

Attila Vértés
Sándor Nagy
Zoltán Klencsár
Rezső G. Lovas
Frank Rösch
Editors

SPRINGER
REFERENCE

VOLUME 1

Handbook of Nuclear Chemistry

Second Edition

Basics of Nuclear Science

 Springer

Handbook of Nuclear Chemistry



Attila Vértes, Sándor Nagy, Zoltán Klencsár, Rezső G. Lovas,
Frank Rösch (Eds.)

Handbook of Nuclear Chemistry

Second Edition

With 907 Figures and 312 Tables

Editors

Attila Vértés, Professor Emeritus
Institute of Chemistry
Eötvös Loránd University
P.O. Box 32
Budapest, 1518
Hungary

Sándor Nagy, Professor
Institute of Chemistry
Eötvös Loránd University
P.O. Box 32
Budapest, 1518
Hungary

Zoltán Klencsár, Dr.
Chemical Research Center
Hungarian Academy of Sciences
Pusztaszeri út 59-67
Budapest, 1025
Hungary

Rezső G. Lovas, Professor
Institute of Nuclear Research (ATOMKI)
Hungarian Academy of Sciences
P.O. Box 51
Debrecen, 4001
Hungary

Frank Rösch, Professor
Institute of Nuclear Chemistry
Fritz-Strassmann-Weg 2
Johannes Gutenberg University Mainz
55128 Mainz
Germany

ISBN 978-1-4419-0719-6

e-ISBN 978-1-4419-0720-2

DOI 10.1007/978-1-4419-0720-2

Print and electronic bundle ISBN: 978-1-4419-0721-9

Springer Dordrecht Heidelberg London New York

Library of Congress Control Number: 2010935459

© Springer Science+Business Media B.V. 2011

No part of this work may be reproduced, stored in a retrieval system, or transmitted in any form or by any means, electronic, mechanical, photocopying, microfilming, recording or otherwise, without written permission from the Publisher, with the exception of any material supplied specifically for the purpose of being entered and executed on a computer system, for exclusive use by the purchaser of the work.

Printed on acid-free paper

Springer is part of Springer Science+Business Media (www.springer.com)

Foreword

The Future of Nuclear Energy and Research

New ideas are hard to accept; popular mistrust and opposition often hinder the exploration and application of new sciences and technologies. We have to look only at the work and struggle of Galileo, Newton, and Einstein, among many others, to realize what obstacles there were in their paths.

There can be no question that nuclear energy will become more important in the future in spite of the fact that there is general opposition toward the use of this form of energy. Conventional energy sources will soon become less available. Oil and gas are becoming more expensive and no great reserves appear to be available. Coal supplies are likely to last longer but I expect it to become more expensive even within this century. The other sources, like hydroelectricity, solar energy and geothermal energy will be in many cases important, but they will remain local and limited. I firmly expect that the source that will become of lasting and general importance for the world is nuclear energy.

As we see it at the present, uranium will remain a satisfactory energy source for the third millennium. Energy from thorium (by transformation into uranium 233) is likely to remain available even longer. One obstacle appears to remain: fear of radioactivity. My main point is that the fear is not justified.

Consider the damage in the last few decades due to the use of nuclear reactors, divided by the amount of available energy produced. Two well-known examples of such damage are at Three Mile Island in the United States in 1979, and even more at Chernobyl in the Soviet Union in 1986. Both of these were caused by human error. At Three Mile Island, the economic damage was great, but there was hardly any effect on health. In Chernobyl, the effect on human health was considerable, but still small compared to the publicity it generated.

The main problem in nuclear energy is the fight against hysteria. I hope and believe that ways will be found to overcome such hysteria. I want to make just one recommendation. In developing nuclear energy for the future, primary emphasis should be given to one problem with double aspect. One aspect is safety of future nuclear reactors; the other is the public understanding of this safety. This is the field in which innovations are most necessary.

For this, we need three things: one is careful planning and operation of nuclear energy production; other improvements in nuclear energy production will be made, but these are unimportant compared to the needed improvements in safety. The second point is the review of past damage in all phases connected with nuclear energy. The third and most important part is the work for and execution of plans for the use of nuclear energy for the whole world, advanced and underdeveloped, with primary emphasis on safety and objective reporting.

An important part of all this is widespread understanding of a field that is novel, but basically not particularly difficult to understand. This major five-volume publication is exceedingly useful for further research, understanding and application of the chemical aspect of nuclear science.

E. Teller[†]

[†]**Editors' note:** The above sentences were dictated by Professor Edward Teller to his secretary in March 2003. The text was to be the Foreword of the first edition of the Handbook of Nuclear Chemistry (HNC) published in November 2003. Professor Teller died on September 9, 2003, just a few months before the book was released. We still deeply regret that we lost the opportunity to present him with a complimentary copy of HNC as a token of our gratitude for his support. However, his words have not lost their timeliness over the years. We have decided to have them published unchanged thus expressing our respect for his memory.

Preface

In the twentieth century, 57 Nobel Prizes honored the chemical and physical results achieved by theoreticians and experimenters who can be rightly called nuclear scientists. This number alone proves that nuclear science was recognized as one of the most powerful engines pushing science to new heights in the past century, often referred to as the **Nuclear Age**.

It is interesting to mention that until the middle of the twentieth century, the ratio of Nobel Prizes that honored nuclear results was 2:1 for physics and chemistry. However, after 1950, only two chemical results were awarded by this prize: E. M. McMillan and G. T. Seaborg for the production of $_{93}\text{Np}$ and $_{94}\text{Pu}$ in 1951, and W. F. Libby for working out the ^{14}C age determination in archeology and geophysics in 1960. R.S. Yalow was honored by the Nobel Prize in 1977 for a medical result. She developed the radioimmunoassays of peptide hormones. All other Nobel Prizes for nuclear results were awarded in the field of physics. The Nobel Prizes achieved by nuclear scientists are listed in [▶ Table 1](#).

A correlation between the period of the research work and the date of the award is demonstrated in [▶ Fig. 1](#).

One needs little imagination to foretell that the flagships of science will be informatics and biology in the twenty-first century. Nevertheless, there are many signs making us firmly believe that nuclear science will remain important in the future as well, in spite of the antinuclear sentiments caused by the unfortunate Chernobyl accident in 1986. Radiopharmaceutical chemistry is stimulating biomedical research and nuclear medicine (diagnosis and therapy). The development of particle physics keeps its dynamism as demonstrated by the Nobel Prizes awarded in this century (2002, 2004, and 2008.)

There are well-supported opinions that nuclear fission and fusion will be among the important sources of energy in the twenty-first century. We cite George A. Olah who was awarded the Nobel Prize for his contributions to carbocation chemistry in 1994. He wrote (Olah GA (1998) Oil and hydrocarbons in the 21st century. In: Barkan P (ed) Chemical research 2000 and beyond. Amer Chem Soc, Washington, DC/OUP, New York, pp 40–54):

- ▶ *Generating energy by burning non-renewable fossil fuels including oil, gas and coal is feasible only for the relatively short future and even so, faces serious environmental problems. The advent of the atomic age opened up a wonderful new possibility, but also created dangers and concerns of safety. I feel that it is tragic that the latter considerations practically brought further development of atomic energy to a stand still at least in most of the Western world. Whether we like it or not we have in the long run no alternative but to rely increasingly on clean atomic energy, but we must solve safety problems including those of disposal and storage of radioactive waste-products. Pointing out difficulties and hazards as well as regulating them (within reason) is necessary. Finding solutions to overcome them, however, is essential.*

(Olah 1998, pp 40–54)

The editors of this handbook hope that this work contributes to the activity of a research field that helps us to learn more and more about nature and will remain dynamic for a long time.

■ Table 1

The results of nuclear scientists honored by Nobel Prizes

The honored results as phrased by the Nobel Committee	The period of the activity resulting the Nobel Prize	The name(s) of the awarded person(s)	The year of distinction
In recognition of the extraordinary services he has rendered by his discovery of spontaneous radioactivity	1896	H. A. Becquerel	1903 (physics)
In recognition of the extraordinary services they have rendered by their joint researches on the radiation phenomena discovered by Professor Henri Becquerel	1897–1903	M. Curie P. Curie	
In recognition of her services to the advancement of chemistry by the discovery of the elements radium and polonium, by the isolation of radium and the study of the nature and compounds of this remarkable element	1898	M. Curie	1911 (chemistry)
For his investigations into the disintegration of the elements, and the chemistry of radioactive substances	1898–1900	E. Rutherford	1908 (chemistry)
In recognition of the services he rendered to the advancement of physics by his discovery of energy quanta	1901	M. Planck	1918 (physics)
For his services to theoretical physics, and especially for his discovery of the law of the photoelectric effect	1905	A. Einstein	1921 (physics)
For his work on the elementary charge of electricity and on the photoelectric effect	1910–1914	R. A. Millikan	1923 (physics)
For his method of making the paths of electrically charged particles visible by condensation of vapor	1912	C. T. R. Wilson	1927 (physics)
For his discovery of cosmic radiation	1912	V. F. Hess	1936 (physics)
For his work on the use of isotopes as tracers in the study of chemical processes	1913–1935	G. Hevesy	1943 (chemistry)
For his contributions to our knowledge of the chemistry of radioactive substances, and his investigations into the origin and nature of isotopes	1913–1916	F. Soddy	1921 (chemistry)
For his discovery of the effect named after him	1923	A. H. Compton	1927 (physics)
For the discovery of the Exclusion Principle, also called the Pauli Principle	1925	W. Pauli	1945 (physics)
For the discovery of new productive forms of atomic theory	1926	E. Schrödinger P. A. M. Dirac	1933 (physics)

For the invention and development of the cyclotron and for results obtained with it, especially with regard to artificial radioactive elements	1929–1932	E. O. Lawrence	1939 (physics)
For his resonance method for recording the magnetic properties for atomic nuclei	1930–1939	I. I. Rabi	1944 (physics)
For the coincidence method and his discoveries made therewith	1930–1940	W. Bothe	1954 (physics)
For his development of the Wilson cloud chamber method, and his discoveries therewith in the field of nuclear physics and cosmic radiation	1931–1933	P. M. S. Blackett	1948 (physics)
For the discovery of the neutron	1932	J. Chadwick	1935 (physics)
For his discovery of the positron	1932	C. D. Anderson	1936 (physics)
For their pioneering work on the transmutation of atomic nuclei by artificially accelerated atomic particles	1932	J. D. Cockcroft E. T. S. Walton	1951 (physics)
For his contributions to the development of the molecular ray method and his discovery of the magnetic moment of the proton	1933	O. Stern	1943 (physics)
For his contributions to the theory of the atomic nucleus and the elementary particles, particularly through the discovery and application of fundamental symmetry principles	1933–1937	E. P. Wigner	1963 (physics)
In recognition of their synthesis of new radioactive elements	1934	F. J. Curie I. Curie	1935 (chemistry)
For the discovery and the interpretation of the Cherenkov effect	1934–1937	P. A. Cherenkov I. M. Frank I. E. Tamm	1958 (physics)
For his demonstrations of the existence of new radioactive elements produced by neutron irradiation, and for his related discovery of nuclear reactions brought about by slow neutrons	1934–1936	E. Fermi	1938 (physics)
For his prediction of the existence of mesons on the basis of theoretical work on nuclear forces	1935	H. Yukawa	1949 (physics)
For his contributions to the theory of nuclear reactions, especially his discoveries concerning the energy production in stars	1938	H. A. Bethe	1967 (physics)
For his discovery of the fission of heavy nuclei	1938	O. Hahn	1944 (chemistry)

Table 1 (Continued)

The honored results as phrased by the Nobel Committee	The period of the activity resulting the Nobel Prize	The name(s) of the awarded person(s)	The year of distinction
For their discoveries in the chemistry of the transuranium elements	1940	E. M. McMillan G. T. Seaborg	1951 (chemistry)
For his method to use carbon-14 for age determination in archaeology, geology, geophysics, and other branches of science	1946	W. F. Libby	1960 (chemistry)
For their development of new methods for nuclear magnetic precision measurements and discoveries in connection therewith	1946–1948	F. Bloch E. M. Purcell	1952 (physics)
For their fundamental work in quantum electrodynamics, with deep-ploughing consequences for the physics of elementary particles	1946–1948	S.-I. Tomonaga J. Schwinger R. P. Feynman	1965 (physics)
For his development of the photographic method of studying nuclear processes and his discoveries regarding mesons made with this method	1946–1950	C. F. Powell	1950 (physics)
For their discoveries concerning nuclear shell structure	1948–1954	O. M. Goeppert-Mayer J. H. D. Jensen	1963 (physics)
For the invention of the bubble chamber	1952	D. A. Glaser	1960 (physics)
For the discovery of the connection between collective motion and particle motion in atomic nuclei and the development of the theory of the structure of the atomic nucleus based on this connection	1953	A. N. Bohr B. R. Mottelson L. J. Rainwater	1975 (physics)
For his pioneering studies of electron scattering in atomic nuclei and for his thereby achieved discoveries concerning the structure of the nucleons	1953–1960	R. Hofstadter	1961 (physics)
For the detection of the neutrino	1953–1960	F. Reines	1995 (physics)
For his contribution to the development of high-resolution electron spectroscopy	1954–1958	K. M. Siegbahn	1981 (physics)
For their discovery of the antiproton	1955	E. G. Segre O. Chamberlain	1959 (physics)

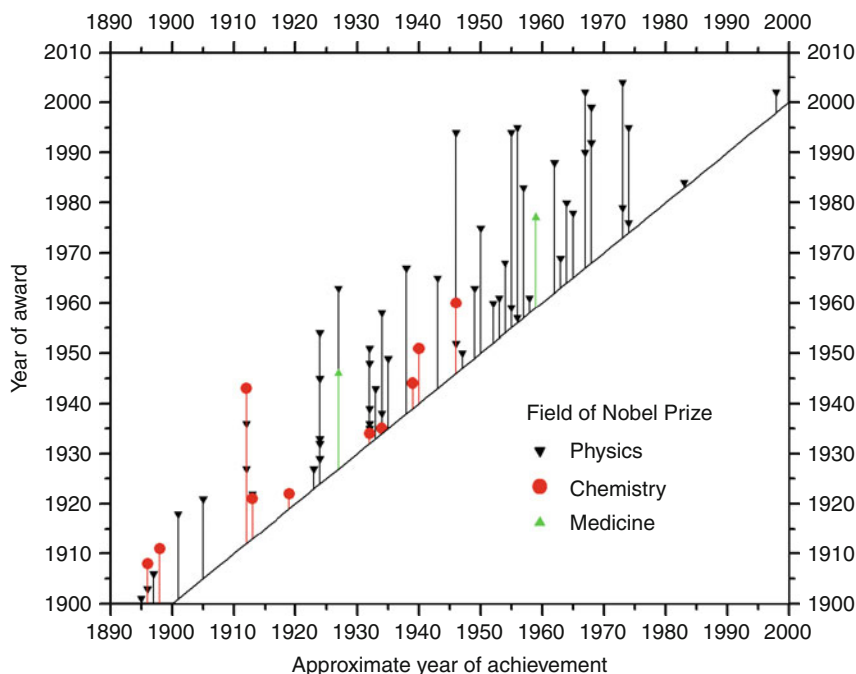
For his decisive contributions to elementary particle physics, in particular, the discovery of a large number of resonance states, made possible through his development of the technique of using hydrogen bubble chamber and data analysis	1955–1957	L. W. Alvarez	1968 (physics)
For the development of neutron spectroscopy	1955–1960	B. N. Brockhouse C. G. Shull	1994 (physics)
For pioneering contributions to astrophysics, in particular, for the detection of cosmic neutrinos	1955–1972	R. Davis M. Koshiba	2002 (physics)
For their penetrating investigation of the so-called parity laws, which has led to important discoveries regarding the elementary particles	1956	T. D. Lee C. N. Yang	1957 (physics)
For his theoretical studies of the physical processes of importance to the structure and evolution of the stars	1962–1971	S. Chandrasekhar	1983 (physics)
For his theoretical and experimental studies of the nuclear reactions of importance in the formation of the chemical elements in the universe	1956–1965	W. A. Fowler	
For his researches concerning the resonance absorption of gamma radiation and his discovery in this connection of the effect that bears his name	1958	R. Mössbauer	1961 (physics)
For their contributions to the theory of the unified weak and electromagnetic interaction between elementary particles, including, inter alia, the prediction of the weak neutral current	1958–1970	S. L. Glashow A. Salam S. Weinberg	1979 (physics)
For the development of radioimmunoassays of peptide hormones	1959	R. S. Yalow	1977 (medicine)
For his contributions and discoveries concerning the classification of elementary particles and their interactions	1960–1965	M. Gell-Mann	1969 (physics)
For the discovery of the mechanism of spontaneous broken symmetry in subatomic physics	1960–1973	Y. Nambu	2008 (physics)
For pioneering contributions to astrophysics, which have led to the discovery of cosmic X-ray sources	1960–1980	R. Giacconi	2002 (physics)

Table 1 (Continued)

The honored results as phrased by the Nobel Committee	The period of the activity resulting the Nobel Prize	The name(s) of the awarded person(s)	The year of distinction
For the neutrino beam method and the demonstration of the doublet structure of the leptons through the discovery of the muon neutrino	1963	L. Lederman	1988 (physics)
		M. Schwartz	
		J. Steinberger	
For the discovery of violations of fundamental symmetry principles in the decay of neutral K-mesons	1964	J. W. Cronin V. L. Fitch	1980 (physics)
For their pioneering investigations concerning deep inelastic scattering of electrons on protons and bound neutrons, which have been of essential importance for the development of the quark model in particle physics	1968	J. I. Friedman	1990 (physics)
		H. W. Kendall	
		R. E. Taylor	
For his invention and development of particle detectors, in particular, the multiwire proportional chamber	1968	G. Charpak	1992 (physics)
For the discovery of the origin of the broken symmetry, which predicts the existence of at least three families of quarks in nature	1970–1973	M. Kobayashi, T. Maskawa	2008 (physics)
		M. J. G. Veltman G. 't Hooft	
For elucidating the quantum structure of electroweak interactions in physics	1972	M. J. G. Veltman G. 't Hooft	1999 (physics)
For his theory for critical phenomena in connection with phase transitions	1972	K. G. Wilson	1982 (physics)
For the discovery of asymptotic freedom in the theory of the strong interaction	1973–1974	D. J. Gross	2004 (physics)
		H. D. Politzer	
		F. Wilczek	
For their pioneering work in the discovery of a heavy elementary particle of a new kind	1974	B. Richter S. C. C. Ting	1976 (physics)
For the discovery of the tau lepton	1974	M. Perl	1995 (physics)
For their decisive contributions to the large project that led to the discovery of the field particles W and Z, communicators of weak interaction	1983	C. Rubbia S. van der Meer	1984 (physics)

■ Fig. 1

A presentation of the time passed between the discoveries and Nobel Prizes related to the development of nuclear science and subatomic concepts (Nagy S (2007) Radiochemistry and nuclear chemistry. In: Encyclopedia of Life Support Systems (EOLSS), Developed under the auspices of the UNESCO. Eolss Publishers, Oxford [<http://www.eolss.net>]). The length of each drop-line shows the delay between award and achievement. Note that some achievements had been awarded almost promptly, whereas the longest delay was almost half a century. The drop-lines of the first few points are meaningless, as the Nobel Prize was first awarded in 1901



The chapter Nuclear and Radiochemistry – the First 100 Years, dealing with the history of nuclear chemistry, was updated by Professors Friedlander and Herrmann in the Fall of 2008 and in the Spring of 2009. Alas, it was submitted for the 2nd edition by Professor Herrmann alone because Professor Friedlander died on September 6, 2009. Gerhart Friedlander was born on July 28, 1916, in Munich. He was a veteran of the Manhattan Project and a pioneer of nuclear chemistry who later exploited the first particle accelerators to do major research as head of the chemistry department at Brookhaven National Laboratory. Many of us, nuclear chemists, used one of Professor Friedlander's monographs to learn the basics of this field of science (e.g., Friedlander G, Kennedy JW, Macias ES, Miller JM (1981) Nuclear and radiochemistry. Wiley, New York). We warmly suggest that those who wish to get a bird's eye view of the field of nuclear science should read the chapter Nuclear and Radiochemistry – the First 100 Years. They will find it not only enjoyable as a 'story' but also useful as a guide to all the main areas of interest, heights, crossroads, and the paths connecting the individual spots of the landscape underneath.

The editors acknowledge the valuable work of Professor Gábor L. Molnár who conceptualized and edited all the appendixes of the first edition. He died on January 6, 2004, and he could not see and enjoy the success of his work as a part of the Handbook of Nuclear Chemistry.

We are sure that Gábor L. Molnár's work, which is mostly integrated into the 2nd edition as well, remains an important contribution to the mission of the Handbook of Nuclear Chemistry.

The 63rd General Assembly of the United Nations adopted a resolution that 2011 would be the Year of Chemistry. The motivation was that Marie Curie was awarded the Nobel Prize of Chemistry a century ago, in 1911. This prize honored results achieved in the field of radio- and nuclear chemistry. It is a great pleasure for us that the 2nd edition of the Handbook of Nuclear Chemistry can welcome the start of the Year of Chemistry.

The Editors
October 2010

Editorial Board



Attila Vértes (Türje, 1934) is a Professor Emeritus of nuclear chemistry at Eötvös Loránd University, Budapest. He studied the scattering of beta particles for his Master's thesis in 1958 and has been dealing with different topics of nuclear chemistry ever since (e.g., Mössbauer and positron annihilation spectroscopy).

Academic career highlights in Hungary include graduating from the Technical University of Budapest (MSc), 1958; Doctor of Science, Hungarian Academy of Sciences, 1973; Corresponding Member of the Hungarian Academy of Sciences, 1993; Ordinary Member of the Hungarian Academy of Sciences, 1998.

Abroad, Prof. Vértes studied at Lomonosov University and became a Candidate of Science, Russian Academy of Sciences, 1965. He was a Visiting Scientist at the University of New Castle (England) and a Humboldt Fellow at the Technical University, Munich (Germany) as well as a Guest Professor at Lehigh University, Bethlehem (USA), Tokyo University (Japan) and Johannes Gutenberg University, Mainz (Germany).

He has published more than 500 papers in scientific periodicals and edited/authored nine monographs. Prof. Vértes is an Honorary Doctor of Glasgow Caledonian University (England, 1996). He was awarded the Széchenyi Prize (given by the President of the Republic of Hungary, 2001) and the Hevesy Medal (Guildford, 2004).

His significant position in the community is seen in his active participation in the Hungarian Academy of Sciences where he chaired the Division of Radiochemistry (1993–2002). He was also a member of the International Board on the Applications of the Mössbauer Effect (IBAME; 1990–1998) and holds editorial spots on some of the top journals in the field.

More about him at his site: www.chem.elte.hu/departments/magkem/vertesa/vertesaeng/index.html.



Sándor Nagy (Budapest, 1949) is a committed teacher of nuclear sciences employed by the Institute of Chemistry, Eötvös Loránd University (ELTE), Budapest. He graduated from chemistry in 1972, but his formal education also includes applied mathematics. He has been working for ELTE since his graduation there with some officially approved detours in the meantime. Thus he spent 14 months at the Sinclair Laboratory of Lehigh University, Bethlehem, USA (1979–1980); another 22 months at the Chemistry Department of Drexel University, Philadelphia (1987–1989); and paid several short visits to Belgium, Canada, Cuba, Denmark, Germany, Kazakhstan, the Netherlands, Romania, and Russia.

Prof. Nagy has published over 100 scientific papers and a number of books and book chapters in English and Hungarian. Between 2005 and 2007, he acted as an Honorary Theme Editor of the theme Radiochemistry and Nuclear Chemistry for EOLSS (www.eolss.net/E6-104-toc.aspx). He is an IUPAC Fellow and a member of the Board of Associate Editors of the Journal of Radioanalytical and Nuclear Chemistry. He also won some professional/teaching awards from the Institute of Chemistry, from the Faculty of Science, from ELTE and also from the Ministry of Education of Hungary. His latest pet project is developing a Nuclear Glossary in Hungarian (inspired by Rick Firestone, one of the Authors of this Handbook) stuffed with animations and simulations provided by scientists and teachers all around the world (www.chem.elte.hu/Sandor.Nagy/NewClearGlossy/).

Apart from science, a few decades ago, he also authored some award-winning books on bicycling, and translated science fiction and children's books etc. to Hungarian. He is also an enthusiastic gardener and the proud father of five daughters.

For more details, visit his site at www.chem.elte.hu/Sandor.Nagy/.



Zoltán Klencsár (Kaposvár, 1971) is a senior research fellow at the Chemical Research Center of the Hungarian Academy of Sciences, Budapest.

Dr. Klencsár received his PhD in physics from Eötvös Loránd University in 1999. He has been working as a researcher for the Hungarian Academy of Sciences (1998–2004, 2008–) and as an assistant and associate professor for the University of Kaposvár, Hungary (2002–2008). His main field is Mössbauer spectroscopy and its applications in physics and chemistry. He has published over 50 articles in international journals, and authored several book chapters and lecture notes in the field of physical sciences. He is also an enthusiastic computer programmer who has developed numerous applications over the past two decades. In the field of Mössbauer spectroscopy he is recognized worldwide as the author of a software package used at many laboratories for the analysis of Mössbauer spectra.

For more details see: www.siaweb.hu/klencsar/



Rezső G. Lovas (Debrecen, 1946) is a Research Professor at the Institute of Nuclear Research of the Hungarian Academy of Sciences in Debrecen, Hungary.

Graduated from the University of Debrecen, he has been affiliated with the Debrecen Institute throughout his career. Meanwhile, he spent sabbatical-like years at the Nuclear Physics Laboratory, Oxford, at Daresbury Laboratory, at Kernforschungszentrum Karlsruhe and medium-term visits at the University of Utrecht, at Manne Siegbahn Laboratory, Stockholm, and at Niigata University. He was Director of the Debrecen Institute from 1997 to 2007. He is a Titular Professor at the University of Debrecen (1993) and a Corresponding Member of the Hungarian Academy of Sciences (2004). Formerly, he was member of the Board of the Nuclear Physics Division of the European Physical Society and of the Editorial Board of Nuclear Physics News International. At present he is Vice-President of the Physics Section of the Academy, member of the Council of the Research Institutions of the Academy, and chairs the Working Group on Energy Strategy of the Academy.

His research field is nuclear theory: reactions, clustering, cluster decay and light exotic nuclei. He is a coauthor of the monograph *Structure and Reactions of Light Exotic Nuclei* (2003).



Frank Rösch (Chemnitz, 1955) is a Professor of nuclear chemistry at Johannes Gutenberg University, Mainz, Germany.

He studied chemistry at the Technical University Dresden from 1976 to 1981. His diploma work was on the *Production of ^{211}At and investigations on cationic species of Astatine and their reactions* and his PhD thesis 1984 *On the chemistry of At(I)-complex formations*.

At the Joint Institute for Nuclear Research, Dubna, Sowjet Union, Laboratory for Nuclear Problems (1984–1987) he investigated *Basics and perspectives of the continuous electromigration measurement of γ -emitting radionuclides in homogeneous aqueous electrolytes free of supporting materials*. Back in Germany, he spent some years (1987–1991) at the Central Institute for Nuclear Research (ZfK) Rossendorf, Department of Radioactive Isotopes, turning his research activities into the application of radionuclides in life sciences. In 1988 he succeeded with his habilitation and obtained the *venia legendi* for radiochemistry.

His research on the production and potential medical application of radionuclides continued at the Institute of Nuclear Chemistry, Research Centre Jülich GmbH, Germany, from 1991–1996. In 1996 he was appointed a University Professor for Nuclear Chemistry at the Institute of Nuclear Chemistry, Johannes Gutenberg-University Mainz, Germany. His current research activities are focused on the development and evaluation of PET radiopharmaceuticals, including radionuclide generator-based radionuclides.

He was honored with scientific awards of the ZfK Rossendorf and the JINR Dubna, and received other national prizes. He has published more than 200 papers in peer review journals and edited/authored various book chapters.



Table of Contents

List of Contributorsxxvii

Volume 1

Basics of Nuclear Science

1 Nuclear and Radiochemistry: the First 100 Years	3
<i>G. Friedlander · G. Herrmann</i>	
2 Basic Properties of the Atomic Nucleus	39
<i>T. Fényes</i>	
3 Nuclear Reactions	143
<i>L. G. Sobotka · V. E. Viola</i>	
4 Nuclear Fission	223
<i>J. O. Denschlag</i>	
5 Tunneling Through Triple-Humped Fission Barriers	281
<i>A. Krasznahorkay</i>	
6 Nuclear Fusion	319
<i>G. Veres</i>	
7 Kinetics of Radioactive Decay	333
<i>S. Nagy</i>	
8 Interaction of Radiation with Matter	363
<i>D. Horváth · A. Vértes</i>	
9 Stochastics and Nuclear Measurements	395
<i>S. Nagy</i>	
10 The Standard Model of Elementary Particles	457
<i>D. Horváth</i>	
11 Appendixes – Reference Data to Part I	475
<i>G. L. Molnár · R. B. Firestone</i>	

Volume 2

Elements and Isotopes Formation, Transformation, Distribution

12	Origin of the Chemical Elements	613
	<i>T. Rauscher · A. Patkós</i>	
13	Natural Radioactive Decay Chains	667
	<i>H. C. Griffin</i>	
14	Radioelements	689
	<i>H. C. Griffin</i>	
15	Isotope Effects	699
	<i>G. Jancsó</i>	
16	Isotopic Paleoclimatology	727
	<i>R. Bowen</i>	
17	Radioactive Dating Methods	761
	<i>R. Bowen</i>	
18	Production and Chemistry of Transuranium Elements	817
	<i>Y. Nagame · M. Hirata · H. Nakahara</i>	
19	Production and Identification of Transactinide Elements	877
	<i>G. Münzenberg · M. Gupta</i>	
20	Chemistry of Transactinides	925
	<i>J. V. Kratz</i>	
21	Superheavy Elements	1005
	<i>D. C. Hoffman · D. A. Shaughnessy</i>	
22	Appendix to Part II – Table of Nuclides	1033
	<i>R. B. Firestone</i>	

Volume 3

Chemical Applications of Nuclear Reactions and Radiations

23	Radiation Chemistry	1265
	<i>L. Wojnárovits</i>	
24	Hot Atom Chemistry	1333
	<i>H. K. Yoshihara · T. Sekine</i>	

25	Mössbauer Spectroscopy	1379
	<i>E. Kuzmann · Z. Homonnay · S. Nagy · K. Nomura</i>	
26	Mössbauer Excitation by Synchrotron Radiation	1447
	<i>M. Seto</i>	
27	Positron Annihilation Spectroscopies	1461
	<i>K. Süvegh · T. Marek</i>	
28	Exotic Atoms and Muonium	1485
	<i>D. Horváth</i>	
29	Neutron Scattering Methods in Chemistry	1515
	<i>L. Pusztai</i>	
30	Activation Analysis	1553
	<i>R. Zeisler · N. Vajda · G. Kennedy · G. Lamaze · G. L. Molnár</i>	
31	Neutron-Induced Prompt Gamma Activation Analysis (PGAA)	1619
	<i>Z. Révay · R. M. Lindstrom · E. A. Mackey · T. Belgya</i>	
32	Applications of Neutron Generators	1673
	<i>J. Csikai · R. Dóczi</i>	
33	Chemical Applications of Ion Accelerators	1695
	<i>E. Koltay · F. Pászti · Á. Z. Kiss</i>	
34	Microscopic X-ray Fluorescence Analysis with Synchrotron Radiation Sources	1737
	<i>F. Adams · B. Vekemans · G. Silversmit · B. De Samber · L. Vincze</i>	
35	Tracer Technique	1761
	<i>H. Haba · S. Motomura · S. Kamino · S. Enomoto</i>	
36	Appendixes – Reference Data to Part III	1793
	<i>Z. Homonnay · Z. Klencsár · R. B. Firestone · Z. Révay · G. L. Molnár · J. Csikai · R. Dóczi</i>	

Volume 4

Radiochemistry and Radiopharmaceutical Chemistry in Life Sciences

37	Introduction to the Fourth Volume	1855
38	Reactor-Produced Medical Radionuclides	1857
	<i>S. Mirzadeh · L. F. Mausner · M. A. Garland</i>	

39	Cyclotron Production of Medical Radionuclides	1903
	<i>S. M. Qaim</i>	
40	Radionuclide Generators	1935
	<i>F. Rösch · F. F. (Russ) Knapp</i>	
41	¹¹C: Labeling Chemistry and Labeled Compounds	1977
	<i>G. Antoni · T. Kihlberg · B. Långström</i>	
42	¹⁸F: Labeling Chemistry and Labeled Compounds	2021
	<i>T. L. Ross · H. J. Wester</i>	
43	^{99m}Tc: Labeling Chemistry and Labeled Compounds	2073
	<i>R. Alberto · U. Abram</i>	
44	Radioiodination Chemistry and Radioiodinated Compounds	2121
	<i>M. Eisenhut · W. Mier</i>	
45	Radiometals (non-Tc, non-Re) and Bifunctional Labeling Chemistry	2143
	<i>M. Fani · S. Good · H. R. Maecke</i>	
46	Radionuclide Therapy	2179
	<i>M. R. Zalutsky</i>	

Volume 5

Instrumentation, Separation Techniques, Environmental Issues

47	Dosimetry and Biological Effects of Ionizing Radiation	2213
	<i>B. Kanyár · G. J. Köteles</i>	
48	Radiation Detection	2259
	<i>H. C. Griffin</i>	
49	Dosimetry Methods	2287
	<i>W. L. McLaughlin · A. Miller · A. Kovács · K. K. Mehta</i>	
50	Particle Accelerators	2319
	<i>S. Biri · E. Koltay · A. Valek</i>	
51	Isotope Separation	2369
	<i>W. A. Van Hook</i>	
52	Solvent Extraction and Ion Exchange in Radiochemistry	2403
	<i>G. Skarnemark</i>	

53	Radiochemical Separations by Thermochromatography	2429
	<i>A. F. Novgorodov · F. Rösch · N. A. Korolev</i>	
54	Methods of Cosmochemical Analysis	2459
	<i>S. Lahiri · M. Maiti</i>	
55	Environmental Radiation Protection	2503
	<i>Y. Maeda · S. Osaki · A. Vincze</i>	
56	Appendix – Reference Data to Part V	2565
	<i>R. B. Firestone · G. L. Molnár</i>	

Volume 6

Nuclear Energy Production and Safety Issues

57	Technical Application of Nuclear Fission	2615
	<i>J. O. Denschlag</i>	
58	Developments and Tendencies in Fission Reactor Concepts	2663
	<i>E. O. Adamov · Y. Fuji-ie</i>	
59	Nuclear Power Sources for Space Systems	2731
	<i>N. E. Kukharkin · N. N. Ponomarev-Stepnoi · V. A. Usov</i>	
60	Technical Developments for Harnessing Controlled Fusion	2759
	<i>G. Veres · S. Zoletnik · W. Jacob</i>	
61	Radioactive Waste Management	2797
	<i>P. A. Baisden · C. E. Atkins-Duffin</i>	
62	Nuclear Forensic Materials and Methods	2837
	<i>I. D. Hutcheon · P. M. Grant · K. J. Moody</i>	
63	Nuclear Safeguards Verification Measurement Techniques	2893
	<i>M. Zendel · D. L. Donohue · E. Kuhn · S. Deron · T. Biró</i>	
Index		3017



List of Contributors

Ulrich Abram

Institute of Inorganic Chemistry
Freie Universität Berlin
Berlin D-14195
Germany
abram@chemie.fu-berlin.de

Evgeny O. Adamov

Research and Development Institute of
Power Engineering (NIKIET)
P.O. Box 788
Moscow 101000
Russia
slp@nikiet.ru

Freddy Adams

Campus Drie Eiken
University of Antwerp
Universiteitsplein 1
Antwerp B-2610
Belgium
freddy.adams@ua.ac.be

Roger Alberto

Institute of Inorganic Chemistry
University of Zurich
Zürich CH-8057
Switzerland
ariel@aci.unizh.ch

Gunnar Antoni

Uppsala University
Uppsala Imanet AB
P.O. Box 967
Uppsala S-751 09
Sweden
gunnar.antoni@ge.com

Cindy E. Atkins-Duffin

Energy and Environment Directorate
Lawrence Livermore National Laboratory
Livermore, California
USA
atkinsduffin1@llnl.gov

Patricia A. Baisden

Chemistry and Materials Science
Directorate
Lawrence Livermore National Laboratory
Livermore, California
USA
baisden1@llnl.gov
trish.baisden@nnsa.doe.gov

Tamás Belgya

Institute of Isotopes
Hungarian Academy of Sciences
P.O. Box 77
Budapest H-1525
Hungary
belgya@iki.kfki.hu

Sándor Biri

Accelerator Center
Institute of Nuclear Research of the
Hungarian Academy of Sciences (ATOMKI)
Bem tér 18/C
Debrecen H-4026
Hungary
biri@atomki.hu

Robert Bowen

Institute of Geology and Paleontology
Westfälische-Wilhelms Universität
Münster
Germany
napierbowen@yahoo.co.uk

Tamás Bíró

Institute of Isotopes
Hungary Academy of Sciences
Pasaréti út 119 1/6
Budapest H-1026
Hungary
tbíro@sunserv.kfki.hu

Julius Csikai

Department of Experimental Physics
University of Debrecen
P.O. Box 105
Debrecen H-4010
Hungary
csikai@falcon.phys.klte.hu

Rita Dóczi

Institute of Nuclear Techniques
Budapest University of Technology and
Economics
P.O. Box 91
Budapest H-1521
Hungary
doczi@reak.bme.hu

Johannes O. Denschlag

Institut für Kernchemie
Universität Mainz
Mainz D-55128
Germany
h.denschlag@uni-mainz.de

Stein Deron

International Atomic Energy Agency
Neustadtgasse 1
Langenzersdorf, Vienna A-2103
Austria
deronfamily@wanadoo.fr

David Lee Donohue

International Atomic Energy Agency
Vienna
Austria
d.donohue@iaea.org

Michael Eisenhut

Department of Radiochemistry and
Radiopharmacology
Cancer Research Center Heidelberg (DKFZ)
Im Neuenheimer Feld, 280
Heidelberg D-69120
Germany
m.eisenhut@dkfz-heidelberg.de

Shuichi Enomoto

RIKEN Nishina Center for Accelerator-Based
Science
RIKEN Wako Institute
2-1, Hirosawa
Wako, Saitama 351-0198
Japan
semo@riken.jp

Melpomeni Fani

Clinic for Nuclear Medicine
University Hospital Freiburg
Hugstetterstrasse 55
Freiburg D-79106
Germany
melpomeni.fani@uniklinik-freiburg.de

Tibor Fényes

Institute of Nuclear Research of the
Hungarian Academy of Sciences
Bem-tér 18/c
Debrecen H-4026
Hungary
h3813fen@ella.hu

Richard B. Firestone

Lawrence Berkeley National Laboratory
MS 88R0192
Berkeley, California 94720
USA
rbfirestone@lbl.gov

Gerhart Friedlander[†]

Brookhaven National Laboratory
Upton, NY 11973
USA

Yoichi Fuji-ie

Hiroshima University, Prof. Emeritus of
Tokyo Institute of Technology
22-1-1221 Shirakawa Koto-ku
Tokyo 135-0021
Japan
fujiie@ll.em-net.ne.jp
ns.fuji-ie@atlas.plala.or.jp

Marc A. Garland

Nuclear Science and Technology Division
Oak Ridge National Laboratory
1 Bethel Valley Road
Oak Ridge, TN 37831-6423
USA
garlandma@ornl.gov

Stephan Good

Division of Radiological Chemistry
University Hospital Basel
Petersgraben 4
Basel CH-4031
Switzerland
stephan.good@unibas.ch

Patrick M. Grant

Forensic Science Center (FSC) and CSD
Livermore National Laboratory
Livermore, CA 94550
USA
grant4@llnl.gov

Henry C. Griffin

Department of Chemistry
University of Michigan
Ann Arbor, Michigan 48109-1055
USA
hcg@umich.edu

Mohini Gupta

MARG
Manipal University
Manipal 576104
Manipal, Karnataka
India
mohini.gupta@manipal.edu

Hiromitsu Haba

RIKEN Nishina Center for Accelerator-Based
Science
RIKEN Wako Institute
2-1, Hirosawa
Wako, Saitama 351-0198
Japan
haba@riken.jp

Günter Herrmann

Institut für Kernchemie
Johannes Gutenberg-Universität
Mainz D-55128
Germany
guen.herrmann@t-online.de

Masaru Hirata

Advanced Science Research Center
Japan Atomic Energy Agency
Tokai, Ibaraki 319-1195
Japan
hirata.masaru@jaea.go.jp

Darleane C. Hoffman

Department of Chemistry
University of California
Berkeley, CA
USA
dchoffman@lbl.gov

Zoltán Homonnay

Institute of Chemistry
Eötvös Loránd University
Pázmány P. s. 1/A
Budapest 1117
Hungary
homonnay@ludens.elte.hu

Dezső Horváth

KFKI Research Institute for Particle and
Nuclear Physics
Budapest H-1525
Hungary
horvath@mail.kfki.hu

Ian D. Hutcheon

Chemical Sciences Division (CSD) and
Seaborg Institute
Livermore National Laboratory
Livermore, CA 94550
USA
hutcheon1@lln.gov

Wolfgang Jacob

Max-Planck-Institut für Plasmaphysik,
Bereich Materialforschung, AG Reaktive
Plasmaprozesse
Boltzmannstrasse 2
Garching D-85748
Germany
wolfgang.jacob@ipp.mpg.de

Gábor Jancsó

KFKI Atomic Energy Research Institute
P.O. Box 49
Budapest H-1525
Hungary
jancso@aeki.kfki.hu

Shinichiro Kamino

Graduate School of Medicine, Dentistry,
and Pharmaceutical Sciences
Okayama University
Okayama Okayama 700-8530
Japan

Béla Kanyár

Institute of Radiochemistry and
Radioecology, University of Pannonia
Veszprém
Hungary
kanyarb@almos.vein.hu

Greg Kennedy

Department of Engineering Physics
Nuclear Engineering Institute, Ecole
Polytechnique de Montreal
P.O. Box 6079
Montreal, QC H3C 3A7
Canada
greg.kennedy@polymtl.ca

Tor Kihlberg

Uppsala University
Uppsala Imanet AB
P.O. Box 967
Uppsala S-751 09
Sweden
tor.kihlberg@ge.com

Árpád Z. Kiss

Laboratory of Ion Beam Applications,
Department of Electrostatic Accelerators
Institute of Nuclear Research (ATOMKI),
Hungarian Academy of Sciences
Bem tér 18/c
Debrecen 4026
Hungary
azkiss@namafia.atomki.hu

Zoltán Klencsár

Chemical Research Center
Hungarian Academy of Sciences
Budapest
Hungary
z.klencsar@somogy.hu

F. F. (Russ) Knapp

Nuclear Medicine Program
Nuclear Science and Technology Division
Oak Ridge National Laboratory
2008
Oak Ridge, TN 37831-6229
USA
knappffjr@ornl.gov

Ede Koltay

Laboratory of Ion Beam Applications,
Department of Electrostatic Accelerators
Institute of Nuclear Research (ATOMKI),
Hungarian Academy of Sciences
Bem tér 18/c
Debrecen 4026
Hungary
koltay@atomki.hu

Nikolai A. Korolev

Joint Institute of Nuclear Research
Dubna RUS-141980
Russian Federation
korolev@nusun.jinr.ru

György J. Köteles

National Research Institute for
Radiobiology and Radiohygiene
Budapest
Hungary
radbiol@hp.osski.hu

András Kovács

Institute of Isotopes
Hungarian Academy of Sciences
P.O. Box 77
Budapest H-1525
Hungary
akovacs@iki.kfki.hu

Attila Krasznahorkay

Division of Nuclear Physics
Institute of Nuclear Research of the
Hungarian Academy of Sciences (ATOMKI)
Bem-tér 18/c
Debrecen Pf. 51, H-4001
Hungary
kraszna@atomki.hu

Jens Volker Kratz

Institute of Nuclear Chemistry, Johannes
Gutenberg University
Fritz Strassmann-Weg 2
Mainz D-55128
Germany
jvkratz@uni-mainz.de

Erwin Kuhn

International Atomic Energy Agency
Huettergasse 23
Wien, Vienna A-1140
Austria
ekuhn@gmx.at

Nikolay E. Kukharkin

Russian Research Center "Kurchatov
Institute"
Kurchatov sq. 1
Moscow 123182
Russia
ztm@adis.vver.kiae.ru

Ernő Kuzmann

Institute of Chemistry
Eötvös Loránd University
Pázmány P. sétány 1/A
Budapest 1117
Hungary
kuzmann@ludens.elte.hu

Susanta Lahiri

Chemical Sciences Division
Saha Institute of Nuclear Physics
1/AF Bidhannagar
Kolkata 700064
India
susanta.lahiri@saha.ac.in

George Lamaze

Analytical Chemistry Division
National Institute of Standards and
Technology
100 Bureau Drive, MS 8395
Gaithersburg, MD 20899-8395
USA
george.lamaze@nist.gov

Bengt Långström

Department of Biochemistry and Organic
Chemistry
Uppsala University
Uppsala Imanet AB
P.O. Box 967
Uppsala S-751 09
Sweden
bengt.langstrom@ge.com

Richard M. Lindstrom

Analytical Chemistry Division
National Institute of Standards and
Technology
100 Bureau Drive
Gaithersburg, MD 20899
USA
richard.lindstrom@nist.gov

Elizabeth A. Mackey

Analytical Chemistry Division
National Institute of Standards and
Technology
100 Bureau Drive
Gaithersburg, MD 20899
USA
lmackey@nist.gov

Helmut R. Maecke

Clinic for Nuclear Medicine
University Hospital Freiburg
Hugstetterstrasse 55
Freiburg D-79106
Germany
helmut.maecke@uniklinik-freiburg.de

Yonezo Maeda

Department of Chemistry
Kyushu University
Hakozaki, Higashi-ku
Fukuoka 812-8581
Japan
y.maescc@osu.bbiq.jp

Moumita Maiti

Chemical Sciences Division
Saha Institute of Nuclear Physics
1/AF Bidhannagar
Kolkata 700064
India
moumita.maiti@saha.ac.in

Tamás Marek

Chemical Research Center
Hungarian Academy of Sciences
Budapest
Hungary
marek@chem.elte.hu

Leonard F. Mausner

Collider Accelerator Department
Brookhaven National Laboratory
P.O. Box 5000, Building 801
Upton, NY 11973-5000
USA
mausner@bnl.gov

William L. McLaughlin[†]

National Institute of Standards and
Technology
Gaithersburg, MD 20902
USA

Kishor K. Mehta

Arbeiterstrandbad Strasse 72
Vienna A-1210
Austria

Walter Mier

Department of Nuclear Medicine
Radiopharmaceutical Chemistry, University
of Heidelberg
Im Neuenheimer Feld, 400
Heidelberg D-69120
Germany
walter.mier@med.uni-heidelberg.de

Arne Miller

Risø High Dose Reference Laboratory
Risø-DTU, Technical University of Denmark
Frederiksborgvej 399, P.O. Box 49
Roskilde DK-4000
Denmark
armi@risoe.dtu.dk

Saed Mirzadeh

Nuclear Science and Technology Division
Oak Ridge National Laboratory
P.O. Box 2008, Mail Stop 6229
Oak Ridge, TN 37831-6229
USA
mirzadehs@ornl.gov

Gábor L. Molnár[†]

Institute of Isotope and Surface Chemistry
Chemical Research Center
Budapest
Hungary

Ken J. Moody

Chemical Sciences Division and FSC
Livermore National Laboratory
Livermore, CA 94550
USA
moody@llnl.gov

Shinji Motomura

RIKEN Center for Molecular Imaging
Science
RIKEN Kobe Institute
Chuo-ku
Kobe, Hyogo 650-0047
Japan
motomura@riken.jp

Gottfried Münzenberg

KPII
GSI Helmholtzzentrum für
Schwerionenforschung mbH
Planckstr. 1
Darmstadt D64291
Germany
g.muenzenberg@gsi.de

Yuichiro Nagame

Advanced Science Research Center
Japan Atomic Energy Agency
Tokai, Ibaraki 319-1195
Japan
nagame.yuichiro@jaea.go.jp

Sándor Nagy

Institute of Chemistry
Eötvös Loránd University
Pázmány P. sétány 1/A
Budapest 1117
Hungary
nagy@chem.elte.hu

Hiromichi Nakahara

Department of Chemistry
Tokyo Metropolitan University
1-7-14 Nakamachi Setagaya
Tokyo 158-0091
Japan
nakahara-hiromichi@c.metro-u.ac.jp

Kiyoshi Nomura

Department of Applied Chemistry,
Graduate School of Engineering
The University of Tokyo
Tokyo
Japan
k-nomura@t-adm.t.u-tokyo.ac.jp

Alexander F. Novgorodov

Joint Institute of Nuclear Research
Dubna RUS-141980
Russian Federation
novgor@nusun.jinr.dubna.su

Susumu Osaki

Radioisotope Center
Kyushu University
Fukuoka
Japan

Ferenc Pászt[†]

KFKI Research Institute for Particle and
Nuclear Physics
Budapest
Hungary

András Patkós

Department of Atomic Physics
Eötvös Loránd University
Pázmány Péter sétány 1/a
Budapest H-1117
Hungary
patkos@galaxy.elte.hu

Zsolt Révay

Institute of Isotopes
Hungarian Academy of Sciences
P.O. Box 77
Konkoly-Thege Miklos street 29-33
Budapest H-1525
Hungary
revay@iki.kfki.hu

Nikolay N. Ponomarev-Stepnoi

Russian Research Center "Kurchatov
Institute"
Kurchatov sq. 1
Moscow 123182
Russia
niknik@kiae.ru

Tobias L. Ross

Institute of Nuclear Chemistry
Johannes Gutenberg-University Mainz
Fritz-Strassmann-Weg 2
Mainz D-55128
Germany
ross@uni-mainz.de

László Pusztai

Research Institute for Solid State Physics
and Optics
Hungarian Academy of Sciences
P.O. Box 49
Budapest H-1525
Hungary
laszlo.pusztai0@gmail.com

Frank Rösch

Institute of Nuclear Chemistry
Johannes Gutenberg-University of Mainz
Fritz-Strassmann-Weg 2
Mainz D-55128
Germany
frank.roesch@uni-mainz.de

Syed M. Qaim

Institut für Nuklearchemie
Forschungszentrum Jülich GmbH
P.O. Box 1913
Jülich D-52425
Germany
s.m.qaim@fz-juelich.de

Björn De Samber

Department of Analytical Chemistry
Ghent University
Krijgslaan 281 – S12
Gent
Belgium
bjorn.desamber@ugent.be

Thomas Rauscher

Department of Physics
University of Basel
Klingelbergstrasse 82
Basel CH-4056
Switzerland
thomas.rauscher@unibas.ch

Tsutomu Sekine

Center for the Advancement of Higher
Education
Tohoku University
41 Kawauchi, Aoba-ku
Sendai
Japan
tsekine@m.tohoku.ac.jp

Makoto Seto

Research Reactor Institute
Kyoto University
Kumatori-cho, Sennan-gun
Osaka 590-0494
Japan
seto@rri.kyoto-u.ac.jp

Dawn A. Shaughnessy

Chemical Sciences Division
Lawrence Livermore National Laboratory
P.O. Box 808, L-236
Livermore, CA 94551
USA
shaughnessy2@llnl.gov

Geert Silversmit

Department of Analytical Chemistry
Ghent University
Krijgslaan 281 – S12
Gent
Belgium
geert.silversmit@ugent.be

Gunnar Skarnemark

Nuclear Chemistry, Department of
Chemical and Biological Engineering
Chalmers University of Technology
Göteborg S-41296
Sweden
gunnar.skarnemark@chalmers.se

Lee G. Sobotka

Departments of Chemistry and Physics
Washington University
St. Louis, Missouri 63130-4899
USA
lgs@wuchem.wustl.edu

Károly Süvegh

Institute of Chemistry
Eötvös Loránd University
Pázmány P. sétány 1/a
Budapest 1117
Hungary
suevghk@chem.elte.hu

Veniamin A. Usov

Russian Research Center “Kurchatov
Institute”
Kurchatov sq. 1
Moscow 123182
Russia
vau@dhtp.kiae.ru

Nóra Vajda

RadAnal Ltd
Budapest
Hungary
vajdanor@gmail.com
vajdanor@reak.bme.hu

Aladár Valek

Accelerator Center
Institute of Nuclear Research of the
Hungarian Academy of Sciences (ATOMKI)
Bem tér 18/C
Debrecen H-4026
Hungary
valek@atomki.hu

W. Alexander Van Hook

Chemistry Department
University of Tennessee
Knoxville, Tennessee 37996-1600
USA
avanhook@utk.edu

Bart Vekemans

Department of Analytical Chemistry
Ghent University
Krijgslaan 281 – S12
Gent
Belgium
bart.vekemans@ugent.be

Gábor Veres

KFKI Research Institute for Particle and
Nuclear Physics
P.O. Box 49
Budapest H-1525
Hungary
veres@rmki.kfki.hu

Attila Vértes

Institute of Chemistry
Eötvös Loránd University
Pázmány P. s. 1/A
Budapest 1117
Hungary
vertesa@chem.elte.hu

Árpád Vincze

Department of Nuclear and Radioactive
Materials
Hungarian Atomic Energy Authority
Budapest
Hungary
vincze@oah.hu

László Vincze

Department of Analytical Chemistry
Ghent University
Krijgslaan 281 – S12
Gent
Belgium
laszlo.vincze@ugent.be

Victor E. Viola

Department of Chemistry and IUCF
Indiana University
Bloomington, Indiana 47405
USA
viola@indiana.edu

Hans-Jürgen Wester

Department of Nuclear Medicine
Klinikum rechts der Isar, Technische
Universität München
München D-81675
Germany
h.j.wester@lrz.tu-muenchen.de

László Wojnárovits

Institute of Isotopes
Hungarian Academy of Sciences
P.O. Box 77
Budapest H-1525

Hungary
wojn@iki.kfki.hu

H. Kenji Yoshihara

Isotope Data Institute
Kusakidai 4-12-13
Iwaki city
Japan
kenji-yoshihara@nifty.com

Michael R. Zalutsky

Departments of Radiology and Biomedical
Engineering
Duke University
Durham, NC 27710
USA
zalut001@mc.duke.edu

Rolf Zeisler

Analytical Chemistry Division
National Institute of Standards and
Technology
100 Bureau Drive, MS 8395
Gaithersburg, MD 20899-8395
USA
rolf.zeisler@nist.gov

Manfred Zendel

Department of Safeguards
International Atomic Energy Agency
Wagramer Strasse 5
P.O. Box 100
Vienna A-1140
Austria
m.zendel@iaea.org

Sándor Zoletnik

KFKI Research Institute for Particle and
Nuclear Physics
P.O. Box 49
Budapest H-1525
Hungary
zoletnik@rmki.kfki.hu

Volume 1

Basics of Nuclear Science



1 Nuclear and Radiochemistry: the First 100 Years

G. Friedlander^{†1} · G. Herrmann²

¹Brookhaven National Laboratory, Upton, NY, USA

²Johannes Gutenberg-Universität, Mainz, Germany

1.1	<i>The Pioneering Years</i>	4
1.2	<i>The Growth Spurt of the 1930s</i>	8
1.2.1	Nuclear Reactions	9
1.2.2	Nuclear Properties	10
1.2.3	New Elements	13
1.2.4	Hot-Atom Chemistry and Tracer Applications	14
1.2.5	Geo- and Cosmochronology	15
1.3	<i>World War II</i>	16
1.4	<i>The Golden Era</i>	18
1.4.1	Nuclear Reactions	19
1.4.2	Nuclear Properties	20
1.4.3	New Elements	22
1.4.4	Hot-Atom Chemistry and Tracer Applications	25
1.4.5	Geo- and Cosmochronology	27
1.5	<i>Current Trends</i>	29

[†]Deceased

Abstract: This chapter gives a brief overview of the development of nuclear and radiochemistry from Mme. Curie's chemical isolation of radium toward the end of the twentieth century. The first four sections deal with fairly distinct time periods: (1) the pioneering years when the only radioactive materials available were the naturally occurring ones; (2) the decade of rapid growth and expansion of both the fundamental science and its applications following the discoveries of the neutron and artificial radioactivity; (3) the World War II period characterized by the intense exploration of nuclear fission and its ramifications; (4) what can be called the "golden era" – the 3 to 4 decades following World War II when nuclear science was generously supported and therefore flourished. In the final section, research trends pursued near the end of the century are briefly touched upon.

1.1 The Pioneering Years

The field that became known as *radiochemistry*, dealing with the chemical manipulation of radioactive materials and the application of radioactivity to basic and applied chemical problems, originated very soon after Henri Becquerel had discovered the phenomenon of radioactivity during his studies of the fluorescence of uranium compounds (Becquerel 1896). The term "radiochemistry" for this field was introduced quite early, as indicated by the fact that it appeared in a book title in 1910 (Cameron 1910). However, the same term was for some time also applied to what is now called "*radiation chemistry*," the chemical action of radioactive (and other ionizing) radiations. Later, after the concept of the atomic nucleus was introduced in 1911 and especially after the discoveries of nuclear transmutations (1919) and of artificially produced radioactivity (1934), chemists became involved more broadly in the study of the production, properties, and reactions of atomic nuclei; in the 1930s, the term "*nuclear chemistry*" gained currency for this branch of the chemical sciences, quite analogous to organic chemistry being concerned with the synthesis, properties, and reactions of organic molecules. The creation, in 1937, of a new chair of "Chimie Nucléaire" for Frédéric Joliot at the Collège de France was perhaps the first official recognition of the new branch of chemistry. At about the same time, Otto Hahn's treatise *Applied Radiochemistry* (Hahn 1936) clearly outlined the now generally accepted definition of "radiochemistry."

Almost immediately after the discovery of radioactivity, Marie Skłodowska Curie and Pierre Curie began more detailed studies of the new phenomenon. Guided by their observation that some natural uranium ores, such as pitchblende, were more highly radioactive than corresponded to their uranium content (Skłodowska Curie 1898), they fractionated the ores chemically, using the intensity of radioactivity in the fractions as evidence for further radioactive substances. The result was the discovery, in June 1898, of a new radioactive element in the bismuth fraction (Curie and Curie, 1898); the Curies named it *polonium* in honor of Marie's homeland. A few months later, in December 1898, they were able to report the discovery of another radioactive element, this one in the barium fraction separated from pitchblende (Curie et al. 1898); they named it *radium*. The subsequent isolation of radium from barium was accomplished by fractional crystallization of barium chloride, with radium chloride always being enriched in the crystalline phase. It soon became possible to characterize radium spectroscopically by optical emission lines (Demarçay 1898) and, thus, to confirm the discovery by an independent identification. By 1902, M. Curie had isolated 120 mg of pure

radium chloride from the residues of about 2 t of pitchblende, a heroic radiochemical enterprise. By then, she was able to determine the atomic weight of radium. The result, 225, provided the final proof that radium is the heaviest alkaline earth element (Curie 1902).

In 1898, M. Curie (Sklodowska Curie 1898) (and independently Gerhard Schmidt) found that not only uranium, but also thorium emits radioactive radiations, and in the following decade numerous other radioactive substances, all of them ultimately assignable to elements between mercury and uranium in the periodic table, were chemically isolated in various fractions from uranium and thorium ores. Eventually, all the newly discovered radioactive substances could be assigned to three separate *decay chains*, originating from uranium (^{238}U), thorium (^{232}Th) and from actinium (^{227}Ac) respectively, the last discovered (Debiere 1899; Giesel 1902) in the lanthanum fraction obtained from pitchblende. Each of the decay series involves a number of α and β decays and terminates in one of the stable lead isotopes ($^{238}\text{U} \rightarrow ^{206}\text{Pb}$, $^{232}\text{Th} \rightarrow ^{208}\text{Pb}$, $^{227}\text{Ac} \rightarrow ^{207}\text{Pb}$). Among the pioneers who contributed to our knowledge of the naturally occurring radioactivities one should further mention Bertram Boltwood, Julius Elster, Kasimir Fajans, Hans Geitel, Georg von Hevesy, Lise Meitner, Stefan Meyer, Fritz Paneth, Egon von Schweidler, and Frederick Soddy (see, e.g., Meyer and Schweidler (1916, 1927), Jauncey (1946), Soddy (1975)).

When the chemical properties of members of the three naturally occurring decay series were investigated, it became clear that some of the radioactive species represented elements that had previously been blank in the periodic table. For example, radium (element 88) was surely the next higher homologue of barium; polonium (84) could be placed below tellurium after it had turned out that it was identical with the radio-tellurium discovered by Wilhelm Marckwald (Marckwald 1903), and actinium (89) was positioned below lanthanum. They were later attributed to ^{226}Ra , with a half-life ($T_{1/2}$) of 1,600 years, ^{210}Po (138 days), and ^{227}Ac (21.8 years). But some of the radioactive species were chemically indistinguishable from existing elements or from each other. For example, the so-called radium D (22 years, ^{210}Pb), a member of the uranium series, could not be chemically separated from ordinary lead. Similarly, ionium (8×10^4 years, ^{230}Th) was chemically indistinguishable from thorium. Furthermore, each of the three series contained at least one relatively short-lived member that was chemically identical with lead, one identical with bismuth, etc. These observations led to the concept of *isotopy*, clearly enunciated by Soddy in 1911 and somewhat later named by him (Soddy 1911, 1913a). Initially it was thought that only radioactive elements have isotopes, i.e., chemically identical species of different atomic weights, but already in 1913, Joseph J. Thomson showed by deflection of positive ions in electric and magnetic fields that ordinary neon consisted of two isotopes of atomic weights 20 and 22 (Thomson 1913). Soon it became apparent that isotopy is a general phenomenon among naturally occurring elements.

Two important developments in the early history of radioactivity were (1) the recognition of the three different *types of radiation*, α , β , and γ rays, distinguished by their very different penetration in matter and (2) the realization that in each of the three decay series there existed a product that behaved chemically like an inert (also called: rare or noble) gas. Through experiments involving deflection in magnetic and electric fields, α and β “rays” were soon identified as streams of helium ions and electrons, respectively, and γ rays, undeflected by such fields, were recognized as a form of electromagnetic radiation akin to X-rays.

As early as 1900, Rutherford was able to show that the erratic electrometer readings he observed when measuring the radioactivity of thorium compounds were due to the emanation of a radioactive gas into the ionization chamber (Rutherford 1900). The observation that a sample of the radioactive gas faded away within a few minutes according to a characteristic

exponential decay law with a well-reproducible decay constant λ (where $\lambda = \ln 2 / T_{1/2}$) was one of the fundamental conclusions from these simple experiments. Perhaps even more surprising was the observation that the gaseous radioactivity could be “milked” repeatedly from the thorium sample and that the buildup with time in the source occurred with the same time constant as the decay process. Furthermore, it was found that even after the emanation had decayed away, radioactivity persisted as an “active deposit” consisting of nonvolatile decay products. Thus, this special case of a natural radiochemical separation of a gaseous component from a solid component gave the first hint that radioactivity is accompanied by a *transmutation of elements*, and it showed clearly that chemical separations are an excellent tool for the unraveling of decay sequences. Radium and actinium compounds were found to exhibit the same phenomenon, i.e., gaseous emanations leading to active deposits, but with quite different half-life patterns. Detailed studies identified the emanations as inert gases of high molecular weight, attributed to a new element, the heaviest noble gas, radon (element 86).

The various developments just mentioned led Rutherford and Soddy to formulate a *theory of radioactive transformation* published in a remarkable series of papers that has remained valid in its essentials to this day (Rutherford and Soddy 1902, 1903). They posited that radioactive decay involves the spontaneous transformation of atoms of one element into those of another, accompanied by the emission of particles. With this hypothesis, they thus introduced the rather revolutionary notion that atoms, previously thought to be immutable “elementary particles,” are in fact composite structures capable of subatomic change. This was a particularly remarkable proposal when one considers that it preceded by some 8 years the concept of the atomic nucleus.

Once the nature of α and β particles had been established and radioactive decay had been recognized as involving subatomic change, it became possible to formulate rules for the placement of radioelements in the periodic table. These so-called *displacement laws*, enunciated in 1913 (Fajans 1913; Soddy 1913b), state that the product of α decay is the element two columns to the left of the parent element, whereas β decay involves a one-column shift to the right. On the basis of these rules it was now possible to place all the known, naturally occurring radioactive species of the three decay series into the periodic table with the inclusion, as already mentioned, of numerous isotopic species. Each of the series also contains examples of so-called branching decays, i.e., instances of a given species decaying by both α and β decay. With the discovery of the long-lived ^{231}Pa (3.3×10^4 years) as the parent of ^{227}Ac (Hahn and Meitner 1918), the major routes of the three decay series were established. The observation (Hahn 1922) that the position of ^{234}Pa in the uranium decay series is shared by two species with different half-lives (1.17 min and 6.7 h) remained a curiosity for many years, until it was understood as the discovery of *nuclear isomerism*, representing the ground and a metastable, excited state. Further work on the natural series was devoted to rare decay branches.

The first realization that radioactivity was not confined to the heaviest elements came with the observation in 1906 of weak β radioactivity in potassium and rubidium (Campbell and Wood 1906). As measurement techniques became more and more sensitive, weak radioactivity was discovered in several other naturally occurring elements (e.g., In, Nd, Sm, Gd, Lu, Hf, and Re).

The identification of radioactive decay as a subatomic process led, of course, to theories of atomic structure. After various models had been suggested – none of them totally satisfactory – the big breakthrough came with Rutherford’s classic 1911 paper (Rutherford 1911) in which he proposed, on the basis of careful, quantitative experiments on the scattering of α particles from thin metallic foils, that most of the mass of an atom must be concentrated in a *positively charged*

nucleus, extremely small when compared to the size of the atom; the positive nuclear charge was thought to be balanced by an equal negative charge carried by electrons surrounding the nucleus. Based on this concept and on Coulomb's law, Rutherford was able to derive a formula that gives detailed predictions of α -particle scattering and its dependence on nuclear charge. Experimental verification of these predictions led to a widespread acceptance of the nuclear model and to the realization that an element's *atomic number*, hitherto merely indicating the element's placement in the periodic table, is in fact its nuclear charge (in units of the electronic charge e). Once Rutherford's *nuclear model of the atom* was accepted, elucidation of atomic structure made rapid strides, important milestones being Niels Bohr's theory of electron orbits (Bohr 1913) and the quantum revolution of the mid-1920s.

With time, the pioneers of radiochemistry developed a great variety of *chemical separation techniques* for the unraveling of the natural decay series, including co-crystallization, adsorption, volatilization, and electrochemical deposition. The quantities of the radioisotopes handled – as estimated from the decay rate – were often smaller by orders of magnitude than could be detected by any other method. Hence, studies of the chemistry of extremely low, “imponderable” quantities became a major research field of radiochemists during the first decades of the twentieth century (see, e.g., Hahn 1936). At such a level, deviations from the behavior of macroscopic amounts are not unexpected. For example, the vapor pressure and the evaporation rate are normally governed by the cohesive forces between the molecules of the species itself. In case of a monomolecular layer covering a backing, they depend, however, largely on the interaction between species and backing material. On the other hand, when radiochemists want to ensure “normal” chemical behavior of a trace quantity of a radionuclide, they add a macroscopic quantity of a *nonradioactive carrier*, usually of the same element in the same chemical form in which the trace element is thought to be present.

Path-breaking work that eventually spawned whole new fields was done in those early years. For example, the potential of *radioactive decay* to serve as a *clock* for geological processes was realized by Rutherford as early as 1906 (Rutherford 1906) when he proposed the amount of helium in uranium ores as a measure of the time since crystallization of the ore. This *He/U method* provided the first proof that geological processes must have occurred over times of the order of 10^8 to 10^9 years, orders of magnitude longer than indicated by previous methods. This revolutionary conclusion was confirmed in 1907 when lead was recognized as the final, stable product of uranium decay (Boltwood 1907), which meant that the Pb/U ratio could be used as a chronometer. Further refinement of this Pb/U method became possible when precise atomic weight determinations showed (Richards and Lambert 1914; Hönigschmid and Horovitz 1914) the lead in some uranium ores had an atomic weight close to 206 rather than the usual 207.2, thus identifying it as radiogenic.

Also of far-reaching consequences was the idea (Hevesy and Paneth 1913) to use *radioisotopes as indicators or tracers* in chemical, physical, and biological studies because radioactive and stable isotopes are chemically indistinguishable. Hevesy and Paneth determined the solubility of sparingly soluble lead salts by labeling the samples with radioactive lead and measuring the radioactivity in the solution after equilibration. The result can be obtained by other techniques too, but not in such a simple way as with radioactive indicators. This holds for most indicator applications.

However, it was realized early on that there is a category of problems that can be attacked *only* with radioactive (or stable isotope) indicators: the behavior of an element in some chemical form in the presence of the same element in a different chemical form. The first example was Hevesy's work on the exchange of lead between solid lead metal and its ions in

solution (Hevesy 1915), in which the dynamical exchange process postulated as a fundamental concept of chemical kinetics was directly verified. Even the fate of a species in an identical environment can be followed, as he showed for the self-diffusion of lead in molten (1920) and solid (1929) lead metal. The most seminal development was the extension of the tracer technique to life sciences by Hevesy and his coworkers. In 1923, they studied the uptake and transport of lead in plants (horse beans) including the proof that transport and fixation occur in ionic form (Hevesy 1923); a year later came the first tracer study in animals, a report on the circulation of bismuth in rabbits (Christiansen et al. 1924). As early as 1927, an application to human subjects was reported (Blumgart and Weiss 1927), the study of blood circulation by injection of ^{222}Rn decay products. This work represents also a generalization of the tracer concept beyond the original idea of isotopic tracers.

Though the potential of the tracer technique was clearly demonstrated in such studies, the input to chemistry and other fields remained somewhat limited as long as radioactivity was confined to the heaviest elements occurring in the natural decay series. The epoch-making event that led to a vast expansion of nuclear and radiochemistry was Irène Curie's and Frédéric Joliot's discovery of *artificially produced radioactivity* (Curie and Joliot 1934). Nuclear transmutation by α -particle bombardment – specifically the nuclear reaction $^{14}\text{N}(\alpha, \text{p})^{17}\text{O}$ – had been discovered by Rutherford in 1919 when he observed energetic protons during the bombardment of nitrogen with α particles from a natural source (Rutherford 1919). The new phenomenon of induced radioactivity appeared, e.g., in bombardments of aluminum with α particles as a nuclide decaying with 3 min half-life that could be chemically identified with phosphorus. The process involved was immediately understood as a nuclear reaction, $^{27}\text{Al}(\alpha, \text{n})^{30}\text{P}$, this time leading to an unstable rather than a stable product nucleus.

1.2 The Growth Spurt of the 1930s

The discovery of artificially produced radioactivity came on the heels of several other crucial events: the discoveries of the neutron (Chadwick 1932) and of deuterium, the heavy isotope of hydrogen (Urey et al. 1932), and the invention of devices – electrostatic generator (Van de Graaff et al. 1933), cyclotron (Lawrence and Livingston 1931), voltage multiplier (Cockcroft and Walton 1930, 1932) – capable of accelerating charged particles to energies needed for nuclear transformations. The invention of a very versatile, electronic counter for radioactivity (Geiger and Müller 1928) was another important step. *Neutron capture* in nuclei was discovered by Enrico Fermi and coworkers (Fermi et al. 1934) as an alternative and efficient method for the production of radioisotopes, such as ^{128}I ($T_{1/2} = 25$ min) from the $^{127}\text{I}(\text{n}, \gamma)$ reaction. The activations could be carried out with small neutron sources consisting of beryllium powder mixed with ^{226}Ra as α -particle source (i.e., using the $^9\text{Be}(\alpha, \text{n})^{12}\text{C}$ reaction) soon available in many radiochemical laboratories, and the yields could be increased substantially with neutrons slowed down in hydrogen-containing material (Fermi and Rasetti 1935; Pontecorvo 1935).

Also in 1934, Leo Szilard and T. A. Chalmers observed that neutron capture is accompanied by chemical effects (Szilard and Chalmers 1934); when ethyl iodide was irradiated with neutrons, about half of the produced ^{128}I was not organically bound, but could be extracted with water in the form of iodide. The recoil energy transferred to the iodine atom by the emitted γ ray exceeds by more than one order of magnitude the energy of the carbon-iodine

chemical bond and is thus sufficient to break the bond. This work opened the new research field of chemical effects of nuclear transformations, often referred to as *hot-atom chemistry*.

These developments, all within a time span of 5 years, led to rapid burgeoning of nuclear physics and chemistry in the 1930s. *New nuclear species* – nuclides as they came to be called – were discovered every week, with half-lives ranging from fractions of a second to thousands of years. Among the newly discovered nuclides were many that later gained great importance as tracers in medical practice and in industry, including ^{131}I , ^{60}Co , ^{32}P , and ^{14}C . By the outbreak of World War II in 1939, several hundred artificially produced radioactive nuclides were known (see, e.g., Seaborg 1940) and at the end of the century the number was somewhere around 3,000.

One might ask why chemists, along with physicists, got into the game of discovering, identifying, and studying radioactive nuclei and their properties as well as investigating the mechanisms of the nuclear reactions producing them. To some extent this came about because irradiation of a given target element with a given projectile often led to a variety of radioactive products that had to be separated and identified chemically. But there was also the intrinsic interest of the subject matter and the obvious parallels between chemical and nuclear reactions, as well as between atomic and nuclear structures.

1.2.1 Nuclear Reactions

By the late 1930s, the systematic study of nuclear reactions induced by various projectiles – protons, neutrons, deuterons, and α particles – at the range of particle energies then available (up to about 40 MeV) led to an understanding of the prevalent reaction mechanism in terms of Niels Bohr's *compound-nucleus model* (Bohr 1936). In this model, the incident particle amalgamates with the target nucleus to form a so-called compound nucleus, in which the particle's kinetic and potential energy is shared by all the nucleons. The compound nucleus may be thought of as the nuclear analogue of the excited, quasi-stationary transition state in chemical reactions. After many collisions among the nucleons, taking typically 10^{-14} – 10^{-19} s (a long time in nuclear dimensions), enough excitation energy may be concentrated by statistical fluctuations on one nucleon (or cluster of nucleons such as an α particle) to allow it to escape from its confinement in the potential well of the nucleus. This slow second step is called “*evaporation*,” in analogy to the escape of molecules from a drop of hot liquid, a concept introduced into nuclear physics in the mid-1930s (Frenkel 1936; Bohr and Kalckar 1937) and soon widely accepted. An essential point of the compound-nucleus model is the independence of the evaporation step from the mode of formation of the compound nucleus, and this was confirmed in the 1950s and 1960s by radiochemical studies of the production of radioactive nuclides via the same compound nucleus formed in different ways.

Although the compound-nucleus model accounts well for a large body of nuclear reactions, it became clear early on that there are exceptions. For example, in some deuteron irradiations it was found that protons are emitted preferentially in the forward direction, whereas the compound-nucleus picture (evaporation) would predict an essentially isotropic emission. These (d,p) reactions are interpreted as “stripping” reactions, i.e., the deuteron's neutron is stripped off by the target nucleus and the proton just continues on its path (Oppenheimer and Phillips 1935). This is an example of so-called *direct reactions*, which can occur with the transfer of larger pieces also, e.g., transfer of an α particle from a ^{12}C projectile to the target nucleus.

Direct reactions in the opposite direction, i.e., transfers from target to projectile, also occur and are referred to as “pick-up” processes.

Another major turning point in the history of nuclear science came with the *discovery of fission* by Otto Hahn and Fritz Strassmann in December 1938 (Hahn and Strassmann 1939a, b). In several laboratories in Rome, Berlin, and Paris, a complex series of β -decay chains resulting from neutron irradiation of uranium had been investigated since 1934, and these chains had been assigned to putative transuranium elements formed by neutron capture in uranium with subsequent β^- transitions increasing the atomic numbers (see [Sect. 1.2.3](#)). But then evidence appeared that known elements in the vicinity of uranium, such as radium, were produced as well. When Hahn and Strassmann attempted to prove this by a classical fractional crystallization separation of radium from barium serving as its carrier, the radioactivity turned out to be barium, not radium; hence, new and totally unexpected type of nuclear reaction had to be invoked.

Lise Meitner and Otto Frisch immediately provided the basic explanation of the fission process, again relying on the liquid-drop model of the nucleus (see [Sect. 1.2.2](#)) and the formation of a compound nucleus (Meitner and Frisch 1939). In the very heavy uranium nucleus, collective vibrations were thought to take place after neutron capture, leading to elongation and eventual breakup into two major pieces. Most stunning was the conclusion that in this breakup about 200 MeV of energy should be liberated, far more than in any other nuclear reaction. These energetic fragments were very soon observed in several, almost simultaneously performed experiments, the first carried out by Frisch (Frisch 1939). Niels Bohr supported this explanation of the process and suggested that fission should be more probable in the rare isotope ^{235}U than in the abundant ^{238}U (Bohr 1939), as soon was experimentally confirmed with tiny samples separated in a mass spectrometer (Nier et al. 1940). As early as the summer of 1939, a comprehensive *theory of fission* was worked out by Bohr and John Wheeler on the basis of the liquid-drop model (Bohr and Wheeler 1939). Cornerstone is the concept of a fission barrier, which stabilizes heavy nuclei although they are thermodynamically unstable against breakup into two fragments. A certain energy is required to deform a nucleus until a critical shape (the saddle point) is reached from where it moves to scission. The capture of a thermal neutron in the rare ^{235}U provides just enough energy to carry it over the barrier, whereas this is not the case in the more tightly bound, abundant ^{238}U .

In 1940, Georgi Flerov and Konstantin Petrzhak showed that natural uranium *fissions spontaneously*, albeit with an extremely low rate (Flerov and Petrzhak 1940; Petrzhak and Flerov 1940). As spontaneous fission was subsequently studied in other nuclei, it was found that its rate increases steeply with atomic number. This decay mode may thus finally terminate the periodic table of elements.

The ramifications of the discovery of fission were, of course, vast – the twin developments of nuclear reactors and nuclear bombs having had scientific, political, military, economic, and social impacts worldwide. For nuclear chemists, fission opened a rich field of research in the identification and characterization of *fission products* with half-lives ranging over about 13 orders of magnitude.

1.2.2 Nuclear Properties

Another field of basic nuclear science that became a major preoccupation of chemists, starting in the 1920s, was the study of the nuclear properties of radioactive nuclides – their half-lives and the radiations emitted by them.

In many ways, α decay presents the simplest situation. As early as 1906, Rutherford had noted that the shorter the half-life of an α emitter, the longer is the range of the emitted α particles in air (i.e., the larger is its kinetic energy), and in 1911, a quantitative relation between decay constant and range was formulated (Geiger and Nuttall 1911). The theoretical basis for understanding this relationship came with the advent of quantum mechanics: In 1928, George Gamow as well as Ronald Gurney and Edward Condon, developed the theory of α decay as a tunneling phenomenon through the energy barrier that confines the α particle within the nucleus (Gamow 1928; Gurney and Condon 1928, 1929). This concept explains the very steep inverse dependence of the half-life on the α -particle energy: for energies spanning a factor of five, the half-life covers 30 orders of magnitude (according to current data). *Quantum-mechanical tunneling* was thus introduced as a concept soon taken over in many scientific fields. Since the kinetic energy carried by the α particles reflects the mass difference between the initial and final nucleus, nuclear masses for unstable nuclei became available. When in the 1930s, α -particle spectra began to be studied with high resolution by magnetic deflection, it became obvious that α particles of more than one energy can be emitted by a given species (Rosenblum 1930). The product nucleus is formed not only in its ground state but also in various excited states, which then de-excite by γ -ray emission. The detailed study of the energy levels involved and their quantum-mechanical properties turned into the field of *nuclear spectroscopy*.

Whereas α -particle spectra consist of discrete lines, β particles are emitted with a broad continuous energy distribution in which the energy difference between decaying and product nucleus appears only as the very weakly populated end point of the energy spectrum and is therefore difficult to determine with great accuracy. The average energy carried by the β particle is only about one third of that “expectation value.” This was very hard to reconcile with a transition between discrete energy levels of the initial and final nucleus. Further problems were noted with the balance of angular momentum and spin in β transitions. This raised the troubling question whether the fundamental laws of energy and momentum conservation are invalid at nuclear dimensions. In 1930, Wolfgang Pauli came up with a privately communicated (Pauli, 1994), surprising suggestion for resolving this puzzle: He postulated a neutral, massless particle, emitted along with the β particle and carrying away the missing energy, momentum, and spin. In 1934, Fermi then developed a complete *theory of β decay* incorporating this idea and naming the particle neutrino (Fermi 1934a), at that time a purely hypothetical construct. Its reality was experimentally proven in 1953 by Fred Reines and Clyde Cowan with the intense neutrino fluxes provided by a nuclear reactor (Reines and Cowan 1953; Reines et al. 1960).

Since β decay occurs throughout the periodic table, it offers a wider field of study than α decay, which is largely confined to heavy elements. The term β decay encompasses both β^- (negatron) and β^+ (positron) emission (Curie and Joliot 1934) as well as the process of *orbital electron capture* discovered in 1937 (Alvarez 1937) which, like β^+ emission, leads to a one-unit decrease in atomic number. In each of the three processes a neutrino is emitted (in β^- emission it is an antineutrino). The systematic of β decay has been worked out and selection rules for β transitions in terms of spin and parity changes have been established. Many if not most β transitions lead to excited states of the product nuclei.

Excited states of nuclei, whether formed through α or β decay or through any other nuclear process, decay to lower-lying states (including the ground state) by the emission of γ rays. It is in fact the spectroscopy of γ rays occurring in coincidence with preceding α or β particles and within γ -ray cascades, and the measurement of lifetimes in such decay sequences that are most

essential to the determination of *decay schemes*. This term denotes the detailed assignment of all the modes of decay of a given nuclide, the energies, transition rates, and sequences of all the γ transitions involved in the de-excitation of excited states, and the energies, lifetimes, and quantum numbers of all the levels populated in the product nucleus. When highly excited states are populated in β decay, enough energy may be available to evaporate a neutron, proton, or α particle, as was first observed in 1939 as *β -delayed neutron emission* from fission products (Roberts et al. 1939). With every advance in instrumentation and detector technology, increasing amounts of detail and increasingly rare branch decays became accessible, and generations of nuclear chemists and physicists have devoted themselves to the study of decay schemes.

Gamma-ray transitions between states with large differences in spin turned out to be highly forbidden by angular momentum selection rules, which leads to measurable lifetimes for certain excited states, the *nuclear isomers*. A transition from an isomeric to a lower state often takes place by *internal conversion* of the γ radiation, i.e., the emission of an orbital electron (most often an electron from the K shell) instead of the γ ray; the electron energy then equals the transition energy minus the electron's binding energy. Like in electron capture, the vacancy in an inner electron shell is filled by outer electrons and this process is accompanied by the emission of X-rays characteristic of the product nucleus. The measurement of such *characteristic X-rays* is an important tool for the determination of the atomic number of unknown radionuclides. As electrons cascade in from outer shells, the product atom becomes highly ionized and may appear in a chemical form different from that of the decaying isomeric state; this can be used for the *chemical separation of nuclear isomers*, first reported in 1939 (Segrè et al. 1939) for the isomers of ^{80}Br ; when the isomeric state ($T_{1/2} = 4.4$ h) was incorporated into an organic bromide, the ground state (18 min) formed by decay could selectively be extracted into an aqueous phase.

Decay-scheme studies have provided theoretical physicists with a broad range of experimental data for the development of models to interpret nuclear properties. Interestingly, such models take up ideas established for the description of atomic, molecular, or macroscopic systems, in spite of the many orders of magnitude difference in dimensions.

Particularly important was a model describing *nuclear masses* as they were becoming available in the 1930s from mass spectroscopic measurements and nuclear decay and reaction studies. Such a model should form the basis of nuclear thermodynamics and allow predictions of the energetics of nuclear transformations in cases not yet investigated. A first step was Gamow's recognition of the analogy between atomic nuclei and macroscopic drops of a liquid (Gamow 1929). In both systems, an attractive force acts between the constituents, increasing the binding energy with size and leading to spherical shapes maintained by surface tension. In nuclei, however, this trend is counteracted by the Coulomb repulsion between protons, which decreases the binding energy as Z increases. Carl Friedrich von Weizsäcker pursued the *liquid-drop model* further in 1935, after the neutron had been established as a constituent of nuclei (Weizsäcker 1935). His semiempirical *equation for nuclear masses* takes as the leading term the binding energy proportional to the number of nucleons, with corrections for surface nucleons, Coulomb repulsion, and the fact that equal numbers of protons and neutrons are energetically preferred. This equation is, in its modern versions, still the backbone of nuclear thermodynamics in that it covers the major, smooth trends of nuclear masses with proton and neutron number.

With improved knowledge of excited nuclear states, it became obvious that they frequently exhibited patterns similar to those known from molecular spectroscopy: vibrations of a (slightly perturbed) harmonic oscillator as well as rotations of a nonspherical structure.

Hence, nuclei can vibrate around the spherical ground state. Moreover, they can be permanently deformed into *prolate* (cigar-like) or *oblate* (disk-like) shapes rotating around an internal symmetry axis. Overlaid on the smooth trends are properties of nuclei with certain proton and neutron numbers (2, 8, 20, 28, 50, 82, 126) standing out in many different respects, as already recognized in the 1930s (Elsasser 1933, 1934). For example, lead nuclei ($Z = 82$) are the end points of the natural decay chains, and extraordinarily high energies are released in the α decay from polonium (84) into lead nuclei. Among the stable nuclei, ^{48}Ca ($Z = 20$, $N = 28$) is unusually neutron rich, and tin ($Z = 50$) has more isotopes than any other element. Most directly, the extra stability associated with these “*magic*” numbers becomes evident in their nuclear masses. The situation was clearly reminiscent of the closed electron shells in atoms, but it was only in 1949 that a quantum-mechanical concept for nuclear shells was developed (see ▶ Sect. 1.4.2).

1.2.3 New Elements

One major field of endeavor of nuclear chemists has long been the *search for* and characterization of *new elements*, i.e., elements not previously found in nature. This field was much stimulated by H. G. J. Moseley’s X-ray studies (Moseley 1913, 1914) indicating still existing gaps in the main body of the periodic table. Further gaps remained even after the extensive studies of the natural decay chains had filled in most of the elements between bismuth and uranium. In the 1930s, the elements 43, 61, 85, and 87 were still missing. Each of them had at various times been claimed to exist in nature, but none of these claims could be substantiated. The growing knowledge of nuclear transformations now made it possible to consider synthesizing missing elements in the laboratory.

Element 43 was the first element produced by an induced nuclear transformation; it was discovered in 1937 (Perrier and Segrè 1937a, b) as a 92 d activity present in molybdenum sheets exposed to deuterons at a cyclotron, i.e., produced by the $^{96}\text{Mo}(\text{d}, \text{p})^{97}\text{Tc}$ reaction. The element followed the chemistry of its supposed homologue rhenium. When it became clear that no stable or extremely long-lived isotopes of element 43 exist in nature, the discoverers proposed in 1947 the name *technetium* for this element, emphasizing its status as the first artificial element. Element 61 in the lanthanide series was unambiguously identified in 1945 (Marinsky et al. 1947) among the fission products of uranium, thanks to the ion-exchange techniques for separating rare earths developed in the Manhattan Project. The discoverers named the new element *promethium*.

Elements 85 and 87 fall into the region covered by the natural decay series and could therefore be expected to be fed by rare decay branches. As early as 1914, α particles were observed in carefully purified ^{227}Ac ($Z = 89$), which implied the formation of element 87 (Meyer et al. 1914). However, the work of Marguerite Perey in 1939 is credited with the discovery of element 87 – the last discovery of a new element in nature (Perey 1939a, b). She proved that a 21 min β^- emitter ($^{223}\text{87}$) growing from ^{227}Ac had chemical properties akin to cesium, and named the element *francium* (Fr). Element 85, *astatine* (At), the heaviest known halogen, was first produced artificially in 1940 as $^{211}\text{85}$ ($T_{1/2} = 7$ h) by ($\alpha, 2\text{n}$) reaction on ^{209}Bi (Corson et al. 1940a, b) before short-lived isotopes were found also in rare branches of the decay series.

Extension of the periodic table beyond uranium by the transmutation of elements was first attempted by neutron irradiation of uranium. Because neutron capture reactions in heavy

isotopes of an element are generally followed by β^- decay to the next heavier element, neutron capture in uranium should yield element 93. After preliminary studies in Rome (Fermi 1934b), more extended studies in Berlin (Hahn et al. 1936; Meitner et al. 1937) presented evidence for several transuranium elements, chemically identified on the premise that element 93 should be a homologue of rhenium, and the elements 94 to 96 should follow the chemistry of the platinum metals. In 1938, contradictory results in Paris (Curie and Savitch 1938) led Hahn and Strassmann to experiments culminating in the discovery of fission (Hahn and Strassmann 1939a, b) (see ► Sect. 1.2.1). Quite soon, it became clear that all these supposed “transuranium” nuclides were in fact fission products.

Now the question whether *transuranium elements* were within range was again open. Edwin McMillan obtained a first hint when he irradiated thin uranium layers with neutrons (McMillan 1939). Whereas the fission products recoiled out of the target, the already known 23 min ^{239}U formed by neutron capture in ^{238}U remained in the target along with a β^- emitter with 2.3 d half-life. A year later, he and Philip Abelson were able to show by a radiochemical milking experiment that the 2.3 d nuclide is the decay product of ^{239}U ; hence it is $^{239}\text{93}$, the first transuranium element (McMillan and Abelson 1940). They named it *neptunium* (after Neptune, the next planet after Uranus). Their further chemical studies of element 93 on the tracer scale revealed uranium-like properties with two oxidation states similar to U(IV) and U(VI), completely different from the expected rhenium-like behavior. Thus, it became clear that the periodic table must have some unexpected features in the vicinity of uranium, later associated with the onset of the *5f electron series* (see ► Sect. 1.3). Since ^{239}Np decays by β^- emission, its daughter clearly had to be another new transuranium element, 94, of mass number 239. Its discovery turned out to be difficult, however.

1.2.4 Hot-Atom Chemistry and Tracer Applications

As mentioned at the beginning of ► Sect. 1.2, *hot-atom chemistry*, i.e., the chemistry of atoms originating from nuclear transformations with kinetic energies far in excess of the usual thermal reaction energies, began in 1934 with the observation that ^{128}I formed by neutron capture in an organic iodide appears as an inorganic species (Szilard and Chalmers 1934). Since the extract contained only traces of stable iodine, this effect allowed, even with the weak neutron fluxes then available, the production of radioactive samples with high specific activity (i.e., activity per weight unit) as often required in tracer applications. Very soon, such so-called *Szilard–Chalmers procedures* were developed for a variety of nuclides accessible by (n, γ) and (n,p) reactions.

In a first study of the organic fraction remaining after such a procedure (Glückauf and Fay 1936), it turned out that a considerable part of the radioactive ^{128}I was present not in the form of the irradiated molecule, but appeared as derivatives. For example, irradiation of CH_3I produced not only CH_3^*I , but also $\text{CH}_2\text{I}^*\text{I}$ ($^*\text{I} = ^{128}\text{I}$) and, when a mixture of CH_3I with C_6H_6 was irradiated, $\text{C}_6\text{H}_5^*\text{I}$ was one of the reaction products. Since in gaseous organic halides all carbon–halogen bonds were found to break in the nuclear process, the apparent “*retention*” of the radioisotope in the original compound observed in condensed states must be due to secondary interactions of the liberated hot atoms with their environment. Hot-atom reactions were also observed in inorganic systems. Already during the Rome group’s systematic exploration of neutron activations (Fermi et al. 1934), it was found that most of the ^{56}Mn ($T_{1/2} = 2.6$ h) produced by irradiation of solid KMnO_4 can be collected, after dissolution, as MnO_2

(D'Agostino 1935). Studies of hot atoms, their reaction mechanism, and use for labeling molecules became a hot topic for radiochemists in the following decades.

With radioisotopes now available for many elements, the tracer technique became generally applicable. New variants were developed, such as *neutron activation analysis*, which was introduced in 1936 for the determination of dysprosium in rare-earth samples (Hevesy and Levi 1936) and subsequently became a widely used technique for sensitive trace analyses, particularly when much larger neutron fluxes became available with the advent of nuclear reactors. Another frequently applied method for trace determination is *isotope dilution*: the species to be determined in the sample is diluted by addition of a known amount of the same species labeled with known specific activity. From the specific activity then resulting and measured, the original quantity of the species is derived, even if only a fraction of the species is finally recovered. The impact on biosciences was revolutionary, when suitable isotopes of key elements in the biosphere were soon discovered: ^{13}N ($T_{1/2} = 10$ min) was one of I. Curie and Joliot's early discoveries, and ^{32}P (14 d) and ^{128}I (25 min) were reported by Fermi's group; ^{11}C (20 min), ^{15}O (2.0 min), ^{35}S (88 d), ^{131}I (8.0 d), and ^3H (12 years) followed soon at the early charged-particle accelerators. Of particular importance was the 1940 discovery of the long-lived ^{14}C (5,730 years) (Ruben and Kamen 1940a, 1941, see also Kamen 1963).

Hevesy was the first to apply the new tracers to *biosystems* in a series of studies all performed with ^{32}P , which was produced by the $^{32}\text{S}(\text{n},\text{p})$ reaction in large volumes of carbon disulfide and isolated by extraction with water. The pioneering experiment, performed in 1935 (Chiewitz and Hevesy 1935), was devoted to phosphorus metabolism in rats. It showed that the skeleton is not static but is dynamically replaced with an average holdup time for a phosphorus atom of about 2 months. Other early work dealt with ^{32}P -labeling of red blood corpuscles for the determination of blood volume; this method became a standard in medical practice.

Early tracer studies with cyclotron-produced nuclides were reported beginning in 1937. Most seminal was the first work on *photosynthesis*, performed in 1940 with the short-lived ^{11}C (Ruben et al. 1940; Ruben and Kamen 1940b). The tracer, made by $^{10}\text{B}(\text{d},\text{n})$, was fed as $^{11}\text{CO}_2$ to *Chlorella* algae, which were killed after various times, and the appearance of ^{11}C in various chemical fractions was followed. The authors concluded that carbon fed as CO_2 is fixed only in the dark and that, in the first step, it is incorporated in the carboxyl group of a species with molecular weight of about 1,000. Some studies were done early on with organic molecules chemically synthesized with ^{11}C labels at specific carbon positions. The study of the uptake of ^{131}I in the thyroid gland of human patients with thyroid malfunctions or goiter, performed by recording the ^{131}I activity in vivo with a counter placed close to the thyroid gland was also path breaking (Hamilton and Soley 1939, 1940).

Although these pioneering studies paved the way for a rich panoply of biological and medical tracer applications, the field came nearly to a halt during World War II and was revived with new vigor after a hiatus of several years.

1.2.5 Geo- and Cosmochronology

As noted in Sect. 1.1, the potential of radioactive decay to serve as a “clock” for geological processes was recognized very early. The amount of helium in uranium and thorium ores should generally be considered to give only lower limits for the ages of mineral deposits because of the likelihood of helium loss during geological times. The probability that there have been no losses (or gains) is intrinsically greater for lead than for helium, and the lead/uranium and lead/

thorium age determination methods, based solely on chemical analyses for Pb, U, and Th, were therefore thought to be more definitive than the He/U and He/Th methods. However, major progress in the reliability of *age determinations* came only with the advent of isotopic analyses by mass spectrometry. The first investigations of the isotopic compositions of lead from various sources were published in 1938 (Nier 1938). The realization that the amount of ^{204}Pb , the only non-radiogenic lead isotope, could be used to correct for the contributions of the other lead isotopes present at the time of formation of a uranium or thorium mineral paved the way for much improved geological age determinations.

Although potassium had been known since 1906 to be radioactive, it was only in 1935 that the rare isotope ^{40}K was discovered mass-spectrometrically (Nier 1935) and found to be responsible for the radioactivity. In 1937, Weizsäcker speculated – correctly as it turned out – that ^{40}K decays to ^{40}Ar by electron capture and proposed the measurement of ^{40}Ar in potassium minerals as a *geochronological dating* method (Weizsäcker 1937). This was the key to the postwar development of the potassium–argon method of age determination which, because of the ubiquity of potassium in nature, has much wider applicability than the methods based on uranium and thorium. Weizsäcker’s speculation was supported by the observation that the abundance of ^{40}Ar is anomalously large in the Earth’s atmosphere as a result of the decay of ^{40}K in the Earth’s crust.

Other techniques that later found extensive use in nuclear geology and other fields also had their roots in the 1930s. An apparatus for obtaining long ocean cores was first described in 1936 (Piggott 1936). In the following years, it was applied in the first investigations of the radioactivity in such cores to deduce time relations from the results. The preparation of thick photographic emulsions for α -particle autoradiography was published in 1935 (Baranov and Kretschmer 1935) for precisely locating radioactive constituents in rocks. This work led to the development of a variety of thick photographic emulsions of different compositions and grain sizes, collectively known as *nuclear emulsions*. In addition to being important in mineralogy and geology, they became widely used after World War II as particle detectors in cosmic-ray research as well as in nuclear and particle physics.

Quite early in the development of nuclear science it had been realized that the huge amounts of *energy radiated by stars* like our Sun must be produced by nuclear rather than chemical processes. The notion that *nuclear fusion* might be what fuels the stars was first proposed in 1919 by Jean Perrin (he called it “la condensation d’atomes légers en atomes lourds”) (Perrin 1919). In 1926, Arthur Eddington refined this idea by postulating the conversion of hydrogen into helium as the most likely candidate (Eddington 1926). But it was only with the more detailed understanding of nuclear reactions achieved in the 1930s that specific mechanisms for this conversion could be formulated. In 1938, Hans Bethe described a sequence of reactions now known as the carbon–nitrogen cycle that fills the bill (Bethe 1939). It starts with the reaction $^{12}\text{C}(\text{p},\gamma)^{13}\text{N}$ and, after a series of such (p,γ) reactions interspersed with positron decays, ends with the reaction $^{15}\text{N}(\text{p},\alpha)^{12}\text{C}$; thus ^{12}C is regenerated in this cycle and can be thought of as a catalyst, with the net reaction being the conversion of four protons to ^4He (plus two positrons and two neutrinos). Bethe’s paper spawned the important and fascinating field of *nuclear astrophysics*.

1.3 World War II

Within a few months of the discovery of nuclear fission, it became evident that this reaction involves a very large energy release as well as the emission of neutrons, and this quickly led to

speculation about the possibility of a chain reaction. With the outbreak of World War II and the possibility of developing a bomb based on an *explosive nuclear chain reaction*, further work on fission in a number of countries soon became shrouded in secrecy, with the US effort (known as the *Manhattan Project*) being by far the most ambitious (for a comprehensive history of the Manhattan Project, see Rhodes 1986). On December 2, 1942, only 4 years after the discovery of fission, the first man-made self-sustained chain reaction was achieved in Chicago by Fermi and his team, using natural uranium as nuclear fuel, embedded in a lattice of very pure graphite as moderator. By then, the US government had decided on a crash program to achieve its goal of a fission bomb and it took a mere 2½ years more to produce the two nuclear bombs dropped on Hiroshima and Nagasaki. The realization of an explosive chain reaction on this incredibly short timescale involved a veritable army of scientists charged with finding solutions to an enormous variety of nuclear, chemical, and engineering problems. Thus, a whole new generation of chemists and physicists was rapidly trained and educated in nuclear science. This new supply of highly skilled nuclear experts, along with the spectacular success of the Manhattan Project, set the stage for the burgeoning of nuclear physics and chemistry in the postwar decades. The massive wartime effort, involving the collaboration of many scientists and interdisciplinary teams, also presaged the age of “*big science*.” Subsequently, this “big science” emerged as the prevalent mode of doing research, first in particle physics and later also in nuclear science and consequently it has become increasingly difficult to single out individual contributions among the large group efforts.

The initial thinking about achieving an explosive chain reaction focused on separating fissile ^{235}U from ^{238}U , and several *isotope separation methods* (thermal diffusion, gaseous diffusion, electromagnetic separation, and centrifugation) were pursued in parallel. But another key development was the *discovery of element 94* and its fissionability by slow neutrons, which opened a second path to a fission bomb. As mentioned in [Sect. 1.2.3](#), the identification of ^{239}Np as a β^- emitter led inevitably to a search for the next element. However, because of its long half-life and unknown chemistry, the decay product ^{239}Pu was difficult to find. Rather, element 94 was discovered in February 1941 in the form of the shorter-lived isotope ^{238}Pu ($T_{1/2} = 88$ years) by deuteron bombardment of uranium (Seaborg et al. 1946a, b). First studies of its chemical behavior were performed on the tracer scale (Seaborg and Wahl 1948). A few months later, Glenn Seaborg’s team (Kennedy et al. 1946) was able to produce a sufficient quantity (about 0.5 μg) of ^{239}Pu to detect its α activity and to find that ^{239}Pu is even more fissile by slow neutrons than ^{235}U . The half-life was later measured to be 2.41×10^4 years. The new element was called *plutonium* (Pu) after the planet Pluto, as uranium and neptunium had been named after Uranus and Neptune.

Initial studies of the *chemistry of neptunium and plutonium* actually preceded the official establishment of the Manhattan Project. But as soon as the project got underway, they became the subject of intensive investigation at several of the Manhattan Project laboratories (Seaborg and Katz 1954). Both elements turned out to have four major oxidation states +3, +4, +5, +6, similar to uranium, but plutonium is unique in that these four states can all exist simultaneously in aqueous solution. Microchemical techniques were applied to prepare and study microgram quantities, such as the first weighable sample of a man-made element, 2.77 μg PuO_2 , in September 1942 (Cunningham and Werner 1949). At the Los Alamos Laboratory, chemists and metallurgists learned to produce metallic plutonium and studied its complex properties, which eventually turned out to involve no less than six allotropic phases, more than any other element.

Quite remarkable is the fact that, based on laboratory experiments on a microgram scale, radiochemists under the leadership of Seaborg were able to devise the methods that were soon

successfully used to separate kilograms of plutonium from reactor-irradiated uranium and fission products. This was achieved by coprecipitation of Pu(IV) with bismuth phosphate. In the first postwar years this batchwise procedure was replaced by continuous solvent extraction processes such as the extraction of both Pu(IV) and U(VI) from nitric acid into tributyl-phosphate, followed by selective reduction of Pu(IV) to Pu(III) and its back-extraction into an aqueous phase.

Also already during World War II the next two elements, 95 and 96, subsequently named *americium* (Am) and *curium* (Cm), were synthesized (Seaborg et al. 1949a, b), using α -particle bombardments of uranium and plutonium, respectively: ^{241}Am (432 years) resulted from (α ,n) reaction on ^{238}U via the β decay of the primary product ^{241}Pu (14.4 years); ^{242}Cm (163 d) was directly formed in the $^{239}\text{Pu}(\alpha, n)$ reaction. The studies of their chemical properties were started, although the realization that their most stable oxidation state is +3 did not come until shortly after the end of the war. It was this observation more than anything else that led Seaborg to his daring concept of the actinide series (Seaborg 1945, 1954) – a major revision of the periodic table.

Detailed studies of the vast array of fission products occupied a small army of chemists at the “Metallurgical Laboratory” in Chicago (Coryell and Sugarman 1951, see also Siegel 1946). The individual nuclides had to be identified, their nuclear properties determined, and their yields in fission measured. One of the important general results was the realization that, under slow-neutron bombardment, ^{235}U and ^{239}Pu split *asymmetrically* into two fragments of unequal mass, whereas the liquid-drop model predicts a symmetric mass split. This behavior remained an intriguing puzzle for 3 decades.

Although the focus has been on the US developments during World War II, one should note that work along some of the same lines went on in other countries as well, albeit on a much more modest scale. In Germany, a small group of chemists in Otto Hahn’s laboratory, using fairly weak neutron sources and unaware of the secret work in the USA, managed to accumulate considerable information on fission products (Seelmann-Eggebert and Strassmann 1947) and on neptunium chemistry on a tracer scale (Strassmann and Hahn 1942). A search for element 94 emerging from the β^- decay of ^{239}Np was not undertaken, however. The German efforts to achieve a self-sustaining chain reaction with natural uranium as fuel and heavy water as moderator never came to fruition.

1.4 The Golden Era

As already indicated, the early postwar decades saw an enormous growth of both basic and applied nuclear research. Almost everywhere, certainly in the USA, Western Europe, the Soviet Union, and Japan, governments supported nuclear science on a scale never before experienced. At the first “*Atoms for Peace*” Conference convened in 1955 at Geneva under the auspices of the United Nations, a vast amount of previously classified information was publicly presented for the first time (PUAE 1956). This conference gave a considerable impetus to the dissemination of nuclear research and the worldwide use of nuclear technology.

The development of new tools, some of them the direct outgrowth of wartime work, was another crucial ingredient. Nuclear reactors provided neutron fluxes many orders of magnitude greater than had ever been available before, and with these fluxes it became possible to make a wide variety of radioactive nuclides of almost any desired intensity, either by (n, γ) reactions or as fission products. *New accelerator designs* – betatrons, synchrocyclotrons, synchrotrons, and linear accelerators – opened up new energy regions for the study of nuclear reactions

(see, e.g., Livingston and Blewett 1962). Moreover, the invention of *new detector types* – solid and liquid scintillators as well as semiconductors – revolutionized radiation detection (see, e.g., Price 1958; Bertolini and Coche 1968). As *computers* became more and more powerful and available, they transformed the performance and interpretation of experiments, the collection and analysis of data, and the calculation of theoretical models. *Textbooks* (Friedlander and Kennedy 1949, 1955; Wahl and Bonner 1951) helped disseminate the rapidly evolving knowledge and educate a new generation of students.

1.4.1 Nuclear Reactions

At the *higher bombarding energies* that became available after World War II – first in the hundreds of MeV with synchrocyclotrons, later into the GeV region with proton synchrotrons – the compound nucleus picture that had accounted well for most nuclear reactions up to about 40 or 50 MeV excitation energy began to fail. As with fission, these high-energy reactions were found to lead to multitudes of radioactive (and stable) products with a wide range of mass and atomic numbers. The unraveling of these complicated mixtures was a natural task for chemists, since the first step normally involved chemical separation of individual elements.

The observed reaction patterns, with a great variety of products formed even in the bombardment of a given target with a given projectile, were accounted for by a two-step model proposed in 1947 by Robert Serber (Serber 1947). In the first step, the high-energy incident particle is thought to interact with individual nucleons, thus setting off a so-called *intranuclear cascade*. In this phase, energy is transferred among a relatively small number of nucleons, some of which may have sufficient energy to escape from the potential well, while others will make further collisions and thus distribute energy among other nucleons. This cascade phase lasts of the order of 10^{-22} s and leaves behind a highly excited nucleus, which can then emit additional particles by *evaporation* (or undergo fission) on a much slower timescale. This cascade/evaporation model, when incorporated in computer codes (Metropolis et al. 1958a; Dostrovsky et al. 1959), was quite successful in accounting for the cross sections of a large body of reactions, referred to as *spallation reactions* because they involve the spalling-off of small fragments from the excited nucleus (in contrast to fission that is essentially a binary breakup). The observed energy spectra of particles emitted in these reactions are also fairly well reproduced by the model.

In the high-energy region just discussed, proton-induced reactions were the ones most widely studied, but other projectiles including deuterons and α particles were also used, and some work on pion-induced reactions has been reported. In the energy regime above a few hundred MeV, the production and subsequent interactions of pions during the intranuclear-cascade phase of reactions are believed to play an important part in facilitating the deposition of large amounts of energy in nuclei. It was only with the inclusion of pion production and pion interactions that the theoretical models were able to account for the pattern of spallation reactions experimentally observed (Metropolis et al. 1958b).

In the early 1950s, the study of the reactions induced by ions heavier than α particles was started (see, e.g., Bromley 1984), and since the 1960s the investigation of *heavy-ion reactions* has become one of the most active areas of nuclear research. New accelerators, designed specifically for producing increasingly intense beams of heavy ions all the way up to uranium ions were developed and, as a result, an enormous variety of reactions became accessible. The basic mechanisms mentioned for light-ion reactions, including *compound nucleus formation*, stripping reactions, and other forms of *direct interactions* appear to be of importance for heavy ions also. But an

additional process, first invoked in 1959 (Kaufmann and Wolfgang 1959, 1961) and later termed *damped collision*, has been found to play an important role in heavy-ion interactions. Projectile and target stick together in a transitory collision complex, but instead of continuing to amalgamate into a compound nucleus, the system is driven apart under the action of the Coulomb repulsion in a fission-like process, yielding a broad distribution of fragment masses and charges (Wilczynski et al. 1967, see also Schroeder and Huizenga 1977).

As will be discussed in [Sect. 1.4.3](#), heavy ion reactions made possible the upward extension of the periodic table that has been one of the triumphs of nuclear chemistry in recent decades.

An overwhelming amount of information on fission was accumulated. The *asymmetric mass split* (see [Sect. 1.3](#)) was found to be a general phenomenon in low-energy fission (see, e.g., von Gunten 1969). Regardless of the mass of the fissioning nucleus, the heavy fragment is located around mass number 130 (i.e., by fragments from tellurium to barium) whereas the light fragment moves with increasing fissioning mass toward the heavy fragment until fission becomes symmetric for fermium nuclei ($Z = 100$). The fact that the heavy fragments are positioned close to the $Z = 50$, $N = 82$ shells led to the suggestion that shell effects in the nascent fragments play a role. V. M. Strutinsky (Strutinsky 1967) showed how to correct the liquid-drop fission barrier (see [Sect. 1.2.1](#)) for shell effects in spherical as well as deformed nuclear shapes. It turned out that the barrier is double humped with a first saddle point located close to the ground state of the fissioning nucleus and a second saddle in a strongly deformed shape state close to the scission point. In between is a minimum at a certain deformation due to the shell closure in the deformed shape. This new picture of the fission barrier was supported by several experimental observations, most convincingly by the shape isomers discovered by Sergei Polikanov (Polikanov et al. 1962), which are spontaneously fissioning elongated nuclei located in the minimum; $^{242\text{f}}\text{Am}$ ($T_{1/2} = 14$ ms) was the first case. The new picture suggested that the mass asymmetry is formed late in the deformation process. Model calculations (Wilkins et al. 1976) showed indeed that at the scission point the fissioning nucleus is asymmetrically deformed. The asymmetric mass distributions and other features of low-energy fission were well reproduced.

In 1972, the chance discovery by French scientists (Bodu et al. 1972; Neuilly et al. 1972; Maurette 1976) that uranium from a uraninite ore in the *Oklo mine* in Gabon was markedly depleted in ^{235}U led to the realization that a *naturally occurring chain reaction* had taken place. Isotopic compositions of rare earth elements and other elements in the Oklo ore labeled them unmistakably as fission products. Various dating techniques (see [Sect. 1.4.5](#)) established that the Oklo reactors had been active about 1.9×10^9 years ago (when the abundance of ^{235}U was 3%, approximately the same as in modern light-water power reactors). From detailed studies of isotopic abundances it was possible to deduce that the reactors contained 800 tons of uranium and operated for almost 10^6 years at a power level of approximately 10 kW. About six tons of ^{235}U were consumed, with about two tons of it originating from the decay of ^{239}Pu formed by neutron capture in ^{238}U . An interesting aspect of the Oklo phenomenon, with possible implications for the storage of nuclear wastes from man-made reactors, is that the ore deposit has retained most fission products over geological times.

1.4.2 Nuclear Properties

Like nuclear reaction studies, research on nuclear properties and nuclear structure made rapid strides in the postwar years. *Advances in instrumentation* played an important role, first the

development of the sodium iodide scintillation detectors in the 1950s, which made it possible to record γ radiation with high efficiency and reasonable energy resolution, followed a decade later by the germanium-based semiconductor detectors with even much better resolution. For α - and other charged particles, silicon-based semiconductors became the standard. (see, e.g., Price 1964; Bertolini and Coche 1968).

A breakthrough in understanding nuclear properties came in 1950 with the development of a quantum-mechanical nuclear model by Maria Goeppert Mayer (Mayer 1950) and – independently – by Otto Haxel, Hans Jensen, and Hans Suess (Haxel et al. 1950). They considered the states of a single nucleon, either proton or neutron, in a spherical potential due to all other nucleons. The particles successively fill energy states determined by quantum numbers, which also prescribe how many particles can occupy a given state with pair-wise cancellation of particle spins to zero. After completion of certain states, a large energy gap occurs in the energy level diagram, thus establishing a nuclear shell structure. By introducing strong coupling between spin and orbital angular momentum of the particles, the magic numbers (see [Sect. 1.2.2](#)) could be reproduced. Furthermore, this so-called *single-particle model* accounted for properties like the ground-state nuclear spins of odd-mass (i.e., odd- A) nuclei in terms of the quantum numbers of the unpaired nucleon.

Single-particle and liquid-drop models (see [Sect. 1.2.2](#)) emphasize quite opposite aspects of nuclei: individual versus cooperative effects in a many-nucleon system. As experimental data show, collective and single-particle excitations interfere and mix, often leading to quite complex patterns of nuclear energy levels. A *unified nuclear model* successfully treating collective and single-particle properties on a common basis was developed by Aage Bohr and Ben Mottelson (Bohr and Mottelson 1953). Sven Gösta Nilsson's comprehensive calculations (Nilsson 1955) of single-particle states in regularly deformed nuclei showed that energy gaps occur also at certain deformations, albeit at proton and neutron numbers different from those for spherical nuclei. Novel approaches with emphasis on the interactions of paired nucleons led to an even more general understanding of nuclear structures (Arima and Iachello 1975).

New forms of radioactivity were reported. Proton emission from ground states, predicted as the simplest decay mode of proton-rich nuclei and long searched for, was observed in 1982 for ^{151}Lu (81 ms) produced by a heavy-ion reaction (Hofmann et al. 1982). Unusual large nuclear radii were found for some very light nuclei (Tanihata et al. 1985) and later attributed to neutron haloes, e.g., for ^{11}Li (8.5 ms) to a halo of two neutrons around a ^9Li core. Even a new kind of natural radioactivity was discovered in 1984 (Rose and Jones 1984): emission of ^{14}C nuclei from ^{223}Ra (11 d) leading to ^{209}Pb . Discoveries of other rare decay modes involving the emission of a variety of fragments from very heavy nuclei soon followed.

The exploration of the nuclear landscape on both the neutron-rich and the proton-rich side of the belt of stable nuclei occupied legions of nuclear chemists and physicists. The study not only of the ground-state properties (half-lives, radiations, masses, radii, shapes, spins, and parities) of nuclei but also of the characteristics of their often numerous excited states has revealed the major features of this landscape. Expansion to more *exotic nuclides* required novel, powerful separation techniques, since with increasing distance from stability the half-lives become shorter and shorter and the production processes more and more complex. Since the late 1960s, automated, computer-operated techniques have been developed to separate nuclides at timescales of seconds to microseconds and to provide, by continuous online operation, steady sources of short-lived nuclides for long observation times. The essential step can be the separation of recoil atoms in flight by magnetic and electric fields (see, e.g., Mueller and Sherrill 1993), of ion beams emitted from ion sources by magnetic fields

(see, e.g., Ravn 1979), and of thermalized reaction products by rapid chemical procedures (see, e.g., Herrmann and Trautmann 1982). Laser and ion-trap techniques online opened new avenues such as the precise determination of nuclear radii and masses far off the stability line (see, e.g., Otten 1989; Kluge and Bollen 1992).

About 3,000 nuclides are known and about 7,000 are predicted to exist. They fill – nearly without gaps – the banana-shaped chart of nuclides on both sides of the belt of stable nuclei. The coordinates are the magic numbers at closed neutron and proton shells of spherical shape. Between the shells, nuclei are regularly deformed, either prolate or oblate, and in transition regions between different shapes, more complicated forms are observed. At the proton-rich side, β^+ decay and electron capture dominate, at the neutron-rich side, β^- decay. Somewhere at proton-rich nuclei, an additional proton cannot be bound anymore; this marks the so-called *proton drip line*. This line, located not too far from the stability line, has been reached experimentally over a wide region of the chart up to about lead. The analogously defined *neutron drip line* lies much further away from stability because of the weak binding force and larger distances between neutrons. It is touched only in very light nuclei up to about neon, where the line quickly bends away and soon lies outside the region accessible with present-day nuclear reactions. Its location is a matter of theoretical predictions. Very neutron-rich nuclei may show quite unusual properties: neutron skins or haloes in general, new magic numbers replacing the spherical ones, new modes of collective excitation, etc. At the heaviest elements, α decay and spontaneous fission become essential for the stability limits. There, the chart looks quite different from what had been expected in the 1960s: it extends beyond the actinide elements continuously without forming an island (see ► Sect. 1.4.3). Ultimately the chart of nuclides and, hence, the periodic table may be terminated not by vanishing stability against fission, but by the inability to produce still heavier elements in the laboratory at a detectable level.

1.4.3 New Elements

As discussed in ► Sects. 1.2.3 and ► 1.3, by the end of World War II the periodic table was complete and without gaps up to atomic number 96. The elements 97, *berkelium* (Bk), and 98, *californium* (Cf), were made by bombardment of americium and curium, respectively, with α particles (Thompson et al. 1950a, b). They were chemically identified by cation exchange chromatography: they exactly followed the pattern of their homologous lanthanide elements. This bootstrap method of jumping up two atomic numbers was possible because long-lived americium and curium isotopes were available as target materials, accumulated in reactors by multiple neutron capture in plutonium.

Very unexpectedly, the elements 99 (*einsteinium*, Es) and 100 (*fermium*, Fm) were detected in 1952 in the debris from a thermonuclear explosion. The Es and Fm isotopes found and identified by a collaborative effort of American laboratories (Ghiorso et al. 1955b) were ^{253}Es ($T_{1/2} = 20.5$ d) and ^{255}Fm (20 h). They were presumably produced by the successive capture of 15 or even more neutrons in ^{238}U in an enormous neutron flux on such a rapid timescale that no radioactive decay occurred between neutron captures until the β^- -decay half-lives of the very neutron-rich uranium isotopes became sufficiently short to compete and, thus, to feed long chains of subsequent β^- -decays ending in the heaviest elements. Macroscopic amounts of the elements berkelium to einsteinium were produced since the late 1960s by multiple neutron capture in curium in a high flux reactor in Oak Ridge.

Element 101 (*mendelevium*, Md) was discovered in 1955 by (α ,n) reaction on a target consisting of about 10^9 atoms of reactor-produced ^{253}Es , and the product was ^{256}Md (1.30 h) (Ghiorso et al. 1955a). Its identification by ion exchange chromatography was probably the first example of one-atom-at-a-time chemistry. Later theoretical studies confirmed that under certain conditions single atoms can indeed represent the behavior of macroscopic quantities (Guillaumont et al. 1989, 1991).

At element 101 the (α ,n) reactions with reactor-produced actinide targets came to an end because fermium targets needed to proceed to element 102 cannot be made. To reach heavier elements, *heavy ions* were required *as projectiles* in order to add more than two protons in a fusion reaction. New accelerators were constructed for providing heavy-ion beams, a linear accelerator in Berkeley and a cyclotron in Dubna (Soviet Union). The Berkeley group applied heavy actinides as targets, the Dubna group relied on light actinides. For example, to synthesize element 105, the former group (Ghiorso et al. 1970) used the reaction $^{249}\text{Cf}(^{15}\text{N},4n)^{260}105$, the latter (Flerov et al. 1971) $^{243}\text{Am}(^{22}\text{Ne},4n)^{261}105$. Since a certain projectile energy is required to amalgamate projectile and target, the compound nuclei are quite hot. They cool down by the evaporation of several neutrons to end as the new element. However, this takes place only for an extremely small fraction of the compound nuclei. Rather, fission is much the dominant decay mode for such fragile, hot nuclei. First evidence for a new element is obtained by the observation of reaction products with unusually high α -particle energy, because α energies increase systematically with atomic number. If it can be shown experimentally that this energetic decay leads to a well-known nuclide of the heaviest (or second heaviest) element, then the atomic number of the new element is unambiguously identified.

Five elements, 102 to 106, emerged between 1958 and 1974 from such “hot fusion” reactions. Several discoveries became controversial between the Berkeley and Dubna groups; even different names for the same element were used in East and West. In order to examine the claims impartially, a Transfermium Working Group was established by the International Unions of Pure and Applied Chemistry (IUPAC) and Physics (IUPAP). The group concluded that the credit for the discovery of element 102 should be given to Dubna, for element 106 to Berkeley, and for the elements 103 to 105 it should be shared (Wilkinson et al. 1993). These conclusions were not generally accepted however. The following names and symbols were adopted after further discussions in the scientific community (IUPAC 1997): 102 *nobelium* (No), 103 *lawrencium* (Lr), 104 *rutherfordium* (Rf), 105 *dubnium* (Db), and 106 *seaborgium* (Sg).

In the late 1960s, the perspective for further extension of the periodic table seemed to be limited because of the obviously more and more dominating role of fission in accordance with the liquid-drop model. This perspective changed drastically in 1966 by two theoretical predictions: (1) spontaneous fission should strongly be hindered around the next, yet unknown magic proton number after $Z = 82$ (Myers and Swiatecki 1966), and (2) this should occur at *proton number 114*, not at 126 as one might expect in analogy to the $N = 126$ shell (Meldner 1966; Sobiczewski et al. 1966). A predicted shell closure at $N = 184$ should further contribute to the existence of an *island of stability* around the doubly magic nucleus $^{298}114^{184}$. According to early estimates, the half-lives of these so-called *superheavy elements* could even be long enough to be found in nature (Nilsson et al. 1969; Fiset and Nix 1972). Not unlike “gold fever,” many searches were undertaken (see, e.g., Herrmann 1979) to find evidence for such relic nuclei in all sorts of natural environments. Even with a simple microscope, but with an ingenious choice of a sample, an outstanding discovery could be made. Also, many attempts were made to jump by heavy-ion reactions from the known territory to the superheavy island. Positive claims were raised from time to time but could not stand up under further scrutiny.

In retrospect (Herrmann 2003), this period appears as a colorful intermezzo in superheavy element research.

The element-by-element advance to new elements continued in 1975 with a new concept, “cold fusion,” introduced by Yu. Ts. Oganessian (Oganessian et al. 1975): use of the stable, magic ^{208}Pb and ^{209}Bi as targets to keep the excitation energy of the compound nucleus at a minimum, as is evident from the evaporation of a single neutron. This approach was first pursued for the synthesis of new elements by Peter Armbruster’s group at a new linear accelerator in Darmstadt (Germany). Element 107, *bohrium* (Bh), made in 1981 by the $^{209}\text{Bi}(^{54}\text{Cr},n)^{262}107$ reaction, was the first success (Münzenberg et al. 1981). Five more elements followed until 1996: 108 *hassium* (Hs), 109 *meitnerium* (Mt), 110 *darmstadtium* (Ds), 111 *roentgenium* (Rg), and 112 *copernicium* (Cn). Common to all these discoveries were the low rates of only a few observed events in several days or even weeks of running time and the short half-lives, typically milliseconds. Key to the success was a sophisticated experimental technique: the new elements were separated in flight from the huge surplus of projectiles and concurrent reaction products by passing through electric and magnetic fields. At the end of their flight path, they were implanted in a detector system, which allowed the successive decay events at the point of impact to be followed. Thus, a new element was linked to a long chain of well-known α -particle emitters. In the case of meitnerium, a single event was sufficient to discover a new element (Münzenberg et al. 1982). According to the liquid-drop nuclear model, the barrier against fission should disappear around atomic number 106. Hence, the existence of heavier nuclei decaying by α -particle emission can only be understood as due to the stabilizing action of *nuclear shells preventing fission* (Armbruster 1984).

Evidence for *element 114* and *element 116* was obtained at Dubna in bombardments of ^{244}Pu and ^{248}Cm with ^{48}Ca , an extremely neutron-rich, doubly magic projectile (Oganessian et al. 2000a, b). The decay chains observed in these hot-fusion reactions soon ended in fission with no link to known nuclei, however. The supposed reaction $^{244}\text{Pu}(^{48}\text{Ca},4n)^{288}114$ would represent the closest approach to the $Z = 114$, $N = 184$ “holy grail” possible with present-day techniques, but the neutron number reached, 174, is still far below that goal. According to recent theoretical calculations, however, the next doubly magic spherical nuclei may be located at $Z = 120$, $N = 172$ or $Z = 126$, $N = 184$ (Bender et al. 1999), perhaps not as a peak structure, but as a mesa-like region.

Some basic *chemical properties* of the first *transuranium elements* became already evident in the discovery experiments, in which chemical separations played a crucial role. With time, a vast amount of information has been amassed on the chemistry of the elements available in macro quantities, i.e., all the elements through californium and, to a lesser degree, einsteinium (see, e.g., Katz et al. 1986).

A new research field in the chemistry of neptunium, plutonium, and other light actinides developed in the late 1970s in the context of environmental contaminations and nuclear waste management. The aim was to unravel their *behavior in natural environments* (see, e.g., Watters et al. 1983; Kim 1986). This is a difficult task because of the complex chemistry: many oxidation states, polymerization, interaction with less defined natural partners such as humic acids, clays, and various rocks play a role. Included is also the development of techniques for the determination of actinide elements and their speciation in extremely low concentrations.

Beyond einsteinium, the amount of chemical information becomes increasingly sparse but significant data were obtained in exploratory studies at the tracer scale (see, e.g., Silva 1986) for elements up to the last actinide element, lawrencium (103), and the first transactinide elements, rutherfordium (104) and dubnium (105). From curium on, the chemical properties

resemble closely those of the homologous 4f lanthanide elements. The results are, thus, in full agreement with the concept of the actinide series of 5f elements (see ▶ Sect. 1.3).

Extension of chemical studies to *transactinide elements* became possible in the late 1980s through the availability of isotopes with half-lives in the order of seconds. A strong motivation was the expectation that, with increasing proton number, the electron shell structure should eventually be significantly affected by *relativistic effects* due to the high electron velocity (see, e.g., Fricke 1975). This could result in unexpected chemical properties: element 114 for example, naively located below lead in the periodic table, may rather behave like an inert gas (Pitzer 1975). Sophisticated techniques had to be developed to explore the characteristic chemical properties with single, short-lived atoms on a fast timescale, to detect them by their specific radiation and to run such experiments online over days or weeks to catch the very few atoms produced. Automated, computer-operated procedures were required, based on experience in studies of short-lived fission products (see ▶ Sect. 1.4.2) and pioneering work by Ivo Zvara (Zvara et al. 1971). For a detailed comparison, homologous elements were also studied under the same experimental conditions. Preferred chemical steps were the distribution of transactinide species between aqueous solutions and ion exchangers (Kratz et al. 1989) and their volatilization and deposition on solid surfaces (Gäggeler et al. 1992). *Rutherfordium* and *dubnium* were found to fit, in general, the periodic table as expected, namely as homologues of hafnium and tantalum. In detail, however, there are inversions in the trend within the groups, which can be traced back to relativistic effects, as theoretical studies showed. A particular challenge is the first exploration of the chemistry of a new element and its inauguration in the periodic table. This succeeded for *seaborgium* (Schädel et al. 1997), *bohrium* (Eichler et al. 2000), and *hassium* (Düllmann et al. 2002). Their placement below tungsten, rhenium, and osmium, respectively, seems to be justified too.

1.4.4 Hot-Atom Chemistry and Tracer Applications

Since the fall of 1946, radioisotopes produced in the Oak Ridge nuclear reactor were available to the general public. This gave an enormous impetus to all kinds of tracer applications, strongest in life sciences where compounds labeled with the long-lived tracers ^{14}C and ^3H soon became an essential, often indispensable tool. Labeling was performed by conventional chemical synthesis starting from simple radioactive molecules, or by *biosynthesis* in living organisms that had been fed with labeled precursors (Calvin et al. 1949). The progress thus made becomes evident in an early application – Melvin Calvin and Andrew Benson's work on *photosynthesis*. Using ^{14}C (instead of ^{11}C , see ▶ Sect. 1.2.4), they were able to follow in *Chlorella* algae how carbon dioxide is converted into sucrose via a sequence of reaction products (Calvin and Benson 1949). Most stunning was the short timescale: half a minute after the addition of labeled carbon dioxide, the major portion of the radiocarbon was found in complicated compounds, such as phosphoglyceric acids and hexose phosphates.

Other fields benefited, too, from the strong neutron fluxes now accessible for irradiations. New phenomena were observed, such as the annealing of *hot-atom effects* in inorganic solids by postirradiation heating, leading to an increased retention in the form of the original species (Green and Maddock 1949; Rieder et al. 1950). A new and powerful tool was discovered by Rudolph Mössbauer in 1958: *recoilless emission of γ rays* with natural or nearly natural line width from nuclei embedded in a solid lattice (Mössbauer 1958, 1962). Resonant absorption of such emissions, e.g., the 14.4 keV transition of ^{57}Fe fed in the decay of ^{57}Co ($T_{1/2} = 270$ d), provides

information on the magnetic and electric environment of either the disintegrating nucleus (in so-called source experiments performed with ^{57}Co -bearing samples) or the absorbing nucleus (e.g., in transmission experiments performed with ^{57}Fe -containing samples).

Hot-atom reactions of hydrogen, carbon, and halogens in organic systems became a major research topic in radiochemistry, aimed at exploring the chemical reactivity of such hot-atom species in the context of chemical dynamics (see, e.g., Willard 1953; Wolf 1964). Furthermore, hot-atom reactions offered an elegant alternative for *labeling organic molecules* (see, e.g., Wolf 1960). As early as in 1946, the formation of ^{14}CO , $^{14}\text{CO}_2$, $^{14}\text{CH}_4$, H^{14}CN , and H^{14}COOH during the $^{14}\text{N}(\text{n},\text{p})$ process was observed in irradiations of simple nitrogen compounds (Yankwich et al. 1946). Hot atoms were found to react only as they approach the end of the recoil track, i.e., at energies below about 20 eV. The product spectra are very broad. Radiocarbon, for example, can (1) replace a C or N atom in the substrate, (2) add one additional carbon to the parent compound, (3) react with smaller molecules produced by fragmentation, and (4) find its way into larger buildup products as well as into polymers. Alongside these hot-atom reactions, similar reactions of thermal carbon atoms also occur, which complicate the interpretation of the results. Within a molecule, the labels are neither randomly distributed nor specifically located at a particular atom. Hence, *recoil labeling* is useful mainly for tracer experiments in which the molecule remains intact throughout, rather than for studies on the fate of a particular part of a molecule.

The application of radiotracers in medical diagnostics grew rapidly with the development of labeling techniques. *Radiopharmaceuticals* labeled with ^{131}I (8.0 d) were introduced in the early 1950s. *Radioimmunoassay*, invented in 1956 by Salomon Berson and Rosalyn Yalow became a widely applied in vitro technique for sensitive measurements of body constituents, e.g., hormones and enzymes (Berson and Yalow 1957, see also Yalow 1978). Based on the principle of isotope dilution analysis, it uses the competitive binding of natural and ^{131}I -labeled antigens to antibodies. The in vivo diagnostics of thyroid diseases with ^{131}I was greatly improved by imaging techniques for extended γ -ray distributions: first by the step-by-step radioactivity scanners (Cassen et al. 1951; Curtis and Cassen 1952) and in 1958 by the NaI scintillation camera (Anger 1958). A later example of a widely applied tracer technique is the study of myocardial perfusion with ^{201}Tl (73 h) (Lebowitz et al. 1975).

For in vivo diagnosis of humans, short-lived tracers are most desirable in order to minimize the damaging effects of radiations, but there were not many places where facilities and staff for isotope production, chemical labeling, and medical diagnostics were at hand. An important step was therefore the development of *radionuclide generators* for short-lived nuclides that grow from long-lived parents. The parent nuclide can then be shipped to the user in a form that allows repeated stripping of the short-lived decay product. Most successful was the *technetium generator*, developed in 1958 (see, e.g., Richards et al. 1982; Molinski 1982). The generator contains the parent ^{99}Mo (66 h), a fission product, fixed on a column from which the grown-in $^{99\text{m}}\text{Tc}$ (6.0 h) is eluted from time to time. Later, “kits” were developed with all ingredients required to release $^{99\text{m}}\text{Tc}$ from the generator in the chemical form to be administered to the patient (Eckelman and Richards 1970). This made $^{99\text{m}}\text{Tc}$ – an isotope of an element that does not occur naturally on Earth – into the backbone of routine imaging in nuclear medicine (see, e.g., Jones 1995), often replacing other radiotracers such as the iodine isotopes and ^{201}Tl .

In the late 1960s, cyclotrons were installed in medical institutions, and in the following decade computer tomography was introduced for the scanning of the γ radiation. This led to a revival of ^{11}C for the specific labeling of organic molecules (see, e.g., Wolf and Redvanly 1977) starting from ^{11}CO , $^{11}\text{CO}_2$, or H^{11}CN produced when ^{11}C is made by the $^{11}\text{B}(\text{p},\text{n})$ or $^{14}\text{N}(\text{p},\alpha)$

nuclear reactions in the presence of oxygen or hydrogen, respectively, and applying a new technology of automated fast chemical synthesis (see, e.g., Stöcklin and Pike 1993). The positron emitter ^{11}C became one of the first tracers for *positron emission tomography* (PET), a technique for the in vivo three-dimensional location of the radiation source based on the fact that the two 511 keV quanta in positron annihilation are emitted in opposite directions. PET found its widest application with ^{18}F (1.83 h) produced by the $^{18}\text{O}(\text{p},\text{n})$ or $^{20}\text{Ne}(\text{d},\alpha)$ reactions. It is introduced into organic molecules by replacement of a hydrogen atom. A breakthrough in PET came in 1978 with the development of ^{18}F -labeled 2-FDG by Alfred P. Wolf's group. (Ido et al. 1978); 2-FDG is a fluoro derivative of deoxy-D-glucose, which is phosphorylated in cells like glucose but does not undergo further metabolic degradation. It is still the only method for measuring quantitatively and in an essentially noninvasive manner the local glucose metabolism in the human brain, the heart, and in tumors. Thus, PET has become an important tool for understanding the functional anatomy and biochemical activity of the normal human brain and in pathological conditions including Alzheimer's disease and the effects of drug abuse. It is also important for diagnosis of heart disease, cancer, stroke, and epilepsy. Thanks to the development of relatively compact, tailored cyclotrons combined with automated chemical synthesizers for standard radiopharmaceuticals, positron emission tomography is becoming more and more incorporated in medical practice.

1.4.5 Geo- and Cosmochronology

The postwar period saw the rapid development of new and improved ways of using *radioactive decay as a clock* for a great variety of processes in the Earth's crust, the atmosphere, the biosphere, the oceans, meteorites, and eventually the Moon. These processes were spurred by advances in instrumentation, such as improved mass spectrometers for precise measurements of isotopic ratios.

A very important observation, made in 1956 by Claire Patterson (Patterson 1956), was that a plot of the relative abundances $^{207}\text{Pb}/^{204}\text{Pb}$ vs. $^{206}\text{Pb}/^{204}\text{Pb}$ for many meteorites differing widely in these individual ratios is a straight line, termed an *isochron*, with a slope corresponding to an age of 4.55×10^9 years. Since the isotope ratios of ordinary terrestrial (non-radiogenic) lead fall on the same isochron, the *age of the Earth* as an isolated system is also inferred to be about 4.55×10^9 years. From the close coincidence between the age of the Earth and the time of solidification of the much smaller (and therefore rapidly cooling) parent bodies of meteorites it followed that the entire solar system originated about 4.6×10^9 years ago (see, e.g., Kirsten 1978). Taking history even further back, the time between the production of the heavy elements composing the solar system and the formation of the solar system was estimated as only about one or two hundred million years, as deduced from the presence, in meteorites, of the decay products of extinct radionuclides such as ^{129}I ($T_{1/2} = 1.57 \times 10^7$ years) and ^{244}Pu (8.08×10^7 years) (see, e.g., Wetherill 1975).

Once the decay of ^{40}K (1.28×10^9 years) to ^{40}Ar was established (see ▶ Sect. 1.2.5), the potassium/argon method for *geological age determination* was on a sound footing, particularly through the pioneering work of Wolfgang Gentner (Gentner and Kley 1955, see also Schaeffer and Zähringer 1966). Because argon is an inert gas, it can be safely assumed that at the time of crystallization of a potassium-bearing rock all previously formed ^{40}Ar had escaped. Any ^{40}Ar found in a sample has thus presumably been accumulated since crystallization and serves as a measure of the geological age of the sample. In principle, any long-lived radionuclide and its

stable descendant can serve as a chronometer. Probably the most important parent–daughter pair for geological dating is ^{87}Rb (4.8×10^{10} years) and its decay product ^{87}Sr (Hahn et al. 1943, see also Faure and Powell 1972). One of the triumphs of isotopic dating came in the 1970s when an enormous amount of detailed information on the history of the Moon was gleaned from examination of returned lunar samples with all the available techniques (see, e.g., Wetherill 1971).

When Fritz Paneth's group in 1953 tried to determine meteorite ages by the He/U method (Paneth et al. 1953), they found much larger amounts of helium than could be accounted for by uranium decay and thus stumbled on the discovery of *cosmic-ray-induced nuclear reactions* in meteorites that subsequently became the subject of extensive research. Many radionuclides with half-lives ranging from days to millions of years as well as some stable spallation products have been identified in meteorites. From the amounts found, the exposure ages of meteorites in space and the average cosmic-ray flux and its time variation can be deduced (see, e.g., Schaeffer 1968).

The cosmic-ray impact that has found the most wide-ranging application is the formation of ^{14}C in the Earth's atmosphere by the $^{14}\text{N}(\text{n},\text{p})$ reaction. The ^{14}C dating technique proposed by Willard Libby in 1946 (Libby 1946, 1952) is based on the assumptions that (1) the cosmic-ray intensity has been essentially constant over many ^{14}C half-lives and (2) the ^{14}C produced in the atmosphere becomes equilibrated with the entire biosphere, so that all living matter has the same specific activity. Thus, the time since any carbon-containing material has been removed from the exchange reservoir can be determined from its residual ^{14}C content. With low-level counting techniques, the method has been used to date innumerable objects of archaeological and historic interest with ages up to about 40,000 years; accelerator mass spectrometer methods for measuring $^{14}\text{C}/^{12}\text{C}$ ratios have extended the range even further (see, e.g., Litherland 1980).

Since all the elements and isotopes in various parts of the universe were presumably formed from primordial matter by nuclear reactions, the details of this so-called *nucleosynthesis* have been of great general interest. Whereas hydrogen and helium and lesser amounts of a few other light elements are believed to have been created in the *big bang*, first proposed by George Gamow (Gamow 1946), the synthesis of other elements occurred and is still occurring in stellar interiors. As a starting point for any theory of nucleosynthesis, it was important to know the elemental and isotopic abundances in the Earth, meteorites, the Moon, the planets, the Sun, and other stars. By the mid-1950s, thanks to the work particularly of Hans Suess and Harold Urey, fairly detailed information on *elemental abundances* in the solar system was available (Suess and Urey 1956). Based on these data, and on measurements of stellar spectra and nuclear reaction rates, it was then possible to develop the comprehensive picture of nucleosynthesis and *stellar evolution* that was first presented in the famous 1957 paper by M. Burbidge, G. Burbidge, W. Fowler, and F. Hoyle (often referred to as BBFH) (Burbidge et al. 1957).

In basic outline, the BBFH picture is still valid (Fowler 1984). A newly formed star contracts gravitationally until the temperature in its center can sustain the reaction $\text{p} + \text{p} \rightarrow \text{d} + \text{e}^+ + \nu$. This reaction and the follow-up reactions $\text{p} + \text{d} \rightarrow {}^3\text{He} + \gamma$ and ${}^3\text{He} + {}^3\text{He} \rightarrow {}^4\text{He} + 2\text{p}$, in other words the *thermonuclear fusion* of four protons to form a ${}^4\text{He}$ nucleus, provide the energy output of the Sun and all so-called main-sequence stars; this fusion energy counterbalances the gravitational force thus stabilizing the star. When hydrogen becomes depleted, contraction takes over again and successively more complex fusion reactions set in, eventually followed by (α,n) reactions, which in turn provide sufficient neutron fluxes to allow (n,γ) reactions. This continues until iron and nickel are reached with the most stable nuclei in terms of binding energy per nucleon.

Elements beyond the iron/nickel region are believed to be built up by neutron capture followed by β^- decay to the next higher element. There are two quite different processes. In the so-called *s-process*, neutrons are captured on a timescale slow enough to allow β^- decay to proceed before another neutron is captured; this process happens around the stability valley. The *r-process*, rapid neutron capture, takes place in such a high neutron flux that many neutrons are captured successively before β^- decay can compete. Its pathways involve nuclides far on the neutron excess side of stability, a largely unexplored region (see [Sect. 1.4.2](#)). Hence, theoretical models often have to be invoked. About half of the solar abundances of elements beyond iron and most of the heaviest elements are believed to be created by the *r-process*, but its mechanism and astrophysical side remain major questions in nucleosynthesis. Nevertheless, on the basis of calculated production rates for very long-lived natural nuclides such as ^{232}Th , ^{235}U , and ^{238}U and their observed solar abundances, the age of the Galaxy is predicted to lie in the range of $(12\text{--}15) \times 10^9$ years (Cowan et al. 1991).

An area that was pioneered by nuclear chemists is the search for *solar neutrinos*. Although main-sequence stars, of which the Sun is a typical representative, have for decades been believed to derive their energy from the series of fusion reactions mentioned above, there was no direct observational evidence for this until Raymond Davis in the 1960s undertook to measure the flux of neutrinos from the Sun which accompany these reactions (Davis et al. 1968; Cleveland et al. 1998). The experiment involved measuring the number of ^{37}Ar atoms (35.0 d) formed by neutrino capture in ^{37}Cl in a tank of perchloroethylene. With only a few atoms of ^{37}Ar per month extracted from over 600 t of liquid, this was indeed the ultimate low-level radiochemical separation. Nevertheless, the experiment was successful in detecting the neutrinos, but ever since the first data appeared in 1968, the measured neutrino flux persisted in being only one third of what was expected from model calculations, and this so-called solar neutrino puzzle literally gave rise to a whole new field – *neutrino astronomy*.

Davis's experiment motivated additional experiments. In the early 1980s, two international collaborations undertook radiochemical experiments with massive gallium detectors in deep underground facilities in the Gran Sasso Tunnel (Italy) (Anselmann et al. 1992a, b) and the Baksan Valley (Caucasus) (Abazov et al. 1991), respectively. Here the aim was neutrino capture in ^{71}Ga to form ^{71}Ge (11.4 d), a reaction principally sensitive to the low-energy neutrinos from the primary $p + p$ reaction in the Sun, whereas the chlorine experiment detects only high-energy neutrinos from rare branch reactions. These gallium experiments showed that, indeed, fewer low-energy neutrinos arrive at the Earth than expected from the energy production in the Sun. Physical experiments with real-time detection of neutrinos followed. Eventually the totality of the experiments and theoretical developments led to the unequivocal conclusion that the expected quantities of electron neutrinos are indeed produced in the Sun, but that some of them are transformed by so-called *neutrino oscillations* into other types of neutrinos, which are not detectable by the chlorine and gallium detectors. Since neutrino oscillations are possible only if one or more of the neutrino types have a finite rest mass, the “solar neutrino puzzle” posed by a radiochemical experiment led to a profound new result in particle physics.

1.5 Current Trends

There is no sharp endpoint to the “golden era.” But the climate for nuclear research and development markedly changed in the 1980s. Government budgets for nuclear science tended to level off after 3 decades of remarkable growth; institutions established for nuclear research

focused on other fields, fewer university departments offered courses in nuclear and radiochemistry, and when nuclear chemistry faculty positions fell vacant, they were often filled with chemists in other specialties.

Several contributing factors are easily identifiable: The accidents at the nuclear power plants at Three Mile Island (1979) and Chernobyl (1986) greatly increased the public's fear of everything nuclear. In the USA and the former Soviet Union, vast amounts of waste streams containing fission products and actinides were left over from plutonium production plants that must be disposed of safely. Furthermore, any country using nuclear energy on a large scale is confronted with the problem how to treat nuclear waste and store it permanently. This negative attitude, however, seems to change in recent years in the context of the worldwide concern about the Earth's climate. Nuclear power becomes more and more accepted as a large-scale energy source with no output of greenhouse gases; its future role is currently not yet recognizable, however.

Another significant change that has gradually come about is that many techniques pioneered by radiochemists turned out to be so successful that they became subsumed in other fields. In particular, the use of radioactive tracers is so pervasive in various areas of chemistry and life sciences that it has simply become a standard tool, like microscopy, mass spectrometry, and nuclear magnetic resonance in the chemist's or biologist's arsenal rather than a branch of chemistry with a clear identity. Thus, tracer techniques play an important role also in such forefront areas as molecular biology and genetic engineering. Needless to say, there still are areas in which the skills of radiochemists are indispensable, such as the development and preparation of complex radiopharmaceuticals labeled with short-lived nuclides for nuclear medicine applications, e.g., for positron emission tomography.

An obvious way to counteract the scarcity of resources and manpower for nuclear research is the collaboration of scientists from many institutions, large and small, and frequently of long duration. Good examples are the efforts to solve the nuclear waste problem in nationwide coordinated programs as established in several countries. The basic decision – disposal of used fuel elements without reprocessing or chemical treatment with solidification of the waste in form of glasses or ceramics – has to be met at the political level. The next decision, whether storage in granite, tuff, clay, or salt is to be preferred, depends on the geological situation. But once a site is envisaged, its suitability has to be proven by a thorough multidisciplinary research program. The task of the radiochemists is to study, at a strictly scientific level, the interactions of long-lived fission products and actinides with the barrier materials including the geological shield in order to ascertain that they protect the environment over very long times. An unconventional approach to the nuclear waste problem is the “incineration” of very long-lived radionuclides into much shorter-lived components by bombardment with intense proton beams.

Collaboration on an international level is essential in “big” science. These trends began with work centered at large facilities such as big accelerators but have also penetrated into areas of “small” science. Research on the chemistry of the heaviest elements concentrated at the few suitable heavy-ion accelerators is an obvious and successful example. Small groups take over at their home institutions a considerable part of the development of fast single-atom chemistry; each element and each class of compounds requires a specific approach; they test it in model experiments at smaller facilities. Eventually, the external groups and the in-house experimentalists join up at the heavy-ion accelerator to perform the major experiment.

Production and properties of exotic nuclei are the focus of another forefront development: accelerators capable of producing, in a first step, beams of radioactive nuclei, which are then

used, in a second step, as projectiles for nuclear reactions. Beams of neutron-rich projectiles, generated, e.g., by nuclear fission, could thus give access to the still unexplored region of extremely neutron-rich nuclei where unique nuclear properties are expected and the r-process path is located, the key to understanding the nucleosynthesis of the heavy chemical elements. Several such facilities are at the planning stage.

One can perhaps take it as a sign of the continued vitality of nuclear and radiochemistry reviewed in this brief chapter that the field's first century is framed by two Nobel Prizes: the 1903 Prize awarded to Becquerel and the Curies, and Raymond Davis's 2002 Prize. That both were awarded in the field of physics should not detract from the fact that the work honored could not have been done without a great deal of chemistry. It is indeed a major strength of our field that it has had wide-ranging impacts on other sciences.

References

- Abazov AI, Anosov OL, Faizov EL et al (1991) Search for neutrinos from the sun using the reaction $^{71}\text{Ga}(\nu_e, e^-)^{71}\text{Ge}$. *Phys Rev Lett* 67:3332
- Alvarez LW (1937) Nuclear K electron capture. *Phys Rev* 52:134
- Anger HO (1958) Scintillation camera. *Rev Sci Instrum* 29:27
- Anselmann P, Hampel W, Heusser G et al (1992a) Solar neutrinos observed by GALLEX at Gran Sasso. *Phys Lett B* 285:376
- Anselmann P, Hampel W, Heusser G et al (1992b) Implications of the GALLEX determination of the solar neutrino flux. *Phys Lett B* 285:390
- Arima A, Iachello F (1975) Collective nuclear states as representations of a SU(6) group. *Phys Rev Lett* 35:1069
- Armbruster P (1984) On the production of heavy elements by cold fusion: the elements 106 to 109. *Ann Rev Nucl Part Sci* 35:135
- Baranov VI, Kretschmer SI (1935) Verwendung von Lichtplatten mit dicker Emulsionsschicht zur Erforschung der Verteilung radioaktiver Elemente in Naturobjekten. *Compt Rend Acad Sci URSS* 1:546
- Becquerel H (1896) Sur les radiations émises par phosphorescence. *Compt Rend* 122:420; Sur les radiations invisibles émises par les corps phosphorescents. *Compt Rend* 122:501, 559, 689, 762, 1086
- Bender M, Rutz K, Reinhard PG et al (1999) Shell structure of superheavy nuclei in self-consistent mean-field models. *Phys Rev C* 60:034304
- Berson SE, Yalow RS (1957) Kinetics of reaction between insulin and insulin-binding antibody. *J Clin Invest* 36:873
- Bertolini G, Coche A (eds) (1968) *Semiconductor Detectors*. North-Holland, Amsterdam
- Bethe HA (1939) Energy production in stars. *Phys Rev* 55:434
- Blumgart HL, Weiss S (1927) Studies of the velocity of blood flow II, The velocity of blood flow in normal resting individuals and a critique of the method used. *J Clin Invest* 4:16
- Bodu R, Bouzigues H, Morin N et al (1972) Sur l'existence d'anomalies isotopiques rencontrées dans l'uranium du Gabon. *Compt Rend D* 275:1731
- Bohr A, Mottelson BR (1953) Collective and individual particle aspects of nuclear structure. *Danske Vidensk Selsk Mat-fys Medd* 27, No. 16
- Bohr N (1913) Constitution of atoms and molecules I, II. *Phil Mag* 26:1, 476
- Bohr N (1936) Neutron capture and nuclear constitution. *Nature* 137:344
- Bohr N (1939) Resonance in uranium and thorium disintegrations and the phenomenon of nuclear fission. *Phys Rev* 55:418
- Bohr N, Kalckar F (1937) On the transmutation of atomic nuclei by impact of material particles I, General theoretical remarks. *Danske Vidensk Selsk Mat-fys Medd* 14, No. 10
- Bohr N, Wheeler JA (1939) The mechanism of nuclear fission. *Phys Rev* 56:426
- Boltwood B (1907) On the ultimate disintegration products of the radioactive elements. *Am J Sci* 23:77
- Bromley DA (1984) The development of heavy-ion nuclear physics. In: Bromley DA (ed) *Treatise on heavy-ion science*, vol 1. Plenum, New York, pp 3–50
- Burbidge EM, Burbidge GR, Fowler WA, Hoyle F (1957) Synthesis of the elements in stars. *Rev Mod Phys* 29:547
- Calvin M, Benson AA (1949) The path of carbon in photosynthesis IV. The identity and sequence of the intermediates in sucrose synthesis. *Science* 109:140
- Calvin M, Heidelberger Ch, Reid JC et al (1949) *Isotopic carbon: techniques in its measurement and chemical manipulation*. Wiley, New York

- Cameron AT (1910) Radiochemistry. J. M. Dent, London
- Campbell NR, Wood A (1906) The radioactivity of the alkali metals. *Proc Cambr Philos Soc* 14:15
- Cassen B, Curtis L, Reed C et al (1951) Instrumentation for I^{131} use in medical studies. *Nucleonics* 9(2):46
- Chadwick J (1932) The existence of a neutron. *Proc Roy Soc A (Lond)* 136:692
- Chiewitz O, Hevesy G (1935) Radioactive indicators in the study of phosphorus metabolism in rats. *Nature* 136:754
- Christiansen JA, Hevesy G, Lomholt S (1924) Recherches, par une méthode radiochimique, sur la circulation du bismuth dans l'organisme. *Compt Rend* 178:1324
- Cleveland BT, Daily T, Davis R Jr et al (1998) Measurement of the solar electron neutrino flux with the Homestake chlorine detector. *Astrophys J* 496:505
- Cockcroft JD, Walton ETS (1930) Experiments with high velocity positive ions. *Proc Roy Soc A (Lond)* 129:477
- Cockcroft JD, Walton ETS (1932) Further developments in the method of obtaining high-velocity positive ions. *Proc Roy Soc A (Lond)* 136:619
- Corson DR, MacKenzie KR, Segrè E (1940a) Possible production of radioactive isotopes of element 85. *Phys Rev* 57:459
- Corson DR, MacKenzie KR, Segrè E (1940b) Artificially radioactive element 85. *Phys Rev* 58:672
- Coryell CD, Sugarman N (eds) (1951) Radiochemical studies: the fission products, vol 1–3. McGraw-Hill, New York
- Cowan JJ, Thielemann F-K, Truran JW (1991) The r-process and nucleochronology. *Phys Rep* 208:267
- Cunningham BB, Werner LB (1949) The first isolation of plutonium. *J Am Chem Soc* 71:1521
- Curie I, Joliot F (1934) Un nouveau type de radioactivité. *Compt Rend* 198:254; Séparation chimique des nouveaux radioéléments émetteurs d'électrons positifs. *Compt Rend* 198:559
- Curie I, Savitch P (1938) Sur les radio-éléments formés dans l'uranium irradié par les neutrons II. *J Phys Radium* 9:355
- Curie M (1902) Sur le poids atomique du radium. *Compt Rend* 135:161
- Curie P, Curie MS (1898) Sur une substance nouvelle radio-active, contenue dans la pechblende. *Compt Rend* 127:175
- Curie P, Curie M, Bémont G (1898) Sur une nouvelle substance fortement radio-active contenue dans la pechblende. *Compt Rend* 127:1215
- Curtis L, Cassen B (1952) Speeding up and improving contrast of thyroid scintigrams. *Nucleonics* 10(9):58
- D'Agostino O (1935) Nuovi elementi radioattivi artificiale. *Gazz Chim Ital* 65:1071
- Davis R Jr, Harmer DS, Hoffman KC (1968) Search for neutrinos from the sun. *Phys Rev Lett* 20:1205
- Debierne A (1899) Sur une nouvelle matière radio-active. *Compt Rend* 129:593
- Demarçay E (1898) Sur l'espectre d'une substance radio-active. *Compt Rend* 127:1218
- Dostrovsky I, Fraenkel Z, Friedlander G (1959) Monte Carlo calculations of nuclear evaporation processes III, Applications to low-energy reactions. *Phys Rev* 116:683
- Düllmann Ch, Bröchle W, Dressler R et al (2002) Chemical investigation of hassium (element 108). *Nature* 418:859
- Eckelman WC, Richards P (1970) Instant ^{99m}Tc DTPA. *J Nucl Med* 11:761
- Eddington AS (1926) The source of stellar energy. *Nature* 117(Suppl):25
- Eichler R, Bröchle W, Dressler R et al (2000) Chemical characterization of bohrium (element 107). *Nature* 407:63
- Elsasser WR (1933) Sur le principe de Pauli dans les noyaux I. *J Phys Radium* 4:549
- Elsasser WR (1934) Sur le principe de Pauli dans les noyaux II, III. *J Phys Radium* 5:389, 635
- Fajans K (1913) Die Stellung der Radioelemente im Periodischen System. *Physik Z* 14:136
- Faure G, Powell JL (1972) Strontium isotope geology. Springer, Berlin
- Fermi E (1934a) Versuch einer Theorie der β -Strahlen. *Z Phys* 88:161
- Fermi E (1934b) Possible production of elements of atomic number higher than 92. *Nature* 133:898
- Fermi E, Amaldi E, D'Agostino O et al (1934) Artificial radioactivity produced by neutron bombardment. *Proc Roy Soc A (Lond)* 146:483
- Fermi E, Rasetti F (1935) Ricerche sui neutroni lenti. *Nuovo Cimento* 12:201
- Fiset EO, Nix JR (1972) Calculations of half-lives for superheavy nuclei. *Nucl Phys A* 193:647
- Flerov GN, Petrzhak KA (1940) Spontaneous fission of uranium. *Phys Rev* 58:89
- Flerov GN, Oganessian YuTs, Lobanov YuV et al (1971) On the synthesis of element 105. *Nucl Phys A* 160:181
- Fowler WA (1984) Experimental and theoretical nuclear astrophysics, The quest for the origin of the elements. *Rev Mod Phys* 56:149
- Frenkel Y (1936) Über das Festkörpermodell schwerer Kerne. *Physik Z Sowj* 9:533
- Fricke B (1975) Superheavy elements. A prediction of their chemical and physical properties. *Struct Bond* 21:89
- Friedlander G, Kennedy JW (1949) Introduction to radiochemistry. Wiley, New York
- Friedlander G, Kennedy JW (1955) Nuclear and radiochemistry. Wiley, New York
- Frisch OR (1939) Physical evidence for the division of heavy nuclei under neutron bombardment. *Nature* 143:276

- Gäggeler HW, Jost DT, Kovacs U et al (1992) Gas phase chromatography experiments with bromides of tantalum and element 105. *Radiochim Acta* 57:93
- Gamow G (1928) Zur Quantentheorie des Atomkerns. *Z Phys* 51:204
- Gamow G (1929) Über die Struktur der Atomkerne. *Physik Z* 30:717
- Gamow G (1946) Expanding universe and the origin of elements. *Phys Rev* 70:572
- Geiger H, Müller W (1928) Elektronenzählrohr zur Messung schwächster Aktivitäten. *Naturwiss* 16:617
- Geiger H, Nuttall JM (1911) The ranges of the α -particles from various radioactive substances and a relation between range and period of transformation. *Phil Mag* 22:613
- Gentner W, Kley W (1955) Zur geologischen Altersbestimmung nach der Kalium-Argon-Methode. *Z Naturforsch* 10a:832
- Ghiorso A, Harvey BG, Choppin GR et al (1955a) New element mendelevium, atomic number 101. *Phys Rev* 98:1518
- Ghiorso A, Thompson SG, Higgins GH et al (1955b) New elements einsteinium and fermium, atomic numbers 99 and 100. *Phys Rev* 99:1048
- Ghiorso A, Nurmia M, Eskola K et al (1970) New element hahnium, atomic number 105. *Phys Rev Lett* 24:1498
- Giesel F (1902) Über Radium und radioaktive Stoffe. *Ber Dtsch Chem Ges* 35:3608
- Glückauf E, Fay JWJ (1936) Direct production of organic compounds containing artificial radioelements. *J Chem Soc* 1936:390
- Green JH, Maddock AG (1949) (n, γ) Recoil effects in potassium chromate and dichromate. *Nature* 164:788
- Guillaumont R, Adloff JP, Peneloux A (1989) Kinetic and thermodynamic aspects of tracer-scale and single-atom chemistry. *Radiochim Acta* 46:169
- Guillaumont R, Adloff JP, Peneloux A et al (1991) Sub-tracer scale behaviour of radionuclides, Application to actinide chemistry. *Radiochim Acta* 54:1
- Gurney RW, Condon EU (1928) Wave mechanics and radioactive disintegration. *Nature* 122:439
- Gurney RW, Condon EU (1929) Quantum mechanics and radioactive disintegration. *Phys Rev* 33:127
- Hahn O (1922) Über das Uran Z und seine Muttersubstanz. *Z Physik Chem* 103:461
- Hahn O (1936) Applied radiochemistry. Cornell University Press, Ithaca
- Hahn O, Meitner L (1918) Die Muttersubstanz des Actiniums, ein neues radioaktives Element von langer Lebensdauer. *Physik Z* 19:208
- Hahn O, Meitner L, Strassmann F (1936) Neue Umwandlungs-Prozesse bei Neutronen-Bestrahlung des Urans: Elemente jenseits Uran. *Ber Dtsch Chem Ges* 69:905
- Hahn O, Strassmann F (1939a) Über den Nachweis und das Verhalten der bei der Bestrahlung des Urans mittels Neutronen entstehenden Erdalkalimetalle. *Naturwiss* 27:11
- Hahn O, Strassmann F (1939b) Nachweis der Entstehung aktiver Bariumisotope aus Uran und Thorium durch Neutronenbestrahlung, Nachweis weiterer aktiver Bruchstücke bei der Uranspaltung. *Naturwiss* 27:89
- Hahn O, Strassmann F, Mattauch J et al (1943) Geologische Altersbestimmung mit der Strontiummethode. *Chemiker Ztg* 67:55
- Hamilton JG, Soley MH (1939) Studies in iodine metabolism by the use of a new radioactive isotope of iodine. *Am J Physiol* 127:557
- Hamilton JG, Soley MH (1940) Studies in iodine metabolism of the thyroid gland in situ by the use of radio-iodine in normal subjects and in patients with various types of goiter. *Am J Physiol* 131:135
- Haxel O, Jensen JHD, Suess HE (1950) Modellmässige Deutung der ausgezeichneten Nukleonenzahlen im Kernbau. *Z Phys* 128:295
- Herrmann G (1979) Superheavy-element research. *Nature* 280:543
- Herrmann G (2003) Historical reminiscences. In: Schädel M (ed) *The chemistry of the superheavy elements*. Kluwer, Dordrecht, pp 291–316
- Herrmann G, Trautmann N (1982) Rapid chemical methods for identification and study of short-lived nuclides. *Ann Rev Nucl Part Sci* 32:117
- Hevesy G (1915) Über den Austausch der Atome zwischen festen und flüssigen Phasen. *Physik Z* 16:52
- Hevesy G (1923) Absorption and translocation of lead by plants, A contribution to the application of the method of radioactive indicators to the investigation of the change of substance in plants. *Biochem J* 17:439
- Hevesy G, Levi H (1936) The action of neutrons on rare earth elements. *Danske Vidensk Selsk Mat-fys Medd* 14, No. 5
- Hevesy G, Paneth F (1913) Die Löslichkeit des Bleisulfids und Bleichromats. *Z Anorg Chem* 82:323
- Hofmann S, Reisdorf W, Münzenberg G et al (1982) Proton radioactivity of ^{151}Lu . *Z Phys A* 305:111
- Hönigschmid O, Horowitz S (1914) Sur le poids atomique du plomb de la pechblende. *Compt Rend* 158:1796
- Ido T, Wan C-N, Casella V et al (1978) Labeled 2-deoxy-D-glucose analogs, ^{18}F -labeled 2-deoxy-2-fluoro-D-glucose, 2-deoxy-2-fluoro-D-mannose and ^{14}C -2-deoxy-2-fluoro-D-glucose. *J Labelled Compd Radiopharm* 14:175
- IUPAC (1997) International Union of Pure and Applied Chemistry: names and symbols of transfermium elements. *Pure Appl Chem* 69:2471
- Jauncey GEM (1946) The early years of radioactivity. *Am J Phys* 14:226

- Jones AG (1995) Technetium in nuclear medicine. *Radiochim Acta* 70/71:289
- Kamen MD (1963) Early history of carbon-14. *Science* 140:584
- Katz JJ, Morss LR, Seaborg GT (1986) Summary and comparative aspects of the actinide elements. In: Katz JJ, Seaborg GT, Morss LR (eds) *The chemistry of the actinide elements*, 2nd edn. Chapman & Hall, London, pp 1121–1193
- Kaufmann R, Wolfgang R (1959) Complex nucleon transfer reaction of heavy ions. *Phys Rev Lett* 3:232
- Kaufmann R, Wolfgang R (1961) Nucleon transfer reactions in grazing collisions of heavy ions. *Phys Rev* 121:192
- Kennedy JW, Seaborg GT, Segrè E, Wahl AC (1946) Properties of 94 (239). *Phys Rev* 70:555
- Kim JL (1986) Chemical behaviour of transuranic elements in natural aquatic systems. In: Freeman AJ, Keller C (eds) *Handbook on the physics and chemistry of the actinides*, vol 4. North-Holland, Amsterdam, pp 413–455
- Kirsten T (1978) Time and the solar system. In: Dermott SF (ed) *Origin of the solar system*. Wiley, Chichester, pp 267–346
- Kluge H-J, Bollen G (1992) Ion traps: recent applications and developments. *Nucl Instr Meth B* 70:473
- Kratz JV, Zimmermann HP, Scherer UW et al (1989) Chemical properties of element 105 in aqueous solution, Halide complex formation and anion exchange into triisooctyl amine. *Radiochim Acta* 48:121
- Lawrence EO, Livingston MS (1931) The production of high-speed protons without the use of high voltages. *Phys Rev* 38:834
- Lebowitz E, Greene MW, Fairchild R et al (1975) Thallium-201 for medical use. *J Nucl Med* 16:151
- Libby WF (1946) Atmospheric helium three and radio-carbon from cosmic radiation. *Phys Rev* 69:671
- Libby WF (1952) Radiocarbon dating. University of Chicago Press, Chicago
- Litherland AE (1980) Ultrasensitive mass spectrometry with accelerators. *Ann Rev Nucl Part Sci* 30:437
- Livingston MS, Blewett JP (1962) *Particle accelerators*. McGraw-Hill, New York
- Marckwald W (1903) Über den radioaktiven Bestandtheil des Wismuths aus Joachimsthaler Pechblende. *Ber Dtsch Chem Ges* 36:2662
- Marinsky JA, Glendenin LE, Coryell CD (1947) The chemical identification of radioisotopes of neodymium and of element 61. *J Am Chem Soc* 69:2781
- Maurette M (1976) Fossil nuclear reactors. *Ann Rev Nucl Sci* 26:319
- Mayer MG (1950) Nuclear configurations in the spin-orbit coupling model I, Empirical evidence. *Phys Rev* 78:16; II, Theoretical considerations. *Phys Rev* 78:22
- McMillan E (1939) Recoils from uranium activated by neutrons. *Phys Rev* 55:510
- McMillan E, Abelson PH (1940) Radioactive element 93. *Phys Rev* 57:1185
- Meitner L, Frisch OR (1939) Disintegration of uranium by neutrons. A new type of nuclear reaction. *Nature* 143:239
- Meitner L, Hahn O, Strassmann F (1937) Über die Umwandlungsreihen des Urans, die durch Neutronenbestrahlung erzeugt werden. *Z Phys* 106:249
- Meldner H (1966) Predictions of new magic regions and masses for super-heavy nuclei from calculations with realistic shell model single particle Hamiltonians. In: Forsling W, Herrlander CJ, Ryde H (eds) *Nuclides far off the stability line*, Almqvist & Wiksell, Stockholm, pp 593–601; also *Arkiv Fysik* 36:593
- Metropolis N, Bivins R, Storm M et al (1958a) Monte Carlo calculations on intranuclear cascades I, Low-energy studies. *Phys Rev* 110:185
- Metropolis N, Bivins R, Storm M et al (1958b) Monte Carlo calculations on intranuclear cascades II, High energy studies and pion processes. *Phys Rev* 110:204
- Meyer St, Hess VF, Paneth F (1914) Neue Reichweitenbestimmungen an Polonium, Ionium und Actiniumpräparaten. *Sitzungsber Akad Wiss Wien, Math-naturw Kl IIa* 123:1459
- Meyer St, Schweidler ER von (1916, 1927) Radioaktivität, 1st and 2nd edn. B. G. Teubner, Leipzig.
- Molinski VI (1982) A review of ^{99m}Tc generator technology. *Int J Appl Radiat Isot* 33:811
- Moseley HGJ (1913, 1914) The high-frequency spectra of the elements I. *Phil Mag* 26:1024; II *Phil Mag* 27:703
- Mössbauer RL (1958) Kernresonanzfluoreszenz von Gammastrahlung in ^{191}Ir . *Z Phys* 151:124
- Mössbauer RL (1962) Recoilless nuclear resonance absorption. *Ann Rev Nucl Sci* 12:123
- Mueller AC, Sherrill BM (1993) Nuclei at the limits of particle stability. *Ann Rev Nucl Part Sci* 43:529
- Münzenberg G, Hofmann S, Hessberger FP et al (1981) Identification of element 107 by correlation chains. *Z Phys A* 300:107
- Münzenberg G, Armbruster P, Hessberger FP et al (1982) Observation of one correlated α -decay in the reaction ^{58}Fe on $^{209}\text{Bi} \rightarrow ^{267}\text{109}$. *Z Phys A* 309:89
- Myers WD, Swiatecki WJ (1966) Nuclear masses and deformations. *Nucl Phys* 81:1
- Neuilly M, Bussac J, Frèjaques C et al (1972) Sur l'existence dans un passé reculé d'une réaction en chaîne naturelle de fissions, dans le gisement d'uranium d'Oklo (Gabon). *Compt Rend D* 275:1847
- Nier AO (1935) Evidence for the existence of an isotope of potassium of mass 40. *Phys Rev* 48:283
- Nier AO (1938) Variations in the relative abundances of the isotopes of common lead from various sources. *J Am Chem Soc* 60:1571

- Nier AO, Booth ET, Dunning JR et al (1940) Nuclear fission of separated uranium isotopes. *Phys Rev* 57:546, 748
- Nilsson SG (1955) Binding states of individual nucleons in strongly deformed nuclei. *Danske Vidensk Selsk Mat-fys Medd* 29, No. 16
- Nilsson SG, Thompson SG, Tsang CF (1969) Stability of superheavy nuclei and their possible occurrence in nature. *Phys Lett B* 28:458
- Oganessian YuTs, Iljinov A, Demin AG et al (1975) Experiments on the production of fermium neutron-deficient isotopes and new possibilities of synthesizing elements with $Z > 100$. *Nucl Phys A* 239:353
- Oganessian YuTs, Utyonkov VK, Lobanov YuV et al (2000a) Synthesis of superheavy nuclei in the $^{48}\text{Ca} + ^{244}\text{Pu}$ reaction: $^{288}114$. *Phys Rev C* 62:041604
- Oganessian YuTs, Utyonkov VK, Lobanov YuV et al (2000b) Observation of the decay of $^{292}116$. *Phys Rev C* 63:011301
- Oppenheimer JR, Phillips M (1935) Note on the transmutation function for deuterons. *Phys Rev* 48:599
- Otten EW (1989) Nuclear radii and moments of unstable isotopes. In: Bromley DA (ed) *Treatise on heavy-ion science*, vol 8. Plenum, New York, pp 517–638
- Paneth FA, Reasbeck P, Mayne KI (1953) Production by cosmic rays of helium-3 in meteorites. *Nature* 172:200
- Patterson C (1956) Age of meteorites and the Earth. *Geochim Cosmochim Acta* 10:230
- Pauli W (1994) On the earlier and more recent history of the neutrino. In: Pauli W (ed) *Writings on physics and philosophy* (English trans: Enz CP, von Meyenn K). Springer, Berlin, pp 193–217
- Perey M (1939a) Sur un élément 87, dérivé de l'actinium. *Compt Rend* 208:97
- Perey M (1939b) L'élément 87: AcK, dérivé de l'actinium. *J Phys Radium* 10:435
- Perrier C, Segrè E (1937a) Radioactive isotopes of element 43. *Nature* 140:193
- Perrier C, Segrè E (1937b) Some chemical properties of element 43. *J Chem Phys* 5:712
- Perrin J (1919) Matière et lumière, Essai de synthèse de la mécanique chimique #49: L'évolution des astres. *Ann Physique* 11:89
- Petrzhak KA, Flerov GN (1940) Über die spontane Teilung von Uran. *Compt Rend Acad Sci URSS* 28:500
- Piggott CS (1936) Apparatus to secure core samples from the ocean bottom. *Bull Geol Soc Am* 47:675
- Pitzer KS (1975) Are elements 112, 114, and 118 relatively inert gases? *J Chem Phys* 63:1032
- Polikanov SM, Druin VA, Karnaukhov VA et al (1962) Spontaneous fission with an anomalously short period. *Sov Phys JETP* 15:1016; *J Exptl Theor Phys USSR* 42:1464
- Pontecorvo B (1935) Sulle proprietà dei neutroni lenti. *Nuovo Cimento* 12:211
- Price WJ (1958, 1964) *Nuclear radiation detection*, 1st and 2nd edn. McGraw-Hill, New York
- PUAE (1956) *Proceedings of the international conference on the peaceful uses of atomic energy*, vols 1–17. United Nations, New York
- Ravn HL (1979) Experiments with intense secondary beams of radioactive ions. *Phys Rep* 54:201
- Reines F, Cowan CL (1953) Detection of the free neutrino. *Phys Rev* 92:830
- Reines F, Cowan CL, Harrison FB et al (1960) Detection of the free antineutrino. *Phys Rev* 117:159
- Rhodes R (1986) *The making of the atomic bomb*. Simon & Schuster, New York
- Richards P, Tucker WD, Srivastava SC (1982) Technetium-99m: an historical perspective. *Int J Appl Radiat Isot* 33:793
- Richards TW, Lambert ME (1914) The atomic weight of lead of radioactive origin. *J Am Chem Soc* 36:1309
- Rieder W, Broda E, Erber J (1950) Dissoziation von Permanganationen durch lokale Energiezufuhr. *Monatsh Chem* 81:656
- Roberts RB, Hafstad LR, Meyer RC et al (1939) The delayed neutron emission which accompanies fission of uranium and thorium. *Phys Rev* 55:664
- Rose HJ, Jones GA (1984) A new kind of natural radioactivity. *Nature* 307:245
- Rosenblum S (1930) Structure fine du spectre magnétique des rayons α . *Compt Rend* 190:1124
- Ruben S, Kamen MD (1940a) Radioactive carbon of long half-life. *Phys Rev* 57:549
- Ruben S, Kamen MD (1940b) Photosynthesis with radioactive carbon IV, Molecular weight of the intermediate products and a tentative theory of photosynthesis. *J Am Chem Soc* 62:3451
- Ruben S, Kamen MD (1941) Long-lived radioactive carbon: C^{14} . *Phys Rev* 59:349
- Ruben S, Kamen M, Hassid WZ (1940) Photosynthesis with radioactive carbon II, Chemical properties of the intermediates. *J Am Chem Soc* 62:3443
- Rutherford E (1900) A radio-active substance emitted from thorium compounds. *Phil Mag* 49:1
- Rutherford E (1906) The mass and velocity of the α particles expelled from radium and actinium. *Phil Mag* 12:348
- Rutherford E (1911) The scattering of α and β particles by matter and the structure of the atom. *Phil Mag* 21:669
- Rutherford E (1919) Collision of α particles with light atoms IV, An anomalous effect in nitrogen. *Phil Mag* 37:581
- Rutherford E, Soddy F (1902) The cause and nature of radioactivity I, II. *Phil Mag* 4:370, 569
- Rutherford E, Soddy F (1903) Radioactive change. *Phil Mag* 5:576

- Schädel M, Brüchle W, Dressler R et al (1997) Chemical properties of element 106 (seaborgium). *Nature* 388:55
- Schaeffer OA (1968) Nuclear chemistry of the earth and meteorites. In: Yaffe L (ed) *Nuclear chemistry*, vol 2. Academic, New York, pp 371–393
- Schaeffer OA, Zähringer J (1966) Potassium-argon dating. Springer, Berlin
- Schroeder WU, Huizenga JR (1977) Damped heavy-ion collisions. *Ann Rev Nucl Sci* 27:465
- Seaborg GT (1940) Artificial radioactivity. *Chem Revs* 27:199
- Seaborg GT (1945) The chemical and radioactive properties of the heavy elements. *Chem Eng News* 23:2190
- Seaborg GT (1954) Coordination of properties as actinide transition series. In: Seaborg GT, Katz JJ (eds) *The actinide elements*. McGraw-Hill, New York, pp 733–768
- Seaborg GT, Katz JJ (eds) (1954) *The actinide elements*. McGraw-Hill, New York
- Seaborg GT, Wahl AC (1948) The chemical properties of elements 94 and 93. *J Am Chem Soc* 70:1128
- Seaborg GT, McMillan EM, Kennedy JW, Wahl AC (1946a) Radioactive element 94 from deuterons on uranium. *Phys Rev* 69:366
- Seaborg GT, Wahl AC, Kennedy JW (1946b) Radioactive element 94 from deuterons on uranium. *Phys Rev* 69:367
- Seaborg GT, James RA, Morgan LO (1949a) The new element americium (atomic number 95). In: Seaborg GT, Katz JJ, Manning WM (eds) *The transuranium elements, research papers II*. McGraw-Hill, New York, pp 1525–1553
- Seaborg GT, James RA, Ghiorso A (1949b) The new element curium (atomic number 96). In: Seaborg GT, Katz JJ, Manning WM (eds) *The transuranium elements, research papers II*. McGraw-Hill, New York, pp 1554–1571
- Seelmann-Eggebert W, Strassmann F (1947) Über die bei der Uranspaltung noch zu erwartenden Bruchstücke. *Z Naturforsch* 2a:80
- Segrè E, Halford RS, Seaborg GT (1939) Chemical separation of nuclear isomers. *Phys Rev* 55:321
- Serber R (1947) Nuclear reactions at high energies. *Phys Rev* 72:1114
- Siegel JM (1946) Nuclei formed in fission: decay characteristics, fission yields, and chain relationships. *J Am Chem Soc* 68:2411
- Silva RJ (1986) Transeinsteinium elements. In: Katz JJ, Seaborg GT, Morss LR (eds) *The chemistry of the actinide elements*, 2nd edn. Chapman & Hall, London, pp 1085–1115
- Skłodowska Curie M (1898) Rayons émis par les composés de l'uranium et du thorium. *Compt Rend* 126:1101
- Sobiczewski A, Gareev FA, Kalinkin BN (1966) Closed shells for $Z > 82$ and $N > 128$ in a diffuse potential well. *Phys Lett B* 22:500
- Soddy F (1911) Radioactivity. *Ann Rep Progr Chem* 7:285
- Soddy F (1913a) Intra-atomic charge. *Nature* 92:400
- Soddy F (1913b) The radio-elements and the periodic law. *Chem News* 107:97
- Soddy F (1975) In: Trenn TT (ed) *Radioactivity and atomic theory: facsimile reproduction of the annual progress reports on radioactivity 1904–1920 to the chemical society by Frederick Soddy F.R.S.* Taylor & Francis, London
- Stöcklin G, Pike VW (eds) (1993) *Radiopharmaceuticals for positron emission tomography: methodological aspects*. Kluwer, Dordrecht
- Strassmann F, Hahn O (1942) Über die Isolierung und einige Eigenschaften des Elements 93. *Naturwiss* 30:256
- Strutinsky VM (1967) Shell effects in nuclear masses and deformation energies. *Nucl Phys A* 95:420
- Suess HE, Urey HC (1956) Abundances of the elements. *Rev Mod Phys* 28:53
- Szilard L, Chalmers TA (1934) Chemical separation of the radioactive element from its bombarded isotope in the Fermi effect. *Nature* 134:462
- Tanihata I, Hamagaki H, Hashimoto O et al (1985) Measurements of interaction cross sections and nuclear radii in the light p-shell region. *Phys Rev Lett* 55:2676
- Thompson SG, Ghiorso A, Seaborg GT (1950a) Element 97. *Phys Rev* 77:838
- Thompson SG, Street K Jr, Ghiorso A, Seaborg GT (1950b) Element 98. *Phys Rev* 78:298
- Thomson JJ (1913) Positive rays of electricity. *Nature* 91:362
- Urey HC, Brickwedde FG, Murphy GM (1932) Hydrogen isotope of mass 2 and its concentration. *Phys Rev* 40:1
- Van de Graaff RJ, Compton KT, Van Atta LC (1933) Electrostatic production of high voltage. *Phys Rev* 43:149
- von Gunten HR (1969) Distribution of mass in spontaneous and neutron-induced fission. *Actinide Revs* 1(4):275
- Wahl AC, Bonner NA (1951) *Radioactivity applied to chemistry*. Wiley, New York
- Watters RL, Hakanson TE, Lane LJ (1983) The behavior of actinides in the environments. *Radiochim Acta* 32:89
- Weizsäcker CF von (1935) Zur Theorie der Kernmassen. *Z Phys* 96:431
- Weizsäcker CF von (1937) Über die Möglichkeit eines dualen β -Zerfalls von Kalium. *Physik Z* 38:623
- Wetherill GW (1971) Of time and the Moon. *Science* 173:383

- Wetherill GW (1975) Radiometric chronology of the early solar system. *Ann Rev Nucl Sci* 25:283
- Wilczynski J, Volkov VV, Decowski P (1967) Some features of the mechanism of many-neutron-transfer reactions. *Sov J Nucl Phys* 5:672; *Yad Fiz* 5:942
- Wilkins BD, Steinberg EP, Chasman RR (1976) Scission-point model of nuclear fission based on deformed-shell effects. *Phys Rev C* 14:1832
- Wilkinson DH, Wapstra AH, Uehla I et al (1993) Discovery of the transfermium elements, Report of the Transfermium Working Group of IUPAC and IUPAP II, Introduction to discovery profiles, III, Discovery profiles of the transfermium elements. *Pure Appl Chem* 65:1757, 1764
- Willard JE (1953) Chemical effects of nuclear transformations. *Ann Rev Nucl Sci* 3:193
- Wolf AP (1960) Labeling of organic compounds by recoil methods. *Ann Rev Nucl Sci* 10:259
- Wolf AP (1964) The reactions of energetic tritium and carbon atoms with organic compounds. *Adv Phys Organ Chem* 2:201
- Wolf AP, Redvanly CS (1977) Carbon-11 and radiopharmaceuticals. *Int J Appl Radiat Isot* 28:29
- Yalow RS (1978) Radioimmunoassay: A probe for the fine structure of biologic systems. *Science* 200:1236
- Yankwich PE, Rollefson GK, Norris TH (1946) Chemical forms assumed by C^{14} produced by neutron irradiation of nitrogenous substances. *J Chem Phys* 14:13
- Zvara I, Belov VZ, Domanov VP et al (1971) Chemical isolation of kurchatovium. *Sov Radiochem* 14:115; *Radiokhimiya* 14:119



2 Basic Properties of the Atomic Nucleus

T. Fényes

Institute of Nuclear Research of the Hungarian Academy of Sciences,
Debrecen, Hungary

2.1	<i>Nucleons and Nuclear Forces</i>	41
2.1.1	Fundamental Constituents and Interactions of Matter	41
2.1.2	Properties of Nuclear Forces	44
2.1.2.1	General Properties of Nuclear Forces	44
2.1.2.2	Phenomenological Nucleon–Nucleon Potentials	46
2.1.2.3	Nucleon–Nucleon Potentials from Meson Field Theories	49
2.2	<i>Properties of Nuclei</i>	51
2.2.1	Nuclear Mass and Binding Energy	51
2.2.2	Spin, Electric, and Magnetic Moments	53
2.2.2.1	Spin	53
2.2.2.2	Electric Moments	53
2.2.2.3	Magnetic Moments	55
2.2.2.4	Experimental Nuclear Moments	56
2.2.3	Size, Parity, and Isospin of Nuclei	57
2.2.3.1	Nuclear Size	57
2.2.3.2	Parity	60
2.2.3.3	Isospin	61
2.2.4	Chart of the Nuclides	61
2.3	<i>Nuclear States and Excitations</i>	63
2.3.1	Shell Model of Atomic Nuclei	63
2.3.1.1	Closed Shells in Atomic Nuclei	63
2.3.1.2	Independent-Particle Shell Model	64
2.3.1.3	Shell Model with Multiparticle Configurations	69
2.3.1.4	Shell Model of Deformed Nuclei	70
2.3.1.5	Calculation of the Total Energy of Nuclei	73
2.3.2	Nuclear Transitions, γ Decay, Conversion Electrons	75
2.3.2.1	Basic Experimental Facts	75
2.3.2.2	Theory of γ Decay	77
2.3.2.3	Experimental γ -Ray Transition Rates: Isomeric States	81
2.3.3	Vibrational Motion	84
2.3.3.1	Basic Experimental Facts	84
2.3.3.2	Theory of Nuclear Vibration: Comparison with Experimental Data	85
2.3.4	Rotational Motion	89

2.3.4.1	Basic Experimental Facts	89
2.3.4.2	Theory of Nuclear Rotation: Comparison with Experimental Data	93
2.3.5	Interacting Boson Models	101
2.3.6	Clustering	107
2.3.7	Recent Developments	109
2.3.7.1	Effective Interactions	109
2.3.7.2	Few Nucleon Systems, Ab Initio Calculations	110
2.4	<i>Nuclear Decay</i>	112
2.4.1	Alpha Decay	112
2.4.1.1	Basic Experimental Facts	112
2.4.1.2	One-Body Theory of α Decay	117
2.4.1.3	Microscopic Theories of α Decay	119
2.4.2	Beta Decay	123
2.4.2.1	Basic Experimental Facts	123
2.4.2.2	Theory of β Decay	127
2.4.2.3	Types of the Weak Interaction	134
2.4.2.4	Selection Rules in β Decay	135
2.4.2.5	Parity Nonconservation in β Decay	135
2.4.3	Special Decay Modes	136

Abstract: In this chapter, four topics are treated. (1) Fundamental constituents and interactions of matter and the properties of nuclear forces (experimental facts and phenomenological and meson-field theoretical potentials). (2) Properties of nuclei (mass, binding energy, spin, moments, size, parity, isospin, and characteristic level schemes). (3) Nuclear states and excitations and individual and collective motion of the nucleons in the nuclei. Description of basic experimental facts and their interpretation in the framework of shell, collective, interacting boson, and cluster models. The recent developments, few nucleon systems, and ab initio calculations are also shortly discussed. (4) In the final section, the α - and β -decays, as well as the special decay modes observed far off the stability region are treated.

2.1 Nucleons and Nuclear Forces

2.1.1 Fundamental Constituents and Interactions of Matter

According to the present knowledge of the science community, the *fundamental constituents* of matter are *quarks* and *leptons*. Both quarks and leptons are pointlike and structureless on a scale of $\leq 10^{-17}$ m. These particles may interact with each other via four apparently different fundamental interactions: strong, weak, electromagnetic, and gravitational interactions. It is generally accepted that any interaction is mediated by the exchange of specific interaction quanta. Some of the most important properties of quarks and leptons are summarized in [Table 2.1](#). The table contains also the properties of quanta of electromagnetic, weak, and strong interactions. (For a detailed review of particle properties see Particle Data Group [2008](#).) The characteristic scale for gluons is < 0.1 fm (i.e., $< 10^{-16}$ m).

Quarks and gluons have quantum numbers called “color.” The primary, basic colors may be called red, green, and blue. Of course, these “colors” have no relation to ordinary, real colors. The quarks interact strongly by color exchange, which means that the quanta of the strong interaction, the gluons, are colored objects. All bound states of quarks observed in nature are “colorless” or “white.” Leptons do not have color quantum numbers.

The visible matter consists of atoms, and atoms contain nuclei and electrons. The constituents of atomic nuclei are called *nucleons*. The two types of nucleons are protons and neutrons.

A nucleus containing Z protons and N neutrons (i.e., $A = Z + N$ nucleons) is to be denoted by A_ZX_N , where X is the chemical symbol of the element with Z protons. Nucleons contain quarks of two types: *up* and *down quarks with some additional dynamical (or sea) quark contributions*, i.e., quark–antiquark pairs created and annihilated in very short time intervals. In nuclear decay electrons, positrons, electron neutrinos, and antineutrinos may also be involved. Thus the visible world (nuclei, atoms, and molecules) is built up mainly from up and down quarks, as well as from electrons, electron neutrinos, and the corresponding antiparticles. Quarks and leptons appear in a variety of types or “flavors.” The flavor quantum numbers define three families of particles. The members of the first family are the u , d quarks and e^- , ν_e leptons. The c , s quarks and μ^- , ν_μ leptons belong to the second, the b , t quarks and τ^- , ν_τ leptons to the third family. The heavier quarks and leptons are similar to the lighter ones (with the same electric charges), except mass. At present, it is not known why quarks and leptons are tripled.

Table 2.1

Properties of fundamental constituents of matter: quarks, leptons, and field quanta (gauge bosons). R, G, and B denote red, green, and blue colors. Neutrinos are longitudinally spin-polarized. If Z denotes the direction of velocity, for neutrinos $S_Z = -1/2$ (left-handed), for antineutrinos $S_Z = +1/2$ (right-handed). Associated with quarks and leptons there are antiquarks and antileptons, too, which have exactly the same mass and half-life as their partners, but opposite electric charge and magnetic moment. The antiquarks have anticolors

	Name	Symbol	Rest energy	Electric charge (e)	Spin (\hbar)
F l a v o r	Color				
	Quarks				
	Up	$u(u_R, u_G, u_B)$	1.5–3.3 MeV	+2/3	1/2
	Down	$d(d_R, d_G, d_B)$	3.5–6.0 MeV	−1/3	1/2
	Charmed	$c(c_R, c_G, c_B)$	1.27 GeV	+2/3	1/2
	Strange	$s(s_R, s_G, s_B)$	104 MeV	−1/3	1/2
	Top	$t(t_R, t_G, t_B)$	171.2 GeV	+2/3	1/2
	Bottom	$b(b_R, b_G, b_B)$	4.20 GeV	−1/3	1/2
	Leptons				
	Electron	e^-	0.511 MeV	−1	1/2
	e^- neutrino	ν_e	<2 eV*	0	1/2
	Muon	μ^-	105.658 MeV	−1	1/2
	μ^- neutrino	ν_μ		0	1/2
	Tau	τ^-	1,777 MeV	−1	1/2
	τ^- neutrino	ν_τ		0	1/2
	Field quanta				
	Photon	γ	0	0	1
	Weak Bosons	W^+	80.398 GeV	+1	1
		W^-	80.398 GeV	−1	1
		Z^0	91.188 GeV	0	1
	Gluons ($i = 1 \dots 8$)	g_i	0	0	1

*From tritium decay.
Data from Particle Data Group (2008).

The nucleons interact through their constituents, and their strong interaction can also be depicted as boson exchange. (All interaction quanta are bosons, i.e., particles with integer spins.) The strongly interacting bosons (particles with integer spins), which take part in the nucleon–nucleon interaction, are called *mesons*. These are π^+ , π^0 , π^- , K^+ , K^0 , K^- , η^0 , ρ^+ , ρ^0 , ρ^- , ω^0 , etc.

The common name of strongly interacting fermions (particles with half-integer spins) is *baryon*. The members of the baryon family are the nucleons (protons and neutrons), as well as different *hyperons*: Λ , Σ^+ , Σ^0 , Σ^- , Ξ^0 , Ξ^- , Ω^- , etc.

Hadron is a common name for baryons and mesons, i.e., for strongly interacting particles.

Of the four *fundamental interactions* – strong, electromagnetic, weak, and gravitational – gravity is far the weakest, so it plays no observable role in nuclear physics. All others do. Some of the particles are electrically charged, some are not. The charged particles take part in electromagnetic interactions. Leptons, in addition, enter into weak interactions. Quarks (and antiquarks) interact with all four interactions. The characteristic features of the interactions are summarized in ► [Table 2.2](#).

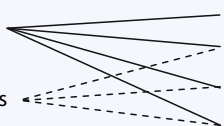
The square of coupling constants, characteristic of the strengths of the interactions, determines the decay probability of the particles and the reaction cross sections primarily. Some examples for the decay and reactions are as follows. (The rest energy of the Δ^{++} baryon is 1,232 MeV.)

Strong interaction	Decay $\Delta^{++} \rightarrow p + \pi^+$
	Reaction $p + \pi \rightarrow p + \pi$
Electromagnetic interaction	Decay $\pi^0 \rightarrow \gamma + \gamma$
	Reaction $p + \gamma \rightarrow p + \pi^0$
Weak interaction	Decay $n \rightarrow p + e^- + \bar{\nu}_e$
	Reaction $p + \bar{\nu}_e \rightarrow n + e^+$

The theories of electromagnetic and weak interactions have been unified in 1967–1968 by Glashow, Salam, and Weinberg. According to the electroweak theory, the coupling of intermediate W^\pm , Z^0 bosons to leptons and quarks is the same, as the coupling of photons to leptons and quarks. Thus, the W^\pm , Z^0 particles behave like heavy photons.

■ **Table 2.2**

Fundamental constituents and interactions of matter according to the “Standard Model.” The data give only rough estimates

Fundamental constituents		Field quanta	Interaction		
<div>Quarks </div> <div>Leptons</div>	Gluon	Strong			
	Photon	Electromagnetic			
	W^{\pm}, Z^0	Weak			
	Graviton	Gravity			
Interactions					
Interaction name	Strong	Electromagnetic	Weak	Gravity	
Source of field	Color charge	Electric charge	Weak charge	Mass	
Relative strength	~ 1 , large distance	$\sim 1/137$	$\sim 10^{-6}$	$\sim 5 \times 10^{-39}$	
	< 1 , small distance				
Range (m)	$\leq 10^{-15}$	∞	$\sim 10^{-18}$	∞	
Typical lifetimes (s)	$10^{-22} - 10^{-24}$	$10^{-18} - 10^{-20}$	$> 10^{-12}$	—	
Typical cross sections (cm ²)	10^{-26}	—	10^{-38}	—	

■ **Table 2.3**

Properties of nucleons (p, n). Quark structure: {symbol, electric charge (e), spin (h) and its direction}. There are three valence quarks both in p and n, such that they are colorless

Particle	Antiparticle	Rest energy	Electric charge	Spin (\hbar),	Isospin		Mean life
		(MeV)	(e)	parity	T	T_z	(s)
{p, 1, 1/2 ↑} = {u, 2/3, 1/2 ↑} + {u, 2/3, 1/2 ↑} + {d, −1/3, 1/2 ↓}							
{n, 0, 1/2 ↑} = {u, 2/3, 1/2 ↑} + {d, −1/3, 1/2 ↑} + {d, −1/3, 1/2 ↓}							
Properties							
p	\bar{p}	938.2720	+1	1/2 ⁺	1/2	+1/2	∞
n	\bar{n}	939.5654	0	1/2 ⁺	1/2	−1/2	885.7

The weak interactions change quark and lepton “flavors,” e.g., a d -quark into u -quark or a muon into an electron (this latter, e.g., in the $\mu^- \rightarrow e^- \bar{\nu}_e \nu_\mu$ process). The quark structures of the proton and neutron as well as the *properties of nucleons* are presented in ▶ [Table 2.3](#). The baryons are built up from three (valence) quarks and massless gluons, but they contain also dynamical (or sea) quarks (quark–antiquark pairs) in a small quantity. The mesons are built up from quark–antiquark pairs and gluons.

The radii of nucleons (see later ▶ [Sect. 2.2.3](#)) can be determined, e.g., from different scattering (i.e., elastic collision) experiments. For the proton the following charge radius has been obtained: 0.875 ± 0.007 fm. The sizes of mesons are between the scales of nucleonic (~ 1 fm) and quark (< 0.01 fm) constituents.

2.1.2 Properties of Nuclear Forces

2.1.2.1 General Properties of Nuclear Forces

One can get *experimental information* on the nucleon–nucleon (NN) interaction from the following sources.

- Properties of the deuteron, the simplest bound-state nuclear system (binding energy, spin, parity, magnetic dipole and electric quadrupole moments, size of the nucleus).
- Characteristic features of the nucleon–nucleon (np, pp, nn) scattering at low, intermediate, and high bombarding energies (differential and integral cross sections, scattering length, effective range, phase shift, polarization, etc.).
- Scattering of pions and heavier mesons on nucleons, pion–pion interaction.
- Properties of light and heavy nuclei (binding energy, volume, density, nuclear moments, excitation levels, compressibility, etc.).

Next some *elementary experimental results* concerning nuclear forces are shortly enumerated.

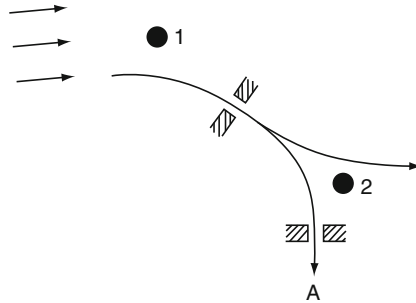
- Nuclear forces are able to keep the nuclei in stable, bound states, in spite of the electric repulsion acting among protons. Consequently, the nuclear forces are basically attractive.
- Rutherford’s α scattering and later the proton–proton scattering experiments have shown that if the interparticle distance in the course of the collision is $> 10^{-14}$ m, only Coulomb

force acts between the particle and nucleus. Thus, the range of nuclear forces, which could modify the scattering picture, is small.

- The proton separation energies (S_p) generally increase with increasing neutron number (N) and neutron separation energies (S_n) increase with increasing proton number (Z). Consequently, a strong attractive interaction must exist between protons and neutrons.
- On the other hand, proton separation energies generally decrease with increasing Z (at constant N) and neutron separation energies decrease with increasing N (at constant Z). This means that the residual interaction (see [Sect. 2.3.1.3](#)) between like nucleons is generally repulsive. An exception from this general rule is the pairing interaction between like nucleons, which causes a fluctuation in the general trends. Nuclei with even numbers of protons and/or neutrons are more stable. There must be a special attractive “pairing” interaction between like nucleons, which couples them to spin-zero, positive parity states.
- Many properties of the deuteron can be explained by supposing that the nuclear potential is central.
- The deuteron occurs in nature only with parallel proton and neutron spin alignments. The spin of even- Z – even- N nuclei in ground state is always zero, and the binding energies in these nuclei are especially large. These facts and also the NN scattering experiments show unambiguously that the nuclear forces depend on the spin states of the nucleons.
- From the study of the deuteron, one can conclude that the nuclear potential energy is ≤ -26 MeV at internucleon distance $d \approx 2 \times 10^{-15}$ m. At the same time, the electrostatic energy of the repulsion between two protons is only ~ 0.7 MeV (at $d = 2 \times 10^{-15}$ m). The magnetic interaction energy, arising from the magnetic dipole moments of the protons is more than one order of magnitude smaller than the electrostatic energy. From these facts it follows that the nuclear interaction is stronger than the electromagnetic, and also the weak and gravitational, interactions ([Table 2.2](#)).
- The similarity of level systems in some light nuclei and also the scattering experiments indicate that the nuclear forces are almost fully independent of the electric charge of nucleons.
- For the interpretation of the observed quadrupole moment of the deuteron, it was necessary to assume that the nucleon–nucleon interaction contains a noncentral, tensor interaction term too (see [Eq. \(2.1\)](#)).
- On the basis of polarization experiments ([Fig. 2.1](#)), one can conclude that the nucleon–nucleon force depends on the relative alignment of the spins with respect to the relative orbital angular momenta. The spin–orbit interaction term depends, indirectly, on the relative velocity.
- The binding energy per nucleon is approximately constant in medium-heavy and heavy nuclei. This property is called the “saturation character” of the nuclear forces. With purely attractive potentials the saturation of nuclear forces cannot be understood. Only the joint effect of a strong repulsion at short distances (≤ 0.5 fm) and the quantum–mechanical exchange interactions can explain the saturation. The existence of strong repulsion at small internucleon distances is shown also by scattering experiments at high energies.
- It is obvious from these properties that the nuclear forces are very intricate. A further complication arises from the fact that many-body interactions (i.e., interactions involving more than three bodies) cannot be treated with exact mathematical methods.
- In principle one cannot exclude the existence of three- or, in general, multinucleon interactions.

■ Fig. 2.1

Schematic drawing of a polarization experiment and illustration of the spin–orbit interaction. The bombarding particle is polarized during the scattering on nucleus No. 1. This means, that its spin will be oriented, e.g., into the reaction plane. As a result, the scattering by nucleus No. 2 will be asymmetric; e.g., more particles will be scattered in direction A than in direction B



- Although the nuclear potentials are very intricate, in simple models one can use short-range, central potentials. The dependence of the nuclear potential on the distance can be approximated in different ways (➤ Fig. 2.2). The parameters of these potentials (such as V_0 , r_0 , R_N , r_c , a) can be adjusted to experimental data. The nuclear force $\mathbf{F}(\mathbf{r})$ is then obtained from the potential by partial derivation: $\mathbf{F}(\mathbf{r}) = -\nabla V(\mathbf{r})$. In quantum mechanics the equation of motion (the Schrödinger equation) contains the potential; therefore the force itself is rarely referred to. This makes it possible to use the sloppy term “force” for the potential itself.

If the treatment of the problem requires the introduction of noncentral (tensor, spin–orbit, etc.) interactions, too, the radial dependence of the potential may be different for the different interaction terms.

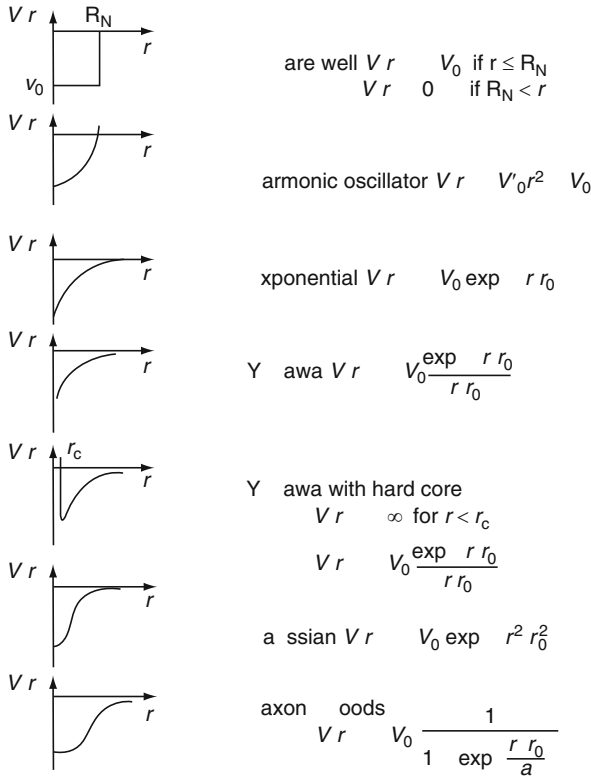
2.1.2.2 Phenomenological Nucleon–Nucleon Potentials

Experience shows that the nuclear forces are very complicated. Therefore, in the construction of phenomenological NN potentials, some general principles are invoked. Such as:

- Limitations from space–time symmetry considerations: translational and Galilean invariances, space reflection and time reversal invariances, rotational invariance in space, and invariance with respect to exchanging neutrons with protons (charge invariance, see ➤ Sect. 2.2.3). These problems are treated in detail, e.g., in Eisenbud and Wigner (1941), Bohr and Mottelson (1969), and Ring and Schuck (1980). It is advisable from the beginning to use only potentials that satisfy the above criteria.
- The generalized Pauli principle allows only certain states for the two-nucleon systems (see, e.g., Fényes 2002).
- As mentioned above, it is generally accepted that all four basic interactions of nature (strong, electromagnetic, weak, and gravitational) are mediated by field quanta. For the nuclear (strong) interaction meson (or, at quark level, gluon) exchange is responsible. The meson field theories have gone through an enormous development from the 1930s,

■ Fig. 2.2

Schematic illustration of simple, central nuclear interaction potentials



and presently they can describe many properties of nuclear forces correctly. Thus, in the construction of NN phenomenological potentials, the predictions of meson field theories are usually taken into account.

- It is usually assumed that the potential energy (V) of a multinucleon system can be composed as a sum of two-nucleon interactions:

$$V(1, 2, \dots, n) = \sum_{i < j=1}^n V(i, j),$$

where n is the number of nucleons. The correctness of this assumption is not perfectly proved, but it seems that one can understand most of the traditional nuclear structure problems without the introduction of three-body forces. For recent results see [Sect. 2.3.7.2](#). Although V is a potential energy, in quantum mechanics it is usually called potential.

In the 1960s, the rapidly growing experimental data made it possible to construct phenomenological potentials that could describe various effects of NN interaction. Such are the Hamada–Johnston potential with hard core (Hamada and Johnston 1962), the Yale potential with hard core (Lassila et al. 1962), the nonlocal Tabakin potential (Tabakin 1964), and the Reid potential with soft core (Reid 1968).

In the hard-core potentials, infinitely strong repulsions are used at distances < 0.5 fm. The Reid potential is also very repulsive in the core region, but it is gradually growing as the distance between the nucleons decreases. The explicit form of the Hamada–Johnston potential is as follows:

$$V = V_C + V_T S_{12} + V_{LS}(\mathbf{LS}) + V_{LL} L_{12}, \quad (2.1)$$

where the subscripts C, T, LS, and LL indicate central, tensor, linear, and quadratic spin–orbit interactions, and

$$V_C(r) = 0.08(0.333m_\pi)(\boldsymbol{\tau}_1 \boldsymbol{\tau}_2)(\boldsymbol{\sigma}_1 \boldsymbol{\sigma}_2)Y(x)[1 + a_c Y(x) + b_c Y^2(x)],$$

$$V_T(r) = 0.08(0.333m_\pi)(\boldsymbol{\tau}_1 \boldsymbol{\tau}_2)Z(x)[1 + a_T Y(x) + b_T Y^2(x)],$$

$$S_{12} = [3(\boldsymbol{\sigma}_1 \mathbf{r})(\boldsymbol{\sigma}_2 \mathbf{r})/r^2] - (\boldsymbol{\sigma}_1 \boldsymbol{\sigma}_2),$$

$$V_{LS}(r) = m_\pi G_{LS} Y^2(x)[1 + b_{LS} Y(x)],$$

$$V_{LL}(r) = m_\pi G_{LL}[Z(x)/x^2][1 + a_{LL} Y(x) + b_{LL} Y^2(x)],$$

$$L_{12} = \delta_{LJ} \mathbf{L}^2 + (\boldsymbol{\sigma}_1 \boldsymbol{\sigma}_2) \mathbf{L}^2 - (\mathbf{LS})^2,$$

$$Y(x) = \frac{e^{-x}}{x}, \quad Z(x) = \left(1 + \frac{3}{x} + \frac{3}{x^2}\right)Y(x).$$

m_π is the pion mass ($m_\pi c^2 = 139.4$ MeV was used in numerical calculations), x is the internucleon distance, measured in m_π^{-1} (see in [Sect. 2.1.2.3](#)), \mathbf{L} is the resulting orbital angular momentum vector, \mathbf{S} is the resulting spin, $\mathbf{S} = \mathbf{s}_1 + \mathbf{s}_2$, $\mathbf{s} = \boldsymbol{\sigma}\hbar/2$ is the spin vector operator (see later in [Sect. 2.2.2](#)), $\mathbf{t} = \boldsymbol{\tau}/2$ is the isospin vector operator (see later in [Sect. 2.2.3](#)), r is the internucleon distance.

The repulsion is infinitely large in the core region, $r_{\text{core}} \leq 0.485$ fm, which corresponds to $x_c \leq 0.343$. The adjusted parameters are as follows:

S	L	a_c	b_c	a_T	b_T	G_{LS}	b_{LS}	G_{LL}	a_{LL}	b_{LL}
0	Even	8.7	10.6	—	—	—	—	−0.000891	0.2	−0.2
1	Even	6.0	−1.0	−0.5	0.2	0.0743	−0.1	0.00267	1.8	−0.4
0	Odd	−8.0	12.8	—	—	—	—	−0.00267	2.0	6.0
1	Odd	−9.07	3.48	−1.29	0.55	0.1961	−7.1	−0.000891	−7.26	6.92

The potential contains 28 fitted (nonzero) parameters. The Hamada–Johnston potential predicts the following data for the deuteron ($S = 1$, L even):

Binding energy	$E_B = 2.226$ MeV
Electric quadrupole moment	$Q_d = +2.85$ mb
D-state probability	$P_D = 6.97\%$

The corresponding experimental data are: $E_B = 2.224566$ MeV (Audi et al. [2003](#)), $Q_d = 2.86(2)$ mb (Stone [2005](#)). There is no direct access to P_D .

2.1.2.3 Nucleon–Nucleon Potentials from Meson Field Theories

According to quantum electrodynamics, the electromagnetic interaction is mediated by photons. For instance, one of the electric charges emits a photon, and the other one absorbs it. Yukawa (1935) supposed that the interaction between nucleons is also mediated by the exchange of field quanta, and the predicted rest energy of the field quantum (called meson) is ~ 140 MeV. After the discovery of π mesons (Lattes et al. 1947) the quanta of the meson field have been identified with π mesons, which have approximately the same rest energy.

According to experiments, the π mesons exist in three charge states: π^+ , π^0 , π^- . From a pseudoscalar theory, taking into account all three charge states in a symmetric way, the following expression was obtained (see, e.g., Bohr and Mottelson 1969) for the asymptotic behavior of the so-called *one-pion exchange nucleon–nucleon potential* (V_{OPEP}):

$$V_{\text{OPEP}} = 0.333 m_\pi c^2 \frac{g^2}{4\pi\hbar c} (\boldsymbol{\tau}_1 \boldsymbol{\tau}_2) [(\boldsymbol{\sigma}_1 \boldsymbol{\sigma}_2) + S_{12} f(r)] \frac{\exp(-r/\lambda)}{r\lambda}, \quad (2.2)$$

where m_π is the mass of the π meson, c is the speed of light in vacuum, g is the “mesonic” charge, analogous to the electric charge, $\hbar = h/2\pi$ is the rationalized Planck constant, $\mathbf{s} = \boldsymbol{\sigma}\hbar/2$ is the spin operator, $\mathbf{t} = \boldsymbol{\tau}/2$ is the isospin operator, $S_{12} = 3(\boldsymbol{\sigma}_1 \mathbf{r})(\boldsymbol{\sigma}_2 \mathbf{r})/r^2 - (\boldsymbol{\sigma}_1 \boldsymbol{\sigma}_2)$, $f(r) = 1 + \frac{3}{r/\lambda} + \frac{3}{(r/\lambda)^2}$, $1/\lambda = m_\pi c/\hbar$, r is the distance between two nucleons.

The potential shows similarity to the interaction potential of two remote, pointlike magnetic dipoles, but the electromagnetic field has vectorial character, while the character of the meson field is pseudoscalar (the spin of π meson is zero).

The one-pion exchange potential (V_{OPEP}) is actually dominant only far from the core region ($r > 2$ fm). The numerical value of the potential can be determined from the analysis of the scattering of π mesons on nucleons.

The values of the parameters are:

$$\frac{1}{\lambda} = \frac{m_\pi c}{\hbar} = 0.70 \text{ fm}^{-1}, \quad \frac{g^2}{4\pi\hbar c} = 0.081 \pm 0.002.$$

It must be remarked that in the short-range region an additional “contact” term appears in [Eq. \(2.2\)](#) that induces a strong repulsion at very small distances.

The one-pion exchange potential contains central and tensor potentials. The interaction has a short range and it is independent of electric charges.

The one-pion exchange potential shows a reasonable agreement with the Hamada–Johnston potential far from the hard core ($r \geq 2$ fm). At small distances there are deviations. A detailed comparison of different nucleon–nucleon potentials can be found, e.g., in Fényes (2002).

If two nucleons are close enough to each other, exchange of two or more π mesons, as well as exchange of heavier mesons (ρ , η , ω) may occur between them, too. Beginning from the 1970s, meson field theoretical potentials have been deduced, which take into account these possibilities and give a better description of experimental data at small distances ($r \leq 2$ fm) than V_{OPEP} does.

Paris potential. Cottingham et al. (1973) and Lacombe et al. (1975) have derived a nucleon–nucleon potential which includes one pion and correlated and uncorrelated two- π and ω meson-exchange potentials. The theory gives a realistic description of the interaction in the

distant and medium-far regions ($r \geq 0.8$ fm). The Paris potential has been parameterized later in a simple analytical form.

Bonn potential. Machleidt et al. (1987) proposed a comprehensive field-theoretical meson-exchange model for nucleon–nucleon interaction. The potential contains many components (one- π , two- π , ρ , η , ω , etc. meson exchange).

The overall description of NN scattering and deuteron data with the Bonn and parameterized Paris potentials is very good. See ▶ Table 2.4 for some deuteron data.

Machleidt et al. (1987) conclude that the many-body forces need not play an important role in traditional nuclear structure calculations. Nevertheless, the recent ab initio Green’s function Monte Carlo calculations show that the three-nucleon interactions give a significant fraction of the nuclear binding energy in few-nucleon systems. The ratio of the expectation values of the three-/two-nucleon interaction potentials ($\langle V_{ijk} \rangle / \langle v_{ij} \rangle$) is about 7% in the $A = 8$ nuclei and $\langle V_{ijk} \rangle$ gives up to one half of their binding energy (Pieper et al. 2001). Details see later in ▶ Sect. 2.3.7.

Although it is widely believed that the fundamental theory of strong interactions can be understood on the basis of quantum chromodynamics (QCD), the non-perturbative character of QCD for low energies raises very serious mathematical problems, and one is far from the quantitative understanding of the NN interaction in the framework of QCD.

Meson-field theoretical NN potentials give a reasonable guidance for the construction of phenomenological potentials, too. At the same time, both the phenomenological and the realistic, meson-field theoretical potentials are very complicated, and their application in nuclear structure calculations is rather difficult.

Therefore, simple “effective” potentials are also widely used in structure calculations. In these potentials, only the main properties of realistic potentials are preserved. In addition to their simplicity, the effective potentials have the advantage that from them it is easier to draw conclusions with clear physical meaning.

■ Table 2.4

The predictions of the Bonn and parameterized Paris meson exchange potentials in comparison with experimental results

Deuteron property	Experimental value ^a	From Bonn ^b full potential	From Paris ^c parameterized potential
Binding energy, E_B (MeV)	2.224575 ± 0.000009	2.22465	2.2249
D-state probability, P_D (%) ^d	(5 ± 2)	4.249	5.77
Quadrupole moment Q_d (fm ²)	0.2859 ± 0.0003	0.2807	0.279
Magnetic dipole moment μ_d (μ_N)	0.857406 ± 0.000001	0.8555	0.853
Root-mean-square radius (fm)	1.9635 ± 0.0045	2.0016	

^aSources of experimental data: see in Machleidt et al. (1987).

^bMachleidt et al. (1987)

^cLacombe et al. (1980)

^dWeight of the $L = 2$ component in the deuteron ground state.

2.2 Properties of Nuclei

2.2.1 Nuclear Mass and Binding Energy

The masses of atomic nuclei can be determined by mass-spectrometers or from nuclear reaction and decay energies. According to Einstein's theory of relativity, the energy (E) and mass (m) are related by equation $E = mc^2$, where c is the speed of light in vacuum. The binding energy U_B is the equivalent mass, obtained by subtracting the mass of the nucleus from the sum of the masses of the constituent nucleons. [Figure 2.3](#) shows the mean binding energy per nucleon (E_B/A) as a function of mass number A for nuclei lying in the stability valley. Above $A \approx 20$ the E_B/A values vary very slowly and regularly: they remain in the 7.5–8.8 MeV/ A interval.

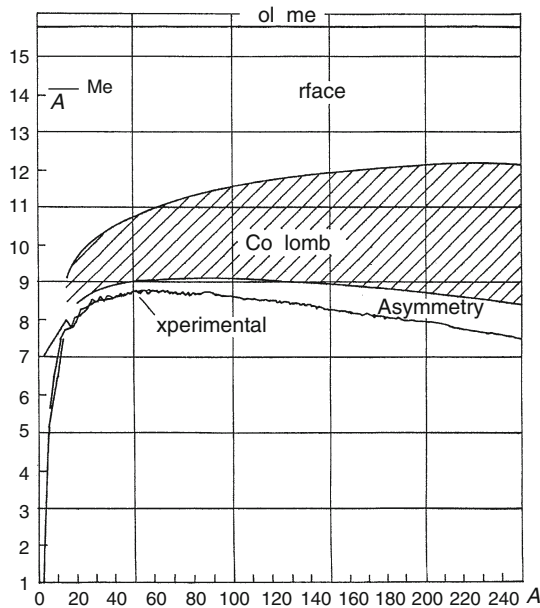
The main features of this behavior can be understood on the basis of the liquid drop model (von Weizsäcker 1935; Bethe and Bacher 1936). According to this model, the nucleus is an incompressible liquid drop, in which the electric charge is distributed uniformly. The binding energy E_B is described by the Weizsäcker formula:

$$E_B = \alpha A - \beta A^{2/3} - \gamma \frac{Z^2}{A^{1/3}} - \zeta \frac{(N - Z)^2}{A} \pm \frac{\delta}{A^{3/4}}, \quad (2.3)$$

where the successive terms express the volume, surface, Coulomb, and asymmetry energies. The last, pairing energy term is equal to $+\delta/A^{3/4}$ for even- Z and even- N , zero for odd- A

■ Fig. 2.3

Mean binding energy per nucleon E_B/A for nuclei lying in the stability valley as a function of the mass number A . The approximate contribution of different terms in [Eq. \(2.3\)](#) is also shown (Based on Kravtsov 1965)



and $-\delta/A^{3/4}$ for odd-odd nuclei. The parameters $\alpha, \beta, \gamma, \zeta, \delta$ are fitted to experimental data. The approximate contribution of different terms to E_B/A is also shown in [Fig. 2.3](#).

A substantial improvement can be obtained, if the parameters in [Eq. \(2.3\)](#) are fitted to experimental values for magic nuclei, and a sixth term ($-\kappa P$) is added to the right-hand side. Here $P = ZN/(Z+N)$ is the “promiscuity” factor. Angeli proposed the following new formula (Angeli 1991b):

$$E_B = \alpha_c A - \beta_c A^{2/3} - \gamma_c \frac{Z^2}{A^{1/3}} - \zeta_c \frac{(N-Z)^2}{A} \pm \frac{\delta_c}{A^{3/4}} - \kappa \frac{ZN}{A}, \quad (2.4)$$

where the subscript c means “closed” shell, and the constants (all values in MeV) are

$$\alpha_c = 15.15, \quad \beta_c = 15.94, \quad \gamma_c = 0.665, \quad \zeta_c = 21.57, \quad \delta_c = 22.4, \quad \text{and} \quad \kappa = 1.42 \pm 0.06. \quad (2.5)$$

In the last 60 years, the binding energy (or mass) formulae have been improved in different directions. One type of formulae is based mainly on the liquid drop model (Myers and Swiatecki 1966, 1967, 1969; Strutinsky 1968; Spanier and Johansson 1988; Möller et al. 1988; Möller and Nix 1988); another type of formulae has been modified starting from the nuclear shell model (Zeldes 1967; Zeldes et al. 1967; Möller et al. 1986, 1992; Tashibana et al. 1988; Han et al. 1992; Lazarev et al. 1994). Finally, some formulae are based on inherent phenomenological relationships between the experimentally determined nuclear masses (Garvey et al. 1969; Garvey 1969; Comay et al. 1988; Jänecke and Masson 1988; Avotina et al. 1995). A survey of mass formulae was given by Tarantin (1995) and Lunney et al. (2003).

Möller et al. (1995) calculated the atomic mass excess and nuclear ground-state deformation for 8,979 nuclei from ^{16}O to $A = 339$ between the proton and neutron drip lines (see [Fig. 2.7](#)). The calculations with the finite-range droplet model (FRDM) contain 16 mass-like and 22 other parameters. In the framework of FRDM it is possible to calculate a large number of nuclear structure properties in addition to the ground-state masses, such as even multipole ground-state deformations ($\varepsilon_2, \varepsilon_4, \varepsilon_6$), β -decay properties, pairing quantities, odd-particle spins, α -decay properties, octupole properties (ε_3), etc.

Proton S_p and neutron S_n (mass-equivalent) separation energies can be derived from the following combinations of atomic masses:

$$S_p = -M(A, Z) + M(A-1, Z-1) + M(1, 1),$$

$$S_n = -M(A, Z) + M(A-1, Z) + M(1, 0),$$

where $M(1,1)$ and $M(1,0)$ are the mass of the hydrogen atom ^1_1H and the neutron ^1_0n , respectively. Evaluated numerical data for masses and binding energies can be found in Wapstra et al. (2003) and Audi et al. (2003). From the separation energies S_p and S_n , one can calculate the pairing energy, which is defined as

$$\begin{aligned} P_p(A, Z) &= 0.25(-1)^{Z+1} [S_p(A+1, Z+1) - 2S_p(A, Z) + S_p(A-1, Z-1)], \\ P_n(A, Z) &= 0.25(-1)^{A-Z+1} [S_n(A+1, Z) - 2S_n(A, Z) + S_n(A-1, Z)]. \end{aligned} \quad (2.6)$$

The pairing energies can also be determined from the ground-state energies of nuclei. The average behavior of pairing energies can be described by a simple expression $P_{n \text{ (or } p)} \approx 12/A^{1/2}$ MeV (Zeldes et al. 1967), although rather large deviations can be observed from this simple formula, especially at closed shells.

2.2.2 Spin, Electric, and Magnetic Moments

2.2.2.1 Spin

One of the measurable properties of atomic nuclei is the total angular momentum (\mathbf{I}) called nuclear spin of the state. (The nuclear spin symbols I and J are used in this chapter alternatively, in accordance with notations in the corresponding literature.) The components of vector \mathbf{I} satisfy the commutation relations

$$I_x I_y - I_y I_x = -\frac{\hbar}{i} I_z$$

and similar expressions with cyclic permutations of the components. According to quantum mechanics, only \mathbf{I}^2 and one of the components of \mathbf{I} (e.g., I_z) can be determined exactly at the same time (they are “commuting” quantities). The eigenvalues of \mathbf{I}^2 and I_z can be written as $I(I+1)\hbar^2$ and $m\hbar$, respectively, where $I \geq 0$ is an integer for even- A , and half-integer for odd- A , and $m = I, I-1, \dots, -I$. The value of I is an important characteristic of a nuclear state.

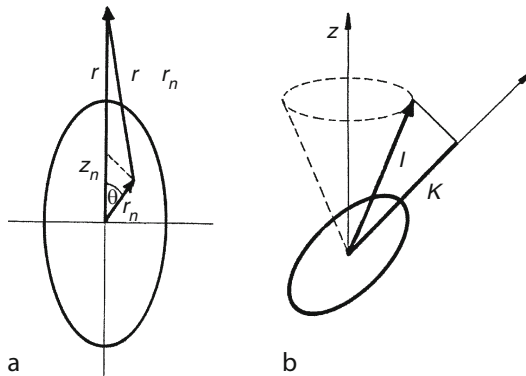
2.2.2.2 Electric Moments

The electric moments of a nucleus can be introduced, e.g., in the following way. Let the origin of a Cartesian coordinate system x_n, y_n, z_n coincide with the center of the nucleus (• Fig. 2.4a). Then the electric potential $V_n(\mathbf{r})$ of the nucleus is given by

$$V_n(\mathbf{r}) = \int \frac{\rho^e(\mathbf{r}_n) dV_n}{|\mathbf{r} - \mathbf{r}_n|}, \quad (2.7)$$

■ Fig. 2.4

(a) Position vector in a coordinate system fixed to the nucleus (illustration to the determination of nuclear electric moments). (b) Angular momentum in an axial-symmetric deformed nucleus. \mathbf{I} is the total angular momentum (spin) of the nucleus. K is the projection of total angular momentum to the symmetry axis



where ρ^e is the nuclear charge density and dv_n is the volume element. The integration must be performed over the whole volume of the nucleus.

Let the vector \mathbf{r} point to the z_n direction. The angle between \mathbf{r} and \mathbf{r}_n is just the polar angle θ . Using the cos law one obtains

$$|\mathbf{r} - \mathbf{r}_n| = \sqrt{\mathbf{r}^2 + \mathbf{r}_n^2 - 2r r_n \cos \theta}.$$

When $(r_n/r) \ll 1$, one can make the following expansion:

$$\frac{1}{|\mathbf{r} - \mathbf{r}_n|} = \frac{1}{r} \sum_{l=0}^{\infty} \left(\frac{r_n}{r} \right)^l P_l(\cos \theta), \quad (2.8)$$

where $P_l(\cos \theta)$ is the Legendre polynomial:

$$P_0(\cos \theta) = 1, \quad P_1(\cos \theta) = \cos \theta, \quad P_2(\cos \theta) = \frac{1}{2}(3\cos^2 \theta - 1), \text{ etc.}$$

Thus the potential $V_n(\mathbf{r})$ can be written in the form:

$$V_n(\mathbf{r}) = \frac{\int \rho^e(\mathbf{r}_n) dv_n}{r} + \frac{\int \rho^e(\mathbf{r}_n) \mathbf{r}_n dv_n}{r^2} + \frac{1}{2} \frac{\int \rho^e(\mathbf{r}_n) (3z_n^2 - r_n^2) dv_n}{r^3} + \dots, \quad (2.9)$$

where, by definition,

$$Ze = \int \rho^e(\mathbf{r}_n) dv_n$$

is the electric monopole moment (i.e., the full nuclear charge), the quantity

$$\int \rho^e(\mathbf{r}_n) z_n dv_n$$

is the electric dipole moment,

$$\int \rho^e(\mathbf{r}_n) (3z_n^2 - r_n^2) dv_n \quad (2.10)$$

is the electric quadrupole moment, and $z_n = r_n \cos \theta$.

Higher multipole moments can also be defined: octupole (2^3 -pole), hexadecapole (2^4 -pole), hexacontatetrapole (2^5 -pole), etc. Nevertheless, higher-order multipoles do not play important roles in nuclear physics, because the weight of subsequent terms in [Eq. \(2.9\)](#) is strongly decreasing.

The definition of the moments becomes unambiguous by specifying the orientation of the nucleus. By convention, in the definition of the electric multipole moments the nuclear angular momentum is assumed to be aligned along the z_n axis. The intrinsic electric quadrupole moment Q_0 is then defined as

$$Q_0 \equiv \int \rho^e(\mathbf{r}_n) (3z_n^2 - r_n^2) dv_n. \quad (2.11)$$

The quadrupole moments are measured in units of barn (b), $1 \text{ b} = 10^{-24} \text{ cm}^2$. If the rotation ellipsoid is prolate, $Q_0 > 0$, if it is oblate, $Q_0 < 0$.

The quadrupole moment can be determined also in a laboratory system, with x, y, z coordinates ([Fig. 2.4b](#)). The quadrupole moment Q in the laboratory frame (also referred

to as spectroscopic quadrupole moment) is expressible in terms of the density in the intrinsic frame similarly. The integral over the rotational variable factors out and yields:

$$Q = \frac{3K^2 - I(I+1)}{(I+1)(2I+3)} Q_0. \quad (2.12)$$

Usually this moment (Q) is measured in experiments. (See later in [Sect. 2.3.4.2](#), “Theory of nuclear rotation.”) This implies that if $I = 0$ (even–even nuclei) or $I = 1/2$, the quadrupole moment is zero in the laboratory system. This is so even if the intrinsic quadrupole moment differs from zero.

2.2.2.3 Magnetic Moments

According to classical electrodynamics, the energy of the nucleus in a magnetic field can be written in the form

$$E = -\boldsymbol{\mu} \mathbf{B},$$

where $\boldsymbol{\mu}$ is the magnetic dipole moment of the nucleus and \mathbf{B} is the magnetic induction. A particle, moving on a circular orbit, generates a magnetic dipole moment

$$\boldsymbol{\mu} = g_l \frac{e}{2m} \mathbf{L},$$

where e and m are the charge and mass of the particle, respectively, c is the speed of light in vacuum, \mathbf{L} is the orbital angular momentum vector and g_l is a dimensionless correction factor, the orbital gyromagnetic ratio. In quantum mechanics, \mathbf{L} is measured in units \hbar , thus \mathbf{L} may be substituted by $\mathbf{L}\hbar$. For an electron, the orbital magnetic moment can be written in the form:

$$\boldsymbol{\mu}^e = \frac{e\hbar}{2m_e} \mathbf{L}.$$

For convenience, the following units have been introduced: the Bohr magneton, μ_B , for the electron:

$$\mu_B = \frac{e\hbar}{2m_e} = 5.7883817555(79) \times 10^{-11} \text{ MeV/T}$$

and the nuclear magneton, μ_N , for nucleons:

$$\mu_N = \frac{e\hbar}{2m_p} = 3.1524512326(45) \times 10^{-14} \text{ MeV/T}.$$

Due to the mass ratio, the nuclear magneton is about 1,836 times smaller than the Bohr magneton. The total magnetic dipole moment is a vectorial sum of the orbital and spin magnetic moments:

$$\boldsymbol{\mu}_j = \boldsymbol{\mu}_l + \boldsymbol{\mu}_s,$$

where $\mathbf{j} = \mathbf{l} + \mathbf{s}$, and $\boldsymbol{\mu}_l = g_l \mathbf{l}$, $g_l^p = 1$, $g_l^n = 0$, $\boldsymbol{\mu}_s = g_s \mathbf{s}$, $g_s^p = 5.586$, $g_s^n = -3.826$, $\boldsymbol{\mu}_j = g_j \mathbf{j}$, the $\boldsymbol{\mu}$ -s are expressed in nuclear magnetons (μ_N), while the \mathbf{l} , \mathbf{s} , \mathbf{j} moments in \hbar units.

Detailed relations between the $\boldsymbol{\mu}_j$ and \mathbf{j} values for protons and separately neutrons were first derived by Schmidt in 1937 (see, e.g., in Fényes (2002), Sect. IV.5.2). By convention, the nuclear

magnetic moment is the value of μ taken in a state in which the nuclear angular momentum is fully aligned with the magnetic field. It is this value that is actually measured. The magnetic moment connected with the spin has no classical analogue, but it may be characterized also by the expression $\boldsymbol{\mu} = g_s \mathbf{s} \mu_N$, where $s = 1/2$ both for a proton and a neutron. The exact magnetic moments of proton and neutron are (Particle Data Group 2008):

$$\mu_p = 2.792847351(28)\mu_N, \quad \mu_n = -1.9130427(5)\mu_N.$$

2.2.2.4 Experimental Nuclear Moments

The nuclear moments can be measured with many different methods. Spin and magnetic moments can be determined from hyperfine splitting of atomic spectra, hyperfine splitting in external magnetic field, deflection of beams in inhomogeneous magnetic field, nuclear magnetic resonance, perturbed angular correlation of γ rays in strong magnetic fields, etc.

Intrinsic quadrupole moments can be obtained by measuring distances between rotational levels, or reduced electromagnetic transition probabilities $B(E2)$.

Spectroscopic quadrupole moments can be determined by many experimental methods: differential perturbed angular distribution of γ rays following nuclear reactions, low temperature nuclear orientation, optical spectroscopy, Coulomb excitation reorientation, different methods of laser spectroscopy, hyperfine splitting of spectrum lines in inhomogeneous electric field, etc.

The experiments show that in the ground states of nuclei the electric moments of 2^l order with odd l and all 2^l -pole magnetic moments with even l are missing. Only electric monopole, magnetic dipole, electric quadrupole, magnetic octupole, etc., moments are observed in experiments. This means that the 2^l -pole character unambiguously determines whether the moment is electric or magnetic, and these latter attributes may be omitted. This rule can be viewed as a consequence of a symmetry property (parity) of the nuclear states.

A compilation and evaluation of experimental nuclear moments has been published in Raghavan (1989) and Stone (2005). On the basis of the available data one can draw some general conclusions.

The spins and magnetic dipole moments in the ground states of all even–even nuclei are zero, without exception. The spins (I) of the odd- A nuclei have half-integer values (in units of \hbar) and $I \leq 11/2$. The magnetic moments (μ in units of μ_N) are in the intervals determined by the “Schmidt curves”: $-0.5 \leq \mu \leq 7$ for odd- Z , even- N , while $-2.2 \leq \mu \leq 1.5$ for even- Z , odd- N nuclei.

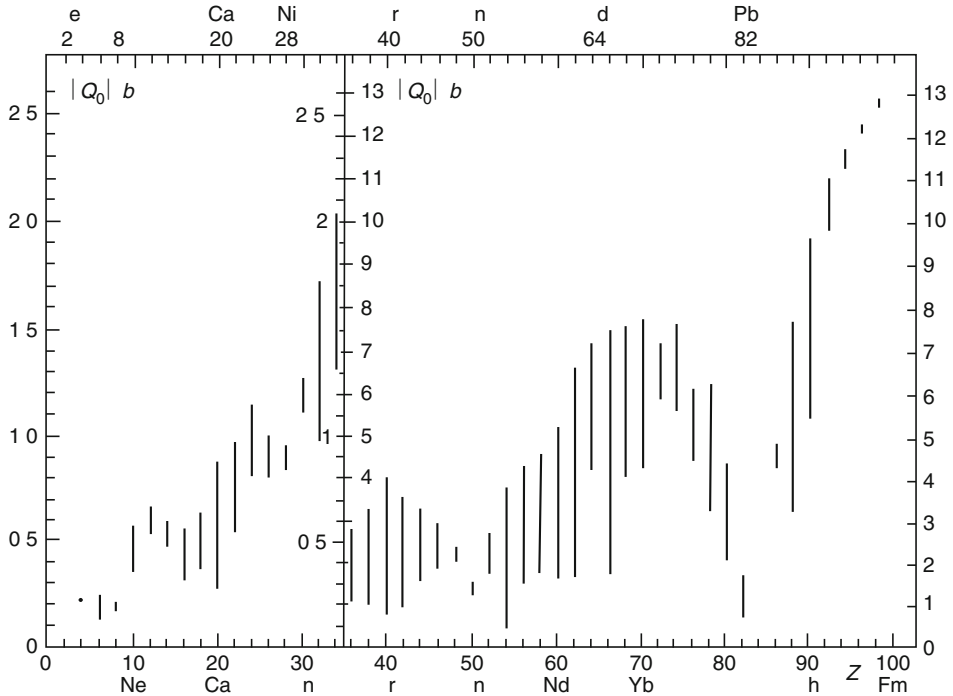
The low values of I and μ show that the orbital and spin angular momenta, as well as the magnetic dipole moments of the individual nucleons, cancel each other to a great extent.

The ground-state spins I of odd–odd nuclei have in all cases integer values (again in units of \hbar) and they remain within the interval $|j_p - j_n| \leq I \leq j_p + j_n$, where j_p and j_n are the total angular momenta of the odd proton and odd neutron, respectively. The magnetic dipole moments of the ground states of the odd–odd nuclei may be either positive or negative, but their absolute values are small (≤ 5 in nuclear magnetons μ_N). In the shell model, the magnetic dipole moments of odd–odd nuclei can be determined from the known configurations of the odd proton and the odd neutron.

The absolute values of the intrinsic quadrupole moments $|Q_0|$ of even–even nuclei are shown in [Fig. 2.5](#). Near magic Z (or/and N) values (2, 8, 20, 28, 50, 82, 126, see in [Sect. 2.3.1.1](#)) the Q_0 moments are close to zero.

■ Fig. 2.5

Absolute values of intrinsic quadrupole moments $|Q_0|$ of even–even nuclei as a function of the atomic number (Z). The $|Q_0|$ values of different isotopes of the given element are scattered within the intervals represented by vertical bars (Data from Raman et al. 1987)



As it was already mentioned, the spectroscopic quadrupole moments of the even–even and $I = 1/2$ nuclei vanish. The reduced $Q/(ZR^2)$ spectroscopic quadrupole moments of the odd- A nuclei are in the range $-10 \times 10^{-28} \leq Q/(ZR^2) \leq 35 \times 10^{-28}$ (for the definition of R , see section “Charge radii”).

Most nuclei have prolate deformation, although small oblate deformations also occur, especially close to magic numbers. In some regions, large quadrupole deformations were measured. In the shell model the spectroscopic quadrupole moments of odd–odd nuclei can be determined from the configurations of the odd proton and odd neutron.

2.2.3 Size, Parity, and Isospin of Nuclei

2.2.3.1 Nuclear Size

Nuclear charge and matter distributions, as well as nuclear radii can be studied by several methods. The most important ones are as follows.

Charge distribution can be extracted from the measurement of elastic electron scattering, X-rays from muonic and ordinary atoms (isotope shifts), and optical spectra (Fricke et al. 1995).

Matter distribution can be determined from elastic p, n, α scattering, π^\pm , K^\pm meson scattering, and cross sections of reactions induced by p, n, antiproton, π , and K beams.

Electrons and muons do not take part in the strong interaction (► Table 2.2) and do not induce substantial rearrangement in the nuclear structure. The laws of electromagnetic interactions are well known. Thus, the methods probing the charge distribution with these projectiles are of primary importance. The nucleon and meson projectiles strongly interact with nuclei, and they are able to give information on the nuclear matter distribution. On the other hand, the evaluation of experimental results is more difficult, because the laws of nuclear interactions are not perfectly known; furthermore, the bombarding particles may perturb the structure of the target nucleus.

Charge Radii

Information on charge radii can be obtained from electron scattering experiments. One can determine the mean square charge radius in a model-independent way:

$$\langle r^2 \rangle = \int_V \rho^e(\mathbf{r}) \mathbf{r}^2 dV, \quad (2.13)$$

where ρ^e is the charge density normalized to the whole charge of the nucleus, dV is the volume element, and V is the volume of the nucleus. From the root-mean-square (r.m.s.) radius, $R_{r.m.s.}$ (which means the square root of the mean square charge radius), one can calculate the radius parameter R of an equivalent uniform charge distribution, for which $\rho^e(r, R) = \rho_0^e$, if $r \leq R$ and $\rho^e(r, R) = 0$, if $r > R$. The ρ_0^e uniform distribution is said to be equivalent to the $\rho^e(r)$ distribution of the nucleus if it contains the same charge and it scatters the low-energy electrons approximately in the same way. The relation between the two radii is:

$$R = 1.291 R_{r.m.s.} \quad (2.14)$$

The experimental charge distribution is shown for some nuclei in ► Fig. 2.6. The nuclear surface is not sharp, the charge density gradually decreases toward larger distances from the center.

The nuclear charge distribution can also be calculated assuming a mean field, in which the nucleons move independently. The short range interactions between the nucleons are replaced usually in a phenomenological way by effective interactions. As ► Fig. 2.6 shows, the theoretical results of Dechargé and Gogny are very close to the experimental ones.

The root-mean-square (charge) radius $R_{r.m.s.}$ depends both on Z and N . At the bottom of the stability valley (see ► Sect. 2.2.4), the atomic number Z_{stab} and mass number A_{stab} are related by

$$Z_{stab} = \frac{A_{stab}}{1.98 + 0.016 A_{stab}^{2/3}}. \quad (2.15)$$

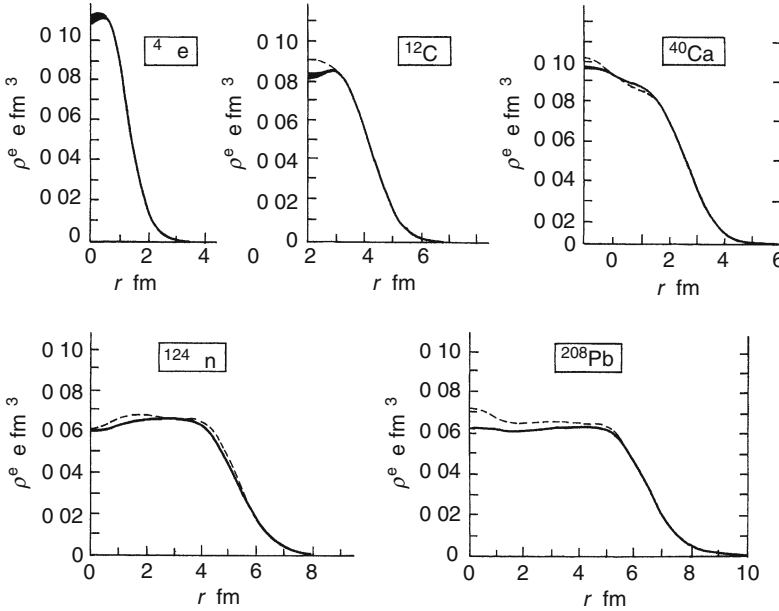
For these nuclei, the dependence of R on the mass number follows the predictions of the uniformly charged liquid-drop model:

$$R = r_0 A^{1/3}, \quad (2.16)$$

where $R = R_{stab}$, $A = A_{stab}$, and $r_0 = 1.23$ fm (for charge distribution). In practice the indices “stab” are usually omitted. According to ► Eq. (2.15), the volume of the nucleus is proportional to the mass number A . The nuclear binding energy per nucleon (► Fig. 2.3)

■ Fig. 2.6

Ground state charge density (ρ^e) distributions in some nuclei from electron scattering and muonic X-ray measurements (Frois 1983). The dashed curves show mean field many-body (microscopic) theoretical results (Dechargé and Gogny 1980)



shows saturation for $A > 10$, which corresponds to $R > 2.6$ fm. The characteristic range of nuclear forces must be close to this distance.

The simple formula [Eq. \(2.15\)](#) only describes the gross structure of nuclear radii. Elton (1961) and Angeli (1991a) proposed formulae which take into account a finite surface thickness.

For isobaric nuclei a symmetry term must be added to the radius formula (see Angeli (1992) and further references therein). Nuclear shell effects were considered in the nuclear r.m. s. radii by Angeli (1991a). A systematics of nuclear charge radii are given in Nadjakov et al. (1994), Angeli (2004), and Fricke and Heilig (2004).

In strongly p- or n-rich nuclei, the diffuseness of the nuclear surface, and thus the radii of nuclei, follows different patterns, and departures are expected from the simple formula [Eq. \(2.16\)](#).

Mass Radii

Nuclear mass distributions can be studied, for example, by the scattering of fast neutrons on nuclei. Such experiments were performed in a wide energy range of bombarding neutrons (14–1,400 MeV) and led to the following result:

$$R = R_0 A^{1/3}, \quad (2.17)$$

where $1.3 \text{ fm} \leq R_0 \leq 1.4 \text{ fm}$. This means that the nuclear mass parameter R_0 is only slightly greater than the charge parameter, $r_0 = 1.23$, shown in [Eq. \(2.15\)](#). In the heavy nuclei

there are usually more neutrons than protons, but the long-range repulsion between proton pairs has a strong effect. A more detailed treatment of nuclear size can be found, e.g., in Fényes (2002).

Note that far from the stability region the separation energy of the outermost nucleons is small. In some cases this may lead to a drastic increase of the size of nucleus: the external nucleon may occupy a distant lying orbit. For example, such proton “halo” exists in ^8B , one-neutron halos in ^{11}Be and ^{19}C , and two-neutron halos in ^6He and ^{11}Li . The radii of these nuclei are extremely large, comparable with that of ^{48}Ca . See Suzuki et al. (2003).

2.2.3.2 Parity

Nuclear states are described in quantum mechanics by eigenvalues and eigenfunctions of the Hamilton operator, to which definite quantum numbers belong. The parity of the wave function is its symmetry property under inversion through the origin of the coordinate system, i.e., when the coordinates x, y, z are transformed into $-x, -y, -z$. This transformation turns a right-handed coordinate system into a left-handed one or vice versa.

The parity is an “observable” physical quantity, which, in the language of quantum mechanics, means that its eigenvalues are real quantities.

It can be proved that an eigenfunction $\Psi(\mathbf{r})$ of the Hamiltonian has definite parity, unless there is degeneracy (i.e., at least two eigenvalues coincide). For stationary states, the wave equation reads:

$$H(\mathbf{r})\Psi(\mathbf{r}) = E\Psi(\mathbf{r}),$$

where $H(\mathbf{r})$ is the Hamilton operator and E is the energy eigenvalue of the state. Inversion through the origin means that one changes the sign of the position vector: $\mathbf{r} \rightarrow -\mathbf{r}$. Experiments show that in strong and electromagnetic interactions the energy of the system is invariant under inversion, that is $H(-\mathbf{r}) = H(\mathbf{r})$. (In [Sect. 2.1.2.2](#) this was an assumption.) Therefore

$$H(\mathbf{r})\Psi(-\mathbf{r}) = E\Psi(-\mathbf{r}).$$

As $\Psi(\mathbf{r})$ and $\Psi(-\mathbf{r})$ satisfy the same equation, $\Psi(\mathbf{r})$ must be proportional to $\Psi(-\mathbf{r})$, $\Psi(\mathbf{r}) = k\Psi(-\mathbf{r})$, where k is a constant (in a nondegenerate case). As \mathbf{r} may take on also value $-\mathbf{r}$, the equation $\Psi(-\mathbf{r}) = k\Psi(\mathbf{r})$ must also be valid. Consequently, k must be either +1 or -1. If $\Psi(-\mathbf{r}) = \Psi(\mathbf{r})$, the function Ψ is said to be even (or it has positive parity $\pi = 1$), if $\Psi(-\mathbf{r}) = -\Psi(\mathbf{r})$, the wave function is odd (it has negative parity $\pi = -1$).

The nuclear states can thus be characterized by a definite parity. It can be shown that the parity is a constant of motion, i.e., it is conserved in closed systems in which only strong and electromagnetic interactions occur. When the weak interaction is included, H contains a term, which changes sign under inversion through the origin, so that the right-handed coordinate system is not equivalent to the left-handed one (see [Sect. 2.4.2.3](#)). But since the weak interaction is almost always negligible in the nuclear structure, the nuclear states can be regarded as having definite parities.

The even- Z -even- N nuclei have even parity in their ground states. The parity of the ground state of odd- A nuclei is determined by $(-1)^l$, where l is the orbital angular momentum of the unpaired nucleon (see in the shell model, [Sect. 2.3.1.2](#)). In the case of the odd-odd nuclei the parity of the ground state is described by the product of the odd proton and odd neutron parities.

2.2.3.3 Isospin

Both the nuclear-binding energies and nucleon–nucleon scattering experiments show that the nuclear forces are almost independent of the types of nucleons; the three types of nuclear interactions (pp)_{nuclear}, pn , and nn are nearly identical.

This property, the charge independence of nuclear forces, can be described conveniently by the isospin formalism introduced by W. Heisenberg. The isospin formalism is completely analogous with the quantum–mechanical formalism of spin 1/2 particles. In the case of a many-nucleon system the total isospin (T) is defined as a sum of the nucleonic isospins:

$$\mathbf{T} = \sum_{i=1}^A \mathbf{t}_i. \quad (2.18)$$

For the z component this reduces to

$$T_z = \sum_{i=1}^A t_{iz}. \quad (2.19)$$

As in ordinary spin algebra, the vector operator \mathbf{T} obeys the angular momentum commutation relations.

The eigenvalues of the operators \mathbf{T}^2 and T_z are thus

$$\mathbf{T}^2 : T(T+1),$$

$$T_z : T, T-1, \dots -T.$$

Here T is either integer or half-integer depending on whether A is even or odd. The eigenvalues of \mathbf{T}^2 and T_z are constructed from those of \mathbf{t}_i^2 and t_{iz} by the rules of angular momentum addition. The eigenvalue of the t_{iz} operator may be either $+1/2$ or $-1/2$ for the two charge states of the nucleon (i.e., $+1$ for p and 0 for n). Here the convention that sign $+$ stands for proton is accepted, but this is arbitrary. As each neutron contributes to T_z with $-1/2$, and each proton with $+1/2$ one can write:

$$T_z = 0.5(Z - N) = Z - A/2. \quad (2.20)$$

Experiments show that in the ground states of most nuclei the isospin is $T = |T_z|$, that is the minimum T value is realized.

The angular momentum and isospin algebras are discussed in detail in basic textbooks of quantum mechanics and nuclear physics (e.g., Schiff 1968; Heyde 1990).

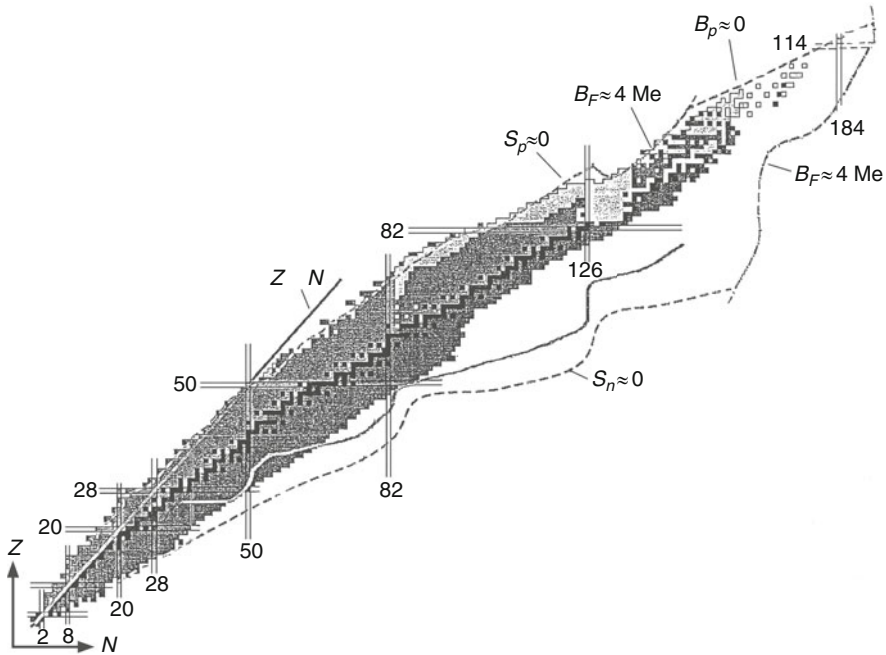
Note, that the isospin symmetry of nuclear forces is not exact. The modern *ab initio* Green's function Monte Carlo calculations show that isospin-breaking terms are necessary in the strong interaction to reproduce the experimental data (Pieper et al. 2001), see later in [Sect. 2.3.7.2](#). The charge symmetry breaking in the strong interaction occurs because the up and down quarks have different masses and quark electromagnetic effects present themselves (Miller et al. 2006).

2.2.4 Chart of the Nuclides

► [Figure 2.7](#) offers a survey of nuclei in the atomic (Z) and neutron (N) number plane. There is experimental information only on $\sim 3,000$ nuclei (including ~ 300 stable ones, with

■ Fig. 2.7

Chart of the nuclides. Black squares show stable nuclides as a function of atomic number Z and neutron number N . S_p zero and S_n zero curves indicate proton and neutron drip lines, respectively, which can be predicted, e.g., from different mass formulae. The B_F curves show limits, where the potential barrier disappears for fission. Grey regions show the domain of known nuclides. Magic numbers are shown by horizontal and vertical lines



$T_{1/2} > 10^9$ years), but approximately 7,000 nuclei can exist in bound states within the proton and neutron drip lines. (At drip lines the separation energies S_p , S_n become zero.) In the light stable nuclei the number of protons is approximately equal to the number of neutrons. This is the result of the exceptionally strong interaction between the protons and neutrons. Furthermore, in the light nuclei the weight of the contribution of the Coulomb interaction to the total energy is much smaller than the contribution of the strong interaction. In the heavier nuclei the neutron number exceeds the number of protons.

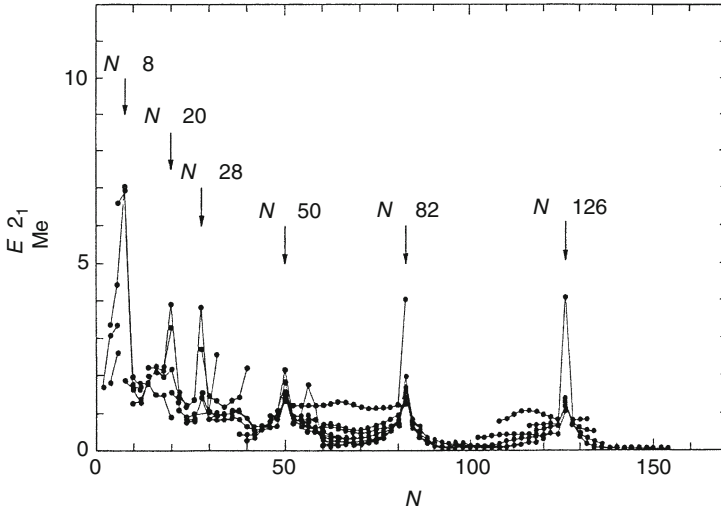
Seeking stability, proton-rich nuclei decay by β^+ emission and/or electron capture, and the neutron-rich nuclei by β^- emission into their isobars. Near magic numbers, the nuclei are more or less spherical; far from them, they are usually deformed.

The low-lying energy levels have definite characteristic features in different regions of the chart of nuclides. ▶ [Figure 2.8](#) shows the excitation energy of the first $I^\pi = 2^+$ states, $E(2_1^+)$, in even-even nuclei as a function of neutron number N . The $E(2_1^+)$ values show a decreasing trend with increasing N . However, at magic numbers the $E(2_1^+)$ values are prominently large, while in the $88 \leq N \leq 120$ and $N > 134$ regions they are extremely small. In the latter two regions the nuclei are strongly deformed and the 2_1^+ states have rotational character.

In odd- A and odd- Z , odd- N nuclei usually there are many low-lying levels. The properties of nuclear excitations will be discussed in more detail in ▶ [Sect. 2.3](#). In ▶ [Sect. 2.3.1](#) one shall

■ Fig. 2.8

Excitation energy E of the first $I^\pi = 2^+$ states in even–even nuclei as a function of neutron number N . The lines connect isotopes (Taken from Spear 1989, based on data compiled by Raman et al. 1987)



see that the most important features of the chart of nuclides can be understood on the basis of shell (and other) models, in which the Pauli principle and the Coulomb interaction between protons play important roles.

2.3 Nuclear States and Excitations

2.3.1 Shell Model of Atomic Nuclei

Although many models have been elaborated for the description of nuclear structure, the shell model is of central importance. In this section, the most important experimental facts indicating the existence of magic numbers (closed shells) in atomic nuclei are summarized. Then the independent-particle shell model of spherical and deformed nuclei, and the shell model with multiparticle configurations will be treated.

2.3.1.1 Closed Shells in Atomic Nuclei

The electron shells of atoms are especially stable in noble gas elements: He, Ne, Ar, Kr, Xe, Rn. This is the consequence of the fact that for the “magic numbers” $Z = 2, 10, 18, 36, 54$, and 86 the electron shells are closed.

Similar distinguished numbers have also been observed in atomic nuclei. For Z or $N = 2, 8, 20, 28, 50, 82$, and $N = 126$ the nuclei are particularly stable. Nuclei with $Z, (N) = 40$ and $Z, (N) = 64$ are also rather stable in some specific mass regions (subshell closures).

The existence of distinguished “magic” numbers in atomic nuclei has been proved by many experimental facts.

Chemical element and isotope abundances. The abundance of chemical elements in the solar system (see ▶ Fig. 12.13 in Chap. 12, Vol. 2), as well as in Earth’s crust and seas usually shows maximum values at magic proton and/or neutron numbers (Firestone et al. 1996). The number of stable isotopes and isotones is remarkably high for magic numbers of Z and N (see ▶ Fig. 2.7).

Nuclear binding, separation, and pairing energies. The effect of magic numbers can be well recognized also in nuclear binding energies, in proton and neutron separation, and pairing energies (Wapstra et al. 2003; Audi et al. 2003).

Quadrupole moments of nuclei. The intrinsic quadrupole moments of even–even nuclei usually show very low values near magic numbers (▶ Fig. 2.5). The effect of magic numbers is well observable also in the quadrupole moments of odd- A nuclei.

Nuclear radii indicate sudden changes at definite proton and neutron numbers, in particular for $Z, N = 28, 50, 82$ and $N = 126$ (Angeli 2004; Fricke and Heilig 2004).

Excited states of nuclei. ▶ Figure 2.8 shows the excitation energies of the first 2^+ states in even–even nuclei as a function of the neutron number N . The effect of magic numbers is well observable; the excitation energies have local maxima at magic numbers in the majority of cases.

Alpha-decay energies. The α -decay energies of some nuclei around $N = 126$ are shown in ▶ Fig. 2.33. There is a sharp change in the systematic trend at the magic number 126.

Beta-decay energies. The β -decay energies also indicate very clearly the effect of magic numbers (see, e.g., ▶ Fig. 2.38).

Reduced γ -ray transition probabilities. According to ▶ Fig. 2.14, the reduced transition probabilities $B(E2; 0_1^+ \rightarrow 2_1^+)$ in even–even nuclei have especially low values at magic numbers. See, for example, data for $_{50}\text{Sn}$ and $_{82}\text{Pb}$.

Nuclear reaction data. The nuclear reactions also clearly show the existence of nuclear shells (Haxel et al. 1952). By reactions, it is harder to break up and it is easier to produce a “magic” nucleus than its neighbors.

2.3.1.2 Independent-Particle Shell Model

The atomic shell phenomena (electrons in a central Coulomb field) can be successfully treated with quantum–mechanical methods. In the case of atomic nuclei, the situation is more complicated, because here there is no well-defined central field, the average field of nucleons substantially differs from the well-known Coulomb field (the nuclear forces are very complicated), and there are two different types of nucleons in nuclei (p and n).

The basic assumption of the independent-particle model is that the valence nucleon(s) move in an average field produced by the inert “core” nucleons.

The average field is expected to be roughly proportional to the nuclear density. ▶ Figure 2.6 shows the ground-state charge distributions in several nuclei, determined from electron scattering and muonic X-ray measurements. Based on these and similar mass distribution curves, it appears promising to use a harmonic oscillator potential for the average field in the light nuclei and a Woods–Saxon potential in heavier ones (▶ Fig. 2.2). Nevertheless, one must keep in mind that the harmonic oscillator potential increases into infinity with the radius,

while the nuclear forces have a short range. Thus, at large distances (e.g., in collisions) the harmonic oscillator potential is not realistic.

Central potential. The Schrödinger equation of a particle moving in central potential $V(r)$ is

$$\left[-\frac{\hbar^2}{2m} \nabla^2 + V(r) \right] \Psi(\mathbf{r}) = E \Psi(\mathbf{r}), \quad (2.21)$$

where m is the mass of the particle. In spherical coordinates, the equation has the form

$$-\frac{\hbar^2}{2m} \left[\frac{1}{r^2} \frac{\partial}{\partial r} \left(r^2 \frac{\partial}{\partial r} \right) + \frac{1}{r^2 \sin \theta} \frac{\partial}{\partial \theta} \left(\sin \theta \frac{\partial}{\partial \theta} \right) + \frac{1}{r^2 \sin^2 \theta} \frac{\partial^2}{\partial \phi^2} \right] \Psi + V(r) \Psi = E \Psi,$$

where r is the length of the vector \mathbf{r} pointing to the particle position, θ and ϕ are its polar and azimuthal angles, respectively.

When the potential is spherically symmetric, [Eq. \(2.20\)](#) has solutions that factorize in the radial and angular coordinates. One can get a complete system of solutions in this way. If one substitutes $\Psi(r, \theta, \phi) = R(r) Y(\theta, \phi)$ and divides both sides by Ψ , one gets

$$\frac{1}{R} \frac{d}{dr} \left(r^2 \frac{dR}{dr} \right) + \frac{2mr^2}{\hbar^2} [E - V(r)] = -\frac{1}{Y} \left[\frac{1}{\sin \theta} \frac{\partial}{\partial \theta} \left(\sin \theta \frac{\partial Y}{\partial \theta} \right) + \frac{1}{\sin^2 \theta} \frac{\partial^2 Y}{\partial \phi^2} \right].$$

As one side of the last equation depends only on r , the other one only on θ and ϕ , both sides must be equal to a constant, say λ . Thus, one arrives at the “radial wave equation”:

$$\frac{d}{dr} \left(r^2 \frac{dR}{dr} \right) + \left(\frac{2mr^2}{\hbar^2} [E - V(r)] - \lambda \right) R = 0 \quad (2.22)$$

and the “angular wave equation”

$$\frac{1}{\sin \theta} \frac{\partial}{\partial \theta} \left(\sin \theta \frac{\partial Y}{\partial \theta} \right) + \frac{1}{\sin^2 \theta} \frac{\partial^2 Y}{\partial \phi^2} + \lambda Y = 0. \quad (2.23)$$

This latter equation possesses single valued solutions only for definite λ values: $\lambda = l(l+1)$, where $l = 0, 1, 2, \dots$

If one substitutes $\lambda = l(l+1)$ in [Eq. \(2.22\)](#) and introduces $u(r)$, defined by $R(r) = u(r)/r$, one obtains the radial wave equation in a form which resembles the one-dimensional wave equation:

$$-\frac{\hbar^2}{2m} \frac{d^2 u(r)}{dr^2} + \left[V(r) + \frac{l(l+1)\hbar^2}{2mr^2} \right] u(r) = E u(r). \quad (2.24)$$

A more detailed treatment of angular momenta and the central force problem in three dimensions can be found in basic textbooks (see, e.g., Schiff 1968; Mandl 1992; Heyde 1990).

For a spherical harmonic oscillator $V(r) = m\omega^2 r^2/2$, where ω is the angular frequency of oscillation. If the valence nucleon is proton, $V(r)$ must also contain a Coulomb term.

The solution of [Eq. \(2.24\)](#) is searched for with conditions $u(r=0) = 0$ (i.e., $\Psi(r=0)$ is finite) and $u(r=\infty) = 0$. The detailed calculations show that the energy eigenvalues of [Eq. \(2.24\)](#) have the form:

$$E = (N + 3/2) \hbar \omega, \quad (2.25)$$

where N is the principal or oscillator quantum number; $N = 0, 1, 2, \dots$, and $N = 2n + l$, n is the radial quantum number; $n = 0, 1, 2, \dots$, l is the angular momentum quantum number; $l = 0, 1, 2, 3, 4, 5, 6, \dots$.

The different l states are often marked with letters: s, p, d, f, g, h, i, ...

The notation of a state often contains its sequence number $n + 1$ as well, e.g., 1s, 1p, 1d, 2s, 2p, etc. (Frequently $n + 1$ is called the radial quantum number. The number n or $n + 1$ counts the radial nodes, thus it differs from the principal or azimuthal quantum number used for the classification of the states of the hydrogen atom.)

The parity of levels is given by $(-1)^l$. One can deduce that the oscillator energy quantum ($\hbar\omega$) decreases with increasing mass number (A) according to the approximate equation

$$\hbar\omega \approx 41A^{-1/3} \text{ MeV}. \quad (2.26)$$

This means that the energy spectrum will be compressed for heavier nuclei. If one uses a square well instead of the harmonic oscillator potential, the oscillator levels split up according to different l values (Schiff 1968; Nilsson and Ragnarsson 1995). The harmonic oscillator level system is shown on the left side of [Fig. 2.9](#). The second column presents the “intermediate” energy spectrum, obtained by interpolation between the harmonic oscillator and square well potential levels.

In the independent-particle model the Pauli principle plays the same role as in atomic physics. Each quantum state can only be occupied by one particle of the same type. The quantum state involves the spin degree of freedom as well, thus a level in a potential well can be filled up by two protons and two neutrons. In the ground state the lowest-lying shells are filled up. The magic numbers are reproduced up to neutron number and atomic number 20, but not beyond.

Spin-orbit interaction. A decisive step in the interpretation of the correct nuclear magic numbers was made by Goeppert Mayer (1949) and by Haxel et al. (1949). They proposed that a new term be added to the potential energy in [Eq. \(2.20\)](#), the so-called spin-orbit term:

$$V_{\text{SO}} = V_{\text{SO}}(r)(\mathbf{l}\mathbf{s}), \quad (2.27)$$

where \mathbf{l} and \mathbf{s} are the orbital angular momentum and spin vectors of the particle, and $\mathbf{l} = \mathbf{r} \times \mathbf{p}$, where \times stands for the vector product of two vectors. As $\mathbf{j} = \mathbf{l} + \mathbf{s}$, it follows that $\mathbf{j}^2 = \mathbf{l}^2 + \mathbf{s}^2 + 2\mathbf{l}\mathbf{s}$, and the spin-orbit potential can be written in the form:

$$V_{\text{SO}} = V_{\text{SO}}(r)(\mathbf{j}^2 - \mathbf{l}^2 - \mathbf{s}^2)/2$$

or, with quantum numbers,

$$V_{\text{SO}} = V_{\text{SO}}(r) \frac{j(j+1) - l(l+1) - s(s+1)}{2}, \quad (2.28)$$

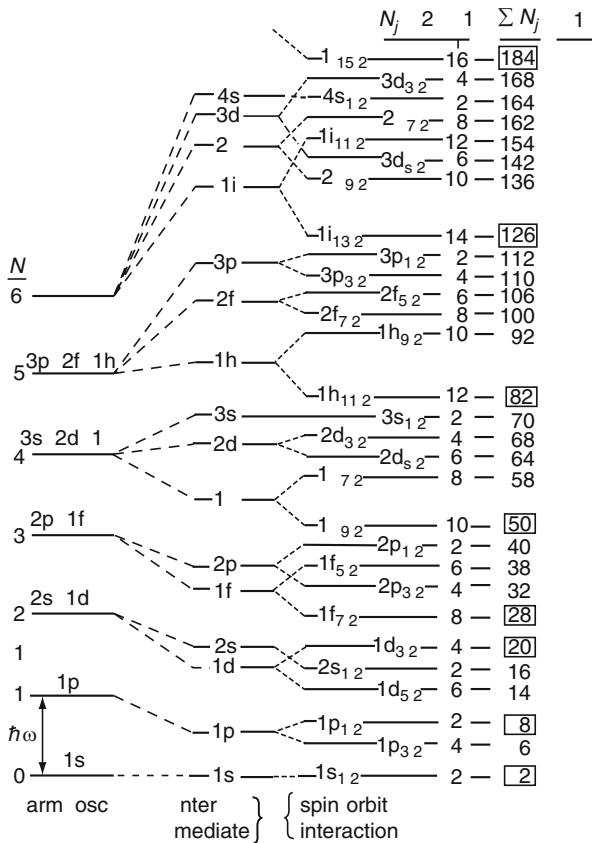
$$V_{\text{SO}} = \begin{cases} V_{\text{SO}}(r) \frac{-l-1}{2} & \text{for } j = l - 1/2, \\ V_{\text{SO}}(r) \frac{l}{2} & \text{for } j = l + 1/2. \end{cases}$$

As shown by [Fig. 2.9](#), with the inclusion of the spin-orbit interaction, the observed magic numbers were properly reproduced. The spin-orbit interaction for atomic electrons is a small quantum-relativistic effect. The nuclear spin-orbit coupling is much stronger and results, in addition to relativistic effects, from the spin dependence of the nucleon-nucleon potential.

The independent-particle model with a Woods-Saxon potential was treated, e.g., by Soloviev (1981).

■ Fig. 2.9

Approximate-level scheme for protons. *First column:* level energies of the harmonic oscillator. *Second column:* interpolated level scheme between the harmonic oscillator and square well solutions. *Third column:* splitting of levels after introducing the spin–orbit interaction. Notation of states: $(n+1)l_j$, where n is the radial quantum number ($n = 0, 1, 2, \dots$). *Fourth column:* the number of protons on the indicated subshell (N_j). *Fifth column:* full number of protons up to the level indicated (ΣN_j). The magic numbers are indicated in frames. *Sixth column:* parity of the level, $(-1)^l$. The level scheme for neutrons is similar; in that case N_j refers to neutrons (Based on Goeppert Mayer and Jensen 1965)



With the use of the Hartree–Fock method (Hartree 1928; Fock 1930), one can calculate the average potential starting from an effective nucleon–nucleon interaction. The Hartree–Fock calculations give a firm basis for the nuclear shell model (see, e.g., Heyde 1990) and allow the calculation of many observables of nuclei (nuclear binding energy, mass, charge radius, see section “Charge radii”).

The independent-particle model is best suited for the treatment of nuclei that have doubly closed-shell core ± 1 nucleon. In this case, the core has a rather well-defined spherical shape and the problem of the residual interaction between valence nucleons does not arise.

Somewhat surprisingly, this simple model gives general agreement with experimental data in a much wider region if one adds to it some simple “*jj*-coupling rules.” In this coupling scheme, the total angular momenta (j) of the valence nucleons are coupled into a resulting one (J) according to the quantum-mechanical addition rules.

The experiments show that the even- Z , even- N nuclei have all zero angular momenta. This fact suggests the “seniority rule”: in the lowest-energy state two particles of the same kind (protons or neutrons) are paired off to angular momentum zero. The strong “pairing force” is the consequence of the large overlap of orbits with the same $|j|$ (but opposite projections m) and the short range of nuclear forces.

In the odd- Z , even- N nuclei, the resulting total angular momentum J will be nearly always the angular momentum j of the odd proton. In some exceptional cases J will take on the value $j - 1$.

If N is odd and Z is even, the same rule holds as in the former case, but the resulting angular momentum is determined now by the odd neutron.

Many problems of the odd-odd nuclei can be successfully treated with the “parabolic rule” (Paar 1979). The rule describes the energy splitting of states arising from different couplings of angular momenta j_p and j_n .

The independent-particle model with *jj*-coupling rules can explain many properties of nuclei. Corresponding results are shortly surveyed below.

According to the shell model and the Pauli principle, in low-lying states low-energy shells will be filled when protons and neutrons are added to the nucleus. The model can explain why Z is approximately equal to N in light nuclei: the protons and neutrons fill up the available low-lying states gradually and independently, striving to reach minimum energy. In the heavy nuclei the Coulomb repulsion is rather strong; consequently more neutron states are occupied than proton states. This can explain the neutron excess observable in the heavy nuclei.

The independent-particle model correctly predicts the magic numbers and the subshell closures (► Figs. 2.8 and ► 2.9).

Furthermore, one can understand, at least qualitatively, why the nuclear radii increase with increasing mass number. The nucleons occupy gradually the higher-lying levels, and for these states, the radial wave functions extend to greater radii.

The spins (J) and parities (π) of the even- Z , even- N nuclei are $J^\pi = 0^+$, in agreement with the predictions of the independent particle model.

The experimental J^π values of some odd- A nuclei are compared with the theoretical ones in ► Table 2.5. The predictions of the shell model agree with experimental data in most cases. In ^{23}Na and ^{21}Ne , the anomalous $J = j - 1$ coupling has been observed. In ^{19}F and ^{19}Ne , there is a strong configuration mixing in the ground states (deformation) and low-lying excited levels have been observed with $J^\pi = 5/2^+$, which is expected on the basis of ► Fig. 2.9. A more complete analysis of the ground-state J^π values of odd- A nuclei was given, e.g., by Goeppert Mayer and Jensen (1965).

The low-lying excited levels of (double-magic ± 1) nuclei can be compared with the predictions of the independent-particle model. In almost all cases, the agreement is very good.

Nevertheless, if there are several nucleons in the valence shell(s), the interaction between the valence nucleons may change the level spectrum. The experimental data show that the level sequence of the independent-particle model (► Fig. 2.9) can only be considered in general as a first approximation. The actual level scheme depends not only on the atomic or the neutron number, but also on the mass number.

■ **Table 2.5**

Comparison of the experimental spins and parities of some odd-*A* nuclei with the predictions of the independent particle model. The central part of the table reproduces the level sequence, shown in ► Fig. 2.9, for easier comparison of experimental data with theory. The exponents over the symbols of the orbits stand for multiple occupancy. Negative exponents mean occupancy with respect to full (sub)shells, “hole” in a (sub)shell

dd Z	ven N	J^π xp	p confi							dd N	ven Z	J^π xp	n confi
1	2	1 2	$1s_{1/2}$		N_j	$2j$	1	ΣN_j	1				
3 i	2	3 2	$1p_{3/2}$		$1h_{11/2}$		12	82		3	2 e	3 2	$1p_{3/2}$
	4	3 2	$1p_{3/2}$		$3s_{1/2}$		2	70		5	4 e	3 2	$1p_{3/2}^3$
5	6	3 2	$1p_{3/2}^3$		$2d_{3/2}$		4	68		5	6 C	3 2	$1p_{3/2}^3$
7 N	6	1 2	$1p_{1/2}$		$2d_{5/2}$		6	64		7	6 C	1 2	$1p_{1/2}$
	8	1 2	$1p_{1/2}$		$1f_{7/2}$		8	58		7	8	1 2	$1p_{1/2}$
9 F	8	5 2	$1d_{5/2}$		$1g_{9/2}$		10	50		9	8	5 2	$1d_{5/2}$
	10	1 2	Mixed		$2p_{1/2}$		2	40		9	10 Ne	1 2	Mixed*
11 Na	12	3 2	$1d_{5/2}^3$		$1f_{5/2}$		6	38		11	10 Ne	3 2	$1d_{5/2}^3$
13 Al	14	5 2	$1d_{5/2}^{-1}$		$2p_{3/2}$		4	32		13	12 M	5 2	$1d_{5/2}^5$
15 P	16	1 2	$2s_{1/2}$		$1f_{7/2}$		8	28		15	14 i	1 2	$2s_{1/2}$
17 Cl	18	3 2	$1d_{3/2}$		$1d_{3/2}$		4	20		17	16	3 2	$1d_{3/2}$
	20	3 2	$1d_{3/2}$		$2s_{1/2}$		2	16		19	16	3 2	$1d_{3/2}^3$
19	20	3 2	$1d_{5/2}^3$		$1d_{5/2}$		6	14		19	18 Ar	3 2	$1d_{3/2}^3$
	22	3 2	$1d_{3/2}^3$		$1p_{1/2}$		2	8		23	20 Ca	7 2	$1f_{7/2}^3$
	24	3 2	$1d_{3/2}^3$		$1p_{3/2}$		4	6		29	24 Cr	3 2	$3p_{3/2}$
21 c	22	7 2	$1f_{7/2}$		$1s_{1/2}$		2	2		31	28 Ni	3 2	$3p_{3/2}^3$
	24	7 2	$1f_{7/2}$							37	30 n	5 2	$1f_{5/2}^{-1}$
31 a	36	3 2	$3p_{3/2}^3$										
49 n	60	9 2	$1g_{9/2}^{-1}$										
51 b	70	5 2	$2d_{5/2}$										
	72	7 2	$1f_{7/2}$										

*The theory of configuration mixing is explained, e.g., in Fényes (2002).

2.3.1.3 Shell Model with Multiparticle Configurations

The interaction between valence nucleons not included in the average field is called the residual interaction. The residual interaction differs from the interaction between free nucleons in that it cannot result in binding into occupied orbits.

If two valence nucleons move in the average field of the core, the residual interaction between them must also be taken into account. As the residual interaction usually gives a weak contribution to the binding, perturbation theory can be applied. In one type of calculation the residual interaction is approximated by a “schematic” (delta, surface delta, Schiffer, etc.) interaction. In another type of calculation, “realistic” interactions are used, which are derived approximately from free nucleon–nucleon interactions. In most calculations, “empirically determined” parameters are used.

The calculations give a reasonable description of the observed energy spectra, electromagnetic and β -decay transition rates, electromagnetic moments, and many other properties of nuclei with closed shells ± 2 nucleons.

It is also possible to perform shell model calculations for nuclei, which have three or more valence nucleons. Nevertheless, the calculations become rapidly very complex with increasing number of valence nucleons. Large-scale shell model calculations were performed mainly for the light nuclides with $A < 70$.

The shell model calculations are explained in detail in several textbooks and review articles: (Brussaard and Glaudemans 1977; Lawson 1980; Brown and Wildenthal 1988; Heyde 1990; Talmi 1993; Fényes 2002).

The shell model calculations for multiparticle configurations are usually very complicated. Nevertheless, several computer programs exist, which help the numerical calculations. The shell model algorithms were reviewed by Vallières and Wu (see Langanke et al. 1991). Several computer programs were described also by Heyde (1990).

Seniority is defined as the number of unpaired nucleons in a state. In the low-seniority scheme, it is supposed that the ground states of even–even semi-magic nuclei consist of pairs of identical nucleons that are coupled to spin zero. In the excited states, one or more pairs are broken. In the ground state of odd- A nuclei, there is one valence nucleon and in the excited states, 1, 3, 5, etc., valence nucleons. The low-seniority scheme calculations (Lawson 1980; Allaart et al. 1988; Talmi 1993) give a reasonable description of numerous semi-magic nuclei that have not too many valence particles (or holes).

If there are many valence protons and neutrons present in the nucleus, traditional shell model calculations lead to insurmountable difficulties. Fortunately, the Bardeen–Cooper–Schrieffer (BCS) theory provides a good approximation method to the seniority-zero shell model, and allows to describe very complex nuclei, too. In the BCS quasiparticle calculations long chains of nuclei can be treated in a relatively simple way. The method was first applied in the theory of superconductivity by Bardeen et al. (1957), then used for nuclear physics by Bohr et al. (1958), Soloviev (1958), and Belyaev (1959). The quasiparticle concept was introduced into nuclear physics by Valatin (1958) and Bogoliubov (1958). The theory is explained in detail in several textbooks (Lawson 1980; Ring and Schuck 1980; Soloviev 1981; Heyde 1990; Nilsson and Ragnarsson 1995; Fényes 2002).

Far from the stability region the density of the outermost nucleons may be very low. According to theoretical predictions, the pairing interaction is probably stronger, while the spin–orbit interaction is weaker in these regions. A reordering of levels was actually observed (► Fig. 2.10). While in $N \approx Z$ nuclei closed shells appear at neutron numbers $N = 8, 20, 28$, in $N \approx 2Z$ nuclei at $N = 6, 16, 32$.

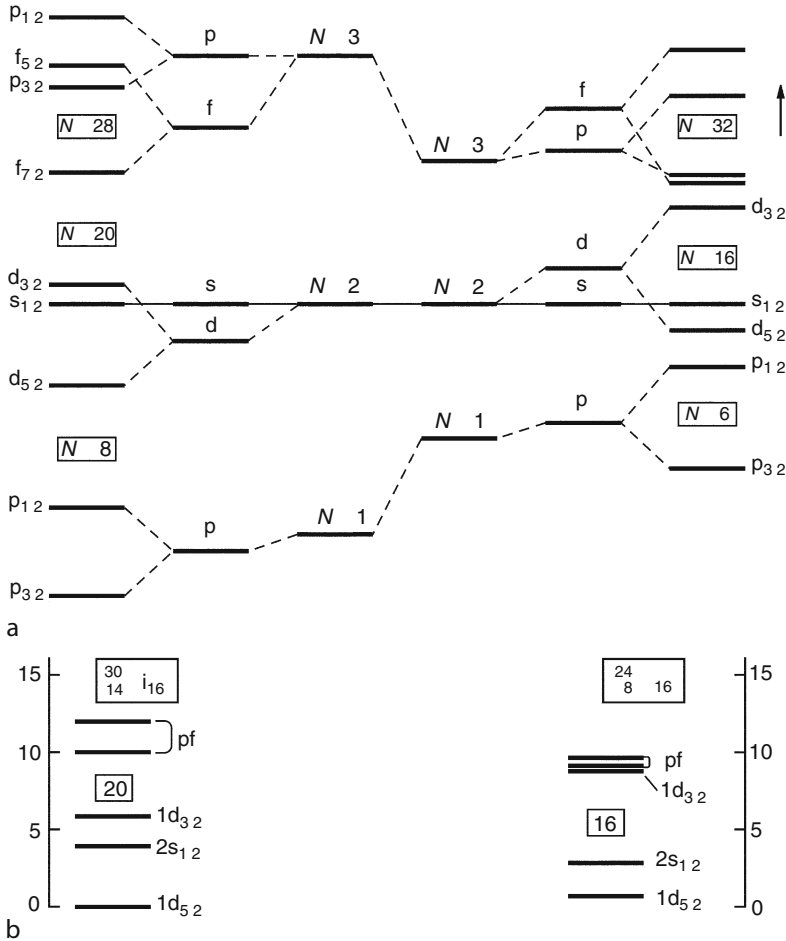
2.3.1.4 Shell Model of Deformed Nuclei

The nuclei are spherical near double closed shells, while in the $150 < A < 190$, $A > 220$ (and other) regions they are deformed. The stable deformation is shown by many experimental facts:

- Large quadrupole moments (► Fig. 2.5).
- Enhanced electric quadrupole transition probabilities (see ► Fig. 2.14).
- Existence of rotational bands. The excitation energies of the “band” members are proportional to $I(I + 1)$, where I is the spin of the state (see ► Sect. 2.3.4).

■ Fig. 2.10

(a) Observed energies of single particle states (E) in the stability region ($N \approx Z$, left side) and far from it ($N \approx 2Z$, right side). (b) Examples for the energy gaps, close to and far from the stability region, are ^{30}Si and ^{24}O , respectively (Based on Dombrádi 2007)



The shell model of deformed nuclei was elaborated by Nilsson (1955) and others. The basic assumptions of the Nilsson model are as follows:

- The shape of the nucleus is an axially symmetric ellipsoid.
- The average potential of the ellipsoidal nucleus is essentially a harmonic oscillator potential (► Fig. 2.2).
- The nuclear matter is incompressible, the nuclear volume is constant.
- There is no friction in nuclear matter.

The detailed mathematical treatment of the theory is described in textbooks (e.g., Nilsson and Ragnarsson 1995). The single particle energies ($\varepsilon_{s,p}$) obtained for medium heavy nuclei are

shown in [Fig. 2.11](#) as a function of the deformation parameter (δ). The explanation of the symbols is as follows.

$\delta \approx \varepsilon_2 - (1/6) \varepsilon_2^2$, $\varepsilon_2 = (c - a)/R_0$, where c and a are half lengths of the longer and shorter axes of the ellipsoid. R_0 is the radius of the sphere, which has the same volume as the ellipsoid.

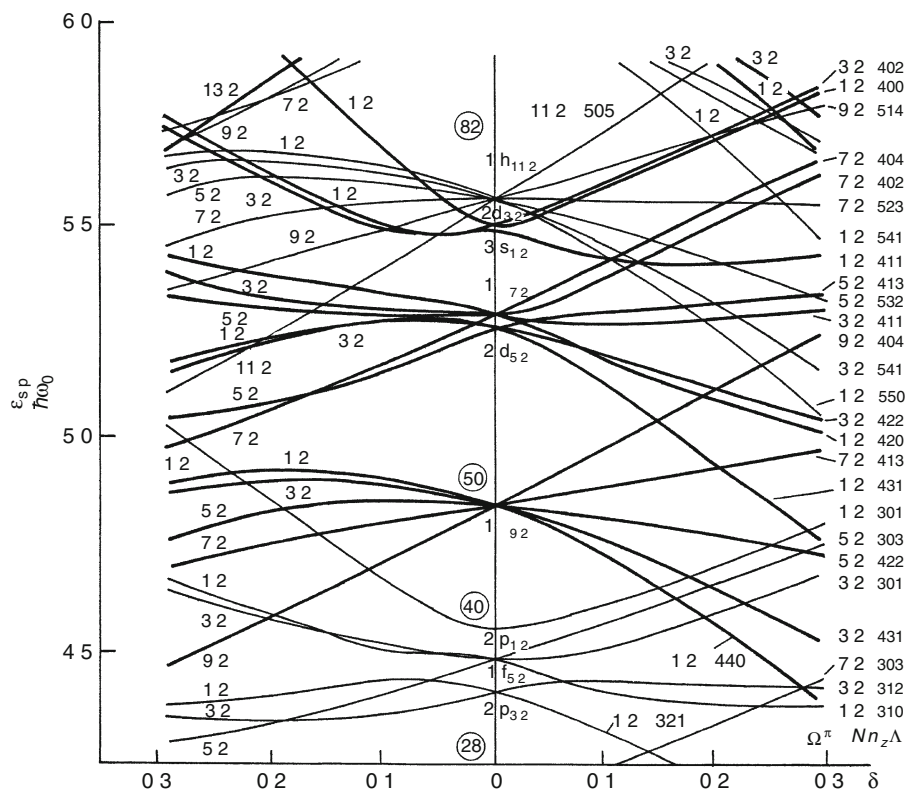
Ω and Λ are the projections of vectors \mathbf{j} and \mathbf{l} on the symmetry axis (z), respectively. The vector \mathbf{j} is the total, \mathbf{l} is the orbital angular momentum of the particle. N and n_z are quantum numbers of the three-dimensional harmonic oscillator potential of an axially symmetric nucleus, $N = n_x + n_y + n_z$.

For small deformations, the energy splitting of the $|Nljm\rangle$ states is proportional to the deformation parameter δ , the oscillator quantum number N , and Ω^2 . For large deformations, the energy again depends on δ and N linearly, but the slopes of the curves are determined by n_z .

With the wave functions of the Nilsson model, it is also possible to calculate the electromagnetic moments and the gamma and beta transition probabilities between single-particle

■ Fig. 2.11

Nilsson diagram. Single-particle energies ($\epsilon_{\text{s.p.}}$ in $\hbar\omega_0 \approx 41A^{-1/3}$ MeV units) as functions of the deformation parameter δ . (Based on Nilsson (1955). The calculations were extended by Bengtsson and Ragnarsson (1985) also to other regions, separately for protons and neutrons and different ϵ_2 , ϵ_4 deformations, see Firestone et al. (1996))



states. The basic formulae can be found, e.g., in Nilsson (1955), Bohr and Mottelson (1974), Soloviev (1981).

A deformed shell model has been elaborated also with the Saxon–Woods potential (see, e.g., Soloviev 1981). In the advanced versions of the theory, pairing correlations, octupole and hexadecapole deformations, and Coriolis mixing have also been included.

The shell model of deformed nuclei was verified for hundreds of nuclei and proved to be very successful. It can account for level schemes, moments, electromagnetic transition probabilities, single-particle transfer reactions, beta-decay properties, etc. in the deformed regions ($A \approx 25$, $150 < A < 190$, $A > 220$).

Note that the quadrupole deformation (which plays a fundamental role in nuclear physics) can be characterized in body-fixed coordinate system by formulae

$$R = R_0[1 + a_{20}Y_{20} + 2a_{22}Y_{22}]$$

or

$$R = R_0[1 + \beta(\cos\gamma)Y_{20} + 2^{1/2}\beta(\sin\gamma)Y_{22}],$$

where R is the radius of the nucleus and Y_{20} , Y_{22} are the spherical harmonic functions. The β parameter describes prolate ($\beta > 0$) or oblate ($\beta < 0$) deformation, while γ characterizes the departure from axial symmetry. In the case of quadrupole deformation $\varepsilon_2 = 0.946 \beta_2$.

2.3.1.5 Calculation of the Total Energy of Nuclei

Taking into account the success of the spherical and deformed shell models, it is tempting to calculate the total energy of nucleus by summation of single-particle proton and neutron energies up to the Fermi level. Then

$$V = \sum_{i=1}^Z e_p^i(\varepsilon_2, \varepsilon_3, \dots) + \sum_{i=1}^N e_n^i(\varepsilon_2, \varepsilon_3, \dots)$$

where V is the sum of single-particle energies in an external potential, e_p^i and e_n^i are the particle energies, and ε_2 , ε_3 are the deformation parameters. (For small values of deformation parameters the radius of the nucleus can be expressed as

$$r = r_0 \left\{ 1 + \frac{2\varepsilon_2}{3} P_2(\cos\theta) - \sum_{\lambda} \varepsilon_{\lambda} P_{\lambda}(\cos\theta) + \dots \right\},$$

where the $P(\cos\theta)$ -s are the Legendre polynomials.) Nevertheless this simple summation of particle energies cannot describe the total energy (and its dependence on deformation parameters) exactly, for example, because problem arises whether or not the contributions from the nucleon–nucleon interactions are double-counted.

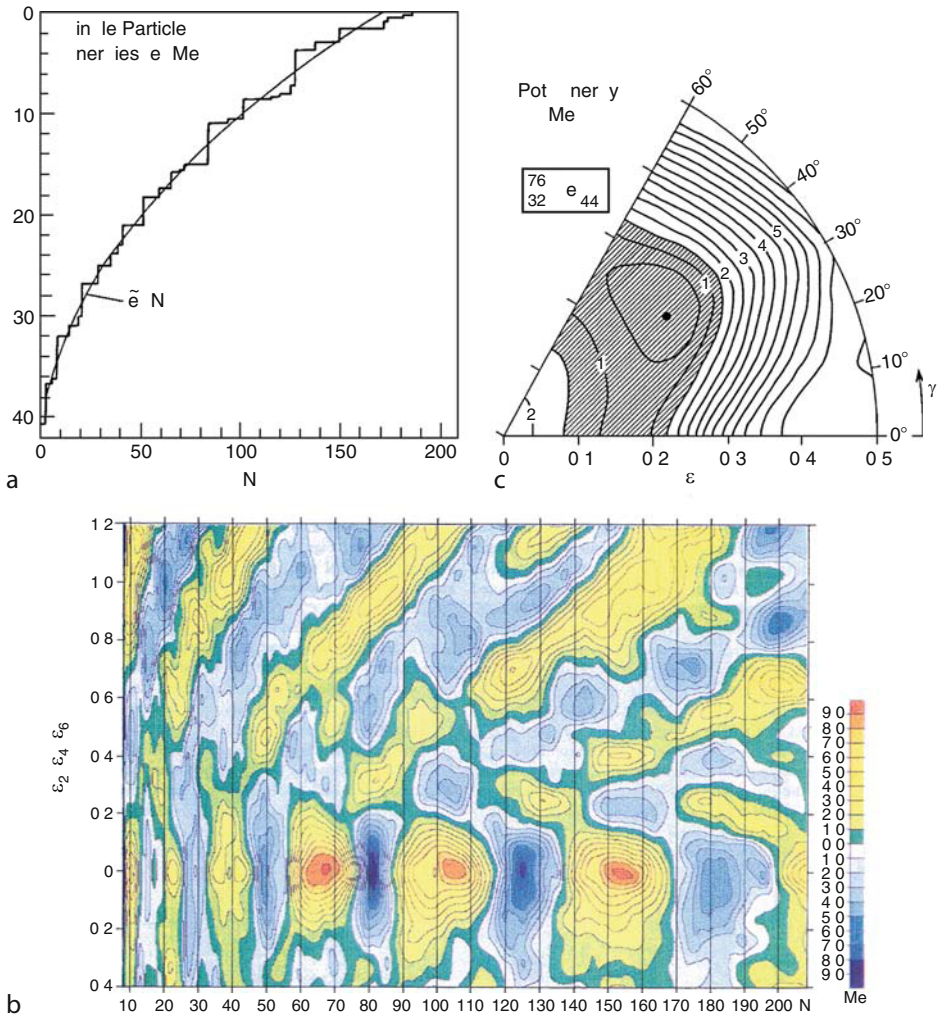
On the other hand, the liquid drop model can correctly reproduce the binding energies of nuclei (see, e.g., [Eq. \(2.3\)](#)), nuclear masses, and the threshold potential of nuclear fission, but it cannot describe the shell effects, ground state spins, and many other quantum characteristics.

Much better results can be obtained, if one combines the shell and liquid drop models, as proposed by Strutinsky (1967, 1968).

[Figure 2.12a](#) shows the theoretical single-neutron energies (e , staircase function) versus neutron number (N). The smooth, average curve $\tilde{e}(N)$ removes local fluctuations. The shell

■ Fig. 2.12

(a) Illustration to the Strutinsky shell correction to liquid drop energy for ^{208}Pb . The figure shows the theoretical single neutron energies ϵ_{STAIR} (staircase function) versus neutron number (N) for a Saxon–Woods-type potential. The smooth, average curve $\bar{\epsilon}(N)$ removes local fluctuations. The shell correction is given by the difference between the two curves up to the given neutron number (Based on Bolsterli et al. 1972). (b) Shell energy (E_{shell}) as a function of the neutron number (N) and deformation parameter ϵ_2 , calculated with a modified oscillator potential using the Strutinsky method. ϵ_2 includes also ϵ_4 and ϵ_6 in such a way that the liquid drop energy should be approximately minimized. The contour line separation is 1 MeV (Taken from Ragnarsson and Sheline 1984). (c) Total (often referred to as “potential”) energy surface for ^{76}Ge as a function of deformation parameters ϵ_2 and γ . The triaxial shape at energy minimum is associated with proton shell gap at $Z = 32$ (From Larsson et al. 1976), see also Ragnarsson et al. (1978). The figure appears in the electronic version in full color



correction (E_{shell}) is given by the difference between the areas under the two curves up to the given neutron number:

$$E_{\text{shell}} = \sum e_i - \sum \tilde{e}_i.$$

If one takes only the fluctuating (staircase) part from the shell model, and the average (smooth) curve is fitted to the liquid drop model values, one can obtain a much better description of the total energies of nuclei. For details of the calculations, see the original publications by Strutinsky or Fényes (2002).

The calculated shell energy (E_{shell}) is shown as a function of neutron number (N) and deformation parameter (ϵ_2) in [Fig. 2.12b](#). One can see that there are numerous local energy minima. The calculations correctly reproduce the magic numbers at zero deformation and predict the existence of many deformed states. The general structure of shell energy is the same for protons and neutrons, and depends on the rotational frequency (see later in [Sect. 2.3.4](#)) only weakly.

[Figure 2.12c](#) shows the potential energy surface of ^{26}Ge in the ϵ_2, γ plane. The energy minimum is obtained at triaxial deformation ($\epsilon_2 \approx 0.27, \gamma \approx 36^\circ$).

2.3.2 Nuclear Transitions, γ Decay, Conversion Electrons

2.3.2.1 Basic Experimental Facts

In atomic nuclei, there are moving protons which have $\rho^e(\mathbf{r}, t)$ charge and $\mathbf{j}(\mathbf{r}, t)$ current densities. Correspondingly, the nuclei can emit or absorb electromagnetic radiation and may have electric and magnetic static moments. As the fundamental laws of the electromagnetic interaction are known, one can obtain valuable information on the nuclear structure from electromagnetic transitions and moments.

The nuclei very often remain in excited state(s) after α or β decay. From these states they decay further to the ground state by γ -ray emission. Nuclear reactions may also lead to excited states, which usually lose their energy first by particle emission (if allowed energetically) and then by γ decay.

The low-lying nuclear states have discrete energies and the corresponding γ rays also have well-defined quantum energies. The wave length of the γ radiation is usually in the range of $10^{-8} < \lambda_\gamma < 10^{-11}$ cm.

The γ quanta may carry away different angular momenta (L). If $L = 1, 2, 3, \dots$ the radiations are called dipole, quadrupole, octupole, etc., respectively. Gamma radiation with $L = 0$ does not exist because the electromagnetic waves have transversal nature (the photons have spin 1). Each multipolarity 2^L is characterized by a specific angular distribution. The radiation may be electric or magnetic, depending on the term of the electromagnetic interaction that is responsible for the particular transition.

For the measurement of lifetimes of excited states, many efficient methods have been elaborated. Some of the direct methods are electronic timing, recoil distance method, Doppler shift and blocking techniques, γ X-ray coincidences; and the indirect methods: Coulomb excitation, (e, e') reactions, resonance fluorescence, particle resonance spectroscopy, etc. The methods were reviewed in Berlovich et al. (1972), Nolan and Sharpey-Schafer (1979), Fényes (1986), and others. Using these techniques, it is possible to measure lifetimes in a very wide ($\geq 10^{-18}$ s) domain.

As an alternative to γ -ray emission, an excited nuclear state can also lose its energy by *internal conversion electron emission*. In this parallel process, the energy of the excited state is transferred directly to an electron of the atomic shell, without previous γ -ray emission. The energy of internal conversion electrons depends on the nuclear transition energy and also on the ionization energy of the K, L, M, ... electrons.

The coefficient of internal conversion is defined as the number of emitted electrons divided by the number of emitted γ quanta:

$$\alpha = N_e/N_\gamma = \alpha_K + \alpha_L + \alpha_M + \dots, \quad (2.29)$$

where $\alpha_K = (N_e)_K/N_\gamma$ is the partial coefficient of internal conversion for K electrons.

The $\alpha_L, \alpha_M, \dots$ coefficients are defined similarly.

According to the theory, the internal conversion coefficient decreases with increasing transition energy and increases with increasing atomic number and multipolarity of γ -radiation. The coefficient α depends also on the electric or magnetic character of the radiation. Internal e^- conversion is possible between 0^+ states, too. If both K and L electron emissions are allowed energetically, the L electron emission is usually weaker ($\alpha_L \approx 0.1\alpha_K$). For $0^+ \rightarrow 0^+$ transitions see the review article by Kibédi and Spear (2005).

The theory of internal conversion is explained in detail, e.g., by Rose (1965). Numerical values of internal conversion coefficients have been published by Band et al. (1976) and Rösler et al. (1978). Selected theoretical partial and total internal conversion coefficients are presented in the form of graphs for M1, M2, M3, M4, E1, E2, E3, and E4 transitions in Firestone et al. (1996). (Here E and M stand for electric and magnetic transitions, and the number following the symbol is just L.) The accuracy of the graphs is 3–5%.

Internal conversion coefficients (ICC) were obtained from relativistic self-consistent-field Dirac–Fock calculations by Band et al. (2002). They presented results for E1,...E5, M1,...M5 transitions in the energy range $E_\gamma = 1 - 2,000$ keV for K, L₁, L₂, L₃ atomic shells of elements $Z = 10 - 126$. The total ICCs and graphs for ICCs were also published. The Dirac–Fock values are in better agreement with experimental results than the relativistic Hartree–Fock–Slater theoretical ones.

A database of available experimental ratios of ICCs for different atomic subshells was published and compared with relevant theoretical results by Raman et al. (2006).

If the energy of the transition is greater than 1.022 MeV, the nucleus may lose its excitation energy also by *internal electron–positron pair emission*. The probability of this mechanism is low; it is usually more than 10^{-3} times smaller than the probability of γ -ray emission. In contrast with the internal conversion electron emission, the internal pair formation coefficient increases with increasing γ -ray energy and decreases with increasing atomic number and multipolarity of transition. A review of internal pair formation was given by Wilson (1965).

The electromagnetic transitions (transition energies, probabilities, multiplicities, selection rules, angular correlation, etc.) offer a very effective tool for the investigation of nuclear states. The systematic study of E0, E1, E2, E3, ... and M1, M2, M3, ... transitions provide information on the quantum numbers of states, on shell structure, core polarization, effective charges, effective gyromagnetic ratios, particle and hole states, collectivity of states, vibrational and rotational excitations, coupling of single particles with collective motion, etc. In this respect, the works of Morinaga and Yamazaki (1976), Brussaard and Glaudemans (1977), Lawson (1980), as well as Ejiri and de Voigt (1989) are referred to.

2.3.2.2 Theory of γ Decay

Basic Formulae

The Hamiltonian of a nuclear system consists of the kinetic and three potential energy terms which contain the strong, electromagnetic, and weak interactions. (The weakest, i.e., the gravitational force can be completely neglected in a nuclear system, see [Table 2.2](#).) The sum of the strong and the electric monopole (Coulomb) interactions determines the wave functions and energy eigenvalues to a very good approximation, and the other electromagnetic multipole interactions (which are at least about two orders of magnitude weaker than the strong interaction) are only perturbations, which may induce transitions between nuclear states. The weak interaction is about four orders of magnitude weaker than the electromagnetic one. Thus, it may play an important role in nuclear processes only in cases when both particle emission (by strong interaction) and γ transition (by electromagnetic interaction) are forbidden. Such a case is the β decay from ground (or long-lived isomeric) states.

The quantum-mechanical transition probability (P) between the initial and final states is given by perturbation theory:

$$P = \frac{2\pi}{\hbar} \left| \int \Psi_f^* H \Psi_i d\nu \right|^2 \frac{dn}{dE}, \quad (2.30)$$

where H is the Hamiltonian of the perturbing electromagnetic interaction, Ψ_i and Ψ_f denote the initial and final wave functions, respectively, $d\nu$ is the volume element, and dn/dE is the number of possible final states per unit energy interval.

This formula of the time-dependent perturbation theory was originally derived by Dirac, but it is often referred to as Fermi's "golden rule No. 2."

The theory of multipole radiation and moments is explained in detail in many monographs and textbooks (e.g., Heitler 1947; Blatt and Weisskopf 1952; Sliv 1961; De Benedetti 1964; Moszkowski 1965; Eisenberg and Greiner 1970; Brussaard and Glaudemans 1977). Only the most important theoretical results shall be summarized here.

The Hamiltonian of the electromagnetic interaction can be approximated by

$$H \approx \int \mathbf{j}(\mathbf{r}, t) \mathbf{A} d\nu, \quad (2.31)$$

where $\mathbf{j}(\mathbf{r}, t)$ is the current density in the nucleus, $\mathbf{A}(\mathbf{r}, t)$ is the vector potential of the electromagnetic field, \mathbf{r} is a spatial vector variable, t is the time.

The scalar potential in the rapidly varying electromagnetic field is supposed to be zero. The vector potential \mathbf{A} satisfies the wave equation in free space:

$$\Delta \mathbf{A} - \epsilon_0 \mu_0 \frac{\partial^2 \mathbf{A}}{\partial t^2} = 0.$$

The transverse nature of electromagnetic waves is expressed by the divergence condition: $\text{div } \mathbf{A} = 0$. Then the electric (\mathbf{E}) and magnetic (\mathbf{B}) fields can be deduced from \mathbf{A} by

$$\mathbf{E} = -\frac{\partial \mathbf{A}(\mathbf{r}, t)}{\partial t} \quad \mathbf{B} = \nabla \times \mathbf{A}(\mathbf{r}, t) \equiv \text{curl } \mathbf{A}(\mathbf{r}, t).$$

The quantities \mathbf{E} and \mathbf{B} satisfy Maxwell's equations. Heitler has shown that the γ quantum carries away L angular momentum (with respect to the source of radiation) in electric (EL) or magnetic (ML) 2^L -pole radiation (Heitler 1936). Thus, the multipole character is closely related to the angular momentum of the radiation.

The transition rate (decay constant) $T(\sigma L; J_i \rightarrow J_f)$ for the transition $J_i \rightarrow J_f$ depends on the electric ($\sigma = E$) or magnetic ($\sigma = M$) character as well as on the multipolarity (2^L) of the radiation. The transition rate has been calculated in the long-wavelength approximation for low-energy γ rays ($E_i - E_f = E_\gamma < 10$ MeV). (In the long-wavelength approximation, it is assumed that $2R\pi \ll \lambda$, where R is the nuclear radius and λ is the wavelength of the γ radiation.) The result is as follows (Blatt and Weisskopf 1952):

$$T(\sigma L; J_i \rightarrow J_f) = G_L(k) B_L^\sigma(J_i \rightarrow J_f), \quad (2.32)$$

where $G_L(k) \equiv \frac{8\pi(L+1)}{L[(2L+1)!!]^2} \frac{k^{2L+1}}{\hbar}$, $k = \frac{E_\gamma}{\hbar c}$, $E_\gamma = \hbar\omega$.

Thus, $G_L(k)$ depends on the energy E_γ and on the multipolarity (2^L) of the transition, where $(2L+1)!! = 1 \cdot 3 \cdot 5 \cdot \dots \cdot (2L+1)$. $B_L^\sigma(J_i \rightarrow J_f)$ is called the reduced transition probability. The reduced transition probability is the factor that contains the effect of the structure of the states involved, without the obvious energy dependence. In principle, between a particular initial and final state several multipole transitions may be possible. Nevertheless, $T(\sigma L; J_i \rightarrow J_f)$ strongly depends on L , and thus usually no more than two multipoles are important in the mixing. For example, M1 transition may be mixed with E2. The square of the mixing ratio is defined as

$$\delta^2 = \frac{I_\gamma(E \text{ or } M, L+1; J_i \rightarrow J_f)}{I_\gamma(M \text{ or } E, L; J_i \rightarrow J_f)}, \quad (2.33)$$

where I_γ is the intensity of γ radiation. The transition rate is related to the time scale of the decaying state:

$$T(\sigma L; J_i \rightarrow J_f) = (\ln 2)/T_{1/2} = 0.6931/T_{1/2} = 1/\tau,$$

where $T_{1/2}$ is the half-life and τ is the mean life. The experimental partial γ -ray half-life $T_{1/2}^{\gamma, \text{exp}}(a)$ for the transition (a) and the measured half-life of the level $T_{1/2}^{\text{exp}}$ are connected by the following relation if the level decays by several (e.g., $x = a, b, c$) transitions of different energies:

$$T_{1/2}^{\gamma, \text{exp}}(a) = T_{1/2}^{\text{exp}} [1 + \alpha_{\text{tot}}(a)] \frac{\sum_{x=a}^c I_{\text{tot}}(x)}{I_{\text{tot}}(a)}, \quad (2.34)$$

where $\alpha_{\text{tot}}(x)$ is the total internal conversion coefficient, $\alpha_{\text{tot}}(x) = \alpha_K(x) + \alpha_L(x) + \alpha_M(x) + \dots$, $I_{\text{tot}}(x)$ is the total transition intensity, $I_{\text{tot}}(x) = I_\gamma(x)[1 + \alpha_{\text{tot}}(x)]$.

The electric reduced transition probability $B(EL)\downarrow$ of de-excitation from an initial (upper) state (J_i) to the final state (J_f) is related to the reduced transition probability $B(EL)\uparrow$ for the excitation of the state J_i by

$$B(EL, J_i \rightarrow J_f) \downarrow = \frac{2J_f + 1}{2J_i + 1} B(EL, J_f \rightarrow J_i) \uparrow. \quad (2.35)$$

This means, for example, that if J_i is a 2_1^+ excited state and J_f is a 0_1^+ ground state, then $B(E2, 2_1^+ \rightarrow 0_1^+) \downarrow = (1/5) B(E2; 0_1^+ \rightarrow 2_1^+) \uparrow$.

The level width (Γ) is defined on the basis of the time-energy uncertainty principle by the following expression:

$$\Gamma \equiv \frac{\hbar}{\tau} = \hbar T, \quad (2.36)$$

where $\hbar = 6.582\,118\,99(16) \times 10^{-22}$ MeV s and T is the transition rate. (The time–energy uncertainty relation expresses that the time τ characteristic of the rate of change of the physical properties of the system is related to the change in energy ΔE , as $\Delta E\tau \geq \hbar$.)

Selection Rules

Owing to angular momentum and parity conservation, some electromagnetic transitions are forbidden. If the initial and final angular momenta of the nucleus are denoted by J_i and J_f , respectively, the conservation of angular momentum sets limits to the possible values of L :

$$|J_i - J_f| \leq L \leq J_i + J_f.$$

This relation is referred to as the triangular rule for vectors \mathbf{J}_i , \mathbf{J}_f and \mathbf{L} .

In [Sect. 2.2.3](#) it was shown that the parity (π) of the wave function of a nuclear state may be either positive or negative; furthermore, the parity is conserved in closed systems in strong and electromagnetic interactions. The parity conservation law can be formulated as follows:

$$\pi_i \pi_\gamma \pi_f = +1,$$

where π_i and π_f are the parities of initial and final states, respectively, and π_γ is the parity of the radiation. From the properties of the electric and magnetic transition operators the following selection rules can be derived:

$$\pi_i \pi_f = (-1)^L \quad \text{for electric radiation,}$$

$$\pi_i \pi_f = (-1)^{L+1} \quad \text{for magnetic radiation.}$$

The electric and magnetic dipole, quadrupole, octupole, etc., transitions are denoted by E1, E2, E3, ... and M1, M2, M3, ..., respectively. The selection rules deduced from angular momentum and parity conservation laws for electric and magnetic multipole radiations are summarized in [Table 2.6](#).

As the table shows, the electromagnetic radiation is forbidden between states $J_i = 0$ and $J_f = 0$. There is no monopole radiation since the electric and magnetic field strengths are perpendicular to the direction of propagation. On the other hand, monopole transitions are often observed in internal conversion electron (or internal pair) spectroscopy.

Table 2.6

Selection rules for electromagnetic radiations. The allowed mixing to the dominating radiation is indicated in parenthesis

Change of angular momentum (ΔJ)	Change of parity between initial and final states			
	$\pi_f / \pi_i = -1$		$\pi_f / \pi_i = +1$	
0 ($0 \rightarrow 0$)	Forbidden		Forbidden	
0 ($1/2 \rightarrow 1/2$)	E1		M1	
0 ($J \rightarrow J$) ($J \geq 1$)	E1	(M2)	M1	(E2)
1	E1	(M2)	M1	(E2)
2	M2	(E3)	E2	(M3)
3	E3	(M4)	M3	(E4)
4	M4	(E5)	E4	(M5)
5	E5	(M6)	M5	(E6)

Single-Particle Transition Rates

The calculation of the transition rate is relatively simple if there is only one particle outside the closed core. The starting assumptions of the calculations may be as follows.

- The spin of the nuclear core is zero and the core does not take part in the process. One needs only to know the wave function of the valence particle in the initial and final states.
- It is assumed that the radial wave functions in the initial and final states are constant within a sphere of radius R , that is $R_{nl}(r) = \text{const.} \neq 0$ if $r \leq R$ and zero if $R < r$. This is a rather crude approximation, not taking into account the real shapes of the radial wave functions, but it simplifies the calculations considerably and it is very useful in practice. The reduced transition probability is evaluated for $J_i = L \pm 1/2$ initial and $J_f = 1/2$ final states.

For electric 2^L -pole radiation (EL) the following single-particle transition rate (T_{sp}) was obtained (in s^{-1}):

$$T_{\text{sp}}[\text{EL}; (L \pm 1/2) \rightarrow 1/2] = \frac{4.4 \times 10^{21} (L+1)}{L[(2L+1)!!]^2} \left(\frac{3}{L+3} \right)^2 \left(\frac{E_\gamma}{197} \right)^{2L+1} R^{2L}, \quad (2.37)$$

where E_γ is the energy of the γ quantum in MeV, R is the radius of the nucleus in fm, and $(2L+1)!! = 1 \cdot 3 \cdot 5 \cdot \dots \cdot (2L+1)$.

Note that in the case of E1 transitions the right-hand side of [Eq. \(2.36\)](#) must be multiplied by effective charge-square correction factors: $(N/A)^2$ for protons and $(Z/A)^2$ for neutrons. For $(J_i = L \pm 1/2) \rightarrow (J_f = 1/2)$ magnetic transitions the following formula was obtained:

$$T_{\text{sp}}[\text{ML}; (L \pm 1/2) \rightarrow (1/2)] = 1.94 \times 10^{21} \frac{(L+1)}{L[(2L+1)!!]^2} \left(\frac{3}{L+3} \right)^2 \left(\frac{E_\gamma}{197} \right)^{2L+1} R^{2L-2}, \quad (2.38)$$

where T_{sp} is given in s^{-1} , E_γ is given in MeV, and R is given in fm.

In a more rigorous treatment, a statistical factor $S(J_i, L, J_f)$ appears on the right-hand side of [Eqs. \(2.37\)](#) and [\(2.38\)](#), too (Moszkowski 1965). In [Eqs. \(2.37\)](#) and [\(2.38\)](#) it was set $S = 1$, which is true for $(J_i = L + 1/2) \xrightarrow{L} (J_f = 1/2)$ transitions. [Equations \(2.37\)](#) and [\(2.38\)](#) are called the Weisskopf estimates, frequently used in nuclear spectroscopy.

Substituting $R = 1.20 A^{1/3}$ fm into the formulae, one can express the electric and magnetic transition rates as functions of mass number A and γ -ray energy E_γ ([Table 2.7](#)). Slightly different results were obtained by Moszkowski for magnetic transition rates, which are also presented in [Table 2.7](#).

Half-lives $T_{1/2} = (\ln 2)/T_L^\sigma$ for electric and magnetic multipole transitions are shown as functions of the γ -ray energy in [Fig. 2.13](#). The half-lives embrace more than 32 orders of magnitude from 10^{16} to 10^{-16} s. For comparison the mean lives ($\tau = T_{1/2}/0.6931$) of atomic levels shall be given here:

In the optical region	10^{-6} to 10^{-8} s
In the X-ray region	10^{-16} to 10^{-17} s
Metastable states	~ 1 to 10^{-3} s

[Figure 2.13](#) shows that the half-lives strongly depend on multipolarity. This means, e.g., that, if the selection rules allow M1 radiation, then M2, M3, etc. can be neglected. Similarly, if E1 is allowed, the E2, E3, ... radiations are negligibly weak. At a given energy E_γ the sequence of transition rates is $T(\text{E1}) > T(\text{M1}) > T(\text{E2}) > T(\text{M2}) > T(\text{E3}) > T(\text{M3}) > T(\text{E4}) > T(\text{M4})$.

■ **Table 2.7**

Single particle estimates for electromagnetic transition rates (T_{sp} in s^{-1}) as functions of mass number (A) and γ -ray energy (E_γ in MeV). The Weisskopf estimates were taken from Wapstra et al. (1959) and Blatt and Weisskopf (1952), the Moszkowski estimates from Moszkowski (1965). The statistical factor (S) is not shown in the table, because $S = 1$ for transitions ($J_i = L + 1/2$) \rightarrow ($J_f = 1/2$), and in other $L = |J_i - J_f|$ cases usually it is not far from one, at least it remains in the same order of magnitude (see in detail, e.g., Moszkowski 1965)

Multipolarity	T_{sp} (Weisskopf)	Multipolarity	T_{sp} (Weisskopf)	T_{sp} (Moszkowski)
E1	$1.0 \times 10^{14} A^{2/3} E_\gamma^{-3}$	M1	$3.1 \times 10^{13} E_\gamma^{-3}$	$2.9 \times 10^{13} E_\gamma^{-3}$
E2	$7.4 \times 10^7 A^{4/3} E_\gamma^{-5}$	M2	$2.2 \times 10^7 A^{2/3} E_\gamma^{-5}$	$8.4 \times 10^7 A^{2/3} E_\gamma^{-5}$
E3	$3.5 \times 10^1 A^2 E_\gamma^{-7}$	M3	$1.1 \times 10^1 A^{4/3} E_\gamma^{-7}$	$8.7 \times 10^1 A^{4/3} E_\gamma^{-7}$
E4	$1.1 \times 10^{-5} A^{8/3} E_\gamma^{-9}$	M4	$3.3 \times 10^{-6} A^2 E_\gamma^{-9}$	$4.8 \times 10^{-5} A^2 E_\gamma^{-9}$
E5	$2.4 \times 10^{-12} A^{10/3} E_\gamma^{-11}$	M5	$7.4 \times 10^{-13} A^{8/3} E_\gamma^{-11}$	$1.7 \times 10^{-11} A^{8/3} E_\gamma^{-11}$

As already mentioned, the Weisskopf estimates are calculated in the single-particle approximation, supposing constant radial wave function. The observed transition rates sometimes strongly deviate from the estimated values. Nevertheless, the Weisskopf units (W. u.) are very useful for comparison. For example, enhanced transition rates (compared to the Weisskopf estimate) signal collectivity.

2.3.2.3 Experimental γ -Ray Transition Rates: Isomeric States

The γ -ray transition rates were compiled and evaluated in different mass number regions: $A = 5-44$ (Endt 1993), $45-90$ (Endt 1979), $91-150$ (Endt 1981), $151-190$ (Andrejtscheff et al. 1975). For recent data see the database Evaluated Nuclear Structure Data File (ENSDF) (<http://www.nndc.bnl.gov/ensdf>).

► **Figure 2.14** presents the reduced transition probabilities for transitions ($E2; 0_1^+ \rightarrow 2_1^+$) \uparrow in even-even nuclei. The $B(E2)$ values have the following characteristics:

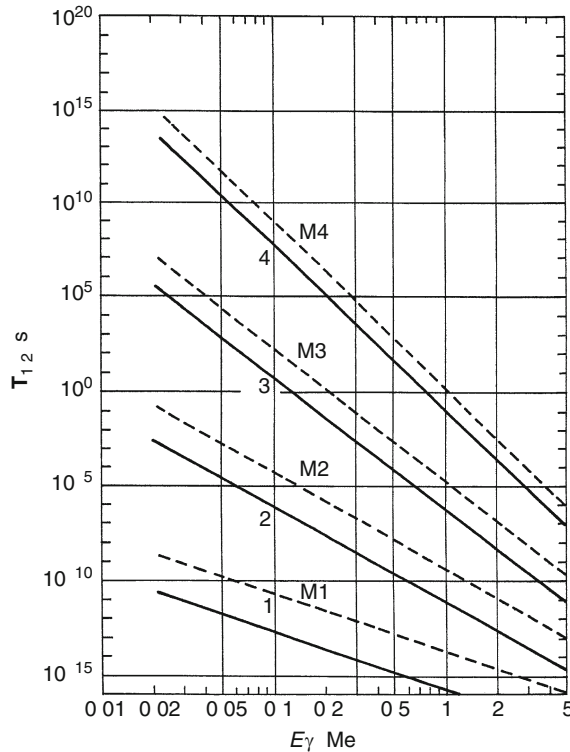
- They are extremely large for strongly deformed nuclei, in the region $160 < A < 180$ and $230 < A$.
- They are very small around magic numbers, e.g. ^8O , ^{50}Sn , ^{82}Pb .
- They are rather large for spherical nuclei elsewhere.

Endt (1981) evaluated 1,340 γ -ray transitions in $A = 91-150$ nuclei. The transition rates were classified according to electric or magnetic multipole character and were expressed in Weisskopf units. Transitions, which can be mixed in principle, are only listed if the mixing ratio has been measured. The strengths $S = T_L^\sigma / (T_L^\sigma)_{sp}$ usually scatter appreciably, nevertheless, upper limits could be established from the data. These are 0.01, 300, 100, and 30 W. u. for E1, E2, E3, and E4; and 1, 1, 10, and 30 W. u. for M1, M2, M3, and M4 radiations, respectively. For upper limits in other regions see (Firestone et al. 1996). The strengths are usually enhanced for E2, and E3, while the E1, M2 transitions are usually hindered.

Note that if there are more than one valence nucleons outside the double-closed core, the residual interaction between the valence nucleons may cause configuration mixing, which may strongly affect the transition rates.

■ Fig. 2.13

Half-lives ($T_{1/2}$) of electric and magnetic transitions vs. γ -ray energy (E_γ) for ^{165}Ho . Weisskopf estimates, based on calculations of Soloviev (1981). At low energies ($E_\gamma < 0.5$ MeV) the internal conversion may reduce the indicated half-lives by orders of magnitude. The half-lives depend also on the mass number. This dependence can be taken into account by different nomograms (Wapstra et al. 1959; Sliv 1961). The half-lives shown in the figure are partial half-lives, which may also have to be corrected for branching, if there are more than one transition from the given level



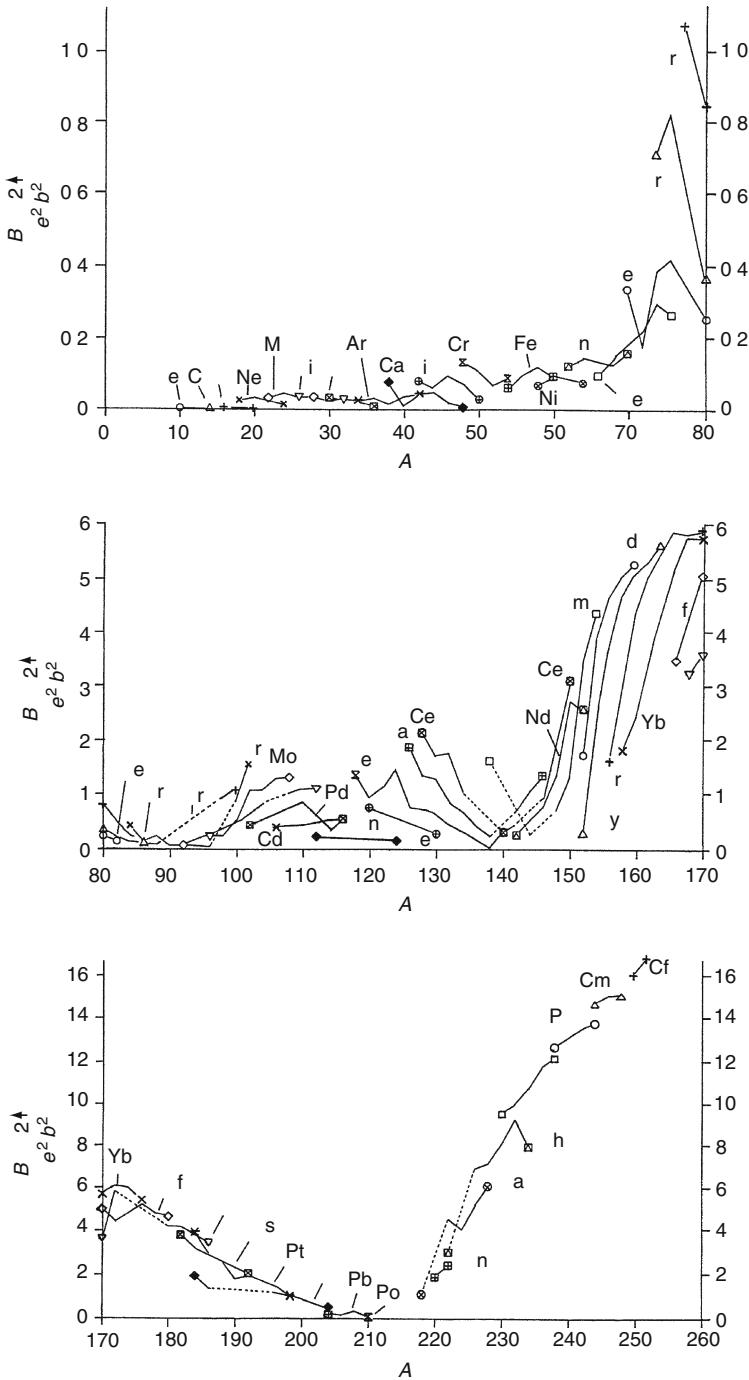
The electromagnetic transitions may be strongly hindered if the spin difference between the isomeric and lower-lying levels is large or the transition energy is very low. The level sequences below magic numbers 50, 82, 126 are as follows (► Fig. 2.9).

Below Z or $N = 50$	Below Z or $N = 82$	Below $N = 126$
$(1g_{9/2})^+$	$(1h_{11/2})^-$	$(1i_{13/2})^+$
$(2p_{1/2})^-$	$(3s_{1/2})^+$	$(3p_{1/2})^-$
$(1f_{5/2})^-$	$(2d_{3/2})^+$	$(3p_{3/2})^-$
$(2p_{3/2})^-$	$(2d_{5/2})^+$	$(2f_{5/2})^-, (2f_{7/2})^-$

This indicates that in these regions large spin differences may occur between levels, and long-lived isomeric states are expected. Indeed, many *long-lived excited (isomeric) states* were observed in these regions. An extensive list of isomeric states (with $T_{1/2} > 10^{-10}$ s) can be found in the

■ Fig. 2.14

Reduced transition probabilities $B(E2; 0_1^+ \rightarrow 2_1^+)$ for even-even nuclei as a function of mass number A . A comprehensive review of the $B(E2; 0_1^+ \rightarrow 2_1^+)$ values is given in Raman et al. (2001)



compilation Kantele and Tannila (1968). See also the database ENSDF mentioned above. The interpretation of many long-lived isomeric states was a great success of the nuclear shell model.

2.3.3 Vibrational Motion

2.3.3.1 Basic Experimental Facts

The experimental evidence on the existence of nuclear surface vibration shall be summarized shortly.

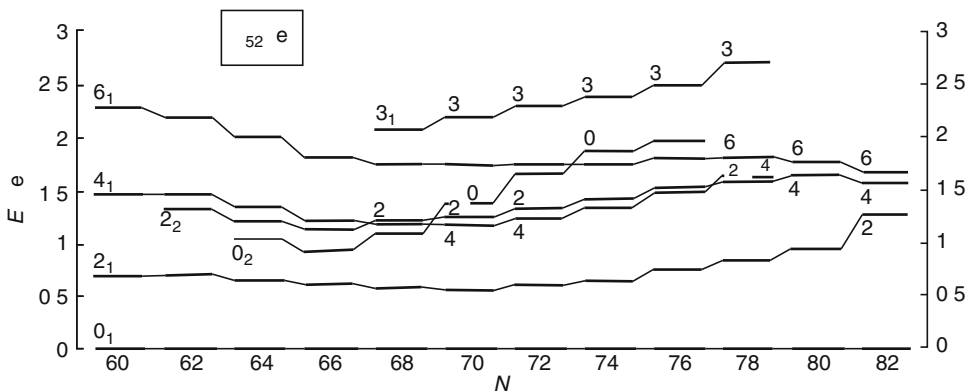
Energy spectra. The systematics of level spectra in even–even nuclei shows that the first excited level is nearly always a 2^+ state with excitation energy $\hbar\omega$, and the next three excited states (with $J^\pi = 2_2^+, 4_1^+$, and 0_2^+) have roughly $2\hbar\omega$ excitation energy. (The subscript on J^π denotes just a sequence number.) Low-lying 3_1^- states have also been observed systematically in even–even spherical nuclei. These regularities can be clearly seen, e.g., in [Fig. 2.15](#) for Te isotopes. [Figure 2.8](#) shows the excitation energies of the first 2^+ states in even–even nuclei as a function of neutron number N . One can see that there exist low-lying 2^+ levels in all even–even nuclei. The level energies generally decrease slowly and monotonously with Z or N , but irregularities are observed at closed- (or nearly closed-) shell nuclei. There are many even–even nuclei in which the $E(4_1^+)/E(2_1^+)$ energy ratio is between ~ 2.0 and 2.4 , characteristic of a vibrator.

Reduced transition probabilities. The systematics of $B(E2; B(E2; 0_1^+ \rightarrow 2_1^+))$ data in even–even nuclei ([Fig. 2.14](#)) shows that the first excited 2^+ states are connected with the 0^+ ground states by fast electric quadrupole transitions. The $B(E2)$ values are usually by order(s) of magnitude larger than the single-particle estimates. The $B(E2)$ probabilities of the $0_2^+, 2_2^+, 4_1^+ \rightarrow 2_1^+$ transitions are comparable with that of the $2_1^+ \rightarrow 0_1^+$ transition (e.g., in ^{114}Cd , [Fig. 2.17](#)). The situation of the 3_1^- states is similar, the $B(E3; 0 \rightarrow 3)$ data are usually order(s) of magnitude larger than the single-particle estimates.

All these data suggest that the lowest states of even–even spherical nuclei cannot be described properly as two (quasi)particle or other single-particle states. These properties are characteristic of a quantum–mechanical vibrator, i.e., an incompressible liquid drop capable of shape vibration.

Fig. 2.15

The positive parity $0_1, 2_1, 0_2, 2_2, 4_1, 6_1$, and negative parity 3_1 levels in even–even Te nuclei



2.3.3.2 Theory of Nuclear Vibration: Comparison with Experimental Data

In [Sect. 2.3.1](#) the *shell model* of spherical and deformed nuclei was discussed. The model gives a good description of various phenomena observed in the light ($A \leq 80$), near double-magic (e.g., around ^{208}Pb) and well-deformed nuclei (e.g., in the regions $150 \leq A \leq 190$, $A \geq 220$). The shell model is a microscopic nuclear model, i.e., it is formulated at the nucleonic level. At the same time, the application of the model far from magic nuclei leads sometimes to very complicated calculations. Furthermore, many observations clearly show the existence of collective behavior in nuclei (surface vibration, collective rotation), which can be treated in macroscopic framework much more simply.

The *liquid drop model* can also explain many nuclear phenomena successfully. The most important ones are as follows: the nuclear volume is proportional to the mass number (A) ([Eq. \(2.15\)](#)); the binding energy per nucleon is approximately constant in a wide mass-number region ([Fig. 2.3](#)); the nuclear masses can be rather well described by the Weizsäcker formula ([Eq. \(2.3\)](#)); nuclear fission (see [Chap. 3](#) in this Volume); Hofstadter's electron scattering experiments show that the nuclear volume is filled up with nucleons rather uniformly. However, the liquid drop model also has its weak points, e.g., it cannot give account of the shell effects.

The basic idea of the *unified model* (Rainwater 1950; Bohr 1952; Bohr and Mottelson 1953) is that the nuclear core can perform collective motion (surface vibration and in the case of deformed nuclei, rotation), while the valence nucleons move on individual orbits.

In the next section, the surface vibration in even–even, odd- A , and odd–odd nuclei shall be discussed.

Even–Even Nuclei

In a hydrodynamical approximation, the nucleus is considered a liquid drop which may perform surface oscillations. The starting assumptions of the theory are as follows.

- The liquid drop has a well-defined surface. This can be described by the radius

$$R(\theta, \phi) = \bar{R} \left[1 + \sum_{\lambda=0}^{\infty} \sum_{\mu=-\lambda}^{\lambda} \alpha_{\lambda\mu} Y_{\lambda\mu}(\theta, \phi) \right] = \bar{R} + \Delta R, \quad (2.39)$$

where \bar{R} is the radius of a sphere which has the same volume as the deformed nucleus, θ and ϕ are the spherical coordinates with respect to an axis fixed to the nucleus, the $Y_{\lambda\mu}$ functions are the spherical harmonics, and μ takes the values $\mu = 0, \pm 1, \dots, \pm \lambda$.

- The nuclear deformation is small, i.e., $\Delta R \ll \bar{R}$.
- The liquid drop is incompressible, i.e., the volume of the droplet ($4\pi\bar{R}^3/3$) does not change during oscillations.
- The fluid moves without friction.
- The velocity field $\mathbf{v}(\mathbf{r})$ of the fluid is irrotational, i.e., $\text{curl } \mathbf{v}(\mathbf{r}) = 0$.
- The oscillation is slow, i.e., the angular frequency of the oscillation is much smaller than the angular frequency of the particle motion ($\omega_{\text{osc}} \ll \omega_{\text{particle}}$).

The hydrodynamical model is described in detail in many publications and books (Bohr and Mottelson 1953; Wohlrab 1960; Alaga 1969; Bohr and Mottelson 1974). Only the most important results of the theory are presented here.

The total energy of the liquid drop consists of three parts: kinetic (T), surface (E_s), and Coulomb (E_C) energies. The calculations give the following result for the total energy of the nucleus (up to second order in $\alpha_{\lambda\mu}$ and in its time derivative):

$$E = E_C(0) + E_s(0) + \frac{1}{2} \sum_{\lambda\mu} B_\lambda \left| \frac{d}{dt} \alpha_{\lambda\mu} \right|^2 + \frac{1}{2} \sum_{\lambda\mu} C_\lambda |\alpha_{\lambda\mu}|^2, \quad (2.40)$$

where $B_\lambda = \frac{1}{\lambda} \frac{3AM}{4\pi} \bar{R}^2$ and $C_\lambda = (\lambda - 1)(\lambda + 2) S_t \bar{R}^2 - \frac{3}{2\pi} \frac{\lambda - 1}{2\lambda + 1} \frac{Z^2 e^2}{\bar{R}}$ are the mass parameter and the stiffness parameter (A is the mass number, M is the average mass of the nucleons), respectively, $\bar{R} = r_0 A^{1/3}$ is the nuclear radius, S_t is the constant of the surface tension, Ze is the charge of nucleus, $E_C(0)$ and $E_s(0)$ are the Coulomb and surface energies of the spherical nucleus, respectively.

As the oscillation is collective, $\alpha_{\lambda\mu}$ and its time derivate are called collective space and velocity parameters, respectively. The third term in [Eq. \(2.39\)](#) is analogous to the classical kinetic energy formula, while the fourth term to the potential energy of the harmonic vibrator ($m\omega^2 r^2/2$). The parameter C_λ corresponds to $m\omega^2$ and $\alpha_{\lambda\mu}$ to the radius. The angular frequency of the 2^λ -pole oscillation is given by

$$\omega_\lambda = \sqrt{C_\lambda / B_\lambda}. \quad (2.41)$$

In the quantum-mechanical theory of collective vibration, one obtains the following energy eigenvalues:

$$E = E_{\text{vibr}} = \sum_{\lambda\mu} \hbar\omega_{\lambda\mu} (n_{\lambda\mu} + 1/2) = \sum_{\lambda} \hbar\omega_{\lambda} \left(n_{\lambda} + \frac{2\lambda + 1}{2} \right), \quad (2.42)$$

where $n_{\lambda} = \sum_{\mu} n_{\lambda\mu} = 0, 1, 2, \dots$, and $n_{\lambda\mu} = 0, 1, 2, \dots$.

This means, that for any λ , the level system of a harmonic oscillator is equidistant. The vibrational quanta with energy $\hbar\omega_{\lambda}$ are called phonons. States with $n_{\lambda} = 0, 1, 2, \dots$ are called $0, 1, 2, \dots$ phonon states. The 2^λ -pole phonons are characterized by their mass (B_λ) and stiffness (C_λ) parameters ($\hbar\omega_{\lambda} = \hbar\sqrt{C_\lambda / B_\lambda}$). Their parity is $(-1)^\lambda$.

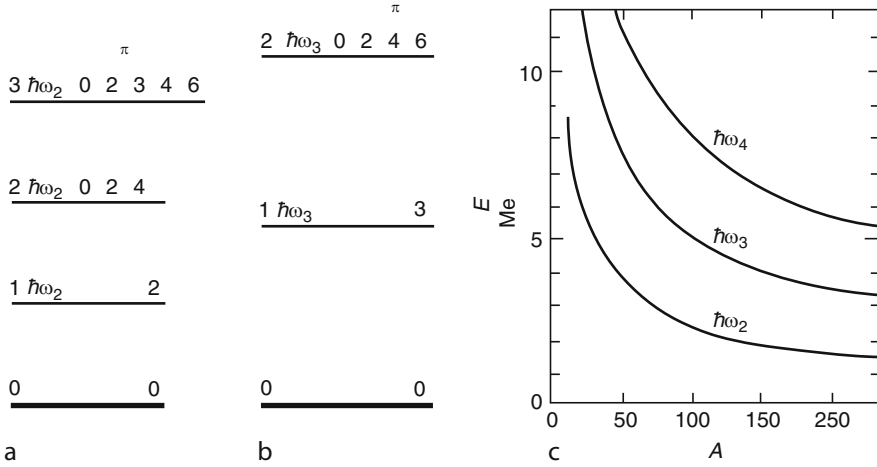
The energy spectra of the harmonic quadrupole and octupole vibrations as well as the phonon energies as functions of mass number are shown in [Fig. 2.16](#). The phonon energies ($\hbar\omega_2, \hbar\omega_3, \dots$) decrease with increasing mass number A . This decrease is very steep for the light nuclei and slow for the heavier ones. The figure also shows the possible spin values of the phonon states. In harmonic approximation, the different $2\hbar\omega_2, 3\hbar\omega_2, 2\hbar\omega_3, \dots$, etc. states are degenerate, i.e., the $n\hbar\omega_{\lambda}$ states are degenerate for each n and λ . For example, the $0^+, 2^+$, and 4^+ states of two quadrupole phonons have the same energy. Nevertheless, if one takes into account higher-order terms in $\alpha_{\lambda\mu}$ and in its time derivative in [Eq. \(2.40\)](#), i.e., in anharmonic approximation, the degenerate levels will split, so that the states with different spins will have different energies (not shown).

Brink et al. (1965) proposed a semiempirical method for the description of the energies of multiphonon states. The method requires the knowledge of the first four excitation energies:

$$\begin{aligned} E(2_1^+), \\ E(0_2^+) &= 2E(2_1^+) + \Delta E_0, \\ E(2_2^+) &= 2E(2_1^+) + \Delta E_2, \\ E(4_1^+) &= 2E(2_1^+) + \Delta E_4, \end{aligned}$$

■ Fig. 2.16

(a, b) Energy spectra of the harmonic quadrupole and octupole vibrations, respectively. (c) Phonon energies $\hbar\omega_2$, $\hbar\omega_3$, and $\hbar\omega_4$ as functions of the mass number A . The results were obtained in the hydrodynamical approximation, with a nuclear radius of $R = 1.44 A^{1/3}$ fm (Based on Bohr and Mottelson 1953)



where ΔE_j is the anharmonic correction to the two-phonon energy $E(J^+)$. Then the three- and higher-phonon level energies are expressed as functions of four parameters: $E(2_1^+)$, ΔE_0 , ΔE_2 , ΔE_4 :

$$E_{I\nu}^{(N)} = NE(2_1^+) + \sum_{j=0,2,4} C_{I\nu j} \Delta E_j, \quad (2.43)$$

where N is the number of phonons, I is the spin of the state, ν is the phonon seniority (number of phonons not coupled pairwise to zero), the symbol $C_{I\nu j}$ stands for the so-called boson fractional parentage coefficient, which depends only on quantum numbers (Bayman and Lande 1966).

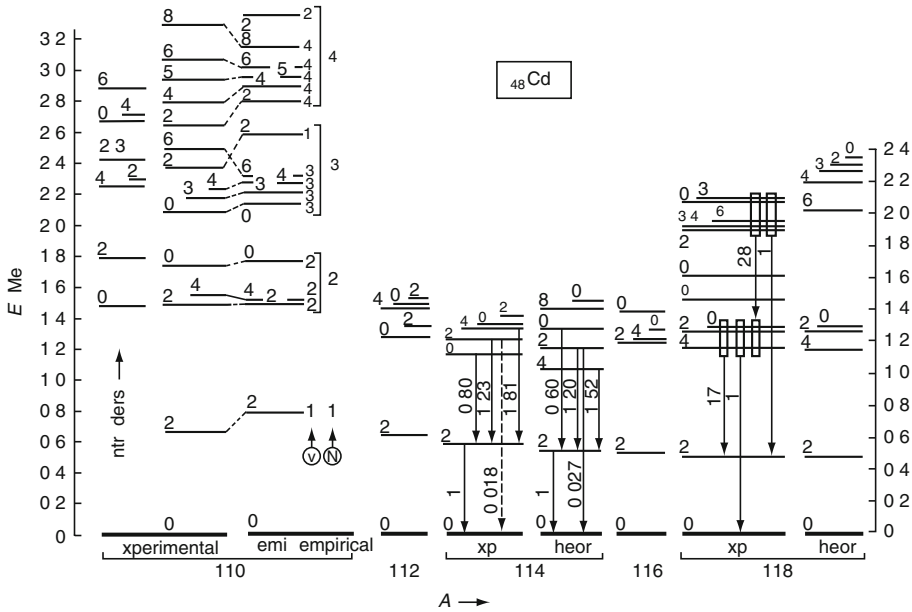
The numerical calculations in the framework of the geometric collective model are helped by different computer codes, e.g., by the code described by Troltenier, Maruhn, and Hess in Langanke et al. (1991). The applied collective Hamiltonian is able to describe both vibrational and rotational excitations of nuclei. The program makes it possible to compute the energy spectra, transition probabilities, and other properties.

The experimental and theoretical low-lying level schemes are compared for the even-even $^{110-118}\text{Cd}$ isotopes in Fig. 2.17. The “intruder” states, shown in the level spectrum of ^{110}Cd , belong mainly to particle-hole excitations across the major closed shell at $Z = 50$. These are not members of the multiphonon excitations. As the figure shows, the theory reproduces both the level energies and the reduced $B(E2)$ transition probabilities fairly well.

In the harmonic vibration approximation the ratio $E(4_1^+)/E(2_1^+)$ is equal to 2. There are really many even-even nuclei, for which this ratio is between 2.0 and 2.4, especially in the $A \leq 140$ region.

■ Fig. 2.17

Low-lying levels of even–even $^{110-118}\text{Cd}$ nuclei. The experimental level data were taken from Bertschy et al. (1995) for ^{110}Cd , otherwise from Firestone et al. (1996). The ^{110}Cd semiempirical calculations were performed by Kern (1997) with Brink's formula. The “intruder states” are out of the scope of the vibrational model. In the case of ^{114}Cd , the reduced E2 transition probabilities are also shown (relative to the $B(E2; 2_1^+ \rightarrow 0_1^+)$ transition) with the corresponding theoretical results (Alaga 1969; Lopac 1967). For the ^{118}Cd transitions the average $B(E2)$ values are shown for different groups of levels. The theoretical ^{118}Cd energy spectrum was obtained for the two-phonon states on the basis of the anharmonic vibrator model (Arahamian 1986; Brink et al. 1965)



Odd-A and Odd–Odd nuclei

If there is a nucleon outside the even–even core, it may interact with the core oscillations. In the particle (hole)–vibration model it is supposed that the nuclear deformation is small; the radius of the nucleus can be described by Eq. (2.38), and the angular frequency of the surface vibrations is much smaller than that of the particle motion ($\omega_{\text{vib}} \ll \omega_{\text{particle}}$). In this case, the particle will follow the changes of the slowly oscillating nuclear average field adiabatically, i.e., the particle will be in an eigenstate belonging to the momentary average field.

The potential of the vibrating core (U) will be a function of the coordinates (r, θ, ϕ). It is assumed that U vibrates together with the nuclear surface:

$$U(r, \theta, \phi) \equiv U\left(\frac{r}{R}\right) = U\left(\frac{r}{1 \pm \sum_{\lambda\mu} \alpha_{\lambda\mu} Y_{\lambda\mu}(\theta, \phi)}\right) \approx V(r) \mp k(r) \sum_{\lambda\mu} \alpha_{\lambda\mu} Y_{\lambda\mu}(\theta, \phi) + \dots, \quad (2.44)$$

where $V(r)$ is the potential of the spherically symmetric nuclear core, $k(r) = r(dV(r)/dr)$, minus and plus signs refer to particles and holes, respectively. (A hole state is a state in which a nucleon is missing from the fully occupied shell.) [Equation \(2.44\)](#) has been obtained by the use of the approximate equality $(1 \pm x)^{-1} \approx 1 \mp x$ (for small x), following from a Taylor expansion. The quadratic and higher-order terms indicated by [Eq. \(2.43\)](#) are usually neglected and $k(r)$ is evaluated at the nuclear surface. Supposing that $V(r)$ is a square-well potential (see [Fig. 2.2](#)) with jump at R_N , at $r = R_N$ one obtains (Bohr and Mottelson 1974; Alaga 1969):

$$k(r) = r \frac{dV}{dr} = R_N V_0 \delta(r - R_N) \approx 50 R_N \delta(r - R_N) \text{ MeV.}$$

The Hamiltonian of the odd-A nucleus consists of three parts:

$$H = H_{\text{sp}} + H_{\text{coll}} + H_{\text{pvc}}, \quad (2.45)$$

where $H_{\text{sp}} = p^2/(2M) + V(r)$ is the single-particle Hamiltonian in the spherical average field, H_{coll} is the collective Hamiltonian (see [Eqs. 2.39](#) and [2.40](#)), and

$$H_{\text{pvc}} = \mp k \sum_{\lambda\mu} \alpha_{\lambda\mu} Y_{\lambda\mu}(\theta, \phi) \quad (2.46)$$

is the term for the particle-vibration coupling. If the particle and the oscillating-field coupling are weak or intermediate, H_{pvc} can be considered a perturbation.

By the use of the particle(hole)-vibration model it was possible to reproduce the level spectra and electromagnetic properties of the odd-A indium isotopes and many other nuclei.

In odd-odd nuclei the total angular momenta of the odd proton (j_p) and odd neutron (j_n) are coupled to a resulting spin $I = |j_p - j_n|, \dots, j_p + j_n$. According to the “parabolic rule” derived by Paar (1979), the energy splitting $\Delta E_2(j_p j_n I)$ of the $|j_p, j_n I\rangle$ multiplet due to a quadrupole interaction through the nuclear core is:

$$\Delta E_2(j_p j_n I) = A[I(I+1)]^2 + BI(I+1) + C, \quad (2.47)$$

where the parameters A , B , and C depend on j_p and j_n , but not on I . The parabolic rule gives a good description of the energy splitting of the proton-neutron multiplets when the quadrupole collective excitation is pronounced. Near-double magic nuclei or very far from closed shells (where the configuration mixing is strong) deviations may occur from the rule. For a more detailed description of vibrational excitations see, e.g., Fényes (2002).

At high (≥ 10 MeV) excitation energies, in several reactions, broad *giant resonances* were observed for virtually all nuclei. These can be attributed to coherent (volume) oscillations of the protons and neutrons. For a review see Harakeh and Van der Woude (2001).

2.3.4 Rotational Motion

2.3.4.1 Basic Experimental Facts

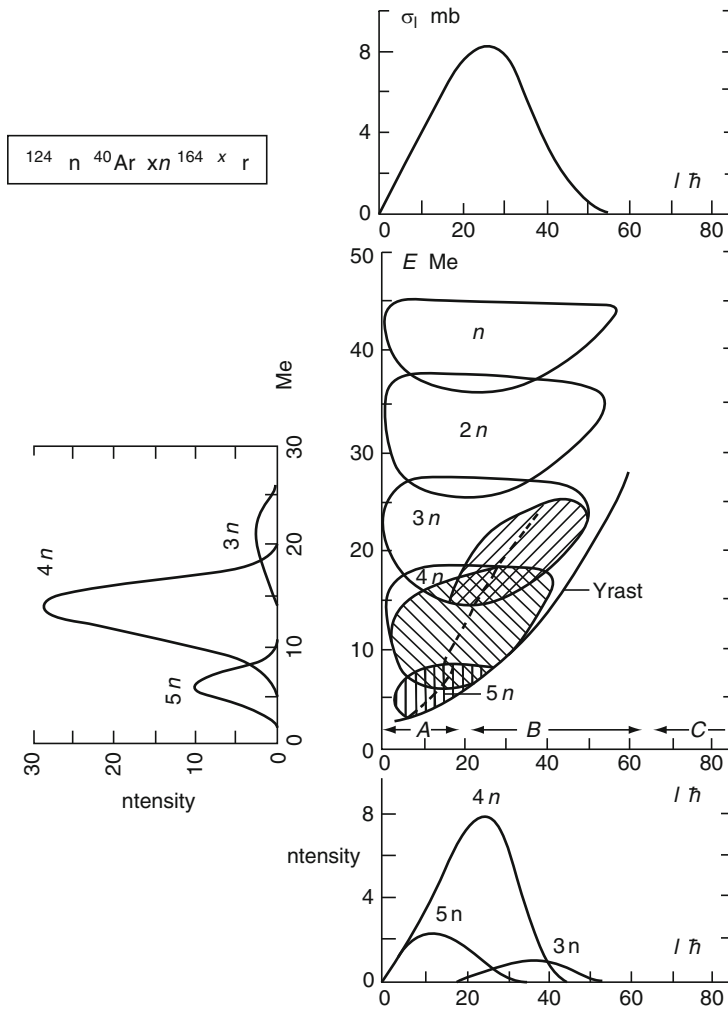
In wide regions of deformed nuclei, one can find low-lying levels with energies approximately proportional to $I(I+1)$, where I is the nuclear spin of the state. As will be seen in [Sect. 2.3.4.2](#), the spectrum of a quantum rotor shows this property. Thus, the existence of such levels may be related to collective nuclear rotation.

Rotational states can be excited in many different ways, through light- and heavy-ion reactions, Coulomb excitation, etc. One of the most effective methods uses heavy-ion fusion reaction.

► **Figure 2.18** shows the statistical model predictions for the reaction $^{124}\text{Sn}(^{40}\text{Ar}, xn)^{164-x}\text{Er}$. The compound nucleus is formed with large average input angular momentum.

■ **Fig. 2.18**

Statistical model predictions for the reaction $^{124}\text{Sn}(^{40}\text{Ar}, xn)^{164-x}\text{Er}$ at 147 MeV bombarding argon energy. The excitation energy of the compound nucleus is 53.8 MeV. Top part: Population of the excited states of the compound nucleus ^{164}Er as a function of input angular momentum I . Middle and lower parts: Calculated population distributions after the emission of 1–5 neutrons as functions of the excitation energy and angular momentum. The hatched areas indicate regions where γ -ray emission competes. Their intensity profiles are shown on the left side and bottom of the figure. The “yrast curve” shows lowest possible energy for a given spin. Based on Hillis et al. (1979). For a detailed analysis of yrast states see Szymański (1983)



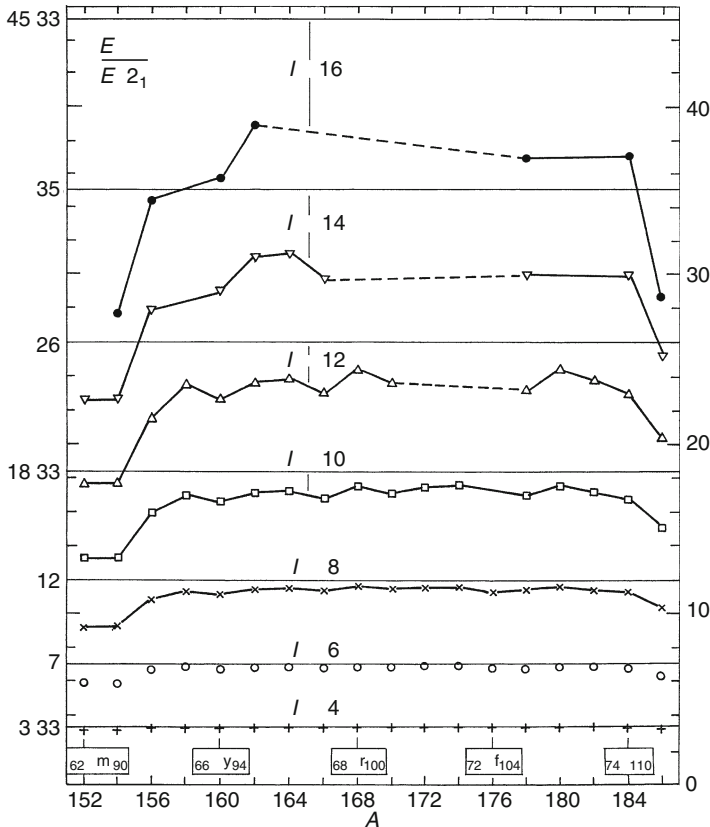
As the evaporated neutrons take away relatively small angular momentum, the residual nucleus remains in a high-spin state (which then decays with successive γ -ray emissions). In this way, rotational bands can be excited up to very high spins (e.g., in ^{152}Dy up to $I \approx 60$).

Properties of Rotational States

One of the characteristic features of rotational excitations is that the first excited states have low energies. This can be seen in [Fig. 2.8](#), where the energies of the first 2^+ states are shown versus the neutron number (N) for even–even nuclei. In the regions of strongly deformed nuclei, $56 \leq Z \leq 78$, $Z > 90$; $90 \leq N \leq 112$, $N > 136$ ([Fig. 2.7](#)) the first 2^+ states have very low-excitation energies. [Figure 2.19](#) shows the systematics of the energy ratio $E(I^+)/E(2_1^+)$ for the ground-state bands of deformed even–even nuclei near the stability curve. The predictions of the $I(I+1)$ rotational energy formula is shown by horizontal lines for states $I = 4^+, 6^+, 8^+, \dots, 16^+$. For low spins the experimental data are close to the predicted values. For higher spins the formula predicts larger values.

Fig. 2.19

The energy ratio $E(I^+)/E(2_1^+)$ in the ground-state bands of even–even nuclei in the mass-number region $152 \leq A \leq 186$. The ratio is shown up to $I^\pi = 16^+$ for nuclei which are closest to the stability curve. Data were taken from (Firestone et al. 1996). The horizontal lines show the predictions of the Bohr–Mottelson $I(I+1)$ formula



Rotational bands can be “built” on the ground state, on various vibrational states, and on different single-particle (Nilsson) states.


The most common type of rotational excitations is *collective rotation*, which is characteristic of the strongly deformed nuclei. In this case, many nucleons contribute coherently to the nuclear motion. The reduced E2 transition probabilities from collective rotational states are usually order(s) of magnitude larger than for single-particle transitions. The moment of inertia of strongly deformed nuclei is large. In the low-lying states, the angular frequency of the collective rotation is much smaller than that of vibrations, let alone internal nucleonic motion: $\omega_{\text{rot}} \ll \omega_{\text{vibr}} \ll \omega_{\text{int}}$. In this case, the rotation does not disturb the nucleonic motion strongly, and an adiabatic description may be successful.

Collective rotational states form series, which are called “bands.” The states belonging to a band are specified by a single “intrinsic” state. The states of a band only differ in the amount of rotation they carry, i.e., in the value of the angular momentum (I) of the rotational motion.

High-spin states were observed also in nearly spherical nuclei, e.g., in $^{147}_{64}\text{Gd}_{83}$. In this case, the level scheme does not show the regular pattern of collective rotation, and the reduced E2 transition probabilities are close to the Weisskopf unit. The high-spin states are produced by the alignment of individual nucleonic orbits. This is the case of *non-collective rotation*. The irregularities are related to the occupation of different single-particle states.


In addition to these two extreme types of rotational motion, a combination of collective and non-collective rotational excitations is also possible.

Structural Changes Induced by Rotation

In the low-spin excitation spectrum (up to angular momentum $\sim 20\hbar$, see region “A” in  Fig. 2.18), the nucleus is relatively cold, and the level structure, density of states, and nuclear equilibrium shape can be described in the framework of the shell model of spherical or deformed nuclei. In the region of well-deformed nuclei, which mostly have axially symmetric shapes in their ground states, the rotational bands can be rather well described by the $I(I+1)$ energy law. The $B(E2)$ reduced transition probabilities are large, showing the collective character of the excitation. The pairing correlations play also an important role. Near the ground state, the nuclei are partly in superfluid phase (i.e., the nucleons are paired to angular momentum zero), which is clearly demonstrated by their reduced moments of inertia.

With increasing angular momentum, increasing centrifugal and Coriolis forces act on the nucleons. The Coriolis force tends to break the nucleon pairs, leading to the “Coriolis antipairing” effect (Mottelson and Valatin 1960). Subsequent investigations showed that the neutron pairing completely disappears at angular momenta of $16\hbar$ – $24\hbar$, while the proton pairing vanishes at $\geq 30\hbar$. This superfluid \rightarrow normal phase transition leads to a substantial increase of the moment of inertia. The Coriolis force is especially strong if the nucleon has a large angular momentum (j). Sometimes, the breaking of one high- j pair and the subsequent alignment of the angular momenta along the rotation axis is sufficient for the explanation of the sudden increase of the moment of inertia of the nucleus.

The “back-bending effect,” i.e., the drastic change of the moment of inertia (at about $I \approx 16\hbar$ for some rare-earth nuclei) was first observed experimentally by Johnson et al. (1971). The explanation of the effect, on the basis of sudden nucleon angular momentum alignment, was given by Stephens and Simon (1972).

With increasing angular momentum (see region “B” in  Fig. 2.18), the strong centrifugal force disturbs the shell structure and drives the prolate nucleus into a triaxial deformed shape.

In the triaxial deformation region a lot more collective states occur than in the region of axially symmetric rotor. These states are characterized by strong intraband and weak interband transitions. The nucleus may perform wobbling motion. Parallel to the yrast line many rotational bands may exist and also band-crossings, producing sudden changes of the moment of inertia.

In the next region “C” (• Fig. 2.18), the shell structure melts and the nucleus acquires an oblate shape. Here the regular pattern of rotational states disappears, and the level scheme is determined by individual nucleons having aligned angular momenta along the rotational axis. The reduced transition probabilities between the states are close to the single-particle values. In this region “yrast traps,” i.e., high-spin, long-lived isomeric levels may also occur.

The potential energy calculations performed for high-spin states show that some nuclei may again acquire triaxial equilibrium shape before fission, and that may lead to collective rotational states.

2.3.4.2 Theory of Nuclear Rotation: Comparison with Experimental Data

Rotation of Even–Even Nuclei

The vast majority of well-deformed nuclei have ellipsoidal or other axial- and reflection-symmetric shapes. The reflection symmetry exists with respect to a plane, going through the center of mass and perpendicular to the axis of rotational symmetry. The rotation of such systems can be described simply (Bohr and Mottelson 1974) because the projection of the total angular momentum on the symmetry axis (• Fig. 2.4b) is a constant of motion. In the following the discussion shall be concentrated on nuclei which have both axial and reflection symmetries.

The Hamilton operator of the system can be written approximately in the form

$$H = H_{\text{in}} + H_{\text{rot}} + H_{\text{vib}},$$

where H_{in} describes the internal motion of particles within the body-fixed coordinate system, H_{rot} is the Hamiltonian of the rotation energy, and H_{vib} describes the surface vibration of the nucleus. Neglecting, for the moment, the internal and vibrational degrees of freedom, the Hamiltonian can be written in the form

$$H \approx H_{\text{rot}} = \frac{R^2}{2\mathfrak{I}},$$

where \mathfrak{I} is the moment of inertia. In an axially symmetric nucleus, the axis of collective rotation is expected to be perpendicular to the symmetry axis. Then the angular momentum (\mathbf{R}) of rotation will also be perpendicular to the axis of symmetry, i.e., $K = 0$ (cf. • Fig. 2.4b). In classical mechanics, the energy of a rotating rigid body is given by $E = \mathfrak{I}\omega^2/2$, where ω is the rotational frequency and $\mathfrak{I}\omega = R$ is the angular momentum. In quantum mechanics, the energy eigenvalues of the rotational Hamiltonian are given by the formula

$$E_{\text{rot}} = \frac{\hbar^2}{2\mathfrak{I}} I(I+1), \quad (2.48)$$

where I is the angular momentum (nuclear spin) quantum number. In the ground states of even–even nuclei, $I = 0$. The systematics of energy ratios $E(I^+)/E(2_1^+)$, presented in • Fig. 2.19, shows that the Bohr–Mottelson $I(I+1)$ formula predicts somewhat higher energies than the

experimental values, indicating that in real nuclei the moment of inertia increases slowly and gradually with increasing energy.

Several phenomenological formulae were proposed that better reproduce the energies of rotational states below the lowest backbending (Harris 1965; Mariscotti et al. 1969; Sood 1967, 1968).

Sood (1967, 1968) had summed up the infinite series

$$E(I) = a_1 I(I+1) + a_2 I^2(I+1)^2 + a_3 I^3(I+1)^3 + \dots$$

taking into account a cue from molecular spectra for the interrelation of the coefficients a_1, a_2, a_3, \dots . His formula reads

$$E(I) = a_1 \left[1 - \frac{(a_2/a_1)I(I+1)}{1 + b(a_2/a_1)I(I+1)} \right] I(I+1), \quad (2.49)$$

where b is determined empirically for each region, e.g., for the actinides $b = 3.00 - (I/30)$. This formula gives excellent description of the experimental data up to high spins both in the rare-earth and actinide regions.

Although the above mentioned phenomenological formulae result in good fits to experimental data, the basis of the theoretical interpretation is not perfectly clear. The main reason for the gradual increase of the moment of inertia is probably the Coriolis antipairing effect. With increasing spin, the Coriolis interaction tends to break the pairs and align the angular momenta of nucleons along the rotation axis. The result is an increase of the moment of inertia. A microscopic description of the moments of inertia near ground states was given by Nilsson and Prior (1961). One can distinguish between two kinds of *moments of inertia*, kinematical $\mathfrak{I}^{(1)}$ and dynamical $\mathfrak{I}^{(2)}$:

$$\begin{aligned} \mathfrak{I}^{(1)} &= \hbar^2 I_x \left(\frac{dE}{dI_x} \right)^{-1} = \hbar \frac{I_x}{\omega}, \\ \mathfrak{I}^{(2)} &= \hbar^2 \left(\frac{d^2 E}{dI_x^2} \right)^{-1} = \hbar \frac{dI_x}{d\omega}, \end{aligned} \quad (2.50)$$

where $I_x = [I(I+1)]^{1/2}$ and $\hbar\omega = dE/dI_x$ (Bohr and Mottelson 1981). For the kinematical moment of inertia, the explicit knowledge of the spin is required:

$$\frac{\mathfrak{I}^{(1)}}{\hbar^2} \approx \frac{2I}{E(I+1) - E(I-1)},$$

while the dynamical moment of inertia can be determined from the differences in transition energies (without knowing I explicitly):

$$\frac{\mathfrak{I}^{(2)}}{\hbar^2} \approx \frac{4}{E(I+2) - E(I) - [E(I) - E(I-2)]}.$$

In the detailed theory, simple expressions were derived for the *reduced electric transition probabilities* $B(E2)$ between rotational levels of the axially symmetric deformed nuclei (Bohr and Mottelson 1974, Sect. 3.2). For example, for the $K = 0, 0_1^+ \rightarrow 2_1^+$ transition (Fig. 2.4b):

$$B(E2; 0_1^+ \rightarrow 2_1^+) = \frac{5}{16\pi} e^2 Q_0^2. \quad (2.51)$$

Note that, according to Eq. (2.34), $B(E2; 0_1^+ \rightarrow 2_1^+) = 5B(E2; 2_1^+ \rightarrow 0_1^+)$. Equation (2.50) means that from the measured reduced transition probabilities $B(E2; 0_1^+ \rightarrow 2_1^+)$ one can determine the *internal quadrupole moment* (Q_0) and also the deformation parameter δ , taking into account that

$$Q_0 \approx 0.8Z\bar{R}^2\delta(1 + 0.667\delta). \quad (2.52)$$

The $B(E2; 0_1^+ \rightarrow 2_1^+)$ values have been determined practically for all even–even nuclei, mainly from Coulomb excitation, lifetime measurements, and electron scattering experiments. The results are summarized in Fig. 2.14. In strongly deformed rare-earth nuclei, δ is around 0.30–0.35, and in the vicinity of magic numbers it is much smaller.

Within the same rotational band Q_0 is constant. In this case the $B(E2)$ ratios for different transitions are determined by the Clebsch–Gordan coefficients (tabulated, e.g., in Lawson (1980) and Bayman and Lande (1966)). These relationships were first formulated by Alaga et al. (1955), and they are called *Alaga rules*. Alaga rules have been derived also for interband transitions for $I_i K_i$ to different $I_f K_f$ and $I_f' K_f'$ states. The rules are widely used by experimental physicists for the construction of rotational bands. As an example, the predictions (Soloviev 1981) of the Alaga rules are given here for E2 transitions from band K_i to ground state band $K_f = 0$:

$$\frac{B(E2; 2_i^+ \rightarrow 4_f^+)}{B(E2; 2_i^+ \rightarrow 0_f^+)} = \begin{cases} 2.57 & \text{for } K_i = 0, \\ 1.15 & \text{for } K_i = 1, \\ 0.075 & \text{for } K_i = 2. \end{cases}$$

The great differences in numerical values help determine unknown K_i quantum numbers. The general agreement of the experimental data with the Alaga rules provides important evidences for the existence of axially symmetric deformation in nuclei and for the separability of a rotational factor from the internal wave function. The calculations lead to the following relationship (cf. Eq. (2.12)) between the *spectroscopic* (Q) and *intrinsic* (Q_0) *quadrupole moments* (Bohr and Mottelson 1974):

$$Q = \frac{3K^2 - I(I+1)}{(I+1)(2I+3)} Q_0.$$

For $I = 0$ and $1/2$ the spectroscopic quadrupole moment is always zero, independently of the value of Q_0 . The sign of Q may differ from that of Q_0 . This is the case, if $K = 0$ or $I(I+1) > 3K^2$. If a prolate nucleus rotates around an axis perpendicular to the body-fixed symmetry axis, the laboratory observer sees oblate deformation.

Expressions have been deduced also for *reduced magnetic dipole transition probabilities* $B(M1)$ and moments (μ) (see, e.g., Bohr and Mottelson 1974; Nathan and Nilsson 1965).

The properties of strongly deformed nuclei can be well described assuming axially symmetric shape. However, in the transitional regions it is necessary to consider also triaxial (i.e., not axially symmetric) shapes. The departure from axial symmetry may be either static (stable deformation) or dynamic (γ surface oscillation). The *theory of γ -soft nuclei* was first developed by Wilets and Jean (1956).

The theory of nuclei unstable against γ deformation was able to explain many properties of transitional nuclei. For instance, in the Wilets–Jean model the value of the ratio $E(4_1^+)/E(2_1^+)$ is ≤ 2.5 , which is much closer to the experimental data than the rigid rotor value 3.33. According to the theory, the $2_2^+ \rightarrow 0_1^+$ crossover transition is forbidden in even–even nuclei.

The experimental data show that when the level sequence $0^+, 2^+, 2^+$ appears, the probability of the $2_2^+ \rightarrow 0_1^+$ transition is indeed much smaller than the probability of the $2_2^+ \rightarrow 2_1^+$ one.

In the theory of γ -unstable nuclei, the central potential changes with time. Consequently, no symmetry axis and no simple constants of motion remain.

The $E(2_1^+) : E(4_1^+) : E(6_1^+) : E(8_1^+)$ energy ratios in different models are as follows:

Harmonic vibrator (► Eq. (2.41))	1:2:3:4,
γ -Unstable rotor	1:(2.5):(4.5):7,
Axial-symmetric rotor (► Eq. (2.47))	1:(3.33):7:12.

The predictions of the γ -unstable rotor model are thus between those of the harmonic vibrator and axial-symmetric rotor models.

The *theory of rigid triaxial rotor* was developed by Davydov and Filippov (1958). The theory makes predictions for the energy of the states and for the electromagnetic transitions. The explicit formulae of the Davydov–Filippov model allow easy comparison with experimental data. Thus, the model was very popular for a long time.

The experimental data and nuclear shape calculations convincingly show that the well-deformed nuclei have axial symmetry at low and moderate angular momenta. At the same time in a wider neutron number region ($N = 84$ – 120), departures were observed from axial symmetry in several Nd, Sm, Gd, Pt, and other nuclei. An analysis performed by Casten (2000) shows that the lack of axial symmetry is associated rather with γ -softness than with stable triaxial deformation.

Nevertheless, one cannot exclude the possibility that rigid triaxial rotors exist in nature. An example is the nucleus ^{76}Ge , for which the potential energy surface calculations, as well as the level spectra and $B(E2)$ values alike demonstrate the occurrence of stable triaxial deformation (Larsson et al. 1976; Ragnarsson et al. 1978).

Note that pure rotational motion is rarely realized in nuclei; the rotational and vibrational excitations are usually mixed. It is very general that there are rotational bands built on the 0_2^+ and 2_2^+ vibrational levels, these are the so-called β - and γ -vibrational bands. The *rotation–vibration coupling* is discussed, e.g., in Bohr and Mottelson (1974) and Garrett (2001) publications.

Rotation of Odd-A Nuclei. Particle-Rotor Model

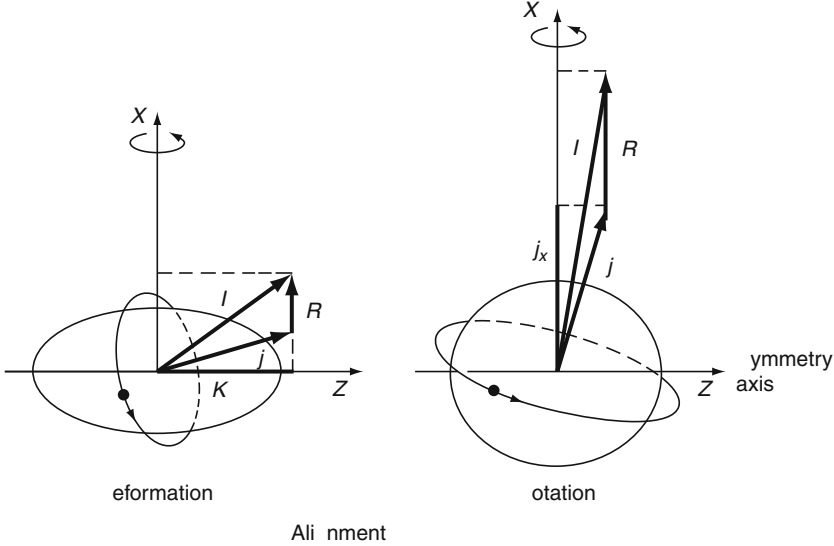
The angular momentum (\mathbf{j}) of a nucleon moving in the average field of an axially symmetric nuclear core may be coupled to the core in different ways. The two possible extreme coupling schemes are illustrated in ► Fig. 2.20. If the deformation is strong, the rotation is slow, and \mathbf{j} is small, then usually the deformation (or strong) coupling scheme is realized in nature. The projections of \mathbf{j} and \mathbf{I} on the symmetry axis (Ω and K , respectively) are equal, and they are constants of motion. However, if the rotation is fast, the strong Coriolis force may decouple \mathbf{j} from the symmetry axis and align it in the direction of the rotation axis. In this case the rotation (or weak) coupling scheme is realized.

In the case of *deformation alignment* (see left part of ► Fig. 2.20), the Hamiltonian of the rotating nucleus can be written in the form

$$H = \frac{\hbar^2}{2\mathfrak{I}} \mathbf{R}^2 = \frac{\hbar^2}{2\mathfrak{I}} (\mathbf{I} - \mathbf{j})^2 = \frac{\hbar^2}{2\mathfrak{I}} (\mathbf{I}^2 + \mathbf{j}^2 - 2\mathbf{jI}), \quad (2.53)$$

■ Fig. 2.20

Illustration of the deformation-alignment and rotation-alignment coupling schemes. j and R are the angular momenta of the particle and the core, respectively. I is the resulting spin of the nucleus. Usually the deformation alignment is realized in nature, if the deformation is strong, the rotation is slow, and j is small, while the rotation alignment is preferred in the opposite case



where \mathfrak{I} is the moment of inertia. Detailed calculations give the following expression for the rotational energy:

$$E_{\text{rot}}(I) = \frac{\hbar^2}{2\mathfrak{I}} \left[I(I+1) + j(j+1) - 2K^2 + \delta_{K,1/2} a(-1)^{I+1/2} (I+1/2) \right], \quad (2.54)$$

where a is the decoupling parameter and $\delta_{K,1/2} = 1$, if $K = 1/2$. If $K \neq 1/2$ and for high j values $j(j+1) \approx K^2$ this formula may be simplified to

$$E_{\text{rot}}(I) \approx \frac{\hbar^2}{2\mathfrak{I}} [I(I+1) - K^2], \quad K \neq 1/2. \quad (2.55)$$

As $I \geq K$, the members of the band have the following spins $I = K, K+1, K+2, \dots$

If the odd particle has a large angular momentum (j), the deformation is not strong, and the rotation of the core is fast, then the Coriolis interaction may align j along the rotation axis and in this way minimize the total energy (Stephens 1975). In the *rotation-aligned case*, when $j \approx j_x$ (► Fig. 2.20), the rotational energy may be written in the form (cf. ► Eq. (2.52)):

$$E_{\text{rot}} \approx \frac{\hbar^2}{2\mathfrak{I}} [I(I+1) + j_x(j_x+1) - 2Ij_x] = \frac{\hbar^2}{2\mathfrak{I}} [(I-j_x)(I-j_x+1) + 2j_x] \quad (2.56)$$

and as $I - j_x \approx R$

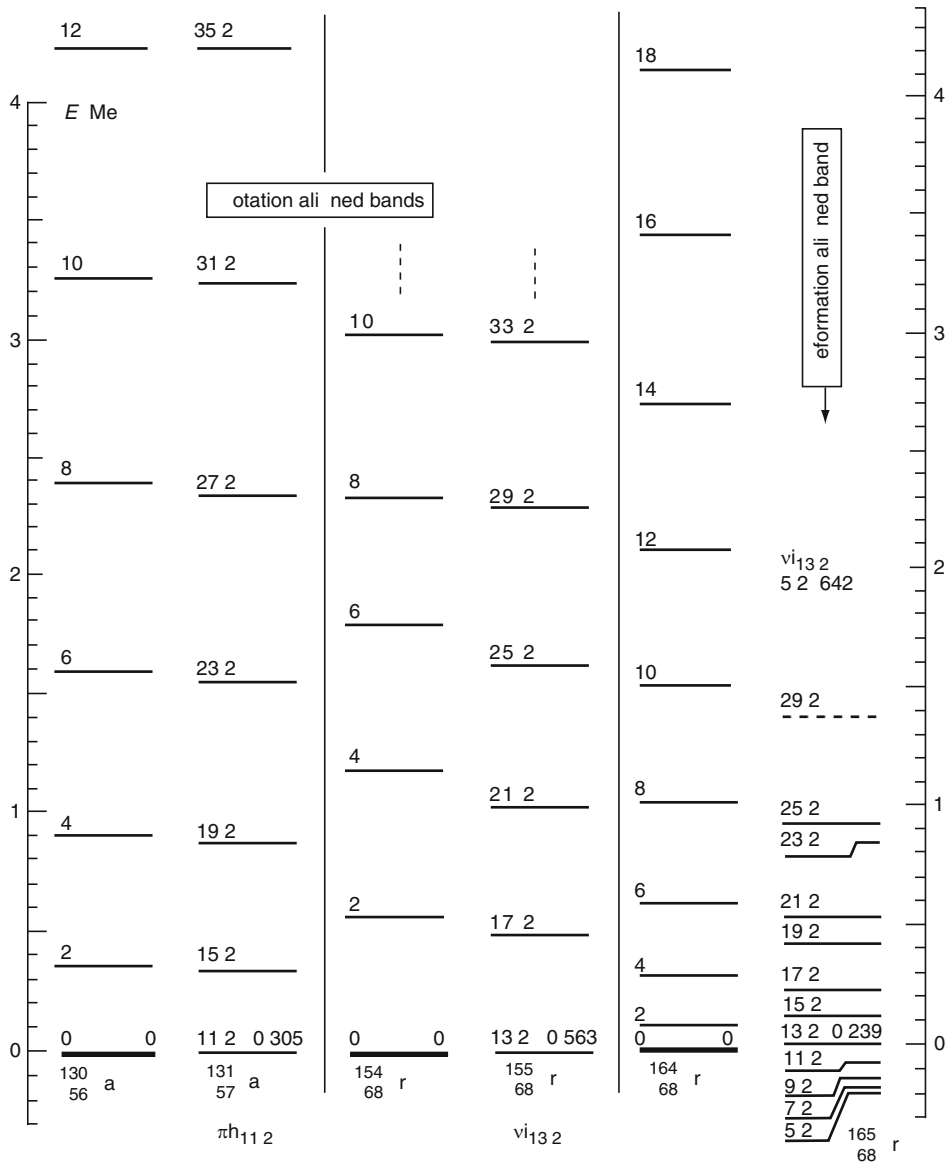
$$E_{\text{rot}} \approx \frac{\hbar^2}{2\mathfrak{I}} R(R+1) + \text{const.} \quad (2.57)$$

The energy spectrum of an odd- A nucleus will thus be very similar to that of its even-even neighbor (see ► Eq. (2.47)) and I will take the values of $j, j+2, j+4, \dots$

Examples for deformation alignment and rotation alignment are shown in [Fig. 2.21](#). The right-hand side of the figure compares the energy spectra of the strongly deformed nuclei ^{164}Er and ^{165}Er . The spectra are quite different because the $i_{13/2}$ neutron of ^{165}Er is deformation-aligned and therefore its spectrum may be described by [Eq. \(2.54\)](#) with $I = K, K + 1, K + 2, \dots$

Fig. 2.21

Examples for rotation and deformation aligned bands. Energy levels in some odd-A nuclei, compared with the ground state bands of neighboring even-even nuclei. The energy scale is shifted in the case of odd-A nuclei. The symbols π and ν stand for proton and neutron, respectively. Data from Lieder and Ryde (1978), completed from Firestone et al. (1996)



As the left-hand side of [Fig. 2.21](#) shows, the rotational band based on the $11/2^-$ 0.305 MeV state of $^{131}_{57}\text{La}$ and the $13/2^+$ 0.563 MeV state of $^{155}_{68}\text{Er}$ are very similar to the ground state bands of the neighboring even–even nuclei $^{130}_{56}\text{Ba}$ and $^{154}_{68}\text{Er}$, respectively. This strongly suggests that the $h_{11/2}$ proton in ^{131}La and the $i_{13/2}$ neutron in ^{155}Er are aligned along the rotation axis, and the rotational spectrum is determined mainly by the even–even core.

The rotation alignment is rather common in the weakly deformed nuclei; however, with increasing deformation, intermediate coupling schemes are realized.

A microscopic description of rotational nuclear motion is also possible by the use of the cranked shell model of Inglis (1954). The model is discussed in detail in several monographs (e.g., Szymański 1983; Nilsson and Ragnarsson 1995; Fényes 2002). The cranking shell model calculations satisfactorily account for the absolute values of aligned angular momenta and for the rotational frequencies, at which the alignment of different orbits occurs.

Rotation of Superdeformed and Hyperdeformed Nuclei

A nucleus is called superdeformed or hyperdeformed in states in which the ratio of its axes is approximately 2 or 3, respectively.

[Fig. 2.12b](#) shows the calculated shell energy (and the local energy minima) in the deformation parameter – neutron number plane. The predicted superdeformed shapes may be stabilized by centrifugal and Coriolis forces in rotating nuclei.

The first rotational band, built on a superdeformed state was discovered by Nyakó et al. (1984) and Twin et al. (1985) in the $^{108}\text{Pd}(^{48}\text{Ca},4n)^{152}\text{Dy}$ reaction. The observed γ -spectrum is shown in [Fig. 2.22a](#), and a partial level scheme of ^{152}Dy in [Fig. 2.22b](#).

The existence of superdeformed (SD-1) states in ^{152}Dy is proved by the following experimental results.

- The level energies can be ordered in a very regular rotational band, with no band crossing. The observed SD-1 band consists of 17 γ -transitions with almost constant spacing of $\Delta E_\gamma = 47$ keV.
- The deduced dynamical moment of inertia $\mathfrak{S}_{\text{SD-1}}^{(2)} = 85\hbar^2 \text{ MeV}^{-1}$ is very large and corresponds to the rigid body value.
- According to the Doppler shift measurements, the SD-1 band members are connected via enhanced E2 transitions with reduced transition probabilities $B(E2)_{\text{exp}} = 2,500 \pm 500 \text{ W. u.}$ This is very close to the theoretical value $B(E2)_{\text{theor}} = 2,390 \text{ W. u.}$ predicted for $\beta_2 = 0.6$ deformation.

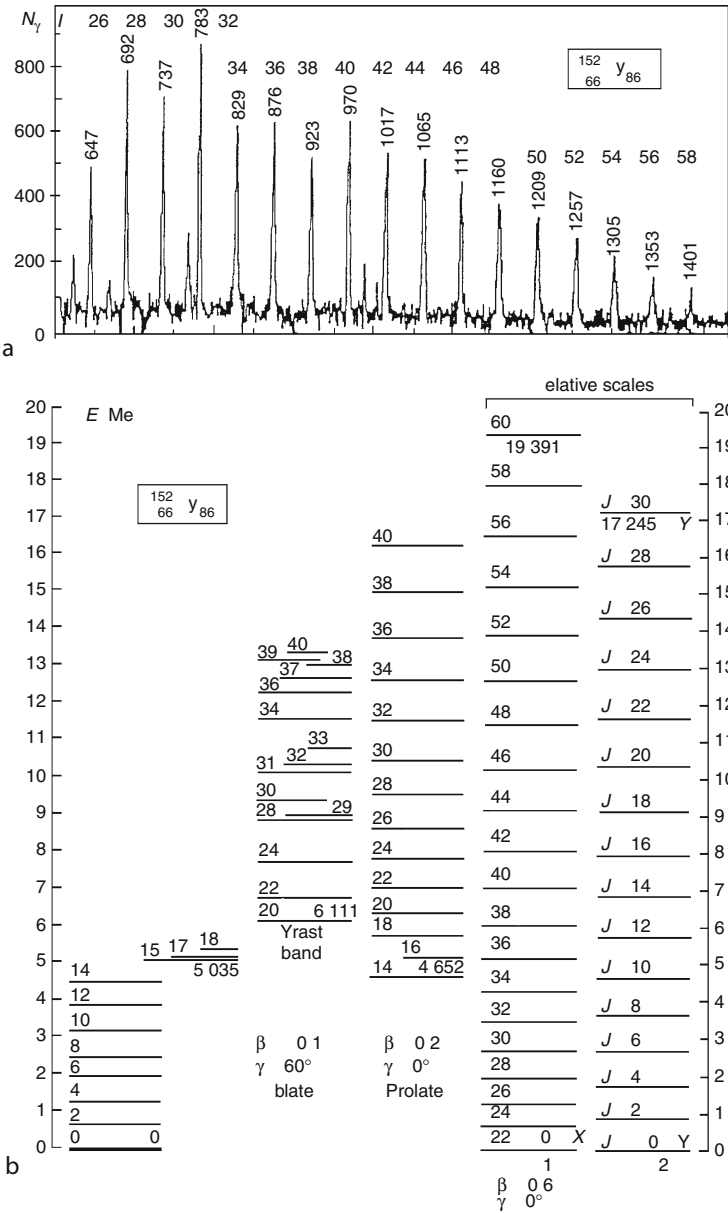
Several other coexisting nuclear shapes have also been identified in ^{152}Dy with different β and γ deformation parameters ([Fig. 2.22b](#)).

The discovery of superdeformed rotational bands in ^{152}Dy was a very impressive achievement of nuclear spectroscopy from many reasons. From the experimental point of view, it has shown that discrete γ cascades can be observed from states whose excitation energy varies from ~ 12 to ~ 30 MeV and spin from (22) to (60) \hbar . From the theoretical point of view, it has demonstrated that the rotation can stabilize very deformed shapes. In this way, a new possibility has been opened to study the quantal effects at very high spins. There are already ≥ 170 superdeformed bands known in the $A \approx 80, 130\text{--}140, 150, 190$ mass number regions. For detailed description, see Szymański (1983), Nilsson and Ragnarsson (1995), and Fényes (2002).

Krasznahorkay et al. (1998, 1999) and Csatlós et al. (2005) have found also hyperdeformed states in ^{234}U and ^{236}U from the study of $^{233}\text{U}(\text{d,pf})^{234}\text{U}$ and $^{235}\text{U}(\text{d,pf})^{236}\text{U}$ reactions. For

Fig. 2.22

(a) γ -ray spectrum of ^{152}Dy from the reaction $^{108}\text{Pd}(^{48}\text{Ca},4n)^{152}\text{Dy}$ at 205 MeV bombarding particle energy. Counts per energy interval (N_γ) as a function of quantum energy of γ -rays (E), I is the probable spin of the γ -emitting state. (b) Partial level scheme of ^{152}Dy . (The known negative parity states are not shown.) SD-1 and SD-2 show different rotational bands built on superdeformed states. The symbols 0 + X, 0 + Y indicate that the absolute positions of the SD-1, SD-2 bands are not known. Level scheme data were taken from Firestone et al. (1996), deformed parameters from Sharpey-Schafer (1990)



example, the deduced moment of inertia of a ^{236}U state was $217 \pm 38 \hbar^2/\text{MeV}$, which corresponds to a hyperdeformed configuration.

Energy Surfaces at Rotating Nuclei

Strutinsky's shell correction method enables the calculation of the static nuclear energy surface as a function of deformation parameters and neutron (or proton) number (see in [▶ Sect. 2.3.1.5](#)). The total energy of nuclei is obtained as a sum of the shell (E_{sh}), liquid drop (E_{LD}), and rotational kinetic energies:

$$E_{\text{tot}}(\epsilon_2, \gamma, \dots, I) = E_{\text{sh}}(\epsilon_2, \gamma, \dots, I) + E_{\text{LD}}(\epsilon_2, \gamma, \dots, I = 0) + \frac{\hbar^2 I^2}{2\mathfrak{I}_{\text{rig}}(\epsilon_2, \gamma, \dots)},$$

where $E_{\text{sh}} = \sum e_i(I) - \sum \tilde{e}_i(I)$, and e_i is the single particle energy, $E_{\text{LD}} = E_{\text{surface}}(\epsilon_2, \gamma, \dots) + E_{\text{Coul.}}(\epsilon_2, \gamma, \dots)$, $\mathfrak{I}_{\text{rig}}(\epsilon_2, \gamma, \dots)$ the moment of inertia of the rigid body. The calculated energy surfaces of ^{158}Yb are presented in [▶ Fig. 2.23a](#).

The cranked shell model of Inglis offers a microscopic description of the rotational motion. The combination of the above methods gives a new possibility for the nuclear energy surface calculations at high spins. In $^{158}\text{Yb}_{88}$ there are only few particles outside the ^{146}Gd core. In the state $I^\pi = 47^+$ terminating the band the angular momenta of the valence nucleons are quantized along the rotational axis as shown in [▶ Fig. 2.23b](#).

2.3.5 Interacting Boson Models

In addition to the shell model and geometric collective model, there exists a third basic approach to nuclear structure, the *interacting boson model* (IBM). A boson is a particle of integer spin. Bosons obey Bose–Einstein statistics, and the wave function of two identical bosons is symmetric under particle exchange.

In the atomic nuclei, one can observe exact and dynamic symmetries, which play important roles in the understanding of nuclear structure. The symmetry connected with the rotation in three-dimensional space (rotational invariance) is an exact, geometrical symmetry. A consequence of rotational invariance is the conservation of angular momentum. Symmetries that arise from a special form of the interaction are called dynamical symmetries. The invariance transformations of dynamical symmetries can usually be formulated in an abstract, higher-dimensional space, which includes, e.g., also the momentum coordinates, in addition to the space coordinates.

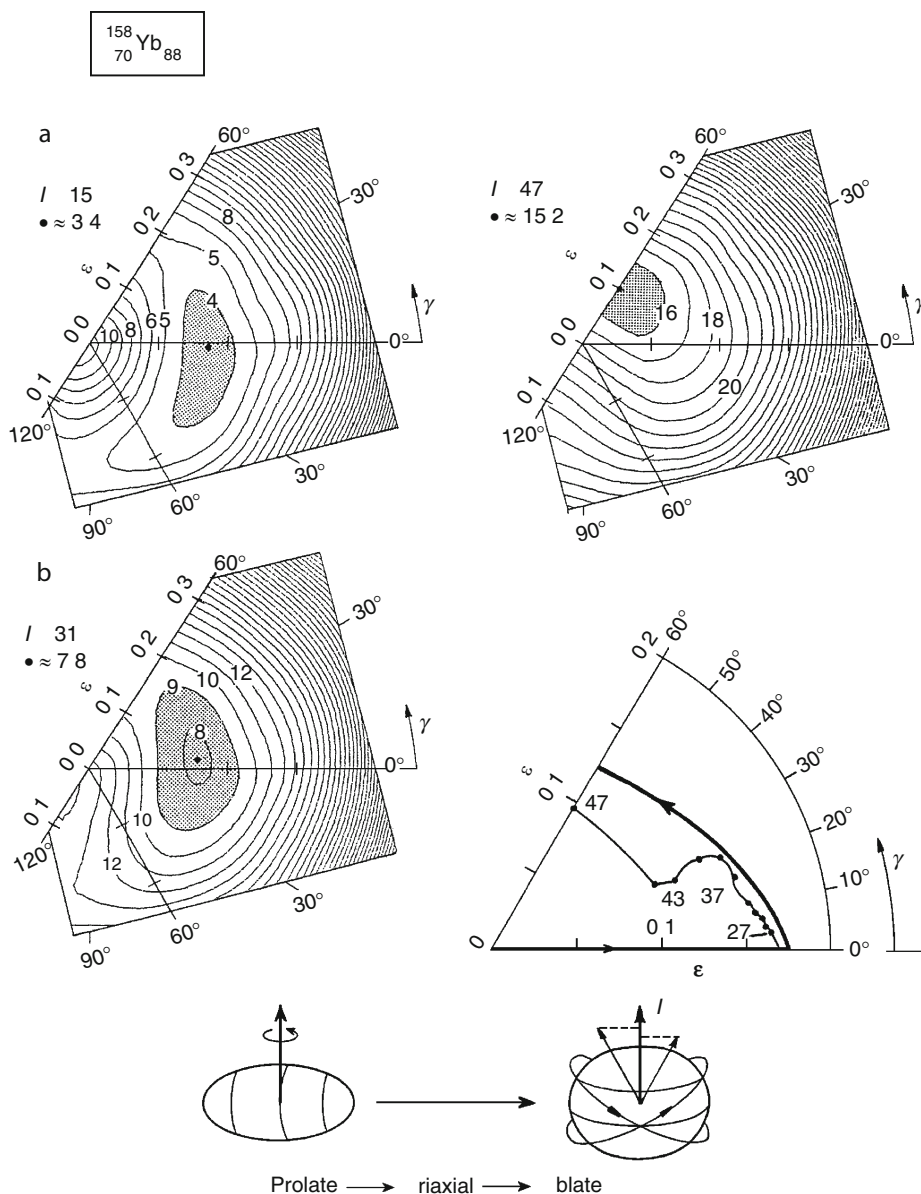
The interacting boson model applies group theoretical (or algebraic) methods and describes nuclear states of various collectivity and symmetry in a uniform framework (see reviews by Iachello and Arima (1987), Iachello and Van Isacker (1991), and Fényes (2002)).

The *starting point* of the interacting boson model is the shell model, but IBM drastically truncates the available configuration space, in order to hold the calculations within reasonable limits. At the same time, the IBM keeps the most important elements substantial for the description of the properties of nuclei.

The first, simplest version of the interacting boson model, the IBM-1 intends to give a description of positive parity levels of medium-heavy even–even nuclei. The model was later considerably extended and now there are versions which are able to treat also negative parity states, both light and heavy, odd-A and odd–odd nuclei, low-lying states and giant resonances, etc.

■ Fig. 2.23

(a) Energy surfaces of ^{158}Yb in the $\varepsilon \equiv \varepsilon_2, \gamma$ plane for configurations terminating in the state $\pi[(d_{5/2})_{3/2}^{-1}(h_{11/2})^6 d_{3/2}] \nu[(f_{7/2} h_{9/2})^4 (i_{13/2})^2]$ at $I^\pi = 47^+$. The subscript 3/2 of $(d_{5/2})_{3/2}^{-1}$ indicates that this hole state contributes to the total spin by 3/2. (b) Shapes of ^{158}Yb corresponding to minimum energy in the $\varepsilon \equiv \varepsilon_2, \gamma$ plane for the above terminating configuration (Based on Bengtsson and Ragnarsson (1985) and Ragnarsson et al. (1986))



The basic assumptions of IBM-1 are as follows:

- The closed proton and neutron shells are inert; they do not take part in the excitations.
- The valence protons and, separately, the valence neutrons are coupled to s and d pairs with angular momenta $J = 0$ and 2 , respectively. See [Fig. 2.24](#).

The numbers of valence protons and neutrons have to be counted from the nearest major closed shells, therefore, the particle and hole states are discussed on equal footing. For example, in $^{176}_{78}\text{Pt}_{98}$ there are $(82 - 78)/2 = 2$ proton bosons and $(98 - 82)/2 = 8$ neutron bosons, altogether 10. In medium-heavy nuclei, the valence protons and neutrons occupy different orbits, therefore, the probability of the creation of pn-pairs is low. IBM-1 does not take into account bosons consisting of pn-pairs.

The bosons are considered, on a phenomenological level, as structureless particles having integer spins. Their states are symmetric with respect to their exchanges, i.e., the interchange of any pair of particles leaves the wave function unchanged. In fact, the bosons may have a rather complicated fermion-pair structure. This structure is investigated in the microscopic theory of the IBM.

The number of valence bosons is finite. This fact leads to important consequences which differ from the predictions of the geometrical collective model.

The truncation of the valence space to s and d bosons is indeed very drastic. Remaining at Talmi's example: $^{154}_{62}\text{Sm}_{92}$ may have $> 3 \times 10^{14}$ different 2^+ states in the shell model. In the IBM this number is reduced by more than 11 orders of magnitude.

- The excitation energy of even-even nuclei depends only on the distribution of valence nucleons into s and d pairs, the energies of the s and d bosons in the field of the central core and the interaction between the bosons, which is assumed to be simple (at most two-body) interaction.

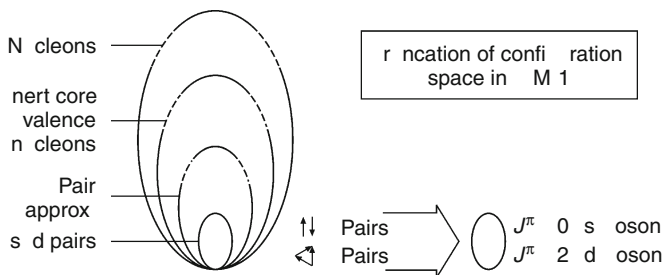
From the above assumptions it follows that group theoretical, algebraic methods can be used in the IBM.

IBM-1 describes the properties of even-even, positive parity levels of medium-heavy and heavy nuclei, the electromagnetic transitions and moments, nuclear radii, transfer reactions, etc. It does not distinguish between pp- and nn-pair bosons.

The IBM-1 is able to treat different collective excitations in a uniform framework. Its *dynamic symmetries* are shown later in [Fig. 2.26](#). The $U(5)$ (five-dimensional unitary group) corresponds to spherical, the $SU(3)$ (three-dimensional special unitary group) to deformed, the $O(6)$ (six-dimensional orthogonal group) to γ -soft nuclei.

Fig. 2.24

Truncation of the configuration space, available for nucleons in IBM-1. The figure is schematic, the truncation is much more drastic in reality



In the IBM-1 simple analytical formulae have been derived for the energy spectra valid in the limiting dynamic symmetries. For example in the U(5) symmetry the level energies (E) are described by the formula

$$E = \varepsilon n_d + \alpha n_d(n_d + 4) + 2\beta v(v + 3) + 2\gamma L(L + 1),$$

where n_d , v , and L are quantum numbers, ε , α , β , and γ are parameters fitted to experimental data. The formula gives a very good description for the energy levels, e.g., built on the ground state of ^{110}Cd (see [Fig. 2.25a](#)).

In contrast with the geometrical collective model, in IBM-1 the number of valence bosons is finite. The consequences of finite boson numbers were verified by the experiments. One can see in [Fig. 2.25b](#), e.g., that the reduced E2 transition probabilities in ^{110}Cd and ^{106}Pd nuclei are better reproduced in IBM-1 calculations than in the harmonic vibrator approximation. In the latter case the allowed phonon number may be infinitely large. (The vibration quanta, i.e., the phonons, are analogous to bosons.)

IBM-1 can also describe rotational bands built on different vibrational levels.

It is a *great merit* of the IBM that it establishes a sound foundation on the connection of the shell model with collective states. It gives an alternative description of collective states based on shell-model considerations.

In view of the simplicity of IBM-1, and the analytical formulae derived from it, the model is used widely for the interpretation of experimental results. Between dynamical symmetries one can use IBM-1 computer programs: PHINT (Scholten 1991) and TQM (Brant et al. 1985, unpublished).

The Bohr–Mottelson geometrical and IBM-1 models give essentially identical results in the phenomenological numerical applications, if the calculations are performed with the same care and with the same number of parameters. Nevertheless the IBM is more comprehensive, and very suitable for numerical calculations with its six parameters. On the other hand, it is rather difficult to find the best IBM fit for individual nuclei; from this point of view the geometrical model can give better results.

The *dynamic symmetries of IBM-1* and the shape transitions among them ([Fig. 2.26](#)) shall now be returned to.

Consider a simple Hamilton operator of the form

$$H = aH_{\text{spher}} - bH_{\text{def}},$$

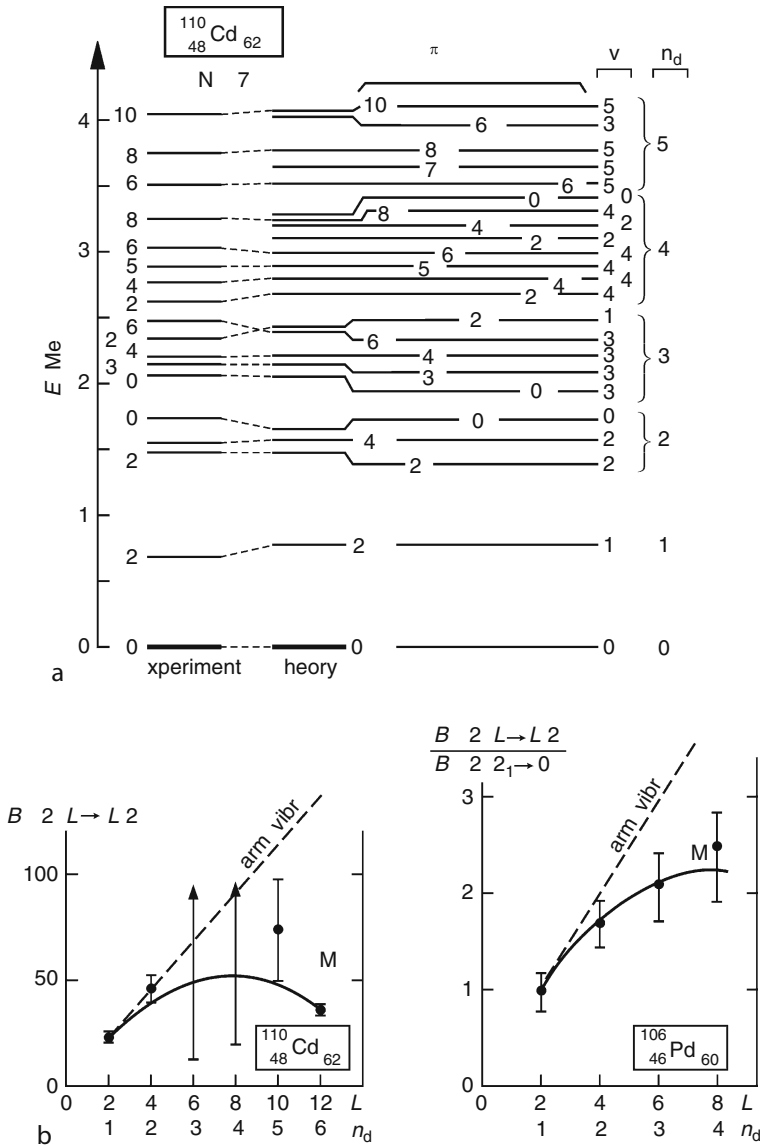
which contains the spherical and deformation driving terms separately (Ising operator). For small b/a values the spherical, for large b/a -s deformed states are characteristic. The Hamilton operator can be written also in the form

$$\hat{H}(N, \eta, \chi) = \eta \hat{n}_d - \frac{1 - \eta}{N} \hat{Q}_\chi \hat{Q}_\chi,$$

where N is the boson number, \hat{n}_d is the number operator of quadrupole bosons, and \hat{Q}_χ is the quadrupole momentum operator of the consistent Q formalism (see, e.g., Iachello and Arima (1987)). Here η and χ are control parameters, playing similar role as the pressure and temperature in statistical physics. The η parameter may change between 0 and 1, the χ between $-\sqrt{7}/2$ (prolate form) and $+\sqrt{7}/2$ (oblate form) values. At $\eta = 0$ the nucleus is deformed and the deformation may be axially symmetric prolate at SU(3), γ -soft at O(6), and axially symmetric oblate at $\bar{\text{SU}}(3)$. If $\eta = 1$, the nucleus is spherical characterized by U(5) dynamic symmetry.

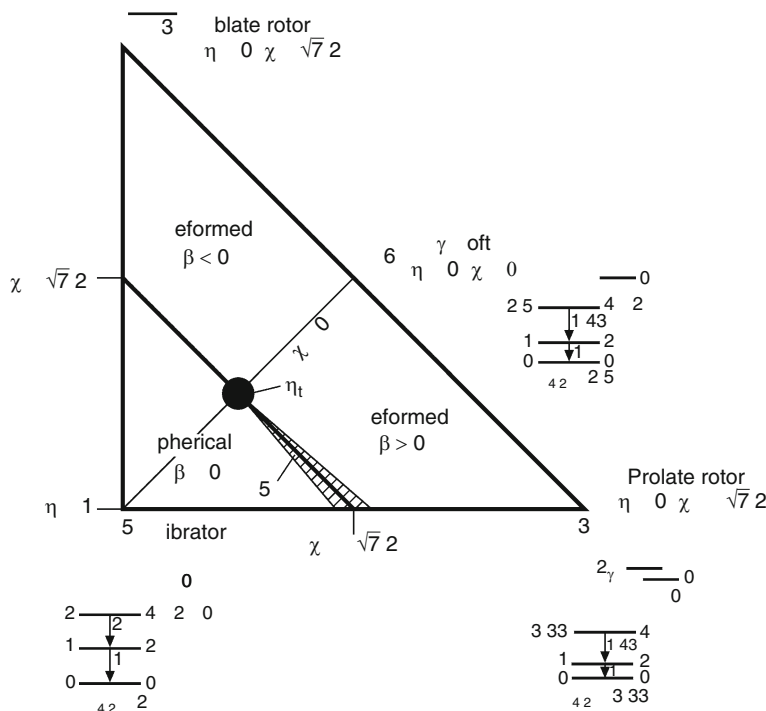
■ Fig. 2.25

(a) The level system built on the ground state of ^{110}Cd . The theoretical results were obtained by the formula $E = \epsilon n_d + \alpha n_d (n_d + 4) + 2\beta\nu (\nu + 3) + 2\gamma L(L + 1)$ of IBM-1 for the U(5) dynamic symmetry. (Based on Bertschy et al. (1995)). (b) Experimental $B(E2; L \rightarrow L-2)$ values (dots) for the ground state bands at ^{110}Cd and ^{106}Pd . The continuous curves denote IBM-1 calculations. The dotted lines show the predictions of harmonic vibrator approximation (Based on Kern (1997))



■ Fig. 2.26

The extended symmetry triangle of IBM-1. At the vertices one can see the dynamic symmetries $U(5)$, $SU(3)$, $O(6)$, $\overline{SU}(3)$, respectively, and some characteristic features of their level systems. The numbers on the transition arrows show relative reduced $B(E2)$ transition probabilities, while $R_{4/2} = E(4_1^+)/E(2_1^+)$ indicates energy ratio. The control parameters of the Ising operator are shown at the key positions. $X(5)$ shows the first-order shape transition between $\beta < 0$ and $\beta > 0$ axially deformed states. η_t denotes a triple point for different transitions (Based on Jolie and Casten (2005) and Iachello (2000, 2001, 2002))



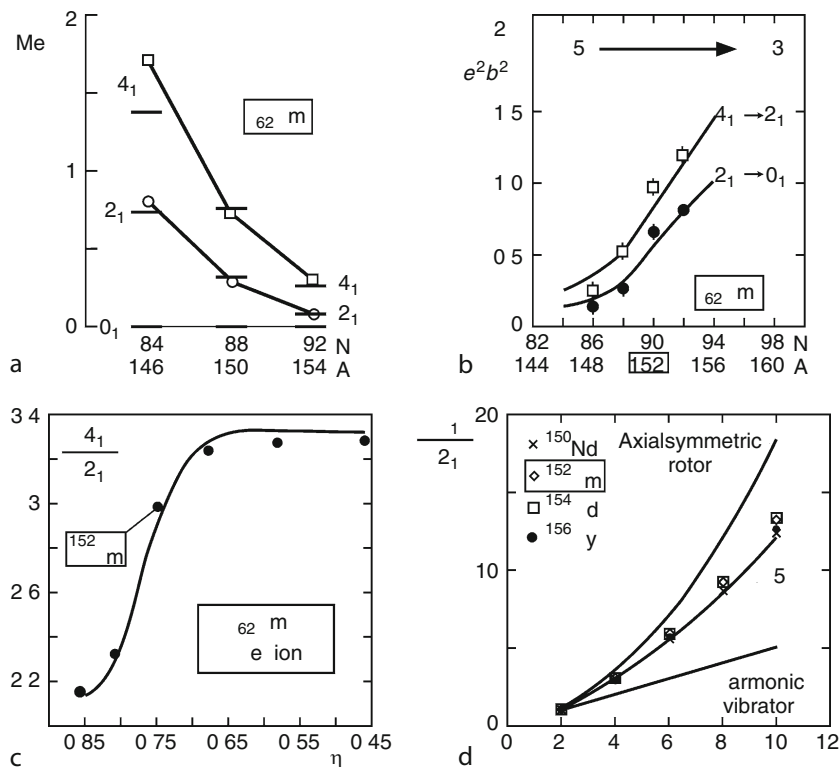
The transition from $U(5)$ to $SU(3)$ symmetry can be seen in ▶ Fig. 2.27a–c for the case of Sm isotopes. Near the magic neutron number $N = 82$, the Sm isotopes are nearly spherical. Here the $E(4_1^+)/E(2_1^+)$ energy ratio is ~ 2 , and the $B(E2; 4_1^+ \rightarrow 2_1^+)$ reduced transition probabilities are small. Far from $N = 82$ the $E(4_1^+)/E(2_1^+)$ energy ratio is ~ 3.3 characteristic of an axially deformed rotor, and the corresponding reduced transition probabilities are large.

^{152}Sm , with some other nuclei, represents an intermediate situation, the $X(5)$ “symmetry” in the coexistence region between the harmonic vibrator and axially symmetric rotor (▶ Fig. 2.27d). At the triple point (η_t) shape transition is possible from spherical to axially symmetric oblate ($\beta < 0$) or prolate ($\beta > 0$) shapes. A good candidate for the triple point behavior is ^{134}Ba . From the triple point, transition is possible also to the triaxial shape (Jolos 2004).

Comprehensive reviews of different versions of the interacting boson and interacting boson–fermion models, as well as surveys of transitions between dynamical symmetries have been published, e.g., by Iachello and Arima (1987), Iachello and Van Isacker (1991), and Fényes (2002).

■ Fig. 2.27

(a) Experimental 2_1^+ and 4_1^+ energy levels (short lines) of $^{146}, ^{150}, ^{154}\text{Sm}$ isotopes compared with IBM-1 theoretical results (dots). (b) Reduced $B(E2)$ transition probabilities for Sm isotopes. Dots show experimental, curves IBM-1 theoretical results. The figures a and b are based on Scholten et al. (1978). (c) $E(4_1^+)/E(2_1^+)$ energy ratios in the Sm region versus the control parameter η (fitted to the number of bosons). Dots: experimental data curve: theoretical results. (Based on Jolie and Casten (2005)). (d) The experimental $E(L_1)/E(2_1^+)$ energy ratios for the ground-state band in some rare earth isotopes as a function of angular momentum (L). The curves show predicted values for different symmetries (Based on Iachello (2002))



2.3.6 Clustering

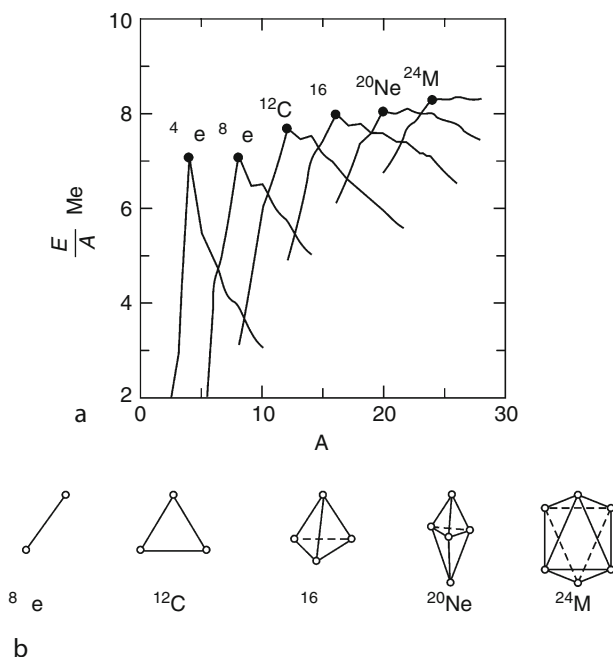
Many nuclear phenomena can be understood better, supposing that the constituents of nuclei are organized into clusters, to be described as coherent superpositions of quasicrystalline structures. The cluster structures were studied already from the very early period of nuclear structure research.

The α -particle is clearly an excellent cluster candidate, as its binding energy per nucleon is extremely high, see Fig. 2.28. The ^8Be , ^{12}C , ^{16}O , ^{20}Ne , and ^{24}Mg nuclei have also outstandingly large binding energy/nucleon indicating α -particle substructures.

A simple phenomenological cluster model has been introduced by Buck et al. (1975). This assumes that some nuclei consist of a structureless core plus an α cluster (i.e., a ^4He nucleus-like composite particle) interacting via simple potentials, and their levels (as well as the

■ Fig. 2.28

(a) Binding energy/nucleon (E_B/A) versus mass number (A) for selected light nuclei. The lines connect data of isotopes of the indicated elements. α -particle cluster candidates are denoted by dots. (b) Possible α -particle quasicrystalline structures in some light nuclei (Based on Hafstad and Teller (1938), Brink (1967), and Freer (2007))

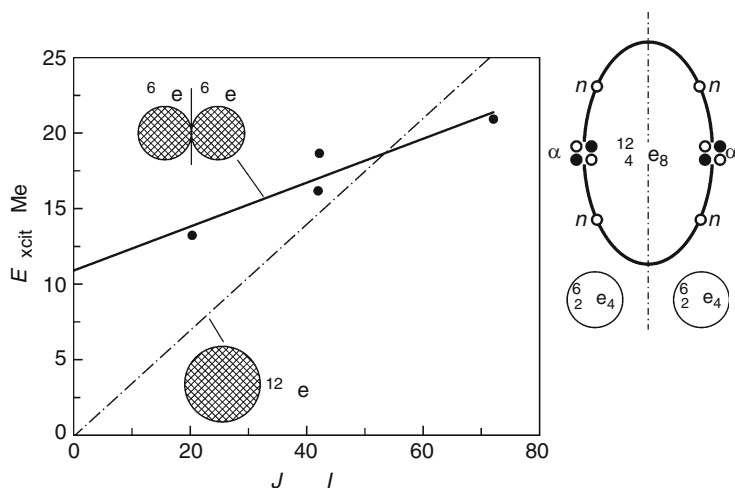


transitions between them) can be understood as the energy levels in this simple potential model. Buck et al. have shown that the model works well for nuclei around the ^{16}O shell closure. Pál and Lovas (1980) applied the alpha-cluster model to nuclei in the ^{40}Ca region, and the basic properties of the lowest-lying rotational-like bands in ^{40}Ca and ^{44}Ti have been well reproduced. In the meantime, the scope of the model has been extended enormously to the Zn, Zr, and Pb regions, to the α -decay, and heavy-cluster decay of all nuclei that decay in these ways; moreover to heavy deformed nuclei, whose decay has not been observed. In the latter cases, the system is described as a composition of two heavy clusters. The model works well in all these cases (Buck et al. 1996, 1997, 1998). More generally, the behavior of light to heavy nuclei is often best understood in terms of their cluster structures.

The existence of cluster substructure in nuclei is supported also by the observation of cluster decay. Besides α particles, the heavy nuclei can emit ^{14}C , ^{24}Ne , ^{28}Mg , ^{32}Si clusters, too. The partial half-lives for these decays depend on the penetrability of the Coulomb barrier in a way very similar to α decay (Mikheev and Tretyakova 1990; see Geiger–Nuttall-type relations in Sect. 2.4.1.1). The heavy cluster decay is a very rare phenomenon. For example, in the decay of ^{223}Ra there were 65×10^9 α particles observed, while only 14 ^{14}C cluster emissions during the same time (Rose and Jones 1984). For the detection of rare clusters solid state track detectors are very suitable.

■ Fig. 2.29

The excitation energy of $^{12}\text{Be}^*$ vs. $J(J+1)$, where J is the angular momentum of the rotating nucleus. The experimental data (dots) are explained supposing $^6\text{He} + ^6\text{He}$ substructure (continuous line) in $^{12}\text{Be}^*$. The dot-dashed line shows extrapolated trajectory of a ground state band in $^{12}\text{Be}^*$ (Based on Freer et al. (1999))



Freer et al. (1999) investigated the breakup of excited $^{12}\text{Be}^*$ nucleus into $^6\text{He} + ^6\text{He}$, using a high-energy ^{12}Be beam inelastically scattered by a C target. The breakup of $^{12}\text{Be}^*$ occurred from rotational states in the 10–25 MeV excitation energy interval, with spins 4–8 \hbar . The inferred moment of inertia is consistent with the decay of $^{12}\text{Be}^*$ from the $(\alpha + 2n) + (\alpha + 2n)$ cluster configuration state (see Fig. 2.29).

For a detailed discussion of cluster structures in nuclei, see the review article of Freer (2007).

2.3.7 Recent Developments

2.3.7.1 Effective Interactions

Nowadays, it is generally accepted that the fundamental theory of the strong interaction is the quantum chromodynamics (QCD). At high energies (and small distances, ≤ 0.1 fm), there is a perturbative theory of the interaction of quarks and gluons, allowing the calculation of measurable physical quantities (cross sections, decay constants, structure functions, etc.) as a function of the coupling constant of the strong interaction. However, at greater distances (≥ 0.5 fm) (in small-energy process) the strength of interaction is so strong that perturbative methods cannot be farther applied. In this region, effective field theories can be used, the meson field theory (see Sect. 2.1.2.3 and Burgess (2007)) and chiral perturbation theory (Bernard and Meissner 2007). These may treat soft hadronic and nuclear processes with success.

For the time being, however, the microscopic theoretical framework for modeling nuclear structure and reactions is mainly quantum mechanics. The most common models are the shell model and its truncated approximations (e.g., IBM), the mean-field theories (like the

Hartree–Fock approach) and the cluster models. The main ingredients of these theories are the effective nucleon–nucleon interactions. The effective interactions usually have simple forms, and are adapted to some special models.

The effective interactions are fitted to nucleon–nucleon collision data and to the properties of nuclei in the stability region. Nevertheless, far from the stability region the effective interactions (e.g., the pairing and spin–orbit interactions) may be different, which must be taken into account.

2.3.7.2 Few Nucleon Systems, Ab Initio Calculations

Recently, major advances have been obtained in the microscopic description of few nucleon systems. Starting from realistic NN -, as well as NNN -interactions (see [Sects. 2.1.2.1](#) and [2.3.1.3](#)), many properties of $3 \leq A \leq 8$ nuclei (energies of ground and excited states, radii, electromagnetic moments, etc.) have been described in agreement with experimental results. These calculations have three different frameworks:

- Variational Monte Carlo (VMC), and a similar Green’s function Monte Carlo (GFMC) method.
- Large-basis no-core shell model (LBNCSM).
- Coupled cluster (CC) expansion methods.

With the latter two methods one can study nuclei up to $A \approx 12$ –16.

These calculations require very large computer capacities, thus they became significant only in the last 2 decades.

The Monte Carlo statistical sampling methods have been known for more than half a century and applied to numerous fields of physics. A simple example for their applications is the determination of the volume of an irregularly shaped body. Let the body be in a unit-volume cube. N points are chosen randomly in the cube, from which N_x falls into the investigated volume. If the number of points is sufficiently large, the expectation value of the sought for volume is N_x/N .

The procedure can be applied also for quantal systems. For example, if one wants to know the ground state energy of a few nucleon system, one may start from a trial wave function $\Psi\{\alpha\}$, where $\{\alpha\}$ denotes variational parameters to be optimized. The expectation value of the Hamiltonian with the trial wave function gives an estimate for the energy of the ground state:

$$E\{\alpha\} = \frac{\langle \Psi | H | \Psi \rangle}{\langle \Psi | \Psi \rangle},$$

where $E\{\alpha\}$ is greater than, or equal to, the true ground-state energy E_0 . If $E\{\alpha\}$ is minimized with respect to all parameters, an approximation to both E_0 and to the wave function of the ground state is obtained. In the variational Monte Carlo procedure the integrals involved in $E\{\alpha\}$ are calculated by the Monte Carlo method.

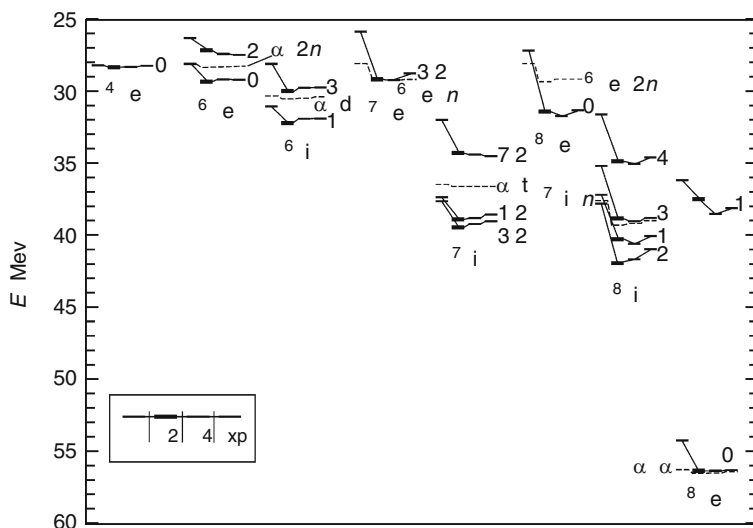
The Green’s function Monte Carlo calculation is very similar; it starts with a trial function Ψ obtained as a result of a variational optimization.

A detailed description of the methods can be found in Carlson and Wiringa (1991), Pudliner et al. (1997), Pieper et al. (2001).

In the calculations of Pieper et al., the Argonne v_{18} two-nucleon potential (v_{ij}), and the Urbana IX (UIX), Illinois 2 (IL2), Illinois 4 (IL4) three-nucleon potentials (V_{ijk}) were used.

For the large-basis no-core shell model calculations see Navrátil et al. (2000), and for coupled cluster calculations Bishop et al. (1990), Heisenberg and Mihaila (1999) as well as Wloch et al. (2005).

Experimental (right-hand side for each nucleus) and Green's function Monte Carlo theoretical energies for the ground and narrow excited states of light nuclei (Pieper et al. 2001). The Argonne v_{18} two-nucleon and Urbana (UIX), Illinois (IL2) and Illinois (IL4) three-nucleon potentials were used in the calculations. The *dashed lines* indicate the breakup thresholds



2.4 Nuclear Decay

2.4.1 Alpha Decay

2.4.1.1 Basic Experimental Facts

Among the neutron deficient isotopes of the heavy ($Z \geq 84$) elements, one of the most common decay modes is the α -particle (i.e., ${}^4\text{He}$ nucleus) emission. One can find α activity also in other regions. For example, a number of strongly neutron deficient ${}_{52}\text{Te}$ – ${}_{55}\text{Cs}$ nuclei, rare-earth isotopes with neutron numbers $N \geq 84$, light isotopes of ${}_{72}\text{Hf}$ – ${}_{83}\text{Bi}$ also decay with α -particle emission.

The energy of α particles can be measured with precision magnetic spectrographs, with high-transmission ionization chambers and semiconductor detector spectrometers.

The α particles are emitted with discrete energies. Some typical α -decay schemes are shown in [Fig. 2.31](#). In the α spectrum of even–even nuclei usually the highest-energy α particles have the highest intensity. With decreasing α -particle energy the intensity of the “fine structure lines” of the α spectrum strongly decreases. See, e.g., the α decay of ${}^{220}\text{Rn}$ and ${}^{240}\text{Cm}$ in [Fig. 2.31](#). In the case of odd- A and odd–odd nuclei this regularity is not always experienced.

In some rare cases, α decay can be observed both from the ground state and the excited states of the parent nucleus (e.g., in ${}^{212}\text{Po}$). The α particles emitted from excited states are called long-range (or β -delayed) α particles.

The α -decay energies (Q_α) can be calculated from the atomic masses (M) using the equation

$$Q_\alpha = [M(Z, A) - M(Z - 2, A - 4) - M(2, 4)]c^2, \quad (2.58)$$

where c is the speed of light in vacuum. The α -decay energy is carried away by the emitted α particle and the recoil (daughter) nucleus:

$$Q_\alpha = E_\alpha + E_d = E_\alpha[1 + m_\alpha/m_d], \quad (2.59)$$

where E_α and E_d denote kinetic energies, m_α and m_d are the masses of the α particle and the daughter nucleus, respectively.

[Equation \(2.58\)](#) follows from the momentum conservation law of classical mechanics. In the heavy element region $m_d \gg m_\alpha$, therefore the daughter nucleus carries away only a small part (a few percent) of the total α -decay energy.

From the measured atomic masses one can calculate the α -decay energies. For nuclei, which are stable against β emission and lie on the “nuclear stability line,” the result is shown in [Fig. 2.32](#). Alpha decay is possible energetically already above $A \approx 140$, but owing to the strong dependence of half-lives on α -decay energy, it is observed only for heavier elements (and for the strongly neutron deficient isotopes of medium heavy nuclei).

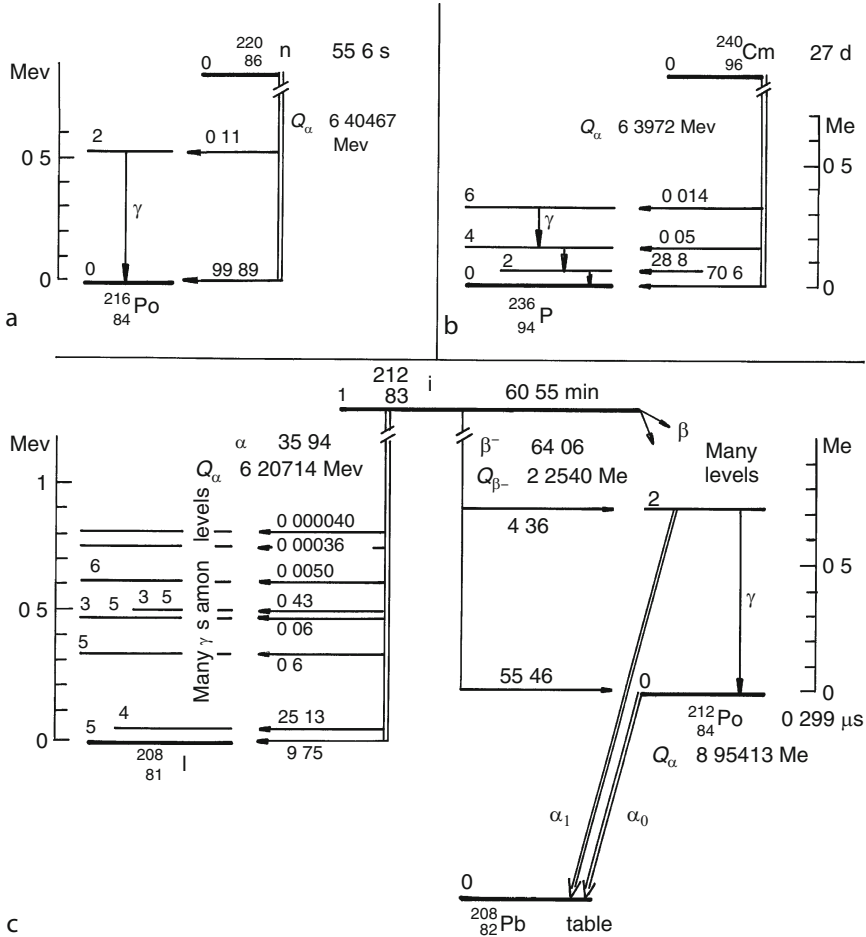
The α -decay energies (Q_α) for some heavy nuclei are shown in [Fig. 2.33](#). It is remarkable that the Q_α curves peak at $N = 128$, which corresponds to the magic $N = 126$ neutron number for the daughter nucleus.

The Weizsäcker semiempirical mass formula ([Eq. \(2.3\)](#)) correctly predicts that α emission can be expected mainly for the heavy elements. Nevertheless, the shell effects, which were not taken into account in the formula, also play an important role in α decay.

The binding energy of the α particle is extremely large, it is 28.3 MeV. The formation of an α particle from two protons and two neutrons leads to a great energy release, provided that the

■ Fig. 2.31

(a) Typical α -decay scheme of an even-even nucleus not too far from the magic atomic number $Z = 82$. (b) Typical α -decay scheme of an even-even nucleus far from magic numbers. (c) α - and β -decay schemes of the odd-odd nucleus ^{212}Bi . From the excited states of ^{212}Po many long-range (i.e., energetic) α -particle groups were observed to the ground state of the double magic ^{208}Pb nucleus, but only two transitions are shown in the figure. The intensity of long-range α_1 particles is several orders of magnitude smaller than the intensity of the α_0 group. The figure is based on data from Firestone et al. (1996)



sum of the binding energies of the decay products exceeds that of the parent nucleus. The heavier the nucleus, the more likely that is the case (cf. [Figs. 2.3](#) and [2.28a](#)). That is why α decay is so common among heavy nuclei, while proton emission occurs only in very neutron-deficient nuclei (e.g., in ^{109}I , $^{112,113}\text{Cs}$, ^{171}Au , and ^{185}Bi).

While the α -decay energies show very little variance ($1.8 \leq Q_\alpha \leq 9.3$ MeV), the observed α partial half-lives span an enormous range from $\sim 10^{-7}$ to $\sim 10^{22}$ s. All the observed half-lives are very long compared to $\leq 10^{-21}$ s, the time needed for an α particle to fly across the nucleus.

Fig. 2.32
 α -decay energies (Q_α) as a function of the mass number (A) for nuclei, which are stable against β emission (Based on Bethe (1937))

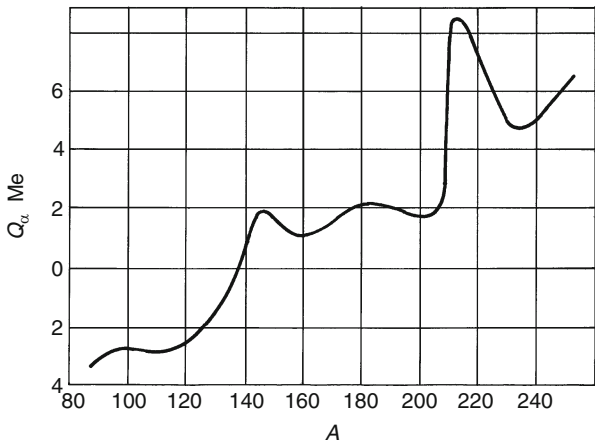
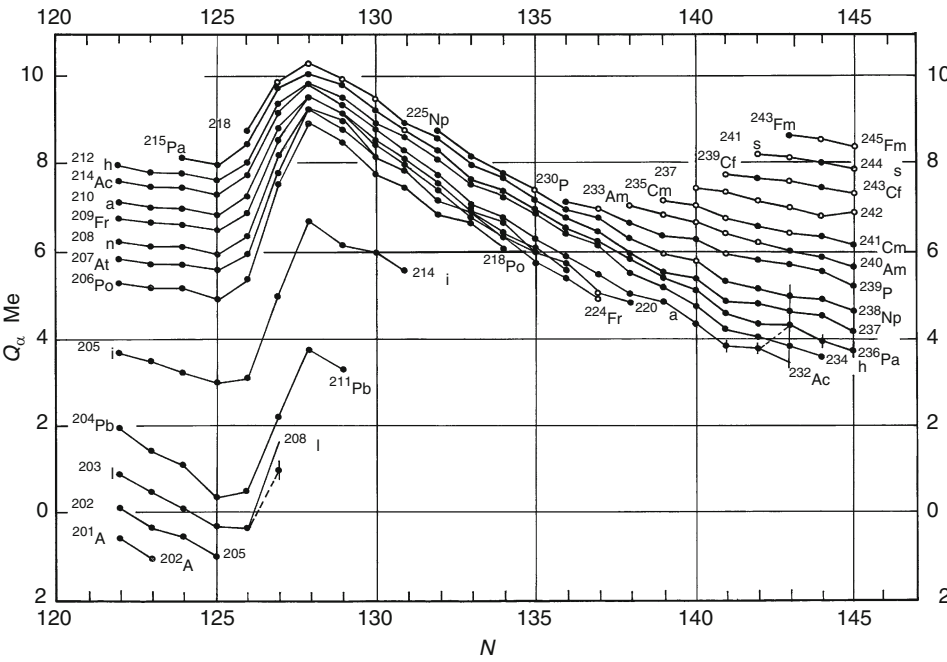


Fig. 2.33
 α -decay energies (Q_α) as a function of neutron number (N) in the $122 \leq N \leq 145$ region. Points denote experimental data; the open circles are estimated values from systematic trends. A comprehensive review of Q_α values in different mass regions was given by Audi et al. (2003)



Geiger and Nuttall (1911, 1912) have proposed a simple linear relationship between $\log \lambda$ and $\log R_\alpha$:


$$\log_{10} \lambda = A \log_{10} R_\alpha + B, \quad (2.60)$$

where λ is the decay constant ($\lambda = \ln 2 / T_{1/2}$, $T_{1/2}$ is the α partial half-life), R_α is the range of the α particle in the air, A and B are empirical constants. The range of the α particle in the air depends on its energy E_α approximately as $R_\alpha \approx 0.3 E_\alpha^{3/2}$, where R_α is measured in centimeters (cm), and E_α in megaelectron volts (MeV).

Note that if the nucleus emits both α and β particles, the total decay constant is the sum of the partial decay constants $\lambda_{\text{total}} = \lambda_\alpha + \lambda_\beta$.

On the basis of a much larger database, Taagepera and Nurmia (1961) proposed the following formula, which relates the α partial half-life ($T_{1/2}$) with the α -particle energy (E_α):



$$\log(T_{1/2}) = C_1(Z_d E_\alpha^{-1/2} - Z_d^{2/3}) - C_2, \quad (2.61)$$

where $C_1 = 1.70 \text{ (MeV)}^{1/2}$, $C_2 = 30.0$, $T_{1/2}$ is measured in years, E_α in MeV, and Z_d is the atomic number of the daughter nucleus. Here the α -particle energy (E_α) was used instead of Q_α , which is allowed because in the $140 \leq A_d \leq 240$ region the ratio E_α/Q_α is nearly one (0.973 ± 0.003).  Figure 2.34 shows the α partial half-lives $T_{1/2}$ as functions of $X = Z_d E_\alpha^{-1/2} - Z_d^{2/3}$. The basic line ($H = 0$) goes through the data of ^{215}Rn , ^{226}Ra , ^{238}U , and ^{232}Th . For this line the following constants were obtained:

$$C_1' = 1.61 \text{ and } C_2' = 28.9. \quad (2.62)$$

It is convenient to define a hindrance factor H as

$$H \equiv \log(T_{1/2\text{exp}}/T_{1/2\text{pred}}), \quad (2.63)$$

where $T_{1/2\text{ pred}}$ is predicted using  Eq. (2.60) with parameters of  Eq. (2.61). The experimental $T_{1/2\text{ exp}}$ data can be found between the $H = 0$ and 1.2 lines for α emitters being far from magic numbers. When the α emitters are close to magic numbers, the observed hindrance is greater. The hindrance factors are usually the smallest for even–even and greatest for odd–odd nuclei.

Note that some authors define the hindrance factor as a measure of hindrance with respect to the ground states of even–even nuclei. A survey of hindrance factors for the α decay of the excited states of even–even nuclei, as well as for the odd- A and odd–odd nuclei is given in the heavy element region by Hyde et al. (1964).

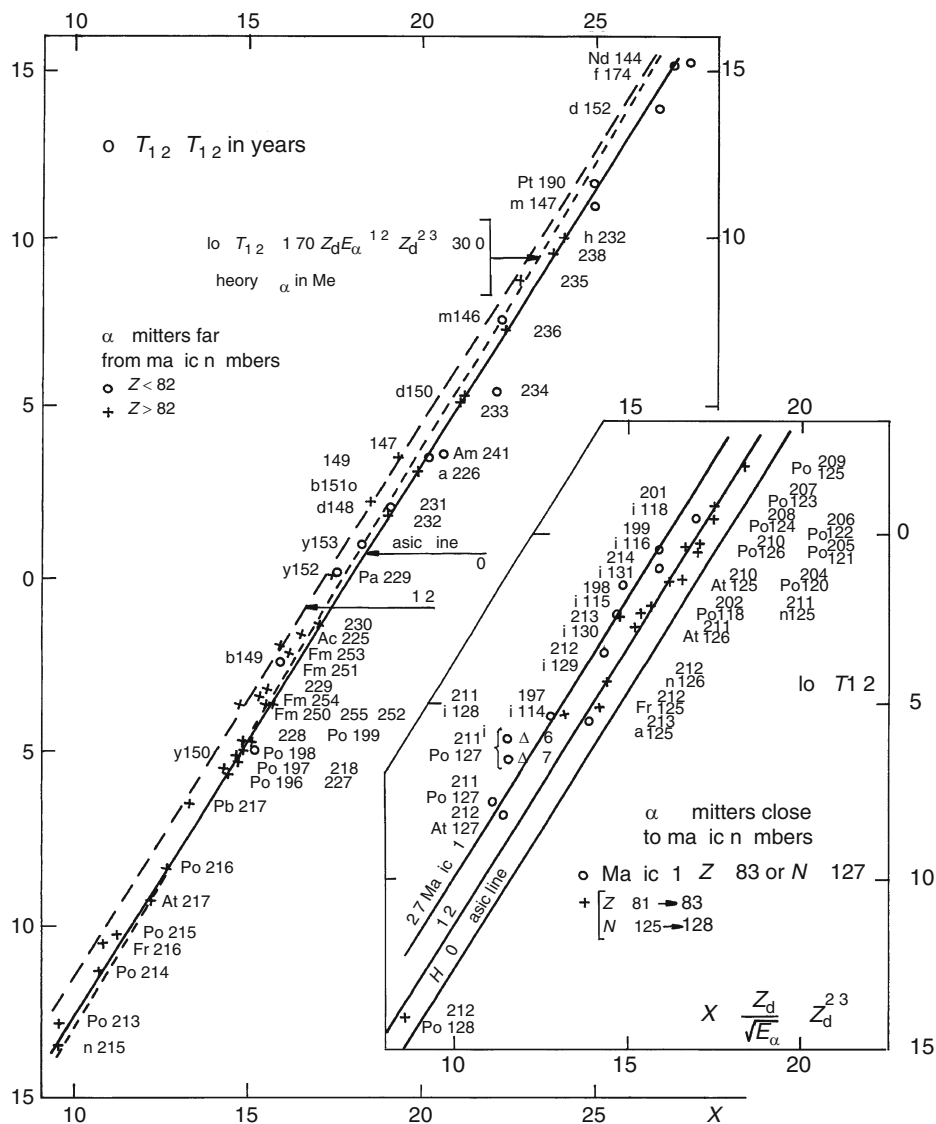
Recently Dasgupta-Schubert and Reyes (2007) proposed a new generalized liquid- drop α -decay formula, which was based on experimental data of 373 α -emitting nuclei. According to this formula

$$\log_{10}(T_{1/2}[\text{s}]) = a + bA^{1/6}\sqrt{Z} + \frac{cZ}{\sqrt{Q_\alpha}},$$

where $T_{1/2}[\text{s}]$ is the alpha partial half-life in seconds, Z , A are the atomic and mass numbers of the mother nucleus, Q_α is the energy of α -decay, a , b , c are constants, which depend on the type of the mother nucleus:

Z	N	a	b	c
Even	Even	−25.31	−1.1629	1.5864
Even	Odd	−26.65	−1.0859	1.5848
Odd	Even	−25.68	−1.1423	1.592
Odd	Odd	−29.48	−1.113	1.6971

Logarithm of α partial half-lives $T_{1/2}$ as a function of $X = Z_d E_\alpha^{-1/2} - Z_d^{3/2}$, where E_α is the α -particle energy in MeV, and Z_d is the atomic number of the daughter nucleus (Based on Taagepera and Nurmia (1961))



Alpha decay can also occur from excited state(s) of the parent nucleus. A necessary condition for the practical observability of such long-range α particles is the excitation of high-energy level(s) of the nucleus, generally through previous β decay, from which the

probability of α decay can be comparable with the γ -decay probability. Delayed α radioactivity is expected usually for strongly neutron-deficient nuclei. In the special case of $^{212}\text{Po} \rightarrow ^{208}\text{Pb}$ (► Fig. 2.31c), the α decay is favored, because ^{208}Pb is a double magic nucleus. For the expected regions of β -delayed α radioactivity, see Fényes and Rupp (1968).

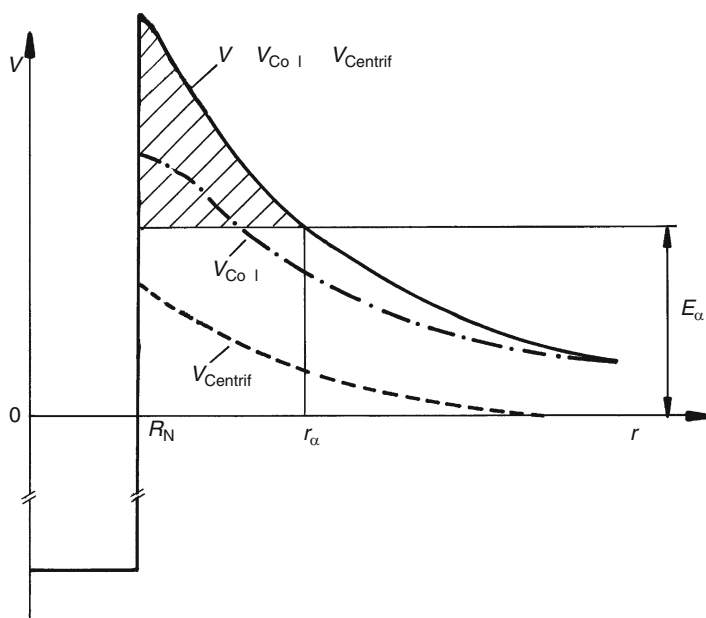
The experimental and theoretical problems of the α decay are discussed in more detail, e.g., in the following books and review articles: Hanna (1959), Hyde et al. (1964), Mang (1964), Rasmussen (1965), Marmier and Sheldon (1969), Mukhin (1974), Lovas et al. (1998). Experimentally determined nuclear structure and decay data have been evaluated and are included in the ENSDF (Evaluated Nuclear Structure Data File) database (<http://www.nndc.bnl.gov/ensdf>).

2.4.1.2 One-Body Theory of α Decay

In 1927 Rutherford observed that the 8.78 MeV energy α particles of ^{212}Po were scattered on heavy nuclei according to the Coulomb scattering formula. This indicated that the repulsive Coulomb interaction between the α particle and the target nucleus gives rise to a barrier higher than 8.78 MeV. At the same time, heavy nuclei can emit α particles even with smaller energies. In the framework of classical physics, it was not clear how an α particle can be emitted from the nucleus with an energy that is smaller than the height of the potential barrier (► Fig. 2.35).

■ Fig. 2.35

Coulomb ($V_{\text{COUL.}}$), centrifugal ($V_{\text{CENTRIF.}}$), and total (V) potentials of the α -nucleus interaction as a function of the distance r from the nuclear center. The probability of α -particle emission through the potential barrier strongly depends on the energy of the α particle (E_α) and on the height (and thickness) of the potential barrier (see shaded area). In the $r < R_N$ region the nuclear potential is by far deeper than the figure shows



Gamow (1928) and independently Condon and Gurney (1928, 1929) have shown that such a penetration of an α particle through the potential barrier is possible in quantum mechanics. The mechanism is called tunneling. One can define a penetration factor (penetrability) P which is the ratio of emergent and incident intensities. A detailed quantum-mechanical approximate theory gives the following expression for the penetration factor:

$$P \approx \exp \left[-\frac{2}{\hbar} \int_{R_N}^{r_\alpha} \sqrt{2m \left(\frac{2Ze^2}{r} - Q_\alpha \right)} dr \right], \quad (2.64)$$

where R_N and r_α are radius parameters (Fig. 2.35), R_N is the radius of the daughter nucleus, m is the reduced mass, $m = m_\alpha m_d / (m_\alpha + m_d)$; for heavy elements $m \approx m_\alpha$, $2Ze^2/r$ is the Coulomb potential, $Z (= Z_d)$ is the atomic number of the daughter nucleus, Q_α is the total α -decay energy; for heavy elements $Q_\alpha \approx E_\alpha$, where E_α is the energy of the α particle.

In the one-body model of α decay it is supposed that the α particle has been formed in the surface region of the nucleus with a probability f (for the probabilistic interpretation of the decay constant, see Sect. 9.3.4 in Chap. 9 or Sect. 7.1.2 in Chap. 7), and the probability of α decay, λ , is given by

$$\lambda = \ln 2 / T_{1/2} = fP \approx f \exp \left[-\frac{2}{\hbar} \int_{R_N}^{r_\alpha} \sqrt{2m \left(\frac{2Ze^2}{r} - Q_\alpha \right)} dr \right]. \quad (2.65)$$

The factor f is also called “reduced transition probability.” As in the theory of β decay (Sect. 2.4.2.2) the quantity $T_{1/2} f$ is a measure of the internal decay rate. In the derivation of the formula (2.64), it was assumed that the α particle is emitted with zero angular momentum (and therefore the centrifugal component shown in Fig. 2.35 is zero).

The wave function of the α particle ($\Psi(r) = u(r)/r$) can be determined from the one-dimensional Schrödinger equation

$$-\frac{\hbar^2}{2m} \frac{d^2 u}{dr^2} + \left(\frac{2Ze^2}{r} - Q_\alpha \right) u = 0 \quad (2.66)$$

with appropriate boundary conditions, where m is the reduced mass, and Q_α is the total decay energy for the bare nucleus. Equation (2.65) can be solved, e.g., in the Wentzel–Kramers–Brillouin (WKB) approximation for different regions of the radius, inside and outside the barrier. Bethe (1937) derived an explicit analytical formula for the decay probability λ . The formula is rather complicated, but it can be simplified with convenient approximations introduced by Taagepera and Nurmia (1961). The approximations are as follows.

The factor f before the exponential function in Eq. (2.64) has been found to be approximately proportional to $Z_d^{-4/3}$. For the region $58 \leq Z_d \leq 98$ its value was taken as a constant: $1.9 \times 10^{20} \text{ s}^{-1} = 6.0 \times 10^{27} \text{ a}^{-1}$.

In the exponential factor of Eq. (2.64) the approximation $R_N \approx 1.36 r_0 Z_d^{1/3}$ was used, where $r_0 = 1.5 \times 10^{-13} \text{ cm}$.

It was assumed that the height of the Coulomb barrier is much greater than Q_α . In the $140 \leq A_d \leq 240$ region the α -particle energy E_α was used instead of Q_α , because the recoil energy of the daughter nucleus is very small. With these approximations and with minor fitting of the constant parameters to the experimental data one obtains the Taagepera–Nurmia formula (Eq. (2.60)).

If the α particle carries away an orbital angular momentum l , the height of potential barrier increases with

$$V_{\text{CENTRIF.}} = l(l+1)\hbar^2/(2mr^2). \quad (2.67)$$

Therefore, in the Schrödinger equation (🔗 Eq. (2.65)) the $V_{\text{COUL.}} = 2Ze^2/r$ term must be replaced by $V = V_{\text{COUL.}} + V_{\text{CENTRIF.}}$. According to the calculations of Winslow and Simpson (1954) the effect of the orbital angular momentum (l), taken away by the α particle, on the penetration factor is as follows (🔗 Table 2.8):

■ Table 2.8

Penetration factor for different values of the orbital angular momentum (l) taken away by the α particle

l	0	1	2	3	4	5	6
P_l/P_0	1.000	0.844	0.601	0.363	0.1854	0.0806	0.0299

Rasmussen (1959) derived the following formula for the calculation of the ratio P_l/P_0 :

$$P_l/P_0 = \exp \left[-2.027l(l+1)Z_d^{-1/2}A_d^{-1/6} \right], \quad (2.68)$$

which agrees with the more exact expression up to $l = 6$. The α decay is governed by the strong interaction. Therefore, both the angular momentum and parity conservation laws are valid in the α -emission process. From these conservation laws come the following selection rules:

$$|I_i - I_f| \leq l \leq I_i + I_f \text{ and } \pi_i/\pi_f = (-1)^l, \quad (2.69)$$

where I_i , π_i , and I_f , π_f are the initial and final spins (I) and parities (π) of the nucleus, and l is the angular momentum carried away by the α particle.

The simple one-body model can give a good description of the α decay of even–even nuclei (or in general of the allowed α transitions). The penetration of α particles through the potential barrier plays a central role in the process. It seems that several factors, which were not taken into account in the above treatment, have the same effect on the allowed transitions of different nuclei.

Nevertheless, the applicability of this simple model has severe limitations. It is not expected to give satisfactory results, if the internal structures of the initial and final states of the nucleus are very different. Especially in the case of odd- A or odd–odd nuclei the internal structure can play an important role.

In the one-body model it is supposed that the nucleus is spherical and the potential barrier has a simple form (🔗 Fig. 2.35). In an exact theory, especially in the case of deformed nuclei, more realistic potential barriers must be taken into account. Furthermore the interaction of the emitted α particle with the asymmetric electric field of the deformed nucleus can also modify the α spectrum.

2.4.1.3 Microscopic Theories of α Decay

The microscopic theories of α decay can be divided into several groups. The statistical models were developed in analogy with the statistical theories of nuclear reactions. The α decay is a surface phenomenon, and reliable information on the nuclear surface is available mostly from

reaction data. In these theories, the probability factor f (Eq. (2.64)) is determined from the average-level densities.

Other microscopic models are based on the shell model. In these models, the formation probability of α particles is calculated starting from the nuclear wave function.

In the resonating group model, α -core cluster model configurations are considered, which contain α particles. The shell model can be combined with the cluster model and in this way it can be applied to the description of α decay.

The detailed description of these microscopic models is beyond the scope of the present survey. The interested readers are referred to the review articles of Mang (1964), Hyde et al. (1964), Rasmussen (1965), and Lovas et al. (1998). Only a few works shall be discussed in some detail below.

Spherical Nuclei

In his classical works Mang (1960, 1964) developed an α -decay model in a fairly general form. According to his theory, the α -decay probability λ depends on the penetration factor P_l and the so-called reduced α width δ_{jl}^2 in the following way:

$$\lambda = \frac{1}{h} \sum_{jl} P_l \delta_{jl}^2. \quad (2.70)$$

Here P_l is the same potential-barrier penetration factor as in the one-body model of α decay, δ_{jl}^2/h gives the probability of α particle formation on the nuclear surface in unit time, expressed in terms of the wave functions of the parent and daughter nuclei, and of the α particle, l is the angular momentum of the α particle, and j is the angular momentum of the daughter nucleus. Combination of angular momenta j and l gives J , the angular momentum of the parent nucleus.

Using the measured α -particle energies, Mang (1960) has calculated the δ^2 values for the ground-state to ground-state transitions of even-even (spherical) Po isotopes. Mang's theoretical results reasonably reproduced the ratios of the experimental δ^2 data, for example, the minimum of δ^2 values at the magic number $N = 126$.

Zeh and Mang (1962) have calculated the α -decay probabilities in the Po–Bi region in the vicinity of the double magic ^{208}Pb . The calculations have shown that it is very important to take into account the residual interaction between the valence nucleons. The consideration of the pairing force leads to a substantial increase of the absolute values of the reduced widths (by a factor of ~ 30 or even more), and to a smoothing of the local fluctuations caused by different subshells. The results are sensitive to the shell-model states included in the calculations. The agreement between experimental and theoretical data for the relative values was especially good for even-even nuclei.

Starting from a general theory of nuclear reactions Thomas (1954) deduced the following expression for the α -decay width $\Gamma \equiv \hbar\lambda = \hbar \ln 2 / T_{1/2}$ of a single transition:

$$\Gamma_l(r_c) = 2P_l(r_c) \frac{\hbar^2}{2mr_c} g_l^2(r_c), \quad (2.71)$$

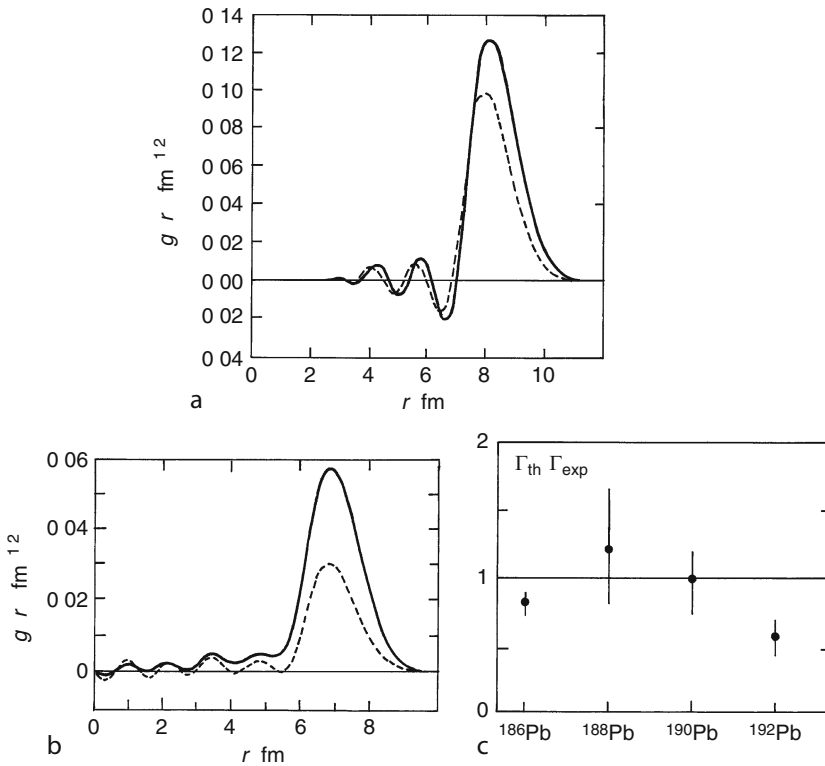
where m is the reduced mass, $g_l(r_c)$ is the formation amplitude of the α particle, which is the projection of the parent state wave function onto the (antisymmetrized) product states of the two fragments, $P_l(r_c)$ is the penetrability of the Coulomb barrier beyond distance r_c from the center.

By using $\Gamma = \hbar\lambda$, one can easily express δ_l^2 in terms of g_l^2 . The width does not depend on r_c , if the latter is chosen beyond the touching point of the α particle and the daughter nucleus, although each factor in ▶ Eq. (2.70) depends on r_c . This formalism, combined with a sophisticated model of the parent nucleus, has been able to reproduce the absolute decay rate (width) of the α decay of ^{212}Po .

By the use of the “cluster-configuration shell model” and the “Gaussian-orbit shell model with preselected random basis,” Varga et al. (1992) and Varga and Liotta (1994) have calculated the $g(r)$ formation amplitude for the $^{212}\text{Po} \rightarrow ^{208}\text{Pb} \alpha$ decay (▶ Fig. 2.36a). For $\Gamma(r_c)$ they obtained 0.72×10^{-15} MeV in the Gaussian shell model and 1.6×10^{-15} MeV in the cluster-configuration shell model, which are close to the experimental value: 1.5×10^{-15} MeV. It was found that the amount of core + α clustering in the ground state of ^{212}Po is 20–30% (Lovas et al. 1998).

■ Fig. 2.36

(a) Radial α -core formation amplitudes $g(r)$ in the ground state of ^{212}Po obtained in the cluster-configuration shell model (solid line) and in the Gaussian shell model (dashed line). See ▶ Eq. (2.70) and Varga and Liotta (1994). (b) Radial α -core formation amplitudes $g(r)$ in the ground state of ^{192}Pb obtained from BCS calculations with proton gaps appropriate for ^{206}Hg (dashed curve) and for ^{188}Hg (full curve) (Insolia et al. 1988). (c) Ratio of theoretical and experimental α -decay widths $\Gamma_{\text{th}}/\Gamma_{\text{exp}}$ for light, spherical Pb isotopes. The theoretical widths were calculated with gaps fitted to the daughter nucleus (Insolia et al. 1988) (The figures were taken from the review article of Lovas et al. (1998))



The pairing interaction gives rise to powerful cluster formation on the nuclear surface, therefore, far from the double magic core nucleus ^{208}Pb , it is reasonable to use the BCS approach to the description of α decay (Lovas et al. 1998).

For the light spherical lead isotopes $^{186,188,190,192}\text{Pb}$ such calculations were performed by Insolia et al. (1988). The results are shown in ► Fig. 2.36b and c. The r_c dependence of the width has a plateau between 8 and 8.5 fm. With such a channel radius and with a prescription simulating the proton–neutron interaction, they obtained a very good agreement with experimental results (► Fig. 2.36c).

Deformed Nuclei

Mang has derived formulae for the treatment of the α decay of deformed nuclei, too, taking into account Nilsson-type wave functions for the nucleons. The calculations of Mang and Rasmussen (1962) for U, Pu, Cm, Cf, Fm isotopes gave reasonable agreement with the experimental results. The calculations again showed that the residual interaction between the valence nucleons plays an important role in the description of α -decay probability.

Following the classical works by Mang (1960, 1964) and using the semiclassical description of barrier penetration by Fröman (1957), the alpha-decay widths Γ_0 have been calculated for the deformed even-even Ra, Rn, and Th isotopes by Insolia et al. (1991) and Delion et al. (1992). They have taken into account the pairing residual interaction and used the BCS approach. The theoretical widths obtained for ground-state to ground-state $l = 0$ transitions are compared with experimental data in ► Table 2.9. The agreement is remarkable. For transitions to the 2^+ states the calculated α -decay widths Γ_2 showed similar agreement with the experimental data.

In the case of spheroidal nuclei the α -particle formation may depend on the direction (in a body-fixed coordinate system). Furthermore, the noncentral electrostatic field of the deformed daughter nucleus may interact with the emitted α particle, causing an increase or decrease of its energy. These problems were discussed by several authors (Hyde et al. 1964). On the basis of these works, one can conclude that the α -particle wave function on the nuclear surface may be quite different for different nuclei. Furthermore, the electric quadrupole field of the strongly deformed daughter nucleus plays an important role in the formation of the intensity of different α -particle groups.

► Table 2.9

Calculated α -decay widths Γ_0 for some even–even deformed nuclei compared with experimental data (Insolia et al. 1991, Delion et al. 1992, Lovas et al. 1998)

Mother nucleus	Experiment (MeV)	Theory (MeV)
^{222}Rn	1.38×10^{-27}	0.70×10^{-27}
^{220}Rn	8.20×10^{-24}	2.7×10^{-24}
^{218}Rn	1.30×10^{-20}	0.25×10^{-20}
^{226}Ra	9.0×10^{-33}	6.6×10^{-33}
^{224}Ra	1.44×10^{-27}	0.83×10^{-27}
^{222}Ra	1.20×10^{-23}	0.52×10^{-23}
^{232}Th	1.01×10^{-39}	0.60×10^{-39}

A systematic survey of a number of At and Rn isotopes shows that the α emission in polar directions is favored mainly by prolate nuclei, while oblate nuclei prefer equatorial emission (Delion et al. 1994).

Note that in some cases the α -particle emission may induce electron knock out from the K or higher electron shells. The effect is very weak. For example the probability of ionization of the K shell in the α decay of ^{210}Po is of the order of 10^{-6} . For a review see Hyde et al. (1964).

2.4.2 Beta Decay

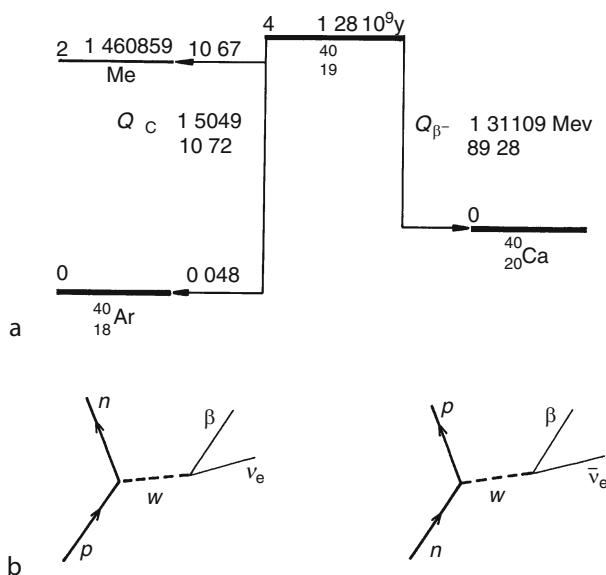
2.4.2.1 Basic Experimental Facts

The β decay of atomic nuclei has three types: β^- and β^+ emission, as well as electron capture (EC). In any of these processes the atomic number of the nucleus changes one unit. In β^- decay electrons (e^-) and in β^+ positrons (e^+) are emitted from the nucleus. In the EC process an electron is captured from the K (or higher) shell. In some cases the same nucleus may undergo β decays of different types (► Fig. 2.37). The β decay may lead to the ground state of the daughter nucleus and/or to excited state(s).

The electron capture process is followed by X-ray and/or Auger electron emission, in which the vacancy in the atomic shell is filled up with an electron from an external shell. As a consequence of the interaction between the nucleus and the electron or positron, a very weak electromagnetic radiation of continuous wavelength distribution (called internal *bremsstrahlung*) is also always present in the radioactive β^\pm and EC decay (Pettersen 1965).

► Fig. 2.37

(a) β -decay modes of ^{40}K (Based on Firestone et al. (1996)). (b) Illustration of the β^+ and β^- decay processes according to the Glashow–Salam–Weinberg theory of weak interaction (see, e.g., Greiner and Müller 1993, Perkins 2000)



Beta decay can take place only when one (or more) of the following mass-energy relations are fulfilled:

$$M(Z, A) > M(Z + 1, A) \quad \beta^- \text{ emission,}$$

$$M(Z, A) > M(Z - 1, A) \quad \text{electron capture,}$$

$$M(Z, A) > M(Z - 1, A) + 2m_0 \quad \beta^+ \text{ emission.}$$

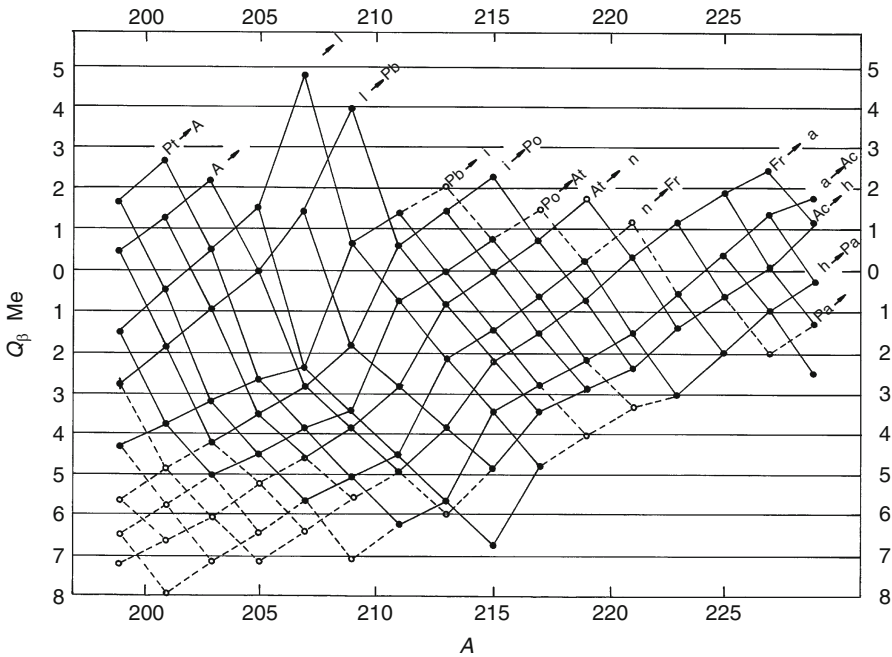
Here the M values denote atomic (not nuclear) masses. $2m_0 = 2 \times 0.511 \text{ MeV}/c^2$ is the sum of rest masses of the emitted β^+ particle and of an atomic electron.

The β -transition energies show a systematic trend, when one plots them as a function of mass number (● Fig. 2.38). The effect of the $Z = 82$ magic number is clearly seen (great gap between the ${}_{81}\text{Tl} \rightarrow {}_{82}\text{Pb}$ and ${}_{82}\text{Pb} \rightarrow {}_{83}\text{Bi}$ transition energies).

The energy of β decay varies from near zero up to 25–30 MeV, while the β partial half-lives vary in a very wide range from $\sim 10^{-3} \text{ s}$ up to $\geq 10^{24} \text{ s}$. The β^+ and β^- energy spectra show continuous distributions (● Fig. 2.39a). As both the initial and final states have well-defined quantum energies, Pauli postulated (in 1931) the existence of a neutral particle (called neutrino), which takes away the missing energy difference. An indirect proof of the existence of the antineutrino was given by Csikai and Szalay (1957) in a cloud chamber photo of the ${}^6\text{He} \rightarrow {}^6\text{Li} \beta^-$ decay (● Fig. 2.39b).

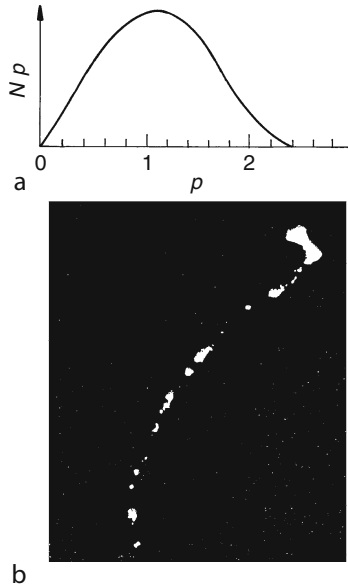
■ Fig. 2.38

β -decay energies (Q_β) of odd- A nuclei from $A = 199$ to 229. Full circles denote experimental values, open circles indicate data estimated from systematic trends. The lines ascending to the right connect isotopes with $N, N + 2, \dots$. The lines descending to the right connect isotones with $Z, Z + 2, \dots$. Open circles are connected by dashed lines for clarity. $Q_{\beta^-} = M(A, Z) - M(A, Z + 1)$, $Q_{\beta^+} = M(A, Z) - M(A, Z - 1)$, where M denotes the atomic mass. A comprehensive review of evaluated Q_β values in different mass regions can be found in Audi et al. (2003)



■ Fig. 2.39

(a) A typical β spectrum. p is the momentum of the β particle (in arbitrary units), $N(p)$ is the number of β particles emitted in a unit momentum interval. (b) Cloud chamber photo of the ${}^6\text{He}$ β^- decay ($T_{1/2} = 0.807$ s). The directions of the tracks of the β^- particle and the recoiled nucleus are not opposite, which indirectly indicates the presence of a third, neutral, undetected particle in the β decay (Csikai and Szalay 1957)



Free antineutrinos were detected directly first from a high-flux reactor through an inverse β -decay process: $p + \bar{\nu}_e \rightarrow n + e^+$ (Reines and Cowan 1959; Reines et al. 1960). The rest mass of the neutrino can be studied, e.g., by a careful analysis of the β spectrum near to the maximum β -ray energy. Some properties of neutrinos (type, mass, charge, spin) are summarized in ► Table 2.1.

The hydrogen burning in the Sun ($4p \rightarrow {}^4\text{He} + 2e^+ + 2\nu_e + Q_{\text{eff}}$) produces low energy (≤ 20 MeV) electron neutrinos, but the flux $\Phi(\nu_e)$ of neutrinos detected fell insistently short of the flux expected. Some of the electron neutrinos produced in the solar core changed flavor. The result, interpreted in this way, is

$$\frac{\Phi(\nu_e)}{\Phi(\nu_e) + \Phi(\nu_{\mu,\tau})} = 0.340 \pm 0.023(\text{stat.}) \pm 0.030(\text{syst.})$$

(Aharmin et al. 2005, Sudbury Neutrino Observatory, Canada). This result clearly shows that $\Phi(\nu_{\mu,\tau})$ is non zero. The KamLAND (Japan) experiment, which studies reactor electron antineutrinos ($\bar{\nu}_e$) traveling ~ 180 km to reach the detector, confirmed the flavor change.

The cosmic rays produce high-energy ($\geq \text{GeV}$) neutrinos in the Earth's atmosphere. One can study the downward-going atmospheric neutrinos in an underground detector, and also the upward-going ones, which come from the opposite side of the Earth, thus traveling much more in the Earth before reaching the detector. The analysis of the Super-Kamiokande (Japan) experimental results shows that some mechanism does change the ν_μ flux

while it is traveling through the Earth. This change-of-flavor effect was confirmed in the accelerator-generated high energy muon neutrino experiments, too. In the MINOS (USA) experiments the accelerator–detector distance was 735 km, in the K2K (Japan) experiments it was 250 km.

Thus there is now compelling evidence that solar, reactor, atmospheric, and accelerator neutrinos change their flavor from one to another.

The neutrino change of flavor can be interpreted also theoretically. It is supposed that the neutrinos are created (or annihilated) in different flavor eigenstates ($|v_e\rangle$, $|v_\mu\rangle$, $|v_\tau\rangle$), which are superpositions of different mass eigenstates ($|v_1\rangle$, $|v_2\rangle$, $|v_3\rangle$). The connection between the different eigenstates can be expressed in matrix form:

$$\begin{pmatrix} |v_e\rangle \\ |v_\mu\rangle \\ |v_\tau\rangle \end{pmatrix} = \begin{pmatrix} U_{e1} & U_{e2} & U_{e3} \\ U_{\mu1} & U_{\mu2} & U_{\mu2} \\ U_{\tau1} & U_{\tau2} & U_{\tau3} \end{pmatrix} \begin{pmatrix} |v_1\rangle \\ |v_2\rangle \\ |v_3\rangle \end{pmatrix}.$$

(Pontecorvo–Maki–Nakagawa–Sakata matrix.)

If all neutrinos were to be massless, there would be no transitions between neutrinos. The above matrix relation assumes that neutrinos have masses, and, if so, the neutrinos in different mass eigenstates may travel with different energies. Thus, according to the Schrödinger equation, phase difference will be created between the neutrino components of different masses, and the difference will depend on the distance. This can lead to the change of neutrino flavor.

If one considers only $v_e \leftrightarrow v_\mu$ transitions, the above matrix equation can be simplified to

$$\begin{pmatrix} |v_e\rangle \\ |v_\mu\rangle \end{pmatrix} = \begin{pmatrix} \cos \theta & \sin \theta \\ -\sin \theta & \cos \theta \end{pmatrix} \begin{pmatrix} |v_1\rangle \\ |v_2\rangle \end{pmatrix}.$$

This transformation contains only one free parameter, the θ mixing angle.

Based on experimental data, one can determine the mass difference square (Δm^2) and mixing angles (θ) for different neutrino transitions. The results are as follows.

From solar and reactor neutrino experiments ($\Delta m_{ij}^2 \equiv m_i^2 - m_j^2$):

$$\Delta m_{\text{solar}}^2 \approx \Delta m_{12}^2 = (7.59 \pm 0.21) \times 10^{-5} \text{eV}^2/\text{c}^4 \text{ and } \tan^2 \theta_{\text{solar}} = 0.47 \pm 0.06.$$

From atmospheric and accelerator neutrino experiments:

$$1.9 \times 10^{-3} \text{eV}^2/\text{c}^4 < \Delta m_{\text{atm}}^2 \approx \Delta m_{23}^2 < 3.0 \times 10^{-3} \text{eV}^2/\text{c}^4 \text{ and } \sin^2(2\theta_{\text{atm}}) > 0.90.$$

This implies that neutrinos have masses and mix. Furthermore the experimental data show quasi-two-neutrino transitions: $v_e \leftrightarrow v_\mu$ for solar and reactor neutrinos, and $v_\mu \leftrightarrow v_\tau$ for atmospheric and accelerator neutrinos.

The neutrino mass, mixing, and flavor change are discussed in detail by Kayser in Particle Data Group (2008).

Detailed investigations show that there are two types of electron neutrinos, which differ in their interactions with matter (different cross sections). The electron neutrino is denoted usually by v_e , the antineutrino by \bar{v}_e . They take part in the β -decay processes as follows:

$$(Z, A) \rightarrow (Z + 1, A) + e^- + \bar{v}_e,$$

$$(Z, A) \rightarrow (Z - 1, A) + e^+ + v_e,$$

$$(Z, A) \rightarrow (Z - 1, A) + v_e,$$

which can be deduced to processes (► Fig. 2.37b)

$$n \rightarrow p + e^- + \bar{\nu}_e,$$

$$p \rightarrow n + e^+ + \nu_e,$$

$$p + e^- \rightarrow n + \nu_e, \text{ respectively.}$$

Since the neutrino does not ionize matter, its magnetic moment (μ_ν) must be very little or zero. It is estimated that $\mu_\nu < 10^{-7} \mu_B$, where μ_B is the Bohr magneton. The measured cross section of the $p + \bar{\nu}_e$ reaction in the experiment by Reines and Cowan (1959) has been found to be $\sigma \approx 10^{-43} \text{ cm}^2$, which, in condensed matter (where the concentration of protons is roughly $n \approx 10^{22} \text{ cm}^{-3}$), corresponds to the average mean free path $\lambda = 1/(n\sigma) \approx 10^{21} \text{ cm} = 10^{16} \text{ km} \approx 1,057 \text{ light years}$. This makes the direct observation of antineutrinos very difficult.

From the relativistic expression of the total energy, $E = m_\nu c^2 (1 - u^2/c^2)^{-1/2}$, it follows that if the neutrino rest mass (m_ν) is close to zero, its speed (u) must be close to the speed of light (c).

The experimental and theoretical problems of β decay are treated in more detail in several review articles and books (Deutsch and Kofoed-Hansen 1959; Wu 1965; Konopinski and Rose 1965; Wu et al. 1965; Wu and Moszkowski 1965; Marmier and Sheldon 1969; Mukhin 1974; Greiner and Müller 1993; Heyde 1999). Experimentally determined nuclear structure and decay data are evaluated and included into the ENSDF (Evaluated Nuclear Structure Data File) database (www.nndc.bnl.gov/ensdf).

2.4.2.2 Theory of β Decay

Based on the analogy with γ radiation, the theory of β decay was formulated first by Fermi (1933, 1934). The basic assumptions of his theory are as follows.

The e^\pm and the neutrino are not present in the nucleus; they are created only in the β -decay process, just as the γ quantum in the γ decay. In contrast with the strong interaction, the “weak interaction” between nucleons can be treated as a very weak perturbation. Then, according to the time-dependent perturbation theory of quantum mechanics, the transition probability in unit time (P_{fi}) between the initial (i) and final (f) states of the system is proportional to the final state density ($\rho_f = dn/dE_0$) and $|H_{fi}|^2$, where H_{fi} is the matrix element of the Hamiltonian H of the weak interaction:

$$P_{fi} = \frac{2\pi}{\hbar} |H_{fi}|^2 \frac{dn}{dE_0}, \quad (2.72)$$

$\hbar \equiv h/(2\pi) \approx 6.582 \times 10^{-16} \text{ eV s}$, E_0 is the total decay energy, and dn is the number of accessible states in the energy interval ($E_0, E_0 + dE_0$) (cf. ► Eq. (2.29)). The matrix element H_{fi} can be expressed as

$$H_{fi} \equiv \int \Psi_f^* H \Psi_i d\tau, \quad (2.73)$$

where $d\tau$ is the volume element, Ψ_i and Ψ_f are the initial and final normalized wave functions. It is useful to consider the different β -decay processes: $n \rightarrow p + e^- + \bar{\nu}_e$ and $p \rightarrow n + e^+ + \nu_e$ in a uniform framework, in which one nucleon is transformed into another one and a pair of leptons are created in the weak interaction. Then “electron” and “neutrino” stand for “positron” and “antineutrino” as well.

The final state density can be derived from Heisenberg's uncertainty relation. The space coordinates shall be denoted by x, y, z , and the momentum coordinates by p_x, p_y, p_z . Then, according to the uncertainty relation (in the form used by Fermi (1934))

$$\Delta x \Delta y \Delta z \Delta p_x \Delta p_y \Delta p_z \approx h^3,$$

that is the product of the uncertainties of the space and momentum coordinates is approximately equal to h^3 . This means a restriction on the possible states in a given phase volume. If the electron can be found in spatial volume $V \approx \Delta x \Delta y \Delta z$, the number of electron states in the momentum interval $(p, p + dp)$ is

$$dn_e = V \frac{4\pi p^2 dp}{h^3}.$$

A similar relation holds for neutrinos. Then the state density dn/dE_0 around the total energy of the electron and neutrino ($E_0 = E + E_v$) can be expressed as a product:

$$\frac{dn}{dE_0} = V^2 \frac{16\pi^2}{h^6} p^2 p_v^2 \frac{dp_v}{dE_0} dp. \quad (2.74)$$

If one considers the neutrino massless, $p_v c = E_v = E_0 - E$ (c is the speed of light in vacuum) and neglecting the small recoil energy of the parent nucleus, one gets

$$\frac{dn}{dE_0} = V^2 \frac{16\pi^2}{c^3 h^6} p^2 (E_0 - E)^2 dp. \quad (2.75)$$

This expression is called a “statistical factor”, which gives the mean density of possible final states in the electron–neutrino field.

The interaction matrix element (Eq. (2.72)) can be written in the form

$$H_{fi} = g \int \psi_f^* \varphi_e^*(\mathbf{r}) \varphi_v^*(\mathbf{r}) M \Psi_i d\tau, \quad (2.76)$$

where $\psi_f, \varphi_e, \varphi_v$ are the wave functions of the final (daughter) nucleus, electron, and neutrino, respectively; g is an empirical coupling constant of the weak interaction. This coupling constant is analogous to the nucleon charge in the γ -ray emission. The full Hamiltonian is gM .

The interaction of neutrinos with the nucleus and surrounding matter is very weak, and therefore the neutrino wave function can be approximated by a plane wave

$$\varphi_v(\mathbf{r}) = V^{-1/2} \exp[i(\mathbf{k}_v \mathbf{r})] \approx V^{-1/2} [1 + i(\mathbf{k}_v \mathbf{r}) - (\mathbf{k}_v \mathbf{r})^2/2 + \dots] \approx V^{-1/2}, \quad (2.77)$$

where $\mathbf{k}_v = \mathbf{p}_v/\hbar$ is the neutrino wave vector and $V^{-1/2}$ is a normalization factor. In the expansion, it is enough to retain only the first term, because the size of the nucleus is very small compared to the volume in which the neutrino can be found, and $p_v = (E_0 - E)/c$. A similar expansion can be applied to the electron wave function, if the electromagnetic interaction between the electron and nucleus is not significant (for light nuclei and electron kinetic energies ≥ 200 keV):

$$\varphi_e(\mathbf{r}) = V^{-1/2} \exp[i(\mathbf{k}_e \mathbf{r})] \approx V^{-1/2} [1 + i(\mathbf{k}_e \mathbf{r}) - (\mathbf{k}_e \mathbf{r})^2/2 + \dots] \approx V^{-1/2}. \quad (2.78)$$

Thus the electron and neutrino wave functions can be considered nearly constant within the nucleus. Then

$$H_{fi} = \frac{g}{V} \int \psi_f^* M \Psi_i d\tau = \frac{g}{V} M_{fi}. \quad (2.79)$$

Here M_{fi} is the transition matrix element between the initial Ψ_i and final ψ_f nuclear states. Its value depends on the overlap of the initial and final wave functions. If they are nearly identical, M_{fi} is large. If Ψ_i and ψ_f are very different, M_{fi} is small. M_{fi} can be computed, if the structures of the parent and daughter nuclei, as well as the Hamilton operator of weak interaction are known. Substituting [Eqs. \(2.74\)](#) and [\(2.78\)](#) into [Eq. \(2.71\)](#) one obtains

$$P_{fi}(p)dp = N(p)dp = C|M_{fi}|^2 p^2 (E_0 - E)^2 dp, \quad (2.80)$$

where $C = g^2/(2\pi^3 c^3 \hbar^7)$ is a constant. Note that the Fermi constant of the weak interaction is defined by the expression $G_F/\sqrt{2} \equiv g^2/(8M_W^2)$ in particle physics (in units $\hbar = 1, c = 1$). The numerical constants of the formula are introduced from historical reasons. M_W is the mass of the W boson. $G_F/(\hbar c)^3 = 1.16637(1) \times 10^{-5} \text{GeV}^{-2}$ (Particle Data Group 2008). The Coulomb interaction between the electric charge of the nucleus and the β^\pm particle can modify the shape of the β spectrum. This effect becomes important especially in the case of heavy nuclei and low-energy β particles. The detailed calculations show that by the introduction of an $F(Z, E)$ factor in [Eq. \(2.79\)](#) this effect can be taken into account:

$$N(p)dp = C|M_{fi}|^2 F(Z, E) p^2 (E_0 - E)^2 dp, \quad (2.81)$$

where Z is the atomic number of the decaying nucleus, E_0 is the total decay energy, E is the kinetic energy of the electron, p is the momentum of the electron,

$$M_{fi} = \int \psi_f^* M \Psi_i d\tau$$

(see [Eq. \(2.78\)](#)), and C is defined as in [Eq. \(2.79\)](#). The numerical values of the Coulomb correction (or Fermi) function $F(Z, E)$ are given in [Fig. 2.40](#).

Experimental and theoretical results can be easily compared by plotting the $[N(p)/(F(Z, E) p^2)]^{1/2}$ values as a function of $(E_0 - E)$, as suggested first by Kurie et al. (1936). [Figure 2.41](#) shows the Kurie plot for the β^- decay of ^{35}S . The straight-line character of the plot indicates that the matrix element $|M_{fi}|^2$ does not depend on the electron energy. The value of $|M_{fi}|^2$ is near to one, as is usual with allowed transitions. For forbidden transitions (see later) $|M_{fi}|^2$ may be much less than one.

The probability of β -decay in unit time (i.e., the decay constant λ) can be calculated by integration of $N(p)dp$ from $p = 0$ up to p_{\max} :

$$\lambda = \frac{\ln 2}{T_{1/2}} = \int_{p=0}^{p_{\max}} N(p)dp = C \int_0^{p_{\max}} |M_{fi}|^2 F(Z, E) p^2 (E_0 - E)^2 dp, \quad (2.82)$$

with $C = g^2/(2\pi^3 c^3 \hbar^7)$. In allowed transitions $|M_{fi}|$ does not depend on the energy thus it can be shifted before the integral. The integral

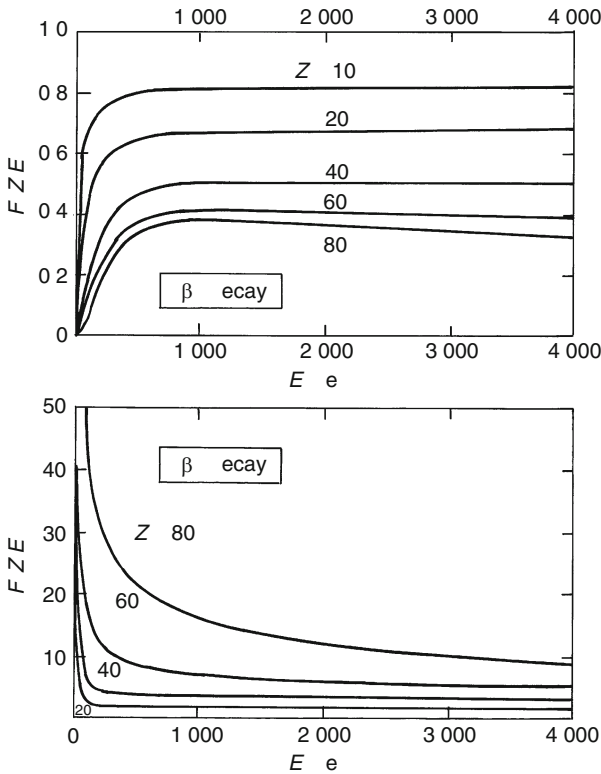
$$\int_{p=0}^{p_{\max}} F(Z, E) p^2 (E_0 - E)^2 dp \equiv f(Z, E_0) \quad (2.83)$$

has been evaluated and tabulated (Wapstra et al. 1959; Dzhelepov et al. 1972) for different Z and E_0 values (see [Fig. 2.42a](#) and [b](#)). The so-called Fermi integral function $f(Z, E_0)$ is approximately proportional to E_0^5 at the highest transition energies. The probability of β decay sharply increases with increasing decay energy. The quantity

$$f(Z, E_0) T_{1/2} \quad (2.84)$$

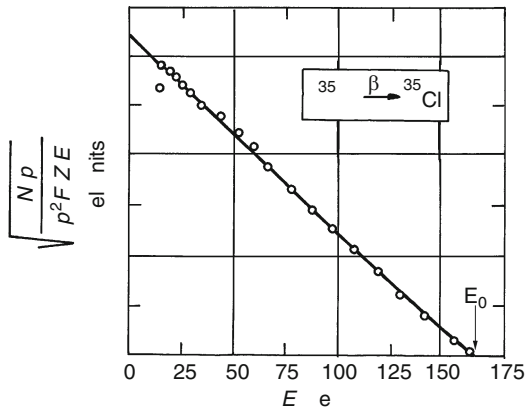
■ Fig. 2.40

Coulomb correction factor $F(Z,E)$ for β^+ and β^- emission as a function of the kinetic energy of the β particle (Based on Dzhelepov et al. (1972))



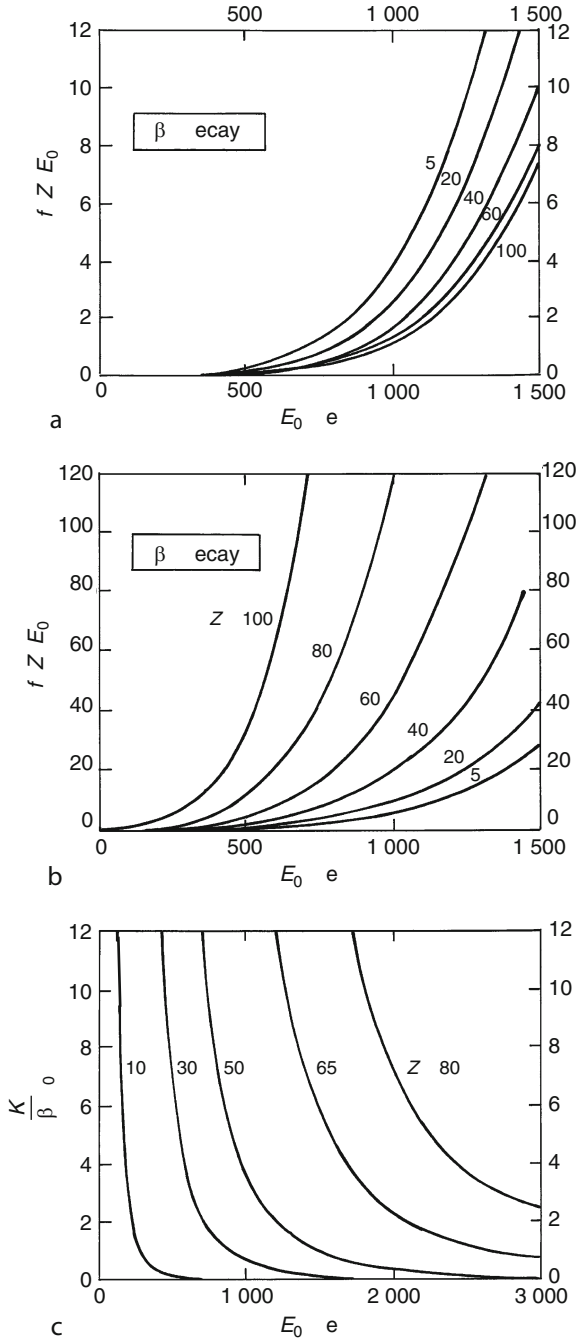
■ Fig. 2.41

Kurie plot for the $^{35}\text{S} \rightarrow ^{35}\text{Cl} \beta^-$ decay ($T_{1/2} = 87.51 \text{ d}$). For notations see Eq. (2.80). Based on Albert and Wu (1948). The intersection with the energy axis is equal to E_0



■ Fig. 2.42

(a, b) The Fermi integral function $f(Z, E_0)$ for β^+ and β^- decay, respectively. E_0 is the maximum kinetic energy of the β particle. (c) K electron capture per β^+ branching ratio $(K/\beta^+)_0$ for allowed transitions as a function of E_0 (The figures are based on Dzhelepov et al. (1972))



is characteristic of the transition matrix element, and it is determined by the structure of the nucleus. The product $f(Z, E_0) T_{1/2}$ is usually denoted by ft , it is measured in seconds and called “comparative half-life.” As the ft values vary in a wide range, the $\log ft$ values are usually given. The β -decay transitions are in general classified according to their comparative half-lives.

For the determination of the $\log ft$ values nomograms have been constructed. The input data are the experimental maximum β^\pm (or K capture) energy, the partial half-life ($T_{1/2}$), and the nuclear charge number (Z) (Wapstra et al. 1959).

Empirical $\log ft$ values for some β decays are presented in ▶ [Table 2.10](#). The first column shows the β transition and the probable valence-orbit shell-model configurations in the mother and daughter nuclei. The next columns give the $\log ft$ value, the spin ($\Delta I = I_f - I_i$), and parity ($\Delta\pi$) changes in the β decay. The table shows that the β transitions can be

■ **Table 2.10**

Empirical $\log ft$ values for some β decays. ΔI and $\Delta\pi$ denote spin and parity changes, respectively. The $\log ft$, ΔI , and $\Delta\pi$ data were taken from Firestone et al. (1996)

	$I_i^\pi \rightarrow I_f^\pi$	$\log ft$	ΔI	$\Delta\pi$	Remark
Superallowed transitions					
$n \rightarrow p$	$s_{1/2+} \rightarrow s_{1/2+}$	3.0	0	No	Mixed Fermi and Gamow–Teller transition
$^1_1\text{H}_2 \rightarrow ^2_2\text{He}_1$	$s_{1/2+} \rightarrow s_{1/2+}$	3.1	0	No	
$^6_6\text{C}_5 \rightarrow ^5_5\text{B}_6$	$p_{3/2-} \rightarrow p_{3/2-}$	3.6	0	No	
$^8_8\text{O}_6 \rightarrow ^7_7\text{N}_7$	$0^+ \rightarrow 0^+$	3.5	0	No	Pure Fermi transition
$^{16}_{16}\text{S}_{15} \rightarrow ^{15}_{15}\text{P}_{16}$	$s_{1/2+} \rightarrow s_{1/2+}$	3.7	0	No	
$^2_2\text{He}_4 \rightarrow ^3_3\text{Li}_3$	$0^+ \rightarrow 1^+$	2.9	1	No	Pure Gamow–Teller transition
$^6_6\text{C}_4 \rightarrow ^5_5\text{B}_5$	$0^+ \rightarrow 1^+$	3.0	1	No	Pure Gamow–Teller transition
$^9_9\text{F}_9 \rightarrow ^8_8\text{O}_{10}$	$1^+ \rightarrow 0^+$	3.6	1	No	Pure Gamow–Teller transition
Allowed transitions					
$^{15}_{15}\text{P}_{18} \rightarrow ^{16}_{16}\text{S}_{17}$	$s_{1/2+} \rightarrow d_{3/2+}$	5.0	1	No	
$^{16}_{16}\text{S}_{19} \rightarrow ^{17}_{17}\text{Cl}_{18}$	$d_{3/2+} \rightarrow d_{3/2+}$	5.0	0	No	
$^{26}_{26}\text{Fe}_{27} \rightarrow ^{25}_{25}\text{Mn}_{28}$	$f_{7/2-} \rightarrow f_{7/2-}$	5.2	0	No	
First forbidden ($n = 1$) transitions					
$^{36}_{36}\text{Kr}_{49} \rightarrow ^{37}_{37}\text{Rb}_{48}$	$g_{9/2+} \rightarrow f_{5/2-}$	9.4	2	Yes	Unique ($\Delta I = n + 1$)
$^{48}_{48}\text{Cd}_{65} \rightarrow ^{49}_{49}\text{In}_{64}$	$h_{11/2-} \rightarrow g_{9/2+}$	9.2	1	Yes	
$^{53}_{53}\text{I}_{80} \rightarrow ^{54}_{54}\text{Xe}_{79}$	$g_{7/2+} \rightarrow h_{11/2-}$	10.0	2	Yes	Unique ($\Delta I = n + 1$)
Second forbidden ($n = 2$) transitions					
$^{11}_{11}\text{Na}_{11} \rightarrow ^{10}_{10}\text{Ne}_{12}$	$3^+ \rightarrow 0^+$	15.1	3	No	Unique ($\Delta I = n + 1$)
$^{40}_{40}\text{Zr}_{53} \rightarrow ^{41}_{41}\text{Nb}_{52}$	$d_{5/2+} \rightarrow g_{9/2+}$	> 12.8	2	No	
$^{43}_{43}\text{Tc}_{56} \rightarrow ^{44}_{44}\text{Ru}_{55}$	$g_{9/2+} \rightarrow d_{5/2+}$	12.3	2	No	
$^{55}_{55}\text{Cs}_{82} \rightarrow ^{56}_{56}\text{Ba}_{81}$	$g_{7/2+} \rightarrow d_{3/2+}$	12.1	2	No	
Third forbidden ($n = 3$) transitions					
$^{19}_{19}\text{K}_{21} \rightarrow ^{18}_{18}\text{Ar}_{22}$	$4^- \rightarrow 0^+$	21.0	4	Yes	Unique ($\Delta I = n + 1$)

approximately divided into groups according to their $\log ft$ values. There are superallowed, allowed, first, second, and third forbidden transitions, with ft values increasing by orders of magnitude.

Nevertheless, the classification of β transitions according to ft values can only be made roughly. For the exact classification one must start from the interaction matrix element H_{fi} given in [Eq. \(2.75\)](#), which involves the overlap integral of initial and final nuclear wave functions and the power expansions of φ_ν and φ_e ([Eqs. \(2.76\)](#) and [\(2.77\)](#)).

The first terms in the expansions of φ_ν and φ_e generate allowed transitions. In this case the matrix element is independent of electron and neutrino energies. In allowed transitions there is no parity change between the initial and final nuclear states (“ $\Delta\pi$ no”), and the orbital angular momentum change is zero. If the electron and neutrino are emitted with antiparallel spins ($\downarrow\uparrow$), the allowed transition is called Fermi transition, and the spin change is $\Delta I = 0$. If the electron and neutrino are emitted with parallel spins ($\uparrow\uparrow$), the allowed transition is called Gamow–Teller transition, and the spin change may be $\Delta I = 0$ or ± 1 .

A strong overlap of initial and final wave functions is expected for mirror nuclei, in which the mass numbers are identical, but the atomic number in one nucleus is equal to the neutron number of the other. The large overlap integral results in a very low ft value (superallowed transitions). Most of the known β emitters decay by allowed or superallowed transitions. Among the light nuclides there are many mirror pairs.

The second and following terms in the expansions of [Eqs. \(2.76\)](#) and [\(2.77\)](#) generate first, second, third, etc., forbidden transitions. As the integration in [Eq. \(2.75\)](#) can be confined to the nuclear volume, where r is very small, the weights of the successive terms in [Eqs. \(2.76\)](#) and [\(2.77\)](#) strongly (by orders of magnitude) decrease.

The first forbidden ($n = 1$) transitions are characterized by $\Delta I = 0, \pm 1, \pm 2$ spin and “ $\Delta\pi$ yes” parity changes. If $\Delta I = n + 1$, the transition is called “unique.”

In the “true” second forbidden ($n = 2$) transitions there is no parity change (“ $\Delta\pi$ no”), and $\Delta I = \pm 2, \pm 3$. In unique second forbidden transitions $|\Delta I| = 3$. In another group of second forbidden transitions the spin change is $\Delta I = 0, \pm 1$, and there is no parity change (“ $\Delta\pi$ no”). These latter selection rules are the same as for allowed transitions, but the corresponding transitions are weak, because of the small $(\mathbf{kr})^2$ factors in the electron and neutrino wave functions.

In n times forbidden transitions $\Delta I = n, n + 1$ and $\pi_i\pi_f = (-1)^n$. In the region $6 < \log ft < 9$ both allowed and first forbidden β -transitions occur. For example, the $^{32}\text{P } \beta^- 1^+ \rightarrow 0^+$ and $^{22}\text{Na } \beta^+ 3^+ \rightarrow 2^+$ decays are allowed Gamow–Teller transitions, although they have rather large $\log ft$ values of 7.9 and 7.4, respectively. Second, third, and fourth forbidden transitions were observed rarely; they are mainly in the region $10 < \log ft$.

In the case of the *electron capture (EC) decay*, the capture of an atomic-shell electron by the nucleus can be considered as an inverse β^+ decay: $p + e^- \rightarrow n + \nu_e$. The main difference is that in EC the neutrino spectrum is discrete, because the energy of the captured electron has a well-defined value. The theory of EC is analogous to the theory of β^\pm decay and also starts from [Eq. \(2.71\)](#).

The capture from K-shell is usually about one order of magnitude more intensive than the capture from L, M, ... shells, because the K-electrons are much closer to the nucleus. Nevertheless, when the K-capture is forbidden owing to energetic reasons, an electron may be captured only from L (or higher) shell.

[Figure 2.42c](#) shows the $(K/\beta^+)_0$ branching ratios for allowed transitions. The EC process always accompanies the β^+ decay, but the electron capture usually becomes dominating only in

heavy nuclei and/or at low decay energies. The overlap of K-electron wave function with the nucleus may be significant. If the decay energy is smaller than $2m_0c^2 = 1,022$ keV, only EC decay can occur. In experiments mostly allowed and superallowed EC transitions have been observed.

2.4.2.3 Types of the Weak Interaction

One of the central problems in the theory of β decay is the determination of the Hamilton operator of the weak interaction (Eqs. (2.71) and (2.72)). H should be invariant against proper Lorentz transformation, otherwise it would be possible to determine an absolute time, which is impossible according to the theory of relativity. Then, from Dirac's relativistic wave mechanics for spin 1/2 particles, it follows that there may be five classes of weak interaction terms, each transforming in a particular way under rotation and space inversion: scalar (S), vector (V), antisymmetric tensor of second rank (T), axial vector (A), and pseudoscalar (P). As one cannot exclude any of these from the beginning, a linear combination of all five interactions must be considered:

$$\overline{H} = g \sum_{i=1}^5 C_i \overline{H}_i; \quad \sum_{i=1}^5 |C_i|^2 = 1. \quad (2.85)$$

Here \overline{H} and \overline{H}_i are the generalized Hamiltonians (Wu and Moszkowski 1965) and the C_i -s are the coupling strengths. The \overline{H}_i operators have different shapes for S, V, T, A, and P classes of weak interaction. They are complicated combinations of the so-called γ matrices of the relativistic quantum mechanics.

One can get information on the possible coupling strengths from general symmetry properties of space and time. From the homogeneity of space and time follow the laws of conservation of momentum and energy, respectively, while from the spatial isotropy follows the law of conservation of angular momentum. (Homogeneity of space means that it has equal structure at all positions \mathbf{r} . Isotropy of space means that all directions are equivalent.) The Schwinger–Lüders–Pauli theorem states that the interaction Hamiltonian is invariant under the combined CPT operation, where C denotes charge conjugation (particle \leftrightarrow antiparticle transformation), P is the parity operation ($\mathbf{r} \rightarrow -\mathbf{r}$, space inversion), and T is the time reversal operator ($t \rightarrow -t$). On the other hand, one can draw conclusions on the possible coupling strengths from different experiments. Some of them are as follows.

- Investigation of pure Fermi $0^+ \rightarrow 0^+$ transitions (e.g., $^{14}\text{O} \rightarrow ^{14}\text{N}$, $^{50}\text{Mn} \rightarrow ^{50}\text{Cr}$ decays), in which both the ft and the M_{fi} can be determined and the g_F constant derived (see E. (2.82)).
- The study of neutron β decay: $n \rightarrow p + \beta^- + \bar{\nu}_e$, where the Fermi and Gamow–Teller transitions are equally allowed. As the n and p are mirror nuclei, the matrix elements $|M_F|^2$ and $|M_{GT}|^2$ can be easily calculated. Consequently, one can derive the $|C_{GT}/C_F|^2$ and also the $|g_{GT}/g_F|^2$ ratios using the experimentally determined ft value.
- Electron-neutrino angular correlation experiments.
- Several experiments in connection with parity nonconservation in β decay.

Based on invariance principles and on experimental results, one can make the following conclusions. The possible forms of weak interaction are the vector (V) and axialvector (A)

interactions. Accordingly, the sums in ► Eq. (2.84) contain only two terms. The respective weights, C_V and C_A , are real numbers and they are related by

$$C_A = -(1.259 \pm 0.004)C_V.$$

The coupling strengths of the weak interaction are: $g_V = g_F = 8.96 \times 10^{-5} \text{ MeV fm}^3$, $g_A = g_{GT} = -11.28 \times 10^{-5} \text{ MeV fm}^3$. The polar and axial vectors are defined by their behavior under rotation and space reflection. The difference is that polar vectors change sign under space reflection, whereas axial vectors do not. The vector interaction is analogous to the electromagnetic interaction. The electromagnetic field can be described by a vector potential, from which both the electric and magnetic field can be deduced through differential operators (see ► Sect. 2.3.2). The vector product of two polar vectors, e.g., the angular momentum $\mathbf{r} \times \mathbf{p}$, is an axial vector. The axial vector interaction has a more complicated electromagnetic counterpart: the emission of two quanta.

For a more detailed treatment of conservation laws see Wu (1965), for the experimental determination of the β interaction see Wu et al. (1965), and for the coupling constants see Kofoed-Hansen (1965). The tests of conservation laws are discussed by Wolfenstein et al. in Particle Data Group (2008).

The strength of the weak interaction is extremely small compared with strong and electromagnetic interactions (► Table 2.2). Therefore it can be neglected in the nuclear structure models.

2.4.2.4 Selection Rules in β Decay

In the exact theory of β decay the selection rules are derived from the transformation properties of operators and orthogonality of wave functions of different angular momentum states. For the actual vector and axial vector interactions the following selection rules have been obtained:

For allowed transitions	$\Delta I = 0 \text{ or } \pm 1$	$\Delta\pi$ no
For first forbidden transitions	$\Delta I = 0, \pm 1, \pm 2$	$\Delta\pi$ yes
For true second forbidden transitions	$ \Delta I = 2, 3$	$\Delta\pi$ no
Corrections to allowed transitions	$ \Delta I = 0, 1$	$\Delta\pi$ no
For true third forbidden transitions	$ \Delta I = 3, 4$	$\Delta\pi$ yes

See in detail separately for vector and axial vector interactions, e.g., Dzhelepov et al. (1972).

It follows from simple qualitative considerations that the probability of β decay is large, if the overlap of the initial and final wave functions of the nucleus is large. This implies that in allowed β transitions the change of angular momentum is small, and there is no parity change.

2.4.2.5 Parity Nonconservation in β Decay

Many experiments have been performed to test the parity conservation or violation in β decay (for a review see Wu et al. (1965)). The experiments gave the following results:

- The preferential emission of β^- particles occurs in antiparallel direction to the nuclear spin orientation.

- The antineutrino has positive (or right-handed) helicity, i.e., the spin vector of antineutrino has the same direction, as the linear momentum vector. On the other hand, the neutrino has negative (left-handed) helicity, i.e., it has antiparallel spin alignment. (The helicity is a constant of motion in the zero-mass approximation.)

The conclusion of these works is that the parity (P) invariance and, separately, the charge conjugation (C) invariance are violated in β decay, while the time reversal (T) or combined CP invariance is not. The parity non-invariance (i.e., non-invariance of the Hamiltonian of the weak interaction under space reflection) can be expressed alternatively by saying that the parity is not conserved. This formulation is a consequence of the fact that the parity P is an observable quantity. The presence of two-pion decay mode in the K_L^0 kaon decay implies, however, that even the CP invariance is violated in the weak interaction (Christenson et al. 1964).

The CP non-invariance is demonstrated also in the semileptonic (l) decay modes of K_L mesons, in the $K_L \rightarrow e^+ \nu_e \pi^-$, and $K_L \rightarrow e^- \bar{\nu}_e \pi^+$ processes, as well as similar ones in which muons are involved instead of electrons. The observed asymmetry (Δ_L) of time-integrated semileptonic decay rates is

$$\Delta_L \equiv \frac{\Gamma(K_L \rightarrow l^+ \nu_l \pi^-) - \Gamma(K_L \rightarrow l^- \bar{\nu}_l \pi^+)}{\Gamma(K_L \rightarrow l^+ \nu_l \pi^-) + \Gamma(K_L \rightarrow l^- \bar{\nu}_l \pi^+)} = (3.32 \pm 0.06) \times 10^{-3}.$$

Here Δ_L is actually a weighted average of electron and muon measurements, as well as K_L decays to $\pi^+ \pi^- \gamma$ and $\pi^+ \pi^- e^+ e^-$; see Kirkby and Nir in Particle Data Group (2008).

CP violation has been experimentally established also in B meson decays. However, the observed matter–antimatter asymmetry of the Universe requires additional sources of CP violation.

2.4.3 Special Decay Modes

In the vicinity of the stability region the dominating decay modes are β decay (for light nuclei), and α and β decays (for heavy nuclei). Far from the stable nuclei other decay modes appear, too.

On the proton-rich side there appear β -delayed proton and alpha emissions. From these the delayed proton emission occurs more often, with >120 cases known. β -delayed two-proton emission has also been observed in several (>8) cases.

Proton decay is possible also from ground states or from long-lived isomeric states. These decay modes are common among the strongly proton-rich nuclei. In the $Z > 50$ region already ≥ 41 proton emitters are known, e.g., ^{105}Sb , ^{109}I , $^{112, 113}\text{Cs}$, ^{117}La , $^{160, 161}\text{Re}$, $^{171, 171^*}\text{Au}$, ^{185}Bi . There are several nuclei emitting protons also in the $Z < 50$ region (e.g., ^{53}Co , ^{69}Br).

The study of proton emission may offer very important information on the nuclear structure near the proton drip line. Spectroscopic factors can be derived, providing information on the configurations of the initial and final states. In contrast to α -decay, the formation probability of a proton need not be calculated. The decay constant (λ) is determined mainly by the penetration probability through the potential barrier and the structure of states.

The systematics of experimental data and the theories of proton emission are discussed for example in the review article of Delion et al. (2006).

The emission of two (or four) protons is also expected from even- Z nuclei, if the emission of one proton is prohibited energetically (Thoennessen 2004). It was predicted from known

proton separation energies that ^{45}Fe , ^{48}Ni , and ^{54}Zn may emit two protons. Such decay modes have been experimentally confirmed. Two-proton decay was observed also from the excited states of ^6Be and ^{12}O , which are beyond the proton drip line. In both cases, the decays happen via a three-body breakup with half-lives of the order $\sim 10^{-21}$ s. The two-proton radioactivity is discussed in detail by Blank and Płoszajczak (2008).

β -delayed d-emission has also been observed, e.g., from the excited state of ^6Li (in the $^6\text{He}_4 \xrightarrow{\beta} ^6\text{Li}_3$ decay).

Among the superheavy nuclei spontaneous fission is a common decay mode. At the same time, the cluster (e.g., ^{14}C -, ^{24}Ne -, ...) decay of heavy nuclei is rather rare (see in [Sect. 2.3.6](#)).

Half-lives for proton emission, α decay, cluster radioactivity, and cold fission processes have been calculated in the framework of an effective liquid drop model by Duarte et al. (2002). The comparison with experimental data shows that the model is very efficient to describe these different decay processes in a unified theoretical framework.

On the neutron-rich side β -delayed neutron radioactivity is a very favored decay mode. From the combination of γ -ray and neutron time-of-flight spectroscopy one can obtain detailed information on the level structure of the daughter nuclei.

Based on the S_{2n} and S_{4n} neutron separation energies and systematics of β -decay energies one can expect also β -delayed $2n$ and even $4n$ emission in strongly neutron rich nuclei (Gelbke et al. 2006).

Similarly to the two-proton emission, two-neutron decay is also expected from the ground states of neutron-rich nuclei (e.g., in the case of ^{26}O). The next generation accelerator facilities will deliver hopefully sufficient beam intensity to explore such weak decay channels, too.

Acknowledgments

The author is grateful to the American Physical Society, Elsevier Science (UK) and Academic Press (USA) publishers granting permission for [Fig. 2.30](#), [Figs. 2.33](#) and [2.38](#), and [Fig. 2.8](#), respectively.

References

- Aharmin B et al (2005) Phys Rev C 72:055502
- Alaga G (1969) Proceedings of the international school of physics Enrico Fermi, Course XL, Varenna, 1967, Academic, New York, p 28
- Alaga G, Alder K, Bohr A, Mottelson BR (1955) Dan Mat Fys Medd 29(9)
- Albert RD, Wu CS (1948) Phys Rev 74:847
- Allaart K, Boeker E, Bonsignori G, Savoia M, Gamhir YK (1988) Phys Reports (Rev Sect Phys Lett) 169:209
- Andrejtscheff W, Schilling KD, Manfrass P (1975) Atomic Data and Nuclear Data Tables 16:515
- Angeli I (1991a) J Phys G Nucl Part Phys 17:439
- Angeli I (1991b) Europhys Lett 16:429
- Angeli I (1992) Proceedings of the 6th international conference on nuclei far from stability, Inst. phys. conf. ser. No 132, Section 1, IOP Publ., Bristol, UK, p 93
- Angeli I (2004) Atomic Data and Nuclear Data Tables 87:185
- Aprahamian A (1986) In: Meyer RA, Paar V (eds) Proc. conf. on nuclear structure, reactions and symmetries, Dubrovnik, 1986. World Sci., Singapore, p 671
- Audi G, Wapstra AH, Thibault C (2003) Nucl Phys A 729:337
- Avotina MP, Voronova NA, Erokhina KT, Lemberg IKh (1995) Yadernaya Fizika 58:248
- Band IM, Trzhaskovskaya MB, Listengarten MA (1976) Atomic Data and Nuclear Data Tables 18:433
- Band IM, Trzhaskovskaya MB, Nestor CW Jr, Tikkanen PO, Raman S (2002) Atomic Data and Nuclear Data Tables 81:1
- Bardeen J, Cooper LN, Schrieffer JR (1957) Phys Rev 108:1175
- Bayman BF, Lande A (1966) Nucl Phys 77:1

- Belyaev ST (1959) *Dan Math Fys Medd* 31, No. 11
- Bengtsson T, Ragnarsson I (1985) *Nucl Phys A* 436:14
- Berlovich EE, Vasilenko SS, Novikov YuN (1972) *Vremena zhizni vozbuzhdennykh sostoyanii atomnykh yader*. Nauka, Leningrad
- Bernard V, Meissner Ulf-G (2007) *Annu Rev Nucl Part Sci* 57:33
- Bertschy M, Drissi S, Garrett PE, Jolie J, Kern J, Mannanal SJ, Vorlet JP, Warr N (1995) *Phys Rev C* 51:103; Erratum, *Phys Rev C* 52:1148
- Bethe HA (1937) *Rev Mod Phys* 9:161
- Bethe HA, Bacher RF (1936) *Rev Mod Phys* 8:82
- Bishop RF et al (1990) *Phys Rev C* 42:1341
- Blank B, Płoszajczak M (2008) *Rep Progr Phys* 71:046301
- Blatt JM, Weisskopf VF (1952) *Theoretical nuclear physics*. Wiley, New York
- Bogoliubov NN (1958) *Nuovo Cimento* 7:794
- Bohr A (1952) *Dan Math Fys Medd* 26, No. 14
- Bohr A, Mottelson BR (1953) *Dan Math Fys Medd* 27, No. 16
- Bohr A, Mottelson BR (1969) *Nuclear structure*, vol 1. Benjamin, New York
- Bohr A, Mottelson BR (1974) *Nuclear structure*, vol 2. Benjamin, New York
- Bohr A, Mottelson BR (1981) *Physica Scripta* 24:71
- Bohr A, Mottelson BR, Pines D (1958) *Phys Rev* 110:936
- Bolsterli M, Fiset EO, Nix JR, Norton JL (1972) *Phys Rev C* 5:1050
- Brink DM (1967) *Nucl Phys A* 91:1
- Brink DM, De Toledo Piza AFR, Kerman AK (1965) *Phys Lett* 19:413
- Brown BA, Wildenthal BH (1988) *Ann Rev Nucl Part Sci* 38:29
- Brussaard PJ, Glaudemans PWM (1977) *Shell-model applications in nuclear spectroscopy*. North-Holland, Amsterdam
- Buck B, Dover CB, Vary JP (1975) *Phys Rev C* 11:1803
- Buck B, Merchant AC, Perez SM (1996) *Phys Rev Lett* 76:380
- Buck B, Merchant AC, Perez SM (1997) *Nucl Phys A* 617:195
- Buck B, Merchant AC, Perez SM (1998) *Phys Rev C* 58:2049
- Burgess CP (2007) *Annu Rev Nucl Part Sci* 57:329
- Carlson JA, Wiringa RB (1991) In: Langanke K et al (eds) *Computational nuclear physics*. Springer, Berlin
- Casten RF (2000) *Nuclear structure from a simple perspective*. Oxford University Press, Oxford
- Christenson JH, Cronin JW, Fitch VL, Turlay R (1964) *Phys Rev Lett* 13:138
- Comay E, Kelson I, Zidon A (1988) *Atomic Data and Nuclear Data Tables* 39:235
- Condon EU, Gurney RW (1928) *Nature* 122:439
- Condon EU, Gurney RW (1929) *Phys Rev* 33:127
- Cottingham WN, Lacombe M, Loiseau B, Richard JM, Vinh Mau R (1973) *Phys Rev D* 8:800
- Csatlós M et al (2005) *Phys Lett B* 615:175
- Csikai J, Szalay A (1957) *International conference on mesons and recently discovered particles*, Padova-Venezia, Ciclografia Borghero, Padova, IV-8
- Dasgupta-Schubert N, Reyes MA (2007) *Atomic Data and Nuclear Data Tables* 93:907
- Davydov AS, Filippov GF (1958) *Nucl Phys* 8:237
- De Benedetti S (1964) *Nuclear interactions*. Wiley, New York
- Dechargé J, Gogny D (1980) *Phys Rev C* 21:1568
- Delion DS, Insolia A, Liotta RJ (1992) *Phys Rev C* 46:1346
- Delion DS, Insolia A, Liotta RJ (1994) *Phys Rev C* 49:3024
- Delion DS, Liotta RJ, Wyss R (2006) *Phys Rep* 424:113
- Deutsch M, Kofoed-Hansen O (1959) β -decay. In: Segré E (ed) *Experimental nuclear physics*, vol III. Wiley, New York
- Dombrádi Zs (2007) *Fizikai Szemle* LVII(7):221
- Duarte SB et al (2002) *Atomic Data and Nuclear Data Tables* 80:235
- Dzhelepov BS, Zyryanova LN, Suslov YuP (1972) *Beta protsessy*. Izd. Nauka, Leningrad
- Eisenberg J, Greiner W (1970, 1972) *Nuclear theory*, vols 1, 2 (1970), 3 (1972). North-Holland, Amsterdam
- Eisenbud L, Wigner EP (1941) *Proc Natl Acad Sci USA* 27:281
- Ejiri H, De Voigt MJA (1989) *Gamma-ray and electron spectroscopy in nuclear physics*. Clarendon, Oxford
- Elton LRB (1961) *Nuclear sizes*. Oxford University Press, Oxford
- Endt PM (1979) *Atomic Data and Nuclear Data Tables* 23:547
- Endt PM (1981) *Atomic Data and Nuclear Data Tables* 26:47
- Endt PM (1993) *Atomic Data and Nuclear Data Tables* 55:171
- Fényes T (1986) In: Meyer RA, Paar V (eds) *Nuclear structure, reactions, and symmetries*, vol 2. World Scientific, Singapore, p 567
- Fényes T (2002) *Structure of atomic nuclei*. Akad Kiadó, Budapest
- Fényes T, Rupp E (1968) *Atomki Közl* 10(2):116
- Fermi E (1933) *La Ricerca Scientifica* 2, No 12
- Fermi E (1934) *Z Physik* 88:161
- Firestone RB, Shirley VS, Baglin CM, Frank Chu SY, Zipkin J (eds) (1996) *Table of isotopes*, vol 1, 2, 8th edn. Wiley, New York
- Fock V (1930) *Z Physik* 61:126
- Freer M (2007) *Rep Progr Phys* 70:2149
- Freer M et al (1999) *Phys Rev Lett* 82:1383
- Fricke G, Heilig K (2004) In: Schopper H (ed) *Landolt-Börnstein, New Series, Group I*, vol 20. Springer, Berlin
- Fricke G, Bernhardt C, Heilig K, Schaller LA, Schellenberg L, Shera EB, De Jager CW (1995) *Atomic Data and Nuclear Data Tables* 60:117

- Frois B (1983) In: Blasi P, Ricci RA (eds) *Proceedings of the international conference on nuclear physics, Florence, 1983*. vol 2, Tipografia Compositori, Bologna, p 221
- Fröman PO (1957) *Kgl Dan Vid Selskab Math Fys Skifter* 1, No 3
- Gamow G (1928) *Z Physik* 51:204
- Garrett PE (2001) *J Phys G Nucl Part Phys* 27:R1
- Garvey GT (1969) *Ann Rev Nucl Sci* 19:433
- Garvey GT, Gerace WJ, Jaffe RL, Talmi I, Kelson I (1969) *Rev Mod Phys* 41:S1
- Geiger H, Nuttall JM (1911) *Phil Mag* [6], 22:613
- Geiger H, Nuttall JM (1912) *Phil Mag* [6], 23:439
- Gelbke CK et al (2006) *Isotope Science Facility at Michigan State University, MSUSCL-1343 report*
- Goeppert Mayer M (1949) *Phys Rev* 75:1966
- Goeppert Mayer M, Jensen JHD (1965) In: Siegbahn K (ed) *Alpha-, beta- and gamma-ray spectroscopy*, vol 1. North-Holland, Amsterdam, p 557
- Greiner W, Müller B (1993) *Gauge theory of weak interactions*. Springer, Berlin
- Hafstad LR, Teller E (1938) *Phys Rev* 54:681
- Hamada T, Johnston ID (1962) *Nucl Phys* 34:382
- Han X-L, Wu C-L, Feng DH, Guidry MN (1992) *Phys Rev C* 45:1127
- Hanna GC (1959) In: Segé E (ed) *Experimental nuclear physics*, vol III, Pt IX. Wiley, New York
- Harakeh MN, Van der Woude A (2001) *Giant resonances*. Clarendon, Oxford
- Harris SM (1965) *Phys Rev* 138:B509
- Hartree DR (1928) *Proc Cambridge Phil Soc* 24:89
- Haxel O, Jensen JHD, Suess HE (1949) *Phys Rev* 75:1766
- Haxel O, Jensen JHD, Suess HE (1952) *Ergebn Ex Naturw* 26:244
- Heisenberg JH, Mihaila B (1999) *Phys Rev C* 59:1440
- Heitler W (1936) *Proc Cambridge Phil Soc* 32:112
- Heitler W (1947) *The quantum theory of radiation*, 2nd edn. Oxford University Press, London
- Heyde KLG (1990) *The nuclear shell model*. Springer, Berlin
- Heyde K (1999) *Basic ideas and concepts in nuclear physics*, 2nd edn. Institute of Physics Publishing, Bristol
- Hillis DL, Garrett JD, Christensen O, Fernandez B, Hagemann GB, Herskind B, Back BB, Folkmann F (1979) *Nucl Phys A* 325:216
- Hyde EK, Perlman I, Seaborg GT (1964) *The nuclear properties of heavy elements*. Prentice-Hall, New Jersey
- Iachello F (2000) *Phys Rev Lett* 85:3580
- Iachello F (2001) *Phys Rev Lett* 87:052502
- Iachello F (2002) *Nucl Phys News* 12(3):17
- Iachello F, Arima A (1987) *The interacting Boson model*. Cambridge University Press, Cambridge
- Iachello F, Van Isacker P (1991) *The interacting Boson-fermion model*. Cambridge University Press, Cambridge
- Inglis DR (1954) *Phys Rev* 96:1059
- Insolia A, Liotta RJ, Maglione E (1988) *Europhys Lett* 7:209
- Insolia A, Curutchet P, Liotta RJ, Delion DS (1991) *Phys Rev C* 44:545
- Jänecke J, Masson PJ (1988) *Atomic Data and Nuclear Data Tables* 39:265
- Johnson A, Ryde H, Sztarkier J (1971) *Phys Lett B* 34:605
- Jolie J, Casten RF (2005) *Nucl Phys News* 15(1):20
- Jolos RV (2004) *Particles and Nuclei (ECHAYA)* 35:408
- Kantele J, Tannila O (1968) *Nucl Data A* 4:359
- Kern J (1997) In: Molnár GL (ed) *Proceedings of the 9th international symposium on capture gamma-ray spectroscopy and related topics, Budapest, 1996*. vol 1, Springer, Budapest, p 175
- Kibédi T, Spear RH (2005) *Atomic Data and Nuclear Data Tables* 89(1):77
- Kofoed-Hansen O (1965) *The coupling constants*. In: Siegbahn K (ed) *Alpha-, beta- and gamma-ray spectroscopy*, vol 2. North-Holland, Amsterdam
- Konopinski EJ, Rose ME (1965) *The theory of nuclear β -decay*. In: Siegbahn K (ed) *Alpha-, beta- and gamma-ray spectroscopy*, vol 2. North-Holland, Amsterdam
- Krasznahorkay A et al (1998) *Phys Rev Lett* 80(10):2073
- Krasznahorkay A et al (1999) *Phys Lett B* 461:15
- Kravtsov VA (1965) *Massy atomov i energii svyazi yader*. Atomizdat, Moskva
- Kurie FND, Richardson JR, Paxton HC (1936) *Phys Rev* 49:368
- Lacombe M, Loiseau B, Richard JM, Vinh Mau R, Pirés P, De Tourreil R (1975) *Phys Rev D* 12:1495
- Lacombe M, Loiseau B, Richard JM, Vinh Mau R, Côté J, Pirés P, De Tourreil R (1980) *Phys Rev C* 21:861
- Langanke K, Maruhn JA, Koonin SE (eds) (1991) *Computational nuclear physics 1, Nuclear structure*, vol 1. Springer, Berlin
- Larsson SE, Leander G, Ragnarsson I, Alenius G (1976) *Nucl Phys A* 261:77
- Lassila KE, Hull MH, Ruppel HM, Mc Donald FA, Breit G (1962) *Phys Rev* 126:881
- Lattes CMG, Muirhead H, Occhialini GPS, Powell CF (1947) *Nature* 159:694
- Lawson RD (1980) *Theory of the nuclear shell model*. Clarendon, Oxford
- Lazarev YuA et al (1994) *Phys Rev Lett* 73:624
- Lieder RM, Ryde H (1978) In: Baranger M, Vogt E (eds) *Advances in Nuclear Physics*, vol 10. Plenum, New York, p 1
- Lopac V (1967) *MSc thesis, University of Zagreb, Zagreb*
- Lovas RG, Liotta RJ, Insolia A, Varga K, Delion DS (1998) *Phys Rep* 294:265
- Lunney D, Pearson JM, Thibault C (2003) *Rev Mod Phys* 75(3):1021
- Machleidt R, Holinde K, Elster Ch (1987) *Phys Rep (Rev Sect Phys Lett)* 149:1
- Mandl F (1992) *Quantum mechanics*. Wiley, Chichester

- Mang HJ (1960) Phys Rev 119:1069
- Mang HJ (1964) Alpha radioactivity. In: Annual review of nuclear science, vol 14. Annual Reviews, Palo Alto
- Mang HJ, Rasmussen JO (1962) Mat Fys Skr Danske Vid Selskab 2:3
- Mariscotti MAJ, Scharff-Goldhaber G, Buck B (1969) Phys Rev 178:1864
- Marmier P, Sheldon E (1969) Physics of nuclei and particles, vol 1. Academic, New York
- Mikheev VL, Tretyakova SP (1990) Joint Institute for Nuclear Research, Heavy Ion Physics, Science Report, 46
- Miller GA, Oppen AK, Stephenson EJ (2006) Annu Rev Nucl Part Sci 56:253
- Möller P, Nix JR (1988) Atomic Data and Nuclear Data Tables 39:213
- Möller P, Leander GA, Nix JR (1986) Z Physik A 323:41
- Möller P, Myers WD, Swiatecki WJ, Treiner J (1988) Atomic Data and Nuclear Data Tables 39:225
- Möller P, Nix JR, Myers WD, Swiatecki WJ (1992) Nucl Phys A 536:61
- Möller P, Nix JR, Myers WD, Swiatecki WJ (1995) Atomic Data and Nuclear Data Tables 59:185
- Morinaga H, Yamazaki T (1976) In-beam gamma-ray spectroscopy. North-Holland, Amsterdam
- Moszkowski SA (1965) In: Siegbahn K (ed) Alpha-, beta- and gamma-ray spectroscopy, vol 2. North-Holland, Amsterdam
- Mottelson BR, Valatin JG (1960) Phys Rev Lett 5:511
- Mukhin KN (1974) Fizika atomnogo yadra. Atomizdat, Moskva
- Myers WD, Swiatecki WJ (1966) Nucl Phys 81:1
- Myers WD, Swiatecki WJ (1967) Ark Fys 36:343
- Myers WD, Swiatecki WJ (1969) Ann Phys 55:395
- Nadjakov EG, Marinova KP, Gangrsky YuP (1994) Atomic Data and Nuclear Data Tables 56:133
- Nathan O, Nilsson SG (1965) In: Siegbahn K (ed) Alpha-, beta- and gamma-ray spectroscopy, vol 1. North-Holland, Amsterdam, p 601
- Navrátil P, Vary JP, Barrett BR (2000) Phys Rev C 62:054311
- Nilsson SG (1955) Dan Mat Fys Medd 29(16):1
- Nilsson SG, Prior O (1961) Dan Mat Fys Medd 32, No 16
- Nilsson SG, Ragnarsson I (1995) Shapes and shells in nuclear structure. Cambridge University Press, Cambridge
- Nolan PJ, Sharpey-Schafer JF (1979) Rep Progr Phys 42:1
- Nyakó BM et al (1984) Phys Rev Lett 52:507
- Paar V (1979) Nucl Phys A 331:16
- Pál KF, Lovas RG (1980) Phys Lett B 96:19
- Particle Data Group (2008) Phys Lett B 667:1
- Perkins DH (2000) Introduction to high energy physics. Cambridge University Press, Cambridge
- Petterson BG (1965) The internal Bremsstrahlung. In: Siegbahn K (ed) Alpha-, beta- and gamma-ray spectroscopy, vol 2. North-Holland, Amsterdam, p 1569
- Pieper SC, Pandharipande VR, Wiringa RB, Carlson J (2001) Phys Rev C 64:014001-1
- Pudliner BS, Pandharipande VR, Carlson J, Pieper SC, Wiringa RB (1997) Phys Rev C 56:1720
- Raghavan P (1989) Atomic Data and Nuclear Data Tables 42:189
- Ragnarsson I, Sheline RK (1984) Phys Scr 29:385
- Ragnarsson I, Nilsson SG, Sheline RK (1978) Phys Rep 45:1
- Ragnarsson I, Xing Z, Bentsson T, Riley MA (1986) Phys Scr 34:651
- Rainwater J (1950) Phys Rev 79:432
- Raman S, Malarkey CH, Milner WT, Nestor CW Jr, Stelson PH (1987) Atomic Data and Nuclear Data Tables 36:1
- Raman S, Nestor CW Jr, Tikkanen P (2001) Atomic Data and Nuclear Data Tables 78:1
- Raman S, Ertugrul M, Nestor CW Jr, Trzhaskovskaya MB (2006) Atomic Data and Nuclear Data Tables 92:207
- Rasmussen JO (1959) Phys Rev 115:1675
- Rasmussen JO (1965) Alpha decay. In: Siegbahn K (ed) Alpha-, beta- and gamma-ray spectroscopy, vol 1. North-Holland, Amsterdam, p 701
- Reid RV (1968) Ann Phys NY 50:411
- Reines F, Cowan CL Jr (1959) Phys Rev 113:273
- Reines F, Cowan CL Jr, Harrison FB, Mc Guire AD, Kruse HW (1960) Phys Rev 117:159
- Ring P, Schuck P (1980) The nuclear many-body problem. Springer, Berlin
- Rose ME (1965) In: Siegbahn K (ed) Alpha-, beta- and gamma-ray spectroscopy, vol 2. North-Holland, Amsterdam, p 887
- Rose HJ, Jones GA (1984) Nature 307:245
- Rösel F, Fries HM, Alder K, Pauli HC (1978) Atomic Data and Nuclear Data Tables 21(91):291
- Schiff LI (1968) Quantum mechanics, 3rd edn. Mc Graw-Hill, New York
- Scholten O (1991) In: Langanke K et al (eds) Computational nuclear physics 1, Nuclear structure. Springer, Berlin
- Scholten O, Iachello F, Arima A (1978) Ann Phys 115:325
- Sharpey-Schafer JF (1990) Physics World September:31
- Sliv LA (ed) (1961) Gamma-luchi. Izd Akad Nauk SSSR, Moskva
- Soloviev VG (1958) Nucl Phys 9:655
- Soloviev VG (1981) Teoriya atomnogo yadra. Yadernye modeli. Energoizdat, Moskva
- Sood PC (1967) Phys Rev 161:1063
- Sood PC (1968) Nucl Data Tables A 4:281
- Spanier L, Johansson SAE (1988) Atomic Data and Nuclear Data Tables 39:259
- Spear RH (1989) Atomic Data and Nuclear Data Tables 42:55
- Stephens FS (1975) Rev Mod Phys 47:43
- Stephens FS, Simon RS (1972) Nucl Phys A 183:257

- Stone NJ (2005) Atomic Data and Nuclear Data Tables, 90(1):75
- Strutinsky VM (1967) Nucl Phys A 95:420
- Strutinsky VM (1968) Nucl Phys A 122:1
- Suzuki Y, Lovas RG, Yabana K, Varga K (2003) Structure and reactions of light exotic nuclei. Taylor & Francis, London
- Szymański Z (1983) Fast nuclear rotation. Clarendon, Oxford
- Taagepera R, Nurmia M (1961) Ann Acad Sci Fennicae Ser A VI:78
- Tabakin F (1964) Ann Phys NY 30:51
- Talmi I (1993) Simple models of complex nuclei. The shell model and interacting Boson model. Harwood, Chur, Switzerland
- Tarantin NI (1995) Physics of Elementary Particles and Atomic Nuclei (ECHAYA) 26(4):1046
- Tashibana T, Uno M, Yamada M, Yamada S (1988) Atomic Data and Nuclear Data Tables 39:251
- Thoennessen M (2004) Rep Progr Phys 67:1187
- Thomas RG (1954) Prog Theor Phys 12:253
- Twin PJ et al (1985) Phys Rev Lett 55:1380
- Valatin JG (1958) Nuovo Cimento 7:843
- Varga K, Liotta RJ (1994) Phys Rev C 50:R1292
- Varga K, Lovas RG, Liotta RJ (1992) Nucl Phys A 550:421
- von Weizsäcker CF (1935) Z Physik 36:431
- Wapstra AH, Nijgh GJ, Van Lieshout R (1959) Nuclear spectroscopy tables. North-Holland, Amsterdam
- Wapstra AH, Audi G, Thibault C (2003) Nucl Phys A 729:129
- Wilets L, Jean M (1956) Phys Rev 102:788
- Wilson R (1965) In: Siegbahn K (ed) Alpha-, beta- and gamma-ray spectroscopy, vol 2. North-Holland, Amsterdam, p 1557
- Winslow GH, Simpson OC (1954) Argonne National Laboratory Report, ANL-5277
- Wloch M et al (2005) Phys Rev Lett 94:212501
- Wohlrab S (1960) In: Hertz G (ed) Lehrbuch der Kernphysik, vol 2. Teubner, Leipzig
- Wu CS (1965) The conservation laws in β -decay. In: Siegbahn K (ed) Alpha-, beta-, and gamma-ray spectroscopy, vol 2. North-Holland, Amsterdam
- Wu CS, Moszkowski SA (1965) Beta decay. Wiley, New York
- Wu CS et al (1965) The experimental determination of the beta interaction. In: Siegbahn K (ed) Alpha-, beta- and gamma-ray spectroscopy, vol 2. North-Holland, Amsterdam
- Yukawa H (1935) Proc Phys Math Soc Jpn 17:48
- Zeh HD, Mang HJ (1962) Nucl Phys 29:529
- Zeldes N (1967) Ark Fys 36:361
- Zeldes N, Grill A, Simievic A (1967) Mat Fys Skr Dan Vid Selsk 3, No. 5



3 Nuclear Reactions

L. G. Sobotka¹ · V. E. Viola²

¹Washington University, St. Louis, Missouri, USA

²Indiana University, Bloomington, Indiana, USA

3.1	<i>Introduction</i>	145
3.2	<i>Basic Concepts</i>	148
3.2.1	Shorthand Notation for Nuclear Reactions	149
3.2.2	Mass-Energy Conservation: The Q-Value	150
3.2.3	The Nuclear Potential Energy: Coulomb Barrier Effects	152
3.2.4	Angular Momentum Effects: The Centrifugal Barrier	154
3.2.5	Summary of Energetic Factors in Nuclear Reactions and the Separation of Thermodynamic and Kinetic Factors	156
3.2.6	Cross Sections: An Introduction	157
3.2.7	Cross Sections, Excitation Functions, and Angular Distributions	159
3.2.8	Cross-Section Measurements	161
3.3	<i>Scattering Theory</i>	161
3.3.1	Preliminaries	161
3.3.2	The Optical Model (OM)	164
3.3.3	The Dispersive Optical Model (DOM)	169
3.4	<i>Near-Barrier Reaction Mechanisms</i>	171
3.4.1	Neutron Capture	173
3.4.2	Nucleon and Heavy-Ion Elastic Scattering	177
3.4.2.1	Nucleon Elastic Scattering	177
3.4.2.2	Heavy-Ion Elastic Scattering	179
3.4.3	Inelastic Excitation	180
3.4.4	Nucleon Knockout Reactions	185
3.4.5	Mean-Field-Dominated HI Reactions	187
3.4.5.1	Impact Parameter Dictates the Reaction Channel	187
3.4.5.2	Surface Reactions: Inelastic Scattering and Nucleon Transfer	188
3.4.5.3	Damped Collisions	189
3.4.5.4	Composite-Nucleus Formation	190
3.5	<i>Statistical Decay</i>	192
3.5.1	Preliminaries	192
3.5.2	The Hauser–Feshbach Treatment of Particle Emission	193
3.5.3	The Transition-State Treatment of CN Decay	194
3.5.4	The Density of States of Highly Excited Nuclei	195
3.5.5	Thermodynamic Models for Multifragmentation	196

3.6	<i>Mechanisms in the Nucleon-Nucleon Domain</i>	198
3.6.1	Reactions Near the Fermi Energy	201
3.6.2	Models of Collision Dynamics	202
3.6.3	Participant–Spectator Reactions	204
3.6.4	Relativistic Heavy-Ion Collisions: Dense Nuclear Matter	205
3.7	<i>The Nuclear Equation of State</i>	207
3.7.1	Background and Connection to Classical Thermodynamics	207
3.7.2	The Perspective from Energy-Density-Functional Theory	209
3.7.3	The Incompressibility from the Physical LDM-Like Expansion	210
3.7.4	Cluster Formation at Very Low Density	212
3.7.5	Multifragmentation: The Low-Density Regime and the Manifestation of the Liquid–Gas Phase Transition in Nuclear Collisions	213
3.8	<i>Addendum: Cross-Section Calculations</i>	216
3.9	<i>Selected Nuclear Reaction Web Resources</i>	218

Abstract: The investigation and application of nuclear reactions play a prominent role in modern nuclear chemistry research. After a discussion of basic principles and reaction probabilities that govern collisions between nuclei, an overview of reaction theory is presented and the various reaction mechanisms that occur from low to high energies are examined. The presentation strives to provide links to more standard chemical disciplines as well as to nuclear structure.

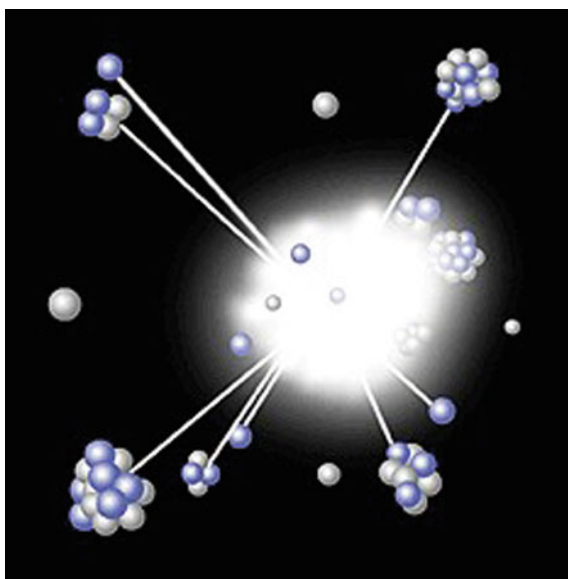
3.1 Introduction

Current understanding of nuclear reactions has been significantly expanded by developments in accelerator technology, which now provide nuclear science with a highly diverse arsenal of nuclear projectiles. It is possible to probe the nucleus with beams of photons, electrons, mesons, neutrons, antiprotons, and virtually all naturally occurring isotopes of elements ranging from hydrogen to uranium. In addition, there is a growing capability to accelerate radioactive nuclei off the line of beta stability.

This arsenal of tools has allowed the response of nuclei to excitation energy, angular momentum, and neutron/proton asymmetry to be studied. Excitation energies from the smallest allowed (excitation to the first allowed quantum state above the ground state) to that corresponding to the capture of a thermal neutron (one binding energy B_N), to that required to totally vaporize a nucleus with A nucleons (► Fig. 3.1), an excitation energy of the order of AB_N , have all been investigated. The study of highly excited nuclei has provided new insights into nuclear systems with bulk densities both higher and lower than the central density

■ Fig. 3.1

Reconstruction of a highly energetic nuclear collision that disintegrates a gold nucleus into multiple nucleons and light clusters



of ground-state nuclei, densities which nature readily accesses in astrophysical objects. Similarly, the nuclear response to angular momentum from zero to that which prompts nuclei to fission (no matter what position in the periodic table) has been examined. Most recently, the use of secondary beams for reaction studies has allowed the study of nuclei formed in nature during nucleosynthesis of the elements – nuclei that previously had been inaccessible to experiment.

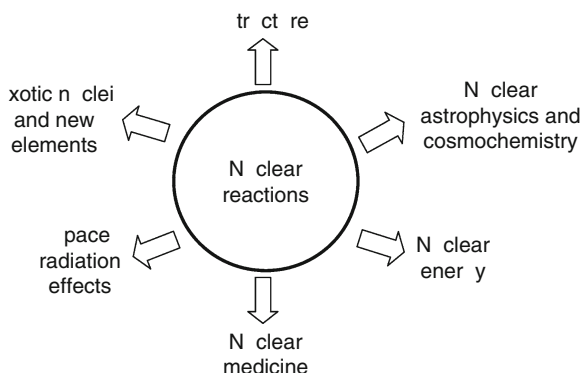
From a broader perspective, progress in related fields of nuclear science has frequently evolved from nuclear reaction studies, as indicated schematically in [Fig. 3.2](#). Reaction studies provide pathways for exploring nuclear structure, the formation of both new elements as well as isotopes of known elements (Loveland 2007), and nuclear astrophysics. At the more practical level, important nuclear applications have resulted from reaction studies, for example, nuclear energy, nuclear medicine (both for diagnostic imaging and therapy), activation analysis, and space-radiation effects due to cosmic-ray exposure.

The vantage point that will be maintained for the bulk of this chapter is that the atomic nucleus can be viewed as a two-component quantum fluid, i.e., the degrees of freedom are those associated with nucleons. Despite the quantum nature of the systems, classical analogs can be of great heuristic value. Leading this list of analogs is that of a charged two-component liquid drop. Here, the quantum aspects are buried in a few well-chosen coefficients of a physical expansion.

The Fermi-Gas Model applies a thin veneer of quantum mechanics to the Liquid-Drop Model (LDM), i.e., the Pauli exclusion principle must be obeyed by the spin $\frac{1}{2}$ nucleons and thus neutrons and protons must occupy distinct quantum levels. The energy of the top-most occupied level in this simple picture is called the Fermi energy, E_F . There is a Fermi energy for neutrons and another for protons, each corresponding to a chemical potential, i.e., the energy associated with the addition or subtraction of a nucleon. The kinetic energies of the nucleons forced by the Pauli principle lead to an internal pressure (intimately related to that which holds up a neutron star against gravitational collapse), but, as the surface of a stable nucleus is stationary, the pressure must return to zero at the periphery (just as it must on the surface of a neutron star or any other self-bound stable object.)

Fig. 3.2

Schematic representation of nuclear reactions as applied to other areas of science and technology



At the next higher level of sophistication, a specific quantization is envisioned by imagining independent particles in a (real) central potential. The consequences of this confinement are the granularization of the single-particle states labeled by orbital angular momentum (ℓ) and its orientation relative to the nucleon's spin (s). The quantum state of the nucleon, either in the entrance or exit channel, can dictate which nuclear reaction channel dominates. Turned around, studying reactions can provide insight into the underlying nuclear structure of the reactants or products.

Beyond the view of nuclei as nucleons moving independently in a mean field, one appreciates that the constituents are often engaged in complex correlations. This is akin to what one finds in water, where correlations (induced by hydrogen bonding) must be understood. However, unlike systems such as water, in which the correlations between identical units determine the interesting material properties, the nuclear system is composed of two distinguishable components.

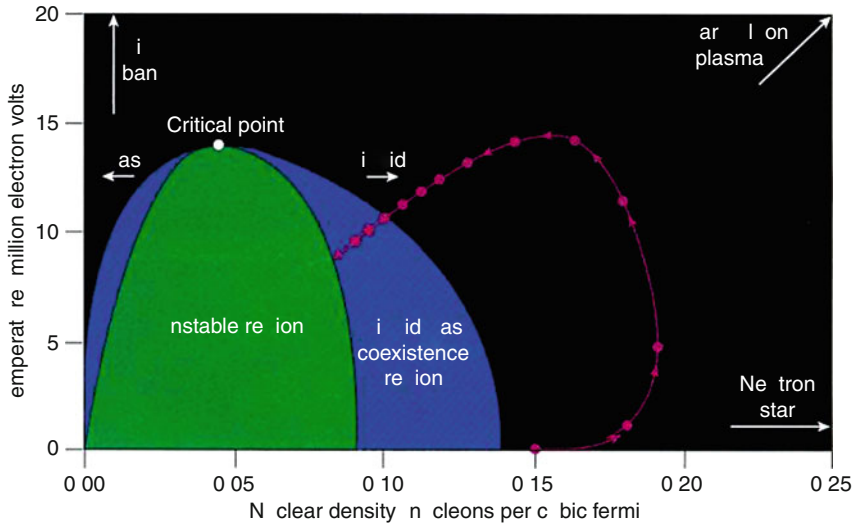
In-medium correlations have many observable effects. They influence the mass of nuclei and if one were to create a one-body potential to mock up their effects, it would cause clustering of levels around the Fermi surface. This, in turn, changes the density of many-body states $\omega(E^*)$; the number of ways nucleons can distribute themselves into the allowed single-particle states within an excitation energy window. The density of states is Boltzmann's *wahrscheinlichkeit* in the expression $S(E^*) = k_B \ln \omega(E^*)$. For all but the lightest nuclei, the state density forms a quasi continuum as long as the excitation energy E^* is greater than the binding energy of a nucleon. This “high level density” allows for statistical treatments of reactions, in which it is the value of $\omega(E^*)$ associated with a given decay path that controls the probability of that decay. Not surprisingly, the entropy (the measure of the density of states that is extensive in macroscopic systems) and the temperature (the inverse of the rate of increase of the extensive measure of the density of states, i.e., S , with excitation energy) turn out to be useful concepts in explaining the competition between decay channels of an excited compound nucleus, including the fission channel(s), by making use of transition-state theory. This theory was developed by a collaboration between Ewing and Wigner in the 1930s. It is perhaps only from the unique perspective of the nuclear chemist that the utility of this theory to treat both chemical and nuclear reaction rates can be appreciated.

These correlated many-body systems can also be viewed as isolated drops of matter, which, if uncharged, could be infinite. Reaction studies have been called upon to explore the equation of state (EoS) of nuclear matter and to extract any phase transitions that punctuate the phase diagram (► [Fig. 3.3](#)). An equation of state is humankind's attempt to interrelate the variable set of thermodynamics, the absolute minimum set required to describe the macroscopic state of a system. Nuclei, being two-component systems, have a “chemical composition” sector (with chemical potentials and numbers of each as the variables, with one or the other chosen as independent), as well as a “mechanical” sector (P, V) and a “thermal” sector (T, S). Reaction data have been able to place rather tight constraints on the incompressibility of symmetric nuclear matter.

The isothermal incompressibility (the inverse of the compressibility) of an ideal gas is $K = -(V)(dP/dV)_T = P$. It is the equivalent science (although general interest is in the adiabatic compressibility) for nuclear systems that is sought. Insight into how this incompressibility changes with neutron–proton asymmetry is just now becoming available. It is this part of the EoS that dictates the behavior of supernovae, the events leading to neutron star formation, and the structure of such stars.

■ Fig. 3.3

The nuclear temperature–density phase diagram, indicating the nuclear landscape now available for reaction studies. The dotted trajectory shows the stepwise evolution of an energetic nuclear collision, in steps of about 1×10^{-23} s (Adapted from Mueller and Serot 1995)



Phase transitions are the delimiting punctuation of the EoS of any matter. One of the great successes of recent nuclear reaction studies has been to elucidate this punctuation, in particular, the nuclear analog of a liquid–gas phase transition (► Fig. 3.3).

As mentioned above, the perspective of this chapter is that of a nuclear system composed of neutrons and protons. The subnuclear aspects of the field are not addressed, for example, the origin of the nucleon–nucleon force and spin, quark–gluon degrees of freedom, and weak–interaction physics. For an overview of these subjects, see (NRC 1999).

3.2 Basic Concepts

In simplest terms, a nuclear reaction can be defined as a binary collision that alters the nucleon–nucleon associations, just as a chemical reaction is one that alters atom–atom associations. This change in association can produce different nuclei (via the exchange of nucleons or fusion) or can simply excite the nuclei (different correlations within the nucleus that no longer correspond to the ground state.) The latter type of reaction is called *inelastic* excitation. The former type might, or might not, proceed through an intermediate.

The case in which an intermediate state is formed can be written as



where the reactants A and a are the target and projectile that form an excited intermediate species C^* , or *composite nucleus*. The intermediate usually decays into a binary exit channel indicated by the product nuclei b and B . If the reaction loses all recollection of the entrance channel aside from quantities fixed by conservation laws (energy and angular momentum), the

intermediate composite is called a *compound nucleus* (CN), (► Fig. 3.4). In this case, exit-channel products are formed via statistical decay on a time scale longer than $\sim 10^{-21}$ s, a time commensurate with those that characterize either collective nuclear motion (rotation or vibration) or nucleon transit across a nucleus. At the other extreme, *direct reactions* occur on a much shorter time scale ($\sim 10^{-23}$ s), effectively bypassing the composite nucleus state. In reality, there is a continuum of time-dependent processes between compound and direct reactions. Intellectually, this continuum of mechanisms can be organized as viewing each step proceeding toward a CN as a fixed “generation” of nucleon-nucleon collisions. In a simple direct reaction the final state – right-hand side of ► Eq. (3.1) – is reached in the first step. Several steps are required to dissipate entrance channel energy and disperse it statistically among all the nucleon degrees of freedom. In the language of statistical mechanics, the CN is the case where the allowed phase space (that piece of the many-body $6N$ dimensional phase space allowed by conservation laws) has been fully sampled. The kinetic process by which this happens, organized by collision generation, is called the Multistep Compound Model, a model developed by Feshbach, Kerman, and Koonin (Feshbach et al. 1980), and often called FKK for short. The FKK codes commonly in use today are: EMPIRE, TALYS, and GNASH, which can be found on the Web.

In principle, the products of a nuclear reaction can be any species permitted by conservation laws. In practice, direct reaction final channels will be strong if they possess substantial overlap with those of the initial state. Similarly, if the reaction proceeds all the way to a CN, strong channels will be those that capture large portions of the available phase space. Compound nucleus wave functions are intractable objects. This, coupled with the myriad of equally complex final states, allows a statistical analysis to be employed. Even so, the full $6N$ dimensional phase space is far too large to cope with and so insight must be used to calculate the phase space area of relevant parts (e.g., the part of phase space well described by two large clumps of matter, rather than one, will be proportional to the fission yield.)

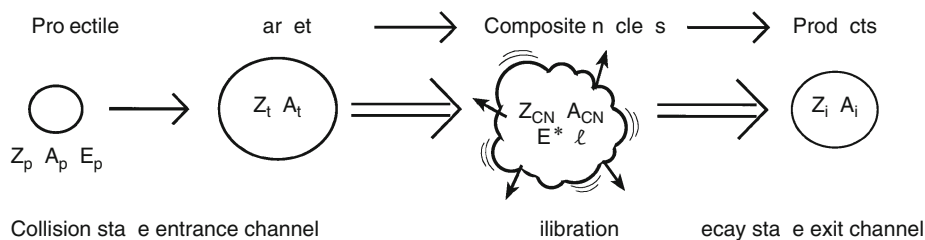
3.2.1 Shorthand Notation for Nuclear Reactions

The following shorthand notation is frequently employed:

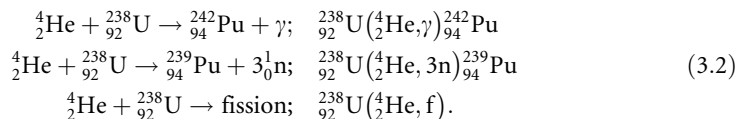
target (projectile, light products) heavy products, or
 $A(a, b)B$.

► Fig. 3.4

Nomenclature for the time evolution of a nuclear reaction in which a composite nucleus is produced and then forms product nuclei

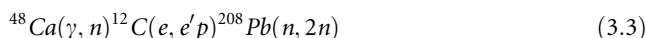


Note that the “products” are in plural; however, either can indicate a single particle. Typical examples, presented in both long- and shorthand notations, for reactions between ${}^4\text{He}$ projectiles and a ${}^{238}\text{U}$ target are:



Note that “one-way” arrows are used in the standard longhand reaction notation. Reaction studies are usually “one-way” exercises, i.e., equilibrium between reactants and products is not achieved. (Notable exceptions are bombs and the National Ignition Facility – NIF). On the other hand, Nature does achieve equilibrium (for many reactions) in the core of stars.

Using the shorthand notation, examples of photon capture, electron knockout and neutron-induced reactions are, respectively:



3.2.2 Mass-Energy Conservation: The Q-Value

The most fundamental constraint on any nuclear reaction is established by mass-energy ($E = Mc^2$) conservation. The **Q-value** for a reaction is the rest-mass energy difference between the reacting nuclei and the product nuclei:

$$Q = \sum M_0(\text{reactants})c^2 - \sum M_0(\text{products})c^2, \quad (3.4)$$

where M_0 is the rest mass of the nucleus. Nuclear mass-energy is tabulated in terms of *mass excess* Δ , which is often given in units of energy rather than mass (see [Sect. 11.6](#) of the Appendix of this Volume, where it is denoted by D):

$$\Delta = (M_0 - A \text{ u})c^2, \quad (3.5)$$

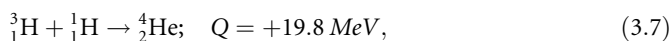
where A is the mass number and u is the *unified atomic mass unit* ($1 \text{ u } c^2 = 931.494 \text{ MeV}$). The Q-value can be rewritten as

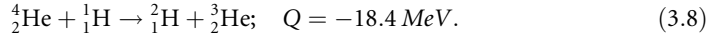
$$Q = [\Delta(\text{projectile}) + \Delta(\text{target})] - \sum \Delta(\text{products}) \quad (3.6)$$

Sources of mass-excess values, as well as reaction and structure data, can be found in NNDC (2010). If the rest mass of the reactants exceeds that of the products, the reaction is *exothermic* ($Q > 0$) and there is no energy threshold for the reaction. If Q is negative, the reaction is *endothermic* and projectile kinetic energy must be converted into rest-mass energy to compensate for this deficiency. Elastic scattering is defined by $Q = 0$.

In terms of writing energy-balanced (chemical-like) equations, Q-values correspond to product-side energy release. This is opposite to the sign convention for enthalpies, which can be viewed as reactant-side energy inputs. (Thus a negative enthalpy corresponds to a positive Q-value, i.e., the energy released in the reaction.) In a chemical reaction, the energy change comes from alteration of the atom associations, while in a nuclear reaction, the energy release comes from a change in the associations (i.e., correlations) at the nucleon level.

Two examples of concern in Big Bang nucleosynthesis, also discussed in [Chap. 12](#) of Vol. 2, are:

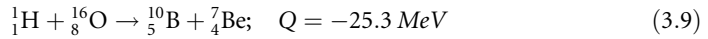




The first reaction (with a positive Q -value) is an important pathway in element formation; the second (with a negative Q -value) hinders destruction of ${}^4\text{He}$ in stellar environments.

All (n, γ) reactions (called *neutron capture*) on stable target nuclei are exothermic, as are all (p, γ) reactions on stable nuclei. These Q -values are no more than the release of energy corresponding to the binding energy of that nucleon. One can think of this energy as the energy difference between an unbound nucleon at zero energy and the Fermi energy, which while approximately 30 MeV above the bottom of a one-body potential is, by definition, 1 B_N below zero. The condition $B_N = 0$ defines the drip lines, i.e., the limits of nuclear stability with respect to the strong force.

Charged-particle reactions with heavier nuclei can have positive or negative Q -values. If the collective binding energies of the products are greater than that of the reactants, as it would be the case if the products were closer to the peak in the binding-energy curve than the reactants, the Q -value will be positive. Negative Q -values occur, for example, when nuclei on the leading edge of the binding energy curve, such as ${}^{12}\text{C}$ and ${}^{16}\text{O}$, are broken up into still lighter nuclei or when nuclei heavier than Fe fuse to build a heavier nucleus. Cosmic-ray-induced reactions that occur in the atmosphere, relevant to Li, Be, and B nucleosynthesis in nature and also to space travel, are examples of reactions with negative Q -values. (Such reactions are perhaps the principal impediment to long-duration space travel by humans.)



In reactions involving complex nuclei, two important quantities related to the Q -value, and also to the incident beam energy, are the excitation energy E^* (or equivalently U) and the threshold energy E_{th} . The *excitation energy* is the excess energy deposited in the product nucleus (► Fig. 3.5). For excitation energies below one B_N , the discretized nature of E^* is important.

The *threshold energy* is the minimum projectile energy required to form the product nucleus in its ground state. Compound nucleus formation provides a simple example of this concept: target (t) + projectile (p) → CN. In this case, energy and linear momentum conservation require (in the nonrelativistic limit):

$$\text{mass-energy :} \quad \Delta_t + \Delta_p + E_p = \Delta_{CN} + E_{CN} + E^*, \quad (3.10)$$

$$\text{linear momentum :} \quad p_p = \sqrt{2M_p E_p} = \sqrt{2M_{CN} E_{CN}} = p_{CN}, \quad (3.11)$$

$$\text{which gives :} \quad E^* = (A_t/A_{CN}) E_p + Q. \quad (3.12)$$

$$\text{Since when :} \quad E^* = 0, E_p = E_{th}, \text{ then} \quad (3.13)$$

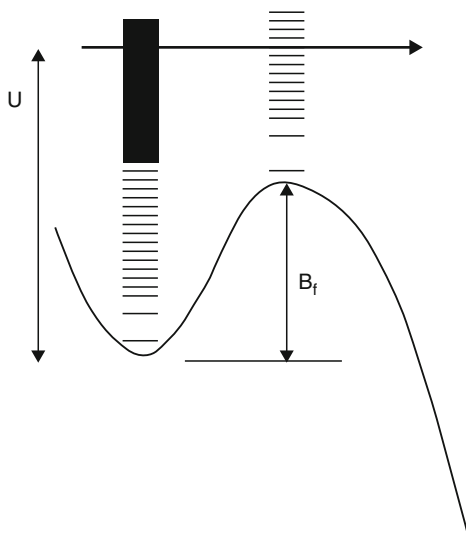
$$E_{th} = (A_{CN}/A_t)(-Q). \quad (3.14)$$

If Q is positive, there is no energetic threshold to limit the reaction. If Q is negative, energy in excess of the Q -value must be supplied to account for the center-of-mass motion of the composite nucleus. Equations for the situation in which two products are formed can be found in standard texts (e.g., Krane 1988; Cottingham and Greenwood 2001).

Under common reaction conditions during the first 50 years of nuclear reaction studies, the lighter of the two partners was the projectile incident on a heavier target at rest. However, with the advent of modern heavy-ion accelerators, this situation can now be interchanged, permitting the study of systems in which a heavy projectile is used to bombard a lighter target (*reverse*

■ Fig. 3.5

Schematic description of the increasing density of nuclear levels as the excitation energy U increases above the minimum in the potential energy (ground state). The abscissa in this plot is a deformation coordinate that represents the “reaction coordinate” and shows the change in level density as the system follows a one-dimensional path toward one possible decay mode, i.e., fission. The lowest density of states along this path is indicated for the height of the fission barrier B_f . In this figure U is used for the excitation energy. This is consistent with the use of U in thermodynamics to indicate the internal energy. The excitation energy E^* is the energy above the ground-state energy (mass) and in this example is indicated by the horizontal arrow



kinematics). This situation provides a unique experimental environment in which the reaction products are focused forward. Most recently, it has become possible to create reactions between colliding beams of heavy nuclei (e.g., Au + Au), thereby retrieving the available energy lost to center-of-mass motion in conventional fixed-target collisions.

3.2.3 The Nuclear Potential Energy: Coulomb Barrier Effects

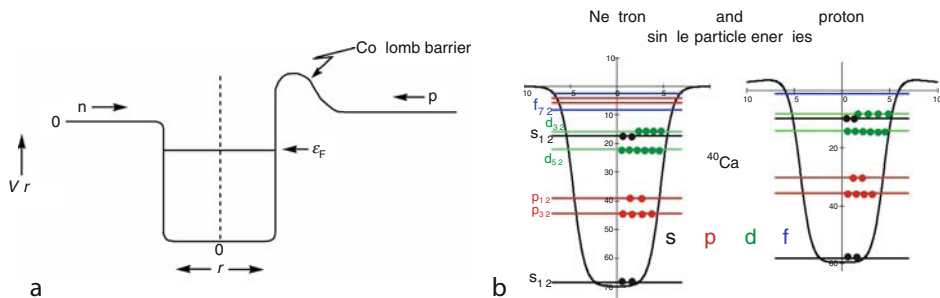
A second energetic factor, independent of the Q -value, is imposed by the *nuclear potential energy*, which summarizes the respective forces at play in atomic nuclei. As shown in ► Fig. 3.6, the potential energy for a complex nucleus is the sum of

1. A *central attractive well* created by the strong nuclear force acting at short range on the constituent neutrons and protons, and
2. A *repulsive Coulomb interaction* of long range acting between the positive charges of the target and projectile.

The saturated, short-ranged nature of the attractive nucleon-nucleon interaction creates an approximately uniform *mean field* inside the nucleus, giving rise to a nearly flat behavior of the nuclear potential. Near the nuclear periphery, the long-range Coulomb repulsive interaction overpowers the short-range nuclear attraction, giving rise to the *Coulomb barrier* and

■ Fig. 3.6

(a) A schematic representation of the nuclear potential energy as a function of the distance from the center of a complex nucleus is shown. Neutrons (*left*) do not experience Coulomb repulsion, as do protons (*right*). The Fermi energy level is indicated by ϵ_F . (b) A potential plot to scale for neutrons and protons in ^{40}Ca



a subsequent decrease in the potential at large distances according to the $1/r$ law. The actual nuclear potential energy will be multidimensional if spherical symmetry is broken by the ground state being deformed, as always happens at midshell, or when fission-like phenomena are being treated.

Using Gauss' Law and assuming that the charge is uniformly distributed within a sphere of radius R_C , the Coulomb potential (i.e., electric potential energy) has the following form:

$$V_C(r) = \frac{Z_p Z_t e^2}{r} = \frac{1.44 Z_p Z_t}{r} \text{ MeVfm}; \quad r \geq R_C$$

$$V_C(r) = \frac{Z_p Z_t e^2}{2R_C} \left(3 - \frac{r^2}{R_C^2} \right); \quad r < R_C. \quad (3.15)$$

Here Z_p and Z_t are the respective charges of the projectile and target nuclei and r is the separation distance between the centers of charge of the colliding nuclei.

The Coulomb barrier B_C^{cm} (in the center of mass) can be estimated as the interaction of nearly touching spheres, i.e., $B_C^{\text{cm}} = V_C(R_C)$, where $R_C = r_C(A_p^{1/3} + A_t^{1/3})$. Empirical studies suggest a value of $r_C \approx 1.4\text{--}1.6$ fm, also discussed in ▶ Sect. 2.2.3.1 of Chap. 2 in this volume. As with the Q -value, it is necessary to correct for center-of-mass motion, so that in the laboratory frame, the projectile energy required to surmount the Coulomb barrier is

$$B_C^{\text{lab}} = (A_{CN}/A_t) B_C^{\text{cm}}. \quad (3.16)$$

For charged particles with kinetic energies below the Coulomb barrier, the projectile usually elastically scatters from the target (discussion of Coulomb excitation below), leaving the reactants unchanged. Once the relative kinetic energy of the colliding pair becomes comparable to the Coulomb barrier, the projectile can classically penetrate into the attractive nuclear potential and produce a nuclear reaction. (Barrier penetration with lab energies below B_C^{lab} can occur but the probability is low.) This energy can be supplied by particle accelerators or in nature by either the high temperatures achieved in the core of a star or by the various cosmic accelerators that generate the high-energy nuclei found in cosmic rays. The Coulomb barrier is the energetic factor that determines the rate of reactions between charged nuclei at low energy.

This barrier also controls the decay rate for channels for which a charge separation is generated. Examples of the latter are all decay channels of an excited CN producing charged particles in the exit channel, ground-state (radioactive) decay via alpha-particle emission and fission.

Reactions between charged species first become probable when the projectile kinetic energy increases to values near the Coulomb barrier energy, permitting the tails of the nuclear matter distributions to overlap, ▶ Fig. 3.7. Because of the diffuse tail of the matter distribution and quantum penetration, it is possible for reactions to occur below the nominal Coulomb barrier. Most often, such reactions involve Coulomb excitation or the transfer of one or a few nucleons at the nuclear surface. However, more complex reactions can occur, including amalgamation of target and projectile, although with low probability. As the overlap between the two nuclear matter distributions increases, the probability for nuclear reactions involving many or all nucleons becomes increasingly probable.

3.2.4 Angular Momentum Effects: The Centrifugal Barrier

A second repulsive energetic factor is due to the orbital angular momentum associated with noncentral collisions. As shown in ▶ Fig. 3.8, initial projectile trajectories can be characterized semiclassically in terms of an *impact parameter* b , which is the distance between a given trajectory and one that passes through the center of the target.

The orbital angular momentum $\ell\hbar$ is quantized, so that for a projectile of mass m and velocity v ,

$$\ell\hbar = (mv)b, \quad (3.17)$$

For the case of two colliding spheres with sharp surfaces, the maximum value of the impact parameter is determined by the touching condition

$$b_{\max} = R_p + R_t, \quad (3.18)$$

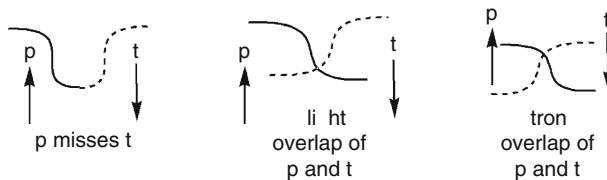
where R_p and R_t are the respective radii of projectile and target nuclei as shown in the left panel of ▶ Fig. 3.9.

In a classical geometrical model, the maximum angular momentum for the collision of objects with a sharp surface is then,

$$\ell_{\max}\hbar = mvb_{\max} = mv(R_p + R_t) = mvr_0(A_p^{1/3} + A_t^{1/3}). \quad (3.19)$$

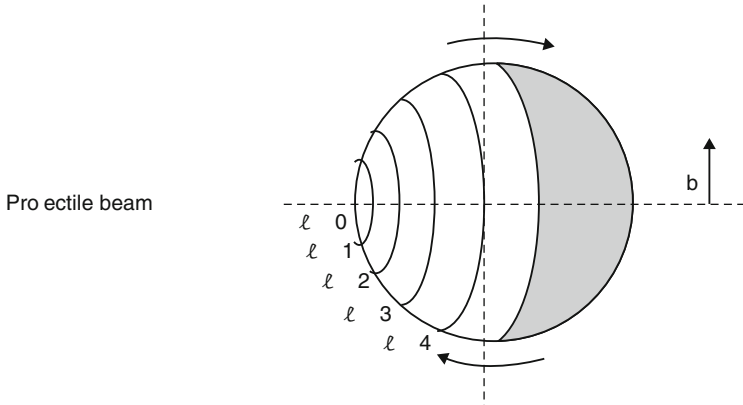
■ Fig. 3.7

Schematic picture of the increasing density overlap between projectile p and target t as two complex nuclei pass by one another



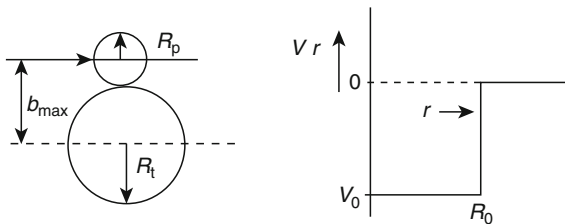
■ Fig. 3.8

Generation of angular momentum $\ell\hbar$ for projectiles with different impact parameters b . Each annular ring corresponds to the area defined by a given impact-parameter range and its associated ℓ -value. The indicated direction of rotation corresponds to “glancing” collisions represented by the two upper projectile trajectories. The middle trajectory leads to a “head-on” collision without angular momentum generation



■ Fig. 3.9

Left: Touching-spheres model of a nuclear collision. **Right:** Square-well nuclear potential, corresponding to a nucleus with a sharp surface



The amount of energy tied up in *rotational energy* E_{rot} depends on the impact parameter and constitutes a *centrifugal barrier*,

$$E_{\text{rot}}(\ell) = \frac{\hbar^2 \ell(\ell+1)}{2\mu r^2} = \frac{(\hbar c)^2 \ell(\ell+1)}{2 \left(\frac{A_p A_t}{A_p + A_t} \right) u r^2}; \quad \ell = 0, 1, 2 \dots \ell_{\text{max}}, \quad (3.20)$$

where μ is the reduced mass of the system, proportional to $A_p A_t / (A_p + A_t)$. (The constant $\hbar c = 197.3 \text{ MeV fm}$ simplifies calculations when combined with the numerical value of $u = 931.5 \text{ MeV}/c^2$).

Three additional points should be noted about this “barrier.” First, it drops off with distance much faster than the Coulomb barrier, i.e., $1/r^2$ versus $1/r$. Second, it is not the result of a real interaction. Rather, it can be viewed as removing that fraction of the energy from the

entrance channel that must be “spent” in angular momentum conservation and is thus not available for a reaction. In the standard language of chemistry, the relative separation is the reaction coordinate. The energy tied up in conserving angular momentum is not available to advance the reaction coordinate. Finally, it is this term in the expression for the energy that when put into the quantum mechanics (one-body) problem forces the wave functions to go to zero at the origin. The combined effects of the Coulomb and centrifugal barriers form independent constraints on the probability for a nuclear reaction.

The angular momentum involved in a reaction has important consequences, ranging from nuclear spectroscopic studies at low-angular momentum to the rotational instabilities that lead to fission, rotating dinuclear configurations (▶ Sect. 3.4.2), and for populating the highly deformed local minima responsible for fission isomers and super-deformed nuclei. For example, in a $^{238}\text{U} + ^{238}\text{U}$ collision, angular momenta up to $\ell_{\text{max}}\hbar \approx 1,000\hbar$ are possible. However, for values above $\ell\hbar \approx 80\text{--}100\hbar$ the composite system becomes rotationally unstable and cannot fuse. Thus all of the cross section associated with angular momentum above this stability limit is associated with reaction channels other than CN formation.

3.2.5 Summary of Energetic Factors in Nuclear Reactions and the Separation of Thermodynamic and Kinetic Factors

To form a composite nucleus, the threshold energy must be exceeded and the available energy must exceed the combined Coulomb and centrifugal barriers for the reaction probability to be appreciable. The threshold energy is imposed by mass-energy conservation and is important only for negative Q -values. The Coulomb barrier applies only to charged-particle reactions. The centrifugal barrier is not a fundamental constraint since $\ell = 0$ is always possible. (Also recall that ℓ is not a good quantum number if the potential is not spherically symmetric. This means that ℓ -waves can mix in such cases. However, as parity is a good quantum number, even values of ℓ mix with even and odd with odd.) As a general rule, the Coulomb barrier dominates for charged-particle-induced reactions, except for some cases where light nuclei are involved. For (n,γ) reactions on stable nuclei, the Q -value is always positive and the Coulomb barrier is zero, so only the centrifugal barrier constraint is relevant.

If the nuclei on either side of the reaction can exist only in one (i.e., the ground) or a few (as in the products of a direct reaction) states, the entropy of the participants is small as is the temperature T . Under these conditions, a thermodynamic discussion reduces to one of enthalpy (as the “ SdT ” term, i.e., the thermal term, in the free energies is tiny.) The Q -value represents the negative of the enthalpy, so a positive Q -value represents a spontaneous reaction. At $T = 0$, there are only two possible values of the degree of reaction: 0 (i.e., none) or 1 (all). So given enough time, something thermodynamics cannot give insight into, a positive Q -value will yield 100% products. (An energetically downhill reaction at equilibrium will yield 100% products at $T = 0$, a case realized in simple radioactive decay.) The barriers (both Coulomb and centrifugal) are kinetic factors. They do not influence ultimate equilibrium constants but they do determine rates (in the same way that the height of a chemical transition state determines the rate of a chemical reaction).

With the exception of the case of stars, or perhaps ultimately earth-bound fusion reactors, rates rather than true equilibrium are the concern. (As the reverse reactions required for true equilibrium do not occur.) Thus the description of the decay of a CN is a kinetic model.

3.2.6 Cross Sections: An Introduction

The compound nucleus scenario described in the previous section provides a useful framework for discussing the probability for a nuclear reaction as characterized by its *cross section*. As long as the excitation energy is not so high that internal thermal equilibration is short circuited, one can separate the formation process from the decay. When this is the case, the reaction probability can be factored into two terms: (1) the total probability for the projectile and target to fuse (entrance channel), and (2) the individual probabilities for formation of each product nucleus (exit channel). The total cross section can be defined more precisely in terms of the difference between the incoming and outgoing flux of beam particles. For specific exit channels, the production cross section is the fraction of the total cross section that yields a given product nucleus. Such a description fits equally well for direct reactions, which do not involve the intermediate composite-nucleus step.

In estimating the total reaction probability, a simple geometric touching-spheres model provides a useful benchmark calculation (► Fig. 3.9). In this model, a reaction will occur if the impact parameter b is less than or equal to the sum of the nuclear radii. For larger values of b there will be no reaction. The cross-sectional area defined by this geometry leads to a classical or *geometric cross section*,

$$\sigma^{\text{geo}} = \pi b_{\text{max}}^2 = \pi(R_p + R_t)^2 = \pi r_0^2 \left(A_p^{1/3} + A_t^{1/3} \right)^2; \quad r_0 \approx 1.40 - 1.60 \text{ fm}. \quad (3.21)$$

For medium-mass nuclei, this value has dimensions of order 10^{-24} cm^2 , which defines the unit for cross sections, the *barn* (b); i.e.,

$$1 \text{ barn} \equiv 1.0 \times 10^{-24} \text{ cm}^2 = 100 \text{ fm}^2. \quad (3.22)$$

For projectile energies well above the threshold and/or Coulomb barrier, ► Eq. (3.21) serves as a good approximation for the *total reaction cross-section*, $\sigma_R \approx \sigma^{\text{geo}}$.

For *neutron-capture* (n, γ) reactions at very low energies ($\ll 1 \text{ MeV}$), microscopic effects come into play, leading to significantly enhanced cross sections. Since (n, γ) reactions can proceed without threshold or Coulomb barrier limitations, reactions can occur at very low energies. More importantly, the wave nature of matter becomes the dominant factor. At very low energies (thermal, i.e., 300 K, energies correspond to an average kinetic energy of 0.025 eV) the neutron reduced *de Broglie wave length* ($\lambda = \hbar/p = 1/k$) is much larger than the nuclear radius; i.e., $\lambda > R$. The reduced de Broglie wave length is the reciprocal of the wave number $\lambda = 1/k$, where $k = (2mE)^{1/2}/\hbar$. Thus, for very low neutron energies, the values of σ_R can greatly exceed σ^{geo} .

Between the thermal and geometric extremes (i.e., between where the de Broglie wave length dominates and the width of the average state greatly exceeds the spacing between states) there is a resonance region where the cross section is characterized by sharp spikes at well-defined energies. All three of these regions are illustrated schematically in ► Fig. 3.10.

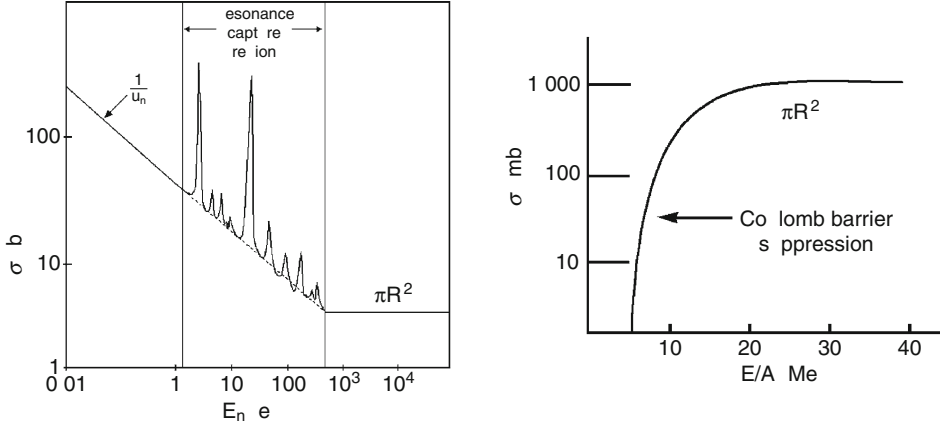
On the other hand, *charged-particle-induced reactions* at low energies are suppressed by the Coulomb barrier. To account for this effect, a simple modification of the form

$$\sigma_R = \sigma^{\text{geo}} (1 - B_C/E_p); \quad E_p \geq B_C \quad (3.23)$$

provides a good first approximation to the cross-section dependence on bombarding energy. By employing more sophisticated models that account for the diffuse nuclear surface and diffraction effects, a more quantitative description of the reaction cross section can be obtained.

■ Fig. 3.10

Left: Schematic representation of the excitation function for the capture of neutrons in a (n, γ) reaction. In this figure the velocity of the neutron is indicated by u_n . **Right:** Total cross section dependence on bombarding energy per nucleon for a charged-particle reaction



An important component of the reaction cross section is the relative distribution of angular momenta, or ℓ -wave distribution, generated in a collision. Angular momentum affects the population of quantum states of a given spin in direct reactions and is also a major factor in generating rotating nuclei that stretch axially into highly deformed nuclear shapes (Janssens and Khoo 1991). Angular momentum also destabilizes nuclei toward fission, much as a high-charge content does. In the geometric model the angular momentum is given by $\ell\hbar = mvb$ and $\ell_{\max}\hbar = mv(R_p + R_t)$, as shown in ► Fig. 3.8, and thus it is possible to partition the cross section by impact parameters,

$$\sigma_{\ell}^{\text{geo}} = \pi(b_{\ell+1}^2 - b_{\ell}^2) = \pi\lambda^2[(\ell+1)^2 - \ell^2] = \pi\lambda^2(2\ell+1). \quad (3.24)$$

By summing over all ℓ -waves the total reaction cross section, σ_R^{geo} , is then given by

$$\sigma_R^{\text{geo}} = \pi\lambda^2 \sum_{\ell=0}^{\ell_{\max}} (2\ell+1) = \pi\lambda^2(\ell_{\max}+1)^2. \quad (3.25)$$

In the simple black-disk model described above, nuclear effects of the diffuse nuclear surface and the discrete (i.e., quantum) nature of the allowed nuclear structure have been ignored and it is assumed that nuclear matter is perfectly opaque. The *optical model* addresses these omissions and is the subject of the next major section. One of the major results of this model is the introduction of ℓ -dependent *transmission coefficients*, T_{ℓ} , where $0 \leq T_{\ell} \leq 1$. The reaction cross section then becomes

$$\sigma_R = \sum_{\ell} \sigma_{\ell} \pi\lambda^2 \sum_{\ell} (2\ell+1) T_{\ell}. \quad (3.26)$$

These transmission coefficients are then the probability that the target-projectile collision will penetrate the interaction barrier and produce a nuclear reaction. Thus as ℓ increases, T_{ℓ} decreases; that is, $T_{\ell} = 1$ corresponds to complete absorption and $T_{\ell} = 0$ to pure elastic scattering.

3.2.7 Cross Sections, Excitation Functions, and Angular Distributions

Experimentally, evidence for a target-projectile interaction can be gained from measuring the probability for formation of the products that populate the various exit channels. This information then serves as the basis for interpretation of the reaction mechanism through which a nuclear collision proceeds. It may also provide essential data for nuclear astrophysics, as described in [Chap. 12](#) of Vol. 2, and for evaluating and implementing nuclear applications, discussed in [Chaps. 38](#) and [39](#) of Vol. 4).

The total reaction cross section is the sum of all possible reaction channels: $\sigma_R = \sum_b \sigma(a, b)$. Exit channels may involve only a single heavy nuclear product, as in the case of (n, γ) , reactions two fragments (as in fission) or even multiple fragments, as in multifragmentation. By measuring all possible exit channels, σ_R can be determined. Alternatively, σ_R can be measured with beam-attenuation measurements by measuring the rates [particle/s] of the beam reaching a detector with the target in and with it out (see the Addendum).

Measurements of production cross sections are performed with a wide range of both radiochemical and direct counter techniques. Historically, radiochemical techniques were particularly useful for measuring heavy residues, for which discrete Z and A identification are difficult to determine with nuclear particle detectors in reactions with normal kinematics. However, with the availability of very heavy-ion beams and the widespread use of reverse kinematics, the measurement of mass ($d\sigma_A/dA$), charge ($d\sigma_Z/dZ$), and isotope ($d\sigma_Z d\sigma_A/dAdZ$) distributions from direct counter techniques are now routinely done. For heavy residues, these values are frequently summarized graphically in terms of an *excitation function*, or cross section as a function of projectile energy, as in [Fig. 3.11](#). Extensive listings of production cross sections are maintained in several databases (IAEA 2010; NEA 2010; NNDC 2010; RNDC 2003).

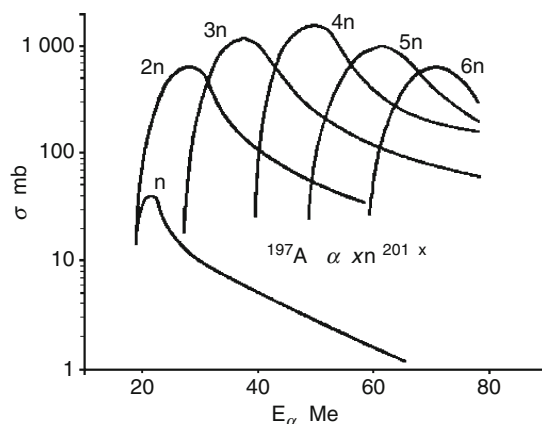
In conducting direct counter experiments, the emission of reaction products over the full 4π of solid angle (θ, ϕ) must be taken into account, as well as the transformation of laboratory data into the center-of-mass system (Krane 1988). Thus, measurements of the *angular distribution*, i.e., differential cross section as a function of angle $d\sigma(\theta, \phi)/d\Omega$, must be made. In the absence of spin-polarized targets or projectiles, the cross section is independent of azimuthal angle ϕ . In this case, the angular distribution is characterized by the single differential cross section, $d\sigma(\theta)/d\Omega$, where Ω is the solid angle into which the particles are emitted. The production cross section is then given by

$$\sigma(a, b) = \int_0^{2\pi} \int_0^\pi \frac{d\sigma(\theta, \phi)}{d\Omega} d\Omega = 2\pi \int_0^\pi \frac{d\sigma(\theta)}{d\Omega} \sin\theta d\theta. \quad (3.27)$$

For statistical decay of a composite nucleus with no angular momentum, particles are emitted isotropically; that is, $d\sigma(\theta)/d\Omega$ is independent of angle in the center-of-mass system. Thus, $d\sigma(\theta)/d\Omega = \text{constant}$ or $d\sigma(\theta)/d\theta \propto \sin\theta$. If the composite nucleus is formed in a state of high angular momentum with the axis of rotation oriented perpendicular to the beam direction (i.e., from an ensemble of reactions, the angular momenta are uniformly distributed in a plane perpendicular to the beam), as in the approximate case in heavy-ion reactions, then one observes strong forward-backward peaking, reaching a limiting value of $d\sigma(\theta)/d\Omega$, $\propto 1/\sin\theta$ or $d\sigma(\theta)/d\theta = \text{constant}$. Schematic angular distributions for these two extremes are shown in [Fig. 3.12](#).

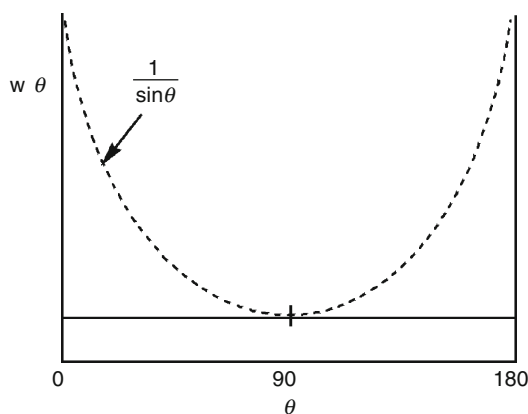
■ Fig. 3.11

Excitation function for the $^{197}\text{Au}(^4\text{He}, xn)^{201-x}\text{Tl}$ reaction (Lanzafame and Blann 1970)



■ Fig. 3.12

Schematic angular distributions for particle emission from an equilibrated hot nucleus. Solid line is for a system with no angular momentum and dashed line is an upper limit for very high angular momentum



On the other hand, for direct reactions, the projectile-like products tend to be focused in the direction of the incident beam momentum vector. Depending on the quantum state, collision energy and time scale, forward peaking or peaking at specific angles will be observed. Thus, angular distributions serve as key indicators of the degree of equilibration achieved in a reaction, as well as providing a means of evaluating the reaction mechanism and imparted angular momentum.

One of the most sensitive tests of any nuclear reaction model is its success in reproducing absolute doubly differential cross sections $d^2\sigma/d\Omega dE$. In order to obtain the differential cross section for a given exit channel, it is necessary to integrate over the full kinetic energy distribution of the emitted particles at a specific angle,

$$\frac{d\sigma(\theta)}{d\Omega} = \int_0^\infty \frac{d^2\sigma(\theta, E)}{d\Omega dE} dE. \quad (3.28)$$

It is the kinetic energy distribution as a function of angle that reveals the physics content of a nuclear reaction most transparently. For a fully equilibrated CN, the spectra of evaporated light particles are Maxwellian in shape and unchanging in angle in the center-of-mass system. The spectra of charged particles are suppressed at low energies by the Coulomb barrier. Two-body direct reactions exhibit discrete spectral lines or resonances, depending on the nuclear structure sampled in the collision. The two-body (simple momentum balance) scenario also produces a good first-order description of fission, yielding Gaussian-like fragment energy spectra resulting from highly stretched breakup configurations.

3.2.8 Cross-Section Measurements

Determination of the cross section for a nuclear reaction product requires measurement of the *reaction rate*, R = number of events/unit time. As in any two-body collision (second-order rate process), the rate is the product of a target-projectile collision factor $cn_p n_t$ and the “probability” σ that if a collision occurs, a specific product will be formed, i.e.,

$$\frac{dN(a, b)}{dt} = R(a, b) = cn_p n_t \sigma(a, b), \quad (3.29)$$

where c is a coefficient and the dimensions of $n_p n_t$ are defined by the geometry of the experiment. Three cases are of general interest:

1. Accelerator-based bombardments in which a beam of particles n_p is incident on a planar target.
2. Nuclear reactors, where a gas of neutrons permeates n_t target nuclei.
3. Stellar interiors, where the reactants act as two interacting gases.

Practical aspects of cross-section calculations are discussed in the Addendum at the end of the chapter.

3.3 Scattering Theory

The presentation in the preceding section is meant to give a general overview of relevant concepts needed to describe nuclear reactions. In this section a treatment of quantum scattering is presented. This presentation is meant to facilitate a comparison between various types of scattering and to link nuclear reactions to structure. Additional background on scattering theory can be found in (Bertulani 2009).

3.3.1 Preliminaries

Before dealing with the scattering problem, the quantum objects under study should be considered. If the neutron and proton constituents of the nucleus were noninteracting, self-bound nuclei would not exist. One might posit that the binding energy is the sum of attractive

two-body interactions, all $A(A - 1)/2$ of them. This amounts to making two assumptions: (1) that neutrons and protons are the only constituents in nuclei, i.e., nucleons are elementary particles and (2) that the interaction is *pair-wise additive*. The former assumption is formally incorrect, but not bad when the available energy is less than the mass of the pion, the lightest field particle that mediates the residual strong force (nuclear force). The second assumption is also likely wrong. Most nucleon-based descriptions of the residual strong force include 3-body forces between nucleons, but the origin of these – beyond *pair-wise additive* contributions – is unclear. Such interaction terms could come from the fact that nucleons are not truly elementary and the employed degrees of freedom (DoF), those of the nucleons, is an incomplete set. (Axilrod and Teller 1943 first introduced 3-body forces in an attempt to explain the crystal structure of solid Ar as a patch when they simplified the many-body problem by dropping all of the degrees of freedom associated with the electrons and retaining only those associated with the nuclear positions. Their assumption being that, if they could have solved the problem employing all degrees of freedom, a 3-body force would not be needed.) However, because the field-mediating bosons of Quantum Chromodynamics do interact with one another, while they do not in Quantum Electrodynamics, pair-wise additivity would not be expected in the former. Whatever the reason, nucleon-based theories require 3-body terms (see also [Chap. 2](#) in this Volume).

High-energy electron reaction studies measuring $(e,e'p)$ cross sections have shown that only 70–80% of the protons participate in independent-particle motion of the type imagined in one-body potential models. This low “occupancy” of one-body states is caused by strong correlations within the nucleus. These correlations are primarily between pairs of nucleons, but α -particle clustering, sometimes called “quarteting,” in any low-density region also suppresses one-body behavior. Nucleons are somewhat different objects inside and outside a nucleus, as they effectively lose 0.8% of their mass, i.e., the binding energy, when transported inside a nucleus. Often, the term “dressed” is used to describe nucleons in the nucleus.

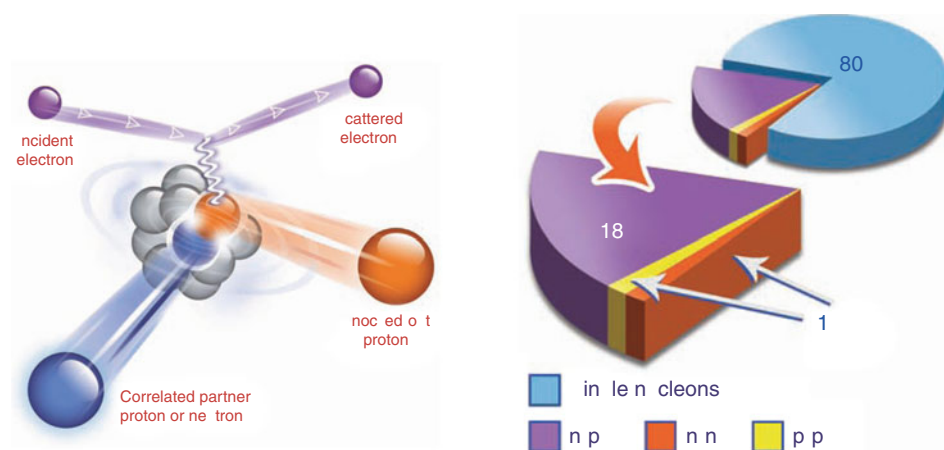
Very recent electron scattering studies using two-nucleon knockout reactions $(e,e'pp)$ and $(e,e'pn)$, have shed considerable light on these in-medium correlations (Subedi et al. 2008). This work showed that the overwhelming strong pair correlations are between neutrons and protons with large relative momenta and small center-of-mass (CM) momenta ([Fig. 3.13](#)). Large relative momenta are expected due to the rather hard core of the nucleon-nucleon interaction, but the tensor force undoubtedly plays a role and helps distinguish like-nucleon versus different-nucleon correlations. The tensor force arises because the interaction between nucleons depends on the relative orientation of their spins with respect to their relative spatial vectors (see [Chap. 2](#) in this Volume).

Due to the Pauli principle, only n-p pairs can have their spins aligned and otherwise have the same quantum numbers. These pairs are referred to as short-range correlated (SRC) pairs and their presence strongly affects the properties of cold, dense nuclear matter, such as that found in neutron stars. This nucleon-nucleon interaction is also required to explain the fact that the n-p spin triplet is bound (i.e., the deuteron) while the n-n and p-p, required singlets, are not. Consideration of n-p interactions is also essential to understand the evolution of the phenomenological spin-orbit interaction as a function of n/p asymmetry (Otsuka 2005), one of the most discussed topics in nuclear structure research today.

A focus on like-nucleon singlet (spin zero, i.e., BCS-like) pairing is warranted in an effort to explain the slight variation in mass responsible for the overwhelming dominance of even-even nuclei as well as explaining their ground-state spins. On the other hand, this myopic focus near the Fermi energy misses the source of the bulk of nuclear binding.

■ Fig. 3.13

The initial nucleon correlations as seen from a two-nucleon knockout experiment (left) are summarized in a pie chart on the right (Subedi et al. 2008)



Descriptions of nuclei based on realistic nucleon-nucleon interactions that include the effects mentioned above have, as of this time (2010), only been able to deal with nuclei with $A < 12$ (Pieper et al. 2002). Above this mass number, various approximations are employed. Simplifying this many-body problem all the way down to independent particles moving in an overall potential is of great heuristic value and utility. (This utility does not extend to calculation of the total binding energy. For this, one needs to add a macroscopic correction to the total binding energy. In this macroscopic-microscopic approach, pioneered by Strutinsky (1967), it is the macroscopic part that captures the impact of nucleon-nucleon correlations far removed from the Fermi surface). The single-particle approximation leads to the one-body problem, i.e., the type solved for generating hydrogenic wave functions (in this case, a solitary e^- moving in a $1/r$ potential.) The greatly simplified (“one-body”) potentials (one for neutrons and one for protons) are separately adjusted to explain phenomena that occur *near* the Fermi surfaces for neutrons and protons. In fact, to explain behavior away from the Fermi surfaces, the potential depths have to be made both energy-dependent and complex.

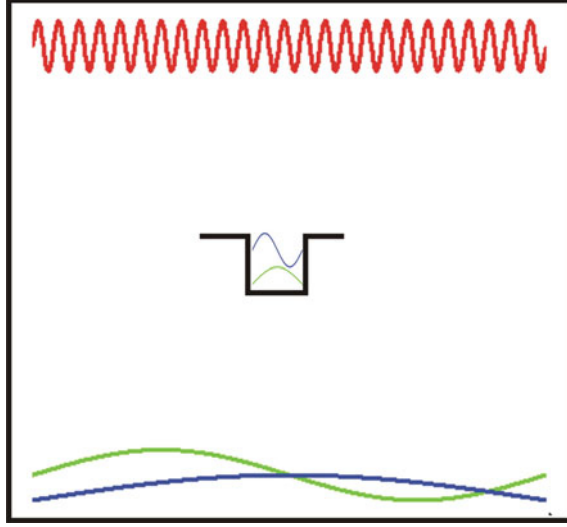
Consider a nucleon interacting with a (one-body) potential well formed by, at least, the $A - 1$ interactions of this nucleon with the others. Now imagine that this potential is itself in a large box of dimensions much larger than the range of the nuclear force (► Fig. 3.14). Considering only the short-ranged nuclear force, outside the well the potential is zero. The box, while large relative to nuclear dimensions, presents a boundary condition, so the box contains (in the absence of the internal potential) all the “particle-in-a box” states. The wave function with the lowest energy has no internal nodes; the more nodes - the higher the energy (eigenvalue).

As the depth and width of the internal potential is “dialed up,” these particle-in-a-box wave functions are modified – increasing the frequency in the region of the potential well and can even localize some of them entirely within the potential well. The latter, having no probability far-removed from the potential well, are the “bound-states.”

The presence of the attractive potential produces a positive phase shift δ of the wave function at large distance, relative to the wave function without the potential (► Fig. 3.15).

■ Fig. 3.14

Nucleon potential in a box. As the potential is made either deeper or wider, states are moved from ones quantized only by the box boundary conditions, essential free waves, to those confined to the central potential. The latter correspond to bound nuclear states



This phase shift is a direct consequence of the higher frequency within the range of the potential. As the potential is made either wider or deeper, states are “sucked” in (from the box) and are localized in the potential well. In the case of a one-dimensional square well of depth V and width L , the number of bound states for a particle of mass m is $N = 1 + [(2mV)^{1/2}L/(\pi\hbar)]$ where the square brackets stand for the integer part. Every time the phase shift passes π , another one of the continuum (particle-in-a-box) states is “sucked” into the well. This phase shift, which plays a central role in scattering problems, records the asymptotic compression of the wave function, but the number of $(1/2)$ oscillations (each producing a bound state) is lost. However, the number of bound states for each ℓ , N_ℓ , can be recovered as it is encoded in the zero energy (i.e., threshold) phase shift, $\delta_\ell(0) = N_\ell \pi$. This is known as Levinson’s Theorem.

3.3.2 The Optical Model (OM)

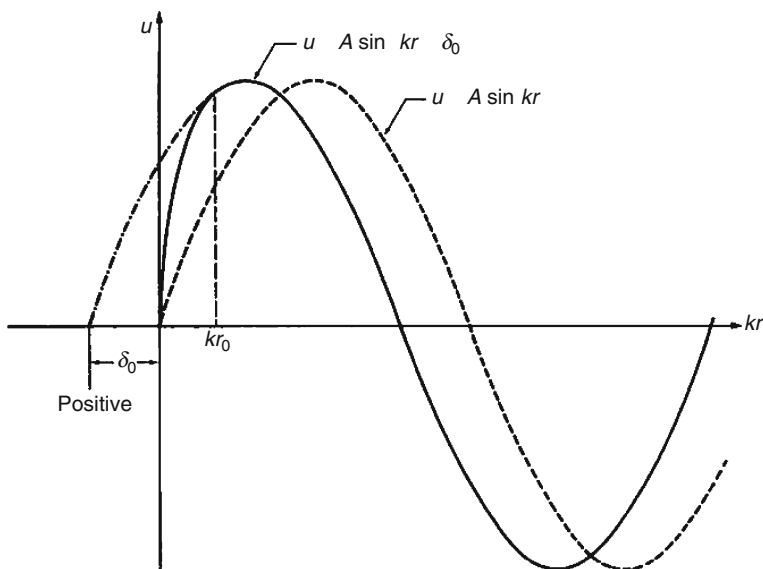
The interaction of a nucleon with a nucleus can be modeled if the potential is made complex (Buck et al. 1960; Hodgson 1967; Messiah 1958). The common form is

$$\begin{aligned}
 U(r, E) &= V(r, E) + iW(r, E) \\
 &= [-V_v(E)f(r, r_v, a_v) + 4a_s V_s(E)f'(r, r_s, a_s) + V_{so}(E)h(r, r_{so}, a_{so})(\ell \mathbf{s}) + V_c(r, a_c)] \\
 &\quad + i\{-W_v(E)f(r, r_v, a_v) + 4a_s W_s(E)f'(r, r_s, a_s) + W_{so}(E)h(r, r_{so}, a_{so})(\ell \mathbf{s})\}.
 \end{aligned} \tag{3.30}$$

where $\ell\hbar$ and $s\hbar$ are angular momentum vectors and $(\ell \mathbf{s})$ is the scalar product of the vectors ℓ and \mathbf{s} .

■ Fig. 3.15

Illustration of the change in a wave function u , with an attractive potential and the associated phase shift



Note that the potential depends on the projectile center-of-mass energy E as well as radius r . The former accounts for the nonlocalities (and thus generates effective masses and spectroscopic factors, which are related to the occupancies of single-particle states). V and W are the real and imaginary parts of the potential, both of which have volume, surface, and spin-orbit-dependent components, V_v , V_s , and V_{so} , respectively. (The spin-dependent term given above is appropriate for the scattering of spin $\frac{1}{2}$ particles by spin 0 nuclei; for the scattering of particles of zero spin, there is no spin-dependent term, while for the scattering of particles of higher spin, more complex forms are required). V_c is the Coulomb potential, a term needed if the incident particle is charged. The refracting potential V elastically scatters the incident particles, and the absorbing potential W takes account of all the inelastic processes.

The unitless form factors (► Fig. 3.16) are most often taken as

$$f(r, r_i, a_i) = \frac{1}{1 + \exp\left(\frac{r - R_i}{a_i}\right)}, \quad (3.31)$$

and

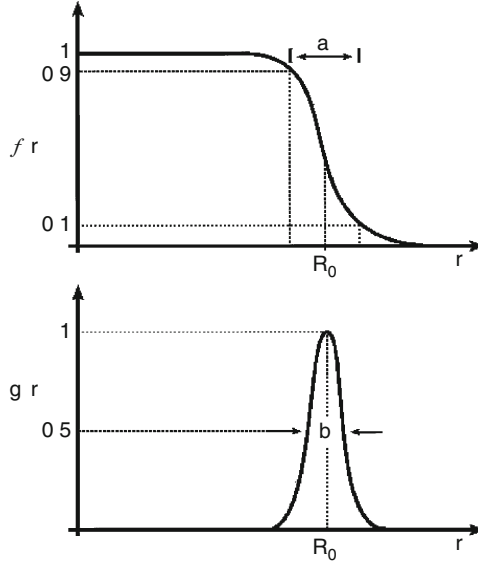
$$h(r, r_i, a_i) = -\frac{1}{2} \left(\frac{\hbar c}{m_\pi c^2} \right)^2 \frac{f'(r, r_i, a_i)}{r}. \quad (3.32)$$

Here $f' = df/dr$.

The nuclear radii are $R_i = r_i A^{1/3}$ and the parameters a_i encode the diffuseness of the nuclear surface. The subscript (i) allows these constants to be different for the different terms in the potential. The spin-orbit form is analogous to the Thomas form for atoms. Relativistic treatments generate such a term, but do not provide insight into the strength or even its sign. The Coulomb potential can be taken to be that for uniformly charged spheres or calculated numerically assuming form factors for the density similar to that for the potential.

■ Fig. 3.16

Form factors of the OM for the real, $f(r)$, and imaginary, $g(r) = -af'(r)$, components



To calculate the observable cross sections for two particles interacting through the above potential, Schrödinger's equation must be solved,

$$\frac{\hbar^2}{2\mu} \nabla^2 \Psi + (E - V) \Psi = 0, \quad (3.33)$$

where the radial part of the kinetic energy operator is (in D -dimensions)

$$\nabla_r^2 = \frac{1}{r^{D-1}} \frac{\partial}{\partial r} r^{D-1} \frac{\partial}{\partial r}. \quad (3.34)$$

As the spin of the incident particle can couple in two ways to the orbital angular momentum ℓ (to give total angular momenta of either $j = \ell \pm 1/2$), there are two solutions for each ℓ to the one-body quantum problem posed above. These solutions are identified with “+” for the “stretched” (i.e., parallel) case and “−” for the “jack-knifed” case. In the solution of the radial problem, the kinetic operator can be reduced to a simple second derivative by solving for the product of r times the radial wave function, sometimes called the reduced radial wave function y . Employing y and defining $\rho = kr$, the resulting radial wave equations become,

$$\frac{d^2 y_\ell^+(\rho)}{d\rho^2} + \left[1 - \frac{V_c}{E} - \frac{(-V_v + iW_v)f(\rho) + 4a_s(V_s + iW)f'(\rho)}{E} - \frac{\ell(V_{so} + iW_{so})h(\rho)}{E} - \frac{\ell(\ell+1)}{\rho^2} \right] y_\ell^+(\rho) = 0 \text{ and} \quad (3.35)$$

$$\frac{d^2 y_\ell^-(\rho)}{d\rho^2} + \left[1 - \frac{V_c}{E} - \frac{(-V_v + iW_v)f(\rho) + 4a_s(V_s + iW)f'(\rho)}{E} + \frac{(\ell+1)(V_{so} + iW_{so})h(\rho)}{E} - \frac{\ell(\ell+1)}{\rho^2} \right] y_\ell^-(\rho) = 0. \quad (3.36)$$

The wave number is $k = (\lambda)^{-1} = \sqrt{(2\mu c^2 E)/\hbar c}$. These (reduced) radial wave functions are zero at the origin and beyond the nuclear field tend asymptotically to the form

$$\begin{aligned} y_\ell^\pm(\rho) &\propto [H_\ell^{\text{in}}(\rho)] - S_\ell^\pm [H_\ell^{\text{out}}(\rho)], \\ &\propto [G_\ell(\rho) - iF_\ell(\rho)] - S_\ell^\pm [G_\ell(\rho) + iF_\ell(\rho)], \end{aligned} \quad (3.37)$$

where the terms in square brackets can be thought of as the incoming and outgoing waves and the $S_\ell^\pm = \exp(2i\delta_\ell)$ are the elements of the so-called scattering matrix, where δ_ℓ are the phase shifts associated with the nuclear potential. (If the potential is spherical, ℓ is a good quantum number and one only needs to be concerned with the diagonal elements of this matrix, indexed by ℓ . If on the other hand, the potential is deformed, ℓ is not a good quantum number and a full matrix – introduced by J. Wheeler – is required). The regular (goes to zero at the origin) and irregular (finite at the origin) Coulomb functions $F_\ell(\rho)$ and $G_\ell(\rho)$ are solutions of [Eqs. 3.35](#) and [3.36](#) without the nuclear terms. These functions have the asymptotic forms

$$\begin{aligned} F_\ell(\rho) &\xrightarrow{\rho \rightarrow \infty} \sin \left[\rho - \eta \ln 2\rho - \frac{1}{2}\ell\pi + \sigma_\ell \right], \\ G_\ell(\rho) &\xrightarrow{\rho \rightarrow \infty} \cos \left[\rho - \eta \ln 2\rho - \frac{1}{2}\ell\pi + \sigma_\ell \right]. \end{aligned} \quad (3.38)$$

The incoming and outgoing waves have the asymptotic forms

$$\begin{aligned} H_\ell^{\text{in}}(\rho) &\xrightarrow{\rho \rightarrow \infty} \exp \left[-i \left(\rho - \eta \ln 2\rho - \frac{1}{2}\ell\pi + \sigma_\ell \right) \right], \\ H_\ell^{\text{out}}(\rho) &\xrightarrow{\rho \rightarrow \infty} \exp \left[+i \left(\rho - \eta \ln 2\rho - \frac{1}{2}\ell\pi + \sigma_\ell \right) \right]. \end{aligned} \quad (3.39)$$

The nonspin-flip $B(\theta)$ and spin-flip $A(\theta)$ scattering amplitudes are

$$A(\theta) = f_C(\theta) + \frac{1}{2ik} \sum_{\ell=0}^{\infty} \{(\ell+1)S_\ell^+ + \ell S_\ell^- - (2\ell+1)\} e^{2i\sigma_\ell} P_\ell(\cos\theta), \quad (3.40)$$

$$B(\theta) = \frac{1}{2ik} \sum_{\ell=0}^{\infty} \{S_\ell^+ - S_\ell^-\} e^{2i\sigma_\ell} P_\ell^1(\cos\theta), \quad (3.41)$$

where σ_ℓ is the (unitless) Coulomb phase shift for the ℓ th partial wave, $f_C(\theta)$ is the (unitless) Coulomb scattering amplitude, and η is the (unitless) Coulomb or Sommerfeld parameter. These are given by

$$\begin{aligned} \sigma_\ell &= \arg\Gamma(\ell+1+i\eta) = \sigma_0 + \sum_{s=0}^{\ell} \tan^{-1}\left(\frac{\eta}{s}\right), \\ f_C(\theta) &= -\frac{\eta}{2k} \csc^2\left(\frac{\theta}{2}\right) \exp \left[2i\sigma_0 - i\eta \ln \left(\sin^2 \frac{\theta}{2} \right) \right], \end{aligned} \quad (3.42)$$

and

$$\eta = \frac{Z_p Z_t e^2}{\hbar v} = \frac{\mu Z_p Z_t e^2}{k \hbar^2} = 0.1575 Z_p Z_t \sqrt{\frac{A_p}{E_{\text{lab}}/\text{MeV}}}. \quad (3.43)$$

(The gamma function Γ is used in the definition of the Coulomb phase shift.) There are three potential observables for elastic scattering. The first is the differential (elastic) scattering cross section,

$$\frac{d\sigma_E}{d\Omega}(\theta) = |A|^2 + |B|^2. \quad (3.44)$$

The above reduces to the famous Rutherford formula when the Coulomb amplitude f_C is all that contributes to the scattering amplitude

$$\frac{d\sigma_{\text{Ruth}}}{d\Omega} = |f_C|^2 = \left(\frac{1.44 Z_p Z_t}{4E/\text{MeV}} \right)^2 \text{fm}^2 = \frac{D_c^2}{16} \csc^4\left(\frac{\theta}{2}\right) \text{fm}^2, \quad (3.45)$$

where D_c is the distance of closest approach.

The second and the third observables are the polarization, $P(\theta)$, and spin rotation, $Q(\theta)$, (Glauber and Osland 1979),

$$P(\theta) = \frac{2 \text{Im}AB^*}{|A|^2 + |B|^2} \quad \text{and} \quad Q(\theta) = \frac{2 \text{Re}AB^*}{|A|^2 + |B|^2}. \quad (3.46)$$

If the incident particle is a neutron, the total elastic cross section is finite and integrates to

$$\sigma_E = \pi\lambda^2 \sum_{\ell=0}^{\infty} \left\{ (\ell+1) |1 - S_{\ell}^+|^2 + \ell |1 - S_{\ell}^-|^2 \right\}. \quad (3.47)$$

To deduce the total inelastic (sometimes called the reaction) cross section, all one needs to note is that for each ℓ -wave, the outgoing wave is reduced in intensity by $|S|^2$ relative to the ingoing wave, therefore

$$\sigma_R = \pi\lambda^2 \sum_{\ell=0}^{\infty} \left\{ (\ell+1) (1 - |S_{\ell}^+|^2) + \ell (1 - |S_{\ell}^-|^2) \right\}. \quad (3.48)$$

The transmission coefficients can be identified with

$$T_{\ell}^{\pm} = 1 - |S_{\ell}^{\pm}|^2 \quad (3.49)$$

and in so doing, one can see that the reaction cross section in the absence of intrinsic spin effects results in [Eq. \(3.26\)](#).

The total cross section, a quantity finite only for neutron scattering, comes from the sum of the elastic and reaction cross sections. Upon canceling terms for each pair of $|1 - S_{\ell}|^2 + 1 - |S_{\ell}|^2$ terms, one gets

$$\sigma_T = \sigma_E + \sigma_R = 2\pi\lambda^2 \sum_{\ell=0}^{\infty} \left\{ (\ell+1) (1 + \text{Re}S_{\ell}^+) + \ell (1 - \text{Re}S_{\ell}^-) \right\}. \quad (3.50)$$

There are several interesting benchmarks related to the results of [Eqs. \(3.47\)–\(3.50\)](#). The elastic scattering cross section (for neutrals) spans from where $S_{\ell} = 1$ (both elastic and inelastic cross sections are zero) to $S_{\ell} = -1$. Thus the cross section for each ℓ lies between

$$0 \leq \sigma_{E,\ell} \leq 4\pi\lambda^2(2\ell+1). \quad (3.51)$$

When $S_{\ell} = 0$,

$$\sigma_{E,\ell} = \sigma_{R,\ell} = \pi\lambda^2(2\ell+1) \quad \text{thus} \quad \sigma_{T,\ell} = 2\pi\lambda^2(2\ell+1). \quad (3.52)$$

► Equation (3.52) demonstrates that the presence of the inelastic scattering implies an elastic contribution. This explains the factor of 2 in ► Eq. (3.50), which indicates that the *total* cross section for neutrals, that is, the case for which the elastic scattering cross section is finite, is *twice* the geometric reaction value. Recalling the initial discussion of the geometric cross section, partial waves with ℓ greater than some value ℓ_{\max} do not contribute significantly to the summations in ► Eqs. (3.48)–(3.50), thus the sums may be truncated.

3.3.3 The Dispersive Optical Model (DOM)

In 1926 R. de L. Kronig noticed that the reflection and absorption of light were interrelated. The next year Hans Kramers explained this relation, essentially allowing for the calculation of *both* the absorption (extinction coefficient) and the index of refraction from the measurement of the 90° reflectance. The key concept is that the response of a system to the stimulus (in this case light and the response in question is called the dielectric response) is dictated by a *complex* quantity, for which the real and imaginary parts are “two-sides of the same coin.” The “sides” are related to one another by energy integrals over the complementary components. (That is, the real part at energy ε is related to an integral over all energies of the imaginary component with a pole at the energy of interest, and vice versa.) For example, in the case of the complex dielectric response (α in the equations below) of matter as a function of the frequency of the stimulus ω

$$\alpha = \alpha_1 + i\alpha_2$$

$$\alpha_1(\omega) = \frac{1}{2}P \int_{-\infty}^{\infty} \frac{\alpha_2(\omega')}{\omega' - \omega} d\omega' ; \quad \alpha_2(\omega) = -\frac{1}{2}P \int_{-\infty}^{\infty} \frac{\alpha_1(\omega')}{\omega' - \omega} d\omega', \quad (3.53)$$

where P stands for the “Cauchy principal value” of the integral whose integrand has a singularity. These relationships are the result of “causality”; that is, the system cannot respond before the stimulus arrives. From the earliest days of the nuclear optical model, it was appreciated that this relationship should be enforced, as it is in all careful optical spectroscopy.

The difficulty in imposing causality is that the interrelationships are in the form of “dispersion relations.” That is, one must know the real (imaginary) part of the response at *all* energies to deduce the imaginary (real) response at any energy. It is the “all” that provides the stumbling block. As a consequence, this dispersive form of the optical model, or dispersive optical model (DOM), has only limited applicability. However, recently, more effort has been directed at the dispersive optical model analyses of data, as they have been shown to be of great value in predicting the behavior of nuclei removed from stability. The utility of this generator is that in addition to using scattering data (at positive energy), structural data (at negative energy, i.e., the position of bound states) is used to fix the real part of the potential, making both parts more robust (via the dispersion interrelationship). A concise discussion of the Kramers–Kronig dispersion relations as applied to the dielectric response can be found in (Kittel 1986). A full presentation of the dispersive optical model can be found in (Mahaux and Sartor 1990) and its most recent application to nuclei as a function of n/p asymmetry can be found in (Charity et al. 2006, 2007). The most important implications of the DOM [based primarily on nucleon knockout reactions (e,e'p) and n and p elastic scattering] are presented below.

First, the connection between the full complex potential and that used in one-body structure models must be unmasked. The imaginary part of the potential vanishes at the Fermi surface. Thus the real one-body potential used as a basis for simple nuclear structure

models is *only* valid near the Fermi surface. Or conversely, if one is interested in phenomena that only involve excitations near the Fermi energy, working with a real potential is valid. On the other hand, at high excitation energies, which are likely to involve particles far above and holes far below the Fermi surface, the imaginary component must be dealt with.

The second feature of this model is that effective masses and spectroscopic factors can be extracted from the energy dependence of the potentials (the former from the real part and the latter, which are related to the occupancy of single-particle states, from the imaginary part). The most striking result of the optical model is that the potential must be made energy-dependent if either the position of the single-particle levels or elastic scattering over a broad range of energies are to be reproduced. While the positions of the levels near the Fermi surface can be extracted from single-nucleon transfer reactions, (e,e'p) reactions are needed to determine the strength functions below the Fermi surface. (These functions will exhibit sharp peaks for orbits slightly below the Fermi surface and broad distributions for deeply bound orbits.) This dependence is shown in [Fig. 3.17](#) for ^{208}Pb .

If the dependence is linear, an effective mass (m^*) can be introduced to allow the single-particle energy to be recast in terms of a fixed potential,

$$\varepsilon = \frac{(\hbar k)^2}{2m} + \left[V_0 + \frac{dV}{d\varepsilon} \varepsilon \right] = \frac{(\hbar k)^2}{2m} + [V_0 + \alpha \varepsilon], \quad (3.54)$$

$$\varepsilon = \frac{(\hbar k)^2}{2m(1-\alpha)} + V_0(r) \left(\frac{1}{1-\alpha} \right) = \frac{(\hbar k)^2}{2m^*} + V_0'(r), \quad (3.55)$$

with

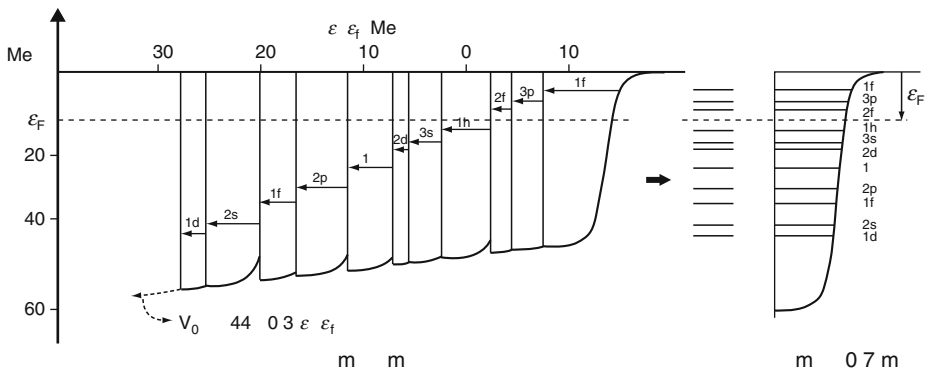
$$\frac{m^*}{m} = 1 - \alpha = 1 - \frac{dV(r, \varepsilon)}{d\varepsilon} \approx 0.7 \quad (3.56)$$

Referring back to the harmonic oscillator, [Fig. 3.18](#) shows that an effective mass greater (less) than the nucleon mass will decrease (increase) the single-particle level spacing, making both the single-particle level density and many-body density of states larger (smaller).

The above discussion is associated with the finite range of the nucleon-nucleon interaction. This can also be viewed (via a Fourier transform) as a momentum dependence of the

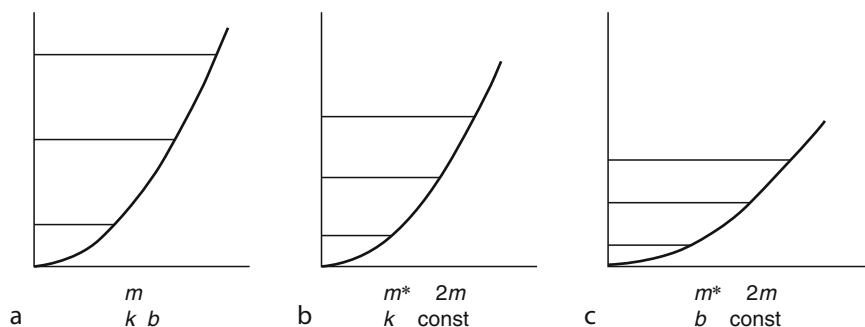
■ **Fig. 3.17**

The energy dependence of the potential needed to reproduce the positions of the single-particle levels for ^{208}Pb (from Mahaux and Sartor 1990)



■ Fig. 3.18

How an effective mass affects the single-particle level spacing



interaction. As a consequence, the effective mass contribution mentioned above is often called the “ k -mass” or the momentum-dependent effective mass. This mass is relevant for matter (i.e., neutron-star calculations) and its dependence on neutron–proton asymmetry has attracted considerable attention (Li et al. 2008).

The description of real nuclei requires more than the k -mass. A second multiplicative effective-mass term, the “omega mass” or m_ω , arises from a time nonlocality of the interaction. (As the exchange involves mesons with mass, the “throwing” and “catching” are not simultaneous events.) This time nonlocality can be viewed as a fundamental energy (or frequency) effect. Following prescriptions developed by Mahaux and collaborators (Mahaux and Sartor 1990), the relative change of the effective mass from real nucleon masses can be represented by two unitless terms,

$$\frac{m^*}{m} = m_k m_\omega. \quad (3.57)$$

The “omega mass” is peaked at the nuclear surface, producing what solid-state scientists would call surface states. In the nuclear case, this just corresponds to low-lying (i.e., near the Fermi surface) collective excitations associated with the physical surface. The combined effective masses and the potentials from which they are derived are shown in ► Fig. 3.19. The k -mass suppresses the effective mass in the interior and the omega-mass produces a peak at the nuclear surface. Also extracted from this analysis are the occupation probabilities of single-particle levels, a subject that will be addressed in the next section when discussing single-particle knockout reactions from nuclei far-removed from stability.

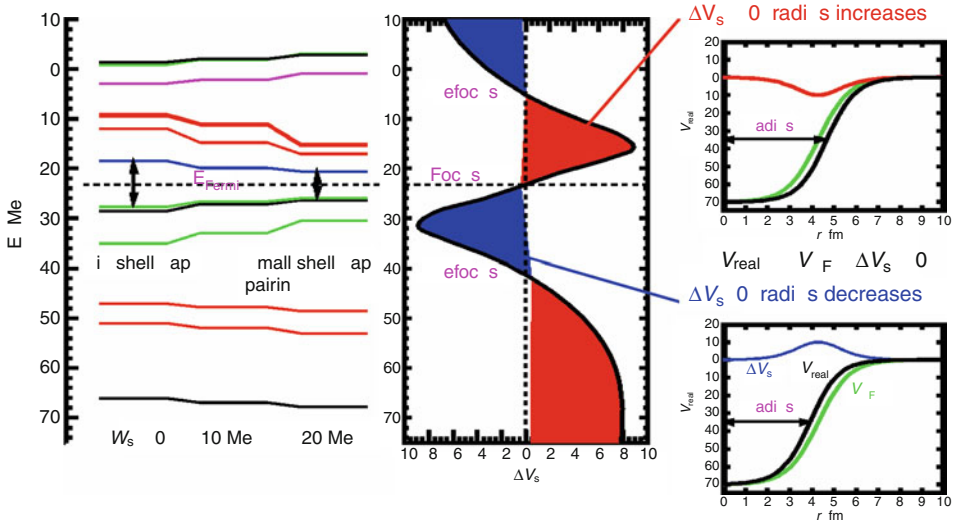
What must also be appreciated is that effective masses: (1) can be viewed as a compact repackaging of other physics, such as momentum dependent potentials, and (2) are required for discussing reactions as well as structure. Examples of the latter (for reactions) stem from the fact that the spacing of single-particle levels near the Fermi surface affects the many-body density of states (ω).

3.4 Near-Barrier Reaction Mechanisms

The study of nuclear reaction mechanisms has revealed a breadth of phenomena that have subsequently stimulated advances in related areas of nuclear research, as well as in nuclear

■ Fig. 3.19

Effect of the omega-mass on the refocusing of single-particle levels near the Fermi surface. This focusing is the result of the requirement that the potential be “pushed in” below the Fermi surface and “pulled out” above the Fermi surface in order to reproduce both the position of bound states and the scattering data (from Charity et al. 2007)



applications. The impetus to obtain a quantitative understanding of these phenomena has motivated the development of increasingly sophisticated measurement technologies, described elsewhere in this Handbook. Here, only an overview of the principal reactions of interest to, or being investigated by, nuclear chemists is provided. Additional references can be found in (Cerny 1974; Durand et al. 2001; Benenson et al. 2002).

Nuclear reaction mechanisms can be schematically separated into two general categories: low-energy reactions that are strongly influenced by structure around the Fermi energy and those at much higher energies where elementary nucleon-nucleon collisions become increasingly important. In either case, the correlations existing within the (ground-state) projectile and target can play determinative roles. This is true at low energy (alpha decay informs about alpha-clustering in the low-density surface of heavy nuclei) as well as high energy (where e^- -induced knockout reactions indicate an overwhelming dominance of high relative-momentum n-p pairs.)


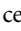
As the model of nuclei composed of nucleons moving independently in a one-body potential is one that is roughly 75% correct, this mean-field approach often provides a rather good initial description of reactions. However, above energies commensurate with the depth of the one-body potential, this potential has little meaning and the best starting point is to consider collisions as sequences of individual nucleon-nucleon collisions. Often a distinction between the *mean-field* and *nucleon-nucleon* (N-N) regimes is made at bombarding energies of about 20 MeV per projectile nucleon (20 MeV/A). Below this energy, individual nucleon-nucleon (N-N) interactions lead to thermalization sufficiently quickly that no individual nucleon has sufficient energy to escape the mean-field potential well. When this has been achieved, a compound nucleus has been formed. As the relative collision energy increases, the

energy dissipation process produces harder N-N collisions with scattered nucleon energies in excess of the mean-field constraints, leading to prompt particle emission. The transition from mean-field to N-N dominance as the bombarding energy increases is a continuous one, mediated by the number of collisions that are not prohibited by the Pauli Principle (*Pauli blocking*). The blocking of 2-body collisions is strong below the Fermi energy, thus leading to surprisingly long mean-free paths at low energy, but weakens as the relative energy per nucleon approaches the Fermi energy.

However, it must also be appreciated that in either regime (mean-field or N-N), the correlations that exist in nuclei can be observed, sometimes as details in the extremes of distributions, other times as an essential ingredient required to explain gross observations, such as the α -particle emission in general.

This section is divided into several parts that focus on the near-barrier domain. The following section addresses N-N dominated reactions. One final comment must be made in an attempt to be forward looking. While the partition of reactions into low and high energy (mean-field dominated or not) has been common in the past, future work must move beyond this mental partition. As mentioned above, due to correlations in the nucleus, the ground state is replete with high-energy nucleons, well above what would be expected from the Fermi-gas model. It is actually this aspect, the correlations that exist in nuclei (for example as a function of n/p asymmetry), that will be the focus of many reaction studies in the future.

3.4.1 Neutron Capture

Recent work at the lowest energies has generated detailed data on (n,x) reactions on nuclei throughout the periodic table. Due to interest in advanced fuel cycles, as well as for possible transmutation of reactor waste, the attention has focused on the actinide elements. (All of these data can be found at the NNDC web site.)  [Figure 3.20](#) shows both fission and capture cross sections over six orders of magnitude in energy for ^{232}Th . The three regions shown schematically in  [Fig. 3.10](#) are clearly seen. The central region is dominated by pronounced resonances, bordered on each side by smoothly varying cross sections. The resonances for heavy nuclei have many-body wave functions, far too complicated to describe. (Only in the lightest nuclei can these resonances be described by simple single-particle excitations.) At higher energy, the number of these many-body resonances is so large per unit energy that they overlap and no experimental resolution would be sufficient to resolve them. At energies lower than the resonance region, one sees capture into the tail of the lowest-lying resonance, but with a probability that increases with the increasing de Broglie wavelength of the neutron (with decreasing energy).

In calculating the capture cross section for the lowest-energy neutrons, it is necessary to consider the energy level width Γ_i and the *natural lifetime* τ_i of resonances. The uncertainty principle gives

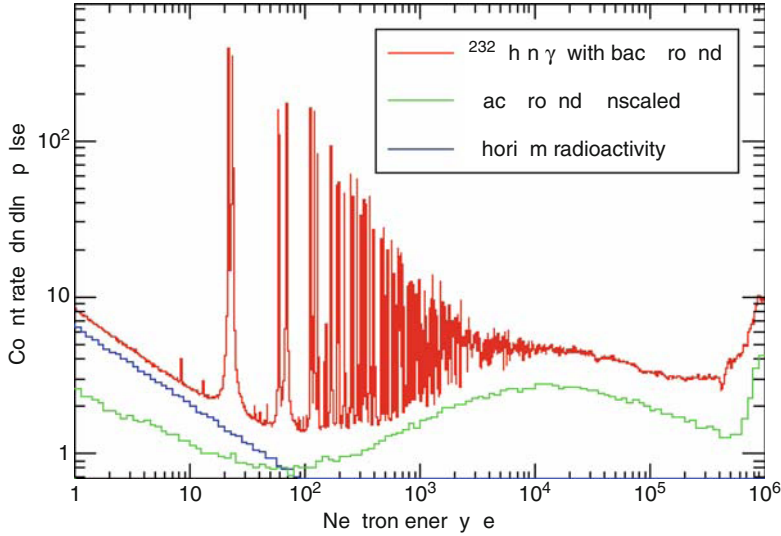
$$\Gamma_i = \hbar/\tau_i, \quad (3.58)$$

i.e., short lifetimes correspond to large level widths. For the general reaction $A + a \rightarrow [\text{CN}] \rightarrow B + b$, the resonance cross section is given by the *Breit–Wigner* form (Breit and Wigner 1936):

$$\sigma(a, b) = \frac{\pi \lambda^2 w(I) \Gamma_a \Gamma_b}{(E_a - E_0)^2 + (\Gamma/2)^2}, \quad (3.59)$$

■ Fig. 3.20

The Th n-capture and fission cross sections from 1 eV to 1 MeV (from Aerts 2006)



where $w(I)$ is a spin factor, a function of the spin of the CN (many-body) state,

$$w(I) = \frac{2I_{\text{CN}} + 1}{(2I_A + 1)(2I_a + 1)}, \quad (3.60)$$

and Γ is the total width composed of the sum of the partial widths $\Gamma = \sum_k \Gamma_k$ (the summation index k includes the exit channel b). E_a is the projectile center-of-mass energy and E_0 is the energy of the resonant state.

At very low energies, comparable to the average thermal energy $(3/2)k_B T \approx 0.025$ eV, (n, γ) is the only open channel. Thus the sum above has only one term, corresponding to gamma-ray emission ($b = \gamma$). These conditions, plus the realization that the neutron capture rate should depend on the velocity v (this is basically a detailed balance argument, more neutrons per unit time will impact the nucleus per unit time at high velocity than low), lead to the following approximations:

$$\begin{aligned} E_a = E_n \approx 0, \quad \text{so that} \quad E_n - E_0 \approx -E_0 \quad \text{and} \\ \Gamma_a = \Gamma_n \propto v_n \Gamma \quad \text{and} \quad \Gamma_b = \Gamma_\gamma = \Gamma. \end{aligned} \quad (3.61)$$

Furthermore, E_0 is a constant close to zero (as the resonance is close to zero energy). Thus the first term in the denominator is small compared to the second and, aside from terms that do not depend strongly on energy, the Breit-Wigner formula – [Eq. \(3.59\)](#) – reduces to a simple $1/v$ dependence,

$$\sigma(n, \gamma) \propto \pi \lambda^2 w(I) \left(\frac{v_n \Gamma \Gamma}{\Gamma^2} \right) \approx \frac{\pi \hbar^2 v_n}{(m v_n)^2} \propto \frac{1}{v_n}. \quad (3.62)$$

That is, for *thermal neutrons*, the lower the energy the higher the cross section.

As the neutron energy increases from thermal to higher energies, the cross section first falls monotonically according to the $1/v$ law. In the vicinity of each resonance state, where $E_n \approx E_0$, sharp spikes are observed in the cross section. When the state density (levels per unit energy) times the mean intrinsic width rises to order one, states are no longer resolved. At this point, the cross section is smoothly varying, of magnitude very roughly equal to the geometric value $\sigma^{\text{geo}} = \pi R^2$.

While the actinide region has achieved much recent attention, (n, γ) reactions throughout the periodic table are important for the analytic tool of neutron activation. Cd is also important for reactor control as the reaction $^{113}\text{Cd}(n, \gamma)$, with $\sigma = 2.0 \times 10^4$ b, is used to control the reactor neutron flux and hence the multiplication factor k in reactor design. The reaction $^{135}\text{Xe}(n, \gamma)$ with $\sigma = 2.6 \times 10^6$ b is a prominent fission-product poison that creates problems in the operation of nuclear reactors by consuming neutrons unproductively.

One of the most important features that can be gleaned from the (n, γ) data mentioned above is the density of states in the excitation energy region near the binding energy of the neutron. Upon capture, a neutron with thermal energy creates a nucleus with $A + 1$ nucleons and $E^* = B_N$. Collecting data from throughout the periodic table has validated the dependences expected for the many-body density of states from the *Fermi-Gas Model*. In this model, which is also needed to calculate the contribution to the heat capacity of the conduction electrons in metals (the component that becomes dominant at very low temperatures), the excitation energy (the thermodynamic internal energy often indicated by U) is proportional to the square of the temperature. The reason for the square rather than the linear dependence in classical gases is that not all the nucleons share in the excitation energy. The number of excited nucleons increases in proportion to T , as does the average energy of each of these (excited) nucleons. The same explanation holds for conduction electrons in metals at very low T .

$$E^* = aT^2. \quad (3.63)$$

As $dU = + SdT - PdV$ and $U = E^*$, the entropy is

$$S = \left(\frac{dE^*}{dT} \right) = 2aT, \quad (3.64)$$

and thus, using the Third Law, $S = k_B \ln \omega(E^*)$, one would expect the density of levels to be roughly

$$\omega^L(E^*) \approx Ce^{2aT} \approx Ce^{2\sqrt{aE^*}}. \quad (3.65)$$

Refer to Huizenga and Moretto (1972) for a general discussion of level densities. Note that the state density ω enumerates each projection of the angular momentum while the level density ω^L does not.

A more careful analysis of a two-component Fermi gas with spin and thermal energy ($U = E^* - E_{\text{rot}}$) yields (Bohr and Mottelson 1969)

$$\omega^L(U) = Ce^{2\sqrt{aU}} / U^2. \quad (3.66)$$

In practical usage the constants a and C are empirically-determined. Only experiments at low E^* , like resonance counting, are sensitive to the prefactor C . Experiments in the region of unresolved states are sensitive only to a relative change in the level density, i.e., $\omega^L(E^* + \Delta) / \omega^L(E^*)$, and thus only the *level density parameter* a can be extracted. It is the parameter a that

relates the excitation energy to the nuclear temperature. This parameter is roughly proportional to A but is reduced near closed shells. For near- ground-state nuclei away from closed shells, the average value is near $a \approx (A/8) \text{ MeV}^{-1}$ (► Fig. 3.21).

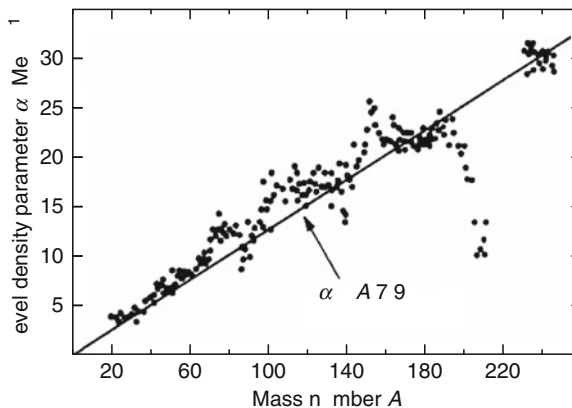
The mass number dependence is what one would expect from “particle-in-a-box logic,” i.e., the larger the box, the greater the number of single-particle levels per unit energy and the greater the number of ways to distribute particles among these levels with a fixed total available energy. However, independent-particle models predict that a should be closer to $(A/12) \text{ MeV}^{-1}$. There are both macroscopic and microscopic explanations for this discrepancy. From a macroscopic view, the nuclear surface, being less dense than the bulk, can accommodate more levels per nucleon. (Lower density, larger volume per particle, larger box, higher density of single-particle states.) This approach was pioneered by Töke and Swiatecki (1981).

These semiclassical formulations for the mass number A and deformation dependence of a are extensively used in statistical decay models. From the microscopic point of view, the augmentation of the density of states at low energy is explained as follows. In a single-particle picture the excitation is “carried” by exciting nucleons to single-particle states (solutions to the one-body potential problem). However, collective rotational bands can be built on any single-particle structure (excitation). Although these states are in principle described in the single-particle picture, they would lie at very high excitation energy in such a model rather than where they really are – low energy. Thus the enhancement in the level density at low energy – the $a \approx (A/8) \text{ MeV}^{-1}$ – can be viewed as a consequence of collective excitations that in a pure single-particle picture belong at very high energy. While the relocation of many-body states from high to low energy greatly increases the ω^L at low energy, it hardly affects the count at high energy as the number of states increases exponentially.

Thus one would expect a to decrease (ω increases, but the rate of increase slows) with excitation. In the last decade this has been confirmed (Shlomo and Natowitz 1990). Modern statistical model calculations (see ► Sect. 3.5) now employ an excitation-energy-dependent a that varies from about $a = (A/7) \text{ MeV}^{-1}$ at low energy to about $a = (A/13) \text{ MeV}^{-1}$ by the time the total excitation energy reaches 100 MeV.

■ Fig. 3.21

Level-density parameter a as a function of mass number. The solid line shows an average fit for $a = (A/7.9) \text{ MeV}^{-1}$ (from Huizenga and Moretto 1972)



3.4.2 Nucleon and Heavy-Ion Elastic Scattering

3.4.2.1 Nucleon Elastic Scattering

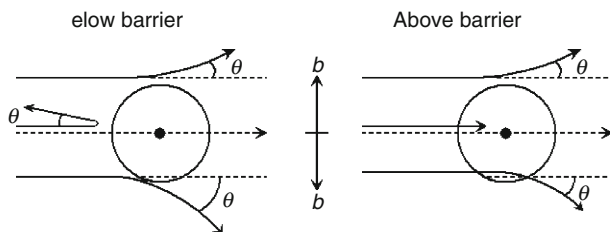
Elastic scattering describes the simplest target-projectile interactions: specifically, those in which the colliding nuclei experience only an angular deflection, but do not change their Z or A composition or their energy state (► Fig. 3.22). For below-barrier projectile energies, the differential cross section for elastic scattering is governed by the Rutherford (Coulomb) scattering equation (► Eq. (3.45)). Rutherford employed this expression to deduce an upper limit to the size of nuclei and, from the angular distribution, the atomic number of the scatterer (Rutherford 1911). This same technique is in common use in analytical surface science work and was notably applied to analyze the elemental composition of lunar samples in situ by observing the scattering of alpha particles emitted from a radioactive source.

Below the Coulomb barrier only elastic and inelastic excitation by Coulomb excitation are likely. Moving above the Coulomb barrier, various inelastic reaction channels compete with each other and with elastic and Coulomb excitation for the partitioning of the income flux. These channels interfere with one another, as do elastic fluxes from near and far-side scattering. ► Figure 3.23 shows all the existing data for nucleon scattering from Ca isotopes. (Shown are the differential cross sections and the analyzing powers. The cited reference also contains spin-rotation data.) Also shown in this figure are the Dispersive Optical Model fits that define the potential, which in turn define the effective masses and occupancies of single-particle states.

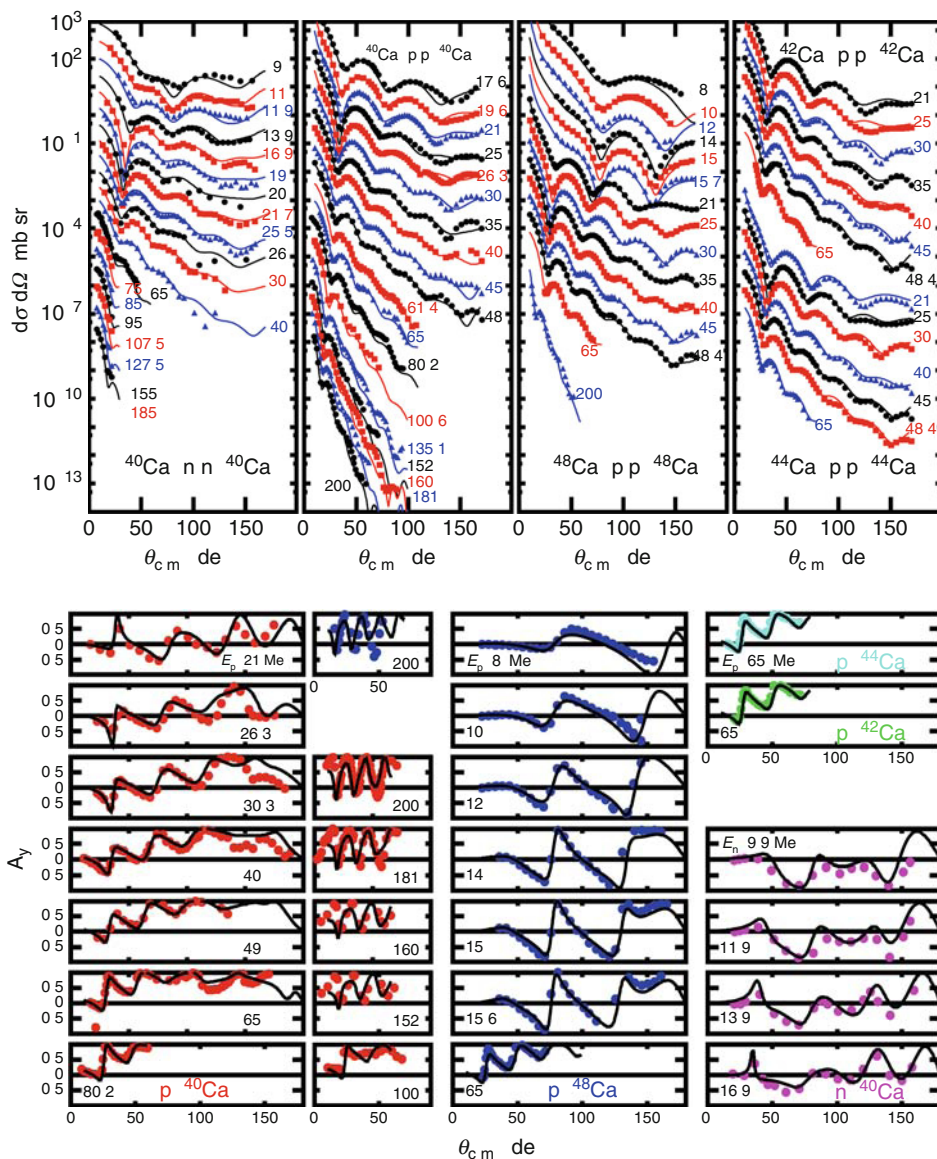
The occupancy of single-particle states was extracted in the 1980s for stable nuclei using $(e,e'p)$ for several nuclei on the line of beta stability. Much recent effort has been spent in attempting to do the same for nuclei off the line of stability and thus extract the asymmetry dependence of spectroscopic factors. Spectroscopic factors expose the deviation from a simple one-body description of the nuclear quantum problem. For example, if removal of a nucleon, from a system with A nucleons and associated quantum numbers, leaves the $A - 1$ system in the ground state, the spectroscopic factor would be unity. However, as the real A (and $A - 1$) systems are strongly correlated, removal of a particle requires a “reorganization” of the others. The spectroscopic factors can be roughly thought of as the fraction of the wave function (of valence particles) that can be described by occupancy of a mean-field quantum solution. Standard shell models predict spectroscopic strength less than one, but such calculations

■ Fig. 3.22

Trajectories of projectiles impinging on a target for reactions below the barrier (*left*), where only elastic scattering occurs and above the barrier (*right*), where the more central trajectories are absorbed. As is seen, nuclear reactions will necessarily decrease the large angle fraction of elastically scattered projectiles



World data set (below 200 MeV) of n and p elastic scattering on Ca isotopes along with DOM fits
(From Charity et al. [2007](#))

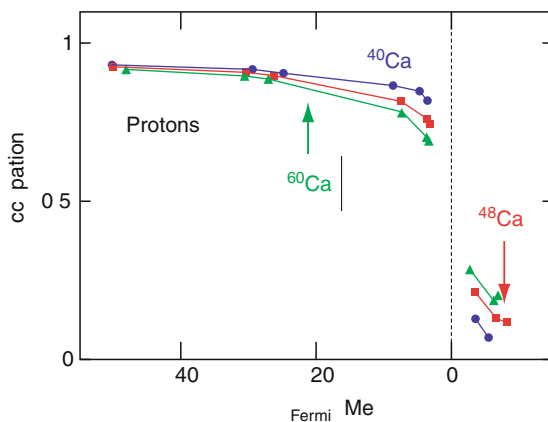


only capture that piece of the correlations contained in the space of the calculation. Particle correlations (for example multiparticle hole strength required to describe the ground state) beyond this very limited space would yield spectroscopic strength with even greater reductions than those predicted by standard shell-model calculations.

Three experimental lines of approach have been used to study the evolution of spectroscopic strength with asymmetry: the dispersive optical model, nucleon knockout reactions, and

■ Fig. 3.24

Proton single-particle occupation probabilities in ^{40}Ca (circles), ^{48}Ca (squares), and ^{60}Ca (triangles) as deduced from a Dispersive Optical Model fit (Charity et al. 2007)



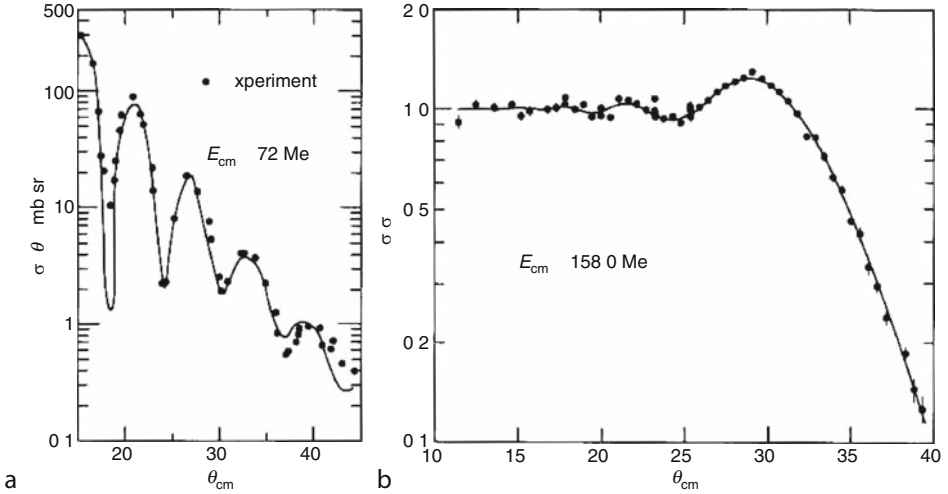
transfer reactions, the latter two projects using secondary beams. The results from these experiments are as follows: there is a general trend that the spectroscopic strength decreases (below the Fermi surface) for the minority (protons in this case) species. That is, for the analysis of the Ca isotopes presented in Fig. 3.23, the proton spectroscopic strength below the Fermi surface decreases in going from ^{40}Ca to ^{48}Ca to ^{60}Ca (^{60}Ca being an extrapolation from the fit), Fig. 3.24. This trend is likely the result of increasing p-n correlations mediated by the tensor force. The same trend is found in nucleon knockout reactions (Gade et al. 2004). However, here the effect mentioned above is found to be much stronger than that found in the DOM analysis. An additional difference is that the knockout work implies that this effect is a function of binding energy (the greater the binding, the greater the correlations), while in the dispersive optical model, the evolution is more subtle, depending on the parity of the levels (of both neutrons and protons) engaging in the correlations. For example, in the DOM case, while the occupancy of single-particle proton states decrease (increase) below (above) the Fermi surface in going from ^{40}Ca to ^{60}Ca ; there is little change in the neutron occupancy over this same range of asymmetry. This latter trend, while in contrast to the knockout results, is in agreement with the transfer studies (Lee et al. 2010). While the elucidation of this trend will be a major focus of research in the coming decade, the present DOM analysis suggests that nucleon correlations increase with the number of possible n-p pairs. (That is, protons become more strongly correlated with increasing neutron number, while neutron correlations do not increase with increasing neutron number.)

3.4.2.2 Heavy-Ion Elastic Scattering

Because of its diffractive nature (Fig. 3.25), elastic scattering measurements provide a useful probe of the nuclear potential near the nuclear surface, thus providing parameters for potential models such as the optical model. Reaction cross sections for reactions induced by heavy ions (HI) can also be determined from elastic scattering experiments (see superscript exp in the

■ Fig. 3.25

Left: Elastic scattering angular distribution for $^{12}\text{C} + ^{16}\text{O}$, illustrating *Fraunhofer scattering* (Hiebert and Garvey 1964). **Right:** ^{16}O ions incident on a ^{208}Pb target, showing a *Fresnel scattering* pattern (Baker and McIntyre 1967). The disappearance of elastic events at large angles is due to the absorption of lower ℓ -waves



following equation), since nuclear reactions preferentially remove elastic events at large scattering angles (low ℓ). Consequently, the ratio of the experimental elastic scattering cross section $d\sigma_{\text{E}}/d\Omega$ to the Rutherford scattering cross section as a function of angle will decrease strongly beyond some critical angle $\theta_{\text{crit}} \sim 30^\circ$ (► Fig. 3.25). The reaction cross section σ_{R} can be estimated from

$$\sigma_{\text{R}} = \int_{\theta_{\text{crit}}}^{\pi} \frac{d\sigma_{\text{Ruth}}}{d\Omega} d\Omega - \int_{\theta_{\text{crit}}}^{\pi} \frac{d\sigma_{\text{el}}^{\text{exp}}}{d\Omega} d\Omega. \quad (3.67)$$

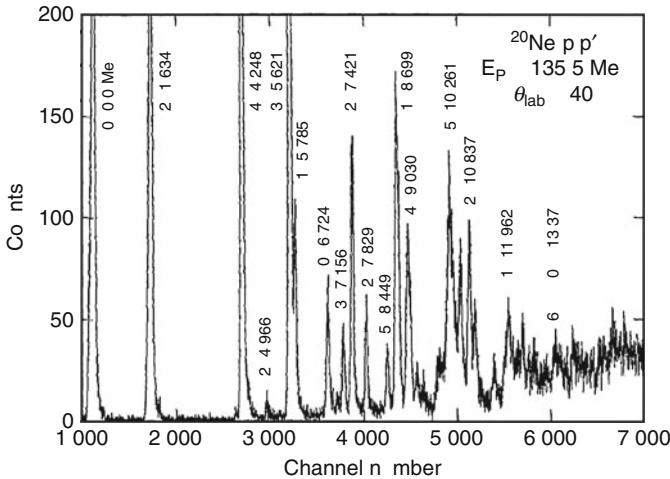
More precise results can be obtained with diffractive models (Frahn 1978), which relate ℓ_{max} to the quarter point (or grazing) angle $\theta_{1/4}$, the angle at which $\sigma_{\text{el}}^{\text{exp}}(\theta)/\sigma_{\text{el}}(\theta) = 0.25$, $\ell_{\text{max}} = \eta \cot(\theta_{1/4}/2)$. The adherence of experiment to the Rutherford values for scattering angles well below $\theta_{1/4}$ makes elastic scattering a valuable technique for cross-section normalizations in heavy-ion reaction studies. The strong Coulomb field for heavy-ion collisions, proportional to $Z_p Z_t$, has important nuclear consequences. Among these are the Coulomb excitation of deformed nuclei to very high rotational levels and the fission of heavy nuclei at relativistic projectile energies.

3.4.3 Inelastic Excitation

Inelastic scattering refers to collisions in which there is a change in the energy state(s) of the target and/or projectile nuclei, but no change in Z and A . Such reactions are useful for

■ Fig. 3.26

Spectrum of protons observed in the $^{20}\text{Ne}(p,p')$ reaction. Elastically scattered protons appear in the 0^+ peak at 0.0 MeV near channel 1,100. Inelastic events populate the excited states of ^{20}Ne (Courtesy of E. J. Stephenson, IUCF)



investigating both the quantal and collective features of nuclear structure. Studies that employ (p,p') and (α,α') reactions are particularly useful for measuring the spins and parities of particle states in stable nuclei. In ▶ Fig. 3.26 the spectrum of protons observed in the $^{20}\text{Ne}(p,p')$ reaction is shown as an example.

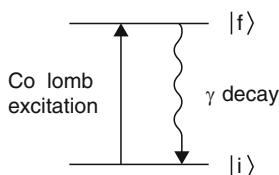
Coulomb excitation is the process by which nuclear excitation occurs without a hard nuclear reaction. Basically, the energy for excitation is extracted from the time-varying Coulomb field as a target and projectile pass one another. This reaction has had a significant rebirth with the availability of fast (>50 MeV/A) heavy-ion beams. The basic process (▶ Fig. 3.27) is strongly energy-dependent (▶ Fig. 3.28) and allows for the extraction of the reduced matrix element for quadrupole excitation (from the probability of exciting the first 2^+ state) as well as studying collective giant resonances. The revival is due to the potential for making these measurements on fast (off β -stability) secondary radioactive beams (Glasmacher 1998).

In the case of the excitation of the first 2^+ state of even-even nuclei, in addition to determination of the energy of this low-lying state, one also measures the reduced matrix element $B(E2)$ from the yield of γ -rays depopulating this state. As the beam energy is increased, the probability for excitation of large-scale collective motion (giant resonances) increases (▶ Fig. 3.28). Fast-beam Coulomb excitation has been a fruitful area of research, because low-intensity secondary beams can be used since cross sections can be significant fractions of a barn. The focus here will be on just one of the interesting findings of this productive research area.

▶ Figure 3.29 shows the energy of the 2_1^+ state for silicon, sulfur, and argon isotopes, $Z = 14, 16, 18$, respectively. (The trailing subscript is used to indicate which level of a specific spin and parity to which one is referring. Thus 0_2^+ is the second 0^+ state in that nucleus.) First, focus on the behavior at $N = 20$. The relatively high energy of the 2_1^+ state in Si and S indicates that $N = 20$ is in fact magic for the corresponding proton numbers. Shifting the focus to the

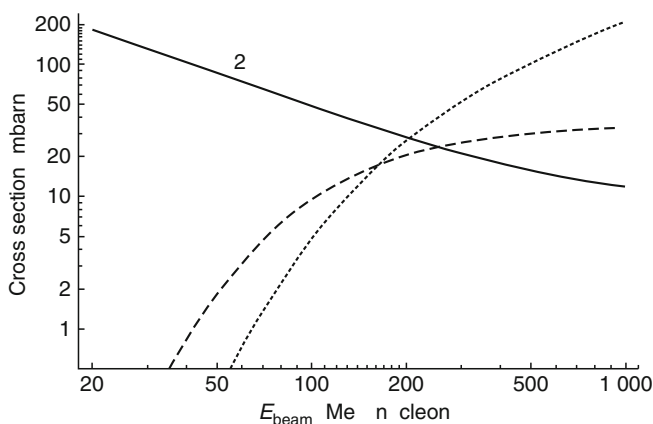
■ Fig. 3.27

Schematic picture of the first-order Coulomb excitation of a nucleus from an initial state to a final bound state and its subsequent γ -decay



■ Fig. 3.28

Calculated cross sections for Coulomb excitation of ^{40}S in the first excited state (2^+), the giant dipole resonance (GDR), and the giant quadrupole resonance (GQR) in ^{40}S using a ^{40}S beam incident on Au, versus the beam energy. The calculation assumes a minimum impact parameter of 16 fm (From Glasmacher 1998)



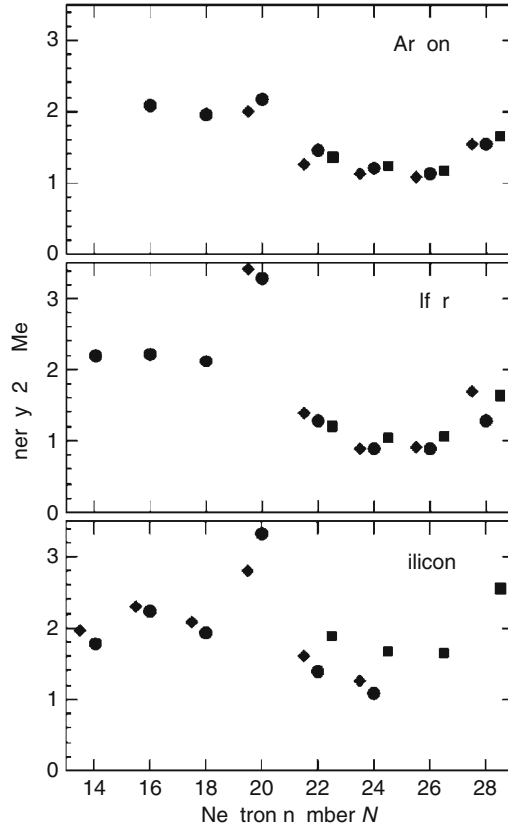
region of $N = 28$, one finds that the same cannot be said, i.e., $N = 28$ is seemingly not magic for these very neutron-rich species. The $B(E2)$ values support this assertion. This loss of “magicity” to the “South-East” of stability on the chart of the nuclides is called the “island of inversion.” More generally, it has been appreciated that the values, or strengths, of the “magic” numbers can change with unusual n/p ratios. This shifting magicity can have universal consequences. For example, it has been postulated that the inversion region mentioned above determines the $^{48}\text{Ca}/^{46}\text{Ca}$ abundance ratio in Nature (Sorlin et al. 1993).

Inelastic excitation via α -particles (i.e., α, α') has provided the bulk of the data on the highly collective giant monopole resonance, often called the “breathing mode.” Data of this type (► Fig. 3.30) have been used to extract the nuclear incompressibility of finite nuclei, and with the aid of models, the incompressibility of symmetric matter (see ► Sect. 3.7).

With greater overlap of the two nuclear potentials, additional channels open up that permit transfer of one or more nucleons, or *direct reactions* (Austern 1970). Classic examples of direct reactions are one-nucleon transfer, or stripping, and pickup reactions. *Stripping* is the transfer of a single nucleon from the projectile to the target, for example a (d,p) reaction. *Pickup* is the

■ Fig. 3.29

Excitation energies of the first excited 2^+ states in argon, sulfur, and silicon plotted versus the neutron number N . Measured values (*solid circles*) are compared to shell-model calculations with a full and a truncated set basis states



reverse reaction, i.e., transfer of a nucleon from target to projectile, as in a (p,d) reaction. At low beam energies, the higher probability for neutron transfer relative to proton transfer demonstrates the charge polarizability that the colliding nuclei experience as they approach one another. This is shown schematically in [Fig. 3.31](#).

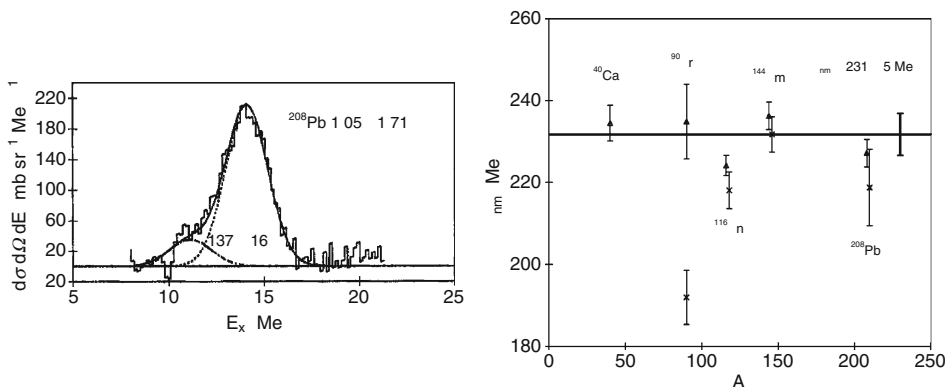
Direct reactions need not be simple one-step processes. The likelihood of a one-step process improves if the momentum transfer q is close to the angular momentum of the transferred nucleon divided by the nuclear radius at which the transfer occurs,

$$q \equiv |\mathbf{k}_{\text{in}} - \mathbf{k}_{\text{out}}| \approx \ell/R. \quad (3.68)$$

If this matching condition is satisfied, the cross sections can be compared to one-step reaction models, such as the Distorted-Wave Born Approximation (DWBA), from which spectroscopic information can be extracted. The common DWBA codes are DWUCK and PTOLEMY.

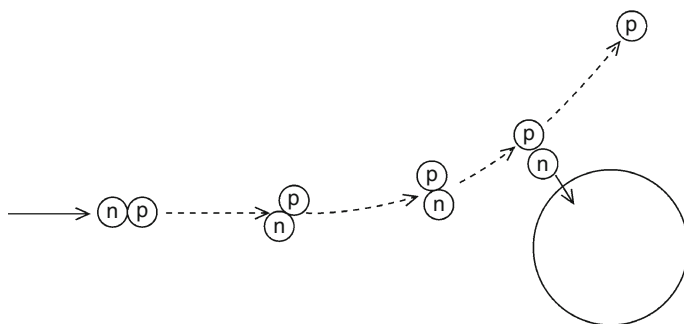
■ Fig. 3.30

Left: Spectra for the giant monopole and isoscalar dipole resonances obtained in (α, α') measurements and **right:** The extracted nuclear matter (nm) incompressibility constant K_{nm} (Figure courtesy, P. H. Youngblood, Texas A&M University)



■ Fig. 3.31

Schematic diagram of a (d, p) transfer reaction. Notice that the deuteron is polarized due to mutual Coulomb repulsion with the target. For a (p, d) pick-up reaction the arrows should be reversed



Stripping and pickup studies with heavy radioactive (secondary) beams on light targets are beginning to provide structure data on nuclei far-removed from stability. Furthermore, since the (d, p) reaction is the analog of neutron capture (n, γ) , it provides an important surrogate pathway for studying nuclear mass buildup in r -process nucleosynthesis (see ▶ Chap. 12 in Vol. 2). Using the $d({}^A_Z X, {}^{A+1}_Z X)p$ reaction, reverse kinematics reactions with beams of neutron-rich radioactive nuclei make it possible to study the structure and neutron-capture probabilities of nuclei nearer the *neutron-drip line* (neutron separation energy near zero).

A similar tool that is useful for studying mirror nuclei and isobaric analog states is the *charge-transfer reaction* of the type (p, n) or (n, p) , the nuclear reaction equivalent of beta-decay. *Mirror nuclei* are pairs of isobars that can be interconverted by exchanging a neutron and a proton, e.g., ${}^{15}_7\text{N}_8$ and ${}^{15}_8\text{O}_7$. An *isobaric analog state* of nucleus ${}^A_Z X_N$ is also a state in the

nucleus for which nucleonic wave functions are the same, as are the masses after correction for the Coulomb energy and the neutron-proton mass difference. One practical application of this process has been the measurement of the $^{37}\text{Cl}(p,n)^{37}\text{Ar}$ and $^{71}\text{Ga}(p,n)^{71}\text{Ge}$ cross sections that are related to understanding measurements of the *flux of solar neutrinos* (Bowles and Gavron 1993).

Numerous theoretical models have been employed in the analysis of direct reactions at low energies. Among the most prominent of these is the coupled-channels approach, which incorporates the quantum structure of the colliding nucleus and its product (Tamura 1965; Dasso and Landowne 1987). The coupled channels can be either inelastic or transfer modes. The coupled-channels model has proven to be among the most successful approaches for obtaining quantitative understanding of direct-reaction probabilities. In addition, it has served as a valuable guide in the interpretation of subbarrier fusion reactions (Broglia et al. 1983).

In heavy-ion reactions, the more general term *quasielastic scattering* is frequently applied to reactions at the nuclear surface. This more inclusive definition covers not only the above mechanisms, but also multiple-nucleon-transfer reactions. In these events, two or more nucleons may be transferred, producing a more diverse array of reaction products. The multiple-nucleon-transfer mechanism can produce nuclei relatively far away from the line of beta stability. Consider the example,



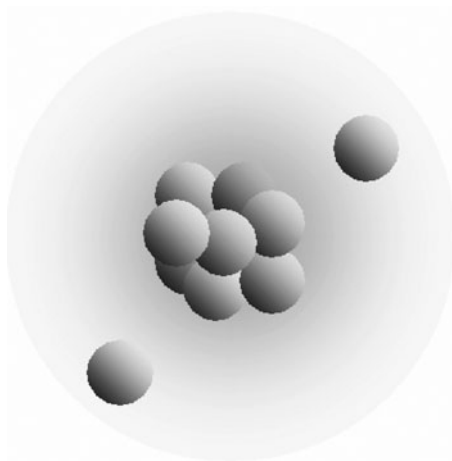
in which four neutrons are transferred from ^{48}Ca to ^{64}Zn and one proton is transferred in the reverse direction. While quantum and collective structure effects play an important role in inelastic scattering and few-nucleon transfer reactions, the primary products may also be formed with significant excitation energies. If the excitation energy exceeds particle binding energies, then secondary decay via statistical emission alters the primary exit channel nucleus.

3.4.4 Nucleon Knockout Reactions

Nucleon knockout reactions have also been the focus of considerable recent effort (both knockout and Coulomb excitation are dealt with in Gade et al. 2004 and Gade and Glasmacher 2008). One famous example of the power of nucleon knockout reactions using secondary beams is that of ^{11}Li , an extremely neutron-rich nucleus. It is thought to have a neutron halo, which would explain its large reaction cross section (Tanihata et al. 1985, [Fig. 3.32](#)). With a half-life of 8.7 ms, ^{11}Li can be produced by fragmentation of a heavier species (usually ^{18}O), separated in flight from other fragmentation products and made into an almost pure beam. Directing this beam toward a second target, a secondary reaction measurement can be performed. Neutron knockout from ^{11}Li forms ^{10}Li , which has no bound states so that the ultimate exit channel is $^9\text{Li} + 2n$. Detecting the ^9Li and a neutron allows for the reconstruction of the ^{10}Li momentum distribution after the knockout of the first neutron, [Fig. 3.33](#). If the target is a spectator, the ^{10}Li momentum distribution is the complement of the momentum distribution of the removed nucleon. Thus, with the caveats concerning the reaction mechanism, the knockout reaction is a measure of the momentum wave function (as opposed to the more standard position representation) of one of the loosely bound nucleons. These data suggest that these valence neutrons are a mixture of $2s_{1/2}$ and $1p_{1/2}$ components. Note that the higher the ℓ value, the broader the (linear) momentum distribution. The admixture of the second s state might seem surprising, as this level usually does not start filling until $N = 14$.

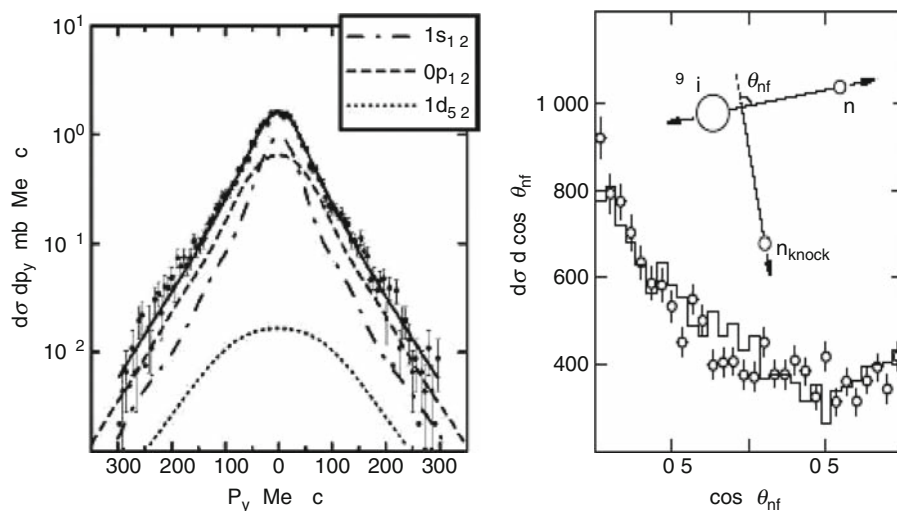
■ Fig. 3.32

Schematic view of the ^{11}Li nucleus, in which the two valence neutrons are in orbits much larger than the ^9Li core (Tanihata et al. 1985)



■ Fig. 3.33

Left: ^{10}Li residue momentum distributions measured following neutron removal from ^{11}Li on ^{12}C at 287 MeV/A. Right: Angular correlations of the decay neutrons measured relative to an axis defined by the ^{10}Li recoil direction as shown in the inset. The points are the experimental data and the histogram is a reconstruction corrected for experimental resolution and acceptance effects. Note the strong forward-backward asymmetry, which reflects interference of the $\ell = 0$ and 1 final states



Its contribution for $N = 8$ (in ^{11}Li) is thought to be a consequence of the tensor interaction between neutrons and protons (Myo et al. 2007).

Knockout reactions, such as (p, α) , (γ, α) , and $(e, e'\alpha)$ in even $N = Z$ (alpha particle) nuclei are also especially important as they provide evidence for *alpha particle clustering* in nuclei. At low energies, such reactions, for example, $^{19}\text{F}(p, \alpha)^{16}\text{O}$ and $^{28}\text{Si}(\gamma, \alpha)^{24}\text{Mg}$, which reduce the mass of the heavy partner, are important competitors to the synthesis pathways leading to the formation of elements just below ^{56}Fe in nova bursts.

3.4.5 Mean-Field-Dominated HI Reactions

3.4.5.1 Impact Parameter Dictates the Reaction Channel

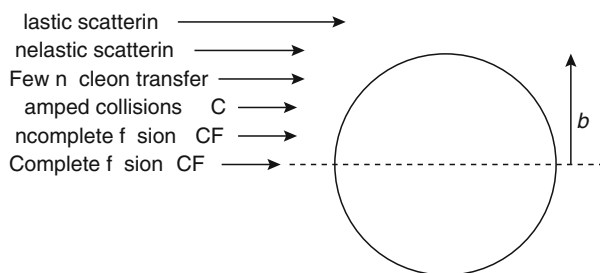
Nuclear chemists have been particularly active in the study of reactions between heavy ions (HI) and heavy nuclei. The interest can be traced to the fact that all heavy elements with $Z > 101$ have been made with HI fusion–evaporation reactions (Loveland 2007). With increasing mass, the distinct quantal features become less important. Classical or quasiclassical reaction models become reasonable when the de Broglie wavelength becomes significantly smaller than nuclear dimensions. However, this condition is not satisfied in HI reactions with energies just exceeding the Coulomb barriers. Thus, quantal descriptions via a Time-Dependent Hartree-Fock (TDHF) approach (Bonche et al. 1976) or some form of quantum molecular dynamics (Feldmeier and Schnack 2000) are needed. In practice, semiclassical methods are usually invoked to describe the range of mechanisms observed at bombarding energies near the Coulomb barrier.

As the energy is increased well above the Coulomb barrier, classical concepts become more applicable and a partition of the impact-parameter space into different reaction types becomes reasonable. ▶ [Figures 3.34](#) and ▶ [3.35](#) illustrate the approximate relationship between reaction mechanism and impact parameter b , or ℓ -wave, for collisions between two complex nuclei at energies of more than a few MeV/A above the barrier.

The classification scheme in ▶ [Fig. 3.35](#) becomes simplified for lighter projectiles, for which fusion and simple surface reactions are the principal exit channels at low relative bombarding energies. For very heavy projectiles, the *damped-collision* (*deep-inelastic*)

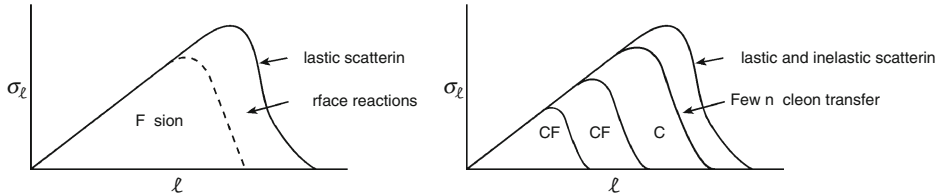
■ [Fig. 3.34](#)

Reaction mechanisms classified schematically according to relative impact parameter b (ℓ -wave). Large values of b are classified as peripheral collisions and small values as central collisions



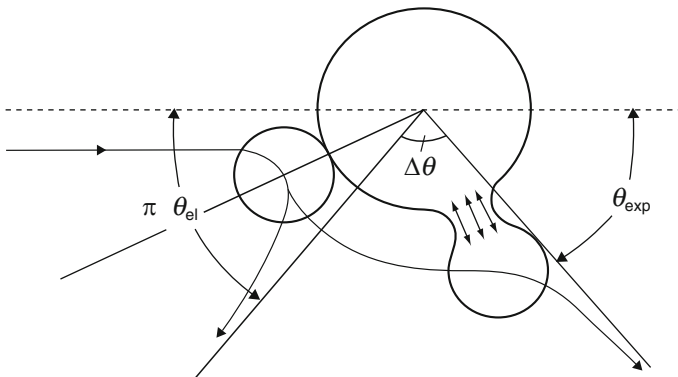
■ Fig. 3.35

Distribution of partial cross sections σ_ℓ as a function of angular momentum quantum number ℓ , decomposed according to reaction mechanism. Left panel is for light-ion-induced reactions (H, He) and right panel for heavy-ion reactions



■ Fig. 3.36

Illustration of a damped (deep inelastic) collision. The projectile trajectory is shown by the heavy curve and the extension of the original Coulomb-scattering trajectory by dashed lines. During the rotation angle of the dinuclear complex, $\Delta\theta = \theta_{el} - \theta_{exp}$, a neck is formed between the reacting species, through which nucleon exchange and energy dissipation proceed



mechanism is dominant as the mutual Coulomb field between the colliding particles becomes very large and inhibits fusion.

In the following subsections, the various mechanisms are discussed in order of decreasing impact parameter, beginning with elastic scattering and finishing with complete fusion.

3.4.5.2 Surface Reactions: Inelastic Scattering and Nucleon Transfer

For impact parameters with trajectories that scatter near the grazing angle, the separation between the colliding nuclei becomes sufficiently small that they begin to sample the attractive component of the nuclear potential. Reactions can then occur at the nuclear surface (leading to two-body final states) that proceed on a time scale comparable to the nuclear transit time. Interactions in this category usually involve excitation of low-lying modes in one or both of the colliding species and are particularly valuable for studying nuclear structure. Experimentally,

reactions at the nuclear surface are distinguished by: (1) angular distributions that peak in the forward direction or near the grazing angle, and (2) distinct spectral peaks, corresponding to energy states in the product nuclei.

3.4.5.3 Damped Collisions

At intermediate impact parameters, the nuclear overlap between target and projectile nuclei becomes sufficiently strong that the nuclear force may compete favorably with the repulsive Coulomb and centrifugal forces. When these competing forces approximately balance one another, it is possible to create short-lived dinuclear complexes, or “*nuclear molecules*” (► Fig. 3.36). These temporal species survive long enough to undergo a partial rotation and significant energy dissipation before undergoing binary breakup. Based on this behavior, these reactions are classified as *damped* or *dissipative* collisions, DC. The importance of the damped-collision mechanism relative to the total reaction cross section depends on the charge product $Z_p Z_t$. If the nuclear charge product is small, the DC cross section is also small. For collisions between very heavy nuclei, damped collisions may consume nearly the entire nuclear reaction cross section (Schröder and Huizenga 1977; Töke and Schröder 1992). While other processes become significant with increasing energy, for collisions between the heaviest nuclei, the bulk of the reaction cross section remains of this dissipative type up to several tens of MeV/A (Baldwin et al. 1995).

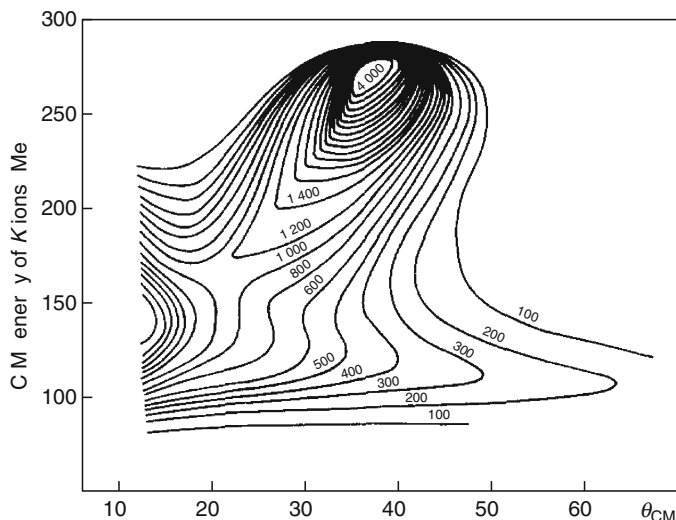
During the contact time, a neck forms between the reacting nuclei, through which statistical diffusion of neutrons and protons occurs in both directions (Planeta et al. 1990). It is this nucleon-exchange process that mediates the dissipation of radial kinetic energy into internal excitation energy. At the same time, extensive nucleon diffusion generates a broad distribution in both charge and mass around the projectile and target values. Thus the distinction between damped collisions and fission is that the product charge and mass distributions are concentrated near those of the projectile and target in the former case, but which for the latter are symmetric, near the total charge and mass divided by two (for all but the lowest excitation energies).

The angular and energy-damping features of the damped-collision mechanism are best illustrated by means of a Wilczynski plot (Wilczynski et al. 1973), shown in ► Fig. 3.37. This type of plot summarizes the probability for observing a projectile-like fragment in the $^{40}\text{Ar} + ^{232}\text{Th}$ reaction as a function of scattering angle and total kinetic energy. Here the most energetic nonelastic fragments form a peak near the grazing angle, as mentioned in ► Sect. 3.4.5.1. As the energy damping increases, a ridge of events develops near the grazing angle, corresponding to quasi-elastic surface reactions. The broad band that appears for the largest kinetic energies defines the damped collision events. The kinetic energies of the fully damped fragments are consistent with fission fragment kinetic energy systematics (Viola et al. 1985). However, the damped-collision angular distribution is peaked near the grazing angle, unlike fission, which is symmetric about 90° in the center-of-mass system.

Theoretical calculations indicate that the rotation angle $\Delta\theta$ (► Fig. 3.36) depends on the impact parameter. Smaller impact parameters lead to greater target and projectile overlap and thus longer rotation times, enhancing the degree of nucleon transfer and energy dissipation. Analysis of the data suggests that for fully damped events, the rotation time is about 10^{-22} s. The dissipated energy appears in the product nuclei as excitation energy. The frictional forces during contact also impart sizeable angular momenta to the primary fragments. These excited,

■ Fig. 3.37

Double-differential cross section (indicated on plot); contours $d\sigma^2/d\Omega dE$ for the 10MeV/A and $^{40}\text{Ar} + ^{232}\text{Th}$ reaction plotted versus scattering angle and kinetic energy of projectile-like fragment (Wilczynski et al. 1973). The grazing angle is near 40° in this reaction



high-spin product nuclei subsequently cool by secondary particle emission to form the observed fragment Z and A distributions.

Because of the statistical nature of nucleon exchange, the nuclide distribution of the products extends over a very broad range of projectile-like and target-like fragments. This has made possible the identification of a large number of exotic nuclei that have significantly expanded knowledge of nuclear properties. By utilizing similar reactions at higher projectile energies (► Fig. 3.38), it becomes possible to create beams of radioactive nuclei for further exploration of important problems in nuclear reactions, structure, and nuclear astrophysics.

In order to explain the dissipation of large amounts of relative kinetic energy into internal excitation and shape degrees of freedom, microscopic transport theories based on statistical nucleon exchange have proven to be of broadest utility. Based upon a master-equation approach (Nörenberg et al. 1974, 1976; Randrup 1978), the macroscopic variables are accounted for qualitatively via a Fokker–Planck equation in which a drift coefficient describes the net flow of nucleons across the target-projectile interface and a diffusion coefficient that accounts for nuclear friction effects.

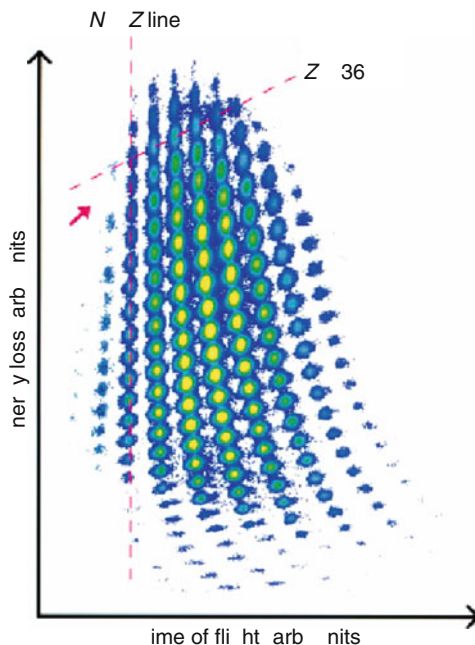
3.4.5.4 Composite-Nucleus Formation

Total amalgamation of target and projectile corresponds to *complete fusion* (CF). If the composite completely samples the mononuclear phase space, a compound nucleus (CN) is formed.

If the barrier is robust, as it is for HI fusion, Wentzel–Kramers–Brillouin (WKB) logic can be used to generate the transmission coefficient (Gamow penetration factor) as a function of the energy of relative motion ε (as it is for spontaneous alpha-decay),

■ Fig. 3.38

Distribution of nuclides produced in the 75 MeV/A $^{78}\text{Kr} + ^{58}\text{Ni}$ reaction. Atomic number increases along the vertical axis and mass number along the horizontal axis (From Pfaff et al. 1996)



$$T_{\ell}(\varepsilon) = \exp \left\{ -\frac{2}{\hbar c} \int_{R_{\text{in}}}^{R_{\text{out}}} \sqrt{2\mu c^2 [V(r) - \varepsilon]} dr \right\} \approx \exp \left\{ -\frac{2\pi}{\hbar \omega} \left[V_C - \varepsilon + \frac{\ell(\ell+1)\hbar^2}{2\mu R_B^2} \right] \right\}. \quad (3.70)$$

Here ε is the energy of relative motion. In the first expression, the general WKB result is given in terms of the real potential $V(r)$ and the classical inner and outer turning points, R_{in} and R_{out} , respectively. The second quantity gives the result if the potential is approximated by an inverted harmonic-oscillator potential of frequency ω . R_B is the intranuclear separation distance at the peak of the barrier.)

From the expression for the transmission coefficient T_{ℓ} it is seen that for sufficiently high angular momenta, the Coulomb plus centrifugal terms may exceed the available beam energy, leading to an upper limit to the angular momentum, ℓ_{max} , that can contribute to fusion (Bass 1974). For slightly higher ℓ -waves this limitation may produce *incomplete fusion* reactions in which only a part of the projectile is captured by the target.

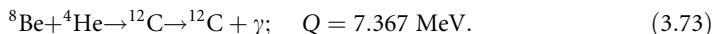
For heavy-ion reactions below the average ℓ -value, fusion saturates as the energy is lowered yielding a transmission coefficient T_{ℓ} and cross section nearly independent of ℓ (Vandenbosch 1992). In this case, the fusion cross section with a center-of-mass energy E , reduces to

$$\sigma_{\text{CF}} = \frac{R_B^2 \hbar \omega}{2E} \exp \left[-\frac{2\pi}{\hbar \omega} (V_C - E) \right]. \quad (3.71)$$

This expression, which predicts an asymptotic slope in energy of $\ln[E\sigma(E)] = 2\pi/\hbar\omega$, describes fusion excitation functions at low energy quite well. For deformed nuclei, R_B will depend on the relative orientation of the colliding pair, resulting in a distribution of effective fusion barriers. As a result, not only is it possible to observe fusion below the mean fusion barrier, but it is also possible to obtain information of the effective distribution of barriers contributing to fusion (Dasgupta et al. 1998). At subbarrier energies, coupling to inelastic channels can be considered as a “doorway” to fusion and thus coupling of such channels to the entrance channel can also be an important consideration (Brogia et al. 1983).

In some heavy-ion reactions a small fraction of the projectile mass may escape capture and proceed forward with the beam momentum. These reactions are called *incomplete fusion* (ICF) or *massive transfer*. The result of such incomplete fusion is, aside from the uncaptured fragment, an excited nucleus that is fully internally equilibrated and thus its decay is suitably treated by statistical models of compound nucleus decay, the subject dealt with in the next major section.

A special case of CN formation occurs when the capture proceeds through an isolated resonance reaction. Such reactions are also of fundamental importance to the nucleosynthesis pathways that form the elements beyond helium (see [Chap. 12](#) in Vol. 2). The classic example here is the $3\alpha \rightarrow {}^{12}\text{C}$ reaction



There are only three levels of ${}^{12}\text{C}$ below $E^* = 10 \text{ MeV}$. One of these levels occurs at 7.654 MeV, just above the Q -value for the ${}^8\text{Be}(\alpha, \gamma)$ reaction (also a resonance reaction). This level was predicted by F. Hoyle before it was observed, based on the fact that C (and life) exists. It is the resonance with this state that magnifies the $3\alpha \rightarrow {}^{12}\text{C}$ cross section and provides the gateway to synthesis of heavier elements. More detailed discussions of resonance and neutron-capture reactions in astrophysics can be found in (Rolfs and Rodney 1988).

The two major decay modes of CN are light-particle emission and fission. The modeling of these decay modes is treated in the next section. In closing this section, it is pointed out that the spectra of light particles (of energy ε and type τ emitted from a CN $P(\varepsilon_\tau)$) is Maxwell–Boltzmann (like) in form, up-shifted in energy by a Coulomb barrier height (B_C) if the ejectile is charged,

$$P(\varepsilon_\tau) \propto \varepsilon_\tau^x e^{-(\varepsilon_\tau - B_C)/T}. \quad (3.74)$$

The variable power x on the exponential prefactor (which determines the spectral rise at low energy) arises from: (a) statistical shape variations which affect the actual barriers, (b) a mixture of “volume” and “surface” emission, (c) the emission of more complex nuclei that subsequently decay into the channel of interest, and (d) quantum penetration. The first factor is the most important, and thus in fitting spectra, often a distribution of B_C values is required.

3.5 Statistical Decay

3.5.1 Preliminaries

Standard statistical-model treatments of compound nucleus decay are predicated on a time-scale separation between the formation of the CN and the time scales for simple (mostly single-particle) decay modes, as well as the massively collective decay process of fission. With

this decoupling of the entrance channel from the exit channel (except for conserved quantities), the CN decays statistically; that is, the decay samples all the phase space allowed by conservation laws (Ericson et al. 1963). The problem is always the identification and quantification of this phase space. As almost all reactions proceed through binary or sequences of binary steps, the rates of decays will be determined by the critical configurations of a binary nature. (The case of multifragmentation is thought to be an exception to this statement: see the end of this section and Sect. 3.7.5.)

There have been two successful approaches to this quantification: the Hauser–Feshbach (HF) and the transition-state (TS) treatments. The former was historically used to treat light-particle emission and the latter to treat fission. Modern codes have extended HF to treat ejectiles as heavy as carbon and with the aid of calculations of conditional barriers, transition-state theory has been used to treat binary divisions with mass asymmetry in the decay channel as a continuous variable.

3.5.2 The Hauser–Feshbach Treatment of Particle Emission

The logic employed in the HF treatment (Hauser and Feshbach 1952), as well as the earlier WE treatment (Weisskopf and Ewing 1940) the which lacks proper consideration of angular momentum coupling, is that the one-way decay rate would be equal to the reverse rate if true reactant-product equilibrium were attained. The one way, state-to-state probability for a fixed ℓ -value and energy is readily given by the transmission through the optical model potential, $T(\varepsilon)$. This rate would be equal, by microscopic reversibility (mechanics is time-reversal invariant), to the outgoing state-to-state probability. Thus an observable rate is simply the microscopic (state-to-state) rate times the density of final states. The latter reflects the number of possible final microstates within an experimental window. This window is naturally quantized by angular momentum and is quantized in energy either by the discrete structure of the quantum system or, at modest excitation energy, by the number of overlapping states in an energy bite determined by an experimental energy resolution, i.e., ωdE , where ω is the state density.

While the forward and backward rates would be equal and thus cancel, giving no net rate in an imagined equilibrium, in the kinetic process the net-rate (unconfined to a box and thus with no backward rate) is equal to the outgoing one-way rate. Thus the rate of emission of nucleons or clusters in any specified state from an initial parent level of excitation energy E_i and spin J_i is the result of a sum over the product intrinsic state-to-state rates and final-state level densities, where the sum is over: (a) the possible ℓ -values (inner sum Eq. (3.76)) and (b) the so called “channel spin” $S = j + s$, where j and s are the intrinsic spin of the residual and ejectile spin (outer sum). With consideration of the possible spin combinations, the HF equation for the emission rate $R_{i \rightarrow f}$ of a particle of type τ energy ε_τ and separation energy S_τ , in terms of the inverse cross section $\sigma_{f \rightarrow i}$ and the density of levels of the parent_{*i*} and the daughter_{*f*} is,

$$R_{i \rightarrow f}(E_i, J_i \rightarrow j, s) dE = \frac{2\lambda^2}{h} \sigma_{f \rightarrow i}(E_i, J_i) \left(\frac{(2s+1)(2j+1)}{(2J_i+1)} \right) \left(\frac{\omega_f^L(E_f, j)}{\omega_i^L(E_i, J_i)} \right), \quad (3.75)$$

with

$$\sigma_{f \rightarrow i}(E_i, J_i) = \pi \lambda^2 \sum_{S=|j-s|}^{S=j+s} \sum_{\ell=|J_i-S|}^{\ell=J_i+S} \left(\frac{2J_i+1}{(2s+1)(2j+1)} \right) T_\ell^\tau(\varepsilon), \quad (3.76)$$

and

$$E_f = E_i - S_\tau - \varepsilon_\tau. \quad (3.77)$$

In order to execute this logic, the following must be known: (1) the ejectile spin, mass, and separation energy and (2) the density of levels (as a function of excitation and angular momentum) of the parent (i) and daughter (f). As the latter has lower mass (and perhaps charge), as well as excitation energy, its level density will be smaller than that of the parent.

Monte Carlo codes are available that execute this logic event-wise, removing energy in each step until particle emission can no longer occur. Some codes seamlessly switch to gamma emission until all products are in their ground states. Since the HF equations treat ejectiles as objects with only one quantum option (there is no ejectile density of final levels), each level in a complex ejectile must be treated as a separate channel. Some modern codes (e.g., GEMINI) have used this logic to treat complex ejectiles (level by level) as heavy as C isotopes (Charity et al. 2001). Such codes are indispensable for calculating decays initiated by the low-energy accelerators located in hospitals for isotope production, for evaluating concepts for transmutation of nuclear reactor waste, and as afterburners for treating the statistical decay that invariably results after fast (nonstatistical) processes originating in high-energy collisions, including those initiated by cosmic rays.

3.5.3 The Transition-State Treatment of CN Decay

In the 1930s Eyring, Polanyi, and Wigner developed transition state (TS) theory, which is a computationally efficient way to compute *classical* reaction rates without integrating trajectories. The main idea is to define a dividing surface that partitions the configuration space into reactant and product sectors and compute the rate from the directional phase-space flux through this surface. One complication (below) is that the dividing surface must be such that it is not recrossed. The transition-state logic was almost immediately applied to fission by Bohr and Wheeler (1939). (See Vandenbosch and Huizenga (1973) or Wagemans (2000) for a detailed presentation of fission data and theory.) In this case, the absolute decay width (at an excitation energy above the ground state $E^* = E - V_{\text{gd.st.}}$) comes from an integral over the density of levels from the point where the energy in the decay channel ε is zero (i.e., maximal energy to be dispersed among the nondecay degrees of freedom and thus maximal level density) to the maximum channel energy (where there is a minimum of energy in the coordinates other than the decay channel),

$$\Gamma_f^{\text{BW}} = \left(\frac{1}{2\pi\omega_{\text{mn}}^{\text{L}}(E^*)} \right) \int_{\varepsilon=0}^{E^*-B_f} \omega_{\text{sp}}^{\text{L}}(E^* - B_f - \varepsilon) d\varepsilon. \quad (3.78)$$

The critical aspect in executing the TS logic is consideration of how the density of levels of the mononuclear (spherical or marginally deformed) parent ($\omega_{\text{mn}}^{\text{L}}$) grows with excitation energy as compared to growth of the density of levels of the highly deformed saddle-point shape ($\omega_{\text{sp}}^{\text{L}}$). The logic employed in statistical model codes is to calculate the level-density parameter via a physical expansion, increasing its value in proportion to the surface area. Following the prescription of Ignatyuk et al. (1975), Reisdorf (1981), and Töke and Swiatecki (1982), the level density parameter a (see Eq. (3.66)) can be written as a physical Liquid Drop Model-like expansion in terms of a deformation parameter q . In such an expansion, one has

constants for the volume c_v and surface c_s contributions, where the latter is multiplied by the surface area at deformation q relative to that of a sphere ($B_s(q)$),

$$a(q) \approx c_v + c_s A^{2/3} B_s(q). \quad (3.79)$$

The complication that the transition state cannot be recrossed was dealt with theoretically by Kramers (1940), where the fission width is reduced relative to the Bohr–Wheeler estimate by saddle recrossing. As the recrossing probability increases with friction, the reduced fission probability can be cast in terms of the friction coefficient γ ,

$$\Gamma_f^{\text{Kram}} = \left[(1 + \gamma^2)^{1/2} - \gamma \right] \Gamma_f^{\text{BW}} \quad (3.80)$$

The importance of this correction is still being debated (McCalla and Lestone 2008). However, it is included in most modern decay codes.

In the early 1980s data on so-called complex fragment (CF) statistical emission became available. Complex fragments are usually defined as those with atomic numbers from three to one half the total mass of the system. The first data, shown in ▶ Fig. 3.39, demonstrated the statistical nature of the emission and were used to extract conditional barriers; that is, barriers that correspond to the minimum energy required to pass from the CN system to an exit channel of fixed mass asymmetry. A general TS theory for treating CF emission was presented by Moretto (1975). This theory exchanges the problem of calculating transmission coefficients (needed for HF) with calculating the barrier and density of levels for the conditional barriers, i.e., barriers with frozen mass asymmetry. As mentioned above, the best modern codes allow for either scheme to be used.

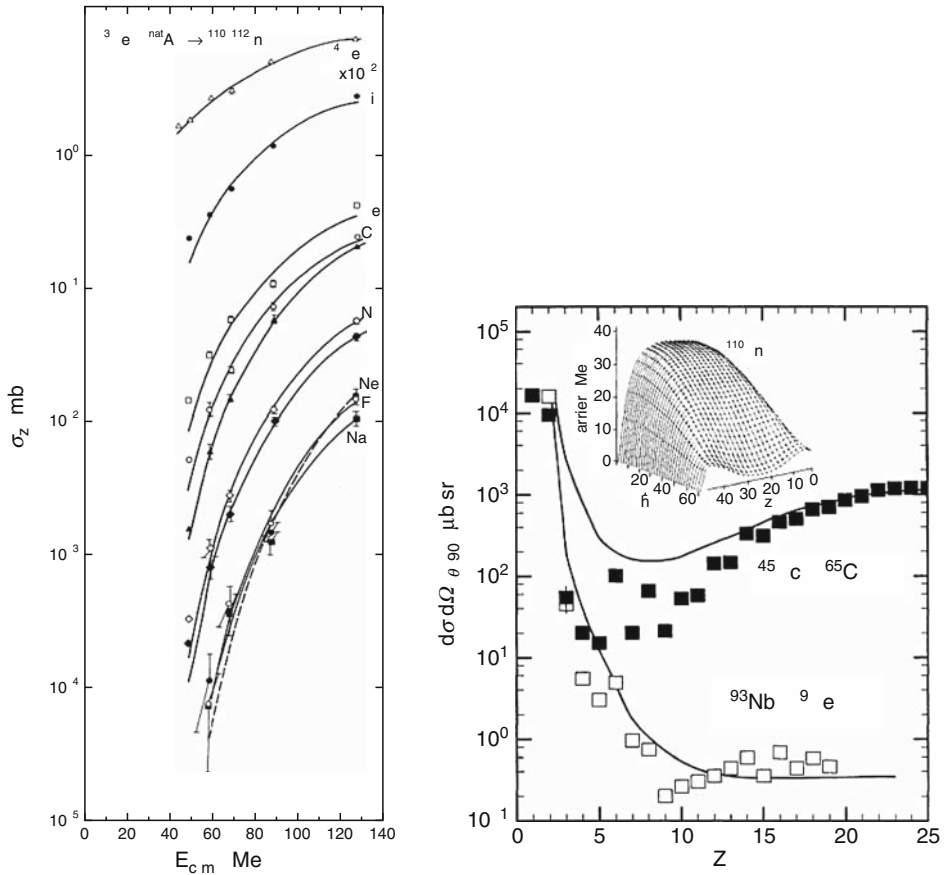
3.5.4 The Density of States of Highly Excited Nuclei

A complete presentation of the issues related to the properties of what are often called “hot nuclei” is given in Shlomo and Kolomietz (2004). One of the assumptions underlying both of the standard treatments is that the reverse process can be considered as capture onto an object that bears significant resemblance to the ground state of the daughter. The macroscopic forward (decay rate) is then just the microscopic rate multiplied by the appropriate density of states. However, at high excitation energy nuclei will expand, with some reduction of the central density and the surface becoming far more extended. This poses two problems. First, the OM might not provide correct transmission coefficients, as the excited objects of relevance have different correlations than those of the ground state. The second problem is that even for uncorrelated fermion systems, the relevant density of states should be for the extended object.

From a schematic model the qualitative effects of expansion are shown in ▶ Fig. 3.40 (Sobotka et al. 2004). Calculations based on realistic effective Hamiltonians (Samaddar et al. 2007, 2008) yield similar results. With increasing excitation energy per nucleon, the equilibrium state (which for an isolated system is that with the maximum entropy) is one with reduced density. This effect increases the level-density parameter (see dotted line in ▶ Fig. 3.40, right hand side). Many-body theory (Prakash et al. 1983) has provided insight into how the effective mass terms evolve with density and excitation energy. In a local-density approximation (i.e., the level density parameter a can be calculated as the sum of contributions from different density regions of a nucleus), the k -mass (m_k , see ▶ Eq. (3.57)) increases from 0.7 to 1 with decreasing density and the peak of the ω -mass (m_ω), at the nuclear surface is removed with excitation energy (see ▶ Sect. 3.3.3). The effect of the k -mass is to suppress a at low excitation but to

■ Fig. 3.39

Left: Excitation functions for complex fragment evaporation from a ^3He -induced reaction (Mcmahan et al. 1987). **Right:** Mass distribution generated from the decay of $A \approx 110$ systems at both low and high angular momenta. The inset shows the finite-ranged Droplet Model conditional-barrier distributions (Sobotka et al. 1987)



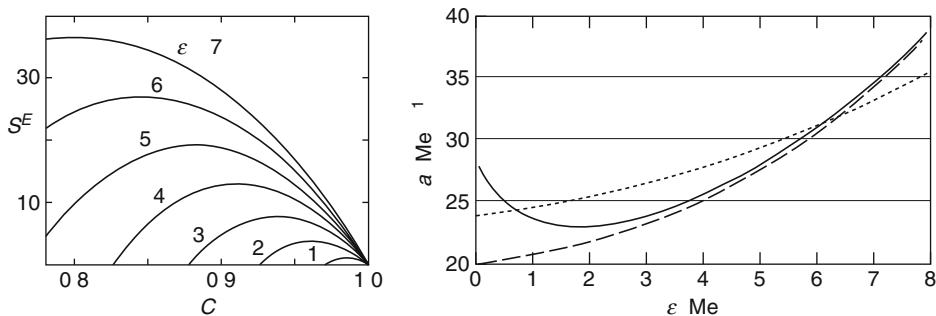
increase it with increasing excitation. This evolution provides positive feedback to expansion, feedback that is active over several MeV/A of excitation. On the other hand, the collapse of the ω -mass at the nuclear surface (which was responsible for increasing a at low excitation) drives a down over the first few MeV/A of excitation energy. The collective effect is a variation of the density of states that yields a “Caloric Curve,” $E^*(T)$, with a pseudo plateau. While not a *phase* transition in the classical sense, these effects represent a transition from a correlated fermion system to one that more closely resembles a hot, but noninteracting Fermi gas.

3.5.5 Thermodynamic Models for Multifragmentation

Multifragmentation is thought to involve a nearly simultaneous breakup of the nucleus into many fragments. This image of the process suggests that the relevant phase space is that

■ Fig. 3.40

Left: The mononuclear excess entropy (above that for a nonexpanded system) as a function of a self-similar expansion coordinate (inverse of scaled radius parameter, i.e., $C = 1$ no expansion), for unit (MeV) steps in the excitation energy per nucleon ϵ . **Right:** The level density parameter with expansion but $m^*/m = 1$ (dotted), considering both expansion and the evolution of m_k (dashed) and expansion with both m_k and m_ω (solid) are shown (Sobotka et al. 2004)



corresponding to any number of fragments in the exit channel (rather than just two as in the HF and TS treatments). Statistical models of this phase space have been generated based on fixed energy and particle number – microcanonical ensemble, Gross (1990) and Bondorf et al. (1985); fixed temperature and particle number – canonical, Das et al. (2005), and fixed temperature and chemical potential – grand-canonical, Randrup and Koonin (1981). As would be expected, such models predict a liquid–gas phase transition for large, uncharged nuclear systems, as discussed in Sect. 3.7. These models do reproduce a considerable amount of data. Having done so, it has been the hope that manifestations of the infinite-system phase transition in a finite system is also represented. To give the flavor of these approaches, the canonical prescription (for one particle type) is presented here.

The first assumption is that the partition function Q is the product of the individual partition functions for the component parts, corrected for indistinguishability,

$$Q_A = \sum \prod_i \frac{1}{n_i!} \left(\frac{V_{\text{free}}}{\Lambda} \right)^{n_i} (q_i)^{n_i}, \quad (3.81)$$

where the sum is over all possible partitions, the product is over the fragments in that partition, n_i is the number of a given fragment type (i) in this partition, q_i is internal partition function for cluster type i , and the factor in parenthesis is the free volume measured in units of the thermal box size

$$\Lambda = \lambda_{\text{th}}^3 = \left[\frac{h}{(2\pi mT)^{1/2}} \right]^3. \quad (3.82)$$

The average number of clusters of type i is

$$\langle n_i \rangle = \left(\frac{V_{\text{free}}}{\Lambda_i} q_i \right) \frac{Q_{A-i}}{Q_A}. \quad (3.83)$$

The partition function (for A particles) can be readily calculated from a recursion relation (Das et al. 2005). The result of particle number conservation in each partition is,

$$Q_A = \frac{1}{A} \sum_{k=1}^A k \left(\frac{V_{\text{free}}}{A_k} q_k \right) Q_{A-k}. \quad (3.84)$$

The execution of this logic then comes down to specifying the internal partition function for each unit q . For nucleons, with no internal degrees of freedom, $q = 1$ (neglecting spin). For clusters, q is calculated from the Helmholtz free energy estimated using a liquid-drop model to calculate the internal energy and the Fermi-gas model to calculate for the entropic contribution to the Helmholtz free energy F , i.e.,

$$q_k = \exp[-F/T] = \exp[(W_0 k - \sigma(T)k^{2/3} + T^2 k/\varepsilon_0)/T]. \quad (3.85)$$

W_0 and ε_0 are constants, while $\sigma(T)$ models a surface free energy that goes to zero at a critical temperature.

This model is logically consistent and when extended to two particle types (for neutrons and protons, see Das et al. 2005) can reproduce many experimental observables. However, its main shortcoming is that it neglects interactions between the clusters. This leads to unphysical effects such as regions of negative heat capacity. This is inconsistent with thermodynamics and is well known to result from unphysical Hamiltonians. This has been made clear by both molecular (Lovett 2007) and mock nuclear systems, simulated with Lennard–Jones-type interactions (Campi et al. 2005). That is, if one considers the interactions that are active at the inter- (as well as intra-) cluster level, regions of negative heat capacity largely disappear as long as the system is truly ergodic. The later well-known qualification is demonstrated by the recent molecular dynamics work of Thirring et al. (2003).

3.6 Mechanisms in the Nucleon-Nucleon Domain

Once the projectile energy significantly exceeds the Coulomb barrier, nucleon-nucleon (N-N) scattering in the early stages of the target–projectile interaction may generate nucleons or clusters that are sufficiently energetic to escape the mean field of the composite system. These fast *nonequilibrium processes* begin to appear when the projectile energy per nucleon approaches the *Fermi energy* ε_F . In the Fermi Gas Model, the nucleus is treated as a degenerate gas of spin $\frac{1}{2}$ particles confined within the nuclear volume. The Fermi energy ε_F can be defined as the kinetic energy measured from the bottom of a one-body potential (a positive quantity) or the binding energy of the last nucleon (a negative quantity). By the former measure, ε_F is about +30 MeV for both neutrons and protons in nuclei near the valley of stability. By the latter measure, ε_F is equal in magnitude to the binding energy but opposite in sign. Thus, by the latter measure, $\varepsilon_F \approx -8$ MeV for both neutrons and protons in nuclei near beta stability but diverge from one another as the neutron/proton asymmetry deviates from stability, with ultimately the value of the nucleon type in excess decreasing to zero at the drip line. The kinetic energy view is a very useful concept for many reactions and is used below, but one has to appreciate that this approach views the nucleus as a collection of independent particles, i.e., no correlations. (The latter definition is more useful for nuclear structure and does not suffer from the one-body model assumption.)

Experimentally, nonequilibrium phenomena become apparent above projectile kinetic energies of about 20 MeV per projectile nucleon, which is comparable to the Fermi energy of nucleons in the nuclear potential well. These processes grow in both probability and complexity with increasing beam energy (Durand et al. 2001).

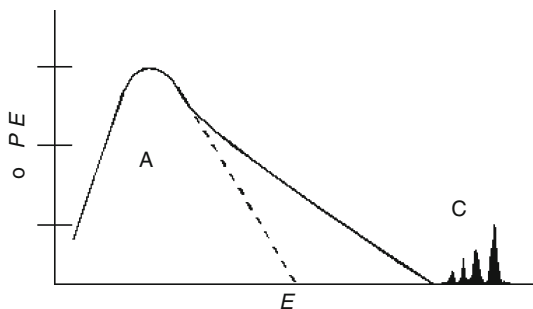
Nonequilibrium phenomena are distinguished by two principal features. First, they occur on a time scale much shorter than the typical equilibration time for statistical decay of a compound nucleus ($\tau \approx 10^{-21}$ s). Second, they produce multiparticle final states that are subsequently followed by statistical decay of the excited heavy product. In normal kinematics ($A_p < A_t$), the energetic light particles or clusters are forward-peaked and form a distinct exponential tail (area B in [Fig. 3.41](#)) on the Maxwellian spectra produced in later evaporation stages (area A in [Fig. 3.41](#)). The preequilibrium component for the nucleon channels is as in by early stage emissions of the multistep compound model, as in by the FKK model for example. At the extreme of nonequilibrium emissions are the discrete peaks (labeled C), which correspond to direct reactions, or the first step in a multistep compound model.

The same partition of the cross section seen in the light-particle emission is observed in the *linear momentum transfer* (LMT) to the heavy reaction partner, [Fig. 3.42](#). The folding angle between correlated binary fission fragments can be used as a gauge for measuring the degree of LMT in a reaction with a highly fissionable target, i.e., one for which $\sigma_R \approx \sigma_F$. In this context, $LMT = 1.0$ corresponds to a complete fusion (CF) reaction in which the total projectile momentum is transferred to the composite system, yielding the maximum excitation energy. $LMT = 0.0$ ($\theta_{\text{corr}} \approx 180^\circ$, [Fig. 3.42](#)) indicates a quasi-elastic mechanism that deposits only a small amount of momentum and excitation energy in the heavy product nucleus. At low bombarding energies, most of the reaction cross section goes into complete fusion reactions, with simple transfer events forming a peak near 180° . With increasing projectile energy, the high LMT peak broadens and shifts toward lower LMT due to the onset of nonequilibrium contributions in which incomplete fusion or prompt light particles carry off some of the projectile momentum, thus decreasing the deposited excitation energy. At the highest bombarding energies, the LMT distribution becomes nearly flat, indicating the deposition of a continuous spectrum of excitation energies, but with diminishing probability for complete fusion of target and projectile as the beam energy increases. Above beam energies of 100 MeV/A, the probability for complete fusion events is very low.

For nonfissionable systems, similar effects of the increase in nonequilibrium phenomena with increasing beam energy can be observed by measuring the velocity distribution of heavy residues relative to the expected velocity for complete fusion events. This approach is especially

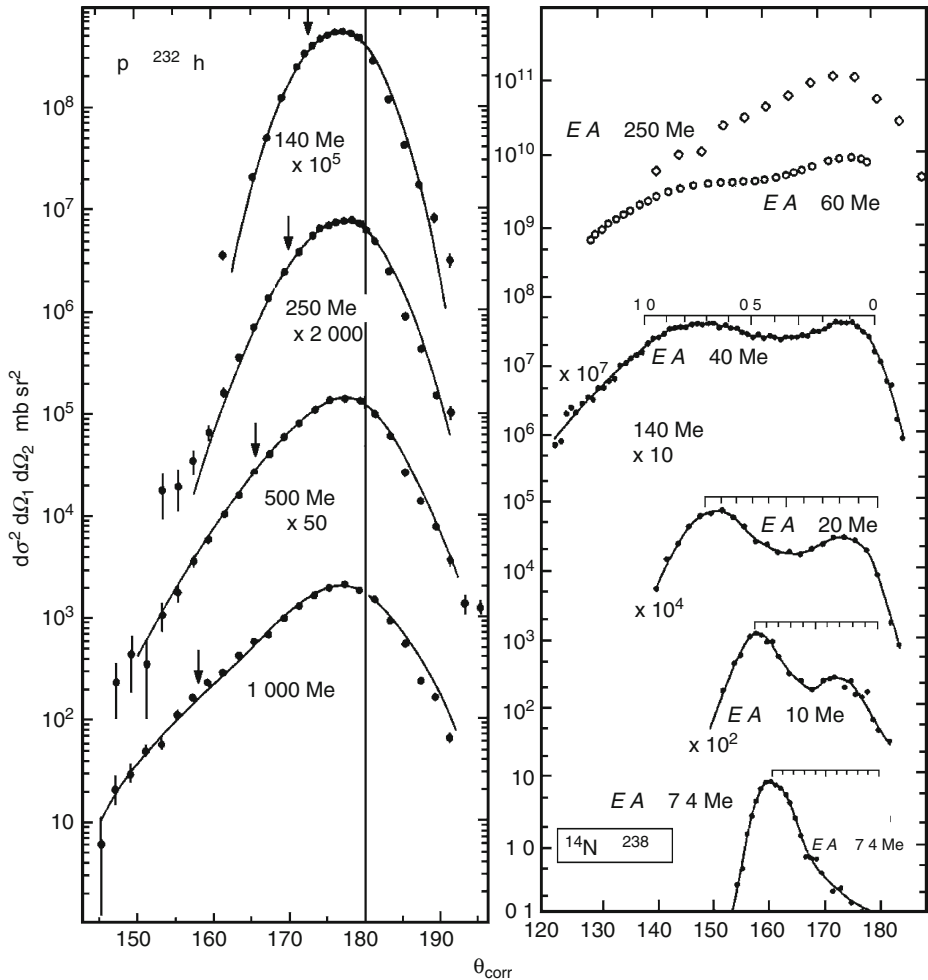
Fig. 3.41

Kinetic energy spectrum at forward angles for emission of light particles. Region A corresponds to evaporation from an equilibrated compound nucleus; region B describes preequilibrium emission, and C indicates the excitation of discrete states in direct reactions



■ Fig. 3.42

Diagram of the evolution of nuclear reaction mechanisms from the mean-field to nucleon-nucleon regimes as a function of projectile kinetic energy per nucleon E/A , as measured by the angle between coincident fission fragments θ_{corr} . Correlation angles nearer 180° designate incomplete momentum transfer. The left frame shows the evolution for a proton-induced reaction on ^{232}Th ; arrows indicate θ_{corr} values for CF (Saint-Laurent et al. 1984). For the right-hand frame, the bar above each plot indicates the LMT scale (1.0 corresponds to CF) for the $^{14}\text{N} + ^{238}\text{U}$ reaction. The two peaks correspond to fusion-like and quasi-elastic processes (Tsang et al. 1984; Fatyga et al. 1985). In all cases, the correlations are broadened by neutron evaporation from the fission fragments



useful in reverse-kinematics studies, where the heavy residues have appreciable kinetic energies. Both the fission-fragment correlations and residue-velocity distributions demonstrate that energetic collisions produce a wide spectrum of nonequilibrium reaction mechanisms that vary with the projectile–target composition and bombarding energy.

The organization of this section proceeds as follows: Relatively simple nonequilibrium phenomena observed in reactions near the Fermi energy are initially discussed. The subsequent sections deal with: models designed to account for the complex reactions that occur at intermediate energies ($E/A > 20$ MeV), a simplified participant–spectator model to account for the reaction observables, and finally, reactions at sufficiently high energy to generate nuclear material with densities significantly in excess of normal nuclear density.

3.6.1 Reactions Near the Fermi Energy

The role of nonequilibrium emission as an intermediate mechanism, linking prompt one-step reactions to statistical particle evaporation from an equilibrated system, is most transparent in the proton spectra of light-ion-induced reactions on complex nuclei (Wu et al. 1979). The exponentially falling, or *preequilibrium*, component (B) in [Fig. 3.41](#) can be viewed as arising from a time-dependent process in which particles are emitted as the energy density in the initial target–projectile interaction zone randomizes throughout the nuclear volume: the lower the particle energy, the later in the process the particle was emitted. Two-component fits to the spectral shapes of components A and B yield slope temperatures consistent with an equilibrated Fermi gas for the statistical component, but slope temperatures are two-to-four times higher for the preequilibrium part, indicating emission from an earlier, hotter stage of the reaction.

Preequilibrium effects also appear in the excitation functions for heavy reaction products in this energy regime. The product yields shown in [Fig. 3.11](#) reach their peaks at bombarding energies consistent with compound nucleus formation; however, all excitation functions have appreciable cross-section tails that extend to higher bombarding energies. For example, in the reaction



the yield of ${}^{198}\text{Tl}$ ([Fig. 3.11](#)) persists to much higher energies than predicted by compound nucleus energetics, because at least one of the emitted neutrons is of preequilibrium origin and carries off more energy than an evaporated neutron. The lowering of the average excitation energy due to preequilibrium emission reduces the probability for sequential evaporative emission and thus serves to hinder attempts to produce nuclei far from stability by increasing the beam energy.

For bombarding energies well above the barrier, one also observes the preequilibrium emission of intermediate-mass fragments ($2 < Z < \sim 20$, or IMFs) in reactions on heavy nuclei. The reaction observables for IMF emission strongly resemble those for light particles and presumably occur on a comparable short time scale. Models based upon a coalescence concept (Bond et al. 1977) have met with some success for light clusters, but encounter more difficulties for IMFs.

The experimental observables ascribed to the preequilibrium mechanism have usually been interpreted in the context of the *exciton model* (Griffin et al. 1966; Blann et al. 1975). In the basic model, the nucleus is treated as a Fermi gas in which the projectile initiates a series of sequential N–N collisions, generating unstable particle-hole states, or excitons (*exciton* = a particle-hole pair). The number of excitons is thus proportional to the degree of thermalization.

Large exciton numbers imply multiple collisions for which the projectile energy is partitioned among many nucleons likely to be in bound (single-particle) states, yielding high

excitation energies. Conversely, when only a few excitons are involved (few collisions), much larger energy transfers must occur and particles are raised to unbound states that yield energetic particle emission, leaving the heavy partner in a low state of excitation. Refinements of the model now include numerous physical effects such as the treatment of the nuclear potential and N-N mean-free path, Pauli blocking, barrier penetration, and finite-state lifetimes (Gadioli and Hodgson 1992; Chadwick and Oblozinsky 1992).

3.6.2 Models of Collision Dynamics

While the exciton model and its derivatives have been relatively successful in describing light-ion-induced reactions near the Fermi energy, the reaction mechanism becomes more complex at higher energies or when heavy-ion projectiles are involved. A major complication is introduced when multiple nonequilibrium processes occur during the evolution from initial target-projectile contact to the internally equilibrated final state. This problem is frequently approximated by a two-step model that assumes a fast collision stage followed by statistical decay of the system at a much later time ($\tau > 10^{-21}$ s). The fast stage (time scale $\tau \approx 10^{-22}$ s) is described by models that attempt to account for mass and energy dissipation during the collision. The second stage is governed by statistical decay mechanisms such as particle evaporation and fission, as discussed in [Sect. 3.5](#).

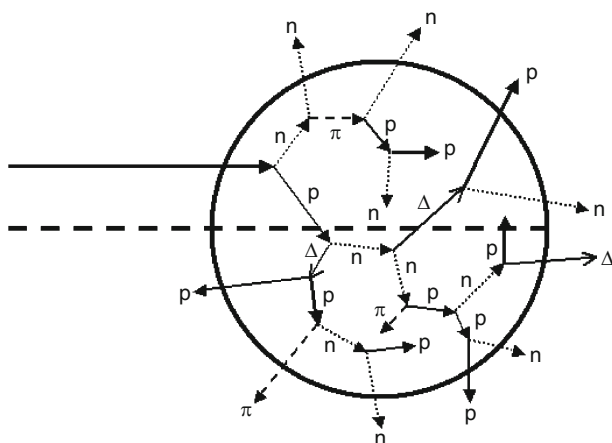
For reactions well above the Fermi energy ($E/A > 100$ MeV), the *intranuclear cascade* (INC) model (Serber 1947) has been frequently employed. For projectiles with de Broglie wavelengths much smaller than the average internucleon separation distance in the nucleus, all nucleon-nucleon collisions can be treated as quasi-free N-N scatterings. The projectile is assumed to follow a semiclassical path and initiate an N-N interaction that generates a cascade of scatterings in three dimensions. The cascade is computed numerically until all available projectile energy is dissipated into either fast cascade particles that leave the system or into internal excitation energy of the target residue. [Figure 3.43](#) shows the schematic concept of the INC model.

The INC model is a phenomenological approach that employs experimental N-N scattering cross sections and angular distributions as a function of energy up to several GeV. Nuclear geometry is incorporated to deal with nuclear surface effects for large impact parameters and a Fermi-gas model with Coulomb barrier effects is used to evaluate the number of fast cascade particles that escape, as well as those that are thermalized and converted into excitation energy. Monte Carlo methods are used to select the impact parameter in each event as well as the scattering angles. For heavy-ion reactions, where multiple primary N-N collisions become possible in the initial contact stage, account must be taken of the vacancies created by these collisions. At energies for which meson production and excitation of the intrinsic resonance states of the nucleon (e.g., Δ , N^* etc.) become possible, the scattering cross section for these types of reactions must be included, as well as the reabsorption probability of the mesons and decay of the nucleon excited states. At proton energies of several GeV and above, the growing number of meson types and resonance states introduces an additional complication, since there is limited experimental guidance for estimating these scattering cross sections.

INC codes – e.g., ISABEL, Yariv and Fraenkel (1981), and QGSM, Toneev et al. (1990) – are relatively successful in reproducing the fast cascade component of the reaction observables for light-ion-induced reactions above 100 MeV. They also predict the qualitative result that a broad distribution of excitation energies will be produced due to impact-parameter-dependent

■ Fig. 3.43

Simplified schematic picture of an intranuclear cascade event for an energetic proton incident on a heavy nucleus. The number of scatterings increases as the impact parameter decreases



transparency effects, with the maximum usually being well below the maximum possible excitation energy. Quantitative predictions of the excitation energy are more problematical. This uncertainty stems from the simple approximations relative to the nuclear potential that became important in terminating the cascade in its latter stages.

For heavy-ion reactions, an additional complication with the INC model is that it ignores mean-field effects, which become relevant when there is extensive mixing of target and projectile nucleons. This shortcoming has been addressed via a microscopic theory based on the *Boltzmann–Uehling–Uhlenbeck* (BUU) formalism (Bertsch et al. 1984); and variations (Gregoire et al. 1985). In this formalism, the time evolution of the mean-field is described by a one-body density-distribution function that is solved simultaneously with a nucleon-nucleon collision integral, thus accounting for both the mean field and N-N collisions. The collision integral is calculated via an intranuclear cascade where only scattering into unoccupied phase space cells is allowed.

Models of this type have proven effective in describing the multiplicities and spectra for energetic nucleons (Durand et al. 2001), as well as small-angle particle-particle correlations and integrated spatial distributions (Bauer et al. 1992). In confronting theory with heavy residue data, BUU-type calculations encounter two principal shortcomings, both of which are also present in INC calculations: first, the time at which thermalization has been achieved and second, the lack of density fluctuations in the model that would provide a mechanism for the formation of nuclear clusters. In an effort to develop a full dynamical theory of fragment production, density fluctuations have been incorporated via the classical *molecular dynamics* (MD) approach (Schlagel and Pandharipande 1987), which has led to several quantal dynamical models (QMD) such as fermionic molecular dynamics (Feldmeier et al. 1995; Feldmeier and Schnack 2000), antisymmetrized molecular dynamics (Ono and Horiuchi 1996), and Brownian one-body dynamics (Chomaz et al. 1994).

Both BUU- and QMD-like models can be used to investigate the *nuclear equation of state* (EOS) and the phase diagram for nuclear matter shown schematically in ▶ Fig. 3.3. One parameter of particular concern is the nuclear incompressibility constant K (a subject dealt

with in the next section). From measurements of spatial flow distributions of emitted light ions, it has been possible to determine the bombarding energy at which the transition from the mean-field to nucleon-nucleon scattering dominance occurs; i.e., the “balance energy” where attractive mean-field scattering becomes equal to repulsive nucleon-nucleon scattering (Magestro et al. 2000).

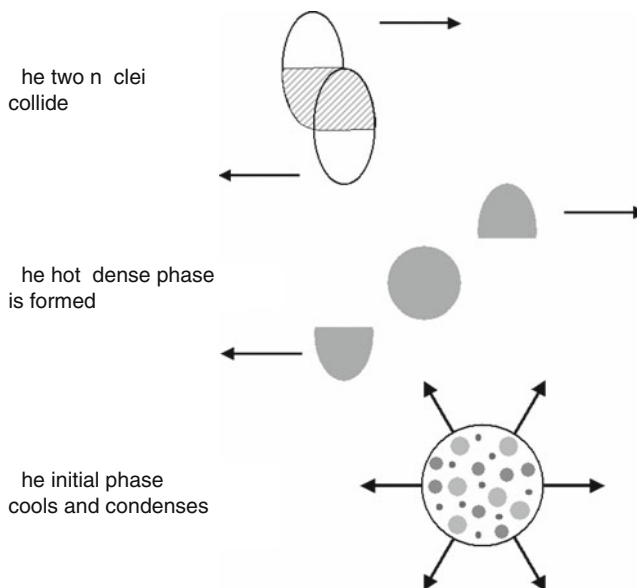
The collision models also demonstrate how nuclear reactions can be used to explore variations from normal nuclear density ρ_0 , ranging from dilute ($\rho < \rho_0$) to compressed ($\rho > \rho_0$) states, by varying the bombarding energy and target–projectile asymmetry. For example, proton-induced reactions above about 5 GeV may leave the heavy partner in a state of depleted density due to the near-instantaneous knockout of several fast cascade particles. At the other extreme, in symmetric heavy-ion collisions, the large target–projectile overlap region in central collisions leads to significant compression and high energy density in the early stages of the reaction.

3.6.3 Participant–Spectator Reactions

For heavy-ion collisions well above the Fermi energy, models predict a low probability for composite-nucleus formation. Instead, most of the cross section is predicted to go into reactions that can be generalized as “*participant–spectator*” reactions (Fig. 3.44). In the participant–spectator scenario, the *participant* source is defined by those nucleons that occupy the geometrical overlap volume of the target and projectile, which is impact-parameter dependent.

■ Fig. 3.44

Schematic picture of the participant-spectator model. The hot participant region is formed from nucleons in the target-projectile overlap region. The target and projectile remnants on the periphery act as spectators, which then decay statistically



The number of participant nucleons and the energy-density of this localized source increase with decreasing impact parameter. The *spectators* are the target and projectile remnants outside the overlap volume and they decouple from the participant source on a time scale that decreases with increasing projectile energy and then decay statistically. The excitation energy of these spectators is a function of the overlap region.

Studies of the projectile spectator, or *projectile fragmentation*, permit investigation of nuclei at extremes of temperature and neutron–proton asymmetry (nuclei with large *isospin* components). By employing reverse kinematics, nuclei of all the elements can be studied. Because of the broad range of impact parameters that contribute to projectile-fragmentation events, the nuclidic yield distribution is very broad in N and Z , with the resultant formation of product nuclei far from stability. Exploitation of this result has led to the discovery of many new neutron- or proton-rich nuclei and provided access to a greatly expanded nuclear landscape for nuclear structure and nuclear astrophysics studies. One of the more intriguing byproducts of such studies has been the discovery of “*halo nuclei*” such as ${}^{11}_3\text{Li}$ (Fig. 3.32 and the discussion of knockout reactions) in which the nuclear radius is abnormally large, since the highest-lying pair of neutrons occupies an extended orbit (Hanson et al. 1995; Hanson and Tostevin 2003).

The participant zone constitutes a unique nuclear environment, analogous to a rapidly evolving plasma decoupled from the nuclear mean field. This zone is the source of energetic nonequilibrium light particles emitted from the neck region between the two separating spectator nuclei. Isospin effects in the overlap volume may subsequently modify the isotope yields. Because of the large multiplicities of particles that may be emitted from both spectator and participant sources, quantitative understanding of these reactions requires large detector arrays with excellent charge, mass, and spatial resolution (see Chap. 48 in Vol. 5).

The fact that the projectile fragments are emitted with velocities near that of the beam also has practical consequences. From the detection point of view, the identification of a fragment’s charge and mass is simplified by the strongly forward-focused kinematics. Projectile fragmentation is also the basis for one of the major radioactive-beam accelerator concepts. By magnetically separating specific fragmentation products, beams of nuclei far from stability can now be provided with intensities high enough to perform nuclear reaction and structure studies. This capability will greatly enhance future efforts to study the effects of neutron–proton asymmetry on the EOS that are predicted to be significant in several nuclear matter theories (Baran et al. 1998; Li 1997). Several accelerator facilities currently exist, or are in the construction/planning stages, for the study of nuclear isospin effects; for example, ATLAS at Argonne National Laboratory, USA (ATLAS 2010), ISAC at TRIUMF, Canada (TRIUMF 2010), CCL at Michigan State University, USA (CCL 2010), SIS at GSI, Germany (GSI 2010), GANIL, France (GANIL 2010), HRIBF at Oak Ridge National Laboratory, USA (HRIBF 2003), JINR in Dubna, Russia (JINR 2003), RARF at RIKEN, Japan (RIKEN 2010), Cyclotron Institute at Texas A&M, USA (TAMU 2010) and the recently approved FRIB facility at Michigan State University, USA (FRIB 2010).

3.6.4 Relativistic Heavy-Ion Collisions: Dense Nuclear Matter

In order to investigate the behavior of nuclear matter at still higher temperatures and densities, it is essential to rely on collisions between heavy ions at relativistic energies (Hermann et al. 1999; Reisdorf and Ritter 1997). At bombarding energies near 1 GeV/A and above, nuclear matter can be compressed to densities considerably higher than in normal nuclei, perhaps

approaching the conditions believed to be present when a neutron star is formed in the core of a collapsing supernova. From event-by-event analysis of the collective trajectories and the momenta of particles emitted during these collisions (► Fig. 3.45), vital tests of the nuclear equation of state can be performed. Two relevant terms often employed in relativistic heavy-ion research are rapidity and flow.

Rapidity is defined by the expression

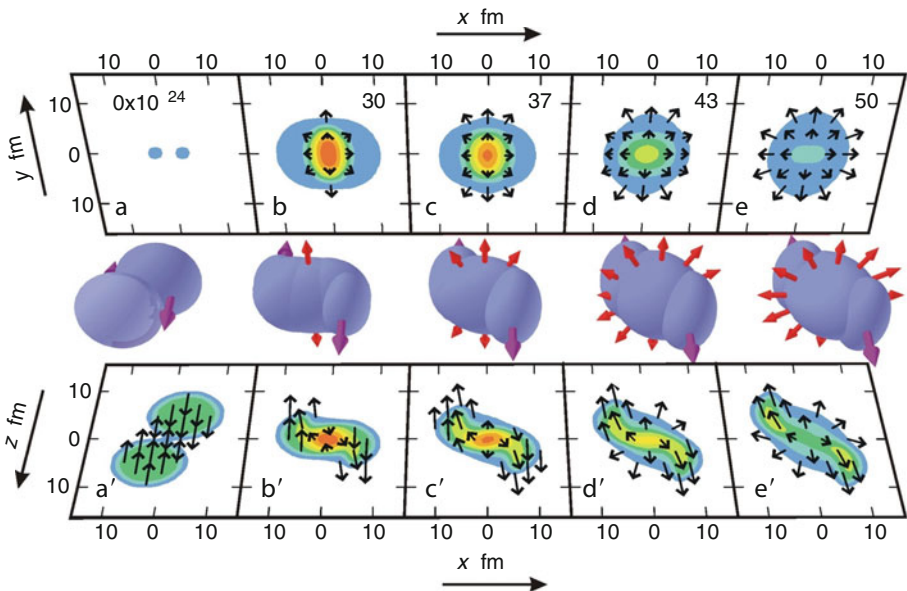
$$y = \frac{1}{2} \ln \left(\frac{E + p_z c}{E - p_z c} \right), \quad (3.87)$$

where p_z is the momentum component parallel to the beam and E is the total energy (rest mass plus kinetic energy). Rapidity, which is a relativistic representation of the velocity parallel to the beam, provides a variable suitable for discussing the kinematical regions generated in collisions of relativistic heavy ions.

Depending on the axis of orientation, different types of flow can be defined by addition of vectors, such as in ► Fig. 3.45. *Transverse flow* (see F in ► Fig. 3.46) is a concept used to examine the emission patterns of spectator nucleons that are emitted transverse to the beam direction (z -axis in ► Fig. 3.45), presumably due to the anomalously large scatterings they undergo when they interact with the compressed region formed in an event. Target and projectile matter can be distinguished on the basis of their respective rapidities. The amount

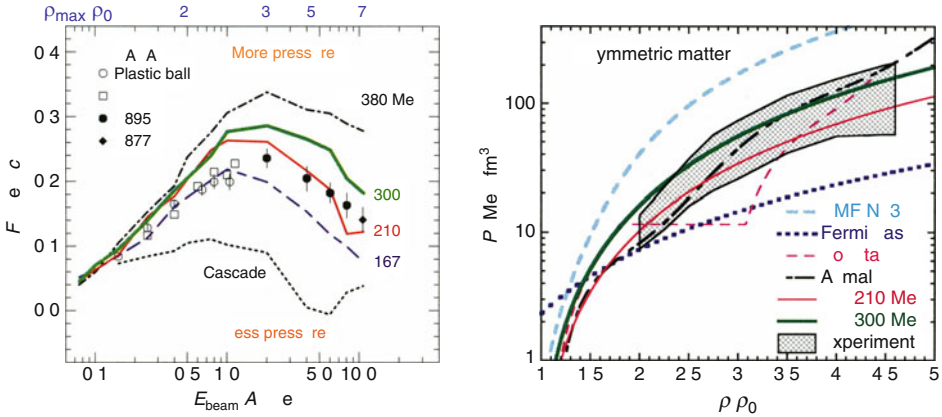
■ Fig. 3.45

Schematic view of a relativistic Au + Au collision with impact parameter $b = 6.0$ fm as a function of time (increasing from left to right as indicated in the cells of the top panel). The middle frame represents matter within a density greater than $0.1 \rho_0$, where ρ_0 is the ground-state density of nuclear matter. Bottom panel shows this projection in the reaction plane (x - z) with respect to the beam direction z . The top panel shows contours of constant pressure in the transverse plane (x - y) (From Danielewicz et al. 2002)



■ Fig. 3.46

Transverse flow F as a function of beam energy (left) and zero-temperature EoS for symmetric nuclear matter (right). Note that the larger the incompressibility coefficient, the larger the pressure P (From Danielewicz et al. 2002)



of flow (Danielewicz et al. 2002) is sensitive to the compressibility of the matter modeled by the transport model. By comparing flow data with the predictions of transport-theory calculations, it is then possible to evaluate the parameters of the EOS at high density (next section).

Flow can be used as a measure of the properties of the N-N interaction in the high density overlap volume, as well as evaluating the densities reached in such collisions. Densities up to $\rho/\rho_0 \approx 2-4$ (Danielewicz et al. 2002) have been estimated from such studies, providing new insights into the nuclear EOS and the related problem of neutron-star formation in supernovae. In addition, the spectra observed at bombarding energies above $E/A \approx 10$ GeV/nucleon reach spectral temperatures of up to $T \approx 150$ MeV. Such temperatures approach the value for deconfinement into a quark-gluon plasma, a plasma of a type not present since the primeval conditions of the Big Bang.

In recent years, the focus of this research has been at the Relativistic Heavy-Ion collider at Brookhaven National Laboratory (RHIC 2005, 2010). One of the most significant findings from the work at RHIC has been that the quark-gluon plasma generated has an ultralow viscosity-to-entropy ratio. The low viscosity implies that the degrees of freedom (quarks and gluons) have short mean-free paths and that the medium itself is still strongly correlated. While this implies that hydrodynamic reaction-model descriptions are valid, fundamental theory is yet to provide a clear insight into why the medium is so strongly coupled. Even higher energy work at the Large Hadron Collider at Conseil Européenne pour la Recherche Nucléaire (LHC, CERN 2010) will produce still higher temperatures and is likely to shed new light on this question.

3.7 The Nuclear Equation of State

3.7.1 Background and Connection to Classical Thermodynamics

In an introduction to thermodynamics, one studies large systems with the aid of “extensive” energy functions. These energy functions have two “sectors” for one-component systems, one

“mechanical” and the other “thermal.” For multicomponent systems another “chemical” sector must be added. The variables are: P and V (or its inverse, the number density ρ) for the “mechanical” sector and S and T for the “thermal” sector. The natural independent variable for the thermal sector is the entropy S for the pure energy functions while T is the independent variable in this sector for the free energies (corresponding to the energy available to do work). For macroscopic systems S and V are extensive, while T and P are intensive, meaning that one and only one of the variables in each set must be extensive.

Equations of state (EoS) are an attempt to capture the interrelationships between the variable set of thermodynamics for *infinite matter*, in the absence of long-range interactions. Thermodynamics itself is the enterprise of trying to describe matter with the absolute minimum number of macroscopic variables. One deduces the EoS from direct measurement of the macroscopic variables and from measureable derivatives such as the isothermal and adiabatic compressibilities for the “mechanical” sector and the constant pressure or volume heat capacities for the thermal sector.

For finite systems such as nuclei, a surface sector must be added. This sector is not extensive (i.e., while proportional to the surface area, it is not proportional to the amount of material). The study of systems where the energy functions are nonextensive has a long history starting with the work of Gibbs. Both small systems (due to surfaces) and systems with long-range interactions (where the interaction energy scales with the number of participants squared) fall into this category. Nuclei suffer from both of these extensivity-destroying features.

Recalling basic (extensive) thermodynamics, the internal energy E of an extensive one-component system is

$$dE^* = TdS - PdV \quad \text{or} \quad d\varepsilon = Tds - Pd v. \quad (3.88)$$

The lower case is employed in the second version to indicate the energy, entropy, and volume per particle. The pressure is no more than the dependence of energy on volume or number density,

$$P = -\left(\frac{\partial \varepsilon}{\partial v}\right)_s = \rho^2 \left(\frac{\partial \varepsilon}{\partial \rho}\right)_s = \rho^2 \left[\left(\frac{\partial \varepsilon_0}{\partial \rho}\right)_s \right] + \rho^2 \left\{ \left(\frac{\partial \varepsilon_{\text{asym}}}{\partial \rho}\right)_s \right\}. \quad (3.89)$$

The second equality makes use of the fact that the volume per unit and the number density are inversely related, $v = \rho^{-1} \rightarrow dv = -\rho^{-2}d\rho$. The final equality separates the isoscalar component of the pressure (the only term present for symmetric matter) from that originating from neutron/proton asymmetry. At large asymmetries, the second term dwarfs the first, so it is this term that is principally responsible for resisting the gravitational collapse of a neutron star.

The compressibility is defined as either the negative of the relative change in the volume with the application of pressure or the relative change in the density with the application of pressure under specified conditions. (The signs are such as to make the coefficient positive for any thermodynamically stable system.) Therefore, the adiabatic compressibility (the version which dictates the speed of sound) is

$$\kappa_s = -\frac{1}{v} \left(\frac{\partial v}{\partial P}\right)_s = \frac{1}{\rho} \left(\frac{\partial \rho}{\partial P}\right)_s. \quad (3.90)$$

Rather than dealing with κ , nuclear science has focused in its inverse, the “*incompressibility*” coefficient” K . Another minor change is that rather than dealing with a problem that is intrinsically 3-dimensional, the analysis is reduced to a one-dimensional problem of the stiffness with respect to harmonic vibrations of a uniform (albeit infinite) sphere of radius R .

(The conversion to a 1-D problem, with the independent variable being R , makes use of $d\rho/dR = -3\rho/R$ twice, yielding the factor of 9). In this case, from [Eq. \(3.89\)](#) one obtains the nuclear matter (nm) incompressibility K_{nm} (with the dimensions of energy):

$$K_{\text{nm}} [\text{MeV}] \equiv 9 \left(\frac{\partial P}{\partial \rho} \right)_s = 9 \rho_{\text{sat}}^2 \left(\frac{\partial^2 \varepsilon}{\partial^2 \rho} \right)_{s, \rho = \rho_{\text{sat}}} . \quad (3.91)$$

This is just the inverse of κ_s , with a slightly different coefficient. (Note that $1/\rho$ for saturated nuclear matter is $V/A = (4/3)\pi R^3/A = (4/3)\pi r_0^3 \approx 7.2 \text{ fm}^3/\text{nucleon}$).

The thermal properties of matter are captured by its ability to absorb energy. The quantum version of the relevant question is: at a given excitation energy, how many ways can a system sustain that energy? At constant volume, the energy-dependent answer to this question is captured in the heat capacity as a function of excitation energy

$$C_V(E^*) \equiv \left(\frac{\partial E^*}{\partial T} \right)_V = T \left(\frac{\partial S}{\partial T} \right)_V = k_B T \left(\frac{\partial \ln \omega(E^*)}{\partial T} \right)_V . \quad (3.92)$$

The effective mass, introduced in [Sect. 3.3](#) and discussed more in [Sect. 3.5](#), is the factor that corrects a single-particle logic for the many-body correlations. Thus, one can say that the study of the evolution in the level-density parameter a , is one of determination of how m^* changes with E^* . This thermal sector was discussed in [Sect. 3.5](#).

Description of the properties of matter is punctuated by phase transitions. While formally such transitions can occur only in the (extensive) matter limit, the manifestations of a matter phase transition in a finite system can profoundly affect the behavior of a finite “clump” of matter. In nuclear science, symmetric matter must undergo a liquid-to-gas-like transition as the matter is heated and the average density reduced, since it has an attractive interaction that can be saturated at short-range. Just as in the case of standard fluids, there will be a coexistence region that self-partitions into low- and high-density phases. Just how this transition is manifest in real charged and finite nuclear (i.e., in the real nonextensive) systems has been the focus of considerable effort.

3.7.2 The Perspective from Energy-Density-Functional Theory

Extraction of an EoS from a fundamental theory is of course desirable, and while there has been progress along this line, presently one must work with functionals of relevant properties such as the density and asymmetry that depend on free parameters that must be determined by some fitting procedure (Bender et al. 2003).

The task is to generate a functional for the energy of a finite system as a function of density and other variables that might be relevant. In fact, this procedure just generates a more rigorous alternative to the Liquid-Drop Model (LDM). This version of developing an expression for the mass of a drop involves an integral over space. The surface term comes from the gradients (inspired by van der Waals) and the asymmetry terms by the dependence on both of the individual densities. The Coulomb term, not included in the expression provided in the text, comes from an integral over the nuclear volume, the same way as it does in the LDM.

Let the energy as a function of density $E(\rho)$ be this function, which in the nuclear case must be a function of the local neutron and proton densities and their derivatives. (Van der Waals appreciated that nature must “pay” for producing nonuniform densities.) The binding energy

for a drop must come from an integral of the nuclear energy density ξ , with corrections for density gradients over the nuclear density,

$$E = \int \left\{ \xi(\rho_n, \rho_p) + \eta(\nabla\rho)^2 + \eta_{\text{asym}}(\nabla\rho_n - \nabla\rho_p)^2 + \dots \right\} d^3r + E_{\text{Coul}}, \quad (3.93)$$

where, in this case, the η 's (one isoscalar and one for the asymmetry) are coefficients to be determined by fitting data in exactly the same fashion as the surface and asymmetry coefficients are fit in the liquid-drop model.

This approach works well for classical fluids, although its convergence has never been proved. The connection to infinite uncharged nuclear matter is that the gradient expansion vanishes and the Coulomb term (which blows up in the infinite limit) is dropped. In that case, the nuclear energy density ξ or the energy per nucleon ε (see [Eq. \(3.94\)](#)) can be viewed as an isoscalar part (with only a density dependence) and an asymmetry component with both a density and an asymmetry dependence as a function of the deviation of the density from saturation and of the asymmetry from symmetry,

$$\xi \equiv \frac{E}{V} = \rho \left\{ \frac{E}{A} \right\} = \rho \varepsilon, \quad (3.94)$$

where

$$\varepsilon(\alpha, \delta) \approx [\varepsilon_0(\alpha)] + \{\varepsilon_{\text{asym}}(\alpha, \delta)\} \approx [\varepsilon_0(\alpha)] + \{S(\alpha)\delta^2\},$$

$$\alpha \equiv \frac{\rho_n + \rho_p}{\rho_0}, \quad \delta \equiv \frac{\rho_n - \rho_p}{\rho_n + \rho_p}. \quad (3.95)$$

The term in square brackets is the energy (per nucleon) of symmetric nuclear matter, while the term in curly brackets captures the change in the energy with asymmetry. Note that the coefficient of the asymmetry term is density-dependent.

Development of the first and second terms (isoscalar and isovector, respectively) in [Eq. 3.94](#) leads to several other coefficients that in principle can be phenomenologically determined. As symmetric matter represents an equilibrium point, an expansion in the density (from the saturation value) cannot have a linear term. The same cannot be said of the asymmetry term. Therefore, an expansion for both the isoscalar and asymmetry terms can be written,

$$\varepsilon(\alpha, \delta) = \left[\varepsilon_0 + \frac{K}{18}(\alpha - \alpha_0)^2 + \dots \right] + \left\{ \left(S_0 + \frac{L}{3}(\alpha - \alpha_0) + \frac{K_{\text{asym}}}{18}(\alpha - \alpha_0)^2 \dots \right) \delta^2 \right\} + \dots, \quad (3.96)$$

where the term in curly parenthesis is the asymmetry contribution is the $S(\alpha)$ in [Eq. 3.94](#). The constants in the coefficients are chosen so that the constants (K , L , and K_{asym}) are consistent with other formulations (Danielewicz and Lee [2009](#)).

3.7.3 The Incompressibility from the Physical LDM-Like Expansion

The incompressibility can also be expressed in a Liquid-Drop Model-like expansion, that is, an expansion where the terms are associated with *physical corrections*, rather than the result of

a Taylor expansion. Doing so provides an expression for the incompressibility of a *finite* charged drop (Youngblood et al. 1999),

$$K_A = K_{\text{nm}} + K_{\text{surf}} A^{-1/3} + K_{\text{asym}} \left(\frac{N-Z}{A} \right)^2 + K_{\text{coul}} \frac{Z^2}{A^{4/3}}. \quad (3.97)$$

The first term K_{nm} is the incompressibility of infinite uncharged nuclear matter (the extensive quantity), the second corrects the matter incompressibility for the presence of the surface, the third term corrects for the neutron–proton asymmetry of the matter and the fourth term (one that blows up for infinite matter) corrects for the charge on the finite drop.

The left-hand side of the physical expansion can be determined from the (mean) energy of the giant-monopole resonance (GMR), and root-mean-square size of the nuclear drop (Colò et al. 2004),

$$E_{\text{GMR}} = \hbar \sqrt{\frac{K_A}{m \langle r^2 \rangle}}. \quad (3.98)$$

Fitting the physical expansion leads to a value of $K_{\text{nm}} = (240 \pm 10)$ MeV (Colò et al. 2004).

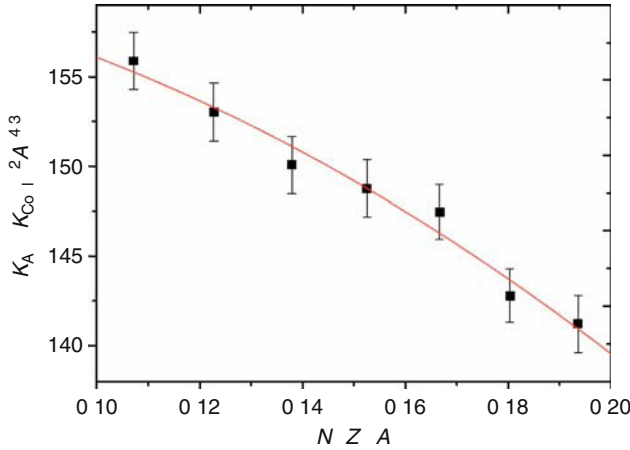
Unfortunately, the GMR data address only tiny variations of the mean density about saturation. The extrapolation to densities far different than saturation is questionable. To gain insight into density variations of more relevance to neutron-star structure, HI “flow” analyses of the type shown in Fig. 3.45 have been used. The momenta transverse to the beam (as a function of the beam energy) are shown in Fig. 3.46 along with a comparison to model (BUU) simulations. The more incompressible the fluid, the greater the momentum “extruded” perpendicular to the beam axis. The constraints on the symmetric matter incompressibility are summarized on the right-hand side of the same figure (Danielewicz et al. 2002). Two statements can be made about the flow results. First, these data are inconsistent with the strongly repulsive nuclear equations of state derived from relativistic mean field theories and weakly repulsive equations of state, which would result from a phase transition at densities less than three times the saturation density. Second, while the uncertainties grow with density, the flow results are consistent with those from the GMR studies.

It is the asymmetry term that has been the focus of much recent effort, as it is this term that provides the internal pressure, holding back the gravitational collapse of a (cold) neutron star. First, results are presented from the perspective of the physical (LDM-like) expansion. As K_{surf} is close in magnitude (but opposite in sign) to K_{nm} , and the Coulomb constant (-5.2 MeV) is essentially model-independent, for sufficiently heavy isotopes, the difference $K_A - K_{\text{Coul}} Z^2 A^{-4/3}$ from Eq. 3.97 can be approximated by the analytic form $y = K_{\text{asym}} \delta^2 + b$, where $\delta = (N - Z)/A$. This approximate relationship has been employed for a series of even- A Sn isotopes for which the giant monopole resonance (GMR) was excited with inelastic alpha-particle scattering at small angles (Li et al. 2007). This work (Fig. 3.47) provided a value $K_{\text{asym}} = (-550 \pm 100)$ MeV. Data on the GMR from isotopes with asymmetries greater or less than those of the natural Sn isotopes would greatly reduce the uncertainty on K_{asym} . This will be one of the focus activities at FRIB in the coming decade. Nevertheless, this result is consistent with the value $K_{\text{asym}} = (-500 \pm 50)$ MeV obtained from analysis of the isotopic transport ratios in medium-energy heavy-ion reactions (Li et al. 2008).

Viewed from the energy-density expansion perspective, the analysis described above will scramble the constant (S_0), linear (L), and quadratic (K_{asym}) terms in Eq. 3.96. Separating the dependences is an active research area, about which several comments can be made.

■ Fig. 3.47

Systematics of the difference $K_A - K_{\text{Coul}} Z^2/A^{4/3}$ in the Sn isotopes as a function of $\delta = (N-Z)/A$; $K_{\text{Coul}} = -5.2$ MeV. The solid line represents least-squares quadratic fit to the data (When plotted in this fashion, the value of K_{asym} comes from the curvature of the best fit) (From Li et al. 2007)



First, there is a cross-correlation (shown in Fig. 3.48) between the constant term (S_0) and the linear term (L) (Tsang et al. 2009). Second, an overall constraint on the density dependence of the asymmetry energy is deduced from HI-reaction data (Danielewicz and Lee 2009; Shetty et al. 2007),

$$S(\rho) \propto \rho^x(1 + c\rho); \quad \frac{2}{3} \leq x \leq 1. \quad (3.99)$$

Again, in an effort to be forward looking, experiments on parity-violating electron scattering on ^{208}Pb (a project called PREX) will be done in the next few years. If successful, this experiment will produce data directly sensitive to the linear term in the dependence of the asymmetry energy on density (Horowitz and Piekarewicz 2002).

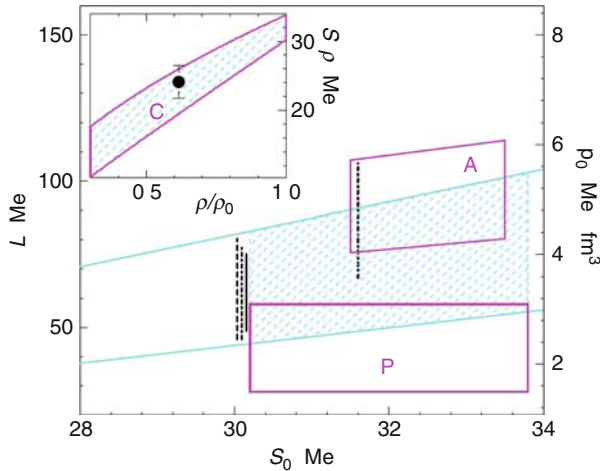
3.7.4 Cluster Formation at Very Low Density

At very low density and temperature, alpha clusters become a significant component of symmetric nuclear matter (Friedman and Pandharipande 1981). The contribution of such clusters is determined by an interplay between the translational phase space (which favors free nucleons with increasing temperature) and binding energy (which favors alpha-particle formation by allowing more energy to be available for translation). One only needs to consider alpha decay of heavy nuclei to appreciate that clustering in the matter tails of heavy (cold) nuclei is significant. As is the case in water, one can consider such clusters as transitory, an existence that increases as the density and temperature decrease.

There have been significant advances on both the theoretical and experimental fronts in elucidating the behavior of nuclear material at very low densities, densities less than 0.1 of saturation. On the theoretical front, a virial (density expansion) EoS has been formulated by

■ Fig. 3.48

Representation of the constraints on parameters S_0 and L in ▶ Eq. 3.96. The right axis corresponds to the neutron-matter-symmetry pressure at saturation density. The region bounded by the *diagonal lines* represents the constraints obtained from analysis of HI collisions. The vertical lines near $S_0 = 31$ MeV are obtained from LDM-like analyses (i.e., masses). The lower and upper boxes are formed by the constraints from the so-called Pigmy Dipole resonances (neutron-rich skin vs. core) and from symmetry-energy analysis on nuclei, respectively. The inset shows the density dependence of the symmetry energy in the shaded region. The symbol in the inset represents the GDR. Note the greatly offset scales on the abscissa and ordinate (From Tsang et al. 2009)



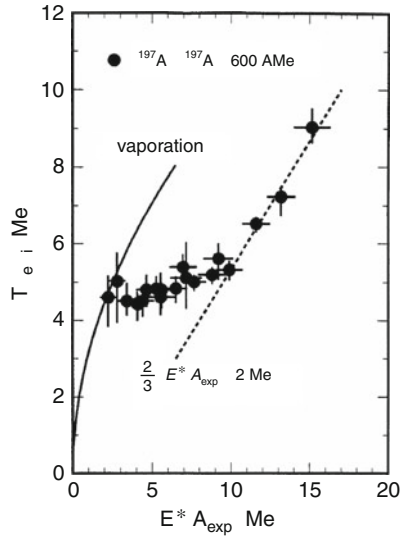
explicitly considering the (N-N), N-alpha and alpha-alpha scattering phase shifts (Horowitz and Schwenk 2006). One of the values of this work has been to quantify the pressure reduction and asymmetry energy enhancement (relative to a nucleon gas), due to alpha-particle clustering. Confirmation of this enhancement at densities of 0.01–0.05 times the ground-state density of symmetric nuclear matter has been observed in an analysis of HI reaction data (Kowalski et al. 2007, Natowitz et al. 2010). This limiting behavior is one aspect of clustering in nuclear systems. The next section deals with perhaps the most significant aspect of this behavior.

3.7.5 Multifragmentation: The Low-Density Regime and the Manifestation of the Liquid–Gas Phase Transition in Nuclear Collisions

When the first high-energy accelerators became available in the 1950s, radiochemical and emulsion studies indicated the existence of a reaction mechanism in which a heavy nucleus is disintegrated into multiple neutrons, H and He ions, and IMFs (▶ Fig. 3.1), a process now called multifragmentation (Lynch 1987; Trautmann 2001; Chomaz 2001). The connection of this phenomenon to the nuclear liquid–gas phase transition in matter was made after construction of a “caloric curve,” i.e., $T(E^*)$, shown in ▶ Fig. 3.49 (Pochodzalla et al. 1995). The ordinate was constructed using isotope ratio “thermometers.” Such thermometers use the

■ Fig. 3.49

Caloric curve (temperature vs. heat) derived from peripheral collisions in $^{197}\text{Au} + ^{197}\text{Au}$ reactions. Temperatures are derived from yield ratios of $^3\text{He}/^4\text{He}$ and $^6\text{Li}/^7\text{Li}$ isotopes and heat (E^*/A) from event-by-event calorimetry. The **solid line** describes the expected behavior for nuclear evaporation. The dashed line is that expected for a hot nuclear gas. The plateau region in between has been interpreted as evidence for a “boiling-like” phase transition in nuclei (Pochodzalla et al. 1995)



difference in the ground-state masses of different isotopes in a Boltzmann expression for the relative yield of the isotopes (Albergo 1985). The experimental isotope ratios are fit by adjusting the temperature.

The only way to have a halt in the increase in T with increasing E^* is for additional degrees of freedom to become available. In the case of the macroscopic liquid–gas transition, it is the access to the full 3-D translational degrees of freedom that halts the increase in the average energy in any one degree of freedom (as energy is poured into the newly accessed ones.)

The observables in high-energy light-ion or intermediate-energy HI collisions all relate to the above-mentioned multifragmentation exit channel. In order to create multifragmentation events, it is necessary to deposit excitation energies in a nucleus in excess of $E^*/A \approx 4\text{--}5$ MeV, i.e., about 1 GeV in a heavy nucleus. Transport codes predict that such events are rare, comprising less than $\sim 5\%$ of the nuclear reaction cross section. Among the methods used to prepare such systems have been light-ion reactions (ISiS, FASA), reverse-kinematics reactions (EOS), peripheral reactions (ALADIN), and near-symmetric heavy-ion ($A + A$) reactions (INDRA, ALADIN and Miniball). The various detector systems (given in square brackets) and earlier devices are referred to in Durand et al. (2001).

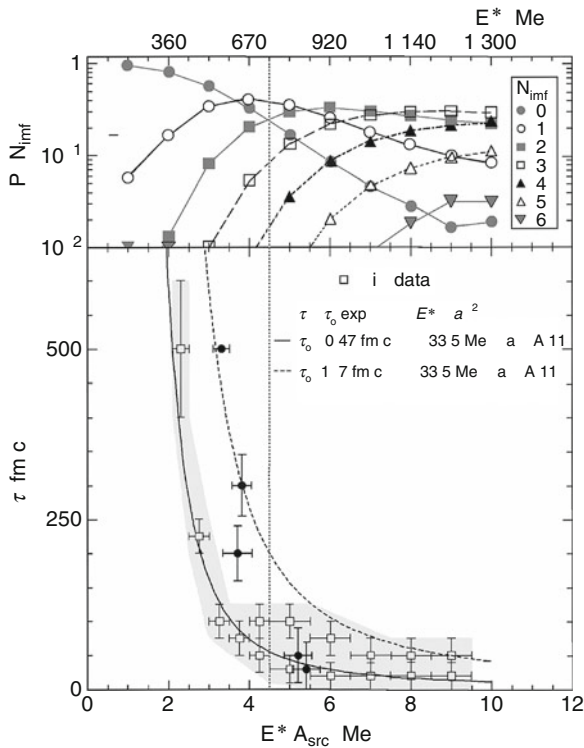
The plateau in the caloric curve is only indicative of access to additional degrees of freedom, not necessarily access to prompt multifragment decay. For example, expansion or greatly increasing the surface diffuseness, or an increase in the level-density parameter all would decrease the rate of increase of T with E^* , as discussed in ► Sect. 3.5. However, numerous

observables do in fact indicate that multifragmentation is the result of a near-instantaneous phenomenon rather than the result of sequential binary decays. Among these observables are evidence for a breakup density of only 20–30% of normal nuclear density ($\rho/\rho_0 \approx 0.2\text{--}0.3$), compression–decompression effects in $A + A$ reactions, and most important, time-scale measurements based on spatial correlations among the clusters. The latter work demonstrates that the breakup time scale is nearly simultaneous ($\tau \approx 10^{-22}$ s), much shorter than expected for a drawn-out sequential evaporative sequence (see [Fig. 3.50](#) and Viola et al. 2006).

Nuclear models based upon both statistical concepts and those for a generalized liquid–gas phase transition dependent on fragment size distribution are in general accord with the phase transition interpretation as long as the models assume expansion to a given breakup volume. In these models, the decay can be that expected from a statistical sampling of the cluster phase space (Bondorf et al. 1985; Gross 1990; Das et al. 2005), that is, without any dynamics, or a time-dependent approach in which emission occurs as the system expands to the breakup volume (Friedman 1990). However, it must be mentioned that as recent fragment–fragment correlation data could not be reproduced by prompt fragmentation models, Gentil et al. (2008), the interpretation of these complex decays is still not fully understood.

Fig. 3.50

Top: Evolution of a multifragmentation reaction as a function of heat E^*/A for the number of $Z \geq 3$ fragments (probability $P(N_{\text{imf}})$, IMF multiplicity N_{imf}). **Bottom:** Breakup time τ in fm/c (1 fm/c $= 3.3 \times 10^{-24}$ s). The growing multiplicity and rapid decrease in the breakup time are consistent with a “boiling-like” phase transition in nuclei (Beaulieu et al. 2000)



Analyses based on the finite-scaling model proposed by Fisher for classical drops (Elliott et al. 2002), percolation theory (Bauer et al. 1992), and a statistical multifragmentation model (Botvina et al. 1999) show generally good agreement with the concept that the transition (halt in the increase in the T with E^*) is associated with accessing the multifragment phase space. The opening of this most complex decay channel in finite nuclei at $T \approx 4\text{--}6$ MeV implies that infinite, uncharged matter cannot exist above $T_{\text{crit}} \approx 17$ MeV (Natowitz et al. 2002).

Perhaps, the most insightful result employing the fragmentation data comes from employing Fisher's model (Elliott et al. 2002). The critical exponents associated with the transition that occurs in the finite system's analog to the infinite matter liquid–gas phase transition are extracted. In addition, using the ubiquitous coexistence behavior for classical fluids, the nuclear phase transition data were added to what are known as “Guggenheim plots” (T/T_{crit} vs. both the low and high reduced densities $\rho_v/\rho_{\text{crit}}$ and $\rho_l/\rho_{\text{crit}}$). However, it should be kept in mind that unlike the macroscopic cases employed by Guggenheim and others to prove reducibility, actual measurements of the two coexisting densities as a function of temperature is not done. Nevertheless, this work shows how nature's systems, while seeming quite different, are often interrelated. The careful reader would have noted a few such cases of this unity of natural systems in this chapter.

3.8 Addendum: Cross-Section Calculations

For the case of a beam of charged particles incident on a thin target of thickness x , as illustrated in Fig. 3.51, the projectile flux can be expressed as $n_p = I/(qe)$. Here I is the electric current in amperes, as measured in a Faraday cup that collects the total charge deposited by projectiles of charge qe . For light ions, the projectile ion is usually fully stripped of its atomic electrons so that $q = Z$, the atomic number of the ion. However, for very low energy or very heavy ions, complete stripping of the atomic electrons may not occur, so that the ionic state of the projectile must be accounted for. The number density of target atoms n_t is given by

$$n_t = (\rho_M/M)N_A, \quad (3.100)$$

where ρ_M is the mass density, M is the molar mass of the target atoms, and N_A is Avogadro's number ($6.022 \times 10^{23} \text{ mol}^{-1}$). For reactions induced by a beam of particles (two dimensional geometry), the surface number density of target nuclei (N_t/area) is the relevant target collision factor, assuming that the beam cross section is smaller than the target area. For a given thickness x the surface number density (usually measured in cm^{-2}) is

$$N_t/S = n_t x. \quad (3.101)$$

where S is the surface area of the target.

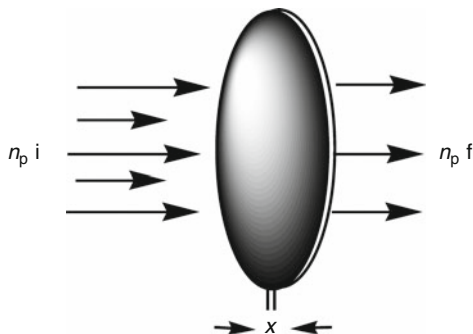
With these definitions the production rate $R(a,k)$ for a given exit channel k becomes

$$R(a,k) = n_p n_t x \sigma(a,k). \quad (3.102)$$

where the quantities are most commonly given in the following units: R (s^{-1}), n_p (s^{-1}), n_t (cm^{-3}), x (cm), and σ (cm^2). For thick targets the above linear behavior does not hold anymore. However, an arbitrarily thick sample can be viewed as being composed of thin slices of thickness dx . The rate of product nucleus formation is then given by the rate of particle removal from the beam as it passes through the slice of the target of thickness dx ,

■ Fig. 3.51

Beam of projectile nuclei impinging on a circular disk of thickness x



$$-dn_p = n_p n_t \sigma(a, k) dx. \quad (3.103)$$

Here $\sigma(a, k)$ stands for the total cross section. Integration over the thickness x of the target gives

$$-\int_i^f \frac{dn_p}{n_p} = \sigma n_t \int_0^x dx, \quad (3.104)$$

where i (initial) and f (final) are to indicate the particle flux entering and leaving the target, respectively, and

$$\frac{n_p(f)}{n_p(i)} = \exp(-n_t \sigma x). \quad (3.105)$$

The production rate then becomes

$$R = n_p(i) - n_p(f) = n_p(i)[1 - \exp(-n_t \sigma x)]. \quad (3.106)$$

If σ is the total reaction cross section, this expression predicts the attenuation of the beam due to all nuclear reactions in a target of thickness x . This expression assumes that the beam intensity and cross section are constants. In reality, this is not necessarily the case and corrections may be required due to time variations in the projectile current and dependence of the cross section on beam energy (► Fig. 3.51).

For an infinitely thin target, that is, one in which there is no appreciable attenuation of the beam due to target thickness, the above expression can be simplified by expanding the exponential term, $\exp(-n_t \sigma x) \approx 1 - n_t \sigma x$. This leads to a commonly-used expression for the rate

$$R(a, b) = \frac{I_0}{z_p e} \sigma(a, b) \frac{N_t}{S}, \quad (3.107)$$

where S is the area of the target containing N_t atoms of weight w and $N_t = (w/M)N_A$. The surface number density (measured, for example, in atoms cm^{-2}) – or its alternative, the surface density (given, for instance, in g cm^{-2}), to which it is proportional – is ordinarily a more accurate and easily determined quantity for thin targets than is the actual thickness. The basic assumption here is that the beam diameter is smaller than that of the target.

In the geometry of a nuclear reactor, the target can be considered to be immersed in a neutron gas, so that all target atoms N_t are exposed to the flux of neutrons. In such cases, target thickness usually does not matter and one can write

$$R = \sigma(a, b)N_t\phi, \quad (3.108)$$

where ϕ is the *neutron flux* (which is usually given in neutrons $\text{cm}^{-2} \text{s}^{-1}$), a parameter of the reactor and the position of the irradiation within it. The same is true for reactions in stars, except that this expression must be modified for the flux of both reactants.

Finally, in the production of radionuclides, it is necessary to include the effects of radioactive decay during bombardment in the rate equation as discussed in [Chap. 7](#) of this volume. The net production rate (dN/dt) will be the difference between the production (R) and decay (λN) rates

$$dN/dt = R - \lambda N. \quad (3.109)$$

The solution to this differential equation gives the number of atoms N produced as a function of time,

$$N = (1/\lambda)R(1 - e^{-\lambda t}), \quad (3.110)$$

where λ is the decay constant of a given radioactive product nucleus and t is the bombardment time. The factor $(1 - e^{-\lambda t})$ is called the *saturation factor*. This factor is an important consideration in production of short-lived medical radionuclides for diagnosis and therapy, and for efficient use of accelerator or reactor time. For bombardment times greater than one half-life, this factor illustrates the *law of diminishing returns*; i.e., half the maximum activity is formed after one half-life, 3/4 after two half-lives, etc.

3.9 Selected Nuclear Reaction Web Resources

Argonne Tandem Linac Accelerator System (ATLAS), <http://www.phy.anl.gov/atlas>
 Australian National University Tandem, Canberra, <http://www.rsphysse.anu.edu.au/nuclear>
 Bhabha Atomic Research Center, <http://www.dae.gov.in/res.htm>
 Canada's National Laboratory for Particle and Nuclear Physics (TRIUMF), <http://www.triumf.ca>
 Centre Européenne pour la Recherche Nucléaire (CERN), <http://public.web.cern.ch>
 China Institute of Atomic Energy, Beijing, <http://www.nti.org/db/china/ciae.htm>
 Chinese Academy of Sciences, Lanzhou, <http://english.imp.cas.cn/>
 Coupled Cyclotron Laboratory, Michigan State University, <http://www.nslc.msu.edu>
 Cyclotron Research Center at Louvain, <http://www.cyc.ucl.ac.be>
 Facility for Rare Isotope Beams (FRIB), <http://www.frib.msu.edu/>
 Fermi National Accelerator Laboratory (FNAL), <http://www.fnal.gov>
 Gesellschaft für Schwerionenforschung (GSI), <http://www.gsi.de>
 Grand Accélérateur des Ions Lourds (GANIL), <http://www.ganil.fr/>
 Holifield Radioactive Ion Beam Facility (HRIBF), <http://www.phy.ornl.gov/hribf/hribf.html>
 Institute for Nuclear Physics, Jülich (COSY), <http://www.fz-juelich.de>
 Joint Institute for Nuclear Research (JINR), <http://www.jinr.dubna.su>
 Kernphysisch Versneller Instituut (KVI), Groningen, <http://www.kvi.nl>
 Laboratory National Legnaro (LNL), <http://www.lnl.infn.it>
 Laboratory of Nuclear Science, Catania, <http://www.ct.infn.it>
 Lawrence Berkeley Laboratory, <http://www.lbl.gov>

Lawrence Livermore National Laboratory, <http://www.llnl.gov>
Los Alamos National Laboratory, <http://www.lanl.gov>
Los Alamos Print Archives (LANL), <http://lib-www.lanl.gov/>
National Nuclear Data Center, NNDC (BNL), <http://www.nndc.bnl.gov/>
Pacific Northwest National Laboratory, <http://www.pnl.gov>
Relativistic Heavy-Ion Collider (RHIC), <http://www.bnl.gov/RHIC>
Research Reactors Database, <http://www.iaea.or.at/worldatom/rrdb/>
RIKEN Accelerator Research Facility (RIKEN), <http://www.rarf.riken.go.jp>
The Svedberg Laboratory (TSL), <http://www.tsl.uu.se>
The Texas A&M Cyclotron Institute, <http://cyclotron.tamu.edu>

References

- Aerts G et al. (2006) Phys Rev C73 : 054610
Albergo S et al (1985) Nuovo Cimento Soc Ital Fis A 89A:1
ATLAS (2010) <http://www.phy.anl.gov/atlas>
Austern N (1970) Direct reaction theories. Wiley, New York
Axilrod BM, Teller E (1943) J Chem Phys 11:299
Baker SD, McIntyre JA (1967) Phys Rev 161:1202
Baldwin SP, Lott B et al (1995) Phys Rev Lett 74:1299
Baran V, Colonna M, Ditoro M, Larimov AB (1998) Nucl Phys A 632:716
Bass R (1974) Nucl Phys A 231:45
Bauer W, Gelbke CK, Pratt S (1992) Annu Rev Nucl Sci 42:77
Beaulieu L et al (2000) Phys Rev Lett 84:5971
Bender M, Heenen P-H, Reinhard P-G (2003) Rev Mod Phys 75:121
Benenson W, Harris JW, Stocker H, Lutz H (eds) (2002) Handbook of physics. Springer, New York
Bertsch GF, Kruse H, Dasgupta S (1984) Phys Rev C 29:673
Bertulani CA (2009) Wiley Encyclopedia of Physics Wiley-VCH, Berlin
Blann HM et al (1975) Annu Rev Nucl Sci 25:123
Bohr A, Mottelson BR (1969) Nuclear structure, vols 1 and 2. W.A. Benjamin, New York
Bohr N, Wheeler JA (1939) Phys Rev 56:426
Bonche P, Koonin S, Negele WG (1976) Phys Rev C 13:1010
Bond P, Johansen PJ, Koonin SE, Garpman S (1977) Phys Lett 71B:43
Bondorf J et al (1985) Nucl Phys A 443:221
Botvina A et al (1999) Phys Rev C 59:3444
Bowles TJ, Gavron VN (1993) Annu Rev Nucl Part Sci 43:117
Breit G, Wigner EP (1936) Phys Res 49:519
Broglia RA et al (1983) Phys Lett 133B:34
Buck B, Maddison RN, Hodgson PE (1960) Phil Mag 5:1181
Campi X, Krivine H, Plagnol E, Sator N (2005) Phys Rev C 17:041601
CCL (2010) <http://www.nsl.msu.edu>
CERN (2010) <http://public.web.cern.ch>
Cerny J (ed) (1974) Nuclear reactions and spectroscopy. Academic, New York/London
Chadwick MB, Oblozinsky P (1992) Phys Rev C 46:2028
Charity RJ et al (2001) Phys Rev C 63:024611
Charity RJ, Sobotka LG, Dickhoff WH (2006) Phys Rev Lett 97:162503
Charity RJ, Mueller JM, Sobotka LG, Dickhoff WH (2007) Phys Rev C 76:044314
Chomaz P (2001) International nuclear physics conference, <http://proceedings.aip.org/proceedings>
Chomaz P, Colonna M, Guarnera A, Randrup J (1994) Phys Lett B 254:340
ColÖ G et al (2004) Phys Rev C 70:024307
Cottingham WA, Greenwood DA (2001) An introduction to nuclear physics. Cambridge University Press, New York
Danielewicz P, Lee J (2009) Nucl Phys A 818:36
Danielewicz P, Lacey R, Lynch WG (2002) Science 298:1592
Das CB, Das Gupta S, Lynch WG, Mekjian AZ, Tsang MB (2005) Phys Rev 406:1
Dasgupta S, Hinde DJ, Rowley N, Stefanini AM (1998) Annu Rev Nucl Part Sci 48:401
Dasso CH, Landowne S (1987) Comp Phys Comm 46:187
Durand D, Suraud E, Tamain B (2001) Nuclear dynamics in the nucleonic regime. Institute of Physics Publishing, Bristol
Elliott JB, Moretto LG, Phair L et al (2002) Phys Rev Lett 88:042701
Ericson T et al (1963) Ann Phys 23:390
Fatyg M et al (1985) Phys Rev Lett 55:1376
Feldmeier H, Schnack J (2000) Rev Mod Phys 72:655
Feldmeier H, Bieler K, Schnack J (1995) Nucl Phys 586:493

- Feshbach H, Kerman A, Koonin S (1980) *Ann Phys* (N.Y.) 125:429; (1993) *Phys Rev C* 47:2255
- Frahn WE (1978) *Nucl Phys A* 302:267
- FRIB (2010) <http://www.nsl.msu.edu>
- Friedman WA (1990) *Phys Rev C* 42:667
- Friedman B, Pandharipande VR (1981) *Nucl Phys A* 361:502
- Gade A, Glasmacher T (2008) *Prog Part Nucl Phys* 60:161
- Gade A et al (2004) *Phys Rev Lett* 93:042501
- Gadioli E, Hodgson PE (1992) *Pre-equilibrium nuclear reactions*. Oxford University Press, New York
- GANIL (2010) <http://www.ganil.fr>
- Gentil E, Le et al (2008) *Phys Rev Lett* 100:022701
- Glasmacher T (1998) *Annu Rev Nucl Part Sci* 48:1
- Glauber RJ, Osland P (1979) *Phys Lett B* 80:401
- Gregoire C et al (1985) *Nucl Phys A* 436:365
- Griffin JJ et al (1966) *Phys Rev Lett* 17:478
- Gross DHE (1990) *Rep Prog Phys* 53:605
- GSI (2010) <http://www.gsi.de>
- Hanson PG, Tostevin JA (2003) *Annu Rev Nucl Part Sci* 53:219
- Hanson PG, Jensen AS, Jonson B (1995) *Annu Rev Nucl Part Sci* 45:591
- Hauser W, Feshbach H (1952) *Phys Rev* 87:366
- Hermann N, Wessels JP, Wienold T (1999) *Annu Rev Nucl Part Phys* 49:581
- Hiebert JC, Garvey GT (1964) *Phys Rev* 135:B346
- Hodgson PE (1967) *Annu Rev Nucl Sci* 17:1
- Horowitz CJ, Piekarewicz J (2002) *Phys Rev C* 66:055803
- Horowitz CJ, Schwenk A (2006) *Nucl Phys A* 776:55
- HRIBF (2003) <http://www.phy.ornl.gov/hribf/hribf.html>
- Huizenga JR, Moretto LG (1972) *Annu Rev Nucl Sci* 22:427
- IAEA (2010) <http://www.iaea.or.at/worldatom/rddb/>
- Ignatyuk AV et al (1975) *Yad Fiz* 21:1185; *Sov J Nucl Phys* 21:612
- Janssens RVF, Khoo TL (1991) *Annu Rev Nucl Sci* 41:321
- JINR (2003) <http://www.jinr.ru/>
- Kittel C (1986) *Elementary statistical physics*. Dover, Mineola, QC174.8K56
- Kowalski S, Natowitz JB, Shlomo S et al (2007) *Phys Rev C* 75:014601
- Kramers HA (1940) *Physica* (Amsterdam) 7:284
- Krane KS (1988) *Introductory nuclear physics*. Wiley, New York
- Lanzafame HM, Blann M (1970) *Nucl Phys* 142:545
- Lee J, Tsang MB et al (2010) *Phys Rev Lett* 104 :112701
- Li B-A, Ko CM (1997) *Nucl Phys A* 618:498
- Li B-A, Chen L-W, Ko CM (2008) *Phys Rep* 464:113
- Li T, Garg U et al (2007) *Phys Rev Lett* 99:162503
- Loveland W (2007) *Phys Rev C* 76:014612
- Lovett R (2007) *Rep Prog Phys* 70:195
- Lynch WG (1987) *Annu Rev Nucl Part Sci* 37:493
- Magestro DJ et al (2000) *Phys Rev C* 61:C21602(R)
- Mahaux C, Sartor R (1990) *Adv Nucl Phys* 20:1
- McCalla SG, Lestone JP (2008) *Phys Rev Lett* 101:032702
- McMahan MA et al (1987) *Phys Rev Lett* 54:1995
- Messiah A (1958) *Quantum Mechanics*, Dover Books
- Moretto LG (1975) *Nucl Phys A* 247:211
- Mueller H, Serot BD (1995) *Phys Rev C* 52:2072
- Myo T, Kato K, Toki H, Ikeda K (2007) *Phys Rev C* 76:024305
- Natowitz J et al (2002) *Phys Rev Lett* 89:212701
- Natowitz J et al (2010) *Phys Rev Lett* 104, 202501
- NEA (2010) <http://www.nea.fr>
- NNDC (2010) <http://www.nndc.bnl.gov>
- Nörenberg W et al (1974) *Phys Lett B* 52:289
- Nörenberg W et al (1976) *Z Phys A* 274:241
- NRC (1999) In: Committee on Nuclear Physics, National Research Council (ed) *Nuclear physics: the core of matter, the fuel of stars*. <http://books.nap.edu/catalog/6288.html>
- Ono A, Horiuchi H (1996) *Phys Rev C* 53:2341, *Ibid.* p. 2958
- Otsuka T (2005) *Phys Rev Lett* 95:232502
- Pfaff R et al (1996) *Phys Rev C* 53:1753
- Pieper SC, Varga K, Wiringa RB (2002) *Phys Rev C* 66:044310
- Polish ł et al (1990) *Phys Rev C* 41:942
- Pochodzalla J et al (1995) *Phys Lett* 75:1040
- Prakash M, Wambach J, Ma ZY (1983) *Phys Lett B* 128:141
- Randrup J (1978) *Ann Phys* (NY) 112:356
- Randrup J, Koonin SE (1981) *Nucl Phys A* 356:223
- Reisdorf W (1981) *Z Phys A* 300:227
- Reisdorf W, Ritter HG (1997) *Annu Rev Nucl Part Sci* 47:663
- RHIC (2005) BRAHMS, PHENIX, PHOBOS, and STAR white papers. *Nucl Phys A* 757:1
- RHIC (2010) <http://www.bnl.gov/RHIC>
- RIKEN (2010) <http://www.rarf.riken.go.jp>
- RNDK (2003) <http://www.ippe.obninsk.ru/podr/cjd/>
- Rolfs CE, Rodney WS (1988) *Cauldrons in the cosmos*. University of Chicago Press, Chicago
- Rutherford E (1911) *Phil Mag* 21:669
- Saint-Laurent F, Conjeaud M, Dayras R, Harar S, Oeschler H, Volant C (1984) *Nucl Phys A* 422:307
- Samaddar SK, De JN, Viñas X, Centelles M (2007) *Phys Rev C* 75:054608
- Samaddar SK, De JN, Viñas X, Centelles M (2008) *Phys Rev C* 78:034607
- Schlagel TJ, Pandharipande VJ (1987) *Phys Rev C* 36:162
- Schröder WU, Huizenga JR (1977) *Annu Rev Nucl Sci* 27:465
- Serber R (1947) *Phys Rev* 72:1114
- Shetty DV, Yennello SJ, Souliotis GA (2007) *Phys Rev C* 76:024606
- Shlomo S, Kolomietz VM (2004) *Rep Prog Phys* 67:1
- Shlomo S, Natowitz JB (1990) *Phys Lett B* 252:187
- Sobotka LG et al (1987) *Phys Rev C* 36:2713
- Sobotka LG, Charity RJ, Töke J, Schröder WU (2004) *Phys Rev Lett* 93:132702

- Sorlin O et al (1993) Phys Rev C 47:2941
Strutinsky VM (1967) Nucl Phys A 95:420
Subedi R et al (2008) Science 320:1476
TAMU (2010) <http://cyclotron.tamu.edu/>
Tamura T (1965) Rev Mod Phys 37:679
Tanihata I et al (1985) Phys Rev Lett 55:2676
Thirring W, Narnhofer H, Posch HA (2003) Phys Rev Lett 91:130601
Töke J, Schröder WU (1992) Ann Rev Nucl Part Sci 42:401
Töke J, Swiatecki WJ (1981) Nucl Phys A372:141
Toneev VD et al (1990) Nucl Phys A 519:463c
Trautmann W (2001) In: Norenberg W, Guerreau D, Metag V (eds) Nucleus-nucleus collisions 2000. North-Holland, Amsterdam
TRIUMF (2010) <http://www.triumf.ca>
Tsang MB et al (1984) Phys Lett 134B: 169
Tsang MB et al (2009) Phys Rev Lett 102:122701
Vandenbosch R (1992) Annu Rev Nucl Part Sci 42:447
Vandenbosch R, Huizenga JR (1973) Nuclear fission. Academic, New York
Viola VE, Kwiatkowski K, Walker M (1985) Phys Rev C 31:155
Viola VE et al (2006) Phys Rep 434:1
Wagemans C (2000) The nuclear fission process. CRC Press, Boca Raton
Weisskopf VF, Ewing DH (1940) Phys Rev 57:672
Wilczynski J et al (1973) Phys Lett 47b:484
Wu J, Chang CC, Holmgren HD (1979) Phys Rev C 19:370
Yarif Y, Fraenkel Z (1981) Phys Rev C 24:488
Youngblood DL, Clark HL, Lui Y-W (1999) Phys Rev Lett 82:691



4 Nuclear Fission

J. O. Denschlag

Universität Mainz, Mainz, Germany

4.1	<i>Introduction</i>	224
4.2	<i>History of the Discovery of Nuclear Fission</i>	224
4.2.1	The Discovery of the Neutron	224
4.2.2	Search for Transuranium Elements	226
4.2.3	Discovery of Alkaline Earth Metals: Identification of Barium	227
4.2.4	Arguments of Nuclear Physicists and Publication	228
4.2.5	Interpretation of the Fission Process by L. Meitner and O. R. Frisch	230
4.2.6	Missed Opportunities	231
4.3	<i>Model Considerations</i>	232
4.3.1	The Liquid Drop Model (LDM)	232
4.3.2	Fission Barrier in the Liquid Drop Model	233
4.3.3	The Fissility Parameter	234
4.3.3.1	Second Derivation of the Fissility Parameter	236
4.3.4	LDM and Fission-Critical Evaluation	238
4.3.5	The Shell Model	239
4.3.6	The Combination of the Liquid Drop Model and the Shell Model According to Strutinsky	242
4.3.7	Further Model Considerations	244
4.4	<i>Experimental Facts and Interpretation</i>	244
4.4.1	Sequence of Events Leading to Fission	244
4.4.2	Chain Yields	245
4.4.2.1	Methods of Measurement	245
4.4.2.2	Experimental Results and Interpretation	249
4.4.3	Nuclear Charge Distribution	262
4.4.3.1	Methods of Measurement of Independent Yields	264
4.4.3.2	Experimental Results and Systematic Description (Z_p -Model)	266
4.4.3.3	Physical Implications of the Nuclear Charge Distribution in Fission	269
4.4.4	Ternary Fission	270
4.4.5	Fission Isomers	272
4.4.5.1	Detection and Measurement of Half-Lives	272
4.4.5.2	Deformation (Charge Plunger Experiment)	275
4.4.5.3	Level Densities in the Isomers	276

Abstract: This chapter first gives a survey on the history of the discovery of nuclear fission. It briefly presents the liquid-drop and shell models and their application to the fission process. The most important quantities accessible to experimental determination such as mass yields, nuclear charge distribution, prompt neutron emission, kinetic energy distribution, ternary fragment yields, angular distributions, and properties of fission isomers are presented as well as the instrumentation and techniques used for their measurement. The contribution concentrates on the fundamental aspects of nuclear fission. The practical aspects of nuclear fission are discussed in [Chap. 57](#) of Vol. 6.

4.1 Introduction

Nuclear fission has had a large impact on human life, probably greater than any other field of radiochemistry. It has truly changed the world for good or for bad. Nuclear power stations are producing electricity for billions of dollars every year, and nuclear weapons changed the military and political equilibrium between nations. Research reactors used as intense sources of neutrons through neutron diffraction have contributed immensely to the knowledge of the structure of biological molecules or to the development of new materials. Nuclear reactors are used for the mass production of radioisotopes required in medical diagnosis and therapy and in modern technology.

The study of the process of nuclear fission as such has also contributed to the fundamental knowledge of matter. A nucleus that undergoes fission has to change its shape from a round-shaped or somewhat deformed ground state to some elongated dumbbell-like configuration, which finally divides into two fragments. Such a large-scale collective motion cannot be observed in other processes at low nuclear temperature. It gives very valuable information on the existence and the survival of shells and nucleon pairs in nuclear matter. This way, it carries information on the viscosity of nuclear matter. The distribution of protons and neutrons between the two fragments formed is informative of the electrical polarizability of nuclear matter. The fission process cannot be understood without taking into account the two complementary aspects of matter: particles and waves.

This chapter, which has been elaborated through giving lectures to students of chemistry, concentrates on these latter fundamental aspects of nuclear fission. The presentation is sometimes more qualitative than quantitative in order to address also the nonspecialist. Due to the large volume of research accomplished in the 7 decades since its discovery and also because of the complexity of the matter, this chapter cannot be exhaustive. Many references have to be made to some more specialized literature. To start with, an early work (Vandenbosch and Huizenga 1973) and a more recent comprehensive volume (Wagemans 1991b) should be mentioned, which will give access to many further references. Partly for didactical reasons, this chapter will more or less follow the historical evolution of experimental techniques used and the knowledge gained. A first point of discussion will be the highly interesting sequence of events that led to the discovery of the process.

4.2 History of the Discovery of Nuclear Fission

4.2.1 The Discovery of the Neutron

The way to nuclear fission was paved by the discovery of the neutron (Chadwick 1932a, b). This discovery was made relatively late compared to the discovery and characterization of the two

other basic (charged) constituents of the atom, the electron (Thomson 1897) and the proton whose fundamental character was probably first recognized by E. Rutherford (Rutherford 1914) (“the suggestion that the hydrogen nucleus is the positive electron”) following some earlier work on electric discharges in gasses (e.g., Goldstein 1886; see Glasstone 1967).

Already in 1920, Rutherford predicted the existence of a sort of neutral particle within the nucleus on the following grounds (Rutherford 1920): From his earlier experiments on the straggling of α particles passing through thin metal foils (Rutherford 1914) it was known that the atom consisted of a small positively charged nucleus surrounded by a cloud of electrons. The charge of the nuclei of the individual elements became known through the pioneering work of Moseley (Moseley 1913, 1914). If one made the reasonable assumption that the nuclear charge of an atomic nucleus was due to a corresponding number of protons, it turned out that the mass of this atom (or atomic nucleus) was generally about twice the value calculated from the number of protons. This observation led Rutherford to predict the presence of electrons besides protons within the nucleus (Rutherford 1920). He viewed these intranuclear electrons as forming “a very close and powerful combination with the charged positive units.” In 1927, after the formulation of the uncertainty principle by Heisenberg (Heisenberg 1927) the proposed existence of electrons as a separate entity within the nucleus even in the form postulated above had to be given up because an electron confined to the small volume of a nucleus would have an energy too high to be stable within the nucleus.

As a consequence, one was searching for a neutral particle. More by chance, Bothe and Becker (Bothe and Becker 1930a, b) found an unusually hard (energetic) “ γ ” radiation emitted when light elements like lithium and beryllium were exposed to α radiation. From the absorption in lead, they calculated an energy of 10 MeV. This radiation was also studied by Curie and Joliot (Curie and Joliot 1932). These authors found that protons were ejected from paraffin and calculated a “ γ ”-ray energy of even 50 MeV – a large discrepancy from the results of Bothe and Becker.

Finally, Chadwick studied the radiation emitted when beryllium was exposed to α particles from ^{210}Po by measuring the energy of recoil protons from paraffin and recoil nitrogen atoms in gaseous nitrogen. His results led to inconsistencies when he assumed that the unknown radiation was γ radiation and that the scattering mechanism was following the law of Compton scattering taking place with the corresponding nuclei (proton or nitrogen) rather than with electrons. The observed recoil energies led however to conclusive results when he assumed that the unknown radiation was composed of particles (of mass one and no charge) rather than photons (Chadwick 1932a, b). The nuclear reaction producing neutrons was



The neutron provided the nuclear physicist (or chemist) for the first time with a simple means to carry out artificial nuclear reactions. The production of neutrons did not require large and expensive accelerators. A mixture of beryllium powder with an α emitter in a little tube was sufficient to produce a neutron source of 10^6 neutrons per second. Neutrons possess no charge. Consequently, they do not have to overcome a Coulomb barrier and therefore do not have to be accelerated to enter an atomic nucleus. On the contrary, “capture cross sections” are usually larger for neutrons of smaller energy (thermal neutrons) because due to their lower velocity their residence time near a particular nucleus is larger.

The capture of a neutron by a nucleus produces an isotope with a mass number one unit higher:



The nucleus formed is often unstable and undergoes a β^- decay in which a neutron within the nucleus is transformed into a proton, an electron, and an antineutrino:



The net result of neutron capture is thus normally a radioactive isotope of the element exposed to neutrons, which, at its decay, will form an isotope of the element with the next higher atomic number. The isotope formed may be stable or may again be radioactive and undergo another nuclear transformation to finally reach stability.

The availability of neutron sources opened the way to the production of radioactive isotopes of most elements and, in fact, practically all the elements of the periodic system were exposed to neutrons within the following years. This was mainly done in three locations: Rome by Fermi and coworkers, Paris by the Curies and coworkers and, a little later in Berlin by Hahn, Meitner, and Strassmann.


4.2.2 Search for Transuranium Elements

A particularly interesting element for these studies was uranium, the heaviest and last element of the periodic system known at that time with the atomic number $Z = 92$. Neutron capture and subsequent β^- decay in this case should lead to a new, hitherto unknown, element (“transuranium element”). What would the chemical properties of element 93 be?

There was a problem: The chemical properties of element 93 were evidently unknown; on the other hand, a certain knowledge of its chemical properties would be required in order to isolate and identify the element or elements formed.

To predict the chemical properties, the periodic system of the elements was resorted to. At the time, however, the last part of the periodic system, including the elements Ac, Th, Pa, and U, was not known correctly. In particular, it was not recognized that these elements belong to the group of the actinides. Due to the most stable oxidation states of the four elements [Ac (III), Th (IV), Pa (V), and U (VI)], they were thought to belong to the group of the transition elements and, hence, were considered homologues of the elements La, Hf, Ta, and W. The elements beyond U were expected to be homologues of Re, Os, Ir, and Pt. Therefore, it was expected that they would form insoluble sulfides and that they could be separated in this way from the uranium and identified. Today it is known that the elements beyond actinium form the group of actinides with different chemical properties and in particular do not form insoluble sulfides.

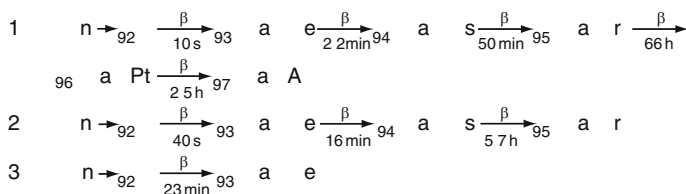
Nevertheless, when, e.g., Fermi and coworkers were irradiating uranium with neutrons and made a precipitation of sulfides from the solution, radioactive products were indeed found. Now it is known that these products were fission products, different isotopes of lighter elements, like tellurium and antimony. The scientists involved in this work assumed, however, for reasons to be discussed later, that elements much lighter than uranium could not be formed in a process induced by slow neutrons. As a consequence, they came to the conclusion that transuranium elements were formed.

The combined results on the “transuranium” elements formed by the irradiation of uranium by neutrons as obtained by the different groups involved and as generally accepted at the time (Meitner et al. 1937) are shown in  Fig. 4.1. The results were, however, surprising (and somewhat suspicious) in two respects.

■ Fig. 4.1


Transuranium elements as believed to be established by 1937; after (Meitner et al. 1937).

The prefix Eka (= one from Sanskrit) indicates a heavy homologue of the corresponding element. Eka is a designation chosen by Mendeleev for unknown elements expected for empty places in his early periodic system



- Whereas in the simple (n, γ) -reactions taking place in other (lighter) elements normally one β transition or at most two β transitions lead to a stable nuclide, here long chains of up to six radioactive isotopes could be identified.
- A second surprise was the observation of more than one such chain. Since ^{238}U represents 99.3% of natural uranium, the contribution of the other isotopes of uranium should be negligible. Consequently, one was expecting one and only one decay chain starting with ^{239}U . Certainly, isomers, i.e., nuclides with the same mass number and nuclear charge but different half-lives were known. Such isomers, if undergoing a β decay, would however decay to the same daughter nucleus and not form a completely separate chain of radionuclides.

Today one understands the above results as due to fission products, i.e., different elements and different isotopes of single elements, as will be discussed later.

In the year 1938, Enrico Fermi received the Nobel Prize among others for the results shown in  Fig. 4.1. Half a year later it was clear that all the information given there was incorrect.

4.2.3 Discovery of Alkaline Earth Metals: Identification of Barium

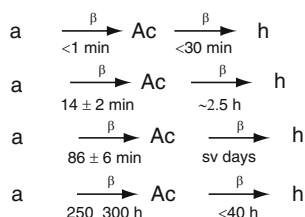
The situation became seemingly more complicated by an observation of Curie and Savitch (Curie and Savitch 1938a, b), of an activation product (half-life of about 3.5 h “that behaved like lanthanum.” Today it is known, the authors had observed the fission products ^{141}La (3.9 h) with an admixture of ^{142}La (92 min). This observation led however to the resolution of all the problems, namely to the discovery of nuclear fission.

Hahn, Meitner, and Strassmann put forward the hypothesis that this nuclide could be an isotope of actinium, the heavy homologue of lanthanum. Actinium could have been formed by the β decay of radium and radium could have been originated from uranium by an $(n, 2\alpha)$ -reaction – actually an unlikely reaction for energetic reasons.

The hypothesis got some support from the fact that the activity coprecipitated from the solution of irradiated uranium with a precipitate of salts of added barium – the lighter homologue of radium. Hahn and coworkers used a coprecipitation with barium chloride from a solution of concentrated hydrochloric acid. Under these conditions, the BaCl_2 precipitate is very clean and one could conclude that a radioactive species coprecipitated would have to be an element belonging to the group of alkaline earths, namely Sr, Ba, or Ra. Since barium

■ Fig. 4.2

Radioisotopes identified after coprecipitation with barium chloride and initially attributed to radium; after (Hahn and Strassmann 1939)



and its lighter homologues were excluded on grounds to be discussed later, the conclusion was that indeed radium was formed. In further studies, again four chains of “isomers” were identified (Hahn and Strassmann 1939) (► Fig. 4.2).

The activity of 3.5 h half-life behaving like lanthanum as claimed by Curie and Savitch was indeed found (Ac II with 2.5 h). In reality, as discussed above, this activity originated from a mixture of 3.93 h ^{141}La and 92.5 min ^{142}La .

In further experiments, Hahn and Strassmann tried to separate the radium from the barium (that was added to carry out the coprecipitation procedure). Such a separation between barium and radium is not easy because of the similar chemical properties of homologues. The chemist uses a procedure of fractionated crystallization in which only “fractions” of the total mixture are precipitated. In the first fractions of the precipitate, the element with a lower solubility is enriched. If a series of such precipitations is carried out in a systematic way, one eventually comes to a clean separation even between elements of similar properties.

Hahn and Strassmann used different salts (bromides, chromates) trying to separate radium from barium. (Lise Meitner had to leave the team in 1938 due to the political situation in Germany. She found a position in the Physical Institute of the Academy of Sciences, Stockholm. She remained, however, in close contact by letters with O. Hahn and F. Strassmann.) Surprisingly no enrichment of the less soluble radium was found in the first fractions. As these chemical procedures are difficult and may not always be successful, they tested the procedure by adding ^{226}Ra , a natural α -emitting isotope of radium. The result of this crucial experiment performed on December 17, 1938 was a big surprise: The natural radium did show enrichment in the first fractions but the radioactive species produced in the neutron irradiation of uranium did not. For a chemist the conclusion could only be that this species was not radium but barium, an element with roughly half the mass of uranium – a conclusion which, with only light-particle emission being known, seemed to disagree with one of the basic laws of physics, namely, energy conservation.

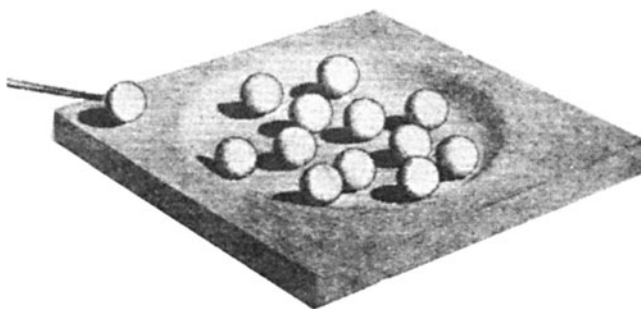
4.2.4 Arguments of Nuclear Physicists and Publication

This argument of the nuclear physicists is perhaps best illustrated by a sketch presented in a popular talk by N. Bohr referred in (Bohr 1936) and shown in ► Fig. 4.3.

The shallow basin filled with billiard balls shown represents a nucleus filled with protons and neutrons. An incoming slow or thermal neutron would share its liberated binding energy (represented here by the difference in height between rim and basin) with other nucleons. This

■ Fig. 4.3

Sketch of a shallow basin with billiard balls shown by N. Bohr in 1936 to illustrate the concept of a nucleus capturing a neutron (Bohr 1936)



would normally lead to an excited state that would return to the ground state by emission of γ rays. In a few cases, it could be that by chance after many collisions the total energy would concentrate on a single neutron again. In that case this neutron would have enough energy to leave the nucleus, a so-called (n,n') -process. If the incoming neutron had a kinetic energy higher than the separation energy of a neutron or of an α particle (a few MeV), the process could lead to the emission of two neutrons in a so-called $(n,2n)$ -process or to the emission of an α particle called (n,α) -process, respectively.

From this picture it is, however, obvious that an incoming thermal neutron could not lead to the loss of nearly half the nucleons. Such a process would indeed violate the basic law of conservation of energy. The qualitative picture presented here was actually backed by some sound theory on α decay (Gamov 1928; Gurney and Condon 1928, 1929).

The physics community was therefore convinced that nuclear reactions induced by thermal neutrons or neutrons with a few MeV of energy could not produce reaction products further away from the original (“target”) nucleus than a few mass units.

Therefore, Hahn and Strassmann were reluctant to accept the consequences of their own discovery. In a letter to Lise Meitner, Hahn wrote on December 19:

- ▶ *Es ist (nämlich) etwas bei den “Radium Isotopen”, was so merkwürdig ist, dass wir es vorerst nur Dir sagen..... Unsere Ra-isotope verhalten sich wie Ba.... Wir wissen dabei selbst, dass es nicht in Ba zerplatzen kann (There is something so strange with the “radium isotopes” that for the moment we tell it only to you. ... Our radium isotopes behave like barium... We know, however, ourselves that it cannot burst into barium...).*

Even though Hahn and Strassmann did not realize fully at this moment the consequences of their discovery, they knew that their results would change fundamental aspects of nuclear physics. They also knew that Curie and Savitch (with their discovery of a β emitter of 3.5 h half-life “that behaved like lanthanum”) were extremely close to the same discovery. Therefore, they wanted to publish their results quickly. They selected the journal *Naturwissenschaften* for its rapidity.

It seemed too time consuming to both to write a new publication. They had a manuscript describing the decay properties of the supposed radium isotopes: “Über den Nachweis und das Verhalten der bei der Bestrahlung des Urans mittels Neutronen entstehenden Radium-Isotope” (On the detection and the properties of the radium isotopes formed in the irradiation of

uranium with neutrons). This manuscript was changed in a few points: In the title, Radium Isotope was changed in Erdalkalimetalle (alkaline earth metals). The article (Hahn and Strassmann 1939) describes the measurements of the radium isotopes as formulated in the original draft. At the end, a few paragraphs were added:

- *Nun müssen wir aber noch auf einige neuere Untersuchungen zu sprechen kommen, die wir der seltsamen Ergebnisse wegen nur zögernd veröffentlichen...* (Now we have to discuss some more recent studies, which we publish with a certain hesitation because of their strange results.)

After the description of the fractionated crystallization it follows:

- *Wir kommen zu dem Schluss: Unsere "Radiumisotope" haben die Eigenschaften des Bariums; Als Chemiker müssten wir eigentlich sagen, bei den neuen Körpern handelt es sich um Barium... Als der Physik in gewisser Weise nahestehende Kernchemiker können wir uns zu diesem, allen bisherigen Erfahrungen der Kernphysik widersprechenden, Sprung noch nicht entschließen...* (We come to the conclusion: our "radium isotopes" behave like barium; as chemists we ought to say the new substances are barium... As nuclear chemists that are in a certain way close to physics, we cannot yet decide to make this leap, which would contradict all the previous knowledge on nuclear physics).

The rapidity of the publication of the results was impressive: After the decisive experiment on December 17 (counting of the samples continued until December 21), the revised manuscript was finished on December 22 (just before Christmas). Otto Hahn called up his friend Paul Rosbaud, a freelance of Die Naturwissenschaften practically in charge of natural science. He came over, got the article, brought it to the printing shop, and replaced another article in press by the one of Hahn and Strassmann. The galley proofs were finished by December 27 and the article was out by January 6, 1939.

4.2.5 Interpretation of the Fission Process by L. Meitner and O. R. Frisch

Besides the letters, Hahn and Strassmann had sent a preprint of the article to Lise Meitner. She took along the news to Kungälv near Göteborg in Sweden, where she spent the Christmas holidays with her nephew Otto R. Frisch. During an extended walk through the wood, they discussed it and suddenly came to the conclusion that indeed fission of a heavy nucleus into two fragments of similar size was certainly possible – and even to be expected. The mechanism of such a reaction would have to be very different from the emission of small particles (neutrons, protons, α particles) and different from what was in a way suggested by a simple picture as shown in ► Fig. 4.3.

Unlike what is suggested by ► Fig. 4.3, a nucleus can get deformed, and actually a quantitative model describing a nucleus as a liquid drop was already existing, 4 years before (Weizsäcker 1935)! This model describes the nucleus as held together by short-range forces. The total binding energy is influenced, among other terms, by the surface energy and by the Coulomb repulsion between the protons. Even while walking through the wood, Meitner and Frisch could estimate that for nuclei with around 92 protons (uranium, with $Z = 92$) the cost of surface energy at deformation could be balanced by a gain in Coulomb energy. Thus, with the excitation energy due to the capture of a neutron, such a nucleus would become unstable against deformation, could evolve into an elongated form, and be driven apart into two fragments. They could estimate that an amount of about 200 MeV would be set free by such

a “fission” reaction, as they chose to call it and that this energy would appear to be about 80% in the form of kinetic energy of the fragments.

In agreement with Hahn and Strassmann, they sent a corresponding manuscript to Nature (on January 16, 1939) (Meitner and Frisch 1939), where, for the first time, the word fission was used. From the estimate that the kinetic energy of the two fragments is about 160 MeV, one could derive that such fragments would make huge signals (of about 80 MeV for each fragment) in an ionization chamber. On his return home, Frisch irradiated a uranium-coated ionization chamber and observed the corresponding pulses with an energy of at least 70 MeV (Frisch 1939).

Lack of space restricts the presentation of details on the history of the discovery of nuclear fission. Detailed accounts of this history and of the scientists involved are published in a number of monographs and journal articles (e.g., Hahn 1962; Frisch 1979; Krafft 1981; Kramish 1986; Lemmerich 1989; Herrmann 1990a, b; Herrmann 1995; Sime 1996).

4.2.6 Missed Opportunities

Three times at least before, one missed the discovery of fission by an inch:

1. Ida Noddack (Noddack 1934) criticized the claim of the discovery of element 93 by “*Es wäre denkbar, dass bei der Beschießung schwerer Kerne mit Neutronen diese Kerne in mehrere größere Bruchstücke zerfallen, die zwar Isotope bekannter Elemente, aber nicht Nachbarn der bestrahlten Elemente sind*” (It would be conceivable that in the bombardment of heavy nuclei with neutrons these nuclei disintegrate into several larger fragments, which are isotopes of known elements but not necessarily neighbors of the irradiated elements). If Noddack had made a pertinent experiment, she would certainly have found the truth 4 or 5 years earlier than Hahn and Strassmann.
2. Experiments using thin layers of uranium or thorium in an ionization chamber like the one made by Frisch to confirm the occurrence of fission were made by many scientists (see, e.g., Herrmann 1995) to study the β decay of radioisotopes produced or to search for high-energy α particles. In these cases, normally the uranium or thorium layer was covered by a thin foil to absorb the high α background of the natural α decay. In some cases, reportedly, the foils were inadvertently omitted and the large fission pulses were observed. They were however interpreted as artifacts of electronics and ignored (see Walton 1961; Flügge 1989).
3. In another case the fission pulses were attributed to high-energy α particles searched for (Braun et al. 1937).

A few months after the discovery of fission, it was clear that neutrons were set free in the process (von Halban jun et al. 1939). This initiation opened the way to speculations for a self-propagating chain reaction that would produce almost unlimited amounts of energy for peaceful and military uses (Flügge 1939). With the beginning of World War II, this had the consequence that from 1940 to the end of the war results on the fission process were kept secret and could not be published. Meanwhile, enormous efforts and money were invested in the development of nuclear reactors and nuclear weapons, particularly in the USA and somewhat later also in the Soviet Union, in Great Britain, France, China, and in other countries. These developments will not be covered here. Further information may be found in [Chap. 1](#) of this Volume. The rest of this chapter will be dedicated to the physics of the fission process, i.e., to the experimental methods used, to the results, and their implications on the structure and behavior of nuclear matter.

4.3 Model Considerations

4.3.1 The Liquid Drop Model (LDM)

The liquid drop model of Weizsäcker (Weizsäcker 1935), which allowed Meitner and Frisch to understand the most important features of fission during the hour of their walk through the woods of Kungälv shall be discussed in the following. Actually, this model, published 4 years before the discovery of nuclear fission, has the inescapable consequence that nuclei with a sufficiently high atomic number must be unstable and ought to undergo fission into fragments of similar sizes. It is astounding that this consequence had not been seen before.

An example for various slightly differing mathematical formulas for the binding energy (E_B) of a nucleus as given in textbooks is (Mayer-Kuckuck 1970)

$$E_B = aA - bA^{2/3} - c \frac{Z^2}{A^{1/3}} - d \frac{(Z - A/2)^2}{A} \pm \frac{p}{A^{1/2}} \quad (4.4)$$

(cf. ► Eq. (2.3) in Chap. 2). The model views an atomic nucleus as a drop of a liquid. A drop of normal liquid is held together by the van der Waals forces well known to the chemist as attractive forces of short range. In the atomic nucleus, these short-ranged forces are the “nuclear forces.” The terms appearing in ► Eq. (4.4) will be discussed briefly.

Term 1 (Volume energy = aA)

The consequence of the short range of nuclear forces is that the total binding of a nucleus (in analogy to a drop) is, to a first approximation, proportional to the number of nucleons. Each nucleon feels only its direct neighbors. As a consequence, the first term in ► Eq. (4.4) is given by a force constant (a) times the number of nucleons (A).

Term 2 (Surface energy = $bA^{2/3}$)

Nucleons on the surface feel an attractive force only from inside, so that their binding energy is smaller. The missing contribution has to be subtracted from term (1). The contribution is proportional to the surface ($S = 4\pi R^2$, for a sphere of radius R). Since nuclear matter is incompressible, the volume (V) of a nucleus is proportional to the number of nucleons, i.e., to the mass number (A). As, generally, the volume of a sphere is given by $V = (4/3)\pi R^3$, the radius is proportional to $V^{1/3} \propto A^{1/3}$. Hence, the surface of a spherical nucleus is proportional to $A^{2/3}$. In term (2) of ► Eq. (4.4), $A^{2/3}$ appears with the constant b .

Term 3 (Coulomb energy = $cZ^2/A^{1/3}$)

The protons all have positive charges and, hence, are repelled by each other. This repulsion diminishes the binding force and the term representing Coulomb repulsion has a negative sign in ► Eq. (4.4). The electrostatic repulsion energy in a uniformly charged spherical drop with radius R and a total electric charge q is

$$\frac{3q^2}{5R} \frac{1}{4\pi\epsilon_0}.$$

Since $q = Ze$ (Z = number of protons) and $R = r_0 A^{1/3}$, one can write $cZ^2/A^{1/3}$.

Term 4 (Asymmetry energy = $d(Z - A/2)^2/A$)

This term is beyond the analogy of a liquid drop and results from the fact that there are two constituents of the atomic nucleus (neutrons and protons) that can occupy two different sets of quantum states. The term becomes zero when the number of protons in a nucleus equals that of neutrons ($Z = A/2$).

Term 5 (Pairing energy = $\pm p/A^{1/2}$)

This term (abbreviated frequently with δ) takes care of the fact that nuclei with even numbers of protons and neutrons are more stable. The constant p has a positive sign for nuclei with even numbers of protons and of neutrons (even–even nuclei) and a negative sign for nuclei with odd numbers of protons and of neutrons (odd–odd nuclei). It is set equal to zero for odd–even and even–odd nuclei. The pairing energy is responsible for the fact that in low energy fission, products with even numbers of nucleons generally dominate. This “odd–even effect” allows theoreticians to study the internal excitation energy (temperature) of a fissioning nucleus at scission.

The following quantitative discussions will be based on a modified version of [Eq. \(4.4\)](#) (Myers and Swiatecki 1966; Friedlander et al. 1981): [Eq. \(4.5\)](#) differs from [Eq. \(4.4\)](#) by the fact that the asymmetry energy is not only subtracted from the volume energy (term 1) but also from the surface energy (term 2). This is consistent and follows from the definition of the surface energy. In addition, a further term, ($f Z^2/A$), is added, which takes into account that nuclear surface is somewhat diffuse.

$$E_B = (aA - bA^{2/3}) \left[1 - d \frac{(Z - A/2)^2}{A} \right] - c \frac{Z^2}{A^{1/3}} + f \frac{Z^2}{A} \pm \frac{p}{A^{1/2}} \quad (4.5)$$

with $a = 15.677$ MeV; $b = 18.56$ MeV; $c = 0.717$ MeV; $d = 1.79$; $p = \pm 11$ MeV or 0 as has been discussed in the context of [Eq. \(4.4\)](#); $f = 1.211$ MeV.

Evidently the liquid drop model can be used to calculate the mass ($M(Z, A)$ in atomic mass units) of any atom as a function of its number of protons (Z) and neutrons (N):

$$M(Z, A) = Z M(1, 1) + (A - Z) M(0, 1) - E_B/c^2. \quad (4.6)$$

Here $M(1, 1)$ and $M(0, 1)$ are the mass of a hydrogen atom (proton and pertinent electron) and neutron, respectively; c is the speed of light in vacuum and E_B is defined by [Eq. \(4.4\)](#) or [Eq. \(4.5\)](#).

4.3.2 Fission Barrier in the Liquid Drop Model

The liquid drop model is a very versatile instrument, which explains not only fission as a process in which the Coulomb energy driving a nucleus apart would overcome the surface energy holding it together but also gives an estimate for the amount of energy set free in the process. Actually, it is very easy to write a little program for [Eqs. \(4.4\)](#), [Eq. \(4.5\)](#) or [Eq. \(4.6\)](#) and study its implications for the stability of matter as a function of A and Z . Some of the implications for the understanding of the fission process shall be discussed in the following.

The first question concerns the region of instability toward fission. A plot of the binding energy of nuclei versus mass derived from experimental masses of stable elements or calculated from [Eq. \(4.4\)](#) or [Eq. \(4.5\)](#) for the optimum neutron to proton ratio shows a maximum of stability around mass $A = 60$. Nevertheless, stable nuclei are found up to a mass number of $A = 209$. This is due to the fact that a barrier exists that prevents these nuclei from decaying into the most stable nuclei around $A = 60$. This barrier is due to the repulsive Coulomb force that a charged particle undergoes when emerging from a heavier nucleus. In order to estimate this barrier height for a heavy nucleus fissioning into two fragments of equal size one can proceed in the following way. One calculates the binding energy of a nucleus, $E_B(Z_f, A_f)$, with mass number

A_f and atomic number Z_f and the binding energy of two fission products of half the mass ($2E_B(Z_f/2, A_f/2)$). The total energy (Q_f) set free in this fission process is then given by

$$Q_f = 2E_B(Z_f/2, A_f/2) - E_B(Z_f, A_f) \quad (4.7)$$

For $A_f = 238$ and $Z_f = 92$ (^{238}U) this gives a value of $Q_f = 193$ MeV. This value is valid for the ground states of the two fission products in infinite distance from each other. In order to obtain a limit for the barrier height, the two fission products will be imagined to approach each other until they touch and then the Coulomb energy that is required to be overcome will be calculated. Mathematically the Coulomb potential V_C (actually: potential energy) between two uniformly charged spheres is given by

$$V_C = \frac{Z_1 Z_2 e^2}{4\pi\epsilon_0(R_1 + R_2)} \quad (4.8)$$

with $e = 1.602 \times 10^{-19}$ As and $\epsilon_0 = 8.854 \times 10^{-12}$ As/(Vm). Setting $Z_1 = Z_2 = Z_f/2$, $R_1 = R_2 = R$ (for two fission fragments of equal size, i.e., symmetric fission), $R = r_0(A_f/2)^{1/3}$, one obtains

$$V_C = \frac{(Z_f/2)^2 e^2}{2(A_f/2)^{1/3} 4\pi\epsilon_0 r_0}. \quad (4.9)$$

Introducing the numerical values of the constants e and ϵ_0 and choosing a value of 1.5×10^{-15} m for r_0 one obtains

$$V_C = 0.151 \frac{Z_f^2}{A_f^{1/3}} (\text{MeV}). \quad (4.10)$$

For the (symmetric) fission of ^{238}U ($Z_f = 92$) one gets $V_C = 206$ MeV. An estimate for the height of the fission barrier (H_B) for the symmetric fission of ^{238}U is obtained according to

$$H_B = V_C - Q_f, \quad (4.11)$$

hence, $H_B = 206 - 193 = 13$ MeV. This value is an upper limit because the picture of two touching spheres is not realistic. In a situation of two touching nuclei, the nuclear force would set in, lowering the total energy. In fact, the experimental barrier height for the specific case is about 7 MeV. This energy corresponds roughly to the binding energy of a neutron. As a consequence, one can imagine that the capture of a (thermal) neutron can induce fission in such a nucleus. Actually in the case of uranium, a thermal neutron will induce fission only in the isotope 235. To induce fission in ^{238}U a neutron has to bring in an additional amount of 1 MeV of kinetic energy.

In order to illustrate the dependence of the fission barrier on the mass of nuclei, [Table 4.1](#) gives values calculated according to [Eq. \(4.11\)](#) for a few selected nuclei.

The results presented confirm the expectation that the fission barrier decreases with increasing mass of the nuclei. Physically this is due to the fact that the Coulomb repulsion driving apart a nucleus increases with $Z^2/A^{1/3}$ and that the surface force holding it together varies only with $A^{2/3}$.

4.3.3 The Fissility Parameter

From a general consideration of [Eq. \(4.11\)](#) a parameter can be extracted, which describes the instability of a nucleus toward fission ("fissility"). For this purpose, one defines a situation where the height of the barrier H_B approaches zero, i.e., according to [Eq. \(4.11\)](#) $Q_f \geq V_C$. Q_f

■ **Table 4.1**

Height of fission barriers in MeV calculated according to the liquid drop model

Nuclide	Atomic number (Z)	Fission barrier H_B (MeV)
^{140}Ce	58	50
^{174}Hf	72	37
^{232}Th	90	16
^{236}U	92	11
^{238}U	92	13
^{250}Cf	98	2

and V_C are defined according to [Eqs. \(4.7\)](#) and [\(4.9\)](#), respectively. E_B in [Eq. \(4.7\)](#) is defined by [Eq. \(4.5\)](#). Writing down [Eq. \(4.7\)](#) again

$$Q_f = 2E_B(Z_f/2, A_f/2) - E_B(Z_f, A_f) \quad (4.12)$$

and replacing E_B by the explicit terms of [Eq. \(4.5\)](#):

$$\begin{aligned} Q_f = 2 & \left[(a(A_f/2) - b(A_f/2)^{2/3}) \times \left(1 - d \frac{(Z_f/2 - A_f/4)^2}{A_f/2} \right) \right. \\ & \left. - c \frac{(Z_f/2)^2}{(A_f/2)^{1/3}} + f \frac{(Z_f/2)^2}{A_f/2} \pm \frac{p}{(A_f/2)^{1/2}} \right] - \left[(aA_f - bA_f^{2/3}) \right. \\ & \left. \times \left(1 - d \frac{(Z_f - A_f/2)^2}{A_f} \right) - c \frac{Z_f^2}{A_f^{1/3}} + f \frac{Z_f^2}{A_f} \pm \frac{p}{A_f^{1/2}} \right]. \end{aligned} \quad (4.13)$$

Inserting the numbers of the constants and rearranging the terms, one comes to the relation:

$$Q_f = 0.265 \frac{Z_f^2}{A_f^{1/3}} - 34.54 \frac{Z_f}{A_f^{1/3}} (1 - Z_f/A_f) + 3.81 A_f^{2/3}. \quad (4.14)$$

Now one can write for $V_C < Q_f$ using [Eqs. \(4.10\)](#) and [\(4.14\)](#):

$$0.151 \frac{Z_f^2}{A_f^{1/3}} < 0.265 \frac{Z_f^2}{A_f^{1/3}} - 34.54 \frac{Z_f}{A_f^{1/3}} (1 - Z_f/A_f) + 3.81 A_f^{2/3}. \quad (4.15)$$

Multiplication of the equation with $A^{-2/3}$ and isolation of the terms with Z^2/A on the left side gives

$$\frac{Z_f^2}{A_f} > 303 \frac{Z_f}{A_f} (1 - Z_f/A_f) - 33.4. \quad (4.16)$$

Since Z/A varies only between 0.38 and 0.42 throughout the periodic system, it is set equal to $Z/A = 0.40 \pm 0.02$. As a consequence, [Eq. \(4.16\)](#) can be rewritten as

$$\frac{Z_f^2}{A_f} > 39.3 \pm 1.2 \quad \text{or} \quad Z > 98.3. \quad (4.17)$$

Z_f^2/A_f (or more simply Z^2/A) appears as a factor that determines the “willingness” of nuclei to fission. Therefore, it is called the fissility parameter. A value of Z^2/A larger than 39 indicates that the nucleus should be unstable toward (spontaneous) fission. Values of Z^2/A larger

than 39 are found for nuclei with $Z \geq 100$. These nuclei should undergo spontaneous fission rapidly. The fact that such nuclei have a certain stability is explained by a stabilization due to shell effects. Actually, the number 39 calculated as the critical value depends on the value of r_0 assumed. Choosing $r_0 = 1.4$ fm rather than 1.5 fm changes the critical value of $Z^2/A = (Z^2/A)_{\text{krit}}$ from 39 to 43.

4.3.3.1 Second Derivation of the Fissility Parameter

Another derivation of the fissility parameter goes back to Bohr and Wheeler (Bohr and Wheeler 1939) and (independently) to Frenkel (Frenkel 1939): Oscillations of a nucleus will be unstable if the gain in Coulomb energy surpasses the loss of surface energy. The volume (V) of a sphere is given by

$$V = \frac{4}{3} \pi R^3 \quad (4.18)$$

If the sphere (drop) is incompressible, a deformation will not change the volume. An ellipsoidal deformation may be described by

$$V = \frac{4}{3} \pi ab^2 \quad (4.19)$$

with a being the long half-axis and b the two short half-axes of the ellipsoid. The half-axes may be described by

$$a = R(1 + \varepsilon) \quad (4.20)$$

and

$$b = R(1 + \varepsilon)^{-1/2} \quad (4.21)$$

with ε a measure for the eccentricity of the ellipsoid. The surface (S) of an ellipsoid can then be approximated by a series (which will be cut after the second term):

$$S = 4\pi R^2 \left[1 + \frac{2}{5} \varepsilon^2 + \dots \right] \quad (4.22)$$

Correspondingly, the surface energy (E_S) will be given by

$$E_S = b' A^{2/3} \left[1 + \frac{2}{5} \varepsilon^2 + \dots \right] \quad (4.23)$$

with

$$b' = b \left[1 - d \frac{(Z - A/2)^2}{A} \right] \quad (4.24)$$

(see [Eq. \(4.5\)](#)). Generally, the Coulomb energy of an ellipsoidal body with charge q is given by

$$E_C = \frac{3q^2}{20\pi e R \varepsilon_0} \left[1 - \frac{1}{5} \varepsilon^2 + \dots \right] \quad (4.25)$$

For the present case of a charged nucleus with atomic number Z and mass number A this results in

$$E_C = c \frac{Z^2}{A^{1/3}} \left[1 - \frac{1}{5} \varepsilon^2 + \dots \right] \quad (4.26)$$

(see [Eq. \(4.5\)](#)). As a consequence, when ε (the deformation) increases, the surface energy E_S will increase and E_C will decrease. Obviously, the decrease of Coulomb energy is due to the increase of the mean distance between the protons. The condition of $|\Delta E_C| > |\Delta E_S|$ results in a nucleus that is unstable to deformation, i.e., the spherical configuration cannot be restored once it gets deformed. As a consequence, one can write for the condition that will lead to spontaneous fission:

$$c \frac{Z^2}{A^{1/3}} \frac{1}{5} \varepsilon^2 > b' A^{2/3} \frac{2}{5} \varepsilon^2 \quad (4.27)$$

or

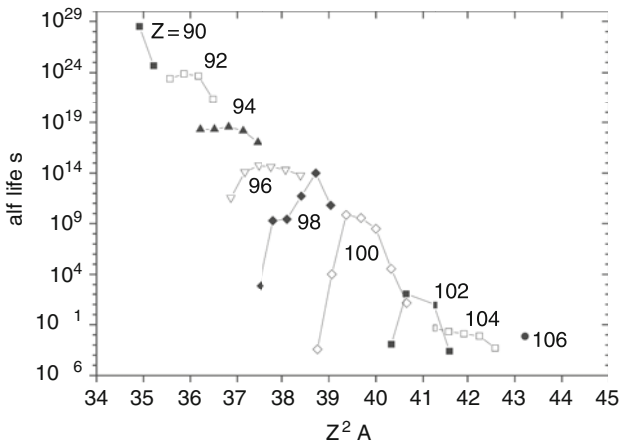
$$\frac{Z^2}{A} > 2 \frac{b'}{c} = 47 \quad (4.28)$$

Like in the derivation based on the height of the fission barrier, Z^2/A appears as the parameter determining fissility. The minimum values obtained for Z^2/A (39 or 47) should not be taken too strictly, as they are based on rather arbitrary assumptions for nuclear constants.

The role of the fissility parameter in the stability of nuclei against fission is documented in [Fig. 4.4](#) where the half-lives of heavy nuclei toward spontaneous fission are plotted. As a general trend, one can observe a gradual decrease over 35 orders of magnitude with increasing Z^2/A in the semilogarithmic plot. At closer look, one can see however that most elements (characterized by their atomic numbers) show a bell-shaped behavior. This deviation from

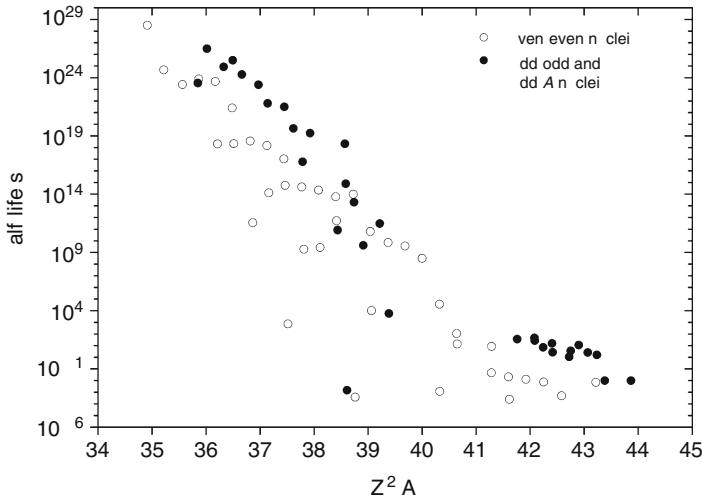
Fig. 4.4

Half-lives for spontaneous fission of heavy elements (characterized by their atomic numbers Z) as a function of their fissility parameters (Z^2/A). (Data from Wagemans [1991a](#), p 37). The data represent even–even nuclei only



■ Fig. 4.5

Half-lives for spontaneous fission of even–even nuclei (as shown in ▶ Fig. 4.4) (open circles) and of odd- A and odd–odd nuclei (full circles) versus the corresponding fissility parameter (Wagemans 1991a)



a simple log-linear dependence has been explained by shell effects in the ground state masses (Swiatecki 1955; Vandenbosch and Huizenga 1973).

In ▶ Fig. 4.4 only even–even nuclei are plotted. Nuclei with an odd number of either neutrons or protons or both, generally, have longer half-lives, as will be discussed later in the context of the influence of nuclear shell structure on fission. For comparison, the half-lives of odd (i.e., odd- A and odd–odd) and even–even nuclei for spontaneous fission as a function of the fissility parameter are shown in ▶ Fig. 4.5. It is obvious that in general the half-lives of odd nuclei are several orders of magnitude longer.

Fission induced by neutrons, charged particles or photons is preceded by an excitation step. This step will allow the nucleus to overcome the barrier. On the other hand, there is a competing process, which allows the nucleus to get rid of the excitation energy by γ -ray emission. The timescale of this competing process does not allow a slow tunneling through the fission barrier. As a consequence, induced fission takes place only if the excitation energy is at least as high as the fission barrier. (Tunneling is only possible in the direct neighborhood of the top of the fission barrier (= sub-barrier fission)).

4.3.4 LDM and Fission-Critical Evaluation

In summary, the liquid drop model explains

1. The existence of a fission barrier as a result of the opposing action of Coulomb and surface forces. It predicts that the barrier diminishes with increasing atomic number of the elements and approaches zero around $Z = 100$.
2. The liberation of about 200 MeV per fission event.

3. The formation of fission products, which are neutron rich and which stabilize by a sequence of several β -decay processes and/or by the emission of prompt neutrons. This is due to the fact that the valley of stability is bent toward the neutron-rich region from the initial $N = Z$ direction due to the Coulomb term.
4. The formation of a compound nucleus in which the excitation energy is redistributed many times between different degrees of freedom (single-particle states of the nucleons and collective degrees of freedom, like deformations and vibrations) before fission occurs (timescale 10^{-14} s).

The liquid drop model does, however, *not* explain some important observations of the fission process:

1. Even though the formation of two fission products of equal mass (half the mass of the fissioning nucleus, “symmetric fission”) would be most exoenergetic, experimentally (as will be shown later) the mass ratio of the two fission products is normally found to be approximately 1/3 to 2/3 (“asymmetric fission”).
2. The deviation from a smooth straight-line behavior and the difference between even–even and odd nuclei, as discussed in the context of [Figs. 4.4](#) and [4.5](#).
3. The existence of elements with atomic number $Z > 100$.
4. Phenomena, like the existence of “fission isomers,” to be discussed later.

The key for the understanding of these observations is the “shell model” (Haxel et al. 1950; Mayer 1950). The shell model is presented in the textbooks of nuclear- and radiochemistry and nuclear physics. Nevertheless, for the reader’s convenience, the basic concept shall be repeated here. A more detailed treatment and other basic information on the physics of nuclei can be found within this volume (see [Chap. 2](#) in this Volume).

4.3.5 The Shell Model

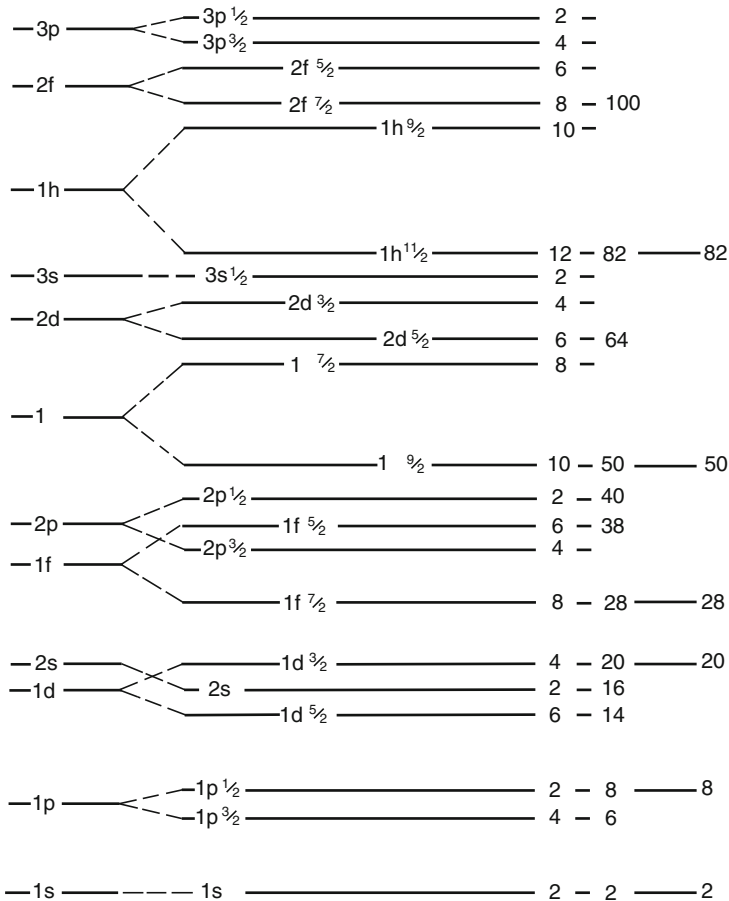
The viewpoint of the shell model is very different from that of the liquid drop model. The nucleons are looked at as standing waves occupying well-defined quantum states in a potential that is formed by the other nucleons. The chemist knows such a system from the behavior of the electrons in the atomic shell. Whereas in the atomic shell the potential and the forces acting are known, this is not the case for nuclei. The form of the nuclear potential well is not known exactly. The form of the nuclear potential well can be parameterized by a harmonic oscillator, by a square well potential or – more realistically – by a Woods–Saxon potential (see [Fig. 2.2](#) in [Chap. 2](#)).

In the nucleus, like in the atom, one has principal quantum numbers (1, 2, 3, ...) and angular momentum quantum numbers (s, p, d, f, ... with $l = 0, 1, 2, 3, \dots$). The latter ones, like in the atom, may be occupied by 2, 6, 10, 14 ... (in general $2(2l + 1)$) nucleons of a particular kind. The numbering is different though. In the atom the nodes pertaining to a p ($l = 1$), d ($l = 2$), f ($l = 3$)-state are added to the main quantum number. In the nucleus this is not so. As a consequence, a sequence of levels of 1s, 2p, 3d, 4f ... in the electron shell corresponds to 1s, 1p, 1d, 1f ... for the nucleus. A level scheme for a spherical nucleus is given in [Fig. 4.6](#).

Another difference between the atomic shell and the nuclear shell is that in the latter spin–orbit coupling has an important energetic effect. This effect changes the energetic sequence of levels. For instance, the $1d_{5/2}$ -level in [Fig. 4.6](#) ends up underneath the 2s-level. The gap due to

■ Fig. 4.6

Level scheme calculated for a Woods–Saxon like potential well (*left*) and the effect of spin–orbit coupling (*middle*). The numbers in parenthesis give the maximum number of neutrons or protons that can occupy the subshell. The numbers in square brackets are the sums of the former from the lowest level up through the level concerned. Proton or neutron numbers that produce particular stability “magic numbers” are given further right



spin–orbit coupling increases with increasing angular momentum quantum number (l) (see levels $1p_{1/2}$ and $1p_{3/2}$ or $1h_{9/2}$ and $1h_{11/2}$ in ▶ Fig. 4.6). Generally, nuclei with fully occupied shells are highly stable. In nuclear physics, a shell is defined by large gaps in the energies of single-particle states. In the electron shell, shell closures occur in the rare gasses, where the p-shell is occupied and the s-shell of the next higher principal quantum number is at a considerably higher level. The numbers of electrons in these shells of particular stability are 2 (He), 10 (Ne), 18 (Ar), 36 (Kr), 54 (Xe), and 86 (Rn). In the nuclear case these “magic numbers” may be read from ▶ Fig. 4.6: 2, 8, 20, 28, 50, 82, etc. One can also see further below that the shell closures at 28 and, especially at 50, have an important influence on the fission process.

The atomic subshells host a number of $(2l + 1)$ pairs of electrons. So the p subshell hosts three pairs of electrons designated by the quantum numbers $m_l = +1, 0, -1$. These states differ in their orientation within the electron shell and possess normally identical energy. Physicists, for some obscure reason, call such levels “degenerate.” When, however, an external electric field or magnetic field is applied, the orientation of the magnetic moment of the p-, d-electrons, etc., makes a difference, and the three levels of the p term mentioned above ($m_l = +1, 0, -1$) will differ in energy (Stark effect, Zeeman effect).

The situation is analogous in the nucleus: The $p_{1/2}$ and $p_{3/2}$ -levels (created from the p-level by the spin–orbit coupling) host six nucleons of the same kind ($p_{1/2}$: $+1/2, -1/2$ and $p_{3/2}$: $+3/2, +1/2, -1/2, -3/2$). Their energies are the same as long as the nucleus is spherical, but when the nucleus is deformed the degenerate levels split up.

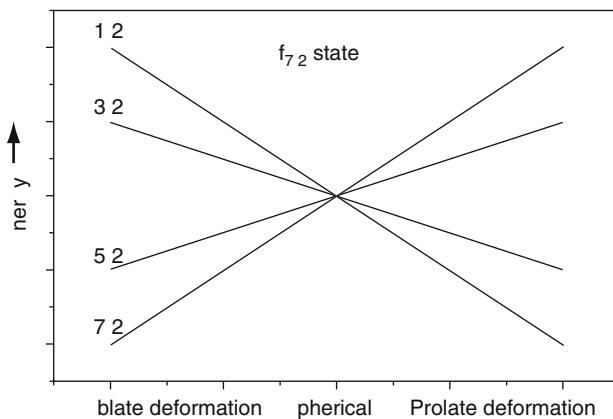
Apparently, in a nonspherical nucleus, the orientation of a wave within the nucleus influences the energies of single-particle states. Obviously, deformation is important for a nucleus on the way to fission and important aspects of fission can be explained by the effect of deformation on nuclear levels. The effect of deformation on nuclear levels is shown schematically in [Fig. 4.7](#) in the case of an $f_{7/2}$ -state. A realistic situation for a nucleus with its different principal and angular momentum quantum states is shown in [Fig. 2.11 of Chap. 2](#).

The splitting of levels leads to an increased level density. Energetic gaps (“closed shells”) found in a spherical nucleus may disappear in a deformed nucleus. New gaps may be formed at different nuclide numbers at specific deformations. The sum of the energetic effects of all the occupied quantum states in a nucleus shows an oscillating behavior, i.e., the stability of a nucleus (as far as shells are concerned) as a function of deformation shows maxima and minima.

The true behavior of a fissioning nucleus can be described only by combining the liquid drop model and the shell model.

Fig. 4.7

Schematic diagram of the energy of an $f_{7/2}$ -state with deformation (oblate = pancake-shaped, prolate = cigar-shaped)



4.3.6 The Combination of the Liquid Drop Model and the Shell Model According to Strutinsky

For the case of fission, Strutinsky (1967) chose a simple but very successful way to describe the energy of a nucleus by combining liquid drop energy (E_{LDM}) with local shell (δU) and pairing (δP) corrections:

$$E = E_{\text{LDM}} + \sum_{p,n} (\delta U + \delta P). \quad (4.29)$$

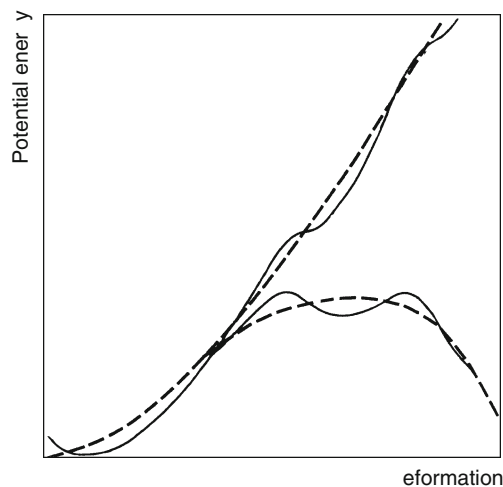
The result of his approach for the potential energy as a function of deformation is shown in [Fig. 4.8](#). These calculations result in a two-humped, double fission barrier ([Fig. 4.8](#)), which is confirmed by multiple experimental evidence, such as the asymmetry of fission, the existence of elements with $Z > 100$ and of fission isomers as will be discussed further below.

A quasi-three-dimensional presentation of the potential energy surface of a fissioning nucleus as a function of deformation and asymmetry is shown in [Fig. 4.9](#).

The way to fission starts at symmetry with a neck radius of 7 fm and a potential energy of $E_{\text{pot}} = 0$ MeV. The nucleus has to pass a first saddle at 6.5 fm ($E_{\text{pot}} = 4.3$ MeV). Beyond the subsequent valley ($E_{\text{pot}} = 1$ MeV) a second barrier appears at 5 fm neck radius. The height of this barrier depends on the degree of asymmetry of the fragments formed. It is 8 MeV for symmetric fission and 5.7 MeV for the saddle at a fragment mass ratio of 88:148. This barrier is responsible for the asymmetric character of low energy fission. As will be shown later, this is due to the shell closures for protons at $Z = 50$ and 28 and for neutrons at $N = 82$. Beyond the second barrier, the fissioning nucleus finds a smooth descent toward scission (at 0 fm neck radius). A return to symmetry on this way is hindered by a mountain ridge of several MeV.

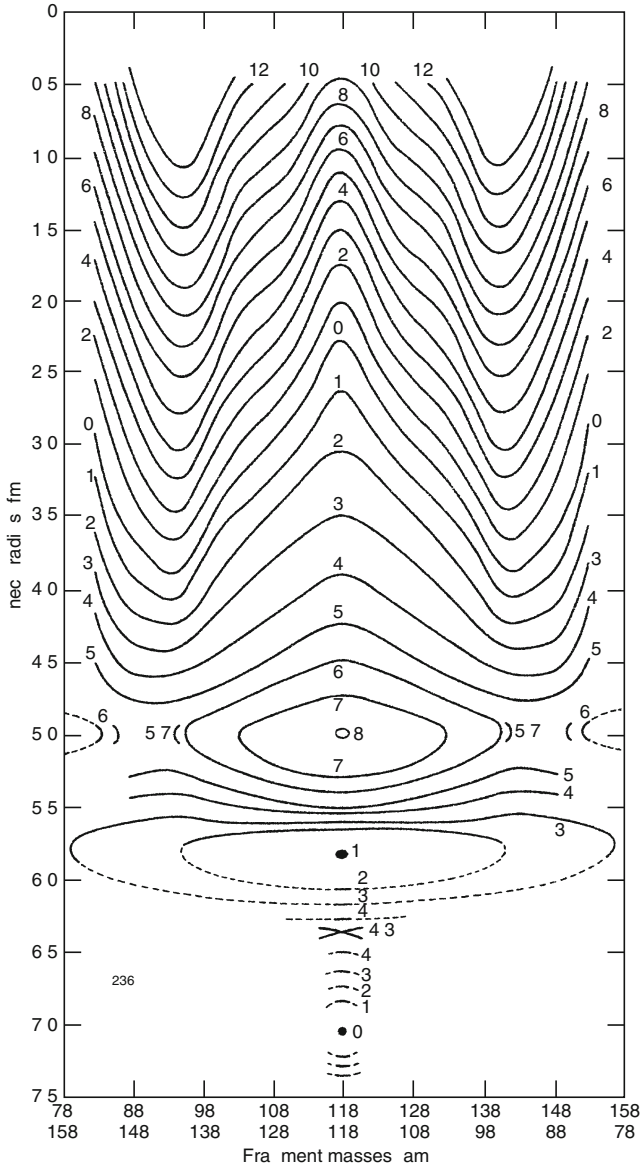
Fig. 4.8

Illustration of the method of Strutinsky to merge shell model and liquid drop model as a function of deformation. Upper full curve shows energetic oscillations due to shell effects around a mean (upper dashed curve). The upper dashed curve has been “adjusted” to the low-deformation part of the lower dashed curve, which is calculated using the liquid drop model; from (Vandenbosch and Huizenga 1973)



■ Fig. 4.9

Potential energy surface of the compound nucleus $^{236}\text{U}^*$ on its way to fission. The path to fission is given in terms of the neck radius. (Fission is achieved when the neck radius drops to zero). The degree of asymmetry is given by the mass ratio of light and heavy fragments formed. The potential energy is shown in the form of contour lines as in geographical maps; after (Mustafa et al. 1973)



4.3.7 Further Model Considerations

Many attempts have been made to understand the fission process and to calculate the measurable quantities (yields, kinetic energies of fragments, etc.). These attempts have not been fully successful yet. Nevertheless, important progress has been made in recent years and new insight has been gained. Due to limitation in space, only two approaches will be mentioned here.

A model, based on the construction of a potential energy surface from a combination of liquid drop terms for protons and neutrons as a function of deformation and shell corrections, has been published by Wilkins, Steinberg, and Chasman (Wilkins et al. 1976). In the model, a specific excitation energy (nuclear temperature) is assumed at scission and the probability to reach this specific state is calculated. The general trends of mass–yield curves in the fission of very different nuclides from ^{211}Po to ^{258}Fm and for different excitation energies of the fissioning nucleus from 0 MeV (spontaneous fission) to highly excited fission reactions are reproduced correctly. In particular, the transition from the symmetric fission of (the compound nuclei) ^{212}Po to a triple-humped mass–yield curve for ^{227}Ra to double-humped yield curves for ^{236}U , ^{246}Cm , and ^{252}Cf and, finally, a partial return to symmetry for ^{258}Fm is reproduced correctly. However all the yield curves are by far too narrow, so that a quantitative prediction of fission yields is not possible.

The latter problem has been solved by Brosa et al. (1990) by introducing fluid dynamics. One may imagine the scission configuration as a dumbbell-like structure with two spheres connected by a neck. When this neck elongates, its diameter becomes increasingly smaller. In this case, fluid dynamics reveals that the location of rupture of the neck is not well defined and this leads to broader mass distributions. In addition, Brosa et al. discovered in their calculations the coexistence of different paths to fission. These paths depend on the mass of the fragments formed. A path leading to a fragment with mass number near the double shell closure of $Z = 50$ and $N = 82$ will be influenced by the rigidity of magic nuclei. The consequence is that the scission configuration will be less deformed. The path to fission will be shorter and the fragments will have a higher kinetic energy. On the other hand, a path leading to well-deformed fragments will be long and will produce fission fragments with less kinetic energy.

4.4 Experimental Facts and Interpretation

4.4.1 Sequence of Events Leading to Fission

In order to understand how the fission process can be accessed experimentally, i.e., to have an overview on the different quantities that can be measured, the sequence of events occurring during the fission process will be briefly described.

For induced fission, the first step is the transfer of sufficient excitation energy to overcome the fission barrier. This excitation energy is most frequently provided by the binding energy of a thermal neutron. It can, however, be due to the absorption of a sufficiently energetic photon. Higher excitation energies can be induced by fast neutrons or charged particles.

In the case of low energy fission, the excited nucleus forms a vibrationally excited compound nucleus, which can return to its ground state by emission of γ rays. In competition with this de-excitation process, the nucleus may find a configuration (saddle point), which is unstable toward fission. This configuration, according to the present understanding, has the shape of two spheres

connected with a neck in a dumbbell-like manner. From this saddle point on, the Coulomb force will drive the nucleus apart. The neck will become gradually thinner and finally snap forming two more or less deformed fragments. In rare cases (1 out of 400 events), a small third fragment will also be formed from the snapping neck (“ternary fission”). The deformed fragments will be accelerated due to the Coulomb repulsion and simultaneously will relax into spherical shapes. In this process, the deformation energy will transform into internal excitation energy allowing the boil-off (emission) of a few neutrons within about 10^{-14} s (“prompt neutrons”). The nuclei formed after prompt neutron emission are usually called “fission products” rather than “fission fragments” as they are referred prior to prompt neutron emission.

The fission products are neutron-rich unstable nuclei, which stabilize by a sequence of β decays. Each β decay will transform a nuclide into its neighbor with the next higher atomic number and the same mass number. (In rare cases, the β decay of a fission product is accompanied by the emission of a neutron, called delayed neutron – as opposed to the prompt neutrons discussed above. In these cases, the mass number of the fission product decreases by one. The delayed neutrons are important for the control of nuclear reactors and will be discussed later.)

Historically, the first quantities measured were the yields of the longest-lived members (near-end products) of the β -decay chains. These yields are called chain yields or mass yields.

With the development of fast chemical separation techniques and physical techniques that allows one to differentiate between different elements of an isobaric decay chain, information could be obtained on the fission product distribution prior to β decay. The corresponding yields are called “independent” or “primary” product yields.

A fission product is hence normally produced in two ways: Directly from the fissioning nucleus and indirectly by the β decay of a precursor. Correspondingly, one can distinguish between independent (primary) and secondary yields. The sum of primary and secondary yields is called cumulative yield. The cumulative yield of the last chain member is normally identical to the chain yield. “Fractional” (independent, cumulative, etc.) yields show what fraction of the total chain yield comes from a particular formation path.

In addition to the yields of the fission products, the yields of the fission fragments (prior to prompt neutron emission), as well as the number of prompt neutrons (and γ rays) emitted are of interest. The yields of ternary fragments and their angular distribution with respect to the direction of the two main fragments give some information on the neck. The kinetic energy of the two fragments gives information on the distance of the two charge centers, i.e., on the deformation of the fissioning system at scission.

In the following, the experimental techniques used to measure the quantities mentioned above will be discussed.

4.4.2 Chain Yields

4.4.2.1 Methods of Measurement

Radiochemical methods. Chain yields are obtained by isolating different elements chemically from a fission product mixture and determining the absolute activities of the isotopes found. Since chemical separation is normally rather time consuming, by the end of the separation, the precursors have decayed into the long-lived isotopes whose cumulative yields then represent the corresponding chain yields.

Radiochemical separations and subsequent counting are supposed to be the domain of radiochemists but, motivated by the interest in fission and its possible applications, even physicists were compelled in the early days to do chemical separations as is described about Fermi by A. v. Grosse (1965). (*"It was fascinating to see Fermi disappear in dense fumes of sulfuric acid as he was carrying out some chemical separation in the corner room of the basement of the Pupin Laboratories at Columbia University (1939). His voice could be clearly heard out of the 'London fog' giving instructions as to what should be done next."*) Large laboratories were set up during World War II for this work first in the USA ("Manhattan Project") and later in the Soviet Union and other countries. The results of the US scientists were kept secret during the war and were published in comprehensive form later (Coryell and Sugarman 1951).

In order to obtain fission yields, the number of atoms of a specific nuclide formed (N_X) must be compared to the number of fission events (N_f) in the corresponding target. The yield is then defined as $Y_X = N_X/N_f$. The number N_f could be determined using a fission counter (Engelkemeir et al. 1951). A thin foil of the fissile material placed in a proportional counting tube is irradiated under the same conditions as the target. The fission products leaving the foil and projected into the counting volume produce large pulses that can be counted. Correcting for the different amounts of fissile material in the foil and in the target, the fission rate (or the number of fissions) in the target can be calculated. The absolute fission yield is then given as

$$Y_X = \frac{A_X}{R_f f_X F_T} \quad (4.30)$$

where A_X is the absolute activity (number of disintegrations per second of X in the chemically separated sample), R_f is the fission rate (number of fission events per second) in the target, f_X is the yield of chemical separation of X (expressed as fraction), and F_T is the fraction of saturation activity of X in the chemically separated sample.

The latter can be expressed as

$$F_T = (1 - e^{-\lambda t_b}) e^{-\lambda t_a} \quad (4.31)$$

where λ is the decay constant of X, t_b is the irradiation time and t_a is the time between end of irradiation and start of measurement.

The yield of the chemical isolation (f) of a particular element can be determined, e.g., by adding a known amount of this element before the chemical separation and determining the amount present in the sample after the chemical separation.

Once the absolute fission yield of a nuclide has been determined accurately in a particular fission reaction, this nuclide could serve as a monitor if it is isolated and counted simultaneously with the nuclide of interest.

Mass spectroscopy. In addition to radiochemical separations, in which the different isotopes of one element were isolated, mass separations can be carried out (De Laeter 1988). A sample is introduced into the ion source of a mass separator; it is heated, vaporized, ionized, accelerated, separated, intercepted on a catcher foil, and counted. In some cases, the separated ions can be counted directly when the accelerated ions impinge on a detector. In mass separation one has the problem that the separation yield is not known, but one knows that this yield is identical for all isotopes of one element (as long as the precursors have decayed completely). Therefore, if one knows the fission yield of one nuclide, one can determine the fission yields of the other isotopes of this element. It is often possible to determine the same chain yield by identifying more than one isotope. These cases may be used to interrelate the separation yields of different elements. Finally, when sufficient yields are known, one

has the possibility to check whether the sum of all chain yields equals 200% (as it should be in the case of a “binary” fission).

Measurements based on momentum conservation. Purely physical methods to determine mass yields are based on the laws of the conservation of energy and momentum. They became possible when the technique of the measurement of the kinetic energy (or the velocity) of the fission fragments became precise enough. The most convenient detectors for this purpose are surface barrier detectors, but proportional counters can also be used. In principle, the masses m_1 and m_2 and the velocities u_1 and u_2 of two fission fragments, produced by a fissioning nucleus at rest, obey the following equation:

$$m_1 u_1 = m_2 u_2. \quad (4.32)$$

In addition, one has the relation

$$u = \sqrt{\frac{2E}{m}}, \quad (4.33)$$

where E is the kinetic energy of either of the fission fragments. As a consequence, one can also write

$$m_1 E_1 = m_2 E_2. \quad (4.34)$$

One can set $m_1 + m_2 = m_f$, the mass of the compound nucleus, which is known. By measuring the kinetic energy of both fragments, one can calculate the mass of each fragment according to

$$m_1 = m_f \frac{E_2}{E_1 + E_2}. \quad (4.35)$$

A great number of such measurements have been performed. A few typical examples are given in the following publications (Schmitt et al. 1966; Pleasonton 1968; Derengowski and Melkonian 1970; Unik et al. 1973; Asghar et al. 1981; Thierens et al. 1981; Thierens et al. 1984; Barreau et al. 1985; Wagemans et al. 1996).

Alternatively, the velocity (u) of the fission fragments can be measured. This is normally done by determining the time of flight across a known distance. Such measurements have been performed quite early for the spontaneous fission of ^{252}Cf (Whetstone 1963). The formula used for mass determination is now

$$m_1 = m_f \frac{u_2}{u_1 + u_2}. \quad (4.36)$$

Finally, the simultaneous measurement of the energy and the velocity of the same fragment also make it possible to calculate its mass as has been shown by Schmitt et al. (1965), Derengowski and Melkonian (1970), and Schillebeeckx et al. (1994). The calculation is based on [Eq. \(4.33\)](#).

The problem with the above methods is that [Eqs. \(4.35\)](#) and [\(4.36\)](#) are only valid for fission *fragments* (prior to prompt neutron emission). As shown above, the formation of fission fragments is followed within about 10^{-14} s by the emission of up to about three prompt neutrons. This neutron emission affects the measured quantities (E or u) to a different extent.

The *velocity* of the fission fragments is changed due to the recoil of the neutrons, which are emitted with an energy of about 1 MeV. This effect is small (about 0.01 MeV) and since the emission of neutrons is isotropic from the fragments in flight, it does not change the mean velocity but widens the distribution and leads to a loss in mass resolution.

The energy of the fragments in flight is changed by two factors: (1) by the change of velocity as discussed above and (2) by the loss of mass due to neutron emission of the fragment in flight. This loss of mass decreases the kinetic energy according to the relation $E = mv^2/2$. As can be estimated easily, the second effect amounts to about 1 MeV per neutron emitted.

As a consequence, mass yields based on a double velocity measurement are in principle more accurate than those based on energy measurements. However, in practice, a velocity measurement (based on the flight time of a fragment through a defined distance) is generally less accurate than an energy measurement.

Examples of sophisticated instruments are “Cosí fan tutte” at the Institute Laue-Langevin (ILL) (Grenoble) (Oed et al. 1984) and a similar one attached to the reactor of the Moscow Engineering and Physics Institute (Alexandrov et al. 1991).

The physical measurements of mass yields based on momentum conservation (double energy, double velocity or energy, and velocity determination) – as opposed to the radiochemical measurements discussed further above – have the advantage of producing a more or less complete mass–yield curve in one experiment using up only small amounts of the possibly exotic fissile material (in one thin target). The mass resolution in the yield curves obtained is, however, not quite as good as that of the radiochemical methods, so that fine details of the mass–yield curve cannot be observed.

In addition, the physical measurements (after some corrections for prompt neutron emission) allow one to obtain fragment mass distributions (prior to prompt neutron emission). A comparison of these fission fragment yield curves with fission product yield curves makes it possible to extract information on prompt neutron emission. This will be discussed in the next subsection.

A very interesting instrument based on the measurement of the energy and the velocity of one fission fragment is Hiawatha (Diiorio and Wehring 1977). In this instrument, the measurement of the kinetic energy of the fission fragments is done by an electrostatic analyzer with an energy resolution of 0.3% unaffected by prompt neutron emission. As a consequence, the mass resolution, in contrast to the instrumentation discussed above, is sufficiently good to measure product yields without disturbance by neighboring masses.

Mass separation of unslowed fission products (Lohengrin). The most successful instrument for the study of fission yields, as will be shown below, is the mass separator Lohengrin (Moll et al. 1975, 1977) (ILL, Grenoble). In contrast to the instruments discussed above (including Hiawatha), which provide mass identification event by event, it provides a true spatial separation of fragments of different masses. Lohengrin achieves the mass separation of fission products by using magnetic and electric sector fields. As a consequence, fission products of one mass can be collected with Lohengrin and may be studied online or off-line, e.g., by γ -ray spectroscopy.

Thin targets of nuclei that are fissile by thermal neutrons are irradiated at the European High Flux Reactor at Institute Laue-Langevin, Grenoble, France. The fission fragments escaping from the target possess almost the whole kinetic energy (60–110 MeV) that they obtained in the fission process. A narrow beam of fission products enters the magnetic and electric sector fields. The separation takes place according to the ratio (A/q) of mass number to ionic charge state and to E/q the ratio of kinetic energy to ionic charge state of the fragments. The ionic charge states range from about $15e$ to $30e$ as a result of the dynamical equilibrium established when fission fragments with their full kinetic energy move through the thin targets. The resolution of the separator is sufficiently good to separate generally single mass numbers in spite of the multiplicity of the q values.

Lohengrin is, in principle, not able to separate identical A/q -ratios (e.g., $100/25 = 96/24 = 92/23 = 4.0$) thus delivering multiplets. Such a multiplet can be resolved using a surface barrier

detector or ionization chamber attached to the collector side and measuring the kinetic energies of the fragments because the members of the multiplet possess the same velocity and different masses and, hence, different kinetic energies.

One problem with Lohengrin is a less efficient use of beam time compared with the measurements based on momentum conservation: whereas in the latter case the information on the total mass and energy distribution is obtained in one shot, Lohengrin requires a measurement for each mass and kinetic energy setting. In addition, measurements of several ionic charge states have to be performed in order to exclude an influence of this parameter on the results.

The advantage of Lohengrin and the reason for its success in contributing more complete data sets on mass, charge, and energy distributions than any other method is its good resolution due to the fact that it is not influenced by prompt neutron emission. Another great advantage of Lohengrin is the almost complete absence of background, which allows the measurement of very low yields (under certain conditions down to about $10^{-7}\%$).

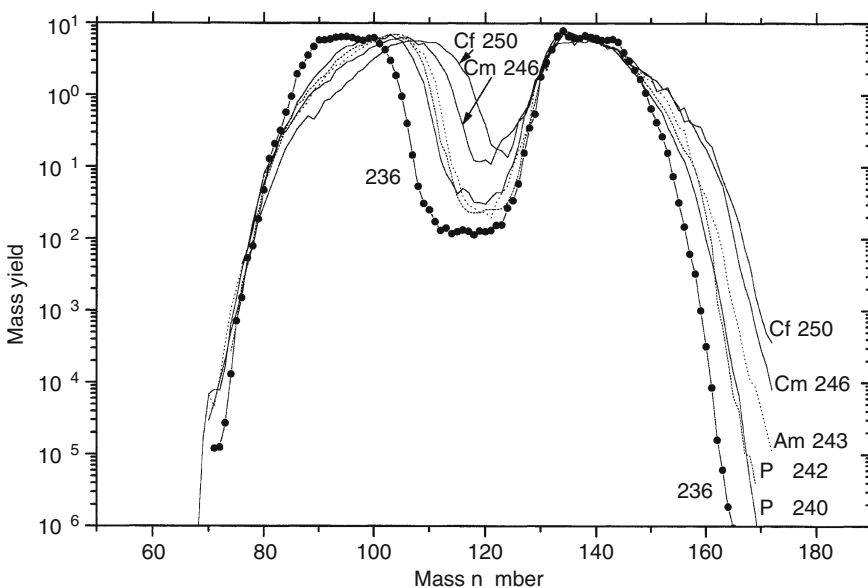
All the physical measurements discussed above have the general advantage to give some information on the kinetic energy of the fission fragments (and, hence, on the deformation of the scission configuration).

4.4.2.2 Experimental Results and Interpretation

Fission products (post-neutron emission). Chain yields as a function of the mass number of the fission product are given in ▶ Fig. 4.10 for different fission reactions. There are several remarkable points in ▶ Fig. 4.10. They will be discussed in the following.

■ Fig. 4.10

Mass-yield distributions for thermal-neutron-induced fission of the following nuclides: ^{235}U , ^{239}Pu , ^{241}Pu , ^{242}Am , ^{245}Cm , and ^{249}Cf . The labels in the figure refer to the respective compound nuclei; after (Tsekhanovich et al. 2001)



First, the curves show two maxima, thus providing the experimental proof of asymmetric fission that has already been referred to. The observation of the mass asymmetry in fission was surprising because the liquid drop model predicts that the formation of two fragments with about equal size would be preferred on energetic grounds. The asymmetry of fission really remained a puzzle from the time of its discovery in 1939 (Jentschke and Prankl 1939a, b) until 1976 (i.e., for 37 years) when the problem was understood in the sense that qualitatively correct predictions could be made (Wilkins et al. 1976). The suspicion that asymmetric fission had to do with nuclear shells was however put forward already in 1948 by M. Goeppert-Mayer together with the formulation of the shell model itself (Goeppert-Mayer 1948) and in 1950 by Lise Meitner (Meitner 1950). These authors argued that fission would occur in such a way that one fragment has at least 82 neutrons and the other one at least 50 neutrons. It turned out subsequently that it is the proton shells (at $Z = 50$ and $Z = 28$) that play the decisive role. This point will be discussed later.

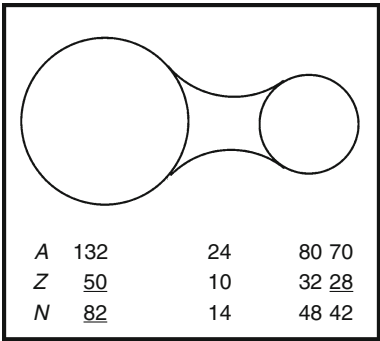
The dip between the two peaks is most pronounced for the fission of ^{235}U and decreases with increasing mass or rather with increasing fissility parameter (Z^2/A) of the fissioning nucleus. This is in agreement with the expectation that shell effects will become less important with increasing excitation energy of the nucleus at the scission point.

The yield curves are shifted along the mass axis according to the mass of the compound nucleus. However, there are two regions where all the curves coincide: one region is around mass number 132 and the other one around mass number 80.

The results shown in Fig. 4.10 and a number of additional experimental findings to be discussed further below can be interpreted in terms of a picture (see Fig. 4.11), which illustrates – with some simplifications – the theoretical findings discussed above.

The configuration of the fissioning nucleus just before scission is understood as a dumbbell-like configuration with a larger sphere and a smaller sphere connected by a neck. The following assumption will explain the experimental yield curves: In the vast majority of the cases, the configuration will break (undergo scission) at the neck and to a first approximation the neck diameter at a specific location will determine the probability of scission at this location.

Fig. 4.11
Dumbbell configuration of a fissioning nucleus ($^{236}\text{U}^*$) just before scission. The numbers refer to the number of nucleons (A), protons (Z), and neutrons (N) contained by the large sphere, the neck, and the small sphere, respectively. (The numbers in parenthesis for the small sphere represent a subunit, the experimental evidence of which will be discussed later)



Assuming the numbers of nucleons as shown in ▶ Fig. 4.11 for the two spheres and the neck, one would predict a mass–yield curve, which starts essentially with a low yield at mass 80 (scission point between the small sphere and the neck), hence producing fragments with mass 80 and (e.g., for ^{236}U) the corresponding complementary fragment with mass 156. When the scission point moves away from the small sphere toward the large one, fragments heavier than $A = 80$ and lighter than $A = 156$ will be formed in increasing yields reaching a plateau in the mass range around 144/92 ($132 + 12$ and $80 + 12$). Further on, when the breaking point approaches the sphere with $A = 132$ (and the complementary mass 104 (for ^{236}U)), the yield curve will show a steep decrease. This is exactly what is shown in ▶ Fig. 4.10.

As appears from ▶ Fig. 4.10, the area of steep descent around mass 132 and mass 80 is found not only for the fission of $^{236}\text{U}^*$ but also for the other compound nuclei shown: $^{240}\text{Pu}^*$, $^{242}\text{Pu}^*$, $^{243}\text{Am}^*$, $^{246}\text{Cm}^*$, and $^{250}\text{Cf}^*$. This can be interpreted as follows. The two spheres in the dumbbell configuration do not change with the mass of the compound nucleus but rather the change in mass of the compound nucleus only affects the size of the neck connecting the two spheres. Surprisingly enough, the steep areas mentioned coincide not only on the mass axis but also on the yield axis, i.e., the different compound nuclei show nearly identical yields around $A = 132$ and 80. This inference may indicate that the two onsets of the neck (toward heavy and light spheres, respectively) are also more or less independent of the mass of the compound nucleus. A comparison of the very light nucleus ^{227}Th with the very heavy nucleus ^{249}Cf (▶ Fig. 4.12) confirms the stability of the mass range around $A = 132$ in an even more spectacular way: The mass–yield curves agree around $A = 132$ (and – not shown in the figure – basically around $A = 80$ as well). The rest of the curve is shifted according to the mass of the compound nucleus.

The middle of the valley (▶ Figs. 4.10 and ▶ 4.12) represents symmetric fission. It has a different (symmetric) shape at scission that is connected with a path over the symmetric barrier indicated in ▶ Fig. 4.9. Since this path crosses a region with higher potential energy, the fraction of symmetric fission depends on the excitation energy available for the nucleus at scission. It appears from ▶ Fig. 4.10 that the depth of the valley decreases with increasing mass (or more precisely increasing fissility parameter, Z^2/A) of the compound nucleus. This is due to the decreasing fission barrier and increasing exoenergetic character of fission with increasing fissility.

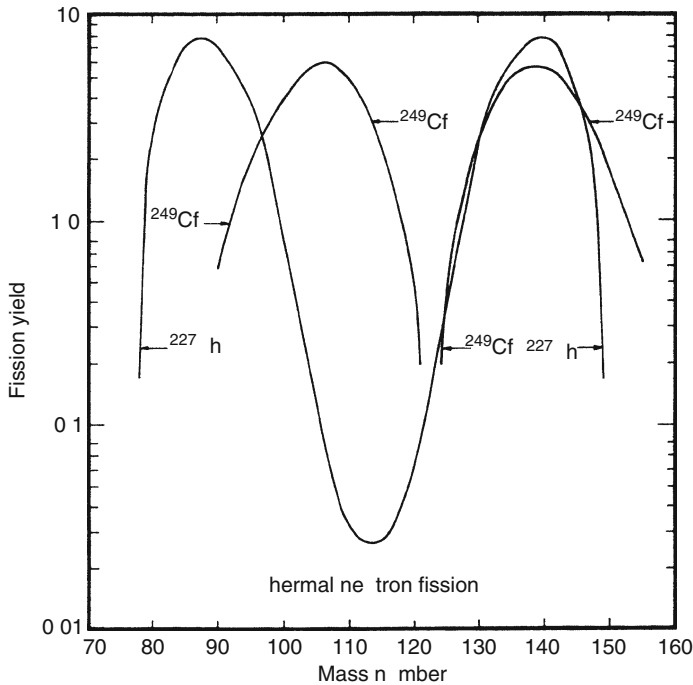
▶ Figure 4.13 shows yield curves for various nuclei undergoing spontaneous fission. In the case of spontaneous fission, the barrier is crossed by tunneling. As a consequence, the excitation energy at scission is very small. The figure shows that the yield of symmetric fission is extremely low (below the limit of detection), as one would expect.

On the other hand, when more excitation energy is put into the system the peak-to-valley ratio decreases. This can be observed for fission reactions induced by reactor neutrons having about 2 MeV of energy (▶ Fig. 4.14) and by 14 MeV neutrons (▶ Fig. 4.15).

The importance of the shell closures at $Z = 50$ and, to a lesser extent, $N \approx 82$ is demonstrated again in the mass–yield curves of very heavy spontaneously fissioning nuclides. ▶ Figure 4.16 shows the fission yield curves for different isotopes of the elements Cf ($Z = 98$) to Rf ($Z = 104$). Starting with element Fm ($Z = 100$, which allows the formation of two fragments with $Z = 50$), one can observe the occurrence of symmetric fission, whenever the neutron number permits it. The minimum neutron number is 158 (i.e., 2×79) for $Z = 100$ and 154 (2×77) for $Z = 104$. More evidence for the fact that the effect of closed neutron shells can be observed already in the direct neighborhood of the magic number will be presented further on. This fact has certainly to do with the other fact that forming fragments is not the same as

■ Fig. 4.12

Mass–yield curves for the thermal-neutron-induced fission of ^{227}Th and ^{249}Cf ; from (von Gunten 1969)



forming isolated nuclei. It shows the limitations of the simple picture shown in ▶ Fig. 4.11 and the requirement of a more fundamental treatment as presented by (Brosa et al. 1990) and others and as mentioned above.

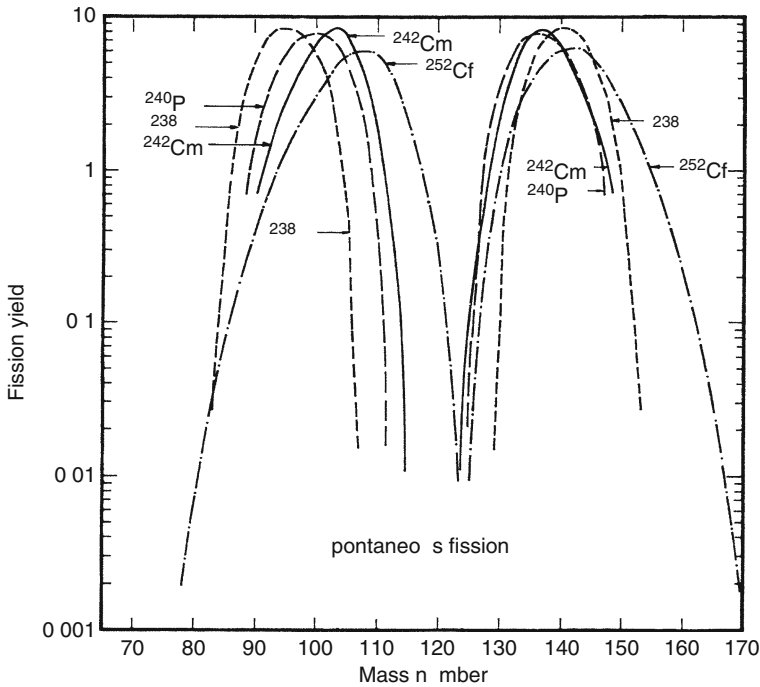
Fission fragments (pre-neutron emission). The yield curves discussed above refer to fission product yields after emission of prompt neutrons. As discussed above, the physical methods based on momentum conservation at scission (double energy, double velocity, or energy and velocity measurements) allow the measurement of the yield distribution of fission fragments (prior to prompt neutron emission). In these cases, simultaneous information is obtained on the kinetic energy of the fragments detected.

▶ Figure 4.17 shows the mass–yield curves determined for the fission fragments as well as for the fission products of ^{235}U for comparison (Schmitt et al. 1966). The two curves are slightly shifted relative to each other along the mass axis due to the emission of neutrons. Accordingly, the number of neutrons emitted can be obtained from a comparison.

Prompt neutron yields and kinetic energy distribution. The evaluation of prompt neutron emission from fission fragment and product yields is based on a method proposed by Terrell (1962). The yields of the single (light) fragments (and products) are plotted cumulatively starting with the lightest mass. This way symmetry is reached at a cumulative yield of 100% (▶ Fig. 4.18). For the heavy fragments (products), one starts from the heaviest fragment and proceeds toward symmetrical fission.

■ Fig. 4.13

Mass–yield curves for the spontaneous fission of ^{238}U , ^{240}Pu , ^{242}Cm , and ^{252}Cf ; from (von Gunten 1969)



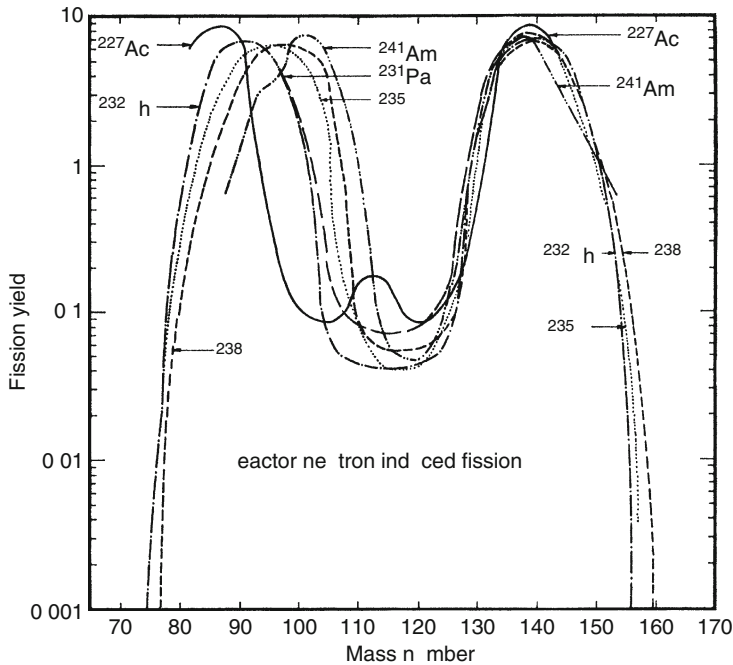
For the fission products, two S-shaped lines are obtained that are separated on the mass axis by the total number of neutrons emitted. For the fission fragments, the two lines naturally coincide. As a consequence, the number of prompt neutrons emitted from light and heavy fragments, respectively (ν_L and ν_H), can be read from the figure, as a function of the mass combination. It is observed that the emission of neutrons varies along the curve. At the location $A = 84/152$ most of the neutrons emitted stem from the heavy fragment whereas at the mass combination with $A = 104/132$ most of the neutrons emitted stem from the light fragment.

➤ Figure 4.19 shows the number of prompt neutrons emitted for various fissioning systems. Within the error margins, these curves follow the same pattern. They show a “sawtooth” shape presenting a minimum around masses 82 and 130 and a linear increase with increasing mass beyond 82 and 132, respectively.

The interpretation is as follows. Prompt neutron emission is due to the excitation energy of the fragments. The excitation arises when fragments deformed at scission relax into their stable nearly spherical configuration. Taking the scission configuration in ➤ Fig. 4.11 seriously, breaking the neck near the heavy sphere ($A = 132$), for instance, would mean that the fragment with $A = 132$ would be practically spherical, but the complementary fragment with $A = 236 - 132 = 104$ (for $^{236}\text{U}^*$) would be composed of a spherical part ($A = 80$) and the entire neck, hence, it would be very deformed. As a consequence, the fragment with $A = 132$ would emit practically no neutrons and all the neutrons would come from the complementary

■ Fig. 4.14

Mass–yield curves in the reactor-neutron-induced fission of ^{227}Ac , ^{232}Th , ^{231}Pa , ^{235}U , ^{238}U , and ^{241}Am ; from (von Gunten 1969)



fragment. As the breaking point is shifted along the neck toward the small sphere, neutron emission from the heavy fragment would gradually increase until a maximum is reached at $A = 156$ ($= 236 - 80$). Correspondingly, the neutron emission from the light fragment will show a minimum around $A = 80$ and will increase with increasing mass. The sawtooth-like curve observed in [Fig. 4.19](#) is in exact agreement with these expectations.

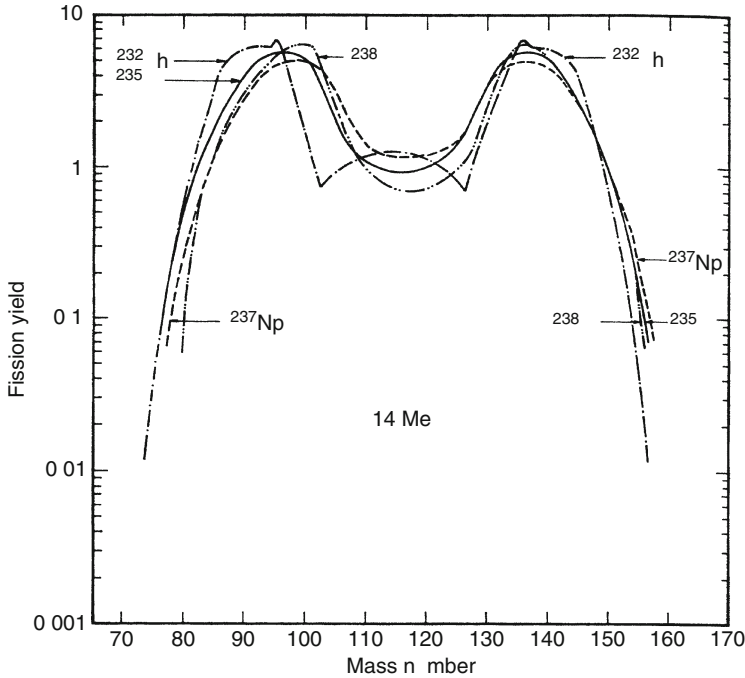
The fact that the lines have the same slope for various fissioning nuclei (from ^{233}U to ^{252}Cf) shows that not only the two spherical parts of the dumb-bell configuration are unchanged but also the neck diameter remains the same. Certainly, the neck for the heavier system (^{252}Cf) will be slightly longer and neutron emission will reach further into the mass region near $A = 120$ and 160 (see [Fig. 4.19](#)).

On these grounds, one would expect that the total number of prompt neutrons emitted will increase with the mass of the compound nucleus. This is found indeed as is documented in [Fig. 4.20](#).

There is, however, an interesting exception in the figure, namely ^{260}Md , which shows a neutron yield of about 2 rather than an extrapolated value of 4. The nucleus of ^{260}Md is the only nucleus among those shown in [Fig. 4.20](#) with a symmetric yield distribution as seen in [Fig. 4.16](#). (The fermium isotopes with $A = 254$, 256 , and 257 ($N = 154$, 156 , and 157) shown also in [Fig. 4.20](#) have an asymmetric mass distribution (see [Fig. 4.16](#))). Unfortunately, no values of prompt neutron emission are known for the other isotopes with $Z \geq 100$ that show a symmetric mass distribution ([Fig. 4.16](#)).

■ Fig. 4.15

Mass–yield curves in the 14 MeV-neutron-induced fission of, ^{232}Th , ^{235}U , ^{238}U , and ^{237}Np ; from (von Gunten 1969)



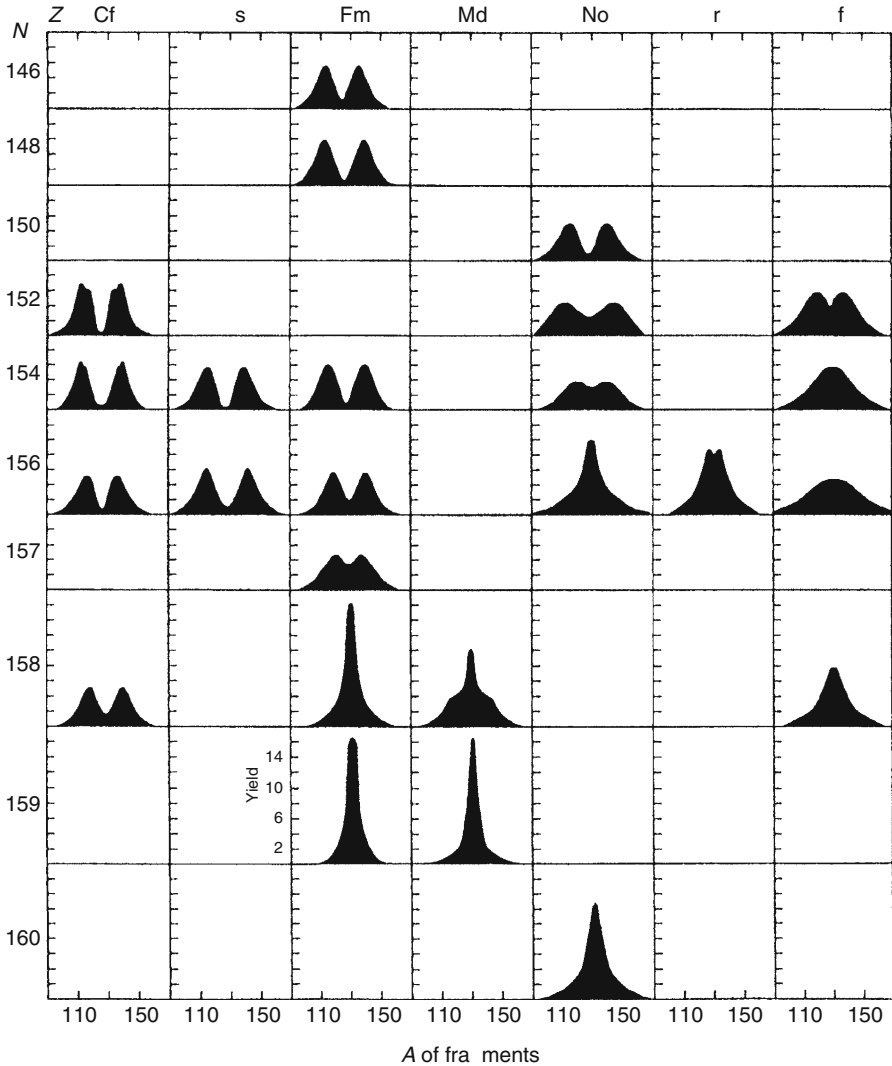
Apparently, the sharp transition from asymmetric fission to symmetric fission (► Fig. 4.16) is accompanied by a sudden change in the scission configuration. When Z and N of the fissioning nucleus allow a scission configuration with two spheres with $Z = 50$ and N sufficiently close to 82, a configuration with two such spheres and nearly no neck is realized. As a consequence, the arising symmetrical fragments show only a small amount of deformation, which may turn into excitation energy and later into neutron emission.

Such a compact configuration with two magic nearly spherical structures at short distance will necessarily lead to a high kinetic energy of the fragments (super-short fission path of Brosa). In fact, the kinetic energy of the fragments has been measured using the methods based on momentum conservation (double energy, double velocity, or energy/velocity techniques discussed above). The results are shown in ► Fig. 4.21.

In ► Fig. 4.21, one can observe the expected steady increase in kinetic energy of the fission products with increasing mass/atomic number of the compound system (or more precisely with the increase in the parameter $Z^2/A^{1/3}$ describing the Coulomb repulsive energy between the two fragments formed). However, one can see that a number of nuclei with $Z \geq 100$ ($^{258,259}\text{Fm}$, $^{259,260}\text{Md}$, and $^{258,262}\text{No}$) show a higher kinetic energy. These are the nuclei that are undergoing symmetric fission as demonstrated in ► Fig. 4.16. For most of these nuclei (^{258}Fm , $^{259,260}\text{Md}$, and $^{258,262}\text{No}$) the kinetic energy distribution can be resolved into two components, a component with low (i.e., normal) kinetic energy (labeled “l” in ► Fig. 4.21) and another

■ Fig. 4.16

Schematic representation of the known mass–yield curves for the spontaneously fissioning isotopes of the elements with $Z = 98$ to $Z = 104$ (Hoffman and Lane 1995)

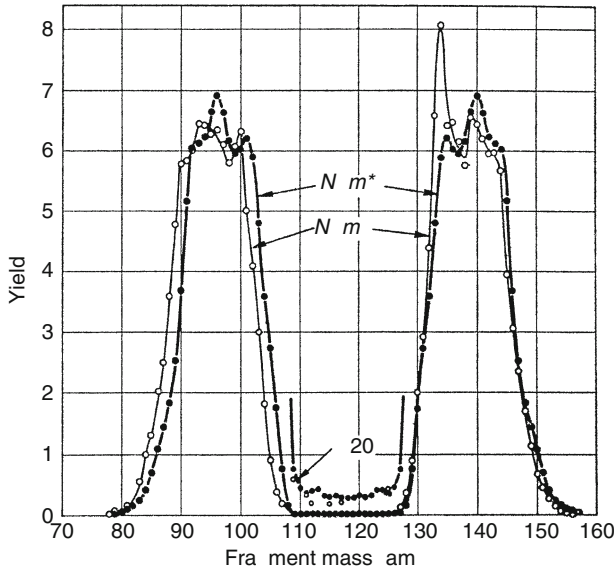


component with high kinetic energy ("h"). Presumably, in these cases there is a coexistence of symmetric and asymmetric fission with the respective scission configurations.

In summary, for compound nuclei with $Z < 100$ one has a scission configuration as shown in ► Fig. 4.11 with two spheres stabilized by the shell closures at $Z = 50/N = 82$ (heavy sphere) and, as it will be shown later, $Z = 28/N \approx 50$ (light sphere). For compound nuclei with $Z \geq 100$ (and $N > 152$) one observes a transition to another scission configuration with two spheres of about $Z = 50$ and N close to 82. The neck between these spheres is small. Therefore,

■ Fig. 4.17

Pre-neutron emission mass distribution, $N(m^*)$, corrected for resolution and post-neutron emission mass distribution, $N(m)$, for the thermal-neutron-induced fission of ^{235}U ; from (Schmitt et al. 1966)



the configuration is compact. This brings about fragments with high kinetic energy and low excitation energy – hence a small number of prompt neutrons are emitted.

The assumption that the emission of prompt neutrons is due to an evaporation of neutrons from excited fragments whose excitation energy comes from the relaxation of potential energy of deformation implies that the neutrons are emitted from flying fragments accelerated by the repulsive Coulomb force between the two positively charged nuclei. As a consequence, the vector addition of the velocity of the fragments and the velocity of the neutrons (emitted isotropically from the flying fragments) should lead to a preferential emission of neutrons in the direction of the flying fragments. The angular distribution of the neutrons with respect to the axis of the fragments has been measured and is shown in ▶ Fig. 4.22.

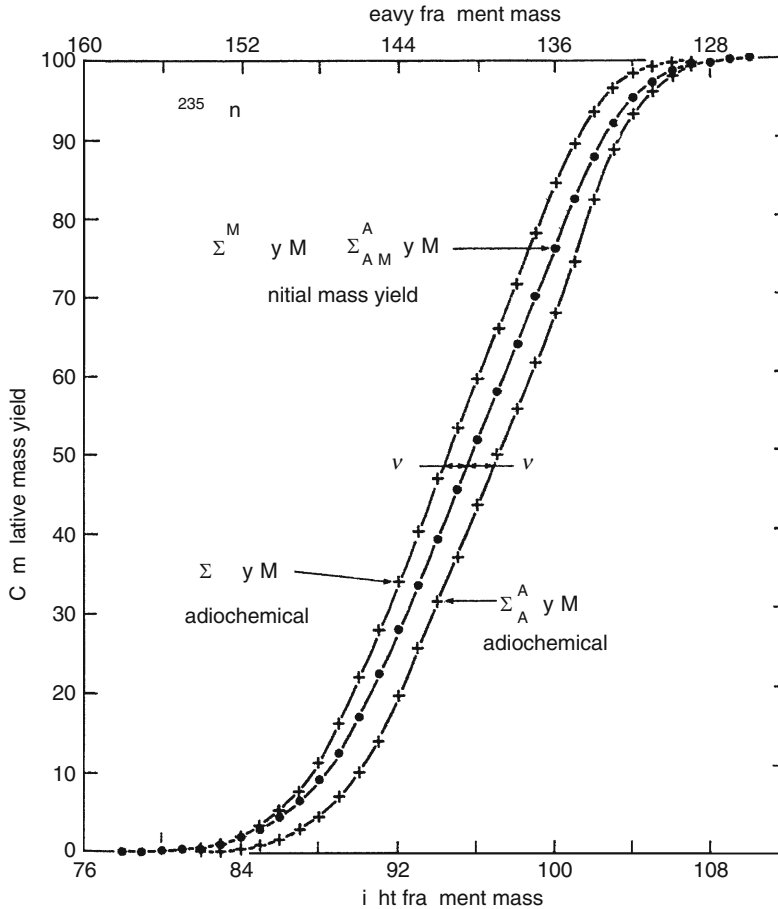
The neutrons are clearly peaked at 0° with respect to the light fragment and at 180° , i.e., along the flight path of the heavy fragment. The peaking in the direction of the heavy fragment is less pronounced because, due to momentum conservation, the velocity of the heavy fragment is smaller than the one of the light fragment.

In addition to the emission of *prompt* neutrons discussed here, there is also an emission of *delayed* neutrons. The delayed neutrons arise from some fission fragments when they undergo β decay. Normally, β decay can lead not only to the ground state of the daughter nucleus but also to some excited states. Such excited states, normally, go over to the ground state by the emission of γ rays. In some fission products, the excited level fed by the β decay of its precursor is higher than the binding energy of the last neutron. In such a case, the nucleus can emit a neutron rather than γ rays.

The longest-lived example of such a delayed neutron emitter (or delayed neutron precursor) is the nuclide ^{86}Br . It undergoes β decay with a half-life of 55 s. The daughter nucleus is the

■ Fig. 4.18

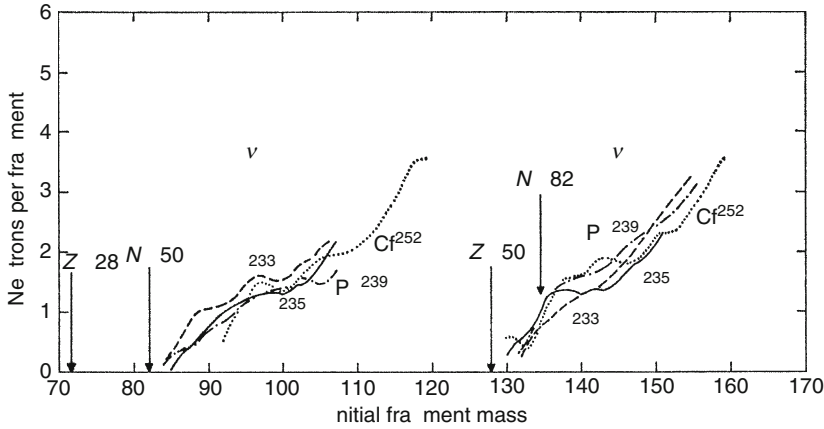
Cumulative plot of the mass yields for thermal-neutron-induced fission of ^{235}U obtained by summing the yields from very asymmetric fission to symmetric fission for fission products (+) and fission fragments (●). The numbers of prompt neutrons emitted (ν_L and ν_H) for light and heavy fragments, respectively, can be obtained from the horizontal distances between the curves using slight corrections for curvature; from (Terrell 1962)



stable ^{86}Kr . The majority of the decays (70%) lead to an excited state in ^{86}Kr , which emits a neutron turning into ^{85}Kr . The neutrons from this process appear with a half-life of 55 s. Among the fission products there are more than 250 such delayed neutron precursors (frequently abbreviated dnp) with half-lives ranging typically between 25 s and 0.2 s. A total number of 17 nuclides out of the above 250 – mainly neutron-rich isotopes of As, Br, Rb, and I – contribute more than 85% of the delayed neutron yield. A list of the delayed neutron precursors and of their properties can be found in (Wahl 1988; England and Rider 1994). The fraction of delayed neutrons among the total amount of neutrons set free is small (e.g., 0.65% and 0.21% for thermal-neutron-induced fission of ^{235}U and ^{239}Pu , respectively). Delayed

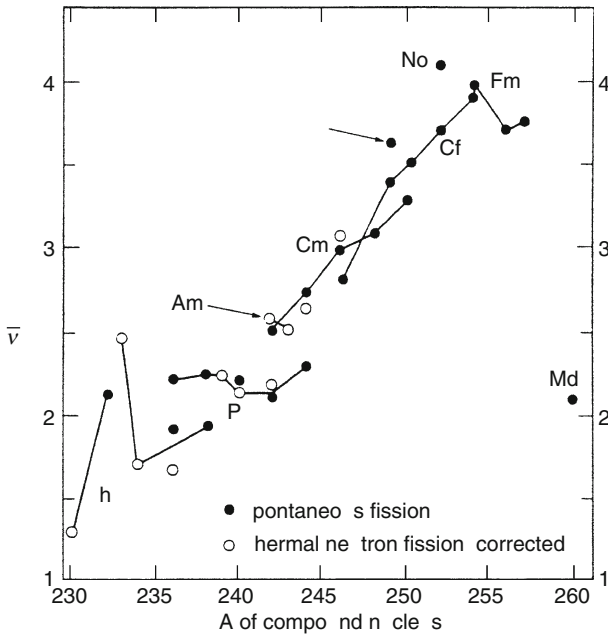
■ Fig. 4.19

Number of prompt neutrons emitted in the thermal-neutron-induced fission of ^{233}U , ^{235}U , and ^{239}Pu and in the spontaneous fission of ^{252}Cf as a function of the initial fragment mass ("Sawtooth" curve); from (Terrell 1962)

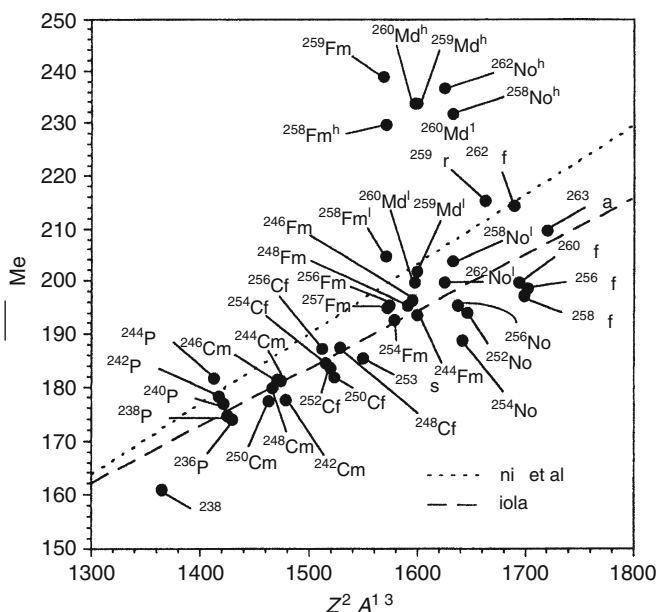


■ Fig. 4.20

Total number of prompt neutrons emitted ($\bar{\nu}_T$) as a function of the mass of the compound nuclei. Full circles: spontaneous fission, blank circles: thermal-neutron-induced fission corrected to zero excitation energy using $d\nu_T/dE_x = 0.11 \text{ MeV}^{-1}$; from (Hoffman 1989)



Average or most probable total kinetic energy of fission products versus ($Z^2/A^{1/3}$), a parameter describing the Coulomb repulsive energy between the two arising fragments. The dashed line is the linear fit of Viola et al. (1985) and the dotted line is the linear fit of Unik et al. (1973); from (Hoffman and Lane 1995)



neutrons are very important for the control of nuclear reactors. Their role is to be discussed in another chapter in this handbook (see [▶ Chap. 57](#) of Vol. 6).

Chain yields in very asymmetric mass distribution. Recently, using the mass separator Lohengrin briefly presented above, it has become possible to measure yields of the light fission fragments down to very low values. Four fission reactions studied are shown in ► Fig. 4.23.

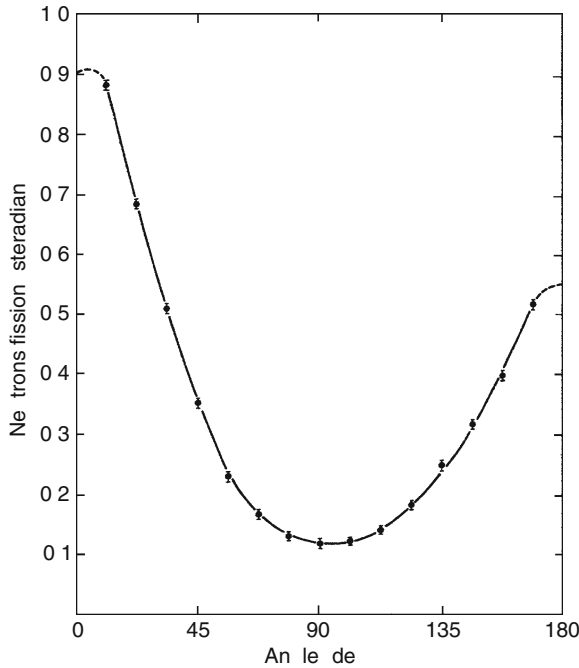
The remarkable observation is a small peak or at least a hump at mass 70. Beyond this hump, the yields are dropping practically to zero. Anticipating some information to be discussed later, it may be said here that the elemental composition is such that the yield of mass 70 consists almost exclusively of nickel with the magic number of 28 protons.

It is concluded therefore that the hump at mass 70 is an effect of the closed shell of 28 protons. At mass 80 in [Fig. 4.23](#), one may vaguely discern another deviation from the general trend. This deviation can be seen more clearly in [Fig. 4.24](#). This figure includes data of additional fission reactions that could be measured down to mass numbers below 80 but not yet down to mass number 70.

A line has been fitted through the data points for masses $A \geq 80$. This is reasonable since the slopes of a Gaussian distribution in a logarithmic display and sufficiently far from the maximum can be approximated very well by a linear relationship. The figure shows that all the curves are broken at mass 80. The yields decrease more rapidly than extrapolated. The effect appears more pronounced if the strongly compressed logarithmic scale is taken into account. The region around $A = 80$ is the region where the mass-yield curves of nearly all low energy

■ Fig. 4.22

Number of prompt neutrons emitted versus the angle with respect to the light fragment direction in spontaneous fission of ^{252}Cf ; from (Bowman et al. 1962), referred to in (Vandenbosch and Huizenga 1973)



fission reactions agree (see Fig. 4.10) and where the neck and the small sphere touch. The tendency to preserve intact the small sphere with $A = 80$ ($Z = 32$ and $N = 48$, near $N = 50$) seems to be at the origin of the more rapid decrease of the yield at masses $A < 80$.

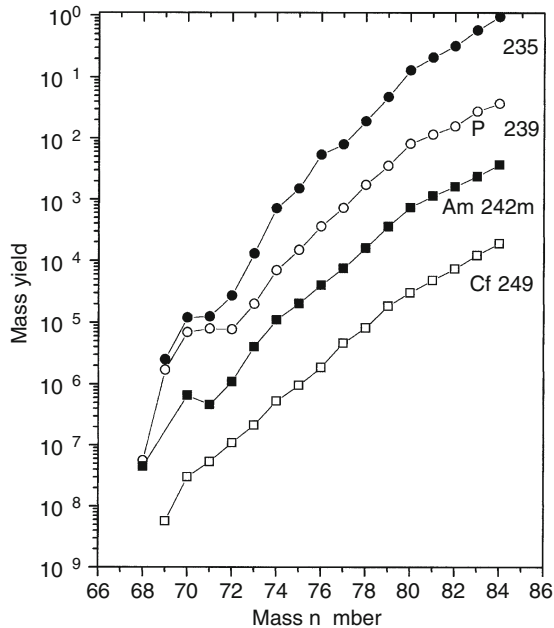
The fact that not $N = 50$ (the magic number for isolated nuclei) but $N = 48$ is the critical number has to do with the fact that the forming fragment is not an isolated nucleus but is part of a scissioning system. In this context, it is worth remembering that in the transition from asymmetric fission to symmetric fission the limiting neutron number is 158 for Fm ($Z = 100$) and 154 for Rf ($Z = 104$) (Fig. 4.16), i.e., a few neutrons less than 164, which would represent twice the magic number of 82.

In contrast to this observation, the shell closures for protons ($Z = 28$, and $Z = 50$) are practically not influenced by the rest of the scissioning nucleus: The transition from asymmetric fission to symmetric fission takes place exactly at Fm $Z = 100$ (2×50) (Fig. 4.16) and the hump at mass 70 (Fig. 4.23) also occurs exactly at $Z = 28$. In this context, it is worth mentioning that – in the framework of astrophysical studies of the r-process (see Chap. 12 in Vol. 2) – it has been revealed that the energetic effect of closed neutron shells is quenched in extremely neutron-rich nuclei (Pfeiffer et al. 2001).

In summary, the light sphere of the dumbbell-like scission configuration possesses an onion-like structure with two shells that are progressively difficult to break into: the total mass

■ Fig. 4.23

Absolute mass yields in the reactions $^{235}\text{U}(n_{\text{th}},f)$ (Sida et al. 1989), $^{239}\text{Pu}(n_{\text{th}},f)$ (Ditz 1991), $^{242\text{m}}\text{Am}(n_{\text{th}},f)$ (Tsekhanovich et al. 1999), and $^{249}\text{Cf}(n_{\text{th}},f)$ (Hentzschel et al. 1994). For clarity of display, the curves have been displaced on the yield axis by dividing the yields labeled Pu-239 by 10, Am-242m by 100, and Cf-249 by 1,000)



of 80 consisting of 32 protons and 48 (nearly 50) neutrons. Inside this structure, a sub-unit of 28 protons and 42 neutrons is found.

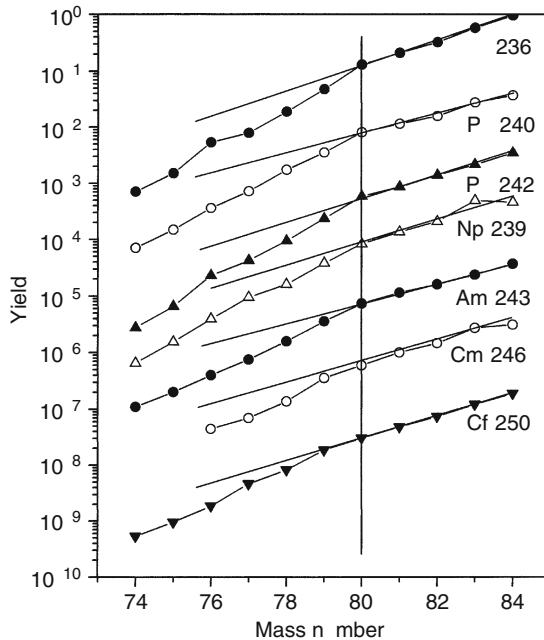
For the nuclear physicist it is interesting to learn from this behavior that nuclear shells document themselves not only as structural elements of nuclei but also as structural elements of subsystems of nuclei.

4.4.3 Nuclear Charge Distribution

So far, essentially mass–yield curves were dealt with. Each point of such a curve represents the formation cross section of isobaric nuclei of mass number A , composed of different combinations of protons and neutrons. Because heavy, fissile nuclei are generally more neutron rich than stable nuclides with about half their mass, fission products are generally also more neutron rich than stable nuclides of the same mass, even after the loss of a few prompt neutrons. (Example: The symmetric fission of the compound nucleus ^{236}U ($Z = 92$, $N = 144$) would form two *fragment* nuclei of ^{118}Pd ($Z = 46$, $N = 72$). Assuming the emission of one prompt neutron, the corresponding primary fission product would be ^{117}Pd . The stable isobar in mass chain with $A = 117$ is, however, ^{117}Sn ($Z = 50$, $N = 67$). As a consequence, the nucleus ^{117}Pd would have to undergo a sequence of four β decays to reach stability.) Thus, the products

■ Fig. 4.24

Mass yields of various thermal-neutron-induced fission reactions characterized by their compound nuclei ($^{236}\text{U}^*$ (Sida et al. 1989), $^{240}\text{Pu}^*$ (Ditz 1991), $^{242}\text{Pu}^*$ (Friedrichs et al. 1998, Friedrichs 1998), $^{239}\text{Np}^*$ (Tsekhanovich et al. 2001), $^{243}\text{Am}^*$ (Tsekhanovich et al. 1999), $^{246}\text{Cm}^*$ (Friedrichs et al. 1998, Friedrichs 1998), and $^{250}\text{Cf}^*$ (Hentzschel et al. 1994)). For clarity of display the single yield curves have been shifted by a factor of 10 among each other. The (logarithmic) yield values at $A \geq 80$ have been fitted to a linear relationship



of the fission process are generally radioactive and decay (by β decay) into some less neutron-rich daughter products until stability is reached. The yields of the primary fission products show a distribution along these β -decay chains. Primary fission yields generally comprise nuclides one to six charge units away from stability with correspondingly different half-lives ranging from less than 1 s to days or, in a few cases, even years. As a consequence, these chain members are generally produced directly in fission and via the β decay of precursors.

The question whether, e.g., the primary products in chain with $A = 70$ are mainly nickel ($Z = 28$, $N = 42$) or cobalt ($Z = 27$, $N = 43$) is decisive for the question whether the closed shell with $Z = 28$ plays a role. The lengths of the β -decay chains are important for the safety of reactors, as β decay produces heat even after the shutdown of a reactor and this heat has to be carried off even in case of an accident. An emergency cooling system has to be designed accordingly. Prompt neutron emission competes with β decay. The number of prompt neutrons emitted determines the possibility for a chain reaction.

Due to these reasons, attempts were made very early to determine the distribution of “primary” or “independent” yields of single nuclides within the isobaric mass chains. The different approaches will be described in the following.

4.4.3.1 Methods of Measurement of Independent Yields

Radiochemical techniques. The first attempts were based on radiochemical techniques. From the preceding discussion, it is clear that, for the measurements of independent yields, time is an important factor. Therefore, the determination of the primary (or “independent”) yield of a nuclide, which is being formed directly and by the decay of precursors, requires a chemical separation from these precursors before they could decay into it in a disturbing amount. Therefore, the determinations of independent yields require short irradiation times and fast chemical separations. In the early years, there were hardly any such procedures available. The first independent yields were obtained for a few exceptional cases where a neutron-rich stable or long-lived nuclide was interrupting the decay chain, producing a “shielded nuclide.” (Example: ^{136}Cs shielded by the stable ^{136}Xe .) Wherever independent yields could be measured, they concerned generally the part of the decay chains near stability, where half-lives were longer than in the very neutron-rich part of the decay chains.

Later, many fast radiochemical separations and ingenious automatic chemical separation methods were developed (Herrmann and Denschlag 1969, 1982; Rengan and Meyer 1993) and were applied to the determination of independent fission yields (Denschlag 1986, 1997). Summarily, one can say that the methods developed allow isolating any element formed from the complex mixture of fission products within the time span of a few seconds (exception: rare earth elements that require a time span of minutes).

γ -ray spectroscopy of unseparated mixtures. The development of γ -ray detectors with high resolution (Ge detectors) led to attempts to use the selectivity of γ rays to identify single isotopes in an unseparated mixture of fission products and to measure their independent yields. Unfortunately, γ -ray spectra of short-lived fission product mixtures are so complicated that they are very difficult to analyze. As a consequence, the results are of limited accuracy and have been restricted mostly to measuring chain yields and a few independent yields of nuclides with favorable γ -decay properties. Moreover, the absolute line intensities required to convert count rates into yields that are often not known accurately. This problem can be partly overcome by the analysis of growth and decay curves of parent/daughter systems. The method has been applied to the thermal-neutron-induced fission of a number of fissile nuclides like ^{229}Th (Dickens and McConnell 1983), ^{239}Pu (Dickens and McConnell 1980, Dickens et al. 1981), ^{241}Pu (Dickens 1979), ^{245}Cm (Dickens and McConnell 1981a), and ^{249}Cf (Dickens and McConnell 1981b).

Conventional fast mass separation with γ -ray spectroscopy. The combination of online mass separation (of fission products stopped in the target, volatilized, ionized, and separated) with γ -ray spectroscopy would be an ideal tool to determine both independent and cumulative yields, because mass separation of nuclides diffusing out of a target under irradiation can be performed within seconds. The selection of a single mass chain would simplify the γ -ray spectra dramatically, so that even short-lived nuclides could be measured. Unfortunately, problems arise with the volatilization from the targets and ionization in the ion source that show different yield and time characteristics for different elements (“chemical selectivity”). Therefore, yields obtained with this technique have frequently been considered unreliable.

Later, high-temperature ion sources were developed (Münzel et al. 1981; Jacobsson et al. 1987) ($T = 2500^\circ\text{C}$), which show a faster release of fission products and less chemical selectivity. Also careful studies of the release and ionization mechanisms (Rudstam 1987; Kirchner 1992) of the elements involved indicate that the previous problems may be overcome.

The technique has been used by Rudstam and coworkers to measure systematically a large part of the independent yield distribution in the fission of ^{235}U , including many isomeric pairs and the region of symmetry (Rudstam et al. 1990), and in the fission of ^{233}U (Galy et al. 2000).

Information on both the distribution of independent yields among different isomeric states and the charge distribution in the region of symmetry is still scarce, as these values are practically inaccessible to most other techniques.


Z-identification by specific energy loss. A more recently developed technique has been adapted from heavy ion research, which consists in identifying the atomic number Z of unslowed fission fragments, i.e., fission fragments with kinetic energies of 60–100 MeV. This Z -identification is based on the fact that the stopping power of matter for fast heavy ions depends (among others) on their atomic number Z , since a higher Z of the ion causes stronger interaction with the electronic shells of the atoms of the stopping material.

The method can be employed in principle in combination with any of the instruments that have been discussed above in the context of the measurement of mass yields provided that they use mass separation or mass identification of unslowed fission fragments; i.e., with instruments like Lohengrin, Hiawatha, and the equipment using momentum conservation to identify fragment masses (energy and/or velocity correlation experiments). Unfortunately, only Lohengrin and Hiawatha possess sufficiently good mass resolutions to produce unbiased yields. In addition, the Z -resolution of the method at the typical kinetic energies of fission fragments is only good enough to distinguish single isotopes up to $Z = 47$, i.e., for the light mass peak. This is, however, not a real problem. As the Z -distributions of light and heavy mass peaks are complementary around Z_f the atomic number of the compound nucleus, a measurement of the light mass peak gives the information on the heavy mass peak as well.

The fact that the technique operates with unslowed fission fragments allows the study of the yield distribution as a function of the kinetic energy of the fragments, i.e., as a function of different degrees of deformation of the fissioning system at scission. Another important advantage is the rapidity of the method. The separation or identification of fragment mass, atomic number, and kinetic energy takes only a time in the order of microseconds. This time is short relative to the time of β decay (>100 ms). Therefore, an undisturbed primary distribution is obtained automatically.

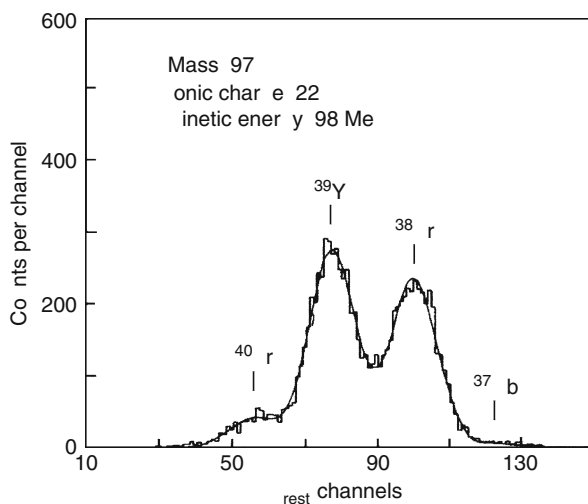
In practice, Z -identification has been added to the mass-separator Lohengrin (Clerc et al. 1975; Bocquet et al. 1988), to Hiawatha (Strittmatter and Wehring 1978; Strittmatter and Wehring 1979) and to the mass identification system Cosí fan tutte (Oed et al. 1983; Boucheneb et al. 1989). It is possible to combine such measurements of Z -identification with a simple double-energy coincidence technique if the analysis is limited to high kinetic energy events not disturbed by prompt neutron emission (Butz-Jørgensen et al. 1987). Finally, at the expense of the mass information, Mariolopoulos et al. were able to measure the plain nuclear charge distribution by combining a measurement of specific energy loss dE/dx , rest-energy, and (for calibration purposes) X-rays (Mariolopoulos et al. 1981).

The actual techniques of Z -identification are based on measuring the specific energy loss (dE/dx) of the fast fragments when they pass through a thin layer of matter (solid or gaseous) in which the fission fragments deposit about half their kinetic energy. Different variants of this technique are given in review articles (e.g., in Denschlag 1997).

The Z -resolutions of these variants are fairly similar. Differences are due to the properties of the detectors and the resolution also depends on the nuclear charge and kinetic energy of the fragments. A typical example of a spectrum of different members of a nuclear decay chain is given in  Fig. 4.25.

■ Fig. 4.25

Pulse height spectrum of the residual energy (kinetic energy of the fragments minus energy loss in the absorber) of fission products after passing through an absorber. The experimental data are shown in histogram form. The smooth curve is the result of a computer fit to four Gaussian curves. The area under each Gaussian is proportional to the relative independent yield of the particular nuclide indicated; after (Quade et al. 1979)



As it appears from ► Fig. 4.25, the most important elements contributing to the total mass chain can be well separated. A fit with equidistant Gaussians provides the contributions. However, the figure demonstrates that contributions of fractional yields smaller than 5% are difficult to ascertain with this method and should be treated with caution.

4.4.3.2 Experimental Results and Systematic Description (Z_p -Model)

The number of independent fission yield values obtained so far is enormous. Because of their multitude and theoretical and practical importance, these values have been compiled in special data banks, e.g., (James et al. 1991; England and Rider 1994). The latter data bank, which is accessible on the Internet, includes 132,000 values from 60 fission reactions (fission of different nuclei induced by different particles of varying energy). The work of collecting, evaluating, and compiling fission yields is coordinated by the International Atomic Energy Agency, Vienna (IAEA 2000).

The best way to deal with the enormous body of data is using a systematic description, which has been developed by A.C. Wahl first for the fission of ^{233}U , ^{235}U , and ^{239}Pu induced by thermal neutrons and for the spontaneous fission of ^{252}Cf (Wahl 1988). This method has been extended to other fission reactions with varying excitation energies later (Wahl 1989; IAEA 2000). The model comes in two variants (Z_p - and A_p '-model). The following discussion will be limited to the Z_p -model.

In this model the fractional independent yields in an isobaric chain (mass chain) are described by a Gaussian curve with a maximum (most probable charge, Z_p) and a width

parameter (standard deviation, $\sigma(Z)$). Both parameters may be obtained by a fit of a Gaussian to the experimental fractional yield values. Z_p may be compared to Z_{UCD} , which represents the nuclear charge of a fission product calculated assuming unchanged charge density of this fragment with respect to the compound nucleus. Z_{UCD} is calculated according to

$$Z_{UCD} = (A + \nu) \frac{Z_f}{A_f} \quad (4.37)$$

with A = the mass number of the fission product, ν = the (average) number of prompt neutrons emitted in producing this fission product, and Z_f and A_f the nuclear charge and mass of the fissioning (compound) nucleus, respectively. The difference of the two values:

$$\Delta Z = Z_p - Z_{UCD} \quad (4.38)$$

represents a charge polarization between the two fragments formed.

At a direct inspection of experimental fractional independent yields and their fits by Gaussian curves one can observe that yield values with even proton and/or neutron numbers tend to lie above the curve and those with odd numbers tend to lie below it. This is taken into account by two factors EOZ and EON, the even–odd (or odd–even) factors for protons and neutrons, respectively. These values may be given in percentage. In this way, an EOZ-value of, e.g., 15% corresponds to a factor 1.15 by which a value read from the Gaussian curve has to be multiplied (even- Z nuclide) or divided (odd- Z nuclide) in order to obtain the predicted yield.

As a consequence, the Z_p model allows one to describe the nuclear charge distribution of a specific fission reaction by four parameters:

$$\Delta Z, \sigma(Z), \text{EOZ, and EON.}$$

In general, these parameters depend on the mass number of the isobaric chain considered. In the region of “normal asymmetric fission” (>99% of the fission yields), e.g., ΔZ can be given as a linear function of the mass of the heavier fragment:

$$\Delta Z(A_H) = \Delta Z(140) + s(A_H - 140). \quad (4.39)$$

Here A_H is the mass of the heavy primary fragment, s a parameter for the slope, and $\Delta Z(140)$, the ΔZ -value for mass $A_H = 140$, arbitrarily taken as a reference (Fig. 4.26). The value of s is generally small and comparable to its error margins.

In this mass region of “normal asymmetric fission,” the parameters $\sigma(Z)$, EOZ, and EON can be generally assumed to be constant and independent of the mass ratio of heavy and light fragments.

In the region of symmetric fission or in the neighborhood of shell closures, the four parameters behave differently and show some abrupt changes. The behavior of the four parameters mentioned, as a function of the fission fragment mass and also as a function of the mass, charge, and excitation energy of the fissioning nuclide, is the subject of the fission yield systematics mentioned (Wahl 1988, 1989; IAEA 2000). A version (YCALC) of the model calculations is attached to ref. IAEA 2000, and it is also available for downloading (YCALC 2003).

The program YCALC allows the calculation of the independent yields of any fission product for 12 different fission reactions (i.e., the spontaneous fission of ^{252}Cf , the thermal-neutron-induced fission of ^{229}Th , ^{233}U , ^{235}U , ^{238}Np , ^{239}Pu , ^{241}Pu , ^{242}Am , and ^{249}Cf , the reactor-neutron-induced fission of ^{232}Th , and ^{238}U , and the 14 MeV-neutron-induced fission of ^{238}U).

Numerical values of the parameters mentioned (for the yield range of “normal asymmetric fission”) are given in Table 4.2.

Fig. 4.26

Illustration of the systematic description of nuclear charge distribution. The outer frame shows a part of a chart of nuclides with a plot of the atomic number (Z) versus the neutron number (N). The location of stable nuclides is shown by the "Line of Stability." Products formed by the fission of a heavy neutron-rich nucleus (^{235}U) with an "Unchanged Charge Density" of both fragments would be located on or around the line labeled "UCD." The maximum of the experimental distribution of fractional yields (shown as protruding from the paper plane) (Z_p) is shifted by ΔZ to even more neutron-rich nuclei for heavy fission fragments and, correspondingly, toward less neutron-rich nuclei for light fission fragments. The amount of charge polarization at the arbitrarily chosen reference mass $A = 140$ is given by $\Delta Z^{140} = Z_p^{140} - Z_{\text{UCD}}^{140}$ for mass $A = 140$ or, generally, for $\Delta Z(A) = Z_p^A - Z_{\text{UCD}}^A = \Delta Z(140) + s(A - 140)$. The insert shows a cut through the three-dimensional yield distribution and allows to illustrate the significance of the parameters ΔZ , σ , EOZ, and EON. The open circles in the insert represent experimental yields (of isobaric nuclides) serving as a basis for the determination of Z_p and σ

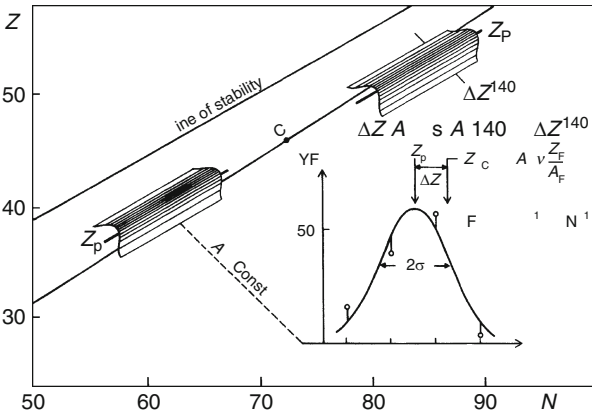


Table 4.2

Numerical values for the parameters of the Z_p -model (asymmetric region) for the thermal-neutron-induced fission of ^{233}U , ^{235}U , ^{239}Pu , and the spontaneous fission of ^{252}Cf (from (Wahl 1988))

Fissile nucleus	σ	ΔZ^{140}	s	EOZ	EON
^{233}U	0.52	-0.47	-0.010	1.27	1.08
^{235}U	0.54	-0.50	-0.015	1.26	1.05
^{239}Pu	0.55	-0.48	-0.015	1.06	1.00
^{252}Cf	0.61	-0.47	-0.005	1.00	1.00
(Estimated uncertainty)	(± 0.02)	(± 0.02)	(± 0.005)	(± 0.03)	(± 0.03)

4.4.3.3 Physical Implications of the Nuclear Charge Distribution in Fission

The fact that ΔZ^{140} is different from zero shows that polarization occurs in the fissioning nucleus. As appears from the negative sign for ΔZ^{140} and as is also visible from [Fig. 4.26](#), heavy fission fragments are more neutron rich than would correspond to an unchanged charge density. Correspondingly, light fission fragments are less neutron rich. This is due to the Coulomb force between protons that favors neutron-rich structures for heavier nuclei.

The width of the distribution (characterized by standard deviation σ) is nearly constant between 0.5 and 0.6, which indicates that within a β -decay chain the direct formation from fission is concentrated to 3–4 nuclides (see insert in [Fig. 4.26](#) and the experimental yield distribution in chain 97 in [Fig. 4.25](#)). The width of this nuclear charge dispersion (σ) is a rough indication of the excitation energy of the nucleus at scission. Surprisingly, σ is not really larger in fission reactions induced by fast particles and, hence, with a larger initial excitation energy. The conclusion supported by other experimental observations is that in these cases particle emission takes place prior to fission, cooling down the compound nucleus.

The even–odd factors for protons (EOZ) and for neutrons (EON) are also indicators of the nuclear temperature before scission. [Table 4.2](#) shows that EOZ approaches one with increasing mass (or fissility Z^2/A) of the fissile nucleus. It is a general observation that even–odd effects tend to decrease or even disappear with increasing fissility parameter. This is probably due to the fact that fission reactions with higher fissility set free more energy leading to higher excitation energy of the nuclei at scission. The observation that the selection of fragments of high kinetic energy (which is possible, e.g., in Lohengrin) shows increased values of EOZ (Denschlag 1986; Gönnerwein 1991) is in agreement with this statement, as the selection of fragments with high kinetic energy leaves correspondingly less excitation energy in the system.

The even–odd effect for neutrons (EON) shows a similar decrease with increasing fissility ([Table 4.2](#)). The absolute values of EON are however smaller than for EOZ. This observation was initially attributed to the fact that neutrons are emitted from the fission fragments smearing out an initially stronger effect. It was however observed that EON was smaller than EOZ even for fragments of sufficiently high kinetic energy to exclude an emission of neutrons (Armbruster et al. 1981; Knitter et al. 1992). This discrepancy, which remained a puzzle until recently, will be discussed below.

In general, the odd–even effects were interpreted for a long time to indicate the survival of the pairing of protons and neutrons on the way of the nucleus from saddle point to scission (Bjornholm 1974; Nifenecker et al. 1980). The preservation of pairing would mean that nuclear matter would remain in a state of superfluidity on the way to scission. This explanation would imply no odd–even effect (i.e., $\text{EOZ} = 1.00$) for the fission of odd Z nuclei (like Np with $Z = 93$ or Am with $Z = 95$). The recent discovery that these odd fissile nuclei also show an odd–even effect (of a slightly different character and in very asymmetric fission) (Stumpf et al. 1992; Davi et al. 1998; Tsekhanovich et al. 1999; Tsekhanovich et al. 2001) demonstrates that preservation of pairing cannot be the only reason for the effect. (The odd–even effect for protons in even fissile nuclei as discussed above means that all fission fragments (light or heavy) with even numbers of protons are formed EOZ times the value expected without odd–even factor (for EOZ, see [Table 4.2](#)). For odd nuclei (which necessarily always form one even and one odd fission fragment), the odd–even effect means that **light** fission fragments with even numbers of protons are formed EOZ times the value expected without odd–even factor and that correspondingly **heavy** fission fragments with odd numbers of protons are formed EOZ times the

value expected without odd–even factor. The situation for neutrons is analogous; it is however complicated by the fact that, after fission, neutrons are emitted obscuring the initial situation.)

The discovery of an odd–even effect in the (again, very asymmetric) fission of lighter odd- Z fissioning systems studied in “inverse kinematics” (Steinhäuser et al. 1998) has confirmed the findings obtained in thermal-neutron-induced fission.

Based on these experimental findings, Nifenecker’s theory (Nifenecker et al. 1982) of the odd–even effect should be modified. The argument is that the level density at a certain excitation energy (phase space) has to be taken into account (Steinhäuser et al. 1998; Rejmund et al. 2000). The level density in a larger nucleus is higher than in a smaller one. Therefore, at scission of an odd- Z nucleus the last unpaired proton will see a larger phase space in the larger fragment and will more likely be attached to it. As a consequence, the heavy fragment will preferably be odd and the light fragment correspondingly even, and that is the observed odd–even effect.

The model also explains the old puzzle mentioned above, i.e., that the odd–even effect for protons is higher than for neutrons even if a high kinetic energy of the fragments excludes the emission of neutrons from the fragments. The argument is as follows (Rejmund et al. 2000). In the mass range considered the number of neutrons exceeds that of protons. Accordingly, the single-particle level density of the neutrons exceeds that of the protons. As a consequence, for a given amount of excitation energy, neutron pairs are broken up more frequently than proton pairs. Thus, the odd–even effect will be smaller for neutrons than for protons.

The limitation in space does not allow a more detailed discussion of nuclear charge distribution in fission. The interested reader should be referred to special literature like (Gönnenwein 1991; Wagemans 1991a; Denschlag 1997). A few specific points have already been presented above. The fact that the fine structure at $A = 70$ shown in ▶ Fig. 4.23 consists practically only of nickel ($Z = 28$) has already been used as an argument for the role of the 28-proton shell in fission. In addition, it has been mentioned in the context of ◀ Fig. 4.24 that the fission products with $A = 80$ are predominantly $Z = 32$ and $N = 48$ (not exactly $N = 50$), in agreement with other observations showing that closed shells of neutrons may be influenced more by nuclear surroundings than proton shells.

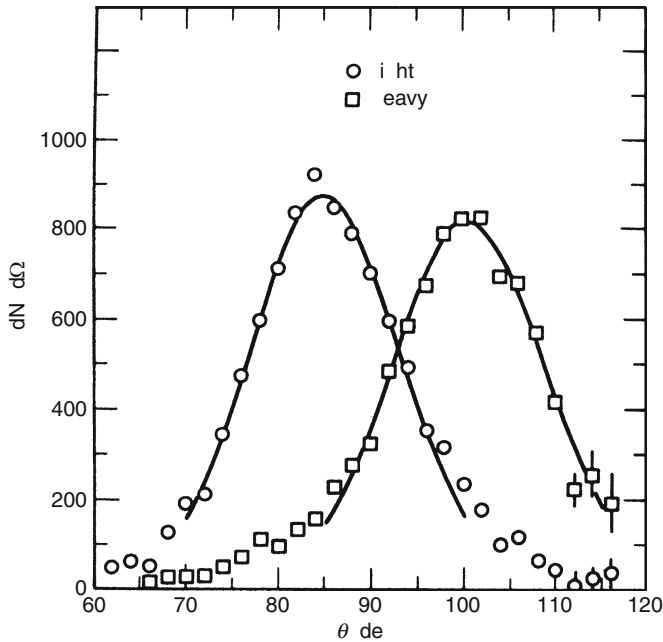
4.4.4 Ternary Fission

So far only binary fission was considered, i.e., the fission into two fragments (plus a few neutrons). In about one fission event out of 400 the nucleus splits, however, into three charged particles. In most cases the third particle is an α particle. It is assumed that these third particles stem from the neck of the scission configuration (see ▶ Fig. 4.11). The experimental evidence for this assumption is provided by the angular distribution of the fragments. This was measured, e.g., by “Diogenes” (Heeg et al. 1983) a cylindrical, position sensitive detector surrounding a source of fissile material. The detector registers heavy, light, and ternary fragments and their directions in space. Results of an (earlier) measurement (Fluss et al. 1973) are presented in ▶ Fig. 4.27.

The configuration assumed to be responsible for the observed angular distribution is shown in ▶ Fig. 4.28. The α particles are focused to a direction of about 90° with respect to the axis formed by the two fission fragments. The focusing is not exactly 90° but somewhat more inclined toward the light fragment because the Coulomb repulsion of the larger fragment is stronger.

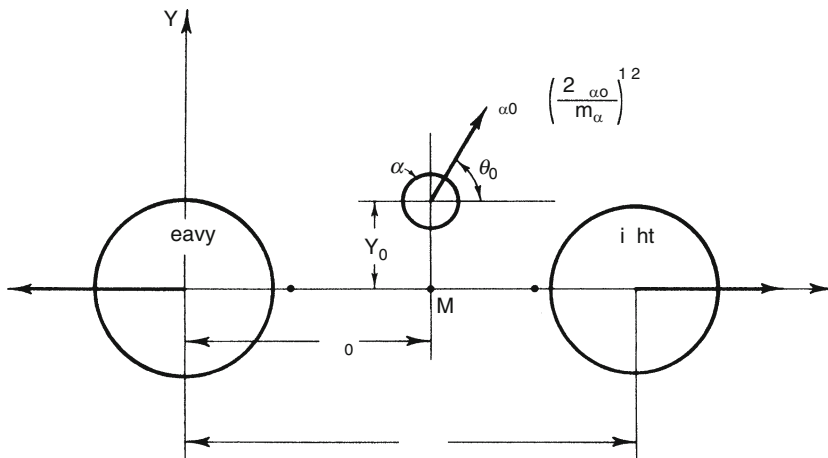
■ Fig. 4.27

Angular distribution of the α particles (with energy greater than 11 MeV) in coincidence with heavy (squares) and light (circles) fission fragments; from (Fluss et al. 1973). The angle θ is defined with respect to the flight direction of the heavy/light fragment as indicated in the figure



■ Fig. 4.28

Diagram illustrating the focusing of the ternary fragment by the two heavier fragments to an angle θ of about 90° with respect to the axis formed by the two heavier fission fragments. Due to the stronger Coulomb interaction with the heavy fragment, the angle of the third particle is around 80° with respect to the light fragment and around 100° with respect to the heavy fragment; from (Vandenbosch and Huizenga 1973)



Alpha particles are by far the most prominent ternary fragments. Other lighter and heavier fragments are, however, also emitted. The extreme sensitivity of the mass separator Lohengrin has allowed to measure yields of ternary fragments down to values of $10^{-7}\%$. A survey of yields of ternary products as a function of their atomic number (Z) is given in [Fig. 4.29](#) for the thermal-neutron-induced fission of ^{233}U and ^{249}Cf .

It is interesting to note that the spectra of ternary particles extend to different atomic numbers, which coincide nearly with the size of the neck that results from the postulate extracted from the mass yield and nuclear charge distributions. To correlate the data, it has been postulated that the two spheres of the dumbbell configuration shown in [Fig. 4.11](#) for the fission of $^{236}\text{U}^*$ are practically the same for all asymmetrically fissioning nuclei from $Z = 90$ to about 99 and, consequently, that the variation in the neutron/proton numbers of the different compound nuclei must be connected with the size of the neck. [Fig. 4.29](#) is the direct experimental proof for this assumption: in the fission of uranium, the neck size is $(92 - 82 =) 10$ protons; in the fission of californium, the neck size is $(98 - 82 =) 16$ protons. The situation is similar for neutrons and for the total mass. This is, however, less convincing due to prompt neutron emission.

4.4.5 Fission Isomers

4.4.5.1 Detection and Measurement of Half-Lives

Considering the minimum in the potential energy barrier as shown in [Figs. 4.8](#) and [4.9](#), one cannot exclude that a nucleus may be trapped in this minimum.

This is indeed the case, and such a short-lived state is called a fission isomer. Actually, it was the discovery of a spontaneously fissioning nucleus with an abnormally short period that led Polikanov et al. to postulate the existence of shape isomers and brought Strutinsky to formulate his theory (Strutinsky 1967). Polikanov's experimental setup is shown in [Fig. 4.30](#).

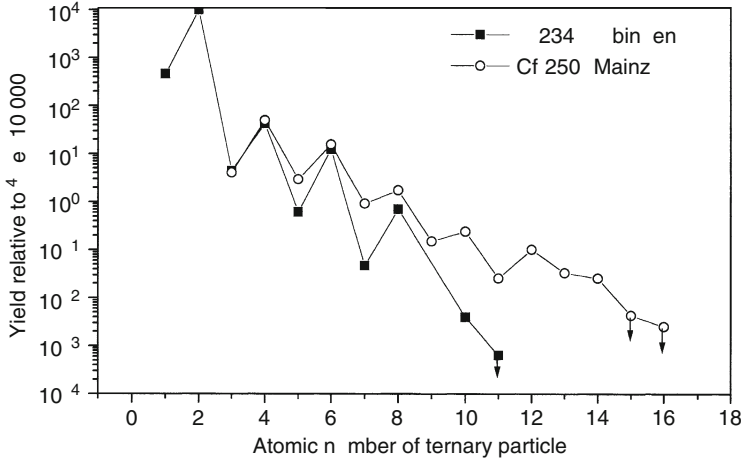
A beam of ^{22}Ne or ^{16}O was directed on a target of ^{238}U . By the impact, the fission isomers formed were projected onto a rotating collector wheel and transported in front of two ionization chambers. Any fission fragments formed from a spontaneously fissioning nuclide on the wheel were to be detected by the ionization chambers. The beam of ^{22}Ne or ^{16}O ions was stopped in a Ta-collector connected to a current meter for monitoring the beam intensity. The apparatus was equipped to allow a calibration of the chambers using fission fragments from the reaction $^{238}\text{U}(n_{\text{th}}, f)$.

The ratio of count rates in the two ionization chambers at a known rotational speed of the wheel (800–1,400 rpm) allowed to calculate the half-life of the spontaneously fissioning nuclides. The value obtained was 0.02 s – about 10^{10} times shorter than expected for a normal spontaneously fissioning nuclide of this fissility parameter (see [Fig. 4.4](#)). (The shortest-lived normal spontaneously fissioning nuclide that could be considered is ^{252}Fm formed in the reaction $^{238}\text{U}(^{16}\text{O}, 2n)^{252}\text{Fm}$. Its fissility parameter would be $Z^2/A = 39.7$. The half-life extrapolated from the systematics ([Fig. 4.4](#)) would be of the order of 10^8 – 10^9 s. The species observed here was later identified to be a shape isomer of ^{242}Am (fissility parameter of 37.3). The ground state of ^{242}Am decays by β^- decay and electron capture with a half-life of 16 h.)

Soon after this discovery, fission isomers were observed in a multitude of other fission reactions (Michaudon 1973; Wagemans 1991a) ([Fig. 4.31](#)). Most of these fission isomers are

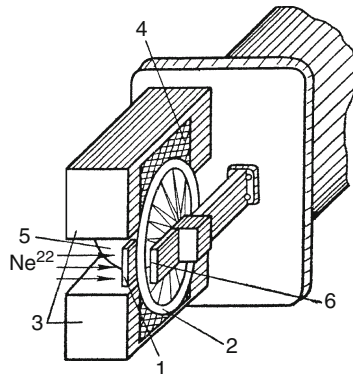
■ Fig. 4.29

Yields of light charged particles (ternary products) emitted in the reactions $^{233}\text{U}(n_{\text{th}},f)$ (Wöstheinrich et al. 1998) and $^{249}\text{Cf}(n_{\text{th}},f)$ (Davi 1997) relative to the yield of ^4He in these reactions (set arbitrarily to 10,000). Data points with arrows represent upper limits



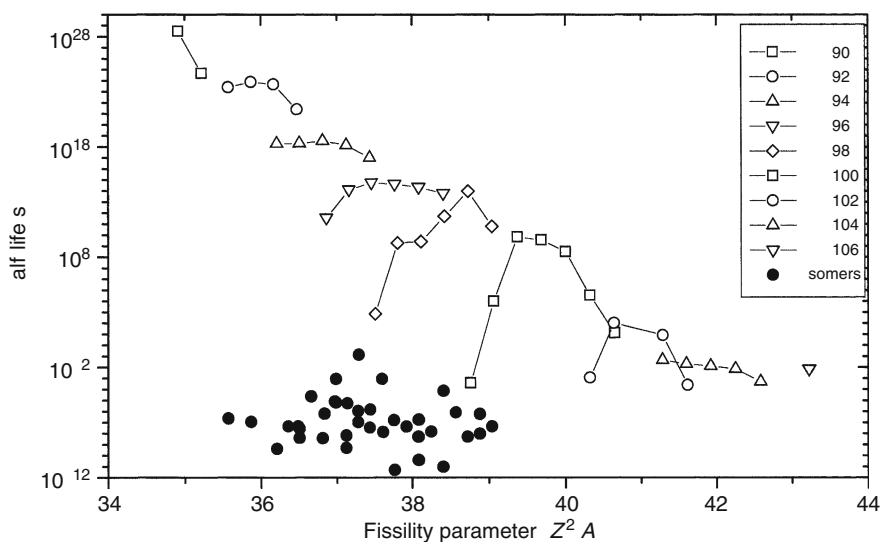
■ Fig. 4.30

Setup used to detect the first fission isomer (Polikanov et al. 1962). (1) Target (^{238}U , 1 mg/cm² on a foil of Al, 5.8 μm thick) exposed to the beam of ^{22}Ne - or ^{16}O -ions (energy 80–139 MeV). (2) Rotating collector wheel intercepting the reaction products (fission isomers) and assuring the transport in front of two ionization chambers. (3) Where any fission fragments originating from nuclei on the wheel were detected. (4) Thin nylon windows of the ionization chambers. (5) Fitting permitting the calibration of the chambers using fragments from the reaction $^{238}\text{U}(n_{\text{th}},f)$. (6) Beam stop connected to a current meter for monitoring the beam intensity



■ Fig. 4.31

Half-lives for spontaneous fission from the second minimum of the potential energy curve as shown schematically in Fig. 4.8 (fission isomers) (*full points*) as a function of the fissility parameter compared to the corresponding half-lives from the ground states (*open points*). The latter points are identical to those in Fig. 4.4. All data are from the compilation of (Wagemans 1991a)



considerably shorter-lived than the isomer of 0.02 s (later identified as ^{242m}Am with its half-life determined more accurately to be 0.014 s).

It was a lucky circumstance for Polikanov et al. that they chose a reaction leading to the longest-lived of the fission isomers; their experimental setup would not have been able to detect any other fission isomer.

For the detection of these shorter-lived isomers a different instrumentation had to be developed. This method is also based on the transfer of momentum from the incoming beam of heavy fragments to the compound nuclei, which will then have sufficient energy to escape from the thin target. Whereas prompt fission will occur in or very near the target, any shape isomers will undergo fission while in flight along a detector plate (Michaudon 1973). The geometrical arrangement is such that prompt fission events are not allowed to enter the detector. The detector plate may be a solid-state track detector such as a foil of Makrofol or another position sensitive detector for fission fragments. (Makrofol KG is a 2,2 bis (4-hydroxy-phenyl) propane polycarbonate available in thin foils. The impact of a fission fragment produces local radiation damage. Such an event, magnified by etching, is visible under a microscope.) The number of fission events per cm^2 can be counted as a function of distance from the target and, since the velocity of the fission isomers is known from momentum conservation, the distance can be converted into time, hence obtaining the half-life of the fissioning isomers. The method in different variants is applicable to half-lives in the range of microseconds to nanoseconds and even below (Metag et al. 1974).

4.4.5.2 Deformation (Charge Plunger Experiment)

A particularly interesting variant of the measurements described above is the “charge plunger experiment.” It allows one to obtain some direct experimental information on the spectroscopic transitions in the second minimum and from this on the degree of deformation of the fission isomers. The experimental setup is shown in ► Fig. 4.32.

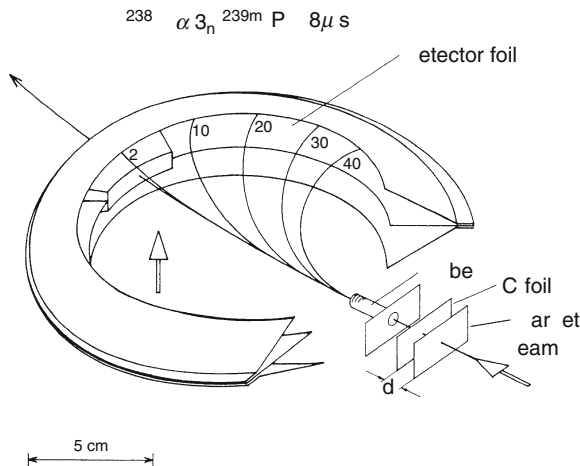
A beam of α particles of 33 MeV is impinging on the target (a thin layer of ^{238}U). Due to the impact, the reaction products (ions of $^{239\text{m}}\text{Pu}$, which have escaped prompt fission) are knocked out of the target, pass through a thin carbon foil and a collimator tube into a volume with a strong magnetic field (B), where they are separated according to their ionic charge (2+ to 40+). The volume is surrounded by a detector foil. The nuclei of $^{239\text{m}}\text{Pu}$ (half-life 8 μs) are intercepted on the foil and undergo fission there leaving an etchable mark at the location of their interception.

The ions of $^{239\text{m}}\text{Pu}$ are produced with high angular momentum and decay by conversion electrons to the “isomeric ground state.” The corresponding Auger cascades produce ionic charges in $^{239\text{m}}\text{Pu}$ up to 40+. These charges can be reset to the equilibrium values (1+ and 2+) by the passage through the thin carbon foil. As a consequence, Auger cascades taking place before the ions have reached the carbon foil are reset to low ionic charges. Auger cascades taking place later are not reset. Since the velocity of the ions can be calculated assuming momentum conservation from the known energy of the α particles and the distance of the target to the carbon foil can be measured, the time difference between the formation of $^{239\text{m}}\text{Pu}$ and the passage through the carbon foil can be calculated. The overall timescale of the rotational de-excitation in the fission isomer $^{239\text{m}}\text{Pu}$ can be determined by varying the distance of the carbon foil to the target. The half-life resulting in the present case is about 20 ps.

The lifetime information of the rotational excitations can be converted to the quadrupole moments of the corresponding nuclei using the rotational model. If the shape of the nucleus for

► Fig. 4.32

Setup of the “charge plunger experiment” (Habs et al. 1977; Metag et al. 1980). See text for details



the isomeric state is described by a prolate spheroid, the quadrupole moments obtained correspond to an axis ratio of about 2:1 for the isomers. The 2:1 ratio of the axes is sometimes called the superdeformed shape (Thirolf and Habs 2002). This ratio is in very good agreement with the calculations of Strutinsky (Strutinsky 1967) discussed in the context of Fig. 4.8. A thorough discussion of the double-humped fission barrier (including its experimental and theoretical implications) is given in (Bjornholm and Lynn 1980).

It is interesting to note that in some fissioning nuclei, like ^{234}U , the potential energy surface has been shown to have a third minimum, and the fissioning system may stay in the states supported by this third pocket (Blons et al. 1978; Krasznahorkay et al. 1998; Thirolf and Habs 2002). The length of the system in such an elongated transient state is three times as large as its breadth, thus the state fulfills the definition of a hyperdeformed state.

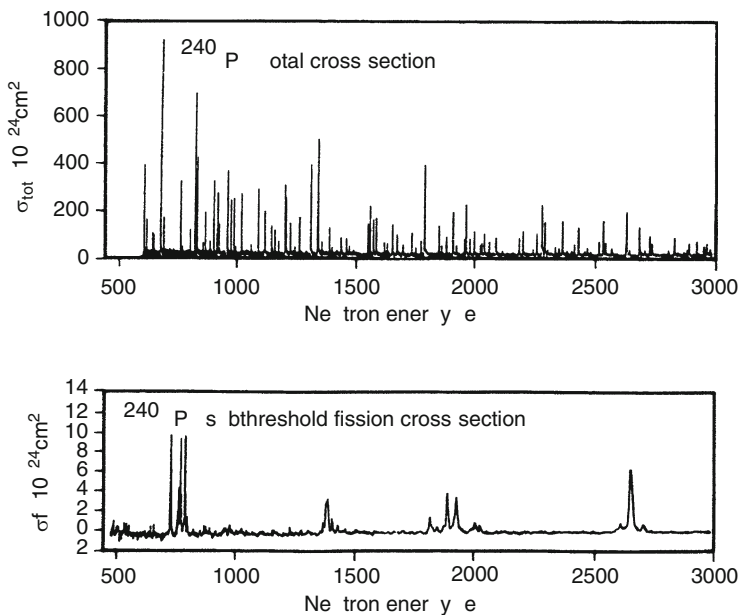
4.4.5.3 Level Densities in the Isomers

Besides the information on the deformation of the fission isomers based on rotational excitations described above, some information can also be obtained on the level density of vibrational and single-particle excitations in fission isomers.

Back in 1968, a grouping of resonances was observed when the fission cross section was measured as a function of the energy of the neutrons for the neutron-induced (sub-barrier)

Fig. 4.33

The neutron total (Kolar and Böckhoff 1968) and sub-barrier (Migneco and Theobald 1968) fission cross sections of ^{240}Pu as a function of neutron energy between 0.5 and 3 keV; from (Weigmann 1991)



fission of ^{240}Pu (Migneco and Theobald 1968) and for ^{237}Np (Fubini et al. 1968). The behavior for the example of the reaction $^{240}\text{Pu}(n,f)$ can be studied in ► Fig. 4.33.

Whereas the resonances observed for the total cross section (upper part of ► Fig. 4.33) show a spacing of about 14 eV, characteristic of a usual compound nucleus, the fission cross section shows groups of resonances interrupted by larger empty spaces of about 450 eV. The interpretation of this behavior is that, in this region of sub-barrier fission, the fissioning system goes over to the isomeric state in the second well by tunneling. The tunneling is facilitated by the existence of two levels (of identical energy, spin, and parity) in the first and second minimum of the potential barrier. As a consequence, the grouped resonances are a measure of the level density in the first and second well of the potential barrier. The distance between the groups reflects the level density in the isomeric state (second well), and the splitting within each group results from mixing with states in the first well.

References

- Alexandrov AA, Alexandrova IA, Ermolenko AV, Korjuk YA, Nikulin DS, Pevchev YF, Podshibyakin SL, Pyatkov YV, Sitnikov SI, Slyusarenko AI, Shemetov AN, Shehmatetiev RA (1991) Nucl Instr Meth Phys Res A 303:323
- Armbruster P, Quade U, Rudolph K, Clerc H-G, Mutterer M, Pannicke J, Schmitt C, Theobald JP, Engelhardt W, Gönnerwein F, Schrader H (1981) The cold fragmentation of ^{234}U in $^{233}\text{U}(n,h,f)$. In: International conference on nuclei far from stability. Helsinki, p 675
- Asghar M, Caitucoli F, Leroux B, Perrin P, Barreau G (1981) Nucl Phys A 368:328
- Barreau G, Sicre A, Caitucoli F, Asghar M, Doan TP, Leroux B, Martinez G, Benfoughal T (1985) Nucl Phys A 432:411
- Bjornholm S (1974) Physica Scripta 10A:110
- Bjornholm S, Lynn JE (1980) Rev Mod Phys 52:725
- Blons J, Mazur C, Paya D, Ribrag M (1978) Phys Rev Lett 41:1282
- Bocquet JP, Brissot R, Faust HR (1988) Nucl Instr Meth Phys Res A 267:466
- Bohr N (1936) Nature 137:351
- Bohr N, Wheeler JA (1939) Phys Rev 56:426
- Bothe W, Becker H (1930a) Nat Wiss 18:705
- Bothe W, Becker H (1930b) Z Physik 66:289
- Boucheneb N, Geltenbort P, Asghar M, Barreau G, Doan TP, Gönnerwein F, Leroux B, Oed A, Sicre A (1989) Nucl Phys A 502:261c
- Bowman HR, Thompson SG, Milton JCD, Swiatecki WJ (1962) Phys Rev 126:2120
- Braun A, Preiswerk P, Scherrer P (1937) Nature 140:682
- Brosa U, Großmann S, Müller A (1990) Physics Reports 197:167
- Butz-Jörgensen C, Knitter H-H, Straede Ch, Hamsch F-J, Vogt RA (1987) Nucl Instr Meth Phys Res A 258:209
- Chadwick J (1932a) Proc Royal Soc (London) A136:692
- Chadwick J (1932b) Nature 129:312
- Clerc H-G, Schmidt K-H, Wohlfarth H, Lang W, Schrader H, Pferdekämper KE, Jungmann R, Asghar M, Bocquet JP, Siegert G (1975) Nucl Instr Meth 124:607
- Coryell CD, Sugarman N (eds) (1951) NNES radiochemical studies: the fission products. McGraw-Hill, New York
- Curie I, Joliot F (1932) C R Acad Sciences, Paris 194:273
- Curie I, Savitch P (1938a) C R Acad Sciences, Paris 206:1643
- Curie I, Savitch P (1938b) C R Acad Sciences, Paris 206:906
- Davi M (1997) Messung von Ausbeuten in der Spaltung von ^{250}Cf und ^{239}Np am Massenseparator Lohengrin. Dissertation, Johannes Gutenberg Universität, Mainz
- Davi M, Denschlag HO, Faust HR, Gönnerwein F, Oberstedt S, Tsekhanovitch I, Wöstheinrich M (1998) Odd-even effects in the fission of odd-Z nuclides. In: Fioni G, Faust H, Oberstedt S, Hamsch FJ (eds) Nuclear fission and fission-product spectroscopy. American Institute of Physics, Woodbury, pp 239–246
- De Laeter JR (1988) Mass Spectrom Rev 7:71
- Denschlag HO (1986) Nucl Sci Engin 94:337
- Denschlag HO (1997) Fission fragment mass charge and energy distributions. In: Poenaru DN, Greiner W (eds) Experimental techniques in nuclear physics. Walter de Gruyter, Berlin, New York, pp 535–582
- Derengowski M, Melkonian E (1970) Phys Rev C 2:1554
- Dickens JK (1979) Nucl Sci Engin 70:177
- Dickens JK, Mcconnell JW (1980) Nucl Sci Engin 73:42
- Dickens JK, Mcconnell JW (1981a) Phys Rev C 23:331
- Dickens JK, Mcconnell JW (1981b) Phys Rev C 24:192
- Dickens JK, Mcconnell JW (1983) Phys Rev C 27:253

- Dickens JK, McConnell JW, Northcutt KJ (1981) Nucl Sci Engin 77:146
- Diiorio G, Wehring BW (1977) Nucl Instr Meth 147:487
- Ditz W (1991) Messung von Massen- und Nuklidausbeuten in der stark asymmetrischen Spaltung von ^{239}Pu . Dissertation, Johannes Gutenberg Universität, Mainz
- Engelkemeir DW, Novey TB, Schover DS (1951) Determination of absolute slow-neutron fission yields in ^{235}U . In: Coryell CD, Sugarman N (eds) Radiochemical studies: the fission products. McGraw-Hill, New York, pp 1334–1343
- England TR, Rider BF (1994) Fission product yields, Report: LA-UR-94-3106. Los Alamos National Laboratory, Los Alamos, NM. <http://ie.lbl.gov/fission.html>
- Flügge S (1939) Nat wiss 23/24:403
- Flügge S (1989) How fission was discovered, fifty years with nuclear fission, Gaithersburg, MD. In: Behrens JW, Carlson AD (eds) (American Nuclear Society, La Grange Park, IL) pp 26–29
- Fluss MJ, Kaufmann SB, Steinberg EP, Wilins BD (1973) Phys Rev C 7:353
- Frenkel JA (1939) Phys Rev 55:987
- Friedlander G, Kennedy JW, Macias ES, Miller JM (1981) Nuclear and radiochemistry. Wiley, New York
- Friedrichs T (1998) Untersuchung der neutroneninduzierten Spaltung von ^{245}Cm und ^{241}Pu sowie Bestimmung von Kernmassen mittels β , gamma-Koinzidenzspektroskopie. Dissertation, Universität Braunschweig, Braunschweig
- Friedrichs T, Faust H, Fioni G, Groß M, Köster U, Münnich F, Oberstedt S (1998) Investigation of mass, charge, and energy of thermal neutron induced fission of ^{245}Cm and ^{241}Pu . In: Fioni G, Faust H, Oberstedt S, Hamsch FJ (eds) Nuclear fission and fission-product spectroscopy. American Institute of Physics (AIP), Woodbury, NY, pp 231–238
- Frisch OR (1939) Nature 143:276
- Frisch OR (1979) Energy from nuclei. In: What little I remember. University Press, Cambridge, pp 113–119
- Fubini A, Blons J, Michaudon A, Paya D (1968) Phys Rev Lett 20:1373
- Galy J, Fogelberg B, Storrer F, Mach H (2000) Europ Phys J A 8:331
- Gamov G (1928) Z Physik 51:204
- Glasstone S (1967) The proton, antiproton, and positron. In: Sourcebook on atomic energy. von Nostrand, Princeton, pp 42–43
- Gönnenwein F (1991) Mass, charge, kinetic energy of fission fragments. In: Wagemans C (ed) The nuclear fission process. CRC-Press, Boca Raton, pp 287–473
- Grosse AV (1965) Introductory note to paper No. 137. In: Fermi E (ed) Note e Memorie; collected papers. Accademia Nazionale dei Cincei/University of Chicago Press, Rome, p 41
- Gurney RW, Condon EU (1928) Nature 122:439
- Gurney RW, Condon EU (1929) Phys Rev 33:127
- Habs D, Metag V, Specht HJ, Ulfert G (1977) Phys Rev Lett 38:387
- Hahn O (1962) Vom radiothor zur uranspaltung. Friedr. Vieweg & Sohn, Braunschweig
- Hahn O, Strassmann F (1939) Nat wiss 27:11
- Haxel O, Jensen JHD, Suess HE (1950) Z Physik 128:295
- Heeg P, Hoffmann KE, Mutterer M, Theobald JP, Weingärtner K, Pannicke J, Gönnenwein F, Barreau G, Leroux B (1983) Nucl Phys A 409:379c
- Heisenberg W (1927) Z Physik 43:172
- Hentschel R, Faust HR, Denschlag HO, Wilkins BD, Gindler J (1994) Nucl Phys A 571:427
- Herrmann G (1990a) Angewandte Chemie 102:469
- Herrmann G (1990b) Angew Chem Int Ed 29:481
- Herrmann G (1995) Radiochim Acta 70/71:51
- Herrmann G, Denschlag HO (1969) Ann Rev Nucl Sci 19:1
- Herrmann G, Trautmann N (1982) Ann Rev Nucl Part Sci 32:117
- Hoffman DC (1989) Spontaneous fission of the heaviest elements, fifty years with nuclear fission. National Institute of Standards and Technology, Gaithersburg, MD, pp 83–91
- Hoffman DC, Lane MR (1995) Radiochim Acta 70/71:135
- IAEA (2000) Compilation and evaluation of fission yield nuclear data, Report: IAEA-TECDOC-1168, available through INIS Clearinghouse, IAEA, Vienna, Austria
- Jacobsson L, Fogelberg B, Ekström B, Rudstam G (1987) Nucl Instr Meth Phys Res B 26:223
- James MF, Mills RW, Weaver DR (1991) A new evaluation of fission product yields and the production of a new library (UKFY2), Parts I to III, Report: AEA-TRS-1015, -1018, -1019, AEA (Atomic Energy Agency), Thermal Reactor Services. Winfrith, Dorchester, UK
- Jentschke W, Prankl F (1939a) Anz Akad Wiss Wien mathem-naturw Klasse, 1939, 19
- Jentschke W, Prankl F (1939b) Nat wiss 27:134
- Kirchner R (1992) Nucl Instr Meth Phys Res B 70:186
- Knitter H-H, Hamsch F-J, Butz-Jørgensen C (1992) Nucl Phys A 536:221
- Kolar W, Böckhoff KH (1968) Final results on the neutron total cross section of ^{240}Pu . In: International conference on neutron cross sections and technology, (National Bureau of Standards, Special Publication No. 299) p 519
- Krafft F (1981) Im Schatten der Sensation, Leben und Wirken von Fritz Straßmann. Verlag Chemie, Weinheim
- Kramish A (1986) The griffin. Houghton Mifflin Company, Boston

- Krasznahorkay A et al (1998) *Phys Rev Lett* 80:2073
- Lemmerich J (1989) Die Geschichte der Entdeckung der Kernspaltung, Katalog zur Ausstellung in der Technischen Universität Berlin. (Berlin, Technische Universität Berlin, available from Universitätsbibliothek, Abt. Publikationen, ISBN 3 7983 1257 5)
- Mariolopoulos G, Hamelin C, Blachot J, Bocquet JP, Brissot R, Crancon J, Nifenecker H, Ristori C (1981) *Nucl Phys A* 361:213
- Mayer MG (1948) *Phys Rev* 74:235
- Mayer MG (1950) *Phys Rev* 78:16
- Mayer-Kuckuck T (1970) *Physik der atomkerne*. B.G. Teubner, Stuttgart
- Meitner L (1950) *Nature* 165:561
- Meitner L, Frisch OR (1939) *Nature* 143:239
- Meitner L, Hahn O, Strassmann F (1937) *Z Physik* 106:249
- Metag V, Habs D, Specht HJ (1980) *Phys Rep* 65:1
- Metag V, Liukkonen E, Sletten G, Glomset O, Bjornholm S (1974) *Nucl Instr Meth* 114:445
- Michaudon A (1973) Nuclear fission. In: Baranger M, Vogt E (eds) *Advances in nuclear physics*. Plenum Press, New York, pp 1–217
- Migneco E, Theobald JP (1968) *Nucl Phys A* 112:603
- Moll E, Schrader H et al (1975) *Nucl Instr Meth* 123:615
- Moll E, Schrader H, Siegert G, Hammers H, Asghar M, Bocquet JP, Armbruster P, Ewald H, Wollnik H (1977) *Kerntechnik* 19:374
- Moseley HGJ (1913) *Phil Mag* 26:1024
- Moseley HGJ (1914) *Phil Mag* 27:703
- Münzel J, Wollnik H, Pfeiffer B, Jung G (1981) *Nucl Instr Meth* 186:343
- Mustafa MG, Mosel U, Schmitt HW (1973) *Phys Rev C* 7:1519
- Myers WD, Swiatecki WJ (1966) *Nucl Phys* 81:1
- Nifenecker H, Mariolopoulos G, Bocquet JP, Brissot R, Hamelin C, Crancon J, Ristori C (1982) *Z Physik A* 308:39
- Nifenecker HA, Blachot J, Bocquet JP, Brissot R, Crancon J, Hamelin C, Mariolopoulos G, Ristori C (1980) Experimental approach to the dynamics of fission, physics and chemistry of fission, Jülich, Germany, (IAEA, Vienna, Austria) pp 35–64.
- Noddack I (1934) *Angewandte Chemie* 47:653
- Oed A, Geltenbort P, Brissot R, Gönnerwein F, Perrin P, Aker E, Engelhardt D (1984) *Nucl Instr Meth Phys Res* 219:569
- Oed A, Geltenbort P, Gönnerwein F (1983) *Nucl Instr Meth* 205:451
- Pfeiffer B, Kratz KL, Thielemann F-K, Walters WB (2001) *Nucl Phys A* 693:282
- Pleasanton F (1968) *Phys Rev* 174:1500
- Polikanov SM, Druin VA, Karnaukhov VA, Mikheev VL, Plev AA, Skobelev NK, Subbotin VG, Ter-Akop'yan GM, Fomichev VA (1962) *Soviet Physics JETP* 15:1016
- Quade U, Rudolph K, Siegert G (1979) *Nucl Instr Meth* 164:435
- Rejmund F, Ignatyuk AV, Junghans AR, Schmidt K-H (2000) *Nucl Phys A* A678:215
- Rengan K, Meyer RA (1993) Ultrafast chemical separations. Report: Nuclear Science Series: NAS-NS-3118 (Radiochemical Techniques). National Academy Press, Washington, DC
- Rudstam G (1987) *Nucl Instr Meth Phys Res A* 256:465
- Rudstam G, Aagard P, Ekström B, Lund E, Göcktürk H, Zwicky HU (1990) *Radiochim Acta* 49:155
- Rutherford E (1914) *Phil Mag* 27:488
- Rutherford E (1920) *Proc Royal Soc (London)* A97:374
- Schillebeeckx P, Wagemans C, Geltenbort P, Gönnerwein F, Oed A (1994) *Nucl Phys A* 580:15
- Schmitt HW, Kiker WE, Williams CW (1965) *Phys Rev* 137:B837
- Schmitt HW, Neiler JH, Walter FJ (1966) *Phys Rev* 141:1146
- Sida JJ, Armbruster P, Bernas M, Bocquet JP, Brissot R, Faust HR (1989) *Nucl Phys A* 502:233c
- Sime RL (1996) *Lise Meitner: a life in physics*. University of California Press, San Francisco
- Steinhäuser S, Benlliure J, Böckstiegel C, Clerc H-G, Heinz A, Grewe A, De Jong M, Junghans AR, Müller J, Pfützer M, Schmidt KH (1998) *Nucl Phys A* 634:89
- Strittmatter RB, Wehring BH (1979) *Nucl Instr Meth* 166:473
- Strittmatter RB, Wehring BW (1978) Direct measurement of nuclide yields in thermal-neutron fission using HIAWATHA. In: International conference on neutron physics and nuclear data for reactors and other applied purposes, OECD, Harwell, p 223
- Strutinsky VM (1967) *Nucl Phys A* 95:420
- Stumpf P, Güttler U, Denschlag HO, Faust HR (1992) Odd-even effects in the reaction ^{241}Am (2n, f). In: Qaim SM (ed) *Nuclear data for science and technology*. Springer, Berlin, p 145
- Swiatecki WJ (1955) *Phys Rev* 100:937
- Terrell J (1962) *Phys Rev* 127:880
- Thierens H, De Clercq A, Jacobs E, De Frenne D, D'hondt P, De Gelder P, Deruyter AJ (1981) *Phys Rev C* 23:2104
- Thierens H, Jacobs E, D'hondt P, De Clerc A, Piesens M, De Frenne D (1984) *Phys Rev C* 29:498
- Thirolf PG, Habs D (2002) *Prog Part Nucl Phys* 49:245
- Thomson JJ (1897) *Phil Mag* 44:293
- Tsekhanovich I, Denschlag HO, Davi M, Büyükmumcu Z, Gönnerwein F, Oberstedt S, Faust HR (2001) *Nucl Phys A* 688:633
- Tsekhanovich I, Denschlag HO, Davi M, Büyükmumcu Z, Wösthelrich M, Gönnerwein F, Oberstedt S, Faust HR (1999) *Nucl Phys A* 658:217
- Unik JP, Gindler JE, Glendenin LE, Flynn KE, Gorski A, Sjöblom RK (1973) Fragment mass and kinetic

- energy distributions for fissioning systems ranging from mass 230–256, physics and chemistry of fission. IAEA, Rochester, p 19
- Vandenbosch R, Huizenga JR (1973) Nuclear fission. Academic, New York
- Viola VE, Kwiatowski K, Walker M (1985) Phys Rev C 31:1550
- Von Gunten HR (1969) Actin Rev 1:275
- Von Halban Jun H, Joliot F, Kowarski L (1939) Nature 143:470
- Wagemans C (1991a) Spontaneous fission. In: Wagemans C (ed) The nuclear fission process. CRC Press, Boca Raton, pp 35–61
- Wagemans C (ed) (1991b) The nuclear fission process. CRC Press, Boca Raton, pp 1–596
- Wagemans C, Dematte L, Pomme S, Schillebeeckx P (1996) Nucl Phys A 597:188
- Wahl AC (1988) At Data Nucl Data Tables 39:1
- Wahl AC (1989) Nuclear charge and mass distributions from fission. In: Behrens JW, Carlson AD (eds) Fifty years with nuclear fission (American Nuclear Society, La Grange Park, IL/Gaithersburg, MD) pp 525–532
- Walton GN (1961) Q Rev Chem Soc 40:71–98
- Weigmann H (1991) Neutron induced fission cross sections. In: Wagemans C (ed) The nuclear fission process. CRC Press, Boca Raton, pp 63–102
- Weizsäcker CFV (1935) Z Physik 96:431
- Whetstone SL Jr (1963) Phys Rev 131:1232
- Wilkins BD, Steinberg EP, Chasman RR (1976) Phys Rev C 14:1832
- Wöstheinrich M, Pfister R, Gönnerwein F, Denschlag HO, Faust H, Oberstedt S (1998) Ternary particles from the reactions $^{229}\text{Th}(\text{n}, \text{f})$, $^{233}\text{U}(\text{n}, \text{f})$ and $^{239}\text{Pu}(\text{n}, \text{f})$. In: Fioni G, Faust H, Oberstedt S, Hamsch FJ (eds) Nuclear fission and fission-product spectroscopy. American Institute of Physics (AIP), Woodbury, NY, pp 330–337
- YCALC (2003) <http://www.kernchemie.uni-mainz.de/institut/links.html>

5 Tunneling Through Triple-Humped Fission Barriers

A. Krasznahorkay

Institute of Nuclear Research of the Hungarian Academy of Sciences
(ATOMKI), Debrecen, Hungary

5.1	<i>Introduction</i>	282
5.2	<i>Theoretical Predictions for the Fission Potential</i>	283
5.2.1	The Liquid Drop Model (LDM)	283
5.2.2	The Shell Correction Method	284
5.2.3	Shape Classification of Excited States	288
5.3	<i>Excited States Related to the Fission Barrier</i>	288
5.3.1	Resonances in the Fission Probability	289
5.3.2	Description of the Fission Probability Without Damping	290
5.4	<i>High-Resolution Study of the Transmission Resonances in ^{240}Pu</i>	291
5.4.1	Experimentally Resolved Intermediate Structure	293
5.4.2	Excitation Energy of the Ground State in the Second Minimum	295
5.5	<i>Experimental Evidence for Hyperdeformed States in U Isotopes</i>	297
5.5.1	Hyperdeformed States in ^{236}U	297
5.5.2	Reinvestigation of the Fission Resonances in ^{236}U	300
5.5.2.1	The Depth of the Third Minimum in ^{236}U	303
5.5.2.2	The Innermost Barrier of Uranium Isotopes	303
5.5.2.3	Clustering in the Actinide Region	305
5.5.3	Hyperdeformed Rotational Bands in ^{234}U	305
5.5.3.1	High-Resolution Study of the Fission Resonances in ^{234}U	306
5.5.3.2	The Depth of the Third Minimum in ^{234}U	310
5.5.4	Subbarrier Fission Resonances and Transitional States Observed in ^{232}U	311
5.6	<i>The Fission-Barrier Landscape</i>	315

Abstract: This chapter gives a survey of the latest results obtained for the fission process that takes place when the energy of the compound system is smaller than the energy of the fission barrier. The tunneling and resonant tunneling processes play a role in this energy region. The transmission resonances were studied in high-energy-resolution experiments and the excitation energies, J^π and K values of the states were determined. Rotational bands were constructed, from which the moment of inertia and the degree of the deformation were determined. The implications of these results to the present knowledge of the fission potential extracted from experiments are discussed.

5.1 Introduction

Nuclear fission is quite a complicated large-scale collective motion. In spite of several decades of intense work, the experimental information on nuclear fission is still rather limited. Knowledge of the nuclear fission phenomenon acquired up to 1972 was summarized by Vandenbosch and Huizenga (1973) and in a comprehensive volume by Wagemans (1991). In [Chap. 4](#) of this Volume, Denschlag has given an overview concentrating mostly on the fundamental aspects of nuclear fission.

In the last decades, studying nuclei with exotic shapes became one of the liveliest fields in modern nuclear structure physics. Especially, studying superdeformed shapes with an axis ratio of 2:1 and hyperdeformed shapes with an axis ratio of 3:1 in the actinide region belong to the frontiers of this field.

The fission of nuclei of this region presents a very rich variety of nuclear shapes. The fissioning nucleus undergoes a continuous sequence of nuclear surface shapes from more or less spherical to elongated, followed by super- and/or hyperdeformed shapes, then neck and split into two fission fragments. The fission potential, which holds the two fragments together, is very complicated and has a lot of structure (minima, maxima, and saddle points) as a function of its parameters. If the energy of the system is lower than the fission barrier, then the system can spend more time in the different potential minima and one can study the cold nuclear system under such extreme conditions.

The focus of this chapter is to review the latest results obtained for the excited states in the second and third minima of the potential barrier. In addition to these exotic shapes, it is also an interesting and longstanding question, at which points of the fission path the mass and energy distributions of the fission fragments are determined. Can one get different mass distributions after the fission of the super- and hyperdeformed states as suggested by Cwiok et al. (1994)? What kind of clusterization is expected in these exotic nuclear states? Does the predicted cold valley exist in the fission barrier? These are very interesting questions but the presently available experimental information is still not sufficient to answer them.

In the seven decades since the discovery of nuclear fission, experimental studies on low-energy fission have been restricted to about 80 fissionable nuclei. They represent only about 15% of all known nuclei with $Z \geq 82$. However, recently a novel experimental technique has been introduced. The fission of relativistic secondary projectiles has now been studied in flight. The benefit of the radioactive beams for studying the fission process is clear, but no fission probabilities below the fission barrier have been determined so far (Schmidt et al. 1994).

Starting with a brief discussion of the theoretical model predictions for the fission potential as a function of the deformation of the nucleus, the consequences of the multiple-humped potential barrier on the fission probabilities will be discussed. During the last decade

a considerable amount of high-resolution experimental data were collected for the fission resonances. These data will be reviewed and their implications for the present experimental knowledge of the fission potential will be discussed.

Such fission potentials might also have practical relevance. The possibility of transmutation of nuclear waste and the production of energy by accelerator-driven systems is under consideration. Accurate fission potentials are needed, particularly in the actinide region, to predict the fission cross sections for these applications.

5.2 Theoretical Predictions for the Fission Potential

5.2.1 The Liquid Drop Model (LDM)

Immediately after the discovery of fission (Hahn and Strassmann 1939), Meitner and Frisch (1939) gave a quantitative explanation of the process using the picture of the LDM. Bohr and Wheeler (1939) developed this picture into their classical theory, which remained the basis for the description of the nuclear fission process for many years to come.

The liquid drop model introduced by von Weizsäcker (1935) treats the nucleus macroscopically similarly to a uniformly charged liquid drop. The total energy is expressed as a sum of a volume energy E_v proportional to the volume (and, consequently, to the mass number) of the nucleus, a surface energy E_s proportional to the surface of the drop, the Coulomb energy E_C , the symmetry energy E_{sy} , and the pairing energy E_p :

$$E = E_v + E_s + E_C + E_{sy} + E_p. \quad (5.1)$$

In application to the fission process, in which the dependence on the deformation is relevant, only the surface and Coulomb terms come into play.

The deformation of the nucleus can be described by a multipole expansion of the nuclear surface

$$R(\theta, \vartheta) = R_0 \left[1 + \sum_{\lambda\mu} a_{\lambda\mu} Y_{\lambda\mu}(\theta, \vartheta) \right] \quad (5.2)$$

For small deformations, if limited to quadrupole deformations (only $a_{20} \neq 0$), the surface and Coulomb energies are given by

$$E_s = E_s(0) \left(1 + \frac{2}{5} a_{20}^2 \right), \quad (5.3)$$

$$E_C = E_C(0) \left(1 - \frac{1}{5} a_{20}^2 \right). \quad (5.4)$$

Consequently, the condition for stability of a spherical nucleus is $E_C(0) < 2E_s(0)$. According to Bohr and Wheeler (1939), one can define the fissility parameter

$$x = \frac{E_C(0)}{2E_s(0)} = \frac{0.71Z^2/A^{1/3}}{2 \times 17.5A^{2/3}} \approx \frac{1}{50} \frac{Z^2}{A}. \quad (5.5)$$

Hence, according to the liquid drop model, nuclei with $x > 1$ or $Z^2/A > 50$ are unstable against spontaneous fission.

For $x < 1$, the deformation energy has a local minimum at the spherical shape. For the common actinide nuclei ($0.68 < x < 0.76$) the deformation energy also has a maximum with positive energy relative to the ground state at positive values of the deformation parameter (a_{20}). That defines the fission barrier. Numerical calculations including multipoles up to $\lambda \approx 16$ led to fission barrier heights

$$E_B = 0.83 E_s(0)(1 - x)^3 \quad (5.6)$$

relative to the ground state.

In spite of several refinements of the LDM, see, e.g., (Myers and Swiatecki 1969; Krappe et al. 1979; Möller and Nix 1981), it seemed to be clearly inadequate to explain some of the basic properties of the actinide nuclei (Wagemans 1991).

When the fission isomeric states were discovered (Polikhanov et al. 1962), it became clear that the fission potential should have a second minimum as a function of the deformation and the observed fission isomers are shape isomers in such a second minimum. Strutinsky's proposal (see [Chap. 2](#) in this Volume) was to combine the virtues of both the LDM and shell models to describe such a second minimum of the fission potential.

5.2.2 The Shell Correction Method

In the nuclear shell model, the mutual interaction between the nucleons adds up to a single-particle average potential consisting of a (spherical) central potential and a spin–orbit interaction. The nucleons are assumed to move independently in this potential. The solutions of the Schrödinger equation yield single-particle energy levels and wave functions for the individual nucleons (Haxel et al. 1949; Goepfert-Mayer 1949).

Nilsson (1955) extended the single-particle shell model to deformed potentials. The solutions of the Schrödinger equation then depend on deformation also. In the independent-particle model (Wagemans 1991) the sum of the single-particle energies of an even–even nucleus is given by

$$U = \sum_{\mu} 2n_{\mu} \varepsilon_{\mu}, \quad (5.7)$$

where the n_{μ} are the occupation numbers of the energy levels ε_{μ} . Unfortunately, in the above expression the errors due to the approximate nature of the shell model potential and the neglect of residual interactions will tend to accumulate. Thus, the final result will be much less accurate than the total energy obtained from the LDM.

The LDM is thus a suitable starting point for an accurate calculation of the total energy, but it has to be corrected for the fluctuations due to the shell structure. Such a combined macroscopic–microscopic method should then hopefully reproduce both the smooth trends and the local fluctuations.

The method in its present form was developed in 1967 (Strutinsky 1967) and has since revolutionized the calculation of fission barriers. There had been a number of studies that employed very similar techniques before Strutinsky's work as well. Swiatecki (1964) had introduced the idea of a macroscopic–microscopic method, but the simplified procedure that he used to calculate the microscopic fluctuations worked only for small deformations. However, even in this form, the method correctly predicted many features of nuclear ground-state masses and deformations, fission-barrier heights, and the probable existence of

superheavy nuclei. Somewhat similar approaches had been used even earlier by Hill and Wheeler (1953). The importance of single-particle effects on the nuclear potential energy, particularly on nuclear ground-state masses, had been recognized and discussed frequently since the early days of nuclear physics.

Strutinsky's "macroscopic-microscopic" or "shell correction" method (SCM) amounts to correcting the LDM energy according to

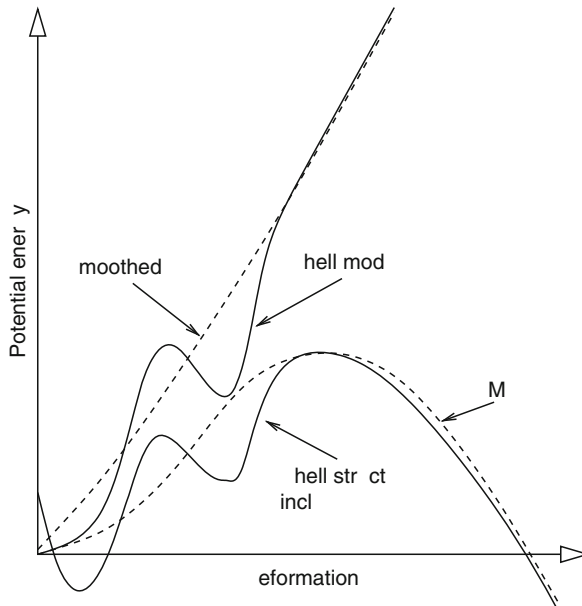
$$E = E_{\text{LDM}} + U - \langle U \rangle = E_{\text{LDM}} + \delta U. \quad (5.8)$$

Here $\langle U \rangle$ means a smoothed deformation dependence of the shell model energy as defined in Wagemans (1991) and δU means the so-called shell correction energy. The qualitative behavior of the shell correction δU with deformation is easily understood. See [Fig. 5.1](#).

The liquid drop energy contains the contributions of both the kinetic energy and of the potential energy, and the right-hand side of [Eq. \(5.8\)](#) contains a correction for the shell effects as well. The quantity E is not an operator, but a value, which depends on various parameters, and it is usually considered a function of the deformation parameters. It is referred to as the energy curve or energy surface depending on the number of parameters that are allowed to vary. The deformation parameters express the properties of the system that are most important in fission, and are considered dynamical variables, just as in the collective model ([Chap. 2](#) in this Volume). That is an intuitive step guided by the success of the collective model. The collective variables are actually expressible in terms of the single-particle

Fig. 5.1

Illustration of the method of Strutinsky to merge the liquid drop model (LDM) and the shell model as a function of deformation. The upper curve shows the oscillations due to shell effects around a mean (upper dashed curve). The difference of the two (δU) was used to correct the LDM energy (lower dashed curve)



coordinates (Buck et al. 1979), and thus it is justifiable to regard them as dynamical variables. (Then, of course, E should be evaluated in terms of intrinsic coordinates from which the collective coordinates have been removed, but that distinction is disregarded.) It is plausible that the dynamics of the system is determined by the energy surface just as that of a particle by the potential, and that it should be complemented by a kinetic energy dependent on the same coordinates. The role of the energy surface as a potential justifies its calling a potential energy surface or a potential energy curve. The energy surface shows a varied landscape of valleys and mountain ridges called (fission) barriers, with peaks and saddle points. In principle, the kinetic energy of the motion of the surface could also be expressed in terms of the single-particle kinetic energies, but that is also beyond the scope of the model. This treatment is fully consistent with that of the potential energy. Overall, in the model of the fission adopted in this report, the Hamiltonian is the sum of the kinetic energy and of the (potential) energy surface/curve, both expressed in terms of the deformation parameters.

Whenever the density of states as a function of deformation is comparatively low (high), the shell correction is negative (positive). Such gaps in the single-particle energy levels occur not only at zero deformation (magic numbers) but also at nonzero deformation. Particularly, strong negative shell corrections are found for nuclear shapes corresponding to a ratio of major and minor axes of the deformed nuclear shape of 2:1, which is now called the superdeformed shape.

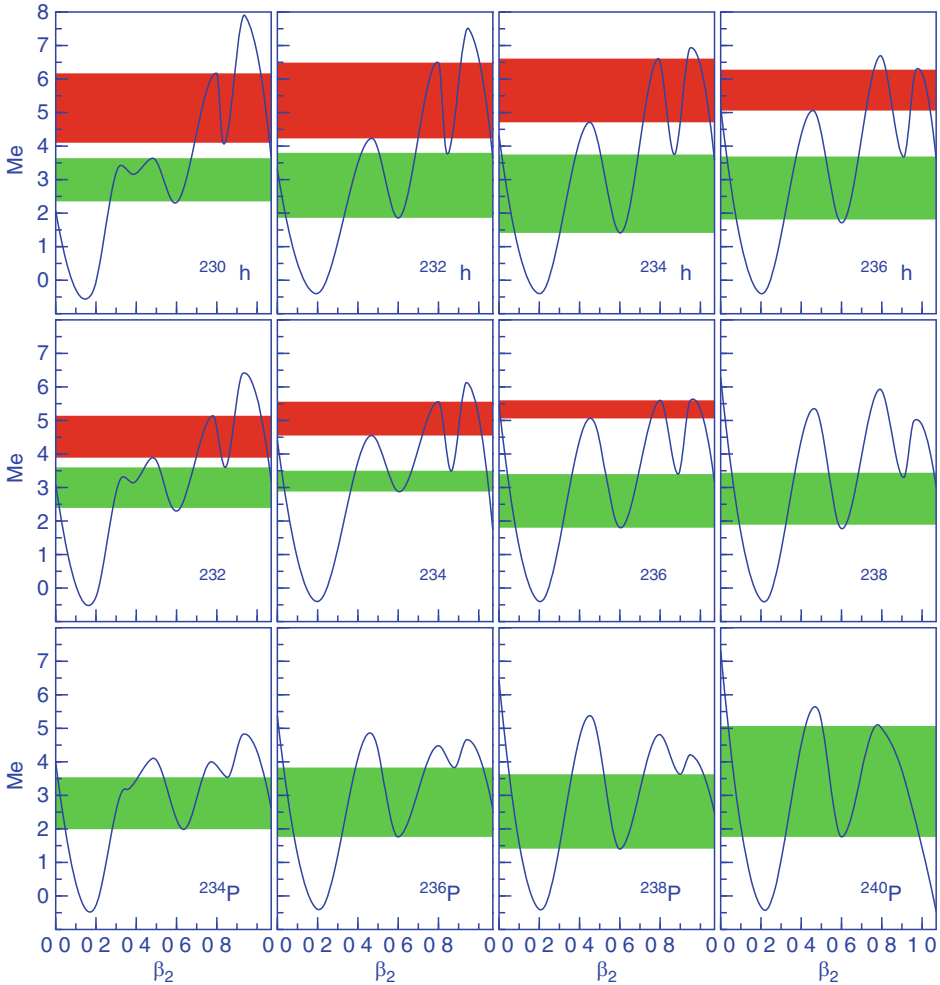
Theoretical progress later on also enabled purely microscopic calculations for the fission potential. Self-consistent mean-field calculations within the Hartree–Fock–Bogolyubov (HFB) approach (Berger 1989) for the fission potential in ^{230}Th clearly exhibit even a third minimum at large quadrupole deformations. In recent years, fission potentials have also been calculated within the relativistic mean-field model (Blum 1994), approximately reproducing the double-humped fission barrier of ^{240}Pu . Even the triple-humped fission barrier of ^{232}Th was described by the relativistic calculations with a quality comparable to the nonrelativistic models (Rutz et al. 1995). While early shell-correction calculations (Howard and Möller 1980) as well as HFB (Berger et al. 1989) and relativistic mean-field calculations predicted rather shallow third minima ($\sim 0.2\text{--}0.5$ MeV), shell-correction calculations by Cwiok et al. (1994) predicted much deeper hyperdeformed third minima ($\sim 1\text{--}3$ MeV), in better agreement with experimental findings, which will be discussed in [Sect. 5.5](#).

Cwiok et al. (1994) performed systematic calculations of potential energy surfaces for even–even Rn, Ra, Th, and U isotopes using the shell correction approach with the axially deformed average Woods–Saxon potential (Cwiok et al. 1987), while for the macroscopic part the Yukawa-plus-exponential liquid-drop mass formula of Möller and Nix (1988) was used. The energies of the local minima in the potential energy surface were obtained by performing a multiparameter minimization of the total energy with respect to the deformation parameters $\beta_3\text{--}\beta_7$. According to these calculations third minima appear in many actinide nuclei, characterized by very large elongations ($\beta_2 \approx 0.9$) and significant reflection asymmetry, $0.35 < \beta_3 < 0.65$. This model does not contain any free parameter adjusted to the properties of these hyperdeformed configurations. In the nuclei around ^{234}U the hyperdeformed minimum splits into two distinct minima with very different values of β_λ ($\lambda = 3\text{--}7$). [Figure 5.2](#) shows the resulting fission potentials for Th, U, and Pu isotopes as a function of the quadrupole deformation β_2 .

The deepest third minima are predicted for the thorium isotopes, while the lowering of the outer barrier with increasing proton number prevents the formation of pronounced third minima beyond uranium.

■ Fig. 5.2

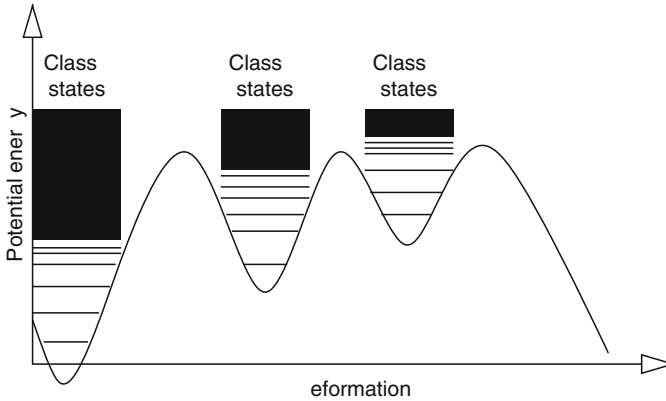
Potential energy as a function of the quadrupole deformation parameter for Th, U, and Pu isotopes. The energy and location of the saddle points and minima (except for the third one) were taken from Howard and Möller (1980), while the energy of the third minimum for the less reflection asymmetric hyperdeformed minimum ($\beta_3 \approx 0.4$) was taken from Cwiok et al. (1994). The energy scale was slightly shifted in order to reproduce the energy of the ground states in the first well (Krasznahorkay et al. 1998b). The best energy regions for studying the super- and hyperdeformed states are marked by green and red shadowed regions, respectively. See ▶ Sect. 5.3.1 for more details. Based on Krasznahorkay (1998a)



The analysis of experimental data for thorium isotopes resulted in values for the moment of inertia $2\Theta/\hbar^2$ close to 500 MeV^{-1} . For comparison, moments of inertia have been calculated using Nilsson and Woods–Saxon potentials as a function of deformation (Boldeman and Walsch 1985). For large deformations ($\beta_2 \approx 0.9$) the results are close to the rigid-body value.

■ Fig. 5.3

Schematic illustration of class I, class II, and class III compound states



5.2.3 Shape Classification of Excited States

For energies of the system below the inner maxima of the fission barrier, the model wave functions are normally concentrated within one of the minima of the deformation potential. This process leads to a classification of the wave functions as class I (with major amplitude within the first well), class II (centered in the second well), and class III (centered in the third well). A schematic illustration of this classification of vibrational states is shown in [Fig. 5.3](#).

Obviously, the tails of these wave functions penetrate the intermediate barriers, and, consequently, there is a certain degree of mixing of idealized pure class I, class II, and class III excitations. The main factors determining the amount of mixing are the penetrability factors of the internal barriers, which can be small below the barriers.

5.3 Excited States Related to the Fission Barrier

It has been known for a long time that the fission barrier can be studied by measuring the fission probability as a function of the excitation energy. If the energy is well below the fission barrier, then one is dealing with a classical tunneling process via the barrier. The fission probability increases exponentially with the energy. In the WKB approximation, the probability of tunneling through the barrier can be calculated (Hill and Wheeler 1953).

Assuming a parabolic fission barrier with a height of V_0 and curvature of $\hbar\omega$, then one can get the well-known Hill–Wheeler transmission coefficient

$$T_{\text{HW}} = \frac{1}{1 + \exp\left(2\pi \frac{V_0 - E}{\hbar\omega}\right)}. \quad (5.9)$$

The experimentally determined fission probabilities can then be compared to the results obtained with the expression above and the height and the curvature of the barrier can be determined. If the fission barrier is more complicated, then this simple formula cannot be used. More sophisticated calculations – including double- and triple-humped fission barriers – have been published recently by Sin et al. (2006, 2008). The situation is complicated by the presence

of the transitional states introduced already by Bohr (1956), which are expected to give more structure in the fission probability above the top of the fission barrier.

5.3.1 Resonances in the Fission Probability

Bohr suggested that in a saddle-point configuration a nucleus is in a very cold state and that the spectrum of **transition states** resembles the spectra near the ground states of stably deformed nuclei. These transition states could cause resonances in the fission probability. Therefore, first the low-lying excited states of even–even nuclei shall be discussed briefly.

Two-particle states in these nuclei have $\sim 1\text{--}2$ MeV of excitation energy, and the excited states lying lower than those states correspond to collective motions. These collective motions are expected to form a sequence of collective vibrational and rotational states.

When developing the analogy of the transition state spectra to these excited state spectra of stably deformed nuclei, the following points must be taken into consideration:

- β -vibration cannot exist at the saddle-point configuration of the outermost barrier, since it is a vibration in the fission direction, and is unstable.
- The energy of a two-particle excitation is higher at the saddle point than that in the stably deformed configuration. Thus, it is sufficient to consider only collective excited states as transition states.

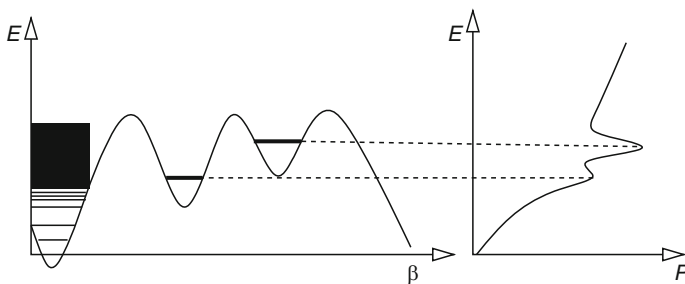
Several experiments support the existence of transition states, and give their spectra (Kikuchi and An 1970). However, there are also many misidentified resonances in the literature, which are actually below the fission barrier and can best be described as resulting from class II and class III states of the multiple-humped fission barrier.

Thanks to the resonant tunneling effect, such excited states (class-II and class-III) can be mapped by measuring the fission probability as a function of the excitation energy (see [Fig. 5.4](#)). If one measures also the angular distribution of the fragments arising from fission induced by some reaction, then one can get information on the spin and K values of such excited states as well.

If the excitation energy is higher than the inner barrier of the second well, but lower than the barriers of the third well then the transmission resonances corresponding to class II and class III states could in principle be distinguished by their widths. The widths of class II

■ Fig. 5.4

Schematic illustration of the resonant tunneling process through the fission potential



resonances should be much broader due to the strong coupling to class I states, while the damping of class III resonances is hindered by the higher barriers of the third well. Therefore, the best energy region for studying the hyperdeformed states by measuring the transmission resonances in the actinides is indicated in [Fig. 5.2](#), illustrating the potential barriers for the Th, U, and Pu isotopes.

5.3.2 Description of the Fission Probability Without Damping

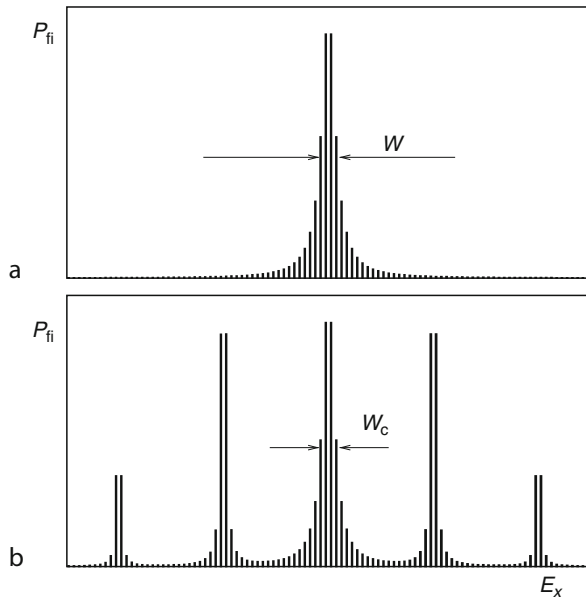
For double-humped potential barriers, detailed calculations were performed by Glässel, Röser, and Specht (Glässel 1974; Glässel et al. 1976). The results of the calculations were summarized by Thierolf and Habs (2002). A schematic illustration of the character of an undamped transmission resonance and a damped (i.e., not fragmented and fragmented) transmission resonance is shown in [Fig. 5.5](#).

For a pure and undamped transmission resonance, where the strength of the β -vibrational state is not distributed over the neighboring intrinsic states in the second minimum, the fission probability P_{fi} of a class-I state can be described as (Glässel et al. 1976)

$$P_{fi} = \frac{D_I}{2\pi} \frac{\Gamma_A \Gamma_B / \Gamma_{\gamma I}}{(E - E_\beta)^2 + W^2/4}, \quad (5.10)$$

Fig. 5.5

Undamped and damped transmission resonances. Panel (a) shows the Lorentzian of the fission probability for class-I states. Panel (b) displays the strength function of the β -vibration in the case of damping into class-II states. Constant level distances D_I for states in the first and D_{II} for states in the second minimum were assumed



where the width W of the resonance is given by



$$W = \left\{ (\Gamma_A + \Gamma_B + \Gamma_{\gamma I})^2 + \frac{2}{\pi} \Gamma_A \Gamma_B \frac{D_I}{\Gamma_{\gamma I}} \right\}^{1/2}. \quad (5.11)$$

Here $\Gamma_{\gamma I}$ ($\Gamma_{\gamma II}$) represents the γ -decay width in the first (second) minimum. D_I describes the level distance between class-I states and E_β stands for the excitation energy of the β -vibrational state. The widths Γ_A and Γ_B caused by the tunneling of a state through the inner and outer fission barrier, respectively, can be determined using the transmission probabilities $P_{A,B}$ through a single barrier with height E_A and E_B , respectively, calculated by Hill and Wheeler (1953):

$$\Gamma_{A,B} = P_{A,B} \frac{\hbar\omega_{II}}{2\pi} = \{1 + \exp(2\pi(E_{A,B} - E)/\hbar\omega_{A,B})\}^{-1} \frac{\hbar\omega_{II}}{2\pi}. \quad (5.12)$$

The $\hbar\omega_{II}$ corresponds to the β -phonon energy in the second minimum, while $\hbar\omega_{A,B}$ denotes the curvature of the parabolic parameterization of the fission barrier. The experimentally accessible fission cross section σ can be obtained from the cross section σ_{cl} for the formation of a compound state $|cl\rangle$ in the first minimum and the fission probability

$$\sigma = \sigma_{cl} P_{II}. \quad (5.13)$$

As shown in  Fig. 5.5, the fission probability is distributed among the class-I states. The width of the distribution is determined by barrier penetration probabilities (P_A and P_B). If one wants to observe sharp transmission resonances in the fission probability, then one should go well below the fission barriers. A more detailed analysis of the transmission resonances will be given in  Sect. 5.4 for ^{240}Pu .

5.4 High-Resolution Study of the Transmission Resonances in ^{240}Pu

After the discovery of fission isomerism in the actinide region, great efforts were directed toward the spectroscopic studies of excited states in superdeformed (SD) nuclei (Strutinsky 1967; Wagemans 1991; Bjornholm and Lynn 1980). The appearance of such elongated shapes with an axis ratio of 2:1 in the actinides is the consequence of a second minimum in the shell-corrected potential energy surface. Low-lying SD excitations were mostly observed in conversion electron experiments, which resulted in the successful identification of rotational bands upon the fission isomeric ground states (Specht et al. 1972; Metag et al. 1980).

In contrast to the first minimum, β -vibrations at higher excitation energies can be investigated in the second minimum as transmission resonances in the prompt fission probability, since the β -vibrations manifest themselves as doorway states to fission. A few members of the vibrational series were systematically observed in actinide isotopes just below the fission barrier (Bjornholm and Lynn 1980). Due to the damping of the vibrational motion, their large fission widths are distributed over many compound states in their vicinity. The fine structure due to compound levels in the first minimum (class I states) cannot be resolved, but the gross structure of the β -vibrational transmission resonances, the intermediate structure due to SD class II compound states can be resolved due to their lower level density. High-energy-resolution studies of fission resonances can therefore give spectroscopic information on SD compound states with specific spin J^π and spin projection K at excitation energies below the fission barrier.

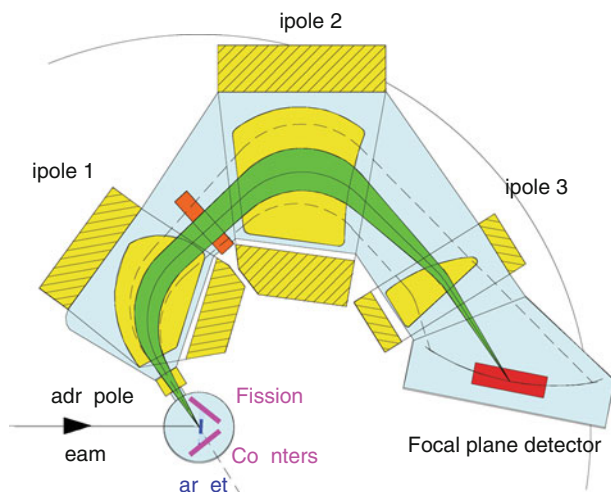
The more one can probe with efficient detector systems, the subbarrier regions of vibrational damping, the better one should be able to observe isolated levels with small widths in the fission channel. The transmission resonances observed in ^{240}Pu at excitation energies, with respect to the ground state in the first minimum, $E^* = 5.1$ MeV (Specht et al. 1969; Specht 1970; Pedersen and Kuzminov 1969) and at $E^* = 4.6$ MeV (Goldstone et al. 1978; Goerlach 1978; Goerlach 1980; Goerlach et al. 1982; Just 1978; Just et al. 1979) were repeatedly interpreted as best examples for damped vibrational resonances. In the experiment of Glässel et al. (1976) on ^{240}Pu , the $E^* = 5.1$ MeV resonance group was investigated with a high-energy resolution of 3 keV. With the aid of a detailed model description (Glässel et al. 1976), all experimentally resolved class-II states that are predominantly populated in the (d,p) reaction were identified as $(K^\pi, J^\pi) = (0^+, 2^+)$ states, but the two states were not resolved due to their fission widths. The $E^* = 4.6$ MeV resonance group was studied by Goldstone et al. (1978), Just (1978) with modest resolution. With good statistics and high-energy resolution, however, individual $K^\pi = 0^+$ SD rotational band members were identified with spin and parity of $J^\pi = 0^+, 2^+, 4^+$.

The high-energy-resolution experiment on ^{240}Pu was carried out at the Munich Accelerator Laboratory employing the $^{239}\text{Pu}(\text{d},\text{pf})^{240}\text{Pu}$ reaction ($Q = 4.309$ MeV) with a deuteron beam of $E_d = 12.5$ MeV, and using an enriched (99.9%) ~ 30 $\mu\text{g}/\text{cm}^2$ thick target of ^{239}Pu on a 30 $\mu\text{g}/\text{cm}^2$ thick carbon backing (Krasznahorkay et al. 2001c; Hunyadi et al. 2001). Protons were detected in coincidence with the fission fragments. The excitation energy E^* of the ^{240}Pu compound nucleus was directly deduced from the kinetic energy of the protons, which was analyzed by a Q3D magnetic spectrograph (Enge and Kowalsky 1970) (see ► Fig. 5.6) set at $\Theta_{\text{Lab}} = 130^\circ$ relative to the incoming beam ($\Omega = 10$ msr).

The spectrograph is equipped with two position-sensitive parallel-plate avalanche counters for the detection of fission fragments in coincidence with proton ejectiles registered by a light-ion focal plane detector (Zanotti et al. 1991).

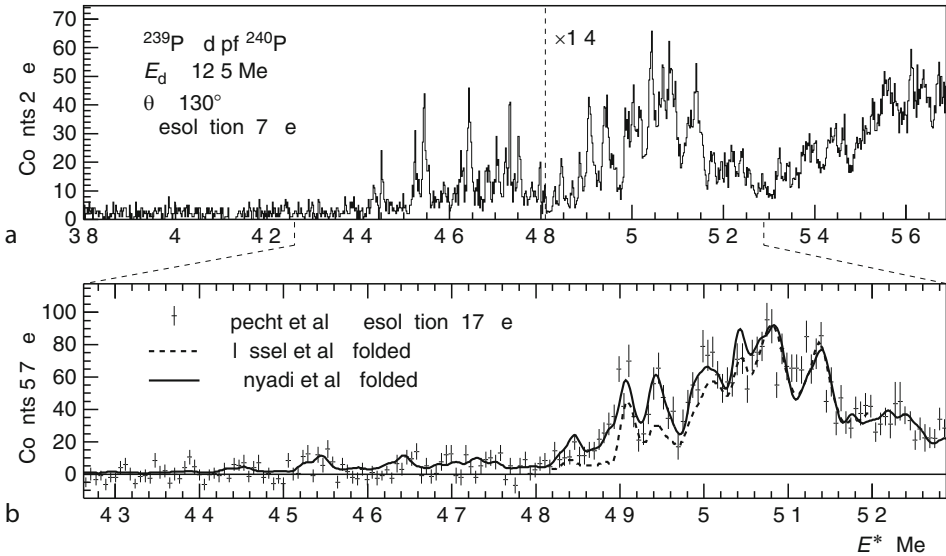
■ Fig. 5.6

Experimental setup for the transmission resonance experiments performed at the Munich Q3D magnetic spectrograph



■ Fig. 5.7

(a) Proton coincidence spectrum of the $^{239}\text{Pu}(\text{d},\text{pf})$ reaction measured by Hunyadi et al. (2001). (b) Proton coincidence spectrum at $E_d = 12.5$ MeV and $\theta = 140^\circ$ from Specht et al. (1969). For comparison the spectra folded with a resolution of 17 keV from Hunyadi et al. (2001) (solid line) and Glässel et al. (1976) (dashed line) are also shown. Based on Hunyadi et al. (2001)



The measured proton energy spectrum from the (d,p) reaction in coincidence with the fission fragments (after subtraction of random coincidences) is shown in ▶ Fig. 5.7a in terms of the excitation energy of the compound nucleus ^{240}Pu . The spectrum is proportional to the product of the fission probability and the known smoothly varying (d,p) cross section, which shows no fine structure (Specht et al. 1969).

In ▶ Fig. 5.7b, the Munich measurement is compared with previous high-resolution measurements of the same reaction: The (d,pf)-spectrum of ▶ Fig. 5.7b was measured with a resolution of 17 keV by Specht et al. (1969). It is nicely reproduced in all fine structures after folding the spectrum from Hunyadi et al. (2001) with the reduced resolution and applying a global shift of 120 keV to higher energies on the experimental data of Specht et al. (1969) to correct partially for the proper Q-value. When folding the measurement by Glässel (1974), which was performed at $E_d = 12.5$ MeV and $\theta = 125^\circ$ with an experimental resolution of 3 keV, only a small overall shift of 12 keV was necessary.

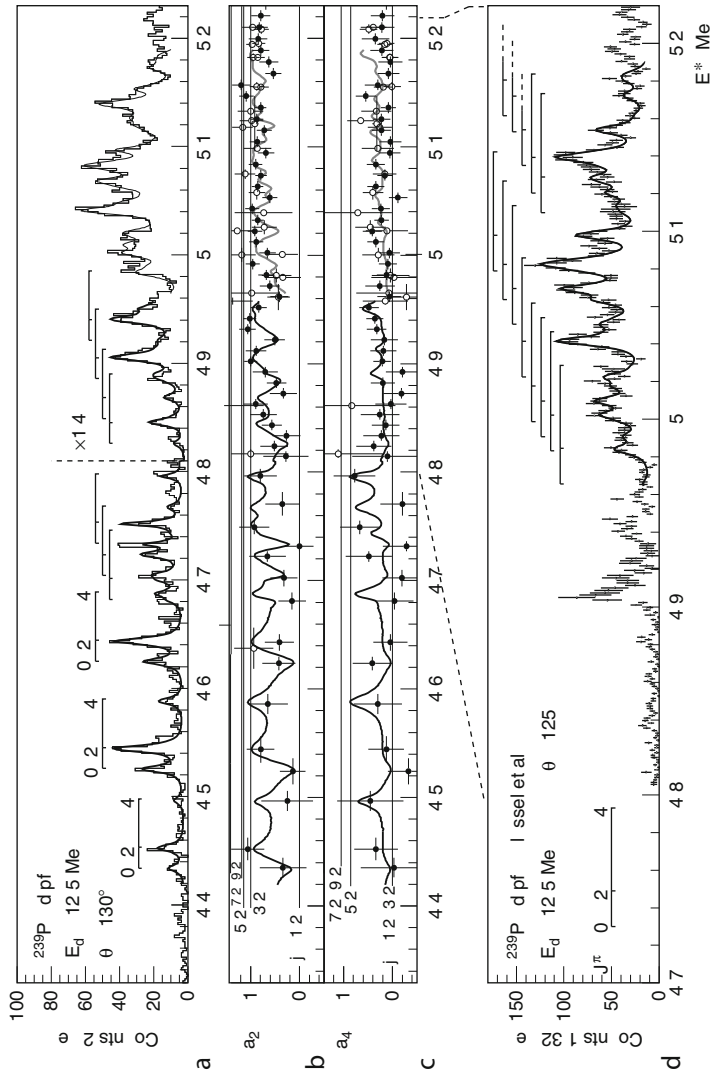
5.4.1 Experimentally Resolved Intermediate Structure

The overall features of ▶ Fig. 5.8a (Hunyadi et al. 2001) show gross structures with a damping width of about 200 keV in the region of the two transmission resonances at 4.6 MeV and 5.1 MeV.

Besides these features, the proton spectrum exhibits a rich structure of individual transitions. The resolved intermediate structure of the lower resonance shows a regular pattern of well-resolved triplets, with weaker lower and upper peaks, which are separated by 19 keV and

■ Fig. 5.8

Panel (a) Proton spectrum of the reaction $^{239}\text{Pu}(\text{d},\text{pf})$ measured with 7 keV resolution (Hunyadi et al. 2001). Also shown is a fit of the data with rotational $K^\pi = 0^+$ bands. The $0^+, 2^+, 4^+$ picket fences show the rotational bands used in the fit. In the upper part of the 5.1 MeV resonance, the fit (thin line), is based on the positions of the rotational bands extracted from panel (d). Panels (b), (c) The full dots represent the a_2 (a_4) fission angular distribution coefficients determined in the same measurement, while the open symbols are the a_2 (a_4) coefficients taken from Glässel et al. (1976). The thick full line results from the fit to spectrum (a). The thin lines correspond to the theoretical a_2 (a_4) coefficients for different angular momentum values j of the transferred neutron. Panel (d) Proton spectrum of the reaction $^{239}\text{Pu}(\text{d},\text{pf})$ from Glässel et al. (1976) measured at 3 keV resolution together with a fit of the spectrum using rotational bands as indicated. Based on Hunyadi et al. (2001)



43 keV, respectively, from the stronger central peak. These separations are very close to the 0^+-2^+ and 2^+-4^+ separation energies (20 keV, 46.6 keV) of the $K^\pi = 0^+$ ground-state rotational band in the second minimum, strongly suggesting that these structures are due to excited $K^\pi = 0^+$ rotational bands in the superdeformed minimum of ^{240}Pu . Thus, at the lower resonance at 4.6 MeV, a series of “pure” resonance states have been observed with $K^\pi = 0^+$ and spins $0^+, 2^+, 4^+$ with rotational energy spacings as known from the ground-state band in the second minimum (Specht 1970; Specht et al. 1972). This is in contrast to the excitation-energy region above 5 MeV, where Hunyadi et al. (2001) confirmed the bunching of peaks “without any systematic trend” observed earlier (Specht et al. 1969; Glässel 1974).

The part of the 5.1 MeV resonance region in the spectrum of Glässel et al. (1976), which sufficiently overlaps with the spectrum of Hunyadi et al. (2001) was fitted with $K^\pi = 0^+$ rotational bands assuming a Lorentzian line shape for the band members. The position and amplitude of each band were treated as individual parameters, and a common moment of inertia (Θ) was used. For the intensity ratio of the band members, the value of Glässel et al. (1976) was accepted as a starting value for the fitting procedure. The fit nicely reproduced the experimental data with 13 rotational bands (see [Fig. 5.8d](#) and Hunyadi et al. 2001). Satisfactory description of the experimental data was achieved again by fitting the line width and the relative amplitudes of the bands, as shown in [Fig. 5.8a](#) with a thin curve. The 4.6 MeV group and the lower part of the 5.1 MeV group obtained in the experiment of Hunyadi et al. was also fitted by the same procedure; however, the rotational parameters $\hbar^2/2\Theta$ and the intensity ratios I_{2+}/I_{0+} and I_{4+}/I_{0+} were determined separately for the bands with prominent band heads at $E^* = 4,434, 4,526, 4,625, 4,685, 4,703$ and $4,733$ keV.

In order to confirm the spin and K -assignments of the observed compound levels in the second minimum, the corresponding fission fragment angular correlations with respect to the recoil axis were analyzed, describing them in the usual way with coefficients a_2 and a_4 of Legendre polynomials (LPs). In [Fig. 5.8](#), the measured proton coincidence spectrum ([Fig. 5.8a](#)) is shown together with the coefficients a_2 ([Fig. 5.8b](#)) and a_4 ([Fig. 5.8c](#)). For comparison, the spectrum of Glässel et al. (1976) is also shown in [Fig. 5.8](#) together with their a_2 and a_4 coefficients marked by open circles in [Fig. 5.8b, c](#). The horizontal lines in [Fig. 5.8b, c](#) show the theoretical a_2 and a_4 coefficients for different values of the angular momentum j of the neutron transferred in the (d,p) reaction, leading to ^{240}Pu states with $K = 0$ and $J = |1/2 \pm j|$. Due to the low ground-state spin ($J_i^\pi = 1/2^+$) of ^{239}Pu , in ^{240}Pu only low total angular momenta J are populated. 0^+ states can easily be identified in the fission-fragment angular correlations through their isotropic emission characteristics. The large and positive a_2 and a_4 coefficients point to a dominant $K = 0$ character of both resonances. From $^{240}\text{Pu}(\gamma, f)$ data (Rabotnov et al. 1970) a “suppression of the $K^\pi = 0^-$ – channel by more than two orders of magnitude relative to the $K^\pi = 0^+$ channel” was deduced (Glässel et al. 1976). For the lower 4.6 MeV resonance a $K^\pi = 0^-$ contribution was discussed as well, however, as will be described below, a reasonable description of the fission probability was achieved assuming a $K^\pi = 0^+$ channel (Goerlach 1978; Just 1978; Just et al. 1979).

5.4.2 Excitation Energy of the Ground State in the Second Minimum

From the experimental findings discussed in [Sect. 5.4.1](#), it seems that a complete spectroscopy of $K^\pi = 0^+$ bands is possible in the regions of vibrational damping. In order to check this completeness and the consistency of the observed level density with the excitation energy in

the second minimum, a statistical analysis of the level distances was performed using the band head energies. The statistical distribution of the ratio of experimental and calculated average 0^+ level distances, using the back-shifted Fermi-gas formula by Rauscher et al. (1995), was generated. The shape of the resulting distribution was successfully approximated by a Wigner-type distribution (Brody et al. 1981), as expected for repelling states with the same angular momentum and parity.

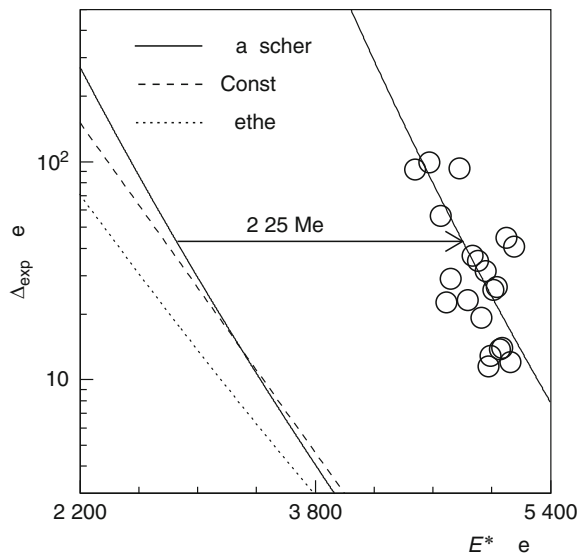
In [Fig. 5.9](#) the experimentally observed 0^+ level distances in the transmission resonance groups of ^{240}Pu (full circles) are compared to calculations of the level density in the first minimum according to different models. The solid line on the left side of the figure corresponds to the level distances in the first minimum calculated in the framework of the back-shifted Fermi gas model in the parameterization by Rauscher et al. (1997). In order to reproduce the experimentally observed 0^+ level distances, this curve has had to be shifted by 2.25 MeV, corresponding to the ground-state energy in the second minimum of ^{240}Pu . For comparison, also shown are the level distances in the first minimum calculated with the Bethe formula and within the “constant temperature” formalism in a parameterization by von Egidy et al. (1988).

The value of $E_{\text{II}} = (2.25 \pm 0.20)$ MeV – extracted for the excitation energy of the ground state in the second minimum of ^{240}Pu – is in good agreement with the fission isomer energy obtained from the well-known method of extrapolated excitation functions of various experiments (see, e.g., Wagemans 1991 and references therein). Thus having proven the reliability of this method, an excellent tool has been obtained to address the question of the depth of the (hyperdeformed) third minimum of the potential surface. This tool will be discussed in

[Sect. 5.5](#).

Fig. 5.9

Distance of the $J^\pi = 0^+$ levels in ^{240}Pu as a function of the excitation energy. The solid line on the left side of the figure corresponds to the level distances in the first minimum calculated in the framework of the back-shifted Fermi gas model in a parameterization by Rauscher et al. (1997). Based on Hunyadi (1999)



5.5 Experimental Evidence for Hyperdeformed States in U Isotopes

5.5.1 Hyperdeformed States in ^{236}U

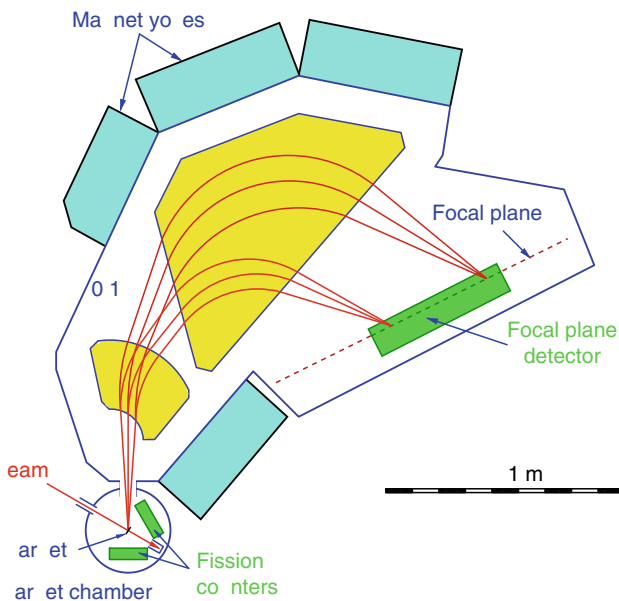
Subbarrier resonances, at about 5-MeV excitation energy, have been observed previously in many actinide nuclei (Back et al. 1972; Blons et al. 1978, 1984; Bjornholm and Lynn 1980). Based on the modest energy-resolution measurements, these subbarrier resonances were believed to arise from the coupling of compound nuclear states in the first potential well to vibrations of the fission degree of freedom in the second potential well. Goldstone et al. (1978) proposed that the observed transmission resonances in ^{234}U and in ^{236}U might be due to states in the second well, which consist of a fission vibration coupled to low-lying states in the second well such as rotations and $K^\pi = 0^+, 0^-, 2^+, 1^- \dots$ collective vibrations. Blons et al. (1988) were able to resolve the fine structure of the resonances in ^{234}U , and they measured also the angular distribution of the fission fragments, but their results were not consistent with the angular distributions calculated with the assumption of single pure J resonances.

The first high-resolution study of the transmission resonances in ^{236}U was carried out at $E_d = 9.73$ MeV at the Debrecen 103-cm isochronous cyclotron and at $E_d = 13.0$ MeV at the Munich Tandem accelerator. Enriched (97.6–99.89%) 88–250 $\mu\text{g}/\text{cm}^2$ thick targets of ^{235}U were used.

The energy of the outgoing protons was analyzed in Debrecen by a split-pole magnetic spectrograph (Spencer and Enge 1967), which had a solid angle of 2 msr and was set at $\Theta_{\text{Lab}} = 140^\circ$ with respect to the incoming beam (see in [Fig. 5.10](#)). The position and energy

Fig. 5.10

Experimental setup for the transmission resonance experiments performed at the Debrecen split-pole magnetic spectrograph



of the protons were analyzed by two Si solid-state, position-sensitive, focal-plane detectors. The overall proton energy resolution of the system, including the effects of target thickness and long-term stability, was estimated to be less than 20 keV.

In Munich, the energy of the outgoing protons was analyzed by a Q3D magnetic spectrograph (Enge and Kowalsky 1970), which was set at $\Theta_{\text{Lab}} = 130^\circ$ relative to the incoming beam and the solid angle amounted to 10 msr. The position in the focal plane was measured by a light-ion, focal-plane detector of 1.8-m active length. Using that detector with the spectrograph, a line-width of <3 keV has been observed for elastic scattering of 20 MeV deuterons.

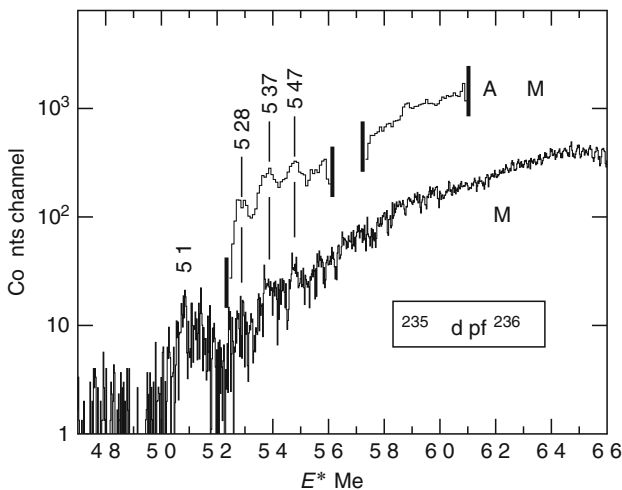
Fission fragments were detected in both experiments by two position-sensitive avalanche detectors (PSAD) (Crouzen 1988) having two wire planes (with delay-line read-out) corresponding to horizontal and vertical directions. Protons were measured in coincidence with fission fragments. Typical proton energy spectra are shown in [Fig. 5.11](#) as a function of excitation energy.

A highly damped superdeformed (SD) vibrational resonance, which is very close to the top of the first barrier, is clearly seen at 5.1 MeV (Goldstone et al. 1978). Above this resonance, one observes some sharper peaks (FWHM ≈ 30 keV) similar to the modest energy-resolution work (FWHM = 60–70 keV) of Goldstone et al. (1978) and to previous results (Krasznahorkay et al. 1996, 1998a). These resonances do not appear to be appreciably damped although they are above the top of the inner barrier, so these sharp resonances cannot be associated with SD states lying in the second well. These results support the presence of a deep HD minimum as predicted by Cwiok et al. (1994).

In the third well of the potential, the reflection asymmetry permits almost degenerate levels of both parities in the rotational spectrum. These kinds of rotational levels have been nicely observed in the experimental fission probability of ^{231}Th (Blons et al. 1975). Assuming that each of the observed resonances also contains a whole rotational band, the experimental results

Fig. 5.11

Proton spectra in coincidence with the fission fragments measured in Debrecen (ATOMKI) and in Munich (LMU). Based on Krasznahorkay et al. (1998b)



were fitted by simple Gaussian functions for describing the different members of the band following the procedure of Blons et al. (1975).

The relative excitation probabilities for members of the rotational band were taken from the work of Back et al. (1972) who performed Distorted Wave Born Approximation (DWBA) calculations for the (d,p) reaction at the same bombarding energy. The width of the Gaussians was set by the experimental resolution.

The following free parameters were introduced: (1) energy of the band head, (2) absolute intensity of the band, and (3) rotational parameter of the band. The last parameter was kept identical for all of the groups, i.e., the 5.28, 5.37 and 5.47 MeV groups. A fit to the measured spectrum was performed with the above parameters using the least squares method. The nonresonant part of the fission probability was taken into account as an exponential “background.”

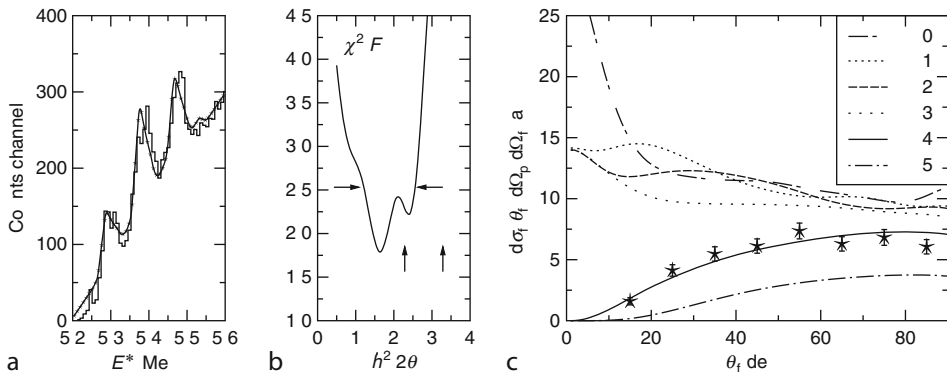
The best fit was obtained with $K = 4$ as shown in Fig. 5.12a. The K value of the target was $K = 7/2$. At the low bombarding energy (9.73 MeV) the $\ell = 0$ transfer is the most probable, which implies the excitation of mainly $K = 3$ and 4 states.

The calculated χ^2 values as a function of $\hbar^2/2\Theta$ are plotted in Fig. 5.12b. The predicted values of $\hbar^2/2\Theta$ for the hyperdeformed and superdeformed states are indicated by HD and SD, respectively. The best fit results in $\hbar^2/2\Theta = 1.6^{+1.0}_{-0.4}$ keV is in good agreement with the value predicted for the hyperdeformed state $(\hbar^2/2\Theta)_{\text{Theo.}} = 2.0$ keV (Bengtsson et al. 1987).

Fission-fragment angular distributions were generated for the 5.47 MeV line as well as for the continuous nonresonant part of the fission probability and normalized to the known (d,f) angular distribution (George et al. 1963). The angular distribution is shown in Fig. 5.12c. All distributions were fitted with even Legendre polynomials (LPs) up to fourth order. For the nonresonant region, the LP coefficients are in good agreement with the previously published data (Britt et al. 1968; Specht et al. 1966; Vandebosch et al. 1967). The measured angular

Fig. 5.12

(a) Proton spectrum measured for ^{236}U in coincidence with the fission fragments as a function of excitation energy, compared to the fitted rotational bands; (b) the results of the χ^2 analysis (F is the number of degrees of freedom of the fit); the theoretical predictions for the HD and SD rotational parameters are indicated by arrows; (c) experimental fission-fragment angular distribution for the 5.47 MeV resonance with respect to the recoil axis (z-axis) compared to the calculated ones. Based on Krasznahorkay et al. (1998b)



distribution was compared to the calculated ones assuming different K values, in order to get information on the K value of the hyperdeformed rotational band. From the comparison, the most probable K value of the band is $K = 4$ (see ► Fig. 5.12c), which is in perfect agreement with the analysis of the proton spectrum.

5.5.2 Reinvestigation of the Fission Resonances in ^{236}U

In the experiment discussed in ► Sect. 5.5.1, the resonances observed at 5.27, 5.34 and 5.43 MeV have been identified as hyperdeformed resonances (Krasznahorkay et al. 1998a, b), however without resolving their rotational structure.

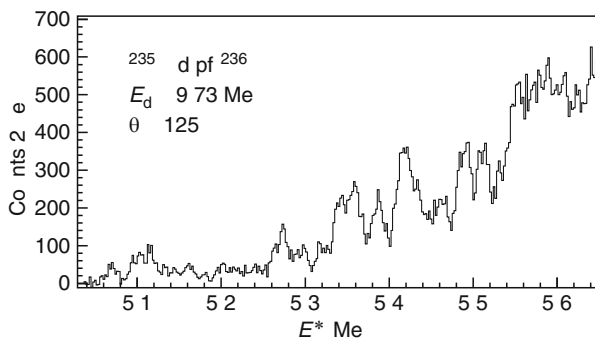
A second experiment aiming at a better energy resolution and a more convincing statistics was carried out at the Munich Accelerator Laboratory to investigate the $^{235}\text{U}(\text{d}, \text{pf})$ reaction with a deuteron beam of $E_d = 9.75$ MeV. The energy of the proton ejectiles was analyzed with a Q3D magnetic spectrograph. The Q3D spectrometer was placed at $\Theta_L = 125^\circ$ relative to the incident beam and the solid angle was 10 msr. The energy resolution obtained from the $^{208}\text{Pb}(\text{d}, \text{p})$ reaction was 3 keV at 8.7 MeV proton energy. Furthermore, this reaction was used for the energy calibration. Fission fragments were detected by two position-sensitive avalanche detectors (PSAD) (Hunyadi et al. 2001). An active area of $16 \times 16 \text{ cm}^2$ resulted in a relatively large solid-angle coverage of the detectors. The measured high-resolution fission probability as a function of the excitation energy of the compound nucleus ^{236}U is shown in ► Fig. 5.13. It was obtained by dividing the proton energy spectrum measured in coincidence with fission fragments by the smoothly varying proton spectrum from the (d,p) reaction.

The structures of the previously identified resonances at 5.27, 5.34, and 5.43 MeV have been nicely resolved as shown in ► Fig. 5.14. The resonance structure around 5.1-MeV excitation energy was formerly interpreted by Goldstone et al. (1978), Just et al. (1979) and Just et al. (1980) as a vibrational resonance in the second minimum.

In the first step of the analysis, the resonance structure between 5.2 and 5.5 MeV was analyzed. In order to describe the rotational structure, overlapping rotational bands were assumed with the same moment of inertia, inversion-splitting parameter and intensity ratio for the band members. Simple Gaussians were used for describing the different band members.

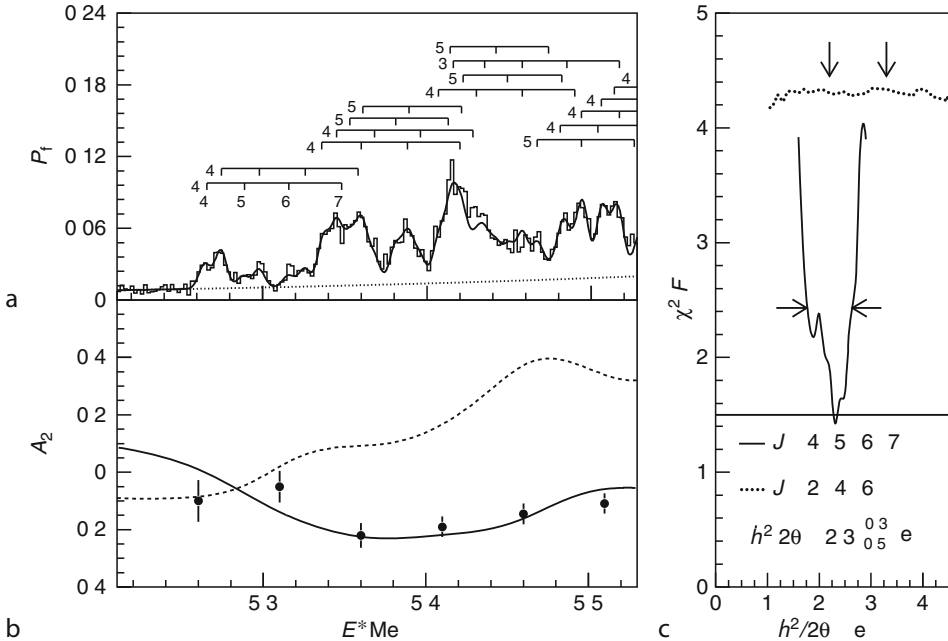
■ Fig. 5.13

Proton spectrum in coincidence with the fission fragments measured in Munich. Based on Csátlós et al. (2005)



■ Fig. 5.14

(a) Fission probability P_f for the $^{235}\text{U}(\text{d},\text{p})^{236}\text{U}$ in the excitation-energy region above 5.2 MeV. The solid line shows a fit to the data assuming rotational bands. The tick marks indicate the positions of the band heads with K values as indicated by the numbers. (b) Consistent description of the angular correlation coefficient A_2 from Just et al. (1979) (data points) with the fit function from panel (a) based on the distribution of K values as indicated there. (c) Normalized χ^2 values for the fit to the spectrum of panel (a). The best fit has been obtained by hyperdeformed rotational bands with $\hbar^2/2\Theta = 2.3 \pm 0.4$ keV. Based on Csátlós et al. (2005)



The width of the Gaussians was fixed by the experimental resolution. The relative excitation probabilities for the members of the rotational bands were taken from DWBA calculations for the (d,p) reaction by Back et al. (1971), calculated around 5.4 MeV excitation energy. During the fitting procedure, three free parameters were used for each band, the first two parameters being the energy of the band head and the absolute intensity of the band. A common rotational parameter ($\hbar^2/2\Theta$) and inversion-splitting parameter (ΔE^\pm) were adopted for all bands. Since the ground-state spin and parity of the target is $7/2^-$, and because at the relatively low bombarding energy the $\ell = 0$ transfer is the most probable one, mainly $J^\pi = 3^-$ and $J^\pi = 4^-$ states were excited. For the reproduction of the angular correlation coefficients, the K value of each rotational band was an additional free parameter.

The HD states are characterized by the presence of alternating parity bands with very large moments of inertia because of the very large quadrupole and octopole moments (Blons et al. 1988). Assuming alternating parity bands with $K = 3, 4$, and 5 band heads, the fission probability between 5.2 and 5.5 MeV was fitted, resulting in the fit curve superimposed on the data in Fig. 5.14a. The corresponding normalized χ^2 values are presented in Fig. 5.14c as a function of $\hbar^2/2\Theta$. The horizontal line represents the 99.9% (3σ) confidence level for the

χ^2 test. The deduced rotational parameter is $\hbar^2/2\Theta = (2.3 \pm 0.4)$ keV, which is consistent with the small inversion parameters, obtained by Blons et al. (1988).

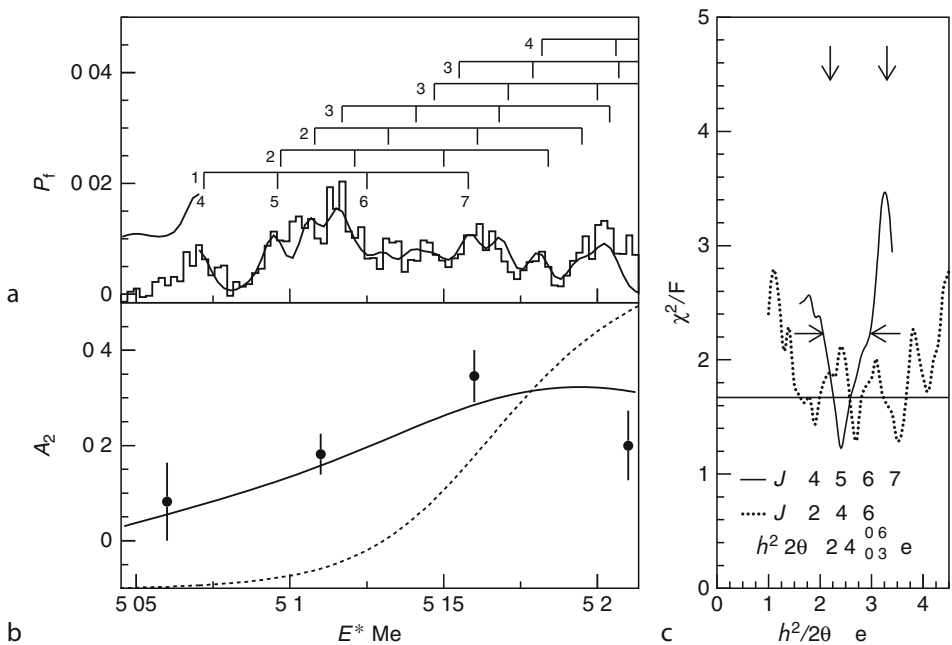
Fitting the fission probability with rotational bands with opposite parity assignments resulted in a fit of similar quality as the one shown in [Fig. 5.14a](#), thus indicating that the analysis is not sensitive to parity. With the series of 15 rotational bands shown in [Fig. 5.14a](#) not only the fission probability, but also the angular correlation coefficient A_2 measured by Just et al. (1979) could be reproduced (data points in [Fig. 5.14b](#)). The extracted rotational parameter corresponds to a value characterizing HD rotational resonances. The moment of inertia $\Theta = (217 \pm 38) \hbar^2/\text{MeV}$ is in good agreement with the values (Shneidman et al. 2000) for ^{234}U and ^{232}Th , with assumed exotic heavy clustering as predicted by Cwiok et al. (1994).

In the second step of the analysis, the proton energy spectrum below 5.2 MeV was analyzed. In the $^{234}\text{U}(t, \text{pf})$ reaction, Back et al. (1974) observed a weak, narrow resonance at 5.0 MeV and a distinct shoulder (or resonance) around 5.15 MeV. Goldstone et al. (1975) and Just et al. (1979) reported the first clear observation of a series of narrow subbarrier fission resonances in ^{236}U produced in the (d, pf) reaction. In their analysis, the underlying states of these resonances were assumed to originate from the second well, close to the top of the inner barrier.

The result of the analysis in the excitation-energy region between 5.05 and 5.2 MeV is shown in [Fig. 5.15](#), where the prompt fission probability is displayed (panel a) together with the results of a fit by rotational bands similar to the procedure described above for the upper resonance region. Again the spin-dependent excitation probabilities of the rotational band members were based on DWBA calculations by Back et al. (1971) for $E^* = 5.1$ MeV.

Fig. 5.15

Fission probability P_f for the $^{235}\text{U}(d, p)^{236}\text{U}$ in the excitation-energy region below 5.2 MeV. Based on Csatlós et al. (2005). The panels are similar to those of [Fig. 5.14](#)



The optimized fit curve shown in [Fig. 5.15a](#) required modifications of the DWBA calculations by Back et al. (1971). However, it is apparent already from the work of Back et al. (1971) that variations of the excitation energy by only a few hundred keV result in variations of the excitation probabilities of up to a factor of 3. Moreover, it should be kept in mind that the Nilsson single-particle structure underlying the DWBA calculations – see also Andersen et al. (1970) – inherently carries large uncertainties in the region of heavy nuclei and high excitation energies in question here. Thus, modifications of the spin-dependent excitation probabilities can very well be justified. In order to allow for a consistent description of the fission probability and the angular correlation coefficient A_2 from Just et al. (1979), a distribution of K values rising from $K = 1$ to $K = 4$ between 5.05 MeV and 5.2 MeV had to be chosen.

The tick marks in [Fig. 5.15a](#) indicate the positions of the band heads with their respective K values marked as numbers. The sign change of the A_2 coefficient already indicates the tendency toward lower K values with decreasing excitation energy. The resulting curve for the A_2 angular-correlation coefficient calculated based on the fit function derived from the fission probability in panel (a) is displayed in panel (b) of [Fig. 5.15](#). The quality of the fit can be judged from [Fig. 5.15c](#), where the normalized χ^2 values are displayed with the horizontal solid line representing the 99.9% confidence level.

The rotational parameter derived from the best fit is $\hbar^2/2\Theta = (2.4 \pm 0.7)$ keV, corresponding to a hyperdeformed configuration. This result is in contrast to the old assumption that the decaying vibrational excitations originate from the superdeformed second minimum. It is impossible to reproduce the data with overlapping rotational bands in the second well with a spin sequence of $J^\pi = 2^+ - 4^+ - 6^+ - 8^+$ and a typical rotational parameter for superdeformed bands $\hbar^2/2\Theta \approx 3.3$ keV.

5.5.2.1 The Depth of the Third Minimum in ^{236}U

The depth of the third well (as shown in [Fig. 5.16](#)) was determined by comparing the experimentally obtained average level distances of the $J = 5$ members of the rotational bands with $K = 4, 5$ of [Fig. 5.15a](#) with calculated ones using the back-shifted Fermi-gas description (Rauscher et al. 1997) as described in [Sect. 5.4.2](#).

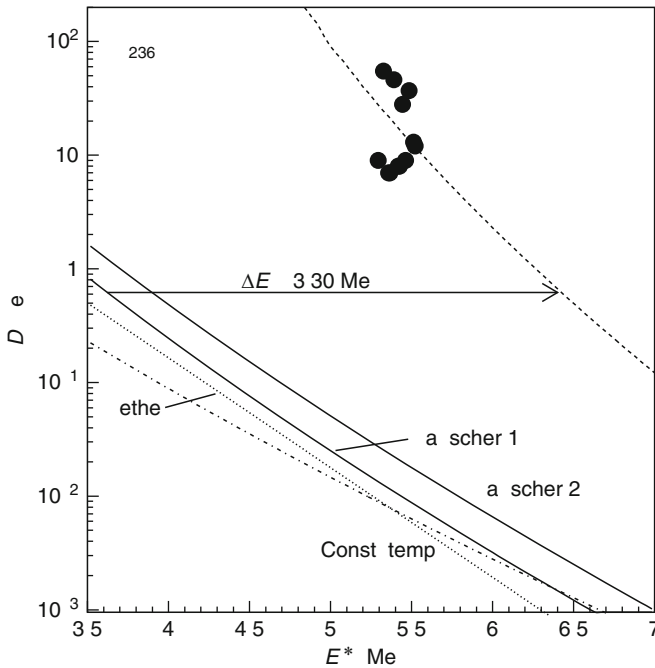
The theoretical prediction for the depth of the third minimum in ^{236}U according to Cwiok et al. (1994) is 3.8 MeV. This experimental result is in a good agreement with that prediction and is also consistent with another experimentally determined value of $E_{\text{III}} = (3.1 \pm 0.4)$ MeV for ^{234}U (see in [Sect. 5.5.3.1](#)).

5.5.2.2 The Innermost Barrier of Uranium Isotopes

The new interpretation of the 5.1 MeV transmission resonance group in ^{236}U as a resonance in the third and not in the second minimum leads to a determination of the parameters of the innermost barrier. Previously the interpretation as a resonance in the second minimum led to the requirement that the inner barrier height E_A was approximately equal to the outer barrier E_B , because a strong resonance requires penetrabilities of both barriers with comparable values. Based on the present interpretation, the innermost barrier has to be reduced to the excitation energy of the lowest transmission resonance in order to achieve a good mixing between the first and second minima.

■ Fig. 5.16

Average distances of the $J = 5$ spin states in the third minimum of ^{236}U as a function of excitation energy. The solid, dotted, and dash-dotted curves show calculated values by different formulas (explained in Krasznahorkay et al. 1999), the full points correspond to experimental values. The dark dotted curve is shifted from curve labeled “Rauscher 1” to fit the data. In this way the value for the ground-state energy is estimated to be $E_{\text{III}} = (3.30 \pm 0.40)$ MeV. Based on Csatlós et al. (2005)

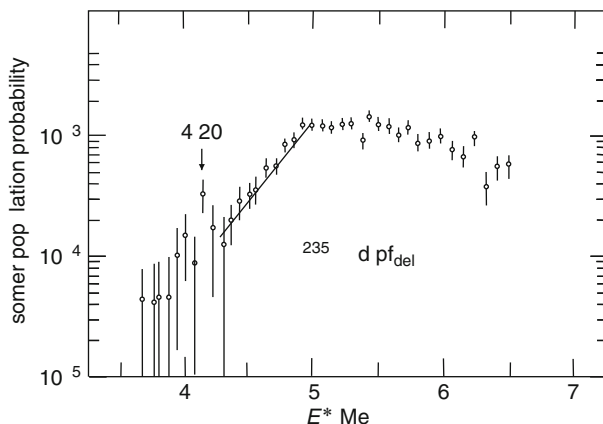


With a back-shifted Fermi-gas formula, the level spacing for 0^+ compound states in the second minimum at a total excitation energy of 5.1 MeV is calculated to be about 80 keV. The damping width of these states due to tunneling through the inner barrier $\Gamma = \hbar\omega_{\text{II}}/2\pi \cdot P_A$ is about 100 keV at the top of the barrier with $P_A \approx 1$. Therefore, the occurrence of a transmission resonance in the third well at 5.1 MeV requires a rather complete damping and an inner-barrier height E_A lower than 5.2 MeV.

On the other hand, one can obtain a lower limit for the inner-barrier height E_A from the previously measured isomer population probability. This is shown in Fig. 5.17 with data from Goerlach (1978). For excitation energies between ~ 4.4 and ~ 4.9 MeV, the weak coupling limit is valid, and the isomer population probability is proportional to the square root of the penetrability P_A of the inner barrier (Goerlach 1978). The data show a clear exponential increase. At an excitation energy of 5.1 MeV, the isomer population probability starts to saturate because the compound states of the first and second minima become largely mixed. Above 6 MeV, one observes a drop of the isomer population probability because the competing fission and neutron channels open up. From the exponential rise of the isomer population probability, for low energies it can be inferred that the inner barrier E_A has to be larger than 4.9 MeV.

■ Fig. 5.17

Isomer population probability from Goerlach et al. (1978)



From these two limits, one obtains $E_A = (5.05 \pm 0.20)$ MeV. Furthermore, from the exponential rise and the estimate of the penetrability from the γ back-decay one obtains $\hbar\omega_A = 1.2$ MeV.

In summary, study of the prompt fission probability of ^{236}U reveals the shape of the fission barrier. The rotational parameter extracted is $\hbar^2/2\Theta = (2.3 \pm 0.4)$ keV. The corresponding moment of inertia ($\Theta = (217 \pm 38) \hbar^2/\text{MeV}$) agrees with a theoretical value (Shneidman et al. 2000). The hyperdeformed rotational-band structure in the excitation-energy region around 5.1 MeV supports that there is a rather deep third minimum in ^{236}U . The lowest transmission resonance in the third well sets limits on the height of the inner barrier E_A .

An extrapolation of the height of the inner barrier indicates that for Th isotopes it should be about 4.5 MeV, which is different from a former interpretation (Bjornholm and Lynn 1980), but agrees with a theoretical prediction (Howard and Möller 1980).

5.5.2.3 Clustering in the Actinide Region

The clustering phenomenon is a dramatic manifestation of the shell structure at very large deformations. From such a di-nuclear system one may expect strong fission decay to the components, similarly to the case of the enhanced α decay of light α + core nuclei above the α + core threshold.

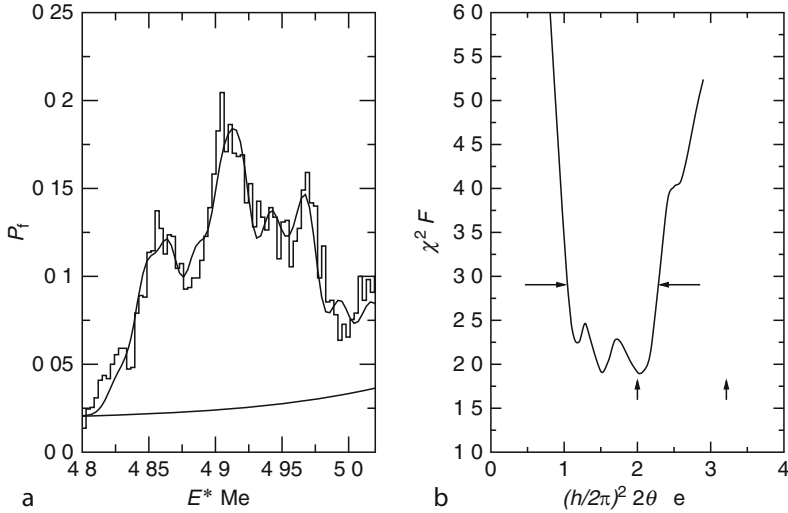
The HD states lying in the third well of the fission barrier may play the role of a doorway-like state before fission, from which the fission can only occur through a limited number of fission paths, resulting in a sharper mass distribution (Krasznahorkay et al. 2000, 2001a, b, 2003, 2004).

5.5.3 Hyperdeformed Rotational Bands in ^{234}U

The experimental results of Blons et al. (1988) concerning ^{234}U were reanalyzed similarly. Each of the resonances observed (see Fig. 5.18) was assumed to consist of a complete rotational band.

■ Fig. 5.18

(a) Fission probability of ^{234}U as a function of excitation energy. The full curve is a result of the fit with $\hbar^2/2\Theta = 1.8$ keV according to the deepest χ^2 minimum; (b) the results of the χ^2 analysis. Based on Krasznahorkay et al. (1998b)



The energies of the band heads, the absolute intensities of the bands, and an inertia parameter ($\hbar^2/2\Theta$) were fitted to the experimental data. The obtained inertia parameter is $\hbar^2/2\Theta = 1.8_{-0.7}^{+0.5}$ keV, which is the average of the values of the equivalent χ^2 minima, and again agrees well with the predicted value for the HD states.

The angular distribution of the fission fragments was also calculated and compared to the experimental data (see Fig. 5.19). Good agreement has been obtained, which also supports that each of the peaks observed contains a complete rotational band with $K = 1$ or 2, instead of one definite state with a well-defined J^π as assumed by Blons et al. (1988). The K value of the target was 5/2, which implies the excitation of $K = 2$ or 3 states with $\ell = 0$ transfer.

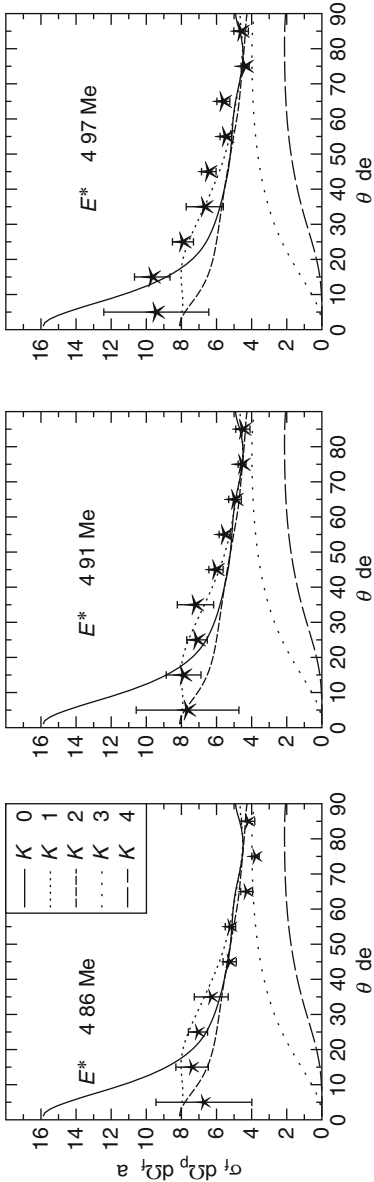
5.5.3.1 High-Resolution Study of the Fission Resonances in ^{234}U

The $^{233}\text{U}(\text{d,pf})^{234}\text{U}$ reaction was also studied with better energy resolution, to resolve the HD rotational bands and, from the level densities, to estimate the depth of the third minimum.

In order to investigate the HD bands, the excitation energy was chosen between the energy of the inner and outer barriers of the second well, i.e., between 4.5 MeV and 5.2 MeV (Krasznahorkay et al. 1998a). In this energy range, the SD resonances in the second well should be much broader than the HD states due to the strong coupling to the normal deformed states. The widths of the HD states due to the higher outer barriers of the third well remain below the actual experimental resolution of ~ 5 keV.

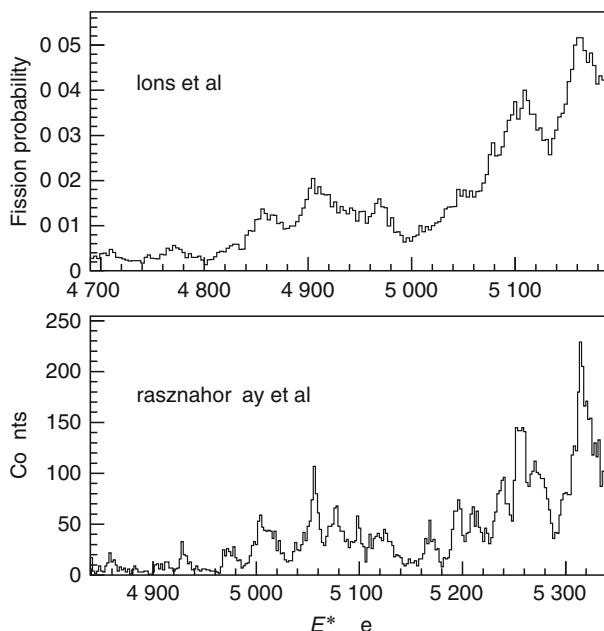
The experiment was carried out with an $E_d = 12.5$ MeV deuteron beam of the Munich Tandem accelerator. The energy of the outgoing protons was analyzed by a Q3D magnetic spectrograph, in coincidence with the fission fragments.

Fig. 5.19 Fission fragment angular distributions for the 4.86, 4.91, and 4.97 resonances in ^{234}U compared to the theoretically calculated curves assuming different K values for the rotational bands. Based on Krasznahorkay et al. (1998)



■ Fig. 5.20

Part of the proton spectrum measured in coincidence with the fission fragments and compared to the result of Blons et al. (1988). Based on Krasznahorkay et al. (1999)



The obtained widths of the peaks show the experimental energy resolution up to about 5.3 MeV. Above this excitation energy, the peaks get increasingly broader due to the increasing fission width when one approaches the top of the fission barrier. The low-energy part of the spectrum, which was analyzed before (Krasznahorkay et al. 1998b), is compared to the one published by Blons et al. (1988) in ▶ Fig. 5.20.

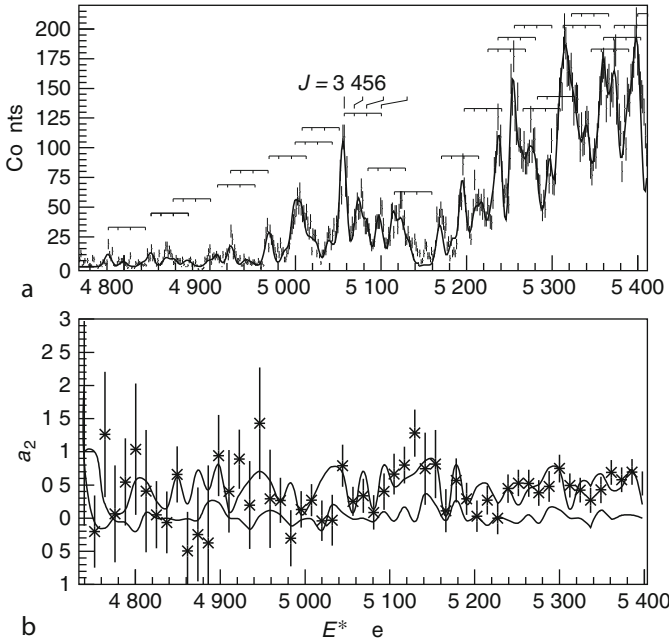
The energy resolution has been considerably improved and one can clearly see the fine structure of the peaks. Experimentally, the very large quadrupole and octopole moments of the HD states should manifest themselves by the presence of alternating parity bands with very large moments of inertia (Blons et al. 1988). Assuming overlapping rotational bands with the same moment of inertia, inversion parameter (Ackermann et al. 1993) and intensity ratio for the members in a band, the spectrum was fitted in the same way as in the previous work (Krasznahorkay et al. 1998b). The result of the fit is shown in ▶ Fig. 5.21a.

The relative intensities of the members of the rotational bands have been taken from Back et al. (1971). These values have been calculated by DWBA for $^{235}\text{U}(\text{d},\text{p})$. These relative intensities depend sensitively on the distribution and widths of the single-particle states involved in the (d,p) process at the given excitation energy. These relative intensities have been adopted as initial parameters for the fitting procedure.

The jump in the relative intensities going from $J = 2^+$ to 3^- , as predicted by Back et al. (1971) might be a consequence of the alternating parities within the rotational bands, although the fit was actually not very sensitive to the relative intensity of the 2^+ state. Increasing this intensity by a factor of two worsens the χ^2 by less than 8%. After fixing the relative intensities of

■ Fig. 5.21

(a) Part of the measured proton energy spectrum fitted with 24 rotational bands of the same rotational parameter. The spectrum was divided into two parts at $E^* = 5,150$ keV for the fitting; (b) Experimental fission-fragment angular-distribution coefficients as a function of excitation energy compared to the calculated ones using $K = 1$ (upper curve) and $K = 3$ (lower curve) for all of the bands. The $K = 0$ curve is very close to the $K = 1$ curve while that with $K = 2$ is between those with $K = 1$ and $K = 3$. The latter are not shown. Based on Krasznahorkay et al. (1999)



the band members, two specific parameters for each band were used during the fitting procedure: the energy of the band head and the absolute intensity of the band. A common rotational ($\hbar^2/2\Theta$) parameter was adopted for all bands.

Although the statistics in the second part of the spectrum is better, the density of the states is about twice as large, making the determination of the rotational parameter more uncertain. The rotational parameter was therefore determined for both parts separately and the weighted average was calculated. The result is $\hbar^2/2\Theta = (2.2 \pm 0.2)$ keV.

The low-lying rotational bands have been investigated in the $^{233}\text{U}(\text{d},\text{pf})$ reaction at 13 MeV by Bjornholm et al. (1968). They obtained intensity distributions, which peak around $J = 2$, distinctly lower than those found by Back et al. (1971). Although Bjornholm et al. (1968) only investigated rotational bands consisting of states of the same parity, and it is known that the intensities depend strongly on parity; the relative intensities were also used to fit the data as an alternative scenario. Using alternatively the relative intensities of Bjornholm et al. (1968) almost as good a fit was obtained as above with $\hbar^2/2\Theta = (1.5 \pm 0.5)$ keV. The somewhat different value obtained by assuming these two very different sets of relative intensities indicates the sensitivity of the rotational parameter to the assumed relative intensities.

Fission-fragment angular distributions were generated as functions of the excitation energy, normalized to the known (d,f) angular distribution (George et al. 1963) and fitted with even Legendre polynomials (LPs) up to fourth order. The a_2 angular distribution coefficient is shown in [Fig. 5.3b](#) as a function of the excitation energy. In order to get information on the spins and K values of the observed rotational bands, or to check the assumptions made for fitting the energy spectrum, the angular distribution coefficients of the fission fragments have been calculated and compared with experiment.

The $a_2(E^*)$ shown in [Fig. 5.21b](#) has been calculated by using the parameters obtained from a fit of the energy spectrum. The amplitudes of the different band members obtained from the fit were then multiplied by the corresponding theoretical Legendre coefficients $A_\lambda(J_f, K_f)$. The final distribution was then obtained by normalizing it with a similar function calculated with the $A_0(J_f, K_f)$ values (Krasznahorkay et al. 1999).

Since the spins J_f of the excited states are already fixed by the energy spacings of the peaks as shown in [Fig. 5.21a](#), in the next step only the K values of the bands were varied between 0 and 3. The measured angular distribution coefficients were compared to the calculated values in [Fig. 5.21b](#).

With the assumption of quadrupole rotational bands with intensities peaking at $J^\pi = 2^+$ it was impossible to explain even the gross structure of the measured angular distribution. The calculated a_2 coefficients were always too low compared to the experimental ones. In order to explain the experimentally measured $a_2 \approx 0.5$ values, one should assume an intensity distribution, which peaks at higher J values than 2, most probably at $J = 3$ as assumed before.

5.5.3.2 The Depth of the Third Minimum in ^{234}U

The density of the $J = 3$ states determined from the experimental data (Krasznahorkay et al. 1999) is close to a Wigner quasi-probability distribution (Brody et al. 1981) but the mixing-in of some Poisson type distribution is also visible. The density of $J = 3$ states has also been calculated using the back-shifted Fermi-gas description with parameters determined by Rauscher et al. (1997). The calculated curve had to be shifted by 2.7 MeV to reproduce the experimental values (Krasznahorkay et al. 1999). The energy of the ground state in the third well is obtained to be $E_{\text{III}} = (3.1 \pm 0.4)$ MeV.

Two different HD minima were predicted (Cwiok et al. 1994) for ^{234}U with very different β_λ ($\lambda = 3-7$) values. One of them has an octopole deformation parameter of $\beta_3 \approx 0.4$ and a minimum of $E_{\text{III}} = 3.5$ MeV, while the other is more reflection-asymmetric and has an octopole deformation parameter of $\beta_3 \approx 0.6$ and a minimum of $E_{\text{III}} = 2.7$ MeV. The experimental value of $E_{\text{III}} = (3.1 \pm 0.4)$ MeV is in between the two predicted values with an error bar, which overlaps with both theoretical values.

In summary, the fission probability of ^{234}U has been measured as a function of excitation energy with high energy resolution using the (d,pf) reaction. The rotational parameter obtained from fitting the energy spectrum around $E^* \approx 5$ MeV is found to be $\hbar^2/2\Theta = (2.1 \pm 0.2)$ keV, which is characteristic of the hyperdeformed nuclear shape. The level density of the most strongly excited $J = 3$ states has been compared to the prediction of the back-shifted Fermi-gas formula, and the energy of the ground state in the third minimum has been estimated to be $E_{\text{III}} = (3.1 \pm 0.4)$ MeV, which agrees well with the predicted value (Cwiok et al. 1994).

5.5.4 Subbarrier Fission Resonances and Transitional States Observed in ^{232}U

In contrast to the $^{234,236}\text{U}$ isotopes, where sharp HD fission resonances have been identified (Blons et al. 1988; Krasznahorkay et al. 1998b, 1999; Csatlós et al. 2005), in ^{232}U no clear resonance structures have been observed so far, but rather a broad shoulder around $E^* = 5.0$ MeV, which was assumed to consist of resonances with $K^\pi = 0^+$ and $K^\pi = 2^+$ (Back et al. 1974). However, according to the calculations on the height of the fission barriers and on the depth of the third potential well (Cwiok et al. 1994; Möller et al. 1972), the appearance of fission resonances representing HD states is expected also in the case of ^{232}U .

The most recent experiment was carried out at the tandem accelerator of the Munich Accelerator Laboratory (now called Maier-Leibnitz Laboratory, MLL) at Garching employing the $^{231}\text{Pa}(^3\text{He},\text{df})$ reaction with a ^3He beam of $E = 38.1$ MeV to investigate the fission probability of ^{232}U in the excitation-energy region of $E^* = 4.0$ –6.5 MeV. An enriched (99%) $70\text{ }\mu\text{g}/\text{cm}^2$ thick radioactive target of ^{231}Pa was used. The excitation energy of ^{232}U was determined from the kinetic energy of the deuteron ejectiles.

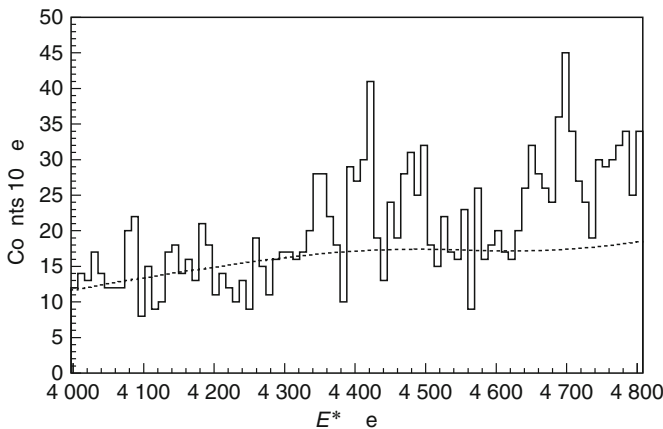
The kinetic energy of the outgoing deuterons was analyzed by the Q3D magnetic spectrograph (see in Fig. 5.6.) set at $\Theta_{\text{lab}} = 35^\circ$ relative to the beam direction. The experimental energy resolution was deduced to be $\Delta E = 11$ keV (FWHM) in the energy region of interest. Fission fragments were detected in coincidence with the outgoing deuterons by two position-sensitive avalanche detectors (PSAD), allowing for a detection of the fission fragment angular correlation with respect to the recoil axis ($30^\circ \leq \Theta_R \leq 90^\circ$) and solid-angle coverage of 10% of 4π .

The measured high-resolution excitation-energy spectrum of ^{232}U is shown in Fig. 5.22 as a function of the excitation energy of the compound nucleus in the region of $E^* = 4.0$ –4.8 MeV together with the contribution of the random coincidence events (dashed line).

A number of sharp transmission resonances have been observed in the excitation-energy region of $E^* = 4.0$ –4.8 MeV with widths of $\Delta E \approx 30$ keV. Considering their narrow width, these resonances do not appear to be considerably damped; thus, they cannot be associated with states in the second minimum. The damping width of class II (SD) resonances should be much

■ Fig. 5.22

Excitation-energy spectrum of ^{232}U between $E^* = 4.0$ MeV and $E^* = 4.8$ MeV. Based on Csige et al. (2009)



broadener (~ 200 keV (Bjornholm and Lynn 1980) due to the strong coupling to class I states, while the damping of class III (HD) resonances is hindered by the higher barriers of the third well.

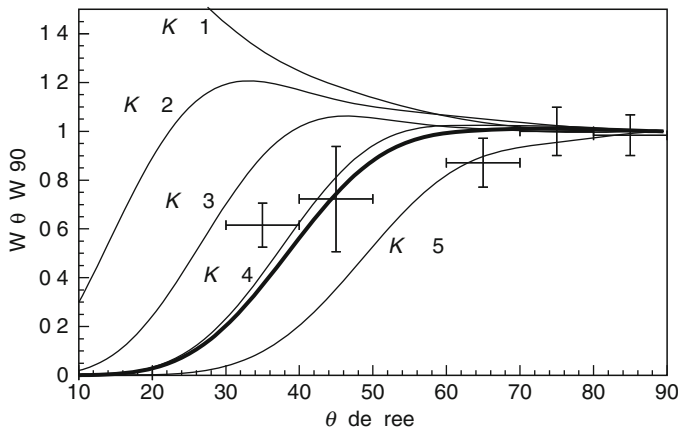
The angular distribution of the fragments was measured by gating on the energies of all observed resonances with respect to the recoil axis and the values were normalized to the value at 90° as can be seen in [Fig. 5.23](#). Angular data for random coincidence events were subtracted, while the efficiency of the PSADs was taken into account by dividing the angular distribution spectrum with the spectrum of random events gated by excitation energies above the fission barrier, where numerous fission channels are open. Errors are caused not only by the statistical contribution but also by the uncertainty coming from the small continuous nonresonant part of the fission probability.

The measured angular distribution was compared to calculated ones in order to derive information on the K value of the rotational bands. The results of these calculations based on different K values are displayed in [Fig. 5.23](#) as continuous lines. These rather high K values ($K = 4, 5$), indicated by the comparison of theoretical and experimental results, can be understood by considering the most probable angular momentum transfer of $L = 3$ and $L = 4$ in the ($^3\text{He}, d$) reaction (Back et al. 1974) and the spin of the ^{231}Pa target nucleus ($J^\pi = 3/2^+$).

Gaussians were used for describing the different band members, as explained before, while the nonresonant part of the fission probability, which is caused by simple tunneling through the fission barrier, was treated as an exponential background. The relative excitation probabilities $\alpha(E, J^\pi)$ for the members of the rotational band were taken from Back et al. (1974). The rotational parameter has been determined to be $\hbar^2/2\Theta = (1.96 \pm 0.11)$ keV, which is far smaller than the corresponding values characterizing SD shapes ($\hbar^2/2\Theta \approx 3.3$ keV) as described in Krasznahorkay et al. (1999); Csatlós et al. (2005). The results have been obtained assuming $K = 4, 4, 4, 4, 5$, and 4 for the seven rotational bands at band head energies $E^* = 4,080(5)$, $4,160(7)$, $4,345(6)$, $4,402(4)$, $4,468(3)$, $4,651(4)$, and $4,678(3)$ keV, respectively. In [Fig. 5.23](#),

Fig. 5.23

Comparison of theoretical and experimental fission fragment angular distributions $W(\theta)/W(90^\circ)$ with respect to the recoil axis. The theoretical curves were obtained by assuming different K values for the rotational bands. The thick line was calculated using K values that were assigned to the experimentally identified rotational bands during the fitting procedure. Based on Csige et al. (2009)



the thick line represents the resulting angular distribution obtained with these assignments. The experimental and calculated values are in very good agreement, supporting the validity of the analysis (► Fig. 5.23).

For the determination of the fission-barrier parameters an analytical expression for the fission probability was used, which was fitted to the experimental values. The details of the fitting procedure are described elsewhere (Csige et al. 2009). The result of the fitting procedure is presented in ► Fig. 5.25.

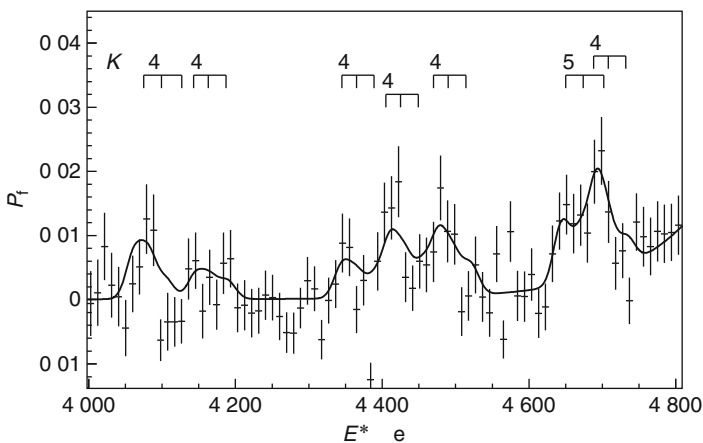
Considering the results for the fission-barrier parameters of ^{232}U , the discrepancy from the fitted function around $E^* = 5.0$ MeV seems to be a nice signature of the existence of transition states, which are assigned to states built on the second barrier.

According to Bohr's transition state concept (Bohr 1956), at excitation energies near the barrier, when the nucleus is passing over a saddle point, most of its energy is expended into deformation energy. Therefore, at this highly deformed configuration, the system should be thermodynamically rather "cold" and exhibit a discrete spectrum of low-lying collective excitations, similar to the ground-state deformation. Within Bohr's concept, it is assumed that near-barrier fission proceeds through these discrete transition states. The fragment angular distributions are then determined by the quantum numbers of the transition states involved. The consequences of such transition states are found to be important in describing both the fission probabilities and the angular distribution of the fission fragments. However, these states usually have large damping widths, which usually prevents their observation separately.

► Figure 5.26 shows the fission probability spectrum $E^* = 4.0$ MeV and $E^* = 4.8$ MeV. In order to describe the rotational structure of these resonances, overlapping rotational bands were assumed again with the same moment of inertia (Θ) and intensity ratio for the band members as described previously for the HD-bands. The angular distribution of the fission fragments showed a $K = 0$ character of the band, but the statistics was insufficient to determine

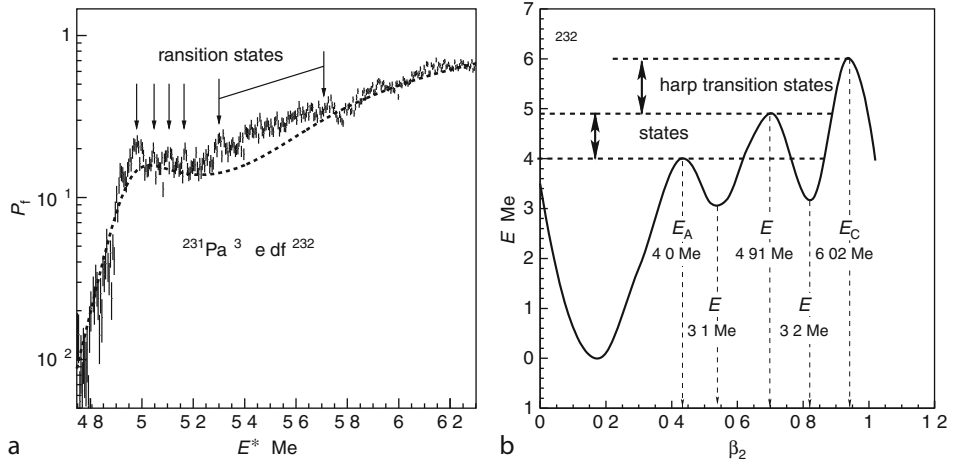
■ Fig. 5.24

Fission probability with error bars as a function of the excitation energy between $E^* = 4.0$ MeV and $E^* = 4.8$ MeV. The result of the fitting procedure assuming seven rotational bands with overlapping band members as described in the text is indicated by the continuous line. The picket fence structures indicate the positions of the rotational band members used in the fit. Based on Csige et al. (2009)



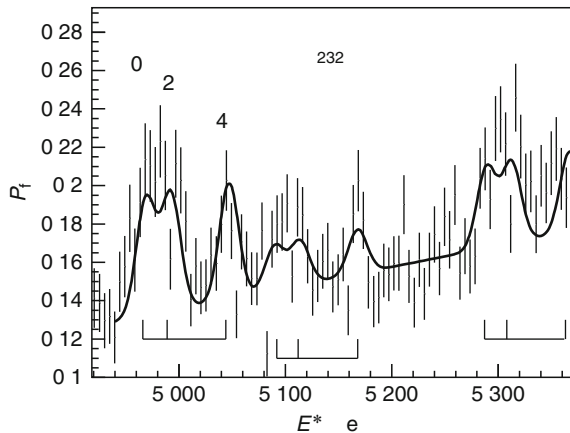
■ Fig. 5.25

(a) Fission probability of ^{232}U as a function of the excitation energy. The result of the fitting procedure assuming five parabolas is indicated by a continuous line. (b) The potential energy of ^{232}U as a function of the quadrupole deformation parameter (β_2) obtained from the fitting procedure. Based on Csige et al. (2009)



■ Fig. 5.26

Fission probability with error bars as a function of the excitation energy between $E^* = 4.8$ MeV and $E^* = 5.4$ MeV. The result of the fitting procedure assuming three rotational bands with overlapping band members as described in the text is indicated by the continuous line. Based on Csige et al. (2009)



the spins of the individual states. The energies and intensities of the resonances could best be described with quadrupole rotational bands, whose members are indicated in Fig. 5.26 for the ground-state band. The energy of the band head was found to be $E^* = (4,970 \pm 3)$ keV. Two other similar bands located at $(5,085 \pm 5)$ keV and $(5,285 \pm 5)$ keV were also included in the fitting procedure. The rotational parameter obtained from the fit was $\hbar^2/2\Theta = (3.38 \pm 0.10)$

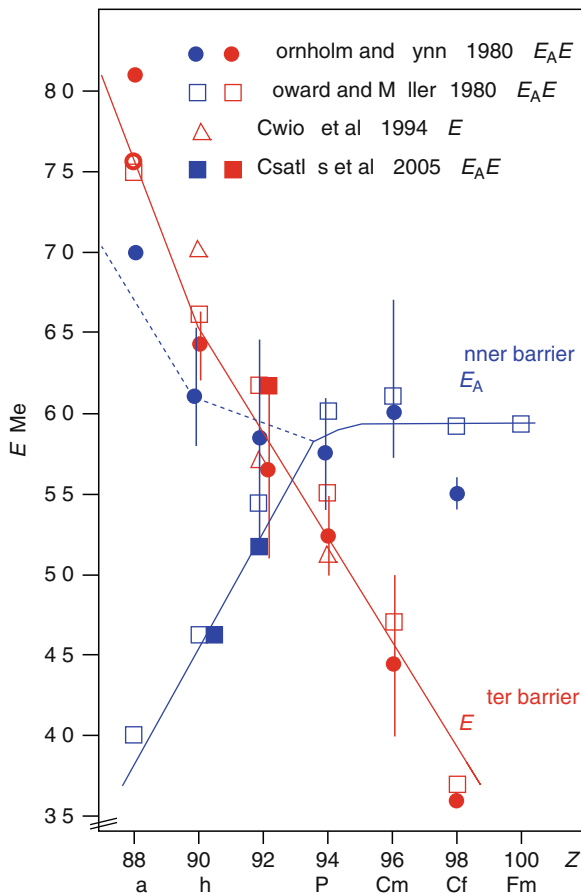
keV, which is characteristic of superdeformed nuclear shape in this mass region (Hunyadi et al. 2001). This result implies that the fission potential might be somewhat distorted.

5.6 The Fission-Barrier Landscape

All presently available information on fission-barrier parameters in the actinide mass region is shown in [Fig. 5.27](#).

Fig. 5.27

Fission-barrier parameters of actinide isotopes. Red symbols indicate the outermost fission barrier E_B , while blue symbols stand for the innermost barrier E_A . The experimental data points from the compilation by Bjornholm and Lynn (1980) are given by the full circles, indicating the centroid of the barrier parameters for a given Z with the error bars denoting the respective range of barrier heights. Open circles indicate the average value of the two outer barriers for the triple-humped barrier in Ra and Th. Open squares show calculated barrier heights taken from Howard and Möller (1980), while open triangles contain, in addition to the calculations by Howard, information on the depth of the third potential well according to Cwiok et al. (1994)

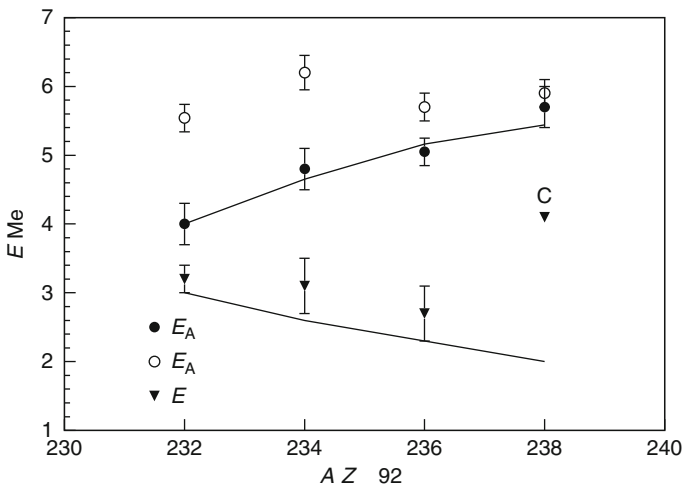


Solid blue and red squares display the barrier heights for ^{236}U as derived in ▶ Sect. 5.5 as well as an estimate for the inner barrier in ^{232}Th . The solid lines visualize the trends visible in the data. While previous publications favored the increase of E_A with decreasing Z (Bjornholm and Lynn 1980) as shown by the dashed blue line, the more recent experimental information, in agreement with earlier calculations, indicates a lowering of E_A as illustrated by the solid blue line below Pu. This discrepancy is explained by the fact that at the time of Bjornholm and Lynn (1980) the existence of a deep third minimum was not known. In the paper of Britt et al. (1973), unease about the obvious discrepancy to the theoretical expectations for E_A in ^{228}Th is explicitly expressed; however, the interpretation of the experimental data was misguided by the assumption of a double-humped fission barrier. In view of the present knowledge, the theoretical trend of a drastic lowering of the inner barrier height with decreasing Z is clearly confirmed. ▶ Figure 5.27 impressively locates the occurrence of the island of fission isomers in the mass region of the light actinides. With the continuous decrease of the outer barrier height E_B with increasing Z , the corresponding half-life of isomeric fission drops below the pico-second region for $Z > 98$. Quite similarly, the decrease of the inner barrier height E_A with decreasing Z results in sub-picosecond half-lives for the γ back-decay in the region of $Z < 88$ thus marks the lower limit for the island of shape isomers.

▶ Figure 5.28 shows the experimentally determined fission-barrier parameters for U isotopes as a function of mass number. The innermost barrier heights and the depths of the third well are marked by full circles and triangles, respectively.

■ Fig. 5.28

The heights of the innermost barrier (E_A) and the depths of the third well (E_{III}) for even-even uranium isotopes. The experimental data for ^{232}U , ^{234}U , ^{236}U , and ^{238}U indicated by full circles and full triangles were taken from Csige et al. (2009); Krasznahorkay et al. (1999); Csatlós et al. (2005); Krasznahorkay (2006); Royer and Bonilla (2007), while the experimental data represented by open circles were taken from Back et al. (1974). Data points marked by (C) are results of calculation taken from Royer and Bonilla (2007). The upper full curve represents theoretical results for the height of the inner barrier (Howard and Möller 1980), while the lower full curve shows the theoretical E_{III} values (Cwiok et al. 1994)



The value for the third minimum of the fission barrier of ^{238}U results from a theoretical calculation, taken from Royer and Bonilla (2007). In [Fig. 5.28](#), the fission-barrier parameters (assuming double-humped fission barrier) obtained by Back et al. (1974) are indicated by open circles. The data for the inner barrier heights E_A (full circles) reveal a clear trend within the isotopic chain. [Figure 5.28](#) also shows a nice agreement between the latest experimental and theoretical results for the fission-barrier parameters supporting strongly the claim that a third minimum exists. The findings presented in this chapter assemble into a firm evidence for the existence of a deep third minimum of the fission potential.

Acknowledgments

The work has been supported by DFG under HA 1101/12-2 and UNG 113/129/0, the DFG cluster of excellence “Origin and Structure of the Universe,” and the Hungarian OTKA Foundation No. K72566.

References

- Ackermann B et al (1993) Nucl Phys A 559:61
- Andersen BL, Back BB, Bang JM (1970) Nucl Phys A 147:33
- Back BB, Bondorf JP, Otroshenko GA, Pedersen J, Rasmussen B (1971) Nucl Phys A 165:449
- Back BB et al (1972) Phys Rev Lett 28:1707
- Back BB, Hansen O, Britt HC, Garrett JD (1974) Phys Rev C 9:1924
- Bengtsson R et al (1987) Nucl Phys A 473:77
- Berger JE, Girod M, Gogny D (1989) Nucl Phys A 502:85c
- Bjornholm S, Dubois J, Elbek B (1968) Nucl Phys A 118:241
- Bjornholm S, Lynn JE (1980) Rev Mod Phys 52:725
- Blons J, Mazur C, Paya D (1975) Phys Rev Lett 35:1749
- Blons J et al (1978) Phys Rev Lett 41:1282
- Blons J, Mazur C, Paya D, Ribrag M, Weigmann H (1984) Nucl Phys A 414:1
- Blons J et al (1988) Nucl Phys A 477:231
- Blum V, Maruhn JA, Reinhard P-G, Greiner W (1994) Phys Lett B 323:262
- Bohr A (1956) On the theory of nuclear fission. In: Proceedings of the Geneva conference 1955, vol 2, p 220
- Bohr N, Wheeler JA (1939) Phys Rev 56:426
- Boldeman JW, Walsch RL (1985) In: Proceedings of the international conference Santa Fe, New Mexico, vol 1, p 317
- Britt HC, Rickey FA, Hall WS (1968) Phys Rev 175:1525
- Britt HC, Bolsterli M, Nix JR, Norton JL (1973) Phys Rev C 7:801
- Brody TA et al (1981) Rev Mod Phys 53:385
- Buck B, Biedenharn LC, Cusson RY (1979) Nucl Phys A 317:205
- Crouzen PCN (1988) PhD thesis, Rijksuniversiteit Groningen
- Csatlós M et al (2005) Phys Lett B 615:175
- Csige L et al (2009) Phys Rev C 80:011301
- Cwiok S et al (1987) Comput Phys Commun 46:379
- Cwiok S, Nazarewicz W, Saladin JX, Plociennik W, Johnson A (1994) Phys Lett B 322:304
- Enge HA, Kowalsky SB (1970) In: Proceedings of the 3rd international conference on magnet technology, Hamburg (Deutsches Elektronen-Synchrotron, Hamburg)
- George L et al (1963) Phys Rev 131:722
- Glässel P (1974) Dissertation, Univ. München
- Glässel P, Röser H, Specht HJ (1976) Nucl Phys A 256:220
- Goeppert-Mayer M (1949) Phys Rev 75:1969
- Goerlach U (1978) Diploma thesis, Univ./MPI Heidelberg
- Goerlach U (1980) Dissertation, Univ. Heidelberg
- Goerlach U et al (1978) Z Phys A 287:171
- Goerlach U et al (1982) Phys Rev Lett 48:1160
- Goldstone PD et al (1975) Phys Rev Lett 35:1141
- Goldstone PD, Hopkins F, Malmin RE, Paul P (1978) Phys Rev C 18:1706
- Hahn O, Strassmann F (1939) Naturwissenschaften 27:11
- Haxel O, Jensen JHD, Suess HE (1949) Phys Rev 75:1766
- Hill DL, Wheeler JA (1953) Phys Rev C 89:1102
- Howard WM, Möller P (1980) Atom Data Nucl Data 25:219, and references therein
- Hunyadi M (1999) PhD thesis, Lajos Kossuth University Debrecen
- Hunyadi M et al (2001) Phys Lett B 505:27
- Just M (1978) PhD thesis, University Heidelberg

- Just M et al (1979) In: Proceedings of the symposium physics and chemistry of fission. IAEA, Jülich, p 71
- Just M, Goerlach U, Habs D, Metag V, Specht HJ (1980) In: Symposium on physics and chemistry of fission, Jülich 1979, IAEA, Vienna, SM-241/A4, p 71
- Kikuchi Y, An S (1970) J Nucl Sci Technol 7:157
- Krappe HJ, Nix JR, Sierk AJ (1979) Phys Rev C 20:992
- Krasznahorkay A et al (1996) Acta Phys Pol B 27:139
- Krasznahorkay A et al (1998a) In: Proceedings of the international symposium on exotic nuclear shapes, Debrecen 1997 APH N.S. Heavy Ion Physics, 7, 35
- Krasznahorkay A et al (1998b) Phys Rev Lett 80:2073
- Krasznahorkay A et al (1999) Phys Lett B 461:15
- Krasznahorkay A et al (2000) In: Poenaru D, Stoica S (eds) Proceedings of the international symposium on advances in nuclear physics, Bucharest, Romania, 9–10 Dec 1999. World Scientific, Singapore, p 328
- Krasznahorkay A et al (2001a) Acta Phys Hung NS H 13:111
- Krasznahorkay A et al (2001b) Acta Phys Pol B 32:657
- Krasznahorkay A et al (2001c) In: Bonsignori GC et al (eds) Proceedings of the conference: Bologna 2000. Structure of the nucleus at the dawn of the century, Bologna, Italy, 29 May–3 June 2000. World Scientific, New Jersey, 2, p 306
- Krasznahorkay A et al (2003) Acta Phys Hung NS-H 18:323
- Krasznahorkay A et al (2004) In: Mueller AC, Mirea M, Tassan-Got L(ed) International workshop of new applications of nuclear fission. Bucharest, Romania, 7–12 Sept 2003. Proceedings. World Scientific, New Jersey, p 95
- Krasznahorkay A et al (2006) In: Woehr A, Aprahamian A (eds) 12th international symposium on capture gamma spectroscopy and related topics, Notre Dame, Indiana, 4–9 Sept 2005. Proceedings. AIP (AIP Conference Proceedings 819), New York, p 439
- Meitner L, Frisch OR (1939) Nature 143:239
- Metag V, Habs D, Specht HJ (1980) Phys Rep 65:1
- Möller P, Nix JR (1981) Nucl Phys A 461:117
- Möller P, Nix JR (1988) Atom Data Nucl Data 39:213
- Möller P, Nilsson SG, Sheline RK (1972) Phys Lett B 40:329
- Myers WD, Swiatecki WJ (1969) Ann Phys NY 55:385
- Nilsson SG (1955) Kgl Dan Vid Selsk Mat-Fys Medd 29(16)
- Pedersen J, Kuzminov BD (1969) Phys Lett B 29:176
- Polikhonov SM et al (1962) Sov Phys JETP 15:1016
- Rabotnov NS et al (1970) Sov J Nucl Phys 11:285
- Rauscher T, Thielemann FK, Kratz KL (1995) Phys Rev C 56:185
- Rauscher T, Thielemann FK, Kratz KL (1997) Phys Rev C 56:1613
- Royer G, Bonilla C (2007) J Radioanal Nucl Ch 272:237
- Rutz K, Maruhn JA, Reinhard P-G, Greiner W (1995) Nucl Phys A 590:680
- Shneidman TM et al (2000) Nucl Phys A 671:119
- Schmidt K-H et al (1994) Phys Lett B 325:313
- Sin M et al (2006) Phys Rev C 74:014608
- Sin M et al (2008) Phys Rev C 77:054601
- Specht HJ (1970) Habilitationsschrift, Univ. München
- Specht HJ, Fraser JS, Milton JC (1966) Phys Rev Lett 17:1187
- Specht HJ, Fraser JS, Milton JCD, Davies WG (1969) In: Proceedings of the symposium on physics and chemistry of fission. IAEA, Vienna, p 363
- Specht HJ, Weber J, Konecny E, Heunemann D (1972) Phys Lett B 41:43
- Spencer JE, Enge HA (1967) Nucl Instrum Meth 49:181
- Strutinsky VM (1967) Nucl Phys A 95:420
- Swiatecki WJ (1964) Proc Int Conf Nuclidic Masses, Vienna, 1963, Springer-Verlag, Vienna, pp 58–66
- Thirolf PG, Habs D (2002) Prog Part Nucl Phys 49:245
- Vandenbosch R, Huizenga J (1973) Nuclear fission. Academic, New York
- Vandenbosch R, Wolf KL, Unik J, Stephan C, Huizenga JR (1967) Phys Rev Lett 19:1138
- von Egidy T, Smidt HH, Behkami AN (1988) Nucl Phys A 481:189
- Wagemans C (1991) The nuclear fission process. CRC Press, Boca Raton
- Weizsäcker CFV (1935) Z Phys 96:431
- Zanotti E, Bisenberger M, Hertenberger R, Kader H, Graw G (1991) Nucl Instrum Meth A 310:706

6 Nuclear Fusion

G. Veres

KFKI Research Institute for Particle and Nuclear Physics, Budapest,
Hungary

6.1	<i>Introduction</i>	320
6.2	<i>Basics of Nuclear Physics</i>	321
6.3	<i>The Cross Section of the Coulomb (Rutherford) Scattering</i>	324
6.4	<i>The Elements of Plasma Physics</i>	326
6.5	<i>Nuclear Reactions and Reaction Rates in the Sun</i>	330

Abstract: This chapter is devoted to the fundamental concepts of nuclear fusion. To be more precise, it is devoted to the theoretical basics of fusion reactions between light nuclei such as hydrogen, helium, boron, and lithium. The discussion is limited because our purpose is to focus on laboratory-scale fusion experiments that aim at gaining energy from the fusion process. After discussing the methods of calculating the fusion cross section, it will be shown that sustained fusion reactions with energy gain must happen in a thermal medium because, in beam-target experiments, the energy of the beam is randomized faster than the fusion rate. Following a brief introduction to the elements of plasma physics, the chapter is concluded with the introduction of the most prominent fusion reactions ongoing in the Sun.

6.1 Introduction

Since the times of ancient civilizations, it has been known that the Sun plays a crucial role in sustaining life on Earth. The inevitable question regarding the source of the Sun's energy also arose very long ago.

Until the birth of nuclear science, only chemical reactions seemed to be available as candidates for the production of the heat that comes from the Sun. While this explanation was held correct, the age of the Earth was believed to be only a few thousand years, as chemical reactions alone would be capable of powering the Sun for only a few thousand years.

Einstein's theory about the equivalence of mass and energy opened the way for finding the real source of the Sun's power, namely nuclear reaction, or – more precisely – nuclear fusion.

The phenomenon called *nuclear fusion* (the merging of nuclei and/or nucleons) is a very broad and complex subject on its own and covers all physical and technological aspects of fusion between nuclei and/or nucleons regardless of whether it happens on the Earth, in a laboratory, or in distant stellar objects. Those aspects of fusion that are relevant to laboratory experiments are covered in this chapter. The processes going on in stellar objects are considered here if they are also relevant to terrestrial experiments.

At the present stage of controlled nuclear fusion experiments, exclusively light elements (isotopes of hydrogen, helium, boron, and lithium) are considered as possible fuel candidates for a future fusion power station; this chapter, therefore, deals only with fusion reactions between light elements. Moreover, this chapter is devoted only to the basics of physics, the technological aspects of the field being covered by [▶ Chap. 60 of Vol. 5](#).

One should emphasize that in stellar media, fusion between heavier elements is also of primary importance. The reader is advised to consult textbooks on astrophysics.

The basic structure of this chapter is as follows.

After a brief introduction to the nuclear physics of fusion (reaction types, cross sections, reaction rates), it is shown first that sustained nuclear fusion reactions with positive energy balance must also be thermonuclear, i.e., they should take place in a thermal medium. To be precise, the thermal medium where sustained fusion can and should take place is a special medium called *high temperature plasma*.

After an introduction to the elements of plasma physics, the chapter is concluded with the introduction of the most prominent fusion reactions going on in the Sun. After studying those reaction channels, one will be able to better understand the choice of the reactions to be used for terrestrial energy production.

Throughout the chapter, ε_0 denotes the permittivity of vacuum and k_B , the Boltzmann constant, and, of course, the SI system of units is used.

6.2 Basics of Nuclear Physics

As already shown in [Chap. 2](#) of this Volume, the average binding energy of a nucleon in a nucleus as a function of mass number has – for β -stable nuclei – a maximum at around the element iron. Consequently, unification (*fusion*) of two light nuclei can release energy. The energy released in the form of the kinetic energy of the particles in this process is exactly the mass difference between the initial nuclei and the final nucleus. Eventually, other particles (e.g., protons, neutrons, electrons, positrons, etc.) may also be borne in the reaction and thus influence the energy balance of the reaction.

It is obvious that many different reactions are possible between light nuclei. The list below summarizes only those possible combinations that are (or might be) relevant in terrestrial fusion applications. For the reactions that occur in the interior of stars (and so in the Sun), see [Sect. 6.5](#).

The following list summarizes the most prominent fusion reactions between light nuclei and the energies released in the reactions. The percentages represent branching ratios. Note that (as throughout this chapter) the element symbols below refer to bare nuclei without the electron shell – a special notation common in the field of fusion.

1. $D + t \rightarrow {}^4\text{He} + n + 17.6 \text{ MeV}$
2. $D + d \rightarrow T + p + 4.03 \text{ MeV}$ 50%
3. $\rightarrow {}^3\text{He} + n + 3.27 \text{ MeV}$ 50%
4. $D + {}^3\text{He} \rightarrow {}^4\text{He} + p + 18.5 \text{ MeV}$
5. $T + t \rightarrow {}^4\text{He} + 2n + 11.3 \text{ MeV}$
6. ${}^3\text{He} + {}^3\text{He} \rightarrow {}^4\text{He} + 2p + 12.9 \text{ MeV}$
7. ${}^3\text{He} + t \rightarrow {}^4\text{He} + p + n + 12.1 \text{ MeV}$ 51%
8. $\rightarrow {}^4\text{He} + D + 14.3 \text{ MeV}$ 43%
9. $\rightarrow {}^4\text{He} + n + p + 14.3 \text{ MeV}$ 6%
10. $D + {}^6\text{Li} \rightarrow 2 {}^4\text{He} + 22.4 \text{ MeV}$
11. $p + {}^6\text{Li} \rightarrow {}^4\text{He} + {}^3\text{He} + 4.0 \text{ MeV}$
12. ${}^3\text{He} + {}^6\text{Li} \rightarrow 2 {}^4\text{He} + p + 16.9 \text{ MeV}$
13. $p + {}^{11}\text{B} \rightarrow 3 {}^4\text{He} + 8.7 \text{ MeV}$

D refers to deuteron (${}^2\text{H}$) and T to triton (${}^3\text{H}$) in target or residual nucleus position, while d and t are the same, respectively, in projectile or ejectile position.

Without going into the details of the *nuclear interaction*, which governs the interaction of two colliding nuclei, the rather simple, qualitative picture given below is adequate to understand the most important points of the fusion process.

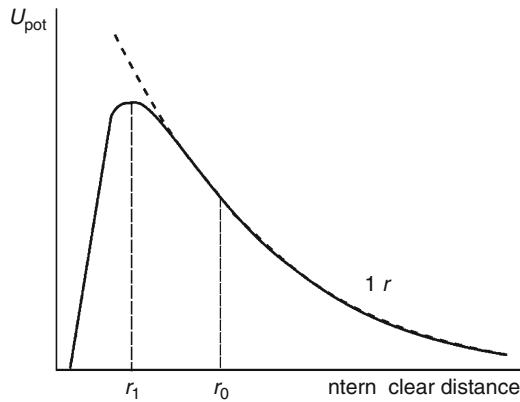
The two colliding nuclei have charges of identical (positive) sign, and so they experience a repelling Coulomb force when the distance between them is larger than some distance r_0 . At distances smaller than this r_0 , the nuclear interaction starts to come into play, and the force between the two nuclei gradually becomes attractive. The exact value of r_0 is dependent on the type of the fusing particles, but is approximately of the order of the nuclear radius, i.e., of a few femtometers.

[Figure 6.1](#) depicts the potential energy between two fusing nuclei as a function of the distance between them. The exact behavior of the potential is unknown near the nucleus but, at larger distances, it is Coulomb-like and decreases as the inverse of the distance. The potential barrier resulting from the two interactions is called the *Coulomb barrier*.

In his celebrated paper, George Gamow (Gamow 1928) had investigated the dynamics of the α -decay of heavy elements. Based on general quantum mechanical considerations, he had

■ Fig. 6.1

The qualitative behavior of the potential energy between two colliding nuclei as a function of the internuclear distance



derived an empirical formula that described the dependence of the decay constant on the energy of the α -particle.

Based on Gamow's investigations and the results of cross-section measurements done in the early 1940s mainly for the four most important reactions, $D(d, n)^3\text{He}$, $D(d, p)\text{T}$, $D(t, n)^4\text{He}$ and $^3\text{He}(d, p)^4\text{He}$, two approximate representations of the fusion cross sections have been proposed and widely used ever since. One of these representations, which is also listed in the NRL Plasma formulary (Huba 2009), was derived by Duane (1972) and the other by Peres (1979). Duane's cross sections pose particular difficulties if they are extrapolated to energies below about 20 keV because of the unphysical parameterization of the penetrabilities that was used. In general, both approximations as well as the corresponding parameterizations for the Maxwellian reactivity $\langle\sigma v\rangle$ (where σ is the cross section and v is the speed) calculated by Hively (1977, 1983) (on the basis of Duane's cross-section formula) and by Peres (1979) need to be improved (Bosch and Halle 1992) mainly for two reasons:

1. While in the past the detection of fusion reaction products was used as a qualitative measure for the success of the thermonuclear fusion experiment, modern fusion experiments use the measured fusion rates as plasma diagnostic tools. If people want to draw reliable conclusions about the plasma parameters from these measurements, detailed knowledge of the fusion cross sections becomes more important than ever.
2. As the experimental devices become larger from one generation to the next, it becomes increasingly more important for the design to predict their behavior reliably. Among other parameters, the fusion rate in these plasmas must be determined accurately. In addition, for reactor design and blanket studies, it is necessary to know the energy dependence of the fusion cross sections with the greatest possible precision.

The proposed improvements, however, did not alter the very basics of how the cross sections are parameterized, and therefore, for the sake of simplicity, the analysis of Peres is followed here.

As said earlier, when a nucleus approaches another one, at large distances they feel each other's Coulomb force, and at short distances they also feel the nuclear force. If the energy of

the collision is not enough to overcome the Coulomb barrier (most collisions are such), quantum mechanical tunneling is the only available channel for fusion. It is thus expected that the nature and energy dependence of fusion cross sections will be influenced by both phenomena: electrostatics and nuclear physics.

Quantum mechanics shows that the fusion reaction probability is also proportional to a geometrical factor $\pi\lambda^2 \propto 1/E$, where λ in this context is the de Broglie wavelength. The strong energy dependence of this factor and the barrier penetrability have prompted the introduction of the astrophysical S -function (Burbidge et al. 1957), defined by writing the cross section as a product of three factors:

$$\sigma(E) = S(E) \frac{1}{E} \exp\left(-\frac{B_G}{\sqrt{E}}\right). \quad (6.1)$$

The motivation for this definition is that the two well-known, strongly energy-dependent factors (which describe the Coulomb and velocity space parts of the incident channel) are separated, leaving the S -function to represent mainly the presumably slowly varying nuclear part of the fusion reaction probability.

This form of the cross section is the extrapolation of the original Gamow formula,

$$\sigma(E) = \frac{A(E)}{E[\exp(B_G/\sqrt{E}) - 1]} \quad (6.2)$$

to low energies, where $A(E) \equiv S(E)$ is a slowly varying function of the center-of-mass energy E and

$$B_G = \pi\alpha Z_1 Z_2 (2m_{\text{cm}} c^2)^{1/2} \quad (6.3)$$

is the *Gamow factor* for nuclei of charges Z_1 and Z_2 and reduced mass m_{cm} , expressed in terms of the fine structure constant $\alpha = e^2/\hbar c$.

The S -functions for the four reactions – $\text{D}(\text{d}, \text{n})^3\text{He}$, $\text{D}(\text{d}, \text{p})\text{T}$, $\text{D}(\text{t}, \text{n})^4\text{He}$, and $^3\text{He}(\text{d}, \text{p})^4\text{He}$ – shown in [Fig. 6.2b](#) demonstrate very clearly the advantages of using the S -functions instead of the cross sections themselves ([Fig. 6.2a](#)):

1. The S -function describes mainly the intrinsic nuclear physics of the reaction and therefore shows clearly the difference between the reactions considered here. The $\text{D} + \text{d}$ reactions do not have resonances close to the threshold, resulting in weak energy dependence, while the other two reactions involve a near-threshold resonance. This is very evident in the S -function, while in the cross section it is masked by the strong energy dependence of the penetrability of the Coulomb barrier.
2. In all cases, the S -functions only vary by a factor of 20 over the whole energy range shown here, rather than by several orders of magnitude as the cross sections do. Therefore, it is much easier to calculate a fit to the experimental data.

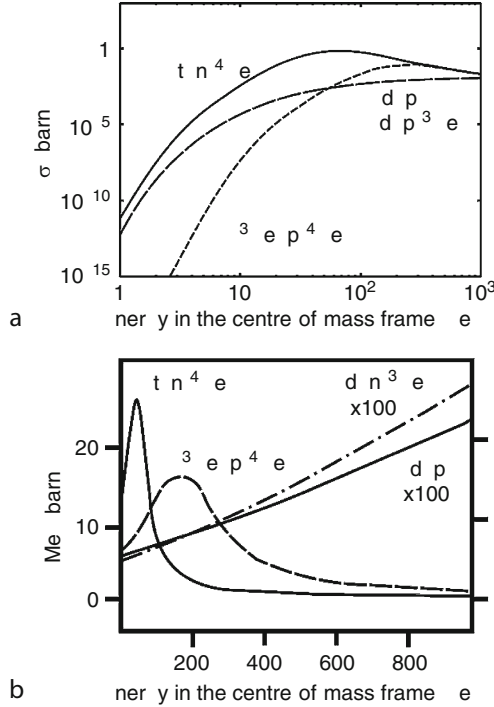
If an analytic fit to the measured cross-section data is available, the reaction rates $\langle\sigma v\rangle$ (Maxwellian averages) can easily be calculated for *weak plasma coupling* approximation as

$$\langle\sigma v\rangle = \text{Const.} \times T^{-\frac{3}{2}} \int_0^\infty E \sigma(E) \exp(-E/k_B T) dE. \quad (6.4)$$

For *strongly coupled plasmas*, an appropriate enhancement factor must be introduced. [Figure 6.3](#) shows, again, for the most important fusion reactions, the energy dependence of the Maxwellian averaged fusion reaction rate.

■ Fig. 6.2

(a) Fusion cross sections for the most important fusion reactions as a function of the center-of-mass energy of the reacting particles. The curves are calculated from the Peres formula (Peres 1979). (b) The S -functions for these reactions as derived from Eq. (6.1). For the $D + d$ reactions, the ordinate values have been multiplied by 100 to improve visibility



6.3 The Cross Section of the Coulomb (Rutherford) Scattering

In nuclear physics, the low-energy collision of two nuclei with positive charges, governed by the Coulomb interaction, is called Rutherford scattering. In this chapter, the identical term *Coulomb scattering* is used, which is more common in plasma physics.

As has already been pointed out in the Introduction, self-sustained fusion reactions with positive energy balance must happen in a thermal medium. This statement can be justified by comparing the effective cross section of individual Coulomb scattering to the fusion cross section.

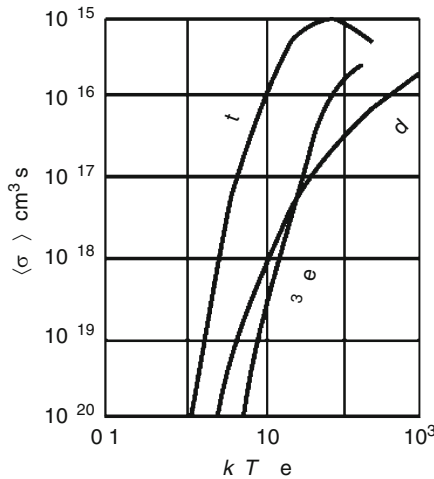
Due to the long range of the Coulomb interaction, the definition of the collision cross section requires some attention. By solving coupled equations for the conservation of energy and momentum for two colliding particles of identical charge, the deflection angle φ can be obtained as a function of the collision parameter b as follows:

$$\tan \frac{\varphi}{2} = \frac{q_T q_P}{4\pi\epsilon_0 b m v_0^2}. \quad (6.5)$$

Here q_T and q_P are charges of the target and the projectile, m is the reduced mass, and v_0 is the relative velocity in the center-of-mass frame. It is clear that small collision parameters

■ Fig. 6.3

The dependence of the fusion reaction rate on the plasma temperature



correspond to large deflection angles, and large collision parameters to small deflection angles. Collision parameter zero corresponds to *central collision*, and there is a well-defined collision parameter called $b_{\pi/2}$ that corresponds to $\pi/2$ deflection angle. It is a bit arbitrary, but collisions with collision parameters smaller than $b_{\pi/2}$ are called *large-angle collisions*, and collisions with collision parameters larger than $b_{\pi/2}$ are called *small-angle collisions*.

A large angle collision event resulting in 90° deflection can happen not only in a single large-angle collision with $b < b_{\pi/2}$ but also as a consequence of a series of small-angle scattering events. The cross section corresponding to a single large-angle scattering is simply $\sigma_{\text{large}} \approx \pi b_{\pi/2}^2$. It is easy to show (Bellan 2006) that the σ^* cumulative cross section corresponding to the series of small-angle scattering events that result in the same 90° deflection as in a single large-angle event is:

$$\sigma^* = 8 \ln \left(\frac{\lambda_{\text{De}}}{b_{\pi/2}} \right) \sigma_{\text{large}} = 8 \ln(\Lambda) \sigma_{\text{large}}. \quad (6.6)$$

Here λ_{De} is the electron Debye length – a distance at which the diverging integral for the Coulomb cross section must be cut off – and Λ is the plasma parameter. For the physical meaning of the Debye length and an explanation of the plasma parameter, see the next section. In a solid, a liquid, or a gas, the cut-off length for the integral (λ_{De}) is the size of the atom, at which the electron cloud shields the Coulomb potential. In plasmas, this distance can be considerably larger, but as this parameter is included logarithmically, the effect is not dramatically different.

The name of the expression $\ln(\Lambda)$ is *Coulomb logarithm*. Depending on the values of the parameters in Eq. (6.6), the cumulative small-angle cross section can be much larger than the cross section that corresponds to a single large-angle scattering.

The cross section in the center-of-mass frame of the Coulomb scattering (cumulative or large angle) is inversely proportional to the fourth power of the relative velocity of the two colliding particles.

The Coulomb scattering cross section at the energy where the fusion cross section has its maximum is estimated as follows. The maximum cross section of the $D(t, n)^4\text{He}$ reaction (see ► Fig. 6.2) is at around 100 keV and has a value of the order of 1 barn = 10^{-28} m^2 . At 100-keV center-of-mass energies, the large-angle Coulomb scattering cross section (see ► Eq. (6.6)) is around 10 barns. Depending on the value of the Coulomb logarithm – that varies from neutral atoms to plasmas between 10 and 20 – the total Coulomb scattering cross section exceeds the fusion cross section by at least a factor of 1,000.

In principle, if the energy released in a single fusion event were 1,000 times the beam energy, one could make an energy multiplication of the order of unity, even if the Coulomb scattering cross section was so large. However, since the energy released per fusion event is only 100–200 times the beam energy, the beam-target scheme cannot be used for energy production.

There is only one way to overcome this problem. Since it is not possible to increase the released energy per fusion event, the effect of the Coulomb scattering must be mitigated. This happens when the energy distribution of the colliding particles is thermal, in which case collisions do not represent an energy loss. For the energies required for fusion, this means plasma state as the binding energy of electrons on the nuclei is several orders of magnitude lower than the energies required for fusion. In these high-temperature plasmas, Coulomb scattering only redistributes the energy between the particles, and any particle can take part in a fusion event, unlike in a beam-target experiment, where only beam particles have enough energy to react with the target particles.

Before proceeding further, some elements of plasma physics must be introduced along with a few figures of merit that describe a high-temperature ensemble of charged particles (plasma). Readers interested in more details than given below may refer to textbooks on the subject (Bellan 2006; Freidberg 2007; Fitzpatrick 2008).

6.4 The Elements of Plasma Physics

Plasma is an ensemble of charged (and possibly neutral) particles. For a medium to qualify to be plasma, it is of crucial importance that the coupled interactions of its charged constituents dominate the behavior of the whole system. In plasmas, the particles move freely around, in a sense that their motion is only influenced by electromagnetic fields – both external and generated by the plasma particles themselves – and the species are not bound to any special place in the space, unlike the atoms in a solid lattice or the electrons bound to a molecule. This is because the temperature of plasmas is sufficiently high, so that the thermal motion of the particles is so intense that atoms can leave their fixed positions and electrons can be stripped off (fully or partly) from the atoms.

In *fully ionized plasmas*, there are only electrons and ions, but not all the electrons are necessarily stripped off the atoms – ions of different states of ionization may be present in the plasma at the same time. In *partially ionized plasmas* electrons, ions, and neutral atoms coexist. In this chapter, the different particles (atoms, electrons, and ions of different types and charges) are denoted by σ .

Plasmas are macroscopically neutral, and since the particles are free to move in the plasma, any excess charge is screened at some spatial distance via the modification of charge densities. This eventually means that the vacuum Coulomb potential of charged particles is modified,

namely the fall-off of the potential changes from $\sim 1/r$ in a vacuum to $\sim (1/r) \times \exp(-r/\lambda_D)$, where

$$\lambda_D = \left(\sum_{\sigma} \frac{1}{\lambda_{\sigma}^2} \right)^{-1/2} \quad (6.7)$$

is the so-called *Debye length*, which is a function of the individual Debye lengths of particles σ :

$$\lambda_{\sigma} = \left(\frac{\epsilon_0 k_B T_{\sigma}}{n_{\sigma} q_{\sigma}^2} \right)^{1/2}. \quad (6.8)$$

Here, n_{σ} is the number density (number of particles per unit volume), T_{σ} is the temperature, and q_{σ} is the charge of species σ . The decrease with the distance of the actual potential in plasmas is much faster than in a vacuum, such that

$$\varphi(\mathbf{r}) = \frac{q_T}{4\pi\epsilon_0 r} \exp(-r/\lambda_D). \quad (6.9)$$

Here, q_T is the charge of a test particle, and r is the distance measured from it. This expression essentially means that outside the distance given by the Debye length (i.e., outside the *Debye sphere*), any excess electric charge is completely screened, and internal as well as external electrostatic fields must vanish. Although hidden in the derivation of the Debye length, it is still very important that the test particles are much slower than the plasma particles, and so even the heaviest and slowest plasma particles have enough time to contribute to the screening.

The Debye length is one of the most important figures of merit that characterizes plasmas.

Another important quantity is the *plasma parameter*. This parameter virtually quantifies the intensity of electrostatic interaction between the plasma particles relative to their kinetic energy.

The average distance between the particles of type σ is defined as:

$$r_D \equiv n_{\sigma}^{-1/3}. \quad (6.10)$$

The distance of closest approach between two particles of the same kind can be obtained as:

$$r_C \equiv \frac{q_{\sigma}^2}{2\pi\epsilon_0 k_B T_{\sigma}}. \quad (6.11)$$

This relationship is derived from the fact that, at the distance of the closest approach, all energy of the two-particle system is potential energy.

The ratio r_C/r_D plays a crucial role in the description of plasmas. When this ratio is small, charged particles are dominated by one another's electrostatic influence more or less continuously, because many particles are inside the virtual sphere available for a particle, and their kinetic energies are small compared to the interaction potential energies. Such plasmas are termed *strongly coupled*. On the other hand, when this ratio is large, strong electrostatic interactions between individual particles are occasional and relatively rare events. A typical particle is electrostatically influenced by all of the other particles within its Debye sphere, but this interaction very rarely causes any sudden change in its motion. Such plasmas are termed *weakly coupled*.

Based on the concepts of these two special distances for the electrons (r_C and r_D), the following definition of the plasma parameter is straightforward:

$$\Lambda = 4\pi n_e \lambda_e^3. \quad (6.12)$$

Here, n_e and λ_e refer to the electron number density and electron Debye length, respectively. The meaning of the plasma parameter is clear: if it is large, then the Debye sphere is heavily populated (this is the case of the weakly coupled plasma), whereas if it is small, then the Debye sphere is only sparsely populated and the plasma is strongly coupled. Some authors define the plasma parameter as 1/3 of the value in [Eq. \(6.12\)](#). In this case, the plasma parameter is exactly the number of particles inside the Debye sphere, whereas in the definition given by [Eq. \(6.12\)](#), it is only proportional to it. The plasma parameter is defined for the electrons only. One could, in principle, define a plasma parameter for the ions also, but that is not common.

After recasting [Eq. \(6.12\)](#) one obtains:

$$A = \frac{1}{\sqrt{4\pi}} \left(\frac{r_D}{r_C} \right)^{3/2} = \frac{\sqrt{2\pi}\epsilon_0^{3/2} (k_B T_e)^{3/2}}{q_e^3 n_e^{1/2}}. \quad (6.13)$$

It can be inferred from [Eq. \(6.13\)](#) that strongly coupled plasmas tend to be cold and dense, whereas weakly coupled plasmas are diffuse and hot. Examples of strongly coupled plasmas include solid-density laser ablation plasmas, the very “cold” (i.e., with kinetic temperatures similar to the ionization energy) plasmas found in “high pressure” arc discharges, and the plasmas which constitute the atmospheres of collapsed objects such as white dwarfs and neutron stars. On the other hand, the hot diffuse plasmas – typically encountered in ionospheric physics, astrophysics, nuclear fusion, and space plasma physics – are invariably weakly coupled.

Another expression that shows the meaning of the plasma parameter very clearly is:

$$\frac{k_B T}{E_{\text{Coulomb}}} = 4\pi (n_\sigma \lambda_D^3)^{2/3}. \quad (6.14)$$

In strongly coupled plasmas (small $n_\sigma \lambda_D^3$), the Coulomb energy dominates, whereas in weakly coupled plasmas (large $n_\sigma \lambda_D^3$), the kinetic energy of the particles dominates.

A subtle but important point in the above introduction of the plasma parameter is that its expression with the Debye radius is only valid as long as the Debye radius has a meaning at all. The above introduction of the Debye radius is valid if the number of particles inside the Debye sphere is “statistically significant,” and this number does not fluctuate “too much.” If there are very few particles inside the Debye sphere, and so the plasma is very strongly coupled, the above formulas must be modified. Very strongly coupled plasmas, however, are outside the scope of this chapter.

As an illustration, [Table 6.1](#) lists the key parameters for some typical plasmas, both terrestrial and celestial. The temperatures in the table, as customary in plasma physics, are expressed in electron volts using the correspondence $E = k_B T$.

In the rest of this section, some further elements of plasma physics are introduced, which are not directly necessary to follow the content of this chapter, but essential for the understanding of a later one ([Chap. 60 of Vol. 5](#)).

The *plasma frequency* is a figure of merit of plasmas worth mentioning:

$$\omega_p = \left(\sum_{\sigma} \omega_{p\sigma}^2 \right)^{1/2}. \quad (6.15)$$

As in the case of the Debye length, the plasma frequency ω_p is a function of plasma frequencies $\omega_{p\sigma}$ of individual particles of type σ .

$$\omega_{p\sigma} = \left(\frac{n_\sigma q_\sigma^2}{\epsilon_0 m_\sigma} \right)^{1/2}. \quad (6.16)$$

The plasma frequency arises from the fact that in plasmas, the densities of different charged particle fluids are coupled through emerging electrostatic forces. When charge neutrality is locally broken, a restoring force appears and an oscillation in particle densities arises with the plasma frequency. The electron plasma frequency ω_{pe} is the frequency of electron oscillations in a zero-temperature homogeneous plasma. In homogeneous nonmagnetized plasma, this oscillatory motion is capable of screening electric fields; therefore, electromagnetic waves (light) cannot propagate below the plasma frequency.

In controlled fusion experiments, as well as in astrophysics, magnetized plasmas play a very important role. Plasmas are said to be magnetized if the plasma is “immersed” into an equilibrium external magnetic field.

Charged particles move quite differently in a magnetized plasma than in a not magnetized medium. This is because they can only move freely along the field lines of the magnetic field. In the perpendicular direction, they gyrate around the field lines and no net perpendicular motion is present in zero order. Their motion can be described as follows.

The Lorentz equation for the movement of a particle of charge q and mass m in an electric field of strength \mathbf{E} and magnetic field of flux density \mathbf{B} is

$$m\dot{\mathbf{v}} = q(\mathbf{E} + \mathbf{v} \times \mathbf{B}). \quad (6.17)$$

If there is no electric field and the magnetic field is homogeneous, then the particle's gyration frequency around the magnetic field lines is $q|\mathbf{B}|/m$ along the perimeter of a circle with radius $m v_\perp / q|\mathbf{B}|$. Here, v_\perp is the component of the velocity perpendicular to the magnetic

■ Table 6.1

Some key plasma parameters for typical laboratory and celestial plasmas. Numbers are correct to only orders of magnitude

	Number density (m^{-3})	Temperature (eV)	λ_D (m)	Λ	Spatial size (m)
Solar corona	10^{15}	10^2	10^{-3}	10^7	10^8
Solar wind	10^7	10	10	10^9	10^8
Sun's core	10^{32}	10^3	10^{-11}	10	10^5
Earth's ionosphere	10^{11}	10^{-1}	10^{-2}	10^4	10^5
Magnetic fusion	10^{20}	10^4	10^{-4}	10^9	10
Inertial fusion	10^{31}	10^4	10^{-10}	10^2	10^{-5}
Dense laboratory plasma	10^{20}	1	10^{-6}	10^3	10^{-1}
Dilute laboratory plasma	10^{16}	1	10^{-4}	10^5	10^{-1}

field. The gyration frequency (gyrofrequency or *cyclotron frequency*) and the gyration radius (*Larmor radius*) are the two most important parameters that characterize magnetized plasmas.

If there is an electric field and/or the magnetic field is not quite homogeneous (however, the scale length of the inhomogeneity cannot be shorter than the Larmor radius), then there is a slow drift motion of the center of the Larmor circle in the direction perpendicular to both the direction of the inhomogeneity and the magnetic field. The value of this drift velocity is:

$$\mathbf{v}_{\text{drift}} = \frac{\mathbf{E} \times \mathbf{B}}{B^2} - \frac{mv_{\perp}^2}{2qB^3} \nabla |\mathbf{B}| \times \mathbf{B} + \frac{mv_{\parallel}^2}{qB^2} \boldsymbol{\kappa} \times \mathbf{B}, \quad (6.18)$$

where the first term is due to the electric field (**EcrosB drift**), the second term is due to the change in the magnitude of the magnetic field (**gradB drift**), and the third term is due to the curvature $\boldsymbol{\kappa}$ of the magnetic field (*curvature drift*).

To describe a plasma via the calculation of the paths of individual particles by solving the Lorentz equation would be not only computationally impossible, but also inadequate, as plasmas are *collective* ensembles of charged particles and one needs a set of equations that is capable of describing this collective character. One such set of equations is the equations of *magnetohydrodynamics (MHD)*. The three most important equations of MHD are the continuity equation, describing the advection of the mass density ρ with velocity \mathbf{U}

$$\frac{\partial}{\partial t} \rho + \nabla \cdot (\rho \mathbf{U}) = 0, \quad (6.19)$$

the equation of motion describing the advection of the momentum density $\rho \mathbf{U}$

$$\rho \left(\frac{\partial}{\partial t} \mathbf{U} + \mathbf{U} \cdot \nabla \mathbf{U} \right) = \mathbf{J} \times \mathbf{B} - \nabla P, \quad (6.20)$$

and the equation of state describing the advection of the pressure P

$$\frac{\partial}{\partial t} P + \mathbf{U} \cdot \nabla P = -\gamma P \nabla \cdot \mathbf{U}. \quad (6.21)$$

Here, γ is the adiabatic constant (the ratio of the specific heats) and \mathbf{J} is the electric current density flowing through the plasma.

After this small bypass into plasma physics, the journey can be continued toward the Sun.

6.5 Nuclear Reactions and Reaction Rates in the Sun

The conditions in the interior of the stars are quite different from those that scientists want to create inside a controlled fusion experiment on the Earth. In this section, only processes occurring in the core of lower branch main-sequence stars (like the Sun) will be dealt with. Stars of the upper branch of the main sequence are out of the scope of this article, not to mention Giants of different size and Dwarfs of different color.

When comparing a star with a terrestrial device of any kind, the most striking difference is in their size: stars are many million times more massive than anything humans can build. Consequently, gravity is the main force that confines the plasma inside a star.

The second very important difference is that stars must continuously produce energy for some billion years, whereas in a power plant steady state energy production is foreseen only for

days or maybe months. This comment is important because the cross sections of the reactions introduced in ▶ Sect. 6.2, although not as large as desired, are far too large to sustain the energy production in the stars. A star would simply burn out in some million years if it used a D–T mixture.

Stars of mass comparable to that of the Sun burn their fuel during most of their lives in two ways. One way involves the simplest hydrogen isotope, the proton, and the sequence of reactions is called the *proton–proton (p–p) chain* or *proton–proton cycle*. The other way uses ^{12}C isotopes as “catalysts” and is called the *carbon–nitrogen–oxygen (CNO) cycle*. Both reaction cycles are advantageous, because they involve a beta-decay event, and so the fusion rate is low enough for the fusion fuel to last for billions of years. The end product of both the proton–proton and the CNO cycle is ^4He because, compared to its neighbors in the chart of nuclides, ^4He is the most deeply bound.

In the case of the Sun, around 98% of the power comes from the p–p chain and only the remaining 2% from the CNO cycle.

▶ Figure 6.4 shows a block diagram of the complete p–p chain. As can be seen, there are several branches of the chain, with the most probable chain on the left-hand side.

▶ Table 6.2 shows the main reactions of the CNO cycle. Note the reactions that involve beta decay (those that involve an electron or a positron).

■ Fig. 6.4

The complete proton–proton chain with all its branches. This chain is the main source of energy in the stars of mass comparable to that of the Sun

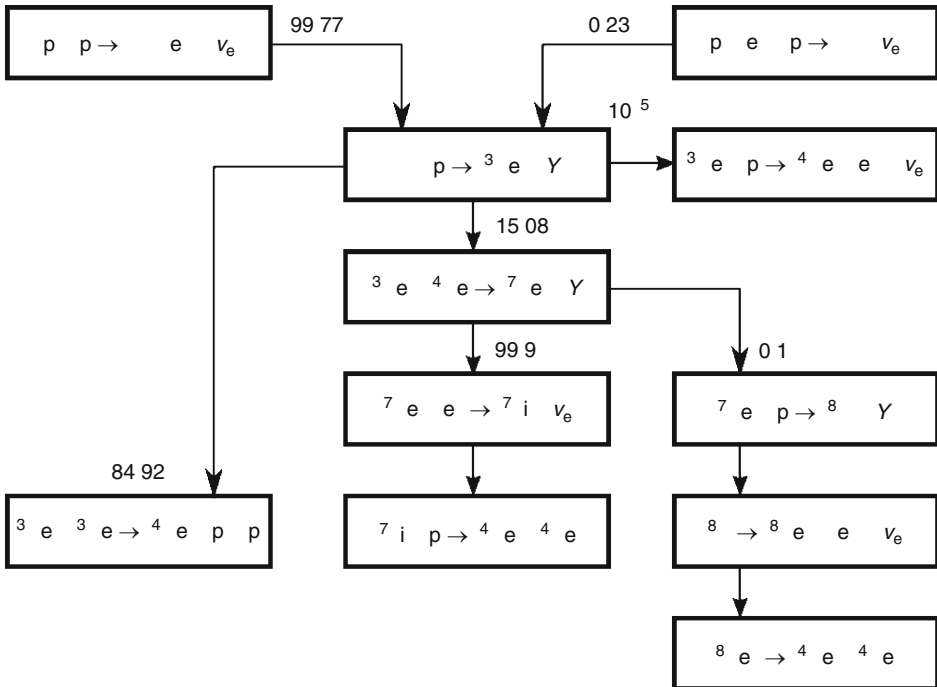


Table 6.2

Main reactions of the CNO cycle

^{12}C	+	p	\rightarrow	^{13}N	+	γ			+	1.95 MeV
^{13}N			\rightarrow	^{13}C	+	e^+	+	ν_{e}	+	2.22 MeV
^{13}C	+	p	\rightarrow	^{14}N	+	γ			+	7.54 MeV
^{14}N	+	p	\rightarrow	^{15}O	+	γ			+	7.35 MeV
^{15}O			\rightarrow	^{15}N	+	e^+	+	ν_{e}	+	2.75 MeV
^{15}N	+	p	\rightarrow	^{12}C	+	^4He			+	4.96 MeV

None of these reaction chains is suitable for terrestrial applications, because the reactions rates are so small that the maximum power that can be extracted from the plasma even in an optimum situation is only a few hundred milliwatts.

Acknowledgments

The author would like to thank Dr. S. Zoletnik for valuable discussions and hints.

References

Bellan PM (2006) Fundamentals of plasma physics. Cambridge University Press, Cambridge

Bosch H-S, Halle GM (1992) Nucl Fusion 32:611

Burbidge EM, Burbidge GR, Fowler WA, Hoyle F (1957) Rev Mod Phys 29:547

Duane BH (1972) Fusion cross section theory, Report BNWL-1685. Brookhaven National Laboratory

Fitzpatrick R (2008) The physics of plasmas. Lulu Publishing

Freidberg JP (2007) Plasma physics and fusion energy. Cambridge University Press, Cambridge

Gamow G (1928) Zeitschrift für Physik 56:204

Hively LM (1977) Nucl Fusion 17:873

Hively LM (1983) Nucl Technol/Fusion 3:199

Huba JD (2009) NRL plasma formulary. Naval Research Laboratory, Washington

Peres A (1979) J Appl Phys 50:5569

7 Kinetics of Radioactive Decay

S. Nagy

Eötvös Loránd University, Budapest, Hungary

7.1	<i>The Exponential Law of Decay</i>	334
7.1.1	Phenomenological Approach	334
7.1.2	Stochastic Approach	336
7.2	<i>Independent Decays: Radionuclide Mixtures</i>	338
7.3	<i>Branching Decays</i>	338
7.4	<i>Successive Processes</i>	342
7.4.1	General Kinetics of Decay Chains	342
7.4.2	Radioactive Equilibrium and Nonequilibrium	346
7.4.3	Decay After Activation	352
7.5	<i>Decay Constant (Half-Life) Systematics</i>	353
7.5.1	Alpha Decay	354
7.5.2	Beta Decay	356
7.5.3	Gamma Decay	359
7.5.4	Spontaneous Fission	361
7.6	<i>Editors' Note</i>	362

Abstract: At present there are over 3,000 known nuclides (see the [Appendix in Vol. 2](#) on the “Table of the Nuclides”), 265 of which are stable, while the rest, i.e., more than 90% of them, are radioactive. The chemical applications of the specific isotopes of chemical elements are mostly connected with the latter group, including quite a number of metastable nuclear isomers, making the kinetics of radioactive decay an important chapter of nuclear chemistry. After giving a phenomenological and then a statistical interpretation of the exponential law, the various combinations of individual decay processes as well as the cases of equilibrium and nonequilibrium will be discussed. Half-life systematics of the different decay modes detailed in [Chaps. 2](#) and [4](#) of this volume are also summarized.

7.1 The Exponential Law of Decay

7.1.1 Phenomenological Approach

The most fundamental quantity of radioactive decay is the activity A , meaning the number of atoms decaying in the specimen per time.

Historical units of activity. The formerly used unit of radioactivity – the curie (Ci) – was introduced in 1930. One curie was originally defined as the disintegration rate of 1 gram of pure ^{226}Ra . Radium was chosen as a reference because of its then importance among radioactive elements. However, it was rather disturbing that the value of the unit had to be changed from time to time as more accurate data were obtained for the decay of radium. Finally, the value of curie was fixed arbitrarily at 3.7×10^{10} disintegrations per second (1950). (During the 1930s, another unit: 10^6 disintegrations per second – called rutherford – was also suggested but it has never become widely known.)

SI unit of activity. Since 1975, the internationally recommended unit is the becquerel (Bq) defined as 1 disintegration per second (1 dps), but workers in nuclear and radiochemistry, especially those handling high activities, still stick to the old unit curie. Some authors prefer the notation “dps” to Bq and the acronym “dpm” (meaning decays per minute) also occurs as a unit of activity.

Intensive quantities related to the activity. In most samples, the radionuclides are not carrier free but inactive isotopes “carry” them and/or an inactive substance called matrix contains them. (The term no-carrier-added or n.c.a. only means that the production process of a radionuclide sample does not involve adding carrier to it. However, it may not be carrier free.) The specific activity of a radioactive sample is defined as the (absolute) activity of the radioactive sample divided by its mass (unit: Bq/kg). Similar quantities are the molar activity (unit: Bq/mol) and the activity concentration (unit: Bq/dm³), defined as the activity of the sample divided by its molar amount and volume, respectively.

Note that the term ‘specific activity’ is also used in the sense of the activity caused by a radioisotope of an element in a sample per the total mass of the element (or a compound of it) contained by the sample. Some authors use the term “specific radioactivity” in the sense of molar activity, although according to International Union of Pure and Applied Physics (IUPAP) and International Union of Pure and Applied Chemistry (IUPAC) recommendations the adjective “specific” should be reserved for naming quantities that are divided by mass. So the use of the term in the latter sense should be avoided.

Basic equations of activity. The activity A , being the measure of disintegration rate, is related to the number of radioactive atoms N through the following expression:

$$A = -\frac{\Delta N}{\Delta t} \approx -\frac{dN}{dt}, \quad (7.1)$$

where Δt is the observation period and $|\Delta N|$ is the number of atoms that have decayed during Δt .

It has been shown in the above equation that if Δt as well as $|\Delta N|/N$ are small enough – if a large number of atoms is observed in a short time interval – then $N(t)$ can be considered as a “smooth” enough function for which the ratio $\Delta N/\Delta t$ can be replaced by the derivative dN/dt .

Radioactive decay usually produces radiation particles (α , β) or photons (γ) that can be detected with some probability. Under favorable conditions, the observed activity A' thus determined will be proportional to the actual activity (also called absolute activity) A :

$$A' = \eta A, \quad (7.2)$$

where η (≤ 1) is the efficiency of detection.

It is also an empirical fact that if there are a larger number of atoms (e.g., if a large sample is prepared from the same homogeneous radioactive material), then the activity will be proportionally larger. Therefore, for a given type of radionuclide it can be written

$$A = \lambda N, \quad (7.3)$$

where the factor λ (dimension: 1/time; unit: s^{-1}) is called the decay constant.

Note that according to [Eq. \(7.3\)](#) the quantity of a radionuclide can be specified by its activity. (This is the “theoretical” background of the common practice that radioactive sources are sold/bought by the megabecquerel or millicurie.)

Determination of the decay constant. The above equation, combined with [Eq. \(7.2\)](#), also serves as a basis for the determination of the decay constant of long-lived radionuclides having very long half-lives (see [Eq. \(7.17\)](#)), which means that neither their activity nor their number is expected to change appreciably within a reasonable period of time that can be spent for their observation:

$$\lambda = \frac{A}{N} = \frac{A'}{\eta N}. \quad (7.4)$$

Comparing [Eqs. \(7.1\)](#) and [Eq. \(7.3\)](#) one gets

$$\frac{dN}{dt} = -\lambda N, \quad (7.5)$$

which is essentially the same differential equation that is characteristic of first-order reactions in chemistry with λ playing the role of the rate constant.

The solution of [Eq. \(7.5\)](#) yields the formula generally referred to as the exponential law of radioactive decay:

$$N = N(0)e^{-\lambda t}, \quad (7.6)$$

where $N(0)$ is the number of radioactive atoms present at $t = 0$.

Multiplying [Eq. \(7.6\)](#) by λ and then by η , and comparing the results with [Eqs. \(7.3\)](#) and [Eq. \(7.2\)](#) one finds that the same type of exponential law holds for the activities as well:

$$A = A(0)e^{-\lambda t}, \quad (7.7)$$

$$A' = A'(0)e^{-\lambda t}. \quad (7.8)$$

Note that [Eq. \(7.8\)](#) is especially useful for the determination of the decay constant of radionuclides with medium half-lives, i.e., whenever it is possible to “sit out” the change of activity, because observed activities are a lot easier to measure than either (absolute) activities or numbers of atoms (of specific nuclides). The latter is unavoidable, e.g., in the case of long-lived radionuclides when the determination of λ can only be done by using [Eq. \(7.4\)](#).

In the case of extremely short half-lives, the starting point of decay-constant determination is still something like [Eq. \(7.8\)](#), but special tricks/equipment (coincidence circuit, time-to-amplitude converter, multichannel analyzer) as well as special conditions (available start and stop signals informing of the “birth” and “death,” respectively, of individual nuclei/particles) are also needed. The waiting-time distribution shown in [Fig. 9.13 of Chap. 9 in Vol. 1](#) has also been obtained with such an apparatus, which is the standard equipment of Positron Annihilation Spectroscopy (PAS) measurements (see [Chap. 27 in Vol. 3](#)).

In olden times the lifetime distribution of short-lived nuclides was measured without a multichannel analyzer using the method of delayed coincidences. In this case, the start signals were delayed and the coincidence rate was plotted against the time of delay. The resulted graph showed the characteristic features of the exponential law, from which the decay constant could be determined by calculating the slope of the semilogarithmic (semilog) plot.

In the case of man-made chemical elements (e.g., transactinides) a different type of problem arises, namely, the number of decays that can be observed is just not enough to measure out the exponential law because only a couple of like atoms are produced at a time. The determination of the decay constant – or, more directly, that of the mean-life (see [Eq. \(7.18\)](#)) – in such a case can be performed by the method explained in [Sect. 19.3.4 of Chap. 19, Vol. 2](#). Some statistical background to this type of analysis is given in remark (#33), [Sect. 9.3.4, Chap. 9](#) in this volume.

There is another problem with man-made chemical elements, namely that their isotopes are short lived too. This, together with the need for their identification, calls for fast separation methods. The Automated Rapid Chemistry Apparatus (ARCA) II system and the Short-lived Isotopes Studied by the AKUFVE-technique (SISAK) equipment (both described in [Sect. 59.2.2 of Chap. 59, Vol. 6](#), on “Solvent Extraction and Ion Exchange in Radiochemistry”) are able to handle radionuclides with half-lives of ~ 10 s and ~ 1 s, respectively.

7.1.2 Stochastic Approach

The connection between the exponential law and some of the special distributions – binomial, Poisson, and exponential – will be detailed later in [Chap. 9](#), “Stochastics and Nuclear Measurements.” However, a simple illustration of the stochastic features will also be given here.¹

Consider a single radioactive atom of some kind. Let p denote the probability that it will disintegrate within a certain observation period Δt . Suppose that the atom is ageless in the sense that p is independent of how long it had existed before its observation was started. It stands to reason that the chance of decay increases with the length of the observation period. Moreover, it also seems reasonable to assume that for short enough Δt there is a proportionality

$$p = \lambda \Delta t, \quad (7.9)$$

where the proportionality constant λ only depends on the type of the atom (or, more specifically, on its readiness to decay).

The complementary event means that the atom is still intact after the period Δt . The probability of this is

$$P(\Delta t) = 1 - p = 1 - \lambda \Delta t. \quad (7.10)$$

Suppose that the atom has indeed survived the first Δt period of observation. Then the probability of its being “alive” even after the next Δt period is again $1 - p = 1 - \lambda \Delta t$.

According to probability theory, for the total observation time $2\Delta t$ one can write

$$P(2\Delta t) = (1 - \lambda \Delta t)^2. \quad (7.11)$$

Thus the probability that the atom will survive a period of $n\Delta t$ is

$$P(n\Delta t) = (1 - \lambda \Delta t)^n \quad (7.12)$$

which, with the notation $n\Delta t = t$, can be rewritten as

$$P(t) = \left(1 - \lambda \frac{t}{n}\right)^n. \quad (7.13)$$

For $n \rightarrow \infty$ (i.e., when the division of t to single periods of observation is infinitely fine) one can get the following expression for the probability that the atom does not decay in an arbitrarily long period t :

$$P(t) = e^{-\lambda t}. \quad (7.14)$$

For a large number of identical atoms, the exponential factor in [Eq. \(7.14\)](#) represents the fraction of survivors $N(t)/N(0)$ as a function of the time t . Thus the initial number of atoms $N(0)$ is expected to drop to $N(t)$ according to the following formula:

$$N(t) = N(0)e^{-\lambda t}. \quad (7.15)$$

Note that what has been just “derived” is the exponential law of decay (see [Eq. \(7.6\)](#)) justifying the notation λ (reserved for the decay constant throughout this chapter) for the proportionality constant in [Eq. \(7.9\)](#).

Using [Eq. \(7.15\)](#), one can introduce a more expressive quantity than the decay constant for the description of the “decayability” of radionuclides. The half-life $T_{1/2}$ is the time in which half of the atoms are expected to decay:

$$N(T_{1/2}) = N(0)e^{-\lambda T_{1/2}} = \frac{N(0)}{2}, \quad (7.16)$$

where

$$T_{1/2} = \frac{\ln 2}{\lambda} \approx \frac{0.693}{\lambda}. \quad (7.17)$$

Another characteristic time parameter of radioactive decay is the mean life τ , which is the expected value of the γ ($1, \lambda$) exponential distribution associated with radioactive decay (see [Chap. 9](#) in this Volume):

$$\tau = \int_0^{\infty} t f(t) dt = \lambda \int_0^{\infty} t e^{-\lambda t} dt = \frac{1}{\lambda}, \quad (7.18)$$

where $f(t) = \lambda e^{-\lambda t}$ is the density function of the lifetime distribution.

Comparing this result with [Eq. \(7.17\)](#), one can see that the mean life is proportional to the half-life:

$$\tau = \frac{T_{1/2}}{\ln 2} \approx 1.44 T_{1/2}. \quad (7.19)$$

It is common knowledge that τ is the time necessary for the atoms to be reduced to 1/e of their initial number

$$N(\tau) = N(0)e^{-\lambda\tau} = \frac{N(0)}{e} \approx 0.37N(0). \quad (7.20)$$

► Equation (7.20) shows that the drop in the number of survivors is larger than in the case of the half-life. The reason is obvious: according to ► Eq. (7.19), $\tau > T_{1/2}$.

Note that the “1/e rule” expressed by ► Eq. (7.20) is not a general criterion for mean times: it is a specific feature of the exponential distribution associated with the exponential law of simple decays. (See also the comment after ► Eq. (7.44).)

7.2 Independent Decays: Radionuclide Mixtures

If it turns out that the logarithmic plot of activity versus time is not a straight line, then this is an indication that the sample contains more than one radionuclide. The radionuclides thus detected may be genetically related to each other (i.e., one is produced by the other through radioactive transformation), or they can be independent of each other, forming a simple mixture (see ► Fig. 7.1). In this section the latter case will only be discussed.

In order to determine the individual decay constants of the mixture, count rates (i.e., observed activities) are to be measured as a function of time, provided that the half-lives are moderately long and comparable with each other. The number of measured points should be at least twice the number of radioactive components plus one (or, preferably, a lot more).

The analysis of the “nuclear spectrum” thus obtained (see ► Chap. 9 in this Volume) is based on the fact that the observed activities are additive and also that they are subject to the exponential law expressed by ► Eq. (7.8). Hence, for n radioactive components one can write

$$A'(t) = \sum_{i=1}^n A'_i(t) + b = \sum_{i=1}^n A'_i(0)e^{-\lambda_i t} + b \quad (7.21)$$

where $A'(t)$ is the observed activity of the mixture at time t , $A'_i(0)$ is the observed activity of the i th component at $t = 0$ and b is the background. The parameters ($2n + 1$ altogether), including the decay constants, can then be estimated by a least-square fit (see ► Chap. 9 in this Volume).

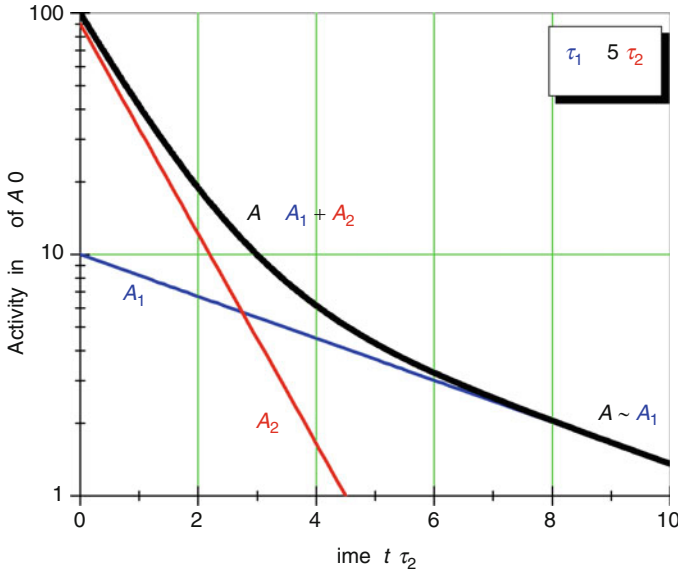
7.3 Branching Decays

Some radionuclides can disintegrate in two or more competing ways leading to different products. In the case of odd–odd nuclei, e.g., sitting nearest to the apex of one of the mass parabolas, negative β decay and electron capture (and in energetically favorable cases: positive β decay) are equally possible. For instance, the nucleus of ^{40}K , a nuclide used in radioactive dating (see ► Sects. 17.2, 17.15, and 17.16 in Chap. 17 of Vol. 2), can undergo both electron capture and β^- decay (see ► Fig. 7.2 and ref. Vértés et al. (1998) for more detail)



■ Fig. 7.1

Schematic representation of the logarithm of activity for a source containing the mixture of two radionuclides. Note that nuclide 1, due to its longer mean life, will survive nuclide 2, although its initial activity at $t = 0$ is much lower (10% of the total). This fact used to be the basis of the graphical decomposition of the decay curves of mixtures in the “pre-PC” age of nuclear science. The idea for obtaining the $A_2(t)$ values (red line) from the thick (black) curve of the experimental $A(t)$ values was to subtract the values of $A_1(t)$ extrapolated back along the blue line representing the asymptote of the thick line for $t \rightarrow \infty$



In the case of the decay series shown by ► Figs. 7.4–7.7, another type of branching decay occurs: α decay competes with β^- decay. For instance, ^{227}Ac , the eponymous member of the actinium ($4n + 3$) series (see ► Fig. 7.7), undergoes the following disintegration:



The additive property of the partial decay constants indicated above follows from the same property of the respective partial decay rates. In the case of ^{40}K , e.g., one can write

$$-\frac{dN_K}{dt} = \frac{dN_{\text{Ar}}}{dt} + \frac{dN_{\text{Ca}}}{dt} = \lambda_{\text{EC}}N_K + \lambda_\beta N_K = (\lambda_{\text{EC}} + \lambda_\beta)N_K = \lambda N_K. \quad (7.24)$$

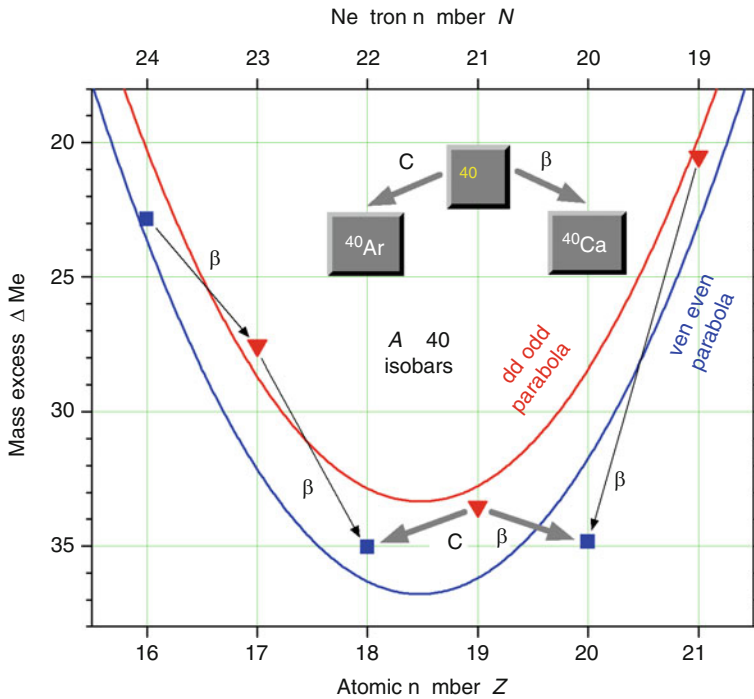
Hence the half-life of ^{40}K according to ► Eq. (7.17) is

$$T_{1/2} = \frac{\ln 2}{\lambda} = \frac{\ln 2}{\lambda_{\text{EC}} + \lambda_\beta}. \quad (7.25)$$

According to ► Eqs. (7.24) and ► (7.6) the growth rates of ^{40}Ar and ^{40}Ca are

■ Fig. 7.2

Mass parabolas explaining the branching decay of ^{40}K . This type of branching is always associated with odd-odd nuclei. The parabolic dependence of the nuclear mass on the atomic number Z comes from a similar (but negative) dependence of the binding energy as expressed by the Weizsäcker formula (2.3) in Chap. 2. (The odd-odd parabola and the even-even one are shifted relative to each other by $2\delta/A^{3/4}$ according to the Weizsäcker formula. Note that in the case of odd- A isobars there is only one mass parabola (and therefore one minimum, see Fig. 14.5 in Chap. 14, Vol. 2) because the pairing energy term of the Weizsäcker formula is the same (zero) for even-odd and odd-even nuclei.) The mass access data used for the figure are taken from Sect. 11.6 of the Appendix of this Volume. Note that $^{40}_{20}\text{Ca}_{20}$ is a doubly magic nuclide, which explains why it has a lower mass (higher stability) than expected from the general trend expressed by the lower (blue) parabola



$$\frac{dN_{\text{Ar}}}{dt} = \lambda_{\text{EC}} N_{\text{K}} = \lambda_{\text{EC}} N_{\text{K}}(0) e^{-\lambda t}, \quad (7.26)$$

$$\frac{dN_{\text{Ca}}}{dt} = \lambda_{\beta} N_{\text{K}} = \lambda_{\beta} N_{\text{K}}(0) e^{-\lambda t}. \quad (7.27)$$

The numbers of the respective nuclides that are present at time t can be calculated by integration. Assuming that at $t = 0$ neither ^{40}Ar , nor ^{40}Ca was present, then

$$N_{\text{Ar}} = \lambda_{\text{EC}} \frac{N_{\text{K}}(0)(1 - e^{-\lambda t})}{\lambda}, \quad (7.28)$$

$$N_{\text{Ca}} = \lambda_{\beta} \frac{N_{\text{K}}(0)(1 - e^{-\lambda t})}{\lambda}. \quad (7.29)$$

Thus, it turns out that the atomic ratio of ^{40}Ar to ^{40}Ca is equal to the ratio of the partial decay constants called branching ratio at any moment:

$$\frac{N_{\text{Ar}}}{N_{\text{Ca}}} = \frac{\lambda_{\text{EC}}}{\lambda_{\beta}}. \quad (7.30)$$

(The schematic representation of such decay is shown by [Fig. 7.3](#).)

Therefore, the atomic fraction of either product is indicative of the contribution of the respective partial decay constant to the total λ . For instance, in the case of ^{40}Ar produced by electron capture (EC) one obtains

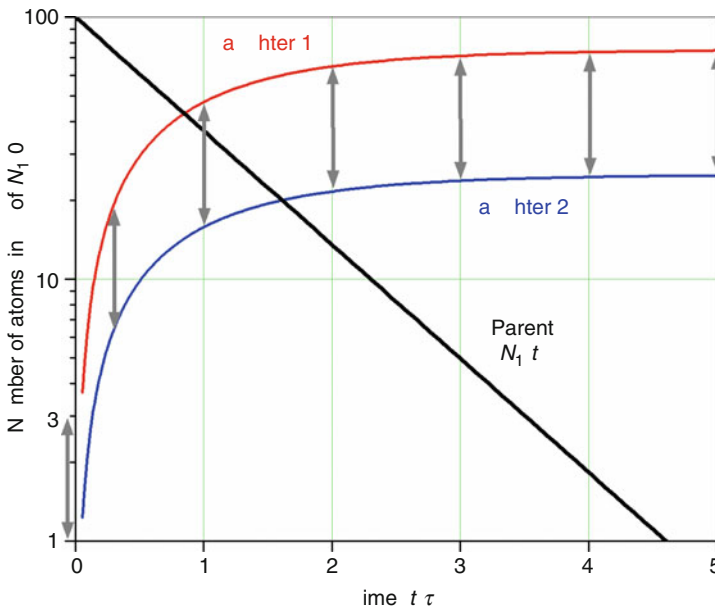
$$x_{\text{Ar}} = \frac{N_{\text{Ar}}}{N_{\text{Ar}} + N_{\text{Ca}}} = \frac{\lambda_{\text{EC}}}{\lambda_{\text{EC}} + \lambda_{\beta}} = \frac{\lambda_{\text{EC}}}{\lambda}. \quad (7.31)$$

Hence, for the products of several parallel decays the following equation holds:

$$\lambda_i = x_i \sum_{k=1}^n \lambda_k = x_i \lambda. \quad (7.32)$$

Fig. 7.3

Schematic representation of branching decay for $\lambda_1/\lambda_2 = 3$. The arrows shown between the curves of the daughters have the same length as the one displayed at the vertical axis between 1 and 3. The constant separation – considering that the vertical scale is logarithmic – means that the upper curve, representing daughter 1, is a scaled-up version of the lower curve. The value of the scaling factor (3) is determined by the ratio λ_1/λ_2 (See [Eq. \(7.30\)](#))



7.4 Successive Processes

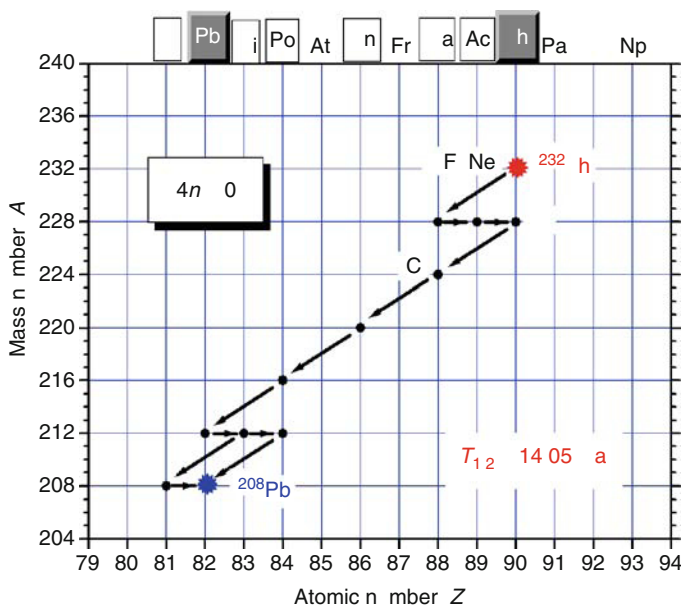
7.4.1 General Kinetics of Decay Chains

It often happens that the decay product itself is also radioactive. Thus, a whole chain of radioactive transformations may evolve, forming a radioactive decay series (see ▶ Figs. 7.4–7.7).

Most of the naturally occurring radionuclides belong to one of three series shown in ▶ Figs. 7.4, ▶ 7.6, and ▶ 7.7 where the symbols of the elements that are represented in the given series are put in boxes. (See also ▶ Chap. 13 in Vol. 2 on “Natural Radioactive Decay

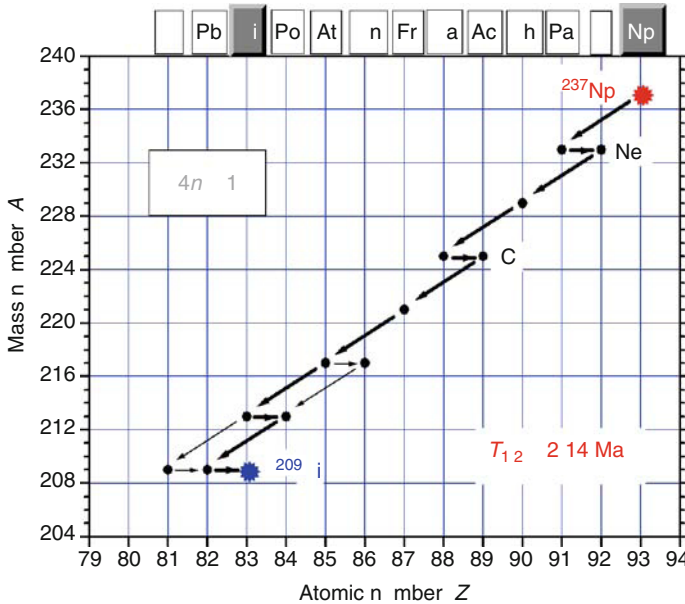
■ Fig. 7.4

The thorium ($4n + 0$) series is one of the four decay series, out of which three (including this one) are naturally occurring, while one (the $4n + 1$ series) is extinct on Earth. The numbering – $4n + 0$, $4n + 1$, $4n + 2$, and $4n + 3$ – refer to the residue class (modulo 4) of the possible mass numbers in each series. The explanation for the notation is that these series (see also ▶ Figs. 7.5–7.7 showing the same range of Z and A for better comparison) only include α decay (slanting arrows) and β decay (horizontal arrows), so the change of the mass number is either 4 or 0. Therefore, the members of the whole series belong to the same residue class (modulo 4) as their primary parent. (There are also some very weak branches of decay indicated in parentheses like spontaneous fission (SF) and different types of cluster decay when a C, O or even a Ne nucleus is emitted instead of an α particle.) Each of the four series represents an example for secular equilibrium due to the very long half-life of the primary parent of the series in comparison with any of the members. For instance, the half-life of ^{232}Th is $T_{1/2} = 1.405 \times 10^{10} \text{ a}$ – a value close to the estimated age of the Universe – while that of the longest-lived daughter, ^{228}Ra , is only $T_{1/2} = 5.75 \text{ a}$



■ Fig. 7.5

The neptunium ($4n + 1$) series is now extinct on Earth. This is due to the relatively short half-life of the primary parent ^{237}Np ($T_{1/2} = 2.14 \times 10^6$ a, which is less than the age of the human race). The nearly 2,136 half-lives, that have elapsed since the creation of our planet (about 4.57×10^9 years ago), have practically wiped out this process because only 1 out of 10^{643} neptunium-237 atoms is expected to survive. Now, the odds of survival are really bad, considering that 10^{643} Np atoms would “weigh” about 3×10^{618} kg, whereas the mass of the Sun is a mere 2×10^{30} kg, and even that of the Milky Way is only estimated to about 2×10^{41} kg



Chains.”) The primary parent and the final product of each series are indicated by shading the box of the respective elements.

It can be useful to determine the activity of a given member of a series at a given time t . The simplest case is when the first two members (the parent X_1 and its daughter X_2) are only considered:



where N_1 and N_2 are the numbers of atoms of X_1 and X_2 , respectively. (Some authors prefer to use the term mother rather than parent.)

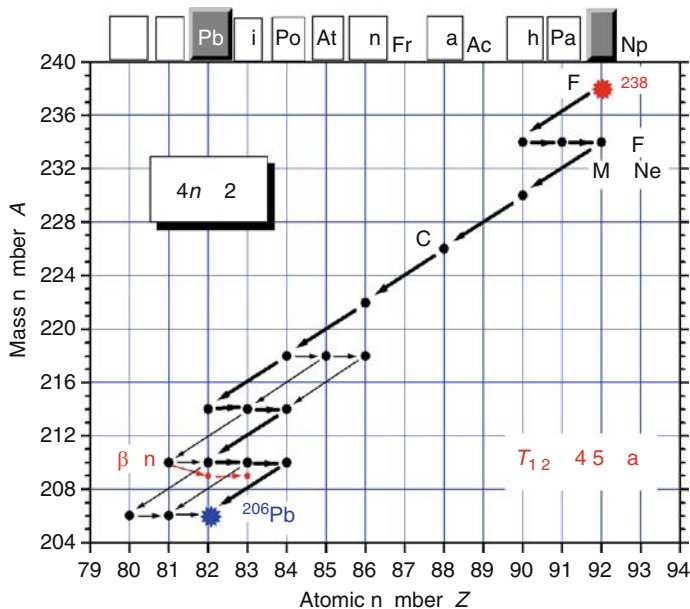
The time dependence of the number of atoms and the activity (decay rate) of the parent X_1 follows directly from Eqs. (7.6) and (7.7):

$$N_1 = N_1(0)e^{-\lambda_1 t}, \quad (7.34)$$

$$A_1 = -\frac{dN_1}{dt} = \lambda_1 N_1 = \lambda_1 N_1(0)e^{-\lambda_1 t} = A_1(0)e^{-\lambda_1 t}. \quad (7.35)$$

■ Fig. 7.6

The uranium ($4n + 2$) series is the second of the three naturally occurring decay series on Earth. The half-life of the primary parent ^{238}U ($T_{1/2} = 4.5 \times 10^9$ a) nearly matches the estimated age of the Earth, so about half of the ^{238}U atoms that once existed are still around. In this series, Mg emission also occurs some of the ^{210}Tl nuclei undergo beta-delayed neutron emission. This establishes a vague interconnection with the ($4n + 1$) series



The daughter X_2 forms at a rate equal to the decay rate of the parent and simultaneously disintegrates at a rate determined by λ_2 :

$$\frac{dN_2}{dt} = \lambda_1 N_1 - \lambda_2 N_2. \quad (7.36)$$

Substituting \blacktriangleright Eq. (7.34) into \blacktriangleright Eq. (7.36) yields

$$\frac{dN_2}{dt} + \lambda_2 N_2 = \lambda_1 N_1(0) e^{-\lambda_1 t}. \quad (7.37)$$

The solution of ► Eq. (7.37) for the initial conditions $t = 0$: $N_1 = N_1(0)$, $N_2 = 0$ is

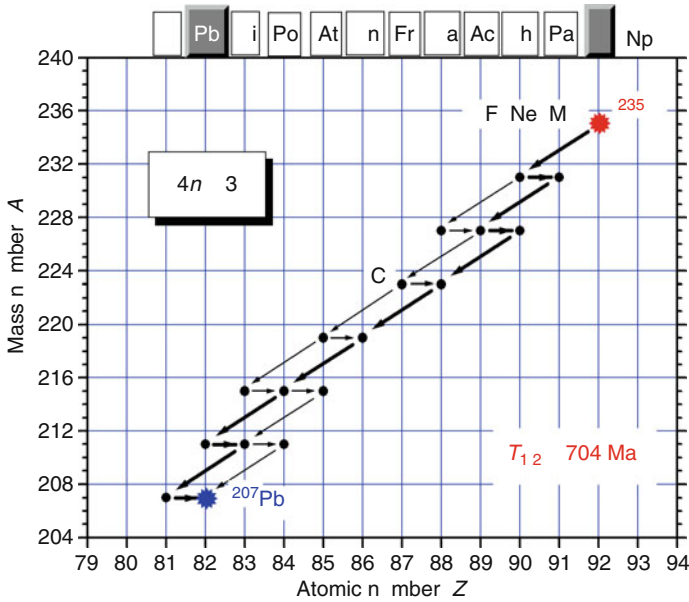
$$N_2 = N_1(0) \frac{\lambda_1}{\lambda_2 - \lambda_1} (e^{-\lambda_1 t} - e^{-\lambda_2 t}). \quad (7.38)$$

Thus the activity of the daughter is

$$A_2 = \lambda_2 N_2 = A_1(0) \frac{\lambda_2}{\lambda_2 - \lambda_1} (e^{-\lambda_1 t} - e^{-\lambda_2 t}). \quad (7.39)$$

■ Fig. 7.7

The actinium ($4n + 3$) series is the third one of the naturally occurring decay series on Earth. The half-life of the primary parent ^{235}U ($T_{1/2} = 7.04 \times 10^8$ a – note, for comparison, that the Cambrian Period started some 5.7×10^8 years ago) is approximately one sixth of the estimated age of the Earth. Thus, nearly 2^{-6} part (or, more exactly, just about 1%) of the ^{235}U atoms that once existed are still potentially available as nuclear fuel



More generally, the following system of differential equations is to be solved:

$$\begin{aligned}
 \frac{dN_1}{dt} &= -\lambda_1 N_1, \\
 \frac{dN_2}{dt} &= \lambda_1 N_1 - \lambda_2 N_2, \\
 \frac{dN_3}{dt} &= \lambda_2 N_2 - \lambda_3 N_3, \\
 &\vdots \\
 \frac{dN_n}{dt} &= \lambda_{n-1} N_{n-1} - \lambda_n N_n.
 \end{aligned} \tag{7.40}$$

The initial conditions considered are

$$\text{for } t = 0 : N_1 = N_1(0); \quad N_2 = N_3 = \dots N_n = 0. \tag{7.41}$$

The solution of the above system of equations can be found, e.g., in Vértés and Kiss (1987), Ehmann and Vance (1991) as well as several authors of this handbook refer to the result summarized by Eqs. (7.42)–(7.43) as the Bateman equation (Bateman 1910, see also in Choppin and Rydberg 1980). Other authors refer to the whole series of equations shown in Eq. (7.40) as Bateman equations.) For the n th member of the series ($n = 1, 2, 3, \dots$) one gets

$$N_n = N_1(0) \frac{f_n(t)}{\lambda_n} \equiv N_1(0) \sum_{k=1}^n a_{kn} e^{-\lambda_k t} \quad (7.42)$$

where $a_{11} = 1$, and the rest of the summation coefficients a_{kn} are given by the expression

$$a_{kn} = \frac{\prod_{i=1}^{n-1} \lambda_i}{\prod_{\substack{i>0 \\ i \neq k}} (\lambda_i - \lambda_k)}. \quad (7.43)$$

For more generalized forms of the above Bateman equations including activation by neutron capture see [Eqs. \(1.29\)–\(1.30\) in Chap. 38, Vol. 4](#), cited from Rubinson (1949).

For all the sophistication of the above result, some questions are easy to answer without using the explicit formulas. Such a question is, e.g., the mean time needed for the parent nucleus (X_1) to go through n steps of subsequent transformations. (For instance, one may be interested in the mean time needed for a ^{238}U atom to transform to ^{206}Pb through the series of decays shown in [Fig. 7.6](#).) Instead of integrating [Eq. \(7.42\)](#) (or, actually, $t f_n(t)$), one can translate the problem to a probability problem in the following way.

The subsequent periods of time T_i that are spent by a nucleus at the i th “stage” ($i = 1, 2, \dots, n$) are random variables with $\gamma(1, \lambda_i)$ exponential distributions (see [Chap. 9](#) for the notation). The total waiting time to get through n stages is $T = T_1 + \dots + T_n$. (Note that according to Rényi (1979) the function $f_n(t)$ in [Eq. \(7.42\)](#) plays the role of the density function of T .) What is actually needed is the expected value (τ) of T . According to [Eq. \(9.45\) in Chap. 9](#) one can directly write up the following result:

$$\tau = \sum_{i=1}^n \tau_i = \sum_{i=1}^n \frac{1}{\lambda_i}. \quad (7.44)$$

Note that the “1/e rule” (see [Eq. \(7.20\)](#)) does not apply to τ , because the distribution of T is only exponential in the trivial case of $n = 1$. To give a numerical example, suppose that the decay constants are nearly equal. If $\lambda_1 \approx \lambda_2 \approx \lambda$, then T has a $\gamma(n, \lambda)$ gamma distribution (see [Chap. 9](#) in this Volume) for which $\tau = n/\lambda$. One can easily verify, e.g., for $n = 2$, that the factor in question would then be $1 - F_2(2/\lambda) = 3e^{-2} \approx 0.41$ rather than $e^{-1} \approx 0.37$, where $F_2(t)$ is the distribution function of the $\gamma(2, \lambda)$ gamma distribution. In the given example, this would mean that about 59% ($= 100 - 41\%$) of the initial atoms rather than 63% ($= 100 - 37\%$) are expected to undergo both decays by the time $t = \tau \equiv 2/\lambda$. For large values of n , on the other hand, one gets 50%, because the gamma distribution can be approximated by normal distribution for which the expected value (τ) and the median ($T_{1/2}$) are equal (see [Chap. 9](#) in this Volume).

In one particular (however important) type of radioactive series, the “1/e rule” is still working. This happens when the half-life (and therefore the mean life) of one of the members is overwhelmingly large compared with all the others. This case, called secular equilibrium, is discussed separately due to its importance.

7.4.2 Radioactive Equilibrium and Nonequilibrium

It is often not necessary to bother with the general solution of the successive decay problem, because after some time the whole series can be analyzed stepwise, comparing the decay

constants of the individual decays. In order to introduce the concepts of equilibrium and nonequilibrium, it is worth starting with the analysis of the first two decays of the series shown by [Eq. \(7.33\)](#). Then, the decay of the second daughter will also be included, in order to be able to draw more general conclusions concerning the whole of the series. Under certain conditions some kind of equilibrium is established between the (primary) parent and its (first) daughter.

The condition for transient equilibrium – or *any* equilibrium for that matter – is $\lambda_1 < \lambda_2$ (or $\tau_1 > \tau_2$). In this case, after some time, the following relation holds:

$$e^{-\lambda_1 t} \gg e^{-\lambda_2 t}, \quad (7.45)$$

and therefore the second term becomes negligible in [Eqs. \(7.38\)](#) and [\(7.39\)](#).

Thus, the asymptotic behavior of the number of the daughter's atoms N_2 is described by the following formula:

$$N_2 \Rightarrow \frac{\lambda_1}{\lambda_2 - \lambda_1} N_1(0) e^{-\lambda_1 t} = \frac{\lambda_1}{\lambda_2 - \lambda_1} N_1. \quad (7.46)$$

From [Eq. \(7.46\)](#) one can easily get the asymptotic ratio of the numbers of atoms

$$\frac{N_2}{N_1} \Rightarrow \frac{\lambda_1}{\lambda_2 - \lambda_1}, \quad (7.47)$$

which shows that, for large enough t , the ratio of the number of daughter atoms to that of the parent atoms (N_2/N_1) becomes approximately constant.

The asymptotic behavior of the daughter's activity A_2 is obtained from [Eq. \(7.39\)](#) using [Eq. \(7.45\)](#):

$$A_2 \Rightarrow \frac{\lambda_2}{\lambda_2 - \lambda_1} A_1(0) e^{-\lambda_1 t} = \frac{\lambda_2}{\lambda_2 - \lambda_1} A_1. \quad (7.48)$$

Thus the asymptotic ratio of the activities is

$$\frac{A_2}{A_1} \Rightarrow \frac{\lambda_2}{\lambda_2 - \lambda_1}, \quad (7.49)$$

that is, the ratio of the activities becomes constant after some time. This can also be observed in [Fig. 7.8](#), where proportionality reveals itself as a constant separation between the logarithmic curves of A_1 and A_2 .

It can also be concluded from [Eq. \(7.49\)](#) that in transient equilibrium the daughter is more active than the parent. (This can also be seen in [Fig. 7.8](#).)

The following criterion can be set up for the minimum time required to approach the equilibrium condition defined by [Eq. \(7.49\)](#) to a given relative accuracy α :

$$\frac{\frac{\lambda_2}{\lambda_2 - \lambda_1} - \frac{A_2}{A_1}}{\frac{\lambda_2}{\lambda_2 - \lambda_1}} \leq \alpha, \quad (7.50)$$

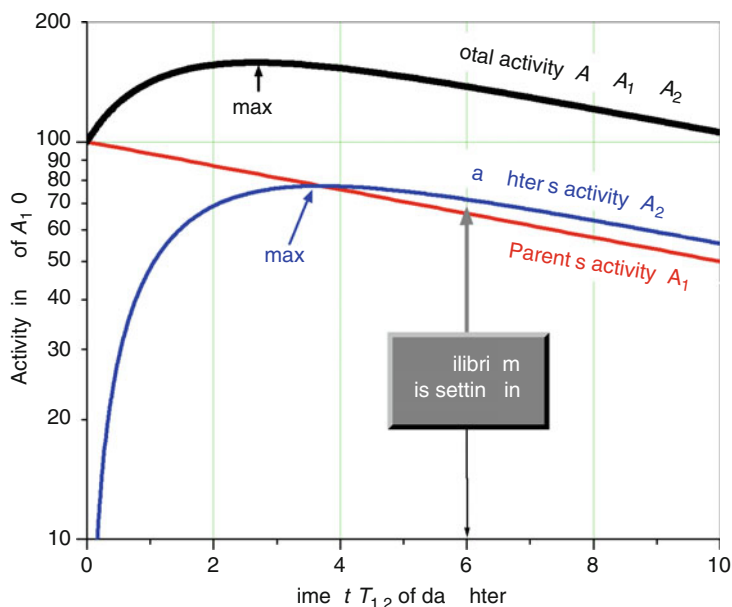
where A_2/A_1 is the actual ratio of the activities as a function of time, i.e.,

$$\frac{A_2}{A_1} = \frac{\lambda_2}{\lambda_2 - \lambda_1} (1 - e^{-(\lambda_2 - \lambda_1)t}) \quad (7.51)$$

as follows from [Eqs. \(7.39\)](#) and [\(7.35\)](#).

■ Fig. 7.8

Schematic representation of (transient) equilibrium. The half-life of the parent nuclide considered is 10 units, while that of the daughter is 1 unit. Note that the maximum of the daughter's activity (see Eq. (7.58)) is reached somewhat later than that of the total activity. Note also that Eq. (7.53) works quite well, i.e., the logarithmic curves of A_1 and A_2 are already practically parallel at $t \approx 6.6$, which means that the ratio A_2/A_1 is nearly constant



Hence, criterion Eq. (7.50) can be rewritten in the following form:

$$e^{-(\lambda_2 - \lambda_1)t} \leq \alpha, \quad (7.52)$$

which eventually yields

$$t > \tau_2 \ln \frac{1}{\alpha}, \quad (7.53)$$

where τ_2 is the mean life of the (shorter-lived) daughter nuclide.

If, e.g., a criterion of 1% is set, then Eq. (7.53) yields $t > 4.6 \tau_2 \approx 6.6 T_{1/2}$. In other words, after about 6–7 half-lives (4–5 mean lives) of the daughter nuclide, the equilibrium condition is only about 1% away.

The condition for secular equilibrium is $\lambda_1 \ll \lambda_2$ (or $\tau_1 \gg \tau_2$). In this case, λ_1 can be neglected in comparison with λ_2 and Eq. (7.49) becomes even simpler:

$$\frac{A_2}{A_1} \Rightarrow 1, \quad (7.54)$$

that is, in secular equilibrium the activities are about equal

$$A_1 \approx A_2. \quad (7.55)$$

Secular equilibrium is illustrated by ► Fig. 7.9 in the special case of ^{226}Ra as the parent ($T_{1/2} = 1,600 \text{ a} = 584,000 \text{ d}$) and ^{222}Rn as its daughter ($T_{1/2} = 3.82 \text{ d}$).

If $\lambda_1 > \lambda_2$, then no equilibrium is reached at any time. Still, similarly to the case of equilibrium, the activity of the daughter passes through a maximum (see ► Fig. 7.10).

The asymptotic behavior of the daughter's activity A_2 is now different from that shown by ► Eq. (7.48), because it is the first term that becomes negligible in ► Eq. (7.39)

$$A_2 \Rightarrow \frac{\lambda_2}{\lambda_1 - \lambda_2} A_1(0) e^{-\lambda_2 t}. \quad (7.56)$$

Note that the above equation would describe the activity of a source prepared from the daughter's atoms, with the initial activity

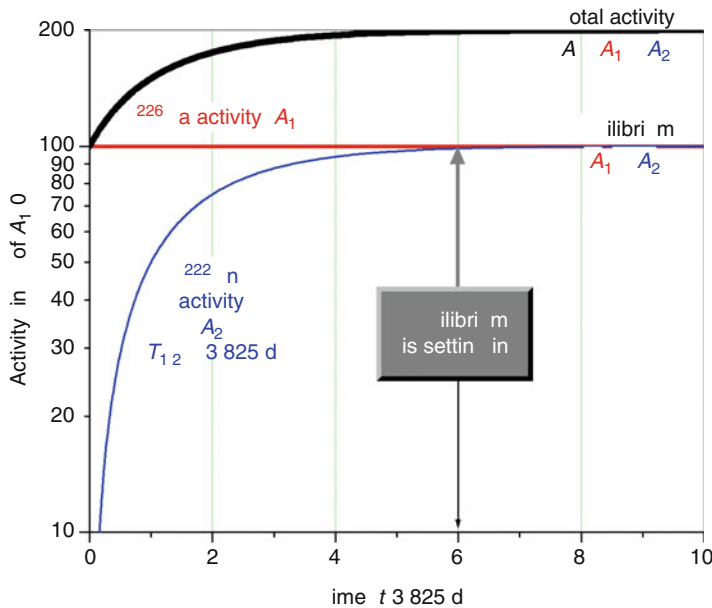
$$A_2(0) = \frac{\lambda_2}{\lambda_1 - \lambda_2} A_1(0). \quad (7.57)$$

(See the intersection of the dotted line with the vertical axis in ► Fig. 7.10.)

It can be useful to know the time when the daughter reaches maximum activity, especially when the aim is to collect a radionuclide produced by radioactive decay.

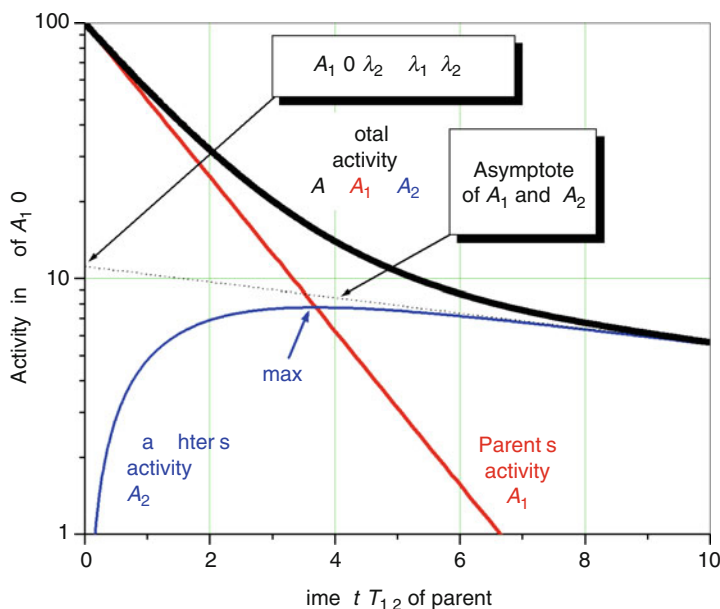
■ Fig. 7.9

The change of activity in the case of secular equilibrium. The half-life of the parent nuclide ^{226}Ra is $T_{1/2} = 1,600 \text{ a}$, and that of the daughter ^{222}Rn is $T_{1/2} = 3.825 \text{ d}$. The time unit is the half-life of the daughter. Note that after the equilibrium has been reached, the activities of Ra and Rn become practically equal – the distinguishing feature of secular equilibrium. This means that the total activity doubles after 6–8 half-lives of the daughter



■ Fig. 7.10

Schematic representation of nonequilibrium. The half-life of the parent nuclide is taken as the time unit, and that of the daughter is 10 times longer. Note that the asymptote of the daughter's activity reflects the time characteristics of the daughter's own, whereas in the case of equilibrium it is determined by that of the parent (See the horizontal red line in Fig. 7.9, representing both the parent's activity and the asymptotic activity curve of the daughter)



The maximum of $A_2(t)$ (as well as of $N_2(t)$) is reached at the time

$$t_{\max} = \frac{1}{\lambda_2 - \lambda_1} \ln \frac{\lambda_2}{\lambda_1} \quad (7.58)$$

as one can easily verify by differentiating Eq. (7.39) (or Eq. (7.38)).

The analysis will now be extended to the three first decays of the series:



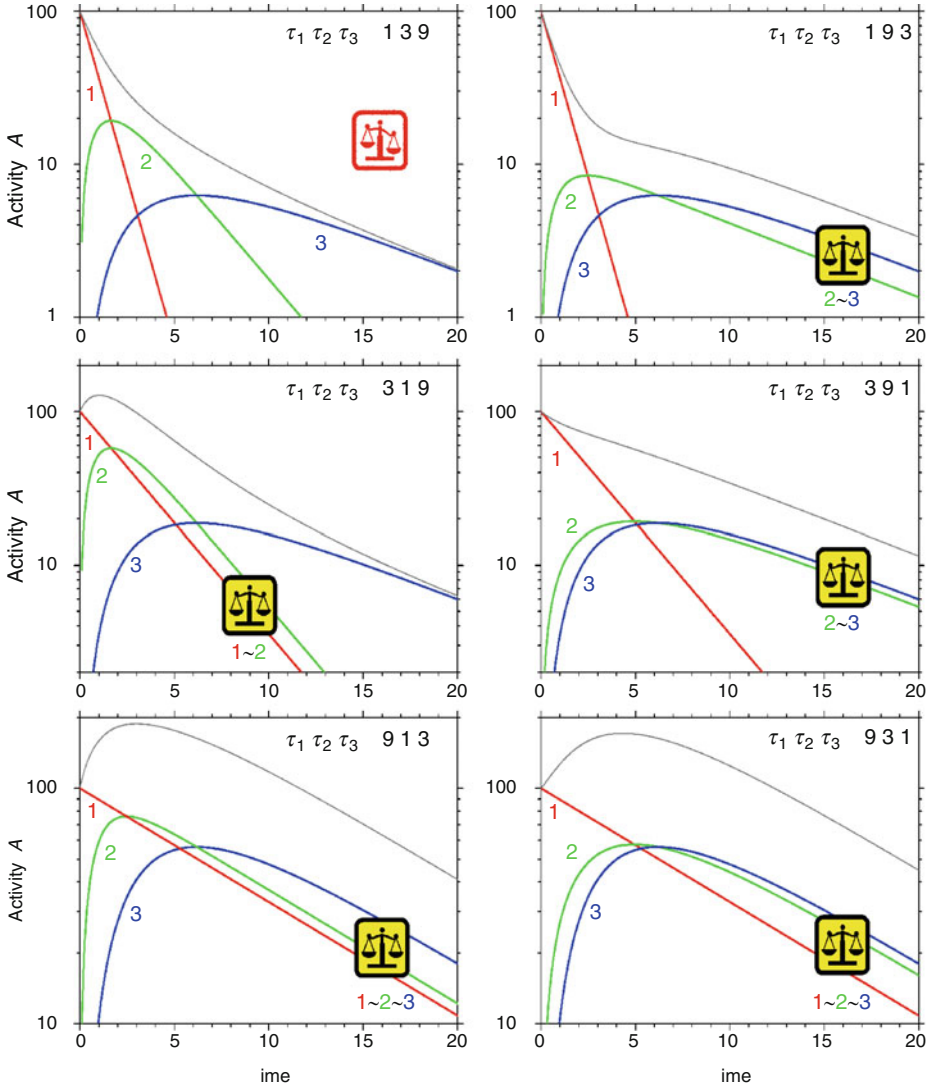
Using Eqs. (7.42) and (7.43), one can write for the activity of the second daughter

$$A_3 = \lambda_3 N_3 = A_1(0) \lambda_2 \lambda_3 \left(\frac{e^{-\lambda_1 t}}{(\lambda_2 - \lambda_1)(\lambda_3 - \lambda_1)} + \frac{e^{-\lambda_2 t}}{(\lambda_1 - \lambda_2)(\lambda_3 - \lambda_2)} + \frac{e^{-\lambda_3 t}}{(\lambda_1 - \lambda_3)(\lambda_2 - \lambda_3)} \right). \quad (7.60)$$

Figure 7.11 shows the activities versus time for the first three nuclides of a series as calculated from Eqs. (7.35), (7.39), and (7.60). The individual graphs represent the six possible permutations of a fast, a medium, and a slow decay characterized by mean lives 1, 3,

■ Fig. 7.11

Basic cases of decay series consisting of three steps. The balanced scales draw attention to the range where the logarithms of activities become parallel, an indication of equilibrium (\sim). The shortest mean life is selected as the time unit for each graph. The most interesting case is represented by the bottom left graph, showing that whenever the parent of the series is the longest-lived nuclide, sooner or later equilibrium will prevail along the whole series, no matter how the individual decay constants of the daughters are related to each other. According to the four upper graphs, the longest-lived member will eventually survive (all of) its predecessor(s)



and 9 time units, respectively. Careful analysis of the graphs makes possible to draw general conclusions about the asymptotic behavior of any series:

If X_k is the longest-lived member of the series, then – after a sufficiently long time – the members X_1, \dots, X_{k-1} will die out, and the series will be shortened to the subseries X_k, X_{k+1}, \dots with X_k as the primary parent.

No matter how the decay constants ($\lambda_{k+1}, \lambda_{k+2}, \dots$) of the daughters of X_k are related to each other, the fact that λ_k is smaller than the rest of the decay constants enforces an equilibrium between X_k and all of its daughters.

For instance, the first member of any of the naturally occurring radioactive series has a half-life of several orders of magnitude longer than any of its descendants (see [Figs. 7.4–7.7](#)). Therefore its decay constant (λ_1) is negligible in comparison with those of the decay products ($\lambda_1, \lambda_2, \dots, \lambda_n$). Similarly, the exponentials

$$e^{-\lambda_2 t}, e^{-\lambda_3 t}, \dots, e^{-\lambda_n t}, \dots \quad (7.61)$$

can also be neglected in comparison with $e^{-\lambda_1 t}$ after some time.

Everything considered, the first member of such a series is in secular equilibrium with all the others, i.e., [Eq. \(7.55\)](#) applies to any of the daughter nuclides:

$$A_1 \approx A_2 \approx \dots \approx A_n \approx \dots \quad (7.62)$$

If, therefore, all the decay products of uranium or thorium remain together in a rock or in an ancient compound, their activities become equal (after a period of time).

7.4.3 Decay After Activation

A special case of successive processes is that in which the parent (X_1) is stable, but it is induced to transformation by a nuclear reaction, the product of which (the “daughter” X_2) is radioactive. For instance, in the case of neutron activation instead of [Eq. \(7.33\)](#) one can write



where ϕ is the neutron flux density (neutrons $\text{cm}^{-2} \text{s}^{-1}$) and σ_1 is the cross section of the nuclear reaction induced by the neutrons (e.g., neutron capture):



Similar processes have an important part in neutron activation analysis (NAA, see [Chap. 30 in Vol. 3](#)) as well as in natural processes such as the formation of radiocarbon (see [Sect. 17.17 in Chap. 17 of Vol. 2](#)) in the atmosphere via the reaction



The equivalent of [Eq. \(7.36\)](#) is now

$$\frac{dN_2}{dt} = \phi\sigma_1 N_1 - \lambda_2 N_2. \quad (7.66)$$

When solving the above equation, it is usually assumed that ϕ and N_1 are constant. (The latter assumption means that only a tiny fraction of X_1 will be activated.) Therefore, the integration between 0 and t is straightforward, resulting in

$$A_2 = \lambda_2 N_2 = \phi \sigma_1 N_1 (1 - e^{-\lambda_2 t}). \quad (7.67)$$

The above equation shows that for a constant time of activation, the activity of the product will be proportional to N_1 , offering a simple technique for the quantitative analysis of the nuclide X_1 by NAA. According to [Fig. 7.12](#), the asymptotic limit of the activity is also proportional to N_1 . This fact is used, e.g., in the case of radiocarbon dating, in which the date of the death of an organism is eventually determined from the following type of equation:

$$A_2(t) = A_2(0)e^{-\lambda_2 t} \propto \phi \sigma_1 N_1 e^{-\lambda_2 t}. \quad (7.68)$$

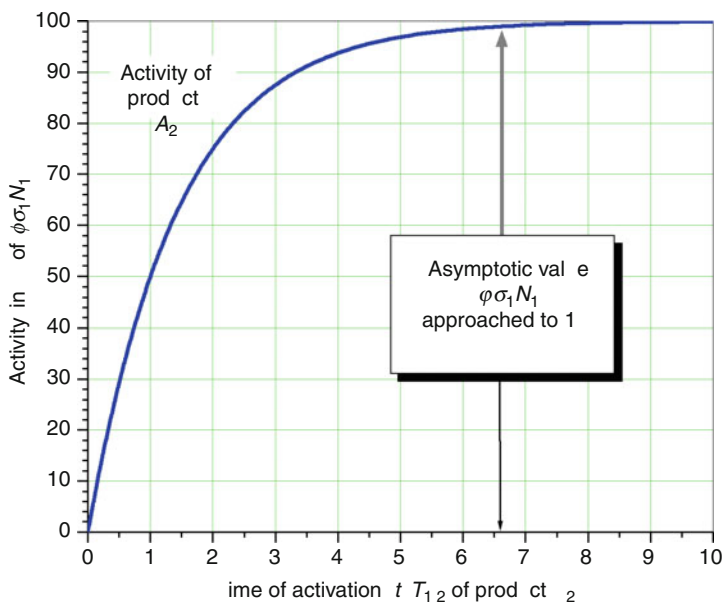
For a general and detailed discussion of activation kinetics see [Chap. 38, Vol. 4](#), on the “Reactor-Produced Medical Radionuclides.”

7.5 Decay Constant (Half-Life) Systematics

This section gives a short summary of some results discussed in more detail in various parts of [Chap. 2](#) (“Basic Properties of the Atomic Nucleus”) and [Chap. 4](#) (“Nuclear Fission”) concerning the dependence of the decay constant on various physical parameters for the most

Fig. 7.12

Schematic representation of the activity of the radioactive product X_2 as a function of the time of activation. The time unit is the half-life of the product. The arrows point to the time calculated from [Eq. \(7.53\)](#), which now provides the minimum activation time needed to get 100% close to the asymptotic (i.e., the highest possible) value of the activity $A_2 \Rightarrow \phi \sigma_1 N_1$. It is clear that the gain in product activity halves in each subsequent half-life period, which makes longer irradiation times increasingly uneconomical from the viewpoint of radionuclide production



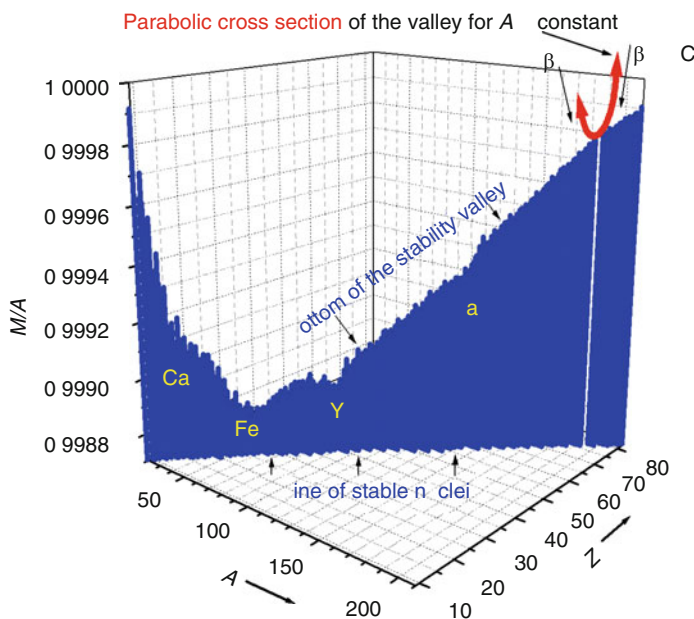
important decay modes. Since the notation in [Chap. 2](#) follows the “jargon” of nuclear physics, a “translation” between this chapter and [Chap. 2](#) will also be given. For instance, the text “decay constant (\rightarrow transition rate)” is meant to indicate that the decay constant is called transition rate in that particular part of [Chap. 2](#), which is referred to. The reader can find a very good theoretical introduction to this field in Friedlander et al. (1981) or in Lefort (1968).

7.5.1 Alpha Decay

Alpha emitters are found among the large- Z nuclides (e.g., $^{144}_{60}\text{Nd}_{84}$ and above) for which, not too far from the bottom of the stability valley (see [Fig. 7.13](#)), the number of neutrons exceeds that of the protons, i.e., the ratio N/Z is greater than 1. Under such conditions, the alpha decay,

Fig. 7.13

The stability valley of nuclei. The vertical projection of the bottom of the valley on the $Z \times A$ plane follows the line of stable nuclei (cf. [Fig. 2.7 in Chap. 2](#)) at an “altitude” expressed by the ratio of the nuclidic mass (M) and the mass number (A). The horizontal projection of the bottom of the valley onto the $(M/A) \times A$ plane is essentially the same as the graph labeled “experimental” in [Fig. 2.3 in Chap. 2](#), except that it is upside down. The isobaric cross sections of the valley are parabolic as a consequence of the Weizsäcker formula [\(2.3\) in Chap. 2](#). (See also the legend of [Fig. 7.2](#) in this chapter, as well as [Fig. 14.5 in Chap. 14, Vol. 2.](#)) The local dips marked are related to magic numbers (Ca: $N = 20$; Fe–Ni: $N = 28$, $Z = 28$; Y: $N = 50$; Ba: $N = 82$). Beta decay occurs all along the valley. On the near side of the valley β^- decay is predominant, on the far side β^+ decay and electron capture (EC) compete with each other as indicated on the parabola. Alpha decay occurs for $A > 60$ mainly on the far side of the valley





will further increase this ratio

$$\frac{N-2}{Z-2} > \frac{N}{Z} > 1. \quad (7.70)$$

Therefore, if a nuclide is situated at the low- N side of the valley (i.e., its N/Z ratio is less than for its most stable neighbors), alpha decay can move it closer to the bottom of the valley and so the nuclide is apt to undergo alpha decay. (In certain cases, even neutron-rich nuclei, e.g., some Po isotopes, may undergo α decay because the Q -value of the process turns out to be positive.)

During the early decades of nuclear physics it had been thought that the alpha radiation of each alpha-emitting nuclide was monoenergetic. It was not till 1929 that Rosenblum (1930) discovered the alpha radiation of ${}^{212}_{83}\text{Bi}$ consisting of alpha particles of different energies. Further experiments have demonstrated that alpha energies are always discrete even in such cases, and the energy excess still possessed by the nucleus above its ground level is emitted in the form of a gamma photon.

It should be noted that a different value of λ belongs to each different value of E_α . Thus the effective λ (as well as the effective $T_{1/2}$) for an α -emitting nucleus is determined by the sum of partial decay constants: $\sum \lambda_i$. (Note that this is a special type of branching decay consisting of α branches only.)

Alpha energies are usually between 4–6 MeV and these limits are exceeded only in a few cases. The total variation is marked by ${}^{144}_{60}\text{Nd}$ (1.8 MeV) and ${}^{212\text{m}}_{84}\text{Po}$ (11.7 MeV). On the other hand, the half-lives cover about 30 decimal magnitudes from ${}^{213}_{85}\text{At}$ (10^{-7} s) to ${}^{148}_{62}\text{Sm}$ (10^{16} a $\approx 3 \times 10^{23}$ s). Note that the above figures do not include those of the process ${}^8_4\text{Be} \rightarrow 2\alpha$ that keeps the alpha burning in massive stars under control. The half-life of this cosmologically important decay is only about 10^{-16} s or so (see [Chapter 12 in Vol. 2](#), on “The Origin of the Chemical Elements”).

As shown in [Chapter 2](#), there is a negative correlation between half-life and alpha energy. The strong energy dependence of partial half-lives explains why the complexity of alpha spectra remained undetected for such a long time: the branch producing the most energetic alpha particles often dominates the whole decay process.

The first decay-constant systematics proposed is called the Geiger–Nuttall rule (see [Eq. \(2.60\) in Chap. 2](#)). This rule, set up originally as a decay-constant – alpha-range relationship, can be readily converted into the following half-life – alpha-energy relationship:

$$\log\{T_{1/2}\} = a \log\{E_\alpha\} + b, \quad (7.71)$$

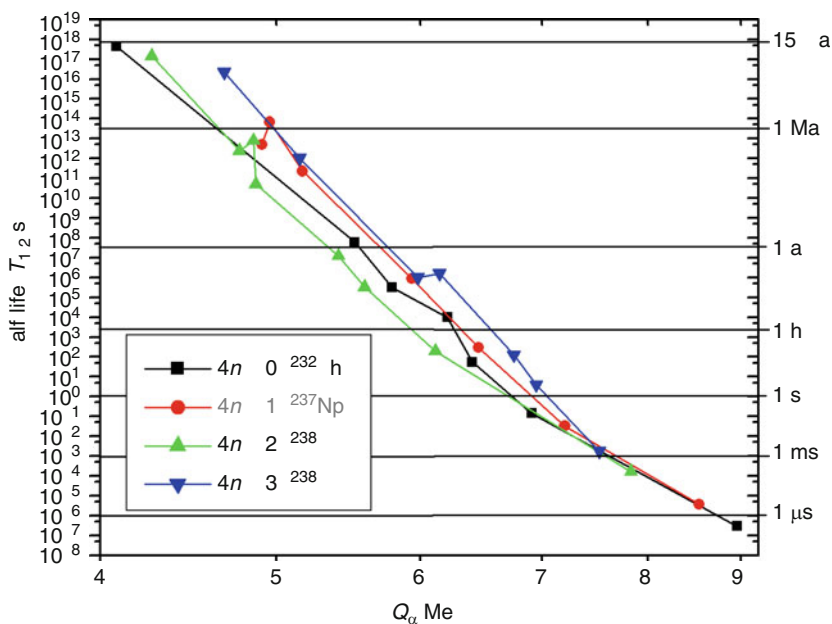
where $a < 0$ is a constant and $\{x\}$ stands for the numerical value of the physical quantity x in some unit $[x]$. On the other hand, b has a different (but constant) value for each decay series. So the logarithmic plots of the individual series are represented by parallel straight lines shifted according to the difference in the parameter b .

Note that the Geiger–Nuttall plot of the $4n + 3$ series is way above the $4n + 0$ and $4n + 2$ series (see [Fig. 7.14](#)). This is so because odd- Z and odd- N nuclei decay more slowly than even–even ones owing to shell effects. This kind of hindrance has saved, e.g., the very important even–odd nuclide ${}^{235}_{92}\text{U}_{143}$ – the primary parent of the $4n + 3$ series – from extinction on Earth (Friedlander et al. 1981).

Chapter 2 contains further expressions describing such systematics.

■ Fig. 7.14

Modern Geiger–Nuttall plot for the α -decaying nuclides of the four major decay chains including the three naturally occurring ones (starting from ^{232}Th , ^{238}U , and ^{235}U) once studied by the eponyms of this type of log–log presentation. The label of the fourth series (starting from ^{237}Np) is in gray color to indicate that this series has been wiped out from Earth due to its relatively short half-life. Note that the α half-lives sweep the range from less than a microsecond (see the labels along the right vertical axis) to 15 billion years (the estimated age of our Universe), which means a scale of ~ 24 decimal or ~ 80 binary orders of magnitude. The Q -values ($\sim E_\alpha$), on the other hand, only drop from 9 MeV to about 4 MeV, a range just about a little wider than 1 binary order of magnitude (i.e., a range covered by a factor of 2).



The empirical Taagepera–Nurmia formula (► Eq. (2.61), Chap. 2) describes the alpha half-life as the function of alpha-energy and the atomic number of the daughter nucleus. ► Figure 2.34 in Chap. 2 illustrates the relationship.

The theoretical Gamow–Condon–Gurney formula (► Eq. (2.65), Chap. 2) describes the alpha decay constant as a function of the alpha-energy (or rather the Q -value of the alpha decay), as well as the nuclear radius and the atomic number of the daughter.

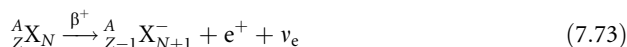
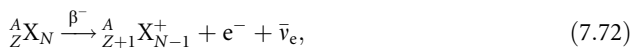
The Gamow–Condon–Gurney formula only applies when the alpha particle is emitted with zero angular momentum. The probability for alpha decay taking away angular momentum is considerably smaller (see ► Eq. (2.68) and ► Table 2.8 in Chap. 2).

7.5.2 Beta Decay

Beta emitters are found all along the stability valley (see ► Fig. 7.13) starting from ^3_1H up to $^{253}_{98}\text{Cf}$.

If, as a result of β decay, excited nuclei are formed, the ground state will be reached through the emission of monoenergetic gamma photons. One might expect, therefore, that β radiation, too, is “monochromatic,” consisting of electrons with energy $Q_\beta - E_\gamma$ each. In reality, however, β spectra are of continuous character with an energy distribution extending from zero to $E_\beta = Q_\beta - E_\gamma$. The energy distribution of the neutrinos is also continuous, being the mirror image of the bell-shaped electron-energy distribution.

This holds both for negative and positive beta decay:



but not for electron capture, the alternative to positive beta decay



in which monoenergetic neutrinos are emitted since there is no third particle in the final state.

Maximum beta energies (E_β) span even wider range than alpha energies from the extremely soft 17–18 keV negatron (i.e., β^-) radiation of ${}_1^3\text{H}$ and ${}_{82}^{210}\text{Pb}$, to the very hard 14 MeV positron (i.e., β^+) radiation of ${}_5^8\text{B}$. The typical E_β range – from a few hundred keV to a few MeV – is lower than the usual range of alpha energies (4–7 MeV). Beta half-lives range from fractions of a second for nuclides far from the bottom of the valley of beta stability to billions of years exemplified by ${}_{19}^{40}\text{K}$ (1.25×10^9 a) and ${}_{37}^{87}\text{Rb}$ (4.7×10^{10} a), both of them being important for radioactive dating.

Double beta (2β) decay should also be mentioned here in which two beta particles and two neutrinos are emitted simultaneously. The typical half-life is on the order of 10^{20} a, and therefore such primordial radionuclides can be considered stable for any practical purpose. (Note that the estimated age of our Universe is only about 1.4×10^{10} a according to some recent measurements mentioned in [▶ Chap. 12 of Vol. 2.](#))

The energy dependence of the decay constant for negative β decay can be very roughly described by the following empirical formula similar to the Geiger–Nuttall rule:

$$\log(\lambda) = \alpha \log(E_\beta) + \beta, \quad (7.75)$$

where $\alpha > 0$ and β are constant for separate groups of β -decaying nuclides (Sargent 1933). The Sargent rule, expressed by the above formula, predicts a very steep increase of the decay constant as a function of the beta energy.

The theory of beta decay developed by Fermi is summarized in [▶ Chap. 2](#). The theoretical relationship describing the dependence of the beta decay constant on beta energy E_β ($\rightarrow E_0$) and atomic number Z is given by [▶ Eqs. \(2.82\) and \(2.83\) in Chap. 2](#). For allowed transitions one can approximately write

$$\lambda = \frac{\ln 2}{T_{1/2}} \propto f(Z, E_\beta) \quad (7.76)$$

where $f(Z, E_\beta)$ is the Fermi integral function defined by [▶ Eq. \(2.83\) in Chap. 2](#).

The product

$$ft \equiv f(Z, E_\beta) T_{1/2} \quad (7.77)$$

is called comparative half-life. The function f contains the trivial dependence of $(T_{1/2})^{-1}$ on the nuclear charge and size, on the decay energy and multipolarity (change of angular

momentum). Thus ft should only depend on the nuclear matrix elements, i.e., on the nontrivial nuclear structure effects. The ft varies in a wide range as shown in [Table 2.10 of Chap. 2](#), depending on the structure of the nucleus and the type of transition.

Still, the Fermi integral function $f(Z, E_\beta)$ is very useful even in the general case, because it can help visualize the overall dependence of the decay constant λ on the beta energy E_β and the atomic number Z . For instance, [Figs. 42A and B in Chap. 2](#) (as well as [Fig. 7.15](#)) show that (1) the probability for beta decay steeply increases with beta energy (this is equally true for positive and negative beta decay), (2) negative beta decay becomes more probable as the atomic number increases, (3) positive beta decay becomes less probable as the atomic number increases.

Friedlander et al. (1981) cite empirical formulas for the energy- and atomic-number dependence of the Fermi integral function. The following formulas (see also [Fig. 7.15](#)) are valid in the intervals $0 < Z \leq 100$ and $0.1 < E_\beta < 10$ (where Z is the atomic number of the daughter and E_β is the maximum of the beta energy):

$$\log f_{\beta^-} = 4 \log (E_\beta/\text{MeV}) - 0.005(Z - 1) \log (E_\beta/\text{MeV}) + 0.02 Z + 0.78, \quad (7.78)$$

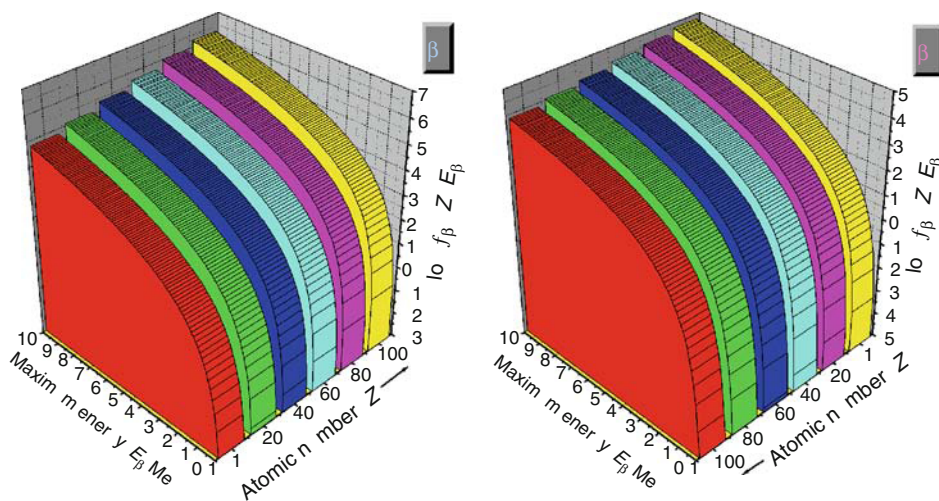
$$\log f_{\beta^+} = 4 \log (E_\beta/\text{MeV}) - 0.009(Z + 1) \left(\log \frac{E_\beta/\text{MeV}}{3} \right)^2 - 0.007 Z + 0.79. \quad (7.79)$$

The respective EC formula gives best approximation for $E_\beta > 0.5$ MeV and for low values of Z (see also [Fig. 7.16](#)):

$$\log f_{\text{EC}} = 2 \log (E_\beta/\text{MeV}) + 3.5 \log (Z + 1) - 5.6. \quad (7.80)$$

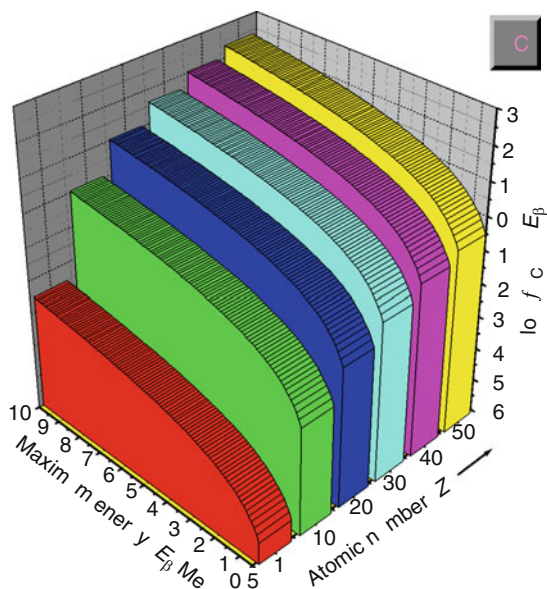
Fig. 7.15

The Fermi integral function for negative (to the left) and positive beta decay (to the right) calculated from [Eqs. \(7.78\) and \(7.79\)](#). Note that the directions of the Z axes are different in accordance with an opposite trend in the Z dependence of f



■ Fig. 7.16

The Fermi integral function for electron capture calculated from ▶ Eq. (7.80). The figure shows that EC is most likely for larger values of Z



As mentioned before, electron capture is the alternative process to positive beta decay. For lower decay energies, electron capture often comes out on top from the competition, due to its less demanding energetic condition (see ▶ Sect. 2.4.2 in Chap. 2).

▶ Figure 2.42C in Chap. 2 shows the branching ratio $\lambda_{EC}/\lambda_{\beta^+}$ ($\rightarrow K/\beta^+$) as a function of E_{β} for different values of the atomic number. The figure demonstrates that, for a constant value of Z (i.e., when comparing different isotopes of the same chemical element), larger beta energy favors β^+ decay. At any given energy, on the other hand, heavier nuclides prefer to undergo EC. (Note that the larger Z , the larger is the probability to find a shell electron in the nucleus – a necessary condition for electron capture.)

Friedlander et al. (1981) also cite an approximate formula for the branching ratio of L- and K-capture in allowed transitions:

$$\frac{\lambda_L}{\lambda_K} = (0.0011 Z + 0.06) \left[\frac{E_L(v)}{E_K(v)} \right]^2, \quad (7.81)$$

where $E_L(v)$ and $E_K(v)$ are the energy of the neutrino for L- and K-capture, respectively. (The neutrino energy equals E_{β} less the binding energy of the electron.)

7.5.3 Gamma Decay

If, for some reason (e.g., as a consequence of α or β decay), an excited nucleus is formed, the excited state will sooner or later de-excite via gamma decay or alternative processes like internal

conversion or the emission of an electron-positron pair. The latter (rather rare) process is called pair emission. (Internal conversion and pair emission are the analogues of photoelectric effect and pair production, both discussed in [Chap. 8](#) on the “Interaction of Radiation with Matter.”)

In the case of γ decay,



the excitation energy (or, in other words, the transition energy $E_T = E_e - E_g$) is carried away by a γ photon (γ emission) as well as by the recoil of the nucleus:

$$E_T = E_\gamma + E_R. \quad (7.83)$$

Long-lived excited nuclei ($T_{1/2} \geq 1 \mu\text{s}$) are sometimes referred to as excited nuclear isomers and are indicated by a left superscript “m” standing for “metastable”:



In such cases the transition is referred to as isomeric transition (IT).

Excitation may sometimes provide protection against other types of (actual nuclear) decay. The excited isomer ${}^{114\text{m}}\text{In}$ serves with a good example of this. In this case first de-excitation takes place through γ emission ($T_{1/2} = 50 \text{ d}$, a very long half-life indeed for an excited state), and then the ground-state isomer ${}^{114}\text{In}$ is transformed by β^- decay ($T_{1/2} = 72 \text{ s}$).

It may also occur that, instead of a gamma photon, a shell electron is emitted. This alternative process for nuclear de-excitation is called internal conversion. Electron emission is then followed by the rearrangement of the electronic shell structure, which, in turn, is accompanied by X-ray emission, characteristic of the element concerned, or by the emission of another electron via Auger process.

The kinetic energy of a conversion electron is given by

$$E_{\text{ce}} = E_T - E_b > 0, \quad (7.85)$$

where E_b is the binding energy of the emitted shell electron and E_T is the transition energy.

Since the binding energy is different for the K-, L-, and M-shells, the kinetic energy of a conversion electron depends on the shell it was emitted from.

The so-called internal conversion coefficient (α) is defined as the ratio of the probability of electron emission (p_e) to that of gamma emission (p_γ):

$$\alpha = \frac{p_e}{p_\gamma} \quad (7.86)$$

The value of α is usually between 10^{-4} and 10^2 . It is calculated as the sum of partial values characteristic of the individual electronic shells:

$$\alpha = \alpha_K + \alpha_L + \alpha_M + \dots \quad (7.87)$$

where

$$\alpha_K = \frac{p_e(n=1)}{p_\gamma}; \alpha_L = \frac{p_e(n=2)}{p_\gamma}; \alpha_M = \frac{p_e(n=3)}{p_\gamma}; \dots \quad (7.88)$$

and n is the principal quantum number.

It is an empirical fact that $\alpha_K > \alpha_L > \alpha_M \dots$ whenever it is energetically possible to emit K, L, M, ... electrons (see [Eq. \(7.85\)](#)).

The dependence of the decay constant (\rightarrow transition rate) of low-energy excited isomers ($E_\gamma < 10$ MeV) on the energy (E_γ), electric ($\rightarrow \sigma = E$) or magnetic ($\rightarrow \sigma = M$) character, and on the multipolarity ($\rightarrow 2^L$; with a common notation: EL or ML) of the radiation as well as on the initial and final value of the nuclear spin ($\rightarrow J_i, J_f$) (and other structural properties of the nucleus) is given by [Eq. \(2.32\) in Chap. 2](#).

[Equations \(2.37\) and \(2.38\) in Chap. 2](#) show the explicit dependence of the decay constant (\rightarrow transition rate) of electric (EL) and magnetic (ML) 2^L -pole transitions, respectively, on the energy and multipolarity of the radiation, as well as on the nuclear radius in the special case of nuclei containing one single nucleon outside the closed core. The different sub-cases representing $E1, E2, \dots$ as well as $M1, M2, \dots$ transitions are summarized in [Table 2.7 of Chap. 2](#), as algebraic expressions of the mass number and the gamma energy. The energy dependence of the half-life is shown by [Fig. 2.13 in Chap. 2](#) for different multipole radiations. The logarithmic plot reveals that (1) the larger the transition energy, the faster the transition, (2) the lower the multipolarity, the faster the transition (the rule holds for allowed transitions and separately for EL and ML radiations); if therefore $E1$ (or $M1$) is allowed, then $E2, E3, \dots$ ($M2, M3, \dots$) can be neglected, (3) for any given multipolarity the electric transition is faster than the magnetic transition, (4) for any given energy, the transition rate decreases in the following order: $E1 > M1 > E2 > M2 > E3 > M3 > E4 > M4$.

The half-life of excited states (isomers) depends on the change of nuclear spin (ΔI) and parity in the transition as well as on the transition energy (E_T). The greater is ΔI , the longer is $T_{1/2}$, but an increase in E_T causes a decrease in the half-life.

7.5.4 Spontaneous Fission

It is known that the fission of heavy nuclei to lighter ones is an energy-producing process above about $A = 100$, however actual fission is only observed for $A \geq 230$. The reason why the instability of heavy nuclides does not lead to prompt fission automatically lies in the existence of the so-called fission barrier analogous to the potential barrier of alpha decay. Nevertheless, spontaneous fission *does* exist, in spite of the fission barrier. This can be explained (similarly to α decay) by tunneling. Since the probability for heavier particles to get across the barrier is less than that for α particles, the half-life for spontaneous fission is usually much longer than for α decay. However, some of the heavy transuranium elements fission with relatively short half-lives. ^{235}U nuclei undergo α decay with $T_{1/2} = 7 \times 10^8$ a and spontaneous fission with $T_{1/2} = 2 \times 10^{17}$ a, i.e., only one out of 300 million atoms disintegrates by fission. ^{254}Cf , on the other hand, decays only by spontaneous fission with a half-life of just 55 d, which is too short a time to be explained by tunneling.

The partial half-lives for spontaneous fission of even–even nuclei are shown in [Fig. 4.4 in Chap. 4](#) as the function of the fissility parameter Z^2/A . Note that there is a general trend for the half-life to decrease as the fissility parameter increases. However, the lines connecting the points representing the same (even- Z) element go through a maximum owing to shell effects. One can also observe that heavier elements (larger Z) tend to undergo spontaneous fission more easily. (Note that as the atomic number increases from $Z = 90$ to $Z = 106$, the partial half-life decreases about 30 orders of magnitude.)

It is interesting to note that when either Z or N is odd, the half-life tends to be much longer (see [Fig. 4.5 in Chap. 4](#)). On the other hand, the half-lives of the fission isomers are many orders of magnitude below the general trend (see [Fig. 4.31 in Chap. 4](#)).²

7.6 Editors' Note

1. The statistical nature of radioactive decay is a quantum effect and, as such, emerges from an intrinsic indefiniteness in the quantum mechanical state of each nucleus of a sample. Decay can thus be described as a time-dependent evolution of a single nucleus. However, quantum mechanics does not allow the existence of purely exponential decay. One can convince oneself of this statement by recognizing that (1) a pure exponential decay must have been started an infinitely long time ago and must last up to infinity; (2) in such a state the probability of finding the emitted particle in the vicinity of any point of space must decrease exponentially in time at the same rate. From proposal (2) it follows that such a state cannot be normalized, thus it cannot be a genuine quantum mechanical state. Nevertheless, one can introduce the exponential time dependence as an approximation in the Schrödinger equation, and end up with a generalized eigenvalue problem for the spatial factor of the wave function of the decaying state. This eigenfunction is called the Gamow wave function, and it turns out to be a good approximation to the exact time-dependent decaying state. The exact state departs from the exponential law at the time of its birth in a way that is specific to each nucleus and, again, toward the end of its life, i.e., after a great many half-lives have passed since its birth. These deviations from the decay law are, however, too delicate to have any practical consequences (p. 336).
2. It may be mentioned that there exist decay modes in between α decay and fission, which are called (heavy-) cluster decay. The typical clusters emitted are ^{14}C , ^{18}O , etc. (see [Figs. 7.4–7.7](#)). These decay modes are regarded as types of radioactivity, like α decay, since, the cluster is emitted in its ground state and the residual nucleus is brought about either in its ground state or in some low-lying excited state. In fission, the products are usually highly excited and de-excite partly via neutron emission. However, recently cold fission was also discovered; in that process the nucleus disintegrates into two nearly equal fragments with low excitation energies and hardly any particle emission. Cold fission is half-way between fission and cluster decay. All these exotic processes are extremely rare (p. 361).

References

- | | |
|---|--|
| Bateman H (1910) <i>Proc Cambridge Philos Soc</i> 15:423 | Rosenblum SJ (1930) <i>J Phys Radium Paris</i> 1:438 |
| Choppin GR, Rydberg J (1980) <i>Nuclear chemistry: theory and applications</i> . Pergamon, Oxford | Rubinson W (1949) <i>J Chem Phys</i> 17:542 |
| Ehmann WD, Vance DE (1991) <i>Radiochemistry and nuclear methods of analysis</i> . Wiley, New York | Sargent BW (1933) <i>Proc Roy Soc A</i> 139:569 |
| Friedlander G, Kennedy JW, Macias ES, Miller JM (1981) <i>Nuclear and radiochemistry</i> . Wiley, New York | Vértes A, Kiss I (1987) <i>Nuclear chemistry</i> . Elsevier, Amsterdam |
| Lefort M (1968) <i>Nuclear chemistry</i> . Nostrand, London | Vértes A, Nagy S, Süvegh K (1998) <i>Nuclear methods in mineralogy and geology</i> , Chap. 1. Plenum, New York |
| Rényi A (1979) <i>Wahrscheinlichkeitsrechnung. Mit einem Anhang über Informationstheorie</i> , 6. Aufl. VEB Deutscher Verlag der Wissenschaften, Berlin | |

8 Interaction of Radiation with Matter

D. Horváth^{1,2} · A. Vértés³

¹KFKI Research Institute for Particle and Nuclear Physics, Budapest, Hungary

²Institute of Nuclear Research, Debrecen, Hungary

³Eötvös Loránd University, Budapest, Hungary

8.1	<i>Introduction</i>	365
8.2	<i>Heavy Charged Particles</i>	365
8.2.1	The Bethe–Bloch Equation	365
8.2.2	Stopping Power at Low Energies	370
8.2.3	Energy Loss in Mixtures and Compounds	372
8.2.4	Fluctuations in the energy loss	373
8.2.5	Secondary Electrons, Ionization Yields	374
8.2.6	Single Scattering	374
8.3	<i>Interaction of Electrons with Matter</i>	376
8.3.1	Energy Loss of Electrons by Ionization	376
8.3.2	Energy Loss of Electrons by Radiation	378
8.3.2.1	Nuclear Bremsstrahlung	378
8.3.2.2	Electron-Electron Bremsstrahlung	378
8.3.2.3	Critical Energy	378
8.3.2.4	Radiation Length	379
8.3.3	Electron Stopping Power	380
8.3.4	Electron Scattering	380
8.3.5	Absorption of β Radiation	381
8.3.6	Cherenkov Radiation and Transition Radiation	382
8.3.6.1	Cherenkov Radiation	382
8.3.6.2	Transition Radiation	383
8.4	<i>Interaction of Photons with Matter</i>	384
8.4.1	Compton Effect	384
8.4.2	Thomson and Rayleigh Scattering	387
8.4.3	Photoelectric Effect	387
8.4.4	Pair Production	388
8.4.5	Photon-Photon Interaction	388
8.4.6	Photon Attenuation	389

8.5 *Complex Interactions* **390**
8.5.1 Electron-Photon Showers 390
8.5.2 Auger Effect 390

Abstract: The effects of interactions of the various kinds of nuclear radiation with matter are summarized with special emphasis on relations to nuclear chemistry and possible applications. The Bethe–Bloch theory describes the slowing down process of heavy charged particles via ionization, and it is modified for electrons and photons to include radiation effects like bremsstrahlung and pair production. Special emphasis is given to processes involved in particle detection, the Cherenkov effect and transition radiation. Useful formulae, numerical constants, and graphs are provided to help calculations of the stopping power of particles in simple and composite materials.

8.1 Introduction

The interaction of nuclear radiation with matter is one of the most important aspects in nuclear chemistry, since most phenomena and applications of the discipline are, in one way or another, related to it. As a result of the interactions, changes may occur in the physical parameters and in the state (energy, direction, absorption) of the radiation particles as well as in the atoms and molecules of the substance (via ionization, excitation, nuclear reaction and, as a secondary effect, chemical reaction). The possible changes are summarized in [▶ Table 8.1](#).

The notation and units of the present review are summarized in [▶ Table 8.2](#). Relativistic notation is used: the particle speed β is given in units of c (speed of light in vacuum) and the (total) energy of the incident particle is $E = \gamma Mc^2$ (where γ is the relativistic Lorentz factor) which formula is then equally applicable to electrons and heavy particles. Throughout this chapter, the symbol E stands for the total (relativistic) energy of a particle including its rest energy Mc^2 , where M (without the subscript 0 used, e.g., in [▶ Chap. 3](#)) is the rest mass. The only exception is E_β , the maximum β -particle energy, which is a kinetic type of energy denoted elsewhere in this chapter by T .

For heavy particles and at low energies $E = \gamma Mc^2$ reduces to the classical $E = Mc^2 + Mu^2/2$, that is, the sum of rest energy and kinetic energy.

The effects of the interaction are classified according to the acting particle and the reacting constituents of the substance (shell electrons or atomic nuclei). The probabilities of different reactions are characterized by individual cross sections.

Basically, there are four different types of incident radiation: heavy charged particles, electron, photon, and neutron. (For neutron interactions see [▶ Chaps. 3 and 4](#) in this Volume as well as [▶ Chap. 38](#) in Vol. 4.) In this review the logic of Bichsel et al. (2002) is followed; however, while discussing the low-energy phenomena extensively, high-energy aspects are enlarged upon rather sparingly since the latter are much less important in nuclear chemistry.

8.2 Heavy Charged Particles

8.2.1 The Bethe–Bloch Equation

At not too high energies, the charged particles other than electrons or positrons (i.e., muons, pions, protons, or atomic nuclei like the α particle) lose their kinetic energy primarily by ionization. The possible interactions are summarized in [▶ Table 8.3](#).

Table 8.1

Classification of radiation-matter interactions, phenomena involved, and examples of application in chemistry

Interacting partner		Radiation				Matter			
Phenomenon	Energy loss	Scattering		Absorption		Stopping in matter (decay, atomic or nuclear absorption)	Ionization, atomic excitation (chemical changes)	Nuclear excitation	Nuclear reaction
		Elastic	Inelastic	Transformation (pair production, annihilation)					
Example of application	Fluorescence spectroscopy, synchrotron radiation	Rutherford back-scattering on surfaces		Positron annihilation spectroscopy	Muon spin resonance spectroscopy		Radiation detectors, radiochemistry	Mössbauer effect	Nuclide production, activation analysis

■ **Table 8.2**

Summary of the physical quantities used in this chapter. The notation of Bichsel et al. (2002) is followed

Symbol	Definition	Value and/or unit
$\alpha = e^2/(4\pi\epsilon_0\hbar c)$	Fine structure constant	1/137.036
c	Speed of light in vacuum	299 792 458 m/s
$\beta = u/c$	Relative speed of the incident particle	
$\gamma = \sqrt{1/(1 - \beta^2)}$	Relativistic factor	
M	Rest mass of incident particle	MeV/ c^2 , GeV/ c^2
$E = \gamma Mc^2$	Particle energy	MeV, GeV
$T = Mu^2/2$	Non-relativistic kinetic energy	
ze	Particle charge	
$m_e c^2$	Electron rest mass $\times c^2$	0.511 MeV
$r_e = e^2/(4\pi\epsilon_0 m_e c^2)$	Classical electron radius	2.817940×10^{-15} m
Z	Atomic number of absorber	
A	Molar mass of absorber atoms	g/mol
N_A	Avogadro's constant	6.022142×10^{23} mol $^{-1}$
$K = 4\pi N_A r_e^2 m_e c^2$	Constant in stopping power	0.307075 MeV cm 2
ρ	Density of medium	g/cm 3
I	Mean (electronic) excitation energy of an element	eV
δ	Density effect correction	
N_e	Electron (number) density	Units of r_e^{-3}
$\hbar\omega_p = \sqrt{4\pi N_e r_e^2 m_e c^2}/\alpha$	Plasma energy	$28.816 \sqrt{\rho (Z/A)}$ eV
ω_j	Mass fraction of j th element in a compound or mixture	
n_j	Number of j th kind of atom in a compound or mixture	
X_0	Radiation length (in surface density)	g/cm 2
E_c	Critical energy for electrons	MeV
$E_{\mu c}$	Critical energy for muons	GeV
$E_s = \sqrt{4\pi/\alpha} m_e c^2$	Scale energy	21.2052 MeV

The mean rate of energy loss, i.e., the **stopping power** is given by the Bethe–Bloch equation (Bethe and Ashkin 1953; Leo 1987; Bichsel et al. 2002):

$$-\frac{dE}{dx} = K Z^2 \frac{Z}{A} \frac{1}{\beta^2} \left[\frac{1}{2} \ln \frac{2m_e c^2 \beta^2 \gamma^2 T_{\max}}{I^2} - \beta^2 - \frac{\delta}{2} - \frac{C}{Z} \right] \quad (8.1)$$

where T_{\max} is the maximum kinetic energy which the incident particle can impart to a free electron in a collision, C/Z is the shell correction, C and δ are adjustable constants, characteristic of the medium, and the other quantities are defined in ► Table 8.2.

■ **Table 8.3**

Classification of the interactions of heavy charged particles in matter

Reacting constituent	Changes in	
	Radiation	Substance
Crystal lattice	Channeling	None
Shell electrons	Slowing down	Excitation, ionization, transition radiation Cherenkov radiation
	Atomic capture	Chemical changes
Atomic nuclei	Nuclear absorption particle decay	Nuclear reaction, chemical changes
Coulomb field of the nucleus	Scattering Slowing down	Recoil of atoms

In order to make the stopping power formulation applicable to both gases and condensed media, surface density is used instead of thickness, or in other words, the thickness x of the medium is measured in units of g/cm^2 .

The Bethe–Bloch equation reproduces the experimental data in the energy region from a few MeV to a few GeV with the precision of about 1%. At lower energies atomic shell effects, at higher energies radiation losses come into play.

At low and intermediate energies (i.e., practically for all purposes of the present book) for a particle with rest mass M and momentum $M\beta\gamma c$ the maximum imparted energy can be approximated as i

$$T_{\max} = \frac{2m_e c^2 \beta^2 \gamma^2}{1 + 2\gamma \frac{m_e}{M} + \left(\frac{m_e}{M}\right)^2} \approx 2m_e c^2 \beta^2 \gamma^2 \left(\frac{2m_e \gamma}{M} \ll 1 \right). \quad (8.2)$$

This approximation introduces, e.g., a ~6% error for the stopping power of muons in copper at 100 GeV.

Using ► Eq. (8.2) in ► Eq. (8.1) one gets the simplified form of the Bethe–Bloch equation

$$-\frac{dE}{dx} = K z^2 \frac{Z}{A} \frac{1}{\beta^2} \left[\ln \frac{2m_e c^2 \beta^2}{I(1 - \beta^2)} - \beta^2 \right] \quad (8.3)$$

where the density effect correction and the shell correction have been also neglected.

The effective ionization energy (or excitation energy) can roughly be approximated as $I = 10 Z \text{ eV}$. A better approximation is given by Leo (1987):

$$\frac{1}{z} = \begin{cases} 12 + 7/Z & Z < 13 \\ 9.76 + 58.5 Z^{-1.19} & Z \geq 13 \end{cases} \quad (8.4)$$

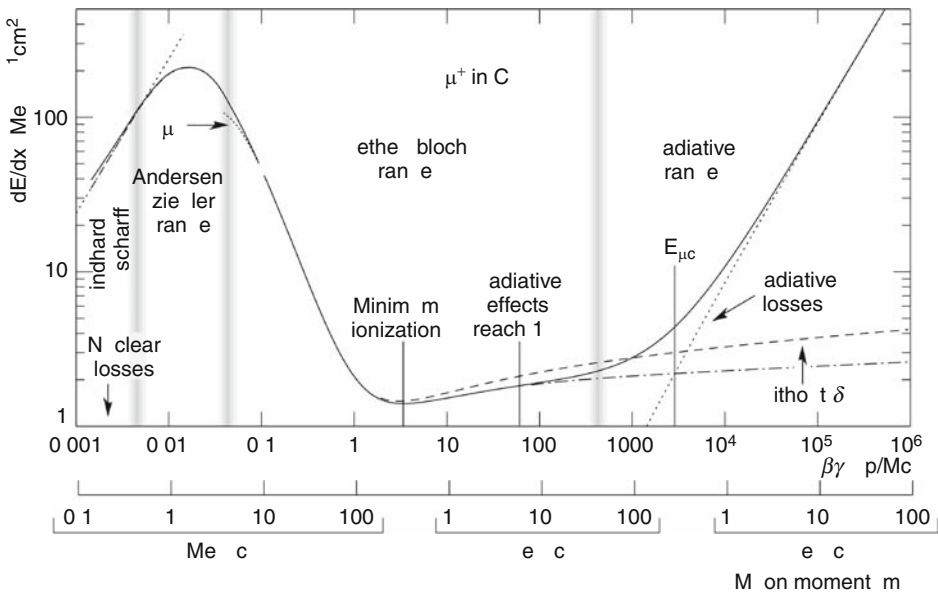
and experimentally adjusted values are tabulated by Groom et al. (2001).

Thus the stopping power depends on the charge and velocity of the incident particle as well as on the effective ionization potential and the atomic and mass numbers of the atoms of the medium.

The stopping power as computed for muons in copper (Bichsel et al. 2002; Groom et al. 2001) is shown in ► Fig. 8.1. Nuclear losses are significant at the lowest energies only, where the

■ Fig. 8.1

Stopping power vs. relative momentum, $\beta\gamma = p/Mc$, for muons in copper. The solid curve indicates the total stopping power, the dash-dotted and dashed lines the Bethe–Bloch equation with and without density effect correction. The vertical bands separate the validity regions of various approximations indicated in the figure. The dotted line denoted with μ^- indicates the Barkas effect. In the Bethe–Bloch region the stopping power scales with the particle mass and Z/A of the medium



difference between positive and negative particles is also noticeable due to the polarization of the medium (**Barkas effect**, Barkas et al. 1956). The Bethe–Bloch curve (dashed and dash-dotted lines) goes through a flat minimum (minimum ionizing region) and then slowly increases again due to radiation losses. The density effect correction δ is important at very high energies only. Most relativistic particles of laboratory energies have energy loss rates close to the minimum; those are called **minimum ionizing particles** or MIPs.

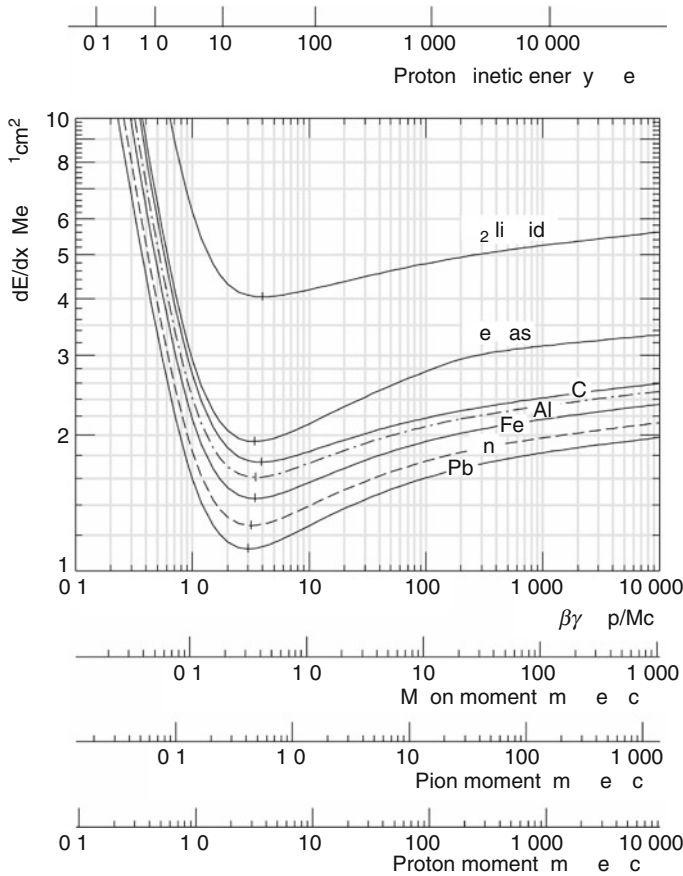
One can get an estimate (Bichsel et al. 2002) of the stopping power of various particles in various substances using ▶ Fig. 8.2. In ▶ Fig. 8.3 the ionization stopping power is plotted for various charged particles as measured in copper as a function of kinetic energy: one can see the scaling with particle mass.

Note, however, the substantial difference at high energies due to the strong interaction: pions are only slightly heavier than muons, and high-energy muons are almost impossible to contain in matter (all high-energy calorimeters are encircled by detectors to detect the escaping muons), whereas even the highest-energy pions produced in particle collisions are contained in materials of moderate thickness (e.g., the so-called hadron calorimeters of high-energy detectors).

One can deduce via integration of the Bethe–Bloch equation the R range of particles losing energy in matter via ionization only. As the stopping power scales with momentum, R/M will

■ Fig. 8.2

Stopping power due to ionization according to the Bethe–Bloch equation vs. relative momentum $\beta\gamma = p/Mc$ of heavy charged particles in liquid hydrogen, gaseous helium, carbon, aluminum, iron, tin and lead. Momentum scales are shown below the plot for muons, pions and protons and an energy scale for protons above



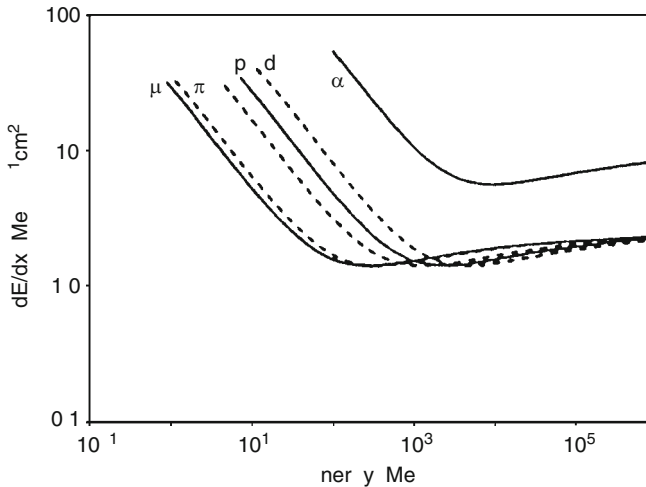
scale with $\beta\gamma$. Ranges in surface density units are presented in ▶ Fig. 8.4 for various particles and elements.

8.2.2 Stopping Power at Low Energies

At low energies electron shell effects should also be taken into account by using the C/Z shell correction, see (Groom et al. 2001) for details. The Bethe–Bloch equation (▶ Eq. (8.1)) is based on first-order Born approximation. Higher order effects, important at low energies only, can be included by adding a term $z^2 L_2(\beta)$ in the square brackets of ▶ Eq. (8.1) where $L_2(\beta)$ is an empirical function of particle speed.

■ Fig. 8.3

Stopping power due to ionization, according to the Bethe–Bloch equation, vs. kinetic energy of heavy charged particles in copper



The Barkas effect, which makes the stopping power for negative and positive particles different in matter, can also be included there as a term $zL_1(\beta)$; it makes the energy loss for a slow negative particle lower than for a positive one under identical conditions due to polarization of the medium. This effect is studied in detail at the Antiproton Decelerator at CERN (Moeller et al. 2002).

For low particle speeds ($0.01 < \beta < 0.05$) there is no satisfactory theory and so semi-empirical formulae are used. The most popular ones are those proposed by Groom et al. (2001), Andersen and Ziegler (1977) and Lindhard (1954). At the lowest energies, for example, for protons below a few hundred eV, non-ionizing nuclear energy loss dominates the stopping power (Groom et al. 2001; Ziegler et al. 1985).

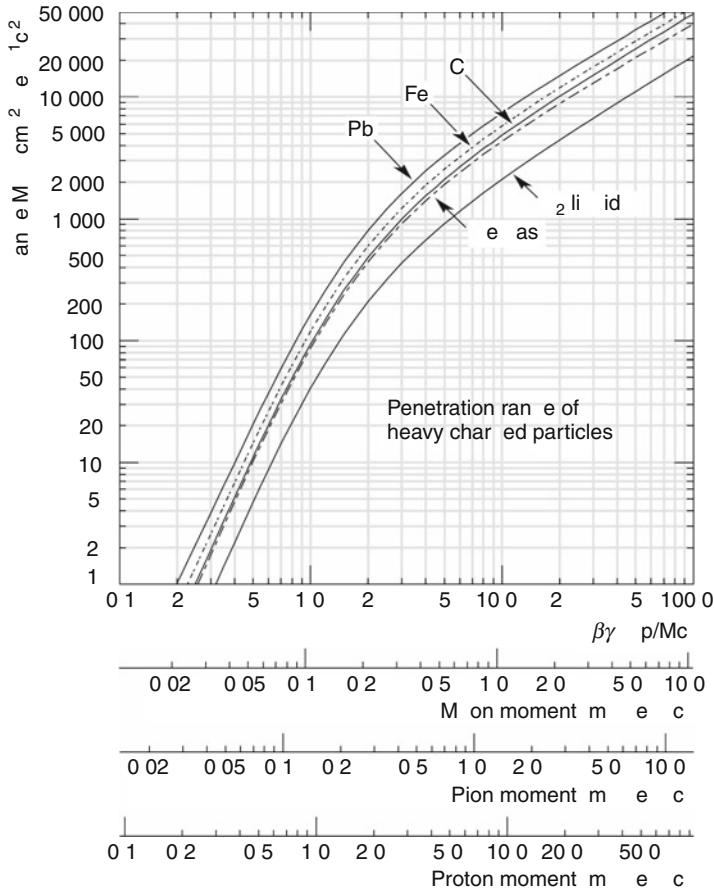
Thus, for instance, for protons in copper, the nuclear plus electronic stopping power is $113 \text{ MeV}/(\text{g cm}^{-2})$ at $T = 10 \text{ keV}$ kinetic energy ($4.3 \text{ MeV}/c$ momentum), then it rises to a maximum of $210 \text{ MeV}/(\text{g cm}^{-2})$ at $100\text{--}150 \text{ keV}$ ($15 \text{ MeV}/c$), and then it falls to $120 \text{ MeV}/(\text{g cm}^{-2})$ at 1 MeV ($44 \text{ MeV}/c$); see the lower momentum part in ▶ Fig. 8.1. Above $0.5\text{--}1 \text{ MeV}$ the Bethe–Bloch equation is adequate (Groom et al. 2001).

As the energy decreases, the stopping power increases according to the Bethe–Bloch formula. The plot of energy loss (which can be related to specific ionization) along the path of a charged particle penetrating a medium is called the **Bragg curve**. A typical Bragg curve is depicted in ▶ Fig. 8.5 for a proton of $\sim 26 \text{ MeV}$ initial energy (Besserer et al. 1997).

The sharp peak at the end of the penetration track of the charged particles is very important in nuclear medicine (e.g., when irradiating living tissue) as it ensures that most of the energy is deposited where the particle is stopped. This is especially promising for pions and antiprotons as they form **exotic atoms** (i.e., an atom where a pion or an antiproton is bound in an atomic orbit) and get absorbed by the nucleus, causing its fragmentation or fission (see ▶ Chap. 28 in Vol. 3). After nuclear capture in an exotic atom, the energy deposited by the nuclear fission fragments (created when the particle is absorbed by the nucleus) significantly increases the

■ Fig. 8.4

Penetration range (R) per particle mass vs. $\beta\gamma = p/Mc$ for heavy charged particles in liquid hydrogen, gaseous helium, carbon, aluminum, iron and lead. Momentum scales are shown for muons, pions and protons



local damage of the tissue. The energy of the particle should be chosen so that the region of stopping be concentrated on the malignant tissue (Lea 1962).

8.2.3 Energy Loss in Mixtures and Compounds

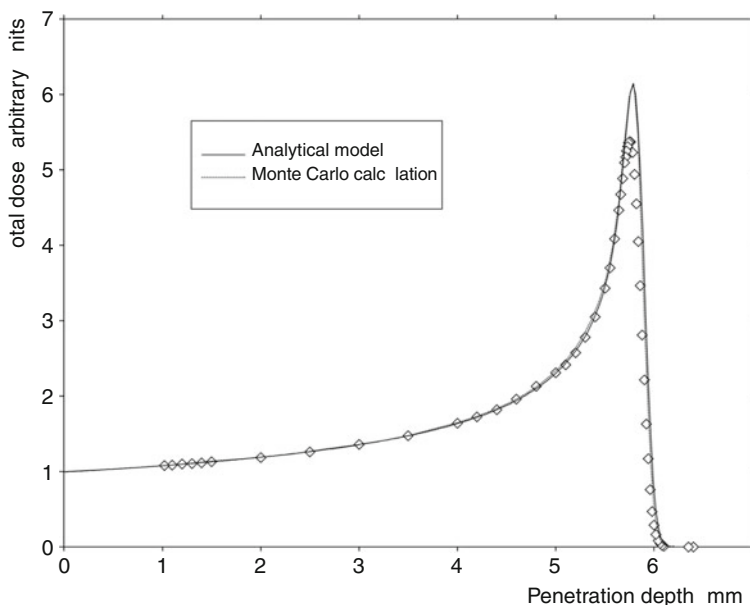
A mixture or compound can be treated as consisting of thin layers of pure elements in the correct proportion according to their mass fractions w_j (Bragg additivity):

$$\left\langle \frac{dE}{dx} \right\rangle = \sum_j w_j \left. \frac{dE}{dx} \right|_j \quad (8.5)$$

where $dE/dx|_j$ is the mean rate of energy loss in the j th element.

■ Fig. 8.5

Typical Bragg curve: deposited energy per distance (dE/dx) vs. penetration depth for protons of ~26 MeV initial energy. The experimental data are reasonably well described by theory and simulation



In principle, similar expressions can be used to estimate average $\langle Z/A \rangle$, $\langle I \rangle$ and $\langle \delta \rangle$ values; for instance,

$$\left\langle \frac{Z}{A} \right\rangle = \sum_j w_j \frac{Z_j}{A_j} = \frac{\sum_j n_j Z_j}{\sum_j n_j A_j}. \quad (8.6)$$

Note that this type of approximation underestimates $\langle I \rangle$ as in a compound the electrons are more tightly bound than in the elements, and $\langle \delta \rangle$ has no relevance as it is the effective electron density that matters. Those quantities have been tabulated for many compounds and nearly 200 mixtures by Sternheimer et al. (1984) and Seltzer and Berger (1984).

8.2.4 Fluctuations in the energy loss

In practice one uses the quantity $(-dE/dx)\Delta x$, the mean energy loss in a layer of Δx thickness. For finite Δx there will be fluctuations in the actual values, the distribution will be skewed toward higher values (**Landau tail**, Landau 1944) and only for thick layers ($T_{\max} \ll (-dE/dx)\Delta x$) will the distribution be Gaussian (see ▶ Sect. 9.3.6 in Chap. 9 on the “Stochastics and Nuclear Measurements”).

The fluctuations in energy loss are due to high-energy knock-on electrons and to the small number of collisions involving large energy transfers. In practice, one measures the *deposited* rather than the *lost* energy. When large amounts of energy are carried away by knock-on

electrons one may prefer to consider a mean energy loss by excluding single energy transfers greater than a given cutoff T_{cut} . This restricted loss rate (Bichsel et al. 2002) with a modified Bethe–Bloch equation is

$$-\frac{dE}{dx}\bigg|_{T < T_{\text{cut}}} = K_Z^2 \frac{Z}{A} \frac{1}{\beta^2} \left[\frac{1}{2} \ln \frac{2 m_e c^2 \beta^2 \gamma^2 T_{\text{upper}}}{I^2} - \frac{\beta^2}{2} \left(1 + \frac{T_{\text{upper}}}{T_{\text{max}}} \right) - \frac{\delta}{2} - \frac{C}{Z} \right] \quad (8.7)$$

where T_{upper} is the smaller of T_{cut} and T_{max} .

8.2.5 Secondary Electrons, Ionization Yields

The distribution of energetic knock-on electrons (δ rays) with kinetic energies $T \gg I$ is given by Rossi (1952) as

$$-\frac{d^2N}{dTdx} = \frac{1}{2} K_Z^2 \frac{Z}{A} \frac{1}{\beta^2} \frac{F(T)}{T^2} \quad (I \ll T \leq T_{\text{max}}), \quad (8.8)$$

where N is the number of electrons and the value of the $F(T)$ function is about unity for $T \ll T_{\text{max}}$; explicit formulae are given by Rossi (1952).


The total energy loss can be related to the number of ion pairs produced near the particle track. This relation becomes complicated for relativistic (β approaches to 1) particles due to the escape of energetic knock-on electrons whose range may exceed the dimensions of the sample. The mean local energy dissipation per ion pair produced, W , is essentially constant for relativistic particles and slowly increases at lower energies (Bichsel et al. 2002). It can be sensitive to the presence of contaminants in gases and may be influenced by subsequent recombination. The ionization yields are very important for a number of applications, especially for radiation detectors.

8.2.6 Single Scattering

A charged particle moving in a medium is deflected many times at small angles. This is mostly due to Coulomb scattering on nuclei, but for hadronic particles at low energies, the strong interaction also contributes. For really heavy projectiles (like the α particle) in very thin targets multiple scattering has a low probability and the angular dependence of the cross section can be described in the following way (Vértes and Kiss 1987).

Due to the Coulomb interaction a nucleus at rest forces an approaching α particle to follow a hyperbolic orbital. For this orbital one can write:

$$\cot \frac{\theta}{2} = l \frac{Mu_{\alpha}^2}{2Ze^2}, \quad (8.9)$$

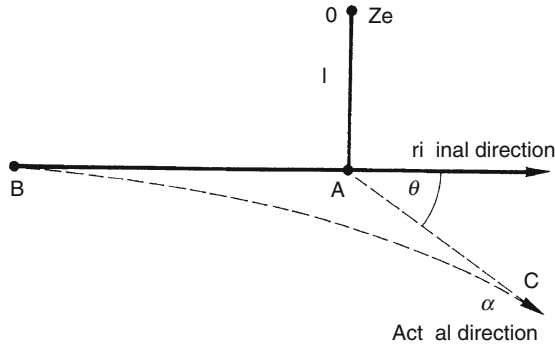
where $l = \overline{OA}$ as shown in  Fig. 8.6, and M and u_{α} are the mass and speed of the α particle, respectively.

If a flux of Φ_0 of α particles per unit area per unit time is being used, the number of particles per unit time crossing the ring-shaped cross section marked off by radii l and $(l + dl)$ around the nucleus is:

$$dN_{\theta} = \Phi_0 2\pi l dl. \quad (8.10)$$

■ Fig. 8.6

The trajectory of an alpha particle in the vicinity of an atomic nucleus with charge Ze



By substituting the expression of l from ► Eq. (8.9) into ► Eq. (8.10) one can write:

$$dN_\theta = \Phi_0 2\pi \left(\cot \frac{\theta}{2} \right) \left(\frac{2Ze^2}{Mu_\alpha^2} \right)^2 \frac{1}{\sin^2 \frac{\theta}{2}} d\left(\frac{\theta}{2} \right). \quad (8.11)$$

The quantity dN_θ can also be expressed as

$$dN_\theta = n_\theta d\omega \quad (8.12)$$

where n_θ is – apart from a constant factor – a probability density function (see ► Chap. 7 in this Volume) characterizing the “frequency” of scattering events per unit time in the solid angle $d\omega$ defined by θ and $\theta + d\theta$. Therefore:

$$d\omega = 2\pi \sin \theta d\theta. \quad (8.13)$$

Using ► Eqs. (8.11–8.13), one obtains:

$$\frac{n_\theta}{\Phi_0} = \left(\frac{Ze^2}{Mu_\alpha^2} \right)^2 \frac{1}{\sin^4(\theta/2)}. \quad (8.14)$$

The inverse proportionality to $\sin^4(\theta/2)$ ensures that single scattering leads to very small angles.

The fraction of energy retained by the scattered particle is (Turkevich et al. 1967)

$$\frac{E_\theta}{E_0} = \left[\frac{(4/A) \cos \theta + \sqrt{1 - (4/A)^2 \sin^2 \theta}}{1 + 4/A} \right]^2. \quad (8.15)$$

In thick samples the multiple Coulomb scattering distribution is well described by the **Molière distribution** (Molière 1947, 1948, 1955; Bichsel et al. 2002), which can be approximated for many applications by a Gaussian angular distribution of a width (i.e., standard deviation)

$$\theta_0 = \frac{13.6 \text{ MeV}}{\beta c p} z \sqrt{\frac{x}{X_0}} \left[1 + 0.038 \ln \frac{x}{X_0} \right], \quad (8.16)$$

where p , β , c and z are the momentum, velocity and charge number of the incident particle, and x/X_0 is the thickness in units of radiation length (defined as follows, in ► Sect. 8.3.2.4).

► Eq. (8.16) is accurate to 11% for thicknesses $10^{-3} < x/X_0 < 100$ (Bichsel et al. 2002).

8.3 Interaction of Electrons with Matter

The interaction of electrons with matter is different from that of heavier charged particles for two reasons. One of them is the electron mass which is more than two orders of magnitude lower than that of the second lightest charged particle, the muon; this makes photon radiation very important in the stopping power of electrons even at lower energies. The other reason is that at low energies, the interaction with shell electrons dominates and that is collision between identical particles, which has to be taken into account in the calculations.

Electrons (β radiation) excite and ionize the atoms and molecules of the substance, they are scattered by the electric field of the atomic nuclei and undergo inelastic collisions with shell electrons. They give kinetic energy to shell electrons or emit energy in the form of bremsstrahlung (an expression taken from German meaning *brake radiation*) while slowing down in the Coulomb field of nuclei. Thus part of the initial electron energy gets absorbed in the substance while another part can get out. These interactions are summarized in [Table 8.4](#).

At low energies electrons and positrons lose their energy predominantly via ionization although other processes can also contribute. Among the latter are Møller (electron-electron) scattering, $e^-e^- \rightarrow e^-e^-$, Bhabha (electron-positron) scattering, $e^+e^- \rightarrow e^+e^-$, and positron annihilation, $e^+e^- \rightarrow \gamma\gamma$ on the electrons of the substance. The total stopping power of the substance for electrons is the sum of the fractional energy losses by collisional and radiation processes (ionization and bremsstrahlung):

$$\frac{dE}{dx} = \left(\frac{dE}{dx} \right)_{\text{ion}} + \left(\frac{dE}{dx} \right)_{\text{brems}}. \quad (8.17)$$

8.3.1 Energy Loss of Electrons by Ionization

The Bethe–Bloch equation has to be modified for this case, and it will be valid both for electrons and positrons. The maximal energy transfer will become $T_{\text{max}} = T_e/2$ and the Bethe–Bloch formula becomes (Leo 1987)

$$-\left(\frac{dE}{dx} \right)_{\text{ion}} = \frac{K Z}{2 A \beta^2} \left[\ln \frac{\tau^2(\tau + 2)}{2(I/m_e c^2)^2} + F(\tau) - \delta - 2 \frac{C}{Z} \right] \quad (8.18)$$

where $\tau = T_e/(m_e c^2)$, T_e is the kinetic energy of the electron and

Table 8.4

Classification of the interactions of electrons (β radiation) in matter

Reacting constituent	Changes in	
	Radiation	Medium
Shell electrons	Slowing-down, absorption	Excitation, ionization, transition radiation, Cherenkov radiation, chemical changes
Coulomb field of the nucleus	Scattering, slowing-down, absorption	Nuclear reaction, chemical changes

$$F(\tau) = \begin{cases} 1 - \beta^2 + \frac{\tau^2/8 - (2\tau+1)\ln 2}{(\tau+1)^2} & \text{for } e^- \\ 2 \ln 2 - \frac{\beta^2}{12} \left(23 + \frac{14}{\tau+2} + \frac{10}{(\tau+2)^2} + \frac{4}{(\tau+2)^3} \right) & \text{for } e^+. \end{cases} \quad (8.19)$$

Note that Cherenkov radiation is very important for fast electrons, but its contribution to the energy loss is small and it is included in [Eq. \(8.18\)](#) (Leo 1987).

The ionization energy loss of non-relativistic electrons can be approximated (Vértes and Kiss 1987) as

$$-\left(\frac{dE}{dx}\right)_{\text{ion}} = \frac{2\pi e^4}{T_e} \frac{N_A Z}{A} \ln \frac{1.66 T_e}{I}. \quad (8.20)$$

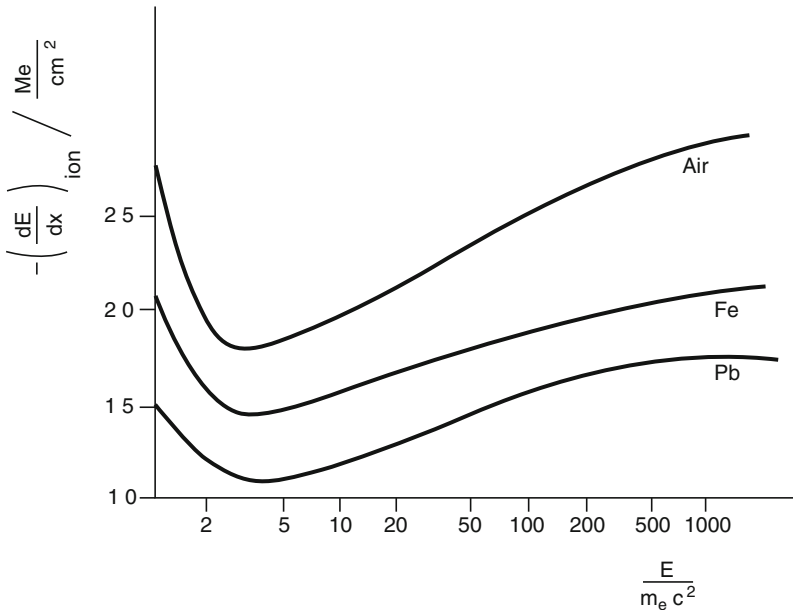
For relativistic electrons or positrons the following equation can be used (Vértes and Kiss 1987)

$$-\left(\frac{dE}{dx}\right)_{\text{ion}} = \frac{2\pi e^4}{m_e c^2} \frac{N_A Z}{A} \left(\ln \frac{E^3}{2m_e c^2 I^2} + \frac{1}{8} \right). \quad (8.21)$$

[Figure 8.7](#) presents ionization energy loss curves for electrons in some common materials.

Fig. 8.7

Energy loss of electrons owing to ionization in different absorbers (Vértes and Kiss 1987)



8.3.2 Energy Loss of Electrons by Radiation

8.3.2.1 Nuclear Bremsstrahlung

Bremsstrahlung accompanies the slowing down of charged particles in the Coulomb field of nuclei and atomic electrons. For a detailed treatment of bremsstrahlung the reader is referred to (Leo 1987); here some practical approximations are only given.

Since bremsstrahlung is a result of the interaction of the fast electron with the Coulomb field of the nucleus, the screening of the latter by atomic electrons plays an important role. This screening is characterized by the parameter (Leo 1987)

$$\xi = \frac{m_e c^2 E_f}{E_i E_f \alpha Z^{1/3}} \quad (8.22)$$

where E_i and E_f are the initial and final energy of the scattered electron ($E_f = E_i - E_\gamma$). Parameter ξ is related to the Thomas-Fermi radius of the atom ($\propto Z^{1/3}$); for no screening $\xi \gg 1$, and for complete screening $\xi = 0$.

At moderate energies ($m_e c^2 \ll E \ll m_e c^2 / Z^{1/3} \alpha$) the incident electron will feel no screening of the nucleus by the atomic electrons ($\xi \gg 1$), and the stopping power due to bremsstrahlung will be

$$-\left(\frac{dE}{dx}\right)_{\text{brems}} = 4r_e^2 \alpha \frac{N_A Z^2}{A} E \left[\ln \frac{2E}{m_e c^2} - \frac{1}{3} - f(\alpha Z) \right] \quad (8.23)$$

where (with the notation $a = \alpha Z$)

$$f(\alpha Z) = f(a) = a^2 \left[\frac{1}{1+a^2} + 0.20206 - 0.0369 a^2 + 0.0083 a^4 - 0.002 a^6 \right] \quad (8.24)$$

is the Coulomb correction which takes into account the interaction of the outgoing electron with the Coulomb field of the nucleus (Davies et al. 1954). High-energy electrons ($\xi \approx 0$; $E \gg m_e c^2 / Z^{1/3} \alpha$) will sense complete screening and their bremsstrahlung stopping power will become (Leo 1987)

$$-\left(\frac{dE}{dx}\right)_{\text{brems}} = 4r_e^2 \alpha \frac{N_A Z^2}{A} E \left[\ln(183 Z^{1/3}) + \frac{1}{18} - f(\alpha Z) \right]. \quad (8.25)$$

8.3.2.2 Electron-Electron Bremsstrahlung

Fast electrons also radiate in the field of the atomic electrons. This electron-electron bremsstrahlung has cross section very similar to that of the nuclear one except that it is proportional to Z instead of Z^2 . Thus, for the total energy loss, one approximately includes electron-electron bremsstrahlung as well if in the aforementioned equations Z^2 is replaced by $Z(Z+1)$ (Leo 1987).

8.3.2.3 Critical Energy

Critical energy, in general, is defined as the particle energy at which the ionization energy loss equals the radiation one. As the radiation losses depend very sensitively on the absorber

■ **Table 8.5**

Critical electron energies of selected absorbers (Leo 1987) including some detector materials

Material	Critical energy (MeV)
Air (STP)	102
H ₂ O	92
Al	51
Fe	27.4
Cu	24.8
Pb	9.51
Anthracene	105
Lucite	100
Nal	17.4
Polystyrene	109

material, the critical energy for electrons, E_c , is considered to be an important material constant. It can be roughly estimated by (Bethe and Ashkin 1953)

$$E_c = \frac{1600 m_e c^2}{Z}. \quad (8.26)$$

Critical electron energies of some commonly used materials are listed in ► [Table 8.5](#).

8.3.2.4 Radiation Length

Radiation length is a material constant similar to the critical energy and it is more widely used: it is the thickness over which the energy of an electron is reduced to a fraction $1/e$ of its original value due to radiation only. As in first order ► [Eqs. \(8.23\)](#) and ► [\(8.25\)](#) linearly depend on energy, the energy of a high-energy electron having passed through an absorber will depend on the absorber's surface density x as

$$E(x) = E_0 \exp(-x/X_0) \quad (8.27)$$

where X_0 is the radiation length of the absorber. Thus the fractional energy loss is roughly independent of the type of material when the absorber thickness is expressed in radiation lengths. ► [Table 8.6](#) quotes radiation lengths for some materials.

There is a simple formula to estimate the radiation lengths of elements (Bichsel et al. 2002):

$$X_0 = \frac{716.4 A}{Z(Z+1) \ln(287/\sqrt{Z})} \quad (8.28)$$

(in units of g/cm^2) and for mixtures and compounds one can use the Bragg additivity rule:

$$\frac{1}{X_0} = \sum_i w_i \frac{1}{X_0^i} \quad (8.29)$$

where w_i is the mass fraction of element i with radiation length X_0^i .

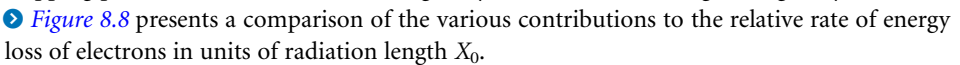
Note that the radiation length cannot be defined for low-energy electrons as their rest mass $m_e c^2$ cannot “disappear” and the kinetic energy may not be large enough to cover the energy loss required.

■ **Table 8.6**

Radiation lengths of selected absorbers (Leo 1987) including some detector materials

Material	Radiation length	
	X_0	
	(g/cm ²)	(cm)
Air (STP)	36.20	30,050
H ₂ O	36.08	36.1
Al	24.01	8.9
Fe	13.84	1.76
Cu	12.86	1.43
Pb	6.37	9.51
Nal	9.49	2.59
Polystyrene	43.80	42.9
BaF ₂	9.91	2.05
Bismuth germanate (BGO)	7.98	1.12

8.3.3 Electron Stopping Power

The ionization loss varies logarithmically with energy and linearly with Z , whereas the radiation loss increases almost linearly with energy and quadratically with Z . Thus the electron stopping power is dominated at low energies by ionization, and at high energies by radiation.  [Figure 8.8](#) presents a comparison of the various contributions to the relative rate of energy loss of electrons in units of radiation length X_0 .

Bremsstrahlung is very important for electrons and positrons: as its emission probability is inversely proportional to the particle mass, its contribution to the energy loss is four orders of magnitude less for the second lightest particle, muon ($M_\mu = 106 \text{ MeV}/c^2$), than for electron.

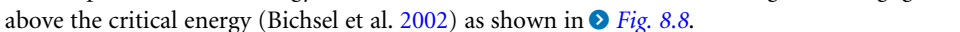
With scattering effects neglected, the total stopping power of low to intermediate energy electrons (β radiation) is approximately

$$-\left(\frac{dE}{dx}\right)_{\text{electron}} = -\left(\frac{dE}{dx}\right)_{\text{ion}} - \left(\frac{dE}{dx}\right)_{\text{brems}}, \quad (8.30)$$

and the ratio of ionization to bremsstrahlung energy loss rates is (Vértés and Kiss 1987)

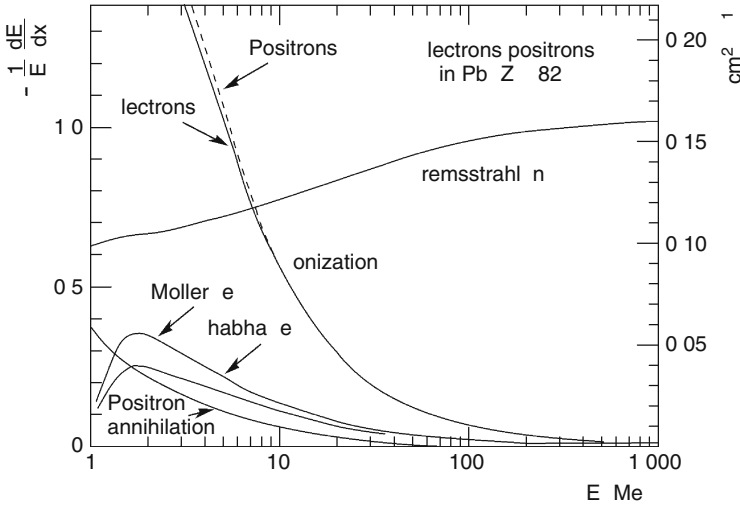
$$\left(\frac{dE}{dx}\right)_{\text{brems}} / \left(\frac{dE}{dx}\right)_{\text{ion}} \approx \frac{Z T_e}{800 \text{ MeV}}. \quad (8.31)$$

8.3.4 Electron Scattering

Electrons and positrons can scatter on the nuclei and on the electrons of the medium. The role of these processes in the energy loss of electrons in matter is small at low energies and negligible above the critical energy (Bichsel et al. 2002) as shown in  [Fig. 8.8](#).

■ Fig. 8.8

Contributions of various processes to the relative rate of energy loss for electrons and positrons in lead. On the left scale x is given in units of radiation length ($X_0(\text{Pb}) = 6.37 \text{ g/cm}^2$), whereas on the right one it is in g/cm^2



8.3.5 Absorption of β Radiation

For the description of β absorption at low energies empirical relations can be used (see, e.g., Vértés and Kiss 1987). The absorption equation is

$$I(x) = I_0 e^{-\mu_m x} \quad (8.32)$$

where I_0 and $I(x)$ are the numbers of electrons entering and leaving the sample of thickness x (measured in g/cm^2) and μ_m is the mass attenuation coefficient depending on E_β , the maximum (kinetic) energy of the electrons produced by the given β decay, and the properties of the absorber. Vértés and Kiss (1987) quote the following empirical formulae:

$$\{\mu_m\} = \begin{cases} \frac{35Z}{\{A\} \{E_\beta\}^{1.14}} & (Z < 13) \\ \frac{7.7 Z^{0.31}}{\{E_\beta\}^{1.14}} & (Z \geq 13), \end{cases} \quad (8.33)$$

where the braces indicate numerical values of the respective quantities measured in the following units: $[A] = \text{g/mol}$, $[E_\beta] = \text{MeV}$ and $[\mu_m] = \text{g}^{-1}\text{cm}^2$. For mixtures and compounds, the attenuation coefficient can be averaged in the usual way:

$$\mu_m = \sum_i w_i \mu_m^i \quad (8.34)$$

where w_i is the mass fraction of component i in the compound and μ_m^i is its mass attenuation coefficient. See ▶ Fig. 2.39 in Chap. 2 of this Volume for a typical β spectrum as well as ▶ Fig. 48.23 in Chap. 48, Vol. 5, for the energy spectra of various β decays.

8.3.6 Cherenkov Radiation and Transition Radiation

There are two kinds of radiation which are characteristic of all fast charged particles, heavy or light, in all kinds of matter: Cherenkov radiation and transition radiation. Although these processes are not that important when estimating energy losses, both are widely used in detecting and identifying charged particles, especially in nuclear and particle physics experiments (Cherenkov and transition radiation detectors, see [Chap. 48](#) in Vol. 5). Here they are treated as radiation induced by electrons as both are characteristic of very fast (more or less relativistic) particles and so play a most important role for the lightest charged particles, electrons and positrons.

8.3.6.1 Cherenkov Radiation

In a medium with refraction index $n > 1$ the speed of light is $u_{\text{rad}} = c/n$. Relativistic particles can propagate there faster than the light and they lose energy via Cherenkov radiation, visible light along a cone under the angle (see [Fig. 8.9](#))

$$\cos \theta = \frac{1}{n\beta} \quad (8.35)$$

or, equivalently,

$$\theta = \arccos \frac{1}{n\beta} \approx \sqrt{1 - 1/(n\beta)^2} \quad (8.36)$$

for small θ (Bichsel et al. 2002), as the interference of waves will prevent radiation in any other direction.

According to Frank and Tamm (1937) in this case the medium becomes polarized and the polarization ceases via the emission of electromagnetic waves. The energy loss via Cherenkov radiation is

$$-\left(\frac{dE}{dx}\right)_C = \frac{4\pi e^2}{\rho c^2} \int_{\beta n(\omega) > 1} \left(1 - \frac{1}{n^2 \beta^2}\right) \omega d\omega, \quad (8.37)$$

where $n(\omega)$ is the refraction index as a function of the photon angular frequency ω . This energy loss is included in the Bethe–Bloch equation, and it is small as compared to the collisional loss (Leo 1987): for condensed substances it is about $10^{-3} \text{ MeV cm}^2 \text{ g}^{-1}$, for hydrogen gas it is $0.1 \text{ MeV cm}^2 \text{ g}^{-1}$ and for heavier gases $0.01 \text{ MeV cm}^2 \text{ g}^{-1}$.

The number of Cherenkov photons produced in a unit path length x and unit photon energy $E_{\text{rad}} = \hbar\omega$ interval by a particle of charge ze is (Bichsel et al. 2002)

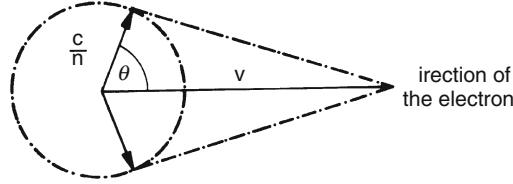
$$\frac{d^2 N}{dE_{\text{rad}} dx} = \frac{\alpha z^2}{\rho \hbar c} \sin^2[\theta(E_{\text{rad}})] \approx (370 \text{ eV}^{-1} \text{ cm}^{-1}) \sin^2[\theta(E_{\text{rad}})] \quad (8.38)$$

where $\theta(E_{\text{rad}})$ is the energy dependent angle shown in [Fig. 8.9](#). The approximation expressed by the second half of the formula is valid only for $z = 1$.

In order to get the total number of observed photons, the aforementioned formula has to be multiplied by the response function of the optical transducer (i.e., the absorption characteristics of the light guide) and integrated over all E_{rad} .

■ Fig. 8.9

Propagation cone of the Cherenkov radiation of a certain frequency in a medium of refraction index n . Note that because the refraction index n depends on the radiation frequency and thus on the radiation energy $E_\gamma = \hbar\omega$, the angle θ is also energy dependent as expressed by ► Eq. (8.35)



8.3.6.2 Transition Radiation

In a medium containing N_e quasi-free electrons in unit volume, an electromagnetic radiation with ω frequency will have a phase velocity (i.e., velocity at which the phase of the wave of a given frequency propagates)

$$u_{\text{rad}} = \frac{c}{n} = \frac{c}{\sqrt{1 - \frac{N_e e^2}{\epsilon_0 m_e \omega^2}}} \quad (8.39)$$

where n is the refraction index.

The radiation can propagate if the refraction index is real, i.e.

$$\omega > \omega_p = \sqrt{\frac{N_e e^2}{\epsilon_0 m_e}} \quad (8.40)$$

where ω_p is the **plasma frequency** of the medium (see, e.g., Bichsel et al. 2002). As in real media the electrons cannot always be considered quasi-free, the plasma frequency is an empirical constant characterizing the substance.

Transition radiation is emitted when a fast charged particle passes the boundary of two media with different relative permittivity. It is caused by the fact that the electric displacement, $\mathbf{D} = \epsilon\epsilon_0\mathbf{E}$ changes continuously through a boundary, but the electric field strength \mathbf{E} jumps (however, if there is a surface charge, then \mathbf{D} jumps). When a charged particle approaches a boundary, with its mirror charge on the boundary they make a dipole which changes in time; that is why the radiation is emitted. This is significant for extreme relativistic particles only with $\gamma = 1/\sqrt{1 - \beta^2} \gg 1$.

When such a particle passes through a thin absorber (foil) with plasma frequency ω_{p1} and enters a medium with ω_{p2} it radiates photons of frequency $\omega \gg \omega_{p1}$ with a double differential energy distribution

$$\frac{dE_{\text{tr}}}{d\omega d\Omega} = \frac{\hbar d_1 \omega}{2c} \left[\gamma^{-1} + \theta^2 + \frac{\omega_{p1}^2}{\omega^2} \right]^{-1} \quad (8.41)$$

where d_1 is the thickness of the foil. This is a radiation in the X-ray region, which is strongly forward peaked with a cone angle of $\theta \approx 1/\gamma$. The total energy radiated for $\omega_{p1} \gg \omega_{p2}$ is $E_{\text{tr}} = \alpha z^2 \gamma \hbar \omega_{p1}/3$.

■ **Table 8.7**

Classification of the interactions of photons (X-ray and γ radiation) in matter. The Z -dependence of the σ cross section of the interaction is also shown

Reacting constituent	Absorption	Scattering	
		Elastic	Inelastic
Shell electrons	Photoelectric effect: $\sigma \propto Z^4$	Rayleigh scattering: $\sigma \propto Z^2$	Compton effect: $\sigma \propto Z$
		Thomson scattering: $\sigma \propto Z$	
Atomic nuclei	Photonuclear reaction (γ, n), (γ, p), etc.: $\sigma \propto Z$	(γ, γ) scattering: $\sigma \propto Z^2$	(γ, γ') scattering
	resonance absorption		
Coulomb field of nuclei	Pair production: $\sigma \propto Z^2$		

8.4 Interaction of Photons with Matter

When photons penetrate a substance, they can interact with the nuclei or with the shell electrons. ▶ [Table 8.7](#) shows a classification of the interactions of photons (X-ray and γ radiation) in matter. The dependence of the cross section σ of the interaction on the atomic number Z of the medium is also shown. Note that the Compton effect is inelastic for the atom but it is treated theoretically as elastic scattering on *free* electrons as the binding energy of the atomic electron is much smaller than that of the scattered electron.

The cross sections (Bichsel et al. 2002) of various kinds of photon interactions with matter are compared in ▶ [Figs. 8.10](#) and ▶ [8.11](#). ▶ [Figure 8.10](#) is restricted to the MeV energy region of nuclear γ rays, whereas ▶ [Fig. 8.11](#) encompasses the widest possible range.

8.4.1 Compton Effect

In the Compton effect, part of the energy and the momentum of the photon is transferred to a shell electron. As a consequence, the energy and the direction of propagation of the photon will change (see ▶ [Fig. 8.12](#)).

Since the binding energy of the electron is negligible as compared to E_γ , the electron is assumed to have been free before the collision. Using energy and momentum conservation, one obtains that the photon energy changes as

$$E_\gamma - E'_\gamma = \frac{E_\gamma E'_\gamma}{m_e c^2} (1 - \cos \theta), \quad (8.42)$$

and the wavelength changes as

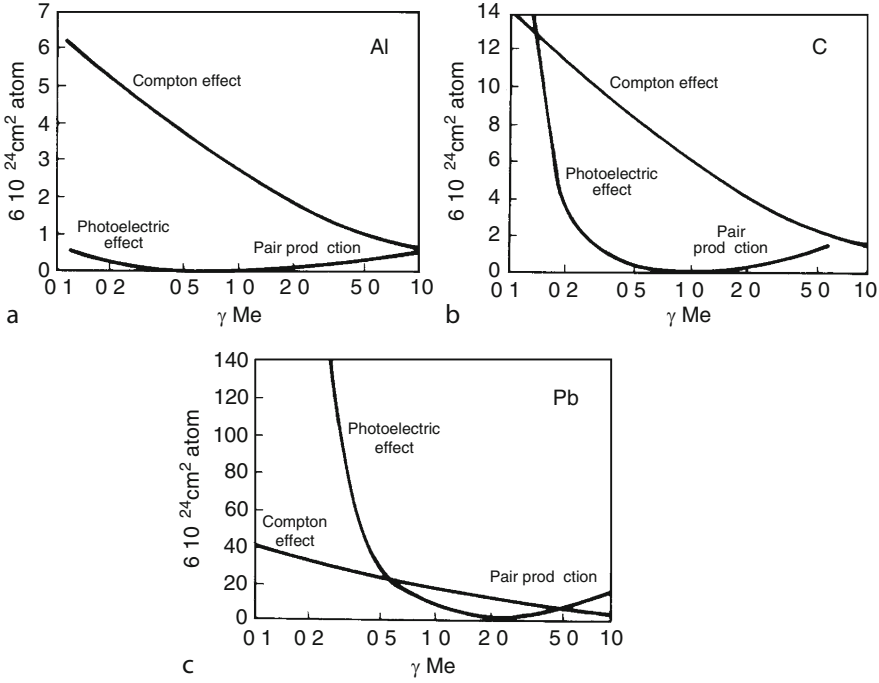
$$\lambda' - \lambda = \frac{h}{m_e c} (1 - \cos \theta). \quad (8.43)$$

Klein and Nishina (1929) performed a full quantum mechanical calculation using Dirac's equation for the electron. For unpolarized incident photons they obtained for the differential cross section

$$\frac{d\sigma_C}{d\Omega} = \frac{1}{2} \left[\frac{r_e}{1 + a(1 - \cos \theta)} \right]^2 \left[1 + \cos^2 \theta + \frac{a(1 - \cos \theta)^2}{1 + a(1 - \cos \theta)} \right] \quad (8.44)$$

■ Fig. 8.10

Energy dependence of the cross sections of Compton effect, photoelectric effect and pair production in various materials: (a) aluminum, (b) copper, and (c) lead



and for the total cross section

$$\sigma_C = \frac{2\pi e^4}{(m_e c^2)^2} \times \left\{ \frac{1+a}{a^2} \left[\frac{2(1+a)}{1+2a} - \frac{1}{a} \ln(1+2a) \right] + \frac{1}{2a} \ln(1+2a) - \frac{1+3a}{(1+2a)^2} \right\} \quad (8.45)$$

where $a = E_\gamma/(m_e c^2)$ and $d\Omega$ is the solid angle between the cones of angles θ and $\theta + d\theta$. The maximum kinetic energy of the scattered electron is

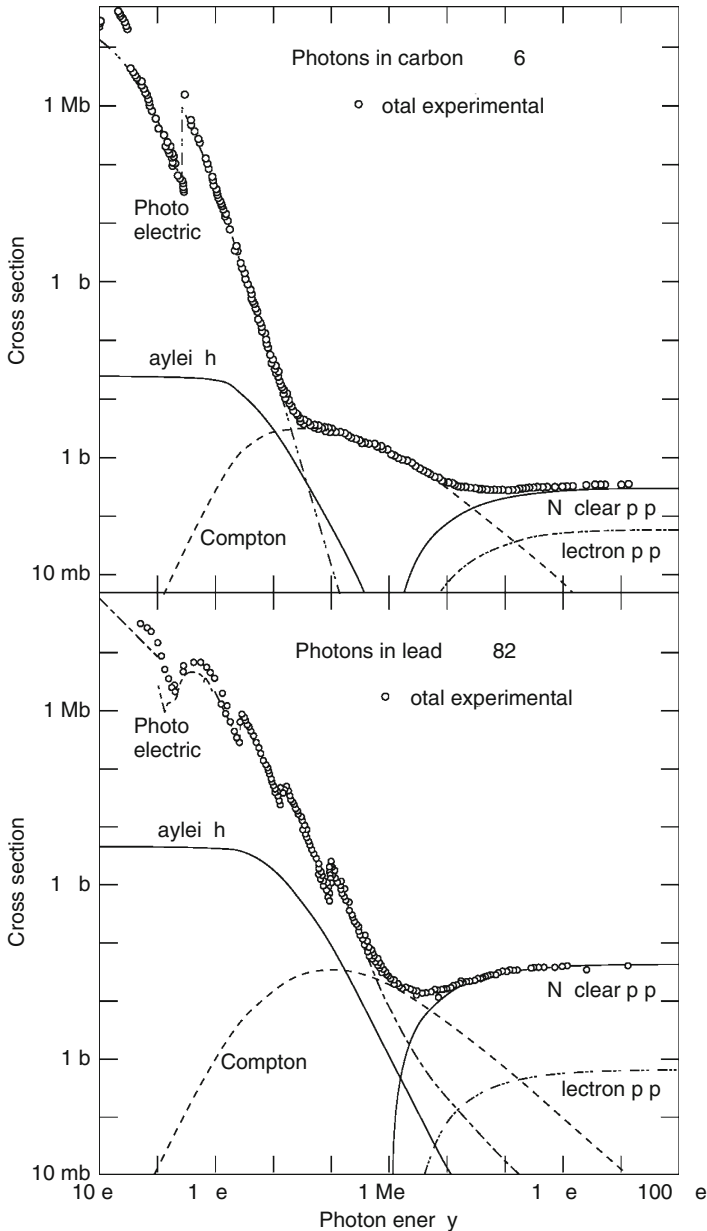
$$T_e^{(\max)} = E_\gamma \frac{2a}{1+2a} < E_\gamma. \quad (8.46)$$

There is a sharp drop at the end of the continuous energy spectrum of the Compton electrons, the **Compton edge**, distinctly below the full energy of the original photon. The electron energy reaches its maximum when the photon is totally back scattered ($\theta = 180^\circ$). The energy of such backscattered photons $E_\gamma' = E_\gamma - T_e^{(\max)}$ is therefore at minimum, but for this minimum one has $E_\gamma' > 0$ owing to [Eq. \(8.46\)](#).

The Compton scattering was the first observation of the dual – wave and particle – nature of electromagnetic radiation.

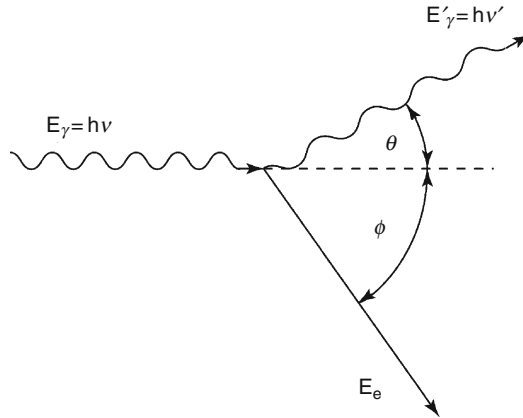
■ Fig. 8.11

Total cross section (in units of 1 barn = 10^{-28} m²) of photon interaction in carbon and lead as a function of photon energy and the contributions of the following processes: photoelectric effect, Rayleigh and Compton scattering, pair production in the field of the nucleus (nuclear p.p.) and of the shell electrons (electron p.p.). Note the resonances ("edges" as they are called) in photoelectric effect. The total cross section curve is flat for another two orders of magnitude in energy beyond the plot



■ Fig. 8.12

Geometrical scheme of the Compton effect. An incoming photon of energy $E_\gamma = h\nu$ kicks out a shell electron which acquires energy E_e ; the scattered photon proceeds at angle θ with energy $E'_\gamma = h\nu'$



8.4.2 Thomson and Rayleigh Scattering

Thomson and Rayleigh scattering are the classical equivalents of the Compton effect with the exception that no (internal) energy is transferred to the atoms, they are neither ionized nor excited, just the direction of the photon is changed.

The electromagnetic field of the propagating photon polarizes the atoms and molecules of the medium and induces electric dipoles which then create secondary electromagnetic radiation in all directions. For moderately low energy ($E \approx 100$ keV) photons, the medium can be considered to be practically homogeneous, the photon is scattered by an atom as a whole, and one speaks of **Rayleigh or coherent scattering**.

If the photon energy is so low that it cannot cause Compton effect, one has elastic scattering on free electrons (**Thomson scattering**). In the classical limit, the Klein-Nishina formula reduces to the Thomson cross section:

$$\sigma = \frac{8\pi}{3} r_e^2. \quad (8.47)$$

8.4.3 Photoelectric Effect

As a result of the photoelectric effect, the total energy of the photon is transferred to a shell electron. If the binding energy of the shell electron is E_b , the emitted electron will have the kinetic energy

$$T_e = E_\gamma - E_b. \quad (8.48)$$

Momentum conservation prohibits photoelectric effect on free electrons; the atom has to absorb the recoil momentum. Electrons with the largest binding energy still accessible for the photon are preferred in the cross section; as the photon energy approaches from above the binding energy of the K-electrons, the cross section increases, followed by a sharp drop

(K absorption edge) when it becomes lower, and this is repeated at the L- and M-energies. As shown by [Fig. 8.11](#), photon absorption at low energies is dominated by the photoelectric effect. In carbon there is a very prominent K absorption edge whereas the spectrum of lead shows several absorption edges.

The partial mass attenuation coefficient (in units of $\text{g}^{-1} \text{cm}^2$) of the photoelectric effect is determined by the empirical formula

$$\{\mu_{\gamma, \text{ph}}\} = 8.9 \times 10^{-6} \frac{Z^{4.1}}{\{A\}} \{\lambda\}^n, \quad (8.49)$$

where $n \approx 3$ and the numerical values are understood in the following units: $[\mu_{\gamma, \text{ph}}] = \text{g}^{-1} \text{cm}^2$, $[A] = \text{g}^{-1} \text{mol}$, and for the photon wavelength $[\lambda] = \text{nm}$.

The photoelectric effect is followed by the deexcitation of the atom via X-ray transitions or by the emission of a secondary electron (**Auger effect**, see later in [Sect. 8.5.2](#)). As above the K edge absorption dominates, one can collect a complete X-ray spectrum from the subsequent electron transitions. The energy and intensity of the X-rays are characteristic of the composition of the emitter. Thus, γ sources can be used to induce photoelectric effect and subsequent X-ray transitions in order to make qualitative and quantitative analyses of samples, which is called the **X-ray fluorescence** method.

Internal conversion can be considered as a special case of the photoelectric effect, occurring when the γ -photon emitted after nuclear decay does not leave the atom but transfers its whole energy to a shell electron.

8.4.4 Pair Production

If the photon energy is greater than the total rest energy of an electron-positron pair, 1.022 MeV, it can create one. For energy-momentum conservation pair production requires a third body, so pairs are usually created in the Coulomb field of an atomic nucleus. Theoretically, it is related to bremsstrahlung, and the cross section (Leo 1987) depends on the energy of the photon and the atomic number of the element. At “moderate” energies ($m_e c^2 \ll E_\gamma \ll m_e c^2 Z^{1/3}/\alpha$) the pair production cross section is

$$\sigma_{\text{pair}} = 4Z^2 \alpha r_e^2 \left[\frac{7}{9} \left(\ln \frac{2E_\gamma}{m_e c^2} - f(\alpha Z) \right) - \frac{109}{54} \right], \quad (8.50)$$

and at high energies (complete screening, $E_\gamma \gg m_e c^2 Z^{1/3}/\alpha$),

$$\sigma_{\text{pair}} = 4Z^2 \alpha r_e^2 \left\{ \frac{7}{9} [\ln(183 Z^{1/3}) - f(\alpha Z)] - \frac{1}{54} \right\}, \quad (8.51)$$

where the Coulomb correction factor $f(\alpha Z)$ is defined in [Eq. \(8.24\)](#).

Similarly to bremsstrahlung, pair production can occur in the field of the atomic electrons as well, and, to include this mechanism in the cross section approximately, Z^2 should be replaced by $Z(Z+1)$ (Leo 1987).

8.4.5 Photon-Photon Interaction

At “moderate” energies photons do not interact with each other. A propagating photon can, however, convert into a (virtual) particle-antiparticle pair for very short times and distances as

allowed by Heisenberg's uncertainty principle. Thus a high-energy photon ($E_\gamma > 1$ GeV) can interact with the virtual constituents of another photon as well. For instance, in high-energy electron-positron scattering emission of quark pairs can be observed. This is explained to be the result of an interaction between two photons emitted by the colliding particles (Nisius 2000).

8.4.6 Photon Attenuation

The energy loss of photons in matter can be characterized by the cross section of the process and also by the **mean free path** of photons between interactions. The latter can be expressed in units of surface density, and then it is called **mass attenuation length**. Photon attenuation lengths for various elements are shown in Fig. 8.13 as taken from Bichsel et al. (2002).

With increasing photon energy pair production dominates and at high energies (complete screening) the differential cross section becomes

$$\frac{d\sigma}{dE_\pm} = \frac{A}{X_0 N_A} \left[\frac{4}{3} a(1-a) \right], \quad (8.52)$$

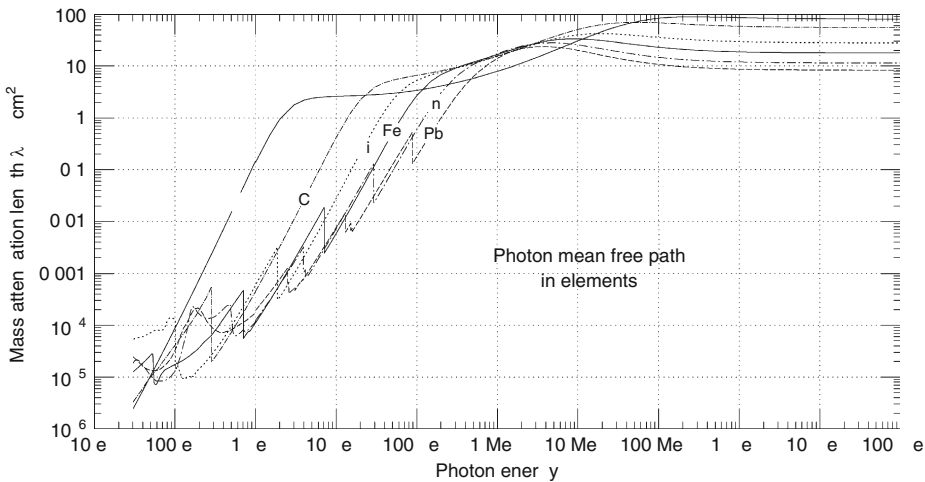
where $a = E_\pm/E_\gamma$ is the fraction of photon energy transferred to the electron or positron. Note that the cross section is symmetric for a and $1-a$. In the high-energy limit the total cross section is

$$\sigma = \frac{7}{9} \frac{A}{X_0 N_A}. \quad (8.53)$$

According to Bichsel et al. (2002), the aforementioned equation is valid within a few percent down to 1 GeV, especially for high- Z materials.

Fig. 8.13

The photon mean free path (mass attenuation length) as a function of photon energy for various absorbers (Bichsel et al. 2002). The photon intensity after traversing the absorber of thickness x is $I = I_0 \exp(-x/\lambda)$



8.5 Complex Interactions

The interaction of nuclear radiation with matter is usually a multi-step process. If the primary particle does not lose all of its energy in a single step, it will enter other interactions. Moreover, secondary particles (emitted electrons or photons) can emerge and take part in secondary interactions. The chain of subsequent effects stops only when the whole energy of the primary particle has been dispersed in such small quantities that they cannot cause changes in the substance any more.

8.5.1 Electron-Photon Showers

As fast electrons create photons and photons create electron-positron pairs and kick out atomic electrons while slowing down, one always detects cascades (showers) of fast electrons and high-energy photons together. Moreover, as mentioned earlier, the phenomenological quantum-mechanical treatments of, e.g., bremsstrahlung and pair production are the same. Experimentally, these cascades are well described by electron-gamma-shower (EGS) simulations using the Monte Carlo method. The substances can be characterized by radiation lengths X_0 for electron and photon attenuation: comparing the pair production and bremsstrahlung cross sections, the **pair production length** of a high-energy photon will be approximately $(9/7) X_0$.

8.5.2 Auger Effect

As a common consequence of any interaction of nuclear radiation with matter, electron vacancies are created in the K, L, M shells of the atoms. Radioactive decay can also create vacancies in the daughter atoms (electron capture, internal conversion). Electron vacancies can cause X-ray transitions or – as shown by Auger (1925) – the vacancy is filled at the expense of a shell electron emission with the energy

$$E_A = \Delta E_b - E_b, \quad (8.54)$$

where E_b is the binding energy of the emitted electron and ΔE_b is the energy released by the shell rearrangement process (Nix 2002).

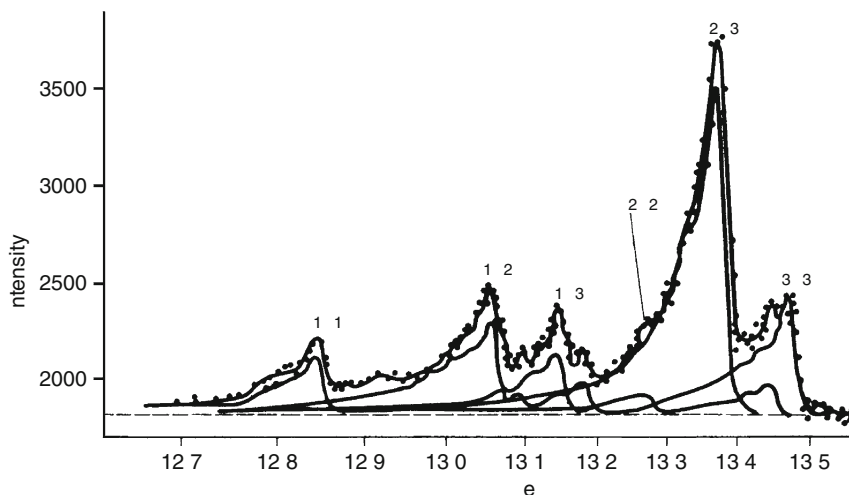
Formally, the Auger effect can be interpreted as a two-step process: first an X-ray photon is emitted, which is then absorbed via photoelectric effect in the same atom. The Auger effect may cause further ionization of a given atom and so multiply ionized atoms can be formed in Auger cascades, especially in high- Z atoms. This, in turn, can cause chemical changes, so the Auger effect has an important role in the mechanism of radiochemical reactions.

A special symbolism has been developed for the Auger effect for indicating the kind of internal rearrangement as well as the origin of the emitted electron. For example, the meaning of KLL is that a primary vacancy in the K shell was filled by an L electron and another L electron was released. Subshells can also be distinguished by precise measurements. For instance, the L shell has three subshells and so six kinds of KLL Auger electrons exist: KL_1L_1 , KL_1L_2 , KL_1L_3 , KL_2L_2 , KL_2L_3 and KL_3L_3 .

➤ *Figure 8.14* shows the measured energy spectrum of KLL Auger electrons of zirconium (Hörnfeldt et al. 1962).

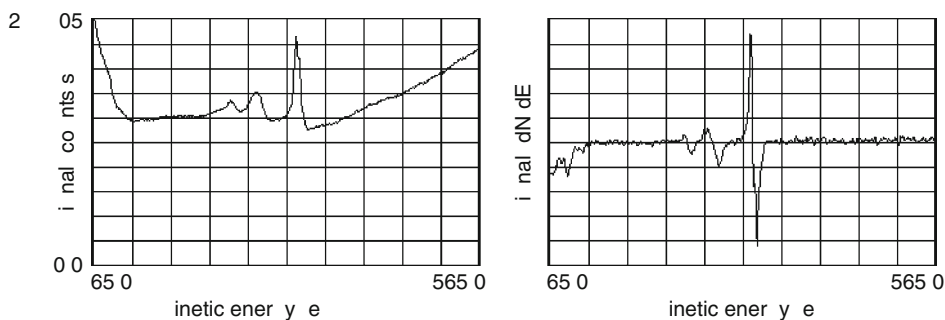
■ Fig. 8.14

The energy spectrum of KLL Auger electrons in Zr. The full lines indicate the resolved components



■ Fig. 8.15

Typical energy spectra of Auger electrons measured in palladium (Nix 2002). The differential spectrum on the right is obtained by differentiating the integral one on the left. Most of recent works present differential spectra

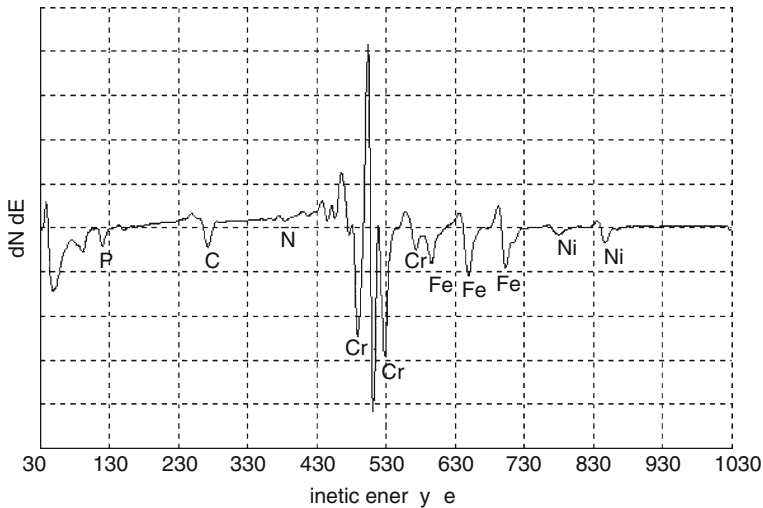


In practice one measures the kinetic energy of the emitted electrons. Figure 8.15 presents (Nix 2002) the energy spectrum of Auger electrons emerging from palladium when bombarded by a 2.5 keV electron beam. The differential spectrum on the right is obtained by differentiating the energy spectrum on the left. Most of the contemporary works present differential Auger spectra (see, e.g., Figure 8.16 and Handbook of Analytical Methods 2002) for several reasons: the peaks are easier to locate and there are ways to measure differential Auger spectra directly.

The binding energy of shell electrons, and, consequently, the kinetic energies of the released Auger electrons are influenced by chemical bonds, and that enables Auger spectroscopy to provide important information on the chemical structure via the energy distribution of Auger electrons. However, Auger electrons formed well within the bulk of a sample cannot get out due

■ Fig. 8.16

The differential energy spectrum of Auger electrons in stainless steel



to their short range; Auger spectra like that in Fig. 8.16 can be measured for electrons originating from a thin ($<10^{-6}$ m) surface layer. This makes Auger spectroscopy a surface-testing method.

Acknowledgments

This work was supported by the Hungarian Scientific Research Fund (OTKA) under contracts NK67974 and K72172.

References

- Andersen HH, Ziegler JF (1977) Stopping and ranges of ions in matter, vol 3. Pergamon Press, Elmsford, New York
- Auger P (1925) *Compt Rend* 180:65
- Barkas WH, Birnbaum W, Smith FM (1956) *Phys Rev* 101:778
- Besserer J et al (1997) LMU, München. http://www.bl.physik.uni-muenchen.de/bl_rep/jb1997/
- Bethe HA, Ashkin J (1953) Passage of radiations through matter. In: Segrè E (ed) *Experimental nuclear physics*, vol 1. Wiley, New York
- Bichsel H, Groom DE, Klein SR (2002) In: *Particle physics review*, Hagiwara K et al, *Phys Rev D* 66, 010001–195. <http://pdg.lbl.gov/>
- Davies H, Bethe HA, Maximon LC (1954) *Phys Rev* 93:788
- Frank I, Tamm I (1937) *C R Acad Sci USSR* 14:109
- Groom DE, Mokhov NV, Striganov SI (2001) *Atom Data Nucl Data* 78:183. <http://pdg.lbl.gov/AtomicNuclearProperties>, <http://physics.nist.gov/PhysRefData>
- Handbook of analytical methods (2002) *Materials Evaluation and Engineering*. <http://www.mee-inc.com/sam>
- Hörnefeldt O, Fahlman A, Nordling C (1962) *Arkiv Fysik* 23:155
- Klein O, Nishina G (1929) *Z Physik* 52:853
- Landau LD (1944) *J Exp Phys (USSR)* 8:201
- Lea D (1962) *Actions of radiations on living cells*. Cambridge University Press, Cambridge
- Leo WR (1987) *Techniques for nuclear and particle physics experiments*, Chapter 2. Springer, Berlin
- Lindhard J (1954) *Kgl Danske Videnskab Selskab Mat-Fys Medd* 28:Nr. 8
- Moeller SP et al (2002) *Phys Rev Lett* 88:193201

- Molière G (1947) *Z Naturforschung* 2a:133
- Molière G (1948) *Z Naturforschung* 3a:78
- Molière G (1955) *Z Naturforschung* 10a:177
- Nix R (2002) An introduction to surface chemistry. Queen Mary University of London. <http://www.chem.qmw.ac.uk/surfaces/scc/>
- Nisius R (2000) *Phys Rep* 332:165
- Rossi B (1952) *High energy particles*. Prentice-Hall, Englewood Cliffs, NJ
- Seltzer SM, Berger MJ (1984) *Int J Appl Radiation* 30:665
- Sternheimer RM, Seltzer SM, Berger MJ (1984) *Atom Data Nucl Data* 30:261
- Turkevich A, Franzquote E, Patterson J (1967) *Science* 158:635
- Vértes A, Kiss I (1987) *Nuclear chemistry*. Elsevier, Amsterdam
- Ziegler JF, Biersac JF, Littmark U (1985) *The stopping and range of ions in solids*. Pergamon Press, New York



9 Stochastics and Nuclear Measurements

S. Nagy

Eötvös Loránd University, Budapest, Hungary

9.1	<i>Introduction</i>	397
9.2	<i>Distributions of Random Variables</i>	397
9.2.1	Measures of the “Location” of a Distribution	397
9.2.2	Useful Tools: Generating Function and Characteristic Function	400
9.2.3	Measures of the “Dispersion” of a Distribution	403
9.2.4	Estimation of Expected Value and Variance	404
9.2.5	Measures of the “Association” of Two Distributions	406
9.3	<i>Sums and Products, Error Propagation</i>	407
9.3.1	Expected Value and Variance of Linear Expressions	407
9.3.2	The Central Limit Theorem	409
9.3.3	Convolution and Deconvolution	409
9.3.4	Random Sums	411
9.3.5	General Approximation of Error Propagation	412
9.3.6	Formulas for Products/Ratios of Independent Random Variables	413
9.4	<i>Special Distributions</i>	413
9.4.1	Bernoulli Distribution: $B(1, p)$	413
9.4.2	Binomial Distribution: $B(n, p)$	414
9.4.2.1	Properties	416
9.4.3	Poisson Distribution: $\Pi(\mu)$	417
9.4.3.1	Properties	418
9.4.4	Exponential Distribution: $\gamma(1, \lambda)$	420
9.4.4.1	Connection with the Exponential Law of Radioactive Decay	423
9.4.4.2	Exponential Law in a Binomial Way	424
9.4.4.3	The Poisson Connection	426
9.4.5	Gamma Distribution: $\gamma(r, \nu)$	430
9.4.5.1	Properties	431
9.4.6	Normal Distribution: $N(\mu, \sigma^2)$	432
9.4.6.1	Properties	435
9.4.7	The χ^2 Distribution: $\chi^2(k)$	436
9.4.7.1	Properties	437

9.4.8 Cauchy Distribution: $C(m, \gamma)$ 438

9.4.8.1 Properties 440

9.5 Applications of Stochastic Processes 442

9.5.1 Renewal Processes 442

9.5.1.1 The Poisson Process as Renewal 443

9.5.1.2 Consideration of Dead Time 443

9.5.1.3 The “Primeval” Shape of the Photoelectric Peak 445

9.5.1.4 Statistical Effects Smearing the Photoelectric Peak 446

9.5.2 Markov Chains 447

9.5.2.1 Branching Processes 447

9.6 Fitting Nuclear Spectra 448

9.6.1 Spectra, Fitting, Model Functions 448

9.6.2 The Maximum Likelihood Principle 449

9.6.3 Weighted Least Squares as a Maximum Likelihood Method 450

9.6.4 Weighted Least Squares Method in Nuclear Spectroscopy 451

9.7 Summarizing Tables 453

Abstract: The term “stochastics” in the title roughly translates into “random features.” So it refers to anything related to probability theory, statistics, and, of course, stochastic processes. Some of the facts of probability and statistics, including special distributions relevant to nuclear measurements, have been summarized. Examples of the nuclear applications of stochastic processes have also been given. A separate section has been devoted to the analysis of nuclear spectra.

9.1 Introduction

Louis Lyons writes in the preface of his book *Statistics for Nuclear and Particle Physicists* (Lyons 1986) that “one cannot learn statistics simply by reading a book on the subject.” This also applies to “stochastics”, defined by Hans-Otto Georgii as “a term comprising both probability theory and statistics” in Footnote 1 of his book titled *Stochastics: Introduction to Probability and Statistics* (Georgii 2008). Therefore, the author of this chapter must be content with summarizing the relevant facts of probability and statistics and pointing out possible connections with nuclear measurements. As regards sampling distributions, parameter estimation, etc., the reader is referred to Lyons (1986) as well as to Press et al. (1999). The only exception will be the χ^2 distribution, which is a valuable goodness-of-fit tool in nuclear spectroscopy. A few examples of the nuclear applications of stochastic processes, a field usually excluded from short studies of this type, will also be cited.

Nuclear aspects (as well as some other important points of reference) will be phrased in the form of remarks numbered thus: (#1), (#2), etc. Such remarks also serve occasionally as an interface between the (mathematical) terminology used in this chapter and the terminologies used by other authors from different fields of nuclear science. The numbering of the remarks may also help to follow a train of thought that is unfolded over several sections or subsections.

9.2 Distributions of Random Variables

To establish uniform notation and to provide the reader with a convenient reference/vocabulary, some of the concepts and formulas of probability theory and statistics are summarized here because they will be referred to later in this chapter.

9.2.1 Measures of the “Location” of a Distribution

Expected value. Among the location parameters, designed to show where the “bulk” of a distribution is concentrated, the expected value (denoted by μ , also called mean) is considered as standard (provided that it exists). If it is necessary to emphasize that the expected value belongs to the random variable X , then the notation $E(X)$ is used. Alternative notations are $\langle X \rangle$ and μ_X .

(#1) Frequently used synonyms for the expected value/mean are *expectation value*, *mathematical expectation* or just *expectation*. In physics and other fields of science (except mathematics), the expected value is often referred to, in a rather careless way, as “average,” but this

term will be reserved here for the estimate of the mean as defined by [Eq. \(9.29\)](#). In physics, it is also customary to use the symbol \bar{X} for the mean, but – in this chapter at least – the horizontal overbar will denote the sample mean, in other words, the “real” average.

The expected value of a discrete distribution is calculated from its mass function $p(x) \equiv P(X = x)$, where P means probability. The formula is

$$E(X) \equiv \sum_{\forall i} x_i p_i \quad (9.1)$$

where p_i is the weight of the i th spectrum point x_i . (The expression “spectrum point” refers to any of the “allowed” values of a discrete random variable in this context, and therefore it has nothing to do with the nuclear spectra discussed in [Sect. 9.6](#).) For spectrum points $P(X = x_i) \equiv p_i$. If x is not a spectrum point, then $P(X = x) = 0$.

The distribution function of discrete distributions is calculated from the following sum:

$$F(x) \equiv \sum_{\forall i: x_i < x} p_i \quad (9.2)$$

For normalized distributions, $F(\infty) = 1$.

Integral valued random variables are an important class of discrete distributions. Their spectra consist of the integers: 0, 1, 2, ... The expected value is

$$E(X) \equiv \sum_{i=0}^{\infty} i p_i. \quad (9.3)$$

For continuous distributions, the expected value of X is calculated from the density function f as follows:

$$E(X) \equiv \int_{-\infty}^{+\infty} x f(x) dx. \quad (9.4)$$

The distribution function of continuous distributions is calculated from the following integral:

$$F(x) \equiv \int_{-\infty}^x f(u) du. \quad (9.5)$$

For normalized distributions, $F(\infty) = 1$.

It follows from [Eq. \(9.5\)](#) that the density function is the derivative of the distribution function:

$$f(x) = \frac{dF(x)}{dx}. \quad (9.6)$$

(#2) Note that in various fields of science, when people talk about averaging a physical quantity, they usually mean calculating the expected value of that quantity (considered but not necessarily declared as a random variable). The truth is revealed by the fact that they use formulas like [Eqs. \(9.1\)](#) and [Eq. \(9.4\)](#) for those calculations. Also, the mass function and the density function are often not distinguished, but they are referred to by the same expressions: *probability density* or *differential distribution function* and sometimes, rather loosely, as “distribution function” or just “distribution.”

The explanation of the adjective “differential” is made clear by [Eq. \(9.6\)](#).

If the density function or the mass function is referred to as “distribution function,” then the “real” distribution function is normally called *integral distribution function*. The reason for the name is clear from [Eq. \(9.5\)](#).

As a matter of fact, very often no reference is made to any distribution at all, although a careful analysis of the problem reveals that some of the quantities are *un-normalized density functions*. The various quantities referred to as *neutron flux* – actually different types of joint density functions of multivariate distributions – are good examples of this. These are usually denoted by the same symbol (either φ , ϕ , or Φ) no matter how many and which of the possible variables (space coordinates, solid angle, speed or energy or, alternatively, lethargy) are considered or made to disappear by integration. (See, for instance, [Chap. 38 in Vol. 4](#) and [Chap. 57 in Vol. 6](#).) To make things even more confusing, the only related quantity “defined” by Union of Pure and Applied Physics (IUPAP) bears the name *neutron flux density*, (unit: number of neutrons per square centimeter per second), although this is the least “density-function-like” of the whole family of related quantities. When in doubt as regards the type of neutron flux that is encountered, *dimensional analysis* can be suggested as a guide.

The “distributions” scientists do their “averaging” with are in fact un-normalized density functions most of the time. That is, in the continuous case, e.g., the “averaging” in physics typically goes like this:

$$\langle x \rangle = \frac{\int_{-\infty}^{+\infty} x g(x) dx}{\int_{-\infty}^{+\infty} g(x) dx} = \frac{1}{A} \int_{-\infty}^{+\infty} x g(x) dx. \quad (9.7)$$

where A^{-1} is called the normalizing factor converting the un-normalized density function $g(x)$ to the normalized one, $f(x) = A^{-1} g(x)$, for which

$$\int_{-\infty}^{+\infty} f(x) dx = \frac{1}{A} \int_{-\infty}^{+\infty} g(x) dx = \frac{A}{A} = 1. \quad (9.8)$$

as it should be. (Needless to say, the integration limits can be different from those indicated.)

(#3) Note also that [Eq. \(9.7\)](#) is written in the way as usually done outside mathematics, i.e., the symbol x is used both for denoting the random variable (*on the left*) and for indicating the assumed values of that same variable (*on the right*). (According to the convention followed in this chapter, the notation should be X on the left.) However, this does not affect the results of such calculations at all; only the notation is somewhat confusing (to a mathematician anyway), but that is how most people do it in practice. (As a matter of fact, the author himself has to concentrate very hard to keep to his chosen role as a “mathematician,” but he probably fails occasionally, anyway.)

(#4) Another type of “averaging” mentioned here is actually beyond the scope of this chapter. In *quantum physics*, the most common symbolism for the calculation of the expected value of a physical quantity q (characterized by the operator \hat{q}) in the quantum state described by the (complex) wave function $\Psi(\mathbf{r})$ is

$$\langle q \rangle = \langle \Psi | \hat{q} | \Psi \rangle \equiv \int \Psi^* \hat{q} \Psi dV. \quad (9.9)$$

where the integration goes by the volume element dV (over the whole space) and Ψ^* is the complex conjugate of Ψ . Here the product $\Psi^* \Psi$ is referred to as probability density too. It is indeed normalized to 1 as one would rightly expect from a density function:

$$\int \Psi^* \Psi dV = 1. \quad (9.10)$$

Median. The median $X_{1/2}$ is the point along the x -axis that represents the middle of the distribution, in the sense that X values smaller and greater than $X_{1/2}$ are equally probable. For a continuous distribution, this is the point where the distribution function $F(x)$ reaches half of the maximum:

$$F(X_{1/2}) = \frac{1}{2}. \quad (9.11)$$

For statistical samples the median is either the middle element (for an odd sample size) or the average of the two middle elements (for an even sample size) when the elements are arranged in increasing order (ordered sample).

(#5) As a familiar example of the median in nuclear science, the half-life $T_{1/2}$ of a radio-nuclide should be mentioned. (See ▶ Sect. 9.4.4 as well as the right-hand panels in ▶ Fig. 9.1.)

Mode. The mode m represents the local maximum (or one of the local maxima) of the density/mass function. It is usually referred to as the most probable value in physics and chemistry. (In the case of discrete distributions, only the spectrum points are considered when looking for maxima.) If there is only one maximum, the distribution is called *unimodal*; if there are two maxima, the distribution is called *bimodal* and so on.

Connection between location parameters. The existence of expected value depends on the convergence of the sum/integral from which it is calculated. If the expected value does not exist, the rest of the location parameters can still be used as substitutes. (For multimodal distributions, the modes can be actually more useful than the single expected value because they also convey information about the shape of the distribution.)

For symmetrical unimodal distributions the location parameters coincide with the center of symmetry c of the mass/density function (like the normal or Gaussian distribution whose density function is shown on the upper left graph in ▶ Fig. 9.1 as well as in ▶ Fig. 9.2):

$$\mu = X_{1/2} = m = c. \quad (9.12)$$

For asymmetrical unimodal distributions (see the upper right graph in ▶ Fig. 9.1) the following “rule of thumb” is often cited: The median divides the distance between the mode and the mean in the approximate ratio 2:1, i.e.,

$$(X_{1/2} - m) : (\mu - X_{1/2}) \approx 2 : 1. \quad (9.13)$$

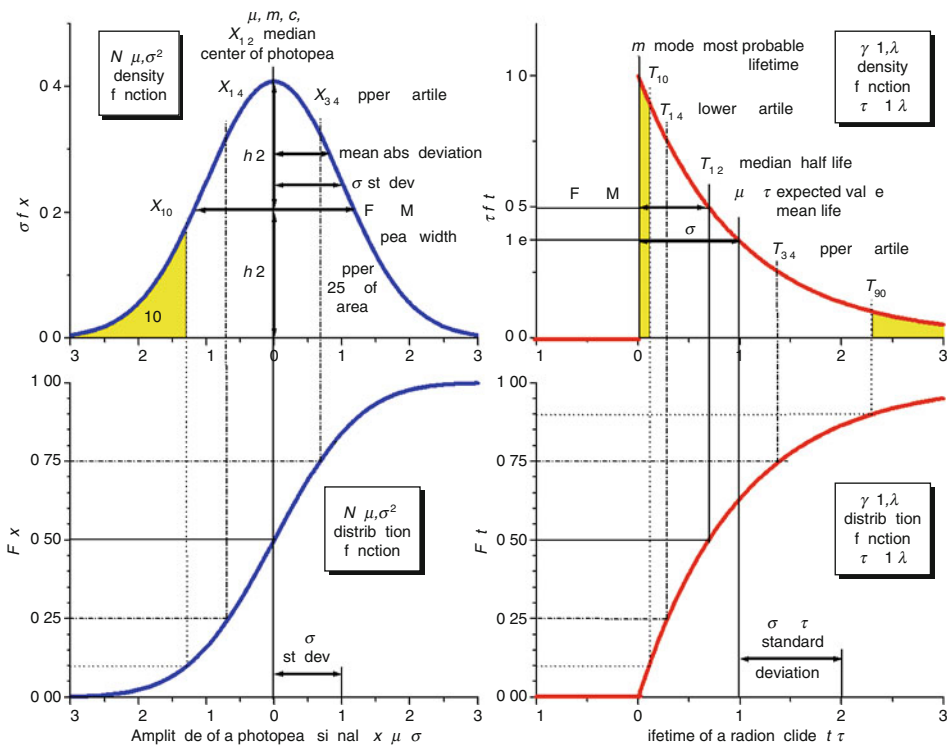
9.2.2 Useful Tools: Generating Function and Characteristic Function

Law of the Unconscious Statistician (Goodman 1988). The expected value of the random variable Y obtained by the function/transformation $Y = g(X)$ is calculated analogously to ▶ Eqs. (9.1) and ▶ (9.4) using the mass/density function of X :

$$E(g(X)) = \sum_{\forall i} g(x_i) p_i; \quad E(g(X)) = \int_{-\infty}^{+\infty} g(x) f(x) dx. \quad (9.14)$$

Fig. 9.1

Presentation of the location and dispersion parameters of a symmetric (normal) and an asymmetric (exponential) distribution by the help of the density function (*upper panels*) and the distribution function (*lower panels*). The shaded areas under the density curves represent 10% of the total area under them in accordance with the meaning of the 10 percentile ($X_{10\%}$) and with the meaning of the percentile and with the relationship between the density function and the distribution function shown by Eq. (9.5). Note that for an asymmetric distribution the “+” and “−” error intervals measured from the mean to complementary values of quantiles/percentiles are different, whereas for a symmetric distribution the estimate of the mean obtained from a single observation of X can always be given as $x \pm \Delta x$ no matter how the error Δx is calculated (e.g., it can be given in terms of the 95% (+) and 5% (−) percentiles, or it can be set equal to 2σ as usual). In practice, most people give their measured or calculated “results” with the “ \pm ” convention without paying any attention to the actual shape of the “error distribution”



Special applications of the above formula are the moments of a distribution. The n th moment is defined as follows:

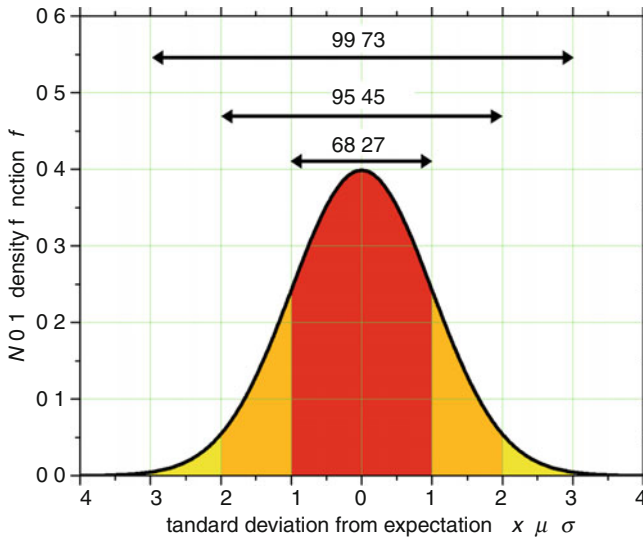
$$M_n \equiv E(X^n). \quad (9.15)$$

In particular, the first moment is equal to the expected value

$$M_1 \equiv E(X) = \mu. \quad (9.16)$$

■ Fig. 9.2

Normal distribution is a well-studied distribution. If one has a good reason to believe (e.g., if this belief is based on the central limit theorem) that a distribution is normal (or Gaussian as often called) one can foretell that ~68% of the data will be within $\mu \pm \sigma$, where the mean μ is estimated by ▶ Eq. (9.29) and the standard deviation σ by ▶ Eq. (9.32), for instance. It is also clear that ~95.5% of the data should be within $\mu \pm 2\sigma$, and less than 0.3% is expected to be outside the $\mu \pm 3\sigma$ interval



The square root of the second moment (also called mean-square) – one of the “effective means” used – is usually referred to as the root mean square or rms:

$$\text{rms} \equiv \sqrt{M_2} = \sqrt{E(X^2)}. \quad (9.17)$$

Beside the rms, other types of effective means can be defined by the formula

$$\text{effective mean} \equiv g^{-1}\{E[g(X)]\} \quad (9.18)$$

where g^{-1} is the inverse of the function g . A further example of the effective means is the harmonic mean, i.e., the reciprocal of the mean-reciprocal:

$$\text{harmonic mean} \equiv [E(X^{-1})]^{-1}. \quad (9.19)$$

(#6) Note that the reduced mass $m_r = m_1 m_2 / (m_1 + m_2)$ of two masses m_1 and m_2 often cited in this book is exactly one half of their harmonic mean as the reader can easily check by assigning the same weight $p_i = 1/2$ when applying ▶ Eq. (9.1) to the simple calculation. Division by two causes the reduced mass to deserve its name inasmuch as it is always less than either of the masses. On the other hand, the harmonic mean itself always lies between m_1 and m_2 as one can rightly expect from a mean of any type. (See also ▶ Sect. 9.6.4.)

Generating function. The generating function is defined for integral valued random variables, the spectra of which consist of $0, 1, 2, \dots$ with weights p_0, p_1, p_2, \dots . The generating function of X is defined as the expected value of the exponential function s^X :

$$G(s) \equiv E(s^X) = \sum_{k=0}^{\infty} p_k s^k. \quad (9.20)$$

Since the distribution is normalized, $G(1) = 1$. The generating function (just like the mass function) contains all the information about the distribution. For instance, the expected value and the variance of X (see later on) can be calculated from its derivatives as follows:

$$E(X) = \mu = G'(1); \quad D^2(X) = G''(1) + \mu(1 - \mu). \quad (9.21)$$

Characteristic function. The characteristic function of continuous distributions is the expected value of the complex exponential function e^{iuX} (where $i^2 = -1$). In other words, it is the Fourier transform of the density function f :

$$\varphi(u) \equiv E(e^{iuX}) = \int_{-\infty}^{+\infty} e^{iuX} f(x) dx. \quad (9.22)$$

Since the distribution is normalized, $\phi(0) = 1$. The characteristic function (just like the density function) contains all the information about the distribution. For instance, the expected value and the variance of X can be calculated from its derivatives as follows:

$$E(X) = \mu = \frac{1}{i} \varphi'(0); \quad D^2(X) = -\varphi''(0) - \mu^2. \quad (9.23)$$

Both the characteristic function and the generating function represent a transformation T for which the following theorem holds (Korn and Korn 1968). Let X and Y denote independent random variables with density/mass functions f_X and f_Y . Let f_{X+Y} denote the density/mass function of the sum $X + Y$. Then one can write

$$T(f_{X+Y}) = T(f_X)T(f_Y). \quad (9.24)$$

The above formula serves as a basis for the deconvolution as well as for the addition theorems that will be cited later on in connection with different distributions.

9.2.3 Measures of the “Dispersion” of a Distribution

Variance. Among the dispersion parameters characterizing the “spread” of a distribution, the variance is considered as standard (provided that it exists). The variance is denoted by σ^2 or, if it has to be emphasized that it is the variance of the random variable X , the notation is $D^2(X)$, $\text{Var}(X)$, or σ_X^2 . The variance of X is calculated as follows:

$$D^2(X) \equiv E[(X - \mu)^2] = M_2 - \mu^2. \quad (9.25)$$

where $M_2 \equiv E(X^2)$ is the second moment of X . (The first moment is $M_1 \equiv \mu$.)

Standard deviation. The standard deviation of X is calculated from the variance

$$D(X) \equiv \sqrt{D^2(X)}. \quad (9.26)$$

Further notations: σ or σ_X . The relative deviation is the ratio of the standard deviation to the expected value

$$\sigma_{\text{rel}} \equiv \frac{\sigma}{\mu}. \quad (9.27)$$

Mean absolute deviation. The (mean) absolute deviation of X is

$$\text{AbsD}(X) \equiv E(|X - \mu|). \quad (9.28)$$

Whenever the expected value exists, so does the absolute deviation. (The standard deviation may not exist, even if the expected value exists.)

Interquantile range. This type of “measure” works even if the expected value does not exist.

The p quantile/fractile is a (not necessarily unique) point X_p along the x -axis, where the distribution function reaches a given p fraction of the maximum, i.e., where $F(X_p) = p$. Special types of quantiles are the quartiles ($p = 1/4, 1/2, 3/4$), the deciles ($p = 0.1, 0.2, \dots, 0.9$), and the percentiles ($p = 0.01, 0.02, \dots, 0.99$).

Quantiles can be used for the characterization of the spread of the distribution by giving the distance between the points X_p and X_{1-p} . For instance, the 10–90-percentile range means the difference $X_{0.9} - X_{0.1}$, where $X_{0.1}$ and $X_{0.9}$ are the 10 and the 90 percentile, respectively. It follows from the definition that about 80% of the observed values of X are supposed to lie in this range and about 20% outside.

The interquartile range characterizes the spread of the distribution with the distance between the lower and the upper quartiles: $X_{3/4} - X_{1/4}$. (The lower, middle, and the upper quartiles mean the 25, 50, and 75 percentiles, respectively.)

According to the above terminology, the median can be either considered as the middle quartile ($X_{2/4}$), or as the 50 percentile ($X_{0.5}$) of the distribution.

Halfwidth. The spread of a unimodal (continuous) distribution is sometimes characterized by its halfwidth meaning its full width at half maximum abbreviated as FWHM. The term refers to the total width of the density function (peak) between the points, where its height is half of the maximum.

The relative width is the ratio of the FWHM to the expected value: $\text{FWHM}_{\text{rel}} = \text{FWHM}/\mu$.

9.2.4 Estimation of Expected Value and Variance

Estimation of the expected value. The expected value is estimated by the average (also called the sample mean or arithmetic mean):

$$\hat{\mu} = \bar{X} \equiv \frac{1}{n} \sum_{k=1}^n X_k \quad (9.29)$$

where “ $\hat{\mu}$ ” reads “the estimate of μ .” According to [Eq. \(9.45\)](#), this estimate is unbiased, that is,

$$E(\bar{X}) = \mu. \quad (9.30)$$

(#7) As mentioned before, in physics, the horizontal overbar above a variable is often used to indicate its expected value, but this notation will be reserved here for the average.

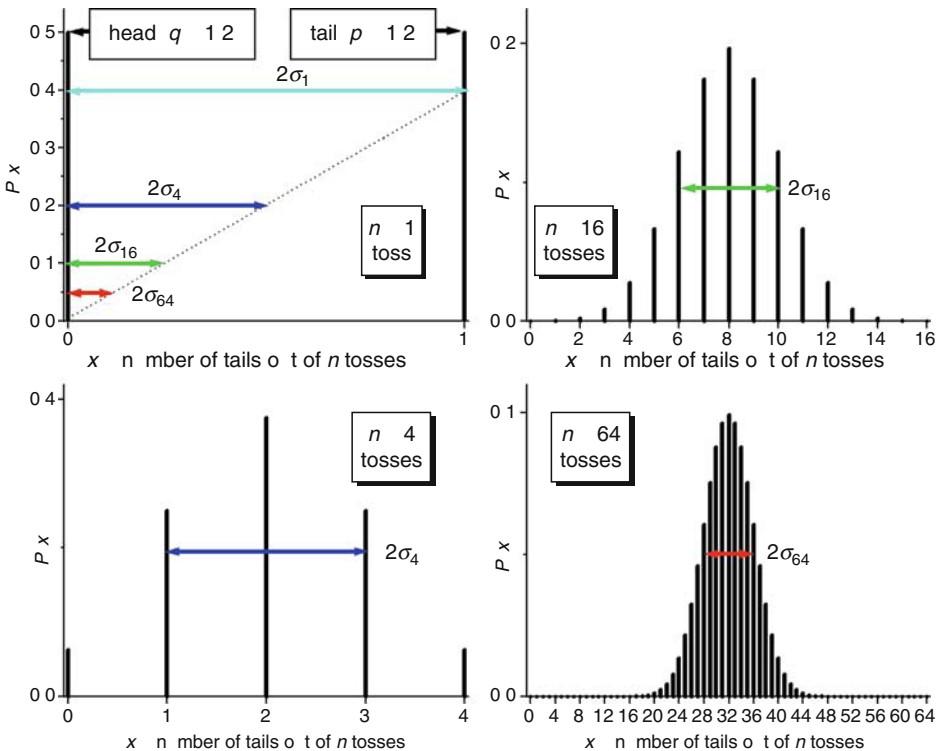
According to [Eq. \(9.47\)](#), the uncertainty of expected-value estimation is determined by the variance of the average

$$D^2(\bar{X}) = \frac{1}{n} D^2(X) \equiv \frac{1}{n} \sigma^2; \quad D(\bar{X}) = \frac{1}{\sqrt{n}} D(X) = \frac{1}{\sqrt{n}} \sigma \quad (9.31)$$

i.e., if the accuracy of expected-value estimation is to be increased by a factor of 2, 3, or N , then 4, 9, N^2 times as many data need to be averaged (see [Fig. 9.3](#)).

■ Fig. 9.3

The above sequence of graphs shows the distributions of the possible outcomes of four series of coin tossing – four series of Bernoulli trials – each representing one particular $B(n, p)$ binomial distribution (see later on). The probability of heads/tails has been fixed to $q = p = 0.5$, and the number of tosses ($n = 1, 4, 16, 64$) has been increased by a factor of 4 in the subsequent Bernoulli series. The graphs demonstrate several things at the same time. (1) Central limit theorem: The sum of a large enough number of independent random variables having a common distribution (such as the total number of tails obtained in a long series of single tosses) is normally distributed. (2) The binomial distribution can be approximated by normal distribution if n is large enough. (3) According to the upper left graph, if the number of data is quadrupled, then the accuracy of the average will double. (Note that the lengths of the $2\sigma_n$ double arrows copied from the rest of the graphs halve as n gets four times larger.) The average comes into the picture because the ratio x/n (lying between 0 and 1) can also be interpreted as the average of n Bernoulli random variables that can only assume the values 0 and 1 (see later on). (4) Law of large numbers: As n increases, the relative width of the binomial distribution gradually diminishes, which guarantees that the relative frequency x/n observed will eventually match the probability $p = 0.5$ as $n \rightarrow \infty$ (Note that the ratio x/n represents not only the average value of the Bernoulli variable, but also the relative frequency of tails in a concrete Bernoulli series)



Estimation of variance. The variance is normally estimated by the following formula of the empirical variance/sample variance (note that the sample mean \bar{X} is determined from the same set of data as the sample variance itself):

$$\hat{\sigma}^2 = s^{*2} \equiv \frac{1}{n-1} \sum_{k=1}^n (X_k - \bar{X})^2. \quad (9.32)$$

The above formula looks rather surprising having the form of a “spoiled” average. Its use, however, is justified since the variance estimate thus obtained is unbiased, i.e.,

$$E(s^{*2}) = \sigma^2. \quad (9.33)$$

If the expected value μ is exactly known, then the “unspoiled” averaging

$$\hat{\sigma}^2 = s^2 \equiv \frac{1}{n} \sum_{k=1}^n (X_k - \mu)^2 \quad (9.34)$$

delivers the unbiased estimate for the variance. Note that the estimate calculated from [Eq. \(9.32\)](#) tends to be greater than that obtained from [Eq. \(9.34\)](#) by a factor of $n/(n-1)$. Thus, the difference is only significant when the sample size n is small. However, for small samples variance estimation is rather meaningless anyway. Therefore in most practical cases the choice between the two formulas is only a matter of taste/convenience (i.e., whichever formula is available it will do). The estimate of standard deviation in either case is

$$\hat{\sigma} = \sqrt{\hat{\sigma}^2}. \quad (9.35)$$

Weighted average. It is a common situation that the value of a physical quantity is determined from different types of experiments, and the experimental values (X_k) obtained for those quantities have their own (different) accuracies characterized by the standard deviation (σ_k). When the error distribution of each experimental value can be considered normal, then the maximum likelihood estimate of the expected value of the physical quantity is given by the following weighted average (Orear 1987):

$$\hat{\mu} = \frac{\sum_{k=1}^n \frac{1}{\sigma_k^2} X_k}{\sum_{k=1}^n \frac{1}{\sigma_k^2}}. \quad (9.36)$$

The variance of the expected-value estimate is now (Leo 1987)

$$D^2(\hat{\mu}) = \frac{1}{\sum_{k=1}^n \frac{1}{\sigma_k^2}}. \quad (9.37)$$

It is easy to verify that if the errors of the X_k variables are equal (i.e., when the experimental values have been determined from the same experiment with the same experimental error $\sigma_k \equiv \sigma$), then [Eq. \(9.36\)](#) changes over to the usual formula of simple arithmetic average as shown by [Eq. \(9.29\)](#) whose uncertainty is given by [Eq. \(9.31\)](#).

9.2.5 Measures of the “Association” of Two Distributions

In the following formulas, the subscripts 1 and 2 refer to the random variables X and Y respectively. The independence of the random variables X and Y means that their joint

distribution function is equal to the product of their respective (one-dimensional) distribution functions:

$$F(x, y) = F_1(x)F_2(y). \quad (9.38)$$

In the case of continuous distributions, independence also means that the joint density function is equal to the product of the individual density functions:

$$f(x, y) = f_1(x)f_2(y). \quad (9.39)$$

The covariance of X and Y is defined as

$$\sigma_{12} \equiv \text{Cov}(X, Y) \equiv E((X - \mu_1)(Y - \mu_2)) = E(XY) - \mu_1\mu_2. \quad (9.40)$$

The correlation coefficient of X and Y is given by

$$\rho_{12} \equiv R(X, Y) \equiv \frac{\text{Cov}(X, Y)}{D(X)D(Y)} \equiv \frac{\sigma_{12}}{\sigma_1\sigma_2}. \quad (9.41)$$

The correlation coefficient is a number lying in the interval $[-1, +1]$.

If X and Y are independent, then they are also uncorrelated, i.e.,

$$\rho_{12} = 0. \quad (9.42)$$

If there is a linear relationship between X and Y , then

$$|\rho_{12}| = 1 \quad (9.43)$$

i.e., the correlation reaches its maximum. More exactly, if $Y = aX + b$, then

$$\rho_{12} = \begin{cases} +1 & \text{if } a > 0 \\ -1 & \text{if } a < 0 \end{cases}. \quad (9.44)$$

Owing to this result, one might conclude (erroneously) that whenever there is a strong relationship between X and Y (e.g., when Y is the function of X), then the variables must be correlated. However the truth is that one can find such distributions and such a strong (however nonlinear) relationship between X and Y , which makes them uncorrelated.

All things considered, one can only state with certainty that if X and Y are correlated, they cannot be independent.

9.3 Sums and Products, Error Propagation

In this section, the “algebra” of random variables will be rehearsed from the viewpoint of error propagation. Convolution, central limit theorem, as well as random sums (i.e., sums of a random number of random variables) are also included here because of their importance in nuclear applications.

9.3.1 Expected Value and Variance of Linear Expressions

Expected value of linear combinations. For any sequence of random variables as well as constants a and b_k one can write

$$E\left(a + \sum_{k=1}^n b_k X_k\right) = a + \sum_{k=1}^n b_k \mu_k. \quad (9.45)$$

Corollaries	
Expected value of a constant	$E(a) = a$
Shift in general	$E(a + X) = a + E(X)$
Change of scale in general	$E(bX) = bE(X)$
Addition/subtraction in general	$E(X \pm Y) = E(X) \pm E(Y)$

Variance of the sum of random variables. One can write for any choice of two random variables that

$$D^2(X \pm Y) = D^2(X) + D^2(Y) \pm 2\text{Cov}(X, Y). \quad (9.46)$$

For independent random variables, the covariances are zero, thus the following formula holds for the variance of the linear combination of several variables:

$$D^2\left(a + \sum_{k=1}^n b_k X_k\right) = \sum_{k=1}^n b_k^2 D^2(X_k). \quad (9.47)$$

Corollaries	
Standard deviation of a constant	$D(a) = 0$
Shift in general	$D(a + X) = D(X)$
Change of scale in general	$D(bX) = b D(X)$
Addition/subtraction for independence	$D^2(X \pm Y) = D^2(X) + D^2(Y)$

Note that the variances add up even if the variables are subtracted, i.e., the errors do not cancel each other out. (Actually, the standard deviations of independent random variables are related to each other like the lengths of orthogonal vectors from which the length of the resultant vector is calculated according to the multidimensional version of the Pythagorean theorem.)

Standardization. Standardization is a special application of the shifting and scale-changing transformations:

$$Y = \frac{X - E(X)}{D(X)} = \frac{X - \mu}{\sigma}. \quad (9.48)$$

The standardized random variable Y obtained this way has 0 for its expected value and 1 for its standard deviation as well as for its variance.

Standardization usually leads out from the distribution family of X . For instance, if X is distributed as Poisson, then Y is certainly not. However, if X happens to be $N(\mu, \sigma^2)$ normal, then Y is an $N(0, 1)$ standard normal random variable. For instance, the left panel in [Fig. 9.1](#) makes use of standardization to show the properties of one-dimensional normal distributions. As standardization shifts the distribution such that the mean becomes 0, this transformation applied to the exponential distribution on the right panel in the same figure would result in a shifted exponential, which however is not considered an exponential distribution. (The exponential distribution is kind of “attached to the soil” as its mode is at $t = 0$ by definition.)

9.3.2 The Central Limit Theorem

Let X be a random variable with any distribution, having expected value μ and standard deviation σ . Let X_i denote the random variable representing the i th result of n independent trials to observe X . (The random variables X_i are obviously independent of each other and they have the same distribution as X .) Then the sample mean $\bar{X} \equiv (X_1 + X_2 + \cdots + X_n)/n$ is asymptotically $N(\mu, \sigma^2/n)$ normal (as a random variable).

The practical content of the central limit theorem is as follows. If one wants to figure out the “exact” value of a physical quantity by calculating the average of measured data, then (1) the estimate thus obtained is still not completely accurate. However, (2) the accuracy is better than that of the original data (it is clear: otherwise the averaging would not make any sense at all). Moreover it is also reasonable to assume that (3) the somewhat erroneous estimates that can be obtained for the “exact” value in this way are normally distributed about the said “exact” value, no matter what the original data distribution was like (e.g., it could be uniform or exponential or anything provided that the expected value and the variance exist).

The central limit theorem makes normal distribution one of the most important continuous distributions. Also, the fact that a lot is known about normal distribution makes the central limit theorem a very practical thing, namely, whenever it is in action, it is easy to judge how large deviations are to be expected from a given mean and how often a given deviation is likely to occur (see [Fig. 9.2](#)).

Note that the theorem can be phrased not only for averages but also for sums (see [Fig. 9.3](#)) and, moreover, with much weaker conditions than specified above. For n -sums, e.g., the central limit theorem can be phrased like this: Under the conditions specified above, the sum $\Sigma_n \equiv (X_1 + X_2 + \cdots + X_n)$ is asymptotically $N(n\mu, n\sigma^2)$ normal.

9.3.3 Convolution and Deconvolution

The convolution and the sum of independent random variables. If X and Y are independent (continuous) random variables with density functions f_X and f_Y , as well as distribution functions F_X and F_Y , respectively, then the density function f_{X+Y} and the distribution function F_{X+Y} of the random variable $Z = X + Y$ are given by the following convolutions:

$$f_{X+Y}(z) = f_X * f_Y(z) \equiv \int_{-\infty}^{+\infty} f_X(z-u)f_Y(u) du, \quad (9.49)$$

$$F_{X+Y}(z) = F_X * F_Y(z) \equiv \int_{-\infty}^{+\infty} F_X(z-u) dF_Y(u) = \int_{-\infty}^{+\infty} F_X(z-u)f_Y(u) du. \quad (9.50)$$

The integral determining f_{X+Y} is called the convolution of density functions, that determining F_{X+Y} is referred to shortly as the convolution of the distributions. (The latter can also be calculated when X is discrete with a finite number of spectrum points. Then, in the case of continuous distributions, the density function f_{X+Y} can be obtained by differentiation if necessary.) The convolution as an operation is commutative, just like the addition. If the distributions are such that $f_i(u) = 0$, for $u \leq a_i$, then

$$f_1 * f_2(z) = \int_{a_2}^{z-a_1} f_1(z-u)f_2(u) du. \quad (9.51)$$

If therefore $a_1 = a_2 = 0$, then the integration proceeds between 0 and z .

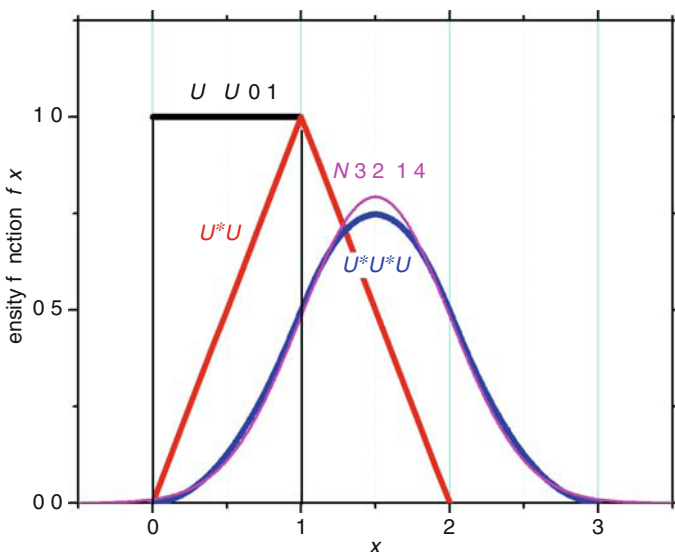
(#8) Uniform distribution: $U(a, b)$. Later on it will be convenient sometimes to refer to the (continuous version of the) uniform distribution that is characterized by a rectangular density function between the limits a and b . More precisely, the density function of the $U(a, b)$ uniform distribution is $f(x) = 1/(b-a)$ in the interval (a, b) and $f(x) = 0$ elsewhere. Its expected value is $\mu = (a+b)/2$ and its variance is $\sigma^2 = (b-a)^2/12$. The density function of the uniform distribution $U(0, 1)$ is shown in [Fig. 9.4](#).

Deconvolution. Making use of the property of the characteristic function (Fourier transform) expressed by [Eq. \(9.24\)](#), a simple solution exists for expressing one of the components from a (density) function having the form of a convolution

$$\varphi(f_{X+Y}) = \varphi(f_X * f_Y) = \varphi(f_X)\varphi(f_Y). \quad (9.52)$$

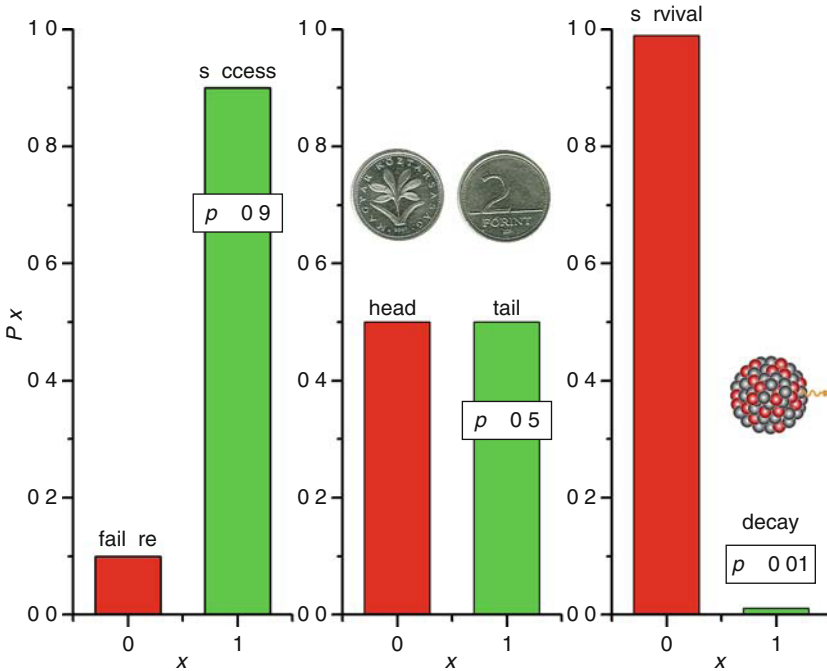
Fig. 9.4

This figure shows the rectangular density function of the uniform distribution $U(0, 1)$ together with its convolutions. Generating $U(0, 1)$ (pseudo) random numbers is a standard feature of many “scientific” calculators. The convolution power $U*U$ represents the distribution of the sum of two such numbers. Similarly, if three such numbers are added, the distribution of the sum will be $U*U*U$. The example demonstrates how soon central limit theorem can be caught in the act even in the case of a distribution far from being bell shaped. Note that the density function of $U*U*U$ is composed of parabolic fragments but still it is rather close in shape to that of a normal distribution of the same mean and variance



■ Fig. 9.5

Three basic types of Bernoulli distribution classified according to the ratio of p ("success" $\Leftrightarrow 1$) to q ("failure" $\Leftrightarrow 0$). Any series of Bernoulli trials results in binomial distribution (see ► Fig. 9.3), however only the third type, characterized by a low probability of success, leads to Poisson distribution. Radioactive decay usually belongs to the latter category



In this case, namely, the density function of X , e.g., can be expressed by the inverse Fourier transform

$$f_X = \varphi^{-1} \left(\frac{\varphi(f_X * f_Y)}{\varphi(f_Y)} \right). \quad (9.53)$$

(#9) The significance of convolution/deconvolution exceeds the boundaries of probability theory. Some nuclear spectra can also be described by a convolution-type integral. For instance, a transmission *Mössbauer spectrum* (see ► Chap. 25 in Vol. 3) is the convolution of two functions one of which is characteristic of the source of radiation while the other of the absorber (sample). The latter function contains all the parameters that the spectroscopist can be interested in, which explains why some methods of spectrum evaluation include the calculation of deconvolution as well.

9.3.4 Random Sums

Sums of a random number of random variables – in short: random sums – are often encountered at several stages of radiation detection. The problem usually presents itself disguised as a product.

Consider about μ_N items, each consisting of about μ_X parts (or, alternatively, each weighing/measuring/worth about μ_X kg/m/dollars). Obviously the whole lot of parts (mass/length/value) adds up to about $\mu_N\mu_X$ (kg/m/dollars). The question to be answered is the following. What is the error of this “product”?

The answer is given by the following theorem (Feller 1968; Korn and Korn 1968). This theorem gives the solution for the recurring problem of Bernoulli sampling that will be discussed later on.

Let X_1, X_2, \dots, X_N be a sequence of mutually independent (integral valued) random variables with a common distribution. Let N be itself an integral valued variable, being independent of the others. Let $\Sigma_N = X_1 + X_2 + \dots + X_N$. Let $G_X(s)$ denote the (common) generating function of the variables X_1, X_2, \dots, X_N . Let $G_N(s)$ be the generating function of N , and $G_\Sigma(s)$ that of the random sum Σ_N . One can write

$$G_\Sigma(s) = G_N(G_X(s)). \quad (9.54)$$

Applying the chain rule of differentiation to [Eq. \(9.54\)](#), the expected value and the variance of the random sum can be easily calculated using [Eq. \(9.21\)](#):

$$\mu_\Sigma = \mu_N\mu_X; \quad \sigma_\Sigma^2 = \mu_X^2\sigma_N^2 + \mu_N\sigma_X^2 \quad (9.55)$$

Thus the square of the relative deviation of the random sum is

$$\left(\frac{\sigma_\Sigma}{\mu_\Sigma}\right)^2 = \left(\frac{\sigma_N}{\mu_N}\right)^2 + \frac{1}{\mu_N} \left(\frac{\sigma_X}{\mu_X}\right)^2. \quad (9.56)$$

This asymmetrical result implies that if the (expected) number of terms is large enough, then the variance of the random sum is principally determined by the variance of the number of these terms (i.e., the variance of the individual terms is of relatively less importance). It is worthwhile to compare this result with [Eq. \(9.61\)](#), showing the formula of error propagation for “real” products.

9.3.5 General Approximation of Error Propagation

For any sequence of random variables, the following approximation holds for the error of the formula $f(X_1, X_2, \dots, X_n)$ calculated from these variables:

$$D^2(f) \approx \sum_{i=1}^n \left[\left(\frac{\partial f}{\partial x_i} \right)_{x=\mu}^2 D^2(x_i) \right] + 2 \sum_{i < j} \left[\left(\frac{\partial f}{\partial x_i} \right)_{x=\mu} \left(\frac{\partial f}{\partial x_j} \right)_{x=\mu} \text{Cov}(x_i, x_j) \right]. \quad (9.57)$$

If the variables are mutually independent, then the second sum containing the covariances becomes zero and therefore

$$D^2(f) \approx \sum_{i=1}^n \left[\left(\frac{\partial f}{\partial x_i} \right)_{x=\mu}^2 D^2(x_i) \right]. \quad (9.58)$$

The subscript $x = \mu$ is to indicate that the derivatives must be calculated at the expected values of the variables. (In practical terms, the expected value is the “exact” value around which the “measured” value of the variable fluctuates.)

[Equations \(9.57\)–\(9.58\)](#) have been obtained from the (first-order) differential – from a linear approximation – of the function $f(X_1, X_2, \dots, X_n)$. Therefore, the related formulas are

quite general in the sense that f can be any type of differentiable function; however, the approximation can only be used for continuous variables and for relatively small errors. On the other hand, \blacktriangleright Eqs. (9.46)–(9.47) obtained for linear expressions – actually the special cases of \blacktriangleright Eqs. (9.57)–(9.58) – are exact.

9.3.6 Formulas for Products/Ratios of Independent Random Variables

For the expected value of products/ratios, the following exact formula holds:

$$E\left(\frac{XY}{Z}\right) = E(X)E(Y)E\left(\frac{1}{Z}\right). \quad (9.59)$$

If $D^2(Z)/E^3(Z)$ is small enough, then the following approximation can be derived by expanding the expression $1/Z$ into Taylor series about $E(Z)$:

$$E\left(\frac{XY}{Z}\right) \approx \frac{E(X)E(Y)}{E(Z)}. \quad (9.60)$$

The approximation of standard deviation of products/ratios can be obtained from the appropriate form of \blacktriangleright Eq. (9.58):

$$\left[\frac{D\left(\frac{XY}{Z}\right)}{E\left(\frac{XY}{Z}\right)}\right]^2 \approx \left[\frac{D(X)}{E(X)}\right]^2 + \left[\frac{D(Y)}{E(Y)}\right]^2 + \left[\frac{D(Z)}{E(Z)}\right]^2. \quad (9.61)$$

One can see that, in the case of multiplication and division, it is the squares of the relative deviations that add up, rather than the variances. Note that the last term representing division is also added rather than subtracted in the above formula.

As shown earlier, \blacktriangleright Eq. (9.56) gives a different error formula for a different type of “product.” In the case of products therefore it is worthwhile to think it over whether or not a random sum is hiding behind the problem. This can only happen, of course, when one of the variables is an integer having no dimension.

9.4 Special Distributions

The distributions summarized on the next few pages play important role in nuclear measurements as well as in the evaluation of nuclear spectra.

9.4.1 Bernoulli Distribution: $B(1, p)$

Mass function: $P(X = x; p) = \begin{cases} p & \text{if } x = 1 \\ q & \text{if } x = 0 \end{cases}$ where $q = 1 - p$	
Generating function: $G(s) = q + ps$	
Expected value: p	Mode: $\begin{cases} 1 & \text{if } p \geq q \\ 0 & \text{if } p \leq q \end{cases}$
Variance: pq	Relative deviation: $\sqrt{\frac{q}{p}}$

Some authors consider the terms Bernoulli distribution and binomial distribution synonyms. As it will turn out later, it has some advantages to handle this simplest variant of binomial distributions separately.

Interpretation. Consider a dichotomous experiment that has only two possible outcomes (alternative events) like a “coin toss.” One of the alternative outcomes (e.g., “heads”) is generally called “success” while the other (e.g., “tails”) “failure.” The probability of “success” is denoted by p , that of “failure” by $q = 1 - p$. Now, the Bernoulli variable X is defined as follows:

$$X(\text{“success”}) \equiv 1; \quad X(\text{“failure”}) \equiv 0. \quad (9.62)$$

(#10) The repeated independent trials associated with such a dichotomous “game” are called Bernoulli trials.

(#11) As regards nuclear methods, another dichotomous game comes to mind: the fate of a radioactive nucleus in a period of time. The alternative outcomes are “decay” (characterized by probability p) and “survival” (characterized by probability q).

(#12) $B(1, p)$ Bernoulli random numbers can be easily obtained from $U(0, 1)$ random numbers uniformly distributed in the interval $(0, 1)$. (As mentioned before, such random numbers are readily available using “scientific” calculators.) The algorithm is straightforward: one chooses $X = 1$, whenever the $U(0, 1)$ uniform random number happens to be less than p , and chooses $X = 0$ otherwise.

9.4.2 Binomial Distribution: $B(n, p)$

Mass function: $P(X = x; n, p) = \binom{n}{x} p^x q^{n-x} \quad (x = 0, 1, \dots, n) \quad q = 1 - p$	
Generating function: $G(s) = (q + ps)^n$	
Expected value: $\mu \equiv np$	Mode: $\begin{cases} \mu - q & \text{and} \\ \mu + p \\ \lfloor \mu + p \rfloor \end{cases} \quad \begin{cases} \text{if } \mu + p \text{ is integer} \\ \\ \text{if } \mu + p \text{ is not integer} \end{cases}$
Variance: $npq = \mu q$	Relative deviation: $\sqrt{\frac{q}{\mu}} = \sqrt{\frac{q}{pn}}$

Interpretation. Consider a dichotomous “game.” Let p denote the probability of “success” in a single trial. Suppose that a series of n Bernoulli trials have been performed. Let X_1, X_2, \dots, X_n denote the independent Bernoulli variables belonging to the respective trials. Then the random variable $X \equiv X_1 + \dots + X_n$ has a $B(n, p)$ binomial distribution.

(#13) Note that X means the number of successful outcomes in the series of n Bernoulli trials. Note also that the above interpretation justifies the use of the symbol $B(1, p)$ for the Bernoulli distribution.

(#14) The above remark provides a straightforward recipe for the simulation of $B(N, p)$ random numbers if a $U(0, 1)$ random number generator is available. One only has to generate N random numbers of $B(1, p)$ Bernoulli distribution according to remark (#12). The sum of the N Bernoulli numbers will then result in a $B(N, p)$ random number.

(#15) The coin-toss game can be performed either by tossing one single coin n times, or by tossing n coins simultaneously. If the only question is the probability of tossing exactly x “heads” out of n tosses, then the two games are essentially identical, and the answer is provided by the mass function of the $B(n, p)$ binomial distribution. (It follows from symmetry that by swapping the roles one gets a similar formula for the number of “tails,” too.)

(#16) Referring to remark (#11), the simultaneous “coin-toss game” can be paraphrased thus: Consider n identical radioactive nuclei, any of which decays with the same probability p during a certain period of observation. What is the probability that exactly x nuclei will decay? The answer is given by the mass function of the $B(n, p)$ distribution. In other words, the fluctuation of the number of nuclei that actually decay over a given period of time can be described by the binomial distribution. (It follows from symmetry that by swapping roles – let p denote the probability of “survival,” and x the number of nuclei escaping decay over the same period – the same distribution will be obtained for the number of “survivors.”)

(#17) Let n denote the number of radionuclei like before. Let p represent the probability that a selected nucleus will decay within a given period of time, and η the probability that the decay of a nucleus will be actually observed with the given detector system. Then $p\eta$ obviously measures the probability that a given nucleus decays over the period of time *and* this decay will be actually observed. What is the probability that exactly x nuclei will be observed to decay? The answer is given by the mass function of the $B(n, p\eta)$ distribution. In other words, the fluctuation of the number of counts measured (without background) over a given period of time can be described by the binomial distribution.

This result will be referred to as the Bernoulli sampling of binomial distribution, because the problem can also be presented in the following way: The number of decayed nuclei has a $B(n, p)$ distribution. Let X denote the actual number of nuclei that have decayed over the given period of time. Now a $B(1, \eta)$ Bernoulli sampling is performed on the decayed nuclei, i.e., the individual decays are considered one after the other and either accepted with probability η (meaning that the decay of the nucleus has been detected) or discarded with probability $1 - \eta$ (the decay of the nucleus has escaped detection). The question is how many decay events have been detected altogether and how these detected numbers are distributed in a whole series of like experiments. Thinking it over, one has a series of Bernoulli trials here, the length of which (X) itself is a random variable with a $B(n, p)$ distribution. Therefore the task is to add up X random variables having $B(1, \eta)$ Bernoulli distribution each. Using [Eq. \(9.54\)](#) obtained for random sums, one finds that this sum – the number of decay events actually observed or, which is the same, the number of counts has $B(n, p\eta)$ distribution, where p is the probability of decay and $\eta < 1$ is the probability/efficiency of detection.

(#18) It is easy to verify that for large values of n , i.e., for large μ , the mode(s) of binomial distribution is (are) practically equal to the expected value, which means that the expected value doubles as the most probable value. On the other hand, the relative deviation rapidly decreases with increasing n or μ . This means that the distribution – obeying the law of large numbers – is gradually “shrinking” on the expected value (see [Fig. 9.3](#)).

Owing to this, if a large enough number of counts have been measured, that single number can be considered as a fairly good estimate of the expected value. (This statement is not at all true for any distribution.) Of course, in the case of such a one-point estimate it is impossible to find out whether or not the measured data point squares with the assumption that the equipment has been faultless.

9.4.2.1 Properties

Addition theorem. If X_1 and X_2 are independent random variables with $B(n_1, p)$ and $B(n_2, p)$ distribution, respectively, then the random variable $X = X_1 + X_2$ has $B(n_1 + n_2, p)$ distribution.

(#19) As regards the example mentioned in remark (#16), the above property means that if there are two “heaps” of identical radionuclei, then not only the separate counts have binomial distribution (with expected values n_1p and n_2p as well as variances n_1pq and n_2pq , respectively), but the total number of counts as well (with expected value $(n_1 + n_2)p$ and variance $(n_1 + n_2)pq$). Choosing 1 s as the time of observation, the addition theorem expresses the additive property of activity.

Normal approximation (De Moivre–Laplace limit theorem). It follows from the interpretation as well as from the central limit theorem that for large enough values of npq ($npq \geq 6$ suffices already) the binomial distribution can be approximated by a normal distribution with expected value $\mu = np$ and variance $\sigma^2 = npq$ (see [Figs. 9.3](#) and [9.6](#)):

$$B(n, p) \approx N(np, npq). \quad (9.63)$$

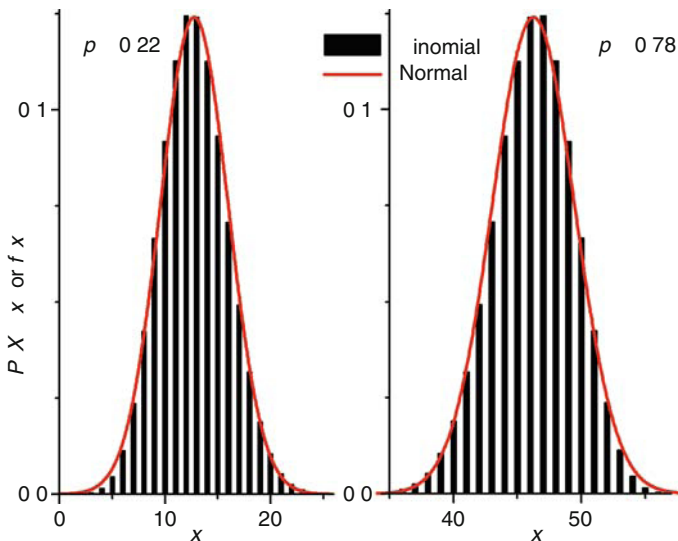
Poisson approximation. For small enough values of p and large enough values of n ($p \leq 0.1$ and $n \geq 20$ will do) the binomial distribution can be approximated by a Poisson distribution with parameter (expected value) $\mu = np$ (see [Figs. 9.5](#) and [9.7](#)):

$$B(n, p) \approx \Pi(np). \quad (9.64)$$

(#20) Consider again the example in remarks (#16)–(#17). If the observation period is very short compared to the half-life of the radionuclide in question (i.e., $p \ll 1$) and if the total number of nuclei observed is large enough, then the number of decay events/counts has a

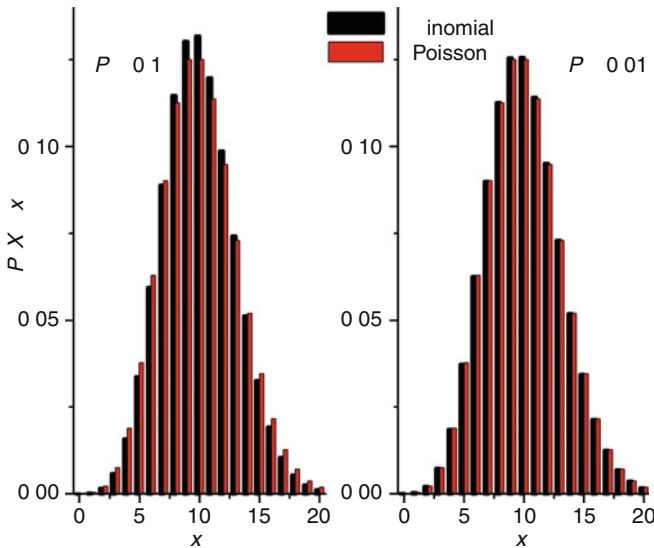
■ Fig. 9.6

The $N(np, npq)$ normal distribution provides a rather good approximation for the $B(n, p)$ binomial distribution irrespective of the value of p provided that $npq \geq 6$. In the example shown n is merely 59, and npq is only 10, however the “fit” is quite good already



■ Fig. 9.7

The $B(n, p)$ binomial distribution can be approximated with the $\Pi(np)$ Poisson distribution even for small values of $\mu = np$ provided that the probability of success in a single trial is small ($p \leq 0.1$). Note that the “fit” is reasonably good at $p = 0.1$, although the value of μ is only $np = 10$. For $p = 0.01$, on the other hand, the “fit” looks almost perfect (see ► Fig. 9.5)



Poisson distribution. This serves with a simple “recipe” for the estimation of the standard deviation:

$$s \approx \sigma = \sqrt{\mu} \approx \sqrt{\bar{X}}. \quad (9.65)$$

(#21) Continuing from the previous remark the following conclusion can be drawn: If the number n of the radionuclides is large enough, which is usually the case, then the number of decay events/counts is normally distributed. Therefore, the expected fluctuation of counts, e.g., can be judged by the “rules” of normal distribution (see ► Table 9.3). For instance, the counts X_i collected over the same length of time are supposed to lie in the error intervals “ $\mu \pm 1\sigma$,” “ $\mu \pm 2\sigma$,” and “ $\mu \pm 3\sigma$ ” with the following frequencies (provided that the total time needed for the series of measurements is short enough compared to the half-life of the radionuclide):

$$\bar{X} \pm \sqrt{\bar{X}} : 68\%; \quad \bar{X} \pm 2\sqrt{\bar{X}} : 95.4\%; \quad \bar{X} \pm 3\sqrt{\bar{X}} : 99.7\%. \quad (9.66)$$

9.4.3 Poisson Distribution: $\Pi(\mu)$

Mass function: $P(X = x; \mu) = \frac{\mu^x}{x!} e^{-\mu} \quad (x = 0, 1, 2, \dots)$	
Generating function: $G(s) = e^{\mu(s-1)}$	
Expected value: μ	Mode: $\begin{cases} \mu - 1 & \text{and} \\ \mu \\ \lfloor \mu \rfloor \end{cases} \quad \begin{cases} \text{if } \mu \text{ is integer} \\ \text{if } \mu \text{ is not integer} \end{cases}$
Variance: μ	Relative deviation: $\frac{1}{\sqrt{\mu}}$

Interpretation. Consider a recurring instantaneous rare event (like the arrival of a background pulse), which repeats itself at random over time. The task of the experimenter is to count such events over a certain observation period ΔT . Suppose that the following general conditions are satisfied:

1. The outcome of the observation does not depend on the location of ΔT along the time axis.
2. The occurrences of the event in separated time intervals are stochastically independent. Suppose that the following “rarity” and “time-proportionality” conditions are also fulfilled in the case of very short periods of time $\Delta t \ll \Delta T$:
3. If the observation period ΔT is divided to n equal intervals – “time cells” – of length $\Delta t = \Delta T/n$, then the majority of such intervals would not contain any event at all, while the rest contain exactly one event each, provided that n is large enough ($n \rightarrow \infty$). That is, the possibility of events appearing in doublets is excluded if the “time cells” considered are small enough.
4. At the above fine time-scale the (single) occurrence of the event within a “time cell” is proportional to the length Δt of the interval:

$$p = P(1) = \frac{\mu}{\Delta T} \Delta t = \frac{\mu}{n}. \quad (9.67)$$

If the above assumptions are satisfied, then the total number of events observed (i.e., the number of counts X) has a $\Pi(\mu)$ Poisson distribution.

(#22) Condition 4 can be better understood, if μ is regarded as the expected number of events occurring over the observation period ΔT . (According to the data in the box of characteristic parameters, this interpretation is justified, because $E(X) = \mu$ for the Poisson distribution.) Thus the ratio μ/n equals the average number of events occurring in a single “time cell.” Note that as n approaches infinity, this average sooner or later drops below 1, however large the value of μ is (e.g., $\mu/n \approx k/m$, where $k < m$). Owing to condition 3, this means that – asymptotically – on an average k cells out of m contain exactly one event each, while the rest are empty. In other words, the probability that a cell is “filled” with an event is $k/m (\approx \mu/n)$, i.e., condition 4 is satisfied.

(#23) The above conditions are fulfilled, e.g., in the case of the background caused by cosmic radiation and the like. Therefore, background counts observed over a given period of time have Poisson distribution.

(#24) It is clear that, for large values of μ , the mode(s) is(are) practically equal to the expected value, i.e., the expected value doubles as the most probable value in the case of the Poisson distribution. On the other hand, the relative deviation rapidly decreases as μ increases. Thus, the distribution is gradually “shrinking” on the expected value.

Consequently, if a large enough background is measured, then this single measurement can provide a fair estimate for the expected value, the square root of which can be used for the estimation of the standard deviation. (See also remark (#18) on the unreliability of such one-point estimates.)

9.4.3.1 Properties

Bernoulli sampling. Consider a random variable with a $\Pi(\mu)$ Poisson distribution, which counts the occurrences of certain types of events (e.g., events of radioactive decay). Now a

$B(1, \eta)$ Bernoulli sampling is performed on the counted events, meaning that the events are either accepted with probability η , or discarded with probability $(1 - \eta)$. For instance, η can indicate the efficiency of detection, in which case “acceptance” means that the decay event in question has been actually detected. It follows from [Eq. \(9.54\)](#) that the number of events passing such a sampling (e.g., the number of detector pulses caused by the radiation of decaying nuclei) has a $\Pi(\mu\eta)$ Poisson distribution. (See also remark (#17).)

Addition theorem. If X_1 and X_2 are independent random variables with Poisson distributions $\Pi(\mu_1)$ and $\Pi(\mu_2)$, respectively, then the random variable $X = X_1 + X_2$ has a $\Pi(\mu_1 + \mu_2)$ Poisson distribution.

(#25) As a consequence of remark (#20) as well as due to the addition theorem, the following conclusion can be drawn: Suppose that decay events are observed in a specimen that contains a mixture of two (or more) radionuclides. If the observation period is short enough in comparison with any of the half-lives (i.e., any single nucleus will survive the period with a high probability), then the total number of decay events has a Poisson distribution. It follows from the property of Bernoulli sampling that the same applies to the total number of counts.

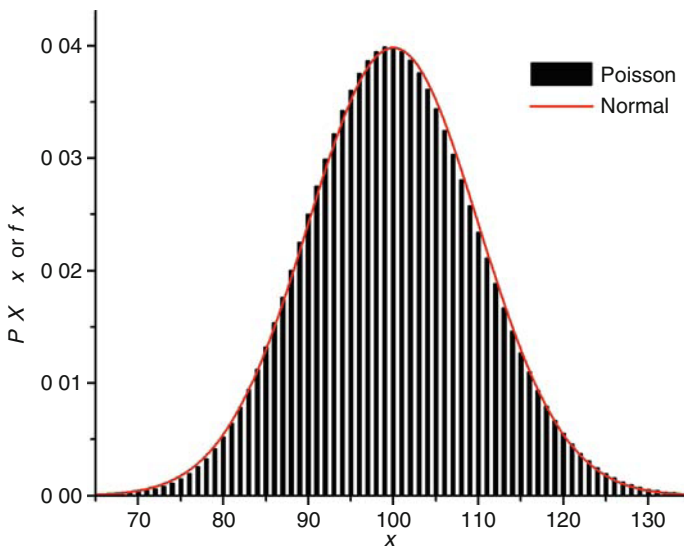
(#26) Continuing from the previous remark as well as remark (#23), the following conclusion can be drawn: The number of counts measured with background also has a Poisson distribution.

Normal approximation. It follows from the addition theorem and from the central limit theorem that for large enough μ the Poisson distribution can be approximated by a normal distribution (see [Fig. 9.8](#))

$$\Pi(\mu) \approx N(\mu, \mu). \quad (9.68)$$

■ Fig. 9.8

The $N(\mu, \mu)$ normal distribution provides an almost perfect fit for the $\Pi(\mu)$ Poisson distribution at as low a parameter value as $\mu = 100$



(#27) Continuing from the previous remarks, the following conclusion can be drawn: If the counts measured together with background are large enough, then their fluctuation can be judged by the “rules” of the normal distribution in the same way as suggested in remark (#21). See [Eq. \(9.66\)](#) and [Table 9.3](#).

9.4.4 Exponential Distribution: $\gamma(1, \lambda)$

Density function: $f(t) = \begin{cases} \lambda e^{-\lambda t} & \text{if } t > 0 \\ 0 & \text{if } t \leq 0 \end{cases}$	
Distribution function: $F(t) = 1 - e^{-\lambda t}$	
Characteristic function: $\varphi(u) = (1 - iu/\lambda)^{-1}$	
Expected value: $\tau \equiv \frac{1}{\lambda}$	Median: $T_{1/2} \equiv \frac{\ln 2}{\lambda} \approx \frac{0.7}{\lambda}$
Variance: $\frac{1}{\lambda^2}$	Relative deviation: 1

Interpretation. Consider an “ageless” but “mortal” entity the lifetime of which is characterized by the random variable $T \in (0, \infty)$. Agelessness means that – at any moment of its life – the life expectancy of such an entity is independent of its age, i.e., of the time it has already lived up to that point. Therefore if it is still alive at the moment $t > 0$ (i.e., if $T > t$), then the (conditional) probability of still finding it alive at a later moment $t + s$ only depends on the time elapsed since the moment t (i.e., it only depends on s):

$$P(T > t + s | T > t) = P(T > s). \quad (9.69)$$

Suppose that the probability that the entity’s “death” (or “decay” as is usually called) occurs within a given time interval is proportional to the length Δt of that interval, provided that Δt is small enough. In other words, $P_{\text{decay}} = 1 - P(T > \Delta t) = \lambda \Delta t$, where λ is the decay constant.

If the above conditions are satisfied, then the lifetime T is a random variable with $\gamma(1, \lambda)$ exponential distribution.

(#28) It is obvious that the above conditions have been “tailored” to fit the disintegration of radioactive nuclei. Consequently, the lifetime distribution of radionuclei is exponential. The same is true for the excited states of nuclei as well as atoms.

There are cases when the exponential distribution is related to waiting times between random events rather than to lifetimes. In such cases the adjective “ageless” is swapped for “memoryless” (Goodman 1988). Anyway, both metaphors are verbal expressions for the same mathematical condition and as such they determine the same (exponential) distribution.

Another phenomenon related to exponential distribution is the absorption (attenuation) of gamma photons in a homogeneous absorber. The correspondence between the roles is as follows: $t \Leftrightarrow d$ (depth of penetration), $\lambda \Leftrightarrow \mu_1$ (linear attenuation coefficient), $T_{1/2} \Leftrightarrow D_{1/2}$ (halving thickness), $\tau \Leftrightarrow \delta$ (mean free path). Agelessness is translated now to indefatigability meaning that the photons – in contrast to ionizing particles – are not losing energy in a continuous way as they proceed in the absorber. However, being mortal, they may “drop dead” suddenly via photoelectric effect, for instance.

(#29) The distribution function (see the red curve in [Fig. 9.9](#)) expresses the monotonically increasing probability that the nucleus will decay sometime over the period $(0, t)$. The “mortality” of the atom is expressed by the normalization condition $F(\infty) = 1$ (which is fulfilled). The fact, on the other hand, that the atom was actually found “living” at the moment

0 corresponds to the condition $F(0) = 0$ (also fulfilled). Thus the probability that the atom will survive t is

$$1 - F(t) = e^{-\lambda t}. \quad (9.70)$$

(#30) Using the above equation, one can get exponentially distributed random numbers from uniformly distributed ones having $U(0, 1)$ distribution. If, namely, the random number/variable X is uniformly distributed in the interval $(0, 1)$, then the random number/variable T calculated from the formula

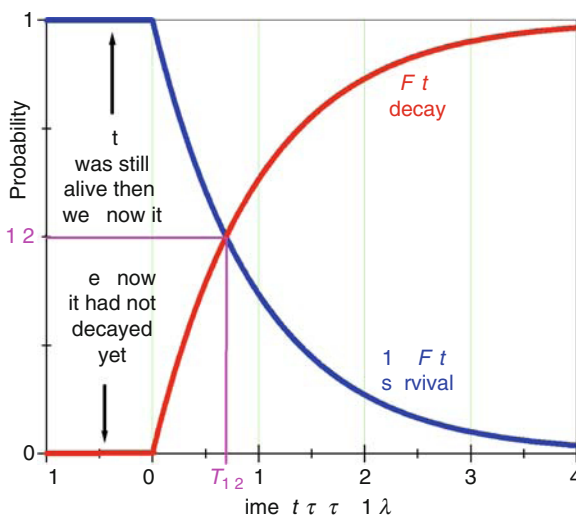
$$T = -\frac{\ln X}{\lambda} \quad (9.71)$$

will have a $\gamma(1, \lambda)$ exponential distribution (Goodman 1988; Lux and Koblinger 1991).

(#31) In the case of the lifetime distribution of radionuclides, excited states, etc., the expected value τ is called the mean life, while the median $T_{1/2}$ is referred to as the half-life. The explanation for the name “half-life” is given in the next subsection on the exponential law of radioactive decay. It will be shown that the half-life is independent of the time elapsed, which is an obvious proof of the agelessness of radionuclides. Note that physicists often use the term lifetime not only in the sense it is used in this chapter, but also in the sense mean life. Fortunately, in the really important cases, i.e., when quantitative statements are made (e.g., “the lifetime of the radionuclide is 10 s”), the ambiguity is removed and the reader can be sure that such a statement actually refers to the mean life.

■ Fig. 9.9

The exponential distribution function $F(t)$ (red curve) expresses the probability that the “entity” – looking at it from the present moment 0 – will be “dead” by the moment t (i.e., that it will decay somewhere between 0 and t). The blue curve, on the other hand, shows the probability of the complementary event, i.e., that the same “entity” will survive the period $(0, t)$. For $t > 0$ the curve of the exponential density function is obtained from the blue curve by multiplying the latter with λ (However, for $t \leq 0$, the density function is zero, not 1, as shown in ► Fig. 9.1)



(#32) Looking at the location parameters of exponential distribution, it must be clear that the rule of thumb expressed by [Eq. \(9.13\)](#) works fairly well for the mode (0), median ($T_{1/2}$), and mean (τ), the ratio of their respective distances being 0.7:0.3 (= 2.1:0.9). This ratio is almost equal to the predicted ratio 2:1 (see also the upper right diagram in [Fig. 9.1](#)).

(#33) The relative-deviation formula ($\sigma_{\text{rel}} = 1$) explains why it is practically hopeless to give a usable mean-life estimate from the observation of the decay of a single atom. (Remember, however, that in the case of the Poisson distribution a large enough observed value could be considered as a fairly good estimate of the expected value.) On the other hand, if the time-scale is changed to logarithmic, e.g., by one of the following transformations:

$$w = \ln t \quad \text{or} \quad u = \ln \frac{t}{\tau} \quad (9.72)$$

(but decimal logarithm will also do), then the density function of the new variable (readily obtained from the exponential distribution function by differentiation using the chain rule):

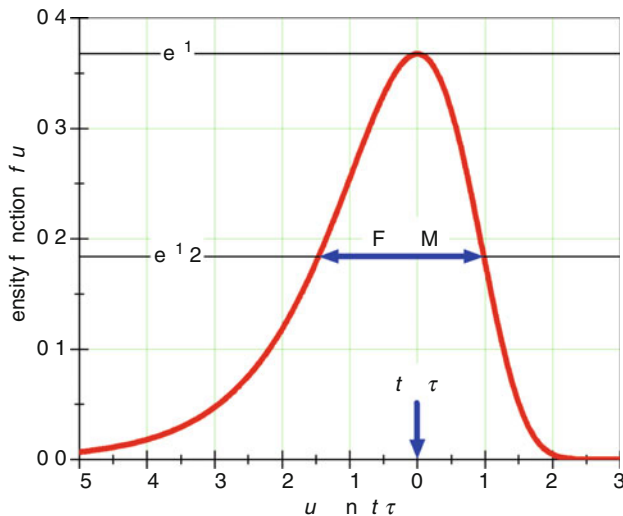
$$f(w) = \frac{1}{\tau} \exp\left(w - \frac{e^w}{\tau}\right) \quad \text{or} \quad f(u) = \exp(u - e^u) \quad (9.73)$$

reaches its maximum at the value corresponding to the condition $t = \tau$ (Schmidt et al. 1984).

The halfwidth of the asymmetric bell-shaped curve in [Fig. 9.10](#) is rather large (FWHM ≈ 2.5 representing about a decimal order of magnitude in uncertainty); however, it can serve as a basis for estimating the mean life τ from the mode of a histogram that has been drawn using the logarithm of a few dozens of lifetime data. For an interesting application of this method used

Fig. 9.10

The density function of the logarithm of exponentially distributed lifetimes. Using this trick, the estimation of the mean life can be reduced to the determination of the mode (i.e., the most frequent value) of a logarithmized lifetime histogram related to the above distribution. This method can be used whenever the number of lifetimes that can be measured is so small that the standard method of mean life determination ($\tau = 1/\lambda$) based on the exponential fit of lifetime data fails. See also remark (#35)



for identifying a couple of man-produced transactinide atoms, see [Sect. 19.3.5, Chap. 19, Vol. 2](#).

9.4.4.1 Connection with the Exponential Law of Radioactive Decay

Suppose that at moment zero there are N_0 atoms “alive.” The question is how many atoms will live at moment t . Let $N(t)$ denote this number. Now if the experiment is repeated several times starting with the same number of atoms (N_0), then the number of the survivors would vary showing that $N(t)$ is a random variable. In other words, the $N(t)$ values would fluctuate about their time-dependent mean $\langle N \rangle(t)$. For any fixed value of t , $N(t)$ has a $B[N_0, p(t)]$ binomial distribution for which the value of $p(t)$ – the probability that a given atom is still intact at moment t – is calculated from [Eq. \(9.70\)](#) as explained in remark (#29) and [Fig. 9.9](#):

$$P(N(t) = k) = \binom{N_0}{k} (e^{-\lambda t})^k (1 - e^{-\lambda t})^{N_0 - k} \quad (k = 0, 1, \dots, N_0). \quad (9.74)$$

Now if the question is put this way: How many atoms *are expected* to live at moment t ?, then the answer is provided by the expected value of the binomial distribution is

$$\langle N \rangle(t) \equiv E_B(N(t)) = N_0 e^{-\lambda t}. \quad (9.75)$$

One can easily recognize the exponential law of radioactive decay in the above formula. The correspondence $\langle N \rangle(t) \Leftrightarrow N$ means that the exponential law applies to the expected number of atoms rather than to the concrete numbers that are measured. The latter show a fluctuation about those expectations according to the standard deviation of the binomial distribution

$$\sigma_N(t) = D_B(N)(t) = \sqrt{N_0 e^{-\lambda t} (1 - e^{-\lambda t})} = \sqrt{\langle N \rangle(t) (1 - e^{-\lambda t})}. \quad (9.76)$$

Note that the above formula gives $\sigma = 0$ both for $t = 0$ and for $t = \infty$. This is due to the following certainties: (1) all of the N_0 atoms were intact at time 0; (2) all of them will decay sooner or later.

As for medium lengths of time (i.e., for periods that are commensurable with the mean life of the atoms), the acceptability of the approximation $\langle N \rangle(t) \approx N$ can be judged by the relative deviation formula

$$\sigma_{\text{rel}}(t) = \frac{\sigma_N(t)}{\langle N \rangle(t)} = \sqrt{\frac{1 - e^{-\lambda t}}{\langle N \rangle(t)}} < \frac{1}{\sqrt{\langle N \rangle(t)}}. \quad (9.77)$$

The above result conveys a reassuring message, namely, if the number of intact atoms is still large enough, then the uncertainty of their number (as expressed by the relative deviation) is negligible. That means that the deterministic expression

$$N = N_0 e^{-\lambda t} = N_0 e^{-t/\tau} = N_0 2^{-t/T_{1/2}} \quad (9.78)$$

usually referred to as the exponential law of radioactive decay stands the test of statistics as well.

(#34) The reason for calling the median “half-life” can be best understood from that variant of the exponential law in which the usual base e is changed to 2. The last expression in [Eq. \(9.78\)](#) shows that N_0 – representing the number of atoms present at time $t = 0$ – will drop to $N_0/2$ by the time $t = T_{1/2}$. Then, after another half-life, the number of survivors will be halved again, and so on. Experience shows that the half-life of radionuclei is independent of both the choice of the origin and the number of halving cycles that have already elapsed. This

can be regarded as a proof for the agelessness of radionuclei. (If they were subject to aging, then the half-life should gradually decrease – an indication that the rest of the population is getting closer to the end of their lives.)

(#35) The exponential law can be written formally as

$$\mu(t) = \mu(t; b) = \mu(t; b_1, b_2) = b_1 e^{-b_2 t}. \quad (9.79)$$

The above expression is an example of a model function, which fits the nuclear spectrum consisting of the spectrum points

$$(t_i, N(t_i)) \quad i = 1, 2, \dots, k \quad (9.80)$$

at an appropriately chosen value (\mathbf{a}) of the parameter vector \mathbf{b} :

$$\mathbf{b} = (b_1, b_2) = (N_0, \lambda) \equiv \mathbf{a} \quad (9.81)$$

The term fitting ideally means that [Eq. \(9.79\)](#) will produce the expected value of $N(t_i)$ for any value of the independent variable t_i . (See [Sect. 9.6](#) on fitting nuclear spectra.) Note that the expression “spectrum point” is used here in the same sense as in [Sect. 9.6](#). See in contrast one of the comments after [Eq. \(9.1\)](#).

9.4.4.2 Exponential Law in a Binomial Way

[Figures 9.11](#) and [9.12](#) help to understand the connection between exponential law on the one part as well as binomial distribution and exponential distribution on the other.

[Figure 9.11](#) shows the possible “fate” of 1,000 atoms through 28 subsequent periods of time – time units – by taking a census of the population at the end of each period. The population numbers $N(t)$ have been simulated by a sequence of random numbers with $B(N, p)$ distributions. (See remark (#14) for the recipe.) The value of the parameter p – representing the probability that a single atom will survive the next period – has been fixed to $p = 0.9$. Thus the starting value of $N(t) \equiv N_t$ has been $N_0 = 1,000$, then the number of survivors has been decreased stepwise by using the recursion algorithm $B(N_{t-1}, p) \Rightarrow N_t$.

The time-dependence of the expected number of survivors is expressed by the monotonically decreasing sequence of the binomial expected values $N_0 p, (N_0 p)p, [(N_0 p)p]p, \dots, N_0 p^{[t]}$. Note that this sequence consists of the substitution values of a decreasing exponential function taken at the end of each period. The explanation for this is as follows. Since no atoms are born in any of the periods, each “census” simplifies to a survival test. The mathematical equivalent of this is the $B(1, p)$ Bernoulli sampling of the $B(N_{t-1}, p)$ distribution of the previous population. Note that the exponential character of the expected value as a function of time is explained by the fact that the Bernoulli sampling has been performed with the assumption that the probability of survival is the same for each period ($p \equiv 0.9$). This assumption, on the other hand, is equivalent to the assumption of agelessness, which, in turn, implies the exponential character of the lifetime distribution.

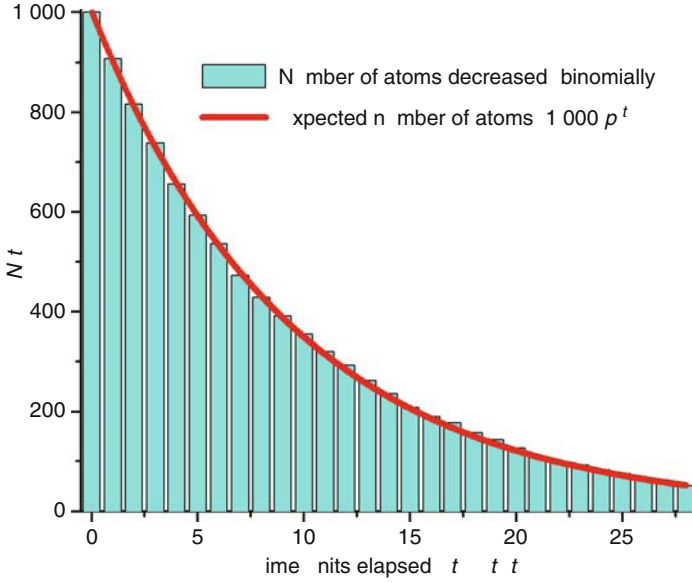
The exponential function obtained for the expected value can be rewritten in e-based form as well with the notation $\{\lambda\} = \ln(1/p)$, and if the unit $[\lambda] = [t]^{-1}$ is attributed to the “new” physical quantity λ (which may be called the “decay constant”) one can write

$$\langle N \rangle(t) = N_0 p^{[t]} = N_0 e^{-\ln(1/p)\{t\}} = N_0 e^{-\{\lambda\}\{t\}} = N_0 e^{-\lambda t}, \quad (9.82)$$

which can be considered as the stochastic reinterpretation of the decay law.

■ Fig. 9.11

The possible fate of 1,000 atoms followed by simulation. The probability that a given atom will survive a single time unit has been fixed at $p = 0.9$. The number of survivors decreases monotonically according to a step function that follows the curve of an exponential function. On the abscissa, the standard notation is used as recommended by IUPAP to express the physical quantity t as a product of a numerical value $\{t\}$ and a unit $[t]$ (See the text for more detail)



If the probability of decay ($q = 1 - p$) is small (e.g., in the given case it is only 0.1), then the factor $\ln(1/p)$ can be expanded into a Taylor series, yielding a probabilistic interpretation for the decay constant λ :

$$\lambda[t] = \frac{\lambda}{[\lambda]} = \{\lambda\} = \ln \frac{1}{p} = -\ln(1 - q) \approx q. \quad (9.83)$$

Thus λ measures the probability that a selected atom will decay during the time unit, provided that this probability (and, consequently, λ) is small enough ($q \ll 1$), which, in turn, depends on how long a time unit has been selected. In other words, the numerical value of the decay constant must be sufficiently small ($\ll 1$) at the given choice of time unit, in order that the probabilistic interpretation can work. (Note that this interpretation corresponds to the second condition fixed at the interpretation of the exponential distribution.)

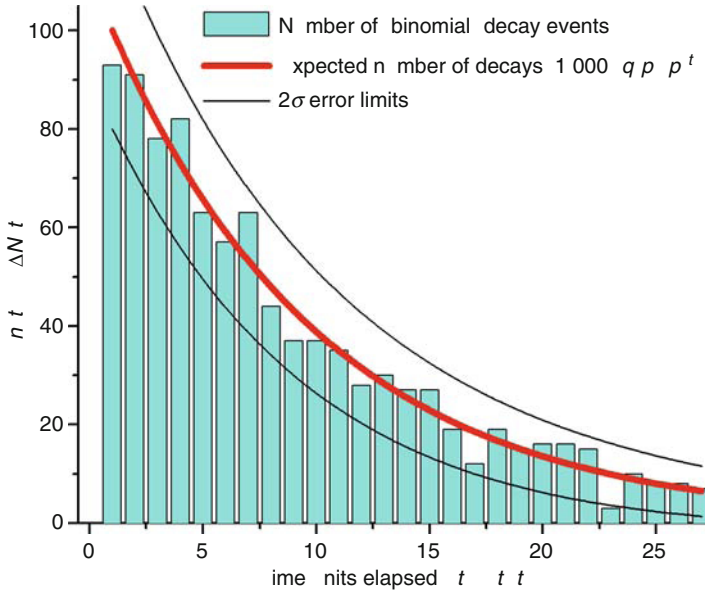
► Figure 9.12 shows the change of the simulated $N(t)$ values, i.e., the simulated numbers of decay events occurring in the time unit. The corresponding expected value is

$$\langle n \rangle(t) = -\Delta \langle N \rangle(t) = -N_0(p^{\{t\}} - p^{\{t\}-1}) = -N_0(p - 1)p^{\{t\}-1} = N_0 \frac{q}{p} p^{\{t\}} = N_0 \frac{q}{p} e^{-\lambda t}. \quad (9.84)$$

Comparing ► Eqs. (9.82) and ► (9.84) as well as ► Figs. 9.11 and ► 9.12 one can see that the time dependence of the number of decay events follows the same exponential rule as that of the number of intact atoms themselves.

■ Fig. 9.12

The numbers of decay events pictured have been obtained by forming the difference of the subsequent step-heights of the simulated step function in ► Fig. 9.11. Note that the “observed” numbers of decay events are not at all monotonically decreasing in time. However, fluctuating up and down, they follow the same exponential curve as the numbers of atoms themselves



9.4.4.3 The Poisson Connection

If the parameter μ of the Poisson distribution means the expected number of pulses arriving over a certain time interval t , then the equation

$$\nu \equiv \mu/t \quad (9.85)$$

will define the mean frequency of such pulses.

The probability that in the period t exactly x pulses arrive at a given mean frequency ν can be calculated from the mass function of the $\Pi(\nu t)$ Poisson distribution

$$P(X = x; \nu, t) = \frac{(\nu t)^x}{x!} e^{-\nu t} \quad (x = 0, 1, 2, \dots). \quad (9.86)$$

Hence the probability that no pulse is counted in the observation period t is

$$P(X = 0; \nu, t) = e^{-\nu t}. \quad (9.87)$$

Note that ► Eq. (9.87) also expresses the probability that the waiting time T (i.e., the time elapsed between subsequent pulses) – a continuous random variable – will be greater than t :

$$P(T > t) = e^{-\nu t}. \quad (9.88)$$

Thus the distribution function of the waiting time T is identical with that of the $\gamma(1, \nu)$ exponential distribution

$$F(t) = P(T \leq t) = 1 - P(T > t) = 1 - e^{-\nu t}. \quad (9.89)$$

(#36) This statement can be reversed, i.e., if the waiting time between pulses has a $\gamma(1, \nu)$ distribution, then the number $X(t)$ of the pulses counted over the period t is a random variable with a $\Pi(\nu t)$ Poisson distribution. Since the time is an explicit parameter here, the word “process” appears to be an appropriate expression. As a matter of fact, the “function” $X(t)$ is referred to as Poisson process in the theory of stochastic processes.

(#37) Continuing from remark (#26), the following conclusion can be drawn: Consider a radioactive specimen. If the detector pulses (including the background) arrive at a mean frequency ν , then the counts registered over the counting period t have a $\Pi(\nu t)$ Poisson distribution, and the waiting times between pulses have a $\gamma(1, \nu)$ exponential distribution.

(#38) Continuing from the previous remark, the following conclusion can be drawn: If the background can be neglected, then the mean frequency ν equals the source strength or observed activity. Thus it is the observed activity rather than the decay constant, which directly appears in the exponential density function of the waiting times (see [Fig. 9.13](#)). The value of the decay constant comes into the picture only indirectly through the expression

$$\nu = \eta \lambda N \quad (9.90)$$

where η is the efficiency of the detecting system for the radiation produced by the decay and N is the number of radionuclei that are still intact.

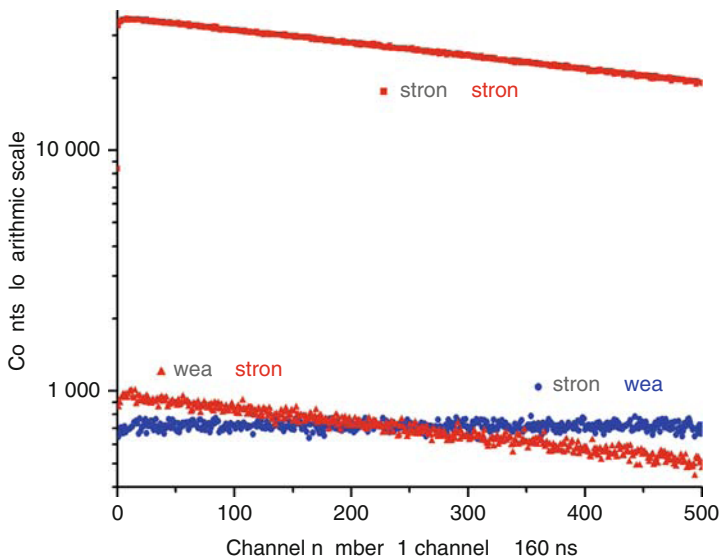
(#39) The Poisson process can be used for the estimation of the count rate of chance coincidences. Let ν_1 and ν_2 denote the mean frequencies of pulses/signals coming from two independent detectors (signal channels). The resolving time of the coincidence circuit is θ , and the counting time is t . (A coincidence circuit only sends out an output signal, if – within the resolving time θ – an input signal coming from channel 1 is followed by an input signal from channel 2 or vice versa. Since the two types of successful events exclude each other, the coincidences estimated separately are to be added up in order to get the total number of coincidences over the counting time t .)

Suppose that an input signal is received from channel 1. The probability that no signal will arrive from channel 2 within the resolving time θ is $\exp(-\nu_2\theta)$, because the waiting times have exponential distribution. (It follows from the memorylessness of the exponential distribution that no matter when one starts measuring the subsequent waiting times, the same time distribution evolves. In other words – see [Fig. 9.13](#) – it does not matter whether one uses the previous pulse of the very same sequence as a starting signal, or one just starts measuring the time at a random moment by leaving the business of starting to the pulses of another sequence.) The probability of the complementary event (i.e., that a signal will arrive from channel 2 within the resolving time θ) is $1 - \exp(-\nu_2\theta)$. Since the coincidence circuit is used for sorting out chance coincidences, one can assume that the exponent is so small that Taylor expansion is allowed. Hence the probability in question is $\nu_2\theta$. This probability can be considered as a type of “efficiency of detection” by which the coincidence circuit “filters” (i.e., performs Bernoulli sampling on) the signals coming from channel 1. Since the latter have a $\Pi(\nu_1 t)$ Poisson distribution, the Bernoulli sampling will result in a number of chance coincidences with a $\Pi(\nu_1 \nu_2 \theta)$ distribution. Due to symmetry, the same result is obtained when channel 2 provides the start signal and channel 1 the stop signal. All in all, the total number of chance coincidences have a $\Pi(2\nu_1 \nu_2 \theta)$ distribution owing to the addition theorem of the Poisson distribution. Thus the expected number of chance coincidences is about $2\theta\nu_1\nu_2 t$, from which the mean frequency of chance coincidences is as follows:

$$\nu_{12} = 2\theta\nu_1\nu_2. \quad (9.91)$$

■ Fig. 9.13

Experimental distribution of the waiting times between the pulses coming from two independent radioactive sources containing ^{22}Na . The labels (e.g., strong–strong) refer to the strengths (i.e., the observed activities) of the sources, which produced the start signal and the stop signal, respectively, for the time measurement. One can see that the slope of each curve is determined by the mean frequency (strength) of the source producing the stop signals. Note also that the start signals are released at random moments and their sequence is completely independent of the sequence of the stop signals. This result well demonstrates the memorylessness of exponential distribution. The same experiment is usually suggested to produce “white” noise (i.e., random signals that are uniformly distributed in time) for the Positron Annihilation Spectroscopy (PAS) measurements (see ● Chap. 27 in Vol. 3). Our results clearly indicate, however, that the noise obtained this way can only be considered “white” in the same way as a finite section of the exponential curve can be regarded horizontal



(#40) It is a common mistake with “beginners” that they directly apply the Poisson-type error estimation to the count rate $v = n/t$ calculated from the count n registered over a period of t in the belief that the “error” of the count rate is $\pm \sqrt{v}$. Dimensional analysis, however, reveals that this cannot be the case, because if one chooses to “measure” v in s^{-1} , then the unit of its “error” calculated this way will be $\text{s}^{-1/2}$, which does not make any sense. Actually, the “square-root” rule applies to “unprocessed” counts only, i.e., to n in the given case.

Now, the correct error calculation of the count rate v goes like this. For clarity’s sake, the notation recommended by IUPAP for scalar-type physical quantities will be used, i.e., $a = \{a\}[a]$, where a is a physical quantity, $\{a\}$ is its numerical value, and $[a]$ is the unit in which a is given (Cohen and Giacomo 1987). Thus the error of the counts is $\sqrt{n} = \sqrt{vt} = \sqrt{\{v\}[v]\{t\}[t]} = \sqrt{\{v\}\{t\}}$, because $[v] = [t]^{-1}$. Since v is obtained from n by dividing it by t , the “change-of-scale” rule of standard deviation yields for the error of v $\sqrt{n}/t = \sqrt{\{v\}\{t\}}/(\{t\}[t]) = \sqrt{\{v\}/\{t\}}/[t]$. Note that the error calculation is performed on dimensionless numbers with the time unit fixed for all the quantities involved. So the correct data presentation of count rates can be either $(\{v\} \pm \sqrt{\{v\}/\{t\}})[t]^{-1}$ or simply $n/t \pm \sqrt{n}/t$.

Note also that, owing to the erroneous practice mentioned above (which, dimension aside, can be rewritten in the form $\{v\} \pm \sqrt{\{v\}}$ for better comparison), the standard deviation will be either over- or underestimated depending on whether the counting time t is shorter or, respectively, longer than the time unit used for the count-rate calculation. In the case of a 1-min measurement, e.g., if the time unit is the second, then the error is overestimated; if the unit is the hour, then it is underestimated. The (numerically) correct result is only obtained if the time unit happens to be the minute.

(#41) It is a fairly common task in nuclear science to tell whether a hypothetical decay would occur. The problematic part is represented by measurements, which have a negative outcome, when none of the atoms subjected to surveillance are found to decay during the observation period. Then the original question always remains open and new questions arise. (1) What would have happened, if the observation period had been longer (in which case [Eq. \(9.87\)](#) would have given more chance for a positive result)? (2) What would have happened, if more “suspicious” atoms had been subjected to the surveillance (in which case [Eq. \(9.90\)](#) would have provided larger v value, and therefore [Eq. \(9.87\)](#), again, would have increased the chances of a positive outcome)?

It is clear that the possibility of decay can never be excluded in cases like that. However, one can still specify a finite upper boundary v_0 , so that the “real” frequency v of the decay is lower than this limit with certain probability. Therefore, this upper boundary depends on the confidence level α set in advance (Leo 1987):

$$v_0 = \eta \lambda_0 N = -\frac{\ln(1 - \alpha)}{t}. \quad (9.92)$$

For instance, 90% certainty means a confidence level $\alpha = 0.9$.

[Equation \(9.92\)](#) can be “deduced” from [Eq. \(9.87\)](#) using common-sense considerations. Suppose that an experimenter decides to make a guess at the value of v . There is only one piece of information available for him or her, namely, that no signal could be detected over a certain observation period t . Then, the best thing he or she can do is form the weighted “average” of all the possible ($0 \leq v < \infty$) values of v , using the weights provided by [Eq. \(9.87\)](#):

$$\bar{v} = \frac{\int_0^{\infty} v e^{-vt} dv}{\int_0^{\infty} e^{-vt} dv} = \int_0^{\infty} v t e^{-vt} dv$$

The advantage of this type of weighting is that it tends to suppress large values of v , for which negative outcome is not likely to occur. On the other hand, it accentuates small values of v , which are more compatible with the negative result.

Note that, according to [Eq. \(9.4\)](#), the integral on the right-hand side of the above equation has the shape of an expected-value formula with the (exponential) density function

$$f(v) = t e^{-vt}$$

in which the variable and the parameter have swapped roles with each other. Hence the “probability” of $v \leq v_0$ is

$$\alpha \equiv P(v \leq v_0) = \int_0^{v_0} f(v) dv = 1 - e^{-v_0 t}$$

which yields [Eq. \(9.92\)](#).

9.4.5 Gamma Distribution: $\gamma(r, \nu)$

The relation of gamma distribution to exponential distribution is similar to that of binomial distribution to Bernoulli distribution in so far as the former (i.e., gamma and binomial) is the convolution power of the latter (i.e., exponential and Bernoulli, respectively), while the latter is a special case of the former. Gamma distribution is also related to the Poisson process (see the interpretation given below). However, in the case of the Poisson process one is looking for the distribution of $X(t)$, the number of signals that arrive over a fixed period of time t . In the case of the gamma distribution, on the other hand, one is interested in the distribution of the time T that is needed for a given number of random signals to arrive.

Density function: $f_r(t) = \begin{cases} \frac{(vt)^{r-1}}{\Gamma(r)} v e^{-vt} & \text{if } t > 0 \\ 0 & \text{if } t \leq 0 \end{cases}$	
Characteristic function: $\varphi(u) = (1 - iu/\nu)^{-r}$	
Mean frequency: $\tau_r^{-1} = \frac{\nu}{r}$	
Expected value: $\tau_r \equiv \frac{r}{\nu}$	Mode: $\frac{r-1}{\nu}$
Variance: $\frac{r}{\nu^2}$	Relative deviation: $\frac{1}{\sqrt{r}}$

In the above expressions the order r and the parameter ν are positive real numbers, and $\Gamma(r)$ is the complete gamma function.

Interpretation. Let T_1, T_2, \dots, T_n be a sequence of independent random variables with $\gamma(1, \nu)$ exponential distribution. Then the random variable defined by the sum $T = T_1 + \dots + T_n$ has a gamma distribution of the n th order with parameter ν . In other words, T has a $\gamma(n, \nu)$ gamma distribution (See Rényi 1970, 1979).

(#42) Note that, according to this interpretation, the exponential distribution of parameter ν can be rightly considered as a $\gamma(1, \nu)$ distribution, i.e., it belongs to the family of the gamma distributions (see [Fig. 9.14](#)). Later on it will be pointed out that the sum of squares of independent random variables with $N(0, 1)$ standard normal distribution also has a special type of gamma distribution called χ^2 distribution.

(#43) For the complete gamma function

$$\Gamma(r) \equiv \int_0^{\infty} e^{-x} x^{r-1} dx \quad (9.93)$$

the following recursion formula holds: $\Gamma(r+1) = r \Gamma(r)$.

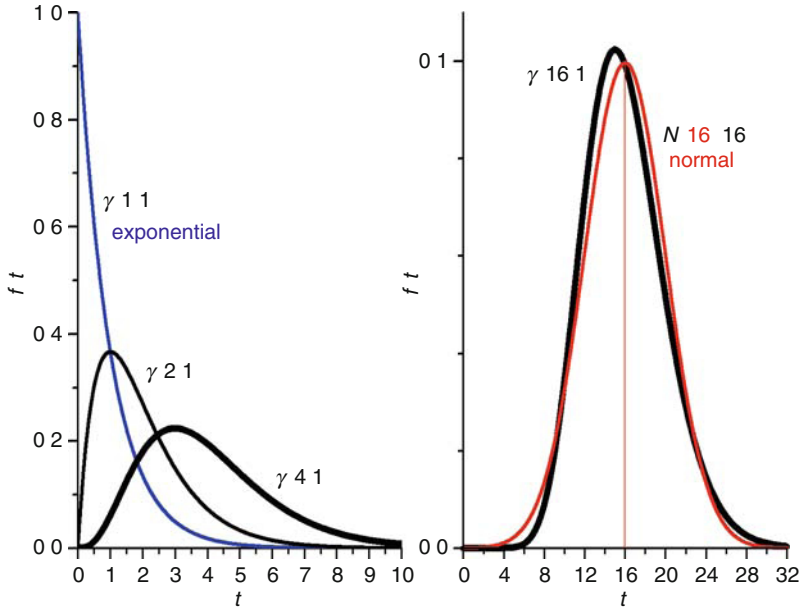
In particular, $\Gamma(1/2) = \sqrt{\pi}$, $\Gamma(1) = 1$, and $\Gamma(n) = (n-1)!(n=1, 2, \dots)$.

(#44) Note that the relative deviation rapidly decreases with the increasing number of waiting periods ($n = r$). This property of the gamma distribution is utilized by the scalers, which only produce an output signal on the arrival of the n th input signal. (In this context n is called the scaling factor.) The actual signal frequencies of scalers are, therefore, much more uniform (i.e., the signals follow the “rhythm” of the mean frequency much more “smoothly”), than the original signals themselves (see [Fig. 9.14](#)).

(#45) The decimal display of regular counters is in fact a realization of a series of scalers with scaling factors $n = 10^0, 10^1, 10^2$, etc. (see [Fig. 9.15](#)). Consequently, while the “switching times” of the lowest digit ($n = 10^0 = 1$) have exponential distribution in accordance with the

■ Fig. 9.14

Density functions of gamma distributions of integral order with the parameter value fixed at $\nu = 1$. The order $r = 1$ is characterized by the well-known asymmetric density function of the exponential distribution. However, as the order increases, the asymmetry decreases, and for as low an order as $r = 16$, an appropriately chosen normal distribution gives an acceptable fit. The gamma distribution is characteristic of the waiting times between scaled events (scalar signals). In that context the order r is called the scaling factor, and ν is the mean frequency of the original (i.e., unscaled) signals



Poisson process, those of the rest are characterized by the density functions of the gamma distributions of the order $n = 10^1, 10^2$, etc.:

$$f_n(t) = \frac{(vt)^{n-1}}{(n-1)!} v e^{-vt}. \quad (9.94)$$

Thus the relative deviation of the “switching time” of the third (10^2) digit is about 10%, and that of the fifth (10^4) digit is only about 1%, which means that the figures at the fifth decimal place seem to “rotate” almost steadily (See Knoll 1979).

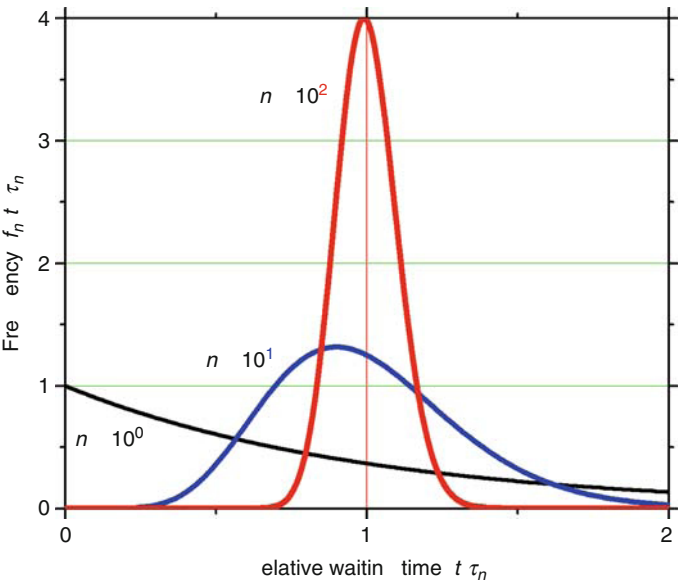
9.4.5.1 Properties

Addition theorem. If X_1 and X_2 are independent random variables with $\gamma(r_1, \nu)$, and $\gamma(r_2, \nu)$ gamma distribution, respectively, then the random variable $X = X_1 + X_2$ has a $\gamma(r_1 + r_2, \nu)$ gamma distribution.

Normal approximation. For large enough values of r , the $\gamma(r, \nu)$ gamma distribution can be approximated by an $N(r/\nu, r/\nu^2)$ normal distribution (see the graph in ► Fig. 9.14 to the right). (If the order $r = n$ is an integer, then this follows directly from the interpretation and from the

Fig. 9.15

When counting the particles/photons emitted by a radioactive specimen, each decimal digit of the counter switches to the next figure after a waiting time determined by a gamma distribution the order of which (n), in turn, is determined by the decimal place of the digit. Note that a narrower distribution means a steadier rhythm of switching. For better comparison, the density functions have been renormalized so that the geometric area under each curve is the same



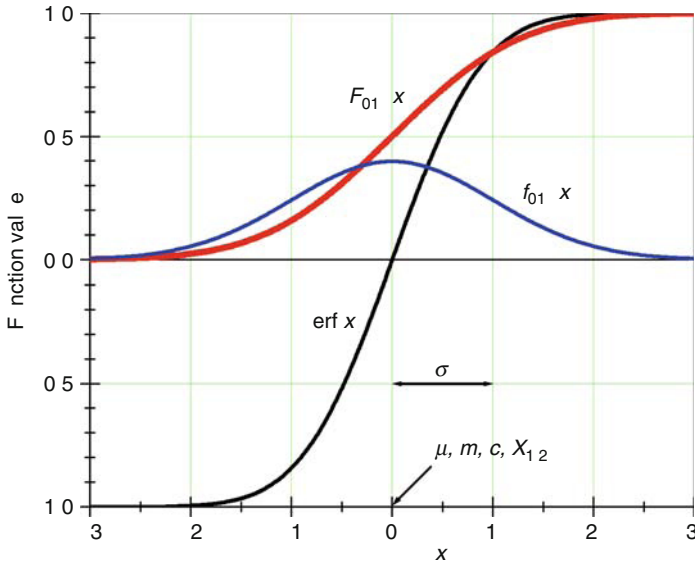
central limit theorem.) The normal probabilities for deviations from the mean ($\mu \pm d\sigma$) can be found in [Table 9.3](#).

9.4.6 Normal Distribution: $N(\mu, \sigma^2)$

Density function: $f(x) = \frac{1}{\sigma} f_{01}\left(\frac{x-\mu}{\sigma}\right) = \frac{1}{\sqrt{2\pi}\sigma} \exp\left[-\frac{1}{2}\left(\frac{x-\mu}{\sigma}\right)^2\right]$	
Distribution function: $F(x) = F_{01}\left(\frac{x-\mu}{\sigma}\right) = \frac{1}{2}\left[1 + \operatorname{erf}\left(\frac{1}{\sqrt{2}}\frac{x-\mu}{\sigma}\right)\right]$	
Error function: $\operatorname{erf} x = -\operatorname{erf}(-x) = \frac{2}{\sqrt{\pi}} \int_0^x e^{-t^2} dt$	
Characteristic function: $\varphi(u) = \exp\left(i\mu u - \frac{\sigma^2}{2} u^2\right)$	
Expected value, median, mode, center of symmetry: μ	
Variance: σ^2	Mean abs. deviation: $\sqrt{2/\pi} \sigma \approx 0.798\sigma$
Interquartile range: 1.348σ	Point of inflection of f : $\mu \pm \sigma$
Full width at half maximum (FWHM): $2\sqrt{2 \ln 2} \sigma \approx 2.355\sigma$	

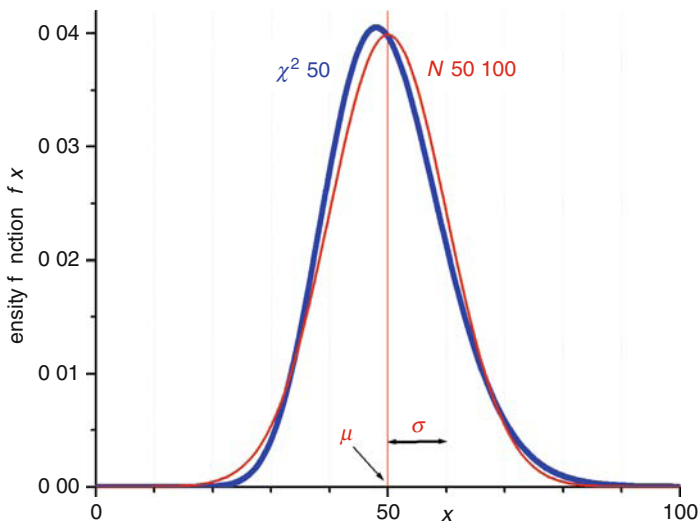
■ Fig. 9.16

Comparison of the error function (erf) with the density function (f_{01}) and the distribution function (F_{01}) of the $N(0, 1)$ standard normal distribution. The intervals 0 ± 1 , 0 ± 2 , and 0 ± 3 correspond to the error limits $\mu \pm \sigma$, $\mu \pm 2\sigma$, and $\mu \pm 3\sigma$, respectively. The normal probabilities for deviations from the mean ($\mu \pm d\sigma$) can be found in ► Table 9.3



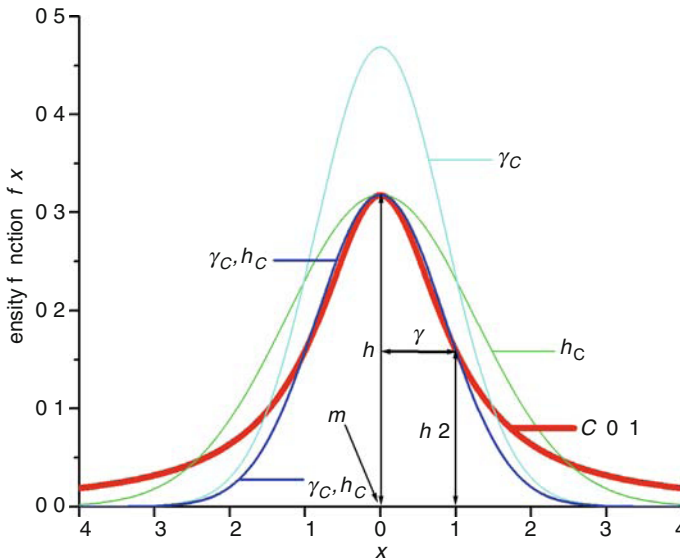
■ Fig. 9.17

The $\chi^2(k)$ distribution can be fairly well approximated with the $N(k, 2k)$ distribution for as low a degree of freedom as $k = 50$



■ Fig. 9.18

The density function of the $C(0, 1)$ Cauchy distribution (*thick red line*, also called Lorentzian curve) compared with different Gaussians. The green and turquoise curves indicate normal density functions (the area under each curve is 1). In one case the height (h_C), in the other case the width (γ_C) is fixed to be equal with that of the Lorentzian. The thicker blue curve shows a Gaussian having the same height and width as the Lorentzian (γ_C, h_C). (With both parameters fixed, the Gaussian could not be normalized. Thus the area under the curve is 0.678 this time.) The difference between the distributions is quite obvious here: the Lorentzian approaches 0 much more slowly than the Gaussian, which is in accordance with the nonexistence of the expected value and the variance in the case of the Cauchy distribution



In the above expressions f_{01} and F_{01} are the $N(0, 1)$ standard normal density function and distribution function, respectively (see Fig. 9.16). In physics and engineering normal distribution is often called Gaussian distribution. However, the expression Gaussian curve will only be used here meaning an un-normalized normal distribution function as shown in Fig. 9.18.

Interpretation. Let X be any random variable with existing expected value (μ) and variance (σ^2). Let X_i denote the random variable representing the outcome of the i th ($i = 1, 2, \dots, n$) independent experiment to observe the value of X . (The random variables X_i are obviously independent and have the same distribution as X .) Then the sample mean $\bar{X} \equiv (X_1 + X_2 + \dots + X_n)/n$ is asymptotically normal with $N(\mu, \sigma^2/n)$ distribution.

(#46) The above interpretation is the Lindberg–Lévy version of the central limit theorem. The $[N(np, npq)]$ normal distribution could also be interpreted as the limiting case of the $B(n, p)$ binomial distribution (De Moivre–Laplace theorem), but that is only a special case of the general theorem phrased for sums when the limiting distribution in general is $N(n\mu, n\sigma^2)$ normal.

(#47) When the normal distribution is referred to as the limiting case of an integral valued ($x = 0, 1, 2, \dots$) discrete distribution (e.g., Poisson or binomial distribution), then the continuous density function $f(x)$ is actually a substitute for the mass function p_x . This is so,

because the latter can be considered as a step function jumping at integral values. Therefore, since $\Delta x = 1$, one can write $p_x \approx f(x)\Delta x \equiv f(x)$ whenever x is an integer.

9.4.6.1 Properties

Standardization. Shifting and/or rescaling a normal random variable will result in another normally distributed random variable. Therefore, the standardization of the $N(\mu, \sigma^2)$ normal random variable X will result in an $N(0, 1)$ standard normal random variable Y :

$$Y = \frac{X - \mu}{\sigma}. \quad (9.95)$$

(#48) The random numbers produced by common calculators usually have a uniform distribution between 0 and 1. However, such $U(0, 1)$ random numbers can be easily converted to normally distributed random numbers by summing them n at a time (see remark (#46)). Considering large enough values for n , the summation will result in random numbers with an $N(n/2, n/12)$ distribution (see remark (#8)). Thus, for $n = 12$, an $N(6, 1)$ distribution is obtained. In this case, the result can be easily converted to $N(0, 1)$ standard normal distribution by subtracting 6 from the sum.

(#49) The $N(0, 1)$ random numbers simulated according to the above remark can be used, e.g., for the simulation of nuclear spectra. Nuclear spectrum points (see in [Sect. 9.6](#)) have $N(\mu_i, \mu_i)$ distribution. If the μ_i values are calculated from the fitting function and R_i is an $N(0, 1)$ random number, then the formula $Y_i \equiv \mu_i + \sqrt{\mu_i}R_i$ defines a random number with $N(\mu_i, \mu_i)$ distribution as required.

Addition theorem. If X_1 and X_2 are independent random variables with $N(\mu_1, \sigma_1^2)$, and $N(\mu_2, \sigma_2^2)$ normal distribution, respectively, then the random variable $X \equiv X_1 + X_2$ has an $N(\mu_1 + \mu_2, \sigma_1^2 + \sigma_2^2)$ normal distribution.

Bernoulli sampling. Suppose that the aim of an experiment is to observe certain objects (e.g., all the “visible” photons belonging to a light pulse that was produced as a result of the detection of a single radiation particle in the scintillator). Suppose that the number of these objects is a random variable with $N(\mu, \sigma^2)$ distribution. The objects are taken one by one and either “accepted” with probability η or “discarded” with probability $1 - \eta$. In other words: a $B(1, \eta)$ Bernoulli sampling is applied to them. (Returning to the above example, η can represent the probability that a “visible” photon will produce a photoelectron due to its interaction with the photocathode of the multiplier.) The question is, how many objects have been accepted altogether in the experiment, i.e., how many objects have passed the test of Bernoulli sampling (e.g., how many photoelectrons have formed on the photocathode as a result of the detection of a single radiation particle) and how these accepted numbers are distributed if a whole series of like experiments is considered. The $N(\mu, \sigma^2)$ distribution mentioned above is, of course, the integral-valued “discrete” version of normal distribution, for which the substitution values $f(n)$ of the density function act as mass function at the integral values of the x -axis. Therefore the question can be answered by reversing the De Moivre–Laplace theorem, i.e., if $\mu > \sigma^2$ and $\mu \gg 1$, then there is a $B(n, p)$ binomial distribution, which provides a fair approximation for the $N(\mu, \sigma^2)$ distribution. In the case of the binomial distribution, it has been shown that the result of Bernoulli sampling is a $B(n, p\eta)$ distribution. Thus one only needs to find the $N(\mu_\eta, \sigma_\eta^2)$ distribution that approximates this Bernoulli-sampled binomial distribution according to

the De Moivre–Laplace theorem. It is easy to show that the parameters of the “sampled” and “un-sampled” normal distributions are related as follows:

$$\mu_\eta = \eta\mu; \quad \sigma_\eta^2 = \eta^2\sigma^2 + \eta(1-\eta)\mu; \quad \frac{\sigma_\eta}{\mu_\eta} = \frac{\sigma}{\mu} \sqrt{1 + \frac{1-\eta}{\eta} \frac{\mu}{\sigma^2}}. \quad (9.96)$$

(#50) According to the above formula, the normal distribution can broaden considerably as a result of Bernoulli sampling. Referring to the above example, this means that the resolution of scintillation detectors is limited (among others) by the fact that typically only 1 “visible” photon out of 10 produces a photoelectron at the photocathode. In the case of the NaI(Tl) scintillator, moreover, there is also a previous Bernoulli sampling, i.e., only one excitation out of three will produce a photon that is suitable for the production of photoelectrons at all. The fact that the number of excitations (occurring, e.g., due to the absorption of a gamma photon) has a normal distribution will be shown in the frame of the renewal process.

9.4.7 The χ^2 Distribution: $\chi^2(k)$

Density function: $f_k(x) = \begin{cases} \frac{x^{k/2-1} e^{-x/2}}{2^{k/2} \Gamma(k/2)} & \text{if } x > 0 \\ 0 & \text{if } x \leq 0 \end{cases}$	
Characteristic function: $\varphi(u) = (1 - 2iu)^{-k/2}$	
Expected value: k	Mode: $k-2$
Variance: $2k$	Relative deviation: $\sqrt{\frac{2}{k}}$

Interpretation. Let Z_1, Z_2, \dots, Z_k be a sequence of independent $N(0, 1)$ random variables. Then the sum of squares $Z_1^2 + Z_2^2 + \dots + Z_k^2$ produces a random variable having a χ^2 distribution with k degrees of freedom – in short: $\chi^2(k)$ distribution.

(#51) If Y_1, Y_2, \dots, Y_k are a sequence of independent random variables having the same $N(\mu, \sigma^2)$ distribution with exactly known expected value and variance, then the sum of squares of the standardized variables will have a $\chi^2(k)$ distribution.

(#52) Continuing from the previous remark, the following conclusion can be drawn: If μ is not known, and therefore it is replaced by the average $\bar{Y} = (Y_1 + Y_2 + \dots + Y_k)/k$ when forming the standardized variables, then the sum of squares of the standardized variables will have a $\chi^2(k-1)$ distribution.

(#53) If Y_1, Y_2, \dots, Y_k are a sequence of independent random variables, which have $N(\mu_i, \sigma_i^2)$ normal distributions ($i = 1, 2, \dots, k$) with known expected values and variances, then the sum of squares of the standardized variables will have a $\chi^2(k)$ distribution.

(#54) Continuing from the previous remark, the following conclusion can be drawn: Suppose that there is a model function $\mu(x) = \mu(x; b_1, b_2, \dots, b_n)$, which is linear in all of its n parameters (b_1, b_2, \dots, b_n) and that model function (now: fitting function) produces the expected values $\mu_i (i = 1, 2, \dots, k)$ whenever the parameter vector \mathbf{b} is set to the value $\mathbf{b} = \mathbf{a}$:

$$\mu_i = \mu(x_i; a_1, a_2, \dots, a_n). \quad (9.97)$$

Consider now the sum of squares

$$S_k = \sum_{i=1}^k \left(\frac{Y_i - \mu(x_i; b_1, b_2, \dots, b_n)}{\sigma_i} \right)^2. \quad (9.98)$$

Suppose that the parameter values $\hat{a}_1, \hat{a}_2, \dots, \hat{a}_n$ minimize the above sum. Then the minimized sum of squares

$$\hat{S}_k = \sum_{i=1}^k \left(\frac{Y_i - \mu(x_i; \hat{a}_1, \hat{a}_2, \dots, \hat{a}_n)}{\sigma_i} \right)^2 \quad (9.99)$$

has a $\chi^2(k - n)$ distribution (Press et al. 1999).

(#55) Continuing from the previous remark, the following conclusion can be drawn: According to remark (#53), the sum of squares taken at the parameter values a_1, a_2, \dots, a_n would have a $\chi^2(k)$ distribution because in this case the “exact” expected values (μ_i) would show up in the sum. It is important to stress this, because it will be shown in the section on the evaluation of nuclear spectra that the values $\hat{a}_1, \hat{a}_2, \dots, \hat{a}_n$ are the maximum likelihood estimates of the “exact” values a_1, a_2, \dots, a_n . Therefore, one might expect that the relation of \hat{a} to the concrete measured spectrum is the same as that of the parameter vector \mathbf{a} that it estimates. Well, the decrease of the degree of freedom indicates that this assumption is false. The reason is that minimization tends to divert the estimated values from the “exact” parameter values so that they can attribute the largest possible likelihood to the concrete spectrum. And this will be so even if the concrete spectrum has a rather low likelihood when calculated with the “exact” values of the parameters.

(#56) The symbol $\Gamma(k/2)$ showing up in the density function denotes the complete gamma function. This is not by chance because the χ^2 distribution is actually a special case of the gamma distribution. (Looking at the density function f_k , one can easily recognize it as the density function of the $\gamma(k/2, 1/2)$ gamma distribution. The characteristic functions are still easier to compare.

(#57) Note that when the degree of freedom (k) is large, then the expected value is practically equal to the mode, i.e., the expected value doubles as the “most probable” value. (The reason for the quotation marks is that with continuous distributions any x value has 0 for probability. What this statement really means is that the probability $dP = f(x)dx$ is at its maximum if dx is considered constant.) When evaluating nuclear spectra, χ^2 distributions with about 2,000 degrees of freedom quite often occur (2,048-channel spectra). In such cases the relative deviation is about 3%, i.e., the value of the $\chi^2(2,000)$ random variable is most probably $2,000 \pm 3\%$ ($2,000 \pm 60$). For more detail, see the next remark. (The p -quantiles for χ^2 distributions $\chi^2(k)$ with degree of freedom $1 \leq k \leq 30$ can be found in [Table 9.4](#).)

9.4.7.1 Properties

Normal approximation. It follows from the interpretation as well as from the central limit theorem that for large enough values of k (i.e. $k \geq 30$) the $\chi^2(k)$ distribution can be approximated with the $N(k, 2k)$ normal distribution (see [Fig. 9.17](#)).

(#58) Continuing from the previous remark, the following conclusion can be drawn: According to the properties of the normal distribution (see [Table 9.3](#)), the value of the $\chi^2(2,000)$ random variable will be $2,000 \pm 3\%$ ($2,000 \pm 60$) in 68% of the cases, $2,000 \pm 6\%$ ($2,000 \pm 120$) in 95% of the cases, and $2,000 \pm 9\%$ ($2,000 \pm 180$) in 99.7% of the cases (i.e., nearly always).

(#59) The relative χ^2 is the scaled-down version of the $\chi^2(k)$ random variable with the scaling factor $1/k$. Consequently, both the expected value and the standard deviation decrease by the same factor $1/k$ resulting in $\mu_{\text{rel}} = 1$ and $\sigma_{\text{rel}} = \sqrt{2/k}$, respectively. Continuing from the previous remark the following conclusion can be drawn: This means that the value of the relative χ^2 will be 1 ± 0.03 in 68% of the cases, 1 ± 0.06 in 95% of the cases, and 1 ± 0.09 in 99.7% of the cases (i.e., nearly always). Relative χ^2 values out of this range are to be considered therefore with suspicion. (Of course, if k is smaller, then the error range is broader.)

Addition theorem. If X_1 and X_2 are independent random variables having χ^2 distributions with k_1 and k_2 degrees of freedom, respectively, then the sum $X = X_1 + X_2$ has a χ^2 distribution with $k_1 + k_2$ degrees of freedom.

9.4.8 Cauchy Distribution: $C(m, \gamma)$

Density function: $f(x) = \frac{1}{\pi\gamma} \frac{1}{1 + \left(\frac{x-m}{\gamma}\right)^2}$
Distribution function: $F(x) = \frac{1}{2} + \frac{1}{\pi} \arctan \frac{x-m}{\gamma}$
Characteristic function: $\varphi(u) = \exp(imu - \gamma u)$
Expected value, variance, standard deviation: do not exist
Median, mode, center of symmetry: m
Full width at half maximum (FWHM), interquartile range: 2γ
Point of inflection of the density function: $m \pm \gamma/\sqrt{3}$

All of the distributions mentioned so far lie within the range of attraction of normal distribution, i.e., the central limit theorem is valid for distributions that are quite dissimilar to the normal distribution such as the discrete Bernoulli distribution and the asymmetric exponential distribution. The Cauchy distribution presented below is, on the contrary, very similar in shape to the normal distribution (see [Fig. 9.18](#)), but it has neither an expected value, nor a (finite) variance, and therefore is exempt from the rule.

Interpretation. Let Θ be a random variable uniformly distributed in the interval $(-\pi/2, \pi/2)$. Then the random variable

$$Y = m + \gamma \tan \Theta \quad (9.100)$$

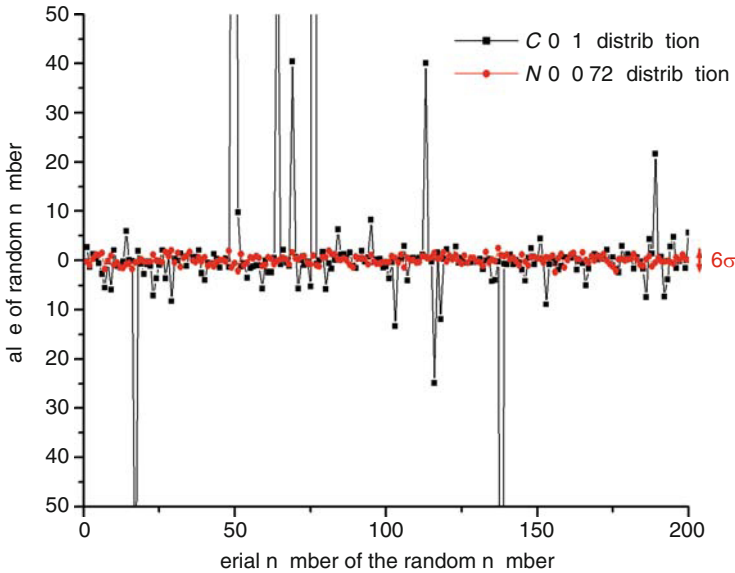
has a $C(m, \gamma)$ Cauchy distribution. In other words: consider the xy -plane and two lines – one (line 1) passing through the origin and another (line 2) parallel to the y -axis and intersecting the x -axis at the point $x = 1$. Now spin line 1 around the origin at constant angular velocity. Measure the y -coordinate of the intersection of lines 1 and 2 at random moments. The Y values obtained in this way will have a $C(0, 1)$ distribution (Hogg and Tanis 1988).

(#60) Using the above interpretation, it is easy to convert uniformly distributed $U(-\pi/2, \pi/2)$ random numbers to random numbers with Cauchy distribution. Such a simulated sequence (200 data) is shown in [Fig. 9.19](#), together with as many normally distributed random numbers having the same FWHM. Note that all of the normal random numbers lie within a few FWHMs from the origin. The Cauchy-type random numbers, on the other hand, behave in a much more disorderly way, i.e., there are quite a number of points that are way out of the same range.

(#61) Another possibility for interpretation (and simulation) is provided by the formula $X = Y_0/Y_1$, where Y_0 and Y_1 are independent random numbers/variables with $N(0, 1)$ distribution. This transformation results in $C(0, 1)$ distribution. The recipe is based on the

■ Fig. 9.19

Comparison of normal random numbers with random numbers having Cauchy distribution. Both distributions have the same halfwidth (FWHM = 2). Note that some of the Cauchy-type random numbers are as large as 500 in this particular sequence. On the other hand, all of the normal random numbers lie in the narrow range of $6\sigma = 5$ determined by the $0 \pm 3\sigma$ limits



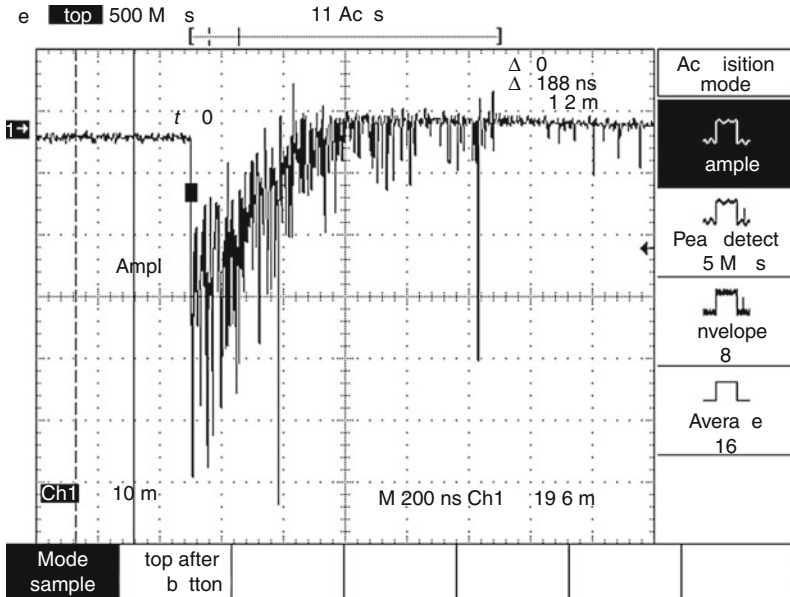
fact that the Cauchy distribution can be considered as a special case of the (Student's) t distribution (not discussed here).

(#62) In Mössbauer spectroscopy (see ▶ Chap. 25 in Vol. 3), the density function of Cauchy distribution is called a Lorentzian curve. In nuclear physics, the same function is also called the Breit–Wigner curve (Lyons 1986). (See also ▶ Chap. 2 in this Volume.) This curve is characteristic of the energy uncertainty of excited (nuclear) states, which follows from the fact that excited states have exponential distribution with a finite mean life τ . The natural linewidth Γ , i.e., the FWHM of the Lorentzian energy density, is twice of the parameter γ ($\Gamma = 2\gamma$).

(#63) The lack of expected value and variance can be quite a shock for those who had been familiar with the physical meaning of the Lorentzian curve but learned about this mathematical “defectiveness” at a later date. (The confrontation with this defectiveness often fails to occur. For instance, Bevington, in his often-cited work (Bevington 1969), writes about Cauchy distribution as if it had an expected value.) This is so, because the nonexistence of these parameters makes them believe that the distribution is hopelessly smeared over the energy axis. However, this is not the case, which is quite clear from the viewpoint of physics, because otherwise no sharp spectrum lines could exist. The expected value (and the variance built on that) fails, because the “central tendency” of the distribution is simply not sufficient for the convergence of the respective formula(s). Note that the density function is asymptotically proportional to x^{-2} , and therefore the integrand in the expected value formula is proportional to x^{-1} , hence the integral itself ($\sim \ln x$) is boundless. Other parameters describing the “location” and “dispersion” of the distribution (mode, interquartile range, etc.) still may and actually *do* work.

■ Fig. 9.20

Fine structure of the detector signal of 0.1 mm NaI(Tl) scintillator at gamma energy of 14.4 keV. The high time resolution of the digital oscilloscope helps to visualize the elementary processes that make up the signal. The steep rise of the pulse is an indication of the promptness of the formation of the excited states. The individual “hairs” sticking out from the fuzzy contour represent photoelectrons (or rather the results of cascades started by these in the multiplier) produced by individual visible photons at the photocathode. The multitude of partly merging elementary pulses outlines the exponential law of the “decay” of excited states



(#64) Continuing from remarks (#62)–(#63), the following conclusion can be drawn: The formula $\tau \Gamma = \hbar$ is often used for the estimation of the natural linewidth. This formula is sometimes interpreted as the time–energy equivalent of the Heisenberg relation, where τ is the uncertainty (standard deviation) of the lifetime and Γ (FWHM) is that of the energy state. It should be stressed, however, that while τ can play the assigned role (because the standard deviation is equal to the expected value in the case of the exponential distribution), the quantity Γ cannot be interpreted as standard deviation, since the Cauchy distribution does not have any.

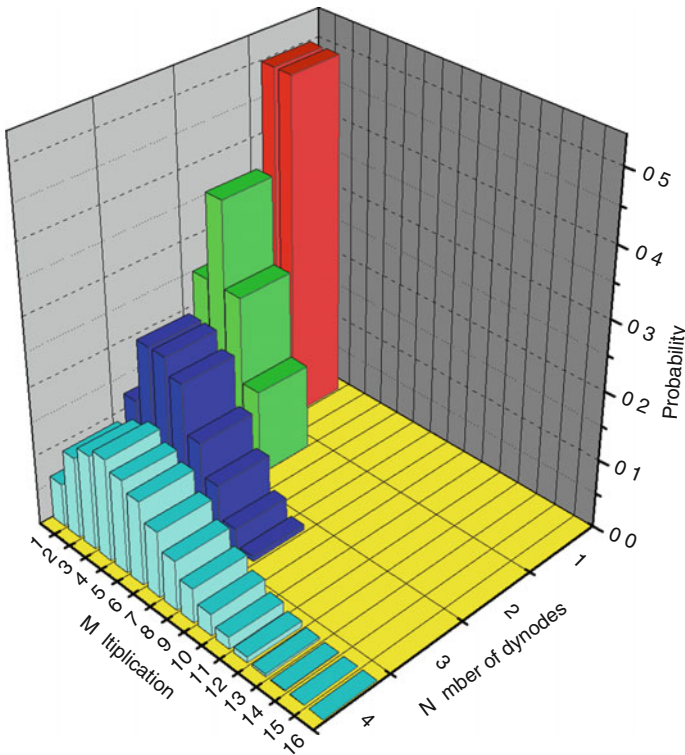
Nevertheless, the formula works not only in theory but also in practice as is proven for the 30 or so nuclides for which the values of Γ and τ have been determined by independent methods (Belgys et al. 1993).

9.4.8.1 Properties

Standardization. The rescaling and shifting of Cauchy distribution results in another Cauchy distribution. Therefore the following transformation of the random variable X having a $C(m, \gamma)$ Cauchy distribution

■ Fig. 9.21

Distributions of the multiplication by a “photomultiplier” calculated for 1, 2, 3, and 4 dynodes



$$Y = \frac{X - m}{\gamma} \quad (9.101)$$

generates a random variable Y with $C(0, 1)$ Cauchy distribution.

(#65) Note that in the above formula, the “substitutes” of the expected value and standard deviation appear as location and dispersion parameters.

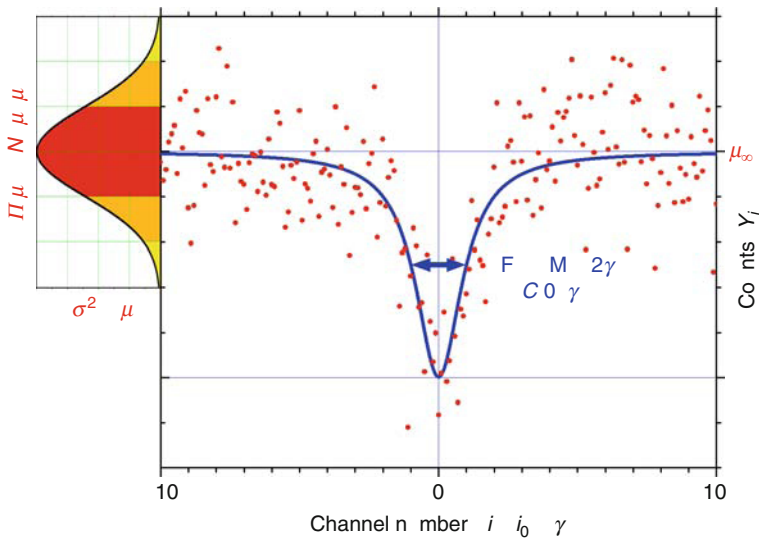
Addition theorem. If X_1 and X_2 are independent random variables with $C(m_1, \gamma_1)$ and $C(m_2, \gamma_2)$ Cauchy distribution, respectively, then the random variable $X = X_1 + X_2$ has a $C(m_1 + m_2, \gamma_1 + \gamma_2)$ Cauchy distribution.

(#66) In Mössbauer spectroscopy, the peak-shape of the transmission spectrum (measured with a thin absorber, see ▶ Fig. 9.22) is described as the convolution of the Lorentzians characteristic of the source and the absorber. According to the addition theorem, the result of such a convolution will be another Lorentzian with a halfwidth equal to the sum of both halfwidths. In other words, in this case, the FWHM is twice of the natural linewidth Γ .

(#67) Note that in the case of the Cauchy distribution, the scaling-up of the random variable with the factor 2 leads to the same result as the addition of two independent random variables with the same distribution (i.e., both parameters m and γ will double). In the case of distributions “more normal” than the Cauchy distribution, on the other hand, the width will only increase by the factor $\sqrt{2}$ when two like (although independent) variables are added up.

■ Fig. 9.22

An example for a nuclear spectrum. The main graph shows a single-peak Mössbauer spectrum “measured” at transmission geometry. Such a spectrum can be fitted with a Lorentzian curve (blue line), whose shape is identical with the density function of a Cauchy distribution. Due to standardization, the tick distance on the horizontal axis is half of the full width at half maximum (FWHM) of the Lorentzian (γ). As mentioned in remark (#66), $\text{FWHM}/2 = \gamma$ gives the natural line width Γ provided that the absorber is ideally thin. On the other hand, the vertical scattering of the counts (red dots) is characterized by the normal distribution. The colored graph on the left, e.g., shows the normal density function belonging to the baseline (μ_∞). The color code is explained by ► Fig. 9.2. On the vertical axis the distance between the ticks equals to σ



As shown before, this is due to the “Pythagorean theorem” of the standard deviations, which means that it is the variances that add up rather than the standard deviations themselves.

9.5 Applications of Stochastic Processes

In this section, a few examples will be given to show the applicability of stochastic processes in nuclear science. It should be stressed that the aim is to present *illustrations* rather than to derive formulas that serve as the final solutions for the problems cited. Reading the next couple of pages can hopefully help to arouse interest in this field (See for more detail in Karlin and Taylor 1975, 1984).

9.5.1 Renewal Processes

The “prototype” of the renewal process is the following. Consider a part of equipment the lifetime of which, T_1 is a random variable with expected value μ and variance σ^2 . The first such part started to work at time 0. Having broken down at time T_1 , it was promptly replaced with a

new part, which was working for a period T_2 , i.e., it broke down at time $T_1 + T_2$, and so on. The n th renewal took place at time: $S_n = T_1 + \dots + T_n$. The renewal process N_t counts the number of renewals occurring in the time interval $[0, t]$, i.e.,

$$N_t = n, \quad \text{if } S_n \leq t < S_{n+1}, \quad \text{where } n = 0, 1, 2, \dots \quad (9.102)$$

The following theorems are very important as regards the above process:

Renewal theorem. $E(N_t) \approx t/\mu$, if t is large enough. (This is in agreement with the expectation based on common sense: If a part works for a period μ on an average, then about t/μ parts will be needed over the total operating period t .)

Central limit theorem for renewals. N_t is asymptotically normal with $N(t/\mu, t\sigma^2/\mu^3)$ distribution.

9.5.1.1 The Poisson Process as Renewal

It is not difficult to recognize the renewal process in the Poisson process discussed earlier, where the random variable T had a $\gamma(1, \nu)$ exponential distribution, as a consequence of which N_t (or, with the earlier notation: X) turned out to have a $\Pi(\nu t)$ Poisson distribution. The Poisson process represents one of the few cases where the distribution of the renewal process is known for any value of t . The importance of the central limit theorem for renewals lies in the very fact that, for large enough values of t , one can count on normal distribution even if the exact distribution of N_t is unknown. The validity of the theorem can be easily checked in this particular case, since by substitution one gets the well-known result that for large enough μ the approximation $\Pi(\mu) \approx N(\mu, \mu)$ can be used.

(#68) The fact that the Poisson process can be interpreted as a renewal makes it possible to generate random numbers with Poisson distribution using exponentially distributed random numbers (Goodman 1988; Lux and Koblinger 1991). (For the generation of exponentially distributed random numbers see remark (#30).) If, namely, T_1, T_2, \dots are a sequence of random numbers/variables with a $\gamma(1, \nu)$ exponential distribution, then the random number/variable N determined by the condition

$$T_1 + T_2 + \dots + T_N \leq t < T_1 + T_2 + \dots + T_N + T_{N+1} \quad (9.103)$$

will have a $\Pi(\nu t)$ Poisson distribution according to inequality (9.102).

(#69) The discrete equivalent of the Poisson process is related to a series of Bernoulli trials, in which case the individual trials (e.g., coin tosses) can be assigned to individual discrete moments (i.e., to the serial number of the toss, n). It is clear that the process $X(n)$ has a $B(n, p)$ binomial distribution – the distribution characteristic of the number of heads turning up in a series of n tosses.

9.5.1.2 Consideration of Dead Time

The Poisson process is connected with a (nonexistent) type of particle/signal detection, when the detecting system is promptly able to deal with a new signal after having received the previous one. In reality, however, any detecting system can only deal with a new signal after a certain period of time Θ_i called the dead time. During this period (which should be treated as a random variable in general), the detecting system is recovering (e.g., GM counter), or it is busy

with signal processing (e.g., pulse height analysis). The dead time is followed by the waiting time T_i having exponential distribution, the same as the one discussed at the Poisson process (see ▶ Eq. (9.89)), with the same mean frequency ν . (This is the consequence of the memorylessness of the exponential distribution.) The total waiting time (including the dead time) connected with the i th (actually detected) signal therefore is $Z_i = \Theta_i + T_i$. Thus the n th signal is detected at the moment $S_n = Z_1 + \dots + Z_n$.

Considering the independence of Θ_i and T_i , as well as that the distributions of both Θ_i and T_i are concentrated to the half-line $t > 0$, the distribution function of Z_i is given by the following convolution (see ▶ Eq. (9.51)):

$$F(z) = G * h(z) = \int_0^z G(z-x)h(x)dx = \int_0^z G(z-x)\nu e^{-\nu x}dx$$

where G is the distribution function of Θ_i , and h is the (exponential) density function of T_i . The subscripts have been omitted, because the Θ_i s have the same distribution and so do the T_i s (separately). The density function of $Z_i(f)$ can be obtained by differentiation. The density function of $S_n(f_n)$ can be obtained by forming the n th convolution power of $f = F'$:

$$f_n(z) = f * \dots * f(z)$$

In particular, if the dead time is constant (θ), then $f = \nu \exp[-\nu(t - \theta)]$, which is the exponential density function shifted to $\theta(t > \theta)$. Therefore, S_n has a shifted gamma distribution with the following density function:

$$f_n(t) = \frac{[\nu(t - n\theta)]^{n-1}}{(n-1)!} \nu e^{-\nu(t-n\theta)} \quad (t > n\theta).$$

The following results hold even if the concrete distribution of the process N_t is unknown:

$$\mu \equiv E(Z) = E(\Theta) + E(T) = \theta + \frac{1}{\nu} \quad (9.104)$$

$$\sigma^2 \equiv D^2(Z) = D^2(\Theta) + D^2(T) = D^2(\Theta) + \frac{1}{\nu^2} \quad (9.105)$$

where θ is the mean dead time, and ν is the mean signal frequency (mean count rate with zero dead time). If the dead time is constant, the latter equation becomes simpler:

$$\sigma^2 = \frac{1}{\nu^2}. \quad (9.106)$$

The mean count rate in the case of constant dead time θ is

$$\nu_\theta = \frac{1}{\mu} = \frac{\nu}{1 + \theta\nu}. \quad (9.107)$$

Using this, one can easily calculate the mean signal frequency ν (i.e., the mean count rate without dead time) from the measured value of the mean count rate ν_θ (i.e., the apparent mean signal frequency) provided that θ is known:

$$\nu = \frac{\nu_\theta}{1 - \theta\nu_\theta}. \quad (9.108)$$

According to the central limit theorem for renewals, N_t is asymptotically $N(t/\mu, t\sigma^2/\mu^3)$ normal. In the case of long enough counting times and constant dead time, therefore, the expected value and the variance of the counts are

$$E(N_t) = \frac{v}{1 + \theta v} t = v_\theta t, \quad (9.109)$$

$$D^2(N_t) = \frac{v}{(1 + \theta v)^3} t = (1 - \theta v_\theta)^2 v_\theta t. \quad (9.110)$$

(#70) It follows from above result that

$$D^2(N_t) = (1 - \theta v_\theta)^2 E(N_t) \leq E(N_t) \quad (9.111)$$

where the equals sign only holds for $\theta v_\theta \ll 1$. Thus, in the case of measured counts, the Poisson approximation (when the variance is taken to be equal to the expected value) tends to overestimate the actual standard deviation.

(#71) The product θv_θ represents the fraction of the counting time t that is “covered” by the dead-time intervals associated with the individual measured signals. The percentage of dead time displayed by some detecting systems is therefore equal to $100\theta v_\theta$.

9.5.1.3 The “Primeval” Shape of the Photoelectric Peak

The initial stage of the detection is the transferring of the energy of a radiation particle – or a gamma photon – to the substance of the detector. Owing to this process ionized/excited states are produced, the number of which is proportional to the absorbed energy, serving as a basis for the energy determination of the detected particle.

The renewal story can also be recounted with the following exchange of roles: $t \Leftrightarrow E$, $N_t \Leftrightarrow N_E$, $T_i \Leftrightarrow \varepsilon_i$, $\mu \Leftrightarrow \varepsilon$, $\sigma \Leftrightarrow \sigma_\varepsilon$. Consider, therefore, a gamma photon, the energy (E) of which breaks up to random portions (ε_i) while it is transferred to the detector crystal following photoelectric effect. The renewal process N_E now counts the number of portions – a random variable – to which the energy of the photon has happened to split. Each energy portion is spent on the production of one charge carrier (or one excited state relevant from the viewpoint of detection). Therefore, N_E also means the number of charge carriers produced by the detected photon, which – assuming linear amplification – will be proportional to the pulse height. If further statistical effects can be neglected, then the density function of N_E will be characteristic of the pulse height distribution as well, which has a Gaussian shape according to experience.

The distribution of the ε_i -values is concentrated to the energy range (V, E), where V is the minimum of energy (ionization potential), which is just enough for the production of one charge carrier in the given detector substance. Further characteristic parameters of the distribution are $\varepsilon \equiv \langle \varepsilon_i \rangle$, the mean energy spent on the production of one charge carrier/excited state, as well as σ_{rel} , the relative deviation of the ε_i -values.

According to the central limit theorem of renewals, N_E will be asymptotically normal with the following parameters:

$$N\left(\frac{E}{\varepsilon}, \sigma_{\text{rel}}^2 \frac{E}{\varepsilon}\right). \quad (9.112)$$

The shape of the photoelectric peak is therefore determined by the density function of the above normal distribution (i.e., by a Gaussian curve), the mode/expected value (MAX) and halfwidth (FWHM) of which are

$$\text{MAX} = \frac{E}{\varepsilon}; \quad \text{FWHM} = 2\sqrt{2 \ln 2} \sigma_{\text{rel},\varepsilon} \sqrt{\frac{E}{\varepsilon}}. \quad (9.113)$$

Thus the position of the maximum is proportional to the photon energy E , and the low-energy peaks are narrower than the high-energy peaks. Hence, the relative peak width turns out to be inversely proportional to the square root of the energy:

$$\text{FWHM}_{\text{rel}} \equiv \frac{\text{FWHM}}{\text{MAX}} = 2\sqrt{2 \ln 2} \sigma_{\text{rel},\varepsilon} \sqrt{\frac{E}{\varepsilon}}. \quad (9.114)$$

The above formulas show that this simple stochastic model not only explains the shape of the photoelectric peak, but also predicts that the smaller is the average energy spent on the production of one charge carrier/excited state in a detector, the better is its energy resolution.

9.5.1.4 Statistical Effects Smearing the Photoelectric Peak

It has been assumed above that there are no statistical effects at later stages of pulse formation that could change the shape of the photoelectric peak. However, such effects *do* exist. Consider the scintillation detectors, for instance, which waste much of the potential of energy resolution hidden in the “primeval” shape of the photoelectric peak.

In the case of scintillation detectors, the production of excited states is practically instantaneous in comparison with the time scale of de-excitation. The excited states are characterized by the same exponential-type lifetime distribution as the radioactive atoms. A large number of excited states start to “decay” at the same moment ($t = 0$), as a result of which visible photons are formed (see [Fig. 9.20](#)).

The temporal density of photons as a function of time – in other words, the shape of the light pulse – shows the characteristic features of the exponential law of decay. If the electronics does not mix up the elementary processes too much, then the shape of the light pulse will be reflected in the shape of the voltage pulse as well, the latter being the object of pulse height analysis. All in all, the pulse height of the detector signal will be determined by the number of photons emitted between $t = 0$ (the moment when the excited states were formed) and a moment a little later: $t = 0 + \Delta t = \Delta t$. (The length of Δt depends on the details of the signal processing/pulse height analysis, however it is surely shorter than the mean life τ of the excited states.) The number of photons responsible for the pulse height is determined therefore by the $B(N_E, \exp(-\Delta t/\tau))$ binomial distribution for any value of N_E . Since the “primeval” shape is very narrow, N_E can be replaced by its expected value (MAX). If the binomial expected value $\text{MAX} \times \exp(-\Delta t/\tau)$ and the variance $\text{MAX} \times \exp(-\Delta t/\tau) \times [1 - \exp(-\Delta t/\tau)]$ are not too small, then the binomial distribution can be approximated with normal.

Hence, the number of photons determining the pulse height is normally distributed:

$$N\left(A \frac{E}{\varepsilon}, B \frac{E}{\varepsilon}\right) \quad (9.115)$$

where A and B are constants. Note that the result is another Gaussian that is considerably broader than the “primeval” one, but otherwise has the same properties, the most important being the proportionality between pulse height (Ampl.) and energy:

$$\text{pulse height} \equiv \text{Ampl.} \propto \frac{E}{\varepsilon}. \quad (9.116)$$

From now on, only the fate of those photons will be followed that are characterized by the above distribution. The production of photoelectrons at the photocathode can be described by Bernoulli sampling (see at the normal distribution). Bernoulli sampling will broaden the distribution (in the relative sense); however, it will not lead out from the family of normal distributions:

$$N\left(\eta A \frac{E}{\varepsilon}, \eta[(1 - \eta)A + \eta B] \frac{E}{\varepsilon}\right) = N\left(a \frac{E}{\varepsilon}, b \frac{E}{\varepsilon}\right). \quad (9.117)$$

The electron multiplier will further modify the shape of the peak (see at the branching processes), but, fortunately, the proportionality between pulse height and energy will not suffer.

9.5.2 Markov Chains

A Markov chain is a stochastic process defined by the condition

$$P(a < X_n \leq b | X_1 = x_1, X_2 = x_2, \dots, X_{n-1} = x_{n-1}) = P(a < X_n \leq b | X_{n-1} = x_{n-1}) \quad (9.118)$$

which means that the current outlook of such a process is determined by the latest information to such an extent that no earlier information can add anything to it.

9.5.2.1 Branching Processes

The story of the branching processes is the following. Consider an entity (0th generation), which produces X_1 identical offspring in one single reproductive cycle (1st generation). The offspring of the n th generation constitute the $(n + 1)$ th generation. The entities belonging to each generation proliferate independently of each other and of their predecessors according to the same distribution. The aim is to follow X_n , the population of the subsequent generations of entities. Such entities can be, e.g., neutrons multiplied by a chain reaction or electrons “breeding” on the dynodes of a multiplier.

The X_1 is a discrete random variable that can assume the values $k = 0, 1, 2, \dots$ with different probabilities $P(X_1 = k) = p_k$. Let μ denote the expected value, and σ^2 the variance of the distribution. Let $G(s) \equiv G_1(s)$ be the generating function of the distribution

$$G(s) \equiv \sum_{k=1}^{\infty} p_k s^k. \quad (9.119)$$


Then, the generating functions of the subsequent generations can be calculated from the following recursion formula (Feller 1968):

$$G_{n+1}(s) = G(G_n(s)). \quad (9.120)$$

The expected value and the variance of the branching process are (Feller 1968)

$$E(X_n) = \mu^n; \quad D^2(X_n) = (\mu^{2n-2} + \mu^{2n-3} + \dots + \mu^{n-1})\sigma^2. \quad (9.121)$$

Note that the result obtained for the expected value is in accordance with the common-sense expectation.

(#72)  *Figure 9.21* shows a sequence of distributions resulted from such a calculation. The model can represent, e.g., a photomultiplier, the dynodes of which “double” the incident electrons with a probability of 50%, i.e., half of the electrons have 2 offspring, while the other

half only 1. Thus the mean multiplication factor of the dynodes is $\mu = 3/2$, with a standard deviation of $\sigma = 1/2$.

According to [Eq. \(9.121\)](#), the relative deviation of multiplication is

$$\sigma_{\text{rel}}(X_n) \equiv \frac{D(X_n)}{E(X_n)} = \frac{\sigma}{\mu} \sqrt{1 + \mu^{-1} + \mu^{-2} + \dots + \mu^{-n+1}}. \quad (9.122)$$

For a large number of dynodes, the relative deviation approaches the following limit:

$$\sigma_{\text{rel}}(X_{\infty}) = \frac{\sigma}{\mu} \frac{1}{\sqrt{1 - \mu^{-1}}} = \frac{\sigma}{\sqrt{\mu(\mu - 1)}}. \quad (9.123)$$

(#73) Continuing from the previous remark, the following conclusion can be drawn: In the case of one stage, the relative deviation is about 33%. By increasing the number of dynodes, the relative deviation increases asymptotically to about 58%. The above formula reveals, however, that by increasing the (mean) multiplication factor of the dynode (μ), the relative deviation becomes smaller (for the same σ). If, e.g., the dynodes triple/quadruple the incident electron with equal probability instead of doubling it (i.e., σ remains $1/2$, while μ increases from $3/2$ to $7/2$), then the asymptotic value of the relative deviation will decrease to about 17%.

(#74) Note that multiplication goes by electrons. When, e.g., the photocathode emits N electrons as a result of a light pulse, then each electron will be multiplied to a different extent by the dynodes. The total number of electrons collected by the anode is obtained by summation

$$\Sigma_N = \sum_{i=1}^N X_{n,i}. \quad (9.124)$$

Note that the above equation shows a random sum. According to the results discussed at renewals (see [Eq. \(9.117\)](#)), the random variable N is asymptotically normal with the following parameters:

$$N \left(a \frac{E}{\varepsilon}, b \frac{E}{\varepsilon} \right). \quad (9.125)$$

According to [Eq. \(9.55\)](#), the expected value and the variance of Σ_N are as follows:

$$E(\Sigma_N) = \mu^n a \frac{E}{\varepsilon} \propto \frac{E}{\varepsilon}, \quad (9.126)$$

$$D^2(\Sigma_N) = [b\mu^{2n} + a\sigma^2(\mu^{2n-2} + \mu^{2n-3} + \dots + \mu^{n-1})] \frac{E}{\varepsilon} \propto \frac{E}{\varepsilon}. \quad (9.127)$$

Thus the expected value of the pulse height remains proportional to the energy even after the photomultiplier. (The peak-width also remains proportional to the square root of the energy.)

9.6 Fitting Nuclear Spectra

In this section, the evaluation of certain parameterized data sequences called nuclear spectra will be discussed. For a more general treatment of similar problems, see Press et al. (1999).

9.6.1 Spectra, Fitting, Model Functions

Spectrum. A spectrum is a set of data pairs (spectrum points)

$$(x_i, Y_i) \quad i = 1, 2, \dots, k \quad (9.128)$$

where x_i is the exact value of some independent variable x (one of a number of set values chosen by the spectroscopist), and the corresponding value of the dependent variable Y_i is considered as a random variable. It will be assumed that the expected value μ_i of Y_i is provided by the appropriate member of a parameterized family of functions

$$\{\mu(x; \mathbf{b})\}_{\mathbf{b}} \quad (9.129)$$

called the model functions. (The subscript above is to remind that there is an element in the set of functions $\{\dots\}_{\mathbf{b}}$ for each different value of \mathbf{b} .)

The vector

$$\mathbf{b} \equiv (b_1, b_2, \dots, b_n) \quad (9.130)$$

is called the vector of the fitting parameters. (See the example mentioned in remark (#35).)

Let \mathbf{a} denote that particular choice of the parameter vector \mathbf{b} at which the fitting actually takes place, i.e., for which

$$E(Y_i) \equiv \mu_i = \mu(x_i; \mathbf{a}) \quad i = 1, 2, \dots, k. \quad (9.131)$$

The function determined by \mathbf{a} :

$$\mu(x) = \mu(x; \mathbf{a}) \quad (9.132)$$

will be referred to as the fitting function. The purpose of fitting is to give the best possible estimate for the parameter vector \mathbf{a} on the basis of the concrete spectrum. The estimate of \mathbf{a} will be denoted by $\hat{\mathbf{a}}$.

Nuclear spectra. Before sketching out the solution for the fitting problem in general, a special class of spectra called nuclear spectra will be considered, in the case of which the Y_i s are counts, for which the Poisson approximation and the normal approximation equally hold. In other words, for the spectra considered, the Y_i -values have $N(\mu_i, \sigma_i^2)$ distributions with $\sigma_i^2 = \mu_i$ as a heritage of the Poisson distribution. (See [Fig. 9.22](#))

9.6.2 The Maximum Likelihood Principle

The maximum likelihood principle is based on the following train of thought. Suppose that the shape of the model function is exactly known (in principle), but the exact value of the parameter vector \mathbf{a} (providing the fitting function common to all spectra that could be measured under the given conditions) remains hidden from the experimenter. One can only state with certainty (because of physical considerations) that such a parameter vector *does* exist. The measured spectrum

$$S_0(\mathbf{a}) \equiv \{(x_i, Y_i)_{i=1, 2, \dots, k}\} \quad (9.133)$$

can therefore be considered as a concrete member – realized by a concrete measurement – of the manifold of spectra $\{S_{\mathbf{a}}(\mathbf{a})\}_{\mathbf{a}}$ the elements of which are characterized by the same “exact” parameter vector \mathbf{a} . The different elements of $\{S_{\mathbf{a}}(\mathbf{a})\}_{\mathbf{a}}$ are not equally likely to occur in an actual measurement. Since the spectrum points have normal distribution and they represent independent random variables, the following “probability” – or rather: likelihood – can be assigned to the different spectra

$$P(\mathbf{a}; \mathbf{a}) \Leftrightarrow \prod_{i=1}^k \left[\frac{1}{\sqrt{2\pi}\sigma_i} \exp\left(-\frac{1}{2} \left(\frac{Y_i - \mu(x_i; \mathbf{a})}{\sigma_i}\right)^2\right) \Delta Y \right] = L(Y_i; \mathbf{a})(\Delta Y)^k \quad (9.134)$$

where $\mathcal{L}(Y_i; \mathbf{a})$ is called the likelihood function that can be considered as a k -dimensional density function characterizing the “probability” of the spectrum in question (Orear 1987)

$$\mathcal{L}(Y_i; \mathbf{a}) = \frac{1}{\prod_{i=1}^k \sqrt{2\pi}\sigma_i} \exp\left(-\frac{1}{2} \sum_{i=1}^k \left(\frac{Y_i - \mu(x_i; \mathbf{a})}{\sigma_i}\right)^2\right). \quad (9.135)$$

Note that the factor ΔY was needed in [Eq. \(9.134\)](#) so that the normal density function could be converted to probability. Now if one has to take a guess at the “position” of the measured spectrum $S_0(\mathbf{a})$ in the manifold $\{S_\alpha(\mathbf{a})\}_\alpha$, then the most sensible thing to do would be to look for it around the maximum of the above likelihood. In other words – like all experimenters – one should *trust* that the single result of that particular measurement (the spectrum measured maybe for several days) exemplifies a typical case rather than a rare and extreme one

$$P(0; \mathbf{a}) \approx \max_\alpha P(\alpha; \mathbf{a}). \quad (9.136)$$

Laying this down, one can continue arguing like this. Since one would like to *believe* that the measured spectrum $S_0(\mathbf{a})$ is a likely realization associated with the “real” – alas, unknown – parameter vector \mathbf{a} , the best thing that one can do is select the estimate $\hat{\mathbf{a}}$ so that it (of all the possible values of the parameter vector \mathbf{b}) assigns the greatest likelihood to the measured spectrum

$$P(0; \hat{\mathbf{a}}) \approx \max_{\mathbf{b}} P(0; \mathbf{b}). \quad (9.137)$$

The above maximum condition is an expression of the maximum likelihood principle. Note that the maximum likelihood principle – rationality aside – does not provide a guarantee that the “real” \mathbf{a} will be found, since it is based on belief rather than on strict mathematical foundations. However, the results shown below can be interpreted mathematically as well, speaking for the “strength” of the principle.

9.6.3 Weighted Least Squares as a Maximum Likelihood Method

Because of the monotony of the logarithmic function, the above maximum condition can be converted to the following minimum condition:

$$-\log P(0; \hat{\mathbf{a}}) \approx \min_{\mathbf{b}} (-\log P(0; \mathbf{b})). \quad (9.138)$$

In the concrete situation this condition provides the estimate $\hat{\mathbf{a}}$ as the solution of the following minimization:

$$\chi^2 \equiv \sum_{i=1}^k \left(\frac{Y_i - \mu(x_i; \hat{\mathbf{a}})}{\sigma_i}\right)^2 \Rightarrow \text{minimum} \quad (9.139)$$

Note that the above sum of squares is proportional to the weighted average of the squared deviation from the expected value as defined by [Eq. \(9.36\)](#).

There are commercial programs for solving the above type of minimization. They provide not only the estimates of the unknown parameters but also their variances and the correlation coefficients between them. Instead of going into details of such evaluations, only a couple of remarks will be made concerning the minimum of χ^2 that is characteristic of the goodness of fit.

(#75) The notation χ^2 is not accidental. It was pointed out at the χ^2 distribution that when the model function is linear in the fitting parameters, then the minimized sum of squares has a $\chi^2(k - n)$ distribution, i.e., the goodness of fit can be judged accordingly.

(#76) If the model function is not linear in all of the parameters, then, perhaps, it can be linearized by a transformation or using a power series. After linearization, the sum of squares will certainly have a χ^2 distribution with *some* degree of freedom. In order to find the minimum, however, the model function need not be linearized (Press et al. 1999). The possibility of linearization is only necessary for the declaration of the “competence” of the χ^2 distribution as a goodness-of-fit measure, as well as for finding the value of n pointing to the concrete χ^2 distribution “in charge.” Considering that the value of k can be as large as several thousand in the case of nuclear spectra, the value of n (which is much less than k) does not matter too much, because the sum of squares will approximately have a $\chi^2(k - n) \approx \chi^2(k) \approx N(k, 2k)$ distribution anyway.

(#77) Some types of linearization require the (nonlinear) transformation of the measured spectrum. As an example, one can mention the logarithmic conversion of decay data for the determination of the decay constant. Logarithmic conversion spoils the initially normal distribution of the spectrum points, thus breaking the connection with the χ^2 distribution as a goodness-of-fit measure.

9.6.4 Weighted Least Squares Method in Nuclear Spectroscopy

It has not yet been made use of the fact that $\sigma_i^2 = \mu_i$ for nuclear spectra. Before including this relationship in the least squares method, a very simple nuclear spectrum will be considered consisting of the counts measured with a long-lived radionuclide for equal periods of time. The model function is obviously very simple in this case. It only contains one single parameter representing the common expected value of the measured counts. The minimization problem therefore can be expressed like this

$$\chi^2 \equiv \sum_{i=1}^k \left(\frac{Y_i - \hat{a}}{\sigma_i} \right)^2 \Rightarrow \text{minimum} \quad (9.140)$$

where \hat{a} is the estimate of the constant $\mu = E(Y_i)$. In this particular case there are three – equally sensible – choices for giving the value of σ_i^2 . The question is, whether or not they lead to the same estimate.

Case 1: $\sigma_i^2 = \sigma^2 = \text{constant}$. The only constraint is that the points have the same variance

$$\chi^2 \equiv \sum_{i=1}^k \left(\frac{Y_i - \hat{a}}{\sigma} \right)^2 \Rightarrow \text{minimum.} \quad (9.141)$$

Case 2: $\sigma_i^2 = \sigma^2 = \mu \approx \hat{a}$. It is also utilized here that the data come from nuclear measurement, and also that \hat{a} is the estimate of μ :

$$\chi^2 \equiv \sum_{i=1}^k \frac{(Y_i - \hat{a})^2}{\hat{a}} \Rightarrow \text{minimum.} \quad (9.142)$$

Case 3: $\sigma_i^2 = \sigma^2 = \mu \approx Y_i$. It is utilized that the data come from nuclear measurement, and also that, in the case of Poisson distribution, a single measured value is a fair estimate of the

expected value (see remark (#24)), provided that the measured (and thus the expected) value is large enough

$$\chi^2 \equiv \sum_{i=1}^k \frac{(Y_i - \hat{a})^2}{Y_i} \Rightarrow \text{minimum.} \quad (9.143)$$

Differentiating the above expressions with respect to \hat{a} , one can see that each minimum problem has a different solution. The result will always be some type of an average of the Y_i -values, however, in case 1 it is the arithmetical mean (i.e., the sample mean, see [Eq. \(9.29\)](#)), in case 2 the harmonic mean (see [Eq. \(9.19\)](#)), while in case 3 the root mean square (see [Eq. \(9.17\)](#)), which provides the concrete solution.

Consider now the problem in general. However tempting case 1 seems to be (note that it proved to be related to the sample mean that is both the unbiased estimate of the expected value and, as shown before, its maximum likelihood estimate), it cannot serve as a general model, because the model function is not usually constant and therefore [Eq. \(9.141\)](#) does not represent a maximum likelihood condition in general.

Although case 2 conveys the nuclear character of the spectra quite accurately, it has two major drawbacks. First, the derivatives are more complicated and, second, the statistical interpretation is more difficult. Consider, e.g., that all the advantages of a linear model function disappear as soon as that same model function appears in the denominator as well (see [Eq. \(9.142\)](#)).

In case 3, the nuclear character is only expressed approximately, but the approximates (Y_i) can be considered as constants from the viewpoint of differentiation and therefore the following minimum condition/merit function is accepted in the practice of spectrum evaluation

$$\chi^2 \equiv \sum_{i=1}^k \frac{(Y_i - \mu(x_i; \hat{a}))^2}{Y_i} \Rightarrow \text{minimum} \quad (9.144)$$

As regards the relationship between χ^2 -values and confidence intervals, see the excellent literature available (Press et al. 1999). Only a few general remarks will be made below.

(#78) For rather obvious reasons, the following relationships hold between the above-mentioned means:

$$\text{harmonic mean} \leq \text{sample mean} \leq \text{root mean square} \quad (9.145)$$

It is reassuring, however, that in the case of the Poisson distribution the actual difference between the above “averages” is relatively small. It is easy to check (e.g., with random numbers of $\Pi(\mu)$ distribution) that the difference – varying μ between 10^2 – 10^6 and “averaging” ten data at a time – does not usually exceed 1. On the other hand, for $\mu = 10^2$, 10^4 , and 10^6 the standard deviations are 10, 100, and 1,000, respectively, showing that the three methods of “averaging” are practically equivalent, because the standard deviations are much larger than the difference between them.

(#79) In spite of the fact that the χ^2 -value is the result of minimization, the same “protocol” should be followed as usual, i.e., when the confidence/acceptability of an estimate is judged by using any other distribution as a measure. Therefore, the fit giving the smallest χ^2 -value is not necessarily the best. The best fit is the one whose χ^2 -value is nearest to the expected value (determined by the degrees of freedom) of the corresponding χ^2 distribution. It is true, however, that in 99 cases out of 100 the spectroscopist is unsatisfied with the fit because he or she finds the χ^2 -value too large.

One possible reason for this can be that the model function used is unsatisfactory. It is a serious error, e.g., when the dimension of the vector \mathbf{b} is taken too small (this happens, e.g., when a Mössbauer spectrum is fitted with fewer peaks than it actually contains). Another source of such error can be that the shape of the elementary model function is imperfect (e.g., the peaks of a Mössbauer spectrum cannot always be described perfectly by Lorentzians).

Spectrum points that are way out of range (mainly “dropped” points) can also lead astray the fitting process.

(#80) If the relative χ^2 is too small, it can be an indication that the fitting program tends to overestimate the degrees of freedom. This can happen, e.g., when the model function is not linear in each of the parameters, and the degree of freedom is calculated (according to the general practice) simply by subtracting the number of fitted parameters from the number of spectrum points.

Too small (i.e., too good) a χ^2 can be obtained, when the dead time is so large that the Poisson approximation built into the merit function of ▶ Eq. (9.144) overestimates the variance in the denominator. In such a case, a more realistic result is obtained, if – on the basis of ▶ Eq. (9.111) – the calculated χ^2 -value is divided by $(1 - \theta v_0)^2$, where θv_0 is the percentage of dead time divided by 100.

9.7 Summarizing Tables

■ Table 9.1

Addition theorems. The addition theorems summarized below are only valid if the random variables X_1 and X_2 are independent of each other

Distribution of X_1	Distribution of X_2	Distribution of $X_1 + X_2$
$B(n_1, p)$	$B(n_2, p)$	$B(n_1 + n_2, p)$
$\Pi(\mu_1)$	$\Pi(\mu_2)$	$\Pi(\mu_1 + \mu_2)$
$\gamma(r_1, v)$	$\gamma(r_2, v)$	$\gamma(r_1 + r_2, v)$
$N(\mu_1, \sigma_1^2)$	$N(\mu_2, \sigma_2^2)$	$N(\mu_1 + \mu_2, \sigma_1^2 + \sigma_2^2)$
$\chi^2(k_1)$	$\chi^2(k_2)$	$\chi^2(k_1 + k_2)$
$C(m_1, \gamma_1)$	$C(m_2, \gamma_2)$	$C(m_1 + m_2, \gamma_1 + \gamma_2)$

■ Table 9.2

Limiting distributions. The conditions given below are practical substitutes for the exact limits (such as $p \rightarrow 0$ and $n \rightarrow \infty$ in the case of the first row). Under the practical conditions given in the middle column, the limiting distribution given in the third column gives a fair approximation of the distribution given in the first column

Distribution of X	Conditions	Limiting distribution of X
$B(n, p)$	$p \leq 0.1, n \geq 20$	$\Pi(np)$
$B(n, p)$	$npq \geq 6, q \equiv (1 - p)$	$N(np, npq)$
$\Pi(\mu)$	$\mu \geq 20$	$N(\mu, \mu)$
$\gamma(r, v)$	$k \geq 30$	$N(r/v, r/v^2)$
$\chi^2(k)$	$k \geq 50$	$N(k, 2k)$

■ **Table 9.3**

Normal distribution. Probabilities expressed in percentage for deviations from the mean higher than $\mu \pm d\sigma$ for the random variable X having $N(\mu, \sigma^2)$ normal distribution

d	$100 \times P(X - \mu \geq d\sigma)$	d	$100 \times P(X - \mu \geq d\sigma)$
0.67449	50	2.1	3.57
0.7	48.39	2.2	2.78
0.8	42.37	2.3	2.14
0.9	36.81	2.4	1.64
1.0	31.37	2.5	1.24
1.1	27.13	2.6	0.932
1.2	23.01	2.7	0.693
1.3	19.36	2.8	0.511
1.4	16.15	2.9	0.373
1.5	13.36	3.0	0.27
1.6	10.96	3.5	0.0465
1.7	8.91	4	0.00634
1.8	7.19	5	0.0000573
1.9	5.74	6	0.0000002
2.0	4.55	7	0.00000000026

■ **Table 9.4**

χ^2 distribution. The p -quantiles of $\chi^2(k)$ distributions for different degrees of freedom k

$k \backslash p$	0.01	0.05	0.10	0.25	0.50	0.75	0.90	0.95	0.99
1	0.0002	0.0039	0.0148	0.102	0.455	1.32	2.71	3.84	6.33
5	0.554	1.15	1.61	2.67	4.35	6.63	9.24	11.1	15.1
10	2.56	3.94	4.87	6.74	9.34	12.5	16.0	18.3	23.2
15	5.23	7.26	8.55	11.0	14.3	18.2	22.3	25.0	30.6
20	8.26	10.9	12.4	15.5	19.3	23.8	28.4	31.4	37.6
25	11.5	14.6	16.5	19.9	24.3	29.3	34.4	37.7	44.3
30	15.0	18.5	20.6	24.5	29.3	34.8	40.3	43.8	50.9

Acknowledgments

The author gratefully acknowledges Dr. Károly Süvegh's help in doing the positron lifetime measurements for [Fig. 9.13](#). He also thanks Dr. György Vankó for giving permission to use his diagram in [Fig. 9.20](#), as well as Prof. György Michaletzky, of the Department of Probability Theory and Statistics, for his helpful advice.

References

- Belgya T, Fazekas B, Molnár G, Gatenby RA, Johnson EL, Baum EM, Wang D, DiPrete DP, Yates SW (1993) In: Eighth International Symposium on Capture Gamma-Ray Spectroscopy, Fribourg, Switzerland, 20–24 September 1993, pp 878–887
- Bevington PR (1969) Data reduction and error analysis for the physical sciences. McGraw-Hill, New York
- Cohen ER, Giacomo P (1987) *Physica A* 146:1–68
- Feller W (1968) An introduction to probability theory and its applications, vol I, 3rd edn. Wiley, New York
- Georgii H-O (2008) Stochastics: introduction to probability and statistics. Gruyter, Berlin
- Goodman R (1988) Introduction to stochastic models. Benjamin/Cummings, Menlo Park
- Hogg RV, Tanis EA (1988) Probability and statistical inference, 3rd edn. Macmillan, New York
- Jánosy L (1965) Theory and practice of the evaluation of measurements. Clarendon, Oxford
- Karlin S, Taylor HM (1975) A first course in stochastic processes. Academic, New York
- Karlin S, Taylor HM (1984) An introduction to stochastic modeling. Academic, Orlando
- Knoll GF (1979) Radiation detection and measurement. Wiley, New York, pp 104–147
- Korn GA, Korn TM (1968) Mathematical handbook for scientists and engineers, 2nd edn. McGraw-Hill, New York, pp 84–144
- Leo WR (1987) Techniques for nuclear and particle physics experiments. Springer, Berlin, pp 75–106
- Lux J, Koblinger L (1991) Monte Carlo particle transportation methods: neutron and photon calculations. CRC Press, Boston
- Lyons L (1986) Statistics for nuclear and particle physicists. Cambridge University Press, Cambridge
- Orear J (1987) Notes on statistics for physicists. In: Bhat MR (ed) Procedures manual for the evaluated nuclear structure data file. National Nuclear Data Center, Brookhaven National Laboratory, Upton
- Press WH, Teukolsky SA, Vetterling WT, Flannery BP (1999) Numerical recipes in C – the art of scientific computing, 2nd edn. Cambridge University Press, Cambridge, pp 609–706
- Rényi A (1970) Foundations of probability. Holden-Day, San Francisco
- Rényi A (1979) Wahrscheinlichkeitsrechnung. Mit einem Anhang über Informationstheorie, 6. Aufl. VEB Deutscher Verlag der Wissenschaften, Berlin
- Schmidt K-H, Sahn CC, Pielenz K, Clerc HG (1984) *Z Phys A* 316:19



10 The Standard Model of Elementary Particles

D. Horváth

KFKI Research Institute for Particle and Nuclear Physics, Budapest,
Hungary

Institute of Nuclear Research (ATOMKI), Debrecen, Hungary

10.1	<i>Elementary Particles</i>	458
10.2	<i>Symmetries</i>	459
10.3	<i>Antiparticles and CPT Invariance</i>	461
10.4	<i>The Quark Model</i>	462
10.5	<i>The Three Families of Fermions</i>	464
10.6	<i>Interactions</i>	465
10.7	<i>The Higgs Mechanism</i>	466
10.8	<i>The Peculiarities of the Weak Interaction</i>	469
10.8.1	Parity and CP Violation	469
10.8.2	State Mixing	469
10.9	<i>The Present and Future of the Standard Model</i>	470

Abstract: The present experimental evidence seems to support the Standard Model of elementary particles, which interprets the world as consisting of 12 basic fermions: six quarks and six leptons with their antiparticles, 13 bosons mediating the strong, electromagnetic and weak interactions, and the mysterious Higgs boson. This chapter attempts to overview the basic features of the Standard Model with a minimal mathematical apparatus.

10.1 Elementary Particles

A traditional way of studying Nature is to dig deeper and deeper in the structure of matter ever increasing the spatial resolution, i.e., studying smaller and smaller objects. In this process each major step resulted in a new set of particles believed to be *elementary*: the four atoms of Democritus (*a-tom* means indivisible), the elements, atoms of Dalton and Mendeleev, the atomic nucleus of Rutherford, and the so-called elementary particles of which the electron, the proton and the neutron are the most common, constituting most of the visible world. It will be shown that, in fact, the proton and the neutron are also composite particles.

In this review the present knowledge of particle physics is summarized on a popular level, with no attempt to go into the very difficult mathematical formalism involved. If the reader is confused, it is the fault of the author and not of the physical theory: that is very precisely elaborated and its predictions beautifully agree with the experimental observations, as shown in some detail at the end of this review. All present-day experimental evidence is summarized in the biennial *Particle Physics Review* of the Particle Data Group (Amsler et al. 2008); for a theoretical introduction the textbooks of Halzen and Martin (1984) and Perkins (2000) are recommended; the latter provides a nice glance at the experimental evidence as well.

The elementary particles can be categorized from various points of view. The most important property is their intrinsic angular momentum or *spin*. It cannot be connected to a rotation of the particle, but it is additive to the other, ordinary angular momenta like the orbital momentum. Its unit is the reduced Planck constant, $\hbar = h/(2\pi)$. The **fermions**, the particles with half-integer spin ($S = 1/2, 3/2, 5/2, \dots$), and the **bosons**, those with integer spin ($S = 0, 1, 2, \dots$) have very different symmetries and other properties. Fermions follow *Fermi–Dirac statistics* whereas bosons follow *Bose–Einstein* one: that is the origin of their names. The fermion number is conserved whereas bosons can be created and absorbed: a lamp can irradiate any number of photons ($S = 1$) and an antenna can absorb them, provided that the energy, momentum, etc. are conserved. At the same time the electrons ($S = 1/2$), in order to illuminate the cathode tube of one’s TV set, have to be brought there and then conducted away. Another very important difference is that any number of bosons, but only one fermion, can be put in any particular quantum state. This restriction concerning fermions is called **Pauli’s exclusion principle** (Pauli 1926). That is why the electrons of the atom fill discrete energy levels and that is the underlying force that prevents the atoms of matter and the nucleons in the nucleus from penetrating each other; this principle provides macroscopic forms for the material objects.

Another way to classify the particles is by the interaction they participate in. The four basic forms of interaction are **gravitational**, **electromagnetic**, **weak**, and **strong** interaction. Gravity affects all particles, but it is negligibly weak under laboratory conditions (although can be very strong in astronomy) and so it will be ignored. All fermions are exposed to the weak interaction, and the particles having an electric charge or magnetic moment also to **electromagnetism**. The composite particles that partake in the strong interaction are called **hadrons**,


among them the **baryons** are fermions and the **mesons** are bosons. The **leptons** are fermions that are not influenced by strong interactions. These names are coming from the masses of the first observed particles of each type: the first leptons (the electron and its neutrino) are light particles, the first mesons (the pion, $m_\pi \approx 139$ MeV is 273 times heavier than the electron) have intermediate masses and the baryons (like the proton and the neutron) are much heavier ($m_p = 938$ MeV $\approx 1,836$ m_e). According to Einstein's mass equation $E = mc^2$ the mass is expressed with energy. The correct notation would be $m_p = 938$ MeV/ c^2 , where m_p means the rest mass of the proton. However, particle physicists prefer to use a “natural” unit system where $\{c\} = 1$ and $\{\hbar\} = 1$ and everything (including time and distance) is measured in energy units.

10.2 Symmetries

Symmetries in particle physics are even more important than in chemistry or solid-state physics. Just like in any theory of matter, the inner structure of the composite particles is described by symmetries, but in particle physics everything is deduced from the symmetries (or invariance properties) of the physical phenomena or from their violation: the conservation laws, the interactions, and even the masses of the particles, as it will be shown later.

The conservation laws are related to symmetries: the conservation of momentum and energy are deduced from the translational invariance of space–time: the physical laws do not depend upon where one places the zero point of the coordinate system or time measurement; and the fact that one is free to rotate the coordinate axes at any angle is the origin of angular momentum conservation.

The symmetry properties of particles with half-integer spin (fermions) differ from those with integer spin (bosons). The wave function describing a system of fermions changes sign when two identical fermions are exchanged, whereas in the case of bosons there is no change; all other differences can be deduced from this property. The spin is also strange: the spin of the electron is added to its orbital momentum, but it has two eigenstates only: it is either left or right polarized (i.e., points either up or down) in any coordinate system. Thus, it is characterized by two independent quantities in three dimensions: by its length and one of its vector components.

The characteristic symmetries of the particles are described in terms of **group theory** (Wigner 1939). The language of physics is mathematics: the difference between theory and speculation is established via the mathematical formalism with the use of which one gets numerical predictions for measurable quantities. In most of the cases the symmetries can be expressed in terms of coordinate transformations and the mathematical apparatus is chosen that way. A simple example, the rotation of a two-dimensional coordinate system by angle Θ is shown in  Fig. 10.1.

The new coordinates (x', y') of point P are obtained from the old ones (x, y) with the well-known transformation

$$x' = a + b = x \cos \Theta + y \sin \Theta, \quad (10.1)$$

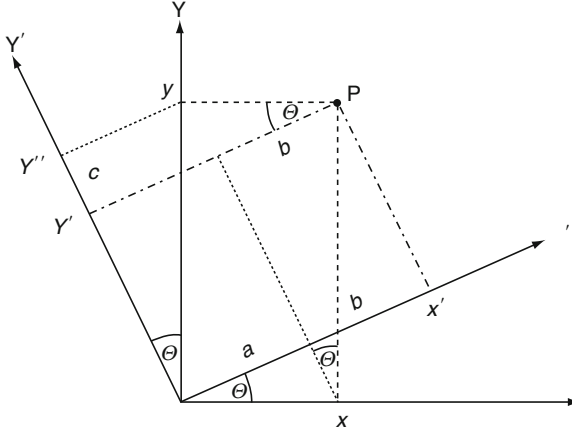
$$y' = y'' - c = y \cos \Theta - x \sin \Theta, \quad (10.2)$$

or, in vector/matrix formalism,

$$\begin{pmatrix} x' \\ y' \end{pmatrix} = \begin{pmatrix} x \cos \Theta + y \sin \Theta \\ -x \sin \Theta + y \cos \Theta \end{pmatrix} = \begin{pmatrix} \cos \Theta & \sin \Theta \\ -\sin \Theta & \cos \Theta \end{pmatrix} \begin{pmatrix} x \\ y \end{pmatrix}. \quad (10.3)$$

■ Fig. 10.1

Rotation of a coordinate system in two dimensions: the $[X', Y']$ system is obtained by rotating $[X, Y]$ by angle Θ



An important property of these rotation transformations is that they do not change the length of vector \mathbf{P} (its absolute value) as

$$x'^2 + y'^2 = (x^2 + y^2)(\cos^2 \Theta + \sin^2 \Theta) = x^2 + y^2. \quad (10.4)$$

Particle physics, however, works with complex quantities of the form $x = a + ib$, where i is the imaginary unit, $i^2 = -1$. The measurable physical quantities are always real, so they contain the absolute values of the complex numbers,

$$x^2 = x^* x = (a - ib)(a + ib) = a^2 + b^2 \quad (10.5)$$

where x^* is the complex conjugate of x . In the case of complex matrices, conjugation must be accompanied by the transposition of its elements around the diagonal, thus the requirement that a rotation whose matrix is \mathbf{U} does not change the lengths of vectors demands that the matrix be *unitary*, i.e., $\mathbf{U}^\dagger \mathbf{U} = \mathbf{I}$ where \mathbf{I} is the unit matrix. In the case of the above matrix this is of course fulfilled:

$$\mathbf{U}^\dagger \mathbf{U} = \begin{pmatrix} U_{11}^* & U_{21}^* \\ U_{12}^* & U_{22}^* \end{pmatrix} \begin{pmatrix} U_{11} & U_{12} \\ U_{21} & U_{22} \end{pmatrix} = \begin{pmatrix} |U_{11}|^2 + |U_{21}|^2 & U_{11}^* U_{12} + U_{21}^* U_{22} \\ U_{12}^* U_{11} + U_{22}^* U_{21} & |U_{12}|^2 + |U_{22}|^2 \end{pmatrix} = \begin{pmatrix} 1 & 0 \\ 0 & 1 \end{pmatrix}. \quad (10.6)$$

Rotations of the above type have the following properties:

- They are additive: consecutive rotations by angles Θ_1 and Θ_2 are equivalent to a rotation by $\Theta = \Theta_1 + \Theta_2$.
- The addition is associative: $(\Theta_1 + \Theta_2) + \Theta_3 = \Theta_1 + (\Theta_2 + \Theta_3)$.
- They have a unit element as rotation with angle $\Theta = 0$ does not do anything.

Sets consisting of objects of such properties constitute a *group*, in the given case the **rotation group**. This particular group in two dimensions is commutative as well: $\Theta_1 + \Theta_2 = \Theta_2 + \Theta_1$.

Being an angular momentum, the spin should be associated with the symmetry of the rotation group. Thus the rotation group can be described by Special (their *determinant* is 1) Unitary 2×2 matrices and so this group is called SU(2). The determinant of matrix **A** is unity if

$$\text{Det} \begin{pmatrix} A_{11} & A_{12} \\ A_{21} & A_{22} \end{pmatrix} = A_{11}A_{22} - A_{12}A_{21} = 1. \quad (10.7)$$

The SU(2) symmetry group describes not only the spin, but any quantity of similar symmetry properties. Such an example, that of **isospin**, will be shown later.

When the degree of freedom is increased, one gets higher symmetry groups of similar properties. The next one, SU(3), which will be used later, is the symmetry group of Special Unitary 3×3 matrices. It can be visualized the following way. A half-spin particle has two possible fundamental states (two *eigenstates*), spin up and spin down. In the case of the SU(3) symmetry group there are three eigenstates with an SU(2) symmetry between any two of them.

One can also *decrease* the degrees of freedom and get the U(1) group of unitary 1×1 matrices, which are simply complex numbers of unit absolute values. This is the symmetry group of the **gauge transformations** of electromagnetism. This **gauge symmetry** means, e.g., in the case of electricity a free choice of potential zero: as it is demonstrated by the birds sitting on high-voltage electric wires, the *potential difference* is the meaningful physical quantity, not the potential itself. The U(1) symmetry of Maxwell's equations leads to the conservation of the electric charge and, in the more general case, the U(1) symmetry of the Dirac equation (Dirac 1928), the general equation describing the movement of a fermion, causes the conservation of the number of fermions (Halzen and Martin 1984).

10.3 Antiparticles and CPT Invariance

All fermions have **antiparticles**, anti-fermions that have identical properties with charges and some quantum numbers of the opposite sign. The interaction of a particle with its antiparticle leads to *annihilation*. When an anti-electron, the **positron**, annihilates with an electron, they produce two or three photons depending on their relative spin states, whereas the annihilation of an **antiproton** with a proton releases so much energy that half a dozen various particles can be emitted. The different abundance of particles and antiparticles in the Universe is one of the mysteries of astrophysics: apparently there is no antimatter in the Universe in significant quantities (see, e.g., Cohen et al. 1998). If there were **antimatter galaxies** they would radiate antiparticles and one would see zones of strong radiation at their borders with matter galaxies, but the astronomers do not see such a phenomenon anywhere.

An extremely interesting property of free *antiparticles* is that they can be treated mathematically as if they were *particles* of the same mass and of oppositely signed charge of the same absolute value *going backward in space and time*. This is the consequence of one of the most important symmetries of Nature: **CPT invariance** (Kostelecký 2002). It states that the following three operations:

- Charge conjugation (i.e., changing particles into antiparticles), $C\psi(\mathbf{r}, t) = \bar{\psi}(\mathbf{r}, t)$,
- Space reflection, $P\psi(\mathbf{r}, t) = \psi(-\mathbf{r}, t)$, and
- Time reversal, $T\psi(\mathbf{r}, t) = \psi(\mathbf{r}, -t)$

when done together, i.e., $\text{CPT}\psi(r, t) = \bar{\psi}(-r, -t)$, do not change the measurable physical properties of the system.

This means that, e.g., the annihilation of a positron with an electron can be described as if an electron came to the point of collision, emitted two or three photons and then went out backwards in space–time. In field theory such incoming and outgoing particles are described as **particle currents** in (some) analogy with the electric current; in the above example the incoming electron and positron constitute a lepton current.

A simple particle collision is described as a particle current exchanging an **interaction boson** with another similar current. The appearance of an extra boson is made possible by the **uncertainty principle** of Heisenberg which implies that for sufficiently short times and distances the conservation laws of energy and momentum can be violated: $\Delta E \Delta t \geq \hbar/2$ and $\Delta p \Delta x \geq \hbar/2$, where ΔA means a small uncertainty or deviation in A ($A = E, p, t, x$), E and p are the energy and momentum of the particle, t and x are time and spatial coordinates. The smallness of the reduced (sometimes called *rationalized*) Planck constant, $\hbar = 1.055 \times 10^{-34}$ Js ensures that in the macroworld the conservation laws are exactly fulfilled. The exchanged boson may be *real* or *virtual* depending on whether or not the conservation laws are fulfilled for its creation; if it is real, then it is emitted and so it can be detected; if it is virtual, then it is absorbed and one can see the result of the boson exchange only, i.e., the effect of the interaction on the motion of the particles involved.

CPT invariance is so far fully supported by the available experimental evidence and it is absolutely fundamental in field theory. Nevertheless, there are many experiments trying to test it. The simplest way to do that is to compare the mass or charge of particles and antiparticles. The most precise measurement of this type is that of the relative mass difference between the neutral K meson and its antiparticle that has so far been found to be less than 10^{-18} (Amsler et al. 2008). In 1999, an *Antiproton Decelerator* facility (CERN 2009) was constructed at the European Particle Physics Laboratory, CERN, in order to test the CPT invariance by comparing the spectra of hydrogen and antihydrogen, the latter being the bound state of an antiproton and a positron (see [Chap. 28 in Vol. 3](#)).

10.4 The Quark Model

The similarity of the proton and neutron was one of the earliest observations indicating a possible compositeness of the *elementary* particles: they have almost identical masses and – in spite of the fact that the proton has electric charge and the neutron has none – they have very similar potentials in the nuclear field. The concept of the *nucleon* was introduced with two eigenstates, neutron and proton, and a quantum number, the **isospin**. Its only similarity to spin is that it belongs to the same symmetry group, SU(2). *Iso* stands for *isobaric*: isobars are a set of nuclei of the same mass number but different charge and they can be identified using the isospin quantum number.

As the technique of experiments improved, more and more hadrons (strongly interacting particles) were discovered and all of them had isospin, i.e., they could be grouped into *isospin multiplets* of very similar properties. The nucleon has an isospin $I = 1/2$ with two eigenstates, so, in analogy with the spin, the third isospin component can take two values, $I_3 = \pm 1/2$; the upward state, $I_3 = +1/2$, is assigned to the proton and the downward one, $I_3 = -1/2$, to the neutron. (In nuclear physics often a converse convention is used, so that $I_3 = +1/2$ is associated with the neutron.)

The lightest hadron, the π meson or *pion* has isospin $I = 1$ and, correspondingly, the three possible isospin states are characterized by $I_3 = -1, 0, +1$ and it has three charge states, positive, neutral and negative. Thus the isospin became a basic quantum number in the classification of particles.

When a new quantum number, called **strangeness**, was discovered, which could be combined with isospin, producing new and new hadrons, Gell-Mann (1964) and Zweig (1964) suggested the **quark model** of hadrons. All observed hadrons could be described as consisting of three quarks. The first two quarks carry the isospin and so the $I_3 = +1/2$ quark is called *up* (u) and the $I_3 = -1/2$ quark *down* (d) quark. The third quark's quantum number is the strangeness, so that is the *strange* (s) quark. The quark model postulates that for some reason the quarks can combine in two ways only: three quarks make a baryon (and of course three antiquarks an antibaryon) and the mesons are quark–antiquark bound states. The quarks have spin $1/2$, they are fermions, and so the baryons are also fermions, whereas the mesons have integer spins, i.e., they are bosons. The quarks have fractional charges: $+2/3$ and $-1/3$ (► Table 10.1) of that of the electron, thus, e.g., the charge of the proton, $p = (uud)$ is 1 and that of the neutron $n = (udd)$ is 0. That is why a unit increase of the isospin's third component increases the charge of the particle: a d quark is replaced by a u quark with a charge increase of $+2/3 - (-1/3) = 1$. The quarks in the baryons and mesons fill states with various spin states and orbital momenta just like the electrons in the atoms, and that explains the series of excited states observed for the hadrons.

The quark model, although very successful in explaining particle properties, had serious inconsistencies. Nobody understood, for instance, why only those two combinations exist, why there are no free quarks in Nature, and why there could be more than one quark in a particle in exactly the same quantum state in spite of the Pauli principle. An excellent example for the latter is the Δ^{++} particle: it has double charge and spin $3/2$ and so it consists of three u quarks in the same spin state. In the course of the history of particle physics, whenever some new unexplained behavior was observed, new quantum numbers were introduced. In order to explain the magic combination of three identical quarks, a new quantum number was suggested: **color**, in analogy with the three basic colors seen by the eye, with three possible values, *red* (R), *green* (G), and *blue* (B). Color solves the above-mentioned problem: the new quantum number makes each quark state in the observed particles specific, and so the Pauli principle is fulfilled. Moreover, color is considered to play the same role for the strong quark–quark interaction as the electric charge does in electrodynamics: it is the **strong charge**. The existence of all observed particles is consistent with the assumption that only colorless particles are allowed to exist in unbound states in Nature. The condition of colorlessness accounts for

► Table 10.1

Leptons and quarks, the three families of basic fermions. T_3 is the third component of the weak isospin, the rest of the notation is explained in the text step by step. The meaning of the subscript L and the apostrophe after some of the symbols is explained in ► Sect. 8

	Family 1	Family 2	Family 3	Charge	T_3
Leptons	$\begin{pmatrix} \nu_e \\ e \end{pmatrix}_L$	$\begin{pmatrix} \nu_\mu \\ \mu \end{pmatrix}_L$	$\begin{pmatrix} \nu_\tau \\ \tau \end{pmatrix}_L$	0 −1	$+\frac{1}{2}$ $-\frac{1}{2}$
Quarks	$\begin{pmatrix} u \\ d' \end{pmatrix}_L$	$\begin{pmatrix} c \\ s' \end{pmatrix}_L$	$\begin{pmatrix} t \\ b' \end{pmatrix}_L$	$+\frac{2}{3}$ $-\frac{1}{3}$	$+\frac{1}{2}$ $-\frac{1}{2}$

the nonexistence of free quarks (*quark confinement*). In other words, only combinations of color + anticolor (i.e., the complementary color) or that of all three colors (R + G + B corresponding to white in the perception of the eye) are allowed to exist.

10.5 The Three Families of Fermions

A great step from the simple quark model to the Standard Model of particle physics was made by Glashow et al. (1970) by introducing what became known as the **GIM mechanism**. On the basis of various experimental observations they postulated that the quarks and leptons exist in pairs and they predicted the existence of a fourth quark, the *charm* (c) quark (► Table 10.1) with a charge of $+2/3$. In 1974 two groups (Aubert et al. 1974; Augustin et al. 1974) succeeded at the same time in discovering the $(c\bar{c})$ bound state (they named it differently and so it is now called **J/ψ meson**, a combination of the two names originally given). For the discovery, Richter and Ting received the Nobel Prize in 1976. (In the large collaborations of high-energy physics the authors usually appear in alphabetical order, so it is not necessarily the first author who is awarded the Nobel Prize.)

According to the GIM mechanism there should be as many lepton pairs as quark pairs (these groups are called *families*), because in order to prevent the theory from having anomalies, the sum of charges of all particles has to be zero. This is fulfilled for each family (► Table 10.1) as the charge sum from the top down is $0 - 1 + 3(2/3 - 1/3) = 0$, where the factor 3 stands for the number of colors. Of course, as soon as Perl's group (Perl et al. 1975) observed a third lepton, the τ (discovery in 1976, Nobel Prize in 1995) another pair of quarks was immediately predicted and later discovered. Thus, one has the menagerie of basic fermions listed in ► Table 10.1. The place of a fermion in the table is determined by its *weak isospin* (T) introduced by analogy with the isospin: for the upper particles its third component has an eigenvalue of $T_3 = +1/2$, for the lower ones it is $T_3 = -1/2$ and the pairs are **weak isospin doublets**. Note that the weak isospin is quite different from isospin: the isospin is a property of the two lightest quarks only, whereas all fermions have a weak isospin. Moreover, the isospin is a quantum number of the strong interaction, and the weak isospin is a characteristic of the weak interaction.

At this point one could ask how many more such families are hidden by Nature at higher energies. The answer was given by experiments performed on the high-energy electron-positron **colliders** (ordinary accelerators hit standing targets with fast particles; colliders can achieve much higher energies by accelerating two beams in opposite direction for collision, see also ► Chap. 50 in Vol. 5 on "Particle Accelerators") of CERN and Stanford: none, there are three families only. The proof is that the Z boson produced by the above machines can decay in various ways and the Standard Model quantitatively describes all of them; detecting all products the only unknown is the number of different neutrinos which cannot be seen there. By comparing the total decay lifetime with that of the detected modes one can deduce the contribution of the invisible ones. It turned out that there are just three kinds of light neutrinos, ν_e , ν_μ and ν_τ , and so there are three families only. A possible heavy neutrino would not carry a charged lepton and quarks, because those should have been observed already from their low-energy effects.

Thus, according to the present knowledge, ► Table 10.1 contains all basic fermions allowed by the Standard Model. The reader should not be frightened by the extraordinary caution of the above statement. Theoretically, the Standard Model was extended in numerous ways and all

those extensions predicted numerous hypothetical new basic particles (Collins et al. 1989). Although up to now no real evidence was found against the Standard Model, there are many possible extensions which do not contradict the present experimental data and so one cannot *a priori* exclude their validity.

10.6 Interactions

As mentioned before, ignoring gravity, there are three fundamental interactions in particle physics. Their basic properties are summarized in [Table 10.2](#).

According to the Standard Model, the interactions are deducible from local symmetries, their source is some “charge” and they are mediated by bosons characteristic of the given interaction. These bosons are real particles in the sense that they exist not only as virtual particles mediating interactions, but they can also be emitted and observed experimentally. A fermion enters into an interaction if it possesses the corresponding charge; the weak interaction operates on all fermions, the electromagnetic one on those having electric charges or magnetic moments and the strong interaction on the colored fermions, i.e., on the quarks.

The photon (γ) mediates the electromagnetic interaction, and the three weak bosons (W^+ , W^- , and Z^0) the weak interaction. In the strong interaction of two quarks they exchange color so the mediating boson, the **gluon** (from glue) should carry a color and an anticolor. This means eight different gluons: the $3 \times 3 = 9$ combinations has one less degree of freedom as the combination $R\bar{R} + G\bar{G} + B\bar{B}$ changes white to white and so does not carry color.

The pion decay provides an excellent example for comparison of the strengths of the electromagnetic and weak interactions. The decay of the neutral pion to two photons, $\pi^0 \rightarrow \gamma\gamma$, is a typical electromagnetic reaction with a mean lifetime of 8×10^{-17} s. The charged pion can decay via the weak interaction to a muon and its neutrino: $\pi^- \rightarrow \mu^- + \bar{\nu}_\mu$ and its lifetime is 26 ns = 2.6×10^{-8} s, eight orders of magnitude longer than that of its neutral partner. Note that in the above reaction a boson disappeared and a lepton was created together with an anti-lepton: the fermion number is conserved, whereas the boson number is not.

The properties of the electromagnetic interaction have been well known for a long time: its source is the electric charge, its mediator is the photon, and it originates from the local form of

Table 10.2

The fundamental interactions. In column 3, r is the distance from the source and R is the range of interaction. In column 4 the mean lifetime of a particle that decays due to the interaction specified is presented in parentheses. The last column gives the rest masses of the mediating bosons

Interaction	Relative strength	Potential	Mean life	Mediating boson	M (GeV/ c^2)
Strong (color)	1	$\propto r$	10^{-23} s	8 gluons	0
			($\Delta \rightarrow p\pi$)		
Electromagnetic	10^{-2}	$\propto \frac{1}{r}$	10^{-20} – 10^{-16} s	Photon	0
			($\pi^0 \rightarrow \gamma\gamma$)		
Weak	10^{-7}	$\propto \frac{1}{r} \exp(-\frac{r}{R})$	$>10^{-12}$ s	W^+, W^-	80
		$R \approx \frac{\hbar}{M_w c}$	($\pi^- \rightarrow \mu^- \bar{\nu}$)	Z^0	91

the $U(1)$ gauge symmetry of Maxwell's equations. Their global $U(1)$ gauge symmetry, a particular demonstration of which is the arbitrariness of potential zero, leads to the conservation of the electric charge. The requirement of local symmetry means that the equation of motion has to be invariant under a gauge transformation with an arbitrary space–time function: that function will give rise to the interaction field after some mathematical manipulations. It can be shown that the range of the interaction is inversely proportional to the mass of the mediating boson. As the photon has mass zero the electromagnetic interaction has an infinite range and its *Coulomb* potential is inversely proportional to the distance. Freely propagating photons are detected by the eyes (visible light) or by the TV sets (radio waves) and so their real existence and their ability to propagate to infinity are evident.

Similarly to the role of the electric charge in the electromagnetic interaction, the source of strong interaction is the **color charge**. It is mediated by the eight gluons and, according to the three colors, its origin is the local $SU(3)$ symmetry. The mass of the gluons is also zero and so the range of color interaction is also infinite; its potential at short distances is of the Coulomb form, but at long distances it is roughly proportional to the distance of the colored objects. This is the consequence of the fact that – as opposed to the photons which are not charged – the gluons themselves carry color, the charge of the interaction, and so they interact with each other. When one tries to separate two quarks, the energy of the field will grow with the distance as the gluons will produce more gluons and quark–antiquark pairs, and the quarks will combine into hadrons until only colorless objects remain: that is how **quark confinement** works.

Nonetheless, one can see quarks experimentally in the form of hadron showers, *jets*, many hadrons going into the same direction, produced in high-energy particle collisions. In a high-energy electron–positron collision, e.g., quark–antiquark pairs are produced (▶ Fig. 10.2, upper left), which are emitted back-to-back in the center-of-mass system. As they are moving away from each other, they exchange color and many hadrons are produced, 10–20 particles per jet; such a reaction cannot be interpreted in any other way. The actual existence of gluons is proven by the observation of events with three jets: the third one has to originate from a gluon emitted by one of the quarks as conservation laws prohibit all other explanations (▶ Fig. 10.2, upper right).

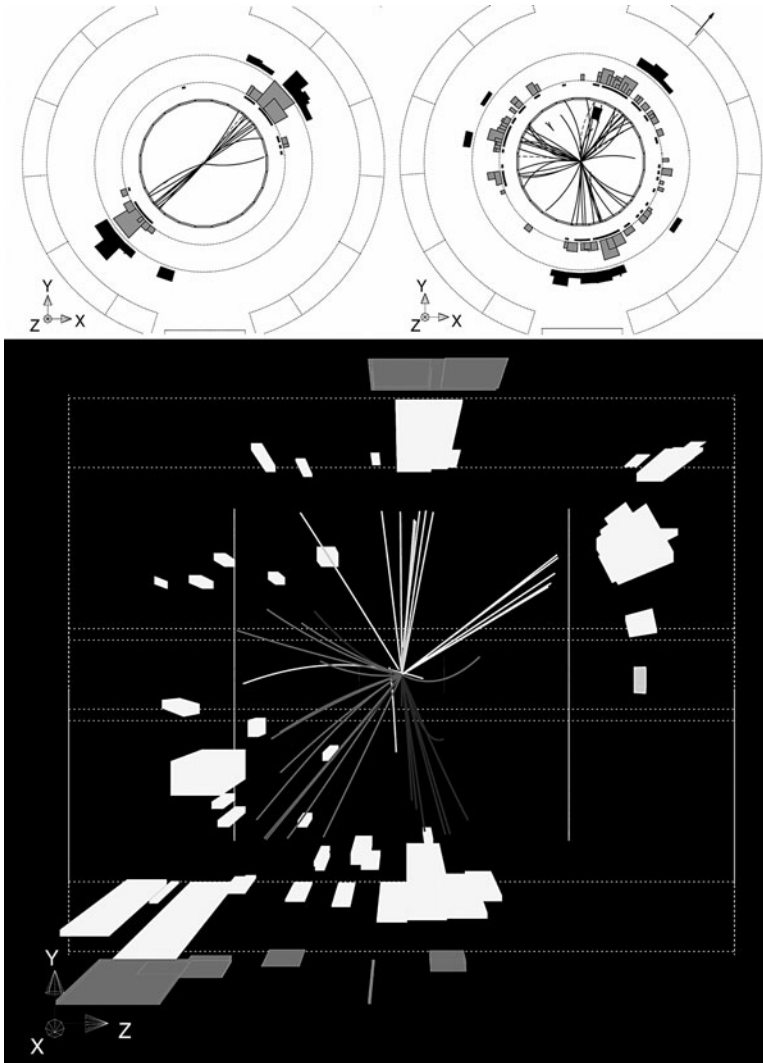
As a result of quark confinement, the observed range of the strong interaction between two hadrons is quite limited, it is about $1 \text{ fm} = 10^{-15} \text{ m}$, close to the size of the atomic nucleus. That means that the nuclear force binding the nucleus is the relatively weak *tail* of the color interaction appearing outside the nucleons, similarly to the chemical bond or to the van der Waals forces acting among neutral molecules or atoms, due to the Coulomb interaction within the atom.

10.7 The Higgs Mechanism

It seems to be quite natural to deduce the weak interaction from local $SU(2)$ symmetry as that is the symmetry group of the weak isospin. There are, however, several problems. First, such a theory predicts zero mass for the *weak bosons*, W^+ , W^- , and Z^0 , mediating the weak interaction, although from the short range of the interaction it follows that they should be quite heavy. As mentioned before, Heisenberg's uncertainty principle allows a particle of mass M to violate energy conservation for a time $\sim \hbar/(2Mc^2)$; that is how the W^- boson with a mass of 80 GeV can transfer, e.g., the 1.3 MeV (five orders of magnitude smaller!) energy released

■ Fig. 10.2

Hadron showers (jets) from quarks and gluons produced in the decay of weak bosons as detected in high-energy electron–positron collisions by the OPAL Collaboration (OPAL 2003) at the Large Electron Positron Collider at CERN. *Upper left:* the decay of a Z boson to a quark and an antiquark, $e^- + e^+ \rightarrow Z \rightarrow q + \bar{q}$ (two jets). *Upper right:* a Z boson decays to a pair of b quarks (as identified by jet properties) and one of them emits a gluon, $e^- + e^+ \rightarrow Z \rightarrow b + \bar{b} + g$ (three jets). *Below:* a W^+W^- pair decays to two quark–antiquark pairs (four jets). The sizes of boxes indicate the particle energies deposited in the detector elements



at the decay of the neutron. Neutron decay, $n \rightarrow p + e^- + \bar{\nu}_e$, is described at quark level as $d \rightarrow u + W^-$; $W^- \rightarrow e^- + \bar{\nu}_e$. The range of the weak interaction is $R = \hbar/(M_W c) \approx 2 \times 10^{-3}$ fm, about three orders of magnitude smaller than the nuclear radius. A problem occurs when calculating cross sections (or probabilities) of reactions involving the weak interaction: infinite

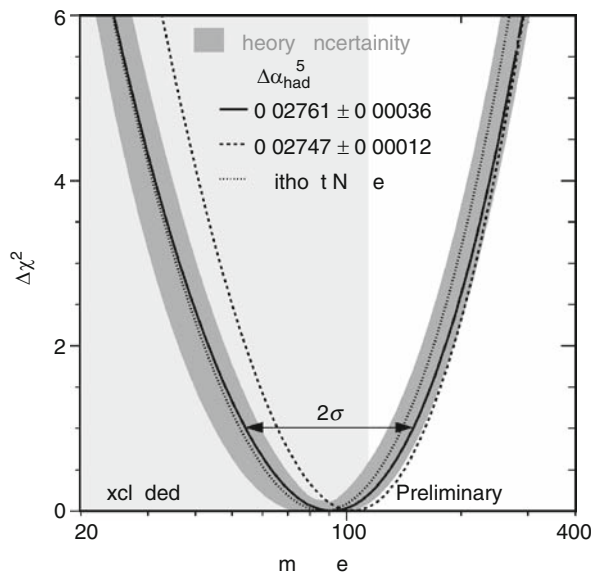
integrals come in which cannot be eliminated. Yet another problem is how to give mass to the fermions: the local SU(2) symmetry does not allow for that.

All of these problems are solved by the theory of **spontaneous symmetry breaking** which is called *Higgs mechanism* after its inventor (Higgs 1964a, b). It assumes the existence of a four-component field (complex isospin doublet) that is added to the fermion function as if it moved in that field. The fermions gain their mass in interaction with this Higgs field similarly to the additional inertia of a charged particle moving in a polarizable liquid as compared to vacuum. The Higgs field violates the local SU(2) symmetry and so – similarly to the quasi-particles of solid-state physics – it produces four new states; three of them are absorbed by the weak bosons, whereby the three weak bosons gain masses, and the fourth state, as a by-product, creates a heavy, neutral, spinless particle, the **Higgs boson**. The latter takes care of the divergences of the theory mentioned above, i.e., helps to eliminate the infinite integrals.

At the time of writing this review, the Higgs boson has not yet been found experimentally. In [Fig. 10.3](#) the goodness of fit of the Standard Model parameters is presented against the mass of a hypothetical Higgs boson. The fit is made by the LEP Electroweak Working Group and it combines the results of the four LEP experiments with those of several other major particle physics experiments. The place of the minimum implies a light Higgs boson around 100 GeV/c², whereas the direct LEP searches excluded, at a confidence level of 95%, all possible


Fig. 10.3

Search for the Higgs boson of the Standard Model: Goodness of fit of the Standard Model parameters against the mass of a hypothetical Higgs boson (LEP Electroweak Working Group 2009). The minimum implies a light Higgs boson with a mass around 100 GeV/c² whereas the LEP experiments excluded at a confidence level of 95% all possible Standard Model Higgs bosons with masses below 114.4 GeV/c² (shaded area) (LEP Working Group for Higgs Boson Searches 2003). The various curves and the shaded band around one illustrate the possible theoretical deviations ($\Delta\alpha_{\text{had}}^{(5)}$); NuTeV is one of the experiments involved. (The horizontal arrow at the level $\Delta\chi^2 = 1$ represents the $\pm\sigma$ limits. The 95% level of significance corresponds to $\pm 1.64\sigma$)



Standard Model Higgs bosons with masses below $114.4 \text{ GeV}/c^2$ as shown by the shaded area (LEP Working Group for Higgs Boson Searches 2003). A combination of all this information indicates that the Higgs boson mass should be between 114 and $250 \text{ GeV}/c^2$.

10.8 The Peculiarities of the Weak Interaction

In  [Table 10.1](#) there is a subscript L at the doublets and an apostrophe at the quark symbols. They indicate peculiarities of the weak interaction.

10.8.1 Parity and CP Violation

If one builds a clock looking at its design in a mirror, it should work properly except that its hands will rotate the opposite way and the lettering will be inverted. The laws governing the work of the clock are invariant under space inversion. In a system obeying such laws the **parity** of the wave function is conserved. Most physicists thought that physics has perfect mirror symmetry, until the experiment of Madame Wu (Wu et al. 1957) who has shown that a decaying cobalt nucleus emits its beta electron in a direction opposite to its spin. Since the spin direction is not reversed at mirror reflection, the mirror image of this decay process cannot take place, which amounts to a **violation of the mirror symmetry of Nature**. Thus, the weak interaction does not conserve parity.

The other two interactions *do* conserve the *parity* of a system, i.e., remember which way a particle was polarized before the interaction, whereas the weak interaction “maximally” violates it. This maximal violation manifests itself in the fact that the particles emitted in weak interaction tend to be polarized left (their spin pointing preferentially against the direction of the momentum) and the antiparticles polarized right (spin and momentum having the same direction) independently of any former polarization; this is indicated by the symbol L for *left* at the weak isospin doublets of the particles. The case of the neutrino is extreme: in the limit of zero mass the neutrino can only exist left-polarized and the antineutrino only right-polarized.

After the discovery of parity violation the CP symmetry, i.e., the invariance of the physical laws against the simultaneous transformation of charge and space reflection, was still assumed to be exact. However, in 1964 Cronin and Fitch (Nobel Prize 1980) discovered (Christenson et al. 1964) that the weak interaction violates that as well, although this violation is tiny, not maximal, like that of the P invariance. **CP violation** makes it possible to differentiate between a world and an antiworld and may be related to the matter – antimatter asymmetry.

As stated before, CPT invariance is still assumed to be absolute. Returning to the example of the clock, a P reflection means switching left to right, a C transformation means changing the matter of the clock to antimatter, and the time reversal T that one plays the video recording of the movement of the clock backward.

10.8.2 State Mixing

As opposed to the other two interactions, the weak interaction does not respect the kind of the quark (called *flavor*) either: heavy quarks can decay into lighter ones via emitting a W^+ or

W^- boson. This is interpreted as a signature that the weak interaction *mixes* the quark states. It is sufficient to assume that either the upper or the lower quark states are mixed. The lower quark states are taken to be mixed, and that is indicated by the apostrophes in [Table 10.1](#) on the symbols of the lower quarks. There is experimental evidence, neutrino oscillations, for the neutrinos also having a tiny little mass (Fukuda and et al. 1998); then of course the lepton states will be mixed as well for the weak interaction (Maki et al. 1962).

This mixing is described by *mixing angles*. If the three lower quark states correspond to the three axes of a rectangular coordinate system, then one needs three angles to describe any possible quark mixing. From those three angles one can get the **Cabibbo–Kobayashi–Maskawa (CKM) mixing matrix**, which transforms a (d,s,b) vector into (d',s',b') . The CP violation can be quantitatively described by simply bringing a complex phase as a fourth parameter into this matrix (Cabibbo 1963; Kobayashi and Maskawa 1973, Nobel Prize in 2008).

Another famous mixing is the **weak mixing** that emerged when the electromagnetic and weak interactions were united by Glashow, Weinberg, and Salam (Nobel Prize 1979) under the name of **electroweak interaction** (Glashow and Weinberg 1968; Weinberg 1967; Salam 1968). Generally, if two states can be mixed in the microworld (i.e., mixing is not prohibited by conservation laws or different quantum numbers), then they surely will; that means that the states observed in the experiment will be mixtures of the primary ones. This is what happens between the neutral currents of the weak and electromagnetic interaction (the concept of current is used here as defined in [Sect. 3](#)). This mixing, which yields the photon and the Z boson is described by an angle, the *Weinberg* or *weak mixing* angle, Θ_w . The Weinberg angle (Weinberg 1972) provides information about the relative strengths of weak and electromagnetic interactions and so it can be considered to be the *coupling constant* associated with the weak interaction, similarly to the *fine structure constant*, α , of the electromagnetic interaction.

All these mixing angles are free parameters of the Standard Model and so, together with the fermion masses, have to be determined using the experimental data.

10.9 The Present and Future of the Standard Model

The Standard Model assumes the existence of three fermion families and three local gauge symmetries, which create the three particle interactions and the $3 + 1 + 8$ **gauge bosons** mediating them. In order to create the masses and to eliminate the divergences of the theory one also needs the Higgs mechanism that produces the **Higgs boson** as well.

The Standard Model has 19 parameters. Each of the three interactions has a strength or coupling constant: the strong coupling, the fine structure constant, and the Weinberg angle. Free parameters are the nine fermion masses (those of the neutrinos can be generally neglected in the calculations), plus the mass of the Higgs boson and the four elements of the CKM matrix. Two more parameters are added by the Higgs potential (Halzen and Martin 1984) and by the theory of strong interaction, **quantum chromodynamics** (Greiner et al. 2002). If one wants to include the neutrino masses one needs three more masses and three or four additional mixing matrix elements (Maki et al. 1962).

All experimental evidence seems to support the validity of the Standard Model. Right at its birth it predicted the masses of the weak bosons and their other properties that were nicely verified experimentally by Arnison et al. (1983, UA1 Collaboration) (C. Rubbia, Nobel Prize 1984). Since its conception, experiment has reproduced every prediction of the Standard

Model quantitatively, and there is not a single observation that would contradict it. Some of the recent experimental data are compared with the predictions of the Standard Model in [Table 10.3](#), and the agreement is generally very good. Note the high precision of both the measurements and the predictions, the latter being usually even more precise. From time to time, as both experiment and theory developed, significant deviations occurred and later proved to be errors in theory or experiment. As the table shows, at present there are two such deviations: the forward–backward asymmetry observed in fermion pair production at electron–positron scattering and the anomalous magnetic moment of the muon represent some small disagreement between theory and experiment. Although these differences are in the range of 2–3 standard deviations only, they cause significant activities in both theory and experiment.

■ **Table 10.3**

Comparison of quantities observable in electron–positron collisions of energies near the Z mass with the predictions of the Standard Model of elementary particles (Amsler et al. 2008). Note the high precision of the calculations and the good agreement between theory and experiment. At present the largest deviation is in the electron–positron forward–backward asymmetry and the anomalous magnetic moment of the muon. If a measured quantity has two uncertainties, the first one is the statistical and the second the systematic error

Group	Quantity	Experiment	Prediction
Top quark	Mass [GeV]	$170.9 \pm 1.8 \pm 0.6$	171.1 ± 1.9
W boson	Mass [GeV]	$80.428 \pm 0.039(\text{pp})$	80.375 ± 0.015
		$80.376 \pm 0.033(e^-e^+)$	
Z boson	Mass [GeV]	91.1876 ± 0.0021	91.1874 ± 0.0021
Z decay	σ_{hadrons}	41.541 ± 0.037	41.466 ± 0.009
	Width Γ_{total} [GeV]	2.4952 ± 0.023	2.4968 ± 0.0010
	Γ_{hadrons} [GeV]	1.7444 ± 0.020	1.7434 ± 0.0010
	Γ_{leptons} [MeV]	83.984 ± 0.086	83.988 ± 0.016
	$\Gamma_{\text{neutrinos}}$ [MeV]	499.0 ± 1.5	501.59 ± 0.08
Z-width ratios	Hadrons/ e^-e^+	20.804 ± 0.050	20.758 ± 0.011
	Hadrons/ $\mu^-\mu^+$	20.785 ± 0.033	20.758 ± 0.011
	Hadrons/ $\tau^-\tau^+$	20.764 ± 0.045	20.803 ± 0.011
	$b\bar{b}/\text{hadrons}$	0.21629 ± 0.00066	0.21584 ± 0.00006
	$c\bar{c}/\text{hadrons}$	0.1721 ± 0.0030	0.17228 ± 0.00004
Forward–backward asymmetry A_{FB}	$e^-e^+ \rightarrow e^-e^+$	0.0145 ± 0.0025	0.01627 ± 0.0023
	$e^-e^+ \rightarrow \mu^-\mu^+$	0.0169 ± 0.0013	0.01627 ± 0.0023
	$e^-e^+ \rightarrow \tau^-\tau^+$	0.0188 ± 0.0017	0.01627 ± 0.0023
	$e^-e^+ \rightarrow b\bar{b}$	0.0992 ± 0.0016	0.1033 ± 0.0007
	$e^-e^+ \rightarrow c\bar{c}$	0.0707 ± 0.0035	0.0738 ± 0.0006
	$e^-e^+ \rightarrow s\bar{s}$	0.0976 ± 0.0114	0.1034 ± 0.0007
Weak mixing	$\sin^2\theta_w(A_{\text{FB}}^{\text{had}})$	0.2324 ± 0.0012	0.23149 ± 0.0013
Muon g-factor	$\frac{1}{2}(g_\mu - 2 - \frac{\alpha}{\pi}) \times 10^9$	4511.07 ± 0.74	4509.08 ± 0.10

Thus, every constituent of the Standard Model has been observed and studied experimentally except the Higgs boson, and Nature seems to faithfully follow its predictions. Even the observation of the (very small) mass of the neutrinos (Fukuda et al. 1998) is easily accommodated in the framework of the Standard Model.

One may ask why there is a need for those expensive accelerators and particle physicists at all if one has finally arrived at this theory describing everything correctly. The answer is contained in the name of what this chapter is about: it is just a model, not a comprehensive theory, and it is not really understood why it functions so well.

One took three different gauge theories, supplied them with some free parameters, added an *ad hoc* Higgs mechanism to make it work, and the result seems to function properly. It is not known exactly why those three symmetries create the three interactions although the $U(1)$ symmetry is clearly related to the electromagnetic charge, the $SU(2)$ to the weak isospin, and $SU(3)$ to the three colors. It is not clear why there are exactly three fermion families and how the fermions of a family are related to each other (apart from the sum of their charges). It is not known why there is no antimatter in the Universe, and there is the deep mystery of **dark matter**: astronomical observations indicate that about 90% of the mass of the Universe is invisible, probably non-baryonic matter that cannot be explained within the framework of the Standard Model (Amsler et al. 2008).

Furthermore, there are indications that there may be a unified, deeper theory behind the Standard Model. The coupling constants of the three interactions have different energy dependencies, but the three converge to the same value at very high energies, as if they were different facets of the same interaction. There are also several theoretical inconsistencies and peculiarities of the Standard Model, which are too involved to discuss here (Collins et al. 1989).

In order to resolve the problems a great number of extensions of the Standard Model have been proposed in the last three decades and much further experimental and theoretical work is needed to see whether any one of them is viable. Most of those models have been disproved with growing experimental information, but one class of them, the **supersymmetric models** (Nilles 1984), persists, although so far no direct evidence is available either for or against it. Such models postulate a symmetry between fermions and bosons assuming that each particle has a *supersymmetric partner* of the other kind. Thus, in this model the quarks and leptons of half spin ($S = 1/2$) have $S = 0$ boson partners called **sleptons** (selectron, smuon, stau, and sneutrinos) and **squarks** (“s” stands for scalar), whereas the $S = 1$ gauge bosons (photon, W^\pm , Z^0 , and the 8 gluons) have $S = 1/2$ fermion partners (*photino*, *wino*, *zino*, *gluinos*), even the Higgs boson has a partner, the *higgsino*. The simplest model of this family, the **Minimal Supersymmetric Standard Model**, solves all theoretical problems of the Standard Model in a very elegant way but at a high price. In addition to the many new particles it has many new free parameters as well, so many indeed that the total set of all available experimental data is not sufficient to determine them. One has to make rather rough approximations in order to reduce their number. The lightest, neutral supersymmetric particle could make the missing part of the dark matter as it interacts with ordinary particles very weakly, and thus it can be “seen” through its gravitational effects only. Although much effort has been made to observe these new particles, none of them has been successful. These experiments are nevertheless useful to help to confine the parameter space of the models. For further references see, e.g., the proceedings of the latest conference on supersymmetry (SUSY 2009).

The greatest question is of course the Higgs boson: whether it exists and its properties agree with the predictions of the Standard Model. It is expected that the Large Hadron Collider

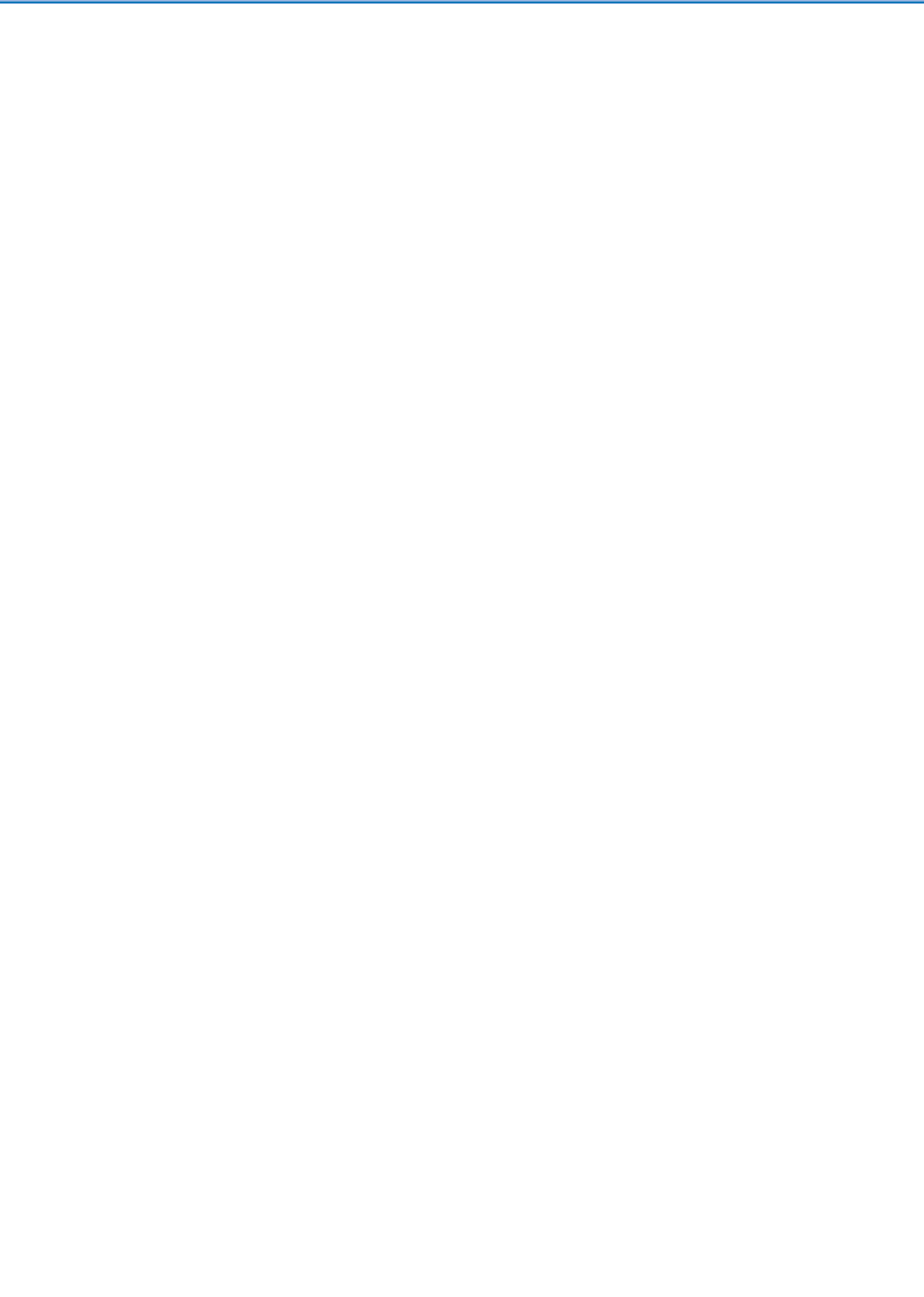
(LHC 2009), the 14 TeV proton–proton collider accelerator of CERN that started to work in late 2009, will answer these questions.

Acknowledgments

This work was supported by the Hungarian National Science Foundation under contracts NK67974, NK81447 and K72172.

References

- Amsler C et al (2008) Phys Lett B 667:1 (For updates see the home page of the Particle Data Group <http://pdg.lbl.gov>)
- Arnison G et al (UA1 Collaboration) (1983) Phys Lett B 122:103
- Aubert JJ et al (1974) Phys Rev Lett 33:1404
- Augustin JE et al (1974) Phys Rev Lett 33:1406
- Cabibbo N (1963) Phys Rev Lett 10:531
- CERN (2009) <http://psdoc.web.cern.ch/PSdoc/acc/ad/index.html>
- Christenson JH et al (1964) Phys Rev Lett 13:138
- Cohen AG, De Rujula A, Glashow SL (1998) Astrophys J 495:539
- Collins PD, Martin AD, Squires EJ (1989) Particle physics and cosmology. Wiley, New York, p 496
- Dirac PAM (1928) Proc Roy Soc 133:60
- Fukuda Y et al (Super-Kamiokande Collaboration) (1998) Phys Rev Lett 81:1562
- Gell-Mann M (1964) Phys Lett 8:214
- Glashow SL, Iliopoulos J, Maiani L (1970) Phys Rev D 2:1285
- Glashow SL, Weinberg S (1968) Phys Rev Lett 20:224–227
- Greiner W, Schramm S, Stein E (2002) Quantum chromodynamics. Springer, Berlin, p 551
- Halzen F, Martin AD (1984) Quarks and leptons: an introductory course in modern particle physics. Wiley, New York
- Higgs PW (1964a) Phys Lett 12:132
- Higgs PW (1964b) Phys Rev Lett 13:508
- Kobayashi M, Maskawa T (1973) Prog Theor Phys 49:652
- Kostelecký VA (ed) (2002) CPT and lorentz symmetry. In: Proceedings of the 2nd Meeting on CPT and lorentz symmetry, 15–18 Aug. 2001, Bloomington, Indiana, (Singapore: World Scientific) p 355
- LEP Electroweak Working Group, ALEPH, DELPHI, L3, and OPAL Collaborations (2009) <http://lepewwg.web.cern.ch/LEPEWWG/>
- LEP Working Group for Higgs Boson Searches, ALEPH, DELPHI, L3, and OPAL Collaborations (2003) Search for the Standard Model Higgs Boson at LEP, preprint CERN-EP-2003-011. Phys Lett B 565:61
- LHC (Large Hadron Collider) (2009) <http://lhc.web.cern.ch/lhc/>
- Maki Z, Nakagawa M, Sakata S (1962) Prog Theor Phys 28:870
- Nilles HP (1984) Phys Rep 110:1
- OPAL (2003) <http://opal.web.cern.ch/Opal/welcome.html>
- Pauli W (1926) Quantum theory. Handbuch der Physik 23:1
- Perl ML et al (1975) Phys Rev Lett 35:1489
- Perkins DH (2000) Introduction to high energy physics. Cambridge University Press, Cambridge
- Salam A (1968) Elementary particle theory. In: Svartholm N (ed) Almquist and Wiksells, Stockholm, p 367
- SUSY (2009) <http://nuweb.neu.edu/susy09/>
- Weinberg S (1967) Phys Rev Lett 19:1264
- Weinberg S (1972) Phys Rev D 5:1962
- Wigner EP (1939) Annals Math 40:149
- Wu CS et al (1957) Phys Rev 105:1413
- Zweig G (1964) Report CERN-TH-412



11 Appendixes – Reference Data to Part I

G. L. Molnár^{1,†} · R. B. Firestone²

¹Chemical Research Center, Budapest, Hungary

²Lawrence Berkeley National Laboratory, Berkeley, California, USA

11.1	<i>The International System of Units (SI)</i>	476
11.1.1	The SI Units of Measurement	476
11.1.1.1	Units Outside the SI	477
11.1.2	Decimal Multiples and Submultiples of SI Units	478
11.2	<i>Fundamental Physical Constants</i>	481
11.2.1	Frequently Used Constants	481
11.2.2	Conversion Factors	485
11.3	<i>Elements and Isotopes</i>	487
11.3.1	Chemical Elements and Their Properties	487
11.3.2	Atomic Weights and Isotopic Compositions	487
11.4	<i>Atomic Data</i>	504
11.4.1	Atomic-Electron Binding Energies	504
11.4.2	X-Ray Energies and Intensities	510
11.4.3	Internal Conversion Coefficients	515
11.5	<i>Absorption of Radiation in Matter</i>	520
11.5.1	X- and γ -ray Attenuation Coefficients	520
11.5.2	Stopping Power and Range of Charged Particles	520
11.6	<i>Nuclear Masses and Separation Energies</i>	540

[†]Deceased

11.1 The International System of Units (SI)

G. L. Molnár · R. B. Firestone

The modern metric system of measurement has become the standard in scientific practice. The official name is *International System of Units*, abbreviated *SI* from the French *Le Système International d'Unités*. The SI was established in 1960 by the 11th General Conference on Weights and Measures. The defining document, commonly called the SI Brochure, has been published by the International Bureau of Weights and Measures (BIPM) in French original and in English translation (BIPM 1991). It has been complemented with a series of international consensus standards to promote international uniformity in the practical use of the SI in science and technology (ISO 1993). Several national standards organizations have prepared practical guides to promote the implementation and practical use of the SI in their country. This chapter is mainly based on the guide prepared by the National Institute of Standards and Technology (NIST), USA (Taylor 1995), which is also available electronically on the NIST Web site on constants, units, and uncertainty (NIST 2003).

11.1.1 The SI Units of Measurement

There are two classes of SI units: base units and derived units. The system is founded on seven base units for seven base quantities, which are assumed to be mutually independent. They are given in ▶ Table 11.1. The definition of the *SI base units* can be found in the aforementioned documents. All other SI units can be expressed in terms of the base units via a system of quantity equations; hence, they are named derived units. Examples of SI derived units are listed in ▶ Table 11.2, using standard notations.

Several *SI derived units* have special names and symbols. They are listed in ▶ Table 11.3 with their definitions in terms of other SI units. Examples of SI derived units without special names can be found in ▶ Table 11.4.

■ Table 11.1

The base units of SI

Base quantity	Standard notation	Name	Symbol
Length	l	meter	m
Mass	m	kilogram	kg
Time	t	second	s
Electric current	I	ampere	A
Thermodynamic temperature	T	kelvin	K
Amount of substance	n	mole	mol
Luminous intensity		candela	cd

■ **Table 11.2**

Examples of SI derived units

Derived quantity	Definition	Name	Symbol
Area	$A = l^2$	Square meter	m^2
Volume	$V = l^3$	Cubic meter	m^3
Molar volume	$V_m = V/n$	Cubic meter per mole	m^3/mol
Specific volume	$v = V/m$	Cubic meter per kilogram	m^3/kg
Volume fraction ^a	$\varphi_B = x_B \cdot V_{m,B} / \sum (x_A \cdot V_{m,A})$	Cubic meter per cubic meter	$m^3/m^3 = 1$
Speed, velocity	$v = l/t$	Meter per second	m/s
Acceleration	$a = l/t^2$	Meter per second squared	m/s^2
Wave number	$k = 1/\lambda$	Reciprocal meter	m^{-1}
Mass density (density)	$\rho = m/V$	Kilogram per cubic meter	kg/m^3
Molar mass	$M = m/n$	Kilogram per mole	kg/mol
Mass fraction ^a	$w_B = m_B/m$	Kilogram per kilogram	$\text{kg}/\text{kg} = 1$
Amount-of-substance Concentration ^a	$c_B = n_B/V$	Mole per cubic meter	mol/m^3
Amount-of-substance fraction ^a (mole fraction)	$x_B = n_B/n$	Mole per mole	$\text{mol}/\text{mol} = 1$
Molality ^b	$b_B = n_B/m_A$	Mole per kilogram	mol/kg
Current density		Ampere per square meter	A/m^2
Magnetic field strength		Ampere per meter	A/m
Luminance		Candela per square meter	cd/m^2

^aOf substance B, for a mixture of substances A, B, C, . . .

^bOf solute B in a solution, divided by the mass of solvent A.

11.1.1.1 Units Outside the SI

There are several traditional units, which are so important for everyday life or for a certain field that they have been accepted for use with the SI. The *accepted units* are listed in ▶ [Table 11.5](#), together with their value in SI units. It is noteworthy that two of them – the *unified atomic mass unit* and the *electronvolt energy unit* – do not have an exact equivalent in SI units. Their values are fundamental constants, which are obtained experimentally (Mohr 1999, 2000). There are some other traditional units, which have been accepted only temporarily, as shown in ▶ [Table 11.6](#).

In basic science, the values of quantities are expressed in terms of *fundamental constants* of nature or so-called “natural units.” In theoretical atomic physics and chemistry, the customarily called “atomic units” have been widely used. Both classes are permissible when their use is absolutely necessary. Examples of physical quantities used as natural and atomic units are given in ▶ [Tables 11.7](#) and ▶ [11.8](#), respectively (Mohr 1999, 2000). More about fundamental constants can be found in ▶ [Section 11.2](#).

Table 11.3
SI derived units with special names and symbols

Derived quantity	Name	Symbol	Expression in terms of other SI units	Expression in terms of SI base units
Plane angle	Radian	rad		$\text{m}\cdot\text{m}^{-1} = 1$
Solid angle	Steradian	sr		$\text{m}^2\cdot\text{m}^{-2} = 1$
Frequency	Hertz	Hz		s^{-1}
Force	Newton	N		$\text{m}\cdot\text{kg}\cdot\text{s}^{-2}$
Pressure, stress	Pascal	Pa	N/m^2	$\text{m}^{-1}\cdot\text{kg}\cdot\text{s}^{-2}$
Energy, work, quantity of heat	Joule	J	$\text{N}\cdot\text{m}$	$\text{m}^2\cdot\text{kg}\cdot\text{s}^{-2}$
Power, radiant flux	Watt	W	J/s	$\text{m}^2\cdot\text{kg}\cdot\text{s}^{-3}$
Electric charge	Coulomb	C		$\text{s}\cdot\text{A}$
Electric potential	Volt	V	W/A	$\text{m}^2\cdot\text{kg}\cdot\text{s}^{-3}\cdot\text{A}^{-1}$
Capacitance	Farad	F	C/V	$\text{m}^{-2}\cdot\text{kg}^{-1}\cdot\text{s}^4\cdot\text{A}^2$
Electric resistance	Ohm	Ω	V/A	$\text{m}^2\cdot\text{kg}\cdot\text{s}^{-3}\cdot\text{A}^{-2}$
Electric conductance	Siemens	S	A/V	$\text{m}^{-2}\cdot\text{kg}^{-1}\cdot\text{s}^3\cdot\text{A}^2$
Magnetic flux	Weber	Wb	$\text{V}\cdot\text{s}$	$\text{m}^2\cdot\text{kg}\cdot\text{s}^{-2}\cdot\text{A}^{-1}$
Magnetic flux density	Tesla	T	Wb/m^2	$\text{kg}\cdot\text{s}^{-2}\cdot\text{A}^{-1}$
Inductance	Henry	H	Wb/A	$\text{m}^2\cdot\text{kg}\cdot\text{s}^{-2}\cdot\text{A}^{-2}$
Celsius temperature	Degree Celsius	$^{\circ}\text{C}$		K
Luminous flux	Lumen	lm	$\text{cd}\cdot\text{sr}$	$\text{cd}\cdot\text{m}^2\cdot\text{m}^{-2}$
Illuminance	Lux	lx	lm/m^2	$\text{cd}\cdot\text{m}^2\cdot\text{m}^{-4}$
Activity (of a radionuclide)	Becquerel	Bq		s^{-1}
Absorbed dose ^a	Gray	Gy	J/kg	$\text{m}^2\cdot\text{s}^{-2}$
Dose equivalent ^b	Sievert	Sv	J/kg	$\text{m}^2\cdot\text{s}^{-2}$

^aAlso specific energy (imparted), kerma.
^bAlso ambient dose equivalent, directional dose equivalent, personal dose equivalent, organ dose equivalent.

11.1.2 Decimal Multiples and Submultiples of SI Units

It is often necessary to form decimal multiples and submultiples of the SI unit, in order to avoid very large or very small numbers, respectively. These multiples, called *SI prefixes*, are summarized in Table 11.9, where the standard notations are also given. A prefix attaches directly to the name of the unit, and a prefix symbol attaches directly to the symbol for a unit. For example, one kilometer (symbol: 1 km) is equal to one thousand meters, symbol: 1,000 m or 10³ m.

■ Table 11.4

Some SI derived units expressed with units having special names and symbols

Derived quantity	Name	Symbol	Expression in terms of SI base units
Heat capacity, entropy	Joule per kelvin	J/K	$\text{m}^2 \cdot \text{kg} \cdot \text{s}^{-2} \cdot \text{K}^{-1}$
Specific heat capacity, specific entropy	Joule per kilogram per kelvin	J/(kg·K)	$\text{m}^2 \cdot \text{s}^{-2} \cdot \text{K}^{-1}$
Specific energy	Joule per kilogram	J/kg	$\text{m}^{-1} \cdot \text{s}^{-2}$
Energy density	Joule per cubic meter	J/m ³	$\text{m}^{-1} \cdot \text{kg} \cdot \text{s}^{-2}$
Molar energy	Joule per mole	J/mol	$\text{m}^2 \cdot \text{kg} \cdot \text{s}^{-2} \cdot \text{mol}^{-1}$
Molar entropy, molar heat capacity	Joule per mole kelvin	J/(mol·K)	$\text{m}^2 \cdot \text{kg} \cdot \text{s}^{-2} \cdot \text{mol}^{-1} \text{K}^{-1}$
Exposure (X and γ rays)	Coulomb per kilogram	C/kg	$\text{kg}^{-1} \cdot \text{s} \cdot \text{A}$
Absorbed dose rate	Gray per second	Gy/s	$\text{m}^2 \cdot \text{s}^{-3}$

■ Table 11.5

Units accepted for use with the SI

	Name	Symbol	Value in SI units
Time	Minute	min	1 min = 60 s
	Hour	h	1 h = 60 min = 3,600 s
	Day	d	1 d = 24 h = 86,400 s
Plane angle	Degree	°	1° = ($\pi/180$) rad
	Minute	'	1' = (1/60)° = ($\pi/10,800$) rad
	Second	"	1" = (1/60)' = ($\pi/648,000$) rad
Volume	Liter	l, L	1 L = 1 dm ³ = 10 ⁻³ m ³
Mass	Metric ton	t	1 t = 10 ³ kg
	Unified atomic mass unit ^a	u	1 u = 1.66053873(13) × 10 ⁻²⁷ kg
Energy	Electronvolt ^b	eV	1.602176462(63) × 10 ⁻¹⁹ J

^aThe unified atomic mass unit is equal to 1/12 of the mass of an atom of the nuclide ¹²C.^bThe electronvolt is the kinetic energy acquired by an electron in passing through a potential difference of 1 V in vacuum.

Table 11.6

Some units temporarily accepted for use with the SI

Quantity	Name	Symbol	Value in SI units
Length	Ångström	Å	1 Å = 0.1 nm = 10 ⁻¹⁰ m
Cross section	Barn	b	1 b = 100 fm ² = 10 ⁻²⁸ m ²
Pressure	Bar	bar	1 bar = 0.1 Mpa = 100 kPa = 1,000 hPa = 10 ⁵ Pa
Activity	Curie	Ci	1 Ci = 3.7 × 10 ¹⁰ Bq
Absorbed dose	Roentgen	R	1 R = 2.58 × 10 ⁻⁴ C/kg
	Rad	rad ^a	1 rad = 1 cGy = 10 ⁻² Gy
Dose equivalent	Rem	rem	1 rem = 1 cSv = 10 ⁻² Sv

^aWhen there is risk of confusion with the symbol for the radian, rd may be used as the symbol for rad.

Table 11.7

Natural units accepted for use with the SI

Quantity	Symbol	Value	Unit	Relative std. uncert.
Velocity: Speed of light in vacuum	c, c_0	299,792,458	m·s ⁻¹	(exact)
Action: reduced Planck constant ($\hbar/2\pi$)	\hbar	1.054571596 (82) × 10 ⁻³⁴	J·s	7.8 × 10 ⁻⁸
		6.58211889 (26) × 10 ⁻¹⁶	eV·s	3.9 × 10 ⁻⁸
Mass: electron mass	m_e	9.10938188 (72) × 10 ⁻³¹	kg	7.9 × 10 ⁻⁸
Energy:	$m_e c^2$	8.18710414 (64) × 10 ⁻¹⁴	J	7.9 × 10 ⁻⁸
		0.510998902 (21)	MeV	4.0 × 10 ⁻⁸
Momentum:	$m_e c$	2.73092398 (21) × 10 ⁻²²	kg·m·s ⁻¹	7.9 × 10 ⁻⁸
		0.510998902 (21)	MeV/c	4.0 × 10 ⁻⁸
Length: ($\hbar/2\pi m_e c$)	λ_c	386.1592642 (28) × 10 ⁻¹⁵	m	7.3 × 10 ⁻⁹
Time:	$\hbar/m_e c^2$	1.2880886555 (95) × 10 ⁻²¹	s	7.3 × 10 ⁻⁹

Table 11.8

Examples of atomic units accepted for use with the SI

Quantity	Symbol	Value	Unit	Relative std. uncert.
Charge: elementary charge	e	1.602176462 (63) × 10 ⁻¹⁹	C	3.9 × 10 ⁻⁸
Mass: electron mass	m_e	9.10938188 (72) × 10 ⁻³¹	kg	7.9 × 10 ⁻⁸
Action: reduced Planck constant($\hbar/2\pi$)	\hbar	1.054571596 (82) × 10 ⁻³⁴	J·s	7.8 × 10 ⁻⁸
Length: Bohr radius (bohr) ($\alpha/4\pi R_\infty$)	a_0	0.5291772083 (19) × 10 ⁻¹⁰	m	3.7 × 10 ⁻⁹
Energy: Hartree energy (hartree) ($2R_\infty hc = \alpha^2 m_e c^2$)	E_h	4.35974381 (34) × 10 ⁻¹⁸	J	7.8 × 10 ⁻⁸

■ Table 11.9

SI prefixes and their symbols

Factor	Prefix	Symbol	Factor	Prefix	Symbol
10^{24}	Yotta	Y	10^{-1}	Deci	d
10^{21}	Zetta	Z	10^{-2}	Centi	c
10^{18}	Exa	E	10^{-3}	Milli	m
10^{15}	Peta	P	10^{-6}	Micro	μ
10^{12}	Tera	T	10^{-9}	Nano	n
10^9	Giga	G	10^{-12}	Pico	p
10^6	Mega	M	10^{-15}	Femto	f
10^3	Kilo	k	10^{-18}	Atto	a
10^2	Hecto	h	10^{-21}	Zepto	z
10^1	Deka	da	10^{-24}	Yocto	y

11.2 Fundamental Physical Constants

G. L. Molnár

Basic physical theories and their application to other fields of science and technology always involve certain fundamental invariant quantities, called briefly *fundamental constants*. Well-known examples of such constants are the speed of light in vacuum, the elementary charge (electron charge), the mass of the electron, and so on. It is important to know the numerical values of the fundamental constants with the highest possible accuracy, because the attained accuracy determines the accuracy of the quantitative predictions of fundamental theories. Moreover, the accurate numerical values of the fundamental constants test the overall consistency and correctness of those theories.

The Committee on Data for Science and Technology (CODATA) was established in 1966 as an interdisciplinary committee of the International Council of Science and Technology (ICSU). The CODATA Task Group on Fundamental Constants was established in 1969, with the aim to provide internationally accepted values of the fundamental physical and chemical constants and related conversion factors. The first such CODATA set was established in 1973, while the latest one in 1998 (Mohr and Taylor 1999, 2000). The latest recommended values of the fundamental constants are also available on an Internet page (CODATA 2003), on which the following presentation is based. Those interested in all recommended values or in the earlier versions of the CODATA set are referred to that Internet page.

11.2.1 Frequently Used Constants

In this section, an arbitrarily selected subset of constants is presented in tabular form. The first category is the most fundamental quantities, listed in [Table 11.10](#) together with their relative

■ **Table 11.10**

Selected fundamental constants

Quantity	Symbol	Value	Unit	Relative std. uncert.
<i>Universal constants</i>				
Speed of light in vacuum	c, c_0	299,792,458	$\text{m}\cdot\text{s}^{-1}$	Exact
Magnetic constant	μ_0	$4\pi \times 10^{-7} = 12.566370614\dots \times 10^{-7}$	$\text{N}\cdot\text{A}^{-2}$	Exact
Electric constant $1/\mu_0 c^2$	ϵ_0	$8.854187817\dots \times 10^{-12}$	$\text{F}\cdot\text{m}^{-1}$	Exact
Characteristic impedance of vacuum $\sqrt{\mu_0/\epsilon_0} = \mu_0 c$	Z_0	376.730313461...	Ω	Exact
Newtonian constant of gravitation	G	$6.673(10) \times 10^{-11}$	$\text{m}^3\cdot\text{kg}^{-1}\cdot\text{s}^{-2}$	1.5×10^{-3}
Planck constant	h	$6.62606876(52) \times 10^{-34}$	$\text{J}\cdot\text{s}$	7.8×10^{-8}
		$4.13566727(16) \times 10^{-15}$	$\text{eV}\cdot\text{s}$	3.9×10^{-8}
Reduced Planck constant $\hbar/2\pi$	\hbar	$1.054571596(82) \times 10^{-34}$	$\text{J}\cdot\text{s}$	7.8×10^{-8}
		$6.58211889(26) \times 10^{-16}$	$\text{eV}\cdot\text{s}$	3.9×10^{-8}
<i>Adopted constants</i>				
Molar mass of ^{12}C	$M(^{12}\text{C})$	12×10^{-3}	$\text{kg}\cdot\text{mol}^{-1}$	Exact
Molar mass constant $M(^{12}\text{C})/12$	M_{u}	1×10^{-3}	$\text{kg}\cdot\text{mol}^{-1}$	Exact
Conventional value of Josephson constant ^a	$K_{\text{J-90}}$	483,597.9	GHz V^{-1}	Exact
Conventional value of von Klitzing constant ^b	$R_{\text{K-90}}$	25,812.807	Ω	Exact
Standard atmosphere		101,325	Pa	Exact
Standard acceleration of gravity	g_{n}	9.80665	$\text{m}\cdot\text{s}^{-2}$	Exact

^aValue of $2e/h$ adopted internationally for realizing representations of the volt using the Josephson effect.

^bAdopted internationally for realizing representations of the ohm using the quantum Hall effect.

standard uncertainty. Some of the *universal constants*, such as the speed of light in vacuum, form the basis of the SI system of measurement, hence their established value is considered exact. There are other constants, such as the basis of the atomic mass unit, which are not fundamental in nature but play an important practical role. Therefore, their value has also been adopted as exact.

The rest of the constants presented are grouped according to the scientific field where they belong. Physicochemical constants are given in ▶ [Table 11.11](#), followed by atomic and nuclear constants in ▶ [Tables 11.12](#) and ▶ [11.13](#), respectively.

Table 11.11

Selected physicochemical constants

Quantity	Symbol	Value	Unit	Relative std. uncert.
Avogadro constant	N_A, L	$6.02214199(47) \times 10^{23}$	mol^{-1}	7.9×10^{-8}
Atomic mass constant $m(^{12}\text{C})/12 = 1 \text{ u} = 10^{-3} \text{ kg} \cdot \text{mol}^{-1}/N_A$	m_u	$1.66053873(13) \times 10^{-27}$	kg	7.9×10^{-8}
Energy equivalent	$m_u c^2$	$1.49241778(12) \times 10^E$	J	7.9×10^{-8}
		931.494013(37)	MeV	4.0×10^{-8}
Faraday constant $N_A e$	F	96.4853415(39)	$\text{C} \cdot \text{mol}^{-1}$	4.0×10^{-8}
Molar Planck constant	$N_A h c$	$3.990312689(30) \times 10^{-10}$	$\text{J} \cdot \text{s} \cdot \text{mol}^{-1}$	7.6×10^{-9}
Molar gas constant	R	8.314472(15)	$\text{J} \cdot \text{mol}^{-1} \cdot \text{K}^{-1}$	1.7×10^{-6}
Boltzmann constant R/\cdot	k	$1.3806503(24) \times 10^{-23}$	$\text{J} \cdot \text{K}^{-1}$	1.7×10^{-6}
		$8.617342(15) \times 10^{-5}$	$\text{eV} \cdot \text{K}^{-1}$	1.7×10^{-6}
Stefan-Boltzmann constant $(\pi^2/60)k^4/\hbar^3 c^2$	σ	$5.670400(40) \times 10^{-8}$	$\text{W} \cdot \text{m}^{-2} \cdot \text{K}^{-4}$	7.0×10^{-6}

Table 11.12

Selected atomic constants

Quantity	Symbol	Value	Unit	Relative std. uncert.
<i>General</i>				
Fine-structure constant $e^2/4\pi\epsilon_0\hbar c$	α	$7297,352,533(27) \times 10^{-3}$		3.7×10^{-9}
Inverse fine-structure constant	α^{-1}	137.03599976(50)		3.7×10^{-9}
Rydberg constant $\alpha^2 m_e c/2h$	R_∞	10,973,731.568549(83)	m^{-1}	7.6×10^{-12}
	$R_\infty \hbar c$	13.60569172(53)	eV	3.9×10^{-8}
Bohr radius $\alpha/4\pi R_\infty$	a_0	$0.5291772083(19) \times 10^{-10}$	m	3.7×10^{-9}
Hartree energy $2R_\infty \hbar c = \alpha^2 m_e c^2$	E_h	$4.35974381(34) \times 10^{-18}$	J	7.8×10^{-8}
<i>Electron (e^-)</i>				
Electron mass	m_e	$9.10938188(72) \times 10^{-31}$	kg	7.9×10^{-8}
Relative mass	$A_r(e)$	$5.485799110(12) \times 10^{-4}$	u	2.1×10^{-9}
Energy equivalent	$m_e c^2$	$8.18710414(64) \times 10^{-14}$	J	7.9×10^{-8}
Electron molar mass $N_A m_e$	M_e	$5.485799110(12) \times 10^{-7}$	kg mol^{-1}	2.1×10^{-9}
		0.510998902(21)	MeV	4.0×10^{-8}

Table 11.12 (Continued)

Quantity	Symbol	Value	Unit	Relative std. uncert.
Electron charge (elementary charge)	e	$1.602176462(63) \times 10^{-19}$	C	3.9×10^{-8}
Electron charge to mass quotient	$-e/m_e$	$-1.758820174(71) \times 10^{11}$	$\text{C}\cdot\text{kg}^{-1}$	4.0×10^{-8}
Bohr magneton $eh/2m_e$	μ_B	$927.400899(37) \times 10^{-26}$	$\text{J}\cdot\text{T}^{-1}$	4.0×10^{-8}
		$5.788381749(43) \times 10^{-5}$	$\text{eV}\cdot\text{T}^{-1}$	7.3×10^{-9}
Electron magnetic moment	μ_e	$-928.476362(37) \times 10^{-26}$	$\text{J}\cdot\text{T}^{-1}$	4.0×10^{-8}
to Bohr magneton ratio	μ_e/μ_B	$-1.0011596521869(41)$		4.1×10^{-12}
Electron g-factor	g_e	$-2.0023193043737(82)$		4.1×10^{-12}
Compton wavelength $h/m_e c$	λ	$2.426310215(18) \times 10^{-12}$	m	7.3×10^{-9}
Reduced Compton wavelength $\lambda/2\pi$	λ_C	$386.1592642(28) \times 10^{-15}$	m	7.3×10^{-9}
Classical electron radius $\alpha^2 a_0$	r_e	$2.817940285(31) \times 10^{-15}$	m	1.1×10^{-8}
Thomson cross section $(8\pi/3)r_e$	σ_e	$0.665245854(15) \times 10^{-28}$	m^2	2.2×10^{-8}

Table 11.13

Selected nuclear constants

Quantity	Symbol	Value	Unit	Relative std. uncert.
<i>Muon (μ^-)</i>				
Muon mass	m_μ	105.6583568(52)	MeV	4.9×10^{-8}
Muon-electron mass ratio	m_μ/m_e	206.7682657(63)		3.0×10^{-8}
Muon-proton mass ratio	m_μ/m_p	0.1126095173(34)		3.0×10^{-8}
<i>Tau (τ^-)</i>				
Tau mass	m_τ	1,777.05(29)	MeV	1.6×10^{-4}
Tau-muon mass ratio	m_τ/m_μ	16.8188(27)		1.6×10^{-4}
Tau-proton mass ratio	m_τ/m_p	1.89396(31)		1.6×10^{-4}
<i>Proton (p)</i>				
Proton mass	m_p	$1.67262158(13) \times 10^{-27}$	kg	7.9×10^{-8}
		1.00727646688(13)	u	1.3×10^{-10}
Energy equivalent of mass	$m_p c^2$	$1.50327731(12) \times 10^{-10}$	J	7.9×10^{-8}
		938.271998(38)	MeV	4.0×10^{-8}
Proton-electron mass ratio	m_p/m_e	1,836.1526675(39)		2.1×10^{-9}
Proton Compton wavelength $h/m_p c$	$\lambda_{C,p}$	$1.321409847(10) \times 10^{-15}$	m	7.6×10^{-9}

■ Table 11.13 (Continued)

Quantity	Symbol	Value	Unit	Relative std. uncert.
Nuclear magneton $eh/2m_p$	μ_N	$5.05078317(20) \times 10^{-27}$	J·T ⁻¹	4.0×10^{-8}
Proton magnetic moment	μ_p	$1.410606633(58) \times 10^{-26}$	J·T ⁻¹	4.1×10^{-8}
To Bohr magneton ratio	μ_p/μ_B	$1.521032203(15) \times 10^{-3}$		1.0×10^{-8}
To nuclear magneton ratio	μ_p/μ_N	2.792847337(29)		1.0×10^{-8}
Proton g-factor $2\mu_p/\mu_N$	g_p	5.585694675(57)		1.0×10^{-8}
Neutron (n)				
Neutron mass	m_n	$1.67492716(13) \times 10^{-27}$	kg	7.9×10^{-8}
		1.00866491578(55)	u	5.4×10^{-10}
Energy equivalent of mass	$m_n c^2$	$1.50534946(12) \times 10^{-10}$	J	7.9×10^{-8}
		939.565330(38)	MeV	4.0×10^{-8}
Neutron–electron mass ratio	m_n/m_e	1,838.6836550(40)		2.2×10^{-9}
Neutron–proton mass ratio	m_n/m_p	1.00137841887(58)		5.8×10^{-10}
Neutron Compton wavelength $h/m_n c$	$\lambda_{C,n}$	$1.319590898(10) \times 10^{-15}$	m	7.6×10^{-9}
Neutron magnetic moment	μ_n	$-0.96623640(23) \times 10^{-26}$	J·T ⁻¹	2.4×10^{-7}
To Bohr magneton ratio	μ_n/μ_B	$-1.04187563(25) \times 10^{-3}$		2.4×10^{-7}
To nuclear magneton ratio	μ_n/μ_N	-1.91304272(45)		2.4×10^{-7}
Neutron g-factor $2\mu_n/\mu_N$	g_n	-3.82608545(90)		2.4×10^{-7}
Deuteron (d)				
Deuteron mass	m_d	1,875.612762(75)	MeV	4.0×10^{-8}
Alpha particle (α)				
Alpha particle mass	m_α	3,727.37904(15)	MeV	4.0×10^{-8}

11.2.2 Conversion Factors

It is often necessary to convert the adopted value of a fundamental constant to another (SI or non-SI) unit. Useful *conversion factors for energy equivalent quantities* can be derived using the following relations:

$$E = mc^2 = hc/\lambda = h\nu = kT$$

$$1 \text{ eV} = (e/CJ)$$

$$1 \text{ u} = m_u = (1/12) m(^{12}\text{C}) = 10^{-3} \text{ kg mol}^{-1} / N_A$$

These equations allow, for example, expressing the energy in temperature units or energy-equivalent mass units. During the conversion, however, the precision inherent in the values of the fundamental constants involved must be kept as much as possible and care should be taken of the correlation of uncertainties. For this reason, the safest procedure is to use the set of

Table 11.14
Energy equivalents

	J	kg	m ⁻¹	Hz	K	eV	u
1 J	(1 J) = 1	$1.112650056 \times 10^{-17}$	$5.03411762(39) \times 10^{-24}$	$(1 \text{ J})/h = 1.50919050(12) \times 10^{-33}$	$(1 \text{ J})/k = 7.242964(13) \times 10^{22}$	$(1 \text{ J}) = 6.24150974(24) \times 10^{18}$	$(1 \text{ J})/c^2 = 6.70053662(53) \times 10^9$
1 kg	$(1 \text{ kg}) c^2 = 8.987551787 \times 10^{16}$	$(1 \text{ kg}) = 1$	$(1 \text{ kg}) c/h = 4.524443929(35) \times 10^{41}$	$(1 \text{ kg}) c^2/h = 1.35639277(11) \times 10^{50}$	$(1 \text{ kg}) c^2/k = 6.509651(11) \times 10^{39}$	$(1 \text{ kg}) c^2 = 5.60958921(22) \times 10^{35}$	$(1 \text{ kg}) = 6.02214199(47) \times 10^{26}$
1 m ⁻¹	$(1 \text{ m}^{-1}) hc = 1.98644544(16) \times 10^{-25}$	$(1 \text{ m}^{-1}) h/c = 2.21021863(17) \times 10^{-42}$	$(1 \text{ m}^{-1}) = 1$	$(1 \text{ m}^{-1}) c = 299792458$	$(1 \text{ m}^{-1}) hc/k = 1.4387752(25) \times 10^{-2}$	$(1 \text{ m}^{-1}) hc = 1.239841857(49) \times 10^{-6}$	$(1 \text{ m}^{-1}) h/c = 1.331025042(10) \times 10^{-15}$
1 Hz	$(1 \text{ Hz}) h = 6.62606876(52) \times 10^{-34}$	$(1 \text{ Hz}) h/c^2 = 7.37249578(58) \times 10^{-51}$	$(1 \text{ Hz})/c = 3.335640952 \times 10^{-9}$	$(1 \text{ Hz}) = 1$	$(1 \text{ Hz}) h/k = 4.7992374(84) \times 10^{-11}$	$(1 \text{ Hz}) h = 4.13566727(16) \times 10^{-15}$	$(1 \text{ Hz}) h/c^2 = 4.439821637(34) \times 10^{-24}$
1 K	$(1 \text{ K}) k = 1.3806503(24) \times 10^{-23}$	$(1 \text{ K}) k/c^2 = 1.5361807(27) \times 10^{-40}$	$(1 \text{ K}) k/h c = 69.50356(12)$	$(1 \text{ K}) k/h = 2.0836644(36) \times 10^{10}$	$(1 \text{ K}) = 1$	$(1 \text{ K}) k = 8.617342(15) \times 10^{-5}$	$(1 \text{ K}) k/c^2 = 9.251098(16) \times 10^{-14}$
1 eV	$(1 \text{ eV}) = 1.602176462(63) \times 10^{-19}$	$(1 \text{ eV})/c^2 = 1.782661731(70) \times 10^{-36}$	$(1 \text{ eV})/hc = 8.065544477(32) \times 10^5$	$(1 \text{ eV})/h = 2.417989491(95) \times 10^{14}$	$(1 \text{ eV})/k = 1.1604506(20) \times 10^4$	$(1 \text{ eV}) = 1$	$(1 \text{ eV})/c^2 = 1.073544206(43) \times 10^{-9}$
1 u	$(1 \text{ u}) c^2 = 1.49241778(12) \times 10^{-10}$	$(1 \text{ u}) = 1.66053873(13) \times 10^{-27}$	$(1 \text{ u}) c/h = 7.513006658(57) \times 10^{14}$	$(1 \text{ u}) c^2/h = 2.252342733(17) \times 10^{23}$	$(1 \text{ u}) c^2/k = 1.0809528(19) \times 10^{13}$	$(1 \text{ u}) c^2 = 931.494013(37)$	$(1 \text{ u}) = 1$

energy equivalent conversion factors, provided in [Table 11.14](#). Those who prefer to perform unit conversions online can do that using the CODATA Internet page (CODATA 2003).

11.3 Elements and Isotopes

G. L. Molnár

11.3.1 Chemical Elements and Their Properties

The chemical elements are uniquely distinguished by their *atomic number*, Z , which is the number of protons in an atom. According to the IUPAC terminology, the atom is the smallest part of an element with no net electric charge, which can enter into chemical combinations. Each neutral atom contains as many electrons as protons in its nucleus. Atoms of the same element with the same atomic number, but different number of neutrons are called *isotopes*. The *isotopic abundance* (isotope abundance or atom abundance) is the relative number of atoms of a particular isotope in a mixture of the isotopes of a chemical element, expressed as a fraction (%) of all the atoms of the element. The isotopic abundances of the elements vary depending on the source of materials. The *natural isotopic abundance* is the isotopic abundance in the element as found on Earth. Because of natural radioactivity, this quantity may not be well defined for some isotopes.

The *mass number*, A , of an isotope of a given element is defined by the sum of the number of protons, Z , and neutrons, N , in its nucleus. Elements have more than one isotope with varying numbers of neutrons. For example, there are two common isotopes of carbon, ^{12}C and ^{13}C , which have six and seven neutrons, respectively. The *atomic mass* is primarily determined by the number of protons and neutrons in the nucleus. The average atomic mass of an element is called *atomic weight*, see [Sect. 3.2](#).

The chemical properties of an element are determined by the *electron configuration*: the distribution of electrons according to the energy sublevels (subshells) in uncharged atoms. The known elements, their basic physical parameters and electron configurations are listed in [Table 11.15](#) after Hanukoglu (2003). The noble gas shown in square brackets (e.g., [He]), marks that all the subshells associated with that element are fully occupied by electrons. More about the properties of elements and compounds formed by them can be found in numerous handbooks (Lide 2003; Dean 1992; Kaye and Laby 1993). A convenient on-line source of chemical and physical properties of the elements is WebElements (Winter 2003).

The elements can be arranged into a periodic table according to their chemical likeliness. The periodic table of elements is shown in [Fig. 11.1](#), in the form recommended by the IUPAC Commission on the Nomenclature of Inorganic Chemistry (Moss 2003). The atomic weights in [Table 11.15](#) and [Fig. 11.1](#) are approximate. See [Sect. 3.2](#) for the precise values and the standard uncertainties. The temporary names for *superheavy elements* are given separately, in [Table 11.16](#). At the end of 2009 the discovery of the element with $Z = 112$ was also accepted by IUPAC.

11.3.2 Atomic Weights and Isotopic Compositions

The *relative atomic mass* is the atomic mass divided by the unified atomic mass unit. This unit is defined as 1/12 of the mass of a ^{12}C neutral atom in its nuclear and electronic ground state,

■ **Table 11.15**

The elements and their basic properties

Z	Atomic weight	Name	Symbol ^a	Melting point (°C)	Boiling point (°C)	Density ^b (g/cm ³)	Group	Electron configuration
89	227	Actinium	Ac [*]	1,050	3,200	10.07	3	[Rn] 6d ¹ 7s ²
13	26.9815	Aluminum	Al	660	2,467	2.7	13	[Ne] 3s ² 3p ¹
95	243	Americium	Am [*]	994	2,607	13.67	9	
51	121.76	Antimony	Sb	630	1,750	6.68	15	[Kr] 4d ¹⁰ 5s ² 5p ³
18	39.948	Argon	Ar	−189	−186	1.78	18	[Ne] 3s ² 3p ⁶
33	74.9216	Arsenic	As	81	613	5.72	15	[Ar] 3d ¹⁰ 4s ² 4p ³
85	210	Astatine	At [*]	302	337		17	[Xe] 4f ¹⁴ 5d ¹⁰ 6s ² 6p ⁵
56	137.327	Barium	Ba	725	1,140	3.59	2	[Xe] 6s ²
97	247	Berkelium	Bk [*]	986		14.78	11	
4	9.0122	Beryllium	Be	1,278	2,970	1.85	2	[He] 2s ²
83	208.9804	Bismuth	Bi	271	1,560	9.75	15	[Xe] 4f ¹⁴ 5d ¹⁰ 6s ² 6p ³
107	264	Bohrium	Bh [*]				7	
5	10.811	Boron	B	2,300	2,550	2.34	13	[He] 2s ² 2p ¹
35	79.904	Bromine	Br	−7	59	3.12	17	[Ar] 3d ¹⁰ 4s ² 4p ⁵
48	112.411	Cadmium	Cd	321	765	8.65	12	[Kr] 4d ¹⁰ 5s ²
20	40.078	Calcium	Ca	839	1,484	1.55	2	[Ar] 4s ²
98	251	Californium	Cf [*]	900		15.1	12	
6	12.0107	Carbon	C	3,500	4,827	2.26	14	[He] 2s ² 2p ²
58	140.116	Cerium	Ce	795	3,257	6.77	4	[Xe] 4f ¹ 5d ¹ 6s ²
55	132.9055	Cesium	Cs	29	678	1.87	1	[Xe] 6s ¹
17	35.453	Chlorine	Cl	−101	−35	3.21	17	[Ne] 3s ² 3p ⁵
24	51.9961	Chromium	Cr	1,857	2,672	7.19	6	[Ar] 3d ⁵ 4s ¹
27	58.9332	Cobalt	Co	1,495	2,870	8.9	9	[Ar] 3d ⁷ 4s ²
29	63.546	Copper	Cu	1,083	2,567	8.96	11	[Ar] 3d ¹⁰ 4s ¹
96	247	Curium	Cm [*]	1,340		13.5	10	
105	262	Dubnium	Db [*]				5	
66	162.5	Dysprosium	Dy	1,412	2,562	8.55	12	[Xe] 4f ¹⁰ 6s ²
99	252	Einsteinium	Es [*]	860			13	
68	167.259	Erbium	Er	1,522	2,510	9.07	14	[Xe] 4f ¹² 6s ²
63	151.964	Europium	Eu	822	1,597	5.24	9	[Xe] 4f ⁷ 6s ²
100	257	Fermium	Fm [*]	1,527			14	
9	18.9984	Fluorine	F	−220	−188	1.7	17	[He] 2s ² 2p ⁵

Table 11.15 (Continued)

Z	Atomic weight	Name	Symbol ^a	Melting point (°C)	Boiling point (°C)	Density ^b (g/cm ³)	Group	Electron configuration
87	223	Francium	Fr [*]	27	677		1	[Rn] 7s ¹
64	157.25	Gadolinium	Gd	1,311	3,233	7.9	10	[Xe] 4f ⁷ 5d ¹ 6s ²
31	69.723	Gallium	Ga	30	2,403	5.91	13	[Ar] 3d ¹⁰ 4s ² 4p ¹
32	72.64	Germanium	Ge	937	2,830	5.32	14	[Ar] 3d ¹⁰ 4s ² 4p ²
79	196.9665	Gold	Au	1,064	2,807	19.32	11	[Xe] 4f ¹⁴ 5d ¹⁰ 6s ¹
72	178.49	Hafnium	Hf	2,150	5,400	13.31	4	[Xe] 4f ¹⁴ 5d ² 6s ²
108	277	Hassium	Hs [*]				8	
2	4.0026	Helium	He	−272	−269	0.18	18	1s ²
67	164.9303	Holmium	Ho	1,470	2,720	8.8	13	[Xe] 4f ¹¹ 6s ²
1	1.0079	Hydrogen	H	−259	−253	0.09	1	1s ¹
49	114.818	Indium	In	157	2,000	7.31	13	[Kr] 4d ¹⁰ 5s ² 5p ¹
53	126.9045	Iodine	I	114	184	4.93	17	[Kr] 4d ¹⁰ 5s ² 5p ⁵
77	192.217	Iridium	Ir	2,410	4,527	22.4	9	[Xe] 4f ¹⁴ 5d ⁷ 6s ²
26	55.845	Iron	Fe	1,535	2,750	7.87	8	[Ar] 3d ⁶ 4s ²
36	83.8	Krypton	Kr	−157	−153	3.75	18	[Ar] 3d ¹⁰ 4s ² 4p ⁶
57	138.9055	Lanthanum	La	920	3,469	6.15	3	[Xe] 5d ¹ 6s ²
103	262	Lawrencium	Lr [*]	1,627			17	
82	207.2	Lead	Pb	327	1,740	11.35	14	[Xe] 4f ¹⁴ 5d ¹⁰ 6s ² 6p ²
3	6.941	Lithium	Li	180	1,347	0.53	1	[He] 2s ¹
71	174.967	Lutetium	Lu	1,656	3,315	9.84	17	[Xe] 4f ¹⁴ 5d ¹ 6s ²
12	24.305	Magnesium	Mg	639	1,090	1.74	2	[Ne] 3s ²
25	54.938	Manganese	Mn	1,245	1,962	7.43	7	[Ar] 3d ⁵ 4s ²
109	268	Meitnerium	Mt [*]				9	
101	258	Mendelevium	Md [*]				15	
80	200.59	Mercury	Hg	−39	357	13.55	12	[Xe] 4f ¹⁴ 5d ¹⁰ 6s ²
42	95.94	Molybdenum	Mo	2,617	4,612	10.22	6	[Kr] 4d ⁵ 5s ¹
60	144.24	Neodymium	Nd	1,010	3,127	7.01	6	[Xe] 4f ⁴ 6s ²
10	20.1797	Neon	Ne	−249	−246	0.9	18	[He] 2s ² 2p ⁶
93	237	Neptunium	Np [*]	640	3,902	20.2	7	

■ Table 11.15 (Continued)

Z	Atomic weight	Name	Symbol ^a	Melting point (°C)	Boiling point (°C)	Density ^b (g/cm ³)	Group	Electron configuration
28	58.6934	Nickel	Ni	1,453	2,732	8.9	10	[Ar] 3d ⁸ 4s ²
41	92.9064	Niobium	Nb	2,468	4,927	8.57	5	[Kr] 4d ⁴ 5s ¹
7	14.0067	Nitrogen	N	–210	–196	1.25	15	[He] 2s ² 2p ³
102	259	Nobelium	No [*]	827			16	
76	190.23	Osmium	Os	3,045	5,027	22.6	8	[Xe] 4f ¹⁴ 5d ⁶ 6s ²
8	15.9994	Oxygen	O	–218	–183	1.43	16	[He] 2s ² 2p ⁴
46	106.42	Palladium	Pd	1,552	2,927	12.02	10	[Kr] 4d ¹⁰
15	30.9738	Phosphorus	P	44	280	1.82	15	[Ne] 3s ² 3p ³
78	195.078	Platinum	Pt	1,772	3,827	21.45	10	[Xe] 4f ¹⁴ 5d ⁹ 6s ¹
94	244	Plutonium	Pu [*]	640	3,235	19.84	8	
84	209	Polonium	Po [*]	254	962	9.3	16	[Xe] 4f ¹⁴ 5d ¹⁰ 6s ² 6p ⁴
19	39.0983	Potassium	K	64	774	0.86	1	[Ar] 4s ¹
59	140.9077	Praseodymium	Pr	935	3,127	6.77	5	[Xe] 4f ³ 6s ²
61	145	Promethium	Pm [*]	1,100	3,000	7.3	7	[Xe] 4f ⁵ 6s ²
91	231.0359	Protactinium	Pa	1,568		15.4	5	[Rn] 5f ² 6d ¹ 7s ²
88	226	Radium	Ra [*]	700	1,737	5.5	2	[Rn] 7s ²
86	222	Radon	Rn [*]	–71	–62	9.73	18	[Xe] 4f ¹⁴ 5d ¹⁰ 6s ² 6p ⁶
75	186.207	Rhenium	Re	3,180	5,627	21.04	7	[Xe] 4f ¹⁴ 5d ⁵ 6s ²
45	102.9055	Rhodium	Rh	1,966	3,727	12.41	9	[Kr] 4d ⁸ 5s ¹
37	85.4678	Rubidium	Rb	39	688	1.63	1	[Kr] 5s ¹
44	101.07	Ruthenium	Ru	2,250	3,900	12.37	8	[Kr] 4d ⁷ 5s ¹
104	261	Rutherfordium	Rf [*]				4	
62	150.36	Samarium	Sm	1,072	1,900	7.52	8	[Xe] 4f ⁶ 6s ²
21	44.9559	Scandium	Sc	1,539	2,832	2.99	3	[Ar] 3d ¹ 4s ²
106	266	Seaborgium	Sg [*]				6	
34	78.96	Selenium	Se	217	685	4.79	16	[Ar] 3d ¹⁰ 4s ² 4p ⁴
14	28.0855	Silicon	Si	1,410	2,355	2.33	14	[Ne] 3s ² 3p ²
47	107.8682	Silver	Ag	962	2,212	10.5	11	[Kr] 4d ¹⁰ 5s ¹
11	22.9897	Sodium	Na	98	883	0.97	1	[Ne] 3s ¹
38	87.62	Strontium	Sr	769	1,384	2.54	2	[Kr] 5s ²
16	32.065	Sulfur	S	113	445	2.07	16	[Ne] 3s ² 3p ⁴
73	180.9479	Tantalum	Ta	2,996	5,425	16.65	5	[Xe] 4f ¹⁴ 5d ³ 6s ²

Table 11.15 (Continued)

Z	Atomic weight	Name	Symbol ^a	Melting point (°C)	Boiling point (°C)	Density ^b (g/cm ³)	Group	Electron configuration
43	98	Technetium	Tc*	2,200	4,877	11.5	7	[Kr] 4d ⁵ 5s ²
52	127.6	Tellurium	Te	449	990	6.24	16	[Kr] 4d ¹⁰ 5s ² 5p ⁴
65	158.9253	Terbium	Tb	1,360	3,041	8.23	11	[Xe] 4f ⁹ 6s ²
81	204.3833	Thallium	Tl	303	1,457	11.85	13	[Xe] 4f ¹⁴ 5d ¹⁰ 6s ² 6p ¹
90	232.0381	Thorium	Th	1,750	4,790	11.72	4	[Rn] 6d ² 7s ²
69	168.9342	Thulium	Tm	1,545	1,727	9.32	15	[Xe] 4f ¹³ 6s ²
50	118.71	Tin	Sn	232	2,270	7.31	14	[Kr] 4d ¹⁰ 5s ² 5p ²
22	47.867	Titanium	Ti	1,660	3,287	4.54	4	[Ar] 3d ² 4s ²
74	183.84	Tungsten	W	3,410	5,660	19.35	6	[Xe] 4f ¹⁴ 5d ⁴ 6s ²
92	238.0289	Uranium	U	1,132	3,818	18.95	6	[Rn] 5f ³ 6d ¹ 7s ²
23	50.9415	Vanadium	V	1,890	3,380	6.11	5	[Ar] 3d ³ 4s ²
54	131.293	Xenon	Xe	−112	−108	5.9	18	[Kr] 4d ¹⁰ 5s ² 5p ⁶
70	173.04	Ytterbium	Yb	824	1,466	6.9	16	[Xe] 4f ¹⁴ 6s ²
39	88.9059	Yttrium	Y	1,523	3,337	4.47	3	[Kr] 4d ¹ 5s ²
30	65.39	Zinc	Zn	420	907	7.13	12	[Ar] 3d ¹⁰ 4s ²
40	91.224	Zirconium	Zr	1,852	4,377	6.51	4	[Kr] 4d ² 5s ²

^aSymbol of element; the elements marked with an asterisk have no stable isotopes.

^bDensity of elements with boiling points below 0°C is given in g/l.

and its value in SI units is given in ► Table 11.5. Hence, the relative atomic mass of isotope X of element E is given by:

$$A_r(X) = \frac{m(X)}{m(^{12}\text{C})/12}$$

where m is the mass of isotope X. The *atomic weight*, $A_r(E)$, of element E can be determined by averaging the relative atomic masses of the isotopes of that element, using the *isotopic abundances* as weighting factors. The isotopic masses and abundances are determined experimentally. As the isotopic composition depends on the origin and treatment of the material used in the experiment, regional and other variations have to be taken into account when deducing universally applicable values for atomic weights.

The IUPAC Commission on Atomic Weights and Isotopic Abundances reviews the experimental data and updates the recommended set of atomic weights and isotopic compositions biennially. The latest recommended set of atomic weights of the elements is from the year 2007

Periodic table of the elements

^b Actinide series	89 Ac*	90 Th	91 Pa*	92 U	93 Np*	94 Pu*	95 Am*	96 Cm*	97 Bk*	98 Cf*	99 Es*	100 Fm*	101 Md*	102 No*	103 Lr*
------------------------------	-----------	----------	-----------	---------	-----------	-----------	-----------	-----------	-----------	-----------	-----------	------------	------------	------------	------------

The temporary names of possible superheavy elements. Note that the discovery of element 112 was already accepted by IUPAC at the end of 2009, but the name and the chemical symbol were only proposals at that time

Z	Name	Symbol
110	Darmstadtium	Ds
111	Roentgenium	Rg
112	Copernicium	Cn
114	Ununquadium	Uuq
116	Ununhexium	Uuh
118	Ununoctium	Uuo

The IUPAC recommended values for *standard atomic weights* and the related quantities used for their derivation are presented in [Table 11.17](#) for element 1 through 116 according to the Internet page by Coursey et al. (2001), which combines data from Coplen (2001), Rosman and Taylor (1998a), and Audi and Wapstra (1995). The relative atomic masses are given in atomic mass units according to the above equation, while the representative *isotopic*

■ Table 11.17

Recommended atomic weights and isotopic compositions for the elements

Isotope			Relative At. Mass	Isotopic Composition (%)
Z	Element	A	Std. At. Weight (u)	
1	H	1	1.0078250321(4)	99.9885(70)
	(D)	2	2.0141017780(4)	0.0115(70)
			1.00794(7)	
2	He	3	3.0160293097(9)	0.000137(3)
		4	4.0026032497(10)	99.999863(3)
			4.002602(2)	
3	Li	6	6.0151223(5)	7.59(4)
		7	7.0160040(5)	92.41(4)
			6.941(2)	
4	Be	9	9.0121821(4)	100
			9.012182(3)	
5	B	10	10.0129370(4)	19.9(7)
		11	11.0093055(5)	80.1(7)
			10.811(7)	
6	C	12	12.0000000(0)	98.93(8)
		13	13.0033548378(10)	1.07(8)
			12.0107(8)	
7	N	14	14.0030740052(9)	99.632(7)
		15	15.0001088984(9)	0.368(7)
			14.0067(2)	
8	O	16	15.9949146221(15)	99.757(16)
		17	16.99913150(22)	0.038(1)
		18	17.9991604(9)	0.205(14)
			15.9994(3)	
9	F	19	18.99840320(7)	100
			18.9984032(5)	
10	Ne	20	19.9924401759(20)	90.48(3)
		21	20.99384674(4)	0.27(1)
		22	21.99138551(23)	9.25(3)
			20.1797(6)	
11	Na	23	22.98976967(23)	100
			22.98976928(2)	
12	Mg	24	23.98504190(20)	78.99(4)
		25	24.98583702(20)	10.00(1)
		26	25.98259304(21)	11.01(3)
			24.3050(6)	

Table 11.17 (Continued)

Isotope			Relative At. Mass	
Z	Element	A	Std. At. Weight (u)	Isotopic Composition (%)
13	Al	27	26.98153844(14)	100
			26.9815386(8)	
14	Si	28	27.9769265327(20)	92.2297(7)
		29	28.97649472(3)	4.6832(5)
		30	29.97377022(5)	3.0872(5)
			28.0855(3)	
15	P	31	30.97376151(20)	100
			30.973762(2)	
16	S	32	31.97207069(12)	94.93(31)
		33	32.97145850(12)	0.76(2)
		34	33.96786683(11)	4.29(28)
		36	35.96708088(25)	0.02(1)
			32.065(5)	
17	Cl	35	34.96885271(4)	75.78(4)
		37	36.96590260(5)	24.22(4)
			35.453(2)	
18	Ar	36	35.96754628(27)	0.3365(30)
		38	37.9627322(5)	0.0632(5)
		40	39.962383123(3)	99.6003(30)
			39.948(1)	
19	K	39	38.9637069(3)	93.2581(44)
		40	39.96399867(29)	0.0117(1)
		41	40.96182597(28)	6.7302(44)
			39.0983(1)	
20	Ca	40	39.9625912(3)	96.941(156)
		42	41.9586183(4)	0.647(23)
		43	42.9587668(5)	0.135(10)
		44	43.9554811(9)	2.086(110)
		46	45.9536928(25)	0.004(3)
		48	47.952534(4)	0.187(21)
			40.078(4)	
21	Sc	45	44.9559102(12)	100
			44.955912(6)	
22	Ti	46	45.9526295(12)	8.25(3)
		47	46.9517638(10)	7.44(2)
		48	47.9479471(10)	73.72(3)
		49	48.9478708(10)	5.41(2)

■ Table 11.17 (Continued)

Isotope			Relative At. Mass	Isotopic Composition (%)
Z	Element	A	Std. At. Weight (u)	
		50	49.9447921(11)	5.18(2)
			47.867(1)	
23	V	50	49.9471628(14)	0.250(4)
		51	50.9439637(14)	99.750(4)
			50.9415(1)	
24	Cr	50	49.9460496(14)	4.345(13)
		52	51.9405119(15)	83.789(18)
		53	52.9406538(15)	9.501(17)
		54	53.9388849(15)	2.365(7)
			51.9961(6)	
25	Mn	55	54.9380496(14)	100
			54.938045(5)	
26	Fe	54	53.9396148(14)	5.845(35)
		56	55.9349421(15)	91.754(36)
		57	56.9353987(15)	2.119(10)
		58	57.9332805(15)	0.282(4)
			55.845(2)	
27	Co	59	58.9332002(15)	100
			58.933195(5)	
28	Ni	58	57.9353479(15)	68.0769(89)
		60	59.9307906(15)	26.2231(77)
		61	60.9310604(15)	1.1399(6)
		62	61.9283488(15)	3.6345(17)
		64	63.9279696(16)	0.9256(9)
			58.6934(4)	
29	Cu	63	62.9296011(15)	69.17(3)
		65	64.9277937(19)	30.83(3)
			63.546(3)	
30	Zn	64	63.9291466(18)	48.63(60)
		66	65.9260368(16)	27.90(27)
		67	66.9271309(17)	4.10(13)
		68	67.9248476(17)	18.75(51)
		70	69.925325(4)	0.62(3)
			65.38(2)	
31	Ga	69	68.925581(3)	60.108(9)
		71	70.9247050(19)	39.892(9)
			69.723(1)	

Table 11.17 (Continued)

Isotope			Relative At. Mass	Isotopic Composition (%)
Z	Element	A	Std. At. Weight (u)	
32	Ge	70	69.9242504(19)	20.84(87)
		72	71.9220762(16)	27.54(34)
		73	72.9234594(16)	7.73(5)
		74	73.9211782(16)	36.28(73)
		76	75.9214027(16)	7.61(38)
			72.64(1)	
33	As	75	74.9215964(18)	100
			74.92160(2)	
34	Se	74	73.9224766(16)	0.89(4)
		76	75.9192141(16)	9.37(29)
		77	76.9199146(16)	7.63(16)
		78	77.9173095(16)	23.77(28)
		80	79.9165218(20)	49.61(41)
		82	81.9167000(22)	8.73(22)
			78.96(3)	
35	Br	79	78.9183376(20)	50.69(7)
		81	80.916291(3)	49.31(7)
			79.904(1)	
36	Kr	78	77.920386(7)	0.35(1)
		80	79.916378(4)	2.28(6)
		82	81.9134846(28)	11.58(14)
		83	82.914136(3)	11.49(6)
		84	83.911507(3)	57.00(4)
		86	85.9106103(12)	17.30(22)
			83.798(2)	
37	Rb	85	84.9117893(25)	72.17(2)
		87	86.9091835(27)	27.83(2)
			85.4678(3)	
38	Sr	84	83.913425(4)	0.56(1)
		86	85.9092624(24)	9.86(1)
		87	86.9088793(24)	7.00(1)
		88	87.9056143(24)	82.58(1)
			87.62(1)	
39	Y	89	88.9058479(25)	100
			88.90585(2)	
40	Zr	90	89.9047037(23)	51.45(40)
		91	90.9056450(23)	11.22(5)
		92	91.9050401(23)	17.15(8)

■ Table 11.17 (Continued)

Isotope			Relative At. Mass	
Z	Element	A	Std. At. Weight (u)	Isotopic Composition (%)
		94	93.9063158(25)	17.38(28)
		96	95.908276(3)	2.80(9)
			91.224(2)	
41	Nb	93	92.9063775(24)	100
			92.90638(2)	
42	Mo	92	91.906810(4)	14.84(35)
		94	93.9050876(20)	9.25(12)
		95	94.9058415(20)	15.92(13)
		96	95.9046789(20)	16.68(2)
		97	96.9060210(20)	9.55(8)
		98	97.9054078(20)	24.13(31)
		100	99.907477(6)	9.63(23)
			95.96(2)	
43	Tc	98	97.907216(4)	
			[98]	
44	Ru	96	95.907598(8)	5.54(14)
		98	97.905287(7)	1.87(3)
		99	98.9059393(21)	12.76(14)
		100	99.9042197(22)	12.60(7)
		101	100.9055822(22)	17.06(2)
		102	101.9043495(22)	31.55(14)
		104	103.905430(4)	18.62(27)
			101.07(2)	
45	Rh	103	102.905504(3)	100
			102.90550(2)	
46	Pd	102	101.905608(3)	1.02(1)
		104	103.904035(5)	11.14(8)
		105	104.905084(5)	22.33(8)
		106	105.903483(5)	27.33(3)
		108	107.903894(4)	26.46(9)
		110	109.905152(12)	11.72(9)
			106.42(1)	
47	Ag	107	106.905093(6)	51.839(8)
		109	108.904756(3)	48.161(8)
			107.8682(2)	
48	Cd	106	105.906458(6)	1.25(6)
		108	107.904183(6)	0.89(3)
		110	109.903006(3)	12.49(18)

■ Table 11.17 (Continued)

Isotope			Relative At. Mass	
Z	Element	A	Std. At. Weight (u)	Isotopic Composition (%)
		111	110.904182(3)	12.80(12)
		112	111.9027572(30)	24.13(21)
		113	112.9044009(30)	12.22(12)
		114	113.9033581(30)	28.73(42)
		116	115.904755(3)	7.49(18)
			112.411(8)	
49	In	113	112.904061(4)	4.29(5)
		115	114.903878(5)	95.71(5)
			114.818(3)	
50	Sn	112	111.904821(5)	0.97(1)
		114	113.902782(3)	0.66(1)
		115	114.903346(3)	0.34(1)
		116	115.901744(3)	14.54(9)
		117	116.902954(3)	7.68(7)
		118	117.901606(3)	24.22(9)
		119	118.903309(3)	8.59(4)
		120	119.9021966(27)	32.58(9)
		122	121.9034401(29)	4.63(3)
		124	123.9052746(15)	5.79(5)
			118.710(7)	
51	Sb	121	120.9038180(24)	57.21(5)
		123	122.9042157(22)	42.79(5)
			121.760(1)	
52	Te	120	119.904020(11)	0.09(1)
		122	121.9030471(20)	2.55(12)
		123	122.9042730(19)	0.89(3)
		124	123.9028195(16)	4.74(14)
		125	124.9044247(20)	7.07(15)
		126	125.9033055(20)	18.84(25)
		128	127.9044614(19)	31.74(8)
		130	129.9062228(21)	34.08(62)
			127.60(3)	
53	I	127	126.904468(4)	100
			126.90447(3)	
54	Xe	124	123.9058958(21)	0.09(1)
		126	125.904269(7)	0.09(1)
		128	127.9035304(15)	1.92(3)
		129	128.9047795(9)	26.44(24)

■ Table 11.17 (Continued)

Isotope			Relative At. Mass	Isotopic Composition (%)
Z	Element	A	Std. At. Weight (u)	
		130	129.9035079(10)	4.08(2)
		131	130.9050819(10)	21.18(3)
		132	131.9041545(12)	26.89(6)
		134	133.9053945(9)	10.44(10)
		136	135.907220(8)	8.87(16)
			131.293(6)	
55	Cs	133	132.905447(3)	100
			132.9054519(2)	
56	Ba	130	129.906310(7)	0.106(1)
		132	131.905056(3)	0.101(1)
		134	133.904503(3)	2.417(18)
		135	134.905683(3)	6.592(12)
		136	135.904570(3)	7.854(24)
		137	136.905821(3)	11.232(24)
		138	137.905241(3)	71.698(42)
			137.327(7)	
57	La	138	137.907107(4)	0.090(1)
		139	138.906348(3)	99.910(1)
			138.90547(7)	
58	Ce	136	135.907140(50)	0.185(2)
		138	137.905986(11)	0.251(2)
		140	139.905434(3)	88.450(51)
		142	141.909240(4)	11.114(51)
			140.116(1)	
59	Pr	141	140.907648(3)	100
			140.90765(2)	
60	Nd	142	141.907719(3)	27.2(5)
		143	142.909810(3)	12.2(2)
		144	143.910083(3)	23.8(3)
		145	144.912569(3)	8.3(1)
		146	145.913112(3)	17.2(3)
		148	147.916889(3)	5.7(1)
		150	149.920887(4)	5.6(2)
			144.242(3)	
61	Pm	145	144.912744(4)	
			[145]	
62	Sm	144	143.911995(4)	3.07(7)
		147	146.914893(3)	14.99(18)

Table 11.17 (Continued)

Isotope			Relative At. Mass	Isotopic Composition (%)
Z	Element	A	Std. At. Weight (u)	
		148	147.914818(3)	11.24(10)
		149	148.917180(3)	13.82(7)
		150	149.917271(3)	7.38(1)
		152	151.919728(3)	26.75(16)
		154	153.922205(3)	22.75(29)
			150.36(2)	
63	Eu	151	150.919846(3)	47.81(3)
		153	152.921226(3)	52.19(3)
			151.964(1)	
64	Gd	152	151.919788(3)	0.20(1)
		154	153.920862(3)	2.18(3)
		155	154.922619(3)	14.80(12)
		156	155.922120(3)	20.47(9)
		157	156.923957(3)	15.65(2)
		158	157.924101(3)	24.84(7)
		160	159.927051(3)	21.86(19)
			157.25(3)	
65	Tb	159	158.925343(3)	100
			158.92535(2)	
66	Dy	156	155.924278(7)	0.06(1)
		158	157.924405(4)	0.10(1)
		160	159.925194(3)	2.34(8)
		161	160.926930(3)	18.91(24)
		162	161.926795(3)	25.51(26)
		163	162.928728(3)	24.90(16)
		164	163.929171(3)	28.18(37)
			162.500(1)	
67	Ho	165	164.930319(3)	100
			164.93032(2)	
68	Er	162	161.928775(4)	0.14(1)
		164	163.929197(4)	1.61(3)
		166	165.930290(3)	33.61(35)
		167	166.932045(3)	22.93(17)
		168	167.932368(3)	26.78(26)
		170	169.935460(3)	14.93(27)
			167.259(3)	
69	Tm	169	168.934211(3)	100
			168.93421(2)	

■ Table 11.17 (Continued)

Isotope			Relative At. Mass	Isotopic Composition (%)
Z	Element	A	Std. At. Weight (u)	
70	Yb	168	167.933894(5)	0.13(1)
		170	169.934759(3)	3.04(15)
		171	170.936322(3)	14.28(57)
		172	171.9363777(30)	21.83(67)
		173	172.9382068(30)	16.13(27)
		174	173.9388581(30)	31.83(92)
		176	175.942568(3)	12.76(41)
			173.054(5)	
71	Lu	175	174.9407679(28)	97.41(2)
		176	175.9426824(28)	2.59(2)
			174.9668(1)	
72	Hf	174	173.940040(3)	0.16(1)
		176	175.9414018(29)	5.26(7)
		177	176.9432200(27)	18.60(9)
		178	177.9436977(27)	27.28(7)
		179	178.9458151(27)	13.62(2)
		180	179.9465488(27)	35.08(16)
			178.49(2)	
73	Ta	180	179.947466(3)	0.012(2)
		181	180.947996(3)	99.988(2)
			180.94788(2)	
74	W	180	179.946706(5)	0.12(1)
		182	181.948206(3)	26.50(16)
		183	182.9502245(29)	14.31(4)
		184	183.9509326(29)	30.64(2)
		186	185.954362(3)	28.43(19)
			183.84(1)	
75	Re	185	184.9529557(30)	37.40(2)
		187	186.9557508(30)	62.60(2)
			186.207(1)	
76	Os	184	183.952491(3)	0.02(1)
		186	185.953838(3)	1.59(3)
		187	186.9557479(30)	1.96(2)
		188	187.9558360(30)	13.24(8)
		189	188.9581449(30)	16.15(5)
		190	189.958445(3)	26.26(2)
		192	191.961479(4)	40.78(19)
			190.23(3)	

Table 11.17 (Continued)

Isotope			Relative At. Mass	
Z	Element	A	Std. At. Weight (u)	Isotopic Composition (%)
77	Ir	191	190.960591(3)	37.3(2)
		193	192.962924(3)	62.7(2)
			192.217(3)	
78	Pt	190	189.959930(7)	0.014(1)
		192	191.961035(4)	0.782(7)
		194	193.962664(3)	32.967(99)
		195	194.964774(3)	33.832(10)
		196	195.964935(3)	25.242(41)
		198	197.967876(4)	7.163(55)
			195.084(9)	
79	Au	197	196.966552(3)	100
			196.966569(4)	
80	Hg	196	195.965815(4)	0.15(1)
		198	197.966752(3)	9.97(20)
		199	198.968262(3)	16.87(22)
		200	199.968309(3)	23.10(19)
		201	200.970285(3)	13.18(9)
		202	201.970626(3)	29.86(26)
		204	203.973476(3)	6.87(15)
			200.59(2)	
81	Tl	203	202.972329(3)	29.524(14)
		205	204.974412(3)	70.476(14)
			204.3833(2)	
82	Pb	204	203.973029(3)	1.4(1)
		206	205.974449(3)	24.1(1)
		207	206.975881(3)	22.1(1)
		208	207.976636(3)	52.4(1)
			207.2(1)	
83	Bi	209	208.980383(3)	100
			208.98040(1)	
84	Po	209	208.982416(3)	
			[209]	
85	At	210	209.987131(9)	
			[210]	
86	Rn	222	222.0175705(27)	
			[222]	
87	Fr	223	223.0197307(29)	
			[223]	

■ Table 11.17 (Continued)

Isotope			Relative At. Mass	Isotopic Composition (%)
Z	Element	A	Std. At. Weight (u)	
88	Ra	226	226.0254026(27)	
			[226]	
89	Ac	227	227.0277470(29)	
			[227]	
90	Th	232	232.0380504(22)	100
			232.03806(2)	
91	Pa	231	231.0358789(28)	100
			231.03588(2)	
92	U	234	234.0409456(21)	0.0055(2)
		235	235.0439231(21)	0.7200(51)
		238	238.0507826(21)	99.2745(106)
			238.02891(3)	
93	Np	237	237.0481673(21)	
			[237]	
94	Pu	244	244.064198(5)	
			[244]	
95	Am	243	243.0613727(23)	
			[243]	
96	Cm	247	247.070347(5)	
			[247]	
97	Bk	247	247.070299(6)	
			[247]	
98	Cf	251	251.079580(5)	
			[251]	
99	Es	252	252.082970(50)	
			[252]	
100	Fm	257	257.095099(7)	
			[257]	
101	Md	258	258.098425(5)	
			[258]	
102	No	259	259.10102(11) ^a	
			[259]	
103	Lr	262	262.10969(32) ^a	
			[262]	
104	Rf	261	261.10875(11) ^a	
			[261]	
105	Db	262	262.11415(20) ^a	
			[262]	

Table 11.17 (Continued)

Isotope			Relative At. Mass	Isotopic Composition (%)
Z	Element	A	Std. At. Weight (u)	
106	Sg	266	266.12193(31) ^a	
			[266]	
107	Bh	264	264.12473(30) ^a	
			[264]	
108	Hs	269	269.13411(46) ^a	
			[269]	
109	Mt	268	268.13882(34) ^a	
			[268]	
110	Ds	271	271.14608(20) ^a	
			[271]	
111	Rg	272	272.15348(36) ^a	
			[272]	
112	(Cn)	277		
			[277]	
114	Uuq	289		
			[289]	
116	Uuh	292		
			[292]	

^aThe value and its standard uncertainty were derived not from purely experimental data, but at least partly from systematic trends

compositions (mole fractions of the various isotopes) are shown in percentages. The derived standard atomic weight is included at the end of the isotopic list for each element, in italics. For elements not found in nature, brackets [] indicate the mass number of the most stable isotope. The standard uncertainties are given as numbers in parentheses after the least significant digits, i.e., 99.9885(70)% means $(99.9885 \pm 0.0070)\%$. These uncertainties reflect the accuracy of measurement and the terrestrial and other variabilities as well.

11.4 Atomic Data

R. B. Firestone

11.4.1 Atomic-Electron Binding Energies

Tables 11.18–11.20 list the *atomic-electron binding energies* (Larkins 1977) for elements with $Z = 1\text{--}104$. These binding energies are referenced to the Fermi level for solid systems, except for Ne, Cl, Ar, Br, Kr, Xe, and Rn, which are vapor phase systems where the binding energy is referenced to the vacuum level. The binding energy uncertainties are 1–2 eV for most subshells in the lighter elements or outer orbitals in the heavier elements, but may be 10–20 eV for the

■ **Table 11.18**

Atomic-electron binding energies for the K-M5 subshells in keV units

Z	Element	K	L1	L2	L3	M1	M2	M3	M4	M5
1	H	0.0136								
2	He	0.0246								
3	Li	0.0548	0.0053							
4	Be	0.1121	0.0080							
5	B	0.1880	0.0126	0.0047	0.0047					
6	C	0.2838	0.0180	0.0064	0.0064					
7	N	0.4016	0.0244	0.0092	0.0092					
8	O	0.5320	0.0285	0.0071	0.0071					
9	F	0.6854	0.0340	0.0086	0.0086					
10	Ne	0.8701	0.0485	0.0217	0.0216					
11	Na	1.0721	0.0633	0.0311	0.0311	0.0007				
12	Mg	1.3050	0.0894	0.0514	0.0514	0.0021				
13	Al	1.5596	0.1177	0.0732	0.0727	0.0007	0.0055	0.0055		
14	Si	1.8389	0.1487	0.0995	0.0989	0.0076	0.0030	0.0030		
15	P	2.1455	0.1893	0.1362	0.1353	0.0162	0.0099	0.0099		
16	S	2.4720	0.2292	0.1654	0.1642	0.0158	0.0080	0.0080		
17	Cl	2.8224	0.2702	0.2016	0.2000	0.0175	0.0068	0.0068		
18	Ar	3.2060	0.3263	0.2507	0.2486	0.0292	0.0159	0.0158		
19	K	3.6074	0.3771	0.2963	0.2936	0.0339	0.0178	0.0178		
20	Ca	4.0381	0.4378	0.3500	0.3464	0.0437	0.0254	0.0254		
21	Sc	4.4928	0.5004	0.4067	0.4022	0.0538	0.0323	0.0323	0.0066	0.0066
22	Ti	4.9664	0.5637	0.4615	0.4555	0.0603	0.0346	0.0346	0.0037	0.0037
23	V	5.4651	0.6282	0.5205	0.5129	0.0665	0.0378	0.0378	0.0022	0.0022
24	Cr	5.9892	0.6946	0.5837	0.5745	0.0741	0.0425	0.0425	0.0023	0.0023
25	Mn	6.5390	0.7690	0.6514	0.6403	0.0839	0.0486	0.0486	0.0033	0.0033
26	Fe	7.1120	0.8461	0.7211	0.7081	0.0929	0.0540	0.0540	0.0036	0.0036
27	Co	7.7089	0.9256	0.7936	0.7786	0.1007	0.0595	0.0595	0.0029	0.0029
28	Ni	8.3328	1.0081	0.8719	0.8547	0.1118	0.0681	0.0681	0.0036	0.0036
29	Cu	8.9789	1.0961	0.9510	0.9311	0.1198	0.0736	0.0736	0.0016	0.0016
30	Zn	9.6586	1.1936	1.0428	1.0197	0.1359	0.0866	0.0866	0.0081	0.0081
31	Ga	10.3671	1.2977	1.1423	1.1154	0.1581	0.1068	0.1029	0.0174	0.0174
32	Ge	11.1031	1.4143	1.2478	1.2167	0.1800	0.1279	0.1208	0.0287	0.0287
33	As	11.8667	1.5265	1.3586	1.3231	0.2035	0.1464	0.1405	0.0412	0.0412
34	Se	12.6578	1.6539	1.4762	1.4358	0.2315	0.1682	0.1619	0.0567	0.0567
35	Br	13.4737	1.7820	1.5960	1.5499	0.2565	0.1893	0.1815	0.0701	0.0690
36	Kr	14.3256	1.9210	1.7272	1.6749	0.2921	0.2218	0.2145	0.0950	0.0938
37	Rb	15.1997	2.0651	1.8639	1.8044	0.3221	0.2474	0.2385	0.1118	0.1103
38	Sr	16.1046	2.2163	2.0068	1.9396	0.3575	0.2798	0.2691	0.1350	0.1331

Table 11.18 (Continued)

Z	Element	K	L1	L2	L3	M1	M2	M3	M4	M5
39	Y	17.0384	2.3725	2.1555	2.0800	0.3936	0.3124	0.3003	0.1596	0.1574
40	Zr	17.9976	2.5316	2.3067	2.2223	0.4303	0.3442	0.3305	0.1824	0.1800
41	Nb	18.9856	2.6977	2.4647	2.3705	0.4684	0.3784	0.3630	0.2074	0.2046
42	Mo	19.9995	2.8655	2.6251	2.5202	0.5046	0.4097	0.3923	0.2303	0.2270
43	Tc	21.0440	3.0425	2.7932	2.6769	0.5440	0.4449	0.4250	0.2564	0.2529
44	Ru	22.1172	3.2240	2.9669	2.8379	0.5850	0.4828	0.4606	0.2836	0.2794
45	Rh	23.2199	3.4119	3.1461	3.0038	0.6271	0.5210	0.4962	0.3117	0.3070
46	Pd	24.3503	3.6043	3.3303	3.1733	0.6699	0.5591	0.5315	0.3400	0.3347
47	Ag	25.5140	3.8058	3.5237	3.3511	0.7175	0.6024	0.5714	0.3728	0.3667
48	Cd	26.7112	4.0180	3.7270	3.5375	0.7702	0.6507	0.6165	0.4105	0.4037
49	In	27.9399	4.2375	3.9380	3.7301	0.8256	0.7022	0.6643	0.4508	0.4431
50	Sn	29.2001	4.4647	4.1561	3.9288	0.8838	0.7564	0.7144	0.4933	0.4848
51	Sb	30.4912	4.6983	4.3804	4.1322	0.9437	0.8119	0.7656	0.5369	0.5275
52	Te	31.8138	4.9392	4.6120	4.3414	1.0060	0.8697	0.8187	0.5825	0.5721
53	I	33.1694	5.1881	4.8521	4.5571	1.0721	0.9305	0.8746	0.6313	0.6194
54	Xe	34.5644	5.4528	5.1037	4.7822	1.1487	1.0021	0.9406	0.6894	0.6767
55	Cs	35.9846	5.7143	5.3594	5.0119	1.2171	1.0650	0.9976	0.7395	0.7255
56	Ba	37.4406	5.9888	5.6236	5.2470	1.2928	1.1367	1.0622	0.7961	0.7807
57	La	38.9246	6.2663	5.8906	5.4827	1.3613	1.2044	1.1234	0.8485	0.8317
58	Ce	40.4430	6.5488	6.1642	5.7234	1.4346	1.2728	1.1854	0.9013	0.8833
59	Pr	41.9906	6.8348	6.4404	5.9643	1.5110	1.3374	1.2422	0.9511	0.9310
60	Nd	43.5689	7.1260	6.7215	6.2079	1.5753	1.4028	1.2974	0.9999	0.9777
61	Pm	45.1840	7.4279	7.0128	6.4593	1.6500	1.4714	1.3569	1.0515	1.0269
62	Sm	46.8342	7.7368	7.3118	6.7162	1.7228	1.5407	1.4198	1.1060	1.0802
63	Eu	48.5190	8.0520	7.6171	6.9769	1.8000	1.6139	1.4806	1.1606	1.1309
64	Gd	50.2391	8.3756	7.9303	7.2428	1.8808	1.6883	1.5440	1.2172	1.1852
65	Tb	51.9957	8.7080	8.2516	7.5140	1.9675	1.7677	1.6113	1.2750	1.2412
66	Dy	53.7885	9.0458	8.5806	7.7901	2.0468	1.8418	1.6756	1.3325	1.2949
67	Ho	55.6177	9.3942	8.9178	8.0711	2.1283	1.9228	1.7412	1.3915	1.3514
68	Er	57.4855	9.7513	9.2643	8.3579	2.2065	2.0058	1.8118	1.4533	1.4093
69	Tm	59.3896	10.1157	9.6169	8.6480	2.3068	2.0898	1.8845	1.5146	1.4677
70	Yb	61.3323	10.4864	9.9782	8.9436	2.3981	2.1730	1.9498	1.5763	1.5278
71	Lu	63.3138	10.8704	10.3486	9.2441	2.4912	2.2635	2.0236	1.6394	1.5885
72	Hf	65.3508	11.2707	10.7394	9.5607	2.6009	2.3654	2.1076	1.7164	1.6617
73	Ta	67.4164	11.6815	11.1361	9.8811	2.7080	2.4687	2.1940	1.7932	1.7351
74	W	69.5250	12.0998	11.5440	10.2068	2.8196	2.5749	2.2810	1.8716	1.8092
75	Re	71.6764	12.5267	11.9587	10.5353	2.9317	2.6816	2.3673	1.9489	1.8829
76	Os	73.8708	12.9680	12.3850	10.8709	3.0485	2.7922	2.4572	2.0308	1.9601
77	Ir	76.1110	13.4185	12.8241	11.2152	3.1737	2.9087	2.5507	2.1161	2.0404

■ **Table 11.18 (Continued)**

Z	Element	K	L1	L2	L3	M1	M2	M3	M4	M5
78	Pt	78.3948	13.8805	13.2726	11.5638	3.2976	3.0270	2.6453	2.2015	2.1211
79	Au	80.7249	14.3528	13.7336	11.9187	3.4249	3.1478	2.7430	2.2911	2.2057
80	Hg	83.1023	14.8393	14.2087	12.2839	3.5616	3.2785	2.8471	2.3849	2.2949
81	Tl	85.5304	15.3467	14.6979	12.6575	3.7041	3.4157	2.9566	2.4851	2.3893
82	Pb	88.0045	15.8608	15.2000	13.0352	3.8507	3.5542	3.0664	2.5856	2.4840
83	Bi	90.5259	16.3875	15.7111	13.4186	3.9991	3.6963	3.1769	2.6876	2.5796
84	Po	93.1000	16.9280	16.2370	13.8100	4.1520	3.8440	3.2930	2.7940	2.6800
85	At	95.7240	17.4820	16.7760	14.2070	4.3100	3.9940	3.4090	2.9010	2.7810
86	Rn	98.3970	18.0480	17.3280	14.6100	4.4730	4.1500	3.5290	3.0120	2.8840
87	Fr	101.1300	18.6340	17.8990	15.0250	4.6440	4.3150	3.6560	3.1290	2.9940
88	Ra	103.9150	19.2320	18.4840	15.4440	4.8220	4.4830	3.7850	3.2480	3.1050
89	Ac	106.7560	19.8460	19.0810	15.8700	4.9990	4.6550	3.9150	3.3700	3.2190
90	Th	109.6500	20.4720	19.6930	16.3000	5.1820	4.8310	4.0460	3.4910	3.3320
91	Pa	112.5960	21.1050	20.3140	16.7330	5.3610	5.0010	4.1740	3.6060	3.4420
92	U	115.6020	21.7580	20.9480	17.1680	5.5480	5.1810	4.3040	3.7260	3.5500
93	Np	118.6690	22.4270	21.6000	17.6100	5.7390	5.3660	4.4350	3.8490	3.6640
94	Pu	121.7910	23.1040	22.2660	18.0570	5.9330	5.5470	4.5630	3.9700	3.7750
95	Am	124.9820	23.8080	22.9520	19.5100	6.1330	5.7390	4.6980	4.0960	3.8900
96	Cm	128.2410	24.5260	23.6510	18.9700	6.3370	5.9370	4.8380	4.2240	4.0090
97	Bk	131.5560	25.2560	24.3710	19.4350	6.5450	6.1380	4.9760	4.3530	4.1270
98	Cf	134.9390	26.0100	25.1080	19.9070	6.7610	6.3450	5.1160	4.4840	4.2470
99	Es	138.3960	26.7820	25.8650	20.3840	6.9810	6.5580	5.2590	4.6170	4.3680
100	Fm	141.9260	27.5740	26.6410	20.8680	7.2080	6.7760	5.4050	4.7520	4.4910
101	Md	146.5260	28.3870	27.4380	21.3560	7.4400	7.0010	5.5520	4.8890	4.6150
102	No	149.2080	29.2210	28.2550	21.8510	7.6780	7.2310	5.7020	5.0280	4.7410
103	Lr	152.9700	30.0830	29.1030	22.3590	7.9300	7.4740	5.8600	5.1760	4.8760
104	Rf	156.2880	30.8810	29.9860	22.9070	8.1610	7.7380	6.0090	5.3360	5.0140

■ **Table 11.19**

Atomic-electron binding energies for the N1-O3 subshells in keV units

Z	Element	N1	N2	N3	N4	N5	N6	N7	O1	O2	O3
31	Ga	0.0015	0.0008	0.0008							
32	Ge	0.0050	0.0023	0.0023							
33	As	0.0085	0.0025	0.0025							
34	Se	0.0120	0.0056	0.0056							
35	Br	0.0273	0.0052	0.0046							
36	Kr	0.0275	0.0147	0.0140							

Table 11.19 (Continued)

Z	Element	N1	N2	N3	N4	N5	N6	N7	O1	O2	O3
37	Rb	0.0293	0.0148	0.0140							
38	Sr	0.0377	0.0199	0.0199							
39	Y	0.0454	0.0256	0.0256	0.0024	0.0024					
40	Zr	0.0513	0.0287	0.0287	0.0030	0.0030					
41	Nb	0.0581	0.0339	0.0339	0.0032	0.0032					
42	Mo	0.0618	0.0348	0.0348	0.0018	0.0018					
43	Tc	0.0680	0.0389	0.0389	0.0020	0.0020					
44	Ru	0.0749	0.0431	0.0431	0.0020	0.0020					
45	Rh	0.0810	0.0479	0.0479	0.0025	0.0025					
46	Pd	0.0864	0.0511	0.0511	0.0015	0.0015					
47	Ag	0.0952	0.0626	0.0559	0.0033	0.0033					
48	Cd	0.1076	0.0669	0.0669	0.0093	0.0093			0.0022	0.0022	0.0022
49	In	0.1219	0.0774	0.0774	0.0162	0.0162			0.0001	0.0008	0.0008
50	Sn	0.1365	0.0886	0.0886	0.0239	0.0239			0.0009	0.0011	0.0011
51	Sb	0.1520	0.0984	0.0984	0.0314	0.0314			0.0067	0.0021	0.0021
52	Te	0.1683	0.1102	0.1102	0.0398	0.0398			0.0116	0.0023	0.0023
53	I	0.1864	0.1227	0.1227	0.0496	0.0496			0.0136	0.0033	0.0033
54	Xe	0.2133	0.1455	0.1455	0.0695	0.0675			0.0234	0.0134	0.0121
55	Cs	0.2308	0.1723	0.1616	0.0788	0.0765			0.0227	0.0131	0.0114
56	Ba	0.2530	0.1918	0.1797	0.0925	0.0899			0.0291	0.0166	0.0146
57	La	0.2704	0.2058	0.1914	0.0989	0.0989			0.0323	0.0144	0.0144
58	Ce	0.2896	0.2233	0.2072	0.1100	0.1100	0.0001	0.0001	0.0378	0.0198	0.0198
59	Pr	0.3045	0.2363	0.2176	0.1132	0.1132	0.0020	0.0020	0.0374	0.0223	0.0223
60	Nd	0.3152	0.2433	0.2246	0.1175	0.1175	0.0015	0.0015	0.0375	0.0211	0.0211
61	Pm	0.3310	0.2420	0.2420	0.1204	0.1204	0.0040	0.0040	0.0380	0.022	0.022
62	Sm	0.3457	0.2656	0.2474	0.1290	0.1290	0.0055	0.0055	0.0374	0.0213	0.0213
63	Eu	0.3602	0.2839	0.2566	0.1332	0.1332			0.0318	0.022	0.022
64	Gd	0.3758	0.2885	0.2709	0.1405	0.1405	0.0001	0.0001	0.0361	0.0203	0.0203
65	Tb	0.3979	0.3102	0.2850	0.1470	0.1470	0.0026	0.0026	0.0390	0.0254	0.0254
66	Dy	0.4163	0.3318	0.2929	0.1542	0.1542	0.0042	0.0042	0.0629	0.0263	0.0263
67	Ho	0.4357	0.3435	0.3066	0.1610	0.1610	0.0037	0.0037	0.0512	0.0203	0.0203
68	Er	0.4491	0.3662	0.3200	0.1767	0.1676	0.0043	0.0043	0.0598	0.0294	0.0294
69	Tm	0.4717	0.3859	0.3366	0.1796	0.1796	0.0053	0.0053	0.0532	0.0323	0.0323
70	Yb	0.4872	0.3967	0.3435	0.1981	0.1849	0.0063	0.0063	0.0541	0.0234	0.0234
71	Lu	0.5062	0.4101	0.3593	0.2048	0.1950	0.0069	0.0069	0.0568	0.028	0.028
72	Hf	0.5381	0.4370	0.3804	0.2238	0.2137	0.0171	0.0171	0.0649	0.0381	0.0306
73	Ta	0.5655	0.4648	0.4045	0.2413	0.2293	0.0275	0.0256	0.0711	0.0449	0.0364
74	W	0.5950	0.4916	0.4253	0.2588	0.2454	0.0379	0.0358	0.0771	0.0468	0.0356
75	Re	0.6250	0.5179	0.4444	0.2737	0.2602	0.0481	0.0457	0.0828	0.0456	0.0346

■ Table 11.19 (Continued)

Z	Element	N1	N2	N3	N4	N5	N6	N7	O1	O2	O3
76	Os	0.6543	0.5465	0.4682	0.2894	0.2728	0.0538	0.0510	0.0837	0.058	0.0454
77	Ir	0.6901	0.5771	0.4943	0.3114	0.2949	0.0640	0.0610	0.0952	0.063	0.0505
78	Pt	0.7240	0.6076	0.5191	0.3307	0.3138	0.0745	0.0711	0.1017	0.0653	0.051
79	Au	0.7588	0.6437	0.5454	0.3520	0.3339	0.0878	0.0841	0.1078	0.0717	0.0587
80	Hg	0.8030	0.6810	0.5769	0.3785	0.3593	0.1040	0.0999	0.1203	0.084	0.065
81	Tl	0.8455	0.7213	0.6090	0.4066	0.3862	0.1231	0.1188	0.1363	0.0996	0.073
82	Pb	0.8936	0.7639	0.6445	0.4352	0.4129	0.1412	0.1363	0.1473	0.1048	0.083
83	Bi	0.9382	0.8053	0.6789	0.4636	0.4400	0.1624	0.1571	0.1593	0.1168	0.093
84	Po	0.9870	0.8510	0.7150	0.4950	0.4690	0.1840	0.1780	0.1760	0.132	0.102
85	At	1.0380	0.8970	0.7510	0.5270	0.4990	0.2060	0.1990	0.1920	0.144	0.113
86	Rn	1.0900	0.9440	0.7900	0.5580	0.5300	0.2290	0.2220	0.2080	0.158	0.123
87	Fr	1.1480	0.9990	0.8340	0.5970	0.5670	0.2580	0.2490	0.2290	0.178	0.138
88	Ra	1.2080	1.0550	0.8790	0.6360	0.6030	0.2870	0.2790	0.2510	0.197	0.153
89	Ac	1.2690	1.1120	0.9240	0.6760	0.6400	0.3160	0.3070	0.2720	0.217	0.168
90	Th	1.3300	1.1680	0.9670	0.7130	0.6770	0.3440	0.3350	0.2900	0.236	0.18
91	Pa	1.3830	1.2170	1.0040	0.7430	0.7080	0.3660	0.3550	0.3050	0.245	0.188
92	U	1.4410	1.2710	1.0430	0.7790	0.7370	0.3890	0.3790	0.3240	0.257	0.194
93	Np	1.5010	1.3280	1.0850	0.8160	0.7710	0.4140	0.4030	0.3380	0.274	0.206
94	Pu	1.5590	1.3800	1.1230	0.8460	0.7980	0.4360	0.4240	0.3500	0.283	0.213
95	Am	1.6200	1.4380	1.1650	0.8800	0.8290	0.4610	0.4460	0.3650	0.298	0.219
96	Cm	1.6840	1.4980	1.2070	0.9160	0.8620	0.4840	0.4700	0.3830	0.313	0.229
97	Bk	1.7480	1.5580	1.2490	0.9550	0.8980	0.5110	0.4950	0.3990	0.326	0.237
98	Cf	1.8130	1.6200	1.2920	0.9910	0.9300	0.5380	0.5200	0.4160	0.341	0.245
99	Es	1.8830	1.6830	1.3360	1.0290	0.9650	0.5640	0.5460	0.4340	0.357	0.255
100	Fm	1.9520	1.7490	1.3790	1.0670	1.0000	0.5910	0.5720	0.4520	0.373	0.262
101	Md	2.0240	1.8160	1.4240	1.1050	1.0340	0.6180	0.5970	0.4710	0.389	0.272
102	No	2.0970	1.8850	1.4690	1.1450	1.0700	0.6450	0.6240	0.4900	0.406	0.28
103	Lr	2.1800	1.9630	1.5230	1.1920	1.1120	0.6800	0.6580	0.5160	0.429	0.296
104	Rf	2.2370	2.0350	1.5540	1.2330	1.1490	0.7250	0.7010	0.5350	0.448	0.319

■ Table 11.20

Atomic-electron binding energies for the O4-P5 subshells in keV units

Z	Element	O4	O5	O6	O7	P1	P2	P3	P4	P5
71	Lu	0.0046	0.0046							
72	Hf	0.0066	0.0066							
73	Ta	0.0057	0.0057							
74	W	0.0061	0.0061							

■ **Table 11.20 (Continued)**

Z	Element	O4	O5	O6	O7	P1	P2	P3	P4	P5
75	Re	0.0035	0.0035							
76	Os									
77	Ir	0.0038	0.0038							
78	Pt	0.0021	0.0021							
79	Au	0.0025	0.0025							
80	Hg	0.0098	0.0078							
81	Tl	0.0153	0.0131							
82	Pb	0.0218	0.0192			0.0031	0.0007	0.0007		
83	Bi	0.0265	0.0244			0.008	0.0027	0.0027		
84	Po	0.034	0.03			0.009	0.004	0.001		
85	At	0.041	0.037			0.013	0.006	0.001		
86	Rn	0.048	0.043			0.016	0.008	0.002		
87	Fr	0.06	0.055			0.024	0.014	0.007		0.0038
88	Ra	0.072	0.066			0.031	0.02	0.012		0.0047
89	Ac	0.084	0.076			0.037	0.024	0.015	0.0044	0.0054
90	Th	0.094	0.087			0.041	0.024	0.017	0.0055	0.0059
91	Pa	0.097	0.09	0.0073		0.043	0.027	0.017	0.0046	0.0056
92	U	0.104	0.095	0.0085		0.044	0.027	0.017	0.0046	0.0057
93	Np	0.109	0.101	0.0097		0.047	0.029	0.018	0.0046	0.0058
94	Pu	0.113	0.102	0.007		0.046	0.029	0.016		0.0054
95	Am	0.116	0.106	0.0079	0.0066	0.048	0.029	0.016		0.0055
96	Cm	0.124	0.11	0.0129	0.0113	0.05	0.03	0.016	0.0045	0.0061
97	Bk	0.13	0.117	0.014	0.0122	0.052	0.032	0.016	0.0044	0.0062
98	Cf	0.137	0.122	0.0105	0.0087	0.054	0.033	0.017		0.0057
99	Es	0.142	0.127	0.0113	0.0094	0.057	0.035	0.017		0.0058
100	Fm	0.149	0.133	0.017	0.0147	0.059	0.036	0.017	0.0042	0.0065
101	Md	0.154	0.137	0.0129	0.0105	0.061	0.037	0.017		0.0059
102	No	0.161	0.142	0.0136	0.0111	0.063	0.038	0.018		0.006
103	Lr	0.174	0.154	0.0199	0.017	0.071	0.044	0.021	0.0039	0.0069
104	Rf	0.19	0.171	0.026	0.0228	0.082	0.055	0.033	0.005	0.0075

inner orbitals of heavy elements. Significant atomic-electron binding energy shifts for the non-valence shells may occur with changes of chemical state (Shirley et al. 1977).

11.4.2 X-Ray Energies and Intensities

The X-ray transitions between the inner K atomic shell and the subshells of higher lying shells have been classified by Siegbahn according to ➤ [Table 11.21](#). Due to the

■ Table 11.21

Siegbahn notation for X-ray transitions

Siegbahn Notation	Transition
$K_{\alpha 1}$	$K-L_1$
$K_{\alpha 2}$	$K-L_2$
$K_{\beta 1}$	$K-M_3$
$K_{\beta 2}$	$K-N_{2+3}$
$K_{\beta 3}$	$K-M_2$
$K_{\beta 4}$	$K-N_{4+5}$
$K_{\beta 5}$	$K-M_{4+5}$

■ Table 11.22

K X-ray energies, relative intensities, and fluorescence yields

Z	Element	$E(I)-K_{\alpha 2}$	$E(I)-K_{\alpha 1}$	$E(I)-K_{\beta 1}'$	$E(I)-K_{\beta 2}'$	ω_K
5	B	0.183(49.6)	0.183(100.0)			0.0014
6	C	0.277(49.5)	0.277(100.0)			0.0026
7	N	0.392(49.8)	0.392(100.0)			0.0043
8	O	0.525(49.7)	0.525(100.0)			0.0069
9	F	0.677(49.8)	0.677(100.0)			0.010
10	Ne	0.848(50.0)	0.849(100.0)			0.015
11	Na	1.041(49.9)	1.041(100.0)			0.021
12	Mg	1.254(49.9)	1.254(100.0)			0.029
13	Al	1.486(49.8)	1.487(100.0)	1.554(0.9)		0.039
14	Si	1.739(49.8)	1.740(100.0)	1.836(2.6)		0.050
15	P	2.009(50.1)	2.010(100.0)	2.136(4.5)		0.064
16	S	2.307(50.0)	2.308(100.0)	2.464(7.0)		0.080
17	Cl	2.621(49.9)	2.622(100.0)	2.816(9.3)		0.099
18	Ar	2.955(50.0)	2.957(100.0)	3.190(12.1)		0.120
19	K	3.311(50.1)	3.314(100.0)	3.590(14.0)		0.143
20	Ca	3.688(50.1)	3.692(100.0)	4.013(15.7)		0.169
21	Sc	4.086(50.2)	4.091(100.0)	4.461(16.2)		0.196
22	Ti	4.505(50.3)	4.511(100.0)	4.932(16.8)		0.226
23	V	4.945(50.4)	4.952(100.0)	5.427(17.1)		0.256
24	Cr	5.405(50.5)	5.415(100.0)	5.947(17.0)		0.288
25	Mn	5.888(50.5)	5.899(100.0)	6.490(17.7)		0.321
26	Fe	6.391(50.5)	6.404(100.0)	7.058(18.0)		0.355
27	Co	6.915(50.9)	6.930(100.0)	7.649(18.1)		0.388
28	Ni	7.461(51.0)	7.478(100.0)	8.265(18.2)		0.421

■ **Table 11.22 (Continued)**

<i>Z</i>	Element	$E(I)-K_{\alpha 2}$	$E(I)-K_{\alpha 1}$	$E(I)-K_{\beta 1}'$	$E(I)-K_{\beta 2}'$	ω_K
29	Cu	8.028(50.9)	8.048(100.0)	8.905(18.0)		0.454
30	Zn	8.616(50.9)	8.639(100.0)	9.572(18.3)		0.486
31	Ga	9.225(51.0)	9.252(100.0)	10.263(18.8)	10.366(0.1)	0.517
32	Ge	9.855(51.3)	9.886(100.0)	10.980(19.2)	11.101(0.3)	0.546
33	As	10.508(51.3)	10.544(100.0)	11.724(19.7)	11.864(0.6)	0.575
34	Se	11.182(51.6)	11.222(100.0)	12.494(20.2)	12.652(1.0)	0.602
35	Br	11.878(51.5)	11.924(100.0)	13.290(20.7)	13.469(1.4)	0.628
36	Kr	12.598(51.7)	12.651(100.0)	14.109(21.1)	14.312(1.9)	0.652
37	Rb	13.336(51.8)	13.395(100.0)	14.958(21.6)	15.186(2.3)	0.674
38	Sr	14.098(52.0)	14.165(100.0)	15.832(21.9)	16.088(3.0)	0.696
39	Y	14.883(52.0)	14.958(100.0)	16.734(22.3)	17.016(3.3)	0.716
40	Zr	15.691(52.2)	15.775(100.0)	17.663(22.8)	17.973(3.7)	0.734
41	Nb	16.521(52.4)	16.615(100.0)	18.618(23.1)	18.957(3.9)	0.751
42	Mo	17.374(52.5)	17.479(100.0)	19.602(23.6)	19.970(4.1)	0.767
43	Tc	18.251(52.5)	18.367(100.0)	20.613(23.9)	21.011(4.3)	0.782
44	Ru	19.150(52.6)	19.279(100.0)	21.650(24.2)	22.081(4.5)	0.796
45	Rh	20.074(52.9)	20.216(100.0)	22.716(24.5)	23.179(4.6)	0.807
46	Pd	21.020(53.0)	21.177(100.0)	23.810(24.9)	24.308(4.8)	0.820
47	Ag	21.990(53.1)	22.163(100.0)	24.933(25.2)	25.465(5.0)	0.831
48	Cd	22.984(53.3)	23.174(100.0)	26.084(25.5)	26.655(5.3)	0.842
49	In	24.002(53.3)	24.210(100.0)	27.264(25.8)	27.873(5.4)	0.851
50	Sn	25.044(53.4)	25.271(100.0)	28.473(26.1)	29.121(5.5)	0.860
51	Sb	26.111(53.5)	26.359(100.0)	29.711(26.3)	30.402(5.6)	0.868
52	Te	27.202(53.7)	27.472(100.0)	30.979(26.6)	31.713(5.8)	0.875
53	I	28.317(53.7)	28.612(100.0)	32.277(26.9)	33.057(6.1)	0.882
54	Xe	29.461(54.0)	29.782(100.0)	33.605(27.1)	34.431(6.4)	0.888
55	Cs	30.625(54.1)	30.973(100.0)	34.966(27.4)	35.833(6.7)	0.894
56	Ba	31.817(54.2)	32.194(100.0)	36.355(27.7)	37.272(7.0)	0.900
57	La	33.034(54.5)	33.442(100.0)	37.776(27.9)	38.745(7.3)	0.905
58	Ce	34.279(54.6)	34.720(100.0)	39.230(28.2)	40.251(7.6)	0.910
59	Pr	35.550(54.8)	36.026(100.0)	40.719(28.3)	41.791(7.9)	0.914
60	Nd	36.847(54.9)	37.361(100.0)	42.239(28.5)	43.366(8.3)	0.918
61	Pm	38.171(55.1)	38.725(100.0)	43.791(28.8)	44.975(8.5)	0.922
62	Sm	39.522(55.2)	40.118(100.0)	45.377(29.0)	46.613(8.6)	0.926
63	Eu	40.902(55.5)	41.542(100.0)	46.997(29.1)	48.288(8.8)	0.929
64	Gd	42.309(55.5)	42.996(100.0)	48.650(29.4)	49.998(8.9)	0.932
65	Tb	43.744(55.7)	44.482(100.0)	50.335(29.9)	51.739(8.9)	0.935
66	Dy	45.208(56.0)	45.998(100.0)	52.061(30.4)	53.517(8.9)	0.938

Table 11.22 (Continued)

Z	Element	$E(I)-K_{\alpha 2}$	$E(I)-K_{\alpha 1}$	$E(I)-K_{\beta 1}'$	$E(I)-K_{\beta 2}'$	ω_K
67	Ho	46.700(56.2)	47.547(100.0)	53.820(30.7)	55.332(8.8)	0.940
68	Er	48.221(56.4)	49.128(100.0)	55.613(31.0)	57.181(8.8)	0.942
69	Tm	49.773(56.5)	50.742(100.0)	57.441(31.4)	59.066(8.7)	0.945
70	Yb	51.354(56.5)	52.389(100.0)	59.313(31.8)	60.997(8.7)	0.947
71	Lu	52.965(56.9)	54.070(100.0)	61.215(32.1)	62.961(8.6)	0.949
72	Hf	54.611(57.3)	55.790(100.0)	63.162(32.6)	64.970(8.5)	0.950
73	Ta	56.280(57.4)	57.535(100.0)	65.136(33.0)	67.008(8.5)	0.952
74	W	57.981(57.6)	59.318(100.0)	67.152(33.3)	69.094(8.6)	0.954
75	Re	59.718(57.7)	61.141(100.0)	69.210(33.8)	71.220(8.6)	0.955
76	Os	61.486(58.1)	63.000(100.0)	71.308(34.3)	73.387(8.7)	0.957
77	Ir	63.287(58.1)	64.896(100.0)	73.448(34.6)	75.601(8.9)	0.958
78	Pt	65.122(58.4)	66.831(100.0)	75.630(35.1)	77.859(9.1)	0.959
79	Au	66.991(58.7)	68.806(100.0)	77.855(35.2)	80.162(9.3)	0.960
80	Hg	68.894(58.7)	70.818(100.0)	80.119(35.2)	82.511(9.6)	0.962
81	Tl	70.833(59.1)	72.873(100.0)	82.429(35.3)	84.909(9.9)	0.962
82	Pb	72.805(59.4)	74.969(100.0)	84.784(35.4)	87.352(10.2)	0.963
83	Bi	74.815(59.4)	77.107(100.0)	87.185(35.4)	89.843(10.5)	0.964
84	Po	76.863(59.7)	79.290(100.0)	89.633(35.4)	92.383(10.8)	0.965
85	At	78.948(60.1)	81.517(100.0)	92.129(35.4)	94.971(11.0)	0.966
86	Rn	81.069(60.2)	83.787(100.0)	94.671(35.5)	97.609(11.3)	0.967
87	Fr	83.231(60.6)	86.105(100.0)	97.265(35.6)	100.297(11.5)	0.967
88	Ra	85.431(60.7)	88.471(100.0)	99.908(35.7)	103.037(11.7)	0.968
89	Ac	87.675(61.2)	90.886(100.0)	102.606(36.1)	105.829(11.8)	0.969
90	Th	89.957(61.3)	93.350(100.0)	105.355(36.3)	108.679(12.0)	0.969
91	Pa	92.282(61.7)	95.863(100.0)	108.159(36.4)	111.585(12.1)	0.970
92	U	94.654(61.8)	98.434(100.0)	111.018(36.5)	114.550(12.3)	0.970
93	Np	97.069(62.1)	101.059(100.0)	113.937(36.6)	117.572(12.4)	0.971
94	Pu	99.525(62.6)	103.734(100.0)	116.922(36.2)	120.655(12.5)	0.971
95	Am	102.030(62.9)	105.472(100.0)	119.950(36.6)	123.802(12.6)	0.971
96	Cm	104.590(63.2)	109.271(100.0)	123.051(36.7)	127.018(12.8)	0.972
97	Bk	107.185(63.7)	112.121(100.0)	126.208(37.1)	130.287(13.0)	0.972
98	Cf	109.831(64.2)	115.032(100.0)	129.428(37.4)	133.624(13.2)	0.972
99	Es	112.531(64.5)	118.012(100.0)	132.718(37.6)	137.033(13.3)	0.972
100	Fm	115.285(64.9)	121.058(100.0)	136.077(37.8)	140.515(13.5)	0.973
101	Md	119.088(65.2)	125.170(100.0)	140.506(37.8)	145.067(13.6)	0.973
102	No	120.953(65.5)	127.357(100.0)	143.010(38.1)	147.698(13.7)	0.973
103	Lr	123.867(66.1)	130.611(100.0)	146.585(38.3)	151.402(13.9)	0.973
104	Rf	126.302(66.6)	133.381(100.0)	149.714(38.5)	154.672(14.0)	0.973

unmeasurably small energy differences, it is practical to group together certain K_{β} transitions as:

$$\begin{aligned} K_{\beta 1}' &\rightarrow K_{\beta 1} + K_{\beta 3} + K_{\beta 5} \\ K_{\beta 2}' &\rightarrow K_{\beta 2} + K_{\beta 4} + \dots \end{aligned}$$

➤ **Table 11.22** lists the energies E and intensities I (with the latter in parentheses) of the most prominent K X-rays defined according to ➤ **Table 11.21** and the above equations. The X-ray energies have been determined from the differences in the corresponding atomic shell binding energies (Bearden and Burr 1967). The energies of complex X-ray transitions, e.g., $K-N_{2+3}$, are intensity-weighted averages of the single-line components.

The X-ray intensities have been determined from the experimental relative emission probabilities of Salem et al. (1974) and the atomic yields of Krause (1979). Theoretical emission probabilities (Scofield 1974) were used when experimental values were not available.

■ **Fig. 11.2**
Theoretical total internal conversion coefficients for electric (E) and magnetic (M) multipole transitions in the energy range 10 keV to 1 MeV for the atomic number 10

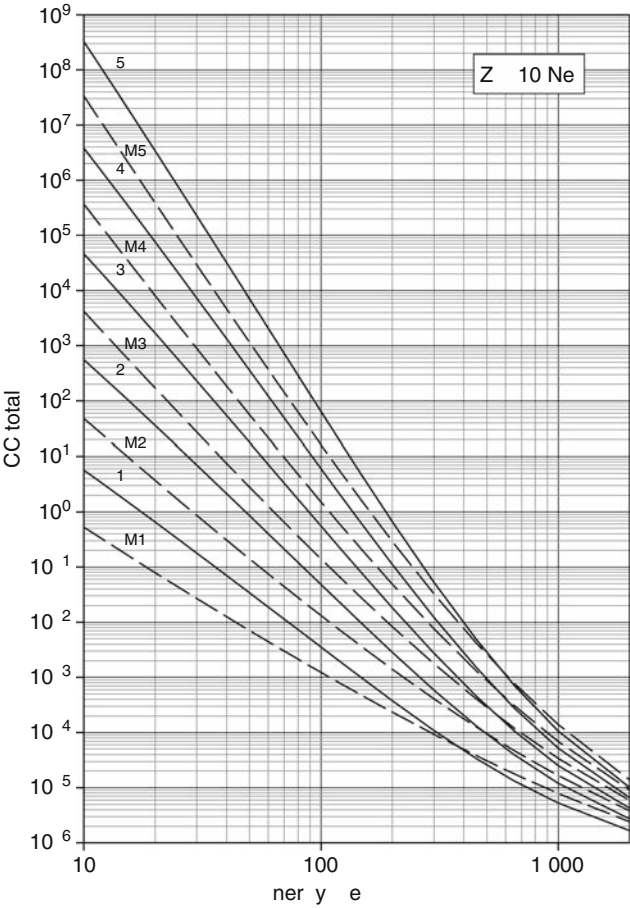
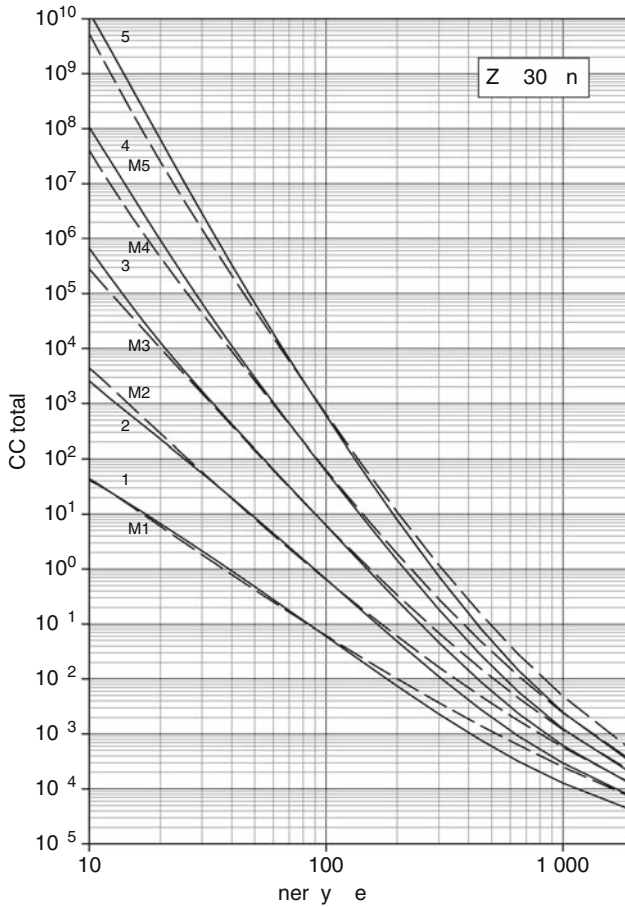


Fig. 11.3

Theoretical total internal conversion coefficients for electric (E) and magnetic (M) multipole transitions in the energy range 10 keV to 1 MeV for the atomic number 30



The relative intensities of X-rays from the same initial atomic shells are independent of the processes creating the shell vacancies. They are normalized to $I(K_{\alpha 1}) = 100$ in [Table 11.22](#). The ω_K fluorescence yields are from a polynomial fit of experimental data (Bambynek 1984).

11.4.3 Internal Conversion Coefficients

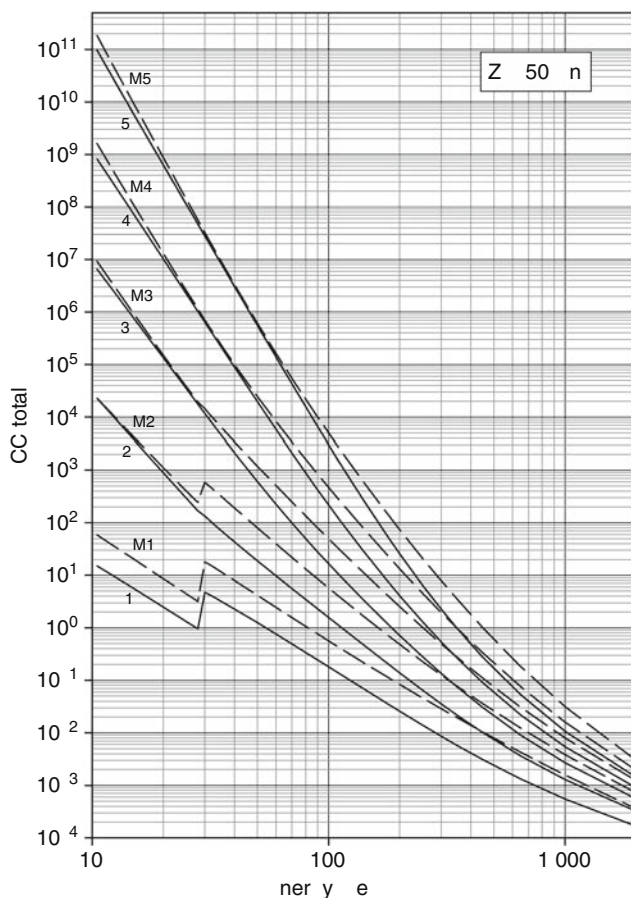
The *internal conversion coefficient (ICC)* of a transition between nuclear levels is defined as the ratio of conversion electron emission intensity to γ -ray emission intensity. For the innermost shell, the K shell, this is:

$$\alpha_K = \frac{I_e}{I_\gamma}$$

The total conversion coefficient α or α_{tot} is the sum of all subshell coefficients.

■ Fig. 11.4

Theoretical total internal conversion coefficients for electric (E) and magnetic (M) multipole transitions in the energy range 10 keV to 1 MeV for the atomic number 50



Recently new ICCs have been obtained from relativistic self-consistent-field Dirac-Fock (DF) calculations for each Z between 10 and 126, for K , L_1 , L_2 , and L_3 atomic shells for nuclear-transition multipolarities $E1$ – $E5$ and $M1$ – $M5$, and for nuclear-transition energies from 1 keV above the L_1 threshold to 2,000 keV (Band et al. 2002). The *total ICC* values were calculated from the sum of partial ICC values from all atomic shells. The calculated K and total values are, on average, about 3% lower than the theoretical relativistic Hartree-Fock-Slater values, and agree better with the most accurate experimental ICC values. A selection of total ICCs is plotted in ► Figs. 11.2–11.7, for atomic numbers $Z = 10, 30, 50, 70, 90$, and 110. The full set of tables and graphs can be found in the original publication.

■ Fig. 11.5

Theoretical total internal conversion coefficients for electric (E) and magnetic (M) multipole transitions in the energy range 10 keV to 1 MeV for the atomic number 70

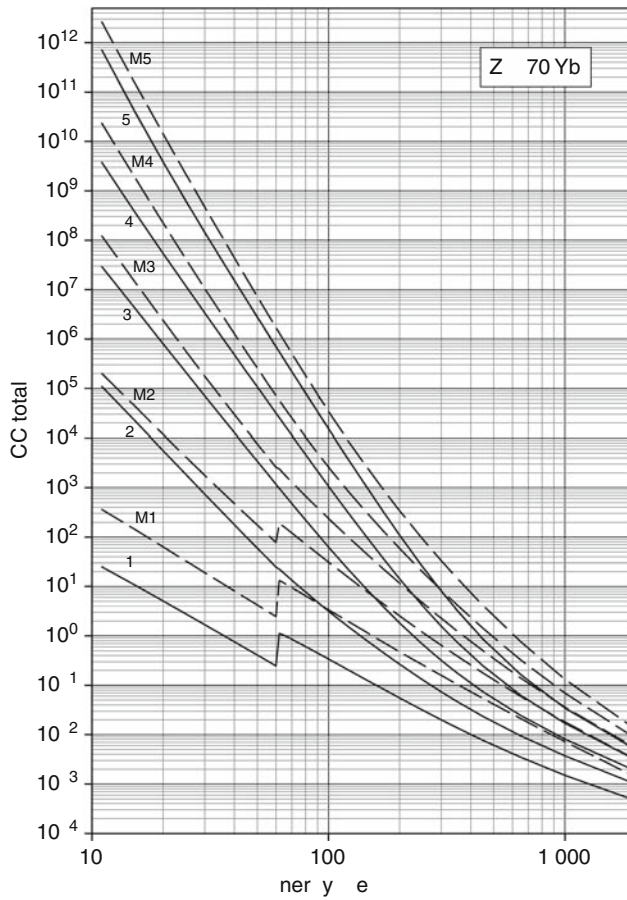
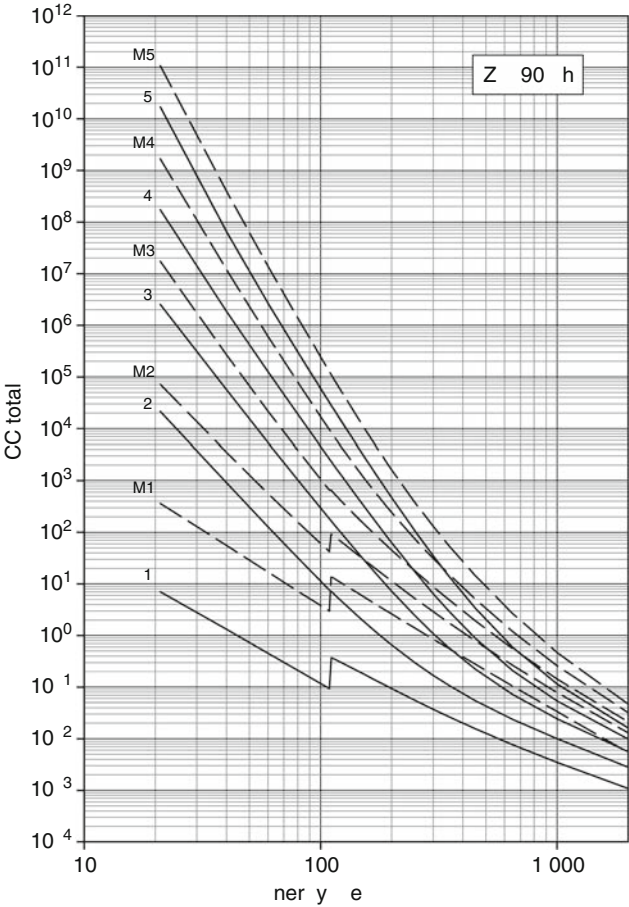
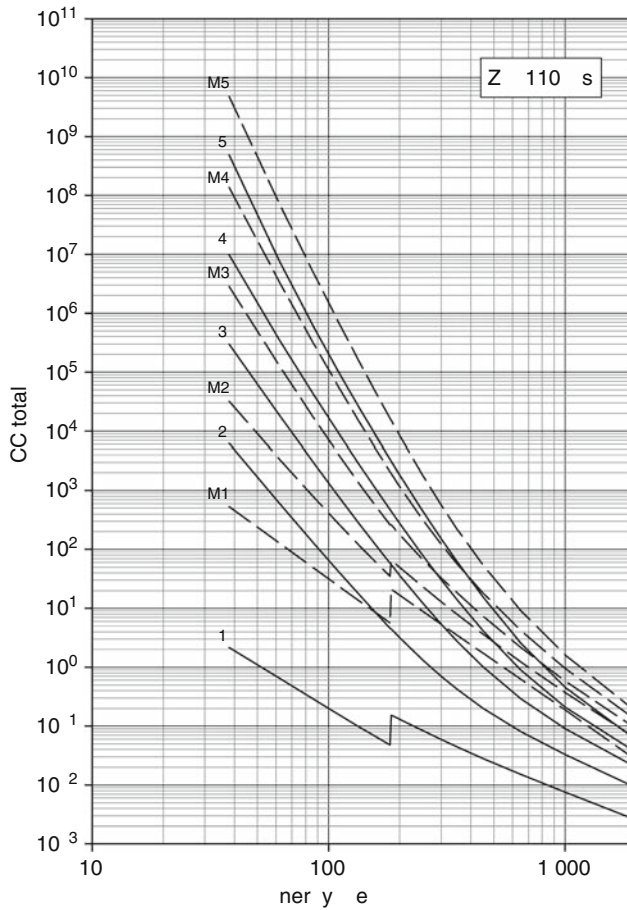


Fig. 11.6
Theoretical total internal conversion coefficients for electric (E) and magnetic (M) multipole transitions in the energy range 10 keV to 1 MeV for the atomic number 90



■ Fig. 11.7

Theoretical total internal conversion coefficients for electric (E) and magnetic (M) multipole transitions in the energy range 10 keV to 1 MeV for the atomic number 110



11.5 Absorption of Radiation in Matter

G. L. Molnár

11.5.1 X- and γ -ray Attenuation Coefficients

When penetrating a matter of thickness d , a collimated beam of X-rays or γ -rays with initial intensity I_0 is attenuated exponentially:

$$I = I_0 \exp(-\mu d) = I_0 \exp(-\ln 2 d / d_{1/2})$$

Here μ is the γ -ray *linear attenuation coefficient*, usually measured in cm^{-1} units. It is a sum of the interaction terms described in [Chap. 6](#) in this Volume, hence it is also called total attenuation coefficient. Its inverse is called the *mean free path*, while the thickness reducing the photon beam by half is the *half-thickness* $d_{1/2}$; both are measured in cm. Frequently the *mass attenuation coefficient* μ/ρ is used, because it does not depend on the physical state of the material. Its dimension is cm^2/g if the density ρ is given in g/cm^3 units. Another important quantity is the *mass-energy absorption coefficient* μ_{en}/ρ , measured in the same units, which characterizes the energy deposition by photons. All these quantities, their units and usage have been defined by the International Commission on Radiation Units and Measurements (ICRU) in ICRU Report 33 (ICRU 1980), which has recently been superseded by two new ones (ICRU 1993c, 1998).

Tables and graphs of μ/ρ and μ_{en}/ρ were presented for elements with $Z = 1$ –92, and for 48 compounds and mixtures of radiological interest (ICRU 1989b) for the energy range of photons from 1 keV to 20 MeV, i.e., for X-rays, γ -rays and bremsstrahlung, by Hubbell and Seltzer (1995). This document is also available on the Internet (Hubbell and Seltzer 1997). A most comprehensive photon cross section database, extended to any element, compound or mixture (with $Z \leq 100$) and up to 100 GeV photon energy was constructed (Berger et al. 1999; Berger and Hubbell 1987) to calculate photon cross sections for coherent and incoherent scattering, photoelectric absorption and pair production, as well as total attenuation coefficients. Interpolation to arbitrary energy and data plotting is done by the computer program XCOM, which can be used online or downloaded for individual use (Berger et al. 1999).

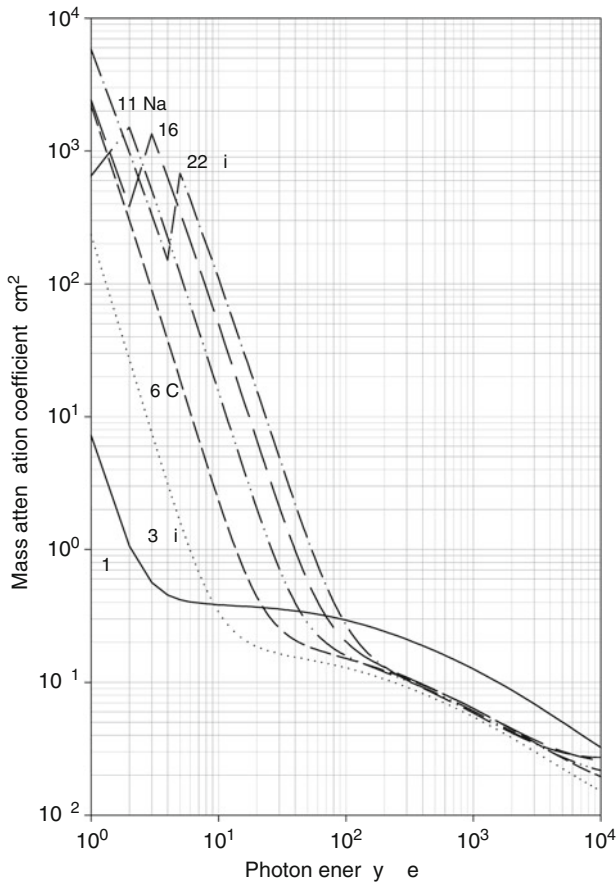
Another useful program is the PC code XMuDat by Nowotny (1998) which is furnished with the databases of Hubbell and Seltzer (1995) and Boone and Chavez (1996). Total mass attenuation coefficients, mass-energy absorption coefficients and half-thicknesses of some representative elements and materials have been calculated with XMuDat and plotted in [Figs. 11.8–11.13](#) for illustration.

11.5.2 Stopping Power and Range of Charged Particles

The penetration of charged particles into matter is characterized by the *stopping power* S defined as the energy loss per unit path length. The most frequently used version is S/ρ , which is measured in $\text{MeV cm}^2/\text{g}$ units. A related quantity is the *range*, which is the path length traveled by a charged particle as it slows down to rest. The continuous-slowing-down approximation range, or *CSDA range*, is obtained by integrating the reciprocal of S with respect to energy from the initial value to zero. The *projected range* is the average value of the depth of

■ Fig. 11.8

Mass attenuation coefficients for light elements from 1 keV to 10 MeV photon energy



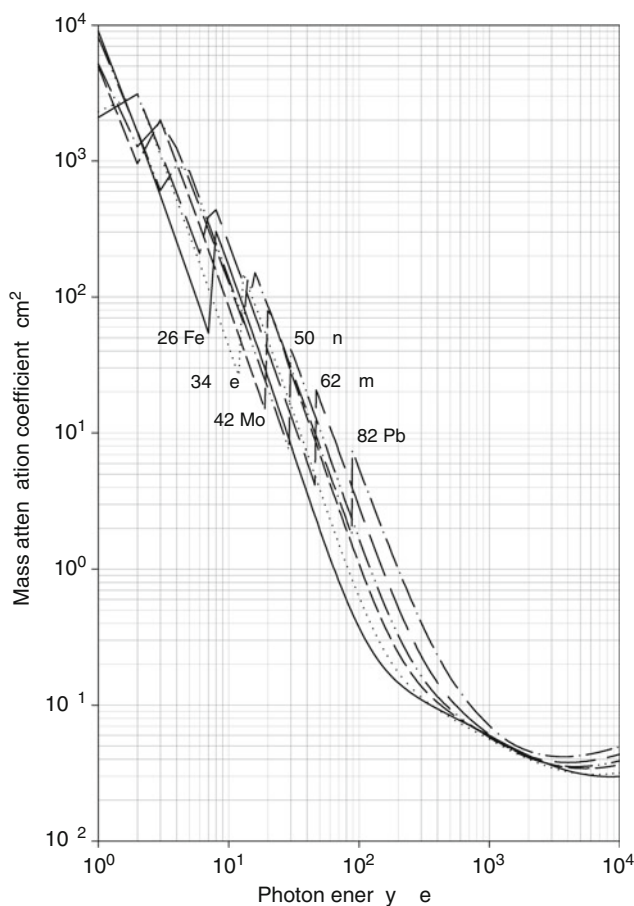
penetration, measured along the initial direction of the particle. The ratio of projected range to the CSDA range is called the detour factor, which is always smaller than unity due to multiple scattering effects. More about these definitions can be found in the ICRU Report 33 (ICRU 1980), and its successors (ICRU 1993c, 1998).

The total stopping power for *electrons* is the sum of collision and radiative stopping powers, as described in ► Chap. 6 in this Volume. These quantities have been tabulated in the ICRU Report 37 for electrons and positrons (ICRU 1989a). The total stopping power for *protons*, *alpha particles* (helium ions) and heavy ions is the sum of collision (atomic) and nuclear stopping powers, the latter being important only at low energies.

Stopping power data for protons and alpha particles have been tabulated in the ICRU Report 49 (ICRU 1993a). While at high energies the Bethe–Bloch theory is accurate to a few percent, at low energies sufficiently accurate values are obtained by fitting experimental data, and in the

■ Fig. 11.9

Mass attenuation coefficients for heavy elements against the photon energy



intermediate range interpolation is performed. The most comprehensive collection of such data has been provided by Ziegler et al. (1985). The extended version of this database is available on the Internet, and is used by the SRIM code (the successor of TRIM) to calculate stopping power and range for protons and heavy ions ($Z = 1-92$) in all elements for the energy range 1.1 eV to 2 GeV per nucleon (Ziegler 2003). The deviation of SRIM values from experiment for more than 25,000 data points has been reduced to 4.6% in the most recent version.

A convenient package of computer codes, consisting of ESTAR for electrons, PSTAR for protons and ASTAR for alpha particles is available for online use and downloading (Berger et al. 2000). They are based on the ICRU data (ICRU 1989, 1993). ESTAR calculates total, collision and radiative stopping powers, CSDA range and *radiation yield* (fraction of kinetic energy converted into bremsstrahlung) for over 250 common materials and any user-specified material in the energy range 10 keV to 10 GeV. The smallest uncertainties are 1–2% above 100 keV for collision stopping powers, and 2% above 50 MeV for radiative stopping powers. PSTAR and ASTAR calculate total, electronic (collision) and nuclear stopping powers, as

■ Fig. 11.10

Mass attenuation coefficients for common shielding materials

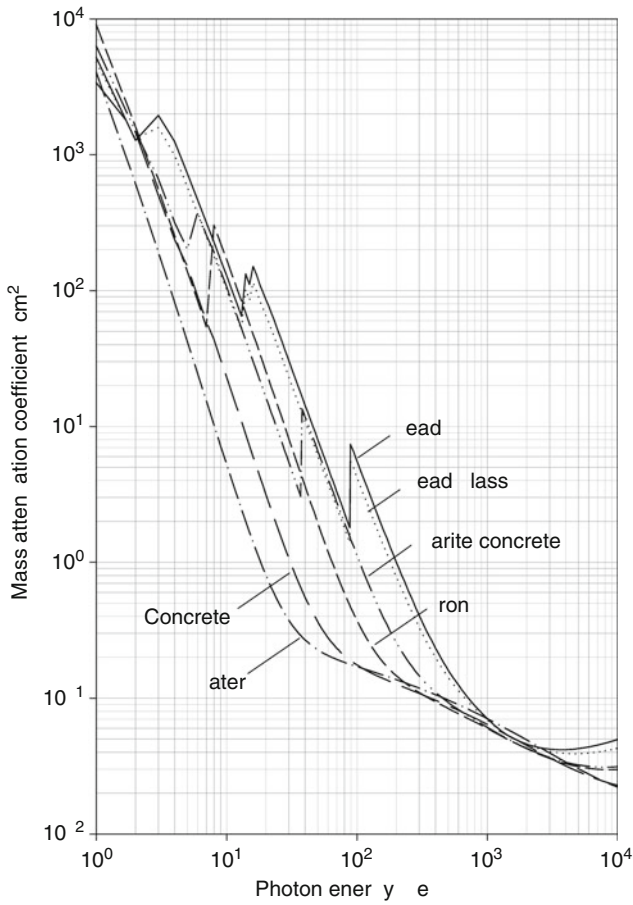
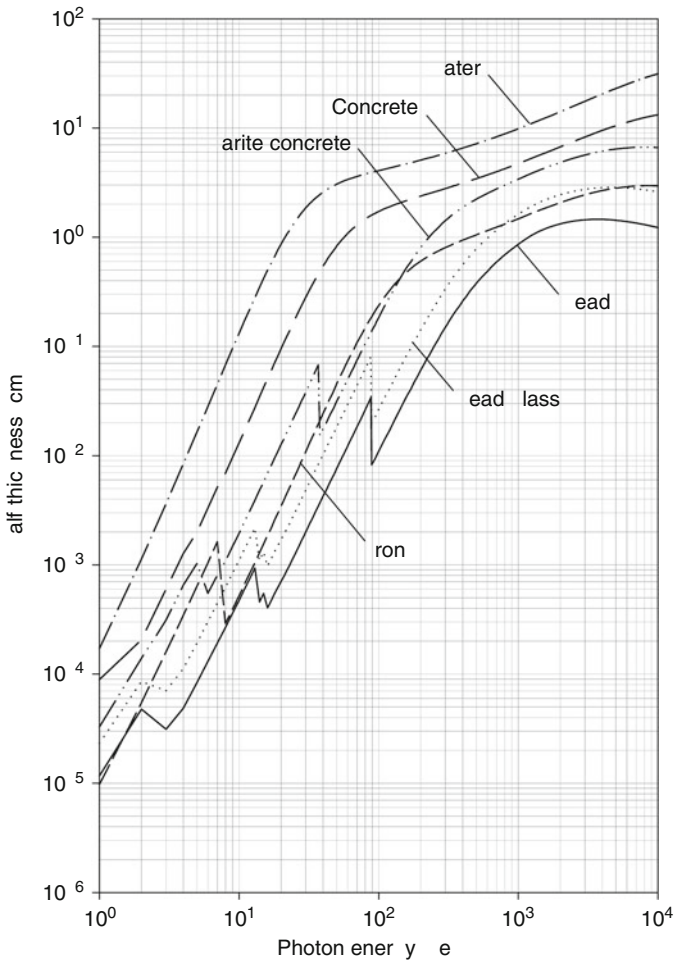


Fig. 11.11
Half-thicknesses for common shielding materials



■ Fig. 11.12

Half-thicknesses for common thin-foil and absorber materials

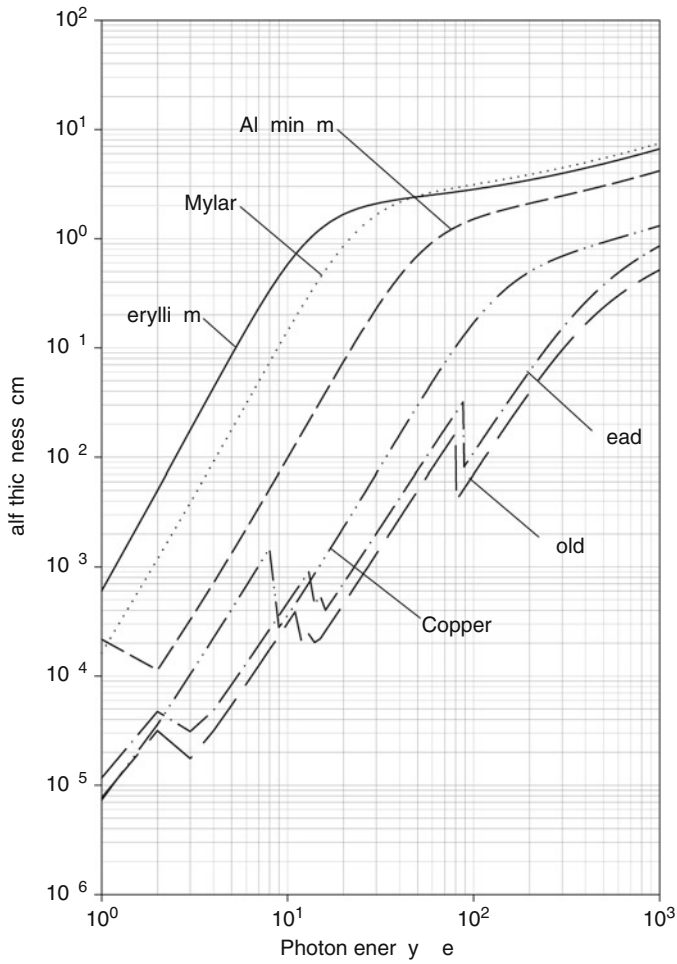
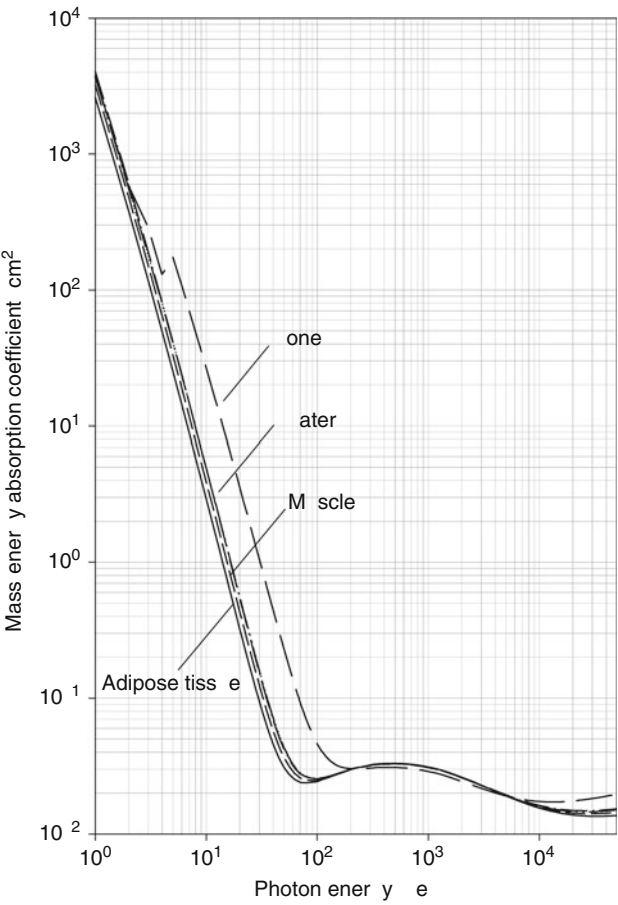


Fig. 11.13
Mass-energy absorption coefficients for various human tissues (ICRU-44) and liquid water



■ Fig. 11.14

Full and radiative stopping power for electrons in aluminum, copper and lead

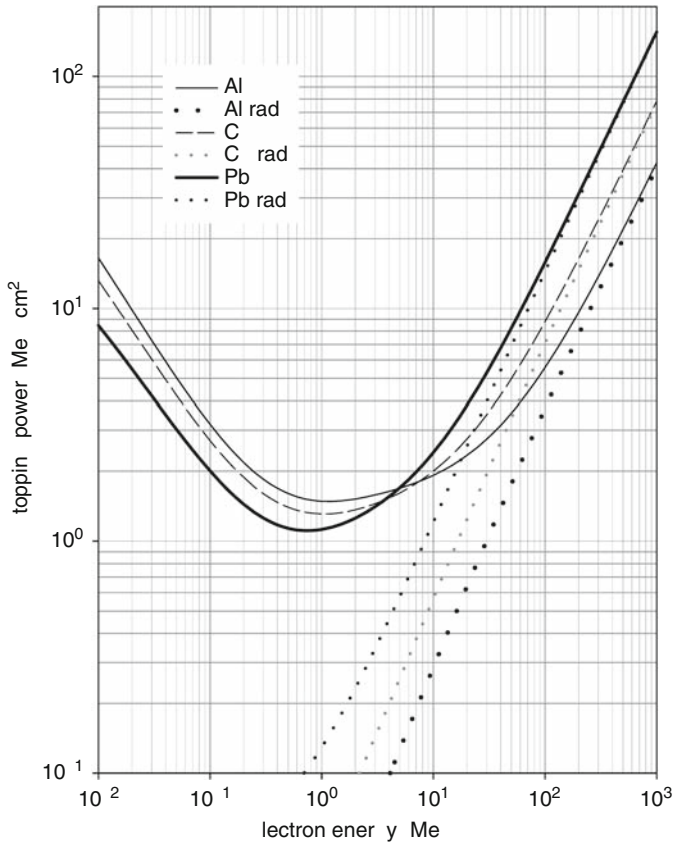
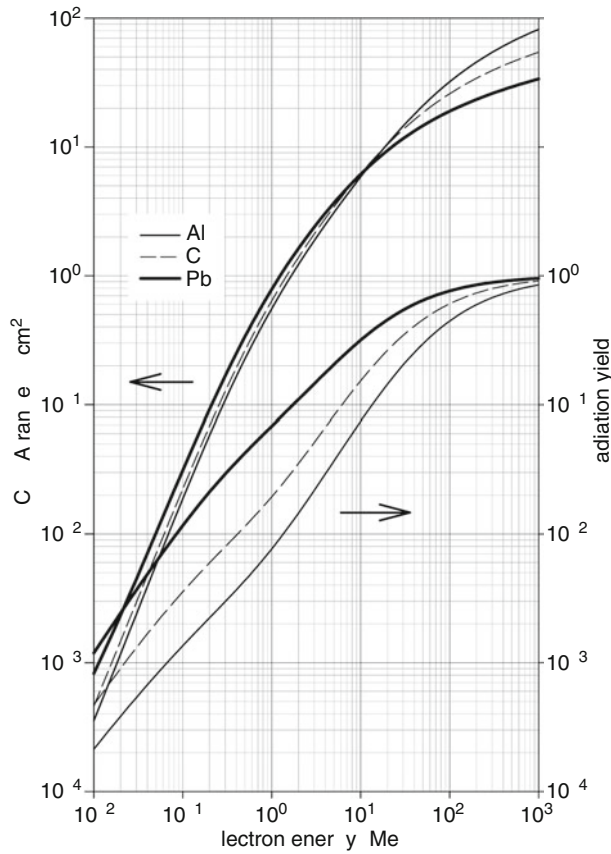


Fig. 11.15
CSDA range and radiation yield for electrons in aluminum, copper and lead



■ Fig. 11.16

Stopping power for electrons in human adipose and bone tissues and water

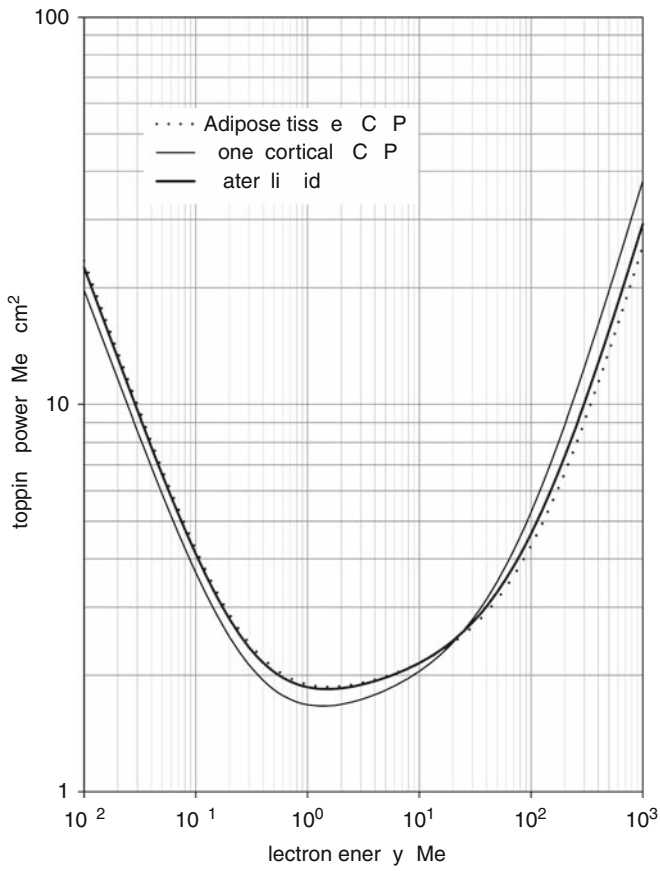
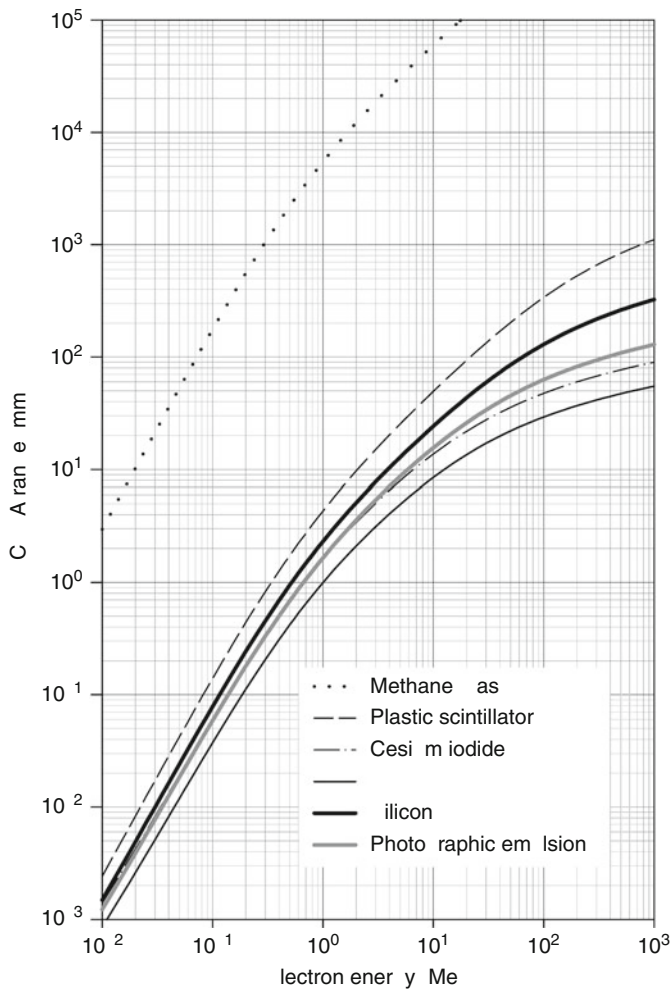


Fig. 11.17
CSDA range for electrons in various detector materials



■ Fig. 11.18

CSDA range for electrons in common thin-foil and absorber materials

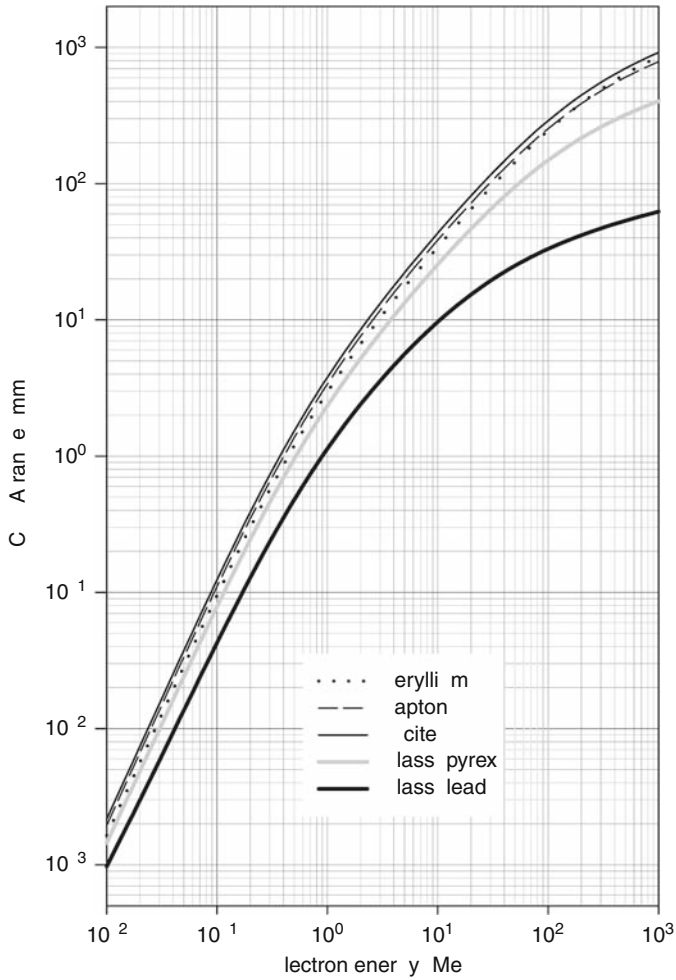
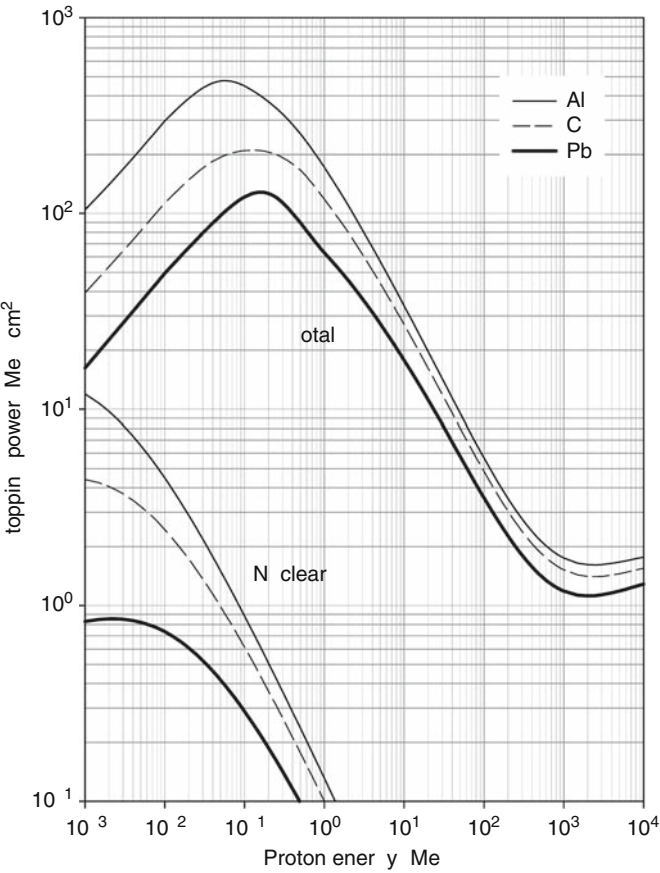


Fig. 11.19

Total and nuclear stopping power for protons in aluminum, copper and lead



■ Fig. 11.20

Projected and CSDA range of protons for aluminum, copper and lead

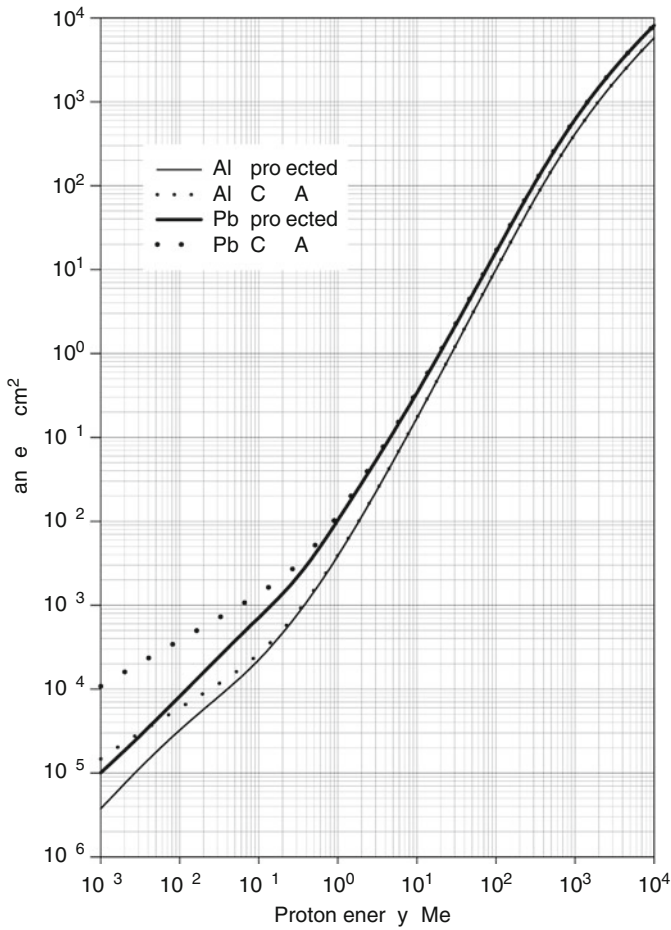
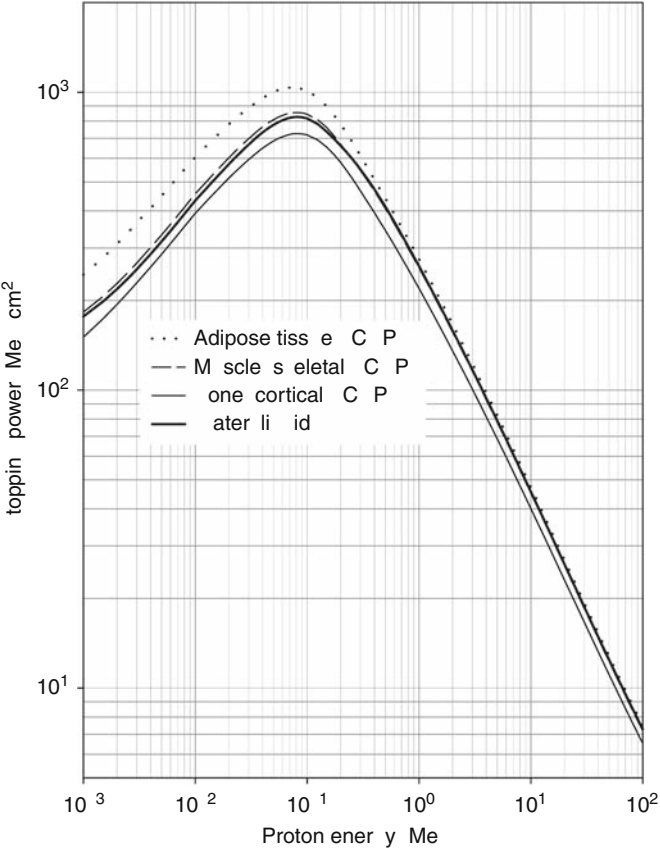


Fig. 11.21

Stopping power for protons in various human tissues and liquid water



■ Fig. 11.22

Projected range for protons in various detector materials

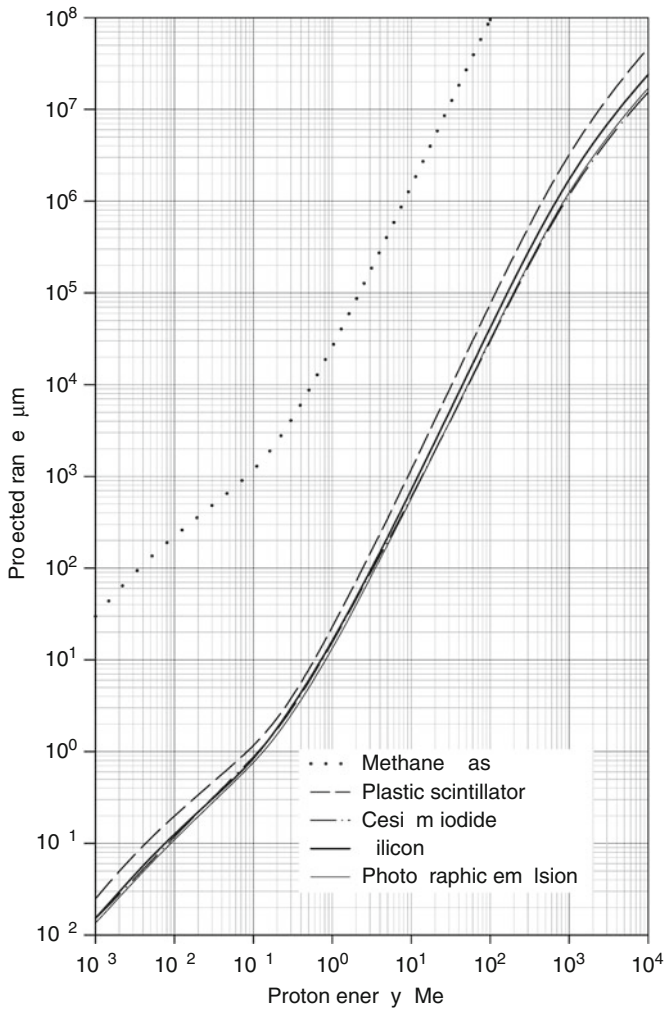
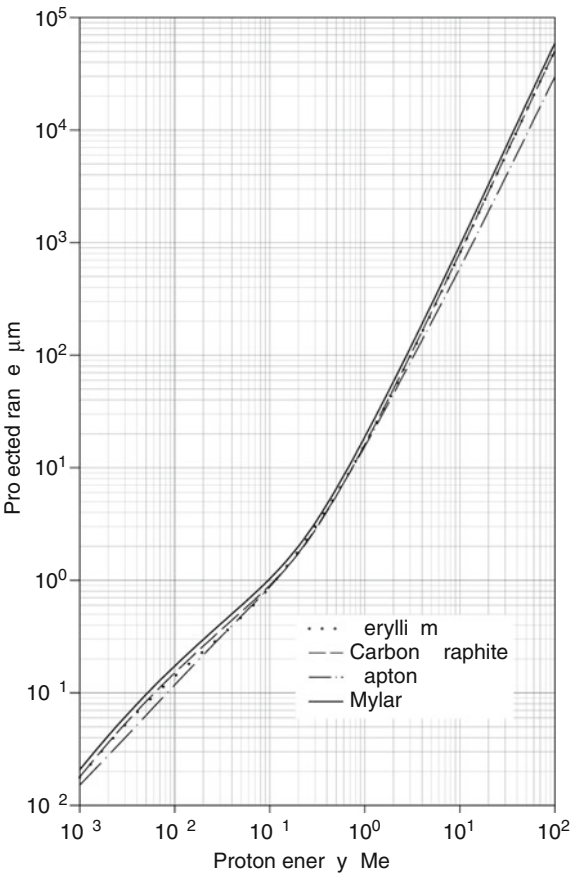


Fig. 11.23
Projected range for protons in common thin-foil materials



■ Fig. 11.24

Total and nuclear stopping powers for helium ions in aluminum, copper and lead

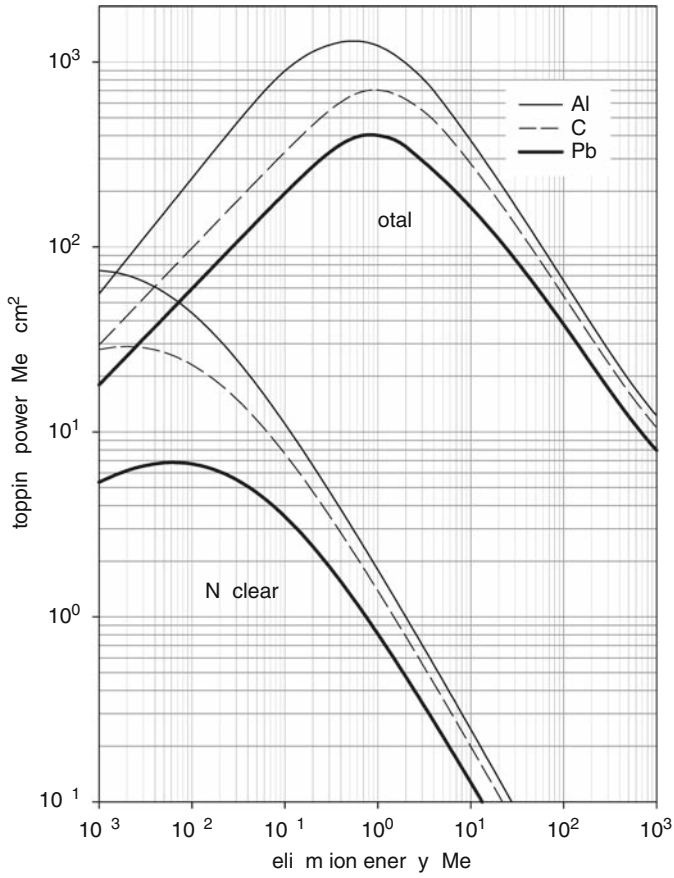
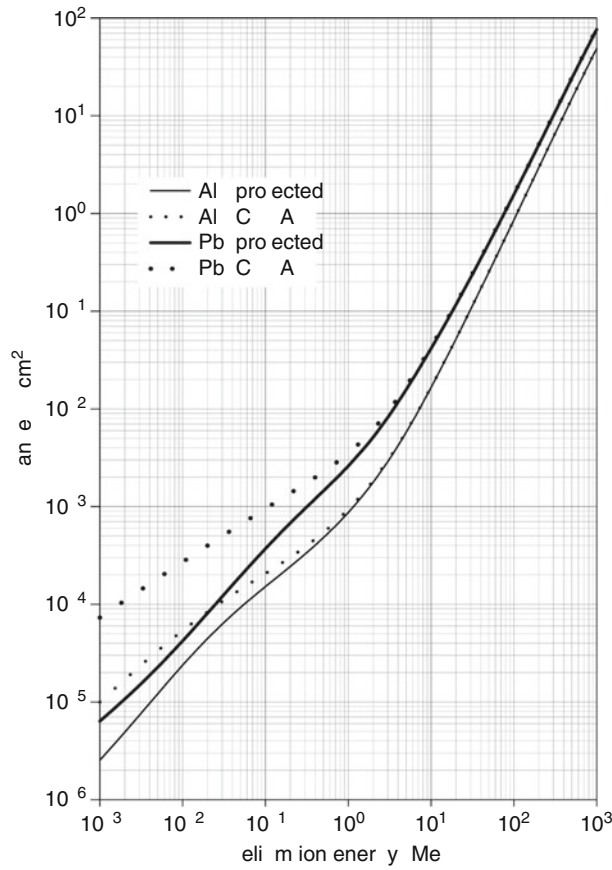
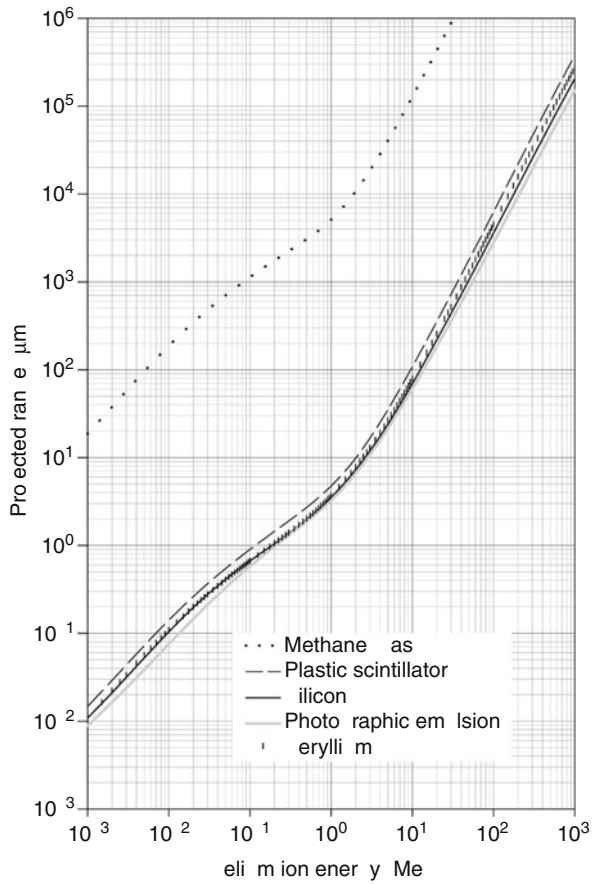


Fig. 11.25
Projected and CSDA ranges for helium ions in aluminum and lead



■ Fig. 11.26

Projected range for helium ions in various detector materials and beryllium



well as CSDA and projected ranges for 74 materials (26 elements, 48 compounds and mixtures) in the energy range 1 keV to 10 GeV (protons) or 1 GeV (helium ions). An extension is the MSTAR code (Paul and Schinner 2003), which is applicable to ions with $Z = 3\text{--}18$. In [Figs. 11.14–11.26](#) representative results are plotted for electrons, protons and helium ions, as obtained using the online versions of ESTAR, PSTAR and ASTAR, respectively.

11.6 Nuclear Masses and Separation Energies

G. L. Molnár

With very few exceptions, data on masses of nuclei refer to “atomic” masses or to masses of singly ionized atoms. The *nuclear mass* of an isotope with mass number A of element Z can be calculated from the atomic mass as:

$$M_N(A, Z) = M_A(A, Z) - Zm_e + B_e(Z) \quad (11.1)$$

where m_e is the electron mass, and B_e is the total atomic binding energy. The atomic masses are usually given in *atomic mass units* as relative atomic masses A_r (see [Section 11.3](#)) and the derived quantities in energy units. The electronvolt (eV) maintained in standard laboratories by using the internationally adopted value for the ratio of frequency and voltage in the Josephson effect ([Section 11.2, Table 11.10](#)) was introduced by Audi and Wapstra in 1993 (Audi and Wapstra 1993a) for the atomic mass evaluation, because at that time it gave more consistent and accurate values than the international volt. Their adopted mass–energy conversion constant (Audi et al. 1993)

$$1 \text{ u} = 931, 493.86 \pm 0.07 \text{ keV} \quad (11.2)$$

is smaller by a factor of only 1.6×10^{-7} than the most recent international value given in [Section 11.2](#). Therefore, the evaluated data remain practically unaffected.

The quantity most frequently tabulated is the *mass excess*:

$$D = M_A - A \quad (11.3)$$

i.e., the difference between the atomic mass and the mass number A (Audi and Wapstra 1995). The total *binding energy* of the atom is:

$$B = Z D(\text{H}) + N D(\text{n}) - D \quad (11.4)$$

where $D(\text{H})$ and $D(\text{n})$ denote the mass excess for the hydrogen atom and the neutron, respectively.

Other important derived quantities are the characteristic energies or Q -values for beta decay and alpha decay, and the neutron and proton *separation energies* $S(\text{n})$ and $S(\text{p})$, respectively:

$$\begin{aligned} Q(\beta^-) &= M(A, Z) - M(A, Z + 1) \\ Q(\beta^+) &= M(A, Z) - M(A, Z - 1) \\ S(\text{n}) &= -M(A, Z) + M(A - 1, Z) + M(\text{n}) \\ S(\text{p}) &= -M(A, Z) + M(A - 1, Z - 1) + M(^1\text{H}) \end{aligned} \quad (11.5)$$

Here the subscript A has been omitted for brevity. The Q -values for more complex nuclear reactions can be derived from the related atomic masses in a similar manner (Audi and Wapstra 1993b).

■ Table 11.23

Mass excess, decay and separation energies in keV units

A	Z	Element	Mass excess	$Q(\beta^-)$	$Q(\alpha)$	$S(n)$	$S(p)$
1	0	n	8,071.323(2)	782.353(2)	^a	0	^a
	1	H	7,288.969(1)	^a	^a	^a	0
2	1	H	13,135.720(1)	^a	^a	2,224.57	2,224.57
3	1	H	14,949.794(1)	18.591(1)	^a	6,257.25	^a
	2	He	14,931.204(1)	^a	^a	^a	5,493.49
4	1	H	25,930(110)	23,500(110)	^a	−2,907(110)	^a
	2	He	2,424.911(1)	^a	0	20,577.62	19,813.85
	3	Li	25,320(210)	22,900(210)	^a	^a	−3,100(210)
5	1	H	36,830(950)	25,450(950)	^a	−2,835(950)	^a
	2	He	11,390(50)	^a	890(50)	−890(50)	21,831(120)
	3	Li	11,680(50)	290(70)	1,965(50)	21,713(220)	−1,965(50)
	4	Be	38,000(4,000) ^b	26,320(4,000) ^b	^a	^a	−5,386(4,000) ^b
6	1	H	41,860(260)	24,270(260)	^a	3,042(980)	^a
	2	He	17,594.1(10)	3,507.8(9)	^a	1,863(50)	26,529(950)
	3	Li	14,086.3(5)	^a	−1,474.3(5)	5,664(50)	4,589(50)
	4	Be	18,374(5)	4,288(5)	^a	27,692(4,000) ^b	593(50)
7	2	He	26,110(30)	11,203(30)	^a	−445(30)	23,042(270)
	3	Li	14,907.7(5)	^a	−2,467.0(5)	7,249.96(9)	9,975.4(9)
	4	Be	15,769.5(5)	861.815(18)	−1,586.6(5)	10,676(5)	5,605.79(9)
	5	B	27,870(70)	12,100(70)	^a	^a	−2,204(70)
	6	C	35,094(23)	12,173(23)	^a	^a	63(70)
8	2	He	31,598(7)	10,652(7)	^a	2,584(30)	^a
	3	Li	20,946.2(5)	16,004.5(5)	−7,407(110)	2,032.80(12)	12,453(30)
	4	Be	4,941.66(4)	^a	91.84(4)	18,899.2(5)	17,255.0(5)
	5	B	22,921.0(11)	17,979.3(11)	−4,824(210)	13,018(70)	137.5(10)
	6	C	35,094(23)	12,173(23)	^a	^a	63(70)
	7	N	39,700(400) ^b	24,000(400) ^b	^a	^a	−3,496(400) ^b
9	2	He	40,820(60)	15,860(60)	^a	−1,149(60)	^a
	3	Li	24,953.9(19)	13,606.3(19)	−14,305(950)	4,063.6(20)	13,933(7)
	4	Be	11,347.6(4)	^a	−2,464(50)	1,665.4(4)	16,887.6(6)
	5	B	12,415.7(10)	1,068.1(9)	−1,688(50)	18,576.6(15)	−185.1(10)
	6	C	28,913.7(22)	16,497.9(24)	−11,507(4,000) ^b	14,252(23)	1,296.3(24)
	7	N	39,700(400) ^b	24,000(400) ^b	^a	^a	−3,496(400) ^b
10	2	He	48,810(70)	15,760(70)	^a	80(90)	^a
	3	Li	33,050(15)	20,444(15)	−11,238(270)	−25(15)	15,057(60)
	4	Be	12,606.6(4)	555.8(5)	−7,412.5(11)	6,812.33(6)	19,636.3(19)
	5	B	12,050.8(4)	^a	−4,460.5(6)	8,436.3(11)	6,585.8(5)
	6	C	15,698.6(4)	3,647.81(9)	−5,101(5)	21,286.4(22)	4,006.1(11)
	7	N	39,700(400) ^b	24,000(400) ^b	^a	^a	−3,496(400) ^b
	8	O	48,810(70)	15,760(70)	^a	^a	−3,496(400) ^b
11	3	Li	40,796(27)	20,622(28)	^a	326(30)	15,303(80)
	4	Be	20,174(6)	11,506(6)	−8,361(30)	504(6)	20,165(16)
	5	B	8,668.0(4)	^a	−8,664.6(6)	11,454.10(20)	11,227.6(6)
	6	C	10,650.5(10)	1,982.5(9)	−7,543.9(11)	13,119.4(9)	8,689.2(9)
	7	N	24,960(180)	14,310(180)	−5,332(190)	22,809(440) ^b	−1,973(180)

Table 11.23 (Continued)

A	Z	Element	Mass excess	$Q(\beta^-)$	$Q(\alpha)$	$S(n)$	$S(p)$
12	3	Li	50,100(1,000) ^b	25,020(1,000) ^b	^a	−1,229(1,000) ^b	^a
	4	Be	25,076(15)	11,708(15)	−8,946(17)	3,169(16)	23,008(30)
	5	B	13,368.9(14)	13,368.9(14)	−10,002.2(15)	3,370.4(15)	14,094(7)
	6	C	0(0)	^a	−7,366.57(4)	18,721.9(10)	15,957.0(4)
	7	N	17,338.1(10)	17,338.1(1)	−8,007.8(15)	15,694(180)	601.4(14)
	8	O	32,048(18)	14,710(18)	−5,471(30)	^a	202(180)
13	4	Be	33,660(500)	17,100(500)	−9,585(510)	−511(500)	23,726(1,120) ^b
	5	B	16,562.2(11)	13,437.2(11)	−10,816.6(22)	4,878.0.0(18)	15,803(15)
	6	C	3,125.011(1)	^a	−10,647.5(4)	4,946.31	17,532.9(14)
	7	N	5,345.46(27)	2,220.45(27)	−9,495.2(10)	20,064.0.0(10)	1,943.51(27)
	8	O	23,111(10)	17,765(10)	−8,228(10)	17,008(21)	1,516(10)
14	4	Be	39,880(110)	16,220(110)	−11,353(130)	1,847(510)	^a
	5	B	23,664(21)	20,644(21)	−11,811(26)	970(21)	17,284(500)
	6	C	3,019.892(4)	156.475(4)	−12,011.6(4)	8,176.44	20,831.3(11)
	7	N	2,863.417(1)	^a	−11,612.3(4)	10,553.36(27)	7,550.56
	8	O	8,006.46(7)	5,143.04(7)	−10,117.0(4)	23,176(10)	4,627.97(28)
	9	F	33,610(400) ^b	25,600(400) ^b	−8,515(570) ^b	^a	−3,209(400) ^b
15	5	B	28,967(22)	19,094(22)	−14,254(40)	2,768(30)	18,204(110)
	6	C	9,873.1(8)	9,771.7(8)	−12,726(6)	1,218.1(8)	21,080(21)
	7	N	101.438(1)	^a	−10,991.5(4)	10,833.3	10,207.42
	8	O	2,855.4(5)	2,753.9(5)	−10,220.1(11)	13,222.4(5)	7,297(5)
	9	F	16,780(130)	13,920(130)	−10,608(220)	24,903(420) ^b	−1,482(130)
16	5	B	37,080(60)	23,390(60)	−15,439(1,000) ^b	−43(60)	^a
	6	C	13,694(4)	8,011(4)	−13,807(15)	4,250(4)	22,562(23)
	7	N	5,683.4(26)	10,420.4(26)	−10,110.4(30)	2,489.3(26)	11,478.7(27)
	8	O	−4,736.998(1)	^a	−7,161.91	15,663.7(5)	12,127.41
	9	F	10,680(8)	15,417(8)	−9,083(8)	14,168(130)	−536(8)
	10	Ne	23,992(20)	13,312(22)	−10,480(28)	^a	74(140)
17	5	B	43,720(140)	22,680(140)	^a	1,437(150)	^a
	6	C	21,037(17)	13,166(23)	−15,047(500)	729(18)	23,334(60)
	7	N	7,871(15)	8,680(15)	−11,116(15)	5,884(15)	13,112(15)
	8	O	−809.00(21)	^a	−6,358.92(21)	4,143.33(21)	13,781.4(26)
	9	F	1,951.70(25)	2,760.7(3)	−5,818.7(4)	16,800(8)	600.27(25)
	10	Ne	16,490(50)	14,530(50)	−9,050(50)	15,579(50)	1,484(50)
18	5	B	52,320(800) ^b	27,400(800) ^b	^a	−534(810) ^b	^a
	6	C	24,920(30)	11,810(40)	−17,383(110)	4,184(30)	26,081(140)
	7	N	13,117(20)	13,899(20)	−12,972(29)	2,825(25)	15,208(26)
	8	O	−782.1(8)	^a	−6,226.9(8)	8,044.4(8)	15,942(15)
	9	F	873.4(6)	1,655.5(6)	−4,414.9(6)	9,149.6(6)	5,606.5(6)
	10	Ne	5,306.8(15)	4,433.4(16)	−5,124.6(15)	19,250(50)	3,933.9(15)
	11	Na	25,320(400) ^b	20,010(400) ^b	−10,715(570) ^b	^a	−1,544(400) ^b
19	5	B	59,360(400) ^b	26,530(420) ^b	^a	1,029(900) ^b	^a
	6	C	32,830(110)	16,970(110)	^a	162(110)	26,778(810) ^b

Table 11.23 (Continued)

A	Z	Element	Mass excess	$Q(\beta^-)$	$Q(\alpha)$	$S(n)$	$S(p)$
	7	N	15,860(16)	12,527(17)	–15,531(28)	5,328(26)	16,353(30)
	8	O	3,334(3)	4,821(3)	–8,964(3)	3,956(3)	17,073(20)
	9	F	–1,487.40(7)	^a	–4,013.75(7)	10,432.2(6)	7,994.3(8)
	10	Ne	1,751.1(6)	3,238.5(6)	–3,529.2(8)	11,627.1(16)	6,411.3(8)
	11	Na	12,929(12)	11,178(12)	–6,273(130)	20,461(400) ^b	–333(12)
20	6	C	37,560(200)	15,790(210)	^a	3,345(230)	29,093(450) ^b
	7	N	21,770(50)	17,970(50)	–17,740(80)	2,165(60)	18,356(120)
	8	O	3,796.9(12)	3,814.3(12)	–12,322(4)	7,608(3)	19,353(16)
	9	F	–17.40(8)	7,024.53(8)	–8,125.7(26)	6,601.31(5)	10,640(3)
	10	Ne	–7,041.930(2)	^a	–4,729.84	16,864.3(6)	12,843.49(7)
	11	Na	6,845(7)	13,887(7)	–6,260(11)	14,155(14)	2,195(7)
	12	Mg	17,571(27)	10,726(28)	–8,847(30)	^a	2,647(30)
21	6	C	45,960(500) ^b	20,730(510) ^b	^a	–329(540) ^b	^a
	7	N	25,230(90)	17,170(90)	–20,909(160)	4,606(100)	19,617(220)
	8	O	8,062(12)	8,109(12)	–15,400(21)	3,807(12)	20,994(50)
	9	F	–47.6(18)	5,684.1(18)	–10,343(15)	8,101.5(18)	11,133.5(22)
	10	Ne	–5,731.72(4)	^a	–7,347.63(21)	6,761.11(4)	13,003.29(9)
	11	Na	–2,184.3(7)	3,547.5(7)	–6,560.9(7)	17,100(7)	2,431.3(7)
	12	Mg	10,912(16)	13,096(16)	–7,998(50)	14,730(30)	3,222(18)
22	13	Al	26,120(300) ^b	15,210(300) ^b	^a	^a	–1,260(300) ^b
	6	C	52,580(900) ^b	20,500(930) ^b	^a	1,448(1,030) ^b	^a
	7	N	32,080(200)	22,800(200)	–22,666(830) ^b	1,222(220)	21,168(540) ^b
	8	O	9,280(60)	6,490(60)	–18,065(60)	6,849(60)	23,237(110)
	9	F	2,794(12)	10,818(12)	–12,748(24)	5,230(13)	12,557(17)
	10	Ne	–8,024.34(22)	^a	–9,667.2(8)	10,363.95(22)	15,265.7(18)
	11	Na	–5,182.1(5)	2,842.2(4)	–8,480.5(8)	11,069.2(8)	6,739.4(5)
	12	Mg	–396.8(14)	4,785.3(14)	–8,128.5(20)	19,380(16)	5,501.5(15)
23	13	Al	18,180(90) ^b	18,580(90) ^b	–9,560(410) ^b	16,008(310) ^b	18(100) ^b
	14	Si	32,160(200) ^b	13,980(220) ^b	^a	^a	1,244(360) ^b
	7	N	37,740(710) ^b	23,120(720) ^b	–24,054(810) ^b	2,417(740) ^b	22,137(1,150) ^b
	8	O	14,620(100)	11,290(130)	–20,642(150)	2,739(120)	24,753(220)
	9	F	3,330(80)	8,480(80)	–14,956(80)	7,536(80)	13,244(100)
	10	Ne	–5,153.64(25)	4,375.84(2)	–10,912(3)	5,200.62(12)	15,236(12)
	11	Na	–9,529.49(21)	^a	–10,466.99(22)	12,418.7(4)	8,794.11(16)
	12	Mg	–5,472.7(13)	4,056.8(12)	–9,648.6(14)	13,147.2(18)	7,579.5(13)
24	13	Al	6,767(25)	12,240(25)	–8,586(28)	19,487(100) ^b	125(25)
	14	Si	23,770(200) ^b	17,010(200) ^b	^a	16,464(280) ^b	1,700(220) ^b
	7	N	47,040(500) ^b	28,070(590) ^b	^a	–1,234(870) ^b	^a
	8	O	18,970(310)	11,430(320)	–21,011(370)	3,713(320)	26,049(770) ^b
	9	F	7,540(70)	13,490(70)	–16,647(80)	3,856(100)	14,361(120)
	10	Ne	–5,948(10)	2,470(10)	–12,169(10)	8,865(10)	16,566(80)
	11	Na	–8,417.60(22)	5,515.78(16)	–10,825.12(23)	6,959.44(5)	10,552.93(20)
	12	Mg	–13,933.38(19)	^a	–9,316.36(19)	16,532.0(12)	11,692.86(15)

Table 11.23 (Continued)

A	Z	Element	Mass excess	$Q(\beta^-)$	$Q(\alpha)$	$S(n)$	$S(p)$
	13	Al	−55(4)	13,878(4)	−9,325(8)	14,894(25)	1,871(4)
	14	Si	10,755(19)	10,810(20)	−9,241(30)	21,088(200) ^b	3,301(30)
	15	P	32,000(500) ^b	21,240(500) ^b	^a	^a	−936(540) ^b
25	8	O	27,140(370) ^b	15,880(380) ^b	−21,241(630) ^b	−98(480) ^b	27,186(630) ^b
	9	F	11,270(80)	13,330(90)	−16,390(120)	4,349(100)	14,997(320)
	10	Ne	−2,060(40)	7,300(40)	−12,545(50)	4,183(50)	16,892(80)
	11	Na	−9,357.5(12)	3,835.3(12)	−11,734.8(22)	9,011.2(12)	10,699(10)
	12	Mg	−13,192.73(19)	^a	−9,885.92(19)	7,330.67(4)	12,064.09(16)
	13	Al	−8,915.7(7)	4,277(7)	−9,156.4(10)	16,932(4)	2,271.3(7)
	14	Si	3,825(10)	12,741(10)	−9,511(19)	15,001(22)	3,409(11)
	15	P	18,870(200) ^b	15,050(200) ^b	−9,672(360) ^b	21,196(540) ^b	−828(200) ^b
	16	S	35,160(430) ^b	16,880(450) ^b	−19,844(1,000) ^b	51(570) ^b	^a
26	8	O	35,160(430) ^b	16,880(450) ^b	−19,844(1,000) ^b	51(570) ^b	^a
	9	F	18,290(120)	17,860(140)	−16,218(230)	1,050(150)	16,145(390) ^b
	10	Ne	430(50)	7,330(60)	−11,279(80)	5,583(70)	18,125(90)
	11	Na	−6,902(14)	9,312(14)	−12,121(19)	5,616(14)	12,133(50)
	12	Mg	−16,214.48(19)	^a	−10,615.04(20)	11,093.07(4)	14,146.0(12)
	13	Al	−12,210.34(20)	4,004.14(6)	−9,453.2(5)	11,365.9(7)	6,306.58(5)
	14	Si	−7,145(3)	5,066(3)	−9,173(3)	19,041(10)	5,518(3)
	15	P	10,970(200) ^b	18,120(200) ^b	−9,635(220) ^b	15,970(280) ^b	141(200) ^b
27	9	F	25,050(420)	17,960(430)	−15,110(820) ^b	1,309(440)	17,403(600) ^b
	10	Ne	7,090(90)	12,670(100)	−9,948(140)	1,408(110)	18,484(150)
	11	Na	−5,580(40)	9,010(40)	−11,335(90)	6,750(40)	13,300(70)
	12	Mg	−14,586.5(2)	2,610.33(17)	−11,857.77(24)	6,443.35(4)	14,973(14)
	13	Al	−17,196.83(13)	^a	−10,092.25(20)	13,057.81(17)	8,271.32(16)
	14	Si	−12,384.43(16)	4,812.4(1)	−9,336.7(13)	13,311.1(30)	7,463.06(19)
	15	P	−750(40)	11,630(40)	−9,945(40)	19,797(200) ^b	897(40)
	16	S	17,510(200) ^b	18,260(200) ^b	−8,690(280) ^b	16,534(360) ^b	755(280) ^b
28	9	F	33,230(510) ^b	21,950(530) ^b	−16,239(720) ^b	−105(660) ^b	^a
	10	Ne	11,280(110)	12,310(140)	−10,121(330)	3,886(140)	21,060(430)
	11	Na	−1,030(80)	13,990(80)	−11,003(100)	3,524(80)	15,416(120)
	12	Mg	−15,018.8(20)	1,831.8(2)	−11,496(10)	8,503.6(20)	16,727(40)
	13	Al	−16,850.55(14)	4,642.24(14)	−10,857.86(21)	7,725.05(6)	9,553.02(18)
	14	Si	−21,492.793(2)	^a	−9,984.32(19)	17,179.69(16)	11,584.93(13)
	15	P	−7,161(4)	14,332(4)	−9,531(5)	14,479(40)	2,066(4)
	16	S	4,070(160)	11,230(160)	−9,107(160)	21,505(260) ^b	2,463(160)
29	17	Cl	26,560(500) ^b	22,480(530) ^b	−7,865(710) ^b	^a	−1,761(540) ^b
	9	F	40,300(580) ^b	22,280(650) ^b	^a	1,001(770) ^b	^a
	10	Ne	18,020(300)	15,400(310)	−11,548(480) ^b	1,329(320)	22,495(590) ^b
	11	Na	2,620(90)	13,280(90)	−11,073(120)	4,419(120)	15,949(140)
	12	Mg	−10,661(29)	7,554(29)	−11,027(50)	3,714(29)	16,917(80)
	13	Al	−18,215.5(12)	3,679.5(12)	−11,283.0(17)	9,436.3(12)	10,485.7(23)
	14	Si	−21,895.025(28)	^a	−11,127.21(19)	8,473.55(3)	12,333.44(14)

■ Table 11.23 (Continued)

A	Z	Element	Mass excess	$Q(\beta^-)$	$Q(\alpha)$	$S(n)$	$S(p)$
30	15	P	−16,951.9(7)	4,943.1(7)	−10,461.1(10)	17,862(4)	2,748.1(7)
	16	S	−3,160(50)	13,790(50)	−9,409(50)	15,303(170)	3,287(50)
	17	Cl	13,140(200) ^b	16,300(200) ^b	−8,154(280) ^b	21,485(540) ^b	−1,781(250) ^b
	10	Ne	22,240(820)	13,640(830)	−15,352(930) ^b	3,855(880)	25,349(1,010) ^b
	11	Na	8,590(90)	17,480(110)	−12,119(160)	2,096(130)	16,715(320)
	12	Mg	−8,880(70)	6,990(70)	−11,737(90)	6,292(70)	18,790(110)
	13	Al	−15,872(14)	8,561(14)	−11,395(20)	5,728(14)	12,500(30)
	14	Si	−24,432.88(4)	^a	−10,643.32(20)	10,609.18(3)	13,506.4(12)
	15	P	−20,200.6(4)	4,232.3(4)	−10,415.1(5)	11,320.0(8)	5,594.5(4)
	16	S	−14,063(3)	6,138(3)	−9,343(4)	18,975(50)	4,400(3)
31	17	Cl	4,440(200) ^b	18,510(200) ^b	−8,955(280) ^b	16,771(280) ^b	−313(200) ^b
	18	Ar	20,080(300) ^b	15,640(360) ^b	−8,312(420) ^b	^a	349(360) ^b
	10	Ne	30,840(900) ^b	18,180(920) ^b	^a	−534(1,220) ^b	^a
	11	Na	12,660(160)	15,880(180)	−14,811(450)	4,002(190)	16,862(840)
	12	Mg	−3,220(80)	11,740(80)	−12,734(120)	2,404(100)	19,098(120)
	13	Al	−14,954(20)	7,995(20)	−11,798(40)	7,153(25)	13,361(70)
	14	Si	−22,948.96(7)	1,492.03(19)	−10,787.37(21)	6,587.40(5)	14,366(14)
	15	P	−24,440.99(18)	^a	−9,669.07(22)	12,311.8(4)	7,297.08(19)
	16	S	−19,044.9(15)	5,396.1(15)	−9,085.4(15)	13,053(3)	6,133.3(16)
	17	Cl	−7,060(50)	11,980(50)	−8,736(60)	19,579(200) ^b	291(50)
32	18	Ar	11,300(210) ^b	18,360(200) ^b	−8,636(290) ^b	16,859(360) ^b	437(280) ^b
	10	Ne	37,180(880) ^b	18,870(1,000) ^b	^a	1,737(1,260) ^b	^a
	11	Na	18,300(480)	19,100(490)	−17,348(700) ^b	2,431(510)	19,827(1,020) ^b
	12	Mg	−800(100)	10,270(130)	−14,499(150)	5,652(120)	20,748(190)
	13	Al	−11,060(90)	13,020(90)	−12,453(120)	4,179(90)	15,136(120)
	14	Si	−24,080.9(22)	224.5(22)	−11,487.0(30)	9,203.2(22)	16,416(20)
	15	P	−24,305.32(19)	1,710.66(21)	−9,879.68(23)	7,935.65(4)	8,645.33(20)
	16	S	−26,015.98(11)	^a	−6,948.10(11)	15,042.4(15)	8,863.96(21)
	17	Cl	−13,331(7)	12,685(7)	−8,595(8)	14,338(50)	1,575(7)
	18	Ar	−2,180(50)	11,150(50)	−8,677(170)	21,546(210) ^b	2,404(70)
33	19	K	20,420(500) ^b	22,600(510) ^b	−8,563(710) ^b	^a	−1,834(540) ^b
	11	Na	25,510(1,490)	20,310(1,500)	−17,211(1,600) ^b	865(1,570)	18,955(1,730) ^b
	12	Mg	5,200(150)	13,710(160)	−15,241(330)	2,071(170)	20,388(500)
	13	Al	−8,500(70)	11,990(70)	−13,549(110)	5,514(110)	14,998(120)
	14	Si	−20,492(16)	5,845(16)	−12,256(30)	4,483(16)	16,719(90)
	15	P	−26,337.7(11)	248.5(11)	−10,547.1(16)	10,103.7(11)	9,545.8(24)
	16	S	−26,586.24(11)	^a	−7,116.12(11)	8,641.58(3)	9,569.89(21)
	17	Cl	−21,003.5(5)	5,582.7(5)	−6,476.5(9)	15,744(7)	2,276.5(5)
	18	Ar	−9,380(30)	11,620(30)	−8,647(60)	15,274(60)	3,340(30)
	19	K	6,760(200) ^b	16,140(200) ^b	−8,806(280) ^b	21,727(540) ^b	−1,653(200) ^b
34	11	Na	32,510(1,050) ^b	24,060(1,090) ^b	^a	1,072(1,830) ^b	^a
	12	Mg	8,450(260)	11,310(280)	−16,211(860)	4,825(300)	24,348(1,510)
	13	Al	−2,860(90)	17,090(90)	−13,882(130)	2,429(110)	15,355(170)

Table 11.23 (Continued)

A	Z	Element	Mass excess	$Q(\beta^-)$	$Q(\alpha)$	$S(n)$	$S(p)$
	14	Si	−19,957(14)	4,601(15)	−13,499(70)	7,536(21)	18,741(70)
	15	P	−24,558(5)	5,374(5)	−11,110(15)	6,291(5)	11,354(17)
	16	S	−29,931.85(10)	^a	−7,923.88(11)	11,416.94(5)	10,883.1(11)
	17	Cl	−24,440.57(12)	5,491.28(7)	−6,664.9(4)	11,508.4(5)	5,143.30(5)
	18	Ar	−18,378(3)	6,062(3)	−6,740(4)	17,068(30)	4,664(3)
	19	K	−1,480(300) ^b	16,900(300) ^b	−8,349(360) ^b	16,315(360) ^b	−611(300) ^b
	20	Ca	13,150(300) ^b	14,630(420) ^b	−9,355(420) ^b	^a	899(360) ^b
35	11	Na	41,150(1,550) ^b	24,860(1,610) ^b	^a	−573(1,870) ^b	^a
	12	Mg	16,290(440) ^b	16,350(460) ^b	−16,975(1,000) ^b	230(510) ^b	23,506(1,140) ^b
	13	Al	−60(140)	14,300(150)	−15,147(220)	5,267(170)	15,798(300)
	14	Si	−14,360(40)	10,500(40)	−13,570(80)	2,475(40)	18,786(100)
	15	P	−24,857.6(19)	3,988.8(19)	−12,328(20)	8,371(5)	12,190(14)
	16	S	−28,846.37(9)	167.14(8)	−8,322.32(11)	6,985.84(4)	11,578(5)
	17	Cl	−29,013.51(4)	^a	−6,997.43(19)	12,644.27(11)	6,370.63(9)
	18	Ar	−23,048.2(8)	5,965.3(8)	−6,428.2(17)	12,741(3)	5,896.6(8)
	19	K	−11,167(20)	11,881(20)	−6,528(50)	17,757(300) ^b	78(20)
	20	Ca	4,440(70) ^b	15,610(70) ^b	−9,282(220) ^b	16,785(310) ^b	1,369(310) ^b
36	12	Mg	20,910(900) ^b	15,000(940) ^b	−18,689(1,260) ^b	3,451(1,000) ^b	27,530(1,790) ^b
	13	Al	5,920(270)	18,320(290)	−14,812(550)	2,097(300)	17,664(510) ^b
	14	Si	−12,400(100)	7,850(100)	−14,030(140)	6,112(110)	19,632(170)
	15	P	−20,251(13)	10,413(13)	−11,614(90)	3,465(13)	13,180(40)
	16	S	−30,663.96(23)	−1,142.07(25)	−9,008.0(22)	9,888.91(25)	13,095.3(19)
	17	Cl	−29,521.89(8)	708.55(26)	−7,641.48(20)	8,579.70(7)	7,964.48(11)
	18	Ar	−30,230.44(25)	^a	−6,639.37(27)	15,253.6(8)	8,505.09(25)
	19	K	−17,425(8)	12,805(8)	−6,519(10)	14,329(21)	1,666(8)
	20	Ca	−6,440(40)	10,990(40)	−6,685(60)	18,949(80) ^b	2,561(40)
	21	Sc	13,900(500) ^b	20,340(510) ^b	−8,945(710) ^b	^a	−2,170(510) ^b
	22	Ti	−17,337.5(10)	−1,142.07(25)	−9,008.0(22)	9,888.91(25)	13,095.3(19)
37	12	Mg	29,100(900) ^b	19,500(1,050) ^b	^a	−117(1,280) ^b	^a
	13	Al	9,600(540)	16,130(550)	−18,331(1,590)	4,384(600)	18,597(1,050) ^b
	14	Si	−6,520(130)	12,470(130)	−14,153(190)	2,195(160)	19,730(300)
	15	P	−18,990(40)	7,900(40)	−12,915(80)	6,815(40)	13,883(110)
	16	S	−26,896.22(25)	4,865.3(25)	−8,829(16)	4,303.58(9)	13,934(13)
	17	Cl	−31,761.52(5)	^a	−7,848.7(11)	10,310.96(9)	8,386.53(23)
	18	Ar	−30,948.0(3)	813.5(3)	−6,786.7(3)	8,788.9(4)	8,715.1(3)
	19	K	−24,799.24(27)	6,148.8(4)	−6,220.6(6)	15,445(8)	1,857.77(9)
	20	Ca	−13,161(22)	11,639(22)	−6,204(40)	14,793(50)	3,025(24)
	21	Sc	2,840(300) ^b	16,000(300) ^b	−6,347(360) ^b	19,128(590) ^b	−1,991(300) ^b
38	13	Al	15,740(560) ^b	19,490(620) ^b	−19,192(1,190) ^b	1,933(780) ^b	20,647(1,060) ^b
	14	Si	−3,740(270)	10,720(300)	−14,620(380)	5,292(300)	20,637(600)
	15	P	−14,470(140)	12,390(140)	−14,029(170)	3,543(140)	15,231(190)
	16	S	−26,861(7)	2,937(7)	−9,329(16)	8,036(7)	15,155(40)
	17	Cl	−29,797.98(11)	4,916.8(5)	−7,665(5)	6,107.78(10)	10,190.73(27)
	18	Ar	−34,714.8(5)	^a	−7,207.8(5)	11,838.1(6)	10,242.2(5)

Table 11.23 (Continued)

A	Z	Element	Mass excess	$Q(\beta^-)$	$Q(\alpha)$	$S(n)$	$S(p)$
39	19	K	−28,801.7(7)	5,913.1(6)	−6,786.0(7)	12,073.8(8)	5,142.6(8)
	20	Ca	−22,059(5)	6,743(5)	−6,106(5)	16,970(23)	4,549(5)
	21	Sc	−4,940(300) ^b	17,120(300) ^b	−5,881(420) ^b	15,849(420) ^b	−935(300) ^b
	22	Ti	9,100(250) ^b	14,040(390) ^b	−6,477(390) ^b	^a	1,029(390) ^b
	13	Al	20,400(600) ^b	18,260(720) ^b	−23,179(1,660) ^b	3,414(820) ^b	^a
	14	Si	2,140(400) ^b	14,790(430) ^b	−16,574(590) ^b	2,184(480) ^b	20,889(690) ^b
	15	P	−12,650(150)	10,510(160)	−15,017(210)	6,255(200)	16,194(310)
	16	S	−23,160(50)	6,640(50)	−11,226(60)	4,372(50)	15,984(150)
	17	Cl	−29,800.7(17)	3,441(5)	−7,368.0(26)	8,074(17)	10,229(7)
	18	Ar	−33,242(5)	565(5)	−6,820(5)	6,598(5)	10,733(5)
	19	K	−33,806.84(28)	^a	−7,218.24(28)	13,076.5(7)	6,381.0(5)
	20	Ca	−27,276.3(18)	6,530.6(18)	−6,653.0(20)	13,289(5)	5,763.5(19)
40	21	Sc	−14,168(24)	13,108(24)	−5,426(30)	17,302(300) ^b	−602(24)
	22	Ti	1,230(100) ^b	15,400(100) ^b	−5,631(120) ^b	15,940(270) ^b	1,120(320) ^b
	14	Si	5,400(500) ^b	13,740(540) ^b	−17,934(1,030) ^b	4,811(640) ^b	22,286(780) ^b
	15	P	−8,340(200)	14,510(300)	−16,678(330)	3,759(250)	17,768(450) ^b
	16	S	−22,850(230)	4,710(240)	−12,874(250)	7,760(240)	17,489(280)
	17	Cl	−27,560(30)	7,480(30)	−9,732(30)	5,828(30)	11,685(60)
	18	Ar	−35,039.890(4)	−1,504.87(27)	−6,800.84(23)	9,869(5)	12,528.2(17)
	19	K	−33,535.02(27)	1,311.09(12)	−6,438.04(28)	7,799.50(8)	7,582(5)
	20	Ca	−34,846.11(29)	^a	−7,040.6(4)	15,641.2(18)	8,328.24(9)
	21	Sc	−20,526(4)	14,320(4)	−5,526(9)	14,430(24)	539(4)
	22	Ti	−8,850(160)	11,680(160)	−4,836(160)	18,154(190) ^b	1,971(160)
	23	V	10,330(500) ^b	19,180(530) ^b	−5,993(710) ^b	^a	−1,809(510) ^b
41	14	Si	11,830(600) ^b	16,670(760) ^b	−19,695(1,080) ^b	1,644(780) ^b	^a
	15	P	−4,840(470)	13,760(510)	−16,872(710)	4,578(510)	17,535(690) ^b
	16	S	−18,600(210)	8,740(220)	−14,503(250)	3,824(320)	17,554(290)
	17	Cl	−27,340(60)	5,730(60)	−10,769(80)	7,853(70)	11,779(240)
	18	Ar	−33,067.3(7)	2,491.6(7)	−8,596.0(7)	6,098.7(7)	12,799(30)
	19	K	−35,558.87(26)	^a	−6,222.26(26)	10,095.18(10)	7,807.95(26)
	20	Ca	−35,137.5(4)	421.39(28)	−6,614.4(5)	8,362.70(26)	8,891.44(27)
	21	Sc	−28,642.2(3)	6,495.28(27)	−6,267.9(4)	16,187(4)	1,085.07(9)
	22	Ti	−15,710(40) ^b	12,930(40) ^b	−4,978(40) ^b	14,934(160) ^b	2,476(40) ^b
	23	V	−240(250) ^b	15,470(250) ^b	−5,508(390) ^b	18,644(560) ^b	−1,319(300) ^b
42	14	Si	15,000(700) ^b	14,910(860) ^b	^a	4,904(920) ^b	^a
	15	P	80(500) ^b	17,330(600) ^b	−18,083(750) ^b	3,144(690) ^b	19,035(780) ^b
	16	S	−17,240(330)	7,750(340)	−15,922(420)	6,711(390)	19,687(570)
	17	Cl	−24,990(110)	9,430(120)	−12,946(180)	5,720(130)	13,674(240)
	18	Ar	−34,420(40)	600(40)	−9,986(40)	9,426(40)	14,372(80)
	19	K	−35,021.3(3)	3,525.4(3)	−7,648.3(3)	7,533.77(15)	9,243.0(7)
	20	Ca	−38,546.8(4)	^a	−6,256.9(5)	11,480.60(6)	10,276.86(28)
	21	Sc	−32,120.9(4)	6,425.84(13)	−5,744.2(8)	11,550.04(28)	4,272.41(12)
	22	Ti	−25,121(5)	7,000(5)	−5,487(7)	17,479(40) ^b	3,768(5)

Table 11.23 (Continued)

A	Z	Element	Mass excess	$Q(\beta^-)$	$Q(\alpha)$	$S(n)$	$S(p)$
43	23	V	−8,170(200) ^b	16,950(200) ^b	−5,657(360) ^b	15,998(320) ^b	−255(200) ^b
	24	Cr	5,990(300) ^b	14,160(360) ^b	−5,536(390) ^b	^a	1,057(390) ^b
	15	P	3,080(500) ^b	15,570(980) ^b	−19,741(780) ^b	5,072(710) ^b	19,203(860) ^b
	16	S	−12,480(840)	11,550(850)	−17,049(930) ^b	3,311(900)	19,855(980) ^b
	17	Cl	−24,030(160)	7,950(180)	−13,805(220)	7,113(200)	14,076(360)
	18	Ar	−31,980(70)	4,620(70)	−11,241(90)	5,627(80)	14,279(130)
	19	K	−36,593(9)	1,815(9)	−9,217(9)	9,643(9)	9,460(40)
	20	Ca	−38,408.4(5)	^a	−7,592(5)	7,933(3)	10,676.1(4)
	21	Sc	−36,187.6(19)	2,220.8(19)	−4,805.7(19)	12,138.0(19)	4,929.8(19)
	22	Ti	−29,320(7)	6,867(7)	−4,469(7)	12,271(9)	4,488(7)
	23	V	−18,020(230) ^b	11,300(230) ^b	−6,281(230) ^b	17,927(300) ^b	192(230) ^b
	24	Cr	−2,140(90) ^b	15,890(250) ^b	−5,793(130) ^b	16,197(310) ^b	1,256(210) ^b
44	15	P	9,200(700) ^b	20,080(860) ^b	^a	1,951(860) ^b	^a
	16	S	−10,880(500) ^b	9,110(550) ^b	−18,707(710) ^b	6,469(980) ^b	21,252(710) ^b
	17	Cl	−19,990(220)	12,270(220)	−14,079(300)	4,033(270)	14,798(870)
	18	Ar	−32,262(20)	3,550(40)	−11,837(230)	8,356(70)	15,522(160)
	19	K	−35,810(40)	5,660(40)	−10,677(50)	7,289(40)	11,122(80)
	20	Ca	−41,469.1(9)	^a	−8,854.1(9)	11,132.0(8)	12,165(9)
	21	Sc	−37,815.8(18)	3,653.3(19)	−6,705.7(18)	9,699.5(26)	6,696.3(17)
	22	Ti	−37,548.3(8)	267.5(19)	−5,127.1(7)	16,299(7)	8,649.6(20)
	23	V	−23,850(80) ^b	13,700(80) ^b	−5,745(80) ^b	13,893(250) ^b	1,815(80) ^b
	24	Cr	−13,540(130) ^b	10,310(160) ^b	−7,109(210) ^b	19,470(160) ^b	2,799(270) ^b
	25	Mn	6,400(500) ^b	19,930(520) ^b	−6,356(710) ^b	^a	−1,246(510) ^b
	26	Fe	13,560(400) ^b	18,680(500) ^b	^a	^a	126(640) ^b
45	15	P	14,100(800) ^b	18,930(1,000) ^b	^a	3,172(1,060) ^b	^a
	16	S	−4,830(600) ^b	14,080(880) ^b	−19,080(840) ^b	2,017(780) ^b	21,317(920) ^b
	17	Cl	−18,910(650)	10,810(650)	−16,490(800)	6,990(690)	15,318(820) ^b
	18	Ar	−29,720(60)	6,890(60)	−13,542(220)	5,529(60)	17,017(230)
	19	K	−36,608(10)	4,205(10)	−11,694(70)	8,869(40)	11,635(23)
	20	Ca	−40,812.5(9)	256.8(9)	−10,170.2(11)	7,414.77(30)	12,291(40)
	21	Sc	−41,069.3(11)	^a	−7,935.4(11)	11,324.9(20)	6,889.2(9)
	22	Ti	−39,006.9(12)	2,062.4(5)	−6,294.3(12)	9,529.9(14)	8,480.1(21)
	23	V	−31,874(17)	7,133(17)	−5,656(17)	16,099(90) ^b	1,614(17)
	24	Cr	−19,410(100) ^b	12,460(100) ^b	−6,124(110) ^b	13,949(170) ^b	2,855(130) ^b
	25	Mn	−5,110(300) ^b	14,300(320) ^b	−7,297(390) ^b	19,585(590) ^b	−1,132(330) ^b
	26	Fe	13,560(400) ^b	18,680(500) ^b	^a	^a	126(640) ^b
46	15	P	22,200(900) ^b	22,600(1,140) ^b	^a	−23(1,210) ^b	^a
	16	S	−400(700) ^b	14,390(860) ^b	−17,823(990) ^b	3,647(920) ^b	21,792(1,060) ^b
	17	Cl	−14,790(500) ^b	14,930(510) ^b	−17,301(710) ^b	3,954(820) ^b	17,256(780) ^b
	18	Ar	−29,720(40)	5,700(40)	−14,904(330)	8,073(70)	18,100(650)
	19	K	−35,419(16)	7,716(16)	−12,857(110)	6,882(19)	12,989(60)
	20	Ca	−43,134.9(24)	−1,376.3(24)	−11,138(40)	10,393.7(24)	13,816(10)
	21	Sc	−41,758.6(11)	2,366.7(7)	−9,162.2(11)	8,760.62(11)	8,235.1(10)
	22	Ti	−44,125.3(11)	^a	−8,003.5(11)	13,189.8(8)	10,345.0(7)

Table 11.23 (Continued)

A	Z	Element	Mass excess	$Q(\beta^-)$	$Q(\alpha)$	$S(n)$	$S(p)$
	23	V	−37,073.9(15)	7,051.4(1)	−7,377.9(15)	13,272(17)	5,356.0(13)
	24	Cr	−29,471(20)	7,603(20)	−6,775(21)	18,130(100) ^b	4,886(26)
	25	Mn	−12,370(110) ^b	17,100(110) ^b	−6,626(230) ^b	15,328(320) ^b	247(150) ^b
	26	Fe	760(350) ^b	13,130(370) ^b	−7,660(460) ^b	20,879(540) ^b	1,421(460) ^b
47	16	S	7,100(800) ^b	18,320(1,000) ^b	^a	573(1,060) ^b	22,388(1,210) ^b
	17	Cl	−11,230(600) ^b	14,680(600) ^b	−16,733(780) ^b	4,504(780) ^b	18,113(920) ^b
	18	Ar	−25,910(100)	9,790(100)	−15,851(840)	4,259(110)	18,405(510) ^b
	19	K	−35,697(8)	6,643(8)	−14,092(160)	8,349(16)	13,265(40)
	20	Ca	−42,339.7(23)	1,991.9(12)	−12,787(70)	7,276.1(5)	14,210(16)
	21	Sc	−44,331.6(21)	600.1(19)	−10,164(9)	10,644.3(21)	8,485.7(13)
	22	Ti	−44,931.7(10)	^a	−8,948.2(10)	8,877.7(10)	10,462.1(11)
	23	V	−42,003.9(11)	2,927.8(1)	−8,241.2(22)	13,001.3(10)	5,167.56(7)
	24	Cr	−34,552(14)	7,452(14)	−7,657(16)	13,153(24)	4,767(14)
	25	Mn	−22,260(160) ^b	12,290(160) ^b	−6,663(280) ^b	17,964(190) ^b	81(160) ^b
	26	Fe	−6,620(260) ^b	15,640(310) ^b	−6,912(280) ^b	15,449(440) ^b	1,542(280) ^b
48	16	S	12,100(900) ^b	16,900(1,140) ^b	^a	3,069(1,210) ^b	^a
	17	Cl	−4,800(700) ^b	18,430(760) ^b	−16,425(990) ^b	1,644(920) ^b	19,184(1,060) ^b
	18	Ar	−23,220(300) ^b	8,900(300) ^b	−14,767(590) ^b	5,385(310) ^b	19,287(670) ^b
	19	K	−32,124(24)	12,090(24)	−14,558(220)	4,499(25)	13,505(100)
	20	Ca	−44,215(4)	278(5)	−14,378(20)	9,946(4)	15,807(7)
	21	Sc	−44,493(5)	3,994(5)	−11,108(40)	8,233(5)	9,442(5)
	22	Ti	−48,487(1)	^a	−9,442.8(11)	11,626.59(4)	11,444.3(19)
	23	V	−44,474.7(26)	4,012.3(24)	−9,084(3)	10,542.1(26)	6,831.9(24)
	24	Cr	−42,815(7)	1,659(8)	−7,692(7)	16,334(16)	8,100(7)
	25	Mn	−29,000(70) ^b	13,820(70) ^b	−7,576(110) ^b	14,806(170) ^b	1,734(70) ^b
	26	Fe	−18,110(100) ^b	10,890(130) ^b	−6,999(170) ^b	19,557(280) ^b	3,135(190) ^b
49	27	Co	1,640(400) ^b	19,750(410) ^b	−7,185(640) ^b	^a	−973(480) ^b
	16	S	20,500(1,000) ^b	20,610(1,280) ^b	^a	−331(1,350) ^b	^a
	17	Cl	−100(800) ^b	16,500(950) ^b	−16,630(1,130) ^b	3,377(1,060) ^b	19,492(1,210) ^b
	18	Ar	−16,600(500) ^b	13,720(510) ^b	−14,199(780) ^b	1,448(590) ^b	19,091(860) ^b
	19	K	−30,320(70)	10,970(70)	−13,836(660)	6,267(70)	14,387(310) ^b
	20	Ca	−41,290(4)	5,262(3)	−13,996(60)	5,146.6(4)	16,455(24)
	21	Sc	−46,552(4)	2,006(4)	−12,369(11)	10,131(6)	9,627(3)
	22	Ti	−48,558(1)	^a	−10,170.4(11)	8,142.36(5)	11,354(5)
	23	V	−47,956.2(13)	601.9(8)	−9,311.8(14)	11,552.8(26)	6,758.2(8)
	24	Cr	−45,325.4(26)	2,630.7(26)	−8,743.4(27)	10,581(8)	8,140(3)
	25	Mn	−37,611(24)	7,715(24)	−8,162(29)	16,684(80) ^b	2,084(25)
50	26	Fe	−24,580(160) ^b	13,030(160) ^b	−7,595(190) ^b	14,545(190) ^b	2,874(170) ^b
	27	Co	−9,580(260) ^b	15,010(310) ^b	−6,887(400) ^b	19,287(480) ^b	−1,244(280) ^b
	17	Cl	7,200(900) ^b	20,300(1,140) ^b	−17,422(1,280) ^b	768(1,210) ^b	20,591(1,350) ^b
	18	Ar	−13,100(700) ^b	12,260(750) ^b	−15,121(990) ^b	4,569(860) ^b	20,283(1,060) ^b
	19	K	−25,350(280)	14,220(280)	−12,985(580) ^b	3,104(290)	16,042(580) ^b
	20	Ca	−39,571(9)	4,966(17)	−12,276(40)	6,353(8)	16,540(70)

■ Table 11.23 (Continued)

A	Z	Element	Mass excess	$Q(\beta^-)$	$Q(\alpha)$	$S(n)$	$S(p)$
	21	Sc	−44,538(16)	6,888(16)	−11,543(21)	6,057(15)	10,536(15)
	22	Ti	−51,425.8(10)	−2,208.3(11)	−10,715.9(22)	10,939.13(4)	12,163(4)
	23	V	−49,217.5(13)	1,036.9(4)	−9,883.8(15)	9,332.7(14)	7,948.5(11)
	24	Cr	−50,254.5(13)	^a	−8,554.0(15)	13,000.4(22)	9,587.3(14)
	25	Mn	−42,621.5(14)	7,632.99(28)	−7,972.5(18)	13,082(24)	4,585.0(22)
	26	Fe	−34,470(60)	8,150(60)	−7,425(60)	17,961(170) ^b	4,150(60)
	27	Co	−17,200(170) ^b	17,280(180) ^b	−7,250(200) ^b	15,691(310) ^b	−98(230) ^b
	28	Ni	−3,790(260) ^b	13,400(310) ^b	−6,971(440) ^b	^a	1,504(370) ^b
51	17	Cl	12,600(1,000) ^b	18,900(1,220) ^b	^a	2,669(1,350) ^b	^a
	18	Ar	−6,300(700) ^b	15,710(860) ^b	−15,820(1,060) ^b	1,271(990) ^b	20,786(1,140) ^b
	19	K	−22,000(500) ^b	13,890(510) ^b	−13,202(780) ^b	4,721(580) ^b	16,194(860) ^b
	20	Ca	−35,890(90)	7,330(90)	−12,403(140)	4,386(90)	17,823(290)
	21	Sc	−43,219(20)	6,508(20)	−9,947(21)	6,753(25)	10,936(22)
	22	Ti	−49,726.9(13)	2,470.6(15)	−9,812.1(23)	6,372.3(9)	12,478(16)
	23	V	−52,197.5(13)	^a	−10,290.8(22)	11,051.28(9)	8,060.6(11)
	24	Cr	−51,444.8(13)	752.73(24)	−8,937.9(12)	9,261.62(30)	9,516.19(25)
	25	Mn	−48,237.0(13)	3,207.8(5)	−8,657.9(15)	13,686.8(5)	5,271.5(4)
	26	Fe	−40,217(15)	8,020(15)	−8,090(21)	13,817(60)	4,885(15)
	27	Co	−27,270(150) ^b	12,940(150) ^b	−7,436(220) ^b	18,150(220) ^b	92(160) ^b
	28	Ni	−11,440(260) ^b	15,840(300) ^b	−7,241(370) ^b	15,719(370) ^b	1,532(310) ^b
52	18	Ar	−1,710(900) ^b	14,490(1,140) ^b	−16,230(1,280) ^b	3,479(1,140) ^b	21,597(1,350) ^b
	19	K	−16,200(700) ^b	16,310(840) ^b	−13,826(990) ^b	2,268(860) ^b	17,191(990) ^b
	20	Ca	−32,510(470)	7,870(520)	−11,712(550) ^b	4,694(470)	17,796(690) ^b
	21	Sc	−40,380(230)	9,080(230)	−10,681(230)	5,233(230)	11,783(250)
	22	Ti	−49,464(7)	1,973(7)	−7,674(8)	7,808(7)	13,534(22)
	23	V	−51,437.4(13)	3,975.4(11)	−9,370(5)	7,311.24(23)	8,999.5(15)
	24	Cr	−55,412.8(14)	^a	−9,350.7(14)	12,039.4(11)	10,504.3(11)
	25	Mn	−50,701.1(24)	4,711.7(2)	−8,651(3)	10,535.5(22)	6,545.4(22)
	26	Fe	−48,329(10)	2,372(10)	−7,939(13)	16,183(18)	7,381(10)
	27	Co	−33,920(70) ^b	14,410(70) ^b	−7,343(100) ^b	14,713(160) ^b	987(70) ^b
	28	Ni	−22,650(80) ^b	11,260(110) ^b	−6,971(130) ^b	19,287(270) ^b	2,669(170) ^b
	29	Cu	−2,630(260) ^b	20,030(270) ^b	−6,691(480) ^b	^a	−1,523(370) ^b
53	18	Ar	5,800(1,000) ^b	17,800(1,220) ^b	−17,127(1,410) ^b	566(1,350) ^b	^a
	19	K	−12,000(700) ^b	15,900(860) ^b	−14,320(1,060) ^b	3,870(990) ^b	17,582(1,140) ^b
	20	Ca	−27,900(500) ^b	10,070(590) ^b	−13,724(710) ^b	3,460(690) ^b	18,989(860) ^b
	21	Sc	−37,970(300) ^b	8,860(310) ^b	−10,073(310) ^b	5,659(380) ^b	12,748(550) ^b
	22	Ti	−46,820(100)	5,020(100)	−7,959(100)	5,432(100)	13,733(250)
	23	V	−51,845(3)	3,436(3)	−7,717(5)	8,479(3)	9,670(8)
	24	Cr	−55,280.6(14)	^a	−9,147.5(14)	7,939.16(16)	11,132.2(11)
	25	Mn	−54,683.6(14)	597(4)	−9,152.4(17)	12,053.8(20)	6,559.8(4)
	26	Fe	−50,941.3(21)	3,742.4(17)	−8,040.8(29)	10,683(10)	7,529.1(25)
	27	Co	−42,639(18)	8,302(18)	−7,454(30)	16,795(70) ^b	1,599(21)
	28	Ni	−29,380(160) ^b	13,260(160) ^b	−7,222(220) ^b	14,797(180) ^b	2,753(170) ^b

Table 11.23 (Continued)

A	Z	Element	Mass excess	$Q(\beta^-)$	$Q(\alpha)$	$S(n)$	$S(p)$
54	29	Cu	–13,460(260) ^b	15,920(310) ^b	–6,309(370) ^b	18,905(370) ^b	–1,905(270) ^b
	19	K	–5,600(900) ^b	17,990(1,140) ^b	–15,224(1,280) ^b	1,672(1,140) ^b	18,688(1,350) ^b
	20	Ca	–23,590(700) ^b	10,880(840) ^b	–12,914(990) ^b	3,759(860) ^b	18,877(990) ^b
	21	Sc	–34,470(470)	11,300(520)	–11,538(540)	4,569(550) ^b	13,856(690) ^b
	22	Ti	–45,760(230)	4,120(230)	–8,618(230)	7,011(250)	15,086(380) ^b
	23	V	–49,887(15)	7,042(15)	–7,774(22)	6,113(15)	10,351(100)
	24	Cr	–56,928.3(14)	–1,377.1(1)	–7,927.4(14)	9,719.01(25)	12,373(3)
	25	Mn	–55,551.3(17)	697.1(11)	–8,758.7(15)	8,939.0(11)	7,559.6(10)
	26	Fe	–56,248.4(13)	^a	–8,418.9(10)	13,378.5(16)	8,853.8(6)
	27	Co	–48,005.3(13)	8,243.08(22)	–7,808.8(10)	13,438(18)	4,353.0(17)
	28	Ni	–39,210(50)	8,800(50)	–7,160(80)	17,898(170) ^b	3,856(50)
	29	Cu	–21,690(210) ^b	17,510(220) ^b	–6,924(270) ^b	16,306(340) ^b	–396(270) ^b
55	30	Zn	–6,570(400) ^b	15,130(450) ^b	–5,201(480) ^b	^a	396(480) ^b
	19	K	–570(1,000) ^b	17,550(1,220) ^b	–15,598(1,410) ^b	3,043(1,350) ^b	^a
	20	Ca	–18,120(700) ^b	12,220(1,240) ^b	–14,246(990) ^b	2,603(990) ^b	19,808(1,140) ^b
	21	Sc	–30,340(1,030) ^b	11,470(1,050) ^b	–10,762(1,140) ^b	3,945(1,130) ^b	14,042(1,240) ^b
	22	Ti	–41,810(240)	7,340(260)	–8,344(260)	4,112(340)	14,629(520)
	23	V	–49,150(100)	5,960(100)	–8,353(100)	7,332(100)	10,672(250)
	24	Cr	–55,103.3(14)	2,603.1(5)	–7,801.4(17)	6,246.3(4)	12,506(15)
	25	Mn	–57,706.4(13)	^a	–7,933.8(11)	10,226.4(11)	8,067.0(4)
	26	Fe	–57,475.0(13)	231.38(1)	–8,455.2(10)	9,297.92(29)	9,212.7(11)
	27	Co	–54,023.7(14)	3,451.3(4)	–8,211.7(10)	14,089.7(4)	5,064.3(3)
	28	Ni	–45,330(11)	8,694(11)	–7,538(19)	14,195(50)	4,614(11)
	29	Cu	–31,620(300) ^b	13,710(300) ^b	–6,775(330) ^b	18,001(370) ^b	–293(300) ^b
	30	Zn	–14,920(250) ^b	16,700(390) ^b	–5,909(360) ^b	16,427(470) ^b	517(330) ^b
56	20	Ca	–13,240(900) ^b	12,230(1,140) ^b	–13,957(1,280) ^b	3,190(1,140) ^b	19,955(1,350) ^b
	21	Sc	–25,470(700) ^b	13,670(750) ^b	–11,693(990) ^b	3,200(1,240) ^b	14,638(990) ^b
	22	Ti	–39,130(280)	7,110(370)	–9,048(540)	5,398(370)	16,082(1,060) ^b
	23	V	–46,240(240)	9,050(240)	–8,284(340)	5,163(260)	11,723(340)
	24	Cr	–55,289(10)	1,617(9)	–8,249(12)	8,257(10)	13,430(100)
	25	Mn	–56,905.6(14)	3,695.5(3)	–7,893.1(11)	7,270.49(30)	9,091.2(6)
	26	Fe	–60,601.0(14)	^a	–7,613.1(5)	11,197.32(19)	10,183.59(17)
	27	Co	–56,035.0(24)	4,566(2)	–7,758.8(28)	10,082.6(21)	5,849.0(20)
	28	Ni	–53,900(11)	2,135(11)	–7,995(15)	16,641(16)	7,165(11)
	29	Cu	–38,600(140) ^b	15,300(140) ^b	–7,110(150) ^b	15,048(330) ^b	560(140) ^b
	30	Zn	–25,730(260) ^b	12,870(300) ^b	–5,499(270) ^b	18,877(360) ^b	1,393(400) ^b
	31	Ga	–4,740(260) ^b	20,990(370) ^b	–4,539(370) ^b	^a	–2,892(360) ^b
57	20	Ca	–7,120(1,000) ^b	14,270(1,220) ^b	–15,346(1,420) ^b	1,955(1,350) ^b	^a
	21	Sc	–21,390(700) ^b	13,170(1,160) ^b	–11,814(990) ^b	3,991(990) ^b	15,440(1,140) ^b
	22	Ti	–34,560(930) ^b	9,820(970) ^b	–9,085(1,060) ^b	3,498(970) ^b	16,380(1,160) ^b
	23	V	–44,380(250)	8,020(270)	–8,834(390) ^b	6,208(350)	12,533(380)
	24	Cr	–52,390(90)	5,090(90)	–7,993(140)	5,176(90)	13,443(260)
	25	Mn	–57,485(3)	2,691(3)	–8,065(4)	8,651(3)	9,485(10)

Table 11.23 (Continued)

A	Z	Element	Mass excess	$Q(\beta^-)$	$Q(\alpha)$	$S(n)$	$S(p)$
	26	Fe	−60,175.7(14)	^a	−7,320.0(5)	7,646.03(10)	10,559.1(4)
	27	Co	−59,339.7(14)	836(4)	−7,081.0(7)	11,376.0.0(20)	6,027.6(4)
	28	Ni	−56,075.5(29)	3,264.2(26)	−7,559(3)	10,247(11)	7,329(3)
	29	Cu	−47,305(16)	8,770(16)	−7,091(24)	16,775(140) ^b	695(19)
	30	Zn	−32,690(140) ^b	14,620(140) ^b	−5,732(210) ^b	15,030(300) ^b	1,374(200) ^b
	31	Ga	−15,900(260) ^b	16,790(300) ^b	−4,865(370) ^b	19,231(370) ^b	−2,538(370) ^b
58	21	Sc	−15,770(800) ^b	15,800(1,060) ^b	−12,597(1,210) ^b	2,454(1,060) ^b	15,939(1,280) ^b
	22	Ti	−31,570(700) ^b	8,810(750) ^b	−10,408(990) ^b	5,081(1,160) ^b	17,470(990) ^b
	23	V	−40,380(260)	11,550(360)	−8,340(530)	4,075(360)	13,111(970) ^b
	24	Cr	−51,930(240)	3,970(240)	−8,591(340)	7,609(260)	14,843(350)
	25	Mn	−55,900(30)	6,247(30)	−8,440(30)	6,489(30)	10,798(100)
	26	Fe	−62,148.8(14)	−2,307.4(11)	−7,645.4(5)	10,044.46(29)	11,953(3)
	27	Co	−59,841.4(17)	381.6(12)	−6,715.1(16)	8,573.1(11)	6,954.7(11)
	28	Ni	−60,223.0(14)	^a	−6,399.5(7)	12,218.9(26)	8,172.3(6)
	29	Cu	−51,660.0(25)	8,563(21)	−6,079.6(22)	12,426(16)	2,873(3)
	30	Zn	−42,290(50)	9,370(50)	−5,512(70)	17,678(150) ^b	2,277(50)
	31	Ga	−23,990(210) ^b	18,310(220) ^b	−4,716(300) ^b	16,157(340) ^b	−1,411(260) ^b
	32	Ge	−8,370(320) ^b	15,610(380) ^b	−4,232(510) ^b	^a	−238(410) ^b
59	21	Sc	−11,140(900) ^b	14,980(1,140) ^b	−12,995(1,350) ^b	3,441(1,210) ^b	^a
	22	Ti	−26,120(700) ^b	11,790(770) ^b	−10,426(990) ^b	2,622(990) ^b	17,638(1,060) ^b
	23	V	−37,910(330)	9,940(410)	−9,998(1,080) ^b	5,603(420)	13,632(770) ^b
	24	Cr	−47,850(250)	7,620(250)	−8,470(350)	3,991(350)	14,760(360)
	25	Mn	−55,473(29)	5,185(29)	−8,751(100)	7,642(40)	10,831(240)
	26	Fe	−60,658.4(14)	1,565.2(6)	−7,980.0(7)	6,580.90(20)	12,045(30)
	27	Co	−62,223.6(14)	^a	−6,942.1(6)	10,453.5(11)	7,363.7(6)
	28	Ni	−61,151.1(14)	1,072.5(6)	−6,101.0(6)	8,999.43(14)	8,598.7(12)
	29	Cu	−56,351.5(17)	4,799.6(9)	−4,752.8(11)	12,762.9(23)	3,417.5(9)
	30	Zn	−47,260(40)	9,090(40)	−4,352(40)	13,036(60)	2,886(40)
	31	Ga	−34,120(170) ^b	13,140(170) ^b	−4,921(340) ^b	18,206(270) ^b	−884(180) ^b
	32	Ge	−17,000(280) ^b	17,120(330) ^b	−4,502(380) ^b	16,697(420) ^b	303(350) ^b
60	22	Ti	−22,690(800) ^b	10,380(980) ^b	−11,880(1,210) ^b	4,643(1,060) ^b	18,840(1,210) ^b
	23	V	−33,070(560)	13,760(620)	−10,026(900) ^b	3,228(650)	14,238(900) ^b
	24	Cr	−46,830(260)	6,090(380)	−10,119(380)	7,047(360)	16,203(420)
	25	Mn	−52,910(270)	8,490(270)	−9,100(360)	5,513(270)	12,353(370)
	26	Fe	−61,407(4)	237(3)	−8,543(10)	8,820(3)	13,223(29)
	27	Co	−61,644.2(14)	2,823.9(5)	−7,163.6(7)	7,491.93(8)	8,274.8(6)
	28	Ni	−64,468.1(14)	^a	−6,292.0(6)	11,388.3(5)	9,533.5(5)
	29	Cu	−58,341.2(25)	6,126.9(21)	−4,731.1(29)	10,061.0.0(23)	4,479.1(21)
	30	Zn	−54,183(11)	4,158(11)	−2,708(15)	14,997(40)	5,121(11)
	31	Ga	−40,000(110) ^b	14,190(110) ^b	−3,822(180) ^b	13,949(200) ^b	30(120) ^b
	32	Ge	−27,770(230) ^b	12,230(260) ^b	−4,465(350) ^b	18,839(360) ^b	936(290) ^b
	33	As	−6,400(600) ^b	21,370(640) ^b	−4,083(650) ^b	^a	−3,311(660) ^b
61	22	Ti	−16,750(900) ^b	13,610(1,140) ^b	−12,055(1,350) ^b	2,130(1,210) ^b	^a

Table 11.23 (Continued)

A	Z	Element	Mass excess	$Q(\beta^-)$	$Q(\alpha)$	$S(n)$	$S(p)$
	23	V	−30,360(700) ^b	12,410(750) ^b	−11,395(990) ^b	5,361(900) ^b	14,955(1,060) ^b
	24	Cr	−42,760(280)	8,970(380)	−10,631(970) ^b	4,010(380)	16,986(620)
	25	Mn	−51,740(260)	7,180(260)	−9,784(360)	6,892(380)	12,198(370)
	26	Fe	−58,917(20)	3,978(20)	−8,949(90)	5,582(20)	13,292(270)
	27	Co	−62,895.0(16)	1,321.7(9)	−7,835(3)	9,322.2(9)	8,777(4)
	28	Ni	−64,216.8(14)	^a	−6,466.0(6)	7,820(13)	9,861.5(5)
	29	Cu	−61,979.6(18)	2,237.2(12)	−5,064.8(13)	11,709.7(24)	4,800.4(12)
	30	Zn	−56,342(16)	5,637(16)	−2,692(17)	10,231(19)	5,290(16)
	31	Ga	−47,350(200) ^b	9,000(200) ^b	−2,467(200) ^b	15,421(230) ^b	454(200) ^b
	32	Ge	−33,730(300) ^b	13,620(360) ^b	−3,468(330) ^b	14,033(380) ^b	1,020(320) ^b
	33	As	−18,050(600) ^b	15,680(670) ^b	−4,577(650) ^b	19,724(840) ^b	−2,427(640) ^b
62	23	V	−25,020(700) ^b	16,150(790) ^b	−11,675(1,060) ^b	2,734(990) ^b	15,559(1,140) ^b
	24	Cr	−41,170(370)	7,290(450)	−12,029(790) ^b	6,478(470)	18,104(790) ^b
	25	Mn	−48,470(260)	10,430(260)	−10,510(370)	4,802(370)	12,990(380)
	26	Fe	−58,898(15)	2,530(25)	−9,392(240)	8,052(25)	14,452(260)
	27	Co	−61,428(20)	5,315(20)	−7,951(40)	6,604(20)	9,800(28)
	28	Ni	−66,742.7(14)	^a	−7,018.8(7)	10,597.2(5)	11,136.6(7)
	29	Cu	−62,795(4)	3,948(4)	−5,378(4)	8,886(4)	5,867(4)
	30	Zn	−61,167(10)	1,627(11)	−3,369(10)	12,896(19)	6,477(10)
	31	Ga	−51,996(28)	9,171(26)	−2,761(28)	12,720(200) ^b	2,943(30)
	32	Ge	−42,240(140) ^b	9,750(140) ^b	−2,375(150) ^b	16,585(330) ^b	2,184(240) ^b
	33	As	−24,960(300) ^b	17,280(330) ^b	−3,403(370) ^b	14,983(670) ^b	−1,476(420) ^b
63	23	V	−21,660(900) ^b	13,870(1,140) ^b	−12,942(1,280) ^b	4,709(1,140) ^b	^a
	24	Cr	−35,530(700) ^b	11,230(750) ^b	−11,833(990) ^b	2,426(790) ^b	17,796(990) ^b
	25	Mn	−46,750(280)	9,030(340)	−11,265(430)	6,357(380)	12,869(470)
	26	Fe	−55,780(190)	6,060(190)	−10,353(310)	4,953(190)	14,603(320)
	27	Co	−61,837(20)	3,672(20)	−8,789(40)	8,480(28)	10,228(25)
	28	Ni	−65,509.2(14)	66.945(5)	−7,275.7(7)	6,837.85(7)	11,370(20)
	29	Cu	−65,576.2(14)	^a	−5,777.5(5)	10,853(4)	6,122.44(7)
	30	Zn	−62,209.3(21)	3,366.9(16)	−3,483.1(17)	9,113(10)	6,704(4)
	31	Ga	−56,690(100)	5,520(100)	−2,763(100)	12,764(100)	2,811(100)
	32	Ge	−46,910(200) ^b	9,780(220) ^b	−2,078(200) ^b	12,738(240) ^b	2,203(200) ^b
	33	As	−33,820(500) ^b	13,090(540) ^b	−2,127(530) ^b	16,930(590) ^b	−1,132(520) ^b
64	24	Cr	−33,350(700) ^b	9,750(770) ^b	−13,081(1,060) ^b	5,892(990) ^b	18,979(1,140) ^b
	25	Mn	−43,100(330)	11,980(430)	−12,457(650)	4,420(430)	14,862(770) ^b
	26	Fe	−55,080(280)	4,710(280)	−10,678(380)	7,371(340)	15,617(400)
	27	Co	−59,789(20)	7,307(20)	−9,300(270)	6,024(28)	11,299(190)
	28	Ni	−67,095.9(14)	−1,675.1(2)	−8,114(3)	9,658.01(19)	12,548(20)
	29	Cu	−65,420.8(14)	578.7(9)	−6,201.5(5)	7,915.96(11)	7,200.55(11)
	30	Zn	−65,999.5(17)	^a	−3,956.3(10)	11,861.6(15)	7,712.3(9)
	31	Ga	−58,835(4)	7,165(4)	−2,918(4)	10,217(100)	3,914(4)
	32	Ge	−54,420(250)	4,410(250)	−2,667(250)	15,586(320) ^b	5,024(270)
	33	As	−39,520(360) ^b	14,900(440) ^b	−1,948(380) ^b	13,770(620) ^b	−100(300) ^b

Table 11.23 (Continued)

A	Z	Element	Mass excess	$Q(\beta^-)$	$Q(\alpha)$	$S(n)$	$S(p)$
65	24	Cr	–27,600(900) ^b	13,290(1,060) ^b	–13,275(1,280) ^b	2,324(1,140) ^b	^a
	25	Mn	–40,890(560)	10,400(620)	–12,960(900) ^b	5,864(650)	14,834(900) ^b
	26	Fe	–51,290(280)	7,880(280)	–10,948(400)	4,280(400)	15,477(430)
	27	Co	–59,164(13)	5,958(13)	–9,854(260)	7,446(24)	11,374(280)
	28	Ni	–65,122.6(15)	2,137.1(1)	–8,630(20)	6,098.01(20)	12,622(20)
	29	Cu	–67,259.7(17)	^a	–6,789.6(12)	9,910.2(10)	7,452.8(10)
	30	Zn	–65,907.8(17)	1,351.9(3)	–4,115.9(11)	7,979.6(5)	7,775.9(9)
	31	Ga	–62,652.9(18)	3,254.9(9)	–3,098.3(10)	11,890(4)	3,942.4(7)
	32	Ge	–56,410(100)	6,240(100)	–2,493(100)	10,057(270)	4,865(100)
	33	As	–47,060(390) ^b	9,360(400) ^b	–2,133(440) ^b	15,606(530) ^b	–80(300) ^b
	34	Se	–32,920(600) ^b	14,140(710) ^b	–1,615(670) ^b	^a	687(700) ^b
66	25	Mn	–36,500(700) ^b	13,820(770) ^b	–13,901(990) ^b	3,675(900) ^b	16,185(1,140) ^b
	26	Fe	–50,320(330)	5,730(430)	–11,572(500)	7,103(430)	16,716(650)
	27	Co	–56,050(270)	9,980(270)	–10,012(380)	4,959(270)	12,053(390)
	28	Ni	–66,029(16)	226(16)	–9,556(22)	8,977(16)	14,153(21)
	29	Cu	–66,254.3(17)	2,642(12)	–7,251(20)	7,065.93(11)	8,420.7(10)
	30	Zn	–68,896.3(15)	^a	–4,578.5(8)	11,059.9(12)	8,925.6(12)
	31	Ga	–63,721(3)	5,175(3)	–3,352(5)	9,140(3)	5,103(3)
	32	Ge	–61,620(30)	2,100(30)	–2,879(30)	13,282(100)	6,257(30)
	33	As	–51,820(200) ^b	9,800(200) ^b	–2,250(200) ^b	12,837(440) ^b	2,700(230) ^b
	34	Se	–41,720(300) ^b	10,100(360) ^b	–1,903(330) ^b	16,874(670) ^b	1,955(490) ^b
	35	Br	–32,800(500) ^b	13,690(540) ^b	–1,400(710) ^b	^a	–1,635(590) ^b
67	25	Mn	–33,700(800) ^b	12,870(930) ^b	–14,469(1,210) ^b	5,277(1,060) ^b	^a
	26	Fe	–46,570(470)	8,750(540)	–13,472(840) ^b	4,327(570)	17,368(840) ^b
	27	Co	–55,320(280)	8,420(280)	–10,995(400)	7,340(390)	12,291(430)
	28	Ni	–63,742(19)	3,558(21)	–10,388(190)	5,785(25)	14,979(270)
	29	Cu	–67,300(8)	577(8)	–7,888(22)	9,117(8)	8,560(18)
	30	Zn	–67,877.2(16)	^a	–4,792.9(9)	7,052.2(4)	8,911.8(13)
	31	Ga	–66,876.7(18)	1,000.5(13)	–3,725.4(15)	11,227(3)	5,269.4(13)
	32	Ge	–62,654(5)	4,223(5)	–2,869(5)	9,104(30)	6,221(6)
	33	As	–56,640(100)	6,010(100)	–2,379(140)	12,894(230) ^b	2,311(100)
	34	Se	–46,490(200) ^b	10,150(220) ^b	–2,006(280) ^b	12,841(360) ^b	1,959(280) ^b
	35	Br	–32,800(500) ^b	13,690(540) ^b	–1,400(710) ^b	^a	–1,635(590) ^b
68	26	Fe	–44,240(700) ^b	7,590(770) ^b	–13,314(990) ^b	5,733(840) ^b	17,824(1,060) ^b
	27	Co	–51,830(330)	11,660(330)	–11,153(460)	4,578(430)	12,543(570)
	28	Ni	–63,486(17)	2,060(50)	–10,832(280)	7,815(25)	15,454(280)
	29	Cu	–65,540(50)	4,460(50)	–8,177(50)	6,313(50)	9,088(50)
	30	Zn	–70,004.0(16)	^a	–5,333.0(10)	10,198.2(5)	9,993(8)
	31	Ga	–67,082.9(20)	2,921.1(12)	–4,087.0(16)	8,277.6(18)	6,494.7(13)
	32	Ge	–66,977(6)	106(6)	–3,402(6)	12,395(8)	7,389(6)
	33	As	–58,880(100)	8,100(100)	–2,467(100)	10,305(140)	3,512(100)
	34	Se	–54,150(300) ^b	4,730(310) ^b	–2,148(390) ^b	15,728(360) ^b	4,793(310) ^b
	35	Br	–38,890(540) ^b	15,260(610) ^b	–1,796(650) ^b	14,165(740) ^b	–310(500) ^b
	36	Kr	–51,900(100) ^b	11,600(100) ^b	–1,400(710) ^b	^a	–1,635(590) ^b
69	26	Fe	–39,400(800) ^b	11,640(880) ^b	–14,227(1,210) ^b	3,237(1,060) ^b	^a

Table 11.23 (Continued)

A	Z	Element	Mass excess	$Q(\beta^-)$	$Q(\alpha)$	$S(n)$	$S(p)$
	27	Co	−51,050(370)	9,330(400)	−12,578(670)	7,289(500)	14,098(790) ^b
	28	Ni	−60,380(140)	5,360(140)	−11,515(310)	4,963(140)	15,838(350)
	29	Cu	−65,740(8)	2,675(8)	−9,001(15)	8,269(50)	9,543(18)
	30	Zn	−68,414.9(17)	906(29)	−5,717.3(11)	6,482.2(5)	10,162(50)
	31	Ga	−69,321(3)	^a	−4,486(3)	10,309(3)	6,605.9(29)
	32	Ge	−67,094(3)	2,227.3(5)	−3,611(3)	8,188(7)	7,300(3)
	33	As	−63,080(30)	4,010(30)	−2,853(30)	12,275(100)	3,393(30)
	34	Se	−56,300(30)	6,780(40)	−2,312(110)	10,221(300) ^b	4,710(110)
	35	Br	−46,410(310) ^b	9,890(320) ^b	−1,778(500) ^b	15,588(620) ^b	−450(100) ^b
	36	Kr	−32,300(500) ^b	14,110(590) ^b	−1,810(780) ^b	^a	701(740) ^b
70	27	Co	−46,750(700) ^b	12,730(770) ^b	−12,681(990) ^b	3,777(790) ^b	14,638(1,060) ^b
	28	Ni	−59,490(330)	3,480(330)	−11,591(460)	7,179(350)	15,728(500)
	29	Cu	−62,960(15)	6,599(14)	−9,333(270)	5,292(16)	9,872(140)
	30	Zn	−69,559(3)	−654.7(16)	−5,956(16)	9,216(3)	11,108(7)
	31	Ga	−68,905(3)	1,656(3)	−5,075(3)	7,655.1(8)	7,778.8(30)
	32	Ge	−70,560.3(17)	^a	−4,088.9(17)	11,538(3)	8,528(3)
	33	As	−64,340(50)	6,220(50)	−3,044(50)	9,331(60)	4,536(50)
	34	Se	−61,940(210) ^b	2,400(200) ^b	−2,744(210) ^b	13,714(210) ^b	6,149(210) ^b
	35	Br	−51,590(360) ^b	10,350(300) ^b	−2,194(420) ^b	13,253(480) ^b	2,582(370) ^b
	36	Kr	−40,980(400) ^b	10,610(540) ^b	−1,680(500) ^b	16,744(640) ^b	1,857(510) ^b
71	27	Co	−44,960(800) ^b	10,930(880) ^b	−13,687(1,130) ^b	6,283(1,060) ^b	^a
	28	Ni	−55,890(370)	6,870(370)	−11,740(600)	4,476(500)	16,427(790) ^b
	29	Cu	−62,760(40)	4,560(40)	−9,868(280)	7,875(40)	10,568(330)
	30	Zn	−67,322(11)	2,815(11)	−6,004(21)	5,834(10)	11,650(17)
	31	Ga	−70,136.8(18)	^a	−5,262(8)	9,303(3)	7,866(3)
	32	Ge	−69,904.9(17)	231.9(3)	−4,452.7(16)	7,415.90(5)	8,289(3)
	33	As	−67,892(4)	2,013(4)	−3,440(4)	11,623(50)	4,621(4)
	34	Se	−63,090(200) ^b	4,800(200) ^b	−2,863(200) ^b	9,223(290) ^b	6,041(210) ^b
	35	Br	−56,590(300) ^b	6,500(360) ^b	−2,373(320) ^b	13,073(470) ^b	1,941(360) ^b
	36	Kr	−46,100(300) ^b	10,490(420) ^b	−2,034(360) ^b	13,195(500) ^b	1,798(470) ^b
	37	Rb	−32,300(500) ^b	13,800(590) ^b	−1,931(710) ^b	^a	−1,383(640) ^b
72	27	Co	−40,600(800) ^b	14,080(930) ^b	^a	3,712(1,130) ^b	^a
	28	Ni	−54,680(470)	5,380(510) ^b	−12,867(840) ^b	6,860(600)	17,004(930) ^b
	29	Cu	−60,060(200) ^b	8,070(200) ^b	−10,659(380) ^b	5,370(200) ^b	11,462(420) ^b
	30	Zn	−68,128(6)	458(6)	−7,067(18)	8,878(12)	12,653(40)
	31	Ga	−68,586.5(20)	3,999.1(23)	−5,470(50)	6,521(10)	8,554(11)
	32	Ge	−72,585.6(15)	^a	−5,006.4(21)	10,752.0.0(20)	9,737.7(21)
	33	As	−68,229(4)	4,356(4)	−3,571(5)	8,409(6)	5,614(5)
	34	Se	−67,894(12)	335(13)	−3,342(14)	12,874(200) ^b	7,291(13)
	35	Br	−59,150(260)	8,740(260)	−2,701(280)	10,632(400) ^b	3,350(330) ^b
	36	Kr	−54,110(270)	5,040(80)	−2,390(400) ^b	16,084(400) ^b	4,810(400) ^b
	37	Rb	−38,120(500) ^b	16,000(570) ^b	−1,650(740) ^b	13,884(710) ^b	−694(590) ^b
73	28	Ni	−50,230(600) ^b	8,930(670) ^b	−13,249(1,000) ^b	3,619(760) ^b	16,911(1,000) ^b

Table 11.23 (Continued)

A	Z	Element	Mass excess	$Q(\beta^-)$	$Q(\alpha)$	$S(n)$	$S(p)$
	29	Cu	−59,160(300) ^b	6,250(300) ^b	−10,538(480) ^b	7,168(360) ^b	11,769(550) ^b
	30	Zn	−65,410(40)	4,290(40)	−7,457(140)	5,353(40)	12,636(200) ^b
	31	Ga	−69,704(6)	1,593(6)	−6,389(10)	9,189(7)	8,864(9)
	32	Ge	−71,297.1(15)	^a	−5,307.1(21)	6,782.90(5)	9,999.6(23)
	33	As	−70,956(4)	341(4)	−4,060(5)	10,798(5)	5,660(4)
	34	Se	−68,216(11)	2,740(10)	−3,548(11)	8,393(16)	7,276(11)
	35	Br	−63,530(130)	4,680(130)	−2,877(140)	12,451(220)	2,927(130)
	36	Kr	−56,890(140)	6,650(190)	−3,013(140)	10,844(300)	5,021(290)
	37	Rb	−46,230(480) ^b	10,650(500) ^b	−2,250(580) ^b	16,188(700) ^b	−590(400) ^b
	38	Sr	−31,700(600) ^b	14,540(770) ^b	−1,819(780) ^b	^a	871(780) ^b
74	28	Ni	−48,520(700) ^b	7,180(810) ^b	^a	6,367(920) ^b	^a
	29	Cu	−55,700(400) ^b	10,010(400) ^b	−11,377(810) ^b	4,615(500) ^b	12,766(720) ^b
	30	Zn	−65,710(50)	2,340(90)	−8,649(330)	8,371(60)	13,839(300) ^b
	31	Ga	−68,050(70)	5,370(70)	−7,519(70)	6,421(70)	9,933(80)
	32	Ge	−73,422.0(15)	−2,562.4(17)	−6,288(4)	10,196.20(6)	11,007(6)
	33	As	−70,859.6(22)	1,353(18)	−4,380(4)	7,975(4)	6,851.4(17)
	34	Se	−72,212.6(15)	^a	−4,077.2(21)	12,068(11)	8,545(4)
	35	Br	−65,306(15)	6,907(15)	−3,391(50)	9,845(130)	4,379(18)
	36	Kr	−62,170(60)	3,140(60)	−2,654(220) ^b	13,356(150)	5,926(150)
	37	Rb	−51,730(720)	10,440(720)	−2,560(810) ^b	13,563(870) ^b	2,129(730)
75	38	Sr	−40,700(500) ^b	11,030(880) ^b	−2,145(640) ^b	17,070(780) ^b	1,752(700) ^b
	28	Ni	−43,810(800) ^b	10,500(950) ^b	^a	3,358(1,060) ^b	^a
	29	Cu	−54,310(500) ^b	8,160(510) ^b	−11,768(950) ^b	6,674(640) ^b	13,074(860) ^b
	30	Zn	−62,470(70)	6,000(70)	−9,004(380)	4,831(90)	14,054(410) ^b
	31	Ga	−68,464(7)	3,392(7)	−8,125(40)	8,482(70)	10,044(50)
	32	Ge	−71,855.9(15)	1,176.5(1)	−6,959(11)	6,505.22(8)	11,091(70)
	33	As	−73,032.5(16)	^a	−5,320.6(22)	10,244.2(19)	6,899.4(10)
	34	Se	−72,168.8(15)	863.6(8)	−4,688.8(21)	8,027.53(8)	8,598.2(18)
	35	Br	−69,139(14)	3,030(14)	−3,672(14)	11,904(20)	4,215(14)
	36	Kr	−64,242(15)	4,897(21)	−3,574(200) ^b	10,143(60)	6,225(22)
76	37	Rb	−57,222(8)	7,019(17)	−3,055(300) ^b	13,568(720)	2,342(60)
	38	Sr	−46,650(300) ^b	10,570(300) ^b	−2,974(420) ^b	14,024(590) ^b	2,213(780) ^b
	28	Ni	−41,610(900) ^b	8,700(1,080) ^b	^a	5,873(1,210) ^b	^a
	29	Cu	−50,310(600) ^b	11,730(610) ^b	−12,131(1,000) ^b	4,075(780) ^b	13,791(1,000) ^b
	30	Zn	−62,040(120)	4,160(80)	−9,789(480)	7,646(140)	15,026(520) ^b
	31	Ga	−66,200(90)	7,010(90)	−8,565(220) ^b	5,810(90)	11,023(110)
	32	Ge	−73,212.9(15)	−923.3(9)	−7,509(6)	9,428.3(5)	12,038(7)
	33	As	−72,289.6(16)	2,962(8)	−6,128.0(24)	7,328.44(7)	7,722.6(10)
	34	Se	−75,251.6(15)	^a	−5,090.9(6)	11,154.07(29)	9,508.1(8)
	35	Br	−70,289(9)	4,963(9)	−4,484(10)	9,221(17)	5,409(9)
	36	Kr	−68,979(11)	1,310(14)	−3,509(16)	12,808(16)	7,129(17)
	37	Rb	−60,481(8)	8,498(13)	−3,753(260)	11,329(11)	3,528(17)
	38	Sr	−54,390(300) ^b	6,090(300) ^b	−2,702(400) ^b	15,812(420) ^b	4,456(300) ^b

Table 11.23 (Continued)

A	Z	Element	Mass excess	$Q(\beta^-)$	$Q(\alpha)$	$S(n)$	$S(p)$
77	28	Ni	−36,490(1,000) ^b	12,000(1,220) ^b	^a	2,948(1,350) ^b	^a
	29	Cu	−48,480(700) ^b	10,120(710) ^b	^a	6,246(920) ^b	14,163(1,140) ^b
	30	Zn	−58,600(130)	7,270(120)	−10,803(610) ^b	4,633(180)	15,583(610) ^b
	31	Ga	−65,870(60)	5,340(60)	−9,140(300) ^b	7,743(110)	11,120(130)
	32	Ge	−71,214.1(18)	2,702(21)	−8,229(40)	6,072.6(11)	12,300(90)
	33	As	−73,916.2(22)	682.9(18)	−6,637(6)	9,697.9(19)	7,992.3(18)
	34	Se	−74,599.0(15)	^a	−5,726.8(6)	7,418.81(7)	9,598.4(8)
	35	Br	−73,234(3)	1,365.1(28)	−4,703(5)	11,017(10)	5,271.3(28)
	36	Kr	−70,171(9)	3,063(9)	−4,380(14)	9,264(11)	7,172(13)
	37	Rb	−64,826(8)	5,346(12)	−3,718(130)	12,417(10)	3,136(13)
	38	Sr	−57,970(150)	6,850(150)	−3,514(200)	11,656(330) ^b	4,783(150)
78	39	Y	−46,930(300) ^b	11,050(330) ^b	−3,120(570) ^b	^a	−172(420) ^b
	28	Ni	−33,720(1,100) ^b	10,240(1,360) ^b	^a	5,305(1,480) ^b	^a
	29	Cu	−43,960(800) ^b	13,270(820) ^b	^a	3,544(1,060) ^b	14,760(1,280) ^b
	30	Zn	−57,220(160)	6,440(140)	−11,125(720) ^b	6,689(210)	16,027(720) ^b
	31	Ga	−63,660(80)	8,200(80)	−10,384(410) ^b	5,859(100)	12,347(160)
	32	Ge	−71,862(4)	954(10)	−8,578(50)	8,719(4)	13,277(60)
	33	As	−72,816(10)	4,209(10)	−7,187(70)	6,971(10)	8,891(10)
	34	Se	−77,025.7(15)	−3,574(4)	−6,028.6(6)	10,497.95(26)	10,398.5(18)
	35	Br	−73,452(4)	708(8)	−5,017(4)	8,289(5)	6,142(4)
	36	Kr	−74,160(7)	^a	−4,372(7)	12,060(7)	8,215(7)
	37	Rb	−66,936(8)	7,224(10)	−4,055(17)	10,181(10)	4,053(12)
79	38	Sr	−63,175(8)	3,761(11)	−3,430(60)	13,271(150)	5,638(10)
	39	Y	−52,630(400) ^b	10,550(400) ^b	−3,329(820) ^b	13,772(500) ^b	1,944(430) ^b
	29	Cu	−41,660(900) ^b	11,740(940) ^b	^a	5,771(1,210) ^b	15,225(1,420) ^b
	30	Zn	−53,400(270) ^b	9,090(240) ^b	−12,015(850) ^b	4,247(310) ^b	16,730(850) ^b
	31	Ga	−62,490(120)	7,000(80)	−10,607(520) ^b	6,897(140)	12,555(200)
	32	Ge	−69,490(90)	4,150(90)	−9,444(110)	5,697(90)	13,115(120)
	33	As	−73,636(6)	2,281(5)	−7,597(9)	8,891(11)	9,063(7)
	34	Se	−75,916.9(15)	151(17)	−6,485.9(7)	6,962.58(28)	10,390(10)
	35	Br	−76,068.0(19)	^a	−5,460.4(18)	10,687(4)	6,331.3(16)
	36	Kr	−74,442(4)	1,626(3)	−4,698(4)	8,354(8)	8,279(5)
	37	Rb	−70,797(7)	3,646(8)	−4,083(15)	11,932(10)	3,926(7)
80	38	Sr	−65,477(9)	5,319(11)	−3,661(18)	10,374(11)	5,831(11)
	39	Y	−58,360(450)	7,120(450)	−3,560(450)	13,799(600) ^b	2,472(450)
	40	Zr	−47,360(400) ^b	11,000(600) ^b	−3,133(500) ^b	^a	2,017(570) ^b
	29	Cu	−35,500(900) ^b	16,280(920) ^b	^a	1,914(1,280) ^b	^a
	30	Zn	−51,780(170)	7,290(120)	−12,592(920) ^b	6,451(320) ^b	17,410(920) ^b
	31	Ga	−59,070(120)	10,380(120)	−11,183(610) ^b	4,651(170)	12,959(300) ^b
	32	Ge	−69,448(23)	2,670(18)	−9,830(120)	8,031(90)	14,249(120)
	33	As	−72,118(21)	5,641(21)	−8,340(90)	6,553(22)	9,919(90)
	34	Se	−77,759.4(19)	−1,870.6(3)	−6,971.4(16)	9,913.8(16)	11,412(5)
	35	Br	−75,888.8(19)	2,004(4)	−6,024.2(18)	7,892.19(20)	7,260.9(17)

■ Table 11.23 (Continued)

A	Z	Element	Mass excess	$Q(\beta^-)$	$Q(\alpha)$	$S(n)$	$S(p)$
	36	Kr	−77,893(4)	^a	−5,067(4)	11,522(5)	9,114(4)
	37	Rb	−72,173(7)	5,721(8)	−4,309(12)	9,448(9)	5,020(8)
	38	Sr	−70,305(8)	1,868(10)	−3,751(13)	12,899(11)	6,797(10)
	39	Y	−61,170(400) ^b	9,140(400) ^b	−3,109(400) ^b	10,879(600) ^b	2,976(400) ^b
	40	Zr	−55,380(300) ^b	5,790(500) ^b	−3,412(420) ^b	16,091(500) ^b	4,309(540) ^b
81	30	Zn	−46,130(400) ^b	11,860(440) ^b	−12,066(1,070) ^b	2,422(440) ^b	17,917(990) ^b
	31	Ga	−57,980(190)	8,320(150)	−11,923(730) ^b	6,986(230)	13,494(260)
	32	Ge	−66,300(120)	6,230(120)	−10,124(180)	4,926(120)	14,524(170)
	33	As	−72,533(6)	3,856(5)	−9,084(60)	8,486(22)	10,374(24)
	34	Se	−76,389.1(20)	1,585.3(26)	−7,599.9(21)	6,701(6)	11,560(21)
	35	Br	−77,974.4(28)	^a	−6,483(3)	10,156.8(26)	7,503.9(25)
	36	Kr	−77,693.6(29)	280.7(5)	−5,519.5(28)	7,872(3)	9,093.8(26)
	37	Rb	−75,456(6)	2,237(7)	−4,647(7)	11,355(9)	4,852(7)
	38	Sr	−71,527(8)	3,930(10)	−3,780(12)	9,293(11)	6,643(10)
	39	Y	−66,020(60)	5,510(60)	−3,615(60)	12,923(410) ^b	3,000(60)
	40	Zr	−58,860(300)	7,160(290)	−3,306(330)	11,550(420) ^b	4,980(500) ^b
	41	Nb	−47,460(400) ^b	11,400(500) ^b	−2,956(500) ^b	^a	−629(500) ^b
82	30	Zn	−42,070(400) ^b	10,880(500) ^b	−10,771(1,170) ^b	4,010(570) ^b	^a
	31	Ga	−52,950(300) ^b	12,680(390) ^b	−11,414(860) ^b	3,035(360) ^b	14,108(500) ^b
	32	Ge	−65,620(240)	4,700(140)	−10,826(290)	7,392(270)	14,930(310)
	33	As	−70,320(200)	7,270(200)	−9,086(220)	5,862(200)	11,310(230)
	34	Se	−77,593.4(21)	−97.5(24)	−8,156(4)	9,275.7(13)	12,350(5)
	35	Br	−77,495.9(28)	3,092.6(15)	−7,105(10)	7,592.90(20)	8,395.8(26)
	36	Kr	−80,588.6(26)	^a	−5,987.8(25)	10,966.2(15)	9,903.2(15)
	37	Rb	−76,189(7)	4,400(7)	−5,162(8)	8,804(9)	5,784(7)
	38	Sr	−76,009(6)	180(9)	−4,274(9)	12,554(9)	7,841(8)
	39	Y	−68,190(100)	7,820(100)	−3,682(100)	10,248(120)	3,955(100)
	40	Zr	−64,190(510)	4,000(500)	−3,443(510)	13,408(590)	5,466(510)
	41	Nb	−52,970(300) ^b	11,220(590) ^b	−2,770(500) ^b	13,586(500) ^b	1,407(420) ^b
83	31	Ga	−49,490(500) ^b	11,510(590) ^b	−10,259(1,030) ^b	4,615(590) ^b	14,713(640) ^b
	32	Ge	−61,000(300) ^b	8,880(370) ^b	−10,030(400) ^b	3,451(390) ^b	15,346(420) ^b
	33	As	−69,880(220)	5,460(220)	−9,817(250)	7,628(300)	11,546(330)
	34	Se	−75,340(4)	3,669(5)	−8,277(90)	5,818.0.0(30)	12,306(200)
	35	Br	−79,009(4)	973(4)	−7,798(7)	9,584(5)	8,705(4)
	36	Kr	−79,982(3)	^a	−6,490(3)	7,465(4)	9,775(4)
	37	Rb	−79,073(6)	909(7)	−5,430(6)	10,955(9)	5,773(6)
	38	Sr	−76,797(9)	2,276(6)	−4,780(9)	8,860(10)	7,897(11)
	39	Y	−72,330(40)	4,470(40)	−3,956(40)	12,207(110)	3,608(40)
	40	Zr	−66,460(100)	5,870(80)	−3,408(100)	10,339(520)	5,556(140)
	41	Nb	−58,960(310)	7,500(300)	−3,028(550)	14,057(430) ^b	2,056(600)
	42	Mo	−47,750(500) ^b	11,210(590) ^b	−2,816(640) ^b	^a	2,063(590) ^b
84	31	Ga	−44,400(600) ^b	14,000(720) ^b	−11,321(1,080) ^b	2,976(780) ^b	^a
	32	Ge	−58,400(400) ^b	7,690(500) ^b	−9,043(440) ^b	5,463(500) ^b	16,194(640) ^b

Table 11.23 (Continued)

A	Z	Element	Mass excess	$Q(\beta^-)$	$Q(\alpha)$	$S(n)$	$S(p)$
	33	As	−66,080(300) ^b	9,870(300) ^b	−9,437(320) ^b	4,271(370) ^b	12,366(420) ^b
	34	Se	−75,950(15)	1,827(27)	−8,927(27)	8,681(15)	13,359(220)
	35	Br	−77,776(25)	4,655(25)	−8,083(30)	6,839(26)	9,725(26)
	36	Kr	−82,431(3)	−2,680.9(23)	−7,097(3)	10,520.5(19)	10,711(4)
	37	Rb	−79,750(3)	894(3)	−6,286(4)	8,749(6)	7,057.3(29)
	38	Sr	−80,644(3)	^a	−5,176(5)	11,919(9)	8,861(7)
	39	Y	−74,160(90)	6,490(90)	−4,410(90)	9,902(100)	4,650(90)
	40	Zr	−71,490(200) ^b	2,670(220) ^b	−3,612(200) ^b	13,103(220) ^b	6,453(200) ^b
	41	Nb	−61,880(300) ^b	9,610(360) ^b	−3,139(500) ^b	10,990(430) ^b	2,708(310) ^b
	42	Mo	−55,810(400) ^b	6,070(500) ^b	−2,853(500) ^b	16,129(640) ^b	4,135(510) ^b
85	32	Ge	−53,380(500) ^b	10,140(590) ^b	−9,681(640) ^b	3,060(640) ^b	16,278(780) ^b
	33	As	−63,520(300) ^b	8,910(300) ^b	−7,961(360) ^b	5,510(420) ^b	12,412(500) ^b
	34	Se	−72,429(30)	6,182(23)	−8,551(120)	4,550(30)	13,637(300) ^b
	35	Br	−78,611(19)	2,870(19)	−8,503(20)	8,906(30)	9,950(24)
	36	Kr	−81,480.6(30)	687.1(19)	−7,516(3)	7,121(4)	10,993(26)
	37	Rb	−82,167.7(23)	^a	−6,618(3)	10,488.9(30)	7,026(3)
	38	Sr	−81,103(3)	1,065(27)	−5,834(4)	8,530(4)	8,641(4)
	39	Y	−77,848(25)	3,255(25)	−4,816(26)	11,761(90)	4,492(25)
	40	Zr	−73,150(100)	4,690(100)	−4,053(100)	9,734(220) ^b	6,285(140)
	41	Nb	−67,150(220)	6,000(200)	−3,563(230)	13,347(370) ^b	2,951(300) ^b
	42	Mo	−59,070(400) ^b	8,090(460) ^b	−2,635(500) ^b	11,332(570) ^b	4,476(500) ^b
	43	Tc	−47,560(500) ^b	11,500(640) ^b	−2,527(640) ^b	^a	−955(640) ^b
86	32	Ge	−50,050(600) ^b	9,350(720) ^b	−10,408(720) ^b	4,737(780) ^b	^a
	33	As	−59,400(400) ^b	11,140(400) ^b	−8,880(500) ^b	3,954(500) ^b	13,306(640) ^b
	34	Se	−70,541(16)	5,099(11)	−7,342(240)	6,184(30)	14,311(300) ^b
	35	Br	−75,640(11)	7,626(11)	−7,741(200)	5,101(22)	10,500(30)
	36	Kr	−83,265.9(11)	−518.6(25)	−8,097.4(23)	9,857(3)	11,944(19)
	37	Rb	−82,747.3(23)	1,774.2(14)	−7,676(3)	8,651.0.0(10)	8,555.7(22)
	38	Sr	−84,521.6(22)	^a	−6,358(3)	11,490(3)	9,642.8(16)
	39	Y	−79,282(14)	5,240(14)	−5,517(16)	9,505(29)	5,468(14)
	40	Zr	−77,810(30)	1,480(30)	−4,221(30)	12,722(110)	7,246(40)
	41	Nb	−69,830(90)	7,980(80)	−4,059(130)	10,744(240)	3,961(130)
	42	Mo	−64,560(440)	5,270(430)	−2,789(670)	13,562(590) ^b	4,691(490)
	43	Tc	−53,210(300) ^b	11,350(530) ^b	−2,658(420) ^b	13,716(590) ^b	1,430(500) ^b
87	33	As	−56,280(500) ^b	10,300(510) ^b	−9,216(710) ^b	4,951(640) ^b	13,521(780) ^b
	34	Se	−66,580(40)	7,280(40)	−8,004(300) ^b	4,113(40)	14,470(400) ^b
	35	Br	−73,857(18)	6,853(18)	−6,402(220)	6,289(21)	10,606(24)
	36	Kr	−80,710.0(13)	3,885.1(27)	−7,795(4)	5,515.4(8)	12,359(11)
	37	Rb	−84,595.0(25)	283.3(15)	−8,011(5)	9,919.1(20)	8,618.1(27)
	38	Sr	−84,878.4(22)	^a	−7,321(4)	8,428.12(17)	9,420.0(14)
	39	Y	−83,016.8(26)	1,861.6(14)	−6,369(6)	11,807(14)	5,784.2(14)
	40	Zr	−79,348(8)	3,669(8)	−4,976(12)	9,614(30)	7,355(16)
	41	Nb	−74,180(60)	5,170(60)	−4,280(70)	12,427(100)	3,667(70)

Table 11.23 (Continued)

A	Z	Element	Mass excess	$Q(\beta^-)$	$Q(\alpha)$	$S(n)$	$S(p)$
88	42	Mo	−67,690(220)	6,490(210)	−3,659(240)	11,209(490)	5,157(240)
	43	Tc	−59,120(300) ^b	8,570(370) ^b	−2,587(430) ^b	13,986(420) ^b	1,854(530) ^b
	44	Ru	−47,340(600) ^b	11,780(670) ^b	−2,015(780) ^b	^a	1,421(670) ^b
	33	As	−51,640(600) ^b	12,240(600) ^b	−9,672(840) ^b	3,432(780) ^b	^a
	34	Se	−63,880(50)	6,850(30)	−7,908(400) ^b	5,367(60)	14,886(510) ^b
	35	Br	−70,730(40)	8,960(40)	−7,077(300) ^b	4,946(40)	11,439(50)
	36	Kr	−79,692(13)	2,914(14)	−6,167(20)	7,053(13)	13,124(22)
	37	Rb	−82,606(4)	5,313(4)	−7,255(26)	6,083(4)	9,185(5)
	38	Sr	−87,919.7(22)	^a	−7,914(3)	11,112.63(22)	10,613.6(15)
	39	Y	−84,297.1(27)	3,622.6(15)	−6,972(4)	9,351.6(20)	6,707.7(15)
	40	Zr	−83,624(10)	673(10)	−5,404(11)	12,347(13)	7,896(10)
	41	Nb	−76,420(200) ^b	7,200(200) ^b	−4,690(220) ^b	10,312(210) ^b	4,365(200) ^b
	42	Mo	−72,701(20)	3,720(200) ^b	−3,633(200) ^b	13,077(220)	5,807(60)
	43	Tc	−62,570(300) ^b	10,130(300) ^b	−3,114(420) ^b	11,518(420) ^b	2,163(370) ^b
	44	Ru	−55,500(500) ^b	7,070(590) ^b	−2,118(640) ^b	16,231(780) ^b	3,665(590) ^b
89	33	As	−47,290(600) ^b	12,310(670) ^b	^a	3,721(840) ^b	^a
	34	Se	−59,600(300) ^b	8,970(300) ^b	−8,638(590) ^b	3,790(300) ^b	15,244(670) ^b
	35	Br	−68,570(60)	8,155(30)	−7,476(300) ^b	5,909(70)	11,981(80)
	36	Kr	−76,720(50)	4,990(50)	−6,721(60)	5,104(50)	13,282(60)
	37	Rb	−81,711(6)	4,496(5)	−5,525(20)	7,176(7)	9,308(15)
	38	Sr	−86,207.0(22)	1,495.1(22)	−7,151.4(25)	6,358.71(13)	10,890(4)
	39	Y	−87,702.1(23)	^a	−7,959.3(25)	11,476.4(27)	7,071.4(22)
	40	Zr	−84,869(3)	2,832.7(25)	−6,192(4)	9,317(10)	7,861(4)
	41	Nb	−80,580(40)	4,290(40)	−5,156(40)	12,226(200) ^b	4,244(40)
	42	Mo	−75,003(15)	5,580(40)	−4,274(100)	10,374(25)	5,869(200) ^b
	43	Tc	−67,490(210)	7,510(210)	−2,764(310)	12,996(370) ^b	2,082(210)
	44	Ru	−59,510(500) ^b	7,980(550) ^b	−2,872(640) ^b	12,086(710) ^b	4,234(590) ^b
	45	Rh	−47,150(500) ^b	12,360(710) ^b	−2,015(710) ^b	^a	−1,057(710) ^b
90	34	Se	−56,430(400) ^b	8,180(410) ^b	−8,806(720) ^b	4,904(500) ^b	16,427(720) ^b
	35	Br	−64,610(80)	10,350(70)	−7,637(410) ^b	4,115(100)	12,305(310) ^b
	36	Kr	−74,963(19)	4,392(17)	−6,847(25)	6,310(60)	13,682(60)
	37	Rb	−79,355(8)	6,587(8)	−6,140(14)	5,716(10)	9,919(50)
	38	Sr	−85,941.9(27)	546(14)	−5,100.8(29)	7,806.1(26)	11,520(6)
	39	Y	−86,487.9(23)	2,280.1(16)	−6,165.5(25)	6,857.08(15)	7,569.8(22)
	40	Zr	−88,767.9(22)	^a	−6,671.3(24)	11,969.8(28)	8,354.8(16)
	41	Nb	−82,657(5)	6,111(4)	−5,800(15)	10,150(40)	5,076(5)
	42	Mo	−80,168(6)	2,489(4)	−4,788(30)	13,236(16)	6,879(40)
	43	Tc	−71,210(240)	8,960(240)	−3,805(260)	11,785(320)	3,493(240)
	44	Ru	−65,410(400) ^b	5,800(470) ^b	−3,277(590) ^b	13,968(640) ^b	5,205(450) ^b
	45	Rh	−53,220(500) ^b	12,190(640) ^b	−2,434(590) ^b	14,135(710) ^b	992(710) ^b
91	34	Se	−50,890(500) ^b	10,620(510) ^b	^a	2,529(640) ^b	^a
	35	Br	−61,510(70)	9,800(40)	−7,655(510) ^b	4,969(110)	12,370(410) ^b
	36	Kr	−71,310(60)	6,440(60)	−7,155(70)	4,421(60)	13,989(100)

■ Table 11.23 (Continued)

A	Z	Element	Mass excess	$Q(\beta^-)$	$Q(\alpha)$	$S(n)$	$S(p)$
	37	Rb	−77,748(8)	5,891(9)	−6,315(20)	6,464(11)	10,074(21)
	38	Sr	−83,639(6)	2,707(6)	−5,354(6)	5,768(6)	11,573(10)
	39	Y	−86,346.3(28)	1,544.8(18)	−4,176(3)	7,929.8(25)	7,693.4(28)
	40	Zr	−87,891.1(22)	^a	−5,437.7(24)	7,194.5(5)	8,692.2(17)
	41	Nb	−86,638(3)	1,253.4(24)	−6,046(4)	12,052(5)	5,158.8(24)
	42	Mo	−82,204(11)	4,434(11)	−5,281(14)	10,107(13)	6,836(12)
	43	Tc	−75,980(200)	6,220(200)	−4,226(210)	12,848(310)	3,105(200)
	44	Ru	−68,580(500)	7,400(540)	−3,309(550)	11,241(640) ^b	4,661(560)
	45	Rh	−59,100(400) ^b	9,480(640) ^b	−2,406(500) ^b	13,958(640) ^b	983(570) ^b
	46	Pd	−47,060(600) ^b	12,040(720) ^b	−2,145(840) ^b	^a	1,132(780) ^b
92	34	Se	−47,200(600) ^b	9,390(600) ^b	^a	4,383(780) ^b	^a
	35	Br	−56,580(50)	12,200(50)	−7,366(600) ^b	3,144(90)	12,985(510) ^b
	36	Kr	−68,788(12)	5,987(10)	−7,335(50)	5,547(60)	14,566(70)
	37	Rb	−74,775(7)	8,100(7)	−6,468(40)	5,099(10)	10,751(60)
	38	Sr	−82,875(7)	1,940(10)	−5,608(15)	7,307(8)	12,416(10)
	39	Y	−84,815(9)	3,639(9)	−4,634(10)	6,540(9)	8,465(11)
	40	Zr	−88,454.6(21)	−2,005.6(18)	−2,959.8(24)	8,634.8(4)	9,397.2(19)
	41	Nb	−86,449.0(27)	357(4)	−4,577(3)	7,882.5(30)	5,846.8(18)
	42	Mo	−86,805(4)	^a	−5,607(11)	12,673(11)	7,457(4)
	43	Tc	−78,935(26)	7,870(26)	−4,936(200) ^b	11,023(200)	4,020(28)
93	44	Ru	−74,410(300) ^b	4,530(300) ^b	−4,132(300) ^b	13,900(580) ^b	5,713(360) ^b
	45	Rh	−63,360(400) ^b	11,050(500) ^b	−3,217(500) ^b	12,328(570) ^b	2,070(640) ^b
	46	Pd	−55,500(500) ^b	7,860(640) ^b	−2,425(710) ^b	16,511(780) ^b	3,684(640) ^b
	35	Br	−53,000(300) ^b	11,020(310) ^b	−8,135(670) ^b	4,490(300) ^b	13,092(670) ^b
	36	Kr	−64,030(100)	8,600(100)	−6,854(310) ^b	3,309(100)	14,732(110)
	37	Rb	−72,626(8)	7,462(9)	−6,481(60)	5,922(10)	11,127(14)
	38	Sr	−80,088(8)	4,137(12)	−5,788(50)	5,284(10)	12,601(10)
	39	Y	−84,224(11)	2,893(10)	−4,938(12)	7,480(14)	8,638(12)
	40	Zr	−87,117.4(21)	91.4(16)	−3,335.2(24)	6,734.1(6)	9,591(9)
	41	Nb	−87,208.7(22)	^a	−1,931.6(22)	8,831.1(20)	6,043.2(16)
94	42	Mo	−86,804(4)	405(3)	−4,359(5)	8,069.71(9)	7,644(4)
	43	Tc	−83,603(4)	3,200.9(1)	−5,450(40)	12,739(26)	4,086.5(10)
	44	Ru	−77,270(90)	6,340(80)	−4,688(90)	10,930(310) ^b	5,620(90)
	45	Rh	−69,170(400) ^b	8,090(410) ^b	−4,104(450) ^b	13,884(570) ^b	2,054(500) ^b
	46	Pd	−59,700(400) ^b	9,470(570) ^b	−2,611(640) ^b	12,272(640) ^b	3,628(570) ^b
	35	Br	−47,800(400) ^b	13,340(500) ^b	^a	2,874(500) ^b	^a
	36	Kr	−61,140(300) ^b	7,410(300) ^b	−7,136(500) ^b	5,186(320) ^b	15,428(420) ^b
	37	Rb	−68,551(9)	10,291(10)	−6,363(80)	3,996(11)	11,814(100)
	38	Sr	−78,842(7)	3,508(8)	−6,304(20)	6,826(10)	13,505(10)
	39	Y	−82,350(8)	4,917(7)	−5,420(11)	6,197(13)	9,551(11)
94	40	Zr	−87,266.3(23)	−901.4(22)	−3,749.3(28)	8,220.2(19)	10,331(11)
	41	Nb	−86,364.9(22)	2,045.4(19)	−2,301.9(22)	7,227.47(9)	6,536.5(16)
	42	Mo	−88,410.3(18)	^a	−2,067.3(21)	9,678(4)	8,490.6(19)

Table 11.23 (Continued)

A	Z	Element	Mass excess	$Q(\beta^-)$	$Q(\alpha)$	$S(n)$	$S(p)$
	43	Tc	−84,155(4)	4,256(4)	−3,923(6)	8,623(6)	4,640(5)
	44	Ru	−82,568(13)	1,587(13)	−4,825(14)	13,373(90)	6,254(13)
	45	Rh	−72,940(450) ^b	9,630(450) ^b	−4,156(510) ^b	11,837(600) ^b	2,961(460) ^b
	46	Pd	−66,350(400) ^b	6,590(600) ^b	−3,366(570) ^b	14,722(570) ^b	4,467(570) ^b
	47	Ag	−53,300(500) ^b	13,050(640) ^b	−2,509(710) ^b	^a	890(640) ^b
95	36	Kr	−56,040(400) ^b	9,800(400) ^b	−7,576(640) ^b	2,969(500) ^b	15,523(570) ^b
	37	Rb	−65,839(19)	9,279(19)	−6,753(80)	5,359(20)	11,987(300) ^b
	38	Sr	−75,117(8)	6,087(8)	−6,229(60)	4,347(10)	13,855(11)
	39	Y	−81,204(8)	4,453(7)	−5,881(11)	6,926(10)	9,651(10)
	40	Zr	−85,657.6(23)	1,124.8(19)	−4,444(6)	6,462.7(9)	10,597(8)
	41	Nb	−86,782.5(19)	925.6(5)	−2,861.1(27)	8,488.9(20)	6,805.1(20)
	42	Mo	−87,708.1(18)	^a	−2,241.9(20)	7,369.06(10)	8,632.2(19)
	43	Tc	−86,017(5)	1,691(5)	−1,805(6)	9,934(7)	4,896(5)
	44	Ru	−83,450(12)	2,567(13)	−3,671(16)	8,953(14)	6,584(13)
	45	Rh	−78,340(150)	5,110(150)	−4,781(250)	13,473(470) ^b	3,061(150)
	46	Pd	−70,150(400) ^b	8,190(430) ^b	−3,997(640) ^b	11,872(570) ^b	4,502(600) ^b
	47	Ag	−60,100(400) ^b	10,050(570) ^b	−3,422(570) ^b	14,871(640) ^b	1,039(570) ^b
96	36	Kr	−53,030(500) ^b	8,180(500) ^b	−8,256(780) ^b	5,063(640) ^b	^a
	37	Rb	−61,214(26)	11,740(27)	−7,056(60)	3,447(26)	12,464(400) ^b
	38	Sr	−72,954(25)	5,387(15)	−6,591(27)	5,908(25)	14,404(29)
	39	Y	−78,341(22)	7,100(22)	−5,990(23)	5,208(23)	10,512(23)
	40	Zr	−85,441(3)	164(4)	−4,990(7)	7,854.3(25)	11,525(8)
	41	Nb	−85,604(4)	3,187(3)	−3,214(10)	6,893(3)	7,236(4)
	42	Mo	−88,791.0(18)	−2,973(5)	−2,761.4(20)	9,154.26(5)	9,297.5(5)
	43	Tc	−85,818(5)	254(10)	−1,794(6)	7,872(7)	5,399(5)
	44	Ru	−86,072(8)	^a	−1,692(9)	10,694(10)	7,344(9)
	45	Rh	−79,626(13)	6,446(10)	−3,116(29)	9,357(150)	3,465(14)
	46	Pd	−76,180(150)	3,450(150)	−4,193(330) ^b	14,096(430) ^b	5,125(210)
	47	Ag	−64,570(400) ^b	11,610(430) ^b	−3,636(570) ^b	12,542(570) ^b	1,709(570) ^b
	48	Cd	−56,100(500) ^b	8,470(640) ^b	−3,030(710) ^b	^a	3,293(640) ^b
97	36	Kr	−47,920(500) ^b	10,450(500) ^b	^a	2,957(710) ^b	^a
	37	Rb	−58,365(28)	10,427(27)	−7,788(300) ^b	5,222(30)	12,624(500) ^b
	38	Sr	−68,792(19)	7,468(16)	−7,191(100)	3,909(30)	14,867(29)
	39	Y	−76,260(12)	6,688(11)	−6,059(14)	5,991(24)	10,595(27)
	40	Zr	−82,949(3)	2,658.1(19)	−5,286(8)	5,580(3)	11,897(22)
	41	Nb	−85,606.9(26)	1,933.9(19)	−3,808(11)	8,074(4)	7,455(3)
	42	Mo	−87,540.8(18)	^a	−2,848.4(20)	6,821.14(25)	9,226(3)
	43	Tc	−87,221(5)	320(4)	−2,437(5)	9,474(7)	5,719(4)
	44	Ru	−86,112(8)	1,108(9)	−1,733(9)	8,111.5(28)	7,584(10)
	45	Rh	−82,590(40)	3,520(40)	−1,411(40)	11,035(40)	3,806(40)
	46	Pd	−77,800(300)	4,790(300)	−2,958(310)	9,695(340)	5,463(300)
	47	Ag	−70,790(400) ^b	7,010(500) ^b	−4,046(570) ^b	14,294(570) ^b	1,907(430) ^b
	48	Cd	−60,600(400) ^b	10,190(570) ^b	−3,328(570) ^b	12,570(640) ^b	3,321(570) ^b

■ Table 11.23 (Continued)

A	Z	Element	Mass excess	$Q(\beta^-)$	$Q(\alpha)$	$S(n)$	$S(p)$
98	37	Rb	−54,300(30)	12,326(24)	−8,923(400) ^b	4,009(40)	13,676(500) ^b
	38	Sr	−66,629(26)	5,823(10)	−7,912(300) ^b	5,908(30)	15,553(40)
	39	Y	−72,452(24)	8,824(15)	−6,326(25)	4,263(26)	10,949(30)
	40	Zr	−81,276(20)	2,250(20)	−4,859(21)	6,399(20)	12,305(22)
	41	Nb	−83,526(6)	4,586(6)	−3,602(9)	5,991(6)	7,867(6)
	42	Mo	−88,112.0(18)	−1,684(3)	−3,270.6(20)	8,642.50(7)	9,794.0(19)
	43	Tc	−86,428(4)	1,796(7)	−2,488(4)	7,279(5)	6,176(3)
	44	Ru	−88,224(6)	^a	−2,239(6)	10,183(10)	8,293(8)
	45	Rh	−83,167(12)	5,057(10)	−1,437(13)	8,649(40)	4,344(14)
	46	Pd	−81,300(21)	1,867(24)	−1,157(22)	11,572(300)	6,000(40)
	47	Ag	−72,880(150)	8,420(150)	−2,367(470) ^b	10,158(430) ^b	2,370(340)
99	48	Cd	−67,460(210) ^b	5,420(140) ^b	−3,535(450) ^b	14,928(450) ^b	3,956(450) ^b
	49	In	−53,800(500) ^b	13,660(540) ^b	−2,928(710) ^b	^a	489(640) ^b
	37	Rb	−50,840(150)	11,280(110)	^a	4,609(150)	^a
	38	Sr	−62,120(140)	8,090(140)	−8,503(420) ^b	3,559(140)	15,103(140)
	39	Y	−70,202(24)	7,567(14)	−6,789(30)	5,822(30)	10,863(40)
	40	Zr	−77,769(20)	4,558(15)	−5,077(21)	4,565(28)	12,606(30)
	41	Nb	−82,327(13)	3,639(13)	−3,548(15)	6,872(14)	8,340(24)
	42	Mo	−85,966.1(18)	1,357.2(1)	−2,733.4(19)	5,925.39(15)	9,729(6)
	43	Tc	−87,323.3(19)	293.7(14)	−2,965.8(11)	8,967(3)	6,500.3(10)
	44	Ru	−87,617(2)	^a	−2,333.8(16)	7,464(7)	8,478(4)
	45	Rh	−85,574(7)	2,043(7)	−1,982(9)	10,479(14)	4,639(9)
100	46	Pd	−82,188(15)	3,387(15)	−1,163(18)	8,959(25)	6,310(19)
	47	Ag	−76,760(150)	5,430(150)	−843(210)	11,949(210)	2,747(150)
	48	Cd	−69,850(210) ^b	6,910(250) ^b	−2,127(450) ^b	10,464(290) ^b	4,262(260) ^b
	49	In	−60,910(500) ^b	8,940(540) ^b	−3,235(640) ^b	15,179(710) ^b	739(540) ^b
	37	Rb	−46,700(300) ^b	13,520(320) ^b	^a	3,927(340) ^b	^a
	38	Sr	−60,220(130)	7,070(100)	−9,614(520) ^b	6,174(190)	16,668(200)
	39	Y	−67,290(80)	9,310(70)	−8,505(80)	5,164(80)	12,467(160)
	40	Zr	−76,600(40)	3,335(25)	−6,075(40)	6,906(40)	13,691(40)
	41	Nb	−79,939(26)	6,245(25)	−4,024(30)	5,683(28)	9,459(30)
	42	Mo	−86,184(6)	−168(6)	−3,169(6)	8,290(6)	11,146(12)
	43	Tc	−86,016.4(22)	3,202.4(17)	−2,837(4)	6,764.4(10)	7,339.3(14)
101	44	Ru	−89,218.8(20)	^a	−2,852.7(17)	9,673.16(14)	9,184.5(14)
	45	Rh	−85,589(20)	3,630(20)	−2,196(21)	8,086(21)	5,261(20)
	46	Pd	−85,227(11)	361(23)	−1,580(13)	11,111(19)	6,942(13)
	47	Ag	−78,180(80)	7,050(80)	−980(80)	9,494(170)	3,282(80)
	48	Cd	−74,310(100)	3,880(70)	−554(180)	12,524(230) ^b	4,836(180)
	49	In	−64,130(380)	10,170(390)	−1,988(550) ^b	11,295(630) ^b	1,570(430) ^b
	50	Sn	−56,860(430) ^b	7,270(200) ^b	−3,185(660) ^b	^a	3,243(660) ^b
	37	Rb	−43,600(170)	11,810(110)	^a	4,973(340) ^b	^a
	38	Sr	−55,410(120)	9,500(80)	−9,917(520) ^b	3,260(180)	16,001(320) ^b
	39	Y	−64,910(100)	8,550(90)	−8,973(100)	5,690(120)	11,982(160)

Table 11.23 (Continued)

A	Z	Element	Mass excess	$Q(\beta^-)$	$Q(\alpha)$	$S(n)$	$S(p)$
	40	Zr	−73,460(30)	5,485(25)	−7,091(40)	4,925(50)	13,452(80)
	41	Nb	−78,943(19)	4,569(18)	−5,107(22)	7,075(30)	9,627(40)
	42	Mo	−83,512(6)	2,824(24)	−2,988(6)	5,398.50(20)	10,861(25)
	43	Tc	−86,336(24)	1,613(24)	−3,154(24)	8,391(24)	7,441(24)
	44	Ru	−87,949.6(20)	^a	−2,833.7(17)	6,802.1(7)	9,222.2(18)
	45	Rh	−87,408(17)	541(17)	−2,612(18)	9,891(26)	5,478(17)
	46	Pd	−85,428(18)	1,980(4)	−1,741(20)	8,272(21)	7,128(27)
	47	Ag	−81,220(100)	4,200(100)	−1,060(110)	11,115(130)	3,286(100)
	48	Cd	−75,750(150)	5,480(110)	−373(340)	9,514(180)	4,856(170)
	49	In	−68,410(300) ^b	7,340(330) ^b	−40(500) ^b	12,346(490) ^b	1,393(310) ^b
	50	Sn	−59,560(500) ^b	8,850(590) ^b	−1,382(640) ^b	10,767(660) ^b	2,714(630) ^b
102	37	Rb	−38,000(500) ^b	15,080(520) ^b	^a	2,469(530) ^b	^a
	38	Sr	−53,080(110)	8,810(70)	^a	5,741(170)	16,769(200)
	39	Y	−61,890(90)	9,850(70)	−10,015(90)	5,051(130)	13,774(150)
	40	Zr	−71,740(50)	4,605(30)	−7,539(60)	6,356(60)	14,119(110)
	41	Nb	−76,350(40)	7,210(40)	−6,321(50)	5,476(40)	10,179(50)
	42	Mo	−83,558(21)	1,010(23)	−4,706(29)	8,117(20)	11,904(27)
	43	Tc	−84,568(9)	4,530(9)	−3,466(11)	6,303(26)	8,345(10)
	44	Ru	−89,097.9(20)	−2,323(5)	−3,410.8(17)	9,219.59(5)	10,051(24)
	45	Rh	−86,775(5)	1,151(5)	−2,772(6)	7,439(18)	6,115(5)
	46	Pd	−87,926(3)	^a	−2,126(7)	10,569(18)	7,807(17)
	47	Ag	−81,970(70)	5,950(70)	−1,229(70)	8,819(130)	3,832(70)
	48	Cd	−79,380(70)	2,587(8)	−509(70)	11,708(170)	5,449(130)
	49	In	−70,130(390)	9,250(380)	321(420)	9,797(490) ^b	1,676(410)
	50	Sn	−64,750(400) ^b	5,390(560) ^b	287(450) ^b	13,260(640) ^b	3,628(500) ^b
103	38	Sr	−47,550(500) ^b	11,190(590) ^b	^a	2,546(520) ^b	16,846(710) ^b
	39	Y	−58,740(300) ^b	9,630(320) ^b	−10,325(340) ^b	4,919(310) ^b	12,951(320) ^b
	40	Zr	−68,370(110)	6,950(80)	−8,683(180)	4,703(120)	13,771(140)
	41	Nb	−75,320(70)	5,530(30)	−7,542(70)	7,043(80)	10,866(80)
	42	Mo	−80,850(60)	3,750(60)	−5,505(60)	5,363(60)	11,791(70)
	43	Tc	−84,599(10)	2,660(10)	−4,697(17)	8,103(13)	8,331(23)
	44	Ru	−87,258.9(20)	763.4(21)	−3,717.8(18)	6,232.39(30)	9,980(9)
	45	Rh	−88,022.3(28)	^a	−3,123.9(26)	9,318(5)	6,213.4(21)
	46	Pd	−87,479.2(29)	543.1(8)	−2,287.2(24)	7,624.7(15)	7,993(5)
	47	Ag	−84,792(17)	2,688(17)	−1,642(18)	10,891(70)	4,155(17)
	48	Cd	−80,650(15)	4,142(10)	−887(22)	9,337(70)	5,967(70)
	49	In	−74,600(25)	6,050(20)	−267(150)	12,537(390)	2,504(70)
	50	Sn	−66,950(300) ^b	7,650(300) ^b	481(360) ^b	10,270(500) ^b	4,101(490) ^b
	51	Sb	−55,780(500) ^b	11,170(590) ^b	2,708(710) ^b	^a	−1,681(640) ^b
104	38	Sr	−44,400(700) ^b	10,140(810) ^b	^a	4,923(860) ^b	^a
	39	Y	−54,540(400) ^b	11,800(570) ^b	−10,268(500) ^b	3,870(500) ^b	14,275(640) ^b
	40	Zr	−66,340(400) ^b	5,890(420) ^b	−8,546(420) ^b	6,038(420) ^b	14,890(500) ^b
	41	Nb	−72,230(110)	8,100(90)	−7,359(130)	4,980(130)	11,143(150)

Table 11.23 (Continued)

A	Z	Element	Mass excess	$Q(\beta^-)$	$Q(\alpha)$	$S(n)$	$S(p)$
	42	Mo	−80,330(60)	2,160(40)	−6,154(70)	7,555(90)	12,303(90)
	43	Tc	−82,490(50)	5,600(50)	−4,974(50)	5,960(50)	8,928(80)
	44	Ru	−88,091(4)	−1,141(4)	−4,332(7)	8,904(3)	10,781(9)
	45	Rh	−86,950.0(28)	2,441(5)	−3,358.5(28)	6,999.05(6)	6,980.1(21)
	46	Pd	−89,391(5)	^a	−2,597(5)	9,983(5)	8,658(5)
	47	Ag	−85,112(6)	4,279(4)	−1,948(21)	8,392(18)	4,922(7)
	48	Cd	−83,976(10)	1,136(11)	−1,173(15)	11,398(17)	6,473(18)
	49	In	−76,070(140)	7,910(140)	−311(160)	9,539(140)	2,707(140)
	50	Sn	−71,550(150)	4,520(60)	328(180)	12,677(340) ^b	4,242(160)
	51	Sb	−59,350(360) ^b	12,200(390) ^b	2,361(530) ^b	11,642(620) ^b	−309(210) ^b
	51	Sb	−59,350(360) ^b	12,200(390) ^b	2,361(530) ^b	11,642(620) ^b	−309(210) ^b
105	39	Y	−51,150(500) ^b	11,220(640) ^b	−9,976(530) ^b	4,681(640) ^b	14,033(860) ^b
	40	Zr	−62,360(400) ^b	8,490(410) ^b	−9,381(420) ^b	4,094(570) ^b	15,114(570) ^b
	41	Nb	−70,850(100)	6,490(70)	−8,367(140)	6,698(150)	11,803(410) ^b
	42	Mo	−77,340(70)	4,950(40)	−6,307(80)	5,078(90)	12,400(130)
	43	Tc	−82,290(60)	3,640(60)	−5,772(60)	7,873(70)	9,245(80)
	44	Ru	−85,930(4)	1,917(4)	−4,843(7)	5,910.07(19)	10,730(50)
	45	Rh	−87,847(5)	566.7(25)	−3,936(24)	8,968(5)	7,045(4)
	46	Pd	−88,414(5)	^a	−2,889(5)	7,094.1(7)	8,753(5)
	47	Ag	−87,068(11)	1,345(11)	−2,085(20)	10,027(12)	4,966(11)
	48	Cd	−84,330(11)	2,738(4)	−1,327(21)	8,426(14)	6,507(12)
	49	In	−79,481(17)	4,849(13)	−682(110)	11,485(140)	2,794(19)
106	50	Sn	−73,220(90)	6,260(90)	98(180)	9,743(180)	4,446(170)
	51	Sb	−63,780(150)	9,440(180)	2,203(340) ^b	12,504(390) ^b	−483(15)
	39	Y	−46,370(700) ^b	13,330(860) ^b	−10,799(860) ^b	3,293(860) ^b	^a
	40	Zr	−59,700(500) ^b	7,190(590) ^b	−9,047(520) ^b	5,407(640) ^b	15,840(710) ^b
	41	Nb	−66,890(300) ^b	9,370(300) ^b	−7,423(310) ^b	4,107(310) ^b	11,816(500) ^b
	42	Mo	−76,257(22)	3,520(17)	−6,940(60)	6,989(70)	12,691(100)
	43	Tc	−79,777(14)	6,547(11)	−5,855(40)	5,559(60)	9,726(70)
	44	Ru	−86,324(8)	39.4(21)	−5,192(22)	8,466(8)	11,323(60)
	45	Rh	−86,364(8)	3,541(6)	−4,221(12)	6,588(7)	7,723(8)
	46	Pd	−89,905(5)	−2,965.3(28)	−3,232(5)	9,562.6(4)	9,347.0(26)
	47	Ag	−86,940(5)	194(8)	−2,589(7)	7,943(11)	5,815.0(29)
107	48	Cd	−87,134(6)	^a	−1,633(7)	10,875(12)	7,354(12)
	49	In	−80,610(14)	6,523(12)	−1,064(70)	9,201(22)	3,569(17)
	50	Sn	−77,430(50)	3,190(50)	−466(90)	12,272(100)	5,233(50)
	51	Sb	−66,360(310) ^b	11,070(320) ^b	1,353(500) ^b	10,648(350) ^b	422(330) ^b
	52	Te	−58,030(400) ^b	8,330(510) ^b	4,293(9)	^a	1,539(430) ^b
	40	Zr	−55,090(600) ^b	9,830(720) ^b	−9,961(780) ^b	3,460(780) ^b	16,008(920) ^b
	41	Nb	−64,920(400) ^b	8,030(430) ^b	−8,601(500) ^b	6,097(500) ^b	12,505(640) ^b
	42	Mo	−72,940(160)	6,160(60)	−6,991(190)	4,755(160)	13,339(340) ^b
	43	Tc	−79,100(150)	4,820(80)	−6,206(160)	7,395(150)	10,132(150)
	44	Ru	−83,920(120)	2,940(120)	−5,496(140)	5,668(120)	11,432(120)
	45	Rh	−86,861(12)	1,511(13)	−4,687(16)	8,569(14)	7,826(14)

Table 11.23 (Continued)

A	Z	Element	Mass excess	$Q(\beta^-)$	$Q(\alpha)$	$S(n)$	$S(p)$
108	46	Pd	−88,372(6)	33(3)	−3,538(7)	6,539(7)	9,297(9)
	47	Ag	−88,405(6)	^a	−2,808(6)	9,537(7)	5,789(6)
	48	Cd	−86,988(7)	1,417(4)	−1,934(7)	7,926(9)	7,338(8)
	49	In	−83,562(13)	3,426(11)	−1,196(21)	11,023(19)	3,717(14)
	50	Sn	−78,560(90)	5,010(90)	−331(90)	9,202(90)	5,235(90)
	51	Sb	−70,650(300) ^b	7,900(310) ^b	1,521(300) ^b	12,368(430) ^b	517(300) ^b
	52	Te	−60,510(300) ^b	10,140(420) ^b	4,008(5)	10,554(500) ^b	1,445(430) ^b
	40	Zr	−51,900(700) ^b	8,640(860) ^b	−9,923(990) ^b	4,886(920) ^b	^a
	41	Nb	−60,540(500) ^b	10,650(540) ^b	−8,424(640) ^b	3,693(640) ^b	12,738(780) ^b
	42	Mo	−71,190(200) ^b	4,750(150) ^b	−7,269(450) ^b	6,316(260) ^b	13,559(450) ^b
	43	Tc	−75,940(130)	7,720(50)	−6,132(170)	4,906(200)	10,283(210)
	44	Ru	−83,660(120)	1,360(60)	−5,747(140)	7,806(170)	11,843(190)
	45	Rh	−85,020(110)	4,510(100)	−4,953(110)	6,227(110)	8,385(160)
	46	Pd	−89,522(4)	−1,918(6)	−3,855(5)	9,221(7)	9,949(12)
	47	Ag	−87,604(6)	1,649(8)	−3,078(6)	7,269.6(6)	6,520(3)
	48	Cd	−89,253(6)	^a	−2,287(7)	10,336(9)	8,136(8)
	49	In	−84,100(40)	5,160(40)	−1,408(40)	8,605(40)	4,396(40)
	50	Sn	−82,000(40)	2,092(25)	−453(40)	11,519(80)	5,730(50)
	51	Sb	−72,510(210) ^b	9,500(210) ^b	1,135(250) ^b	9,925(360) ^b	1,241(220) ^b
109	52	Te	−65,680(150)	6,830(260) ^b	3,445(4)	13,241(340) ^b	2,318(340) ^b
	53	I	−52,820(360) ^b	12,860(390) ^b	4,099(50)	^a	−400(200) ^b
	41	Nb	−58,100(500) ^b	9,150(590) ^b	−9,374(710) ^b	5,631(710) ^b	13,483(860) ^b
	42	Mo	−67,250(300) ^b	7,620(370) ^b	−7,306(500) ^b	4,130(360) ^b	13,996(590) ^b
	43	Tc	−74,870(210) ^b	5,990(200) ^b	−6,437(230) ^b	7,003(250) ^b	10,971(290) ^b
	44	Ru	−80,850(70)	4,160(60)	−5,937(100)	5,268(140)	12,206(150)
	45	Rh	−85,012(12)	2,591(12)	−5,147(60)	8,067(110)	8,646(120)
	46	Pd	−87,604(4)	1,115.9(2)	−4,099(5)	6,153.30(30)	9,876(110)
	47	Ag	−88,720(3)	^a	−3,298(5)	9,187(6)	6,486.9(20)
	48	Cd	−88,505(4)	214.3(29)	−2,517(6)	7,324(6)	8,191(7)
	49	In	−86,485(6)	2,020(6)	−1,842(12)	10,461(40)	4,522(5)
	50	Sn	−82,636(10)	3,850(11)	−730(15)	8,703(40)	5,829(40)
	51	Sb	−76,256(19)	6,380(16)	801(26)	11,820(210) ^b	1,541(50)
110	52	Te	−67,570(70)	8,680(80)	3,226(50)	9,963(170)	2,355(220) ^b
	53	I	−57,570(150)	10,000(170)	3,782(16)	12,821(390) ^b	−819.5(19)
	41	Nb	−53,390(600) ^b	12,060(720) ^b	−9,448(920) ^b	3,367(780) ^b	^a
	42	Mo	−65,460(400) ^b	5,910(570) ^b	−8,182(640) ^b	6,283(500) ^b	14,648(640) ^b
	43	Tc	−71,360(400) ^b	8,780(460) ^b	−6,896(500) ^b	4,566(450) ^b	11,406(500) ^b
	44	Ru	−80,140(230)	2,810(50)	−6,307(230)	7,359(240)	12,562(310) ^b
	45	Rh	−82,950(220)	5,400(220)	−5,597(220)	6,009(220)	9,387(230)
	46	Pd	−88,350(11)	−892(11)	−4,450(13)	8,818(11)	10,627(5)
	47	Ag	−87,458(3)	2,892.2(16)	−3,519(8)	6,809.20(10)	7,142.8(20)
	48	Cd	−90,349.7(30)	^a	−2,870(6)	9,916(3)	8,919.0(16)
	49	In	−86,472(12)	3,878(12)	−1,957(13)	8,058(13)	5,255(12)

Table 11.23 (Continued)

A	Z	Element	Mass excess	$Q(\beta^-)$	$Q(\alpha)$	$S(n)$	$S(p)$
	50	Sn	–85,835(16)	637(19)	–1,126(17)	11,270(17)	6,638(16)
	51	Sb	–77,540(200) ^b	8,300(200) ^b	651(200) ^b	9,350(200) ^b	2,188(200) ^b
	52	Te	–72,280(50)	5,260(210) ^b	2,723(16)	12,775(90)	3,310(60)
	53	I	–60,350(310) ^b	11,930(310) ^b	3,584(50)	10,845(350) ^b	63(320) ^b
	54	Xe	–51,720(400) ^b	8,630(510) ^b	3,885(14)	^a	1,435(430) ^b
111	42	Mo	–61,000(500) ^b	8,810(640) ^b	–8,340(780) ^b	3,619(640) ^b	14,899(780) ^b
	43	Tc	–69,820(400) ^b	6,980(500) ^b	–7,325(570) ^b	6,525(570) ^b	11,648(570) ^b
	44	Ru	–76,790(300) ^b	5,500(360) ^b	–6,276(340) ^b	4,724(380) ^b	12,720(500) ^b
	45	Rh	–82,290(210) ^b	3,740(210) ^b	–5,612(250) ^b	7,410(300) ^b	9,437(310) ^b
	46	Pd	–86,030(40)	2,190(40)	–4,533(130)	5,750(40)	10,368(230)
	47	Ag	–88,217(3)	1,036.8(14)	–3,781(12)	8,831.2(22)	7,156(11)
	48	Cd	–89,254.2(30)	^a	–3,307(7)	6,975.84(19)	9,085.7(16)
	49	In	–88,389(5)	865(5)	–2,408(8)	9,988(12)	5,328(5)
	50	Sn	–85,944(7)	2,445(8)	–1,381(10)	8,181(16)	6,761(14)
	51	Sb	–80,840(200) ^b	5,100(200) ^b	293(200) ^b	11,381(280) ^b	2,298(200) ^b
112	52	Te	–73,480(70)	7,370(210) ^b	2,655(110)	9,270(90)	3,230(210) ^b
	53	I	–64,950(300) ^b	8,530(310) ^b	3,282(50)	12,671(430) ^b	–41(310) ^b
	54	Xe	–54,370(300) ^b	10,580(430) ^b	3,719(50)	10,720(500) ^b	1,311(430) ^b
	42	Mo	–58,830(600) ^b	7,080(780) ^b	–9,355(920) ^b	5,901(780) ^b	^a
	43	Tc	–65,910(500) ^b	9,960(740) ^b	–7,800(710) ^b	4,168(640) ^b	12,198(710) ^b
	44	Ru	–75,870(540) ^b	3,670(200) ^b	–7,107(570) ^b	7,146(620) ^b	13,341(670) ^b
	45	Rh	–79,540(500) ^b	6,800(500) ^b	–6,027(520) ^b	5,320(540) ^b	10,034(580) ^b
	46	Pd	–86,337(18)	288(17)	–5,107(120)	8,379(40)	11,338(210) ^b
	47	Ag	–86,625(17)	3,956(17)	–4,033(110)	6,479(17)	7,885(40)
	48	Cd	–90,581.0(28)	–2,586(5)	–3,484(3)	9,398.1(22)	9,652.6(26)
113	49	In	–87,995(5)	664(5)	–2,816(8)	7,678(6)	6,030(5)
	50	Sn	–88,659(4)	^a	–1,831(7)	10,786(6)	7,559(5)
	51	Sb	–81,604(23)	7,055(23)	67(40)	8,831(200) ^b	2,949(24)
	52	Te	–77,260(170)	4,350(170)	2,322(160)	11,852(180)	3,702(260) ^b
	53	I	–67,100(210) ^b	10,160(270) ^b	2,987(50)	10,220(370) ^b	909(220) ^b
	54	Xe	–59,930(150)	7,170(260) ^b	3,330(6)	13,629(340) ^b	2,269(340) ^b
	55	Cs	–46,270(300) ^b	13,660(340) ^b	4,133(210) ^b	^a	–814(7)
	42	Mo	–54,000(600) ^b	9,970(840) ^b	^a	3,237(840) ^b	^a
	43	Tc	–63,970(600) ^b	8,190(780) ^b	–8,293(780) ^b	6,125(780) ^b	12,422(840) ^b
	44	Ru	–72,150(500) ^b	6,630(640) ^b	–7,334(590) ^b	4,358(740) ^b	13,530(710) ^b
113	45	Rh	–78,790(400) ^b	4,910(400) ^b	–6,343(450) ^b	7,320(640) ^b	10,208(670) ^b
	46	Pd	–83,690(40)	3,340(40)	–5,266(80)	5,428(40)	11,445(500) ^b
	47	Ag	–87,033(17)	2,016(17)	–4,446(20)	8,480(24)	7,985(24)
	48	Cd	–89,049.9(28)	316(3)	–3,871(3)	6,540.2(6)	9,714(17)
	49	In	–89,366(3)	^a	–3,072(4)	9,443(5)	6,074(3)
	50	Sn	–88,330(4)	1,036(28)	–2,250(5)	7,742.9(18)	7,624(5)
	51	Sb	–84,414(22)	3,917(22)	–353(23)	10,881(30)	3,044(22)
	52	Te	–78,310(200) ^b	6,100(200) ^b	1,897(200) ^b	9,129(260) ^b	3,999(200) ^b

Table 11.23 (Continued)

A	Z	Element	Mass excess	$Q(\beta^-)$	$Q(\alpha)$	$S(n)$	$S(p)$
114	53	I	−71,120(50)	7,190(210) ^b	2,706(50)	12,101(220) ^b	1,157(180)
	54	Xe	−62,050(90)	9,070(100)	3,095(50)	10,197(180)	2,247(230) ^b
	55	Cs	−51,660(150)	10,390(180)	3,484(7)	13,470(340) ^b	−973.5(26)
	43	Tc	−59,730(600) ^b	11,070(700) ^b	−8,759(840) ^b	3,833(840) ^b	13,018(840) ^b
	44	Ru	−70,790(360) ^b	4,800(200) ^b	−7,763(540) ^b	6,712(620) ^b	14,117(700) ^b
	45	Rh	−75,590(300) ^b	7,900(300) ^b	−6,657(500) ^b	4,880(500) ^b	10,730(590) ^b
	46	Pd	−83,494(25)	1,451(25)	−5,779(230)	7,872(50)	11,997(400) ^b
	47	Ag	−84,945(26)	5,076(26)	−4,420(230)	5,983(30)	8,540(50)
	48	Cd	−90,021.3(28)	−1,452(3)	−4,096(11)	9,042.71(30)	10,277(17)
	49	In	−88,569(3)	1,988.7(7)	−3,537(4)	7,274.4(12)	6,809(3)
	50	Sn	−90,558(3)	^a	−2,633(4)	10,299.0(28)	8,480.7(13)
	51	Sb	−84,680(200)	5,880(200)	−630(200)	8,334(200)	3,635(200)
	52	Te	−81,920(200) ^b	2,760(280) ^b	1,491(200) ^b	11,676(280) ^b	4,794(200) ^b
	53	I	−72,800(300) ^b	9,120(360) ^b	2,313(360) ^b	9,743(300) ^b	1,771(360) ^b
	54	Xe	−66,930(210) ^b	5,860(360) ^b	2,920(200) ^b	12,950(220) ^b	3,096(210) ^b
	55	Cs	−54,570(310) ^b	12,370(370) ^b	3,357(50)	10,972(340) ^b	−199(320) ^b
	56	Ba	−45,700(450) ^b	8,870(540) ^b	3,598(200) ^b	^a	1,322(470) ^b
115	43	Tc	−57,490(700) ^b	9,290(920) ^b	^a	5,836(920) ^b	^a
	44	Ru	−66,780(600) ^b	7,630(780) ^b	−8,200(780) ^b	4,056(700) ^b	14,340(840) ^b
	45	Rh	−74,400(500)	6,000(500)	−7,013(640) ^b	6,881(590) ^b	10,898(620) ^b
	46	Pd	−80,400(60)	4,580(50)	−6,036(300) ^b	4,981(70)	12,098(310) ^b
	47	Ag	−84,990(30)	3,100(30)	−5,124(210) ^b	8,114(40)	8,782(40)
	48	Cd	−88,090.9(28)	1,446(4)	−4,487(40)	6,140.9(6)	10,435(26)
	49	In	−89,537(4)	496(4)	−3,744(5)	9,039(4)	6,804(4)
	50	Sn	−90,032.6(30)	^a	−3,203(4)	7,545.8(17)	8,752.2(18)
	51	Sb	−87,003(20)	3,030(20)	−1,039(21)	10,397(200)	3,733(20)
	52	Te	−82,360(110)	4,640(100)	1,155(110)	8,517(230) ^b	4,976(230)
	53	I	−76,460(470) ^b	5,910(480) ^b	1,960(510) ^b	11,734(550) ^b	1,829(510) ^b
	54	Xe	−68,430(240) ^b	8,030(520) ^b	2,621(250) ^b	9,569(320) ^b	2,922(380) ^b
	55	Cs	−59,670(430) ^b	8,760(490) ^b	2,850(300) ^b	13,178(520) ^b	29(470) ^b
	56	Ba	−48,710(600) ^b	10,970(730) ^b	3,237(670) ^b	11,081(750) ^b	1,431(670) ^b
	44	Ru	−65,060(700) ^b	6,010(860) ^b	−8,647(920) ^b	6,348(920) ^b	14,853(990) ^b
	45	Rh	−71,060(500) ^b	8,900(500) ^b	−7,573(710) ^b	4,729(710) ^b	11,571(780) ^b
116	46	Pd	−79,960(60)	2,607(30)	−6,519(540) ^b	7,629(80)	12,847(510)
	47	Ag	−82,570(50)	6,150(50)	−5,456(500) ^b	5,652(60)	9,454(80)
	48	Cd	−88,720(3)	−470(4)	−4,808(18)	8,700.2(21)	11,021(30)
	49	In	−88,250(4)	3,275(4)	−4,050(17)	6,784.3(8)	7,448(4)
	50	Sn	−91,524.7(30)	^a	−3,369(3)	9,563.41(11)	9,277(4)
	51	Sb	−86,818(6)	4,707(5)	−1,248(7)	7,886(21)	4,074(5)
	52	Te	−85,310(90)	1,510(90)	928(90)	11,013(140)	5,592(90)
	53	I	−77,560(140)	7,750(110)	1,618(140)	9,173(490) ^b	2,486(180)
	54	Xe	−72,900(250) ^b	4,660(200) ^b	1,931(300) ^b	12,543(340) ^b	3,731(530) ^b
	55	Cs	−62,490(350)	10,410(430) ^b	2,181(410) ^b	10,889(550) ^b	1,349(420) ^b

Table 11.23 (Continued)

A	Z	Element	Mass excess	$Q(\beta^-)$	$Q(\alpha)$	$S(n)$	$S(p)$
117	56	Ba	−54,330(500) ^b	8,170(610) ^b	3,178(530) ^b	13,688(780) ^b	1,941(660) ^b
	44	Ru	−60,740(800) ^b	8,790(1,000) ^b	−9,169(1,000) ^b	3,759(1,060) ^b	^a
	45	Rh	−69,540(600) ^b	7,000(670) ^b	−7,995(840) ^b	6,546(780) ^b	11,769(920) ^b
	46	Pd	−76,530(300) ^b	5,730(300) ^b	−6,803(590) ^b	4,642(300) ^b	12,759(590) ^b
	47	Ag	−82,270(50)	4,160(50)	−5,905(400) ^b	7,769(70)	9,594(70)
	48	Cd	−86,426(3)	2,517(6)	−5,157(40)	5,777.2(10)	11,147(50)
	49	In	−88,943(6)	1,455(5)	−4,334(18)	8,765(6)	7,512(6)
	50	Sn	−90,398.0(29)	^a	−3,773(3)	6,944.6(11)	9,437(4)
	51	Sb	−88,641(9)	1,757(9)	−1,700(9)	9,895(10)	4,406(9)
	52	Te	−85,107(19)	3,535(17)	799(19)	7,872(90)	5,578(20)
	53	I	−80,440(70)	4,670(70)	1,552(70)	10,947(160)	2,420(110)
	54	Xe	−73,990(180)	6,440(180)	1,895(270) ^b	9,164(280) ^b	3,722(200)
	55	Cs	−66,470(50)	7,520(190)	2,228(80)	12,053(360)	860(250) ^b
	56	Ba	−56,950(650) ^b	9,520(650) ^b	2,677(650) ^b	10,698(820) ^b	1,751(740) ^b
	57	La	−46,570(890) ^b	10,390(1,110) ^b	2,675(910) ^b	^a	−470(1,030) ^b
118	44	Ru	−58,660(900) ^b	7,080(1,140) ^b	^a	5,985(1,210) ^b	^a
	45	Rh	−65,740(700) ^b	9,730(730) ^b	−8,433(920) ^b	4,271(920) ^b	12,282(1,060) ^b
	46	Pd	−75,470(210)	4,100(200)	−7,097(420) ^b	7,006(370) ^b	13,219(630) ^b
	47	Ag	−79,570(60)	7,140(60)	−6,397(310) ^b	5,372(80)	10,323(310) ^b
	48	Cd	−86,709(20)	521(22)	−5,640(30)	8,355(20)	11,732(50)
	49	In	−87,230(8)	4,423(8)	−4,710(27)	6,358(6)	8,093(9)
	50	Sn	−91,653.1(29)	^a	−4,057(3)	9,326.5(14)	9,999(5)
	51	Sb	−87,996(4)	3,656.6(3)	−1,852(4)	7,426(10)	4,887(3)
	52	Te	−87,723(16)	273(16)	410(16)	10,688(25)	6,371(18)
	53	I	−80,690(80)	7,030(80)	1,561(220)	8,325(110)	2,873(80)
	54	Xe	−77,710(1,000)	2,980(1,000)	1,780(1,020) ^b	11,791(1,020)	4,566(1,000)
	55	Cs	−68,414(13)	9,300(1,000)	1,958(300) ^b	10,013(60)	1,709(180)
	56	Ba	−62,000(500) ^b	6,410(500) ^b	2,507(540) ^b	13,120(820) ^b	2,817(510) ^b
	57	La	−49,770(800) ^b	12,230(950) ^b	2,371(860) ^b	11,276(1,200) ^b	107(1,030) ^b
119	45	Rh	−63,940(800) ^b	8,090(860) ^b	−8,871(1,060) ^b	6,274(1,060) ^b	12,571(1,210) ^b
	46	Pd	−72,020(300) ^b	6,530(310) ^b	−7,669(670) ^b	4,628(370) ^b	13,577(760) ^b
	47	Ag	−78,560(90)	5,350(40)	−6,578(510)	7,062(110)	10,380(230)
	48	Cd	−83,910(80)	3,800(80)	−5,928(100)	5,269(80)	11,630(100)
	49	In	−87,704(8)	2,364(8)	−5,141(40)	8,545(9)	8,284(22)
	50	Sn	−90,067.2(28)	^a	−4,401(3)	6,485.4(14)	10,126(8)
	51	Sb	−89,473(8)	594(8)	−2,361(9)	9,548(8)	5,109(8)
	52	Te	−87,180(8)	2,293(2)	427(8)	7,528(18)	6,473(8)
	53	I	−83,670(60)	3,510(60)	912(70)	11,047(90)	3,232(70)
	54	Xe	−78,660(120)	5,010(110)	1,278(160)	9,018(1,010)	5,259(140)
	55	Cs	−72,311(14)	6,350(120)	1,723(470) ^b	11,969(19)	1,886(1,000)
	56	Ba	−64,220(1,020)	8,090(1,020)	1,780(1,050) ^b	10,296(1,140) ^b	3,100(1,020)
	57	La	−54,970(700) ^b	9,260(1,240) ^b	2,280(820) ^b	13,269(1,060) ^b	256(860) ^b
	58	Ce	−44,000(900) ^b	10,960(1,140) ^b	2,279(1,080) ^b	^a	1,523(1,210) ^b

Table 11.23 (Continued)

A	Z	Element	Mass excess	$Q(\beta^-)$	$Q(\alpha)$	$S(n)$	$S(p)$
120	45	Rh	−59,820(800) ^b	10,950(900) ^b	^a	3,954(1,130) ^b	^a
	46	Pd	−70,770(400) ^b	4,880(410) ^b	−8,135(810) ^b	6,814(500) ^b	14,117(900) ^b
	47	Ag	−75,650(70)	8,330(70)	−7,012(510) ^b	5,163(120)	10,914(310) ^b
	48	Cd	−83,973(19)	1,760(40)	−6,437(60)	8,138(80)	12,705(90)
	49	In	−85,730(40)	5,370(40)	−5,590(60)	6,101(40)	9,116(90)
	50	Sn	−91,103.3(25)	−2,681(7)	−4,808(4)	9,107.4(22)	10,689(7)
	51	Sb	−88,423(8)	982(13)	−2,598(8)	7,021(11)	5,644(7)
	52	Te	−89,405(10)	^a	−305(11)	10,296(13)	7,221(13)
	53	I	−83,790(18)	5,615(15)	603(19)	8,195(70)	3,899(20)
	54	Xe	−81,830(40)	1,960(40)	1,051(100)	11,241(130)	5,453(80)
	55	Cs	−73,888(10)	7,940(50)	1,248(140)	9,648(17)	2,516(120)
	56	Ba	−68,890(300)	5,000(300)	1,588(390) ^b	12,734(1,060)	3,866(300)
	57	La	−57,690(600) ^b	11,200(670) ^b	2,378(690) ^b	10,791(920) ^b	752(1,180) ^b
	58	Ce	−49,710(800) ^b	7,980(1,000) ^b	2,195(950) ^b	13,772(1,210) ^b	2,026(1,060) ^b
121	45	Rh	−57,680(900) ^b	9,220(1,030) ^b	^a	5,929(1,210) ^b	^a
	46	Pd	−66,900(500) ^b	7,760(520) ^b	−8,582(950) ^b	4,206(640) ^b	14,368(950) ^b
	47	Ag	−74,660(150)	6,400(120)	−7,547(610) ^b	7,082(160)	11,182(430) ^b
	48	Cd	−81,060(80)	4,780(80)	−6,952(310) ^b	5,157(90)	12,699(110)
	49	In	−85,838(27)	3,365(27)	−5,998(60)	8,176(50)	9,154(30)
	50	Sn	−89,202.8(25)	390.1(21)	−5,202(4)	6,170.8(6)	10,758(40)
	51	Sb	−89,592.9(23)	^a	−3,075(6)	9,242(7)	5,778.6(21)
	52	Te	−88,557(25)	1,036(25)	−584(25)	7,224(26)	7,424(26)
	53	I	−86,288(11)	2,269(26)	−72(15)	10,569(16)	4,172(4)
	54	Xe	−82,543(24)	3,745(27)	139(30)	8,784(50)	6,042(30)
	55	Cs	−77,143(14)	5,400(20)	869(70)	11,327(16)	2,602(50)
	56	Ba	−70,340(300)	6,800(300)	1,228(350)	9,524(430)	3,742(300)
	57	La	−62,400(500) ^b	7,940(590) ^b	1,646(510) ^b	12,785(780) ^b	802(590) ^b
	58	Ce	−52,470(700) ^b	9,930(860) ^b	2,056(950) ^b	10,838(1,060) ^b	2,073(920) ^b
122	59	Pr	−41,580(800) ^b	10,890(1,060) ^b	2,562(1,200) ^b	^a	−837(50)
	46	Pd	−65,390(500) ^b	6,040(540) ^b	−9,160(1,030) ^b	6,562(710) ^b	15,002(1,030) ^b
	47	Ag	−71,430(210) ^b	9,150(290) ^b	−8,116(730) ^b	4,840(250) ^b	11,816(540) ^b
	48	Cd	−80,570(210) ^b	3,000(210) ^b	−7,533(290) ^b	7,587(220) ^b	13,205(250) ^b
	49	In	−83,580(50)	6,370(50)	−6,435(80)	5,809(60)	9,807(100)
	50	Sn	−89,944.9(27)	−1,616.4(28)	−5,661(20)	8,813.5(25)	11,396(27)
	51	Sb	−88,328.5(22)	1,982.5(2)	−3,523(8)	6,806.9(10)	6,414.7(22)
	52	Te	−90,311.1(19)	^a	−1,083(3)	9,825(25)	8,007.1(21)
	53	I	−86,077(5)	4,234(5)	−506(7)	7,860(12)	4,809(26)
	54	Xe	−85,190(90)	890(90)	112(90)	10,715(90)	6,188(90)
	55	Cs	−78,132(16)	7,050(90)	134(80)	9,060(20)	2,878(29)
	56	Ba	−74,280(300) ^b	3,860(300) ^b	1,011(1,040) ^b	12,008(430) ^b	4,423(300) ^b
	57	La	−64,540(500) ^b	9,730(590) ^b	1,446(500) ^b	10,214(710) ^b	1,491(590) ^b
	58	Ce	−57,740(600) ^b	6,800(780) ^b	1,832(780) ^b	13,344(920) ^b	2,632(780) ^b
	59	Pr	−45,040(800) ^b	12,710(1,000) ^b	2,307(1,130) ^b	11,531(1,130) ^b	−144(1,060) ^b

Table 11.23 (Continued)

A	Z	Element	Mass excess	$Q(\beta^-)$	$Q(\alpha)$	$S(n)$	$S(p)$
123	46	Pd	−61,240(600) ^b	8,720(670) ^b	^a	3,917(780) ^b	^a
	47	Ag	−69,960(300) ^b	7,360(300) ^b	−8,442(860) ^b	6,600(360) ^b	11,853(590) ^b
	48	Cd	−77,310(40)	6,120(30)	−7,712(300) ^b	4,808(210) ^b	13,173(210) ^b
	49	In	−83,426(24)	4,394(24)	−7,294(90)	7,921(60)	10,140(210) ^b
	50	Sn	−87,819.5(27)	1,403(28)	−6,338(80)	5,945.9(12)	11,532(50)
	51	Sb	−89,222.5(20)	^a	−3,944(8)	8,965.3(22)	6,566.5(29)
	52	Te	−89,169.2(18)	53.3(18)	−1,526.9(29)	6,929.4(5)	8,129.6(20)
	53	I	−87,935(4)	1,234(3)	−887(9)	9,929(6)	4,913(3)
	54	Xe	−85,259(15)	2,676(15)	−504(18)	8,144(90)	6,471(16)
	55	Cs	−81,049(12)	4,210(20)	192(60)	10,989(20)	3,151(90)
	56	Ba	−75,590(300) ^b	5,460(300) ^b	645(320) ^b	9,385(420) ^b	4,748(300) ^b
	57	La	−68,710(400) ^b	6,880(500) ^b	1,179(400) ^b	12,235(640) ^b	1,719(500) ^b
124	58	Ce	−60,070(500) ^b	8,640(640) ^b	1,728(1,140) ^b	10,400(780) ^b	2,818(710) ^b
	59	Pr	−50,340(700) ^b	9,730(860) ^b	2,205(990) ^b	13,372(1,060) ^b	−116(920) ^b
	47	Ag	−66,570(400) ^b	10,140(410) ^b	−9,178(900) ^b	4,690(500) ^b	12,626(720) ^b
	48	Cd	−76,710(60)	4,170(40)	−8,369(410) ^b	7,471(70)	14,044(310) ^b
	49	In	−80,880(50)	7,360(50)	−7,653(90)	5,522(50)	10,855(60)
	50	Sn	−88,236.1(14)	−617.5(21)	−6,688(19)	8,488.0(25)	12,100(24)
	51	Sb	−87,618.6(20)	2,904.5(15)	−4,310(40)	6,467.45(7)	7,088.1(28)
	52	Te	−90,523.1(15)	−3,159.6(19)	−1,844.7(25)	9,425.2(11)	8,589.6(15)
	53	I	−87,363.5(24)	294(29)	−1,366(8)	7,500(4)	5,483.3(22)
	54	Xe	−87,657.5(20)	^a	−678(10)	10,470(16)	7,012(4)
	55	Cs	−81,743(12)	5,915(12)	−378(22)	8,765(16)	3,773(19)
	56	Ba	−79,095(14)	2,648(18)	310(50)	11,575(300) ^b	5,334(18)
125	57	La	−70,300(300) ^b	8,800(300) ^b	1,163(300) ^b	9,664(500) ^b	1,998(420) ^b
	58	Ce	−64,720(500) ^b	5,580(590) ^b	1,743(590) ^b	12,719(710) ^b	3,302(640) ^b
	59	Pr	−53,130(600) ^b	11,590(780) ^b	2,130(840) ^b	10,866(920) ^b	349(780) ^b
	47	Ag	−64,700(400) ^b	8,660(410) ^b	−9,448(990) ^b	6,199(570) ^b	^a
	48	Cd	−73,360(70)	7,120(60)	−8,883(510) ^b	4,719(90)	14,073(410) ^b
	49	In	−80,480(30)	5,418(30)	−8,246(150)	7,675(60)	11,059(70)
	50	Sn	−85,897.8(15)	2,363.3(3)	−7,264(80)	5,733(6)	12,311(50)
	51	Sb	−88,261.1(28)	766.7(21)	−4,848(28)	8,713.8(30)	7,314.0(29)
	52	Te	−89,027.8(19)	^a	−2,249.9(28)	6,576.0(14)	8,698.1(21)
	53	I	−88,842.0(19)	185.77(6)	−1,674.0(25)	9,549.9(23)	5,607.9(14)
	54	Xe	−87,189.5(20)	1,652.6(26)	−1,057(25)	7,603.3(4)	7,115.0(29)
	55	Cs	−84,091(8)	3,099(8)	−228(14)	10,419(14)	3,722(8)
126	56	Ba	−79,530(250)	4,560(250)	587(250)	8,507(250)	5,077(250)
	57	La	−73,900(300) ^b	5,640(390) ^b	823(300) ^b	11,667(420) ^b	2,090(300) ^b
	58	Ce	−66,570(400) ^b	7,330(500) ^b	1,351(500) ^b	9,916(640) ^b	3,554(500) ^b
	59	Pr	−57,910(500) ^b	8,650(640) ^b	2,065(710) ^b	12,850(780) ^b	480(710) ^b
	47	Ag	−61,010(400) ^b	11,310(400) ^b	^a	4,383(570) ^b	^a
	48	Cd	−72,330(50)	5,490(40)	−9,361(510) ^b	7,040(90)	14,914(400) ^b
	49	In	−77,810(40)	8,210(40)	−8,811(210) ^b	5,404(50)	11,744(80)

■ Table 11.23 (Continued)

A	Z	Element	Mass excess	$Q(\beta^-)$	$Q(\alpha)$	$S(n)$	$S(p)$
	50	Sn	−86,020(11)	378(30)	−7,870(210) ^b	8,193(11)	12,829(30)
	51	Sb	−86,400(30)	3,670(30)	−5,246(60)	6,208(30)	7,789(30)
	52	Te	−90,070.3(19)	−2,155(4)	−2,550.3(30)	9,113.8(4)	9,098.2(22)
	53	I	−87,915(4)	1,258(5)	−2,011(4)	7,144(4)	6,176(4)
	54	Xe	−89,173(6)	^a	−1,287(6)	10,055(7)	7,620(6)
	55	Cs	−84,349(12)	4,824(14)	−697(13)	8,329(14)	4,448(12)
	56	Ba	−82,676(14)	1,673(18)	86(90)	11,216(250)	5,874(16)
	57	La	−75,110(300) ^b	7,570(300) ^b	601(300) ^b	9,282(420) ^b	2,865(390) ^b
	58	Ce	−70,700(400) ^b	4,410(500) ^b	1,152(500) ^b	12,207(570) ^b	4,094(500) ^b
	59	Pr	−60,260(500) ^b	10,440(640) ^b	1,860(710) ^b	10,419(710) ^b	983(640) ^b
	60	Nd	−53,030(700) ^b	7,230(860) ^b	2,288(920) ^b	^a	2,408(860) ^b
127	47	Ag	−58,800(500) ^b	9,730(510) ^b	^a	5,854(640) ^b	^a
	48	Cd	−68,530(70)	8,470(60)	−9,714(600) ^b	4,270(90)	14,802(410) ^b
	49	In	−76,990(40)	6,510(30)	−9,463(300) ^b	7,252(60)	11,956(70)
	50	Sn	−83,508(25)	3,201(24)	−8,622(50)	5,559(27)	12,984(50)
	51	Sb	−86,709(6)	1,581(5)	−5,708(25)	8,382(30)	7,978(12)
	52	Te	−88,290(3)	698(4)	−2,895(4)	6,290.5(28)	9,181(30)
	53	I	−88,987(4)	^a	−2,190(4)	9,143.4(27)	6,206(4)
	54	Xe	−88,325(4)	662.4(21)	−1,580(4)	7,223(6)	7,699(3)
	55	Cs	−86,240(9)	2,085(9)	−730(9)	9,963(15)	4,356(10)
	56	Ba	−82,790(100)	3,450(100)	44(100)	8,186(100)	5,730(100)
	57	La	−78,100(220) ^b	4,690(250) ^b	528(220) ^b	11,061(370) ^b	2,710(220) ^b
128	58	Ce	−71,960(300) ^b	6,140(370) ^b	1,208(420) ^b	9,329(500) ^b	4,141(420) ^b
	59	Pr	−64,430(400) ^b	7,530(500) ^b	1,851(570) ^b	12,244(640) ^b	1,020(570) ^b
	60	Nd	−55,420(600) ^b	9,010(720) ^b	2,223(780) ^b	10,465(920) ^b	2,455(780) ^b
	48	Cd	−67,290(290)	7,070(290)	^a	6,836(300)	15,784(580) ^b
	49	In	−74,360(50)	8,980(40)	−10,212(400) ^b	5,438(60)	13,124(90)
	50	Sn	−83,336(27)	1,274(15)	−9,051(70)	7,900(40)	13,632(50)
	51	Sb	−84,610(25)	4,384(25)	−6,159(60)	5,973(26)	8,392(40)
	52	Te	−88,993.6(18)	−1,252(4)	−3,182.4(22)	8,775(4)	9,574(6)
	53	I	−87,742(4)	2,119(4)	−2,548(4)	6,826.07(5)	6,741(4)
	54	Xe	−89,860.8(14)	^a	−1,762.7(19)	9,607(4)	8,163(4)
	55	Cs	−85,932(6)	3,929(5)	−994(6)	7,764(10)	4,897(7)
128	56	Ba	−85,410(11)	523(12)	−177(11)	10,691(100)	6,459(14)
	57	La	−78,760(400)	6,650(400)	558(400)	8,735(460) ^b	3,259(410)
	58	Ce	−75,570(300) ^b	3,190(500) ^b	1,098(300) ^b	11,686(420) ^b	4,765(370) ^b
	59	Pr	−66,320(400) ^b	9,250(500) ^b	1,553(500) ^b	9,962(570) ^b	1,653(500) ^b
	60	Nd	−60,180(600) ^b	6,140(720) ^b	2,111(780) ^b	12,831(840) ^b	3,041(720) ^b
	61	Pm	−48,200(900) ^b	11,990(1,080) ^b	2,512(1,080) ^b	^a	61(1,080) ^b
129	48	Cd	−63,100(400) ^b	9,880(420) ^b	^a	3,880(500) ^b	^a
	49	In	−72,980(130)	7,660(30)	−10,698(420) ^b	6,686(140)	12,974(320)
	50	Sn	−80,630(120)	4,000(120)	−9,697(140)	5,365(120)	13,559(130)
	51	Sb	−84,626(21)	2,380(21)	−6,571(40)	8,087(30)	8,579(30)

Table 11.23 (Continued)

A	Z	Element	Mass excess	$Q(\beta^-)$	$Q(\alpha)$	$S(n)$	$S(p)$
	52	Te	−87,006(3)	1,498(3)	−3,533(3)	6,083.3(27)	9,685(25)
	53	I	−88,504(3)	194(3)	−2,667(4)	8,833(5)	6,799(3)
	54	Xe	−88,697.4(8)	^a	−2,094.5(20)	6,907.9(16)	8,244(4)
	55	Cs	−87,501(5)	1,196(5)	−1,084(5)	9,640(7)	4,930(5)
	56	Ba	−85,070(11)	2,432(11)	−305(12)	7,731(16)	6,427(13)
	57	La	−81,350(50)	3,720(50)	316(50)	10,661(400)	3,229(50)
	58	Ce	−76,300(210) ^b	5,050(200) ^b	806(320) ^b	8,799(360) ^b	4,829(450) ^b
	59	Pr	−69,990(300) ^b	6,310(360) ^b	1,478(420) ^b	11,741(500) ^b	1,709(420) ^b
	60	Nd	−62,170(360) ^b	7,820(470) ^b	1,967(540) ^b	10,061(700) ^b	3,140(540) ^b
	61	Pm	−52,950(800) ^b	9,230(880) ^b	2,540(950) ^b	12,822(1,210) ^b	51(1,000) ^b
130	48	Cd	−61,500(400) ^b	8,500(400) ^b	^a	6,469(570) ^b	^a
	49	In	−70,000(50)	10,250(40)	−11,409(400) ^b	5,093(130)	14,187(400) ^b
	50	Sn	−80,246(29)	2,148(15)	−10,344(60)	7,687(130)	14,560(130)
	51	Sb	−82,394(25)	4,959(25)	−7,006(50)	5,839(30)	9,053(120)
	52	Te	−87,352.9(19)	−420(4)	−3,758(11)	8,418.6(29)	10,016(21)
	53	I	−86,933(3)	2,949(3)	−2,960(30)	6,500.33(4)	7,216(3)
	54	Xe	−89,881.8(9)	−2,979(8)	−2,236.4(21)	9,255.8(9)	8,667(3)
	55	Cs	−86,903(8)	369(11)	−1,413(9)	7,473(10)	5,494(8)
	56	Ba	−87,271(7)	^a	−523(9)	10,273(11)	7,059(8)
	57	La	−81,670(210) ^b	5,600(210) ^b	250(210) ^b	8,395(210) ^b	3,893(210) ^b
	58	Ce	−79,460(610) ^b	2,210(650) ^b	788(610) ^b	11,234(650) ^b	5,401(620) ^b
	59	Pr	−71,370(300) ^b	8,090(680) ^b	1,310(420) ^b	9,450(420) ^b	2,360(360) ^b
	60	Nd	−66,340(500) ^b	5,030(590) ^b	1,934(640) ^b	12,239(620) ^b	3,638(590) ^b
	61	Pm	−55,470(700) ^b	10,870(860) ^b	2,363(860) ^b	10,596(1,060) ^b	586(790) ^b
	62	Sm	−47,850(900) ^b	7,620(1,140) ^b	2,754(1,140) ^b	^a	2,194(1,210) ^b
131	49	In	−68,220(80)	9,174(22)	−11,845(510) ^b	6,290(90)	14,007(410) ^b
	50	Sn	−77,390(70)	4,632(20)	−11,289(100)	5,214(80)	14,681(90)
	51	Sb	−82,020(70)	3,190(70)	−7,453(80)	7,699(70)	9,064(80)
	52	Te	−85,211.3(20)	2,233.5(23)	−4,129(25)	5,929.7(5)	10,106(25)
	53	I	−87,444.8(11)	970.8(6)	−3,161(6)	8,584(4)	7,380.8(23)
	54	Xe	−88,415.6(10)	^a	−2,551(3)	6,605.1(13)	8,772(4)
	55	Cs	−88,063(5)	352(5)	−1,501(6)	9,232(10)	5,470(5)
	56	Ba	−86,693(7)	1,370(7)	−794(8)	7,493.50(30)	7,080(11)
	57	La	−83,730(100)	2,960(100)	82(100)	10,131(230) ^b	3,751(100)
	58	Ce	−79,710(410)	4,020(400)	652(420)	8,322(450) ^b	5,329(460) ^b
	59	Pr	−74,460(440)	5,250(150)	1,208(490) ^b	11,164(530) ^b	2,290(430) ^b
	60	Nd	−67,900(460)	6,560(150)	1,630(550) ^b	9,634(680) ^b	3,821(550) ^b
	61	Pm	−59,800(600) ^b	8,100(760) ^b	2,205(720) ^b	12,403(920) ^b	750(780) ^b
	62	Sm	−50,400(900) ^b	9,400(1,080) ^b	2,596(1,080) ^b	10,624(1,280) ^b	2,222(1,140) ^b
132	49	In	−62,490(70)	14,140(60)	^a	2,341(100)	^a
	50	Sn	−76,621(26)	3,103(12)	−11,755(300)	7,303(80)	15,694(80)
	51	Sb	−79,724(23)	5,486(20)	−7,788(50)	5,774(70)	9,623(80)
	52	Te	−85,210(11)	493(4)	−4,298(30)	8,070(12)	10,477(70)

Table 11.23 (Continued)

A	Z	Element	Mass excess	$Q(\beta^-)$	$Q(\alpha)$	$S(n)$	$S(p)$
	53	I	−85,703(11)	3,577(11)	−3,517(27)	6,329(11)	7,780(11)
	54	Xe	−89,279.5(11)	−2,119(3)	−2,710.8(21)	8,935.3(8)	9,123.7(10)
	55	Cs	−87,160(3)	1,279.5(22)	−1,843(5)	7,168(6)	6,033(3)
	56	Ba	−88,440(3)	^a	−1,004(3)	9,818(7)	7,665(6)
	57	La	−83,730(40)	4,710(40)	−224(50)	8,070(110)	4,327(50)
	58	Ce	−82,450(200) ^b	1,290(200) ^b	538(200) ^b	10,804(460) ^b	6,002(220) ^b
	59	Pr	−75,340(200) ^b	7,110(280) ^b	996(450) ^b	8,947(480) ^b	2,915(460) ^b
	60	Nd	−71,610(300) ^b	3,730(360) ^b	1,534(420) ^b	11,781(550) ^b	4,439(530) ^b
	61	Pm	−61,710(500) ^b	9,900(590) ^b	2,186(640) ^b	9,981(780) ^b	1,097(680) ^b
	62	Sm	−55,130(700) ^b	6,590(860) ^b	2,633(920) ^b	12,794(1,140) ^b	2,613(920) ^b
	63	Eu	−42,700(900) ^b	12,430(1,140) ^b	3,071(1,280) ^b	^a	−414(1,280) ^b
133	49	In	−57,440(400) ^b	13,530(410) ^b	^a	3,022(410) ^b	^a
	50	Sn	−70,970(80)	7,990(25)	−10,292(410) ^b	2,418(80)	15,770(100)
	51	Sb	−78,960(80)	4,003(13)	−8,406(150)	7,305(80)	9,625(80)
	52	Te	−82,960(80)	2,920(70)	−4,754(140)	5,822(80)	10,525(80)
	53	I	−85,878(26)	1,771(26)	−3,676(30)	8,247(28)	7,957(28)
	54	Xe	−87,648(4)	427.4(24)	−3,068(5)	6,440(4)	9,235(11)
	55	Cs	−88,075.7(30)	^a	−1,997(4)	8,986.9(19)	6,085(3)
	56	Ba	−87,558(3)	517.4(1)	−1,286(3)	7,189.9(4)	7,687.1(22)
	57	La	−85,330(200)	2,230(200)	−252(200)	9,668(200)	4,178(200)
	58	Ce	−82,390(200) ^b	2,940(280) ^b	254(200) ^b	8,015(280) ^b	5,948(200) ^b
	59	Pr	−78,060(200) ^b	4,330(280) ^b	866(200) ^b	10,791(280) ^b	2,902(280) ^b
	60	Nd	−72,460(300) ^b	5,600(360) ^b	1,414(360) ^b	8,919(420) ^b	4,411(360) ^b
	61	Pm	−65,470(500) ^b	7,000(590) ^b	2,102(590) ^b	11,825(710) ^b	1,141(590) ^b
	62	Sm	−57,070(600) ^b	8,390(780) ^b	2,676(700) ^b	10,018(920) ^b	2,650(780) ^b
	63	Eu	−47,600(900) ^b	9,470(1,080) ^b	2,922(1,210) ^b	12,971(1,280) ^b	−238(1,140) ^b
134	49	In	−51,550(500) ^b	15,090(510) ^b	^a	2,184(640) ^b	^a
	50	Sn	−66,640(100)	7,370(90)	−7,563(410) ^b	3,740(130)	16,489(410) ^b
	51	Sb	−74,010(50)	8,390(40)	−6,433(70)	3,120(90)	10,328(100)
	52	Te	−82,400(30)	1,550(30)	−4,578(40)	7,511(80)	10,732(80)
	53	I	−83,949(15)	4,175(15)	−3,980(29)	6,143(30)	8,279(80)
	54	Xe	−88,124.4(8)	−1,229(3)	−3,196.4(21)	8,547(4)	9,536(26)
	55	Cs	−86,895.9(30)	2,058.7(4)	−2,388(4)	6,891.54(1)	6,536.6(24)
	56	Ba	−88,954.5(30)	^a	−1,498(3)	9,467.7(11)	8,167.9(4)
	57	La	−85,241(26)	3,713(26)	−764(27)	7,984(200)	4,972(26)
	58	Ce	−84,740(200)	500(200)	105(200)	10,422(280) ^b	6,702(280)
	59	Pr	−78,550(300) ^b	6,190(220) ^b	697(360) ^b	8,564(360) ^b	3,450(360) ^b
	60	Nd	−75,780(330) ^b	2,770(150) ^b	1,256(700) ^b	11,392(450) ^b	5,011(390) ^b
	61	Pm	−66,610(390) ^b	9,170(200) ^b	2,335(490) ^b	9,217(640) ^b	1,439(490) ^b
	62	Sm	−61,460(500) ^b	5,150(640) ^b	2,456(710) ^b	12,459(780) ^b	3,284(710) ^b
	63	Eu	−50,000(700) ^b	11,460(860) ^b	3,043(990) ^b	10,475(1,140) ^b	219(920) ^b
135	50	Sn	−60,800(400) ^b	8,910(410) ^b	^a	2,234(410) ^b	16,539(640) ^b
	51	Sb	−69,710(110)	8,120(50)	−3,915(130)	3,771(120)	10,359(150)

Table 11.23 (Continued)

A	Z	Element	Mass excess	$Q(\beta^-)$	$Q(\alpha)$	$S(n)$	$S(p)$
	52	Te	−77,830(90)	5,960(90)	−2,861(120)	3,497(100)	11,109(110)
	53	I	−83,788(23)	2,648(24)	−4,191(70)	7,909(28)	8,677(40)
	54	Xe	−86,436(10)	1,151(10)	−3,649(10)	6,383(10)	9,775(18)
	55	Cs	−87,587(3)	269.3(12)	−2,567(3)	8,762.0(10)	6,751(3)
	56	Ba	−87,855.9(30)	^a	−1,865(3)	6,972.7(5)	8,249.0(7)
	57	La	−86,656(10)	1,200(10)	−1,018(11)	9,486(28)	4,990(10)
	58	Ce	−84,630(11)	2,026(5)	−362(13)	7,960(200)	6,678(28)
	59	Pr	−80,910(150)	3,720(150)	398(180)	10,430(330) ^b	3,458(250)
	60	Nd	−76,160(210) ^b	4,750(250) ^b	1,130(460) ^b	8,449(390) ^b	4,897(360) ^b
	61	Pm	−70,220(320) ^b	5,940(250) ^b	1,820(550) ^b	11,679(510) ^b	1,727(470) ^b
	62	Sm	−63,020(500) ^b	7,200(600) ^b	2,463(680) ^b	9,627(710) ^b	3,693(640) ^b
	63	Eu	−54,290(600) ^b	8,730(780) ^b	3,090(840) ^b	12,356(920) ^b	116(780) ^b
	63	Eu	−54,290(600) ^b	8,730(780) ^b	3,090(840) ^b	12,356(920) ^b	116(780) ^b
136	50	Sn	−56,500(500) ^b	8,090(590) ^b	^a	3,777(640) ^b	^a
	51	Sb	−64,590(300) ^b	9,830(300) ^b	−4,529(310) ^b	2,956(320) ^b	11,080(500) ^b
	52	Te	−74,420(50)	5,070(60)	−228(60)	4,669(100)	12,007(110)
	53	I	−79,500(50)	6,930(50)	−2,200(60)	3,782(50)	8,962(100)
	54	Xe	−86,424(7)	−80(8)	−3,640(13)	8,060(12)	9,926(23)
	55	Cs	−86,344(4)	2,548.2(19)	−3,067(11)	6,828.9(22)	7,197(10)
	56	Ba	−88,892.4(30)	−2,870(70)	−2,038(3)	9,107.74(4)	8,594.7(12)
	57	La	−86,020(70)	470(80)	−1,287(70)	7,438(70)	5,455(70)
	58	Ce	−86,500(50)	^a	−480(50)	9,936(50)	7,128(50)
	59	Pr	−81,370(50)	5,126(18)	−62(70)	8,530(160)	4,027(50)
	60	Nd	−79,160(60)	2,211(25)	864(200) ^b	11,070(210) ^b	5,536(160)
	61	Pm	−71,310(210)	7,850(200)	1,606(290) ^b	9,160(380) ^b	2,438(290) ^b
	62	Sm	−66,790(400) ^b	4,520(450) ^b	2,400(500) ^b	11,844(640) ^b	3,858(520) ^b
	63	Eu	−56,360(500) ^b	10,430(640) ^b	2,931(710) ^b	10,139(780) ^b	629(710) ^b
	64	Gd	−49,300(700) ^b	7,050(860) ^b	3,397(990) ^b	^a	2,305(920) ^b
137	50	Sn	−50,500(600) ^b	9,760(720) ^b	^a	2,063(780) ^b	^a
	51	Sb	−60,260(400) ^b	9,300(420) ^b	−5,247(570) ^b	3,740(500) ^b	11,043(640) ^b
	52	Te	−69,560(120)	6,940(120)	−1,018(150)	3,207(130)	12,259(320) ^b
	53	I	−76,501(28)	5,877(27)	31(80)	5,074(60)	9,367(60)
	54	Xe	−82,379(7)	4,173(7)	−1,844(80)	4,025.46(27)	10,169(50)
	55	Cs	−86,551.1(30)	1,175.63(17)	−3,098(26)	8,278.3(19)	7,416(7)
	56	Ba	−87,726.8(30)	^a	−2,503.4(25)	6,905.74(3)	8,671.6(19)
	57	La	−87,130(50)	600(50)	−1,476(50)	9,176(80)	5,523(50)
	58	Ce	−85,900(50)	1,222.1(16)	−771(50)	7,480.7(4)	7,171(80)
	59	Pr	−83,200(50)	2,702(10)	−299(210)	9,905(21)	3,996(10)
	60	Nd	−79,510(70)	3,690(50)	453(210) ^b	8,426(60)	5,433(60)
	61	Pm	−73,860(140) ^b	5,660(110) ^b	1,779(240) ^b	10,619(240) ^b	1,987(130) ^b
	62	Sm	−67,960(110)	5,900(120) ^b	2,080(320) ^b	9,239(420) ^b	3,937(230)
	63	Eu	−60,350(500) ^b	7,600(520) ^b	2,689(710) ^b	12,067(710) ^b	852(640) ^b
	64	Gd	−51,560(600) ^b	8,790(780) ^b	3,090(840) ^b	10,326(920) ^b	2,492(780) ^b
138	51	Sb	−55,000(500) ^b	10,940(540) ^b	−5,871(710) ^b	2,808(640) ^b	11,788(780) ^b

Table 11.23 (Continued)

A	Z	Element	Mass excess	$Q(\beta^-)$	$Q(\alpha)$	$S(n)$	$S(p)$
	52	Te	−65,930(210) ^b	6,370(220) ^b	−1,720(230) ^b	4,443(240) ^b	12,962(450) ^b
	53	I	−72,300(80)	7,820(70)	−718(100)	3,869(80)	10,029(150)
	54	Xe	−80,120(40)	2,770(40)	−145(50)	5,812(40)	10,907(50)
	55	Cs	−82,893(10)	5,374(9)	−1,369(18)	4,413(9)	7,804(12)
	56	Ba	−88,267.2(30)	−1,738(4)	−2,568(3)	8,611.72(4)	9,005(18)
	57	La	−86,529(4)	1,044(11)	−2,058(4)	7,474(50)	6,092(4)
	58	Ce	−87,574(11)	^a	−1,044(11)	9,741(50)	7,736(50)
	59	Pr	−83,137(15)	4,437(10)	−320(30)	8,006(50)	4,521(50)
	60	Nd	−82,040(200) ^b	1,100(200) ^b	280(280) ^b	10,596(210) ^b	6,123(210) ^b
	61	Pm	−75,040(320) ^b	7,000(250) ^b	1,090(440) ^b	9,253(350) ^b	2,813(330) ^b
	62	Sm	−71,220(300) ^b	3,820(440) ^b	2,134(450) ^b	11,338(320) ^b	4,655(330) ^b
	63	Eu	−61,990(400) ^b	9,230(500) ^b	2,196(560) ^b	9,711(640) ^b	1,324(420) ^b
	64	Gd	−55,920(500) ^b	6,070(640) ^b	3,117(710) ^b	12,431(780) ^b	2,855(710) ^b
	65	Tb	−43,900(800) ^b	12,020(950) ^b	3,676(1,060) ^b	^a	−368(1,000) ^b
139	51	Sb	−50,570(600) ^b	10,230(720) ^b	^a	3,647(780) ^b	^a
	52	Te	−60,800(400) ^b	8,050(400) ^b	−2,425(570) ^b	2,939(450) ^b	13,092(640) ^b
	53	I	−68,840(30)	6,806(23)	−1,563(110)	4,616(90)	10,201(210) ^b
	54	Xe	−75,650(21)	5,057(21)	−249(90)	3,602(40)	10,639(80)
	55	Cs	−80,707(4)	4,213(3)	656(24)	5,885(10)	7,876(40)
	56	Ba	−84,919.3(30)	2,316.8(26)	−909(10)	4,723.43(4)	9,315(9)
	57	La	−87,236(3)	^a	−2,074.4(29)	8,778.0(26)	6,257.9(26)
	58	Ce	−86,958(8)	278(7)	−1,527(7)	7,456(12)	7,718(7)
	59	Pr	−84,829(8)	2,129(3)	−598(13)	9,764(16)	4,544(13)
	60	Nd	−82,040(50)	2,790(50)	163(50)	8,077(210) ^b	6,194(50)
	61	Pm	−77,540(60)	4,504(29)	948(160)	10,572(330) ^b	2,790(210) ^b
	62	Sm	−72,375(15)	5,160(60)	1,359(210) ^b	9,225(300) ^b	4,627(320) ^b
	63	Eu	−65,360(150) ^b	7,020(150) ^b	2,439(360) ^b	11,436(430) ^b	1,422(330) ^b
	64	Gd	−57,680(500) ^b	7,680(530) ^b	2,913(710) ^b	9,832(710) ^b	2,976(640) ^b
	65	Tb	−48,410(700) ^b	9,270(860) ^b	3,453(920) ^b	12,580(1,060) ^b	−219(860) ^b
140	52	Te	−57,100(500) ^b	6,980(550) ^b	−3,021(710) ^b	4,373(640) ^b	13,819(780) ^b
	53	I	−64,080(210) ^b	8,920(220) ^b	−1,913(370) ^b	3,305(220) ^b	10,568(450) ^b
	54	Xe	−73,000(60)	4,060(60)	−997(80)	5,418(60)	11,441(70)
	55	Cs	−77,056(9)	6,220(10)	17(50)	4,421(9)	8,695(22)
	56	Ba	−83,276(8)	1,050(8)	724(11)	6,428(8)	9,858(9)
	57	La	−84,326(3)	3,761.9(19)	−407(3)	5,160.97(5)	6,695.5(26)
	58	Ce	−88,088(3)	^a	−1,620.2(29)	9,201(7)	8,140.5(19)
	59	Pr	−84,700(7)	3,388(6)	−1,102(70)	7,942(10)	5,030(9)
	60	Nd	−84,477(19)	222(20)	−407(50)	10,507(50)	6,937(21)
	61	Pm	−78,430(30)	6,047(23)	514(60)	8,964(70)	3,677(60)
	62	Sm	−75,459(15)	2,970(30)	1,274(60)	11,156(21)	5,211(60)
	63	Eu	−66,990(50)	8,470(50)	1,894(210)	9,705(160) ^b	1,903(50)
	64	Gd	−61,530(400) ^b	5,460(400) ^b	2,834(570) ^b	11,923(650) ^b	3,463(430) ^b
	65	Tb	−50,730(900) ^b	10,800(800) ^b	3,201(1,030) ^b	10,391(1,140) ^b	340(1,030) ^b

Table 11.23 (Continued)

A	Z	Element	Mass excess	$Q(\beta^-)$	$Q(\alpha)$	$S(n)$	$S(p)$
141	66	Dy	−43,040(900) ^b	7,690(1,270) ^b	3,835(1,140) ^b	^a	1,924(1,140) ^b
	52	Te	−51,800(500) ^b	8,910(590) ^b	−3,729(780) ^b	2,771(710) ^b	^a
	53	I	−60,710(300) ^b	7,620(310) ^b	−2,872(500) ^b	4,699(370) ^b	10,894(590) ^b
	54	Xe	−68,330(90)	6,150(90)	−1,194(150)	3,404(110)	11,540(230) ^b
	55	Cs	−74,479(10)	5,251(11)	−402(30)	5,494(13)	8,772(60)
	56	Ba	−79,730(8)	3,213(9)	224(11)	4,525(11)	9,963(11)
	57	La	−82,943(5)	2,502(4)	1,183(5)	6,689(4)	6,956(9)
	58	Ce	−85,445(3)	580.7(11)	−143.0(29)	5,428.6(7)	8,408.1(20)
	59	Pr	−86,026(3)	^a	−1,324(50)	9,397(6)	5,226.9(12)
	60	Nd	−84,203(4)	1,823(28)	−723(50)	7,797(19)	6,792(7)
	61	Pm	−80,475(27)	3,728(27)	303(60)	10,116(40)	3,287(30)
	62	Sm	−75,946(12)	4,529(27)	1,142(70)	8,558(19)	4,805(30)
	63	Eu	−69,968(28)	5,978(26)	1,462(140) ^b	11,050(60)	1,798(30)
	64	Gd	−63,150(300) ^b	6,820(300) ^b	2,385(320) ^b	9,688(500) ^b	3,446(300) ^b
	65	Tb	−54,810(600) ^b	8,340(670) ^b	3,117(780) ^b	12,151(1,080) ^b	569(720) ^b
	66	Dy	−45,470(700) ^b	9,340(920) ^b	3,667(920) ^b	10,493(1,140) ^b	2,026(1,140) ^b
142	52	Te	−47,970(600) ^b	7,750(720) ^b	^a	4,243(780) ^b	^a
	53	I	−55,720(400) ^b	9,760(410) ^b	−3,151(640) ^b	3,088(500) ^b	11,211(640) ^b
	54	Xe	−65,480(100)	5,040(100)	−1,975(230) ^b	5,224(140)	12,065(320) ^b
	55	Cs	−70,521(11)	7,307(10)	−647(80)	4,114(14)	9,482(90)
	56	Ba	−77,828(6)	2,211(4)	−134(40)	6,169(10)	10,638(12)
	57	La	−80,039(6)	4,504(5)	429(11)	5,167(7)	7,598(10)
	58	Ce	−84,543(3)	−745.3(24)	1,300(3)	7,169.1(25)	8,889(5)
	59	Pr	−83,797(3)	2,162.2(15)	307(3)	5,843.06(10)	5,641.4(11)
	60	Nd	−85,959.5(28)	^a	−811(10)	9,828(3)	7,222.9(15)
	61	Pm	−81,090(40)	4,870(40)	−374(40)	8,682(50)	4,172(40)
	62	Sm	−78,997(11)	2,090(40)	615(200) ^b	11,122(16)	5,811(29)
	63	Eu	−71,350(30)	7,645(29)	1,260(320) ^b	9,455(40)	2,695(30)
	64	Gd	−66,850(300) ^b	4,500(300) ^b	1,945(420) ^b	11,778(420) ^b	4,173(300) ^b
	65	Tb	−56,950(760) ^b	9,900(700) ^b	2,614(860) ^b	10,215(970) ^b	1,095(820) ^b
	66	Dy	−50,050(790) ^b	6,900(200) ^b	3,440(940) ^b	12,658(1,050) ^b	2,532(990) ^b
	67	Ho	−37,390(1,000) ^b	12,660(1,270) ^b	4,086(1,280) ^b	^a	−787(1,220) ^b
143	53	I	−52,100(400) ^b	8,550(460) ^b	−3,953(720) ^b	4,448(570) ^b	11,415(720) ^b
	54	Xe	−60,650(220) ^b	7,040(230) ^b	−2,276(460) ^b	3,240(250) ^b	12,217(460) ^b
	55	Cs	−67,691(22)	6,253(20)	−1,273(40)	5,241(24)	9,499(100)
	56	Ba	−73,945(13)	4,246(18)	−720(25)	4,188(14)	10,712(16)
	57	La	−78,191(15)	3,426(15)	91(16)	6,223(16)	7,652(16)
	58	Ce	−81,616(3)	1,461.4(18)	878(3)	5,145.11(26)	8,866(5)
	59	Pr	−83,078(3)	933.9(14)	1,733.4(27)	7,351.9(20)	5,824.2(18)
	60	Nd	−84,011.8(28)	^a	521(7)	6,123.59(13)	7,503.4(15)
	61	Pm	−82,970(4)	1,041.4(24)	−566(8)	9,956(40)	4,299.9(24)
	62	Sm	−79,528(4)	3,443(4)	90(50)	8,602(11)	5,731(40)
	63	Eu	−74,253(13)	5,275(14)	860(60)	10,971(30)	2,545(17)

■ Table 11.23 (Continued)

A	Z	Element	Mass excess	$Q(\beta^-)$	$Q(\alpha)$	$S(n)$	$S(p)$
	64	Gd	−68,240(200)	6,010(200)	1,708(200)	9,461(360) ^b	4,179(200)
	65	Tb	−60,780(400) ^b	7,460(450) ^b	2,150(430) ^b	11,899(860) ^b	1,217(500) ^b
	66	Dy	−52,320(500) ^b	8,460(640) ^b	2,931(710) ^b	10,341(940) ^b	2,659(910) ^b
	67	Ho	−42,210(700) ^b	10,120(860) ^b	3,779(990) ^b	12,887(1,220) ^b	−557(1,050) ^b
144	53	I	−46,940(500) ^b	10,600(590) ^b	^a	2,911(640) ^b	^a
	54	Xe	−57,540(320) ^b	5,780(320) ^b	−2,863(590) ^b	4,960(390) ^b	12,729(510) ^b
	55	Cs	−63,316(28)	8,464(27)	−1,664(220) ^b	3,696(30)	9,955(230) ^b
	56	Ba	−71,780(14)	3,120(60)	−1,210(60)	5,907(18)	11,378(25)
	57	La	−74,900(60)	5,540(60)	−269(60)	4,780(60)	8,244(60)
	58	Ce	−80,441(4)	318.7(8)	410(9)	6,896(3)	9,539(15)
	59	Pr	−80,760(4)	2,997.5(24)	1,141(3)	5,753.4(28)	6,433(3)
	60	Nd	−83,757.5(28)	−2,331.7(22)	1,905.2(18)	7,817.02(7)	7,968.6(14)
	61	Pm	−81,426(4)	550.5(25)	849(7)	6,526.7(15)	4,703.0(22)
	62	Sm	−81,976(3)	^a	76(19)	10,520.1(24)	6,294.9(27)
	63	Eu	−75,661(18)	6,315(17)	344(30)	9,480(22)	3,423(17)
	64	Gd	−71,920(200) ^b	3,740(200) ^b	1,113(200) ^b	11,750(280) ^b	4,958(200) ^b
	65	Tb	−62,850(300) ^b	9,070(360) ^b	1,717(300) ^b	10,139(500) ^b	1,894(360) ^b
	66	Dy	−56,760(400) ^b	6,090(500) ^b	2,349(570) ^b	12,505(640) ^b	3,265(570) ^b
	67	Ho	−45,050(600) ^b	11,710(720) ^b	3,257(1,080) ^b	10,912(920) ^b	14(780) ^b
	68	Er	−36,710(800) ^b	8,340(1,000) ^b	3,909(1,210) ^b	^a	1,793(1,060) ^b
145	54	Xe	−52,470(400) ^b	7,710(400) ^b	−3,096(640) ^b	3,004(510) ^b	12,822(640) ^b
	55	Cs	−60,190(50)	7,880(40)	−1,905(300) ^b	4,941(40)	9,936(320) ^b
	56	Ba	−68,070(60)	4,920(70)	−2,166(110)	4,361(60)	12,043(60)
	57	La	−72,990(70)	4,110(70)	−940(70)	6,165(90)	8,502(70)
	58	Ce	−77,100(40)	2,530(40)	203(40)	4,732(40)	9,491(70)
	59	Pr	−79,636(8)	1,805(7)	882(8)	6,948(7)	6,484(8)
	60	Nd	−81,441.6(28)	^a	1,578.4(19)	5,755.4(6)	7,970.6(25)
	61	Pm	−81,279(4)	163(22)	2,322.1(27)	7,924.0(15)	4,810.0(22)
	62	Sm	−80,662(3)	616.4(24)	1,116(4)	6,757.10(30)	6,525.3(25)
	63	Eu	−78,002(4)	2,660(28)	48(27)	10,412(18)	3,314.7(27)
	64	Gd	−72,950(40)	5,050(40)	574(40)	9,098(200) ^b	4,575(40)
	65	Tb	−66,250(230) ^b	6,700(220) ^b	1,296(230) ^b	11,471(370) ^b	1,615(300) ^b
	66	Dy	−58,730(300) ^b	7,520(200) ^b	1,993(420) ^b	10,043(500) ^b	3,169(420) ^b
	67	Ho	−49,480(600) ^b	9,250(670) ^b	2,903(840) ^b	12,505(840) ^b	14(720) ^b
	68	Er	−39,630(700) ^b	9,860(920) ^b	3,416(990) ^b	10,987(1,060) ^b	1,868(920) ^b
146	54	Xe	−49,090(400) ^b	6,650(410) ^b	−3,543(720) ^b	4,690(570) ^b	^a
	55	Cs	−55,740(80)	9,370(40)	−2,442(410) ^b	3,625(70)	10,557(410) ^b
	56	Ba	−65,110(80)	4,100(40)	−2,049(130)	5,107(80)	12,209(70)
	57	La	−69,210(70)	6,530(50)	−1,114(70)	4,288(90)	8,429(80)
	58	Ce	−75,740(70)	1,030(40)	−337(70)	6,710(70)	10,036(90)
	59	Pr	−76,770(60)	4,170(60)	848(60)	5,201(60)	6,954(70)
	60	Nd	−80,935.5(28)	−1,472(4)	1,182.2(22)	7,565.25(14)	8,588(7)
	61	Pm	−79,464(5)	1,542(3)	1,909(4)	6,257(5)	5,311(4)

Table 11.23 (Continued)

A	Z	Element	Mass excess	$Q(\beta^-)$	$Q(\alpha)$	$S(n)$	$S(p)$
	62	Sm	−81,006(4)	^a	2,528.9(29)	8,415(3)	7,016(3)
	63	Eu	−77,128(7)	3,878(6)	1,533(40)	7,197(7)	3,755(7)
	64	Gd	−76,098(5)	1,030(8)	474(11)	11,222(40)	5,385(5)
	65	Tb	−67,830(50)	8,270(50)	1,097(50)	9,655(230) ^b	2,172(60)
	66	Dy	−62,670(110)	5,160(100)	1,757(320) ^b	12,015(320) ^b	3,712(250) ^b
	67	Ho	−52,070(500) ^b	10,600(520) ^b	2,457(910) ^b	10,661(780) ^b	632(590) ^b
	68	Er	−44,600(600) ^b	7,470(780) ^b	3,028(990) ^b	13,046(920) ^b	2,408(840) ^b
	69	Tm	−31,210(700) ^b	13,390(920) ^b	3,755(1,220) ^b	^a	−1,127(5)
147	54	Xe	−43,770(500) ^b	8,520(530) ^b	^a	2,752(640) ^b	^a
	55	Cs	−52,290(150)	9,200(180)	−2,616(430) ^b	4,623(140)	10,489(430) ^b
	56	Ba	−61,490(90)	5,750(50)	−3,261(240) ^b	4,452(120)	13,036(120)
	57	La	−67,240(80)	4,950(60)	−1,969(80)	6,097(110)	9,419(110)
	58	Ce	−72,180(50)	3,290(40)	−661(60)	4,512(80)	10,260(90)
	59	Pr	−75,470(40)	2,690(40)	295(40)	6,776(70)	7,020(70)
	60	Nd	−78,156.3(28)	896(9)	1,035.3(22)	5,292.07(15)	8,679(60)
	61	Pm	−79,052.3(29)	224.1(3)	1,600.7(17)	7,660(4)	5,405.7(9)
	62	Sm	−79,276.4(29)	^a	2,310.5(11)	6,342.0(30)	7,102(4)
	63	Eu	−77,555(4)	1,721.3(23)	2,990.5(29)	8,498(7)	3,838(4)
	64	Gd	−75,368(4)	2,187.4(28)	1,735.0(20)	7,341(4)	5,529(7)
	65	Tb	−70,759(12)	4,609(12)	1,069(18)	10,999(50)	1,950(12)
	66	Dy	−64,390(50)	6,370(50)	1,431(210)	9,787(120)	3,844(70)
	67	Ho	−56,040(400) ^b	8,350(400) ^b	2,316(570) ^b	12,039(640) ^b	657(420) ^b
	68	Er	−47,220(500) ^b	8,820(640) ^b	2,680(710) ^b	10,689(780) ^b	2,436(710) ^b
	69	Tm	−36,250(600) ^b	10,970(780) ^b	3,528(920) ^b	13,114(920) ^b	−1,058(3)
148	55	Cs	−47,600(590)	10,450(600)	−3,087(770) ^b	3,381(590)	11,118(770) ^b
	56	Ba	−58,050(140)	5,110(60)	−2,935(350) ^b	4,634(170)	13,048(210)
	57	La	−63,160(130)	7,260(50)	−2,272(130)	3,999(150)	8,967(160)
	58	Ce	−70,430(120)	2,060(70)	−1,070(120)	6,317(130)	10,479(140)
	59	Pr	−72,490(90)	4,930(90)	−11(110)	5,087(100)	7,594(100)
	60	Nd	−77,418(3)	−540(6)	599(3)	7,332.9(17)	9,236(40)
	61	Pm	−76,878(7)	2,468(6)	1,457(7)	5,897(6)	6,011(6)
	62	Sm	−79,346.6(29)	−3,107(17)	1,986.0(12)	8,141.5(7)	7,583.3(7)
	63	Eu	−76,239(18)	41(17)	2,762(17)	6,756(17)	4,252(17)
	64	Gd	−76,280(3)	^a	3,271.21(3)	8,983.9(14)	6,014.2(26)
	65	Tb	−70,520(30)	5,760(30)	2,721(30)	7,828(30)	2,437(30)
	66	Dy	−67,830(30)	2,682(10)	1,663(200) ^b	11,518(60)	4,363(30)
	67	Ho	−58,430(270) ^b	9,400(270) ^b	1,990(400) ^b	10,466(480) ^b	1,336(280) ^b
	68	Er	−51,750(400) ^b	6,680(480) ^b	2,577(570) ^b	12,608(640) ^b	3,004(570) ^b
	69	Tm	−39,540(700) ^b	12,210(810) ^b	3,080(920) ^b	11,360(920) ^b	−387(860) ^b
	70	Yb	−30,960(800) ^b	8,580(1,060) ^b	3,322(1,130) ^b	^a	1,999(1,000) ^b
149	55	Cs	−44,040(300) ^b	9,560(500) ^b	^a	4,513(660) ^b	^a
	56	Ba	−53,600(400) ^b	7,540(500) ^b	−3,552(570) ^b	3,621(430) ^b	13,287(710) ^b
	57	La	−61,130(300) ^b	5,660(310) ^b	−3,373(300) ^b	6,042(320) ^b	10,374(330) ^b

Table 11.23 (Continued)

A	Z	Element	Mass excess	$Q(\beta^-)$	$Q(\alpha)$	$S(n)$	$S(p)$
	58	Ce	−66,800(80)	4,190(70)	−1,153(100)	4,444(140)	10,924(150)
	59	Pr	−70,988(11)	3,397(10)	−420(70)	6,574(90)	7,851(120)
	60	Nd	−74,385(3)	1,691(3)	292(40)	5,038.68(10)	9,188(90)
	61	Pm	−76,076(4)	1,071(4)	1,136(8)	7,269(7)	5,947(3)
	62	Sm	−77,146.8(29)	^a	1,869.9(13)	5,871.5(9)	7,557(6)
	63	Eu	−76,451(5)	695(4)	2,402(4)	8,284(18)	4,394(4)
	64	Gd	−75,138(4)	1,314(4)	3,100(3)	6,929(3)	6,187(18)
	65	Tb	−71,500(5)	3,638(4)	4,077.2(24)	9,056(30)	2,509(4)
	66	Dy	−67,688(11)	3,812(10)	2,835(40)	7,926(30)	4,462(30)
	67	Ho	−61,674(22)	6,014(19)	2,148(230) ^b	11,312(270) ^b	1,130(40)
	68	Er	−53,860(470) ^b	7,810(470) ^b	2,438(560) ^b	10,182(620) ^b	2,720(540) ^b
	69	Tm	−44,110(600) ^b	9,760(760) ^b	2,950(840) ^b	12,636(920) ^b	−359(720) ^b
	70	Yb	−34,020(700) ^b	10,090(920) ^b	3,183(990) ^b	11,127(1,060) ^b	1,765(990) ^b
150	55	Cs	−39,150(500) ^b	11,500(710) ^b	^a	3,181(590) ^b	^a
	56	Ba	−50,660(500) ^b	6,570(640) ^b	−3,990(640) ^b	5,128(640) ^b	13,903(590) ^b
	57	La	−57,220(400) ^b	7,770(420) ^b	−3,908(410) ^b	4,159(500) ^b	10,912(570) ^b
	58	Ce	−64,990(120)	3,010(90)	−2,313(140)	6,267(140)	11,149(320) ^b
	59	Pr	−68,000(80)	5,690(80)	−1,219(110)	5,087(80)	8,494(110)
	60	Nd	−73,694(4)	−87(20)	−379(70)	7,379.8(27)	9,994(10)
	61	Pm	−73,607(20)	3,454(20)	734(60)	5,603(20)	6,511(20)
	62	Sm	−77,061.1(29)	−2,261(6)	1,449.5(12)	7,985.7(7)	8,274(4)
	63	Eu	−74,801(7)	971(4)	2,238(7)	6,420(7)	4,943(6)
	64	Gd	−75,772(7)	^a	2,809(6)	8,706(7)	6,609(7)
	65	Tb	−71,116(8)	4,656(9)	3,587(5)	7,687(9)	3,267(8)
	66	Dy	−69,322(5)	1,794(9)	4,351.1(16)	9,705(11)	5,111(6)
	67	Ho	−62,080(100) ^b	7,240(100) ^b	3,324(110) ^b	8,479(100) ^b	1,683(100) ^b
	68	Er	−57,970(100) ^b	4,108(15) ^b	2,272(150) ^b	12,181(480) ^b	3,589(100) ^b
	69	Tm	−46,880(500) ^b	11,090(510) ^b	2,764(710) ^b	10,847(780) ^b	307(690) ^b
151	70	Yb	−39,130(600) ^b	7,750(780) ^b	3,043(840) ^b	13,185(920) ^b	2,315(840) ^b
	71	Lu	−25,460(700) ^b	13,670(920) ^b	3,325(990) ^b	^a	−1,269.6(28)
	55	Cs	−35,400(700) ^b	10,530(920) ^b	^a	4,317(860) ^b	^a
	56	Ba	−45,920(600) ^b	8,510(780) ^b	−4,577(780) ^b	3,339(780) ^b	14,061(780) ^b
	57	La	−54,440(500) ^b	7,010(590) ^b	−4,571(530) ^b	5,286(640) ^b	11,071(710) ^b
	58	Ce	−61,440(300) ^b	5,410(300) ^b	−2,381(310) ^b	4,519(320) ^b	11,509(500) ^b
	59	Pr	−66,860(40)	4,100(40)	−2,045(90)	6,923(90)	9,151(130)
	60	Nd	−70,957(4)	2,442(4)	−1,201(50)	5,334.43(20)	10,242(80)
	61	Pm	−73,399(6)	1,187(5)	−354(40)	7,863(21)	6,995(4)
	62	Sm	−74,586.2(29)	76.7(5)	1,145.1(12)	5,596.44(10)	8,268(20)
	63	Eu	−74,662.9(29)	^a	1,964.4(11)	7,934(6)	4,890.8(6)
	64	Gd	−74,199(4)	464.1(28)	2,652.7(29)	6,498(7)	6,687(7)
	65	Tb	−71,634(5)	2,565(4)	3,497(4)	8,589(9)	3,151(7)
	66	Dy	−68,763(4)	2,870(5)	4,179.6(26)	7,513(5)	4,937(8)
	67	Ho	−63,639(12)	5,124(12)	4,695.1(19)	9,628(100) ^b	1,606(12)

Table 11.23 (Continued)

A	Z	Element	Mass excess	$Q(\beta^-)$	$Q(\alpha)$	$S(n)$	$S(p)$
152	68	Er	−58,260(300) ^b	5,380(300) ^b	3,706(300) ^b	8,353(320) ^b	3,463(310) ^b
	69	Tm	−50,830(140) ^b	7,430(330) ^b	2,786(420) ^b	12,017(520) ^b	143(90) ^b
	70	Yb	−41,690(320) ^b	9,140(310) ^b	3,107(590) ^b	10,624(680) ^b	2,092(590) ^b
	71	Lu	−30,600(600) ^b	11,080(680) ^b	3,226(850) ^b	13,214(920) ^b	−1,241(100) ^b
	56	Ba	−42,700(700) ^b	7,500(920) ^b	^a	4,848(920) ^b	14,592(990) ^b
	57	La	−50,200(600) ^b	9,060(720) ^b	−5,023(840) ^b	3,833(780) ^b	11,565(840) ^b
	58	Ce	−59,260(400) ^b	4,450(500) ^b	−3,638(430) ^b	5,892(500) ^b	12,114(640) ^b
	59	Pr	−63,710(300) ^b	6,440(300) ^b	−2,976(320) ^b	4,930(300) ^b	9,562(420) ^b
	60	Nd	−70,160(30)	1,110(80)	−2,157(120)	7,272(30)	10,592(50)
	61	Pm	−71,270(70)	3,500(70)	−1,207(110)	5,940(70)	7,600(70)
	62	Sm	−74,772.6(29)	−1,874.3(7)	220.3(21)	8,257.7(7)	8,662(5)
	63	Eu	−72,898.3(29)	1,818.8(11)	1,555(6)	6,306.72(10)	5,601.1(6)
	64	Gd	−74,717.1(30)	^a	2,204.6(14)	8,589.6(30)	7,343.1(11)
	65	Tb	−70,730(40)	3,990(40)	3,087(40)	7,165(40)	3,817(40)
	66	Dy	−70,129(5)	600(40)	3,727(4)	9,437(5)	5,784(6)
	67	Ho	−63,580(30)	6,550(30)	4,507.2(13)	8,016(30)	2,109(30)
	68	Er	−60,470(30)	3,109(10)	4,934.4(16)	10,290(300) ^b	4,124(30)
	69	Tm	−51,880(300) ^b	8,590(300) ^b	4,124(400) ^b	9,127(330) ^b	918(420) ^b
	70	Yb	−46,420(360) ^b	5,460(200) ^b	2,910(540) ^b	12,805(480) ^b	2,880(380) ^b
	71	Lu	−33,900(700) ^b	12,520(780) ^b	3,220(990) ^b	11,366(920) ^b	−499(770) ^b
153	56	Ba	−37,620(900) ^b	9,460(1,140) ^b	^a	2,995(1,140) ^b	^a
	57	La	−47,090(700) ^b	8,260(860) ^b	−5,471(760) ^b	4,960(920) ^b	11,676(990) ^b
	58	Ce	−55,350(500) ^b	6,460(590) ^b	−4,176(640) ^b	4,159(640) ^b	12,440(780) ^b
	59	Pr	−61,810(300) ^b	5,550(300) ^b	−3,096(420) ^b	6,162(420) ^b	9,832(500) ^b
	60	Nd	−67,352(27)	3,336(25)	−2,979(80)	5,266(40)	10,927(300) ^b
	61	Pm	−70,688(11)	1,881(11)	−2,125(15)	7,491(70)	7,819(30)
	62	Sm	−72,569.0(29)	808.2(8)	−608.8(21)	5,867.72(23)	8,590(70)
	63	Eu	−73,377.3(29)	^a	274(4)	8,550.28(12)	5,893.6(8)
	64	Gd	−72,892.9(30)	484.4(11)	1,829(13)	6,247.08(13)	7,283.5(11)
	65	Tb	−71,324(5)	1,569(4)	2,703(5)	8,668(40)	3,896(4)
	66	Dy	−69,153(5)	2,170.4(19)	3,559(4)	7,096(6)	5,715(40)
	67	Ho	−65,023(6)	4,130(6)	4,052(4)	9,512(30)	2,184(7)
	68	Er	−60,460(11)	4,563(11)	4,802.7(15)	8,058(30)	4,166(30)
	69	Tm	−54,001(22)	6,459(19)	5,248.4(14)	10,188(300) ^b	816(40)
	70	Yb	−47,310(300) ^b	6,690(300) ^b	4,129(560) ^b	8,963(460) ^b	2,715(420) ^b
	71	Lu	−38,480(600) ^b	8,830(670) ^b	3,201(840) ^b	12,654(920) ^b	−650(690) ^b
154	57	La	−42,480(800) ^b	10,320(1,000) ^b	−5,750(950) ^b	3,460(1,060) ^b	12,142(1,210) ^b
	58	Ce	−52,800(600) ^b	5,520(720) ^b	−4,567(780) ^b	5,519(780) ^b	12,999(920) ^b
	59	Pr	−58,320(400) ^b	7,370(420) ^b	−3,524(570) ^b	4,588(500) ^b	10,260(640) ^b
	60	Nd	−65,690(110)	2,740(140)	−3,117(170)	6,405(120)	11,170(320) ^b
	61	Pm	−68,420(70)	4,040(70)	−2,842(110)	5,804(70)	8,358(80)
	62	Sm	−72,465.3(30)	−717.3(11)	−1,196.5(24)	7,967.6(9)	9,066(11)
	63	Eu	−71,748.0(29)	1,968.4(11)	−566(20)	6,441.98(30)	6,467.9(8)

Table 11.23 (Continued)

A	Z	Element	Mass excess	$Q(\beta^-)$	$Q(\alpha)$	$S(n)$	$S(p)$
	64	Gd	−73,716.3(29)	−3,560(50)	919.9(12)	8,894.77(17)	7,628.0(11)
	65	Tb	−70,150(50)	250(50)	2,221(50)	6,902(50)	4,550(50)
	66	Dy	−70,400(9)	^a	2,947(5)	9,318(9)	6,366(9)
	67	Ho	−64,649(9)	5,751(11)	4,042(4)	7,697(10)	2,785(9)
	68	Er	−62,618(6)	2,032(10)	4,279.6(26)	10,229(12)	4,883(7)
	69	Tm	−54,560(110) ^b	8,050(110) ^b	5,094(50)	8,634(110) ^b	1,392(110) ^b
	70	Yb	−50,080(100) ^b	4,490(50) ^b	5,474.3(19)	10,836(320) ^b	3,363(100) ^b
	71	Lu	−39,960(500) ^b	10,110(510) ^b	4,496(710) ^b	9,552(780) ^b	−61(590) ^b
	72	Hf	−33,300(700) ^b	6,660(860) ^b	3,406(920) ^b	^a	2,110(920) ^b
155	57	La	−39,000(900) ^b	9,400(1,140) ^b	−6,030(1,140) ^b	4,597(1,210) ^b	^a
	58	Ce	−48,400(700) ^b	7,500(860) ^b	−4,903(920) ^b	3,675(920) ^b	13,213(1,060) ^b
	59	Pr	−55,900(500) ^b	6,860(530) ^b	−3,887(710) ^b	5,649(640) ^b	10,391(780) ^b
	60	Nd	−62,760(150)	4,220(150)	−3,739(340) ^b	5,141(190)	11,723(430) ^b
	61	Pm	−66,980(30)	3,224(30)	−2,547(50)	6,627(80)	8,580(120)
	62	Sm	−70,201.2(30)	1,626.9(12)	−1,669.3(25)	5,807.20(30)	9,069(70)
	63	Eu	−71,828.0(29)	252.1(11)	−854(5)	8,151.4(4)	6,651.7(12)
	64	Gd	−72,080.1(29)	^a	81.2(12)	6,435.13(30)	7,621.1(11)
	65	Tb	−71,259(12)	821(12)	979(12)	9,176(50)	4,832(12)
	66	Dy	−69,164(12)	2,094.5(19)	2,610(12)	6,835(14)	6,299(50)
	67	Ho	−66,062(23)	3,102(20)	3,146(24)	9,485(25)	2,951(25)
	68	Er	−62,220(50)	3,840(60)	4,119(50)	7,674(50)	4,860(50)
	69	Tm	−56,643(13)	5,580(50)	4,571(5)	10,150(110) ^b	1,314(14)
	70	Yb	−50,490(300) ^b	6,150(300) ^b	5,336.7(27)	8,490(320) ^b	3,219(320) ^b
156	71	Lu	−42,630(130) ^b	7,860(330) ^b	5,771(16) ^b	10,742(520) ^b	−154(90)
	72	Hf	−34,690(600) ^b	7,940(610) ^b	4,571(680) ^b	9,459(920) ^b	2,017(780) ^b
	58	Ce	−45,400(800) ^b	6,650(1,000) ^b	−5,126(1,060) ^b	5,072(1,060) ^b	13,688(1,210) ^b
	59	Pr	−52,050(600) ^b	8,310(720) ^b	−4,279(840) ^b	4,224(780) ^b	10,940(920) ^b
	60	Nd	−60,360(400) ^b	3,860(400) ^b	−3,524(570) ^b	5,677(430) ^b	11,751(640) ^b
	61	Pm	−64,220(40)	5,160(40)	−2,928(300) ^b	5,311(50)	8,751(160)
	62	Sm	−69,372(10)	722(8)	−1,639(30)	7,242(9)	9,684(30)
	63	Eu	−70,094(6)	2,451(5)	−1,251(70)	6,337(5)	7,182(5)
	64	Gd	−72,545.2(29)	−2,444(4)	−197.4(12)	8,536.37(12)	8,006.1(11)
	65	Tb	−70,101(5)	434(7)	373(4)	6,913(12)	5,310(4)
	66	Dy	−70,534(7)	^a	1,758(6)	9,441(10)	6,564(10)
	67	Ho	−65,470(200) ^b	5,060(200) ^b	2,828(200) ^b	7,483(200) ^b	3,599(200) ^b
	68	Er	−64,260(70)	1,220(210) ^b	3,445(70)	10,111(90)	5,486(80)
	69	Tm	−56,810(60)	7,440(40)	4,344(50)	8,243(60)	1,884(80)
157	70	Yb	−53,240(30)	3,580(50)	4,812(7)	10,815(300) ^b	3,884(40)
	71	Lu	−43,870(300) ^b	9,370(300) ^b	5,593(50)	9,306(330) ^b	661(430) ^b
	72	Hf	−37,960(360) ^b	5,910(200) ^b	6,033(10)	11,344(700) ^b	2,618(380) ^b
	73	Ta	−26,370(600) ^b	11,590(700) ^b	5,101(920) ^b	^a	−1,029(13)
	58	Ce	−40,670(900) ^b	8,540(1,140) ^b	−5,471(1,280) ^b	3,339(1,210) ^b	^a
	59	Pr	−49,210(700) ^b	7,360(860) ^b	−4,549(990) ^b	5,230(920) ^b	11,099(1,060) ^b

Table 11.23 (Continued)

A	Z	Element	Mass excess	$Q(\beta^-)$	$Q(\alpha)$	$S(n)$	$S(p)$
	60	Nd	−56,570(500) ^b	5,650(590) ^b	−3,645(710) ^b	4,280(640) ^b	11,807(780) ^b
	61	Pm	−62,220(300) ^b	4,510(300) ^b	−2,844(420) ^b	6,078(300) ^b	9,152(500) ^b
	62	Sm	−66,740(50)	2,730(50)	−1,810(60)	5,437(50)	9,809(60)
	63	Eu	−69,471(6)	1,363(6)	−1,208(12)	7,449(8)	7,388(11)
	64	Gd	−70,833.9(30)	^a	−689.7(12)	6,360.04(15)	8,029(5)
	65	Tb	−70,773.8(30)	60.05(3)	178.6(11)	8,744(4)	5,517.6(3)
	66	Dy	−69,432(7)	1,341(6)	1,036(6)	6,969(6)	6,621(7)
	67	Ho	−66,890(50)	2,540(50)	2,006(50)	9,489(210) ^b	3,647(50)
	68	Er	−63,390(80)	3,500(60)	3,336(80)	7,205(110)	5,207(220) ^b
	69	Tm	−58,910(110)	4,480(70)	3,687(110)	10,168(120)	1,941(130)
	70	Yb	−53,410(50)	5,500(120)	4,622(50)	8,247(60)	3,887(80)
	71	Lu	−46,480(22)	6,930(50)	5,096(3)	10,685(300) ^b	532(40)
	72	Hf	−39,000(300) ^b	7,480(300) ^b	5,881(50)	9,114(470) ^b	2,427(430) ^b
	73	Ta	−29,670(600) ^b	9,330(670) ^b	6,382(50)	11,373(850) ^b	−999(700) ^b
158	59	Pr	−44,920(800) ^b	9,230(1,000) ^b	−4,865(1,130) ^b	3,777(1,060) ^b	11,537(1,210) ^b
	60	Nd	−54,150(600) ^b	4,830(720) ^b	−3,776(840) ^b	5,649(780) ^b	12,226(920) ^b
	61	Pm	−58,970(400) ^b	6,240(410) ^b	−3,077(570) ^b	4,820(500) ^b	9,692(640) ^b
	62	Sm	−65,220(80)	1,999(15)	−1,955(140)	6,550(90)	10,281(310) ^b
	63	Eu	−67,210(80)	3,490(80)	−1,219(110)	5,815(80)	7,766(90)
	64	Gd	−70,699.9(30)	−1,220(9)	−659.5(13)	7,937.33(12)	8,518(6)
	65	Tb	−69,479.9(30)	936.7(24)	−156.8(14)	6,777.4(9)	5,935.0(9)
	66	Dy	−70,417(4)	^a	874.8(24)	9,056(6)	6,931.8(24)
	67	Ho	−66,190(30)	4,230(30)	1,543(60)	7,366(60)	4,043(30)
	68	Er	−65,290(100) ^b	900(100) ^b	2,689(110) ^b	9,966(130) ^b	5,683(120) ^b
	69	Tm	−58,690(120) ^b	6,600(50) ^b	3,537(120) ^b	7,847(160) ^b	2,584(140) ^b
	70	Yb	−56,022(10)	2,670(120) ^b	4,171(8)	10,680(50)	4,400(110)
	71	Lu	−47,350(120) ^b	8,670(120) ^b	4,790(50)	8,940(120) ^b	1,224(130) ^b
	72	Hf	−42,250(100) ^b	5,100(70) ^b	5,403(4)	11,313(320) ^b	3,055(100) ^b
	73	Ta	−31,330(510) ^b	10,920(520) ^b	6,209(50)	9,726(780) ^b	−388(590) ^b
159	74	W	−24,280(700) ^b	7,050(860) ^b	6,600(30)	^a	1,891(920) ^b
	59	Pr	−41,700(900) ^b	8,230(1,140) ^b	−5,126(1,280) ^b	4,858(1,210) ^b	^a
	60	Nd	−49,940(700) ^b	6,760(860) ^b	−3,962(990) ^b	3,861(920) ^b	12,310(1,060) ^b
	61	Pm	−56,700(500) ^b	5,520(590) ^b	−3,226(710) ^b	5,798(640) ^b	9,841(780) ^b
	62	Sm	−62,220(300) ^b	3,830(300) ^b	−1,894(340) ^b	5,079(310) ^b	10,540(500) ^b
	63	Eu	−66,057(8)	2,514(7)	−1,505(30)	6,914(80)	8,131(80)
	64	Gd	−68,571.9(30)	970.6(7)	−795.6(13)	5,943.29(15)	8,646(80)
	65	Tb	−69,542.4(30)	^a	−139.3(13)	8,133.9(5)	6,131.5(7)
	66	Dy	−69,177(3)	365.6(12)	478.4(13)	6,831.5(25)	6,985.9(13)
	67	Ho	−67,339(4)	1,837.7(27)	1,495(12)	9,224(30)	4,211(4)
	68	Er	−64,570(5)	2,768.6(2)	2,169(12)	7,355(100) ^b	5,673(30)
	69	Tm	−60,730(70)	3,850(70)	2,912(70)	10,109(130) ^b	2,727(120) ^b
	70	Yb	−55,750(90)	4,980(90)	4,048(100)	7,796(90)	4,348(150) ^b
	71	Lu	−49,730(50)	6,020(90)	4,490(50)	10,450(130) ^b	995(50)

Table 11.23 (Continued)

A	Z	Element	Mass excess	$Q(\beta^-)$	$Q(\alpha)$	$S(n)$	$S(p)$
160	72	Hf	−42,850(300) ^b	6,880(310) ^b	5,223(50)	8,671(320) ^b	2,786(330) ^b
	73	Ta	−34,550(120) ^b	8,300(330) ^b	5,662(50)	11,289(520) ^b	−412(70)
	74	W	−25,820(600) ^b	8,720(610) ^b	6,443(50)	9,617(920) ^b	1,783(780) ^b
	60	Nd	−47,140(800) ^b	5,960(1,000) ^b	−4,167(1,130) ^b	5,277(1,060) ^b	12,729(1,210) ^b
	61	Pm	−53,100(600) ^b	7,310(720) ^b	−3,477(840) ^b	4,476(780) ^b	10,456(920) ^b
	62	Sm	−60,420(400) ^b	2,960(450) ^b	−2,481(570) ^b	6,264(500) ^b	11,006(640) ^b
	63	Eu	−63,370(200) ^b	4,580(200) ^b	−1,580(200) ^b	5,386(200) ^b	8,437(360) ^b
	64	Gd	−67,951.9(30)	−105.6(1)	−1,005(9)	7,451.4(7)	9,184(7)
	65	Tb	−67,846.3(30)	1,835.3(13)	−177(5)	6,375.18(29)	6,563.4(8)
	66	Dy	−69,682(3)	^a	438.7(13)	8,576.1(15)	7,428.2(13)
	67	Ho	−66,392(15)	3,290(15)	1,284(15)	7,124(15)	4,504(15)
	68	Er	−66,060(50)	330(50)	2,047(50)	9,563(50)	6,012(50)
	69	Tm	−60,460(300)	5,600(300)	2,587(360) ^b	7,809(310)	3,181(300)
	70	Yb	−58,160(210) ^b	2,300(360) ^b	3,672(220) ^b	10,487(230) ^b	4,726(220) ^b
	71	Lu	−50,280(230) ^b	7,880(100) ^b	4,107(240) ^b	8,626(240) ^b	1,825(250) ^b
	72	Hf	−45,910(30)	4,370(230) ^b	4,902.7(30)	11,135(300) ^b	3,471(60)
	73	Ta	−36,000(310) ^b	9,920(310) ^b	5,446(50)	9,521(330) ^b	438(430) ^b
	74	W	−29,460(360) ^b	6,530(210) ^b	6,072(10)	11,715(700) ^b	2,208(380) ^b
	75	Re	−17,250(600) ^b	12,220(700) ^b	6,699(13)	^a	−1,285(50)
161	60	Nd	−42,540(900) ^b	7,890(1,140) ^b	−4,297(1,280) ^b	3,470(1,210) ^b	^a
	61	Pm	−50,430(700) ^b	6,550(860) ^b	−3,645(990) ^b	5,398(920) ^b	10,577(1,060) ^b
	62	Sm	−56,980(500) ^b	4,800(590) ^b	−2,835(710) ^b	4,634(640) ^b	11,164(780) ^b
	63	Eu	−61,780(300) ^b	3,740(300) ^b	−1,978(420) ^b	6,476(360) ^b	8,649(500) ^b
	64	Gd	−65,516(3)	1,955.6(14)	−1,204(50)	5,635.4(10)	9,433(200) ^b
	65	Tb	−67,472(3)	593.1(14)	−425(6)	7,696.6(6)	6,808.6(10)
	66	Dy	−68,065(3)	^a	344.3(13)	6,454.36(9)	7,507.3(13)
	67	Ho	−67,206(4)	858.9(27)	1,143.2(29)	8,885(15)	4,813.1(27)
	68	Er	−65,203(10)	2,002(9)	1,804(11)	7,212(50)	6,101(18)
	69	Tm	−62,040(90)	3,160(90)	2,428(100)	9,648(320)	3,266(100)
	70	Yb	−57,890(220) ^b	4,150(200) ^b	3,078(230) ^b	7,798(300) ^b	4,716(380) ^b
	71	Lu	−52,590(240) ^b	5,300(100) ^b	3,897(260) ^b	10,378(330) ^b	1,716(320) ^b
	72	Hf	−46,270(70)	6,320(250) ^b	4,722(50)	8,428(80)	3,273(240) ^b
	73	Ta	−38,780(50)	7,490(90)	5,280(50)	10,852(310) ^b	154(60)
	74	W	−30,660(310) ^b	8,120(310) ^b	5,924(50)	9,263(470) ^b	1,950(430) ^b
	75	Re	−20,810(600) ^b	9,850(670) ^b	6,439(50)	11,633(850) ^b	−1,366(700) ^b
162	61	Pm	−46,310(800) ^b	8,450(1,000) ^b	−3,813(1,130) ^b	3,945(1,060) ^b	11,052(1,210) ^b
	62	Sm	−54,750(600) ^b	3,890(720) ^b	−3,030(840) ^b	5,845(780) ^b	11,611(920) ^b
	63	Eu	−58,650(400) ^b	5,640(400) ^b	−2,099(570) ^b	4,942(500) ^b	8,956(640) ^b
	64	Gd	−64,291(5)	1,390(40)	−1,500(80)	6,846(4)	9,803(300) ^b
	65	Tb	−65,680(40)	2,510(40)	−895(90)	6,284(40)	7,457(40)
	66	Dy	−68,190(3)	−2,140(4)	84.7(13)	8,196.95(12)	8,007.7(14)
	67	Ho	−66,050(4)	296(4)	1,005(4)	6,916(4)	5,274(4)
	68	Er	−66,346(4)	^a	1,646(3)	9,214(9)	6,429(3)

Table 11.23 (Continued)

A	Z	Element	Mass excess	$Q(\beta^-)$	$Q(\alpha)$	$S(n)$	$S(p)$
	69	Tm	−61,510(30)	4,840(30)	2,255(40)	7,538(90)	3,592(30)
	70	Yb	−59,850(210) ^b	1,660(210) ^b	3,013(230) ^b	10,030(300) ^b	5,098(220) ^b
	71	Lu	−52,890(220) ^b	6,960(80) ^b	3,374(250) ^b	8,370(330) ^b	2,288(310) ^b
	72	Hf	−49,180(11)	3,710(220) ^b	4,417(6)	10,985(70)	3,880(240) ^b
	73	Ta	−39,920(130) ^b	9,260(130) ^b	5,007(50)	9,213(140) ^b	939(150) ^b
	74	W	−34,150(100) ^b	5,770(90) ^b	5,674.5(29)	11,562(320) ^b	2,661(120) ^b
	75	Re	−22,630(510) ^b	11,520(520) ^b	6,274(50)	9,891(790) ^b	−738(590) ^b
	76	Os	−15,070(700) ^b	7,560(870) ^b	6,779(30)	^a	1,552(920) ^b
163	61	Pm	−43,300(900) ^b	7,600(1,140) ^b	−4,018(1,280) ^b	5,063(1,210) ^b	^a
	62	Sm	−50,900(700) ^b	5,730(860) ^b	−3,384(990) ^b	4,215(920) ^b	11,881(1,060) ^b
	63	Eu	−56,630(500) ^b	4,860(590) ^b	−2,350(710) ^b	6,050(640) ^b	9,161(780) ^b
	64	Gd	−61,490(300) ^b	3,120(300) ^b	−1,689(420) ^b	5,269(300) ^b	10,130(500) ^b
	65	Tb	−64,605(5)	1,785(4)	−972(9)	6,992(40)	7,603(6)
	66	Dy	−66,390(3)	^a	−242.9(13)	6,270.93(7)	7,994(40)
	67	Ho	−66,387(3)	2,565(14)	730.2(13)	8,409(4)	5,486.01(7)
	68	Er	−65,177(5)	1,210(5)	1,575(5)	6,903(5)	6,416(6)
	69	Tm	−62,738(6)	2,439(3)	2,176(6)	9,303(30)	3,682(6)
	70	Yb	−59,370(100)	3,370(100)	2,777(100)	7,591(230) ^b	5,151(100)
	71	Lu	−54,770(220)	4,600(200)	3,532(230)	9,951(310) ^b	2,209(300) ^b
	72	Hf	−49,320(320) ^b	5,450(390) ^b	4,005(330) ^b	8,207(320) ^b	3,717(390) ^b
	73	Ta	−42,550(70)	6,760(320) ^b	4,749(50)	10,709(150) ^b	663(70)
	74	W	−34,900(310) ^b	7,650(310) ^b	5,520(50)	8,825(320) ^b	2,274(330) ^b
	75	Re	−26,110(110) ^b	8,790(330) ^b	6,008(50)	11,555(520) ^b	−746(50)
	76	Os	−16,720(600) ^b	9,390(610) ^b	6,674(50)	9,721(920) ^b	1,383(790) ^b
164	62	Sm	−48,180(800) ^b	4,930(1,000) ^b	−3,459(1,130) ^b	5,351(1,060) ^b	12,170(1,210) ^b
	63	Eu	−53,100(600) ^b	6,640(720) ^b	−2,425(840) ^b	4,550(780) ^b	9,497(920) ^b
	64	Gd	−59,750(400) ^b	2,340(410) ^b	−1,754(570) ^b	6,329(500) ^b	10,409(640) ^b
	65	Tb	−62,090(100)	3,890(100)	−1,140(220) ^b	5,553(100)	7,888(310) ^b
	66	Dy	−65,977(3)	−986.8(22)	−449.6(13)	7,658.08(12)	8,661(4)
	67	Ho	−64,990(3)	962.8(23)	431.6(23)	6,673.8(22)	5,888.9(22)
	68	Er	−65,953(3)	^a	1,304.1(25)	8,847(5)	6,854.2(25)
	69	Tm	−61,990(19)	3,963(19)	1,977(24)	7,323(19)	4,102(19)
	70	Yb	−60,990(100) ^b	1,000(100) ^b	2,643(120) ^b	9,697(140) ^b	5,545(100) ^b
	71	Lu	−54,760(130) ^b	6,240(70) ^b	3,280(330) ^b	8,061(260) ^b	2,678(160) ^b
	72	Hf	−51,770(200) ^b	2,990(230) ^b	3,967(290) ^b	10,525(370) ^b	4,291(300) ^b
	73	Ta	−43,250(400) ^b	8,520(450) ^b	4,608(460) ^b	8,767(410) ^b	1,222(510) ^b
	74	W	−38,210(30)	5,040(400) ^b	5,278.8(21)	11,377(310) ^b	2,942(80)
	75	Re	−27,650(310) ^b	10,560(310) ^b	5,923(50)	9,606(330) ^b	35(440) ^b
	76	Os	−20,560(360) ^b	7,090(210) ^b	6,478(21)	11,910(700) ^b	1,738(380) ^b
165	62	Sm	−43,800(900) ^b	6,760(1,140) ^b	−3,682(1,280) ^b	3,693(1,210) ^b	^a
	63	Eu	−50,560(700) ^b	5,910(860) ^b	−2,555(990) ^b	5,528(920) ^b	9,674(1,060) ^b
	64	Gd	−56,470(500) ^b	4,190(540) ^b	−1,913(710) ^b	4,792(640) ^b	10,652(780) ^b
	65	Tb	−60,660(200) ^b	2,960(200) ^b	−1,307(360) ^b	6,644(220) ^b	8,202(450) ^b

Table 11.23 (Continued)

A	Z	Element	Mass excess	$Q(\beta^-)$	$Q(\alpha)$	$S(n)$	$S(p)$
	66	Dy	−63,621(3)	1,286.1(19)	−530.1(16)	5,715.89(10)	8,824(100)
	67	Ho	−64,907.3(30)	^a	139.4(20)	7,988.8(12)	6,219.6(19)
	68	Er	−64,531(3)	376(2)	1,108.4(25)	6,650.1(7)	6,830.5(23)
	69	Tm	−62,939(4)	1,592.5(15)	1,842(3)	9,020(19)	4,275.2(16)
	70	Yb	−60,177(20)	2,762(20)	2,602(22)	7,254(100) ^b	5,476(27)
	71	Lu	−56,260(80)	3,920(80)	3,358(120)	9,571(150) ^b	2,551(130) ^b
	72	Hf	−51,660(370) ^b	4,600(380) ^b	3,803(430) ^b	7,962(420) ^b	4,193(390) ^b
	73	Ta	−45,810(220) ^b	5,850(440) ^b	4,351(330) ^b	10,635(460) ^b	1,332(300) ^b
	74	W	−38,810(90)	7,000(240) ^b	5,032(50)	8,675(90)	2,850(410) ^b
	75	Re	−30,690(70)	8,120(110)	5,658(50)	11,116(320) ^b	−225(80)
	76	Os	−21,910(310) ^b	8,780(320) ^b	6,317(50)	9,424(470) ^b	1,555(440) ^b
	77	Ir	−11,570(400) ^b	10,350(510) ^b	6,815(720) ^b	^a	−1,703(540) ^b
166	63	Eu	−46,600(800) ^b	7,800(1,000) ^b	−2,723(1,130) ^b	4,112(1,060) ^b	10,093(1,210) ^b
	64	Gd	−54,400(600) ^b	3,310(670) ^b	−2,071(840) ^b	6,003(780) ^b	11,127(920) ^b
	65	Tb	−57,710(300) ^b	4,890(300) ^b	−1,484(500) ^b	5,118(360) ^b	8,528(590) ^b
	66	Dy	−62,593(3)	486.2(19)	−728(4)	7,043.5(4)	9,223(200) ^b
	67	Ho	−63,079.6(30)	1,854.9(9)	180(40)	6,243.64(2)	6,747.4(19)
	68	Er	−64,934.5(29)	^a	830.9(19)	8,474.5(20)	7,316.2(9)
	69	Tm	−61,895(11)	3,040(11)	1,730(12)	7,027(11)	4,653(11)
	70	Yb	−61,591(8)	304(14)	2,330(8)	9,485(22)	5,941(8)
	71	Lu	−56,110(160)	5,480(160)	2,971(160)	7,925(180)	3,223(160)
	72	Hf	−53,790(300) ^b	2,320(340) ^b	3,630(360) ^b	10,204(480) ^b	4,826(310) ^b
	73	Ta	−46,140(300) ^b	7,660(420) ^b	4,327(370) ^b	8,395(370) ^b	1,765(480) ^b
	74	W	−41,899(12)	4,240(300) ^b	4,857(4)	11,160(90)	3,374(220) ^b
	75	Re	−31,860(140) ^b	10,040(140) ^b	5,637(50)	9,233(160) ^b	334(170) ^b
167	63	Eu	−43,730(900) ^b	6,970(1,080) ^b	−2,863(1,280) ^b	5,202(1,210) ^b	^a
	64	Gd	−50,700(600) ^b	5,140(720) ^b	−2,229(920) ^b	4,373(840) ^b	11,388(1,000) ^b
	65	Tb	−55,840(400) ^b	4,100(410) ^b	−1,642(640) ^b	6,208(500) ^b	8,733(720) ^b
	66	Dy	−59,940(60)	2,350(60)	−880(300) ^b	5,420(60)	9,525(300) ^b
	67	Ho	−62,293(6)	1,007(5)	−113(7)	7,284(5)	6,988(5)
	68	Er	−63,299.2(29)	^a	665.7(20)	6,436.1(4)	7,508.6(9)
	69	Tm	−62,551(3)	748.4(15)	1,411.5(23)	8,727(11)	4,905.4(15)
	70	Yb	−60,597(5)	1,954(4)	2,156(6)	7,077(9)	5,991(12)
	71	Lu	−57,470(100)	3,130(100)	2,847(100)	9,427(190)	3,165(100)
	72	Hf	−53,470(210) ^b	4,000(230) ^b	3,476(230) ^b	7,745(360) ^b	4,646(260) ^b
	73	Ta	−48,460(430) ^b	5,010(480) ^b	3,881(490) ^b	10,397(530) ^b	1,958(530) ^b
	74	W	−42,220(310) ^b	6,240(300) ^b	4,668(50)	8,395(310) ^b	3,375(430) ^b
	75	Re	−34,870(130) ^b	7,350(340) ^b	5,257(110) ^b	11,089(190) ^b	262(130) ^b
	76	Os	−26,500(310) ^b	8,380(340) ^b	5,979(50)	8,977(330) ^b	1,931(340) ^b
	77	Ir	−17,190(100) ^b	9,300(330) ^b	6,495(50)	11,763(520) ^b	−1,110(10)

Table 11.23 (Continued)

A	Z	Element	Mass excess	$Q(\beta^-)$	$Q(\alpha)$	$S(n)$	$S(p)$
168	64	Gd	−48,100(700) ^b	4,400(860) ^b	−2,350(1,060) ^b	5,472(920) ^b	11,658(1,140) ^b
	65	Tb	−52,500(500) ^b	5,970(590) ^b	−1,819(780) ^b	4,727(640) ^b	9,087(780) ^b
	66	Dy	−58,470(300) ^b	1,620(300) ^b	−1,149(500) ^b	6,599(300) ^b	9,916(500) ^b
	67	Ho	−60,085(29)	2,914(29)	−423(100)	5,863(29)	7,431(70)
	68	Er	−62,999.0(29)	−1,679.1(19)	552.7(20)	7,771.07(25)	7,995(5)
	69	Tm	−61,320(3)	257(4)	1,245.0(23)	6,840.3(18)	5,309.6(18)
	70	Yb	−61,577(4)	^a	1,951(4)	9,052(5)	6,315(4)
	71	Lu	−57,100(80)	4,470(80)	2,463(80)	7,707(130)	3,794(80)
	72	Hf	−55,300(100) ^b	1,800(130) ^b	3,267(150) ^b	9,906(230) ^b	5,125(140) ^b
	73	Ta	−48,640(370) ^b	6,670(380) ^b	3,696(390) ^b	8,245(570) ^b	2,458(420) ^b
	74	W	−44,840(200) ^b	3,800(420) ^b	4,506(12)	10,687(370) ^b	3,665(480) ^b
	75	Re	−35,760(400) ^b	9,080(450) ^b	5,063(13)	8,961(420) ^b	827(510) ^b
	76	Os	−29,960(30)	5,800(400) ^b	5,818.0(29)	11,538(310) ^b	2,381(140) ^b
	77	Ir	−18,660(330) ^b	11,300(330) ^b	6,561(110) ^b	9,540(350) ^b	−546(450) ^b
	78	Pt	−11,150(360) ^b	7,520(240) ^b	6,991(20)	^a	1,242(370) ^b
169	64	Gd	−43,900(800) ^b	6,190(1,000) ^b	−2,527(1,210) ^b	3,870(1,060) ^b	^a
	65	Tb	−50,100(600) ^b	5,510(670) ^b	−1,959(920) ^b	5,668(780) ^b	9,282(920) ^b
	66	Dy	−55,610(300)	3,200(300)	−1,565(590) ^b	5,208(420) ^b	10,397(590) ^b
	67	Ho	−58,807(20)	2,124(20)	−573(200) ^b	6,793(40)	7,626(300) ^b
	68	Er	−60,930.8(29)	351.1(11)	265.5(20)	6,003.13(28)	8,135(29)
	69	Tm	−61,281.9(29)	^a	1,200.4(13)	8,033.4(15)	5,571.9(11)
	70	Yb	−60,373(4)	909(4)	1,734(4)	6,867.2(3)	6,342(4)
	71	Lu	−58,080(5)	2,293(3)	2,434(5)	9,049(80)	3,792(3)
	72	Hf	−54,810(80)	3,270(80)	2,941(80)	7,579(130) ^b	4,998(110)
	73	Ta	−50,380(210) ^b	4,440(220) ^b	3,457(220) ^b	9,810(420) ^b	2,361(230) ^b
	74	W	−44,940(320) ^b	5,440(380) ^b	4,300(200) ^b	8,169(370) ^b	3,589(480) ^b
	75	Re	−38,350(210) ^b	6,590(380) ^b	5,039(90) ^b	10,660(450) ^b	800(280) ^b
	76	Os	−30,670(90)	7,680(220) ^b	5,717(4)	8,776(90)	2,196(410) ^b
	77	Ir	−21,990(90)	8,680(120)	6,276(50)	11,401(340) ^b	−683(100)
	78	Pt	−12,650(310) ^b	9,340(330) ^b	6,840(50)	9,574(480) ^b	1,276(460) ^b
170	65	Tb	−46,340(700) ^b	7,060(810) ^b	−2,164(1,060) ^b	4,317(920) ^b	9,729(1,060) ^b
	66	Dy	−53,400(400) ^b	2,850(400) ^b	−1,428(720) ^b	5,867(500) ^b	10,596(720) ^b
	67	Ho	−56,250(50)	3,870(50)	−967(300) ^b	5,513(50)	7,930(300)
	68	Er	−60,118(3)	−314.4(18)	50.2(24)	7,258.8(16)	8,600(20)
	69	Tm	−59,803.9(29)	968(8)	850.8(16)	6,593.3(11)	6,162.1(14)
	70	Yb	−60,771.9(29)	^a	1,737.6(15)	8,470(3)	6,778.9(12)
	71	Lu	−57,313(19)	3,459(19)	2,157(22)	7,304(19)	4,229(19)
	72	Hf	−56,220(200) ^b	1,100(200) ^b	2,950(200) ^b	9,477(210) ^b	5,425(200) ^b
	73	Ta	−50,220(200) ^b	6,000(280) ^b	3,469(250) ^b	7,913(280) ^b	2,695(210) ^b
	74	W	−47,240(470) ^b	2,980(510) ^b	4,133(560) ^b	10,371(570) ^b	4,150(510) ^b
	75	Re	−38,970(400) ^b	8,270(620) ^b	4,741(500) ^b	8,693(450) ^b	1,324(510) ^b
	76	Os	−33,935(13)	5,040(400) ^b	5,539(3)	11,338(90)	2,874(210) ^b

Table 11.23 (Continued)

A	Z	Element	Mass excess	$Q(\beta^-)$	$Q(\alpha)$	$S(n)$	$S(p)$
171	77	Ir	−23,260(150) ^b	10,680(150) ^b	6,173(50)	9,336(180) ^b	−123(170) ^b
	78	Pt	−16,460(100) ^b	6,790(110) ^b	6,704(6)	11,886(330) ^b	1,760(140) ^b
	65	Tb	−43,500(800) ^b	6,350(950) ^b	−2,192(1,210) ^b	5,230(1,060) ^b	^a
	66	Dy	−49,850(500) ^b	4,680(780) ^b	−1,577(780) ^b	4,522(640) ^b	10,801(860) ^b
	67	Ho	−54,530(600)	3,200(600)	−1,110(720) ^b	6,352(600)	8,415(720) ^b
	68	Er	−57,729(3)	1,490.5(12)	−211(60)	5,681.5(5)	8,769(50)
	69	Tm	−59,219.0(29)	96.4(1)	649(5)	7,486.4(14)	6,389.6(12)
	70	Yb	−59,315.4(28)	^a	1,559.0(14)	6,614.8(7)	6,800.5(10)
	71	Lu	−57,837(3)	1,478.8(19)	2,289.4(24)	8,595(19)	4,353.6(19)
	72	Hf	−55,430(200) ^b	2,400(200) ^b	2,738(200) ^b	7,289(280) ^b	5,409(200) ^b
	73	Ta	−51,740(210) ^b	3,700(280) ^b	3,307(230) ^b	9,590(280) ^b	2,808(280) ^b
	74	W	−47,080(280) ^b	4,660(350) ^b	3,965(350) ^b	7,913(550) ^b	4,150(340) ^b
	75	Re	−41,410(340) ^b	5,670(200) ^b	4,630(550) ^b	10,508(530) ^b	1,461(580) ^b
	76	Os	−34,430(310) ^b	6,980(460) ^b	5,370(5)	8,565(310) ^b	2,746(510) ^b
	77	Ir	−26,290(130) ^b	8,140(340) ^b	6,159.2(26)	11,102(200) ^b	−358(130) ^b
	78	Pt	−17,470(310) ^b	8,820(340) ^b	6,607(50)	9,073(330) ^b	1,497(350) ^b
	79	Au	−7,660(250) ^b	9,800(400) ^b	7,106(220) ^b	^a	−1,512(230) ^b
172	66	Dy	−47,400(600) ^b	4,000(720) ^b	−1,726(920) ^b	5,621(780) ^b	11,192(1,000) ^b
	67	Ho	−51,400(400) ^b	5,090(400) ^b	−1,326(640) ^b	4,943(720) ^b	8,835(640) ^b
	68	Er	−56,493(5)	891(5)	−448(300) ^b	6,836(4)	9,254(600)
	69	Tm	−57,384(6)	1,880(5)	276(29)	6,236(5)	6,944(5)
	70	Yb	−59,263.8(28)	^a	1,310.3(14)	8,019.72(27)	7,333.8(10)
	71	Lu	−56,745(3)	2,519.3(24)	2,150(3)	6,979.3(27)	4,718.1(24)
	72	Hf	−56,390(50)	350(50)	2,757(50)	9,033(200) ^b	5,847(50)
	73	Ta	−51,470(190)	4,920(180)	3,202(200)	7,811(280) ^b	3,330(270) ^b
	74	W	−48,980(270) ^b	2,500(200) ^b	3,903(290) ^b	9,968(390) ^b	4,528(340) ^b
	75	Re	−41,650(310) ^b	7,320(410) ^b	4,560(200) ^b	8,315(460) ^b	1,863(420) ^b
	76	Os	−37,190(200) ^b	4,460(360) ^b	5,227(10)	10,830(370) ^b	3,069(400) ^b
	77	Ir	−27,350(400) ^b	9,840(450) ^b	5,991(10)	9,129(420) ^b	206(510) ^b
173	78	Pt	−21,070(30)	6,270(400) ^b	6,465(4)	11,681(320) ^b	2,075(140) ^b
	79	Au	−9,210(330) ^b	11,860(340) ^b	7,024(50)	9,622(420) ^b	−962(460) ^b
	66	Dy	−43,370(700) ^b	5,730(810) ^b	−1,894(1,060) ^b	4,038(920) ^b	^a
	67	Ho	−49,100(400) ^b	4,560(450) ^b	−1,428(720) ^b	5,771(570) ^b	8,984(720) ^b
	68	Er	−53,650(200) ^b	2,610(200) ^b	−472(360) ^b	5,232(200) ^b	9,543(450) ^b
	69	Tm	−56,262(5)	1,298(5)	120(21)	6,950(7)	7,058(6)
	70	Yb	−57,560.0(28)	^a	945.9(15)	6,367.6(5)	7,465(6)
	71	Lu	−56,889.2(28)	670.8(17)	1,967.8(20)	8,216.0(23)	4,914.4(16)
	72	Hf	−55,280(100) ^b	1,610(100) ^b	2,664(100) ^b	6,961(110) ^b	5,829(100) ^b
	73	Ta	−52,590(230) ^b	2,690(200) ^b	3,061(230) ^b	9,191(290) ^b	3,489(230) ^b
	74	W	−48,590(380) ^b	4,000(300) ^b	3,791(380) ^b	7,691(460) ^b	4,409(420) ^b
	75	Re	−43,720(450) ^b	4,870(590) ^b	4,228(500) ^b	10,142(550) ^b	2,036(530) ^b
	76	Os	−37,450(310) ^b	6,270(550) ^b	5,057(50)	8,338(370) ^b	3,092(440) ^b

Table 11.23 (Continued)

A	Z	Element	Mass excess	$Q(\beta^-)$	$Q(\alpha)$	$S(n)$	$S(p)$
174	77	Ir	−30,080(230) ^b	7,370(390) ^b	5,844(100) ^b	10,806(460) ^b	182(300) ^b
	78	Pt	−21,890(100)	8,190(250) ^b	6,353(50)	8,888(110)	1,834(410) ^b
	79	Au	−12,670(100)	9,220(140)	6,897(50)	11,528(350) ^b	−1,115(110)
	67	Ho	−45,500(500) ^b	6,340(590) ^b	−1,587(860) ^b	4,476(640) ^b	9,422(860) ^b
	68	Er	−51,850(300) ^b	2,030(300) ^b	−869(500) ^b	6,264(360) ^b	10,037(500) ^b
	69	Tm	−53,870(40)	3,080(40)	−50(70)	5,683(40)	7,508(200) ^b
	70	Yb	−56,953.3(28)	−1,374.3(16)	740.1(16)	7,464.60(10)	7,980(5)
	71	Lu	−55,579.0(28)	273.3(22)	1,800.0(20)	6,761.1(15)	5,307.9(16)
	72	Hf	−55,852(3)	^a	2,494.8(25)	8,639(100) ^b	6,252.0(22)
	73	Ta	−52,010(80)	3,840(80)	2,881(80)	7,484(240) ^b	4,012(130) ^b
	74	W	−50,150(300) ^b	1,860(310) ^b	3,639(360) ^b	9,629(480) ^b	4,846(370) ^b
	75	Re	−43,680(410) ^b	6,480(510) ^b	4,116(460) ^b	8,025(610) ^b	2,370(560) ^b
	76	Os	−39,940(470) ^b	3,740(360) ^b	4,872(10)	10,556(560) ^b	3,506(650) ^b
	77	Ir	−30,920(400) ^b	9,020(620) ^b	5,624(10)	8,913(460) ^b	757(510) ^b
	78	Pt	−25,326(13)	5,600(400) ^b	6,184(5)	11,507(100)	2,535(230) ^b
	79	Au	−14,050(150) ^b	11,280(150) ^b	6,782(10)	9,451(180) ^b	−552(180) ^b
175	67	Ho	−42,800(600) ^b	5,700(720) ^b	−1,726(1,000) ^b	5,370(780) ^b	^a
	68	Er	−48,500(400) ^b	3,820(400) ^b	−1,074(640) ^b	4,727(500) ^b	10,288(640) ^b
	69	Tm	−52,320(50)	2,390(50)	−216(600)	6,517(70)	7,761(300) ^b
	70	Yb	−54,704.3(28)	470(13)	599.3(16)	5,822.33(12)	8,120(40)
	71	Lu	−55,174.3(26)	^a	1,619.7(17)	7,666.7(10)	5,510(13)
	72	Hf	−54,490(3)	684.7(2)	2,400.9(24)	6,708.7(5)	6,199.6(22)
	73	Ta	−52,490(100) ^b	2,000(100) ^b	2,922(100) ^b	8,554(130) ^b	3,926(100) ^b
	74	W	−49,580(200) ^b	2,910(220) ^b	3,425(280) ^b	7,503(360) ^b	4,865(210) ^b
	75	Re	−45,280(450) ^b	4,310(490) ^b	4,033(490) ^b	9,673(610) ^b	2,414(540) ^b
	76	Os	−39,980(300) ^b	5,300(540) ^b	4,673(410) ^b	8,112(560) ^b	3,594(510) ^b
	77	Ir	−33,270(340) ^b	6,710(460) ^b	5,709(4)	10,423(530) ^b	624(580) ^b
	78	Pt	−25,830(310) ^b	7,450(460) ^b	6,178.3(26)	8,570(310) ^b	2,192(510) ^b
176	79	Au	−17,190(240) ^b	8,640(390) ^b	6,678(200) ^b	11,206(280) ^b	−853(240) ^b
	80	Hg	−8,000(320) ^b	9,180(400) ^b	7,039(50)	^a	1,240(350) ^b
	68	Er	−46,310(400) ^b	3,070(410) ^b	−1,326(720) ^b	5,873(570) ^b	10,791(720) ^b
	69	Tm	−49,380(100)	4,120(100)	−402(410) ^b	5,129(110)	8,163(410) ^b
	70	Yb	−53,497.2(29)	−106.2(17)	571(4)	6,864.2(11)	8,467(50)
	71	Lu	−53,391.0(26)	1,192.8(9)	1,568(6)	6,287.98(15)	5,975.7(13)
	72	Hf	−54,583.8(27)	^a	2,255.0(17)	8,165.6(18)	6,698.5(10)
	73	Ta	−51,470(100)	3,110(100)	2,846(100)	7,055(140) ^b	4,273(100)
	74	W	−50,680(200) ^b	790(220) ^b	3,287(200) ^b	9,170(280) ^b	5,482(220) ^b
	75	Re	−45,110(200) ^b	5,570(280) ^b	3,937(270) ^b	7,907(490) ^b	2,818(280) ^b
	76	Os	−41,960(200) ^b	3,150(280) ^b	4,585(340) ^b	10,055(360) ^b	3,976(490) ^b
	77	Ir	−33,990(300) ^b	7,980(360) ^b	5,237(50)	8,787(460) ^b	1,298(430) ^b
	78	Pt	−28,880(200) ^b	5,110(360) ^b	5,886.1(22)	11,123(370) ^b	2,892(400) ^b
	79	Au	−18,380(400) ^b	10,500(450) ^b	6,542(10)	9,266(470) ^b	−157(510) ^b
	80	Hg	−11,720(40)	6,660(400) ^b	6,925(10)	11,795(320) ^b	1,829(240) ^b

Table 11.23 (Continued)

A	Z	Element	Mass excess	$Q(\beta^-)$	$Q(\alpha)$	$S(n)$	$S(p)$
177	68	Er	−42,500(600) ^b	4,970(670) ^b	−1,559(920) ^b	4,271(720) ^b	^a
	69	Tm	−47,470(300) ^b	3,520(300) ^b	−795(500) ^b	6,163(310) ^b	8,453(500) ^b
	70	Yb	−50,993(3)	1,399.2(2)	236(200) ^b	5,566.8(12)	8,904(100)
	71	Lu	−52,391.9(26)	498.3(8)	1,445(5)	7,072.2(6)	6,183.7(16)
	72	Hf	−52,890.2(25)	^a	2,244.9(16)	6,377.7(13)	6,788.2(10)
	73	Ta	−51,724(4)	1,166(3)	2,740(3)	8,322(100)	4,429(3)
	74	W	−49,720(300) ^b	2,000(300) ^b	3,136(320) ^b	7,112(360) ^b	5,538(310) ^b
	75	Re	−46,320(200) ^b	3,400(360) ^b	3,846(300) ^b	9,282(280) ^b	2,930(280) ^b
	76	Os	−41,880(280) ^b	4,450(340) ^b	4,294(470) ^b	7,983(350) ^b	4,052(340) ^b
	77	Ir	−36,170(450) ^b	5,710(530) ^b	5,127(50)	10,252(540) ^b	1,495(490) ^b
	78	Pt	−29,390(310) ^b	6,780(550) ^b	5,643.5(28)	8,581(370) ^b	2,685(440) ^b
	79	Au	−21,220(230) ^b	8,160(390) ^b	6,431(7)	10,916(460) ^b	−363(300) ^b
	80	Hg	−12,730(110)	8,500(260) ^b	6,738(50)	9,074(120)	1,637(420) ^b
	81	Tl	−2,910(230) ^b	9,820(250) ^b	7,340(200) ^b	^a	−1,530(230) ^b
178	69	Tm	−44,120(400) ^b	5,590(400) ^b	−1,037(640) ^b	4,718(500) ^b	8,900(720) ^b
	70	Yb	−49,701(10)	645(10)	−279(300) ^b	6,780(10)	9,521(300) ^b
	71	Lu	−50,346(3)	2,099.2(21)	1,102(40)	6,025.4(19)	6,642.3(28)
	72	Hf	−52,445.2(25)	^a	2,083.2(16)	7,626.33(29)	7,342.3(9)
	73	Ta	−50,530(100)	1,910(100)	2,621(100)	6,880(100)	4,932(100)
	74	W	−50,440(100)	91.3(2)	2,985(100)	8,790(320) ^b	6,007(100)
	75	Re	−45,780(210)	4,660(180)	3,800(220)	7,530(280) ^b	3,348(360) ^b
	76	Os	−43,460(200)	2,330(290)	4,271(360) ^b	9,652(350) ^b	4,422(280) ^b
	77	Ir	−36,250(360) ^b	7,210(300) ^b	5,000(200) ^b	8,152(580) ^b	1,664(460) ^b
	78	Pt	−31,940(470) ^b	4,310(300) ^b	5,573.4(26)	10,626(560) ^b	3,060(650) ^b
	79	Au	−22,380(400) ^b	9,560(620) ^b	6,118(50)	9,226(460) ^b	283(510) ^b
	80	Hg	−16,323(15)	6,060(400) ^b	6,578(6)	11,667(110)	2,388(230) ^b
	81	Tl	−4,450(210) ^b	11,880(210) ^b	7,180(150) ^b	9,611(310) ^b	−993(240) ^b
179	69	Tm	−41,600(500) ^b	4,820(590) ^b	−1,223(780) ^b	5,556(640) ^b	^a
	70	Yb	−46,420(300) ^b	2,650(300) ^b	−338(500) ^b	4,786(300) ^b	9,590(500) ^b
	71	Lu	−49,067(6)	1,406(5)	827(50)	6,793(5)	6,655(11)
	72	Hf	−50,472.9(25)	^a	1,806.5(16)	6,099.03(10)	7,415.9(21)
	73	Ta	−50,362(6)	111(5)	2,387(6)	7,900(100)	5,206(5)
	74	W	−49,302(16)	1,060(16)	2,762(16)	6,932(100)	6,058(100)
	75	Re	−46,590(50)	2,710(50)	3,472(120) ^b	8,882(210)	3,439(110)
	76	Os	−42,890(230) ^b	3,700(240) ^b	4,265(310) ^b	7,509(310) ^b	4,401(310) ^b
	77	Ir	−38,050(400) ^b	4,840(460) ^b	4,800(200) ^b	9,873(540) ^b	1,885(450) ^b
	78	Pt	−32,160(300) ^b	5,890(500) ^b	5,395(7)	8,290(560) ^b	3,198(470) ^b
	79	Au	−24,770(340) ^b	7,390(460) ^b	6,082(21)	10,459(530) ^b	115(580) ^b
	80	Hg	−16,970(310) ^b	7,800(460) ^b	6,431(5)	8,717(310) ^b	1,879(510) ^b
	81	Tl	−7,950(140) ^b	9,020(340) ^b	6,810(210) ^b	11,576(260) ^b	−1,085(140) ^b
180	70	Yb	−44,400(400) ^b	2,280(410) ^b	−525(570) ^b	6,059(500) ^b	10,093(640) ^b
	71	Lu	−46,690(70)	3,100(70)	266(120)	5,691(70)	7,559(310) ^b
	72	Hf	−49,789.5(25)	−854.1(29)	1,282.8(18)	7,387.90(24)	8,011(5)

Table 11.23 (Continued)

A	Z	Element	Mass excess	$Q(\beta^-)$	$Q(\alpha)$	$S(n)$	$S(p)$
	73	Ta	−48,935(3)	708(4)	2,031(3)	6,645(5)	5,751.5(29)
	74	W	−49,643(5)	^a	2,516(5)	8,412(15)	6,570(6)
	75	Re	−45,840(30)	3,800(30)	3,208(110)	7,320(60)	3,828(40)
	76	Os	−44,390(180) ^b	1,460(190) ^b	3,873(270) ^b	9,562(300) ^b	5,081(190) ^b
	77	Ir	−37,960(190) ^b	6,430(60) ^b	4,732(270) ^b	7,975(440) ^b	2,350(300) ^b
	78	Pt	−34,270(200) ^b	3,690(60) ^b	5,275(9)	10,176(360) ^b	3,502(450) ^b
	79	Au	−25,710(300) ^b	8,550(360) ^b	5,851(21)	9,018(460) ^b	842(430) ^b
	80	Hg	−20,190(200) ^b	5,520(360) ^b	6,258(4)	11,295(370) ^b	2,715(400) ^b
	81	Tl	−9,140(450) ^b	11,060(490) ^b	6,820(200) ^b	9,256(470) ^b	−546(550) ^b
181	70	Yb	−40,850(400) ^b	3,890(500) ^b	−767(720) ^b	4,513(570) ^b	^a
	71	Lu	−44,740(300) ^b	2,670(300) ^b	304(420) ^b	6,124(310) ^b	7,624(500) ^b
	72	Hf	−47,413.9(26)	1,027.2(27)	1,153.9(23)	5,695.7(7)	8,016(70)
	73	Ta	−48,441.1(29)	^a	1,525.9(27)	7,577.0(13)	5,940.6(26)
	74	W	−48,253(5)	188(5)	2,212(5)	6,681(6)	6,607(5)
	75	Re	−46,515(14)	1,739(15)	2,785(15)	8,745(40)	4,160(15)
	76	Os	−43,520(200)	2,990(200)	3,774(360) ^b	7,211(270) ^b	4,973(200)
	77	Ir	−39,460(210)	4,070(60)	4,442(290) ^b	9,572(280) ^b	2,360(280) ^b
	78	Pt	−34,300(280) ^b	5,160(350) ^b	5,150(50)	8,107(340) ^b	3,634(340) ^b
	79	Au	−27,990(450) ^b	6,310(530) ^b	5,752.0(30)	10,351(540) ^b	1,017(490) ^b
	80	Hg	−20,670(310) ^b	7,320(550) ^b	6,287(4)	8,552(370) ^b	2,249(430) ^b
	81	Tl	−12,200(380) ^b	8,480(490) ^b	6,600(300) ^b	11,136(590) ^b	−705(430) ^b
182	82	Pb	−3,060(160) ^b	9,140(410) ^b	7,241(120) ^b	^a	1,216(480) ^b
	71	Lu	−41,720(300) ^b	4,340(300) ^b	−31(500) ^b	5,053(420) ^b	8,165(500) ^b
	72	Hf	−46,060(7)	373(7)	1,217(12)	6,717(6)	8,609(300) ^b
	73	Ta	−46,432.7(29)	1,813.5(18)	1,488(3)	6,062.96(16)	6,307.8(27)
	74	W	−48,246.2(29)	^a	1,774.1(28)	8,064(5)	7,094.1(18)
	75	Re	−45,450(100)	2,800(100)	2,662(140)	7,003(100)	4,482(100)
	76	Os	−44,538(25)	910(100)	3,479(100)	9,085(200)	5,313(29)
	77	Ir	−39,000(140)	5,530(140)	4,353(250)	7,619(260)	2,768(250)
	78	Pt	−36,080(200)	2,920(140)	4,952(5)	9,850(340) ^b	3,912(290)
	79	Au	−28,300(360) ^b	7,780(300) ^b	5,527(4)	8,377(580) ^b	1,288(460) ^b
	80	Hg	−23,520(470) ^b	4,780(300) ^b	5,997(5)	10,917(560) ^b	2,815(650) ^b
	81	Tl	−13,400(400) ^b	10,120(620) ^b	6,550(10)	9,276(550) ^b	19(510) ^b
	82	Pb	−6,822(17)	6,580(400) ^b	7,076(9)	11,832(160) ^b	1,912(380) ^b
183	71	Lu	−39,520(300) ^b	3,760(300) ^b	−348(590) ^b	5,873(420) ^b	^a
	72	Hf	−43,290(30)	2,010(30)	706(300) ^b	5,297(30)	8,853(300) ^b
	73	Ta	−45,295.6(29)	1,070(18)	1,347(6)	6,934.18(20)	6,525(7)
	74	W	−46,365.6(27)	^a	1,682.4(28)	6,190.7(10)	7,221.9(17)
	75	Re	−45,810(8)	556(8)	2,128(9)	8,435(100)	4,852(8)
	76	Os	−43,680(100) ^b	2,130(100) ^b	3,200(100) ^b	7,211(110) ^b	5,520(150) ^b
	77	Ir	−40,230(140) ^b	3,450(100) ^b	3,940(150) ^b	9,295(200) ^b	2,978(150) ^b
	78	Pt	−35,650(230) ^b	4,580(270) ^b	4,819(50)	7,642(310) ^b	3,935(270) ^b
	79	Au	−30,160(400) ^b	5,490(460) ^b	5,465.6(30)	9,934(540) ^b	1,371(450) ^b

Table 11.23 (Continued)

A	Z	Element	Mass excess	$Q(\beta^-)$	$Q(\alpha)$	$S(n)$	$S(p)$
184	80	Hg	−23,700(300) ^b	6,470(500) ^b	6,039(4)	8,248(560) ^b	2,686(470) ^b
	81	Tl	−16,120(390) ^b	7,580(490) ^b	6,224(190) ^b	10,785(560) ^b	−112(610) ^b
	82	Pb	−7,520(310) ^b	8,600(500) ^b	7,027(50)	8,766(310) ^b	1,402(510) ^b
	71	Lu	−36,170(400) ^b	5,330(400) ^b	^a	4,718(500) ^b	^a
	72	Hf	−41,500(40)	1,340(30)	479(400) ^b	6,286(50)	9,266(300) ^b
	73	Ta	−42,840(26)	2,866(26)	1,422(80)	5,616(26)	6,843(40)
	74	W	−45,706.0(27)	−1,483(4)	1,658.6(28)	7,411.74(27)	7,699.4(18)
	75	Re	−44,223(5)	31(4)	2,287(5)	6,485(9)	5,147(4)
	76	Os	−44,254.5(30)	^a	2,964(4)	8,648(100) ^b	5,734(8)
	77	Ir	−39,690(270)	4,560(270)	3,724(270)	7,536(310) ^b	3,304(290) ^b
	78	Pt	−37,360(180) ^b	2,340(330) ^b	4,602(9)	9,780(290) ^b	4,419(230) ^b
	79	Au	−30,300(190) ^b	7,060(60) ^b	5,232(5)	8,208(440) ^b	1,937(300) ^b
	80	Hg	−26,180(200) ^b	4,120(60) ^b	5,662(5)	10,553(360) ^b	3,305(450) ^b
	81	Tl	−16,990(300) ^b	9,190(360) ^b	6,298(50)	8,944(490) ^b	584(420) ^b
	82	Pb	−10,990(200) ^b	6,000(360) ^b	6,775(5)	11,547(360) ^b	2,164(440) ^b
185	72	Hf	−38,400(300) ^b	3,000(300) ^b	25(500) ^b	4,967(300) ^b	9,515(500) ^b
	73	Ta	−41,396(14)	1,992(14)	918(300) ^b	6,628(30)	7,185(40)
	74	W	−43,388.4(28)	433(9)	1,600.5(28)	5,753.74(30)	7,837(26)
	75	Re	−43,821.4(28)	^a	2,194.7(20)	7,669(4)	5,404.4(9)
	76	Os	−42,808.6(28)	1,012.8(4)	3,020(5)	6,625.4(9)	5,874(4)
	77	Ir	−40,440(200) ^b	2,370(200) ^b	3,653(200) ^b	8,815(330) ^b	3,471(200) ^b
	78	Pt	−36,560(210)	3,880(290) ^b	4,542(50)	7,271(280) ^b	4,154(340)
	79	Au	−31,850(210)	4,710(40)	5,181(4)	9,624(280) ^b	1,782(280) ^b
	80	Hg	−26,100(280) ^b	5,750(350) ^b	5,778(11)	7,991(340) ^b	3,089(340) ^b
	81	Tl	−19,470(400) ^b	6,630(490) ^b	6,100(200) ^b	10,549(500) ^b	579(450) ^b
	82	Pb	−11,570(310) ^b	7,900(510) ^b	6,680(50)	8,647(360) ^b	1,868(430) ^b
	83	Bi	−2,140(230) ^b	9,430(380) ^b	7,639(440) ^b	^a	−1,569(110) ^b
186	72	Hf	−36,400(300) ^b	2,210(300) ^b	^a	6,078(420) ^b	^a
	73	Ta	−38,610(60)	3,900(60)	686(300) ^b	5,285(60)	7,503(300) ^b
	74	W	−42,511.3(29)	−581.6(17)	1,123(7)	7,194.2(17)	8,404(14)
	75	Re	−41,929.8(28)	1,069.5(9)	2,078.0(21)	6,179.7(7)	5,830.3(11)
	76	Os	−42,999.3(29)	^a	2,822.0(17)	8,262.0(12)	6,466.8(11)
	77	Ir	−39,168(20)	3,831(20)	3,853(100)	6,803(200) ^b	3,649(20)
	78	Pt	−37,790(30)	1,380(40)	4,325(20)	9,302(210)	4,641(200) ^b
	79	Au	−31,670(140)	6,120(140)	4,906(15)	7,894(260)	2,404(250)
	80	Hg	−28,450(200)	3,230(140)	5,206(15)	10,421(340) ^b	3,886(290)
	81	Tl	−19,980(370) ^b	8,470(310) ^b	5,892(50)	8,585(540) ^b	1,173(460) ^b
	82	Pb	−14,620(470) ^b	5,360(300) ^b	6,471(7)	11,125(560) ^b	2,444(620) ^b
	83	Bi	−3,280(450) ^b	11,340(650) ^b	7,700(200) ^b	9,215(500) ^b	−1,001(540) ^b
187	73	Ta	−36,880(300) ^b	3,030(300) ^b	221(420) ^b	6,339(300) ^b	7,764(420) ^b
	74	W	−39,906.7(29)	1,311.2(13)	954(30)	5,466.72(21)	8,585(60)
	75	Re	−41,217.9(28)	2,663(19)	1,652.8(23)	7,359.4(14)	5,995.5(13)
	76	Os	−41,220.5(28)	^a	2,720.2(15)	6,292.6(14)	6,579.7(14)

Table 11.23 (Continued)

A	Z	Element	Mass excess	$Q(\beta^-)$	$Q(\alpha)$	$S(n)$	$S(p)$
188	77	Ir	−39,718(7)	1,502(6)	3,667(10)	8,621(21)	4,008(6)
	78	Pt	−36,740(180) ^b	2,980(180) ^b	4,513(150) ^b	7,023(190) ^b	4,861(180) ^b
	79	Au	−33,010(150) ^b	3,730(100) ^b	4,793(50)	9,408(210) ^b	2,511(160) ^b
	80	Hg	−28,150(240) ^b	4,870(280) ^b	5,080(70) ^b	7,768(310) ^b	3,761(280) ^b
	81	Tl	−22,200(400) ^b	5,950(470) ^b	5,539(8)	10,287(540) ^b	1,039(450) ^b
	82	Pb	−14,880(300) ^b	7,320(500) ^b	6,395(7)	8,324(560) ^b	2,183(470) ^b
	83	Bi	−6,090(380) ^b	8,780(480) ^b	7,599(100) ^b	10,886(590) ^b	−1,240(600) ^b
	73	Ta	−33,800(300) ^b	4,870(300) ^b	−59(500) ^b	4,997(420) ^b	^a
	74	W	−38,669(4)	349(3)	406(40)	6,834(3)	9,080(300) ^b
	75	Re	−39,018.1(28)	2,120.4(4)	1,397(26)	5,871.60(30)	6,400.4(13)
	76	Os	−41,138.5(28)	^a	2,142.6(15)	7,989.29(30)	7,209.6(30)
	77	Ir	−38,329(7)	2,809(7)	3,469(8)	6,682(9)	4,398(7)
	78	Pt	−37,823(6)	506(7)	4,007(5)	9,154(180) ^b	5,394(8)
	79	Au	−32,520(100) ^b	5,300(100) ^b	4,745(290) ^b	7,584(180) ^b	3,071(210) ^b
	80	Hg	−30,220(180) ^b	2,300(150) ^b	4,710(20)	10,149(300) ^b	4,501(240) ^b
	81	Tl	−22,430(220) ^b	7,790(290) ^b	5,443(290) ^b	8,304(460) ^b	1,574(330) ^b
	82	Pb	−17,640(200) ^b	4,790(300) ^b	6,111(4)	10,837(360) ^b	2,733(450) ^b
	83	Bi	−7,290(300) ^b	10,350(360) ^b	7,275(25)	9,268(480) ^b	−296(420) ^b
189	74	W	−35,480(200)	2,500(200)	493(360) ^b	4,881(200)	8,964(360) ^b
	75	Re	−37,979(9)	1,009(8)	993(17)	7,032(8)	6,598(9)
	76	Os	−38,987.8(28)	^a	1,975.7(16)	5,920.6(5)	7,258.6(7)
	77	Ir	−38,455(13)	532(13)	2,941(13)	8,198(14)	4,606(13)
	78	Pt	−36,485(11)	1,971(14)	3,899(11)	6,734(12)	5,445(13)
	79	Au	−33,640(200) ^b	2,850(200) ^b	4,376(280) ^b	9,184(220) ^b	3,101(200) ^b
	80	Hg	−29,690(280) ^b	3,950(200) ^b	4,448(350) ^b	7,534(340) ^b	4,451(300) ^b
	81	Tl	−24,510(350) ^b	5,180(200) ^b	4,917(410) ^b	10,149(410) ^b	1,575(390) ^b
	82	Pb	−17,810(270) ^b	6,700(440) ^b	5,863(60) ^b	8,240(340) ^b	2,669(350) ^b
	83	Bi	−9,780(400) ^b	8,030(480) ^b	7,267(4)	10,556(500) ^b	−577(450) ^b
190	74	W	−34,300(220)	1,270(70)	−320(370) ^b	6,891(300)	^a
	75	Re	−35,570(210)	3,140(210)	617(220)	5,661(210)	7,378(290)
	76	Os	−38,708.0(28)	−2,000(200)	1,378.4(16)	7,791.6(9)	8,018(8)
	77	Ir	−36,710(200)	620(200)	2,797(200)	6,324(200)	5,009(200)
	78	Pt	−37,325(6)	^a	3,249(6)	8,911(10)	6,159(13)
	79	Au	−32,883(16)	4,442(15)	3,860(26)	7,319(200) ^b	3,687(18)
	80	Hg	−31,410(150) ^b	1,470(150) ^b	3,951(150) ^b	9,799(320) ^b	5,067(250) ^b
	81	Tl	−24,410(430) ^b	7,000(400) ^b	4,835(450) ^b	7,976(550) ^b	2,017(510) ^b
	82	Pb	−20,330(200)	4,090(470) ^b	5,698(5)	10,586(340) ^b	3,106(400) ^b
	83	Bi	−10,700(370) ^b	9,630(310) ^b	6,862(5)	8,990(540) ^b	174(450) ^b
	84	Po	−4,560(470) ^b	6,140(310) ^b	7,643(20)	^a	2,068(620) ^b
191	75	Re	−34,350(11)	2,045(10)	103(300) ^b	6,853(210)	7,341(220)
	76	Os	−36,395.4(28)	313.7(11)	1,086.4(16)	5,758.66(16)	8,116(210)
	77	Ir	−36,709.1(29)	^a	2,083.9(15)	8,072(200)	5,290(12)
	78	Pt	−35,691(5)	1,019(4)	3,105(4)	6,437(6)	6,271(200)

Table 11.23 (Continued)

A	Z	Element	Mass excess	$Q(\beta^-)$	$Q(\alpha)$	$S(n)$	$S(p)$
	79	Au	−33,860(50)	1,830(50)	3,433(50)	9,049(50)	3,825(50)
	80	Hg	−30,680(90)	3,180(70)	3,635(200) ^b	7,339(170) ^b	5,087(90)
	81	Tl	−26,190(220) ^b	4,490(200) ^b	4,397(270) ^b	9,846(480) ^b	2,064(270) ^b
	82	Pb	−20,310(210) ^b	5,880(310) ^b	5,413(110) ^b	8,053(290) ^b	3,183(480) ^b
	83	Bi	−12,990(400) ^b	7,320(450) ^b	6,781(5)	10,368(540) ^b	−45(450) ^b
	84	Po	−4,980(300) ^b	8,010(500) ^b	7,471(20)	8,496(560) ^b	1,574(470) ^b
	192	75 Re	−31,710(200) ^b	4,170(200) ^b	−329(360) ^b	5,429(200) ^b	^a
		76 Os	−35,882(3)	−1,046.2(23)	362(4)	7,558.0(21)	8,821(10)
		77 Ir	−34,835.8(29)	1,459.7(19)	1,757.4(16)	6,198.08(20)	5,729.4(12)
		78 Pt	−36,296(3)	^a	2,418.1(24)	8,676.3(30)	6,875.4(19)
		79 Au	−32,779(16)	3,516(16)	3,125(17)	6,990(50)	4,378(16)
		80 Hg	−32,070(280) ^b	710(280) ^b	3,329(280) ^b	9,460(300) ^b	5,498(290) ^b
		81 Tl	−25,950(200) ^b	6,120(200) ^b	4,149(220) ^b	7,833(300) ^b	2,558(220) ^b
		82 Pb	−22,580(180) ^b	3,370(270) ^b	5,221(5)	10,342(280) ^b	3,678(280) ^b
	193	83 Bi	−13,630(220) ^b	8,950(290) ^b	6,376(5)	8,709(460) ^b	612(310) ^b
		84 Po	−7,900(200) ^b	5,730(300) ^b	7,320(7)	10,988(360) ^b	2,195(450) ^b
		76 Os	−33,396(4)	1,140.5(24)	−342(200)	5,585.1(9)	8,977(200) ^b
		77 Ir	−34,536.3(29)	^a	1,017(8)	7,771.85(20)	5,943.3(23)
		78 Pt	−34,479.7(29)	56.64(3)	2,083.2(15)	6,255.5(19)	6,932.9(4)
		79 Au	−33,411(9)	1,069(9)	2,619(16)	8,703(18)	4,405(9)
		80 Hg	−31,071(19)	2,340(17)	2,989(22)	7,073(280) ^b	5,581(25)
		81 Tl	−27,430(250) ^b	3,640(250) ^b	3,776(320) ^b	9,556(320) ^b	2,654(380) ^b
	194	82 Pb	−22,280(190) ^b	5,150(310) ^b	4,979(340) ^b	7,776(260) ^b	3,621(270) ^b
		83 Bi	−15,780(350) ^b	6,500(390) ^b	6,305(5)	10,220(410) ^b	491(390) ^b
		84 Po	−8,290(280) ^b	7,490(440) ^b	7,096(50)	8,463(340) ^b	1,948(350) ^b
		85 At	180(400) ^b	8,460(490) ^b	7,526(30)	^a	−783(450) ^b
		76 Os	−32,435(4)	96.6(2)	−562(220)	7,111(3)	^a
		77 Ir	−32,531.9(29)	2,246.8(16)	611(210)	6,066.8(4)	6,425.0(25)
		78 Pt	−34,778.6(29)	^a	1,504.5(19)	8,370.3(16)	7,531.3(16)
		79 Au	−32,287(12)	2,492(11)	1,997(200)	6,947(14)	5,096(11)
	195	80 Hg	−32,247(23)	40(20)	2,653(24)	9,247(30)	6,125(25)
		81 Tl	−26,960(210) ^b	5,280(210) ^b	3,494(210) ^b	7,601(260) ^b	3,182(210) ^b
		82 Pb	−24,250(150) ^b	2,710(260) ^b	4,738(20)	10,040(240) ^b	4,105(290) ^b
		83 Bi	−16,070(430) ^b	8,180(400) ^b	5,918(5)	8,362(550) ^b	1,077(470) ^b
		84 Po	−10,910(200)	5,160(470) ^b	6,987(3)	10,696(340) ^b	2,424(400) ^b
		85 At	−960(400) ^b	9,960(340) ^b	7,312(160) ^b	9,205(570) ^b	−41(480) ^b
		76 Os	−29,690(500)	2,000(500)	^a	5,328(500)	^a
		77 Ir	−31,692.4(29)	1,120(16)	233(10)	7,231.87(11)	6,546.1(20)
	195	78 Pt	−32,812.4(29)	^a	1,158.1(19)	6,105.06(12)	7,569.5(16)
		79 Au	−32,586(3)	226.8(1)	1,698.6(19)	8,370(11)	5,095.9(10)
		80 Hg	−31,080(50)	1,510(50)	2,190(50)	6,900(60)	6,078(50)
		81 Tl	−28,270(130) ^b	2,810(140) ^b	3,165(140) ^b	9,378(190) ^b	3,313(130) ^b

Table 11.23 (Continued)

A	Z	Element	Mass excess	$Q(\beta^-)$	$Q(\alpha)$	$S(n)$	$S(p)$
196	82	Pb	−23,780(410) ^b	4,490(430) ^b	4,475(400) ^b	7,601(440) ^b	4,106(460) ^b
	83	Bi	−17,930(220) ^b	5,850(350) ^b	5,833(5)	9,932(480) ^b	969(270) ^b
	84	Po	−11,140(220) ^b	6,800(310) ^b	6,746(50)	8,294(300) ^b	2,355(480) ^b
	85	At	−3,210(400) ^b	7,930(460) ^b	7,356(50)	10,323(570) ^b	−414(450) ^b
	76	Os	−28,300(40)	1,160(60)	^a	6,675(500)	^a
	77	Ir	−29,450(40)	3,210(40)	−171(200) ^b	5,833(40)	7,050(500)
	78	Pt	−32,662.9(29)	−1,505.7(29)	794.2(28)	7,921.88(15)	8,259.5(16)
	79	Au	−31,157(4)	686(3)	1,254(3)	6,643(3)	5,633.8(29)
	80	Hg	−31,843(4)	^a	2,027(4)	8,839(50)	6,547(3)
	81	Tl	−27,470(140) ^b	4,380(140) ^b	2,889(140) ^b	7,266(160) ^b	3,679(150) ^b
	82	Pb	−25,420(140) ^b	2,050(200) ^b	4,224(320) ^b	9,712(440) ^b	4,439(190) ^b
	83	Bi	−18,060(210) ^b	7,360(250) ^b	5,460(50)	8,205(300) ^b	1,573(460) ^b
	84	Po	−13,500(180) ^b	4,570(270) ^b	6,657(3)	10,431(290) ^b	2,854(280) ^b
	85	At	−4,000(230) ^b	9,490(290) ^b	7,201(50)	8,864(460) ^b	157(320) ^b
	86	Rn	2,150(200) ^b	6,150(310) ^b	7,623(30)	^a	1,928(450) ^b
197	77	Ir	−28,283(20)	2,155(20)	^a	6,901(40)	7,276(40)
	78	Pt	−30,438.1(29)	718.9(6)	532.9(29)	5,846.4(3)	8,273(40)
	79	Au	−31,157.0(29)	^a	954.5(17)	8,071.1(28)	5,783(7)
	80	Hg	−30,557(4)	600(3)	1,497(4)	6,785.4(15)	6,689(3)
	81	Tl	−28,380(30)	2,180(30)	2,609(30)	8,983(140) ^b	3,823(30)
	82	Pb	−24,800(100) ^b	3,580(110) ^b	3,849(100) ^b	7,447(170) ^b	4,620(170) ^b
	83	Bi	−19,620(240)	5,170(260) ^b	5,387(50) ^b	9,630(320) ^b	1,491(280) ^b
	84	Po	−13,450(190) ^b	6,180(310) ^b	6,412(50)	8,021(260) ^b	2,670(280) ^b
	85	At	−6,250(350) ^b	7,190(400) ^b	7,103(50)	10,318(420) ^b	44(390) ^b
	86	Rn	1,550(280) ^b	7,800(450) ^b	7,411(50)	8,675(350) ^b	1,739(360) ^b
198	77	Ir	−25,820(200) ^b	4,100(200) ^b	^a	5,609(200) ^b	^a
	78	Pt	−29,923(4)	−325(3)	87(4)	7,556.6(30)	8,929(20)
	79	Au	−29,598.0(29)	1,372.5(5)	509.0(17)	6,512.34(11)	6,448.9(6)
	80	Hg	−30,970.5(29)	^a	1,383.3(9)	8,484(3)	7,102.5(6)
	81	Tl	−27,510(80)	3,460(80)	2,351(80)	7,205(90)	4,242(80)
	82	Pb	−26,100(90) ^b	1,410(120) ^b	3,721(100) ^b	9,375(140) ^b	5,013(100) ^b
	83	Bi	−19,540(180)	6,560(200) ^b	5,000(100) ^b	7,987(230)	2,031(210) ^b
	84	Po	−15,520(150) ^b	4,020(240) ^b	6,309.1(21)	10,143(250) ^b	3,183(290) ^b
	85	At	−6,750(430) ^b	8,760(400) ^b	6,893.3(27)	8,573(550) ^b	596(470) ^b
	86	Rn	−1,140(200)	5,620(470) ^b	7,352(5)	10,755(350) ^b	2,175(400) ^b
199	77	Ir	−24,420(40)	2,990(40)	^a	6,667(200) ^b	^a
	78	Pt	−27,408(4)	1,703(3)	−141(500)	5,556.1(5)	8,876(200) ^b
	79	Au	−29,111.0(29)	452.3(7)	156.5(17)	7,584.36(15)	6,477(3)
	80	Hg	−29,563.3(29)	^a	824.2(10)	6,664.2(6)	7,254.3(7)
	81	Tl	−28,120(100)	1,450(100)	2,042(100)	8,679(130)	4,437(100)
	82	Pb	−25,230(70)	2,880(90)	3,416(80)	7,206(110) ^b	5,013(100)
	83	Bi	−20,890(120)	4,350(120)	4,959(50) ^b	9,420(160)	2,075(150) ^b

Table 11.23 (Continued)

A	Z	Element	Mass excess	$Q(\beta^-)$	$Q(\alpha)$	$S(n)$	$S(p)$
200	84	Po	−15,280(410) ^b	5,610(430) ^b	6,074.3(20)	7,836(440) ^b	3,031(450) ^b
	85	At	−8,730(220) ^b	6,560(350) ^b	6,780(50)	10,045(480) ^b	498(270) ^b
	86	Rn	−1,580(230) ^b	7,150(320) ^b	7,135(50)	8,510(300) ^b	2,113(480) ^b
	78	Pt	−26,618(20)	660(60)	−747(40)	7,282(20)	9,490(50)
	79	Au	−27,280(50)	2,240(50)	−247(60)	6,236(50)	7,157(50)
	80	Hg	−29,520.2(29)	^a	717.8(10)	8,028.25(25)	7,698.2(7)
	81	Tl	−27,064(6)	2,456(6)	1,668(6)	7,017(100)	4,790(6)
	82	Pb	−26,254(13)	811(14)	3,165(13)	9,090(70)	5,424(100)
	83	Bi	−20,360(90)	5,890(90)	4,680(100) ^b	7,545(120)	2,415(110)
	84	Po	−17,010(140) ^b	3,350(170) ^b	5,981.5(20)	9,804(440) ^b	3,416(180) ^b
	85	At	−9,040(210) ^b	7,970(250) ^b	6,596.4(14)	8,388(300) ^b	1,050(460) ^b
	86	Rn	−4,030(180) ^b	5,020(270) ^b	7,043.5(26)	10,523(290) ^b	2,590(290) ^b
	87	Fr	6,050(240) ^b	10,080(300) ^b	7,632(50)	^a	−340(330) ^b
201	78	Pt	−23,760(50)	2,660(50)	^a	5,209(50)	^a
	79	Au	−26,416(4)	1,263(3)	−558(21)	7,212(50)	7,087(21)
	80	Hg	−27,679.1(29)	^a	334.1(11)	6,230.2(6)	7,692(50)
	81	Tl	−27,196(15)	483(15)	1,536(15)	8,203(16)	4,965(15)
	82	Pb	−25,290(30)	1,900(30)	2,839(30)	7,111(30)	5,518(30)
	83	Bi	−21,450(30)	3,840(40)	4,500(6)	9,162(90)	2,487(30)
	84	Po	−16,570(100) ^b	4,880(110) ^b	5,799.0(17)	7,630(170) ^b	3,501(140) ^b
	85	At	−10,720(240)	5,850(260) ^b	6,473.3(16)	9,753(320) ^b	999(280) ^b
	86	Rn	−4,160(200) ^b	6,570(310) ^b	6,861(50)	8,203(270) ^b	2,405(290) ^b
	87	Fr	3,710(350) ^b	7,870(410) ^b	7,538(50)	10,412(420) ^b	−450(400) ^b
202	78	Pt	−22,600(300) ^b	1,820(340) ^b	^a	6,913(300) ^b	^a
	79	Au	−24,420(170)	2,950(170)	−1,020(260) ^b	6,071(170)	7,949(170)
	80	Hg	−27,362.1(29)	^a	136(3)	7,754.31(23)	8,235(3)
	81	Tl	−25,997(15)	1,365(15)	1,176(15)	6,873(21)	5,607(15)
	82	Pb	−25,948(10)	50(15)	2,598(10)	8,726(30)	6,041(18)
	83	Bi	−20,800(50)	5,150(50)	4,289(100)	7,416(60)	2,792(60)
	84	Po	−17,980(90) ^b	2,820(110) ^b	5,701.0(17)	9,473(140) ^b	3,812(100) ^b
	85	At	−10,760(180)	7,210(200) ^b	6,353.7(14)	8,107(230)	1,477(210) ^b
	86	Rn	−6,320(150) ^b	4,440(240) ^b	6,773.6(19)	10,230(250) ^b	2,882(290) ^b
	87	Fr	3,060(430) ^b	9,380(400) ^b	7,389(9)	8,722(560) ^b	68(470) ^b
203	79	Au	−23,159(4)	2,124(4)	−1,167(40)	6,815(170)	7,850(300) ^b
	80	Hg	−25,283(3)	491.8(12)	−300(4)	5,992.7(17)	8,157(170)
	81	Tl	−25,775.3(29)	^a	910.8(15)	7,849(15)	5,702.2(13)
	82	Pb	−24,801(7)	975(6)	2,338(6)	6,924(11)	6,092(16)
	83	Bi	−21,547(21)	3,253(22)	4,146(100)	8,822(60)	2,888(23)
	84	Po	−17,310(70)	4,230(60)	5,496(5)	7,411(110) ^b	3,807(80)
	85	At	−12,250(120)	5,060(120)	6,210.3(8)	9,563(160)	1,566(150) ^b
	86	Rn	−6,230(410) ^b	6,030(430) ^b	6,629.9(23)	7,980(440) ^b	2,755(450) ^b
	87	Fr	980(230) ^b	7,200(360) ^b	7,277(50)	10,157(490) ^b	−5(280) ^b
	88	Ra	8,580(230) ^b	7,600(330) ^b	7,730(50)	^a	1,772(490) ^b

Table 11.23 (Continued)

A	Z	Element	Mass excess	$Q(\beta^-)$	$Q(\alpha)$	$S(n)$	$S(p)$
204	79	Au	−20,770(200) ^b	3,940(200) ^b	^a	5,679(200) ^b	^a
	80	Hg	−24,707(3)	−347.5(15)	−514(20)	7,495.2(19)	8,837(3)
	81	Tl	−24,359.8(29)	763.72(18)	491(50)	6,655.86(29)	6,365.4(13)
	82	Pb	−25,123.5(29)	^a	1,971.8(14)	8,394(6)	6,637.2(3)
	83	Bi	−20,674(26)	4,449(26)	3,965(27)	7,198(30)	3,163(27)
	84	Po	−18,344(13)	2,331(29)	5,484.9(14)	9,101(70)	4,086(25)
	85	At	−11,870(90)	6,480(90)	6,069.9(15)	7,685(120)	1,841(110)
	86	Rn	−8,040(140) ^b	3,820(170) ^b	6,545.6(19)	9,889(440) ^b	3,081(180) ^b
	87	Fr	550(210) ^b	8,600(250) ^b	7,169.8(27)	8,495(310) ^b	511(460) ^b
	88	Ra	6,030(180) ^b	5,480(280) ^b	7,636(8)	10,617(290) ^b	2,232(290) ^b
205	79	Au	−18,990(300) ^b	3,310(300) ^b	^a	6,297(360) ^b	^a
	80	Hg	−22,304(5)	1,531(4)	−972(50)	5,668(4)	8,825(200) ^b
	81	Tl	−23,834.8(30)	^a	157(3)	7,546.3(5)	6,416.5(15)
	82	Pb	−23,783.7(29)	51.1(5)	1,470.4(12)	6,731.51(15)	6,712.87(23)
	83	Bi	−21,075(8)	2,708(7)	3,696(17)	8,472(27)	3,241(7)
	84	Po	−17,544(29)	3,531(28)	5,324(10)	7,272(30)	4,159(40)
	85	At	−13,010(30)	4,540(40)	6,019.7(17)	9,213(90)	1,952(30)
	86	Rn	−7,760(110) ^b	5,250(120) ^b	6,386(50)	7,789(180) ^b	3,184(150) ^b
	87	Fr	−1,240(240)	6,520(260) ^b	7,055(50)	9,868(320) ^b	490(280) ^b
	88	Ra	5,760(210) ^b	7,010(310) ^b	7,497(50)	8,342(270) ^b	2,079(290) ^b
206	80	Hg	−20,960(21)	1,307(20)	−787(300) ^b	6,728(21)	9,256(300) ^b
	81	Tl	−22,267.1(30)	1,533.5(7)	−276(170)	6,503.6(4)	7,252(4)
	82	Pb	−23,800.6(29)	^a	1,136.6(12)	8,088.2(4)	7,254.8(6)
	83	Bi	−20,043(8)	3,758(8)	3,529(17)	7,039(10)	3,548(8)
	84	Po	−18,197(10)	1,847(12)	5,326.5(13)	8,724(30)	4,410(12)
	85	At	−12,480(50)	5,710(50)	5,888.4(19)	7,547(60)	2,227(60)
	86	Rn	−9,170(90) ^b	3,320(110) ^b	6,383.8(17)	9,476(150) ^b	3,448(100) ^b
	87	Fr	−1,410(180)	7,760(200) ^b	6,926(4)	8,236(220)	937(210) ^b
	88	Ra	3,520(150) ^b	4,930(240) ^b	7,416(5)	10,311(260) ^b	2,521(280) ^b
	89	Ac	11,270(230) ^b	7,790(360) ^b	7,864(50)	^a	−454(280) ^b
207	80	Hg	−16,230(150)	4,810(150)	^a	3,341(150)	^a
	81	Tl	−21,044(6)	1,423(5)	−310(6)	6,849(6)	7,374(21)
	82	Pb	−22,467.1(29)	^a	391.5(13)	6,737.79(11)	7,489.0(7)
	83	Bi	−20,069(4)	2,398.2(21)	3,281.5(22)	8,097(8)	3,557.2(21)
	84	Po	−17,160(7)	2,909(6)	5,215.9(10)	7,035(11)	4,406(10)
	85	At	−13,250(21)	3,910(22)	5,873(3)	8,838(60)	2,342(23)
	86	Rn	−8,640(70)	4,610(60)	6,251.0(17)	7,543(110) ^b	3,444(80)
	87	Fr	−2,930(120)	5,710(120)	6,901(50)	9,587(150)	1,049(150) ^b
	88	Ra	3,470(420) ^b	6,400(430) ^b	7,273(50)	8,122(440) ^b	2,408(450) ^b
	89	Ac	11,270(230) ^b	7,790(360) ^b	7,864(50)	^a	−454(280) ^b
208	80	Hg	−13,100(300) ^b	3,670(300) ^b	^a	4,939(330) ^b	^a
	81	Tl	−16,762.6(29)	5,001(17)	1,580(200) ^b	3,789(6)	7,822(150)
	82	Pb	−21,763.6(29)	^a	518.8(15)	7,367.82(9)	8,008(5)
	83	Bi	−18,884(4)	2,879.1(2)	3,050.5(20)	6,887.0(27)	3,706.4(20)

Table 11.23 (Continued)

A	Z	Element	Mass excess	$Q(\beta^-)$	$Q(\alpha)$	$S(n)$	$S(p)$	
	84	Po	−17,483(3)	1,401.3(24)	5,215.5(13)	8,395(7)	4,703.3(25)	
	85	At	−12,498(26)	4,985(26)	5,751.1(22)	7,320(30)	2,628(27)	
	86	Rn	−9,658(13)	2,840(29)	6,260.5(17)	9,092(70)	3,698(25)	
	87	Fr	−2,670(80)	6,990(80)	6,771(50)	7,816(100)	1,321(100)	
	88	Ra	1,650(140) ^b	4,320(160) ^b	7,273(5)	9,889(440) ^b	2,709(180) ^b	
	89	Ac	10,700(210) ^b	9,040(250) ^b	7,721(15)	8,639(310) ^b	63(460) ^b	
	209	81	Tl	−13,647(10)	3,982(10)	2,921(300) ^b	4,956(10)	7,839(300) ^b
	82	Pb	−17,629(3)	644.2(11)	2,250(4)	3,936.5(14)	8,155.1(22)	
	83	Bi	−18,272.9(30)	^a	3,137.0(8)	7,459.8(19)	3,798.3(8)	
	84	Po	−16,380(3)	1,893.3(16)	4,979.2(14)	6,967.8(19)	4,784.1(25)	
	85	At	−12,893(8)	3,486(7)	5,757.3(20)	8,466(27)	2,699(7)	
	86	Rn	−8,964(29)	3,929(28)	6,155.3(20)	7,377(30)	3,755(40)	
	87	Fr	−3,800(30)	5,160(40)	6,777(4)	9,206(80)	1,435(30)	
	88	Ra	1,810(130) ^b	5,620(130) ^b	7,147(50)	7,915(190) ^b	2,808(150) ^b	
	89	Ac	8,910(240)	7,100(270) ^b	7,733(50)	9,856(320) ^b	30(280) ^b	
	210	81	Tl	−9,254(11)	5,489(11)	^a	3,678(15)	^a
	82	Pb	−14,743(3)	63.5(5)	3,792(20)	5,185.3(13)	8,384(10)	
	83	Bi	−14,806.1(30)	1,162.1(8)	5,036(8)	4,604.58(13)	4,466.4(12)	
	84	Po	−15,968.2(29)	^a	5,407.46(7)	7,660.0(14)	4,984.3(8)	
	85	At	−11,987(8)	3,981(8)	5,631.1(10)	7,165(11)	2,896(8)	
	86	Rn	−9,613(10)	2,374(12)	6,158.5(22)	8,720(30)	4,009(12)	
	87	Fr	−3,355(22)	6,258(24)	6,703(50)	7,622(40)	1,680(40)	
	88	Ra	420(90) ^b	3,770(100) ^b	7,157(5)	9,466(160) ^b	3,069(100) ^b	
	89	Ac	8,620(190)	8,210(210) ^b	7,607(50)	8,362(240)	477(230) ^b	
	90	Th	14,000(150) ^b	5,380(240) ^b	8,053(17)	^a	2,202(290) ^b	
	211	82	Pb	−10,496.6(30)	1,372(6)	3,308(150)	3,825(3)	8,532(12)
	83	Bi	−11,869(6)	579(6)	6,750.5(5)	5,134(6)	4,415(6)	
	84	Po	−12,447.7(30)	^a	7,594.5(5)	4,550.8(5)	4,930.5(9)	
	85	At	−11,662(4)	786.1(25)	5,982.4(13)	7,746(8)	2,982.3(25)	
	86	Rn	−8,770(7)	2,892(7)	5,965.2(14)	7,228(12)	4,071(10)	
	87	Fr	−4,164(21)	4,605(21)	6,660(5)	8,881(30)	1,840(23)	
	88	Ra	830(70)	5,000(60)	7,046(5)	7,654(110) ^b	3,101(70)	
	89	Ac	7,120(130)	6,290(130)	7,625(50)	9,570(160)	580(160) ^b	
	90	Th	13,840(420) ^b	6,720(440) ^b	7,943(50)	8,232(450) ^b	2,072(460) ^b	
	212	82	Pb	−7,556.7(27)	573.8(2)	3,115(300) ^b	5,131.5(27)	^a
	83	Bi	−8,130.5(29)	2,254(17)	6,207.14(4)	4,333(6)	4,923(3)	
	84	Po	−10,384.5(29)	−1,753.9(29)	8,954.13(11)	6,008.2(5)	5,805(5)	
	85	At	−8,631(4)	43(4)	7,828.9(20)	5,040(4)	3,471.9(29)	
	86	Rn	−8,673(4)	^a	6,385.0(26)	7,975(7)	4,301(4)	
	87	Fr	−3,544(26)	5,129(26)	6,529.1(18)	7,451(30)	2,064(27)	
	88	Ra	−202(14)	3,343(29)	7,031.9(18)	9,106(70)	3,326(25)	
	89	Ac	7,280(90)	7,480(90)	7,521(50)	7,919(120)	845(110)	
	90	Th	12,030(140) ^b	4,760(170) ^b	7,952(10)	9,880(440) ^b	2,382(190) ^b	

■ Table 11.23 (Continued)

A	Z	Element	Mass excess	$Q(\beta^-)$	$Q(\alpha)$	$S(n)$	$S(p)$
213	82	Pb	−3,260(100) ^b	1,980(100) ^b	^a	3,774(100) ^b	^a
	83	Bi	−5,240(8)	1,427(7)	5,982(6)	5,181(7)	4,972(7)
	84	Po	−6,667(4)	^a	8,536.7(26)	4,354.0(29)	5,826(3)
	85	At	−6,594(6)	73(5)	9,254(5)	6,035(5)	3,498(5)
	86	Rn	−5,712(7)	882(8)	8,243(6)	5,110(7)	4,370(7)
	87	Fr	−3,563(8)	2,148(10)	6,905.1(18)	8,090(27)	2,179(8)
	88	Ra	322(30)	3,885(29)	6,861(4)	7,547(30)	3,422(40)
	89	Ac	6,120(60)	5,800(70)	7,503(50)	9,224(100)	964(60)
	90	Th	12,070(130) ^b	5,950(150) ^b	7,838(50)	8,029(190) ^b	2,492(160) ^b
	91	Pa	19,730(250)	7,660(280) ^b	8,394(50)	^a	−411(290) ^b
214	82	Pb	−188.0(25)	1,024(11)	^a	5,000(100) ^b	^a
	83	Bi	−1,212(11)	3,272(11)	5,616.8(10)	4,044(13)	5,241(100) ^b
	84	Po	−4,484(3)	−1,090(4)	7,833.46(6)	5,888.4(29)	6,533(7)
	85	At	−3,394(5)	941(10)	8,987(4)	4,871(6)	4,016(5)
	86	Rn	−4,335(10)	^a	9,208(9)	6,695(11)	5,030(10)
	87	Fr	−974(9)	3,361(13)	8,589(4)	5,482(12)	2,551(11)
	88	Ra	85(11)	1,059(14)	7,273(4)	8,309(30)	3,641(13)
	89	Ac	6,420(50)	6,340(60)	7,351(50)	7,774(80)	1,190(60)
	90	Th	10,670(90) ^b	4,250(110) ^b	7,826(7)	9,478(160) ^b	2,746(110) ^b
	91	Pa	19,320(190)	8,650(220) ^b	8,271(50)	8,485(250)	44(240) ^b
215	83	Bi	1,710(100)	2,250(100)	^a	5,152(100)	5,394(100)
	84	Po	−545.3(29)	720(7)	7,526.4(8)	4,132(3)	6,622(11)
	85	At	−1,266(7)	^a	8,178(4)	5,943(8)	4,070(7)
	86	Rn	−1,184(8)	82(10)	8,839(8)	4,920(12)	5,079(9)
	87	Fr	304(8)	1,487(10)	9,540(7)	6,794(11)	2,650(11)
	88	Ra	2,519(8)	2,215(10)	8,864(4)	5,637(13)	3,796(11)
	89	Ac	6,010(50)	3,490(50)	7,748(50)	8,483(80)	1,365(60)
	90	Th	10,920(70)	4,910(80)	7,666(6)	7,815(120) ^b	2,787(90)
	91	Pa	17,790(140)	6,870(140)	8,240(50)	9,600(180)	166(170) ^b
216	83	Bi	5,780(100) ^b	4,000(100) ^b	^a	4,003(140) ^b	^a
	84	Po	1,774.7(27)	−469(4)	6,906.5(5)	5,751.4(25)	7,221(100)
	85	At	2,244(4)	2,003(8)	7,949(3)	4,562(8)	4,500(4)
	86	Rn	240(8)	^a	8,200(7)	6,647(10)	5,783(10)
	87	Fr	2,969(13)	2,729(14)	9,175(12)	5,406(14)	3,136(15)
	88	Ra	3,277(9)	308(15)	9,526(8)	7,313(11)	4,315(11)
	89	Ac	8,124(27)	4,846(28)	9,243(8)	5,956(60)	1,684(28)
	90	Th	10,294(16)	2,170(30)	8,071(8)	8,701(70)	3,004(60)
	91	Pa	17,800(110)	7,510(110)	8,099(50)	8,060(140)	412(120)
217	84	Po	5,830(100) ^b	1,440(100) ^b	6,660(4)	4,021(100) ^b	7,239(140) ^b
	85	At	4,387(8)	741(8)	7,201.9(14)	5,928(8)	4,677(7)
	86	Rn	3,646(5)	^a	7,888.6(29)	4,665(8)	5,886(5)
	87	Fr	4,300(7)	654(8)	8,469(4)	6,741(14)	3,229(10)
	88	Ra	5,874(10)	1,574(11)	9,161(6)	5,475(13)	4,384(16)

Table 11.23 (Continued)

A	Z	Element	Mass excess	$Q(\beta^-)$	$Q(\alpha)$	$S(n)$	$S(p)$
218	89	Ac	8,693(13)	2,819(16)	9,832(10)	7,502(30)	1,873(15)
	90	Th	12,170(30)	3,480(30)	9,424(9)	6,194(30)	3,242(40)
	91	Pa	17,040(80)	4,860(80)	8,487(50)	8,836(130)	547(80)
	84	Po	8,351.6(25)	265(12)	6,114.68(9)	5,545(100) ^b	^a
	85	At	8,087(12)	2,883(12)	6,874(30)	4,372(14)	5,027(100) ^b
	86	Rn	5,204(3)	−1,842(5)	7,263.0(19)	6,514(4)	6,472(8)
	87	Fr	7,045(5)	409(12)	8,014.3(20)	5,326(8)	3,890(6)
	88	Ra	6,636(11)	^a	8,546(6)	7,309(14)	4,953(13)
	89	Ac	10,830(50)	4,190(50)	9,377(50)	5,936(50)	2,334(50)
	90	Th	12,359(14)	1,530(50)	9,849(9)	7,884(30)	3,623(19)
	91	Pa	18,640(70)	6,280(80)	9,791(50)	6,470(110)	823(80)
	92	U	21,880(100) ^b	3,240(120) ^b	8,786(25)	^a	2,447(120) ^b
219	85	At	10,520(80)	1,700(80)	6,391(50)	5,635(80)	5,118(80)
	86	Rn	8,825.7(28)	218(7)	6,946.1(3)	4,449(4)	6,550(12)
	87	Fr	8,608(7)	^a	7,448.6(18)	6,509(8)	3,885(7)
	88	Ra	9,379(9)	771(11)	8,138(3)	5,328(14)	4,955(9)
	89	Ac	11,560(50)	2,180(50)	8,827(50)	7,345(70)	2,370(50)
	90	Th	14,460(50)	2,900(70)	9,514(50)	5,972(50)	3,660(70)
	91	Pa	18,520(70)	4,060(90)	10,085(50)	8,190(100)	1,129(70)
	92	U	23,210(80)	4,690(110)	9,860(50)	6,741(130) ^b	2,718(110)
220	85	At	14,250(110) ^b	3,650(110) ^b	6,053(50)	4,341(140) ^b	^a
	86	Rn	10,604.3(27)	−865(4)	6,404.67(10)	6,292.8(25)	7,207(80)
	87	Fr	11,469(5)	1,209(11)	6,800.7(19)	5,210(8)	4,645(5)
	88	Ra	10,260(10)	^a	7,595(7)	7,190(13)	5,637(12)
	89	Ac	13,740(50)	3,480(50)	8,347(50)	5,885(70)	2,926(50)
	90	Th	14,655(22)	910(60)	8,953(20)	7,874(60)	4,189(60)
	91	Pa	20,380(60)	5,720(60)	9,829(50)	6,212(90)	1,369(80)
	92	U	23,020(200) ^b	2,640(210) ^b	10,300(200) ^b	8,261(220) ^b	2,789(210) ^b
221	85	At	16,900(300) ^b	2,500(320) ^b	^a	5,427(320) ^b	^a
	86	Rn	14,400(100) ^b	1,130(100) ^b	6,146(3)	4,279(100) ^b	7,146(150) ^b
	87	Fr	13,270(8)	315(9)	6,457.9(14)	6,271(8)	4,623(7)
	88	Ra	12,955(7)	^a	6,884(5)	5,376(12)	5,803(8)
	89	Ac	14,510(50)	1,550(50)	7,784(50)	7,304(70)	3,040(50)
	90	Th	16,927(10)	2,420(50)	8,628(4)	5,800(24)	4,104(50)
	91	Pa	20,370(50)	3,440(50)	9,248(50)	8,083(80)	1,578(60)
	92	U	24,550(110) ^b	4,180(120) ^b	9,950(100) ^b	6,544(230) ^b	3,121(120) ^b
222	85	At	20,800(300) ^b	4,430(300) ^b	^a	4,168(420) ^b	^a
	86	Rn	16,366.8(25)	25(21)	5,590.3(3)	6,101(100) ^b	7,819(300) ^b
	87	Fr	16,342(21)	2,033(21)	5,830(24)	4,999(22)	5,343(100) ^b
	88	Ra	14,309(5)	^a	6,681(4)	6,717(8)	6,249(8)
	89	Ac	16,607(6)	2,298(7)	7,137.4(20)	5,973(50)	3,637(8)
	90	Th	17,190(13)	582(14)	8,129(6)	7,808(16)	4,608(50)

■ Table 11.23 (Continued)

A	Z	Element	Mass excess	$Q(\beta^-)$	$Q(\alpha)$	$S(n)$	$S(p)$
223	91	Pa	22,100(70) ^b	4,910(70) ^b	8,847(50) ^b	6,337(90) ^b	2,115(70) ^b
	92	U	24,280(100) ^b	2,180(120) ^b	9,500(100) ^b	8,334(150) ^b	3,371(110) ^b
	85	At	23,600(400) ^b	3,310(500) ^b	^a	5,268(500) ^b	^a
	86	Rn	20,300(300) ^b	1,920(300) ^b	^a	4,141(300) ^b	7,792(420) ^b
	87	Fr	18,379.0(27)	1,149.1(9)	5,432(80)	6,034(21)	5,276.7(24)
	88	Ra	17,230.0(28)	^a	5,979.31(26)	5,151(5)	6,401(21)
	89	Ac	17,816(7)	586(7)	6,783.1(10)	6,863(9)	3,783(8)
	90	Th	19,371(10)	1,555(12)	7,567(4)	5,891(16)	4,526(10)
	91	Pa	22,320(70)	2,950(70)	8,342(50)	7,850(100) ^b	2,157(70)
	92	U	25,820(70)	3,500(100)	8,941(50)	6,531(120) ^b	3,566(100) ^b
224	86	Rn	22,440(300) ^b	800(300) ^b	^a	5,929(420) ^b	8,453(500) ^b
	87	Fr	21,640(50)	2,830(50)	4,966(120) ^b	4,807(50)	5,942(300) ^b
	88	Ra	18,818.0(27)	−1,403(4)	5,788.87(15)	6,483.3(25)	6,850.0(23)
	89	Ac	20,221(5)	232(13)	6,326.9(7)	5,666(8)	4,298(5)
	90	Th	19,989(12)	^a	7,304(7)	7,453(15)	5,116(14)
	91	Pa	23,860(50)	3,870(50)	7,694(4)	6,533(90)	2,799(50)
	92	U	25,700(25)	1,840(60)	8,620(12)	8,195(80)	3,911(80)
225	86	Rn	26,490(300) ^b	2,640(300) ^b	^a	4,019(420) ^b	^a
	87	Fr	23,853(10)	1,865(10)	4,530(300) ^b	5,862(50)	5,876(300) ^b
	88	Ra	21,987(3)	358(7)	5,166(100) ^b	4,902.0(30)	6,945(50)
	89	Ac	21,630(8)	^a	5,935.2(14)	6,663(8)	4,477(7)
	90	Th	22,301(7)	671(10)	6,921.4(21)	5,759(14)	5,209(8)
	91	Pa	24,330(70)	2,020(70)	7,393(50)	7,605(90)	2,952(70)
	92	U	27,370(50)	3,050(90)	8,020(50)	6,400(60)	3,778(70)
	93	Np	31,580(70)	4,210(90)	8,787(50)	^a	1,412(80)
	94	Pu	35,040(100)	7,670(100)	9,590(100)	7,990(100)	3,280(100)
226	86	Rn	28,770(400) ^b	1,440(410) ^b	^a	5,789(500) ^b	^a
	87	Fr	27,330(90)	3,670(90)	4,108(310) ^b	4,591(90)	6,447(310) ^b
	88	Ra	23,662.3(25)	−640(3)	4,870.63(25)	6,396.4(29)	7,479(10)
	89	Ac	24,303(4)	1,117(5)	5,536(21)	5,399(8)	4,974(4)
	90	Th	23,186(5)	^a	6,451.2(10)	7,187(8)	5,733(8)
	91	Pa	26,019(12)	2,834(12)	6,987(10)	6,378(70)	3,571(13)
	92	U	27,330(19)	1,311(22)	7,715(14)	8,113(50)	4,285(70)
	93	Np	32,720(90) ^b	5,390(90) ^b	8,197(50)	6,926(110) ^b	1,938(100) ^b
227	86	Rn	32,980(420) ^b	3,330(430) ^b	^a	3,864(580) ^b	^a
	87	Fr	29,650(100)	2,480(100)	3,623(410) ^b	5,752(130)	6,410(410) ^b
	88	Ra	27,172.3(25)	1,326.2(24)	4,450(300) ^b	4,561.34(27)	7,450(90)
	89	Ac	25,846.1(27)	44.8(8)	5,042.19(14)	6,528(3)	5,105.2(24)
	90	Th	25,801.3(28)	^a	6,146.43(15)	5,456(5)	5,790(4)
	91	Pa	26,821(8)	1,019(8)	6,580.0(21)	7,270(14)	3,654(9)
	92	U	29,007(17)	2,186(18)	7,211(14)	6,394(25)	4,301(20)
	93	Np	32,560(70)	3,560(70)	7,816(14)	8,230(110) ^b	2,055(70)
	94	Pu	35,920(100)	7,020(100)	8,620(100)	7,920(100)	3,280(100)
228	86	Rn	35,480(470) ^b	2,200(510) ^b	^a	5,578(630) ^b	^a
	87	Fr	33,280(200) ^b	4,340(200) ^b	^a	4,448(220) ^b	6,994(470) ^b

Table 11.23 (Continued)

A	Z	Element	Mass excess	Q(β [−])	Q(α)	S(n)	S(p)
	88	Ra	28,936.0(25)	45.9(9)	4,071(300) ^b	6,307.6(24)	8,005(100)
	89	Ac	28,890.1(26)	2,127(3)	4,821(50)	5,027.3(28)	5,571.2(26)
	90	Th	26,763.1(27)	^a	5,520.12(22)	7,109.6(25)	6,372.0(23)
	91	Pa	28,911(5)	2,148(4)	6,264.5(15)	5,981(9)	4,180(5)
	92	U	29,218(16)	307(16)	6,804(10)	7,861(23)	4,892(17)
	93	Np	33,700(200) ^b	4,480(200) ^b	7,416(200) ^b	6,933(210) ^b	2,594(200) ^b
	94	Pu	36,070(30)	2,370(200) ^b	7,950(20)	^a	3,778(80)
	229	87	Fr	35,790(360) ^b	3,360(360) ^b	^a	5,554(410) ^b
	88	Ra	32,430(60)	1,760(40)	3,518(300) ^b	4,572(60)	8,130(210) ^b
	89	Ac	30,670(50)	1,100(50)	4,397(50)	6,287(50)	5,550(50)
	90	Th	29,579.9(29)	^a	5,167.6(10)	5,254.5(28)	6,599.2(29)
	91	Pa	29,890(9)	310(9)	5,836(5)	7,092(10)	4,162(9)
	92	U	31,201(8)	1,311(11)	6,475(3)	6,087(17)	4,998(9)
	93	Np	33,760(90)	2,560(90)	7,013(50)	8,009(210) ^b	2,743(90)
	94	Pu	37,390(70)	3,630(110)	7,593(50)	6,757(80)	3,601(210) ^b
	230	87	Fr	39,600(450) ^b	5,050(450) ^b	^a	4,266(570) ^b
	88	Ra	34,540(30)	990(110)	3,345(400) ^b	5,962(70)	8,538(360) ^b
	89	Ac	33,560(100)	2,700(100)	3,799(140)	5,189(110)	6,167(120)
	90	Th	30,857.2(20)	−1,309.7(28)	4,770.0(15)	6,794.0(23)	7,107(50)
	91	Pa	32,167(3)	564(5)	5,439.4(7)	5,795(9)	4,702(4)
	92	U	31,603(5)	^a	5,992.7(7)	7,670(9)	5,576(10)
	93	Np	35,220(50)	3,620(50)	6,778(50)	6,613(100)	3,268(50)
	94	Pu	36,930(24)	1,710(60)	7,175(15)	8,531(80)	4,123(90)
	231	87	Fr	42,300(520) ^b	3,900(600) ^b	^a	5,373(690) ^b
	88	Ra	38,400(300) ^b	2,490(310) ^b	2,990(300) ^b	4,219(300) ^b	8,491(540) ^b
	89	Ac	35,910(100)	2,100(100)	3,833(140)	5,718(140)	5,923(110)
	90	Th	33,810.5(20)	389.5(17)	4,213.3(16)	5,118.04(20)	7,036(100)
	91	Pa	33,421.0(26)	^a	5,149.9(8)	6,817(3)	4,725.2(17)
	92	U	33,803(4)	382(3)	5,576.9(30)	5,871(6)	5,653(5)
	93	Np	35,610(50)	1,810(50)	6,368(50)	7,680(70)	3,278(50)
	94	Pu	38,430(100) ^b	2,820(110) ^b	7,000(100) ^b	6,569(100) ^b	4,079(110) ^b
	95	Am	42,440(300) ^b	4,010(320) ^b	7,451(310) ^b	^a	1,780(300) ^b
232	87	Fr	46,250(640) ^b	5,550(730) ^b	^a	4,115(820) ^b	^a
	88	Ra	40,700(360) ^b	1,560(370) ^b	2,800(300) ^b	5,768(470) ^b	8,886(630) ^b
	89	Ac	39,140(100)	3,700(100)	3,443(220) ^b	4,838(140)	6,541(310) ^b
	90	Th	35,443.7(20)	−495(8)	4,082.8(14)	6,438.1(12)	7,756(100)
	91	Pa	35,939(8)	1,337(7)	4,624(8)	5,554(8)	5,161(8)
	92	U	34,601.5(27)	^a	5,413.55(14)	7,273(4)	6,108.4(22)
	93	Np	37,350(100) ^b	2,750(100) ^b	6,016(100) ^b	6,334(110) ^b	3,741(100) ^b
	94	Pu	38,358(19)	1,010(100) ^b	6,716(10)	8,145(100) ^b	4,545(50)
	95	Am	43,400(300) ^b	5,040(300) ^b	7,272(360) ^b	7,112(420) ^b	2,322(320) ^b
233	88	Ra	44,710(470) ^b	3,210(560) ^b	^a	4,064(590) ^b	8,834(790) ^b
	89	Ac	41,500(300) ^b	2,770(300) ^b	3,280(200) ^b	5,717(310) ^b	6,491(470) ^b

Table 11.23 (Continued)

A	Z	Element	Mass excess	$Q(\beta^-)$	$Q(\alpha)$	$S(n)$	$S(p)$
	90	Th	38,728.6(20)	1,245.1(14)	3,869(60)	4,786.35(25)	7,704(100)
	91	Pa	37,483.5(23)	570.1(2)	4,384(50)	6,526(8)	5,249.1(14)
	92	U	36,913.4(28)	^a	4,908.6(12)	5,759.4(27)	6,314(8)
	93	Np	37,940(50)	1,030(50)	5,627(50)	7,481(110) ^b	3,949(50)
	94	Pu	40,040(50)	2,100(70)	6,416(50)	6,387(50)	4,598(110) ^b
	95	Am	43,290(220) ^b	3,250(220) ^b	7,100(200) ^b	8,181(370) ^b	2,359(220) ^b
	96	Cm	47,320(400) ^b	4,030(460) ^b	7,506(410) ^b	^a	3,367(500) ^b
	234	88	Ra	47,090(540) ^b	1,980(670) ^b	^a	5,694(710) ^b
	89	Ac	45,100(400) ^b	4,490(400) ^b	3,080(200) ^b	4,466(500) ^b	6,893(620) ^b
	90	Th	40,609(4)	273(3)	3,640(30)	6,191(3)	8,178(300) ^b
	91	Pa	40,336(5)	2,195(4)	4,354(100)	5,219(5)	5,682(5)
	92	U	38,140.6(20)	^a	4,858.5(7)	6,844.2(21)	6,631.9(13)
	93	Np	39,950(9)	1,810(8)	5,359(9)	6,063(50)	4,252(9)
	94	Pu	40,338(7)	388(11)	6,310(5)	7,776(50)	4,893(50)
	95	Am	44,520(210) ^b	4,180(210) ^b	6,872(200) ^b	6,840(300) ^b	2,812(210) ^b
	96	Cm	46,800(300) ^b	2,280(360) ^b	7,444(300) ^b	8,593(500) ^b	3,779(370) ^b
	235	89	Ac	47,600(420) ^b	3,350(430) ^b	2,880(300) ^b	5,573(580) ^b
	90	Th	44,250(50)	1,930(70)	3,429(300) ^b	4,430(50)	8,142(400) ^b
	91	Pa	42,320(50)	1,410(50)	3,989(110)	6,083(50)	5,574(50)
	92	U	40,914.1(20)	^a	4,678.7(7)	5,297.84(23)	6,711(4)
	93	Np	41,037.8(21)	123.7(9)	5,191.9(18)	6,984(8)	4,391.8(9)
	94	Pu	42,179(21)	1,142(21)	5,951(20)	6,230(22)	5,060(22)
	95	Am	44,740(210) ^b	2,560(210) ^b	6,700(200) ^b	7,852(290) ^b	2,888(210) ^b
	96	Cm	48,060(220) ^b	3,320(310) ^b	7,200(200) ^b	6,813(370) ^b	3,752(310) ^b
	97	Bk	52,700(400) ^b	4,650(460) ^b	7,840(500) ^b	^a	1,383(500) ^b
	236	89	Ac	51,400(500) ^b	5,090(580) ^b	2,720(400) ^b	4,275(650) ^b
	90	Th	46,310(300) ^b	960(360) ^b	3,180(200) ^b	6,017(300) ^b	8,586(520) ^b
	91	Pa	45,340(200)	2,900(200)	3,772(220)	5,055(210)	6,198(210)
	92	U	42,440.6(19)	−930(50)	4,572.0(9)	6,544.8(6)	7,172(50)
	93	Np	43,370(50)	480(50)	5,007(50)	5,739(50)	4,833(50)
	94	Pu	42,893.5(27)	^a	5,867.07(8)	7,357(21)	5,433.2(19)
	95	Am	46,170(100) ^b	3,280(100) ^b	6,397(140) ^b	6,637(230) ^b	3,295(100) ^b
	96	Cm	47,880(200) ^b	1,710(220) ^b	7,100(200) ^b	8,245(300) ^b	4,145(290) ^b
	97	Bk	53,400(400) ^b	5,520(450) ^b	7,579(500) ^b	7,373(570) ^b	1,943(460) ^b
	237	90	Th	50,200(360) ^b	2,570(370) ^b	3,070(300) ^b	4,174(470) ^b
	91	Pa	47,640(100)	2,250(100)	3,713(310) ^b	5,776(220)	5,957(310) ^b
	92	U	45,386.1(20)	518.6(6)	4,232.5(11)	5,125.9(5)	7,244(200)
	93	Np	44,867.5(20)	^a	4,959.1(12)	6,574(50)	4,862.1(3)
	94	Pu	45,087.8(23)	220.3(13)	5,749.5(23)	5,877.0(24)	5,571(50)
	95	Am	46,550(50)	1,460(50)	6,181(5)	7,697(110) ^b	3,635(50)
	96	Cm	49,270(210) ^b	2,720(210) ^b	6,800(200) ^b	6,687(290) ^b	4,195(230) ^b
	97	Bk	53,210(300) ^b	3,950(360) ^b	7,500(200) ^b	8,260(500) ^b	1,959(360) ^b
	98	Cf	57,820(500) ^b	4,600(580) ^b	8,073(640) ^b	^a	2,874(640) ^b

Table 11.23 (Continued)

A	Z	Element	Mass excess	$Q(\beta^-)$	$Q(\alpha)$	$S(n)$	$S(p)$
238	90	Th	52,390(360) ^b	1,630(370) ^b	2,880(400) ^b	5,884(510) ^b	^a
	91	Pa	50,760(60)	3,460(60)	3,236(410) ^b	4,944(120)	6,727(360) ^b
	92	U	47,303.7(20)	−147.1(11)	4,269.8(29)	6,153.7(12)	7,621(100)
	93	Np	47,450.7(20)	1,292(7)	4,690(4)	5,488.09(20)	5,224.3(6)
	94	Pu	46,158.7(20)	^a	5,593.20(19)	7,000.5(14)	5,997.8(7)
	95	Am	48,420(50)	2,260(50)	6,042(50)	6,202(70)	3,960(50)
	96	Cm	49,380(40)	970(60)	6,621(40)	7,955(210) ^b	4,452(60)
	97	Bk	54,270(290) ^b	4,890(290) ^b	7,330(200) ^b	7,010(410) ^b	2,282(350) ^b
	98	Cf	57,200(400) ^b	2,930(490) ^b	7,980(500) ^b	8,686(640) ^b	3,299(500) ^b
239	91	Pa	53,220(300) ^b	2,650(300) ^b	3,190(300) ^b	5,619(300) ^b	6,462(470) ^b
	92	U	50,568.7(20)	1,263.5(15)	3,894(50)	4,806.26(21)	7,484(60)
	93	Np	49,305.3(21)	721.8(9)	4,556(50)	6,216.8(10)	5,287.4(15)
	94	Pu	48,583.5(20)	^a	5,244.50(23)	5,646.5(3)	6,156.2(6)
	95	Am	49,386.4(28)	802.9(2)	5,923.7(18)	7,102(50)	4,061.3(20)
	96	Cm	51,190(100) ^b	1,800(100) ^b	6,582(100) ^b	6,269(110) ^b	4,520(110) ^b
	97	Bk	54,360(290) ^b	3,180(300) ^b	7,200(200) ^b	7,982(410) ^b	2,310(290) ^b
	98	Cf	58,290(230) ^b	3,930(370) ^b	7,810(60) ^b	6,983(460) ^b	3,272(370) ^b
240	91	Pa	56,800(300) ^b	4,090(300) ^b	2,980(400) ^b	4,485(420) ^b	^a
	92	U	52,709(5)	388(16)	3,980(300) ^b	5,931(5)	7,796(300) ^b
	93	Np	52,321(15)	2,200(15)	4,555(200)	5,056(15)	5,537(15)
	94	Pu	50,121.3(19)	^a	5,255.78(15)	6,533.5(5)	6,472.9(10)
	95	Am	51,500(14)	1,379(14)	5,705(50)	5,957(14)	4,372(14)
	96	Cm	51,715.7(27)	215(14)	6,397.2(6)	7,542(100) ^b	4,959.7(27)
	97	Bk	55,660(150) ^b	3,940(150) ^b	7,057(180) ^b	6,779(320) ^b	2,820(180) ^b
	98	Cf	58,030(200) ^b	2,370(250) ^b	7,719(10)	8,336(310) ^b	3,626(350) ^b
	99	Es	64,200(400) ^b	6,170(450) ^b	8,371(570) ^b	^a	1,382(460) ^b
241	92	U	56,200(300) ^b	1,940(310) ^b	3,570(200) ^b	4,584(300) ^b	7,894(420) ^b
	93	Np	54,260(70)	1,300(70)	4,195(120)	6,136(70)	5,742(70)
	94	Pu	52,951.0(19)	20.82(2)	5,140.1(5)	5,241.60(19)	6,659(15)
	95	Am	52,930.2(20)	^a	5,637.81(12)	6,641(14)	4,480.06(27)
	96	Cm	53,697.6(23)	767.4(12)	6,184.9(6)	6,089.4(24)	5,092(14)
	97	Bk	56,100(200) ^b	2,400(200) ^b	7,125(210) ^b	7,629(250) ^b	2,907(200) ^b
	98	Cf	59,350(260) ^b	3,250(320) ^b	7,659(150) ^b	6,747(330) ^b	3,593(300) ^b
	99	Es	63,960(300) ^b	4,610(390) ^b	8,320(40) ^b	8,311(500) ^b	1,357(360) ^b
242	92	U	58,610(200) ^b	1,200(290) ^b	3,800(300) ^b	5,654(360) ^b	^a
	93	Np	57,410(210) ^b	2,700(210) ^b	4,224(220) ^b	4,914(220) ^b	6,073(360) ^b
	94	Pu	54,713(2)	−751(7)	4,984.4(9)	6,309.4(7)	6,832(70)
	95	Am	55,464(2)	664.8(7)	5,588.34(25)	5,537.57(10)	4,776.03(22)
	96	Cm	54,799.2(20)	^a	6,215.56(8)	6,969.8(13)	5,420.0(7)
	97	Bk	57,800(200) ^b	3,000(200) ^b	6,957(210) ^b	6,370(280) ^b	3,187(200) ^b
	98	Cf	59,330(40)	1,530(200) ^b	7,516(4)	8,097(260) ^b	4,061(200) ^b
	99	Es	64,920(330) ^b	5,600(330) ^b	8,224(150) ^b	7,106(440) ^b	1,717(410) ^b
	100	Fm	68,400(400) ^b	3,480(520) ^b	8,772(570) ^b	^a	2,848(500) ^b

Table 11.23 (Continued)

A	Z	Element	Mass excess	$Q(\beta^-)$	$Q(\alpha)$	$S(n)$	$S(p)$
243	93	Np	59,870(30) ^b	2,120(30) ^b	4,228(300) ^b	5,615(210) ^b	6,034(200) ^b
	94	Pu	57,750(3)	581.6(28)	4,756.2(28)	5,034.5(26)	6,952(210) ^b
	95	Am	57,168.3(22)	^a	5,438.1(9)	6,367.0(11)	4,833.7(12)
	96	Cm	57,177.2(22)	8.9(14)	6,168.8(10)	5,693.3(11)	5,575.8(12)
	97	Bk	58,686(5)	1,508(5)	6,874(4)	7,185(200) ^b	3,403(5)
	98	Cf	60,940(140) ^b	2,250(140) ^b	7,328(100) ^b	6,458(150) ^b	4,149(250) ^b
	99	Es	64,860(290) ^b	3,920(320) ^b	8,072(10)	8,134(430) ^b	1,754(290) ^b
	100	Fm	69,410(240) ^b	4,550(370) ^b	8,689(50)	7,065(470) ^b	2,807(400) ^b
244	93	Np	63,200(300) ^b	3,400(300) ^b	3,974(420) ^b	4,739(300) ^b	^a
	94	Pu	59,800(5)	−76(5)	4,665.5(10)	6,021(4)	7,359(30) ^b
	95	Am	59,875.9(21)	1,428.1(9)	5,130(15)	5,363.7(9)	5,162.9(28)
	96	Cm	58,447.8(19)	^a	5,901.61(5)	6,800.7(11)	6,009.4(10)
	97	Bk	60,703(14)	2,256(14)	6,778(4)	6,053(15)	3,763(14)
	98	Cf	61,470(3)	766(15)	7,329.1(18)	7,541(140) ^b	4,505(5)
	99	Es	66,110(180) ^b	4,640(180) ^b	8,026(100) ^b	6,825(340) ^b	2,121(230) ^b
	100	Fm	69,000(280) ^b	2,900(340) ^b	8,550(200) ^b	8,475(370) ^b	3,148(400) ^b
245	94	Pu	63,098(14)	1,205(15)	4,476(300) ^b	4,773(14)	7,393(300) ^b
	95	Am	61,893(4)	894.1(28)	5,213(70)	6,054(3)	5,195(6)
	96	Cm	60,999.4(27)	^a	5,623.5(19)	5,519.7(19)	6,165.4(21)
	97	Bk	61,809.6(25)	810.2(24)	6,454.5(15)	6,965(14)	3,927.2(15)
	98	Cf	63,380(100) ^b	1,570(100) ^b	7,256(100) ^b	6,163(100) ^b	4,614(100) ^b
	99	Es	66,430(200) ^b	3,050(220) ^b	7,909(3)	7,746(270) ^b	2,327(200) ^b
	100	Fm	70,210(280) ^b	3,780(340) ^b	8,435(100) ^b	6,861(400) ^b	3,184(330) ^b
	101	Md	75,470(380) ^b	5,260(470) ^b	9,084(230) ^b	^a	824(470) ^b
246	94	Pu	65,389(15)	401(14)	4,350(200) ^b	5,780(20)	^a
	95	Am	64,989(18)	2,376(18)	5,151(210) ^b	4,976(18)	5,398(23)
	96	Cm	62,612.7(22)	^a	5,474.8(10)	6,458.0(22)	6,570(4)
	97	Bk	63,960(60)	1,350(60)	6,074(60)	5,918(60)	4,326(60)
	98	Cf	64,085.7(22)	120(60)	6,861.6(10)	7,364(100) ^b	5,012.9(19)
	99	Es	67,970(220) ^b	3,880(220) ^b	7,742(100) ^b	6,537(300) ^b	2,701(250) ^b
	100	Fm	70,120(40)	2,160(230) ^b	8,374(14)	8,159(280) ^b	3,596(200) ^b
	101	Md	76,320(390) ^b	6,200(390) ^b	8,971(210) ^b	7,219(540) ^b	1,181(470) ^b
247	94	Pu	69,000(300) ^b	1,850(310) ^b	^a	4,465(300) ^b	^a
	95	Am	67,150(100) ^b	1,620(100) ^b	4,853(110) ^b	5,913(100) ^b	5,531(100) ^b
	96	Cm	65,528(4)	45(7)	5,353(3)	5,156(4)	6,750(18)
	97	Bk	65,483(6)	^a	5,889(5)	6,551(60)	4,419(5)
	98	Cf	66,129(8)	646(6)	6,527(8)	6,028(8)	5,123(60)
	99	Es	68,600(30) ^b	2,480(30) ^b	7,494(30) ^b	7,433(230) ^b	2,770(30) ^b
	100	Fm	71,560(150) ^b	2,950(150) ^b	8,192(50)	6,639(160) ^b	3,699(270) ^b
	101	Md	76,200(370) ^b	4,640(390) ^b	8,914(220) ^b	8,191(530) ^b	1,213(370) ^b
248	95	Am	70,560(200) ^b	3,170(200) ^b	4,930(360) ^b	4,663(220) ^b	5,728(360) ^b
	96	Cm	67,386(5)	−690(70) ^b	5,161.73(25)	6,213(5)	7,050(100) ^b
	97	Bk	68,070(70) ^b	840(70) ^b	5,773(70) ^b	5,480(70) ^b	4,743(70) ^b

Table 11.23 (Continued)

A	Z	Element	Mass excess	$Q(\beta^-)$	$Q(\alpha)$	$S(n)$	$S(p)$
	98	Cf	67,233(5)	^a	6,361(5)	6,967(9)	5,538(7)
	99	Es	70,290(50) ^b	3,060(50) ^b	7,160(50) ^b	6,387(60) ^b	3,129(50) ^b
	100	Fm	71,897(12)	1,610(50) ^b	8,002(11)	7,731(150) ^b	3,996(30) ^b
	101	Md	77,230(240) ^b	5,330(240) ^b	8,697(150) ^b	7,042(440) ^b	1,616(280) ^b
249	95	Am	73,100(300) ^b	2,360(300) ^b	^a	5,524(360) ^b	^a
	96	Cm	70,744(5)	901(5)	5,221(14)	4,713.46(30)	7,101(200) ^b
	97	Bk	69,843(3)	124(14)	5,525.0(23)	6,302(70) ^b	4,832(5)
	98	Cf	69,719.4(28)	^a	6,295.0(7)	5,585(5)	5,643(70) ^b
	99	Es	71,170(30) ^b	1,450(30) ^b	6,936(30) ^b	7,190(60) ^b	3,352(30) ^b
	100	Fm	73,610(140) ^b	2,440(150) ^b	7,808(100) ^b	6,358(140) ^b	3,967(150) ^b
	101	Md	77,320(220) ^b	3,710(270) ^b	8,459(100) ^b	7,984(330) ^b	1,870(220) ^b
	102	No	81,810(340) ^b	4,490(410) ^b	9,170(200) ^b	^a	2,711(420) ^b
250	96	Cm	72,983(11)	37(12)	5,169(18)	5,832(10)	7,409(300) ^b
	97	Bk	72,946(4)	1,780(3)	5,532(18)	4,969(4)	5,087(6)
	98	Cf	71,166.1(22)	^a	6,128.44(19)	6,624.6(23)	5,966.2(27)
	99	Es	73,270(100) ^b	2,100(100) ^b	6,878(120) ^b	5,976(100) ^b	3,742(100) ^b
	100	Fm	74,068(12)	800(100) ^b	7,557(12)	7,614(140) ^b	4,392(30) ^b
	101	Md	78,700(300) ^b	4,630(300) ^b	8,309(200) ^b	6,687(380) ^b	2,199(330) ^b
	102	No	81,500(200) ^b	2,800(360) ^b	8,950(200) ^b	8,379(400) ^b	3,106(300) ^b
251	96	Cm	76,641(23)	1,420(20)	5,221(300) ^b	4,413(25)	^a
	97	Bk	75,221(11)	1,093(10)	5,649(100) ^b	5,796(11)	5,051(15)
	98	Cf	74,128(5)	^a	6,175.8(10)	5,109(4)	6,106(5)
	99	Es	74,504(6)	376(7)	6,596.7(26)	6,833(100) ^b	3,951(6)
	100	Fm	75,979(8)	1,474(7)	7,425.1(20)	6,160(14)	4,576(100) ^b
	101	Md	79,100(200) ^b	3,120(200) ^b	8,072(200) ^b	7,670(360) ^b	2,255(200) ^b
	102	No	82,870(180) ^b	3,770(270) ^b	8,885(100) ^b	6,705(270) ^b	3,123(350) ^b
	103	Lr	87,900(300) ^b	5,030(350) ^b	9,271(470) ^b	^a	892(360) ^b
252	96	Cm	79,060(300) ^b	530(360) ^b	^a	5,657(300) ^b	^a
	97	Bk	78,530(200) ^b	2,500(200) ^b	5,547(280) ^b	4,765(200) ^b	5,402(200) ^b
	98	Cf	76,028(5)	−1,260(50)	6,216.87(4)	6,172(5)	6,482(11)
	99	Es	77,290(50)	480(50)	6,789(50) ^b	5,287(50)	4,129(50)
	100	Fm	76,811(6)	^a	7,152.7(20)	7,239(10)	4,982(8)
	101	Md	80,700(200) ^b	3,880(200) ^b	7,982(200) ^b	6,477(280) ^b	2,572(200) ^b
	102	No	82,871(13)	2,180(200) ^b	8,549(5)	8,066(180) ^b	3,519(200) ^b
253	103	Lr	88,800(300) ^b	5,930(300) ^b	9,145(380) ^b	7,168(420) ^b	1,356(350) ^b
	97	Bk	80,930(360) ^b	1,630(360) ^b	5,400(200) ^b	5,671(410) ^b	5,416(470) ^b
	98	Cf	79,295(6)	288(6)	6,126(4)	4,804(4)	6,522(200) ^b
	99	Es	79,007(3)	^a	6,739.16(5)	6,352(50)	4,310(5)
	100	Fm	79,341(5)	334(4)	7,197(4)	5,541(7)	5,236(50)
	101	Md	81,300(210) ^b	1,960(210) ^b	7,705(210) ^b	7,466(280) ^b	2,799(210) ^b
	102	No	84,440(250) ^b	3,140(320) ^b	8,403(200) ^b	6,504(250) ^b	3,545(310) ^b
	103	Lr	88,730(230) ^b	4,290(340) ^b	8,992(40) ^b	8,138(380) ^b	1,428(230) ^b
	104	Rf	93,780(450) ^b	5,050(510) ^b	9,550(300) ^b	^a	2,307(540) ^b

Table 11.23 (Continued)

A	Z	Element	Mass excess	$Q(\beta^-)$	$Q(\alpha)$	$S(n)$	$S(p)$
254	97	Bk	84,390(300) ^b	3,060(300) ^b	^a	4,607(470) ^b	^a
	98	Cf	81,335(12)	−652(13)	5,926(5)	6,032(12)	6,883(360) ^b
	99	Es	81,986(4)	1,088(3)	6,615.7(15)	5,092(5)	4,598(7)
	100	Fm	80,898(3)	^a	7,307.2(20)	6,514(5)	5,398(3)
	101	Md	83,580(100) ^b	2,680(100) ^b	7,887(140) ^b	5,794(230) ^b	3,052(100) ^b
	102	No	84,718(18)	1,140(100) ^b	8,226(13)	7,792(250) ^b	3,872(210) ^b
	103	Lr	89,970(340) ^b	5,250(340) ^b	8,846(150) ^b	6,833(410) ^b	1,757(420) ^b
	104	Rf	93,300(290) ^b	3,330(440) ^b	9,380(200) ^b	8,549(540) ^b	2,717(370) ^b
255	98	Cf	84,800(200) ^b	720(200) ^b	5,736(200) ^b	4,603(200) ^b	6,880(360) ^b
	99	Es	84,083(11)	290(10)	6,436.3(13)	5,975(12)	4,541(16)
	100	Fm	83,793(5)	^a	7,239.7(18)	5,177(5)	5,482(6)
	101	Md	84,836(7)	1,043(8)	7,907(4)	6,814(100) ^b	3,351(7)
	102	No	86,845(12)	2,009(11)	8,442(8)	5,944(21)	4,022(100) ^b
	103	Lr	90,140(210) ^b	3,300(210) ^b	8,614(40) ^b	7,902(400) ^b	1,867(210) ^b
	104	Rf	94,540(210) ^b	4,400(290) ^b	9,248(100) ^b	6,837(350) ^b	2,721(400) ^b
	105	Db	100,040(420) ^b	5,500(470) ^b	9,720(300) ^b	^a	552(510) ^b
256	98	Cf	87,040(300) ^b	−140(310) ^b	5,558(420) ^b	5,835(360) ^b	^a
	99	Es	87,180(100) ^b	1,700(100) ^b	6,227(220) ^b	4,974(100) ^b	4,912(220) ^b
	100	Fm	85,480(7)	^a	7,027(5)	6,384(7)	5,892(12)
	101	Md	87,610(50)	2,130(50)	7,897(16)	5,298(50)	3,472(50)
	102	No	87,817(8)	210(50)	8,581(5)	7,099(14)	4,308(10)
	103	Lr	92,000(220) ^b	4,180(220) ^b	8,877(100) ^b	6,214(300) ^b	2,137(220) ^b
	104	Rf	94,248(27)	2,250(220) ^b	8,952(23)	8,362(210) ^b	3,181(210) ^b
	105	Db	100,700(360) ^b	6,460(360) ^b	9,480(200) ^b	7,408(560) ^b	1,124(410) ^b
257	99	Es	89,400(410) ^b	820(410) ^b	6,050(200) ^b	5,848(420) ^b	4,924(510) ^b
	100	Fm	88,584(6)	^a	6,863.8(14)	4,967(6)	5,885(100) ^b
	101	Md	88,990(3)	406(7)	7,557.6(10)	6,691(50)	3,779(7)
	102	No	90,220(30)	1,230(30)	8,452(30)	5,671(30)	4,681(60)
	103	Lr	92,780(210) ^b	2,560(210) ^b	9,057(30) ^b	7,287(300) ^b	2,324(210) ^b
	104	Rf	96,010(270) ^b	3,230(340) ^b	9,147(100) ^b	6,309(270) ^b	3,276(350) ^b
	105	Db	100,470(230) ^b	4,460(350) ^b	9,312(50) ^b	8,306(430) ^b	1,068(240) ^b
	106	Sg	105,400(410) ^b	3,460(540) ^b	9,670(300) ^b	^a	2,359(480) ^b
258	100	Fm	90,420(200) ^b	−1,260(200) ^b	6,660(200) ^b	6,236(200) ^b	6,273(460) ^b
	101	Md	91,683(5)	210(200) ^b	7,271.3(19)	5,379(5)	4,190(7)
	102	No	91,470(200) ^b	^a	8,150(200) ^b	6,816(200) ^b	4,806(200) ^b
	103	Lr	94,900(100) ^b	3,430(220) ^b	8,900(20)	5,950(230) ^b	2,604(110) ^b
	104	Rf	96,470(200) ^b	1,570(230) ^b	9,330(200) ^b	7,609(330) ^b	3,598(290) ^b
	105	Db	101,940(340) ^b	5,470(400) ^b	9,546(70) ^b	6,600(420) ^b	1,359(440) ^b
	106	Sg	105,400(410) ^b	3,460(540) ^b	9,670(300) ^b	^a	2,359(480) ^b
	107	Bh	109,330(410) ^b	3,460(540) ^b	9,670(300) ^b	^a	2,359(480) ^b
259	100	Fm	93,700(280) ^b	80(350) ^b	6,470(200) ^b	4,793(350) ^b	^a
	101	Md	93,620(200) ^b	^a	7,110(200) ^b	6,136(200) ^b	4,091(280) ^b
	102	No	94,100(100) ^b	490(220) ^b	7,885(100) ^b	5,441(220) ^b	4,868(100) ^b
	103	Lr	95,940(70) ^b	1,830(120) ^b	8,674(70) ^b	7,039(120) ^b	2,827(210) ^b
	104	Rf	98,390(70) ^b	2,460(100) ^b	9,121(70) ^b	6,153(210) ^b	3,800(130) ^b

Table 11.23 (Continued)

A	Z	Element	Mass excess	$Q(\beta^-)$	$Q(\alpha)$	$S(n)$	$S(p)$
260	105	Db	102,210(290) ^b	3,810(300) ^b	9,640(200) ^b	7,808(450) ^b	1,557(350) ^b
	106	Sg	106,800(210) ^b	4,590(360) ^b	9,834(30)	6,673(460) ^b	2,432(400) ^b
	101	Md	96,550(320) ^b	940(370) ^b	6,940(300) ^b	5,144(370) ^b	4,442(420) ^b
	102	No	95,610(200) ^b	^a	7,700(200) ^b	6,570(220) ^b	5,302(280) ^b
	103	Lr	98,340(120) ^b	2,740(230) ^b	8,306(100) ^b	5,666(140) ^b	3,052(150) ^b
	104	Rf	99,140(200) ^b	800(230) ^b	8,900(200) ^b	7,321(210) ^b	4,082(210) ^b
	105	Db	103,790(230) ^b	4,650(310) ^b	9,371(70)	6,483(370) ^b	1,887(240) ^b
	106	Sg	106,600(40)	2,800(240) ^b	9,923(30)	8,273(210) ^b	2,898(290) ^b
	107	Bh	113,460(620) ^b	6,860(620) ^b	10,330(500) ^b	^a	628(650) ^b
261	102	No	98,500(300) ^b	^a	7,490(300) ^b	5,177(360) ^b	5,335(440) ^b
	103	Lr	99,620(200) ^b	1,120(360) ^b	8,200(200) ^b	6,797(230) ^b	3,279(280) ^b
	104	Rf	101,300(110) ^b	1,690(230) ^b	8,659(100) ^b	5,912(230) ^b	4,327(160) ^b
	105	Db	104,430(230) ^b	3,130(260) ^b	9,219(100) ^b	7,439(330) ^b	2,005(310) ^b
	106	Sg	108,240(280) ^b	3,810(360) ^b	9,803(70) ^b	6,429(280) ^b	2,844(360) ^b
	107	Bh	113,460(240) ^b	5,220(360) ^b	10,562(50)	8,074(660) ^b	429(240) ^b
262	102	No	100,150(540) ^b	^a	7,310(500) ^b	6,416(620) ^b	^a
	103	Lr	102,180(300) ^b	2,020(620) ^b	8,070(300) ^b	5,509(360) ^b	3,610(420) ^b
	104	Rf	102,390(280) ^b	210(410) ^b	8,490(200) ^b	6,985(300) ^b	4,516(350) ^b
	105	Db	106,330(180) ^b	3,950(340) ^b	9,005(150) ^b	6,165(290) ^b	2,258(210) ^b
	106	Sg	108,500(280) ^b	2,170(340) ^b	9,600(200) ^b	7,812(400) ^b	3,217(370) ^b
	107	Bh	114,580(380) ^b	6,080(470) ^b	10,216(150) ^b	6,945(450) ^b	945(470) ^b
263	103	Lr	103,760(360) ^b	^a	7,720(300) ^b	6,486(470) ^b	3,681(650) ^b
	104	Rf	104,830(190) ^b	1,070(410) ^b	8,302(160) ^b	5,629(340) ^b	4,636(350) ^b
	105	Db	107,190(170) ^b	2,360(250) ^b	8,834(150) ^b	7,210(250) ^b	2,483(330) ^b
	106	Sg	110,210(120) ^b	3,010(210) ^b	9,391(100) ^b	6,361(310) ^b	3,414(220) ^b
	107	Bh	114,710(420) ^b	4,500(430) ^b	10,080(300) ^b	7,944(560) ^b	1,077(500) ^b
	108	Hs	119,890(370) ^b	5,180(550) ^b	10,670(300) ^b	^a	1,979(530) ^b
264	104	Rf	106,170(450) ^b	^a	8,140(400) ^b	6,732(480) ^b	4,882(580) ^b
	105	Db	109,430(230) ^b	3,260(500) ^b	8,660(200) ^b	5,840(290) ^b	2,694(300) ^b
	106	Sg	110,780(280) ^b	1,350(370) ^b	9,210(200) ^b	7,502(310) ^b	3,706(330) ^b
	107	Bh	116,190(280) ^b	5,410(400) ^b	9,967(150) ^b	6,596(500) ^b	1,311(300) ^b
	108	Hs	119,610(50)	3,430(280) ^b	10,591(20)	8,352(370) ^b	2,387(420) ^b
265	105	Db	110,530(280) ^b	^a	8,490(200) ^b	6,967(370) ^b	2,929(530) ^b
	106	Sg	112,770(140) ^b	2,240(320) ^b	9,045(90) ^b	6,077(320) ^b	3,942(270) ^b
	107	Bh	116,620(380) ^b	3,850(400) ^b	9,770(300) ^b	7,636(470) ^b	1,445(470) ^b
	108	Hs	121,100(300) ^b	4,470(480) ^b	10,432(120) ^b	6,587(310) ^b	2,379(410) ^b
	109	Mt	127,210(470) ^b	6,120(560) ^b	11,330(400) ^b	^a	−311(470) ^b
266	106	Sg	113,580(290) ^b	^a	8,762(50)	7,268(320) ^b	4,244(400) ^b
	107	Bh	118,310(350) ^b	4,730(450) ^b	9,550(300) ^b	6,385(520) ^b	1,753(380) ^b
	108	Hs	121,130(410) ^b	2,830(540) ^b	10,210(300) ^b	8,034(510) ^b	2,777(560) ^b
	109	Mt	128,490(350) ^b	7,360(540) ^b	11,483(160) ^b	6,792(580) ^b	−106(460) ^b
267	107	Bh	118,990(340) ^b	^a	9,370(300) ^b	7,390(490) ^b	1,875(450) ^b
	108	Hs	122,750(100) ^b	3,760(360) ^b	10,114(70) ^b	6,458(430) ^b	2,850(370) ^b

■ Table 11.23 (Continued)

A	Z	Element	Mass excess	$Q(\beta^-)$	$Q(\alpha)$	$S(n)$	$S(p)$
	109	Mt	128,110(580) ^b	5,360(590) ^b	10,970(400) ^b	8,457(670) ^b	317(710) ^b
	110	Ds	134,090(380) ^b	5,990(690) ^b	11,777(110) ^b	^a	1,685(520) ^b
268	108	Hs	123,100(410) ^b	^a	9,900(300) ^b	7,716(430) ^b	3,176(540) ^b
	109	Mt	129,310(320) ^b	6,200(520) ^b	10,695(150) ^b	6,870(660) ^b	730(330) ^b
	110	Ds	133,700(500) ^b	4,390(590) ^b	11,660(500) ^b	8,469(630) ^b	1,697(770) ^b
269	108	Hs	124,930(420) ^b	^a	9,730(400) ^b	6,247(590) ^b	^a
	109	Mt	129,580(550) ^b	4,650(700) ^b	10,530(400) ^b	7,801(640) ^b	815(690) ^b
	110	Ds	135,200(290) ^b	5,620(620) ^b	11,680(100) ^b	6,567(580) ^b	1,394(430) ^b
270	109	Mt	131,080(610) ^b	^a	10,350(500) ^b	6,565(820) ^b	1,133(740) ^b
	110	Ds	134,720(650) ^b	3,640(890) ^b	11,160(500) ^b	8,554(710) ^b	2,147(850) ^b
271	109	Mt	131,550(610) ^b	^a	10,140(500) ^b	7,600(860) ^b	^a
	110	Ds	136,070(180) ^b	4,520(630) ^b	10,899(150) ^b	6,719(670) ^b	2,301(640) ^b
272	110	Ds	136,290(650) ^b	^a	10,760(500) ^b	7,855(670) ^b	2,556(890) ^b
	111	Rg	142,960(330) ^b	6,680(730) ^b	11,232(100) ^b	^a	397(380) ^b
273	110	Ds	139,020(440) ^b	^a	11,669(110) ^b	5,338(780) ^b	^a

^aNot calculable.^bDerived from systematic trends.

In ► Table 11.23 the *mass excesses* in keV units are given for 2,931 nuclides in their ground states according to the 1995 update to the atomic mass evaluation (Audi and Wapstra 1995), also available in electronic form (AME 1995). The deduced beta and alpha *decay energies*, as well as the *neutron separation energy* and the *proton separation energy* have been added after rounding the uncertainties from the original data files (AME 1995) in a similar manner as it was done by the authors for the masses. For those nuclides exhibiting β^+ /EC decay the Q -value is given as the $Q(\beta^-)$ of the preceding isobar. Reaction energies for more complex reactions can be retrieved from the original computer files at the Atomic Mass Data Center (AME 1995).

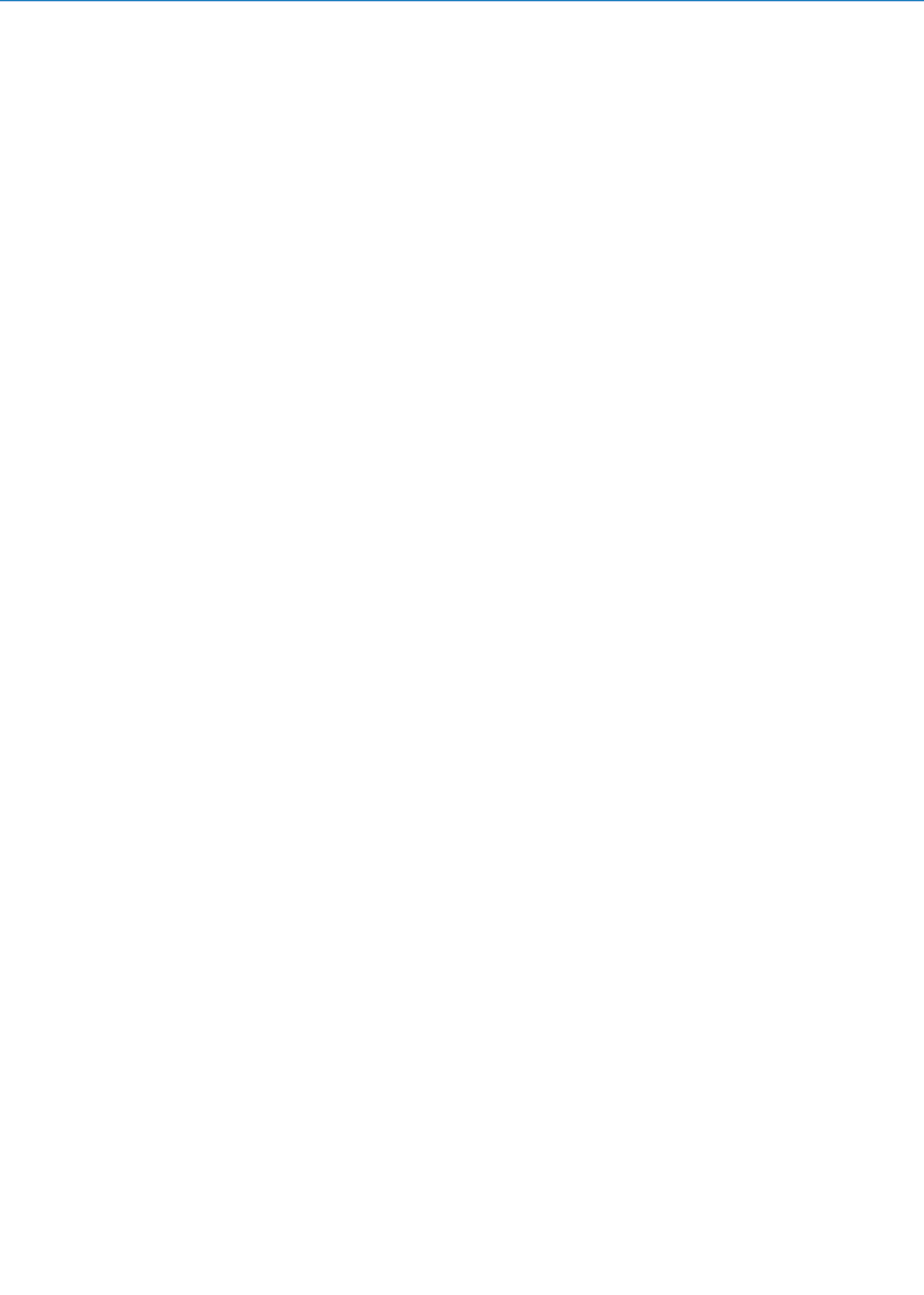
References

- AME (1995) The 1995 update to the atomic mass evaluation. Atomic Mass Data Center. <http://www-csns.m.in2p3.fr/AMDC/web/masseval.html>
- Audi G, Wapstra AH (1993a) Nucl Phys A 565:1–65
- Audi G, Wapstra AH (1993b) Nucl Phys A 565:66–157
- Audi G, Wapstra AH (1995) Nucl Phys A 595:409–480
- Audi G, Wapstra AH, Dedieu M (1993) Nucl Phys A 565:193–397
- Audi G, Wapstra AH, Thibault C (2003) Nucl Phys A 729:337
- Bambynek W (1984) In: Meisel A (ed) Proceedings of the conference on X-ray and inner shell processes in atoms and solids, Leipzig, 20–24 Aug
- Band IM, Trzhaskovskaya MB, Jr Nestor CW, Tikkanen PO, Raman S (2002) At Data Nucl Data Tables 81:1
- Bearden JA, Burr AF (1967) Rev Mod Phys 39:125
- Berger MJ, Hubbell JH (1987) NIST X-ray and gamma-ray attenuation coefficients and cross sections database, NIST standard reference database 8. National Institute of Standards and Technology, Gaithersburg
- Berger MJ, Hubbell JH, Seltzer SM, Coursey JS, Zucker DS (1999) XCOM: photon cross section database, version 1.2. Online, National Institute of Standards and Technology, Gaithersburg. <http://physics.nist.gov/xcom>
- Berger MJ, Coursey JS, Zucker DS (2000) ESTAR, PSTAR and ASTAR: computer programs for calculating stopping-power and range tables for electrons, protons, and helium ions, version 1.2.2, April 2000. Online, National Institute of Standards and Technology, Gaithersburg. <http://physics.nist.gov/Star>

- BIPM (1991) Le Système International d'Unités (SI), The international system of units (SI), 6th edn. Bur. Intl. Poids et Mesures, Sèvres
- Boone JM, Chavez AE (1996) *Med Phys* 23:1997
- CODATA (2003) CODATA internationally recommended values of the fundamental physical constants 1998. National Institute of Standards and Technology, Gaithersburg. <http://physics.nist.gov/cuu/constants>
- Coplen TB (2001) *Pure Appl Chem* 73:667
- Coursey JS, Schwab DJ, Dragoset R (2001) Atomic weights and isotopic compositions, version 2.3.1. Online, National Institute of Standards and Technology, Gaithersburg. <http://physics.nist.gov/Comp>
- Dean JA (ed) (1992) *Lange's handbook of chemistry*, 14th edn. McGraw-Hill, New York
- Hanukoglu I (ed) (2003) Israel science and technology homepage. <http://www.science.co.il/PTElements.asp>
- Hubbell JH, Seltzer SM (1995) Tables of X-ray mass attenuation coefficients and mass-energy absorption coefficients from 1 keV to 20 MeV for elements $Z = 1-92$ and 48 additional substances of dosimetric interest, report NISTIR 5632. National Institute of Standards and Technology, Gaithersburg
- Hubbell JH, Seltzer SM (1997) Tables of X-ray mass attenuation coefficients and mass-energy absorption coefficients from 1 keV to 20 MeV for elements $Z = 1-92$ and 48 additional substances of dosimetric interest (version 1.03, online). National Institute of Standards and Technology, Gaithersburg. <http://physics.nist.gov/xaamdi>
- ICRU (1980) Radiation quantities and units, report 33. International Commission on Radiation Units and Measurements, Bethesda
- ICRU (1989a) Stopping powers for electrons and positrons, report 37. International Commission on Radiation Units and Measurements, Bethesda
- ICRU (1989b) Tissue substitutes in radiation dosimetry and measurement, report 44. International Commission on Radiation Units and Measurements, Bethesda
- ICRU (1993a) Stopping powers for protons and alpha particles, report 49. International Commission on Radiation Units and Measurements, Bethesda
- ICRU (1993b) Stopping powers for protons and alpha particles, with data disk, report 49D. International Commission on Radiation Units and Measurements, Bethesda
- ICRU (1993c) Quantities and units for use in radiation protection, report 51. International Commission on Radiation Units and Measurements, Bethesda
- ISO (1993) ISO standards handbook quantities and units. International Organization for Standardization, Geneva
- ICRU (1998) Fundamental quantities and units for ionizing radiation, report 60. International Commission on Radiation Units and Measurements, Bethesda
- James AM, Lord MP (1992) *Macmillan's chemical and physical data*. Macmillan, London
- Kaye GWC, Laby TH (1993) *Tables of physical and chemical constants*, 15th edn. Longman, London
- Krause MO (1979) *J Phys Chem Ref Data* 8:307
- Larkins FB (1977) *At Data Nucl Data Tables* 20:313
- Lide DR (ed) (2002) *CRC handbook of chemistry and physics*, 83rd edn. CRC Press, Boca Raton
- Mohr PJ, Taylor BN (1999) *J Phys Chem Ref Data* 28(6):1713–1852
- Mohr PJ, Taylor BN (2000) *Rev Mod Phys* 72(2):351–495
- Moss GP (2003) World wide web version of the periodic table. Department of Chemistry, Queen Mary and Westfield College, London. <http://www.chem.qmul.ac.uk/iupac/AtWt>
- NIST (2003) The NIST reference on constants, units and uncertainty. National Institute of Standards and Technology, Gaithersburg. Available: <http://physics.nist.gov/cuu>
- Nowotny R (1998) Photon attenuation data on PC; program XMuDat (version 1.0.1, August 1998), report IAEA-NDS-195. International Atomic Energy Agency, Vienna
- Paul H (2002) Stopping power for light ions; program Mstar, version 3.00, November 2002. Johannes Kepler Universität, Linz. <http://www.exphys.uni-linz.ac.at/stopping>
- Paul H, Schinner A (2003) *Nucl Instrum Meth B* 209:252
- Rosman KJR, Taylor PDP (1998a) *J Phys Chem Ref Data* 27:1275
- Rosman KJR, Taylor PDP (1998b) *Pure Appl Chem* 70:217
- Rosman KJR, Taylor PDP (1998c) *J Anal At Spectrom* 13:45N
- Rosman KJR, Taylor PDP (1999) *J Anal At Spectrom* 14:5N
- Salem SI, Panossian SL, Krause RA (1974) *At Data Nucl Data Tables* 14:91
- Scofield JH (1974) *At Data Nucl Data Tables* 14:121
- Shirley DA, Martin RL, Kowalczyk SP, McFeely FR, Ley L (1977) *Phys Rev B* 15:544
- Taylor BN (1995) Guide for the use of the international system of units (SI), National Institute of Standards and Technology special publication 811, 1995 edn. U.S. Government Printing Office, Washington
- Wieser ME, Berglund M (2009) *Pure Appl Chem* 81:2131–2156
- Winter M (2003) WebElements TM, the periodic table on the WWW. The University of Sheffield and WebElements Ltd, UK. <http://www.webelements.com>
- Ziegler JF (2003) Program SRIM, version 2003.20. <http://www.srim.org>
- Ziegler JF, Biersack JP, Littmark U (1985) *The stopping and range of ions in solids*. Pergamon, New York, New edition in progress

Volume 2

Elements and Isotopes Formation, Transformation, Distribution



12 Origin of the Chemical Elements

T. Rauscher¹ · A. Patkós²

¹University of Basel, Basel, Switzerland

²Eötvös Loránd University, Budapest, Hungary

12.1	<i>Introduction</i>	615
12.2	<i>Creation and Early Evolution of Matter in the Universe</i>	615
12.2.1	Evolution of the Energy Density in the Early Universe	615
12.2.1.1	Observations of CMBR	616
12.2.1.2	Inflationary Interpretation of the CMBR	618
12.2.1.3	Dark Matter: Indications, Candidates, and Signals	619
12.2.1.4	Dark Energy, the Accelerating Universe, and the Problem of Distance Measurements	621
12.2.2	Origin of the Matter–Antimatter Asymmetry	625
12.2.3	Evolution of the Expanding Universe	627
12.2.4	Gravitational Clustering of Matter	628
12.3	<i>Primordial Nucleosynthesis</i>	629
12.3.1	Weak Decoupling	629
12.3.2	The Reaction Network and the Production Process of Nucleosynthesis	630
12.3.3	Comparison of Calculations and Observed Primordial Abundances	634
12.4	<i>Stellar Nucleosynthesis</i>	637
12.4.1	Stellar Evolution	637
12.4.1.1	Birth of Stars	637
12.4.1.2	Hertzsprung–Russell Diagram	638
12.4.1.3	Supernova Explosions	639
12.4.1.4	Core-Collapse Supernovae	640
12.4.2	Hydrogen Burning: Proton–Proton Chain, CNO-Cycle	641
12.4.3	Helium Burning: Nucleosynthesis of Carbon and Oxygen	645
12.4.4	Advanced Burning Stages	647
12.4.5	Nucleosynthesis Beyond Fe	648
12.4.5.1	The Main and Weak s-Process Components	649
12.4.5.2	Explosive Nucleosynthesis in the Outer Layers of a Massive Star	651
12.4.5.3	Explosive Burning in the Deep Layers of a Massive Star	651
12.4.6	Nucleosynthesis by Spallation	652
12.5	<i>Nucleosynthesis in Binary Star Systems</i>	652
12.5.1	General Considerations	652
12.5.2	Novae	654

12.5.3 Type Ia Supernovae 655

12.5.4 X-ray Bursts and the rp-Process 655

12.5.5 Neutron Star Mergers 656

12.6 *The Abundance of Elements in the Universe* 657

12.6.1 Experiments and Observations 657

12.6.2 Solar Abundances 659

12.6.3 Meteoritic Inclusions 659

12.6.4 Galactical Chemical Evolution: Putting it all Together 661

Abstract: This chapter provides the necessary background from astrophysics, nuclear, and particle physics to understand the cosmic origin of the chemical elements. It reflects the year 2008 state of the art in this extremely quickly developing interdisciplinary research direction. The discussion summarizes the nucleosynthetic processes in the course of the evolution of the Universe and the galaxies contained within, including primordial nucleosynthesis, stellar evolution, and explosive nucleosynthesis in single and binary systems.

12.1 Introduction

Chemical elements are central for the existence of life and the richness and variety of our environment. Therefore, one of the basic questions concerns the origin of the chemical elements. The answer is complex because it relies on dynamical processes from elementary particles and nuclei to stars and galaxies. An interdisciplinary effort of various fields of science achieved considerable progress in this direction of research. This chapter summarizes the state of knowledge obtained mainly from particle and nuclear physics, astrophysics, and astronomy.

➤ Sections 12.2 and ➤ 12.3 concentrate on the two most important information sources concerning the earliest history of the Universe, i.e., the cosmic microwave background radiation and the primordial synthesis of the nuclei of the lightest chemical elements. The aim is to describe, in the simplest qualitative terms, the empirical facts and the way their interpretation is connected with the physics of the epoch immediately following the Big Bang. It should become clear that the structures observed today on the largest distance scales reflect the nature of the quantum fluctuations of the earliest period. Moreover, nuclear physics combined with the basic facts of cosmology provide a perfect account of the primordial abundance of the lightest nuclei. In ➤ Sect. 12.4, the production mechanism of the elements will be discussed as they occur in the different stages of stellar evolution. Explosive events occurring in binary stellar systems and their roles in nucleosynthesis are discussed in ➤ Sect. 12.5. The concluding part – ➤ Sect. 12.6 is devoted to the description and the interpretation of the abundance of chemical elements in the Sun and in the Galaxy. This includes abundance determinations from astronomical observations as well as from the analysis of presolar grains. The experimental methods to determine abundances and to study the nuclear physics relevant to nucleosynthesis processes are outlined. Finally, the basic ideas of galactic chemical evolution are laid out, which combine all the knowledge concerning production and distribution of nuclides to a grander picture. The chapter is completed by a list of references, where textbooks and review articles appear alongside the relevant original publications.

12.2 Creation and Early Evolution of Matter in the Universe

12.2.1 Evolution of the Energy Density in the Early Universe

The basic question addressed when investigating the history of the Universe as a whole in the framework of modern physics is the following: Why do we see something instead of detecting nothing? It originates from the common wisdom that any isolated system after long enough evolution will reach thermal equilibrium, characterized by a homogeneous structureless

distribution of its energy. Nearly 14 billion years after the Big Bang, one observes the presence of complicated hierarchical structures on all scales, starting from the subnuclear world, through chemical elements, and up to the scale of galaxy clusters. This section will review our present understanding of how the structured evolution of the Universe could be sustained for a time more than 60 orders of magnitude longer than the characteristic timescale of the particle physics processes present at the moment of its “birth.”

The information concerning the constitution of the early Universe has increased tremendously during the past decade, mainly due to improved observations of the cosmic microwave background radiation (CMBR). The most important cosmological parameters (the total energy density, the part contained in baryonic matter, the part of nonbaryonic dark matter (DM), other components, etc.) have been determined with percent level accuracy as a result of projects completed in the first decade of the twenty-first century and now appear in tables of fundamental physical data (Amsler et al. 2008).

12.2.1.1 Observations of CMBR

The existence of CMBR was predicted by Alpher et al. (1948) as a direct consequence of the Hot Big Bang Universe of Gamow (Lamarre and Puget 2001). It was discovered by Penzias and Wilson (1965). It originates from the combination of the once free electrons and protons into neutral atoms when the temperature of the Universe dropped below $kT = 13.6$ eV (the ionization energy of the H-atom, i.e., $T = 1.58 \times 10^5$ K) to nearly 1 eV (1.16×10^4 K). (Note that in certain branches of physics it is customary to express temperature in eV units through the equation $E = kT$. The conversion is given by 1 eV corresponds to 1.16045×10^4 K.) After the recombination, the Universe became transparent to this radiation, which at present reaches the detectors with a redshift determined by the kinematics of the expansion of the Universe (Lamarre and Puget 2001). It appears to be a perfect thermal radiation with Planckian power distribution over more than three decimal orders of magnitude of frequency, having a temperature of $T = 2.725 \pm 0.001$ K.

The first quantitative evidence for the temperature anisotropy of CMBR was provided by the COBE (Cosmic Background Explorer) satellite in 1992. The angular resolution of its detectors was 7° . This enabled the collaboration to determine the first 20 multipole moments of the fluctuating part of CMBR beyond its isotropic component. It has been established that the degree of anisotropy of CMBR is one part in one hundred thousand (10^{-5}). There are two questions of extreme importance related to this anisotropy:

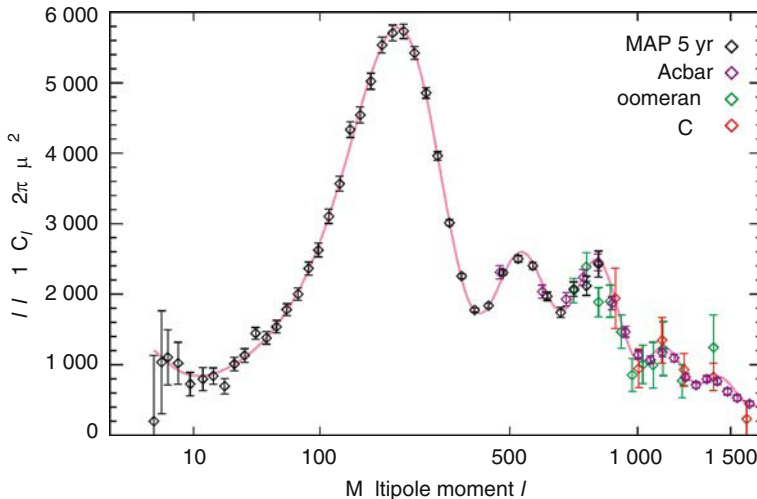
1. Is this anisotropy the origin of the hierarchical structure one observes today in the Universe?
2. What is the (micro)physical process behind this anisotropy?

► **Section 12.2.4** returns to the answer to the first question. To the second question, the answer will be briefly outlined below.

Following the success of the COBE mission several more refined (ground based and balloon) measurements of the CMBR fluctuations were performed between 1998 and 2001. An angular resolution of about 1° has been achieved, which was further refined to the arc-minute level by the satellite mission Wilkinson Microwave Anisotropy Probe (WMAP). The combined efforts of these investigations allowed the determination of the multipole projection of CMBR on the sky up to angular moments $l = 2,000$. The fluctuation information extracted

■ Fig. 12.1

Multipole fluctuation strength of the cosmic microwave background radiation as a function of the spherical harmonic index l . The location and the height of the first minimum favors a spatially flat Universe, while the level of the fluctuations in the higher multipoles ($l > 400$) indicates the presence of a low-density baryonic component ($< 5\%$). The measurements cover already the damping region ($l > 1,000$). Wilkinson Microwave Anisotropy Probe (WMAP) data are displayed together with results of earlier balloon observations (Reprinted from Nolte et al. 2009 with kind permission of the first author, the WMAP Science Team, and AAS)



until 2007 is presented in Fig. 12.1 with $l_{\max} = 2,000$. One easily recognizes the presence of three pronounced maxima in this figure (possible additional, weaker maxima are discussed further below).

Another important characteristic of the CMBR anisotropy is its spectral power distribution. The measured distribution is nearly scale invariant; it is the so-called Zel'dovich–Harrison spectrum (see Peebles 1993). This means that every unit in the logarithm of the wave number contributes almost equally to the total power.

The small-amplitude and almost scale-invariant nature of the fluctuation spectra, described above, reflects the very early fluctuations of the gravitational field. First of all, one has to emphasize that the coupled electron–proton–photon plasma near recombination was oscillating in a varying gravitational field (Hu 2001). Where the energy density was higher the plasma experienced the effect of a potential well, and the radiation emerging from this region was hotter than average. On the contrary, diminutions of the energy density led to a colder emission. Still, an observer located far from the sources detects lower temperature from denser sources due to the Sachs–Wolfe effect (Peebles 1993). In any case, the CMBR anisotropy actually traces the inhomogeneity of the gravitational potential (or total energy density) in the era of recombination.

Thomson scattering of the anisotropic CMBR on the ionized hot matter of galaxy clusters and galaxies results in roughly 5% linear polarization of CMBR. Its presence in CMBR was first detected by the Degree Angular Scale Interferometer (DASI) experiment (Kovac et al. 2002). Starting from 2003, the WMAP experiment also measured the temperature–polarization cross

correlation jointly with the temperature–temperature correlation. The significance of this type of measurement is obvious since the presence of ionized gases corresponds to the beginning of the epoch of star formation.

12.2.1.2 Inflationary Interpretation of the CMBR

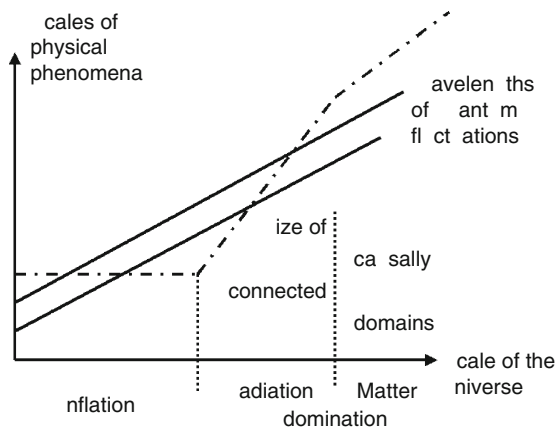
A unique particle physics framework has been proposed, which can account for the energy density fluctuations with the characteristics found in CMBR. One conjectures that the large-scale homogeneity of the Universe is due to a very early period of exponential inflation in its scale (Peebles 1993).

One assumes that during the first era after the Big Bang the size of the causally connected regions (the horizon) remained constant, while the global scale of the Universe increased exponentially. This is called inflationary epoch. The wavelength of any physical object is redshifted in proportion with the global scale. Therefore, at a certain moment, fluctuations with a wavelength bigger than the horizon were “felt” as constant fields and did not influence anymore the gravitational evolution of the matter and radiation at smaller length scale.

The inflationary period in the evolution of the Universe ended at about 10^{-32} s after the Big Bang. At this moment, the constant ordered potential energy density driving the inflation decayed into the particles observed today. Some of them may have belonged to a more exotic class, which can contribute to the violation of the matter–antimatter symmetry if they exhibit sufficiently long lifetimes (see ▶ Sect. 12.2.2). The rate of expansion of the horizon in the subsequent radiation- and matter-dominated eras was always faster than the global expansion of the Universe (see ▶ Fig. 12.2). Radiation-dominated means

■ Fig. 12.2

Variation of the characteristic length scales during the history of the Universe. On both axes the logarithm of the corresponding length is measured. The wavelengths of physical phenomena (full lines) grow linearly with the scale parameter of the Universe. The size of the causally connected domains (dot-dashed line) stagnates during the exponential growth (inflation), whereas it increases faster than the length scale of the Universe later, i.e., quadratically in the radiation era and with 3/2 power under matter domination



that the main contribution to the energy density comes from massless and nearly massless particles with much lower rest energy than the actual average kinetic energy. Therefore, the long-wavelength fluctuations having left during inflation continuously reentered the horizon and their gravitational action was “felt” again by the plasma oscillations. The first maximum of the CMBR multipole moments corresponds to the largest wavelength fluctuations that were just entering the horizon in the moment of the emission of CMBR.

Since during its evolution beyond the horizon, any dynamical change in the fluctuation spectra was causally forbidden, the fluctuating gravitational field experienced by the recombining hydrogen atoms was directly related to the fluctuation spectra of the inflationary epoch, determined by the quantum fluctuations of the field(s) of that era. This observation leads promptly to the conclusion that the spectra should be very close to the Zel’dovich–Harrison spectra. Detailed features of the power spectra seem to effectively rule out some of the concurrent inflationary models.

Also the simplest version of the field-theoretical realization of inflation predicts a total energy density very close to the critical density ρ_c , which separates the parameter region of a recollapsing Universe from the region where a non-accelerating expansion continues forever. Such a Universe is spatially flat. In the apparently relevant case of accelerated expansion, the borderline is shifted and universes somewhat above the critical densities might expand with no return. It is customary to measure the density of a specific constituent of the Universe in proportion to the critical density: $\Omega_i = \rho_i/\rho_c$.

An important prediction of the inflationary scenario for the origin of CMBR anisotropy is a sequence of maxima in the multipole spectrum (Hu 2001). The latest results (see [Fig. 12.1](#)) confirm the existence of at least two further maxima, in addition to the main maximum known before. The new satellite-based CMBR observations by the European satellite PLANCK launched in May 2009 will improve the accuracy of the deduced cosmological parameters to 0.5% and determine the multipole projection of the anisotropy up to angular momentum $l \sim 2,500$.

The positions and the relative heights of these maxima allow the determination of the relative density of baryonic constituents among the energy carriers. The increased level of accuracy leads to the conclusion that the baryonic matter (building up also the nuclei of all chemical elements) constitutes no more than 5% of the energy content of the Universe. This conclusion agrees very convincingly with the results of the investigation of the primordial abundance of the light chemical elements to be described in detail in [Sect. 12.3](#). These facts lead us to the unavoidable conclusion that about 95% of the energy content of the Universe is carried by some sort of nonbaryonic matter. (More accurate numbers will be given at the end of this section). The discovery of its constituents and the exploration of its extremely weak interaction with ordinary matter is one of the greatest challenges for the scientific research in the twenty-first century.

12.2.1.3 Dark Matter: Indications, Candidates, and Signals

Beyond CMBR, growing evidence is gathered on a very wide scale for the existence of an unknown massive constituent of galaxies and galaxy clusters. It is tempting to follow a unified approach describing the “missing gravitating mass” from the galactic to cosmological scale (i.e., from a few tens of kpc to Mpc, with $1 \text{ pc} = 3.26 \text{ light-years} = 3.0856 \times 10^{13} \text{ km}$). In this

subsection the main evidence already found and the ongoing experimental particle physics efforts for direct detection of the dark matter (DM) constituents are shortly reviewed.

First hints of some sort of gravitating Dark Matter below the cosmological scale came from galactic rotation curves (some tens of kpc), then from gravitational lensing (up to 200 kpc), and from the existence of hot gas in galaxy clusters. The anomalous flattening of the rotation curves of galaxies was discovered in the 1970s. Following Kepler's law, one expects a decrease of the orbiting velocity of all objects (stars as well as gas particles) with increasing distance from the galactic center. Instead, without exception a tendency for saturation in the velocity of bright objects in all studied galaxies is observed. The simplest explanation is the existence of an enormous dark matter halo. Since velocity measurements are based on the 21 cm hydrogen hyperfine radiation, they cannot trace the galactic gravitational potential farther than a few tens of kiloparsecs. Therefore, with this technique only the rise of the galactic dark matter (DM) haloes can be detected but one cannot find their extension.

Dark supermassive objects of galactic cluster size are observable by the lensing effect exerted on the light of farther objects located along their line of sight. According to general relativity the light of distant bright objects (galaxies, quasars, γ ray bursts (GRBs)) will be bent by massive matter located between the light source and the observer along the line of sight. Multiple and/or distorted images arise, which allow an estimate of the lensing mass. The magnitude of this effect, as measured in the Milky Way, requires even more DM out to larger distances than it was called for by the rotation curves (Adelmann-McCarthy et al. 2006).

The large-scale geometry of the galactic DM profile semiquantitatively agrees with results of Newtonian many-body simulations, though there are definite discrepancies between the simulated and observed gravitating densities at shorter distances. Interesting propositions were put forward by Milgrom to cure the shorter-scale deviations with a modified Newtonian dynamics (MOND) (reviewed by Milgrom 2008).

Gravitational lensing combined with X-ray astronomy can trace the separation of bright and dark matter, occurring when two smaller galaxies collide. The motion of the radiating matter is slowed down more than that of the DM components. As a consequence, the centers of the lensing and X-ray images are shifted relative to each other. A recent picture taken by the Chandra X-ray Telescope is considered as the first direct evidence for the existence of DM on the scale of galaxy clusters (Clowe et al. 2006).

Another way to estimate the strength of the gravitational potential in the bulk of large galaxy clusters is offered by measuring spectroscopically the average kinetic energy (e.g., the temperature) of the gas. One can relate the very high temperature values (about 10^8 K) to the depth of the gravitational potential assuming the validity of the virial theorem for the motion of the intergalactic gas particles. Without the DM contribution to the binding potential the hot gas would have evaporated long ago.

Three most popular DM candidates could contribute to the explanation of the above wealth of observations. Historically, faint stars/planetary objects constituted of baryonic matter were invoked first, with masses smaller than 0.1 solar mass (this is the mass limit minimally needed for nuclear burning and the subsequent electromagnetic radiation). The search for massive compact halo objects (MACHOs) was initiated in the early 1990s based on the so-called microlensing effect – a temporary variation of the brightness of a star when a MACHO crosses the line of sight between the star and the observer. This effect is sensitive to all kind of dark matter, baryonic or nonbaryonic. The very conservative combined conclusion from these observations and some theoretical considerations is that at most 20% of the galactic halo can be made up of stellar remnants (Alcock et al. 2000).

Complementary to this astronomy-based proposition elementary particle physics suggests two distinct nonbaryonic “species,” which originate from the extreme hot period of the Universe and therefore could be present nearly homogeneously on all scales. *Axions* are hypothetical particles of small ($10^{-(3-6)}$ eV/ c^2) rest energy. They were introduced (Peccei and Quinn 1977) for the theoretical explanation of the strict validity of the symmetry of strong interactions (QCD) under the combined application of space- and charge reflections (CP-invariance). Although they are very light, their kinetic energy is negligible, since they are produced in nonthermal processes. This way they represent the class of cold dark matter. The parameter space was and is thoroughly searched for axions in all particle physics experiments of the last 2 decades. The presently allowed mass range is close to the limit of the astrophysical significance of these particles.

The most natural DM candidates from particle physics are weakly interacting massive particles (WIMPs). Assuming that the thermal abundance of the WIMPs is determined by the annihilation and pair-production processes with themselves, one can estimate their present density as a function of the annihilation cross section. It is quite remarkable (even qualified sometimes as “WIMP miracle”) that, using cross sections typical of the supersymmetric extension of the standard particle physics model, just the gravitating density missing on the cosmological scale is found. By this coincidence, one identifies WIMPs with the lightest stable supersymmetric particle (called neutralino). The neutralino’s mass is on the scale of heavy nuclei; usually one assumes it to equal the mass of the tungsten atom. It would constitute pressureless cold dark matter, with a density calculable by analyzing its decoupling from thermal equilibrium.

An important milestone in the WIMP-story will be reached once the Large Hadron Collider (LHC) at CERN begins working. The available energy covers the expected mass range of the most popular variants of supersymmetric extensions. Currently, extensive strategies are worked out for the identification of prospective new massive particles to be observed at LHC, along with their cosmologically motivated counterparts (Baltz et al. 2006).

A positive identification at CERN would give new impetus to the underground direct searches for WIMPs. Such research is based on looking for heat deposition by particles arriving from the nearest galactic neighborhood into cryogenic detectors, well isolated from any other type of heat exchange. At present, only a single such experiment, i.e., the Dark Matter (DAMA) experiment in Gran Sasso, Italy, has reported a positive signal in the DM particle search. For more than 5 years now, a seasonal variation in the heat deposition rate is observed, which may be caused by the DM particle flux variation along the orbit of the Earth (Bernabei et al. 2003).

Although the analysis of CMBR excludes the domination of hot dark matter, i.e., relativistic weakly interacting particles, like light neutrinos, there still exists a plethora of more exotic propositions for the constituents of dark matter, not yet accessible for experimental verification, like primordial black holes, nonthermal WIMPzillas, and the so-called Kaluza–Klein excitations of higher-dimensional theories.

12.2.1.4 Dark Energy, the Accelerating Universe, and the Problem of Distance Measurements

The expansion of the Universe is conventionally characterized by the Hubble law, stating that cosmological objects uniformly recede from the observer with a velocity proportional to their distance. The proportionality factor H has not remained constant during the

evolution of the Universe, the rate of change being characterized by the deceleration parameter $q_0 = dH^{-1}/dt - 1$ (Peebles 1993).

The deceleration can be probed by distance measurements using type Ia supernovae. As explained in ▶ Sect. 12.5.3 these very energetic cosmic events occur in a rather narrow mass range of compact objects, with a minimal scatter in their energy output or *luminosity* L , which determines also the energy flux F reaching the observer at distance d_L called *luminosity distance*. Therefore, type Ia supernovae are standardizable light sources (standard candles), their light curves can be transformed into a universal form.

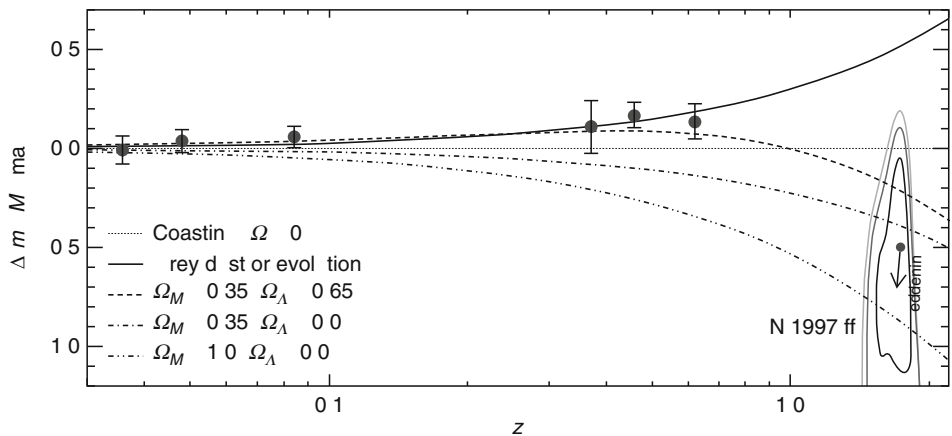
Standard candles are important tools to measure astronomical distances. Knowing the luminosity (i.e., energy output) of an object, it is straightforward to calculate its distance by the observed brightness, which drops with the inverse square of the distance $1/r^2$. The advantage of using SN Ia is that they are outshining all the stars in a regular galaxy and thus can be seen and studied over vast distances.

More recently, the method of measuring distances with SN Ia has acquired some fame by showing that the Universe is expanding faster at large distances than expected by the standard cosmological model (Perlmutter et al. 1999; Riess et al. 1998; Leibundgut 2001a, b).

The luminosities of 42 SN Ia were analyzed in these pioneering publications as a function of their redshift. The survey comprised objects with redshift $z \leq 1$, which corresponds to an age ≤ 10 Ga (gigayears). Assuming that the absolute magnitude of these objects is independent of the distance (excluding evolution effects) the apparent luminosities were detected on an average 60% fainter than expected in a Universe, whose energy density is dominated by nonrelativistic matter. A number of data points with $z \leq 0.7$ are displayed in ▶ Fig. 12.3, all having positive deviation for the difference of the apparent and absolute luminosities, $m - M$

■ Fig. 12.3

Variation of the difference of the observed (m) and absolute (M) luminosity for the SN Ia with redshift z , measured in a special astronomical unit, called *magnitude*. The zero level corresponds to supernovae in an empty ($\Omega = 0$) Universe. A positive difference signals sources that are fainter than expected. A brighter (negative) value is naturally interpreted as the decelerating action of the gravitational force exerted on the source by a nonzero rest energy ($\Omega_M \neq 0$). See text for models corresponding to the different curves possibly producing positive values (Reprinted from Riess et al. 2001 with kind permission of the first author and AAS)




(note that the fainter is a source the larger is its magnitude). The simplest interpretation is to assume the scattering of the light on its way from the source by some sort of “dust” (full line) leading to objects that are fainter than foreseen. A less conventional interpretation is to assume positive acceleration of the global expansion. (An accelerating source is located farther away, and will appear to be fainter at a certain z than expected in standard cosmology.)

The quantitative argument is based on relating the measurements to the deceleration parameter defined above. In fact the luminosity distance of an object at redshift z can be expressed as an integral of an expression of the varying Hubble-parameter $H(z)$ on the interval $(0, z)$, where $z = 0$ corresponds to the observer’s position today. When the redshift is not too large, one can expand this integral into a series of z and arrive in the first approximation at a simple linear relation expressing Hubble’s law of the dependence of the luminosity distance on the redshift. Its first nonlinear correction involves the deceleration parameter: $d_L = (c/H_0)z[1 + (1 - q_0)z/2 + \dots]$. Dust absorption diminishes the source brightness irrespective of the value of z . On the other hand, the presence of both matter and a cosmological constant will change the sign of the deceleration parameter with z .

In the past decade several projects contributed to the luminosity distance measurements and by now (i.e., as of 2009) the list includes over 200 events. Specifically with the help of the Hubble telescope 13 new Sn Ia were found with spectroscopically confirmed redshifts exceeding $z = 1$ and at present the full sample contains already 23 $z > 1$ objects (Riess et al. 2007). Such objects most strongly influence the value of the deceleration parameter. A combined analysis of all Sn Ia data yields a deceleration parameter value of -0.7 ± 0.1 (Kowalski et al. 2008). Its negative value signals an accelerating expansion rate at distance scales comparable to the size of the Universe.

A nonzero cosmological constant Λ in the equations describing the dynamics of the Universe can account for such an acceleration. The cosmological constant is related to a vacuum energy density (ρ) characterized by negative pressure (equation of state $p = w\rho$, with $w = -1$). Nowadays, the more general term “dark energy” is used for the hypothetical agent of such an accelerating effect (acceleration requires $w < -1/3$).

The fraction of the total energy density stored in Λ is not constant in time. Although Λ is constant by definition, the energy densities in the radiation and matter components are varying respectively as quartic and cubic inverse powers of the distance scale of the Universe. The early Universe until the decoupling of the photons is radiation-dominated and the Λ energy density is negligible. Initially, the matter density (including nonbaryonic dark matter) is dominating after decoupling, exerting a conventional decelerating effect on the motion of cosmological objects. Because of the reduction of the matter density with the expansion of the Universe, its contribution to the total energy density (and total $\Omega = \Omega_M + \Omega_\Lambda$) may become smaller than the one of Λ at a given point in time. How early this crossover happens depends on the absolute value of Λ , which is not constrained by any current theory. From this point of view, it is remarkable that Ω_M and Ω_Λ are of the same order of magnitude in the Universe at present. Because of this and the rather small value of Λ its impact on the cosmic expansion can only be detected over large distances, i.e., when studying distances of objects with large redshift z . In the distant future, the repulsive action of a nonzero Λ will more and more dominate. Without any additional effect, this leads to a “Big Rip” scenario in which smaller and smaller volumes become causally isolated because the repulsion will be pushing everything apart faster than the speed of light.

The different fits in  Fig. 12.3 correspond to different matter – dark energy compositions. Without cosmological constant, the deviation is always negative but its rate of decrease

depends on Ω_M . The two lower curves show cases ($\Omega_M = 0.35$ and 1.00 , respectively), which do not fit the measurements at all. Evidently, if the measurements are correct, some sort of dust or dark energy will be needed.

Because of the important consequences of these observations on cosmology, astronomers seriously investigate possible alternatives or data biases, such as possible effects of the evolution of SN Ia objects (deviation from the “standard candle” behavior at low metallicity), effects of light absorption by the galaxy clusters hosting the supernovae, and by the intergalactic dust, lensing effects, etc. Although the actual dust content in the line of sight is not well determined, dust is not a problem in recent observations because astronomers make use of an empirical relation between the width of the SN Ia lightcurve (between rise and decay) and its absolute magnitude. By studying samples of closer SN Ia it was found that more energetic, brighter explosions also lead to a wider lightcurve. This is called the Phillips relation. It is not affected by dust absorption and the only assumption entering is that it is universally valid for all SN Ia. Thus, knowing the easily determinable lightcurve width, the absolute magnitude can be derived and the distance calculated by comparison to the observed relative magnitude of the explosion.

The best fit rather indicates the presence of dark energy. This conclusion was largely determined by the object with largest z observed to date. In 2001, a SN Ia with $z = 1.6$ was reported with larger apparent luminosity than expected in a matter dominated or in an empty Universe (Riess et al. 2001, see [Fig. 12.3](#)). It can be reconciled with the small z observations by assuming that it exploded in an epoch when the matter part of the energy density was still dominant and the rate of the expansion was decreasing. Quantitatively, the fit led to $\Omega_M = 0.35$, $\Omega_A = 0.65$.

The important question to be addressed in this context is the one regarding alternatives concerning the nature of the repulsive force. A cosmological constant implies an equation-of-state with $w = -1$ but any $w < -1/3$ yields repulsion. An additional, previously unknown, form of energy has been postulated as an alternative to the cosmological constant: Quintessence (Caldwell et al. 1998; Armendariz-Picon et al. 2000). It has repulsive properties but $w \neq -1$. Therefore, it can be time-dependent and even have different values at different spatial points, contrary to a cosmological constant. Detailed SN Ia investigations try to put bounds not just on the size of the acceleration but also on the type of dark energy, i.e., the equation-of-state of the Universe.

The most recent analyses (Riess et al. 2007; Wood-Vasey et al. 2007) employing much larger data sets than before are all compatible with the cosmological constant ($w = -1$) interpretation of the data and give $\Omega_M = 0.274$ with 20% statistical error. A final conclusion concerning the acceleration driven by a substantial cosmological constant might be reached by the proposed Supernova Acceleration Probe space mission. The project aims at the observation of around 2,000 SN Ia up to a redshift $z \leq 1.2$. Its launch is tentatively scheduled for 2013.

The results of 5 years of WMAP satellite mission were published and their cosmological interpretation was studied (Komatsu et al. 2009), taking into account the effect of the above-listed investigations. The results were interpreted by assuming that our Universe is flat and its energy content is a mixture of ordinary matter, gravitating dark matter, and dark energy. The most important cosmological parameters were determined with unprecedented accuracy. The accuracy was substantially increased by combining the WMAP CMBR data, type Ia supernova luminosity distance measurements, and the largest scale components of the 2dF galaxy cluster catalogue (Percival et al. 2007). The supernova data are sensitive to the energy density component of cosmological constant type, while the galaxy clusters represent the

aggregates of the gravitating (mainly dark) matter. The analysis results in a value of the Hubble parameter H at present time of $(70.1 \pm 1.3) \text{ km s}^{-1} \text{ Mpc}^{-1}$. The ordinary matter content is $(4.62 \pm 0.15)\%$, the cold (nonrelativistic) dark matter represents $(23.3 \pm 1.3)\%$, the part of the dark energy in the full energy density is $72.1 \pm 1.5\%$. The projection of the motion of such a Universe back in time leads to a highly accurate estimate of its age: 13.73 ± 0.12 billion years.

Concluding, it becomes a more and more established fact that the chemical elements formed from baryonic matter contribute less than 5% to the total energy density of the present Universe. In view of the complete symmetry of laws governing matter and antimatter in our present-day Universe it is actually a rather nontrivial fact that baryonic matter did not completely annihilate into radiation in the hot Universe directly after the inflationary epoch and also that the original energy density was transformed into a high-temperature gas of ordinary elementary particles.

12.2.2 Origin of the Matter–Antimatter Asymmetry

On the interface of neighboring domains of baryonic and antibaryonic matter, quark–antiquark (proton–antiproton) annihilation would lead to the emission of hard X-rays. The absence of this signal makes it highly probable that even if antibaryons were present in the early, hot Universe they had disappeared before the CMBR was emitted. Therefore, the observed baryonic density actually proves the presence of a matter–antimatter asymmetry within the present horizon in our Universe (Rubakov and Shaposhnikov 1996; Riotto and Trodden 1999).

In 1967, Sakharov analyzed the conditions that might lead to this asymmetry dynamically, instead of simply assuming it to be fixed by some initial conditions (Sakharov 1967). If, in a certain moment,

1. The elementary interactions violate the symmetry under the combined transformation consisting of spatial reflection (P) followed by charge conjugation (C) – the so-called CP symmetry,
2. The elementary interactions violate the baryon-antibaryon symmetry,
3. The Universe is out of thermal equilibrium,

then a matter–antimatter density difference is produced. One can deduce the actual amount of asymmetry with detailed quantitative calculations.

Without going into details, some of the scenarios proposed by theoretical particle physicists for the creation process of this fundamental asymmetry will be outlined below. For this, a short account of the Standard Model of elementary interactions (Perkins 2000) is given first. (See also [Chap. 10, Vol. 1.](#))

Known elementary constituents of matter are quarks and leptons (see [Table 12.1](#)). Three families have been discovered. In each family one has two flavors of quarks and one lepton with the associated neutrino. The decay of the free neutron observed in 1932 and described first by the Fermi theory of weak interactions is understood today as the decay of a d-quark (one of three quarks composing the neutron) into a u-quark (which forms the final proton with the unchanged other two quarks) and an electron plus its antineutrino. The particles participating in this process constitute the lightest (first) particle family of the Standard Model.

Three elementary interactions act among these particles. Each of them is mediated by vector particles. The electromagnetic quanta, the photons, bind nuclei and electrons into

■ Table 12.1

Elementary particles in the Standard Model. For each family, the first line in the center column refers to quark species of left- and right-handedness (L, R), the second line gives the same for the leptons, not participating in strong interaction processes. Those appearing in a bracket form a doublet with respect to $SU(2)_L$ transformations. The field quanta mediating strong, electromagnetic, and weak interactions are listed in the last column. They are not specific to any particle family

Particle families	Matter constituents (each has its own anti-particle)	Interaction vector particles
1st	$(u_L, d_L), u_R, d_R$	8 gluons
	$(e_L, \nu_{eL}), e_R$	
2nd	$(c_L, s_L), c_R, s_R$	Photon (γ)
	$(\mu_L, \nu_{\mu L}), \mu_R$	Weak quanta (Z^0, W^\pm)
3rd	$(t_L, b_L), t_R, b_R$	
	$(\tau_L, \nu_{\tau L}), \tau_R$	

atoms and molecules. Weak interactions are mediated by three vector fields, the W^\pm and the Z^0 , all discovered in 1983. Gluon fields bind the quarks into protons and neutrons. The strong interaction quanta come in eight different, so-called colored states and also each quark can appear in one of three different colored states.

It has been shown that the three Sakharov conditions might be fulfilled simultaneously in the Standard Model at high temperatures. The CP-violation, which allows the oscillation of the K^0 and of the B^0 mesons into their antiparticles and back, has been observed experimentally (in 1967 and 2001, respectively) and can be quantitatively understood with the present theory (Amsler et al. 2008).

On the other hand, no sign of baryon number violation has been observed to date in any elementary particle physics experiment. In the Standard Model, one cannot find any process that would involve the transformation of a proton into mesons or leptons. However, in the early 1970s, 't Hooft (1976) showed that in the presence of specific configurations of electro-weak vector fields, fermions (leptons and quarks) can be created or annihilated, but the difference of the baryon number and of lepton number ($B-L$) should stay constant (quarks and antiquarks actually carry $\pm 1/3$ unit of baryon charge, while the lepton charge of the known species is ± 1). Today the chance for such transitions to occur is negligible (the probability is estimated to about 10^{-170}). However, they must have occurred frequently when the temperature was of the order of 100 GeV (about 10^{15} K).

It is a very interesting coincidence that exactly at that temperature scale one expects the transformation of all elementary particles from massless quanta into the massive objects observed in today's experiments. The creation of the mass is due to the so-called Higgs effect. This consists of the condensation of an elementary scalar field (a close relativistic analogue of the Cooper-pairing in superconductivity). If this transformation had proceeded via a sufficiently strong first-order phase transition, the third of Sakharov's criteria had been also fulfilled by the behavior of the known elementary interactions in the very early Universe.

In a first-order phase transition, the low-temperature (massive) phase would appear via thermal nucleation, which is a truly far-from-equilibrium process. Inside the bubbles of the new phase the baryon number-violating processes are stopped. So the question is this: What is the net baryon concentration frozen?

Quarks and antiquarks traverse the phase boundaries, which represent a potential barrier for them. As a consequence of the complex CP-violating phase in the Hamiltonian describing weak interactions, the reflection and transmission amplitudes for matter and antimatter turn out to be different leading to an asymmetry in the constitution of matter and antimatter inside the bubbles.

The quantitative details of this beautiful scenario critically depend on a single parameter: the strength of the self-coupling of the so-called Higgs field, whose condensation determines the masses of all particles. This parameter is still unknown. The latest lower bound (Amsler et al. 2008) lies in a region where the phase transformation is actually continuous (beyond the end point of the first-order transition line). The situation could be different in supersymmetric extensions of the Standard Model. The one explored best is the electroweak phase transition within the so-called Minimal Supersymmetric Standard Model (Carena et al. 2009). One expects considerable guidance from measurements at the Large Hadron Collider in constraining the parameter space to search for the origin of baryon–antibaryon asymmetry. Another avenue could be the very late (low-energy density) exit from the inflationary period of evolution (Garcia-Bellido et al. 1999; Krauss and Trodden 1999; van Tent et al. 2004). If this energy scale coincides with the electroweak mass scale then the reheating of the Universe from its cold inflationary state would offer an out-of-equilibrium situation. This is the basis of the proposition of the cold baryogenesis scenario (Tranberg et al. 2007).

The resolution of the matter–antimatter asymmetry problem is an issue of central importance in particle physics in the twenty-first century.

12.2.3 Evolution of the Expanding Universe

The equilibrium in the hot particle “soup” is maintained through frequent elementary particle reactions mediated by the quanta of the three fundamental interactions. The expansion of the Universe dilutes the densities and, consequently, the reaction rates get gradually lower. The adiabatic expansion lowers monotonically also the temperature (the average energy density). (Actually, there is a one-to-one mapping between time and temperature.) The following milestones can be listed in the thermal history of the Universe (Kolb and Turner 1990).

First, the weak interaction quanta became massive at the temperature scale of 100 GeV. Since then, weak reactions have only occurred in contact interactions of the particles. At about the same time the *t*-quark and the Higgs quanta also decoupled from the “soup.” The same decoupling happened for the other heavy quark species (*b*-quark, *c*-quark) and for the heaviest of the leptons (τ -particle) in the range 1–5 GeV (a few times 10^{13} K) of the average energy density. The τ -neutrinos remain in thermal equilibrium via weak neutral interactions.

The strong interaction quanta, the gluons became extremely short ranged at around the temperature $kT \sim 100\text{--}200$ MeV (a few times 10^{12} K). Computer-aided quantum field theoretical investigations have demonstrated that quarks and gluons are confined to the interior of nucleons (protons and neutrons) and excited baryonic resonances below this temperature range (Petreczky 2007). This transformation was smooth for baryonic matter

densities characteristic of our Universe at that epoch and for the actual mass values of the light quarks, very similar to the process of atomic recombination.

At this stage no nuclear composite objects can be formed yet, since they would instantly disintegrate in collisions with hard electromagnetic quanta. The stabilization occurs for temperatures below 0.1 MeV. Primordial synthesis of light nuclei took place at that cooling stage of the Universe (► Sect. 12.3).

Below this temperature, light nuclei and electrons form a globally neutral plasma, in which thermal equilibrium is maintained exclusively by electromagnetic interactions. The gravitational attraction of the massive and electrically screened constituents of matter was balanced by the radiation pressure. This dynamical equilibrium is described by coupled fluid equations and results in acoustic oscillations modulating the essentially homogeneous distribution of the constituents (Hu 2001). The dominant wavelength of these oscillations is determined by those density fluctuation modes that left the horizon during inflation and are continuously reentering, since during the radiation-dominated period, the horizon expands faster than the global scale parameter of the Universe increases.

The last qualitative change occurred at the energy scale around 1 eV ($\sim 10^4$ K), when at the end of atomic recombinations the Universe became transparent to the propagation of electromagnetic radiation. At this moment the size of the Universe was about 1/1000 of its present radial scale. Today, the light emitted in the act of the last scattering is detected as cosmic microwave background radiation. A consistent interpretation of the details of its features represents (together with the primordial abundance of light nuclei) a unique test of all ideas concerning the earlier evolution of the Universe.

12.2.4 Gravitational Clustering of Matter

At the moment of the decoupling of light, the matter in the Universe became gravitationally unstable against density fluctuations. The key feature in understanding the emergence of a large-scale structure in the Universe is the statistical characterization of the density fluctuations at this moment. These fluctuations are determined by the spectra of the acoustic oscillations, which are in turn determined by the reentering density fluctuations of inflationary origin. This line of thought leads us to the hypothesis of the quantum origin of the largest-scale structures observed in the Universe.

Amplitudes of density fluctuations at different wavelengths follow independent Gaussian (also called normal) statistics (see ► Sect. 9.3.6, Chap. 9, Vol. 1), and their mean spectral power is distributed in an almost scale-invariant manner, described above. The absolute normalization was determined by the COBE satellite to be 1 part in 100,000. Their evolution can be analyzed initially with the help of the linearized gravitational equations. The classical analysis, originally performed by Jeans (1902), leads to the conclusion that fluctuations above the Jeans-scale are unstable and they are at the origin of the formation of the oldest structures (for a modern textbook on the subject, see Peacock 1999).

The nonlinear stage of the clustering process can only be followed by numerical integration of Newton's equations of motion for a very large number (typically 10^6 – 10^7) of equal-mass particles. The most interesting question studied in these N -body simulations concerns the mass distribution of the first galaxies. This feature determines the frequency of the occurrence of densities sufficiently high to start nuclear fusion reactions in these first gravitationally bound galactic objects.

The semiempirical theory (Press and Schechter 1974) assumes that this distribution is determined by the probability of matter fluctuations obeying a Gaussian distribution to exceed an empirically determined threshold value. This simple idea results in an $\sim M^{-2/3}$ power scaling for the statistics of the collapsed objects with different mass M . This means that the earliest collapsed gas clouds were small, about 10^5 solar masses, and had a temperature of a few hundred Kelvin. The thermal excitation of H_2 molecules provides the microscopic mechanism for the further radiative cooling, which might have led to the formation of the first minigalaxies and/or quasars. If sufficient quantities of H_2 molecules were present, then the first stars and black holes were born very early, at a redshift $z \sim 20$ i.e., some 12 billion years ago, when the characteristic size of the Universe was $z + 1$ times smaller than it is at present). If the dominant radiative cooling mechanism was the excitation of the atomic hydrogen, then the first objects with nearly 10^8 solar masses were formed at a temperature of 10^4 K. The first galaxies appeared in this case only for a redshift $z \sim 10$. One expects that astronomical surveys of the coming years will be able to reach the distance that can be calculated from the Hubble law $d = H/\nu$, where the Hubble parameter H was defined in [Sect. 12.2.1.4](#). The exploration of this distance scale should bring evidence for the existence of the first galaxies. According to the latest WMAP results (Komatsu et al. 2009) the first galaxies were formed at $z = 10.8 \pm 1.4$.

The Millenium simulation (Springel et al. 2005) is an N -body simulation tracing over 10 billion mass points, representing fractions of the primordial gas, from the time of the CMBR decoupling to the present-day Universe. This simulation showed that it was necessary to assume cold dark matter (consisting of slowly moving, heavy particles) to reproduce the large-scale structures found in galactic surveys. It was also able to show that bright quasars are formed already at very early stages, thus confirming the observational results from the Sloan Digital Sky Survey (Anderson et al. 2001; Abazajian et al. 2009) that challenged traditional models of structure formation.

The radiative cooling and further gravitational evolution of the collapsed clouds lead to the appearance of the first stars (see [Sect. 12.4.1.1](#)).

12.3 Primordial Nucleosynthesis

12.3.1 Weak Decoupling

Since the quark–hadron phase transition no free quarks or gluons exist anymore. The hot plasma is composed of neutrons, protons, electrons, positrons, photons, and the electron-, muon-, and tau-neutrinos and their antineutrinos. Basically, all particles with masses $2m < kT/c^2$ are present because the respective particle–antiparticle pairs can be created in photon collisions. Scattering reactions thermalize all plasma constituents to the same temperature and forward and reverse reactions are in equilibrium. For instance, protons can be converted into neutrons by electron capture $e^- + p \leftrightarrow n + \nu_e$, neutrons into protons by positron capture $e^+ + n \leftrightarrow p + \nu_e$. While all other constituents are highly relativistic, the nucleons are slower due to their large mass. Their kinetic energy exhibits a Maxwell–Boltzmann distribution appropriate for the given plasma temperature. Although formation and destruction reactions are in equilibrium, protons will be more abundant because of their lower mass. The ratio of neutron to proton number densities only depends on the temperature

and the mass difference Δm between the nucleons as long as the reaction equilibria apply (Börner 1988; Kolb and Turner 1990; Peacock 1999):

$$\frac{n_n}{n_p} = \exp\left(-\frac{\Delta mc^2}{kT}\right). \quad (12.1)$$

Once $kT \leq 1$ MeV (i.e., at about 10^{10} K), the electrons are not energetic enough anymore to overcome the mass difference between neutrons and protons in electron captures. Also, photons cannot produce positrons anymore in pair-production processes to support positron capture on neutrons. Such weak transitions will thus cease to exist. Since the neutrinos were produced in such reactions, thermal communication of the neutrinos with the other constituents comes to an end. This phase is called weak freeze-out and weak decoupling because the neutrinos become decoupled from the rest of the particles and can assume different temperatures. Since there is little, if any, interaction between this neutrino background and the remaining particles, its evolution is governed predominantly by the expansion rate of the Universe similar to the photon background radiation after electromagnetic decoupling that gives rise to the cosmic microwave background (see [Sect. 12.2.1.1](#)). Thus, in addition to the cosmic microwave background there is a cosmic neutrino background stemming from the era of weak decoupling. Its temperature is lower by a factor of 0.714 because of the heating of the photons by $e^+ - e^-$ annihilation after weak decoupling.

With the ceasing of electron and positron capture, the ratio of neutrons to protons gets frozen at the decoupling temperature, yielding a value of about 1/6. However, after the weak freeze-out, photons still dominate the total energy of the Universe and thus the temperature is decreasing as the inverse square root of the time, according to the law valid for a radiation-dominated Universe. The ratio between baryon and photon number densities $\eta = n_b/n_\gamma$ characterizes a particular solution of the equations for the expanding early Universe and, therefore, the solutions can be labeled by the parameter η (Kolb and Turner 1990; Coles and Lucchin 1996; Riotto and Trodden 1999). Assuming a globally valid η , the baryon density can be written as a function of temperature: $\rho_b = 3.376 \times 10^4 \eta T_9^3 \text{ g cm}^{-3}$ (T_9 is the temperature in units of 10^9 K.) In fact, η is inversely proportional to the total entropy of the Universe, which has to remain constant.

Together with the equation for the evolution of the temperature $T_9 = 13.336/t^{1/2}$, this sets the conditions for primordial nucleosynthesis. The strength of the standard Big Bang scenario is that only one free parameter – the above-introduced baryon-to-photon ratio η – must be specified to determine all of the primordial abundances ranging over 10 orders of magnitude.

The parameter η also depends on $\Omega_b = \rho_b / \rho_c$, i.e., the ratio of the baryon density to the critical density ρ_c needed for a flat Universe.

Thus, a fit of η to observed primordial abundances not only probes the conditions in the early Universe at the time of nucleosynthesis but can also reveal the curvature of the Universe, or at least the baryonic contribution to that curvature (Schramm and Turner 1998). Historically, primordial nucleosynthesis was the first tool for determining the geometry of the Universe. With the increased accuracy in the resolution of the angular multipole expansion of the CMBR temperature fluctuations delivered by WMAP, the total density of the Universe (and not just the baryonic one) can be determined independently now (see [Sect. 12.2.1](#)).

12.3.2 The Reaction Network and the Production Process of Nucleosynthesis

After the weak freeze-out, the baryonic matter part essentially consists of free neutrons and protons interacting with each other. Deuterium is constantly formed via neutron captures on

protons. However, due to the low binding energy of the deuteron the created deuterons will preferably be destroyed by photodisintegration as long as the (photon) temperature is higher than 10^9 K. Below that temperature, photodisintegration is no longer effective, and more heavy elements can be built up by further reactions on the deuterons. Thus, although free neutrons and protons had already existed earlier, the onset of further primordial nucleosynthesis is delayed until about 2 s after the Big Bang (Boesgaard and Steigman 1985; Bernstein et al. 1991).

Because free neutrons are not stable, but decay with a half-life of $T_{1/2} = (10.25 \pm 0.015)$ min, the neutron-to-proton ratio will change from 1/6 to 1/7 until the onset of primordial nucleosynthesis.

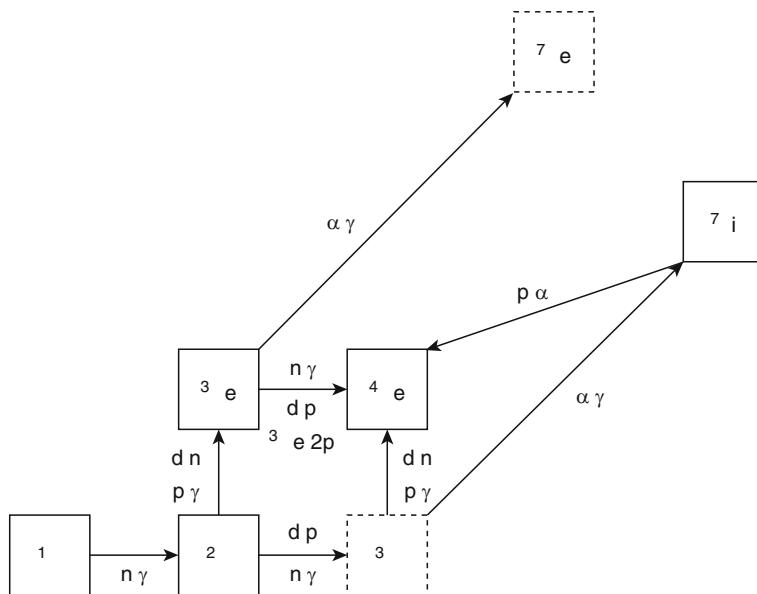
While the Universe expands further, it cools down and the decreased energy of the photons cannot prevent significant formation of deuterons anymore. Thereafter, heavier nuclides can be created by reactions involving protons, neutrons, and the newly formed nuclear species (Schramm and Turner 1998; Sarkar 1996). This is nothing else than a freeze-out from a high-temperature, low-density nuclear statistical equilibrium (NSE), similar to the one occurring in late and explosive phases of nucleosynthesis (see ▶ Sects. 12.4.4 and ▶ 12.4.5) but at different density. An NSE is defined by all reactions via the strong and electromagnetic forces being in equilibrium. The equilibrium abundances are then only determined by the (baryon) density, the temperature, and the binding energy of the nuclei, as well as by the initial composition of the material, i.e., the neutron-to-proton ratio. The latter is set by the weak freeze-out and the subsequent neutron decay. In a high-temperature NSE, all nuclei are completely dismantled into their constituents: the protons and neutrons. Assuming a quick freeze-out in such a manner that late-time nonequilibrium reactions will not significantly alter the NSE abundances, the resulting abundances can already be determined without detailed reaction network calculations. With decreasing temperature, simply the most strongly bound nuclei at the given neutron-to-proton ratio will be formed. Thus, mainly unprocessed protons and ^4He nuclei are expected to be present, which exhibit a high binding energy, with all neutrons having been incorporated into the ^4He nuclides. Formation of elements beyond He is hindered by the fact that there are no nuclei with mass numbers 5 and 8. The 3α reaction (see ▶ Sect. 12.4.3) could convert ^4He to ^{12}C but is not in equilibrium because it is strongly dependent on the density and too slow at the conditions in the early Universe. Nuclei close to ^4He are produced according to their binding energies.

The important reactions and the produced nuclear species are shown in ▶ Fig. 12.4. The conditions at the onset of and during the nucleosynthesis are given by the initial values and parameters discussed above, with η being a free parameter.

A typical result of a full network calculation for a specific η is shown in ▶ Fig. 12.5 (Tytler et al. 2000; Kolb and Turner 1990). As can be seen, practically no nucleosynthesis occurs during the first 2 s, the temperature remains above 10^{10} K, and no other nuclides than free nucleons are favored. Only after a sufficient drop in temperature, deuterons are formed, ^3H and ^3He nuclei are produced, quickly followed by ^4He . The neutron abundance is determined by slow β -decay in the early phase. During the formation of ^4He , the neutron abundance suddenly drops because most of the neutrons are incorporated into the α particles. Slightly delayed, traces of ^7Li and ^7Be nuclei are formed. During the decline of the temperature, charged particle reactions freeze out quickly and after about 15–30 min nucleosynthesis ceases. The very few free neutrons decay into protons, ^3H eventually also decays and so does ^7Be , which forms further ^7Li . Finally, by far the most abundant species are hydrogen (protons) and helium (^4He , i.e., α particles), which together give more than 99.9% of the baryonic material. Although this calculation did not assume NSE at all times, the resulting abundances are very close to the ones obtained from equilibrium abundances and fast freeze-out. Realizing the dominance of ^4He due to its high

■ Fig. 12.4

The reaction network of standard Big Bang nucleosynthesis. Unstable nuclear species are marked by dashed boxes. When all reactions are stopped, the unstable ${}^7\text{Be}$ decays to ${}^7\text{Li}$ and ${}^3\text{H}$ decays to ${}^3\text{He}$



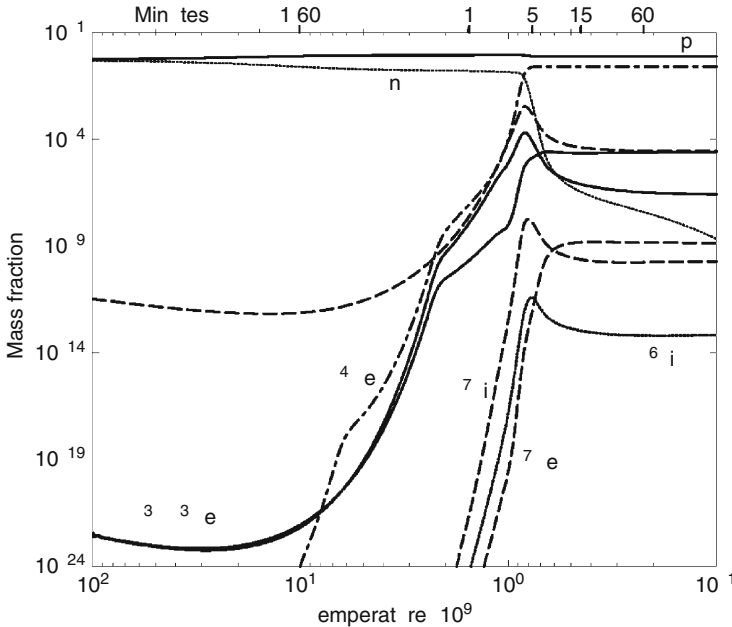
binding energy, it is easy to understand that about 25% of the gas is made up of helium. The initial n/p ratio of $1/7$ translates into mass fractions $X_n = 0.125$ and $X_p = 0.875$ (i.e., 12.5% of the gas mass consists of neutrons). Assuming that all neutrons combine with protons to form ${}^4\text{He}$, the mass fraction of ${}^4\text{He}$ has to be $X_\alpha = 2X_n$ because it contains two neutrons and two protons. Thus, $X_\alpha = 0.25$, i.e., 25%.

An interesting result was obtained from the fact that the initial n/p ratio depends on the weak freeze-out (see above). The freeze-out time and temperature and thus also the resulting n/p ratio depends on the change in the degrees of freedom during freeze-out (Kolb and Turner 1990). Although only three neutrino families were known originally ($N_\nu = 3$), it remained an open question for a while whether there are more families containing light (nearly massless) neutrinos. Increasing the number of neutrino species increases the number of degrees of freedom and has a similar effect to that of a faster expansion resulting from larger pressure. Thus, a larger number of neutrino families would lead to an earlier weak decoupling at a still higher temperature. This results in a higher n/p ratio and consequently leads to more ${}^4\text{He}$.

Primordial nucleosynthesis calculations performed along these lines were able to put the limit $N_\nu \leq 3.3$, ruling out any further families long before any particle physics experiments. This was possible due to several facts: helium is very abundant and can be easily measured in astronomical observations; it is strongly bound and therefore robust during galactical chemical evolution; its abundance only weakly depends on η ; the primordial production reactions are well determined; and the half-life of the neutron (determining the change of the n/p ratio between weak freeze-out and onset of nucleosynthesis) is measured to high accuracy.

■ Fig. 12.5

Primordial abundances of different nuclear species as a function of time and temperature for a fixed ratio of baryon to proton number densities, $\eta = 5.1 \times 10^{-10}$ (Reprinted from Tytler et al. 2000 with kind permission of the first author and IOP)



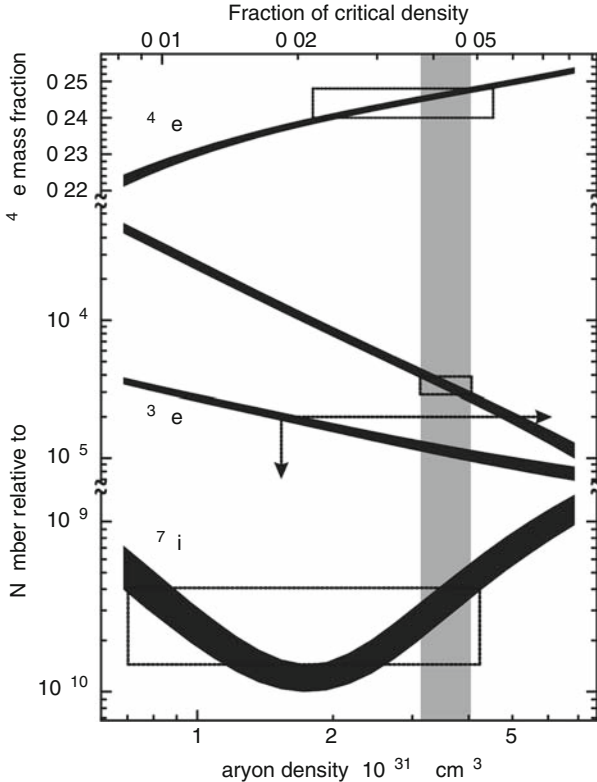
This prediction on the number of neutrino species was later confirmed by experiments at CERN (see the article of D. Karlen in Hagiwara et al. 2002) directly measuring the decay widths of the Z^0 boson in the weak interaction.

The nuclear reaction rates (cross section) for the reactions specified in ► Fig. 12.4 are well determined, also at the interaction energies relevant to primordial nucleosynthesis, which are comparatively low by nuclear physics standards. Thus, once the initial conditions are determined, the evolution of the different species with time and the final abundances can be calculated with high accuracy. The only open parameter in the standard Big Bang nucleosynthesis model is η . Since the baryon density is proportional to η and the reaction rates are density dependent, the final abundances will also depend on the choice of η .

► Figure 12.6 shows this dependence for a typical range of the baryon density and equivalently its fraction of the critical density Ω_b . Immediately catching the eye is the difference between the density dependences of the different species: the ^4He fraction increases slightly with increasing density while the deuterium and ^3He fractions strongly decrease (note that the vertical scale of the upmost curve is linear, while those of the rest are logarithmic). The simple explanation is that a high density during the nucleosynthesis phase gives rise to a larger number of capture reactions on deuterium and ^3He , producing more ^4He but leaving less of the targets. ^7Li shows a more complex behavior with a pronounced minimum. At low densities ^7Li is produced by α -capture on ^3H but is preferably destroyed at higher densities by the reaction

■ Fig. 12.6

Primordial abundances as a function of baryon density ρ_b or fraction of critical density Ω_b (these two quantities are directly related to the baryon-to-photon ratio η , see text). The widths of the curves give the nuclear physics uncertainties. The boxes specify the ranges of abundances and densities constrained by observation (there is only an upper limit for ${}^3\text{He}$ from observation) as given in Burles et al. (1999, 2001). The shaded area marks the density range consistent with all observations (Burles et al. 1999, 2001). Symbol D represents deuterium, ${}^2\text{H}$ (Reprinted from Tytler et al. 2000 with kind permission of the first author and IOP)



${}^7\text{Li}(p,\alpha){}^4\text{He}$. However, at higher densities the production of ${}^7\text{Be}$ via ${}^3\text{He}(\alpha,\gamma){}^7\text{Be}$ also increases. This ${}^7\text{Be}$ is not destroyed by any further primordial process but eventually decays to ${}^7\text{Li}$ after nucleosynthesis has ceased. The different density dependences of the three main reactions involved give rise to the minimum shown in Fig. 12.6.

12.3.3 Comparison of Calculations and Observed Primordial Abundances

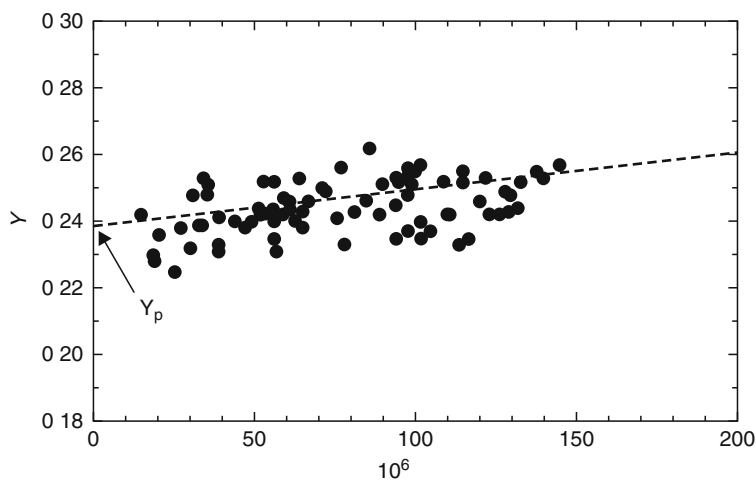
Except for helium, the abundances of the primordial isotopes change by orders of magnitude when varying the baryon density or η , respectively. On the other hand, ${}^4\text{He}$ is very abundant and thus it can be observed with high accuracy. Therefore, it is possible to determine η from

comparison with primordial abundances. As outlined above, this means nothing less than determining the total baryon density and thus the baryonic contribution to the curvature of our Universe! The allowed abundance range for each primordial species is shown in ▶ Fig. 12.6, combined with the calculated baryon density. It is reassuring that the independent observations for each species still permit a consistent range of η , i.e., all the observations are consistent with the same baryon density.

Serious complications arise from the fact that the calculations have to be compared to primordial abundances, not to the ones currently found in stars or the interstellar medium (Boesgaard and Steigman 1985; Olive et al. 2000; Tytler et al. 2000; Olive 2001; Steigman 2006). During the further evolution of the Universe, when stars are formed and destroyed, the abundances within a galaxy change with time (see ▶ Sect. 12.6.4) due to the stellar production and destruction processes (see ▶ Sect. 12.4). Thus, it is not trivial to determine the primordial values, especially those for isotopes that are weakly bound and therefore easily destroyed in stars such as deuterium, ^3He , or ^7Li nuclei. In order to trace the effects of chemical evolution, the standard practice is to correlate the abundance of the nuclide in question with the abundance of a nuclide, which becomes monotonically enriched in the interstellar medium during the course of the chemical evolution, e.g., oxygen. This other nuclide serves as a tracer of the metallicity of an object, i.e., the content of elements beyond hydrogen and helium (a technical term borrowed from astronomy). From the observation of different sites with different metallicities, one hopes to find trends that can be extrapolated to zero metallicity, i.e., to the primordial values. ▶ Figure 12.7 shows an example of such an extrapolation.

■ Fig. 12.7

Example of the extrapolation to primordial values. The primordial value of ^4He (Y_p) for zero metallicity (zero oxygen) is inferred from a series of observations (filled circles) (Olive 2001). For other primordial isotopes the slope of the interpolation would be steeper, for ^7Li there would be a steep rise at higher metallicities and a flat line with nearly constant abundance at low metallicity (Reprinted from Olive 2001 with permission by Springer)



The spectra of ^4He are easy to observe due to its high abundance. This He isotope can be identified in clouds of ionized interstellar gas around bright, young stars (HII regions). Although the abundance in an object can be determined with high precision, a large systematic uncertainty remains due to observations of different objects. On the other hand, the observation of ^3He is difficult and an extrapolation carries a large uncertainty because different stars both produce and destroy it effectively. Due to its weak lines it cannot be seen in low-metallicity stars. The chemical evolution of ^7Li is also complex but it can at least be seen in old stars. Such stars contain a factor of 0.03–0.0003 less “metals” (in astronomy: all elements except H and He) than the Sun. Studying such stars, a remarkable discovery was made: below a certain metallicity the content of ^7Li remains almost constant, i.e., a plateau appears in the abundance plots. The ^7Li -plateau was thought to give the primordial value. However, the question of possible depletion in early stars remains to be addressed (Korn et al. 2006) as well as the dependence of the data on the underlying assumptions, such as model atmospheres (Charbonnel and Primas 2005; Asplund et al. 2006a). These problems give rise to a large systematic uncertainty also for ^7Li . Until recently, deuterium was usually observed in the local interstellar medium. However, the situation has greatly improved in recent years. It became possible to observe ^2H absorption lines in quasar spectra (Tytler et al. 2000). Quasar light passes through clouds at high redshift, i.e., far away and at the same time far back in time, which contain (almost) primordial amounts of deuterium, ^2H . Because of the brightness of quasars such lines can still be identified although the photons have traveled a long distance. In summary, only upper limits can be given for primordial ^3He and the primordial values of ^4He and ^7Li have a smaller individual observational error compared to ^3He but a considerable systematic uncertainty in the observations. The averaged ^2H values from far objects seem to give the tightest constraint for Big Bang Nucleosynthesis (BBN) calculations (Steigman 2007).

The dependence of primordial abundances on Ω_b are shown in [Fig. 12.6](#). Using the available abundance information, it is found that it has to lie between about 0.038 and 0.048, also somewhat depending on the choice of the value of the Hubble constant (Schramm and Turner 1998; Burles et al. 2001; Steigman 2007). Most recently, an independent value for η_b was derived from the WMAP data of the CMBR (see Komatsu et al. 2009 for latest results). The CMBR value of $\eta_b = (6.11 \pm 0.2) \times 10^{-10}$ is in excellent agreement with the value derived from the BBN abundances for ^2H and ^3He . Depending on improvements in the observations and theoretical models of the evolution of ^4He and ^7Li with metallicity, their required η_b may or may not remain in agreement with the CMBR value. However, the BBN model still is in good standing when considering the CMBR data due to the large systematic uncertainties inherent in the observations of the latter isotopes (Steigman 2007).

Assuming only baryonic matter, the small value of $\Omega = \Omega_b$ would indicate an open Universe, i.e., one expanding forever. However, theory of inflation demands that $\Omega = 1$ (exactly) and thus a flat Universe (Kolb and Turner 1990; Peacock 1999). This is in agreement with the latest observations of the CMBR as discussed in [Sect. 12.2.1.2](#). Then the missing mass required to close the Universe must be nonbaryonic. Indeed, there are other indications (in the initial creation and later dynamics of galaxies) that there is more gravitational interaction than can be accounted for by standard baryonic matter. Of further interest is the value of the cosmological constant (see [Sect. 12.2.1.4](#)), which was found to be nonzero in recent distance measurements (Perlmutter et al. 1997; Schmidt et al. 1998; Perlmutter et al. 1999; Wood-Vasey et al. 2007; Riess et al. 2007), using type Ia supernovae as “standard candles” ([Sects. 12.2.1.4](#) and [12.5.3](#)). The cosmological constant Λ also provides a contribution Ω_Λ to the expansion of the Universe so that the new requirement reads $\Omega_M + \Omega_\Lambda = \Omega_b +$

$\Omega_s + \Omega_A = 1$, with Ω_s being the nonbaryonic contribution (Steigman et al. 2000). At the time of writing, it is not clear yet what constitutes the nonbaryonic mass. A quite general name for possible new, exotic particles is WIMP, an acronym for “weakly interacting massive particle” (see ► Sects. 12.2.1.3 and ► 12.2.1.4 for details).

12.4 Stellar Nucleosynthesis

12.4.1 Stellar Evolution

12.4.1.1 Birth of Stars

Stars are formed within molecular clouds, vast aggregations of molecules residing in the galactic disks. These clouds that often contain the mass of a million stars, are much denser and colder than the surrounding interstellar gas. Stars are born out of the collapse of small condensation areas that are scattered throughout the much larger volume of a molecular cloud. The collapse can occur due to random density fluctuations or be externally triggered, e.g., by shockwaves from supernovae or galaxy collisions. Soon after the collapse begins, a small pressure-supported protostar at the very center of the collapse flow develops. During the main collapse phase, the central protostar is surrounded by an inward flow of gas and dust. As the protostar evolves both the temperature and the density increase inside. Finally, the central core of the protostar heats up so much that nuclear “burning” is initiated and the star begins its energy production through nuclear fusion.

Star formation is a process complicated by the details of cloud fractionation, rotation, turbulence, and magnetic fields. While the formation of low-mass stars (below 8 solar masses) is thought to be understood and proceeding through an accretion disk, the mechanism to form more massive stars is not quite understood as well. Due to the larger radiation pressure of their emissions, the accretion disk would be blown away. The current model assumes, consistent with observations, the formation of a directed jet, transporting a small fraction of material but clearing a cavity through which most of the radiation can escape without interaction with the accretion disk (Bannerjee and Pudritz 2007). In this way, low-mass and high-mass stars could be formed in a similar manner. Other models assume coalescence of two or more light stars or competitive accretion of a low- and a high-mass star feeding from the same molecular cloud (Bonnell et al. 1997; Bonnell and Bate 2006).

The galactic mass distribution of the newborn stars is known as the initial mass function. To sustain nuclear burning in their interiors, stars must have at least 8% of the mass of the Sun. During their formation, stars with a smaller mass do not release sufficient gravitational binding energy to heat the gas to temperatures required for igniting nuclear fusion. These are called brown dwarfs. The lower-mass stars between about 8 and 40% of the mass of our Sun are called red dwarfs, because of their small size and their low surface temperature. At the other end of the mass range stars more than 100 times as massive as the Sun are highly unstable due to spontaneous pair production of electrons and positron from plasma interactions and therefore do not exist in our Universe. During their enormous life spans, stars produce energy through nuclear fusion and shine continuously over millions to billions of years. Lower-mass stars consume their fuel very quietly and survive for several billion years. Massive stars, on the other hand, burn out in a few millions of years.

12.4.1.2 Hertzsprung–Russell Diagram

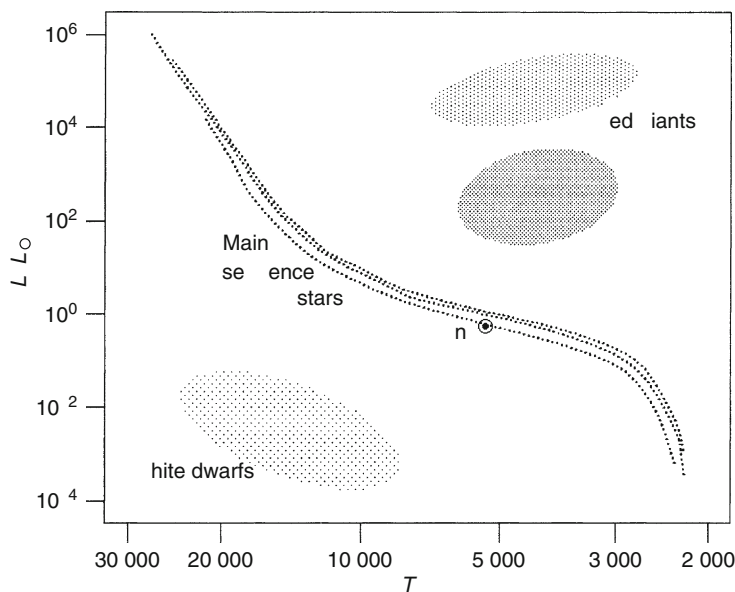
Stars undergo drastic changes during their evolution. One of the best methods for charting the course of stellar evolution is the Hertzsprung–Russell (HR) diagram shown in ► Fig. 12.8, a particular type of graph developed in the early twentieth century by the astronomers Hertzsprung and Russell. In this diagram, the luminosity or energy output of a star is plotted on the vertical axis, and the surface temperature of the star on the horizontal axis. For historical reasons, the surface temperatures along the horizontal axis are plotted backward, so that they increase toward the left. In the HR diagram the various stars are then plotted according to their luminosity and surface temperature. As one can see, the stars are not distributed randomly in the HR diagram, but are rather grouped in certain areas.

Most of the stars line up along a well-defined band on the HR diagram known as the main sequence and are therefore also called main-sequence stars. This trend is no coincidence. Stars that lie along the main sequence have the proper internal configurations to support fusion of hydrogen to helium. Since stars spend most of their lifetime in this hydrogen burning state, most stars in the HR diagram are lying on the main-sequence band. Our Sun is also a typical main-sequence star.

After the hydrogen supply in the core of the star is exhausted and converted to helium, the central temperature is too low to fuse helium into heavier elements. Therefore, the core lacks an energy source and cannot support anymore the overlying bulk of the star. Through the gravitational pressure, the size of the core shrinks and the temperature of the central region

■ Fig. 12.8

The Hertzsprung–Russell (HR) diagram. In this schematic diagram, various stars are plotted according to their relative luminosity L/L_{\odot} (where L_{\odot} is the absolute luminosity of the Sun) and their surface temperature, T



increases accordingly. The heat released by the core increases steadily the luminosity of the star. Paradoxically, even though the helium core is shrinking, the radius of the star, determined by the outer hydrogen layer, increases by factors of 100 to 1,000. Through this expansion, the surface temperature drops by as much as 50% and the star becomes redder. Therefore, these stars are called red giants and are found in the HR diagram in the upper right corner.

When the core temperature of the red giant reaches about one hundred million degrees, a new sequence of nuclear reactions called helium burning begins in the core where helium nuclei fuse to carbon and oxygen. Our Sun has lived for 4.5 billion years and has already burnt half of its hydrogen in the core. After about another 5 billion years our Sun will also become a red giant and will thereby increase its size so much that the radius of the Sun will reach about the Earth's orbit.

The further evolution of a star and the nature of its stellar death depend on the initial mass. If the initial mass of a star is less than about 8 solar masses, it is burning He in an unstable way (see also [Sect. 12.4.3](#)) and the resulting pulsations lead to the loss of huge quantities of hot gases toward the end of its life. This cloud moving away from the star is called a planetary nebula. The central small and hot core of the star that is left over is a white dwarf and consists of the ashes of helium burning, i.e., carbon and oxygen. Even though the surface temperature of the white dwarf is still very hot its luminosity is small, because nuclear fusion has ceased. Therefore, the white dwarfs are found in the lower left corner of the HR diagram.

If the initial mass of a star is more than about 8 solar masses further burning phases will take place. These are called advanced burning phases and consist of carbon, neon, oxygen, and silicon burning, being named after the nuclei mainly destroyed in that phase. In these subsequent burning phases, heavier and heavier nuclei are built up, and the ashes of the preceding burning phases provide the fuel for the subsequent burning phases. However, in the outer and therefore cooler and less dense regions of the star the previous burning phases are still continuing. This leads to shell burning with distinct adjacent shells of different chemical compositions, in which different burning phases prevail. In the outermost shell of the star still hydrogen is burnt into helium (hydrogen burning), in the next shell helium to carbon and oxygen (helium burning), and finally, in the fully evolved star, there follow still carbon, oxygen, neon, and silicon burning shells ([Fig. 12.9](#)). In the core of the star significant amounts of iron are accumulating through silicon burning. A detailed discussion of the nuclear burning phases is given in [Sects. 12.4.2](#) through [12.4.4](#).

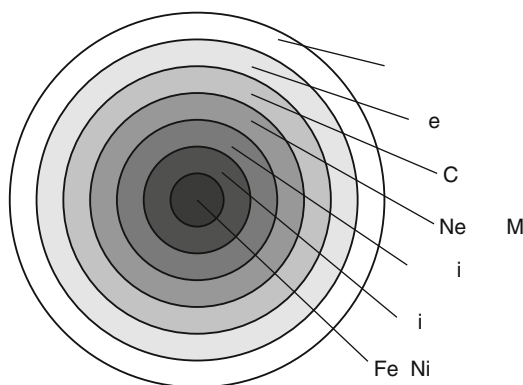
A detailed introduction to stellar evolution is given in the following books: Clayton ([1984](#)), Hansen and Kawaler ([1994](#)), Kippenhahn and Weigert ([1994](#)), Phillips ([1994](#)), Tayler ([1994](#)). Books and reviews discussing stellar nucleosynthesis are Rolfs and Rodney ([1988](#)), Arnett ([1996](#)), Thielemann et al. ([2001b](#)). Tables of nuclear reaction rates and cross sections can be found in Rauscher and Thielemann ([2000](#)).

12.4.1.3 Supernova Explosions

The endpoint in the evolution of stars with more than 8 solar masses is a type II supernova. One should not confuse novae with supernovae and even the two types (i.e., type I and type II) of supernovae are quite different. It will become evident in the following that the sites of these explosive events are only loosely related, despite the similarity in the name. There is a major difference in the underlying mechanism between type I (SN I) and type II supernovae (SN II). The confusing choice of names is, once again, historical. Astronomy is guided by observations

■ Fig. 12.9

Schematic structure of the different shells of a fully evolved massive star with their prominent constituents. At the bottom of each shell, different burning phases take place. The iron core in the center has been accumulated in silicon burning. The outer part of the star consists of a thick envelope of unburned hydrogen. Note that the relative thickness of the layers is not drawn to scale



and early astronomers did not have the equipment to investigate the objects in any detail. Obviously, even today, it is impossible to view the events in binary systems directly. Much more detail can be seen in light curves (i.e., brightness as a function of time) and spectra.

Historically, the comparatively frequent novae (see ▶ Sect. 12.5.2) were named first. Subsequently, much brighter eruptions of light were observed in the sky. Since they are brighter by more than a factor of 10^6 , they were appropriately termed supernovae. The light curve of a supernova is somewhat different from that of a nova: its rise time is only a few hours instead of days and it exponentially decays after having reached its peak. Closer investigations showed that several classes of supernovae can be found, according to features in their spectra: type I do not show hydrogen lines, whereas they are found in type II eruptions. This indicates whether the exploding object has an extended hydrogen envelope (such as massive stars). A more detailed classification scheme is shown in ▶ Table 12.2. Type Ia supernovae are further discussed in ▶ Sect. 12.5.3, while the unique scenario producing all other types (SN Ib,c; SN II) is shortly introduced in the following.

12.4.1.4 Core-Collapse Supernovae

When the stellar core becomes dominated by iron, the fusion into heavier elements does not lead to the release of energy, but rather requires absorption of energy. (See, e.g., ▶ Fig. 7.13 in Chap. 7, Vol. 1, showing the cross section of the stability valley of nuclei with iron at its lowest point.) Therefore, the core lacks an energy source and is unable to support itself against gravity anymore leading to a collapse of the star. In a single second the innermost regions are compressed to nuclear densities of about 10^{12} kg/m^3 and temperatures of about 10^{11} K . The iron nuclei, which have been synthesized just before in silicon burning are broken up again into protons and neutrons through the high-energy thermal radiation. The innermost regions are

■ **Table 12.2**

Supernova classification by observed properties. Different lines can be identified in the spectra. The assumed scenario causing the light burst is also given

Characteristic explosion energy (10^{44} J) and light curve				
No H lines			H lines	
Si lines	No Si lines		Exponential decay of light curve	Plateau feature in light curve
	He lines	No He lines		
White dwarf disruption	Core collapse (binary system?)	Core collapse (binary system?)	Core collapse	Core collapse
SN Ia	SN Ib	SN Ic	SN II L	SN II P

compressed so much that the core density becomes sufficiently high for electrons and protons to combine, producing neutrons and neutrinos. As the collapse continues, this giant ball of neutrons generally reaches a state of maximum density, and then bounces back. The bounce drives an extraordinarily powerful shock wave outward through the outer parts of the star. Investigations within the last 3 decades have made it clear that this prompt shock will not have enough energy to explode the remaining outer layers of the star. Only with the additional supply of energy through neutrino heating can the shock wave be supported to blow apart the star completely. This powerful explosion can explain supernovae of type II, but also of type Ib,c. At the center of the supernova explosion, the dense core of neutrons may be left behind as a neutron star. Alternatively, if the remaining core becomes heavier than a few solar masses through partial fallback of material, it can even collapse into a black hole. The dual explosion mechanism with prompt shock and delayed explosion by neutrinos is still not understood well. A proper treatment of the neutrino transport requires detailed three-dimensional hydrodynamic simulations, which are currently beyond the capability of modern computers and thus one has to refrain to approximations whose merits are debatable. For an overview, see, e.g., Janka et al. (2007).

The physics of the remaining compact objects after stellar death, e.g., white dwarfs, neutron stars, and black holes are discussed by Shapiro and Teukolsky (1983).

12.4.2 Hydrogen Burning: Proton–Proton Chain, CNO-Cycle

For nuclear reactions to take place in the interiors of stars, a temperature of at least 10 million degrees is necessary. This high temperature is needed because nuclei have positive charge and therefore repel each other through the Coulomb potential. The typical kinetic energy of nuclei in stellar interior range from between a few keV to a few 100 keV being much smaller than the typical height of a few MeV of the Coulomb barrier between reaction partners. Therefore, nuclear reactions in stars proceed mainly by barrier penetration exploiting the quantum mechanical tunnel effect. The cross sections decrease exponentially with the kinetic energies of the nuclei because of the decreasing penetration probability through the Coulomb barrier. The dependence on the relative kinetic energy E between interacting nuclei can be represented most simply by a formula in which a factor proportional to the inverse of the relative kinetic energy $1/E$ and the barrier penetration factor $G(E)$ is factored out from the cross

section: $\sigma(E) = (1/E) G(E) S(E)$. This leaves a function $S(E)$ called the astrophysical S -factor that varies smoothly with the kinetic energy E of the interacting nuclei in the absence of resonances. Neutron-induced reactions would not have to overcome the Coulomb barrier. However, neutrons are not very abundant in stellar interiors. They still play a major role for the nucleosynthesis of heavy nuclei through the so-called s - and r -processes, to be discussed in [Sect. 12.4.5](#).

The reaction rate, expressed as the number of reactions per volume and per time, is proportional to the astrophysical S -factor. At the temperatures and densities relevant to the stellar environments the interacting nuclei have a Maxwell distribution of speeds. This distribution has also to be taken into account when determining the reaction rate. An introduction to astrophysical S -factors and reaction rates can be found in many textbooks on nuclear astrophysics, e.g., Arnett (1996), Rolfs and Rodney (1988), Iliadis (2007), Boyd (2008).

Nuclear burning in late hydrostatic phases (see, e.g., silicon burning) and in different explosive scenarios proceeds at high temperatures and densities. This leads to equilibrium between forward and reverse reactions, e.g., capture and photodisintegration. It gives rise to equilibrium abundances depending only on the supply of free neutrons and protons and on certain nuclear properties. High temperatures favor the creation of light nuclei because photodisintegration processes dominate. High densities lead to heavy nuclei, and intermediate conditions yield the highest abundances for nuclei with high binding energies. Such an equilibrium can be established within a group of nuclear species where individual reactions link different groups. This is called quasi-statistical equilibrium (QSE). The full nuclear statistical equilibrium (NSE) is reached when all nuclei are equilibrated.

In the following, the different burning stages will be described one by one, starting with hydrogen burning, being the first burning stage of every star.

In hydrogen burning, occurring in the cores of main-sequence stars like our Sun, ordinary hydrogen nuclei (i.e., protons) are burnt through a chain or cycle of nuclear reactions into ^4He nuclei. In this stellar plasma there are two processes burning hydrogen: the proton–proton chain (pp-chain) ([Fig. 12.10](#)) and the carbon, nitrogen, and oxygen (CNO)-cycle ([Fig. 12.11](#)).

The pp-chain proceeds through a sequence of two-body reactions. The first reaction in the pp-chain is the exothermic fusion of two protons p into the deuteron d consisting of a proton p and a neutron n through the reaction



For this reaction to take place a proton p must be converted into a neutron n through $p \rightarrow n + e^+ + \nu$, releasing a positron e^+ and a neutrino ν . Such a conversion can only proceed through the weak interaction (see [Sect. 12.3.1](#)). Therefore, the rate of the reaction in [Eq. \(12.2\)](#) is very low, which makes the reaction the bottleneck of the pp-chain.

Once the deuteron d is formed, it very rapidly undergoes the reaction



There are two alternatives for the next step, leading to a branching of the pp-chain into the ppI- and ppII-chain. In the ppI-chain, occurring in 86% of the cases, two ${}^3\text{He}$ nuclei fuse to a final ${}^4\text{He}$ nucleus while two protons are released:



Fig. 12.10

The proton–proton chain of hydrogen burning

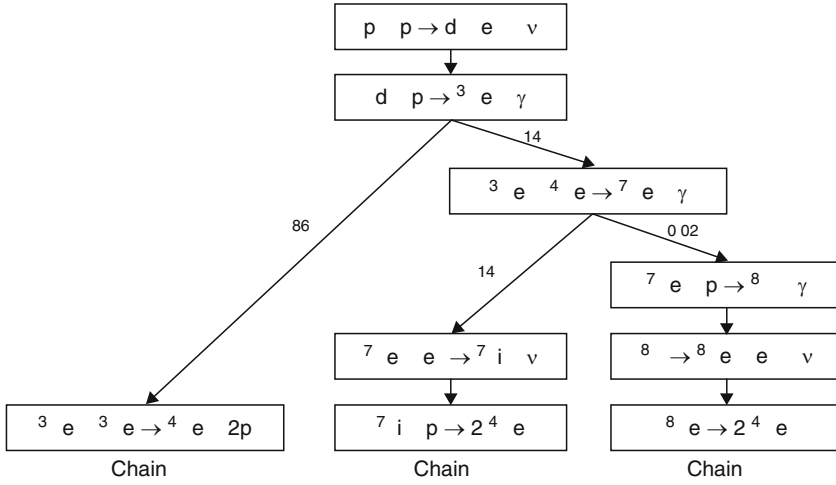
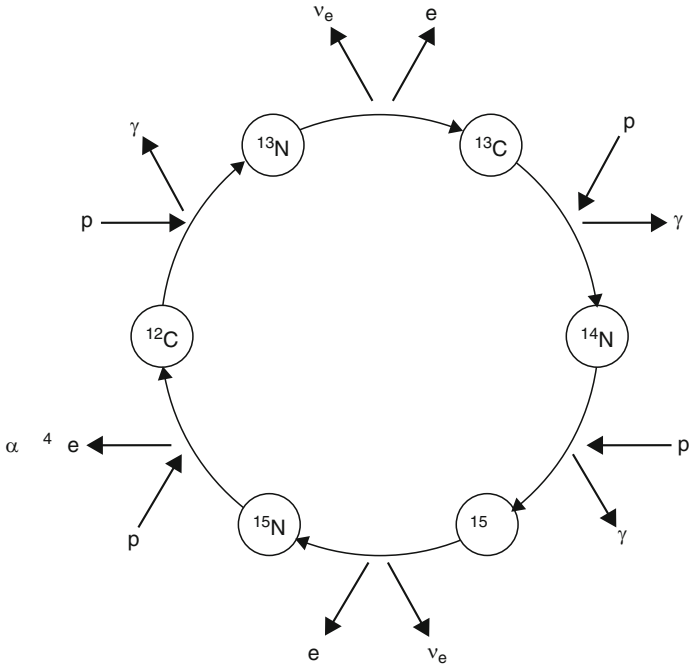


Fig. 12.11

The carbon, nitrogen, and oxygen (CNO)-cycle of hydrogen burning



In the ppII-chain, occurring in 14% of the cases, a ^3He nucleus fuses with a ^4He nucleus creating a ^7Be nucleus and thereby releasing a photon, γ :



In almost all cases, this reaction is followed by the capture of an electron and emission of a neutrino ν , thereby converting a ^7Be nucleus into ^7Li . This is followed by the capture of another proton, creating two ^4He nuclei:



Another branching into the ppIII-chain occurs in a very small percentage of cases with a total probability of only 0.02%. In this chain, reaction (12.5) is followed by the following sequence of reactions:

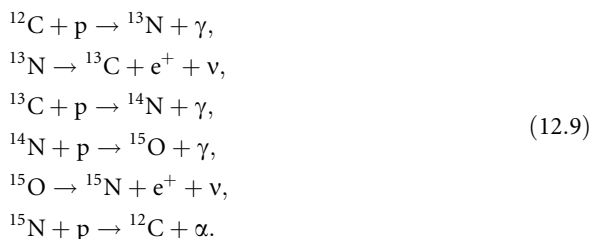


The net reaction of all three pp-chains



leads to a transformation of four protons into a ^4He nucleus releasing two positrons e^+ , two neutrinos ν and a total energy of 26.73 MeV. A fraction of this energy is carried away by the neutrinos, which leave the star practically unhindered due to their negligible interaction with the solar material.

Fusion of hydrogen into helium may also be achieved through another sequence called CNO-cycle (Fig. 12.11), which is notably different from the pp-chain:



In this sequence the C, N, and O nuclei only act as “catalysts” and the net reaction of the CNO-cycle is again given by Eq. (12.8).

For main-sequence stars lighter than about 2 solar masses, the pp-chain dominates in hydrogen burning, whereas the CNO-cycle is favored over the pp-chain in stars that are more than twice as massive as the Sun.

In our Sun the pp-chain dominates over the CNO-cycle, producing about 98% of the total energy. A prerequisite for CNO-cycles is, of course, the existence of the elements C, N, O in the stellar plasma. Stars formed early in the Galaxy (first-generation stars) contain only primordial elements and thus are not able to burn hydrogen through a CNO-cycle at all.

The Sun’s temperature in the core is about 1.5×10^7 K, whereas the surface temperature is only about 5,600 K. The Sun has already lived for 4.6 billion years, and will have enough hydrogen supply to live for about another 5 billion years. This leads to a long lifetime of about 10 billion years before its fuel is exhausted.

How can information be obtained from the Sun's core, where hydrogen burning takes place? The photons reaching us from the Sun are emitted from the solar surface. They have changed their energy enormously by many scattering processes on their way from the hot solar core to the relatively cool surface of the Sun. Therefore, in the visible region only the solar surface and not the solar interior can be observed. One possibility to obtain information about the Sun's core is helioseismology, i.e., by observing the vibration modes of the Sun. It was confirmed through helioseismology that our standard solar model is correct (Fiorentini and Ricci 2000; Bahcall et al. 2001a; Christensen-Dalsgaard 2001).

Another possibility is to observe the neutrinos that are set free in nuclear reactions of the pp-chain and CNO-cycle and reach the surface practically unhindered. Presently four neutrino detectors measuring solar neutrinos exist: HOMESTAKE (USA), GALLEX (Italy), (SUPER) KAMIOKANDÉ (Japan), and SNO (Canada). All these neutrino detectors are underground in order to shield out the cosmic rays that would give unwanted background signals in the neutrino detectors. The existing solar neutrino detectors measure only about 1/3 to 1/2 of the electron neutrino flux compared to the value calculated from the standard solar model (Bahcall 2000). This discrepancy is called the solar neutrino problem (Bahcall 1989, 1999). Possible problems both with the neutrino measurements and with our standard solar model have been ruled out. Recently, at SNO it was possible to observe not only the solar electron neutrinos, but also the μ - and τ -neutrinos in the same experiment (Heger 2001; SNO Collaboration et al. 2002a, b). The measured total neutrino flux agrees with the value expected from the standard solar model. The solution to the solar neutrino problem implies some new physics by the introduction of the so-called neutrino oscillations (see [Sect. 10.8.2 in Chap. 10, Vol. 1](#)). Through such oscillations, the electron neutrinos ν emitted in the solar core by the nuclear reactions given in [Eqs. \(12.2\)](#), [\(12.6\)](#), and [\(12.7\)](#) can change into other types of neutrinos. Thus, mainly μ -neutrinos emerge on their way from the core of the Sun to the detector. Experiments measuring electron neutrinos thus show a smaller flux than initially emitted in the solar core (Bahcall 2001; Bahcall et al. 2001b; Fiorentini et al. 2001). This physical picture is the culmination of about 40 years of solar neutrino detection and research.

Recently, these findings have been combined with the results of the so-called atmospheric neutrino anomaly, where μ -neutrinos generated in pion decays oscillate over into, mainly, τ -neutrinos. In addition, terrestrial experiments performed with neutrino fluxes (produced either at nuclear power plants or with accelerators) provide substantial information on the mixing pattern among the different neutrino species. Searches for possible oscillations into further light neutrino flavors, which would be of clear cosmological significance, have not yet provided a clear answer to the question of their existence. (See [Sect. 10.8.2 in Chap. 10, Vol. 1](#))

12.4.3 Helium Burning: Nucleosynthesis of Carbon and Oxygen

The fusion of protons into helium continues until the star has exhausted its hydrogen. When this happens, the star undergoes a gravitational collapse and the temperature rises to about a few times 10^8 K in the core of the star, which makes the fusion of helium into heavier nuclei possible. In the first reaction of helium burning, the fusion of two ^4He nuclei creates the ^8Be nucleus. However, the ^8Be nucleus has an extremely short mean life of only 10^{-16} s, before it

decays back again to two ${}^4\text{He}$ nuclei. This process is in equilibrium, where the rate of production equals the rate of destruction of the ${}^8\text{Be}$ nucleus:



The ${}^8\text{Be}$ just produced can, however, capture another ${}^4\text{He}$ nucleus creating the ${}^{12}\text{C}$ nucleus through the reaction



The reactions (12.10) and (12.11) are called the triple- α reaction, because three ${}^4\text{He}$ nuclei or α particles are necessary for the creation of ${}^{12}\text{C}$. This reaction can only create carbon in appreciable amounts because of the existence of a resonance in ${}^{12}\text{C}$ at the relevant energy for helium burning. Through this resonance, reaction (12.11) is enhanced by many orders of magnitude.

In helium burning, about half of the carbon nuclei produced are converted to oxygen nuclei ${}^{16}\text{O}$ by the capture of another ${}^4\text{He}$ nucleus:



Further captures of helium nuclei ${}^4\text{He}$ by oxygen nuclei ${}^{16}\text{O}$ occur only to a much lesser extent and therefore helium burning comes to an end after the creation of ${}^{12}\text{C}$ and ${}^{16}\text{O}$.

Carbon and oxygen are the two most important elements for carbon-based life. Carbon is needed for the complex nuclei of the DNA and proteins, whereas oxygen is needed even for water. Interestingly enough, these two elements are extremely fine-tuned with respect to the nuclear force. If the strength of this force were 0.5% larger or smaller, the average abundance of carbon or oxygen in our Universe would be reduced by more than two orders of magnitude. This would make the existence of carbon-based life in our Universe very improbable (Oberhummer et al. 2000; Schlattl et al. 2004).

Outside the stellar core burning helium, hydrogen burning continues in a shell around the core. If the initial mass of a star is less than about 8 solar masses no more burning phases will take place after helium burning and nuclear burning stops. A white dwarf with a surrounding expanding planetary nebula will be the endpoint of the star's life. Charbonnel et al. (1999) and Marigo (2001) review the chemical yields in light and intermediate-mass stars between 0.8 and 8 solar masses.

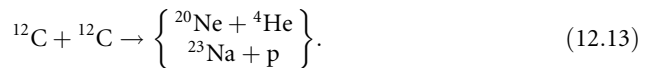
Two interesting effects happen in helium burning of low-mass stars. Firstly, stars with less than about 2 solar masses undergo a core He flash instead of igniting stable He burning after the H burning phase. This is because the cores of lower-mass stars are more dense than those of higher-mass stars. For stars with less than about 2 solar masses, the contracted He core is so dense that it cannot be described as an ideal gas. Rather, it is a degenerate gas, in which pressure is only depending on density but not on temperature. Once the triple- α reaction, being very efficient at high density, is ignited, a thermonuclear runaway ensues because the rising temperature does not raise the pressure and therefore does not cause an expansion of the burning zone. Thus, the usual self-regulation mechanism of hydrostatic burning is not working anymore and He burning proceeds quickly to high temperature. Very high temperatures lift the degeneracy of the gas and its equation-of-state becomes temperature dependent again very suddenly. This causes an explosive expansion of the outer core, also ejecting the outer layers of the star as a planetary nebula.

The second phenomenon occurs in stars between 2 and 8 solar masses, the so-called Asymptotic Giant Branch (AGB) stars. Regular He burning takes place in the core of these stars in their red giant phase. With the exhaustion of He in the center of the star, the burning zone moves outward and becomes a burning shell. Thus, there are two shells burning, a H-burning shell and a He-burning shell. The He-burning shell is very thin and does not generate sufficient energy to balance the mass layers on top of it through radiation pressure. This squashes the shell more and more. Because of the nonlinear dependence on density of the triple- α rate, which is actually two reactions one after another, the energy release will considerably increase but still not be enough to expand and self-regulate the shell against the pressure from the surrounding layers. Further contraction enhances the triple- α rate nonlinearly and so on. Although the gas is not degenerate, a similar thermonuclear runaway as in the degenerate case occurs. When a critical temperature is reached, enough energy is released to expand the shell explosively against its surroundings. This rapid expansion, the He-shell flash, is so strong that it also blows out the H-burning shell. Due to the expansion, the density drops and the triple- α reaction ceases. Quickly, the star contracts again, the outer material settles, and first the H-burning shell and then the He-burning shell is ignited again. This sets the stage for another such cycle. AGB stars undergo a large number of such pulses, where the thermonuclear runaway phase with the flash lasts only a few hundred years whereas the time between pulses is a hundred to a thousand times longer. Oscillations and vibrations are induced into the stellar plasma by these pulses, leading to increased mass loss from the surface of the star. AGB stars have strong stellar winds, which considerably decrease their total mass during their evolution. The shell flashes have another important impact: they cause large convection zones, mixing the plasma constituents across large distances within the star. This is important for the production of the s-process nuclei (see [Sect. 12.4.5.1](#)).

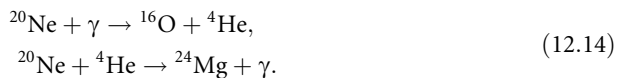
He-shell flashes only occur in low-mass stars because they are caused by thin He-burning shells and the size of the shells scale with the stellar mass.

12.4.4 Advanced Burning Stages

In a massive star with more than 8 solar masses, the next stage after helium burning is carbon burning. This starts when the carbon/oxygen core has shrunk so that the temperature at its center has reached about 5×10^8 K. Then two carbon nuclei fuse together creating ^{20}Ne or ^{23}Na nuclei:



The next stage is neon burning starting at 10^9 K, in which photons first disintegrate ^{20}Ne and liberate ^4He , which in turn reacts with the undissociated ^{20}Ne to build up ^{24}Mg and further nuclei:



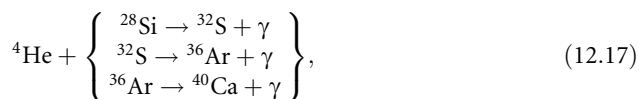
Oxygen burning occurs when the temperature reaches 2×10^9 K, the most important reaction being the one producing ^{28}Si :



The final stage is reached at a temperature of 5×10^9 K, when silicon burning begins. At this high temperature, a series of reactions takes place beginning with the photodisintegration of ^{28}Si :



Then the released ^4He nuclei build up heavier nuclei by successive capture reactions



and so on. At such high temperatures, capture and photodisintegration reactions are in equilibrium. In this so-called nuclear statistical equilibrium (NSE) the knowledge of individual reactions or reaction rates is not important anymore to calculate the abundances. The produced abundances only depend on the temperature and density of the plasma and the nuclear binding energies (Iliadis 2007; Boyd 2008). The result of this series of photodisintegration and capture reactions is the steady buildup of heavier elements up to the elements grouped around iron (Hix and Thielemann 1998), with ^{56}Ni preferentially produced because it is the nucleus with the highest binding energy and having equal number of protons and neutrons.

The sequence of stellar burning is terminated when the core of the star is largely composed of elements in the mass region of nickel and iron, because no more energy is to be gained from further nuclear reactions. As soon as the energy produced is not enough to maintain the hydrostatic equilibrium, the core cannot support the outer layers anymore, and it begins to collapse due to its gravitation, leading to a core-collapse supernova (see [Sect. 12.4.1.3](#)).

In a core-collapse supernova explosive nucleosynthesis also takes place through the outward proceeding shock wave (Thielemann et al. 2001a), modifying the elemental abundance pattern of the outer layers of the pre-supernova star. This explosive burning of the C-, Ne-, O-, and Si-layers in the star mainly leads to modifications of the abundances in the region from Ca to Fe (Rauscher et al. 2002). Photodisintegration of heavy nuclei also leads to the production of proton-rich stable nuclides, the so-called p-nuclides (see also [Sect. 12.4.5.2](#)). The strong neutrino emission caused by the formation of a neutron star in the core collapse influences nucleosynthesis in the deepest, barely ejected layers of the star as well as in the outer layers ([Sects. 12.4.5.2 and 12.4.5.3](#)).

Nucleosynthesis of massive stars is reviewed by Rauscher et al. (2002), Woosley and Heger (2007). An overview of stellar nucleosynthesis including hydrogen, helium, neon, silicon, and explosive burning as well as the basics of the s- and r-process are given by Rauscher and Thielemann (2001). Explosive burning and the s- and r-processes are also introduced below.

12.4.5 Nucleosynthesis Beyond Fe

As it has been seen in the preceding sections, stellar burning phases only lead to the production of nuclei up to Fe. A review by National Research Council of the National Academies identified 11 key questions to be addressed in science in the next decade (Turner et al. 2003). Ranked three on the list is “How were the elements from Fe to U produced?” Although the ground to answer this question has been laid by Burbidge et al. (1957), Cameron (1957) and much progress has

been made since then, there remain a number of problems regarding the astrophysical sites of certain nucleosynthesis processes and also concerning the properties of certain, highly unstable nuclei in such processes. In the following subsections, a brief summary is given of the current knowledge of how elements beyond Fe were synthesized.

12.4.5.1 The Main and Weak s-Process Components

Due to the lack of a Coulomb barrier, the most likely process for the formation of elements heavier than those grouped around iron is neutron capture. If a supply of neutrons is available, they can accrete by sequential neutron captures on a “seed nucleus” in the region of iron to build up neutron-rich nuclei. As the neutron number of the nucleus increases, it will become unstable to β^- decay, transforming a neutron into a proton in the nucleus, and emitting an electron and an antineutrino. Successive neutron captures, interspersed by β^- decays build up many, but not all of the heavier stable nuclei.

There are two basic timescales in this scenario of heavy-element nucleosynthesis by neutron captures: (1) the β -decay lifetimes, and (2) the time intervals between successive captures that are inversely proportional to the neutron capture reaction rates and the neutron flux. If the rate of neutron capture is slow compared to the relevant β decays, the synthesis path will follow the bottom of the stability valley very closely. On the other hand, if the rate of neutron capture is faster than the relevant β^- decays, highly neutron-rich nuclei will be formed. After the neutron flux has ceased, those nuclei will be transformed to stable nuclei by a series of β^- decays. The above two processes are called s- and r-process, respectively, according to their slow or rapid rate of neutron capture. The observed abundances of nuclei in the solar system, especially in the regions of closed-shell nuclei, suggest that the s- and r-processes contributed more or less equally to the formation of the elements above the iron region (see [Fig. 12.12](#)).

Two important reactions provide neutrons for the s-process:

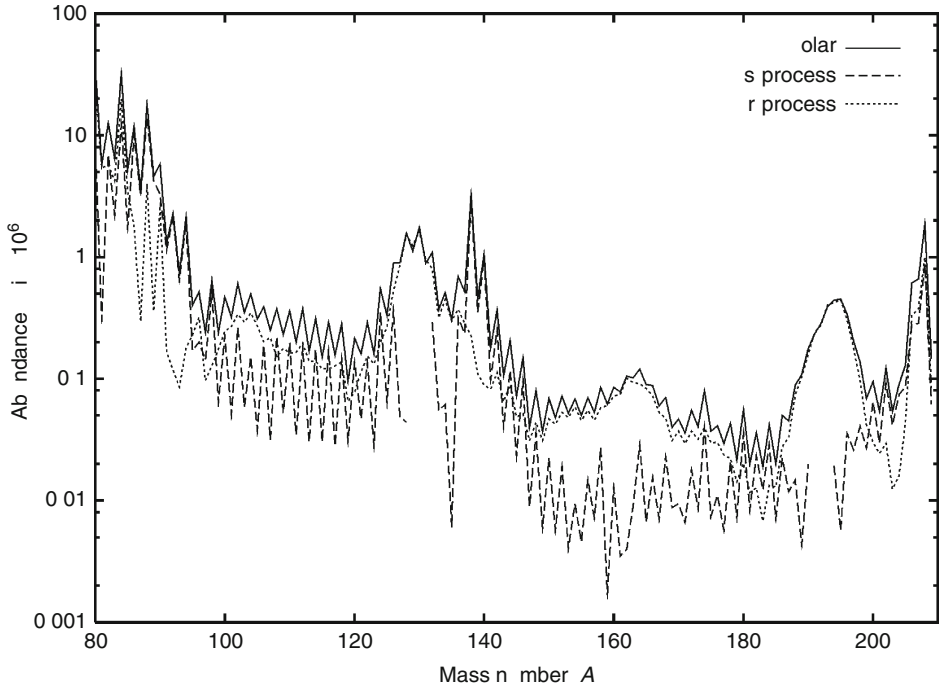


The reaction on ${}^{13}\text{C}$ is much more efficient in releasing neutrons because it is strongly exothermic, as opposed to the second reaction. However, ${}^{13}\text{C}$ normally does not occur in He-burning zones whereas ${}^{22}\text{Ne}$ does. This proved to be a longstanding problem in complete stellar simulations of s-process nucleosynthesis.

Early observations (see Burbidge et al. 1957) had already found Tc on the surface of AGB stars. Since Tc isotopes are short lived compared to the age of such a star, they had to be produced in that star and brought up to the surface. Only in recent years, sophisticated stellar models were able to follow the complicated convection and nucleosynthesis processes inside AGB stars with sufficient accuracy to confirm them as the production sites. He-shell flashes (see [Sect. 12.4.3](#)) and the mixing brought about by them turned out to be the key (Busso et al. 2001; Boothroyd 2006). Such a flash can mix down protons from the unburnt outer layer of the star, which can then be used to produce ${}^{13}\text{C}$ by proton capture on ${}^{12}\text{C}$ and subsequent β -decay of the resulting ${}^{13}\text{N}$. With this ${}^{13}\text{C}$ neutrons can be very sufficiently released even during the interpulse phase. Additionally, the reaction on ${}^{22}\text{Ne}$ can release further neutrons during the high temperature phase of the flash itself. Thus, the nuclides in the stellar plasma are irradiated with neutrons in bursts over millennia. The large convection zones appearing in the flash phase bring up the newly synthesized material to the surface.

■ Fig. 12.12

Contribution of s- and r-process to the solar abundances of the isobars for heavy elements (p-isotopes cannot be seen in this figure because of their very small abundances). Solar system abundances are measured (Anders and Grevesse 1989), s- and r-abundances are calculated. The peaks in the solar abundances around mass numbers $A = 88, 138, 208$ are formed in the s-process, whereas the broader companion peaks shifted to slightly lower mass number are r-process peaks



In the manner described above, AGB stars produce the majority of the s-process nuclei, the so-called main component. It was known for a long time that there must be a second site of s-processing, producing light s-nuclei. Because they exhibit smaller abundances than those of the main component, this was called the weak component. Such a weak s-process is found in massive stars (i.e., stars with more than 8 solar masses), where capture of ^4He by ^{22}Ne is the main neutron source. Massive stars reach higher temperatures than AGB stars already in their late evolution stages, which help to release neutrons. Even more neutrons can be released during explosive burning, when the temperature rises due to the supernova shock wave passing through the outer layers of the star. Because of the inefficiency of the ^{22}Ne neutron release and the short timescale, this mechanism cannot proceed much beyond Fe in massive stars.

For nucleosynthesis of the heavy elements through the s-process in both AGB and massive stars, there already must be nuclei present in the iron region, which were produced in previous generations of stars. Thus, the s-process will be stronger in stars formed more recently than in older stars containing less heavy elements.

12.4.5.2 Explosive Nucleosynthesis in the Outer Layers of a Massive Star

Since the buildup of nuclei in the s- (and r-) process follows the neutron-rich side of the stability valley (see, e.g., ► Fig. 7.13 in Chap. 7, Vol. 1), 32 proton-rich isotopes cannot be produced in either process. These so-called p-nuclides occur naturally but with abundances many orders of magnitude lower than the other nuclides. The hypothetical process synthesizing these nuclides was termed p-process and several models have been suggested. The commonly favored one is photodisintegration of preexisting nuclei in the Ne/O shells of massive stars. When a supernova shockfront is passing through these layers, the high temperatures of 2–4 GK enable photodisintegration, starting with γ -induced emission of several neutrons, leading to proton-rich nuclei. The photodisintegration path can branch when proton or α emission becomes more favorable than neutron emission in such proton-rich nuclei. The bulk of p-nuclides can be explained in such a model but some problems remain (Rauscher et al. 2002; Arnould and Goriely 2003; Boyd 2008). Especially the production of the light p-isotopes, in particular $^{92,94}\text{Mo}$ and $^{96,98}\text{Ru}$, is not understood. Among the p-nuclei they have by far the highest abundance but cannot be produced concurrently with the others. It remains an open question whether the stellar models have to be revised or an additional production mechanism has to be invoked for these light p-nuclei.

The neutrino flux of a core-collapse supernova is high enough to contribute to the nucleosynthesis of certain rare elements and isotopes, even in the outer layers of the star. In this so-called ν -process, inelastic scattering of a neutrino leads to formation of an excited daughter nuclide, which then decays by particle emission. This process can contribute significantly to the production of light (^{11}B , ^{19}F) and heavy (^{138}La , ^{180}Ta) nuclides (Woosley and Weaver 1995; Heger et al. 2005).

12.4.5.3 Explosive Burning in the Deep Layers of a Massive Star

In addition to s-process nucleosynthesis, about half of the nuclides beyond Fe are produced through rapid neutron captures on short timescales in the r-process. The site of the r-process is controversial. Mostly favored are core-collapse supernovae where appropriate r-process conditions are thought to be found close to the region of neutron star formation. These innermost layers, which are barely ejected, move outward within a strong neutrino flux, driving the material to become very neutron rich. With a high neutron density, neutron captures can proceed much faster than β -decays and produce very neutron-rich nuclei far from stability. Through simultaneously occurring captures, photodisintegrations with neutron emission, and β -decays, heavier elements are synthesized within a few seconds. When the ejected material cools down, those highly unstable nuclei decay back to stability, thus supplying the needed fraction of heavy elements. While the s-process is confined to the region up to Bi, the r-process is thought to also reach the region of fissionable nuclei and produce natural, long-lived elements such as U. The endpoint of the r-process path is highly debated since it depends on fission barriers of very neutron-rich, heavy nuclei, for which there is no consensus among theoretical models yet.

The conditions in those innermost regions of a core-collapse supernova are closely linked to the working of the explosion mechanism. Since the latter is not yet fully understood, it is not yet clear whether the required conditions can actually be established. Therefore, a number of alternative scenarios are still discussed, such as jet outflows from asymmetrically exploding stars. The search for the site of the r-process remains a major focus of research.

Recently, an additional nucleosynthesis process in the deep layers of the exploding star has been suggested (Fröhlich et al. 2006). It was discovered that the combined flux of neutrinos and antineutrinos from the emerging, hot neutron star initially creates very proton-rich conditions before the matter becomes neutron rich at later times and/or larger radii. The high temperature and density environment gives rise to rapid proton captures, thus synthesizing nuclei beyond Fe but on the proton-rich side of stability. A small number of neutrons are required to speed up the matter flow to heavier elements and these are produced by antineutrino captures on protons. The vp-process could perhaps explain the surprisingly high abundance of Sr, Y, and Zr found in very old stars (Travaglio et al. 2004; Frebel et al. 2005). Again, the details of this so-called vp-process (including the question of how efficiently it can produce elements beyond Fe) depend strongly on the conditions in the deep layers of the exploding star and the explosion mechanism. Among the suggested alternative scenarios are wind outflows from the accretion disks around black holes formed by core collapse of very massive stars (Surman et al. 2006). These are also thought to be the cause of so-called γ -ray bursts, which are the most energetic phenomena observed in our Universe today (MacFadyan and Woosley 1999; Mészáros 2006).

12.4.6 Nucleosynthesis by Spallation

The light and fragile elements lithium, beryllium, and boron (LiBeB) are not primarily produced in primordial or stellar nucleosynthesis. In fact, the abundance curve in [Fig. 12.13](#) shows a huge dip (almost a gap, actually) for the mass numbers 8–11, reflecting the scarcity of LiBeB-nuclei in the solar system. Only the nuclide ${}^7\text{Li}$ can be produced both in primordial (see [Sect. 12.3](#)) and in stellar nucleosynthesis (see [Sect. 12.4.2](#)), whereas the nuclides ${}^6\text{Li}$, ${}^9\text{Be}$, ${}^{10}\text{B}$, and ${}^{11}\text{B}$ are almost pure spallation products of heavier elements.

The high-energetic galactic cosmic rays (GCRs) originate probably from supernovae (Erlykin and Wolfendale 2001). GCRs consist mainly of fast-moving bare hydrogen and helium nuclei and, to a lesser amount, of carbon, nitrogen, and oxygen nuclei (CNO)-nuclei. Hydrogen and helium nuclei of interstellar clouds can spall the CNO-nuclei in flight of the fast GCRs. Therefore, the GCRs are by about a million times enriched in LiBeB-nuclei compared to the solar system abundance.

The most plausible origin of the main bulk of LiBeB-nuclei is that hydrogen and helium nuclei of GCRs hit and spall CNO-nuclei contained in interstellar clouds. However, this process alone seems unable to produce LiBeB at the observed level. Therefore, another production site of LiBeB-nuclei has been proposed. This invokes in-flight fragmentation of carbon and oxygen nuclei by collision with hydrogen and helium nuclei in interstellar clouds. The sites of this process are mainly the surroundings of massive stars, which are able to furnish freshly synthesized carbon and oxygen nuclei and accelerate them via shock waves. Finally, spallation through neutrinos in supernova explosions also produces the nuclides ${}^7\text{Li}$ and ${}^{11}\text{B}$ (Hartmann et al. 1999).

A review of nucleosynthesis by spallation is given by Vangioni-Flam et al. (2000).

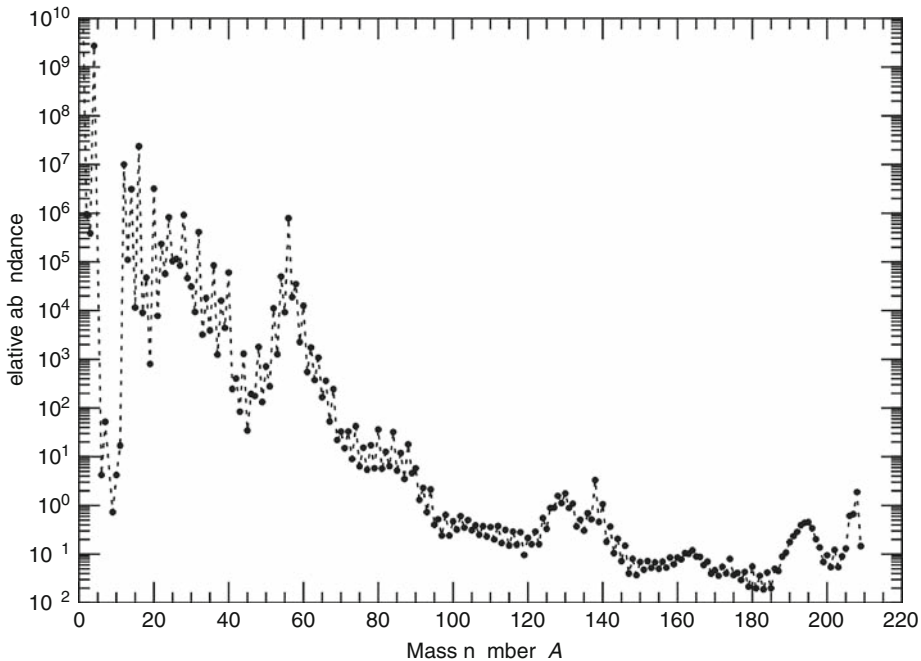
12.5 Nucleosynthesis in Binary Star Systems

12.5.1 General Considerations

Observations reveal that more than half of the known stars are associated in binary or multiple systems. In many such systems, the stars are so well separated that there is negligible influence

■ Fig. 12.13

Relative solar abundances by mass number. Data are from Anders and Grevesse (1989). The abundances are arbitrarily renormalized to yield a value of 10^6 for silicon



on each other's evolution. However, when the constituents of such a system are close, a range of interesting physical phenomena can ensue. Mass can be transferred from one star to the other when the donating star becomes so large that its atmosphere extends beyond the limiting region where the gravitational attraction of the two stars is equal. Material is then escaping from the gravitational well of the donor and flowing into the attractive field of the other object. It can be shown that there is a single point of gravitational equilibrium between the two objects, through which the mass transfer will occur. The volume around a star enclosed by the equipotential surface containing this point is called the Roche lobe. A star can fill or exceed its Roche lobe when it either increases its radius in the normal course of evolution (e.g., by becoming a Red Giant), or when the orbital separation of the two objects is decreasing due to the emission of gravitational waves. The latter situation corresponds to shrinking their respective Roche lobes. The inflow onto the surface of the companion can alter its surface properties, which is manifested, for instance, in the observed spectra. The further evolution might even lead to powerful explosions. A broad review of such phenomena is given by Warner (1995).

From the point of view of nucleosynthesis, explosive burning in such binary systems proves to be especially important as nuclides created in such an environment can be injected into the interstellar medium by the explosion. Furthermore, the nucleosynthetic signature will be different from stellar hydrostatic and explosive scenarios due to the different initial and burning conditions. Thus, different isotopic ratios can be obtained and, in some cases, it is possible to synthesize nuclides not accessible in other sites. In the following, therefore the main focus is put on outlining only such scenarios, which might have an impact on the abundances

of elements observed in our Galaxy and the Universe. It has to be emphasized, however, that it is not yet possible to model all details of the explosive processes, due to the complexity of a multidimensional hydrodynamic problem including scales differing by many orders of magnitude. The problems are similar to those occurring in core-collapse supernova models. In scenarios where neutron stars are involved, additional uncertainties in the nuclear equation of state enter. As a result, a detailed, quantitative understanding of some of the processes is still lacking. Nevertheless, the basic features of all the processes can be described qualitatively in simplified models.

12.5.2 Novae

Historically, the Nova phenomenon is one of the oldest observed. Already astronomers of ancient civilizations were aware of sudden appearances of bright stars in the sky, at a position where no star had been observed before. This was termed “nova” as in “new star.” Modern astronomy was able to identify nova progenitors. These are faint stars (mostly undetectable by the naked eye), which suddenly increase their brightness by several stellar magnitudes (i.e., their energy output increases by a factor of 100–100,000) within a few days. The star returns to its initial brightness after several months. In rare cases, the same star experiences another nova outburst within several years. This is called a recurring nova. In general, classical novae reappear only every 100 to 10,000 years.

The modern explanation of the Nova phenomenon invokes a binary system with a regular star in its early burning phases and a white dwarf (Fujimoto 1982; Truran 1984; Gehrz et al. 1998; Starrfield 1999). The latter is too faint to be directly observed. Such a system can have originated from two low-mass stars, one of them slightly more massive than the other. More massive stars evolve faster and thus the heavier star already underwent its complete stellar evolution and left a white dwarf as a remnant, while the other star has not yet even completed its early phases. From the atmosphere of the main sequence or red giant star, hydrogen-rich material is flowing across the Roche surface. It is captured by the gravitation of the white dwarf forming an accretion disk around it. Subsequently, the gas is accreted on the surface of the companion, forming a thin layer. Close to the surface, the gas becomes degenerate, delaying the onset of hydrogen burning. As soon as the necessary density and temperature is reached, hydrogen burning ignites explosively, pushing outward and ejecting part of the outer accreted layer. With the sudden expansion, temperature and density are dropping again and the burning ceases. It can reoccur as soon as a sufficient amount of new material has been accreted, which usually takes several thousand years at typical accretion rates of less than 1 Earth mass per 10 years.

In terms of nucleosynthesis it should be obvious that nova ejecta are mainly hydrogen and that they more or less retain the surface composition of the accompanying star. However, it was found observationally that they are also strongly enriched in C, N, and O. This has been a puzzle for over 2 decades (Rosner et al. 2001). In the thermonuclear runaway triggered by hydrogen ignition the main reaction sequences are those of the CNO-cycles. However, they can account neither for the observed enrichment nor for the energy production required for a fast nova burst. Currently, it is thought that material from the surface of the white dwarf might be dredged up and efficiently mixed into the burning layer and the outer zones. This would increase the CNO energy production and also provide a mechanism for the enrichment. However, to date one-dimensional and multidimensional simulations have not been able to account for the observations (Starrfield et al. 2000; Kercek et al. 1999). Nevertheless, it seems

that novae are “digging up the ashes” of previous stars and distributing them throughout the Galaxy. They are considered to be the major sources of ^{15}N , ^{17}O , and ^{13}C , and to have minor contributions to a number of additional species, mainly ^7Li and ^{26}Al . For current reviews on the nucleosynthetic contribution of novae, see Jordi and Hernanz (2007, 2008).

12.5.3 Type Ia Supernovae

Given a binary system consisting of a white dwarf and a companion star as in the nova case, the accretion rate on the surface of the white dwarf is essential for further development. Low accretion rates lead to a nova as described above. When the accretion rate exceeds about 10^{-8} solar masses per year, hydrogen can be quiescently burned during accretion and the burning products will sediment on the surface of the white dwarf, forming a He layer. The details on the further fate of the object are complicated and have not been fully simulated yet. Basically, two ways of explosion can be envisioned. In the first, the ignition of the He layer leads to a thermonuclear runaway, this time mainly burning via the triple- α reaction, not depending on CNO elements, contrary to novae. Nevertheless, the resulting explosion would lead to an expulsion of the outer layers, like in a nova, only much more powerful. The second type of explosion occurs when the accretion rate is even higher, about 10^{-6} solar masses per year. The energy released by the accretion and by burning layers heats the C/O core of the white dwarf sufficiently to ignite core C burning. This is followed by a complete disruption of the white dwarf because the nuclear energy exceeds the gravitational binding energy (Leibundgut 2001a, b).

The latter is the currently most widely accepted scenario explaining SN Ia (Nomoto et al. 1984; Hillebrandt and Niemeyer 2000). It is encouraging that observations can confirm also the basic nucleosynthesis features expected. In each explosive event, a quantity of material of the order of 0.6–0.8 solar masses is produced in the ^{56}Ni region, which later decays to its stable isobars. Thus, the larger part of the Fe found in the solar system stems from SN Ia. In addition, some intermediate elements like Mg, Si, S, and Ca are also produced.

The details of the shockwave propagation and explosive burning are not fully understood yet. However, the total energy production remains robust due to the fact that the initial white dwarf mass is always close to the Chandrasekhar limit of 1.4 solar masses. This fact, in combination with the observational evidence that there are no compact central objects (i.e., neutron stars) found in SN Ia remnants, puts a strong constraint on the achieved explosion energy. This is why type Ia supernovae are thought to be excellent standard candles with very low variation in the effective energy output (Dominguez et al. 2001; Leibundgut 2001a, b). Type Ia supernovae as standard candles are important tools to measure astronomical distances although there is no firm theoretical grounding of the Phillips relation (see ► Sect. 12.2.1.4) yet.

12.5.4 X-ray Bursts and the rp-Process

Bursts have been observed not only in the optically visible frequency range of light. Powerful, brief bursts of X-rays are also observed throughout the Galaxy. A binary system is suggested to be responsible for one subclass of these bursts. Their duration is from several seconds up to minutes and they show a fast rise and a slowly decaying tail. In the assumed scenario, a main-sequence star and a neutron star are orbiting the common center of mass. As in the nova and SN Ia case, material is flowing from the atmosphere of the companion star and is accreted on

the surface of the compact object. Due to the increased gravitational field of the neutron star in comparison with a white dwarf, the thermonuclear runaway after ignition of hydrogen burning can proceed differently from the one in novae and supernovae (Taam et al. 1996; Schatz et al. 1998; Wiescher and Schatz 2000; Boyd 2008). Hydrogen and subsequently also helium, burn explosively at higher temperatures as before. First, the so-called hot CNO-cycle (also found in certain massive stars) is established, followed by further CNO-type cycles beyond Ne. The energy production from these cycles leads to a breakout to further CNO-type cycles beyond Ne at temperatures surpassing 4×10^8 K. The additional cycles generate additional energy, further increasing the temperature. In the next stage of the ignition process, He is also burned in the triple- α reaction. The CNO-type cycles break up toward more proton-rich nuclides by (α , p) and (p, γ) reactions.

Finally, the rp-process (rapid proton capture) sets in. In the rp-process, similar to the r-process for neutrons, proton captures and photodisintegrations are in equilibrium. Thus, the abundances within an isotonic chain are only determined by temperature, density, and the proton separation energy of a nucleus. The timescales of flows from one chain into the next are given by β -decay half-lives. The reaction path basically follows the proton dripline. The processing of matter is hampered at nuclides with long half-lives, the so-called waiting points, which determine the processing timescales. A final endpoint of the rp-process path was found in a closed reaction cycle in the Sn–Sb–Te region, due to increasing instability against α decay of heavy proton-rich nuclides (Schatz et al. 2001).

Time-dependent calculations showed that the structure of type I X-ray bursts can be explained by the energy generation of the proposed processes. Regarding nucleosynthesis, it is being discussed whether a fraction of or all light p-nuclei (see [Sect. 12.4.5.2](#)) originate from X-ray bursters. Since the rp-process synthesizes very proton-rich nuclei, they would decay to p-nuclei after the burning ceased. Since it proved to be problematic to synthesize the light p-nuclei with mass numbers $A < 110$ in the γ -process by photodisintegration ([Sect. 12.4.5.2](#)), the rp-process provides a compelling alternative to such models, especially after the discovery of its endpoint, preventing the production of nuclides with mass numbers $A > 110$. Although it was shown that the isotopes in question can be produced in large quantities, it is still speculative whether any of the material is ejected. There could be a very small fraction of material lost from the outer atmosphere of the accreted layer on the neutron star surface but the rp-process burning takes place further down. Therefore, some convection has to be invoked to bring the freshly produced nuclei to the outer layers. Comparatively small amounts of ejecta would be sufficient to explain solar p-abundances but detailed hydrodynamic studies of the burning, convection, and possible ejection are still needed.

12.5.5 Neutron Star Mergers

Another interesting binary system is that of two neutron stars. Such systems are known to exist; four have been detected by now. They can be created when two massive stars complete their stellar evolution and both explode in a core-collapse supernova, each leaving a neutron star behind. In such a configuration, the system loses angular momentum by emission of gravitational radiation (Taylor 1994) and the two neutron stars spiral inward. At timescales of 10^8 years or less, the objects collide at their center of mass. Such a merger can lead to the ejection of neutron-rich material (Rosswog et al. 1999; Ruffert and Janka 2001). Since this material is even more neutron rich than the deep, high-entropy layers thought to be a possible site of the

r-process in core-collapse supernovae, nucleosynthesis in decompressed neutron star matter could be a viable alternative site for the r-process (Freiburghaus et al. 1999). Detailed hydrodynamic calculations coupled to a complete r-process reaction network have not been undertaken yet, but parameterized r-process studies indicate the possibility that such mergers could even account for all heavy r-process matter in the Galaxy. However, detailed galactic chemical evolution models (Argast et al. 2004) show that neutron star mergers, occurring at late time in the life of a galaxy, cannot account for the r-process nuclei found in very old stars (Snedden et al. 2000; Cayrel et al. 2001; Frebel et al. 2005). Therefore, there may be several sites producing r-process nuclei, perhaps similar to the two components of the s-process (but occurring in different sites than the s-process, of course).

12.6 The Abundance of Elements in the Universe

12.6.1 Experiments and Observations

The essence of every science is the ability to validate theories by comparison to experiments. The ability to perform guided experiments is somewhat limited in astrophysics because of the large scales and extreme conditions involved. Nevertheless, there is a wealth of data to be exploited. Atomic transitions and certain nuclear reactions (Käppeler et al. 1998) can be studied in the laboratory with current methods.

Since the s-process (Sect. 12.4.5.1) involves mainly stable nuclei, an important experimental contribution is the one studying neutron capture at low energy. Special focus is put on reactions at s-process branchings. For the majority of unstable nuclei reached through the s-process, β -decays are much faster than the neutron captures. At several places in the nuclear chart, however, the s-process path encounters long-lived nuclei for which the decay rate becomes comparable to the neutron capture rate. This leads to a splitting of the path: a fraction of the s-process flow proceeds through neutron capture, the other through the decay, bypassing certain isotopes. A comparison of abundances of nuclei reached through one or the other branch provides information on the relation between decay and capture rate. Due to the different temperature dependence of capture and decay, the branching ratio is dependent on temperature, becoming a sensitive s-process “thermometer.” The capture rate also depends on the neutron density and thus such a branching can also be used as a neutron pycnometer. This yields detailed information on the conditions inside an AGB star. To be useful, neutron capture cross sections have to be known with an accuracy of better than 1% below about 50 keV neutron energy. This has been achieved for some target nuclei but remains a challenge for others. High-resolution time-of-flight experiments are most promising to give the required accuracy and provide cross sections within the required energy range. The cross sections have to be converted to reaction rates to be applied in astrophysical models. The Karlsruhe group (Käppeler et al. 1989) has had a leading role in directly determining rates by using a neutron spectrum created by the ${}^7\text{Li}(p, n){}^7\text{Be}$ reaction. Through this trick, the resulting energy distribution of the released neutrons is very similar to the one of neutrons in stellar plasma with thermal energy of 25 keV, coinciding with s-process conditions. The limitation of this technique is that it can only provide the spectrum at this energy.

The predictions of reaction models giving cross sections relevant to the production of p-nuclei and of the nuclear properties required in such calculations can also be tested by using neutron and charged particle reactions on stable targets (Descouvemont and Rauscher 2006).

Some of the accessible reactions are directly important in the nucleosynthetic processes while other experiments can only serve as tests of the theoretical approaches (Kiss et al. 2008). The reactions can either be studied in online beam experiments detecting directly emitted γ -rays or particles. Another important type of experiment is that of activation (see, e.g., Gyürky et al. 2006, and references therein). A material sample is activated by neutron, proton, or α beams at the energy of interest and the long-term radiation is counted over an extended period of time. Alternatively, the amount of the nuclei produced by the activation can be measured by the very sensitive accelerator mass spectrometry (AMS), which has become an important tool also for astrophysical measurements. It is especially well suited to study neutron-induced reactions producing different isotopes of the same element.

The advent of radioactive ion beam (RIB) facilities in nuclear physics allows studying the properties of and reactions with unstable nuclei (Käppeler et al. 1998; Thielemann et al. 2001b; Rauscher and Thielemann 2001). In addition to the few, already existing, smaller RIB facilities in Europe, Japan, and the USA, one large-scale facility is under construction at GSI Darmstadt, Germany, and another large-scale facility has recently been funded in the USA, the Facility for Rare Isotope Beams (FRIB) at Michigan State University. Both the GSI FAIR (Facility for Antiproton and Ion Research) and FRIB will allow producing highly unstable nuclides, both on the proton- and neutron-rich side of the chart of nuclides. For the first time, this will enable us to study nuclear properties of the p- and rp-processes directly, and also close to the r-process path. These investigations will largely improve the understanding of explosive nucleosynthetic processes.

Plasma physics experiments describe the properties of hot and thin plasmas. Utilizing data from laser-induced plasmas or nuclear testing allows drawing conclusions on the behavior of matter under conditions that are to a certain extent close to those found in stellar environments. Hydrodynamic simulations can also be validated against test cases drawn from experiments and terrestrial experience. However, large nuclear reaction networks involving highly unstable nuclei, extended stellar atmospheres with complicated mixing processes, or macroscopic amounts of matter at and beyond nuclear densities are only accessible by theoretical methods. The models have then to be tested ultimately against astronomical data. The latter have almost exclusively been observations in the electromagnetic spectrum, starting from the ancient observations of visible light coming from the Sun and the stars, to modern satellite observatories also exploring other frequency ranges and studying emissions of compact objects, faint galaxies, accretion disks, quasars, and the echo of the Big Bang, the cosmic microwave background. It is amazing how much has already been learned about the structure and history of the whole Universe by just examining the faint light reaching the surface of our tiny planet. The upcoming new missions of ground- and space-based observatories guarantee an increasing inflow of data, securing the development of the related fields and ensuring that this research field stays exciting and is still able to provide new insights.

In addition to the observation in the electromagnetic spectrum, other means of obtaining astrophysically relevant information become increasingly important. Among those are measurements of cosmic rays, on the surface and in the atmosphere of Earth, as well as in low-earth orbits (Westphal et al. 1998, 2001). Such investigations provide insights regarding the particle flux in our solar system, originating from the Sun and from galactic sources. In the future, it will be possible to study another type of radiation in addition to the electromagnetic one: gravitational waves emitted, e.g., by neutron star mergers, black hole formation, and other interactions between highly massive or relativistic objects (Sathyaprakash and Schutz 2009). Even more important for studying nucleosynthesis and stellar evolution are the isotopic ratios found in

certain meteoritic inclusions (Lugmair et al. 1983; Lewis et al. 1987; Hoppe and Zinner 2000). Using advanced chemical extraction methods, these data can be utilized to deduce the composition of the material in the early solar system. Because of its growing importance for nucleosynthesis studies, the field is introduced in a separate subsection (► Sect. 12.6.3).

12.6.2 Solar Abundances

As might have become evident from the previous sections, the origin of the elements can only be understood in detail when the physics of the nucleosynthesis sites is also understood. Complete simulations of nucleosynthetic events that account for all data are required, not just those giving details of elemental or isotopic abundances. Nevertheless, the determination of abundances remains central if one wants to study nucleosynthesis.

By inspection of the absorption lines in stellar spectra, it is possible to measure the contents of the stellar atmosphere. A theoretical model has to explain how many of those nuclides were inherited from the proto-cloud from which the star formed and what amount was produced in the central, nuclear burning regions of the star itself and brought up by convection.

Similar considerations apply to the observation of absorption and emission lines from other objects, such as supernova ejecta, planetary nebulae, and interstellar clouds. Some methods and results were already presented in ► Sect. 12.3.3.

On the way to understand the origin of elements on Earth, the abundances in the Sun have to be explained first because the planets and the Sun formed from the same interstellar cloud. Due to their low gravitation, the smaller planets subsequently lost those light elements that were not chemically bound in their crust whereas the Sun was able to retain more or less the original composition. In planets, physical and chemical fractionation processes then separated certain elements or isotopes and concentrated them in different regions, leading to the heterogeneous distribution found, e.g., in geological surveys. The solar composition is shown in ► Fig. 12.13. As an example of how the solar composition affects nucleosynthesis studies is shown in ► Fig. 12.12. In order to constrain the relative contributions of the s- and r-process, the solar abundances are used to represent the current composition of the local interstellar medium.

The accurate determination of solar abundances is, therefore, central to all investigations of nucleosynthesis. This is reflected in the recent commotion caused by a new study of solar abundances (Asplund et al. 2006a, b), revising the previously widely used tables of Anders and Grevesse (1989). The new abundances are based on modern three-dimensional model atmospheres (describing the region in the Sun where line absorption occurs). The content of elements beyond H and He was found to be lower by a factor of two compared to the previous study. This finding impacts all kinds of comparative nucleosynthesis studies but mainly those involving C, N, and O, which are the most abundant (apart from H and He). The new abundances resolved previous problems regarding the consistency of solar abundances and those of the solar neighborhood. On the other hand, they challenge current models of the solar interior, especially regarding the comparison of predictions of the local sound speed (which is also dependent on the abundances of C, N, O, Ne) and helioseismological results.

12.6.3 Meteoritic Inclusions

In addition to abundance determinations from stellar spectra, another way to obtain information about the composition of the early solar system as well as of environments that are

more distant has become increasingly important in the last years. Certain types of meteorites contain inclusions wherein the composition of the early presolar cloud is conserved. This also enables one to study some isotopic compositions that cannot be extracted from the solar spectrum. More surprisingly, some meteorites contain so-called presolar grains, which are supposed to have been formed from material of other stars. The grains traveled through interstellar space with their inherent speed at formation and were incorporated into the protosolar cloud from which the Sun and its planets formed. Some of them survived the formation of the solar system and also the fall as a meteorite. This requires that their host material never experienced temperature above about 1,000 K. Various types of meteorites, most prominently carbon-rich ones (carbonaceous chondrites) carry such nm- to μm -sized inclusions, which were incorporated into the presolar cloud and were since then shielded from any chemical or physical fractionation and mixing processes occurring during planet formation or in the Sun.

Literally being “stardust,” presolar grains provide information not just on the isotopic composition of other stars that cannot be determined through their spectra. Additionally, they may show the composition of different layers of a star depending on their formation process. There are a number of excellent reviews on the topic (e.g., Nittler 2003; Clayton and Nittler 2004; Zinner et al. 2006; and the book by Lugaro 2005). Therefore, here only a summary of the most important aspects regarding types and origins of presolar grains and the methods to analyze them (see also [Chap. 54 of Vol. 5](#)) is presented.

Presolar grains are foremost identified by their nonsolar isotopic composition. They are subsequently classified by the mineral phase carrying the isotopes and by the isotopic ratios of certain elements (mainly C, N, O, Si, Al, and Fe). Most abundant but the least understood are nanodiamonds. Best studied are the second most abundant SiC grains. Further phases include, in order of abundance, graphite, TiC, ZrC, MoC, RuC, FeC, Fe–Ni metal, Si_3N_4 , corundum, spinel, hibonite, and TiO_2 .

The well-studied SiC grains can be subdivided into different classes according to the isotopic anomalies (relative to solar) they exhibit. The bulk of 90% is made up of so-called mainstream grains, which are thought to originate from AGB stars, showing almost pure s-process isotopic ratios. They are inferred to have formed in the winds of AGB stars or planetary nebulae. Therefore, they are a snapshot of the surface composition of the star but AGB stars, contrary to other types of stars, have strong convection, carrying freshly synthesized nuclides from the burning zone deep inside the star to the surface ([Sect. 12.4.5.1](#)). Much of the recent progress on the nucleosynthetic details of the s-process in recent years is due to the analysis of presolar grains.

A small subclass of SiC grains, the so-called type X grains, contain a large $^{26}\text{Mg}/^{24}\text{Mg}$ ratio and large excess of ^{44}Ca , pointing to a core-collapse supernova origin. The radionuclides ^{26}Al and ^{44}Ti are concurrently produced only in such supernovae and decay to ^{26}Mg and ^{44}Ca , respectively. The SiC X grains are thought to be formed in supernova ejecta. As these consist of a large fraction of the progenitor star, grains can also condensate from material of inner layers or from a mixture of different layers of the star. There is some success in reproducing X grain compositions by mixing abundances predicted by current stellar models.

The origin of other types of grains is still debated and a unique identification with a site is not always possible. They could have been produced in supernovae, AGB stars, or novae.

The analysis of the content of a grain requires a combination of chemical and physical methods to separate the grain from the surrounding meteoritic material and to determine the isotopic abundances contained within. Luckily, mineral phases condensing in the vicinity of stars contain acid-resistant phases, which can be separated from the meteorite by essentially

dissolving everything else away. Until recently, this was the way to go but it has the disadvantage that other, less acid-resistant, presolar phases, e.g., silicates, may be lost in the process. Once the grain material has been isolated and concentrated, standard mass spectrometric methods (with AMS being the most sensitive) can be applied. A complete analysis of the presolar content, including more easily dissolvable materials, requires new analytic methods, currently under development. Among those is resonance ionization mass spectrometry (RIMS), which allows measuring ppm-level trace elements in μm -sized grains with elimination of isobaric interferences. Even more promising is the NanoSIMS, an ion microprobe with high sensitivity and high spatial resolution (Stadermann et al. 1999; Marhas et al. 2008). The NanoSIMS allows studying a grain in a slice of a meteorite to obtain isotopic abundances with information on their location within the sample. This enables studies of layered grains in their meteoritic matrix and also grains made up of easily dissolvable phases. This is superior to TEM (transmission electron microscope) analysis, which requires ultrathin samples cut with diamond knives and losing some depth information. Nevertheless, the TEM can sometimes be complementary to a NanoSIMS analysis.

Presolar grains open a new, promising window into the Universe by enabling us “hands on” analysis of nonsolar, stellar matter. With improved preparation and analysis methods, this line of research will remain important for many types of nucleosynthesis studies, even directly impacting the theory of stellar structure and evolution.

12.6.4 Galactical Chemical Evolution: Putting it all Together

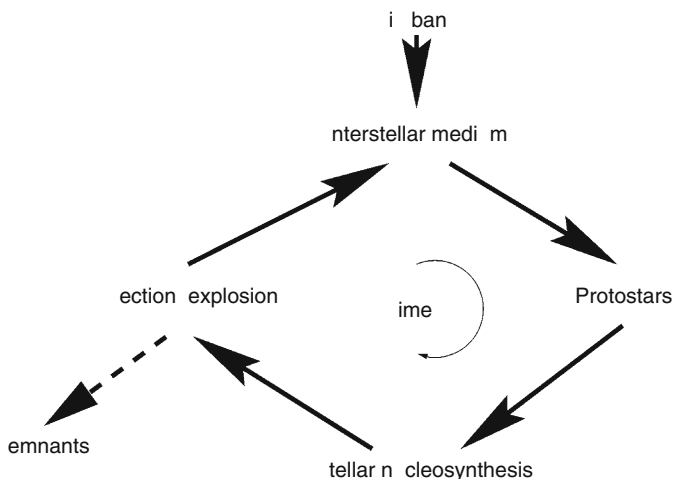
Although the Sun is considered to exhibit a composition typical of the disk of the Galaxy, it has to be realized that its abundances are only a snapshot in time. As is evident from the discussion in the preceding sections, the Sun contains elements, which have been produced in other stars or galactic sites and the solar abundances (● Fig. 12.13) are only a snapshot of the composition of the interstellar medium. After the first stars in the galaxies lit up, numerous generations of stars have contributed to the elemental contents of the interstellar material from which new stars form. The current stars, on the other hand, are building up material that will be incorporated in future stellar generations. All this is illustrated by the fact that a gradient in metallicity is observed depending on the age of the star (see ● Sect. 12.3.3). Older stars contain less “metals,” i.e., elements other than H and He, because the interstellar medium from which they formed contained less. Therefore, it becomes obvious that the interstellar medium in a galaxy becomes enriched with elements over time. The general picture is that of a cycle of matter within a galaxy as shown in ● Fig. 12.14.

The primordial galactic material is processed and reprocessed in star-forming regions many times. Indeed, a general enrichment can actually be found when comparing galaxies of different ages.

We do not know how many generations of stars have contributed to the solar abundances and how well the products were mixed into the proto-solar cloud. Therefore, a comparison with abundances in old stars allows drawing conclusions on the relevant processes. For example, recent observations in stars found in the halo of the Galaxy show that the relative r-process abundances are very similar to the ones in the Sun, although very much depleted (Snedden et al. 2000; Cayrel et al. 2001; Frebel et al. 2005). This indicates that the r-process seems to be robust, i.e., occurring under almost the same conditions and giving almost the same elemental yield in each event.

■ Fig. 12.14

Schematic view of the cycle of matter in a galaxy



For a complete understanding of the chemical evolution of a galaxy it is necessary to integrate over the yields of all possible contributors. With the advent of advanced stellar models, galactic chemical evolution has become a field of its own, providing further constraints to the nucleosynthetic models. Many considerations enter, such as the amount and composition of ejecta per event, frequency of events, and mixing processes that distribute matter within a galaxy (Pagel 1997). Thus, all available knowledge is combined to reach an improved level of understanding. However, the young field of galactic chemical evolution still faces major difficulties due to the timescales involved, the limitations in observations and models, and the impossibility of accurately dating stars and galaxies. One of the big questions is how material is mixed and transported. Nevertheless, recent promising trends in modeling galactic evolution might even provide constraints, e.g., on individual supernova models rather than only on global properties of SN II and SN Ia. The reason for this possibility is the fact that there is no instantaneous mixing of ejecta with the interstellar medium, and therefore early phases of galactic evolution can present a connection between low metallicity star observations and a single supernova event (Argast et al. 2000).

To summarize, it is worth emphasizing again the tremendous achievements obtained over the last decades. Accurate and detailed studies made it possible that, coming from more simple observations of the Sun and nearby stars, one reached the stage where details of the origin of chemical elements and their isotopes on our planet as well as the evolution of their abundances in entire galaxies and in the early Universe can be studied. It is especially amazing that all this knowledge was gathered without really or just barely leaving the surface of our planet.

Future efforts in nuclear physics and astronomy ensure that the stream of data will not be cut off and will greatly improve our detailed knowledge not only of the origin of the elements but also of the position of our Galaxy, our planet, and ourselves within a vast, evolving Universe.

References

- Abazajian KN et al (2009) *Astrophys J Suppl* 182:543
- Adelmann-McCarthy JK et al (2006) *Astrophys J Suppl* 162:38
- Alcock CR et al (2000) *Astrophys J* 542:281
- Alpher RA, Gamow G, Hermann R (1948) *Phys Rev* 74:1198
- Amsler C et al (2008) *Phys Lett B* 667:1
- Anders E, Grevesse N (1989) *Geochim Cosmochim Acta* 53:197
- Anderson SF et al (2001) *Astronomical J* 122:503
- Argast D, Samland M, Gerhard OE, Thielemann F-K (2000) *Astron Astrophys* 356:873
- Argast D, Samland M, Thielemann F-K, Qian Y-Z (2004) *Astron Astrophys* 416:997
- Armendariz-Picon C, Mukhanov V, Steinhardt PJ (2000) *Phys Rev Lett* 85:4438
- Arnett D (1996) *Supernovae and nucleosynthesis*. Princeton University Press, Princeton
- Arnould M, Goriely S (2003) *Phys Rep* 384:1
- Asplund M et al (2006a) *Astrophys J* 644:229
- Asplund M, Grevesse N, Sauval J (2006b) *Nucl Phys A* 777:1
- Bahcall JN (1989) *Neutrino astrophysics*. Cambridge University Press, Cambridge
- Bahcall JN (1999) *Nucl Phys B (Proc Suppl)* 77:64, astro-ph/9808162
- Bahcall JN (2000) *Nucl Phys B (Proc Suppl)* 91:9, hep-ph/0009044
- Bahcall JN (2001) *Nature* 412:29
- Bahcall JN, Pinnonseault MH, Basu S (2001a) *Astrophys J* 555:990, astro-ph/0010346
- Bahcall JN, Gonzales-Garcia MC, Pena-Garay C (2001b) *JHEP* 0108:014, hep-ph/0106258
- Baltz EA, Battaglia M, Peskin ME, Wizansky T (2006) *Phys Rev D* 74:103521
- Bannerjee R, Pudritz RE (2007) *Astrophys J* 660:479
- Bernabei R et al (2003) *Riv Nuovo Cim* 26:1
- Bernstein J, Brown L, Feinberg G (1991) *Rev Mod Phys* 61:25
- Boesgaard AM, Steigman G (1985) *Ann Rev Astron Astrophys* 23:319
- Bonnell IA et al (1997) *MNRAS* 285:201
- Bonnell IA, Bate MR (2006) *MNRAS* 370:488
- Boothroyd AI (2006) *Science* 314:1690
- Boyd RN (2008) *An introduction to nuclear astrophysics*. University of Chicago Press, Chicago
- Börner G (1988) *The early Universe: facts and fiction*. Springer, Berlin
- Burbidge EM, Burbidge GR, Fowler WA, Hoyle F (1957) *Rev Mod Phys* 29:547
- Burles S, Nollet KM, Truran JN, Turner MS (1999) *Phys Rev Lett* 82:4176
- Burles S, Nollet KM, Turner MS (2001) *Astrophys J* 552:L1
- Busso M, Gallino R, Lambert DL, Travaglio C, Smith VV (2001) *Astrophys J* 557:802, astro-ph/0104424
- Caldwell RR, Dave R, Steinhardt PJ (1998) *Phys Rev Lett* 80:1582
- Cameron AGW (1957) Chalk River laboratory report CRL-41. Atomic Energy of Canada Ltd, Chalk River
- Carena M, Nardini G, Quirós M, Wagner CEM (2009) *Nucl Phys B* 812:243
- Cayrel R et al (2001) *Nature* 409:691
- Charbonnel C et al (1999) *Astron Astrophys Suppl* 135:405
- Charbonnel C, Primas F (2005) *Astron Astrophys* 442:961
- Christensen-Dalsgaard J (2001) *Europhys News* 32:229
- Clayton DD (1984) *Principles of stellar evolution and nucleosynthesis*. University of Chicago Press, Chicago
- Clayton DD, Nittler LR (2004) *Annu Rev Astron Astrophys* 42:39
- Clowe D et al (2006) *Astrophys J* 648:L109
- Coles P, Lucchin F (1996) *Cosmology: The Origin and Evolution of Cosmic Structure*. Wiley and Sons, New York
- Descouvemont P, Rauscher T (2006) *Nucl Phys A* 777:137
- Dominguez I, Höflich P, Straniero O (2001) *Astrophys J* 557:279
- Erlykin AD, Wolfendale AW (2001) *Europhys News* 32:246
- Fiorentini G, Ricci B, Villante FL (2001) *Nucl Phys B (Proc Suppl)* 95:116, astro-ph/0012239
- Fiorentini G, Ricci B (2000) *Nucl Phys B (Proc Suppl)* 81:95, astro-ph/9905341
- Frebel A et al (2005) *Nature* 434:871
- Freiburghaus C et al (1999) *Astrophys J* 516:381
- Fröhlich C et al (2006) *Phys Rev Lett* 96:142502
- Fujimoto MY (1982) *Astrophys J* 257:752
- Garcia-Bellido J, Grigoriev D, Kusenko A, Shaposhnikov ME (1999) *Phys Rev D* 60:123504
- Gehrz RD, Truran JW, Williams RE, Starrfield S (1998) *Publ Astron Soc Pac* 110:3
- Gyürky G et al (2006) *Phys Rev C* 74:025805
- Hagiwara K et al (2002) *Phys Rev D* 66:01001
- Hansen CJ, Kawaler SD (1994) *Stellar interiors: physical principles, structure and evolution (A&A Library)*. Springer, New York
- Hartmann D, Myers J, Woosley S, Hoffman R, Haxton W (1999) In: Ratamay R, Vangioni-Flam E, Casse M, Olive K (eds) *LiBEB cosmic rays and γ -ray astronomy*. ASP conference series, vol 171. Astronomical Society of the Pacific, San Francisco, pp 235–260

- Heger A et al (2005) *Phys Lett B* 606:258
- Heger KM (2001) *Europhys News* 32:180
- Hillebrandt W, Niemeyer JC (2000) *Ann Rev Astron Astrophys* 38:191
- Hix WR, Thielemann F-K (1998) *Astrophys J* 511:862, astro-ph/9808032
- 't Hooft G (1976) *Phys Rev Lett* 37:8
- Hoppe P, Zinner E (2000) *J Geophys Res – Space Phys* 105:10371
- Hu W (2001) In: de Vega HJ, Khalatnikov IM, Sanchez N (eds) *Phase transitions in the early Universe: theory and observation*, vol 40, NATO science series: mathematics, physics, and chemistry. Kluwer Academic, Dordrecht, pp 183–205
- Iliadis C (2007) *Nuclear physics of stars*. Wiley-VCH, Weinheim
- Janka H-T et al (2007) *Phys Rep* 442:38
- Jeans JH (1902) *Phil Trans* 129:44
- Jordi J, Hernanz M (2007) *J Phys G* 34:R431
- Jordi J, Hernanz M (2008) *J Phys G* 35:014024
- Käppeler F, Beer H, Wisshak K (1989) *Rep Prog Phys* 52:945
- Käppeler F, Wiescher M, Thielemann F-K (1998) *Ann Rev Nucl Part Sci* 48:175
- Kercek A, Hillebrandt W, Truran JW (1999) *Astron Astrophys* 345:831
- Kippenhahn R, Weigert A (1994) *Stellar structure and evolution* (A&A Library). Springer, Heidelberg
- Kiss GG et al (2008) *Phys Rev Lett* 101:191101
- Kolb EW, Turner MS (1990) *The early Universe*. Addison-Wesley, Redwood City
- Komatsu E et al (2009) *Astrophys J Suppl* 180:330
- Korn AJ et al (2006) *Nature* 442:657
- Kovac J et al (2002) *Nature* 420:772
- Kowalski M et al (2008) *Astrophys J* 686:749
- Krauss LM, Trodden M (1999) *Phys Rev Lett* 83:1502
- Lamarre JM, Puget J-L (2001) *Europhys News* 32:212
- Leibundgut B (2001a) *Ann Rev Astron Astrophys* 39:67
- Leibundgut B (2001b) *Europhys News* 32:4
- Lewis RS, Tang M, Wacker JF, Anders E, Steel E (1987) *Nature* 326:160
- Lugaro M (2005) *Stardust from meteorites: an introduction to presolar grains*. World Scientific, Singapore
- Lugmair G, Shimamura T, Lewis RS, Anders E (1983) *Science* 222:1015
- Marhas KK et al (2008) *Astrophys J* 689:622
- Marigo P (2001) *Astron Astrophys* 370:194, astro-ph/01121181
- MacFadyan AI, Woosley SE (1999) *Astrophys J* 524:262
- Mészáros P (2006) *Rep Prog Phys* 69:2259
- Milgrom M (2008) *The MOND paradigm*. arXiv: 0801.3133
- Nittler LR (2003) *Earth Planet Sci Lett* 209:259
- Nolta M et al (2009) *Astrophysical J Suppl* 180:296
- Nomoto K, Thielemann F-K, Yokoi K (1984) *Astrophys J* 286:644
- Oberhummer H, Csótó A, Schlattl H (2000) *Science* 289:88, astro-ph/0007178
- Olive KA, Steigman G, Walker TP (2000) *Phys Rep* 333:389
- Olive KA (2001) In: Klapdor-Kleingrothaus HV (ed) *Dark matter in astro and particle physics*. Springer, Berlin, p 176
- Pagel BEJ (1997) *Nucleosynthesis and chemical evolution of galaxies*. Cambridge University Press, Cambridge
- Peacock J (1999) *Cosmological physics*. Cambridge University Press, Cambridge
- Peccei RD, Quinn HR (1977) *Phys Rev Lett* 38:1440
- Peebles PJE (1993) *Principles of physical cosmology*. Princeton University Press, Princeton
- Penzias AA, Wilson RW (1965) *Astrophys J* 142:419
- Percival W et al (2007) *MNRAS* 381:1053
- Perkins DH (2000) *Introduction to high energy physics*. Cambridge University Press, Cambridge
- Perlmutter S et al (1997) *Astrophys J* 483:565
- Perlmutter S et al (1999) *Astrophys J* 517:565
- Petreczky P (2007) *J Phys G* 35:044033
- Phillips AC (1994) *The physics of stars*. Wiley, Chichester
- Press WH, Schechter PL (1974) *Astrophys J* 181:425
- Rauscher T, Thielemann F-K (2000) *Atomic Data Nuclear Data Tables* 75:1, astro-ph/0004059
- Rauscher T, Thielemann F-K (2001) *Europhys News* 32:224
- Rauscher T, Heger A, Hoffman RD, Woosley SE (2002) *Astrophys J* 576:323
- Riess AG et al (1998) *Astron J* 116:1009
- Riess AG et al (2001) *Astrophys J* 560:49
- Riess AG et al (2007) *Astrophys J* 659:98
- Riotto A, Trodden M (1999) *Ann Rev Nucl Part Sci* 49:35
- Rolfs CE, Rodney WS (1988) *Cauldrons in the cosmos*. The University of Chicago Press, Chicago
- Rosner R, Alexakis A, Young Y-N, Truran JW, Hillebrandt W (2001) *Astrophys J Lett* 562:L177
- Rosswog S, Liebendörfer M, Thielemann F-K, Davies MB, Benz W, Piran T (1999) *Astron Astrophys* 341:499
- Rubakov VA, Shaposhnikov M (1996) *Usp Fiz Nauk* 166:493
- Ruffert M, Janka H-T (2001) *Astron Astrophys* 380:544
- Sakharov A (1967) *JETP Lett* 5:24
- Sarkar S (1996) *Rep Prog Phys* 59:1493
- Sathyaprakash BS, Schutz BF (2009) *Living Rev Relativity* 12:2, <http://relativity.livingreviews.org/Articles/lrr-2009-2/>
- Schatz H et al (1998) *Phys Rep* 294:167
- Schatz H et al (2001) *Phys Rev Lett* 86:3471
- Schlattl H, Heger A, Oberhummer H, Rauscher T, Csoto A (2004) *Astrophys Space Sci* 291:27
- Schmidt BP et al (1998) *Astrophys J* 507:46
- Schramm DN, Turner MS (1998) *Rev Mod Phys* 70:303
- Shapiro SL, Teukolsky SA (1983) *Black holes, white dwarfs, and neutron stars*. Wiley-Interscience, New York

- Snedden C et al (2000) *Astrophys J* 533:L139
- SNO Collaboration, Ahmad G et al (2002a) *Phys Rev Lett* 89:011301, nucl-ex/0204008
- SNO Collaboration, Ahmad G et al (2002b) *Phys Rev Lett* 89:011302, nucl-ex/0204009
- Springel V et al (2005) *Nature* 435:629
- Stadermann FJ, Walker RM, Zinner E (1999) *Meteoritics Planet Sci* 34:A111
- Starrfield S, Sparks WM, Truran JW, Wiescher MC (2000) *Astrophys J Suppl* 127:485
- Starrfield S (1999) *Phys Rep* 311:371
- Steigman G (2007) *Ann Rev Nucl Part Sci* 57:463
- Steigman G, Walker TP, Zentner A (2000) Global constraints on key cosmological parameters, astro-ph/0012149.
- Surman R, McLaughlin GC, Hix WR (2006) *Astrophys J* 643:1057
- Taam RE, Woosley SE, Lamb DQ (1996) *Astrophys J* 459:271
- Taylor J (1994) *Rev Mod Phys* 66:711
- Tayler R (1994) *The stars: their structure and evolution*. Cambridge University Press, Cambridge
- Thielemann F-K et al (2001a) Proceedings of 27th international cosmic ray conference. Copernicus Gesellschaft, Katlenburg-Lindau, Germany, astro-ph/0202453
- Thielemann F-K et al (2001b) *Prog Part Nucl Phys* 46:5
- Tranberg A, Smit J, Hindmarsh M (2007) *JHEP* 0701:034
- Travaglio C et al (2004) *Astrophys J* 601:864
- Truran JW (1984) *Ann Rev Nucl Part Sci* 34:53
- Turner MS et al (2003) Connecting quarks with the cosmos, eleven science questions for the new century. National Academies Press, Washington DC
- Tytler D, O'Meara JM, Suzuki N, Lubin D (2000) *Physica Scripta* T85:12, astro-ph/0001318
- Vangioni-Flam E, Casse M, Audouze J (2000) *Phys Rep* 333:365
- Van Tent B, Smit J, Tranberg A (2004) *JCAP* 0407:003
- Warner B (1995) *Cataclysmic variable stars*. Cambridge University Press, Cambridge
- Westphal AJ, Price PB, Weaver BA, Afanasiev VG (1998) *Nature* 396:50
- Westphal AJ, Weaver BA, Tarl G (2001) *Adv Space Res* 27:797
- Wiescher MC, Schatz H (2000) *Prog Theor Phys Suppl* 140:11
- Wood-Vasey WM et al (2007) *Astrophys J* 666:694
- Woosley SE, Heger A (2007) *Phys Rep* 442:269
- Woosley SE, Weaver TA (1995) *Astron Astrophys Suppl* 101:181
- Zinner E, Nittler LR, 'D Alexander CMO, Gallino R (2006) *New Astron Rev* 50:574



13 Natural Radioactive Decay Chains

H. C. Griffin

University of Michigan, Ann Arbor, Michigan, USA

13.1	<i>Introduction</i>	668
13.1.1	<i>4n Chain</i>	671
13.1.2	<i>4n + 2 Chain</i>	673
13.1.3	<i>4n + 3 Chain</i>	673
13.1.4	<i>4n + 1 Chain</i>	673
13.2	<i>Island of Stability</i>	673
13.3	<i>Time Dependence</i>	674
13.3.1	<i>Approach to Equilibrium</i>	675
13.3.2	<i>Branching Decay</i>	676
13.3.3	<i>Multiple Step Series</i>	676
13.3.4	<i>Multiple Separations</i>	676
13.4	<i>Physical Properties</i>	678
13.4.1	<i>Alpha Rays</i>	679
13.4.2	<i>Gamma Rays</i>	679
13.4.3	<i>Recoil</i>	682
13.4.4	<i>Heavy Ion Emission</i>	685
13.5	<i>Chemical Properties</i>	686

Abstract: Shell effects on nuclear stability have created an island of relative stability for nuclides near $A = 230$ – 240 and $Z = 90$ – 92 . Three nuclides, ^{232}Th , ^{238}U , and ^{235}U , have half-lives long enough for significant amounts to have survived since the heavy elements in the Earth's crust were created. When one of these nuclides decays, it starts a journey that ends with an isotope of lead ($Z = 82$, $A \approx 208$). The predominant steps in this journey are α and β decays, so that each of the long-lived parents heads a distinct chain. Each chain, as well as a fourth one that is extinct, is described.

13.1 Introduction

Radioactivity was discovered (1896) from observations of radioactivity occurring in natural radioactive chains. There are other instances of natural radioactivity, such as ^{14}C , ^{40}K , and ^{187}Re , but none of these nuclides leads to a radioactive product and therefore starts a chain. Note that many radionuclides occur in chains, e.g., $^{100}\text{Sn} \rightarrow 6 \text{ EC}/\beta^+ \rightarrow ^{100}\text{Ru}$, but early members of the chains have short half-lives and disappear before the chain is completed. The distinguishing characteristic of the natural chains is that they begin with a radionuclide with a long enough half-life that some of it has survived since the Earth was formed and leads to intermediate components with short – sometimes very short – half lives.

Details of the natural radioactive decay series are particularly important for several radioactive dating methods (🔗 Chap. 17 of this Volume). These methods depend on differences in chemical properties of chain components in a geological environment and on growth-and-decay among the components. See 🔗 Chap. 7 in Vol. 1.

There is considerable variety in the modes of decay of heavy elements; if spontaneous fission is considered a mode of radioactive decay, then there are many chains that meet this criterion of long-to-short. However, this chapter does not include fission except as a mechanism of terminating a chain.

The natural radioactive chains are represented in 🔗 Figs. 13.1–13.4. The relative intensities of various decay modes given in those figures do not show the full precision of current information. See the appendix “Table of Nuclides” by R. B. Firestone for current values.

The dominant steps in the chains are α and β decays, which either decrease the mass number by 4 (α decay) or leave it unchanged (β decay). Therefore, there are four chains (including one which is extinct on Earth) corresponding to mass numbers $A = 4n$ (^{232}Th and descendants) through $A = 4n + 3$ (^{235}U and descendants), where n is an integer. In the figures, rows correspond to elements, with atomic number increasing from the bottom to the top. Columns have constant $N-Z$; they contain nuclides that are related by α decay. For a given chain only half of the cells in such a row-and-column array are members of the given chain. (The other half corresponds to a chain differing by 2 mass numbers.) The components are in shaded boxes, and the chains progress two steps down (α decay) or one step up and to the left (β decay). The long-lived parent and the stable end-product have a deeper shade. For α decay of a particular nuclide, the percentage of decays that use that mode is given below it, followed (in italics) by the energies (in keV) of the most intense α groups. If there is no competing β decay, the α percentage is 100. If both α and β decay occur, the fraction of β decay is the complement of the α fraction. For example, in 🔗 Fig. 13.1 ^{212}Bi α decays 35.9% of the time, so 64.1% of the time β decays.

Fig. 13.1

The $4n$ (^{232}Th) chain. The “rules of the game” are shown by the arrows in the lower right corner. See text for more details

					^{236}Th 2.3×10^7 years	
					100 4494 4445	
		d h	^{228}Th 1.91 years		^{232}Th 1.4×10^{10} years	
		Ms h ₂	100 5423 5340	^{228}Ac 6.1 h	100 4013 3950	
		h	^{224}Ac 3.64 days		^{228}Ra 5.76 years	Ms h ₁
			100 5686 5449			
		n	^{220}Rn 56 s			
			100 6288			
hC	^{212}Po 0.3 μs		^{216}Po 0.15 s	hA		
hC	100 8784	^{212}I 61 min	100 6779			β
	^{208}Pb	35.9 6051	^{212}Pb 10.6 h	h		α
hC		^{208}Tl 3.1 min				

Many individual components in the series are referred to by names derived from their positions in the series and other details that are no longer of much interest except to reveal the history of discovery of structure of each series. The most common names of this type for the ^{232}Th series are given in Fig. 13.1. Since ^{228}Ra and ^{228}Ac are sandwiched between two isotopes of thorium, they were called mesothorium 1 and 2 (*meso*: intermediate or in the middle), with symbols MsTh_1 and MsTh_2 . ^{228}Th has higher specific activity (activity per unit mass) than ^{232}Th and was called radiothorium (RdTh). Tn (^{220}Rn) is short for thoron, the gaseous component similar to *radon* from *radium*. Relatively simple chemical procedures could show that there were three species following Tn, and these were named

Fig. 13.2

The $4n + 2$ (^{238}U) chain. *Note that the decay of ^{234}Th leads to $1.17\text{ min }^{234\text{m}}\text{Pa}$, most of which decays directly to ^{234}U . In 0.16% of the cases, $6.7\text{ h }^{234}\text{Pa}$ is formed by IT

					^{234}Th 0.24 My		^{238}U 4470 My
					100 4776 4715	$^{234\text{m}}\text{Pa}$ 1.17 min 0.16% 6.7 h	100 4196 4147
					^{230}Th 7.5×10^4 years		^{234}U 24.1 days
					100 4688 4621		
					^{226}Ra 1599 years		
					100 4784 4602		
			^{218}Po 35 ms		^{222}Rn 3.8 days		
			100 7133	^{218}At 1.5 s	100 5490		
	^{210}Po 138 days		^{214}Po 164 μs	99.9 6694	^{218}Po 3.1 min		
	100 5304	^{214}Pb 5.0 days	100 7687	^{214}Bi 20 min	99.98 5490	 β α	
	^{206}Pb	1.3×10^4 4648	^{210}Pb 22 years	100 5450 5513	^{214}Pb 26 min		
		^{206}Pb 4.2 min	1.9×10^6 3720	^{210}Pb 1.3 min			
			^{206}Pb 8.15 min				

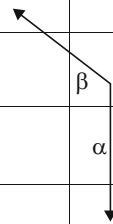
ThA (^{216}Po), ThB (^{212}Pb), and ThC (^{212}Bi). Later it was determined that ^{212}Po (ThC') and ^{208}Tl (ThC'') are also involved.

Each of the chains could be extended (with many branches) to shorter-lived precursors. Although these precursors are not properly considered members of the natural chains, several

Fig. 13.3

The $4n + 3$ (^{235}U) chain

					^{239}P 24 1 y		
					100 5156 5143	^{239}NP 2 4 days	
					^{235}U 7×10^8 years		239 23 min
				^{231}pa 3.3×10^4 years	100 4400 4365		
			^{227}h 18 7 days	100 5013 4950	^{231}h 25 6 h		
			100 6038 5978	^{227}Ac 21 8 years			
			^{223}a 11 4 days	1 38 4953 4941			
			100 5716 5607	^{223}Fr 22 min			
			^{219}n 4 0 s	6×10^{-3} 5340			
			100 6819 6553	^{219}At 0 9 min			
	^{211}Po 0 52 s		^{215}Po 1 8 ms	97 6280			
	100 7450	^{211}i 2 2 min	100 7386	^{215}i 7 4 min			
	^{207}Pb 99 72 6623 6278		^{211}Pb 36 min				
		207 4 8 min					

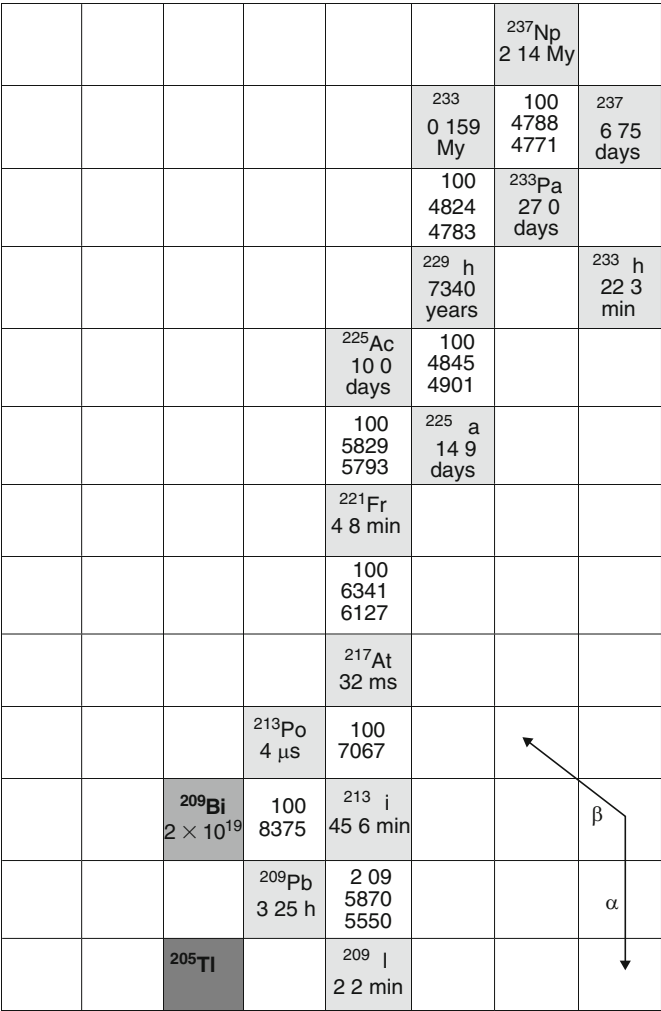


of them are included in the diagrams to show likely production paths of the chains in the nuclear fuel cycle. For example, neutron capture in ^{232}Th produces short-lived ^{233}Th , which decays to ^{233}Pa and then to ^{233}U (see Fig. 13.4), which can be used as reactor fuel.

13.1.1 $4n$ Chain

The chain is defined in Fig. 13.1. Because α decay changes mass number by 4, the overall loss of 24 mass numbers between ^{232}Th and ^{208}Pb requires six α 's. But six α 's would change atomic

Fig. 13.4
The $4n + 1$ (^{237}Np) chain



number by 12, and the overall change is only 8; there must be a net of four β decays (β decays less electron captures), each increasing atomic number by 1 without changing mass number. In fact there are no electron capture decays in any of the chains – for reasons related to general trends in nuclear stability – and there are exactly four β decays in this chain.

The parent of the $4n$ series, 1.405×10^{10} year ^{232}Th , is the longest-lived nuclide in the Th–U region. It is comparable to the age of the universe, so more than half of all of the ^{232}Th ever produced (and not consumed by nuclear reactions) is still present. Because of the long half-life, ^{232}Th has unusually low specific activity (rate of decay per unit mass). Little easily absorbed radiation, such as α particles and low-energy electrons and photons, escapes the necessarily thick samples of moderate activity.

The last steps in the chain are unusual; ^{212}Po has a remarkably short half-life (and high decay energy), and ^{208}Tl emits a high energy γ ray (2,615 keV). This γ ray is a distinctive feature of background spectra of most γ ray spectrometers (See [Fig. 13.7](#)).

13.1.2 $4n + 2$ Chain

The $4n + 2$ chain is very similar to the $4n$ chain. They both pass through two isotopes of the parent element and of the element two units below it. The outstanding feature of the $4n + 2$ chain is that it populates the longest-lived isotopes of radium (1,599 year ^{226}Ra) and radon (3.82 days ^{222}Rn).

13.1.3 $4n + 3$ Chain

The $4n + 3$ chain is the only one that (barely) includes every element from uranium to thallium. Although included, francium and especially astatine are very minor components. The parent, 704×10^6 year ^{235}U , has a half-life considerably smaller than the $\sim 4,500 \times 10^6$ year age of the Earth. It is long enough for significant amounts (0.720% of the atoms in natural uranium) to remain. The chain includes by far the longest-lived isotopes of protactinium (32.8×10^3 year ^{231}Pa) and actinium (21.77 year ^{227}Ac).

13.1.4 $4n + 1$ Chain

The $4n + 1$ series is extinct on Earth except (presumably) for vanishingly small amounts arising from capture of stray neutrons by ^{232}Th . Even the end-product ($\sim 2 \times 10^{19}$ year ^{209}Bi) appears to be slightly radioactive. The longest-lived member is ^{237}Np , but the most important is ^{233}U . This isotope of uranium has fission properties similar to ^{235}U (and ^{239}Pu). The mechanisms for large-scale production are similar to those for ^{239}Pu .

The following sections explain how the long-lived parents arise ([Sect. 13.2](#)), describe the growth and decay relations within the chains ([Sect. 13.3](#)), list the physical (i.e., nuclear physics) properties of members of the chains ([Sect. 13.4](#)), and indicate sources of information on the chemical properties of the elements in the chains ([Sect. 13.5](#)).

13.2 Island of Stability

The general trend in stability of various combinations of protons and neutrons can be understood in terms of the Weizsäcker formula, which is given as [Eq. \(2.3\)](#) in “Basic Properties of the Atomic Nucleus” ([Chap. 2](#) of Vol. 1). The first two terms of this semiempirical formula are related to the volume and surface of a nucleus; together they prefer large nuclei. The third term is proportional to the Coulomb energy of a charged sphere; it prefers a neutral nucleus. The fourth term has no classical interpretation, but it can be understood as arising from quantum mechanical exclusion; it prefers equal numbers of protons and neutrons. When these terms are combined, the lowest energy (most stable) combination of A nucleons is given by

$$Z_A(A) = \frac{A \left(2 - \frac{m_n - m_H}{a_s} \right)}{4 + \frac{a_c}{a_s} A^{2/3}} \quad (13.1)$$

where a_a is the asymmetry coefficient and a_c is the Coulomb coefficient. Note that Z_A is the minimum on the parabolic mass curve for mass number A . For small A the minimum corresponds to nearly equal numbers of protons and neutrons; the symmetry term dominates. For large A , Z is considerably less than N , e.g., ^{208}Pb with $N = 126$ and $Z = 82$. These general trends are displayed in N vs. Z plot, such as [▶ Fig. 2.7 in Chap. 2](#) of Vol. 1 on “Basic Properties of the Atomic Nucleus.” The main relevant feature of the figure is the distribution of stable nuclides in the vicinity of $A \approx 200$.

[▶ Figure 21.11 of Chap. 21](#), “Superheavy Elements,” gives a clearer picture of the nuclides beyond $A \approx 200$. There is an abrupt absence of nuclides with moderate much less long half-lives between ^{208}Pb and ^{232}Th . This is due to shell effects that are not included in the semiempirical equation. Of course shell effects are crucial for stabilizing the several “islands” of stability among heavy elements, which include the parents of the natural decay series as well as surprisingly stable isotopes of elements well beyond uranium.

[▶ Table 13.1](#) shows the α -decay energies of the $4n$ series and the energies predicted by the semiempirical equation without shell effects. The equation agrees with the facts near the middle — at ^{220}Rn . The predicted half-lives are too short in the Th–U region, and too long for Po (just above the shell). The Hg–Pb isotopes are predicted to have rather short half-lives for α decay. To be sure some of them are energetically unstable, but not enough that barrier penetration proceeds at an appreciable rate.

13.3 Time Dependence

The equations for growth and decay of genetically related radioactive materials were developed (Bateman 1910) in order to understand the complicated relations among the components of the natural decay chains. Time dependence remains important. First, it is of interest to

■ **Table 13.1**

Shell effects on α -decay energies (in MeV) and half-lives in the $4n$ chain. Note that for very rare α decays it is difficult to obtain experimental Q_α values. (In the case of ^{228}Ra nuclides, e.g., 19 ppb are only expected to undergo α decay, while the rest disintegrates by β decay according to

[▶ Fig. 13.1](#))

Nuclide	Q_α	Q from eqn.	α half-life	Half-life from mass eqn.
^{236}U	4.572	7.62	2.3×10^7 years	0.9 s
^{232}Th	4.083	6.92	1.4×10^{10} years	20 s
^{228}Ra	~ 4.1	6.21	$(3 \times 10^8 \text{ years})$	5×10^3 s
^{228}Th	5.520	7.63	1.911 years	0.02 s
^{224}Ra	5.789	6.95	3.66 days	5 s
^{220}Rn	6.405	6.25	56 s	150 s
^{216}Po	6.907	5.53	0.146 s	1 day
^{212}Pb	~ 3.1	4.80	(Not known)	3 years
^{212}Bi	6.207	5.56	2.8 h	5 h
^{212}Po	8.954	6.29	0.3 μs	10 s

anticipate how radioactivity will develop in freshly prepared samples. Second, processes such as weathering of waste deposits disturb the growth and decay relations, and analysis of the relative activities of the several components can indicate the rates and times of the disturbances. Third, the processes have been valuable in dating very old geological samples.

See ▶ Chap. 7 of Vol. 1 for information on the rates of genetically related radioactive materials and, in particular, the Bateman equations describing members of arbitrarily long chains. Note that each set of equations describes the components of a chain defined for particular branches. Different branches require different set of equations. These points are illustrated in the following sections.

The time dependence of a genetically related pair can be described as equilibrium (if the half-life of parent is longer than that of the descendant) or no equilibrium (half-life of parent shorter than that of the descendant). Cases involving equilibrium are further classified as secular (half-life of the parent is long compared to the descendant and to the time duration of interest) or transient (decay of parent must be considered); the distinction depends on one's criterion for change. In most cases it is difficult to measure rates with uncertainties less than 0.1%, so one might require that less than 0.1% of the parent decay and that the rate of decay of descendant be more than 99.9% of the initial activity of the parent. For these conditions to obtain, the half-life of the parent must be at least 7,000 times the half-life of the descendant.

13.3.1 Approach to Equilibrium

If one excludes the extinct $4n + 1$ series, the parents of all three natural series have decayed less than 0.1% during human history, and the smallest parent/descendant ratio of half-lives (18,000 for $4n + 2$) is greater than 7,000 (see above). Therefore they can be in secular equilibrium with their descendants. For geological time scales, the entire series will follow the decay curve of the parent within 0.1%.

Parts of chains, such as the important genetic pair ^{226}Ra – ^{222}Rn , may also demonstrate secular equilibrium. The growth and decay relations of radon isotopes are perhaps of greatest general interest. About half of the radiation exposure of the general population is due to ^{222}Rn and its descendants. Its immediate parent, ^{226}Ra , has a long half-life ($160,000 \times$ that of ^{222}Rn) and is often displaced from its Th and U ancestors. For example, Ra in groundwater might be absorbed on a deionizer column, while any associated Rn would pass through unless embedded in the support material by recoil. If there is no flow for a period of time, the Rn will build up and eventually (perhaps within a month) reach secular equilibrium. For any given shorter time, the radon activity A_{Rn} will follow the simple growth curve given by $(1 - e^{-\lambda t}) A_{\text{Ra}}$, where λ is the decay constant for radon and t is the time since radium was freed from radon. The case is represented in ▶ Fig. 7.9 of Chap. 7 in Vol. 1.

The decay of ^{227}Ac to ^{227}Th is an example of transient equilibrium. (See ▶ Fig. 13.3 for half-lives and branching ratios.) An initially pure sample of ^{227}Ac will have increasing amounts of ^{227}Th until the rate of decay of ^{227}Th is nearly the same as the rate of decay of ^{227}Ac to it. If the ^{227}Th were fed at a constant rate, it would reach 99.9% of that rate in 9.966×18.7 days ≈ 186.6 days. However, during that time the ^{227}Ac would decay by 1.61%. Therefore the proper Bateman equation must be used to include both growth of ^{227}Th and decay of ^{227}Ac . The maximum in the decay rate of ^{227}Th occurs when it is equal to the production rate, namely, 0.9858 of the initial rate of decay of ^{227}Ac to ^{227}Th at 3,930 h (164 days).

Note that the weak 1.38% branch from ^{227}Ac to ^{223}Fr has been ignored and only a genetically related pair has been considered. When these factors are included, the correct equations are essential.

13.3.2 Branching Decay

When one takes into consideration that only 98.62% of the decay of ^{227}Ac goes to ^{227}Th and that 1.38% goes to ^{223}Fr , one finds that the maximum fractional activities for ^{227}Th and ^{223}Fr are 0.975 and 0.0138, respectively. Note that the ^{223}Fr reaches maximum sooner (when the production rate is nearly equal to the initial production rate); it meets the criterion for secular equilibrium. A subtle point is that one must distinguish between total and partial decay constants. The total describes the rate of disappearance of a species, while the partial decay constants describe the rate of production of the product of a particular branch. These points are developed in more detail in the next section.

13.3.3 Multiple Step Series

Consider one more step in the series originating from ^{227}Ac , passing through the branches described above, and rejoining at ^{223}Ra . Separate equations are required for the separate branches.

One can consider the terms in the Bateman equations to have three parts: a product of λ 's in the numerator, a product of *differences* in λ 's in the denominator, and an exponential factor. For branched decay of component i , the λ_i in the numerator is the partial decay constant, and the λ_i 's in the denominator and the exponential for i are the total decay constants. Another way to view the use of partial decay constants in the numerator is to multiply the entire equation by the fraction for that particular branch. This is not a simplification, because chains with different branches have different numerators and some different exponential factors.

These calculations for $^{227}\text{Ac} \rightarrow ^{223}\text{Ra}$ for several times are given in [▶ Table 13.2](#) and [▶ Fig. 13.5](#). Note that the weak branch through 21.8 min ^{223}Fr produces ^{223}Ra more quickly, but eventually the main branch dominates. The total amount of ^{223}Ra at any time is the sum of the amounts coming through separate branches. If the calculations had been made for longer times, it would be clear that ^{223}Ra is in transient equilibrium with ^{227}Ac .

13.3.4 Multiple Separations

As a final example of time dependence, consider the effect of several chemical purifications on the relative amounts of Th and Ra components of the $4n$ (^{232}Th) series. Assume that these components initially are in secular equilibrium. This would *not* be the case if the sample consisted of thorium that had been isolated from an ore in modern times.

If the object is to obtain pure ^{228}Ra , isolation from the equilibrium chain does not suffice; an equal amount of ^{224}Ra will be obtained. Of course, aging the sample will improve purity, because the ^{224}Ra will decay more quickly than the ^{228}Ra . These trends are shown in [▶ Fig. 13.6](#). The amount of ^{228}Ra will decrease slowly, but that effect is ignored in this example. After about 22 days, the amount of ^{224}Ra growing from ^{228}Ra will be equal to the residual amount from the initial purification. If nothing is done, the sample will become progressively less pure. If the

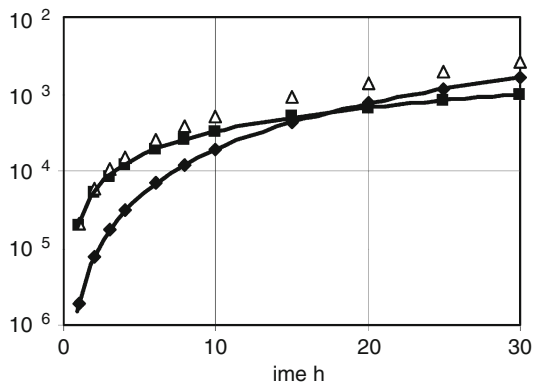
■ Table 13.2

Calculations for the relative activities of ^{227}Ac , ^{227}Th , ^{223}Fr , and ^{223}Ra in aged samples of initially pure ^{227}Ac . The convention used for representing numbers is $aE \pm b \equiv a \times 10^{\pm b}$. The Ac activity is not given; the final rate is 0.99982 times the initial rate. The fractions of each nuclide's production rate are given in the body of the table. The actual activities, relative to the activity of Ac, are obtained by multiplying Th and the Ra growing from it by 0.986. For Fr and the Ra obtained from it, the factor is 0.0138

Time (h)	Th-227	Ra-223	Fr-223	Ra-223
0	0.00E+00	0.00E+00	0.00E+00	0.00E+00
1	1.54E-03	1.95E-06	8.52E-01	1.40E-03
2	3.08E-03	7.80E-06	9.78E-01	3.76E-03
3	4.62E-03	1.75E-05	9.97E-01	6.26E-03
4	6.16E-03	3.11E-05	1.00E+00	8.77E-03
6	9.22E-03	6.99E-05	1.00E+00	1.38E-02
8	1.23E-02	1.24E-04	1.00E+00	1.88E-02
10	1.53E-02	1.93E-04	1.00E+00	2.37E-02
15	2.29E-02	4.31E-04	1.00E+00	3.60E-02
20	3.04E-02	7.62E-04	1.00E+00	4.81E-02
25	3.79E-02	1.18E-03	1.00E+00	6.01E-02
30	4.53E-02	1.69E-03	1.00E+00	7.20E-02
35	5.26E-02	2.29E-03	1.00E+00	8.36E-02
40	5.99E-02	2.97E-03	1.00E+00	9.52E-02
45	6.71E-02	3.73E-03	1.00E+00	1.07E-01
50	7.43E-02	4.57E-03	1.00E+00	1.18E-01

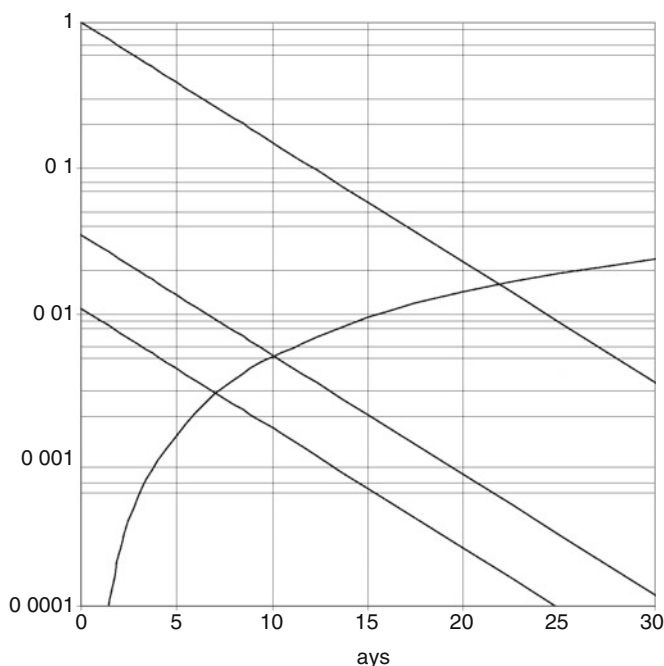
■ Fig. 13.5

Growth of ^{223}Ra in initially pure ^{227}Ac as a fraction of the initial ^{227}Ac activity. The squares show the Ra produced through Fr, the diamonds through Th. The triangles show the sum, the actual amount of Ra produced by all available paths



■ Fig. 13.6

Growth and decay of ^{224}Ra after isolation of radium from $4n$ series at secular equilibrium. The top curve gives the decay of ^{224}Ra after the first isolation relative to the secular rate. The growth curve shows the time dependence of ^{224}Ra that comes from ^{228}Ra (via ^{228}Ac and ^{228}Th). The middle decay curve shows ^{224}Ra that decays (with the clock restarted) after thorium is removed when growth and decay are equal (about 22 days from $t = 0$). The bottom decay curve shows decay following a third purification (about 10 days after the second)



^{228}Th is removed, growth is interrupted and decay in the fraction of ^{224}Ra resumes. However, for this purer ^{228}Ra sample, growth and decay effects become equal sooner, in this case about 10 days. Seven days later the $^{224}\text{Ra}/^{228}\text{Ra}$ ratio will be about 0.006; if higher purity were needed, more (and more frequent) purifications would be required.

The thorium after the initial purification would have equal activities of ^{228}Th and ^{232}Th . If pure ^{232}Th were needed, a similar series of purifications would eventually (about 20 years for 99.9% ^{232}Th) suffice. Even without subsequent processing, it would take many decades for the ^{228}Th to return to equilibrium with ^{232}Th . Getting pure ^{228}Th would be easier; the thorium growing into the purified radium would be pure ^{228}Th .

13.4 Physical Properties

The most sensitive detection of natural radioactive materials is by α spectroscopy. However, to realize good resolution it is necessary to have thin sources, which requires radiochemical purification in most cases. Therefore, γ rays are most convenient for measuring the components in complex mixtures, but γ rays emphasize the β -decay steps.

In addition to β decay and γ -ray emission, the elements near and beyond Pb in the chart of nuclides are unstable with respect to breakup, such as emission of α particles or heavier nuclei. The α , β , and γ emissions preserve the $4n + x$ chains, but emission of heavy ions might not, and fission certainly will not preserve the chains.

13.4.1 Alpha Rays

The energies of the most intense α groups are given in [Figs. 13.1–13.4](#). The lower members of the chains emit the highest energy α particles, and the energies of different nuclides are generally quite different. A semiconductor detector can give ~ 20 keV resolution (full width at half maximum – FWHM) for α spectroscopy if thin sources are used. In the ^{232}Th chain, all of the intense α groups differ by more than 50 keV except the main group of ^{228}Th (5,423 keV, 71%) and the secondary group of ^{224}Ra (5,449 keV, 5%). Note that it would be difficult to obtain a thin source of a mixture of components without using chemical procedures, and chemistry would emphasize a few elements.

Similarly, the various isotopes of a given element isolated from a mixture of natural chains are likely to be resolvable. Radium occurs in all four chains, but ^{225}Ra in the $4n + 1$ chain is a nearly pure β emitter ([Table 13.3](#)).

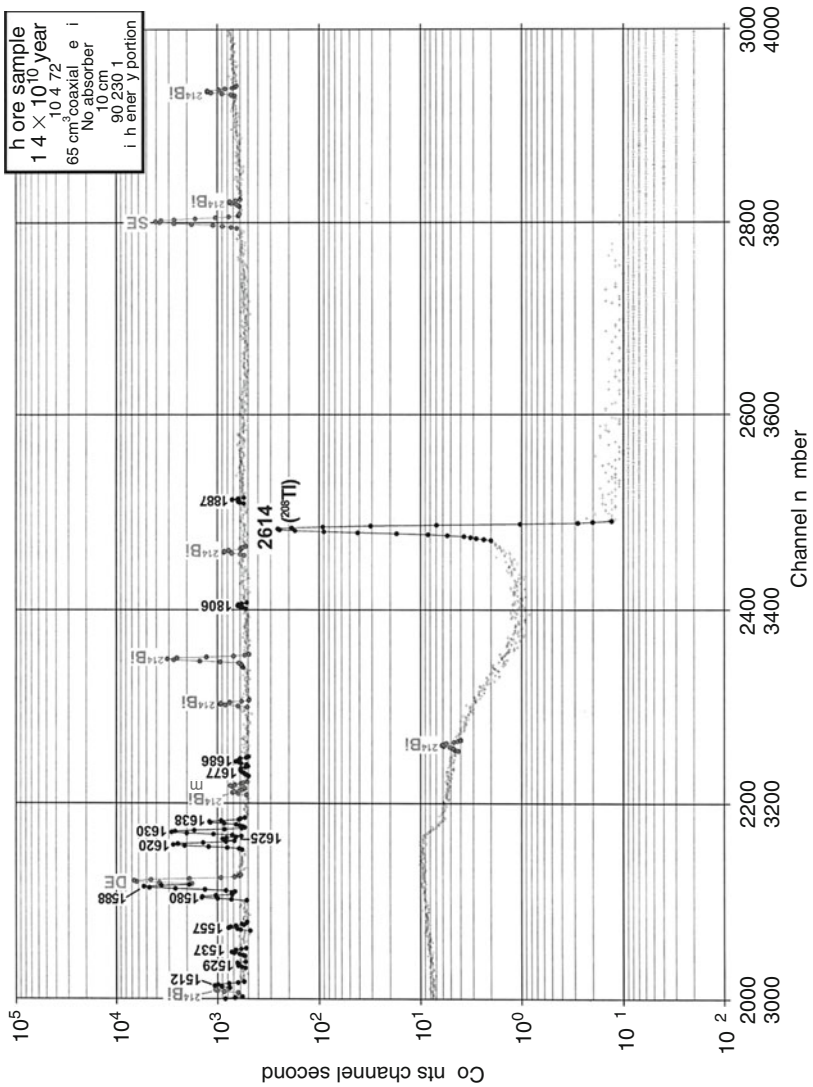
13.4.2 Gamma Rays

Most of the γ rays emitted in the decay chains are emitted following β decay. Most of the Q values for α decay are considerably larger than those for β decay, but β decay is much more likely to populate states that are just barely accessible energetically. Therefore, the use of γ -ray spectroscopy to measure the amounts of various components in a mixture emphasizes the β decays. [Figure 13.7](#) shows the γ -ray spectrum (Helmer et al. 1999) of a sample of thorium ore, i.e., a sample that has been undisturbed for long enough time that the chain is in secular equilibrium. [Table 13.4](#) lists the energies and intensities of the most intense γ rays emitted by components of the chain.

Table 13.3

Energies of α groups from Ra isotopes

Chain	Isotope	α energy/keV	Abundance/%
$4n$	^{224}Ra	5,685	94
		5,449	6
$4n + 1$	^{225}Ra	4,006	Very weak
$4n + 2$	^{226}Ra	4,784	94
		4,602	6
$4n + 3$	^{223}Ra	5,747	9
		5,716	53
		5,607	26
		5,540	9



■ **Table 13.4**
Energies and intensities of γ rays in the $4n$ chain

Nuclide	γ -ray energy/keV	γ -ray intensity/%	Nuclide	γ -ray energy/keV	γ -ray intensity/%
^{232}Th	63.8	0.27	^{220}Rn	549.7	0.07
	410.88	0.018	^{216}Po	804.9	0.0018
^{228}Ra	13.5	14	^{212}Pb	238.6	43.6
^{228}Ac	911.2	29	^{212}Bi	727.3	6.7
	969.0	17.4	^{212}Po	None	
^{228}Th	84.9	1.21	^{208}Tl	583.0	86
	215.8	0.28		2614.4	100
^{224}Ra	240.8	3.9			

It is difficult under any circumstances to observe the γ rays emitted by ^{232}Th itself. The Q value for α decay is small and transition rates are very sensitive to small changes in the energy available for α decay. Because of the high atomic number of the daughter Ra , the transition from the excited state to the ground state mostly occurs via internal conversion rather than γ emission. Because of the long half-life and corresponding low specific activity, attenuation in the source material is serious. Finally, the detector used for ▶ Fig. 13.7 had a thick layer of “dead” Ge , which would limit the detection efficiency at energies as low as 64 keV.

It is easier to detect the γ rays emitted in α decay of ^{224}Ra . The Q value is higher (hence the shorter half-life) and less sensitive to high excitation energy of the 240 keV first excited state of ^{220}Rn . There is less competition from internal conversion. The peak due to the 240 keV γ ray is a shoulder (easily resolved by current detectors) on the 238 keV peak of ^{212}Pb .

The high excitation energy of the first excited state accessible by α decay of ^{220}Rn and ^{216}Po dominates the increase in Q , and the γ -ray intensities are low. The 549 keV peak is barely discernable, and the 804 keV peak is below the limit of detection in γ -ray singles.

The dominant features of the spectrum are the peaks at 238 (^{212}Pb) and 2,614 keV (^{208}Tl). The actual intensities are about the same (recall that only 36% of the chain passes through ^{208}Tl), but the detection efficiency for the lower-energy γ ray is higher. The 2,614 keV stands out for lack of spectral competition.

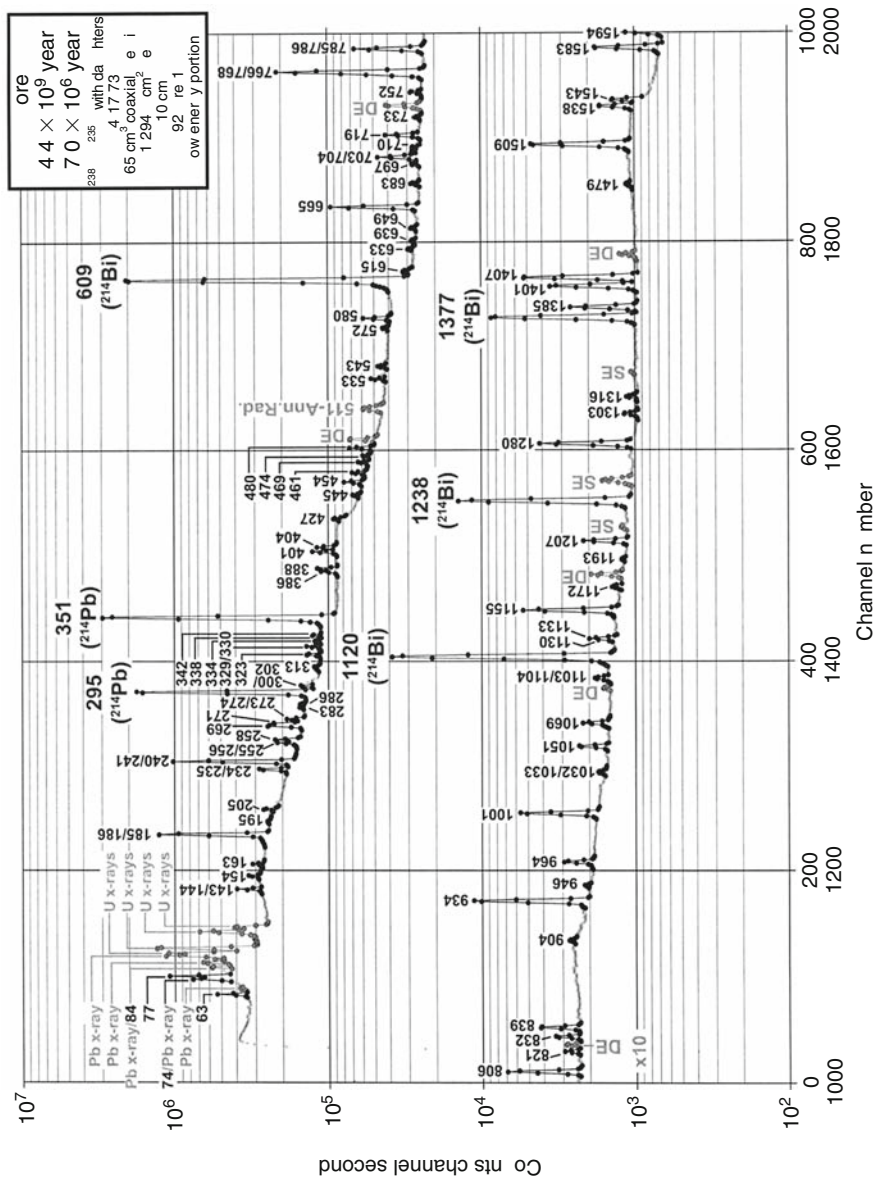
Many of the other γ rays are associated with the ^{228}Ac . Beta decays of both ^{228}Ac and ^{208}Tl have high Q values.

▶ Figure 13.8 shows the γ -ray spectrum of uranium ore (Helmer et al. 1999). The spectrum of recently purified uranium is considerably different; most of the high-energy γ rays emitted by the ore arise from decays of the chain members near the end (primarily ^{214}Bi). Their growth is slowed by long-lived intermediates, such as ^{230}Th and ^{231}Pa .

13.4.3 Recoil

The substantial energy imparted to the residual nucleus in α decay is important because, in the chains, the residual nucleus may itself be radioactive and its fate is observable. For example, in α decay of ^{228}Th to the ground state of ^{224}Ra , the α particle has 5,423 keV of energy. The ^{224}Ra “recoils” with an initial energy of 97 keV, which is large compared with the energy required

Fig. 13.8
Gamma-ray spectrum of U series (Helmer et al. 1999)



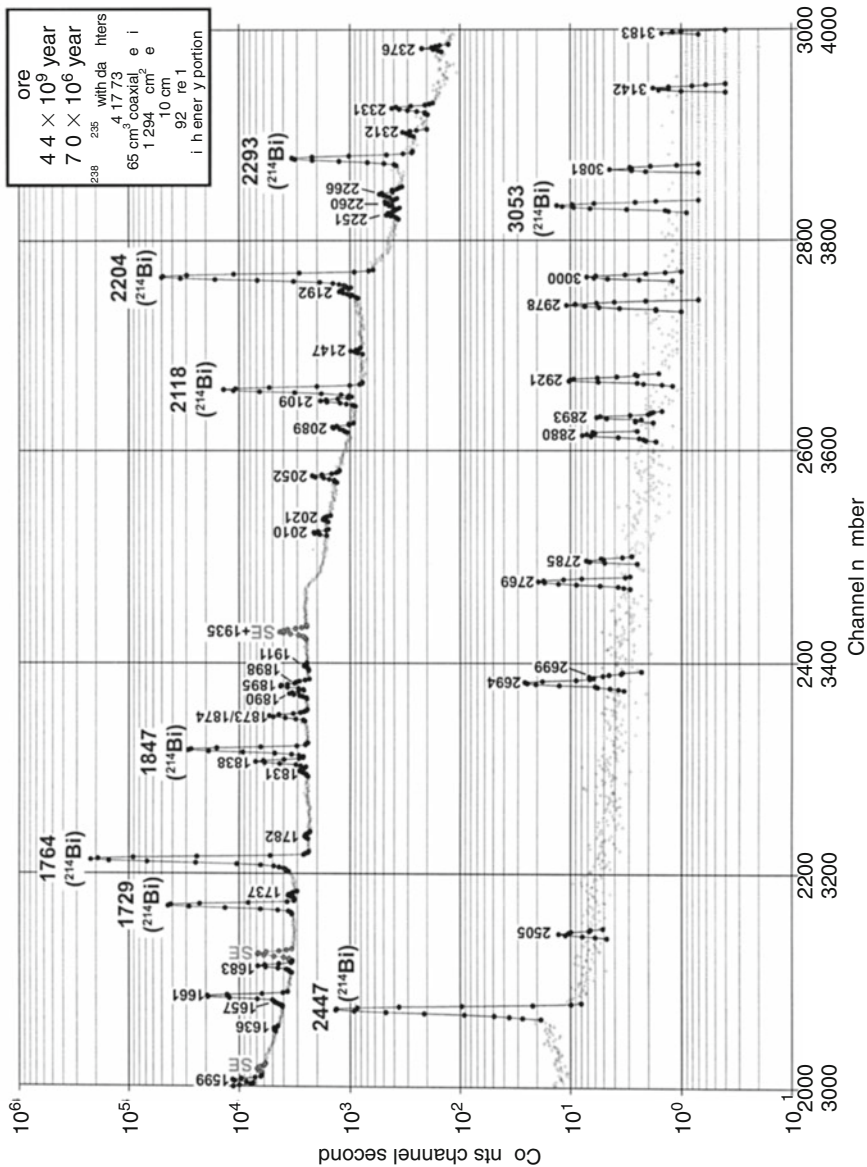


Fig. 13.8
(Continued)

to vaporize one atom of Ra. If the thorium is in a thin deposit in a vacuum, the recoil will move in a direct line (opposite the direction of the emission of the α particle) until it strikes an object.

The recoil can be used to prepare thin sources. The recoils can embed in a catcher, such as a metal disk, placed close to a thin deposit. Of course, the process can repeat; subsequent α decays can produce other recoils, but each such cycle eliminates one member of the chain in the catcher.

If the source is covered with a thin layer such as evaporated gold or a VYNS film, the recoils will be retained. It is important to do so in order to prevent contamination of an α detector, particularly a semiconductor spectrometer operated with a vacuum between the source and the detector.

If a radon atom decays in a gas, although the recoils will stop in the gas, they often will be charged and can be collected by electrostatic attraction to a charged plate.

Recoils can interfere with ordinary chemical processing. If a parent nuclide is adsorbed on a surface, such as a bead of ion-exchange resin or the surface of a container, the recoil can embed deep in the support material and not be in equilibrium with the external chemical environment.

13.4.4 Heavy Ion Emission

All of the members of the natural decay chains are unstable with respect to spontaneous fission, but the probabilities are small. The decay chains follow the side of the valley of stability where the fissionability parameter Z^2/A is relatively small. However, fission is such an extraordinary event that even a few events can be detected, as long as they can be distinguished from events such as muon-induced fission. For the natural chains ^{238}U has the highest fraction of decays by spontaneous fission, 5.4×10^{-7} . Although this leads to a multitude of natural decay chains consisting of fission followed by decays through fission product chains, the process will not be considered in this chapter.

Because fusion reactions such as $3\ ^4\text{He} \rightarrow\ ^{12}\text{C} + Q$ and $4\ ^4\text{He} \rightarrow\ ^{16}\text{O} + Q'$ are exothermic ($Q = 7.275\ \text{MeV}$ and $Q' = 11.16\ \text{MeV}$), when several α decays occur in sequence, the corresponding “crossover” decays can occur. For example, in the $4n$ chain the primary flow from ^{228}Th is a sequence of four α decays to ^{212}Pb . The crossover process would be $^{228}\text{Th} \rightarrow\ ^{16}\text{O} + ^{212}\text{Pb} + 39.06\ \text{MeV}$. In fact, the process $^{228}\text{Th} \rightarrow\ ^{20}\text{O} + ^{208}\text{Pb} + 44.72\ \text{MeV}$ is even more energetically favorable and is found to occur in $1.13 \times 10^{-11}\%$ of the decays of ^{228}Th . The low probability corresponds to the improbability of such a large particle as ^{20}O to tunnel through the Coulomb barrier. In this case the crossover does not lead to a product outside the chain. In some cases the mass number of the emitted heavy ion is not a multiple of 4 (e.g., ^{14}C), and the process crosses to another chain. Several known cases of heavy ion emission are listed in [Table 13.5](#). (A more complete list is given in [Chap. 18](#) in this Volume.) None is sufficiently probable as there are significant violations of the $4n + x$ rule for chains.

In some cases, heavy ion emission has been characterized in considerable detail. The structure in the ^{14}C emissions from ^{223}Ra has been observed. The energies are 29.8, 29.1, and 28.6 MeV, which populate ^{209}Pb levels at 0 (9/2+), 779 (11/2+), and 1,423 keV (spins and parities, in parenthesis) with relative intensities 15, 84, and 4, respectively.

The nuclides in the natural radioactive decay chains are not the most favorable candidates for heavy ion emission; they have unfavorable N/Z ratios. As shown in the example of emission of oxygen isotopes by ^{228}Th , emission of a $Z = N$ fragment leads to a product that is far from the center of β stability. Of course, emitting a fragment with $N > Z$ (e.g., ^{20}O) displaces the emitted

Table 13.5

Instances of heavy ion emission by members of the natural decay chains

Chain	Emitter	Heavy ion	Probability	Product	Q value	Partial $T_{1/2}$
$4n$	^{228}Th	^{20}O	1.13×10^{-13}	^{208}Pb	44.7 MeV	1.7×10^{13} years
	^{224}Ra	^{14}C	4.3×10^{-11}	^{210}Pb		2.3×10^8 years
$4n + 1$	^{225}Ac	^{14}C	6.4×10^{-12}	^{211}Bi		
	^{221}Ra	^{14}C	1.2×10^{-12}	^{207}Pb		
	^{221}Fr	^{14}C	8.8×10^{-13}	^{207}Tl		
$4n + 2$	^{234}U	Ne	9×10^{-12}	Pb		
	^{234}U	Mg	1.4×10^{-11}	Hg		
	^{230}Th	^{24}Ne	5.6×10^{-13}	^{206}Hg		
	^{226}Ra	^{14}C	3.2×10^{-11}	^{212}Pb	28.2 MeV	5×10^{13} y
	^{222}Ra	^{14}C	3.5×10^{-8}	^{208}Pb	33.0 MeV	34 years
$4n + 3$	^{235}U	^{20}Ne	8×10^{-12}	^{215}Pb		
	^{223}Ra	^{14}C	6×10^{-10}	^{209}Pb		

particle from β stability. If the emitter is on the proton excess side of stability, its decay benefits from extra “push” and can reach more stable products. The partial half-lives for heavy particle emission are very sensitive functions of the Q values. Although 38 s ^{222}Ra is not a member of a natural chain, it is included in the table to illustrate this point. Even though ^{222}Ra has a much shorter physical half-life than ^{226}Ra , the fraction of decays that involve ^{14}C emission is much higher — 3.5×10^{-8} versus 3.2×10^{-11} . The ratio of partial half-lives (see the last column of the table) is even more striking.

Heavy ion emission would be grouped with spontaneous fission and not considered in this chapter were it not for the convenience the chains afford as a source of radioactive materials with which to study the process. Products such as ^{222}Ra can be produced in charged-particle bombardments, but that implies the presence of energetic ions, which can complicate the detection of a few heavy ions from decay. The ranges of the heavy ions emitted by processes analogous to α decay are a few milligrams per square centimeter. Thin sources are needed, and the carrier-free materials that can be isolated from the chains serve this purpose well. It is likely that heavy particle emission will be found to be a decay mode for most heavy elements.

13.5 Chemical Properties

The most significant chemical property of most members of the chains is that each element is carrier-free — there are no inactive atoms to compete with the radioactive ones for chemical sites, such as ion-exchange sites on the inner surface of a container. In extreme cases, such as polonium in the ^{232}Th chain, there will be few if any atoms at a given time. The specific activity of ^{232}Th is 4,070 Bq/g. If 1 g of thorium is in equilibrium with its chain, the activities of 0.15 s ^{216}Po and 0.3 μs ^{212}Po will be 4,070 Bq and 2,609 Bq (64.1%), respectively. On average there will be 881 atoms of ^{216}Po present at any given time. Only 0.1% of the time is even one atom of ^{212}Po present. Francium is even more rare. It occurs only in the ^{235}U chain (and the extinct $4n + 1$), and then only in a 1.4% branch. There are only a few grams of Fr in the entire crust of the Earth.

■ **Table 13.6**

Chemistry of the chain elements. *Astatine and francium were discovered as the products of nuclear reactions. They are present in only one of the natural chains (^{235}U), and even then not in the main branch (see ► [Fig. 13.3](#)). The masses given in the last three columns refer to undisturbed (secular) equilibrium along the whole chain. See text for more details

Element	Oxidation state(s)	Monograph NAS-NS 30xx	Year of discovery	Mass/g of ^{232}Th	Mass/g of ^{238}U	Mass from ^{235}U /g of U
Thallium	1 3		1861	136 ag	0.1	82 ag
Lead	2 4	3040	Ancient	Various	Various	Various
Bismuth	3 5	3061	1753	7.6 fg	7.7 pg	38 ag
Polonium	2 4	3037	1898	0.3 ag	75 pg	~3 atoms
Astatine	–1 1 3 5 7	3012	1940*	–	–	<1atom
Radon	0	3025	1900	120 ag	2.2 pg	1.2 ag
Francium	1	3003	1939*	–	–	5.6 ag
Radium	2	3057	1898	0.4 ng	340 ng	303 fg
Actinium	3	3020	1899	49 fg	–	215 pg
Thorium	4	3004	1828	1 g	44 ng	1.2 pg
Protactinium	4 5	3016	1913		757 ag	332 ng
Uranium	3 4 5 6	3050	1789		1 g	7.2 mg

The chemical properties span a range similar to the representative elements in the first few rows of the periodic table. Francium and radium are certainly characteristic of alkali and alkaline earth elements. Both Fr and Ra have only one oxidation state in chemical combinations and have little tendency to form complexes. Thallium in the 1+ oxidation state has alkali-like properties, but it does form complexes and has extensive chemistry in its 3+ state. Similarly, lead can have alkaline earth characteristics, but differs from Ra in forming complexes and having a second, 4+, oxidation state. Bismuth and actinium form 3+ ions in solution and are similar to the lanthanides and heavy ($Z > 94$) actinides. Thorium also has a relatively simple chemistry, with similarities to zirconium and hafnium. Protactinium is famous for difficult solution chemistry; it tends to hydrolyze and deposit on surfaces unless stabilized (e.g., by $>6\text{ M}$ sulfuric acid). The chemistry of uranium as the uranyl ion UO_2^{2+} is fairly simple, but several other oxidation states are possible.

These properties and references for monographs giving detailed radiochemical characteristics (published by the U.S. National Academy of Sciences beginning in 1960 in a series NAS-NS 30xx, e.g., NAS-NS 3040 for lead) are given in ► [Table 13.6](#) (see also LANL [2004](#)).

References

Bateman H (1910) Proc Cambridge Philos Soc 15:423
 Helmer RG, Gehrke RJ, Davidson JR (1999) Gamma-ray
 spectrum catalogue. Idaho National Engineering
 and Environmental Laboratory

LANL (2004) <http://library.lanl.gov/radiochemistry/>



14 Radioelements

H. C. Griffin

University of Michigan, Ann Arbor, Michigan, USA

<i>14.1 Introduction</i>	690
<i>14.2 Discovery of Technetium</i>	690
<i>14.3 Discovery of Promethium</i>	692
<i>14.4 Why Do Tc and Pm Have No Stable Isotopes?</i>	694
<i>14.5 Chemical and Physical Properties</i>	697

Abstract: Technetium (Tc) ($Z = 43$) and promethium ($Z = 61$) are the only elements below bismuth ($Z = 83$) in atomic number that have no stable isotopes. The discovery of these unusual elements is described, and the physical factors leading to their instability are discussed.

14.1 Introduction

The last of the naturally occurring stable elements were discovered in 1923 ($_{72}\text{Hf}$) and 1925 ($_{75}\text{Re}$). This concluded over a century of rapid discovery of elements found in the earth's crust. Two holes among atomic numbers below $_{83}\text{Bi}$ remained: 43 and 61. Moseley's correlation of atomic number with the energies of transitions involving inner atomic electrons made it clear that the gaps were real.

The steps and missteps in the process of discovering new elements led to caution in accepting a previously unidentified spectroscopic feature as evidence for a new element (Boyd 1959). Chemical characterization was required. For example, "masurium" was proposed for element 43, and "illium" and "florentium" were proposed for element 61 based on atomic spectroscopy of extracts from minerals. In retrospect, it is clear that there was evidence for unusual conditions for these elements. For example, above $_{7}\text{N}$ the only mass numbers of stable isotopes of elements with odd atomic number are also odd, and there is only one stable isobar for each odd A . Molybdenum (Mo) has stable isotopes 92, 94–98, and 100. Ruthenium has 96, 98–102, and 104. Niobium has 93, and rhodium 103. Nothing is left for technetium, which would have the best chance for stability at mass numbers 97 and 99. Similarly, either neodymium or samarium has a β -stable isotope from 142 to 150; nothing is left for promethium.

There is little difference between protons and neutrons with respect to nuclear properties, but our interest in elements leads to an emphasis on atomic numbers. There are more missing neutron numbers (19, 35, 39, 45, 61, 89, 115, and 123).

The development of the cyclotron and, later, the fission reactor gave the means for a variety of artificial transmutations, but it often was difficult to identify the element and mass number of a radioactive product. In many cases, individual radionuclides could be characterized only by simple features, such as half-life or attenuation of radiations in absorbers, which did not allow discriminating the components of a complex mixture. Chemical evidence was required in order to make definite identification with a particular element.

Except when original observations are relevant, nuclear properties are taken from compilations (Browne et al. 1986; Firestone et al. 1996; Baum et al. 2002).

14.2 Discovery of Technetium

According to the periodic table, the missing element at atomic number 43 should be between manganese and rhenium with regard to chemical properties. The group that discovered rhenium in 1925 (Noddack et al. 1925) claimed to have detected element 43 ("masurium") in the same minerals. They subsequently were able to isolate weighable quantities of rhenium (more than a gram in 1928), but neither they nor others could confirm detection of element 43.

Technetium was finally discovered by Perrier and Segrè in 1937 (Perrier and Segrè 1937). E.O. Lawrence had bombarded a Mo plate with deuterons (and secondary neutrons) in the

Berkeley cyclotron for several months prior to shipping the plate to Segrè's group in Italy in late December, 1936. Perrier and Segrè began their radiochemical studies in late January, more than 6 weeks after the end of bombardment. On the surface exposed to the deuterons, they found "strong activity, chiefly due to very slow electrons" ascribed to "more than one substance of a half-value period of some months" in addition to ^{32}P (which they could not explain, but did not attribute to reactions with molybdenum).

Subsequent work (Cacciapuoti and Segrè 1937) revealed that most of the Tc activity arose from what are now known to be 61-day $^{95\text{m}}\text{Tc}$ and 90.1-day $^{97\text{m}}\text{Tc}$.

► **Table 14.1** shows a nuclide chart corresponding to charged particle reactions with Mo. Both (d,n) and (d,2n) reactions are energetically allowed (have energy requirements, Q , that are met by the bombarding particle) and lead directly to Tc. For example, the Q values for ^{95}Mo (d,n) ^{96}Tc and ^{95}Mo (d,2n) $^{95\text{m}}\text{Tc}$ are -3.25 and -4.74 MeV, respectively. The Q value for ^{97}Mo (d,2n) $^{97\text{m}}\text{Tc}$ is -3.42 MeV. In addition, (d,p) reactions with ^{98}Mo and ^{100}Mo produce Mo isotopes that subsequently decay to Tc. Therefore, the bombardments produced many different radioactive products, but after a few months 61-day $^{95\text{m}}\text{Tc}$ and 90.1-day $^{97\text{m}}\text{Tc}$ dominate the activity. Note that both of these are isomeric levels. One, $^{95\text{m}}\text{Tc}$, decays primarily (96%) by electron capture (EC) and subsequent γ -ray emission. The other, $^{97\text{m}}\text{Tc}$, decays by a highly converted 96.6 keV transition, which presumably produced the "slow electrons" reported (Perrier and Segrè 1937).

The chemical identification consisted of three parts: (1) removing ^{32}P , (2) showing that the remaining activity was not due to zirconium, niobium, or molybdenum, and (3) showing that the element was similar, but not identical, to rhenium.

Until recognized for what it was, the ^{32}P was very confusing. Once recognized, it was removed by precipitating magnesium ammonium phosphate.

Zirconium was isolated as a hydroxide, molybdenum as a sulfide, and niobium as sodium metaniobate. None carried a significant part of the activity.

In solutions containing inactive manganese and rhenium carriers as well as the activity under study, the activity generally followed rhenium. This is consistent with the greater chemical similarities of heavy members of a group in the periodic table as compared to differences among lighter members. However, Tc_2O_7 is more volatile than Re_2O_7 , and the chloride is less volatile. Other chemical properties of Tc are summarized in ► Sect. 14.5.

■ **Table 14.1**

Nuclide chart showing stable molybdenum isotopes and radioactive products from deuteron bombardments

^{92}C	^{93}C	^{94}C	^{95}C	^{96}C	^{97}C	^{98}C	^{99}C	^{100}C	^{101}C	^{102}C
4 2 min	43 min 2 73 h	52 min 4 88 h	61 days 20 h	52 min 4 3 days	91 days 4 2 My	4 2 My	6 01 h 0 21 My	15 8 s	14 2 min	4 4 min 5 3 s
^{91}Mo	^{92}Mo	^{93}Mo	^{94}Mo	^{95}Mo	^{96}Mo	^{97}Mo	^{98}Mo	^{99}Mo	^{100}Mo	^{101}Mo
1 08 min 15 5 min	14 84	6 9 h 3 5 y	9 25	15 92	16 68	9 55	24 12	2 75 days	9 63	14 6 min

Stable isotopes are shaded and list natural abundances in percentage. When isomers exist and relative energies of the states are known, the half-life of the isomer is given above that of the ground state. See also ► **Table of Nuclides** in this volume's appendix (My = Ma, i.e., 10^6 years; ky = ka, i.e., 10^3 years).

14.3 Discovery of Promethium

In principle, $_{61}\text{Pm}$ could have been discovered by techniques similar to those used for $_{43}\text{Tc}$ – bombardment of $_{60}\text{Nd}$ with charged particles from a cyclotron and demonstration that some of the products were isotopes of element 61. Indeed the bombardments were done, and several radionuclides that might have been isotopes of element 61, for example, “cyclonium” (Pool and Quill 1938), were produced, but the essential chemical proof was lacking. Whereas technetium and its neighbors differ considerably in chemical properties, variations among neighboring rare earths are very slight. This chemical characterization was beyond the capabilities of the groups carrying out the bombardments.

Conventional chemistry is illustrated by the chemistry used to support the claim of “illinium” (Harris et al. 1926). This report is one (*Observations on the Rare Earths XXIII*) of a series of studies in which concentrates rich in one or more rare earths were studied by arc spectroscopy. Harris et al. chose a concentrate prepared by methods that were intermediate between those found to enhance $_{60}\text{Nd}$ and $_{62}\text{Sm}$. The visible and infrared emissions were found to have about 130 lines that were not unique to either Nd or Sm fractions. They found support for their claims in absorption spectra of solutions and L X-ray emission spectra associated with the concentrate.

The chart of the nuclides in the region of promethium is given in ▶ Table 14.2. It is obvious now that there is a negligible amount of promethium in natural materials, and if macroscopic amounts were present, the radioactivity would be intense. The isotope with the longest half-life is 17.7-year ^{145}Pm . If it were present at 1 ppm in a 1-g sample, the activity would be 6 MBq.

In order to separate adjacent elements and to isolate very small quantities, a new chemistry was needed. This chemistry, ion-exchange chromatography (see ▶ Chap. 51 in Vol. 5) with synthetic resins (Walton 1976), was developed during the Manhattan project in order to study the products of nuclear fission, which include several light rare earths. The technique was borrowed in order to identify element 61.

■ Table 14.2
Chart of the nuclides in the vicinity of promethium

^{143}Pm 265 days	^{144}Pm 360 days	^{145}Pm 17.7 years	^{146}Pm 5.53 years	^{147}Pm 2.62 years	^{148}Pm 41.3 days 5.37 days	^{149}Pm 2.21 days	^{150}Pm 2.68 h	^{151}Pm 1.18 days	^{152}Pm 13.8 min 4.1 min	
^{142}Nd 27.2	^{143}Nd 12.2	^{144}Nd 23.8 2.1×10^{15} years	^{145}Nd 8.3	^{146}Nd 17.2	^{147}Nd 10.98 days	^{148}Nd 5.7	^{149}Nd 1.73 h	^{150}Nd 5.6	^{151}Nd 12.4 min	
^{141}Pr 100						↖ 2.25		↖ 1.08		↖ 0.419
^{140}Ce 88.45		^{142}Ce 11.11								

The columns contain isotones. The fission yields for ^{235}U are given for several mass chains (i.e., isobars situated along the lines shown by the slanted arrows). Stable isotopes are shaded and list natural abundances in percentage. (The upmost cells show the stable and primordial Sm isotopes.) See also ▶ Table of Nuclides in this volume’s appendix.

By mid-1945, over 30 fission products had been characterized as isotopes of yttrium or one of the lanthanides, but few could be definitely assigned by element and mass numbers. The work that ultimately identified element 61 began with a mixture of radioactive materials that concentrated elements between cerium and samarium. This mixture included a soft β emitter with a half-life of ~ 4 years and a γ emitter of ~ 11 days.

Marinsky, Glendenin, and Coryell reported their discovery of promethium in part as follows:

- In the comprehensive studies of the radioactive species produced in the fission of uranium it has been found that over thirty are members of the rare earth family (isotopes of yttrium and the group lanthanum through europium). The chemical and physical identification of these was an important part of the research program of the Manhattan Project. Standard oxidative separations and fractional precipitations and the use of radiochemical methods based on chain relations served to distinguish the activities of yttrium, lanthanum, cerium, and some of praseodymium, and those of samarium and europium. The characterization of the sequence praseodymium, neodymium, and element 61 presented very difficult problems that were solved only with the intensification of ion exchange methods originally developed by Boyd and co-workers and applied to the rare earth field by Cohn and co-workers. (Marinsky et al. 1947)

The ion-exchange medium was Amberlite IR-1, a sulfonated phenol-formaldehyde resin, and the eluting agent was 5% ammonium citrate at pH 2.75. The order of elution of the rare earths had been established in a series of experiments with radioactive cerium, lanthanum, europium, and yttrium produced by fission, and praseodymium and europium produced by neutron capture. The lanthanides elute in reverse order of atomic number, and yttrium precedes the fission-product lanthanides. Although the technique was a vast improvement over conventional chemical procedures, the physical form of the resin was quite inferior to modern, uniform beads. Resolution was barely better than the separation between adjacent elements, and there was considerable tailing. It is fortunate that the elution order puts low yield products before higher yield ones; this minimized the interference from tailing.

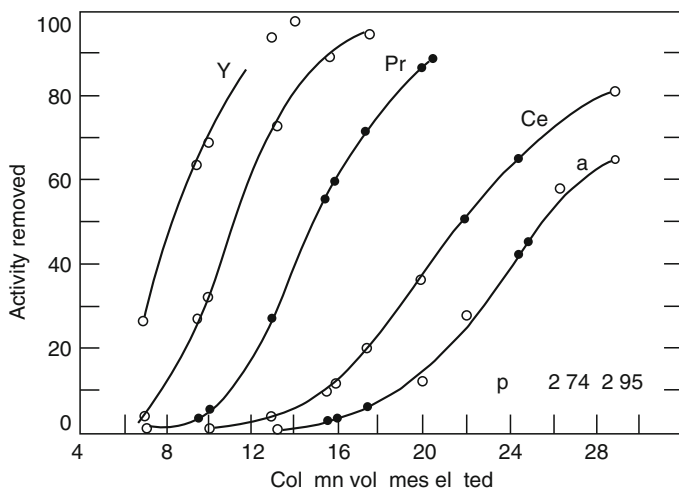
A sample of the praseodymium group (praseodymium, neodymium, and element 61; most of the cerium, samarium, europium, and yttrium fission products had been removed, cerium by ceric iodate precipitations and the others by potassium carbonate digestions) was absorbed on an Amberlite IR-1 column. The elution curve is shown in ► Fig. 14.1. The soft β emitter (now known to be 2.62-year ^{147}Pm ; see ► Table 14.2) appeared in the position expected (by interpolation) for element 61 and became the first isotope identified as the element subsequently named promethium. The ~ 11 -day γ emitter eluted in the position expected for neodymium (10.98-day ^{147}Nd). The praseodymium peak was primarily 13.6-day ^{143}Pr . The yttrium peak was primarily 58.5-day ^{91}Y ; the fission yields of ^{143}Pr and ^{91}Y were high, $\sim 6\%$, and the yttrium peak represented $\sim 0.001\%$ of the fission yield.

Subsequent experiments with neutron-activated neodymium, described in the same report, revealed a 1.7-h isotope of neodymium (too short to be isolated from fission with the available columns) and a 47-h isotope of element 61 (also detected in fission).

Mass number assignments were based on quantitative analysis of the chemically resolved fractions. Fission is known to produce primarily products with neutron/proton ratios similar to the fissioning nuclide (here ^{235}U , two to three neutrons less which accompany the fragments). For $A = 147$, the most likely products are 4-s ^{147}La and 56-s ^{147}Ce , which join their short-lived isobars by quickly cumulating in 11-day ^{147}Nd . Very little ^{147}Pm is produced as a primary fission product; just as in neutron activation of Nd, ^{147}Pm is a product of decay of ^{147}Nd .

■ Fig. 14.1

Elution curve for the praseodymium group of fission products from Amberlite IR-1 (Reprinted with permission from Marinsky et al. 1947. © 1947 American Chemical Society)



The general form of the mass-yield distribution was also known; the yield drops rapidly with increasing mass number above 144. By showing that the cumulative fission yield of the “~4-year” product was about twice that of the “48-h” product, combined with the results of activation measurements, ^{147}Pm and ^{149}Pm were identified by mass number as well as atomic number.

14.4 Why Do Tc and Pm Have No Stable Isotopes?

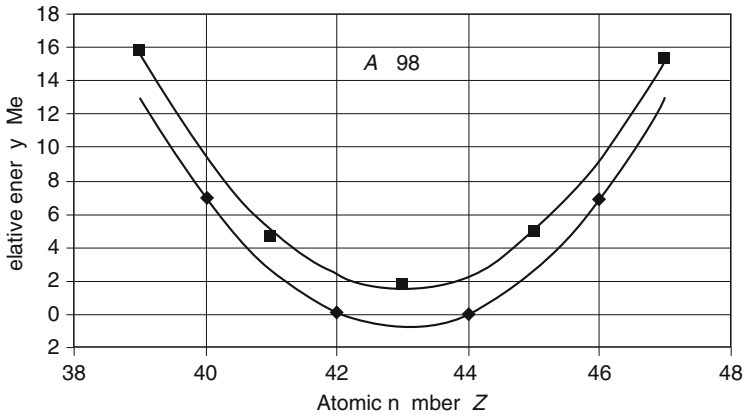
There is nothing remarkable about atomic numbers 43 and 61, except that they are odd integers and, in terms of nuclear stability, unlucky. In random assemblages of neutrons and protons, there are equal probabilities for even A versus odd A or even Z versus odd Z . However, far fewer odd- Z nuclides are stable. These generalizations can be understood in terms of the symmetry and pairing terms in the semiempirical mass equation (Choppin et al. 2002; Friedlander et al. 1981). The symmetry term is proportional to $(N-Z)^2$ and leads to a parabolic dependence on Z at constant A . The pairing term raises odd- Z odd- N nuclides and lowers even- Z even- N nuclides, producing two parabolas for even- A isobars. The effect is exemplified by the $A = 98$ isobars shown in Fig. 14.2. Both parabolas are centered on $Z = 43.0$, and they are separated by ~ 2.22 MeV; ^{98}Tc would be at the bottom and, therefore, stable, were it not for the pairing term.

For mass numbers above ~ 40 , and certainly by $A \sim 98$, Coulomb energies are significant, and stable nuclides have more neutrons than protons. The parabolic minima define $Z_A(A)$, which increases by ~ 0.45 per mass unit in the vicinity of Tc. Therefore, the minima should be $\sim 43.0 - 0.45 = 42.55$ at $A = 97$ and should be 43.45 at $A = 99$. Both of these are closer to 43 than to the adjacent atomic numbers. If masses were exactly parabolic, both ^{97}Tc and ^{99}Tc would be stable. These are the conditions that lead to two stable isotopes for some odd- Z elements.

Although the masses (energies) are nearly parabolic, as shown in Fig. 14.3, valence neutrons are slightly more stable than valence protons. According to the mass equation, energy

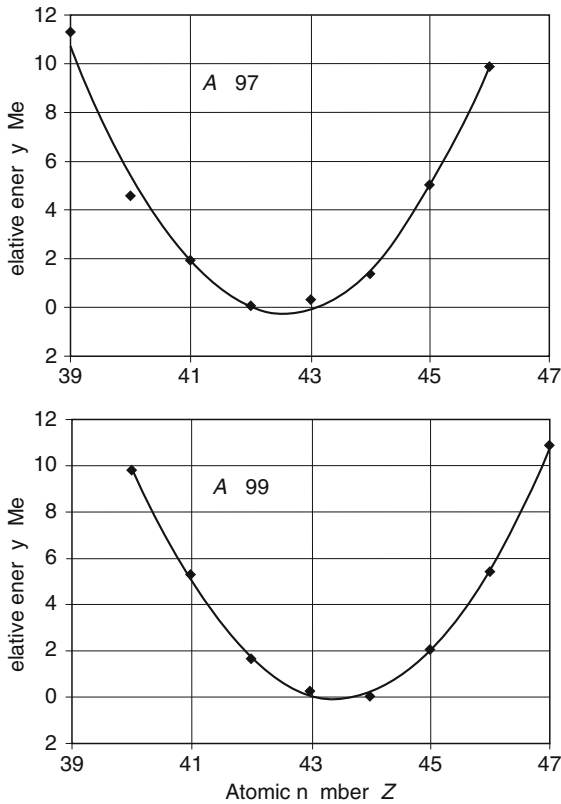
■ Fig. 14.2

Relative energies of the $A = 98$ isobars. The odd- Z and even- Z elements are represented by *squares* and *diamonds*, respectively. The lines are quadratic (parabolic) fits to the data of each type



■ Fig. 14.3

Relative energies of the $A = 97$ (top) and $A = 99$ (bottom) isobars



differences between adjacent isobars should be linear with atomic number. These energy differences are just the Q values for β decay (β^- and EC). These energy differences are shown in ▶ Fig. 14.4. The upper part gives EC energies for $A = 97$ isobars for comparison with ^{97}Tc , which decays by this mode. The lower part gives β^- energies for $A = 99$ for comparison with ^{99}Tc . In both parts, linear fits to odd- Z and even- Z elements are shown. For both chains, the small positive decay energy for Tc would disappear if the neutron–proton separation were removed.

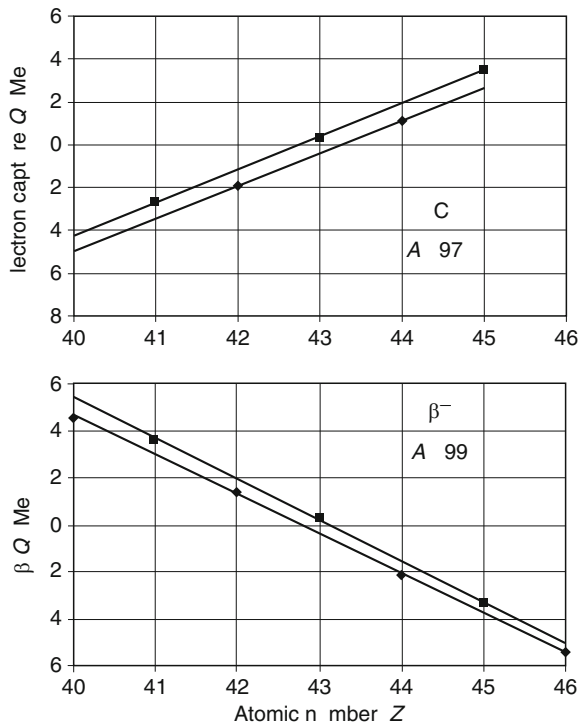
The same analysis applies to promethium. ▶ Figure 14.5 shows the decay energies for isobars of ^{145}Pm (17.7-year EC decay) and ^{147}Pm (2.62-year β^- decay). Just as for technetium, the most favored isotopes of promethium just miss being stable because of small differences in neutron–proton stabilities.

Although these promethium isotopes have much shorter half-lives than the corresponding technetium isotopes, the decay energies for promethium are actually lower. Decay of the technetium isotopes is hindered by large angular momentum changes.

Because of a small difference in stability of valence neutrons and protons, combined with fortuitous combinations of symmetry and Coulomb energies, technetium and promethium have no stable isotopes.

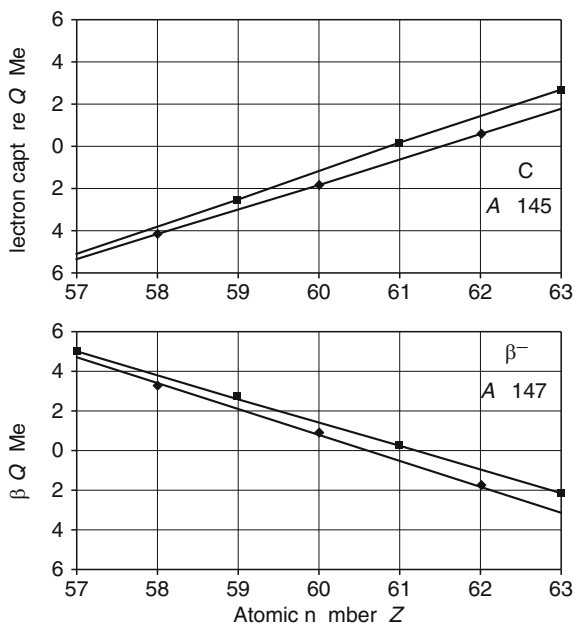
■ Fig. 14.4

Q values for electron capture (EC) decay of $A = 97$ isobars (top) and β decay of $A = 99$ isobars (bottom)



■ Fig. 14.5

Q values for electron capture (EC) decay of $A = 145$ isobars (top) and β^- decay of $A = 147$ isobars (bottom)



Since Z_A increases ~ 0.4 per mass number, the neutron number must increase by ~ 0.6 per unit A . Therefore it is *expected* that all isotones for some odd N would be unstable. As pointed out in [Sect. 14.1](#), there are eight such neutron numbers.

14.5 Chemical and Physical Properties

Neither element is unusual except for the absence of stable isotopes. Of course this means that either pure element can have high specific activity; there are no nonradioactive forms to dilute the activity.

On the earth, the most likely source of macroscopic amounts for technetium and promethium is the reprocessing of irradiated uranium and plutonium from fission reactors. This mechanism produces only a few, and not the longest-lived, isotopes.

For technetium, most of the mass consists of 2.1×10^5 -year ^{99}Tc . Heavier isotopes are short lived, and lighter isotopes are “shielded” by stable isotopes of molybdenum (here “shielded” means not fed by chain decay). The cumulative fission yield of ^{99}Tc is $\sim 6\%$ for both ^{235}U and ^{239}Pu . Because of the long half-life, this isotope contributes little to the total activity of fission products for the first 100 years, but it is the dominant fission product after 1,000 years. There is little energetic γ emission; it is difficult to detect ^{99}Tc in impure matrices without chemical processing. The dominant mode of decay is 293.5-keV β^- decay to the ground state of ^{99}Ru . Only 0.0016% of the β^- decays goes to excited states. The only γ -ray is the $\sim 6 \times 10^{-4}\%$ 89.7-keV γ .

The most important isotope of technetium is 6.0-h $^{99\text{m}}\text{Tc}$. It is a valuable tool of medical diagnostics because of its chemical versatility and the energy of its γ -ray. This application is described in detail in ► Chap. 43 of Vol. 4.

For promethium, most of the mass in aged fission products consists of 2.62-year ^{147}Pm , which (except for half-life) has decay characteristics similar to ^{99}Tc . The dominant decay mode is 224-keV β decay to the ^{147}Sm ground state. Only 0.0057% of decays feeds excited states. The most intense γ -ray is the 0.0029% 121.2-keV γ -ray. Because of its high specific activity and the absence of penetrating radiation, ^{147}Pm has been used as a source of energy in thermoelectric converters for remote applications.

Anders (1960) summarized the chemical properties of technetium in his monograph on radiochemistry.

- In many respects, the analytical behavior of Tc is similar to that of Re. Both form stable XO_4^- anions that give insoluble salts with large cations; both form volatile heptoxides; and both form acid-insoluble heptasulfides. However, there are subtle differences between the two elements that can cause them to behave very differently under certain conditions. The vapor pressure of Tc_2O_7 is much higher than that of Re_2O_7 at low temperatures (e.g., 10^{-1} mm at 100°C , compared to $\sim 3 \times 10^{-5}$ mm for Re_2O_7). In contrast to rhenium, technetium (VII) is therefore easily lost upon evaporation of acid solutions unless a reducing agent is present or the evaporation is conducted at a very low temperature. Ignorance of these factors has led to a multitude of conflicting statements concerning the volatility of technetium.

The chemistry of promethium must be understood in terms of the trends in properties within the rare earth, or lanthanide, series. The radiochemistry of these elements (plus scandium and yttrium) has been described by Stevenson and Nervik (1961).

References

- Anders E (1960) The radiochemistry of technetium, NAS-NS 3021. Natural Academy of Sciences, Washington, DC
- Baum EM, Knox HD, Miller TR (2002) Nuclides and isotopes, 16th edn. KAPL, Schenectady, NY
- Boyd GE (1959) J Chem Ed 36:3
- Browne E, Firestone RB, Shirley VS (1986) Table of radioactive isotopes. Wiley, New York
- Cacciapuoti BN, Segrè E (1937) Phys Rev 52:1252
- Choppin GR, Liljenzin J-O, Rydberg J (2002) Radiochemistry and nuclear chemistry, 3rd edn. Butterworth-Heinemann, Woburn, MA
- Firestone RB, Shirley VS, Baglin CM, Zipkin J, Chu SYF (1996) Table of isotopes, 8th edn. Wiley, New York
- Friedlander G, Kennedy JW, Macias ES, Miller JM (1981) Nuclear and radiochemistry, 3rd edn. Wiley, New York
- Harris JA, Yntema LE, Hopkins BS (1926) J Am Chem Soc 48:1585
- Marinsky JA, Glendenin LE, Coryell CD (1947) J Am Chem Soc 69:2781
- Noddack W, Tacke I, Berg O (1925) Naturwissenschaften 13:567
- Perrier C, Segrè E (1937) J Chem Phys 5:712
- Pool ML, Quill LL (1938) Phys Rev 53:436
- Stevenson PC, Nervik WE (1961) The radiochemistry of the rare earths, scandium, yttrium, and actinium, NAS-NS 3020. Natural Academy of Sciences, Washington, DC
- Walton FW (1976) Ion-exchange chromatography. Halsted Press, Wiley, Stroudsburg, PA

15 Isotope Effects

G. Jancsó

KFKI Atomic Energy Research Institute, Budapest, Hungary

15.1	<i>Introduction</i>	700
15.2	<i>Mechanical Effects</i>	701
15.3	<i>Isotope Effects in Spectroscopy</i>	702
15.4	<i>Isotope Effects in Chemical Equilibria</i>	704
15.4.1	Isotope Exchange Equilibria	705
15.4.2	Calculation of the Equilibrium Constant	706
15.5	<i>Isotope Effects on Phase Equilibria</i>	708
15.5.1	Vapor Pressure Isotope Effects	708
15.5.2	Isotope Effects on Other Phase Equilibria	711
15.6	<i>Isotope Effects on Some Physicochemical Properties</i>	713
15.7	<i>Kinetic Isotope Effects</i>	715
15.7.1	Classification and Determination of Kinetic Isotope Effects	715
15.7.2	Theory of Kinetic Isotope Effects	717
15.8	<i>Mass-Independent Isotope Effects</i>	719
15.9	<i>Biochemical and Biological Isotope Effects</i>	720
15.9.1	Physiological Effects of Heavy Water	721
15.9.2	Isotope Fractionation in Biological Processes	722

Abstract: Isotope effects, that is, differences brought about by isotopic substitution in the physical and chemical properties of atoms and molecules, are reviewed from the point of view of spectroscopy, chemical equilibria, phase equilibria, physicochemical properties, reaction kinetics, and biology. The theory of isotope effects is discussed in some detail.

15.1 Introduction

If naturally occurring water, containing deuterium in low concentration, evaporates then the concentration of deuterium in the liquid phase increases because H_2O is more volatile than HDO . (Note that deuterium ^2H will be denoted by D in this chapter, whereas protium ^1H , the common isotope of hydrogen, will be denoted by H , as customary in this field.) The viscosity of D_2O is higher than that of H_2O . The diffusion rate of ^{36}Ar is higher than that of the heavier argon isotope ^{40}Ar . The infrared spectrum of CH_4 is different from that of CD_4 . The reaction of an organic compound becomes substantially slower if, in the rate-determining step of the reaction, a $\text{C}-\text{D}$ bond is being broken instead of a $\text{C}-\text{H}$ bond. Other examples abound.

These differences brought about by isotopic substitution in the physical and chemical properties of atoms and molecules are called *isotope effects*. The differences in the characteristic parameters of nuclear transformations (half-life, energy of radiation, cross section) are not considered as isotope effects. The molecules that differ in their isotopic composition are usually called *isotopic molecules* in the literature. However, according to the IUPAC terminology, a molecular entity that differs solely in isotopic composition (number of isotopic substitutions), for example, CH_4 , CH_3D , CH_2D_2 , CD_4 , is called *isotopologue*. Isomers having the same number of each isotopic atom but differing in their positions are called *isotopomers* (the term is a contraction of “isotopic isomer”). Isotopomers can be either constitutional isomers (e.g., $\text{CH}_2\text{DCH}=\text{O}$ and $\text{CH}_3\text{CD}=\text{O}$) or isotopic stereoisomers (e.g., (*R*)- and (*S*)- CH_3CHDOH). The term isotopologue is preferable to the customary “isotopomer,” which ought to be restricted to species that are constitutionally or stereochemically isomeric because of isotopic substitution.

Isotope effects are usually based on the differences between the masses of the atoms and therefore they are referred to sometimes as “isotope-mass effects” (the so-called mass-independent isotope effects, for example, the “magnetic isotope effects,” which are due to the differences between the nuclear spins of isotopes, will be discussed in [Sect. 15.8](#)). The geometrical and electronic structures of isotopic molecules are much the same because isotopic nuclei differ only in the number of neutrons, while it is the number of protons that determines the nuclear charge and thus the electron distribution and molecular structure. This fact leads to a great simplification in theoretical calculations of isotope effects.

Isotope effects can be divided in two main groups: phenomena that are directly connected to the differences in the molecular mass (thermal motion, motion in gravitational, electric, and other fields) and those connected to different mass distributions within the molecule (isotope effects on molecular spectra, chemical equilibria, reaction rate, etc.). Isotope effects may also be classified according to the field in which they are observed: physics, chemistry, biology, geology, spectroscopy, etc. Isotope effects play an important role in the variation of stable isotope compositions in nature. The differences in chemical and physical properties of the isotopes form the basis of their separation from each other and make possible the production of enriched isotopes for industrial, military, medical, and research purposes (see [Chap. 51](#) in Vol. 5).

Extensive information about isotope effects can be found in a number of books, book chapters, and review papers (e.g., Brodsky 1961; Roginski 1962; Wolfsberg 1969c; Krumbiegel 1970; Rabinovich 1970; Collins and Bowman 1971; Wolfsberg 1972; Bigeleisen et al. 1973; Bigeleisen 1975, 1984; Vértés and Kiss 1987; Criss 1999).

15.2 Mechanical Effects

The average speed of gas molecules at a given temperature depends on their masses, therefore, in a gas made up of molecules containing different isotopic species, those molecules containing the light isotope will, on average, have speeds slightly higher than those that contain the heavy isotope. In the gaseous diffusion process used for the enrichment of ^{235}U isotope, the maximal theoretical separation that can be achieved is equal to the square-root of the ratio of the masses of the gas molecules. In the diffusion process, utilizing uranium hexafluoride, this ratio is 1.00429. Because this number is so close to unity, the degree of enrichment that can be achieved in a single diffusion stage is very small, but the effect can be multiplied by making use of a cascade consisting of a number of stages.

Isotope effects can also be observed in the concentration distribution of gaseous substances in mechanical fields. In the earth's gravitational field, the pressure decreases with increasing altitude, which can be described by the barometric formula

$$p_h = p_0 \exp\left(-\frac{Mgh}{RT}\right) \quad (15.1)$$

where p_h and p_0 are the pressures at altitude h , and at zero altitude, respectively, g is the gravitational acceleration, M is the molar mass, R is the gas constant, and T is the temperature. (It should be noted that during the derivation of Eq. (15.1), the h dependence of T and g has been neglected, therefore it is only a rough approximation to actual atmospheric pressures). As a consequence of Eq. (15.1), the ratio of the concentrations (c'_h/c_h) of two isotopic variants with molecular masses M' and M , respectively, changes with the altitude according to the following equation

$$\frac{c'_h}{c_h} = \frac{c'_0}{c_0} \exp\left(-\frac{(M - M')gh}{RT}\right). \quad (15.2)$$

Similarly, the ratio of the concentrations of the two isotopic species will be different at the axis of a gas centrifuge and at a distance r from the axis:

$$\frac{c'_r}{c_r} = \frac{c'_0}{c_0} \exp\left(-\frac{(M - M')(\omega r)^2}{2RT}\right) \quad (15.3)$$

where ω is the angular velocity of the centrifuge. This effect is utilized in the enrichment of ^{235}U isotope. The magnitude of the separation factor $\alpha = (c'_r/c_r)/(c'_0/c_0)$ in this case is the function of the absolute mass difference of the isotopic molecules, not of the relative mass difference, which is the case in the other processes. This fact is especially advantageous for isotope separation of heavier elements.

In electric and magnetic fields, the deflection of ions from the original direction of motion also depends on their mass m . The deflection (X) of an ion with velocity u and charge q in an electric field E can be given as

$$X \propto \frac{Eq}{mu^2}. \quad (15.4)$$

The magnitude of the deflection (Y) caused by a magnetic field strength H is

$$Y \propto \frac{qH}{mu}. \quad (15.5)$$

► Equations (15.4) and ► (15.5) show that the deflections of the ions of the lighter isotope are greater than those of the heavier isotope, provided that their velocities and charges are the same. The isotope analysis by mass spectrometry and the electromagnetic isotope separation method using large-scale mass spectrometers, called Calutrons because of their early development at the University of California Cyclotron Laboratory, are based on these effects.

The kinetic theory of gases yields theoretical expressions for the thermal conductivity and other transport properties of gases. For ideal gases around atmospheric pressure, where the mean free path is much less than the smallest dimension of the container, the ratio of the thermal conductivities of the isotopic molecules is inversely proportional to the ratio of the square-roots of their molecular masses. At lower pressures, where the mean free path becomes comparable to, or larger than the dimensions of the container, the thermal conductivity will be strongly pressure dependent. The isotope analysis of isotopic gas mixtures by using a catharometer is based on the fact that, to a first approximation, the relationship between the thermal conductivity and isotopic composition of the mixture is linear (Müller et al. 1969). The isotope ratio of the viscosities of gases is equal, to a first approximation, to the square-root of the molecular mass ratio.

On the basis of the mass dependence of the different forms of motions of isotopic molecules, one can expect isotope effects also in the rate of evaporation, condensation, dissolution, and crystallization as well as in electric mobilities of ions.

15.3 Isotope Effects in Spectroscopy

Isotope effects in atomic spectroscopy can be illustrated using the example of the visible spectra of hydrogen that led Urey et al. (1932) to the discovery of deuterium (the first public announcement of the discovery was made at the 1931 Christmas meeting of the American Association for the Advancement of Science in New Orleans). The spectral lines of the visible spectra of hydrogen (Balmer series) can be given by the Rydberg equation, which describes the energy change accompanying the jump of an electron from the n th orbital to the 2nd

$$\frac{1}{\lambda_H} = R \left(\frac{1}{2^2} - \frac{1}{n^2} \right), \quad (n > 2) \quad (15.6)$$

where λ_H is the wavelength of a spectral line, R is the Rydberg constant that depends on the mass of the nucleus; its values for hydrogen and deuterium are 109,677.58 and 109,707.42 cm^{-1} , respectively. Urey et al. (1932) observed weak satellites for four of the Balmer lines of hydrogen ($n = 3, \dots, 6$), which were shifted to shorter wavelengths and the magnitudes of these shifts were found to be in exact agreement with the predictions of ► Eq. (15.6) if one assumed the existence of a nucleus with a mass of “2.”

In a diatomic molecule isotope effects appear in the vibrational, rotational, and electronic spectra. Isotope effects on vibrational spectra can be interpreted within the framework of the *Born–Oppenheimer approximation*, which is the cornerstone of most theories dealing with the effects of isotopic substitution on molecular properties. In this approximation, the potential energy surface for the vibrational-rotational motions of a molecular system is taken as being independent of the masses of the nuclei. Thus, the nuclei of different masses move on the same potential surface because to good approximation the electronic structure is independent of isotopic substitution. Then, the harmonic vibrational frequencies of the two isotopic variants of a diatomic molecule (prime denotes the lighter molecule) can be given as

$$\frac{\omega'}{\omega} = \sqrt{\frac{\mu}{\mu'}} \quad (15.7)$$

where ω is the frequency and μ is the reduced mass ($= m_a m_b / (m_a + m_b)$), m_a and m_b are the atomic masses of the atoms in the diatomic molecule. Vibrational and rotational lines cannot always be observed separately; changes in the vibrational state are accompanied by changes of the rotational state and the rotational constant is dependent on the vibrational quantum number. It should also be noted that quite often the potential curve is significantly anharmonic.

The effect of isotopic substitution appears also in the electronic spectra of diatomic molecules that led to the discovery of ^{18}O , ^{17}O , ^{13}C , and ^{15}N by the methods of optical molecular spectroscopy in 1929 (see, e.g., Nash 1975).

Isotopic substitution plays an important role in the determination of vibrational force constants of small polyatomic molecules from observed vibrational frequencies.

In the general valence force field of an N -atomic nonlinear molecule, there are $\frac{1}{2}(3n - 6) \times (3n - 5)$ force constants, but maximum only $3n - 6$ vibrational frequencies may be observed. Isotope substitution changes the vibrational frequencies without changing the force constants (within the Born–Oppenheimer approximation) and thus increases the number of data from which the force constants can be determined.

If hydrogen is replaced by deuterium in one of the substituents connected to an asymmetric carbon atom, the optical activity may change by several per cent. Similar shifts can be observed when the solvent is changed for its deuterated variant. Isotopic substitution can create asymmetry in a molecule, for example, by replacing one of the hydrogen atoms in a compound of the type $\text{R}_1\text{-CH}_2\text{-R}_2$, and thereby induce optical activity. In this case, the molecular chirality arises solely from an isotopic substitution and the phenomenon can be well understood in terms of vibronic interactions that differ for isotopically substituted and parent molecules (Polavarapu et al. 1981). One example is the α -deuteroethyl benzene molecule in which one of the hydrogen atoms of the methylene group is replaced by deuterium and the optical activity of this compound is $\alpha_D^{25} = -0.30^\circ$. The replacement of H by D in the C–H bond will result in a shortening of the average length of the bond, while the rest of the molecule remains unchanged. This very small difference in the average bond lengths of C–H and C–D bonds renders the carbon atom of the methylene group asymmetric and is the principal cause of the optical activity (Dezentje and Dekkers 1976).

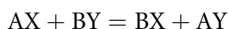
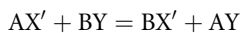
The isotope effects observed in different spectral regions are often used for isotopic analysis. For example, in a certain range of the emission spectra of nitrogen there is an isotopic shift of $3. \dots 8 \text{ \AA}$ between ^{14}N and ^{15}N isotopes, on the basis of which an analytical method was developed for ^{15}N -analysis. Emission molecular spectroscopy has also been used for isotope

analysis of hydrogen, lithium, boron, carbon, and oxygen (Müller et al. 1969). The IR absorption intensity of the OH-stretching vibration of HDO at $3,500\text{ cm}^{-1}$ makes possible the high precision deuterium analysis of heavy water. On the other hand, the intensity of the OD-stretching vibration of HDO at $2,510\text{ cm}^{-1}$ can be used for the determination of deuterium content of natural water samples (see, e.g., Fusch et al. 1993). Other interesting applications of spectroscopic isotope effects are described by Nash (1975).

There is a considerable difference between the values of the index of refraction of H_2O and D_2O , 1.33250 and 1.32796 (at 25°C , Na D-line), respectively. This difference can be used for a rapid, although not very precise (± 0.4 atom percent of D) deuterium analysis of water samples by means of a simple immersion refractometer (Müller et al. 1969).

15.4 Isotope Effects in Chemical Equilibria

One of the most characteristic manifestations of the chemical differences between isotopic molecules is the difference between the equilibrium constants for a given chemical reaction. Compare the following chemical equilibria:



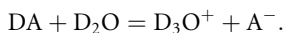
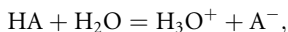
where X and X' are different isotopes (the prime denotes the lighter isotope). The equilibrium constants can be written as

$$K'_A = \frac{[\text{BX}'][\text{AY}]}{[\text{AX}'][\text{BY}]} \quad (15.8)$$

$$K_A = \frac{[\text{BX}][\text{AY}]}{[\text{AX}][\text{BY}]} \quad (15.9)$$

where [] denotes the concentration. If there were no difference between the chemical properties of the isotopic molecules, then K'_A would be equal to K_A . However, the vibrational frequencies and, consequently, the zero-point energies and dissociation energies of isotopic molecules are different; therefore the equilibrium constants of the above reactions are also different. The deviation of K'_A/K_A from unity is the isotope effect on the equilibrium constant.

The isotope effect on chemical equilibria can be illustrated with the example of acid–base equilibria. Consider the ionization reactions of the weak acids HA and DA in water and heavy water, respectively



The isotope effect can be characterized by the ratio of the dissociation constants ($K_{\text{H}}/K_{\text{D}}$). For example, it was found experimentally that for OH-, NH-, SH-, and CH-acids K_{D} is less than K_{H} ($K_{\text{H}}/K_{\text{D}} \approx 2.5\text{--}3.9$), that is, the strength of these acids is less in D_2O than in H_2O and the weaker acids exhibit higher $K_{\text{H}}/K_{\text{D}}$ values.

For water and heavy water, the values of the ionization constant at 25°C are 1.00×10^{-14} and 1.38×10^{-15} , which correspond to pH and pD values of 7.0 and 7.43, respectively. This has a practical consequence in the determination of pD values by glass electrodes (Glasoe and Long 1960): if the pH meter is calibrated by using buffer solutions prepared with H_2O , then one must

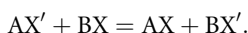
add 0.40 to the value shown by the instrument (“pH meter reading”) in the case of a solution prepared with D₂O in order to obtain the value of pD (i.e., pD = pH meter reading + 0.40).

15.4.1 Isotope Exchange Equilibria

The ratio of the equilibrium constants K'_A and K_A (Eqs. (15.8) and (15.9))

$$K = \frac{K'_A}{K_A} = \frac{[AX][BX']}{[AX'][BX]} \quad (15.10)$$

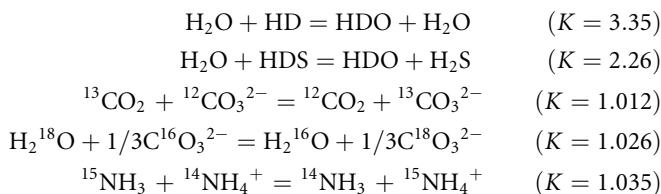
gives the equilibrium constant of the isotope exchange reaction



K indicates how the two isotopes are distributed between the two chemical compounds. Instead of K , very often the elementary *separation factor* (fractionation factor) is used, which is defined by

$$\alpha = \left(\frac{N}{N'} \right)_{AX} / \left(\frac{N}{N'} \right)_{BX} \quad (15.11)$$

where N and N' are the atom fractions of the heavier and lighter isotopes in the compounds AX and BX. In general, α is defined in such a way that its value be larger than 1, that is, the compound in which the heavier isotope is enriched is in the numerator of Eq. (15.11). It should be noted that α is only equal to K , if one atom in each molecule takes place in the isotope exchange (the relationship between α and K for the general case is given, for example, by Criss 1999). A separation factor of 1.050 is often referred to as a 5% isotope effect. Some examples for isotope exchange reactions (the values of K for 25°C are given in parenthesis):

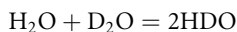


The equilibrium constants for isotope exchange reactions are functions of temperature, similarly to those of ordinary chemical reactions. However, contrary to expectations that the magnitudes of the equilibrium constants decrease monotonically with increasing temperature, their temperature dependences may show striking “anomalies,” such as maxima, minima, inflections, and single and multiple inversions (“cross-overs”) as shown by Stern et al. (1968). The temperature dependence of the separation factor constitutes the basis of the “dual temperature” processes used for the production of heavy water (Rae 1978). For example, in the water–hydrogen sulfide (Girdler–Spevack) exchange process, in the hot tower ($\alpha = 1.8$ at 138°C) deuterium passes from the liquid to the gas, whereas in the cold tower ($\alpha = 2.2$ at 30°C) the equilibrium of the exchange reaction shifts to the right, so in the net process deuterium passes from the gas to the liquid.

Isotope effects can also be readily detected in exchange reactions for other light elements. For example, the $^{15}\text{N}/^{14}\text{N}$ ratio is 3.5% higher in solution than in the NH_3 gas when ammonia gas and aqueous solutions of ammonium salts are in equilibrium. The heavier carbon isotope (^{13}C) enriches ($\sim 1\%$) in aqueous carbonate compared with gaseous carbon dioxide.

When stable isotopes are used, for example, as tracers for in vivo metabolic studies, typically the tracer flux is being measured and inferences are made about the flux of the material being traced (“tracee”). When there is no isotope fractionation, the flux of the heavy tracer is equal to the flux of the lighter major isotope and hence the tracee flux. However, when there is isotope fractionation the fluxes of the heavy tracer and tracee are not equal and thus the flux derived from the kinetic analysis of the tracer is not equal to that of the tracee. For example, ^{18}O is fractionated between water and carbon dioxide ($\alpha = 1.041$ at 25°C) thus the rate of removal of ^{18}O by CO_2 is 4.1% greater than the rate of ^{16}O removal. Because ^{16}O comprises 99.8% of the oxygen pool, the rate of CO_2 production is essentially equal to the rate of ^{16}O removal by CO_2 , which will be less by 4.1% than that measured from ^{18}O . Without taking this correction into account, the calculated tracee flux will be in error. On the other hand, the isotope effect becomes negligible in the distribution of the isotopes of heavier elements; therefore, no corrections are necessary in the tracer experiments.

The distribution of isotopes between isotopic molecules is a special case of isotope exchange reactions, for example,



It should be noted that the HDO molecules cannot be isolated from the liquid H_2O - D_2O mixture owing to the above disproportionation reaction (which is fast). The question arises how the isotopes are distributed between the different isotopic molecules. By assuming random isotope distribution, the mole fractions of the isotopic molecules AX_2 , AXX' , and AX_2' are $(1 - x)^2$, $2(1 - x)x$, and x^2 , respectively, where x is the atom fraction of the lighter isotope (X'). This means, for example, that in natural water that contains about 0.015 atom percent D (abbreviated as 0.015 at% D), practically all the deuterium atoms are in the form of HDO. In reality, however, isotope effects can be observed even in these reactions. The equilibrium constant for the above reaction is 3.75 at 25°C instead of 4 (which would correspond to the random distribution).

15.4.2 Calculation of the Equilibrium Constant

The statistical thermodynamic method used for the calculation of equilibrium constants of chemical reactions becomes considerably easier in the case of isotopic exchange reactions. The reason for this is that within the framework of the Born–Oppenheimer approximation, the zero of energy is the same for the isotopic molecules, thus ΔE of the reaction from the zero of energy of reactants to that of the products does not enter into the calculations. Consider the following isotope exchange reaction



the equilibrium constant (K) for this reaction can be written as

$$K = \frac{Q_{\text{A}_2}^a Q_{\text{B}_1}^b}{Q_{\text{A}_1}^a Q_{\text{B}_2}^b} = \left(\frac{Q_{\text{A}_2}}{Q_{\text{A}_1}} \right)^a \left(\frac{Q_{\text{B}_2}}{Q_{\text{B}_1}} \right)^b \quad (15.13)$$

where Q is the partition function of the molecule. It can be seen that the equilibrium constant can be expressed through the ratio of the partition functions of isotopic molecules. These have been calculated for many compounds and are available for different temperatures in the literature (e.g., Urey and Greiff 1935; Urey 1947; Richet et al. 1977; Knyazev et al. 2001).

The calculation of partition functions and of K is based on the following assumptions: the Born–Oppenheimer approximation is valid, that is, the electronic potential energy is independent of isotopic substitution; the partition function can be factored into contributions from translational, rotational, and vibrational motions; the translational and the rotational motions of the molecule can be treated in the classical approximation; the vibrations are harmonic. Corrections to the effect of anharmonicity and to the Born–Oppenheimer approximation on isotopic exchange equilibria have been discussed by Wolfsberg (1969a, b) and by Kleinman and Wolfsberg (1973, 1974), respectively.

In the calculation of equilibrium constants and in the theory of isotope effects, the so-called reduced partition function ratio (RPFR) introduced by Bigeleisen and Mayer (1947) plays an important role. The RPFR (f) is the quantum mechanical partition function divided by the classical partition function, and in the case of an ideal gas is given by the expression

$$f = \prod_i^{3n-6} \frac{u_i}{u'_i} \frac{1 - \exp(-u'_i)}{1 - \exp(-u_i)} \exp\left(\frac{u'_i - u_i}{2}\right) \quad (15.14)$$

where $u_i = h\nu_i/(kT)$ (ν_i is the harmonic frequency of mode i in cm^{-1}), $3n - 6$ is the number of vibrational modes if the number of atoms in the molecule is n . The equilibrium constant for the isotope exchange reaction (Eq. (15.12)) can be written in terms of the reduced partition function ratios as

$$K = \left(\frac{s_{A_1}}{s_{A_2}}\right)^a \left(\frac{s_{B_2}}{s_{B_1}}\right)^b \frac{f_A^a}{f_B^b} \quad (15.15)$$

where the s values are the symmetry numbers of the molecules. The ratio of the symmetry numbers corresponds to the random isotope distribution and to the equilibrium constant derived using classical statistical mechanics. For example, as the symmetry numbers for H_2O , D_2O , and HDO are 2, 2, and 1, respectively, the symmetry number ratios in Eq. (15.15) give a value of 4. The symmetry number factor leads to no fractionation of isotopes, the isotope effect is reflected by the RPFRs; in other words *any isotope separation by an isotopic exchange reaction must be a quantum effect*.

In terms of the RPFRs, some simple and practical relationships can be derived that help understand the direction and magnitude of isotope fractionation between different molecules (Vojta 1960, 1962; Bigeleisen 1961b):

1. At very high temperatures ($T \rightarrow \infty$) $f = 1$.
2. $f > 1$, since $u_i < u'_i$.
3. For pairs of isotopic molecules in which the substitution occurs at the same site by different isotopes of an element, $f - 1$ is roughly proportional to the isotopic mass difference. For example, $f - 1$ is twice as large for the molecule pair with ^{14}C and ^{12}C than for the molecule pair with ^{13}C and ^{12}C , thus, at 0°C

$$f\left(\frac{^{13}\text{CO}_2}{^{12}\text{CO}_2}\right) - 1 = 0.2199, \quad f\left(\frac{^{14}\text{CO}_2}{^{12}\text{CO}_2}\right) - 1 = 0.4469.$$

The following rule is also valid approximately: the larger the relative mass difference between the isotopes, the larger the isotope effect. For instance, H–D isotope effects are much larger than $^{235}\text{U} - ^{238}\text{U}$ isotope effects.

4. The larger isotope molecule has a larger f value because it has more vibrational degrees of freedom, for example, at 0°C

$$\left[f \left(\frac{(\text{S}^{18}\text{O}_3)^{2-}}{(\text{S}^{16}\text{O}_3)^{2-}} \right) \right]^{1/3} = 1.080, \quad \left[f \left(\frac{(\text{S}^{18}\text{O}_4)^{2-}}{(\text{S}^{16}\text{O}_4)^{2-}} \right) \right]^{1/4} = 1.100.$$

5. An atom with higher valency is characterized by a larger value of f , for example, the values of f for the $^{34}\text{S}/^{32}\text{S}$ isotope effects (at 0°C) in the molecule SO_2 , SO_3 , and $(\text{SO}_4)^{2-}$ are 1.053, 1.096, and 1.101, respectively.
6. For pairs of molecules with multiple isotopic substitution (with the exception of D and T substitution) f is independent of the isotopic composition of the other atoms in the molecule, for example, for carbon dioxide:

$$f \left(\frac{^{13}\text{C}^{16}\text{O}_2}{^{12}\text{C}^{16}\text{O}_2} \right) = f \left(\frac{^{13}\text{C}^{18}\text{O}_2}{^{12}\text{C}^{18}\text{O}_2} \right).$$

7. A useful rule of thumb is the following: the heavier isotope enriches in that isotopic molecule that has a larger f , in other words, *the heavier isotope accumulates where the binding is stronger*.

The value of the equilibrium constant for the isotope exchange reaction between real gases can be taken, to a good approximation, to be equal to that of ideal gases. For reactions taking place in the liquid phase, K can be obtained from its value in the gaseous phase and the vapor pressures of the isotopic compounds.

15.5 Isotope Effects on Phase Equilibria

15.5.1 Vapor Pressure Isotope Effects

The difference between the isotope distributions of two phases that are in thermodynamic equilibrium is a manifestation of the differences between the properties of isotopic molecules. The differences between the equilibrium isotope compositions of the condensed and gaseous phases, that is, the different volatilities of isotopic molecules, are called *vapor pressure isotope effects* (VPPIE) and they represent the most often and thoroughly investigated thermodynamic isotope effects (Rabinovich 1960; Van Hook 1968; Rabinovich 1970; Jancsó and Van Hook 1974). The direction and magnitude of the vapor pressure differences between isotopic molecules vary in a wide range. Some examples (in some cases, the magnitude of the relative vapor pressure difference is given in parenthesis): $p(^{20}\text{Ne}) > p(^{22}\text{Ne})$; $p(^{11}\text{BF}_3) > p(^{10}\text{BF}_3)$ (0.2–1.8%); $p(^{11}\text{BCl}_3) > p(^{10}\text{BCl}_3)$ (0.2–0.3%); $p(\text{B}^{35}\text{Cl}_3) > p(\text{B}^{37}\text{Cl}_3)$ (0.3%); $p(\text{H}_2\text{O}) > p(\text{D}_2\text{O})$, $p(\text{H}_2\text{O}) = p(\text{D}_2\text{O})$ at 220°C (“cross-over temperature”), and above this temperature $p(\text{H}_2\text{O}) < p(\text{D}_2\text{O})$; $p(\text{HT}) > p(\text{D}_2)$; $p(\text{o-dideuterobenzene}) < p(\text{p-dideuterobenzene}) < p(\text{m-dideuterobenzene})$ (0.003%!).

One can see from the above examples that the lighter isotopic molecule is usually more volatile than the heavier one (“normal vapor pressure isotope effect”). Sometimes, however, the heavier molecule has a higher vapor pressure (“inverse vapor pressure isotope effect”) and in some cases the direction of the isotope enrichment between the liquid and gaseous phases changes its direction with temperature at the “cross-over temperature.” There are very small, but still measurable differences between different diduterobenzenes.

The vapor pressure difference between isotopic compounds is usually expressed in terms of logarithm of the vapor pressure ratio, $\ln(p'/p)$ (the prime, as usual, denotes the lighter

molecule). The use of this quantity is very convenient because it expresses the relative difference in the vapor pressures for small differences, $\ln(p'/p) \approx \Delta p/p = (p' - p)/p$. The vapor pressure isotope effect is called normal if $\ln(p'/p) > 0$, that is, if the lighter isotopic molecule has a higher vapor pressure than the heavier one, and inverse if $\ln(p'/p) < 0$. The temperature at which the vapor pressures of the isotopic molecules are the same ($\ln(p'/p) = 0$) is called the cross-over temperature.

The best possible precision for the determination of VPIE can be obtained by measuring Δp and p simultaneously using a differential technique. Another and quite different approach to determine the VPIE involves a measurement of the separation factor (α) defined by the equilibrium between the liquid phase and its saturated vapor in a one-plate fractionation experiment

$$\alpha = (y'/y)/(x'/x) \quad (15.16)$$

where y and x are the concentrations in the vapor and liquid phase, respectively. The accuracy of this method is limited by the accuracy of the isotopic analysis of the two phases in equilibrium; an improvement can be achieved by multiplication of the elementary separation process, for example, by using distillation columns.

The relationship between α and the vapor pressures of the pure isotopic molecules is given to a good approximation by the equation (the exact relationship is given, e.g., in Jancsó and Van Hook 1974)

$$\ln \alpha \approx \ln \frac{p'}{p}. \quad (15.17)$$

The isotope separation factor can be expressed in terms of the equilibrium constant for the liquid–vapor phase equilibrium

$$X'_{\text{liq}} + X_{\text{vap}} = X_{\text{liq}} + X'_{\text{vap}} \quad (15.18)$$

where X and X' denote different isotope molecules.

The equilibrium constant K itself

$$K = \frac{[X_{\text{liq}}][X'_{\text{vap}}]}{[X'_{\text{liq}}][X_{\text{vap}}]} \quad (15.19)$$

is thus equal to the distillation separation factor. Consequently, α and the VPIE may be expressed in terms of the reduced partition function ratios (f) of the liquid phase and gas phase

$$K = \frac{f_{\text{liq}}}{f_{\text{vap}}} \approx \alpha \approx \frac{p'}{p}. \quad (15.20)$$

The theory of VPIE was worked out by Bigeleisen (1961a). In model calculations of f_{vap} it is often assumed that in the case of an ideal gas, the molecules are freely rotating and translating and the $3n - 6$ vibrational modes (n is the number of atoms in the molecule, $3n - 6$ is the number of internal degrees of freedom) can be treated as harmonic oscillators and f_{vap} is given by ► Eq. (15.14). In the liquid phase, the reduced partition function ratio for the “average” liquid-phase molecule (f_{liq}) will be calculated within the framework of a simplified cell model in which the molecule has $3n$ degrees of freedom, of these $3n - 6$ are similar to the vibrational modes of the gas-phase molecule (Stern et al. 1963). The other six external degrees of freedom correspond to the gas-phase translations and rotations, which have become bound (hindered) in the liquid phase. In this approximation,

$$f_{\text{liq}} = \prod_i^{3n} \frac{u_i}{u'_i} \frac{1 - \exp(-u'_i)}{1 - \exp(-u_i)} \exp\left(\frac{u'_i - u_i}{2}\right). \quad (15.21)$$

The most common approximation applied to the calculation of the VPIE makes use of the fact that very often the $3n$ molecular frequencies happen to fall neatly into two groups. The first group contains the low translational and rotational frequencies (ν_{ext}) of the molecule in the liquid phase, which are treated in the so-called first-order quantum correction (first term on the right-hand side of [Eq. \(15.22\)](#)). The second group contains the high frequencies, usually the internal vibrational frequencies, for which $u_i = h\nu_i/(kT) \gg 1$, these may be treated in the so-called zero-point energy approximation (second term on the right hand side of [Eq. \(15.22\)](#)).

$$\ln \alpha = \ln \frac{f_{\text{liq}}}{f_{\text{vap}}} \approx \frac{1}{24} \left(\frac{hc}{kT} \right)^2 \left[\sum_{\text{ext}} (\nu_{\text{ext}}'^2 - \nu_{\text{ext}}^2) \right] - \frac{1}{2} \frac{hc}{kT} \sum_{\text{int}} (\Delta \nu' - \Delta \nu) = \frac{A}{T^2} - \frac{B}{T} \quad (15.22)$$

where $\Delta \nu' = \nu_{\text{vap}}' - \nu_{\text{liq}}'$ and $\Delta \nu = \nu_{\text{vap}} - \nu_{\text{liq}}$.

[Equation \(15.22\)](#) makes it easier to understand the contributions of the different molecular motions to the vapor pressure isotope effect. One can see that the hindered translations and rotations will always work in the direction of a normal isotope effect, since in this case $\nu' > \nu$. Consequently, for monatomic substances, which have only translational degrees of freedom, always a normal VPIE is observed. For polyatomic molecules, the effect of intermolecular forces on the internal vibrations of the molecules must also be considered. The frequencies of the internal vibrations shift in most cases toward lower frequencies (“red shift”) when the molecule passes from the vapor phase to the liquid phase, and this leads in the direction of an inverse isotope effect. The observed VPIE is the result of the interplay between the normal isotope effect from hindered translations and rotations and the inverse isotope effect arising from the zero-point energy contribution of the internal vibrations. The temperature dependence of the effects is different: the normal isotope effect usually falls off more steeply with temperature (proportionally to T^{-2}) than does the inverse isotope effect (T^{-1}). With internal and external effects of opposite sign, each proportional to different powers of temperature, it is not surprising that VPIE can and often *does* cross from positive to negative (cross-over effect). A good example that illustrates the cross-over is the case of heavy water/light water: H_2O has a higher vapor pressure than D_2O up to 220°C , but above this temperature D_2O is more volatile than H_2O (Harvey and Lemmon [2002](#)). At yet higher temperatures, the inverse effect would decay to zero, but before the decay gets complete the critical point is reached, and the distinction between condensed and vapor phase vanishes, and the point becomes moot.

A frequently used relationship for the vapor pressure isotope effects is the “rule of the geometric mean” (Bigeleisen [1955](#)). For example, for the vapor pressures of H_2O , HDO , and D_2O

$$p_{\text{HDO}} = (p_{\text{H}_2\text{O}} p_{\text{D}_2\text{O}})^{1/2}. \quad (15.23)$$

The rule of the geometric mean is an exact one if the temperature dependence of the VPIE follows the A/T^2 rule (see [Eq. \(15.22\)](#)). For molecules with appreciable B/T terms, however, it is found that [Eq. \(15.23\)](#) is obeyed only approximately, and thus the exponent is $1/1.91$ for $\text{HOH}/\text{DOD}/\text{HOD}$ instead of $1/2$ (Van Hook [1972a, b](#)).

In order to calculate the VPIE within the framework of the above model, one has to know (1) the hindered translational and rotational frequencies of the molecule in the liquid phase and (2) the internal vibrational frequencies (and thus the vibrational force constants) of the molecule (at least of one of the isotopic species) in the vapor and liquid phase.

The theoretical analysis of experimentally observed VPIE data has furnished information, among others, (1) about the details of the intermolecular interactions in the liquid phase, (2) on the vibrational coupling between internal vibrations and molecular translations and/or rotations, which occurs in the condensed phase, (3) on the density dependence of the force constants, which govern the external molecular motions and internal vibrations in the liquid, (4) on changes in vibrational anharmonicity, which occur on condensation, as well as (5) on the magnitude of the “dielectric correction” to IR absorption peaks in condensed phases.

The statistical mechanical theory of the vapor pressure isotope effect can be applied to the interpretation of isotope effects on other phase equilibria (e.g., solid–liquid, liquid–liquid miscibility, solubility of gases in liquids, etc.).

An interesting question, which is closely related to the VPIE, is the deviation of *isotopic mixtures* from the ideal behavior. Isotopic mixtures, that is, mixtures of isotopic molecules (e.g., benzene and deuterated benzene), have long been considered as textbook examples of ideal solutions: “statistical theory predicts that mixtures of very similar species, in particular isotopes, will be ideal”; “the only truly ideal solutions would thus involve isotopic species”; “molecules which differ only by isotopic substitution... form ideal solutions”; “except for isotope mixtures, ideal solutions will occur rather rarely”; “we expect binary solutions to have ideal properties when the two components are isotopes of each other.”

The ideal behavior of isotopic mixtures is expected if one assumes that the intermolecular forces between pairs of like molecules of each type and between unlike molecules are all the same, and further assumes the isotopic molecules to have the same size. Both assumptions are reasonable to a first approximation. Highly precise vapor pressure measurements on isotopic mixtures have shown, however, that even these mixtures exhibit small, but still significant, deviations from ideal behavior (Jancsó et al. 1993, 1994). Theoretical analysis has demonstrated that the origin of nonideality is closely connected with the difference between the molar volumes of isotopic molecules (“molar volume isotope effect”).

15.5.2 Isotope Effects on Other Phase Equilibria

Ice–water equilibrium is a well-known example for the isotope effect on solid–liquid phase equilibrium. It has been found that both deuterium and ^{18}O enrich in the solid phase by 2.1 and 0.30%, respectively. This is in harmony with the rule of thumb (see “rule” (7) in ► Sect. 15.4.2), according to which the heavier isotope enriches in the phase where the bonding is stronger. The triple point temperatures (at the triple point solid, liquid, and vapor phases are in equilibrium) of the isotopic water molecules containing the heavier isotopes are also higher than that of ordinary water (3.82°C, 0.38°C, and 0.01°C for D_2O , H_2^{18}O , and H_2^{16}O , respectively). Isotope effects on triple points and melting temperatures of different compounds have been discussed by Van Hook (1994).

Whereas the differences in vapor pressure between isotopic substances have received much attention, relatively little is known about the isotope effects on the solubility of gases in liquids; the available experimental information has been recently reviewed by Jancsó (2002). The isotope effect is manifested in the isotope fractionation of natural gases, for example, in studies of the solubility of nitrogen and oxygen in water it was found that the heavier molecular species, $^{14}\text{N}^{15}\text{N}$ and $^{16}\text{O}^{18}\text{O}$ are more soluble in water than the respective lighter ones, $^{14}\text{N}_2$ and $^{16}\text{O}_2$, by 0.085% and 0.080%, respectively, at 0°C and both effects decrease to approximately 0.055% at 27°C. In general, the *solubility isotope effect* is normal, that is, the heavier isotopic

species is more soluble than the lighter one. The largest effect was observed for the solubilities of pure hydrogen and deuterium gases in water (8.6% at 5°C). The first inverse isotope effect (the lighter isotopic species is more soluble than the heavier one) on gas solubility was observed in the study of isotopic fractionation between gaseous carbon dioxide and the equilibrated aqueous solution of the gas between 0 and 60°C (Vogel et al. 1970). It was observed that $^{13}\text{C}^{16}\text{O}_2$ is slightly less soluble than $^{12}\text{C}^{16}\text{O}_2$ (by 0.012% at 0°C) while the oxygen isotopes exhibit a normal isotope effect ($^{12}\text{C}^{16}\text{O}^{18}\text{O}$ is about 0.08% more soluble than $^{12}\text{C}^{16}\text{O}_2$). Dang et al. (1989) demonstrated that the solubility isotope effect can be interpreted using the same theoretical framework as developed for vapor pressure isotope effects (see ▶ Sect. 15.5.1). For example, using available spectroscopic data Bacsik et al. (2002) were able to predict the order of magnitude of the inverse and normal solubility isotope effects of methane observed in water for H/D and $^{12}\text{C}/^{13}\text{C}$ substitution, respectively.

There are some differences (up to about 30%) between the solubilities of inorganic salts in ordinary and heavy water. In general, the solubilities of salts in D_2O are markedly less than in H_2O (e.g., at 20°C NaCl and KCl are 6.7% and 9.8% less soluble in D_2O than in H_2O , respectively), with the exception of LiF and LiCl-aq, which have higher solubilities (e.g., by 13% and 2% at 25°C) in heavy water. The magnitude of the isotope effect decreases with increasing temperature and the less soluble the salt, the larger the isotope effect.

The solubility of heavy water in different organic solvents is smaller than that of ordinary water. The differences in the solubility of H_2O and D_2O can be expressed as $100 (N_{\text{H}} - N_{\text{D}})/N_{\text{H}}$, where N_{H} and N_{D} are the solubilities of H_2O and D_2O in mole fractions. For example, at room temperature the solubility differences in triethylamine, carbon disulfide, benzene, chloroform, and diethylether are 30%, 21%, 17%, 15%, and 7%, respectively. The deuterium isotope effects in liquid–liquid phase diagrams have been reviewed by Rabinovich (1970) and Fenby et al. (1981). The experimental investigations showed that the replacement of H by D usually, but not always, leads to an enlargement of the domain of partial miscibility; the upper critical solution temperature usually increases, while the lower critical solution temperature always decreases. The study on the miscibility behavior of methanol–cyclohexane binary mixture revealed that whereas the replacement of hydrogen atoms involved in hydrogen bonding (OH group of methanol) leads to an increase of the miscibility gap, the replacement of hydrogen atoms not involved in hydrogen bonding (CH_3 , $\text{c-C}_6\text{H}_{12}$) by deuterium leads to a reduction of the miscibility gap (Schön et al. 1986). There are some even more striking isotope effects on miscibility behavior of liquids, for example, while 2-methylpyridine and 3-methylpyridine are completely miscible in all proportions at all temperatures with water, they are only partially miscible with heavy water. Isotope effects on coexistence curves, similarly to the vapor–liquid and gas–liquid solubility equilibria, can be interpreted in terms of the theory of condensed phase isotope effects, inasmuch as the necessary spectroscopic information for the two phases in equilibrium is available (Singh and Van Hook 1987).

The difference in the adsorption isotherms of isotopic molecules has long been known and it has been used for isotope separation and isotope analysis. For example, deuterium gas exhibits an enrichment factor of 40 (!) at 20 K on silica gel, but the enrichment factor decreases steeply with increasing temperature (Krumbiegel 1970). Another example is the behavior of CH_4/CD_4 system in a capillary column with activated glass surface: at 153 K the retention time of CH_4 is larger than that of CD_4 , at 130 K they are equal to each other and at lower temperatures CH_4 leaves earlier the column than CD_4 (Bruner et al. 1966). Similarly to the gas–solid chromatographic separations, gas–liquid separation techniques have also been widely used for isotopic separation and for rapid and convenient analysis of mixtures of

isotopic molecules. Isotopic fractionation of organic compounds observed in different chromatographic techniques has been reviewed by Filer (1999). The isotope effects observed in gas chromatography can be interpreted analogously to the vapor pressure isotope effect (Van Hook 1969). The VPIE is governed by the “solute–solute” interactions in the pure liquid state, whereas in the infinitely dilute solution “solvent–solute” (gas–liquid chromatography) and in the dilute surface-adsorbed state “surface-adsorbate” (gas–solid chromatography), intermolecular forces are operative.

Isotope effects in ion exchange chromatography and extraction chromatography have also been studied, with the aim of investigating the possibility of separation of ^6Li and ^7Li isotopes (Lee 1969). It was found that the lighter isotope enriches in the resin phase and the separation factor (in general, less than 1.005) is determined by the difference in the states of the ion in the solution and in the resin. With resin having monobenzo-15-crown-5 as a functional group, a single separation factor as high as 1.053 can be achieved for the separation of Li isotopes (Kim et al. 1991). A method for uranium isotope separation has been developed by Asahi Chemical Industries in Japan using redox ion exchange chromatography (see ▶ Sect. 51.6.2, Chap. 51, Vol. 5). The isotope separation factor anomalies observed in this process are discussed in ▶ Sect. 15.8.

15.6 Isotope Effects on Some Physicochemical Properties

Beside spectroscopic and thermodynamic isotope effects treated in the preceding sections, isotope effects related to the structure of the molecules manifest themselves in a variety of physical and physicochemical properties, such as density, permittivity, compressibility, dipole moment, surface tension, etc. It is not possible to give a comprehensive treatment of the subject here; useful reviews have been given among others by Rabinovich (1970) and Jancsó and Van Hook (1974). For illustration of the magnitude of the isotope effects, differences in various physical properties between water and *heavy water* are collected in ▶ Table 15.1.

The density difference between H_2O and D_2O can be used for the determination of the deuterium content of heavy water (Schattenstein 1960). It is interesting to note that the 10% difference in density is within 0.5% entirely due to the molecular weight difference. The molar volume of D_2O is *larger* only by 0.34% and that of H_2^{18}O is *smaller* by 0.15% than the molar volume of H_2^{16}O . The isotope effect on the dielectric constant and dipole moment is very small, which plays an important role in the interpretation of solvent isotope effects in aqueous systems (Van Hook 1975).

The compressibility of liquid water is anomalous in that it decreases with increasing temperature, passes through a minimum at 46°C , and then increases again. The compressibility of heavy water follows a similar pattern, but the minimum is about 3°C higher than for H_2O . The ratio of the viscosities of liquid D_2O and H_2O is 1.23 at 25°C , which is much larger than the ratio of the square-roots of the molecular masses (1.0544). However, according to Vedamuthu et al. (1996) the “thermal offset effect,” that is, the difference (6.498°C) between the temperatures of the maximum densities of H_2O (3.984°C) and D_2O (11.185°C) should be taken into account when one compares the different properties of the two liquids. Thus, for example, the viscosity of D_2O at 26.498°C would be the viscosity of H_2O at 20°C multiplied by 1.0544, the square-root of the mass ratio of the two isotopic molecules (Cho et al. 1999). This supports the view that the viscosity isotope effect on liquid water is not a rotational, but a translational mass effect. The concept of thermal offset effect can be used in correlating the various thermodynamic properties of liquid H_2O , D_2O , and T_2O .

■ Table 15.1

Some physical properties of water and heavy water

	H ₂ O	D ₂ O
Melting point (°C)	0.00	3.81
Triple point (°C)	0.01	3.82
Temperature of maximum density (°C)	3.984	11.185
Normal boiling point (°C)	100.00	101.42
Critical temperature (°C)	374.0	370.7
Critical pressure (MPa)	22.06	21.67
Critical volume (cm ³ /mol)	55.3	55.0
Density at 25°C (g/cm ³)	0.997048	1.104468
Heat of fusion at the melting point (J/mol)	6,008	6,339
C _p (liquid at 25°C) (J deg ⁻¹ mol ⁻¹)	75.27	84.35
C _v (liquid at 25°C) (J deg ⁻¹ mol ⁻¹)	74.48	83.7
Vapor pressure at 20°C (kPa)	2.3370	1.9997
Dipole moment in benzene solution at 25°C (Cm)	5.87×10^{-30}	5.94×10^{-30}
Dipole moment (vapor) at 100–200°C (Cm)	6.14×10^{-30}	6.14×10^{-30}
Dielectric constant at 25°C	78.304	77.937
Refractive index, <i>n_D</i> at 25°C	1.33250	1.32796
Viscosity at 25°C (N s m ⁻²)	8.904×10^{-4}	1.095×10^{-3}
Surface tension at 25°C (N/m)	0.07197	0.07193
Compressibility at 25°C (TPa ⁻¹)	447.0	459.5

Experimental measurements of the molar volumes of benzene, toluene, cyclohexane, and methylcyclohexane and their deuterated analogs have shown that the lighter species have a greater volume by about 0.3% (Bartell and Roskos 1966). This difference in molar volumes (*molar volume isotope effect*) arises from the fact that C–H bonds are longer than C–D bonds by about 0.005 Å. Whereas in the above case, the hindered translational motion of the molecules as a whole plays a negligible role, for small molecules (e.g., ethylene) the vibrations of the molecules give important contributions to the molar volume isotope effect (Menes et al. 1970). The volume dependence of the vibrational frequencies may also influence the molar volume isotope effect as was shown in the case of polyethylene (Lacks 1995).

The question sometimes arises whether the *deuterium bond* is stronger or weaker than the hydrogen bond. While the electronic contribution to the strength of the H-bond is unaffected by deuterium substitution since the H-bonded and D-bonded species have the same potential surface, some of the vibrational frequencies in the complex will be smaller because of the larger mass of deuterium (Buckingham and Fan-Chen 1981). Consequently, the zero-point vibrational energy of the D-bond will be lower than that of the H-bond, and thus the *D-bond can be considered stronger than the H-bond*. It was found from ab initio calculations, carried out on complexes containing H-bond forming organic functional groups (such as hydroxyl, carbonyl, carboxyl, and amide) and water molecules (Čuma and Scheiner 1997), that deuterium substitution increases the strength of the hydrogen bond by several tenths of a kcal/mol. In contrast

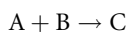
to the hydrogen bonds in complexes pairing neutral molecules, *in ionic complexes* (e.g., $\text{H}_2\text{O}\cdots\text{H}^+\cdots\text{OH}_2$) *the H-bond is stronger than the D-bond*.

Some interesting isotope effects in the solid phase include those on superconductivity and ferroelectricity. For simple metals like Hg, Pb, Sn, and Zn, the relationship between the characteristic temperature at which the metal becomes superconductor (T_c) and the mass of the isotope (m) can be given as $T_c \propto m^{-1/2}$. Very large isotope effects can be observed on ferroelectricity of crystals. A ferroelectric crystal exhibits a spontaneous electric dipole moment, that is, even in the absence of an applied electric field the center of the positive charges does not coincide with that of the negative charges. At the Curie temperature, the crystal changes from the polarized state to the unpolarized state. For example, the Curie temperature of KH_2PO_4 crystal is 123 K, whereas that of KD_2PO_4 is 213 K. In some crystals (e.g., Seignette salt, sodium potassium tartrate- $4\text{H}_2\text{O}$) there are two Curie points, an upper and a lower one, and between these temperatures the crystal is ferroelectric. In the Seignette salt, the lower Curie point decreases (by 4°C), while the upper one increases (by 11°C) when H_2O is replaced by D_2O in the crystal.

The differences between isotopic molecules in the majority of the physical properties are still awaiting interpretation on the molecular level.

15.7 Kinetic Isotope Effects

Isotopic molecules may react at different rates in the same chemical reaction and the effect of isotopic substitution on a rate constant is referred to as a *kinetic isotope effect*. For example, in the reaction



the effect of isotopic substitution in reactant A is expressed as the ratio of rate constants k'/k , where the superscripts with prime and without prime represent reactions in which the molecules A contain the light and heavy isotopes, respectively.

The phenomenon was first observed in the electrolysis of water when it was found that the decomposition rate of H_2O may be several times higher than that of D_2O . This observation led to the preparation of the first pure heavy water sample electrolytically and forms the basis of one of the methods of industrial production of heavy water. The study of isotope effects on reaction rates provides one of the most powerful and subtle methods for elucidation of reaction mechanisms and plays an important role in investigations using isotope labeling.

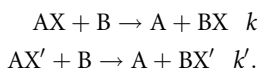
The experimental determination, theory, and application of kinetic isotope effects are treated in a number of excellent monographs and book chapters (Bigeleisen and Wolfsberg 1958; Melander 1960; Van Hook 1971; Wolfsberg 1972; Shiner 1975; Buddenbaum and Shiner 1977; Cleland et al. 1977; Melander and Saunders 1980; Willi 1983; Sims and Lewis 1984; Vértés and Kiss 1987).

15.7.1 Classification and Determination of Kinetic Isotope Effects

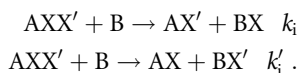
Kinetic isotope effects can be divided into different groups. The term *primary isotope effect* is used when in the rate-determining step of the reaction the bond to the isotope in question will be broken (or formed). *Secondary isotope effects* are those in which the bonds to the isotopically

substituted atom are not broken or formed in the course of the reaction. Secondary isotope effects are, in general, about one order of magnitude smaller than primary isotope effects. *Intermolecular isotope effect* causes the difference between the reaction rates of two isotopic molecules. The *intramolecular isotope effect* reflects the difference between the reaction rates of two functional groups of the same molecule, which differ only in their isotopic compositions. The different types of kinetic isotope effects can be illustrated by the following general reaction schemes (the prime refers to the lighter isotope).

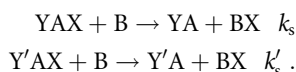
Primary intermolecular isotope effect, k'/k , e.g.,



Primary intramolecular isotope effect, k'_i/k_i , e.g.,



Secondary intermolecular isotope effect, k'_s/k_s , e.g.,



As a rule, lighter isotope molecules react at a higher rate (*normal isotope effect*, $k'/k > 1$), however, there are some cases in which $k'/k < 1$ (*inverse isotope effect*).

The ratio of the rate of a reaction in light water to that in heavy water (or in $\text{H}_2\text{O}/\text{D}_2\text{O}$ mixtures) is referred to as a *solvent isotope effect*. For example, many enzymatic properties, including catalytic rates, differ when the enzyme is dissolved in D_2O rather than in H_2O . Solvent isotope effects including those on chemical equilibria have been reviewed, among others, by Arnett and McKelvey (1969), Laughton and Robertson (1969), Schowen (1977), and Conway (1981).

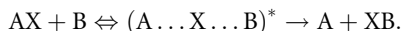
The simplest method of the experimental determination of kinetic isotope effects is to compare the reaction rates of the pure isotopic variants under the same experimental conditions. This technique is simple and does not require the isotope analysis of the reactants and products; however, it requires pure isotopic compounds. In addition to that, the reaction rate should be measured with an accuracy that is at least one order of magnitude higher than the difference between the reaction rates of the isotopic variants.

It is often more advantageous to use comparative methods, that is, to work with the mixture of the two compounds in the experiments, which ensures identical experimental conditions for the parallel reactions. The isotope competition method does not require pure isotopic compounds, it can be used even with compounds of natural isotopic composition, and thus it can be applied to the determination of ^{13}C , ^{15}N , and ^{18}O isotope effects. However, the isotopic composition must be measured with high accuracy, in the case of stable isotopes usually by mass spectrometry, in the case of radioisotopes by measuring the change in the specific activity. In order to obtain the kinetic isotope effect, one needs to determine the isotopic composition of the test compound, first at the start of the reaction then again after the reaction has taken place to a known extent. The isotope effect can also be obtained from the isotopic analysis of the reaction products. In the latter case, the method of the evaluation of k'/k from the experimental data can be found, for example, in the book of Vértés and Kiss (1987).

15.7.2 Theory of Kinetic Isotope Effects

The method of calculating the isotope effect on equilibrium constants was extended to the rates of chemical reactions by Bigeleisen (1949), and the formal theory of kinetic isotope effects was developed by Bigeleisen and Wolfsberg (1958) within the framework of transition-state theory.

According to the transition-state theory, reactions proceed through an activated or transition state (molecules in this state will be designated as “activated complexes”). The first step of the process is the formation of the activated complex and in the second step the activated complex dissociates to reaction products:



The reactants are considered to be in equilibrium with the activated complex.

The equilibrium constant (K) can be written as

$$K = \frac{[\text{A} \dots \text{X} \dots \text{B}]^*}{[\text{AX}][\text{B}]} \quad (15.24)$$

and can be expressed through the corresponding partition functions (Q)

$$K = \frac{Q_t^*}{Q_{\text{AX}} Q_{\text{B}}} \quad (15.25)$$

where Q_t^* is the total partition function of the activated complex. For the ratio of the rate constants of the reactions of AX and AX' (k'/k) one obtains

$$\frac{k'}{k} = \frac{\kappa'}{\kappa} \frac{\tau'}{\tau} \frac{Q^{*'}_{\text{AX}}}{Q^*_{\text{AX'}}} \quad (15.26)$$

where κ is the transmission coefficient, which expresses the probability that an activated system moving in the forward direction will cross to the product side; κ is assumed to be independent of isotopic substitution therefore the κ'/κ ratio in [Eq. \(15.26\)](#) cancels. The factor τ corresponds to the tunnel effect, which takes into account that according to quantum mechanics, it is possible for systems with insufficient energy to surmount the energy barrier to leak or to “tunnel” through. The tunnel effect is significant only for particles whose de Broglie wavelength is comparable to the thickness of the barrier that must be penetrated. Protons at ordinary temperatures have wavelengths of the order of 1–2 Å, which is similar to the width expected for an energy barrier to a proton reaction, therefore the tunnel effect should have some influence on the rate of proton transfer reactions. The tunnel corrections to kinetic isotope effects are discussed in detail by Weston (1975), Kresge (1977), and Bell (1980). Contrary to Q_t^* in [Eq. \(15.25\)](#), Q^* in [Eq. \(15.26\)](#) does not include the normal vibrational mode that corresponds to the transformation of the activated complex back to reactants or forward into products and has a zero or imaginary frequency (in the literature, this mode is referred to as the “reaction coordinate”). Therefore, in the calculation of Q^* one is supposed to use only $3n - 7$ real vibrational frequencies of the transition state (n is the number of atoms).

The expression for the isotope effect on the rate constant has the same form as the one for the equilibrium isotope effect (see [Eqs. \(15.14\)](#) and [Eq. \(15.15\)](#))

$$\frac{k'}{k} = \frac{u^{*'} }{u^*} \prod_i^{3n-7} \frac{u_i^{*'} }{u_i^*} \frac{1 - \exp(-u_i^*)}{1 - \exp(-u_i^{*'})} \exp\left(\frac{u_i^{*'} - u_i^*}{2}\right) \prod_i^{3n-6} \frac{u_i}{u_i^{*'}} \frac{1 - \exp(-u_i^{*'})}{1 - \exp(-u_i)} \exp\left(\frac{u_i' - u_i}{2}\right) \quad (15.27)$$

where u^* refers to the zero or imaginary frequency (ν^*) of the transition state and $u_i = h\nu_i/(kT)$. (ν_i is the harmonic frequency of mode i in cm^{-1} , T is the temperature.)

A straightforward conclusion that can be drawn (e.g., from [Eq. \(15.27\)](#)) is that isotope effects are determined almost entirely by the changes in vibrational force constants on going from the reactants to transition state.

Very often, one assumes that the vibrational frequencies in the reacting molecule are identical with those in the activated complex with the exception of the vibrational frequency corresponding to the rupture of the bond (ν_k). In this approximation, and at low temperatures or high vibrational frequency for the bond of interest, the logarithm of the isotopic rate ratio k'/k is given by

$$\ln \frac{k'}{k} = \frac{hc}{2kT} (\nu'_k - \nu_k). \quad (15.28)$$

Very often, isotope effects are dominated by zero-point energy differences and this contribution plays an important role in the qualitative discussions explaining isotope effects. [Equation \(15.28\)](#) can be used for the estimation of the primary kinetic isotope effect. For example, the zero-point energy of a typical C–H stretching vibration with $\nu = 3,000 \text{ cm}^{-1}$ is 18 kJ/mol; deuterium substitution reduces the frequency to $2,200 \text{ cm}^{-1}$ and the zero-point energy to 13.4 kJ/mol. The difference (4.6 kJ/mol) gives $k_{\text{H}}/k_{\text{D}} = 6.4$ for the primary kinetic isotope effect for C–H bond breaking at room temperature.

On the basis of [Eq. \(15.27\)](#), it is possible to estimate the maximal values of primary kinetic isotope effects for different isotopic substitutions. For example, at room temperature the maximal values of k'/k for some isotopes are as follows: $\text{H/D} = 18$, $\text{H/T} = 60$, $^{12}\text{C}/^{13}\text{C} = 1.25$, $^{12}\text{C}/^{14}\text{C} = 1.5$, $^{14}\text{N}/^{15}\text{N} = 1.14$, $^{16}\text{O}/^{18}\text{O} = 1.19$, $^{32}\text{S}/^{34}\text{S} = 1.05$, and $^{127}\text{I}/^{131}\text{I} = 1.02$ (see, e.g., Vértés and Kiss [1987](#)). Similarly, for the maximal secondary isotope effects one obtains for H/D isotope substitution in C–H and O–H bonds 1.74 and 2.02, respectively. For $^{12}\text{C}/^{13}\text{C}$ substitution in C–C bond one has $k'_s/k_s = 1.012$.

A very simple expression can be derived for the estimation of intramolecular isotope effects. In this case, the reacting molecules are identical and thus only the breaking bond of the activated complex may exhibit isotope effect, therefore

$$\frac{k'_{\text{intra}}}{k_{\text{intra}}} = \frac{\nu^{*'} }{\nu^*} = \sqrt{\frac{\mu}{\mu'}} \quad (15.29)$$

where μ is the reduced mass calculated from the masses of the two atoms joined by the bond being broken or from the masses of the molecular fragments to be separated in the reaction. It can be seen that the intramolecular isotope effect is independent of temperature, which is in agreement with the experimental observations.

Computer programs are available for the calculation of kinetic isotope effects within the framework of [Eq. \(15.27\)](#), which use as input data the geometry and force constants of reactants and transition states (Wolfsberg and Stern [1964](#)).

Melander and Saunders ([1980](#)) have given a comprehensive description of the development of methods of computer calculations of isotope effects on the kinetics of chemical reactions. Such techniques, originally proposed by Wolfsberg and Stern ([1964](#)), Shiner ([1975](#)), Buddenbaum and Shiner ([1977](#)), and Schowen ([1977](#)), marry the methods of Eyring's absolute rate (activated complex) theory with detailed modeling of molecular vibrational properties. Input parameters are a mix of spectroscopically determined or quantum mechanically calculated force constants and/or force constant shifts. The method has resulted in informative and detailed molecular description of the molecular changes that occur as the system proceeds from reactant to product along the reaction coordinate. As a result, kinetic isotope effect studies now constitute one of the most important methods employed in the development of detailed

models of the mechanisms of organic and enzymatic reactions (see, e.g., Francisco et al. 2002; Knapp et al. 2002).

15.8 Mass-Independent Isotope Effects

In the previous sections, it has been demonstrated that both equilibrium and kinetic isotope effects can be well understood in terms of mass differences between different isotopes. However, there are some isotope effects that either do not depend on mass or exhibit an anomalous mass-dependence.

Different isotopes may have different nuclear spins (e.g., H: 1/2, D: 1; ^{12}C : 0, ^{13}C : 1/2; ^{16}O , ^{18}O : 0, ^{17}O : 5/2), which may result in the so-called nuclear spin isotope effect (also called “magnetic isotope effect”). This type of isotope effect may be observed in chemical processes that involve triplet-singlet transition. The energy characterizing such transitions contains a term that depends on the interaction between the spins of electrons and nuclei. Thus, the probability of the chemical process is a function of hyperfine coupling describing the above interaction. Hence, in the case of elements that have isotopes with different nuclear spins, the reaction rates may be different, thus leading to the nuclear-spin isotope effect. The term “magnetic isotope effect” refers to the fact that the magnitude of the isotope effect can be influenced by the strength of the applied external magnetic field. The magnetic isotope effect was discovered in 1976 by Buchachenko et al. (1976) in the photolysis of dibenzyl ketone (DBK). During photolysis triplet pairs of acyl and benzyl radicals are formed as primary products. The fate of the pair depends on whether it carries magnetic (^{13}C) or nonmagnetic (^{12}C) nuclei. The magnetic radical pair (with, e.g., ^{13}C in the carbonyl position) undergoes a fast triplet-singlet conversion, induced by the hyperfine coupling between the unpaired electron and the magnetic nucleus ^{13}C , which is followed by the recombination into the starting DBK molecule. The nonmagnetic pair (with ^{12}C in the carbonyl group) predominantly dissociates and forms the reaction products (dibenzyl and carbon monoxide). Thus, the DBK regenerated is enriched in ^{13}C while the reaction products are depleted in it. Some characteristics of the nuclear spin isotope effects are as follows (Turro and Kraeutler 1984; Buchachenko 2001). The isotope effect increases with increasing value of the hyperfine coupling constant; its magnitude does not depend on temperature and the expression describing the isotope effect does not contain any mass-dependent term. The magnetic isotope effect can be used to separate ^{13}C from ^{12}C and also to separate the magnetic ^{17}O selectively from the nonmagnetic isotopes ^{16}O and ^{18}O . It is interesting to note that the efficiency of the separation of ^{13}C from ^{12}C by use of the magnetic isotope effect mechanism surpasses considerably the separation efficiencies possible via mechanisms involving conventional isotope mass effects.

Another type of “anomalous mass effect” resulting from the uneven charge distributions in the isotopic nuclei was discussed by Bigeleisen (1996a, b) in order to explain the anomalies revealed by the precise measurements of equilibrium separation factors for uranium isotopes during the U(IV)/U(VI) redox equilibrium carried out on an anion exchange resin (Fujii et al. 1989): (1) separation factors for all the uranium isotopes appeared to be unexpectedly high; (2) heavy isotopes are enriched in compounds characterized by the lower oxidation states; (3) the dependence of the logarithm of the separation factor ($\ln\alpha$) on the reciprocal of the isotopic masses exhibits distinct deviations from the expected linear pattern for odd masses. The experimental finding that in the redox exchange system of U(IV)–U(VI) α for the $^{238}\text{U}/^{235}\text{U}$ isotope pair did not fit the linear interpolation between $^{238}\text{U}/^{234}\text{U}$ and $^{238}\text{U}/^{236}\text{U}$ explains why the phenomenon is sometimes called the “even-odd effect” or “even-odd staggering

of the isotopes.” Bigeleisen suggested that the anomalies are the result of a nuclear field shift of the electronic energy levels; the differences in the size and shape of nuclei of different isotopes bring about a displacement of the ground-state electronic energy of the atom or molecule. The contribution of the field effect to the U(IV)–U(VI) isotope separation factors was found to be about three times that of the vibrational effect due to the mass differences between uranium isotopes and the two effects are opposite in sign. It was suggested later that there is a nuclear quadrupole (Knyazev et al. 1999) and a chemical type isotope effect contribution (Mioduski 1999) to the even-odd effect. The study of the fractionation of ytterbium isotopes (the rare earth ytterbium has five isotopes with even mass numbers and two with odd) in Yb(III)-acetate/Yb-amalgam system represents another example for the occurrence of the “even-odd effect” (Dembiński et al. 1998). The problems that occur during the numerical estimation of nuclear size equilibrium isotope effects have been reviewed by Knyazev and Myasoedov (2001).

In order to understand the *mass-independent isotope effect*, which was first observed by Thiemens and Heidenreich (1983) in a laboratory experiment, the so-called δ -notation will be introduced. In the mass spectrometric determination of isotopic abundances, the isotopic ratios are typically reported in terms of the delta value (δ), which is the relative difference between the isotope ratio of the sample and that of a standard with known isotopic composition:

$$\delta = \frac{R_{\text{sample}} - R_{\text{standard}}}{R_{\text{standard}}} \quad (15.30)$$

where R is the ratio of the concentrations (atom fractions) of the heavy and light isotopes (e.g., $^{18}\text{O}/^{16}\text{O}$ isotope concentration ratios). The value of δ depends on the standard chosen, and as the differences between the samples and the standard are usually quite small, it is convenient to express the δ values in parts per thousand (“per mil”) $\delta (\text{‰}) = \delta \times 1,000$ (the δ values are widely used to describe the variations of stable isotope ratios in nature). For the relative fractionation of ^{18}O and ^{17}O isotopes, the theory of “mass-dependent” isotope effects predicts (see [Eq. \(15.15\)](#) and “rule” (3) in [Sect. 15.4.2](#)) that $\delta ^{17}\text{O} \approx 0.52 \times \delta ^{18}\text{O}$. Thiemens and Heidenreich (1983) measured the oxygen isotope fractionation, which occurs during the formation of ozone by an electric discharge in molecular oxygen. They found quite unexpectedly that the ^{18}O and ^{17}O isotopes were approximately equally enriched in the ozone product and equally depleted in the residual oxygen, that is, ^{17}O and ^{18}O isotope effects were found to be nearly equal ($\delta ^{17}\text{O} \approx \delta ^{18}\text{O}$). Since then, a number of experiments have been carried out in different laboratories and the existence of the anomalous relationship between ^{17}O and ^{18}O isotope effects was confirmed; see the critical reviews of the field published by Krankowsky and Mauersberger (1996), Weston (1999), and by Gao and Marcus (2001). The ozone isotope effect plays an important role in atmospheric processes (Mauersberger et al. 2001). Different models have been put forward to explain the observed experimental results (see, e.g., Janssen et al. 2001). According to the theory of Marcus and his coworkers (Gao and Marcus 2001, 2002; Gao et al. 2002), which is based on RRKM calculations of rate constants, the isotope effects can be regarded as “symmetry driven” and the calculations are consistent with most of the available experimental data.

15.9 Biochemical and Biological Isotope Effects

The sensitivity of living organisms to different isotopes of a given element is more difficult to explain than are physical and chemical isotope effects. After the discovery of deuterium in

1932, interest in the biological properties of deuterium was immediately aroused, however, early experimentation with deuterium was severely hindered by the extreme scarcity of the separated isotope (then produced by the electrolysis of water).

The first biological experiment with heavy water took place in 1933 in the laboratory of Urey where one of his assistants put few drops of deuterium-enriched water on his tongue and reported that it tasted the same as ordinary water (Rittenberg 1964). In another early experiment, Lewis, the famous physical chemist, administered 1 g of heavy water to a mouse; however, he was not able to draw any definite conclusion concerning the effect of deuterium, because he ran out of the supply of heavy water (Bigeleisen 1984). With the growth of nuclear technology, heavy water became readily available in the mid-1950s in quantities of hundred tons at a reasonable price. This circumstance greatly facilitated the research on the effects of deuterium in biological systems and the results obtained have been discussed in detail in monographs and review papers (Thomson 1963; Katz and Crespi 1971; Katz et al. 1975).

On the basis of isotope effects observed in physical and chemical properties, one can expect that *the replacement of hydrogen by deuterium in a living organism* may result in differences in the biological activity. Some of the factors that play an important role are the following. A significant part of a living organism consists of water and the properties of H_2O and D_2O differ from each other; the rate of reaction involving the breaking of a C–H bond is about six times faster than that of the C–D bond; deuterium bonds ($\text{OD} \cdots \text{O}$, $\text{ND} \cdots \text{O}$) are supposed to be stronger than hydrogen bonds ($\text{OH} \cdots \text{O}$, $\text{NH} \cdots \text{O}$); the substitution of D for H has a large effect on the rate of enzymatic reactions and on the three-dimensional structure of naturally occurring macromolecules, etc. It is very difficult to separate solvent isotope effects, primary and secondary isotope effects in living organisms and biochemical systems.

Since the metabolic rates of isotopically labeled compounds are different, variations in the concentration of the stable isotopes in organic compounds can be expected to depend on their biosynthetic pathway. Some examples are given by Rittenberg (1964): the concentration of deuterium in fermentation alcohol is less by 33 ppm than that of tap water (150 ppm); stearic acid and cholesterol are 21 and 34 ppm “lighter” than tap water, glucose and mannose are enriched in deuterium by 11 and 15 ppm, respectively, with respect to tap water. The application of isotope separation occurring in biological systems to large-scale separation of isotopes has been also considered; however, the low efficiency of the biological processes does not make the method feasible (Syrett 1961).

15.9.1 Physiological Effects of Heavy Water

The effect of heavy water on various living organisms has been widely investigated and this section is based on the excellent review of Katz and Crespi (1971). Algae are autotrophic systems in which water represents the only source required for the biosynthesis of organic compounds. The early experiments indicated that the incorporation of deuterium into algae was incompatible with life, however, it turned out later that by gradually changing the deuterium concentration of water, algae can be fully adapted to grow in D_2O . It is interesting to note that the phenomena observed when organisms are transferred from H_2O to D_2O should not be ascribed to the toxicity of deuterium, since they occur under the reversed conditions as well, that is, H_2O is “toxic” to organisms grown in D_2O . Algae are cultivated in heavy water on a large scale and the fully deuterated algae produced are available on the market and used for isotope effect studies in biological systems. There are some striking effects of heavy

water on simple organisms. For example, the yeast *Torulopsis utilis* grows well in a medium containing glucose and inorganic salts; however, it can only grow in D₂O if the sulfur-containing vitamin thiamine is added to the medium. This indicates that the presence of deuterium hinders the ability of the yeast to biosynthesize thiamine. Another example is *Aspergillus niger* that grows well in media containing D₂O, but loses its ability to synthesize its characteristic black pigment and becomes alabaster-white.

Whereas simple organisms can be adapted to grow in D₂O, higher plants as well as animals resist full deuteration. Experiments carried out with mice showed that animals drinking 30% D₂O, and deuterated to about 25% in the body fluids, live normal life span; however, their reproductive capacity becomes severely impaired. When the deuterium content of drinking water is higher than 30%, the animals do not survive. Deuterium content of 15–20% in the body fluids was found to be the *threshold for toxicity* in animals. Since deuterium substitution results in a decrease of the rates of reactions, the question arose already at an early stage after the discovery of deuterium whether the growth of tumors could be inhibited by the administration of heavy water. Experiments carried out on mice with mammary cancer showed that although the administration of 40% D₂O decreased the growth rate of the tumors, the mice treated died more rapidly due to the toxic effects of deuterium.

It is an interesting question how toxic deuterium or heavy water is to humans. If it is accepted on the basis of animal experiments that the “critical” deuterium concentration (the double of which would cause severe physiological effects) is about 10%, then one can easily estimate that a person of 70 kg may drink 4.8 l heavy water or 1.2 l per day for 4 days without serious consequences (Förstel 1978). Thus, heavy water cannot be considered toxic to humans. This is an important conclusion, since stable isotopes (e.g., heavy water for the estimation of total body water) are widely used in clinical research and diagnosis (Krumbiegel 1991). In the literature, one can find also some more conservative estimates as far as the application risk of the deuterium in the form of heavy water is concerned, for example, Jones and Leatherdale (1991) suggest that the threshold for noticeable side-effects exists at the dosage between 70 and 140 g of 100% D₂O.

While the effect of increased deuterium concentration on various physiological processes has been extensively investigated in different biological systems, very little is known about the sensitivity of biological processes to *reduced deuterium concentrations*. It was demonstrated by Somlyai et al. (1993) that subnormal deuterium concentration leads to the inhibition of cell division in cultured proliferating animal cells, indicating that naturally occurring deuterium is essential for normal growth rate of cells.

15.9.2 Isotope Fractionation in Biological Processes

Natural differences in the stable isotope composition of biological compounds result from differences in a variety of predictable factors, such as kinetic isotope effects, fractionating via diffusion, enzyme selectivity, etc. Stable isotope studies have been extensively used for solving problems in geochemistry and cosmochemistry (Craig et al. 1964) for a long time. Applications of stable isotope analysis in biological and ecological sciences have been expanding rapidly during the past 20 years (Rundel et al. 1988; Gebauer et al. 1993; Ivlev 2001; Zarzycki et al. 2002).

One of the most extensively studied biological isotope fractionation process is the *photosynthetic carbon fixation* (O’Leary 1981; Rundel et al. 1988; Ivlev 2001). It was found that plants with C₃ (e.g., rice, beet, potatoes, wheat, barley, legumes), C₄ (e.g., corn, sugar cane, sorghum,

pearl millet), and CAM (Crassulacean acid metabolism: e.g., pineapple) photosynthetic pathways show different discriminations against ^{13}C during photosynthesis. For example, while atmospheric carbon dioxide contains ^{12}C and ^{13}C in the ratio 89:1, C_3 plants generally contain proportionally less ^{13}C than does the air, their $^{12}\text{C}:^{13}\text{C}$ ratio is typically 91:1. Photosynthesis leads to an enrichment of the lighter carbon isotope (^{12}C) in organic materials; in other words they are depleted in ^{13}C (C_4 plants and CAM plants are richer in ^{13}C than C_3 plants). The difference in isotopic composition has become one of the methods by which C_4 plants can be distinguished from C_3 plants. Isotope fractionation in the photosynthesis of C_3 plants is due to the carboxylating enzyme ribulose biphosphate (RuBP) carboxylase, which discriminates strongly against the heavier carbon isotope. In C_4 and CAM plants, diffusional processes and recarboxylation play an important role in determining the carbon isotope composition since phosphoenolpyruvate (PEP) carboxylase does not discriminate against ^{13}C .

In plant samples collected in a salt marsh and lagoon, Smith and Epstein (1970) observed that the organic hydrogen of the dried plants contained 5.5% less deuterium than the environmental water, and the lipid fraction of the plant was even more depleted in deuterium. Investigations with plants grown under controlled conditions indicated that photosynthesis is the major process in fractionating the stable hydrogen isotopes in plants (Estep and Hoering 1980, 1981). The relationship between hydrogen isotope fractionation processes in plant tissues and different photosynthetic pathways has been thoroughly studied and significant differences were observed in discrimination against deuterium (Ziegler et al. 1976; Ziegler 1989).

Further biological fractionation takes place in animals and the measurement of the animals' isotopic ratios can be used to study animal ecology (Rundel et al. 1988). Finally, the isotopic composition of humans may reflect the composition of their diets and the principle "we are what we eat" can be used in archeological research to reconstruct the diet of prehistoric humans (Chen and Orna 1996) and hominids that predate the genus *Homo* (Sponheimer and Lee-Thorp 1999).

References

- Arnett EM, McKelvey DR (1969) In: Coetzee JF, Ritchie CD (eds) *Solute-solvent interactions*, Chapter 6. Marcel Dekker, New York, pp 344–398
- Bacsik Z, Canongia Lopes JN, Costa Gomes MF, Jancsó G, Mink J, Pádúa AAH (2002) *J Chem Phys* 116:10816
- Bartell LS, Roskos RR (1966) *J Chem Phys* 44:457
- Bell RP (1980) *The tunnel effect in chemistry*. Chapman and Hall, London
- Bigeleisen J (1949) *J Chem Phys* 17:675
- Bigeleisen J (1955) *J Chem Phys* 23:2264
- Bigeleisen J (1961a) *J Chem Phys* 34:1485
- Bigeleisen J (1961b) In: London H (ed) *Separation of isotopes*, Chapter 5. George Newnes, London, pp 95–122
- Bigeleisen J (1975) *ACS Symp Ser* 11:1
- Bigeleisen J (1984) *J Chem Educ* 61:108
- Bigeleisen J (1996a) *Proc Natl Acad Sci USA* 93:9393
- Bigeleisen J (1996b) *J Am Chem Soc* 118:3676
- Bigeleisen J, Mayer MG (1947) *J Chem Phys* 15:261
- Bigeleisen J, Wolfsberg M (1958) *Adv Chem Phys* 1:15
- Bigeleisen J, Lee MW, Mandel F (1973) *Ann Rev Phys Chem* 24:407
- Brodsky AE (1961) *Isotopenchemie*. Akademie-Verlag, Berlin
- Bruner F, Cartoni GP, Liberti A (1966) *Anal Chem* 38:298
- Buchachenko AI (2001) *J Phys Chem A* 105:9995
- Buchachenko AI, Galimov EM, Nikiforov GA (1976) *Dokl Akad Nauk SSSR* 228:379
- Buckingham AD, Fan-Chen L (1981) *Int Rev Phys Chem* 1:253
- Buddenbaum WE, Shiner VJ Jr (1977) In: Cleland WW, O'Leary MH, Northrop DB (eds) *Isotope effects on enzyme-catalyzed reactions*. University Park Press, Baltimore, pp 1–36
- Chen W, Orna MV (1996) *J Chem Educ* 73:485
- Cho CH, Urquidí J, Singh S, Robinson GW (1999) *J Phys Chem B* 103:1991
- Cleland WW, O'Leary MH, Northrop DB (eds) (1977) *Isotope effects on enzyme-catalyzed reactions*. University Park Press, Baltimore

- Collins NS, Bowman S (eds) (1971) Isotope effects in chemical reactions. Van Nostrand Reinhold, New York
- Conway BE (1981) Ionic hydration in chemistry and biophysics, Chapter 26. Elsevier, Amsterdam, pp 551–568
- Craig H, Miller SL, Wasserburg GJ (eds) (1964) Isotope and cosmic chemistry. North-Holland, Amsterdam
- Criss RE (1999) Principles of stable isotope distribution. Oxford University Press, Oxford
- Čuma M, Scheiner S (1997) *J Phys Org Chem* 10:383
- Dang LX, Bopp P, Wolfsberg M (1989) *Z Naturforsch* 44a:485
- Demiński W, Poniński M, Fiedler R (1998) *Separ Sci Technol* 33:1693
- Dezentje RFR, Dekkers HPJM (1976) *Chem Phys* 18:189
- Estep MF, Hoering TC (1980) *Geochim Cosmochim Acta* 44:1197
- Estep MF, Hoering TC (1981) *Plant Physiol* 67:474
- Fenby DV, Kooner ZS, Khurma JR (1981) *Fluid Phase Equilib* 7:327
- Filer CN (1999) *J Labelled Compd Rad* 42:169
- Förstel H (1978) Report Jül-1539, Kernforschungsanlage Jülich GmbH, Jülich
- Francisco WA, Knapp MJ, Blackburn NJ, Klinman JP (2002) *J Am Chem Soc* 124:8194
- Fujii Y, Nomura M, Okamoto M, Onitsuka H, Kawakami F, Takeda K (1989) *Z Naturforsch* 44a:395
- Fusch CH, Sprig N, Moeller H (1993) *Eur J Clin Chem Clin Biochem* 31:639
- Gao YQ, Marcus RA (2001) *Science* 293:259
- Gao YQ, Marcus RA (2002) *J Chem Phys* 116:137
- Gao YQ, Chen WC, Marcus RA (2002) *J Chem Phys* 117:1536
- Gebauer G, Förstel H, Rating D (eds) (1993) In: Proceedings of the annual meeting of Arbeitsgemeinschaft stabile isotope e.V., Isotopenpraxis Environmental and Health Studies, vol 29, pp 3–198
- Glasoe PK, Long FA (1960) *J Phys Chem* 64:188
- Harvey AH, Lemmon EW (2002) *J Phys Chem Ref Data* 31:173
- Ivlev AA (2001) *Separ Sci Technol* 36:1819
- Jancsó G (2002) *Nukleonika* 47(suppl 1):53
- Jancsó G, Van Hook WA (1974) *Chem Rev* 74:689
- Jancsó G, Rebelo LP, Van Hook WA (1993) *Chem Rev* 93:2645
- Jancsó G, Rebelo LP, Van Hook WA (1994) *Chem Soc Rev* 93:257
- Janssen C, Guenther J, Mauersberger K, Krankowsky D (2001) *Phys Chem Chem Phys* 3:4718
- Jones PJH, Leatherdale ST (1991) *Clin Sci* 80:277
- Katz JJ, Crespi HL (1971) In: Collins CL, Bowman NS (eds) Isotope effects in chemical reactions, Chapter 5. Van Nostrand Reinhold, New York, pp 286–363
- Katz JJ, Uphaus RA, Crespi HL, Blake MI (1975) *ACS Symp Ser* 11:184
- Kim DW, Jeon YS, Eom TY, Suh MY, Lee CH (1991) *J Radioanal Nucl Chem* 150:417
- Kleinman LI, Wolfsberg M (1973) *J Chem Phys* 59:2043
- Kleinman LI, Wolfsberg M (1974) *J Chem Phys* 60:4749
- Knapp MJ, Rickert K, Klinman JP (2002) *J Am Chem Soc* 124:3865
- Knyazev AD, Myasoedov NF (2001) *Separ Sci Technol* 36:1677
- Knyazev DA, Semin GK, Bochkarev AV (1999) *Polyhedron* 18(20):2579
- Knyazev DA, Bochkarev AV, Myasoedov NF (2001) *Separ Sci Technol* 36:1595
- Krankowsky D, Mauersberger K (1996) *Science* 274:1324
- Kresge AJ (1977) In: Cleland WW, O'Leary MH, Northrop DB (eds) Isotope effects on enzyme-catalyzed reactions. University Park Press, Baltimore, pp 37–63
- Krumbiegel P (1970) *Isotopieeffekte*. Akademie-Verlag, Berlin
- Krumbiegel P (1991) Stable isotope pharmaceuticals for clinical research and diagnosis. Gustav Fischer Verlag, Jena
- Lacks DJ (1995) *J Chem Phys* 103:5085
- Laughton PM, Robertson RE (1969) In: Coetzee JF, Ritchie CD (eds) Solute-solvent interactions, Chapter 7. Marcel Dekker, New York, pp 399–538
- Lee DA (1969) *Adv Chem Ser* 89:57
- Mauersberger K, Lämmerzahl P, Krankowsky D (2001) *Geophys Res Lett* 28:3155
- Melander L (1960) Isotope effects on reaction rates. Ronald Press, New York
- Melander L, Saunders WH (1980) Reaction rates of isotopic molecules. Wiley, New York
- Menes F, Dorfmueller T, Bigeleisen J (1970) *J Chem Phys* 53:2869
- Mioduski T (1999) *Comments Inorg Chem* 21:175
- Müller G, Mauersberger K, Sprinz H (1969) Analyse stabiler isotope durch spezielle Methoden. Akademie-Verlag, Berlin
- Nash CP (1975) *ACS Symp Ser* 11:29
- O'Leary MH (1981) *Phytochemistry* 20:553
- Polavarapu PL, Nafle LA, Benner SA, Morton TH (1981) *J Am Chem Soc* 103:5349
- Rabinovich IB (1960) *Usp Khim* 31:101
- Rabinovich IB (1970) Influence of isotopy on the physicochemical properties of liquids. Consultants Bureau, New York
- Rae HK (ed) (1978) Separation of hydrogen isotopes, ACS Symp Ser 68. American Chemical Society, Washington
- Richet P, Bottinga Y, Javoy M (1977) *Ann Rev Earth Planet Sci* 5:65
- Rittenberg D (1964) In: Craig H, Miller SL, Wasserburg GJ (eds) Isotope and cosmic chemistry, Chapter 6. North-Holland, Amsterdam, pp 60–69

- Roginski SS (1962) Theoretische Grundlagen der Isotopenchemie. VEB Deutscher Verlag d. Wissenschaften, Berlin
- Rundel PW, Ehleringer JR, Nagy KA (eds) (1988) Stable isotopes in ecological research. Springer, New York
- Schatenstein AI (1960) Isotopenanalyse des Wassers. VEB Deutscher Verlag d. Wissenschaften, Berlin
- Schön W, Wiechers R, Woermann D (1986) *J Chem Phys* 85:2922
- Schowen RL (1977) In: Cleland WW, O'Leary MH, Northrop DB (eds) Isotope effects on enzyme-catalyzed reactions. University Park Press, Baltimore, pp 64–99
- Shiner VJ Jr (1975) *ACS Symp Ser* 11:163
- Sims LB, Lewis DE (1984) In: Buncl E, Lee CC (eds) Isotope effects: recent developments in theory and experiment, Chapter 4. Elsevier, Amsterdam, pp 161–259
- Singh RR, Van Hook WA (1987) *J Chem Phys* 87:6097
- Smith BN, Epstein S (1970) *Plant Physiol* 46:738
- Somlyai G, Jancsó G, Jáklí GY, Vass K, Barna B, Lakics V, Gaál T (1993) *FEBS Lett* 317:1
- Sponheimer M, Lee-Thorp JA (1999) *Science* 283:368
- Stern MJ, Van Hook WA, Wolfsberg M (1963) *J Chem Phys* 39:3179
- Stern MJ, Spindel W, Monse EU (1968) *J Chem Phys* 48:2908
- Syrett PJ (1961) In: London H (ed) Separation of isotopes, Chapter 13. George Newnes, London, pp 416–428
- Thiemens MH, Heidenreich JE III (1983) *Science* 219:1073
- Thomson JF (1963) Biological effects of deuterium. Pergamon, Oxford
- Turro NJ, Kraeutler B (1984) In: Buncl E, Lee CC (eds) Isotope effects: recent developments in theory and experiment, Chapter 3. Elsevier, Amsterdam, pp 107–160
- Urey HC (1947) *J Chem Soc* 562
- Urey HC, Greiff LJ (1935) *J Am Chem Soc* 57:321
- Urey HC, Brickwedde FG, Murphy GM (1932) *Phys Rev* 40:1
- Van Hook WA (1968) *Isotopenpraxis* 4:161
- Van Hook WA (1969) *Adv Chem Ser* 89:99
- Van Hook WA (1971) In: Collins CL, Bowman NS (eds) Isotope effects in chemical reactions, Chapter 1. Van Nostrand Reinhold, New York, pp 1–89
- Van Hook WA (1972a) *J Phys Chem* 76:3040
- Van Hook WA (1972b) *J Chem Soc Chem Comm* 479
- Van Hook WA (1975) *ACS Symp Ser* 11:101
- Van Hook WA (1994) *Z Naturforsch* 50a:337
- Vedamuthu M, Singh S, Robinson GW (1996) *J Phys Chem* 100:3825
- Vértes A, Kiss I (1987) Nuclear chemistry, Chapter 10. Akadémiai Kiadó, Budapest
- Vogel JC, Grootes PM, Mook WG (1970) *Z Physik* 230:225
- Vojta G (1960) *Kernenergie* 3:917
- Vojta G (1962) In: Hertz G (ed) *Lehrbuch der Kernphysik, Band III*, Chapter C. B. G. Teubner Verlagsgesellschaft, Leipzig, pp 88–116
- Weston RE Jr (1975) *ACS Symp Ser* 11:29
- Weston RE Jr (1999) *Chem Rev* 99:2115
- Willi AV (1983) Isotopeneffekte bei chemischen Reaktionen. Georg Thieme Verlag, Stuttgart
- Wolfsberg M (1969a) *Adv Chem Ser* 89:185
- Wolfsberg M (1969b) *J Chem Phys* 50:1484
- Wolfsberg M (1969c) *Ann Rev Phys Chem* 20:449
- Wolfsberg M (1972) *Accounts Chem Res* 5:225
- Wolfsberg M, Stern MJ (1964) *Pure Appl Chem* 8:225
- Zarzycki R, Chmielewski AG, Zakrzewska-Trznadel G (eds) (2002) Stable isotopes – some new fields of application. Polish Academy of Sciences, Łódź
- Ziegler H (1989) In: Rundel PW, Ehleringer JR, Nagy KA (eds) Stable isotopes in ecological research, Chapter 8. Springer, New York, pp 105–123
- Ziegler H, Osmond CB, Stichler W, Trimbom P (1976) *Planta (Berl)* 128:85



16 Isotopic Paleoclimatology

R. Bowen

Westfälische Wilhelms-Universität, Münster, Germany

16.1	<i>Urey and His Geologic Thermometer</i>	728
16.1.1	The Paleotemperature Concept	729
16.1.2	First Carbonate/Water Paleotemperature Scale	730
16.1.3	Other Paleotemperature Scales	731
16.1.4	Working Standards (PDB, SMOW, SNOW, SLAP)	731
16.2	<i>Milankovitch, Ice, and Sediment Cores</i>	732
16.2.1	Basic Considerations	734
16.2.2	Dole Effect and the Meteoric Water Line	735
16.2.3	Continental Glaciation	736
16.3	<i>Ice Volume Versus Paleotemperatures</i>	737
16.3.1	Isotopes and Ice Age Impacts	738
16.3.2	The Geography of the Last Ice Age	739
16.4	<i>The Quaternary Global Carbon Cycle</i>	741
16.4.1	Past Atmospheric Carbon Dioxide in Ice Cores	741
16.4.2	Carbon Cycle Changes	742
16.5	<i>O–H–C Isotopes in Trees and Seas</i>	743
16.6	<i>Orbital Frequency Rhythms in the ¹⁸O Records</i>	744
16.6.1	Modeling Pleistocene Climatic Response	744
16.6.2	Simulating the Ice Age	746
16.6.3	Pleistocene/Holocene Climatic Changes	747
16.7	<i>Quantifying Isotopic Chronostratigraphy</i>	748
16.8	<i>Time’s Arrow Reversed: Pliocene Paleoclimates</i>	750
16.8.1	Middle Tertiary Paleooceanographic Changes	751
16.8.2	The Eocene Ocean	751
16.8.3	Oxygen and Carbon Isotopic Variations in Foraminifera Across the Cretaceous/Tertiary (K/T) Boundary	753
16.8.4	Isotopes and Mass Extinctions	753
16.8.5	Isotopes as Mesozoic Climate Indicators	754
16.8.6	The Permo/Triassic (P/Tr) Boundary	755
16.8.7	Oxygen and Carbon Isotopic Paleozoic Ocean Data	757
16.8.8	The Precambrian Eons	757
16.8.8.1	Archean/Proterozoic Transition	758

Abstract: Paleotemperature scales were calculated by H. C. Urey and others in the 1950s to assess past temperatures, and later work using the stable isotopes of oxygen, hydrogen, and carbon employed standards such as Peedee belemnite (PDB) and Standard Mean Ocean Water (SMOW). Subsequently, subjects as diverse as ice volume and paleotemperatures, oceanic ice and sediment cores, Pleistocene/Holocene climatic changes, and isotope chronostratigraphy extending back to the Precambrian were investigated.

16.1 Urey and His Geologic Thermometer

Oxygen isotopes of masses 17 and 18 were discovered in atmospheric oxygen in 1929. Deuterium, the heavy stable isotope of hydrogen, was detected in 1931, and by 1938 the carbon dioxide–water exchange technique for the oxygen isotope analysis of water had been developed. By the end of the 1930s, the existence of variations in the hydrologic cycle of both hydrogen and oxygen had been elaborated. Isotope paleoclimatology started with H. C. Urey's researches both on the empirical and theoretical aspects of isotope chemistry that followed his award of the Nobel Prize in 1934. In that year, he had already examined oxygen isotopes in stony meteorites and terrestrial rocks and claimed that they are constant to 2.5%. Later refinements produced per mill (‰, parts per thousand) accuracies and, after his World War II involvement in the separation of uranium isotopes, he treated the thermodynamics of isotope equilibria, also geochemical and cosmic problems. A seminal paper on the thermodynamic properties of isotopic substances appeared in 1947 (Urey 1947).

A mass spectrometer was described for measuring the isotopic variations in gas samples with high accuracy (Nier 1947). Urey improved its precision and started taking the paleotemperatures of Cretaceous belemnites. He did this by assessing the oxygen isotope fractionation between ocean water and the calcium carbonate precipitated by these animals (Urey et al. 1951). This was probably one of the greatest developments in the earth sciences and spans a wide range of disciplines from biology through isotopic fractionation to the history of the Earth.

In 1958, Urey relocated from Chicago to California, where at the Scripps Institution of Oceanography a School of Chemistry was formed. H. A. Lowenstam and S. Epstein continued the examination of Mesozoic belemnites following development of a paleotemperature scale (later modified by H. Craig and others) that will be discussed below. Attempts were later made to use two other mineral phases, i.e., biogenic silica/water and biogenic phosphate/water. They were successful, but the difference in values of carbonate, silica and phosphate in equilibrium with water were constant. Thus, it proved impossible to use either silica or phosphate to assess the temperature and isotopic composition from the measurements of delta (δ) oxygen-18 values in pairs of biogenic carbonate, silica, and phosphate. Parenthetically, delta is a parameter defined in per mill as ‰. This is fully explained later in the text (see ► Table 16.1).

Additional and ongoing research has accelerated the accumulation of more knowledge about the climates of the past essentially based on what some physicists scornfully described as “Urey's plumbing” beside the Pacific Ocean at La Jolla at Urey's lunch table. As well as oxygen isotopes, the isotopes of hydrogen, carbon, and, to a lesser degree, nitrogen, strontium, sulfur, etc., have been investigated. And the further back in time, the less the reliability of the data, the scantier the available evidence. Almost all interesting information relates to the isotopic paleoclimatology of the period, which started about 66.5 million years ago at the

■ Table 16.1

A comparison of hydrogen, oxygen, and carbon isotopic standards

Element	Isotope	Natural abundance variation (%)	Standard	Abbreviation
H	$^1\text{H}(\text{H})$	D/H:700	Artificial (Vienna) SMOW	V-SMOW
	$^2\text{H}(\text{D})$			
C	^{12}C	$^{13}\text{C}/^{12}\text{C}$:110	Vienna peedee belemnite	V-PDB
	^{13}C			
O	^{16}O	$^{16}\text{O}/^{18}\text{O}$:100	Standard mean ocean water	SMOW
	^{18}O		Artificial (Vienna) SMOW	V-SMOW
			Standard light Antarctic precipitation	SLAP
O in carbonates			<i>Belemnitella americana</i> from the peedee	
			Formation, cretaceous, North Carolina	PDB
			Vienna peedee belemnite	V-PDB

Cretaceous/Tertiary (K/T) Boundary. Significant topics include ice volume versus paleotemperatures, sediment core data from deep oceans, ice core information, and the extension of the paleotemperature scale from belemnites to other organisms such as foraminifera and brachiopods. Associated matters involve the missing carbon problem, the global carbon cycle, simulation of the ice age, modeling climatic response for the Pleistocene, climate forcing, quantifying isotopic chronostratigraphy, ice-free oceans, and geochemical changes possibly connected with mass extinctions.

16.1.1 The Paleotemperature Concept

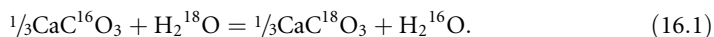
In 1950, the phosphoric acid technique for obtaining carbon dioxide from carbonates for mass spectrometric analysis was described (McCrea 1950). An improved version of Nier's mass spectrometer was used to determine the temperatures of Cretaceous belemnites by assessing the oxygen isotope fractionation between ocean water and the carbonate precipitated by these extinct animals (Urey et al. 1951). An oxygen isotope scale for evaluating paleotemperatures was developed in the 1950s following Urey's realization that if calcium carbonate is slowly crystallized in the presence of water at 0°C , the ratio of the oxygen isotopes in it should be 1.026:500 if the ratio of the oxygen isotopes in the water is 1:500, that is to say that the oxygen-18 is very slightly concentrated in the calcium carbonate in relation to water. If the temperature is 25°C , the oxygen isotopes will be concentrated only to the extent of 1.022:500 compared to 1:500 in water. From these considerations, a slight temperature coefficient for the abundance of oxygen-18 in the calcium carbonate as compared to that in the water was inferred. The degree of this fractionation is so small that the atomic weight of oxygen in the calcium carbonate will be changed by only 0.0000007 atomic weight units as the temperature is changed by 1°C . Hence

it was calculated that a change in temperature from 0°C to 25°C entails a change in the atomic weight of the oxygen of a mere 0.00002 atomic weight units. In this way, Urey wrote that “*I suddenly found myself with a geologic thermometer on my hands.*” With his group, he went on to develop the PDB standard.

This standard is significant because of the **calcareous-shelled abundance of carbonates** in the geological record. Urey and others used constant temperature baths to grow marine animals at known temperatures and also collected at various places so as to solve what he called “*the toughest chemical problem I ever faced,*” that is to say setting up a paleotemperature scale. The following paleotemperature equations are based on empirical data either obtained through growth experiments under controlled conditions (Epstein et al. 1953) or by the inorganic precipitation of minerals (Tarutani et al. 1969).

16.1.2 First Carbonate/Water Paleotemperature Scale

The first carbonate/water paleotemperature scale was based on the fact that the isotopic composition of oxygen from calcium carbonate differs from that of the water and depends on the temperature when the carbonate in question is precipitated under equilibrium conditions. This difference arises from an isotope-exchange reaction that can be represented by the expression



As only two thirds of the oxygen reacts to carbon dioxide when carbonate is treated with phosphoric acid, it is necessary to know the relevant fractionation factor which is

$$K = \alpha = R_c/R_w \quad (16.2)$$

where R_c and R_w represent the oxygen-18/oxygen-16 ratios of carbonate and water respectively. In the system calcite/water, the fractionation factor found is 1.0286 at 25°C so that the calcite precipitated in equilibrium will be enriched in oxygen-18 to 2.86‰ or 28.6‰ in δ -notation. The fractionation is temperature-dependent with values near unity and carbonate can either be enriched or depleted in heavy oxygen isotopes. Of course, the isotopic composition of seawater is unaffected because the mass of this is larger by orders of magnitude than that of the CaCO_3 equilibrated with it.

The temperature dependence of oxygen isotope fractionation between water and the important carbonate phases was established, the fractionation being normalized to the form as follows: $\delta^{18}\text{O}$ (CaCO_3 versus PDB) – $\delta^{18}\text{O}$ (water versus SMOW). Details regarding PDB and SMOW follow below, see ► [Table 16.1](#).

One of several equations is

$$T/^{\circ}\text{C} = 16.0 - 4.14(\delta_c - \delta_w) + 0.13(\delta_c - \delta_w)^2, \quad (16.3)$$

later revised so that 16.0 became 16.9 and 4.14 became 4.2. A later relationship was proposed for the aragonite/water paleotemperature scale by Grossman and Ku (1986). This is as follows:

$$T/^{\circ}\text{C} = 21.8 - 4.69(\delta_{\text{aragonite}} - \delta_w). \quad (16.4)$$

In all these cases, T is the derived temperature in °C, δ_c is the $\delta^{18}\text{O}$ of carbon dioxide liberated by the reaction of carbonate with 100% phosphoric acid at 25°, and δ_w is the $\delta^{18}\text{O}$ of

carbon dioxide equilibrated at 25°C with the water in which the shell was precipitated. The second factor is a problem because it refers, in their cases, mostly to oceanic water in a paleo-ocean, the isotopic composition of which is not known precisely. Urey assumed a value of zero for it, but later work has refined this approach. Doubtless, changes in the isotopic composition of seawater occurred through geological time and affected the $\delta^{18}\text{O}$ and also the δD contents as well as some significantly dissolved constituents such as the $\delta^{13}\text{C}$ of bicarbonate and the $\delta^{34}\text{S}$ of sulfate.

16.1.3 Other Paleotemperature Scales

Epstein et al. (1953) determined empirically the temperature dependence of the oxygen-18 of calcite in equilibrium with water, the delta values of these being later modified by Craig (1965). The expression for the temperature (T in °C) is as follows:

$$T/^{\circ}\text{C} = 16.9 - 4.2(\delta_{\text{c}} - \delta_{\text{w}}) + 0.13(\delta_{\text{c}} - \delta_{\text{w}})^2, \quad (16.5)$$

where δ_{c} is the $\delta^{18}\text{O}$ of carbon dioxide obtained from a sample of carbonate by reaction with 100% H_3PO_4 with respect to the mass spectrometer standard working gas, and δ_{w} is the corrected oxygen-18 of carbon dioxide equilibrated isotopically at the same temperature with the water from which the carbonate was precipitated, again measured against the same mass spectrometer standard working gas. Subsequently, extended studies have been done taking into account the new information regarding the paleotemperature scales and problems arising from the further development of the method. The estimation of paleotemperatures by measuring the oxygen isotope ratios of calcium carbonate from marine fossils had great significance as regards interpreting the history of climatic changes in the past, although it must be admitted that paleotemperatures have to be interpreted carefully if reliable data are to result. Unrealistic results can derive from various factors such as salinity, diagenetic alteration of samples, ice volume effects, mixing with freshwater, life habits, biological fractionation, or the mineralogical structure of the calcium carbonate. Although these parameters might influence and limit the value of temperature determinations in the past, each one of them offers opportunities for obtaining more paleoecological information, particularly if comparable data gained through faunal or floral analyses are available.

Clearly, these considerations necessitated initial chemical work using appropriate standards and various isotopic geochemical laboratories employ different reference gases or working standards in order to measure relative isotopic ratios using mass spectrometers. In [Table 16.1](#) there is a list of the most important isotopes involved.

16.1.4 Working Standards (PDB, SMOW, SNOW, SLAP)

All the stable and relevant standards are listed starting with the lightest isotope and proceeding upward. As well as oxygen and hydrogen, carbon is included in the following [Table 16.1](#) because it has proved to be useful in paleotemperature and allied work, for instance in dating groundwater aquifers. Information as to how these standards were derived follows below. Some of them have now been exhausted and have had to be replaced and some details as to how this was accomplished follow below the table under the headings PDB and SMOW.

Measurement of these isotopes produces data expressible in units of delta, δ , a parameter defined as follows:

$$\delta = \delta_{\text{sample to standard}} = \frac{R_{\text{sample}} - R_{\text{standard}}}{R_{\text{standard}}} \times 10^3, \quad (16.6)$$

and stated in parts per mill (‰). R_{sample} can be D/H, $^{18}\text{O}/^{16}\text{O}$, $^{13}\text{C}/^{12}\text{C}$, etc., the subscript “sample” denoting isotope ratio in a sample and the subscript “standard” denoting that in an appropriate standard.

PDB refers to a standard derived from *Belemnitella americana* from the Cretaceous Peedee Formation, South Carolina, USA. This standard is exhausted but referred to in the literature, so isotope ratios are measured against other standards and related to PDB as follows:

$$\delta_{\text{sample to PDB}} = \delta_{\text{sample to standard}} \times \delta_{\text{standard to PDB}} + \delta_{\text{sample to standard}} + \delta_{\text{standard to PDB}}, \quad (16.7)$$

where the result is expressed in parts per thousand (per mill). Vienna-PDB (V-PDB) standard was introduced in 1985 with NBS-19 as a reference material.

SMOW is Standard Mean Ocean Water, and it is now exhausted. It was originally made from seawater distilled into fractions and measured for deuterium and oxygen-18. The fractions were so combined and adjusted as to produce $\delta^{18}\text{O} = 0\text{‰}$ relative to what was originally defined as SMOW relative to NBS standard water. The oxygen-18 value was exactly 0‰ (to $\pm 0.02\text{‰}$). The D/H delta was negative because of the effects of distillation, so heavy water was added to bring the D/H delta to 0‰ (to $\pm 0.02\text{‰}$). As regards SLAP, H. Craig proposed SNOW (Standard Non-Ocean Water) for the light water standard, a proposal which did not find favor with the International Atomic Energy Agency (IAEA) on the grounds that it could be confused with SMOW. Urey wrote:

- ▶ *the temperature coefficient for the abundance of the oxygen isotope in calcium carbonate makes possible a new thermometer of great durability which may have been buried in the rocks for hundreds of millions of years after recording the temperature of some past geological record and then having remained to the present.* (Urey 1948)

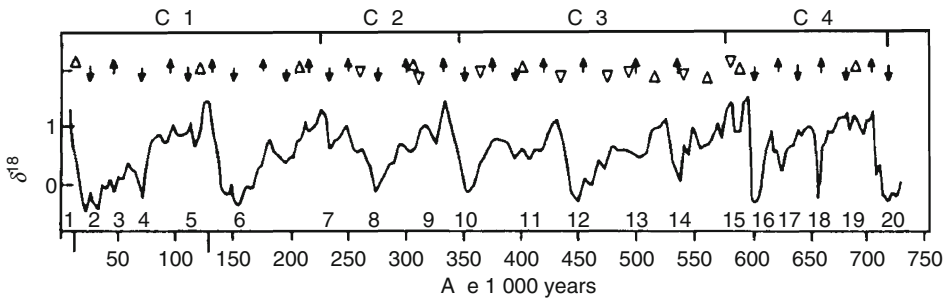
The oxygen isotope compositions of foraminiferal tests from oceanic cores are a function of two variables, namely the oceanic temperatures and the oxygen isotope composition of the waters in which these animals lived. It was calculated that almost 85% of the isotopic change between glacial and interglacial planktonic foraminifera resulted from oceanic temperature changes, the remaining 20% or so coming from changes in the isotopic composition of water in the oceans through this transition due to the expansion and contraction of continental ice sheets (Emiliani 1955). Such changes were expressed in terms of 16 isotope stages, odd numbered ones representing warmer periods of Earth history and even numbered ones colder periods. Broecker and Van Donk referred to the changes from cold to warm stages as “terminations” (🔗 Fig. 16.1); thus, Termination I is the transition between Stages 2 and 1, Termination II that between Stages 6 and 5, etc. (Broecker and Van Donk 1970).

16.2 Milankovitch, Ice, and Sediment Cores

Greenhouse states occurred throughout Earth history, and they were occasionally irregularly interrupted by icehouse states during glaciations (ice ages). There is probably a greenhouse effect at present and this is quite different from the situation prevailing through the rest of the

■ Fig. 16.1

The oceanic isotope record and the timescale of planetary orbital changes showing an accurate chronology of first-order climatic variations through the last 0–75 million years. It can be seen that the record is saw-toothed in shape. Data composed from Cores P6304-9 (275,000–730,000 years) show $\delta^{18}\text{O}_{\text{‰}}$ -values against Chicago PDB-1 of *Globigerinoides sacculifer* (with correction of 2‰ for the section from Core 280). Absolute timescales were based on age 0 for core top, 125,000 years for the peak of Stage 5, and 700,000 years for the peak of Stage 19 (representing the Brunhes/Matuyama Boundary). Interpolations were based on average stage thicknesses from the Caribbean (Stages 1–6) and on the thicknesses of Stage 6–20 in Core V28-238. *Upward pointing arrows* show obliquity maxima and vice versa. *Upward pointing triangles* show eccentricity maxima and vice versa. *Circles* show times of maximum eccentricity when the northern summer was at perihelion. SCT 1–4 are superclimatherms and an earlier fifth covers isotope Stages 21–25. The foregoing SCT6 is a Late Cenozoic climatic boundary connected with the first continental ice sheet glaciations of Europe and the maximum glaciations in North America and Patagonia. Transitions from cold to warm episodes are called “terminations.” The last was Termination I (TI) between Stage 2 and 1. It was preceded by Termination II (TII) between Stages 6 and 5 (After Emiliani 1955, 1978)



Holocene Epoch that commenced some 10,000 years ago. Prior to that, the Pleistocene was characterized by ice episodes comprising the last Ice Age. Large quantities of ice remain even today, and examination of ice cores and their oxygen isotope profiles have shown climatic variations through the past 100,000 years. The parameter $\delta^{18}\text{O}$ measured in the water molecules produces basic information in an ice core. The temperature at which ice crystals form clouds determines the $\delta^{18}\text{O}$ ratio of the ice deposited at the surface so that the $\delta^{18}\text{O}$ of an ice core provides a proxy record of precipitation temperatures. In 1987, Dansgaard recorded many abrupt climatic changes in the North Atlantic during the last ice-age and deep-sea sediment analyses have confirmed that the southern hemisphere was affected as well. Ocean sediment cores are also important in understanding past climates since they embody relevant data on timescales of 1,000–10,000 years at sample resolutions claimed to be in the range of 1,000–10,000 years. The Deep Sea Drilling Project (DSDP) sampled 600 sites and gave records up to tens of millions of years in age. The most interesting areas for sediment core studies is probably within 10° of the equator in mid- to high latitudes and along coastal margins. Such ice ages occurred irregularly throughout Earth history, and long-term climatic trends entail astronomical cycles of 100,000 years (eccentricity of the planetary orbit), 41,000 years (obliquity signal), and 23,000 and 19,000 years (Milankovitch 1930). **CLIMAP (Climate Long-Range Investigation and Mapping)** deep-sea ocean core stratigraphy and associated isotope analyses have been used to determine whether smaller fluctuations in an isotope curve correspond to

those predicted by Milankovitch theory. The history of the North Atlantic and North Pacific oceans during the Brunhes Epoch of normal magnetic polarity extends back to 690,000 years before the present. Brunhes himself noted that magnetization of lava flows and underlying baked clays indicated that the direction opposed that of the present field (Brunhes 1906). It became apparent that the Earth's magnetic field reversed itself during the past. A preceding reversed polarity time interval extended from 690,000 to 2.4 million years before the present and this is termed the Matuyama Epoch.

16.2.1 Basic Considerations

Damage to the ecosystem increases through acid rain, ozone depletion, and supernovae may well induce ozone drops through the emission of a proton burst that might add an equivalent of solar possible greenhouse effects. Some of these factors are beyond human control, e.g., it has been suggested that ionizing radiation to the terrestrial atmosphere can produce NO_x molecules capable of reducing the ozone layer to as little as 10% of its present concentration and that the Tunguska event of June 1908 actually caused a 40% drop in this layer, which probably entailed the release of a nitric oxide cloud. It has been proposed that the transition from an ice-free “greenhouse” Earth to a glacial cycle “icehouse” regime could be produced from a northern hemisphere ice sheet model if there was a slow general cooling on the continents perhaps due to plate tectonic shifting (Oerlemans 1984). Implications of the coral reef record from New Guinea in regard to the astronomical theory of ice ages may provide a means for quantitatively evaluating ice volume and the temperature factor from their oxygen isotope contents and sea-level changes. An even more startling application of isotopes to Pleistocene ice age events was an indication that detailed heavy isotope and dust concentration profiles from Greenland ice cores imply that the North Atlantic regional climate became milder and less stormy because of a rapid retreat of the sea ice cover occurring in less than 20 years. As regards mass extinctions, e.g., at the K/T Boundary, supportive records show a high $^{87}\text{Sr}/^{86}\text{Sr}$ ratio in some planktonic fossils, which could reflect continental-derived strontium. Curiously, at the K/T Boundary, there was a change in the carbon isotope ratios, but not in the sulfur ones. Lower values of the carbon ones may imply lowered oceanic productivity that eliminated the usual state between surface and deep waters to give “**Strangelove**” conditions. Later, higher values were restored with vigorous oceanic circulation. Productive oceans have a biologically mediated gradient in the carbon isotopes between surface and deep waters and it is this that disappeared at the K/T Boundary to initiate “Strangelove” conditions, i.e., a “Strangelove” ocean, one where the above-mentioned biologically mediated gradient in carbon isotopes between surface and deep waters characteristic of productive oceans disappears. A similar carbon drop was recorded for the largest mass extinction in the Phanerozoic era, namely that which took place at the Permo/Triassic (P/T) Boundary about 237.2 Ma ago. Several magnetic reversals around this time have been noted from core records and, curiously, the carbon record does not revert as rapidly back to normal as was the case in the wake of the K/T one. However, apparently global changes in the carbon cycle started in the Late Permian and continued smoothly across the stratigraphical P/T Boundary to culminate in the Early Triassic.

Greenland ice cores may record a milder and less stormy climate in the North Atlantic region because of a rapid retreat of the sea-ice cover occurring in less than 2 decades (Dansgaard et al. 1989). This produced a wide belt of open seawater of intermediate temperatures lying between tropical and polar water masses. In fact, it is feasible that a bi-stable

climatic regime existed there in the course of the glacial period and may have been connected to a flip-flop mechanism in the North Atlantic Ocean. This could perhaps be correlated with switching from “strong” to “weak” modes of deepwater production there, a process that could have been driven, at least to some extent, by an influx of cold freshwater from melting continental ice sheets. Isotopic data have been applied also to mass extinctions of which the best known is that occurring at the K/T Boundary about 66.5 Ma ago. This may have contributed to the extinction of the dinosaurs and other life-forms and could have resulted from the impact of an “extinction bolide” striking a shallow marine terrane on Earth or even an asteroid if the Chicxulub crater really is an impact relic.

16.2.2 Dole Effect and the Meteoric Water Line

Melting ice releases isotopically light water, that is to say water enriched in ^{16}O . Freezing has the opposite effect. Variation in oxygen-18 ocean contents between maximum and minimum glaciations might have been about 1.5‰, therefore glaciation can be more significant than temperature as regards the isotopic composition of marine carbonates, for instance in foraminifera in tropical oceans (Craig 1965). This is because their environmental temperatures will not vary much during glacial or interglacial episodes. And, while oxygen-18 temperature effects produce approximately 0.7‰ increase in the heavy stable isotope in precipitation for every 1°C rise in temperature, the isotopic difference between shells formed during maximum or minimum glaciation in equatorial surface waters in the Atlantic Ocean and in the Caribbean Sea is only about 1.6‰. From this, it may be inferred that freshwater systems respond far more to climatic changes than do marine ones.

Today atmospheric oxygen is not in isotopic equilibrium with ocean water (Dole effect) and there is a considerable oxygen-18 enrichment relative to V-SMOW, $\sim 23.5\text{‰}$, possibly accounted for by global respiratory processes. As for δD , the hydrosphere now has an overall value ranging from roughly zero relative to V-SMOW. Since magmatic water has values ranging from -50‰ to -90‰ relative to V-SMOW, it cannot have originated from the hydrosphere. Of course it is possible that the hydrogen isotope composition of the original sources of water on the surface of the Earth may have been different from that of those waters incorporated into the planetary interior.

Examination of the ranges of relative deuterium concentrations in various terrestrial and meteoric materials shows that seawater is on the heavy side of most samples, including those from carbonaceous chondrites. This may be due to a stepwise distillation process during which hydrogen moves faster than the heavier deuterium. It may be described by a modified Rayleigh equation and determines that precipitation falling furthest from its source will be isotopically enriched in the lighter stable isotopes hydrogen and oxygen-16. Also, natural waters in high latitudes and altitudes are isotopically light and those in subtropical regions with low rainfall are often heavier than seawater. A linear correlation exists between deuterium and oxygen-18 in meteoric waters and this can be expressed by the following relationship

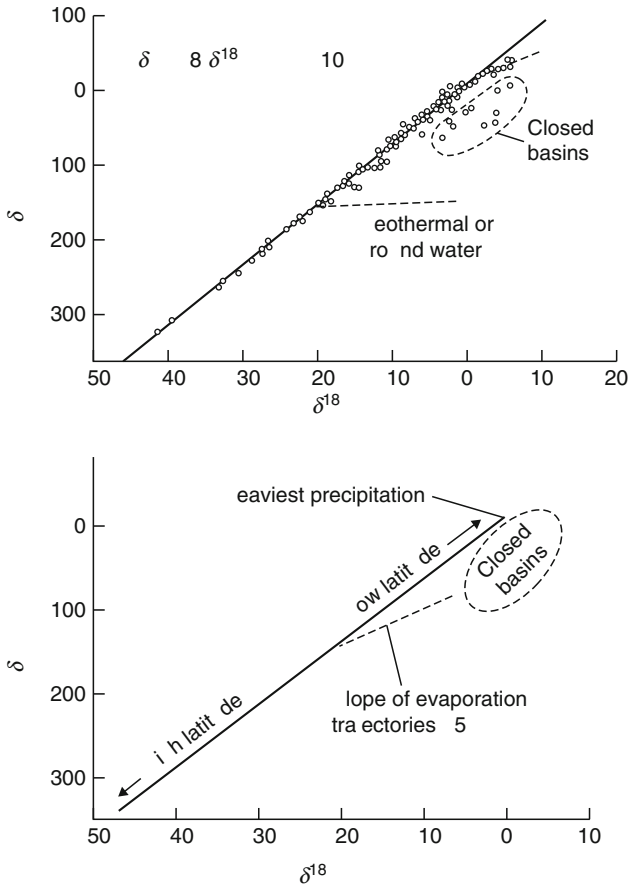
$$\delta\text{D} = 8 \delta^{18}\text{O} + 10 \quad (16.8)$$

which is called the “meteoric water line” (see upper graph in [Fig. 16.2](#)). Deviations occur in lakes and other enclosed water bodies undergoing extensive evaporation.

There are other effects to consider. They are temperature, altitude, and latitude. The above correlation confirms that atmospheric precipitation follows a Rayleigh distillation process at

■ Fig. 5.2

The relationship between δD and $\delta^{18}O$ in meteoric water. The linear relationship is the “meteoric water line”



liquid–vapor equilibrium and the slope of the meteoric water line roughly corresponds to the ratio of equilibrium fractionations at 25°C. Decreasing δD and $\delta^{18}O$ values along this line are connected to increasing altitude and latitude and decreasing mean annual temperature. As for groundwater, their isotopic compositions in temperate and humid regions resemble those of precipitation in their recharge areas. Another effect of evaporation may be a rise in salinity, but, if such a rise does not occur, the isotopic composition of the evaporating water body may increase monotonically to a steady-state condition.

16.2.3 Continental Glaciation

Continental glaciation exerts effects on the isotopic composition of the oceans arising from isotopic fractionation in the meteoric cycle. High-latitude precipitation is depleted in the heavy stable isotopes relative to ocean water so that when continental glaciers grow, the light

isotopic species are preferentially removed from seawater and the $\delta^{18}\text{O}$ and δD contents of the residual oceans increase. The reverse takes place when glaciers or ice sheets melt. Consequently, the advance and retreat of continental glaciers during the Pleistocene must have altered the $\delta^{18}\text{O}$ in seawater and this so-called ice volume effect is calculable. It must have been paralleled during earlier ice ages in Earth history, and notable $\delta^{18}\text{O}$ shifts in the records of Tertiary deep-sea carbonates may be due to the development of such continental glaciers.

16.3 Ice Volume Versus Paleotemperatures

A composite curve of isotopic variations for the past 700,000 years was constructed (Emiliani 1978). It implied that glacial/interglacial cycles have a periodicity of about 100,000 years. Fluctuations were saw-toothed in a pattern that suggested rapid change from one condition to the other. Subsequently, the original idea that ice effect was less than temperature was reversed and an improved timescale devised. Obtaining an improved timescale entailed deciding between one based on radiocarbon dating linked to a presumed fit to Milankovitch fluctuations and another based on the dating of raised coral reefs (Broecker and Van Donk 1970). The so-called Broecker scale was vindicated.

Continental glaciation exerts effects on the isotopic composition of the oceans arising from isotopic fractionation in the meteoric cycle. High-latitude precipitation is depleted in the heavy stable isotopes relative to ocean water so that when continental glaciers grow the light isotopic species are preferentially removed from seawater and the $\delta^{18}\text{O}$ and δD contents of the residual oceans increase. The reverse takes place when glaciers or ice sheets melt. Consequently, the advance and retreat of continental glaciers during the Pleistocene must have altered the $\delta^{18}\text{O}$ in seawater and this so-called ice volume effect is calculable. It must have been paralleled during earlier ice ages in Earth history and notable $\delta^{18}\text{O}$ shifts in the records of Tertiary deep-sea carbonates may be due to the development of such continental glaciers. Attempts to estimate variations in $\delta^{18}\text{O}$ in seawater through geological time could be improved by analyzing two mineral phases, both of which equilibrated with the seawater at the same temperature. Two independent equations could be constructed relating the δ -value of the water and the temperature, the latter then becoming determinable. Two such phases have been proposed, namely biogenic silica and phosphate, but unfortunately the slopes of lines drawn from derived equations parallel that of the calcium carbonate paleothermometer; therefore, the difference in the δ -values of carbonate and silica in equilibrium with water is constant and independent both of δ -values of the relevant water and also of the temperature. The situation between biogenic carbonate and biogenic phosphate is similar. Hence, it is not possible to use either approach for assessment of both temperature and the isotopic composition of water from measurements of $\delta^{18}\text{O}$ values in pairs of biogenic carbonate, silica, or phosphate.

Variations in the oxygen isotopic compositions of Quaternary foraminifera relate to paleoclimatic events, but the extent to which temperature changes and **ice volume** actually correlate is unclear. Oxygen isotope analysis of deep-sea cores implies that massive destruction of the Antarctic ice sheet occurred during glacial terminations I and II. It should be mentioned that although most references allude to marine environments, there are data regarding oxygen and carbon isotopes in freshwater shells, terrestrial plants, etc. If diagenetic changes have not taken place, there can be little doubt that the isotopic composition of fossil shells and limestones from freshwater deposits embody information showing much greater variability because of the large-scale fractionation of oxygen isotopes in the meteoric water cycle. Thus,

the oxygen isotopic composition of freshwater systems varies by a factor of 10 more than that of seawater and it is not directly applicable to paleotemperature determinations. The carbon-13 isotopic composition of fresh-water mollusks was studied and its distribution and that of oxygen-18 in such shells from Dutch estuaries showed no significant deviation from the isotopic equilibrium values expected, which implies that vital effects did not occur. The latter are disequilibrium fractionations shown by oxygen and carbon isotopic analyses of calcite shells or tests from certain organisms such as living benthic foraminifera like *Heterostegina depressa*. All recent species of planktonic foraminifera seem to be in isotopic disequilibrium with respect to the $\delta^{13}\text{C}$ of equilibrium calcite. The disequilibrium fractionation is species-specific and very large in small spinose species in the euphotic zone.

Various mechanisms have been proposed to explain vital effects. One is uptake of metabolic carbon dioxide calcification. A second is physiological changes with ontogeny, that is to say a possible physiological control being exerted on the carbon and oxygen isotope compositions of skeletons of some marine organisms such as echinoderms. A third is kinetic isotope effects in the transport of carbonate ions to the calcification sites. And where symbiotic algae are present, their photosynthetic activities may play a part also. Honestly, the fact of the matter is that such **vital effects** have been recorded, but so far not properly understood. An important fact is that isotope effects involving radiocarbon are greater than those for carbon-13 by a factor of about 2 and this offers a basis for correcting $\delta^{13}\text{C}$ values from organic matter. The total range of this is ca 30‰, hence 60‰ for radiocarbon. Hence, the measured age difference between an isotopically heavy and light wood would be almost 350 years. Resolving this is done conventionally by normalizing all radiocarbon dates to a $\delta^{13}\text{C} = 25\text{‰}$, which is a value close to the average for all terrestrial plants.

Deuterium has been sampled from organic matter for use as a paleoclimatological tool and, since the average ratio of hydrogen to this isotope is 6,419:1, only minuscule isotopic variations can be anticipated. However, because of the relatively enormous mass difference between the two stable isotopes of hydrogen, the isotopic effects are strongly accentuated. But the problem is that plants constitute complicated chemical systems and so isotopic differences between various chemical compounds in any particular plant could have a great influence on the recorded D/H ratio for the plant. To overcome this, cellulose was investigated and showed that two types of hydrogen are found in plants, and also that carbon-bound hydrogen in cellulose is not exchangeable in contrast to hydroxyl- and oxygen-bound hydrogen which are exchangeable. There is an excellent correlation between the D/H ratio in plants and that of the water available to them. Hence, since the δD of freshwater is dependent on climatic parameters, information from plants must relate to this as well. Obviously plants growing and living for centuries are optimal for study. Depletion in D and ^{18}O in growth rings points to lower temperatures, while enrichment in these isotopes shows higher overall temperatures and less fractionated rainwater or groundwater. The approach has been applied to fossil, but not decomposed, wood from the Pleistocene.

16.3.1 Isotopes and Ice Age Impacts

Four ice age episodes were recognized in the Pleistocene Epoch that commenced about 2 million years ago and ended about 10,000 years ago. Each was succeeded by warmer episodes and there were an estimated 22 ice episodes during this time interval. Numerous possible causes for this last ice age and earlier ones have been put forward. One is a decrease in solar energy output. Another is variations in the geometry of the Earth's orbit and precessional cycle,

which could have produced significant changes in the pattern of incident radiation on timescales from 10,000 to 400,000 years, such changes entailing three orbital parameters, namely eccentricity, obliquity (tilt), and the precession index. It has also been proposed that abrupt sliding of huge sections of the Antarctic ice sheet into the ocean might well have initiated climatic changes ending in an ice age. Another model envisaged an ice age starting when, for a short time, the Arctic Ocean is ice-free and open to warm currents from the North Atlantic (a state of affairs that looks likely to recur shortly if present trends continue). Evaporative increases added (or will add) excess water vapor to the overlying air, and this in turn gives greater snowfall on surrounding land areas. Escalating glaciation might trigger an ice age, deglaciation following when temperatures drop enough to permit the Arctic Ocean to refreeze. Later, with the moisture source removed, ice sheets would shrink, sea level would rise with its eustatic elevation inundating continental shelves, and warm North Atlantic Ocean currents could start melting Arctic ice once again. Since an historic sequence of events is involved, this should be recorded in Arctic Ocean sediments so that, in principle, the hypothesis can be tested. Such sediments ought to have fossils of organisms that colonized sunlit waters, but none has been found and also the sediments in question demonstrate that the Arctic Ocean has not been ice-free during the past several million years.

Another suggestion is that an ice age, however caused, could be terminated through postulated greenhouse conditions, which are worsening today because of fossil fuel burning and a correlated rise in carbon dioxide levels in the atmosphere. This gas comprises 0.033% of air and, while reasonably transparent to solar shortwave radiation, is rather opaque to reflected long-wave radiation and returns most of it to Earth as infrared light. This makes the atmosphere act like glass covering a greenhouse, hence the environment heats up through an accompanying entrapment of incoming incident radiant energy. Data from Antarctic ice cores show that over the past 160,000 years, ice ages indeed coincided with reduced carbon dioxide levels and warmer, interglacial periods were characterized by increased production of this gas.

16.3.2 The Geography of the Last Ice Age

In the 1960s, isotope analytical work was applied to a number of paleoclimatic problems and only then did it become possible to attempt to reconstruct conditions on Earth at the culmination of the last ice age. Ten years later, quantification followed and entailed the use of multivariate statistical methods using both biological and geological data. Transfer functions were integral to this approach and their use was based on the assumption that biological changes, for instance in the distribution of species, relate to climatic factors. Basically, they are regressive equations relating modern fauna and floral census information to oceanic characteristics such as the temperature of the sea surface. Further observations on them are included in [Sect. 16.6.1](#) below. They facilitate the estimating of past ocean properties from past census information (Imbrie and Kipp 1971). CLIMAP contributions were valuable because they involved the determination of oxygen isotope stratigraphy for hundreds of ocean cores in each of which the inferred maximum ice volume was estimated and correlated from one core to another. The climate 18,000 years ago was compared with that of today and this took into account relevant factors such as bioturbation, inaccurate stratigraphic correlation, and imprecise absolute dating – these could cause individual sampling points to have ages ranging from 15,000 to 20,000 years B.P. The main objective was to reconstruct the surface of the Earth during the last glacial maximum about 18,000 years ago and the final oceanic reconstruction

was based on 450 worldwide cores. The main conclusions were that during the last glacial maximum, there were several vast land-based ice sheets as much as 3 km thick in the northern hemisphere, while in the southern hemisphere there was much more sea ice than there is today. Global sea level dropped by at least 100 m and the average sea surface temperatures were about 1.7°C cooler in August and 1.4°C in February. The average surface albedo then was higher than now, and the ice age ocean was characterized by a steepening of thermal gradients along frontal systems as well as by an equatorial shift of subtropical convergences in the southern hemisphere and a displacement of the Gulf Stream which flowed east at 40°N. As for the last interglacial, it seems that it resembled current conditions to a great extent. However, there is evidence that the stable isotope record of the planktonic foraminifera from the Fram Strait and central Arctic Ocean could refine the response of that ocean to climatic change. Until 1988, the paleo-oceanography of the Fram Strait–Norwegian/Greenland seas was interpreted mainly from sediment core studies and only four isotope records were available. The longest was V28-56 and this was interpreted as reaching Isotope Stage II (about 420,000 years ago).

The opinion offered was that during the last glacial/interglacial transition about 10,000–18,000 years B.P., the North Atlantic Ocean responded to orbital-induced insolation changes which suggested that when glaciation sets in, the ice pack retreated to higher latitudes and allowed a northerly extension of the warm North Atlantic drift to reach higher latitudes (Broecker et al. 1985). There, heat emitted by this warm current would reach adjacent ice caps and leave residual surface water cold and dense. Actually, it would be dense enough to sink and form Norwegian/Greenland Sea Deep Water (**NGDW**).

Waning of ice caps could have produced a melt-water spike over huge areas of high-latitude seas to throw the climatic system back toward the glacial mode and the isotopic composition of planktonic foraminifera would record such changes. Since orbital positioning caused increased insolation to overwhelm the glacial pulse, the climatic system would have entered the now prevailing interglacial mode. This explains the “pulsed” nature of the isotope records from high-latitude seas, namely glacial toward interglacial then back to glacial and eventually to full interglacial. The explanation of the “pulsed” high-latitude isotopic records suggests that once in the interglacial phase of the climatic cycle the increased production of **NGDW** may induce spillage over the Iceland/Faroe Sill to produce **NADW** for most of the world’s ocean basins. Further light was shed on the subject through a claim that a comparison of stable isotope and textural records of sediment cores from the Fram Strait and central Arctic Ocean with low-latitude oceans showed that the Arctic/Mediterranean responded dynamically to climate change during the Pleistocene (Morris 1988). Core MG-123 from this strait had a minimum of four significantly low $\delta^{18}\text{O}$ intervals with low amounts of coarse sediments also. The association of high $\delta^{18}\text{O}$ values with high amounts of such sediments indicated increased glacial ice in the Fram Strait during the glacial phases of the climate cycle. Peaks within the low $\delta^{18}\text{O}$ intervals increased in size from oldest to youngest, implying a progressive intensification in the oceanographic response to glacial/interglacial transitions in the Fram Strait during the past 524,000 years. Time series spectral analyses suggested this age for the oldest sediment in core MG-123 that would then have had a rate of sedimentation of about 1.66 cm per 1,000 years. Isotope records support the established central Arctic Ocean lithostratigraphy, but coarse sediment deposition in the Arctic is not so clearly related to glacial conditions as it is in the Fram Strait. The oxygen isotope range of central Arctic Ocean records is accentuated relative to the global ice volume signal recorded from lower latitude cores, perhaps because of variations in salinity, temperature, and thickness of the low salinity surface area of the Arctic Ocean. Paleoceanographic responses to climatic changes recorded in the Fram Strait are

paralleled in the central Arctic Ocean, but with decreased resolution due to the great difference in the rates of sedimentation between the two. All this and other work led to a new outlook on the Earth during the ice age. Earlier studies were based on terrestrial data, mostly from midlatitudes, and they showed the growth of ice sheets and accompanying equatorial compression of climate zones. However, data from ocean cores also show a similar compression inwards towards the centers of subtropical oceanic gyres forming thermally and geographically stable parts of the climate system with areas of modest cooling around them, those with maximum effects being located in the higher latitudes.

16.4 The Quaternary Global Carbon Cycle

As regards recent natural events and CO₂ anomalies, increase of about 9 ppm between 1976 and 1982 suggested a mean global rate for the atmosphere of 1.5 ± 0.2 ppm annually. The total production of this gas from fossil fuel use and current manufacturing through this time interval was estimated at about 38×10^{13} g C (=16.8 ppm atmospheric equivalent). Such data facilitate understanding the response of the atmosphere/ocean/biosphere systematic anthropogenic perturbations. Trapped air bubbles in cores showed variations of up to 100 ppm in atmospheric carbon dioxide, which are thought to have taken place in periods as short as a century in the course of the last ice age. The cause might be rapid uptake or removal of enormous amounts of carbon from a reservoir (maybe the oceans) through some mechanism. Natural events such as the El Niño/Southern Oscillation (ENSO) may be involved. There is some evidence for this because, in 1993, it was shown that a slowing of the growth rate of atmospheric carbon dioxide due to anthropogenic emissions by more than in any preceding year in a 35-year record from samples from Mauna Loa correlated, after removing the long-term trend and seasonal signal, with huge changes in the oceanic and atmospheric circulation of just this oscillation. After such events, atmospheric carbon dioxide usually rises, but during them the ocean reduced its content. Aberrant results came from the eruption of Mt. Pinatubo in June 1991 and a “**Pinatubo carbon anomaly**” had reached Mauna Loa by May 1993. If this were applied globally in the northern hemisphere, a loss of 1.6 Pg (1.6×10^{15} g) of carbon would be entailed. An oceanic sink for it would give an oxygen/carbon dioxide ratio of between 2 and 8 and a terrestrial sink ratio of ca 1. La Jolla observations demonstrated a positive **Pinatubo eruption anomaly** approximately twice that of the negative carbon one. Hence, though a terrestrial sink may account for part of the anomaly, the oxygen data suggest that much is due to the oceans. The coincidence of the onset of carbon and oxygen anomalies with the Pinatubo eruption connotes a causal relationship, e.g., iron fertilization of the oceans since removal of over 1.6 Pg of carbon would need ca 10^5 t of iron.

16.4.1 Past Atmospheric Carbon Dioxide in Ice Cores

The history of such CO₂ was obtained from deep ice cores embodying continuous sequences formed up to 100,000 years ago. The preindustrial age concentration is believed to have been in the range 260–270 ppm. Basic information from an ice core derives from $\delta^{18}\text{O}$ measurements from water molecules, periods of high values (positive) recording warmer times and vice versa. At about 10,000 B.P. for Dye 3 1981, there was a marked shift paralleled at Camp Century 1967, both corresponding to the last warming from the Pleistocene into the Holocene. Both cores

recorded an earlier $\delta^{18}\text{O}$ increase around 13,000 B.P. Plotting these values against depth and carbon dioxide and beryllium-10 concentrations showed that the increase to higher values at the first warming transition around 13,000 B.P. occurred within 100 years. In fact, since data from ancient air compositions came from ice layers about a century older than those containing the oxygen-18 information, the two transitions took place during the same time interval within ± 100 years. Interestingly, at 1,890 m depth (corresponding to an estimated age of about 40,000 years), there is a relatively high carbon dioxide concentration coinciding with one of the high $\delta^{18}\text{O}$ periods during the Wisconsin glaciation. Further work on the $\text{CO}_2/\delta^{18}\text{O}$ relationship in the 30,000–40,000-years-old level of the Dye ice core showed that all rapid $\delta^{18}\text{O}$ oscillations are accompanied by simultaneous and well-correlated carbon dioxide oscillations. It was concluded that changes in both of these parameters took place at about the same time (phase shift $< \pm 100$ years). Therefore, the observed carbon dioxide concentrational changes in air occluded in ice may represent atmospheric carbon dioxide changes.

16.4.2 Carbon Cycle Changes

The average carbon-13/carbon-12 ratio on Earth is $\sim 1.12 \times 10^{-2}$, although it varies because the physicochemical properties of the molecules are mass-dependent, e.g., the carbon dioxide exchange between the atmosphere and the oceans causes a 9‰ lower $^{13}\text{C}/^{12}\text{C}$ ratio of atmospheric CO_2 relative to ocean bicarbonate. $^{13}\text{C}/^{12}\text{C}$ ratios are expressed as $\delta^{13}\text{C}$, this being the relative deviation from PDB standard in per mill.

Radiocarbon is present in atmospheric carbon dioxide with a $^{14}\text{C}/^{12}\text{C}$ ratio of about 10^{-12} and it is produced continuously in the stratosphere through interactions between thermal neutrons and nitrogen. For further details, see [Chap. 6](#). Precise radiocarbon determinations need large samples and long counting times. For instance, a typical tree ring counting precision of 1.5‰ was obtained at a Quaternary Isotope Laboratory for 6 g carbon samples counted for 4 days. The optimal material is dendrochronologically dated tree samples, the cellulose annually formed in each ring ceasing to exchange carbon thereafter. However, even when the removal is not 100% total, resultant errors in natural $\Delta^{14}\text{C}$ values are reducible to a few tenths per mill. The radiocarbon age is obtained from the ratio of residual sample activity to oxalic acid standard activity.

In 1989, Suess noted that measured carbon-14 values deviate consistently from those calculated from tree rings and the “wiggles” involved showed the existence of a geophysical parameter valid for the entire terrestrial atmosphere (Suess 1989). Fourier spectra showed the consistency of the results and supported the contention that secular variations of radiocarbon in atmospheric carbon dioxide are related to variations in solar activity. Using varve deposits, it is possible to extend the study of radiocarbon variations beyond dendrochronological limits. Some temperature regional lakes contain rhythmites, sedimentary successions of interbedded laminae, and such sediments in the Lake of the Clouds, Minnesota, have over 10,000 couplets. The problem is that varve chronologies assume that no duplication of annual couplets occurred, no parts are missing, and also that constant radiocarbon reservoir deficiency occurred. Obviously it would be valuable if agreement with radiocarbon tree ring data over the last 8,600 years or so up to as much as 9,200 years could be reached. But this has only been achieved at the Lake of the Clouds. Much less is known about atmospheric $\Delta^{14}\text{C}$ before 13,000 B.P., but a good agreement between carbon-14 and ionium dates in Searles Lake sediments showed that departures from the oxalic acid baseline are restricted to about 10%

between 23,000 and 32,000 years ago. Also, a comparison between carbon-14 and ionium dates of a stalagmite showed a 50% increase in $\Delta^{14}\text{C}$ about 18,000 B.P. and a roughly normal level near 29,000 B.P. These data imply carbon-14 levels one and a half to twice the present ones for the time interval between 35,000 and 40,000 years B.P.

During glacial episodes mutually antagonistic and different processes affected the atmospheric levels of radiocarbon and carbon dioxide and these include reduction in radiocarbon atmosphere–ocean exchange caused by a lowered sea-level and increased ice cover, less downward advection due to a reduced rate of bottom water formation in the Atlantic and a concomitant reduction in the global rate of upwellings bringing less carbon-14-deficient water to the surface plus changes in the biological productivity of high-latitude surface waters. The first two of these considerations indicate a higher atmospheric carbon-14 level, but downward eddy diffusion transport of the radioisotope over the oceanic thermocline increases during glacial episodes because oceanic thermal gradients are less. Changes in atmospheric carbon dioxide content and $\Delta^{14}\text{C}$ are interrelated. A 100 ppm decrease in the former during the previous glacial would have caused a 2.5% increase in atmospheric $\Delta^{14}\text{C}$ if all other global reservoirs stayed constant. And this would suggest an estimated 7% reduction of $\delta^{14}\text{C}$ in deep oceans because of a 7% increase in inactive oceanic carbon-12 during glacial times. Such a change in carbon content would take place if the concept of phosphorus extraction on continental shelves is correct.

The missing carbon concept arose because radiocarbon-calibrated carbon cycle models predict that the quantity of carbon remaining in the atmosphere after fossil fuel release should exceed that suggested by the direct observation of rising concentrations of carbon dioxide. Three solutions have been proposed. One is that current ocean models cannot be adequately calibrated using radiocarbon. A second is that the biosphere currently acts as a sink for carbon. The third is that the biosphere has been a net source of carbon in the past.

16.5 O–H–C Isotopes in Trees and Seas

The early work of Emiliani (1955) reflected his belief that the isotopic record related to variations in sea surface temperatures, but it was later suggested that ice volume changes were more influential and the isotopic record actually records mainly the changes in continental volumes of ice (Shackleton 1967). Later work provided support from equatorial Pacific Ocean Core V28-238 (stated to have an accumulation rate of about 1.5 cm per 1,000 years). An original 16 isotopic stages were extended to 22 and similar isotopic fluctuations both for planktonic and benthic foraminifera were noted. If temperature had been the main factor controlling the isotopic values, the isotope record of the benthic forms should have showed low variability since bottom water temperatures are relatively stable. In fact, however, they showed great variability that might imply a significant contribution from changes in the water chemistry. Later, core work was extended back to the Plio-Pleistocene Boundary to provide a complete record of Quaternary climatic changes. Also, the Brunhes/Matuyama Boundary and the Jaramillo and Olduvai events were recognized. From these data, an average rate of accumulation of 1 cm per 1,000 years was inferred. However, the Brunhes Chron showed steadier accumulation rates, these being sufficiently reliable for it to be taken as the Later Pleistocene stratotype.

The above-mentioned researches demonstrate that Urey's confident assertions have been realized, albeit in a slightly different form as regards glacial episodes in the history of the Earth. Oxygen isotope ratios can be interpreted in terms of the changing chemistry of both oceans and atmosphere in accordance with the growth and decline of the polar and subpolar ice sheets.

Actually, they provide the standard stratigraphic framework into which Pleistocene climatic events can be placed. In this respect, radiometric dating has been invaluable in establishing an absolute stratigraphy for the past 800,000 years. A model was developed in which the isotope is envisaged as a response of a single exponential system induced by variations in obliquity and precession of the orbit of the Earth (Imbrie et al. 1984).

Stable isotope investigations were made on plants and tree-rings. Variations in the widths of annual growth rings in many temperate and subpolar tree species are valuable proxy indicators of past climatic fluctuations and led to the science of dendrology. Progress has led to the creation of a parallel research field, that of dendroclimatology.

Apropos tree-ring isotope chemistry, the important isotopes are oxygen-16, 17, and 18; hydrogen-1 and 2 (deuterium); and carbon-12, 13, and 14 (radiocarbon). Again it was Urey who first suggested in 1947 that the carbon-13 content of plant material might be related to temperature and subsequently, it was shown that the $^{13}\text{C}/^{12}\text{C}$ ratio of atmospheric carbon dioxide is a function of temperature-dependent exchange reactions with the oceans (Craig 1954). It is interesting that oak $\delta^{13}\text{C}$ values were proposed as potential paleo-rain gauges and paleo-thermometers (Tans, Unpublished Dissertation).

16.6 Orbital Frequency Rhythms in the ^{18}O Records

The oceanic core isotope record can be fitted to a timescale of planetary orbital changes so as to construct an accurate chronology of first-order climatic variations over the past hundred million years that confirmed the significance of orbital-frequency rhythms in this record and made small, but crucial, adjustments in the timescale of the last 400,000 years (Hayes et al. 1976). The consequent power spectrum of the $\delta^{18}\text{O}$ signal indicated a dominance of 100,000-year power with lesser 41,000- and 23,000-year responses. Also, it has been observed that the $\delta^{18}\text{O}$ signal from the high-latitude planktonic species *Globigerina bulloides* resembles other signals of this type known to be subject to the effects of ice volume. Probably this species changed its season and/or depth of occurrence chronologically so as to observe a narrow temperature regime despite localized climatic changes (► Fig. 16.3).

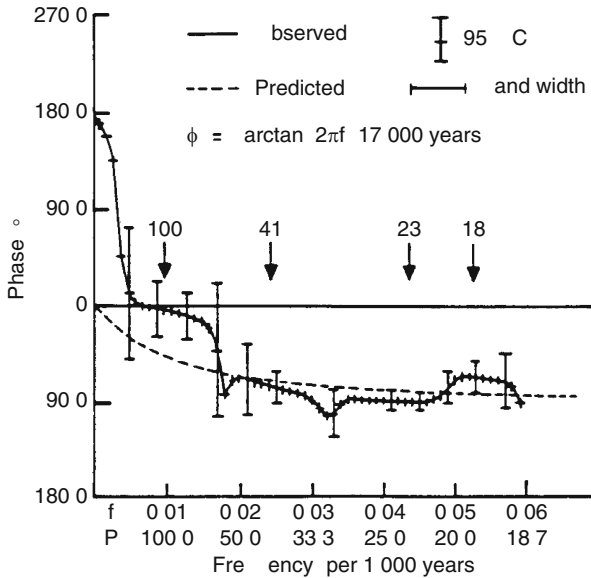
16.6.1 Modeling Pleistocene Climatic Response

This takes into account the hypotheses of Milankovitch and J. Croll requiring that the Earth's climate must respond to orbital forcing (Imbrie 1985). Suitable models include spectral and cross-spectral, gain-and-phase, and dynamic, but cannot be discussed here. However, the first involved four of the main Milankovitch frequencies, i.e., at 100,000, 41,000, 23,000, and 19,000 years, the second including two attempts. One aimed at simulating the entire 782,000-year record, again using the Milankovitch four, which are 100,000 = eccentricity, 41,000 = obliquity, 23,000 and 19,000 = precessional factors (► Fig. 16.4).

A second treated younger and older data separately with the boundary between the two placed at 400,000 years B.P. Dynamic models are useful in showing how strong or weak a response is elicited by any given forcing function. Variations in climate in other frequency bands have also been considered. Over the decadal band, there is evidence to show that Alpine glaciers altered greatly in size through periodic volcanic explosions and solar activity and lunisolar tides affected regional patterns of precipitation and temperature. On the millennial

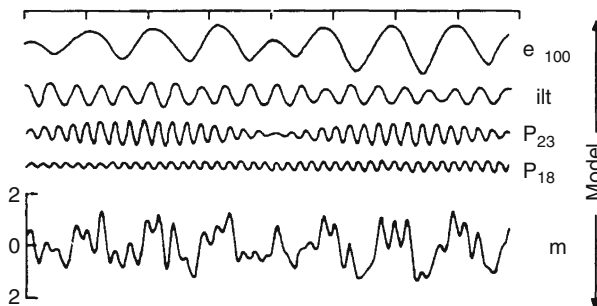
■ Fig. 16.3

Theoretical and observed phase spectra relating $\delta^{18}\text{O}$ and orbital variation over the past 782,000 years. The *dashed line* represents the predicted phase response of a single-exponential system with a time constant of 17,000 years (From Imbrie et al. 1984)



■ Fig. 16.4

This is a model of $\delta^{18}\text{O}$ variation over the past 782,000 years. The model curve is the sum of four components, each being an orbital curve multiplied by an appropriate gain and shifted by an appropriate phase. The difference from others is due to the incorporation of these frequency components, namely the 100,000 year one of eccentricity, the obliquity signal (variance concentrated near to 41,000 years) and the 23,000 and 19,000 year components of precession. The result is the model that has a correlation of 0.71 with the data and a pattern of residuals in time (not included) suggesting a change in the response characteristics of the system about 400,000 years ago. A spectrum of these residuals indicates model failures near 59,000 years and at periods rather longer than 100,000 years (From Imbrie et al. 1985)



band, mountain glaciers probably expanded and contracted during the Holocene and the periphery of the Laurentide ice sheet must have fluctuated during the late Pleistocene. Indeed, orbital variations may well have initiated Pleistocene ice episodes. They were pre-Pleistocene glacial episodes also, for instance in the Middle Oligocene about 30 million years ago when small glaciers were widespread in Antarctica and at the end of the Eocene about 38 million years ago. These events constitute the Late Cenozoic Glacial Age commencing about 10 million years ago and culminating in the Pliocene. A similar extensive event, the Permo-Carboniferous Glaciation, occurred about 300 million years ago and there were even earlier ones, for instance during the Late Devonian to Late Permian and glacial deposits have been found in Africa near the Ordovician/Silurian Boundary. This probably indicates a glaciation and it is interesting that glaciations appear to have been more the norm than the exception in the Paleozoic and may even have synchronized with relatively “warm” oceans. Over 700 million years ago, early in the Precambrian, glaciations lasting from 10 to 20 million years took place in the Early and Late Proterozoic and could have coexisted with “hot” ($>60^{\circ}\text{C}$) oceans. Modeling arrays, transformations, multivariate procedures, and climate forcing are all entailed regarding the reconstruction of past climates as a multivariate function of time and space, relating them to frequency domains (Imbrie 1985). Some remarks on using multivariate statistical methods on biological and geological information as well as transfer functions were made above in ▶ Sect. 16.3.2. Transforming and condensing numerous observations into estimates of small sets of climatic indices are not just paleoclimatologically exclusive but also applicable to modern climatology, oceanography, and meteorology. This has been done in an attempt to understand the climatic anomalies known as ENSO (see ▶ Sect. 16.4 above). The relevant transformations comprised conversions of sets of observations about climate at a particular time and in a particular place into a smaller number of informational indices such as assessments of salinity or air-mass frequency.

16.6.2 Simulating the Ice Age

Several models have been presented. All have to recognize the complicated interrelationships and interactions of the many terrestrial components such as the atmosphere, the cryosphere, the oceans, and land. Simpler ones can be used to compute the spatial distribution at equilibrium of any one key climatic parameter, e.g., temperature as a function of latitude. Such models facilitate understanding changes in gross climatic conditions occurring when the near equilibrium between energy gain and loss of the relevant climatic system is changed to another equilibrium state. More elegant models reflect the development of general circulation models (GCMs) that can be used not merely to simulate ice age conditions, but also to predict future developments of terrestrial climates, e.g., how continued rise in the carbon dioxide levels in the atmosphere are likely to change it. Of course, all models are simplifications of the real world because the complex processes of the existing climatic system are far from being fully understood. The results of using GCMs to simulate February and August paleoclimates for 18,000 years B.P. on the basis of CLIMAP data utilized at the National Center of Atmospheric Research, the Geophysical Fluid Dynamics Laboratory, and Oregon State University have been described (Heath 1979). Later, final CLIMAP data were used in conjunction with a new simulation. Ice age conditions used were a sea-level drop of 150 m and a drop in the carbon dioxide content of the atmosphere from 320 to 220 ppm. The carbon dioxide decline was based on observations of levels for this gas assessed from ice cores (Neftel et al. 1982).

The ice simulation showed both in February and August a zonally averaged cooling of the surface air temperatures at all latitudes with a maximum effect at about 10°N. Averaged cooling was approximately 3.4°C globally and, in tropical regions, the average temperature change was about 2°C. Rates of precipitation during the ice age altered at most latitudes from 3% in February to 9% in August and there was a narrowing of the subtropical dry zone near 14°N accompanied by a southward displacement of the zonally averaged midlatitude precipitation maximum from 34°N to 26°N. All this revealed the ice age as cooler and dryer over much of the Earth. Earlier in the history of the Earth, plate tectonics provide a unified model that can explain such variations over the past several hundreds of millions of years at least. It is clear that plate tectonic movements produced alterations in the distribution of land and seas together with changes in the relative percentages of each. These profoundly affected past climates. A zonally averaged energy-balanced model (EBM) was used to examine possible mechanisms determining the warm equable climate of the Middle Cretaceous 100 million years ago (Thompson and Schneider 1981; Barron et al. 1979). The implication is that such geographical changes were highly significant. However, it must be remembered that **EBMs** are usually one-dimensional and employ only simplified relationships. But, *faute de mieux*, they are widely used (Crowley and North 1985). The atmosphere/ocean/cryosphere system now has been discussed, particularly as regards its significance in controlling simulations of the climate under altered external forcing systems. An optimal approach entails formulation of a Newtonian mechanics problem for geophysical fluids and integration of the system of differential equations forward in time to be followed by assembling of statistics. The technique is feasible because of the availability of the digital computer and the installation of a global network of observational stations originated by the **IAEA** and World Meteorological Organization (**WMO**) termed the **Global Network for Isotopes in Precipitation** (GNIP) that can initialize the problem and verify the numerical solutions. Over 30 years' experience with **GCMs** of the global atmosphere showed their value in weather prediction and such huge numerical models could be valuable in generating climatic experiments. The output ought to include a complete description of the present model climate, but the problem is more complex because the equations are nonlinear and their interrelationships are so very complicated that they become mathematically unstable. Hence, small errors amplify with integration to cause a degradational effect in effective determinations that may explain why meteorologists cannot provide good weather forecasts 2 weeks ahead. Obviously, there is still a very long way to go in modeling Pleistocene and earlier climatic changes with large scale models.

16.6.3 Pleistocene/Holocene Climatic Changes

The last ice age caused reductions in the diversity of terrestrial vertebrate faunas in most continents and many islands at the end of the Pleistocene and the start of the Holocene. Such extinctions were not random because species of large body size were more severely affected than those with body masses under 25–50 kg. Human predation played a part as well. However, if environmental fluctuations are offered in order to explain Late Pleistocene extinctions, why did similar ones not occur during previous glacial/interglacial cycles of which there have been a minimum of 22 during the past 870,000 years? The unsolved question is whether the Pleistocene/Holocene change was triggered by some factor or factors which were fundamentally different from other environmental fluctuations and if so what were they.

Similar extinctions took place on a much larger scale at the end of the Cretaceous about 66.5 million years ago when dinosaurs, ammonites, and many other plant and animal groups declined and often disappeared. This is evidenced by the accumulation of deposits containing anomalous iridium accumulations of up to 160 times the background level. A similar iridium anomaly was recorded in the Lower to Middle Jurassic of the Venetian area of northern Italy. These earlier extinction episodes cannot be related to human hunters, but rather to astronomical and other forcing factors. Ice ages must have been important also and they too were influenced by these same factors.

Some ambiguity has arisen. Recent US Geological Survey work at Devil's Hole, Nevada, at a site where water flowing in from a large catchment area, deposited a calcite vein over the last 250,000 years. Calculation of ages was effected layer by layer by measuring $^{230}\text{Th}/^{234}\text{U}$ or $^{234}\text{U}/^{238}\text{U}$ ratios, and the oxygen isotope record was also examined. Results from both approaches did not accord with those from deep-sea cores and air bubbles trapped in ice sheets, although a similar pattern was apparent. It was inferred that the previous interglacial episode may have started as long ago as 163,000 years B.P., although conventional techniques put it at its warmest about 122,000 years ago. This agrees with changes in the angle of obliquity of the Earth and its precession implying that, in the northern hemisphere, summers were especially warm about 125,000 years B.P. Despite this seeming disparity between the Milankovitch model and these data, the latter do not undermine the former. In fact, the model is claimed as inadequate to account for the timing of several major paleoclimatic events that occurred during the time interval from 100,000 to 300,000 years ago. Additionally, there are $\delta^{18}\text{O}$ records from deep-sea sediments (Core CH73-1390 from the Rockall Plateau, northeast Atlantic Ocean) showing relatively slow glacial buildup, the end of the ice age occurring rapidly in about 10,000 years.

16.7 Quantifying Isotopic Chronostratigraphy

The method has been used in the Gulf of Mexico and improved stratigraphic resolution across a basin in an effort to improve hydrocarbon prediction (Williams and Trainor 1986). It was extended globally and each isotope record was regarded as a time series, common analyses being used to develop criteria about the identification of common events in records and how accurately these can be recognized and interpreted (McKenna et al. 1988). The limiting factors include insufficient knowledge on the paleo-evolutionary behavior of foraminifera, inadequate data on oceans, not enough information on isotope processes with time, nonlinearity in the atmosphere/ocean climate system and diagenetic effects. These combine to cause a “noise” effect in every record, that is to say they introduce a factor with no discernible relationship to any geological process of interest. Sampling is another problem because this may be carried out at a set of discrete times over a finite geological interval and may be fine in depth at some point in time and coarser at another. Established methods based on information theory were used for the signal processing strategy. Initial quantitative analysis of Plio-Pleistocene $\delta^{18}\text{O}$ records necessitated using interpolative filters, semblance and coherence analyses, autocorrelation and cross-correlation, and non-minimization filters. Two sections were involved. One was a formulation of a $\delta^{18}\text{O}$ -type record for the Plio-Pleistocene and the second compared this with other $\delta^{18}\text{O}$ records for the same time range. In the first, a high-quality $\delta^{18}\text{O}$ record from **DSDP** piston-core V-28-239 was transformed into the TYPE record that had a lower noise level than the original. In the second, the TYPE record was compared with $\delta^{18}\text{O}$ records from **DSDP** sites 502B, 504, and 522A. Because much of the isotope signal represents global isotopic

changes in ocean chemistry induced by the volume of Pleistocene ice sheets in the northern hemisphere, a common global signal in the Plio-Pleistocene $\delta^{18}\text{O}$ must exist. If such a global signal is subtracted from an individual record, what remains must reflect other constituents in the $\delta^{18}\text{O}$ signal, e.g., temperature, melt-water impulses, the disturbance of sediments, etc. A common signal is recorded in the behavior of similar record types at different locations as the latter merge so that the record types reflect a degree of coherence. Coherent events are spread through some time range.

Here the concept of semblance can be introduced. This is derived from geophysics and functions to provide a more meaningful measure of coherent signals. Semblance can detect small timescale correlations (high semblance) over a few datum points in each record when a small window is used and long-term correlatable trends when a large window is used. On the other hand, uncorrelated or anti-correlated events appear as low semblance areas and the range and/or strength of a correlated or uncorrelated event is determinable by high- or low-semblance contours closing as the window width increases around a given time.

A **TYPE** record can be made for the Pleistocene $\delta^{18}\text{O}$ signal with time and can be used as a template against which other Plio-Pleistocene isotope records can be compared. To select a **TYPE** record entails meeting certain requirements. One is a relatively fine, continuously sampled record with depth and a second is a rate of sediment accumulation that preserves isotopic shifts at specific times in preference to small thicknesses of sediment covering large time spans. Thirdly, a relative abundance of biostratigraphic and paleomagnetic time horizons should be included. Lastly, the core sample should have simple structure and stratigraphy. Piston core V28-239 from an open ocean area fulfills all these desiderata relative to most other Pleistocene records and so it was selected as the initial **TYPE** section. The $\delta^{18}\text{O}$ record from another sample, core 522A, came from benthic foraminifera, data from other sites from planktonic ones. No attempt was made to normalize the benthic information to the planktonic data due to $\delta^{18}\text{O}$ -temperature fractionation. The $\delta^{18}\text{O}$ depth record of V-28-239 was converted to time using suitable time horizons and assuming constant rates of sedimentation between the “known” time horizons. The so-constructed time record was sampled at 5,000-year intervals to produce a $\delta^{18}\text{O}$ time series with a time range of 5,000–1,870,000 years. This $\delta^{18}\text{O}$ record contains the basic input data for ensuing analyses. It showed a marked break at about 930,000 years, the younger part comprising broad peaks and troughs and the older part narrower ones. The top of the record (5,000–935,000 years) was designated V28-239T and the bottom part (940,000–1,870,000 years) was designated V28-239B. Application of a Wiener filter revealed increased high-frequency structures and the Fourier transformation of the two pre- and post-Wiener filter sets from the time to the frequency domain enabled determination of the power at discrete frequencies in the records from power spectra to be made. There are 94 harmonics in them with harmonic spacing equal to $1/T$, where T is the total length of the record (930,000 years). The zeroth was suppressed so as to obtain scaling clarity and some dominant peaks were labeled in thousands of years. There was a roughly constant low power above harmonic 44, this being the “noise” power extracted by the Wiener filter. Noise is defined as all frequency components above harmonic 44 (period of 21,000 years). This destroys a component of the precession signal interpreted by some, but provides objective data analysis. Removing “noise” from raw data showed that most of the basic characteristics in the input record were preserved and exactly the same procedure was applied to the older part of the Plio-Pleistocene record. In this way, it was possible to create a noise-free $\delta^{18}\text{O}$ record with time from 5,000 to 1,870,000 years together with a reconstructed record designated **TYPE** used for the rest of the analyses.

A common periodic signal of $95,000 \pm 30,000$ years in **TYPE**, 502B, 552A, and 504 was identified, this being close to that derived from the orbital eccentricity parameter by Milankovitch in 1930 and also by others (Berger 1976; Kominz et al. 1979). In addition, this periodicity was reflected in power spectra, cross-spectra versus **TYPE** and spectral coherency versus **TYPE** within resolution limits. Other global periodicities of about 1,355,000, 41,000 \pm 2,000, and 24,000 \pm 3,000 years were noted in the average (global) spectral coherency. The relevant work introduced a new dimension into both correlative and interpretive researches into isotope records.

16.8 Time's Arrow Reversed: Pliocene Paleoclimates

The Pliocene embraced a thermal optimum, which, through a new technique termed climostratigraphy that includes micropaleontological, isotopic, “radiological,” and paleomagnetic data, facilitated subdividing the Epoch, identifying datum planes and global paleoclimatic events (climathems). An accuracy of 50,000–100,000 years has been claimed and such events grouped into superclimathems (SCTs) and hyperclimathems (HCTs), the first containing 100,000–300,000-year episodes and the second longer time intervals of which 30 were diagnosed between 7.3 and 1.2 million years ago. Through this latter (which extends into the Late Miocene), both types were observed, for instance the Messinian salinity crisis correlated with the seventh hyperclimathem and a warm, dry time interval in the Mediterranean and seven climathems in the Black Sea. SCTs were numbered from the present to the past, the first spanning Stages 1–7 of the deep-sea cores scale, the second Stages 8–10, the third Stages 16–20, and the fifth Stages 21–25. The sixth is the Late Cenozoic climate boundary connected with the first continental ice sheet glaciation in Europe, the maximum glaciation in North America and in Patagonia (Zubakov and Borsenkova 1988). It really marked the onset of the Pleistocene. SCTs and HCTs probably relate to variations in orbital parameters, mostly in the eccentricity. The so-called Climatic Optimum of the Pliocene occurred between 4.4 and 3.3 million years ago, and during it the atmosphere may have contained about twice as much carbon dioxide as now. This may be an analog of anticipated climatic conditions in the middle of the twenty-first century if the supposed and probably actual greenhouse conditions continue that long.

A curve has been postulated describing variations in the strontium isotope composition of seawater in the Late Neogene 9–2 million years ago, these based on $^{87}\text{Sr}/^{86}\text{Sr}$ analyses of marine carbonate at the five DSDP sites 502, 519, 588, 590, and 593 (Hodell et al. 1989). The strontium isotope contents of the oceans rose during the time interval, but from 9 to 5.5 million years ago these ratios were practically constant at about 0.708925. Between 5.5 and 4.5 million years ago, they increased monotonically at a rate of about 1×10^{-4} per million years. The steep slope then could serve to facilitate high-resolution strontium isotope stratigraphy across the Miocene/Pliocene Boundary. The rate of change in the isotope ratios decreased almost to zero again during the time interval 4.5 to 2.5 million years ago and ratios averaged 0.709025. The relatively rapid increase between 5.5 and 4.5 million years ago could be connected with changes in flux of average $^{87}\text{Sr}/^{86}\text{Sr}$ ratios of the major inputs of strontium to the oceans. Quantitative modeling of these inputs implies that the increase may have been caused by an increase in the dissolved riverine flux of strontium into the oceans or an increase in the average $^{87}\text{Sr}/^{86}\text{Sr}$ composition of the river water or maybe by a combination of both of these factors. On the other hand, the 5.5–4.5-million-years age period can be modeled as a simple transition from one steady state to another if the oceanic residence time of strontium was eight times less than

the currently accepted value of 4 million years. During the time interval when the strontium isotope ratios steeply increased, sediment accumulation rates may have risen too and there might have been a drop in the calcite compensation depth (CCD) together with a decrease in the $\delta^{13}\text{C}$ of dissolved bicarbonate. Hodell and his coworkers thought that the simplest mechanism to explain all this would have been an increase in chemical fluxes carried by rivers to the oceans, reflecting increased chemical denudation of continents and shelves in the Late Neogene. Increased chemical weathering rates could be due to increased exposure of continents and shelves as a result of eustatic regression accompanied by intensified glacial/interglacial cycles and accelerated rates of global tectonism during the latest Miocene. Today the intra-continental shields of North America, Eurasia, and Antarctica mostly comprise Precambrian basement with high $^{87}\text{Sr}/^{86}\text{Sr}$ ratios. For the latest Miocene, evidence exists implying a cooling episode and pulsed ice sheet expansion with oxygen isotope records suggesting a magnitude for glacial/interglacial episodes of about one third of the ice volume changes of the late Pleistocene.

16.8.1 Middle Tertiary Paleoceanographic Changes

The analyses of Oligocene and Miocene planktonic and benthonic foraminifera and calcareous nannofossils (unicellular algae) from DSDP Site 354 in the equatorial Atlantic led to the taking of the isotopic composition of *Cibicidoides pseudoungerianus* as representative of bottom water changes, the $\delta^{18}\text{O}$ deviating in isotopic composition about 0.4‰ from that of *Uvigerina* (Biolzi 1983). In the older part of the section analyzed, the isotopic composition remained constant at about +1.6‰, but toward the top of the Oligocene two minor fluctuations in $\delta^{18}\text{O}$ values occurred and were followed by a positive shift reaching a maximum of +2‰. Until the end of the Early Miocene, the oxygen-18 values for *Cibicidoides* ranged between +1.6‰ and +1.7‰. Then came a hiatus, but succeeding that was an increase of 0.5‰ to reach +2‰. The genus was benthic and so to estimate pelagic water conditions, planktonic foraminifera were used. These showed a general trend toward higher $\delta^{18}\text{O}$ values and *Globigerina venezuelana* was selected as a reference for these conditions from the Oligocene into the Miocene. Its oxygen isotope composition increased from about -1.5‰ in the Middle Oligocene to about +0.5‰ in the Middle Miocene. If this represents temperature changes, then there must have been a marked cooling in the Middle Oligocene about 30 million years ago. There is supportive evidence of small glaciers at that time. The associated ice age culminated in the Pliocene after the Middle Miocene accumulation of the Antarctic ice sheet. Further confirmation of this pre-Pleistocene ice age came from the deuterium contents of interstitial waters of cores as part of the **Joint Oceanographic Institutions Deep Earth Sampling (JOIDES)** work. It was estimated that allowing for diffusion effects, there was an increase of 10‰ in δD (corresponding to a $\delta^{18}\text{O}$ change of about 1.2‰) between the Early and Late Miocene. A similar analysis of Pleistocene to Holocene changes showed a δD increase of 8‰ during the time of maximum continental ice (corresponding to a $\delta^{18}\text{O}$ increase of about 1‰). It was thought that there was no change in the parameter from the Cretaceous to the Tertiary.

16.8.2 The Eocene Ocean

In the Early Tertiary, the Earth experienced rather warm conditions as shown by benthic foraminifera from deep-sea sediments. With planktonic ones, there is the problem that it is very difficult to be sure whether the species in question actually lived at the sea surface and so

would have recorded the relevant temperature. Analyses of foraminiferal species from the Paleocene were affected and results from the ones consistently registering higher temperatures, i.e., with the isotopically lightest oxygen isotope composition, used. This was justified by reference to the carbon isotope composition (Shackleton and Boersma 1981).

The important vertical carbon isotope gradient in the upper part of the ocean water column results from the photosynthetic removal of isotopically light carbon from the dissolved inorganic carbon in the photic zone. The return of this carbon to the oceanic carbon reservoir occurs in deep water. The difference between the carbon-13 content of surface and deep water is about 2‰ and parallels that between *Globigerinoides sacculifera* and species of *Uvigerina*. However, a much greater difference was observed (sometimes as much as 4‰) between planktonic and benthonic species in the Late Paleocene and through much of the Eocene from carbon and oxygen isotope variations in at **DSDP** Site 384. While not all samples were synchronous, they were plotted on a global reconstruction representing 50 million years ago at those localities where it was thought they occurred. Paleolatitudes were similarly estimated. Temperatures were calculated on the basis of an oceanic isotopic composition of -1.2‰ versus PDB (which refers to the time interval prior to the Middle Miocene accumulation of the Antarctic ice sheet). Some interesting conclusions were drawn. The overall range of surface water temperatures turned out to be lower than is the case now. This compares favorably with previous deep sediment work, but not with the anomalously high apparent temperature derived from the isotopic analyses of mollusks in the North Sea Basin (Burchardt 1978). This may have been the result of localized and salinity-related isotopic anomalies or represent diagenetic changes. In the North Atlantic and, to a lesser extent, the South Atlantic also, there appeared to have been strong Western Boundary currents and the east–west temperature gradient across the latter has been reported consistently. However, in the North Atlantic, there has been found an anomalous temperature estimate in its north-eastern part (Vergnaud-Grazzini et al. 1978). If the surface- and deep-water temperatures estimated for each sample are plotted as a function of paleolatitude and compared with the average temperature distribution in existing oceans as a function of latitude, it is clear that more measurements are necessary before an accurate estimate of the global average surface temperature can be made. However, if the available data are considered, they are adequate for averaging over 10° bands of paleolatitudes and an average temperature of 18°C weighted according to area has been proposed. This compares with about 16°C in the oceans today. Therefore, on the scale of global average, the difference between then and now is about 2°C despite the tremendous changes that occurred in some regions, e.g., tropical vegetation grew in the Early Eocene where London is now. By the end of the epoch, sea ice probably formed around Antarctica. In this regard, it is interesting that the difference between the last glacial and now was also of the order of 2°C when averaged. To a first approximation, the latitudinal temperature gradient in the last glacial was similar to the present one, so heat transport mechanisms must have operated in the same way as now. But the latitudinal temperature gradient of the Eocene Ocean was less than half of its present value, thus the transportation of solar energy from high to low attitudes must have proceeded differently. Maybe much of this was through the oceans because of the inability of the atmosphere to transport heat through the reduced temperature gradient. But the way in which heat could have been transported effectively when temperature gradients were as low as they were during the Eocene remains unclear.

A major climatic event occurred near the end of the Eocene, namely the development of the psychrosphere, the deep and very cold waters of the world ocean. This was first detected at the Eocene/Oligocene Boundary as a major reorganization of deep water ostracodan faunas. Also,

oxygen isotope measurements demonstrated a dramatic drop of almost 5°C during the Late Eocene (foraminiferal Zones P15 to P16) in the Atlantic. A similar phenomenon was recorded in the equatorial Pacific. Also, there was a parallel decrease in bottom water temperatures found in samples from the earliest Oligocene of the Campbell Plateau south of New Zealand. All may signal the start of Antarctic bottom water formation at near-freezing temperatures. Stratigraphic problems arising from the time-regressive nature of stratigraphic zones between temperate and tropical regions have been invoked to explain the appearance of cold water in the south-western Pacific, but there is a possibility that the time lag is real.

16.8.3 Oxygen and Carbon Isotopic Variations in Foraminifera Across the Cretaceous/Tertiary (K/T) Boundary

Species of *Rugoglobigerina* or *Pseudoguembelina* were used for the Maastrichtian and species of *Guembelitra*, *Acarinina*, and *Morozovella* for the Paleocene as having lived nearest to the ocean surface (Boersma 1970). Then the situation was unusual because of the apparent dominance of heterohelids in the surface zone. Several species showed anomalously negative carbon isotope values. However, during the Paleocene, the heterohelids adopted deep-dwelling habits and other surface-dwelling species gave more positive carbon isotope values. As regards surface water carbon isotope values, problems exist apropos interpreting them in the *Globigerina eugubina* Zone and early Zone P1 since the planktonic foraminiferal species, which registered the warmest temperatures consistently gave more negative carbon values than cooler living species. It appears that through most of the Tertiary and in recent times also many of the warmest living species record more positive carbon isotope values while deeper (i.e., cooler water) dwellers have more negative (i.e., isotopically lighter) carbon isotope ratios. The carbon isotope difference recorded between recent *Globigerinoides sacculifera* and the average recent benthic foraminifera is roughly equal to the recorded gradient in the water column. There is as yet no satisfactory explanation for these anomalous carbon isotope profiles in the Early Paleocene. Boersma selected the highest carbon values in samples from this time interval, although the surface carbon isotope values are sufficiently alike to be treated together. Those from the latest Campanian Age through the Early and Middle Maastrichtian Age cluster around +2‰, the values rising through the Late Maastrichtian to reach +2.3–2.6‰ in the *Abathomphalus mayaroensis* Zone just below the Cretaceous/Tertiary Boundary. Across this boundary, there was a significant excursion everywhere, carbon isotope ratios becoming more negative by 1–1.5‰ in the earliest *Globigerina eugubina* Zone. Measurement of bulk carbonates gave values at Sites 384 and 152 that showed similar drops across the boundary. In sum, it can be inferred that a temperature drop of 5–6°C took place from the Late Cretaceous to the Early Tertiary.

16.8.4 Isotopes and Mass Extinctions

As well as around the K/T Boundary, there were earlier ones, for instance at the Permian/Triassic (P/T) Boundary about 248 million years ago. When the former took place, there may have been an alteration in sea-floor spreading rates and a drop in the carbonate compensation depth (CCD) in the Atlantic, succeeded by a rise. Another such drop occurred in the Early Tertiary and may have been the result of a supernova. Four episodes were recognized in the

evolution of the stable isotope and carbonate records across the K/T Boundary and in the Early Paleocene at **DSDP** Site 577 (Zachos et al. 1989).

Event I at 66.5 million years ago preceded the boundary and showed an enrichment in planktonic and benthonic microfossil carbon records together with a decrease in the barium accumulation rate. The $\delta^{13}\text{C}$ rise may reflect a change in that of the oceanic total dissolved carbonate reservoir caused by increased organic carbon burial on continental margins (or decreased carbon fluxes from weathering) triggered by the latest Cretaceous transgression commencing 66.5 Ma ago.

Event II was the main plankton extinction and productivity crisis connected to the rapid collapse of the surface-to-deep water carbon isotope gradient and drops in barium and carbonate accumulation rates. Curiously, there was a hundredfold increase in the concentration of foraminifera relative to total carbonate. It could be due to intensified deep circulation with winnowing of the fine fraction. Or possibly to better the preservation of the dissolution-prone planktonic forms through deepening of the **CCD** and/or lowered rates of in situ dissolution caused by decreased decay of organic carbon in sediment pore waters. There is support for this idea from the fact that coccoliths tend to be more dissolution-resistant than foraminifera, also from calcite dissolution above the calcite saturation horizon is driven mainly by titration by metabolic carbon dioxide derived from organic carbon decay at or near the sediment–water interface.

Event III (65.9 Ma ago) entailed the gradual return of the surface-to-deep water carbon isotope signal, a slight increase in barium accumulation rates and a gradual decline in planktonic foraminiferal accumulations. This implies that surface water productivity started rising about 0.5 Ma after the Cretaceous/Tertiary Boundary event. Temperature fluctuations of several degrees Celsius are inferred from variations in nannofossil and foraminiferal $\delta^{18}\text{O}$ values.

Event IV (65.3 Ma ago) expressed the surface-to-deep water carbon isotope gradient associated with a decrease in planktonic foraminiferal concentrations to more normal levels. Aluminum accumulation rates rose and, since they probably reflect a flux of eolian debris to the site, may mirror a climatic change together with an increase in wind strength. Environmental stability is indicated by a practically constant $\delta^{13}\text{C}$ gradient, relatively stable $\delta^{18}\text{O}$ values and low rates of change of accumulation of planktonic foraminifera. An abrupt extinction of phytoplankton and zooplankton plus the disappearance of the carbon isotope gradient took place, probably within 10,000 years or so. Only such a rapid environmental change could have triggered such a drastic collapse of the marine ecosystem. A bolide encounter could have triggered an “instantaneous” environmental stress factor that went on to engender the collapse of primary productivity, but could not have done so for long. It is possible that the 500,000 years “**Strangelove**” **Ocean** might have existed just long enough to provide the recovery time for the biosphere regarded as normal after such a mass extinction period. A Strangelove Ocean is one in which the dissolved carbon dioxide became enriched due to reduced plankton lasting at least a 1,000 years and followed by increased productivity of plankton.

16.8.5 Isotopes as Mesozoic Climate Indicators

Ice-free oceans are involved. Not much information is available from deep-sea cores at more than a 100 sites from **DSDP** Legs 1–75 penetrating the Cretaceous and yielding foraminifera. A temperature maximum based on $\delta^{18}\text{O}$ values from belemnites at paleolatitudes considered to

have been tropical appears to have occurred in the Albian Age. If a mean $\delta^{18}\text{O}$ of -1‰ for ocean water on an ice-free Earth be assumed, the planktonic foraminifera analyzed recorded paleotemperatures ranging from 25°C to 27°C and this agrees closely with belemnite results. If neither was altered diagenetically, then the surface temperatures in Cretaceous tropical oceans were hotter than today. Of course, if the mean value for ocean water differs from that cited above, these values might be shifted by a couple of degrees either way. As regards diagenetic alteration, this induces a shift in the measured $\delta^{18}\text{O}$ in an isotopically lighter, i.e., negative, direction and thus produces a paleotemperature which is too high. Luckily belemnites are usually translucent and so diagenetic changes are optically visible. Isotopic paleotemperature data are very numerous and suggest that much more equable climates existed during the Mesozoic than was the case in the Tertiary.

Oxygen isotope data from Pacific-cores foraminifera and belemnites showed that low-latitude bottom water temperatures fell from $>15^{\circ}\text{C}$ to about $10\text{--}12^{\circ}\text{C}$ at the end of the Cretaceous. A Cretaceous maximum occurred in the Albian (Teis et al. 1969). This did not agree with other data indicating a climatic temperature maximum in the Coniacian/Santonian almost 11 million years later. The disparity might have been due to a different $^{16}\text{O}/^{18}\text{O}$ ratio in the Teis Group standards, also its specimens came from isolated Santonian waters so that temperatures calculated from their belemnites were lower than the usual ones. There is general agreement that there was an Aptian temperature minimum preceding Albian and continuing an earlier Hauterivian one.

Toward the end of the Jurassic, a low-latitude arid zone extended northwards into much of Europe and south central Asia and caused replacement of corals and limestones by evaporates together with a spreading of limestones at the expense of siliclastics. The transition into the Cretaceous produced humid conditions again with seasonal rains over a vast area including North America, Europe, North Africa, and the Middle East, although southeast Asia stayed dry. This is shown by the abrupt replacing of shallow marine limestones by coarse siliclastics. Large deposits of bauxite and coal relate to such humid conditions and an equatorial humid zone is shown by coals and ironstones in Nigeria and Colombia. Huge salt deposits record Early Cretaceous aridity in the low-latitude South Atlantic region. Isotope data confirm the expansion of the humid zones in the Late Cretaceous as against their extent in the Late Jurassic. Evidence came from strontium isotope ratios in marine carbonates that are believed to reflect seawater values accurately. The $^{87}\text{Sr}/^{86}\text{Sr}$ ratios correlate with the amount of continental run-off that depends on the extent of land and quantity of precipitation falling on it. Allowing for the regional spread of epicontinental seas, the ratio is significantly higher in the Late Cretaceous than it was in the Lower Jurassic. This is the opposite of what happened in the Neogene Ocean. Such changes are due to alterations in the flux of changes in the flux of average $^{87}\text{Sr}/^{86}\text{Sr}$ ratios of the major inputs of strontium to the oceans.

16.8.6 The Permo/Triassic (P/Tr) Boundary

Data from a geochemical record at the P/Tr Boundary recorded in a core, GK-1, in the Carnic Alps, Austria, that started in the Muschelkalk Conglomerate (Middle Triassic) and ended in the lowermost part of the Triassic (as evidenced by the presence of the conodont species *Hindeodus parvus*) are very interesting (Holser et al. 1989). The paleomagnetic record of this core showed several polarity reversals and a carbon isotope profile showed $\delta^{13}\text{C}$ -enriched values of about $+3 \pm 0.3\text{‰}$, a drop occurring in the younger parts of the core. The $\delta^{18}\text{O}$ values also showed

consistent variations at certain intervals with a marked depletion across the P/Tr Boundary that is interpreted as showing a temperature rise of possibly 5°C. A smooth decrease in $\delta^{13}\text{C}$ in Unit 1B (Upper Bellerophon Formation) continued through Unit 2 (the Tesero Horizon, including the P/Tr Boundary) at an accelerating rate, the drop signaling the inception of a zone of low $\delta^{13}\text{C}$ values and chemical changes, e.g., the first and third of three carbon minima are marked by high concentrations of pyrite. The group found two peaks in iridium data that are well above background, but an order of magnitude lower (at least) than the iridium spike at the K/T Boundary. The drop in $\delta^{13}\text{C}$ started in the core at about 50 m below the P/Tr Boundary and showed a net oxidation of the world reservoir of organic carbon as sea level fell to expose paralic and shallow shelves to erosion. The Holser Group claimed that the $\delta^{13}\text{C}$ profile confirmed an accelerated organic carbon oxidation as the boundary is approached and a similar situation was found at Tesero in Italy. An abrupt change to anoxic conditions shown by a rise in Ce^*/La^* and high S/C ratios plus the appearance of pyrite at the top of Unit 2. If this is the case and the $\delta^{13}\text{C}$ dropped through zero for the first time, anomalous concentrations of iridium and other metals may have resulted. The Holser Group took the maximum of the anoxic zone to correspond with the initial minimum of the $\delta^{13}\text{C}$ and claimed that a similar sequence is repeated during a later $\delta^{13}\text{C}$ minimum at the top of Unit 3A and that this was, again, accompanied by high concentrations of metals and sulfides. Actually a single minimum zone of $\delta^{13}\text{C}$ at the base of the Triassic has been validated globally. The interesting question is why many of the above-mentioned changes occurred so fast after the primary global longer-term shifts of the carbon cycle. It is possible that all were the result of the same sea-level regression that first exposed organic carbon to oxidation and finally created anoxic conditions to precipitate metals at least in this part of the Tethys Ocean. This would agree with increased erosion of elevated red beds of the underlying Gröden Formation and precipitated at the oxidation–reduction interface (compare the metal-rich shales of the Kupferschiefer that include platinum group elements). Metal accumulation may have been assisted by algae, as is perhaps shown by observed lamellar texture. If the anoxia and metal concentrations turn out to be localized in the Bellerophon Basin, the cause might be an estuarine-type top flow of freshwater from the lands to the west during the maximum regress of the Tethys Ocean. Alternatively, on a larger scale, a last phase of a deep-sea oxygen minimum zone believed to have existed during much of the Paleozoic Era may have been involved after having been brought near to the surface during the maximum regress event. A prevalent incidence of freshwater eroding continental rocks during this regression is shown by the high values of $^{87}\text{Sr}/^{86}\text{Sr}$ compared with those of the earlier Permian.

The above-mentioned considerations make it clear that the P/Tr Boundary was a very significant event associated with what may well have been the greatest of all mass extinctions. The carbon and oxygen isotope values recorded a drop in $\delta^{13}\text{C}$ values and a depletion in $\delta^{18}\text{O}$ values with a related temperature rise of about 5°C. These phenomena are apparent in other regions, for instance West Spitsbergen where a number of non-allochthonous brachiopods were analyzed. These were Late Permian in age and selected because they do not fractionate carbon and oxygen isotopes significantly. Associated conodonts suggested that the range reached the end of the Permian. The lower part of the carbon isotope curve scattered round a $\delta^{13}\text{C}$ value of +4‰, which is globally typical of Permian rocks. However, there is marked decline of more than 10‰ in the upper part to produce very negative values and it is thought to have taken place over a few million years. The oxygen isotope curve parallels the carbon one. The most startling feature of the data is the size of the carbon shifts that imply that the Late Permian Ocean was first relatively impoverished and later enriched in carbon-12. Is it possible that this reflects a diminished uptake of the light isotope by the biosphere? Or does it mirror an

increased input of the light isotope to the system in the form of organic carbon from land ($\delta^{13}\text{C} = -25\text{‰}$), marine deposits ($\delta^{13}\text{C} = -15\text{‰}$ to -20‰), or juvenile carbon dioxide ($\delta^{13}\text{C} = -5\text{‰}$)? Some prefer the idea that the global process demonstrated by the carbon isotope measurements are attributable to an increased burial of organic matter (spike) succeeded by its oxidation (drop). This would be consistent with the oxygen isotope curve because oxidation of organic matter must lead through kinetic fractionation processes to a decline in the $\delta^{18}\text{O}$ values as measured in all species of dissolved carbon. Such processes may have occurred in the ocean rather than in another carbon reservoir and a similar phenomenon may have taken place at the Precambrian/Cambrian Transition.

16.8.7 Oxygen and Carbon Isotopic Paleozoic Ocean Data

The $\delta^{18}\text{O}$ values of marine chemical sediments tend to decrease with age not just in carbonates but also in cherts, phosphorites, and glauconites. Of course, this could be due to postdepositional equilibrium with oxygen-18-depleted meteoric waters, such equilibration increasing with increasing age. On the other hand, it is possible that it indicates a higher overall temperature for ancient oceans with Archean and Early Proterozoic waters having values exceeding 60°C , although this must be regarded as inherently improbable. Then again, the oxygen isotope composition of the oceans changed through geological time, becoming depleted in the heavy stable isotope. This trend is said to have occurred in carbonates, but to a lesser extent in the Cenozoic and Mesozoic compared to the Paleozoic and Precambrian (Veizer and Hoefs 1976). In the Late Paleozoic, there may have been a major step in the $\delta^{18}\text{O}$ age curve, which, if postdepositional alteration were the sole cause of the secular trend recorded, may be significant in understanding the diagenetic evolution of (bio)chemical sediments.

Secular oscillations have been detected in the $\delta^{13}\text{C}$ of marine bicarbonates. On timescales of 10^7 years, the $\delta^{13}\text{C}_{\text{carbonate}}$ correlates negatively with $\delta^{34}\text{S}_{\text{sulphate}}$ and both correlate with $^{87}\text{Sr}/^{86}\text{Sr}_{\text{carbonate}}$ and the Phanerozoic “sea-level stands.” It seems that the inverse S–C isotopic relationship probably implies oxygen transfer and hence a redox balance between sulfur and oxygen exogenic cycles.

16.8.8 The Precambrian Eons

The Precambrian is extremely long and includes two eons, i.e., the earlier Archean and the later Proterozoic, starting about 4.4 Ga ago and ending with the onset of the Cambrian Period initiating the Paleozoic Era about 570 million years ago. Large-scale ice ages occurred in the Precambrian (Salop 1983). Thus, rock sequences show wide fluctuations in paleoclimates and in many ways similarly to such changes in the Phanerozoic. There was an ice age, the Vendian, in the Eocambrian (570–650 Ma B.P.) and this is indicated by the last Precambrian “tillites,” assuming that these really are tillites and really do show a glaciation situation. This led to the suggestion of a major Varangian global ice age between 630 and 670 Ma ago (Harland 1964). Contrary evidence comes from associated dolomites and/or red beds typical of tropical conditions as well as from paleomagnetic data, poor but indicative of a low-latitude situation. It has been suggested that the tillites were indeed glacial, but the paleomagnetic information is incorrect either because the geomagnetic field was not a dipole of the type found through the

rest of Earth history or the data are too poor in quality. If the tillites were in fact polar, very fast polar wandering would be necessary to account for their apparently widespread distribution, i.e., if distances 30° from the poles were involved. Clearly there is a potential problem in distinguishing paleopolar tillites from the rest. For instance, 47 tillite-like beds have been recorded in the 750 m thick Garvallack sequence of the Late Precambrian of Scotland and claimed to represent at least 17 separate glacial advances (Spencer 1971). These might have been the result of an ecliptic-type wobble that brought ice to the equator every few score thousand years to produce alternation between glacial facies with tropical oxidation and dolomitization. Such wobble-induced ice could have been the mechanism that eroded laterites and tills in their turn would have been oxidized and dolomitized. The requisite time interval has been estimated as 40,000 years. The association of red beds and dolomites with tillites has been accepted and a very different tilt of the Earth's spin axis with respect to the orbital plane could have produced this intimate mixture of hot and cold facies (Williams 1975). The tilt would have varied between $21\frac{1}{2}^\circ$ and $24\frac{1}{2}^\circ$ in the Milankovitch model, but the potential range is clearly between 0° and 90° . The inference is that the Earth formed from a solar prominence with the spin axis in the plane of the planetary orbit, i.e., with an obliquity of the ecliptic of 90° .

Say a change of 1° occurred in 7 million years, then a complete cycle of the spin axis through 360° with respect to the orbital plane would take place every 2.5 Ga. If the polar axis were to lie near or actually in the plane of the Earth's orbit, equatorial latitudes would on average be colder than polar ones. An ecliptic obliquity of 54° would represent an intermediate stage between average hotter pole and average hotter equator. In this state, the Earth would have practically no climatic zonations, hence the climate would effectively be the same everywhere. Such a tilt would fit with the concept of a global glaciation. The area of the planet lying within $20\text{--}30^\circ$ of the equator is much greater than that within $20\text{--}30^\circ$ of the poles, therefore the geological record is biased toward low-latitude phenomena. It was proposed that such a drastic tilt of the terrestrial spin axis could not have been a short-term episode, but rather a much longer one. If so, geological evidence below and above the Varangian glacial deposits showing signs of low-latitude deposition and hot conditions argues against the proposed tilt. The main advantages of Williams' major obliquity hypotheses are that it would associate minimum obliquity with warm or equable climates in the Late Phanerozoic Era and maximum obliquity times would include the Early and Late Proterozoic. However, the Witwatersrand glacial sequence in South Africa constitutes an objection to this because it falls in the middle of a supposedly non-glacial time interval. In this case, if the Williams hypothesis is true, the relevant ice would have had to have been at high latitude. An even more telling argument against Williams is that the Milankovitch wobble of a mere $2\text{--}3^\circ$ caused a marked climatic effect much later in Earth history and this implies that the Williams ecliptic megacycle incorporating major changes in the obliquity of the ecliptic should have had much greater effects on paleoclimates than those actually observed.

16.8.8.1 Archean/Proterozoic Transition

Metasedimentary rocks formed in these two eons extending from 590 to 4,000 Ma B.P., but differ both in lithological abundances and geochemistry, for instance their $^{87}\text{Sr}/^{86}\text{Sr}$ ratios in carbonates are <0.703 for the Archean and <0.704 for the post-Archean. As might be expected almost all such rocks have undergone extensive metamorphism. Carbonates have been used to evaluate the history of the isotopic composition of seawater. As postdepositional alteration is

believed to have been more likely to have increased rather than diminished this ratio, the lowest $^{87}\text{Sr}/^{86}\text{Sr}$ values for a given suite of samples is taken as the best available estimate for strontium isotope composition in their contemporary oceans. The Transition was investigated by examining the geochemistry of rocks from Guyana and Montana (Gibbs et al. 1986). The Guyana material came from the greenstone belts of the Guyana Shield. Metapelites and volcanoclastic metagreywackes of the Early Proterozoic proved similar to many Archean greenstone belts in rare earth elements, trace and major element compositions. Other Archean continental basin sediments turned out to resemble their post-Archean counterparts, implying that the upper continental crusts of the relevant time intervals did not differ to any great extent. Dolomitic limestone from a greenstone belt in northern Guyana has an anomalously low $^{87}\text{Sr}/^{86}\text{Sr}$ ratio of 0.7007, which may mirror the local influence of mantle-derived volcanics during carbonate deposition, diagenesis, or metamorphism. Gibbs and his associates thought that their results made a reconsideration of the Archean/Proterozoic Transition necessary with regard to its attributes of substantial increases in continental area, changes in weathering and erosion together with alterations to the average isotope compositions of upper continental crust.

If it can be shown that the Archean/Proterozoic Transition is an artifact, Archean epicontinental basins and Proterozoic greenstone belts must have been more important than has been previously recognized. The greenstone belts may have formed in some pre-cratonic stage and later comprised part of the basement. Hence they are found at deeper crustal levels than continental sedimentary basins and must have been less vulnerable to erosion or involvement in the internal zones of collision orogens. The transitional event has been interpreted as diachronous so that comparisons of 2–2.5 Ga with 2.7 Ga old metasediments can be regarded as another demonstration of this. But similarly consistent associations of geochemical compositions and geological settings have been reported from both older and younger rocks as well as from modern sediments. Both pre-cratonic and cratonic crust apparently coexisted through Earth history, and change from one to the other probably proceeded throughout as well.

References

- Barron EJ, Thompson SL, Schneider SH (1979) *Science* 21:501
- Berger AL (1976) *Astron Astrophys* 51:127
- Biolzi M (1983) *Mar Micropal* 8:121
- Boersma A (1984) In: Beggren WA, van Couvering JA (eds) *Catastrophes and earth history*. Princeton University Press, Princeton, p 247
- Bowen R (1966) *Paleotemperature analysis*. Elsevier, London/New York
- Broecker WS, Peteet DM, Rind D (1985) *Nature* 315:21
- Broecker WS, Van Donk J (1970) *Rev Geophys Space Phys* 8:169
- Brunhes B (1906) *J Phys* 5:705
- Burchardt B (1978) *Nature* 275:121
- Craig H (1954) *J Geol* 62:115
- Crowley TJ, North GR (1985) *J Geol Soc London* 142:475
- Dansgaard W, White JWC, Johnsen SJ (1989) *Nature* 339:552
- Emiliani C (1955) *J Geol* 63:538
- Emiliani C (1978) *Earth Planet Sci Lett* 37:349
- Epstein S, Buchsbaum R, Lowenstam HA, Urey HC (1953) *Bull Geol Soc Am* 64:1315
- Gibbs AK, Montgomery CW, O'Day PA, Erslev E (1986) *Geochim Cosmochim Acta* 50:2125
- Harland WB (1964) In: Nairn AEM (ed) *Problems in palaeoclimatology*. Wiley, London, p 179
- Hays JD, Imbrie J, Shackleton NJ (1976) *Science* 194:1121
- Heath GR (1979) *Palaeogeog Palaeoclim Palaeoecol* 26:291
- Hodell DA, Mueller P, McKenzie JA, Mead JA (1989) *Earth Planet Sci Lett* 92:165
- Holser WT, Schönlaub H-P, Attrep M, Boecklemann K, Klein P, Margaritz P, Orth CJ, Fenniger A, Jenny C, Kralik C, Mauritsch H, Pak E, Schramm J-F, Statteger K, Schmöller R (1989) *Nature* 337:39
- Imbrie J (1985a) *J Geol Soc London* 142:417
- Imbrie J (1985b) In: Hecht AD (ed) *Paleoclimate analysis and modelling*. Wiley, New York, p 197

- Imbrie J, Kipp N (1971) In: Turekian KK (ed) Late cenozoic glacial ages. Yale University Press, New Haven, CT, p 71
- Imbrie J, Hays JD, Martinson DG, McKintyre A, Mix AC, Morley JJ, Pisias NG, Prell WL, Shackleton NJ (1984) In: Berger A, Imbrie J, Hayes J, Kukla G, Saltzman B (eds) Milankovitch and climate. NATO Scientific Affairs Division: Reidel Publishing Company, Dordrecht, p 269
- Kominz MA, Heath GR, Ju T-L, Pisias NG (1979) *Earth Planet Sci Lett* 45:394
- Lowenstam HA, Epstein S (1954) *J Geol* 62:207
- McCrea JM (1950) *J Chem Phys* 81:849
- McKenna TE, Lerche I, Williams DF, Full W (1988) *Palaeogeog Palaeoclimatol Palaeoecol* 64:241
- Milankovitch M (1930) In: Köppen W, Geiger R (eds) *Handbuch der klimatologie*. Gebruder Borntraeger, Berlin, p 1
- Morris TH (1988) *Palaeogeog Palaeoclimat Palaeoecol* 64:201
- Nefel A, Oeschger H, Schwander J, Stauffer B, Zumbun R (1982) *Nature* 295:220
- Nier AO (1947) *Rev Sci Instr* 11:212.X
- Oerlemans J (1984) In: Berger A, Imbrie J, Hays J, Kukla G, Saltzman B (eds) *Milankovitch and climate*. NATO Scientific Affairs Division: Reidel Publishing Company, Dordrecht, p 565
- Salop LJ (1983) *Geological evolution of the earth during the precambrian*. Springer, Berlin
- Shackleton NJ (1967) *Nature* 215:15
- Shackleton NK, Boersma A (1981) *J Geol Soc London* 138:153
- Spencer AM (1971) *Mem Geol Soc London* 6:1
- Suess H (1989) Abstr., Mtg of Royal Society and Academie des Sciences, Org. In: Pecker JC, Runcorn SK
- Tans PP, Ph.D. Dissertation University of Groningen, Netherlands
- Tarutani T, Clayton RN, Mayeda T (1969) *Geochim Cosmochim Acta* 33:987
- Thompson SL, Schneider SH (1981) *J Geophys Res* 84:2401
- Teis RV, Naidin DP, Zadorozhny IK (1969) *Geokhimiya* II:1286
- Urey HC (1947) *J Chem Soc* 562
- Urey HC (1948) *Science* 108:489
- Urey HC, Lowenstam HA, Epstein S, McKinney CR (1951) *Bull Geol Soc Am* 62:399
- Veizer J, Hoefs J (1976) *Geochim Cosmochim Acta* 40:137
- Vergnaud-Grazzini C, Pierre C, Letolle R (1978) *Oceanolog Acta* 1:381
- Williams DF, Trainor D (1986) *Trans Gulf Coast Assoc Geol Soc* 36:589
- Williams GE (1975) *Geol Mag* 112:441
- Zachos JC, Arthur MA, Dean WE (1989) *Nature* 337:61
- Zubakov VA, Borsenkova II (1988) *Palaeogeog Palaeoclimat Palaeoecol* 65:35

17 Radioactive Dating Methods

R. Bowen

Westfälische-Wilhelms Universität, Münster, Germany

17.1	<i>Introduction</i>	764
17.2	<i>Argon/Argon</i>	765
17.2.1	Incremental Heating	766
17.2.2	Stony Meteorites	767
17.2.3	Argon Losses	767
17.2.4	Some Important Applications	769
17.3	<i>Cesium</i>	769
17.4	<i>Cosmogenic Radionuclides</i>	770
17.4.1	Aluminum-26	770
17.4.2	Argon-39	770
17.4.3	Beryllium-7	771
17.4.4	Beryllium-10	771
17.4.5	Chlorine-36	772
17.4.6	Krypton-81 and Krypton-85	773
17.4.7	Silicon-32	773
17.5	<i>Electron Spin Resonance (ESR)</i>	773
17.6	<i>Fission Track Dating</i>	774
17.7	<i>Iodine/Xenon</i>	775
17.8	<i>Lanthanum/Cerium</i>	775
17.9	<i>Lutetium/Hafnium</i>	776
17.10	<i>Manganese</i>	777
17.11	<i>Nickel</i>	777
17.12	<i>Osmium/Osmium</i>	777
17.13	<i>Pleochroic Haloes</i>	778
17.14	<i>Polonium/Lead</i>	779

17.15	<i>Potassium/Argon</i>	781
17.15.1	The Metamorphic Veil Concept	783
17.16	<i>Potassium/Calcium</i>	783
17.17	<i>Radiocarbon (Carbon-14)</i>	784
17.17.1	Conversion of Radiocarbon Years to Calendar Years	785
17.17.2	Atmospheric Radiocarbon in the Past	785
17.17.3	Radiocarbon in Dead Animals and Plants	786
17.17.4	The De Vries Effect	787
17.17.5	Bomb, Reactor, and Accelerator Radiocarbon in the Environment	787
17.17.6	Separating Bomb-Produced ^{14}C from Natural Radiocarbon	787
17.17.7	Variation of Bomb Radiocarbon in Oceans	788
17.17.8	Dendrochronology and Radiocarbon	788
17.17.9	Radiocarbon and Dating Groundwaters	789
17.17.10	Fractionation of Carbon Isotopes in Nature	790
17.18	<i>Rhenium/Osmium</i>	790
17.18.1	Rhenium/Osmium in Meteorites and the Mantle	791
17.19	<i>Rubidium/Strontium</i>	791
17.19.1	Fictitious Isochrons in the Rift Valley	793
17.19.2	Meteorites, BABI, LUNI, and FUN	794
17.19.3	Some Caveats	794
17.20	<i>Samarium/Neodymium</i>	795
17.20.1	Apollo-12, ADOR, and CHUR	796
17.21	<i>Thermoluminescence (TL)</i>	796
17.22	<i>Tritium</i>	797
17.22.1	Dating Using Tritium and Tritogenic ^3He	798
17.22.2	A Danubian Application of the Tritium/ ^3He Dating Method	799
17.23	<i>Uranium Series Disequilibrium</i>	800
17.23.1	Ionium (^{230}Th)	800
17.23.2	Ionium/Protactinium	801
17.23.3	Lead-210	801
17.23.4	Snow, Ice, and Volcanoes	802
17.23.5	Thorium-230, Uranium-234, Uranium-238	803
17.23.6	The Uranium-234, Uranium-238 Geochronometer	803
17.24	<i>Uranium/Thorium/Lead</i>	804
17.24.1	Radioactive Series	805
17.24.2	Concordia and Discordia	807
17.24.3	Common Lead	809
17.24.4	The Holmes/Houtermans Model	810

17.24.5	Anomalous Lead	811
17.24.6	Multistage Leads	812
17.24.7	Whole-Rock Dating	813
17.25	<i>Uranium/Xenon, Uranium/Krypton</i>	813
17.25.1	Pitchblendes	814
17.26	<i>Editors' Notes</i>	815

Abstract: This chapter provides a necessarily brief summary of radioactive dating techniques, which can produce dates (“ages”) ranging from tens to thousands through millions to billions of years often with assumptions not universally accepted, especially those involving the assessments of half-lives and radioactive decay constants.

17.1 Introduction

Radioactive dating methods involve use of radioactive isotopes of various elements. Of the more than 1,500 presently known nuclides, over four fifths are unstable although most do not occur naturally on Earth, because of their very rapid rates of radioactive decay. To date, rocks, minerals, and naturally occurring radioisotopes are used that continued to exist long after the so-called Big Bang because of their extremely slow rates of radioactive decay. These include uranium-238, uranium-235, thorium-232, rubidium-87, and potassium-40. Some result from the radioactive decay of long-lived, naturally occurring radioactive parents, and among these are uranium-234, thorium-230, and radium-226. Others may have been created by natural nuclear reactions, and these include radiocarbon (carbon-14) and tritium (hydrogen-3). Today, artificial radionuclides have been introduced into the environment as a result of thermonuclear testing and the operation of nuclear fission reactors and particle accelerators.

Whatever its sources, radioactivity is significant as regards geochronology and radioactive dating began in an attempt to determine the age of the Earth once the phenomenon was discovered and uranium and thorium minerals were found to emit radiation. Two new elements were identified, namely polonium and radium, and the word “radioactivity” was derived from the latter. Ever accelerating progress has been made in determining the ages of minerals, rocks, archeological and historical objects, and so on to such an extent that numerous approaches have become routine. Major methods for achieving these data are presented alphabetically in abbreviated form in order to provide a brief but useful perspective of what is in fact a vast and continuously expanding subject. The techniques include four radiation damage techniques, namely electron spin resonance (ESR), fission track dating (FTD), pleochroic haloes, and thermoluminescence.

Great advances resulted from Hans Oeschger’s development of the *Oeschger Counter* that has a lower background than other such instruments. It became the leading instrument for measuring the activity of a variety of naturally occurring radionuclides such as tritium, radiocarbon, aluminium-26, argon-37, argon-39, krypton-81, and krypton-85. Using this method, Oeschger and his team were able to quantify exchange processes between different components of the Earth System. There is a final caveat to make here, and this refers to the words “assuming,” “presuming,” “implying,” and “inferring” appearing occasionally in the text regarding certain dating methods, and in a number of cases, dubiety apropos half-lives and radioactive decay constants are mentioned. From this, it is apparent that there is still some way to go to improve and, if possible, perfect many of the relevant techniques.

In this chapter, the following shorthand notation is used. $[^AX]$ denotes the number of atoms/concentration of nuclide AX , where X stands for the chemical symbol of some element and A is the mass number of one of its isotopes. (^AX) is the activity (either absolute or specific) of nuclide AX . Symbols such as $[^AX/^BY]$ actually mean atomic ratios of nuclides AX and BY ; i.e., they represent the ratio $[^AX]/[^BY]$. Similarly, the ratio of activities $(^AX)/(^BY)$ will be abbreviated sometimes as $(^AX/^BY)$. An asterisk as a right superscript such as $^AX^*$ or $[^AX]^*$ is to stress that the nuclide in question or the specified number of them is of radiogenic origin.

17.2 Argon/Argon

For a better understanding of the argon/argon method, it is recommended that ▶ Sect. 17.15 on potassium/argon dating be read first. The method presented below can be considered as a special variant of the K/Ar method in which the potassium content is monitored by an argon isotope that is readily formed by the neutron irradiation of potassium.

The argon/argon method is partly based on the formation of argon-39 by irradiation of potassium-bearing samples using both thermal and fast neutrons in a nuclear reactor. The relevant reaction is



Argon-39 is radioactive, decaying by beta emission with a half-life of 269 years, a fact that makes it stable in terms of the relatively insignificant analytical times involved in research. A counting technique for the assessment of argon-39 was superseded in the middle 1960s by mass spectrometric determination of the $^{40}\text{Ar}/^{39}\text{Ar}$ ratio. It is assumed that all argon-40 in the irradiated sample is either radiogenic or atmospheric in origin and that argon-39 is produced by the (n,p) reaction as shown by ▶ Eq. (17.1).

During the irradiation process, reactions that involve potassium, calcium, and chlorine occur, but the only one of interest is that cited above. The number of radiogenic $^{40}\text{Ar}^*$ atoms present in a sample due to the radioactive decay of potassium-40 during its geological history is given by

$$[^{40}\text{Ar}^*] = \frac{\lambda_{\text{EC}}}{\lambda} [^{40}\text{K}] (e^{\lambda t} - 1), \quad (17.2)$$

where λ_{EC} is the decay constant of potassium-40 for electron capture, λ is the total decay constant of potassium-40 (including β^- decay):

$$\lambda = \lambda_{\text{EC}} + \lambda_{\beta} \quad (17.3)$$

and t is the age. For the decay scheme of ^{40}K , see ▶ Eq. (7.22) in Chap. 7, Vol. 1, presented as an example for branching decays.

After the neutron irradiation process, the $^{40}\text{Ar}/^{39}\text{Ar}$ ratio can be determined and compared with the $^{40}\text{Ar}/^{39}\text{Ar}_{\text{fm}}$ ratio of a flux monitor the age of which is known. Various mineral concentrates can be used as flux monitors. One is MMHb-1. It is assumed that all argon-40 in the irradiated sample derives either from a radiogenic or an atmospheric origin, argon-36 is purely atmospheric, and also that all argon-39 is produced by the (n,p) reaction shown in ▶ Eq. (17.1).

Several corrections have to be introduced, especially as regards younger samples ($\sim 10^6$ years) and those having $[\text{K}/\text{Ca}] < 1.0$. Particularly important are interfering reactions involving calcium isotopes. For instance, argon-36 is produced by the reaction



and removed by the reaction



both reactions interfering with the correction for atmospheric air, which is based on argon-36.

In addition, an atmospheric argon-40 correction is relevant both to conventional potassium/argon and to $^{40}\text{Ar}/^{39}\text{Ar}$ dating methods. The assumption is made that argon-36 is of

atmospheric origin and that the ratio $[^{40}\text{Ar}/^{36}\text{Ar}]$ in the atmosphere is 295.5. However, both argon-40 and argon-36 may become incorporated into minerals when they crystallize so that the $[^{40}\text{Ar}/^{36}\text{Ar}]$ ratio of this argon may differ significantly from that of atmospheric argon today. Consequently, the observed quantity of argon-36 in a mineral or rock may not allow an accurate correction to be made for the presence of non-radiogenic argon-40. Where the $[^{40}\text{Ar}/^{36}\text{Ar}]$ ratio of the inherited argon exceeds 295.5, an apparent excess of radiogenic argon will result. But if the value of this ratio is below 295.5, an apparent deficiency of radiogenic argon will result. This latter result might mistakenly be attributed to a partial loss of argon-40.

It is possible to calculate a date from the $[^{40}\text{Ar}/^{39}\text{Ar}]$ ratio of a sample that has been irradiated by neutrons and so a set of such dates can be obtained for the sample if argon is liberated from it in steps following temperature increases. If the sample was a closed system for both argon and potassium since it first cooled, the dates obtained from each step should be constant. However, if some loss of radiogenic argon occurred and took place in regard to some, but not all, crystallographic sites, the $[^{40}\text{Ar}/^{36}\text{Ar}]$ ratios of the gas released at different temperatures will vary and a range of dates will result. From this result, the time elapsed since initial cooling can be derived.

It has been indicated that the $^{40}\text{Ar}/^{39}\text{Ar}$ approach has several advantages over potassium/argon method of which perhaps the greatest is that only ratios of argon isotopes have to be measured in order to calculate an age rather than absolute quantities. Hence, it is not necessary to extract all radiogenic argon from a mineral to derive an accurate age, thus mitigating a problem inherent in the potassium/argon dating of sanidine, which is that K/Ar ages for this mineral tend to be anomalously young since the melt usually forms a viscous mass, which retains some radiogenic argon under ultrahigh vacuum. Even at maximum attainable temperatures in standard induction heaters and resistance furnaces, 5–10% of the gas can stay trapped in such viscous sanidine melts. The problem was obviated by using a $^{40}\text{Ar}/^{39}\text{Ar}$ analytical system (Dalrymple 1989).

17.2.1 Incremental Heating

The concept of stepwise heating (Merrihue and Turner 1966) was incorporated into a model used to forecast the $[^{40}\text{Ar}^*/^{39}\text{Ar}]$ spectrum of a potassium-bearing mineral grain that underwent a partial loss of radiogenic argon-40 (i.e., $^{40}\text{Ar}^*$) caused by heating during a metamorphic event. A mineral grain that underwent partial loss of argon-40 may become a closed system again when the relevant metamorphic event ended. If uniformly sized grains of a particular potassium-bearing mineral with such a geological history is incrementally heated, the $[^{40}\text{Ar}^*/^{39}\text{Ar}]$ ratios of the gas fractions liberated at different temperatures will vary systematically. The first will emerge at the lowest temperature and come from grain surfaces with a low ratio. This reflects the time interval elapsed since the accumulation of radiogenic argon-40 recommenced after the metamorphic event. Succeeding fractions released through rising temperatures will have progressively higher $[^{40}\text{Ar}^*/^{39}\text{Ar}]$ ratios representing the removal of the gas from increasingly retentive locations, which lost ever smaller fractions of the argon-40 during the event. Finally, the $[^{40}\text{Ar}^*/^{39}\text{Ar}]$ ratios may reach a plateau that corresponds to a date approaching the time, which has passed subsequently to the original cooling of the mineral.

The stepwise heating procedure applied to a mineral sample, which underwent partial loss of radiogenic argon, permits a set of dates to be calculated, and this procedure ideally includes

the actual time of the metamorphic event (low temperature release). This is advantageous because a date can be derived which nears, if sometimes underestimating, the original cooling age of potassium-bearing minerals in rocks, which suffered partial loss of radiogenic argon in the course of a metamorphic event.

17.2.2 Stony Meteorites

Investigations have been made on stony meteorites including severely shocked chondrites. Also, the effect of implanting argon isotopes during a similar shock metamorphism on $^{40}\text{Ar}^*/^{39}\text{Ar}$ dates of both terrestrial and lunar rocks has been examined. Many data have been obtained from samples derived from metamorphic terranes on Earth, for instance Barberton Mountain komatiites, extrusive igneous rocks of peridotitic composition with much higher melting temperatures than basalts.

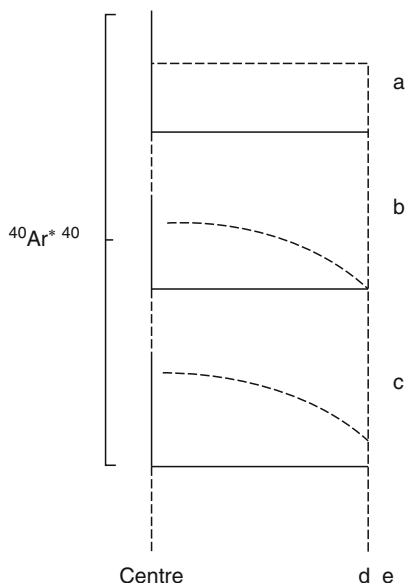
The validity of the technique was scrutinized by dating minerals and rocks with ages already known from alternative isotope methods. Whole-rock samples of diabase with excess radiogenic argon from dykes in western Libya were analyzed in order to assess the stepwise approach. Results showed that minerals from slowly cooled metamorphic and intrusive igneous rocks normally yield $^{40}\text{Ar}^*/^{39}\text{Ar}$ ages younger than their real crystallization ages because radiogenic argon-40 continues to escape from the mineral crystals in appreciable amounts until they cool below some critical temperature range (► Fig. 17.1). Such loss is a volume diffusion process. The integrated closure temperature corresponding to the temperature of the mineral at the time conforming to its apparent integrated age can be regarded as a function of the diffusivity of argon-40 in the mineral, a dimension over which diffusive loss occurs and the rate of cooling.

17.2.3 Argon Losses

Argon-39 may be lost or relocated in a sample because of its recoil arising from the emission of a proton during the (n,p) nuclear reaction shown in ► Eq. (17.1). If much is lost from an irradiated sample, the $[^{40}\text{Ar}/^{39}\text{Ar}]$ ratio will increase proportionally and so the total release date will exceed the real geological age. Loss of argon-39 from a potassium-bearing mineral grain may occur from a surface layer 0.08 μm thick and the effect of such recoil-induced loss is related to the particle size of the mineral, i.e., fractured or fine-grained minerals lose more of the isotope during irradiation than do coarse-grained ones. The implication is that the $^{40}\text{Ar}/^{39}\text{Ar}$ method may be unsuitable if applied to the dating of potassium-rich clay minerals of the glauconite type, which normally comprise green pellets made of aggregates of platy crystals about a micrometer thick. Of course, recoil loss from potassium-rich mineral grains may entail gas entering adjacent grains of potassium-poor minerals. Then the $[^{40}\text{Ar}/^{39}\text{Ar}]$ ratio of the former would increase and that of the latter would decrease. The amount of increase would depend on grain sizes, namely the surface-to-volume ratio of the relevant grains. Where this ratio is large, that is to say where the grains are small, there will be a larger increase in the $[^{40}\text{Ar}/^{39}\text{Ar}]$ ratio due to the argon-39 recoil loss than in a similar sample with larger grains of potassium-bearing minerals. Potassium-depleted minerals taking up expelled argon-39 include pyroxene and they are more retentive as a rule than potassium-rich minerals. Therefore, argon freed at high temperatures may have lower $[^{40}\text{Ar}/^{39}\text{Ar}]$ ratios because it is derived from pyroxenes containing argon-39 expelled from potassium-bearing minerals during

■ Fig. 17.1

(a) Uniform distribution of the radiogenic $[^{40}\text{Ar}^*/^{40}\text{K}]$ ratio in a spherical mineral grain closed since crystallization, (b) partial loss of radiogenic $^{40}\text{Ar}^*$ through diffusion induced by heating, which reduced the relevant ratio to zero at the surface of the grain while leaving it unaltered at the center, (c) distribution of the $[^{40}\text{Ar}^*/^{40}\text{K}]$ ratio at a time after partial argon loss after the system again became closed to $^{40}\text{Ar}^*$. The value of the $[^{40}\text{Ar}^*/^{40}\text{K}]$ ratio on the surface of the grain is a function of that time, which elapsed subsequently to partial outgassing, and at the center of the grain, it corresponds to the age of the mineral sample



neutron irradiation of the sample. This may explain why the stepwise release spectra of some lunar rocks showed a decrease of this ratio at the highest gas release temperatures.

The $^{40}\text{Ar}/^{39}\text{Ar}$ age spectra of a whole-rock sample and mineral concentrates can be altered by the occurrence of minerals, which may lose argon at a continuous rate even at low temperatures and perhaps also of minerals younger than the main minerals. These latter can be produced by thermal metamorphic episodes involving low temperatures. Alternatively, they may exist as inclusions in the main minerals. Either way, it is hard to separate them and, since they are characterized by their inability to retain argon, their presence in irradiated samples contributes to low dates commonly derived from low temperature-derived gas fractions freed by incremental heating. The problem has been approached using a precisely focused laser beam to release gas from individual grains of retentive minerals. In one experiment, a pulsed ruby laser melted less than a $1\ \mu\text{g}$ sample of the neutron-irradiated sample to create a pit $10\text{--}100\ \mu\text{m}$ wide, the beam being focused through a petrographic microscope on to a polished surface of the sample sealed in a vacuum chamber on the stage. The gas was collected on charcoal at the temperature of liquid nitrogen and later a gas source mass spectrometer used to obtain the required $[^{40}\text{Ar}/^{39}\text{Ar}]$ ratio. Another technique involved applying continuous argon-ion lasers to melt individual mineral grains previously irradiated by fast neutrons. Dates were obtained from biotite, hornblende, and muscovite of Precambrian age and could not be distinguished from total release dates resulting from fusion of the relevant minerals by radio frequency

induction. Using lasers is valuable because individual mineral grains can be dated so that their inclusions and any alteration products can be excluded.

The laser method has been used to study the occurrence of argon in lunar rocks from the Mare Serenitatis, but there were drawbacks. They resulted from the fact that the date obtained was a total release that could underestimate the ages of samples, which lost argon-40 after crystallization. Also, the laser beam may stimulate the release of argon from other minerals when penetrating the target material. However, it was claimed that less than 1% of the gas freed from pits comes from an area exceeding 10 μm from their peripheries.

Dating sulfide minerals is complicated because they lack radioactive elements such as uranium, thorium, and rubidium. However, some contain potassium, e.g., the mineral rasvumite, KFe_2S_3 . Samples of this mineral were collected from an alkali-rich igneous rock at Coyote Peak near Arcata, northern California, and they gave a date of 26.5 ± 0.5 Ma, while associated phlogopite mica yielded a total release date from $^{40}\text{Ar}/^{39}\text{Ar}$ measurements of 28.3 ± 0.4 Ma. This confirms that potassium-bearing sulfide minerals can be dated on the basis of the radioactive decay scheme



17.2.4 Some Important Applications

K/Ar ages and paleomagnetic data from geological mapping of the Jemez Mountains in northern Mexico were used as a basis for recognition of the Jaramillo Normal Subchron (JNS) and obtaining calibration points near the Matuyama/Brunhes Boundary (MBB). Sanidine and obsidian were used. The isotopic ages of volcanic rocks significant both for the JNS and MBB were reported following $^{40}\text{K}/^{40}\text{Ar}$ and $^{40}\text{Ar}/^{39}\text{Ar}$ analyses of rhyolite domes of the Valles caldera, which formed just prior to the MBB. New information was obtained by measuring $^{40}\text{Ar}/^{39}\text{Ar}$ ages of basalt flow extruded during the Matuyama/Brunhes magnetic field reversal. The age of the MBB was further constrained by dating of sanidine from the reversely magnetized Oldest Toba Tuff in Sumatra.

Other applications of the $^{40}\text{Ar}/^{39}\text{Ar}$ technique include a Burdigalian (Miocene 1) age for extensional ductile tectonics in the Edough Massif, Kabylies, Algeria, a preliminary $^{40}\text{Ar}/^{39}\text{Ar}$ age spectrum and laser probe dating of the Manson Impact Structure (MI core), a Cretaceous/Tertiary (K/T) Boundary crater candidate, use of the $^{40}\text{Ar}/^{39}\text{Ar}$ technique to date mylonitic deformation associated with the regionally extensive Norumbega fault zone in south-central Maine, USA, meteorites (acapulcoites and lodranites, also dating shock-melted phases of the Chico chondrite as well as an argon isotope study of lunar meteorite Asuka 881757. Also studied were diamonds some of which are known to be 2–3 Ga old, the formation of which from the Earth's mantle might have entailed incorporating large quantities of “excess” radiogenic argon in association with potassium. If this is true, the dating projects may turn into studies of the ancient mantle fluids.

17.3 Cesium

The natural isotope ^{133}Cs is stable, but two radioactive isotopes are of interest. These are ^{135}Cs and ^{137}Cs . Both are radioactive with half-lives of 2.3 Ma and 30 a, respectively. They are produced with equal yields of about 6–7% in binary fission of actinide nuclides. The nuclei

enter the environment through atmospheric testing of nuclear devices and release from the nuclear industries. ^{137}Cs is a well-known radiotracer and time marker while ^{135}C has been neglected because its much longer half-life precludes detection by counting. In addition, in conventional mass spectrometers, the tail from the stable ^{133}Ca swamps its signal (since its abundance is typically 10^{-9} smaller). The first measurement of the relevant isotopes was made using two coastal sediment samples and a thermal ionization mass spectrometer equipped with a retarding potential quadrupole lens filter. The $[^{135}\text{Ca}/^{133}\text{Cs}]$ ratio was about 1×10^{-9} , and the $[^{137}\text{Cs}/^{135}\text{Cs}]$ ratio was about five due to the decay occurring through the past 30 years from their production ratio of about one. It was noted that this appeared to be the first detection of fallout ^{135}Cs in nature and it may be inferred that the isotope ratio $[^{137}\text{Cs}/^{135}\text{Cs}]$ is much more powerful as a tracer than ^{137}Cs alone. Two models were given to illustrate how the ratio may be used in order to quantify estimates of recent sedimentation and rates of erosion (Lee et al. 1993).

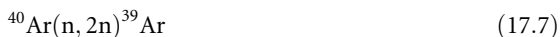
17.4 Cosmogenic Radionuclides

17.4.1 Aluminum-26

This radionuclide enters the oceans in ionic form and mixes with stable aluminium-27, later becoming adsorbed on various particles. Its concentration rises with depth and its half-life is 0.716×10^6 years. Its residence time was estimated as 1,400 years and that makes it valuable for dating authigenic minerals, although detecting it is not easy. It has been employed to determine the rates of growth of manganese nodules of which one estimate is 2.3 mm Ma^{-1} . When it is measured with beryllium-10 from the same sample, the ratio of their respective rates of radioactive decay decreases with time. The geochronometer is useful because the time-dependent variations in the rates of production and the geochemical paths of the two tend to annul each other (Lal and Somanyajulu 1984). The Oeschger Counter has been a valuable asset in measuring this radionuclide.

17.4.2 Argon-39

This radionuclide forms in the atmosphere through the nuclear reaction



and decays by beta emission to ^{39}K with a half-life of 269 years.

Its contribution to atmospheric radioactivity is about $1.87 \pm 0.17 \text{ Bq m}^{-3}$ and of this, less than 5% is due to thermonuclear testing. It has a long residence time that damps down fluctuations in its production rate and contributes to probable constancy of its concentration in terms of time and latitude. This makes it valuable for dating glacial ice and groundwaters. At about 70 m depth, névé (also called firn) is converted to glacial ice and air bubbles become trapped and can be analyzed to assess disintegration rates for ^{39}Ar as well as for radiocarbon and krypton-81. The main problem in using it is that it is chemically inert and so does not interact with solids (unlike radiocarbon, silicon-32, and chlorine-36). Also, because it and other inert gases occur mostly in the atmosphere, concentrations in groundwater depend on the time elapsed since the water was in contact with the atmosphere. In addition, analyzing

argon-39 entails collecting very large volumes of water as with silicon-32. Finally, excess argon-39 may arise from potassium-39 as shown in ► Eq. (17.1), i.e., through the (n,p) reaction



in rocks containing measurable amounts of uranium and thorium.

17.4.3 Beryllium-7

Beryllium-7 occurs naturally and is radioactive with a half-life of 53.29 days, after which it decays to lithium-7 by electron capture. It is a cosmogenic product of various high-energy spallation reactions between cosmic-ray neutrons and nitrogen in the atmosphere about 1.5 km above the surface of the Earth. It forms BeO molecules, which diffuse until encountering dust particles to which they adhere, most forming cloud nuclei with their beryllium-7 incorporating into atmospheric precipitation. Once deposited on the terrestrial surface, it enters the geochemical cycle of beryllium. Although it has low production rate, it is easy to detect because it is found practically carrier-free in the atmosphere. Years ago, it was suggested that beryllium-7 might be useful in dating and its rapid radioactive decay facilitates examining various atmospheric processes, surface water in the oceans, and the mixing of sediments in offshore marine and lake environments.

17.4.4 Beryllium-10

As with beryllium-7, this is a spallation product formed by cosmic rays in the atmosphere, and it descends in precipitation to reach sea-bottom sediments and continental ice sheets. Its half-life is 1.5×10^6 years and its global production rate has been estimated as between 1.5×10^{-2} and 3×10^{-2} atoms $\text{cm}^2 \text{s}^{-1}$, although a lower value has been claimed for Antarctic snow. Like aluminium-26 and beryllium-7, it is introduced into seas in ionic form and mixes with the stable isotopes such as beryllium-9 and aluminium-27. Having high ionic potentials, they may become adsorbed on both organic and inorganic particles. Seawater has a very low concentration of beryllium-10 compared to river waters and lower concentrations at the surface than in deep waters. The residence has been calculated as being about 1,600 years, and so it is useful for dating authigenic minerals, which take it up in ionic solution in the oceans. But there are difficulties because of its low level of activity and its disintegration rate varies sporadically with depth in cores (associated abundances depending not just on the time elapsed since deposition, but on the rate of deposition and secular variations in the production rates). It cannot be assumed that the rates of sedimentation in oceans at any particular place were constant for geologically significant time intervals of ~ 1 Ma. As well as sediment dating in oceans, beryllium-10 concentrations on land, for instance in soils, can be examined. However, few data are available again due to the low activities involved.

Beryllium-10 gave a rate of growth for the manganese nodule (alluded to above in aluminium-26) of about $2.8 \pm 0.06 \text{ mm Ma}^{-1}$. Tektites of various origins were analyzed and it has been concluded that the beryllium-10 arose from sediments on the Earth's surface. It may be noted that a pair of older tektites (moldavites) about 15 million years old had a content of less than 2×10^6 atoms of $^{10}\text{Be g}^{-1}$ that could mean that decay occurred after their formation as

a consequence of meteoritic impact on the Earth and so a terrestrial origin is confirmed (Pal et al. 1982).

17.4.5 Chlorine-36

This radionuclide is produced in the atmosphere through the nuclear reaction



mostly in the stratosphere and its formation is latitude-dependent because of the effects of terrestrial magnetism on cosmic-ray intensities. Mixing there is rapid and the concentration of chlorine-36 is constant. Its atoms attach to atmospheric aerosols in the submicron range and these are progressively removed by precipitation from the lower troposphere. Entry from the stratosphere into the troposphere varies seasonally, and the fallout rate is greater in middle latitudes than it is at the poles or equator. This rate was determined at 57° N latitude at Stripa, Sweden, as about 14 ± 3 atoms $\text{m}^{-2} \text{s}^{-1}$ (Lal and Peters 1967). Its half-life is 3.01×10^5 years. This makes it useful for dating glacial, groundwater, etc. Neutron irradiation of oceanic aerosols following thermonuclear testing at low altitudes induced increased fallout through the nuclear reaction $^{35}\text{Cl}(n, \gamma)^{36}\text{Cl}$, an effect rising from 1953 to a 1964 maximum of 70,000 atoms $\text{m}^{-2} \text{s}^{-1}$ (Bentley et al. 1986). Because such tests began earlier over oceans, the chlorine-36 bomb-peak predated that of tritium by about 10 years. A residence time in the atmosphere for chlorine ions as less than 3 years has been proposed, which may be why the bomb pulse of chlorine-36 was transient with fallout rates returning to normal by the early 1970s when low altitude testing was terminated (Elmore et al. 1982). This bomb pulse was used to study the migration of water through the unsaturated zone into groundwater aquifers and also the stratification of waters in unconfined aquifers.

There is subterranean production of chlorine-36 and the world average chlorine contents of granite and basalt have been given as around 50 and 200 ppm, respectively. Sedimentary rocks have variable contents ranging from 10 ppm in sandstones to 20,000 ppm in deep-sea limestones. Rock outcrops are exposed to the cosmic neutron flux so that some chlorine-36 results from neutron capture by chlorine-35, but, below a few meters, it is ineffectual. Nonetheless, some chlorine-36 results from an in situ neutron flux in rock matrices caused by (α, n) reactions triggered by alpha particles from uranium and thorium radioactive decay systems. This flux may be of the order of $10^{-4} \text{ cm}^{-2} \text{s}^{-1}$ (Kuhn et al. 1984).

At Stripa, efforts were made to use data to obtain generalized groundwater regimes. These regimes were presented as “A,” “B,” and “C.” “A” showed groundwater evolution in a granite where salinity arises from interaction with the rock matrix, the [$^{36}\text{Cl}/\text{Cl}$] atomic ratio of the dissolved chloride characterizing the rock. “B” had the groundwater recharging a formation with lower content of radionuclides (thus lower neutron flux) than the granite so that a lower [$^{36}\text{Cl}/\text{Cl}$] atomic ratio resulted as chlorinity rose. If chlorinity evolution stopped before this groundwater reached the granite, the ratio would increase with increasing residence time in the granite and the length of this could be estimated from the extra ^{36}Cl in-growth in the granite. “C” assumed chlorinity to derive from a source with a low [$^{36}\text{Cl}/\text{Cl}$] ratio (possibly an evaporite). Later infiltration into a formation with a higher content of radionuclides will produce ^{36}Cl in-growth in the dissolved chloride and, if the groundwater resides long enough, the chloride will reach the saturation ratio for the in situ neutron flux. Subsequent flow into a granite fracture system would induce a further time-dependent rise in the [$^{36}\text{Cl}/\text{Cl}$] atomic

ratio if no additional matrix chloride was dissolved. Chlorine-36 deposits in snow on the Greenland ice sheets and in Antarctica can be used to date ice or detect variations in production rates in the atmosphere.

17.4.6 Krypton-81 and Krypton-85

Krypton-81 resembles both argon-39 and the short-lived argon-37 in that it is a cosmogenic radionuclide occurring in the atmosphere, in groundwater that has been in contact with the atmosphere and in air occluded in glacial ice. Both ^{81}Kr and ^{85}Kr result from spallation reactions involving protons and also from (n,γ) reactions from the stable ^{80}Kr and unstable ^{84}Kr . Krypton-81 has a half-life of 2.13×10^5 years and undergoes radioactive decay by electron capture to the stable bromine-81. It is not a fission product and has an activity of 0.067 ± 0.003 dpm L^{-1} . This value exceeds expectations by a factor of up to two that might imply an extraterrestrial influence of some sort (Kuzimov and Pomansky 1980). Krypton-81 has been used to date glacial ice.

Krypton-85 is a fission product continuously being released into the atmosphere during the reprocessing of spent nuclear fuel. Because major reprocessing plants are located in the northern hemisphere, krypton-85 concentrations in the southern hemisphere are systematically lower. In addition, part of the krypton-85 released at mid-northern latitudes decays before it can be transported to the southern hemisphere. It has a half-life of 10.76 years and decays to the stable nuclide rubidium-85 by beta emission. The specific activity of anthropogenic krypton-85 has been reported as about 3×10^4 dpm L^{-1} (Alburger et al. 1986). Both krypton-81 and krypton-85 have been investigated using the Oeschger Counter.

17.4.7 Silicon-32

Silicon-32 is produced by the cosmic-ray spallation of argon in the upper atmosphere from whence it descends to mix with surface water so that, as a radiotracer, it may be applied to measuring ocean water mixing and currents, glacier formation, the accumulation of sediments, and the stability of groundwater over centuries. However, there is a problem with the half-life of which estimates range from 60 to 700 years or more. A fairly recent value was 172 ± 4 years (Alburger et al. 1986). Of course, this constrains its utility, and another disadvantage is that its extremely low concentration in planetary waters requires using relatively enormous samples of around 10 t of water for analytical purposes.

17.5 Electron Spin Resonance (ESR)

When dielectric (paramagnetic) solids meet ionizing radiation, metastable electrons occur and are detectable. Measuring them is feasible using electron spin resonance (ESR) spectrometers that can sense the adsorption of microwave radiation by the trapped electrons when these are subjected to a strong magnetic field. Splitting of the energies of unpaired electrons is promoted and how this happens depends on whether their magnetic moments are aligned parallel to or opposite to the applied field. ESR-dating is based on such measurements of unpaired electrons trapped in crystal defects. Such quasi-“free” electrons are produced through geological time by

natural radiation arising from the decay of radioactive atoms and also from cosmic radiation. Paramagnetic centers in crystals revealed by ESR can be used to date samples of animal or human bones, fossil shells, corals, stalactites, quartz grains in fault gauges, etc., in the Quaternary Era (Ikeya and Miki 1980). Also, early Pleistocene volcanic rocks have been dated using quartz (Shimokawa et al. 1984). However, it has been shown that defects in quartz may have lasted for at least 1.5 Ga and, since quartz is the most abundant mineral in the Earth's crust, this may have laid the foundation for a greatly extended ESR geochronometer capable of dating numerous geological features over practically the last third of the history of the Earth (Odom and Rink 1988).

Some matters still have to be resolved. The relevant centers can be attributed to *Schottky–Frenkel defects* in the crystal lattice of quartz and measuring their number is difficult because of the fact that the characteristic ESR lines are frequently small and close to the background signal. Extreme spectrum accumulation has been proposed as a remedy. Also, the defects were created by elastic collisions of recoiling α -emitting nuclei with silicon and oxygen atoms and the precise amount of α -particle emitting nuclides have to be determined. They belong to the uranium and thorium decay chains, but normally have concentrations in quartz in the ppb range that makes them very hard to assess. In addition, the number of centers per unit of radioactive nuclides can vary as a function of the type of quartz examined.

17.6 Fission Track Dating

Energy is transferred from charged particles passing through a solid to its atoms and a damage trail is left behind. Such tracks were noted during the examination of irradiated solids using an electron microscope with high magnification ($\times 50,000$). Later it was found that such tracks could be both enlarged and made visible under the optical microscope by etching with an appropriate chemical solution, this reflecting the preferential solubility of the damaged areas. Tracks have dimensions of about 10 μm and are created by spontaneous fission fragments of uranium-238. These tracks not only have a large individual mass each but also release a large quantity of energy amounting to some 200 MeV during the process. It was proposed that track densities might be used for dating various types of mica. Natural minerals such as biotite and muscovite may have track densities up to $5,000\text{ cm}^{-2}$. The actual numbers relate to the time interval during which they accumulated and the uranium concentration in the samples. Any selected sample must have enough uranium content to produce a track density greater than 10 tracks/cm^2 during the time interval from cooling of the sample until now. And the tracks must be stable at ordinary temperatures for periods of time comparable to the age being measured. Tracks can be created artificially by induced fission of uranium-235 through irradiation of a sample using thermal neutrons in a nuclear reactor, this procedure being termed the “zeta” method of calibrating fission track dating (FTD) against other radiometric techniques (Hurford and Green 1983). Clearly, fission tracks must be reasonably free of defects and lattice ruptures so that they can be counted after etching and also the distribution of uranium in a sample must be close to uniform in order to permit the concentration to be determined from the density of induced tracks. Obviously, weathering is adverse to fission tracks and interestingly can reduce the assessed date of apatite while having little or no effect on zircon or sphene. However, the apparent reduction of the assessed date may have resulted from difficulty in identifying tracks in corroded crystals and perhaps also because they may have partially faded through the action of groundwater.

An age equation has been proposed, bearing in mind that the vast majority of tracks is due to the spontaneous fission of uranium-238 so that the effects of uranium-235 and thorium-232 can be neglected as can those due to decay by spontaneous of naturally occurring radionuclides of high atomic numbers. It is also assumed that induced ^{235}U fission resulting from the adsorption of thermal neutrons arising from the spontaneous fission of ^{238}U is insignificant unless the mineral, being dated, was embedded in uranium ore. The radioactive decay constant for the spontaneous fission of uranium-238, λ_6 , is uncertain, but it could be $(8.46 \pm 0.06) \times 10^{-17} \text{ a}^{-1}$.

With the usual assumptions, the relevant dating equation is as follows:

$$t = 6.446 \times 10^9 \ln \left(1 + 7.715 \times 10^{-18} \frac{\rho_s}{\rho_i} \Phi \right) \quad (17.10)$$

where ρ_s is the area density of spontaneous fission tracks on the surface of the mineral that is being analyzed and ρ_i is the area density of the induced tracks. The time t can be derived after measurement of ρ_s/ρ_i and the relevant dose from the monitor, Φ . Zeta calibration became necessary because of systematic errors arising from uncertainty regarding the value of λ_6 , these possibly affecting FTD dates.

17.7 Iodine/Xenon

In all, iodine has 33 isotopes, of which 16 are radioactive. The one of interest is iodine-129 with a half-life of 15.7×10^7 years. Common iodine is iodine-127. Xenon is an inert gas present in the atmosphere in minute amounts of around 0.006 ppm. It has 36 isotopes, of which the one of interest is xenon-129 produced by iodine-129 via β^- decay. This has an abundance in the naturally occurring element of 26.4 atom %. The I/Xe system could be a potentially precise geochronometer, especially of events in the solar system.

17.8 Lanthanum/Cerium

Both these elements are lanthanides (rare earths) and, like all members of that group have properties resembling those of aluminum. Cerium is a member of the inner transition elements. The lanthanum/cerium geochronometer is based on ^{138}La with a natural abundance of 0.09%, which undergoes branched radioactive decay by negatron emission to produce stable ^{138}Ce and by electron capture to yield the stable isotope barium-138. The initial values for partial half-lives have been given as $(2.69 \pm 0.24) \times 10^{11} \text{ a}$ (beta decay) and $(1.51 \pm 0.10) \times 10^{11} \text{ a}$ (electron capture), respectively. It became apparent that both of the radioactive decay constants had to be refined before the technique could be used. The Oeschger Counter was useful in promoting it.

Constraints on the ^{138}La β -decay half-life must be discussed. It was recognized that the La/Ce isotope scheme could be a powerful adjunct to the samarium/neodymium approach for petrogenetic studies. However, counting of the β -decay half-life of lanthanum gave $3.02 \times 10^{11} \text{ a}^{-1}$ and this did not accord with the geological half-life determinations from lanthanum/cerium and samarium/neodymium mineral isochrons (Dickin 1987). Further examination of this matter led to a six-point La/Ce isochron on whole-rock samples of Lewisian granulite facies of Archean gneiss from northwest Scotland. Based on the

above-mentioned half-life, a La/Ce age of 2.99 ± 0.4 Ga (2σ) resulted and this came within the error of a whole-rock samarium/neodymium date from Lewisian granulites of 2.895 ± 0.1 Ga (2σ). The above-mentioned half-life is equivalent to a La β -decay constant of $2.30 \times 10^{-12} \text{ a}^{-1}$ and it can be recommended for geological application of the method.

17.9 Lutetium/Hafnium

As with rhenium/osmium and potassium/calcium, this depends on the β decay of a naturally occurring radioactive isotope and all three techniques can be applied to rocks and minerals that cannot be dated by other conventional methods. Also, studying their radiogenic daughters gives information about the terrestrial mantle as well as about the accreting of continental crust. For a long time, it was not possible to use the Lu/Hf approach because of the difficulty in determining the half-life of ^{178}Lu by dating appropriate minerals of which the age was known from other methods. Another problem was that of separating pure hafnium from other elements, but this has been overcome (Patchett and Tatsumoto 1980). Thereafter great progress has been made with dating both minerals and rocks.

Lutetium-176 is radioactive and subject to branched decay by β emission, mostly to ^{176}Hf , though approximately $3 \pm 1\%$ decays to ^{176}Yb . However, the latter can be disregarded because of the long half-life of ^{176}Lu . Thus, the decay scheme of interest is



which leads to an excited state of hafnium-176 first that “decays” to the ground state by γ emission.

Two approaches were used to determine the half-life of lutetium-176. These were analysis of lutetium-bearing minerals with known ages and direct counting. Variable results range from 2 to 7×10^{10} years and a calculation from the slope of a Lu/Hf isochron formed by ten achondrites (eucrites) with an age of 4.55×10^9 years gave a value of $(3.53 \pm 0.14) \times 10^9$ years. This value accords with a recent estimate of 3.8×10^9 years.

Hafnium is a dispersed element found in many minerals where it replaces zirconium and to a lesser extent titanium. In lutetium-bearing rocks, the radioactive decay of ^{176}Lu means that the abundance of ^{176}Hf increases as a function of time. To assess the age of a mineral or rock sample, the concentrations of lutetium and hafnium have to be measured and also the $[^{176}\text{Hf}/^{177}\text{Hf}]$ ratio after which an appropriate age equation can be applied. If a suite of samples has a common age, but differing $[^{176}\text{Lu}/^{177}\text{Hf}]$ ratios with the same initial $[^{176}\text{Hf}/^{177}\text{Hf}]_i$ ratio, all its members will lie on a straight-line isochron in the graph of $[^{176}\text{Hf}/^{177}\text{Hf}]$ vs. $[^{176}\text{Lu}/^{177}\text{Hf}]$, its slope being a monotonic function of their age (which, for relatively short ages, simplifies to proportionality) and its intercept being the initial $[^{176}\text{Hf}/^{177}\text{Hf}]_i$ ratio. (For a similar case, see [Sect. 17.16](#).) Data have been published on a suite of whole-rock samples and separated zircons from the Amitsoq gneiss, West Greenland, and the relevant isochron gave an age of 3.59 ± 0.22 Ga and an initial ratio of 0.280482 ± 0.000033 (Pettingell et al. 1981). This result agreed closely with others obtained using the rubidium/strontium method and quite well with uranium, thorium, and lead dating as well. Therefore, this date is probably a very reasonable estimate of the time elapsed since the sources of the Amitsoq gneiss were transferred up from the mantle.

From the Murchison chondrite meteorite, the $[\text{Lu}/\text{Hf}]$ ratio was taken as 0.24 and, assuming that the age of the chondritic reservoir is 4.55 Ga, the present value of the

[$^{176}\text{Hf}/^{177}\text{Hf}$] ratio would be 0.2828, taking into account the corresponding [$^{176}\text{Lu}/^{177}\text{Hf}$] ratio of this chondrite, which is 0.0334. These data define a hafnium growth curve valuable as a reference for the isotopic composition of hafnium in terrestrial rocks and minerals. In basalts from mid-oceanic ridges (MORB) and oceanic islands (OIB), the [$^{176}\text{Hf}/^{177}\text{Hf}$] ratio ranged from the above-mentioned 0.2828 to 0.2835 and usually exceeded the present ratio in the chondritic reservoir. It may be inferred that such basalts derived from mantle sources depleted in hafnium relative to lutetium during earlier episodes of partial melting, therefore having higher [Lu/Hf] ratios than do chondrites. Curiously, the [$^{176}\text{Hf}/^{177}\text{Hf}$] ratios of oceanic basalts correlate negatively with [$^{87}\text{Sr}/^{86}\text{Sr}$] ratios, but positively with [$^{143}\text{Nd}/^{144}\text{Nd}$] ratios (Patchett and Tatsumoto 1980).

Zircon crystals may contain detrital cores with ages preceding the crystallization of the igneous rocks that contain them and also they can acquire overgrowths during the metamorphism of their host. In such zircons, the hafnium may well have a wide range of isotopic compositions that produces a scattering of data points about the isochron and introduces systematic errors into the derived ages. However, zircons have low [Lu/Hf] ratios and so can be used to extend the [Lu/Hf] ratios of data points on isochrons as well as to calculate the initial [$^{176}\text{Hf}/^{177}\text{Hf}$]_i ratios of igneous rocks by using their ages after these ratios have been determined by alternative methods.

17.10 Manganese

Manganese has a naturally occurring stable isotope, ^{55}Mn , and 12 radioactive isotopes. The one of interest is ^{53}Mn that has a half-life of 3.7×10^6 years and decays by K-capture into the stable ^{53}Cr . It may be possible to use it in assessing the terrestrial ages of meteorites and extraterrestrial dust abundances in ice and sediments.

17.11 Nickel

Nickel has 5 stable and 11 unstable isotopes. The one of interest is ^{59}Ni with a half-life of 7.5×10^4 years. It decays by electron capture and is the longest-lived of the unstable isotopes. It has been employed to assess the terrestrial ages of meteorites and extraterrestrial dust abundances in ice and sediments.

17.12 Osmium/Osmium

Since negative thermal ion mass spectrometry (N-TIMS) for rhenium/osmium dating (see [Sect. 17.18](#)) was developed about 1990, not too much work has been published. This is probably due to the high rhenium blanks from the current generation of “clean” platinum filaments and to problems in achieving isotopic exchange and equilibrium between sample and spike for osmium. Another drawback is the non-homogeneity of samples. Because of this, rhenium and osmium concentrations may vary by up to 40% in the same sample.

Obviating such difficulties may be possible using “Os/Os,” that is to say $^{187}\text{Os}/^{186}\text{Os}$ and $^{187}\text{Os}/^{188}\text{Os}$, dating (Yin et al. 1993). The approach is a high-precision one, and its use with a molybdenite sample implied that it can become a geochronological tool even capable

of dating such minerals from meteorites. Irradiating a rhenium-bearing sample with thermal neutrons in a nuclear reactor enriches ^{186}Os and ^{188}Os proportionally to the neutron flux and the Re/Os ratio of the relevant sample. After free decay (i.e., after a short “cooling” period during which short-lived intermediate nuclides decay), the increments of ^{186}Os and ^{188}Os contents caused by thermal neutrons can be measured. (The relevant branching ratio is 0.922.)

Although very difficult to use, Os/Os dating could eliminate problems characteristic of conventional rhenium/osmium analyses and enable both the Re/Os ratio and the osmium isotopic composition to be derived from a single measurement. It is clear that the precision of age determination will reflect the instrumental precision of osmium isotope ratio measurements using N-TIMS. The method may offer the possibility of dating open systems, i.e., to say of obtaining age spectra by selective leaching or by in situ measurement of irradiated samples. However, the analytical procedure must be further refined, particularly as regards the flux monitor. Obviously establishing and certifying an appropriate monitor would facilitate extending the Os/Os method. And, since ^{186}Os , ^{187}Os , and ^{188}Os are variable and for ^{189}Os , there is significant ^{188}Os interference, e.g., in molybdenites; only $^{190}\text{Os}/^{192}\text{Os}$ can be used for the fractionation correction in all Os/Os dating measurements. MPI-Os is an available standard.

17.13 Pleochroic Haloes

These are bands or zones of discoloration surrounding uranium- and thorium-bearing inclusions in minerals, which show such radiation damage effects as a result of the interaction of α particles with atoms in the relevant crystal lattices to produce either displacement of the atoms or their electrons from their equilibrium positions. Such phenomena occur not only in colored minerals, but also in such colorless ones as muscovite and fluorite. The inclusions involved are centrally located with respect to the haloes and commonly comprise zircon, apatite, or sphene. Correlation with radioactivity was established as long ago as 1907. Pleochroic haloes are composed of concentric rings with radii ranging from 20 to 50 μm . They are produced by specific α particles emitted by the radionuclides occurring in the central inclusions. The radii record the kinetic energies of the corresponding α particles. Rings form because the ionizing power of such α particles maximize near the end of their ranges in particular media. (See the Bragg curve in [Fig. 8.5 in Chap. 8, Vol. 1.](#)) Probably the optimal mineral in which to examine them is biotite because of its perfect cleavage and also because radiation damage discoloration is easily observed. Although numerous attempts have been made to identify which radioisotope is responsible for which ring with any specific radius, in biotite, the matter is not yet completely solved. Controversy exists regarding giant haloes with diameters that may reach 110 μm . Some are caused by energetic α particles emitted for instance by polonium isotopes. Some have radii of about 54 μm and derive from uncommon 10.5 MeV α particles of ^{212}Po , a daughter of thorium.

The origin of haloes with greater radii is speculative. They may come from the diffusion of radioactive daughters of uranium and thorium. Otherwise, they could be due to the occurrence of residual primordial ^{244}Pu , which emits α particles with energies far exceeding 15 MeV during spontaneous fission. Another suggestion is that such giant haloes are produced by the radioactive decay of superheavy elements (SHEs) with atomic numbers up to 127. (See [Sect. 21.2.1, Chap. 21 in this Volume.](#))

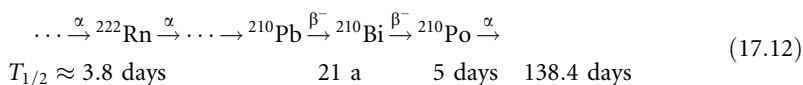
Pleochroic haloes have been used to date minerals and rocks. The method depends on the fact that the intensity of their colors increases with the alpha dose to which they have been exposed. The relationship between the two may fall into any one of three categories. In the first place, a normal stage exists in which color increases linearly with radiation dose. Secondly, there is a saturated stage in which the color reaches a maximum density and does not show any further increase with increasing radiation dose. Thirdly, there is an inversion stage in which coloration actually decreases with the intensity of the radiation dose – this is caused by extreme radiation damage. Only those from the first category are used for age determinations.

A number of assumptions have to be made. One is that the coloration really is a linear function of the received alpha dose. A second is that concentrations of radionuclides emitting alpha particles have not altered except through radioactive decay processes. Consequently, to date a mineral using this method entails measuring the alpha activity of the inclusion at the center of the pleochroic halo as well as assessing the intensity of color of this feature. Also, it is essential to know the relationship between the alpha dose and the intensity of color in the mineral to be dated. This latter can be established experimentally by irradiation of the mineral sample with alpha particles from an artificial source or by examining haloes in other samples of the same mineral with known ages.

Mineral dating using pleochroic haloes is possible, but drawbacks must be noted. One is that the haloes are to some extent erased by heating of the mineral during metamorphism (Fowler and Lang 1977; Hashemi-Nezhad et al. 1979). Secondly, the alpha activities in the inclusions are hard to measure. Finally, there is some ambiguity surrounding the exact relationship between the alpha dose and coloration in biotite, which is the best mineral for use in age determinations using pleochroic haloes.

17.14 Polonium/Lead

Polonium is a radioactive element with 27 isotopes, of which the longest-lived has a half-life of 103 years. The isotope of interest in this new geochronometer is ^{210}Po found in some uranium ores to the extent of one part in 10^{10} . It is a member of the uranium-238 series (see Fig. 7.6 in Chap. 7, Vol. 1) of which the most relevant steps are as follows:



In an undisturbed (closed) system, that is to say one at secular or radioactive equilibrium, ^{210}Po has the same activity as other radionuclides in this series. Preceded by ^{210}Bi , its immediate parent (half-life 5.013 days), fractionation occurs, and it equilibrates with its “grandparent,” namely ^{210}Pb .

The method described here has been suggested to date glassy eruption products within a few years after eruption (Rubin et al. 1994). The method is based on the fact that during eruption degassing occurs, which affects not only the obvious ^{222}Rn , but also ^{210}Po as its compounds (e.g., its halogenides) are rather volatile (even the pure metal has a fairly low boiling point of 962°C). So it is thought to be completely gaseous in volcanic eruptions at about 400°C . Due to the very short half-lives between ^{222}Rn and ^{210}Pb , equilibrium gets reestablished again within a few weeks all the way down to ^{210}Pb , so that the activity of the latter can be considered constant.

The calculation was based on a simplified form of the Bateman equation – see [Eq. \(7.42\) in Chap. 7, Vol. 1](#) – for closed system radioactive decay to describe the ^{210}Po content of degassed lavas as a function of time. Using appropriate initial conditions for solving [Eq. \(7.36\) in Chap. 7, Vol. 1](#), one obtains the following relationship for the activities:

$$(^{210}\text{Po}) \equiv (^{210}\text{Po})_t = (^{210}\text{Po})_0 e^{-\lambda t} + (^{210}\text{Pb})(1 - e^{-\lambda t}) \quad (17.13)$$

where t is the time elapsed since the eruption and λ is the decay constant of ^{210}Po .

For the numbers of atoms there is a slightly more complicated formula involving the decay constant λ_{Pb} of ^{210}Pb :

$$[^{210}\text{Po}] \equiv [^{210}\text{Po}]_t = [^{210}\text{Po}]_0 e^{-\lambda t} + [^{210}\text{Pb}] \frac{\lambda_{\text{Pb}}}{\lambda} (1 - e^{-\lambda t}). \quad (17.14)$$

To calculate t from one measurement of (^{210}Po), it is necessary to know both (^{210}Pb) and (^{210}Po)₀. While for a totally degassed lava, the latter term would be zero, it is probable that only partial degassing may take place in the case of submarine lavas, which erupted under high hydrostatic pressure. However, it is feasible to calculate a unique maximum value to t by assuming that total degassing occurred and fitting an exponential function to a set of measurements made on a sample as ^{210}Po grows into equilibrium with ^{210}Pb (Rubin et al. 1994). The maximum age corresponds to (^{210}Po)₀ = 0 on the best fit growth curve. The approach was applied to East Pacific Rise (EPR) lavas and repeated measurements of (^{210}Po) over several years were made on aliquots of each sample together with in-growth curves having the functional form of the above equation. They were fitted to the data using the time interval between sequential measurements in order to constrain t . The regression results gave a function for (^{210}Po) and the known analysis times linked the results to calendar time.

If degassing was not complete at eruption, the eruption time cannot be accurately ascertained, but is bracketed in every case by the “window” between collection of sample and calculated maximum age. Such “windows” (eruption dates) are most accurately determinable for samples either having the lowest (^{210}Po) when collected or for which the initial (^{210}Po)₀ can be estimated independently. Samples have been obtained from mid-ocean ridge basalts (MORBs), and these have similar chemical compositions and were erupted at the same water depth, both factors possibly affecting the efficiency of degassing. Hence, it can be anticipated that all will have more or less the same initial (^{210}Po)₀. But the degassing content may not be as high as the subaerial value of 100%. Two samples were analyzed by Rubin et al. (1994) and had the same ^{210}Po contents at the time of collection, which were only about 25% of the secular equilibrium value (25.1% and 25.6%, respectively), implying that all samples were minimally 75% degassed in the course of the eruption.

Best-estimate “windows” are about 2 months long and allow investigation of MORB eruption chronology on a much finer scale than was hitherto possible. If Po degassing turns out usually to be larger than the “conservative” minimum estimate of 75%, the resolution of the process may improve although such improvement would require analyses of ^{210}Po in a number of young MORBs having eruption dates, which are well-known so that the normal degree of degassing could be established. It was proposed that making remote observations of potential eruption indicators such as seismicity or mega-plumes that fall within an eruption “window” could also be valuable in constraining eruption dates and the range of initial (^{210}Po)₀ in MORBs.

17.15 Potassium/Argon

Potassium has 18 isotopes, of which the majority are unstable. The naturally occurring unstable one is potassium-40 and this undergoes branched radioactive decay to calcium-40 and argon-40 so that argon-40 abundance in the atmosphere is orders of magnitude greater than would be expected by comparison with abundances of the other inert gases. Hence, excess ^{40}Ar should occur in ancient potassium-bearing minerals, and once this was found to be the case, the foundation of the K/Ar dating method was laid. The relative abundances of the three significant potassium isotopes are ^{39}K 93.2581%, ^{40}K 0.1167%, and ^{41}K 6.7302%. Those of the interesting argon isotopes are ^{36}Ar 0.337%, ^{38}Ar 0.063%, and ^{40}Ar 99.6%.

Radioactive decay of potassium-40 to stable argon-40 takes place by electron capture (and also by positron decay) with the emission of γ quanta (energy 1.51 MeV). (See the decay scheme in [Eq. \(7.22\) in Chap. 7, Vol. 1.](#)) Eleven percent of the potassium-40 decays by electron capture to an excited state of argon-40 that de-excites by emitting a gamma ray. About 0.16% of the decays take a more direct route by electron capture straight to the ground state of argon-40. Positron decay is rare, taking place only about 0.001% of the time with an E_{max} of 0.49 MeV. It is followed by two annihilation gamma rays with a combined energy of 1.02 MeV.

Negatron (β^-) decay to stable calcium-40 involves most of the potassium-40 atoms and in fact only 11% of them decay to ^{40}Ar . In a potassium-bearing system closed to all external influences through geological time, the growth of radiogenic argon-40 and calcium-40 can be represented as

$$[^{40}\text{Ar}] + [^{40}\text{Ca}] = [^{40}\text{K}](e^{\lambda t} - 1) \quad (17.15)$$

where $\lambda = \lambda_{\text{EC}} + \lambda_{\beta}$ is the total decay constant of potassium-40, and all numbers of atoms including that of ^{40}K refer to the same moment t .

Each branch of the decay mode has its own decay constant and these are as follows. For ^{40}K to ^{40}Ar , it is $\lambda_{\text{EC}} = 0.581 \times 10^{-10} \text{ a}^{-1}$, and for ^{40}K to ^{40}Ca , it is $\lambda_{\beta} = 4.962 \times 10^{-10} \text{ a}^{-1}$. Summing gives a value for λ of $5.543 \times 10^{-10} \text{ a}^{-1}$ and the corresponding half-life is 1.25×10^9 years. The branching ratio is about 0.11. It should be added that there are other, slightly different, values for the decay constants in the literature.

The growth of radiogenic ^{40}Ar atoms in potassium-bearing minerals is given by

$$[^{40}\text{Ar}] = \frac{\lambda_{\text{EC}}}{\lambda} [^{40}\text{K}](e^{\lambda t} - 1) \quad (17.16)$$

where λ_{EC} is the decay constant for the decay of ^{40}K to ^{40}Ar .

The total number of argon-40 atoms will be the sum of the radiogenic ones and those that were present when the mineral formed. It is assumed that none was present initially and if this is the case, then, if the ^{40}Ar concentration and the amount of accumulated radiogenic argon-40 in a mineral are known, its age t can be derived from

$$t = \frac{1}{\lambda} \ln \left(1 + \frac{\lambda}{\lambda_{\text{EC}}} \frac{[^{40}\text{Ar}]}{[^{40}\text{K}]} \right). \quad (17.17)$$

Some other assumptions have to be made in order to derive values for t from various minerals. One is that none of the radiogenic ^{40}Ar arising from the radioactive decay of ^{40}K in the mineral during its geological history has escaped by diffusion. Another is that the mineral closed to ^{40}Ar soon after crystallization, hence rapid cooling must have occurred.

It is implicit in the method that no excess ^{40}Ar became incorporated in the mineral when it crystallized or during any subsequent metamorphic episodes. Finally, it is assumed that the mineral remained closed to potassium throughout its geological history so that the isotopic composition of the potassium in it must have altered solely through radioactive decay of the ^{40}K originally present and no isotopic fractionation took place. A correction is necessary for the presence of atmospheric ^{40}Ar . Also, the potentially disturbing effects of argon being overpressurized in extremely old basement rocks have to be considered because the gas might be released during metamorphism (Roddick 1983). However, it has been claimed that this may not always happen because analyses of Alpine muscovites in granites from the Helvetic basement (Aar Massif) in the central Swiss Alps showed that no argon overpressure, either of radiogenic or atmospheric origins, existed (Dempster 1986).

If argon loss occurred in a mineral, it happened usually because of metamorphism, this phenomenon showing the inability of argon to bond with other atoms in a crystal lattice. In fact, minerals have difficulty in retaining the gas even at quite low temperatures and at atmospheric pressure. So it is not surprising that the concept of closure temperatures below which, when minerals formed, crystallization ages were recorded, has been increasingly criticized. In the western Alps and Norway, old ages were retained despite later metamorphic temperatures believed to have exceeded the supposed closure temperatures (Chopin and Maluski 1980; Verschure et al. 1980). Clearly, other factors such as chemical weathering, deformation, ex-solution, and recrystallization may affect mineral age relationships. Naturally, only potassium-bearing minerals, rocks, and minerals able to resist as many as possible of these adverse influences are appropriate for dating by the K/Ar method. In fact, such rocks and minerals are quite common and, among igneous rock, include volcanics, although those containing devitrified glass must be avoided, as also should those containing such secondary minerals as xenocrysts. Basaltic glass can retain argon well, but hydrated glass cannot, especially if devitrified. Devitrified glass data revealed a lowering of K/Ar dates. Xenocrysts may produce the opposite effect if they possess excess radiogenic argon-40.

Such excess radiogenic argon-40 may occur in some potassium-bearing minerals, and its effects on K/Ar ages are most marked in young minerals or those with low potassium content. However, while beryl, cordierite, and tourmaline often contain such excess radiogenic argon-40, other minerals do not. The excess gas can result from the relevant minerals having been exposed to high partial pressure of the gas during an episode of regional metamorphism when pegmatites crystallize or kimberlite pipes are emplaced. In addition, it may diffuse into minerals as a result of the outgassing of older potassium-bearing minerals in the crust and mantle of the Earth or from older xenoliths or xenocrysts. Whenever it happens, K/Ar ages are increased and therefore give overestimates for the ages of minerals containing it. Minerals used in such dating have different blocking temperatures, e.g., that of biotite is lower than that of hornblende in deep-seated plutons and so the K/Ar “clock” of the hornblende starts before that of biotite since cooling is in progress. If temperature decrease was smooth and both minerals constituted closed systems since crystallization, the hornblende will register an older date than the biotite. If two such different dates are obtained, they can be used to infer the cooling rate.

Discordant K/Ar dates from coexisting minerals have been recorded in metamorphic rock samples from metamorphic rocks having two separate temperature histories. In such cases, either all the minerals were totally degassed during the metamorphic episode and slow cooling followed or the degassing process did not go to completion and the fraction of argon lost from a particular mineral will relate to the retentivity of that mineral for the gas.

17.15.1 The Metamorphic Veil Concept

Many biotites from granitic gneisses and schists of Precambrian age shields and orogenic belts have been dated by the method and results often reflected times elapsed after cooling through blocking temperatures rather than real ages. If such dates are plotted on a map, they form a conceptual surface termed the metamorphic veil (Armstrong 1966). The meaning of this is that the K/Ar dates veil the real ages of the host rocks and show only the metamorphic episode and the later cooling histories of the rocks. Regional homogeneity for such dates in shields and orogens implies that large parts of the continental crust may have undergone metamorphism, later cooling in large-scale systematic patterns perhaps induced by the uplifting of vast cratonic blocks bordered by extensive fracture zones extending far below the surface. Perhaps the K/Ar dates from an individual mineral of such a cratonic block might represent the time interval that elapsed since rocks now exposed at the surface were upthrust across the isotherm corresponding to the blocking temperature. Contours drawn to represent equal times since cooling through blocking temperatures have been termed thermochrons or chronochrons. In the Grenville Province, Canada, they run roughly parallel to the Grenville Front to form a southeasterly dipping surface. Rocks that are now exposed were uplifted through the blocking temperature isotherm between 850 Ma and 1.125 Ga ago, and the western edge of the Grenville craton was uplifted before the eastern. However, if the lower dates along the eastern edge are a result of argon loss induced thermally during the Appalachian orogeny, this would be an alternative explanation. Data from the Canadian shield cluster around certain values may relate to the presumed ages of orogenies, of which there were at least four for which the timescale was determined using K/Ar dating as well as whole-rock Rb/Sr and U/Th (Stockwell 1982). In association with this, eight structural provinces have been recognized on this shield and each stabilized at the end of a particular orogeny as is shown by the clustering of K/Ar mica dates around a so-called magic number. But the metamorphic veiling must be remembered – it conceals the real ages so that, for instance, the Grenville Province has rocks formed much earlier than the Grenville orogeny. A similar timescale has been constructed for the USA.

Coexisting minerals with the same presumed initial $[\text{}^{40}\text{Ar}/\text{}^{36}\text{Ar}]_i$ ratio and the same age can be represented by points defining a straight line in coordinates of the measured $[\text{}^{40}\text{Ar}/\text{}^{36}\text{Ar}]$ and $[\text{}^{40}\text{K}/\text{}^{36}\text{Ar}]$ ratios, this constituting an isochron. The slope of such an isochron, m , can be used to derive an equation for calculating relevant ages, which is as follows:

$$t = \frac{1}{\lambda} \ln \left(m \frac{\lambda}{\lambda_{\text{EC}}} + 1 \right) \quad (17.18)$$

where t is the time elapsed since crystallization.

Such K/Ar isochrons have been used extensively and clearly, they only form when all the samples involved are closed systems with respect to potassium and argon, this ensuring that the data points define the relevant slopes satisfactorily. The isochron approach is probably more advantageous than conventional K/Ar dating because the degree of good fit of such data points to a straight line expresses the degree of closure of the samples analyzed through geological time as well as the similarity or concordance of their initial $[\text{}^{40}\text{Ar}/\text{}^{36}\text{Ar}]_i$ isotopic ratios.

17.16 Potassium/Calcium

Calcium has six stable isotopes, the commonest being calcium-40 with an abundance of 96.98215%. The isotopic composition in minerals and rocks varies through the formation of

^{40}Ca by the negatron decay of ^{40}K (along one path of branched decay, the other leading to ^{40}Ar) and also because of the fractionation of calcium isotopes during several physicochemical processes. The possibility of calcium isotopes fractionating is great because of the considerable difference in their masses (about 20% of ^{48}Ca relative to ^{40}Ca). The decay constant for the decay of ^{40}K to ^{40}Ca is about $\lambda_\beta = 4.962 \times 10^{-10} \text{ a}^{-1}$. Co-genetic rocks or minerals with the same initial $[^{40}\text{Ca}/^{42}\text{Ca}]_i$ ratio and of the same age lie on an isochron in coordinates of $[^{40}\text{Ca}/^{42}\text{Ca}]$ and $[^{40}\text{K}/^{42}\text{Ca}]$ with a slope, m , of

$$m = \frac{\lambda_\beta}{\lambda} (e^{\lambda t} - 1) \quad (17.19)$$

and an intercept b equal to the original $[^{40}\text{Ca}/^{42}\text{Ca}]_i$ ratio. High precision values for this ratio relative to $[^{42}\text{Ca}/^{44}\text{Ca}]$ were about 0.31221, a useful reference for making fractionation corrections. The Pikes Peak batholith, Colorado, USA, was dated at $1.041 \pm 0.032 \text{ Ga}$ by isochron and this agreed closely with results from other isotopic geochronometers (Marshall and DePaolo 1982). The initial $[^{40}\text{Ca}/^{42}\text{Ca}]_i$ ratio was 151.024 ± 0.016 , and this is almost the same as that obtained from two stony meteorites and three mantle-derived rocks and minerals.

17.17 Radiocarbon (Carbon-14)

Radiocarbon is produced in the atmosphere through the impact of cosmic-ray neutrons on a small proportion of nitrogen-14 atoms in the following manner:



It then becomes incorporated into molecules of carbon dioxide by reaction with oxygen or by exchange with stable carbon isotopes in molecules of carbon dioxide or monoxide. Molecules of $^{14}\text{CO}_2$ mix rapidly into the atmosphere and hydrosphere as well as living organisms to attain a constant level of concentration representing a steady-state equilibrium maintained because of the continuous production of ^{14}C and its on-going radioactive decay; hence,



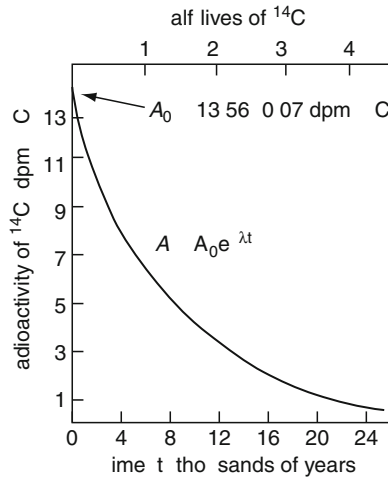
The Q -value of the above decay is only $Q = 0.156 \text{ MeV}$, and the ground state of nitrogen-14 is reached directly without γ emission. Thus, the result is a rather “soft” β radiation with $E_{\text{max}} = 156 \text{ keV}$.

Radiocarbon dating can be performed on objects made from once-living organisms such as wood or the remnants of such organisms. The idea behind the method is that the steady-state equilibrium stops between the organism and its environment as soon as it stops living. From that moment on, the specific activity of ^{14}C incorporated by the organism starts to decline (due to the above decay) according to the exponential law with a half-life of $5,730 \pm 40 \text{ years}$ (see [Chap. 7 in Vol. 1](#) as well as [Fig. 17.2](#) and [Eq. \(17.22\)](#) later on).

A multi-wire counter was used by Libby to measure the radiocarbon content in archeological artifacts. The first sample he dated was a piece of acacia wood from furniture in Pharaoh Zoser's tomb at Saqqara, Egypt. About 20 g were used, and the date determined was $2,030 \pm 350 \text{ years BC}$. The technique developed rapidly, and only 10 mg of the same sample were dated in 1992 in the new National Ocean Sciences Accelerator mass spectrometry facility at Woods Hole Oceanographic Institution and gave an age of $4,115 \pm 34 \text{ years}$, i.e., within one σ error of the first (Libby) analysis. The Oeschger Counter is another indispensable tool on

■ Fig. 17.2

The radioactive decay of radiocarbon in plant or animal tissues originally in equilibrium with atmospheric or hydrospheric $^{14}\text{CO}_2$ molecules. Exchange ceases after the deaths of the organism involved. The radioactivity diminishes as a function of time (half-life of ^{14}C is 5730 ± 40 years). When the residual radiocarbon activity is measured, the age of the sample is obtainable from this graph



measuring the activity of the naturally occurring radioisotope (carbon-14). Oeschger, together with F. T. Houtermans (Bern), built the first Radiocarbon Dating Laboratory in Switzerland and was the first to date the “age” of Pacific deep water. The Oeschger Counter facilitated the application of the ^{14}C method to geophysical problems.

17.17.1 Conversion of Radiocarbon Years to Calendar Years

To do this conversion, it requires corrections accounting for fluctuations of radiocarbon content in atmospheric carbon dioxide in the past. These are based on measurements of radiocarbon concentrations in a series of tree rings dated using dendrochronological techniques. The tree ring calibrated age for the modern carbon-14 AMS equipment analysis of the Zoser wood gives two solutions with a 95% degree of confidence: 2877–2800 BC and 2780–2580 BC. This fact accords with archeological estimates. However, a marked step in the calibration curve during Zoser’s reign precludes a high precision calibrated age estimate for this particular material.

17.17.2 Atmospheric Radiocarbon in the Past

There have been systematic variations in the radiocarbon content of the atmosphere in the past, which cause inaccuracies where dating is concerned. One reason for such variations is that the rate of formation by the (n,p) reaction shown by [Eq. \(17.20\)](#) depends mostly on the density of the cosmic-ray-produced neutron flux (see [Eq. \(7.68\)](#) in Chap. 7, Vol. 1), which increases

with altitude to attain a maximum between 12,000 and 15,000 m above the surface of the Earth. Also, the flux is greater by a factor of four in the polar regions. Consequently, the rate of production of radiocarbon there should mean that living tissues in that region ought to have more radiocarbon in them than those at the equator. However, it has been shown that specific ^{14}C activity may be independent of location probably because of rapid mixing in the upper atmosphere, a process believed to last less than 2 years. The effect of this may well tend to produce uniformity at the surface of the Earth. In addition, the neutron flux will vary as the intensity of the solar proton flux does, so that the ^{14}C content of the atmosphere doubtless varied with time in conjunction with alternating solar activity. Additionally, the cosmic-ray flux may be modified by changes in the Earth's magnetic field during the past 40,000 years or so, although data have been published implying that the initial radiocarbon in a set of archeologically dated samples was compatible with present day values (Arnold and Libby 1949).

17.17.3 Radiocarbon in Dead Animals and Plants

The radioactivity of a carbon sample from a plant or animal tissue, which died t years ago is given by $A = A_0 e^{-\lambda t}$, where A is the specific activity now and A_0 is the specific activity of ^{14}C in the same sample when death occurred. A value for the estimated specific activity of ^{14}C was 226 ± 1.2 Bq/kg and the half-life, $T_{1/2}$, was given as $5,730 \pm 40$ years with a decay constant of 1.209×10^{-4} . A “dead” sample containing carbon can be considered no longer in equilibrium with the ^{14}C of the atmosphere.

From the exponential law of decay applied to (specific) activities one obtains

$$t = \frac{1}{\lambda} \ln \left(\frac{A_0}{A} \right) \quad (17.22)$$

which, substituting the value of λ , gives

$$t = 8271.3 \ln \left(\frac{A_0}{A} \right) \text{ years.} \quad (17.23)$$

The initial activity is a known constant through the past 70,000 years independent of passing time and with a value independent of geographical location and the species of dead plant or animal from which the relevant tissues are taken. It is assumed that the sample to be dated was not contaminated by modern radiocarbon and that its observed activity is unaffected by radioactive impurities. Research has shown that the initial carbon-14 activity of modern plant and animal tissues is constant to a first approximation and also that the radiocarbon activity in archeological materials of known age is measurable with sufficient precision to provide radiocarbon dates that agree satisfactorily with the known historical ages.

Materials suitable for radiocarbon dating include charcoal, peat, wood, grains and seeds, ivory, burnt bones, collagen, cloth, inorganic and organic carbon in shells, lake marls, lake and deep-sea sediments, pottery, and iron. Amounts needed for analysis vary from about 25 g for wood to 5,000 g for iron. To measure the radiocarbon contents, liquid scintillation has been used and is adequate for dates <30,000 years old. Ultrasensitive high-voltage tandem mass spectrometers offer direct counting of ^{14}C ions, but the technique is expensive.

17.17.4 The De Vries Effect

It has been shown that the radiocarbon content of the atmosphere varied systematically in the past so that the radiocarbon activity around 1,500 and 1,700 was approximately 2% higher than it was during the nineteenth century. This phenomenon has been termed the De Vries effect, and another such effect (called the Suess effect) has been observed in twentieth century activity and is ascribed to the introduction of “dead” CO₂ into the atmosphere through the combustion of fossil fuels after the start of the Industrial Revolution (De Vries 1958).

17.17.5 Bomb, Reactor, and Accelerator Radiocarbon in the Environment

Larger effects came from atmospheric thermonuclear explosions then and later by the operation of nuclear reactor and particle accelerators. Bomb-produced radiocarbon is detectable in the oceans and also in the biosphere. To narrow uncertainty of estimates of fossil fuel, anthropogenic carbon dioxide uptake by the oceans is important in quantifying the contemporary carbon budget. Using ocean general circulation models (OGCMs) may be the best way of tackling this problem, but first the model has to be calibrated with the distribution of bomb-produced radiocarbon in the ocean. Natural, i.e., cosmic ray-produced, radiocarbon is most sensitive to processes operating over century timescales, whereas anthropogenic (i.e., bomb testing-produced) radiocarbon is most sensitive to processes operating over 10-year periods. If the bomb-produced radiocarbon is not separated from the natural radiocarbon, it will not be possible to determine whether the disagreements between model and observation reflect the deficiencies in the model's simulation of the steady-state distribution of natural radiocarbon or in its simulation of the distribution of the bomb radiocarbon transient. Therefore, the separation of bomb-produced radiocarbon from the natural radiocarbon in the overall radiocarbon measurements is essential if radiocarbon distribution is to be used to constrain the ocean models.

17.17.6 Separating Bomb-Produced ¹⁴C from Natural Radiocarbon

A method of achieving such a separation has been developed. It involves the strong correlation between natural radiocarbon and dissolved silica. For global coverage, radiocarbon measurements made on samples collected during the Geochemical Ocean Sections Study (GEOSECS) in 1972–1978 were analyzed for bomb radiocarbon inventory in the ocean. Later measurements made in the Atlantic Ocean during Transient Tracers in the Ocean (TTO) in the early 1980s and South Atlantic Ventilation Experiment (SAVE) in the late 1980s were also analyzed for temporal variations in bomb radiocarbon inventory. Recent radiocarbon measurements on the NOAA/OACES 1993 cruise in the Atlantic have also been analyzed for bomb radiocarbon inventory. In the Pacific Ocean, radiocarbon measurements from samples collected in the WOCE program are gradually becoming available for bomb radiocarbon inventory analysis. Continuing efforts in analyzing WOCE data have been proposed.

Comparison of results between GEOSECS and TTO/SAVE shows that the bomb radiocarbon inventory has increased by 36% for the region north of 10° N, by 69% for the equatorial region and by 71% for the region south of 10° S. These data reflect the radiocarbon uptake for the Atlantic Ocean between 1973 (GEOSECS) and 1985 (TTO/SAVE). Along with global bomb radiocarbon distribution, this information provides crucial constraints for the carbon cycle in the ocean. Preliminary results from CGC-91, one of the WOCE cruises, show that the observed increase in bomb radiocarbon inventory from 1974 to 1991 in the northern Pacific Ocean is consistent with the first-order prediction from a box-diffusion ocean model.

17.17.7 Variation of Bomb Radiocarbon in Oceans

Variation of bomb radiocarbon in oceans has been applied to the analysis of banded corals and so to lower latitudes. A shell-derived chronological history of bomb ^{14}C on Georges Bank and its Labrador Sea implications offered high latitude data resulting from the analysis of a 54-year-old mollusk (age assessed from annual growth bands) using accelerator mass spectrometry. This finding gave a time history from 1939 to 1990 and so widened the scope of such investigations. Other significant information came from the southern Great Barrier Reef in Australia (Druffel and Griffin 1993). Radiocarbon and stable isotope ($\delta^{18}\text{O}$ and $\delta^{13}\text{C}$) data for biannual samples were obtained from a 323 years banded coral series collected from the region. The high precision $\Delta^{14}\text{C}$ record showed variations on an interannual timescale that were especially large from 1,680 to 1,730. This observation may have nothing to do with atmospheric changes, but perhaps involved in vertical mixing and large-scale advective changes of source waters to the western Coral Sea. Low values from 1,935 to 1,875 may relate to El Niño/Southern Oscillation (ENSO) events in the eastern tropical Pacific. But these values cannot explain all the variations, especially those from 1,875 to 1,920 characterized by high $\Delta^{14}\text{C}$ values. The time interval 1,635 to 1,795 appears to embody a 6-year periodicity, a coherency later lost. It may be inferred that secular changes take place in the nature and properties of the ENSO as manifested in the southwestern Pacific. Interestingly, no trace of the Suess effect was found from the coral record.

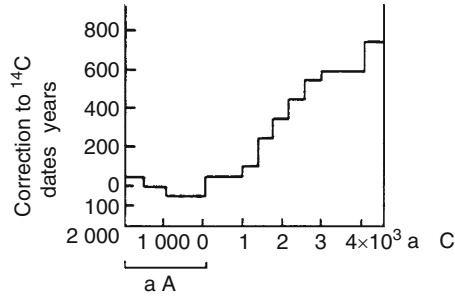
17.17.8 Dendrochronology and Radiocarbon

Further to previous remarks regarding Zoser's tomb and the converting of radiocarbon years to calendar ones, analyzing old trees facilitated investigation of the secular variations of the radiocarbon content of the atmosphere. Such trees can be dated using tree rings, annual accretions of woody tissue to the circumferences of their trunks.

Layers deposited earlier cannot receive radiocarbon from the atmosphere anymore so that their radiocarbon contents decrease by radioactive decay. Two tree species that have been used are *Pinus aristato* (bristlewood pine) and *Sequoia gigantea* (sequoia). Combining dendrochronology with isotopic investigations enables age-corrected deviations of the radiocarbon contents of such trees to be used in calculating corrections applicable to conventional radiocarbon dates (► Fig. 17.3). The drawback is that the technique is valid only back about 12,000 years into the past. However, examination of varve chronologies of sediments deposited in glacial lakes extends the approach further back. The researches imply that the radiocarbon content of the atmosphere varied by about $\pm 10\%$ of the nineteenth century value.

■ Fig. 17.3

The graph gives the corrections that have to be added to radiocarbon dates so as to bring them into agreement with tree ring dates based on 143 analyses of the wood of bristlecone pine (*Pinus aristata*) and sequoia (*Sequoia gigantea*), which gave dendrochronological dates



17.17.9 Radiocarbon and Dating Groundwaters

Radiocarbon is important for dating groundwaters on the basis that the soil-zone carbon dioxide is of biogenic origin resulting from the respiration of plant roots and also from the decay of plants. So, indirectly, it contains radiocarbon from the atmosphere. The actual content of the radioisotope decays steadily since the gas is no longer in contact with the atmosphere and the fraction of the original content remaining is a measure of the time elapsed since this happened through infiltration. The time since this occurred, t , is given by

$$t = 8,720 \ln \left(\frac{C_0}{C} \right) \text{ years} \quad (17.24)$$

where 8,270 is the mean life of radiocarbon in years, C_0 is the initial concentration of the radiocarbon, and C is the concentration recorded in the sample.

Since radiocarbon is measured relative to the total carbon content of the sample, the origin of the stable carbon present must be examined as well. Not all of it is similar in origin to the atmospheric radiocarbon since infiltrating water contains carbon dioxide dissolved out of the soil zone, which dissolves carbonate minerals in the soil. However, water from limestone contains no radiocarbon and therefore that which reaches the water table contains dissolved carbon in the chemical forms H_2CO_3 , HCO_3^- and CO_3^{2-} with a radiocarbon content lower than that occurring in the soil (biogenic) carbon dioxide. The evaluation of the dilution of soil carbon dioxide originally containing 100% modern radiocarbon with radiocarbon-free (“dead”) carbonate in order to estimate the initial radiocarbon concentration in recharge water reaching the water table is one of the most difficult problems of radiocarbon age determination.

An interesting study of the frequency distribution of radiocarbon ages in groundwater samples collected in the Sahara has appeared (IAEA 2002). It has been known for at least a century that large reserves of groundwater lie beneath the Sahara, the largest desert in the world. Radiocarbon dating made it possible to estimate the age of these groundwaters. From a graph based on 350 samples collected in Algeria, Libya, Egypt, and the Southern Sahara, it was shown that aquifers in Northern Africa were recharged mainly during the pluvial periods of the Holocene and during the interstadials of the last glacial period. A well-marked minimum in the distribution curve ranging from approximately 12 to 20,000 years B.P. reflects the time interval

of maximum aridity in Northern Africa. This estimate of the groundwater age is critical in exploiting this groundwater resource, all the more so since absence of tritium and low concentrations of radiocarbon strongly imply that the aquifer in question is not being replenished at present.

17.17.10 Fractionation of Carbon Isotopes in Nature

Fractionation of the carbon isotopes in nature entails small systematic errors in radiocarbon dates that can be eliminated when the isotopic composition of stable carbon to be dated can be assessed using a mass spectrometer. The value is expressed as $\delta^{13}\text{C}\%$. Such fractionation during photosynthesis alters the abundances of the stable isotopes ^{12}C and ^{13}C from those prevailing in the atmosphere and plants usually become enriched in ^{12}C and depleted both in ^{13}C and ^{14}C .

17.18 Rhenium/Osmium

The beta decay scheme of rhenium-187 to osmium-187 may be applied to the study of sulfide minerals of molybdenum and osmium-rich minerals such as iridosmine. Together with rubidium/strontium, samarium/neodymium, lutetium/hafnium, and uranium/lead methods, it has been used to examine mantle differentiation and the accretion of continental crust. In molybdenites, rhenium concentrations vary from a few ppm to as much as 1.88%. The element has two naturally occurring isotopes, and these are the stable rhenium-185 with a relative abundance of 37.398% and the radioactive rhenium-187 with a relative abundance of 62.602%. This decays as follows:



with a Q-value about 2.5 keV. This makes it difficult to determine its half-life by direct counting, but it is about 4.56 Ga and its decay constant is about $(1.64 \pm 0.05) \times 10^{-11} \text{ a}^{-1}$.

The growth of osmium in a rhenium-bearing system is expressible as

$$\left[\frac{^{187}\text{Os}}{^{186}\text{Os}} \right] = \left[\frac{^{187}\text{Os}}{^{186}\text{Os}} \right]_i + \left[\frac{^{187}\text{Re}}{^{186}\text{Os}} \right] (e^{\lambda t} - 1). \quad (17.26)$$

The first term is the isotope ratio of the isotopes now, the second that which prevailed initially when the system closed to both elements, and the third includes the present ratio of rhenium-187 to osmium-186, λ being the decay constant of ^{187}Re . Of course, the second term must necessarily be an assumption. This equation is applicable to a suite of samples with a common age and presumably, the same initial $[^{187}\text{Os}/^{186}\text{Os}]_i$ ratio and these form an isochron in coordinates of $[^{187}\text{Os}/^{186}\text{Os}]$ and $[^{187}\text{Re}/^{186}\text{Os}]$ of which the relevant slope is proportional to their age. Taylor expansion of the exponential expression in [Eq. \(17.26\)](#), namely, yields the following approximation for relatively short ages:

$$\left[\frac{^{187}\text{Os}}{^{186}\text{Os}} \right] \approx \left[\frac{^{187}\text{Os}}{^{186}\text{Os}} \right]_i + \left[\frac{^{187}\text{Re}}{^{186}\text{Os}} \right] \lambda t \quad (17.27)$$

where the zero intercept of the isochron will give the initial $[^{187}\text{Os}/^{186}\text{Os}]_i$ ratio.

The concentrations of both elements have been determined in iron meteorites and these plus the metallic grains of chondrules were found to fit the same isochron, implying that they formed from the solar nebula (thought to have contained isotopically homogeneous osmium) in a very short time interval estimated to be about 90 Ma. The primordial $^{187}\text{Os}/^{186}\text{Os}$ ratio has been given as 0.807 ± 0.006 . And the isotopic compositions of both rhenium and osmium in meteorites are compatible with terrestrial sample values.

17.18.1 Rhenium/Osmium in Meteorites and the Mantle

Molybdenites are particularly suitable for rhenium/osmium dating because their $[\text{Re}/\text{Os}]$ ratio is very high. The rhenium contents of molybdenites have been recorded as ranging from 2 to 230 ppm in 19 samples. From these samples, ages ranging from 105 Ma to 2.54 Ga were obtained. Osmium-bearing minerals may record the isotopic evolution of the element in the mantle as is implied by the genetic association of iridosmine with ultramafic rocks. Data have been published on measurements of $^{187}\text{Os}/^{186}\text{Os}$ ratios from iridosamine samples with known ages and, when shown in coordinates of $^{187}\text{Os}/^{186}\text{Os}$ and time t , fitted a straight line with slope m .

The collinearity of these data points indicates that the mantle sources of these samples probably had a homogeneous $[\text{Re}/\text{Os}]$ ratio (Luck et al. 1980) that changed solely through the decay of rhenium-187. The value of this ratio was calculated from the slope of the osmium-development line shown by [Eq. \(17.27\)](#):

$$\left[\frac{^{187}\text{Re}}{^{186}\text{Os}} \right] = \frac{m}{\lambda}. \quad (17.28)$$

Considering this equation and the concrete value determined for m , if $\lambda = 1.52 \times 10^{-11} \text{ a}^{-1}$, then the $^{187}\text{Re}/^{186}\text{Os}$ ratio in the mantle is 3.34 ± 0.14 and the corresponding $[\text{Re}/\text{Os}]$ ratio is about 0.085. The intercept of the osmium-development line gives a value for the $^{187}\text{Os}/^{186}\text{Os}$ ratio in the mantle at present, i.e., at $t = 0$, of 1.040 ± 0.01 . Both ratios in the mantle fit the Re/Os isochron for meteorites and the agreement suggests that the Earth and the parental bodies of the meteorites formed at about the same time from a primordial source containing rhenium and osmium, both with a homogeneous isotopic composition. Since a unique osmium-development line exists, it can be inferred that, despite internal magmatic activity accompanying the formation of the crust, the mantle is homogeneous as regards its rhenium/osmium ratio. Granites, ultrabasics, and basalts have similar concentrations; therefore, the element Re was not appreciably partitioned during partial melting and fractional crystallization, the geochemical differentiation of the mantle not having changed its rhenium concentration much. As osmium is depleted in granites and basalts compared to ultra-mafics, it could be that only a small fraction of mantle osmium has been transferred into the crust. Hence, while the $[\text{Re}/\text{Os}]$ ratio appears to have been rather stable through geological time, the crust appears to have undergone more variation with respect to it. Thus, its variability could be a useful indicator of crustal contamination of magma.

17.19 Rubidium/Strontium

Rubidium has an ionic radius sufficiently close to that of potassium that it can substitute for the latter in all potassium-bearing minerals, and hence it occurs as a dispersed element forming

measurable parts of micas, potassium feldspar, some clay minerals, and evaporites. Two isotopes occur in nature, namely rubidium-85 and the radioactive rubidium-87 with isotopic abundances of 72.17% and 27.83%, respectively. Rubidium-87 undergoes decays by negatron emission to strontium-87 with a half-life, $T_{1/2}$, of 4.8×10^{10} years. Regarding this, other values have been proposed, which affect the value of the decay constant, although $1.49 \times 10^{-11} \text{ a}^{-1}$ must be close to the true figure.

The decay process is



where $Q = 275 \text{ keV}$.

Strontium has four naturally occurring isotopes, strontium-87 having a relative abundance of 7% and a metastable state with a γ energy of 388 keV for the isomeric transition. This decays by electron capture in a time interval determined by the half-life of 2.81 h. The abundance varies reflecting the formation of radiogenic ^{87}Sr by the decay of ^{87}Rb . Therefore, the precise isotopic composition of strontium in a mineral or rock containing rubidium depends on the age and the $[\text{Rb}/\text{Sr}]$ ratio of either.

The growth of radiogenic ^{87}Sr in a rubidium-enriched mineral over a time interval t is given by the following expression:

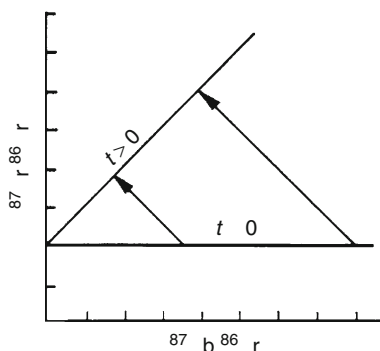
$$[^{87}\text{Sr}] = [^{87}\text{Sr}]_0 + [^{87}\text{Rb}](e^{\lambda t} - 1) \quad (17.30)$$

where $[^{87}\text{Sr}]$ and $[^{87}\text{Rb}]$ are the total numbers of atoms of the respective isotopes in a unit mass of the mineral now and $[^{87}\text{Sr}]_0$ is the amount of ^{87}Sr incorporated in it when crystallized, λ is the decay constant of ^{87}Rb , and t is the age of the mineral sample.

An equation for age determination has been presented and based on real isochrons. A rubidium/strontium three-isotope plot (see [Fig. 17.4](#)) is constructed involving $[^{87}\text{Sr}/^{86}\text{Sr}]$ against $[^{87}\text{Rb}/^{86}\text{Sr}]$. When a rock cools, all of its minerals have the same ratio of strontium-87 to strontium-86 though they will have varying amounts of rubidium. As the rock ages, rubidium decreases by changing to strontium-87. For any given age, the composition can be represented by a line through the points, and this line can be extrapolated back to zero to

■ Fig. 17.4

A rubidium/strontium “three-isotope” diagram showing the time-dependent isotopic evolution of rock systems after they crystallize from a homogeneous magma



obtain the initial $[^{87}\text{Sr}/^{86}\text{Sr}]_0$ ratio. This ratio is about 0.70775, but for the K/T Boundary it is 0.70790, a rise attributed to acid rain. Values at this boundary have been given as 1.6 for Denmark, 1.3 for Colorado, and 1.1 for New Zealand. The age of the rock is determinable from the slope of the isochron. This slope is a monotonic function of the age of the rock and the older the rock, the steeper the line. If the slope of the line is m , the age t is given by

$$t = \frac{1}{\lambda} \ln(m + 1) = \frac{T_{1/2}}{\ln 2} \ln(m + 1). \quad (17.31)$$

Measuring rubidium and strontium concentrations in suitable minerals can be effected using standard chemical and mass-spectrometric procedures, X-ray fluorescence, or isotope dilution.

Real isochrons may be altered through metamorphism when heat causes minerals to deviate from the whole-rock isochron and each acquires its own isochron. Also, new minerals may form, and existing minerals may recrystallize. The entire situation is one of mobility entailing ionic diffusion. Metasomatism may occur and involve both the bulk chemical composition and the trace element composition. The phenomenon can affect the parent/daughter relationships of all naturally occurring radioactive element systems in a particular rock. A suitable age equation for t is available and, to implement it, the best rocks to utilize are igneous acidic ones such as granite because they contain both micas and potassium feldspars. However, both concordant and discordant results may be obtained. The latter results are due to gain or loss of radiogenic ^{87}Sr caused by geological events usually connected to metamorphism. And when forming, such igneous rocks undergo fractional crystallization of magna involving the separation of crystals from an ever-diminishing liquid magma so that suites of comagmatic igneous rocks have different chemical compositions. However, if it is assumed that the strontium in such a magma stayed isotopically homogeneous through the cooling process, all the various suites formed will have the same initial $[^{87}\text{Sr}/^{86}\text{Sr}]_0$ ratio. It is reasonable to assume that all rocks formed will have about the same age because cooling and crystallization times are negligible compared to the age of the event. In this way, the age equation may be regarded as relating to a set of suites and creating a group of straight lines on a plot having a slope intercept such that

$$y = b + mx. \quad (17.32)$$

All rock samples from a comagmatic suite plot as points on a straight line in coordinates of $[^{87}\text{Sr}/^{86}\text{Sr}]$ (y) and $[^{87}\text{Rb}/^{86}\text{Sr}]$ (x), that is to say that they form an isochron. Its slope is related to t as

$$m = e^{\lambda t} - 1 \quad (17.33)$$

and the value of the initial $[^{87}\text{Sr}/^{86}\text{Sr}]_0$ ratio may be provided by the y -intercept b .

17.19.1 Fictitious Isochrons in the Rift Valley

Fictitious isochrons have slopes devoid of any geochronological significance. If a set of samples resulted from the mixing of two components with different $[^{87}\text{Rb}/^{86}\text{Sr}]$ and $[^{87}\text{Sr}/^{86}\text{Sr}]$ ratios, they will fall on a straight line, which links the end members in coordinates of these ratios. The result is a fictitious isochron, which may have a positive or a negative slope depending on the relative values of the end members. An instance was obtained from potassic lava flows found in

volcanic centers lying along the western Great Rift Valley north of Lake Tanzania and west of Lake Victoria, these centers being about 160 km apart (Bell and Powell 1969). Identified as Pliocene to Recent in age, their volcanic activity is believed to have continued into historical times so there is no doubt that the relevant rocks are young and ought to give an isochron with practically zero slope. However, a significant positive correlation between the average $[^{87}\text{Sr}/^{86}\text{Sr}]$ and the $[^{87}\text{Rb}/^{86}\text{Sr}]$ ratios of the rock types was found and the straight line drawn through the data points was not an isochron, rather a mixing line. It had a slope yielding a fictitious age of 773 Ma because the $[^{87}\text{Sr}/^{86}\text{Sr}]$ ratios of the rocks resulted from mixing and do not relate to the radioactive decay of rubidium-87 in them after crystallization took place.

17.19.2 Meteorites, BABI, LUNI, and FUN

Rubidium/strontium analyses of chondritic meteorites gave an average age of about 4.49 Ga as did those of achondrites and it was suggested that crystallization occurred fast and that they had similar initial $[^{87}\text{Sr}/^{86}\text{Sr}]_0$ ratios. Basaltic achondrite analyses gave the value for the primordial $[^{87}\text{Sr}/^{86}\text{Sr}]_p$ ratio of 0.6987 ± 0.00003 and this is termed BABI (Basic Achondrite Best Initial). Isotope anomalies in meteorites imply that the solar nebula could not have been isotopically homogeneous with respect to some elements. The concert of Fractionation and Unknown effects as possible causes produced the term FUN (Papanastassiou and Wasserburg 1969). The Rb/Sr method was used to help in unveiling the seismological history of the Moon and an age for the satellite of about 4.5 Ga was obtained. BABI is paralleled by LUNI of which a value has been given as 0.69892 ± 0.00009 (Nyquist 1977).

17.19.3 Some Caveats

It must be added that there is a number of things that can present difficulties for the Rb/Sr dating method and include the following. One is the case where a rock contains some minerals that are older than the main part of the rock. Occasionally, magma inside the Earth will take up unmelted minerals from the surrounding rock as it moves through a magma chamber. Normally, such “xenoliths” are distinguishable from the younger minerals surrounding them. If they are not used for dating the rock, the points represented by these minerals will be off the line made by the rest of the points. Another problem arises if a rock has suffered metamorphism during which it became extremely hot but not sufficiently hot to completely remelt the rock. Then, dates will be confused and not lie along a line. Some minerals will have completely melted others not at all. Thereafter, some minerals will try to give the igneous age, while some others will try to give the metamorphic age. In such cases, there will not be a straight line and no valid date is determined.

In some rare cases, the Rb/Sr method gave straight lines giving wrong ages. This may result when the rock being dated was formed from a magma that was not well mixed and had two separate batches of rubidium and strontium. One magma batch had rubidium and strontium compositions near the upper end of a line and one batch had compositions near the lower end of the line. Then, the minerals received a mixture of both batches and the resulting composition ended near a line *between* the two batches. Such a state of affairs is termed a two-component

mixing line. Among tens of thousands of rubidium/strontium dates, at least 30 cases have been documented. Of course, if a two-component mixture is suspected, a second dating method must be employed in order to either confirm or disprove the rubidium/strontium date. In general, it may be stated that agreement between several dating methods is by far the best way to date rocks.

17.20 Samarium/Neodymium

Both of these elements are lanthanides (rare earth elements), and each has 26 isotopes, of which seven occur naturally. Samarium-147 is radioactive and decays by α emission to a stable isotope of neodymium, ^{143}Nd :



The half-life of ^{147}Nd is 1.06×10^{11} a with a corresponding decay constant of $6.54 \times 10^{-12} \text{ a}^{-1}$, and the decay scheme is applicable to dating terrestrial rocks, stony meteorites, and lunar materials.

Samarium, neodymium, and the other rare earth elements occur in high concentrations in minerals such as monazite (CePO_4) and as trace elements in common rock-forming ones such as biotite and plagioclase feldspar. The atomic $[\text{Sm}/\text{Nd}]$ ratio on Earth varies from 0.1 to 0.5 and the relative abundances are 15% for ^{147}Sm and 12.18% for ^{143}Nd . It has been suggested that neodymium is more concentrated than samarium during the fractional crystallization of magma and that crustal rocks usually have lower $[\text{Sm}/\text{Nd}]$ ratios than rocks originating from the upper mantle such as oceanic tholeiites. Also, during the formation of silicate liquids by partial melting of rocks in the crust or mantle of the Earth, the liquid phase may enrich in neodymium relative to samarium. This may be because Nd^{3+} has a larger ionic radius than samarium, which gives it a lower ionic potential as a result of which it forms weaker ionic bonds that can be more easily ruptured than those involving Sm^{3+} .

The growth of radiogenic ^{147}Nd due to the decay of ^{147}Sm can be given as

$$\left[\frac{^{143}\text{Nd}}{^{144}\text{Nd}} \right] = \left[\frac{^{143}\text{Nd}}{^{144}\text{Nd}} \right]_0 + \left[\frac{^{147}\text{Sm}}{^{144}\text{Nd}} \right] (e^{\lambda t} - 1) \quad (17.35)$$

where ^{144}Nd acts as the reference since the number of its atoms in a unit quantity of any given sample remains constant so long as the host system remains closed to neodymium. The decay constant of ^{147}Sm , λ , is taken to be $6.54 \times 10^{-12} \text{ a}^{-1}$.

Determination of ages by the Sm/Nd method entails analyzing either individual minerals or cogenetic rock suites in which the ratios between the two are sufficiently different to define the slope of an isochron in coordinates of $[^{143}\text{Nd}/^{144}\text{Nd}]$ and $[^{147}\text{Sm}/^{144}\text{Nd}]$. The method is especially suitable for mafic and ultramafic rocks, cf. the Rb/Sr method, which is best suited for acidic and intermediate igneous rocks enriched in rubidium and depleted in strontium. Since the rare earth elements are less mobile than the alkali metals and the alkaline earths, phenomena such as regional metamorphism have less effect on them. Hence, suitable rocks can be dated by the Sm/Nd method even if they have lost or gained rubidium and strontium and this makes the Sm/Nd method a useful complement to the R/Sr method.

17.20.1 Apollo-12, ADOR, and CHUR

Volcanics from the Onverwacht Group, Swaziland and South Africa, comprise the basal part of the Early Precambrian Barberton greenstone belt found both in Swaziland and the Transvaal. Data from them gave an age of about 3.54 Ga calculated using an initial $^{143}\text{Nd}/^{144}\text{Nd}$ ratio of 0.50809 ± 0.0004 (Hamilton et al. 1979). The strontium and neodymium isotopic record of *Apollo-12 basalts* from the Moon were examined. Isochrons were derived for an achondrite (eucrite) and another meteorite and gave ages of about 4.58 and 4.562 Ga, respectively, with primordial $^{143}\text{Nd}/^{144}\text{Nd}$ ratios of 0.50684 ± 0.00008 and 0.506664 . An initial $^{87}\text{Sr}/^{86}\text{Sr}$ ratio was termed *ADOR*. The isotopic evolution of neodymium in the Earth has been described by means of a model termed *CHUR* (CHondritic Uniform Reservoir). And the present value of the $^{143}\text{Nd}/^{144}\text{Nd}$ ratio is 0.512638 relative to a $^{146}\text{Nd}/^{144}\text{Nd}$ ratio of 0.7219. The present value of the $^{147}\text{Sm}/^{144}\text{Nd}$ ratio of CHUR is 0.1967, which permits calculation of $^{143}\text{Nd}/^{144}\text{Nd}$ ratio in any past time interval.

17.21 Thermoluminescence (TL)

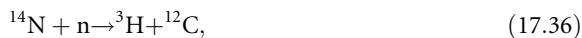
This is a phenomenon occurring as a result of increase in temperature of a body and it takes place when electrons trapped in crystal defects are released by heat. When ionizing radiation impinges on a dielectric solid, electrons may be stripped off and so become trapped in metastable states associated with the said defects. Heat frees this energy as light emissions when the trapped electrons resume their stable ground states. Such light emissions are independent of the normal incandescence shown by thermally activated solids and increase linearly with the radiation dose until saturation is reached. Once electron traps are drained by heating, thermoluminescence disappears unless the sample is irradiated again. In TL dating, a sample is heated at increasing temperatures and its light output recorded as a glow curve, the area underneath this measures the radiation dose to which the sample was subjected since it was last heated to about 450°C . The annual radiation dosage can be assessed from the concentrations of uranium, thorium, and potassium in the rock sample and the time elapsed since the last heating, t , is given by accumulated radiation dose/annual radiation dose. The accumulated radiation dose is given by the glow curve. In the 1950s, it was suggested that the method could be used in order to date geological materials and shown that TL can be induced by pressure and the recrystallization of solids.

Later, archeological materials and even Pleistocene sediments have been analyzed and yielded important data. TL dates have been obtained from loess deposits above and below the Old Crow tephra at the Halfway House near Fairbanks, Alaska, and its age restricted to 86 ± 8 ka, which accorded with radiocarbon records from wood and peat less than 6 m above the tephra that gave an age of more than 60 ka. Emission spectra of meteorites showed that neither trapping levels at 170 and 350°C nor the luminescence centers were significantly perturbed by either their shock or thermal histories. A tentative assignment of the luminescence producing the low-temperature broad emission feature was made to Mn^{2+} ions in the oligoclase feldspar (Strain et al. 1986). Interestingly, it has been suggested that induced thermoluminescence may prove to be valuable in terms of understanding metamorphism in chondrites (Batchelor and Sears 1991). Their feldspar has a novel origin and history. Induced thermoluminescence and the thermal history of plagioclase feldspars have been examined (Kim et al. 1995). On the other hand, eucrites were regarded as igneous rocks resembling

terrestrial and lunar basalt. The success of induced TL studies could be used for many types of basalt in which dry, low-level metamorphism took place.

17.22 Tritium

Tritium, ^3H , the radioactive isotope of hydrogen, is produced in the atmosphere by the interaction of cosmic ray-produced neutrons with nitrogen, hence



and also



with a production rate of $0.5 \pm 0.3 \text{ atoms cm}^{-2} \text{ s}^{-1}$.

It also results from solar emissions, the operation of nuclear reactors and particle accelerators on the Earth together with diminishing quantities originating from earlier atmospheric testing of thermonuclear devices. These later added “bomb tritium” and practically eliminated natural tritium as a tracer. However, it offered a new tool, namely the use of the bomb tritium peak as a “dye” that is delivered to natural water systems from the atmosphere on local to global scales. But there are natural limits to the method because tritium decay and dispersion make it increasingly hard to identify the bomb peak in groundwater. A way round this has been presented and this involves using tritium with its decay product ^3He ($^3\text{He}_{\text{trit}}$). This is discussed in detail below. Tritium in the environment from this source reached a prominent peak in the Northern Hemisphere in 1963, thereafter steadily declining. The radioisotope undergoes beta decay,



with $Q = E_{\text{max}} = 18.6 \text{ keV}$ and the half-life is 12.43 years.

As to the inventory, tritium (also denoted by the symbol T) is measured in tritium units. By definition, the abundance of ^3H is 1 TU when the atomic ratio $[^3\text{H}/^1\text{H}]$ equals 1×10^{-18} . In terms of specific activity $1 \text{ TU} = 3.2 \text{ pCi/kg H}_2\text{O} = 0.12 \text{ Bq/kg H}_2\text{O}$, the natural level in precipitation being $\sim 5 \text{ TU}$ as compared to “bomb tritium” maximum levels of $\sim 1,000$ – $2,000 \text{ TU}$ and more. In 1973, natural tritium represented $\sim 2.5\%$, nuclear power plants 0.02% , bombs 97.5% of the total.

Tritium can be assessed mass spectrometrically but results from this approach were improved using the Oeschger Counter, which measures weak radioactivity. Oeschger began determining the tritium content of firn and ice, using them as archives of environmental information. His participation in various expeditions to Greenland and Antarctica from 1964 to 1992 provided his laboratory with direct access to polar ice cores. The analytical methods and drilling technology developed from this access facilitated an unprecedented reconstruction of climatic changes of the last 150,000 years.

Once tritium is formed in the atmosphere, it becomes rapidly incorporated into water molecules and resides in the lower stratosphere for anything between 1 and 10 years. Later such molecules enter the lower troposphere and rainout of the tritiated water (HTO) occurs within five and twenty days. This is how HTO enters the hydrological cycle where it constitutes a radiotracer for water that has been in the atmosphere for the past 35 years. However, as the bomb component diminishes, so does the radio-tracing value.

17.22.1 Dating Using Tritium and Tritogenic ^3He

To compensate for the decline of bomb tritium input into the environment and continue to use tritium as a dating tool for water in aquifers, rivers, springs, etc., the following approach was proposed. Simultaneous measurement of tritium and tritogenic ^3He permits identification of the tritium peak as the sum of $[^3\text{H}]$ and $[^3\text{He}_{\text{trit}}]$, even if most of the tritium has decayed, and also allows direct calculation of age from the radioactivity of mother per quantity of daughter ratio (tritium/ ^3He age). Extensive studies of this methodology and the applicability of tritium/ ^3He dating were commenced in the middle to late 1980s and early 1990s.

Determination of the tritium/ ^3He age of groundwater is straightforward:

$$t = \frac{T_{1/2}}{\ln 2} \ln \left(1 + \frac{[^3\text{He}_{\text{trit}}]}{[^3\text{H}]} \right). \quad (17.39)$$

The hardest step in determining the tritium/ ^3He age is the separating of the $^3\text{He}_{\text{trit}}$ from the total ^3He dissolved in a groundwater. The total ^3He concentration, $[^3\text{He}_{\text{tot}}]$, has a number of sources noted as follows:

$$[^3\text{He}_{\text{tot}}] = [^3\text{He}_{\text{eq}}] + [^3\text{He}_{\text{exc}}] + [^3\text{He}_{\text{terr}}] \quad (17.40)$$

where $^3\text{He}_{\text{eq}} = ^3\text{He}$ in solubility equilibrium with the atmosphere, $^3\text{He}_{\text{exc}} = ^3\text{He}$ due to excess air, and $^3\text{He}_{\text{terr}} =$ terrigenous ^3He (nucleogenic ^3He together with mantle ^3He). Only $^3\text{He}_{\text{tot}}$ and $^3\text{He}_{\text{eq}}$ are determined through measurements. $^3\text{He}_{\text{exc}}$ and $^3\text{He}_{\text{terr}}$ (if they are present in a sample) must be determined by using measurements of ^4He and Ne ($^3\text{He}_{\text{terr}}$).

The total ^4He concentration measured in a groundwater sample, $[^4\text{He}_{\text{tot}}]$, can be presented as

$$[^4\text{He}_{\text{tot}}] = [^4\text{He}_{\text{eq}}] + [^4\text{He}_{\text{exc}}] + [^4\text{He}_{\text{terr}}] \quad (17.41)$$

where $[^4\text{He}_{\text{eq}}] = ^4\text{He}$ concentration equilibrium with the atmosphere, $[^4\text{He}_{\text{exc}}] = ^4\text{He}$ concentration caused by excess air, and $[^4\text{He}_{\text{terr}}] =$ terrigenous ^4He concentration (radiogenic ^4He together with mantle ^4He). If no terrigenous helium is contained in the groundwater sample, $[^3\text{He}_{\text{trit}}]$ can be calculated using the following equation:

$$[^3\text{He}_{\text{trit}}] = [^4\text{He}_{\text{tot}}](R_{\text{tot}} - R_{\text{atm}}) + [^4\text{He}_{\text{eq}}]R_{\text{atm}}(1 - \alpha) \quad (17.42)$$

where $R_{\text{tot}} =$ measured $[^3\text{He}/^4\text{He}]$ ratio of the sample, $R_{\text{atm}} = [^3\text{He}/^4\text{He}]$ ratio of air (1.384×10^{-6}), and α is the solubility isotope effect (about 0.983).

The conversion factor κ by which one has to multiply the above $[^3\text{He}_{\text{trit}}]$ value to switch from $\text{cm}^3 \text{ STP g}^{-1}$ to TU is

$$\kappa = \frac{4.021 \times 10^{14}}{1 - s/1000} \frac{\text{TU}}{\text{cm}^3 \text{ STP g}^{-1}} \quad (17.43)$$

where s is the salinity in ‰.

For the separation of terrigenous helium, neon measurements have to be employed. Two assumptions are (1) that the neon comes only from the atmosphere and also (2) that $[\text{Ne}/^4\text{He}]_{\text{eq}} = [\text{Ne}/^4\text{He}]_{\text{air}}$. The terrigenous ^4He component will then become

$$[^4\text{He}_{\text{terr}}] = [^4\text{He}_{\text{tot}}] - ([\text{Ne}_{\text{tot}}] - [\text{Ne}_{\text{eq}}]) \frac{[^4\text{He}_{\text{atm}}]}{[\text{Ne}_{\text{atm}}]} - [^4\text{He}_{\text{eq}}] \quad (17.44)$$

where $[Ne_{tot}]$ is the measured concentration of neon in the sample, $[^4He_{atm}/Ne_{atm}]$ is atmospheric $[He/Ne]$ ratio (0.288), and $[Ne_{tot}] - [Ne_{eq}] = [Ne_{exc}]$ is the neon concentration originating from excess air.

$[^3He]$ is calculated by multiplying the $[^4He_{terr}]$ calculated from the above equation by the $[^3He/^4He]$ ratio of the terrigenous helium component, which can be radiogenic helium, mantle helium, or a mixture of both.

The best approach to determine R_{terr} is to measure it in groundwater samples from the same aquifer that are free of tritium. If there is no tritium-free groundwater in the relevant aquifer, then an estimate can be obtained in the majority of such cases by plotting $[^3He]$ versus $[^4He]$, such a plot offering quite good clues regarding the origin of the terrigenous helium.

The concentration of the atmospheric $^3He_{atm}$ component may be expressed as follows:

$$[^3He_{atm}] = R_{atm} \{ [^4He_{tot}] - [^4He_{terr}] - [^4He_{eq}](1 - \alpha) \}. \quad (17.45)$$

Other appropriate equations are also available, which will facilitate attaining the concentration of $^3He_{trit}$. Observations have been made on the nonlinearity of the tritium/ 3He age. This age, calculated from [Eq. \(17.39\)](#), is apparently independent of the initial tritium concentration of the water sample, this comprising an advantage since it removes the need to establish the precise time-dependent tritium delivery to the aquifer. Of course, there is always the possibility that mixing and dispersive factors may affect the tritium/ 3He age because this is typically biased toward the age of the water component with the higher tritium concentration. For quantitative studies, it is usual to rule out mixing as a significant influence or try to account for it in the final evaluation of the relevant data.

There are important differences between the apparent tritium/ 3He ages and the real water ages and, as a rule, these occur near the location of the bomb peak. The validity of this remark is ascribed to the high tritium and 3He concentration gradients near the bomb peak as well as the related increased transport of both tracers by dispersive processes. The effect also sets the usual life period over which tritium/ 3He dating is typically applicable. In many aquifers, the tritium/ 3He balance below the bomb tritium peak is dominated by the downwardly directed dispersion of bomb tritium and $^3He_{trit}$ as a result of its radioactive decay. Hence, in cases like these the tritium/ 3He age distribution is constant over a depth of a few to several tens of meters below the location of the bomb peak. It may be added that in aquifers with very low dispersion rates, meaningful tritium/ 3He ages can be provided for periods that precede the bomb peak.

3He is a gas; therefore, using the tritium/ 3He method for the dating of groundwaters is dependent on the extent of confinement of $^3He_{trit}$ in the groundwater, which is primarily determined by the ratio of advection to dispersion in the water parcels moving away from the water table. In aquifers with reasonably high recharge rates and related vertical flow velocities near the water table, loss of $^3He_{trit}$ is smaller than approximately 10–20%.

17.22.2 A Danubian Application of the Tritium/ 3He Dating Method

This was effected using 3H , 3He , 4He , and Ne concentrations in samples from a shallow groundwater system being recharged by bank infiltration from the Danube River in the Szigetköz area, northwestern Hungary (Stute et al. 2002). The $^3H/^3He$ ages were found to increase linearly along the flow lines as a function of distance from the river. For the deeper groundwater (50–100 m below the surface), which is not affected by recharge from local

precipitation, a horizontal flow velocity of about 500 m annually was derived from the age gradient. Variation of ^3H plus ^3He ("initial tritium") groundwater data as a function of the $^3\text{H}/^3\text{He}$ age is consistent with the time series of tritium measurements in the Danube River for the past 30 years. This confirms the reliability of the derived residence times. Deviations between the measured Danube tritium data and ^3H and ^3He data from the aquifer are explicable as a result of dispersive mixing and also by interaction with local surficial recharge.

It is germane to add that the observed content of ^3He in meteorites has been used to determine their $^3\text{H}/^3\text{He}$ age and the method involved dividing the recorded total number of ^3He atoms by the number of ^3He atoms decaying per unit time and making a 30% correction for the directly produced ^3He . Results were dubious in part because of the need to assume that there was a constant ^3He content or a constant cosmic-ray flux at the meteoroid integrated over 25 years.

17.23 Uranium Series Disequilibrium

17.23.1 Ionium (^{230}Th)

Ionium (i.e., ^{230}Th) is a daughter of uranium-234 and produces radium-226 in the uranium-238 radioactive decay series. Its half-life is 7.52×10^4 years and the corresponding decay constant is $9.217 \times 10^{-6} \text{ a}^{-1}$. Differences in geochemical properties induce thorium isotopes to separate from uranium in the oceans, which is the basis for using ionium to date deep-sea sediments. In oxidizing conditions on the Earth's surface, uranium occurs as the uranyl ion, UO_2^{2-} , whereas thorium remains tetravalent and is rapidly abstracted from seawater by adsorption on solid surfaces and also by incorporation into authigenic minerals with uranium concentrating in the aqueous phase. Hence, the residence time of uranium in oceans is longer by orders of magnitude than that of thorium, namely ~ 0.5 million years compared to about 300 years. Most ionium in seawater is formed right there from dissolved ^{234}U , but about a quarter is thought to come from river inputs. The preferential removal of ionium from seawater separates the radionuclide from its parent and produces an excess of unsupported ionium in the sediments. This causes activity that falls off with time, this assuming that both locally formed and river-derived components are altogether removed from seawater.

A sample of sediment from a given depth below the water/sediment interface can be dated from its ($^{230}\text{Th}/^{232}\text{Th}$) activity ratio if this has stayed constant for at least several hundred thousand years in the water body next to the sediment in any given ocean basin and also if there was no migration of the isotopes in the sediments. In addition, their chemical speciation must have been the same in seawater with no isotopic fractionation between this and the mineral phases involving thorium in the sediment. Furthermore, the ionium and thorium found in detrital mineral particles must be excluded from the analysis. Assuming that the contribution made by uranium-supported ionium is negligible, the activity of a sample given as an activity ratio may be related to its age as

$$R = R_0 e^{-\lambda t} \quad (17.46)$$

where R is the ionium/thorium activity ratio of the leachable fraction of sediment obtained at a given depth below the top of a core, R_0 is the same ratio for the newly deposited sediment, λ is the decay constant of ionium, and t is the time elapsed since deposition occurred. R is measured and, if R_0 is known, then

$$t = \frac{1}{\lambda} \ln \left(\frac{R_0}{R} \right). \quad (17.47)$$

This approach has been used to determine the rate of sedimentation in oceans, and this varies greatly due to factors such as the quantity of debris introduced by rivers, the rates of melting of icebergs, and the number of particles transported through and deposited by the atmosphere. The ionium/thorium method covers a range from less than 0.5 mm/1,000 years to 50 mm/1,000 years on a carbonate and opal-free basis, the lower figures applying to the South Pacific and the higher ones to the Atlantic. This is paralleled by variation in ($^{230}\text{Th}/^{232}\text{Th}$) activity ratios at the surfaces from which it has been inferred that there is a greater input of ^{232}Th in the Atlantic. This may be due to the many large rivers that enter it. But an excess thorium-230 method may be applicable for separating ocean sediments into fractions, which form isochrons of which the intercepts decrease with depth in the core. However, the slope of the isochron in young samples was found not to be zero, as expected, but rather showed disequilibrium among the thorium isotopes in the sediment (Bernat and Allegre 1974).

17.23.2 Ionium/Protactinium

Protactinium is a radioactive element with over 20 isotopes, of which the one of interest is ^{231}Pa with a half-life of 32,480 years and a corresponding decay constant of $2.134 \times 10^{-5} \text{ a}^{-1}$. It is a daughter of ^{231}Th in the ^{235}U radioactive decay series. In oceans, its geochemical properties resemble those of thorium since the isotopes are removed from seawater either by adsorption on mineral grains or by incorporation into authigenic minerals. Hence, sediments deposited in oceans may contain not only excess unsupported ^{230}Th , but also unsupported ^{231}Pa . If both are removed from seawater equally efficiently, their activity ratios will change with time in a manner controlled by their decay constants.

The ratios of the activities of the unsupported ionium and ^{231}Pa increase with depth in cores and, if the sediment is deposited at a uniform rate, then the following expression below may be applicable:

$$\ln \left(\frac{^{230}\text{Th}}{^{231}\text{Pa}} \right) = \ln \left(\frac{^{230}\text{Th}}{^{231}\text{Pa}} \right)_0 + \frac{\lambda_{\text{Pa}} - \lambda_{\text{Th}}}{\alpha} h \quad (17.48)$$

where h is the depth in the core and $\alpha = h/t$ is the constant rate of sedimentation.

This is a straight-line equation in coordinates of h and $\ln(^{230}\text{Th}/^{231}\text{Pa})$. Its slope will be inversely proportional to the rate of sedimentation, and its intercept equals the logarithm of the initial value of the activity ratio of the relevant unsupported ionium and ^{231}Pa in the sediment, i.e., $\ln(^{230}\text{Th}/^{231}\text{Pa})_0$. The approach has been used to determine α for a core from the Arctic Ocean, and a value of 0.2 cm/1,000 years was derived (Baxter et al. 1981).

17.23.3 Lead-210

In the uranium series, a daughter of ^{238}U (namely ^{222}Rn) enters the atmosphere and later decays through several short-lived daughters to lead-210 with a half-life of 22.3 years (see also ▶ Sect. 17.14 on the polonium/lead method). This radionuclide is removed by precipitation with a residence time of about 10 days. Later, this may deposit on snow and ice in glaciers as

well as in lakes and coastal regions. The activity of unsupported lead-210 diminished thereafter as a function of time at a rate determined by its half-life. ^{210}Pb can be used to date materials containing it. Owing to the short half-life of ^{210}Pb , the dating range is only a few hundred years. The method has been used for measuring the rates of deposition of snow in Greenland and Antarctica as well as on Alpine glaciers. Lake sediments have been dated using the method, for instance some from Loch Lomond in Scotland.

In addition to the unsupported (excess) ^{210}Pb of atmospheric origin, this radionuclide is also found unsupported by its primary parent ^{238}U but supported by excess ^{226}Ra in sediment minerals, i.e., at equal activity to the latter through in situ production from ^{226}Ra . This component is controlled by sediment mineralogy and so gives no information about time-scales. The unsupported ^{210}Pb is quantified by subtracting the measured activity of supported ^{210}Pb from the total ^{210}Pb inventory at each depth in a core. ^{222}Rn activity is measured and the total inventory assessed by analysis of ^{210}Pb decay products ^{210}Bi or ^{210}Po . In all cases, secular equilibrium is assumed for the parent/daughter pairs. Thus, the conventional dating method is indirect and specialized, involving nuclear counting equipment and radiochemical expertise. A more practical alternative is afforded by a particle track approach, which depends on counting radiation damage tracks produced in selected plastic films by both alpha particles and fission products emitted from essentially in processed dried sediment. Supported ^{210}Pb is measured indirectly by ^{235}U analysis. Because the $[^{235}\text{U}/^{238}\text{U}]$ ratio does not vary significantly in nature, the ^{238}U content of a sample can be calculated and secular equilibrium with ^{210}Pb again invoked. The supported ^{210}Pb profile is then subtracted from the total alpha record and the assumption made that the resultant excess alpha-plot is dominated by the decay of unsupported ^{210}Pb (or ^{210}Po). Using this method depends on an idealized nonmigratory behavior for all other uranium series alpha-emitters and also on total constancy with depth of ^{232}Th and its decay products.

17.23.4 Snow, Ice, and Volcanoes

As regards snow and ice chronology, the time elapsed since a sample of snow deposited at a depth h from the surface can be calculated from the activity of ^{210}Pb if the initial activity of this radioisotope has remained constant so that

$$(^{210}\text{Pb}) = (^{210}\text{Pb})_0 e^{-\lambda t} \quad (17.49)$$

where the first term expresses the activity per unit mass of sample at depth h , $(^{210}\text{Pb})_0$ is the specific activity at the surface (where $h = 0$), λ is the decay constant of ^{210}Pb ($3.11 \times 10^{-2} \text{ a}^{-1}$), and t is the age of the snow sample. From this equation, the following may be derived:

$$t = \frac{1}{\lambda} \ln \left\{ \frac{(^{210}\text{Pb})_0}{(^{210}\text{Pb})} \right\}. \quad (17.50)$$

Excess ^{210}Pb unsupported by ^{238}U occurs in volcanic rocks and arises partly from the radioactive decay of excess ^{226}Ra (half-life 1,602 years). A sample from Mount Vesuvius showed enrichment in ^{226}Ra and so in ^{210}Pb also. There is a high ^{210}Pb activity in the mineral cotunnite (PbCl_2) that occurs as a sublimate in fumaroles around the volcano and its lead probably comes from the volcanization of basalts. Lead-210 activity in volcanic rocks increases through the radioactive decay of excess ^{226}Ra so that deviations in the $(^{210}\text{Pb}/^{238}\text{U})$ activity ratios cannot just be ascribed to elemental fractionation effects in the magma. In the oceans, ^{210}Pb

distribution was examined through the GEOSECS Program, particularly in the Pacific. Oceanic boundaries were envisaged as potential sinks for reactive metals in seawater. The lead-210 deficiency relative to its ancestral ^{226}Ra seemed to increase from oceanic interiors toward continental edges and sea floors where it is more intensively scavenged. Within about 100 m of the latter, a large amount of excess ^{222}Rn relative to ^{226}Ra has been recorded and attributed to supply by sediments through pore water diffusion. This ^{222}Rn decays to ^{210}Pb and so its effects on the distribution of the latter is manifest. However, some vertical profiles in the deep western North Pacific showed no significant variations with depth despite this excess ^{222}Rn . And the apparent box model residence time that is based on $(^{210}\text{Pb}/^{222}\text{Rn})$ activity ratios decreases from ~ 100 years in oceanic interiors to about 10 years near the bottom. The lead-210 data are explicable using a vertical-mixing and first-order scavenging model without enhanced scavenging near the sediment/water interface. This shows that the bottom excess ^{222}Rn can scarcely influence ^{210}Pb in the water and also that the short residence time mentioned may be an artifact not reflecting the chemical reactivity of lead. It may be inferred that the deficiency of ^{210}Pb through scavenging is best estimated using ^{226}Ra not ^{222}Rn . One caveat – the ^{210}Pb scavenging at the sediment/water interface inferred from the oceanic distribution of this radioisotope – appears difficult to detect from bottom ^{210}Pb profile measurements.

17.23.5 Thorium-230, Uranium-234, Uranium-238

Practically no thorium, but substantial amounts of uranium are contained in calcium carbonates deposited in saline lakes and also in the oceans where they sometimes reach 5 ppm. Hence, there is almost no initial ^{230}Th activity in newly deposited carbonates, but due to the radioactive decay of ^{234}U , the activity of ^{230}Th increases with time. Consideration of this lead to the setting up of a method, which has been used to date corals, for instance, those from the three lowest terraces in Barbados, an island apparently emerging from the sea at a uniform rate (Broecker 1963). Data from the $(^{230}\text{Th}/^{234}\text{U})$ activity ratios of coral samples gave dates of 122,000, 103,000, and 82,000 years. These coincide with predicted times of elevated summer radiation at 45° N latitude (Milankovitch 1920). In age determinations, it is necessary that initial activity ratios $(^{230}\text{Th}/^{234}\text{U})_0$ are close to zero, also the sample must have been a closed system as regards uranium and intermediates between ^{238}U and ^{230}Th . In addition, the initial activity ratios $(^{234}\text{U}/^{238}\text{U})_0$ must be known.

It is possible to relate the activity of ^{230}Th to that of its immediate parent, ^{234}U , since, if the ^{234}U is in secular equilibrium with ^{238}U , then the $(^{230}\text{Th}/^{234}\text{U})$ activity ratio is related to time, t , as follows:

$$\left(\frac{^{230}\text{Th}}{^{234}\text{U}}\right) = \left(\frac{^{230}\text{Th}}{^{234}\text{U}}\right)_0 e^{-\lambda t} + (1 - e^{-\lambda t}) \approx 1 - e^{-\lambda t} \quad (17.51)$$

where λ is the decay constant of ^{230}Th . Note that this equation does not take into account the possible presence of excess ^{234}U . This, however, may not make much difference.

17.23.6 The Uranium-234, Uranium-238 Geochronometer

Attainment of secular equilibrium in radioactive decay series starting with uranium-238, uranium-235, and thorium-232 depends on none of relevant daughters leaving or entering the systems concerned. Once this equilibrium is established, the decay rates of the daughters in

any particular system equal that of the parent: $\lambda_1 N_1 = \lambda_2 N_2 = \lambda_3 N_3 = \dots = \lambda_n N_n$ where $\lambda_1 N_1$ is the activity of the parent and the other terms represent those of the daughters. (See [Sect. 7.4 in Chap. 7, Vol. 1](#) on successive processes discussing the cases of equilibrium and nonequilibrium.) Under secular equilibrium conditions, the ratio between the decay rate of any daughter and its parent is equal to one. The production of uranium-234 from its parent proceeds as follows :



so that, where secular equilibrium exists, the rate of decay (i.e., the activity) of ^{234}U in a uranium-bearing mineral equals that of ^{238}U and the activity ratio ($^{234}\text{U}/^{238}\text{U}$) = 1. However, investigations from groundwater samples showed that such secular equilibrium does not exist there and was also absent from minerals deposited from the said groundwater (Thurber 1962). In fact, the value of the ratio usually exceeds unity because the ^{234}U is enriched by such processes as the radioactive decay of its parent dissolved in groundwater. The alpha decay of the parent, namely, damages the crystal lattice and permits the daughter to migrate through micro-capillaries in the mineral and oxidize to form uranyl ions, which dissolve in water and remove it into an aqueous phase. Uranium-238 occurs in stable lattice positions. Thorium-234 can be rejected from grain surfaces through recoil caused by alpha emission, and then it decays to uranium-234 through the short-lived protactinium-234. Generally, activity ratios ($^{234}\text{U}/^{238}\text{U}$) both in surface and groundwaters as well as in secondary minerals containing uranium on continents usually exceed unity and can reach values as high as ten. But the activity ratios of primary uranium minerals in chemically weathered rocks may be less than unity through the preferential removal of uranium-234.

If uranium occurs in solution in groundwaters, it may enter oceans and become isotopically homogenized, the relevant activity ratio ($^{234}\text{U}/^{238}\text{U}$) having a narrow spread of values with a mean around 1.15. The element uranium can be removed from oceans by incorporation into authigenic minerals such as calcium carbonate, also by adsorption on grain surfaces under reducing conditions. Once uranium has become isolated from seawater, ^{234}U decays to ^{230}Th until the activity ratio ($^{234}\text{U}/^{238}\text{U}$) approaches an equilibrium value. However, this is not useful as a dating method because of the possibility that uranium-234 migrated after deposition. Nevertheless, the radioactive decay of excess ^{234}U and the growth of its daughter ^{230}Th have been used for dating of marine and non-marine carbonates of Pleistocene age.

The geochronometer involves determination of γ_0 , the initial ($^{234}\text{U}/^{238}\text{U}$)₀ activity ratio and it has been applied to dating the calcium carbonate of biogenic and inorganic origin deposited both in marine and non-marine environments. The reliability of ages from the latter is restricted by uncertainty regarding the value of the initial ratio. In non-marine areas, this factor shows time-dependent variations since shells of some non-marine mollusks actually acquire uranium after the death of the organisms. However, since groundwater can enrich in uranium-238 relative to its parent, this enables its specific sources to be assessed. In addition, mixing of different water masses characterized by their individual ($^{234}\text{U}/^{238}\text{U}$) activity ratios can be determined (Kronfeld and Rosenthal 1981).

17.24 Uranium/Thorium/Lead

After radioactivity was identified in uranium and thorium minerals, it was used to date them, and methods included Pb/U, Pb/alpha, U/He, U/Th/Pb, and common lead of which the last

two are still utilized. Natural uranium comprises 99.28% ^{238}U with a half-life of 4.5×10^9 years, 0.71% ^{235}U with a half-life of 7.1×10^8 years, and 0.006% ^{234}U with a half-life of 2.5×10^5 years. The common radioactive isotope of thorium is ^{232}Th (half-life 1.4×10^{10} years) and its relative abundance in nature is 100%. From these data, the corresponding decay constants of these primordial radionuclides may be cited. For uranium-238, it is $1.55125 \times 10^{-10} \text{ a}^{-1}$, for uranium-235, $9.8485 \times 10^{-10} \text{ a}^{-1}$; for uranium-234, $2.806 \times 10^{-6} \text{ a}^{-1}$; and for thorium-232, $4.948 \times 10^{-11} \text{ a}^{-1}$. In fact, heavy radioactive elements can be grouped into four radioactive decay series that are designated as thorium ($4n$) series, neptunium ($4n+1$) series, uranium ($4n+2$) series, and actinium ($4n+3$) series. (See [▶ Chap. 7 in Vol. 1](#) and [▶ Chap. 13 in this Volume](#).) The numbers in brackets indicate that the parent and all members of a particular series have mass numbers exactly divisible by four or divisible by four with a remainder of one, two, or three. There is no natural cross-linkage between the series, though this can be achieved artificially. The uranium, thorium, and actinium series occur naturally and each element is the parent of its own series and has the longest half-life of the relevant series. They all decay to lead and all have alpha-decay modes. The neptunium series was added to the list after the discovery of the artificial transuranic elements. Neptunium is a by-product of the manufacture of plutonium in nuclear reactors. The neptunium series ends with ^{209}Bi .

17.24.1 Radioactive Series

The radioactive decay of uranium-238 initiates the uranium series ($A = 4n+2$). This includes ^{234}U as a daughter and ends in stable ^{206}Pb . This series is expressible as follows:



where $Q = 47.4 \text{ MeV}$ per ^{238}U atom.

Thus, each atom of ^{238}U undergoing radioactive decay eventually produces one atom of ^{206}Pb as the result of cumulative emissions of eight α particles (i.e., $^4\text{He}^{2+}$ ions) and six β^- particles (i.e., “normal” electrons with negative electric charge, also called negatrons, as opposed to positrons that are positive). This assumes that the radioactive decay occurred in a closed system as regards uranium, lead, and all intermediate daughters, and Q represents all the associated decay energies of the series. Some intermediate daughters undergo branched decay entailing the emissions of either α particles or β^- particles. However, stable ^{206}Pb remains as the end product of all possible decay paths. (See [▶ Fig. 7.6 in Chap. 7, Vol. 1](#).)

The radioactive decay of ^{235}U produces stable lead-207 after the emissions of seven α particles and four β^- particles and constitutes the actinium series ($A = 4n+3$). The process may be represented as



where $Q = 45.2 \text{ MeV}$ per ^{235}U atom. (See [▶ Fig. 7.7 in Chap. 7, Vol. 1](#).)

The radioactive decay of ^{232}Th produces stable ^{208}Pb after the emissions of six α particles and four β^- particles and constitutes the thorium series ($A = 4n$). The following expression summarizes these data:



where $Q = 39.8 \text{ MeV per } ^{232}\text{Th atom}$. Branched decay again occurs. (See [Fig. 7.4 in Chap. 7, Vol. 1.](#))

The artificial neptunium series has the formula $A = 4n+1$. (See [Fig. 7.5 in Chap. 7, Vol. 1.](#))

Altogether 42 nuclides representing 12 elements are formed as intermediate daughters in the three naturally occurring radioactive decay series, but none is a member of more than one series so that each of the series terminates in specific isotopes of lead. The half-lives of the respective parents are longer by orders of magnitude than those of the various daughters; hence, the decay series fulfill the requirements for the establishment of secular equilibrium, and the decay rates of the intermediate daughters are equal to those of the respective parents.

If the mineral used is a closed system and secular equilibrium exists, the rate of production of the stable daughter at the end of a particular decay series is equal to the rate of decay of the relevant parent. Hence, it is feasible to regard the radioactive decay of the uranium and thorium isotopes in minerals as if it went directly to the respective lead isotopes. This consideration simplifies the equations required to describe the growth of radiogenic lead in uranium- and thorium-bearing minerals. Four naturally occurring lead isotopes are ^{204}Pb , ^{206}Pb , ^{207}Pb , and ^{208}Pb . Their relative abundances are 52.4% for lead-208, 22.1% for lead-207, 24.1% for lead-206, and 1.4% for lead-204. Otherwise, lead has a total of 32 isotopes, the remaining 28 being radioactive and extremely short-lived. Actually, ^{204}Pb is also very slightly radioactive, but can be regarded as practically stable because of its enormously long half-life of 1.4×10^{17} years.

The isotopic composition of lead is determinable mass spectrometrically. An expression for the age, t , of a suitable mineral in the case of uranium-238 is shown in the following expression:

$$t = \frac{1}{\lambda_{238}} \ln \left\{ \frac{[\frac{^{206}\text{Pb}}{^{204}\text{Pb}}] - [\frac{^{206}\text{Pb}}{^{204}\text{Pb}}]_i}{[\frac{^{238}\text{U}}{^{204}\text{Pb}}]} + 1 \right\} \quad (17.56)$$

where $[\frac{^{206}\text{Pb}}{^{204}\text{Pb}}]_i$ is the initial atomic ratio of ^{206}Pb (i.e., the final product of the ^{238}U series) to ^{204}Pb (the non-radiogenic lead isotope used as an inner reference); and λ_{238} is the decay constant of ^{238}U , the primary parent of the series assumed to be in equilibrium with all of its radioactive daughters.

There are also similar equations for both uranium-235 and thorium-232. Results embody three independent ages referring to the three decay series involved and ideally should agree. However, they will only do so if the mineral samples analyzed stayed closed throughout their geological history and also if the isotopic compositions of uranium and thorium were not modified in any way, for instance by fractionation. It is assumed that the values used for the initial lead isotopes are accurate and that no analytical or systematic errors occurred. The ratio $[\frac{^{235}\text{U}}{^{238}\text{U}}]$ is 1/137.88 for uranium of normal composition found in terrestrial minerals, lunar rocks, and meteorites. That this is known is important because it enables a “207/206” date to be obtained without the necessity to know the uranium concentration in the relevant mineral. It is possible, namely, to derive a formula, which contains the ratio $[\frac{^{207}\text{Pb}}{^{206}\text{Pb}}]$ as the only parameter to be measured for a uranium-bearing sample in order to get its age. There are tables from which the age t can be interpolated.

Although uranium and thorium are found in many minerals, only a few of these minerals are suitable for dating using the uranium, thorium, lead method. These comprise those that can retain these elements adequately and probably the most retentive mineral is zircon. In sedimentary rocks, zircon derived from sources underlain by igneous or metamorphic complexes embodies a record both of the orogenic and magmatic histories of these sources. In

zircons, the concentrations of uranium and thorium average 1,330 and 560 ppm respectively, but in pegmatites greater concentrations occur. Uranium and thorium are present in zircons through the isomorphous replacement of Zr^{4+} (ionic radius 0.087 nm) by U^{4+} (ionic radius 0.105 nm) and also through the presence of thorite inclusions. Such substitution is restricted by differences in the ionic radii and Pb^{2+} is excluded altogether because its ionic radius is 0.132 nm. In addition, it carries a lower charge. Therefore, zircon does not contain much lead when it crystallizes and has very high ratios for $[\text{U}/\text{Pb}]$ and $[\text{Th}/\text{Pb}]$ that makes it an invaluable geochronometer. Hydrothermal decomposition in a sealed pressure vessel has been used to extract lead and uranium from zircons.

17.24.2 Concordia and Discordia

The concept of two independent geochronometers arose from consideration of the radioactive decay of the naturally occurring radionuclides of uranium, i.e., ^{238}U and ^{235}U . For the atomic ratio of ^{206}Pb to ^{238}U , one can write

$$\left[\frac{^{206}\text{Pb}}{^{238}\text{U}} \right] = \exp(\lambda_{238}t) - 1 \quad (17.57)$$

where the ^{206}Pb is assumed to be in equilibrium with its primary parent ^{238}U all along the period t . On the other hand, using [Eq. \(17.56\)](#), one can also express the above ratio as a function of time as follows:

$$\left[\frac{^{206}\text{Pb}}{^{238}\text{U}} \right] = \frac{\left[\frac{^{206}\text{Pb}}{^{204}\text{Pb}} \right] - \left[\frac{^{206}\text{Pb}}{^{204}\text{Pb}} \right]_i}{\left[\frac{^{238}\text{U}}{^{204}\text{Pb}} \right]} = \exp(\lambda_{238}t) - 1. \quad (17.58)$$

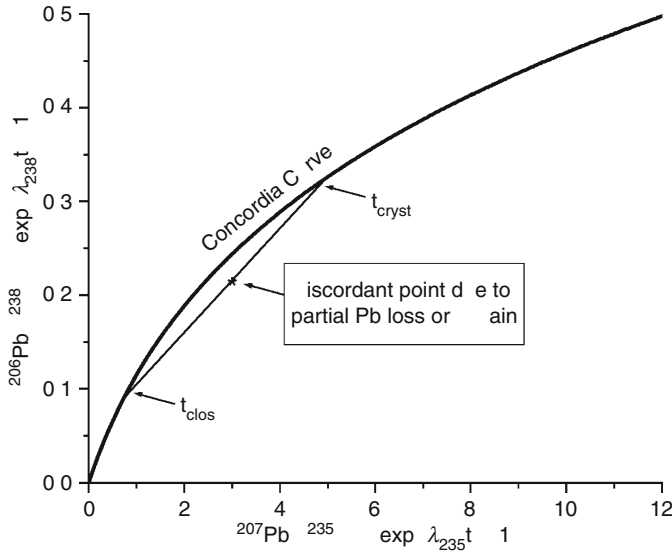
The other decay series can be treated similarly. Such equations give concordant dates if a uranium-bearing mineral that satisfies the necessary assumptions regarding closed systems is analyzed. The expression(s) appearing on the left-hand side of the above equations and the equivalents for the actinium series are connected through the same parameter t that appears in the exponential expression on the right-hand side. Due to the parametric relationship, there is a particular curve representing the loci of all concordant U/Pb systems, this curve being termed the Concordia (see [Fig. 17.5](#)). In other words, the pairs of atomic ratios $[^{206}\text{Pb}/^{238}\text{U}]$ and $[^{207}\text{Pb}/^{235}\text{U}]$ determined from all samples having concordant dates – samples that do not represent episodic lead losses – must plot on this curve. If all radiogenic lead accumulated up to such a lead loss episode is lost during that episode, the system responds in such a manner that those coordinate points that represent it return to the origin and the U/Pb geochronometer restarts; i.e., the geological “clock” is reset. Of course, when this happens, all trace of the earlier geological history of the relevant system disappears. If only some radiogenic lead is lost, points move part way along a chord comprising systems with discordant dates, in other words a discordia.

Concordia plots allow the interpretation of the geological histories of uranium/lead systems and provide information on the past disturbances of these systems. Several concordia models have been developed in order to interpret the discordancy of the U/Pb dates of uranium-bearing minerals.

One is the *dilatancy model* (Goldich and Mudrey 1972). Minerals undergo radiation damage through the alpha decay of uranium, thorium, and their daughters, and the extent

■ Fig. 17.5

Concordia diagram showing the effects of lead loss or uranium gain on U/Pb systems. t_{cryst} is the time elapsed since original crystallization, t_{clos} is the time elapsed since closure of the system after lead loss or uranium gain. λ_{235} and λ_{238} are the decay constants of the respective primary parents ^{235}U and ^{238}U



of this increases with increasing age as well as with the uranium and thorium contents of the relevant minerals. Such damage produces micro-capillaries allowing water to enter crystals. This is retained until uplift and erosion release the pressures on minerals, such consequent dilation of zircons being accompanied by the escape of water and dissolved radiogenic lead. Loss of radiogenic lead probably occurred during the uplift and erosion of crystalline basement complexes in Precambrian shields. Investigations showed that “207/206” dates from these often approximate the true ages of uranium-bearing minerals. Such minerals from different continents may have lost radiogenic lead 500–600 Ma ago as a result of the Pan-African Event and parallel happenings in other parts of Gondwana such as the Brazilian Event.

A second model relates to chemical weathering that affects almost all minerals and rocks that outcrop. A third is a continuous diffusion one in which radiogenic lead diffused from crystals at a rate governed by a diffusion coefficient, D , an effective radius a , and a concentration gradient of $[^{206}\text{Pb}/^{238}\text{U}]$ (ordinate) against $[^{207}\text{Pb}/^{235}\text{U}]$ (abscissa). The crystals are assumed to be spherical and it is also assumed that there has been either no or negligible diffusion of uranium and intermediates. Also, it is assumed that the radiogenic lead diffusion followed Fick’s Law. The appropriate expression for the ^{206}Pb – ^{238}U pair, for instance, describes the change in lead concentration with time for any radial volume element in a sphere as follows:

$$\frac{\partial [^{206}\text{Pb}]}{\partial t} = D \frac{\partial^2 [^{206}\text{Pb}]}{\partial r^2} + \frac{2}{r} \frac{\partial [^{206}\text{Pb}]}{\partial r} + [^{238}\text{U}]_i \exp(-\lambda_{238}t) \quad (17.59)$$

where $[^{206}\text{Pb}]$ is the atom concentration of lead daughter, $[^{238}\text{U}]_i$ is the initial concentration of uranium parental atoms, λ_{238} is the decay constant of the parental uranium, and t is

the time elapsed since crystallization took place. The relevant boundary condition is $[^{206}\text{Pb}] = 0$ at $t = 0$.

17.24.3 Common Lead

Common lead (i.e., lead that had long lost any association with the decay series discussed above) is found in many minerals such as galena (lead sulfide) and cerussite (lead carbonate), which are constituents of ore-forming bodies. Also, it occurs as a trace element in minerals where associated uranium and thorium contents are low as well as in rock-forming minerals such as feldspars. The atomic weight of common lead is less than that of lead associated with uranium. The difference is due to the increased presence of radiogenic lead-206 in the latter. Common lead, namely, contains isotopes of the element with mass numbers 204, 206, 207, and 208. Lead-204 is not the decay product of a radioactive series, but the other three derive from the radioactive series initiated by uranium-238, uranium-235, and thorium-232, respectively. The relevant atom number ratios are denoted as follows:

$$\alpha = \left[\frac{^{206}\text{Pb}}{^{204}\text{Pb}} \right], \quad \beta = \left[\frac{^{207}\text{Pb}}{^{204}\text{Pb}} \right], \quad \gamma = \left[\frac{^{208}\text{Pb}}{^{204}\text{Pb}} \right]. \quad (17.60)$$

Every lead contains a measurable quantity of lead-204 and can be represented by a three-dimensional diagram of the variables α , β , and γ . There are large variations in the isotopic composition of common lead from different sources. Understanding this was initially difficult because earlier observations implied that common lead had a constant average atomic mass. It soon became clear that this supposed constancy was fortuitous and reflected the fact that the increase in the $[^{206}\text{Pb}/^{204}\text{Pb}]$ atomic ratio is often accompanied by a comparable rise in the $[^{208}\text{Pb}/^{204}\text{Pb}]$ ratio. Efforts were made to construct quantitative models for the isotopic evolution in the Earth from which its age and also that of common lead could be derived (Holmes 1946; Houtermans 1946). They supposed that the Earth was originally both fluid and homogeneous with uranium, thorium, and lead uniformly distributed and with primeval lead having the same isotopic composition everywhere. Later the Earth rigidified so that small regional differences in the $[\text{U}/\text{Pb}]$ ratio arose. In any given region, this may have changed only through the radioactive decay of uranium to lead. It was assumed that when a common lead mineral crystallized, the lead separated from uranium and thorium with its isotopic composition thereafter remaining constant. A Holmes/Houtermans model was developed and this facilitated understanding differences in the above-mentioned α , β , and γ parameters for various types of common lead and allowed calculations to be made of the time elapsed since the formation of the Earth's crust and the time when common lead became incorporated into an ore. Most of the lead in the accessible parts of the crust occurs in igneous and sedimentary rocks with contents ranging from a few tenths to say 500 ppm of lead. Only a tiny proportion of crustal lead is in minerals or ore bodies comprising more than 0.1% of lead and this is true for crustal uranium and thorium as well. Hence, the incorporation of lead into a lead mineral is a very rare event implying that the probability of the event occurring twice in the history of any given sample of lead is negligible.

In the source rock from which a sample of common lead is obtained, lead was related to given quantities of uranium and thorium. This relationship can be described by a chemical milieu index μ , the atom number of uranium-238 over lead-204 comprising that milieu from

which the sample of common lead came. As the ^{238}U decays with time, the content may be extrapolated to the present as if the original mother rock still existed. The chemical milieu index can then be defined as follows:

$$\mu = \left[\frac{^{238}\text{U}}{^{204}\text{Pb}} \right]_{\text{today}}. \quad (17.61)$$

In the same way, it is possible to define another chemical milieu index for the mother rock of a given sample of common lead by means of the ratio between the number of atoms of thorium-232 and the atom number of uranium-238 extrapolated to the present day, the following being appropriate:

$$x = \left[\frac{^{232}\text{Th}}{^{238}\text{U}} \right]_{\text{today}}. \quad (17.62)$$

Finally, the present atomic ratio of ^{235}U to ^{238}U is given as

$$\varepsilon = \left[\frac{^{235}\text{U}}{^{238}\text{U}} \right]_{\text{today}} = \frac{1}{139}. \quad (17.63)$$

17.24.4 The Holmes/Houtermans Model

This model assumed that all common lead had an isotopic composition explicable by the adding of radiogenic lead as decay products from uranium-238, uranium-235, and thorium-232 associated with a primeval lead at the time of formation of the Earth (Holmes 1946; Houtermans 1946). This primeval lead was characterized by the relative isotopic abundances α_w , β_w , and γ_w , w being the age of the Earth. It is taken for granted that the chemical milieu indices for a given sample of common lead remained constant from w up to a time p where p is the time elapsed since a given sample of lead became incorporated into a lead mineral to which a model age of p can be assigned. From the general equation of radioactive decay, it is clear that the lead sample changed its isotopic composition only by the addition of the isotopes lead-206, lead-207, and lead-208 from uranium and thorium with which it was linked in the mother rock during the time interval $w - p$.

A further impetus to researches came from the investigation of the isotopic compositions of minuscule amounts of lead in iron meteorites, particularly in the iron and troilite (FeS) phases of Catmon Diablo. The α and β values turned out to be far lower than those obtained from samples of terrestrial lead or lead from stony meteorites. The troilite phase, while containing lead, does not contain uranium and thorium and therefore the isotopic composition of the lead was regarded as practically constant since crystallization. Such lead is the least radiogenic available and may approach primeval lead in composition and the Catmon Diablo lead values may well approximate primeval lead ones initially incorporated into the Earth's crust and also into chondritic material. If the above values are assumed, the age of the Earth would be about 4.5 ± 0.05 Ga. All models of this type for the isotopic changes with time from the formation of the Earth's crust up to a time p of mineralization involve the hypothesis that the lead spent the entire time interval $(w - p)$ in a milieu with a constant value of μ . Interestingly, phenomena such as metamorphism that occurred often in geological history do not appear to have influenced the μ -values of the mother material of lead minerals to any great extent. However, there is a small dispersion in the x -values.

Serious problems arose with the Holmes/Houtermans model, and these problems came from anomalous lead as opposed to common lead that gave meaningful model dates. It is probable that the small number of ore deposits containing ordinary lead reflects the fact that the lead in most of these underwent a more complex history than that envisaged in the Holmes/Houtermans model. To conform with this model, the relevant lead must have had a single-stage history and this can be confirmed if the model dates agree reasonably well with isotopic data obtained for other minerals from the ore and if the isotopic ratios of lead from a particular deposit are constant within experimental error.

17.24.5 Anomalous Lead

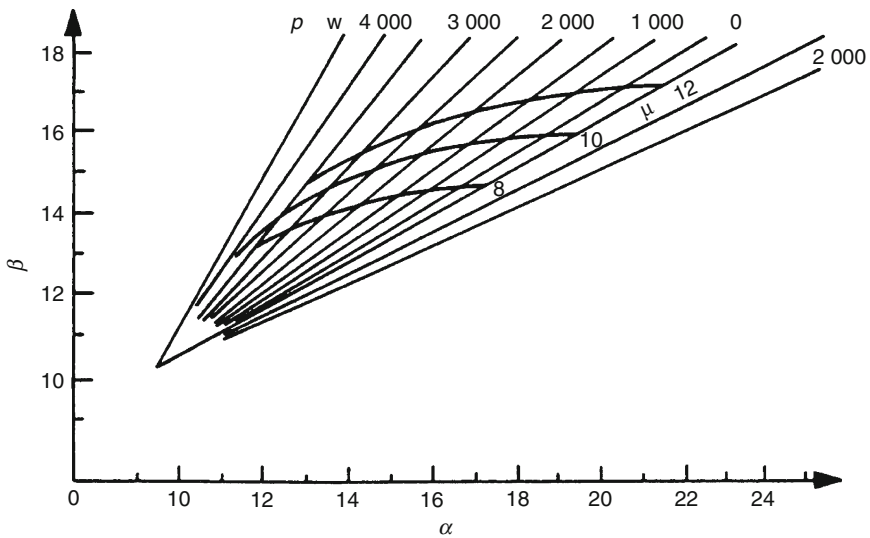
The basic premise regarding the isotopic development of the isotopic composition of lead is the addition of radiogenic lead isotopes such as lead-206, lead-207, and lead-208 stemming from the radioactive decay of uranium and thorium and having values of μ and $x\mu$, which remained constant during the time interval $(w - p)$. Unfortunately, p does not always coincide with the actual time of mineralization as was shown by fossils in beds containing veins of lead ore. Indeed, some absurd results have been obtained that led to negative ages so that common lead ores now existing should form in the far future (up to 2 Ga later, see the last isotherm in [Fig. 17.6](#)).¹ Two types of anomalies are called “B” and “J.” “B” includes those anomalies in which the model age may exceed the geological age of the rock containing lead ores, and it is named after Bleiberg in Austria. Its causes include pneumatolysis, which can redistribute lead minerals in ore bodies or veins and so produce a condition where $g < p$, g being the geological age. J-type anomalies were called after leads at Joplin, Sudbury, Ontario, Canada, and for them, the application of the Holmes/Houtermans model gave negative model ages. However, there are instances of apparently normal leads belonging to this type and giving model ages more or less inferior to the age of mineralization. These are hard to identify, but can sometimes be recognized from their anomalous x -values. Explaining J-type anomalies is straightforward bearing in mind that a basic assumption of the method is that μ had a constant value during the time interval $(w - p)$. Obviously, this cannot be more than, at best, a first approximation of the actual history of a lead sample. So, if purely common lead mixed with a small amount of radiogenic lead, an isotopic composition resembling a J-type anomalous lead would be the result. Such an event could take place at any time during the time interval $(w - p)$ before the uranium and thorium contents of the lead sample dropped to zero.

A single analysis of an anomalous J-type lead gives little information about the date when radiogenic lead was added during the time interval $(w - p)$ or about the isotopic composition and hence the age. Better data are obtainable from a number of samples in a region. Three case histories were offered for three different regions containing lead ore deposits and these are Sudbury and Thunder Bay, Ontario, and Australia. Common leads and highly anomalous leads were used, the former following a lead development line without appreciable alteration in their μ and x values during the time interval $(w - p)$. They have model ages corresponding to the actual time of mineralization (Russell and Farquhar 1960). Of course, the isotopic data alone do not suffice to determine the time of addition of the radiogenic component of such anomalous J-type leads.

Alternatives to the Holmes/Houtermans model have been proposed. The Russell/Standton/Farquhar (RSF) and the Russell/Farquhar/Cumming (RFS) models were proposed based on the work of Alpher and Herman (1951). While the Holmes/Houtermans model presented a fan

■ Fig. 17.6

A graphic presentation of the Holmes/Houtermans model for common lead. The straight lines are isochrones (the p -values are given in million years, positive numbers refer to the past, the negative one to the future), the curved lines are Pb development lines. The relevant constants are as follows: $\alpha_w = 9.41$, $\beta_w = 10.27$, $w = 4.49$ Ga, $\lambda_{238} = 1.54 \times 10^{-10} \text{ a}^{-1}$, $\lambda_{235} = 9.80 \times 10^{-10} \text{ a}^{-1}$. The point (α_w, β_w) represents primeval lead. The extra radiogenic lead accumulated relative to the primeval lead composition during the time interval $(w - p)$ elapsed till crystallization can be represented this way: $\alpha - \alpha_w = \mu [\exp(\lambda_{238}w) - \exp(\lambda_{238}p)]$, $\beta - \beta_w = \mu \epsilon [\exp(\lambda_{235}w) - \exp(\lambda_{235}p)]$. Dividing the second equation by the first helps to eliminate the constant μ , thus $(\beta - \beta_w)/(\alpha - \alpha_w) = \epsilon \{[\exp(\lambda_{235}w) - \exp(\lambda_{235}p)]/[\exp(\lambda_{238}w) - \exp(\lambda_{238}p)]\}$, so that leaves only three constants to be assessed, i.e., α_w , β_w , and p . Hence from two pairs of α and β of known age p , the values for α_w and β_w can be extrapolated and the age of the Earth, w , evaluated



of lead development lines and isochrones starting from a point corresponding to primeval lead (α_w, β_w) or a similar α, γ diagram, both of the others assumed a single global source for all “ordinary” common leads, which could be in the upper mantle. A continuous growth model has been suggested and considered as more feasible since it is more probable that radiogenic contaminants were generated continuously during a time interval commencing with the formation of relevant rocks, for instance granites, and ending with the removal of radiogenic lead from them to mix with other lead prior to or in the course of the formation of a lead ore deposit.

17.24.6 Multistage Leads

Leads in igneous and metamorphic rocks have isotopic compositions determined by a multistage history in the majority of cases. Clearly, they will have past associations with

a number of systems possessing different [U/Pb] and [Th/Pb] ratios. In the complex situation of a sample of lead, which underwent transference through two uranium-bearing systems (at points p_1 and p_2 , respectively) characterized by different [$^{238}\text{U}/^{204}\text{Pb}$] ratios designated as μ_1 and μ_2 , the α -value of the sample is given by

$$\alpha = \alpha_w + \mu_1 [\exp(\lambda_{238} w) - \exp(\lambda_{238} p_1)] + \mu_2 [\exp(\lambda_{238} p_1) - \exp(\lambda_{238} p_2)]. \quad (17.64)$$

When lead is transferred from the first system to the second, this probably entails a physical process of removal, e.g., through the formation of magma in the mantle and its later emplacement in the crust of the Earth. Such a transition from system 1 to system 2 might occur without such a physical removal taking place, i.e., take place solely through changes in the U/Pb system of system 1. These changes would affect the [$^{238}\text{U}/^{204}\text{Pb}$] ratio and so the isotopic composition of the lead, which became incorporated in the ore deposit. A rarer possibility is that lead may be gained and its different isotopic composition would alter the isotopic composition of the final lead. It is clear that all of the above-mentioned considerations would apply to three or more stages also.

17.24.7 Whole-Rock Dating

Considering lead/lead isochrons of igneous and metamorphic rocks, if a magma volume involving homogeneous material crystallizes, a rock suite results, which contains different [U/Pb] and [Th/Pb] ratios. Alternatively, a volcanic rock assemblage might arise after a high-grade regional metamorphic episode and contain lead isotopically homogenized by the event. Either way the lead later evolved along a set of divergent and curved trajectories corresponding to different values of μ in each specimen. If such growth proceeds to the present uninterruptedly, the leads lie along an isochron if the rocks had the same initial isotope ratios of lead, formed at the same time and remained closed to uranium, thorium, and lead. Recent alterations in the concentrations of these elements are permissible if the isotopic composition of the lead is unaffected. An isochron equation can be derived of which the slope, s , is given by the following expression:

$$s = \frac{1}{137.88} \frac{\exp(\lambda_{235} t) - 1}{\exp(\lambda_{238} t) - 1}. \quad (17.65)$$

From this, the age of a rock suite can be obtained (Goldich and Mudrey 1972). A suite of metamorphic rocks from the Lewisian basement complex in northwestern Scotland was depleted in uranium compared to the crustal average. Uranium and lead concentrations were 0.24 and 7.9 ppm, respectively, and the average $^{238}\text{U}/^{204}\text{Pb}$ ratio was 1.76. The isotope ratios of lead scattered about a straight line interpreted as a secondary isochron. A date was found from the point of intersection of this with the primary lead growth curve, which had a value of 8.68 for μ , near to, but lower than the value for conformable lead ores. The result was an age of about 2.9 Ga that was taken to be the time of variable uranium losses during pyroxene/granulite metamorphism of the ancestral Lewisian rocks.

17.25 Uranium/Xenon, Uranium/Krypton

Uranium undergoes spontaneous fission as well as radioactive α decay and this produces fissionogenic xenon and krypton that accumulate in uranium-bearing minerals through

geological time. The determination of the ages of such minerals followed the discovery that xenon is produced by the spontaneous fission of ^{238}U in pitchblende (Khlopin et al. 1947). A U/Xe or U/Kr age may be calculated as follows:

$$t_{\text{U/Xe}} = \frac{1}{\lambda_{\alpha} + \lambda_{\text{sf}}} \ln \left\{ \frac{[^A\text{Xe}_{\text{sf}}](\lambda_{\alpha} + \lambda_{\text{sf}})}{[^{238}\text{U}]^A Y_{\text{sf}} \lambda_{\text{sf}}} + 1 \right\} \quad (17.66)$$

where λ_{α} is the decay constant of uranium-238 for alpha decay, λ_{sf} is the uranium-238 spontaneous fission decay constant, and $[^A\text{Xe}_{\text{sf}}]$ and $^A Y_{\text{sf}}$ are the concentration and mass yield, for the xenon isotope with mass number A resulting from spontaneous fission. Because $\lambda_{\alpha} \gg \lambda_{\text{sf}}$, the above can be reduced as follows (Eikenberg et al. 1993):

$$t_{\text{U/Xe}} = \frac{1}{\lambda_{\alpha}} \ln \left\{ \frac{[^A\text{Xe}_{\text{sf}}] \lambda_{\alpha}}{[^{238}\text{U}]^A Y_{\text{sf}} \lambda_{\text{sf}}} + 1 \right\}. \quad (17.67)$$

Similar equations can be derived for $t_{\text{U/Kr}}$ ages calculated from the concentration of and mass yield of suitable krypton isotopes such as ^{86}Kr .

The yield of the main ^{238}U spontaneous fission isotope ^{136}Xe is about 6% and, because the rate of production ratio $[^{136}\text{Xe}_{\text{sf}}/^{206}\text{Pb}_{\text{rad}}]$ is of the order of 4×10^{-8} , the U/Xe method was initially applied to uranium-rich minerals such as pitchblende, but later uranium-poorer accessory minerals such as monazites and zircons have been investigated as well.

17.25.1 Pitchblendes

Pitchblendes can be affected by geological events causing alteration or dissolution and the subsequent redistribution of uranium and its daughters so that reported U/Xe ages of pitchblendes are often lower than their formation ages. At one time, the disparity was attributed to gas losses by diffusion and it was inferred that pitchblende is unsuited for dating by the U/Xe method. But later work using U/Xe, U/Kr, and U/Pb systems plus electron microprobe analysis demonstrated that the fission gases in pitchblendes could well have survived even greenschist facies metamorphism so that studying them could aid in the interpretation of discordant isotope ages. Obviously, if geologically undisturbed pitchblendes gave concordant U/Pb ages and underwent no losses of fission gases, the U/Xe and U/Kr ages should both be identical and agree with the U/Pb ages if appropriate values for λ_{sf} , $^A Y_{\text{sf}}$, and $[^{136}\text{Xe}_{\text{sf}}/^{86}\text{Kr}_{\text{sf}}]$ are used. Where gas losses *did* take place, krypton seems always to be lost preferentially with respect to xenon and both fissiogenic xenon and lead losses ran almost parallel. When the $[^{136}\text{Xe}_{\text{sf}}/^{86}\text{Kr}_{\text{sf}}]$ atomic ratios are larger than 6.1 ± 0.1 , discordant fission gas ages clearly indicate perturbation of the U/Pb system. Extensive fractionation between xenon and krypton has been observed in pitchblendes.

To use the U/Xe/Kr dating method, the product ($\lambda_{\text{sf}} ^A Y_{\text{sf}}$) must be known and also the concentrations of spontaneous fission xenon and krypton, the relative xenon and krypton spontaneous fission yields, and the $[^{136}\text{Xe}/^{86}\text{Kr}]_{\text{sf}}$ ratio. Any contribution from uranium-238 that underwent fast neutron-induced fission can be neglected. Slow neutron-induced fission of ^{235}U , however, had to be taken into correction:

$$[^{136}\text{Xe}_{\text{sf}}] = [^{136}\text{Xe}_{\text{f}}] - [^{136}\text{Xe}_{\text{nif}}] \quad (17.68)$$

where the subscript “f” refers to all fission events resulting in ^{136}Xe , whereas “nif” stands for neutron-induced fission of ^{235}U .

Iteration was commenced using the following values: 6.39% for $^{136}\text{Y}_{\text{nif}}$ from the slow neutron-induced fission of ^{235}U and 6.3% for $^{136}\text{Y}_{\text{sf}}$ from the spontaneous fission of ^{238}U , both taken from earlier work (Eikenberg et al. 1993). For isotope pairs of Xe 136/131, 134/131, and 132/131, for which the differences between induced and spontaneous compositions are large, a mean value for a factor R was calculated for each sample, where R is the ratio of induced to spontaneous fission events.

Then $\text{U}/^A\text{Xe}$ and $\text{U}/^B\text{Kr}$ ages for each sample were calculated (where A and B are the respective mass numbers of Xe and Kr). While the former were only slightly different, there were significant differences between the $\text{U}/^{136}\text{Xe}$ and $\text{U}/^{86}\text{Kr}$ ages of geologically unaffected pitchblendes, a matter regarded as not surprising on the grounds that varying compositions of fission krypton from $^{238}\text{U}_{\text{sf}}$ have been reported. Keeping $^{136}\text{Y}_{\text{sf}}$ fixed, the $^A\text{Y}_{\text{sf}}$ and $^B\text{Y}_{\text{sf}}$ yields of the deviational $\text{U}/^A\text{Xe}$ and $\text{U}/^B\text{Kr}$ were changed to obtain agreement between all ages. The new yields were inserted into suitable equations so as to calculate a new set of ages, a procedure iterated until all ages agreed satisfactorily within analytical error. Most samples gave $[^{136}\text{Xe}/^{86}\text{Kr}]_{\text{sf}}$ values around 6.1. Back-up information showed that none of the samples was geologically disturbed. However, some of them had undergone xenon, krypton, and lead losses of up to 50%, but they were still suitable to determine the relative $^A\text{Xe}_{\text{sf}}$ and $^B\text{Kr}_{\text{sf}}$ isotopic ratios. This is because minute losses of inert gases have no detectable effect on the isotopic compositions of xenon and krypton. Regarding such geologically undisturbed samples, the product $(\lambda_{\text{sf}}^{136}\text{Y}_{\text{sf}})$ was obtained and required that the minerals assessed remained closed both to uranium and to the fission gases. Only samples with concordant U/Pb ages and the recrystallized pitchblendes (U/Pb discordant, but $\text{U}/\text{Xe}/\text{Kr}$ concordant) were examined, the latter having formation ages determinable from the intercept of the U/Pb discordia with the concordia and also from U/Pb microprobe analyses. All values of $(\lambda_{\text{sf}}^{136}\text{Y}_{\text{sf}})$ were around $5.7 \times 10^{-18} \text{ a}^{-1}$ and agreed within acceptable error. No fractionation between the heavier xenon and the lighter krypton was observed from which it was concluded that the selected minerals retained their fission xenon quantitatively.

17.26 Editors' Notes

1. Douglas Adams's *The Restaurant at the End of the Universe* may turn out to have some scientific support after all (p. 811).

Further Reading

Bowen R (1994) *Isotopes in the earth sciences*. Chapman & Hall, London
 Bowen R, Attendorn H-G (1997) *Radioactive and stable isotope geology*. Chapman & Hall, London

References

Alburger DE, Harbottle G, Norton EF (1986) *Earth Planet Sci Lett* 78:1678
 Alpher RA, Herman RC (1951) *Phys Rev* 84:1111

Armstrong AL (1966) In: Schaeffer DA, Zahringer J (eds) *Potassium-argon dating*. Springer, New York
 Arnold JR, Libby WF (1949) *Science* 110:678
 Batchelor JD, Sears DWGh (1991) *Nature* 349:516
 Baxter MS, Crawford RW, Swan DS, Farmer JG (1981) *Earth Planet Sci Lett* 53:43
 Bell K, Powell JL (1969) *J Petrol* 10:536
 Bentley HW, Phillips FM, Davis SN (1986) In: Fritz P, Fontes J-C (eds) *Handbook of environmental*

- isotope geochemistry, vol 2, The terrestrial environment. Elsevier, Amsterdam, p 427
- Bernat M, Allegre CJ (1974) *Earth Planet Sci Lett* 21:310
- Broecker WS (1963) *J Geophys Res* 68:2817
- Broecker WS, Sutherland S, Smethie W, Sutherland S, Smethie W, Peng T-H, Ostlund G (1995) *Geochem Cycle* V.9:263
- Chopin C, Maluski H (1980) *Cont Min Pet* 74:109
- Dalrymple GB (1989) *US Geol Surv Bull* 1890:89
- Dempster TJ (1986) *Earth Planet Sci Lett* 78:355
- De Vries H (1958) *Proc Koninkl Ned Akad Wetenschap* B61:94
- Dickin AF (1987) *Nature* 325:337
- Druffel ERM, Griffin S (1993) *J Geophys Res* 98:20249
- Eikenberg J, Signer P, Wieler R (1993) *Geochim Cosmochim Acta* 57:1053
- Elmore D, Tubbs LE, Newman D, Ma XZ, Finkel R, Nishiisumi K, Beer J, Oeschger H, Andree M (1982) *Nature* 300:735
- Fowler PH, Lang AR (1977) *Nature* 270:163
- Goldich SS, Mudrey Jr MG (1972) In: Tugarinov AI (ed) *Contribution to recent geochemistry and analytical chemistry (A.P. Vinogradov volume)*, Nauka Publication Office, Moscow, p 415
- Hamilton PJ, Evensen NM, O'Nions RK, Smith HS, Erlank AJ (1979) *Nature* 277:325
- Hashemi-Nezhad SR, Fremlin JH, Durrant SA (1979) *Nature* 278:333
- Holmes A (1946) *Nature* 157:680
- Houtermans FG (1946) *Naturwiss* 33:185
- Hurfurd AJ, Green PF (1983) *Earth Planet Sci Lett* 59:343
- IAEA (2002) *Bull* 382
- Ikeya M, Miki T (1980) *Science* 207:977
- Khlopin VG, Gerling EK, Baruiovaknya NV (1947) *Bull Acad Sci Chim (in Russian)* 599
- Kim TK, Choi HS, Choi IS, Jang HK, Whang CN (1995) *J Korean Phys Soc* 28(4):519
- Kronfeld J, Rosenthal E (1981) *J Hydrol* 50:179
- Kuhn MW, Davis SN, Bentley HW, Zito R (1984) *Geophys Res Lett* 11:607
- Kuzimov VV, Pomansky AA (1980) *Radiocarbon* 22:311
- Lal D, Peters S (1967) In: Sitte K (ed) *Handbuch der Physik*. Springer, Berlin, p 351
- Lal D, Somanyajulu BLK (1984) *Tectonophysics* 105:383
- Luck JM, Birck L, Allègre CJ (1980) *Nature* 283:256
- Marshall BD, DePaolo DJ (1982) *Geochim Cosmochim Acta* 46:2537
- Merrihue CM, Turner G (1966) *J Geophys Res* 71:2852
- Milankovitch M (1920) *Theorie Mathematique des Phenomenes Thermique produits par la radiation solaire*. Gauthier-Villaris, Paris
- Nyquist LE (1977) *Phys Chem Earth* 10:103
- Odom AL, Rink WJ (1988) *Geology* 17:55
- Pal DK, Tuniz C, Moniot RK, Kruse TH, Herzog GF (1982) *Science* 218:787
- Papanastassiou DA, Wasserburg GJ (1969) *Earth Planet Sci Lett* 5:361
- Patchett PJ, Tatsumoto M (1980) *Nature* 288:571
- Pettingell HS, Patchett PJ, Tatsumoto M, Moorbath S (1981) *Earth Planet Sci Lett* 55:150
- Roddick JC (1983) *Earth Planet Sci Lett* 12:300
- Rubin KH, Macdougall JD, Perfit MR (1994) *Nature* 368:841
- Russell RD, Farquhar RM (1960) *Lead isotopes in geology*. Interscience, New York
- Shimokawa K, Imai N, Hirota H (1984) *Isot Geosci* 2:365
- Stockwell CH (1982) *Geol Surv Canada, Paper* 80-19, Pt 1:135
- Strain JA, Townsend PD, Jassemnjad B, McKeever SWS (1986) *Earth Planet Sci Lett* 77:14
- Stute M, Derk J, Révész K, Böhlke JK, Deseö É, Weppernig R, Schlosser P (2002) *Environmental Tracer Group, Danube*, 1
- Thurber DL (1962) *J Geophys Lett* 67:4318
- Verschure RH, Andriessen PAM, Boelrijk NAIM, Hebeda EH, Majjer C, Priem HNA, Verdurmen EATH (1980) *Cont Min Pet* 74:245
- Yin QZ, Jagoutz E, Yerkhovskiy AB, Wänke H (1993) *Geochim Cosmochim Acta* 57:4119

18 Production and Chemistry of Transuranium Elements

Y. Nagame¹ · M. Hirata¹ · H. Nakahara²

¹Japan Atomic Energy Agency, Tokai, Ibaraki, Japan

²Tokyo Metropolitan University, Tokyo, Japan

18.1	<i>Production of Transuranium Elements</i>	818
18.1.1	Discovery of Transuranium Elements	818
18.1.1.1	Neptunium (Np)	818
18.1.1.2	Plutonium (Pu)	819
18.1.1.3	Americium (Am) and Curium (Cm)	819
18.1.1.4	Berkelium (Bk) and Californium (Cf)	820
18.1.1.5	Einsteinium (Es) and Fermium (Fm)	820
18.1.1.6	Mendelevium (Md)	821
18.1.1.7	Nobelium (No) and Lawrencium (Lr)	822
18.1.2	Production of Transuranium Nuclides	823
18.1.2.1	Neutron Capture Reactions	823
18.1.2.2	Charged-Particle-Induced Reactions	826
18.1.3	Experimental Techniques for Production and Identification of Short-Lived Transuranium Nuclei	831
18.1.4	Exotic Nuclear Decay Properties	838
18.1.4.1	Cluster Radioactivities	839
18.1.4.2	Delayed Fission	841
18.1.4.3	Spontaneous Fission	841
18.1.4.4	Progress in Two-Mode Fission	845
18.2	<i>Chemical Properties of Transuranium Elements</i>	846
18.2.1	Actinide Concept	846
18.2.2	Ionic Radii and Oxidation States	849
18.2.3	Separation of Transuranium Elements	851
18.2.3.1	Ion-Exchange Properties	851
18.2.3.2	Solvent Extraction Separation	852
18.2.4	Solid-State Properties of Transuranium Metals and Compounds	855
18.2.5	XAFS: New Methodology for Chemical Studies of Transuranium Elements	861
18.2.6	Computational Chemistry of Transuranium Elements	865

Abstract: This chapter reviews the historical perspective of transuranium elements and the recent progress in the production and study of nuclear properties of transuranium nuclei. Exotic decay properties of heavy nuclei are also introduced. Chemical properties of transuranium elements in aqueous and solid states are summarized based on the actinide concept. For new application of studying transuranium elements, an X-ray absorption fine structure (XAFS) method and computational chemistry are surveyed.

18.1 Production of Transuranium Elements

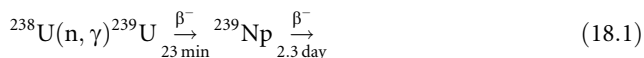
18.1.1 Discovery of Transuranium Elements

The history of the discovery of transuranium elements is a fascinating story that has been described in several articles (e.g., Seaborg and Loveland 1990; Morss and Fuger 1992; Seaborg 1995; Hoffman et al. 2000).

There were at least two difficulties in the discovery of transuranium elements; the first one was the chemical behavior of transuranium elements. Before Seaborg's proposal of the actinide concept (Seaborg 1945), it was believed that thorium, protactinium, uranium, neptunium, plutonium, and the next elements 95 and 96 should be placed as the heavier members of groups 4 through 10. According to the actinide concept, it was expected that the new series should start with actinium as a prototype and end with the filling of the 5f electron shell at element 103, and that the heavier actinides would be trivalent homologs of the lanthanide series in which 4f orbitals were being filled. The second difficulty was the method of identification of transuranium isotopes produced in nuclear reactions. An isotope to be identified had to be isolated before it decayed from large quantities of impurities, especially from fission products.

18.1.1.1 Neptunium (Np)

The first man-made transuranium element, neptunium (Np), was discovered by McMillan and Abelson (1940) while studying the neutron-induced fission of uranium (U). The reaction used in the synthesis was



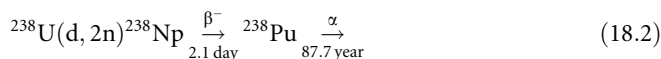
For separating fission products from the neutron capture products, a recoil technique was employed; fission products recoiling out of the target foil with high kinetic energies were removed from the target perse, and the neutron capture products together with the target material were subjected to chemical experiments. It was found that in the presence of the reducing agent, sulfur dioxide, SO₂, the 2.3-day half-life species produced in the growth from the 23-min uranium was quantitatively precipitated as a fluoride. This behavior chemically distinguished the product from uranium.

The later chemical study showed that neptunium was oxidized to hexavalent with the oxidizing agent, bromate ion BrO₃[−]; it resembled uranium, not rhenium (Re), contrary to the expectation from the periodic table at that time. The result was the first evidence that an inner electron shell (i.e., the 5f shell) is filled in the transuranium elements. The isotope of neptunium with the longest half-life ($T_{1/2} = 2.14 \times 10^6$ years) is ²³⁷Np, the mother nuclide of the

neptunium decay series produced in nuclear reactors. Neptunium was named after the planet Neptune, the next planet beyond Uranus.

18.1.1.2 Plutonium (Pu)

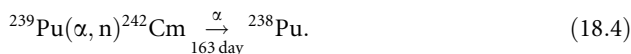
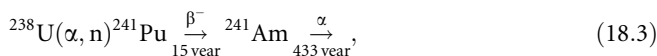
Plutonium (Pu), the second transuranium element, was discovered by Seaborg and coworkers (Seaborg et al. 1946). The first isotope of Pu was synthesized by using the 60 in. cyclotron for the deuteron bombardment of uranium at the University of California, Berkeley,



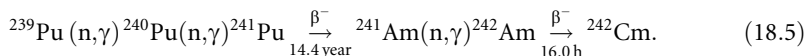
The α -emitting product was identified as a new element from the study of chemical behavior of this isotope. It was distinctly different from both uranium and neptunium in its redox properties; the 3+ and 4+ valence states were more stable. A second isotope of element 94, ^{239}Pu , with a half-life of 24,000 years was synthesized immediately as a daughter of β^- decay of ^{239}Np , which confirmed the presence of element 94. The isotope ^{239}Pu produced in appreciable amounts in nuclear reactors is of major importance, because of its large fission cross section with thermal neutrons. It was named after the planet Pluto in analogy to uranium and neptunium.

18.1.1.3 Americium (Am) and Curium (Cm)

Element 95, americium (Am), and element 96, curium (Cm) were synthesized by Seaborg et al. in 1944–1945 (Seaborg 1945) in bombardments of uranium and plutonium with α particles in a cyclotron:



The isotope ^{242}Cm was identified by observing the known isotope ^{238}Pu as the α -decay daughter of the new nuclide. It was found that successive neutron capture in ^{239}Pu produced ^{241}Am and ^{242}Cm in a reactor according to the following reactions (Ghiorso et al. 1950)



Americium and curium are quite similar to the rare earth elements in their chemical properties; a stable oxidation state is 3+. Thus, it was too difficult for the discovery team to chemically isolate the two elements from each other and from rare earth fission products. For their chemical separation, the development of the ion-exchange technique was required, which also made the separation and identification of subsequent transuranium elements. The identification of ^{241}Am was also confirmed by the volatility measurement of ^{241}Am produced from its parent ^{241}Pu . Element 95, americium, was named after the Americas in analogy with the naming of its rare earth homolog, europium, and curium was named after Marie and Pierre Curie in analogy with the naming of its homolog, gadolinium, that was named after the Finnish rare earth chemist Johann Gadolin.

18.1.1.4 Berkelium (Bk) and Californium (Cf)

The element with the atomic number 97, berkelium (Bk), was produced by irradiation of milligram amounts of ^{241}Am with α particles at Berkeley (Thompson et al. 1950a):



To identify the new nuclide, a rapid cation-exchange separation technique using ammonium citrate as an eluant was employed. Early experiments indicated that element 97 had two oxidation states 3+ and 4+. The actinide concept provided the guidance to search for these two oxidation states, by analogy with the homolog element, terbium (Tb). The chemically separated samples were subjected to the measurement of radiation. Characteristic Cm X-rays associated with the electron capture (EC) decay and low-intensity α particles with a half-life of 4.5 h were detected. Berkelium was named after the city of Berkeley, California where it was discovered, just as the name terbium derived from Ytterby, Sweden.

Californium was synthesized in 1950 by irradiation of a few micrograms of ^{242}Cm with α particles:



The identification of element 98 was accomplished with a total of only 5,000 atoms (Thompson et al. 1950b). The ion-exchange techniques were also used in the separation and identification of californium. Element 98 was eluted in the expected fraction, and the observed half-life and α -particle energy of the radioactivity were also in agreement with predictions. It was named after the state of its discovery, although the chemical analog of element 98 was dysprosium (Dy).

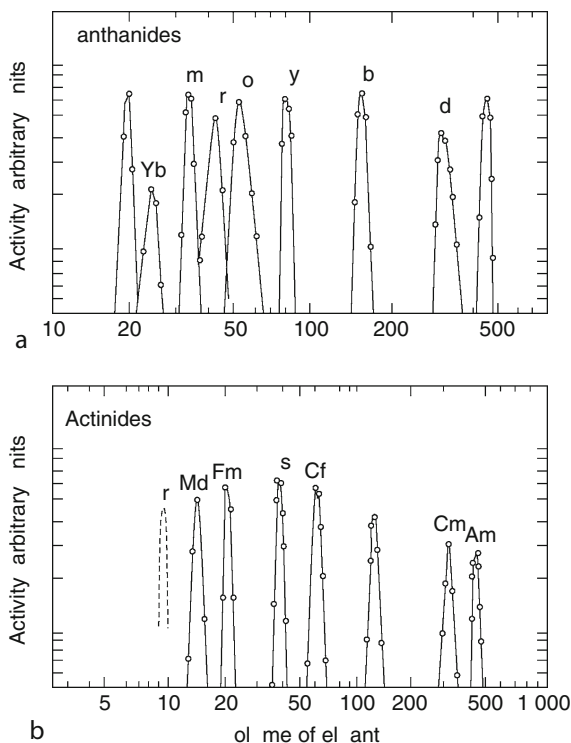
The last four actinides (Am, Cm, Bk, and Cf) have 3+ as their most stable valence state in solution, just as the rare earth elements. The similarity in solution has been commonly used for identification of a particular actinide. ▶ [Figure 18.1](#) shows elution curves for lanthanides and actinides from a cation-exchange column (cited from Katz et al. 1986). Ion-exchange properties of actinides are described in ▶ [Sect. 18.2.3.1](#).

18.1.1.5 Einsteinium (Es) and Fermium (Fm)

Einsteinium (Es) and fermium (Fm) were identified in 1952 in the radioactive debris from the “Mike” thermonuclear explosion that took place in the Pacific. Ion-exchange separation was applied, and the new elements, einsteinium and fermium, were isolated by processing larger amounts of the radioactive coral material (Ghiorso et al. 1955a). Chemical identification was made by ion-exchange separations, while isotopic assignments were made as the result of the corresponding decay sequences: $^{253}\text{Cf} \rightarrow ^{253}\text{99}$ and $^{255}\text{99} \rightarrow ^{255}\text{100}$. A 20-day activity emitting α particles of 6.6 MeV was identified as ^{253}Es and 7.1 MeV α activity with a half-life of 22 h was identified as ^{255}Fm . The elements Es and Fm were named in honor of Albert Einstein and Enrico Fermi. These discoveries confirmed that ^{238}U can suffer as many as 17 successive neutron captures and subsequent β^- decays if the neutron flux is large enough ($1 \times 10^{24} - 4 \times 10^{24} \text{ s}^{-1} \text{ cm}^{-2}$).

■ Fig. 18.1

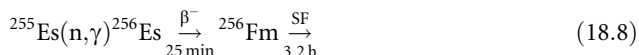
Elution curves for 3+ lanthanide and actinide ions from Dowex-50 ion-exchange resin with ammonium α -hydroxyl isobutyrate eluant (Katz et al. 1986)



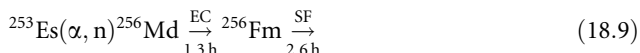
18.1.1.6 Mendelevium (Md)

Mendelevium (Md) was produced in 1955 by irradiation of ^{253}Es with α particles (Ghiorso et al. 1955b). The number of atoms of element 101, N_{101} , expected to be produced was calculated as $N_{101} = N_{\text{Es}} \phi_{\alpha} \sigma t \approx 1$ atom under the experimental conditions characterized by the following parameters. The number of the ^{253}Es target atoms was $N_{\text{Es}} \approx 10^9$ ($\sim 4 \times 10^{-13}$ g), the flux density of α particles was $\phi_{\alpha} \approx 10^{14}$ particles s^{-1} , the cross section was $\sigma \approx 1$ mb ($= 10^{-27}$ cm^2), and the irradiation time was $t \approx 10^4$ s. To detect these single atoms produced in 10^4 s, the recoil technique was applied. The einsteinium target was prepared by electrodeposition on a thin gold foil. The produced element 101, recoiling through a vacuum due to the momentum of the impinging α particles, could be caught on a catcher foil. After irradiation, the catcher foil containing recoiling mendelevium atoms was subjected to the chemical separation by the cation-exchange resin Dowex-50 with an eluant of ammonium α -hydroxy isobutyrate (► Fig. 18.1). The earliest experiments were confined to searching for short-lived α -emitting isotopes of element 101. No α activity, however, was observed that could be attributed to element 101. After longer bombardments, spontaneous fission (SF) events with a half-life of 3.5 h were observed in the fractions corresponding to elements 100 and 101. At that time, it

was assumed that the isotope $^{256}_{101}\text{Es}$ was produced in the $^{253}_{99}\text{Es}(\alpha, n)$ reaction that decayed by electron capture (EC) with a half-life of the order of half an hour to $^{256}_{100}\text{Fm}$, and that $^{256}_{100}\text{Fm}$ then decayed by spontaneous fission (SF) with a half-life of about 3.2 h. In fact, another experiment confirmed the SF decay of $^{256}_{100}\text{Fm}$ produced in the following neutron capture reaction:



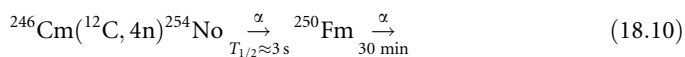
Only 17 atoms of Md were detected by their EC decay into the spontaneously fissioning isotope $^{256}_{100}\text{Fm}$ that is presently known to have the half-life of 2.6 h:



The name mendelevium was suggested for the element, in honor of the Russian chemist, Dmitri Mendeleev.

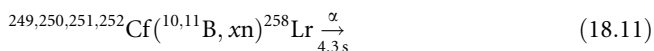
18.1.1.7 Nobelium (No) and Lawrencium (Lr)

The first report of the discovery of element 102 came from the Nobel Institute, Stockholm, Sweden. The research group used the reaction of $^{244}_{98}\text{Cm} + ^{12}_6\text{C}$ in which they found a new α emitter with a half-life of about 10 min. However, experiments neither at Berkeley nor at the Kurchatov Institute in Moscow confirmed the above result. In 1958, Ghiorso et al. (1958) announced the positive identification of $^{254}_{102}\text{No}$ that was supposedly produced in the following reaction by use of the double recoil technique:



$^{250}_{100}\text{Fm}$, the daughter of the new element, was collected using the recoil technique, one atom at a time, and identified as Fm by their position in the cation-exchange elution curve. A half-life of ~ 3 s was assigned to $^{254}_{102}\text{No}$ at that time. However, it is now known that the 3 s radioactivity was $^{252}_{102}\text{No}$ produced in the $^{244}_{98}\text{Cm}(^{12}_6\text{C}, 4n)$ reaction; the used target contained 20 times more $^{244}_{98}\text{Cm}$ than $^{246}_{98}\text{Cm}$. $^{254}_{102}\text{No}$ is now known to have 55 s half-life. The errors in this experiment indicate the difficulty associated with one-atom-at-a-time studies. In subsequent chemical experiments, it was found that the most stable oxidation state of element 102 in solution was 2+. The element was named nobelium after Alfred Nobel.

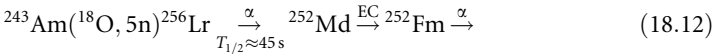
The first identification of an isotope of element 103 was by the Berkeley group in 1961 (Ghiorso et al. 1961). The californium isotopes, $^{249,250,251,252}_{98}\text{Cf}$, were bombarded with boron beams:



Reaction products recoiling from the target were caught by a long-metallized Mylar tape, which was moved past a series of α -particle detectors. A new α -emitting nuclide with α energy of 8.6 MeV and a half-life of ~ 4 s was assigned to $^{257}_{103}\text{Lr}$. But later experiments indicated this activity was due to $^{258}_{103}\text{Lr}$. Subsequent identification of element 103 was made by the Russian group in 1965 using the double-recoil technique (Donets et al. 1965).

$^{256}_{103}\text{Lr}$, now known to have a half-life of ~ 30 s, was deduced from the genetic relation with the known $^{252}_{103}\text{Lr}$. Lr is the first actinide that was identified through a purely instrumental

method, because the half-life of the isotope was too short to allow any chemistry. Silva et al. later conducted the ion-exchange experiments of ^{256}Lr and confirmed that Lr exhibits a stable 3+ state in solution, as expected by the actinide concept (Silva et al. 1970). Lawrencium was named after Ernest O. Lawrence, the inventor of the cyclotron.



The discovery of elements 93 to 103 is summarized in [▶ Table 18.1](#). The names and symbols from element 101 through 103 were approved in 1992 by IUPAC (International Union of Pure and Applied Chemistry) based on the report of the Transfermium Working Group (TWG) (Barber et al. 1992), which consisted of scientists appointed by both IUPAP (International Union of Pure and Applied Physics) and IUPAC.

[▶ Figure 18.2](#) shows the year of discovery of the transuranium elements. Some of the important discoveries related to the transuranium elements are also shown in the figure.

18.1.2 Production of Transuranium Nuclides

There are two kinds of methods for production of transuranium elements as indicated in the previous [▶ Sect. 18.1.1](#): neutron capture reactions in nuclear reactors and charged-particle-induced reactions at accelerators.

18.1.2.1 Neutron Capture Reactions

The method is based on the concept that absorption of neutrons by nuclides with the atomic number Z leads to formation of neutron-rich nuclides that transmute by β^- decay into nuclides with the atomic number $Z + 1$.

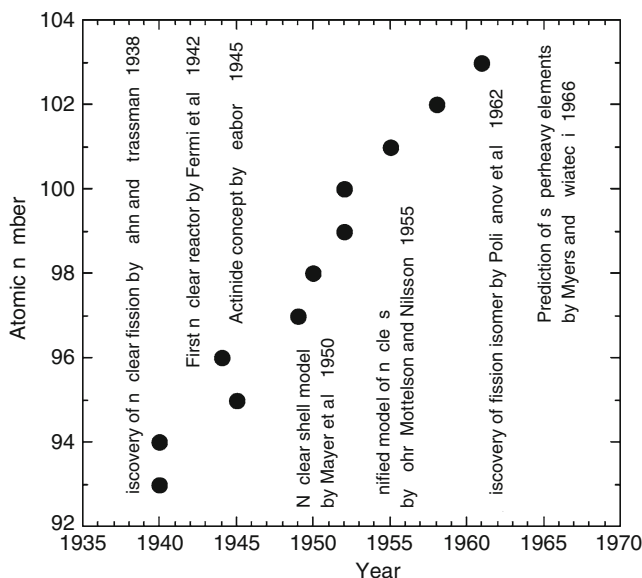
[▶ Table 18.1](#)

Discovery of transuranium elements 93–103

Atomic number	Element	Symbol	Year of discovery	Production reaction
93	Neptunium	Np	1940	$^{238}\text{U} (\text{n}, \gamma) ^{239}\text{U} \rightarrow ^{239}\text{Np}$ (2.3 days)
94	Plutonium	Pu	1940–1941	$^{238}\text{U} (\text{d}, 2\text{n}) ^{238}\text{Np} \rightarrow ^{238}\text{Pu}$ (87.7 years)
95	Americium	Am	1944–1945	$^{238}\text{U} (\alpha, \text{n}) ^{241}\text{Pu} \rightarrow ^{241}\text{Am}$ (433 years)
96	Curium	Cm	1944	$^{239}\text{Pu} (\alpha, \text{n}) ^{242}\text{Cm}$ (163 days)
97	Berkelium	Bk	1949	$^{241}\text{Am} (\alpha, 2\text{n}) ^{243}\text{Bk}$ (4.5 h)
98	Californium	Cf	1950	$^{242}\text{Cm} (\alpha, \text{n}) ^{245}\text{Cf}$ (44 min)
99	Einsteinium	Es	1952	Thermonuclear explosion, ^{253}Es (20 days)
100	Fermium	Fm	1952	Thermonuclear explosion, ^{255}Fm (22 h)
101	Mendelevium	Md	1955	$^{253}\text{Es} (\alpha, \text{n}) ^{256}\text{Md}$ (1.3 h)
102	Nobelium	No	1958	$^{244}\text{Cm} (^{12}\text{C}, 4\text{n}) ^{252}\text{No}$ (~ 3 s)
103	Lawrencium	Lr	1961	$^{249-252}\text{Cf} (^{10,11}\text{B}, \text{xn}) ^{258}\text{Lr}$ (~ 4 s)

■ Fig. 18.2

Historical presentation of the discovery of transuranium elements. Some important discoveries related to the transuranium elements are also shown



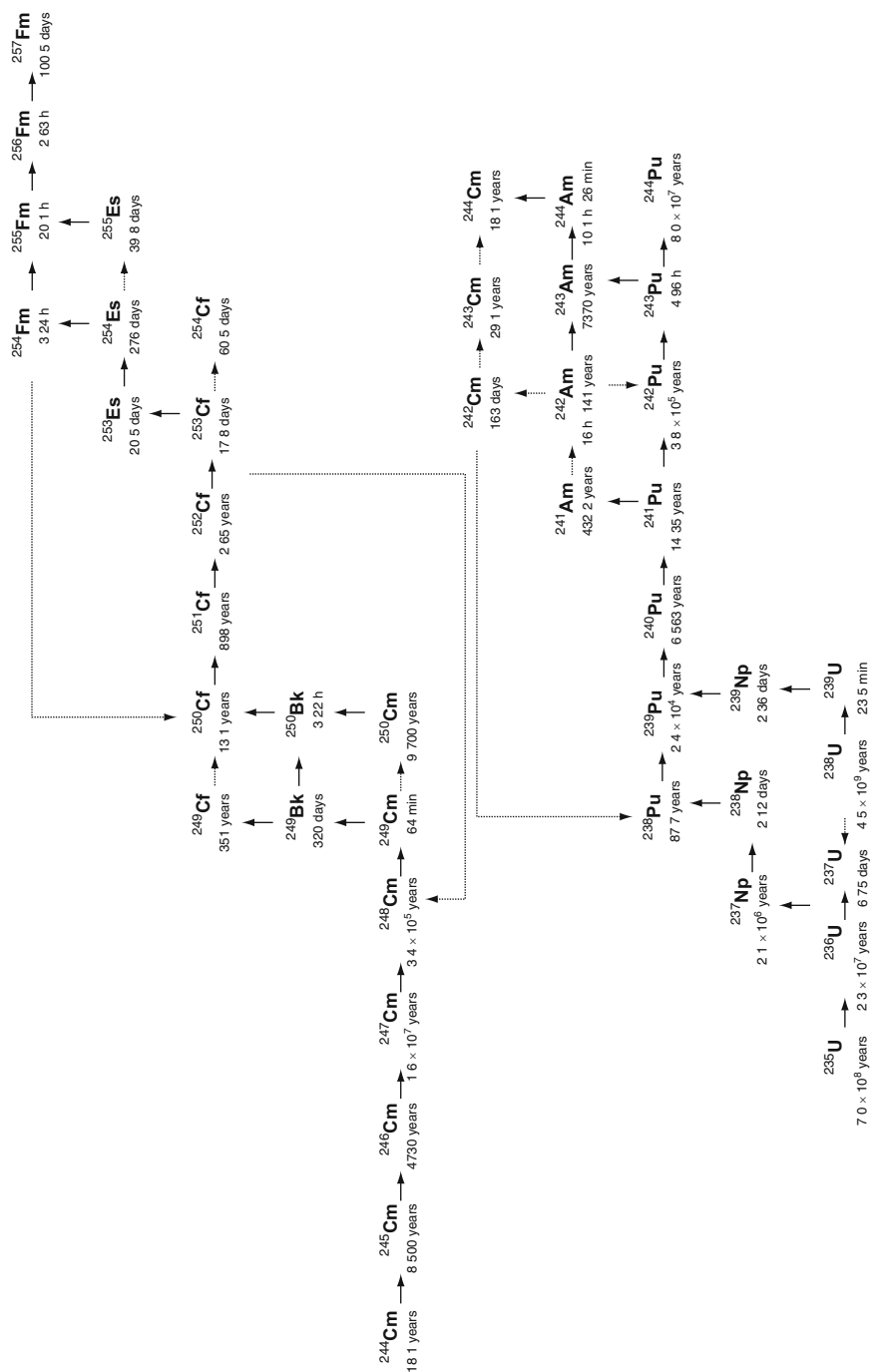
Four of the transuranium elements (Np, Am, Es, and Fm) were first produced using neutron capture reactions. In ▶ Fig. 18.3, the neutron capture paths used for production of transuranium nuclides in nuclear reactors are shown. Starting with ^{238}U , the main path goes to ^{239}Pu that undergoes multiple neutron captures to ^{243}Pu . ^{243}Pu decays to ^{243}Am that successively undergoes captures and decays to ^{244}Cm . Then ^{244}Cm can undergo multiple neutron captures to yield the Cm isotopes up to ^{249}Cm followed by subsequent captures and decays to ^{249}Bk , ^{250}Bk , ^{250}Cf , ^{252}Cf , and finally to ^{257}Fm . The chain ends at the 380 μs spontaneous fission (SF) of ^{258}Fm . As no appreciable amounts of nuclides above ^{244}Cm are produced in power reactors, one needs irradiations of heavy targets such as ^{244}Cm in a specific isotope production reactor for the production of heavier nuclides. As a typical facility for such irradiations, there is the High Flux Isotope Reactor (HFIR) at Oak Ridge National Laboratory, USA that accommodates 300 g of actinide target nuclides in a flux of 2×10^{15} – $5 \times 10^{15} \text{ n cm}^{-2} \text{ s}^{-1}$. Production of the heavier transuranium nuclides at HFIR is shown in ▶ Table 18.2 (cited from Hoffman 1986). Macroscopic quantities of some of these elements are available for studies of their nuclear and chemical properties and also serve as accelerator targets for preparation of other heavy element isotopes.

Successive neutron capture reactions (see ▶ Fig. 18.3) depend on the β -decay constant, λ , and the neutron capture cross section, σ , of each nuclide, as well as on the neutron flux ϕ . In other words, the competition between neutron capture and β^- -decay processes should be considered. The production rate of the i th nuclide with the number of atoms N_i is expressed as

$$\frac{dN_i}{dt} = N_{i-1}\sigma_{i-1}\phi - (\lambda_i + \sigma_i\phi)N_i. \quad (18.13)$$

Fig. 18.3

Neutron capture paths to produce transuranium nuclei in nuclear reactors. The horizontal arrows represent the neutron capture and the vertical ones pointing upward indicate β^- decay. The main paths are shown by the solid arrows



■ **Table 18.2**

Mainline High Flux Isotope Reactor (HFIR) production (elements 96–100) (cited from Hoffman 1986)

Isotope	Half-life (principal decay mode)	Production (amount/year)
Curium-248	3.397×10^5 years (α)	150 mg
Berkelium-249	320 days (β^-)	50 mg
Californium-249	350.6 years (α)	From ^{249}Bk decay
Californium-252	2.64 years (α) ^a	500 mg
Einsteinium-253	20.4 days (α)	2 mg
Einsteinium-254	275.7 days (α)	4 μg
Fermium-257	100.5 days (α)	1 pg

^a ^{252}Cf has neutron output from spontaneous fission (SF) of $2.3 \times 10^{12} \text{ n s}^{-1} \text{ g}^{-1}$.

In the case of $\lambda_i \gg \sigma_i \phi$, the nuclide transmutes by β^- decay into the nuclide with $Z + 1$, while in the case of $\lambda_i \ll \sigma_i \phi$ the nuclide undergoes neutron capture to produce the nuclide with the number of neutrons increased by one. When $\lambda_i \approx \sigma_i \phi$, two processes compete with each other. Assuming the following values, e.g., for the neutron flux and the neutron-absorption cross section of the i th nuclide $\phi = 1 \times 10^{15} \text{ n cm}^{-2} \text{ s}^{-1}$ and $\sigma_i = 10$ barns ($1 \times 10^{-23} \text{ cm}^2$), respectively, the competing processes become comparable if the β half-life of the nuclide is $T_{1/2} = 2.2$ years ($\lambda_i = 1 \times 10^{-8} \text{ s}^{-1}$).

Over a thousand tons of plutonium has been synthesized in commercial and military reactors; the annual global net production rate in nuclear power reactors is $\sim 100 \text{ tons y}^{-1}$, contained in the spent fuel elements. The accumulated amount of higher actinides within the European community is on the level of 1–3 tons for ^{237}Np , ^{238}Pu , and ^{241}Am and over 100 kg for ^{244}Cm ; the amounts in the USA and Russia are of the same magnitudes (Choppin et al. 1995).

For frontier research on both the chemical and nuclear properties of the heaviest elements, large quantities of heavy actinides with relatively long half-lives, such as ^{254}Es and $^{244,248}\text{Cm}$ are needed. In fact, the LEAP (Large Einsteinium Activation Program) project had been proposed by the US national laboratories to investigate the inorganic and nuclear chemistry of elements in the transfermium region and to search for superheavy elements (Hoffman 1986).

18.1.2.2 Charged-Particle-Induced Reactions

Compound nucleus reactions involving light incident charged particles were used for the first production of the transuranium elements Pu, Cm, Bk, Cf, and Md. However, for the production of transuranium nuclei far from the stability line, the emphasis has shifted from using light charged-particle-induced reactions to using heavy-ion-induced reactions. Recent developments in accelerator technology have made the use of high intensity heavy-ion beams as massive as ^{238}U . General description of the heavy-ion reactions appears in some references (see, e.g., Bock 1980; Bass 1980; Bromley 1984).

Successful production of fissionable nuclei, such as transuranium nuclides in nuclear reactions, depends mainly on two factors: fusion cross section, σ_{fusion} , and survival probability, P_{survival}

$$\sigma_{\text{production}} = \sigma_{\text{fusion}} P_{\text{survival}}. \quad (18.14)$$

The first term is the yield of compound nucleus formation or the fusion cross section used in the heavy-ion reaction, while the second term is the survival probability of the produced transuranium nucleus in the process of de-excitation. Fusion cross section can be approximated by the equation

$$\sigma_{\text{fusion}} = \pi \lambda^2 \sum (2l + 1) T_l P_{\text{cn}} \quad (18.15)$$

where λ is the de Broglie wavelength of the incident particle, l is the orbital angular momentum, and T_l indicates the transmission coefficient of the wave (for detailed explanation of nuclear reactions see [▶ Chap. 3 in Vol. 1](#)). P_{cn} is the probability of the compound nucleus formation. On the de-excitation process of transuranium nuclei, competition between the particle emission (mainly neutron) and fission that destroys transuranium nuclei, $\Gamma_{\text{n}}/\Gamma_{\text{f}}$, should be considered. $\Gamma_{\text{n}}/\Gamma_{\text{f}}$ is discussed in detail by Vandenbosch and Huizenga (1973) and the experimental values are compiled for various fissioning nuclei by Schmidt et al. (1980). The $\Gamma_{\text{n}}/\Gamma_{\text{f}}$ values averaged over evaporation of four neutrons are shown in [▶ Fig. 18.4](#) as a function of the neutron number N of the nucleus. It is found that the $\Gamma_{\text{n}}/\Gamma_{\text{f}}$ decreases with the atomic number Z of the nucleus and increases with N for each Z .

For the calculation of $\sigma_{\text{production}}$ via compound nucleus formation followed by the de-excitation process with $\Gamma_{\text{n}}/\Gamma_{\text{f}}$, some computer codes, such as ALICE (Plasil and Blann 1975; Blann 1984), PACE (Gavron 1980), and HIVAP (Reisdorf 1981) are widely used.

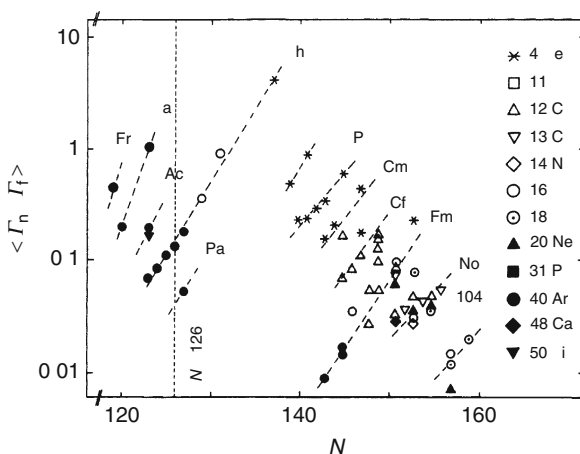
In the production of heavy transuranium nuclei with heavy ions, additional factors that enhance or decrease the yields of transuranium products should be considered. They are fusion enhancement at sub-barrier energy and dynamical hindrance to fusion.

The dynamical hindrance caused by the Coulomb repulsion between two fusing nuclei in heavy nuclear systems brings up a serious problem for heavy element production. A dramatic decrease in fusion probability occurs as the value of $Z_1 \times Z_2$ becomes 1,600–2,000, where Z_1 and Z_2 indicate the atomic numbers of the incident particle and target, respectively. The energy required to make the nuclei to touch is called the interaction barrier, while the extra radial energy above this barrier to make the two nuclei to fuse and form a compound nucleus is called the extra-push energy (Swiatecki 1982). For estimating the interaction barrier, the Bass barrier (Bass 1974) is generally used. Experimental data and recent interpretation of the dynamical fusion hindrance are summarized in the review articles by, e.g., Schmidt and Morawek, and Armbruster (Schmidt and Morawek 1991; Armbruster 1999).

The anomalous sub-barrier fusion of two massive nuclei is the phenomenon that is of several orders of magnitude larger than expected from the quantum tunneling through the interaction barrier. Various theoretical attempts have been made to understand the causes of this enhancement of fusion, such as static deformation of colliding nuclei, neck formation during fusion, vibrational excitation of nuclear surfaces, and nuclear structure effects. As a formal theoretical approach, the channel-coupling picture, the tunneling degree of freedom (entrance channel) coupled to the internal degree of freedom (inelastic channel) of the quantum many-body system (two nuclei), is suggested. The detailed description of the sub-barrier fusion appears in the reviews by Beckerman, Satchler, and Reisdorf (Beckerman 1988;

■ Fig. 18.4

Systematics of the Γ_n/Γ_f values averaged over evaporation of four neutrons. The symbols on the right side are the incident particles to produce heavy nuclei (Schmidt et al. 1980)



Satchler 1991; Reisdorf 1994). For the calculations of sub-barrier fusion cross sections, the computer code CCDEF (Fernandez-Niello et al. 1989) is widely used in which the influence of the static deformation of the colliding nuclei as well as the inelastic coupling to collective excited levels is considered.

Some experimental production cross sections of transuranium nuclides including transactinides in charged-particle-induced reactions of the U isotopes and ^{248}Cm targets are summarized in Table 18.3.

Some cross sections listed in Table 18.3 are plotted as a function of the atomic number Z of the product for various incident charged particles (CP) in Fig. 18.5. The decreasing trend of the cross section with increasing Z is obvious, and it is interesting to note that the slope for $^{238}\text{U}(\text{CP},5n)$ and $^{248}\text{Cm}(\text{CP},5n)$ are about the same, while the absolute values for the ^{248}Cm reactions are slightly larger than those for ^{238}U .

Neutron-rich nuclides are inaccessible via the compound nuclear reaction. To produce neutron-rich transuranium nuclides, heavy-ion-induced transfer reactions of actinide targets ranging from ^{238}U to ^{254}Es with a variety of incident particles ranging from ^{16}O to ^{238}U have been studied.

A typical example of such attempts was the study of the $^{238}\text{U} + ^{238}\text{U}$ reaction at GSI (GSI Helmholtzzentrum für Schwerionenforschung GmbH), Darmstadt, Germany. In Fig. 18.6, the production yields of transuranium isotopes for the reaction of 7.5 MeV/amu ^{238}U ions with thick ^{238}U targets are shown (Schädel et al. 1978). The yield distributions of the heavy actinides were found to show similar bell-shaped variations with the atomic number Z and mass number A as observed in the $^{136}\text{Xe} + ^{238}\text{U}$ reaction (Schädel et al. 1978). However, the yields of each isotope in the $^{238}\text{U} + ^{238}\text{U}$ reaction are much larger than those observed in the $^{136}\text{Xe} + ^{238}\text{U}$ reaction. Schädel et al. (1982) also measured the yields of heavy actinides in the reaction of ^{238}U with ^{248}Cm and the results showed that the shapes and centroids of the isotopic distributions are similar in all cases but the magnitudes of the yields are the greatest in the $^{238}\text{U} + ^{248}\text{Cm}$ reaction.

■ Table 18.3

Production cross sections in the charged-particle-induced reactions of U and ^{248}Cm targets

Reaction	Atomic number of product	$\sigma_{\text{max}}/\mu\text{b}^a$	$E_{\text{max}}/\text{MeV}^a$	Reference
$^{238}\text{U}(\text{p},3\text{n})$	93	79,600	20	Ageev et al. 1987
$^{238}\text{U}(\text{p},4\text{n})$	93	42,800	29	Bellido et al. 1994
$^{235}\text{U}(\text{d},3\text{n})$	93	28,400	18.6	Wing et al. 1959
$^{238}\text{U}(\text{d},4\text{n})$	93	58,000	26	Bellido et al. 1993
$^{233}\text{U}(\alpha,3\text{n})$	94	2,050	33.7	Delagrange et al. 1978
$^{234}\text{U}(\alpha,3\text{n})$	94	6,110	35.2	Delagrange et al. 1978
$^{235}\text{U}(\alpha,3\text{n})$	94	8,630	34.1	Vandenbosch et al. 1958
$^{235}\text{U}(\alpha,3\text{n})$	94	8,730	33.7	Delagrange et al. 1978
$^{238}\text{U}(\alpha,3\text{n})$	94	70,600	32.5	Wing et al. 1959
$^{233}\text{U}(\alpha,4\text{n})$	94	1,130	46.2	Vandenbosch et al. 1958
$^{234}\text{U}(\alpha,4\text{n})$	94	1,170	43.2	Delagrange et al. 1978
$^{235}\text{U}(\alpha,4\text{n})$	94	2,400	42.8	Vandenbosch et al. 1958
$^{235}\text{U}(\alpha,4\text{n})$	94	2,230	42.0	Delagrange et al. 1978
$^{238}\text{U}(\alpha,4\text{n})$	94	23,100	40.2	Coleman 1958
$^{235}\text{U}(^{11}\text{B},4\text{n})$	97	12	58	Williams and Seaborg 1979
$^{233}\text{U}(^{12}\text{C},3\text{n})$	98	0.35	66	Sikkeland et al. 1968a
$^{235}\text{U}(^{12}\text{C},3\text{n})$	98	1.4	67	Sikkeland et al. 1968a
$^{236}\text{U}(^{12}\text{C},3\text{n})$	98	2.7	67	Sikkeland et al. 1968a
$^{234}\text{U}(^{12}\text{C},4\text{n})$	98	4	71	Sikkeland et al. 1968a
$^{235}\text{U}(^{12}\text{C},4\text{n})$	98	8.8	70.5	Sikkeland et al. 1968a
$^{236}\text{U}(^{12}\text{C},4\text{n})$	98	22	70	Sikkeland et al. 1968a
$^{238}\text{U}(^{12}\text{C},4\text{n})$	98	62	67.5	Sikkeland et al. 1968a
$^{238}\text{U}(^{12}\text{C},4\text{n})$	98	60	67	Volkov et al. 1959
$^{235}\text{U}(^{12}\text{C},5\text{n})$	98	5	77.5	Sikkeland et al. 1968a
$^{236}\text{U}(^{12}\text{C},5\text{n})$	98	9.8	77.5	Sikkeland et al. 1968a
$^{238}\text{U}(^{12}\text{C},5\text{n})$	98	100	73.5	Sikkeland et al. 1968a
$^{238}\text{U}(^{13}\text{C},5\text{n})$	98	120	78	Volkov et al. 1959
$^{233}\text{U}(^{16}\text{O},4\text{n})$	100	0.2	94	Nurmia et al. 1967
$^{238}\text{U}(^{16}\text{O},4\text{n})$	100	2.3	92	Shinohara et al. 1986
$^{238}\text{U}(^{18}\text{O},4\text{n})$	100	0.9	90.5	Sikkeland 1966
$^{238}\text{U}(^{18}\text{O},4\text{n})$	100	0.75	88	Donets et al. 1966
$^{233}\text{U}(^{16}\text{O},5\text{n})$	100	0.015	98	Nurmia et al. 1967
$^{238}\text{U}(^{18}\text{O},5\text{n})$	100	4.0	94	Sikkeland 1966
$^{238}\text{U}(^{18}\text{O},5\text{n})$	100	4	94	Donets et al. 1966
$^{238}\text{U}(^{19}\text{F},5\text{n})$	101	0.5	103	Donets et al. 1966
$^{236}\text{U}(^{22}\text{Ne},4\text{n})$	102	6.8×10^{-3}	112	Andreyev et al. 1993a
$^{238}\text{U}(^{22}\text{Ne},4\text{n})$	102	0.04	112	Donets et al. 1966

■ Table 18.3 (Continued)

Reaction	Atomic number of product	$\sigma_{\max}/\mu\text{b}^a$	E_{\max}/MeV^a	Reference
$^{236}\text{U}(^{22}\text{Ne},5\text{n})$	102	0.0179	124	Andreyev et al. 1993a
$^{238}\text{U}(^{22}\text{Ne},5\text{n})$	102	0.2	117	Donets et al. 1966
$^{238}\text{U}(^{26}\text{Mg},3\text{n})$	104	1.1×10^{-5}	122	Gates et al. 2008
$^{238}\text{U}(^{26}\text{Mg},5\text{n})$	104	1.1×10^{-3}	140	Utyonkov et al. 1997
$^{236}\text{U}(^{27}\text{Al},5\text{n})$	105	4.5×10^{-3}	154	Andreyev et al. 1992
$^{238}\text{U}(^{30}\text{Si},4\text{n})$	106	1.8×10^{-4}	158	Ikezoe et al. 1998
$^{238}\text{U}(^{30}\text{Si},4\text{n})$	106	9×10^{-6}	149	Gregorich et al. 2008
$^{238}\text{U}(^{30}\text{Si},5\text{n})$	106	5×10^{-5}	165	Gregorich et al. 2008
$^{238}\text{U}(^{30}\text{Si},6\text{n})$	106	2.3×10^{-5}	165	Gregorich et al. 2008
$^{238}\text{U}(^{34}\text{S},5\text{n})$	108	2.5×10^{-6}	185	Lazarev et al. 1995
$^{233}\text{U}(^{48}\text{Ca},3\text{n})$	112	2.5×10^{-6}	234	Oganessian et al. 2004
$^{238}\text{U}(^{48}\text{Ca},4\text{n})$	112	6×10^{-7}	240	Oganessian et al. 2004
$^{248}\text{Cm}(^{12}\text{C},5\text{n})$	102	0.58	77	Sikkeland et al. 1968b
$^{248}\text{Cm}(^{13}\text{C},5\text{n})$	102	0.66	76	Sikkeland et al. 1968b
$^{248}\text{Cm}(^{15}\text{N},5\text{n})$	103	0.2	87	Eskola et al. 1971
$^{248}\text{Cm}(^{18}\text{O},5\text{n})$	104	0.005	97	Ghiorso et al. 1970
$^{248}\text{Cm}(^{18}\text{O},5\text{n})$	104	0.013	94	Nagame et al. 2002a
$^{248}\text{Cm}(^{19}\text{F},5\text{n})$	105	1.3×10^{-3}	106	Nagame et al. 2002a
$^{248}\text{Cm}(^{19}\text{F},5\text{n})$	105	2×10^{-3}	106	Trubert et al. 2002
$^{248}\text{Cm}(^{22}\text{Ne},4\text{n})$	106	2.5×10^{-5}	121	Türler et al. 1998
$^{248}\text{Cm}(^{22}\text{Ne},5\text{n})$	106	2.4×10^{-4}	123	Türler et al. 1998
$^{248}\text{Cm}(^{26}\text{Mg},5\text{n})$	108	6×10^{-6}	145	Türler et al. 2003
$^{248}\text{Cm}(^{48}\text{Ca},3\text{n})$	116	1.2×10^{-6}	240	Oganessian et al. 2004
$^{248}\text{Cm}(^{48}\text{Ca},4\text{n})$	116	3.3×10^{-6}	247	Oganessian et al. 2004

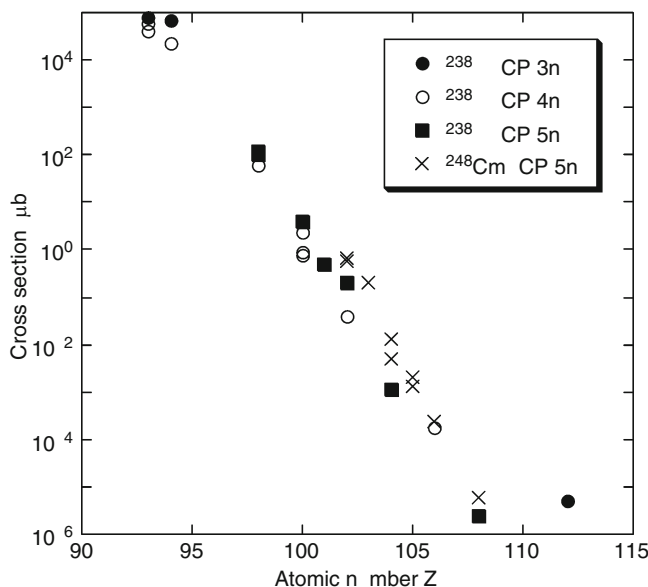
^a Maximum cross section σ_{\max} at the bombarding energy E_{\max} .

The availability of relatively large quantities of curium isotopes has made it possible to use them as target materials, both for the production of heavier elements and new neutron-rich nuclides. ^{248}Cm has been widely used as a target to make superheavy elements and isotopes in other heavy element studies because of its high neutron-to-proton ratio, its long half-life (3.4×10^5 years), its availability in milligram amounts, and its high isotopic purity, especially, if it is produced by milking from ^{252}Cf (e.g., Malmbeck et al. 2001). The transfer reactions for the production of heavy transuranium nuclides using various heavy ions on ^{248}Cm are summarized in ▶ Table 18.4.

Interesting results were reported for the bombardments of ^{248}Cm with the ^{40}Ca , ^{44}Ca , and ^{48}Ca projectiles. Production yields for elements through Fm are shown in ▶ Fig. 18.7a (Türler et al. 1992). Considerable difference is observed in the yields of the below-target elements with the highest yields observed for ^{48}Ca , while for the above-target elements the lowest yields were observed for the ^{48}Ca projectile. The most neutron-rich nuclides in the isotopic yield distribution were observed for the reactions with ^{48}Ca (Hoffman et al. 1985).

■ Fig. 18.5

Cross sections for transuranium elements produced in the charged-particle-induced reactions of ^{238}U and ^{248}Cm



The reactions of ^{40}Ar with ^{233}U , ^{235}U , and ^{238}U were studied at the energy of the Coulomb barrier (Scherer et al. 1990). Contrary to the above $\text{Ca} + ^{248}\text{Cm}$ reactions, the element yields below uranium are the same within the limits of errors for the three target isotopes, while the yields of the above-target elements are in the order of ^{238}U , ^{235}U , and ^{233}U as shown in

► Fig. 18.7b.

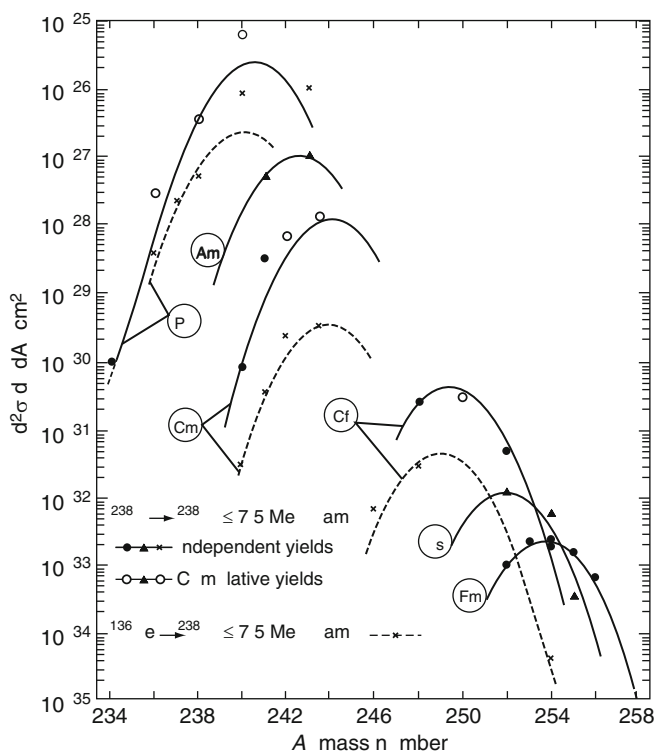
Neutron-rich isotopes of heavier actinides such as ^{262}No and $^{261,262}\text{Lr}$, were produced through transfer reactions by bombardments of highly radioactive ^{254}Es ($T_{1/2} = 275.7$ days) targets with heavy ions (Lougheed et al. 1989; Hulet 1990a). Most recently, it has been suggested that the nuclear shell structure may strongly influence the nucleon flow in the low-energy damped collisions of heavy ions (Zagrebaev et al. 2006; Zagrebaev and Greiner 2008). The production of neutron-rich heavy nuclei has been proposed (Zagrebaev et al. 2006) in the multi-nucleon transfer processes of low-energy heavy-ion collisions that are based on the dynamical multidimensional Langevin equation.

18.1.3 Experimental Techniques for Production and Identification of Short-Lived Transuranium Nuclei

In the study of the mechanism of heavy-ion reaction resulting in transuranium products and for investigating nuclear properties of transuranium nuclei, it is of great importance to isolate and uniquely identify the products by their atomic number Z , mass number A , and production cross sections. The claim to the discovery of a new element must present a clear evidence for unequivocal identification of Z , while that of a new isotope has to be made with the determination of both Z and A .

■ Fig. 18.6

Production cross sections of transuranium isotopes in the reactions $^{238}\text{U} + ^{238}\text{U}$ and $^{136}\text{Xe} + ^{238}\text{U}$ (Schädel et al. 1978)



A review of the experimental techniques is given in several articles (Herrmann and Trautmann 1982; Münzenberg 1988; Seaborg and Loveland 1990; Trautmann 1995). Table 18.5 presents a comparison of characteristics, such as separation time and total efficiency, of various methods generally used for isolating and identifying transuranium reaction products.

For studying fission properties such as mass-yield and total kinetic energy (TKE) distributions of very short-lived spontaneous fission (SF) isotopes, the SWAMI (spinning-wheel analyzer for millisecond isotopes) apparatus was constructed (Hulet et al. 1989). The schematic diagram is shown in Fig. 18.8.

A portion of the recoil products emerging from the target is stopped in $100 \mu\text{g}/\text{cm}^2$ Al foils in continuous band on the rotating disk. These foils rotate between four pairs of detectors that measure the energy deposited by correlated fission fragments when the product nuclei decay by SF. For example, SF properties of $1.2 \text{ ms } ^{258}\text{No}$ produced through the $^{248}\text{Cm}(^{13}\text{C}, 3n)$ reaction were studied with SWAMI. A similar rotating wheel technique was developed by Gäggeler et al. (1984) to measure SF of Fm isotopes.

A gas-jet transport method is conventionally used to identify and study short-lived transuranium nuclei. Nuclei recoiling out of a target are stopped in a volume of gas such as He, which is loaded with aerosols, such as KCl, PbI_2 , C clusters, and MoO_3 . The products

■ Table 18.4

List of the studied transfer reactions for the production of transuranium nuclides in the bombardments of ^{248}Cm with various kinds of incident particles

Projectile	Studied products	Energy/MeV	Reference
^{16}O	Bk–Md	97	Lee et al. 1982
^{18}O	Bk–No	98	Lee et al. 1982
^{18}O	Bk–Fm	97, 104, 113, 122	Lee et al. 1983
^{18}O	Np–Bk	95.5–96.5	Moody et al. 1986
^{20}Ne	Bk–Md	115	Lee et al. 1982
^{22}Ne	Bk–Md	116	Lee et al. 1982
^{31}P	Bk–Fm	174, 190, 207, 233, 239	Leyba et al. 1991
^{40}Ar	Bk–Fm	207, 225, 245, 266, 286	Leyba et al. 1990
^{40}Ca	Bk–Fm	221–234, 246–259, 281–294	Hoffman et al. 1985
^{44}Ca	Th–Fm	231–323	Türler et al. 1992
^{48}Ca	Bk–Fm	223–239, 247–263, 272–288, 304–318	Hoffman et al. 1985
^{48}Ca	Rn–Pu	248–263	Gäggeler et al. 1986
^{86}Kr	Pa–Fm	379–435, 402–457, 436–490, 493–546	Moody et al. 1986
^{129}Xe	Np–Fm	791–769	Welch et al. 1987
^{132}Xe	Np–Fm	817–793	Welch et al. 1987
^{136}Xe	Pa–Fm	624–716, 699–790, 761–808	Moody et al. 1986
^{238}U	Bk–Md	1,761	Schädel et al. 1982

attached to the aerosols are swept out of a target recoil chamber with the He gas and are transported through a capillary to a detection system or other apparatuses.

To search for new transuranium nuclides and to study decay properties of these nuclei, a composite system consisting of the gas-jet transport apparatus and an online isotope separator (JAEA-ISOL) has been developed by Ichikawa et al. (2002). This system enables one to simultaneously determine the mass number via the isotope separator and the atomic number by the measurement of X-rays associated with the EC/ β^\pm decay of a nucleus. The experimental setup is schematically drawn in ► Fig. 18.9.

The reaction products recoiling out of targets are thermalized in the He gas loaded with PbI_2 aerosol clusters. The targets are mounted in the multiple target system. The products attached to the aerosols are swept out of the target chamber and transported to the thermal ion source of ISOL through the gas-jet. The transported nuclides are ionized, mass separated, and collected on an aluminum-coated Mylar tape in the tape transport system or in the rotating catcher foil apparatus. The new isotope ^{241}Bk produced in the $^{239}\text{Pu}(^6\text{Li},4n)$ reaction was identified by the measurement of the characteristic Cm X-rays associated with the electron capture (EC) decay of the nucleus separated for mass 241 (Asai et al. 2003). The other new isotope ^{233}Am produced in $^{233}\text{U}(^6\text{Li},6n)$ was identified through an α - α correlation analysis (Sakama et al. 2000).

The identification of new nuclides $^{243,244}\text{Np}$ with the gas-jet coupled rapid chemical separation method (Moody et al. 1987a) is described as follows. Two different chemical separation procedures were used to isolate Np from other reaction products in the

■ Fig. 18.7

(a) Element yields in the reactions of $^{40,44,48}\text{Ca}$ projectiles with ^{248}Cm (Türler et al. 1992) and
 (b) those for the $^{40}\text{Ar} + ^{233,235,238}\text{U}$ reactions (Scherer et al. 1990)

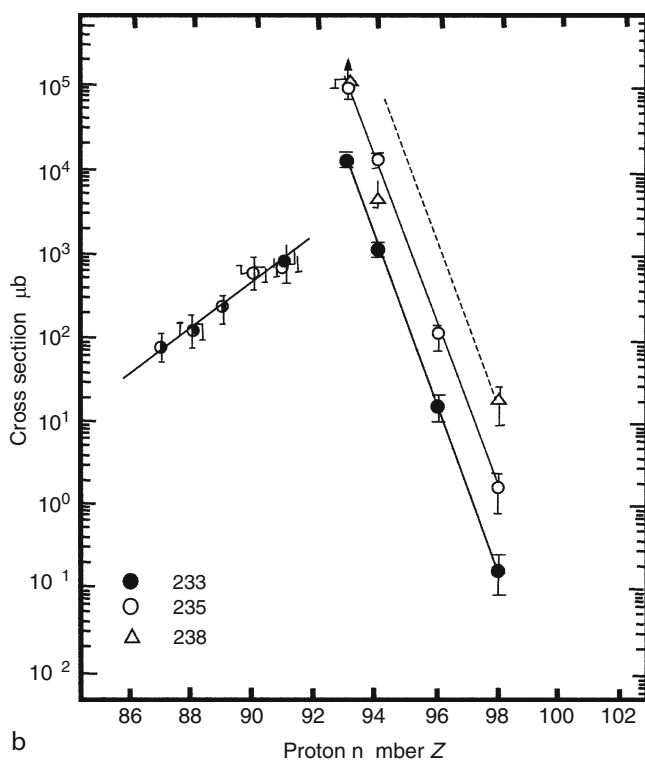
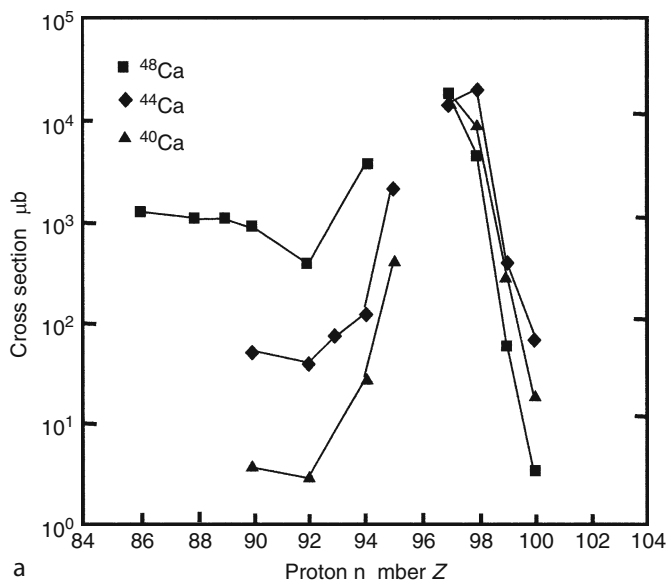
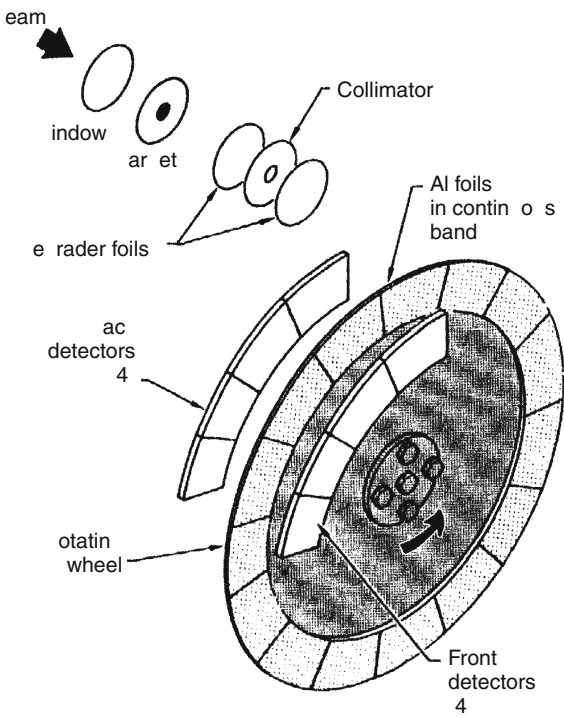


Table 18.5
Comparison of characteristics of experimental techniques for isolating transuranium reaction products

Method	Separation time/s	Total efficiency/%
Rotating wheel catcher	10^{-3}	60
Gas-jet transport	10^{-1}	50
Gas-jet coupled rapid chemical separation	10^1	30–40
Gas-jet coupled ISOL ^a	10^0	~1
Gas-filled separator	10^{-6}	25–45
Velocity separator	10^{-6}	20

^a ISOL: Isotope Separator On-Line.

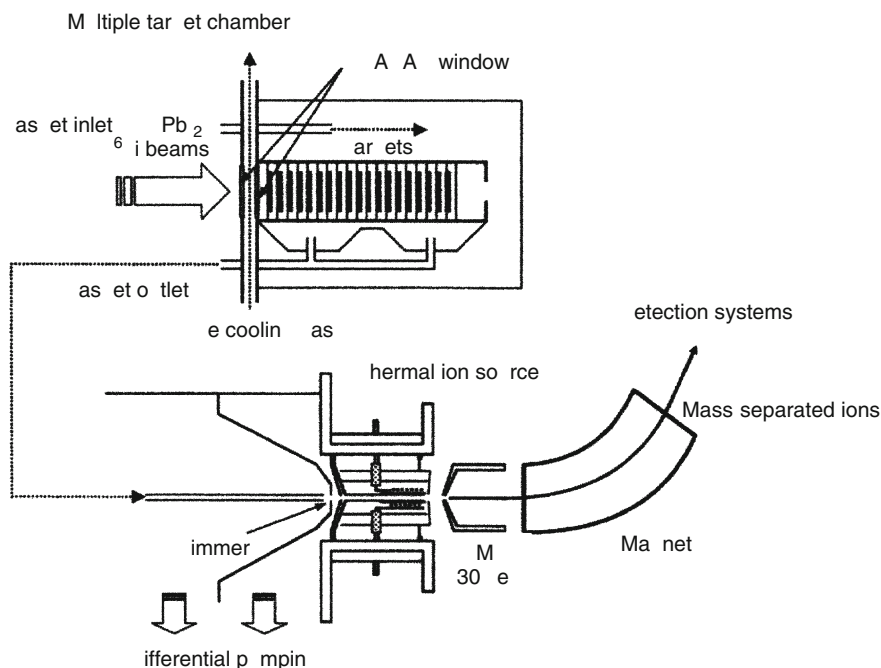
Fig. 18.8
Schematic diagram showing the essential features of the SWAMI (spinning-wheel analyzer for millisecond isotopes) apparatus (Hulet et al. 1989)



$^{136}\text{Xe} + ^{244}\text{Pu}$ reaction. The first method involved a series of solvent extractions performed continuously with the centrifuge system SISAK (Short-lived Isotopes Studied by the AKUFVE Technique) (Skarnemark et al. 1980) and the second one involved the ion-exchange separation apparatus ARCA (Automated Rapid Chemistry Apparatus) (Schädel et al. 1989). In the case of

■ Fig. 18.9

Schematic view of the gas-jet coupled Japan Atomic Energy Agency, JAEA-ISOL (Ichikawa et al. 2002; Nagame et al. 2002b)



the SISAK experiment shown in Fig. 18.10, reaction products were transported with the argon (Ar) gas-jet system to the chemistry laboratory. The transported products were dissolved in dilute HCl containing TiCl_3 , which reduced Np to the 3+ oxidation state. U, Th, and several fission products were extracted into di(2-ethyl-hexyl)orthophosphoric acid in CCl_4 (HDEHP/ CCl_4). Np was extracted in the second HDEHP/ CCl_4 step after oxidation to the 4+ state with HNO_3 , and was back-extracted with phosphoric acid. The neptunium fraction was continuously pumped from the SISAK system through a Teflon tube to the front face of a series of Ge γ -ray detectors. For the detailed description of SISAK see Chap. 52 in Vol. 5.

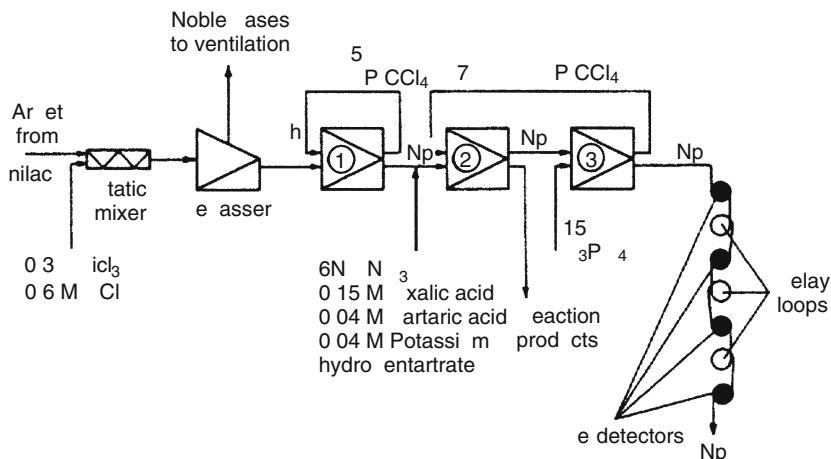
^{253}Md produced in the $^{243}\text{Am}(^{13}\text{C}, 3n)$ reaction was identified by using the Automated Chromatographic Chemical Element Separator System, ACCESS, in which ammonium α -hydroxy isobutyrate (α -HIB) was used for the separation of Md (Kadkhodayan et al. 1992). The other rapid chemical separation apparatus is described in the reviews (Herrmann and Trautmann 1982; Trautmann 1995) and also in Chap. 20 of this Volume.

As indicated in Table 18.5, for the detection and identification of isotopes with $T_{1/2} < 1$ ms, one has to employ in-flight separators based on electromagnetic separation of reaction products. Currently working in-flight separators for studies of transuranium nuclei are listed in Table 18.6. Detailed description of the in-flight separators is given by Münzenberg (1997).

In the region of heavy elements, spectroscopic studies were restricted because of the severe background arising from fission products. This problem was essentially solved by the employment of the new recoil decay tagging (RDT) technique (Paul et al. 1995) that consists of an in-beam γ -ray apparatus and the recoil mass separator.

■ Fig. 18.10

Schematic diagram of the SISAK (Short-lived Isotopes Studied by the AKUFVE Technique) setup used for the identification of $^{243,244}\text{Np}$ (Tetzlaff et al. 1986)



■ Table 18.6

Currently working in-flight separators for studies of transuranium nuclides

Name of apparatus	Institute, type of separator	Reference
GARIS	RIKEN ^a , gas-filled recoil separator	Morita et al. 1992
DGFRS	JINR ^b , gas-filled recoil separator	Lazarev et al. 1993, Subotic et al. 2002
RITU	JYFL ^c , gas-filled recoil separator	Leino et al. 1995
BGS	LBNL ^d , gas-filled recoil separator	Ninov et al. 1998
TASCA	GSI ^e , gas-filled recoil separator	Schädel 2007, Semchenkov et al. 2008
SHIP	GSI ^e , velocity filter	Münzenberg et al. 1979
VASSILISSA	JINR ^b , recoil-energy separator	Yeremin et al. 1989
FMA	ANL ^f , recoil mass separator	Davids et al. 1992
JAEA-RMS	JAEA ^g , recoil mass separator	Ikezoe et al. 1996

^a RIKEN: The Institute of Physical and Chemical Research, Japan.

^b JINR: Joint Institute for Nuclear Research, Dubna, Russia.

^c JYFL: University of Jyväskylä, Finland.

^d LBNL: Lawrence Berkeley National Laboratory, USA.

^e GSI: GSI Helmholtzzentrum für Schwerionenforschung GmbH, Darmstadt, Germany.

^f ANL: Argonne National Laboratory, USA.

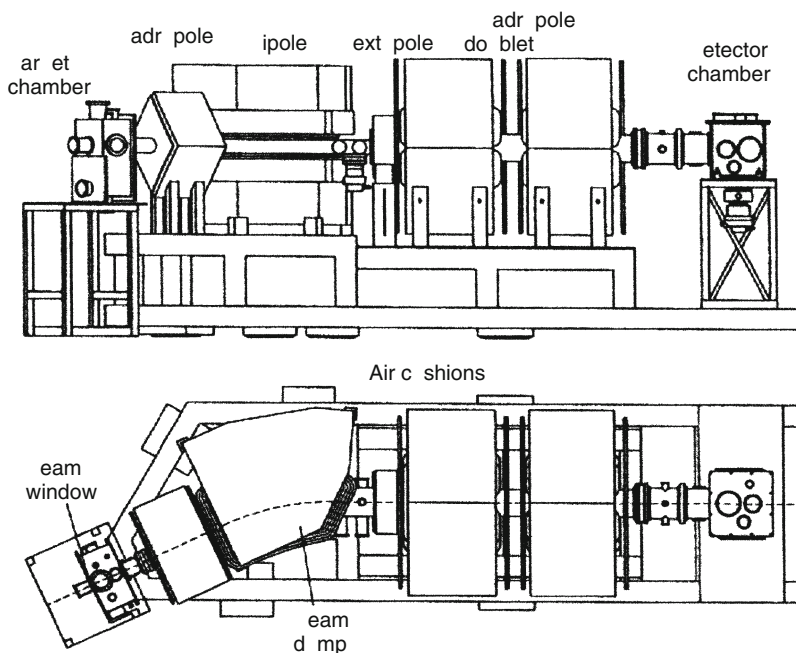
^g JAEA: Japan Atomic Energy Agency, Japan.

The characteristic decay modes offer a signature that a particular nuclide has been produced, and can be efficiently detected by a focal plane detector behind the recoil mass separator. Prompt γ rays at the target are detected by large Ge detector arrays.

The gas-filled recoil separator RITU (Recoil Ion Transport Unit) and the recoil mass separator FMA (fragment mass analyzer) in conjunction with germanium (Ge) detector arrays

■ Fig. 18.11

Scheme of recoil separator RITU (Recoil Ion Transport Unit) (Münzenberg 1997)



have been used for the study of the nuclear structure in the region of No isotopes (Leino et al. 1999; Reiter et al. 1999; 2000; Herzberg et al. 2001).

The schematic of RITU is shown in Fig. 18.11. RITU has been designed to separate nuclides produced through compound nuclear reactions from beam particles and other reaction products, especially fission products. To collect reaction products efficiently in the focal plane of the separator, dilute gas was filled in a dipole magnet (Ghiorso et al. 1988). The nobelium nuclides, ^{254}No and ^{252}No , were produced in the fusion reactions of $^{208}\text{Pb}(^{48}\text{Ca}, 2n)$ and $^{206}\text{Pb}(^{48}\text{Ca}, 2n)$ with the cross sections of $2\ \mu\text{b}$ and $0.2\ \mu\text{b}$, respectively. Recently, Oganessian et al. (2001) measured the excitation functions for the reactions $^{204,206,207,208}\text{Pb}(^{48}\text{Ca}, xn)$.

18.1.4 Exotic Nuclear Decay Properties

Decay properties of transuranium nuclides lead to the understanding of proton excess heavy nuclei: verification of the proton drip line, nuclear structure of large deformed nuclei such as octupole and hexadecapole deformation, and fission barrier heights. There are several textbooks and review articles on nuclear decay properties of transuranium nuclei (e.g., Hyde et al. 1964; Seaborg and Loveland 1985; Poenaru 1996). Theoretical nuclear models of heavy nuclei are presented by Rasmussen (1975) and the nuclear structure with a deformed single-particle model is discussed by Chasman et al. (1977). Radioactive decay properties of transuranium nuclei are tabulated in the **Table of Isotopes** (Firestone and Shirley 1996). Recent nuclear and decay properties of nuclei in their ground and isomeric states are compiled and evaluated by Audi et al. (1997), while the calculated atomic mass excess and nuclear ground-state deformations are tabulated by Möller et al. (1995).

Fission barriers using the ETFSI (extended Thomas–Fermi plus Strutinsky integral) method have been calculated by Mamdouh et al. (1998, 2001) for a large number of nuclei. Möller et al. (2009) presented calculated fission barriers for heavy elements based on the macroscopic–microscopic finite-range liquid drop model.

As described in the previous ► Sect. 18.1.3, the spectroscopic studies of the No isotopes have been vigorously performed with large γ -ray detector arrays, Gammasphere (Lee 1990), Jurosphere and SARI (Segmented Array at RITU) arrays (Leino et al. 1999; Leino 2002), and the electron spectrometer SACRED (Solenoid and Array for Conversion Electron Detection) (Butler et al. 1996, 2002) coupled with the recoil separator. α - γ and α -electron (α -e) decay spectroscopy of the neutron-rich nuclide ^{257}No produced in the $^{248}\text{Cm}(^{13}\text{C},4n)$ reaction was carried out at JAEA using a rotating wheel detection system coupled with the gas-jet and the gas-jet transport coupled to ISOL, respectively. On the basis of the α - and γ -transition energies, α - γ , α -e, and e-e coincidence relations, the decay scheme of ^{257}No was established (Asai et al. 2005). As another interesting topic, enhanced stability of heavy nuclei due to high-spin isomers (*K*-isomers) is predicted (Walker and Dracoulis 1999; Xu et al. 2004). Multi-quasiparticle configurations (high-*K* isomer states) have been identified in ^{254}No (Herzberg et al. 2006). In-beam γ -ray spectroscopic studies of neutron-rich trans-U nuclei, $^{245,246}\text{Pu}$, and $^{249,250}\text{Cm}$, have been conducted through the unique nucleon transfer reactions using neutron-rich beams, such as ^{18}O . The ground-state bands of these nuclei were successfully established (Ishii et al. 2006, 2008; Makii et al. 2007). The recent experimental progress of nuclear structure study of the heaviest nuclei are summarized by Ahmad (2002), Leino and Hessberger (2004), and Herzberg (2008), while theoretical description is reviewed by Sobiczewski and Pomorski (2007).

A high-precision mass measurement system with Penning traps, SHIPTRAP (Block et al. 2007) at GSI has been developed to investigate nuclear structure of rare isotopes far from stability. The direct mass measurements of $^{252-254}\text{No}$ have been successfully performed (Block et al. 2010).

Spectroscopic studies of superdeformed fission isomers have been reviewed (Vandenbosch 1977; Metag et al. 1980; Bjornholm and Lynn 1980), while hyperdeformed nuclear shapes in the third minimum of the potential energy surface was discussed by Möller et al. (1972) and recently by Cwiok et al. (1994). Krasznahorkay et al. (1998) succeeded to observe hyperdeformed rotational bands in actinide nuclei.

In the following, exotic nuclear decay modes of heavy nuclei, cluster radioactivities, delayed fission, and spontaneous fission (SF) together with the recent progress on deformation paths toward fission are briefly introduced.

18.1.4.1 Cluster Radioactivities

A charged particle heavier than an α particle but lighter than a fission fragment, such as C, O, F, Ne, Mg, and Si isotopes, is spontaneously emitted in a cluster decay of a heavy nucleus. The cluster decay was first predicted by Sandulescu et al. (1980) and experimentally discovered by Rose and Jones (1984) in the decay: $^{223}\text{Ra} \rightarrow ^{14}\text{C} + ^{209}\text{Pb}$. Theoretical study of the cluster radioactivities is given by Greiner et al. (Sandulescu and Greiner 1992; Poenaru and Greiner 1996). The probability for the decay was $\sim 10^{-9}$ of the α -decay probability. The data obtained until now on half-lives and branching ratios relative to α decay are summarized in review articles (Price 1989; Bonetti and Guglielmetti 1996; Poenaru et al. 2002; Bonetti and Guglielmetti 2007). Some representative data are tabulated in ► Table 18.7.

■ Table 18.7

A summary of cluster radioactivities: experimental Q -values, half-lives, $T_{1/2}$, and half-lives relative to those of the α decay in terms of the logarithm of $T_{1/2}/T_\alpha$

Parent nucleus	Emitted cluster	Q/MeV	$\log (T_{1/2}/\text{s})$	$-\log (T_{1/2}/T_\alpha)$	Reference
^{221}Fr	^{14}C	31.294	14.53	11.99	Bonetti et al. 1994
^{221}Ra	^{14}C	32.402	13.39	11.47	Bonetti et al. 1994
^{222}Ra	^{14}C	33.052	11.01	9.42	Price et al. 1985
^{223}Ra	^{14}C	31.839	15.15	8.88	Price et al. 1985
^{224}Ra	^{14}C	30.541	15.69	10.16	Price et al. 1985
^{226}Ra	^{14}C	28.198	21.22	10.49	Barwick et al. 1986
^{225}Ac	^{14}C	30.479	17.16	10.93	Barwick et al. 1986
^{226}Th	^{18}O	45.731	>16.76	>13.37	Bonetti et al. 2001
^{228}Th	^{20}O	44.730	20.72	12.80	Bonetti et al. 1993
^{230}Th	^{24}Ne	57.765	24.61	12.10	Tretyakova et al. 1985
^{232}Th	^{24}Ne	54.491	>29.20	>11.44	Bonetti et al. 1995
^{232}Th	^{26}Ne	55.973	>29.20	>11.44	Bonetti et al. 1995
^{231}Pa	^{23}F	51.854	>26.02	>14.90	Price et al. 1992
^{231}Pa	^{24}Ne	60.413	22.88	11.76	Price et al. 1992
^{230}U	^{22}Ne	61.390	19.57	13.14	Bonetti et al. 2001
^{232}U	^{24}Ne	62.312	20.42	10.90	Barwick et al. 1985
^{233}U	^{24}Ne	60.490	24.84	12.06	Price et al. 1991
^{232}U	^{28}Mg	74.32	>22.26	>12.93	Bonetti and Guglielmetti 2007
^{233}U	^{25}Ne	60.736	24.84	12.06	Price et al. 1991
^{233}U	^{28}Mg	74.235	>27.59	>14.81	Price et al. 1991
^{234}U	^{24}Ne	58.831	>25.92	>12.90	Wang et al. 1987
^{234}U	^{26}Ne	59.473	>25.92	>12.90	Wang et al. 1987
^{234}U	^{28}Mg	74.118	25.74	12.72	Tretyakova et al. 1989
^{235}U	^{24}Ne	57.358	27.42	10.85	Bonetti et al. 1991
^{235}U	^{25}Ne	57.717	27.42	10.85	Bonetti et al. 1991
^{235}U	^{28}Mg	72.162	>28.09	>11.52	Bonetti et al. 1991
^{236}U	^{24}Ne	55.96	>25.90	>11.04	Bonetti and Guglielmetti 2007
^{236}U	^{26}Ne	56.75	>25.90	>11.04	Bonetti and Guglielmetti 2007
^{236}U	^{28}Mg	70.558	27.58	12.59	Tretyakova et al. 1994
^{236}U	^{30}Mg	72.280	27.58	12.59	Tretyakova et al. 1994
^{237}Np	^{30}Mg	74.791	>27.57	>13.41	Moody et al. 1992
^{236}Pu	^{28}Mg	79.674	21.67	13.57	Ogloblin et al. 1990
^{238}Pu	^{28}Mg	75.919	25.70	16.11	Wang et al. 1989
^{238}Pu	^{30}Mg	76.801	25.70	16.11	Wang et al. 1989
^{238}Pu	^{32}Si	91.198	25.27	15.68	Wang et al. 1989

■ **Table 18.7** (Continued)

Parent nucleus	Emitted cluster	Q/MeV	$\log (T_{1/2}/s)$	$-\log (T_{1/2}/T_{\alpha})$	Reference
^{240}Pu	^{34}Si	91.038	>25.52	>14.07	Bonetti and Guglielmetti 2007
^{241}Am	^{34}Si	93.931	>25.26	>15.06	Moody et al. 1987b
^{242}Cm	^{34}Si	96.519	23.15	15.87	Ogloblin et al. 2000

18.1.4.2 Delayed Fission

Delayed fission is also an exotic nuclear decay process of heavy nuclei that is observed subsequent to β or EC decay. In the delayed fission process, β decays or electron captures (EC) of the parent nuclide populate excited states of the daughter nucleus, and if these states are of energies comparable to or greater than the fission barrier of the daughter nucleus, then fission may compete with other decay modes of the excited states. The process is schematically shown in ► Fig. 18.12. Reviews give a detailed description of delayed fission (Oganessian and Lazarev 1985; Hall and Hoffman 1992).

Delayed fission permits studies of fission properties of nuclei far from stability and γ de-excitation of nuclear levels in the second minimum of the potential energy surface (► Fig. 18.12). There has been also considerable theoretical interest in β -delayed fission process because it may significantly affect the final abundance of heavy elements produced in the astrophysical r-process and in other multiple neutron capture process taking place in very high neutron flux, such as thermonuclear explosions (Tielemann et al. 1983; Meyer et al. 1989; Cowan et al. 1991; Staut and Klapdor-Kleingrothaus 1992). The experimental data on the delayed fission are presented in ► Table 18.8.

18.1.4.3 Spontaneous Fission

Spontaneous fission (SF) is observed only in elements with $Z \geq 90$ where Coulomb forces make the nucleus unstable toward this mode of decay, although energetically SF is an exothermic process for nuclei with $A \geq 100$. Numerous reviews of SF properties, half-lives, and properties of fission fragments, have been summarized by several authors (von Gunten 1969; Hoffman and Hoffman 1974; Hoffman and Somerville 1989; Hulet 1990b, Wagemans 1991; Hoffman and Lane 1995; Hoffman et al. 1996) and basic properties of nuclear fission are described in ► Chap. 4 of Vol. 1. However, some current topics concerning SF are presented in this Subsection.

Schematic representations of all of the measured mass-yield distributions (normalized to 200% fragment yield) for SF of the trans-Bk isotopes are shown in ► Fig. 18.13 (Hoffman and Lane 1995). It is interesting to observe rather sudden changes from asymmetric to symmetric fission as reflected by the mass distributions changing from asymmetric to symmetric mass distributions as the neutron number increases toward $N \approx 160$ for the elements Fm ($Z = 100$), No ($Z = 102$), and Rf ($Z = 104$).

The other interesting feature in SF of very heavy actinides is bimodal fission. The existence of two distinctively different scission configurations for the same mass division was demonstrated in SF of the heavy actinides (Balagna et al. 1971; Hulet et al. 1986, 1989). The most

■ Table 18.8

Experimental data on delayed fission

Nucleus	$T_{1/2}$	Q_{β}^a / MeV	Production reaction	P_{DF}^b	Reference
^{180}Tl	0.70 s	11.05	$^{144}\text{Sm} (^{40}\text{Ca}, p3n)$	$\sim 10^{-6}$	Lazarev et al. 1987
^{188}Bi	0.21 ± 0.09 s	10.35	$^{153}\text{Eu} (^{40}\text{Ca}, 5n)$	3.4×10^{-4}	Andreyev et al. 1993b
^{196}At	0.3 ± 0.03 s	9.50	$^{159}\text{Tb} (^{40}\text{Ca}, 3n)$	8.8×10^{-4}	Andreyev et al. 1993b
^{228}Fr	39 s	4.34	1 GeV p+U	$< 2 \times 10^{-7}$	Mezilev et al. 1990
^{230}Fr	19 s	5.06	1 GeV p+U	$< 3 \times 10^{-6}$	Mezilev et al. 1990
^{232}Fr	5 s	5.55	1 GeV p+U	$< 5 \times 10^{-5}$	Mezilev et al. 1990
^{230}Ac	122 s	2.70	60 MeV/amu $^{18}\text{O} + ^{232}\text{Th}$	$(1.19 \pm 0.40) \times 10^{-8}$	Yuan et al. 2001
^{232}Ac	35 s	3.70	1 GeV p+U	$< 10^{-6}$	Mezilev et al. 1990
^{234}Pa	6.7 h	2.20	$^{232}\text{Th} (\alpha, pn)$	3×10^{-12}	Gangrskii et al. 1978
^{234m}Pa	1.2 min	2.27	$^{238}\text{U} \rightarrow ^{234}\text{Th} \rightarrow$ $\rightarrow ^{234m}\text{Pa}$	10^{-12}	Gangrskii et al. 1978
^{236}Pa	9.1 min	2.90	$^{238}\text{U} (\gamma, pn)$ $^{238}\text{U} (d, \alpha)$	10^{-9} 3×10^{-10}	Gangrskii et al. 1978
^{238}Pa	2.3 min	3.46	$^{238}\text{U} (n, p)$ $^{238}\text{U} (n, p)$	6×10^{-7} $< 2.6 \times 10^{-8}$	Gangrskii et al. 1978 Bass-May et al. 1985
^{228}Np	61.4 ± 4 s	4.48	$^{233}\text{U} (p, 6n)$	2×10^{-4}	Kreek et al. 1994a
^{232}Am	55 ± 7 s 1.31 ± 0.04 min	5.04	$^{237}\text{Np} (\alpha, 9n)$ $^{237}\text{Np} (\alpha, 9n)$	$(1.3^{+4}_{-0.8}) \times 10^{-2}$ $(6.9 \pm 1.0) \times 10^{-4}$	Habs et al. 1978 Hall et al. 1990a ^c
^{234}Am	2.32 ± 0.08 min	4.18	$^{237}\text{Np} (\alpha, 7n)$	$(6.6 \pm 1.8) \times 10^{-5}$	Hall et al. 1990b ^c
^{238}Bk	144 ± 5 s	4.89	$^{241}\text{Am} (\alpha, 7n)$	$(4.8 \pm 2) \times 10^{-4}$	Kreek et al. 1994b ^c
^{240}Bk	4 min	3.94	$^{232}\text{Th} (^{14}\text{N}, 6n)$	10^{-5}	Gangrskii et al. 1980
^{242}Bk	7 min	3.00	$^{232}\text{Th} (^{14}\text{N}, 4n)$	$< 3 \times 10^{-7}$	Gangrskii et al. 1980
^{242}Es	11 ± 3 s	5.59	$^{233}\text{U} (^{14}\text{N}, 5n)$	0.006 ± 0.002	Shaughnessy et al. 2000
^{244}Es	37 s 37 s	4.64	$^{235}\text{U} (^{15}\text{N}, 5n)$, $^{237}\text{Np} (^{12}\text{C}, 5n)$ $^{237}\text{Np} (^{12}\text{C}, 5n)$	10^{-4} $(1.2 \pm 0.4) \times 10^{-4}$	Gangrskii et al. 1980 Shaughnessy et al. 2002
^{246}Es	8 min 7.7 min	3.89	$^{238}\text{U} (^{14}\text{N}, 6n)$ $^{249}\text{Cf} (p, 4n)$	3×10^{-5} $(3.7^{+8.5}_{-3.0}) \times 10^{-5}$	Gangrskii et al. 1980 Shaughnessy et al. 2001
^{248}Es	28 min 26 min	3.06	$^{238}\text{U} (^{14}\text{N}, 4n)$ $^{249}\text{Cf} (p, 2n)$	3×10^{-7} $(3.5 \pm 1.8) \times 10^{-6}$	Gangrskii et al. 1980 Shaughnessy et al. 2001

Table 18.8 (Continued)

Nucleus	$T_{1/2}$	Q_{β}^a / MeV	Production reaction	P_{Df}^b	Reference
^{256m}Es	7.6 h	1.70	$^{254}\text{Es} (t,p)$	2×10^{-5}	Hall et al. 1989 ^c
^{248}Md	7 s	5.33	$^{239}\text{Pu} (^{14}\text{N},5n)$	$< 5 \times 10^{-4}$	Gangrskii et al. 1980
^{250}Md	52 s	4.63	$^{243}\text{Am} (^{12}\text{C},5n)$	2×10^{-4}	Gangrskii et al. 1980

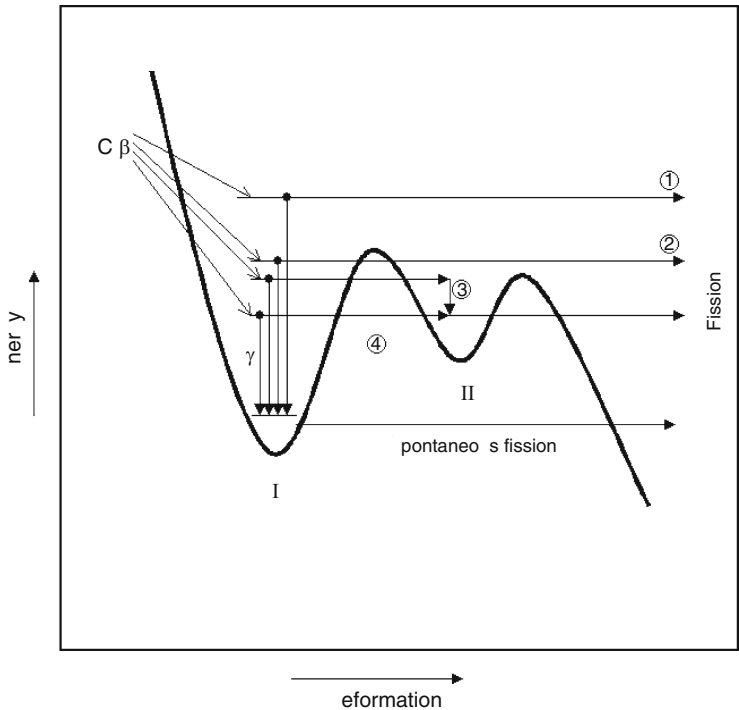
^a Q_{β} values have been taken from (Audi et al. 1997).

^b Delayed fission probability.

^c Based on coincidence measurements of β^- ray and fission or KX-ray associated with the electron capture (EC) decay and fission.

Fig. 18.12

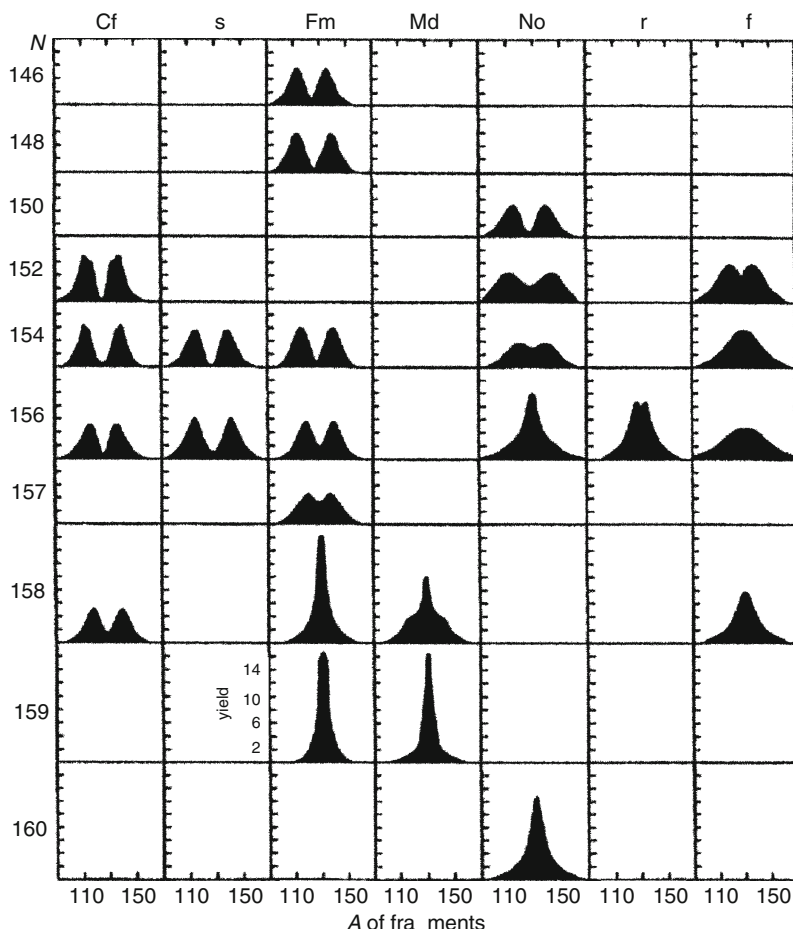
Schematic illustration of the delayed-fission process. The potential energy of the daughter nucleus as a function of deformation is shown, displaying the double-humped fission barrier prevalent in the actinides. Region I is the inner, or ground-state, well (first minimum); region II is the outer, or shape isomer, well (second minimum). The horizontal arrows indicate the various kinds of deformation toward fission



striking and significant features are that the mass-yield distribution is essentially single peaked around the symmetric mass split, resulting in products with the mass number $A \approx 130$, whereas the total kinetic energy (TKE) distribution apparently exhibits the structure with a shoulder that strongly suggests the presence of at least two components in the TKE distribution.

■ Fig. 18.13

Schematic representation of all known mass-yield distributions for spontaneous fission (SF) of trans-Bk isotopes (Hoffman and Lane 1995) (see also ► Fig. 4.16 in Chap. 4, Vol. 1)

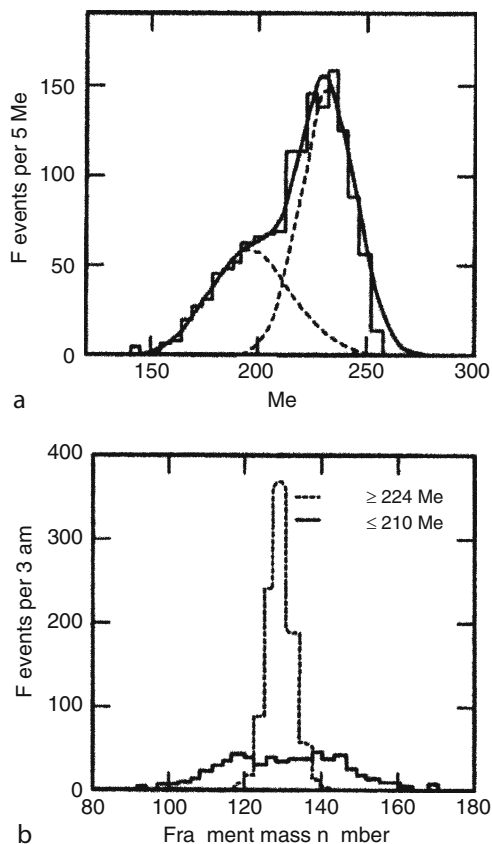


As typical data, the TKE and mass-yield distributions observed in SF of ^{260}Md (Hulet et al. 1989) are depicted in ► Fig. 18.14a, b, respectively; two components are clearly seen in the TKE distribution. The two-component analysis yielded the fact that the high-TKE events mostly constitute the sharp mass-yield curve around symmetry and the low-TKE ones a broad flat-topped distribution. Some theoretical calculations to understand bimodal fission of heavy actinides have been extensively performed (Warda et al. 2002; Asano et al. 2004; Bonneau 2006; Dubray et al. 2008; Ichikawa et al. 2009).

A sudden change of the mass distribution depending on the neutron number of the fissioning isotopes has been reported by Wagemans et al. for SF of plutonium, $^{236,238,240,242,244}\text{Pu}$ (Wagemans et al. 1989; Schillebeeckx et al. 1992; Dematte et al. 1997). The change of neutrons among the isotopes studied yields a drastic change in the mass and TKE

■ Fig. 18.14

(a) Total kinetic energy (TKE) distribution for SF of ^{260}Md . (b) Decomposed mass-yield distributions for the events with TKE ≥ 224 MeV (dashed histogram) and for those with TKE ≤ 210 MeV (solid histogram) (Wild et al. 1990)



distributions. An attempt was made to understand the phenomena in terms of the model of multimodal random neck rupture (Brosa et al. 1990).

Recent studies of SF of ^{252}Cf with large γ -ray detector arrays, Gammasphere (Lee 1990), revealed a new fission mode, cold fission with no neutron emission in the pair fragments of Zr–Ce and Mo–Ba (Ter-Akopian et al. 1994; Hamilton et al. 1995). Cold ternary SF, as $^{252}\text{Cf} \rightarrow ^{146}\text{Ba} + ^{96}\text{Sr} + ^{10}\text{Be}$, has also been identified by measuring the various γ -transitions of these nuclei in coincidence (Ramayya et al. 1998). The use of the high-resolution triple γ -coincidence technique can provide important information on very rare events in fission.

18.1.4.4 Progress in Two-Mode Fission

The presence of two kinds of deformation paths in low-energy fission of actinides has been verified by examining the correlation among saddle-point configurations, scission configurations, and mass-yield distributions (Nagame et al. 1996, 2001). The first path is initiated at

higher threshold energy and ends with an elongated scission configuration, giving a final mass-yield curve centered around symmetric mass division and lower TKE, the symmetric fission path. In the second path, the fissioning nucleus experiences lower threshold energy. This results in a more compact scission configuration, which gives a double-humped mass-yield distribution always centered around the heavy fragment mass number $A = 140$ with higher TKE, the asymmetric fission path. The above picture is well reproduced by the recent theoretical calculations of the potential energy surfaces by Möller et al. (2001); the saddle leading to the mass-symmetric division is found to be a few MeV higher than that of the mass-asymmetric division and the compact scission configuration is related to the asymmetric fission and the elongated one associated with the symmetric fission path. The clear ridge separating the two symmetric and asymmetric fission valleys is also pointed out (Möller et al. 2001).

Systematic features of the mass-yield and TKE distributions in both symmetric and asymmetric fission depending on A and Z of fissioning nuclei are discussed in detail by Ohtsuki et al. (1999) and Zhao et al. (2000). The effects of A and Z on the relative probability of taking either the deformation path or the characteristics of the final mass division phenomena and scission properties resulting from each deformation path have been extensively studied. Elemental yields of fission fragments in the Coulomb fission have been obtained for a number of neutron-deficient actinides and preactinides by using the unique method, relativistic radioactive beams (Schmidt et al. 1994, 2001). In [Fig. 18.15](#), the experimentally measured mass distributions are shown on the chart of nuclides, while the elemental yield distributions after Coulomb fission are depicted as functions of Z and N of the fissioning nuclei in [Fig. 18.16](#) (Schmidt et al. 2000). The transition from a single-humped mass-yield distribution at ^{221}Ac to a double-humped one at ^{234}U is clearly seen. In the transition region around ^{227}Th , triple-humped distributions appear, demonstrating comparable yields for the symmetric and asymmetric fission modes.

18.2 Chemical Properties of Transuranium Elements

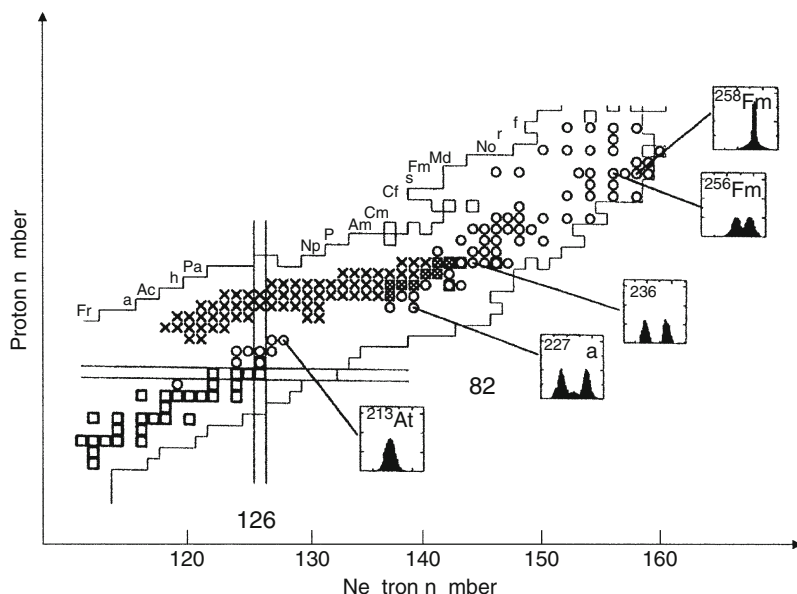
18.2.1 Actinide Concept

The actinide elements are 5f transition elements having partly filled f and d orbitals in the valence states. Compared to the 4f transition elements, lanthanides, in the actinides 5f orbitals have an important role in chemical bonding because of their wider radial distribution and higher energy due to relativistic effects (Pepper and Bursten 1991; Balasubramanian 1997). Relativity becomes important when particles move with speeds comparable to the speed of light. Relativistic effects become significant for heavier elements, and influence energy level structure and radial distribution of wave functions. [Figure 18.17](#) shows the spatial orientations of the atomic orbitals of the general set of seven f orbitals. Because of the variety of the direction of f orbitals, interactions with different atoms of ligands are complicated.

For the lighter actinide elements, such as uranium, neptunium, plutonium, and americium, the promotion energy of $5f \rightarrow 6d$ is smaller than that of $4f \rightarrow 5d$ transition in the lanthanides. Due to this smaller promotion energy, the chemical bonding is complicated in the lighter actinides and these elements take from 3+ to 7+ oxidation states. However, the heavier actinides beyond curium more closely resemble the lanthanides and the trivalent state becomes stable. In order to understand the chemistry of transuranium elements, one has to consider the relative energy of the valence orbitals and the relativistic effects on

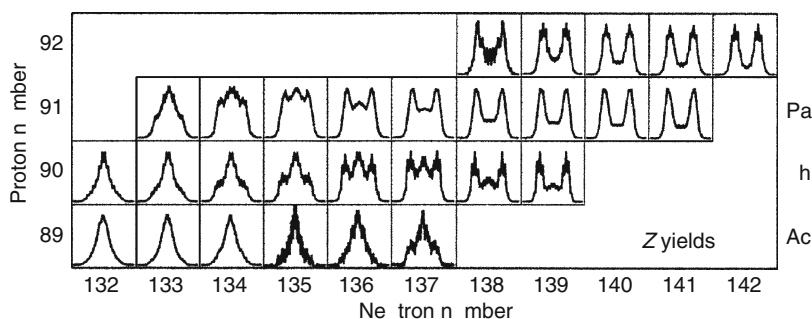
■ Fig. 18.15

Isotopes investigated in low-energy fission are indicated on the chart of nuclides. *Circles:* Mass distributions measured for excitation energies less than 10 MeV above the fission barrier and those from SF. *Crosses:* Data obtained using the Coulomb fission by using the relativistic radioactive beams (Schmidt et al. 2000)



■ Fig. 18.16

Fission-fragment elemental yield distributions in the range $Z = 24$ – 65 observed in Coulomb fission are shown on the chart of nuclides (Schmidt et al. 2000)

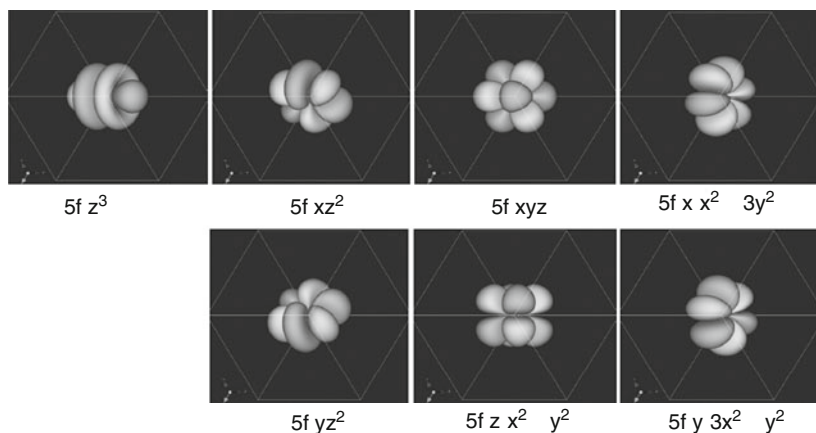


5f electrons. The relative energy between 5f and 6d orbitals strongly affects the oxidation states and ionic radii of the ions.

The energy level structure is particularly important to understand the relativistic effects on the valence states of the actinide atoms. ➤ *Figure 18.18* shows relativistic effects on the energy level structure of Am calculated by the nonrelativistic Hartree–Fock–Slater and the relativistic

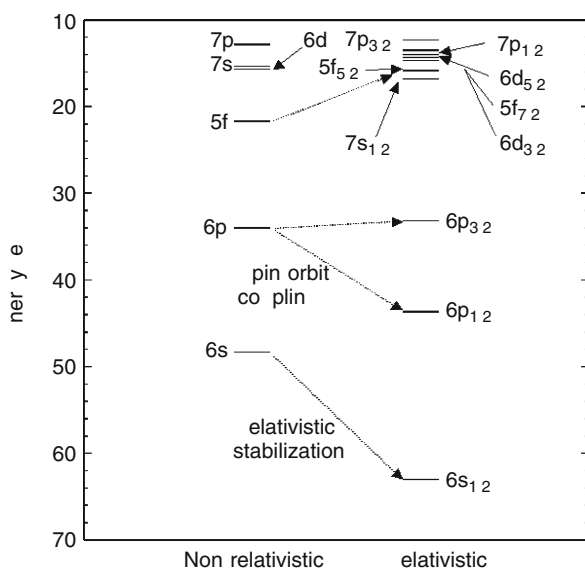
■ Fig. 18.17

The general set of seven f orbitals (Sakane 2009)



■ Fig. 18.18

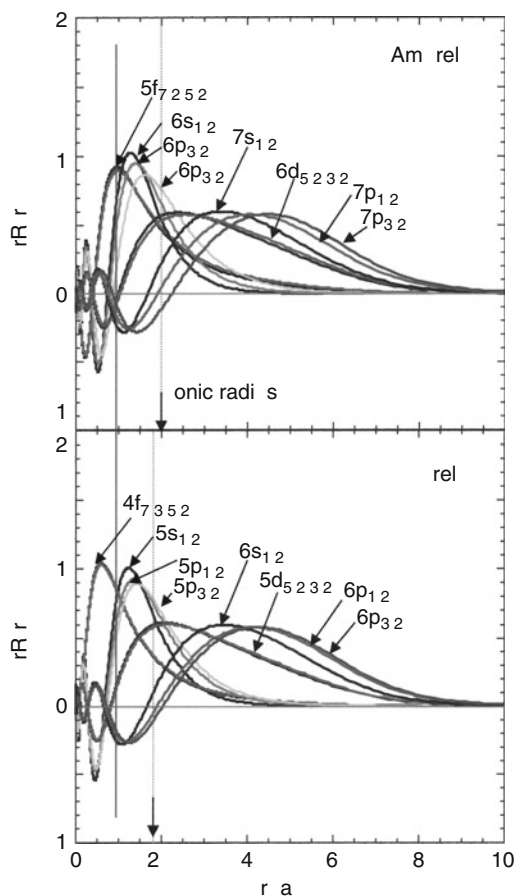
Energy level structures of the valence electrons of Am as a result of nonrelativistic and relativistic calculations



Dirac–Fock–Slater programs. The relativistic effects are also significant in the orbital energy of valence electrons. The 6s orbital is strongly affected by the direct relativistic effect and energetically stabilized, while the 6p orbital splits into the $6p_{1/2}$ and $6p_{3/2}$ orbitals by the spin–orbit coupling. The 5f orbital also splits to the $5f_{5/2}$ and $5f_{7/2}$ orbitals and energetically destabilized by the indirect relativistic effect. The energies of the 5f orbitals become closer to those of the 6d orbitals, which cause the complex configuration of the valence states.

■ Fig. 18.19

Radial wave functions of valence orbitals for the Eu^{3+} and Am^{3+} ions. Solid perpendicular line indicates maximum density of Am 5f orbitals. The arrows indicate the ionic radii of Eu^{3+} and Am^{3+}



It is of interest to compare the radial wave functions between 4f and 5f elements. Figure 18.19 shows relativistic calculations of Eu^{3+} and Am^{3+} valence wave functions of the radial part. This figure indicates that the 4f subshell of Eu^{3+} is “core like” because of the lower density around the ionic radius of the ion. In the corresponding 5f ion, Am^{3+} , 5f subshell penetrates the 6s and 6p orbitals. The wider distribution of the 5f orbital allows much participation in bonding for the actinides than for the lanthanides. The 4f orbitals of lanthanide atoms are mainly localized in the core and do not contribute to the chemical bonding.

18.2.2 Ionic Radii and Oxidation States

Chemical properties of elements are determined by the valence electronic structure, oxidation states, ionic radii, and coordination number. As already described in Sect. 18.2.1, the oxidation states of the actinide elements are more variable than those of the lanthanides.

■ **Table 18.9**

Oxidation states of actinide elements: the most stable oxidation state is bold font, while unstable oxidation states are shown in parentheses (Katz et al. 1986)

Atomic Number	Element		Oxidation States
89	Actinium	Ac	3
90	Thorium	Th	(3) 4
91	Protactinium	Pa	(3) 4 5
92	Uranium	U	3 4 5 6
93	Neptunium	Np	3 4 5 6 7
94	Plutonium	Pu	3 4 5 6 (7)
95	Americium	Am	(2) 3 4 5 6 7 ²
96	Curium	Cm	(2) 3 4 5 ² 6 ²
97	Berkelium	Bk	3 4
98	Californium	Cf	(2) 3 4 5 ²
99	Einsteinium	Es	(2) 3 (4)
100	Fermium	Fm	2 3 4 ²
101	Mendelevium	Md	1 ² 2 3
102	Nobelium	No	2 3
103	Lawrencium	Lr	3

► **Table 18.9** gives oxidation states of actinide elements (Katz et al. 1986). Actinium and transplutonium elements (from Am to Lr) take 3+ as the most stable oxidation state and they behave similar to the lanthanide elements, except element 102, No, which seems to prefer the 2+ state. Because of the itinerancy of the 5f electrons, the lighter actinide elements take broad range of oxidation states. The light transuranium elements, Np, Pu, and Am can behave as 3+ to 7+ cations and the most stable oxidation states of these three elements are 5+, 4+, and 3+, respectively.

Pentavalent and hexavalent actinide elements take oxygenated actinyl ions AnO_2^+ and AnO_2^{2+} (An = actinide elements). Stable pentavalent neptunium takes the NpO_2^+ type structure in solution. The relationship between oxidation states and structural variation is fundamental information for solution and separation chemistry of actinide elements. As these actinyl ions, AnO_2^+ and AnO_2^{2+} , are less acidic than the An^{4+} ions, the tendency of hydrolysis decreases in the order, $\text{An}^{4+} > \text{AnO}_2^{2+} > \text{An}^{3+} > \text{AnO}_2^+$.

► **Table 18.10** shows ionic radii of actinide elements together with those of lanthanide elements (Seaborg and Loveland 1990). The useful data on the ionic radii and coordination number are given by Shannon and Prewitt (1969). They carried out comprehensive study of crystal, or ionic, radii by analyzing the crystal structures of many fluoride, oxide, chloride, and sulfide compounds. Marcus published a data book on the properties of ions (Marcus 1997). The book covers a wide range of information on ionic radii of the actinide elements and other ions. Ionic radii of actinide elements decrease with increasing atomic number. This behavior is called actinide contraction and is one of the important examples of the actinide concept.

Because of the limited production yields and shorter half-lives of heavy actinide elements, the determination of ionic radii and chemical properties for heavier actinides are quite difficult (Hulet 1983; Keller 1984). Brüchle et al. (1988) reported the hydration enthalpies and ionic radii of Md^{3+} and Lr^{3+} by the ion-exchange experiments. Recently, the most stable nobelium

■ Table 18.10

Ionic radii of lanthanide and actinide elements (Seaborg and Loveland 1990)

Z	Element	Ln ³⁺ /nm	Ln ⁴⁺ /nm	Z	Element	An ³⁺ /nm	An ⁴⁺ /nm
57	La	0.1061		89	Ac	0.1119	
58	Ce	0.1034	0.092	90	Th	(0.108)	0.0972
59	Pr	0.1013	0.090	91	Pa	(0.105)	0.0935
60	Nd	0.0995		92	U	0.1041	0.0918
61	Pm	(0.0979)		93	Np	0.1017	0.0903
62	Sm	0.0964		94	Pu	0.0997	0.0887
63	Eu	0.0950		95	Am	0.0982	0.0878
64	Gd	0.0938		96	Cm	0.0970	0.0871
65	Tb	0.0923	0.084	97	Bk	0.0949	0.0860
66	Dy	0.0908		98	Cf	0.0934	0.0851
67	Ho	0.0894		99	Es	0.0925	
68	Er	0.0881		100	Fm	–	
69	Tm	0.0869		101	Md	0.0896 ^a	
70	Yb	0.0858		102	No	0.0894 ^b	
71	Lu	0.0848		103	Lr	0.0882 ^a	

^a Brühlle et al. 1988.^b Bilewicz 2002.

ion, No²⁺, was successfully oxidized to the trivalent state, No³⁺, which was held in α -hydroxyisobutyric acid (α -HIB) solution by a newly developed flow electrolytic chromatography technique (Toyoshima et al. 2008, 2009). It was found that the oxidation state of No on an atom-at-a-time scale is absolutely controlled by the employed apparatus. The new approach is expected to lead to the determination of the ionic radius of No³⁺, which is a key to understanding the contraction of the ionic radii at the end of the actinide series.

18.2.3 Separation of Transuranium Elements

For the study of nuclear and chemical properties of transuranium elements, chemical separation of these elements is indispensable. Especially, in the field of nuclear fuel reprocessing and waste management, it is quite important to separate each transuranium element selectively from fission products of dissolved spent nuclear fuels.

The problems of practical separation of these elements are (1) the separation of actinide elements from the lanthanide group (trivalent actinide ions behave like lanthanide ions), and (2) the separation of the actinide elements from each other. Ion-exchange and solvent extraction methods have so far been extensively studied.

18.2.3.1 Ion-Exchange Properties

Ion exchange is a fundamental technique for selective separation of transuranium elements. Since ion-exchange behavior strongly depends on the oxidation states and ionic radii of

transuranium elements, this technique was applied for the discovery of the heavy actinides as described in ▶ Sect. 18.1.1. The order of elution of these actinide ions generally follows that of their ionic radii.

The pattern of this elution behavior made it possible to identify and predict a new actinide element. The adsorption strength of different oxidation states on cation-exchange resins is $An^{4+} > An^{3+} > AnO_2^{2+} > An^{2+} > AnO_2^+$.

Comprehensive data for ion-exchange separation are available in “Handbook of Ion Exchange Resins” (Korkisch 1989). The essential properties employed for the separation of transuranium elements are the behavior toward strongly basic anion-exchange resins in both hydrochloric acid (HCl) and nitric acid (HNO₃) systems.

Tetravalent uranium, neptunium, and plutonium forming anionic complexes with chloride ions are strongly adsorbed on the anion-exchange resin. The adsorption of these tetravalent actinides increases in the order of $U^{4+} < Np^{4+} < Pu^{4+}$. The $[AnCl_6]^{2-}$ type anion complex (Marcus 1967a, b) is formed in high HCl concentration that are stable and strongly retained by the anion-exchange resin from 8 to 12 M HCl solution. In lower concentration of HCl, the species $[AnCl_3]^+$ (6–9 M HCl), $[AnCl_2]^{2+}$ (4–6 M HCl), $[AnCl]^{3+}$ (2–4 M HCl), and An^{4+} (0.5– M HCl) are formed. Th^{4+} and Pa^{4+} do not form the $[AnCl_6]^{2-}$ type complexes and they are not adsorbed on the anion-exchange resin. Trivalent actinides are not at all or at most only slightly adsorbed on the resin. The trivalent transplutonium elements, however, form more stable anionic chloride complexes than do the trivalent lanthanide elements.

Tetravalent Np and Pu are adsorbed on strongly basic anion-exchange resins even from relatively dilute nitric acid solution by forming the $[An(NO_3)_6]^{2-}$ type anionic nitrate complexes. The adsorption of Np^{4+} and Pu^{4+} increases with the nitric acid concentration. Pu^{4+} is more strongly adsorbed than Np^{4+} and is best adsorbed on the resin from 7 to 9 M HNO₃ solutions. On the contrary to the HCl system, Th^{4+} form the $[Th(NO_3)_6]^{2-}$ type complex in the concentrated nitric acid solution of 4–5 M HNO₃ (Ryan and Wheelwright 1959; Ryan 1960). For the elution of these adsorbed tetravalent actinide ions from nitric acid solution, the oxidation state must be reduced to trivalent one by using hydroxylamine hydrochloride and Fe^{2+} ion (Reynolds and Scott 1975; Scott and Reynolds 1975). The trivalent actinides are very weakly adsorbed on the anion-exchange resin (Shabana and Ruf 1978) and the adsorption property decreases with an increase of the atomic number.

Recently, Arisaka et al. have applied time-resolved laser-induced fluorescence spectroscopy (TRLFS) (Kimura and Choppin 1994) to the study of cation- (Kimura et al. 1998; Arisaka et al. 2001a) and anion- (Arisaka et al. 2001b) exchange behavior of Eu^{3+} and Cm^{3+} . They measured the inner-sphere hydration number of Eu^{3+} and Cm^{3+} in the HCl–CH₃OH mixture/cation-exchange resin system and observed a decrease of hydration number with an increase of methanol molar fraction. The TRLFS is applicable to quantitative and direct observation of the inner-sphere hydration of minor actinides.

18.2.3.2 Solvent Extraction Separation

The solvent extraction separation is one of the major research fields of the chemistry of transuranium elements. Nash and Choppin published selected papers on the separation science of f-elements in 1995 (Nash and Choppin 1995) and Yoshida et al. published “Recent Progress in Actinide Separation Chemistry” in 1997 (Yoshida et al. 1997). Mathur et al. (2001) reviewed actinide partitioning, and more recently, Tachimori and Morita (2009) issued a review article

of solvent extraction chemistry for reprocessing. In a commercial nuclear fuel reprocessing plant, solvent extraction technique is applied for the recovery of uranium and plutonium. The process called PUREX (Plutonium and Uranium Refining by EXtraction) uses tributyl phosphate (TBP) as an extractant. The TBP ligand strongly coordinates to hexavalent uranium (UO_2^{2+}) and tetravalent plutonium (Pu^{4+}). In the PUREX process, these species are co-extracted from nitric acid solution of spent nuclear fuel. However, trivalent actinide and lanthanide elements are not extracted and selective stripping of Pu is accomplished by reduction with U^{4+} and Fe^{2+} (Benedict et al. 1981).

The redox reaction has been utilized in the separation of light actinide elements (U, Np, and Pu) with both ion-exchange process and solvent extraction process. For trivalent heavy actinides with $Z > 94$ (except No), separation of these actinide ions from lanthanide ions is required for safe storage of long-lived nuclear waste and transmutation of these nuclides. Fundamental researches have widely been carried out by several groups for the purpose of quantitative separation of transuranium elements. Recent topics on the development and application of solvent extraction for the separation of transuranium elements are briefly summarized below.

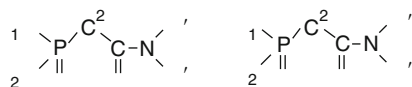
CMP, CMPO system. Horwitz and Kalina (1984), Horwitz et al. (1986) developed neutral bifunctional extractants CMP ($\text{R}_1\text{R}_2\text{-N,N-di(R') carbamoylmethyl phosphonate}$) and CMPO ($\text{R}_1\text{R}_2\text{-N,N,- di(R')-carbamoylmethyl phosphine oxide}$, see [Fig. 18.20](#)) for the separation of trivalent actinide ions. With thiocyanate as a counter ion in the CMPO system, americium is preferentially extracted and the separation factor S.F. ($\text{Am}^{3+}/\text{Eu}^{3+}$) is about seven (Muscatello et al. 1982).

TODGA system. Sasaki and coworkers developed tridentate oxygen donor extractant named TODGA ($\text{N,N,N',N'-tetraoctyl diglycolamide}$, see [Fig. 18.21](#)) for the selective separation of trivalent and tetravalent actinide and lanthanide ions (Sasaki et al. 2001; Sasaki and Tachimori 2002).

They reported the distribution ratios (D_M) of lanthanide and actinide ions and compared the D_M values with that of Am^{3+} in the extraction system of 1 M HNO_3 and 0.1 M TODGA/ n -dodecane as shown in [Table 18.11](#). The order of extractability of actinide ions from 1 M HNO_3 is An^{3+} , $\text{An}^{4+} > \text{AnO}_2^{2+} > \text{AnO}_2^{+}$. The TODGA has an ability of co-extraction of trivalent actinide ions and lanthanide ions from high-level liquid radioactive waste.

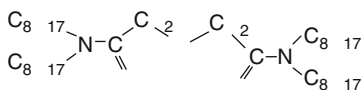
■ Fig. 18.20

Structure of CMP (left) and CMPO (right) molecule (Horwitz and Kalina 1984, Horwitz et al. 1986)



■ Fig. 18.21

Structure of TODGA molecule (Sasaki et al. 2001)



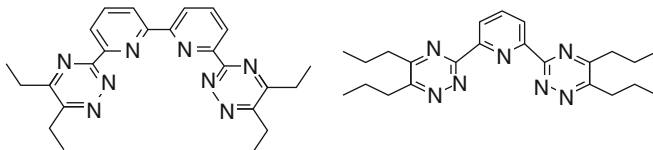
■ **Table 18.11**

D_M values of Ln^{3+} and An^{3+} , and D_M/D_{Am} values in the extraction system 0.1 M TODGA/*n*-dodecane – 1 M HNO_3 (Sasaki et al. 2001)

Element	D_M	D_M/D_{Am}
La^{3+}	5.3	0.18
Eu^{3+}	265	8.8
Lu^{3+}	631	21
Th^{4+}	147	4.9
UO_2^{2+}	0.8	0.027
NpO_2^{+}	0.0056	0.00020
Am^{3+}	30	1.0
Cm^{3+}	78	2.6
Cf^{3+}	156	5.2

■ **Fig. 18.22**

Structure of BTBP, 6,6'-bis-(5,6-diethyl-[1,2,4]triazin-3-yl)-2,2'-bipyridyl (*left*) and BTP, 2,6-bis-(5,6-dipropyl-[1,2,4]triazin-3-yl)pyridine (*right*) molecules (Drew et al. 2005)



These oxygen-donor type extractants have potential for co-extraction of trivalent lanthanide and actinide ions. For the mutual separation between trivalent actinides and lanthanides, so-called soft-donor (nitrogen-donor type and sulfur-donor type) extractants are promising and widely investigated for the application of nuclear waste treatment as follows.

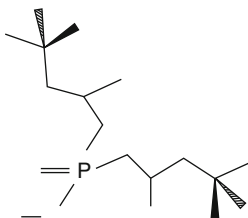
BTP, BTBP system. Kolarik et al. (1999, 2008) and Madic et al. (2000) carried out comprehensive study of the separation of trivalent actinides from lanthanides by the nitrogen donor extractants. They developed several new nitrogen polydentate ligands, BTP [2,6-bis(5,6-dialkyl-1,2,4-triazin-3-yl)-4-alkyl-pyridines] and BTBP [6,6'-bis-(5,6-diethyl-[1,2,4]triazin-3-yl)-2,2'-bipyridyl] (see ● Fig. 18.22).

Cordier et al. (1999) reported S.F. ($\text{Am}^{3+}/\text{Eu}^{3+}$) > 100 in the extraction system of 1 M HNO_3 and 0.01 M *n*-propyl-BTP/tetrapropene + *n*-octanol. The *n*-propyl-BTP extracts Am^{3+} more than ten times higher than the other N-donor ligands like 2,2':6',2'-terpyridine. Although the BTP type extractants have potential for the selective separation of the An^{3+} group, they are not stable against oxidation, acidic hydrolysis, and radiolysis (Hill et al. 2002). Drew et al. (2005) and coworkers applied BTBP/1,1,2,2-tetrachloroethane to the $\text{Am}^{3+}/\text{Eu}^{3+}$ separation from 1 M HNO_3 . They reported exceptional S.F. ($\text{Am}^{3+}/\text{Eu}^{3+}$) > 160.

Cyanex-301 system. The sulfur type soft-donor extractant, thiophosphoric acid has potential for selective separation of trivalent actinides from lanthanides (Musikas 1985). Zhu et al. (Zhu 1995; Zhu et al. 1996) developed dithiophosphinic acid type extractant, Cyanex-301

■ Fig. 18.23

Structure of Cyanex-301 (Zhu 1995)



(bis(2,4,4-trimethylpentyl) dithiophosphinic acid) (see ► Fig. 18.23), for the separation of Am^{3+} . They reported the average separation factor of Am^{3+} against Ln^{3+} being greater than 2,300. Chen et al. (1996) reported that the equilibrium constant for the liquid–liquid extraction of Am^{3+} by Cyanex-301 is 5,900 times larger than that of Eu^{3+} , the homologous lanthanide.

18.2.4 Solid-State Properties of Transuranium Metals and Compounds

The lighter actinide metals, from Pa to Pu, are characterized by the presence of itinerant 5f electrons. The wider radial distribution of 5f orbitals contributes to the chemical bonding in metallic phase and alloys. On the other hand, properties of the heavier actinide metals, having localized 5f electrons, resemble those of the lanthanides, which have localized 4f electrons. The itinerant 5f electrons of lighter actinide metals hybridize with the conduction electrons and contribute to the metallic bonding.

The ionization potential of an element is one of its fundamental properties. It is known that the first ionization potential of heavy elements depends on relativistic effects. The Mainz group, in Germany, systematically determined the first ionization potential of the actinide elements from Ac through Es using laser spectroscopy as shown in ► Table 18.12 (Becke et al. 2002). ► Figure 18.24 shows the comparison of ionization potentials between lanthanide and actinide atoms (Moore 1971; Becke et al. 2002). The atomic level structure of ^{256}Fm (2.7×10^{10} atoms) with a half-life of 20.1 h was studied for the first time by the method of resonance ionization spectroscopy. Two atomic levels were identified at wave numbers $(25,099.8 \pm 0.2) \text{ cm}^{-1}$ and $(25,111.8 \pm 0.2) \text{ cm}^{-1}$ (Sewtz et al. 2003).

► Table 18.13 gives the crystal structures and phase transformations of the transuranium elements (Katz et al. 1986). The lighter actinide elements like Np and Pu have a bcc structure at the melting point and Pu has six distinct allotropic forms. The heavier actinides from Am to Es show face-centered cubic (fcc) structures at the melting point and double hexagonal close-packed (dhcp) structures below the melting point. These heavier actinides behave like lanthanide metals.

Because of the itinerancy of the 5f electrons, magnetic order is not observed in these lighter actinide metals. The localized 5f electrons of the elements heavier than Am do not contribute to the metallic bond, but they contribute to the magnetic order. Since the spin–orbit coupling is significant in the heavy elements, the effective magnetic moment for the actinide compounds depends on the J value ($J = L + S$, where J , L , and S denote total angular momentum, orbital

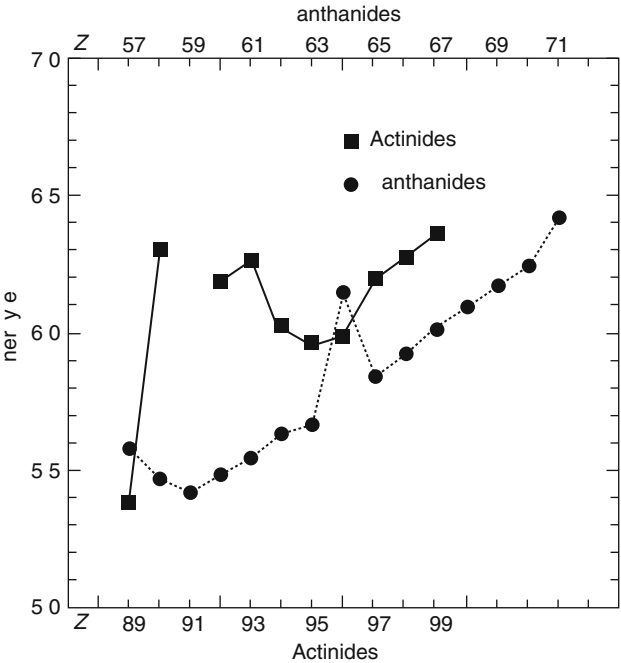
Table 18.12

First ionization potentials of actinide elements (Becke et al. 2002)

Atomic Number	Element	Ionization potentials/cm ⁻¹	Ionization potentials/eV
89	Actinium	43,398(3)	5.3807(3)
90	Thorium	50,867(2)	6.3067(2)
91	Protactinium	–	–
92	Uranium	49,957(1)	6.1939(1)
93	Neptunium	50,535(2)	6.2655(2)
94	Plutonium	48,601(2)	6.0258(2)
95	Americium	48,180(3)	5.9736(3)
96	Curium	48,324(2)	5.9914(2)
97	Berkelium	49,989(2)	6.1979(2)
98	Californium	50,663(2)	6.2814(2)
99	Einsteinium	51,358(2)	6.3676(2)

Fig. 18.24

First ionization potentials of lanthanide and actinide atoms (Moore 1971; Becke et al. 2002)



angular momentum, and resultant spin of the electrons). Therefore, theoretical treatment of a complicated spin state is quite important in the actinide series. These heavy actinide metals have lower cohesive energies and larger atomic volumes than those of the lighter actinide metals. Figure 18.25 shows atomic volumes of lanthanide and actinide metals. The lighter

■ **Table 18.13**

Properties of the transuranium metals (Katz et al. 1986). Radii in the last column are corrected to coordination number 12. bcc: body-centered cubic, fcc: face-centered cubic, dhcp: double hexagonal close-packed

Atomic number	Element	Melting point/ $^{\circ}\text{C}$	Lattice symmetry and temperature range of stability/ $^{\circ}\text{C}$	X-ray density/ g cm^{-3}	Metallic radius/ \AA
93	Neptunium	639	α , orthorhombic (below 280)	20.45	1.503
			β , tetragonal (280–576)	19.36	1.511
			γ , bcc (576–639)	18.04	1.53
94	Plutonium	640	α , monoclinic (below 122)	19.86	1.623
			β , monoclinic (122–207)	17.70	1.571
			γ , orthorhombic (207–315)	17.14	1.588
			δ , fcc (315–457)	15.92	1.640
			δ' , bc tetragonal (457–479)	16.00	1.640
			ϵ , bcc (479–640)	16.51	1.592
95	Americium	1,173	α , dhcp (below 658)	13.6	1.730
			β , fcc (793–1,004)	13.65	1.730
			γ , ? ($\sim 1,050$ –1,173)		
96	Curium	1,345	α , dhcp (below $\sim 1,277$)	13.5	1.743
			β , fcc (1,277–1,345)	12.9	1.782
97	Berkelium	1,050	α , dhcp (below 930)	14.79	1.704
			β , fcc (930–986)	13.24	1.767
98	Californium	900	α , dhcp	15.10	1.694
			β , fcc (below 900)	8.74	2.030
99	Einsteinium	860	α , dhcp	?	
			β , fcc (Below 860)	8.84	2.03

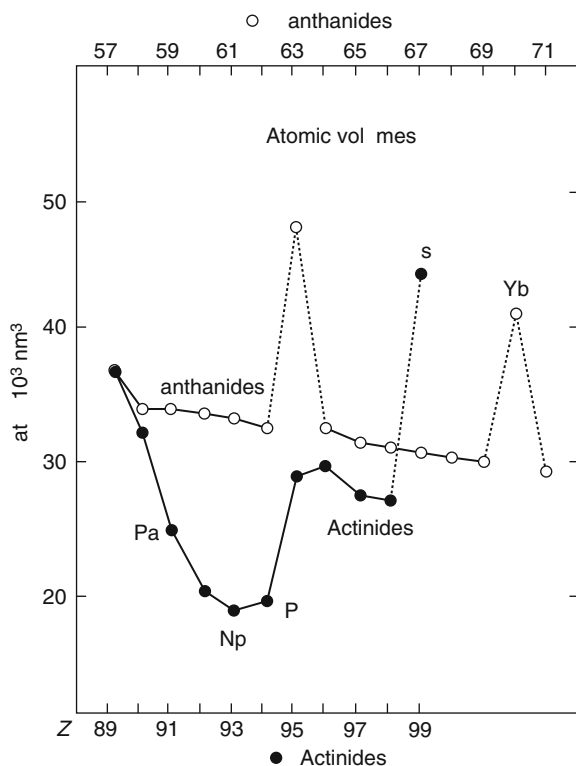
actinide metals from Pa to Pu take smaller atomic volumes and higher densities compared with those of the heavier actinides. The metallic bonding becomes tighter by the contribution of 5f electrons in the lighter actinide metals.

Benedict et al. (Benedict 1987; Benedict and Holzapfel 1993) reviewed the study of pressure-induced structural transitions in the actinide metals. High pressure is the most efficient and cleanest way of changing the interatomic distances in a lattice.

Many physical properties of metals can be changed by pressure, and the pressure dependence supplies information on the electronic processes in the solid. For example, localized 5f electrons tend to be delocalized with increasing pressure. ➤ [Figure 18.26](#) shows high-pressure structural behavior of the actinide metals. The lighter actinide metals have wider pressure ranges without phase transitions, while the heavier actinide metals have several phase transitions with increasing the pressure. The low-symmetry orthorhombic phase appears at higher pressure, indicating that the localized 5f electrons become itinerant with an addition of higher pressure.

■ Fig. 18.25

Atomic volumes of lanthanide and actinide metals. Pa, U, Np, and Pu: density increased by 5f bonding. Low density of Eu, Es, and Yb is due to divalency (Benedict and Holzapfel 1993)

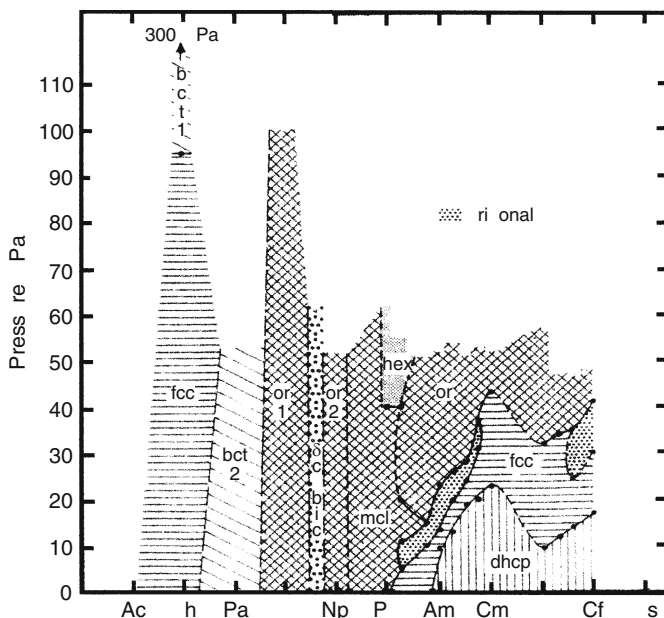


Variation of phase diagrams and behavior of transuranium alloys are attractive for both nuclear energy application and fundamental physics of 5f electrons in metallic phase. Comprehensive data of the phase diagrams of binary actinide alloys are available in the book of Kassner and Peterson (1995). Plutonium alloys with group IIIB metals (Al, Ga, In, or Tl) are well studied since the 1960s (Grison et al. 1961). Small addition of these metals stabilizes the δ phase of plutonium. Because of the six allotropic forms of the plutonium metal, the stabilization of the δ phase is required especially for storage of plutonium metal. Recently, Havela et al. (2002) carried out photoelectron spectroscopy of Pu metal and Espinosa et al. (2001) reported XAFS study of the local atomic structure of α -phase plutonium. Allen et al. (2002) examined local structures of Ga-stabilized δ -phase plutonium and Söderlind et al. (2002) investigated electronic structure of δ -phase plutonium by all-electron full potential linear muffin-tin orbitals (FPLMTO), Korringa–Kohn–Rostoker (KKR), and projector augmented wave (PAW) methods. Savrasov et al. (2001) correctly predicted the behavior of plutonium metal by the dynamical mean-field theory (DMFT) (Georges et al. 1996).

They compared the calculated density of states for δ -plutonium with the recent photoemission experiments and obtained a good agreement between them (Arko et al. 2000). They concluded that the fundamental features of physics and chemistry of actinide compounds are

■ Fig. 18.26

General diagram of the phase relations of actinide metals under pressure (Benedict and Holzapfel 1993). fcc: face-centered cubic, bct: body-centered tetragonal, or: orthorhombic, mcl: monoclinic, hex: hexagonal, dhcp: double hexagonal close-packed



related to the behavior of 5f electrons in the system. The behavior of 5f electrons of the actinides is in between the more localized 4f electrons of the lanthanides and the itinerant d electrons of the transition metals. The combination of structural study and theoretical approaches become popular in the field of condensed-matter physics of actinide elements and their alloys and compounds.

In the following, some other current interesting topics on the metallic properties of actinides are introduced. Recently, Sarrao et al. (2002) discovered new plutonium-based superconductivity in PuCoGa_5 with a transition temperature $T_c = 18.5$ K. The temperature dependence of the magnetic susceptibility was indicative of the local moment behavior close to that expected for Pu^{3+} . Interestingly, the isostructural UCoGa_5 , having no sign of a local moment, is not a superconductor. Akiyama et al. (2001) studied high-performance liquid chromatography (HPLC) elution behavior of the fullerenes encapsulating actinide elements. The elution behavior of U, Np, and Am fullerenes was found extremely similar to that of Ce fullerenes. They concluded that the major products of the U-, Np- and Am- fullerenes are $\text{M}@\text{C}_{82}$ ($\text{M} = \text{U}, \text{Np}, \text{and Am}$) species with the oxidation state of +3.

A huge amount of research has been done on the solid compounds of transuranium elements. In this section, fundamental properties of oxide and some compounds of the transuranium elements are briefly overviewed. The oxygen to metal ratio (O/M ratio) is one of the important parameters to understand the solid-state behavior of these oxides. The fluorite-structure dioxide is well studied in the research of mixed oxide (MOX) nuclear fuels.

► Table 18.14 gives fundamental properties of transuranium oxides (Morss 1991). Neptunium

■ Table 18.14

Properties of the transuranium oxides

Compound	Color	Symmetry	Space group	Lattice parameters, $a_0, b_0, c_0/\text{\AA}$, β/deg
NpO ₂	Apple green	Cubic	<i>Fm</i> 3 <i>m</i>	$a_0 = 5.433$
Np ₂ O ₅	Dark brown	Monoclinic	<i>P</i> 2 ₁ / <i>c</i>	$a_0 = 4.183, b_0 = 6.584, c_0 = 4.086,$ $\beta = 90.32$
Pu ₂ O ₃	Black	Hexagonal	<i>P</i> $\bar{3}$ <i>m</i> 1	$a_0 = 3.841, c_0 = 5.958$
PuO ₂	Yellow-green to brown	Cubic	<i>Fm</i> 3 <i>m</i>	$a_0 = 5.3960$
Am ₂ O ₃	Tan	Hexagonal	<i>P</i> $\bar{3}$ <i>m</i> 1	$a_0 = 3.817, c_0 = 5.971$
Am ₂ O ₃	Reddish brown	Cubic	<i>Ia</i> 3	$a_0 = 11.03$
AmO ₂	Black	Cubic	<i>Fm</i> 3 <i>m</i>	$a_0 = 5.374$
Cm ₂ O ₃	White/faint tan	Hexagonal	<i>P</i> $\bar{3}$ <i>m</i> 1	$a_0 = 3.792, c_0 = 5.985$
Cm ₂ O ₃	White/pale green	Monoclinic	<i>C</i> 2/ <i>m</i>	$a_0 = 14.282, b_0 = 3.641, c_0 = 8.883,$ $\beta = 100.29$
Cm ₂ O ₃	White	Cubic	<i>Ia</i> 3	$a_0 = 11.002$
Cm ₇ O ₁₂	Black	Rhombohedral	<i>R</i> $\bar{3}$	$a_0 = 10.184, c_0 = 9.448$
CmO ₂	Black	Cubic	<i>Fm</i> 3 <i>m</i>	$a_0 = 5.358$
Bk ₂ O ₃	Light green	Hexagonal	<i>P</i> $\bar{3}$ <i>m</i> 1	$a_0 = 3.754, c_0 = 5.958$
Bk ₂ O ₃	Yellow-green	Monoclinic	<i>C</i> 2/ <i>m</i>	$a_0 = 14.197, b_0 = 3.606, c_0 = 8.846,$ $\beta = 100.23$
Bk ₂ O ₃	Yellow-brown	Cubic	<i>Ia</i> 3	$a_0 = 10.887$
BkO ₂	Yellow-brown	Cubic	<i>Fm</i> 3 <i>m</i>	$a_0 = 5.3315$
Cf ₂ O ₃	Pale green	Hexagonal	<i>P</i> $\bar{3}$ <i>m</i> 1	$a_0 = 3.72, c_0 = 5.96$
Cf ₂ O ₃	Lime green	Monoclinic	<i>C</i> 2/ <i>m</i>	$a_0 = 14.121, b_0 = 3.592, c_0 = 8.809,$ $\beta = 100.34$
Cf ₂ O ₃	Pale green	Cubic	<i>Ia</i> 3	$a_0 = 10.83$
Cf ₇ O ₁₂		Rhombohedral	<i>R</i> $\bar{3}$	$a_0 = 10.061, c_0 = 9.375$
CfO ₂	Black	Cubic	<i>Fm</i> 3 <i>m</i>	$a_0 = 5.310$
Es ₂ O ₃	White	Hexagonal	<i>P</i> $\bar{3}$ <i>m</i> 1	$a_0 = 3.7, c_0 = 6.0$
Es ₂ O ₃	White	Monoclinic	<i>C</i> 2/ <i>m</i>	$a_0 = 14.1, b_0 = 3.59, c_0 = 8.80, \beta = 100$
Es ₂ O ₃	White	Cubic	<i>Ia</i> 3	$a_0 = 10.766$

takes pentavalent oxide Np₂O₅, while the other transuranium elements take between trivalent and tetravalent states in the oxides. The chemical forms of these oxides give important information on properties of irradiated nuclear fuels and solidified high-level nuclear wastes.

Plutonium and neptunium nitrides were studied for the application to advanced fast breeder reactor (FBR) fuels. Details on the application of nuclear fuels is available in the reference (Matzke 1986). Fundamental properties of these plutonium and neptunium compounds are reviewed in the “Chemical Thermodynamics of Neptunium and Plutonium” (Lemire et al. 2001) issued by OECD/NEA (Organization for Economic Co-operation and

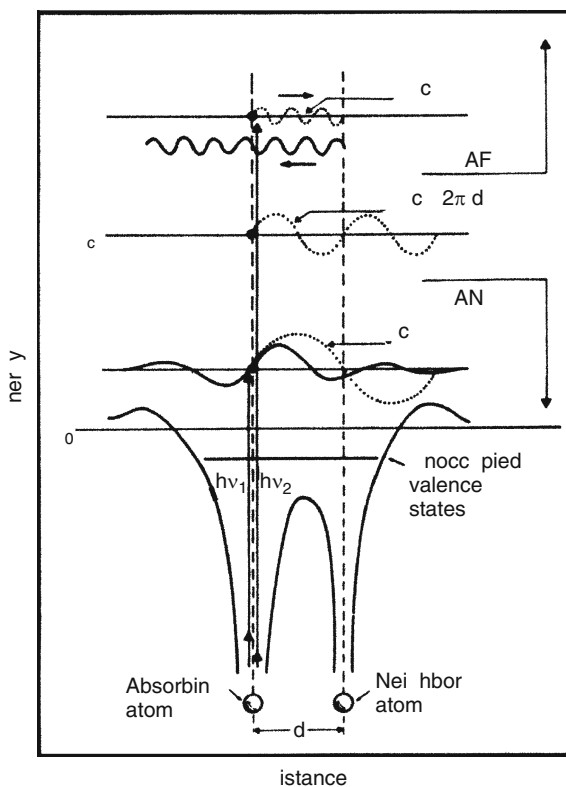
Development/Nuclear Energy Agency). Americium data are also available in the “Chemical Thermodynamics of Americium” (Silva et al. 1995).

18.2.5 XAFS: New Methodology for Chemical Studies of Transuranium Elements

One of the new fields of actinide chemistry since the 1990s is an application of X-ray absorption spectroscopy (Teo 1986) especially by use of the synchrotron radiation. XAFS (X-ray absorption fine structure) is a powerful technique for characterization of the local structure of specific elements, even radioactive elements such as actinides, and their electronic states. XAFS contains two fundamental information, EXAFS (extended X-ray absorption fine structure) and XANES (X-ray absorption near-edge structure). ➤ Figure 18.27 shows a fundamental pictorial view of the XAFS process (Koningsberger and Prins 1987).

■ Fig. 18.27

Pictorial view of the final-state wave functions in the core excitation in a diatomic molecule at high energies, extended X-ray absorption fine structure (EXAFS) region, and in the low-energy, X-ray absorption near-edge structure (XANES) region. The dotted curves are the wave functions of the emitted photoelectron (Koningsberger and Prins 1987)



EXAFS is based on an oscillatory structure observed in X-ray absorption spectra. Kronig (Kronig 1931, 1932) found this oscillation for the first time and Sayers and coworkers (Sayers et al. 1971) successfully explained it in 1971. EXAFS provides considerable information about coordination numbers and distances of each atomic species in complex, polyatomic solids, liquids, and gases.

XANES spectra contain information about the electronic states of a specific target (X-ray absorbing) atom and the local structure surrounding it. The near-edge structure is associated with the excitation process of a core electron to bound and quasi-bound states. Because of the multi-electron process of the excitation, the theoretical assignment of XANES spectra has several difficulties.

Rehr and Albers (2000) reported theoretical approaches to the assignment of XAFS spectroscopy. They described the advantages and the remaining problems of the multiple-scattering (MS) method for the analyses. Multiple-scattering (MS) formalism and first-principle molecular orbital (MO) calculation techniques so far have been proposed for the theoretical analysis of XANES. The *ab initio* XAFS codes FEFF series program is widely used for this purpose. The detailed information of the FEFF code is available in the Web site of the FEFF and in several references (e.g., Ankudinov et al. 1998; FEFF 2009).

Molecular orbital (MO) methods have been studied and reviewed by Kosugi (1996). Ellis and Goodman (1984) first applied local density functional method and Nakamatsu (1995) applied the discrete-variational (DV) $X\alpha$ method to the analyses of XANES.

XAFS studies for the actinide research are being carried out at the synchrotron facilities of the USA and EU. Advanced Photon Source (APS) of Argonne National Laboratory (APS 2009), Advanced Light Source (ALS) of UC Berkeley (ALS 2009), ESRF (European Synchrotron Radiation Facility) of Grenoble (ESRF 2009), and SOLEIL (SOLEIL 2009) in Saint-Aubin, France are the main synchrotron facilities for the actinide research. Useful information is available in the Web site of each facility.

D'Amico et al. (1996) published selected papers on the application of synchrotron radiation techniques in industrial, chemical, and material science. Although there are several papers on the structural research of actinide compounds and complexes, the results are mostly limited to uranium compounds. Allen et al. (1996a) briefly reviewed the application of XAFS to the environmental materials containing plutonium and neptunium. They introduced NpO_2^+ adsorption study of the α -FeOOH (goethite)/water interface reported by Combes et al. (1992). The application of XANES spectroscopy to the analysis of U, Np, and Pu solid compounds with different oxidation states is also reviewed (Petiau et al. 1986; Kalkowski et al. 1987a, b; Bertram et al. 1989).

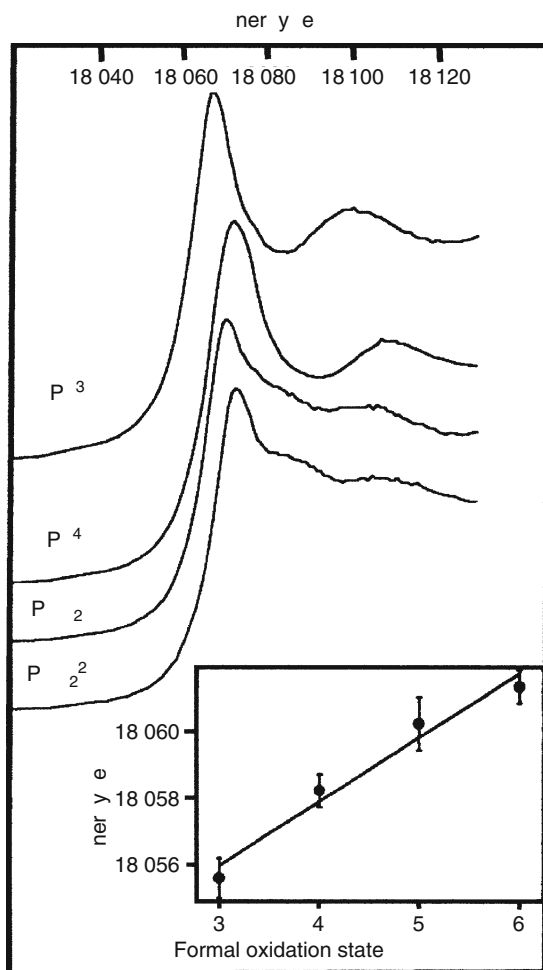
Veirs et al. (1994) carried out structural study of Pu^{4+} in nitric acid solution. They observed coordination of nitrate ligands as bidentate and planar. Allen et al. (1996b) also reported the structural study of Pu^{4+} nitrate complexes by measuring EXAFS spectra as a function of nitric acid concentration and found highly coordinated plutonium complexes with coordination number of 11–12 for the first shell of oxygen nearest neighbors. The average Pu–O(nitrate) bond length was 2.49 Å, while the distance of Pu–O(water) was evaluated to be 2.38 Å. In the anion-exchange separation of Pu^{4+} from nitric acid solution, plutonium is adsorbed quantitatively on the resin. The Pu^{4+} species were considered to form anion complexes in highly concentrated nitrate solution. The 6 coordinated $[\text{Pu}(\text{NO}_3)_6]^{2-}$ species in the 13 M HNO_3 was observed and nitrates were all bidentate. The coordination number was determined to be 12 by the EXAFS technique.

In addition to the nitrate system, Allen et al. (1997) reported a structural study of UO_2^{2+} , NpO_2^+ , Np^{4+} , and Pu^{3+} species in HCl solution by the EXAFS method. They also conducted (Allen et al. 2000) EXAFS experiments on the trivalent lanthanide and actinide ions in HCl solutions. In the dilute HCl solution, on average, the Am^{3+} and Cm^{3+} aqua ions are coordinated by 10.3 oxygens at 2.48 Å and by 10.2 oxygens at 2.45 Å, respectively, while 9.2 water molecules are coordinated to the Pu^{3+} . The average distance between the Pu^{3+} ion and the oxygens of water molecules is 2.51 Å. They observed Cl^- coordination to the Cm^{3+} above the 10.5 M LiCl concentration. However, Pu^{3+} does not form inner sphere chloride complexation.

One of the most significant examples of the application of XANES in the chemistry of actinide elements was reported by Conradson et al. (1998). They measured L_{III} XANES spectra

■ Fig. 18.28

Plutonium XANES spectra for the aqua Pu^{3+} and Pu^{4+} , PuO_2^+ and PuO_2^{2+} species (Conradson et al. 1998)



of four oxidation states of Pu (3+, 4+, 5+, and 6+) at the Stanford Synchrotron Radiation Laboratory. As shown in ▶ Fig. 18.28, clear relation between the edge energies and the oxidation states are observed. The edge energies shifted progressively to higher energy with increasing valence, with an average energy of 1.68 eV per formal oxidation state (see inset of ▶ Fig. 18.28).

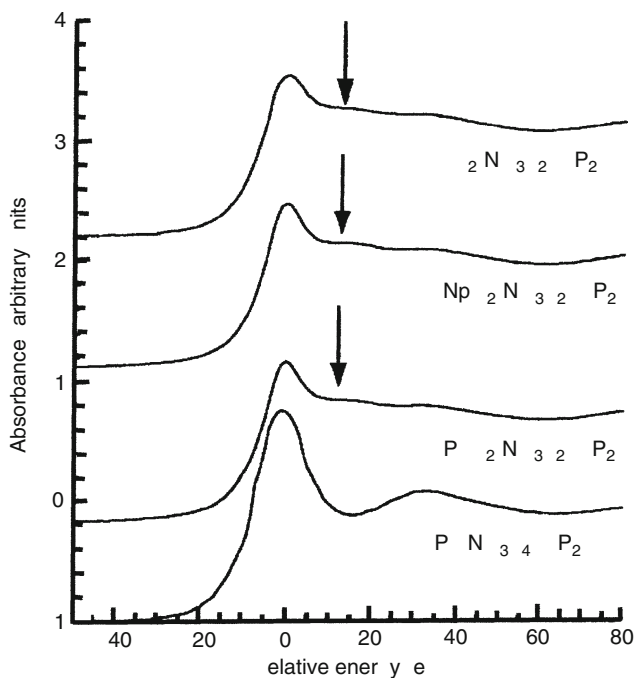
As already mentioned, XANES spectra are strongly affected by the geometry of the first coordination sphere. In ▶ Fig. 18.28, the general spectral shape of the Pu^{3+} and Pu^{4+} species is clearly different from that of the dioxo-containing PuO_2^+ and PuO_2^{2+} species. XANES spectra have potential for the determination of oxidation states and the nearest-neighbor structure in the complex and disordered system.

Ankudinov et al. (1998) conducted real-space multiple-scattering calculation and interpreted these plutonium hydrate spectra with the FEFF8 program package. The different behavior of the Pu^{3+} and Pu^{4+} relative to PuO_2^+ and PuO_2^{2+} can be understood in terms of their first coordination structure. Pu^{3+} and Pu^{4+} are surrounded by nine and eight nearly equidistant oxygen atoms of water molecules. For these species, the white-line intensity calculated by the FEFF8 code agrees well with the experiment.

Den Auwer et al. (1999) applied XAFS to the structural analysis of TBP (Tributyl phosphate) complexes of tetra- and hexavalent U, Np, and Pu. Similar to the results of hydrated Pu complexes, they observed significant difference in the XANES spectra between the Pu^{4+} and PuO_2^{2+} species as shown in ▶ Fig. 18.29. However, the XANES spectra of $\text{AnO}_2(\text{NO}_3)_2(\text{TBP})_2$ (An = U, Np, Pu) solution complexes show no significant difference among them.

■ Fig. 18.29

L_{III} edges of the $\text{AnO}_2(\text{NO}_3)_2(\text{TBP})_2$ solution complexes (An = U, Np, Pu) and $\text{Pu}(\text{NO}_3)_4(\text{TBP})_2$ (Den Auwer et al. 1999)



The separation of trivalent actinides, such as Am^{3+} and Cm^{3+} is of major concern in the field of nuclear technology. Den Auwer et al. (2000) studied the structure of N,N,N',N'-Tetraethylmalonamide (TEMA) complexes of lanthanides and americium by several methods including the X-ray absorption technique. They carried out first the X-ray diffraction study of the single crystals of $\text{Nd}(\text{NO}_3)_3(\text{TEMA})_2$ and $\text{Yb}(\text{NO}_3)_3(\text{TEMA})_2$ and compared the EXAFS spectra of these complexes in a solvent phase. The metal-centered polyhedron in the solvent phase was found to be similar to that of the solid-state complexes. They also measured an EXAFS spectrum of the $\text{Am}(\text{NO}_3)_3(\text{TEMA})_2$ complex in the solvent phase and confirmed the similar coordination spheres with the Nd^{3+} complex.

As briefly described in [Sect. 18.2.3.2](#), soft-donor extractants have potential for selective separation of trivalent actinide ions. To understand the difference in extraction between Am^{3+} and trivalent lanthanide elements, Yaita et al. (2001) studied Am^{3+} and Nd^{3+} complexes with N-donor ligand benzimidazole by EXAFS. Although they found slight difference in the coordination number of water molecules and in the distance, Yaita et al. concluded that the coordination structure of Am^{3+} – benzimidazole complexes is almost similar to that of Nd^{3+} complexes.

Tian et al. (2002) carried out an EXAFS study on the Am^{3+} complexes with di-*n*-octyldithiophosphinic acid and bis(2,4,4-trimethylpentyl) dithiophosphinic acid (S-donor type extractants) in kerosene. These complexes have the same coordination structure with an eight sulfur-coordinated tetrakis configuration. They observed larger steric hindrance in the Am^{3+} – bis(2,4,4-trimethylpentyl) dithiophosphinic acid complex than in the Am^{3+} – di-*n*-octyldithiophosphinic acid one. Jensen and Bond (2002) also studied Cm^{3+} , Nd^{3+} , and Sm^{3+} complexes with bis(2,4,4-trimethylpentyl) phosphinic acid ($\text{R}_2\text{PO}_2\text{H}$), bis(2,4,4-trimethylpentyl) mono-thiophosphinic acid (R_2PSOH), and bis(2,4,4-trimethylpentyl) dithiophosphinic acid ($\text{R}_2\text{PS}_2\text{H}$) in *n*-dodecane by EXAFS. They proposed neutral bidentate complexes, ML_3 , for dithiophosphinate ligand. Comparison of the EXAFS spectra of Cm^{3+} , Nd^{3+} , and Sm^{3+} shows that the structure and metal – donor atom bond distances are indistinguishable within experimental error.

Skanthakumar et al. (2007) and coworkers extensively studied the coordination structure of the hydrated Cm^{3+} ion by EXAFS and high-energy X-ray scattering (HEXS). They also carried out X-ray diffraction of $[\text{Cm}(\text{H}_2\text{O})_9](\text{CF}_3\text{SO}_3)_3$ single crystal to compare the coordination sphere of Cm^{3+} ions. The HEXS data show that the nine water molecules coordinated to the Cm^{3+} ions at 2.48 Å and hydrogen atoms are located at 3.05 Å.

Antonio et al. (2002) reported redox properties of berkelium by both XAFS and cyclic voltammetry. They obtained the formal potential of the $\text{Bk}^{4+}/\text{Bk}^{3+}$ redox couple, $E^{\circ'} = +1.388 \pm 0.005$ eV versus Ag/AgCl by in situ XANES spectroelectrochemistry and Nernst analysis. They also reported the information of coordination sphere for Bk^{3+} and Bk^{4+} . The Bk^{3+} is coordinated to 9 ± 0.5 O atoms at an average distance of 2.43(2) Å, while the Bk^{4+} is coordinated 8 ± 0.5 O atoms at an average distance of 2.32(1) Å.

18.2.6 Computational Chemistry of Transuranium Elements

The quantum chemical calculation and computational prediction of the behavior of transuranium elements has become very popular recently for being useful in the qualitative understanding of their complicated chemical properties. In order to calculate the electronic structure of actinide compounds, relativistic effects must be taken into account. One of the important

tools for the study of chemical properties of heavy elements is computation using first-principle relativistic molecular orbital calculation methods. Several groups have developed empirical, semiempirical, and nonempirical (so-called first-principle or *ab initio*) methods.

The relativistic calculations on the electronic structure of actinide compounds were reviewed by Pyykkö (1987). He also reviewed relativistic quantum chemistry in 1988, whereas the relativistic calculations were limited to small molecules containing one heavy atom only (Pyykkö 1988). Calculations on the uranyl and neptunyl ions were introduced in the review article. The general information on the computational chemistry of heavy elements and relativistic calculation techniques appear in the book written by Balasubramanian (1997). There are several first-principle approaches to the electronic structure of actinide compounds. The relativistic effective core potential (ECP) and relativistic density functional methods are widely used for complex systems containing actinide elements. Pepper and Bursten (1991) reviewed relativistic quantum chemistry, while Schreckenbach et al. (1999) reviewed density functional calculations on actinide compounds in which theoretical background and application to actinide compounds were described in detail. The “Encyclopedia of computational chemistry” also contains examples including lanthanide and actinide elements (Schleyer et al. 1998). The various methods for the computational approach to the chemistry of transuranium elements are briefly described and summarized below.

Semiempirical (INDO) approach. Zerner and coworkers developed the semiempirical, “Intermediate Neglect of Differential Overlap” (INDO) method for the calculation of electronic structures of actinide complexes (Cory et al. 1994). They presented ground-state resonance parameter sets for the actinide elements from Ac to Pu and applied the INDO parameters to the actinide halides, bis(cyclooctatetraenyl) actinide complexes $M(\text{COT})_2$ ($M = \text{Th, Pa, U, Np, Pu}$), the so-called actinocene and imide/amide complexes of uranium. The semiempirical approach is required for large systems, such as biological molecules containing actinide elements.

First-principle approach. Because of the difficulties of parameter generation for the calculation of actinide elements, the nonempirical or first-principle quantum chemical calculations become important. The Gaussian98 program doing *ab initio* calculation (Frische et al. 1998) is one of the most popular programs used for the calculation of actinide compounds. In order to reduce the computational time, core orbitals are not treated explicitly for the calculation of the actinide compounds. This technique is called the ECP (effective core potential) of the Gaussian98 program. Several ECPs have been proposed and these ECPs are available on the Web (Gaussian 2009). Craw et al. discussed the electronic structure of nitrate and sulfate complexes for uranyl and plutonyl by using ECP, and found that both structures of the nitrates were similar to each other (Craw et al. 1995). Tsushima and Suzuki (2000) reported a computational study on the hydration number of penta- and hexavalent uranyl, neptunyl, and plutonyl ions. The calculations showed that the hydration number $N = 5$ is the most stable for all penta- and hexavalent actinyl ions. The MP2 (Møller-Plesset 2) level calculations had good agreement with the experimental measurements.

Balasubramanian (2002) calculated potential energy surfaces of lawrencium and nobelium dihydrides (LrH_2 and NoH_2) by the relativistic effective core potentials with the ALCHEMY II code (Balasubramanian 2000). He predicts that Lr and No exhibit unusual non-actinide properties. 7s and 7p orbitals have major contribution to the bonding compared with 5f and 6d shells and they behave unlike other actinides.

The Dirac–Fock–CI formula is also available in the MOLFDIR program, which is developed by the Nieuwpoort group. Visscher, Nieuwpoort, and coworkers presented applications and

computational details of the MOLFDIR program in 1994 (Visscher et al. 1994). The Dirac program is also available for the calculation of actinide compounds by the fully relativistic all-electron Dirac–Hartree–Fock method. The detail of the program can be found at the Web site of Dirac (Dirac 2009).

Mochizuki and Okamoto applied the Dirac program for the estimation of stabilities of trivalent actinide elements and water or ammine complexes (Mochizuki and Okamoto 2002). Mochizuki and Tatewaki (2002) also carried out the electronic structure calculation on the hexa-hydrated ions of curium and gadolinium. They used the Dirac program and also predicted the fluorescence transition energy using the “Complete Open-Shell Configuration Interaction” (COSCI) method. Even the hexa-hydrate curium ion needs 2,108 basis functions for the fully relativistic four-component calculation.

Relativistic density functional approach. Ellis and his coworkers (Rosen and Ellis 1975; Nakamatsu et al. 1992) developed the relativistic density functional calculation using the discrete-variational (DV) $X\alpha$ formalism. They use numerical wave functions for the generation of molecular potential and molecular orbitals so that the integration becomes quite simple. Fricke and his group (Bastug et al. 1993, 1995) added a precise integration scheme to the relativistic DV- $X\alpha$ method and the program can calculate total energy of the system with several generalized gradient approximation (GGA) corrections (Vosko et al. 1980; Becke 1988). Hirata et al. (1998) studied the stability of actinyl nitrate – triethyl phosphate complexes using the relativistic DV-DFS (Dirac–Fock–Slater) method. They examined the contribution of 5f electrons to the chemical bonding between the actinide ions and donor atoms of the ligand. The bond-overlap population decreases in the order of $U > Np > Pu$. The application of nonrelativistic and relativistic DV- $X\alpha$ method and their development appeared in the special volume of *Advances in Quantum Chemistry* (Löwdin 1997, 2000). Te Velde and coworkers have published a review on the application of ADF (Amsterdam Density Functional) program including relativistic calculations (Te Velde et al. 2001). See also reference (ADF 2009) for its Web site. The ADF has been developed since 1973 (Baerends et al. 1973), which exploits Slater-type functions (STOs) as the basis set. Guillaumont et al. (2006) and coworkers extensively studied the simulation of liquid/liquid extraction systems for actinide/lanthanide separation. This review involves computer simulation techniques for quantum chemistry and molecular dynamics. Challenging application of the ADF program has been reported by Hancock et al. (2006). They estimated chemical properties of element 111, roentgenium (I) and predicted that Rg(I) is a very soft ion but also a stronger Lewis acid than the other monovalent cations.

For the solid-state actinide physics, VASP (Vienna Ab-initio Simulation Package) and Wien2k are widely used. VASP is a program package for ab initio quantum-mechanical molecular dynamics simulations using pseudopotentials or the projector-augmented wave method and a plane wave basis set (VASP 2009). Wolfer et al. (2007) and coworkers applied the VASP to simulate the effect of Ga addition to the stabilization of δ -plutonium and Minamoto et al. (2009) estimated thermodynamic properties of PuO_2 by using the VASP. The Wien2k (2009) program package is also useful for the actinide science. This program allows performing electronic structure calculations based on the DFT using all-electron scheme including relativistic effects. Robert et al. (2003) calculated thermodynamical properties of plutonium metals and Atta-Fynn and Ray (2009) predicted magnetic properties of δ -plutonium and adsorption properties of water molecules on the δ -plutonium (1,1,1) surface. Several applications on the properties of solid-state americium are reported by using the Wien2k program. Penicaud (2005) and Gao and Ray (2006) applied the Wien2k to the metallic americium to evaluate the effect of 5f electrons to the phase transition of americium.

References

- ADF (2009) <http://www.scm.com> (Amsterdam Density Functional software)
- Ageev VA, Golovnya VYa, Gromova EA, Egorov SA, Kovalenko SS, Linev AF, Nemilov YuA, Pozdnyakov AV, Rubchenya VA, Selitskii Yu et al (1987) *Sov J Nucl Phys* 46:392
- Ahmad I (2002) *J Nucl Radiochem Sci* 3:179
- Akiyama K, Zhao Y, Sueki K, Tsukada K, Haba H, Nagame Y, Kodama T, Suzuki S, Ohtsuki T, Sakaguchi K et al (2001) *J Am Chem Soc* 123:181
- Allen PG, Bucher JJ, Denecke M, Edelstein NM, Kaltsoyannis N, Nitsche H, Reich T, Shuh DK (1996a) In: Amico KLD, Terminello LJ, Shuh DK (eds) *Synchrotron radiation techniques in industrial, chemical, and materials science*. Plenum Press, New York, p 169
- Allen PG, Veirs DK, Conradson SD, Smith CA, Marsh SF (1996b) *Inorg Chem* 35:2841
- Allen PG, Bucher JJ, Shuh DK, Edelstein NM, Reich T (1997) *LBNL-4024 (UC-401)*
- Allen PG, Bucher JJ, Shuh DK, Edelstein NM, Craig I (2000) *Inorg Chem* 39:595
- Allen PG, Henderson AL, Sylwester ER, Turchi PEA, Shen TH, Gallegos GF, Booth CH (2002) *Phys Rev B* 65:214107
- ALS (2009) <http://www-als.lbl.gov>
- Andreyev AN, Bogdanov DD, Chepigin VI, Kabachenko AP, Malyshev ON, Oganessian YuTs, Sagaidak RN, Ter-Akopian GM, Yereimin AV, Hessberger FP et al (1992) *Z Phys A* 344:225
- Andreyev AN, Bogdanov DD, Chepigin VI, Kabachenko AP, Malyshev ON, Sagaidak RN, Salamatin LI, Ter-Akopian GM, Yereimin AV (1993a) *Z Phys A* 345:389
- Andreyev AN, Bogdanov DD, Saro S, Ter-Akopian GM, Veselsky M, Yereimin AV (1993b) *Phys Lett B* 312:49
- Ankudinov AL, Ravel B, Rehr JJ, Conradson SD (1998) *Phys Rev B* 58:7565
- Antonio MR, Williams CW, Soderholm L (2002) *Radiochim Acta* 90:851
- APS (2009) <http://www.aps.anl.gov>
- Arisaka M, Kimura T, Suganuma H, Yoshida Z (2001a) *Radiochim Acta* 89:593
- Arisaka M, Kimura T, Suganuma H, Yoshida Z (2001b) *Radiochim Acta* 90:193
- Arko AJ, Joyce JJ, Morales J, Wills J, Jashley J (2000) *Phys Rev B* 62:1773
- Armbruster P (1999) *Rep Prog Phys* 62:465
- Asai M, Tsukada K, Ichikawa S, Sakama M, Haba H, Nagame Y, Nishinaka I, Akiyama K, Toyoshima A, Kaneko T (2003) *Eur Phys J A* 16:17
- Asai M, Tsukada K, Sakama M, Ichikawa S, Ishi T, Nagame Y, Nishinaka I, Akiyama K, Osa A, Oura Y et al (2005) *Phys Rev Lett* 95:102502
- Asano T, Wada T, Ohta M, Ichikawa T, Yamaji S, Nakahara H (2004) *J Nucl Radiochem Sci* 5:1
- Atta-Fynn R, Ray AK (2009) *Eur Phys Lett* 85:27008
- Audi G, Bersillon O, Blachot J, Wapstra AH (1997) *Nucl Phys A* 624:1
- Baerends EJ, Ellis DE, Ros P (1973) *Chem Phys* 2:41
- Balagna JP, Ford GP, Hoffman DC, Knight JD (1971) *Phys Rev Lett* 26:145
- Balasubramanian K (1997) *Relativistic effects in chemistry*, part A and B. Wiley, New York
- Balasubramanian K (2000) *J Chem Phys* 112:7425
- Balasubramanian K (2002) *J Chem Phys* 116:3568
- Barber RC, Greenwood NN, Hryniewicz AZ, Jeannin YP, Lefort M, Sakai M, Uehla I, Wapstra AH, Wilkinson DH (1992) *Prog Part Nucl Phys* 29:453
- Barwick SW, Price PB, Stevenson JD (1985) *Phys Rev C* 31:1984
- Barwick SW, Price PB, Ravn HL, Hourani E, Hussonnois M (1986) *Phys Rev C* 34:362
- Bass R (1974) *Nucl Phys A* 231:141
- Bass R (1980) *Nuclear reactions with heavy ions*. Springer, Berlin
- Bass-May A, Kratz JV, Trautmann N (1985) *Z Phys A* 322:457
- Bastug T, Heinemann D, Sepp WD, Kolb D, Fricke B (1993) *Chem Phys Lett* 211:119
- Bastug T, Sepp WD, Kolb D, Fricke B, Te Velde G, Baerends EJ (1995) *J Phys B At Mol Opt Phys* 28:1833
- Becke AD (1988) *Phys Rev A* 38:3098
- Becke H, Dretzke A, Eberhardt K, Fritzsche S, Grüning C, Gwinner G, Haire RG, Huber G, Kratz JV, Kube G et al (2002) *J Nucl Sci Technol (Suppl. 3)*:86
- Beckerman M (1988) *Rep Prog Phys* 51:1047
- Bellido LF, Robinson VJ, Sims HE (1993) *Radiochim Acta* 62:123
- Bellido LF, Robinson VJ, Sims HE (1994) *Radiochim Acta* 64:11
- Benedict M, Pigford TH, Levi HW (1981) *Nuclear chemical engineering*, 2nd edn. McGraw-Hill, New York
- Benedict U (1987) In: Freeman J, Lander GH (eds) *Handbook on the physics and chemistry of the actinides*. Elsevier Science, Amsterdam, Chapter 3, pp 227–269
- Benedict U, Holzapfel WB (1993) In: Gschneidner KA Jr, Eyring L, Lander GH, Choppin GR (eds) *Handbook on the physics and chemistry of rare earths*, vol 17: *Lanthanides/Actinides: physics -I*. Elsevier Science, Amsterdam, Chapter 113, pp 245–300
- Bertram S, Kaindl G, Jove J, Pages M, Gal J (1989) *Phys Rev Lett* 63:2680
- Bilewicz A (2002) *J Nucl Radiochem Sci* 3:147
- Bjornholm S, Lynn JE (1980) *Rev Mod Phys* 52:725

- Blann M (1984) UCID-20169, Lawrence Livermore National Laboratory, California
- Block M, Ackermann D, Blaum K, Chaudhuri A, Di Z, Eliseev S, Ferrer R, Habs D, Herfurth F, Hessberger FP (2007) *Eur Phys J D* 45:39
- Block M, Ackermann D, Blaum K, Droese C, Dworschak M, Eliseev S, Fleckenstein T, Haettner E, Herfurth F, Hessberger FP et al (2010) *Nature* 463:785
- Bock R (ed) (1980) *Heavy ion collisions*, vol 2. North-Holland, Amsterdam
- Bonetti R, Chiesa C, Guglielmetti A, Migliorino C, Cesana A, Terrani M, Price PB (1991) *Phys Rev C* 44:888
- Bonetti R, Chiesa C, Guglielmetti A, Migliorino C, Cesana A, Terrani M (1993) *Nucl Phys A* 556:115
- Bonetti R, Chiesa C, Guglielmetti A, Migliorino C, Monti P, Pasinetti AL, Ravn HL (1994) *Nucl Phys A* 576:21
- Bonetti R, Chiesa C, Guglielmetti A, Matheoud R, Poli G, Mikheev VL, Tretyakova SP (1995) *Phys Rev C* 51:2530
- Bonetti R, Guglielmetti A (1996) In: Poenaru DN (ed) *Nuclear decay modes*. Institute of Physics Publishing, Bristol/Philadelphia, Chapter 9, pp 370–392
- Bonetti R, Carbonini C, Guglielmetti A, Hussonnois M, Trubert D, Le Naour C (2001) *Nucl Phys A* 686:64
- Bonetti R, Guglielmetti A (2007) *Rom Rep Phys* 59:301
- Bonneau L (2006) *Phys Rev C* 74:014301
- Bromley DA (ed) (1984) *Treaties on heavy-ion science*, vol 2–3. Plenum Press, New York
- Brosa U, Grossmann S, Müller A (1990) *Phys Rep* 197:167
- Brüchle W, Schädel M, Scherer UW, Kratz JM, Gregorich KE, Lee D, Nurmia M, Chasteler RM, Hall HL, Henderson RA et al (1988) *Inorg Chim Acta* 146:267
- Butler PA, Jones PM, Cann KJ, Cocks JFC, Jones GD, Julin R, Trzaska WH (1996) *Nucl Instr Meth Phys Res A* 381:433
- Butler PA, Humphreys RD, Greenless PT, Herzberg R-D, Jenkins DG, Jones GD, Kankaanpää H, Kettunen H, Rakhila P, Scholey C et al (2002) *Phys Rev Lett* 89:202501
- Chasman RR, Ahmad I, Friedman AM, Erskine JR (1977) *Rev Mod Phys* 49:833
- Chen J, Zhu Y, Jiao R (1996) *Sep Sci Technol* 31:2723
- Choppin GR, Liljenzin J-O, Rydberg J (1995) *Radiochemistry and nuclear chemistry*, 2nd edn. Butterworth-Heinemann, Oxford
- Coleman JA (1958) UCRL-8281, University of California Radiation Laboratory, California
- Combes J-M, Chisholm-Brause CJ, Brown GE Jr, Parks GA, Conradson SD, Eller PG, Triay I, Hobart DE, Meier A (1992) *Environ Sci Technol* 26:376
- Conradson SD, Al Mahamid I, Clark DL, Hess NJ, Hudson EA, Neu MP, Palmer PD, Runde WH, Tait CD (1998) *Polyhedron* 17:599
- Cordier PY, Rabbe C, Francois N, Madic C, Kolarik Z (1999) *JAERI-Conf 99-004*:278
- Cory MG, Kostlmeier S, Kotzian M, Rosch N, Zerner MC (1994) *J Chem Phys* 100:1353
- Cowan JJ, Thielemann F-K, Truran JW (1991) *Phys Rep* 208:267
- Craw JS, Vincent MA, Hillier IH, Wallwork AL (1995) *J Phys Chem* 99:10181
- Cwiok S, Nazarewicz W, Saladin JX, Plociennik W, Johnson A (1994) *Phys Lett B* 322:304
- D'Amico KL, Terminello LJ, Shuh DK (eds) (1996) *Synchrotron radiation techniques in industrial, chemical, and materials science*. Plenum Press, New York
- Dauids CN, Back BB, Bindra K, Henderson DJ, Kutschera W, Lauritsen T, Nagame Y, Sugathan P, Ramayya AV, Walters WB (1992) *Nucl Instr Meth Phys Res B* 70:358
- Delagrangé H, Fleury A, Alexander JM (1978) *Phys Rev C* 17:1706
- Dematte L, Wagemans C, Barthelemy R, D'hondt P, Deruytter A (1997) *Nucl Phys A* 617:331
- Den Auwer C, Revel R, Charbonnel MC, Presson MT, Conradson SD, Simoni E, Le Du JF, Madic C (1999) *J Synchrotron Rad* 6:101
- Den Auwer C, Charbonnel MC, Drew MGB, Grigoriev M, Hudson MJ, Iveson PB, Madic C, Nierlich M, Presson MT, Revel R et al (2000) *Inorg Chem* 39:1487
- Dirac (2009) <http://dirac.chem.sdu.dk> (Direct Iterative Relativistic All-electron Calculations)
- Donets ED, Shchegolev VA, Ermakov VA (1965) *Sov J At Energy* 19:995
- Donets ED, Shchegolev VA, Ermakov VA (1966) *Sov J Nucl Phys* 2:723
- Drew MGB, Foreman MRSJ, Hill C, Hudson MJ, Madic C (2005) *Inorg Chem Comm* 8:239
- Dubray N, Goutte H, Delaroche J-P (2008) *Phys Rev C* 77:014310
- Ellis DE, Goodman GL (1984) *Int J Quantum Chem* 25:185
- Eskola K, Eskola P, Nurmia M, Ghiorso A (1971) *Phys Rev C* 4:632
- Espinosa FJ, Vilella P, Lashley JC, Conradson SD, Cox LE, Martinez R, Martinez B, Morales L, Terry J, Pereyra RA (2001) *Phys Rev B* 63:174111
- ESRF (2009) <http://www.esrf.eu>
- FEFF (2009) <http://leonardo.phys.washington.edu/feff/>
- Fernandez-Niello J, Dasso CH, Landowne S (1989) *Comput Phys Commun* 54:409
- Firestone RB, Shirley VS (eds) (1996) *Table of isotopes*. Wiley, New York
- Frische MJ et al (1998) *Gaussian*, www.gaussian.com
- Gäggeler H, Sikkeland T, Wirth G, Brüchle W, Bögl W, Franz G, Herrmann G, Kratz JV, Schädel M, Sümmerer K et al (1984) *Z Phys A* 316:291

- Gäggeler H, Bröchle W, Brügger M, Schädel M, Sümmerer K, Wirth G, Kratz JV, Lerch M, Blaich Th, Herrmann G et al (1986) *Phys Rev C* 33:1983
- Gangrskii YuP, Marinescu GM, Miller MB, Samosyuk VN, Kharisov IF (1978) *Sov J Nucl Phys* 27:475
- Gangrskii YuP, Miller MB, Mikhailov LV, Kharisov IF (1980) *Sov J Nucl Phys* 31:162
- Gao D, Ray AK (2006) *Eur Phys J B* 50:497
- Gates JM, Garcia MA, Gregorich KE, Düllmann ChE, Dragojević I, Dvorak J, Eichler R, Folden CM III, Loveland W, Nelson SL et al (2008) *Phys Rev C* 77:034603
- Gaussian (2009) <http://www.gaussian.com/>
- Gavron A (1980) *Phys Rev C* 21:230
- Georges A, Kotliar G, Krauth W, Rozenberg JJ (1996) *Rev Mod Phys* 68:13
- Ghiorso A, James RA, Morgan LO, Seaborg GT (1950) *Phys Rev* 78:472
- Ghiorso A, Thompson SG, Higgins GH, Seaborg GT, Studier MH, Fields PR, Fried SM, Diamond H, Mech JF, Pyle GL et al (1955a) *Phys Rev* 99:1048
- Ghiorso A, Harvey BG, Choppin GR, Thompson SG, Seaborg GT (1955b) *Phys Rev* 98:1518
- Ghiorso A, Sikkeland T, Walton JR, Seaborg GT (1958) *Phys Rev Lett* 1:18
- Ghiorso A, Sikkeland T, Larsh AE, Latimer RM (1961) *Phys Rev Lett* 6:473
- Ghiorso A, Nurmia M, Eskola K, Eskola P (1970) *Phys Lett* 32B:95
- Ghiorso A, Yashita S, Leino ME, Frank L, Kalnins J, Armbruster P, Dufour J-P, Lemmertz PK (1988) *Nucl Instr Meth Phys Res A* 269:192
- Gregorich KE, Gates JM, Düllmann ChE, Sudowe R, Nelson SL, Garcia MA, Dragojević I, Folden CM III, Neumann SH, Hoffman DC et al (2008) *Phys Rev C* 74:044611
- Grison E, William BH, Fowler RD (eds) (1961) *Plutonium 1960*. Cleaver-Hume Press, London
- Guillaumont D, Guilbaud Ph, Sorel C, Gutierrez F, Chalmet S (2006) *Nucl Sci Eng* 153:207
- Habs D, Klewe-Nebenius H, Metag V, Neumann B, Specht HJ (1978) *Z Phys A* 285:53
- Hall HL, Gregorich KE, Henderson RA, Lee DM, Hoffman DC, Bunker ME, Fowler MM, Lysaght P, Starner JW, Wilhelmy JB (1989) *Phys Rev C* 39:1866
- Hall HL, Gregorich KE, Henderson RA, Gannett CM, Chadwick RB, Leyba JD, Czerwinski KR, Kadkhodayan B, Kreek SA, Hannink NJ et al (1990a) *Phys Rev C* 42:1480
- Hall HL, Gregorich KE, Henderson RA, Gannett CM, Chadwick RB, Leyba JD, Czerwinski KR, Kadkhodayan B, Kreek SA, Lee DM et al (1990b) *Phys Rev C* 41:618
- Hall HL, Hoffman DC (1992) *Ann Rev Nucl Part Sci* 42:147
- Hamilton JH, Ramayya AV, Zhu SJ, Ter-Akopian GM, Oganessian YuTs, Cole JD, Rasmussen JO, Stoyer MA (1995) *Prog Part Nucl Phys* 35:635
- Hancock RD, Bartolotti LJ, Kaltsoyannis N (2006) *Inorg Chem* 45:10780
- Havela L, Gouder T, Wastin F, Rebizant J (2002) *Phys Rev B* 65:235118
- Herrmann G, Trautmann N (1982) *Ann Rev Nucl Part Sci* 32:117
- Herzberg R-D, Amzal N, Becker F, Butler PA, Chewter AJC, Cocks JFC, Dorvaux O, Eskola K, Gerl J, Greenless PT et al (2001) *Phys Rev C* 65:014303
- Herzberg R-D, Greenless PT, Butler PA, Jones GD, Venhart M, Darby IG, Eeckhaudt S, Eskola K, Grahn T, Gray-Jones C et al (2006) *Nature* 442:896
- Herzberg R-D (2008) *Prog Part Nucl Phys* 61:674
- Hill C, Guillauneux D, Berthon L, Madic C (2002) *J Nucl Sci Technol (Suppl. 3)*:289
- Hirata M, Sekine R, Onoe J, Nakamatsu H, Mukoyama T, Takeuchi K, Tachimori S (1998) *J Alloy Comp* 271–273:128
- Hoffman DC, Hoffman MM (1974) *Annu Rev Nucl Sci* 24:151
- Hoffman DC, Fowler MM, Daniels WR, von Gunten HR, Lee D, Moody KJ, Gregorich K, Welch R, Seaborg GT, Bröchle W et al (1985) *Phys Rev C* 31:1763
- Hoffman DC (1986) *Nucl Instr Meth Phys Res A* 249:13
- Hoffman DC, Somerville LP (1989) In: Poenaru DN, Ivascu MS (eds) *Charged particle emission from nuclei*, vol 3. CRC Press, Boca Raton, Chapter 1, pp 1–40
- Hoffman DC, Lane MR (1995) *Radiochim Acta* 70/71:135
- Hoffman DC, Hamilton TM, Lane MR (1996) In: Poenaru DN (ed) *Nuclear decay modes*. Institute of Physics Publishing, Bristol/Philadelphia, Chapter 10, pp 393–432
- Hoffman DC, Ghiorso A, Seaborg GT (2000) *The transuranium people – the inside story*. Imperial College Press, Singapore
- Horwitz EP, Kalina DG (1984) *Solvent Extr Ion Exch* 2:179
- Horwitz EP, Martin KA, Diamond H, Kaplan L (1986) *Solvent Extr Ion Exch* 4:449
- Hulet EK (1983) *Radiochim Acta* 32:7
- Hulet EK, Wild JF, Dougan RJ, Loughheed RW, Landrum JH, Dougan AD, Schädel M, Hahn RL, Baisden PA, Henderson CM et al (1986) *Phys Rev Lett* 56:313
- Hulet EK, Wild JF, Dougan RJ, Loughheed RW, Landrum JH, Dougan AD, Baisden PA, Henderson CM, Dupzyk RJ, Hahn RL et al (1989) *Phys Rev C* 40:770
- Hulet EK (1990) *Very heavy transuranium isotopes*. In: *Proceedings of the Robert A. Welch foundation conference on chemical research XXXIV, fifty years with transuranium elements*, pp 279–310

- Hulet EK (1990) *J Radioanal Nucl Chem Articles* 142:79
- Hyde EK, Perlmann I, Seaborg GT (1964) The nuclear properties of the heavy elements, vol 1 and 2. Prentice-Hall, New Jersey
- Ichikawa S, Tsukada K, Asai M, Haba H, Sakama M, Kojima Y, Shibata M, Nagame Y, Oura Y, Kawade K (2002) *Nucl Instr Meth Phys Res B* 187:548
- Ichikawa T, Iwamoto A, Möller P (2009) *Phys Rev C* 79:014305
- Ikezo H, Nagame Y, Ikuta T, Hamada S, Nishinaka I, Ohtsuki T (1996) *Nucl Instr Meth Phys Res A* 376:420
- Ikezo H, Ikuta T, Mitsuoka S, Nagame Y, Nishinaka I, Tsukada K, Ohtsuki T, Kuzumaki T, Lu J (1998) *Eur Phys J A* 2:379
- Ishii T, Shigematsu S, Makii H, Asai M, Tsukada K, Toyoshima A, Matsuda M, Makishima A, Shizuma T, Kaneko J (2006) *J Phys Soc Jpn* 75:043201
- Ishii T, Makii H, Asai M, Tsukada K, Toyoshima A, Matsuda M, Makishima A, Shigematsu S, Kaneko J, Shizuma T (2008) *Phys Rev C* 78:054309
- Jensen MP, Bond A (2002) *J Am Chem Soc* 124:9870
- Kadkhodayan B, Henderson RA, Hall HL, Leyba JD, Czerwinski KR, Kreek SA, Hannink NJ, Gregorich KE, Lee DM, Nurmia MJ et al (1992) *Radiochim Acta* 56:1
- Kalkowski G, Kaindl G, Bertram S, Schmiester G, Rebizant J, Spirlet JC, Vogt O (1987a) *Solid State Comm* 64:193
- Kalkowski G, Kaindl G, Brewer WD, Krone K (1987b) *Phys Rev B* 35:2667
- Kassner ME, Peterson DE (eds) (1995) Phase diagrams of binary actinide alloys, monograph series on alloy phase diagrams 11. Materials Information Society, USA
- Katz JJ, Seaborg GT, Morss LR (1986) The chemistry of the actinide elements, 2nd edn. Chapman and Hall, London/New York
- Keller OL Jr (1984) *Radiochim Acta* 37:169
- Kimura T, Choppin GR (1994) *J Alloy Comp* 213–214:313
- Kimura T, Kato Y, Takeishi H, Choppin GR (1998) *J Alloy Comp* 271–273:719
- Kolarik Z, Müllich U, Gassner F (1999) *Solvent Extr Ion Exch* 17:1155
- Kolarik Z (2008) *Chem Rev* 108:4208
- Koningsberger DC, Prins R (eds) (1987) X-ray absorption, principles, applications, techniques of EXAFS, SEXAFS and XANES. Wiley, New York
- Korkisch J (ed) (1989) Handbook of ion exchange resins: their application to inorganic analytical chemistry, vol 2. CRC Press, New York
- Kosugi N (1996) In: Iwasawa Y (ed) X-ray absorption fine structure for catalysts and surfaces. World Scientific, Singapore, Chapter 4, pp 60–76
- Krasznahorkay A, Hunyadi M, Harakeh MN, Csatos M, Faestermann T, Gollwitzer A, Graw G, Gulyas J, Habs D, Hertenberg R et al (1998) *Phys Rev Lett* 80:2073
- Kreek SA, Hall HL, Gregorich KE, Henderson RA, Leyba JD, Czerwinski KR, Kadkhodayan B, Nue MP, Kacher CD, Hamilton TM et al (1994a) *Phys Rev C* 50:2288
- Kreek SA, Hall HL, Gregorich KE, Henderson RA, Leyba JD, Czerwinski KR, Kadkhodayan B, Nue MP, Kacher CD, Hamilton TM et al (1994b) *Phys Rev C* 49:1859
- Kronig RD (1931) *Z Phys* 70:317
- Kronig RD (1932) *Z Phys* 75:468
- Lazarev YuA, Oganessian YuTs, Shirokovsky IV, Tretyakova SP, Utyonkov VK, Buklanov GV (1987) *Europhys Lett* 4:893
- Lazarev YuA, Lobanov YuV, Mezentsev AN, Oganessian YuTs, Subbotin VG, Utyonkov VK, Abdullin FSh, Bechtere VV, Iliev S, Kolesov IV et al (1993) In: Oganessian YuTs, Penionzhkevich YuE, Kalpakchieva R (eds) Proceedings of the international school-seminar on heavy ion physics, vol II. (Joint Institute for Nuclear Research Report E7-93-274) pp 497–502
- Lazarev YuA, Lobanov YuV, Oganessian YuTs, Tsyganov YuS, Utyonkov VK, Abdullin FSh, Iliev S, Polyakov AN, Rigol J, Shirokovsky IV et al (1995) *Phys Rev Lett* 75:1903
- Lee D, von Gunten H, Jacak B, Nurmia M, Liu YF, Luo C, Seaborg GT, Hoffman DC (1982) *Phys Rev C* 25:286
- Lee D, Moody KJ, Nurmia MJ, Seaborg GT, von Gunten HR, Hoffman DC (1983) *Phys Rev C* 27:2656
- Lee IY (1990) *Nucl Phys A* 520:641c
- Leino M, Äystö J, Enqvist T, Heikkinen P, Jokinen A, Nurmia M, Ostrowski A, Trzaska WH, Uusitalo J, Eskola K et al (1995) *Nucl Instr Meth Phys Res B* 99:653
- Leino M, Kankaanpää H, Herzberg R-D, Chewter AJ, Hessberger FP, Coz YLe, Becker F, Butler PA, Cocks JFC, Dorvaux O et al (1999) *Eur Phys J A* 6:63
- Leino M (2002) *J Nucl Radiochem Sci* 3:173
- Leino M, Hessberger FP (2004) *Ann Rev Nucl Part Sci* 54:175
- Lemire RJ et al (eds) (2001) Chemical thermodynamics of neptunium and plutonium. Elsevier Science, Amsterdam
- Leyba JD, Henderson RA, Hall HL, Gannett CM, Chadwick RB, Czerwinski KR, Kadkhodayan BA, Kreek SA, Haynes GR, Gregorich KE et al (1990) *Phys Rev C* 41:2092
- Leyba JD, Henderson RA, Hall HL, Czerwinski KR, Kadkhodayan BA, Kreek SA, Brady EK, Gregorich KE, Lee DM, Nurmia MJ et al (1991) *Phys Rev C* 44:1850

- Löwdin P-O (eds) (1997) Electronic structure of clusters. In: *Advances in quantum chemistry*, vol 29. Academic, New York
- Löwdin P-O (2000) DV-X α for atomic spectroscopy and materials science. In: *Advances in quantum chemistry*, vol 37. Academic, New York
- Lougheed RW, Hulet EK, Wild JF, Moody KJ, Dougan RJ, Gannett CM, Henderson RA, Hoffman DC, Lee DM (1989) The discovery and spontaneous fission of properties of ^{262}No . In: *Proceedings of 50 years with nuclear fission*, National Academy of Sciences, Washington, DC; National Institute of Standards and Technology, Gaithersburg, MD; vol II, American Nuclear Society, La Grange Park, IL, pp 694–697
- Madic C, Hudson MJ, Liljenzin JO, Glatz JP, Nannicini R, Facchini A, Kolarik Z, Odoj R (2000) New partitioning techniques for minor actinides, EUR 19149 EN
- Makii H, Ishii T, Asai M, Tsukada K, Toyoshima A, Matsuda M, Makishima A, Kaneko J, Toume H, Ichikawa S (2007) *Phys Rev C* 76:061301(R)
- Malmbeck R, Apostolidis C, Carlos R, Glatz J-P, Molinet R, Morgenstern A, Nicholl A, Pagliosa G, Römer K, Schädel M et al (2001) *Radiochim Acta* 89:543
- Mamdouh A, Pearson JM, Rayet M, Tondeur F (1998) *Nucl Phys A* 644:389
- Mamdouh A, Pearson JM, Rayet M, Tondeur F (2001) *Nucl Phys A* 679:337
- Marcus Y (1967a) *Coor Chem Rev* 2:195
- Marcus Y (1967b) *Coor Chem Rev* 2:257
- Marcus Y (1997) *Ion properties*. Marcel Dekker, New York
- Mathur JN, Murali MS, Nash KL (2001) *Solvent Extr Ion Exch* 19:357
- Matzke H (1986) *Science of advanced LMFBR*. North-Holland, Amsterdam
- McMillan EM, Abelson PA (1940) *Phys Rev* 57:1185
- Metag V, Habs D, Specht HJ (1980) *Phys Rep* 65:1
- Meyer BS, Howard WM, Mathews GJ, Takahashi K, Möller P, Leander GA (1989) *Phys Rev C* 39:1876
- Mezilev KA, Novikov YuN, Popov AV, Sergeev YuYa, Tikhonov VI (1990) *Z Phys A* 337:109
- Minamoto S, Kato M, Konashi K, Kawazoe Y (2009) *J Nucl Mater* 385:18
- Mochizuki Y, Okamoto Y (2002) *Chem Phys Lett* 359:331
- Mochizuki Y, Tatewaki H (2002) *J Chem Phys* 116:8838
- Möller P, Nilsson SG, Sheline RK (1972) *Phys Lett B* 40:329
- Möller P, Nix JR, Myers WD, Swiatecki WJ (1995) *At Data Nucl Data Tables* 59:185
- Möller P, Madland DG, Sierk AJ, Iwamoto A (2001) *Nature (London)* 409:785
- Möller P, Sierk AJ, Ichikawa T, Iwamoto A, Bengtsson R, Uhrenholt H, Åberg S (2009) *Phys Rev C* 79:064304
- Moody KJ, Lee D, Welch RB, Gregorich KE, Seaborg GT, Lougheed RW, Hulet EK (1986) *Phys Rev C* 33:1315
- Moody KJ, Brüchle W, Brügger M, Gäggeler H, Haefner B, Schädel M, Sümmerer K, Tetzlaff H, Herrmann G, Kaffrell N et al (1987a) *Z Phys A* 328:417
- Moody KJ, Hulet EK, Wang S, Price PB, Barwick SW (1987b) *Phys Rev C* 36:2710
- Moody KJ, Hulet EK, Price PB (1992) *Phys Rev C* 45:1392
- Moore CE (1971) Analysis of optical spectra, NSRDS-NBS 34, National Bureau of Standards, Washington, DC
- Morita K, Yoshida A, Inamura TT, Kizumi M, Nomura T, Fujioka M, Shinozuka T, Miyatake H, Sueki K, Kudo H et al (1992) *Nucl Instr Meth Phys Res B* 70:220
- Morss LR (1991) In: Meyer G, Morss LR (eds) *Synthesis of lanthanide and actinide compounds*. Kluwer Academic, Dordrecht, pp 237–258
- Morss LR, Fuger J (eds) (1992) *Transuranium elementse – a half century*. American Chemical Society, Washington, DC
- Münzenberg G, Faust W, Hofmann S, Armbruster P, Güter K, Ewald K (1979) *Nucl Instr Meth* 161:65
- Münzenberg G (1988) *Rep Prog Phys* 51:57
- Münzenberg G (1997) In: Poenaru DN, Greiner W (eds) *Experimental techniques in nuclear physics*, Walter de Gruyter, Berlin, Chapter 11, pp 375–424
- Muscattello AC, Horwitz EP, Kalina DG, Kaplan L (1982) *Sep Sci Technol* 17:859
- Musikas C (1985) Actinide-lanthanide separation. In: Choppin GR, Navratil JD, Schulz WW (eds) *International symposium proceedings*. World Scientific, Singapore, pp 19–30
- Nagame Y, Nishinaka I, Tsukada K, Oura Y, Ichikawa S, Ikezoe H, Zhao YL, Sueki K, Nakahara H, Tanikawa M et al (1996) *Phys Lett B* 387:26
- Nagame Y, Zhao YL, Nishinaka I, Goto S, Kaji D, Tanikawa M, Tsukada K, Asai M, Haba H, Sakama M et al (2001) *Radiochim Acta* 89:681
- Nagame Y, Asai M, Haba H, Goto S, Tsukada K, Nishinaka I, Nishio K, Ichikawa S, Toyoshima A, Akiyama K et al (2002a) *J Nucl Radiochem Sci* 3:85
- Nagame Y, Asai M, Haba H, Tsukada K, Goto S, Sakama M, Nishinaka I, Toyoshima A, Akiyama K, Ichikawa S (2002b) *J Nucl Radiochem Sci* 3:129
- Nakamatsu H, Adachi H, Mukoyama T (1992) *Bull Inst Chem Res Kyoto Univ* 70:16
- Nakamatsu H (1995) *Chem Phys* 200:49
- Nash KL, Choppin GR (eds) (1995) *Separation of f-elements*. Plenum Press, New York
- Ninov V, Gregorich KE, McGrath CA (1998) In: Sherrill BM, Morrissey DJ, Davids CN (eds) *Exotic nuclei and atomic masses, AIP conference proceedings 455*, American Institute of Physics, Woodbury/New York, pp 704–707
- Nurmia M, Sikkeland T, Silva R, Ghiorso A (1967) *Phys Lett* 26B:78

- Oganessian YuTs, Lazarev YuA (1985) In: Bromley DA (eds) *Treatise on heavy-ion sciences*, vol 4. Plenum Press, New York/London, Chapter 1, pp 3–251
- Oganessian YuTs, Utyonkov VK, Lobanov YuV, Abdullin FSh, Polyakov AN, Shirokovsky IV, Tsyganov YuS, Mezentsev AN, Iliev S, Subbotin VG et al (2001) *Phys Rev C* 64:054606
- Oganessian YuTs, Utyonkov VK, Lobanov YuV, Abdullin FSh, Polyakov AN, Shirokovsky IV, Tsyganov YuS, Gulbekian GG, Bogomolov SL, Gikal BN et al (2004) *Phys Rev C* 70:064609
- Ogloblin AA, Venikov NI, Lisin SK, Pirozhkov SV, Pchelin VA, Rodionov YuF, Semochkin VM, Shabrov VA, Shvetsov IK, Shubko VM et al (1990) *Phys Lett B* 235:35
- Ogloblin AA, Bonetti R, Denisov VA, Guglielmetti A, Itkis MG, Mazzocchi C, Mikheev VL, Oganessian YuTs, Pik-Pichak GA, Poli G et al (2000) *Phys Rev C* 61:034301
- Ohtsuki T, Nagame Y, Nakahara H (1999) In: Greiner W, Gupta RJ (eds) *Heavy elements and related new phenomena*. World Scientific, Singapore, Chapter 13, pp 507–535
- Paul ES, Woods PJ, Davinson T, Page RD, Sellin PJ, Beausang CW, Clark RM, Cunningham RA, Forbes SA, Fossan DB et al (1995) *Phys Rev C* 51:78
- Penicaud M (2005) *J Phys Condens Matter* 17:257
- Pepper M, Bursten BC (1991) *Chem Rev* 91:719
- Petiau J, Calas G, Petitmaire D, Bianconi A, Benfatto M, Marcelli A (1986) *Phys Rev B* 34:7350
- Plasil F, Blann M (1975) *Phys Rev C* 11:508
- Poenaru DN (ed) (1996) *Nuclear decay modes*. Institute of Physics Publishing, Bristol/Philadelphia
- Poenaru DN, Greiner W (1996) In: *Nuclear decay modes*. Institute of Physics Publishing, Bristol/Philadelphia, Chapter 6, pp 275–336
- Poenaru DN, Nagame Y, Gherghescu RA, Greiner W (2002) *Phys Rev C* 65:054308
- Price PB, Stevenson JD, Barwick SW, Ravn HL (1985) *Phys Rev Lett* 54:297
- Price PB (1989) *Ann Rev Nucl Part Sci* 39:19
- Price PB, Moody KJ, Hulet EK, Bonetti R, Migliorino C (1991) *Phys Rev C* 43:1781
- Price PB, Bonetti R, Guglielmetti A, Chiesa C, Matheoud R, Migliorino C (1992) *Phys Rev C* 46:1939
- Pyykkö P (1987) *Inorg Chim Acta* 139:243
- Pyykkö P (1988) *Chem Rev* 88:563
- Ramayya AV, Hwang JK, Hamilton JH, Sandulescu A, Florescu A, Ter-Akopian GM, Daniel AV, Oganessian YuTs, Popeko GS, Greiner W et al (1998) *Phys Rev Lett* 81:947
- Rasmussen JO (1975) In: Cerny J (ed) *Nuclear spectroscopy and reactions*, part D. Academic, New York, Chapter IX.B, pp 97–178
- Rehr JJ, Albers RC (2000) *Rev Modern Phys* 72:621
- Reisdorf W (1981) *Z Phys A* 300:227
- Reisdorf W (1994) *J PhysG Nucl Part Phys* 20:1297
- Reiter P, Khoo TL, Lister CJ, Seweryniak D, Ahmad I, Alcorta M, Carpenter MP, Cizewski JA, Davids CN, Gervais G et al (1999) *Phys Rev Lett* 82:509
- Reiter P, Khoo TL, Lauritsen T, Lister CJ, Seweryniak D, Sonzogni AA, Ahmad I, Amzal N, Bhattacharyya P, Butler PA et al (2000) *Phys Rev Lett* 84:3542
- Reynolds SA, Scott TG (1975) *Radiochem Radioanal Lett* 23:269
- Robert G, Pasturel A, Siberchicot B (2003) *J Phys Condens Matter* 15:8377
- Rose HJ, Jones GA (1984) *Nature (London)* 307:245
- Rosen A, Ellis DE (1975) *J Chem Phys* 62:3039
- Ryan JL, Wheelwright EJ (1959) *Ind Eng Chem* 51:60
- Ryan JL (1960) *J Phys Chem* 64:1375
- Sakama M, Tsukada K, Asai M, Ichikawa S, Haba H, Goto S, Oura Y, Nishinaka I, Nagame Y, Shibata M et al (2000) *Eur Phys J A* 9:303
- Sakane G (2009) <http://www.chem.ous.ac.jp/~gsakane>
- Skanthakumar S, Antonio MR, Wilson RE, Soderholm L (2007) *Inorg Chem* 46:3485
- Sandulescu A, Poenaru DN, Greiner W (1980) *Sov J Part Nucl* 11:528
- Sandulescu A, Greiner W (1992) *Rep Prog Phys* 55:1423
- Sarrao JL, Morales LA, Thompson JD, Scott BL, Stewart GR, Wastin F, Rebizant J, Boulet P, Colineau E, Lander GH (2002) *Nature* 420:297
- Sasaki Y, Sugo Y, Suzuki S, Tachimori S (2001) *Solvent Extr Ion Exch* 19:91
- Sasaki Y, Tachimori S (2002) *Solvent Extr Ion Exch* 20:21
- Satchler GR (1991) *Phys Rep* 199:147
- Savrasov SY, Kotliar G, Abrahams E (2001) *Nature* 410:793
- Sayers DE, Stern EA, Lytle FW (1971) *Phys Rev Lett* 27:1204
- Schädel M, Kratz JV, Ahrens H, Bruchle W, Franz G, Gäggeler H, Warnecke I, Wirth G, Herrmann G, Trautmann N et al (1978) *Phys Rev Lett* 41:469
- Schädel M, Bruchle W, Gäggeler H, Kratz JV, Sümmerer K, Wirth G, Herrmann G, Stakemann R, Tittel G, Trautmann N et al (1982) *Phys Rev Lett* 48:852
- Schädel M, Bruchle W, Jäger E, Shimpf E, Kratz JV, Scherer UW, Zimmermann HP (1989) *Radiochim Acta* 48:171
- Schädel M (2007) *Eur Phys J D* 45:67
- Scherer UW, Bruchle W, Brügger M, Frink C, Gäggeler H, Herrmann G, Kratz JV, Moody K, Schädel M, Sümmerer K et al (1990) *Z Phys A* 335:421
- Schillebeeckx P, Wagemans C, Deruytter AJ, Barthelemy R (1992) *Nucl Phys A* 545:623
- Schleyer P von R, Allinger NL, Clark T, Gasteiger J, Kollman P, Schaefer HF (eds) (1998) In: *Encyclopedia of computational chemistry*. Wiley, New York
- Schmidt K-H, Faust W, Münzenberg G, Reisdorf W, Clerc H-G, Vermeulen D, Lang W (1980)

- Experimental determination of fission probabilities for proton-rich nuclei near the $N = 126$ shell. In: *Proceedings of a symposium on physics and chemistry of fission*, vol 1. IAEA, Vienna, pp 409–420
- Schmidt K-H, Morawek W (1991) *Rep Prog Phys* 54:949
- Schmidt K-H, Heinz A, Clerc H-G, Blank B, Brohm T, Czaikowski S, Donzaud C, Geissel H, Hanelt E, Inrich H et al (1994) *Phys Lett B* 325:313
- Schmidt K-H, Steinhäuser S, Böckstiegel C, Grewe A, Heinz A, Junghans AR, Benlliure J, Clerc H-G, de Jong M, Müller J et al (2000) *Nucl Phys A* 665:221
- Schmidt K-H, Benlliure J, Junghans AR (2001) *Nucl Phys A* 693:169
- Schreckenbach G, Hay PJ, Martin RL (1999) *J Comp Chem* 20:70
- Scott TG, Reynolds SA (1975) *Radiochem Radioanal Lett* 23:275
- Seaborg GT (1945) *Chem Eng News* 23:2190
- Seaborg GT, McMillan EM, Kennedy JW, Whal AC (1946) *Phys Rev* 69:366
- Seaborg GT, Loveland WD (1985) In: Bromley DA (ed) *Treatise on heavy-ion sciences*, vol 4. Plenum Press, New York/London, Chapter 2, pp 255–330
- Seaborg GT, Loveland WD (1990) *The elements beyond uranium*. Wiley, New York
- Seaborg GT (1995) *Radiochim Acta* 70/71:69
- Semchenkov A, Brühle W, Jager E, Schimpf E, Schadel M, Muhle C, Klos F, Turler A, Yakushev A, Belov A et al (2008) *Nucl Instr Meth Phys Res B* 266:4153
- Sewtz M, Backe H, Dretzke A, Kube G, Lauth W, Schwamb P, Eberhardt K, Grüning C, Thorle P, Trautmann N et al (2003) *Phys Res Lett* 90:163002
- Shabana R, Ruf H (1978) *J Radioanal Chem* 45:37
- Shannon RD, Prewitt CT (1969) *Acta Crystallogr B* 25:925
- Shaughnessy DA, Adams JL, Gregorich KE, Lane MR, Laue CA, Lee DM, McGrath CA, Patin JB, Strellis DA, Sylwester ER et al (2000) *Phys Rev C* 61:044609
- Shaughnessy DA, Gregorich KE, Lane MR, Laue CA, Lee DM, McGrath CA, Strellis DA, Sylwester ER, Wilk PA, Hoffman DC (2001) *Phys Rev C* 63:037603
- Shaughnessy DA, Gregorich KE, Adams JL, Lane MR, Laue CA, Lee DM, McGrath CA, Ninov V, Patin JB, Strellis DA et al (2002) *Phys Rev C* 65:024612
- Shinohara N, Usuda S, Ichikawa S, Suzuki T, Magara M, Okashita H, Yoshikawa H, Horiguchi T, Iwata Y, Shibata S et al (1986) *Phys Rev C* 34:909
- Sikkeland T (1966) *Ark Phys* 36:539
- Sikkeland T, Maly J, Lebeck DF (1968a) *Phys Rev* 169:1000
- Sikkeland T, Ghiorso A, Nurmia MJ (1968b) *Phys Rev* 172:1232
- Silva RJ et al (eds) (1995) *Chemical thermodynamics of americium*. Elsevier Science, Amsterdam
- Silva R, Sikkeland T, Nurmia M, Ghiorso A (1970) *Inorg Nucl Chem Lett* 6:733
- Skarnemark G, Aronsson PO, Broden K, Rydberg J, Björnstad T, Kaffrell N, Stender E, Trautmann N (1980) *Nucl Instr Meth* 171:323
- Söderlind P, Land A, Sadigh B (2002) *Phys Rev B* 66:205109
- SOLEIL (2009) <http://www.synchrotron-soleil.fr/>
- Sobiczewski A, Pomorski K (2007) *Prog Part Nucl Phys* 58:292
- Staut A, Klapdor-Kleingrothaus HV (1992) *Nucl Phys A* 549:254
- Subotic K, Oganessian YuTs, Utyonkov VK, Lobanov YuV, Abdullin FSh, Polyakov AN, Tsyganov YuS, Ivanov OV (2002) *Nucl Instr Meth Phys Res A* 481:71
- Swiatecki WJ (1982) *Nucl Phys A* 376:275
- Tachimori S, Morita S (2009) In: Moyer BA (ed) *Ion exchange and solvent extraction, a series of advances*, vol 19. Chapter 1, pp 1–64
- Te Velde G, Bickelhaupt FM, Baerends EJ, Gueerra CF, Van Gisbergen SJA, Snijders JG, Ziegler T (2001) *J Comp Chem* 22:931
- Teo BK (1986) *EXAFS, principles and data analysis*. Springer, Berlin
- Ter-Akopian GM, Hamilton JH, Oganessian YuTs, Kormicki J, Popeko GS, Daniel AV, Ramayya AV, Lu Q, Butler-Moore K, Ma WC et al (1994) *Phys Rev Lett* 73:1477
- Tetzlaff H, Herrmann G, Kaffrell N, Kratz JV, Rogowski J, Trautmann N, Skälberg M, Skarnemark G, Alstad J, Fowler MM et al (1986) *J Less-Common Met* 122:441
- Tian G, Zhu Y, Xu J, Hu T, Xie Y (2002) *J Alloy Comp* 334:86
- Tielemann F-K, Metzinger J, Klapdor HV (1983) *Z Phys A* 309:301
- Thompson SG, Ghiorso A, Seaborg GT (1950a) *Phys Rev* 77:838
- Thompson SG, Street K Jr, Ghiorso A, Seaborg GT (1950b) *Phys Rev* 78:298
- Toyoshima A, Kasamatsu Y, Kitatsuji Y, Tsukada K, Haba H, Shinohara A, Nagame Y (2008) *Radiochim Acta* 96:323
- Toyoshima A, Kasamatsu Y, Tsukada K, Asai M, Kitatsuji Y, Ishii Y, Toume H, Nishinaka I, Haba H, Ooe K et al (2009) *J Am Chem Soc* 131:9180
- Trautmann N (1995) *Radiochim Acta* 70/71:237
- Tretyakova SP, Sandulescu A, Mikheev VL, Hasegan D, Lebedev IA, Zamyatnin YuS, Korotkin YuS, Myasoedov BF (1985) *JINR Dubna Rapid Commun* 13:34
- Tretyakova SP, Zamyatnin YuS, Kovantsev VN, Korotkin YuS, Mikheev VL, Timofeev GA (1989) *Z Phys A* 333:349

- Tretyakova SP, Mikheev VL, Ponomarenko VA, Golovchenko AN, Ogloblin AA, Shigin VA (1994) JETP Lett 59:394
- Trubert D, Le Naour C, Monroy Guzman F, Hussonnois M, Brillard L, Le Du JE, Constantinescu O, Gasparro J, Barci V, Weiss B et al (2002) Radiochim Acta 90:127
- Tsushima S, Suzuki A (2000) J Mol Struct (THEOCHEM) 529:21
- Türler A, von Gunten HR, Leyba JD, Hoffman DC, Lee DM, Gregorich KE, Bennett DA, Chasteler RM, Gannett CM, Hall HL et al (1992) Phys Rev C 46:1364
- Türler A, Dressler R, Eichler B, Gäggeler HW, Jost DT, Schädel M, Brühle W, Gregorich KE, Trautmann N, Taut S (1998) Phys Rev C 57:1648
- Türler A, Düllmann ChE, Gäggeler HW, Kirbach UW, Yakushev AB, Schädel M, Brühle W, Dressler R, Eberhardt K, Eichler B et al (2003) Eur Phys J A 17:505
- Utyonkov VK, Lazarev YuA, Lobanov YuV, Oganessian YuTs, Abdullin FSh, Polyakov AN, Rigol J, Shirokovsky IV, Tsyganov YuS, Iliev S et al (1997) In: Oganessian YuTs, Kalpakchieva R (eds) Proceedings of the VI international school- seminar on heavy ion physics. World Scientific, Singapore, pp 400–408
- Vandenbosch R, Thomas TD, Vandenbosch SE, Glass RA, Seaborg GT (1958) Phys Rev 111:1358
- Vandenbosch R, Huizenga JR (1973) Nuclear fission. Academic, New York
- Vandenbosch R (1977) Ann Rev Nucl Sci 27:1
- VASP (2009) <http://cms.mpi.univie.ac.at/vasp/>
- Veirs DK, Smith CA, Berg JM, Zwick BD, Marsh SF, Allen PG, Conradson SD (1994) J Alloy Comp 213:328
- Visscher L, Visser O, Aerts PJC, Merenga H, Nieuwpoort WC (1994) Comput Phys Commun 81:120
- Volkov VV, Guseva LI, Pasyuk AS, Tarantin NI, Filippova KV (1959) Sov Phys JETP 36:536
- von Gunten HR (1969) Actinides Rev 1:275
- Vosko SH, Wilk L, Nusair M (1980) Can J Phys 58:1200
- Wagemans C, Schillebeeckx P, Deruyter A (1989) Nucl Phys A 502:287c
- Wagemans C (1991) In: Wagemans C (ed) The nuclear fission process. CRC Press, Boca Raton, Chapter 3, pp 35–61
- Walker P, Dracoulis G (1999) Nature 399:35
- Wang S, Price PB, Barwick SW, Moody KJ, Hulet EK (1987) Phys Rev C 36:2717
- Wang S, Snowden-Ifft D, Price PB, Moody KJ, Hulet EK (1989) Phys Rev C 39:1647
- Warda M, Egido JL, Robledo LM, Pomorski K (2002) Phys Rev C 66:014310
- Welch RB, Moody KJ, Gregorich KE, Lee D, Seaborg GT (1987) Phys Rev C 35:204
- Wien2k (2009) <http://www.wien2k.at/>
- Williams KE, Seaborg GT (1979) Phys Rev C 19:1794
- Wild JF, van Aarle J, Westmeier W, Loughed RW, Hulet EK, Moody KJ, Dougan RJ, Koop E-A, Glaser RE, Brandt R et al (1990) Phys Rev C 41:640
- Wing J, Ramler WJ, Harkness AL, Huizenga JR (1959) Phys Rev 114:163
- Wolfer WG, Kubota A, Söderlind P, Landa A, Oudot B, Sadigh B, Sturgeon JB, Surh MP (2007) J Alloy Comp 444–445:72
- Xu ER, Zhao EG, Wyss R, Walker PM (2004) Phys Rev Lett 92:252501
- Yaita T, Tachimori S, Edelstein NM, Bucher JJ, Rao L, Shuh DK, Allen PG (2001) J Synchrotron Rad 8:663
- Yeremin AV, Andreyev AN, Bogdanov DD, Chepigin VI, Gorshkov VA, Ivanenko AI, Kabachenko AP, Rubinskaya LA, Smirnova EM, Stepantsov SV et al (1989) Nucl Instr Meth Phys Res A 274:528
- Yoshida Z, Kimura T, Meguro Y (eds) (1997) Recent progress in actinide separation chemistry. World Scientific, Singapore
- Yuan S, Yang W, Xu Y, Pan Q, Xiong B, He J, Wang D, Li Y, Ma T, Yang Z (2001) Eur Phys J A 10:1
- Zagrebaev V, Oganessian YuTs, Itkis MG, Greiner W (2006) Phys Rev C 73:031602(R)
- Zagrebaev V, Greiner W (2008) Phys Rev Lett 101:122701
- Zhao YL, Nagame Y, Nishinaka I, Sueki K, Nakahara H (2000) Phys Rev C 62:014612
- Zhu Y (1995) Radiochim Acta 68:95
- Zhu Y, Chen J, Jiao R (1996) Solvent Extr Ion Exch 14:61

Further Reading

- Aspinall HC (2001) Chemistry of the f-block elements, advance chemistry texts. Gordon and Breach Science, Amsterdam
- Cotton FA, Wilkinson G, Murillo CA, Bochmann M (1999) Advanced inorganic chemistry, 6th edn. Wiley, New York
- Edelmann FT (1997) Synthetic methods of organometallic and inorganic chemistry. In: Herrmann WA (ed) Lanthanides and actinides, vol 6. Georg Thieme Verlag, New York
- Freeman AJ, Keller C (eds) (1991) Handbook on the physics and chemistry of the actinides, vol 1 to 6. North-Holland, Amsterdam
- Gschneidner KA Jr, Eyring L, Choppin GR, Lander GH (eds) (1994) Handbook on the physics and chemistry of rare earths, vol 18, Lanthanides/Actinides: Chemistry, North-Holland, Amsterdam
- Hess BA (2003) Relativistic effects in heavy-element chemistry and physics. Wiley, London
- Kaltsayannis N, Scott P (1999) The f elements. Oxford Science, London
- Kaldor U, Wilson S (2003) Theoretical chemistry and physics of heavy and superheavy elements. Kluwer Academic, New York
- Morss LR, Edelstein NM, Fuger J, Katz JJ (2006) The chemistry of the actinide and transactinide elements, vol 1–5. Springer, New York



19 Production and Identification of Transactinide Elements

G. Münzenberg^{1,2} · M. Gupta²

¹GSI Helmholtzzentrum für Schwerionenforschung mbH, Darmstadt, Germany

²Manipal University, Manipal, Karnataka, India

19.1	<i>Introduction</i>	878
19.2	<i>A Brief History of Discoveries</i>	882
19.2.1	Priorities and Naming	892
19.3	<i>Experimental Methods</i>	892
19.3.1	Accelerators and Ion Sources	892
19.3.2	Separation In-Flight	893
19.3.3	Working with Single Atoms	897
19.3.4	Statistics of Single-Atom Chains	898
19.4	<i>Nuclear Structure of the Transactinide Nuclides</i>	899
19.4.1	Superheavy Elements: The Limits of Stability	899
19.4.2	Alpha-Decay Properties and the New Shell Region Around Hassium	901
19.4.3	Shells and Fission Barriers	902
19.4.4	Theoretical Predictions	904
19.5	<i>Production of the Transactinide Elements</i>	908
19.5.1	Fusion of Massive Nuclear Systems	908
19.5.2	Experiment	910
19.5.3	Future Perspectives	915
19.6	<i>New Experimental Developments and Prospects for SHE Research</i>	916

Abstract: Microscopic nuclear theories predict a region of superheavy elements (SHEs) at the next doubly magic shell closure above ^{208}Pb . Early models locate the shell closure at $Z = 114$, more recent calculations place it at $Z = 120$. The closed neutron shell is located at $N = 184$. These predictions motivated the search for superheavy elements in nature and in the laboratory to explore the limits of the chart of nuclides toward its upper end. A new region of shell stabilization, centered at $Z = 108$ and $N = 162$ has been discovered. It interconnects the transuranium region and the superheavy elements. As of 2009, the heaviest element accepted by the Union of Pure and Applied Chemistry is $Z = 112$. The discovery of elements 113 to 116 and 118 has been reported. All of these elements have been created by the complete fusion of heavy ions. Production rates decrease to less than one atom per month for the heaviest species. Half-lives range down to below microseconds. The elements at the top of the nuclear chart have been discovered on the basis of single-atom decays after separation in-flight. The production and investigation of the transactinide elements with $Z = 104$ and beyond form the subject matter of this chapter. After a brief history of their discoveries and experimental methods, nuclear structure and the production of heavy elements will be discussed. The prospects for the synthesis and investigation of heavy elements using advanced technologies such as new high-current heavy-ion accelerators, radioactive beams, and ion traps will be outlined. The importance of closed nuclear shells for the existence and production of the heaviest elements will be addressed briefly.


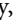
19.1 Introduction

Two fundamental questions involve the number of chemical elements that can be found in nature and the limits of stability of matter in terms of nuclear mass and charge. The search for superheavy elements (SHEs) in nature is an attempt at answering the first question. The heaviest primordial element existing in large amounts is uranium (Herrmann 1979; Seaborg et al. 1979). The discovery of natural plutonium in trace amounts has been reported (Hoffmann et al. 1971). Large-scale searches for superheavy elements in nature, most of them aimed at element 114, have been unsuccessful (Kratz 1983).

The second question can only be answered by laboratory experiments and remains the subject matter of research. The first milestone on the way to the artificial transuranium elements is the work of Hahn and Strassmann, aiming at the synthesis of these elements by using Fermi's method of neutron irradiation and successive β^- decay to transmute a chemical element into its next heavy neighbor (Fermi 1934). In irradiations of ^{238}U with neutrons they found barium isotopes instead of the expected new heavy elements (Hahn and Strassmann 1939a, b). This resulted in the discovery of induced nuclear fission, a new type of nuclear reaction specific to the transuranium elements. (See [Chap. 4 in Vol. 1](#) for more details on fission). Meitner and Frisch interpreted this new phenomenon in terms of the charged nuclear droplet. As the large Coulomb force acting between the many protons cannot be balanced by the cohesive nuclear force, the heavy nucleus breaks into two large fragments (Meitner and Frisch 1939). Meitner and Frisch estimated the upper limit for the existence of chemical elements to be around $Z = 100$. The first experiments already contained two important characteristics of future heavy element research: the identification via a two-step process consisting of the separation and subsequent assignment based on nuclear spectroscopy, and the role of fission in their production and decay. Later McMillan and Abelson applied

Fermi's method successfully to create the first transuranium element $Z = 93$, later named neptunium (McMillan and Abelson 1940). This method worked successfully up to fermium, $Z = 100$.

With the addition of microscopic effects to the nuclear droplet, which add stabilization (Strutinsky 1967), the question arose as to whether superheavy nuclei can exist *only* due to shell stabilization beyond the macroscopic limit estimated by Meitner and Frisch. In a first semi-empirical approach the possible evidence for an island of superheavy nuclei was predicted for 126 protons and 184 neutrons (Myers and Swiatecki 1966). A series of more basic calculations followed to confirm the hypothesis of shell stabilization playing a predominant role in the existence of superheavy elements (Mosel and Greiner 1969; Nilsson et al. 1969; Fizet and Nix 1972). Most of these calculations predicted $Z = 114$ and $N = 184$ as the center of the island of superheavy nuclei located in the sea of macroscopic instability, well separated from the transuranium elements. The situation remained practically unaltered until 1984. With the discovery of element 108 (Münzenberg et al. 1984b) it became clear that the island of superheavy elements is connected to the transuranium elements by a bridge of shell-stabilized nuclei.

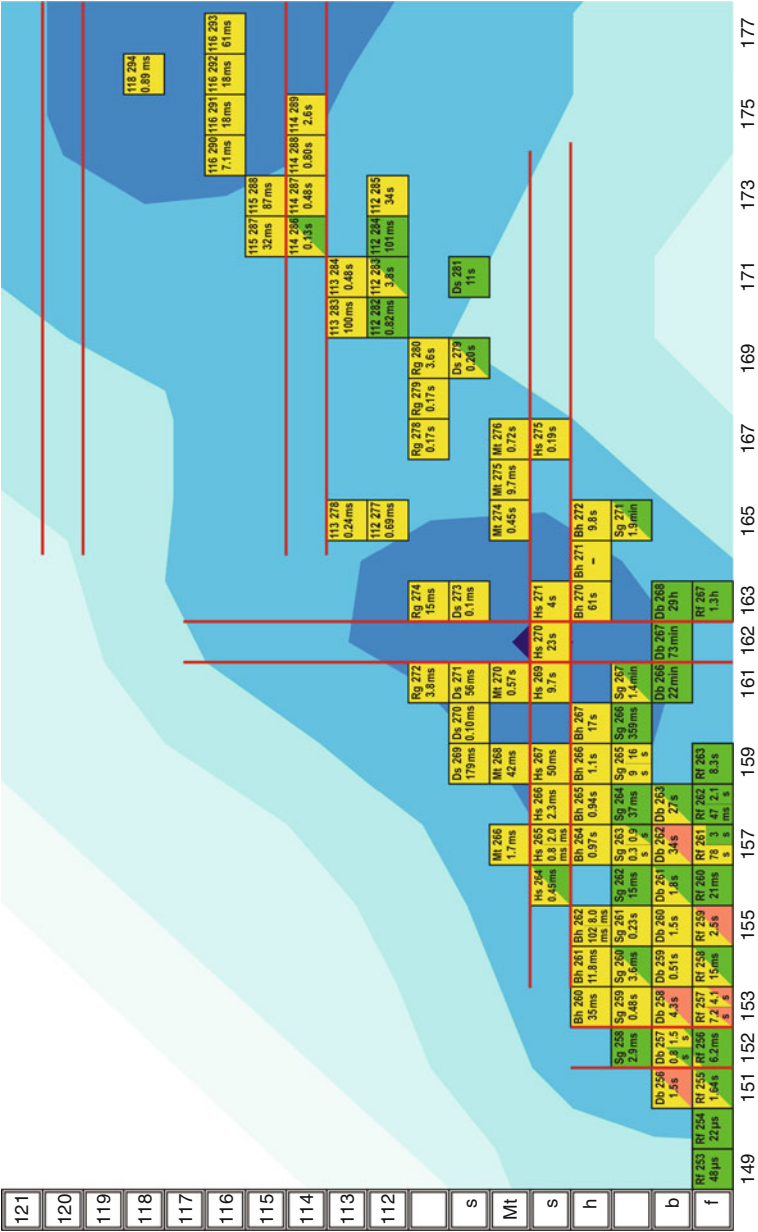
The unexpected discovery of this new subshell challenged theoreticians to reinvestigate their predictions. Calculations were performed with improved macroscopic–microscopic models (Möller et al. 1986; Sobiczewski et al. 1987) predicting a region of deformed shell-stabilized nuclei, centered at $Z = 108$ and $N = 162$. The discovery of the shell-stabilized island around $Z = 108$ and $N = 162$ is the basis of contemporary heavy element research. Without shell stabilization, nuclei could not exist in the region around hassium ($Z = 108$).  Figure 19.1 shows the presently known isotopes of the heaviest elements in the landscape of shell correction energies. At the boundaries of the shell-stabilized region, fission begins to play a role. Element 112, copernicium (Cn), is the heaviest element accepted by the International Union of Pure and Applied Chemistry, IUPAC (Barber et al. 2009,  Fig. 19.2). Element 118 is the heaviest element reported to date. Element 117 has not been observed yet (Oganessian et al. 2007; Oganessian 2007). Attempts to synthesize element 120 have been without success (Hofmann et al. 2008; Oganessian et al. 2009). All known isotopes of the heaviest elements are neutron deficient and still about eight neutrons away from the magic neutron number 184. New systematic calculations with self-consistent mean field models and realistic nucleon–nucleon interactions were carried out to predict nuclear properties of the heavy and superheavy elements (Cwiok et al. 1996; Rutz et al. 1997; Bender et al. 1999; Heenen and Nazarewicz 2002). Besides $Z = 114$, new magic proton numbers at $Z = 120$ and $Z = 126$ were suggested while the magic neutron number remained at $N = 184$ for all predictions. A recent theoretical analysis of the experimental data concludes that the position of the proton shell closure lies beyond $Z = 120$ (Adamian et al. 2009).

Transuranium elements are artificially created. The (n, γ) reaction, first used successfully for the production of neptunium ($Z = 93$), works only up to fermium ($Z = 100$). It ends at ^{257}Fm due to the short half-life of this isotope (e.g., Seaborg and Loveland 1990). With neutron irradiation, transuranium elements can be produced in weighable amounts by breeding in high flux reactors because the cross sections are of the order of barns, neutron fluxes are high, and the usable target thickness is large.

Transfermium elements are created by the complete fusion of heavy nuclei. Energetic heavy ions from accelerators are shot at heavy targets to create a combined nuclear system through complete fusion. The production cross sections are small. For nobelium ($Z = 102$), it is of the order of microbarns, six orders of magnitude below the cross section for neutron capture.

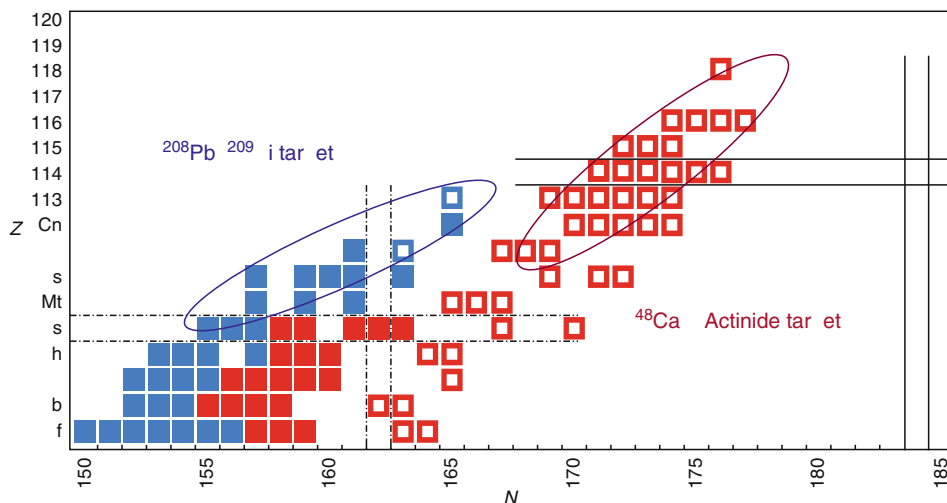
Fig. 19.1

Upper end of the chart of nuclides showing nuclear half-lives. Theoretical shell correction energies (Smolanczuk 1997) are underlain in blue color. The shading indicates the height of the shell correction energy in steps of 1 MeV. The decay modes are as follows: α decay (yellow), β^+ decay (red), spontaneous fission (green) (Courtesy M. Schädel)



■ Fig. 19.2

Known (filled squares) and proposed (hollow squares) transfermium isotopes (Barber et al. 2009). Nuclides marked in blue have been synthesized with cold fusion, while the ones in red have been synthesized with hot fusion. The subshell at $Z = 108$ and $N = 162$ (dashed-dotted lines) and the spherical shell closure $Z = 114$ and $N = 184$ (solid lines) are indicated



For the heaviest elements, cross sections drop to values below 1 pb. Due to the energy loss of the energetic projectile ions in the target and the narrow width of the excitation function, usable target thicknesses are of the order of a milligram. As a consequence, production rates count in quantities of single atoms. For the heaviest elements only one atom per week or even month are available.

The transfermium elements up to seaborgium were created by irradiations of reactor bred actinide targets with light projectiles, typically oxygen or nitrogen (Seaborg and Loveland 1985). Cold fusion with lead or bismuth targets and appropriate beams such as nickel led to the synthesis of element 113 (Hofmann and Münzenberg 2000; Morita 2008). The elements beyond were created by hot fusion with calcium beams together with suitable actinide targets (e.g., Oganessian et al. 2007; Oganessian 2007). It is interesting to note that for both types of fusion reactions doubly magic nuclei, ^{208}Pb and ^{48}Ca , play a key role. Also as with production cross sections, the half-lives decrease steeply toward the heaviest elements dropping more than ten orders of magnitude from 100 days for the longest-lived fermium isotope to about 1 ms for element 118 presently defining the top end of the nuclear chart.

Since transfermium work involves research with one single, short-lived, atom at a time it requires sensitive and fast detection techniques. As chemical techniques are limited to half-lives of seconds, all of the transactinide elements beyond seaborgium have been discovered using separation in-flight with ion optical separators (Münzenberg 1997). The identification is based on the parent–daughter α – α correlation method (Ghiorso et al. 1969), which has been refined by the implantation technique (Hofmann et al. 1984), permitting the identification of new isotopes or even new elements by single-atom decay sequences (Münzenberg et al. 1984a).

Presently superheavy element (SHE) research concentrates on the production and unambiguous identification of elements 114 and above using both physical and chemical methods. Developments include dedicated facilities for SHE production with accelerators delivering high beam intensities, detailed structure investigations with new generation gamma arrays of the highest efficiency, and trapping in ion traps for direct mass measurements and atomic physics (Sewtz and Habs 2007).

19.2 A Brief History of Discoveries

The transactinides are the doorway to the superheavy elements. The region of shell stabilization starts here (► Fig. 19.1) without which the chart of the nuclides would end around seaborgium. For this reason, these elements are sometimes also referred to as “superheavy” nuclei. In this chapter the conventional definition will be adopted when referring to the superheavy elements: spherical nuclei that lie around the next double shell closure above ^{208}Pb .

The first of the transactinide elements rutherfordium ($Z = 104$, Rf), dubnium ($Z = 105$, Db), and seaborgium ($Z = 106$, Sg) were discovered in hot fusion reactions by irradiating actinide targets, bred in high flux reactors, with light projectile beams such as oxygen or carbon (Flerov and Ter Akopian 1983; Seaborg and Loveland 1990). Rutherfordium was discovered in the irradiation of ^{249}Cf with ^{12}C (Ghiorso et al. 1969). After the evaporation of four neutrons from the resulting compound nucleus (CN) the isotope ^{257}Rf was formed. This reaction may be written as $^{249}\text{Cf}(^{12}\text{C}, 4n)^{257}\text{Rf}$. The first experiment to produce dubnium (Flerov et al. 1971) used the reaction $^{243}\text{Am}(^{22}\text{Ne}, 4n)^{261}\text{Db}$. Seaborgium was discovered with $^{249}\text{Cf}(^{18}\text{O}, 4n)^{263}\text{Sg}$ (Ghiorso et al. 1974). Production cross sections are given in ► Table 19.1. The “Criteria that must be satisfied for the Discovery of a New Chemical Element to be recognized” are provided in the report of the Transfermium Working Group (Barber et al. 1992) together with the detailed discovery profiles of the transfermium elements including meitnerium ($Z = 109$).

In the discoveries of the light transactinides, the reaction products recoiling from the thin production target due to the momentum transfer from the projectile, were stopped in a gas cell and transported with a helium gas jet to a detector system where their α decays were observed over several daughter generations. As the α spectra of the daughter nuclides were known, the mother element could be unambiguously identified with the method of α - α parent-daughter correlation (Ghiorso et al. 1974).

At seaborgium, the production cross sections drop below 1 nb and half-lives are shorter than 1 s. To access the region beyond seaborgium innovative methods were devised (Münzenberg 1988; Hofmann and Münzenberg 2000). A new type of synthesis reaction, cold heavy-ion fusion, using lead and bismuth targets (Oganessian 1974) was employed together with fast and sensitive detection methods allowing the identification of new nuclides or even new elements by the observation of single-atom decay chains (Münzenberg et al. 1981b). In irradiations of ^{208}Pb targets with ^{48}Ca , ^{50}Ti , and ^{54}Cr projectiles the cold production of transfermium elements in two-neutron evaporation channels had been observed (Oganessian et al. 1975). The final and most convincing proof of the validity of this new concept was given by the observation of ^{257}Rf in irradiations of ^{208}Pb with ^{50}Ti produced by the evaporation of one neutron from the compound nucleus ^{258}Rf (Münzenberg et al. 1982a). Single-atom detection comprises separation in-flight (Münzenberg 1974; Münzenberg et al. 1979, 1981b) using ion optical methods in combination with the α - α parent-daughter correlation technique. The implantation of the heavy atom, separated in-flight, into a position sensitive silicon

■ Table 19.1

Typical reactions employed to produce the transactinide elements

Isotope	Reference	Reaction	σ /nb
Element 104: Rutherfordium (Rf)			
255	Hessberger et al. (1985)	$^{207}\text{Pb} (^{50}\text{Ti}, 2\text{n})$	4.8
	Hessberger et al. (1997)	$^{208}\text{Pb} (^{50}\text{Ti}, \text{n})$	0.7
	Dragojevic et al. (2008)	$^{208}\text{Pb} (^{48}\text{Ti}, \text{n})$	0.4
256	Hessberger et al. (1985)	$^{208}\text{Pb} (^{50}\text{Ti}, 2\text{n})$	5.2
257	Ghiorso et al. (1969)	$^{249}\text{Cf} (^{12}\text{C}, 4\text{n})$	10
	Hessberger et al. (1985)	$^{208}\text{Pb} (^{50}\text{Ti}, \text{n})$	6.1
	Dragojevic et al. (2008)	$^{208}\text{Pb} (^{50}\text{Ti}, \text{n})$	40
261	Lazarev et al. (2000)	$^{244}\text{Pu} (^{22}\text{Ne}, 5\text{n})$	4.4
	Haba et al. (2009)	$^{248}\text{Cm} (^{18}\text{O}, 5\text{n})$	13
262	Somerville et al. (1985)	$^{248}\text{Cm} (^{18}\text{O}, 5\text{n})$	5
Element 105: Dubnium (Db)			
257	Hessberger et al. (2001, 2009)	$^{209}\text{Bi} (^{50}\text{Ti}, 2\text{n})$	2.3
	Gates et al. (2008)	$^{208}\text{Pb} (^{51}\text{V}, 2\text{n})$	1.7
258	Gates et al. (2008)	$^{208}\text{Pb} (^{51}\text{V}, \text{n})$	2.1
	Hessberger et al. (2001, 2009)	$^{209}\text{Bi} (^{50}\text{Ti}, \text{n})$	4.3
260	Ghiorso et al. (1970)	$^{249}\text{Cf} (^{15}\text{N}, 4\text{n})$	3
261	Flerov et al. (1971)	$^{243}\text{Am} (^{22}\text{Ne}, 4\text{n})$	0.5
262	Kratz et al. (1992)	$^{249}\text{Bk} (^{18}\text{O}, 5\text{n})$	6
	Nagame et al. (2002)	$^{248}\text{Cm} (^{19}\text{F}, 5\text{n})$	1
263	Kratz et al. (1992)	$^{249}\text{Bk} (^{18}\text{O}, 4\text{n})$	10
	Schädel (2006)	$^{249}\text{Cf} (^{18}\text{O}, 4\text{n})$	0.30
Element 106: Seaborgium (Sg)			
258	Folden et al. (2009)	$^{208}\text{Pb} (^{52}\text{Cr}, 2\text{n})$	0.15
259	Münzenberg et al. (1985)	$^{207}\text{Pb} (^{54}\text{Cr}, 2\text{n})$	0.3
	Folden et al. (2009)	$^{208}\text{Pb} (^{52}\text{Cr}, \text{n})$	0.32
260	Münzenberg et al. (1985)	$^{208}\text{Pb} (^{54}\text{Cr}, 2\text{n})$	0.3
261	Streicher et al. (2007)	$^{208}\text{Pb} (^{54}\text{Cr}, \text{n})$	2.2
263	Timokhin et al. (1996)	$^{249}\text{Cf} (^{18}\text{O}, 4\text{n})$	0.3
	Nishio et al. (2006)	$^{238}\text{U} (^{30}\text{Si}, 5\text{n})$	0.07
265	Schädel (2002, 2006)	$^{248}\text{Cm} (^{22}\text{Ne}, 5\text{n})$	0.24
Element 107: Bohrium (Bh)			
260	Nelson et al. (2008a)	$^{209}\text{Bi} (^{52}\text{Cr}, \text{n})$	0.06
261	Münzenberg et al. (1989)	$^{209}\text{Bi} (^{54}\text{Cr}, 2\text{n})$	0.036
	Nelson et al. (2008b)	$^{208}\text{Pb} (^{55}\text{Mn}, 2\text{n})$	0.043
262	Nelson et al. (2008b)	$^{209}\text{Bi} (^{54}\text{Cr}, \text{n})$	0.44
	Nelson et al. (2008b)	$^{208}\text{Pb} (^{55}\text{Mn}, \text{n})$	0.03
266	Schädel (2002)	$^{249}\text{Bk} (^{22}\text{Ne}, 5\text{n})$	0.03–0.25

■ Table 19.1 (Continued)

Isotope	Reference	Reaction	σ /nb
267	Schädel (2002, 2006)	$^{249}\text{Bk} (^{22}\text{Ne}, 4n)$	0.07
Element 108: Hassium (Hs)			
263	Kaji et al. (2009)	$^{206}\text{Pb} (^{58}\text{Fe}, n)$	0.021
	Dragojevic et al. (2009)	$^{208}\text{Pb} (^{56}\text{Fe}, n)$	0.021
264	Münzenberg et al. (1987)	$^{207}\text{Pb} (^{58}\text{Fe}, n)$	0.002
265	Hofmann et al. (1997)	$^{208}\text{Pb} (^{58}\text{Fe}, n)$	0.07
267	Lazarev et al. (1995)	$^{238}\text{U} (^{34}\text{S}, 5n)$	0.0025
269	Türler et al. (2003)	$^{248}\text{Cm} (^{26}\text{Mg}, 5n)$	0.006
270	Dvorak et al. (2006, 2008)	$^{248}\text{Cm} (^{26}\text{Mg}, 4n)$	0.003
271	Dvorak et al. (2008)	$^{248}\text{Cm} (^{26}\text{Mg}, 3n)$	0.0025 ^a
Element 109: Meitnerium (Mt)			
266	Hofmann et al. (1997)	$^{209}\text{Bi} (^{58}\text{Fe}, n)$	0.008
	Nelson et al. (2009)	$^{208}\text{Pb} (^{59}\text{Co}, n)$	0.008
Element 110: Darmstadtium (Ds)			
269	Hofmann et al. (2002)		2.6 ^b
270	Hofmann et al. (2001)	$^{207}\text{Pb} (^{64}\text{Ni}, n)$	13
271	Morita et al. (2004a, b)	$^{208}\text{Pb} (^{64}\text{Ni}, n)$	17
Element 111: Roentgenium (Rg)			
272	Hofmann et al. (2002)	$^{209}\text{Bi} (^{64}\text{Ni}, n)$	2.9
Element 112: Copernicium			
277	Hofmann et al. (2002b)	$^{208}\text{Pb} (^{70}\text{Zn}, n)$	0.5
282	Oganessian et al. (2004a, b)	$^{238}\text{U} (^{48}\text{Ca}, 4n)$	0.6
283	Oganessian et al. (2004a, b)	$^{238}\text{U} (^{48}\text{Ca}, 3n)$	2.5
	Hofmann et al. (2007)	$^{238}\text{U} (^{48}\text{Ca}, 3n)$	0.72
Element 113			
278	Morita et al. (2004d, 2007b)	$^{209}\text{Bi} (^{70}\text{Zn}, n)$	0.031
282	Oganessian et al. (2007)	$^{237}\text{Np} (^{48}\text{Ca}, 3n)$	0.9
Element 114			
286	Oganessian et al. (2004a, b)	$^{242}\text{Pu} (^{48}\text{Ca}, 4n)$	4.5 ^c
287	Oganessian et al. (2004a, b)	$^{242}\text{Pu} (^{48}\text{Ca}, 3n)$	3.6
	Oganessian et al. (2004c)	$^{244}\text{Pu} (^{48}\text{Ca}, 5n)$	1.1
288	Oganessian et al. (2004a, b)	$^{242}\text{Pu} (^{48}\text{Ca}, 2n)$	0.5
	Oganessian et al. (2004c)	$^{244}\text{Pu} (^{48}\text{Ca}, 4n)$	5.3
289	Oganessian et al. (2004c)	$^{244}\text{Pu} (^{48}\text{Ca}, 3n)$	1.7
Element 115			
288	Oganessian et al. (2005)	$^{243}\text{Am} (^{48}\text{Ca}, 3n)$	4.2
287	Oganessian et al. (2004d, 2005)	$^{243}\text{Am} (^{48}\text{Ca}, 4n)$	0.9
Element 116			
290	Oganessian et al. (2006)	$^{245}\text{Cm} (^{48}\text{Ca}, 3n)$	3.7

■ Table 19.1 (Continued)

Isotope	Reference	Reaction	σ /nb
291	Oganessian et al. (2004c); Oganessian et al. (2007)	$^{245}\text{Cm}(^{48}\text{Ca}, 2n)$	0.9
292	Oganessian et al. (2004a, b)	$^{248}\text{Cm}(^{48}\text{Ca}, 4n)$	3.3
293	Oganessian et al. (2004a, b)	$^{248}\text{Cm}(^{48}\text{Ca}, 3n)$	1.2 ^c
Element 118			
294	Oganessian et al. (2006)	$^{249}\text{Cf}(^{48}\text{Ca}, 3n)$	0.5

^aDvorak et al. (2008) and Ch. E. Düllmann (2009, private communications).

^bRevised cross section.

^cCross section provided by V. Utyonkov (2009, private communication).

It should be noted that discrepancies in production cross sections measured with vacuum separators such as SHIP and gas-filled separators may be caused by short-lived states decaying by converted transitions followed by Auger cascades. These lead to charge states considerably higher than the equilibrium charge state. Therefore, at SHIP a thin carbon foil located about 10 cm downstream the target equilibrates the ionic charge state of the passing ions. Species which decay during their flight through SHIP after passing the equilibration foil may be lost (Münzenberg et al. 1984a). The time window is 10^{-8} to 10^{-6} s. Such cases have been observed in systematic cross-section investigations. This problem is less relevant for gas-filled separators where ionic charge states are continuously equilibrated while passing the filling gas. A typical example is ^{257}Rf . Experiments to investigate this problem in more detail are planned.

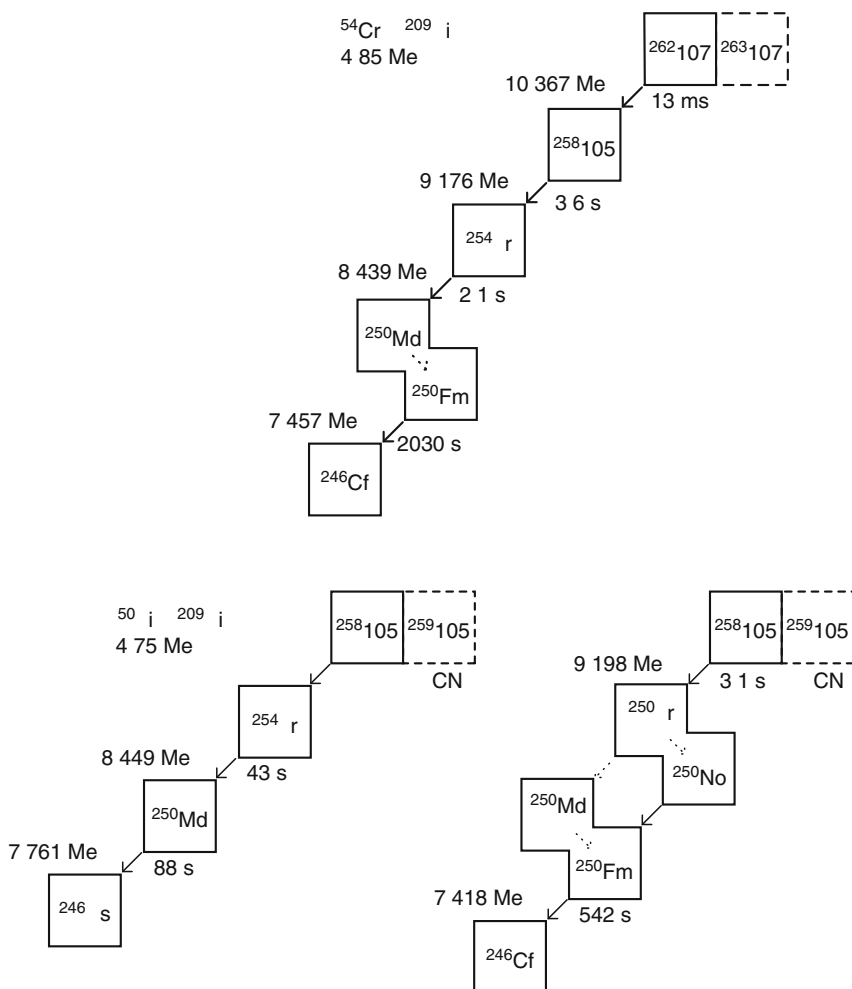
surface-barrier detector allows the observation of its individual decay history over several generations *in situ* (Hofmann et al. 1984). If at least one member of the sequence is known, the whole chain can be identified. At present, 12 isotopes of rutherfordium, 11 of dubnium, and 11 of seaborgium are known.

Bohrium (Bh), $Z = 107$, was the first of a series of elements discovered with this new method (Münzenberg et al. 1981a, 1989). In irradiations of ^{209}Bi with ^{54}Cr six atoms of ^{262}Bh were identified. An example of the observed decay sequence of one atom of ^{262}Bh together with decay chains of two atoms of the daughter nuclide ^{258}Db , observed in a companion experiment, is displayed in (► Fig. 19.3) for comparison. Since then, ten isotopes of bohrium have become known. The proton-rich ones with masses 260, 261, and 262 were directly produced by cold fusion. The isotopes with mass 262 and 264 appear in the discovery chains of the elements 109 and 111 (Hofmann et al. 2002). The neutron-rich isotopes with masses 266, 267 were created in irradiations of actinide targets. The three most neutron-rich ones with masses 270, 271, and 272 appear in decay chains from $^{282}\text{113}$ (Oganessian et al. 2007; Oganessian 2007), $^{287}\text{115}$ (Oganessian et al. 2004d, 2005), and $^{288}\text{115}$ respectively (Dmitriev et al. 2005, Oganessian et al. 2005), which were produced with ^{48}Ca projectiles in a series of experiments done at Dubna. These ten isotopes have half-lives ranging from 8 ms to 61 s. All of them undergo α decay.

Hassium (Hs), $Z = 108$ was discovered in the reaction $^{208}\text{Pb}(^{58}\text{Fe}, n)^{265}\text{Hs}$ (Münzenberg et al. 1984b, 1987) and unambiguously confirmed in a later experiment (Hofmann et al. 1995a). This element was synthesized after meitnerium as theoretical predictions available at that time suggested the predominance of spontaneous fission with half-lives below microseconds for the doubly even hassium isotopes (Randrup et al. 1976). Hence, to proceed with the synthesis of meitnerium was considered to be safer since it was possible to profit twice from the fission hindrance provided by the odd proton and the odd neutron, if an odd-odd nuclide was to be produced. The resulting observation of α decay is necessary for the identification of the new element with the correlation method. The synthesis of hassium with the unexpected

■ Fig. 19.3

A typical decay chain of ^{262}Bh with daughter decays illustrating the method of identification of a new species by single-atom decay sequences (Münzenberg et al. 1981a). Note that lifetimes of the individual nuclei fluctuate according to the “rules” of exponential distribution (see Sect. 9.4.4 in Chap. 9, Vol. 1)



observation of α decay provided the first hint of the existence of a new region of shell stabilization (Münzenberg et al. 1989). It became the cornerstone for paving the way to the creation of the heavier transactinides. The production cross section for ^{265}Hs , measured in a later experiment (Hofmann et al. 1995a) was found to be one order of magnitude larger than that measured in the first experiment. Both unexpected results opened the door to the synthesis of elements $Z = 110$, 111, and 112. The hassium isotopes with masses 264 and 265 were produced in cold fusion reactions. The isotope with mass 263 has been observed recently (Kaji et al. 2009; Dragojevic et al. 2009). The isotopes 265, 266, and 267 appear in the decay chains of

darmstadtium isotopes. The isotopes with mass 269 (Türler et al. 2003), 270, and 271 (Dvorak et al. 2006, 2008) were produced in hot fusion reactions. The most neutron-rich isotope with mass 275 has been observed in the decay chain of $^{283}_{112}$ produced with ^{48}Ca (Oganessian et al. 2004a, b). All eight hassium isotopes known today are α emitters including the doubly even ^{264}Hs for which a fission branch is reported. The half-lives of the hassium isotopes span more than four orders of magnitude from 0.26 ms for ^{264}Hs to 9.3 s for ^{269}Hs .

Meitnerium (Mt), $Z = 109$, was discovered in the reaction $^{209}\text{Bi}(^{58}\text{Fe}, n)^{266}\text{Mt}$ by the observation of the decay chain (► Fig. 19.9) of one single atom (Münzenberg et al. 1982a). The assignment, based on statistical arguments (Münzenberg et al. 1984a), was confirmed in two independent experiments (Münzenberg et al. 1988; Hofmann et al. 1997). At present, six meitnerium isotopes are known. The isotope with mass 266 and a half-life of 1.7 ms was produced directly, the isotope with mass 268 and a half-life of 70 ms was found in the decay chain of ^{272}Rg (Hofmann et al. 1995a), and the isotope with mass 270 was observed in the decay chain of $^{278}_{113}$ (Morita et al. 2004d, 2007b). The three most neutron-rich isotopes with masses 274, 275, and 276 were observed as daughter nuclei in the decay chains of $^{282}_{113}$ (Oganessian et al. 2007), $^{287}_{115}$ (Oganessian et al. 2004d, 2005), and $^{288}_{115}$ (Dmitriev et al. 2005; Oganessian et al. 2005). All known isotopes are α -emitters. Their half-lives range from 1.7 ms to 0.7 s.

Darmstadtium (Ds), $Z = 110$, was discovered in 1994 (Hofmann et al. 1995a). The isotope with mass 269 was observed in irradiations of ^{208}Pb with ^{62}Ni . Four α chains were measured. One of these was retracted later (Hofmann et al. 2002). For the elements up to $Z = 110$ the most neutron-rich beams available in nature were used: ^{50}Ti , ^{54}Cr , ^{58}Fe , and ^{62}Ni each separated by one α . Consequently it was possible to build up the “reversed” decay chains toward the heavier elements step by step. For nickel and heavier projectiles more neutron-rich isotopes of these elements exist. By replacing the projectile ^{62}Ni by ^{64}Ni the production cross section is enhanced by a factor of five (Hofmann et al. 1995b). This led to the synthesis of ^{271}Ds paving the way for the discovery of roentgenium. The production of element 110 was confirmed by the RIKEN (Japan) group (Morita et al. 2004a, b). The isotope with mass 270, the heaviest even–even nucleus identified with the correlation method, was produced by the irradiation of ^{207}Pb with ^{64}Ni (Hofmann et al. 2001). Alpha decay sequences assigned to the isotope with mass 273 have been observed in the bombardment of ^{244}Pu with ^{34}S (Lazarev et al. 1996). The isotopes with masses 279 and 281 undergo fission. They are the endpoints of the α decay chains from $^{291}_{116}$ (Oganessian et al. 2004c; Oganessian 2007) and $^{293}_{116}$ (Oganessian et al. 2004a, b) respectively. Altogether six isotopes of darmstadtium have been reported with half-lives ranging from 0.1 ms to 17 s. They are mostly α emitters except for the two most neutron-rich ones, which fission just at the boundary of the shell-stabilized region around $N = 169$ and $N = 171$ (► Fig. 19.1). For more detailed discovery profiles and priorities of discovery, see the corresponding IUPAC report (Karol et al. 2001).

Because of the strong enhancement of the production cross section for element 110 with the ^{64}Ni beam, roentgenium (Rg), $Z = 111$, was produced in the same series of experiments by proceeding from the ^{208}Pb target to ^{209}Bi (Hofmann et al. 1995b). Three decay chains of ^{272}Rg were measured. The Q_{α} value of this isotope is 10.99 MeV, the half-life is 3.8 ms, and the production cross section is 2.9 pb. This result was confirmed in later experiments (Hofmann et al. 2002; Morita et al. 2004c). The isotope ^{274}Rg has been observed in the decay chain of $^{278}_{113}$ (Morita et al. 2004d, 2007b). The three most neutron-rich isotopes with masses 278, 288, and 289 appear in the decay chains from elements 113 (Oganessian et al. 2007) and 115 (Oganessian et al. 2004d, 2005; Dmitriev et al. 2005). The half-lives of the five observed

isotopes span from 3.8 ms to 3.6 s. For more details of the history of discovery see the corresponding IUPAC report (Karol et al. 2003).

The heaviest element accepted by IUPAC is copernicium (Cn), $Z = 112$ (Barber et al. 2009). It has been discovered in the reaction $^{208}\text{Pb}(^{70}\text{Zn}, n)^{277}112$ (Hofmann et al. 1996). The first atom of $^{277}112$ that was observed, decays over six generations of alphas to ^{253}Fm . The last two generations were known and provided the anchor for its identification. The second chain reported in this paper was retracted after a reanalysis of the original data (Hofmann et al. 2002). The Q_α value is 11.43 MeV, the half-life 0.69 ms, and the production cross section is 0.5 pb corresponding to the production rate of one single atom per 6 weeks. Later experiments (Hofmann et al. 2002; Morita 2005; Morita et al. 2007a) confirmed the discovery chain. The isotopes $^{282}112$ and $^{283}112$ have been observed in irradiations of ^{238}U with ^{48}Ca in 3n and 4n reactions in a series of experiments done at Dubna using ^{48}Ca beams (Oganessian et al. 2007; Oganessian 2007). This new concept will be discussed in more detail with element 114, the first element discovered with this method. The isotope $^{283}112$ was produced in the reaction $^{238}\text{U}(^{48}\text{Ca}, 3n)$ as the first of this new series (Oganessian et al. 1999a). This was followed by more experiments using the same reaction (Oganessian et al. 2004a, b). The properties measured in the second set of experiments were confirmed at Gesellschaft für Schwerionenforschung (GSI) using the Separator for Heavy Ion reaction Products (SHIP) (Hofmann et al. 2007). The heavier isotopes with masses 284 and 285 appear in decay chains from heavier elements and are reviewed in (Oganessian et al. 2007; Oganessian 2007). The five isotopes cover a half-life ranging from 0.7 ms to 29 s. The two even-even isotopes with masses 282 and 284 undergo spontaneous fission, while for the isotope with mass 283 a fission branch is reported. A detailed discovery profile and the priorities for assignment are given in a recent IUPAC report (Barber et al. 2009).

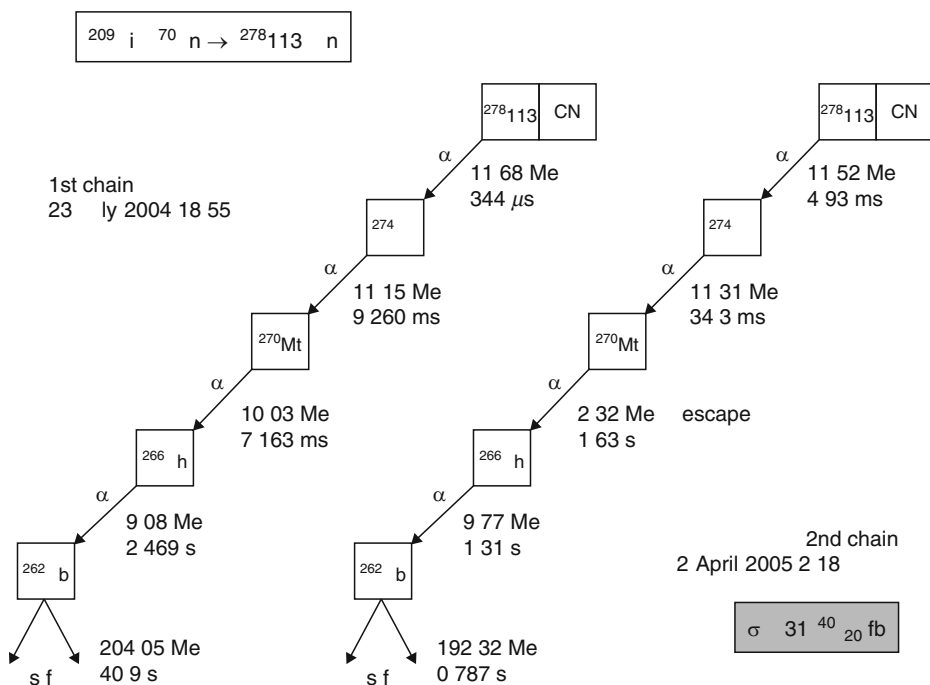
Element 113 has been discovered at RIKEN in the reaction $^{209}\text{Bi}(^{70}\text{Zn}, n)^{278}113$ (Morita et al. 2004d). In an irradiation time of 79 days with a projectile dose of 1.7×10^{19} the α -decay sequence of one atom had been observed. In a second experiment (Morita et al. 2007b) one more chain was found (► Fig. 19.4). The production cross section is 30 fb, the smallest cross section ever measured for the production of a heavy element. The Q_α value is 11.68 MeV and the half-life, 0.24 ms (Morita 2008). The isotope $^{282}113$ has been produced in the reaction $^{237}\text{Np}(^{48}\text{Ca}, 3n)$ (Oganessian et al. 2007), while the isotopes with masses 283 and 284 appear in the decay chains of element 115. The half-lives of the four isotopes range from 0.24 ms to 0.48 s. Element 113 is presently at the experimental limit for heavy-element production by cold fusion, because of the required beam time. A simple extrapolation would require a beam time of the order of 1 year for one atom of element 114. To go beyond, new concepts are needed.

While noting the success of cold fusion to create elements 107 to 113 with the doubly magic ^{208}Pb and its neighbor ^{209}Bi as targets, it is tempting to use hot fusion and another strongly bound doubly magic nucleus ^{48}Ca with actinide targets for the production of the heavier new elements in a more asymmetric target-projectile combination. A first attempt at the production of element 116 by the irradiation of ^{248}Cm with ^{48}Ca was without success (Armbruster et al. 1985). The cross section limit for this experiment was 0.3 nb. From the experimental data available as of 2009, it is evident that beyond element 110 cross sections drop down to the picobarn (pb) region.

In 1999, the Dubna group started a series of experiments with the new concept of using ^{48}Ca beams for the synthesis of unknown elements beyond $Z = 113$ (Oganessian 1996). They upgraded their equipment to enhance the sensitivity by a factor 1,000 over the 1985 experiment and started their series with an attempt to produce the new element 114 with the irradiation of

Fig. 19.4

Two decay chains of $^{278}_{113}$ (Morita 2008). Note that the length of the α decay chains increases for the heavier elements in the region of α emitters generated by the subshell closure at $Z = 108$

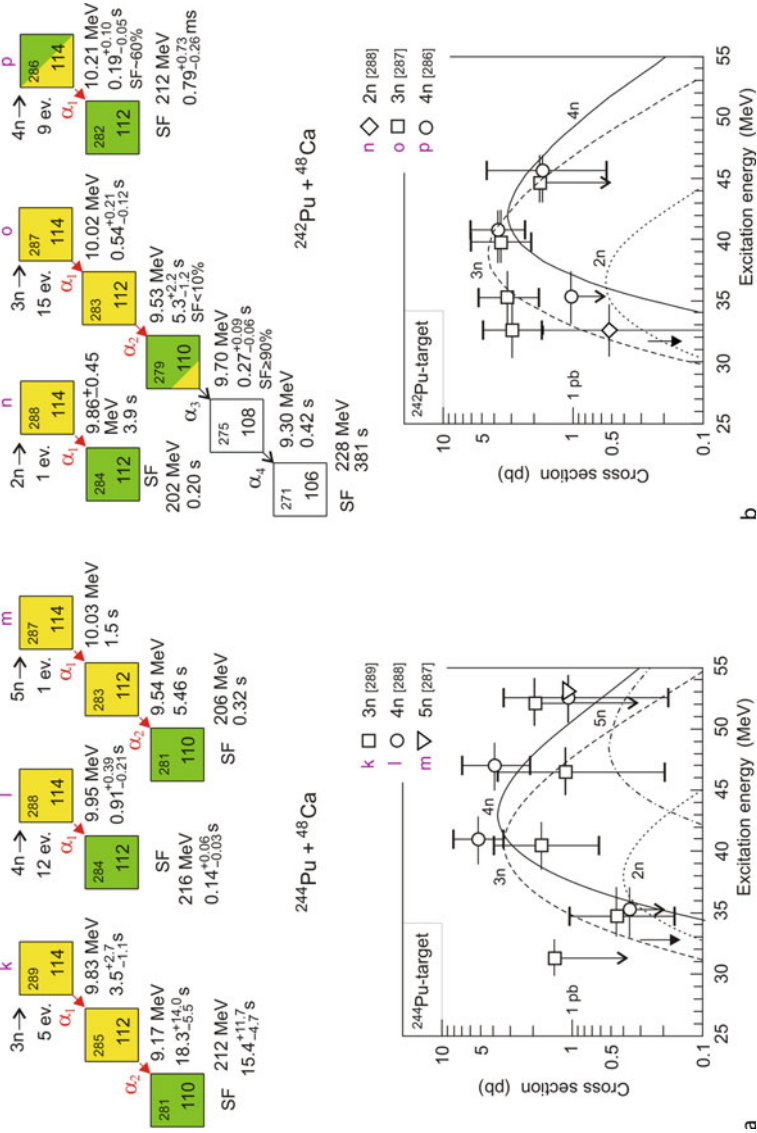


^{244}Pu with ^{48}Ca (Oganessian et al. 1999b) as the first in a series of Superheavy Element synthesis. The isotopes created in irradiations of actinide target with ^{48}Ca beams are on an average richer by three to four neutrons over those produced in cold fusion reactions. Their decay chains traverse the shell-stabilized region of deformed nuclei centered at $Z = 108$ and $N = 162$, and terminate by fission before they enter the region of known transuranium elements (Fig. 19.1). Since the chains end in an unknown region, the parent–daughter correlation method cannot be applied. Therefore, the assignment of new elements and isotopes is based on the assumption that the charge Z of the new element is the sum of the charges Z_t of the target and Z_p of the projectile. This assumption is justified by the observation that charged-particle emission is suppressed in heavy-element synthesis because of the high Coulomb barrier of the heavy compound nuclei. The mass assignment is based on the measurement of excitation functions and comparison to theoretical predictions (Zagrebaev, 2001). Generally, the assignments are supported by Q_α systematics. In the early experiments with ^{48}Ca where the number of evaporated neutrons was simply estimated from the excitation energy of the compound nucleus, the mass number had not been correctly assigned in some cases (Gupta and Burrows 2005).


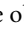
The strategy of the Dubna group is to build up a region of nuclides in an internally consistent manner where descendants appearing in decay chains are, in addition, directly synthesized by the complete fusion of heavy ions including using the technique of cross bombardments (Fig. 19.5). Thus, if one nuclide in this region is safely identified, the whole island is fixed. This process explains the importance of the recent experiment (Hofmann

Fig. 19.5

Upper panel: Decay chains from the irradiations of (a) ^{244}Pu (labeled k, l, m) (b) ^{242}Pu (n, o, p). The lifetimes and fission energies are averaged from all observed events. The numbers of events are indicated (e.g., “5 ev” for $^{289}\text{114}$). Note that the chains l and n as well as m and o belong to the same isotopes. Lower panel: The corresponding excitation functions (Oganessian 2007)



et al. 2007) using SHIP at GSI to confirm the properties and the production cross section of ^{283}Cn . SHIP is a kinematic separator and only sensitive to nuclei produced in complete fusion. Thus, if ^{283}Cn had been produced in another type of reaction, it would not have been observed.

In the first experiment to create element 114 in an irradiation of ^{244}Pu with ^{48}Ca one single decay chain terminated by spontaneous fission, after a sequence of three α decays with lifetimes up to 16.5 min, was observed and proposed as a candidate for $^{289}114$. This nuclide was formed after the evaporation of three neutrons from the compound nucleus $^{292}114$ (Oganessian et al. 1999b). This decay mode has not been confirmed yet. New results (Oganessian et al. 2004c) indicate much shorter lifetimes of the order of seconds with the chains terminating by fission at ^{281}Ds (Oganessian et al. 2007; Oganessian 2007) as indicated in  Fig. 19.1. Four isotopes with masses 286 to 289 and half-lives from 0.13 to 2.6 s have been reported. They were produced in irradiations of ^{244}Pu and ^{242}Pu with ^{48}Ca . All their decay chains end by fission. The even–even chains end at copernicium, the even–odd ones at darmstadtium. The isotopes with masses 288 and 287 (Oganessian et al. 2004a, c) were observed with both targets ( Fig. 19.5). They were also observed in the decay chains from isotopes of element 116, which gives a consistent picture. Nevertheless, the early assignments (e.g., Oganessian et al. 1999a, b) were disputed and many attempts were made to confirm results.

Chemical investigations are being pursued actively. An experiment to investigate the chemical properties of copernicium began with an attempt at producing element 114. Recently, in an irradiation of ^{242}Pu with ^{48}Ca , two decay chains were observed after chemical separation where the daughters were attributed to ^{283}Cn following the (unobserved) decay of $^{287}114$ (Eichler et al. 2007). Although the measured decay properties support the later Dubna assignments (Oganessian et al. 2004a), this experiment in itself cannot be considered as a proof of a Z assignment as the chemical properties of copernicium remain the subject matter of discussion.

Two isotopes of element 115 with masses 287 and 288 have been reported (Oganessian et al. 2004d, 2005; Dmitriev et al. 2005). Both have been produced in irradiations of ^{243}Am . They are α emitters with half-lives of 32 and 87 ms respectively.

In the first successful experiment on the synthesis of element 116 one single α chain was observed (Oganessian et al. 2001) and initially attributed to the isotope with mass 292, produced in the reaction $^{284}\text{Cm}(^{48}\text{Ca}, 4n)$. Subsequently, the parent was reassigned to $^{293}116$ and four new events attributed to the isotope with mass 292 were reported using the same reaction at a higher energy (Oganessian et al. 2004a, b). Three more isotopes have been measured for element 116. The isotope $^{293}116$ was produced in the $3n$ channel (Oganessian et al. 2004a, b) while the isotopes with masses 290 (Oganessian et al. 2004c, 2006) and 291 (Oganessian et al. 2004c) have been observed in irradiations of ^{245}Cm and $^{290}116$ also appears in the decay chain of $^{294}118$. All four of them are α emitters with half-lives ranging from 7 to 61 ms. The production cross section for $^{292}116$ is 3.3 pb, a factor of 100 below the cross section limit of the experiment from 1985 (Armbruster et al. 1985).

Element 117 has not been created yet. Experiments to synthesize this element are still under preparation. It will be produced in irradiations of ^{249}Bk , which is a difficult target because of its short half-life of 320 days. (In December 2009, the experiment on the synthesis of element 117 was in progress at Dubna.)

Element 118 is the heaviest one reported at present. The isotope $^{294}118$ was observed in the reaction $^{249}\text{Cf}(^{48}\text{Ca}, 3n)$. Three chains were measured in total (Oganessian et al. 2004a, 2006). The half-life is 0.9 ms and the α decay energy, 11.65 MeV. The α sequences are quite short,

ending after three generations by the spontaneous fission of ^{282}Cn . With the synthesis of element 118, the reactions using the ^{48}Ca beam are exhausted. There are no targets available with $Z > 98$.

To go beyond element 118, new production techniques are being explored. The first but unsuccessful attempts to synthesize element 120 have been reported recently (Hofmann et al. 2008; Oganessian et al. 2009). New concepts to go beyond element 118 are being discussed (e.g., Zagrebaev and Greiner 2008).

19.2.1 Priorities and Naming

The decision on the priority of the discovery of a new chemical element is the responsibility of the IUPAC. The detailed definition of the criteria for the discovery of a new element was prepared by the Transfermium Working Group (Barber et al. 1992). [Table 19.2](#) displays the elements for which the priority of discovery has been assigned. The IUPAC accepted the following names and symbols for the transactinides (Sargeson 1997). The laboratories associated with their discovery as accepted by IUPAC are given in parentheses (Barber et al. 1992, 2009; Karol et al. 2001, 2003).

19.3 Experimental Methods

19.3.1 Accelerators and Ion Sources

The development of heavy-ion accelerators providing intense beams, even for isotopes appearing with small abundances in nature, and the availability of fast and sensitive detection systems paved the way to the synthesis of the transactinides. The projectile energy for the production of heavy elements is close to the Coulomb barrier, i.e., around 5 A MeV (A is

Table 19.2

Priorities of discovery and associated laboratories as accepted by International Union of Pure and Applied Chemistry (IUPAC)

Element 104	Rutherfordium (Rf) honoring Sir Ernest Rutherford (LBL Berkeley, JINR Dubna, shared).
Element 105	Dubnium (Db) named after Dubna, its place of discovery (LBL Berkeley, JINR Dubna, shared).
Element 106	Seaborgium (Sg) honoring Glenn T. Seaborg (LBL Berkeley).
Element 107	Bohrium (Bh) honoring Niels Bohr (GSI Darmstadt).
Element 108	Hassium (Hs) named after Hessen, Latin: Hassia, its state of discovery (GSI Darmstadt with contribution from Dubna).
Element 109	Meitnerium (Mt) honoring Lise Meitner (GSI Darmstadt).
Element 110	Darmstadtium (Ds) named after Darmstadt, its town of discovery (GSI Darmstadt).
Element 111	Roentgenium (Rg) honoring Wilhelm Conrad Röntgen (GSI Darmstadt).
Element 112	Copernicium (Cn) honoring Nicolaus Copernicus (GSI Darmstadt).

the mass number of the projectile). Accelerators used for heavy-element production are large cyclotrons such as the U400 at Dubna or linear accelerators such as the UNILAC at GSI or the RILAC facility at RIKEN.

The largest production yields for heavy elements are obtained with the most neutron-rich projectiles available in nature. As most of the neutron-rich isotopes used for SHE production occur with low abundances, the ion sources have to be operated with enriched material to provide intense beams. (See ► Chap. 51 in Vol. 5 on isotope separation techniques.) For the production of the elements hassium to copernicium with lead or bismuth targets, beams of the isotopes ^{58}Fe (0.3% natural abundance), ^{64}Ni (0.9% natural abundance), or ^{70}Zn (0.6% natural abundance) were used. For the Dubna series of experiments ^{48}Ca is used, which has a natural abundance of 0.2%. At present, all heavy-element laboratories use electron cyclotron resonance (ECR) ion sources, which have a material consumption of about 0.5 mg/h for ion currents as high as one particle- μA (corresponding to 1 μA of single-charged ions). Because of the excellent long-term stability of this ion source, experiments of several weeks and even months of duration are possible. To further explore the region of superheavy nuclei around $Z = 114$ and beyond, ion sources and accelerators for intense beams of stable isotopes with intensities up to 20 particle- μA , equivalent to 10^{14} ions/s, are under development (U. Ratzinger 2009, private communication; Yu. Ts. Oganessian 2009, private communication).

The small production yields for the heaviest elements need isotopically pure targets to avoid background from contaminants with large cross sections, which is a problem specific to actinide targets that sometimes have lead contaminations. High beam intensities need specialized targets, especially when using lead or bismuth, which melt easily. The optimum target thickness for recoil separators is of the order of 0.5 mg/cm^2 to preserve the reaction kinematics. Thin targets have practically no thermal conduction. Therefore, the target temperature is determined by radiative cooling. Target problems increase for heavy beams, as the energy loss of the beam (i.e., the heat deposition) increases with Z_p^2 (see ► Eq. (8.1) in Chap. 8, Vol. 1). For beam currents in excess of 10^{12} projectiles/s, rotating wheels have been developed to obtain a large effective irradiated surface and to aid radiative cooling. Targets in gas-filled separators profit from cooling of the gas. The technology for the development of new targets intended for high-intensity beams include chemical compounds with high melting points such as sulfides, oxides, or fluorides and efficient gas cooling.

19.3.2 Separation In-Flight

The key to the discovery of the short-lived nuclides at the very limits of nuclear stability is separation in-flight. It is fast, sensitive, and independent of the chemical properties of the species to be separated. The separation time is determined by the flight time through the separator, which is of the order of microseconds. Presently kinematic separators such as velocity- or energy filters and gas-filled separators are used successfully (see Münzenberg 1997; Oganessian 2007; Düllmann 2008, and conference volume Emis-14 (2002) for a review of recent separator developments). Separation, sensitive to the specific kinematic properties of the desired reaction products is most efficient for a clean SHE selection as products from other types of reactions are suppressed. The key to kinematic separation of products from complete fusion is based on the principle that since only nuclei formed by complete fusion, recoil from the target with the full momentum transferred from the projectile, they are the only recoils moving with center-of-mass velocity. Their speed as determined from momentum conservation is

$$v_c = \frac{v_p M_p}{M_c} \quad (19.1)$$

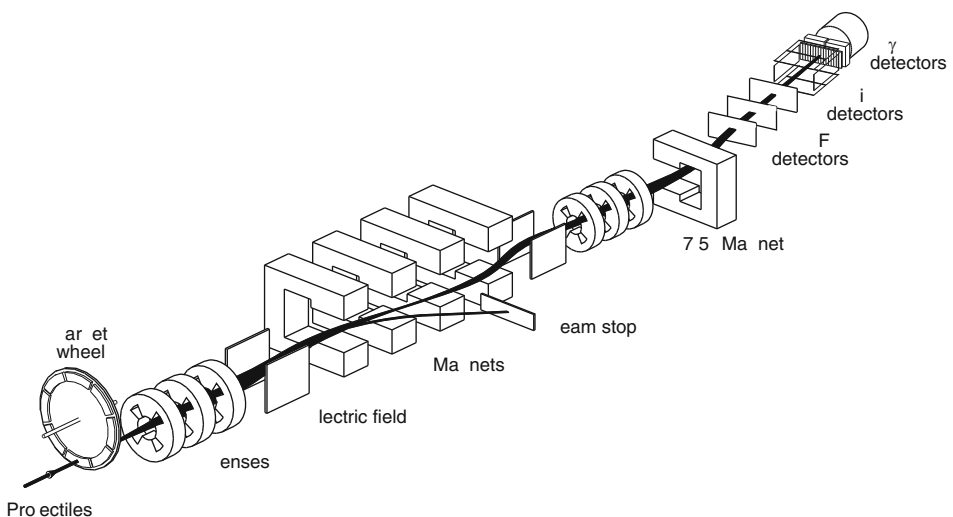
with v_p denoting the speed of the projectile. M_p and M_c are the masses of the projectile and the compound nucleus, respectively. Therefore, velocity filters are the ideal separators for fusion products (Münzenberg 1997).

The velocity filter SHIP (Separator for Heavy Ion reaction Products, [Fig. 19.6](#)) at GSI Darmstadt (Münzenberg 1974; Münzenberg et al. 1979) has been developed for sensitivities down to picobarns. The intense projectile beam is focused onto lead or bismuth targets (which have low melting points) mounted on a rotating wheel. The reaction products recoil almost unretarded from the thin target into SHIP with its combination of two velocity filters with separated electrostatic and magnetic deflection fields. Here, magnetic quadrupole lenses arranged in a triplet at the entrance collect the recoils from nearly the full solid angle. At the symmetry plane, the projectile beam is separated from the recoils. A second quadrupole triplet focuses the separated recoils onto the detector system (see the [Sect. 19.3.3](#) for more detail). Recently a small dipole magnet has been added to further improve the suppression of scattered projectiles and to move the detector out of the zero degree direction (Hofmann et al. 1995a).

The separation characteristic of SHIP is shown in [Fig. 19.7](#). The upper panel displays the reaction $^{175}\text{Lu}(^{40}\text{Ar}, 5n)$, which has its maximum within the velocity window of SHIP while the lower panel shows the reaction $^{175}\text{Lu}(^{40}\text{Ar}, \alpha 4n)$, which has a minimum in this velocity window. The recoil from the α particles emitted from the compound nucleus is large enough to drive the remaining residue out of the velocity window. This results in a strong suppression of α -channels and all channels, which involve the emission of a fragment like an α particle or a heavier product in the exit channel (Faust et al. 1979).

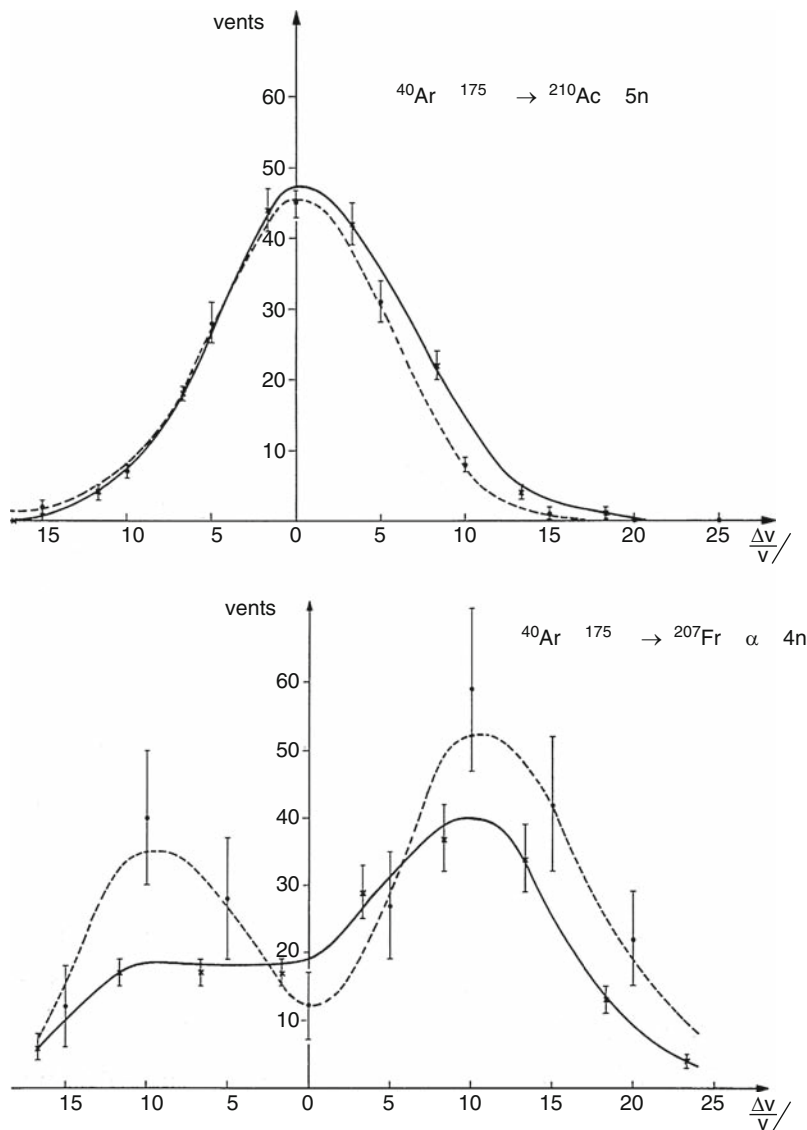
■ **Fig. 19.6**

Schematic view of the velocity filter Separator for Heavy Ion reaction Products (SHIP) in its present configuration with target wheel and detector array (Hofmann and Münzenberg 2000)



■ Fig. 19.7

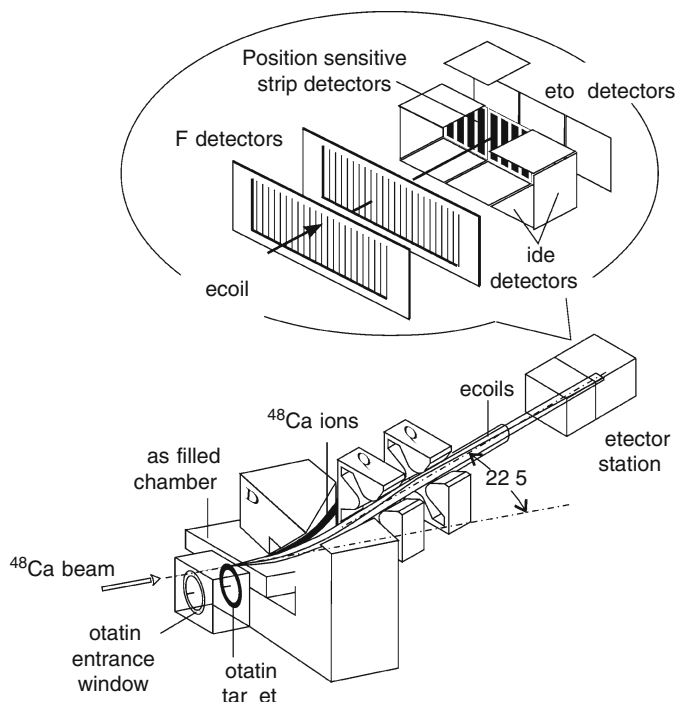
Separation characteristic of SHIP. *Upper panel: 5n channel; lower panel: α , 4n channel. Line and crosses: data; dashed line and dots: Monte-Carlo calculation (Faust et al. 1979). The velocity window of SHIP is indicated in gray*



The experiments at Dubna (Russia) and RIKEN (Japan), and LBNL Berkeley (USA) have been carried out with gas-filled separators. Gas-filled separators (Münzenberg 1997; Oganessian 2007) are filled with helium (GSI, RIKEN, LBNL) or hydrogen (Dubna) and maintained at a pressure of typically 0.5 mbar. A schematic view is given in ► Fig. 19.8. Heavy nuclei recoil from the rotating target into the dipole magnet where they are separated

■ Fig. 19.8

Layout of the Dubna gas-filled recoil separator (DGFRS) with target wheel, dipole magnet, and detector station (Oganessian 2007). A schematic view of the detector system is displayed in the upper part of the figure



from the projectile beam. The separated nuclei are focused by a magnetic quadrupole doublet onto the detector system, displayed in the upper part of the figure. In a gaseous medium, fast-moving ions approach an equilibrium charge expressed usually by the Bohr formula

$$q = \frac{v}{v_0} Z^{1/3} \quad (19.2)$$

where v_0 is the Bohr velocity.

Since the deflection in a magnetic field, $B\rho$, is determined by the momentum to ionic charge ratio $B\rho = mv/q$, the magnetic rigidity of a ion traveling in the filling gas (Oganessian et al. 2007) is


$$B\rho = \frac{0.027A}{Z^{1/3}} \quad (19.3)$$


As A/Z is roughly constant, the separation is proportional to $A^{2/3}$. The deflection of the ions passing the gas-filled separator is independent of velocity and the ionic charge state. Therefore, transmission is high and provides a great advantage for reactions with light projectiles where the relative velocity spread and charge distribution of the ions emerging from the solid target are broad. However, due to scattering in the gas the beam spot is large and the separation poor. Hence, although the resolution is sufficient to achieve an efficient suppression of the projectile

beam, it is not sufficient to discriminate between the SHE created by complete fusion and the products of incomplete fusion or transfer products. The separation can only be achieved with a kinematic separator such as SHIP. Using the combination of both separation methods for the same reaction, a cross section measured with a gas-filled separator when compared to the cross section measured at SHIP for instance, provides a clear proof of complete fusion with the emission of only neutrons or protons. Proton emission cannot be excluded, though the recoil from an emitted proton is too small to drive the recoil out of the velocity window.

19.3.3 Working with Single Atoms

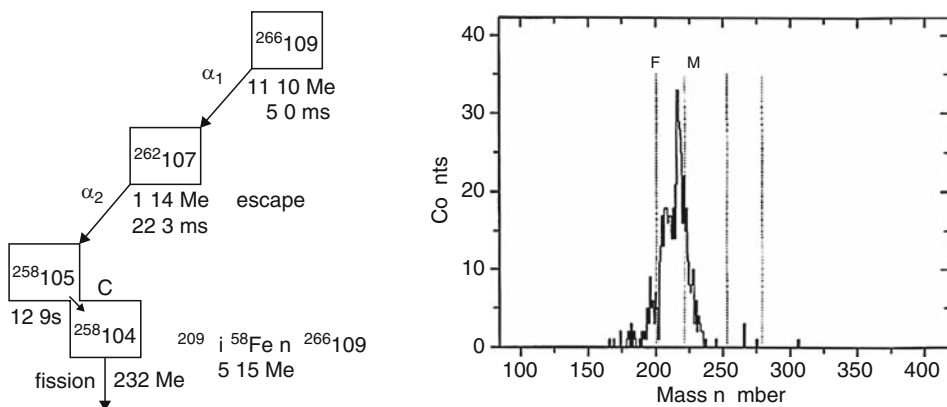
All transactinide elements are identified by their decay properties. An unambiguous method is the parent–daughter α – α correlation. It relies on the identification of an unknown species by its known daughter decays. This method, which has been originally developed in connection with the helium jet gas transport system (Ghiorso et al. 1974), allows extending the nuclear table safely in a stepwise manner. At SHIP the parent–daughter correlation technique has been developed to the highest possible sensitivity: the identification of new isotopes or even elements by single-atom decay chains. The implantation of the energetic recoils into a position-sensitive silicon detector allows the observation of a detailed decay history for each single nucleus over hours or even days, *in situ*. This is possible as all the decay events are localized once the parent atom is stuck to a well-defined position in the detector (Hofmann et al. 1984). The decays originating from an individual mother nucleus are observed at that very position of implantation and can be traced over all generations until the chain is terminated by long-lived daughters, spontaneous fission, or β decay the last of which is not visible in the silicon stop detectors.

The detector arrangement as developed at SHIP (Hofmann and Münzenberg 2000) is similar to all recoil separators used at present for SHE research. As an example see the upper part of  Fig. 19.8. The silicon box with the position-sensitive implantation detector at the back allows for the efficient detection of α decay and fission. The side detectors detect α particles and fission fragments escaping from the implantation detector into the backward hemisphere. This is possible as the heavy nuclei are stopped close to the surface of the silicon chip. With this Si-detector box open in front, it is possible to achieve near 4π geometry (Hofmann et al. 1995a). Thin carbon foil secondary-electron detectors allow for time-of-flight (TOF) measurements, which give approximate information on the recoil mass in combination with the energy signal from the implantation of the SHE into the silicon detector. The TOF detectors simultaneously work in anticoincidence to the implantation array to discriminate between beam particles and decays. In recent experiments the projectile beam is switched off after the implantation of a possible SHE has been detected. This makes it possible to obtain clean decay sequences not contaminated by scattered particles of low energy. Optionally, the system may be complemented by X- and γ -ray detectors.

Meitnerium is an example of the identification of a new element by the decay of only one single atom (Münzenberg et al. 1982, 1984a).  Figure 19.9 displays the discovery chain together with the mass spectrum from the measurement of TOF and implantation energy, the resolution of which is limited by the large pulse-height defect of the slow, large Z -ions implanted into the Si detector. To check the reliability of the experimental results, careful investigations of background, Poisson statistics of the decay sequences, and background and consistency tests of the observed decay properties with theoretical predictions are necessary.

■ Fig. 19.9

The discovery chain of meitnerium (left panel) with the mass spectrum (right panel, Münzenberg et al. 1982)



The general problem is however, that superheavy nuclei are the very definition of “terra incognita” being as they are at the frontiers of the chart of nuclides with unknown properties. Therefore, all such evidence is of limited value for the identification of a new element and while necessary, it is not sufficient to make a conclusive determination according to the rules of IUPAC as elaborated by the transfermium working group (Barber et al. 1992).

19.3.4 Statistics of Single-Atom Chains

The identification of a new element from a correlated single-atom chain requires statistical analysis done in two steps (Münzenberg et al. 1984a). In the first step, the *statistical significance* of the correlation in each decay step must be established. It is determined by the observed time interval t , the background rate r , and the number of leading signals n , observed during the entire experiment. The leading signal is the most relevant event in the sequence, e.g., the decay of the mother nucleus. The error probability

$$p = nrt \quad (19.4)$$

should be below 10^{-3} or 3σ .

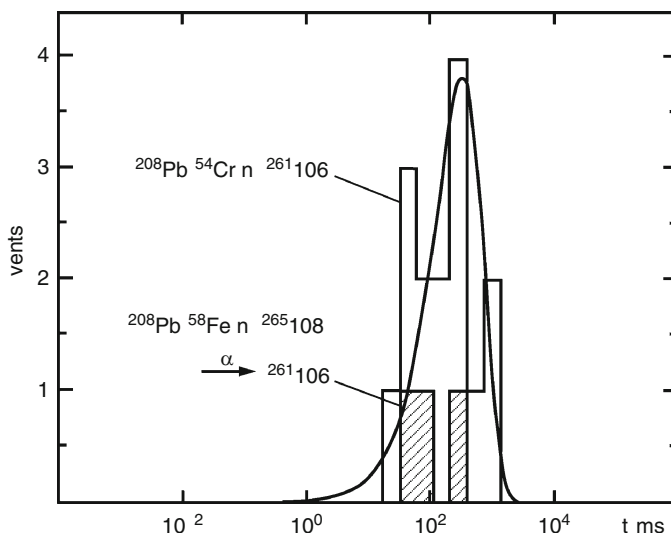
The second step is the *assignment* of each decay step to the known daughter nuclides. For full-energy α decays, the observed decay energy including calibration precision and detector resolution is compared to the known decay energy of the corresponding daughter nuclides. The measured time interval t permits a comparison with the known mean life (see remark (#31) in ► Chap. 9, Vol. 1) (as obtained from the half-life $\tau = 1/\lambda = T_{1/2}/\ln 2$) using the exponential probability density function

$$f(t) = \lambda e^{-\lambda t} = \frac{e^{-t/\tau}}{\tau} \quad (19.5)$$

With this method, all possible assignments can be checked to select the most probable one. It also allows for a compatibility test of measured time intervals assigned to the same transition

■ Fig. 19.10

Decay curve for $^{261}\text{106}$ in logarithmic bins. The histograms show the daughter decays from $^{265}\text{108}$ (hatched) in comparison to the decays from the directly produced $^{261}\text{106}$ (Münzenberg 1988)



to check, for instance, data from different experiments. The half-life estimate is made by the maximum likelihood method. The error is given by Poisson Statistics (see ▶ Sect. 9.4.3 in Chap. 9, Vol. 1) (Schmidt et al. 1984). To test the random distribution of the measured time interval distributions it is convenient to transform the decay curve into a function peaked at the average lifetime (mean life, τ) by a logarithmic binning of the measured time intervals (Schmidt et al. 1984). ▶ Figure 19.10 shows this transformation for the daughter decays of $^{261}\text{106}$ observed in the $^{265}\text{108}$ decay chains in comparison to the directly produced $^{261}\text{106}$. The curve is asymmetric and peaks at the average lifetime. (See also ▶ remark (#33) in Chap. 9, Vol. 1.) This probability distribution also holds for one single decay for which the error amounts to about one order of magnitude for a two σ confidence level (Münzenberg 1988).

19.4 Nuclear Structure of the Transactinide Nuclides

19.4.1 Superheavy Elements: The Limits of Stability

The existence of heavy and superheavy elements is limited by their stability against fission, which finally terminates the chart of nuclides and limits the number of the chemical elements. In the macroscopic description, the limit of stability for heavy nuclei beyond uranium is determined by the balance between the cohesive nuclear force and the disruptive Coulomb force. The stability against fission is described by the fissility parameter x , which is the ratio between Coulomb energy and surface energy of the charged nuclear droplet, normalized to the critical fissility beyond which nuclei promptly disintegrate (Myers and Swiatecki 1966)

(See also ► Sect. 4.3.3 in Chap. 4, Vol. 1, discussing in detail the (un-normalized) fissility parameter Z^2/A):

$$x = \frac{Z^2/A}{(Z^2/A)_{\text{crit}}} \quad (19.6)$$

with

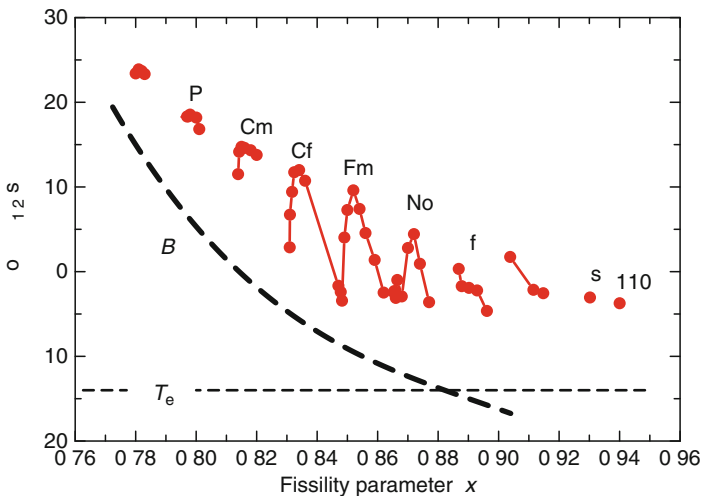
$$(Z^2/A)_{\text{crit}} = 50.883 \left[1 - 1.7826 \left(\frac{N-Z}{A} \right)^2 \right]. \quad (19.7)$$

In ► Fig. 19.11 the partial fission half-lives of the doubly even isotopes of uranium and beyond are plotted on a logarithmic time scale versus the fissility parameter. In accordance with the expectation from the liquid drop model the dashed line labeled B_{LD} , describing the fission half-life calculated with only the liquid drop barrier B_{LD} , crosses the T_e line at nobelium. The time T_e is needed for the formation of the electron shell of the atom, the lower time limit considered beyond which a chemical element cannot be formed (Barber et al. 1992). The experimental half-lives follow this general trend. They decrease from uranium to nobelium over more than 20 orders of magnitude, from the age of the solar system down to fractions of seconds. The structure of the isotopic chains of elements from curium to nobelium is caused by a subshell closure at $N = 152$.

A change in the half-life systematics occurs at rutherfordium. Fission half-lives become independent of the fissility parameter and stay almost constant. A comparison of the data to the calculated liquid-drop half-lives shows an enhancement of the fission half-lives by about 15 orders of magnitude. This stabilization is caused by a new shell at hassium.

■ Fig. 19.11

Partial fission half-lives of the even-even isotopes of the transuranium elements (dots) compared to the fission half-lives as calculated from a macroscopic model. The dashed lines and the labels are explained in the text after ► Eq. (19.7)



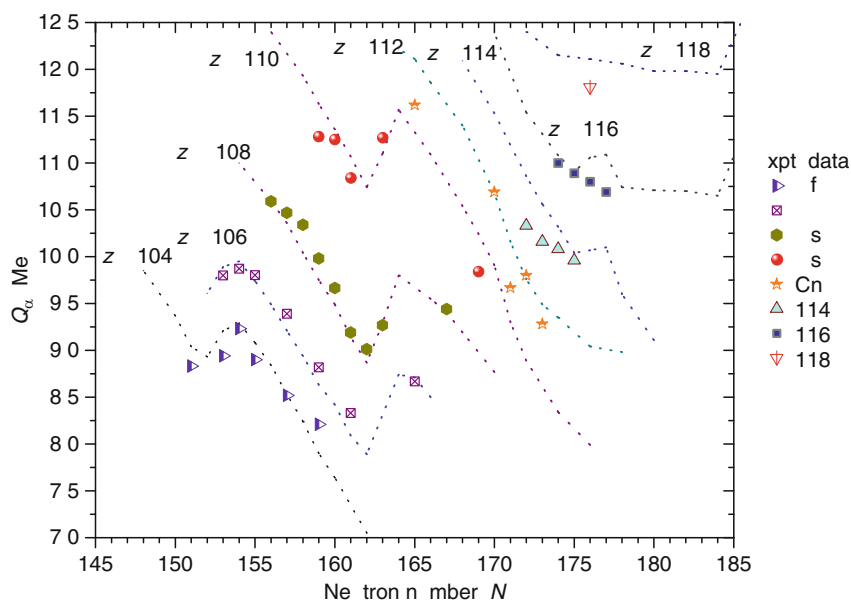
19.4.2 Alpha-Decay Properties and the New Shell Region Around Hassium

The stabilization against fission in the transactinide region makes α decay the dominating decay mode and enables us to extract basic information on the structure of the elements at the top of the chart of nuclei. Dealing with only a few atoms this information is rather scarce and needs support from theory to get some more detailed understanding of the underlying physics. Obviously the decay mode, half-life, and Q_α are the most important pieces of information about the stability and the physical nature of these nuclides. Naturally, structure information is available in greater detail for the lighter transactinide nuclei where fine structure in the α -decay spectra (Hessberger et al. 1997, 2009) and γ transitions have been measured. This information then can be used to help predict the structure of heavier nuclei by investigating their isotones or using appropriate theoretical calculations. Shells in the heaviest nuclei are large and they carry high angular momenta. The level densities are high. As a consequence, high-spin and low-spin states are close together and isomers are observed. Internal conversion has been observed in the light transactinides where statistics for the decay spectra are sufficiently high. As the mother nuclei are implanted in the Si-detector, summing with conversion electrons shifts the measured α -decay energy. An example is the first 2^+ state in ^{256}Rf . An α transition into the 2^+ level is strongly influenced by energy summing with conversion electrons (Hessberger et al. 2009) where the α lines are shifted or show tails.

The Q_α systematics for even- Z transuranium elements (including both even- N and odd- N isotopes) is displayed in [Fig. 19.12](#). The experimental data are compared to

Fig. 19.12

Q_α systematics for the even Z transuranium elements. *Dotted line: theory (Muntian et al. 2003a, b).* Note that very few observations exist for even-even superheavy element (SHE)



predictions with the macroscopic–microscopic model (Muntian et al. 2003a, b). In general, the observations agree well with predictions, including the data from Dubna. Data and calculations show a small shell effect for $N = 152$. Beyond $N = 156$ the Q_α values decrease toward the neutron-rich isotopes, a characteristic associated with the enhancement of stability. The calculations (solid lines) predict a shell closure at $N = 162$, which is reflected in the experimental Q values. The effect of shell closure is also reflected in the half-lives. The nuclide ^{270}Hs , located at the double shell closure has a half-life as long as 23 s (Dvorak et al. 2006).

Detailed spectroscopic data are still scarce. As an example, the ground-state deformation has been derived from spectroscopy for the nucleus ^{256}Rf . It has been obtained from the α decay of ^{260}Sg to a 2^+ rotational level of this nucleus. The quadrupole deformation is $\varepsilon = 0.28$ close to $\varepsilon = 0.25$ following the trend of the actinides and as predicted by theory (Münzenberg 1989a). The investigation of K -Isomers in ^{254}No probes single-particle energies and pairing strengths including the energies of the proton levels that govern the stability of SHE (Tandel et al. 2006). Experimental data favor $Z = 114$ as a SHE-magic proton number. More detailed experimental investigations on the structure of transactinide elements have been undertaken (Hofmann and Münzenberg 2000; Hofmann et al. 2001, 2002; Hessberger et al. 1997, 2009).

19.4.3 Shells and Fission Barriers


A universal definition of nuclear shells including deformed nuclei was given by Strutinsky (1967). He defined a shell as a large-scale nonuniformity in the distribution of the single-particle states. From this definition, shells may be expected for any nuclear shape. The nonuniformity in the level spacing creates the required shell correction to an appropriately chosen average, the liquid drop. The shell correction energy is closely connected to the density fluctuations of the single-particle states near the Fermi surface as calculated with a realistic model. This new concept allowed calculating the deformation energy of a nucleus on its way to fission and fission barriers while including shell effects. In this macroscopic–microscopic picture, the mass of a nucleus is represented as

$$M = M_{\text{LD}} + \delta M + P \quad (19.8)$$

where M_{LD} is the liquid drop mass, δM the shell correction, and P the pairing correction.

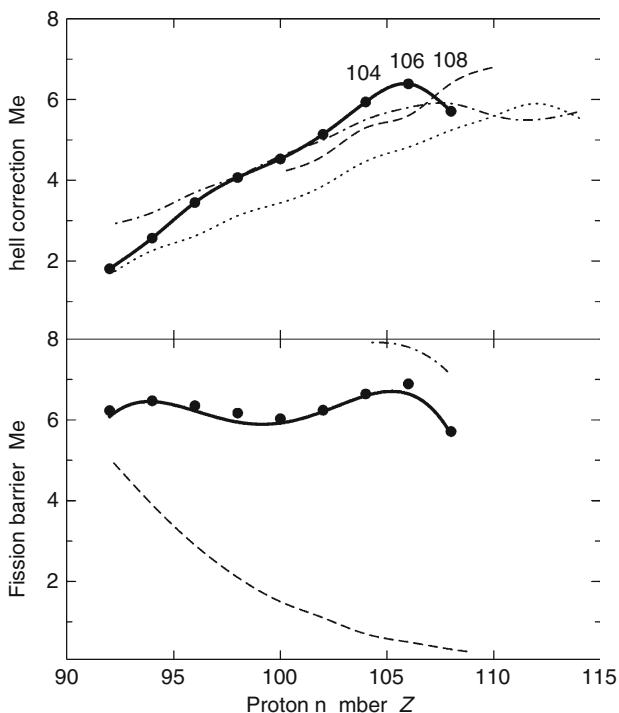
By using the macroscopic–microscopic model, shell correction energies can be extracted from the experimental mass M and a macroscopic (spherical) mass M_{LD} taken from a theoretical model. The shell correction is negative and it stabilizes the nucleus:

$$E_{\text{SH}} = (\delta M + P)c^2. \quad (19.9)$$

The ground state masses are taken from the Q_α values. For doubly even isotopes, α decays are expected to be ground state transitions.  Figure 19.13 shows the experimental shell effects for the $N - Z = 48$ nuclides from uranium to element 108 obtained with the macroscopic mass taken from the finite-range droplet model (Möller and Nix 1988, 1994). The experimental shell correction energies increase from 2 MeV for ^{232}U to more than 6 MeV for $^{264}108$. This is about half the shell strength of the most strongly bound doubly magic nucleus ^{208}Pb . Microscopic calculations (Cwiok et al. 1983; Patyk and Sobizcewski 1991; Möller and Nix 1988, 1994) reproduce the experimental data sufficiently well.

■ Fig. 19.13

Upper panel: Experimental shell correction energies (E_{SH}) for even–even nuclides characterized by the difference $N-Z = 48$ compared to current theoretical predictions. **Lower panel:** Experimental and calculated fission barriers for the same nuclides. The dashed line displays the macroscopic fission barrier as explained after ► Eq. (19.10)



In close analogy, an estimate of an experimental fission barrier can be obtained by superimposing the shell correction energy and the liquid drop barrier B_{LD} :

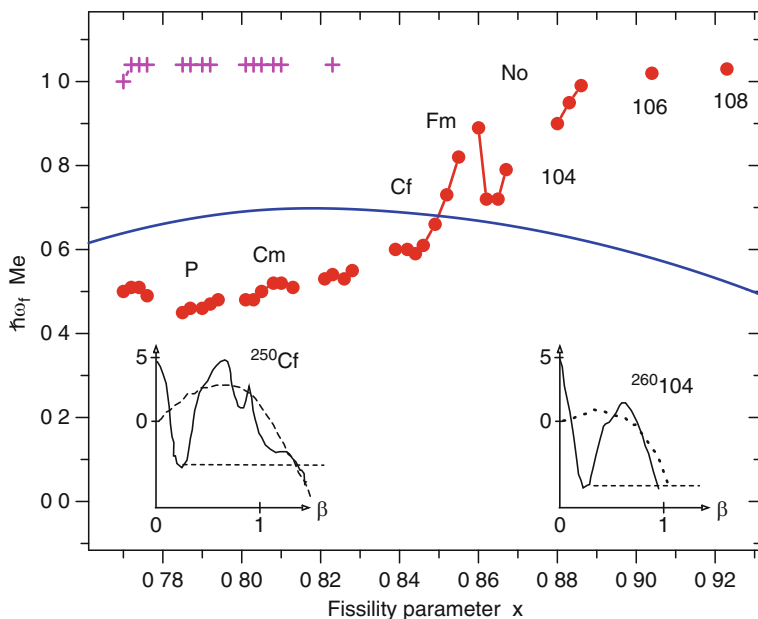
$$B_{\text{F}} = B_{\text{LD}} + E_{\text{SH}}. \quad (19.10)$$

B_{LD} , shown in the lower panel of ► Fig. 19.13 displays the experimental barriers obtained with a liquid drop barrier taken from systematics (Dahlinger et al. 1982). They remain practically constant between 6 and 7 MeV from uranium to hassium and are in reasonable agreement with theory (dashed line, Sobiczewski et al. 1987). Near rutherfordium, the macroscopic contribution to the barrier falls below 0.5 MeV, the calculated zero-point energy, and becomes practically ineffective. The dramatic decrease of the partial fission half-lives from 10^{25} s for uranium to 10^{-3} s for the transactinides despite a constant height of the barrier can be attributed to the small width characteristic of shell-stabilized barriers (Münzenberg et al. 1988). The barrier width can be estimated from the partial fission half-life and the barrier height with a parabolic approximation for the barrier:

$$T_{1/2} = \left[1 + e^{\frac{2\pi B_{\text{F}}}{\hbar\omega_{\text{f}}}} \right] \frac{\ln 2}{n}. \quad (19.11)$$

■ Fig. 19.14

Barrier curvature parameter. *Dots:* experimental data; *crosses:* curvature of the inner barrier; *line:* calculated curvature of the liquid drop barrier; *inserts:* representative barrier shapes for an actinide and a transactinide nucleus



Here $\hbar\omega_f$ is the barrier curvature parameter and n the number of barrier assaults, $n = 2.5 \times 10^{20} \text{ s}^{-1}$. Figure 19.14 shows the experimental barrier curvatures plotted against the fissility parameter. The liquid drop barrier (Nix 1967) is indicated as a line. The actinides show weakly curved thick liquid-drop dominated barriers with a curvature of 0.5 MeV. The transactinide barriers have curvatures close to 1 MeV, compatible with the curvature of the inner barrier measured for the light actinides (Bjornholm and Lynn 1980).

For illustration, the two insets show examples of a typical actinide and transactinide barriers. The actinides exhibit broad and double-humped barriers, dominated by the thick liquid drop barrier. For the transactinides, because of the vanishing liquid drop barrier, the outer hump sitting on top of the liquid drop barrier falls below the ground state. The remaining inner hump of the barrier creates the typical single-humped, thin barrier of shell-stabilized nuclei.

19.4.4 Theoretical Predictions

Superheavy elements mark the limit of nuclear mass and charge. Specific features are the large nuclear shells that carry large angular momenta and the large Coulomb force. The high number of protons creates a large electrostatic repulsion. SHEs are the biggest nuclear objects available and are therefore expected to have a complicated structure. Some developments are reviewed by Heenen and Nazarewicz (2002). Present theoretical models concentrate on mean-field

concepts. Theory suggests that the enhanced stability of the deformed nuclei near hassium and $N = 162$ may be due to a hexadecapole deformation in the ground state (Cwiok et al. 1983; Möller et al. 1986; Sobiczewski et al. 1987). Such nuclei are shaped like a barrel.

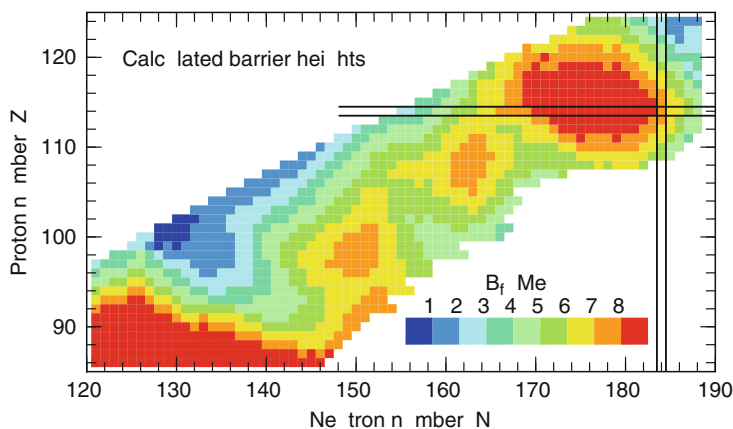
This discovery of a new region of enhanced stability interconnecting the transuranium elements and the spherical superheavies has dramatic consequences for the production of heavy and superheavy elements. It opened the door to the nuclei around the spherical shell closure at or beyond $Z = 114$ and $N = 184$, which can be approached stepwise starting with the transuranium elements. It is not necessary to jump across the “sea of instability” as was expected from the earlier predictions. The long half-lives of the neutron-rich isotopes allow for chemical studies and open up a new field of investigation with ion and atom traps. The macroscopic–microscopic method includes nuclear deformation and nicely reproduces the deformed region whereas most of the early self-consistent models only calculate spherical nuclei and are best suited to predicting the location of the spherical superheavy shell closure (Cwiok et al. 1996; Smolanczuk 1997; Bender et al. 1999; Kruppa et al. 2000).

➤ **Figure 19.15** displays the contour map of fission barriers from a macroscopic–microscopic calculation (Möller et al. 2009) for the region from the last stable spherical double shell closure at ^{208}Pb to the predicted superheavy elements. The colors give the height of the fission barrier. Orange corresponds to a barrier height of 7 MeV, red to 8 MeV or higher. The spherical superheavy nuclei at $Z = 114$ and $N = 184$ have fission barriers of 8 MeV or higher. It is interesting to note that the spherical shell region around $Z = 114$ is quite extended. High fission barriers cover the region up to $Z = 120$ and the region from $N = 170$ to $N = 184$. The deformed-shell nuclei around $Z = 108$ and $N = 162$ have fission barriers of 7 MeV in good agreement with experiment (➤ **Fig. 19.13**) and interconnect the transfermium region and the region of spherical SHEs (Möller and Nix 1988; Smolanczuk 1997; Muntian et al. 2003a, b).

A study of the superheavy region with self-consistent mean field models (employing mean field and Skyrme–Hartree–Fock approaches) yields different results for predicted regions of stability. ➤ **Figure 19.16** displays the single-particle spectra for neutrons and protons (Bender et al. 2001) for ^{132}Sn , the superheavy nucleus $^{310}126$, and the hyperheavy nucleus $^{472}164$. They exhibit a significant difference in the nature of the shells of doubly magic tin (where proton and

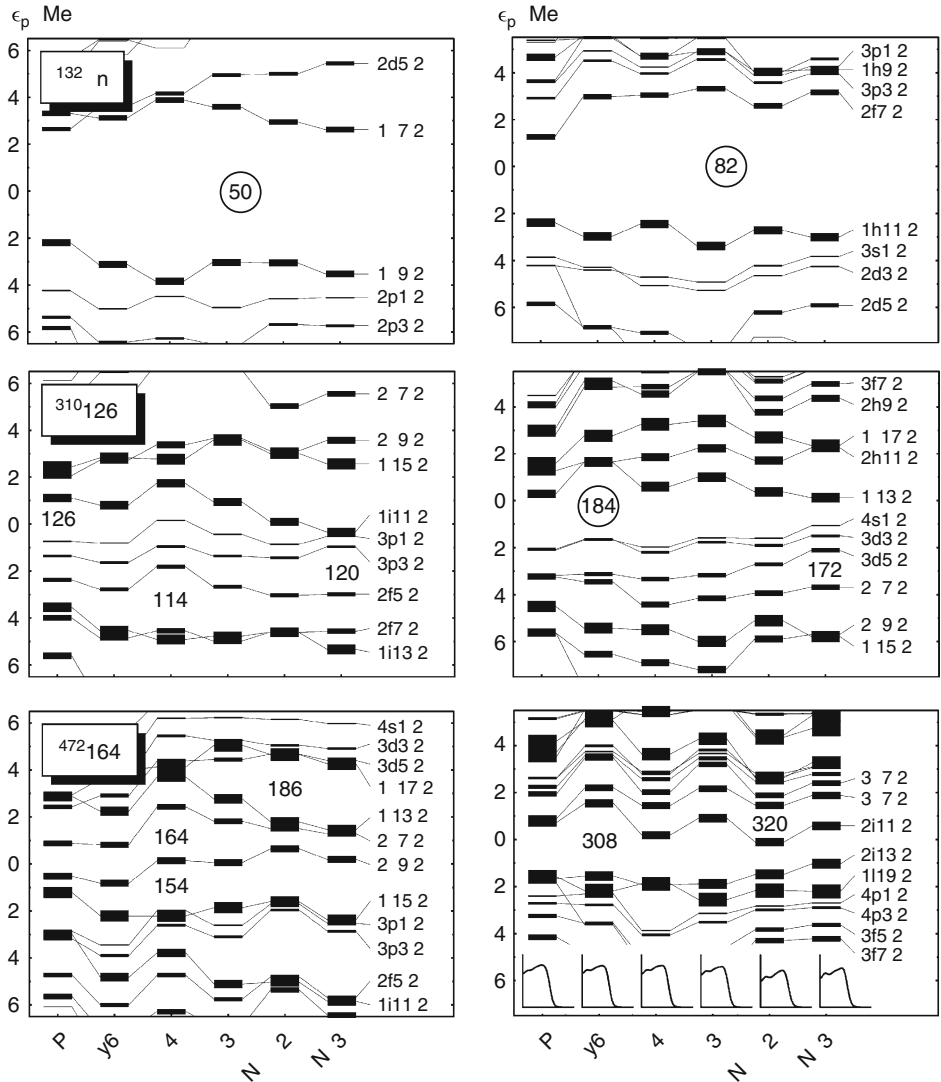
■ **Fig. 19.15**

Map of fission barriers (Möller et al. 2009). See inset for color code



■ Fig. 19.16

Single-particle spectra for protons (left panels) and neutrons (right panels) at spherical shape for different mean-field forces. The small diagrams at the bottom of the right panel show the predicted radial neutron distributions. (Bender et al. 2001)



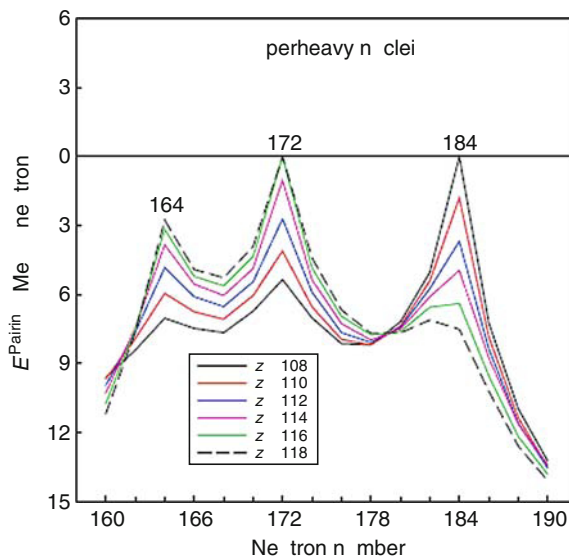
neutron shells are well pronounced) and of the superheavy element $Z = 126$ (where a region of low-level density between $Z = 114$ and $Z = 126$ creates the enhanced stability). Depending on the parameterization of the interaction and the method – Skyrme–Hartree–Fock (SKP, Sly6, SKI4, SKI3) or relativistic mean field (NL-Z2 and NL3) – the shell gap appears at $Z = 114$, $Z = 120$ or $Z = 126$. Nonrelativistic microscopic models such as the Skyrme–Hartree–Fock–Bogoliubov method (Cwiok et al. 1999), where the spin–orbit term so crucial to the prediction of shell closures has to be manually introduced into the calculation, predict that both $Z = 120$

and $Z = 114$ are equally probable. This indicates that magic shells in the SHE region are strongly isotope dependent (Greiner 1995; Rutz et al. 1997).

The neutron shell is located at $N = 184$ for all predictions. The situation for the hyperheavy nucleus $Z = 164$ is similar. Comprehensive microscopic calculations based on relativistic mean field (RMF) theory (NL3) using the double folding and WKB approximations in an internally consistent manner over the observed SHE region (Gambhir et al. 2005) have suggested an additional but weaker shell closure around $N \approx 164$ corresponding to $Z = 108$ – 110 and also around $N \approx 172$. This effect is clearly seen where neutron pairing energies go to zero (► Fig. 19.17, Gambhir et al. 2005). There is some support for these calculations in the observed decay chains from $^{277}_{112}\text{GSI}$ and $^{287,288}_{115}\text{Dubna}$ that traverse this region. The spread in theoretical estimates of closure underscore the fact that predictions remain strongly isotope dependent, i.e., a function of both N and Z . A recent theoretical extrapolation of the experimental data concludes that the position of the proton shell closure lies beyond $Z = 120$ (Adamian et al. 2009). One explanation for the less-pronounced SHE shell gap when compared to the magnitude of closure at $N = 126$ for instance, is the higher-level density prevalent in the large proton and neutron shells. Moreover, according to the calculations, superheavy nuclei have enhanced proton and neutron densities near the nuclear surface, created by the high-spin orbits (as indicated in the lower right panel of ► Fig. 19.16, bottom line). This affects the spin–orbit splitting and hence the location and strength of the shells. Macroscopic–microscopic models tend to overestimate the splitting of levels since the spin–orbit interaction has to be put in by hand. This may affect the location and extent of predicted closures. While RMF theories may do better in this regard, given the high-level densities, SHEs serve as a sensitive probe to distinguish between the various predictions, especially when all models describe stable nuclei with comparable accuracy (Gambhir et al. 2005).

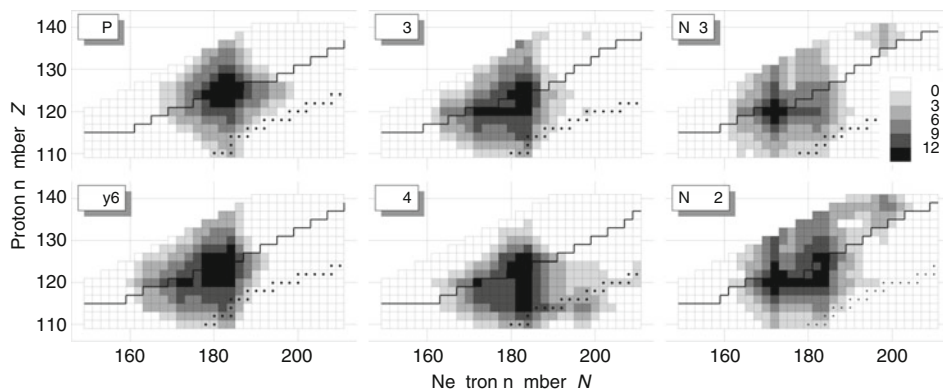
► Fig. 19.17

Neutron pairing energies using relativistic mean field (RMF) calculations (NL3) for even–even nuclei in the region $108 \leq Z \leq 118$ (Gambhir et al. 2005)



■ Fig. 19.18

Maps of shell correction energies obtained from self-consistent calculations plotted versus proton and neutron number. The darker the shading, the larger is the shell correction. The scale of E_{SH} (upper right figure) is in MeV (Bender et al. 2001)



Some results from self-consistent RMF calculations are compiled in Fig. 19.18. The region of superheavy nuclei is centered around $Z = 120$ and $N = 184$ and rather extended in Z . Only for NL3 and NL3+2 is the proton number $Z = 114$ well pronounced. The calculations suggest a diffused region of superheavy nuclei, which is caused by a low-level density in the proton levels around $Z = 112$ rather than a sharp level gap as known for ^{208}Pb . This may be due to the fact that it is difficult to create a pronounced gap in the proton shell with its relatively large spread of levels as shown in Fig. 19.16. Half-life estimates range from 1 year for ^{270}Hs at the center of the deformed region and 10^6 year for ^{292}Hs , at the closed neutron shell $N = 184$ (Smolanczuk 1997) down to 1 h for ^{270}Hs and 100 year for ^{292}Hs (Hofmann and Münzenberg 2000).

19.5 Production of the Transactinide Elements

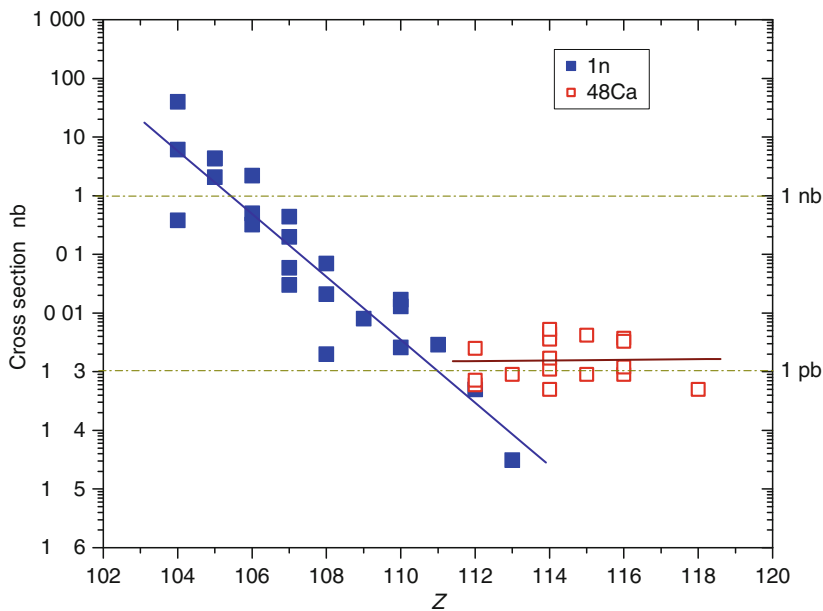
19.5.1 Fusion of Massive Nuclear Systems

The only successful method to synthesize transactinide elements is through the complete fusion of heavy ions (Schmidt and Morawek 1991; Vandenbosch 1992; Reisdorf 1994). Two types of reactions have been employed to create new chemical elements: cold fusion with ^{208}Pb or ^{209}Bi targets and hot fusion with ^{48}Ca projectiles (Fig. 19.19). The success of reactions involving doubly magic nuclei has been explained in the framework of the fragmentation model (Sandulescu et al. 1976).

To start the fusion process, the projectile needs sufficient kinetic energy to overcome the Coulomb repulsion between target and projectile. In a simple model fusion starts at the touching point of the spherical target–projectile configuration, the conventional Coulomb barrier, when the nuclear forces become effective and drive the dinuclear system (DNS) toward a mononucleus. For the creation of superheavy nuclear systems, the minimum kinetic energy of the projectile exceeds the Q -value needed for the formation of the compound system. The compound nucleus is created above its ground state. To reach the ground state, the excitation

■ Fig. 19.19

Experimental production cross sections of heavy and superheavy nuclei for 1n emission (*filled squares*) and ^{48}Ca (*open squares*) induced reactions; the solid lines indicate fits to the data



energy is dissipated by particle-evaporation, generally neutrons, and γ emission. Charged-particle emission is strongly suppressed because of the high Coulomb barrier and the relatively small excitation energy. For these heavy, fissile nuclei the de-excitation process is dominated by fission, which becomes of increasing importance toward the upper end of the periodic table. As the collision is not central in general, the compound nucleus has an angular momentum. Nuclei with an angular momentum above a critical value will not survive but fission.

The fusion–evaporation reaction is a two-step process. The production cross section is determined by the fusion and the de-excitation of the intermediate (compound) nucleus:

$$\sigma = \sigma_{\text{fus}}(E_p - E_B, l) w_x(E^*, l). \quad (19.12)$$

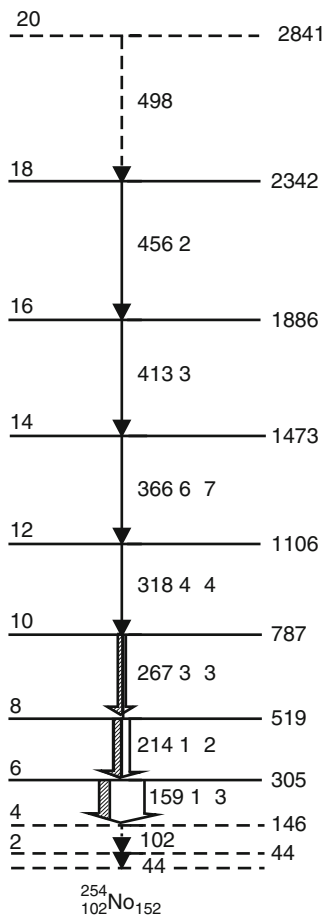
The fusion cross section σ_{fus} depends on the projectile energy E_p , the height of the fusion barrier E_B , and the angular momentum l of the system. The survival probability w_x of the compound nucleus is determined by the excitation energy E^* , which yields the number of evaporated neutrons x . For each step of neutron evaporation there is a strong competition between neutron evaporation and fission given by the ratio of neutron to fission width Γ_n/Γ_f . It is of the order of 10^{-2} to 10^{-3} . The geometric fusion cross section is

$$\sigma_{\text{fus}} = \pi \lambda^2 - \sum_{l=0}^{l_{\text{lim}}} (2l+1) T_l(E_p - E_B), \quad (19.13)$$

where $\lambda = 2\pi\lambda$ is the de Broglie wavelength of the dinuclear system and T_l is the transmission of the l th partial wave through the fusion barrier. The limiting angular momentum l_{lim} of the compound system up to which the partial waves contribute to the fusion cross section can

■ Fig. 19.20

Rotational levels populated in the production of nobelium, measured with in-beam γ spectroscopy, converted transitions: *dashed lines* (Courtesy P. Reiter)



be obtained from the rotating liquid drop model (Cohen et al. 1974). (See Sect. 2.2.1, Chap. 2, Vol. 1 as well as Sect. 4.3, Chap. 4, Vol. 1 for a detailed explanation of the liquid drop model in general.) The limiting angular momentum for elements near fermium (Münzenberg et al. 1981c) is below $15\hbar$ according to this model. Recent in-beam γ measurements with the new recoil–decay–tagging technique for ^{48}Ca on ^{208}Pb to produce ^{254}No show however that the rotational band is populated up to $20\hbar$ (Fig. 19.20, Reiter et al. 2000).

19.5.2 Experiment

The first transuranium elements were produced from actinide targets such as ^{248}Cm , ^{249}Bk , and ^{249}Cf (bred in high flux nuclear reactors) by irradiating them with beams of neutron-rich light ions of ^{15}N or ^{18}O . The idea was to start with a target close in mass to the final nucleus and use

a light projectile. There was a strong physics argument for this procedure. To create a compound nucleus, the dinuclear system must pass the fission barrier. The distance from the point of nuclear contact to the mononuclear system inside the barrier is much closer for asymmetric systems (when a small-sized projectile is added to the heavy target) than for symmetric systems combining two nuclei of similar radii.

The disadvantage is that the compound nuclei are produced at high excitation energy and have to evaporate four to five neutrons, which dramatically reduces their survival probability. The use of ^{208}Pb or its neighbor ^{209}Bi in combination with neutron-rich beams of ^{54}Cr , ^{58}Fe , $^{62,64}\text{Ni}$, and ^{70}Zn profits from the strongly bound doubly magic nucleus and the higher symmetry of target and projectile allowing the formation of “cold” compound systems with excitation energies of 10 to 20 MeV at the Coulomb barrier. Only one or two steps of fission–evaporation competition are necessary to dissipate the excitation energy. In this way, a high survival probability is expected even for the most heavy and fissile nuclei at the upper end of the periodic table (Oganessian 1974). In contrast, compound systems created using the actinides are formed with excitation energies of typically 40 to 50 MeV.

The production cross sections of cold heavy-ion fusion by 1n evaporation, and ^{48}Ca -induced reactions in 3n evaporation channels are displayed in [Fig. 19.19](#) and [Table 19.1](#). The cross sections for cold fusion drop steeply from the order of 1 μb for nobelium to 0.03 pb for element 113, which is more than six orders of magnitude. The ^{48}Ca data do not follow this trend. They stay constant around 1 pb from copernicium to element 118.

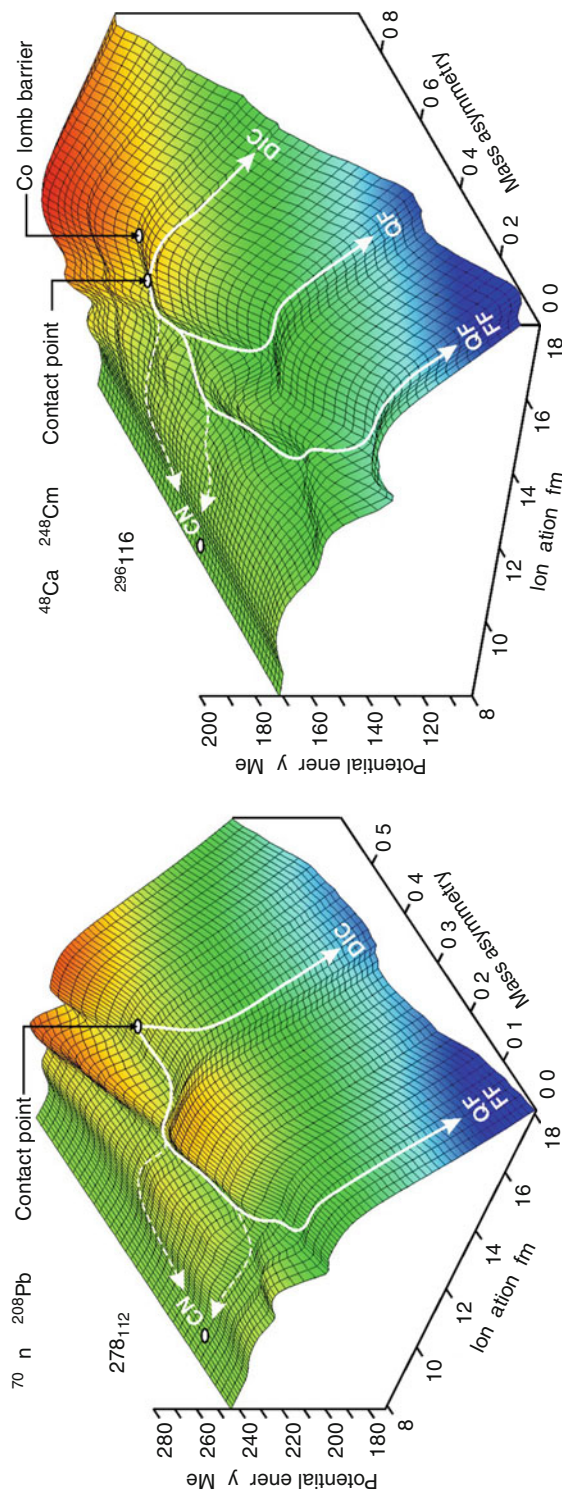
To explain the small cross sections for SHE synthesis and in particular the fast decrease of the cold fusion cross sections, the concept of “extra push” has been developed. In this model, the barrier for complete fusion is shifted dynamically above the Coulomb barrier until the experimental cross section is reproduced (Hessberger et al. 1985). The barrier shift is explained (in terms of a macroscopic approach) as a result of dynamical hindrance of the nuclei on their way to fusion (Swiatecki 1982; Armbruster 1989). However, for the transactinide elements known to exist only due to shell effects, the application of a macroscopic model to explain all structure effects related to their production is questionable if not wrong (Münzenberg 1988). In contrast to the extra push concept, experiment shows that the maximum of the excitation function shifts toward a smaller excitation energy for heavier systems, with ^{278}Cn being the coldest compound nucleus ever produced at an excitation energy of only 10 MeV (Hofmann et al. 1996).

Up to now, there is no fundamental theoretical approach to *quantitatively* explain the fusion of heavy systems in terms of a microscopic theory. The first attempt in that direction is the fragmentation model, a two-center microscopic calculation predicting the most favorable target–projectile combinations employing magic nuclei (Sandulescu et al. 1976). Recently calculations that are more refined have been carried out taking into account microscopic effects. The diffusion model uses a microscopic–macroscopic approach with temperature dependent shell corrections to create a fusion pocket the depth of which is determined by the excitation energy of the system on its way to fusion (Arimoto et al. 1999). The dinuclear system (DNS) concept assumes that complete fusion is achieved by transferring the nucleons shell by shell to the other one. Due to their shell structure, the nuclei keep their individuality all the way toward the formation of the compound nucleus (Cherepanov 1999).

[Figure 19.21](#) illustrates the possible trajectories of collective motion on the potential-energy surface for the fusion of ^{70}Zn with ^{208}Pb to create element 112, and for ^{48}Ca on ^{248}Cm to produce element 116 (Zagrebaev et al. 2003). For the cold fusion example, ^{70}Zn on ^{208}Pb , the system has to move a long distance from the contact point to the compact shape of the

■ Fig. 19.21

Trajectories of collective motion in the potential energy surface for the reactions $^{70}\text{Zn} + ^{208}\text{Pb}$ (left panel) and $^{48}\text{Ca} + ^{248}\text{Cm}$ (right panel) in dependence on the symmetry coordinate of target and projectile and the elongation (Courtesy V. Zagrebaev)

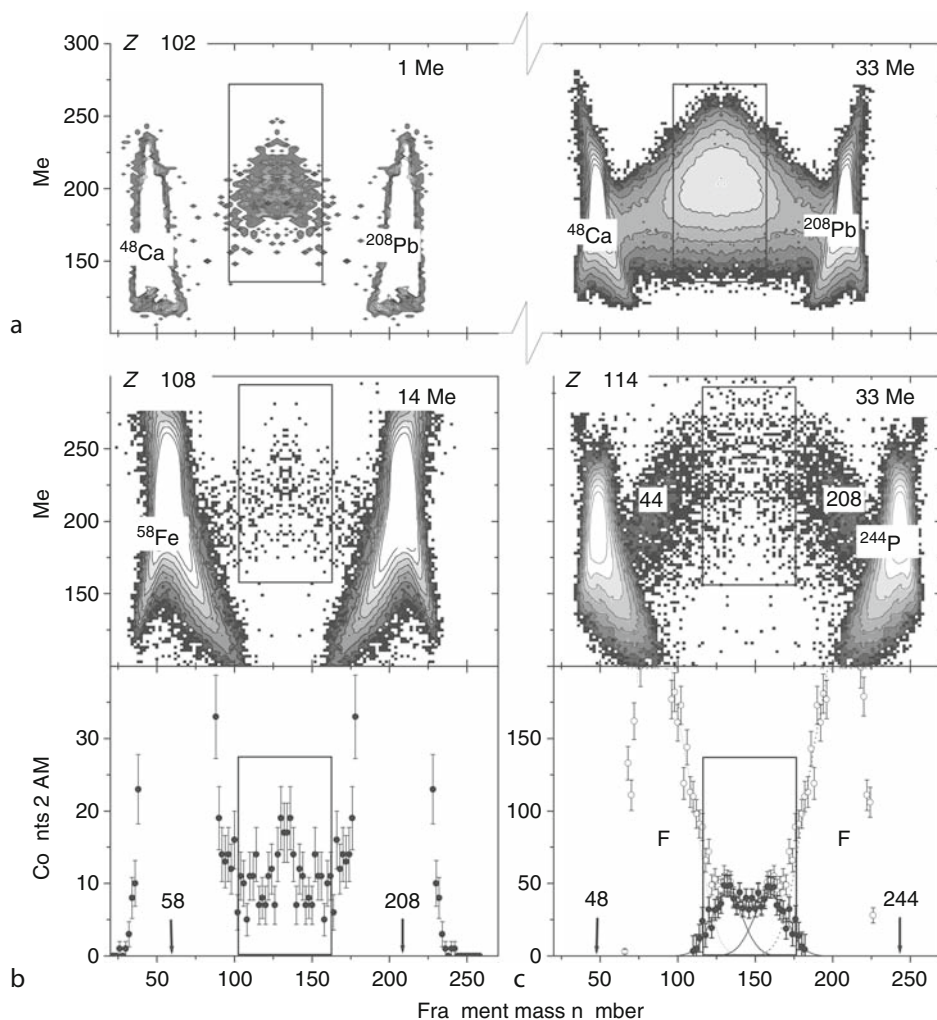


compound nucleus (CN) passing two barriers. Since deep inelastic collisions (DIC) and fast fission (FF) are much more likely, the resulting fusion cross section is small. For the fusion of ^{48}Ca with ^{248}Cm the contact point is much closer to the compound shape. Though only one small barrier has to be passed, quasi fission (QF) and fast fission are competing and the fusion cross section will be higher as with the more symmetric case of cold fusion. The calculations suggest that the fusion of an asymmetric system is favored (Oganessian 2007).

Experimental studies to investigate the fusion of massive systems (Oganessian et al. 2000) support these findings. ▶ Figure 19.22 shows the measured fragment distribution in mass

■ Fig. 19.22

Experimental fission fragment distributions for the production of $Z = 102$ and $Z = 108$ in cold fusion, and $Z = 114$ in hot fusion with a ^{48}Ca beam. In the upper panels the total kinetic energy (TKE) is plotted vs. the mass number of the fission fragment. In the lower panels the counts of the mass distributions of fission fragments are displayed (Oganessian 2001)



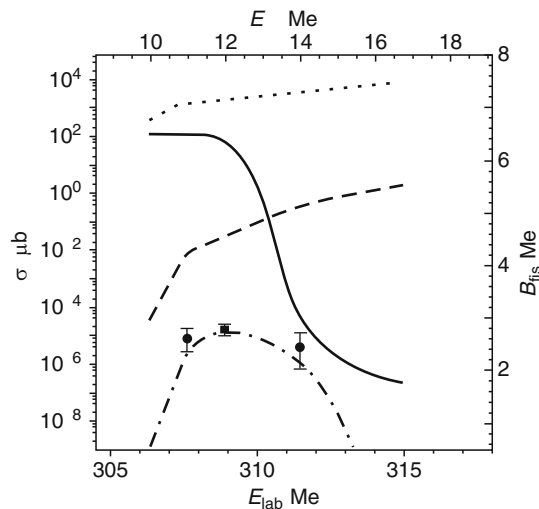
versus energy coordinates as a scatter plot for three reactions: $^{48}\text{Ca} + ^{208}\text{Pb}$, $^{58}\text{Fe} + ^{208}\text{Pb}$, and $^{48}\text{Ca} + ^{244}\text{Pu}$. Between the large asymmetric peaks, there is a symmetric component. From its energy and angular distribution, it has been concluded that it stems from compound fission (e.g., from the equilibrated mononucleus), and hence can be taken as a measure of the fusion cross section. For the light system $Z = 102$, formed in the reaction $^{48}\text{Ca} + ^{208}\text{Pb}$, a strong symmetric component is observed. It is well developed close to the fusion barrier (corresponding to an excitation energy of the compound system $E_x = 17.6$ MeV) and increases strongly with increasing energy. For $Z = 108$ fusion is also well pronounced. For $Z = 114$, some events can still be attributed to the fusion component though the fast-fission components have grown strongly. Experiment shows that in accordance with the fragmentation model there is some influence of shells in the entrance channel, either in the projectile or in the target, which serves to enhance the fusion probability (Münzenberg 1988; Schmidt and Morawek 1991).


The different behavior of the cross section systematics for cold fusion and ^{48}Ca reactions (► Fig. 19.19) is not understood in detail. The steep decrease of the cold fusion cross section is caused by the strong increase of the Coulomb forces in the entrance channel, with the entrance channel fissility scaling with the factor $(Z_p Z_t)$. It increases from 1,640 for calcium on lead to 2,460 for zinc on lead, by a factor of 1.5, whereas the entrance channel fissility for calcium-induced reactions varies from 1,840 for calcium on uranium to 1,960. For calcium on californium, it changes only by a factor of 1.06. Here the exit channel dominates. The shell structure of the compound system becomes important (Oganessian 2007).

The fissility of the compound system increases with Z^2/A very fast toward the upper end of the periodic table. The consequence is a strong competition between penetration probability through the fusion barrier and survival of the compound nucleus as shown by the calculation presented in ► Fig. 19.23 for the example of cold fusion to produce element 110. It leads to an

■ Fig. 19.23

Calculated quasi fission (dotted curve), fusion (dashed curve), and survival cross section of the compound nucleus (CN) (line) for $^{64}\text{Ni} + ^{208}\text{Pb}$. The resulting cross section for the 1n channel is given by the dash-dot line together with the data points from experiment (Giardina et al. 2000)




extremely narrow excitation function for the one-neutron evaporation channel of a width of about 5 MeV, which has also been observed in experiment (Hofmann and Münzenberg 2000; Giardina et al. 2000).  [Figure 19.23](#) also shows the large quasifission cross section of about 1 μb to be compared to a fusion cross section of 10^{-2} μb at the maximum of the 1n excitation function.

The survival probability P_{sur} of the compound nucleus after evaporation of x neutrons is

$$P_{\text{sur}} \approx \prod_{i=1}^n \frac{e^{B_f - B_n}}{T}, \quad (19.14)$$

It is dominated by the difference between the fission B_f and the neutron binding energy B_n of the compound nucleus. For heavy systems beyond $Z = 114$ the fission barrier increases while for very neutron-rich species the neutron binding energy decreases. Consequently, $(B_f - B_n)$ increases for compound systems $Z = 114$ to $Z = 118$ and the net effect results in the cross section remaining almost constant (Oganessian 2007). Recent calculations reproduce the SHE production cross sections in cold fusion as well as from the ^{48}Ca data fairly well (Zagrebayev et al. 2001; Zagrebayev 2001; Oganessian 2007).

19.5.3 Future Perspectives

 [Figure 19.19](#) shows that with the existing experimental capabilities the limit for cold fusion is reached at element 113. A promising way to proceed to the region beyond is through ^{48}Ca -induced reactions using hot fusion. The limit for hot fusion is reached with element 118 due to the unavailability of suitable targets. Since the heaviest target available for hot fusion is californium, to go beyond element 118 projectiles heavier than ^{48}Ca are needed. First attempts to produce element 120 with ^{64}Ni on ^{238}U (Hofmann et al. 2008) and ^{244}Pu on ^{58}Fe (Oganessian et al. 2009) were unsuccessful.

The fragmentation model predicts three paths to the production of superheavy elements (Sandulescu et al. 1976): cold heavy-ion fusion with lead and bismuth targets, fusion with actinides, and symmetric fusion or reversed fission. Presently only cold fusion has been explored systematically while hot actinide-based fusion has recently generated a wealth of data. The exploration of symmetric fusion with a high level of sensitivity is still missing given the argument that the fusion of such massive target–projectile combinations is unlikely because of the large Coulomb force expected in the entrance channel.

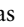
The magic proton number at $Z = 114$ has been arrived at and the synthesis of $Z = 118$ places within reach the other possible magic proton number at $Z = 120$. However, the question as to how the magic neutron number $N = 184$ can be reached remains unanswered. The reaction $^{82}\text{Se}(^{208}\text{Pb}, n)$ leads to the nuclide $^{289}116$ (not observed yet) with 173 neutrons, which is still more than 10 neutrons away from $N = 184$. The reaction $^{48}\text{Ca}(^{248}\text{Cm}, 4n)$ leads to the nuclide $^{292}116$ with only three more neutrons. Even $^{294}118$ with 176 neutrons is still far away from the magic $N = 184$. The most neutron-rich isotope reported to date is $^{293}116_{177}$, which is still 7 neutrons away. There are two possibilities for complete-fusion reactions to come closer to the $N = 184$ shell. In the first case, *overshooting the proton number* may be possible as this would automatically lead to more neutrons due to the increasing neutron excess for heavier projectile–target combinations. The magic region would then be crossed by a later generation of the α -decay chain. A nice example demonstrating this is the chain starting from ^{277}Cn passing by the center of the hexadecapole-stabilized region at hassium. The second possibility is presently

discussed in the context of new radioactive ion beam facilities, which provide energetic exotic nuclear beams (Münzenberg 1998; Hofmann 2001). New ways of SHE synthesis need to be explored including other reactions for fusion such as transfer or deep inelastic collisions (Zagrebaev and Greiner 2008).

19.6 New Experimental Developments and Prospects for SHE Research

In-flight separation is the most important tool for heavy-element research and has been successful in the discovery of new elements together with recently developed detection techniques. These methods have enabled the identification of new elements through a measurement of their gross nuclear properties from the decay of single atoms. Recent heavy-element research led to the discovery of deformed, shell-stabilized nuclei, creating a region of enhanced stability, which extends the nuclear chart to the magic proton number 114 and beyond up to element 118. Though great progress has been made, there is still no convincing evidence for the discovery of superheavy elements. The knowledge of the atomic and nuclear structure of the transactinide elements is still scarce. In-beam spectroscopy and decay spectroscopy with the new generation of X-ray and γ -detection systems of high efficiency will be certainly an important field of future research. The combination of recoil separators and ion traps will address interesting new physics with single atoms such as offering the possibility to make direct mass measurements with high precision and using laser spectroscopy to determine deformations or ionization potentials.

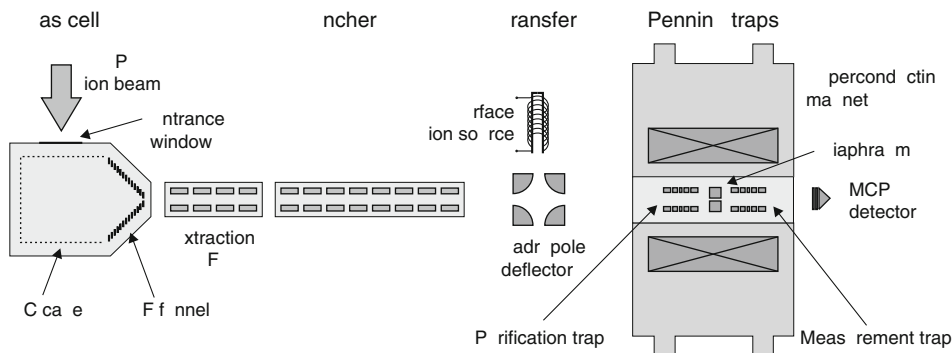
SHE chemistry at the picobarn level gives access to the elements 114 and heavier and is another important issue for future research. This would include addressing the important question of where the Mendeleev systematics will break down due to relativistic effects of the inner electrons of increasingly heavy, proton-rich nuclei. Pre-separation with gas-filled separators such as BGS at LBNL Berkeley, GARIS at RIKEN, or TASCA at GSI have been successfully applied in SHE chemistry experiments (Düllmann 2008).

Presently the only method applicable to identify a new chemical element according to the guidelines set down by IUPAC (Barber et al. 1992) is the α - α parent-daughter correlation method, which is not applicable for nuclides remotely removed from the known region where decay chains may terminate by fission in an unexplored mass region. Even chemical identification is not a safe method as the chemical properties of the new elements are difficult to predict (Schädel 2006). Plans to measure the mass of SHE directly with conventional methods such as online separation with a high resolving spectrometer are under way (Oganessian 2007). New facilities include time-of-flight mass spectrometers (TOF-MS, Plass et al. 2008) and ion traps such as SHIPTRAP (Block et al. 2007).  Figure 19.24 shows SHIPTRAP, an ion trap coupled to SHIP. The in-flight separated ions are injected into a buffer gas cell, stopped and thermalized in high purity helium gas at a pressure of about 50 mbar, and swept out by a supersonic gas jet. Then the ions are transported by a radio-frequency quadrupole (RFQ) ion guide to a cooler for accumulation, cooling, and bunching. Cooled beams have low emittance and are ideally used for high-resolution experiments such as Penning traps. SHIPTRAP has two traps. The first one is used for isobar separation, the second one for high-precision mass measurements. Recently the masses of the isotopes $^{252-254}\text{No}$ have been measured.

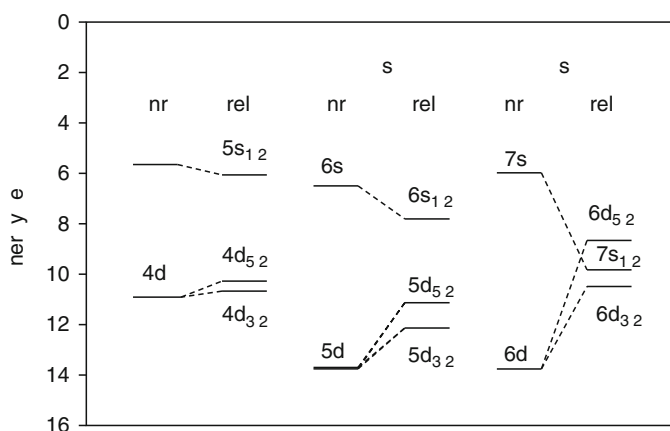
Optical spectroscopy is being considered for various nobelium isotopes (Backe et al. 2007). Here, investigations of the relativistic effects of the inner electrons of nuclei with large Z , which shift the optical levels and ionization potentials are of interest. Relativistic effects are already observed in gold as “nonrelativistic” gold would be white in color. For heavy elements with large

■ Fig. 19.24

SHIPTRAP: a schematic overview (Block et al. 2007)



■ Fig. 19.25

Relativistic and nonrelativistic energy levels of the valence ns and $(n - 1)d$ electrons for the group-8 elements (Pershina 2003)

proton numbers, the inner electrons move with relativistic velocity. The relativistic mass increase causes a shrinkage of the inner electron orbitals, the shielding of the nuclear charge increases and the outer electron orbitals are energetically destabilized and expand. ➤ Figure 19.25 shows the relativistic and nonrelativistic levels of the valence ns and $(n - 1)d$ electrons. It demonstrates the relativistic stabilization of the ns orbitals as well as the relativistic destabilization $(n - 1)d$ orbitals for group-8 elements. The trends of the relativistic and nonrelativistic energies of the valence electrons are opposite from the 5d to the 6d elements. The depression of the levels by relativistic effects increases from 5s to 6s and continues, so that the 7s for hassium falls below the 6d level. A fundamental query of chemical research question is to locate the point at which the dramatic influence of the relativistic effect on atomic levels will cause the breakdown of the Mendeleviev systematic (Pershina 2003).

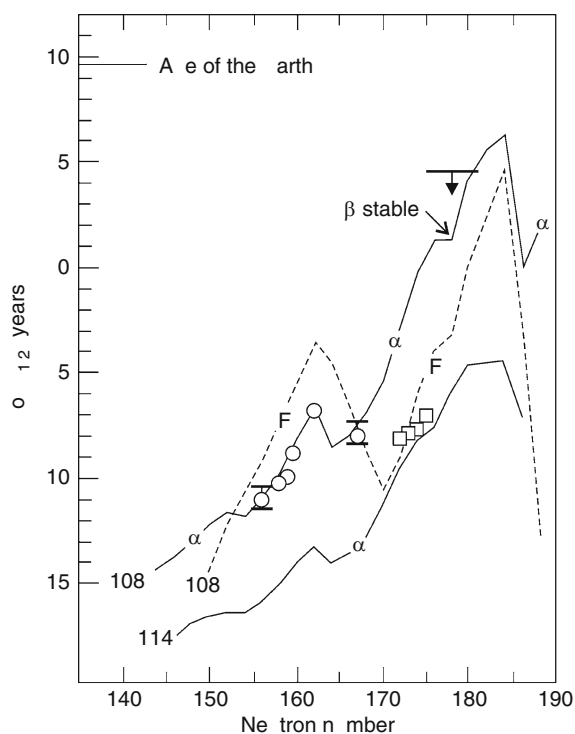
Decay spectroscopy of the heavy elements with the new generation of highly efficient 4π γ -arrays will give detailed structure information to test and improve the nuclear models in that

region and may help to clarify the question for the location of the spherical proton and neutron shells. Highly sensitive in-beam spectroscopy, combined with recoil-decay tagging (Reiter et al. 1999) is extremely sensitive. It will allow in-beam spectroscopy below the microbarn level to extract ground state deformation and level structure information including for the excited levels of the compound nucleus. Nuclear spectroscopy of the transactinide elements will be an important component of future research (Hessberger et al. 2009).

The prerequisite for this new generation of experiments to investigate nuclear, atomic, and chemical properties of the heavy and superheavy elements as well as to proceed beyond $Z = 118$ are high-current accelerators that provide beam intensities of $5 \times 10^{14} \text{ s}^{-1}$. The use of radioactive beams is being explored. First-generation experiments of fusion–fission studies to estimate cross sections for SHE production and to explore new types of reactions should be started. New and upgraded rare-isotope facilities, FAIR-NUSTAR at GSI (Germany), SPIRAL II at GANIL (France), RIKEN (Japan) and its upgrade, MSU and its upgrade (Michigan, USA), as well as HIRFL (Lanzhou, China) are expected to provide beams of unstable neutron-rich nuclei with intensities up to 10^7 s^{-1} for existing laboratories and in excess of 10^{10} s^{-1} for projected facilities. Currently, the most promising way to produce new superheavy elements is through an intensity upgrade of stable beams (U. Ratzinger 2009, private communication; Yu. Ts. Oganessian 2009, private communication).

■ Fig. 19.26

Calculated partial fission and α half-lives for elements 108 and 114. Circles and squares mark experimental partial α half-lives. The limiting half-life for ^{286}Hs according to data from Dubna is indicated (Oganessian 2007)



Finally, the existence of SHEs in nature remains an open question. Experimental results and new calculations do not exclude the possibility that the very heavy elements can be found in nature (► Fig. 19.26). In contrast to numerous earlier searches that concentrated on long-lived nuclides expected to be seen around the magic proton number $Z = 114$, new calculations suggest a search for hassium or a lighter chemical element may be more productive. For these elements, the most stable species are expected with fission half-lives of the order of 10^5 to 10^6 years (Smolanczuk 1997) comparable to the half-life of ^{234}U . New investigations have already begun at Dubna (Oganessian 2007) with renewed interest.

Note added in proof

The experiment on the synthesis of element 117 has been finished successfully at Dubna. The discoveries of isotopes with masses 293 and 294 are reported.
Oganessian YuTs et al. (2010) Phys Rev Lett 104:142502

Acknowledgments

The authors gratefully acknowledge many useful discussions and materials given by S. Hofmann, F. P. Hessberger, D. Ackermann, M. Block, Ch. E. Düllmann, Y. K. Gambhir, W. Greiner, E. M. Kozulin, P. Möller, Yu. Ts. Oganessian, V. Pershina, M. Schädel, P. Reiter, W. Scheid, A. Sobiczewski, V. K. Utyonkov, and A. V. Yeremin.

References

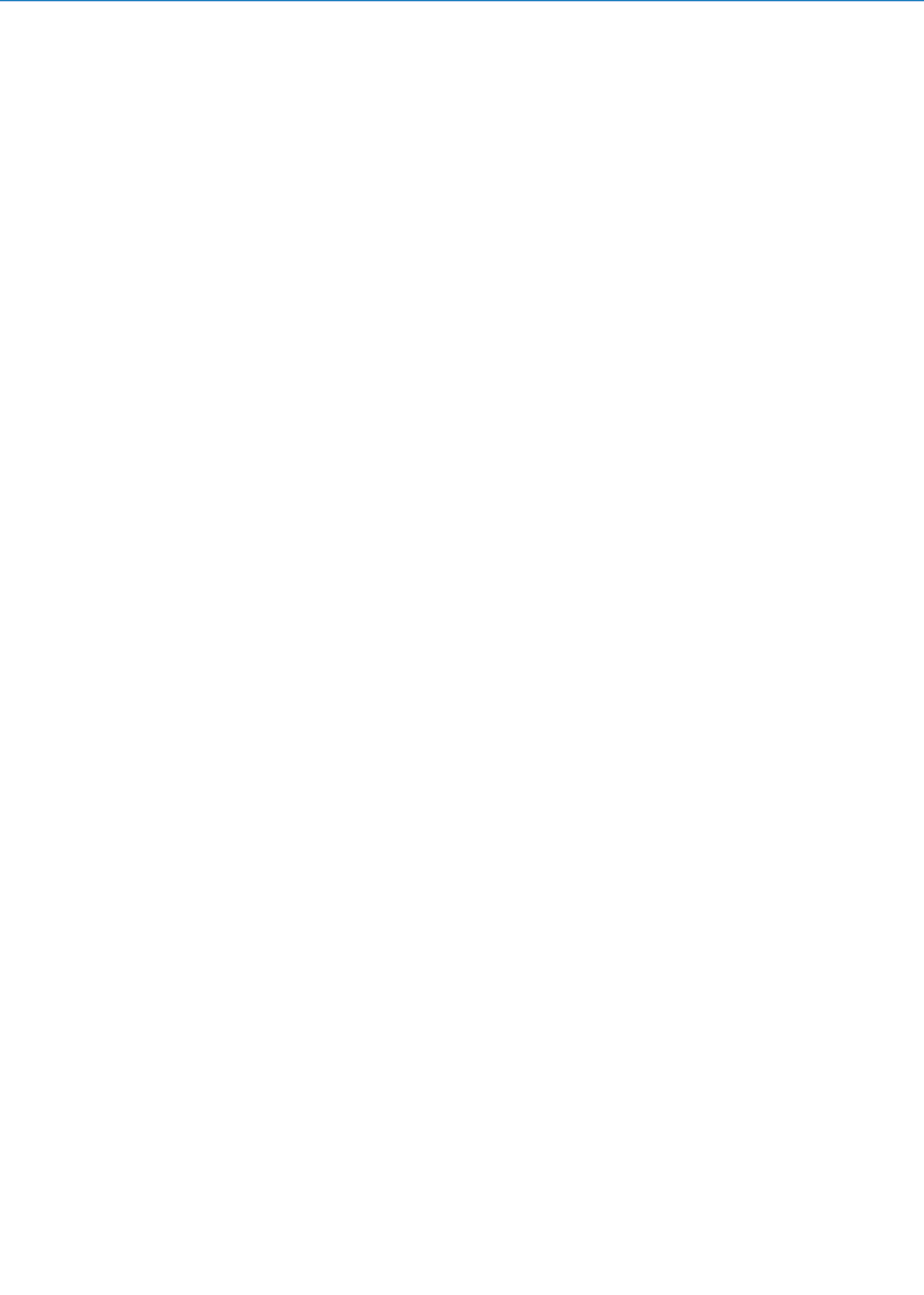
- Adamian GG, Antonenko NV, Sargasyan VV (2009) Phys Rev C 79:054608
- Arimoto Y, Wada T, Ohta M, Abe Y (1999) Phys Rev C 59:796
- Armbruster P, Agarwal YK, Brühle W, Brügger M, Dufour JP, Gäggeler H, Hessberger FP, Hofmann S, Lemmert P, Münzenberg G et al (1985) Phys Rev Lett 54:406
- Armbruster P (1989) Proceedings of the 1989 international nuclear physics conference. World Scientific, New Jersey, pp 313–355
- Backe H, Kunz P, Lauth W, Dretzke A, Horn R, Kolb T, Laatiaoui M, Sewtz M, Ackermann D, Block M et al (2007) Eur Phys J D 45:99
- Barber RC, Greenwood NN, Hryenkiewicz AZ, Jeannin YP, Lefort M, Sakai M, Ulehla I, Wapstra AH, Wilkinson DH (1992) Prog Part Nucl Phys 29:453
- Barber RC, Gäggeler HW, Karol PJ, Nakahara H, Verdaci E, Vogt E (2009) Pure Appl Chem 81:1331
- Bender M, Rutz K, Reinhard P-G, Maruhn JA, Greiner W (1999) Phys Rev C 60:034304
- Bender M, Nazarewicz W, Reinhard P-G (2001) Phys Lett B 515:42
- Bjornholm S, Lynn JE (1980) Rev Mod Phys 52:725
- Block M, Ackermann D, Blaum K, Chaudhuri A, Di Z, Eliseev S, Ferrer R, Habs D, Herfurth F, Hessberger FP et al (2007) Eur Phys J D 45:39
- Cherepanov EA (1999) Pramana J Phys 53:619
- Cohen S, Plasil F, Swiatecki WJ (1974) Ann Phys 82:557
- Cwiok S, Pashkevich VV, Dudek J, Nazarewicz W (1983) Nucl Phys A 410:254
- Cwiok S, Dobaczewski J, Heenen PH, Magierski P, Nazarewicz W (1996) Nucl Phys A 611:211
- Cwiok S, Nazarewicz W, Heenan PH (1999) Phys Rev Lett 83:1108
- Dahlinger M, Vermeulen D, Schmidt KH (1982) Nucl Phys A 376:94
- Dmitriev SN, Oganessian YuTs, Utyonkov VK, Shiskin SV, Yeremin SV, Lobanov YV, Tsyganov YS, Chepigin VI, Sokol EA, Vostokin GK et al (2005) Mendelev Commun 15:1
- Dragojevic I, Gregorich KE, Düllmann ChE, Garcia MA, Gates JM, Nelson SL, Stavsetra L, Sudowe R, Nitsche H (2008) Phys Rev C 78:024605
- Dragojevic I, Gregorich KE, Düllmann ChE, Dvorak J, Ellison PA, Gates JM, Nelson SL, Stavsetra L, Nitsche H (2009) Phys Rev C 79:011602
- Düllmann CE (2008) Nucl Instrum Meth Phys Res B 266:4123

- Dvorak J, Bröchle W, Chelnokov M, Dressler R, Düllmann ChE, Eberhardt K, Gorshkov V, Jäger E, Krücken R, Kuznetsov A et al (2006) *Phys Rev Lett* 97:242501
- Dvorak J, Bröchle W, Chelnikov M, Düllmann ChE, Dvorakova Z, Eberhardt K, Jäger E, Krücken R, Kuznetsov A, Nagame Y et al (2008) *Phys Rev Lett* 100:132503
- Eichler R, Aksenov NV, Belozerov GA, Bozhikov GA, Chepigin VI, Dmitriev SN, Dressler R, Gäggeler HW, Gorshkov VA, Haenssler F et al (2007) *Nature* 447:72
- Emis-14 (2002) In: Proceedings of the international conference on magnetic isotope separators and their applications (conference volume). Victoria, Canada; 2003 *Nucl Instr Meth B* 204
- Faust W, Münzenberg G, Hofmann S, Reisdorf W, Schmidt KH, Armbruster P (1979) *Nucl Instrum Meth* 166:397
- Fermi E (1934) *Nature* 133:898
- Fizet EO, Nix JR (1972) *Nucl Phys A* 193:647
- Flerov GN, Oganessian YuTs, Lobanov YuA, Lasarev YuA, Tretiakova SP, Kolesov IV, Plotko VM (1971) *Nucl Phys A* 160:181
- Flerov GN, Ter Akopian GM (1983) *Rep Prog Phys* 46:817
- Folden CM III, Dragojevic I, Düllmann ChE, Eichler R, Garcia MA, Gates JM, Nelson SL, Sudowe R, Gregorich KE, Hoffman DC et al (2009) *Phys Rev C* 79:027602
- Gambhir YK, Bhagwat A, Gupta M (2005) *Ann Phys New York* 320:429
- Gates JM, Nelson SL, Gregorich KE, Dragojevic I, Düllmann ChE, Ellison PA, Folden CM III, Garcia MA, Stavsetra L, Sudowe R et al (2008) *Phys Rev C* 78:034604
- Ghiorso A, Nurmia M, Harris J, Eskola K, Eskola P (1969) *Phys Rev Lett* 22:1317
- Ghiorso A, Nurmia M, Eskola K, Eskola P (1970) *Phys Lett* 32B:95
- Ghiorso A, Nitschke JM, Alonso JR, Alonso CT, Nurmia M, Seaborg GT (1974) *Phys Rev Lett* 33:1490
- Giardina G, Hofmann S, Muminov AI, Nasirov AK (2000) *Eur Phys J A* 8:205
- Greiner W (1995) *Int J Mod Phys E* 5:1
- Gupta M, Burrows TW (2005) *Nuclear Data Sheets* 106:251; Errata (2006) *Nuclear Data Sheets* 107:789
- Haba H, Kaji D, Komori Y, Kudou Y, Morimoto K, Morita K, Ooe K, Ozeki K, Sato N, Shinohara A et al (2009) *Chem Lett* 38:426
- Hahn O, Strassmann F (1939a) *Die Naturwissenschaften* 27:11
- Hahn O, Strassmann F (1939b) *Die Naturwissenschaften* 27:89
- Heenen PH, Nazarewicz W (2002) *Europhys News* 33:5
- Herrmann G (1979) *Nature* 280:543
- Hessberger FP, Münzenberg G, Hofmann S, Reisdorf W, Schmidt KH, Schmidt HJ, Armbruster P, Hingmann R, Thuma B, Vermeulen D (1985) *Z Phys A* 321:317
- Hessberger FP, Hofmann S, Ninov V, Armbruster P, Folger H, Münzenberg G, Schött HJ, Popeko AG, Yerein AV, Andreyev AN, Saro S (1997) *Z Phys A* 359:415
- Hessberger FP, Hofmann S, Ackermann D, Ninov V, Leino M, Münzenberg G, Saro S, Lavrentev A, Popeko AG, Yerein AV, Stodel Ch (2001) *Eur Phys J A* 12:57
- Hessberger FP, Hofmann S, Streicher B, Sulignano B, Antalic S, Ackermann D, Heinz S, Kindler B, Kojouharov I, Kuusiniemi P et al (2009) *Eur Phys J A* 41:145
- Hoffmann DC, Lawrence FA, Mewether JC, Rourke FM (1971) *Nature* 243:132
- Hofmann S, Münzenberg G, Hessberger F, Schött HJ (1984) *Nucl Instr Meth* 223:312
- Hofmann S, Ninov V, Hessberger FP, Armbruster P, Folger H, Münzenberg G, Schött HJ, Popeko A, Yerein AV, Andreyew A, Saro S, Janik R, Leino ME (1995a) *Z Phys A* 350:277
- Hofmann S, Ninov V, Hessberger FP, Armbruster P, Folger H, Münzenberg G, Schött HJ, Popeko A, Yerein AV, Andreyew A, Saro S, Janik R, Leino ME (1995b) *Z Phys A* 350:281
- Hofmann S, Ninov V, Hessberger FP, Armbruster P, Folger H, Münzenberg G, Schött HJ, Popeko A, Yerein AV, Saro S, Janik R, Leino ME (1996) *Z Phys A* 354:229
- Hofmann S, Hessberger FP, Ninov V, Armbruster P, Münzenberg G, Stodel C, Popeko A, Yerein AV, Saro S, Leino ME (1997) *Z Phys A* 358:377
- Hofmann S, Münzenberg G (2000) *Rev Mod Phys* 72:733
- Hofmann S (2001) *Progr Part Nucl Phys* 46:293
- Hofmann S, Hessberger FP, Ackermann D, Antalic S, Cagarda P, Cwiok S, Kindler B, Kojuharova J, Lommel B, Mann R, Münzenberg G et al (2001) *Eur Phys J A* 10:5
- Hofmann S, Hessberger FP, Ackermann D, Münzenberg G, Antalic S, Cagarda P, Kindler B, Kojuharova J, Lommel B, Mann R et al (2002) *Eur Phys J A* 14:147
- Hofmann S, Ackermann D, Antalic S, Burkhard HG, Comas VF, Dressler R, Gaz Z, Heinz S, Heredia JA, Hessberger FP et al (2007) *Eur Phys J A* 32:251
- Hofmann S, Ackermann D, Antalic S, Gomas VF, Heinz S, Heredia JA, Hessberger FP, Khuyagbataar J, Kindler B, Kojuharov I et al (2008) *GSI Scientific Report 2008*. GSI Darmstadt, NUSTAR-SHE-01
- Kaji D, Morimoto K, Sato N, Ichikawa T, Ideguchi E, Kazutake O, Haba H, Koura H, Kudou Y, Ozawa A et al (2009) *J Phys Soc Jpn* 78:035003
- Karol PJ, Nakahara H, Petley BW, Vogt E (2001) *Pure Appl Chem* 73:959

- Karol PJ, Nakahara H, Petley BW, Vogt E (2003) *Pure Appl Chem* 75:1601
- Kratz JV (1983) *Radiochimica Acta* 32:25
- Kratz JV, Gober MK, Zimmermann HP, Schädel M, Brühle W, Schimpf E, Gregorich KE, Türlér A, Hannink NJ et al (1992) *Phys Rev C* 45:1064
- Kruppa AT, Bender M, Nazarewicz W, Reinhard P-G, Vertse T, Cwiok S (2000) *Phys Rev C* 61:03413-1
- Lazarev YuA, Lobanov YuV, Oganessian YuTs, Tsyganov YuS, Utyonkov VK, Abdullin FSh, Iliev S, Polyakov AN, Rigoli J, Shirokovsky IV et al (1995) *Phys Rev Lett* 75:1903
- Lazarev YuA, Lobanov YuV, Oganessian YuTs, Utyonkov VK, Abdullin FSh, Polyakov AN, Rigol J, Shirokovsky IV, Tsyganov YuTs, Iliev S et al (1996) *Phys Rev C* 54:620
- Lazarev YuA, Lobanov YuV, Oganessian YuTs, Utyonkov VK, Abdullin FSh, Polyakov AN, Rigol J, Shirokovsky IV, Tsyganov YuS, Iliev S et al (2000) *Phys Rev C* 62:064307
- McMillan EM, Abelson PH (1940) *Phys Rev C* 57:1185
- Meitner L, Frisch OR (1939) *Nature* 143:239
- Möller P, Leander GA, Nix JR (1986) *Z Phys A* 323:41
- Möller P, Nix JR (1988) *Atomic Data and Nuclear Data Tables* 39:213
- Möller P, Nix JR (1994) *J Phys G* 20:1681
- Möller P, Sierk AJ, Ichikawa T, Iwamoto A, Bengtsson R, Uhrenholt H, Aberg S (2009) *Phys Rev C* 79:064304
- Morita K, Morimoto K, Kaji D, Haba H, Ideguchi E, Kanungo R, Katori K, Koura H, Kudo H, Ohnishi T et al (2004a) *Eur Phys J A* 21:257
- Morita K, Morimoto K, Kaji D, Haba H, Ideguchi E, Kanungo R, Katori K, Koura H, Kudo H, Ohnishi T et al (2004b) *Nucl Phys A* 738:129
- Morita K, Morimoto K, Kaji D, Haba H, Ideguchi E, Peter JC, Kanungo R, Katori K, Koura H, Kudo H et al (2004c) *J Phys Soc Jpn* 73:1738
- Morita K, Morimoto K, Kaji D, Akiyama T, Goto S, Haba H, Ideguchi E, Kanungo R, Katori K, Koura H et al (2004d) *J Phys Soc Jpn* 73:2593
- Morita K (2005) In: Penionzhkevich YuE, Cherepanov EA (eds) *Proceedings of the international symposium on exotic nuclei*. World Scientific, Singapore, p 188
- Morita K, Morimoto K, Kaji D, Akiyama T, Goto S, Haba H, Ideguchi E, Kanungo R, Katori K, Koura H et al (2007a) *J Phys Soc Jpn* 76:043201
- Morita K, Morimoto K, Kajidaya AT, Goto S-I, Haba H, Ideguchi K, Koura H, Unaga H et al (2007b) *J Phys Soc Jpn* 76:045001
- Morita K (2008) *Nucl Phys A* 805:172c
- Mosel U, Greiner W (1969) *Z Phys* 222:261
- Muntian I, Patyk Z, Sobiczewski A, (2003a) *Yad Fiz* 66:1051; *Phys Atomic Nuclei* 66:1015
- Muntian I, Hofmann S, Patyk Z, Sobiczewski A (2003b) *Acta Phys Pol B* 34:2073
- Münzenberg G (1974) *Int J Mass Spectrom Ion Phys* 14:363
- Münzenberg G, Faust W, Hofmann S, Armbruster P, Güttner K, Ewald H (1979) *Nucl Instr Meth* 161:65
- Münzenberg G, Hofmann S, Hessberger FP, Reisdorf W, Schmidt KH, Schneider JRH, Armbruster P, Sahn CC, Güttner K, Thuma B (1981a) *Z Phys A* 300:107
- Münzenberg G, Faust W, Hessberger FP, Hofmann S, Reisdorf W, Schmidt K-H, Schneider WFW, Schött HJ, Armbruster P, Güttner K et al (1981b) *Nucl Instr Meth* 186:423
- Münzenberg G, Hofmann S, Faust W, Hessberger FP, Reisdorf W, Schmidt K-H, Kitahara T, Armbruster P, Güttner K, Thuma B, Vermeulen D (1981c) *Z Phys A* 302:7
- Münzenberg G, Armbruster P, Faust W, Güttner K, Hessberger FP, Hofmann S, Reisdorf W, Sahn CC, Schmidt K-H, Schött HJ, Thuma B, Vermeulen D (1982a) In: Edelstein NM (ed) *Proceedings of the international conference on actinides in perspective*. Pergamon, New York, p 223
- Münzenberg G, Armbruster P, Hessberger FP, Hofmann S, Poppensieker K, Reisdorf W, Schneider JRH, Schneider WFW, Schmidt KH, Sahn CC, Vermeulen D (1982b) *Z Phys A* 309:89
- Münzenberg G, Reisdorf W, Hofmann S, Agarwal YK, Hessberger FP, Poppensieker K, Schneider JRH, Schneider WFW, Schmidt K-H, Schött HJ, Armbruster P, Sahn CC, Vermeulen D (1984a) *Z Phys A* 315:145
- Münzenberg G, Armbruster P, Folger H, Hessberger FP, Hofmann S, Keller JG, Poppensieker K, Reisdorf W, Quint B, Schmidt KH, Schött HJ, Leino ME, Hingmann R (1984b) *Z Phys A* 317:235
- Münzenberg G, Hofmann S, Folger H, Hessberger FP, Keller J, Poppensieker K, Quint B, Reisdorf W, Schmidt K-H, Schött HJ, Armbruster P (1985) *Z Phys A* 322:227
- Münzenberg G, Armbruster P, Berthes G, Folger H, Hessberger FP, Hofmann S, Keller J, Poppensieker K, Quint AB, Reisdorf W, Schmidt K-H, Schött HJ, Sümmerer K, Zychor I, Leino ME, Hingmann R, Gollerthan U, Hanelt E (1987) *Z Phys A* 328:49
- Münzenberg G (1988) *Rep Prog Part Phys* 51:57
- Münzenberg G, Hofmann S, Hessberger FP, Folger H, Ninov V, Poppensieker K, Quint AB, Reisdorf W, Schött HJ, Sümmerer K et al (1988) *Z Phys A* 339:435
- Münzenberg G, Armbruster P, Hofmann S, Hessberger FP, Folger H, Keller JG, Ninov V, Poppensieker K, Quint AB, Reisdorf W et al (1989) *Z Phys A* 333:163
- Münzenberg G (1989) *Nucl Phys A* 502:571c–590c
- Münzenberg G (1997) In: Greiner W, Poenaru D (eds) *Experimental techniques in nuclear physics*, Chap. 11. Gruyter, Berlin, pp 375–424
- Münzenberg G (1998) *Phil Trans R Soc Lond A* 356:2083
- Myers WD, Swiatecki WJ (1966) *Nucl Phys* 81:1
- Nagame Y, Asai M, Haba H, Goto S, Tsukada K, Nishinaka I, Nishio K, Ichikawa S, Toyoshima A, Akiyama K et al (2002) *J Nucl Radiochem Sci* 3:85

- Nelson SL, Gregorich KE, Dragojewic I, Garcia MA, Gates JM, Sudowe R, Nitsche H (2008a) *Phys Rev Lett* 100:022501
- Nelson SL, Folden CM III, Gregorich KE, Dragojewic I, Düllmann ChE, Eichler R, Garcia MA, Gates JM, Sudowe R, Nitsche H (2008b) *Phys Rev C* 78:024606
- Nelson SL, Gregorich KE, Dragojewic I, Dvorak J, Ellison PA, Garcia MA, Gates JM, Stavsetra L, Ali MN, Nitsche H (2009) *Phys Rev C* 79:027605
- Nilssen SG, Tsang CF, Sobiczewski A, Szymanski Z, Wycech S et al (1969) *Nucl Phys A* 131:1
- Nishio K, Hofmann S, Hessberger FP, Ackermann D, Antalic S, Comas VF, Gan Z, Heinz S, Heredia JA, Ikezoe H et al (2006) *Eur Phys J A* 29:281
- Nix JR (1967) *Ann Phys* 41:52
- Oganessian YuTs (1974) *Lecture notes in physics*, vol 33. Springer, Berlin, p 221
- Oganessian YuTs, Demin AG, Iljinov AS, Tretyakova SP, Pleve AA, Penionzhkevich YuE, Ivanov MP, Tretyakov YuP (1975) *Nucl Phys A* 239:157
- Oganessian YuTs (1996) *Proceedings of the international conference on nuclear physics at the turn of the millenium*. World Scientific, Singapore, p 11
- Oganessian YuTs, Yeremin AV, Gulbekian GG, Bogomolov SL, Chepigin VI, Gikal BN, Gorshkov VA, Itkis MG, Kabachenko AP, Kutner VB et al (1999a) *Eur Phys J A* 5:63
- Oganessian YuTs, Yeremin AV, Popeko AG, Bogomolov SL, Buklanov GV, Chelnokov ML, Chepigin VI, Gikal BN, Gorshkov VA, Gulbekian GG et al (1999b) *Nature* 400:242
- Oganessian YuTs, Utyonkov VK, Lobanov YuV, Abdullin FSh, Polyakov AN, Shirokovsky IV, Tsyganov YuS, Gulbekian GG, Bogomolov SL, Gikal BN et al (1999c) *Phys Rev Lett* 83:3154
- Oganessian YuTs, Utyonkov VK, Lobanov YuV, Abdullin FSh, Polyakov AN, Shirokovsky IV, Tsyganov YuS, Gulbekian GG, Bogomolov SL, Gikal BN (2000) *Phys Rev C* 62:041604(R) 1
- Oganessian YuTs, Utyonkov VK, Lobanov YuV, Abdullin FSh, Polyakov AN, Shirokovsky IV, Tsyganov YuS, Gulbekian GG, Bogomolov SL, Gikal BN et al (2001) *Phys Rev C* 63:011301(R) 1
- Oganessian YuTs (2001) *Nucl Phys A* 685:17c
- Oganessian YuTs, Utyonkov VK, Lobanov YuV, Abdullin FSh, Polyakov AN, Shirikovsky IV, Tsyganov YuS, Gulbekian GG, Bogomolov SL, Gikal BN et al (2004a) *Phys Rev C* 70:064609; Erratum (2005) *Phys Rev C* 71:029902
- Oganessian YuTs, Utyonkov VK, Lobanov YuV, Abdullin FSh, Polyakov AN, Shirokovsky IV, Tsyganov YuS, Gulbekian GG, Bogomolov SL, Gikal BN et al (2004b) *JINR Preprint E7-2004-160*. [http://www.jinr.ru/publish/Preprints/2004/160\(E7-2004-160\).pdf](http://www.jinr.ru/publish/Preprints/2004/160(E7-2004-160).pdf)
- Oganessian YuTs, Utyonkov VK, Lobanov YuV, Abdullin FSh, Polyakov AN, Shirokovsky IV, Tsyganov YuS, Gulbekian GG, Bogomolov SL, Gikal BN et al (2004c) *Phys Rev C* 69:054607
- Oganessian YuTs, Utyonkov VK, Lobanov YuV, Abdullin FSh, Polyakov AN, Shirokovsky IV, Tsyganov YuS, Gulbekian GG, Bogomolov SL, Mezentssev AN et al (2004d) *Phys Rev C* 69:021601(R); Erratum (2004) *Phys Rev C* 69:029902
- Oganessian YuTs, Utyonkov VK, Dmitirev SN, Lobanov YuV, Itkis MG, Polyakov AN, Tsyganov YuS, Mezentssev AN, Yeremin AV, Voinov AA et al (2005) *Phys Rev C* 72:034611
- Oganessian YuTs, Utyonkov VK, Lobanov YuV, Abdullin FSh, Polyakov AN, Sagaidak RN, Shirokovsky IV, Tsyganov YuS, Voinov AA, Gulbekian GG et al (2006) *Phys Rev C* 74:044602
- Oganessian YuTs, Utyonkov VK, Lobanov YuV, Abdullin FSh, Polyakov AN, Sagaidak RN, Shirokovsky IV, Tsyganov YuS, Voinov AA, Gulbekian GG et al (2007) *Phys Rev C* 76:011601(R)
- Oganessian YuTs (2007) *J Phys G Nucl Part Phys* 34: R165
- Oganessian YuTs, Utyonkov VK, Lobanov YuV, Abdullin FSh, Polyakov AN, Sagaidak RN, Shirokovsky IV, Tsyganov YuS, Voinov AA, Mezentssev AN et al (2009) *Phys Rev C* 79:024603
- Patyk Z, Sobiczewski A (1991) *Nucl Phys A* 533:132
- Pershina V (2003) In: Schädel M (ed) *The chemistry of superheavy elements*. Kluwer, Dordrecht, p 31
- Plass WR, Dickel T, Czok U, Geissel H, Petrick M, Reinheimer K, Scheidenberger C, Yavor M (2008) *Nucl Instrum Meth Phys Res B* 266:4123
- Randrup J, Larsson SE, Möller P, Nilsson SG, Pomorski K, Sobiczewski A (1976) *Phys Rev C* 13:229
- Reisdorf W (1994) *J Phys G* 20:1297
- Reiter P, Khoo TL, Lister CJ, Seweryniak D, Ahmad I, Alcorta M, Carpenter MP, Cizewski JA, Davids C, Gervais G et al (1999) *Phys Rev Lett* 82:509
- Reiter P, Khoo TL, Lauritsen T, Lister DJ, Seweryniak D, Songoni AA, Ahmad I, Amzal A, Bhattacharya P, Butler PA (2000) *Phys Rev Lett* 84:3542
- Rutz K, Bender M, Bürvenich T, Schilling T, Reinhard PG, Maruhn JA, Greiner W (1997) *Phys Rev C* 56:238
- Sandulescu A, Gupta RK, Scheid W, Greiner W (1976) *Phys Lett* 60B:225
- Sargeson AM (1997) *Names and symbols of transfermium elements, IUPAC recommendations 1997*. *Pure Appl Chem* 69:2471
- Schädel M (2002) *J Nucl Radiochem Sci* 3:113
- Schädel M (2006) *Angewandte Chemie Int Ed* 45:368
- Schmidt K-H, Sahm CC, Pielenz K, Clerc HG (1984) *Z Phys A* 316:19
- Schmidt K-H, Morawek W (1991) *Rep Prog Phys* 54:949
- Seaborg GT, Loveland W, Morrissey DJ (1979) *Science* 203:711

- Seaborg GT, Loveland WD (1985) In: Bromley DA (ed) *Treatise in heavy-ion science*, vol 4. Plenum, New York, p 255
- Seaborg GT, Loveland W (1990) *The elements beyond uranium*. Wiley, New York
- Sewtz M, Habs D (eds) (2007) In: *Proceedings of the workshop on the atomic properties of the heaviest elements*. Frauenwörth im Chiemsee, Germany; 2006 Eur Phys J D 45
- Smolanczuk R (1997) Phys Rev C 56:812
- Sobiczewski A, Patyk Z, Cwiok S (1987) Phys Lett B 186:6
- Somerville LP, Nurmia MJ, Nitschke JM, Ghiorso A, Hulet EK, Loughheed RW (1985) Phys Rev C 31:1801
- Streichner B, Antalic S, Saro S, Venhart M, Hessberger FP, Hofmann S, Ackermann D, Kindler B, Kojuharov I, Lommel B et al (2007) Acta Phys Pol B 38:1561
- Strutinsky VM (1967) Nucl Phys A 95:420
- Swiatecki WJ (1982) Nucl Phys A 375:275
- Tandel SK, Khoo TL, Seweryniak D, Mukherjee G, Ahmad I, Back B, Blinstrup R, Carpenter MP, Chapman J, Chowdhury P et al (2006) Phys Rev Lett 97:082502
- Timokhin SN, Yakushev AB, Xu H, Pereygin VP, Zvara I (1996) J Radioanal Nucl Chem Lett 212:31
- Türler A, Düllmann ChE, Gäggeler HW, Kirbach UW, Yakushev AB, Schädel M, Bröchle W, Dressler R, Eberhardt K, Eichler B et al (2003) Eur Phys J A 17:505
- Vandenbosch R (1992) Ann Rev Nucl Part Sci 42:477
- Zagrebbaev VI, Arimoto Y, Itkis MG, Oganessian YuTs, Ohta M (2001) Phys Rev C 65:014607
- Zagrebbaev VI (2001) Phys Rev C 64:034606
- Zagrebbaev VI, Itkis MG, Oganessian YuTs (2003) Phys At Nucl 66:1033
- Zagrebbaev VI, Greiner W (2008) Phys Rev C 78:034610



20 Chemistry of Transactinides

J. V. Kratz

Institute of Nuclear Chemistry, Johannes Gutenberg University, Mainz,
Germany

20.1	<i>Introduction</i>	926
20.2	<i>Synthesis and Decay of Transactinides</i>	929
20.3	<i>Single-Atom Chemistry</i>	929
20.4	<i>Experimental Techniques</i>	932
20.4.1	Target and Transport Systems	932
20.4.2	Gas-Phase Chemistry	933
20.4.3	Aqueous Chemistry	937
20.5	<i>Element 104 (Rutherfordium)</i>	943
20.5.1	Theoretical Predictions	943
20.5.2	Experimental Results	944
20.6	<i>Element 105 (Dubnium)</i>	960
20.6.1	Theoretical Predictions	960
20.6.2	Experimental Results	962
20.7	<i>Element 106 (Seaborgium)</i>	969
20.7.1	Theoretical Predictions	969
20.7.2	Experimental Results	972
20.8	<i>Element 107 (Bohrium)</i>	983
20.8.1	Theoretical Predictions	983
20.8.2	Experimental Results	984
20.9	<i>Element 108 (Hassium)</i>	986
20.9.1	Theoretical Predictions	986
20.9.2	Experimental Results	986
20.10	<i>Element 112 (Copernicium)</i>	990
20.10.1	Theoretical Predictions	990
20.10.2	Experimental Results	990
20.11	<i>Outlook</i>	994
20.12	<i>Editors' Notes</i>	995

Abstract: In this chapter, the chemical properties of the man-made transactinide elements rutherfordium, Rf (element 104), dubnium, Db (element 105), seaborgium, Sg (element 106), bohrium, Bh (element 107), hassium, Hs (element 108), and copernicium, Cn (element 112) are reviewed, and prospects for chemical characterizations of even heavier elements are discussed. The experimental methods to perform rapid chemical separations on the time scale of seconds are presented and comments are given on the special situation with the transactinides where chemistry has to be studied with single atoms. It follows a description of theoretical predictions and selected experimental results on the chemistry of elements 104 through 108, and element 112.

20.1 Introduction

At present, 25 man-made transuranium elements are known. The first 11 artificial elements beyond uranium belong to the actinide series. Their chemistry is documented in a number of review articles and books (see, e.g., Seaborg and Loveland 1990; Seaborg 1993, 1995; Morss et al. 2006). According to the actinide concept (Seaborg 1945), the 5f series ends with lawrencium, Lr (element 103), and a new 6d transition series is predicted to begin with rutherfordium, Rf (element 104) (see, e.g., Fricke and Greiner 1969). Hence, the currently known transactinide elements 104 through 112 have been placed in the periodic table under their lighter homologs in the 5d series Hf, Ta, W, Re, Os, Ir, Pt, Au, and Hg. The first 7p element, element 113, eka-thallium, has been synthesized at RIKEN, Japan (Morita et al. 2004). Evidence for the syntheses of elements 112, 114, 115, 116, and 118 in ^{48}Ca -induced fusion reactions with actinide targets with partly mutually inconsistent results reported by the Dubna laboratory (Oganessian et al. 1999a, b, c, 2000, 2001, 2002, 2004a, b, c, d; Oganessian 2007) would mean that further 7p elements, eka-lead, eka-bismuth, eka-polonium, and eka-radon, have been synthesized. In one case, concerning the isotope $^{283}112$, the data obtained (Oganessian et al. 2004c, d) with the dubna gas-filled recoil separator (DGFRS) were reproduced at GSI, Darmstadt, with the velocity filter separator for heavy-ion products (SHIP) (Hofmann et al. 2007). The same decay pattern was measured in a chemistry experiment, where $^{283}112$ (i.e., ^{283}Cn) was produced through α decay of $^{287}114$ in the $^{48}\text{Ca} + ^{242}\text{Pu}$ reaction (Eichler et al. 2007a, b, 2008). Independent verification of $^{286}114$ and $^{287}114$ in the $^{242}\text{Pu}(^{48}\text{Ca}, 3\text{-}4\text{n})$ reaction was reported from Berkeley (Stavsetra et al. 2009).

The peculiar arrangement of the first five actinides in some representations (see, e.g., the cover of the textbook by Adloff and Guillaumont (1993)) of the periodic table in [Fig. 20.1](#) with a shifted position with respect to the other actinides reflects the fact that, due to a large delocalization of their 5f electron orbitals, the 5f electrons take part in their chemistry, a feature that is much less pronounced in the 4f series of the lanthanides. This makes Th a pseudo-homolog of the group-4 elements Zr and Hf, Pa a pseudo-homolog of Nb and Ta, and, to a decreasing extent, U, Np, and Pu, pseudo-homologs of the group-6, group-7, and group-8 elements, respectively. The more uniform actinide behavior is found only in the second half of the actinide series starting with Am.

Investigating the chemical properties of the transactinides is challenging both experimentally and theoretically. Due to increasingly strong relativistic effects, increasing deviations from the periodicity of the chemical properties based on linear extrapolations from the lighter homologs in the periodic table have been predicted for some time (Fricke and Greiner 1969). They result from the increasingly strong Coulomb field of the highly charged nucleus,

1																		18																	
1																		2																	
H																		He																	
1																		2																	
3																		10																	
Li																		Ne																	
4																		10																	
Be																		10																	
11																		18																	
Na																		Ar																	
12																		18																	
Mg																		18																	
3																		18																	
4																		18																	
5																		18																	
6																		18																	
7																		18																	
8																		18																	
9																		18																	
10																		18																	
11																		18																	
12																		18																	
13																		18																	
14																		18																	
15																		18																	
16																		18																	
17																		18																	
18																		18																	
19																		36																	
20																		36																	
21																		36																	
22																		36																	
23																		36																	
24																		36																	
25																		36																	
26																		36																	
27																		36																	
28																		36																	
29																		36																	
30																		36																	
31																		36																	
32																		36																	
33																		36																	
34																		36																	
35																		36																	
36																		36																	
37																		54																	
38																		54																	
39																		54																	
40																		54																	
41																		54																	
42																		54																	
43																		54																	
44																		54																	
45																		54																	
46																		54																	
47																		54																	
48																		54																	
49																		54																	
50																		54																	
51																		54																	
52																		54																	
53																		54																	
54																		54																	
55																		86																	
56																		86																	
57																		86																	
58																		86																	
59																		86																	
60																		86																	
61																		86																	
62																		86																	
63																		86																	
64																		86																	
65																		86																	
66																		86																	
67																		86																	
68																		86																	
69																		86																	
70																		86																	
71																		86																	
72																		86																	
73																		86																	
74																		86																	
75																		86																	
76																		86																	
77																		86																	
78																		86																	
79																		86																	
80																		86																	
81																		86																	
82																		86																	
83																		86																	
84																		86																	
85																		86																	
86																		86																	
87																		118																	
88																		118																	
89																		118																	
90																		118																	
91																		118																	
92																		118																	
93																		118																	
94																		118																	
95																		118																	
96																		118																	
97																		118																	
98																		118																	
99																		118																	
100																		118																	
101																		118																	
102																		118																	
103																		118																	
104																		118																	
105																		118																	
106																		118																	
107																		118																	
108																		118																	
109																		118																	
110																		118																	
111																		118																	
112																		118																	
113																		118																	
114																		118																	
115																		118																	
116																		118																	
117																		118																	
1																																			

Ce	Pr	Nd	Pm	Sm	Eu	Gd	Tb	Dy	Ho	Er	Tm	Yb	Lu
58	59	60	61	62	63	64	65	66	67	68	69	70	71

If rutherfordium (in this chapter, the element names endorsed in 1997 by the International Union of Pure and Applied Chemistry are used. Note that the names Kurchatovium (Ku) and

nielsbohrium (Ns) were used in some original publications of the Dubna group for elements 104 and 105. In publications by the Berkeley group and in earlier publications by the author, the name hahnium has been used for element 105.) exhibits chemical properties similar to those of zirconium and hafnium it should form volatile tetrachlorides. Thus, early experiments exploited the volatility of RfCl_4 in the gas-phase (Zvara et al. 1966, 1969; Chuburkov et al. 1969; Zvara et al. 1971a). In aqueous solutions, the complexing with α -hydroxyisobutyrate (α -HIB) (Silva et al. 1970) and the formation of chloride anions (Hulet et al. 1980) confirmed a behavior radically different from that of the heavy actinides. Although these were key experiments demonstrating that a new transition element series, the 6d series, begins with element 104, none of these experiments provided a detailed study of rutherfordium chemistry. First generation gas-phase experiments with chlorides (Zvara et al. 1974) and bromides (Zvara 1976; Zvara et al. 1976) of dubnium, element 105, indicated also for Db halides a much greater volatility than that of the respective actinide compounds. As the deposition temperature in such thermochromatography experiments depends on the migration time and the latter, in turn, strongly depends on the nuclear half-life, these experiments (Zvara et al. 1966, 1969; Chuburkov et al. 1969; Zvara et al. 1971a, b, 1974; Zvara 1976; Zvara et al. 1976) did not allow detailed comparisons of the volatility of rutherfordium and dubnium with the volatilities of their homologs. The respective correction technique based on a microscopic model of gas–solid interactions (Zvara 1985, 1990) in open columns was outlined later. It was systematically applied by Türlér (1996, 1999). The results from the first generation experiments on the chemistry of the transactinides were summarized by Keller and Seaborg (1977), Hulet (1981), Keller (1984) and Silva (1986).

A renewed interest in studying the chemical properties of the transactinide elements in more detail both experimentally and theoretically arose in the late 1980s, (see, e.g., Hoffman 1990, 1993, 1994; Kratz 1994, 1995; Schädel 1995; Kratz 1999; Schädel 2003; Kratz 2003a, b, c; Schädel 2006) for recent reviews. This extensive series of detailed investigations was made possible by the development of new experimental techniques such as computer-controlled automated systems that have greatly improved one's ability to perform rapidly and reproducibly large numbers of chromatographic separations on miniaturized columns in the liquid phase and to detect the transactinides through their characteristic α decay and preferably by $\alpha\alpha$ -mother-daughter correlations. Also, vastly improved techniques for gas-phase experiments coupled online to versatile detection systems for α -decay chains have been developed. Both techniques have produced detailed and sometimes surprising results that called for a detailed theoretical modeling of the chemical species with improved quantum-chemical codes.

In this chapter, the special conditions of the synthesis and decay of the transactinides are considered followed by some remarks about performing chemistry with only one atom at a time (referred to therefore as one-atom-at-a-time chemistry or single-atom chemistry). The experimental techniques are outlined, and a description of theoretical predictions and experimental results on the chemistry of Rf, Db, Sg, Bh, Hs, and Cn is given and mutually compared. Perspectives to go beyond 112 are also briefly discussed.

It should be noted that chemical studies of the transactinides have added a new dimension to heavy element research. While in the physics experiments, for example, in recent experiments using electromagnetic separators, the transactinides are implanted into a Si detector (see ► Fig. 19.6 in Chap. 19) and thereafter, their radioactive decay and decay properties are registered. In chemistry experiments, the transactinides are transferred into a chemistry apparatus, subsequently chemically manipulated and chemically characterized, before their radioactive decay is registered.

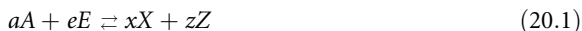
20.2 Synthesis and Decay of Transactinides

Transactinides are being synthesized in nuclear fusion reactions with heavy-ion projectiles. Details of the production and decay of the heaviest elements are discussed in a number of reviews (Armbruster 1985; Münzenberg 1995; Münzenberg and Hofmann 1999), see also ► Chap. 19 on “Production and Identification of Transactinide Elements.” The production rates rapidly decrease from about one atom per minute for element 104 to one atom per several days for the heaviest man-made elements. Half-lives decreasing from about 1 min to the order of magnitude of 1 ms for the longest lived isotope of these elements present an additional challenge, especially for chemical investigations. Low production rates and short half-lives lead to the situation in which, on the average, each synthesized atom has decayed before a new one is made. The consequences for chemical studies performed with one atom at a time are discussed in the next section.

Cold fusion reactions¹ in which ^{50}Ti , ^{54}Cr , ^{58}Fe , $^{62,64}\text{Ni}$, and ^{70}Zn projectiles are fused with ^{208}Pb and ^{209}Bi targets tend to give the highest cross sections, however, the neutron deficient product nuclei in these reactions have half-lives of mostly less than 1 s. This is too short for most existing chemical techniques, in particular for those which allow the study of detailed chemical properties. More neutron rich and, hence, longer-lived products are obtained in hot fusion reactions of ^{18}O , ^{22}Ne , ^{26}Mg , ^{34}S , and ^{48}Ca projectiles with actinide targets such as ^{238}U , $^{242,244}\text{Pu}$, ^{243}Am , ^{248}Cm , ^{249}Bk , and ^{249}Cf . Typical experimental conditions have been heavy-ion beam currents of 3×10^{12} particles per second, and target thicknesses on the order of $800 \mu\text{g}/\text{cm}^2$. Recent chemical studies of rutherfordium have used $78 \text{ s } ^{261\text{a}}\text{Rf}$ produced in the $^{248}\text{Cm}(^{18}\text{O},5\text{n})$ reaction with a cross section on the order of 10 nb. Recent studies of dubnium used $34 \text{ s } ^{262}\text{Db}$ and $27 \text{ s } ^{263}\text{Db}$ produced in 5n- and 4n- reactions of ^{18}O with ^{249}Bk targets with cross sections of about 6 nb at 99 MeV and 10 nb at 93 MeV, respectively. The seaborgium isomers $9 \text{ s } ^{265\text{a}}\text{Sg}$ and $16 \text{ s } ^{265\text{b}}\text{Sg}$ are produced in the 5n- reaction of ^{22}Ne with ^{248}Cm with a cross section of 240 pb around 124 MeV. An isotope of bohrium suitable for chemical studies is $17 \text{ s } ^{267}\text{Bh}$ produced in the $^{249}\text{Bk}(^{22}\text{Ne},4\text{n})$ reaction at 117 MeV with a cross section of about 60 pb. Recently, in 5n-, 4n-, and 3n- reactions of 130, 136, 140, 145, and 150 MeV ^{26}Mg ions with ^{248}Cm , $9 \text{ s } ^{269}\text{Hs}$, $23 \text{ s } ^{270}\text{Hs}$, and $4 \text{ s } ^{271}\text{Hs}$ were produced with cross sections on the order of 6 pb, 3 pb, and 3 pb, respectively, and used for chemical and nuclear studies of element 108, hassium. An isotope suitable for chemical studies of element 112, copernicium is $3.8 \text{ s } ^{283}\text{Cn}$. For element 114, $\sim 0.8 \text{ s } ^{288}\text{114}$ and $\sim 2.6 \text{ s } ^{289}\text{114}$ are candidates for chemical investigations; they are produced in the bombardment of $^{242,244}\text{Pu}$ targets with ^{48}Ca beams. The reactions used for chemical studies are summarized in ► Table 20.1. For completeness, it should be mentioned that in the decay chain of $288(115)$ a long-lived ($\sim 30 \text{ h}$) spontaneously fissioning isotope of dubnium (Stoyer et al. (2007)), presumably ^{268}Db , was chemically identified, that might be a candidate for further chemical studies of dubnium.

20.3 Single-Atom Chemistry

For a chemical reaction



the change of the Gibbs free energy is

■ Table 20.1

Nuclides from nuclear fusion reactions used in transactinide chemistry

Nuclide	Half-life	Target	Proj.	Evap.	σ	Prod. rate ^a	Reference
^{257g} Rf	7.2 s	²⁰⁸ Pb	⁵⁰ Ti	1n	10 nb	2 min ⁻¹	Dragojevic et al. (2008)
^{257m} Rf	4.1 s	²⁰⁸ Pb	⁵⁰ Ti	1n	10 nb	2 min ⁻¹	Dragojevic et al. (2008)
²⁵⁹ Rf	2.5 s	²³⁸ U	²⁶ Mg	5n	EC 0.15		Gates et al. (2008)
^{261a} Rf	78 s	²⁴⁸ Cm	¹⁸ O	5n	10 nb	2 min ⁻¹	Kadkhodayan et al. (1996)
^{261b} Rf	3 s	²⁴⁸ Cm	²⁶ Mg	5n,2 α	6 pb	3 days ⁻¹	Dvorak et al. (2006, 2008)
²⁶² Db	34 s	²⁴⁹ Bk	¹⁸ O	5n	6 nb	2 min ⁻¹	Kratz et al. (1992)
		²⁴⁸ Cm	¹⁹ F	5n	1 nb	0.5 min ⁻¹	Nagame et al. (2002a)
²⁶³ Db ^b	27 s	²⁴⁹ Bk	¹⁸ O	4n	10 nb	2 min ⁻¹	Kratz et al. (1992)
^{263a} Sg	0.9 s	²⁴⁹ Cf	¹⁸ O	4n	0.3 nb	6 h ⁻¹	Ghiorso et al. (1974)
^{265a} Sg	9 s	²⁴⁸ Cm	²² Ne	5n	~240 pb	5 h ⁻¹	Düllmann and Türler (2008)
^{265b} Sg ^b	16 s	²⁴⁸ Cm	²⁶ Mg	5n, α	6 pb	3 days ⁻¹	Düllmann and Türler (2008)
²⁶⁷ Bh	17 s	²⁴⁹ Bk	²² Ne	4n	~70 pb	1.5 h ⁻¹	Eichler et al. (2000b)
²⁶⁹ Hs	9 s	²⁴⁸ Cm	²⁶ Mg	5n	~6 pb	3 days ⁻¹	Türler et al. (2003)
²⁷⁰ Hs ^b	23 s ^c	²⁴⁸ Cm	²⁶ Mg	4n	~3 pb	1.5 days ⁻¹	Dvorak et al. (2006, 2008)
²⁷¹ Hs ^b	4 s ^c	²⁴⁸ Cm	²⁶ Mg	3n	~3 pb	1.5 days ⁻¹	Dvorak et al. (2006, 2008)
²⁸³ Cn	3.8 s	²⁴² Pu	⁴⁸ Ca	3n	~3 pb	1.5 days ⁻¹	Eichler et al. (2008)

^a Assuming typical values of 0.8 mg/cm² target thickness and 3×10^{12} s⁻¹ beam particles.^b Nuclide observed as a “by-product” or discovered in a radiochemical experiment.^c Estimated from measured E_{α} .

$$\Delta G = \Delta G_0 + RT \frac{[X]^x [Z]^z}{[A]^a [E]^e}, \quad (20.2)$$

where the brackets indicate activities (concentrations, partial pressures) of the substances involved. According to the law of “mass action,”

$$\frac{[X]^x [Z]^z}{[A]^a [E]^e} = K, \quad (20.3)$$

where K is the equilibrium constant. In equilibrium, $\Delta G = 0$, and

$$\Delta G_0 = -RT \ln K. \quad (20.4)$$

This is well established for macroscopic quantities where, for example, ions of the metal M are constituents of A and X at the same time, and ➤ Eq. (20.1) characterizes a dynamical, reversible process in which reactants and products are continuously transformed into each other back and forth even at equilibrium. If only one atom of M is present, it cannot be constituent of A and X at the same time, and at least one of the activities on the left or right hand side of ➤ Eq. (20.1) is zero. Consequently, an equilibrium constant can no longer be defined, and the same holds for the thermodynamic function ΔG_0 . Does it make sense, then, to study chemical equilibria with a single atom?

Guillaumont et al. (1989, 1991), in view of this dilemma, have pointed out that chemical speciation of nuclides at the tracer scale is usually feasible with partition methods in which the

species to be characterized is distributed between two phases. This can be an aqueous and an organic phase or a solid phase and the gas phase. According to Guillaumont et al. (1989), single-atom chemistry requires the introduction of a specific thermodynamic function, the single-particle Gibbs free energy. An expression equivalent to the law of mass action is derived by Guillaumont et al. (1989) in which activities (concentrations or partial pressures) are replaced by the probability of finding the species in the appropriate phase. According to this law, an equilibrium constant, that is, the distribution coefficient K_d of M between two phases, is correctly defined in terms of the probabilities of finding M in one phase or the other. If a static partition method is used, this coefficient must be measured many times in repetitive experiments. Since dynamical partition methods (chromatographic separations) can be considered as spatially repetitive static partitions, the displacement of M along the chromatographic column, in itself, is a statistical result and only one experiment is necessary, in principle. This underlines the validity of partition experiments with single atoms and the particular attractivity of chromatographic methods in single-atom chemistry.

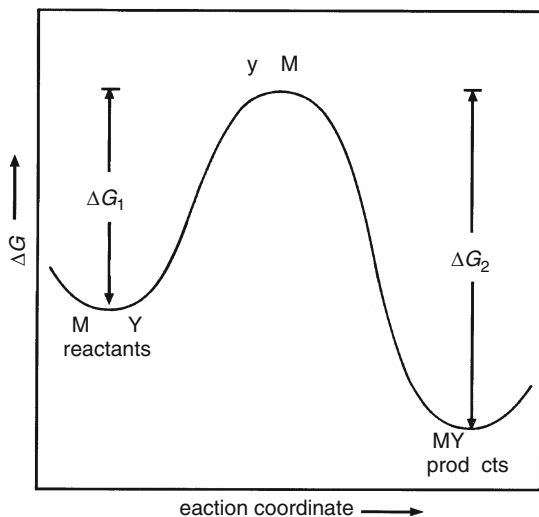
For short-lived atoms, additional considerations with regard to the kinetics are in order. The partition equilibrium must be reached during the lifetime of the atom, which requires high reaction rates. Consider a single-step exchange reaction



Here, M is the single atom that can bind with either X or Y, and k_1 and k_2 are the rate constants for the reactions forth and back. The rate of a chemical reaction depends on the

■ Fig. 20.2

The reaction barrier between two chemical states $MX + Y$ and $MY + X$. The metastable transition state $[Y \cdots M \cdots X]$ has a higher potential energy than the reactants and the products. The energy differences ΔG_1^\ddagger and ΔG_2^\ddagger are the activation energies for the reactions from left to right and from right to left, respectively (Adapted from (Borg and Dienes 1981))



height of the reaction barrier between the states $\text{MX} + \text{Y}$ and $\text{MY} + \text{X}$, because in-between, there is a state of high potential energy (the transition state $[\text{Y} \cdots \text{M} \cdots \text{X}]$), see ► Fig. 20.2.

This state is unstable because the old chemical bond is not completely disrupted and the new one not yet completely formed. If the (Gibbs free) energies of activation ΔG_1^\ddagger and ΔG_2^\ddagger are high, the reaction proceeds very slowly. The transitions from left to right and from right to left do not occur with sufficient frequency and the system is far from its thermodynamical equilibrium. Borg and Dienes (1981) found that if ΔG^\ddagger is less than 15 kcal (60 kJ), then the residence time of M in either state (MX or MY) is rather short (<1 s) and an equilibrium is rapidly reached (in comparison with the nuclear half-lives of the transactinides). Borg and Dienes point out that the average time that M spends as MX or MY is proportional to the equilibrium constant. Thus, a measurement of the partition of M between the states MX and MY with very few atoms of M will already yield an equilibrium constant close to the “true” value provided that both states are rapidly sampled. This shows again that chromatographic systems with fast kinetics are ideally suited for single-atom separations as there is rapid, multiple sampling of the absorbed or mobile species. The fractional average time that M spends as the absorbed species (which is proportional to the equilibrium constant, see above) is closely related to the chromatographic observable, the retention time.

20.4 Experimental Techniques

Recent reviews of fast chemical separation procedures developed for transactinide studies can be found in (Schädel 1995; Trautmann 1995). Nevertheless, the most pertinent techniques are also presented here.

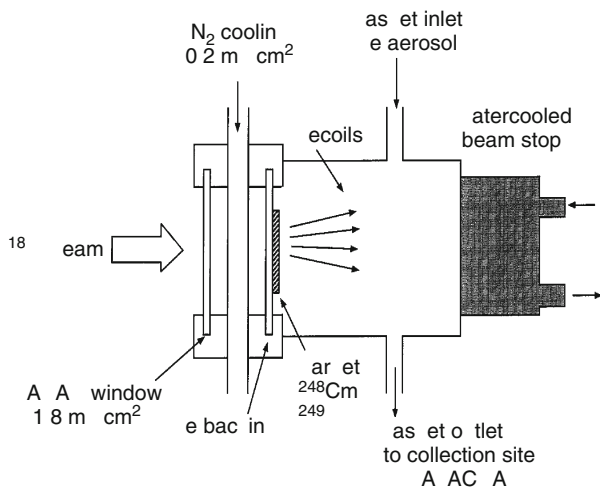
20.4.1 Target and Transport Systems

A scheme of a target- and recoil chamber arrangement is shown in ► Fig. 20.3. Heavy-ion beams pass through a vacuum isolation window, a volume of nitrogen cooling gas, and a target backing before interacting with the target material. Reaction products recoiling out of the target are thermalized in a volume of He gas loaded with aerosol particles of 10–200 nm size to which the reaction products attach. At a flow rate of about 2 l/min the transport gas with the aerosols is transported through capillary tubes (~ 1.5 mm inner diameter) to the chemistry apparatus where it deposits the reaction products. He/aerosol-jets allow transportation over distances of several tens of meters with yields of about 50% (Gregorich et al. 1988; Schädel et al. 1988; Gäggeler et al. 1991; Günther et al. 1995a, b). Transport times are on the order of 2–5 s. Aerosol materials are selected such as to minimize their influence on the chemical procedures. Separations in the aqueous phase often use KCl (Gregorich et al. 1988; Schädel et al. 1988; Günther et al. 1995a, b) as aerosol while MoO_3 and carbon clusters are preferred in gas-phase separations (Gäggeler et al. 1991).

In the early frontal gas-chromatographic experiments with element 104 (Zvara et al. 1966, 1969; Chuburkov et al. 1969), the target- and recoil chamber was bombarded by the internal beam inside the cyclotron. The recoils were stopped in nitrogen heated to 300°C (flow rate 18–20 l/min) and transported into an outlet tube (i.d. 3.5 mm) where, at a distance of 3 cm from the target, a stream of nitrogen (0.5–1.0 l/min), containing the chlorinating reactive gases NbCl_5 and ZrCl_4 , was introduced. The volatile RfCl_4 was transported through the 4 m long outlet tube to mica fission-track detectors outside of the cyclotron.

■ Fig. 20.3

Schematic representation of a target and recoil chamber arrangement with He/aerosol-jet
(Reprinted with the permission of Oldenbourg Wissenschaftsverlag, München, (Trautmann 1995))



Later, the external beam of the cyclotron was used with the chromatography columns coupled directly to the target and recoil chamber (Zvara et al. 1970, 1971a, b, 1974, 1976; Timokhin et al. 1996; Yakushev et al. 1996a, b; Zvara et al. 1998). In this configuration, typically 60% of the recoils reach the column without the use of aerosols. Transport times of <1 s were measured (Zvara et al. 1971b). The disadvantage of this thermochromatography technique is that the detection of the transactinides has to be performed in a hostile chemical environment so that detection of α particles with semiconductor detectors is not possible and the detection is limited to the unspecific spontaneous fission (SF) by solid-state track detectors.

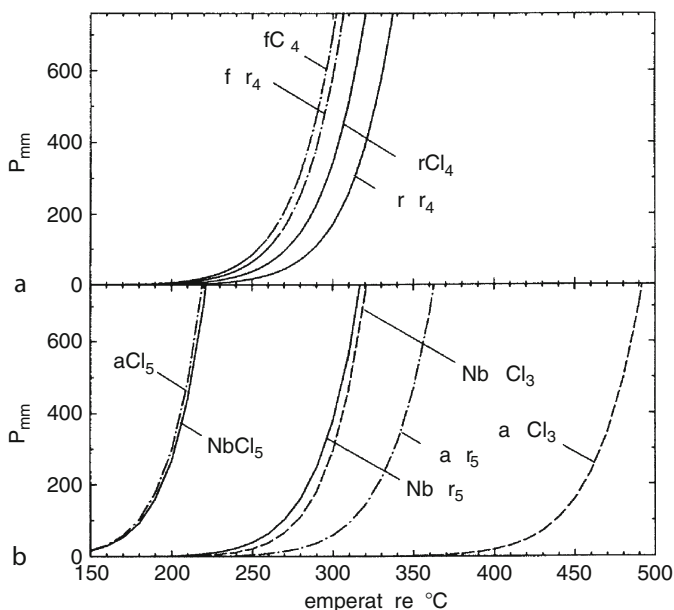
Recent important developments in the field of target and transport systems are the use of (1) rotating target wheels (Eberhardt et al. 2008) that allow for higher beam intensities, and (2) pre-separation of the fusion- evaporation residues in an electro-magnetic separator such as the **Berkeley Gas-Filled Separator BGS** (Omtvedt et al. 2002; Düllmann et al. 2009) or the newly commissioned **TransActinide Separator and Chemistry Apparatus TASCA** at the GSI Helmholtz center for heavy ion research, Darmstadt, (Schädel et al. 2008), both coupling the chemistry apparatus to the separator via a He/KCl gas jet leaving a **Recoil Transfer Chamber RTC** in the focal plane, and (3) avoiding vacuum windows by differential pumping in the target area.

20.4.2 Gas-Phase Chemistry

Vapor pressure curves (Gäggeler 1994; Türler 1996; Gärtner et al. 1997) give a measure of the volatility of compounds. In ► Fig. 20.4, the vapor pressure curves of the monomeric gas over the respective solids for Zr and Hf tetrachlorides and -bromides and for Nb and Ta pentachlorides and -bromides are shown, respectively. Also shown are vapor pressure curves for Nb and Ta oxytrichlorides. These curves are calculated using tabulated standard

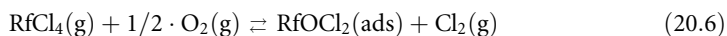
■ Fig. 20.4

Vapor pressure curves of the monomeric gas over the respective solids for (a) ZrCl_4 , ZrBr_4 , HfCl_4 , HfBr_4 , and (b) NbCl_5 , NbBr_5 , TaCl_5 , TaBr_5 , NbOCl_3 and TaOCl_3 (Reprinted with permission of Oldenbourg Wissenschaftsverlag, München, (Türler 1996)⁸)



sublimation enthalpies, $\Delta H_s^{\circ(298\text{ K})}$, and standard sublimation entropies, $\Delta S_s^{\circ(298\text{ K})}$ (Knacke et al. 1991). HfCl_4 and HfBr_4 are slightly more volatile than the Zr homologs, but less volatile than TaCl_5 and NbCl_5 .

It is interesting to note that the chlorides and bromides of Zr and Hf show similar volatilities, whereas NbBr_5 and TaBr_5 are considerably less volatile than the respective pentachlorides. In Fig. 20.4, no vapor pressure curves for ZrOCl_2 and HfOCl_2 are shown because their existence in the gas phase is uncertain. Morozov and Karlova (1971) found that ZrOCl_2 and HfOCl_2 decompose to tetrachloride and oxide when heated. They also determined the vapor pressure curves of the tetrachlorides over their oxychlorides. Domanov and Jin (1989) observed that the deposition temperature for Zr and Hf depends on the O_2 concentration in the reactive gas. Eichler (1996) suggested a transport reaction mechanism (“reaction gas chromatography”) with the tetrachloride in the gas phase and the oxychloride in the adsorbed state, that is,




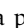
Jost et al. (1996) presented experimental evidence for this transport reaction mechanism. Since in experiments with transactinide elements only single molecules can be studied, $\Delta H_s^{\circ(298\text{ K})}$ of, for example, RfCl_4 cannot be determined directly. The quantity deduced from gas chromatography experiments is $\Delta H_a^{\circ(T)}$, the adsorption enthalpy on the chromatographic surface (usually quartz) at zero coverage. As was demonstrated by Zvara et al. (1970), there exists a linear relationship between $\Delta H_a^{\circ(T)}$ and $\Delta H_s^{\circ(298\text{ K})}$ for chlorides. By measuring $\Delta H_a^{\circ(T)}$ of chlorides of 24 elements on quartz surfaces, Eichler et al. (1976) established the empirical relation

$$-\Delta H_a^{\circ(T)} = (0.655 \pm 0.042) \times \Delta H_s^{\circ(298K)} + (18.0 \pm 8.8) \text{ kJ mol}^{-1}, \quad (20.7)$$

Thus, $\Delta H_a^{\circ(T)}$ is the quantity used to judge the volatility of the transactinide compounds relative to the volatility of their lighter homologs.

There are two experimental approaches to determine $\Delta H_a^{\circ(T)}$, thermochromatography and isothermal gas chromatography. In thermochromatography (Zvara et al. 1970, 1971a, b, 1974, 1976; Zvara 1976, 1985, 1990; Timokhin et al. 1996; Yakushev et al. 1996; Zvara et al. 1998), a longitudinal, negative temperature gradient is established along the chromatography column in the flow direction of the carrier gas.² Volatile species are deposited in the column according to their volatility and form distinct deposition zones. Mica sheets inserted into the chromatography column serve as fission track detectors. The method has the advantage of a very high speed at which the production of volatile species and their separation occurs. The recoiling reaction products are rapidly swept from the target chamber to the entrance of the chromatography column where gaseous halogenating agents are added. Transactinides decaying by SF are registered in the column at a characteristic deposition temperature thus providing information about their volatility. These experiments are simple and relatively easy to perform. However, thermochromatography, as applied in the above references, shows also serious disadvantages. The fact that the position of the deposition zones of homologs can be measured only after completion of the experiment makes the interpretation of the relative volatility of the short-lived transactinides difficult compared to the detected, much longer-lived homologs. In addition, real-time detection of the nuclear decay of transactinides and the determination of their half-lives is not possible. Moreover, SF is an unspecific decay mode of many actinides and transactinides which allows no identification of the decaying nuclide.

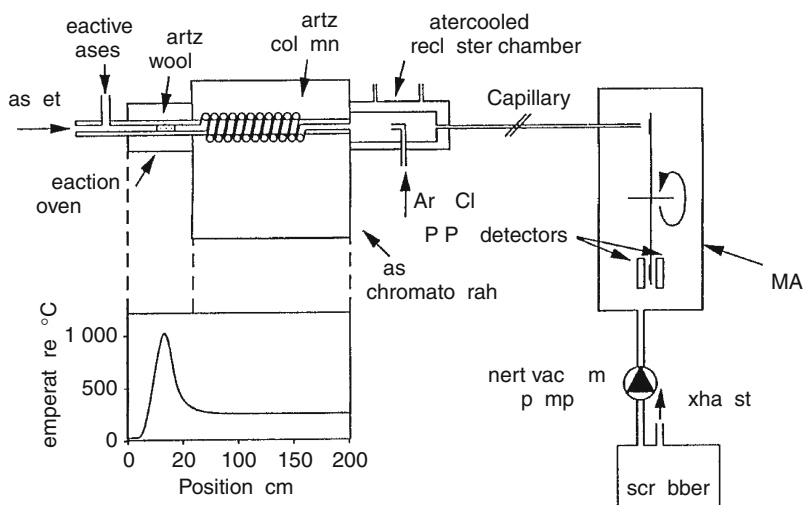
In order to overcome these serious disadvantages, the online isothermal gas chromatography was developed and was successfully applied to study the volatility of Rf, Db, Sg, and Bh halides and oxyhalides (Gäggeler et al. 1991, 1992a, b, Türlér et al. 1992; Gäggeler 1994; Jost et al. 1996; Türlér 1996; Türlér et al. 1996; Kadkhodayan et al. 1996; Yakushev et al. 1996; Gärtner et al. 1997; Gäggeler 1998). The most advanced version of the Online Gas Chemistry Apparatus, OLGA III, is shown in  Fig. 20.5. The reaction products, attached to graphite aerosols, are continuously transported through a capillary to the OLGA setup. In the first section of the chromatography column, the aerosols are stopped on a quartz wool plug. This section is heated to 900–1,000°C. At the position of the quartz wool plug, reactive gases such as HBr, BBr₃, HCl, Cl₂, SOCl₂, and O₂ are added.

The second part of the quartz column serves as isothermal chromatography section. Volatile species pass this section whereby they undergo numerous sorption/desorption steps with retention times indicative of the volatility at the given temperature of the isothermal part of the column. The chemical yield of the volatile species is studied as a function of the temperature of the isothermal part of the column. The chemical yield rises steeply above a certain temperature and reaches a plateau at higher temperatures (see  Fig. 20.11). The retention time of the volatile species is determined by using the nuclear half-life of the radionuclides as a “clock”: at the temperature at which 50% of the plateau yield is observed, $T_{50\%}$, the retention time is equal to one half-life.

To measure the decay of the separated species, they are – after leaving the chromatographic column and entering a water-cooled “recluster chamber” – attached to new aerosols and transported through a capillary to a detection system, a rotating wheel or a moving tape system (Türlér 1996) that positions the deposited activity in front of successive PIPS detectors (Passivated Ion-implanted Planar Silicon), which register α particles and SF events.³ The

■ Fig. 20.5

The OLGA III system used for the study of seaborgium (Gäggeler 1998). The gas jet transports the seaborgium atoms attached to graphite particles in He gas to the reaction oven where the reactive gas $\text{Cl}_2/\text{SOCl}_2/\text{O}_2$ is added to form volatile oxychlorides and to convert the graphite particles into CO_2 . Behind the isothermal chromatography section, the gaseous molecules are attached to new aerosol particles and transported to the rotating-wheel counting device ROMA (Reprinted from Gäggeler 1998), copyright (2009), with the permission from Elsevier)



energies of the events are stored in list mode with the time and detector designation for off-line processing of the data. This allows searching for time-correlated parent-daughter pairs of α events allowing for an unambiguous identification of single events.

Based on a microscopic model of gas-solid thermochromatography in open columns by Zvara (1985), a Monte Carlo code has been made available (Türler 1996), which allows to generate thermochromatographic deposition zones as well as yield versus temperature curves as observed in isothermal chromatography. This model accommodates the influence of the carrier gas flow, the actual temperature profiles, and the different half-lives of the investigated species. For each isothermal temperature, the transport through the column is modeled for a large number of sample molecules. These calculations result in a curve of yield versus temperature for each value of the adsorption enthalpy $\Delta H_a^{\circ(T)}$. The curve for the particular $\Delta H_a^{\circ(T)}$, which best fits the measured data, is chosen by a least-squares method. In the correlation of the retention time with $\Delta H_a^{\circ(T)}$, the adsorption entropy $\Delta S_a^{\circ(T)}$ calculated according to the formalism of Eichler and Zvara (1985) is used.

The most obvious chemical compound of hassium suitable for its chemical separation is the tetroxide, HsO_4 , which is likely to be highly volatile. Zhuikov et al. (1986) have set up an online system in which radioactive Os recoils were thermalized in a gas mixture of 1.2 bar Ar + 2% O_2 whereby volatile OsO_4 was formed in situ and was transported without aerosols through a Teflon capillary to the detection device. This technique has been adapted (Düllmann et al. 2002a; Kirbach et al. 2002; von Zweidorf et al. 2002) in the preparation of the first chemical identification of Hs. The IVO technique developed by Kirbach et al. and Düllmann et al. combines the in situ volatilization of compounds with their online detection in a narrow, ~ 40 cm


long channel consisting of pairs of PIN-diode detectors to which a negative temperature gradient from typically room temperature down to $\sim -180^{\circ}\text{C}$ is applied. This powerful cryo-detection technique has also been instrumental in the studies of the volatility of element 112 (Eichler et al. 2008).

At the velocity filter SHIP (Münzenberg et al. 1979) at GSI in Darmstadt, a Penning trap, SHIPTRAP, has been installed (Marx et al. 2002) in which heavy-ion fusion evaporation residues can be stored for precision mass measurements and manipulated, for example, by laser spectroscopy or by chemical interactions with reactive gases. In order to explore the merits of ion-chemical investigations of heavy elements in a Penning trap, Rieth et al. (2002) have studied the reactions of Ru^+ and Os^+ ions with O_2 , thus demonstrating that ion-molecule reactions may be considered a new way to study the chemical properties of heavy elements.

20.4.3 Aqueous Chemistry

While gas-phase chemistry is generally carried out continuously as an online process, aqueous chemistry has been performed mostly in a discontinuous, batch-wise manner. It is then necessary, in order to get statistically significant result, to repeat the same experiment several hundred or even several thousand times with a cycle time of typically 1 min. These discontinuous studies were either performed manually (Gregorich et al. 1988; Czerwinski et al. 1994a, b; Bilewicz et al. 1996; Kacher et al. 1996a, b) or with the Automated Rapid Chemistry Apparatus ARCA II (Kratz et al. 1989, 1992; Schädel et al. 1992; Gober et al. 1992; Zimmermann et al. 1993; Schädel et al. 1997a, b, Günther et al. 1998; Schädel et al. 1998; Paulus et al. 1999a, b; Strub et al. 2000) or with the Automated Ion-exchange separation apparatus coupled with the Detection system for Alpha spectroscopy AIDA (Nagame et al. 2005).

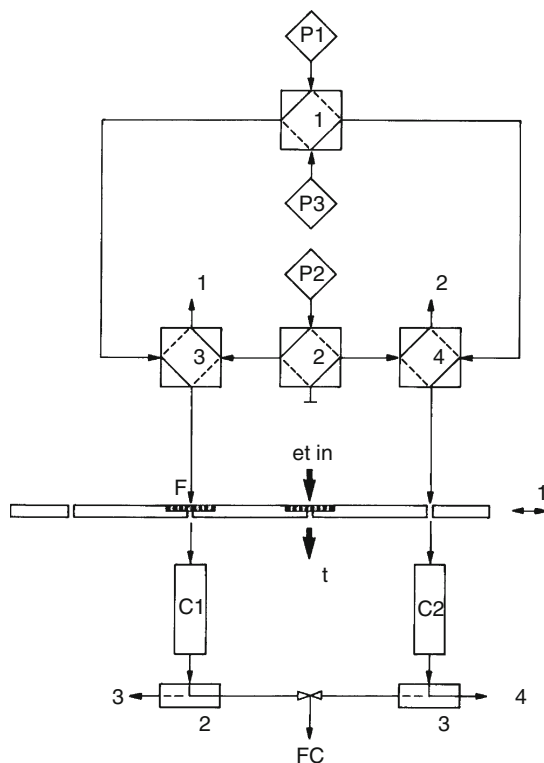
One of the manual separations made use of the characteristic adsorption of the group-5 elements Nb, Ta, and element 105 from nitric acid on glass surfaces (Gregorich et al. 1988). Another used thin film ferrocyanide surfaces for the study of the hydrolysis of rutherfordium (Bilewicz et al. 1996). All other manual separations were liquid-liquid extractions typically comprising the following steps: the KCl aerosol with the reaction products was collected on a platinum or TeflonTM slip for 60 to 90 s, picked up with 10 μl of the aqueous phase and transferred to a 1 ml centrifuge cone containing 20 μl of the organic phase. The phases were mixed ultrasonically for 5 s and centrifuged for 10 s for phase separation. The organic phase was transferred to a glass cover slip, evaporated to dryness on a hot plate, and placed over a PIPS detector. This procedure took about 1 min and was mainly applied to study the aqueous chemistry of element 104 with the isomer $78\text{ s }^{261\text{a}}\text{Rf}$ (Czerwinski et al. 1994a, b; Kacher et al. 1996a, b). A serious drawback of these latter investigations is that only the organic phase was assayed for $^{261\text{a}}\text{Rf}$; the aqueous phase was not counted.

Automated separations with ARCA II were performed with element 104 (Günther et al. 1998; Strub et al. 2000), element 105 (Kratz et al. 1989; Gober et al. 1992; Kratz et al. 1992; Schädel et al. 1992; Zimmermann et al. 1993; Paulus et al. 1999a, b), and element 106 (Schädel et al. 1997a, b, 1998). ARCA II is a computer-controlled apparatus for fast, repetitive High Performance Liquid Chromatography (HPLC) separations (Schädel et al. 1989). A schematic representation of ARCA II is shown in  Fig. 20.6.

ARCA II consists of a central catcher-chemistry part incorporating the sliders SL1-SL3, and two movable magazines containing 20 of the chromatographic columns C_1 , C_2 (1.6 mm i.d. \times 8 mm) each, and peripheral components, that is, three chemically inert HPLC pumps,

■ Fig. 20.6

Schematic representation of the computer-controlled HPLC-system ARCA II; for details see text (Reprinted with the permission of Oldenbourg Wissenschaftsverlag, München, (Schädel et al. 1989))



P_1 - P_3 , and a number of pneumatically driven four-way slider valves, S1-S4. Each pump pumps one eluent, in case of the separations of element 105 in mixed HCl/HF solutions (Kratz et al. 1989), one 12 M HCl/0.02 M HF, another 4 M HCl/0.02 M HF, and the third 6 M HNO₃/0.015 M HF, through Teflon tubing of 0.3 mm inner diameter to the central catcher-chemistry unit. The He(KCl) gas jet deposits the transported reaction products continuously onto one of two polyethylene frits F. After 1 min collection, the frit is moved on top of one of the microcolumns C1, washed with 12 M HCl/0.02 M HF, whereby the reaction products are dissolved, complexed, and extracted into the organic phase (the columns are filled with TeflonTM grains coated with tri-isooctyl amine, TiOA), while the non-extractable species (notably the actinides) run through into the waste, W3. The column is then washed with 4 M HCl/0.02 M HF, and the effluent (containing Nb, Pa, and element 105) is directed through SL 2 to the fraction collector FC where it is collected on a Ta disk and quickly evaporated to dryness by intense IR light and hot He gas. Next, the Ta fraction is eluted with 6 M HNO₃/0.015 M HF, collected on a Ta disk, and evaporated to dryness. The Ta disks are inserted into the counting chambers about 55 s after the end of collection. Five seconds later, the next 1 min collection on the twin frit is complete. That frit is moved on top of the column

C2 contained in the opposite magazine, and the next separation cycle is carried out. After each separation, the magazine is moved by one step, thus introducing a new column into the elution position. In this way, the time-consuming reconditioning of used columns and cross contaminations from previous separations are avoided. After 40 min of continuous collection and separation cycles, the program is stopped, the used magazines are removed, two new magazines are introduced, and another 40 cycles are started. More than 7,800 of such and similar ARCA II experiments have been conducted in the study of element 105 so far.

► **Figure 20.7** shows an example for such a separation (Schädel et al. 1989). The upper part is the result of a manually operated HPLC separation on a TiOA/TeflonTM column (1.7 mm i.d. \times 11 mm). Radioactive tracers of lanthanides (Ln), actinides (An), Zr, Hf, Pa, Nb, and Ta are introduced into the system through a sample loop in 12 M HCl/0.02 M HF. Under these conditions, halide complexes of Pa, Nb, and Ta are extracted into the amine, while Ln, An, Zr, and Hf pass the column (fraction A). Pa and Nb are then eluted together with 4 M HCl/0.02 M HF (fraction B), and finally, Ta is stripped from the column in 6 M HNO₃/0.015 M HF (fraction C). The manually performed separation takes about 75 s. This time does not include the times required for rinsing the tubings when the eluent is changed.

The lower part of ► **Fig. 20.7** shows the same separation performed automatically with ARCA II. A volume of 50 μ l of 12 M HCl/0.02 M HF is used to precondition each column before the tracer activities are loaded onto the column in 25 μ l 12 M HCl/0.02 M HF. The complete extraction and elution cycle is complete in ≤ 35 s. This is achieved by the reduction of the void volumes to a minimum.

Recently, an apparatus similar to ARCA II was constructed at JAERI, now JAEA, Tokai, Japan, called AIDA (Automated Ion-exchange separation apparatus coupled with the Detection system for Alpha spectroscopy) (Haba et al. 2001; Nagame et al. 2002b, 2005), and was used for a start-up of transactinide chemistry in Japan. A schematic diagram of the experimental set-ups at JAEA is shown in ► **Fig. 20.8**. In the modified ARCA, there are two different paths to supply solutions; the first eluent goes through the collection port to the microcolumn, while the other one is directed to the column without going through the collection port. This minimizes contamination of the strip fraction. A schematic drawing of AIDA is given in ► **Fig. 20.9**. The Ta disks with the evaporated samples are automatically inserted into the eight vacuum chambers for α spectroscopy.

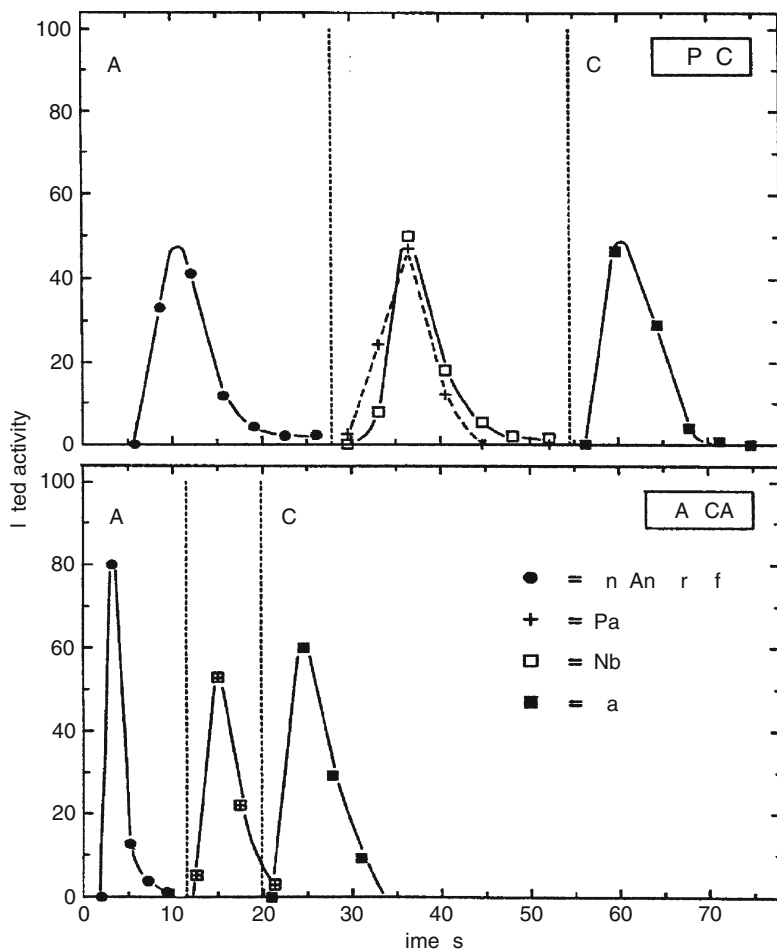
Continuous isolation procedures have also been developed, the first one for nuclear decay studies of Hf, Ta, and W isotopes (Bruchertseifer et al. 1989), which was subsequently applied to element 104 (Szegłowski et al. 1990) in combination with a discontinuous sample preparation step.

Reaction products transported by an aerosol jet were continuously dissolved in the aqueous phase which was pumped through three consecutive ion-exchange columns (multicolumn technique, MCT). Trivalent actinides were retained on the first cation exchange column followed by an anion exchange column to adsorb anionic fluoride complexes of element 104, and a third column filled with a cation exchange resin to collect the trivalent daughter products from the α decay of ^{261a}Rf. At the end of an experiment, the ²⁶¹Rf daughter products, 3.0 d ²⁵³Fm and 20 d ²⁵³Es, were stripped from this third column to prepare a sample for off-line α spectroscopy. The detection of ²⁵³Es in that sample was proof that ^{261a}Rf had formed anionic fluoride complexes that had been retained on the anion exchange column.

Pfreppep et al. (1997, 1998) have developed this technique further, thereby making it a quantitative technique capable of measuring distribution coefficients K_d . In the conventional

■ Fig. 20.7

Separation of trivalent lanthanides (Ln) and actinides (An), Zr, Hf, Nb, Ta, and Pa in an extraction chromatographic system with TiOA (tri-isooctyl amine) on an inert support as stationary phase and 12 M HCl/0.02 M HF (A), 4 M HCl/0.02 M HF (B), and 6 M HNO₃/0.015 M HF (C) as eluents. In the upper part of the figure (HPLC) the chromatogram of a manually performed separation with standard HPLC techniques on a 1.7 × 11 mm column is shown. The lower part of the figure (ARCA) shows a fully automated separation in ARCA II on a 1.6 × 8 mm column at a flow rate of 1.0 ml/min (Reproduced with the permission of Oldenbourg Wissenschaftsverlag, München, (Schädel et al. 1989))



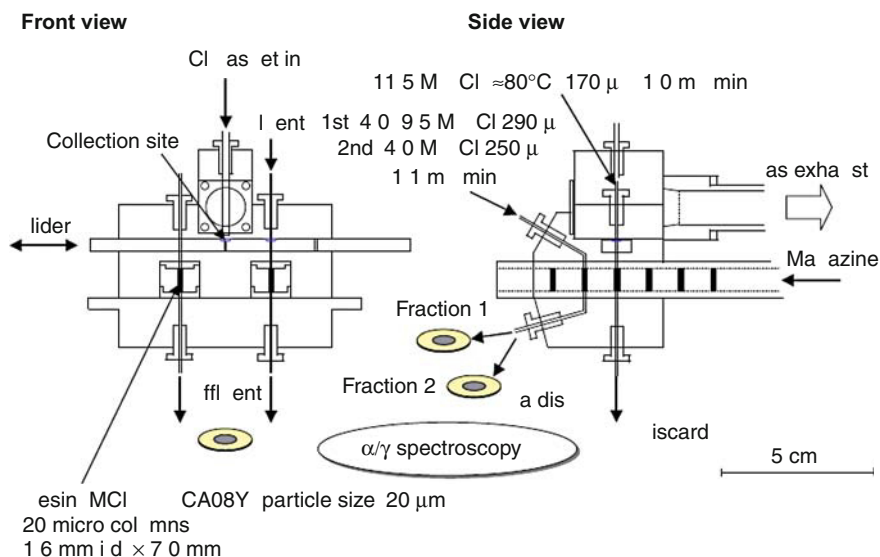
off-line chromatography as performed by ARCA II, the distribution coefficient is determined via the retention time (elution position) as

$$K_d = (t_r - t_0) \frac{V}{M} \quad (20.8)$$

where t_r denotes the retention time, t_0 is the column hold-up time due to the free column volume, V is the flow rate of the mobile phase (ml/min), and M is the mass of the ion exchanger (g).

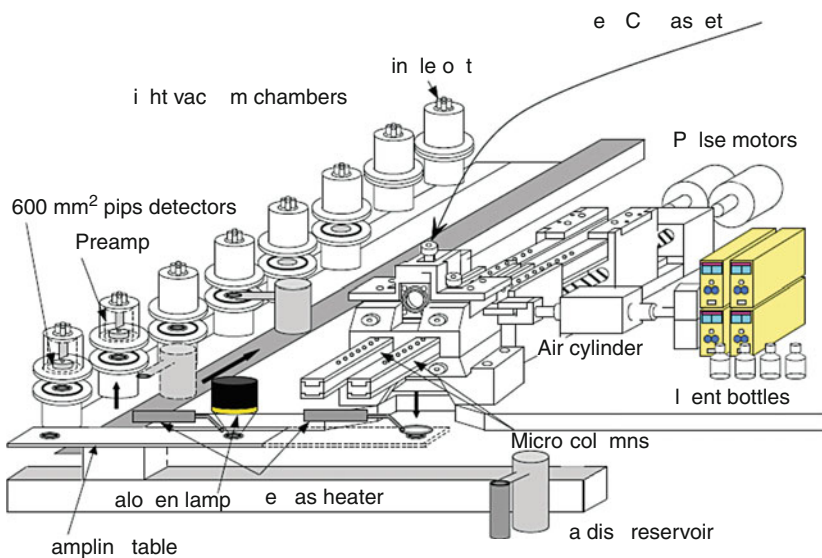
■ Fig. 20.8

Schematic diagram of the modified ARCA in AIDA (Nagame et al. 2005) (Reproduced with the permission of Oldenbourg Wissenschaftsverlag, München)



■ Fig. 20.9

Schematic diagram of AIDA (Reproduced with the permission of Oldenbourg Wissenschaftsverlag, München, (Nagame et al. 2005))



As in (Szegełowski et al. 1990), the detection of the transactinide isotope itself, $^{261\text{a}}\text{Rf}$, is abandoned and replaced by the detection of its long-lived descendant, 20 d ^{253}Es . This way, one gains the possibility of a continuous online mode over many hours. The feeding of $^{261\text{a}}\text{Rf}$ onto the anion exchange column is performed under conditions in which the retention time t_r is on the order of the nuclear half-life $T_{1/2}$, that is, K_d values on the order of 10–50 are selected (Pfrepper et al. 1997). Similarly to the principle used in the online isothermal gas chromatography, one is using the nuclear half-life as an internal clock. As in (Szegełowski et al. 1990), three ion exchange columns are used in series; first a cation exchange column that retains the ^{253}Es from the continuously flowing feed solution. This is necessary as ^{253}Es could be produced directly by transfer reactions. It follows the true chromatographic column filled with an anion exchange resin. The long-lived decay products (whose number is denoted by D_1) that are formed by radioactive decay of $^{261\text{a}}\text{Rf}$ during its retention time on the anion exchange column are eluted from this column as cations and are fixed on the following cation exchange column. The part of the $^{261\text{a}}\text{Rf}$ that survives the retention time on the anion exchange column is eluted from it and passes the following cation exchange column to be subsequently collected in a reservoir in which it decays into the long-lived decay products (D_2). Thus D_1 and D_2 decay products are isolated separately after the end of the online experiment and assayed off-line for α activity of ^{253}Es . From the ratio of D_1 and D_2 and the nuclear half-life of $^{261\text{a}}\text{Rf}$, one obtains the distribution coefficient

$$K_d = \left[\frac{T_{1/2}}{\ln 2} \ln \frac{D_1 + D_2}{D_2} - t_0 \right] \frac{V}{M}. \quad (20.9)$$

This principle has been applied to rutherfordium in fluoride solutions (Pfrepper et al. 1998; Kronenberg et al. 2004a) and in preliminary studies of rutherfordium and dubnium by Le Naour et al. (1999).

The centrifuge system SISAK III (Persson et al. 1989) allows for a continuous separation of nuclides with half-lives down to 1 s⁴. The separation is based on multistage liquid-liquid extractions using static mixers and specially designed mini-centrifuges for subsequent phase separation. SISAK was successfully applied to a large number of γ -spectroscopic studies of lighter elements. Recently, a new detection system based on liquid scintillation counting (LSC) was developed for online α spectroscopy and SF-detection in the flowing organic phase behind SISAK (Wierczinski et al. 1996). Between α energies of 4.8 and 7.4 MeV, energy resolutions of 210 through 330 keV are achieved. Suppression of interfering β and γ radiation is done by pulse-shape discrimination and pile-up rejection. An online model experiment for element 104 was carried out (Wierczinski et al. 1996) using the α emitter 17 s ^{161}Hf . However, in experiments with $^{261\text{a}}\text{Rf}$, due to a high level of interfering β and γ radiation, the number of random $\alpha\alpha$ -mother-daughter correlations due to pile-up was too large to allow an unambiguous identification of $^{261\text{a}}\text{Rf}$ decay chains. Two solutions of this problem have been pursued recently: (1) The Berkeley Gas-Filled Separator (BGS) was used as a preseparator for ^{257}Rf produced in the $^{208}\text{Pb}(^{50}\text{Ti}, \text{In})$ reaction followed by the transfer of ^{257}Rf to a gas jet delivering the activity to the SISAK system (Omtvedt et al. 2002). This reduced the interfering β and γ radiation by more than three orders of magnitude thus enabling the unambiguous detection of ^{257}Rf by LSC. (2) A fast transient recorder was introduced into the data acquisition in order to digitally record the pulse shapes, and a neural network was trained to recognize true α events and to distinguish these from $\beta\beta$ -pileup and $\beta\gamma$ -pileup events (Langrock et al. 2002; Eberhardt et al. 2002).

20.5 Element 104 (Rutherfordium)

20.5.1 Theoretical Predictions

Extrapolating the ground state electron configuration of Ti, Zr, and Hf to Rf gives the configuration $[\text{Rn}]5f^{14}6d^27s^2$ for the latter. This configuration was also indicated by early relativistic calculations (Fricke 1975; Desclaux 1973) in a Dirac-Fock computer code with a single configuration approximation.

After multiconfiguration Dirac-Fock (MCDF) calculations had indicated that, because of the relativistic stabilization of the $p_{1/2}$ orbital, the electronic structure of lawrencium (element 103) is $[\text{Rn}]5f^{14}7s^27p_{1/2}$ rather than $[\text{Rn}]5f^{14}6d7s^2$ (Desclaux and Fricke 1980; Brewer 1984) it was extrapolated that element 104 should have a $7s^2p^2$ rather than a $6d^27s^2$ configuration (Keller 1984). This raised the question whether element 104 might be a “p-element” with properties similar to Pb, which has a ground state configuration $[\text{Xe}]4f^{14}5d^{10}6s^2p^2$. However, it should be noted that, contrary to Rf, Pb has a closed 5d shell and a large energy gap of more than 4 eV between its ground state and the next higher state.

A more recent MCDF calculation using 468 *jj*-configurations gave a (80%) $6d7s^27p$ ground state configuration for Rf (Glebov et al. 1989) with the $6d^27s^2$ level (95%) only 0.5 eV higher. This calculation predicted the $7s^27p^2$ state 2.9 eV above the ground state. The $6d7s^27p$ ground state configuration was confirmed in a similar MCDF calculation (Johnson et al. 1990) with an energy gap of only 0.24 eV to the next higher state.

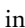
Relativistic coupled-cluster calculations based on the Dirac-Coulomb-Breit Hamiltonian (CCSD) including dynamical correlations (Eliav et al. 1995) reverted to the $6d^27s^2$ configuration as the ground state of Rf. Here, the $6d7s^27p$ state is 0.274 eV above the ground state.

From MCDF calculations, ionization potentials, atomic radii, and ionic radii were deduced (Johnson et al. 1990; Zhuikov et al. 1990). It was found that radii, orbital energies, and ground levels of ionized states of Rf are similar to Hf and much different from Pb (Zhuikov et al. 1990) so that it was concluded that there is no solid ground for expecting a “p-character” for Rf and that its chemical properties will resemble those of Zr and Hf. From a relativistic SCF- $X\alpha$ scattering wave Dirac-Fock computation for RfCl_4 , a lower effective charge of the central metal ion and a higher covalency in the metal-chloride bonds was obtained (Zhuikov et al. 1990). This could give rise to a higher volatility of RfCl_4 as compared to that of ZrCl_4 and HfCl_4 .

Quantum chemical calculations using the Dirac-Slater Discrete Variational Method (DS DVM) were performed to study the electronic structure of the group-4 tetrachlorides and of PbCl_4 (Ryshkov et al. 1992) and of the highest chlorides of the group-4, group-5, and group-6 elements (Pershina and Fricke 1994a). These calculations agree that the electronic structures of RfCl_4 and HfCl_4 are similar and that the bonding is typical of a d-element compound. Both calculations also show that RfCl_4 is a rather covalent compound, more covalent than HfCl_4 . A stronger metal-ligand bond in RfCl_4 should make RfCl_4 thermally more stable than ZrCl_4 and HfCl_4 (Pershina and Fricke 1994a).

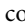
More recently, calculations of the total binding energies of the group-4 tetrachlorides were performed in order to test the predictive power of an improved DVM scheme using the four-component fully relativistic density functional method (Varga et al. 2000). The calculations show the binding energies to be in very good agreement with thermochemical dissociation energies obtained via the Born-Haber cycle, thus demonstrating a new quality in theoretical predictions.



20.5.2 Experimental Results

The pioneering experiments with rutherfordium in the gas phase (Zvara et al. 1966; Chuburkov et al. 1969; Zvara et al. 1969, 1971a) demonstrated that element 104 forms volatile chlorides and that RfCl_4 is much more volatile than the actinide chlorides and similar to HfCl_4 . Originally, the authors claimed (Zvara et al. 1969) that the spatial distribution of fission tracks was compatible with the half-life of 0.3 s that they believed to be associated with the isotope ^{260}Rf . It was also claimed that the volatility of RfCl_4 was somewhat less than that of HfCl_4 (Zvara et al. 1969). These claims are evidently incorrect. Firstly, an isotope of element 104 with a half-life of 0.3 s has never existed (Ter-Akopyan et al. 1985), and secondly, it is impossible to determine both the half-life and the heat of adsorption from a fission track distribution. Later, Zvara et al. (1971b) reinterpreted their original experiments by considering “the possible chromatographic effect of retention” and suggested that they were evidently dealing with 3 s ^{259}Rf , an α emitter discovered earlier at Berkeley (Ghiorso et al. 1969). There has been on-going discussion about the existence of a fission branch in this isotope. New studies (Gates et al. 2008) have found an electron capture branch in the decay of ^{259}Rf leading to ^{259}Lr that partially decays by spontaneous fission. The thermochromatographically determined deposition zones for spontaneously fissioning isotopes in (Zvara et al. 1971b) are shown as full circles in  Fig. 20.10 where they are compared to the distribution of $^{44\text{m}}\text{Sc}$ modeling trivalent actinides and to the distribution of $^{170,171}\text{Hf}$.

The fission tracks designated by open circles were thus assigned to heavy actinides, those designated by the full circles to rutherfordium. Zvara et al. (1971b) also reported a strongly enhanced retention of the RfCl_4 when KCl is provided as the solid phase instead of glass, most likely due to the formation of nonvolatile K_2RfCl_6 .

A careful discussion of the results of online isothermal gas chromatography experiments with the group-4 elements Zr, Hf, and Rf, is given by Türlér (1996). The most recent results are given by Kadkhodayan et al. (1996). In these experiments, a MoO_3 aerosol gas jet was used to transport the activities from the recoil chamber to the chromatography apparatus.

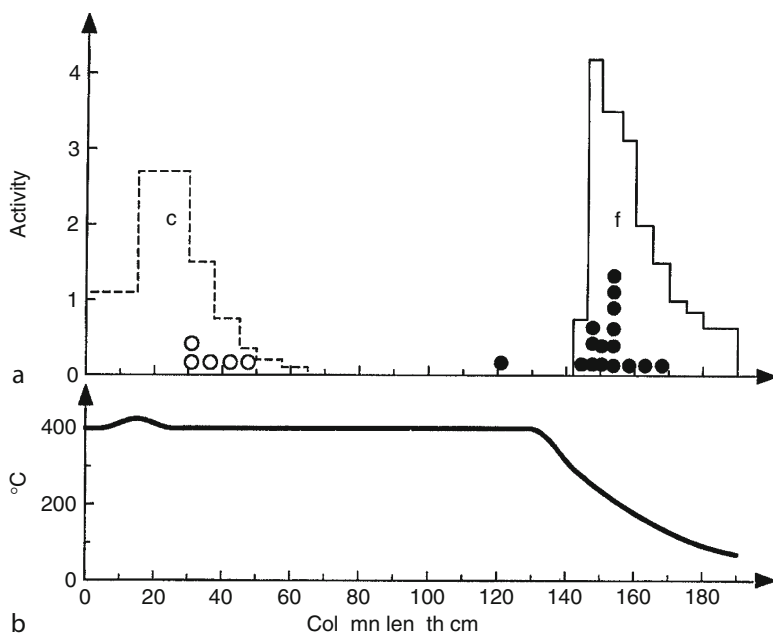
The MoO_3 after reaction with chlorinating reagents forms volatile oxychlorides that do not deposit inside the chromatography column. A total of 837 α particles attributed to the decay of $^{261\text{a}}\text{Rf}$ and its daughter ^{257}No were detected after the gas-phase separation including 170 $\alpha\alpha$ -correlations. A half-life of 78_{-6}^{+11} s resulted from the decay of $^{261\text{a}}\text{Rf}$, in good agreement with the 65 ± 10 s literature value (Ghiorso et al. 1970).⁵ The relative yields measured as a function of the isothermal temperature for chlorides of ^{98}Zr , ^{162}Hf , and ^{261}Rf under similar experimental conditions are shown in  Fig. 20.11.

Chlorinating agent was 100 ml/min HCl in experiments with Zr and Hf. The experimental data were analyzed with the Monte Carlo model mentioned above to yield adsorption enthalpies $\Delta H_{\text{a}}^{\circ(T)}$ for group-4 chlorides on SiO_2 surfaces which are -74 ± 5 kJ/mol for Zr, -96 ± 5 kJ/mol for Hf, and -77 ± 6 kJ/mol for Rf. The lower volatility of Hf chloride is surprising in view of the known vapor pressure curves ( Fig. 20.4) as the experimental conditions were kept as similar as possible to the ZrCl_4 and RfCl_4 experiments (Kadkhodayan et al. 1996). It is not clear whether Hf is more susceptible to trace impurities in the system (O_2 , H_2O) thus forming HfOCl_2 in the adsorbed state, in a similar way as shown by  Eq. (20.6). This would shift the yield versus temperature curve to higher temperatures.

Within the error limits, RfCl_4 exhibits about the same volatility as ZrCl_4 and thus shows the volatility expected from relativistic calculations (Pershina and Fricke 1994a). From “nonrelativistic” extrapolations one would expect a less volatile RfCl_4 . Further experiments under

■ Fig. 20.10

(a) Thermochromatogram of Sc (dashed line) and Hf (solid line) and circles indicating the number and position of SF tracks produced in the $^{242}\text{Pu} + ^{22}\text{Ne}$ reaction at 119 MeV (Adapted from (Zvara et al. 1971b)). The full circles near the Hf deposition zone are interpreted as being due to element 104, the open circles as being due to heavy actinides. (b) Temperature profile along the chromatographic tube



absolutely oxygen-free conditions with also a higher resolution with respect to the determination of the observable $T_{50\%}$ are desirable before quantitative conclusions on the influence of relativistic effects on the volatility of RfCl_4 can be drawn.

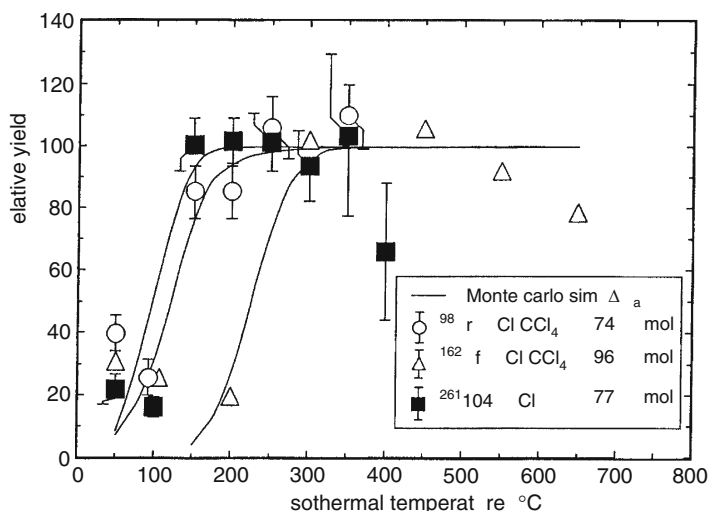
The volatility of short-lived Hf and Rf in chlorinating, oxygen-containing gases was investigated recently by Jost et al. (1996). 150 ml/min Cl_2 , saturated with thionylchloride (SOCl_2) and 20 ml/min O_2 were used as reactive gases. The 50% temperature for Hf was found to be shifted to 390°C whereas for a simple adsorption/desorption process of HfCl_4 $T_{50\%}$ would be expected at $\sim 200^\circ\text{C}$. Preliminary data for Rf are shown in ▶ Fig. 20.12 where the yield versus temperature curves are compared for the reactive gases 300 ml/min HCl and 150 ml/min Cl_2 saturated with SOCl_2 , 20 ml/min O_2 .

A shift of the $T_{50\%}$ value from about 125°C to about 330°C is observed with a much slower increase of the yield in the presence of oxygen. This is strong evidence for the proposed transport reaction, ▶ Eq. (20.6). A modification of the Monte Carlo model to take care of the different transport reaction mechanism (“reaction gas chromatography”) will be discussed in ▶ Sect. 20.7. The data for HCl as chlorinating agent (Jost et al. 1996) are in agreement with those reported by Kadkhodayan et al. (1996).

Preliminary data (Yakushev et al. 1996a) allow comparing the volatility of RfCl_4 with that of the bromide compound, RfBr_4 , which turns out to be less volatile with the yield versus temperature curve of the latter being shifted by about 150°C to higher temperatures. It is

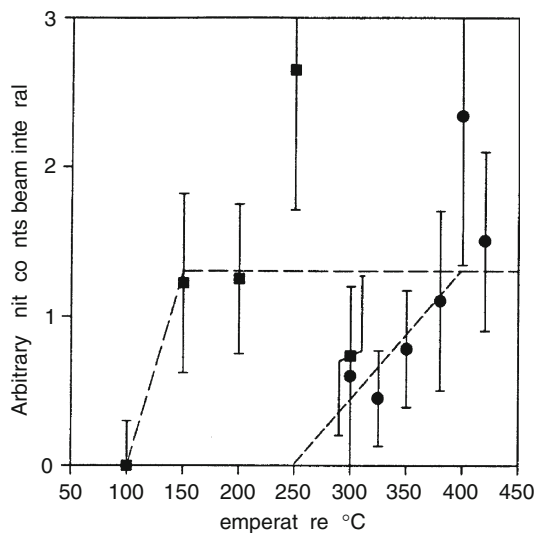
■ Fig. 20.11

Relative chemical yields for Zr (*open circles*), Hf (*triangles*), and Rf (*solid squares*) chlorides as a function of the temperature of the isothermal part of the gas-chromatographic column with Monte Carlo simulations (*solid lines*). Inserted into the figure is information about the chlorinating reagents and the deduced adsorption enthalpies (Türler 1996) (Reproduced with the permission of Oldenbourg Wissenschaftsverlag, München)



■ Fig. 20.12

Chromatographic yield of ²⁶¹Rf as a function of the temperature of the isothermal part of the column in 1 l/min He, 150 ml/min Cl₂, saturated with SOCl₂, 20 ml/min O₂ (*full circles*), and with 1 l/min He, 300 ml/min HCl (pure HCl) (*full squares*). Preliminary data from Jost et al. (1996)



interesting to note that, in these experiments, the simultaneously measured behavior of Hf indicated a lower volatility of both the chloride and the bromide if compared with the corresponding Rf chloride and bromide, respectively.

One experiment in the gas phase was carried out to probe possible p-element behavior of Rf in its atomic state (Zhuikov et al. 1989); p-elements such as Tl, Pb, and Bi in the elemental state show a much higher volatility than the group-4 elements Ti, Zr, and Hf. In analogy to a similar experiment on element 103 (Jost et al. 1988; Eichler et al. 1988), the retention of element 104 in a quartz column at 1,170°C was measured in Ar carrier gas containing some hydrogen. All fission tracks from 2.6 h ^{256}Fm (an unwanted by-product) and from 3 s ^{259}Rf were observed in the region of the column where d-elements deposit. A lower limit for the sublimation enthalpy of $\Delta H_s^\circ(\text{Rf}) \geq 370$ kJ/mol was determined. This result is in agreement with predictions (Zhuikov et al. 1990; Ryshkov et al. 1992) saying that, despite possible $6d7s^27p$ ground state configuration, in the interaction with any chemical environment, Rf will behave similar to Hf.

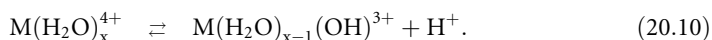
The first aqueous-phase separations of Rf (Silva et al. 1970) were performed with a cation-exchange chromatography column and the chelating reagent α -hydroxyisobutyric acid (α -HIB). Rf was eluted together with Zr and Hf from the column while the trivalent actinides were strongly retained on the column. The chloride complexation of Rf was investigated in an automated solvent extraction chromatography experiment with the quaternary ammonium chloride Aliquat 336 on an inert support as stationary phase and 12 M HCl as the mobile phase (Hulet et al. 1980). Under these conditions, Zr, Hf, and Rf were extracted into the amine while the trivalent actinides were not retained on the column. The Rf, together with the Hf tracer, was then eluted in 6 M HCl. Although only six α decays of ^{261a}Rf were detected, this experiment demonstrated that the chloride complexation of Rf is similar to that of Hf and much stronger than that of the actinides (Hulet et al. 1980).

A series of manually performed separations of ^{261a}Rf from aqueous solutions was performed by the Berkeley group (Czerwinski et al. 1994a, b; Bilewicz et al. 1996; Kacher et al. 1996a, b). Liquid-liquid extractions with TiOA from 12 M HCl (Czerwinski et al. 1994a) confirmed the results of (Hulet et al. 1980). Cationic species were investigated by extraction into thenoyltrifluoroacetone (TTA). A distribution coefficient for Rf between those of the tetravalent pseudo-homologs Th and Pu indicated (Czerwinski 1992) that Rf is less affected by hydrolysis than Zr, Hf, and Pu.

Czerwinski et al. (1994b) performed a series of liquid-liquid extractions with tributylphosphate, TBP, in benzene to study the effect of HCl, Cl^- , and H^+ ion concentration between 8 M and 12 M on the extraction of Zr^{4+} , Hf^{4+} , Th^{4+} , Pu^{4+} , and Rf^{4+} . It was found that Rf extracts efficiently as the neutral tetrachloride into TBP from 12 M HCl (i.e., it behaves like Zr, Th, and Pu) while the extraction of Hf was relatively low and increased seemingly from 20% to 60% between 8 M and 12 M HCl. Extraction of Rf increased from 60% to 100% between 8 M and 12 M HCl, thus defining an extraction sequence $\text{Zr} > \text{Rf} > \text{Hf}$ for the group-4 chlorides. Surprising results were obtained when the chloride concentration was varied at a constant H^+ concentration of 8 M. Above 10 M Cl^- concentration, the extraction of Rf decreased and behaved differently from Zr, Hf, and Th, and resembled that of Pu^{4+} . This was interpreted in terms of stronger chloride complexing in Rf than in Zr, Hf, and Th, leading to the formation of RfCl_6^{2-} (Hoffman 1990), which is not extracted into TBP. Extraction studies at a constant concentration of 12 M Cl^- showed that Rf extraction is sharply increasing with increasing H^+ concentration between 8 M and 12 M (Czerwinski et al. 1994b). Such behavior is not exhibited by Zr and Hf. As some of these extraction experiments suffered from differences in the details of the chemical procedures applied to the different elements, for example, different contact

times and volumes used, it is important to confirm these very interesting findings in an experiment that establishes identical conditions for all homologous elements including Rf.

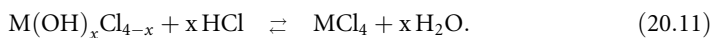
Kacher et al. (1996a) performed some additional chloride extractions into TBP/ benzene with Zr, Hf, and Ti. The reported low extraction yields of Hf by Czerwinski et al. (1994b) could not be reproduced by Kacher et al. (1996a) who reported that they observed that significant amounts of Hf (more than 50% in some cases) stick to Teflon surfaces. (They actually conducted their subsequent experiments with polypropylene equipment because only negligible adsorption was observed with polypropylene surfaces.) The Hf results from the experiments performed by Czerwinski et al. (1994b) were based on online data taken at the cyclotron where the activity was collected on a Teflon disk which according to (Kacher et al. 1996a) accounts for the seemingly low Hf extraction. Surprisingly, a similar loss of Rf due to adsorption in the experiments of Czerwinski et al. (1994b) was not suspected by Kacher et al., and so the latter authors, based on their new Zr-, Hf-, and Ti-results and on the old (Czerwinski et al. 1994b) Rf results, suggested a revised sequence of extraction into TBP/ benzene from around 8 M HCl as $Zr > Hf > Rf > Ti$. In a parallel study of liquid-liquid extractions into TBP/benzene from HBr solutions, extraction of Rf was found to be low and was only increased for bromide concentrations beyond 9 M (Kacher et al. 1996a). The extraction behavior of the group-4 elements into TBP from both HCl and HBr solutions was primarily attributed to their different tendencies to hydrolyze (Kacher et al. 1996a). The latter statement refers to concurrent work by Bilewicz et al. (1996) who studied the sorption of Zr, Hf, Th, and Rf on cobalt ferrocyanide surfaces. These ferrocyanides are known to be selective sorbents for heavy univalent cations such as Fr^+ , Cs^+ , and Rb^+ . However, some ferrocyanides such as Co ferrocyanide have been found to exhibit also particularly high affinities for tetravalent metal ions such as Zr^{4+} , Hf^{4+} , and Th^{4+} involving the formation of a new ferrocyanide phase between the 4+ cation and the $Fe(CN)_6^{4-}$ anion. The first hydrolysis step of a 4+ cation is shown in the following reaction



The left hand side of ► Eq. (20.10) shows the hydrated 4+ cation, whereas the right hand side the first hydrolysis product a 3+ cation. As 3+ cations are essentially not sorbed by ferrocyanide surfaces, the onset of hydrolysis at decreasing HCl concentration in the aqueous phase will be reflected by a rapid decrease of the sorbed activity. This decrease was observed by Bilewicz et al. (1996) below 3 M HCl for Rf, below 1 M HCl for Zr, and below 0.5 M HCl for Hf, establishing seemingly a hydrolysis sequence $Rf > Zr > Hf$. As hydrolysis increases with decreasing radius of the cation, the stronger hydrolysis of Rf is very surprising and in conflict with the results of Czerwinski (1992). Bilewicz et al. (1996) suggested as an explanation that the predominant coordination number (x in ► Eq. (20.10)) for Zr^{4+} and Hf^{4+} is 8, and changes to 6 for Rf due to relativistic effects making the $6d_{5/2}$ orbitals unavailable for ligand bonding of water molecules. Günther et al. (1998) have shown that this does not withstand a critical examination. It is the present author's opinion that some experimental deficiency and not the increased tendency of Rf to hydrolyze produced the surprising results of Bilewicz et al. (1996). For example, the contact time of the aqueous phase with the ferrocyanide surface was only 10 s in the Rf experiments. In a kinetic study, the authors found that Zr and Hf sorbed within 20 s and 40 s, respectively, while Th required more than 90 s to achieve nearly complete sorption (Bilewicz et al. 1996). It is conceivable that, within the 10 s interaction of the aqueous phase in the Rf experiments, no equilibrium was established thus making the Rf data meaningless.

A study of the extraction of fluoride complexes of Ti^{4+} , Zr^{4+} , Hf^{4+} , and Rf^{4+} into TiOA was also reported by Kacher et al. (1996b). This work presents some evidence for extraction of $^{261\text{a}}\text{Rf}$ into TiOA from 0.5 M HF; however, no quantitative assessment of the extraction yield or K_d value is made so that the conclusion of Kacher et al. (1996b) that the extraction into TiOA for the group-4 elements decreases in the order $\text{Ti} > \text{Zr} \approx \text{Hf} > \text{Rf}$ is not reproducible.

In view of the somewhat unsatisfactory situation with the conflicting Hf results by Czerwinski et al. (1994b) and Kacher et al. (1996a) and with the intention to establish an independent set of data characterizing the extraction sequence of Zr, Hf, and Rf from 8 M HCl into TBP, Günther et al. (1998) determined distribution coefficients of these elements from HCl solutions. In 8 M HCl, the K_d of Zr is 1,180 and that of Hf is 64. This difference makes possible a chromatographic separation of Hf from Zr in ARCA II on 1.6 mm i.d. \times 8 mm columns filled with TBP on an inert support. This separation was also studied with the short-lived ^{169}Hf from the $\text{Gd}(^{18}\text{O}, \text{n})$ reaction yielding $K_d = 53^{+15}_{-13}$ in agreement with the above results from batch extraction experiments. 78 s $^{261\text{a}}\text{Rf}$ was produced in the $^{248}\text{Cm}(^{18}\text{O}, 5\text{n})$ reaction at the Philips Cyclotron of the Paul Scherrer Institute, Switzerland, and from the distribution of α events between the Hf and Zr fraction, a K_d value of Rf in 8 M HCl of ~ 150 was determined. This gives the extraction sequence $\text{Zr} > \text{Rf} > \text{Hf}$. Such a sequence is expected from theoretical considerations (Günther et al. 1998; Pershina 1998a, b) of complex formation and the concurrent hydrolysis of complexes



To predict the equilibrium constant of \blacklozenge Eq. (20.11), one has to consider the difference in total energies of the (partially) hydrolyzed species on the left hand side of \blacklozenge Eq. (20.11) that are not extracted and the extractable MCl_4 . (It is assumed that the OH^- -containing species will not extract into the organic phase because of the strong hydrogen bonding interaction between OH^- and H_2O .) This can be done by quantum chemical calculations (Pershina 1996; Pershina and Fricke 1999), allowing to determine the differences in the Coulomb and the covalent parts of the binding energy separately. Calculations for Zr, Hf, and Rf are still to be done, but one can already draw qualitative conclusions based on a parallel study of the hydrolysis of chloro complexes of the group-5 elements Nb, Ta, Pa, and Db (Pershina 1998a, b). For group 5, the order of complex formation described by equilibria similar to the reaction (\blacklozenge 20.11) in 4–12 M HCl solutions was found to be $\text{Pa} > \text{Nb} > \text{Db} > \text{Ta}$ in excellent agreement with experimental data (Paulus et al. 1999a, b) to be discussed in \blacklozenge Sect. 20.6. This sequence is explained by dominant differences in the Coulomb part of the energy of reaction when OH^- groups are replaced by Cl^- anions. Earlier calculations (Pershina and Fricke 1994a) of MCl_4 ($\text{M} = \text{Zr}, \text{Hf}, \text{and Rf}$) have shown that the compounds are very similar, which can also be true for $\text{M}(\text{OH})_x\text{Cl}_{4-x}$. Knowing the analogy in the electronic structure of the halides and oxyhalides of groups 4 and 5 (Pershina 1996, 1998a, b) one can postulate the same order of complex formation $\text{Zr} > \text{Rf} > \text{Hf}$ according to \blacklozenge Eq. (20.11) as it was found for the corresponding group-5 elements. For both group 4 and 5, such a sequence is in full agreement with experimental data for Zr, Hf, and Nb, Ta, respectively, showing that compounds of the 5d elements are more hydrolyzed than those of the 4d elements and are hence less extracted. For these elements, the hydrolysis of complexes (Pershina 1998a, b; Pershina and Fricke 1999) is of opposite order to the hydrolysis of cations. This shows that the statements of Kacher et al. (1996a), concerning the seemingly low extraction of Hf and Rf as being due to their increased tendency to hydrolyze, are incorrect.

Fluoride complexation of the group-4 elements was studied by Bruchertseifer et al. (1989), Szegłowski et al. (1990), Pfrepper et al. (1997, 1998), and Strub et al. (2000). In the work of Szegłowski et al. (1990), $^{261\text{a}}\text{Rf}$ transported to the chemistry apparatus on line was continuously dissolved in 0.2 M HF, and the solution was passed through three ion-exchange columns. In the first cation-exchange column, the transplutonium elements produced directly in the $^{18}\text{O} + ^{248}\text{Cm}$ reaction were removed from the solution. In the next anion-exchange column, $^{261\text{a}}\text{Rf}$ was sorbed as RfF_6^{2-} , while the following cation-exchange column retained its cationic decay products. After the end of bombardment, the descendants ^{253}Fm and ^{253}Es were desorbed from the third column and detected off-line by α spectroscopy. Their detection was proof that Rf forms anionic fluoride complexes, which are sorbed on an anion-exchange resin.

By selecting conditions such that the retention time, t_r , is of the order of the nuclear half-life, $T_{1/2}$, Pfrepper et al. (1997, 1998) developed this technique further, thereby making it a quantitative technique capable of measuring K_d values of short-lived isotopes by online chromatography. Pfrepper et al. have verified the equivalence of \bullet Eqs. (20.8) and \bullet (20.9). They compared K_d values for Hf isotopes obtained, firstly, in batch experiments and by conventional elution chromatography in the anion-exchange system consisting of HS36 (a resin with the quaternary triethyl-ammonium group) and 0.27 M HF/ x M HNO_3 (where x is variable) with, secondly, K_d values obtained in the same system with the MCT technique. They used the short-lived Hf isotopes $^{165,166}\text{Hf}$ and detected the daughter nuclides $^{165,166}\text{Tm}$ and ^{166}Yb by γ -ray spectroscopy. In order to determine the ionic charge of the Hf fluoride complexes, the concentration of the counter ion NO_3^- was varied. K_d values were found to be 12.7 ± 1.8 ml/g with 0.2 M HNO_3 and 2.4 ± 0.8 ml/g with 0.5 M HNO_3 corresponding to an ionic charge of -1.9 ± 0.4 for the fluoride complex of Hf as determined from the slope of the plot of $\log K_d$ versus the logarithm of the concentration of the counter ion. From this it was concluded that Hf probably forms HfF_6^{2-} . This is evidenced also by \bullet Fig. 20.13 in which the K_d values obtained by the online MCT technique are compared with those from a series of batch experiments performed in parallel with the same anion-exchange resin. From the good agreement, it was concluded that with the MCT technique, determination of the ionic charge of complexes of transactinides must be feasible.

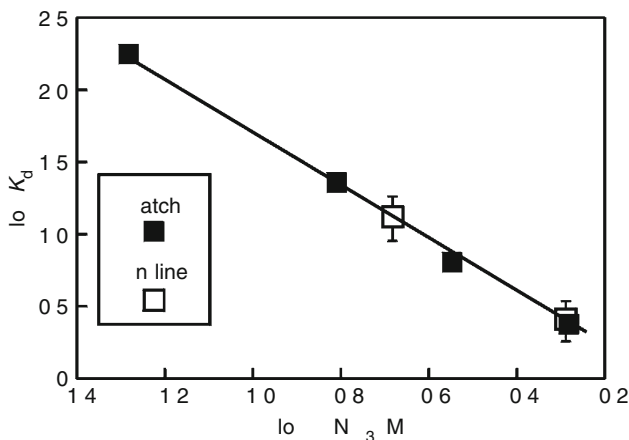
In the application of the MCT technique to $^{261\text{a}}\text{Rf}$, Pfrepper et al. (1998) used about 20 mg (11 mg) of the anion-exchange resin HS36 in the chromatographic column at an elution rate of approximately 0.35 ml/min of 0.27 M HF and 0.2 (0.1) M HNO_3 . The cation-exchange column (s) that sorbed the descendants 23 s ^{257}No , 3 d ^{253}Fm , and 20 d ^{253}Es contained 50 mg of the strongly acidic cation exchanger Wofatit KPS.

For the similar cation-exchange resin Dowex 50 \times 12, it was shown previously by Pfrepper et al. (1997) that, for HNO_3 concentrations <0.3 M, K_d values for trivalent rare earth cations exceed 10^4 ml/g resulting in a breakthrough volume in excess of 500 ml. Assuming the same conditions for their $^{261\text{a}}\text{Rf}$ experiment (Pfrepper et al. 1998), it was decided to renew the cation-exchange columns collecting the descendant fractions D_1 and D_2 every 12 h. This corresponded to eluent volumes of about 260 ml, while the breakthrough volume was estimated to be about 10^3 ml.

Thus, at first sight, breakthrough of the cationic “daughter nuclides” was safely prevented. $^{261\text{a}}\text{Rf}$ and $^{165-169}\text{Hf}$ were produced simultaneously by irradiation of a combined target of ^{248}Cm and $^{152,154,158}\text{Gd}$ with ^{18}O ions at the Dubna U-400 Cyclotron. In the γ -ray spectra of D_1 and D_2 , the nuclides ^{165}Tm , ^{166}Yb , ^{167}Tm , ^{169}Lu , and ^{169}Yb were detected as the decay products of $^{165,166,167,169}\text{Hf}$. K_d values on the order of 14.8 and 47 were determined in 0.27 M HF/0.2 M HNO_3 and 0.27 M HF/0.1 M HNO_3 , respectively, compatible with an ionic charge

■ Fig. 20.13

Value of $\log K_d$ of Hf in the system HS36-0.27 M HF- HNO_3 as a function of the HNO_3 concentration, measured in batch and online experiments (Reprinted with the permission of Oldenbourg Wissenschaftsverlag, München, (Pfrepper et al. 1997))



of the fluoride complex of -1.85 ± 0.1 . For ^{261}Rf , the α decays of its descendant ^{253}Es were evaluated yielding K_d values of about 14 and 50 in 0.27 M HF/0.2 M HNO_3 and 0.27 M HF/0.1 M HNO_3 , respectively, giving an ionic charge of -1.9 ± 0.2 . Pfrepper et al. (1998) concluded that Rf has properties of a close homologue of Hf and forms RfF_6^{2-} , the stoichiometry characteristic of Hf and other group-4 elements.

Kronenberg et al. (2004a) have observed that the K_d values of trivalent lanthanide (Tb^{3+}) and actinide cations (^{241}Am , ^{250}Fm) in mixed HF/0.1 M HNO_3 solutions on the cation-exchange resin Dowex 50W \times 8 exceed 10^4 ml/g only for HF concentrations below 10^{-2} M. For higher HF concentrations, the K_d values decrease to 2,000 in 0.05 M HF/0.1 M HNO_3 , 1,300 in 0.1 M HF/0.1 M HNO_3 , 700 in 0.5 M HF/0.1 M HNO_3 , and 500 in 1 M HF/0.1 M HNO_3 . A simultaneous rise of K_d values on the anion-exchange resin Dowex 1 \times 8 is observed (Kronenberg et al. 2000) for >0.05 M HF/0.1 M HNO_3 with values reaching 170 in 0.1 M HF/0.1 M HNO_3 , 1,600 in 0.5 M HF/0.1 M HNO_3 , and 2,500 in 1 M HF/0.1 M HNO_3 thus indicating that anionic fluoride complexes are formed. The K_d value in 0.27 M HF/0.1 M HNO_3 on a strongly acidic cation-exchange resin can be estimated to be on the order of 800. Thus, the breakthrough volume for lanthanides and actinides in the experiments by Pfrepper et al. was not >500 ml (Pfrepper et al. 1998) but rather <40 ml, that is, both the Hf and the Rf descendants were breaking through the cation-exchange columns in less than 2 h. It is impossible to reconstruct what this did to the K_d values in the work of Pfrepper et al. (1998); however, the enormous differences (orders of magnitude) between the K_d values of Hf and Rf in mixed HF/ HNO_3 solutions observed recently by Toyoshima et al. (2008) do cast doubt on the validity of the results by Pfrepper et al. (1998) where indistinguishable K_d values for Hf and Rf were reported.

Strub et al. (2000) have investigated in batch experiments K_d values of the long-lived tracers ^{95}Zr , ^{175}Hf , and ^{233}Th on a strongly acidic cation-exchange resin, Aminex A5, and on a strongly basic anion-exchange resin (Riedel-de H  en) in 0.1 M HNO_3 solutions containing variable concentrations of HF. On the cation-exchange resin, below 10^{-3} M HF, the K_d values for Zr, Hf,

and Th are $>10^3$ indicating the presence of cations. In the range $10^{-3} \text{ M} < [\text{HF}] < 10^{-2} \text{ M}$, the K_d values of Zr and Hf decrease due to the formation of neutral or anionic fluoride complexes. The behavior of Zr and Hf is very similar (Hf sticking to the resin even at slightly higher HF concentrations). The elution of Th from the resin is observed at more than one order of magnitude higher HF concentrations (see [Fig. 20.14](#)). These off-line data were compared with online data taken with ARCA II at the GSI Helmholtz center for heavy ion research, Darmstadt, UNILAC accelerator where short-lived Hf isotopes $^{166,167,168}\dots\text{Hf}$ were produced in xn-reactions of a ^{12}C beam with an enriched ^{158}Dy target. There is a general agreement between both sets of data.

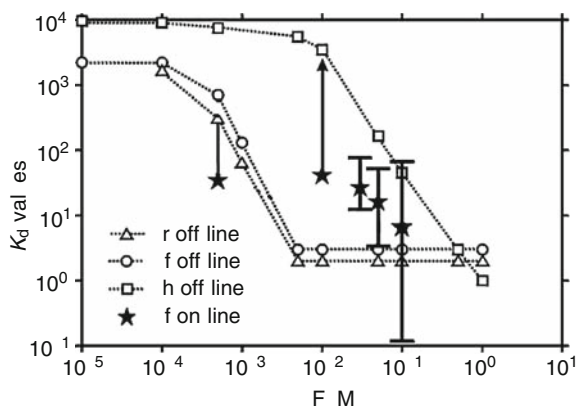
On an anion-exchange resin, as expected, there is little sorption of Zr, Hf, and Th at low HF concentrations. In the range $10^{-3} \text{ M} < [\text{HF}] < 10^{-2} \text{ M}$, the K_d values of Zr and Hf in batch experiments rise simultaneously, that is, in the same range as they decrease on the cation-exchange resin. This shows that the disappearance of the cationic species at low HF concentrations is followed immediately by the formation of anionic fluoride complexes. For Th, the sorption on the anion-exchange resin stays low for all HF concentrations indicating that Th does not form anionic fluoride complexes.

In the Rf experiments (Strub et al. 2000) performed at the PSI Philips Cyclotron, ^{261}Rf was produced in the $^{248}\text{Cm}(^{18}\text{O},5n)$ reaction at 100 MeV. The target contained 10% Gd enriched in ^{152}Gd to produce simultaneously short-lived Hf isotopes that were used to monitor the behavior of Hf and to perform yield checks by γ spectroscopy. Rf and Hf were transported by a $\text{He}(\text{KCl})$ gas jet and were collected for 90 s by impaction inside ARCA II. The deposit was dissolved in 200 μl 0.1 M HNO_3/x M HF (for different values of x) and was fed onto the 1.6×8 mm cation-exchange column at a flow rate of 1 ml/min. The effluent was evaporated to dryness as sample 1. In order to elute remaining Rf and Hf from the column, a second fraction of 200 μl 0.1 M $\text{HNO}_3/0.1$ M HF was collected to strip all group-4 elements from the column. This fraction was referred to as sample 2.

In the anion-exchange experiments, Rf and Hf were transported, collected, and loaded onto the anion-exchange column as in the experiments with the cation-exchange columns. Again,

Fig. 20.14

Sorption of Zr, Hf, Th, and Rf on the cation-exchange resin Aminex A6 in 0.1 M HNO_3 at various HF concentrations. Off-line data are shown for Zr, Hf, and Th, and online data for Rf; re-evaluated data from (Strub et al. 2000)



the effluent was evaporated to dryness as sample 1. In order to elute remaining Rf and Hf from the column, a second fraction of 200 μl 5 M HNO_3 /0.01 M HF was used. This fraction was prepared as sample 2. K_d values are often calculated as follows:

$$K_d = \frac{A_s}{A_l} = \frac{A_{s0} V_1}{A_{l0} m_s} \quad (20.12)$$

with A_s specific activity in the solid phase (Bq/g), A_l activity concentration in the liquid phase (Bq/ml), A_{s0} activity in the solid phase (Bq), A_{l0} activity in the liquid phase (Bq), V_1 volume of the solution (ml), and m_s mass of the resin (g). The K_d values using Eq. (20.12) are obtained such that the activity of sample 1 is attributed to the liquid phase and the activity of sample 2 to the solid phase. However, in elution experiments, Eq. (20.12) yields only correct K_d values for the fortunate situation of equal activities in fraction 1 and 2, that is, cuts between fraction 1 and 2 at the maximum position of the elution curve. To circumvent this deficiency, K_d values shown in Fig. 20.14 were calculated by a computer program that simulates the elution process. The number of theoretical plates (obtained from the shape of tracer elution curves), the free column volume, the volume of fraction 1 and an assumed K_d value are the initial input parameters. In an iteration process, the K_d value is varied until the experimentally observed activity in fraction 1 results.

The results of the online experiments with Rf and Hf on cation-exchange columns are given in Fig. 20.14 together with the results of the off-line batch experiments. The online data for Hf are consistent with the off-line data.

The K_d values for ^{261}Rf at 5×10^{-4} M HF and at 10^{-2} M HF are lower limits as no ^{261}Rf decays were detected in sample 1. It is seen that the decrease of the K_d values for Rf occurs between 0.01 M HF and 0.1 M HF, that is, at one order of magnitude higher HF concentrations than for Zr and Hf. Under the given conditions, the behavior of Rf is intermediate between that of its pseudo-homologue Th and that of its group members Zr and Hf.

The results of the online experiments with the anion-exchange columns are as follows: While the off-line data for Hf clearly indicate that anionic fluoride complexes of Hf are formed for $>10^{-3}$ M HF, one observes that the Hf data taken online are somewhat lower. The reason for this discrepancy is unknown at present. Seemingly, the behavior of Rf is different from that of Zr and Hf, if compared with the off-line data, as there is almost no sorption of Rf on the resin. For HF concentrations for which maximum K_d values are observed for Zr and Hf, there is no indication of a rise in the K_d values for Rf.

This cannot mean that no anionic fluoride complexes exist for Rf at any HF concentration as this would be in contradiction with the results reported by Kacher et al. (1996b), Szegłowski et al. (1990), and Pfrepper et al. (1998). Therefore, the concentration of HNO_3 was varied (Strub et al. 2000) between 0.1 M and 0.01 M at a constant HF concentration of 0.05 M thus varying the concentration of NO_3^- , which acts as a counter ion competing for the binding sites on the anion exchanger. It was observed (Strub et al. 2000) that the K_d values of Hf and Rf rise with decreasing NO_3^- concentration indicating that negatively charged complexes are formed both for Hf and for Rf, but that the counter ion NO_3^- is apparently much more effective in removing Rf from the binding sites on the anion exchanger than in removing Zr and Hf.

This was the starting point for a new series of experiments with anion-exchange chromatography with Aminex A27 in which the HNO_3 and the HF concentration were varied systematically (Strub et al. 2001). The following observations were made:

1. There is a steep dependence of the $\log K_d$ values of Rf on the $\log [\text{NO}_3^-]$ concentration at fixed HF concentration (0.01 M).

2. At fixed $[\text{NO}_3^-]$ concentration (0.003 M), above 0.1 M HF, increasing the HF concentration leads to a decrease in the K_d values for Rf.

Observation (1) suggested that the NO_3^- ion acts as a counter ion competing for the binding sites on the anion-exchange resin with the Rf-fluoride complex. Based on observation (2), a second counter ion discussed by Strub et al. (2001) is the HF_2^- ion, that is, the dominant anion above an initial HF concentration of 0.3 M.

Note that in the work of Kronenberg et al. (2004a) there were two MCT experiments performed with ^{261}Rf using 0.5 M HF/0.1 M HNO_3 and 0.01 M HF, respectively. In the first case, the cation-exchange columns were filled with 330 mg of Dowex 50W \times 8 and were used for 3 h to prevent breakthrough of the cationic descendants. The anion-exchange column in between was filled with 50 mg of the anion exchange resin Dowex 1 \times 8 in the nitrate form. In the second case, the cation-exchange columns were filled with 68 mg Dowex 50W \times 8 and used for 4 h, and the anion-exchange column with 17 mg of Dowex 1 \times 8 in the fluoride form. Each experiment was run for 24 h at an average beam intensity of $3 \times 10^{12} \text{ s}^{-1}$.

The first experiment with 0.5 M HF/0.1 M HNO_3 was performed to corroborate the low K_d values obtained by Strub et al. (2000) with ARCA II on an anion-exchange resin. A total of 80 α decays were observed attributable to ^{253}Es in the sample 1 representing the liquid phase and no event in the strip fraction representing the solid phase. Taking zero to be compatible with three events at 95% confidence level in Poisson statistics, leads to an upper limit for the K_d value of Rf of <3 , which is rather consistent with the data of Strub et al. (2000), but not with the value in 0.27 M HF/0.1 M HNO_3 obtained by Pfrepper et al. (1998).

In the second experiment, performed in pure 0.01 M HF without any HNO_3 , 90 events attributable to ^{253}Es were observed in the strip fraction representing the solid phase and zero events in the liquid phase. This led to a lower limit for the K_d value on the order of 300 compatible with the one measured with ARCA II in pure 0.01 M HF (Strub et al. 2001).

In summary, one can state that the K_d values for Rf obtained with the MCT, that is, low in 0.5 M HF/0.1 M HNO_3 and high in 0.01 M HF, are consistent with the ones determined with ARCA II.

The formation of anionic chloride complexes of Zr, Hf, and Rf above 7 M HCl through 9.5 M HCl was shown in experiments with AIDA (Haba et al. 2002) indicating that the complexing strength in the group-4 elements decreases in the order $\text{Rf} > \text{Zr} > \text{Hf}$. A hypothetical Th-like or Pu-like behavior of Rf was probed with an anion-exchange resin in 8 M HNO_3 in experiments with AIDA. While Th(VI) and Pu(VI) form anionic complexes under these conditions and are sorbed on the anion-exchange resin, Rf remains in solution (Haba et al. 2002) as expected for a typical group-4 element with non Th-like and non Pu-like properties.

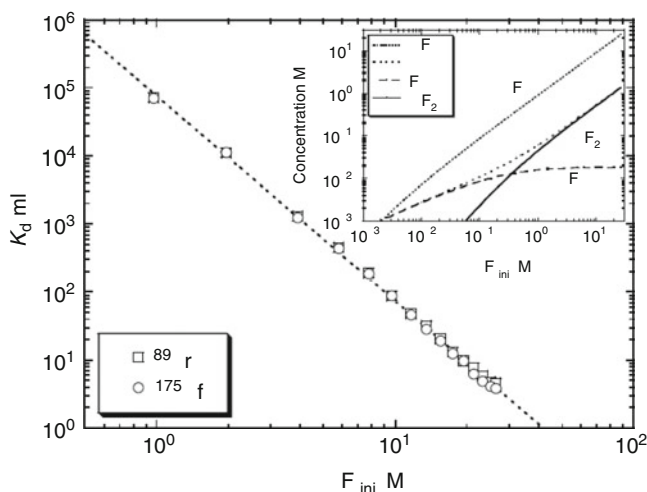
The anion-exchange chromatographic behavior of Rf was investigated by Haba et al. (2004) in 1.9–13.9 M HF and compared to that of Zr and Hf. As HF is a weak acid, equilibration among HF, H^+ , F^- , and HF_2^- in aqueous solution is established by the chemical equations



with $K_1 = 935 \text{ M}^{-1}$ and $K_2 = 3.12 \text{ M}^{-1}$ for the first \bullet Eq. (20.13) and the second \bullet Eq. (20.14) equilibria, respectively. The insert of \bullet Fig. 20.15 shows the variation of $[\text{HF}]$, $[\text{H}^+]$, $[\text{F}^-]$, and $[\text{HF}_2^-]$ as a function of the initial $[\text{HF}]_{\text{ini}}$. Above 1 M HF, the concentration of the HF_2^- anion is more than one order of magnitude higher than that of F^- , and $[\text{HF}_2^-]$ increases linearly with

■ Fig. 20.15

Variation of the distribution coefficient, K_d , of Zr and Hf on the anion-exchange resin CA08Y as a function of the initial HF concentration. The linear relation with a slope of -3.0 ± 0.1 is indicated by a dotted line. The insert shows the variation of $[\text{HF}]$, $[\text{H}^+]$, $[\text{F}^-]$, and $[\text{HF}_2^-]$ as a function of $[\text{HF}]_{\text{ini}}$ (Reprinted with the permission from (Haba et al. 2004). Copyright (2009) American Chemical Society)



increasing $[\text{HF}]_{\text{ini}}$. Thus, the decrease of the K_d values of Zr and Hf with increasing $[\text{HF}]_{\text{ini}}$ shown in Fig. 20.15 are explained as the displacement of the metal complex from the binding sites by HF_2^- as the dominant anionic species in solution. In Fig. 20.16, elution curves for Zr and Hf simultaneously produced are shown with (a) a 1.6 mm i.d. \times 7. mm column in 17.4 and 7.7 M HF and with (b) a 1.0 mm i.d. \times 3. mm column in 9.7 and 5.8 M HF. The percentages of the eluted activities are depicted and are nearly the same as expected from the same K_d values in the batch experiment, see Fig. 20.15. According to the Glöckauf equation of chromatography, the eluted activity $A(v)$ with the effluent volume v is

$$A(v) = A_{\text{max}} \exp \left\{ -N(v_{\text{peak}} - v)^2 / 2v_{\text{peak}}v \right\} \quad (20.15)$$

where A_{max} , N , and v_{peak} are the maximum peak height, the number of theoretical plates, and the peak volume, respectively. The results of the fit of Eq. (20.15) are shown as solid or dotted curves in Fig. 20.16. In the dynamic chromatographic system, the K_d value is

$$K_d = v_{\text{peak}} / m_r \quad (20.16)$$

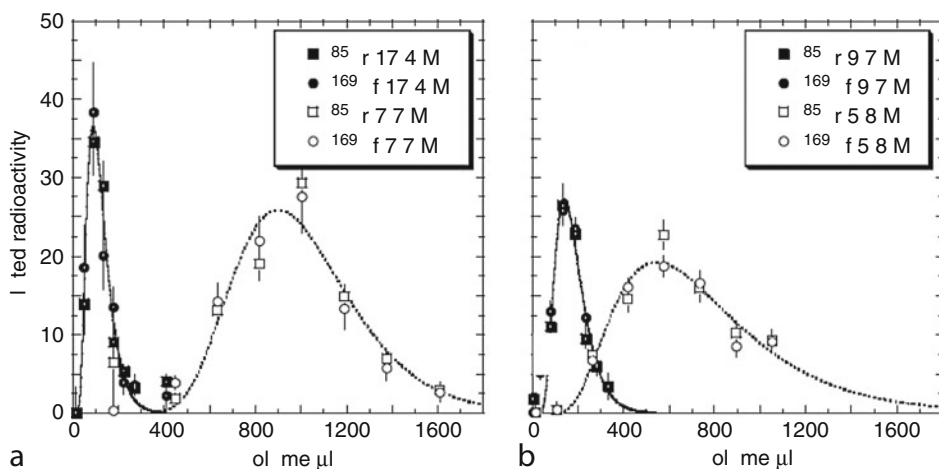
where m_r is the mass of the dry resin. In Fig. 20.17, the K_d values of Zr and Hf calculated with Eq. (20.16) are shown. The K_d values of the different column sizes are consistent with each other.

From the radioactivities A_1 and A_2 observed in fractions 1 and 2, respectively, the percentages %ads were evaluated using the equation

$$\% \text{ads} = 100 A_2 / (A_1 + A_2) \quad (20.17)$$

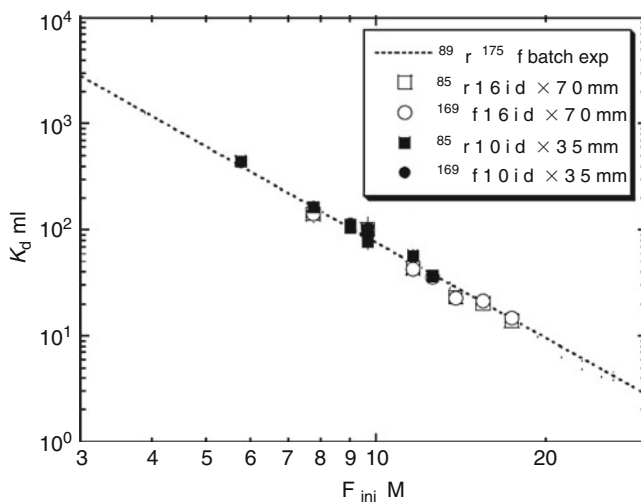
■ Fig. 20.16

Elution curves of Zr and Hf from (a) 1.6 mm i.d. \times 7.0 mm columns in 17.4 and 7.7 M HF and from (b) 1.0 mm i.d. \times 3.5 mm columns in 9.7 and 5.8 M HF. The solid and dotted curves are fits by the Glöckauf equation. The number of theoretical plates results as (a) 4.8 ± 0.5 and (b) 4.6 ± 0.5 (Reprinted with the permission from (Haba et al. 2004). Copyright (2009) American Chemical Society)



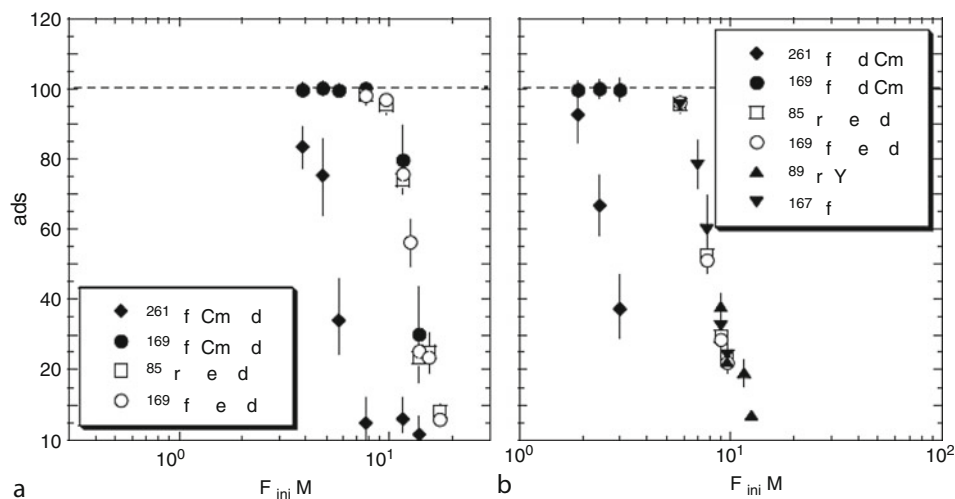
■ Fig. 20.17

Variation of the K_d of Zr and Hf on the anion-exchange resin CA08Y obtained in chromatographic experiments as a function of the initial HF concentration. The *dotted line* indicates the results from batch experiments (Reprinted with the permission from (Haba et al. 2004). Copyright (2009) American Chemical Society)



■ Fig. 20.18

%ads of Zr, Hf, and Rf on the anion-exchange resin CA08Y as a function of the initial HF concentration with (a) the 1.6 mm i.d. \times 7.0 mm columns and with (b) the 1.0 mm i.d. \times 3.5 mm columns (Reprinted with the permission from (Haba et al. 2004). Copyright (2009) American Chemical Society)



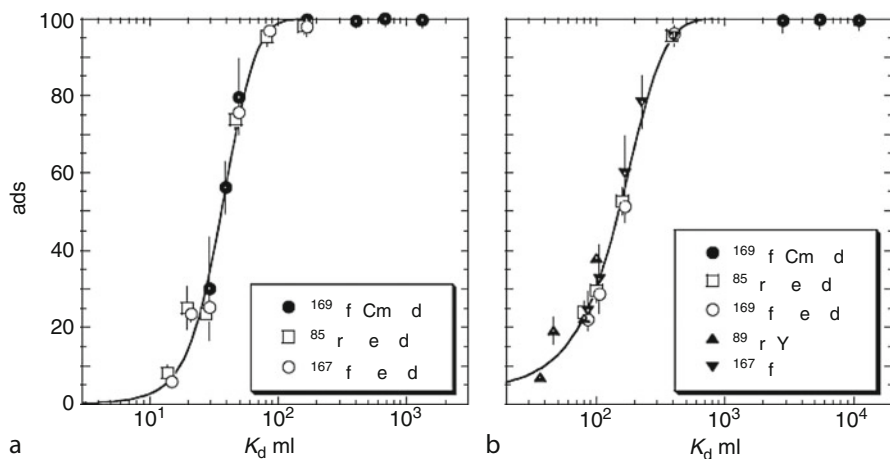
The %ads values of Zr, Hf, and Rf are shown in Fig. 20.18 as a function of $[HF]_{ini}$ for the 1.6 mm i.d. \times 7.0 mm columns (a) for the 1.0 mm i.d. \times 3.5 mm columns (b). The %ads values of Zr and Hf obtained by the online experiments decrease steeply with increasing $[HF]_{ini}$ above 8 M for the larger columns and above 5 M for the smaller ones, while the %ads of Rf decrease at much smaller $[HF]_{ini}$. In Fig. 20.19, the correlations between the %ads values shown in Fig. 20.18 and the K_d values from Fig. 20.15 are plotted with the same symbols as used in Fig. 20.18 and are fitted (solid curves) by

$$\%ads = 100 \exp[-a \exp\{-b(K_d - c)\}] \quad (20.18)$$

Assuming that the kinetics in the complexation and ion-exchange processes of Rf are as fast as those for Zr and Hf, the %ads of Rf from the dynamic column method have been transformed into K_d values using Eq. (20.18). This assumption has subsequently been verified by measuring the elution curve for Rf in 5.4 M HF and by deducing the K_d value according to Eq. (20.16) (Toyoshima et al. 2004). The results from Haba et al. (2004) for Rf are shown as diamonds in Fig. 20.20, together with those of Zr and Hf by the same symbols as used in Fig. 20.17. As shown by a solid line, the K_d values of Rf decrease linearly with increasing $[HF]_{ini}$ and are much smaller than those of Zr and Hf for the same $[HF]_{ini}$. The slope of -2.0 ± 0.3 of $\log K_d$ versus $\log [HF]_{ini}$ for Rf differs from the slope of -3.0 ± 0.1 for Zr and Hf, indicating that different anionic fluoride complexes are formed, that is, RfF_6^{2-} and ZrF_7^{3-} and HfF_7^{3-} . Relativistic molecular density functional calculations (Pershina et al. 2002) – where the free energy change for various fluorination of Rf was compared to those of Zr and Hf – indicated that the complex formation for Rf is much weaker in Rf compared to Zr and Hf in agreement with experiment.

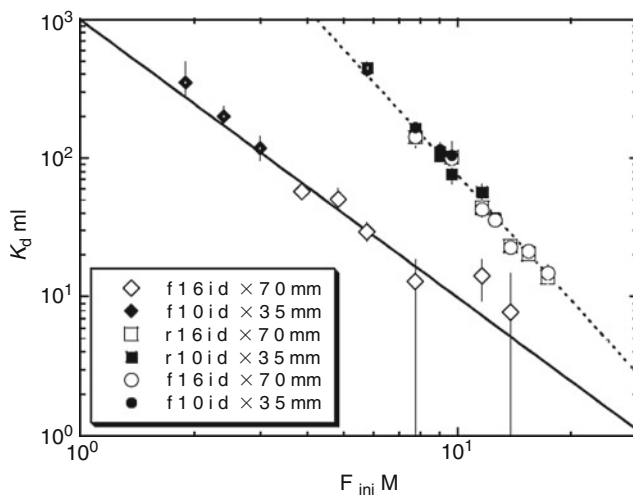
■ Fig. 20.19

Variation of the %ads of Zr and Hf on the anion-exchange resin CA08Y with (a) the 1.6 mm i.d. \times 7.0 mm columns and with (b) the 1.0 mm i.d. \times 3.5 mm columns as a function of the distribution coefficient K_d . The solid lines are a fit of Eq. (20.18) to the data (Reprinted with the permission from (Haba et al. 2004). Copyright (2009) American Chemical Society)



■ Fig. 20.20

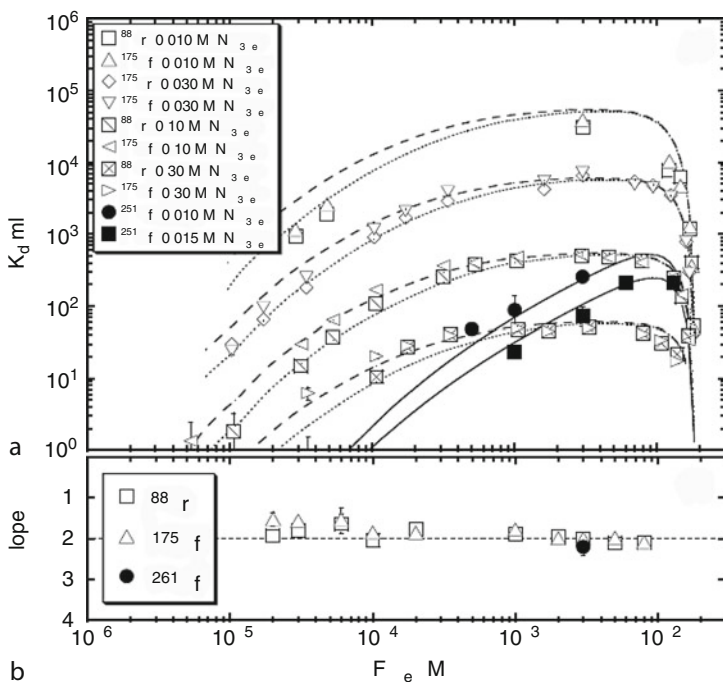
Variation of the distribution coefficient K_d of Zr, Hf, and Rf on the anion-exchange resin CA08Y as a function of the initial HF concentration. The linear relationships with slopes -2.0 ± 0.3 for Rf and -3.0 ± 0.1 for Zr and Hf are indicated by the solid and dotted lines, respectively (Reprinted with the permission from (Haba et al. 2004). Copyright (2009) American Chemical Society)



With reference to (Strub et al. 2000, 2001), Toyoshima et al. (2008) have re-examined the fluoride complexation of Rf in mixed HF/HNO₃ solutions by determining %ads values for Rf and correlating them with the relationship between K_d and %ads for Zr and Hf as in (Haba et al. 2004). The variation of the K_d values of Zr and Hf under static conditions and K_d values of Rf from column chromatography as a function of the equilibrated concentration of free F⁻ ($[F^-]_{eq}$) is shown in ▶ Fig. 20.21a. The solid, dashed, and dotted curves are results of theoretical calculations by Haba et al. in which the log K_d is related to the formation constants K_n ($n = 1-6$). From this, it is concluded that the maximum possible value of the formation constant K_6 of Rf is at least one order of magnitude smaller than K_6 of Zr and Hf. Under the assumption that the equilibrium constant of the exchange reaction of MF_6^{2-} with the anion-exchange resin for Rf is equal to those of Zr and Hf ($D_2 = 5 \times 10^5$), a K_6 for Rf results that is approximately three orders of magnitude smaller than those of the lighter homologs. In ▶ Fig. 20.21b, the slopes of the linear correlations of log K_d versus log $[NO_3^-]$ are plotted, which are consistently -2 , indicating that the stoichiometry of the fluoride complexes is MF_6^{2-} in the given range of $[F^-]_{eq}$. For Rf, this has been shown at a fixed equilibrated concentration

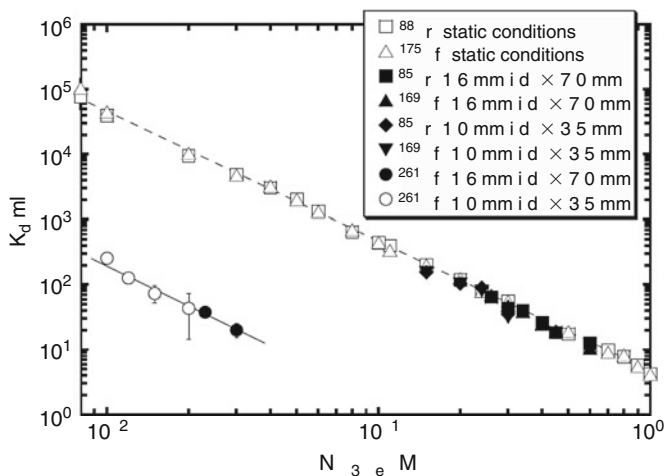
■ Fig. 20.21

(a) Variation of the K_d values of Zr and Hf under static conditions and of Rf in column chromatography as a function of the equilibrated concentration of F⁻ ($[F^-]_{eq}$). Values for Zr and Hf are shown for $[NO_3^-] = 0.01, 0.03, 0.1$, and 0.3 M. Values for Rf are shown for $[NO_3^-] = 0.01$ and 0.015 M. The solid, dashed, and dotted curves represent theoretical calculations of K_d values. (b) Variation of the slopes in the log K_d versus log $[NO_3^-]$ plot as a function of $[F^-]_{eq}$ (Reproduced with the permission of Oldenbourg Wissenschaftsverlag, München, (Toyoshima et al. 2008))



■ Fig. 20.22

Distribution coefficients, K_d of Zr and Hf under static conditions and those of Zr, Hf, and Rf from column chromatography as a function of the equilibrated concentration of NO_3^- ($[\text{NO}_3^-]_{\text{eq}}$) at fixed $[\text{F}^-]_{\text{eq}} = 3.0 \times 10^{-3}$ M. Linear relationships of the $\log K_d$ versus $\log [\text{NO}_3^-]_{\text{eq}}$ for Rf and the homologs are indicated by the solid and dashed lines, respectively (Reproduced with the permission of Oldenbourg Wissenschaftsverlag, München, (Toyoshima et al. 2008))



$[\text{F}^-]_{\text{eq}} = 3.0 \times 10^{-3}$ M, see Fig. 20.22. Here, again, the much weaker complexation of Rf by the fluoride ion is apparent compared to that of its homologs. A qualitative explanation comes from the Hard Soft Acid–Base (HSAB) concept. The small fluoride anions are hard donors and prefer the smaller acceptor ions Zr and Hf. The much larger (softer) Rf acceptor ion tends to prefer larger (softer, more polarizable) donor ligand ions like Cl^- , see (Haba et al. 2002).

The extraction behavior of Rf into tributylphosphate from hydrochloric acid, see (Günther et al. 1998), was re-examined in reversed-phase extraction chromatography by Haba et al. (2007). It was found that Zr shows the largest %ads values and that the values for Rf and Hf are close to each other in qualitative agreement with the previous work. A re-examination of the K_d values of Zr, Hf, Th, and Rf on a cation-exchange resin in 0.1 M HNO_3 as a function of the concentration of the fluoride ion by Ishii et al. (2008) is highly consistent with the results by Strub et al. (2000).

20.6 Element 105 (Dubnium)

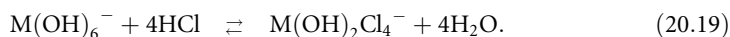
20.6.1 Theoretical Predictions

In the periodic table, Fig. 20.1, element 105 is placed in group 5 below Ta, so that the electronic ground state configuration is expected to be $[\text{Rn}]5f^{14}6d^37s^2$. This is in agreement with early relativistic calculations (Desclaux 1973) and with a more recent MCDF calculation (Fricke et al. 1993). Thus, a significant contribution of the $7p_{1/2}$ state to the ground state is not expected for Db. Atomic and ionic radii and the first through fifth ionization potentials were calculated by Fricke et al. (1993). Differences in the chemical behavior of element 105 to

extrapolated properties of an eka-tantalum could result from a larger ionic radius, a different effective charge, and a different radial extension of the 6d orbitals which are most important in its molecular bondings (Pershina et al. 1992a, b, c; Fricke et al. 1993; Pershina and Fricke 1993, 1994a, b; Pershina 1998a, b). Redox potentials were estimated for the group-5 elements including the pseudo-homolog Pa on the basis of ionization potentials from MCDF calculations (Ionova et al. 1992; Fricke et al. 1993). It was shown that the stability of the pentavalent state is increasing from V to Db, while the stability of the tetra- and trivalent state is decreasing. Although it was found that the stability of the maximum oxidation state decreases when going from element 103 to 105, no extra stability of the trivalent state in element 105 was found (Ionova et al. 1992). It would be interesting to test this prediction in reduction experiments similar to the experiments performed on element 103 (Scherer et al. 1988).

DS DVM calculations allow the degree of covalency in the bonding and the effective charge on the central atom in halide and oxyhalide compounds of the group-5 elements (Pershina et al. 1992a, b, c; Pershina and Fricke 1993). From these, it was inferred (Pershina et al. 1992b) that DbBr_5 should be more volatile than its lighter homologs, whereas classical extrapolations within the periodic table would yield a lower volatility (Türler 1996).

The electronic structure of the group-5 anionic complexes $[\text{MCl}_6]^-$, $[\text{MOCl}_4]^-$, $[\text{M}(\text{OH})_2\text{Cl}_4]^-$, and $[\text{MOCl}_5]^{2-}$ was calculated with the DS DVM code (Pershina et al. 1994). By applying Born's theory of phase transition between the aqueous phase and the organic phase (mixed HCl/HF solutions and TiOA, see (Kratz et al. 1989), the extraction sequence $\text{Pa} > \text{Db} > \text{Nb}$ was predicted, which is the inverse sequence compared to that observed experimentally (Kratz et al. 1989). Due to the complicated situation in mixed HCl/HF solutions with possibilities to form mixed chloride/fluoride- or fluoride complexes, it was recommended to repeat the experiments in the pure HCl system (Pershina et al. 1994). While these new experiments were prepared (Paulus 1997), Pershina (1998a, b) considered hydrolysis and complex formation of Nb, Ta, Pb, and Pa in HCl solutions as competing processes in equilibria such as



Here, the hydrolyzed species on the left is the one staying in the aqueous phase, and the chloride complex on the right is expected to be extracted into the amine phase. Calculations of the electronic structure of the hydrolyzed species of Nb, Ta, Db, and Pa, and of their complexes in HCl solutions were performed (Pershina 1998a, b) using the DS DVM method. On the basis of results of these calculations, relative values of the free energy change of the reactions of complex formation were determined (Pershina 1998a, b). The order of complex formation above 4 M HCl was found to be $\text{Pa} \gg \text{Nb} > \text{Db} > \text{Ta}$. This sequence is predominantly defined by the electrostatic energy of the metal–ligand interaction. The hydrolysis of the chloride complexes, as a reverse process, was found to change as $\text{Ta} > \text{Db} > \text{Nb} \gg \text{Pa}$. Using finally Born's theory of metal-ion extraction, the following trend in the extraction of the anionic species from aqueous solutions containing >4 M HCl was predicted (Pershina 1998b): $\text{Pa} \gg \text{Nb} \geq \text{Db} > \text{Ta}$. This was the first time that detailed predictions of the aqueous-phase properties of these elements were made. It shows that a detailed analysis of the electronic structure of the compounds formed under specific conditions is necessary and leads to the prediction of an inversion of the trend of the properties when going from the 5d to the 6d elements. This has already been observed for the group-4 elements (Günther et al. 1998), and it is of importance to verify this experimentally for the group-5 elements.

20.6.2 Experimental Results

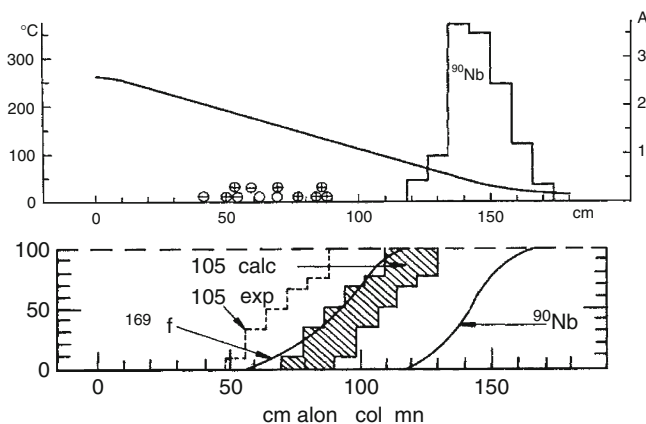
The volatilities of the chlorides and bromides of element 105 were first studied with $1.8 \text{ s } ^{261}\text{Db}$ in a similar thermochromatographic apparatus as used for element 104 (Zvara et al. 1974, 1976). Results from the volatility study of the bromides are shown in [Fig. 20.23](#). In these experiments, the spontaneous-fission track distribution detected on mica track detectors along the chromatographic column was assumed to characterize the behavior of element 105. The measured distribution of ^{261}Db was corrected for the much shorter half-life before comparing it with the adsorption zones of longer-lived tracer activities of various elements including $3.3 \text{ min } ^{169}\text{Hf}$ and $14.6 \text{ h } ^{90}\text{Nb}$. The distance between the integral curve for ^{90}Nb and the center of the shaded zone in [Fig. 20.23](#) is $60 \pm 10^\circ\text{C}$ and characterizes dubnium bromide as being less volatile than niobium bromide and close in volatility to hafnium bromide.

First isothermal gas chromatography experiments with the bromides of the group-5 elements Nb, Ta, and Db (Gäggeler et al. 1992b; Gäggeler 1994) were performed with an earlier version of the OLGA apparatus shown in [Fig. 20.5](#). The results are shown in [Fig. 20.24](#) where the chemical yield as a function of the isothermal temperature is a measure of the volatility. The yields for Nb were measured with HBr as brominating agent, for Ta, HBr plus BBr_3 vapor was used, and for Db both HBr and HBr plus BBr_3 vapor were applied. The solid curves are the results of Monte Carlo simulations with the free parameter $\Delta H_a^{\circ(T)}$ adjusted to the data by a least-squares fit.

Within the error limits, the bromides of Nb and Ta have the same volatility while the Db bromide is less volatile as already indicated by the thermochromatographic data (Zvara et al. 1976). Both sets of experimental data seem, at first glance, to disagree with results from

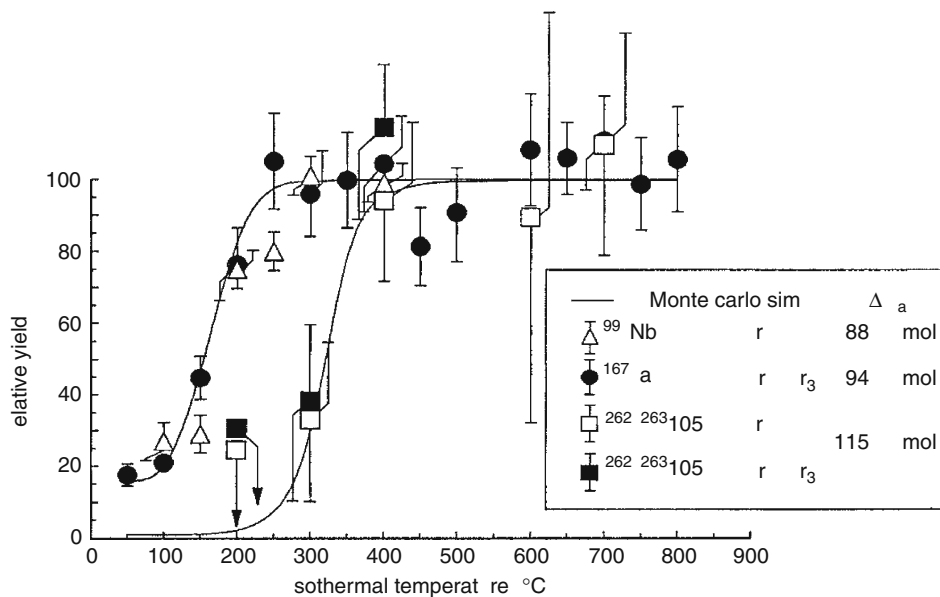
Fig. 20.23

Upper panel: Distribution of fission tracks (circles) attributed to element 105 bromides from three thermochromatographic experiments compared with the deposition zone of $14.6 \text{ h } ^{90}\text{Nb}$ (histogram) and the temperature gradient along the column. **Lower panel:** Integral distribution of $14.6 \text{ h } ^{90}\text{Nb}$ and of $3.3 \text{ min } ^{169}\text{Hf}$ (smooth solid lines) and the integral fission-track distribution (dashed step function). The shaded zone depicts the limits of the “corrected” position of the step function for element 105 after consideration of the difference in the half-life of ^{261}Db and the Hf and Nb isotopes (Adapted from Zvara et al. (1976))



■ Fig. 20.24

Relative yield of Nb (open triangles), Ta (full circles), and Db (squares) bromides as a function of temperature in the isothermal part of the gas-chromatography column. Inserted into the figure is information on the brominating agents and the adsorption enthalpies derived from Monte Carlo simulations (solid lines). After (Gäggeler et al. 1992b) (Reproduced with the permission of Oldenbourg Wissenschaftsverlag, München)



relativistic molecular calculations (Pershina et al. 1992b). Theory predicts that DbBr_5 has the highest covalency and lowest effective charge among the group-5 bromides, which should make DbBr_5 more volatile than its homologs. Also, a “nonrelativistic” thermodynamical model (Eichler 1994) leads to the prediction of a band of DbBr_5 volatilities that are close to those of NbBr_5 and TaBr_5 . This is depicted in Fig. 20.25.

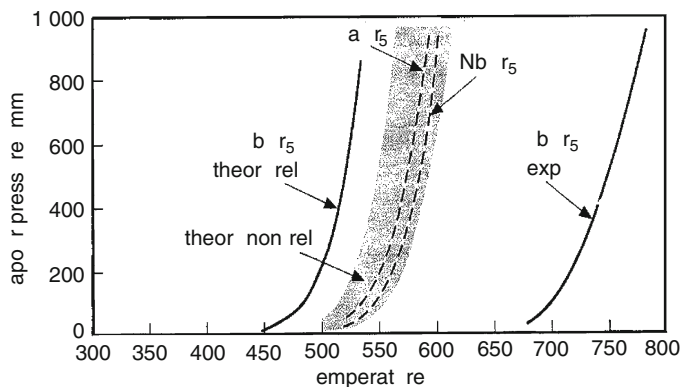
The current interpretation of the low Db-bromide volatility is the possible formation, due to the presence of traces of oxygen in the system, of the oxytribromide DbOBr_3 instead of the pentabromide. This is supported by theoretical calculations, which showed for element 105 a much stronger tendency to form oxyhalide compounds than for Nb and Ta (Pershina et al. 1992c). While the generally lower volatility of the oxyhalide can be inferred from the DS DVM calculations, it remains open whether the DbOBr_3 volatility will be higher or lower than that of the Nb and Ta oxyhalides (Pershina et al. 1992c). Further experiments are needed to clarify the situation.

In a series of experiments investigating the volatility of the chlorides of the group-5 elements, it was observed that the dubnium chlorides are more volatile than the bromides, possibly similar in volatility to NbCl_5 (Kadkhodayan 1993; Türler 1996). This is in agreement with the finding that the group-4 and -5 chlorides are more volatile than the respective bromides. For Ta, only a species with a much lower volatility was observed, presumably TaOCl_3 (Türler 1996).

In the most recent experiment (Türler et al. 1996), either precautions were taken to keep the partial pressure of oxygen as low as possible or controlled partial pressures of free O_2 were

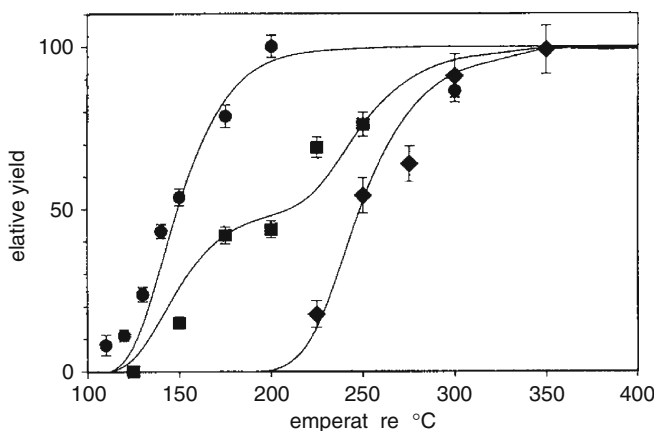
■ Fig. 20.25

Vapor pressure curves for Nb, Ta, and Db bromides. The curve DbBr_5 exp. was deduced from the experimental data shown in ▶ Fig. 20.24. The curve theor.-rel. is from Pershina et al. (1992b). The shaded area denoted theor.-non-rel. is from Eichler (1994)



■ Fig. 20.26

Relative yields of 15 s ^{99g}Nb pentachloride and oxychloride as a function of isothermal temperature and O_2 "partial pressure." Full circles: $^{99g}\text{NbCl}_5$, $p(\text{O}_2) \leq 1$ ppmv, $\Delta H_a^{\circ(T)}(\text{NbCl}_5) = -80$ kJ/mol. Full squares: 50% $^{99g}\text{NbCl}_5 + 50\%$ $^{99g}\text{NbOCl}_3$, $1 \text{ ppmv} \leq p(\text{O}_2) \leq 80$ ppmv. Full diamonds: $^{99g}\text{NbOCl}_3$, $p(\text{O}_2) \geq 80$ ppmv, $\Delta H_a^{\circ(T)}(\text{NbOCl}_3) = -99$ kJ/mol. The solid lines are the results of the Monte Carlo model using $\Delta H_a^{\circ(T)}$ values which best fit the experimental data (Reproduced with the permission of Oldenbourg Wissenschaftsverlag, München, (Türler et al. 1996))



applied to study the volatility of the chlorides of niobium and dubnium. ▶ Figure 20.26 illustrates the response of Nb to the various oxygen concentrations. It shows that the concentration of O_2 and oxygen containing compounds (e.g., H_2O) is critical in volatility experiments with group-5 elements and needs carefully to be controlled.

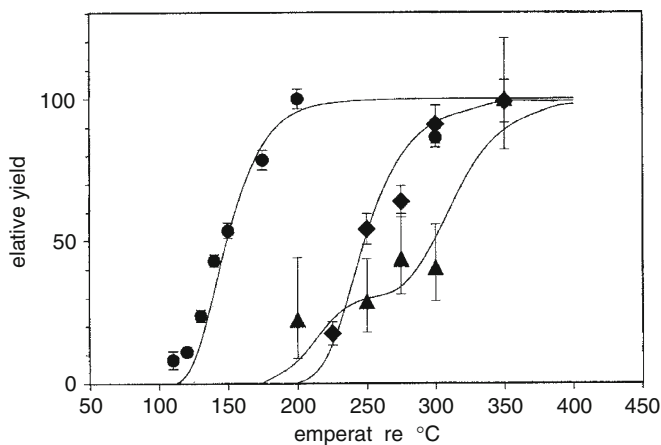
For a “partial pressure” of oxygen below 1 ppmv (parts per million by volume), NbCl_5 is formed with purified HCl as chlorinating agent. For $p(\text{O}_2)$ between 1 ppmv and 80 ppmv two species of different volatilities (NbCl_5 and NbOCl_3) are observed. Both species were produced in about equal amounts, which resulted in a yield curve with two steps. Finally, above $p(\text{O}_2) \geq 80$ ppmv, NbOCl_3 was identified as the volatile species. The conditions at which the subsequent experiments with ^{262}Db were conducted were as close as possible to the conditions where NbCl_5 was formed in the test experiments. The relative yield curve for ^{262}Db is shown in [Fig. 20.27](#) in comparison with the yield curves for NbCl_5 and NbOCl_3 from [Fig. 20.26](#). For element 105, again a yield curve consisting of two steps is observed, suggesting that both DbCl_5 and DbOCl_3 were present (Türler et al. 1996). $\Delta H_a^{\circ(T)}(\text{DbOCl}_3) = -117$ kJ/mol was obtained in the application of the Monte Carlo model at the higher temperatures and only a lower limit of the absorption enthalpy $\Delta H_a^{\circ(T)}(\text{DbCl}_5) > -98$ kJ/mol can be given for the pentachloride. An investigation of the Ta volatility is needed to complete the picture. Also, future experiments should extend the yield measurements of Db chlorides to lower temperatures for a comparison with theoretical predictions. At this time, the data show that, indeed, dubnium has a strong tendency to form the oxychloride as predicted.

First studies of the aqueous phase chemistry of element 105 were conducted by Gregorich et al. (1988). Like Nb and Ta, Db was adsorbed on glass surfaces upon fuming with nitric acid. In 801 manually performed experiments, 24 α events due to the decay of 34 s ^{262}Db or its 3.9 s ^{258}Lr daughter including five $\alpha\alpha$ mother-daughter correlations were observed. In an attempt to study the extraction of the dubnium fluoride complex from 3.8 M HNO_3 /1.1 M HF into methyl isobutyl ketone (MIBK), no decays attributable to ^{262}Db could be observed.

Under these conditions, Ta extracts while Nb does not. From an extrapolation in group 5 it was expected that Db would behave more like Ta than Nb but, surprisingly, Db apparently did

Fig. 20.27

Relative yield of NbCl_5 (full circles) and NbOCl_3 (full diamonds) as a function of the temperature of the isothermal part of the gas-chromatography column (Türler et al. 1996). The data for dubnium (triangles) indicate that both DbCl_5 and DbOCl_3 were formed under the experimental conditions. The solid lines are the results of Monte Carlo simulations with the adsorption enthalpies given in the text (Reproduced with the permission of Oldenbourg Wissenschaftsverlag, München, (Türler et al. 1996))



not extract. The non Ta-like behavior of Db might indicate that Db forms polynegative anions like $[\text{DbF}_7]^{2-}$ under the chosen conditions. The higher charge would then prevent extraction even into solvents with a relatively high dielectric constant such as MIBK.

To investigate this unexpected finding and more facets of the dubnium chemistry, a large number of automated separations were conducted with the Automated Rapid Chemistry Apparatus ARCA II (Schädel et al. 1989). In the first experiments, extraction chromatography separations with the liquid anion exchanger TiOA on an inert support (Kratz et al. 1989) were performed. TiOA extracts all group-5 elements including Pa, irrespective of the formation of mono- or polynegative anions, from HCl solutions above 10 M. At lower concentrations, selective back extractions allowed to distinguish between the chemical behavior of Nb, Ta, Pa, and Db. Small amounts of HF (typically 0.02 M) were added to the HCl solutions as this is recommended in the literature (Korkisch 1989) to prevent hydrolysis and “to maintain reproducible solution chemistry” of the group-5 elements. Element 105 was shown (Kratz et al. 1989) to extract into the TiOA on the chromatographic columns in ARCA II from 12 M HCl/0.02 M HF as do Nb, Ta, and Pa, due to the formation of anionic halide complexes. In subsequent elutions, the elution positions of element 105 relative to those of Nb, Ta, and Pa were determined (Kratz et al. 1989) in 10 M HCl/0.025 M HF, in 4 M HCl/0.02 M HF, and in 0.5 M HCl/0.01 M HF (Zimmermann et al. 1993). Two thousand one hundred and ninety-eight collection and separation cycles on a 1 min time scale (Kratz et al. 1989; Zimmermann et al. 1993) were necessary to obtain the results shown in Fig. 20.28.

It is seen that element 105 shows a striking non Ta-like behavior and that it follows, at all HCl concentrations below 12 M, the behavior of its lighter homolog Nb and that of its pseudo-homolog Pa. From this similarity, it was concluded that the complex structure of Db was $[\text{DbOX}_4]^-$ or $[\text{Db}(\text{OH})_2\text{X}_4]^-$, and the preferential formation of oxyhalide complexes of element 105 was also predicted theoretically (Perschina et al. 1994). As explained in Sect. 20.6.1, due to the complicated situation in mixed HCl/Hf solutions, it was recommended (Perschina et al. 1994) to repeat the experiments in the pure HCl system.

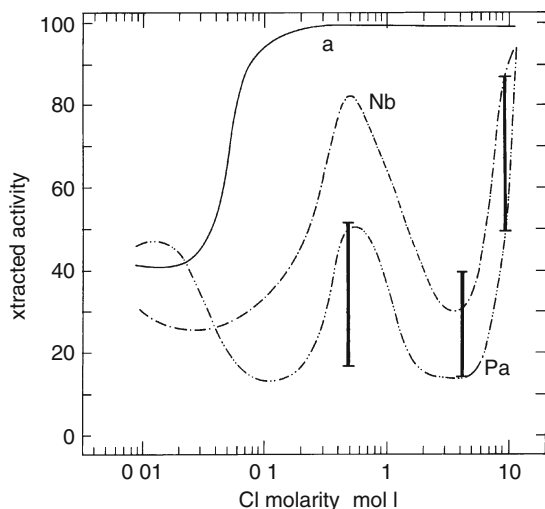
The proximity of the Db behavior in the TiOA experiments to Pa was the reason for performing a series of extractions of Db into diisobutyl carbinol (DIBC), a secondary alcohol, which is a specific extractant for Pa. The extraction from concentrated HBr in ARCA II was followed by the elution of a Nb fraction in 6 M HCl/0.0002 M HF, and a Pa fraction in 0.5 M HCl. The number of ^{262}Db decays observed in the Nb fraction indicated that less than 45% of the Db was extracted into DIBC and the extraction sequence $\text{Db} < \text{Nb} < \text{Pa}$ was established (Gober et al. 1992). This was tentatively attributed to an increasing tendency of these elements to form non-extractable polynegative complex species in the sequence $\text{Pa} < \text{Nb} < \text{Db}$.

Another series of experiments with Db used its complexation by the α -hydroxyisobutyrate anion (α -HIB), $(\text{CH}_3)_2\text{COH-COO}^-$, which depends strongly on the charge of the metal ion (Schädel et al. 1992). Elutions from cation exchange columns in ARCA II with unbuffered 0.05 M α -HIB showed that Db, together with Nb, Ta, and Pa, elutes promptly (within 4 s), while tri- and tetravalent ions are strongly retained on the resin (Schädel et al. 1992). This provided an unambiguous proof that pentavalent Db is the most stable valence state in aqueous solution. These separations, being fast and very clean, were also used to detect the hitherto undiscovered isotope 27 s ^{263}Db produced in the $^{249}\text{Bk}(^{18}\text{O},4n)$ reaction (Kratz et al. 1992; Schädel et al. 1992).

As suggested in (Perschina et al. 1994), the amine extractions of the group-5 elements were systematically revisited by Paulus et al. (Paulus 1997; Paulus et al. 1999a, b). Perschina (1998a, b), by considering the competition between hydrolysis and halide complex formation,

■ Fig. 20.28

Percentage extracted activity of Nb, Ta, and Pa tracers (curves) as a function of HCl concentration in the system TiOA-HCl/0.03 M HF. The **bold bars** encompass the upper and lower limits deduced for the Db extraction from the elution positions in the chromatography experiments (Kratz et al. 1989; Zimmermann et al. 1993). The complete extraction of Db into TiOA from 12 M HCl/0.02 M HF is not indicated for clarity (Reprinted with the permission of Oldenbourg Wissenschaftsverlag, München, (Zimmermann et al. 1993))



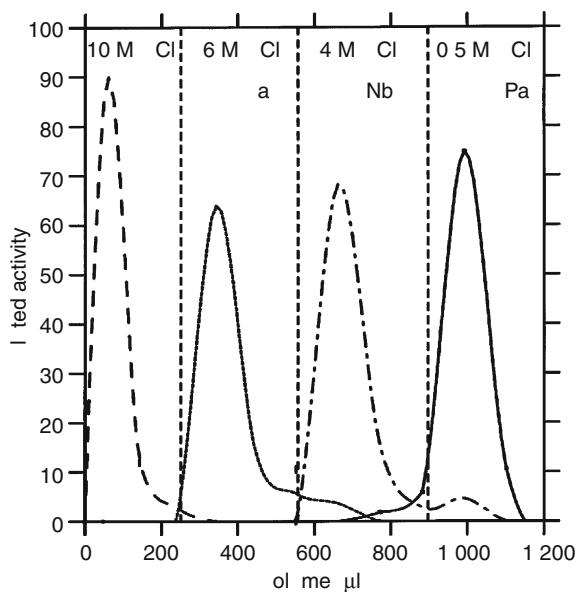
predicted the extraction sequence $\text{Pa} \gg \text{Nb} \geq \text{Db} > \text{Ta}$, as mentioned above. K_d values for Nb, Ta, and Pa were measured in new batch extraction experiments with the quaternary ammonium salt Aliquat 336 and pure HF, HCl, and HBr solutions (Paulus 1997; Paulus et al. 1999a, b). Based on these results, new chromatographic column separations with ARCA II were elaborated to study separately the fluoride and chloride complexation of element 105. As an example, the separation of Eu-, Ta-, Nb-, and Pa tracers in the Aliquat 336/HCl system is shown in ► Fig. 20.29. After feeding of the activities onto the column in 10 M HCl (whereby the disturbing actinides modeled by trivalent Eu run through the column), Ta is eluted in 6 M HCl, Nb in 4 M HCl, and Pa in 0.5 M HCl (Paulus 1997; Paulus et al. 1999a, b).

One thousand three hundred and seven experiments were conducted with element 105 with a cycle time of 50 s. In the system Aliquat 336/HCl, after feeding of the activity onto the column in 167 μl 10 M HCl, a Ta fraction was eluted in 183 μl 6 M HCl as is shown in ► Fig. 20.29. This was followed by stripping of a combined Nb, Pa fraction from the column in 167 μl 6 M HNO_3 /0.015 M HF. From the distribution of α decays between the Ta fraction and the Nb, Pa fraction, a K_d value of 438^{+532}_{-166} for element 105 in 6 M HCl was deduced, which is close to that of Nb and differs from the values for Pa and Ta, see ► Fig. 20.30. Thus, the extraction sequence $\text{Pa} > \text{Nb} \geq \text{Db} > \text{Ta}$ is established exactly as theoretically predicted (Pershina 1998a, b).

In the system Aliquat 336/HF, the reaction products were loaded onto the column in 167 μl 0.5 M HF. In elutions with 133 μl 4 M HF (Pa fraction), and with 167 μl 6 M HNO_3 /0.015 M HF (combined Nb, Ta fraction) all α -decay events of element 105 were observed in the Nb, Ta

■ Fig. 20.29

Elution curves for trivalent cations (Eu), and for Ta, Nb, and Pa from Aliquat 336/Voltalef columns (1.6×8 mm) in ARCA II. The activities are fed onto the column in 10 M HCl. This is followed by separate elutions of a Ta fraction in 6 M HCl, of a Nb fraction in 4 M HCl, and of a Pa fraction in 0.5 M HCl (Reproduced with the permission of Oldenbourg Wissenschaftsverlag, München, (Paulus et al. 1999b))



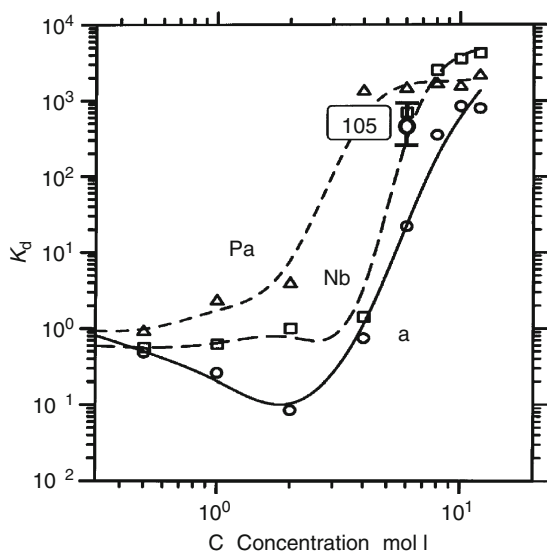
fraction. This results in a lower limit for the K_d value of element 105 in 4 M HF of >570 , which is close to that of Nb and Ta ($\geq 10^3$) and differs markedly from that of Pa (~ 10).

It is satisfying to see that not only the extraction sequence in the system Aliquat 336/HCl is correctly predicted by theory (Pershina 1998b) but that the calculated free energy changes of the reactions of complex formation are on the order of 12 eV for the fluorides, 20 eV for the chlorides, and 22 eV for the bromides (Pershina et al. 1999) (not taking into account the Gibbs free energy of formation of H_2O which is 3 eV), which again is in agreement with the experimental findings: For the fluorides, the equilibrium is always on the right hand side of Eq. (20.19) even at low HF concentrations (Paulus 1997); for the chlorides, it takes >3 M HCl to form extractable chloride complexes and for the bromides, the threshold is shifted to >6 M HBr (Paulus 1997).

Anion-exchange chromatography of Db produced in the $^{248}\text{Cm}(^{19}\text{F},5n)^{262}\text{Db}$ reaction was investigated by Tsukada et al. (2009) together with the homologs Nb and Ta and the pseudo-homolog Pa with the anion-exchange resin CA08Y in 13.9 M HF solution. For Nb and Ta, elution curves were determined and K_d values were determined with fits by the Glöckauf equation. The latter were again correlated with %ads values, and the correlation was used to determine a K_d from the %ads values of ^{262}Db and ^{170}Ta in 13.9 M HF solution. The variation of the K_d values of Db, Nb, Ta, and Pa on the anion-exchange resin CA08Y as a function of $[\text{HF}]_{\text{ini}}$ are shown in Fig. 20.31. The results indicate that the sorption of Db on the resin is significantly different from that of the homologs and that the sorption decreases in the

■ Fig. 20.30

Distribution coefficients of Pa, Nb, and Ta in the system Aliquat 336/HCl. The K_d for Db in 6 M HCl is also indicated (Paulus 1997). The system shows the inverse extraction sequence as compared to the TiOA/HCl/HF system (● Fig. 20.28) as theoretically predicted (Pershina 1998b) (Reproduced with the permission of Oldenbourg Wissenschaftsverlag, München, (Paulus et al. 1999b))



sequence $Ta \approx Nb > Db > Pa$. The measurement of distribution coefficients at different HF concentrations is necessary to determine the chemical forms of the group-5 elements to compare the experimental adsorption sequence with that from theoretical predictions.

20.7 Element 106 (Seaborgium)

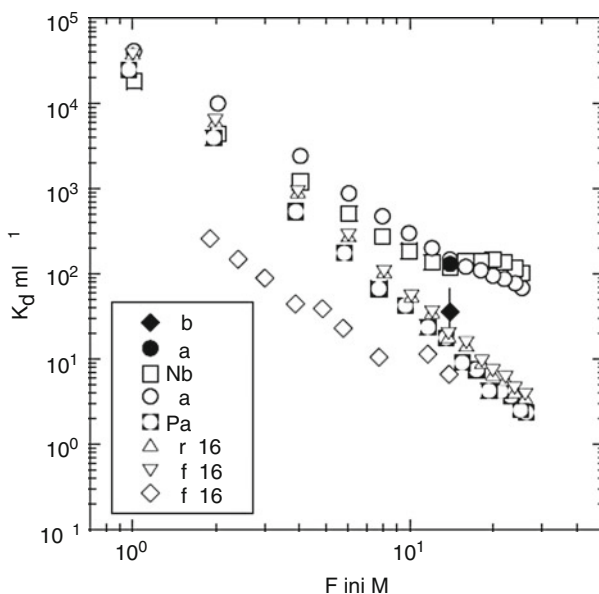
20.7.1 Theoretical Predictions

Relativistic molecular orbital calculations (Pershina and Fricke 1994a, 1995) with the DS DVM code have shown that the volatile species $SgCl_6$ as well as $SgOCl_4$ will decompose at high temperatures by analogy with $MoCl_6$ and $MoOCl_4$ transforming into compounds of Mo(V). Therefore, DS DVM calculations were performed of the electronic structure of the group-6 dioxodichlorides MO_2Cl_2 ($M = Cr, Mo, W, Sg$) and their analysis with respect to the stability of the compounds toward thermal decomposition. In ● Table 20.2, the Mulliken analysis data (Pershina and Fricke 1996; Pershina et al. 1996) effective charges Q_M , overlap populations, OP , and dipole moments, μ , are presented.

The trends in Q_M , OP , and the metal-ligand bond energies estimated on the basis of the data in ● Table 20.2, are reminiscent of those for the group-6 oxotetrachlorides, $MOCl_4$. However, the energy gaps ΔE between the highest occupied molecular orbital (HOMO) and the lowest unoccupied molecular orbital (LUMO) are much larger for the dioxodichlorides, MO_2Cl_2 , than for the oxotetrachlorides. This should prevent the dioxodichlorides from thermal

■ Fig. 20.31

Distribution coefficients K_d of Db, Nb, Ta, and Pa on the anion-exchange resin CA08Y as a function of $[\text{HF}]_{\text{ini}}$. The values of Db and Ta obtained from online column experiments are indicated by the closed symbols, while those of Nb, Ta, and Pa from batch experiments are shown by the open symbols. The K_d values of Rf, Zr, and Hf taken from (Haba et al. 2004) are also plotted (Reproduced with the permission of Oldenbourg Wissenschaftsverlag, München, (Tsukada et al. 2009))



■ Table 20.2

Effective charges, Q_M , overlap populations, OP , and dipole moments, μ , for MO_2Cl_2 (Pershina and Fricke 1996; Pershina et al. 1996)

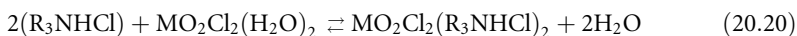
	MoO_2Cl_2	WO_2Cl_2	SgO_2Cl_2
Q_M/e	1.03	1.08	0.97
OP ($M = 2O$)	1.07	1.38	1.48
OP ($M - 2Cl$)	0.64	0.86	0.85
OP (tot)	1.72	2.23	2.34
μ/D	1.04	1.35	1.83

dissociation and should make MoO_2Cl_2 , WO_2Cl_2 , and SgO_2Cl_2 much more stable than MoOCl_4 , WOCl_4 , and SgOCl_4 even though their $M\text{-Cl}$ bond strengths are similar.

The lower volatility of WO_2Cl_2 compared to that of MoO_2Cl_2 was associated (Pershina 1996; Pershina et al. 1996) with the larger dipole moment of the former compound. And from the trend of the dipole moments in Table 20.2, the following sequence in volatility was predicted: $\text{MoO}_2\text{Cl}_2 > \text{WO}_2\text{Cl}_2 > \text{SgO}_2\text{Cl}_2$.

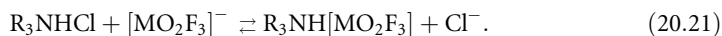
These theoretical results (Pershina and Fricke 1994a, 1995, 1996; Pershina et al. 1996) have influenced the decision (Dressler et al. 1995) of the gas-phase chemists to use oxygen containing chlorinating agents, and the volatility data in ▶ Fig. 20.35 are in agreement with the prediction. Note that the dipole moments in the dioxodichlorides of the group-6 elements are the result of the ds hybridization in MO_2^{2+} giving rise to a cis structure of the oxygen ligands (Pershina and Fricke 1996).

DS DVM calculations (Pershina and Fricke 1994a, 1996; Pershina et al. 1996) confirmed the full analogy between SgO_2Cl_2 and MO_2Cl_2 ($\text{M} = \text{Mo}$ and W). Thus, one can also assume the same type of complexes of seaborgium in HCl and HF solutions as those of Mo and W. Results of the extraction of the Mo, W, and U species from aqueous HCl solutions into organic media have shown the opposite trend in the distribution coefficients, $K_d(\text{U}) > K_d(\text{Mo}) > K_d(\text{W})$, compared with HF solutions where $K_d(\text{U}) < K_d(\text{Mo}) < K_d(\text{W})$. Pershina (1996) associates this with two different extraction mechanisms. In the HCl case the mechanism of the formation of an adduct is valid:



The process of the molecule transfer (ΔG_t) between the aqueous and the organic phase in this case is defined by the strength of the dipole–dipole interaction of the $\text{MO}_2\text{Cl}_2(\text{H}_2\text{O})_2$ species with water molecules. The values of dipole moments obtained as a result of the DS DVM calculations (Pershina and Fricke 1996), ▶ Table 20.2, then define the distribution coefficients in 2–6 M HCl in the sequence $\text{U} > \text{Mo} > \text{W} > \text{Sg}$.

The absence of a dipole moment in $\text{UO}_2\text{Cl}_2(\text{H}_2\text{O})_2$ with a linear structure of the oxygen ligands explains its superior extractability. In HF solutions, anion exchange takes place (Pershina 1996) according to



Here, the free energy of transfer is determined by the sizes of the extracted species leading to the sequence $\text{U} < \text{Mo} < \text{W}$.

The distribution coefficient is finally dependent on the complex formation and on the partition of the complexes between the phases. Details of the electronic structure of the anionic complexes existing in HF solutions still need to be studied.

Based on MCDF calculations of the ionization potentials for all oxidation states of the group-4 elements (Johnson et al. 1999), Pershina et al. (1999b) made use of a linear correlation between the calculated ionization potentials and the redox potentials of the group-6 elements to predict the reduction potentials of the various oxidation states of seaborgium in acid solutions. For example, the reduction potential $E^\circ(\text{Sg}^{\text{VI}}/\text{Sg}^{\text{III}})$ is -0.46 V. Thus, it might be interesting to attempt to reduce seaborgium by contact with a strongly reducing metal such as Al ($E^\circ = -1.662$ V) in future experiments. Throughout the transactinide series, the stability of the maximum oxidation state decreases in the sequence $\text{Rf} > \text{Db} > \text{Sg}$.

Relativistic molecular density-functional calculations of the electronic structure of hydrated and hydrolyzed species have been performed by Pershina and Kratz (2001) for the group-6 elements Mo, W, and Sg. By use of the electronic density distribution data, relative values of the free energy changes and constants of hydrolysis reactions were defined. The results show hydrolysis of the cationic species with the formation of neutral molecules to decrease in the order $\text{Mo} > \text{W} > \text{Sg}$, which is in agreement with experiment for Mo, W, and Sg. For the

further hydrolysis process, with the formation of the anionic species, the trend is predicted to be reversed: Mo > Sg > W. A decisive energetic factor in the hydrolysis process is the predominant electrostatic metal–ligand interaction.

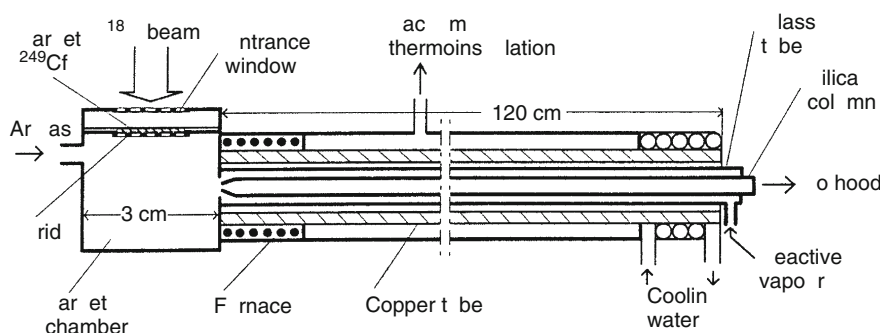
20.7.2 Experimental Results

First attempts to chemically characterize seaborgium were reported by Timokhin et al. in 1992 (Timokhin et al. 1996) and were completed in 1993 and 1995 (Yakushev et al. 1996; Zvara et al. 1998). The authors used the short-lived isotope $0.9\text{ s }^{263}\text{Sg}$ produced in the $^{249}\text{Cf}(^{18}\text{O},4n)$ reaction and their fast online thermochromatography equipment shown in Fig. 20.32. The recoils were thermalized and swept from the target chamber in 1 l/min argon gas directly into the thermochromatographic column; an open, 3.5 mm i.d. tube of fused silica, 120 cm in length. About 60% of the recoils reached the column, the rest deposited on the walls of the target chamber. At the column inlet, the flowing argon was mixed with the reactive gas supplied from the end part of the apparatus through an annular channel formed by the glass jacket of the column. 0.2 l/min of air saturated with SOCl_2 vapor was supplied to yield partial pressures of 20 mmHg ($\sim 2.7\text{ kPa}$ or 2.6 vol %) of SOCl_2 and 25 mmHg ($\sim 3.3\text{ kPa}$ or 3.3 vol %) of O_2 in the resulting carrier gas.

In test experiments with Mo and W radioisotopes with half-lives in the range of seconds to hours, Yakushev et al. (1996) generally observed two deposition zones, a “high temperature zone” at about 250°C and a “low temperature zone” at about 160°C . The distribution of the activities between these zones depended on the half-life such that the percentage deposited in the lower temperature zone increased with increasing half-lives of the nuclides. This was interpreted as evidence for a rapid formation of the dioxodichlorides, MO_2Cl_2 , that are subsequently relatively slowly converted into the more volatile oxotetrachlorides, MOCl_4 . For very short-lived species, a deposition on the quartz surface as the dioxodichloride was expected. Zvara et al. (1998) also report that, in their thermochromatography column, short-lived W isotopes reached their deposition zone in less than 0.8 s.

Fig. 20.32

Schematic representation (Zvara et al. 1998) of the thermochromatographic equipment used by Timokhin et al. (1996), Yakushev et al. (1996) and Zvara et al. (1998) (Reprinted with the permission of Oldenbourg Wissenschaftsverlag, München, (Zvara et al. 1998))



The inner surface of the fused silica column served as a solid state detector for spontaneous fission (SF) events. After the discovery of the α -emitting 0.9 ± 0.2 s ^{263}Sg by Ghiorso et al. (1974) with a cross section on the order of 0.3 nb, Druin et al. (1979), reported observation of a $0.64^{+0.32}_{-0.18}$ s SF activity assigned to ^{263}Sg with 0.6 nb cross section at 95 MeV. This was thought to be the origin of the fission tracks in the fused silica column, which were made visible by etching subsequent 5 cm segments of the column with HF and scanning the surface with an optical microscope. At room temperature, the detection efficiency with this technique is 65%. It decreases at higher temperatures due to annealing of the tracks.

Six experiments with the $^{249}\text{Cf}(^{18}\text{O},4n)^{263}\text{Sg}$ reaction were performed with a total number of ^{18}O ions (called “beam dose”) between 0.8×10^{17} and 2.6×10^{17} in each case. In the first two thermochromatographic runs, a quartz wool filter was present in the start zone as in most ancillary tests. No fission tracks were found in the column. In the four following experiments, this filter was omitted. In the fifth experiment, no chlorinating reagents were added and the column was kept at ambient temperature to test the behavior of the nonvolatile actinides. 18 SF events were detected within the first 15 cm of the column. The number of tracks found in runs 3, 4, and 6 are 10, 20, and 11, respectively, and these are mostly distributed along the first 20–120 cm of the column, see [Fig. 20.33](#).

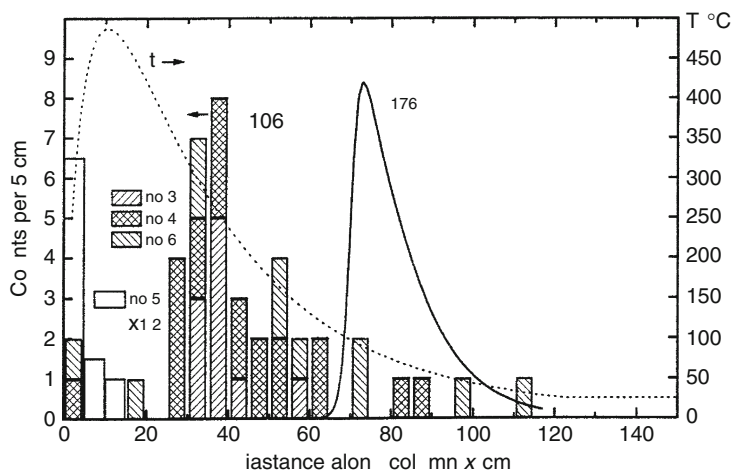
The same data from runs 3, 4, and 6 are shown again in [Fig. 20.34](#) with corrections for the decreased detection efficiency due to annealing in the hotter part of the column. The thick solid line is a fit of the theoretical peak shape in nonequilibrium thermochromatography (Zvara 1990) to the corrected data. One notices a marked difference in the deposition temperatures of element 106 and ^{176}W . According to Zvara et al. (1998), this difference can hardly be associated with the different half-lives, 0.9 s versus 2.5 h, resulting in different migration times (Zvara 1985). Rather, according to Zvara et al. (1998), the different deposition zones for ^{263}Sg and ^{176}W point to nonidentical chemical states of the two homologs: The short-lived ^{263}Sg deposited as SgO_2Cl_2 and decayed long before this compound could be transformed into SgOCl_4 . The long-lived ^{176}W first rather quickly formed WO_2Cl_2 but was completely converted into the more volatile WOCl_4 . In the first two “unsuccessful” experiments, the retention time of seaborgium on the quartz wool filter was assumed (Zvara et al. 1998) to have exceeded the nuclear half-life of the seaborgium isotope(s). A longer retention time on the filters than in the open column was observed earlier by the authors in investigations of the group-4 and -5 elements and attributed to the large effective surface of the quartz filters (equivalent to several meters of an open column).

The work by Zvara et al. (Timokhin et al. 1996; Yakushev et al. 1996; Zvara et al. 1998) has been met with skepticism. This concerns both the assignment of the observed SF activity and the chemical state of the tungsten and seaborgium oxochlorides. The latter is discussed first.

As mentioned above, different deposition temperatures due to different half-lives are a well-known phenomenon (Zvara 1985). It is difficult to understand that the formalism to analyze thermochromatographic data has not been applied by Zvara et al. (1998) to correct quantitatively for the largely different half-lives of ^{263}Sg and ^{176}W and to extract the adsorption enthalpy. Also, before a statement about the possible chemical state of seaborgium is made, the data for short-lived isotopes of the homologous elements Mo and W should be presented and analyzed quantitatively with the formalism developed by Zvara (1985). The latter was used by Türler (1999) and applied to the data in [Fig. 20.34](#) resulting in values of $\Delta H_a^{\circ(\text{T})} = -110$ kJ/mol for ^{263}Sg and $\Delta H_a^{\circ(\text{T})} = -102$ kJ/mol for ^{176}W . These values are much higher than the values reported in (Türler et al. 1999), which are -98 kJ/mol for ^{265}Sg and -96 kJ/mol for ^{168}W .

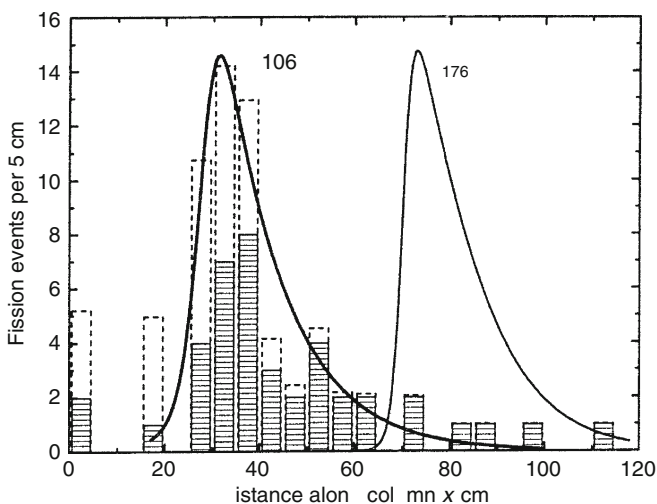
■ Fig. 20.33

Distribution of fission tracks along the thermochromatographic column (Zvara et al. 1998). The *hatched* histograms stand for fission events detected in runs with the carrier gas argon (1 l/min) + air (0.2 l/min) + SOCl_2 (20 mmHg). The white (*not hatched*) histogram depicts the fission events observed in the run with pure argon in a cold column. The *dotted* curve gives the temperature profile along the column. The *solid* line indicates the distribution of gamma activity due to $2.5 \text{ h } ^{176}\text{W}$ in an arbitrary linear scale (Reprinted with the permission of Oldenbourg Wissenschaftsverlag, München, (Zvara et al. 1998))



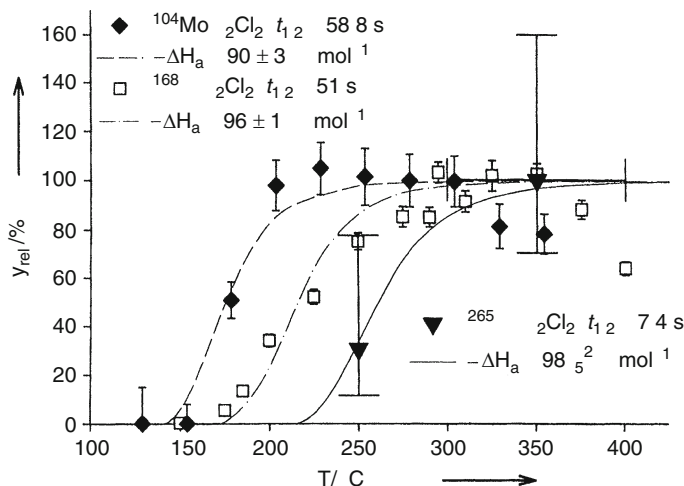
■ Fig. 20.34

The data from ▶ Fig. 20.33 are represented with their correction for the relative detection efficiency (*dashed* histograms) due to annealing at elevated temperatures. The thick solid line is “the smoothed corrected thermochromatogram of element 106” (Zvara et al. 1998) (Reprinted with the permission of Oldenbourg Wissenschaftsverlag, München, (Zvara et al. 1998))



■ Fig. 20.35

Relative yield versus isothermal temperature for $^{104}\text{MoO}_2\text{Cl}_2$ (full diamonds, $T_{1/2} = 59$ s, $\Delta H_a^{\circ(T)} = -90$ kJ/mol), $^{168}\text{WO}_2\text{Cl}_2$ (open squares, $T_{1/2} = 51$ s, $\Delta H_a^{\circ(T)} = -96$ kJ/mol), and $^{265}\text{SgO}_2\text{Cl}_2$ (full triangles, $T_{1/2} = 7.4$ s, $\Delta H_a^{\circ(T)} = -98$ kJ/mol) (Reprinted with the permission of WILEY-VCH, STM Copyright & Licenses (Türler et al. 1999))




The other concern is with the assignment of the observed SF activity. The 70% SF branch deduced on the basis of cross section arguments by Druin et al. (1979) has never been confirmed. In the decay chains of $^{271}\text{110}$ as third generation α decays, 8 α decays of ^{263}Sg grouped around 9.248 MeV were measured (Hofmann et al. 1995a) in excellent agreement with the 9.25 MeV literature value (Ghiorso et al. 1974) for 0.9 s ^{263}Sg , but the half-life of $0.31^{+0.16}_{-0.08}$ s is different. Therefore, and because Hofmann et al. (1995a) did not observe the 9.06 MeV line (intensity ratio of the 9.25 MeV line to the 9.06 MeV line in the work of Ghiorso et al. (1974) is $\sim 9:1$), one must assign the two α lines to two different levels in ^{263}Sg . Both are populated in the $^{249}\text{Cf}(^{18}\text{O},4n)$ reaction, but only the 0.3 s level is populated by α decay in the decay chain of $^{271}\text{110}$. An upper limit for a fission or electron capture branch of the 0.3 s level of 12% was given by Hofmann et al. (1995a).

Hofmann et al. compared the decay pattern of ^{263}Sg with that of the next heavier $N = 157$ isotope $^{265}\text{108}$. Two α lines with energies of 10.31 and 10.58 MeV and an intensity ratio of 2:1 were measured in the case of the direct production in the reaction $^{58}\text{Fe} + ^{208}\text{Pb}$. Only the 10.58 MeV transition was observed in the α decays of $^{269}\text{110}$ (Hofmann et al. 1995b).

Therefore, two levels with approximately the same half-life of 1.5 ms exist in $^{265}\text{108}$. As fission was not observed, one can determine the α decay hindrance factors⁶ as 1.1 (10.31 MeV) and 5.0 (10.58 MeV) both being in agreement with favored α transitions. This also confirms the expectation, based on theoretical predictions (Cwiok et al. 1994), of the existence of isomeric states with similar decay properties. Theory predicts a very similar level structure for the lighter odd- A isotones. If this is the case in ^{263}Sg , the 0.9 s state should also decay by favored α transition. Also, a fission branch of more than 10% in ^{263}Sg would require an odd- N fission hindrance factor of less than 200 (usually on the order of 10^5 for odd neutrons). These

arguments by Hofmann et al. (1995a) do not rule out a large fission branch in $^{263\text{m}}\text{Sg}$ but make it seem unlikely.

A solution to these open questions was recently given by Gregorich et al. (2006) who measured a fission branch of 13% in 0.9-s $^{263\text{a}}\text{Sg}$. Starting from a cross section of 0.3 nb (Ghiorso et al. 1974) and an “effective” cross section of 0.15 nb in the experiment by Zvara et al. (1998), and using this fission branch of 13%, one calculates 32 SF events to be expected under the reported conditions, while twice as many SF events are shown in  Fig. 20.34.

Thus, if the assignment of the observed SF events in the thermochromatography experiments (Zvara et al. 1998) to the decay of 0.9 s $^{263\text{a}}\text{Sg}$ is questionable, it is of crucial importance to show that in the experiments, the other transactinide elements 104 and 105 are much less volatile than the studied 106 compound. Zvara et al. (1998) claimed that elements 104 and 105 do not form volatile compounds with a chlorinating, oxygen-containing carrier gas but the references given do not warrant such a claim. On the other hand, Türler et al. (1996) have shown that DbOCl_3 is volatile above 200°C, and an absorption enthalpy of -117 kJ/mol was deduced. From literature data, it is known that DbOCl_3 is more volatile than TaOCl_3 . Therefore, DbOCl_3 could have been volatile under the experimental conditions of the experiment even if it had been shown that Ta was not volatile. A volatile DbOCl_3 needs to be considered because one cannot exclude an EC decay branch in $^{263\text{a}}\text{Sg}$ leading to SF in ^{263}Db (Kratz et al. 1992) and, after α decay, to SF in ^{259}Lr (Gregorich et al. 1992). Such a “bizarre” explanation of the observed SF events in the seaborgium experiments (Zvara et al. 1998) is not ruled out by the evidence presented.

Also for rutherfordium, Jost et al. (1996) showed that ^{261}Rf is volatile in a carrier gas of 1 l/min He, 150 ml/min Cl_2 saturated with SOCl_2 , and 20 ml/min O_2 , that is, under conditions that are similar to the conditions of the thermochromatography experiments (Zvara et al. 1998). In summary, the conclusion by Zvara et al. (1998) that only element 106 can be responsible for the observed SF decays is not convincing. The evidence presented by Zvara et al. (1998) falls short of demonstrating that other sources of SF tracks are rigorously excluded.

In 1991, an international collaboration centered around the nuclear chemistry groups at GSI, Darmstadt, the University of Mainz, and PSI, Villigen, started to prepare their chemical characterization of seaborgium in a series of test experiments (see, e.g., Brüche et al. 1992; Gäggeler et al. 1992a, Hübener et al. 1992; Dressler et al. 1995; Günther et al. 1995). Generally, their experiments used gas-jet transportation systems and “external” detection systems in which the $\alpha\alpha$ -correlation technique with silicon detectors was used; both being “slow” as compared to the Dubna technique (Zvara et al. 1998). Therefore, based on the predicted enhanced nuclear stability near $N = 162$ and $Z = 108$ due to an especially large negative shell correction (Patyk and Sobiczewski 1991), it was hoped that more neutron-rich nuclides with presumably longer half-lives than the 0.9 s of $^{263\text{m}}\text{Sg}$ could be synthesized, for example, in the $^{22}\text{Ne} + ^{248}\text{Cm}$ reaction. Indeed, in 1993, working at the Dubna gas-filled recoil separator, a Dubna-Livermore collaboration succeeded to synthesize, as they believed, two new isotopes of element 106, ^{265}Sg , and ^{266}Sg , in the $^{248}\text{Cm}(^{22}\text{Ne}, 5n)$ and $^{248}\text{Cm}(^{22}\text{Ne}, 4n)$ reaction at 121 MeV and 116 MeV, respectively (Lazarev et al. 1994). They measured an α energy of 8.63 ± 0.05 MeV for ^{266}Sg and a half-life of 1.2 s for the spontaneously fissioning daughter, ^{262}Rf . For ^{265}Sg , they measured α energies between 8.71 MeV and 8.91 MeV and correlated α decays of the daughter $^{261\text{a}}\text{Rf}$ (8.29 MeV) and the grand-daughter ^{257}No (8.222, 8.27, and 8.32 MeV). The cross sections were reported to be 80 pb at 116 MeV and 60 pb at 121 MeV for production of ^{266}Sg and 260 pb at 121 MeV for production of ^{265}Sg . These were reported to have an estimated

uncertainty of a factor of ~ 3 . Using the phenomenological formula of Viola and Seaborg (Patyk and Sobiczewski 1991) they estimated a partial α half-life for ^{266}Sg of 10–30 s and of 2–30 s for ^{265}Sg , assuming a hindrance factor between 1 and 3. Measurements of the life times could not be performed as the implantation signals in the position-sensitive surface barrier detector were below the detection threshold. The estimated half-lives were felt to be rather encouraging for the planned chemistry experiments with these seaborgium isotopes. Note that due to the work by Dvorak et al. (2006, 2008) and Düllmann and Türler (2008), the assignments in (Lazarev et al. 1994) need to be reexamined.

In 1995, two of the developed techniques (Dressler et al. 1995; Günther et al. 1995) were eventually used to study the chemical properties of seaborgium. A short account of these successful first experiments and their results was published in (Schädel et al. 1997a). A more up-to-date report on the experiments, including the results of a follow-up experiment performed in 1996, is given here.

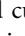
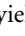
The choice of the chemical system was influenced by the wish to differentiate Sg from the group-4 elements and by theoretical predictions (Pershina and Fricke 1996) showing that SgO_2Cl_2 should be the most stable oxochloride compound. Thus, chlorinating oxygen containing reactive gases were selected. It was also predicted by calculating the dipole moments in the Mo-, W-, and Sg-dioxodichlorides (Pershina and Fricke 1996) that the volatility should decrease in the order $\text{Mo} > \text{W} > \text{Sg}$. With the aid of an empirical correlation between sublimation enthalpy ($\Delta H_s^{\circ(298\text{ K})}$) and adsorption enthalpy on quartz surfaces, $\Delta H_a^{\circ(T)}(\text{SgO}_2\text{Cl}_2)$, between -97 and -108 kJ/mol was predicted (Eichler et al. 1999a).

With the reaction oven temperature kept at 900°C and typically 100 ml/min Cl_2 saturated with SOCl_2 plus 2 ml/min O_2 , the chromatographic behavior of short-lived Mo isotopes from ^{235}U fission and of short-lived W isotopes produced at the PSI Philips cyclotron in the $^{152}\text{Gd}(^{20}\text{Ne}, xn)$ reaction was studied and values of $\Delta H_a^{\circ(T)}$ of -90 kJ/mol were measured for MoO_2Cl_2 and of -100 kJ/mol for the less volatile compound WO_2Cl_2 . Also, the yield versus temperature curve for ^{229}U from the $^{232}\text{Th}(\alpha, 7n)$ reaction was measured yielding a $\Delta H_a^{\circ(T)}$ of -91 kJ/mol indicative of the formation of UCl_6 (Gärtner et al. 1997). It was demonstrated that for isothermal temperatures above 275°C retention times less than 10 s in OLGA III are achieved.

In a first experiment in 1995 at the GSI UNILAC accelerator, a ^{248}Cm target of $950\text{ }\mu\text{g}/\text{cm}^2$ was bombarded with 121 MeV ^{22}Ne ions of 3×10^{12} ions s^{-1} . OLGA III was operated between 300°C and 400°C . As reactive agents, 100 ml/min Cl_2 saturated with SOCl_2 and 2 ml/min O_2 were added. Spontaneous fission decays and α decays were registered in ROMA. The separated activities were deposited on thin polypropylene foils ($30\text{--}40\text{ }\mu\text{g}/\text{cm}^2$) at the periphery of a 64-position wheel. Every 10 s, the wheel was stepped to move the collected activity between 7 pairs of PIPS detectors. All events were registered in an event-by-event mode. Due to a long-lived contamination from ^{212}Po in the 8.8 MeV region, where α decays of ^{265}Sg are expected, the significance of the observed event chains had to be improved. Therefore, a mother-daughter recoil mode for ROMA was implemented. In this mode, every second position on the wheel remained empty. Whenever an α particle with the decay energy of ^{265}Sg or ^{266}Sg (between 8.5 MeV and 8.9 MeV) was detected in a bottom detector, it was assumed that the daughter nucleus, ^{261a}Rf or ^{262}Rf recoiled out of the KCl deposit on the polypropylene foil (KCl was the aerosol in the recluster unit) into the top detector. Such an event initiated the daughter search mode by causing a single step. In this mode, the sources were removed from the detector pairs and empty positions were moved in-between. The system waited for 2 min for the decay of the daughter nuclides, before the parent mode was resumed.

Between 300°C and 400°C isothermal temperature, several $\alpha\alpha$ -correlations observed in the daughter mode allowed the clear identification of ^{265}Sg . In addition, one very significant triple correlation was observed in the parent mode (Gäggeler 1998).

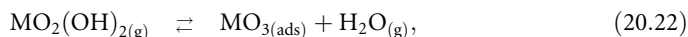
In 1996 the experiment was continued (Gäggeler 1998) and the isothermal temperature was varied in order to determine $\Delta H_a^{\circ(T)}$ for the seaborgium compound. First, the volatility of WO_2Cl_2 was carefully re-examined under conditions that were identical to those of the actual Sg experiment. Short-lived W-isotopes were produced in the 119 MeV ^{22}Ne on ^{152}Gd reaction at the GSI UNILAC accelerator. A He/C-jet (1.0 l/min) was used to rapidly transport the reaction products to the chromatography apparatus. As reactive agents, 144 ml/min Cl_2 saturated with SOCl_2 at room temperature (20 ml/min) and 2 ml/min O_2 were added. The Sg experiment was performed with a mixed $^{248}\text{Cm}/^{152}\text{Gd}$ target ($690 \mu\text{g}/\text{cm}^2$ ^{248}Cm , $22 \mu\text{g}/\text{cm}^2$ ^{152}Gd) at ^{22}Ne beam energy of 123 MeV. The same quartz column with the same quartz wool plug in the same chromatography oven as in the preceding W experiment was used. Spontaneous fission decays and α decays were registered with ROMA. Every 10 s, the wheel was stepped to move the collected activity between 7 pairs of PIPS detectors. Again the mother-daughter recoil mode with a daughter search time of 200 s was implemented. Simultaneously, the yield of short-lived W was monitored with a HPGe detector, in order to ensure that the chemical separation was proceeding with high chemical yield.

The yield curve measured for $^{168}\text{WO}_2\text{Cl}_2$ ($T_{1/2} = 51$ s) is shown in  Fig. 20.35 together with the previously measured yield curve for $^{104}\text{MoO}_2\text{Cl}_2$ ($T_{1/2} = 59$ s) (Gärtner et al. 1997). With the Monte Carlo model, an adsorption enthalpy $\Delta H_a^{\circ(T)}(\text{WO}_2\text{Cl}_2) = -96$ kJ/mol was determined in good agreement with the previous measurement. For ^{265}Sg , at 350°C isothermal temperature and with a “beam dose” of 2.31×10^{17} ^{22}Ne ions, the results of the first experiment were confirmed by observing further ^{265}Sg α -decay chains (Türler et al. 1998). Without changing any of the other experimental parameters, the isothermal temperature was then lowered to 250°C, and a beam dose of 5.22×10^{17} was accumulated. Three decay chains of ^{265}Sg were observed, corresponding to a relative yield of $\sim 30\%$ as compared to the results at 350°C. For the simultaneously produced ^{168}W , a relative yield of $\sim 47\%$ was observed at 250°C as compared to the result at 350°C, which is in agreement with previous measurements. The relative yields for ^{265}Sg are also shown in  Fig. 20.35. Owing to the relatively large error bars on the two Sg data points, a careful statistical analysis was performed which resulted, within the Monte Carlo model, in a value of $\Delta H_a^{\circ(T)}(\text{SgO}_2\text{Cl}_2) = -98_{-5}^{+2}$ kJ/mol. Thus, the sequence in volatility of MO_2Cl_2 ($\text{M} = \text{Mo}, \text{W}, \text{Sg}$) is $\text{MoO}_2\text{Cl}_2 > \text{WO}_2\text{Cl}_2 \approx \text{SgO}_2\text{Cl}_2$. The probability that SgO_2Cl_2 is equally or even more volatile than MoO_2Cl_2 is less than 15% (Türler et al. 1999).

The experimentally determined $\Delta H_a^{\circ(T)}$ values, measured with trace amounts (at zero surface coverage), can be correlated with their macroscopic sublimation enthalpies ΔH_s (Türler et al. 1999). From an empirically derived linear correlation between ΔH_a and ΔH_s , the sublimation enthalpy of SgO_2Cl_2 can be estimated as ~ 127 kJ/mol. This is an important quantity to estimate the sublimation enthalpy of Sg metal. Seaborgium is estimated to have an equal or even higher sublimation enthalpy than W, the least volatile element in the periodic table (Türler et al. 1999).

The assignment of very few decay chains (Türler et al. 1998) to the isotope ^{266}Sg must be revised according to the more recent data by Dvorak et al. (2006) and Dvorak et al. (2008) showing that all decay chains observed in the reaction $^{248}\text{Cm}(^{26}\text{Mg}, \text{xn})^{270-x}\text{Sg}$, which were originally attributed to ^{266}Sg , originated from ^{265}Sg (Düllmann and Türler 2008).

The other gas chromatography approach that has been applied to seaborgium is the online high-temperature gas chromatography of group-6 elements in the $\text{O}_2\text{--H}_2\text{O(g)--SiO}_2\text{(s)}$ system. Hübener et al. (2001) have found that Mo and W are volatile in humid oxygen gas at relatively high temperatures and that the peculiar adsorption behavior both in the thermochromatography and in the isothermal gas chromatography (Hübener et al. 2001), for a detailed account see (Vahle 1996), required the assumption of a dissociative adsorption and associative desorption



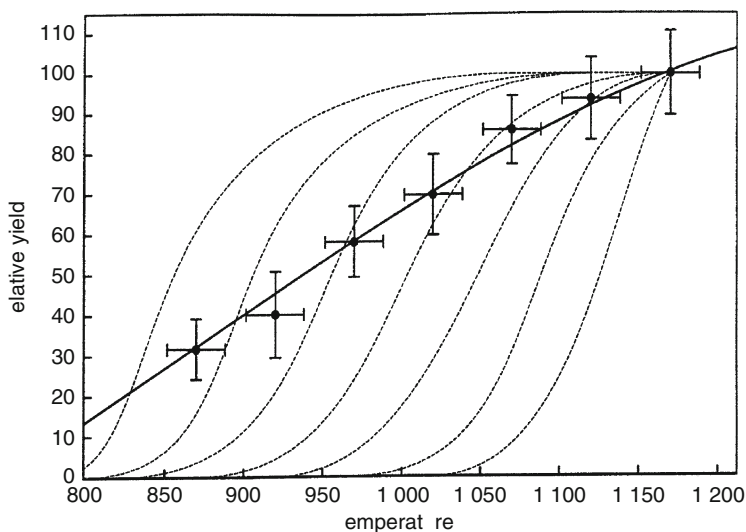
also called “reaction gas chromatography.” ▶ Figure 20.36 shows as an example the relative elution yield of ^{169}W as a function of column temperature in isothermal online gas chromatography at $p(\text{H}_2\text{O}) = 780 \text{ Pa}$, $v_o(\text{He}) = 1 \text{ l/min}$, $v_o(\text{O}_2) = 0.5 \text{ l/min}$ (Vahle 1996). One sees from ▶ Fig. 20.36 that the experimental data cannot be reproduced by the conventional model assuming reversible adsorption. None of the dashed curves is capable of accounting for the experimental observation.

The solid line is the result of a Monte Carlo simulation for dissociative adsorption and associative desorption as formulated above with $\Delta H^\circ_{\text{diss,ads}} = -41 \text{ kJ/mol}$ and $\Delta S^\circ_{\text{diss,ads}} = -41 \text{ J K}^{-1} \text{ mol}^{-1}$. It is tempting to enlarge on this newly developed model.

The residence time of a molecule in the adsorbed state is a random variable. Its expectation value is given by the Frenkel equation

■ Fig. 20.36

Relative elution yield (Vahle 1996) of ^{169}W ($T_{1/2} = 76 \text{ s}$) as a function of isothermal temperature at $p(\text{H}_2\text{O}) = 780 \text{ Pa}$, $v_o(\text{He}) = 1 \text{ l/min}$, $v_o(\text{O}_2) = 0.5 \text{ l/min}$. The dashed lines were calculated with the conventional Monte Carlo model assuming reversible adsorption of $^{169}\text{WO}_2(\text{OH})_2$ with $\Delta H_a^{\circ(\text{T})} = -180 \text{ kJ/mol}$ through -240 kJ/mol in steps of 10 kJ/mol . The solid line is the Monte Carlo result for reaction gas chromatography with $\Delta H^\circ_{\text{diss,ads}} = 41 \text{ kJ/mol}$, $\Delta S^\circ_{\text{diss,ads}} = 41 \text{ J K}^{-1} \text{ mol}^{-1}$ (Adapted from (Vahle 1996))



$$\bar{\tau}_a = \tau_0 e^{-\frac{\Delta H_{\text{ads}}^0}{RT}}. \quad (20.23)$$

In the case of reversible adsorption, τ_0 is the vibrational period of the adsorbed particle perpendicular to the surface of the adsorbing solid; it is typically of the order 10^{-12} to 10^{-14} s. In the case of reaction gas chromatography, τ_a depends essentially on the kinetics of the rate-determining associative desorption and the collision probability of water molecules with the adsorbed species. The mean residence time in the adsorbed state then becomes

$$\bar{\tau}_a = \tau_0^* e^{-\frac{\Delta H_{\text{ads}}^0}{RT}}. \quad (20.24)$$

If the volatility of the gaseous compound ($\text{MO}_2(\text{OH})_{2(\text{g})}$) is much larger than that of the adsorbed species ($\text{MO}_{3(\text{ads})}$) the retention time t_r is equal to the total time of adsorption t_{ads} . This leads to the new expression for the retention time

$$t_r = \frac{LT_0\Phi}{v_0 T} \left\{ 1 + \frac{4}{d} \frac{c_{\text{ads}}^0(\text{MO}_3)}{c_{\text{gas}}(\text{H}_2\text{O})} \exp\left(-\frac{\Delta H_{\text{diss,ads}}^0}{RT}\right) \exp\left(\frac{\Delta S_{\text{diss,ads}}^0}{R}\right) \right\} \quad (20.25)$$

where L denotes the length of the isothermal part of the column, Φ denotes the cross section of the column, d is the inner diameter of the column, $T_0 = 298$ K, T is the isothermal temperature, $c_{\text{ads}}^0(\text{MO}_3)$ is the standard concentration of MO_3 in the adsorbed state, $c_{\text{gas}}(\text{H}_2\text{O})$ is the concentration of water molecules, $\Delta H_{\text{diss,ads}}^0$ is the standard enthalpy of the dissociative adsorption, and $\Delta S_{\text{diss,ads}}^0$ is the standard entropy of the dissociative adsorption. Two important things follow from the above equation:

1. An increase of the water partial pressure in the carrier gas leads to a higher collision probability of water molecules with the adsorbate.
2. The new quantity τ_0^* becomes

$$\tau_0^* = \sqrt{\frac{2\pi M}{RT}} \frac{c_{\text{ads}}^0(\text{MO}_3)}{c_{\text{gas}}(\text{H}_2\text{O})} \exp\left(\frac{\Delta S_{\text{diss,ads}}^0}{R}\right). \quad (20.26)$$

The latter equation means that, while τ_0 was only dependent on temperature and on properties of the adsorbing surface, τ_0^* depends on more parameters, which are connected to the transport process (molar mass of the transported species M , $c_{\text{gas}}(\text{H}_2\text{O})$ and $\Delta S_{\text{diss,ads}}^0$). Therefore, the values of τ_0^* can vary over large ranges and are always orders of magnitude longer than the values of τ_0 . For the transport of tungsten at a water partial pressure of 780 Pa, one obtains $\tau_0^* = 10^{-4}$ s.

The high temperatures visible in [Fig. 20.36](#) that are necessary to obtain high yields (and fast transport, see Vahle 1996) have presented a technological challenge. Nevertheless, the system has been advanced such that a first application to the study of seaborgium oxide hydroxides was conducted (Hübener et al. 2001) in which the formation of a volatile $\text{SgO}_2(\text{OH})_2$ could unambiguously be proven by the observation of two $^{265\text{b}}\text{Sg}$ α decays followed shortly by time-correlated fission of the $^{261\text{b}}\text{Rf}$ daughter. The original assignments to ^{266}Sg and the daughter ^{262}Rf have been corrected here according to the revised decay properties by Düllmann and Türler (2008).

The Automated Rapid Chemistry Apparatus, ARCA II (Schädel et al. 1989), that has been so successful in studying chemical properties of element 105 (Kratz 1994; Paulus et al. 1999a, b)

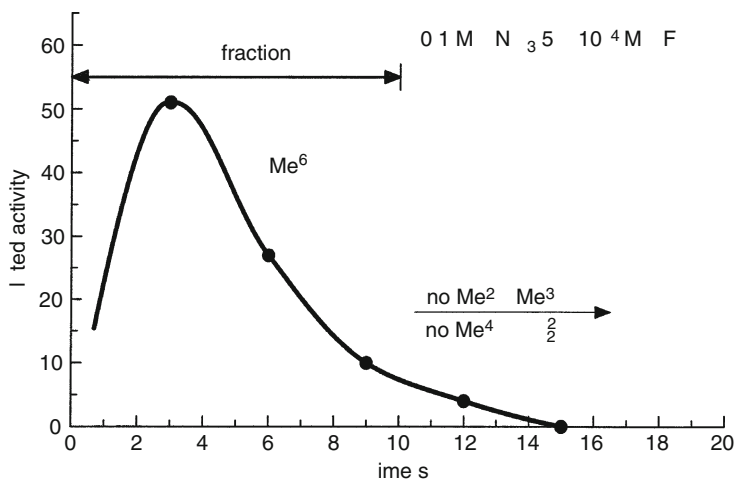
and recently also of element 104 (Günther et al. 1998; Strub et al. 2000, 2001) in aqueous solutions, was foreseen (Brüchle et al. 1992) to perform also the first aqueous chemistry with seaborgium.

Several chemical systems were tested with the fission products ^{93}Y , ^{97}Zr , and ^{99}Mo , and W isotopes produced in the $^{20}\text{Ne} + ^{152}\text{Gd}$ reaction (Brüchle et al. 1992) at the PSI Philips cyclotron. α -hydroxyisobutyric acid solutions of 5×10^{-2} M, pH = 2.65, or pH = 5 used to elute W in a rapid, one-stage separation from cation exchange columns provided a good separation from Hf and Lu. Likewise, solutions with 0.1 M HCl and various HF concentrations between 10^{-4} M and 10^{-2} M were eluting W rapidly while Hf was safely retained on the column below 10^{-3} M HF. Hf was observed to be partially eluted for $\geq 2.8 \times 10^{-3}$ M HF in 0.1 M HCl. Finally, the decision was made to use a solution of 0.1 M $\text{HNO}_3/5 \times 10^{-4}$ M HF to elute a seaborgium fraction from cation exchange columns (Günther et al. 1995) in order to avoid the formation of mixed chloride-fluoride complexes which are difficult to model. $[\text{MO}_2\text{F}_3(\text{H}_2\text{O})]^-$ is a likely form of the complexes that are eluted, but neutral species such as MO_2F_2 cannot be excluded. Some problems were encountered with adsorption of the activities on the slider in ARCA II. Among the various materials tested, titanium showed the lowest losses of W and Hf due to adsorption. Figure 20.37 shows the elution curve for short-lived W isotopes from the reaction of ^{20}Ne with enriched ^{152}Gd .

The activity was transported to ARCA II with a He(KCl)-jet within about 3 s and deposited on a titanium slider, dissolved and washed through the 1.6×8 mm chromatographic column (filled with the cation exchange resin Aminex A6, 17.5 ± 2 μm) at a flow rate of 1 ml/min with 0.1 M $\text{HNO}_3/5 \times 10^{-4}$ M HF. Eighty-five percent of the W are eluted within 10 s. No di- or

■ Fig. 20.37

Elution curve for W-tracer modeling the seaborgium separation (Schädel et al. 1997) in ARCA II using a solution of 0.1 M $\text{HNO}_3/5 \times 10^{-4}$ M HF with a flow rate of 1 ml/min. The 1.6 mm i.d. \times 8 mm columns are filled with the cation exchange resin Aminex A6 (Reprinted with the permission of Oldenbourg Wissenschaftsverlag, München)



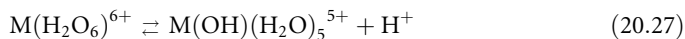
trivalent metal ions and no group-4 ions are eluted within the first 15 s. Also uranium, in the form of UO_2^{2+} , is completely retained on the column.

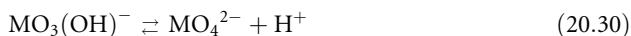
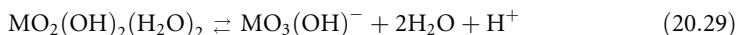
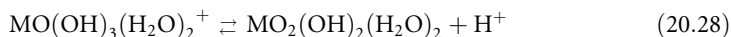
In the seaborgium experiments (Schädel et al. 1997b), a $950 \mu\text{g}/\text{cm}^2$ ^{248}Cm target was bombarded with 3×10^{12} ^{22}Ne ions s^{-1} at 121 MeV. Three thousand nine hundred identical separations were conducted with a collection and cycle time of 45 s and a total beam dose of 5.48×10^{17} ^{22}Ne ions. The transport efficiency of the He(KCl) jet was 45%. On the average, counting of the samples started 38 s after the end of collection. The overall chemical yield was 80%.

Three correlated $\alpha\alpha$ -mother-daughter decays were observed that were assigned to the decay of ^{261}Rf and ^{257}No as the decay products of ^{265}Sg . The three correlated events have to be compared with an expectation value of 0.27 for random correlations. This gives a probability of 0.24% that the three events are random correlations. As the mother decays were not observed, it is important to note that ^{261}Rf and ^{257}No can only be observed if ^{265}Sg passed through the column because group-4 elements and No are strongly retained on the cation exchange columns in ARCA II. Most likely, the decay of ^{265}Sg was not observed because it decayed in the time interval between the end-of-separation and the start-of-measurement, which was equivalent to four half-lives. That the columns really retained ^{261}Rf was demonstrated recently in an experiment where ^{261}Rf was produced directly in the $^{248}\text{Cm}(^{18}\text{O}, \text{n})$ reaction at the PSI Philips cyclotron (Strub et al. 2000), and processed in the seaborgium chemistry in 0.1 M $\text{HNO}_3/5 \times 10^{-4}$ M HF. ^{261}Rf did not elute from the column and was subsequently stripped from the column with 0.1 M $\text{HNO}_3/10^{-1}$ M HF. From the observation of the three correlated α -decay chains of ^{265}Sg daughters it was concluded, that, for the first time, a chemical separation of seaborgium was performed in aqueous solution. Seaborgium shows a behavior typical of a hexavalent element located in group 6 of the periodic table and different from that of the pseudo-group-6 element uranium, which is fixed as UO_2^{2+} on the cation exchange column. Presumably, Sg forms $[\text{SgO}_2\text{F}_3(\text{H}_2\text{O})]^-$ or the neutral species $[\text{SgO}_2\text{F}_2]$, but due to the low fluoride concentration used, the anionic $[\text{SgO}_4]^{2-}$ ("seaborgate" in analogy to molybdate, $[\text{MoO}_4]^{2-}$, or tungstate, $[\text{WO}_4]^{2-}$) could not be excluded.

In order to get experimental information on this latter question, a new series of seaborgium experiments with ARCA II was performed in 1996 in which 0.1 M HNO_3 without HF was used as the mobile aqueous phase and Aminex A6 as stationary phase (Schädel et al. 1998). If the "seaborgate" ion was what was isolated in 1995, it was supposed to show up here again. A $691 \mu\text{g}/\text{cm}^2$ ^{248}Cm target containing $22 \mu\text{g}/\text{cm}^2$ enriched ^{152}Gd was bombarded with 123 MeV ^{22}Ne ions. The simultaneously produced ^{169}W served as a yield monitor. Forty-five second cycles were run in which the effluent was evaporated on thin ($\sim 500 \mu\text{g}/\text{cm}^2$) Ti foils mounted on Al frames. These were thin enough to be counted in close geometry by pairs of PIPS detectors thus increasing the efficiency for $\alpha\alpha$ -correlations by a factor of 4 as compared to the 1995 experiment. A beam dose of 4.32×10^{17} beam particles was collected in 4,575 separations. Only one $\alpha\alpha$ -correlation attributable to the $^{261}\text{Rf} - ^{257}\text{No}$ pair was observed. With an expected number of random correlations of 0.5 this is likely (the probability is 30%) to be a random correlation. From the beam integral and the overall yield as measured simultaneously for ^{169}W (27% including jet transportation and chemical yield), a total of five correlated events was to be expected. This tends to indicate that, in the absence of fluoride ion, there is sorption of seaborgium on the cation-exchange resin.

This non-tungsten-like behavior of seaborgium under the given conditions may be attributed to its weaker tendency to hydrolyze:

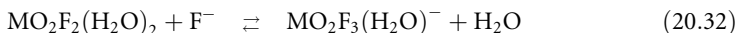
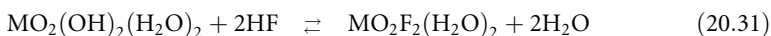


$$\vdots$$


The measured equilibrium constants for this stepwise deprotonation scheme for Mo and W have been collected from the literature (Pershina and Kratz 2001). They show that Mo is more hydrolyzed than W, and that the deprotonation sequence for Mo and W at pH = 1 reaches the neutral species $\text{MO}_2(\text{OH})_2(\text{H}_2\text{O})_2$. Assuming the deprotonation processes for Sg to be similar to those of Mo and W, Eqs. (20.27)–(20.30), Pershina and Kratz (2001) predict that the hydrolysis of the cationic species to the neutral species decreases in the order $\text{Mo} > \text{W} > \text{Sg}$, which is in agreement with the experimental data on hydrolysis of Mo and W and with the results for Sg (Schädel et al. 1998) for which the deprotonation sequence ends earlier with a cationic species such as $\text{SgO}(\text{OH})_3(\text{H}_2\text{O})_2^+$, which sorbs on a cation-exchange resin.

It is interesting to recall that a decreasing tendency to hydrolyze ($\text{Nb} > \text{Ta} > 105 > \text{Pa}$) was reported (Pershina 1998b) to determine the extraction of the group-5 chlorides into aliphatic amines. Thus, a similar behavior in the neighboring group-6 is apparent.

Looking back to the experiments in (Schädel et al. 1997b) where fluoride ions were present, having a strong tendency to replace OH^- ligands, it appears plausible that, in this preceding experiment, neutral or anionic species were formed:



Thus, the presence of fluoride ions seems to be an important prerequisite for planned experiments in which the K_a value of Sg on an anion-exchange resin is to be determined with the MCT technique (Pfrepper et al. 1998; Kronenberg et al. 2000) and to be compared to that of Mo and W.

20.8 Element 107 (Bohrium)

20.8.1 Theoretical Predictions

To assess the influence of relativistic effects on the volatility of BhO_3Cl , fully relativistic density-functional calculations of the electronic structure of the group-7 oxychlorides MO_3Cl ($\text{M} = \text{Tc}$, Re , and Bh) were performed by Pershina and Bastug (2000). These calculations show that the properties of Bh are very similar to those of the lighter homologs. BhO_3Cl is the most covalent

compound in the row TcO_3Cl , ReO_3Cl , and BhO_3Cl , and is relatively stable. In this molecular form, element 107 is the most stable in the highest oxidation state in the group.

Increasing values of dipole moments and electric dipole polarizabilities in the row TcO_3Cl , ReO_3Cl , and BhO_3Cl are the reasons for increasing molecule–surface interactions (Pershina and Bastug 2000), which means that volatility of the compounds changes in the following sequence: $\text{TcO}_3\text{Cl} > \text{ReO}_3\text{Cl} > \text{BhO}_3\text{Cl}$. Using a simple physisorption model for the molecule–surface interaction adjusted to the experimental adsorption enthalpy of ReO_3Cl , results in a value for the adsorption enthalpy of TcO_3Cl of -48 ± 2 kJ/mol in agreement with the experimental value of -51 ± 2 kJ/mol and in a predicted value for the adsorption enthalpy of BhO_3Cl of -78 ± 5 kJ/mol.

Also, classical extrapolations down the group using empirical correlations of thermochemical properties (Eichler et al. 2000a) predict BhO_3Cl to be more stable and less volatile than ReO_3Cl and TcO_3Cl . Bh is thus expected to behave chemically like a typical group-7 element and the volatility of its compound BhO_3Cl is expected to be the lowest within the group.

20.8.2 Experimental Results

The first unambiguous identification of an isotope of element 107 in the nuclear fusion reaction of ^{54}Cr with ^{209}Bi involved $^{262\text{m}}\text{Bh}$ (Münzenberg et al. 1981). The half-life of 8 ms determined for $^{262\text{m}}\text{Bh}$ and even the half-life of 440 ms for the more stable isotope ^{264}Bh (Hofmann et al. 1995c), are too short for an investigation of chemical properties. Therefore, searches for the presumably longer lived, more neutron rich nuclides ^{266}Bh and ^{267}Bh were performed for some time. Early searches applying gas chemical separation techniques for volatile oxide and oxyhydroxide compounds failed (Zvara et al. 1984; Schädel et al. 1995). Recently, the nuclide ^{267}Bh was discovered in the $^{249}\text{Bk}(^{22}\text{Ne}, 4n)$ reaction (Wilk et al. 2000). The production cross section of ^{267}Bh was about 60 pb at a beam energy of 117 MeV. Its half-life is 17^{+14}_{-6} s and the α -decay energy 8.83 ± 0.03 MeV. There was also evidence for the 5n-product ^{266}Bh having a much shorter half-life (Wilk et al. 2000).

In preparation of experiments investigating the chemical properties of bohrium, the adsorption data of the lighter homolog Re as oxide (ReO_3) and hydroxide (HReO_4) on quartz surfaces was studied (Eichler et al. 1999a). In online studies with short-lived Re isotopes, only the formation of the less volatile ReO_3 was observed with an adsorption enthalpy indistinguishable from those for PoO_2 and BiOOH . Po, Pb, and Bi nuclides are often formed in interactions of the heavy-ion beam with lead impurities in the target or target assembly. As these by-products would severely interfere with the unambiguous identification of ^{267}Bh due to their very similar α -decay energies, the high-temperature gas chromatography developed in (Eichler et al. 1999a) was considered less suitable for the chemical characterization of bohrium. Therefore, the oxychloride chemistry of the group-7 elements Tc and Re was investigated and the highly volatile compounds observed in O_2/HCl -containing carrier gas were attributed to MO_3Cl ($\text{M} = \text{Tc}, \text{Re}$) (Eichler et al. 2000a). Adsorption enthalpies on quartz surfaces of -51 kJ/mol and -61 kJ/mol were evaluated for TcO_3Cl and ReO_3Cl , respectively, and an excellent separation from the much less volatile compounds BiOCl and PoOCl_2 was achieved (Eichler et al. 2000a), which made this system the prime choice for experiments with bohrium.

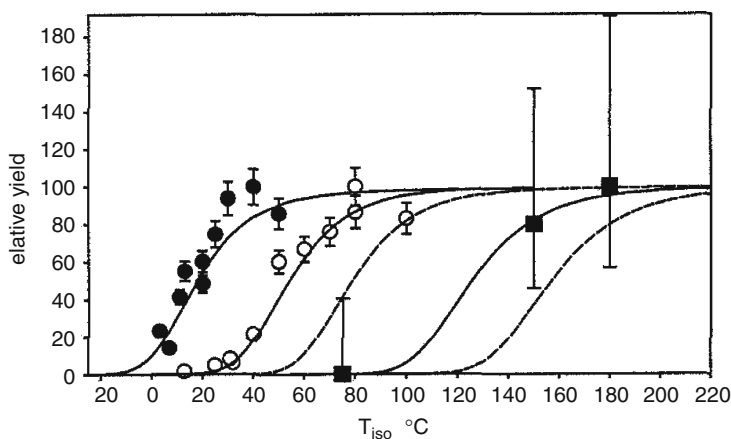
A ^{249}Bk target ($670 \mu\text{g}/\text{cm}^2$) covered with a layer of ^{159}Tb was bombarded for 4 weeks at the Philips cyclotron of the Paul Scherrer Institute with typically 1.6×10^{12} ^{22}Ne particles per second at 119 MeV, producing 17 s ^{267}Bh in the $^{249}\text{Bk}(^{22}\text{Ne}, 4n)$ reaction (Eichler et al. 2000b).

^{176}Re was simultaneously produced in the $^{159}\text{Tb}(^{22}\text{Ne},5\text{n})$ reaction and served as monitor for the chemical separation process. Nuclear reaction products recoiling from the thin ^{249}Bk target were adsorbed on carbon aerosols in the He carrier gas and were transported to the online gas chemistry apparatus. There, the aerosol particles were collected on quartz wool at $1,000^\circ\text{C}$. HCl and O_2 were introduced to form the volatile oxychlorides as well as to oxidize the carbon particles. The chromatographic separation took place downstream in the adjoining isothermal section of the quartz column. The retention time of the compounds in the column is mainly dependent on the adsorption interaction with the chlorinated quartz surface at a given isothermal temperature and on the flow rate of the carrier gas. Oxychlorides leaving the column were attached to CsCl particles and transported to the detection system. Here, the CsCl particles were deposited on thin polyethylene foils mounted on the periphery of a stepwise rotating wheel. Every 10 s, the collected activity was stepped between successive pairs of silicon detectors measuring α and spontaneous fission decays. Four correlated decay chains of ^{267}Bh were observed at 180°C isothermal temperature, two at 150°C , and none at 75°C . The relative yields of ^{267}Bh observed at the three temperatures are shown in [Fig. 20.38](#) together with the data for ^{108}Tc and ^{169}Re .

The adsorption properties of BhO_3Cl were quantified by using the microscopic model of the adsorption process (Zvara 1985). The standard adsorption enthalpy of BhO_3Cl on the quartz surface resulted as $-75^{+9}_{-6}\text{ kJ/mol}$ (68% confidence interval) with $T_{1/2} = 17\text{ s}$ for ^{267}Bh . This value compares well with the predicted value of $-78 \pm 5\text{ kJ/mol}$ (Pershina and Bastug 2000) for BhO_3Cl , applying a physisorption model adjusted to the experimental adsorption enthalpy of ReO_3Cl . Thus, BhO_3Cl exhibits a stronger adsorption interaction with the chlorinated quartz surface than TcO_3Cl and ReO_3Cl as predicted.

■ Fig. 20.38

Isothermal gas chromatographic separation of the group-7 oxychlorides MO_3Cl ($\text{M} = \text{Tc}, \text{Re}, \text{Bh}$) (Eichler et al. 2000b). The error bars indicate a 68% confidence interval. The lines represent the results of the Monte Carlo modeling (Zvara 1985) giving standard adsorption enthalpies of -51 kJ/mol (TcO_3Cl), -61 kJ/mol (ReO_3Cl), and -75 kJ/mol (BhO_3Cl). The dashed lines show the calculated relative yield of BhO_3Cl concerning the 68% confidence interval of the standard adsorption enthalpy of BhO_3Cl ranging from -66 to -81 kJ/mol (Reprinted by permission from Macmillan Publishers Ltd.: (NATURE) (Eichler et al. 2000b), copyright (2009))



An empirical correlation between the standard adsorption enthalpy on quartz and the macroscopic standard sublimation enthalpy for chlorides and oxychlorides (Türler et al. 1999) allows estimating the standard sublimation enthalpy of BhO_3Cl as 89^{+21}_{-18} kJ/mol to be compared to the values of 49 ± 12 kJ/mol and 66 ± 12 kJ/mol for TcO_3Cl and ReO_3Cl , respectively (► Fig. 20.38).

20.9 Element 108 (Hassium)

20.9.1 Theoretical Predictions

As the presumably very volatile tetroxide of hassium is an attractive object for a chemical characterization, fully relativistic density functional calculations of the electronic structure of the group-8 oxides MO_4 ($M = \text{Ru}, \text{Os}, \text{and Hs}$) have been performed by Pershina et al. (2001a). They find that the covalence and stability of the tetroxides increase from OsO_4 to HsO_4 . By using various models of molecule–surface interaction and by adjusting the adsorption enthalpy for OsO_4 to the experimental value (-38 kJ/mol), standard adsorption enthalpies of -40.4 ± 1.5 kJ/mol and -36.7 ± 1.5 kJ/mol were predicted for RuO_4 and HsO_4 , respectively. Thus, HsO_4 has been expected to be as volatile as OsO_4 , with the difference in the adsorption enthalpy being on the order of the experimental uncertainty. The trend in the predicted volatility of the group-8 oxides is, therefore, $\text{RuO}_4 < \text{OsO}_4 \leq \text{HsO}_4$. This sequence would also correspond to the idea that increasing volatility corresponds to increasing covalence of the compounds. More recent theoretical developments triggered by the experimental results are discussed below.

20.9.2 Experimental Results

The discovery of Hs was reported in 1984 (Münzenberg et al. 1984) with the identification of ^{265}Hs with a half-life of 1.5 ms. In 1996, ^{269}Hs with a half-life of about 10 s was observed in the α -decay chain of $^{277}112$ (Hofmann et al. 1996). Its direct production should be possible in the $^{248}\text{Cm}(^{26}\text{Mg}, 5n)$ reaction with a cross section of a few picobarns.

Following the example of Zhuikov (Zhuikov et al. 1986), several groups have adopted the *in situ* production of volatile tetroxides directly behind the target by adding oxygen (typically 10%) to the carrier gas that contains no aerosol particles (Düllmann et al. 2002a, Kirbach et al. 2002; von Zweidorf et al. 2002). Typically, the reaction products were transported with the carrier gas through a quartz column containing a quartz wool plug heated to some 600°C at the exit of the recoil chamber providing a hot surface at which the oxidation of the group-8 elements to their tetroxides was completed. The latter were further transported through a Teflon capillary to the detection system. Using thermochromatography at low temperatures, Düllmann et al. measured the temperature at which HsO_4 deposits with their cryo online detector COLD, which also served as detection system for the isotopes $^{269,270}\text{Hs}$. COLD consists of 12 pairs of silicon PIN-diodes of $1 \times 3 \text{ cm}^2$ mounted at a distance of 1.5 mm inside a copper bar. A temperature gradient from -20°C to -170°C was established along the detector array.⁷ The efficiency for detecting a single α particle was 77%. COLD (Düllmann et al. 2002b) was an improved version of a previous setup called the cryo-thermochromatography separator CTS (Kirbach et al. 2002).

An alternative approach is being followed by von Zweidorf et al. (2002). In their experiment the tetroxides are allowed to deposit on a thin layer of humid NaOH faced at a distance of ca.

1 mm by an array of silicon PIN-diodes. This system has an efficiency of 45% for detecting a single α particle. For OsO_4 the deposition is due to the formation of an osmate (VIII) of the form $\text{Na}_2[\text{OsO}_4(\text{OH})_2]$ where OsO_4 acts as an acid anhydride.

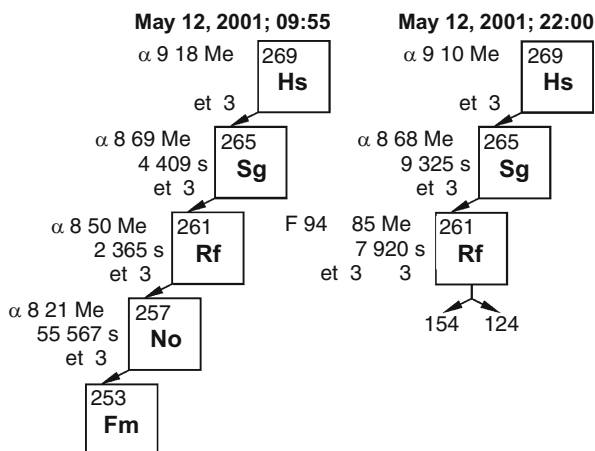
In the first experiment to characterize the volatility of HsO_4 the COLD array was used (Düllmann et al. 2002b). The experimental setup involved three banana-shaped ^{248}Cm targets mounted on a rotating target wheel that was bombarded with up to $8 \times 10^{12} \text{ } ^{26}\text{Mg}^{5+}$ ions per second, delivered by the UNILAC accelerator at GSI, Darmstadt. The projectile energy was $\sim 146 \text{ MeV}$ inside the ^{248}Cm targets. The functioning of the entire experiment was checked at the beginning and after the Hs experiment by mounting a ^{152}Gd target and by producing $19.2 \text{ s } ^{172}\text{Os}$, which has an α -decay branch of 1%. The experiment to produce Hs lasted 64.2 h during which a total of $1.0 \times 10^{18} \text{ } ^{26}\text{Mg}$ ions passed through the targets. Seven correlated decay chains were observed of which two representative ones are shown in Fig. 20.39.

The characteristics of the three first decay chains agree well with data (Hofmann et al. 1996) on ^{269}Hs and its daughter nuclides, while two other chains were attributed (Türler et al. 2003) to the decay of ^{270}Hs . The last two decay chains were incomplete and their assignment to either ^{269}Hs or ^{270}Hs was uncertain. More recently, the results reported in (Dvorak et al. 2006) and (Dvorak et al. 2008) strongly suggest that all decay chains observed in the original work by Düllmann et al. 2002b were starting with ^{269}Hs . All correlated α -decay chains were registered in detector pairs 2 through 4. The background count rate of α particles with energies of 8.0 through 9.5 MeV was so low that the probabilities that any of the five first chains and any of the two last chains are of random origin are less than 7×10^{-5} and 2×10^{-3} , respectively.

As depicted in Fig. 20.40, the α decay of one Hs atom was registered in detector 2, the decay of four atoms in detector 3, and the decay of two atoms in detector 4. The maximum of

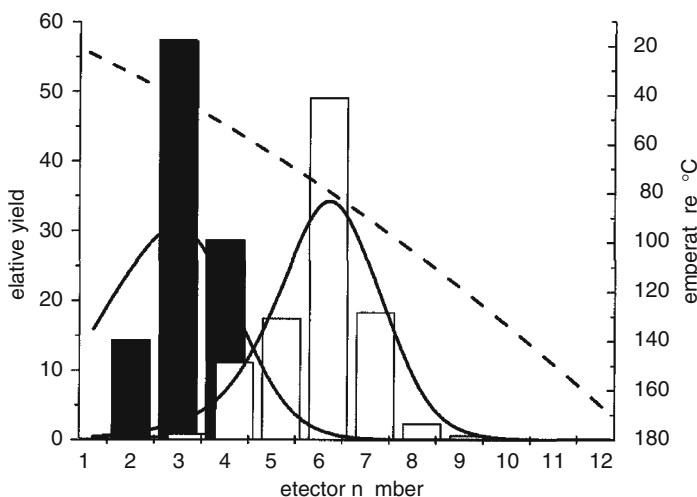
Fig. 20.39

Two of the seven nuclear decay chains originating from Hs isotopes detected in COLD (Düllmann et al. 2002b). Indicated are the energies of α particles and fission fragments in MeV and the lifetimes in s. The detector in which the decay was registered is indicated where T stands for top detector and B for bottom detector. For each chain, the date and time of its registration are given. The two selected chains are typical in the sense that both show $3 \text{ s } ^{261}\text{bRf}$ as grand-daughter of ^{269}Hs decaying either by the emission of an 8.5 MeV α particle or by SF (Adapted by permission from Macmillan Publishers Ltd: (NATURE) (Düllmann et al. 2002b), copyright (2009))



■ Fig. 20.40

Thermochromatograms of HsO_4 and OsO_4 . Measured values are represented by bars (HsO_4 black, OsO_4 white). The dashed line represents the temperature profile. The maxima of the deposition zones are at $-44 \pm 6^\circ\text{C}$ for HsO_4 and $-82 \pm 7^\circ\text{C}$ for OsO_4 . Solid lines represent the results of Monte Carlo simulations with standard adsorption enthalpies of -46 kJ/mol for HsO_4 and -39 kJ/mol for OsO_4 (Reprinted by permission from Macmillan Publishers Ltd: (NATURE) (Düllmann et al. 2002b), copyright (2009))

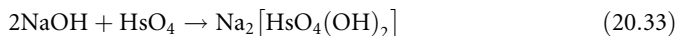


the Hs distribution was found at a temperature of $-44 \pm 6^\circ\text{C}$, that for the Os distribution at $-82 \pm 7^\circ\text{C}$. The adsorption enthalpy was extracted from the data by a Monte Carlo simulation with the value of ΔH_{ads} being a free parameter. The results that best reproduce the experimental data are shown in Fig. 20.40 (solid lines) and suggest a value of the standard adsorption enthalpy of $-46 \pm 2\text{ kJ/mol}$ for HsO_4 and $-39 \pm 1\text{ kJ/mol}$ for OsO_4 on the silicon nitride surface of the detectors. For OsO_4 the value is in good agreement with that using quartz surfaces (Düllmann et al. 2002a). Therefore, a direct analogy between theory and experiment is expected because a comparable adsorption interaction of OsO_4 is ascertained for quartz and silicon nitride surfaces. The significantly lower volatility of HsO_4 as compared to that of OsO_4 has been a surprise as a similar or slightly higher volatility for HsO_4 had repeatedly been predicted (Pershina et al. 2001a, b; Pershina et al. 2005). The apparent discrepancy between experiment and theory has triggered new theoretical efforts (Pershina et al. 2008); in this work, fully relativistic four-component density functional theory calculations were performed on MO_4 ($\text{M} = \text{Ru}, \text{Os}, \text{and Hs}$). Implementation of the noncollinear spin-polarized approximation in the method and the use of large optimized sets of numerical basis functions resulted in a high accuracy of the calculated molecular properties, especially the molecular polarizabilities. The latter have fully reproduced the experimental values for RuO_4 and OsO_4 , and have shown a dramatic increase in the polarizability by 8.95 a.u. for HsO_4 in comparison with the old value (Pershina et al. 2005). This led to a new value for $\Delta H_{\text{ads}} = -45.4 \pm 1\text{ kJ/mol}$ for HsO_4 , which is now in perfect agreement with experiment.

It is noteworthy that the decay properties of ^{261}Rf in Fig. 20.39 are consistent with those observed in the decay chains of element 112 (Hofmann et al. 1996) but deviate from

experimental data where ^{261}Rf was produced directly. In the latter case, a half-life of 78 s and an α -particle energy of 8.28 MeV are observed (Kadkhodayan et al. 1996). Apparently, when ^{261}Rf is formed by α decay of precursors, the α -decay energy is 8.5 MeV, the half-life is about 3 s, and a SF branch of 91% is evident (Düllmann and Türler 2009). Dressler and Türler (2002) have tentatively assigned the hitherto known 78 s state to an $11/2^-$ isomeric state and the 3 s state to the $7/2^+$ ground state in ^{261}Rf .

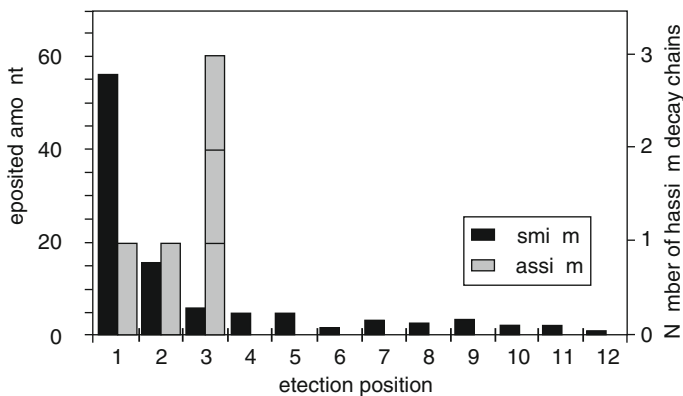
In the work by von Zweidorf et al. (2004), ^{269}Hs was also produced in the $^{248}\text{Cm}(^{26}\text{Mg},5n)$ reaction. In the CALLISTO experiment (Continuously working Arrangement for cLuster-Less transport of In-SiTU produced volatile Oxides), an admixture of ^{152}Gd to one of the three banana shaped rotating target segments simultaneously produced α -emitting 19.2-s ^{172}Os and 22.4-s ^{173}Os . The evaporation residues were oxidized in situ behind the target in a mixture of He and O_2 and transported to a deposition and detection system. The latter consisted of 16 PIN diode detectors facing in close geometry a layer of NaOH which served, in the presence of a certain partial pressure of water in the transport gas, as a reactive surface for the deposition of the volatile tetroxides. For OsO_4 , the deposition involves the formation of a salt, an osmate (VIII). In analogy, the deposition of HsO_4 is likely to involve the reaction



Thus, CALLISTO has shown that HsO_4 like OsO_4 is an acid anhydride and forms with NaOH a hassate(VIII) in analogy to the known osmate(VIII), that is, a salt. [Figure 20.41](#) shows the distribution of the deposited amount of OsO_4 and HsO_4 as a function of the detector position. While the majority of the Os activity is centered in front of detector 1 and tails into the subsequent positions, the five α -decay chains of ^{269}Hs are centered in front of detector position 3. In (von Zweidorf et al. 2004) it was not claimed that this indicates a lower reactivity of HsO_4 with respect to moisturized NaOH as compared to OsO_4 , however, theoretical work by Pershina (2005) predicts interestingly that the hassate(VIII) should be more covalent than the osmate(VIII), and HsO_4 should react slightly weaker with NaOH (by less than 52 kJ/mol) than OsO_4 .

Fig. 20.41

Distribution of the deposited amount of OsO_4 and HsO_4 on a surface of NaOH facing a phalanx of 16 PIN diode detectors as a function of the detector position. While the $^{172,173}\text{Os}$ α activity is centered in front of detector 1, the ^{269}Hs decays are centered around position 3 (Reproduced with the permission of Oldenbourg Wissenschaftsverlag, München, (von Zweidorf et al. 2004))



20.10 Element 112 (Copernicium)

20.10.1 Theoretical Predictions

Based on relativistic calculations, Pitzer (1975) indicated the possibility that element 112 (copernicium, Cn, whose name and symbol was approved by IUPAC in February 2010) in its elementary state should be relatively inert – almost like a noble gas due to its closed electron shells $7s^2$, $6d^{10}$. Therefore, Cn should be more volatile than Hg.

A more recent fully relativistic treatment of the interaction of Cn with metallic surfaces such as Au or Pd, predicts weaker absorption of Cn than Hg on these metals (Perschina et al. 2004); however, due to metal–metal interaction, Cn was predicted to sorb at much higher temperatures than Rn, which sorbs only by van der Waals forces. The capability of Cn to form metallic bonds was also predicted by Eichler and Rossbach (1983). On the other hand, on chemically inert surfaces such as quartz or ice, mercury is found to be adsorbed only at very low temperatures (-100°C) (Soverna et al. 2005) to -160°C (Yakushev et al. 2001, 2003). Thus, the latter surfaces are much less suitable to distinguish between a volatile metal and a noble gas-like behavior of Cn, than sorption on, for example, a Au surface. Recent developments in the four-component Density Functional Theory, that is, the spin-polarized (SP) 4c-DFT allow to make very accurate predictions on the adsorption enthalpy of Cn on a Au surface, which is 20 kJ/mol weaker than that for Hg (Perschina et al. 2009).

20.10.2 Experimental Results

The first two attempts to chemically characterize element 112 with the use of the 3-min SF-isotope $^{283}\text{112}$ (Oganessian et al. 1999a, b, 2004a) were made by Yakushev et al. (2001 and 2003) at the FLNR in Dubna. Products from the $^{48}\text{Ca} + ^{238}\text{U}$ reaction including 49-s ^{185}Hg produced on a small amount of Nd added to the U target were transported in the elementary state in a He gas flow. In the improved second experiment, the 25 m long capillary, i.d., 2 mm, was connected to a detector array of eight pairs of Au-coated PIPS detectors at ambient temperature for the detection of Hg-like 112. Subsequently, the gas flow entered a $5,000\text{ cm}^3$ cylindrical ionization chamber for the detection of a gaseous element 112. This chamber had an aerosol filter at the entrance. A mixture of Ar and CH_4 was added as counting gas. The PIPS detectors and the ionization chamber were placed inside a barrel-shaped neutron detector with 126 ^3He long counters. In this experiment, 95% of the 49-s ^{185}Hg was found on the first pair of Au-coated PIPS detectors at a He flow rate of 500 ml/min. At a He flow rate of 250 ml/min, 99% of the ^{185}Hg deposited on the first detector pair. Eight SF-decays attributed to the decay of $^{283}\text{112}$ were registered in the ionization chamber and none in the PIPS detectors. It was concluded that element 112 does not form a strong metal–metal bond with Au and that it behaves more like a noble gas rather than Hg. A standard adsorption enthalpy for Cn of ≤ 0 kJ/mol was estimated as compared to -100 kJ mol^{-1} for Hg and -29 kJ/mol for Rn (Eichler and Schädel 2002). According to more recent Dubna results (Oganessian et al. 2004d) and GSI results (Hofmann et al. 2007), ^{283}Cn decays by α -particle emission with a half-life of about 4 s. Thus, the results of the first chemical experiments on element 112 are inconclusive.

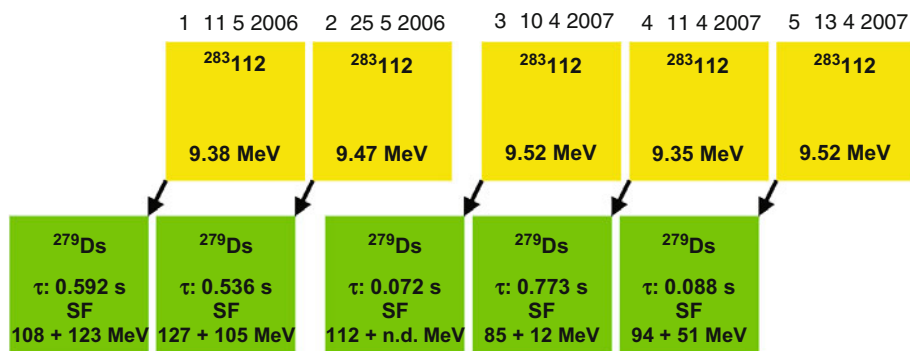
A second series of experiments started in 2003 at GSI (Gäggeler et al. 2004) again with the reaction of $^{48}\text{Ca} + ^{238}\text{U}$ to produce ^{283}Cn . Simultaneously, $^{184-186}\text{Hg}$ was produced on a small amount of Nd in the target as well as ^{220}Rn as a transfer product from U. The aim was to

measure the adsorption behavior of element 112 on Au in comparison with that of Hg and Rn. In a modified version of the COLD detector (Düllmann et al. 2002a), along a Au surface, a temperature gradient from +35°C to −185°C was established. Test experiments had determined the adsorption behavior of Hg and Rn on various transition metal surfaces with some interference due to an ice coverage at the low temperature end (Soverna et al. 2005). In the first experiment on element 112 (Gäggeler et al. 2004), the Au catcher was faced by 32 silicon PIN diodes. The following observations were made: Hg was mainly adsorbed on the Au opposite to the first detector with a tail to lower temperatures in agreement with a Monte Carlo simulation with a standard adsorption enthalpy of −101 kJ/mol. From the adsorption of Rn, beginning at detector 29 and peaking at detector 31, it was deduced that below −95°C, the Au surface was covered with a thin ice layer. At an expected background of 3 SF events, 5 SF events were observed scattered along the entire detector array. A cluster of 7 SF events – interpreted as candidates for 3-min ^{283}Cn – were observed at detectors 29 to 31, that is, in the position of the Rn. If true, this suggests that element 112 behaves as a noble gas. However, the collaboration decided to repeat the experiment with an improved setup in almost 4π geometry (Eichler et al. 2006) and improved sensitivity to shorter half-lives. However, also this experiment did not yield a conclusive result.

In 2006, a series of experiments at FLNR Dubna made possible the first unambiguous detection of element 112 after its chemical separation (Eichler et al. 2007a, b). These chemical experiments with element 112 were focused on the new decay pattern of ^{283}Cn with a half-life of about 4 s and an α -particle decay ($E_\alpha = 9.54$ MeV) to ^{279}Ds , which decays by SF with a half-life of 200 ms (Oganessian et al. 2004d; Hofmann et al. 2007) produced in the fusion reaction of ^{48}Ca with ^{238}U . Even larger production rates have been observed for ^{283}Cn by using the indirect production path $^{242}\text{Pu}(^{48}\text{Ca}, 3n)^{287}114$ ($T_{1/2} = 0.48$ s, $E_\alpha = 10.02$ MeV) \rightarrow ^{283}Cn (Oganessian et al. 2004d). This reaction was used in the subsequent work (Eichler et al. 2008). The chemical setup used in the experiments was based on the thermochromatographic in situ volatilization and online detection technique (IVO) in combination with the cryo-online detector COLD (Eichler et al. 2000b; Düllmann et al. 2002b; Eichler et al. 2006, 2007a, b). From the observation of only two atoms (► Fig. 20.42, chains 1 and 2), assigned unambiguously to ^{283}Cn , a first indication of a volatile metallic element 112 was obtained (Eichler et al. 2007a, b). In 2007, the

► Fig. 20.42

Detected α -SF decay chains assigned to the isotope ^{283}Cn ; n.d. = not determined (Reproduced with the copyright permission of Wiley-VCH, STM-Copyright & Licenses (Eichler et al. 2008))



collaboration was able to increase the overall efficiency by a factor of about three (Eichler et al. 2008) and observed three additional decay chains of ^{283}Cn (Fig. 20.42, chains 3–5). The thermochromatographic deposition patterns for ^{185}Hg , ^{219}Rn , and ^{283}Cn under varied experimental conditions are depicted in Fig. 20.43.

In the first experiment in 2006 (Eichler et al. 2007a, b), a carrier-gas flow of 860 ml/min and a temperature gradient between -24°C and -184°C was applied (Fig. 20.43). A spontaneous, diffusion-controlled deposition of ^{185}Hg was observed in the first eleven detectors. ^{219}Rn deposited almost entirely on the last nine detectors. One decay chain (chain 1) assigned to ^{283}Cn was observed in the second detector (-28°C) together with ^{185}Hg , that is, clearly distinct from ^{219}Rn .

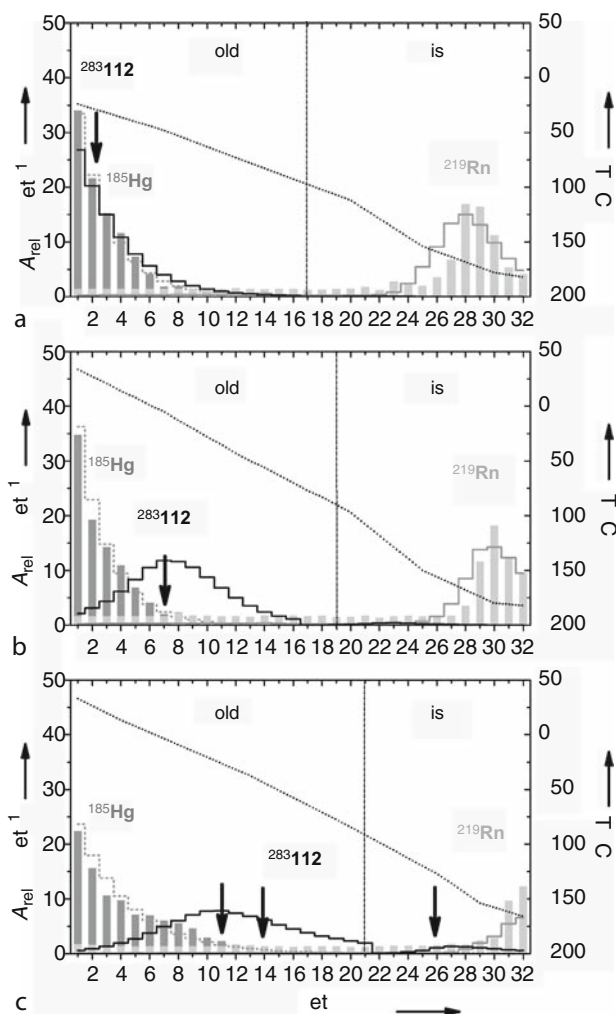
In the second part of the experiment in 2006 (Eichler et al. 2007a, b), a steeper temperature gradient between $+35^\circ\text{C}$ and -180°C (Fig. 20.43b) was established. The gas-flow rate was 890 ml/min. Thus, ^{185}Hg revealed a shorter deposition pattern up to detector eight consistent with an increased diffusion coefficient of Hg in the carrier gas. Only 70% of the ^{219}Rn deposited on the last six detectors due to the slightly increased temperature at the last detectors. A decay chain (chain 2) attributed to ^{283}Cn was observed in the seventh detector (-5°C), again clearly distinct from ^{219}Rn .

In 2007 (Fig. 20.43c), the gas-flow rate was increased to 1,500 ml/min in order to increase the transport efficiency. The temperature gradient was between $+32^\circ\text{C}$ and -164°C . As a result, the ^{185}Hg deposition region broadened considerably to 14 detectors. Only about 30% of the ^{219}Rn deposited on the last four detectors. The faster carrier gas transported three observed atoms of ^{283}Cn further down to detectors at lower temperatures. Chains 3 and 5 were detected in detectors 11 (-21°C) and 14 (-39°C). Chain 4 was detected in detector 26 (-124°C). From dew point measurements in the carrier gas, it has to be concluded that the detector surfaces held below -95°C were covered by a thin ice layer (Fig. 20.43a–c, vertical lines). Thus, it was concluded that four events (chains 1–3, and 5) are attributable to atoms of element 112 deposited on the gold surface, while chain 4 represents an atom of element 112 deposited on ice.

Monte Carlo simulations following (Zvara 1985) were applied to determine the most probable standard adsorption enthalpy on gold surfaces at zero coverage from the chromatographic deposition of Hg, Rn, and element 112 (Eichler et al. 2008). The diffusion controlled deposition of Hg (Fig. 20.43, gray dashed lines) yielded a lower limit for $-\Delta H_{\text{a}}^{\text{Au}}(\text{Hg}) > 65 \text{ kJ/mol}$, in agreement with literature data (Soverna et al. 2005). The deposition of ^{219}Rn (Fig. 20.43, gray solid lines) gave an adsorption enthalpy of $-\Delta H_{\text{a}}^{\text{Au}}(\text{Rn}) = 19 \pm 2 \text{ kJ/mol}$ in agreement with a value of $-20 \pm 2 \text{ kJ/mol}$ measured for Rn on ice (Eichler et al. 2000a). The Monte Carlo simulation of the deposition of ^{283}Cn (Fig. 20.43, black arrows), resulted in an adsorption enthalpy of element 112 on gold surfaces of $-\Delta H_{\text{ads}}^{\text{Au}}(\text{Cn}) = 52_{-3}^{+4} \text{ kJ/mol}$ (68% confidence interval). Using this value, the calculated deposition pattern (Fig. 20.43, black lines) indicates, for the highest gas flow, a probability of 15% for atoms of element 112 to reach detector 21 and to continue the chromatographic process on ice. This explains the observation of chain 4 by detector 26. The expected number of random correlations during the entire experiment was calculated to be 0.05. The enhanced adsorption enthalpy of element 112 on gold compared to a prediction using a physisorption model (Eichler and Schädel 2002) indicates a metallic-bond character of the interaction of element 112 with gold. The calculations of the Cn–Au interaction potential using density functional theory (Pershina et al. 2005; Pershina et al. 2007; Sarpe-Tudoran et al. 2007) predict a metallic-bond character but seem to overestimate somewhat the energetic content of this interaction. In summary, element 112 is chemically not as inert as a noble gas as suggested in 1975 (Pitzer 1975).

■ Fig. 20.43

Thermochromatographic deposition patterns of ^{185}Hg , ^{219}Rn , and ^{283}Cn in the COLD, dependent on experimental parameters. The measured relative activity per detector (A_{rel} , left hand axis) of ^{185}Hg (dark gray bars, MCS: gray dashed line) and ^{219}Rn (gray bars, MCS: gray solid line) is shown. The positions of the detected ^{283}Cn atoms are indicated (black arrows, MCS: black solid line). The temperature gradient is shown (black dashed line, right hand axis). Experimental parameters: (a) gas flow 860 ml/min, temperature gradient from -24°C to -184°C ; (b) gas flow 890 ml/min, temperature gradient from 35°C to -180°C ; (c) gas flow 1,500 ml/min, temperature gradient from 32°C to -164°C . The beginning of ice coverage of the detectors at -95°C is indicated by the vertical lines (Reproduced with the copyright permission of WILEY-VCH, STM Copyright & Licenses (Eichler et al. 2008))



An empirical link between the single-atom quantity ΔH_a and the volatility of macroscopic amounts of an element or compound, determined by the standard sublimation enthalpy ΔH_{aubl} , reveals linear relationships for various elements and compound classes on various surfaces (Eichler and Eichler 2003). A similar correlation was established between ΔH_a^{Au} values of elements and their ΔH_{subl} values (Eichler 2005). By using this correlation, the standard sublimation enthalpy can be estimated as $\Delta H_{\text{subl}}(\text{Cn}) = 38_{-12}^{+10}$ kJ/mol, indicating that element 112 is more volatile than its lighter homologs Zn, Cd, and Hg, reflecting an increasing stabilization of the atomic state due to relativistic effects in group 12 of the periodic table up to element 112.

20.11 Outlook

On behalf of the International Union of Pure and Applied Chemistry (IUPAC), the chemistry of the early transactinides Rf, Db, and Sg, has been critically evaluated by Kratz (2003a, b, c), with the result that for each of these elements there remain open questions that should be clarified in future experiments. The same holds, of course, for Bh and Hs. Nevertheless, it is fashionable to go ahead and design and prepare chemical experiments with even heavier elements.

For meitnerium, element 109, the isotope ^{270}Mt to be produced in the $^{238}\text{U}(^{37}\text{Cl}, 5n)$ or $^{248}\text{Cm}(^{27}\text{Al}, 5n)$ reactions is anticipated to have a half-life on the order of a second and should, thus, be suitable for chemical studies with one of the fastest separation techniques, for example, with SISAK.

Similarly to element 112, one can expect that element 114 will also have an enhanced volatility in the metallic state (Schwerdtfeger and Seth 2002) due to its ground state electron configuration with the quasiclosed electron shell $7s^2 7p_{1/2}^2$ caused by the large spin-orbit splitting of the 7p atomic orbitals and the strong relativistic stabilization of the $7p_{1/2}$ atomic orbital. Thus, the scheme of separation and identification can, in principle, be similar to that used by Eichler et al. (2008). Fully relativistic (four-component) density-functional theory calculations by Pershina et al. (2009) predict that element 114 should be gaseous in its elemental state but should be more reactive toward sorption on a gold surface than element 112. The trend in the binding energies with gold predicted is $\text{Pb} \gg 114 < \text{Hg} < \text{Cn}$. It is expected that element 114 should be observed in the thermochromatography experiments at the very beginning of the chromatography column with a warm end close to the position of Hg. It should be clearly distinguished from the more volatile element 112. At this time, it is one of the most challenging tasks for nuclear chemistry to verify this prediction.

Elements 108–116 are expected to be partially very noble metals. Thus, their electrochemical deposition on suitable electrode materials from aqueous solutions could be an attractive method for their isolation. It is known that the potential associated with the electrochemical deposition of radionuclides in metallic form from solutions of extremely small concentration is strongly influenced by the choice of the electrode material. This is reproduced by Eichler and Kratz (2000) in a model in which the interaction between the microcomponent A and the electrode material B is described by the partial molar adsorption enthalpy and entropy. By combination with the thermodynamic description of the electrode process, a potential is calculated that characterizes the process at 50% deposition:

$$E_{50\%} = E^\circ - \Delta H(A - B)/nF + T\Delta S_{\text{vibr}}(A - B)/nF - (RT/nF)\ln(A_m/1,000) \quad (20.34)$$

Here, $\Delta H(A - B)$ is the partial molar net adsorption enthalpy associated with the transformation of 1 mol of the pure metal A in its standard state into the state of “zero

coverage” on the surface of the electrode material B, ΔS_{vibr} is the difference in the vibrational entropies in the above states, n is the number of electrons involved in the electrode process, F is the Faraday constant, and A_m the surface of 1 mol of A as a monolayer on the electrode material B (Eichler and Kratz 2000). For the calculation of the thermodynamic functions in [Eq. \(20.34\)](#), a number of models were used by Eichler and Kratz (2000) and calculations were performed for Ni-, Cu-, Pd-, Ag-, Au-, and Pt-electrodes and the microcomponents Hg, Tl, Pb, Bi, and Po, thus confirming the decisive influence of the choice of the electrode material on the deposition potential. For Pd and Au, particularly large, positive values of $E_{50\%}$ were calculated, larger than the standard electrode potentials tabulated for these elements. This makes these electrode materials the prime choice for practical applications. An application of the same model for the superheavy elements still needs to be done, but one can anticipate that the preference for Pd and Au will persist. The latter are metals in which, due to the formation of the metallic bond, almost or completely filled d orbitals are broken up so that these metals tend in an extreme way toward the formation of intermetallic compounds with sp-metals. The perspective is to make use of these metals in the form of a tape on which the tracer activities are electrodeposited and the deposition zone is subsequently stepped between pairs of Si detectors for α and SF spectroscopy (Hummrich et al. 2008).

The coupling of chemistry devices to a physical pre-separator, mentioned shortly in [Sect. 20.4](#), opens completely new possibilities for chemical experiments. In experiments without pre-separation, the intense heavy-ion beam creates a plasma in the gas-filled recoil chamber where the fusion evaporation residues are thermalized. In contrast, a so-called recoil transfer chamber RTC behind a physical recoil separator is virtually beam-free and organic ligands can be directly introduced into the RTC, allowing in situ syntheses also of compound classes that would be destroyed by the beam. In a proof-of-principle experiment performed at the BGS in Berkeley, highly volatile β -diketonate complexes of the homologs of Rf, Zr, and Hf, were formed (Düllmann et al. 2009). It was thus shown that this technique indeed allows to expand the range of accessible chemical systems for transactinide research. As an exciting example, studies of organometallic compounds of transactinides appear feasible. First studies in this field could focus on group-6 hexacarbonyls with the ultimate goal of investigating Sg (CO)₆ and the group-8 metallocenes toward an experiment with hassocene, Hs(Cp)₂. Thus, a new interdisciplinary research field is about to open up bringing together experts from transactinide chemistry, organic, and organometallic chemistry, but also the spectroscopic community as the analog compounds with the lighter homologs will be amenable to, for example, XAS-spectroscopy helping to understand the structure of the new transactinide containing compounds.

20.12 Editors' Notes

1. The expressions “cold fusion” and “hot fusion” are explained in [Sect. 21.5 of Chap. 21 in this Volume 2](#) on “Superheavy Elements” (p. 929).
2. See also [Chap. 53 in Vol. 5](#) on “Radiochemical Separations by Thermochromatography” (p. 935).
3. PIPS detectors have been designed to replace SSB (silicon surface barrier) and DJ (diffused junction) detectors in alpha and beta/(conversion-)electron spectroscopies. Passivation normally means a SiO₂ layer on the surface, a key to low noise and relative ruggedness. Due to ion-implanted junctions, PIPS's have a very thin (<50 nm) and well-defined dead

- (window) layer, and those meant for alpha measurements have at least 140 μm (i.e., 140.000 nm) active layer, enough to stop up to 15 MeV alphas (p. 935).
4. See also ► [Sect. 52.2 in Chap. 52, Vol. 5](#), on “Solvent extraction and Ion Exchange in Radiochemistry” (p. 942).
 5. See ► [Fig. 9.1 in Chap. 9, Vol. 1](#), on “Stochastics and Nuclear Measurements” for choices of giving symmetric (\pm) or asymmetric (+ and $-$) error intervals (p. 944).
 6. See ► [Eq. \(2.63\) in Sect. 2.4, Chap. 2, Vol. 1](#), on “Basic Properties of the Atomic Nucleus” (p. 975).
 7. Modern silicon PIN diode detectors – P for p-type, I for intrinsic, N for n-type – have the same old sandwiched layer structure as the older Li-drifted ones; however, they can operate up to 150°C without being damaged. The operation principle is also the same. Being reversed biased, the high-resistivity I layer is completely depleted of free carriers, so when a radiation particle creates electron-hole pairs in the I layer, the electric field drives the holes to the N layer and the electrons to the P layer thus forming a current pulse, the height of which is proportional to the energy deposited in the active layer, that is, I (p. 986).
 8. To get the pressure in Pa, the values on the vertical axis are to be multiplied by ~ 133 (p. 934).

Acknowledgements

The author gratefully acknowledges the assistance of P. Sach-Muth in bringing the manuscript into its final form.

References

- Adloff JP, Guillaumont R (1993) Fundamentals of radiochemistry. CRC Press, Boca Raton
- Armbruster P (1985) *Ann Rev Nucl Part Sci* 35:135
- Bilewicz A, Siekierski S, Kacher CD, Gregorich KE, Lee DM, Stoyer NJ, Kadkhodayan B, Kreek SA, Lane MR, Sylwester ER, Neu MP, Mohar MF, Hoffman DC (1996) *Radiochim Acta* 75:121
- Borg RJ, Dienes GJ (1981) *J Inorg Nucl Chem* 43:1129
- Brewer L (1984) *High Temp Sci* 17:1
- Bruchertseifer H, Eichler B, Estevez J, Zvara I (1989) *Radiochim Acta* 47:41
- Brüchle W, Schausten B, Jäger E, Schimpf E, Schädel M, Kratz JV, Trautmann N, Zimmermann HP, Bruchertseifer H, Heller W (1992) GSI scientific report 1991, GSI 92-1, p 315
- Chuburkov YuTs, Zvara I, Shilov BV (1969) *Sov Radiochem* 11:171
- Cwiok S, Hofmann S, Nazarewicz W (1994) *Nucl Phys A* 573:356
- Czerwinski KR (1992) PhD thesis, Lawrence Berkeley Laboratory report LBL-32233, University of California, Berkeley
- Czerwinski KR, Gregorich KE, Hannink NJ, Kacher CD, Kadkhodayan B, Kreek SA, Lee DM, Nurmia MJ, Türler A, Seaborg GT, Hoffman DC (1994a) *Radiochim Acta* 64:23
- Czerwinski KR, Kacher CD, Gregorich KE, Hamilton TM, Hannink NJ, Kadkhodayan B, Kreek SA, Lee DM, Nurmia MJ, Türler A, Seaborg GT, Hoffman DC (1994b) *Radiochim Acta* 64:29
- Desclaux JP (1973) *At Data Nucl Data Tables* 12:311
- Desclaux JP, Fricke B (1980) *J Phys* 41:943
- Domanov VP, Jin KU (1989) *Radiokhimiya* 31:19
- Dragojevic I, Gregorich KE, Düllmann ChE, Garcia MA, Gates JM, Nelson SL, Stavsetra L, Sudowe R, Nitsche H (2008) *Phys Rev C* 78:024605
- Dressler R, Türler A (2002) Labor für Radio- und Umweltchemie der Universität Bern und des Paul Scherrer Instituts. Annual report 2001, p 4
- Dressler R, Türler A, Jost DT, Piguet D, Eichler B, Gäggeler HW (1995) Labor für Radio- und Umweltchemie der Universität Bern und des Paul Scherrer Instituts. Annual report 1994, p 45
- Druin VA, Bochev B, Lobanov YuV, Sagaidak RN, Kharitonov YuP, Tretyakova SP, Gulbekian GG, Buklanov GN, Yerin EA, Kosyakov VN, Rykov AG (1979) *Sov J Nucl Phys* 29:591
- Düllmann ChE, Türler A (2008) *Phys Rev C* 77:064320

- Düllmann ChE, Eichler B, Eichler R, Gäggeler HW, Jost DT, Piguet D, Türlér A (2002a) *Nucl Instrum Meth A* 479:631
- Düllmann ChE, Brüchle W, Dressler R, Eberhardt K, Eichler B, Eichler R, Gäggeler HW, Ginter TN, Glaus F, Gregorich KE, Hoffman DC, Jäger E, Jost DT, Kirbach UW, Lee DM, Nitsche H, Patin JB, Pershina V, Piguet D, Qin Z, Schädel M, Schausten B, Schimpf E, Schött H-J, Soverna S, Sudowe R, Thörle P, Timokhin SN, Trautmann N, Türlér A, Vahle A, Wirth G, Yakushev AB, Zielinski PM (2002b) *Nature* 418:859
- Düllmann ChE, Gregorich KE, Pang GK, Dragojevic I, Eichler R, Folden CM, Garcia MA, Gates JM, Hoffman DC, Nelson SL, Sudowe R, Nitsche H (2009) *Radiochim Acta* 97:403
- Dvorak J, Brüchle W, Chelnokov M, Dressler R, Düllmann ChE, Eberhardt K, Gorshkov A, Jäger E, Krücken R, Kuznetsov A, Nagame Y, Nebel F, Novackova Z, Qin Z, Schädel M, Schausten B, Schimpf E, Semchenkov A, Thörle P, Türlér A, Wegrzecki M, Wierczinski B, Yakushev A, Yereimin A (2006) *Phys Rev Lett* 97:242501
- Dvorak J, Brüchle W, Chelnokov M, Düllmann ChE, Dvorakova Z, Eberhardt K, Jäger E, Krücken R, Kuznetsov A, Nagame Y, Nebel F, Nishio K, Perego R, Qin Z, Schädel M, Schausten B, Schimpf E, Schuber R, Semchenkov A, Thörle P, Türlér A, Wegrzecki M, Wierczinski B, Yakushev A, Yereimin A (2008) *Phys Rev Lett* 100:132503
- Eberhardt K, Alstad J, Kling HO, Kratz, JV, Langrock G, Omtvedt JP, Skarnemark G, Tharun U, Trautmann N, Wiehl N, Wierczinski B (2002) In: *Proceedings of the international conference on advances in liquid scintillation spectrometry (LSC 2001)*; *Radiocarbon* 2002, pp 19–24
- Eberhardt K, Brüchle W, Düllmann ChE, Gregorich KE, Hartmann W, Hübner A, Jäger E, Kindler B, Kratz JV, Liebe D, Lommel B, Maier HJ, Schädel M, Schausten B, Schimpf E, Semchenkov A, Steiner J, Szerypo J, Thörle P, Türlér A, Yakushev A (2008) *Nucl Instr Meth Phys Res A* 590:134
- Eichler B (1994) Labor für Radio- und Umweltchemie der Universität Bern und des Paul Scherrer Instituts. Annual report 1993, p 38
- Eichler B (1996) *Radiochim Acta* 72:19
- Eichler B, Eichler R (2003) In: Schädel M (ed) *Chemistry of superheavy elements*. Kluwer, Dordrecht, pp 205–236
- Eichler B, Kratz JV (2000) *Radiochim Acta* 88:475
- Eichler B, Rossbach H (1983) *Radiochim Acta* 33:121
- Eichler B, Zvara I (1985) *Radiochim Acta* 38:103
- Eichler B, Domanov VP, Zvara I (1976) *Dubna report* P12-9454
- Eichler B, Hübener S, Gäggeler HW, Jost DT (1988) *Inorg Chim Acta* 146:162
- Eichler B, Türlér A, Jost DT, Gäggeler HW (1994) Labor für Radio- und Umweltchemie der Universität Bern und des Paul Scherrer Instituts. Annual report 1993, p 42
- Eichler B, Türlér A, Gäggeler HW (1999a) *J Phys Chem A* 103:9296
- Eichler B, Zimmermann P, Gäggeler HW (2000a) *J Phys Chem A* 104:3126
- Eichler R, Schädel M (2002) *J Phys Chem B* 106:5413
- Eichler R, Eichler B, Gäggeler HW, Jost DT, Dressler R, Türlér A (1999b) *Radiochim Acta* 87:151
- Eichler R, Eichler B, Gäggeler HW, Jost DT, Piguet D, Türlér A (2000b) *Radiochim Acta* 88:87
- Eichler R, Brüchle W, Dressler R, Düllmann ChE, Eichler B, Gäggeler HW, Gregorich KE, Hoffman DC, Hübener S, Jost DT, Kirbach UW, Laue CA, Lavanchy VM, Nitsche H, Patin JB, Piguet D, Schädel M, Shaughnessy DA, Strellis DA, Taut S, Tobler L, Tsyganov YS, Türlér A, Vahle A, Wilk PA, Yakushev AB (2000c) *Nature* 407:63
- Eichler R (2005) *Radiochim Acta* 93:245
- Eichler R, Brüchle W, Buda R, Bürger S, Dressler R, Düllmann ChE, Dvorak J, Eberhardt K, Eichler B, Folden CM, Gäggeler HW, Gregorich KE, Haenssler F, Hummrich H, Jäger E, Kratz JV, Kuczewski B, Liebe D, Nayak D, Nitsche H, Piguet D, Qin Z, Rieth U, Schädel M, Schausten B, Schimpf E, Semchenkov A, Soverna S, Sudowe R, Trautmann N, Thörle P, Türlér A, Wierczinski B, Wiehl N, Wilk PA, Wirth G, Yakushev AB, von Zweidorf A (2006) *Radiochim Acta* 94:181
- Eichler R, Aksenov NV, Belozero AV, Bozhikov GA, Chepigin VI, Dmitriev SN, Dressler R, Gäggeler HW, Gorshkov VA, Haenssler F, Itkis MG, Laube A, Lebedev VYa, Malyshev ON, Oganessian YuTs, Petrushkin OV, Piguet D, Rasmussen P, Shishkin SV, Shutov AV, Svirikhin AI, Tereshatov EE, Vostokin GK, Wegrzecki M, Yereimin AV (2007a) *Nature* 447:72
- Eichler R, Aksenov NV, Belozero AV, Bozhikov GA, Chepigin VI, Dressler R, Dmitriev SN, Gäggeler HW, Gorshkov VA, Haenssler F, Itkis MG, Lebedev VYa, Laube A, Malyshev ON, Oganessian YuTs, Petrushkin OV, Piguet D, Rasmussen P, Shishkin SV, Shutov AV, Svirikhin AI, Tereshatov EE, Vostokin GK, Wegrzecki M, Yereimin AV (2007b) *Nucl Phys A* 787:373c
- Eichler R, Aksenov NV, Belozero AV, Bozhikov GA, Chepigin VI, Dressler R, Dmitriev SN, Gäggeler HW, Gorshkov VA, Haenssler F, Itkis MG, Lebedev VYa, Laube A, Malyshev ON, Oganessian YuTs, Petrushkin OV, Piguet D, Rasmussen P, Shishkin SV, Shutov AV, Svirikhin AI, Tereshatov EE, Vostokin GK, Wegrzecki M, Yereimin AV (2008) *Angew Chem Int Ed* 47:3262
- Eliav E, Kaldor U, Ishikawa Y (1995) *Phys Rev Lett* 74:1079
- Fricke B (1975) *Struct Bond* 21:89

- Fricke B, Greiner W (1969) *Phys Lett* 30B:317
- Fricke B, Johnson E, Rivera GM (1993) *Radiochim Acta* 62:17
- Gäggeler HW (1994) *J Radioanal Nucl Chem Articles* 183:261
- Gäggeler HW (1998) In: *Proceedings of the international conference on actinides, Baden-Baden, 21–26 Sept 1997; J Alloys Comp* 271–273:277
- Gäggeler HW, Jost DT, Baltensperger U, Weber A, Kovacs J, Vermeulen D, Türlér A (1991) *Nucl Instr Meth Phys Res A* 309:201
- Gäggeler HW, Jost DT, Kovacs J, Schädel M, Brüche W, Becker U, Kratz JV, Eichler B, Hübener S (1992a) GSI scientific report 1991, GSI 92-1, p 321
- Gäggeler HW, Jost DT, Kovacs J, Scherer UW, Weber A, Vermeulen D, Türlér A, Gregorich KE, Henderson RA, Czerwinski KR, Kadkhodayan B, Lee DM, Nurmia MJ, Hoffman DC, Kratz JV, Goyer MK, Zimmermann HP, Schädel M, Brüche W, Schimpf E, Zvara I (1992b) *Radiochim Acta* 57:93
- Gäggeler HW, Brüche W, Düllmann CE, Dressler R, Eberhardt K, Eichler B, Eichler R, Folden CM, Ginter TN, Glaus F, Gregorich KE, Haenssler F, Hoffman DC, Jäger E, Jost DT, Kirbach UW, Kratz JV, Nitsche H, Patin JB, Pershina V, Pguet D, Qin Z, Rieth U, Schädel M, Schimpf E, Schausten B, Soverna S, Sudowe R, Thörle P, Trautmann N, Türlér A, Vahle A, Wilk PA, Wirth G, Yakushev AB, von Zweidorf A (2004) *Nucl Phys A* 734:433
- Gärtner M, Boettger M, Eichler B, Gäggeler HW, Grantz M, Hübener S, Jost DT, Piguat D, Dressler R, Türlér A, Yakushev AB (1997) *Radiochim Acta* 78:59
- Gates JM, Garcia MA, Gregorich KE, Düllmann ChE, Dragojevic I, Dvorak J, Eichler R, Folden CM III, Loveland W, Nelson SL, Pang GK, Stavsetra L, Sudowe R, Türlér A, Nitsche H (2008) *Phys Rev C* 77:034603
- Ghiorso A, Nurmia M, Harris J, Eskola K, Eskola P (1969) *Phys Rev Lett* 22:1317
- Ghiorso A, Nurmia M, Eskola K, Eskola P (1970) *Phys Lett* 32B:95
- Ghiorso A, Nitschke JM, Alonso JR, Alonso CT, Nurmia M, Seaborg GT, Hulet EK, Loughheed RW (1974) *Phys Rev Lett* 33:1490
- Glebov VA, Kasztura L, Nefedov VS, Zhuikov BL (1989) *Radiochim Acta* 46:117
- Goyer MK, Kratz JV, Zimmermann HP, Schädel M, Brüche W, Schimpf E, Gregorich KE, Türlér A, Hannink NJ, Czerwinski KR, Kadkhodayan B, Lee DM, Nurmia MJ, Hoffman DC, Gäggeler H, Jost D, Kovacs J, Scherer UW, Weber A (1992) *Radiochim Acta* 57:77
- Gregorich KE, Henderson RA, Lee DM, Nurmia MJ, Chasteler RM, Hall HL, Bennett DA, Gannett CM, Chadwick RB, Leyba JD, Hoffman DC, Herrmann G (1988) *Radiochim Acta* 43:223
- Gregorich KE, Hall HL, Henderson RA, Leyba JD, Czerwinski KR, Kreek SA, Kadkhodayan BA, Nurmia MJ, Lee DM, Hoffman DC (1992) *Phys Rev C* 45:1058
- Gregorich KE, Gates JM, Düllmann ChE, Sudowe R, Nelson SL, Garcia MA, Dragojevic I, Folden CM III, Neumann SH, Hoffman DC, Nitsche H (2006) *Phys Rev C* 74:044611
- Guillaumont R, Adloff JP, Peneloux A (1989) *Radiochim Acta* 46:169
- Guillaumont R, Adloff JP, Peneloux A, Delamoye P (1991) *Radiochim Acta* 54:1
- Günther R, Paulus W, Posledni A, Kratz JV, Schädel M, Brüche W, Jäger E, Schimpf E, Schausten B, Schumann D, Binder R (1995) *Institut für Kernchemie, Univ. Mainz, Jahresbericht 1994, IKMz 95-1, p 2*
- Günther R, Becker HU, Zauner S, Nähler A, Kratz JV, Schädel M, Brüche W, Jäger E, Schimpf E, Schausten B (1995) *Institut für Kernchemie, Univ. Mainz, Jahresbericht 1994, IKMz 95-1, p 7*
- Günther R, Paulus W, Kratz JV, Seibert A, Thörle P, Zauner S, Brüche W, Jäger E, Pershina V, Schädel M, Schausten B, Schumann D, Eichler B, Gäggeler HW, Jost DT, Türlér A (1998) *Radiochim Acta* 80:121
- Haba H, Tsukada K, Asai M, Nishinaka I, Sakama M, Goto S, Hirata M, Ichikawa S, Nagame Y, Kaneko T, Kudo H, Toyoshima A, Shoji Y, Yokoyama A, Shinohara A, Oura Y, Sueki K, Nakahara H, Schädel M, Kratz JV, Türlér A, Gäggeler HW (2001) *Radiochim Acta* 89:733
- Haba H, Tsukada K, Asai M, Goto S, Toyoshima A, Nishinaka I, Akiyama K, Hirata M, Ichikawa S, Nagame Y, Shoji Y, Shigekawa M, Koike T, Iwasaki M, Shinohara A, Kaneko T, Maruyama T, Ono S, Kudo H, Oura Y, Sueki K, Nakahara H, Sakama M, Yokoyama A, Kratz JV, Schädel M, Brüche W (2002) *J Nucl Radiochem Sci* 3:143
- Haba H, Tsukada K, Asai M, Toyoshima A, Akiyama K, Nishinaka I, Hirata M, Yaita T, Ichikawa S, Nagame Y, Yasuda K, Miyamoto Y, Kaneko T, Goto S, Ono S, Hirai T, Kudo H, Shigekawa M, Shinohara A, Oura S, Nakahara H, Sueki K, Kikunaga H, Kinoshita N, Tsuruga N, Yokoyama A, Sakama M, Enomoto S, Schädel M, Brüche W, Kratz JV (2004) *J Am Chem Soc* 126:5219
- Haba H, Tsukada K, Asai M, Toyoshima A, Ishii Y, Toume H, Sato T, Nishinaka I, Ichikawa T, Ichikawa S, Nagame Y, Sato W, Matsuo M, Kitamoto Y, Tashiro Y, Shinohara A, Saito J, Ito M, Ikezawa T, Sakamaki M, Goto S, Kudo H, Kikunaga H, Arai M, Kamataki S, Yokoyama A, Akiyama K, Sueki K, Oura Y, Schädel M, Brüche W, Kratz JV (2007) *Radiochim Acta* 95:1
- Hoffman DC (1990) In: *The Robert A. Welch Foundation conference on chemical research XXXIV fifty years with transuranium elements, Houston, Texas, 22–23*

- Oct 1990, Lawrence Berkeley Laboratory report LBL-29815, p 255
- Hoffman DC (1993) *Radiochim Acta* 61:123
- Hoffman DC (1994) *Chem Eng News* 72(18):24
- Hofmann S, Ninov V, Hessberger FP, Armbruster P, Folger H, Münzenberg G, Schött HJ, Popeko AG, Yeremin AV, Andreyev AN, Saro S, Janik R, Leino M (1995a) *GSI-Nachrichten* 02–95:4
- Hofmann S, Ninov V, Hessberger FP, Armbruster P, Folger H, Münzenberg G, Schött HJ, Popeko AG, Yeremin AV, Andreyev AN, Saro S, Janik R, Leino M (1995b) *Z Phys A* 350:277
- Hofmann S, Ninov V, Hessberger FP, Armbruster P, Folger H, Münzenberg G, Schött H-J, Popeko A, Yeremin AV, Andreyev A, Saro S, Janik R, Leino ME (1995c) *Z Phys A* 350:281
- Hofmann S, Ninov V, Hessberger FP, Armbruster P, Folger H, Münzenberg G, Schött HJ, Popeko A, Yeremin AV, Saro S, Janik R, Leino ME (1996) *Z Phys A* 354:229
- Hofmann S, Ackermann D, Antaia S, Burkhard HG, Comas VF, Dressler R, Gan Z, Heinz S, Heredia JA, Hessberger F-P, Khuyagbaatar J, Kindler B, Kojouharov I, Kuusiniemi P, Leino M, Lommel B, Mann R, Münzenberg G, Nishio K, Popeko AG, Saro S, Schött H-J, Streicher B, Sulignano B, Uusitalo J, Venhart M, Yeremin AV (2007) *Eur Phys J A* 32:251
- Hübener S, Eichler B, Becker U, Kratz JV, Gäggeler HW, Jost DT, Kovacs J, Schädel M, Brüchle W, Jäger E (1992) *GSI scientific report 1991*, GSI 92-1, p 320
- Hübener S, Taut S, Vahle A, Dressler R, Eichler B, Gäggeler HW, Jost DT, Piguet A, Türlér A, Brüchle W, Jäger E, Schädel M, Schimpf E, Kirbach U, Trautmann N, Yakushev AB (2001) *Radiochim Acta* 89:737
- Hulet EK (1981) In: Edelman NM (ed) *Actinides in perspective*. Pergamon Press, Oxford, p 453
- Hulet EK, Loughhead RW, Wild JF, Landrum JH, Nitschke JM, Ghiorso A (1980) *J Inorg Nucl Chem* 42:79
- Hummrich H, Banik NL, Breckheimer M, Brüchle W, Buda R, Feist F, Jäger E, Kratz JV, Kuczewski B, Liebe D, Niewisch L, Schädel M, Schausten B, Schimpf E, Wiehl N (2008) *Radiochim Acta* 96:73
- Ionova GV, Pershina V, Johnson E, Fricke B, Schädel M (1992) *J Phys Chem* 96:11096
- Ishii Y, Toyoshima A, Tsukada K, Asai M, Toume H, Nishinka I, Nagame Y, Miyashita S, Mori T, Suganuma H, Haba H, Skamaki M, Goto S, Kudo H, Akiyama K, Oura Y, Nakahara H, Tashiro Y, Shinohara A, Schädel M, Brüchle W, Pershina V, Kratz JV (2008) *Chem Lett* 37:288
- Johnson E, Fricke B, Keller OL Jr, Nestor CW, Tucker TC (1990) *J Chem Phys* 93:8041
- Johnson E, Pershina V, Fricke B (1999) *J Phys Chem A* 103:8458
- Jost DT, Gäggeler HW, Vogel Ch, Schädel M, Jäger E, Eichler B, Gregorich KE, Hoffman DC (1988) *Inorg Chim Acta* 146:225
- Jost DT, Buklanov G, Dressler R, Eichler B, Gäggeler HW, Gärtner M, Grantz M, Hübener S, Lebedev V, Piguet D, Timokhin SN, Türlér A, Vedenev MV, Yakushev AB, Zvara I (1996) In: Fourth international conference on nuclear and radiochemistry (NRC-4), Saint Malo, Sept 1996, Extended Abstracts, IPN Orsay, vol 1, A-P14
- Kacher CD, Gregorich KE, Lee DM, Watanabe Y, Kadkhodayan B, Wierczinski B, Lane MR, Sylwester ER, Keeney DA, Hendriks M, Stoyer NJ, Yang J, Hsu M, Hoffman DC, Bilewicz A (1996a) *Radiochim Acta* 75:127
- Kacher CD, Gregorich KE, Lee DM, Watanabe Y, Kadkhodayan B, Wierczinski B, Lane MR, Sylwester ER, Keeney DA, Hendriks M, Hoffman DC, Bilewicz A (1996b) *Radiochim Acta* 75:135
- Kadkhodayan B (1993) PhD thesis, Lawrence Berkeley Laboratory report LBL-33961, University of California, Berkeley
- Kadkhodayan B, Türlér A, Gregorich KE, Baisden PA, Czerwinski KR, Eichler B, Gäggeler HW, Hamilton TM, Hannink NJ, Jost DT, Kacher CD, Kovacs J, Kreek SA, Lane MR, Mohar MF, Neu MP, Stoyer NJ, Sylwester ER, Lee DM, Nurmia MJ, Seaborg GT, Hoffman DC (1996) *Radiochim Acta* 72:169
- Keller OL Jr (1984) *Radiochim Acta* 37:169
- Keller OL Jr, Seaborg GT (1977) *Ann Rev Nucl Sci* 27:139
- Kirbach UW, Folden III CM, Ginter TN, Gregorich KE, Lee DM, Ninov V, Omtvedt JB, Patin JB, Seward NK, Strellis DA, Sudowe R, Türlér A, Wilk PA, Zielinski PM, Hoffman DC, Nitsche H (2002) *Nucl Instr Meth Phys Res A* 484:587
- Knacke O, Kubaschewski O, Hesselmann K (eds) (1991) *Thermochemical properties of inorganic substances II*. Springer, Berlin
- Korkisch J (1989) *Handbook of ion exchange resins: their application to inorganic analytical chemistry*, vol IV. CRC Press, Boca Raton, p 257
- Kratz JV (1994) In: *Proceedings of the international conference on actinides*, Santa Fe, New Mexico, 19–24 Sept 1993, Elsevier, Amsterdam; *J Alloys Comp* 213–214:20
- Kratz JV (1995) *Chemie in unserer Zeit*, 29. Jahrg 4:194
- Kratz JV (1999) In: Greiner W, Gupta RK (eds) *Heavy elements and related new phenomena*, vol 1. World Scientific, Singapore, Chapter 4, pp 129–193
- Kratz JV (2003a) *Pure Appl Chem* 75(1):103
- Kratz JV (2003b) In: Schädel M (ed) *The chemistry of superheavy elements*. Kluwer, Dordrecht, Chapter 5, pp 159–203
- Kratz JV (2003c) In: Vertes A, Nagy S, Klencsár Z (eds) *Handbook of nuclear chemistry*, vol 2. Kluwer, Dordrecht, Chapter 9, pp 324–395

- Kratz JV, Zimmermann HP, Scherer UW, Schädel M, Brüchle W, Gregorich KE, Gannett CM, Hall HL, Henderson RA, Lee DM, Leyba JD, Nurmia MJ, Hoffman DC, Gäggeler H, Jost D, Baltensperger U, Nai-Qi Y, Türlér A, Lienert Ch (1989) *Radiochim Acta* 48:121
- Kratz JV, Guber MK, Zimmermann HP, Schädel M, Brüchle W, Schimpf E, Gregorich KE, Türlér A, Hannink NJ, Czerwinski KR, Kadkhodayan B, Lee DM, Nurmia MJ, Hoffman DC, Gäggeler H, Jost D, Kovacs J, Scherer UW, Weber A (1992) *Phys Rev C* 45:1064
- Kronenberg A, Kratz JV, Mohapatra PK, Brüchle W, Jäger E, Schädel M, Türlér A (2000) Institut für Kernchemie, Univ. Mainz, Jahresbericht 1999, IKMZ 2000-1, p 10
- Kronenberg A, Eberhardt K, Kratz JV, Mohapatra PK, Nähler A, Thörle P, Brüchle W, Schädel M, Türlér A (2004a) *Radiochim Acta* 92:379
- Kronenberg A, Mohapatra PK, Kratz JV, Pfrepper G, Pfrepper R (2004b) *Radiochim Acta* 92:395
- Langrock G, Wiehl N, Alstad J, Breivik JE, Dyve K, Eberhardt K, Hult EA, Johansson M, Kling HO, Mendel M, Nähler A, Omtvedt JP, Stavsetra L, Skarnemark G, Tharun U, Trautmann N, Kratz JV (2002) Institut für Kernchemie, Univ. Mainz, Jahresbericht 2001, IKMZ-2002-1, A8
- Lazarev YuA, Lobanov YuV, Oganessian YuTs, Utyonkov VK, Abdullin FSh, Buklanov GV, Gikal BN, Iliev S, Mezentsev AN, Polyakov AN, Sedykh IM, Shirikovskiy IV, Subbotin IG, Sukov AM, Tsyganov YuS, Zhuchko VE, Loughheed RW, Moody KJ, Wild JF, McQuaid JH (1994) *Phys Rev Lett* 73:624
- Le Naour C, Trubert D, Hussonnois M, Brillard L, Monroy Guzman F, Le Du JF, Constantinescu O, Barci V, Weiss B, Gasparro J, Ardisson G (1999) In: *Extended abstracts of the 1st international conference on the chemistry and physics of the transactinide elements*, Seeheim, Germany, pp 0–12
- Marx G, Dilling J, Kluge H-J, Mukherjee M, Quint W, Rahaman S, Rodriguez D, Sikler G, Tarisien M, Weber C, The Shiptrap Collaboration (2002) SHIPTRAP: a capture and storage facility on its way towards a RIB-facility. In: *Anderegg F, Schweikhard L, Driscoll CF (eds) Non-neutral plasma physics IV. AIP Conference Proceedings 606*, AIP, p 615
- Morita K, Morimoto K, Kaji D, Akiyama T, Goto S, Haba H, Ideguchi E, Kanungo R, Katori K, Koura H, Kudo H, Ohnishi T, Ozawa A, Suda T, Sueki K, Xu H, Yamaguchi T, Yoneda A, Yoshida A, Zhang Y-L (2004) *J Phys Soc Jpn* 73:2593
- Morozov AI, Karlova EV (1971) *Russ J Inorg Chem* 16:12
- Morss LR, Edelstein NM, Fuger J, Katz JJ (eds) (2006) *The chemistry of the actinide and transactinide elements*. Springer, Dordrecht
- Münzenberg G (1995) *Radiochim Acta* 70(71):193
- Münzenberg G, Faust W, Hofmann S, Armbruster P, Güttner K, Ewald H (1979) *Nucl Instrum Meth* 161:65
- Münzenberg G, Hofmann S, Faust W, Hessberger FP, Reisdorf W, Schmidt KH, Kitahara T, Armbruster P, Güttner K, Thuma B, Vermeulen D (1981) *Z Phys A* 302:7
- Münzenberg G, Armbruster P, Folger H, Hessberger FP, Hofmann S, Keller JG, Poppensieker K, Reisdorf W, Quint B, Schmidt K-H, Schött HJ, Leino ME, Hingmann R (1984) *Z Phys A* 317:235
- Münzenberg G, Hofmann S (1999) In: *Greiner W, Gupta RK (eds) Heavy elements and related new phenomena*, vol 1. World Scientific, Singapore, Chapter 1, pp 9–42
- Nagame Y, Asai M, Haba H, Goto S, Tsukada K, Nishinaka I, Nishio K, Ichikawa S, Toyoshima A, Akiyama K, Nakahara H, Sakama M, Schädel M, Kratz JV, Gäggeler HW, Türlér A (2002a) *J Nucl Radiochem Sci* 3:85
- Nagame Y, Asai M, Haba H, Tsukada K, Goto S, Skama M, Nishinaka I, Toyoshima A, Akiyama K, Ichikawa S (2002b) *J Nucl Radiochem Sci* 3:129
- Nagame Y, Haba H, Tsukada K, Asai M, Akiyama K, Hirata H, Nishinaka I, Goto S, Kaneko T, Kudo H, Toyoshima A, Shinohara A, Schädel M, Kratz JV, Gäggeler HW, Türlér A (2003) *Czech J Phys* 53: A299
- Nagame Y, Tsukada K, Asai M, Toyoshima A, Akiyama K, Ishii Y, Kaneko-Sato T, Hirata M, Nishinaka I, Ichikawa S, Haba H, Enomoto S, Matsuo K, Saika D, Kitamoto Y, Hasegawa H, Tani Y, Sato W, Shinohara A, Ito M, Saito J, Goto S, Kudo H, Kikunaga H, Kinoshita N, Yokoyama A, Sueki K, Oura Y, Nakahara H, Sakama M, Schädel M, Brüchle W, Kratz JV (2005) *Radiochim Acta* 93:519
- Oganessian YuTs (2007) *Nucl Phys A* 787:343c
- Oganessian YuTs, Yeremin AV, Popeko AG, Bogomolov SL, Buklanov GV, Chelnokov ML, Chepigin VI, Gikal BN, Gorskochov VA, Gulbekian GG, Itkis MG, Kabachenko AP, Lavrentev AY, Malyshev ON, Rohac J, Sagaidak RN, Hofmann S, Saro S, Giardina G, Morita K (1999a) *Nature* 400:242
- Oganessian YuTs, Yeremin AV, Gulbekian GG, Bogomolov SL, Chepigin VI, Gikal BN, Gorskochov VA, Itkis MG, Kabachenko AP, Kutner VB, Lavrentev YY, Malyshev ON, Popeko AG, Rohac J, Sagaidak RN, Hofmann S, Münzenberg G, Veselsky M, Saro S, Iwasa N, Morita K (1999b) *Eur Phys J A* 5:63
- Oganessian YuTs, Utyonkov VK, Lobanov YuV, Abdullin FSh, Polyakov AN, Shirokovskiy IV, Tsyganov YuS, Gulbekian GG, Bogomolov SL, Gikal BN, Mezentsev AN, Iliev S, Subbotin VG, Sukhov AM, Buklanov GV, Subotic K, Itkis MG, Moody KJ, Wild JF, Stoyer NJ, Stoyer MA, Loughheed RW (1999c) *Phys Rev Lett* 83:3154

- Oganessian YuTs, Utyonkov VK, Lobanov YuV, Abdullin FSh, Polyakov AN, Shirokovsky IV, Isyanov YuS, Gulbekian GG, Bogomolov SL, Gikal BN, Mezentssev AN, Iliev S, Subbotin VG, Sukhov AM, Ivanov OV, Buklanov GV, Subotic K, Itkis MG, Moody KJ, Wild JF, Stoyer NJ, Stoyer MA, Loughheed RW (2000) *Phys Rev C* 62:04160
- Oganessian YuTs, Utyonkov VK, Lobanov YuV, Abdullin FSh, Polyakov AN, Shirokovsky IV, Tsyganov YuS, Gulbekian GG, Bogomolov SL, Gikal BN, Mezentssev AN, Iliev S, Subbotin VG, Sukhov AM, Ivanov OV, Buklanov GV, Subotic K, Itkis MG, Moody KJ, Wild JF, Stoyer NJ, Stoyer MA, Loughheed RW, Laue CA, Karelin YeA, Tatarinov AN (2001) *Phys Rev C* 63:011301
- Oganessian YuTs, Utyonkov VK, Lobanov YuV, Abdullin FSh, Polyakov AN, Shirokovsky IV, Tsyganov YuS, Gulbekian GG, Bogomolov GV, Gikal BN, Mezentssev AN, Iliev S, Subbotin VG, Sukhov AM, Ivanov OV, Buklanov GV, Subotic K, Voinov AA, Itkis MG, Moody KJ, Wild JF, Stoyer NJ, Stoyer MA, Loughheed RW, Laue CA (2002) *Eur Phys J A* 15:201
- Oganessian YuTs, Yeremin AV, Popeko AG, Malyshev ON, Belozero AV, Buklanov GV, Chelnokov ML, Chepigin VI, Gorshkov VA, Hofmann S, Itkis MG, Kabachenko AP, Kindler B, Münzenberg G, Sagaidak RN, Saro S, Schött H-J, Streicher B, Shutov AV, Svirikhin AI, Vostokin GK (2004a) *Eur Phys J A* 19:3
- Oganessian YuTs, Utyonkov VK, Lobanov YuV, Abdullin FSh, Polyakov AN, Shirokovsky IV, Tsyganov YuS, Gulbekian GG, Bogomolov SL, Mezentssev AN, Iliev S, Subbotin VG, Sukhov AM, Voinov AA, Buklanov GV, Subotic K, Zagrebaev VI, Itkis MG, Patin JB, Moody KJ, Wild JF, Stoyer MA, Stoyer NJ, Shaughnessy DA, Kenneally JM, Loughheed RW (2004b) *Phys Rev C* 69:0216601(R)
- Oganessian YuTs, Utyonkov VK, Lobanov YuV, Abdullin FSh, Polyakov AN, Shirokovsky IV, Tsyganov YuS, Gulbekian GG, Bogomolov SL, Gikal BN, Mezentssev AN, Iliev S, Subbotin VG, Sukhov AM, Voinov AA, Buklanov GV, Subotic K, Zagrebaev VI, Itkis MG, Patin JB, Moody KJ, Wild JF, Stoyer MA, Stoyer NJ, Shaughnessy DA, Kenneally JM, Loughheed RW (2004c) *Phys Rev C* 69:054607
- Oganessian YuTs, Utyonkov VK, Lobanov YuV, Abdullin FSh, Polyakov AN, Shirokovsky IV, Zsyganov YuS, Gulbekian GG, Bogomolov SL, Gikal BN, Mezentssev AN, Iliev S, Subbotin VG, Sukhov AM, Voinov AA, Buklanov GV, Subotic K, Zagrebaev VI, Itkis MG, Patin JB, Moody KJ, Wild JF, Stoyer MA, Stoyer NJ, Shaughnessy DA, Kenneally JM, Wilk PA, Loughheed RW, Il'kaev RI, Vesnovskii SP (2004d) *Phys Rev C* 70:064609
- Omtvedt JP, Alstad J, Breivik H, Dyve JE, Eberhardt K, Folden CM III, Ginter T, Gregorich KE, Hult EA, Johansson M, Kirbach UW, Lee DM, Mendel M, Nähler A, Wierczinski B, Wilk PA, Zielinski PM, Kratz JV, Trautmann N, Nitsche H, Hoffman DC (2002) *J Nucl Radiochem Sci* 3:121
- Patyk Z, Sobiczewski A (1991) *Nucl Phys A* 533:132
- Paulus W (1997) Dissertation, Universität Mainz, GSI Diss. 1997, 97-09
- Paulus W, Kratz JV, Strub E, Zauner S, Bröchle W, Pershina V, Schädel M, Schausten B, Adams JL, Gregorich KE, Hoffman DC, Laue C, Lee DM, McGrath CA, Shaughnessy DK, Strellis DA, Sylwester ER (1999a) *Czech J Phys* 49(S1):573
- Paulus W, Kratz JV, Strub E, Zauner S, Bröchle W, Pershina V, Schädel M, Schausten B, Adams JL, Gregorich KE, Hoffman DC, Lane MR, Laue C, Lee DM, McGrath CA, Shaughnessy DK, Strellis DA, Sylwester ER (1999b) *Radiochim Acta* 84:69
- Pershina V (1996) *Chem Rev* 96:1977
- Pershina V (1998a) *Radiochim Acta* 80:65
- Pershina V (1998b) *Radiochim Acta* 80:75
- Pershina V (2005) *Radiochim Acta* 93:373
- Pershina V, Bastug T (1999) *Radiochim Acta* 84:79
- Pershina V, Bastug T (2000) *J Chem Phys* 113:1441
- Pershina V, Bastug T (2005) *Chem Phys* 311:139
- Pershina V, Fricke B (1993) *J Chem Phys* 99:9720
- Pershina V, Fricke B (1994a) *J Phys Chem* 98:6468
- Pershina V, Fricke B (1994b) *Radiochim Acta* 65:13
- Pershina V, Fricke B (1995) *J Phys Chem* 99:144
- Pershina V, Fricke B (1996) *J Phys Chem* 100:8748
- Pershina V, Fricke B (1999) In: Greiner W, Gupta RK (eds) *Heavy elements and related new phenomena*, vol 1. World Scientific, Singapore, Chapter 5, pp 194–262
- Pershina V, Kratz JV (2001) *Inorg Chem* 40:776
- Pershina V, Sepp WD, Fricke B, Rosen A (1992a) *J Chem Phys* 96:8367
- Pershina V, Sepp WD, Fricke B, Kolb D, Schädel M, Ionova GV (1992b) *J Chem Phys* 97:1116
- Pershina V, Sepp WD, Bastug T, Fricke B, Ionova GV (1992c) *J Chem Phys* 97:1123
- Pershina V, Fricke B, Kratz JV, Ionova GV (1994) *Radiochim Acta* 64:37
- Pershina V, Bastug T, Fricke B (1996) GSI scientific report 1995, GSI 96-1, p 15
- Pershina V, Johnson E, Fricke B (1999) *J Phys Chem A* 103:8463
- Pershina V, Bastug T, Fricke B, varga S (2001a) *J Chem Phys* 115:792
- Pershina V, Bastug T, Kratz JV (2001b) *Radiochim Acta* 89:729
- Pershina V, Trubert D, Le Naour C, Kratz JV (2002) *Radiochim Acta* 90:869
- Pershina V, Bastug T, Sarpe-Tudoran C, Anton J, Fricke B (2004) *Nucl Phys A* 734:200
- Pershina V, Bastug T, Fricke B (2005) *J Chem Phys* 122:124301

- Pershina V, Bastug T, Anton J, Fricke B (2007) *Nucl Phys A* 787:381c
- Pershina V, Anton J, Jacob T (2008) *Phys Rev A* 89:729
- Pershina V, Anton J, Jacob T (2009) *J Chem Phys* 131:084713
- Persson H, Skarnemark G, Skålberg M, Alstad J, Liljenzin JO, Bauer G, Haberberger F, Kaffrell N, Rogowski J, Trautmann N (1989) *Radiochim Acta* 48:177; Alstad J, Skarnemark G, Haberberger F, Herrmann G, Nähler A, Pense-Maskow M, Trautmann N (1995) *J Radioanal Nucl Chem* 189:133
- Pfreppe G, Pfreppe R, Yakushev AB, Timokhin SN, Zvara I (1997) *Radiochim Acta* 77:201
- Pfreppe G, Pfreppe R, Krauss D, Yakushev AB, Timokhin SN, Zvara I (1998) *Radiochim Acta* 80:7
- Pitzer KS (1975) *J Chem Phys* 63:1032
- Rieth U, Herlert A, Kratz JV, Schweikhard L, Vogel M, Walther C (2002) *Radiochim Acta* 90:337
- Ryshkov MV, Gubanov VA, Zvara I (1992) *Radiochim Acta* 57:11
- Sarpe-Tudoran C, Fricke B, Anton J, Pershina V (2007) *J Chem Phys* 126:174702
- Schädel M (1995) *Radiochim Acta* 70(71):207
- Schädel M (ed) (2003) *The chemistry of superheavy elements*. Kluwer, Dordrecht
- Schädel M (2006) *Angewandte Chemie international edition* 45:368
- Schädel M, Brüchle W, Haefner B (1988) *Nucl Instr Meth Phys Res A* 264:308
- Schädel M, Brüchle W, Jäger E, Schimpf E, Kratz JV, Scherer U, Zimmermann HP (1989) *Radiochim Acta* 48:171
- Schädel M, Brüchle W, Schimpf E, Zimmermann HP, Gober MK, Kratz JV, Trautmann N, Gäggeler H, Jost D, Kovacs J, Scherer UW, Weber A, Gregorich KE, Türlér A, Czerwinski KR, Hannink NJ, Kadkhodayan B, Lee DM, Nurmia MJ, Hoffman DC (1992) *Radiochim Acta* 57:85
- Schädel M, Jäger E, Brüchle W, Sümmerer K, Hulet EK, Wild JF, Loughheed RW, Dougan RJ, Moody KJ (1995) *Radiochim Acta* 68:7
- Schädel M, Brüchle W, Dressler R, Eichler B, Gäggeler HW, Günther R, Gregorich KE, Hoffman DC, Hübener S, Jost DT, Kratz JV, Paulus W, Schumann D, Timokhin S, Trautmann N, Türlér A, Wirth G, Yakushev A (1997a) *Nature* 388:55
- Schädel M, Brüchle W, Schausten B, Schimpf E, Jäger E, Wirth G, Günther R, Kratz JV, Paulus W, Seibert A, Thörle P, Trautmann N, Zauner S, Schumann D, Andrassy M, Misiak R, Gregorich KE, Hoffman DC, Lee DM, Sylwester ER, Nagame Y, Oura Y (1997b) *Radiochim Acta* 77:149
- Schädel M, Brüchle W, Jäger E, Schausten B, Wirth G, Paulus W, Günther R, Eberhardt K, Kratz JV, Seibert A, Strub E, Thörle P, Trautmann N, Waldek A, Zauner, Schumann D, Kirbach U, Kubica B, Misiak R, Nagame Y, Gregorich KE (1998) *Radiochim Acta* 83:156
- Schädel M, Ackermann D, Andersson L-L, Ballof J, Block M, Buda RA, Brüchle W, Dragojevic I, Düllmann ChE, Dvorak J, Eberhardt K, Even J, Gates JM, Gerl J, Gorshkov A, Golubev P, Graeger R, Gregorich KE, Gromm E, Hartmann W, Hessberger FP, Hild D, Hoischen R, Hübner A, Jäger E, Khuyagbaatar J, Kindler B, Kojouharov I, Kratz JV, Krier J, Kurz N, Lahiri S, Liebe D, Lommel B, Maiti M, Mendel M, Merchan E, Nitsche H, Nayak D, Nilssen J, Omtvedt JP, Opel K, Reichert P, Rudolph D, Sabelnikov A, Samadani F, Schaffner H, Schausten B, Schuber R, Schimpf E, Semchenkov A, Stavsetra L, Steiner J, Szerypo J, Thörle-Pospiech P, Toyoshima A, Türlér A, Uusitalo J, Wiehl N, Wollersheim H-J, Wunderlich T, Yakushev A (2008) GSI scientific report, GSI report 2009-1, p 138, <http://www.gsi.de/tasca>
- Scherer UW, Kratz JV, Schädel M, Brüchle W, Gregorich KE, Henderson RA, Lee DM, Nurmia MJ, Hoffman DC (1988) *Inorg Chim Acta* 146:249
- Schwerdtfeger P, Seth M (2002) *J Nucl Radiochem Sci* F3:133
- Seaborg GT (1945) *Chem Eng News* 23:2190
- Seaborg GT (1993) *Radiochim Acta* 61:115
- Seaborg GT (1995) *Radiochim Acta* 70(71):69
- Seaborg GT, Loveland WD (1990) *The elements beyond uranium*. Wiley, New York
- Silva RJ (1986) In: Katz JJ, Seaborg GT, Morss LR (eds) *The chemistry of the actinide elements*, vol 2, 2nd edn. Chapman and Hill, London, p 1085
- Silva RJ, Harris J, Nurmia M, Eskola K, Ghiorso A (1970) *Inorg Nucl Chem Lett* 6:871
- Sovernia S, Dressler R, Düllmann ChE, Eichler B, Eichler R, Gäggeler HW, Hänssler F, Niklaus J-P, Piguet D, Qin Z, Türlér A, Yakushev AB (2005) *Radiochim Acta* 93:1
- Stavsetra L, Gregorich KE, Dvorak J, Ellison PA, Dragojevic I, Garcia MA, Nitsche H (2009) *Phys Rev Lett* 103:132502
- Stoyer NJ, Landrum JH, Wilk PA, Moody KJ, Kenneally JM, Shaughnessy DA, Stoyer MA, Wild JF, Loughheed RW, Dmitriev SN, Oganessian YuTs, Shishkin SV, Aksenov NV, Tereshatov EE, Bozhikov GA, Vostokin GK, Utyonkov VK, Yerebin AA (2007) *Nucl Phys A* 787:388c
- Strub E, Kratz JV, Kronenberg A, Nähler A, Thörle P, Zauner S, Brüchle W, Jäger E, Schädel M, Schausten B, Schimpf E, Zongwei L, Kirbach U, Schumann D, Jost D, Türlér A, Asai M, Nagame Y, Sakama M, Tsukada K, Gäggeler HW, Glatz JP (2000) *Radiochim Acta* 88:265
- Strub E, Kratz JV, Kronenberg A, Nähler A, Thörle P, Brüchle W, Jäger E, Li Z, Schädel M, Schausten B, Schimpf E, Jost D, Türlér A, Gäggeler HW, Glatz JP

- (2001) Institut für Kernchemie, Univ. Mainz, Jahresbericht 2000, IKMz 2001-1, A3
- Szegłowski Z, Bruchertseifer H, Domanov VP, Gleisberg B, Guseva LJ, Hussonnois M, Tikhomirova GS, Zvara I, Oganessian YuTs (1990) *Radiochim Acta* 51:71
- Ter-Akopyan GM, Sagaidak RN, Pleva AA, Tretyakova SP, Buklanov GN (1985) Dubna report, P7-85-634
- Timokhin SN, Yakushev AB, Xu H, Pereygin VP, Zvara I (1996) Rep. at the NRC-3 International Conference, Vienna, Sept 1992; *J Radioanal Nucl Chem Lett* 212:31
- Toyoshima A, Haba H, Tsukada K, Asai M, Akiyama K, Nishinaka I, Nagame Y, Saika D, Matsuo K, Sato W, Shinohara A, Ishizu H, Ito M, Saito J, Goto S, Kudo H, Kikunaga H, Kinoshita N, Kato C, Yokoyama A, Sueki K (2004) *J Nucl Radiochem Sci* 5:45
- Toyoshima A, Haba H, Tsukada K, Asai M, Akiyama K, Goto S, Ishii Y, Nishinaka I, Sato TK, Nagame Y, Sato W, Tani Y, Hasegawa H, Matsuo K, Saika D, Kitamoto Y, Shinohara A, Ito M, Saito J, Kudo H, Yokoyama A, Sakama M, Sueki K, Oura Y, Nakahara H, Schädel M, Brüchle W, Kratz JV (2008) *Radiochim Acta* 96:125
- Trautmann N (1995) *Radiochim Acta* 70(71):237
- Tsukada K, Haba H, Asai M, Toyoshima A, Akiyama K, Kasamatsu Y, Nishinaka I, Ichikawa S, Yasuda K, Miyamoto Y, Hashimoto K, Nagame Y, Goto S, Kudo H, Sato W, Shinohara A, Oura Y, Sueki K, Kikunaga H, Kinoshita N, Yokoyama A, Schädel M, Brüchle W, Kratz JV (2009) *Radiochim Acta* 97:83
- Türler A (1996) *Radiochim Acta* 72:7
- Türler A (1999) Habilitationsschrift, Universität Bern
- Türler A, Gäggeler HW, Gregorich KE, Barth H, Brüchle W, Czerwinski KR, Guber MK, Hannink NJ, Henderson RA, Hoffman DC, Jost DT, Kacher CD, Kadkhodayan B, Kovacs J, Kratz JV, Kreek SA, Lee DM, Leyba JD, Nurmia MJ, Schädel M, Scherer UW, Schimpf E, Vermeulen D, Weber A, Zimmermann HP, Zvara I (1992) *J Radioanal Nucl Chem* 160:327
- Türler A, Eichler B, Jost DT, Piguet D, Gäggeler HW, Gregorich KE, Kadkhodayan B, Kreek SA, Lee DM, Mohar M, Sylwester E, Hoffman DC, Hübener S (1996) *Radiochim Acta* 73:55
- Türler A, Dressler R, Eichler B, Gäggeler HW, Jost DT, Schädel M, Brüchle W, Gregorich KE, Trautmann N, Taut S (1998) *Phys Rev C* 57:1648
- Türler A, Brüchle W, Dressler R, Eichler B, Eichler R, Gäggeler HW, Gärtner M, Glatz JP, Gregorich K, Hübener S, Jost DT, Lebedev VY, Pershina V, Schädel M, Taut S, Timokhin SN, Trautmann N, Vahle A, Yakushev AB (1999) *Angew Chem Int Ed* 38:2212
- Türler A, Düllmann ChE, Gäggeler HW, Kirbach UW, Yakushev AB, Schädel M, Brüchle W, Dressler R, Eberhardt K, Eichler B, Eichler R, Ginter TN, Glaus F, Gregorich KE, Hoffman DC, Jäger E, Jost DT, Lee DM, Nitsche H, Patin JV, Pershina V, Piguet D, Qin Z, Schausten B, Schimpf E, Schött H-J, Soverna S, Sudowe R, Thörle P, Timokhin SN, Trautmann N, Vahle A, Wirth G, Zielinski PM (2003) *Eur Phys J A* 17:505
- Vahle A (1996) Doctoral dissertation, Technische Universität Dresden
- Varga S, Fricke B, Hirata M, Bastug T, Pershina V, Fritzsche S (2000) *J Phys Chem A* 104:6495
- Von Zweidorf A, Angert R, Brüchle W, Jäger E, Kratz JV, Langrock G, Mendel M, Nähler A, Schädel M, Schausten B, Schimpf E, Stiel E, Trautmann N, Wirth G (2002) Institut für Kernchemie, Univ. Mainz, Jahresbericht 2001, IKMZ 2002-1, A5
- Von Zweidorf A, Angert R, Brüchle W, Bürger S, Eberhardt K, Eichler R, Hummrich H, Jäger E, Kling H-O, Kratz JV, Kuczewski B, Langrock G, Mendel M, Rith U, Schädel M, Schausten B, Schimpf E, Thörle P, Trautmann N, Tsukada K, Wiehl N, Wirth G (2004) *Radiochim Acta* 92:855
- Wierczinski B, Eberhardt K, Herrmann G, Kratz JV, Mendel M, Nähler A, Rocker F, Tharun U, Trautmann N, Weiner K, Wiehl N, Alstad J, Skarnemark G (1996) *Nucl Instr Meth Phys Res A* 370:532
- Wilk PA, Gregorich KE, Türler A, Laue CA, Eichler R, Ninov V, Adams JL, Kirbach U, Lane MR, Lee DM, Patin JB, Shaughnessy DA, Strellis DA, Nitsche H, Hoffman DC (2000) *Phys Rev Lett* 85:2797
- Yakushev A, Buklanov B, Eichler B, Gäggeler HW, Grantz M, Hübener S, Jost DT, Lebedev V, Piguet D, Timokhin S, Türler A, Vedenev MV, Zvara I (1996a) In: Fourth international conference on nuclear and radiochemistry (NRC-4), Saint Malo, Sept 1996a, Extended Abstracts, IPN Orsay, vol 1, A-P26
- Yakushev AB, Timokhin SN, Vedenev MV, Xu H, Zvara I (1996b) *J Radioanal Nucl Chem Articles* 205:63
- Yakushev AB, Buklanov GV, Chelnokov ML, Chepigin VI, Dmitriev SN, Gorshkov VA, Hübener S, Lebedev VYa, Malyshev ON, Oganessian YuTs, Popeko AG, Sokol EA, Timokhin SN, Türler A, Vasko VM, Yerebin AV, Zvara I (2001) *Radiochim Acta* 89:743
- Yakushev AB, Zvara I, Oganessian YuTs, Belozero AV, Dmitriev SN, Eichler B, Hübener S, Sokol EA, Türler A, Yerebin AV, Buklanov GV, Chelnokov ML, Chepigin VI, Gorshkov VA, Gulyaev AV, Lebedev VYa, Malyshev ON, Popeko AG, Soverna S, Szegłowski Z, Timokhin SN, Tretyakova SP, Vasko VM, Itkis MG (2003) *Radiochim Acta* 91:433
- Zhuikov BL, Chepigin VI, Kruz H, Ter-Akopian GM, Zvara I (1986) Experiments for chemical isolation and detecting of spontaneously fissioning and α -active isotopes of element 108, unpublished report 1985; Chepigin VI, Zhuikov BL, Ter-Akopian GM,

- Zvara I (1985) In: Fizika tiazhelykh ioniv 1985. Sbornik annotacii. Report JINR P7-86-322, p 15 (in Russian); Zhuikov BL, Kruz H, Zvara I (1986) Possibilities of chemical identification of short-lived element 108 isotopes. In: Fizika tiazhelykh ioniv 1985. Sbornik annotacii. Report JINR P7-86-322, p 26 (in Russian)
- Zhuikov BL, Chuburkov YuT, Timokhin SN, Jin KU, Zvara I (1989) *Radiochim Acta* 46:113
- Zhuikov BL, Glebov VA, Nefedov VS, Zvara I (1990) *J Radioanal Nucl Chem* 143:103
- Zimmermann HP, Guber MK, Kratz JV, Schädel M, Brühl W, Schimpf E, Gregorich KE, Türler A, Czerwinski KR, Hannink NJ, Kadkhodayan B, Lee DM, Nurmia MJ, Hoffman DC, Gäggeler H, Jost D, Kovacs J, Scherer UW, Weber A (1993) *Radiochim Acta* 60:11
- Zvara I (1976) In: Müller W, Lindner R (eds) *Transplutonium elements*. North-Holland, Amsterdam, p 11
- Zvara I (1985) *Radiochim Acta* 38:95
- Zvara I (1990) *Isotopenpraxis* 26:251
- Zvara I, Chuburkov YuT, Caletka R, Zvarova TS, Shalaevsky MR, Shilov BV (1966) *At Energy* 21:8; *J Nucl Energy* 21:60; *Sov J At Energy* 21:709
- Zvara I, Chuburkov YuTs, Zvarova TS, Caletka R (1969) *Sov Radiochem* 11:153; Zvara I, Chuburkov YuTs, Caletka R, Shalaevsky MR (1969) *Sov Radiochem* 11:161
- Zvara I, Chuburkov YuTs, Belov VZ, Buklanov GV, Zakhvataev BB, Zvarova TS, Maslov OD, Caletka R, Shalaevsky MR (1970) *Sov Radiochem* 12:530; *J Inorg Nucl Chem* 32:1885
- Zvara I, Belov VZ, Chelnokov LP, Domanov VP, Hussonnois M, Korotkin YuS, Shegolev VA, Shalaevsky MR (1971a) *Inorg Nucl Chem Lett* 7:1109
- Zvara I, Belov VZ, Domanov VP, Korotkin YuS, Chelnokov LP, Shalaevsky MR, Shchegolev VA, Hussonnois M (1971b) *Sov Radiochem* 14:115
- Zvara I, Eichler B, Belov VZ, Zvarova TS, Korotkin YuS, Shalaevsky MR, Shegolev VA, Hussonnois M (1974) *Sov Radiochem* 16:709
- Zvara I, Belov VZ, Domanov VP, Shalaevsky MR (1976) *Sov Radiochem* 18:328
- Zvara I, Domanov VP, Hübener S, Shalaevskii MR, Timokhin SN, Zhinikov BL, Eichler B, Buklanov GV (1984) *Sov Radiochem* 26:72
- Zvara I, Yakushev AB, Timokhin SN, Honggui Xu, Pereygin VP, Chuburkov YuT (1998) *Radiochim Acta* 81:179

21 Superheavy Elements

D. C. Hoffman^{1,2} · D. A. Shaughnessy³

¹University of California, Berkeley, CA, USA

²Lawrence Berkeley National Laboratory, Berkeley, CA, USA

³Lawrence Livermore National Laboratory, Livermore, CA, USA

21.1	<i>Early Predictions of Superheavy Elements</i>	1006
21.2	<i>Early Searches for SHEs</i>	1009
21.2.1	In Nature	1009
21.2.2	At Accelerators	1010
21.3	<i>Summary of Results to 1978</i>	1011
21.4	<i>Searches for SHEs Since 1978</i>	1011
21.5	<i>Discovery of Elements 107 Through 112</i>	1012
21.6	<i>Reports of Discoveries of SHEs</i>	1015
21.6.1	1999–2003	1015
21.6.2	2004–2009	1017
21.7	<i>Theoretical Predictions for Half-Lives and Nuclear Properties of Transactinide Elements (2003–2009)</i>	1023
21.8	<i>Future</i>	1025

Abstract: The long quest to detect superheavy elements (SHEs) that might exist in nature and the efforts to artificially synthesize them at accelerators or in multiple-neutron capture reactions is briefly reviewed. Recent reports of the production and detection of the SHEs 113, 114, 115, 116, and 118 are summarized and discussed. Implications of these discoveries and the prospects for the existence and discovery of additional SHE species are considered.

21.1 Early Predictions of Superheavy Elements

The possibility of relatively stable elements well beyond uranium, the heaviest element found in large quantities in nature, was considered in the early 1950s. This interest was sparked by the totally unexpected discovery of the new elements 99 (einsteinium) and 100 (fermium) in debris from the first US thermonuclear device “Mike,” tested on Eniwetok Atoll in the South Pacific on November 1, 1952, by the Los Alamos Scientific Laboratory. Prior to that discovery, only the elements through californium (atomic number 98) were known. Scientists postulated that the enormous, nearly instantaneous, high neutron flux generated in the 10 Mt detonation of Mike resulted in the successive capture of at least 17 neutrons in the uranium-238 (^{238}U) present in the device. In this way, the heavier uranium isotopes through ^{255}U were produced and many of these isotopes decayed rapidly by successive emission of negatively charged beta particles to produce isotopes of known elements with atomic numbers of 93 through 98. The uranium isotopes of masses 253 and 255 decayed all the way to the new elements having proton numbers of 99 and 100 and mass numbers of 253 and 255 as shown in the schematic diagram in [Fig. 21.1](#).

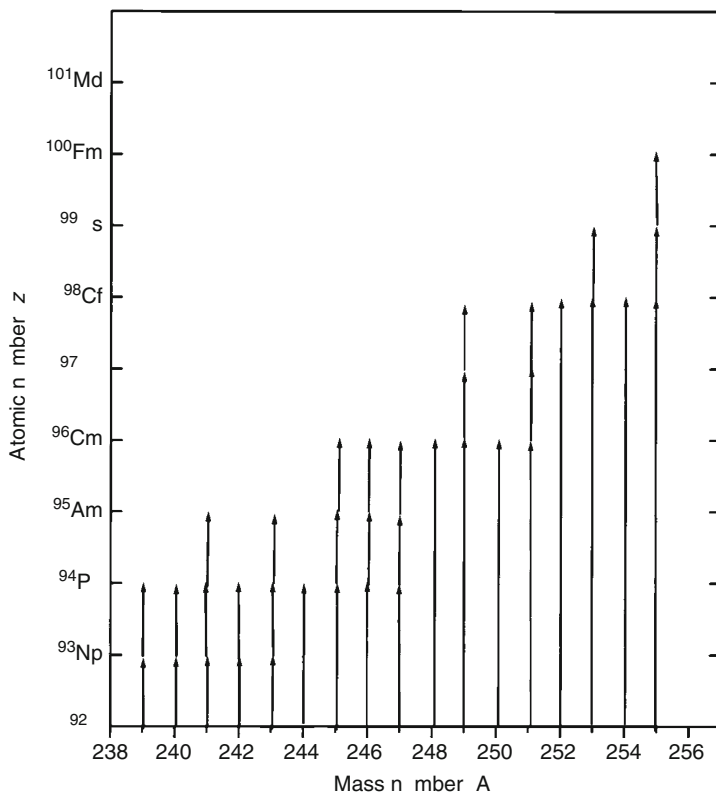
Publication (Ghiorso et al. 1955) of these 1952–1953 discoveries of elements 99 and 100 by Berkeley, Argonne, and Los Alamos scientists was delayed until after the data were declassified in 1955. In that same year, John A. Wheeler published a paper (Wheeler 1955) on nuclear fission and nuclear stability in which he extrapolated the rates of spontaneous fission (SF) and other processes limiting nuclear stability to the region of very large masses. In a talk presented at the 1955 International Conference on the Peaceful Uses of Atomic Energy (Wheeler 1956) he showed a diagram of the estimated limits of nuclear stability within which half-lives would be greater than a ten-thousandth of a second. Although he cautioned that his extrapolations might be appreciably in error, he still concluded that it was reasonable to look for nuclei with masses perhaps twice as heavy as $^{256}\text{100}$, the heaviest nucleus known at the time, i.e., masses of 500 or more! He further suggested that massive neutron irradiation of existing heavy nuclides might be an appropriate method for building such superheavy nuclei.

The possible existence of superheavy elements was also discussed by Gertrude Scharff-Goldhaber (1957). She speculated that there might be another region of relative stability around $^{310}\text{126}$ because it might be expected to have two especially stable, spherical closed nuclear shells (similar to closed electron shells). These spherical shells, or “magic” numbers as they are often called, were thought to be at proton number 126 and neutron number 184, thus making $^{310}\text{126}$ a “doubly magic” nucleus.

Such ideas spurred the quest to produce still heavier elements in subsequent thermonuclear tests. Indeed, the rather long-lived nuclide ^{257}Fm (half-life: $T_{1/2} = 100$ days) was detected in later nuclear tests, indicating capture of at least 19 neutrons in uranium. However, attempts to produce and detect still heavier elements in underground nuclear tests conducted at the Nevada Test Site all failed, thus dashing hopes that heavier long-lived elements could be produced via this multiple neutron-capture process that, as it had been postulated, might

■ Fig. 21.1

Schematic diagram of production of heavy uranium isotopes by successive neutron captures in ^{238}U followed by their subsequent beta-decay to spontaneously fissioning or alpha-decaying nuclides. Mass chains detected in debris from the Mike thermonuclear test are shown

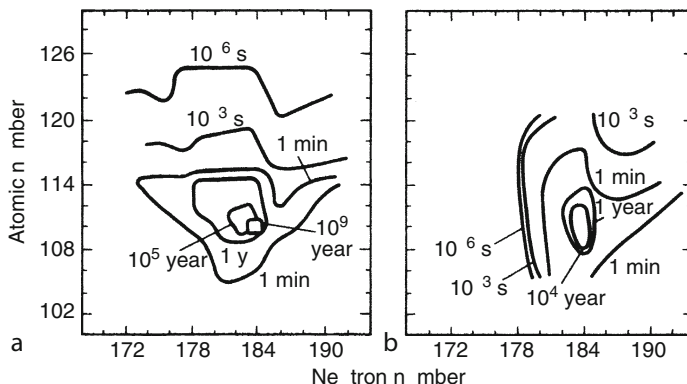


“mimic” production of heavy elements in astrophysical processes. (See ► [Chap. 12 in this Volume.](#)) These unsuccessful attempts were reviewed by R. W. Hoff (1978) at a symposium held at Berkeley in 1978 to commemorate the 25th anniversary of the discovery of elements 99 and 100. He postulated that the neutron fluxes were high enough to have produced masses heavier than 257, but the measured SF half-lives of 0.4 ms for ^{258}Fm and 1.5 s for ^{259}Fm were so short that formation of masses heavier than 257 by additional neutron capture was effectively blocked. It was suggested that perhaps the very neutron-rich, long-lived ($T_{1/2} \approx 9,700$ years) nuclide, ^{250}Cm , formed in rather large quantities in these tests, might be recovered afterward. It could then be used as target material to produce superheavy elements (hereafter to be called SHEs) by bombardments at accelerators with projectiles as heavy as ^{238}U .

Myers and Swiatecki (1966) and Meldner (1967) predicted that an “Island of Superheavy Elements” well beyond uranium might exist around elements with atomic numbers 114 or 126. This raised the possibility that very long-lived SHEs might still exist on earth after having been formed during the last nucleosynthesis in the solar system some 4.5 billion years ago. Later theoretical studies based on new theories of nuclear structure (Strutinsky 1966; Nilsson et al.

■ Fig. 21.2

Contour plots of predicted half-lives of SHEs as a function of proton and neutron number according to (a) Fiset and Nix (1972) and (b) Randrup et al. (1974)



1969a; Fiset and Nix 1972; Randrup et al. 1974) confirmed that an island of nuclear stability stabilized by spherical nuclear shells should be centered around 110–114 protons and 184 neutrons. Such calculations led to the conclusion that these spherical closed nuclear shells or “magic numbers” should be nearly as strong as those at 82 protons and 126 neutrons found in doubly magic, stable (nonradioactive) lead-208 (^{208}Pb), the most abundant isotope of naturally occurring lead. Some calculations even indicated that element 110 with 184 neutrons ($^{294}110$) should be the longest-lived with a half-life in the range of hundreds of thousands to a billion years as shown in the contour plots (Fiset and Nix 1972; Randrup et al. 1974) in Fig. 21.2.

These elements near the predicted islands of nuclear stability around the spherical closed shells at proton numbers 110–114 (or even 126) and 184 neutrons are typically referred to as SHEs. Although arguments have been made (Armbruster and Münzenberg 1989) that the heavy elements that would not exist except for stabilization by nuclear shells, whether or not they are spherical, should be designated as SHEs, the term has usually been reserved for those elements in the region of the predicted spherical doubly magic nuclei.

A 1968 periodic table with the “Superactinide” series proposed by Glenn T. Seaborg (1968) is shown in Fig. 21.3. Seaborg stated that in placing what he called the “Superactinides” at the bottom of the periodic table under the lanthanides and actinides, he had tried for simplicity’s sake to conform as nearly as possible to the current form of the periodic table.

This 32-member “Superactinide” series would begin with element 122 and end with element 153 after filling of the $5g^{18}$ and $6f^{14}$ electron shells, perhaps in mixed electronic configurations. However, Seaborg cautioned that complications from intruding 7d and 8p electrons might also occur and cause deviations from this picture and from the predominantly trivalent character expected for this Superactinide series. The predicted SHE with atomic number 126 would be a member of this series. A few examples of some of the early searches for SHEs in nature and at accelerators will be described in the next sections of this chapter and are discussed in much more detail by Hoffman, Ghiorso, and Seaborg in the *Transuranium People: The Inside Story* (Hoffman et al. 2000).

Fig. 21.3

Representation of Glenn T. Seaborg's "conventional" form of the periodic table showing predicted location of new elements, including Superactinides, in parentheses

1																	2 e
3 i	4 e											5	6 C	7 N	8	9 F	10 Ne
11 Na	12 M											13 Al	14 i	15 P	16	17 Cl	18 Ar
19	20 Ca	21 c	22 i	23	24 Cr	25 Mn	26 Fe	27 Co	28 Ni	29 C	30 n	31 a	32 e	33 As	34 e	35 r	36 r
37 b	38 r	39 Y	40 r	41 Nb	42 Mo	43 c	44	45 h	46 Pd	47 A	48 Cd	49 n	50 n	51 b	52 e	53 l	54 e
55 Cs	56 a	57 f	72	73 a	74	75 e	76 s	77 r	78 Pt	78 Pt	80	81 l	82 Pb	83 i	84 Po	85 At	86 n
87 Fr	88 a	89 Ac	104	105	106	107	108	109	110	111	112	113	114	115	116	117	118
119	120	121	154	155	156	157	158	159	160	161	162	163	164	165	166	167	168
anthanides		58 Ce	59 Pr	60 Nd	61 Pm	62 m	63	64 d	65 b	66 y	67 o	68 r	69 m	70 Yb	71		
Actinides		90 h	91 Pa	92	93 Np	94 P	95 Am	96 Cm	97	98 Cf	99 s	100 Fm	101 Md	102 No	103 r		
peractinides		122	123	124	125	126	127								153		

21.2 Early Searches for SHEs

21.2.1 In Nature

Among the earliest searches for SHEs in nature were those conducted at Berkeley between 1968 and 1972 by S. G. Thompson's group (Nilsson et al. 1969b; Cheifitz et al. 1972). Searches were begun in natural ores for element 110 as eka-platinum and elements 111 through 114 as eka-gold, -mercury, -thallium, and -lead. Initially, they looked specifically for eka-platinum, element 110, using low background counting techniques and sensitive analytical methods. Among the most sensitive measurements are those based on evidence of SF decay. This process is very rare among the known naturally occurring radionuclides and even if SHEs decay by other modes, they were expected to end in SF. The results of the searches were negative, corresponding to a concentration of $<10^{-11}$ g/g. Later, they used their very high efficiency, large liquid scintillator system in an attempt to measure the high multiplicity of neutrons predicted (Nix 1969) to be emitted during the SF of spherical SHE nuclei in the region of element 114. In order to reduce effects from cosmic-ray background, they placed their detector some 250 m deep in a cross passage inside the Bay Area Rapid Transit (BART) system tunnel then under construction between Berkeley and Orinda, California. More than 40 large samples of ores, natural minerals such as galena and gold nuggets, manganese nodules from the ocean floor, moon rocks, and placer platinum were surveyed, but they found no evidence for

increased neutron emission. Assuming a half-life of a billion years, they set a limit of $<10^{-14}$ moles of SHEs per mole of sample.

In 1969, G. N. Flerov and coworkers (Flerov and Pereygin 1969) in Dubna, Russia, reported detecting fission tracks in lead glass, which they attributed to the possible decay of SHEs. Based on additional observations of fission events in lead ore samples, they concluded they had found SF events with an apparent half-life of 4×10^{20} years that they attributed to SHEs. However, other researchers (Price et al. 1970) were not able to observe any fission tracks in old lead- and gold-rich minerals and set lower limits that were in contradiction with the Flerov results.

G. Herrmann (1974) published a review of early searches for SHEs in nature and concluded that no positive results had yet been obtained in either terrestrial or extraterrestrial samples, although many extremely sensitive methods had been developed and used in the search.

In 1976, R. V. Gentry and others (Gentry et al. 1976; Fox et al. 1976) reported evidence for element 126 and possibly elements 116, 124, and 127 in several “Giant Halos” found in mica samples (see [Sect. 17.13 of Chap. 17 in this Volume](#) on pleochroic halos). Gentry suggested that these giant halos had to be caused by 12–14 MeV alpha particles, much higher than the known members of radioactive decay series, and might have been produced by SHEs. Measurements of miniscule samples containing a single giant halo were bombarded with low-energy protons and the induced X-rays were measured. These so-called PIXIE measurements indicated L X-rays at the appropriate energies for the SHEs 126 and possibly 116, 124, and 127 as well. These results created great excitement and elation in the community and, at first it appeared that at last there was some firm physical evidence for SHEs. Unfortunately, the ‘X-rays’ turned out to be nuclear gamma rays induced in cerium-praseodymium isotopes present in the inclusions, and yet another discovery disappeared.

21.2.2 At Accelerators

First attempts to produce SHEs “artificially” were also conducted at Berkeley in 1968 by S. Thompson and A. Ghiorso and coworkers (Thompson 1968; Bowman et al. 1968). They used reactions of heavy ion projectiles with heavy actinide targets, e.g., $^{40}\text{Ar} + ^{248}\text{Cm} \rightarrow ^{288}114$, followed by neutron emission. No SHEs were detected and only limits could be set on the production cross sections and half-lives. (See [remark #33 in Chap. 9 of Vol. 1](#) on estimating such limits.)

Marinov et al. (1971a) published an article in *Nature* in January 1971, claiming production of element 112, eka-mercury, after they observed SF events in a mercury fraction chemically separated from the products of a long irradiation of tungsten with 24 GeV protons. The production mechanism was presumed to be secondary reactions with suitable targets of the heavy recoil products from the interactions of the high-energy protons. Later experiments showed (Marinov et al. 1971b) that some 70% of the observed SF activity was due to contamination from ^{252}Cf , and subsequent attempts by members of the group to repeat the initial results were unsuccessful. Subsequent more sensitive experiments (Bimbot et al. 1971; Batty et al. 1973) also proved to be negative.

Flerov and Oganessian (1972) reported detecting SF activity with a half-life of about 150 days in sulfide fractions containing osmium and bismuth separated from the products of long bombardments of ^{238}U with a variety of ions as heavy as ^{136}Xe . However, the average number of neutrons per fission was typical of actinides rather than SHEs so, again, another report seemed

unlikely. Attempts were initiated to try to produce SHEs in uranium + uranium collisions at the Universal Linear Accelerator (UNILAC) in Darmstadt, Germany, and in reactions of ^{48}Ca projectiles with ^{248}Cm at the SuperHILAC at Berkeley, but no positive results were obtained.

21.3 Summary of Results to 1978

The quest for SHEs continued in spite of the negative results, and in 1978 a large International Symposium on Superheavy Elements (Lodhi 1978) was held to assess the results and to consider future experiments. Most of the researchers working in the field and many other interested scientists attended. Some 15 countries and 50 different institutions were represented. The results of both searches in nature and attempts to synthesize SHEs were summarized. The quest had been extended by Anders et al. (1975) to investigations of anomalous stable xenon ratios arising from fission of SHEs in meteorites, but the results were model-dependent and controversial. The detection of neutrons from SF found in separated samples of hot springs water from the Cheleken Peninsula by Flerov and his group (Flerov 1977) was nonspecific as pointed out by D. C. Hoffman (Hoffman 1978; Hoffman et al. 1980) and remained inconclusive. Investigations of the reaction of ^{48}Ca with ^{248}Cm at Berkeley (Hulet et al. 1977; Illige et al. 1978; Otto et al. 1978) continued to prove fruitless, and resulted only in pushing the limit on the production cross section still lower to 0.1 nanobarn (nb) (10^{-34} cm^2). In the closing summary of the Superheavy Elements Symposium, G. A. Cowan (1978), suggested using uranium beams to bombard ^{248}Cm , or even ^{250}Cm , recovered from underground nuclear tests. The conclusion was that there was still no positive evidence for the discovery of SHEs either in nature or in the products of accelerator bombardments. With the reduction of most of the half-life predictions from 10^9 down to 10^4 years, or even only a year depending on estimates of SF half-lives, most plans for future attempts to find SHEs were focused on production at accelerators.

21.4 Searches for SHEs Since 1978

In 1981, Herrmann summarized (Herrmann 1981) the results of searches for SHEs in damped collisions of ^{238}U with ^{238}U carried out at the UNILAC at Darmstadt utilizing their unique high-energy uranium beams to bombard uranium targets. A wide variety of radiochemical separation techniques and a rotating-wheel system were used to search for elements 108 to 118 and even 126. These experiments were also to no avail and upper limits of 10^{-32} , 10^{-33} , and 10^{-35} cm^2 were set on the cross sections for half-lives of 1 to 100 ms, 100 ms to 1 day, and 1 day to 1 year, respectively. However, he predicted that the planned increases in fluence levels would permit reaching cross sections below these levels. Subsequently, the search for the production of SHEs in damped collisions (see [Chap. 3 in Vol. 1](#)) with ^{238}U (6.2–7.3 MeV/nucleon) at the UNILAC was extended to ^{248}Cm targets (Kratz et al. 1986) because this reaction was predicted to have a higher cross section. Comprehensive aqueous- and gas-phase radiochemical separation techniques were used to isolate SHE fractions that were then assayed for SF activity, including fission-fragment total kinetic energies, and neutron emission. Again, the results were negative with upper cross-section limits of $\sim 10^{-33} \text{ cm}^2$ for half-lives of minutes to hours and $\sim 4 \times 10^{-35} \text{ cm}^2$ for half-lives from days to several years.

About the same time, a large collaboration (Armbruster et al. 1985) of nuclear scientists, both chemists and physicists, from groups in the USA, Germany, and Switzerland conducted an exhaustive “final” investigation of the reaction of ^{248}Cm with ^{48}Ca projectiles in 1982–1983 first at the SuperHILAC at Berkeley, USA, and then at the UNILAC in Darmstadt, Germany. The earlier attempts at Berkeley (Hulet et al. 1977; Otto et al. 1978; Illige et al. 1978) and Dubna (Oganessian et al. 1978) using bombarding energies corresponding to excitation energies of the compound system of 33–53 MeV had all been negative. Therefore, the new experiments were conducted with excitation energies between 16 and 40 MeV, close to the reaction barrier, in an attempt to keep the excitation energy as low as possible in order to minimize losses due to prompt fission.

The recoil fragment separators, Small Angle Separator System (SASSY) at the SuperHILAC, Lawrence Berkeley Laboratory (LBL) and Separator for Heavy Ion Reaction Products (SHIP) at the Universal Linear Accelerator (UNILAC) at the Gesellschaft für Schwerionenforschung (GSI), Darmstadt, Germany, were used to search for nuclides with half-lives as short as microseconds. In addition, both online and off-line radiochemical separation techniques were utilized to search for species with half-lives as short as a few seconds and as long as years. Again, no evidence was found for SHEs with production cross sections larger than 0.1–0.01 nb over a half-life range of 1 μs to 10 years.

Searches for naturally occurring SHEs in *Atlantis II* hot brine reported by Flerov et al. (1979), Halperin et al. (1981), and Feige et al. (1987) also all proved to be negative. By the end of 1987, no credible evidence for SHEs, either in nature or artificially produced, remained and the quest was essentially abandoned.

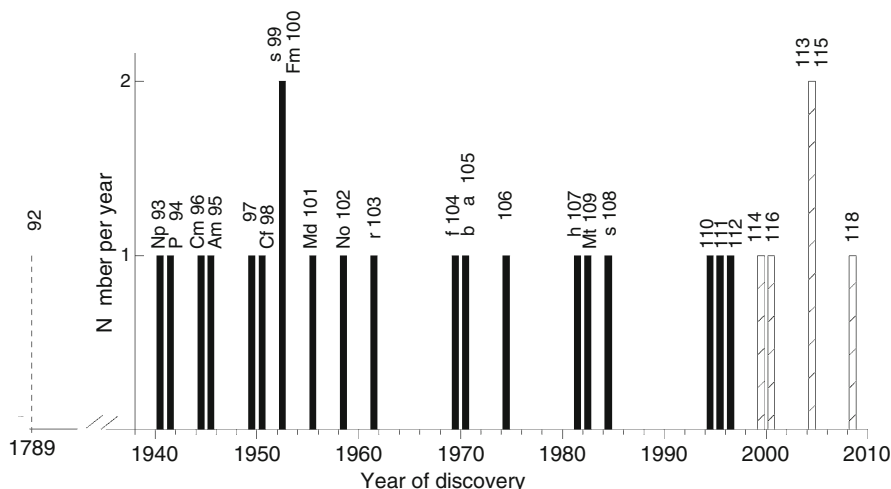
21.5 Discovery of Elements 107 Through 112

Meanwhile, between 1981 and 1984, three new elements, bohrium (107), hassium (108), and meitnerium (109) were discovered (see Chap. 19 in this Volume.) A timeline of the discovery of the transuranium elements is shown in Fig. 21.4. They were produced (Münzenberg et al. 1981, 1982a, b) at the UNILAC using so-called cold fusion production reactions suggested by Oganessian et al. (1975). Targets of doubly magic stable ^{208}Pb or nearby stable ^{209}Bi were bombarded with the appropriate heavy-ion projectiles (e.g., enriched stable ^{54}Cr and ^{58}Fe ions). These “shell-stabilized” targets react with the stable projectiles to give a compound nucleus that is the sum of their proton and neutron numbers. The resulting compound nuclei are produced with much lower excitation energies than those resulting from “hot fusion” reactions in which unstable heavy actinide targets are used. These “cold” compound nuclei are much more likely to de-excite by emitting only a single neutron, and thus, being less likely to be destroyed by fission, they have larger production cross sections. The isotopes $^{262}107$, $^{265}108$, and $^{266}109$ were separated and identified using the in-flight “separator for heavy-ion reaction products” (SHIP), built at GSI under the direction of Peter Armbruster. The names and symbols bohrium (Bh) for 107, hassium (Hs) for 108, and meitnerium (Mt) for 109 were officially adopted for these elements along with rutherfordium (Rf) for element 104, dubnium (Db), formerly called hahnium (Ha) for element 105, and seaborgium (Sg) for 106 by the International Union of Pure and Applied Chemistry (IUPAC) in August 1997 (CNIC 1997).

Evidence for different isotopes of element 110 was reported by several groups of scientists in 1995–1996. Ghiorso et al. (1995a, b) reported production of a single atom of $^{267}110$ in the $^{209}\text{Bi}(^{59}\text{Co},n)$ cold fusion reaction, Lazarev et al. (1996) reported evidence for decay of

■ Fig. 21.4

Timeline of discovery of transuranium elements. The claimed discovery date is indicated rather than the date discovery was confirmed and approved by the IUPAC. Solid lines indicate confirmed elements, dashed lines indicate unconfirmed elements



the neutron-rich nuclide $^{273}_{110}$ produced in the hot fusion reaction $^{244}\text{Pu}(^{34}\text{S}, 5n)$, and Hofmann et al. (1995a) reported evidence for isotopes of element 110 produced in cold fusion reactions. More details on these reports are given in Hoffman (1998).

After many improvements to SHIP, an international team led by S. Hofmann conducted experiments at GSI in 1995 and claimed discovery of element 110 (Hofmann et al. 1995a) produced in the cold-fusion reaction $^{208}\text{Pb}(^{62}\text{Ni}, n)^{269}_{110}$. They reported observation of $^{269}_{110}$ based on four chains that decayed by alpha emission to known daughter nuclides. They proposed the name darmstadtium (Ds), which was approved by the IUPAC in August 2003. The second chain could not be found in subsequent re-examination of the data (Hofmann et al. 2002), but IUPAC ruled that the remaining three chains constituted adequate proof.

In the subsequent experiments conducted in 1995, discovery of element 111 produced via the cold-fusion reaction $^{209}\text{Bi}(^{64}\text{Ni}, n)^{272}_{111}$ was also claimed (Hofmann et al. 1995b) based on observation of three decay chains identified using SHIP. The name “roentgenium” (Rg) in honor of Wilhelm Conrad Roentgen was proposed for element 111 and announced on the 100th anniversary of Roentgen’s 1895 discovery of X-rays. The IUPAC considered the data of high quality but inconclusive because no known daughters were identified in the reported decay chains.

In 2004, Morita et al. (2004a) used the same reaction as the GSI group to produce $^{272}_{111}$. They observed 14 alpha-decay chains in total, thus providing much new information about its decay properties, clearing up some of the ambiguities and confirming the discovery of $^{272}_{111}$ and the alpha-decay properties previously reported by Hofmann et al. (1995b, 2002). The name “roentgenium” with symbol Rg was finally officially approved by IUPAC in November 2004.

Continuing their experiments at GSI using the SHIP separator, Hofmann et al. (1996) identified two decay chains attributed to element 112 produced via the $^{208}\text{Pb}(^{70}\text{Zn}, n)^{277}_{112}$

reaction. Hofmann et al. (2002) later reanalyzed their 1996 data and subsequently reported that one of the decay chains attributed to element 112 could not be found in the original data and performed additional experiments to obtain more data for the isotopes of element 110 through 112 to support their originally reported discoveries. Again, Morita et al. (2005, 2007a) at RIKEN repeated the GSI experiments on production of element 112. Their observation of two of the same decay chains as reported by the GSI team was important in the ultimate assignment of discovery of element 112 to the GSI team of Hofmann et al. (2002).

A Joint Working Party (JWP) appointed by the International Unions of Pure and Applied Chemistry (IUPAC) and Pure and Applied Physics (IUPAP) assigned priority of discovery in May 2009 of element 112 to the international group of scientists led by S. Hofmann (Hofmann et al. 1996, 2002) working at GSI. The discoverers proposed the name “copernicium” with the symbol “Cp” after the Polish astronomer Nicolaus Copernicus. However, the proposed symbol was amended to be “Cn” because Cp for “cassiopeium” had earlier been proposed for element 71. That discovery could not be confirmed, and element 71 was later named lutetium by the acknowledged discoverers. The approval process was initiated by IUPAC in July 2009 and completed in March 2010 (Tatsumi and Corish 2010). The names and symbols for the transactinides approved as of 2010 are shown in [Table 21.1](#). The updated 2010 Periodic table of the Elements is shown in [Fig. 21.5](#).

One of the most significant things about the elements 107 through 112 is that they decay predominantly by alpha emission rather than SF, contrary to earlier predictions. These discoveries helped to give scientists renewed hope that it would be possible to reach the predicted island of SHE stability around element 114. The newly discovered nuclides also helped to substantiate the theoretical model and calculations of A. Sobiczewski and his group (Smolańczuk et al. 1995; Sobiczewski 1997) at the Soltan Institute for Nuclear Studies in Warsaw that predicted a doubly magic deformed region of extra stability around proton number 108 and neutron number 162 in addition to the island of spherical stability around $Z = 114$ and $N = 184$.

Table 21.1

List of IUPAC approved transactinides (TANs) 104–112 (Elements 104–109 approved August 30, 1997)

Z	Name	Symbol
104	Rutherfordium	Rf
105	Dubnium (Hahnium) [#]	Db (Ha) [#]
106	Seaborgium	Sg
107	Bohrium	Bh
108	Hassium	Hs
109	Meitnerium	Mt
110 ^a	Darmstadtium	Ds
111 ^b	Roentgenium	Rg
112 ^c	Copernicium	Cn

^aIUPAC approved August 2003.

^bIUPAC approved November 2004.

^cIUPAC approved March 2010.

[#]Used in publications on chemical properties prior to 1997.

■ Fig. 21.5

Periodic table of the elements as of 2010

1																	18				
1	2															13	14	15	16	17	2
3	4															5	6	7	8	9	10
i	e	ro p															C	N		F	Ne
11	12	3	4	5	6	7	8	9	10	11	12	13	14	15	16	17	18				
Na	M											Al	i	P		Cl	Ar				
19	20	21	22	23	24	25	26	27	28	29	30	31	32	33	34	35	36				
	Ca	c	i		Cr	Mn	Fe	Co	Ni	C	n	a	e	As	e	r	r				
37	38	39	40	41	42	43	44	45	46	47	48	49	50	51	52	53	54				
b	r	Y	r	Nb	Mo	c		h	Pd	A	Cd	n	n	b	e	l	e				
55	56	57	72	73	74	75	76	77	78	79	80	81	82	83	84	85	86				
Cs	a	a	f	a		e	s	r	Pt	A		l	Pb	i	Po	At	n				
87	88	89	104	105	106	107	108	109	110	111	112	113	114	115	116		118				
Fr	a	Ac	f	b a		h	s	Mt	s		Cn										
anthanides		58 Ce	59 Pr	60 Nd	61 Pm	62 m	63	64 d	65 b	66 y	67 o	68 r	69 m	70 Yb	71						
Actinides		90 h	91 Pa	92	93 Np	94 P	95 Am	96 Cm	97	98 Cf	99 s	100 Fm	101 Md	102 No	103 r						

21.6 Reports of Discoveries of SHEs

21.6.1 1999–2003

After the discovery of element 112 in 1996, researchers at GSI attempted to produce element 113 but were unsuccessful. Extrapolation from their previous experiments with lead and bismuth targets led them to believe that the cross sections for producing the elements beyond 112 had dropped so low that they needed to further upgrade and increase the efficiency of their SHIP system before continuing the search.

Bombardment of ^{208}Pb with 449 MeV ^{86}Kr projectiles to produce $^{293}118$ by a 1n out reaction was predicted by Smolańczuk (1999a, b) to have a large production cross section and decay via a unique chain of six high-energy alpha emitters with rather short half-lives. In 1999, the reaction was investigated by researchers at Lawrence Berkeley National Laboratory (LBNL) using the recently completed Berkeley Gas-filled Separator (BGS) at the 88 in. cyclotron. Because of the odd neutron in these nuclides, the half-lives might be as much as a factor of ten longer than these predictions. Due to the very low excitation energy of only 13.3 MeV calculated for the compound nucleus, emission of two neutrons is energetically forbidden, and single neutron emission is much more probable than alpha or proton emission from the compound nucleus. Ninov et al. (1999) reported finding three such decay chains with a cross section of a few picobarns in initial experiments conducted in April and May 1999, but upon re-examination of the original data, these results could not be verified. Later experiments

conducted in 2001 (Gregorich et al. 2003) showed no evidence for these decay chains and an upper limit of about 1 pb for production of this decay chain in the reaction of ^{208}Pb with 449 MeV ^{86}Kr projectiles was set.

Concurrently, under the leadership of Yu. Ts. Oganessian, researchers from the Joint Institute of Nuclear Research (JINR), Dubna, Russia, and the Lawrence Livermore National Laboratory (LLNL) heavy element group used the Dubna gas-filled recoil separator (DGFRS) to investigate production of heavier elements via the “hot fusion” reaction. In bombardments of rotating ^{244}Pu targets with ^{48}Ca projectiles accelerated in the Dubna U-400 heavy ion cyclotron, they found evidence for a single decay chain that they attributed to element 114 in data obtained from some 40 days of running time during November and December 1998. This corresponds to a cross section of about 1 pb or less. Based on the bombarding energy of 236 MeV and the characteristics of the observed alpha-decay chain, they originally attributed the event to $^{289}114$, which corresponded to the calculated maximum for the 3n evaporation reaction of the $^{244}\text{Pu} + ^{48}\text{Ca}$ reaction (Oganessian et al. 1999c). They reported observation of only one alpha-decay chain, a long chain ending with SF of $^{277}108$. The measured time intervals between successive decays and the corresponding alpha-decay energies indicated relatively long half-lives for $^{289}114$ (2–23 s), $^{285}112$ (20–200 min), $^{281}110$ (1–12 min), and $^{277}108$ (16 min). The half-lives they reported for $^{285}112$ and $^{281}110$ are nearly a million times longer than those of the heaviest previously known isotopes ($^{277}112$ and $^{273}110$) of these elements. Because this reaction was not previously studied, the method of genetic correlations to known nuclei for the identification of the parent nucleus could not be used, but the assignment of this one decay sequence to $^{289}114$ seemed reasonable based on predicted excitation functions for the $^{244}\text{Pu} + ^{48}\text{Ca}$ reaction. Evidence for $^{288}114$ via the 4n out reaction was subsequently observed in a continuation of the previous experiment that ran from June through October 1999, using the same bombarding beam energy as the first experiment (Oganessian et al. 2000a). Two decay sequences with similar decay characteristics were observed consisting of an implanted ion, two subsequent alpha-decays and terminated by a spontaneous fission. The decay chains were different than those observed during the first run. Based on previous experimental data as well as theoretical calculations, it was assumed that evaporation of either three or four neutrons from the $^{292}114$ compound nucleus would be expected with similar probabilities (on order of one picobarn) over the range of excitation energies observed in both experiments, $E^* = 31.5\text{--}39$ MeV (Oganessian et al. 2000a). Therefore, observation of two neighboring isotopes of element 114 in these experiments at the same beam energy was not unexpected. The new chains obviously originated from a different parent nucleus than that previously observed during the first $^{244}\text{Pu} + ^{48}\text{Ca}$ reaction that were originally attributed to $^{289}114$. The new nuclides observed in the second experiment were characterized by higher alpha-decay energies and terminated by SF at an earlier stage in the sequence. Comparison of the two chains-supported assignment of the first reported decay chain (three alpha-decays followed by SF) to the odd-mass nucleus $^{289}114$ and the shorter chains consisting of two alpha-decays followed by SF to even-even $^{288}114$ (Oganessian et al. 2000a). However, in further measurements of the $^{244}\text{Pu} + ^{48}\text{Ca}$ excitation function over a range of higher beam energies (see ▶ Sect. 21.6.2), the one event originally attributed to $^{289}114$ could not be reproduced and that result has never been confirmed. The original assignment of $^{288}114$ has since been changed to $^{289}114$ based on excitation function data described in ▶ Sect. 21.6.2.

In mid-April 1999, a multinational collaboration, also led by Oganessian, reported indirect evidence for two events of $^{287}114$ from the $^{242}\text{Pu}(^{48}\text{Ca}, 3\text{n})$ reaction using the Dubna electrostatic recoil vacuum separator VASSILLISSA. These results were published (Oganessian et al. 1999b)

in July 1999. In one event, a 10.29 MeV alpha particle was followed 1.3 s later by SF, while in the other event an escape peak with an alpha energy of only 2.31 MeV followed by SF was detected. The SF lifetimes for the two events were 9.3 and 3.8 min, which the authors claim correspond to the same SF activity (within the limits of the reported uncertainties) of about 1.4 min that they produced previously in the reaction of ^{238}U with ^{48}Ca projectiles (Oganessian et al. 1999a) and had attributed to $^{283}112$. In these experiments with the ^{242}Pu target, it was postulated that $^{283}112$ would be observed as the alpha-decay daughter of $^{287}114$. Based on the two SF events observed in the $^{242}\text{Pu} + ^{48}\text{Ca}$ reaction and the two events attributed to $^{283}112$ produced via the $^{238}\text{U}(^{48}\text{Ca},3n)$ reaction, the SF half-life of $^{283}112$ was estimated to be approximately 3 min (Oganessian et al. 1999b). However, later measurements of the $^{242}\text{Pu} + ^{48}\text{Ca}$ excitation function showed that the reported decay properties of $^{287}114$ were not correct, and the parent 114 nucleus actually decays through a chain consisting of two alpha particles followed by SF with the much shorter SF half-life of only a few seconds (Oganessian et al. 2004b). The shorter $^{283}112$ half-life was later reproduced by Hofmann et al. (2007), which supported the revised $^{287}114$ decay properties (see ▶ Sect. 21.6.2).

In 2000, the Dubna–LLNL collaboration reported evidence for the production of $^{292}116$ in the $^{248}\text{Cm}(^{48}\text{Ca},4n)$ reaction at a center-of-target beam energy of 240 MeV (Oganessian et al. 2000b, Oganessian 2001). One decay chain was observed consisting of an evaporation residue followed by two alpha particles and partial energy deposition of a third alpha followed by a spontaneous fission. The half-life estimated from this one event was ~ 33 ms; a cross-section limit was not given as the experiment was in progress during the reported observation of this nuclide, but subsequent excitation function measurements indicate it was likely on the order of 1 pb (Oganessian et al. 2004b). The daughter nuclides appeared to decay with the same properties as those observed in the second reported $^{244}\text{Pu} + ^{48}\text{Ca}$ experiment where the $^{288}114$ assignment was originally proposed (Oganessian et al. 2000a). Therefore, this first reported isotope of element 116 was assigned to $^{292}116$, but was later changed to $^{293}116$ when it was realized that the assignments of the first two reported isotopes of element 114 were incorrect (see ▶ Sect. 21.6.2 for more details). The earlier experiments of Armbruster et al. (1985) described in ▶ Sect. 21.4 reported no evidence for production of SHEs with cross sections larger than 0.1 nb (100 pb) to 0.01 nb (10 pb) over a half-life range of μs to 10 years. However, these experiments did not have sufficient sensitivity to detect SHE nuclides at the picobarn cross-section level and are not in conflict with the above results.

21.6.2 2004–2009

The complete excitation function of the $^{244}\text{Pu} + ^{48}\text{Ca}$ fusion reaction was not measured until 2004 by Oganessian et al. (2004a). The ^{244}Pu targets were bombarded with ^{48}Ca ions at beam energies ranging from 243 to 257 MeV; these were higher than those studied previously during the first two reported observations of element 114 (Oganessian et al. 1999c, 2000a). At a ^{48}Ca energy of 243 MeV, decay chains consisting of two consecutive alpha-decays followed by SF were observed and had identical decay properties to the two chains previously reported at the lower bombarding energy of 236 MeV that were originally assigned to $^{288}114$ (Oganessian et al. 2000a). In addition, at all three of these higher bombarding energies, very short decay chains consisting of a single alpha-decay followed by SF were observed, and at the highest beam energy of 257 MeV, one chain was detected that included two sequential alpha-decays ending with a SF with decay properties that differed from any of the previous observed

chains (Oganessian et al. 2004a). It was assumed that the longer decay chains observed at the lowest and highest beam energies belonged to odd-mass isotopes of 114, while the short alpha-SF chains originated from an even-even nucleus. Based on predicted excitation functions for the $^{244}\text{Pu} + ^{48}\text{Ca}$ reaction, it now appeared that the single chain observed at the highest bombarding energy was likely due to the previously unreported isotope $^{287}\text{114}$ produced via the 5n evaporation channel and the alpha-SF chain, therefore, originated from $^{288}\text{114}$ produced via the 4n channel. These assignments meant that the decay chains originally attributed to $^{288}\text{114}$ (Oganessian et al. 2000a) were actually from a different isotope, and based on the measurement of the excitation function, the assignment was changed instead to the 3n evaporation product, $^{289}\text{114}$, which would be consistent with a longer, odd-mass decay chain (Oganessian et al. 2004a). The single decay chain originally reported as $^{289}\text{114}$ (Oganessian et al. 1999c) was never duplicated experimentally, and, based on the results subsequently reported by Oganessian et al. (2004a), was probably not due to an isotope of element 114. Maximum cross sections for the production of 114 isotopes via the $^{244}\text{Pu} + ^{48}\text{Ca}$ reaction were reported to be: 2 pb (3n), 5 pb (4n), and 1 pb (5n).

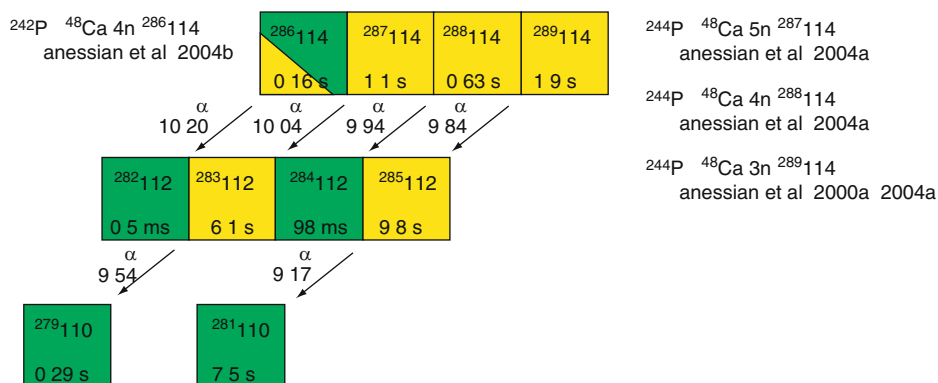
Likewise, the complete excitation function of the $^{242}\text{Pu} + ^{48}\text{Ca}$ reaction was subsequently measured in 2004 over a range of beam energies from 235 to 250 MeV (Oganessian et al. 2004b). During a subsequent experiment, the $^{238}\text{U} + ^{48}\text{Ca}$ reaction was also studied over a range of beam energies from 230 to 240 MeV in order to identify the potential alpha-decay daughter of $^{287}\text{114}$, $^{283}\text{112}$ (Oganessian et al. 2004b). Fifteen decay chains consisting of two alpha-decays followed by SF were observed at three beam energies (235, 238, and 244 MeV) during bombardment of ^{242}Pu with ^{48}Ca . The decay properties matched those reported as $^{287}\text{114}$ produced via the $^{244}\text{Pu}(^{48}\text{Ca},5\text{n})$ reaction (Oganessian et al. 2004a). This assignment was also supported by the direct production of the $^{283}\text{112}$ daughter via the $^{238}\text{U}(^{48}\text{Ca},3\text{n})$ reaction (Oganessian et al. 2004b). $^{283}\text{112}$, produced both directly and as the daughter of $^{287}\text{114}$, was observed to decay in both cases via alpha-decay with a half-life of 4 s followed by a very short SF (Oganessian et al. 2004b). These results disagreed with the original report of $^{283}\text{112}$ (Oganessian et al. 1999b), which indicated that it decayed via SF with a lifetime on the order of several minutes. The alpha-decay of $^{283}\text{112}$ was later confirmed by Hofmann et al. (2007) but the 3 min SF activity was not observed. Hofmann et al. (2007) measured two decay chains from the $^{238}\text{U}(^{48}\text{Ca},3\text{n})$ reaction, confirming data previously reported for this isotope by Oganessian et al. (2004b). Two other events were observed consistent with a 50% SF branch for $^{283}\text{112}$. Decay chains for the observed element 114 isotopes based on the original measurements of their direct production via $^{242,244}\text{Pu} + ^{48}\text{Ca}$ reactions with their current proposed isotopic assignments are shown in [Fig. 21.6](#).

Evidence for $^{286}\text{114}$ was first reported by Oganessian et al. (2004a) as the daughter of $^{290}\text{116}$ produced in the $^{245}\text{Cm}(^{48}\text{Ca},3\text{n})$ reaction shown in [Fig. 21.7](#). The assignment was later substantiated in measurements of cross sections for the $^{48}\text{Ca} + ^{242}\text{Pu}$ reaction (Oganessian et al. 2004b). The maximum cross section measured for production of $^{286}\text{114}$ is approximately 4.5 pb for the $^{242}\text{Pu}(^{48}\text{Ca},4\text{n})$ reaction.

Additional isotopes of element 116, $^{290}\text{116}$, and $^{291}\text{116}$, were observed in the reaction of ^{48}Ca with ^{245}Cm (Oganessian et al. 2004a), with cross sections of about 1 pb at a bombarding beam energy of 243 MeV. Once the final assignments of $^{288}\text{114}$ and $^{289}\text{114}$ were determined by Oganessian et al. (2004a; see discussion above) it was realized that the daughter of what was originally believed to be $^{292}\text{116}$ had decay properties that, in fact, matched those of $^{289}\text{114}$ produced in the $^{244}\text{Pu} + ^{48}\text{Ca}$ reaction (Oganessian et al. 2004a). Therefore, the assignment of the element 116 isotope originally observed in the $^{248}\text{Cm} + ^{48}\text{Ca}$ reaction was changed to

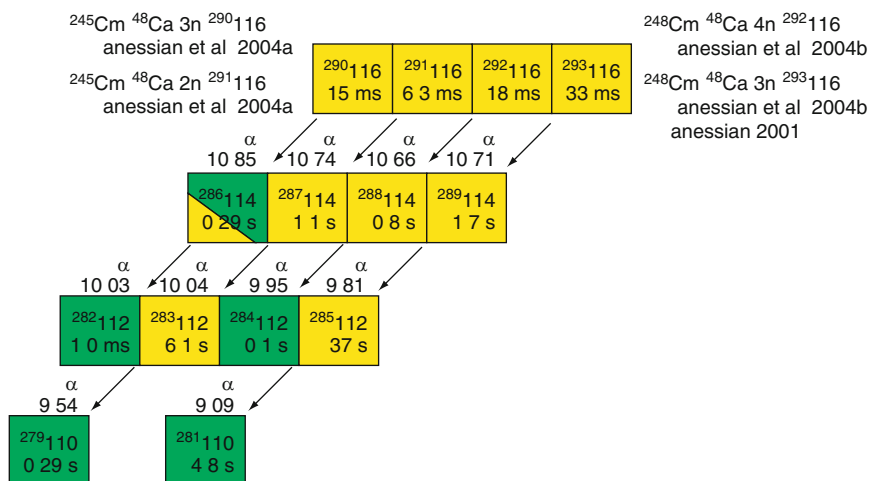
■ Fig. 21.6

Decay chains for $^{286}_{114}$ (Oganessian et al. 2004b), $^{287}_{114}$ (Oganessian et al. 2004a), $^{288}_{114}$ (Oganessian et al. 2004a), and $^{289}_{114}$ (initially reported as $^{288}_{114}$ by Oganessian et al. 2000a, later changed to $^{289}_{114}$ in Oganessian et al. 2004a) as measured from the direct production reactions shown on the figure. Half-lives calculated from average lifetimes; observed alpha energies in megaelectron volts are given. Yellow squares indicate alpha-decay and green squares indicate SF



■ Fig. 21.7

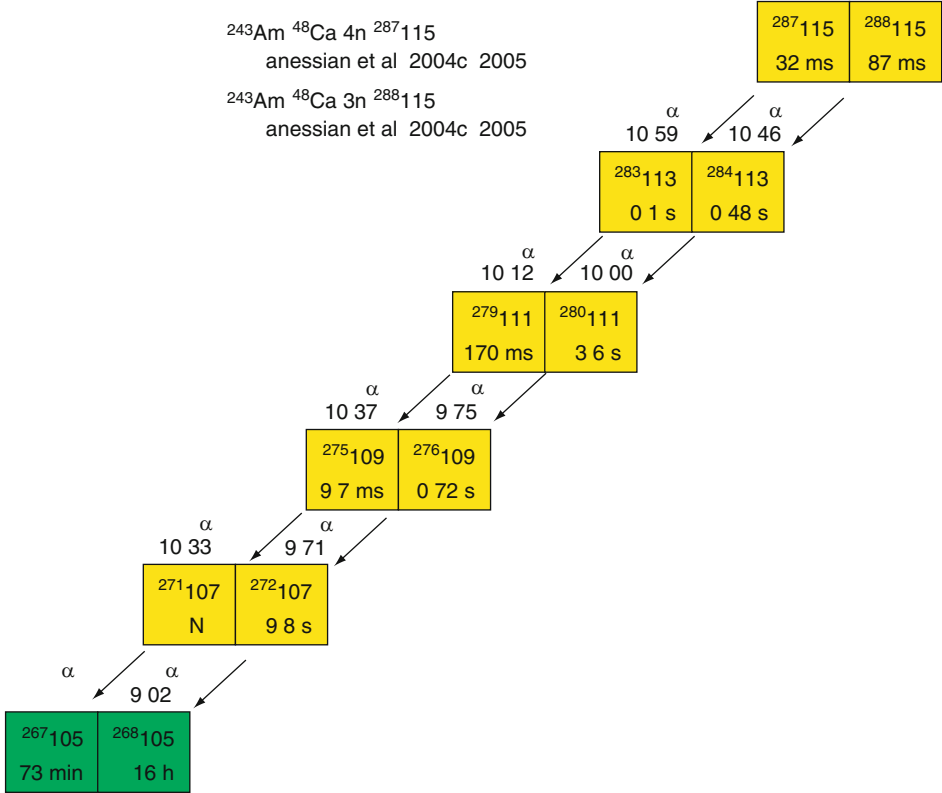
Decay chains for $^{290}_{116}$ (Oganessian et al. 2004a), $^{291}_{116}$ (Oganessian et al. 2004a), $^{292}_{116}$ (Oganessian et al. 2004b), and $^{293}_{116}$ (initially reported as $^{292}_{116}$ by Oganessian et al. 2000b, Oganessian 2001, later changed to $^{293}_{116}$ in Oganessian et al. 2004a) as measured from the direct production reactions shown on the figure. Half-lives calculated from average lifetimes; observed alpha energies in megaelectron volts are given. Yellow squares indicate alpha-decay and green squares indicate SF



$^{293}_{116}$, and $^{292}_{116}$ was later reported in the measurement of the $^{248}\text{Cm}(^{48}\text{Ca},4n)$ reaction at 247 MeV with a cross section of about 1 pb (Oganessian et al. 2004b). Decay chains for the four observed isotopes of element 116 based on the original measurements of their direct production via $^{245,248}\text{Cm} + ^{48}\text{Ca}$ reactions ($^{290,291,292,293}_{116}$) with their current proposed isotopic assignments are shown in Fig. 21.7.

The next reported discovery of a SHE was in 2004 when the Dubna–LLNL collaboration reported the observation of element 115 and its decay daughter 113 for the first time (Oganessian et al. 2004c, 2005). Targets of ^{243}Am were bombarded with 248 MeV ^{48}Ca projectiles resulting in a total beam dose of 4.3×10^{18} ^{48}Ca ions. Three decay chains consistent with the decay of $^{288}_{115}$ and its daughter $^{284}_{113}$ formed via the $^{243}\text{Am}(^{48}\text{Ca},3n)$ reaction were reported resulting in a cross section of about 3 pb. One additional decay chain corresponding to the decay of $^{287}_{115}$ and its daughter $^{283}_{113}$ produced via the $^{243}\text{Am}(^{48}\text{Ca},4n)$ reaction was observed at an increased beam energy of 253 MeV giving a production cross section of about 1 pb (see Fig. 21.8).

Fig. 21.8
Reported decay chains for $^{287,288}_{115}$ (Oganessian et al. 2004c, 2005). $^{271}_{107}$ was not detected (ND). Half-lives calculated from average lifetimes; observed alpha energies in megaelectron volts are given. Yellow squares indicate alpha-decay and green squares indicate SF



The long-lived (16 h) ^{268}Db decay daughter of $^{288}_{115}$ (Oganessian et al. 2004c) was later isolated via chemical methods (Dmitriev et al. 2005) during a subsequent ^{48}Ca bombardment of ^{243}Am . During this procedure, the reaction products that came from the ^{243}Am were caught in a copper block placed directly behind the target. The block was removed after 24 h of irradiation and the surface was removed using a microlathe. The copper was then dissolved in nitric acid and run through a column of Dowex 50×8 cation-exchange chromatography resin. The Groups 4 and 5 elements were eluted together with hydrofluoric acid (Dmitriev et al. 2005; Oganessian et al. 2005; Schumann et al. 2005). The entire effluent was evaporated on a thin polyethylene foil for subsequent alpha and SF counting. The entire procedure from end of bombardment to the beginning of counting was approximately 2–3 h (Oganessian et al. 2005). Fifteen spontaneous fission events were observed with a measured half-life of 32 h (Oganessian et al. 2005), which was consistent within experimental uncertainties with the 16 h half-life observed for ^{268}Db produced as a decay product of the reported $^{288}_{115}$ chain shown in [Fig. 21.8](#) (Oganessian et al. 2004c). However, the chemical method used would not differentiate the Group 4 from Group 5 elements (Schumann et al. 2005). Identification of the atomic number cannot be made via spontaneous fission alone, especially in a case where contamination from other elements may have been present. The cross section for the production of $^{288}_{115}$ via the $^{243}\text{Am}(^{48}\text{Ca}, 3n)$ reaction was determined during the off-line chemical separation to be approximately 4 pb based on the assumption that the 15 observed SF events were from ^{268}Db and not another fissioning nuclide present in the final chemical fraction (Oganessian et al. 2005). This cross section was consistent with the 2.7 pb cross section measured via direct production (Oganessian et al. 2004c).

In a subsequent experiment performed by the LLNL–Dubna collaboration (Stoyer et al. 2007; Wilk et al. 2008), five SF events were detected in an experiment in which the reaction products collected in the copper catcher block were chemically separated to first isolate the Group 5 elements from other interfering products, and then the Group 5 fraction was further separated into Nb- and Ta-like fractions in order to evaluate whether the previously observed fission events were from ^{268}Db , which would be expected to behave as a Group 5 element. After removing the surface of the copper and dissolving it as before, the solution was sorbed on an inert Kel-F resin coated with methyl isobutyl ketone (MIBK). Several chemical fractions were collected by performing gradient elutions with varying concentrations of HCl and HF (Wilk et al. 2008). The Groups 4 and 5 elements were shown to be in different fractions based on the location of tracer radionuclides (^{89}Zr , $^{92\text{m}}\text{Nb}$, ^{177}Ta , ^{175}Hf , ^{167}Tm , and ^{169}Yb) added prior to the start of chemistry (Stoyer et al. 2007). The Group 5 elements were further separated in Nb- and Ta-like fractions through the use of graded HCl/HF elutions followed by a warm-water wash, which removed all of the tantalum (Wilk et al. 2008). All fractions were evaporated onto thin polyethylene foils for subsequent alpha and SF counting. The entire procedure from the end of irradiation to the beginning of counting took approximately 2 h. The five observed SF events all appeared in the Ta fraction, suggesting that the fissions originated from a Group 5 element. The lifetimes of the fission events were between 16 and 37 h. When one incorporates all of the fission events from direct production (Oganessian et al. 2004c) and the two subsequent off-line chemistry experiments (Oganessian et al. 2005; Stoyer et al. 2007; Wilk et al. 2008), the half-life of ^{268}Db is 28 h (Stoyer et al. 2007). The chemistry experiments provide indirect evidence that the daughter activity may come from the same long-lived dubnium nuclide that is part of the element 115 decay chain ([Fig. 21.8](#)). However, direct production will ultimately be required to confirm assignment of $^{288}_{115}$.

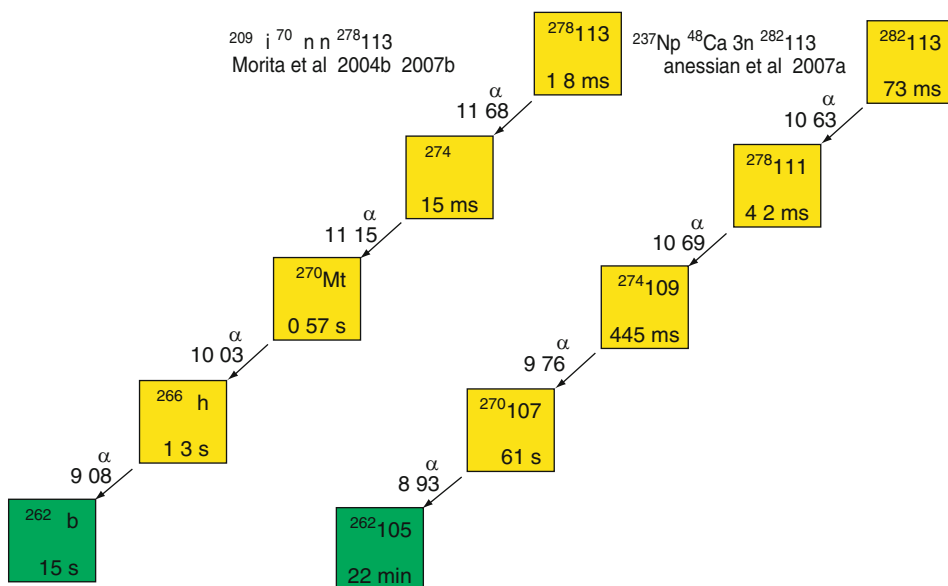
Direct production of two different isotopes of element 113 has also been reported. Morita et al. (2004b, 2007b) reported production of two events of $^{278}113$ via the $^{209}\text{Bi}(^{70}\text{Zn},n)$ cold fusion reaction with the extremely small production cross section of only about 31 fb in two separate experiments at a beam energy of 353 MeV at the Riken Linear Accelerator Facility. These were attributed to $^{278}113$ based on alpha-decay to the previously reported isotopes ^{266}Bh (approximately 1 s; Wilk et al. 2000) and ^{262}Db (34 s). Oganessian et al. (2007a) reported observation of two decay chains of $^{282}113$ produced via the $^{237}\text{Np}(^{48}\text{Ca},3n)$ reaction at a bombarding energy of 244 MeV, corresponding to a production cross section of 0.9 pb. Decay chains for these experiments to produce isotopes of 113 are shown in Fig. 21.9.

Eichler et al. (2007a, b) studied the production of $^{287}114$ via the $^{242}\text{Pu}(^{48}\text{Ca},3n)$ reaction using thermochromatographic separation methods. The reaction products were volatilized and the $^{283}112$ decay daughters were subsequently collected and measured on a detector surface cooled with a temperature gradient from $+35^\circ\text{C}$ to -186°C . The observed decay chains attributed to $^{283}112$ (9.5 MeV alpha-decay with a half-life of about 4 s) were consistent with those reported by Oganessian et al. (2004b) as decay products of $^{287}114$ observed during measurement of the $^{242}\text{Pu} + ^{48}\text{Ca}$ excitation function (Oganessian et al. 2004b). These experiments of Eichler et al. provide indirect proof of production of element 114 through the measurement of its $^{283}112$ decay daughter.

Most recently, a group at LBNL (Stavsetra et al. 2009) has reported production of one event each of $^{286}114$ and $^{287}114$ produced via the $^{242}\text{Pu} + ^{48}\text{Ca}$ reaction with decay properties

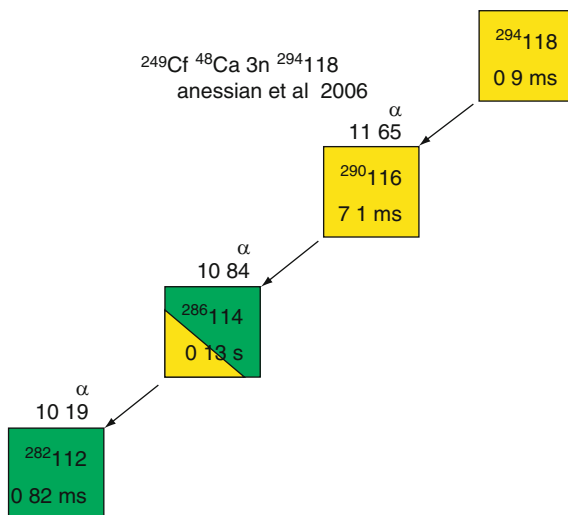
Fig. 21.9

Reported decay chains for Element 113. Left: $^{278}113$, two events reported (Morita et al. 2004b, 2007b). Right: $^{282}113$ (two events, Oganessian et al. 2007a). Half-lives calculated from average lifetimes; observed alpha energies in megaelectron volts are given. Yellow squares indicate alpha-decay and green squares indicate SF



■ Fig. 21.10

Reported decay chain for $^{294}_{118}$ (Oganessian et al. 2006). Half-lives calculated from average lifetimes; observed alpha energies in megaelectron volts are given. Yellow squares indicate alpha-decay and green squares indicate SF



consistent with those reported by Oganessian et al. (2004b). These experiments are the first to provide direct confirmation of production of element 114.

In 2006, Oganessian et al. (2006) reported the observation of three similar decay chains originating from element 118 produced via the $^{249}\text{Cf}(^{48}\text{Ca}, 3n)^{294}_{118}$ reaction at two different excitation energies (29 and 34 MeV) with a cross section of approximately 0.5 pb. The assignment of element 118 to the new decay chains was supported by the genetic correlation with a previously identified isotope of element 116 measured in the $^{245}\text{Cm}(^{48}\text{Ca}, 3n)^{290}_{116}$ reaction (Oganessian et al. 2004a) and its corresponding decay daughters. The decay chain for $^{294}_{118}$ is shown in ► Fig. 21.10.


21.7 Theoretical Predictions for Half-Lives and Nuclear Properties of Transactinide Elements (2003–2009)

Although most nuclear models indicated that half-lives and production rates rapidly decrease beyond Sg, some theoretical calculations (Sobiczewski 1997) predicted a region of nuclear stability around ^{270}Hs , a doubly magic deformed nucleus with 108 protons and 162 neutrons. One of the challenging experiments proposed for the future was to produce isotopes in this region for study of their properties. In recent studies by Dvorak et al. (2006, 2008), the new isotope ^{271}Hs (half-life ~ 4 s) was produced via a 3n out reaction in the bombardment of ^{248}Cm with ^{26}Mg projectiles at below Coulomb barrier energies. The measured cross section of a few picobarns was comparable to the maximum cross sections for the previously known 4 s ^{269}Hs , as well as for the isotope ^{270}Hs , which alpha-decays with a half-life of about 23 s and is an ideal candidate for chemical studies. These experiments suggest that the 3n reaction may be useful

for making more neutron-rich transactinides using relatively light heavy ion beams and actinide targets.

These and other studies and reanalysis of data for Sg decay products of Hs alpha-decay by Düllmann and Türler (2008) have shown that the originally reported 21 s ^{266}Sg (Türler et al. 1998) was in error and was actually due to ^{265}Sg , which has two isomeric states with half-lives of 8.9 s and 16.2 s, respectively. The good news is that the 8.9 s ^{265}Sg isomer is produced preferentially via the $^{248}\text{Cm}(^{22}\text{Ne}, 5n)$ reaction with an estimated cross section of a few hundred picobarns! Now it should be quite feasible to perform more “in-depth” detailed studies of the chemistry of Sg, such as stability of its oxidation states both in solution and in gas-phase studies and complex formation under a variety of conditions.

A review of predicted chemical properties including ionization potentials, ionic radii, and redox potentials for Sg and lighter Group 6 elements is given in Hoffman et al. (2006). These indicate that the (VI) oxidation state will be the most stable both in solution and in the gas phase and that Sg^{4+} will be even less stable than Ta^{3+} and W^{4+} . It will be especially interesting to compare actual comprehensive measurements of the chemical properties of Sg with those of lighter Group 6 homologues and with the predictions of modern relativistic atomic and molecular calculations that include the influence of relativistic effects on chemical properties.

The early predicted doubly magic spherical region of hypothetical long-lived SHEs shown in  Fig. 21.2 has never been reached although some of the recently reported heaviest isotopes of elements 112–118 produced in fusion reactions of heavy actinide nuclei with ^{48}Ca projectiles show significant increases in stability as the number of neutrons increases. Oganessian (2007b) has given a comprehensive review of the reported properties of the heaviest nuclides. He also discusses the theoretical predictions about the “island of stability.”

Zagrebaev and Greiner (2008) considered the use of multinucleon transfer reactions in low-energy collisions of heavy ions for the production of new heavy isotopes along the closed shell at 126 neutrons, which is important in the *r*-process of nucleosynthesis. They predicted that more than 50 new nuclei might be produced in collisions of ^{136}Xe projectiles with ^{208}Pb targets with cross sections of at least a microbarn and although SHEs would not be reached the information gained might be of some value in planning future SHE experiments and would add to the general information on reaction mechanisms.

Pei et al. (2009) investigated isentropic fission barriers using self-consistent nuclear density functional theory and the relationship between isothermal and isentropic descriptions. They found that the dependence of isentropic fission barriers on excitation energy changes rapidly and that shell effects are still important even for compound nuclei with large excitation energy. Fission barriers for nuclides produced in cold fusion reactions and those synthesized in hot fusion reactions are predicted to exhibit quite different behavior. For nuclei around $^{278}112$ produced in cold fusion reactions, they predict a more rapid decrease in the fission barriers with excitation energy compared to nuclei around $^{292}114$ produced in hot fusion reactions. Research to provide reliable theoretical estimates of compound nucleus survivability is in progress.

In a 2005 review article, Ćwiok, Heenan, and Nazarewicz (2005) present new theoretical results for properties of even–even heavy and SHE element nuclei with $94 \leq Z \leq 118$ and with $134 \leq N \leq 188$. They use self-consistent formalism and a modern nuclear energy density functional to formulate the following major conclusions concerning SHEs: (1) SHE nuclei around $Z = 116$ and $N = 176$ are expected to exhibit coexistence of oblate and prolate shapes,

in contrast to actinide and transfermium nuclei which have well-deformed elongated shapes; (2) Inclusion of triaxial shapes in the calculations dramatically reduces barriers between prolate and oblate shapes; (3) Gradual changes are expected along the triaxial energy surfaces although in special cases prolate and oblate shapes may be well separated. The heaviest isotopes recently reported by the Dubna–LLNL group are predicted to belong to a transition region that is subject to dramatic shape changes and/or triaxial softness. These shape effects are predicted to affect the alpha-decay energies, and half-lives may be lengthened due to hindrances in decay rates between parents and daughters with different shapes. Their predictions that the long-lived SHEs can exist in a variety of shapes and in some cases even in metastable states, and the formation of shape isomers will make positive identification of new species even more difficult than formerly anticipated.

21.8 Future

The 1970s predictions of exceedingly long half-lives for nuclei in the region around the spherical doubly magic superheavy nucleus $^{298}114$ have been drastically reduced. For example, calculations of Smolańczuk (1997) indicated that the spherical doubly magic superheavy nucleus $^{298}114$ would decay predominantly by alpha emission with a half-life of only about 12 min, but that $^{292}110$ might alpha-decay with a half-life of about 50 years. Theoretical calculations (Smolańczuk 2001; Chasman and Ahmad 1997) also indicated that nuclei with half-lives of microseconds or longer would exist all along the way to the predicted islands of stability. A 1978 contour plot with some of the nuclei reported in this “transition” region as of mid-2002 is shown in [Fig. 21.11](#).

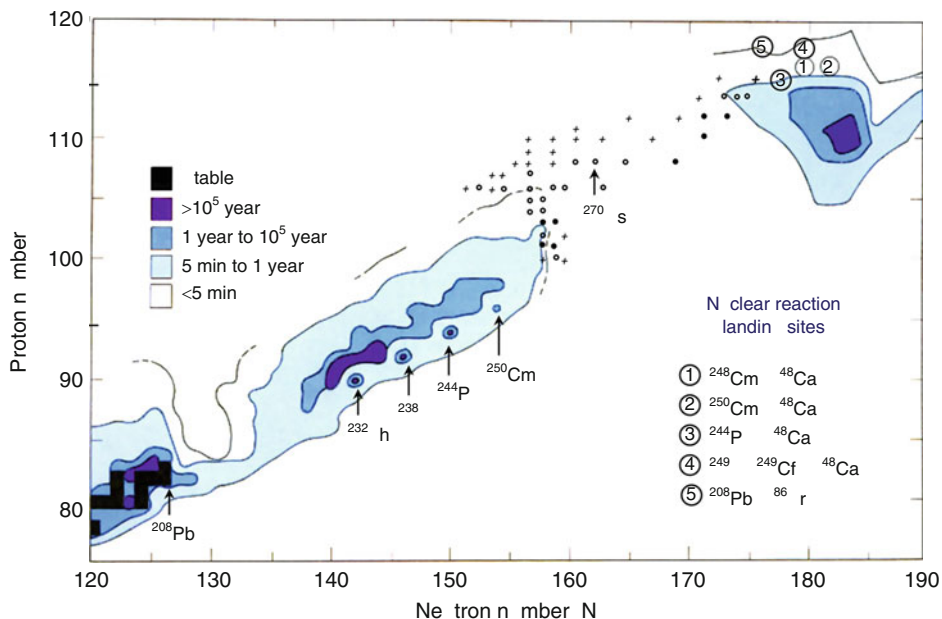
A large number of isotopes have been added to those shown as of mid-2002 for Sg (106) and beyond in [Fig. 21.9](#) of the authors’ previous SHE paper (Hoffman and Lee 2003). Many assignments have changed, some have been dropped entirely, and a host of others have been added and still await confirmation. [Figure 21.12](#) shows a similar representation of the isotopes *reported* (not necessarily confirmed) for Sg(106) through element 118 as of mid-2009 (Düllmann 2009).

Four isotopes each of elements 113 and 114, two of element 115, four of element 116, and one of element 118 have now been reported. It should be noted that none have yet been reported for element 117. Earlier calculations by Smolańczuk (1997) indicated that some of these nuclei would be expected to be nearly spherical with deformation energies ranging from only about 0.1 MeV for $^{292}116$ to 0.2–0.3 MeV for the 114 isotopes, compared to zero deformation energy for the spherical doubly magic $^{298}114$ and 7.8 MeV (Sobiczewski et al. 2001) for the doubly deformed magic nucleus, $^{270}108$. Thus, the nuclei in this region may qualify as spherical SHEs even though they do not have the full complement of 184 neutrons.

A Dubna–LLNL team (Oganessian et al. 2009) recently reported an unsuccessful attempt to synthesize element 120 at Dubna via the $^{244}\text{Pu}(^{58}\text{Fe},\text{xn})^{302-x}120$ reaction. The sensitivity of the experiment corresponded to a cross section of ~ 0.4 pb for the detection of one decay. The production cross section of the evaporation residues in this reaction appeared to be lower by more than an order of magnitude compared to that of the same target with ^{48}Ca . They considered various explanations for this and concluded that additional attempts to synthesize element 120 in this reaction would require much increased sensitivity and proposed

■ Fig. 21.11

Plot of heavy element topology from 1978 showing some landing points for proposed reactions. New heavy element isotopes reported as of mid-2002 are indicated with symbols denoting the following half-life ranges: + = 0.1 ms to 0.1 s; o = 0.1 s to 5 min; • = >5 min



that a more mass-asymmetric reaction, e.g., $^{248}\text{Cm} + ^{54}\text{Cr}$ or $^{249}\text{Cf} + ^{50}\text{Ti}$ might be more favorable.

Subsequent to the authors' mid-2002 review (Hoffman and Lee 2003), some 30 new heavy element isotopes have been reported. However, the longest lifetimes (not yet confirmed) reported to date by the Dubna–LLNL team for elements Rg through element 118 are: ^{280}Rg , 3.6 s; $^{285}\text{112}$, 29 s; $^{284}\text{113}$, 0.5 s; $^{289}\text{114}$, 2.6 s; $^{288}\text{115}$, 0.087 s; $^{293}\text{116}$, 0.05 s; 117, not yet reported; $^{294}\text{118}$, 0.09 ms. All of these decay via emission of an alpha particle. None are confirmed as yet, and none decay to any currently known isotopes, although some of the results for production of element 114 have been duplicated by other groups. Making it still more difficult is that using currently known reactions, accelerators, and detection techniques only an atom every few days may be produced! The half-lives quoted above for Rg, 112, 114, and possibly 113 are long enough for chemical studies provided techniques can be developed to deal with or enhance the low production rates. On the positive side, it has already been demonstrated that it is possible to perform studies of chemical properties at the picobarn level for nuclides with half-lives of seconds. Perhaps some of the predicted longer-lived metastable states and shape isomers of SHEs can be produced with large enough production rates to permit identification and characterization of their nuclear decay properties. It has also been proposed (Armbruster 2008) that the magic proton shell should be shifted from $Z = 114$ to $Z = 122$, which would present an additional challenge for experimentalists to try to produce still more proton rich nuclei.

Fig. 21.12

Chart of the Isotopes for Sg (106) through element 118 reported as of mid-2009 adapted from compilation of C. E. Düllmann, mid-2009 (Düllmann 2009)

[illegible]

Although it now is predicted that many additional, relatively long-lived SHE species can exist, new production reactions, imaginative techniques for optimizing overall yields, and methods for “stockpiling” long-lived products for off-line studies must be devised if these exciting new phenomena are to be fully explored.

References

- Anders EH, Higuchi H, Gros J, Takahashi H, Morgan JW (1975) *Science* 190:1251
- Armbruster P, Agarwal YK, Bröchle W, Brügger M, Dufour JP, Gäggeler H, Hessberger FP, Hofmann S, Lemmert P, Münzenberg G, Poppensieker K, Reisdorf W, Schädel M, Schmidt KH, Schneider JHR, Schneider WFW, Sümmerer K, Vermeulen D, Wirth G, Ghiorso A, Gregorich KE, Lee D, Leino M, Moody KJ, Seaborg GT, Welch RB, Wilmarth P, Yashita S, Frink C, Greulich N, Herrmann G, Hickmann U, Hildebrand N, Kratz JV, Trautmann N, Fowler MM, Hoffman DC, Daniels WR, von Gunten HR, Dornhöfer H (1985) *Phys Rev Lett* 54:406
- Armbruster P, Münzenberg G (1989) *Sci Am* 66:66
- Armbruster P (2008) *Eur Phys J A* 37:159
- Batty CJ, Kilvington AI, Weil JL, Newton GWA, Skarestad M, Hemingway JD (1973) *Nature* 244:429
- Bimbot R, Deprun C, Gardes D, Gauvin H, Le Beyec Y, Lefort M, Peter J, Tamaï B (1971) *Nature* 234:215
- Bowman HR et al (1968) Lawrence Berkeley Laboratory Report, UCRL-17989, 147
- Chasman RR, Ahmad I (1997) *Physics Letters B* 392:255
- Cheifitz E, Jared R, Giusti ER, Thompson SG (1972) *Phys Rev C* 6:1348
- CNIC, Inorganic Chemistry Division Commission on Nomenclature of Inorganic Chemistry (1997) *Pure Appl Chem* 69:2471
- Cowan GA (1978) Superheavy elements. In: *Proceedings of the international symposium on superheavy elements*, Lubbock, Texas, Pergamon Press, New York, 9–11 March 1978, pp 89–101
- Ćwiok Z, Heenan P-H, Nazarewicz W (2005) *Nature* 433:705
- Dmitriev SN, YuTs O, Utyonkov VK, Shishkin SV, Yeremin AV, Lobanov YuV, Tsyganov YuS, Chepygin VI, Sokol EA, Vostokin GK, Aksenov NV, Hussonnois M, Itkis MG, Gäggeler HW, Schumann D, Bruchertseifer H, Eichler R, Shaughnessy DA, Wilk PA, Kenneally JM, Stoyer MA, Wild JF (2005) *Mendeleev Commun* 1:1
- Düllmann ChE, Türlér A (2008) *Phys Rev C* 77:064320
- Dvorak J, Bröchle W, Chelnokov M, Dressler R, Düllmann ChE, Eberhardt K, Gorshkov V, Jäger E, Krücken R, Kuznetsov A, Nagame Y, Nebel F, Novackova Z, Qin Z, Schädel M, Schausten B, Schimpf E, Semchenkov A, Thörle P, Türlér A, Wegrzecki M, Wierczinski B, Yakushev A, Yeremin A (2006) *Phys Rev Lett* 97:242501
- Dvorak J, Bröchle W, Chelnokov M, Düllmann ChE, Dvorakova Z, Eberhardt K, Jäger E, Krücken R, Kuznetsov A, Nagame Y, Nebel F, Nishio K, Perego R, Qin Z, Schädel M, Schausten B, Schimpf E, Schuber R, Semchenkov A, Thörle P, Türlér A, Wegrzecki M, Wierczinski B, Yakushev A, Yeremin A (2008) *Phys Rev Lett* 100:132503
- Düllmann ChE (2009) Adapted from private communication as of mid-2009
- Eichler R, Aksenov NV, Belozero AV, Bozhikov GA, Chepigin VI, Dressler R, Dmitriev SN, Gäggeler HW, Gorshkov VA, Haenssler F, Itkis MG, Lebedev VYA, Laube A, Malyshev ON, Oganessian YuTs, Petruschkin OV, Piguet D, Rasmussen P, Shishkin SV, Shutov AV, Svirikhin AI, Tereshatov EE, Vostokin GK, Wegrzecki M, Yeremin AV (2007a) *Nucl Phys A* 787:373c
- Eichler R, Aksenov NV, Belozero AV, Bozhikov GA, Chepigin VI, Dmitriev SN, Dressler R, Gäggeler HW, Gorshkov VA, Haenssler F, Itkis MG, Laube A, Lebedev VYA, Malyshev ON, Oganessian YuTs, Petruschkin OV, Piguet D, Rasmussen P, Shishkin SV, Shutov AV, Svirikhin AI, Tereshatov EE, Vostokin GK, Wegrzecki M, Yeremin AV (2007b) *Nature* 447:72
- Feige G, Molzahn D, Brandt R, Hoffman DC, Knight SJ, Gancarz A, Knobeloch GW, Lawrence FO (1987) *Radiochim Acta* 41:55
- Fiset EO, Nix JR (1972) *Nucl Phys A* 193:647
- Flerov GN, Perelygin VP (1969) *Sov J At Energy* 36:603
- Flerov GN, Oganessian YT (1972) Joint Institute for Nuclear Research Report, E7-6838
- Flerov GN (1977) Joint Institute for Nuclear Research Report, Superheavy elements, P7-11097
- Flerov GN, Korotkin YS, Ter-Akopyan GM, Zvara I, Oganessian YT, Popeko AG, Chuburkov YT, Chelnokov LP, Maslov OP, Smirnov VI, Gerstenberger R (1979) *Physik A* 292:43
- Fox JD, Courtney WJ, Kemper KW, Lumpkin AH, Fletcher NR, Medsker LR (1976) *Phys Rev Lett* 37:629
- Gentry RV, Cahill TA, Fletcher NR, Kaufmann HC, Medsker LR, Nelson JW, Flocchini RG (1976) *Phys Rev Lett* 37:11

- Ghiorso A, Thompson SG, Higgins GH, Seaborg GT, Studier MH, Fields PR, Fried SM, Diamond H, Mech JF, Pyle GL, Browne CI, Smith HL, Spence RW (1955) *Phys Rev* 99:1048
- Ghiorso A, Lee D, Somerville LP, Loveland W, Nitschke JM, Ghiorso W, Seaborg GT, Wilmarth P, Leres R, Wydler A, Nurmia M, Gregorich K, Czerwinski K, Gaylord R, Hamilton T, Hannink NJ, Hoffman DC, Jarzynski C, Kacher C, Kadkhodayan B, Kreek S, Lane M, Lyon A, McMahan MA, Neu M, Sikkeland T, Swiatecki WJ, Türlér A, Walton JT, Yashita S (1995a) *Nucl Phys* 583:861
- Ghiorso A, Lee D, Somerville LP, Loveland W, Nitschke JM, Ghiorso W, Seaborg GT, Wilmarth P, Leres R, Wydler A, Nurmia M, Gregorich K, Czerwinski K, Gaylord R, Hamilton T, Hannink NJ, Hoffman DC, Jarzynski C, Kacher C, Kadkhodayan B, Kreek S, Lane M, Lyon A, McMahan MA, Neu M, Sikkeland T, Swiatecki WJ, Türlér A, Walton JT, Yashita S (1995b) *Phys Rev C* 51:R2293
- Gregorich KE, Ginter TN, Loveland W, Peterson D, Patin JB, Folden CM III, Hoffman DC, Lee DM, Nitsche H, Omtvedt JP, Omtvedt LA, Stavsetra L, Sudowe R, Wilk PA, Zielinski PM, Aleklett K (2003) *Eur Phys J A* 18:633
- Halperin J, Stoughton RW, Kettele BH, Lund T, Brandt R (1981) *Z Phys A* 300:281
- Herrmann G (1974) *Phys Scr* 10A:71
- Herrmann G (1981) *Pure Appl Chem* 53:949
- Hoff R (1978) In: *Proceedings of symposium commemorating the 25th anniversary of elements 99 and 100*, LBL-7701, UC-34C, pp 39–49
- Hoffman DC (1978) Superheavy elements. In: *Proceedings of the international symposium on superheavy elements*, Lubbock, Texas, Pergamon Press, New York, 9–11 March 1978, pp 89–101
- Hoffman DC, Ford GP, Balagna JP, Veaser LR (1980) *Phys Rev C* 21:637
- Hoffman DC (1998) The transuranium elements: from neptunium and plutonium to element 112. In: *Sterne PA, Gonis A, Borovoi AA (eds) Actinides and the environment*. Kluwer Academic, Norwell, pp 3–22
- Hoffman DC, Ghiorso A, Seaborg GT (2000) *The transuranium people: the inside story*. Imperial College Press/World Scientific, London/Singapore, pp 400–433
- Hoffman DC, Lee DM (2003) Chapter 10: Superheavy elements. In: *Vertes A, Klencsar Z (eds) Handbook of nuclear chemistry*. Kluwer Academic, Norwell, pp 397–416
- Hoffman DC, Lee DM, Pershina V (2006) Chapter 14: Transactinide elements and future elements. In: *Morss L, Edelstein N, Fuger J (eds) The chemistry of the actinide and transactinide elements*. Springer, Dordrecht, pp 1652–1752
- Hofmann S, Ninov V, Hessberger FP, Armbruster P, Folger H, Münzenberg G, Schott HJ, Popeko AG, Yeremin AV, Andreyev AN, Saro S, Janik R, Leino M (1995a) *Z Phys A* 350:277
- Hofmann S, Ninov V, Hessberger FP, Armbruster P, Folger H, Münzenberg G, Schott HJ, Popeko AG, Yeremin AV, Andreyev AN, Saro S, Janik R, Leino M (1995b) *Z Phys A* 350:281
- Hofmann S, Ninov V, Hessberger FP, Armbruster P, Folger H, Münzenberg G, Schott HJ, Popeko AG, Yeremin AV, Saro S, Janik R, Leino M (1996) *Z Phys A* 354:229
- Hofmann S, Hessberger FP, Ackermann D, Münzenberg G, Antalic S, Cagarda P, Kindler B, Kojouharova J, Leino M, Lommel B, Mann R, Popeko AG, Reshitko S, Saro S, Uusitalo J, Yeremin AV (2002) *Eur Phys J A* 14:147
- Hofmann S, Ackermann D, Antalic S, Burkhard HG, Comas VF, Dressler R, Gan Z, Heinz S, Heredia JA, Hessberger FP, Khuyagbaatar J, Kindler B, Kojouharov I, Kuusiniemi P, Leino M, Lommel B, Mann R, Münzenberg G, Nishio K, Popeko AG, Saro S, Schott HJ, Streicher B, Sulignano B, Uusitalo J, Venhart M, Yeremin AV (2007) *Eur Phys J A* 32:251
- Hulet EK, Loughheed RW, Wild JF, Landrum JH, Stevenson PC, Ghiorso A, Nitschke M, Otto RJ, Morrissey DJ, Baisden PA, Gavin BF, Lee D, Silva RJ, Fowler MM, Seaborg GT (1977) *Phys Rev Lett* 39:385
- Illige JD, Hulet EK, Nitschke JM, Dougan RJ, Loughheed RW, Ghiorso A, Landrum JH (1978) *Phys Lett* 78B:209
- Kratz JV, Brüchle W, Folger H, Gäggeler H, Schädel M, Sümmerer K, Wirth G, Greulich N, Herrmann G, Hickmann U, Peuser P, Trautmann N, Hulet EK, Loughheed RW, Nitschke JM, Fergerson RL, Hahn RL (1986) *Phys Rev C* 33:504
- Lazarev YA, Lobanov YV, Oganessian YT, Utyonko VK, Abdulin FS, Polyakov AN, Rigol J, Shirokovsky IV, Tsyganov YS, Iliev S, Subbotin VG, Sukhov AM, Buklanov GV, Gikal N, Kutner VB, Mezentssev AN, Subotic K, Wild JF, Loughheed RW, Moody KJ (1996) *Phys Rev C* 54:620
- Lodhi MAK (ed) (1978) *Superheavy elements*. In: *Proceedings of the international symposium on superheavy elements*, Lubbock, Texas, 9–11 March 1978
- Marinov A, Batty CJ, Kilvington AI, Newton GWA, Borinson VJ, Hemingway JD (1971a) *Nature* 229:464
- Marinov A, Batty CJ, Kilvington AI, Weil JL, Friedman AM, Newton GWA, Robinson VJJ, Hemingway D, Mather DS (1971b) *Nature* 234:212
- Meldner H (1967) *Arkiv Fysik* 36:593
- Morita K, Morimoto K, Kaji D, Haba H, Ideguchi E, Peter JC, Kanungo R, Katori K, Koura H, Kudo H, Ohnishi T, Ozawa A, Suda T, Sueki K, Tanihata I,

- Xu H, Yeremin AV, Yoneda A, Yoshida A, Zhao Y-L, Zheng T, Goto S, Tokanai F (2004a) *J Phys Soc Jpn* 73:1738
- Morita K, Morimoto K, Kaji D, Akiyama T, Goto S, Haba H, Ideguchi E, Kanungo R, Katori K, Koura H, Kudo H, Ohnishi T, Ozawa A, Suda T, Sueki K, Xu H, Yamaguchi T, Yoneda A, Yoshida A, Zhao Y-L (2004b) *J Phys Soc Jpn* 73:2593
- Morita K, Morimoto K, Kaji D, Akiyama T, Goto S, Haba H, Ideguchi E, Koura H, Kujdo H, Ohnishi T, Ozawa A, Suda T, Sujeki K, Xu H, Yamaguchi T, Yoneda A, Yoshida A, Zhao Y-L (2005) *RIKEN Accel Prog Rep* 38:69
- Morita K, Morimoto K, Kaji D, Akiyama T, Goto S, Haba H, Ideguchi E, Katori K, Koura H, Kudo H, Ohnishi T, Ozawa A, Suda T, Sueki K, Tokanai F, Yamaguchi T, Yoneda A, Yoshida A (2007a) *J Phys Soc Jpn* 76:043201
- Morita K, Morimoto K, Kaji D, Akiyama T, Goto S, Haba H, Ideguchi E, Katori K, Koura H, Kikunaga H, Kudo H, Ohnishi T, Ozawa A, Sato N, Suda T, Sueki K, Tokanai F, Yamaguchi T, Yoneda A, Yoshida A (2007b) *J Phys Soc Jpn* 76:045001
- Münzenberg G, Hofmann S, Hessberger FP, Reisdorf W, Schmidt KH, Schneider JHR, Armbruster P, Sahm C-C, Thuma B (1981) *Z Phys A* 300:107
- Münzenberg G, Armbruster P, Hessberger FP, Hofmann S, Poppensieker K, Reisdorf W, Schneider JHR, Schneider WRW, Schmidt KH, Sahm CC, Vermeulen D (1982a) *Z Phys A* 309:89
- Münzenberg G, Armbruster P, Hessberger FP, Hofmann S, Poppensieker K, Reisdorf W, Schneider JHR, Schneider WRW, Schmidt KH, Sahm CC, Vermeulen D (1982b) *Z Phys A* 315:145
- Myers WD, Swiatecki WJ (1966) *Nucl Phys* 81:1
- Nilsson SG, Tsang CF, Sobiczewski A, Szymanski Z, Wycech S, Gustafsson G, Lam IL, Möller P, Nilsson B (1969a) *Nucl Phys A* 131:1
- Nilsson SG, Thompson SG, Tsang CF (1969b) *Phys Lett* 28B:458
- Ninov V, Gregorich KE, Loveland W, Ghiorso A, Hoffman DC, Lee DM, Nitsche H, Swiatecki WJ, Kirbach UW, Laue CA, Adams JL, Patin JB, Shaughnessy DA, Strellis DA, Wilk PA (1999) *Phys Rev Lett* 83:1104
- Nix JR (1969) *Phys Lett* 30B:1
- Oganessian YuTs, Iljinov AAS, Demin AG, Tretyakova SP (1975) *Nucl Phys A* 239:353
- Oganessian YT, Bruchertseifer H, Buklanov GV, Cherpigin VI, Choy VS, Eichler B, Gavrilov KA, Gäggeler H, Korotkin GS, Orlova OA, Reetz T, Seidel W, Ter-Akopyan GM, Tretyakova SP, Zvara I (1978) *Nucl Phys A* 294:213
- Oganessian YuTs, Yeremin AV, Gulbekian GG, Bogomolov SL, Cherpigin VI, Gikal BN, Gorshkov VA, Itkis MG, Kabachenko AP, Kutner VB, Lavrentev AY, Malyshev ON, Popeko AG, Rohác J, Sagaidak RN, Hofmann S, Münzenberg G, Veselsky M, Saro S, Iwasa N, Morita K (1999a) *Eur Phys J A* 5:63
- Oganessian YuTs, Yeremin AV, Popeko AG, Bogomolov SL, Buklanov GV, Chelnokov ML, Cherpigin VI, Gikal BN, Gorshkov VA, Gulbekian GG, Itkis MG, Kabachenko AP, Lavrentev AY, Malyshev ON, Rohac J, Sagaidak RN, Hofmann S, Saro S, Giardinias G, Morita K (1999b) *Nature* 400:242
- Oganessian YuTs, Utyonkov VK, Lobanov YV, Abdullin FS, Polyakov AN, Shirokovsky IV, Tsyganov YS, Gulbekian GG, Bogomolov SL, Gikal BN, Mezentssev AN, Iliev S, Subbotin VG, Sukhov AM, Buklanov GV, Subotic K, Itkis MG, Moody KJ, Wild JF, Stoyer NJ, Stoyer MA, Loughheed RW (1999c) *Phys Rev Lett* 83:3154
- Oganessian YuTs, Utyonkov VK, Lobanov YuV, Abdullin FSh, Polyakov AN, Shirokovsky IV, Tsyganov YuS, Gulbekian GG, Bogomolov SL, Gikal BN, Mezentssev AN, Iliev S, Subbotin VG, Sukhov AM, Ivanov OV, Buklanov GV, Subotic K, Itkis MG, Moody KJ, Wild JF, Stoyer NJ, Stoyer MA, Loughheed RW (2000a) *Phys Rev C* 62:041604 (R)
- Oganessian YuTs, Utyonkov VK, Lobanov YV, Abdullin FS, Polyakov AN, Shirokovsky IV, Tsyganov YS, Gulbekian GG, Bogomolov SL, Gikal BN, Mezentssev AN, Iliev S, Subbotin VG, Sukhov AM, Ivanov OV, Buklanov GV, Subotic K, Itkis MG, Moody KJ, Wild JF, Stoyer NJ, Stoyer MA, Loughheed RW, Laue CA, Karelin YA, Tatarinov AN (2000b) *Phys Rev C* 63:011301 (R)
- Oganessian YuTs (2001) *Nucl Phys A* 685:17c
- Oganessian YuTs, Utyonkov VK, Lobanov YV, Abdullin FSh, Polyakov AN, Shirokovsky IV, Tsyganov YuS, Gulbekian GG, Bogomolov SL, Gikal BN, Mezentssev AN, Iliev S, Subbotin VG, Sukhov AM, Voinov AA, Buklanov GV, Subotic K, Zagrebaev VI, Itkis MG, Patin JB, Moody KJ, Wild JF, Stoyer MA, Stoyer NJ, Shaughnessy DA, Kenneally JM, Loughheed RW (2004a) *Phys Rev C* 69:054607
- Oganessian YuTs, Utyonkov VK, Lobanov YV, Abdullin FSh, Polyakov AN, Shirokovsky IV, Tsyganov YuS, Gulbekian GG, Bogomolov SL, Gikal BN, Mezentssev AN, Iliev S, Subbotin VG, Sukhov AM, Voinov AA, Buklanov GV, Subotic K, Zagrebaev VI, Itkis MG, Patin JB, Moody KJ, Wild JF, Stoyer MA, Stoyer NJ, Shaughnessy DA, Kenneally JM, Loughheed RW, Il'kaev RI, Vesnovskii SP (2004b) *Phys Rev C* 70:064609
- Oganessian YuTs, Utyonkov VK, Lobanov YuV, Abdullin FSh, Polyakov AN, Shirokovsky IV, Tsyganov YuS, Gulbekian GG, Bogomolov SL, Mezentssev AN, Iliev S, Subbotin VG, Sukhov AM, Voinov AA, Buklanov GV, Subotic K, Zagrebaev VI, Itkis MG, Patin JB, Moody KJ, Wild JF, Stoyer MA, Stoyer NJ, Shaughnessy DA, Kenneally JM, Loughheed RW (2004c) *Phys Rev C* 69:021601

- Oganessian YuTs, Utyonkov VK, Dmitriev SN, Lobanov YuV, Itkis MG, Polyakov AN, Tsyganov YuS, Mezentsev AN, Yeremin AV, Voinov AA, Sokol EA, Gulbekian GG, Bogomolov SL, Iliev S, Subbotin VG, Sukhov AM, Buklanov GV, Shishkin SV, Chepygin VI, Vostokin GK, Aksenov NV, Hussonnois M, Subotic K, Zagrebaev VI, Moody KJ, Patin JB, Wild JF, Stoyer MA, Stoyer NJ, Shaughnessy DA, Kenneally JM, Wilk PA, Loughheed RW, Gäggeler HW, Schumann D, Bruchertseifer H, Eichler R (2005) *Phys Rev C* 72:034611
- Oganessian YuTs, Utyonkov VK, Lobanov YuV, Abdullin FSh, Polyakov AN, Sagaidak RN, Shirokovsky IV, Tsyganov YuS, Voinov AA, Gulbekian GG, Bogomolov SL, Gikal BN, Mezentsev AN, Iliev S, Subbotin VG, Sukhov AM, Subotic K, Zagrebaev VI, Vostokin GK, Itkis MG, Moody KJ, Patin JB, Shaughnessy DA, Stoyer MA, Stoyer NJ, Wilk PA, Kenneally JM, Landrum JH, Wild JF, Loughheed RW (2006) *Phys Rev C* 74:044602
- Oganessian YuTs, Utyonkov VK, Lobanov YuV, Abdullin FSh, Polyakov AN, Sagaidak RN, Shirokovsky IV, Tsyganov YuS, Voinov AA, Gulbekian GG, Bogomolov SL, Gikal BN, Mezentsev AN, Subbotin VG, Sukhov AM, Subotic K, Zagrebaev VI, Vostokin GK, Itkis MG, Henderson RA, Kenneally JM, Landrum JH, Moody KJ, Shaughnessy DA, Stoyer MA, Stoyer NJ, Wilk PA (2007) *Phys Rev C* 76:011601
- Oganessian YuTs (2007) *J Phys G Nucl Part Phys* 34:R165
- Oganessian YuTs, Utyonkov VK, Lobanov YuV, Abdullin FSh, Polyakov AN, Sagaidak RN, Shirokovsky IV, Tsyganov YuS, Voinov AA, Mezentsev AN, Subbotin VG, Sukhov AM, Subotic K, Zagrebaev VI, Dmitriev SN, Henderson RA, Moody KJ, Kenneally JM, Landrum JH, Shaughnessy DA, Stoyer MA, Stoyer NJ, Wilk PA (2009) *Phys Rev C* 79:024603
- Otto RJ, Morrissey DJ, Lee D, Ghiorso A, Nitschke JM, Seaborg GT, Fowler MM, Silva RJ (1978) *J Inorg Nucl Chem* 40:589
- Pei JC, Nazarewicz W, Sheikh JA, Kerman AK (2009) *Phys Rev Lett* 102:192501
- Price PB, Fleischer RL, Woods RT (1970) *Phys Rev C* 1:1819
- Randrup J, Larsson SE, Möller P, Sobiczewski A, Kukasiak A (1974) *Phys Scr* 10A:60
- Scharff-Goldhaber G (1957) *Nucleonics* 15:122
- Seaborg GT (1968) *Annu Rev Nucl Sci* 18:53
- Schumann D, Bruchertseifer H, Eichler R, Eichler B, Gäggeler HW, Dmitriev SN, Oganessian YuTs, Utyonkov VP, Shishkin SV, Yeremin AV, Lobanov YuV, Tsyganov YuS, Chepygin VI, Sokol EA, Vostokin GK, Aksenov NV, Hussonnois M, Itkis MG (2005) *Radiochim Acta* 93:727
- Smolańczuk R, Skalski J, Sobiczewski A (1995) *Phys Rev C* 52:1871
- Smolańczuk R (1997) *Phys Rev C* 56:812
- Smolańczuk R (1999a) *Phys Rev C* 59:2634
- Smolańczuk R (1999b) *Phys Rev C* 60:021301
- Smolańczuk R (2001) *Phys Lett B* 509:227
- Sobiczewski A (1997) In: *Proceeding of the Robert A. Welch foundation 41st conference on chemical research: the transactinide elements*, Welch Foundation, Houston, 27–28 October 1997, chapter 13, pp 369–384
- Sobiczewski A, Muntian I, Patyk Z (2001) *Phys Rev C* 63:034306
- Stavsetra L, Gregorich KE, Dvorak J, Ellison PA, Dragojević I, Garcia MA, Nitsche H (2009) *Phys Rev Lett* 103:132502
- Stoyer NJ, Landrum JH, Wilk PA, Moody KJ, Kenneally JM, Shaughnessy DA, Stoyer MA, Wild JF, Loughheed RW, Dmitriev SN, Oganessian YuTs, Shishkin SV, Aksenov NV, Tereshatov EE, Bozhikov GA, Vostokin GA, Utyonkov VK, Yeremin AA (2007) *Nucl Phys A* 787:388c
- Strutinsky VM (1966) *Sov J Nucl Phys* 3:614
- Tatsumi K, Corish J (2010) *Pure Appl Chem* 82(No. 3):753
- Thompson SG (1968) *Bull Am Phys Soc* 13:1442
- Türler A, Dressler R, Eichler B, Gäggeler HW, Jost DT, Schaedel M, Bruchle W, Gregorich KE, Trautmann N, Taut S (1998) *Phys Rev C* 57:1648
- Wheeler JA (1955) *Nuclear fission and nuclear stability*. In: *Niels Bohr and the development of physics*. Pergamon Press, London
- Wheeler JA (1956) In: *Proceedings of the international conference on peaceful uses of atomic energy*, vol 2. IAEA, Vienna, p 155
- Wilk PA, Gregorich KE, Türler A, Laue CA, Eichler R, Ninov V, Adams JL, Kirbach UW, Lane MR, Lee DM, Patin JB, Shaughnessy DA, Strellis DA, Nitsche H, Hoffman DC (2000) *Phys Rev Lett* 85:2697
- Wilk PA, Landrum JH, Shaughnessy DA, Kenneally JM, Stoyer NJ, Stoyer MA, Moody KJ, Aksenov NV, Bozhikov GA, Tereshatov EE, Vostokin GK, Shishkin SV, Dmitriev SN (2008) *J Radioanal Nucl Ch* 275:651657
- Zagrebaev V, Greiner W (2008) *Phys Rev Lett* 101:122701



22 Appendix to Part II – Table of Nuclides

R. B. Firestone

Lawrence Berkeley National Laboratory, Berkeley, California, USA

22.1	<i>Introduction</i>	<i>1034</i>
22.2	<i>Editors' Notes</i>	<i>1034</i>

Abstract: This chapter presents the table of nuclides, i.e., experimental nuclear data concerning isotopes and isomers of the elements.

22.1 Introduction

The table of nuclides shown below is arranged by elements with the atomic number Z starting from 0 (neutron). It lists all isotopes and isomers with half-lives >1 ms for which some experimental data are available.

The data including nuclear spin and parity ($J\pi$) are taken from the Nuclear Wallet Cards (Tuli 2000) and from the Evaluated Nuclear Structure Data File (ENSDF 2002).

Q -values (decay energies for different decay modes) for beta minus ($Q\beta^-$), electron capture ($Q\epsilon$), alpha ($Q\alpha$), and proton decay (Qp) are from Audi and Wapstra (1995). Systematic values are shown in square brackets.

Representative IUPAC isotopic compositions (abundances) of the elements (Rosman and Taylor 1997) are shown in curly brackets. Principal gamma rays and alpha particles for radioactive decay from ENSDF are given. Up to four gamma rays and two alpha particles with intensity greater than 10% of the most intense transition are shown.

Apart from the symbols printed in bold face above (and some trivial cases), the following abbreviations are used in [Table 22.1](#):

- **BR**: percent branching ratio
- β^- (β^-), ϵ (electron capture and/or β^+), **IT** (isomeric transition), and **SF** (spontaneous fission)
- β^- or ϵ delayed n, p, or α emission (β^-n , ϵn , $\epsilon\alpha$, etc.)

22.2 Editors' Notes

A *nuclide* is an atomic species as determined by its atomic number (proton number) Z and mass number (nucleon number) $A = Z + N$, where N is the number of neutrons in its nucleus. Atomic species with the same nuclear composition but different nuclear energy states with measurable lifetime are considered independent nuclides “in their own right.” Nuclides can be classified in different ways. Nuclides having the same atomic number Z (but different mass number A) represent the same chemical element and are called the *isotopes* of that element. Nuclides with the same mass number A (but different atomic number Z) are called *isobars*. Nuclides of the same number of neutrons N (but different atomic number Z) are called *isotones*. Nuclides of the same nuclear composition but different nuclear states are referred to as (nuclear) *isomers*. The terms *isotope*, *isotopic*, *isobar*, *isobaric*, *isotone*, *isotonic*, *isomer*, and *isomeric* can also be applied to *nuclei*, but the terms *nuclide* and *nuclidic* can only be applied to *atoms*.

Table 22.1
Table of Nuclides

	A	Element	Half-life or width	J π	Qmode(%BR){%Abund}	Principal gammas, alphas
0		Neutron				
	1	n	10.23(1) m	1/2+	Q β^- = 782.353(100%)	
1		Hydrogen				
	1	H	Stable	1/2+	{99.9885(70)%}	
	2	H	Stable	1+	{0.0115(70)%}	
	3	H	12.32(2) years	1/2+	Q β^- = 18.591(100%)	
	4	H	4.6(9) MeV	2-	n(100%)	
	5	H	5.7(21) MeV		n(100%)	
	6	H	1.6(4) MeV	(2-)	n(100%)	
2		Helium				
	3	He	Stable	1/2+	{0.000137(3)%}	
	4	He	Stable	0+	{99.999863(3)%}	
	5	He	0.60(2) MeV	3/2-	Q α = 890(100%)	
					n(100%)	
	6	He	806.7(15) ms	0+	Q β^- = 3,507.8(100%)	
	7	He	150(20) keV	(3/2)-	n	
3	8	He	119.1(12) ms	0+	Q β^- = 10,652(100%)	γ 981
					β^- - n(16%)	
	9	He	65(37) keV	1/2+	n(100%)	
	10	He	0.30(20) MeV	0+	2n	
		Lithium				
	4	Li	6.03 MeV	2-	Qp = 3,100(100%)	
	5	Li	~1.5 MeV	3/2-	Q α = 1,970(100%)	
					Qp = 1,970(100%)	

Table 22.1 (Continued)

A	Element	Half-life or width	J^{π}	Qmode(%BR){%Abund}	Principal gammas, alphas
4	6 Li	Stable	1+	{7.59(4)%}	
	7 Li	Stable	3/2−	{92.41(4)%}	
	8 Li	839.9(9) ms	2+	Qβ− = 16,004.5(100%) β − α(100%)	
	8 Li(980.8)	8.2(3) fs	1+	IT(100%)	
	9 Li	178.3(4) ms	3/2−	Qβ− = 13,606.3(100%) β − n(50.8%)	
	10 Li	1.2(3) MeV	(1−,2−)	n	
	11 Li	8.59(14) ms	3/2−	Qβ− = 20,620(100%) β − nα(0.027%) β − n	
	12 Li	<10 ns		n	
	Beryllium				
	5 Be		(1/2+)	Qp = [5,000]	
	6 Be	92(6) keV	0+	2p(100%) α(100%)	
	7 Be	53.22(6) days	3/2−	Qε = 861.815(100%)	γ478
	8 Be	5.57(25) eV	0+	Qα = 91.84(100%)	
	9 Be	Stable	3/2−	{100%}	
	10 Be	1.51(6)E6 years	0+	Qβ− = 555.8(100%)	
	10 Be(3368)	125(12) fs	2+	IT(100%)	
	10 Be(6179)	0.8(3) ps	0+	IT(≈100%)	
	11 Be	13.81(8) s	1/2+	Qβ− = 11,506(100%) β − α(3.1%)	γ2124,4444,7283,5019

	12	Be	21.49(3) ms	0+	Qβ− = 11,708(100%)	
	13	Be	0.17(11) MeV	(1/2−)	β − n(<1%)	
	14	Be	4.35(17) ms	0+	n	
					Qβ− = 16,220(100%)	
5					β − n(81%)	
					β − 2n(5%)	
		Boron				
	7	B	1.4(2) MeV	(3/2−)	Qp = 2,200	
					α,p	
	8	B	770(3) ms	2+	Qε = 17,979.3(100%)	
					εα(100%)	
	9	B	0.54(21) keV	3/2−	Qp = 185.1(100%)	
					2α(100%)	
	10	B	Stable	3+	{19.9(7)%}	
	11	B	Stable	3/2−	{80.1(7)%}	
	12	B	20.20(2) ms	1+	Qβ− = 13,368.9(100%)	γ3215
					β − 3α(1.58%)	
	13	B	17.33(17) ms	3/2−	Qβ− = 13,437.2(100%)	γ3684
	14	B	12.5(5) ms	2−	Qβ− = 20,644(100%)	γ6092,6727
					β − n(6.04%)	
	15	B	9.93(7) ms		Qβ− = 19,094(100%)	
					β − n(93.6%)	
					β − 2n(0.4%)	
	16	B	<190 ps	0−	n	

Table 22.1 (Continued)

	A	Element	Half-life or width	J π	Qmode(%BR){%Abund}	Principal gammas, alphas
6	17	B	5.08(5) ms	(3/2-)	Q β^- = 22,680(100%) β^- - n(63%) β^- - 2n(11%) β^- - 3n(3.5%) β^- - 4n(0.4%)	
	18	B	<26 ns	(4-)	n	
	19	B	2.92(13) ms	(3/2-)	Q β^- = [26,500] β^- - n(72%) β^- - 2n(16%)	
		Carbon				
	8	C	230(50) keV	0+	Qp=-60 α	
	9	C	126.5(9) ms	(3/2-)	Q ε = 16,497.9(100%) ε p(23%) $\varepsilon\alpha$ (17%)	
	10	C	19.290(12) s	0+	Q ε = 3,647.81(100%)	γ 718
	11	C	20.334(24) m	3/2-	Q ε = 1,982.5(100%)	
	12	C	Stable	0+	{98.93(8)%}	
	13	C	Stable	1/2-	{1.07(8)%}	
	14	C	5,700(30) years	0+	Q β^- = 156.475(100%)	
	15	C	2.449(5) s	1/2+	Q β^- = 9,771.7(100%)	γ 5298
	16	C	0.747(8) s	0+	Q β^- = 8,011(100%) β^- - n(99%)	
	17	C	193(13) ms		Q β^- = 13,166(100%) β^- - n(32%)	γ 1374,1850,1907,619

	18	C	92(2) ms		0+	Q β^- = 11,810(100%) β^- – n(31.5%) β^- – n(61%) Q β^- = 16,970 Q β^- = 15,790(100%) β^- – n(72%) n	γ 115,2614,880,2499
	19	C	49(4) ms				
	20	C	14(+6–5) ms		0+		
	21	C	<30 ns		(1/2+)		
	22	C	6.1(+14–12) ms		0+	Q β^- = [20,500](100%) β^- – n(61%) β^- – 2n(<37%)	
7		Nitrogen					
	10	N				Qp = [3,500] p	
	11	N(320)	1.6(+8–5) MeV		1/2+		
	12	N	11.000(16) ms		1+	Q ϵ = 17,338.1(100%) Q ϵ = 2,220.4(100%) {99.632(7)%} {0.368(7)%}	γ 4439,3215
	13	N	9.965(4) m		1/2–		
	14	N	Stable		1+		
	15	N	Stable		1/2–		
	16	N	7.13(2) s		2–	Q β^- = 10,420(100%) β^- – α (0.0012%) Q β^- = 8,680(100%) β^- – n(95.1%)	γ 6129 γ 871,2184
	17	N	4.173(4) s		1/2–		
	18	N	624(12) ms		1–	Q β^- = 13,899(100%) β^- – n(14.3%) β^- – α (12.2%)	γ 1982,822,1652,2473
	19	N	271(8) ms			Q β^- = 12,527(100%) β^- – n(54.6%)	γ 96,3138,709

Table 22.1 (Continued)

A	Element	Half-life or width	J^{π}	Qmode(%BR){%Abund}	Principal gammas, alphas
20	N	130(7) ms		Q β^- = 17,970(100%) β^- - n(57%)	
21	N	85(7) ms	(1/2-)	Q β^- = 17,170(100%) β^- - n(81%)	
22	N	24(5) ms		Q β^- = 22,800(100%) β^- - n(36%) β^- - 2n(<13%)	
23	N	14.5(14) ms		Q β^- = [23,100](100%) β^- - n β^- - 2n n	
24	N	<52 ns			
8	Oxygen				
	O	0.40(25) MeV	0+	Qp = -200	
	O	8.58(5) ms	(3/2-)	Q ϵ = 17,765(100%) ϵ p(~100%)	
	O	70.606(18) s	0+	Q ϵ = 5,143.04(100%)	γ 2313
	O	122.24(16) s	1/2-	Q ϵ = 2,753.9(100%)	
	O	Stable	0+	{99.757(16)%}	
	O	Stable	5/2+	{0.038(1)%}	
	O	Stable	0+	{0.205(14)%}	
	O	26.88(5) s	5/2+	Q β^- = 4,821(100%)	γ 197,1357
	O	13.51(5) s	0+	Q β^- = 3,814.3(100%)	γ 1057
	O	3.42(10) s	(5/2+)	Q β^- = 8,109(100%)	γ 1730,3517,280,1787

9	22	O	2.25(9) s		0+	Qβ− = 6,490(100%) β − n(<22%)	γ637,72,1863,918
	23	O	82(37) ms			Qβ− = 11,290(100%) β − n(31%)	
	24	O	65(5) ms		0+	Qβ− = 11,400(100%) β − n(18%)	γ1832,522,1310
	25	O	<50 ns		(3/2+)	n	
	26	O	<40 ns		0+	n	
		Fluorine					
	14	F			(2−)	Qp = [3,200]	p
	15	F	1.0(2) MeV		(1/2+)	Qp = 1,480(100%) Qp = 536(100%) Qε = 2,760.7(100%) Qε = 1,655.5(100%) {100%}	
	16	F	40(20) keV		0−		
	17	F	64.49(16) s		5/2+		
	18	F	109.77(5) m		1+		
	19	F	Stable		1/2+		
	20	F	11.07(6) s		2+	Qβ− = 7,024.53(100%)	γ1634
	21	F	4.158(20) s		5/2+	Qβ− = 5,684.1(100%)	γ351,1395
	22	F	4.23(4) s		(4+)	Qβ− = 10,818(100%) β − n(<11%)	γ1275,2083,2166,4366
	23	F	2.23(14) s		5/2+	Qβ− = 8,480(100%)	γ1701,2129,1822,3432
	24	F	390(70) ms		(1,2,3)+	Qβ− = 13,490(100%) β − n(<5.9%)	γ1982
	25	F	50(6) ms		(5/2+)	Qβ− = 13,330(100%) β − n(14%)	γ1703,1613,575,2189 γ1982
	26	F	9.6(8) ms		1+	Qβ− = 17,860(100%) β − n(11%)	γ2018,1673

Table 22.1 (Continued)

A	Element	Half-life or width	$J\pi$	Qmode(%BR){%Abund}	Principal gammas, alphas
27	F	5.0(2) ms	(5/2+)	Q β^- = 18,000(100%) β^- – n(77%)	
28	F	<40 ns		n	
29	F	2.5(4) ms	(5/2+)	Q β^- = [22,300](100%) β^- – n(100%) β^- – 2n	
10	Neon				
16	Ne	122(37) keV	0+	Q β^- = –70(100%)	
17	Ne	109.2(6) ms	1/2–	Q ϵ = 14,530(100%) $\epsilon p(\sim 100\%)$ $\epsilon\alpha$	
18	Ne	1.672(8) ms	0+	Q ϵ = 4,433.4(100%)	γ 1042
19	Ne	17.22(2) s	1/2+	Q ϵ = 3,238.5(100%)	γ 110,1357,197
20	Ne	Stable	0+	{90.48(3)%}	
21	Ne	Stable	3/2+	{0.27(1)%}	
22	Ne	Stable	0+	{9.25(3)%}	
23	Ne	37.24(12) s	5/2+	Q β^- = 4,375.84(100%)	γ 440
24	Ne	3.38(2) m	0+	Q β^- = 2,470(100%)	γ 874
25	Ne	602(8) ms	(3/2)+	Q β^- = 7,300(100%)	γ 90,980
26	Ne	192(6) ms	0+	Q β^- = 7,330(100%) β^- – n(0.2%)	γ 234
27	Ne	32(2) ms	(3/2+)	Q β^- = 12,670(100%) β^- – n(2%)	

	28	Ne	18.9(4) ms	0+	Qβ− = 12,310(100%) β − n(11.9%) β − 2n(3.6%)a	γ2063,865
	29	Ne	14.8(3) ms	(3/2+)	Qβ− = 15,400(100%) β − n(28%) β − 2n(4%)	γ2918,1177,224
	30	Ne	7.3(3) ms	0+	Qβ− = 13,600(100%) β − n(13%) β − 2n(8.9%)	γ151
	31	Ne	3.4(8) ms		Qβ− = [18,200](100%) β − n	
	32	Ne	3.5(9) ms	0+	Qβ− = [18,900](100%) β − n	
11		Sodium				
	18	Na		(1 −)	Qp = [1,500] Qε = [20,000] Qp = 333	
	19	Na	<40 ns	(5/2+)	Qε = 13,887(100%) εα(20.05%)	γ1634
	20	Na	447.9(23) ms	2+	Qε = 3,547.5(100%) Qε = 2,842.2(100%) {100%}	γ351 γ1275
	21	Na	22.49(4) s	3/2+	Qβ− = 5,515.78(100%) IT(99.95%) β − (0.05%)	γ1369,2754 γ472
	22	Na	2.6027(10) years	3+		
	23	Na	Stable	3/2+		
	24	Na	14.997(12) h	4+		
	24	Na(472.2)	20.18(10) ms	1+		
	25	Na	59.1(6) s	5/2+	Qβ− = 3,835.3(100%) Qβ− = 9,312(100%)	γ975,585,390,1612 γ1809
	26	Na	1.077(5) s	3+		

Table 22.1 (Continued)

A	Element	Half-life or width	J^{π}	Qmode(%BR){%Abund}	Principal gammas, alphas
27	Na	301(6) ms	5/2+	Q β^- = 9,010(100%)	γ 985,1698
				β^- – n(0.13%)	γ 1809
28	Na	30.5(4) ms	1+	Q β^- = 13,990(100%)	γ 1473,2389
				β^- – n(0.58%)	
29	Na	44.9(12) ms	3/2+	Q β^- = 13,280(100%)	γ 55,2560,1638
				β^- – n(21.5%)	γ 1474
30	Na	48(2) ms	2+	Q β^- = 17,480(100%)	γ 1483,1978,985,4968
				β^- – n(30%)	γ 1040,336
				β^- – 2n(1.17%)	
				β^- – α (0.000055%)	
31	Na	17.0(4) ms	3/2(+)	Q β^- = 15,880(100%)	γ 51,2244,171,2022
				β^- – n(37%)	γ 1483,1978,1821,305
				β^- – 2n(0.9%)	γ 1039,1638
32	Na	13.2(4) ms	(3–,4–)	Q β^- = 19,100(100%)	γ 886,2152,1973,3935
				β^- – n(24%)	γ 171,240,221,895
				β^- – 2n(8%)	γ 1483
33	Na	8.0(3) ms	(3/2+)	Q β^- = 20,300(100%)	γ 547,1243,704,485
				β^- – n(47%)	γ 886,2551
				β^- – 2n(13%)	
34	Na	5.5(10) ms		Q β^- = [24,100](100%)	
				β^- – n(\approx 15%)	
				β^- – 2n	γ 886
35	Na	1.5(5) ms		Q β^- = [24,900](100%)	
				β^- – n	

12	Magnesium						
	20	Mg	90.8(24) ms	0+		Q ε = 10,730(100%)	
						$\varepsilon p(\sim 27\%)$	
	21	Mg	122(2) ms	5/2+		Q ε = 13,096(100%)	γ 332,1384
						$\varepsilon p(32.6\%)$	
						$\varepsilon \alpha(<0.5\%)$	
	22	Mg	3.8755(12) s	0+		Q ε = 4,785.3(100%)	γ 582,74
	23	Mg	11.317(11) s	3/2+		Q ε = 4,056.8(100%)	γ 440
	24	Mg	Stable	0+		{78.99(4)%}	
	25	Mg	Stable	5/2+		{10.00(1)%}	
	26	Mg	Stable	0+		{11.01(3)%}	
	27	Mg	9.458(12) m	1/2+		Q β^- = 2,610.33(100%)	γ 844,1014
	28	Mg	20.915(9) h	0+		Q β^- = 1,831.8(100%)	γ 31,1342,941,401
	29	Mg	1.30(12) s	3/2+		Q β^- = 7,550(100%)	γ 2224,1398,960,1754
	30	Mg	335(17) ms	0+		Q β^- = 6,990(100%)	γ 244,444
	31	Mg	232(15) ms	1/2(+)		Q β^- = 11,740(100%)	γ 1613,947,1626,666
						$\beta^- - n(1.7\%)$	
32	Mg	86(5) ms	0+			Q β^- = 10,270(100%)	γ 2765,736,2467
						$\beta^- - n(5.5\%)$	
33	Mg	90.5(16) ms	(3/2+)			Q β^- = 13,710(100%)	
						$\beta^- - n(17\%)$	
34	Mg	20(10) ms	0+			Q β^- = 11,300(100%)	
						$\beta^- - n$	
35	Mg	70(40) ms	(7/2-)			Q β^- = [16,400](100%)	
						$\beta^- - n(52\%)$	
36	Mg	3.9(13) ms	0+			Q β^- = [15,000]	
						$\beta^- - n$	

Table 22.1 (Continued)

A	Element	Half-life or width	J^{π}	Qmode(%BR){%Abund}	Principal gammas, alphas
13	37 Mg	>260 ns	(7/2-)	Q β^- = [19,500](100%)	
	38 Mg	>260 ns	0+	β^- - n	
				β^-	
	39 Mg	<180 ns		β^- - n	
	40 Mg	>170 ns	0+	n	
				β^-	
	Aluminum				
	21 Al	<35 ns	(5/2+)	Q ρ = [1,300]	
	22 Al	59(3) ms	(3)+	Q ϵ = [18,580](100%)	
				$\epsilon\rho$ (~60%)	
				$\epsilon 2\rho$ (0.9%)	
				$\epsilon\alpha$ (0.31%)	
	23 Al	0.47(3) s	5/2+	Q ϵ = 12,240(100%)	
				$\epsilon\rho$ (0.46%)	
	24 Al	2.053(4) s	4+	Q ϵ = 13,878(100%)	γ 1369,7070,2754,5393
				$\epsilon\alpha$ (0.04%)	
				$\epsilon\rho$ (0.0016%)	
	24 Al(425.8)	131.3(25) ms	1+	IT(82%)	γ 426
				ϵ (18%)	γ 1369,9966,8598
				$\epsilon\alpha$ (0.03%)	
	25 Al	7.183(12) s	5/2+	Q ϵ = 4,277.0(100%)	γ 1612
	26 Al	7.17(24)E5 years	5+	Q ϵ = 4,004.14(100%)	γ 1809
	26 Al(228.3)	6.3452(19) s	0+	ϵ (100%)	

27	Al	Stable	5/2+	{100%}		
28	Al	2.2414(12) m	3+	Qβ− = 4,642.24(100%)	γ1779	
29	Al	6.56(6) m	5/2+	Qβ− = 3,679.5(100%)	γ1273	
30	Al	3.60(6) s	3+	Qβ− = 8,561(100%)	γ2235,1263,3498	
31	Al	644(25) ms	(3/2,5/2)+	Qβ− = 7,995(100%)	γ2317,1695,752,1564	
32	Al	33.0(2) ms	1+	Qβ− = 13,020(100%)	γ1941,3042,4230,3844	
				β − n(0.7%)		
33	Al	41.7(2) ms	(5/2+)	Qβ− = 11,990(100%)		
				β − n(8.5%)		
34	Al	42(6) ms		Qβ− = 17,090(100%)	γ3328,930,125,4257	
				β − n(27%)		
35	Al	38.6(4) ms		Qβ− = 14,300(100%)		
				β − n(41%)		
36	Al	90(40) ms		Qβ− = 18,300(100%)		
				β − n(<31%)		
37	Al	10.7(13) ms		Qβ− = 16,100(100%)		
38	Al	7.6(6) ms		Qβ− = [19,500]		
				β − n		
39	Al	7.6(6) μs		Qβ− = [18,300]		
				β − n		
40	Al	>260 ns		β−		
				β − n		
41	Al	>260 ns		β−		
42	Al	>170 ns		β−		
				β − n		
43	Al	>170 ns		β−		
				β − n		

Table 22.1 (Continued)

14	A	Element	Half-life or width	$J\pi$	Qmode(%BR){%Abund}	Principal gammas, alphas
		Silicon				
	22	Si	29(2) ms	0+	Q ϵ = [13,980](100%) ϵ p(32%)	
	23	Si	42.3(4) ms	(5/2)+	Q ϵ = [17,010](100%) ϵ p(71%) ϵ 2p(3.6%)	
	24	Si	140(8) ms	0+	Q ϵ = 10,810(100%) ϵ p(38%)	
	25	Si	220(3) ms	5/2+	Q ϵ = 12,741(100%) ϵ p	
	26	Si	2.234(13) s	0+	Q ϵ = 5,066(100%)	γ 829,1622
	27	Si	4.16(2) s	5/2+	Q ϵ = 4,812.40(100%)	γ 1014
	28	Si	Stable	0+	{92.2297(7)%} {4.6832(5)%}	
	29	Si	Stable	1/2+	{3.0872(5)%}	
	30	Si	Stable	0+		
	31	Si	157.3(3) m	3/2+	Q β^- = 1,492.03(100%)	γ 1266
	32	Si	153(19) years	0+	Q β^- = 224.5(100%)	
	33	Si	6.11(21) s	(3/2+)	Q β^- = 5,845(100%)	γ 1848,1432
	34	Si	2.77(20) s	0+	Q β^- = 4,601(100%)	γ 1179,429,1608
	35	Si	0.78(12) s		Q β^- = 10,500(100%)	γ 4101,3860,2386,241
	36	Si	0.45(6) s	0+	Q β^- = 7,850(100%) β^- – n(<10%)	γ 250,175,878,425
	37	Si	90(60) ms	(7/2–)	Q β^- = 12,470(100%) β^- – n(17%)	

15	38	Si		> 1 μ s		0+	Q β^- = 10,700(100%)	
							β^- - n	
	39	Si		47.5(20) ms		(7/2-)	Q β^- = [14,800]	
							β^- - n	
	40	Si		33.0(10) ms		0+	Q β^- = [13,700]	
							β^- - n	
	41	Si		40.0(25) ms			Q β^- = [16,700]	
							β^- - n?	
	42	Si		12.5(35) ms		0+	Q β^- = [14,900]	
							β^- - n	
15	43	Si		> 60 ns			Q β^- =	
	44	Si		> 360 ns		0+	Q β^- = [
		Phosphorus						
	24	P				(1+)	Qp = [900]	
							Q ϵ = [21,200]	
	25	P		< 30 ns		(1/2+)	Qp = [830]	
	26	P		43.7(6) ms		(3+)	Q ϵ = [18,120](100%)	
							ϵ p	
	27	P		260(80) ms		1/2+	Q ϵ = 11,630(100%)	
							ϵ p(0.07%)	
15	28	P		270.3(5) ms		3+	Q ϵ = 14,332(100%)	γ 1779,4497
							ϵ p(0.0013%)	
							$\epsilon\alpha$ (0.00086%)	
	29	P		4.142(15) s		1/2+	Q ϵ = 4,943.1(100%)	γ 1273
	30	P		2.498(4) m		1+	Q ϵ = 4,232.3(100%)	γ 2235
	31	P		Stable		1/2+	{100%}	

Table 22.1 (Continued)

A	Element	Half-life or width	J^{π}	Qmode(% β R){%Abund}	Principal gammas, alphas
32	P	14.262(14) days	1+	Q β – = 1,710.66(100%)	
33	P	25.34(12) days	1/2+	Q β – = 248.5(100%)	
34	P	12.43(8) s	1+	Q β – = 5,374(100%)	γ 2127
35	P	47.3(7) s	1/2+	Q β – = 3,988.8(100%)	γ 1572
36	P	5.6(3) s	4–	Q β – = 10,413(100%)	γ 3291,902,1638,2540
37	P	2.31(13) s		Q β – = 7,900(100%)	γ 646,1583
38	P	0.64(14) s	(0–,4–)	Q β – = 12,390(100%) β – n(12%)	γ 1292,2224,3516,3698
39	P	0.28(4) s		Q β – = 10,510(100%) β – n(26%)	
40	P	125(25) ms	(2–,3–)	Q β – = 14,500(100%) β – n(15.8%)	γ 904,3235,3490,4106
41	P	100(15) ms	(1/2+)	Q β – = 13,800(100%) β – n(30%)	γ 1614
42	P	48.5(15) ms		Q β – = [17,300](100%) β – n(50%)	
43	P	36.5(15) ms	(1/2+)	Q β – = [15,600](100%) β – n(100%)	
44	P	18.5(25) ms		Q β – = [20,100] β – n	
45	P	> 200 ns		Q β – = [18,900]	
46	P	> 200 ns		Q β – = [22,600](100%)	

16	Sulfur									
26	S	~10 ms	0+					2p		
27	S	15.5(15) ms	(5/2+)					Q _ε = [18,260](100%)		
								ε2p(1.1%)		
								εp(2.3%)		
28	S	125(10) ms	0+					Q _ε = 11,230(100%)		
								εp(21%)	γ957	
29	S	187(4) ms	5/2+					Q _ε = 13,790(100%)	γ1384,2423,1954,3571	
								εp(47%)	γ1779	
30	S	1.178(5) s	0+					Q _ε = 6,138(100%)	γ677	
31	S	2.572(13) s	1/2+					Q _ε = 5,396.1(100%)	γ1266	
32	S	Stable	0+					{94.93(31)%}		
33	S	Stable	3/2+					{0.76(2)%}		
34	S	Stable	0+					{4.29(28)%}		
35	S	87.51(12) days	3/2+					Q _{β-} = 167.14(100%)		
36	S	Stable	0+					{0.02(1)%}		
37	S	5.05(2) m	7/2-					Q _{β-} = 4,865.30 (100%)	γ3103	
38	S	170.3(7) m	0+					Q _{β-} = 2,937(100%)	γ1942	
39	S	11.5(5) s	(7/2)-					Q _{β-} = 6,640(100%)	γ1302,1697,395,875	
40	S	8.8(22) s	0+					Q _{β-} = 4,710(100%)	γ212,1014,678,432	
41	S	1.99(5) s	(7/2-)					Q _{β-} = 8,740(100%)	γ1405	
								β - n		
42	S	1.013(15) s	0+					Q _{β-} = 7,700(100%)	γ119,1282,724,471	
43	S	0.28(3) s						Q _{β-} = 11,500(100%)		
								β - n(40%)		

Table 22.1 (Continued)

	A	Element	Half-life or width	J^{π}	Qmode(%BR){(%Abund)}	Principal gammas, alphas
17	44	S	100(1) ms	0+	Q β^- = [9,100](100%) β^- – n(18%)	
	45	S	68(2) ms		Q β^- = [14,100](100%) β^- – n(54%)	
	46	S	50(8) ms	0+	Q β^- = [14,400](100%)	
	48	S	>200 ns	0+	Q β^- = [16,900]	
	49	S	<200 ns		n	
		Chlorine				
	28	Cl		(1+)	Qp = [1,800]	
	29	Cl	<20 ns	(3/2+)	Qp = [1,780]	
	30	Cl	<30 ns	(3+)	Qp = [310]	
	31	Cl	150(25) ms		Q ϵ = 11,980(100%) ϵ p(0.7%)	γ 2236
	32	Cl	298(1) ms	1+	Q ϵ = 12,685(100%) $\epsilon\alpha$ (0.05%) ϵ p(0.03%)	γ 2230,4772
	33	Cl	2.511(3) s	3/2+	Q ϵ = 5,582.7(100%)	γ 841,1967,2868
	34	Cl	1.5264(14) s	0+	Q ϵ = 5,491.28(100%)	
	34	Cl(146.4)	32.00(4) m	3+	ϵ (55.4%) IT(44.6%)	γ 2127,1177,3304 γ 146
	35	Cl	Stable	3/2+	{75.78(4)%}	
	36	Cl	3.01(2)E5 years	2+	Q β^- = 708.6(98.1%) Q ϵ = 1,142.07(1.9%)	
	37	Cl	Stable	3/2+	{24.22(4)%}	

38	Cl	37.24(5) m	2−	$Q\beta^- = 4,916.8(100\%)$	$\gamma 2167, 1643$
38	Cl(671.4)	715(3) ms	5−	$IT(100\%)$	$\gamma 671$
39	Cl	56.2(6) m	3/2+	$Q\beta^- = 3,441(100\%)$	$\gamma 1267, 250, 1518$
40	Cl	1.35(2) m	2−	$Q\beta^- = 7,480(100\%)$	$\gamma 1461, 2840, 2622, 3102$
41	Cl	38.4(8) s	(1/2+)	$Q\beta^- = 5,730(100\%)$	$\gamma 4683$
42	Cl	6.8(3) s		$Q\beta^- = 9,430(100\%)$	$\gamma 1208, 2837, 1277, 3208$
43	Cl	3.13(9) s	(1/2+)	$Q\beta^- = 7,950(100\%)$	$\gamma 762, 1032, 679$
44	Cl	0.56(11) s		$Q\beta^- = 12,270(100\%)$	$\gamma 1158, 853, 2796, 2010$
				$\beta^- - n(<8\%)$	
45	Cl	413(25) ms	(1/2+)	$Q\beta^- = 10,800(100\%)$	
				$\beta^- - n(24\%)$	
46	Cl	232(2) ms		$Q\beta^- = [14,900](100\%)$	
				$\beta^- - n(60\%)$	
47	Cl	101(6) ms		$Q\beta^- = [14,700](100\%)$	
				$\beta^- - n$	
48	Cl	>200 ns		$Q\beta^- = [18,400]$	
49	Cl	>170 ns		$Q\beta^- = [16,500]$	
51	Cl	>200 ns	(3/2+)	$Q\beta^- = [18,900]$	
18 Argon					
30	Ar	<20 ns	0+	$Q\beta = [-300]$	
31	Ar	14.4(6) ms	5/2(+)	$Q\epsilon = [18,360](100\%)$	
				$\epsilon p(63\%)$	$\gamma 1192$
				$\epsilon 2p(7.2\%)$	
32	Ar	98(2) ms	0+	$Q\epsilon = 11,150(100\%)$	$\gamma 1168, 702, 466, 1079$
				$\epsilon p(43\%)$	$\gamma 1248$
33	Ar	173.0(20) ms	1/2+	$Q\epsilon = 11,620(100\%)$	$\gamma 811$
				$\epsilon p(38.7\%)$	$\gamma 2231$

Table 22.1 (Continued)

A	Element	Half-life or width	J^{π}	Qmode(% β R){%Abund}	Principal gammas, alphas
34	Ar	844.5(34) ms	0+	Q ε = 6,062(100%)	γ 666,3129,461,2580
35	Ar	1.775(4) s	3/2+	Q ε = 5,965.3(100%)	γ 1219,1763,2694
36	Ar	Stable	0+	{0.3365(30)%}	
37	Ar	34.95(4) days	3/2+	Q ε = 813.5(100%)	
38	Ar	Stable	0+	{0.0632(5)%}	
39	Ar	269(3) years	7/2-	Q β - = 565(100%)	
40	Ar	Stable	0+	{99.6003(30)%}	
41	Ar	109.61(4) m	7/2-	Q β - = 2,491.6(100%)	γ 1294
42	Ar	32.9(11) years	0+	Q β - = 600(100%)	
43	Ar	5.37(6) m	(5/2-)	Q β - = 4,620(100%)	γ 975,738,1440,2345
44	Ar	11.87(5) m	0+	Q β - = 3,550(100%)	γ 183,1703,1886
45	Ar	21.48(15) s	(5/2-7/2-)	Q β - = 6,890(100%)	γ 1020,3703,61,1808
46	Ar	8.4(6) s	0+	Q β - = 5,700(100%)	γ 1944
47	Ar	1.23(3) s	(3/2) -	Q β - = 9,790(100%)	
				β - n(<0.2%)	
48	Ar	170(50) ms	0+	Q β - = [8,900]	
				β - n(65%)	
49	Ar	>170 ns		Q β - = [13,700]	
50	Ar	>170 ns	0+	Q β - = [12,300]	
				β - n(35%)	γ 3832
51	Ar	>200 ns		Q β - = [15,700]	
52	Ar	10 ms	0+	Q β - = [14,500]	
53	Ar	3 ms	(5/2-)	Q β - = [17,800]	
				β - n	

Table 22.1 (Continued)

A	Element	Half-life or width	$J\pi$	Qmode(%BR){%Abund}	Principal gammas, alphas
20	50	K	472(4) ms	(0−,1,2−)	Qβ− = 14,200(100%) β − n(29%) γ1027,4030,4880,3005 γ2023,4073,3354
	51	K	365(5) ms	(1/2+,3/2+)	Qβ− = [13,900](100%) β − n(47%) γ3462,3530 γ1026,1973 γ2563
	52	K	105(5) ms	(2−)	Qβ− = [16,300](100%) β − n(~64%)
	53	K	30(5) ms	(3/2+)	Qβ− = [15,900](100%) β − n(~67%) β − 2n(~17%)
	54	K	10(5) ms		Qβ− = [18,000](100%) β − n(>0%)
	55	K	3 ms		Qβ− = β − n
	Calcium				
	34	Ca	<35 ns	0+	Qp = [−900]
	35	Ca	25.7(2) ms		Qε = [15,610](100%) εp(95.7%) ε2p(4.2%)
	36	Ca	102(2) ms	0+	Qε = 10,990(100%) εp(54.3%) γ1619,1113
	37	Ca	181.1(10) ms	3/2+	Qε = 11,639(100%) εp(82.1%) γ3239,2750,1371
	38	Ca	440(12) ms	0+	Qε = 6,743(100%) γ1568,328
	39	Ca	859.6(14) ms	3/2+	Qε = 6,530.6(100%) γ2522

21	40	Ca	Stable	0+	{96.94(16)%}		
	41	Ca	1.02(7)E5 years	7/2–	Q _ε = 421.4(100%)		
	42	Ca	Stable	0+	{0.647(23)%}		
	43	Ca	Stable	7/2–	{0.135(10)%}		
	44	Ca	Stable	0+	{2.09(11)%}		
	45	Ca	162.61(9) days	7/2–	Q _{β–} = 256.8(100%)	γ12	
	46	Ca	>2.8E15 years	0+	2β–		
					{0.004(3)%}		
	47	Ca	4.536(3) days	7/2–	Q _{β–} = 1,991.9(100%)	γ1297	
	48	Ca	1.9E19(+45–8) years	0+	2β–		
					{0.187(21)%}		
	49	Ca	8.718(6) m	3/2–	Q _{β–} = 5,262(100%)	γ3084	
	50	Ca	13.9(6) s	0+	Q _{β–} = 4,966(100%)	γ257,1519,72,1591	
	51	Ca	10.0(8) s	(3/2–)	Q _{β–} = 7,330(100%)	γ862,1394,1168,1480	
					β – n		
	52	Ca	4.6(3) s	0+	Q _{β–} = 7,900(100%)	γ675,961,1636,2070	
					β – n(<2%)		
	53	Ca	90(15) ms	(3/2–,5/2–)	Q _{β–} = [10,100](100%)		
					β – n(>30%)		
	54	Ca	>300 ms	0+	Q _{β–} = [10,900](100%)		
	55	Ca	30 ms	(5/2–)	Q _{β–} =		
	56	Ca	10 ms	0+	Q _{β–} = [12,200]		
	57	Ca	5 ms	0+	Q _{β–} = [12,200]		
					β – n		
21		Scandium					
	36	Sc			Q _p = [2,200]		
	37	Sc			Q _p = [2,000]		

Table 22.1 (Continued)

A	Element	Half-life or width	J^{π}	Qmode(%BR){%Abund}	Principal gammas, alphas
38	Sc			Qp = [900]	
39	Sc	<300 ns	(7/2-)–	Qp = 602(100%)	
40	Sc	182.3(7) ms	4–	Q ϵ = 14,320(100%)	γ 3737,755,2045,1877
				ϵ p(0.44%)	
				$\epsilon\alpha$ (0.02%)	
41	Sc	596.3(17) ms	7/2–	Q ϵ = 6,495.3(100%)	γ 2575,2959
42	Sc	681.3(7) ms	0+	Q ϵ = 6,425.84(100%)	γ 313,1525
42	Sc(616.3)	61.7(4) s	(7)+	ϵ (100%)	γ 438,1525,1227
43	Sc	3.891(12) h	7/2–	Q ϵ = 2,220.8(100%)	γ 373
44	Sc	3.97(4) h	2+	Q ϵ = 3,653.3(100%)	γ 1157
44	Sc(271.1)	58.61(10) h	6+	IT(98.8%)	γ 271
				ϵ (1.2%)	γ 1002,1126,1157
45	Sc	Stable	7/2–	{100%}	
45	Sc(12.4)	318(7) ms	3/2+	IT(100%)	γ 12
46	Sc	83.79(4) days	4+	Q β – = 2,366.7(100%)	γ 1121,889
46	Sc(142.5)	18.75(4) s	1–	IT(100%)	γ 143
47	Sc	3.3492(6) days	7/2–	Q β – = 600.1(100%)	γ 159
48	Sc	43.67(9) h	6+	Q β – = 3,994(100%)	γ 1312,984,1038
49	Sc	57.18(13) m	7/2–	Q β – = 2,006(100%)	γ 1762,1623
50	Sc	102.5(5) s	5+	Q β – = 6,888(100%)	γ 1554,1121,524
50	Sc(256.9)	0.35(4) s	(2,3)+	IT(>97.5%)	γ 257
				β – (<2.5%)	
51	Sc	12.4(1) s	(7/2)–	Q β – = 6,508(100%)	γ 1437,2144,1568,907
52	Sc	8.2(2) s	3(+)	Q β – = 9,080(100%)	γ 1050,1268,1032,1215

22	53	Sc	> 3 s	(7/2−)	Qβ− = [8,900](100%) β − n	
	54	Sc	0.36(6) s	3+	Qβ− = 11,300(100%)	γ1000,1700,500
	55	Sc	105(6) ms	(7/2−)	Qβ− = [11,500](100%) β − n	
	56	Sc(x)	60(7) ms	(6+,7+)	Qβ− = [13,700]	
	56	Sc(y)	35(5) ms	(1+)	Qβ− = [13,700]	
	57	Sc	13(4) ms	(7/2−)	Qβ− = [13,200](100%) β − n	
	58	Sc	12(5) ms	(3+)	Qβ− =	
	59	Sc	(10 ms)	(3+)	Qβ−	
	60	Sc	(3 ms)	(3+)	Qβ− =	
		Titanium				
	38	Ti		0+	2p	
	39	Ti	31(+6−4) ms	(3/2+)	Qε = [15,400](100%) εp(100%)	
	40	Ti	53.3(15) ms	0+	Qε = 11,680(100%) εp(100%)	
	41	Ti	80.4(9) ms	3/2+	Qε = [12,930](100%) εp(∼100%)	
	42	Ti	199(6) ms	0+	Qε = 7,000(100%)	γ611
	43	Ti	509(5) ms	7/2−	Qε = 6,867(100%)	γ2288,845,2459,1408
	44	Ti	60.0(11) years	0+	Qε = 267.5(100%)	γ78,68
	45	Ti	184.8(5) m	7/2−	Qε = 2,062.4(100%)	γ720,1408,1661

Table 22.1 (Continued)

	A	Element	Half-life or width	J π	Qmode(%BR){%Abund}	Principal gammas, alphas
	46	Ti	Stable	0+	{8.25(3)%}	
	47	Ti	Stable	5/2–	{7.44(2)%}	
	48	Ti	Stable	0+	{73.72(3)%}	
	49	Ti	Stable	7/2–	{5.41(2)%}	
	50	Ti	Stable	0+	{5.18(2)%}	
	51	Ti	5.76(1) m	3/2–	Q β – = 2,470.6(100%)	γ 320
	52	Ti	1.7(1) m	0+	Q β – = 1,973(100%)	γ 124, 17
	53	Ti	32.7(9) s	(3/2)–	Q β – = 5,020(100%)	γ 128, 228, 1676, 101
	54	Ti	1.5(4) s	0+	Q β – = 4,120(100%)	
	55	Ti	1.3(1) s	(\geq 1/2–)	Q β – = 7,300(100%)	
	56	Ti	200(4) ms	0+	Q β – = 7,100(100%)	
	57	Ti	60 (16) ms		β – n Q β – = [9,800](100%)	
	58	Ti	59(9) ms	0+	β – n Q β – = [8,800](100%)	
	59	Ti	30(3) ms	(5/2–)	Q β – = [11,800]	
	60	Ti	22(2) ms	0+	Q β – = [13,600]	
	61	Ti	>300 ns		Q β – = [13,600]	
	62	Ti	(10 ms)	0+	Q β – = [13,600]	
	63	Ti	(3 ms)		Q β – = [13,600] β – n	
23		Vanadium				
	40	V			Qp = [1,800]	
	41	V			Qp = [1,300]	

42	V	<55 ns			Q β = [260]		
43	V	>800 ms			Q ε = [11,300](100%)		
44	V	111(7) ms		(2+)	Q ε = [13,700](100%)		γ 1083,5523,1448,3032
44	V (0 + x)	150(3) ms		(6+)	$\varepsilon\alpha$		
45	V	547(6) ms		7/2–	ε (100%)		γ 1083,1371,1561,2833
46	V	422.50(11) ms		0+	Q ε = 7,133(100%)		γ 40
46	V (801.1)	1.02(7) ms		3+	Q ε = 7,051.4(100%)		γ 4317,1722,889
47	V	32.6(3) m		3/2–	IT(100%)		γ 801
48	V	15.9735(25) days		4+	Q ε = 2,927.8(100%)		γ 1794,160,244,1390
49	V	330(15) days		7/2–	Q ε = 4,012.3(100%)		γ 984,1312
50	V	1.4(4)E17 years		6+	Q ε = 601.9(100%)		
					Q ε = 2,208.3(83%)		γ 1554
					{0.250(4)%}		
					Q β – = 1,036.9(17%)		γ 783
51	V	Stable		7/2–	{99.750(4)%}		
52	V	3.743(5) m		3+	Q β – = 3,975.4(100%)		γ 1434
53	V	1.60(4) m		7/2–	Q β – = 3,436(100%)		γ 1006,1289
54	V	49.8(5) s		3+	Q β – = 7,042(100%)		γ 835,989,2259,3170
55	V	6.54(15) s		(7/2–)	Q β – = 5,960(100%)		γ 518,881
56	V	216(4) ms		1+	Q β – = 9,050(100%)		
					β – n(0.06%)		
57	V	0.35(1) s		(3/2–)	Q β – = 8,000(100%)		
					β – n(0.04%)		
58	V	185(10) ms		(1+)	Q β – = 11,600(100%)		
59	V	75(7) ms		(5/2–, 3/2–)	Q β – = 9,900(100%)		γ 102
60	V	68(5) ms			Q β – = 13,800(100%)		

Table 22.1 (Continued)

A	Element	Half-life or width	J^{π}	Qmode(%BR){%Abund}	Principal gammas, alphas
60	V	122(18) ms		Q β^- = 13,800(100%) β^- – n	
61	V	47(1) ms	(3/2–)	Q β^- = [12,400]	
62	V	> 150 ns		Q β^- = [16,200]	
63	V	17(3) ms	(7/2–)	Q β^- = [13,900]	
64	V	19(8) ms		β^-	
65	V	(10 ms)		Q β^- = 13,800(100%) β^- – n	
24	Chromium				
42	Cr	13(+4–2) ms	0+	Q ϵ = [14,200]	
43	Cr	21.6(7) ms	(3/2+)	Q ϵ = [15,890](100%) ϵ p(23%) ϵ 2p(6%)	
44	Cr	53(+4–3) ms	0+	Q ϵ = [10,310](100%) ϵ p(>7%)	
45	Cr	60.9(4) ms	(7/2–)	Q ϵ = [12,460](100%) ϵ p(34.4%)	γ 1083
46	Cr	0.26(6) s	0+	Q ϵ = 7,603(100%)	
47	Cr	500(15) ms	3/2–	Q ϵ = 7,452(100%)	γ 88
48	Cr	21.56(3) h	0+	Q ϵ = 1,659(100%)	γ 308,112
49	Cr	42.3(1) m	5/2–	Q ϵ = 2,631(100%)	γ 91,153,62
50	Cr	> 1.3E18 years	0+	2 ϵ {4.345(13)%}	

	51	Cr	27.7025(24) days	7/2–	Q ϵ = 752.73(100%)	γ 320
	52	Cr	Stable	0+	{83.789(18)%}	
	53	Cr	Stable	3/2–	{9.501(17)%}	
	54	Cr	Stable	0+	{2.365(7)%}	
	55	Cr	3.497(3) m	3/2–	Q β – = 2.603.1(100%)	γ 1528
	56	Cr	5.94(10) m	0+	Q β – = 1.617(100%)	γ 83,26
	57	Cr	21.1(10) s	(3/2–7/2)–	Q β – = 5.090(100%)	γ 83,850,1752,1535
	58	Cr	7.0(3) s	0+	Q β – = 3.970(100%)	γ 683,126,290,520
	59	Cr	0.46(5) s	(1/2–)	Q β – = 7.620(100%)	γ 1239
	60	Cr	0.57(6) s	0+	Q β – = 6.100(100%)	
	61	Cr	0.27(2) s		Q β – = 9.000(100%)	
	62	Cr	0.19(3) s	0+	Q β – = 7.300(100%)	
	63	Cr	129(2) ms	(1/2–)	Q β – = [11,200](100%)	
	64	Cr	43(1) ms	0+	Q β – = [9,800]	
25	65	Cr	27(3) ms	(1/2–)	Q β – = [13,300]	
	66	Cr	10(6) ms	0+	β – n	
	67	Cr	~50 ms		β – (100%)	
		Manganese			β –	
	44	Mn	<105 ns	(2–)	Q ϵ = [19,900]	
	45	Mn			Qp = [1,200]	
	46	Mn	35(+5–4) ms	[4+]	Qp = [1,100]	
					Q ϵ = [17,100](100%)	
					ϵ p(22%)	

Table 22.1 (Continued)

A	Element	Half-life or width	J^{π}	Qmode(%BR){%Abund}	Principal gammas, alphas
47	Mn	100(50) ms	(5/2 [−])	Q ε = [12,290](100%) ε p(3.4%)	
48	Mn	158.1(22) ms	4 ⁺	Q ε = [13,820](100%) ε p(0.28%) $\varepsilon\alpha$ (<0.00060%)	γ 752,1106,3676,3934 γ 88,58
49	Mn	382(7) ms	5/2 [−]	Q ε = 7,715(100%)	γ 272,2505
50	Mn	283.29(8) ms	0 ⁺	Q ε = 7,633.0(100%)	γ 3628,2844
50	Mn(229)	1.75(3) m	5 ⁺	ε (100%)	γ 783,1098,1443,1282
51	Mn	46.2(1) m	5/2 [−]	Q ε = 3,207.8(100%)	γ 749,1148,1164,2001
52	Mn	5.591(3) days	6 ⁺	Q ε = 4,711.7(100%)	γ 1434,936,744
52	Mn(377.7)	21.1(2) m	2 ⁺	ε (98.25%) IT(1.75%)	γ 1434 γ 378
53	Mn	3.74(4)E6 years	7/2 [−]	Q ε = 597.0(100%)	
54	Mn	312.12(6) days	3 ⁺	Q ε = 1,377.1(100%) Q β^- = 697.1(<0.00029%)	γ 835
55	Mn	Stable	5/2 [−]	{100%}	
56	Mn	2.5789(1) h	3 ⁺	Q β^- = 3,695.5(100%)	γ 847,1811,2113
57	Mn	85.4(18) s	5/2 [−]	Q β^- = 2,691(100%)	γ 122,692,352,136
58	Mn	3.0(1) s	1 ⁺	Q β^- = 6,250(100%)	γ 1447,2433,2066
58	Mn(71.8)	65.2(5) s	(4) ⁺	β^- (~80%) IT(~20%)	γ 811,1323,459,864 γ 72
59	Mn	4.59(5) s	(5/2) [−]	Q β^- = 5,190(100%)	γ 726,473,571,591
60	Mn	51(6) s	0 ⁺	Q β^- = 8,500(100%)	
60	Mn(271.8)	1.77(2) s	3 ⁺	β^- (88.5%) IT(11.5%)	γ 824,1969,493,2299

26	61	Mn	0.67(4) s		(5/2)–	$Q_{\beta^-} = 7,200(100\%)$	$\gamma 629,207$
	62	Mn	0.88(15) s		(3+)	$Q_{\beta^-} = 10,400(100\%)$	$\gamma 877,942,1299,1815$
	63	Mn	0.29(2) s		(5/2–)	$\beta^- n$	
	64	Mn	90(4) ms		(1+)	$Q_{\beta^-} = 9,000(100\%)$	
	64	Mn				$Q_{\beta^-} = 12,000(100\%)$	
	64	Mn (175)	0.50(5) ms		(4+)	$\beta^- n(33\%)$	
	65	Mn	92(1) ms			$\pi\pi(100\%)$	
	65	Mn				$Q_{\beta^-} = 10,400(100\%)$	
	66	Mn	64(2) ms			$\beta^- n(6.92\%)$	
	66	Mn				$Q_{\beta^-} = [13,800](100\%)$	
26	67	Mn	47(2) ms		(5/2–)	$\beta^- n(10.88\%)$	
	67	Mn				$Q_{\beta^-} = [12,900](100\%)$	
	68	Mn	28(4) ms			$\beta^- n$	
	68	Mn				$\beta^- (100\%)$	
	69	Mn	14(4) ms		5/2–	$\beta^- n$	
	69	Mn				$\beta^- (100\%)$	
	45	Fe	1.89(+49–21) ms		(3/2+)	$Q_{\varepsilon=}$	
	45	Fe				$\varepsilon p < 43\%$	
	46	Fe	12(+4–3) ms		0+	p	
	46	Fe				$Q_{\varepsilon} = [13,100]$	
26	47	Fe	21.8(7) ms		(7/2–)	$\varepsilon p > 36\%$	
	47	Fe				$Q_{\varepsilon} = [15,600](100\%)$	
	47	Fe				εp	
26	47	Fe				$2\varepsilon p$	
	47	Fe					
	47	Fe					

Table 22.1 (Continued)

A	Element	Half-life or width	J π	Qmode(%BR){%Abund}	Principal gammas, alphas
48	Fe	44(7) ms	0+	Q ε = [10,890](100%) ε p(3.6%)	
49	Fe	64.7(3) ms	(7/2-)	Q ε = [13,030](100%) ε p(56.7%)	
50	Fe	155(11) ms	0+	Q ε = 8,150(100%) ε p(~0%)	γ 651
51	Fe	305(5) ms	5/2-	Q ε = 8,020(100%)	γ 237
52	Fe	8.275(8) h	0+	Q ε = 2,372(100%)	γ 169
52	Fe(6820)	45.9(6) s	12+	ε (100%)	γ 930,870,622,2038
53	Fe	8.51(2) m	7/2-	Q ε = 3,742.4(100%)	γ 378
53	Fe(3040.4)	2.526(24) m	19/2-	IT(100%)	γ 701,1328,1012,2340
54	Fe	>3.1E22 years	0+	2 ε {5.845(35)%}	
55	Fe	2.737(11) years	3/2-	Q ε = 231.38(100%)	γ 126
56	Fe	Stable	0+	{91.754(36)%}	
57	Fe	Stable	1/2-	{2.119(10)%}	
58	Fe	Stable	0+	{0.282(4)%}	
59	Fe	44.495(9) days	3/2-	Q β^- = 1,565.2(100%)	γ 1099,1292
60	Fe	1.5(3)E6 years	0+	Q β^- = 237(100%)	
61	Fe	5.98(6) m	3/2-,5/2-	Q β^- = 3,978(100%)	γ 1205,1027,298,1646
62	Fe	68(2) s	0+	Q β^- = 2,530(100%)	γ 506
63	Fe	6.1(6) s	(5/2)-	Q β^- = 6,060(100%)	γ 995,1427
64	Fe	2.0(2) s	0+	Q β^- = 4,700(100%)	
65	Fe	1.3(3) s		Q β^- = 7,900(100%)	

27	66	Fe	0.44(6) s	0+	Qβ− = 5,700(100%)	
	67	Fe	0.6(+2−1) s	(5/2+)	Qβ− = 8,700(100%)	
	68	Fe	187(6) ms	0+	Qβ− = [7,600](100%)	
	69	Fe	109(9) ms	1/2−	Qβ− = [11,600](100%)	
	70	Fe	94(17) ms	0+	β−	
	71	Fe	> 150 ns	(7/2+)	β−	
	72	Fe	> 150 ns	0+	β−	
		Cobalt				
	50	Co	44(4) ms	(6+)	Qε = [17,280](100%)	
					εp(54%)	
	51	Co	> 200 ns	(7/2−)	Qε = [12,940]	
	52	Co	115(23) ms	(6+)	Qε = [14,410](100%)	γ849,1535,1329,1942
	53	Co	240(20) ms	(7/2−)	Qε = 8,302(100%)	γ1328
	53	Co(3190.0)	247(12) ms	(19/2−)	ε(~98.5%)	
					Qp = −1,599(~1.5%)	
	54	Co	193.28(7) ms	0+	Qε = 8,243.08(100%)	γ1153
	54	Co(197.4)	1.48(2) m	7+	ε(100%)	γ1407,1130,411
	55	Co	17.53(3) h	7/2−	Qε = 3,451.3(100%)	γ931,477,1409
	56	Co	77.233(27) days	4+	Qε = 4,566.0(100%)	γ847,1238,2598,1771
	57	Co	271.74(6) days	7/2−	Qε = 836.0(100%)	γ122,136,14
	58	Co	70.86(6) days	2+	Qε = 2,307.4(100%)	γ811
	58	Co(24.9)	9.04(11) h	5+	IT(100%)	γ25
	59	Co	Stable	7/2−	{100%}	
	60	Co	1,925.28(14) days	5+	Qβ− = 2,823.9(100%)	γ1333,1173
	60	Co(58.6)	10.467(6) m	2+	IT(99.76%)	γ59
					β − (0.24%)	γ1333

Table 22.1 (Continued)

	A	Element	Half-life or width	J π	Qmode(%BR){%Abund}	Principal gammas, alphas
	61	Co	1.650(5) h	7/2–	Q β – = 1,321.7(100%)	γ 67
	62	Co	1.50(4) m	2+	Q β – = 5,315(100%)	γ 1173,2302,1129
	62	Co(22)	13.91(5) m	5+	β – (>99%)	γ 1173,1164,2004
					IT(<1%)	
	63	Co	27.4(5) s	7/2–	Q β – = 3,672(100%)	γ 87
	64	Co	0.30(3) s	1+	Q β – = 7,307(100%)	γ 1346,931
	65	Co	1.20(6) s	(7/2)–	Q β – = 5,958(100%)	γ 1142,311,964,1211
	66	Co	0.18(1) s	(3+)	Q β – = 10,000(100%)	γ 1425,1246,471
	67	Co	0.425(20) s	(7/2–)	Q β – = 8,400(100%)	γ 694
	68	Co	0.199(21) s	(7–)	Q β – = 11,700(100%)	γ 815,2033,595,709
	68	Co(x)	1.6(3) s	(3+)	β – (100%)	γ 2033,478,2745,815
	69	Co	0.22(2) s	7/2–	Q β – = 9,300(100%)	
	70	Co	119(6) ms	(6–)	Q β – = [12,700](100%)	
	70	Co(x)	0.50(18) s	(3+)	Q β – = [12,700](100%)	
	71	Co	79(5) ms		Q β – = [10,900](100%)	
					β – n(2.61%)	
	72	Co	62(3) ms	(6–,7–)	Q β – = [14,100](100%)	
					β – n(4.8%)	
	73	Co	41(4) ms		β –	
	74	Co	>150 ns	0+	β –	
	75	Co	>150 ns	(7/2–)	β – (100%)	
28		Nickel				
	48	Ni	>0.5 μ s	0+	ϵ	
	49	Ni	7.5(10) ms		ϵ	
					ϵ p(83%)	

50	Ni	12(3) ms	0+	Q ε = [13,400] $\varepsilon p(70\%)$	
51	Ni	>200 ns	(7/2-)	Q ε = [15,800]	
52	Ni	38(5) ms	0+	Q ε = [11,260](100%) $\varepsilon p(17\%)$	
53	Ni	45(15) ms	(7/2-)	Q ε = [13,260](100%) $\varepsilon p(\sim 45\%)$	
54	Ni	104(7) ms	0+	Q ε = 8,800(100%)	$\gamma 937$
55	Ni	204.7(37) ms	7/2-	Q ε = 8,694(100%)	$\gamma 3303$
56	Ni	6.075(10) days	0+	Q ε = 2,135(100%)	$\gamma 158,812,750,270$
57	Ni	35.60(6) h	3/2-	Q ε = 3,264(100%)	$\gamma 1378,127,1920$
58	Ni	Stable	0+	{68.0769(89)%}	
59	Ni	7.6(5)E4 years	3/2-	Q ε = 1,072.5(100%)	
60	Ni	Stable	0+	{26.2231(77)%}	
61	Ni	Stable	3/2-	{1.1399(6)%}	
62	Ni	Stable	0+	{3.6345(17)%}	
63	Ni	100.1(20) years	1/2-	Q β^- = 66.945(100%)	
64	Ni	Stable	0+	{0.9256(9)%}	
65	Ni	2.5172(3) h	5/2-	Q β^- = 2,137.1(100%)	$\gamma 1482,1116,366$
66	Ni	54.6(3) h	0+	Q β^- = 226(100%)	
67	Ni	21(1) s	(1/2)-	Q β^- = 3,558(100%)	$\gamma 1937,1115,822,2841$
68	Ni	29(2) s	0+	Q β^- = 2,060(100%)	
68	Ni(2849)	0.86(5) ms	5-	IT(100%)	
69	Ni	11.4(3) s	9/2+	Q β^- = 5,360(100%)	$\gamma 1871,680,1213,1483$
69	Ni(321)	3.5(5) s	1/2-	Q β^- = 2,060(100%)	

Table 22.1 (Continued)

A	Element	Half-life or width	J π	Qmode(%BR){%Abund}	Principal gammas, alphas
70	Ni	6.0(3) s	0+	Q β^- = 3,500(100%)	
71	Ni	2.56(3) s		Q β^- = 6,900(100%)	
72	Ni	1.57(5) s	0+	Q β^- = [5,400](100%) β^- - n	
73	Ni	0.84(3) s	(9/2+)	Q β^- = [8,900](100%)	γ 166,1010,961,844
74	Ni	0.68(18) s	0+	Q β^- = [7,200](100%) β^- - n	
75	Ni	0.6(2) s	(7/2+)	Q β^- = [10,500](100%) β^- - n(8.43%)	
76	Ni	0.238(+15–18) s	0+	Q β^- = [8,700](100%) β^- - n	
77	Ni	> 150 ns		Q β^- = [12,000]	
78	Ni	> 150 ns	0+	Q β^- = [10,200]	
29	Copper				
	Cu		(3+)	Q p = [1,500]	
	Cu	< 300 ns	(3/2–)	Q ε = [15,900]	
				Q p = [1,900]	
	Cu	< 75 ns	(3+)	Q p = [400]	
	Cu	40 ms	3/2–	Q ε = [13,700](100%)	
	Cu	94(3) ms	4+	Q ε = [15,300]	
	Cu	196.3(7) ms	3/2–	Q ε = 8,770(100%)	γ 1113,769
	Cu	3.204(7) s	1+	Q ε = 8,563.0(100%)	γ 1455,1448,40
	Cu	81.5(5) s	3/2–	Q ε = 4,799.6(100%)	γ 1301,878,339,465
	Cu	23.7(4) m	2+	Q ε = 6,126.9(100%)	γ 1333,1792,826

61	Cu	3.333(5) h	3/2–	$Q_{\varepsilon} = 2,237.2(100\%)$	$\gamma 283,656,67,1185$
62	Cu	9.67(3) m	1+	$Q_{\varepsilon} = 3,948(100\%)$	$\gamma 1173,876,2302$
63	Cu	Stable	3/2–	$\{69.17(3)\%$	
64	Cu	12.701(2) h	1+	$Q_{\varepsilon} = 1,675.10(61\%)$	$\gamma 1346$
				$Q_{\beta-} = 578.7(39\%)$	
65	Cu	Stable	3/2–	$\{30.83(3)\%$	
66	Cu	5.120(14) m	1+	$Q_{\beta-} = 2,642.0(100\%)$	$\gamma 1039$
67	Cu	61.83(12) h	3/2–	$Q_{\beta-} = 577(100\%)$	$\gamma 185,93,91$
68	Cu	31.1(15) s	1+	$Q_{\beta-} = 4,460(100\%)$	$\gamma 1078,1262$
68	Cu(721.6)	3.75(5) m	(6–)	IT(84%)	$\gamma 526,85,111,637$
				$\beta - (16\%)$	$\gamma 1341,1078,1041,152$
69	Cu	2.85(15) m	3/2–	$Q_{\beta-} = 2,675(100\%)$	$\gamma 1008,834,531,1430$
70	Cu	44.5(2) s	(6–)	$Q_{\beta-} = 6,599(100\%)$	$\gamma 885$
70	Cu(101.1)	33(2) s	(3–)	$Q_{\beta-} = 6,599(52\%)$	
				IT(48%)	
70	Cu(242.6)	6.6(2) s	(1+)	$\beta - (93.2\%)$	$\gamma 885,902,1252$
				IT(6.8%)	
71	Cu	19.5(16) s	(3/2–)	$Q_{\beta-} = 4,560(100\%)$	$\gamma 490,595,587,675$
72	Cu	6.6(1) s	(1+)	$Q_{\beta-} = [8,070](100\%)$	$\gamma 652,1005,1658,847$
73	Cu	4.2(3) s	(3/2–)	$Q_{\beta-} = [6,300](100\%)$	$\gamma 450,502,307$
74	Cu	1.594(10) s	(1+3+)	$Q_{\beta-} = [10,000](100\%)$	$\gamma 606,1064,1139,813$
75	Cu	1.224(3) s	(3/2–)	$Q_{\beta-} = [8,200](100\%)$	
				$\beta - n(3.5\%)$	
76	Cu	0.641(6) s		$Q_{\beta-} = [11,700](100\%)$	
				$\beta - n(3\%)$	
76	Cu(0 + x)	1.27(30) s		$\beta - (100\%)$	$\gamma 599,698,1337,341$

Table 22.1 (Continued)

A	Element	Half-life or width	$J\pi$	Qmode(%BR){%Abund}	Principal gammas, alphas
77	Cu	0.469(8) s		$Q\beta^- = [10, 100](100\%)$	
78	Cu	342(11) ms		$Q\beta^- = [13, 300](100\%)$	
79	Cu	188(25) ms		$Q\beta^- = [11, 700](100\%)$ $\beta^- - n(55\%)$	
80	Cu	> 300 ns		$Q\beta^- = [16, 300]$	
30	Zinc				
	Zn		0+	2p	
	Zn	20 ms	5/2-	$Q\epsilon = [16, 700]$	
				$Qp = [-500]$	
	Zn	> 0.5 μ s	0+	$Q\epsilon = [12, 900]$	
				$Qp = [-1, 400]$	
	Zn	38(4) ms	(7/2-)	$Q\epsilon = [14, 620](100\%)$	
				$\epsilon p(> 65\%)$	
	Zn	84(9) ms	0+	$Q\epsilon = 9, 370(100\%)$	$\gamma_{203, 848}$
	Zn	182.0(18) ms	3/2-	$Q\epsilon = 9, 090(100\%)$	$\gamma_{491, 914}$
60	Zn	2.38(5) m	0+	$Q\epsilon = 4, 158(100\%)$	$\gamma_{670, 61, 273, 334}$
61	Zn	89.1(2) s	3/2-	$Q\epsilon = 5, 637(100\%)$	$\gamma_{475, 1660, 970, 690}$
61	Zn(418.1)	0.14(7) s	3/2-	IT	
62	Zn	9.186(13) h	0+	$Q\epsilon = 1, 627(100\%)$	$\gamma_{597, 41, 548, 508}$
63	Zn	38.47(5) m	3/2-	$Q\epsilon = 3, 366.9(100\%)$	$\gamma_{670, 962}$
64	Zn	Stable	0+	{48.63(60)%}	
65	Zn	243.66(9) days	5/2-	$Q\epsilon = 1, 351.9(100\%)$	γ_{1116}
66	Zn	Stable	0+	{27.90(27)%}	

67	Zn	Stable	5/2–	{4.10(13)%}		
68	Zn	Stable	0+	{18.75(51)%}		
69	Zn	56.4(9) m	1/2–	Qβ– = 906(100%)	γ318,872	
69	Zn(438.6)	13.76(2) h	9/2+	IT(99.97%)	γ439	
				β – (0.03%)	γ574	
70	Zn	> 1.3E16 years	0+	2β–		
				{0.62(3)%}		
71	Zn	2.45(10) m	1/2–	Qβ– = 2,815(100%)	γ512,910,390	
71	Zn(157.7)	3.96(5) h	9/2+	β – (100%)	γ386,487,620,512	
				IT(<0.05%)		
72	Zn	46.5(1) h	0+	Qβ– = 458(100%)	γ145,192	
73	Zn	23.5(10) s	(1/2)–	Qβ– = 4,290(100%)	γ218,911,496,1613	
73	Zn(0 + x)	5.8(8) s		IT		
				β–		
73	Zn(195.5)	13.0(2) ms	(5/2+)	IT(100%)		
74	Zn	95.6(12) s	0+	Qβ– = 2,340(100%)	γ49,143,57,192	
75	Zn	10.2(2) s	(7/2+)	Qβ– = 6,000(100%)	γ229,432,156,606	
76	Zn	5.7(3) s	0+	Qβ– = 4,160(100%)	γ199,76	
77	Zn	2.08(5) s	(7/2+)	Qβ– = 7,270(100%)	γ189,474,1832,161	
77	Zn(772.4)	1.05(10) s	(1/2–)	IT(>50%)	γ772	
				β – (<50%)		
78	Zn	1.47(15) s	0+	Qβ– = 6,440(100%)	γ225,182,860,636	
79	Zn	0.995(19) s	(9/2+)	Qβ– = [9,090](100%)	γ702,866,874,979	
				β – n(1.3%)		

Table 22.1 (Continued)

A	Element	Half-life or width	J^{π}	Qmode(%BR){%Abund}	Principal gammas, alphas
31	80 Zn	0.54(2) s	0+	Q β^- = 7,290(100%) β^- – n(1%)	γ 713,715,965,686
	81 Zn	0.29(5) s		Q β^- = [11,900](100%) β^- – n(7.5%)	
	82 Zn	> 150 ns	0+	Q β^- = [10,900]	
	83 Zn	> 150 ns	(5/2+)	β^-	
	Gallium				
	56 Ga			Qp = [2,900]	
	57 Ga			Qp = [2,500]	
	58 Ga			Qp = [1,400]	
	59 Ga			Qp = [880]	
	60 Ga	70(15) ms	(2+)	Q ϵ = [14,190](100%) ϵ p(1.6%) $\epsilon\alpha$ (<0.02%)	γ 1004,3848,2559,1555
	61 Ga	168(3) ms	3/2–	Q ϵ = [9,000](100%)	γ 88,123,418,755
	62 Ga	116.12(23) ms	0+	Q ϵ = 9,170(100%)	
	63 Ga	32.4(5) s	(3/2–)	Q ϵ = 5,520(100%)	γ 637,627,193,650
	64 Ga	2.627(12) m	0+	Q ϵ = 7,165(100%)	γ 992,808,3366,1387
	65 Ga	15.2(2) m	3/2–	Q ϵ = 3,254.9(100%)	γ 115,61,153,752
	66 Ga	9.49(7) h	0+	Q ϵ = 5,175(100%)	γ 1039,2752,834,2190
	67 Ga	3.2617(5) days	3/2–	Q ϵ = 1,000.5(100%)	γ 93,185,300,394
	68 Ga	67.71(9) m	1+	Q ϵ = 2,921.1(100%)	γ 1077
	69 Ga	Stable	3/2–	{60.108(9)%}	

70	Ga	21.14(3) m	1+	$Q\beta^- = 1,656(99.59\%)$ $Q\epsilon = 654.7(0.41\%)$	$\gamma^{1039,176}$
71	Ga	Stable	3/2−	{39.892(9)%}	
72	Ga	14.095(3) h	3−	$Q\beta^- = 3,999.1(100\%)$	$\gamma^{834,2202,630,2508}$
72	Ga(119.7)	39.68(13) ms	(0+)	IT	
73	Ga	4.86(3) h	3/2−	$Q\beta^- = 1,593(100\%)$	$\gamma^{297,326}$
74	Ga	8.12(12) m	(3−)	$Q\beta^- = 5,370(100\%)$	$\gamma^{596,2354,608}$
74	Ga(59.7)	9.5(10) s	(0)	IT(>50%) $\beta^- (<50\%)$	γ^3
75	Ga	126(2) s	(3/2)−	$Q\beta^- = 3,392(100\%)$	$\gamma^{253,575,885,177}$
76	Ga	32.6(6) s	(2+,3+)	$Q\beta^- = 7,010(100\%)$	$\gamma^{563,546,1108,431}$
77	Ga	13.2(2) s	(3/2−)	$Q\beta^- = 5,340(100\%)$	$\gamma^{469,459}$
78	Ga	5.09(5) s	(3+)	$Q\beta^- = 8,200(100\%)$	$\gamma^{619,1186,567,1025}$
79	Ga	2.847(3) s	(3/2−)	$Q\beta^- = 7,000(100\%)$ $\beta^- n(0.09\%)$	$\gamma^{465,516,1187,2140}$
80	Ga	1.676(14) s	(3)	$Q\beta^- = 10,380(100\%)$ $\beta^- n(0.89\%)$	$\gamma^{659,1083,1109,523}$ γ^{205}
81	Ga	1.217(5) s	(5/2−)	$Q\beta^- = 8,320(100\%)$	$\gamma^{216,828,711,937}$
82	Ga	0.599(2) s	(1,2,3)	$\beta^- n(1.9\%)$ $Q\beta^- = [12,700](100\%)$ $\beta^- n(22.3\%)$	γ^{659} $\gamma^{1348,2215,867,1909}$ $\gamma^{711,216,530}$
83	Ga	0.308(1) s		$Q\beta^- = [11,500](100\%)$ $\beta^- n(37\%)$	
84	Ga	0.085(10) s		$Q\beta^- = [14,000](100\%)$ $\beta^- n(70\%)$	
85	Ga	>150 ns	(3/2−)	β^-	
86	Ga	>150 ns		β^-	

Table 22.1 (Continued)

32	A	Element	Half-life or width	J^{π}	Qmode(%BR){%Abund}	Principal gammas, alphas
		Germanium				
	58	Ge		0+	2p	
	59	Ge			2p	
	60	Ge	≈30 ms	0+	Q ϵ = [12,200]	
					2p	
	61	Ge	39(12) ms	(3/2 $-$)	Q ϵ = [13,600](100%)	
					ϵ p(~80%)	
	62	Ge	>150 ns	0+	Q ϵ = [9,750]	
	63	Ge	142(8) ms	(3/2 $-$)	Q ϵ = [9,780](100%)	
	64	Ge	63.7(25) s	0+	Q ϵ = 4,410(100%)	γ 427,667,128,384
	65	Ge	30.9(5) s	(3/2 $-$)	Q ϵ = 6,240(100%)	γ 650,62,809,191
	66	Ge	2.26(5) h	0+	Q ϵ = 2,100(100%)	γ 44,382,273,109
	67	Ge	18.9(3) m	1/2 $-$	Q ϵ = 4,223(100%)	γ 167
	68	Ge	270.95(16) days	0+	Q ϵ = 106(100%)	
	69	Ge	39.05(10) h	5/2 $-$	Q ϵ = 2,227.3(100%)	γ 1107,574,872,1337
	70	Ge	Stable	0+	{20.84(87)%}	
	71	Ge	11.43(3) days	1/2 $-$	Q ϵ = 231.9(100%)	
	71	Ge(198.4)	20.40(17) ms	9/2+	IT(100%)	γ 175
	72	Ge	Stable	0+	{27.54(34)%}	
	73	Ge	Stable	9/2+	{7.73(5)%}	
	73	Ge(66.6)	0.499(11) s	1/2 $-$	IT(100%)	γ 54
	74	Ge	Stable	0+	{36.28(73)%}	
	75	Ge	82.78(4) m	1/2 $-$	Q β^- = 1,176.5(100%)	γ 265,199
	75	Ge(139.7)	47.7(5) s	7/2+	IT(99.97%)	γ 140
					β^- – (0.03%)	γ 136,121,279,400

33	76	Ge	8.0E24 years	0+	2β− {7.61(38)%}		
	77	Ge	11.30(1) h	7/2+	Qβ− = 2,702.0(100%)	γ264,211,216,416	
	77	Ge(159.7)	52.9(6) s	1/2−	β − (81%)	γ216	
					IT(19%)	γ160	
	78	Ge	88.0(10) m	0+	Qβ− = 954(100%)	γ277	
	79	Ge	18.98(3) s	(1/2)−	Qβ− = 4,150(100%)	γ110,1506,100,503	
	79	Ge(186.0)	39.0(10) s	(7/2+)	β − (96%)	γ230,542,755,634	
					IT(4%)	γ186	
	80	Ge	29.5(4) s	0+	Qβ− = 2,670(100%)	γ265,110,1564,937	
	81	Ge	7.6(6) s	(9/2+)	Qβ− = 6,230(100%)	γ336,793,1496,93	
	81	Ge(679.1)	7.6(6) s	(1/2+)	β − (100%)	γ93,336,197,738	
	82	Ge	4.55(5) s	0+	Qβ− = 4,700(100%)	γ1092	
	83	Ge	1.85(6) s	(5/2+)	Qβ− = [8,900](100%)	γ307,1194,1526,1435	
	84	Ge	0.947(11) s	0+	Qβ− = [7,700](100%)	γ242,100	
					β − n(10.8%)		
	85	Ge	535(47) ms		Qβ− = [10,100](100%)	γ102	
					β − n(14%)		
	86	Ge	> 150 ns	0+	Qβ− = [9,400]		
	87	Ge	~0.14 s	(5/2+)	β − (100%)		
					β − n		
	88	Ge	> 150 ns	0+	β−		
	89	Ge	> 150 ns		β−		
33		Arsenic					
	60	As			Qp = [3,300]		

Table 22.1 (Continued)

A	Element	Half-life or width	$J\pi$	Qmode(%BR){%Abund}	Principal gammas, alphas
61	As			Qp = [2,400]	
62	As			Qp = [1,500]	
63	As		(3/2-)	Qp = [1,100]	
64	As	18(+43-7) ms		Q ϵ = [14,900]	
65	As	128(16) ms		Q ϵ = [9,400](100%)	
66	As	95.79(22) ms		Q ϵ = [9,800](100%)	
67	As	42.5(12) s	(5/2-)	Q ϵ = 6,010(100%)	γ 123,121,244,808
68	As	151.6(8) s	3+	Q ϵ = 8,100(100%)	γ 1016,762,651,1778
69	As	15.2(2) m	5/2-	Q ϵ = 4,010(100%)	γ 233,146,87,287
70	As	52.6(3) m	4(+)	Q ϵ = 6,220(100%)	γ 1040,668,1114,745
71	As	65.28(15) h	5/2-	Q ϵ = 2,013(100%)	γ 175
72	As	26.0(1) h	2-	Q ϵ = 4,356(100%)	γ 834
73	As	80.30(6) days	3/2-	Q ϵ = 341(100%)	γ 53
74	As	17.77(2) days	2-	Q ϵ = 2,562.4(66%)	γ 596
				Q β - = 1,353.0(34%)	γ 635
75	As	Stable	3/2-	{100%}	
75	As(303.9)	17.62(23) ms	9/2+	IT(100%)	γ 280,304
76	As	1.0942(7) days	2-	Q β - = 2,962.0(100%)	γ 559,657
77	As	38.83(5) h	3/2-	Q β - = 682.9(100%)	γ 239,521,250,88
78	As	90.7(2) m	2-	Q β - = 4,209(100%)	γ 614,695,1309,828
79	As	9.01(15) m	3/2-	Q β - = 2,281(100%)	γ 96,365,432,879
80	As	15.2(2) s	1+	Q β - = 5,641(100%)	γ 666,1645,1207
81	As	33.3(8) s	3/2-	Q β - = 3,856(100%)	γ 468,491
82	As	19.1(5) s	(1+)	Q β - = 7,270(100%)	γ 654,1731,755,1080

33	82	As(0 + x)	13.6(4) s	(5-)	β^- (100%)	γ 654,344,1895,1731
	83	As	13.4(3) s	(5/2-, 3/2-)	$Q\beta^- = 5,460$ (100%)	γ 735,1113,2077,2203
	84	As	3.24(26) s	(3-)	$Q\beta^- = [9,900]$ (100%) β^- n(0.28%)	γ 1455,667
	85	As	2.021(10) s	(3/2-)	$Q\beta^- = [8,900]$ (100%) β^- n(59.4%)	γ 1112,3749,462,3345 γ 1455,667
	86	As	0.945(8) s		$Q\beta^- = [11,100]$ (100%) β^- n(33%)	γ 704
	87	As	0.56(8) s	(3/2-)	$Q\beta^- = [10,300]$ (100%) β^- n(15.4%)	
	88	As	> 300 ns		$Q\beta^- = [12,200]$	
	89	As	> 300 ns		$Q\beta^- = [12,300]$	
	90	As	> 150 ns		β^-	
	91	As	> 150 ns		β^-	
	92	As	> 300 ns		β^- (100%)	
	Selenium					
	64	Se	> 180 ns	0+	$Q\epsilon = [14,100]$ (100%)	
	65	Se	< 50 ms		$Q\epsilon = [14,100]$ (100%)	
	66	Se	33(12) ms	0+	$Q\epsilon = [10,100]$ (100%)	
	67	Se	136(12) ms		$Q\epsilon = [10,150]$ (100%) ϵp (0.5%)	γ 352
34	68	Se	35.5(7) s	0+	$Q\epsilon = [4,700]$ (100%)	γ 315,161,265,111
	69	Se	27.4(2) s	(1/2-, 3/2-)	$Q\epsilon = 6,780$ (100%) ϵp (0.05%)	γ 98,66,692
	70	Se	41.1(3) m	0+	$Q\epsilon = [2,400]$ (100%)	γ 50,426,377,203
	71	Se	4.74(5) m	5/2-	$Q\epsilon = [4,800]$ (100%)	γ 148,1095,830,1243

Table 22.1 (Continued)

A	Element	Half-life or width	$J\pi$	Qmode(%BR){%Abund}	Principal gammas, alphas
72	Se	8.40(8) days	0+	Q ϵ = 335(100%)	γ 46
73	Se	7.15(8) h	9/2+	Q ϵ = 2,740(100%)	γ 361,67
73	Se(25.7)	39.8(13) m	3/2-	IT(72.6%)	γ 26
				ϵ (27.4%)	γ 67,254,84,393
74	Se	Stable	0+	{0.89(4)%}	
75	Se	119.79(4) days	5/2+	Q ϵ = 863.6(100%)	γ 265,136,280,121
76	Se	Stable	0+	{9.37(29)%}	
77	Se	Stable	1/2-	{7.63(16)%}	
77	Se(162.0)	17.36(5) s	7/2+	IT(100%)	γ 162
78	Se	Stable	0+	{23.77(28)%}	
79	Se	2.95(38)E5 years	7/2+	Q β - = 151.0(100%)	
79	Se(95.8)	3.92(1) m	1/2-	IT(99.94%)	γ 96
				β - (0.06%)	
80	Se	Stable	0+	{49.61(41)%}	
81	Se	18.45(12) m	1/2-	Q β - = 1,585(100%)	γ 276,290,828,566
81	Se(103.0)	57.28(2) m	7/2+	IT(99.95%)	γ 103
				β - (0.05%)	γ 276,260
82	Se	8.3(19)E20 years	0+	2 β - (100%)	
				{8.73(22)%}	
83	Se	22.3(3) m	9/2+	Q β - = 3,669(100%)	γ 357,510,225,718
83	Se(228.5)	70.1(4) s	1/2-	β - (100%)	γ 1031,357,988,674
84	Se	3.10(10) m	0+	Q β - = 1,830(100%)	γ 408
85	Se	31.7(9) s	(5/2+)	Q β - = 6,182(100%)	γ 345,3397,1427
86	Se	15.3(9) s	0+	Q β - = 5,099(100%)	γ 2441,48,2011,208

35	87	Se	5.50(12) s	(5/2+)	Qβ− = 7,280(100%) β − n(0.2%)	γ243,334,573,468
	88	Se	1.53(6) s	0+	Qβ− = 6,850(100%) β − n(0.99%)	γ159,259,1904,1745
	89	Se	0.41(4) s	(5/2+)	Qβ− = [9,000](100%) β − n(7.8%)	γ130
	90	Se	> 300 ns	0+	Qβ− = [8,200]	
	91	Se	0.27(5) s		Qβ− = [10,600](100%) β − n(21%)	
	92	Se	> 300 ns	0+	Qβ− = [9,400](100%)	
	93	Se	> 150 ns	(1/2+)	β −	
	94	Se	> 150 ns	0+	β −	
		Bromine				
	67	Br			Qp = [1,600]	
	68	Br	< 1.2 μs		Qp = [300]	
	69	Br	< 24 ns		Qp = [450]	
	70	Br	79.1(8) ms	0+	Qε = [10,400]	
	70	Br(0 + x)	2.2(2) s	9+	ε	
	71	Br	21.4(6) s	(5/2)−	Qε = [6,500](100%)	γ261,234,172,123
	72	Br	78.6(24) s	1+	Qε = 8,700(100%)	γ862,1317 455,2372
	72	Br(100.9)	10.6(3) s	1−	IT(∼100%)	
					ε	
	73	Br	3.4(2) m	1/2−	Qε = 4,680(100%)	γ65,336,700,126
	74	Br	25.4(3) m	(0−)	Qε = 6,907(100%)	γ635,219,634,2615
	74	Br(13.8)	46(2) m	4(+)	ε(100%)	γ635,728,634
	75	Br	96.7(13) m	3/2−	Qε = 3,030(100%)	γ287

Table 22.1 (Continued)

A	Element	Half-life or width	J^{π}	Qmode(%BR){%Abund}	Principal gammas, alphas
76	Br	16.2(2) h	1−	Q ϵ = 4,963(100%)	γ 559,657,1854,1216
76	Br(102.6)	1.31(2) s	(4)+	IT(>99.4%)	γ 45,57
				ϵ (<0.6%)	
77	Br	57.036(6) h	3/2−	Q ϵ = 1,365(100%)	γ 239,521,297,250
77	Br(105.9)	4.28(10) m	9/2+	IT(100%)	γ 106
78	Br	6.46(4) m	1+	Q ϵ = 3,574(>99.99%)	γ 614
				Q β − = 708(<0.01%)	
79	Br	Stable	3/2−	{50.69(7)%}	
79	Br(207.6)	4.86(4) s	9/2+	IT(100%)	γ 207
80	Br	17.68(2) m	1+	Q β − = 2,004(91.7%)	γ 616
				Q ϵ = 1,870.6(8.3%)	γ 666
80	Br(85.9)	4.4205(8) h	5−	IT(100%)	γ 37
81	Br	Stable	3/2−	{49.31(7)%}	
82	Br	35.282(7) h	5−	Q β − = 3,092.6(100%)	γ 777,554,619,698
82	Br(45.9)	6.13(5) m	2−	IT(97.6%)	γ 46
				β − (2.4%)	γ 777,698
83	Br	2.40(2) h	3/2−	Q β − = 973(100%)	γ 530
84	Br	31.80(8) m	2−	Q β − = 4,655(100%)	γ 882,1898,3928,2484
84	Br(320)	6.0(2) m	6−	β − (100%)	γ 424,882,1463
85	Br	2.90(6) m	3/2−	Q β − = 2,870(100%)	γ 802,925,919,1727
86	Br	55.1(4) s	(2−)	Q β − = 7,626(100%)	γ 1565,2751,1535,1362
87	Br	55.65(13) s	3/2−	Q β − = 6,853(100%)	γ 1420,1476,1578,532
				β − n(2.6%)	
88	Br	16.29(6) s	(2−)	Q β − = 8,960(100%)	γ 775,802
				β − n(6.58%)	γ 532

36	89	Br	4.40(3) s	(3/2 [−] , 5/2 [−])	Qβ [−] = 8,160(100%)	γ1098,29,998,954
					β [−] n(13.8%)	γ775
	90	Br	1.91(1) s		Qβ [−] = 10,350(100%)	γ707,1362,655,1233
					β [−] n(25.2%)	γ411,963,1098
	91	Br	0.541(5) s		Qβ [−] = 9,800(100%)	γ263,803,365,186
					β [−] n(20%)	
	92	Br	0.343(15) s	(2 [−])	Qβ [−] = 12,200(100%)	γ769,1447
					β [−] n(33.1%)	γ301,145,483,707
	93	Br	102(10) ms	(5/2 [−])	Qβ [−] = [11,000](100%)	γ117,242,237,710
					β [−] n(68%)	
	94	Br	70(20) ms		Qβ [−] = [13,300](100%)	
					β [−] n(68%)	
	95	Br	> 150 ns	(3/2 [−])	β [−]	
	96	Br	> 150 ns		β [−]	
					β [−] n(27.6%)	
	97	Br	> 150 ns	(3/2 [−])	β [−]	
36		Krypton				
	69	Kr	32(10) ms		Qε = [14,100](100%)	
	70	Kr	52(17) ms	0+	Qε = [10,600]	
	71	Kr	100(3) ms	(5/2 [−])	Qε = [10,500](100%)	
					εp(5.2%)	
	72	Kr	17.1(2) s	0+	Qε = 5,040(100%)	γ415,310,163,577
	73	Kr	27.3(10) s	3/2 [−]	Qε = 6,650(100%)	γ178,151,454,473
					εp(0.25%)	γ860
	74	Kr	11.50(11) m	0+	Qε = 3,140(100%)	γ90,203,297,63
	75	Kr	4.29(17) m	5/2+	Qε = 4,897(100%)	γ133,155,153

Table 22.1 (Continued)

A	Element	Half-life or width	J π	Qmode(%BR){%Abund}	Principal gammas, alphas
76	Kr	14.8(1) h	0+	Q ϵ = 1,310(100%)	γ 316,270,46,407
77	Kr	74.4(6) m	5/2+	Q ϵ = 3,063(100%)	γ 130,147
78	Kr	>2.3E20 years	0+	2 ϵ {0.35(1)%}	
79	Kr	35.04(10) h	1/2–	Q ϵ = 1,626(100%)	γ 261,398,606,306
79	Kr(129.8)	50(3) s	7/2+	IT(100%)	γ 130
80	Kr	Stable	0+	{2.28(6)%}	
81	Kr	2.29(11)E5 years	7/2+	Q ϵ = 280.7(100%)	γ 276
81	Kr(190.5)	13.10(3) s	1/2–	IT(100%)	γ 190
82	Kr	Stable	0+	ϵ (0.0025%)	
83	Kr	Stable	9/2+	{11.58(14)%}	
83	Kr	Stable	9/2+	{11.49(6)%}	
83	Kr(41.6)	1.83(2) h	1/2–	IT(100%)	γ 9
84	Kr	Stable	0+	{57.00(4)%}	
85	Kr	3,916.8(25) days	9/2+	Q β – = 687.1(100%)	γ 514
85	Kr(304.9)	4.480(8) h	1/2–	β – (78.6%)	γ 151
				IT(21.4%)	γ 305
86	Kr	Stable	0+	{17.30(22)%}	
87	Kr	76.3(5) m	5/2+	Q β – = 3,885(100%)	γ 403,2555,845
88	Kr	2.84(3) h	0+	Q β – = 2,914(100%)	γ 2392,196,2196,835
89	Kr	3.15(4) m	3/2(+)	Q β – = 4,990(100%)	γ 221,586,904,1473
90	Kr	32.32(9) s	0+	Q β – = 4,392(100%)	γ 1119,122,539,242
91	Kr	8.57(4) s	5/2(+)	Q β – = 6,440(100%)	γ 109,507,613,1109
92	Kr	1.840(8) s	0+	Q β – = 5,987(100%)	γ 142,1219,813,548
				β – n(0.03%)	

37	93	Kr	1.286(10) s	1/2+	Qβ− = 8,600(100%) β − n(1.95%)	γ253,324,267,253
	94	Kr	212(5) ms	0+	Qβ− = [7,400](100%) β − n(1.11%)	γ629,765,219,359
	95	Kr	114(3) ms	1/2	Qβ− = [9,800](100%) β − n(2.87%)	
	96	Kr	80(6) ms	0+	Qβ− = [8,200] β − n(3.7%)	
	97	Kr	63(4) ms		Qβ− = [10,400] β − n(8.2%)	
	98	Kr	46(8) ms	0+	β− β − n(7.0%)	
	99	Kr	40(11) ms	(3/2+)	β− β − n(11%)	
	100	Kr	>300 ns	0+	β− β − n	
		Rubidium				
	71	Rb			Qp = [1,400]	
	72	Rb	<1.2 μs	(3+)	Qp = [700]	
	73	Rb	>30 ns		Qε = [10,700] Qp = [600](>0%)	
	74	Rb	64.9(5) ms	(0+)	Qε = 10,400(100%)	
	75	Rb	19.0(12) s	(3/2−)	Qε = 7,019(100%)	γ179,179,187,672
	76	Rb	36.5(6) s	1(−)	Qε = 8,498(100%) εα(3.8E − 7%)	γ2571,424,356,346
	77	Rb	3.77(4) m	3/2−	Qε = 5,346(100%)	γ67,179,393

Table 22.1 (Continued)

A	Element	Half-life or width	$J\pi$	Qmode(%BR){%Abund}	Principal gammas, alphas
78	Rb	17.66(8) m	0(+)	Q ϵ = 7,224(100%)	γ 455,693,562,3438
78	Rb(103.3 + x)	5.74(5) m	4(–)	ϵ (90%)	γ 455,664,1110,693
				IT(10%)	γ 103,47
79	Rb	22.9(5) m	5/2+	Q ϵ = 3,646(100%)	γ 688,183,143,130
80	Rb	33.4(7) s	1+	Q ϵ = 5,721(100%)	γ 617
81	Rb	4.570(4) h	3/2–	Q ϵ = 2,237(100%)	γ 190,446
81	Rb(86.3)	30.5(3) m	9/2+	IT(97.6%)	γ 86
				ϵ (2.4%)	γ 50,644,1195,549
82	Rb	1.273(2) m	1+	Q ϵ = 4,400(100%)	γ 777
82	Rb(68.9)	6.472(6) h	5–	ϵ (100%)	γ 777,554,619,1044
				IT(<0.33%)	
83	Rb	86.2(1) days	5/2–	Q ϵ = 909(100%)	γ 520,530,553
84	Rb	33.1(1) days	2–	Q ϵ = 2,680,9(96.2%)	γ 882
				Q β – = 894(3.8%)	
84	Rb(463.6)	20.26(4) m	6–	IT(100%)	γ 248,464,216
85	Rb	Stable	5/2–	{72.17(2)%}	
86	Rb	18.642(18) days	2–	Q β – = 1,774.2(99.99%)	γ 1077
				Q ϵ = 519(0.0052%)	
86	Rb(556.1)	1.017(3) m	6–	IT(100%)	γ 556
				β – (<0.3%)	
87	Rb	4.81(9)E10 years	3/2–	Q β – = 283.3(100%)	
				{27.83(2)%}	
88	Rb	17.773(11) m	2–	Q β – = 5,313(100%)	γ 1836,898
89	Rb	15.15(12) m	3/2–	Q β – = 4,496(100%)	γ 1032,1248,2196,658

90	Rb	158(5) s	0–	Q β^- = 6,587(100%)	γ 832,1061,4366,4136
90	Rb(106.9)	258(4) s	3–	β^- – (97.4%) IT(2.6%)	γ 832,1375,3317,2753 γ 107
91	Rb	58.4(4) s	3/2(–)	Q β^- = 5,891(100%)	γ 94,2564,3600,346
92	Rb	4.492(20) s	0–	Q β^- = 8,100(100%) β^- – n(0.01%)	γ 815,2821,570,1712
93	Rb	5.84(2) s	5/2–	Q β^- = 7,462(100%) β^- – n(1.39%)	γ 433,986,213,1385 γ 815
94	Rb	2.702(5) s	3(–)	Q β^- = 10,291(100%) β^- – n(10.01%)	γ 837,1309,1578,1089 γ 433,213,986,219
95	Rb	377.5(8) ms	5/2–	Q β^- = 9,279(100%) β^- – n(8.73%)	γ 352,204,681,329 γ 837
96	Rb	203(3) ms	2(–)	Q β^- = 11,740(100%) β^- – n(13.3%)	γ 815,692 γ 352,204,681
97	Rb	169.9(7) ms	3/2+	Q β^- = 10,430(100%) β^- – n(25.1%)	γ 167,585,601,520 γ 815,692,414,813
98	Rb	114(5) ms	(0,1)	Q β^- = 12,326(100%) β^- – n(13.8%) β^- – 2n(0.05%)	γ 144,1693,2172,2316 γ 167,141
98	Rb(270)	96(3) ms	(3,4)	β^- – (100%)	γ 144,290,3011,3031
99	Rb	50.3(7) ms	(5/2+)	Q β^- = 11,280(100%) β^- – n(15.9%)	γ 91,125,1072,981 γ 145,289
100	Rb(0 + x)	51(8) ms	(3+,4+)	Q β^- = [13,500](100%) β^- – n(6%) β^- – 2n(0.16%)	γ 129,288,1201 γ 91,125 γ 145
101	Rb	32(5) ms	(3/2+)	Q β^- = 11,810(100%) β^- – n(28%)	γ 271,252,112,1092

Table 22.1 (Continued)

A	Element	Half-life or width	J π	Qmode(%BR){%Abund}	Principal gammas, alphas
102	Rb	37(5) ms		Q β^- = [15,100](100%) β^- – n(18%)	γ 126
38	Strontium				
	73	>25 ms		Q ϵ = [14,500](100%) $\epsilon p(>0\%)$	
	74	>1.2 μ s	0+	Q ϵ = [11,000]	
	75	88(3) ms	(3/2 $-$)	Q ϵ = [10,600](100%) $\epsilon p(5.2\%)$	
	76	7.89(7) s	0+	Q ϵ = [6,100](100%) $\epsilon p(0.34\%)$	γ 477,101,983,375
	77	9.0(2) s	5/2+	Q ϵ = 6,850(100%) $\epsilon p(<0.25\%)$	γ 147,160
	78	2.5(3) m	0+	Q ϵ = 3,761(100%)	
	79	2.25(10) m	3/2($-$)	Q ϵ = 5,319(100%)	γ 39,105,414,219
	80	106.3(15) m	0+	Q ϵ = 1,868(100%)	γ 589,175,553,379
	81	22.3(4) m	1/2 $-$	Q ϵ = 3,930(100%)	γ 154,148,443,188
	82	25.55(15) days	0+	Q ϵ = 180(100%)	
	83	32.41(3) h	7/2+	Q ϵ = 2,276(100%)	γ 763,382,418
83	Sr(259.2)	4.95(12) s	1/2 $-$	IT(100%)	γ 259
84	Sr	Stable	0+	{0.56(1)%}	
85	Sr	64.84(2) days	9/2+	Q ϵ = 1,065(100%)	γ 514
85	Sr(238.8)	67.63(4) m	1/2 $-$	IT(86.6%) ϵ (13.4%)	γ 232 γ 151

86	Sr	Stable	0+	[9.86(1)%]		
87	Sr	Stable	9/2+	[7.00(1)%]		
87	Sr(388.5)	2.815(12) h	1/2−	IT(99.7%)	γ389	
88	Sr	Stable	0+	ε(0.3%)		
89	Sr	50.53(7) days	5/2+	[82.58(1)%]		
90	Sr	28.90(3) years	0+	Qβ− = 1,495.1(100%)	γ909	
91	Sr	9.63(5) h	5/2+	Qβ− = 546.0(100%)		
92	Sr	2.66(4) h	0+	Qβ− = 2,707(100%)	γ1024,750,653,926	
93	Sr	7.423(24) m	5/2+	Qβ− = 1,940(100%)	γ1384	
94	Sr	75.3(2) s	0+	Qβ− = 4,137(100%)	γ590,876,888,710	
95	Sr	23.90(14) s	1/2+	Qβ− = 3,508(100%)	γ1428	
96	Sr	1.07(1) s	0+	Qβ− = 6,087(100%)	γ686,2717,2933,2248	
97	Sr	429(5) ms	1/2+	Qβ− = 5,387(100%)	γ122,809,932,530	
98	Sr	0.653(2) s	0+	Qβ− = 7,468(100%)	γ1905,954,652,307	
99	Sr	0.269(1) s	3/2+	β − n(<0.05%)		
100	Sr	202(3) ms	0+	Qβ− = 5,823(100%)	γ119,445,428,37	
101	Sr	118(3) ms	(5/2−)	β − n(0.25%)		
102	Sr	69(6) ms	0+	Qβ− = 8,090(100%)	γ125,536,1198,2279	
				β − n(0.1%)		
				Qβ− = 7,080(100%)	γ964,899,65,11	
				β − n(0.78%)		
				Qβ− = 9,510(100%)	γ128,1125,511,1211	
				β − n(2.37%)		
				Qβ− = 8,820(100%)	γ244,150,94,254	
				β − n(4.8%)		

Table 22.1 (Continued)

A	Element	Half-life or width	J π	Qmode(%BR){%Abund}	Principal gammas, alphas
103	Sr	> 150 ns		Q β^- = [11,200]	
104	Sr		0+	Q β^- = [10,100]	
105	Sr	> 150 ns		β^-	
39	Yttrium				
76	Y	> 200 ns		Q ϵ = [11,000](100%)	
				p	
77	Y	57(+22–12) ms	(5/2+)	Q ϵ = [11,000](100%)	
				ϵ p	
				p	
78	Y	50(8) ms	(0+)	Q ϵ = [10,500]	
78	Y (500.0)	5.7(7) s	(5+)	ϵ	
79	Y	14.8(6) s	(5/2+)	Q ϵ = 7,100(100%)	γ 177,1106,153
				ϵ p	
80	Y	30.1(5) s	4–	Q ϵ = [9,100](100%)	γ 386,595,1185,757
80	Y (228.0)	4.8(3) s	1–	ϵ (19%)	
				IT(81%)	
81	Y	70.4(10) s	(5/2+)	Q ϵ = 5,510(100%)	γ 124,79,408,120
82	Y	8.3(2) s	1+	Q ϵ = 7,820(100%)	γ 574,602
83	Y	7.08(6) m	9/2+	Q ϵ = 4,470(100%)	γ 36,882,490,859
83	Y (62.0)	2.85(2) m	3/2–	ϵ (60%)	γ 422,495
				IT(40%)	
84	Y	4.6(2) s	1+	Q ϵ = 6,490(100%)	γ 793
84	Y (0 + x)	39.5(8) m	(5–)	ϵ (100%)	γ 793,974,1040,661
85	Y	2.68(5) h	(1/2)–	Q ϵ = 3,255(100%)	γ 232,504,914

85	Y (19.8)	4.86(13) h	9/2+	ϵ (100%)	γ 232,2124,767,536
86	Y	14.74(2) h	4-	IT(<0.002%)	
86	Y (218.3)	48(1) m	(8+)	$Q\epsilon = 5.240$ (100%)	γ 1077,628,1153,777
87	Y	79.8(3) h	1/2-	IT(99.31%)	γ 10
87	Y (380.82)	13.37(3) h	9/2+	ϵ (0.69%)	γ 627,1153,1077,99
				$Q\epsilon = 1.861.6$ (100%)	γ 485,389
				IT(98.43%)	γ 381
				ϵ (1.57%)	
88	Y	106.626(21) days	4-	$Q\epsilon = 3.622.6$ (100%)	γ 1836,898
89	Y	Stable	1/2-	{100%}	
89	Y (909.0)	15.663(5) s	9/2+	IT(100%)	γ 909
90	Y	64.053(20) h	2-	$Q\beta- = 2.280.1$ (100%)	γ 2186
90	Y (682.0)	3.19(6) h	7+	IT(100%)	γ 203,480
				$\beta- (0.0018\%)$	γ 2319
91	Y	58.51(6) days	1/2-	$Q\beta- = 1.544.8$ (100%)	γ 1205
91	Y (555.6)	49.71(4) m	9/2+	IT(100%)	γ 556
				$\beta- (<1.5\%)$	
92	Y	3.54(1) h	2-	$Q\beta- = 3.639$ (100%)	γ 934,1405,561,449
93	Y	10.18(8) h	1/2-	$Q\beta- = 2.893$ (100%)	γ 267,947,1918
93	Y (758.7)	0.82(4) s	7/2+	IT(100%)	γ 590,168
94	Y	18.7(1) m	2-	$Q\beta- = 4.917$ (100%)	γ 919,1139
95	Y	10.3(1) m	1/2-	$Q\beta- = 4.453$ (100%)	γ 954,2176,3576,1324
96	Y	5.34(5) s	0-	$Q\beta- = 7.100$ (100%)	γ 1750,2226
96	Y (0 + x)	9.6(2) s	8+	$\beta- (100\%)$	γ 1751,915,617,1107
97	Y	3.75(3) s	(1/2-)	$Q\beta- = 6.688$ (100%)	γ 3288,3401,1997,2743
				$\beta- n(0.058\%)$	

Table 22.1 (Continued)

A	Element	Half-life or width	J^{π}	Qmode(%BR){%Abund}	Principal gammas, alphas
97	Y (667.5)	1.17(3) s	(9/2)+	β^- (>99.3%)	γ 1103,161,1091,970
				IT(<0.7%)	γ 668
				β^- - n(<0.08%)	
97	Y (3523.3)	142(8) ms	(27/2-)	IT(>80%)	γ 912,792,990,162
98	Y	0.548(2) s	(0)-	β^- (<20%)	
				Q β^- = 8.824(100%)	γ 1223,2941,1591,4450
98	Y (410)	2.0(2) s	(4,5)	β^- - n(0.33%)	
				β^- (90%)	γ 1223,621,648,1802
				IT(<20%)	
				β^- - n(3.4%)	
99	Y	1.470(7) s	(5/2+)	Q β^- = 7.567(100%)	γ 122,724,536,576
100	Y	735(7) ms	1-,2-	β^- - n(1.9%)	
				Q β^- = 9.310(100%)	γ 213,119,666
				β^- - n(0.92%)	γ 122
100	Y (0 + x)	0.94(3) s	(3,4,5)	β^- (100%)	γ 213,352
101	Y	0.45(2) s	(5/2+)	Q β^- = 8.550(100%)	γ 98,217,759,1300
102	Y (0 + y)	0.30(1) s		β^- - n(1.94%)	
				Q β^- = 9.850(100%)	γ 152,1211,1059,743
				β^- - n(4.9%)	
102	Y (0 + x)	0.36(4) s		β^- (100%)	γ 152,327,1091,579
103	Y	0.23(2) s	(5/2+)	β^- - n(4.9%)	
				Q β^- = [9,600](100%)	γ 98,109
				β^- - n(8%)	
104	Y	180(60) ms		Q β^- = [11,800](100%)	
				β^- - n	

	105	Y	> 150 ns				Qβ– = [11,200]		
	106	Y	> 150 ns				Qβ– = [13,300]		
	107	Y	≈30 ms		(5/2+)		β– (100%)		
	108	Y	(20 ms)				β–		
							β– n		
40		Zirconium							
	78	Zr	> 200 ns		0+		Qε		
	79	Zr	56(30) ms				εp		
							Qε = [11,000]		
							εp		
	80	Zr	4.6(6) s		0+		Qε = [5,800]		
	81	Zr	5.5(4) s		(3/2–)		Qε = 7,200(100%)		
							εp(0.12%)		
	82	Zr	32(5) s		0+		Qε = 4,000(100%)		γ525
	83	Zr	41.6(24) s		(1/2–)		Qε = 5,870(100%)		γ56,105,474,304
							εp		
	84	Zr	25.9(7) m		0+		Qε = [2,670](100%)		γ113,45,373,667
	85	Zr	7.86(4) m		7/2+		Qε = 4,690(100%)		γ454,416,1198
	85	Zr(292.2)	10.9(3) s		(1/2–)		IT(<92%)		γ292
							ε(>8%)		γ417
	86	Zr	16.5(1) h		0+		Qε = 1,480(100%)		γ243,29
	87	Zr	1.68(1) h		(9/2)+		Qε = 3,669(100%)		γ1227,1210,1024

Table 22.1 (Continued)

A	Element	Half-life or width	J π	Qmode(%BR){(%Abund)}	Principal gammas, alphas
87	Zr(335.8)	14.0(2) s	(1/2) [−]	IT(100%)	γ 201,135
88	Zr	83.4(3) days	0 ⁺	Q ϵ = 673(100%)	γ 393
89	Zr	78.41(12) h	9/2 ⁺	Q ϵ = 2,833(100%)	γ 909
89	Zr(587.8)	4.161(17) m	1/2 [−]	IT(93.77%)	γ 588
				ϵ (6.23%)	γ 1507
90	Zr	Stable	0 ⁺	{51.45(40)%}	
90	Zr(2319.0)	809.2(20) ms	5 [−]	IT(100%)	γ 2319,2186
91	Zr	Stable	5/2 ⁺	{11.22(5)%}	
92	Zr	Stable	0 ⁺	{17.15(8)%}	
93	Zr	1.53(10)E6 years	5/2 ⁺	Q β [−] = 91.4(100%)	γ 31
94	Zr	Stable	0 ⁺	{17.38(28)%}	
95	Zr	64.032(6) days	5/2 ⁺	Q β [−] = 1,124.8(100%)	γ 757,724
96	Zr	2.0(4)E19 years	0 ⁺	2 β [−]	
				{2.80(9)%}	
97	Zr	16.744(11) h	1/2 ⁺	Q β [−] = 2,658.1(100%)	γ 743
98	Zr	30.7(4) s	0 ⁺	Q β [−] = 2,250(100%)	
99	Zr	2.1(1) s	(1/2 ⁺)	Q β [−] = 4,558(100%)	γ 469,546,594,462
100	Zr	7.1(4) s	0 ⁺	Q β [−] = 3,335(100%)	γ 504,400
101	Zr	2.3(1) s	(3/2 ⁺)	Q β [−] = 5,485(100%)	γ 119,206,912,2010
102	Zr	2.9(2) s	0 ⁺	Q β [−] = 4,610(100%)	γ 600,535,65,157
103	Zr	1.3(1) s	(5/2 [−])	Q β [−] = 6,950(100%)	γ 248,164,126,120
104	Zr	1.2(3) s	0 ⁺	Q β [−] = [5,900](100%)	γ 101,445,505,264
105	Zr	0.6(1) s		Q β [−] = [8,500](100%)	
106	Zr	> 150 ns	0 ⁺	Q β [−] = [7,200]	

41	107	Zr	≈150 ms			Qβ− = [9,800](100%)	
	108	Zr	(80 ms)	0+		Qβ− = [8,600]	
	109	Zr	>150 ns			β − n	
						β−	
						β − n	
	110	Zr	>150 ns	0+		β−	
		Niobium					
	81	Nb	~0.8 s			Qε = [11,400]	
						εp	
						Qp = [600]	
	82	Nb	50(5) ms	(0+)		Qε = [11,200]	
	83	Nb	4.1(3) s	(5/2+)		Qε = 7,500(100%)	γ24
	84	Nb	9.5(10) s	3+		Qε = [9,600](100%)	γ540,723
						εp	
	85	Nb	20.9(7) s	(9/2+)		Qε = 6,000(100%)	γ50
	86	Nb(0 + x)	56(8) s			Qε = 7,980	γ752,915,1003,670
	86	Nb	88(1) s	(6+)		ε(100%)	
	87	Nb	3.75(9) m	(1/2−)		Qε = 5,170(100%)	γ201,135
	87	Nb(3.8)	2.6(1) m	(9/2+)		ε	γ201,471,1067,1885
	88	Nb	14.55(6) m	(8+)		Qε = [7,200](100%)	γ1083,1057,671,503
	88	Nb(40)	7.78(5) m	(4−)		ε(100%)	γ1057,1083,399,451
	89	Nb	2.03(7) h	(9/2+)		Qε = 4,290(100%)	γ1627,1833,3093,2572
	89	Nb(35)	66(2) m	(1/2)−		ε(100%)	γ588,507
	90	Nb	14.60(5) h	8+		Qε = 6,111(100%)	γ1129,2319,141,2186
	90	Nb(124.7)	18.81(6) s	4−		IT(100%)	
	90	Nb(382.0)	6.19(8) ms	1+		IT(100%)	

Table 22.1 (Continued)

A	Element	Half-life or width	$J\pi$	Qmode(%BR){%Abund}	Principal gammas, alphas
91	Nb	680(130) years	9/2+	Q ε = 1,253.4(100%)	
91	Nb(104.6)	60.86(22) days	1/2-	IT(96.6%) ε (3.4%)	γ 105 γ 1205
92	Nb	3.47(24)E7 years	(7)+	Q ε = 2,005.6(100%) Q β^- = 357(<0.05%)	γ 561,935
92	Nb(135.5)	10.15(2) days	(2)+	ε (100%)	γ 934
93	Nb	Stable	9/2+	{100%}	
93	Nb(30.8)	16.13(14) years	1/2-	IT(100%)	γ 31
94	Nb	2.03(16)E4 years	(6)+	Q β^- = 2,045.4(100%)	γ 871,703
94	Nb(40.9)	6.263(4) m	3+	IT(99.5%) β^- (0.5%)	γ 41 γ 871
95	Nb	34.991(6) days	9/2+	Q β^- = 925.6(100%)	γ 766
95	Nb(235.7)	3.61(3) days	1/2-	IT(94.4%) β^- (5.6%)	γ 236 γ 204
96	Nb	23.35(5) h	6+	Q β^- = 3,187(100%)	γ 778,569,1091,460
97	Nb	72.1(7) m	9/2+	Q β^- = 1,933.9(100%)	γ 658
97	Nb(743.4)	58.7(18) s	1/2-	IT(100%)	γ 743
98	Nb	2.86(6) s	1+	Q β^- = 4,586(100%)	γ 787,1024,645,1432
98	Nb(84)	51.3(4) m	(5+)	β^- (99.9%) IT(<0.2%)	γ 787,723,1169,834
99	Nb	15.0(2) s	9/2+	Q β^- = 3,639(100%)	γ 138,98
99	Nb(365.2)	2.6(2) m	1/2-	β^- (>96.2%) IT(<3.8%)	γ 98,254,2641,2852 γ 365
100	Nb	1.5(2) s	1+	Q β^- = 6,245(100%)	γ 536,528,160,1023

42	100	Nb(314)	2.99(11) s	(5+)	β^- – (100%)	γ 536,601,1281,967
	101	Nb	7.1(3) s	(5/2+)	$Q\beta^- = 4,569(100\%)$	γ 13,276,44,158
	102	Nb	1.3(2) s	1+	$Q\beta^- = 7,210$	γ 949
	102	Nb(0 + x)	4.3(4) s		β^-	γ 296,1633,552,447
	103	Nb	1.5(2) s	(5/2+)	$Q\beta^- = 5,530(100\%)$	γ 103,641,539,139
	104	Nb	4.9(3) s	(1+)	$Q\beta^- = 8,110(100\%)$	γ 192,368,620,836
	104	Nb(215.0)	0.94(4) s		β^- – n(0.06%)	
					β^- – (100%)	
					β^- – n(0.05%)	
	105	Nb	2.95(6) s	(5/2+)	$Q\beta^- = 6,490(100\%)$	γ 95,247,310,138
	106	Nb	0.93(4) s		β^- – n(1.7%)	
					$Q\beta^- = [9,400](100\%)$	γ 172,351,714,725
					β^- – n(4.5%)	
	107	Nb	330(50) ms		$Q\beta^- = [8,000](100\%)$	
	108	Nb	0.193(17) s	(2+)	$Q\beta^- = [10,600](100\%)$	γ 193,590,393,586
					β^- – n(6.2%)	
	109	Nb	0.19(3) s	(5/2)	$Q\beta^- = [9,100](100\%)$	
					β^- – n(31%)	
	110	Nb	0.17(2) s		$Q\beta^- = [12,100](100\%)$	
					β^- – n(40%)	
	111	Nb	(80 ms)	(5/2+)	β^-	
	112	Nb	> 150 ns	(2+)	β^-	
	113	Nb	> 150 ns		β^-	
42		Molybdenum				
	83	Mo	6(+30–3) ms		$Q\epsilon = [11,200](100\%)$	
	84	Mo	3.7(+10–8) s	0+	$Q\epsilon = [6,100](100\%)$	

Table 22.1 (Continued)

A	Element	Half-life or width	$J\pi$	Qmode(%BR){%Abund}	Principal gammas, alphas
85	Mo	3.2(2) s	(1/2 [−])	$\epsilon p(0.14\%)$ Q ϵ = [8, 100]	
86	Mo	19.6(11) s	0 ⁺	Q ϵ = 5,300(100%)	γ 50,47,187
87	Mo	14.02(26) s	7/2 ⁺	Q ϵ = 6,490(100%)	γ 263,397
88	Mo	8.0(2) m	0 ⁺	$\epsilon p(15\%)$ Q ϵ = [3,720](100%)	γ 752,915 γ 171,80,131
89	Mo	2.11(10) m	(9/2 ⁺)	Q ϵ = 5,580(100%)	γ 659,844,1272,1155
89	Mo(387.3)	190(15) ms	(1/2 [−])	IT(100%)	γ 269,119
90	Mo	5.56(9) h	0 ⁺	Q ϵ = 2,489(100%)	γ 257,122
91	Mo	15.49(1) m	9/2 ⁺	Q ϵ = 4,434(100%)	γ 1637,1582,2632,3029
91	Mo(652.9)	64.6(6) s	1/2 [−]	$\epsilon(50\%)$ IT(50%)	γ 1508,1208 γ 653
92	Mo	Stable	0 ⁺	{14.84(35)%}	
93	Mo	4,000(800) years	5/2 ⁺	Q ϵ = 405(100%)	γ 31
93	Mo(2424.9)	6.85(7) h	21/2 ⁺	IT(99.88%) $\epsilon(0.12\%)$	γ 685,1477,263 γ 950,689,385,541
94	Mo	Stable	0 ⁺	{9.25(12)%}	
95	Mo	Stable	5/2 ⁺	{15.92(13)%}	
96	Mo	Stable	0 ⁺	{16.68(2)%}	
97	Mo	Stable	5/2 ⁺	{9.55(8)%}	
98	Mo	Stable	0 ⁺	{24.13(31)%}	
99	Mo	65.94(1) h	1/2 ⁺	Q β^- = 1,357.2(100%)	γ 740,181,141,778
100	Mo	7.3(4)E18 years	0 ⁺	2 β^- – (100%) {9.63(23)%}	γ 591

43	101	Mo	14.61(3) m	1/2+	Qβ− = 2,824(100%)	γ590,192,1012,506
	102	Mo	11.3(2) m	0+	Qβ− = 1,010(100%)	γ212,148,224
	103	Mo	67.5(15) s	(3/2+)	Qβ− = 3,750(100%)	γ83,424,46,688
	104	Mo	60(2) s	0+	Qβ− = 2,160(100%)	γ69,70,36,55
	105	Mo	35.6(16) s	(3/2−)	Qβ− = 4,950(100%)	γ85,77,148,161
	106	Mo	8.73(12) s	0+	Qβ− = 3,520(100%)	γ466,54,619,595
	107	Mo	3.5(5) s	(5/2+)	Qβ− = 6,160(100%)	γ400,66,384,484
	108	Mo	1.09(2) s	0+	Qβ− = [4,750](100%)	γ268,241,372,86
	109	Mo	0.53(6) s	(7/2−)	Qβ− = [7,600](100%)	
	110	Mo	0.30(4) s	0+	Qβ− = [5,900](100%)	γ142,121,223,599
	111	Mo	(200 ms)		Qβ− = [8,800]	
	112	Mo	>150 ns	0+	Qβ− = [7,100]	
	113	Mo	(100 ms)		Qβ− = [10,000]	
43					β − n	
	114	Mo	(80 ms)	0+	β−	
	115	Mo	(60 ms)		β−	
					β − n	
		Technetium				
	85	Tc	~0.5 s		Qε = [11,500]	
	86	Tc	54(7) ms	(0+)	Qε = [11,400]	
	87	Tc	2.2(2) s	(9/2+)	Qε = [8,600](100%)	
	88	Tc(0 + x)	5.8(2) s	(3+)	Qε = [10,100](100%)	γ741,914,972
	88	Tc	6.4(8) s	(6+)	ε(100%)	
	89	Tc	12.8(9) s	(9/2+)	Qε = 7,510(100%)	γ119
	89	Tc(62.6)	12.9(8) s	(1/2−)	ε(100%)	γ269
	90	Tc(0 + x)	8.7(2) s	1+	Qε = 8,960(100%)	γ948

Table 22.1 (Continued)

A	Element	Half-life or width	J^{π}	Qmode(%BR){%Abund}	Principal gammas, alphas
90	Tc(500)	49.2(4) s	(6+)	ε (100%)	γ 1054,948,945,810
91	Tc	3.14(2) m	(9/2)+	Q_{ε} = 6,220(100%)	γ 2451,1640,1605,1565
91	Tc(139.3)	3.3(1) m	(1/2)–	ε (100%)	γ 503
				IT(<1%)	
92	Tc	4.25(15) m	(8)+	Q_{ε} = 7,870(100%)	γ 1510,773,329,148
93	Tc	2.75(5) h	9/2+	Q_{ε} = 3,200.9(100%)	γ 1363,1520,1477
93	Tc(391.8)	43.5(10) m	1/2–	IT(76.6%)	γ 392
				ε (23.4%)	γ 2645,944,3129,1492
94	Tc	293(1) m	7+	Q_{ε} = 4,256(100%)	γ 871,703,850
94	Tc(75.5)	52.0(10) m	(2)+	ε (100%)	γ 871
				IT(<0.1%)	
95	Tc	20.0(1) h	9/2+	Q_{ε} = 1,691(100%)	γ 766
95	Tc(38.9)	61(2) days	1/2–	ε (96.12%)	γ 204,582,835,786
				IT(3.88%)	γ 39
96	Tc	4.28(7) days	7+	Q_{ε} = 2,973(100%)	γ 778,850,813,1127
96	Tc(34.2)	51.5(10) m	4+	IT(98%)	γ 34
				ε (2%)	γ 778,1200,481,720
97	Tc	4.21(16)E6 years	9/2+	Q_{ε} = 320(100%)	
97	Tc(96.5)	91.4(8) days	1/2–	IT(96.06%)	γ 97
				ε (<3.9%4)	
98	Tc	4.2(3)E6 years	(6)+	$Q_{\beta-}$ = 1,796(100%)	γ 745,652
99	Tc	2.111(12)E5 years	9/2+	$Q_{\beta-}$ = 293.7(100%)	γ 90
99	Tc(142.7)	6.0058(12) h	1/2–	IT(100%)	γ 141
				$\beta-$ – (0.0037%)	γ 322

100	Tc	15.46(19) s	1+	Qβ− = 3,202.4(100%) Qε = 168(0.0018%)	γ540,591
101	Tc	14.22(1) m	9/2+	Qβ− = 1,613(100%)	γ307
102	Tc	5.28(15) s	1+	Qβ− = 4,530(100%)	γ475,469,866,628
102	Tc(0 + x)	4.35(7) m	(4,5)	β − (98%) IT(2%)	γ475,628,630,1615
103	Tc	54.2(8) s	5/2+	Qβ− = 2,660(100%)	γ346,136,563,210
104	Tc	18.3(3) m	(3+)	Qβ− = 5,600(100%)	γ358,531,535,884
105	Tc	7.6(1) m	(3/2−)	Qβ− = 3,640(100%)	γ143,108,322,160
106	Tc	35.6(6) s	(1,2)	Qβ− = 6,547(100%)	γ270,2239,1969,2789
107	Tc	21.2(2) s	(3/2−)	Qβ− = 4,820(100%)	γ103,177,106,459
108	Tc	5.17(7) s	(2)+	Qβ− = 7,720(100%)	γ242,466,708,733
109	Tc	0.86(4) s	(5/2+)	Qβ− = [5,990](100%) β − n(0.08%)	γ195,129,96,69
110	Tc	0.92(3) s	(2+)	Qβ− = [8,800](100%) β − n(0.04%)	γ241,372,613,619
111	Tc	.290(20) ms		Qβ− = [7,000](100%) β − n(0.85%)	γ150,368,175,104
112	Tc	0.29(2) s		Qβ− = [10,000](100%) β − n(1.5%)	γ237,287,523,408
113	Tc	0.17(2) s		Qβ− = [8,200](100%) β − n(2.1%)	
114	Tc	0.15(3) s		Qβ− = [11,100] β − n	
115	Tc	73(+32−22) ms		Qβ− = [9,300] β − n	

Table 22.1 (Continued)

	A	Element	Half-life or width	$J\pi$	Qmode(%BR){%Abund}	Principal gammas, alphas
44	116	Tc	(90 ms)		β^-	
	117	Tc	(40 ms)		β^-	
	118	Tc	>150 ns		β^-	
		Ruthenium				
	87	Ru	> 1.5 μ s		Q ϵ = [11,800]	
	88	Ru	1.2(+3 –2) s	0+	Q ϵ = [7,100]	
	89	Ru	1.5(2) s	(9/2+)	Q ϵ = [8,000]	
					ϵ p(<0.15%)	
	90	Ru	11.7(9) s	0+	Q ϵ = [5,800](100%)	γ 1551
	91	Ru	7.9(4) s	(9/2+)	Q ϵ = 7,400(100%)	γ 395,1097,893
	91	Ru(0 + x)	7.6(8) s	(1/2–)	ϵ (>0%)	
					ϵ p(>0%)	
					IT	
	92	Ru	3.65(5) m	0+	Q ϵ = [4,500](100%)	γ 214,259,135,47
	93	Ru	59.7(6) s	(9/2)+	Q ϵ = 6,340(100%)	γ 681,1435
	93	Ru(734.4)	10.8(3) s	(1/2)–	ϵ (78%)	γ 1396,1111,2039
					IT(22%)	γ 734
					ϵ p(0.03%)	
	94	Ru	51.8(6) m	0+	Q ϵ = 1,587(100%)	γ 367,891
95	Ru		1.643(14) h	5/2+	Q ϵ = 2,567(100%)	γ 336,1097,627
96	Ru		Stable	0+	{5.54(14)%}	
97	Ru		2.9(1) days	5/2+	Q ϵ = 1,108(100%)	γ 216,324
98	Ru		Stable	0+	{1.87(3)%}	
99	Ru		Stable	5/2+	{12.76(14)%}	

100	Ru	Stable	0+	{12.60(7)%}		
101	Ru	Stable	5/2+	{17.06(2)%}		
102	Ru	Stable	0+	{31.55(14)%}		
103	Ru	39.26(2) days	3/2+	Q β^- = 763.4(100%)	γ 497	
103	Ru(238.2)	1.69(7) ms	11/2-	IT(100%)	γ 211	
104	Ru	Stable	0+	{18.62(27)%}		
105	Ru	4.44(2) h	3/2+	Q β^- = 1,917(100%)	γ 724,469,676,316	
106	Ru	371.8(18) days	0+	Q β^- = 39.40(100%)		
107	Ru	3.75(5) m	(5/2)+	Q β^- = 2,940(100%)	γ 194,848,463,374	
108	Ru	4.55(5) m	0+	Q β^- = 1,360(100%)	γ 165,150	
109	Ru	34.5(10) s	(5/2+)	Q β^- = 4,160(100%)	γ 206,226,359,1929	
110	Ru	11.6(6) s	0+	Q β^- = 2,810(100%)	γ 112	
111	Ru	2.12(7) s	(5/2+)	Q β^- = [5,500](100%)	γ 304,212,382,1516	
112	Ru	1.75(7) s	0+	Q β^- = [3,670](100%)	γ 327,245,82	
113	Ru	0.80(5) s	(5/2+)	Q β^- = [6,600](100%)	γ 263,212,338,658	
113	Ru(130)	510(30) ms	(11/2-)	β^- - (92%)		
				IT(8%)		
114	Ru	0.52(5) s	0+	Q β^- = [4,800](100%)	γ 127,128,179,53	
115	Ru	740(80) ms		Q β^- = [7,600](100%)	γ 293	
				β^- - n		
116	Ru	(400 ms)	0+	Q β^- = [6,000]		
117	Ru	(300 ms)		Q β^- = [8,800]		
118	Ru	123(+48-35) ms	0+	Q β^- = [7,100]		
				β^- - n		
119	Ru	> 150 ns		β^-		
120	Ru	> 150 ns	0+	β^-		

Table 22.1 (Continued)

45	A	Element	Half-life or width	J π	Qmode(%BR){%Abund}	Principal gammas, alphas
		Rhodium				
	89	Rh	> 1.5 μ s		Q ϵ = [12,400]	
	90	Rh	12(+9–4) ms		Q ϵ = [12,200]	
	90	Rh(x)	1.0(+3–2) s		ϵ	
	91	Rh	1.47(22) s	(9/2+)	Q ϵ = [9,500]	
	91	Rh(x)	1.46(11) s	(1/2–)	ϵ	
	92	Rh	4.66(25) s	(\geq 6+)	Q ϵ = [11,000](100%)	γ 817,990
	92	Rh(x)	0.5(4) s	(2+)	ϵ	
	93	Rh	11.9(7) s	(9/2+)	Q ϵ = [8,100]	
	94	Rh(0 + y)	25.8(2) s	(8+)	Q ϵ = [9,600](100%)	γ 1431,756,312,146
	94	Rh(0 + x)	70.6(6) s	(4+)	ϵ (100%)	γ 1431,756,1073,312
					ϵ p(1.8%)	
	95	Rh	5.02(10) m	(9/2)+	Q ϵ = 5,110(100%)	γ 942,1352

95	Rh(543.3)		1.96(4) m	(1/2)–	IT(88%)	γ 543
					ϵ (12%)	γ 788,3407,4337,3186
96	Rh		9.90(10) m	6+	Q ϵ = 6,446(100%)	γ 833,685,632,742
96	Rh(52.0)		1.51(2) m	3+	IT(60%)	γ 52
					ϵ (40%)	γ 833,1098,1692
97	Rh		30.7(6) m	9/2+	Q ϵ = 3,520(100%)	γ 422,840,879
97	Rh(258.8)		46.2(16) m	1/2–	ϵ (94.4%)	γ 189,2246,422,1587
					IT(5.6%)	γ 259
98	Rh		8.72(12) m	(2)+	Q ϵ = 5,057(100%)	γ 653
98	Rh(0 + x)		3.6(2) m	(5+)	ϵ (11%)	γ 653,745
					IT(89%)	

99	Rh	16.1(2) days	1/2–	$Q_{\alpha} = 2.043(100\%)$	$\gamma 528, 353, 90, 322$
99	Rh(64.3)	4.7(1) h	9/2+	$\epsilon(>99.84\%)$	$\gamma 341, 618, 1261$
				$IT(<0.16\%)$	
100	Rh	20.8(1) h	1–	$Q_{\alpha} = 3.630(100\%)$	$\gamma 540, 2376, 823, 1553$
100	Rh(0 + x)	4.6(2) m	(5+)	$IT(\sim 98.3\%)$	$\gamma 33, 75, 75, 42$
				$\epsilon(\sim 1.7\%)$	$\gamma 540, 687, 1828, 1536$
101	Rh	3.3(3) years	1/2–	$Q_{\alpha} = 541(100\%)$	$\gamma 198, 127, 325$
101	Rh(157.4)	4.34(1) days	9/2+	$\epsilon(92.8\%)$	$\gamma 307$
				$IT(7.2\%)$	$\gamma 157$
102	Rh	207(3) days	(1–, 2–)	$Q_{\alpha} = 2.323(78\%)$	$\gamma 475$
				$Q\beta^{-} = 1,151(22\%)$	$\gamma 557$
102	Rh(140)	≈ 2.9 years	6(+)	$\epsilon(99.77\%)$	$\gamma 475, 631, 697, 1047$
				$IT(0.23\%)$	$\gamma 141$
103	Rh	Stable	1/2–	{100%}	
103	Rh(39.8)	56.114(9) m	7/2+	$IT(100\%)$	$\gamma 40$
104	Rh	42.3(4) s	1+	$Q\beta^{-} = 2,441(99.55\%)$	$\gamma 556$
				$Q_{\alpha} = 1,141(0.45\%)$	$\gamma 358$
104	Rh(129.0)	4.34(3) m	5+	$IT(99.87\%)$	$\gamma 51$
				$\beta^{-} - (0.13\%)$	$\gamma 556$
105	Rh	35.36(6) h	7/2+	$Q\beta^{-} = 567(100\%)$	$\gamma 319, 306$
105	Rh(129.6)	42.9(3) s	1/2–	$IT(100\%)$	$\gamma 130$
106	Rh	30.07(35) s	1+	$Q\beta^{-} = 3,541(100\%)$	$\gamma 512, 622$
106	Rh(137)	131(2) m	(6)+	$\beta^{-} - (100\%)$	$\gamma 512, 1047, 717, 451$
107	Rh	21.7(4) m	7/2+	$Q\beta^{-} = 1,511(100\%)$	$\gamma 303, 392$
108	Rh	16.8(5) s	1+	$Q\beta^{-} = 4,510(100\%)$	$\gamma 434, 619, 497$
108	Rh(0 + x)	6.0(3) m	(5+)	$\beta^{-} - (100\%)$	$\gamma 434, 581, 948, 901$
109	Rh	80(2) s	7/2+	$Q\beta^{-} = 2,591(100\%)$	$\gamma 327, 426, 178, 291$

Table 22.1 (Continued)

	A	Element	Half-life or width	$J\pi$	Qmode(%BR){%Abund}	Principal gammas, alphas
	110	Rh(y)	3.2(2) s	1+	$Q\beta^- = 5.400(100\%)$	$\gamma 374,440$
	110	Rh(x)	28.5(15) s	(≥ 4)	$\beta^- (100\%)$	$\gamma 374,546,688,838$
	111	Rh	11(1) s	(7/2+)	$Q\beta^- = [3,740](100\%)$	$\gamma 275$
	112	Rh(0 + x)	3.45(37) s	1+	$Q\beta^- = [6,800](100\%)$	$\gamma 349,388,778$
	112	Rh(0 + y)	6.73(15) s	(4,5,6)	$\beta^- (100\%)$	$\gamma 349,561,1099,360$
	113	Rh	2.80(12) s	(7/2+)	$Q\beta^- = [4,900](100\%)$	$\gamma 349,190,409,220$
	114	Rh	1.85(5) s	1+	$Q\beta^- = [7,900](100\%)$	
	114	Rh(0 + x)	1.85(5) s	(4,5)	$\beta^- (100\%)$	
	115	Rh	0.99(5) s	(7/2+)	$Q\beta^- = 6,000(100\%)$	$\gamma 128,126,165,297$
	116	Rh	0.68(6) s	1+	$Q\beta^- = [8,900](100\%)$	$\gamma 340,398,738$
	116	Rh(150)	0.57(5) s	(6-)	$\beta^- (100\%)$	$\gamma 340,537,726,744$
	117	Rh	0.44(4) s	(7/2+)	$Q\beta^- = [7,000](100\%)$	$\gamma 132,97,35$
	118	Rh	266(+22-21) ms		$Q\beta^- = [9,700]$	
					$\beta^- n(3.1\%)$	
	119	Rh	> 150 ns		$Q\beta^- = [8,100]$	
	120	Rh	136(+14-13) m		$Q\beta^- = [10,900]$	
					$\beta^- n(<5.4\%)$	
	121	Rh	151(+67-58) ms		$Q\beta^- = [9,200]$	
					$\beta^- n$	
	122	Rh	> 300 ns		β^-	
					$\beta^- n$	
46		Palladium				
	91	Pd	> 1 μ s		$Q\epsilon = [12,000]$	
	92	Pd	0.7(+4-2) s	0+	$Q\epsilon = [7,900](100\%)$	

93	Pd	1.3(2) s	(7/2+,9/2+)	$Q_{\varepsilon} = [9,500](100\%)$	$\gamma 240,382,622,864$
93	Pd(0 + x)	9.3(+25–17) s		εp	
94	Pd	9.0(5) s	0+	ε	
95	Pd	(10 s)		IT	
95	Pd(2000)	13.3(3) s	(21/2+)	$Q_{\varepsilon} = [6,600](100\%)$	$\gamma 558,724,55$
				$Q_{\varepsilon} = [8,200]$	
				$\varepsilon(>91.3\%)$	$\gamma 1351,717,382,913$
				IT(<9.7%)	
96	Pd	122(2) s	0+	$\varepsilon p(0.9\%)$	$\gamma 756,1431,312,146$
97	Pd	3.10(9) m	5/2+	$Q_{\varepsilon} = 3,450(100\%)$	$\gamma 125,762,500,1099$
98	Pd	17.7(3) m	0+	$Q_{\varepsilon} = 4,800(100\%)$	$\gamma 265,475,793,1760$
99	Pd	21.4(2) m	(5/2)+	$Q_{\varepsilon} = 1,867(100\%)$	$\gamma 112,662,107,68$
100	Pd	3.63(9) days	0+	$Q_{\varepsilon} = 3,387(100\%)$	$\gamma 136,264$
101	Pd	8.47(6) h	5/2+	$Q_{\varepsilon} = 361(100\%)$	$\gamma 84,75,126,42$
102	Pd	Stable	0+	$Q_{\varepsilon} = 1,980(100\%)$	$\gamma 296,590,270,24$
103	Pd	16.991(19) days	5/2+	{1.02(1)%}	
104	Pd	Stable	0+	$Q_{\varepsilon} = 543.1(100\%)$	$\gamma 40,357$
105	Pd	Stable	5/2+	{1.14(8)%}	
106	Pd	Stable	0+	{22.33(8)%}	
107	Pd	6.5(3)E6 years	5/2+	{27.33(3)%}	
107	Pd(214.9)	21.3(5) s	11/2–	$Q_{\beta-} = 33(100\%)$	
108	Pd	Stable	0+	IT(100%)	$\gamma 215$
109	Pd	13.7012(24) h	5/2+	{26.46(9)%}	
109	Pd(188.9)	4.696(3) m	11/2–	$Q_{\beta-} = 1,115.9(100\%)$	$\gamma 88$
110	Pd	Stable	0+	IT(100%)	$\gamma 189$
				{11.72(9)%}	

Table 22.1 (Continued)

A	Element	Half-life or width	J^{π}	Qmode(%BR){%Abund}	Principal gammas, alphas
111	Pd	23.4(2) m	5/2+	Q β^- = 2,190(100%)	γ 580,70,1459,650
111	Pd(172.2)	5.5(1) h	11/2-	IT(73%)	γ 172
				β^- - (27%)	γ 70,391,633,575
112	Pd	21.03(5) h	0+	Q β^- = 288(100%)	γ 19
113	Pd	93(5) s	(5/2+)	Q β^- = 3,340(100%)	γ 96,644,740,222
113	Pd(81.3)	0.3(1) s	(9/2-)	IT(100%)	γ 81
114	Pd	2.42(6) m	0+	Q β^- = 1,451(100%)	γ 232,127,359,137
115	Pd	25(2) s	(5/2+)	Q β^- = 4,580(100%)	γ 343,304,397,556
115	Pd(89.3)	50(3) s	(11/2-)	β^- - (92%)	γ 749
				IT(8%)	γ 89
116	Pd	11.8(4) s	0+	Q β^- = 2,610(100%)	γ 115,178,101,91
117	Pd	4.3(3) s	(5/2+)	Q β^- = [5,700](100%)	γ 248,650,324,626
117	Pd(203.2)	19.1(7) ms	(11/2-)	IT(100%)	γ 169,35
118	Pd	1.9(1) s	0+	Q β^- = 4,100(100%)	γ 125,125,224,152
119	Pd	0.92(13) s		Q β^- = [6,500](100%)	γ 130,257,326,70
120	Pd	0.5(1) s	0+	Q β^- = [4,900](100%)	γ 158,90,102,53
121	Pd	> 150 ns		Q β^- = [7,800]	
122	Pd	175(16) ms	0+	Q β^- = [6,000]	
				β^- - n(<2.5%)	
123	Pd	> 150 ns		Q β^- = [8,700]	
124	Pd	38(+38-19) ms	0+	β^-	
	Silver				
93	Ag	> 1.5 μ s		ϵ	
94	Ag	26(+26-9) ms	(0+)	Q ϵ = [13,100](100%)	
				ϵ p	

94	Ag(x)	0.55(6) s	(7+)	$\varepsilon(100\%)$	
				$\varepsilon p(20\%)$	
94	Ag(6670)	0.40(4) s	(21+)	$\varepsilon(100\%)$	$\gamma 814,905,660,979$
				$\varepsilon p(27\%)$	
				P(4.1%)	
95	Ag	2.0(1) s		$Q_{\varepsilon} = [10,100]$	
				εp	
96	Ag(0 + x)	4.40(6) s	(8+)	$Q_{\varepsilon} = [11,600](100\%)$	$\gamma 1416,684,326,107$
96	Ag(0 + y)	6.9(6) s	(2+)	ε	
97	Ag	25.9(4) s	9/2+	$Q_{\varepsilon} = [7,000](100\%)$	$\gamma 687,1295,1257,587$
98	Ag	47.5(3) s	(6+)	$Q_{\varepsilon} = 8,420(100\%)$	$\gamma 863,679,571,452$
				$\varepsilon p(0.0011\%)$	
99	Ag	124(3) s	(9/2)+	$Q_{\varepsilon} = 5,430(100\%)$	$\gamma 264,832,806,816$
99	Ag(506.2)	10.5(5) s	(1/2-)	IT(100%)	$\gamma 343,164$
100	Ag	2.01(9) m	(5)+	$Q_{\varepsilon} = 7,050(100\%)$	$\gamma 666,751,773,450$
100	Ag(15.5)	2.24(13) m	(2)+	ε	$\gamma 666,751,1694,2118$
				IT	
101	Ag	11.1(3) m	9/2+	$Q_{\varepsilon} = 4,200(100\%)$	$\gamma 261,588,667,1174$
101	Ag(274.3)	3.10(10) s	(1/2)-	IT(100%)	$\gamma 98,176$
102	Ag	12.9(3) m	5+	$Q_{\varepsilon} = 5,950(100\%)$	$\gamma 557,719,1745,1582$
102	Ag(9.2)	7.7(5) m	2+	$\varepsilon(51\%)$	$\gamma 557,1835,2055,2159$
				IT(49%)	
103	Ag	65.7(7) m	7/2+	$Q_{\varepsilon} = 2,688(100\%)$	$\gamma 119,148,267,1274$
103	Ag(134.4)	5.7(3) s	1/2-	IT(100%)	$\gamma 134$
104	Ag	69.2(10) m	5+	$Q_{\varepsilon} = 4,279(100\%)$	$\gamma 556,768,942,926$
104	Ag(6.9)	33.5(20) m	2+	$\varepsilon(>99.93\%)$	$\gamma 556$
				IT(<0.07%)	

Table 22.1 (Continued)

A	Element	Half-life or width	J^{π}	Qmode(%BR){%Abund}	Principal gammas, alphas
105	Ag	41.29(7) days	1/2–	Q ϵ = 1,345(100%)	γ 345,280,645,443
105	Ag(25.5)	7.23(16) m	7/2+	IT(99.66%)	γ 25
106	Ag	23.96(4) m	1+	ϵ (0.34%)	γ 319,306
				Q ϵ = 2,965(99.5%)	γ 512
				Q β – = 194(<1%)	
106	Ag(89.6)	8.28(2) days	6+	ϵ (100%)	γ 512,1046,717,451
107	Ag	Stable	1/2–	{51.839(8)%}	
107	Ag(93.1)	44.3(2) s	7/2+	IT(100%)	γ 93
108	Ag	2.37(1) m	1+	Q β – = 1,649(97.15%)	γ 633
				Q ϵ = 1,918(2.85%)	γ 434,619
108	Ag(109.4)	418(21) years	6+	ϵ (91.3%)	γ 723,434,614
				IT(8.7%)	γ 79
109	Ag	Stable	1/2–	{48.161(8)%}	
109	Ag(88.0)	39.6(2) s	7/2+	IT(100%)	γ 88
110	Ag	24.6(2) s	1+	Q β – = 2,892.2(99.7%)	γ 658
				Q ϵ = 892(0.3%)	
110	Ag(117.6)	249.76(4) days	6+	β – (98.64%)	γ 658,885,937,1384
				IT(1.36%)	γ 116
111	Ag	7.45(1) days	1/2–	Q β – = 1,036.8(100%)	γ 342,245
111	Ag(59.8)	64.8(8) s	7/2+	IT(99.3%)	γ 60
				β – (0.7%)	γ 245,620,171
112	Ag	3.130(9) h	2(–)	Q β – = 3,956(100%)	γ 617,1388
113	Ag	5.37(5) h	1/2–	Q β – = 2,016(100%)	γ 299,259,316

113	Ag(43.6)	68.7(16) s	7/2+	IT(64%)	γ_{44}	
				β^- – (36%)	$\gamma_{316,392,298,584}$	
114	Ag	4.6(1) s	1+	$Q\beta^-$ – 5,080(100%)	γ_{558}	
114	Ag(199)	1.50(5) ms	(<7)	IT(100%)	γ_{73}	
115	Ag	20.0(5) m	1/2–	$Q\beta^-$ – 3,100(100%)	$\gamma_{229,213,473,649}$	
115	Ag(41.1)	18.0(7) s	7/2+	β^- – (79%)	$\gamma_{229,132,389,361}$	
				IT(21%)	γ_{41}	
116	Ag	2.68(10) m	(2)–	$Q\beta^-$ – 6,150(100%)	$\gamma_{513,2478,700}$	
116	Ag(81.9)	8.6(3) s	(5+)	β^- – (94%)	$\gamma_{513,706,1029,709}$	
				IT(6%)	γ_{82}	
117	Ag	72.8(+20–7) s	(1/2–)	$Q\beta^-$ – 4,160(~100%)	$\gamma_{135,338,157,426}$	
117	Ag(28.6)	5.34(5) s	(7/2+)	β^- – (94%)	$\gamma_{135,387,298,522}$	
				IT(6%)	γ_{29}	
118	Ag	3.76(15) s	1(–)	$Q\beta^-$ – 7,140(100%)	$\gamma_{488,677,2789,3224}$	
118	Ag(127.7)	2.0(2) s	4(+)	β^- – (59%)	$\gamma_{488,677,1058,2778}$	
				IT(41%)	γ_{128}	
119	Ag(0 + x)	2.1(1) s	(7/2+)	$Q\beta^-$ – 5,350(100%)	$\gamma_{626,366,399,213}$	
119	Ag	6.0(5) s	(1/2–)	β^- – (100%)		
120	Ag	1.23(4) s	3(+)	$Q\beta^-$ – 8,330(100%)	$\gamma_{506,698,817,1323}$	
				β^- – n(<0.003%)		
120	Ag(203)	0.40(3) s	6(–)	β^- – (~63%)	$\gamma_{698,506,926,830}$	
				IT(~37%)	γ_{203}	
121	Ag	0.79(2) s	(7/2+)	$Q\beta^-$ – 6,400(100%)	$\gamma_{315,353,501,1196}$	
				β^- – n(0.08%)		

Table 22.1 (Continued)

A	Element	Half-life or width	J^{π}	Qmode(%BR){(%Abund)}	Principal gammas, alphas
122	Ag(0 + x)	0.529(13) s	(3+)	Q β^- = [9,100](100%) β^- - n(0.186%)	γ 760
122	Ag(0 + y)	0.55(5) s	(1 -)	IT	
122	Ag(80)	0.20(5) s	(9 -)	β^-	
123	Ag	0.300(5) s	(7/2+)	Q β^- = [7,400](100%) β^- - n(0.55%)	γ 264,410,591,116
124	Ag	0.172(5) s		Q β^- = [10,100](100%) β^- - n(1.3%)	γ 613,772,461,539
125	Ag	166(7) ms	(7/2+)	Q β^- = [8,700](100%) β^- - n	
126	Ag	107(12) ms		Q β^- = [11,300](100%)	
127	Ag	79(3) ms	(1/2 -)	Q β^- = [9,700](100%)	
128	Ag	58(5) ms		β^- - (100%) β^- - n	γ 784
129	Ag(0 + x)	46(+5 -9) ms	(9/2+)	β^- - (100%) β^- - n	
129	Ag(0 + y)	\approx 160 ms	(1/2 -)	β^-	
130	Ag	\approx 50 ms		β^-	
48	Cadmium				
	Cd	(5 ms)	0+	Q ε =	
	Cd	\sim 1 s	0+	Q ε = [8,500]	
	Cd	2.8(6) s		Q ε = [10,200]	
				ε p	

98	Cd	9.2(3) s		0+	Q ε = [5,420](100%)	γ 347,1176,107,61
99	Cd	16(3) s		(5/2+)	$\varepsilon p(<0.03\%)$ Q ε = [6,910](100%) $\varepsilon p(0.17\%)$ $\varepsilon \alpha(<0.00010\%)$	γ 343,672,672,1583
100	Cd	49.1(5) s		0+	Q ε = 3,880(100%)	γ 937,140
101	Cd	1.36(5) m		(5/2+)	Q ε = 5,480(100%)	γ 98,1723,1259,925
102	Cd	5.5(5) m		0+	Q ε = 2,587(100%)	γ 481,1036,415,505
103	Cd	7.3(1) m		5/2+	Q ε = 4,142(100%)	γ 1462,1449,1080,387
104	Cd	57.7(10) m		0+	Q ε = 1,136(100%)	γ 84,709,559
105	Cd	55.5(4) m		5/2+	Q ε = 2,738(100%)	γ 962,347,1302,607
106	Cd	>2.6E17 years		0+	2 ε {1.25(6)%}	
107	Cd	6.50(2) h		5/2+	Q ε = 1,417(100%)	γ 93
108	Cd	Stable		0+	{0.89(3)%}	
109	Cd	461.4(12) days		5/2+	Q ε = 214(100%)	γ 88
110	Cd	Stable		0+	{12.49(18)%}	
111	Cd	Stable		1/2+	{12.80(12)%}	
111	Cd(396.2)	48.50(9) m		11/2–	IT(100%)	γ 245,151
112	Cd	Stable		0+	{24.13(21)%}	
113	Cd	7.7(3)E15 years		1/2+	Q β – = 316(100%) {12.22(12)%}	
113	Cd(263.5)	14.1(5) years		11/2–	β – (99.86%) IT(0.14%)	γ 264
114	Cd	Stable		0+	{28.73(42)%}	
115	Cd	53.46(5) h		1/2+	Q β – = 1,446(100%)	γ 336,528,492

Table 22.1 (Continued)

A	Element	Half-life or width	J^{π}	Qmode(%BR){%Abund}	Principal gammas, alphas
115	Cd(181.0)	44.56(24) days	(11/2) [−]	β^- – (100%)	γ 934,1291,484
116	Cd	3.1(4)E19 years	0 ⁺	β^- – {7.49(18)%}	
117	Cd	2.49(4) h	1/2 ⁺	$Q\beta^-$ – = 2,517(100%)	γ 273,1303,344,1577
117	Cd(136.4)	3.36(5) h	(11/2) [−]	β^- – (100%)	γ 1997,1066,564,1433
118	Cd	50.3(2) m	0 ⁺	$Q\beta^-$ – = 521(100%)	
119	Cd	2.69(2) m	3/2 ⁺	$Q\beta^-$ – = 3,800(100%)	γ 293,343,1610,1764
119	Cd(146.5)	2.20(2) m	(11/2) [−]	β^- – (100%)	γ 1025,2021,721,1204
120	Cd	50.80(21) s	0 ⁺	$Q\beta^-$ – = 1,760(100%)	
121	Cd	13.5(3) s	(3/2 ⁺)	$Q\beta^-$ – = 4,780(100%)	γ 324,1040,349,1483
121	Cd(214.9)	8.3(8) s	(11/2) [−]	β^- – (100%)	γ 2059,1021,988,1181
122	Cd	5.24(3) s	0 ⁺	$Q\beta^-$ – = [3,000](100%)	
123	Cd	2.10(2) s	(3/2 ⁺)	$Q\beta^-$ – = 6,120(100%)	γ 1166,1028,2103,2602
123	Cd(317.0)	1.82(3) s	(11/2) [−]	β^- – IT	
124	Cd	1.25(2) s	0 ⁺	$Q\beta^-$ – = 4,170(100%)	γ 180,63,143
125	Cd	0.65(2) s	(3/2 ⁺)	$Q\beta^-$ – = 7,120(100%)	γ 436,1099,2147,1701
125	Cd(50)	0.48(3) s	(11/2) [−]	β^- – (100%)	γ 1028,1173,737,2392
126	Cd	0.515(17) s	0 ⁺	$Q\beta^-$ – = 5,490(100%)	γ 260,428
127	Cd	0.37(7) s	(3/2 ⁺)	$Q\beta^-$ – = 8,470(100%)	γ 1235,376,524,1067
128	Cd	0.28(4) s	0 ⁺	$Q\beta^-$ – = 7,100(100%)	γ 248,857,68,925
129	Cd	0.27(4) s	(3/2 ⁺)	$Q\beta^-$ – = [9,900]	γ 281
130	Cd	162(7) ms	0 ⁺	$Q\beta^-$ – = [8,500](100%) β^- – n(3.5%)	

49	131	Cd	68(3) ms	(7/2−)	β−	
	132	Cd	97(10) ms	0+	β− n(3.5%) Q _ε = [8,500] β− n(60%)	
		Indium				
	97	In	(5 ms)		Q _ε = [13,700]	
	98	In (0 + x)	32(+32−11) ms		Q _ε =	
	98	In (0 + y)	1.2(+12−3) s		Q _ε = [8,900]	
	99	In	3.0 (+8−7) s	(9/2+)	Q _ε = [8,900]	
	100	In	5.9(2) s	(6+,7+)	Q _ε = 10,200(100%) εp(> 3.9%)	
	101	In	15.1(3) s	(9/2+)	Q _ε = [7,300](~100%) εp	γ252,750,421,891
	102	In	23.3(1) s	(6+)	Q _ε = 9,300(100%) εp(0.0093%)	γ777,862,593,923
	103	In	65(7) s	(9/2+)	Q _ε = 6,050(100%)	γ188,720,740,917
	103	In(631.7)	34(2) s	(1/2−)	ε(67%) IT(33%)	γ632
	104	In	1.80(3) m	(6+)	Q _ε = 7,910(100%)	γ658,834,878,943
	104	In(93.5)	15.7(5) s	(3+)	IT(80%) ε(20%)	
	105	In	5.07(7) m	9/2+	Q _ε = 4,849(100%)	γ131,260,604,668
	105	In(674.1)	48(6) s	(1/2−)	IT(~75%) ε(~25%)	γ674
	106	In	6.2(1) m	7+	Q _ε = 6,523(100%)	γ633,861,998,1009
	106	In(28.6)	5.2(1) m	2(+)	ε(100%)	γ633,1715

Table 22.1 (Continued)

A	Element	Half-life or width	$J\pi$	Qmode(%BR){%Abund}	Principal gammas, alphas
107	In	32.4(3) m	9/2+	Q ϵ = 3,426(100%)	γ 205,506,321,1268
107	In(678.5)	50.4(6) s	1/2–	IT(100%)	γ 678
108	In	58.0(12) m	7+	Q ϵ = 5,160(100%)	γ 875,633,243,1033
108	In(29.8)	39.6(7) m	2+	ϵ (100%)	γ 633,1986,3452
109	In	4.167(18) h	9/2+	Q ϵ = 2,020(100%)	γ 204
109	In(650.1)	1.34(7) m	1/2–	IT(100%)	γ 650
109	In(2101)	0.209(6) s	(19/2+)	IT(100%)	γ 674,1428,1025,402
110	In	4.9(1) h	7+	Q ϵ = 3,878(100%)	γ 658,885,937,707
110	In(62.1)	69.1(5) m	2+	ϵ (100%)	γ 658
111	In	2.8047(4) days	9/2+	Q ϵ = 865(100%)	γ 245,171
111	In(537)	7.7(2) m	1/2–	IT(100%)	γ 537
112	In	14.97(10) m	1+	Q ϵ = 2,586(56%) Q β – = 664(44%)	γ 617,606
112	In(156.4)	20.56(6) m	4+	IT(100%)	γ 156
113	In	Stable	9/2+	{4.29(5)%}	
113	In(391.7)	99.476(23) m	1/2–	IT(100%)	γ 392
114	In	71.9(1) s	1+	Q β – = 1,988.7(99.5%) Q ϵ = 1,452(0.5%)	γ 1300 γ 558
114	In(190.3)	49.51(1) days	5+	IT(96.75%)	γ 190
				ϵ (3.25%)	γ 725,558
114	In(502.0)	43.1(6) ms	8–	IT(100%)	γ 312,190
115	In	4.41(25)E14 years	9/2+	Q β – = 496(100%) {95.71(5)%}	
115	In(336.2)	4.486(4) h	1/2–	IT(95%) β – (5%)	γ 336 γ 497

116	In	14.10(3) s	1+	Qβ− = 3,275(99.98%) Qε = 470(0.02%)	γ1293,463
116	In(127.3)	54.29(17) m	5+	β − (100%)	γ1294,1097,417,2112
116	In(289.7)	2.18(4) s	8−	IT(100%)	γ162
117	In	43.2(3) m	9/2+	Qβ− = 1,455(100%)	γ553,159
117	In(315.3)	116.2(3) m	1/2−	β − (52.9%) IT(47.1%)	γ159 γ315
118	In	5.0(5) s	1+	Qβ− = 4,423(100%)	γ1230,528
118	In(60)	4.45(5) m	5+	β − (100%)	γ1230,1051,683
118	In(200)	8.5(3) s	8−	IT(98.6%) β − (1.4%)	γ138 γ1230,1051,254,41
119	In	2.4(1) m	9/2+	Qβ− = 2,364(100%)	γ763,24
119	In(311.4)	18.0(3) m	1/2−	β − (94.4%) IT(5.6%)	γ1066,1250,1164,1090 γ311
120	In	3.08(8) s	1+	Qβ− = 5,370(100%)	γ1173
120	In(0 + x)	47.3(5) s	(8−)	β − (100%)	γ1171,1023,197,90
120	In(70)	46.2(8) s	(5)+	β − (100%)	γ1171,1023,864,1294
121	In	23.1(6) s	9/2+	Qβ− = 3,360(100%)	γ926
121	In(313.6)	3.88(10) m	1/2−	β − (98.8%) IT(1.2%)	γ60 γ314
122	In	1.5(3) s	1+	Qβ− = 6,370(100%)	γ1140,2759
122	In(0 + x)	10.3(6) s	5+	β − (100%)	γ1141,1002,1191,1164
122	In(200)	10.8(4) s	(8−)	β − (100%)	γ1141,1002,104,163
123	In	6.17(5) s	(9/2)+	Qβ− = 4,394(100%)	γ1131,1020
123	In(327.2)	47.4(4) s	(1/2)−	β − (100%)	γ126
124	In	3.12(9) s	(1)+	Qβ− = 7,360(100%)	γ1132,3214,998

Table 22.1 (Continued)

A	Element	Half-life or width	$J\pi$	Qmode(%BR){%Abund}	Principal gammas, alphas
124	In(50)	3.7(2) s	(8-)	β^- – (100%)	γ 1132,970,1073,103
125	In	2.36(4) s	9/2+	$Q\beta^- = 5,420(100\%)$	γ 1335,1032,618
125	In(360.1)	12.2(2) s	1/2(-)	β^- – (100%)	γ 188
126	In	1.53(1) s	3(+)	$Q\beta^- = 8,210(100\%)$	γ 1141,3345,970
126	In(102)	1.64(5) s	(8-)	β^- – (100%)	γ 1141,909,112,1637
127	In	1.09(1) s	(9/2+)	$Q\beta^- = 6,510(100\%)$	γ 1598,646,805,1049
127	In(462)	3.67(4) s	(1/2-)	β^- – n(<0.03%)	
				β^- – (100%)	γ 252
				β^- – n(0.69%)	
128	In	0.84(6) s	(3)+	$Q\beta^- = 8,980(100\%)$	γ 1169,3520,4298,935
				β^- – n(<0.05%)	
128	In(340)	0.72(10) s	(8-)	β^- – (100%)	γ 1169,832,1867,1974
				β^- – n(<0.05%)	
129	In	0.61(1) s	(9/2+)	$Q\beta^- = 7,660(100\%)$	γ 2118,1865,769,1008
				β^- – n(0.25%)	
129	In(380)	1.23(3) s	(1/2-)	β^- – (>99.7%)	γ 315
				β^- – n(2.5%)	
				IT(<0.3%)	
130	In	0.29(2) s	1(-)	$Q\beta^- = 10,250(100\%)$	γ 1905,130,1221,774
				β^- – n(0.93%)	
130	In(50)	0.54(1) s	(10-)	β^- – (100%)	γ 2259,391
				β^- – n(<1.67%)	
130	In(400)	0.54(1) s	(5+)	β^- – (100%)	γ 1221,774,89,2377
				β^- – n(<1.65%)	

50	131	In	0.28(3) s		(9/2+)	Q β^- = 9,174(100%)	γ 2434
						$\beta^- - n(<2\%)$	
	131	In(363)	0.35(5) s		(1/2-)	$\beta^- - (>99.98\%)$	γ 332,1655
						$\beta^- - n(<2\%)$	
	131	In(4270)	0.32(6) s		(21/2+)	IT(<0.02%)	
						$\beta^- - (>99\%)$	γ 4273,2096,284,173
						IT(<1%)	
						$\beta^- - n(0.03\%)$	
	132	In	0.207(6) s		(7-)	Q β^- = 14,140(100%)	γ 375,4041,299,479
						$\beta^- - n(6.3\%)$	
133	In	165(3) ms		(9/2+)	Q β^- = [13,500](100%)	γ 1561,854,2005	
					$\beta^- - n(85\%)$		
134	In	140(4) ms			Q β^- = [15,100](100%)		
					$\beta^- - n(65\%)$	γ 1561,2005,854	
135	In	92(10) ms			$\beta^- - (100\%)$		
					$\beta^- - n(>0\%)$		
	Ti n						
99	Sn	(5 ms)		0+	Q ε =		
100	Sn	1.0(+54-26) s		0+	Q ε = [7,270](100%)		
					$\varepsilon p(<17\%)$		
101	Sn	1.7(3) s		(5/2+)	Q ε = [8,800]		
					$\varepsilon p(26\%)$		
102	Sn	4.5(7) s		0+	Q ε = [5,400](100%)		
103	Sn	7.0(2) s		(5/2+)	Q ε = [7,700](100%)		
					$\varepsilon p(1.2\%)$		
104	Sn	20.8(5) s		0+	Q ε = 4,520(100%)		γ 133,913,401,1407

Table 22.1 (Continued)

A	Element	Half-life or width	$J\pi$	Qmode(%BR){%Abund}	Principal gammas, alphas
105	Sn	34(1) s		Q ε = 6,260(100%)	
				εp	
106	Sn	115(5) s	0+	Q ε = 3,190(100%)	γ 387,253,477,864
107	Sn	2.90(5) m	(5/2+)	Q ε = 5,010(100%)	γ 679,1129,1542,1001
108	Sn	10.30(8) m	0+	Q ε = 2,092(100%)	γ 396,273,669,168
109	Sn	18.0(2) m	5/2(+)	Q ε = 3,850(100%)	γ 1099,650,1321,331
110	Sn	4.11(10) h	0+	Q ε = 637(100%)	γ 283
111	Sn	35.3(6) m	7/2+	Q ε = 2,445(100%)	γ 1153,1915,762,1610
112	Sn	Stable	0+	{0.97(1)%}	
113	Sn	115.09(3) days	1/2+	Q ε = 1,036(100%)	γ 392
113	Sn(77)	21.4(4) m	7/2+	IT(91.1%)	γ 77
				ε (8.9%)	
114	Sn	Stable	0+	{0.66(1)%}	
115	Sn	Stable	1/2+	{0.34(1)%}	
116	Sn	Stable	0+	{14.54(9)%}	
117	Sn	Stable	1/2+	{7.68(7)%}	
117	Sn(314.58)	13.76(4) days	11/2–	IT(100%)	γ 159
118	Sn	Stable	0+	{24.22(9)%}	
119	Sn	Stable	1/2+	{8.59(4)%}	
119	Sn(89.5)	293.1(7) days	11/2–	IT(100%)	γ 24,25
120	Sn	Stable	0+	{32.58(9)%}	
121	Sn	27.03(4) h	3/2+	Q β – = 390.1(100%)	
121	Sn(6.3)	43.9(5) years	11/2–	IT(77.6%)	γ 6
				β – (22.4%)	γ 37

122	Sn	Stable	0+	{4.63(3)%}		
123	Sn	129.2(4) days	11/2–	Q β – = 1,403(100%)	γ 1089	
123	Sn(24.6)	40.06(1) m	3/2+	β – (100%)	γ 160	
124	Sn	Stable	0+	{5.79(5)%}		
125	Sn	9.64(3) days	11/2–	Q β – = 2,363(100%)	γ 1067, 1089, 822, 916	
125	Sn(27.5)	9.52(5) m	3/2+	β – (100%)	γ 332	
126	Sn	2.30(14)E5 years	0+	Q β – = 380(100%)	γ 88, 64, 87, 23	
127	Sn	2.10(4) h	(11/2–)	Q β – = 3,201(100%)	γ 1114, 1096, 823, 806	
127	Sn(4.7)	4.13(3) m	(3/2+)	β – (100%)	γ 491	
128	Sn	59.07(14) m	0+	Q β – = 1,274(100%)	γ 482, 75, 557, 681	
128	Sn(2091.5)	6.5(5) s	(7–)	IT(100%)	γ 832, 1169	
129	Sn	2.23(4) m	(3/2+)	Q β – = 4,000(100%)	γ 645	
129	Sn(35.2)	6.9(1) m	(11/2–)	β – (100%)	γ 1161, 1128, 761, 782	
				IT(<0.002%)		
130	Sn	3.72(7) m	0+	Q β – = 2,148(100%)	γ 192, 780, 70, 229	
130	Sn(1946.9)	1.7(1) m	(7–)	β – (100%)	γ 733, 145, 85, 900	
131	Sn	56.0(5) s	(3/2+)	Q β – = 4,632(100%)		
131	Sn(241.8)	58.4(5) s	(11/2–)	β – (100%)	γ 1226, 450, 799, 304	
				IT(<0.004%)		
132	Sn	39.7(8) s	0+	Q β – = 3,103(100%)	γ 341, 86, 899, 247	
133	Sn	1.45(3) s	(7/2–)	Q β – = 7,990(100%)	γ 962	
				β – n(0.08%)		
134	Sn	1.050(11) s	0+	Q β – = 7,370(100%)	γ 872, 318, 554	
				β – n(17%)		
135	Sn	530(20) ms	(7/2–)	Q β – = [8,900](100%)	γ 282, 923, 732, 1207	
				β – n(21%)	γ 318	

Table 22.1 (Continued)

A	Element	Half-life or width	J^{π}	Qmode(%BR){%Abund}	Principal gammas, alphas
136	Sn	0.25(3) s	0+	Q β^- = [8,100](100%) β^- – n(30%)	
137	Sn	190(60) ms		Q β^- – = [9,800](100%) β^- – n(58%)	
51	Antimony				
103	Sb	> 1.5 μ s		Q ϵ = [11,200]	
104	Sb	0.44(+15–11) s		Q ϵ = [12,200](100%) ϵ p(<7%) Qp = [310](<1%)	
105	Sb	1.22(11) s	(5/2+)	Q ϵ = 9,440(–99%) Qp = 483(–1%) Q ϵ = [11,100]	
106	Sb	0.6(2) s	(2+)		
107	Sb	4.0(2) s	(5/2+)	Q ϵ = [7,900](100%)	γ 1280,819,151,704
108	Sb	7.4(3) s	(4+)	Q ϵ = [9,500](100%)	γ 1206,905,1599,1273
109	Sb	17.0(7) s	(5/2+)	Q ϵ = 6,380(100%)	γ 925,1062,665,1496
110	Sb	23.0(4) s	(3+,4+)	Q ϵ = [8,300](100%)	γ 1212,985,1243,827
111	Sb	75(1) s	(5/2+)	Q ϵ = [5,100](100%)	γ 154,489,1033
112	Sb	51.4(10) s	3+	Q ϵ = 7,055(100%)	γ 1257,991
113	Sb	6.67(7) m	5/2+	Q ϵ = 3,917(100%)	γ 498,332
114	Sb	3.49(3) m	3+	Q ϵ = 5,880(100%)	γ 1300,888
115	Sb	32.1(3) m	5/2+	Q ϵ = 3,030(100%)	γ 497
116	Sb	15.8(8) m	3+	Q ϵ = 4,707(100%)	γ 1294,932,2225
116	Sb(383)	60.3(6) m	8–	ϵ (100%)	γ 1294,973,543,407
117	Sb	2.80(1) h	5/2+	Q ϵ = 1,757(100%)	γ 159

118	Sb	3.6(1) m	1+	$Q_{\varepsilon} = 3,657(100\%)$	$\gamma 1229,1267,529,827$
118	Sb(250)	5.00(2) h	8–	$\varepsilon(100\%)$	$\gamma 1230,254,1051,41$
119	Sb	38.19(22) h	5/2+	$Q_{\varepsilon} = 594(100\%)$	$\gamma 24$
119	Sb(2841.7)	0.85(9) s	(27/2+)	IT(100%)	
120	Sb	15.89(4) m	1+	$Q_{\varepsilon} = 2,681(100\%)$	$\gamma 1171$
120	Sb(0 + x)	5.76(2) days	8–	$\varepsilon(100\%)$	$\gamma 1172,1023,197,90$
121	Sb	Stable	5/2+	{57.21(5)%}	
122	Sb	2.7238(2) days	2–	$Q_{\beta-} = 1,982.5(97.59\%)$	$\gamma 564$
				$Q_{\varepsilon} = 1,616(2.41\%)$	$\gamma 1141$
122	Sb(137.5)	0.53(3) ms	(5)+	IT(100%)	
122	Sb(163.6)	4.191(3) m	(8)–	IT(100%)	$\gamma 61$
123	Sb	Stable	7/2+	{42.79(5)%}	
124	Sb	60.20(3) days	3–	$Q_{\beta-} = 2,904.5(100\%)$	$\gamma 603,1691,723$
124	Sb(10.9)	93(5) s	5+	IT(75%)	$\gamma 11$
				$\beta - (25\%)$	$\gamma 646,603,498$
124	Sb(36.8)	20.2(2) m	(8)–	IT(100%)	$\gamma 26$
125	Sb	2.7586(3) years	7/2+	$Q_{\beta-} = 766.7(100\%)$	$\gamma 428,601,636,463$
126	Sb	12.35(6) days	(8)–	$Q_{\beta-} = 3,670(100\%)$	$\gamma 695,666,415,721$
126	Sb(17.7)	19.15(8) m	(5)+	$\beta - (86\%)$	$\gamma 415,666,695$
				IT(14%)	$\gamma 18$
126	Sb(40.4)	≈ 11 s	(3)–	IT(100%)	
127	Sb	3.85(5) days	7/2+	$Q_{\beta-} = 1,581(100\%)$	$\gamma 686,473,784,252$
128	Sb	9.01(4) h	8–	$Q_{\beta-} = 4,384(100\%)$	$\gamma 743,754,314,527$
128	Sb(0 + x)	10.4(2) m	5+	$\beta - (96.4\%)$	$\gamma 754,743,314$
				IT(3.6%)	
129	Sb	4.40(1) h	7/2+	$Q_{\beta-} = 2,380(100\%)$	$\gamma 813,915,545,1030$

Table 22.1 (Continued)

A	Element	Half-life or width	J^{π}	Qmode(%BR){%Abund}	Principal gammas, alphas
129	Sb(1851.3)	17.7(1) m	(19/2-)	β^- – (85%) π^{π} (15%)	γ 406 γ 1128,723
130	Sb	39.5(8) m	(8-)	$Q\beta^- = 4,959(100\%)$	γ 840,793,331,182
130	Sb(4.8)	6.3(2) m	(4,5)+	β^- – (100%)	γ 840,793,182,1018
131	Sb	23.03(4) m	(7/2+)	$Q\beta^- = 3,190(100\%)$	γ 943,933,642,1124
132	Sb	2.79(5) m	(4+)	$Q\beta^- = 5,486(100\%)$	γ 974,697,990,103
132	Sb(0 + x)	4.10(5) m	(8-)	β^- – (100%)	γ 974,697,151,103
133	Sb	2.5(1) m	(7/2+)	$Q\beta^- = 4,003(100\%)$	γ 1096,818,2755,837
134	Sb	0.78(6) s	(0-)	$Q\beta^- = 8,390(100\%)$	γ 1279,2631,1352,2464
134	Sb(0 + x)	10.07(5) s	(7-)	β^- – (100%) β^- – n(0.091%)	γ 1279,297,706,115
135	Sb	1.679(15) s	(7/2+)	$Q\beta^- = 8,120(100\%)$	γ 1127,1380,1246,1442
136	Sb	0.923(14) s	1-	β^- – n(22%) $Q\beta^- = [9,800](100\%)$ β^- – n(16.3%)	γ 1279,297,115 γ 607,962,2034,1437
137	Sb	450(50) ms	(7/2+)	$Q\beta^- = [9,300]$ β^- – n(49%)	
138	Sb	> 300 ns		$Q\beta^- = [10,900]$ β^- – n	
139	Sb	> 150 ns		$Q\beta^- = [10,200]$	
52	Tellurium				
	Te	0.62(7) μ s	(5/2+)	$Q\alpha =$	
	Te	70(17) μ s	0+	$Q\alpha = 4,293(100\%)$	α 4128
	Te	3.1(1) ms		$Q\alpha = 4,008(70\%)$	α 3833
				$Q\varepsilon = [10,100](30\%)$	

108	Te	2.1(1) s	0+	Q _ε = [6,800](51%) Q _α = 3,445(49%) εp(2.4%)	α3318
109	Te	4.6(3) s	(5/2+)	Q _ε = 8,680(96.1%) εp(9.4%) Q _α = 3,230(3.9%) εα(<0.005%)	α3080
110	Te	18.6(8) s	0+	Q _ε = [5,260](~100%) Q _α = 2,723(~0.003%) Q _ε = [7,370](100%) εp	γ895 α2624
111	Te	19.3(4) s	(5/2+)		
112	Te	2.0(2) m	0+	Q _ε = 4,350(100%)	γ373,296,419,351
113	Te	1.7(2) m	(7/2+)	Q _ε = [6,100](100%)	γ814,1018,1181,645
114	Te	15.2(7) m	0+	Q _ε = [2,800](100%)	γ90,1897,727,244
115	Te	5.8(2) m	7/2+	Q _ε = 4,640(100%)	γ724,1381,1327,1099
115	Te(20)	6.7(4) m	(1/2)+	ε(<100%) IT	γ770,724,1072,1504
116	Te	2.49(4) h	0+	Q _ε = 1,510(100%)	γ94
117	Te	62(2) m	1/2+	Q _ε = 3,535(100%)	γ720,1716,2300,1091
117	Te(296.1)	103(3) ms	(11/2-)	IT(100%)	γ1
118	Te	6.00(2) days	0+	Q _ε = 273(100%)	
119	Te	16.05(5) h	1/2+	Q _ε = 2,293.0(100%) ε(100%) IT(<0.008%) {0.09(1)%}	γ644,700 γ1213,154,271,1137
119	Te(261.0)	4.70(4) days	11/2-		
120	Te	Stable	0+		

Table 22.1 (Continued)

A	Element	Half-life or width	$J\pi$	Qmode(%BR){%Abund}	Principal gammas, alphas
121	Te	19.16(5) days	1/2+	Q α = 1,036(100%)	γ 573,508
121	Te(294.0)	154(7) days	11/2–	IT(88.6%)	γ 212
122	Te	Stable	0+	ϵ (11.4%)	γ 1102,37
123	Te	>9.2E16 years	1/2+	{2.55(12)%}	
				Q α = 53.3(100%)	
				{0.89(3)%}	
123	Te(247.5)	119.2(1) days	11/2–	IT(100%)	γ 159
124	Te	Stable	0+	{4.74(14)%}	
125	Te	Stable	1/2+	{7.07(15)%}	
125	Te(144.8)	57.40(15) days	11/2–	IT(100%)	γ 36
126	Te	Stable	0+	{18.84(25)%}	
127	Te	9.35(7) h	3/2+	Q β – = 698(100%)	γ 418,360
127	Te(88.3)	109(2) days	11/2–	IT(97.6%)	γ 88
				β – (2.4%)	γ 58
128	Te	8.8(4)E18 years	0+	β – β – (100%)	
				{31.74(8)%}	
129	Te	69.6(3) m	3/2+	Q β – = 1,498(100%)	γ 28,460
129	Te(105.5)	33.6(1) days	11/2–	IT(63%)	γ 106
				β – (37%)	γ 696,730
130	Te	>5E23 years	0+	β – β – (100%)	
				{34.08(62)%}	
131	Te	25.0(1) m	3/2+	Q β – = 2,233.5(100%)	γ 150,452
131	Te(182.2)	33.25(25) h	11/2–	β – (74.1%)	γ 774,852,794,1125
				IT(25.9%)	γ 182

131	Te(1940)	93(12) ms	(23/2+)	IT(100%)	
132	Te	3.204(13) days	0+	Qβ− = 493(100%)	γ228,50
133	Te	12.5(3) m	(3/2+)	Qβ− = 2,920(100%)	γ312,408,1333,720
133	Te(334.3)	55.4(4) m	(11/2−)	β − (82.5%)	γ913,648,864,915
				IT(17.5%)	γ334
134	Te	41.8(8) m	0+	Qβ− = 1,550(100%)	γ767,210,278,79
135	Te	19.0(2) s	(7/2−)	Qβ− = 5,960(100%)	γ604,267,870
136	Te	17.63(8) s	0+	Qβ− = 5,070(100%)	γ2078,334,579,2569
				β − n(1.31%)	
137	Te	2.49(5) s	(7/2−)	Qβ− = 6,940(100%)	γ243,554,469,359
				β − n(2.99%)	γ738
138	Te	1.4(4) s	0+	Qβ− = [6,370](100%)	
				β − n(6.3%)	
139	Te	> 150 ns	(7/2−)	Qβ− = [8,000]	
				β − n	
140	Te	> 150 ns	0+	Qβ− = [7,000]	
				β − n	
141	Te	> 150 ns		Qβ− = [8,900]	
				β − n	
142	Te	Te	0+	Qβ− = [7,800]	
	Iodine				
108	I	36(6) ms	(1)	Qα = 4,100(91%)	
				Qε = [12,900](9%)	
				Qp = [400](< 1%)	
109	I	103(5) μs	1/2+	Qp = 819.5(100%)	
53					

Table 22.1 (Continued)

A	Element	Half-life or width	J π	Qmode(%BR){%Abund}	Principal gammas, alphas
110	I	0.65(2) s		Q ϵ = [11,900](83%)	
				Q α = 3,580(17%)	α 3444
				ϵ p(11%)	
				$\epsilon\alpha$ (1.1%)	
111	I	2.5(2) s	(5/2+)	Q ϵ = [8,500](99.9%)	
				Q α = 3,280(~0.1%)	α 3152
112	I	3.42(11) s		Q ϵ = [10,200](100%)	γ 787
				Q α = 2,990(~0.0012%)	α 2880
113	I	6.6(2) s	(5/2+)	Q ϵ = [7,190](100%)	γ 463,622,352,567
				Q α = 2,710(3.3E – 7%)	α 2610
114	I	2.1(2) s	1+	Q ϵ = [9,100](100%)	γ 709,683
				ϵ p	
114	I (265.9)	6.2(5) s	(7)	ϵ (91%)	γ 709,683,775
				IT(9%)	γ 103
115	I	1.3(2) m	(5/2+)	Q ϵ = [5,900](100%)	γ 709
116	I	2.91(15) s	1+	Q ϵ = 7,750(100%)	γ 679,540
117	I	2.22(4) m	(5/2)+	Q ϵ = 4,670(100%)	γ 326,274
118	I (0 + x)	13.7(5) m	2–	Q ϵ = 7,030(100%)	γ 606,545,601
118	I (104 + x)	8.5(5) m	(7–)	ϵ (<100%)	γ 606,601,614,1258
				IT(>0%)	
119	I	19.1(4) m	5/2+	Q ϵ = 3,510(100%)	γ 258
120	I	81.6(2) m	2–	Q ϵ = 5,615(100%)	γ 560,1523,641
120	I (320)	53(4) m	(7–)	ϵ (100%)	γ 560,601,615,1346
121	I	2.12(1) h	5/2+	Q ϵ = 2,270(100%)	γ 212
122	I	3.63(6) m	1+	Q ϵ = 4,234(100%)	γ 564

123	I	13.2235(19) h	5/2+	$Q_{\beta^-} = 1,234(100\%)$	$\gamma 159$
124	I	4.1760(3) days	2-	$Q_{\beta^-} = 3,159.6(100\%)$	$\gamma 603, 1691, 723$
125	I	59.400(10) days	5/2+	$Q_{\beta^-} = 185.77(100\%)$	$\gamma 35$
126	I	12.93(5) days	2-	$Q_{\beta^-} = 2,155(52.7\%)$	$\gamma 666, 754$
				$Q_{\beta^-} = 1,258(47.3\%)$	$\gamma 389$
127	I	Stable	5/2+	{100%}	
128	I	24.99(2) m	1+	$Q_{\beta^-} = 2,119(93.1\%)$	$\gamma 443$
				$Q_{\beta^-} = 1,252(6.9\%)$	$\gamma 744$
129	I	1.57(4)E7 years	7/2+	$Q_{\beta^-} = 194(100\%)$	$\gamma 40$
130	I	12.36(1) h	5+	$Q_{\beta^-} = 2,949(100\%)$	$\gamma 536, 669, 740, 418$
130	I (40.0)	8.84(6) m	2+	IT(84%)	$\gamma 40$
				$\beta^- - (16\%)$	$\gamma 536$
131	I	8.0252(6) days	7/2+	$Q_{\beta^-} = 970.8(100\%)$	$\gamma 364$
132	I	2.295(13) h	4+	$Q_{\beta^-} = 3,577(100\%)$	$\gamma 668, 773, 955, 523$
132	I (120)	1.387(15) h	(8-)	IT(86%)	$\gamma 98$
				$\beta^- - (14\%)$	$\gamma 600, 175, 614, 610$
133	I	20.8(1) h	7/2+	$Q_{\beta^-} = 1,770(100\%)$	$\gamma 530$
133	I (1634)	9(2) s	(19/2-)	IT(100%)	$\gamma 647, 912$
134	I	52.5(2) m	(4)+	$Q_{\beta^-} = 4,175(100\%)$	$\gamma 847, 884, 1073, 595$
134	I (316.5)	3.52(4) m	(8)-	IT(97.7%)	$\gamma 272, 44$
				$\beta^- - (2.3\%)$	$\gamma 885, 847, 234$
135	I	6.58(3) h	7/2+	$Q_{\beta^-} = 2,648(100\%)$	$\gamma 1260, 1132, 1678, 1458$
136	I	83.4(10) s	(1-)	$Q_{\beta^-} = 6,930(100\%)$	$\gamma 1313, 1321, 2290, 2415$
136	I (640)	46.9(10) s	(6-)	$\beta^- - (100\%)$	$\gamma 1313, 381, 197, 370$
137	I	24.5(2) s	(7/2+)	$Q_{\beta^-} = 5,880(100\%)$	$\gamma 1218, 601, 1303, 1220$
				$\beta^- - n(7.14\%)$	

Table 22.1 (Continued)

	A	Element	Half-life or width	J^{π}	Qmode(%BR){%Abund}	Principal gammas, alphas
54	138	I	6.23(3) s	(2-)	Q β^- = 7,820(100%) β^- - n(5.56%)	γ 589,875 γ 601
	139	I	2.280(11) s	(7/2+)	Q β^- = 6,806(100%) β^- - n(10%)	γ 528,571,537,656 γ 589,484
	140	I	0.86(4) s	(4-)	Q β^- = [8,920](100%) β^- - n(9.3%)	γ 377,458,937
	141	I	0.43(2) s		Q β^- = [7,600](100%) β^- - n(21.2%)	
	142	I	~0.2 s		Q β^- = [9,800](100%)	
	143	I	> 150 ns		Q β^- = [8,600]	
	144	I	> 300 ns		Q β^- = [10,600]	
		Xenon				
	109	Xe	13(2) ms	(7/2+)	Q α =	
	110	Xe	93(3) ms	0+	Q α = 3,885(64%) Q ϵ = (36%)	α 3745
	111	Xe	0.74(20) s		Q ϵ = [10,600](92%) Q α = 3,720(8%)	α 3560,3463
	112	Xe	2.7(8) s	0+	Q ϵ = [7,200](99.16%) Q α = 3,330(0.84%)	α 3211
	113	Xe	2.74(8) s	(5/2+)	Q ϵ = 9,070(~100%) ϵ p(7%) Q α = 3,100(~0.01%) ϵ α (~0.007%)	α 2985
	114	Xe	10.0(4) s	0+	Q ϵ = [5,900](100%)	γ 309,162,103

115	Xe	18(4) s	(5/2+)	$Q_{\beta} = [8,000](100\%)$ $\beta p(0.34\%)$	
116	Xe	59(2) s	0+	$Q_{\beta} = [4,660](100\%)$	$\gamma 105,311,248,192$
117	Xe	61(2) s	5/2(+)	$Q_{\beta} = 6,440(100\%)$ $\beta p(0.0029\%)$	$\gamma 29,221,32,519$
118	Xe	3.8(9) m	0+	$Q_{\beta} = 3,000(100\%)$	$\gamma 54,60,120,151$
119	Xe	5.8(3) m	(5/2+)	$Q_{\beta} = 5,010(100\%)$	$\gamma 232,100,462,208$
120	Xe	40(1) m	0+	$Q_{\beta} = 1,960(100\%)$	$\gamma 25,73,178,763$
121	Xe	40.1(20) m	(5/2+)	$Q_{\beta} = 3,750(100\%)$	$\gamma 253,133,445,311$
122	Xe	20.1(1) h	0+	$Q_{\beta} = 890(100\%)$	$\gamma 350,149,417$
123	Xe	2.08(2) h	(1/2)+	$Q_{\beta} = 2,676(100\%)$	$\gamma 149,178,330$
124	Xe	> 1.6E14 years	0+	2ϵ {0.09(1)%}	
125	Xe	16.9(2) h	1/2(+)	$Q_{\beta} = 1,653(100\%)$	$\gamma 188,243,55$
125	Xe(252.6)	56.9(9) s	9/2(−)	IT(100%)	$\gamma 111,141$
126	Xe	Stable	0+	{0.09(1)%}	
127	Xe	36.4(1) days	1/2+	$Q_{\beta} = 662.4(100\%)$	$\gamma 203,172,375$
127	Xe(297.1)	69.2(9) s	9/2−	IT(100%)	$\gamma 125,173$
128	Xe	Stable	0+	{1.92(3)%}	
129	Xe	Stable	1/2+	{26.44(24)%}	
129	Xe(236.1)	8.88(2) days	11/2−	IT(100%)	$\gamma 40,197$
130	Xe	Stable	0+	{4.08(2)%}	
131	Xe	Stable	3/2+	{21.18(3)%}	
131	Xe(163.9)	11.84(4) days	11/2−	IT(100%)	$\gamma 164$

Table 22.1 (Continued)

A	Element	Half-life or width	J^{π}	Qmode(%BR){%Abund}	Principal gammas, alphas
132	Xe	Stable	0+	{26.89(6)%}	
132	Xe(2752.3)	8.39(11) ms	(10+)	IT(100%)	γ 773,538,668,600
133	Xe	5.243(1) days	3/2+	Q β – = 427.4(100%)	γ 81
133	Xe(233.2)	2.19(1) days	11/2–	IT(100%)	γ 233
134	Xe	> 5.8E22 years	0+	{10.44(10)%}	
134	Xe(1958.7)	290(17) ms	7–	IT(100%)	γ 846,880,233
135	Xe	9.14(2) h	3/2+	Q β – = 1,151(100%)	γ 250
135	Xe(526.6)	15.29(5) m	11/2–	IT(>99.4%)	γ 527
				β – (<0.6%)	γ 787
136	Xe	> 2.4E21 years	0+	β – β –	
				{8.87(16)%}	
137	Xe	3.818(13) m	7/2–	Q β – = 4,173(100%)	γ 455
138	Xe	14.08(8) m	0+	Q β – = 2,770(100%)	γ 258,435,1768,2016
139	Xe	39.68(14) s	3/2–	Q β – = 5,057(100%)	γ 219,297,175,290
140	Xe	13.60(10) s	0+	Q β – = 4,060(100%)	γ 806,1414,1315,622
141	Xe	1.73(1) s	5/2(–)	Q β – = 6,150(100%)	γ 909,119,106,459
				β – n(0.04%)	
142	Xe	1.250(25) s	0+	Q β – = 5,040(100%)	γ 571,657,538,618
				β – n(0.21%)	
143	Xe	0.511(6) s	5/2–	Q β – = [7,040](100%)	γ 90
				β – n(1%)	
144	Xe	0.388(7) s	0+	Q β – = [5,800](100%)	
				β – n(3%)	
145	Xe	188(4) ms		Q β – = [7,700](100%)	
				β – n(5%)	

146	Xe	146(6) ms	0+	Qβ− = [6,600](100%)	
147	Xe	0.10(+10−5) s		β − n(6.9%)	
55	Cesium			Qβ− = [8,500]	
				β − n(<8%)	
	112	Cs	(0+,3+)	Qp = 814(100%)	
	113	Cs	(3/2+)	Qp = 974(100%)	
	114	Cs	(1+)	Qα = 3,484	
				Qε = [12,400](~100%)	γ450,698
				εp(8.7%)	γ31,122
				εα(0.19%)	
	115	Cs		Qα = 3,360(0.02%)	α3239
				Qε = [8,800](100%)	
116	Cs	1.4(8) s		εp(~0.07%)	
116	Cs	0.70(4) s	(1+)	Qε = [10,400](100%)	γ394
				εp(2.8%)	
				εα(0.05%)	
116	Cs(100)	3.85(13) s	4+,5,6	ε(100%)	γ394,524,615,622
				εp(0.51%)	
				εα(0.008%)	
117	Cs	8.4(6) s	(9/2+)	Qε = 7,520(100%)	γ205,30,206,160
117	Cs(150.0)	6.5(4) s	(3/2+)	ε(100%)	
118	Cs	14(2) s	2	Qε = 9,300(100%)	
				εp(<0.04%)	
				εα(<0.0024%)	

Table 22.1 (Continued)

A	Element	Half-life or width	$J\pi$	Qmode(%BR){%Abund}	Principal gammas, alphas
118	Cs(0 + x)	17(3) s	6,7,8	ϵ (100%) $\epsilon p(<0.04\%)$ $\epsilon \alpha(<0.0024\%)$	γ 337,473,587,591
119	Cs	43.0(2) s	9/2+	$Q\epsilon = 6.350(100\%)$	γ 176,225,258,260
119	Cs(0 + x)	30.4(1) s	3/2(+)	ϵ (100%)	γ 169,314,246
120	Cs	61.3(11) s	2(+)	$Q\epsilon = 7.940(100\%)$ $\epsilon \alpha(0.000020\%)$ $\epsilon p(7.0E - 6\%)$	
120	Cs(0 + x)	57(6) s	(7 -)	ϵ (100%)	γ 323,473,553,601
121	Cs	155(4) s	3/2(+)	$Q\epsilon = 5.400(100\%)$	γ 154,240,427,179
121	Cs(68.5)	122(3) s	9/2(+)	ϵ (83%) IT(17%)	γ 179,196,460,235 γ 69
122	Cs	21.18(19) s	1+	$Q\epsilon = 7.050(100\%)$	γ 331
122	Cs(127.0)	0.36(2) s	(5) -	IT(100%)	γ 81,46
122	Cs(140)	3.70(11) m	8(-)	ϵ (100%)	γ 331,497,639,1098
123	Cs	5.88(3) m	1/2+	$Q\epsilon = 4.210(100\%)$	γ 97,597,83,307
123	Cs(156.3)	1.64(12) s	(11/2) -	IT(100%)	γ 95,64
124	Cs	30.9(4) s	1+	$Q\epsilon = 5.915(100\%)$	γ 354
124	Cs(462.5)	6.3(2) s	(7)+	IT(100%)	γ 212,90,97,189
125	Cs	46.7(1) m	1/2(+)	$Q\epsilon = 3.099(100\%)$	γ 526,112,412,712
125	Cs(266.1)	0.90(3) ms	11/2 -	IT(100%)	
126	Cs	1.64(2) m	1+	$Q\epsilon = 4.824(100\%)$	γ 389,491,925
127	Cs	6.25(10) h	1/2+	$Q\epsilon = 2.085(100\%)$	γ 412,125
128	Cs	3.66(2) m	1+	$Q\epsilon = 3.929(100\%)$	γ 443

129	Cs	32.06(6) h	1/2+	$Q_{\varepsilon} = 1,196(100\%)$	$\gamma 372,411,549$
130	Cs	29.21(4) m	1+	$Q_{\varepsilon} = 2,979(98.4\%)$	$\gamma 536,586,895$
130	Cs(163.2)	3.46(6) m	5-	$Q_{\beta^-} = 369(1.6\%)$	
131	Cs	9.689(16) days	5/2+	IT(99.84%)	$\gamma 80,51,148$
132	Cs	6.480(6) days	2+	$\varepsilon(0.16\%)$	$\gamma 471,206$
133	Cs	Stable	7/2+	$Q_{\varepsilon} = 352(100\%)$	
134	Cs	2.0652(4) years	4+	$Q_{\varepsilon} = 2,119(98.13\%)$	$\gamma 668$
134	Cs(138.7)	2.912(2) h	8-	$Q_{\beta^-} = 1,279.5(1.87\%)$	$\gamma 464,567$
135	Cs	2.3(3)E6 years	7/2+	{100%}	
135	Cs(1633.3)	53(2) m	19/2-	$Q_{\beta^-} = 2,058.7(100\%)$	$\gamma 605,796,569$
136	Cs	13.04(3) days	5+	$Q_{\varepsilon} = 1,229(0.0003\%)$	$\gamma 847$
136	Cs(x)	19(2) s	8-	IT(100%)	$\gamma 128$
137	Cs	30.08(9) years	7/2+	$Q_{\beta^-} = 269.3(100\%)$	
138	Cs	33.41(18) m	3-	IT(100%)	$\gamma 787,846$
138	Cs(79.9)	2.91(8) m	6-	$Q_{\beta^-} = 2,548.2(100\%)$	$\gamma 819,1048,341,1235$
139	Cs	9.27(5) m	7/2+	IT(>0%)	
140	Cs	63.7(3) s	1-	β^-	
141	Cs	24.84(16) s	7/2+	$Q_{\beta^-} = 1,175.63(100\%)$	$\gamma 662$
142	Cs	1.684(14) s	0-	$Q_{\beta^-} = 5,374(100\%)$	$\gamma 1436,463,1010,2218$
				IT(81%)	$\gamma 80$
				$\beta^- - (19\%)$	$\gamma 1436,463,192$
				$Q_{\beta^-} = 4,213(100\%)$	$\gamma 1283,627,1421$
				$Q_{\beta^-} = 6,220(100\%)$	$\gamma 602,908$
				$Q_{\beta^-} = 5,251(100\%)$	$\gamma 49,562,1194,589$
				$\beta^- - n(0.04\%)$	
				$Q_{\beta^-} = 7,307(100\%)$	$\gamma 360,1326,967,1176$
				$\beta^- - n(0.09\%)$	

Table 22.1 (Continued)

A	Element	Half-life or width	J^{π}	Qmode(%BR){%Abund}	Principal gammas, alphas
143	Cs	1.791(7) s	3/2+	Q β^- = 6,253(100%) β^- – n(1.64%)	γ 196,232,306,660
144	Cs	0.994(4) s	1	Q β^- = 8,460(100%) β^- – n(3.2%)	γ 199,639,759,560
144	Cs(0 + x)	< 1 s	(\geq 4)	β^-	
145	Cs	0.587(5) s	3/2+	Q β^- = 7,880(100%) β^- – n(14.7%)	γ 175,199,112,436
146	Cs	0.321(2) s	1–	Q β^- = 9,370(100%) β^- – n(14.2%)	γ 181,558,332
147	Cs	0.235(3) s	(3/2+)	Q β^- = 9,200(100%) β^- – n(43%)	γ 85,246,110,596
148	Cs	146(6) ms		Q β^- = 10,400(100%) β^- – n(25.1%)	γ 142,687,546,633
149	Cs	> 50 ms		Q β^- = [9,600] β^- – n	
150	Cs	> 50 ms		Q β^- = [11,500] β^- – n	
151	Cs	> 50 ms		Q β^- = [10,500] β^- – n	
56	Barium				
	Ba	0.43(+30–15) s	0+	Q ϵ = [8,900](~100%) ϵ p(20%) Q α = [3,600]	
	Ba	0.45(5) s	(5/2+)	Q ϵ = [11,000](100%) ϵ p(>15%)	

116	Ba	1.3(2) s	0+	Q ϵ = [8,200](100%) ϵp (3%)	
117	Ba	1.75(7) s	(3/2)	Q ϵ = [9,500](100%) $\epsilon p(>0\%)$ $\epsilon \alpha(>0\%)$	
118	Ba	5.5(2) s	0+	Q ϵ = [6,400](100%)	
119	Ba	5.4(3) s	(5/2+)	Q ϵ = 8,100(100%) $\epsilon p(<25\%)$	
120	Ba	24(2) s	0+	Q ϵ = 5,000(100%)	γ 179,270,140,166
121	Ba	29.7(15) s	5/2(+)	Q ϵ = 6,800(100%)	γ 112,992,111,111
122	Ba	1.95(15) m	0+	Q ϵ = [3,900](100%)	γ 551
123	Ba	2.7(4) m	5/2(+)	Q ϵ = [5,500](100%)	γ 95,124,31,116
124	Ba	11.0(5) m	0+	Q ϵ = 2,648(100%)	γ 170,189,1217,253
125	Ba	3.5(4) m	1/2(+)	Q ϵ = 4,560(100%)	γ 78,141,85,55
126	Ba	100(2) m	0+	Q ϵ = 1,673(100%)	γ 234,258,241,682
127	Ba	12.7(4) m	1/2+	Q ϵ = 3,450(100%)	γ 181,115,66,1201
127	Ba(80.3)	1.9(2) s	7/2–	IT(100%)	γ 56
128	Ba	2.43(5) days	0+	Q ϵ = 523(100%)	γ 273
129	Ba	2.23(11) h	1/2+	Q ϵ = 2,432(100%)	γ 214,221,129,554
129	Ba(8.4)	2.16(2) h	7/2+	$\epsilon(<100\%)$ IT	γ 182,1459,202,420
130	Ba	>3.5E14 years	0+	2 ϵ	
130	Ba(2476.2)	9.4(4) ms	8–	{0.106(1)%} IT(100%)	γ 357,545,691,883
131	Ba	11.50(6) days	1/2+	Q ϵ = 1,370(100%)	γ 496,124,216,373
131	Ba(187.5)	14.6(2) m	9/2–	IT(100%)	γ 108

Table 22.1 (Continued)

A	Element	Half-life or width	$J\pi$	Qmode(%BR){%Abund}	Principal gammas, alphas
132	Ba	Stable	0+	{0.101(1)%}	
133	Ba	3.841(7) days	1/2+	Q ϵ = 517.4(100%)	γ 356,81,303,384
133	Ba(288.2)	38.9(1) h	11/2–	IT(99.99%)	γ 276
				ϵ (0.0096%)	γ 633
134	Ba	Stable	0+	{2.417(18)%}	
135	Ba	Stable	3/2+	{6.592(12)%}	
135	Ba(268.2)	28.7(2) h	11/2–	IT(100%)	γ 268
136	Ba	Stable	0+	{7.854(24)%}	
136	Ba(2030.5)	0.3084(19) s	7–	IT(100%)	γ 1048,819,164
137	Ba	Stable	3/2+	{11.232(24)%}	
137	Ba(661.7)	2.552(1) m	11/2–	IT(100%)	γ 662
138	Ba	Stable	0+	{71.698(42)%}	
139	Ba	83.06(28) m	7/2–	Q β – = 2.317(100%)	γ 166
140	Ba	12.7527(23) days	0+	Q β – = 1.050(100%)	γ 537,30,163,305
141	Ba	18.27(7) m	3/2–	Q β – = 3.213(100%)	γ 190,304,277,344
142	Ba	10.6(2) m	0+	Q β – = 2.211(100%)	γ 255,1204,895,232
				β – ν (0.09%)	
143	Ba	14.5(3) s	5/2–	Q β – = 4.246(100%)	γ 211,799,980,1010
144	Ba	11.5(2) s	0+	Q β – = 3.120(100%)	γ 104,430,173,157
				β – ν (3.6%)	
145	Ba	4.31(16) s	5/2–	Q β – = 4.920(100%)	γ 97,92,66,544
146	Ba	2.22(7) s	0+	Q β – = 4.100(100%)	γ 141,251,121,197
147	Ba	0.893(1) s	(3/2+)	Q β – = 5.750(100%)	γ 167,105,196,249
				β – ν (0.06%)	

57	148	Ba	0.612(17) s	0+	Q β^- = 5,120(100%) β^- – n(0.4%)	γ 56,134,416
	149	Ba	0.344(7) s		Q β^- = [7,500](100%) β^- – n(0.43%)	
	150	Ba	0.3 s	0+	Q β^- = [6,600](100%)	
	151	Ba	>300 ns		Q β^- = [8,500]	
	152	Ba	\approx 0.1 s	0+	Q β^- = [7,500]	
	153	Ba	\approx 0.08 s		Q β^- = [9,500]	
		Lanthanum				
	117	La	23.5(26) ms	(3/2 $^+$, 3/2 $-$)	Q β^- = [500](93.9%) Q ϵ = [10,400](6.1%)	
	117	La(151.0)	10(5) ms	(9/2 $^+$)	p(97.4%) ϵ (2.6%)	
	118	La	\approx 1 s		Q ϵ = [12,200]	
	119	La	\approx 2 s		Q ϵ = [9,300]	
	120	La	2.8(2) s		Q ϵ = [11,200](100%) ϵ p(>0%)	
	121	La	5.3(2) s		Q ϵ = [7,900](100%)	γ 139,134,213,98
	122	La	8.6(5) s		Q ϵ = [9,700](100%) ϵ p	γ 703
	123	La	17(3) s		Q ϵ = [6,900](100%)	γ 93,154,937,121
	124	La(0 + x)	21(4) s		Q ϵ = [8,800](100%) ϵ (100%)	γ 230,422,577,1034
	124	La(0 + y)	29.21(17) s	(8 $-$)		
	125	La	64.8(12) s		Q ϵ = [5,600](100%)	γ 68,44
	125	La(107.0)	0.4(2) s		Π	
	126	La	<50 s	(0 $-$, 1, 2 $-$)	Q ϵ = [7,600]	

Table 22.1 (Continued)

A	Element	Half-life or width	$J\pi$	Qmode(%BR){%Abund}	Principal gammas, alphas
126	La(0 + x)	54(2) s	(5+)	ε	γ 625
127	La	5.1(1) m	(11/2-)	Q ε = [4,690](100%)	γ 2272
127	La(14.8)	3.7(4) m	(3/2+)	ε (100%)	γ 56,25
128	La	5.18(14) m	(5+)	IT	
128	La(0 + x)	<1.4 m	(1+,2-)	Q ε = 6,700(100%)	γ 284,479,644,601
129	La	11.6(2) m	3/2+	ε (100%)	γ 2345
129	La(172.1)	0.56(5) s	11/2-	Q ε = 3,720(100%)	γ 279,111,457,254
130	La	8.7(1) m	3(+)	IT(100%)	γ 68,105
131	La	59(2) m	3/2+	Q ε = [5,600](100%)	γ 357,551,908,545
132	La	4.8(2) h	2-	Q ε = 2,960(100%)	γ 108,418,365,285
132	La(188.2)	24.3(5) m	6-	Q ε = 4,710(100%)	γ 465,567,663,1910
133	La	3.912(8) h	5/2+	IT(76%)	γ 136
134	La	6.45(16) m	1+	ε (24%)	γ 465,663,286,899
135	La	19.5(2) h	5/2+	Q ε = 2,230(100%)	γ 279,302,290,633
136	La	9.87(3) m	1+	Q ε = 3,710(100%)	γ 605
136	La(230 + x)	114(3) ms	(8+)	Q ε = 1,200(100%)	γ 481,875
137	La	6(2)E4 years	7/2+	Q ε = 2,870(100%)	γ 819,761,1323
138	La	1.02(1)E11 years	5+	IT(100%)	γ 96,34
				Q ε = 600(100%)	
				Q ε = 1,738(65.6%)	γ 1436
				{0.090(1)%}	
				Q β - = 1,044(34.4%)	γ 789
139	La	Stable	7/2+	{99.910(1)%}	
140	La	1.67855(12) days	3-	Q β - = 3,761.9(100%)	γ 1596,487,816,329

58	141	La	3.92(3) h	(7/2+)	$Q\beta^- = 2,502(100\%)$	γ^{1355}
	142	La	91.1(5) m	2−	$Q\beta^- = 4,504(100\%)$	$\gamma^{641,2398,2543,895}$
	143	La	14.2(1) m	(7/2)+	$Q\beta^- = 3,426(100\%)$	$\gamma^{620,644,621,798}$
	144	La	40.8(4) s	(3−)	$Q\beta^- = 5,540(100\%)$	$\gamma^{397,541,845}$
	145	La	24.8(20) s	(5/2+)	$Q\beta^- = 4,110(100\%)$	$\gamma^{70,356,118,447}$
	146	La	6.27(10) s	2−	$Q\beta^- = 6,530(100\%)$	$\gamma^{258,925,702}$
	146	La(0 + x)	10.0(1) s	(6−)	$\beta^- (100\%)$	$\gamma^{258,410,515,503}$
	147	La	4.015(8) s	(5/2+)	$Q\beta^- = 4,950(100\%)$	$\gamma^{118,186,438,216}$
	148	La	1.26(8) s	(2−)	$\beta^- n(0.04\%)$	
	149	La	1.05(3) s	(3/2−)	$Q\beta^- = 7,260(100\%)$	$\gamma^{158,990,760,602}$
	150	La	0.51(3) s	(3−)	$\beta^- n(0.15\%)$	
	151	La	>300 ns		$Q\beta^- = [5,700](100\%)$	
	152	La	>150 ns		$\beta^- n(1.43\%)$	
	153	La	>100 ns		$Q\beta^- = [7,800](100\%)$	
	154	La	≈0.1 s		$\beta^- n(2.7\%)$	
58	155	La	≈0.06 s		$Q\beta^- = [7,000]$	
		Cerium			$Q\beta^- = [9,100]$	
	119	Ce	≈0.2 s		$Q\beta^- = [8,300]$	
	120	Ce	≈0.25 s	0+	$Q\beta^- = [10,300]$	
	121	Ce	1.1(1) s		$Q\beta^- = [9,400]$	
	122	Ce		0+	$Q\beta^- = [11,000]$	
					$Q\epsilon = [8,000]$	
					$Q\epsilon = [9,900](100\%)$	
					$\epsilon p(\sim 1\%)$	γ^{358}
					$Q\epsilon = [6,800]$	
					ϵp	

Table 22.1 (Continued)

A	Element	Half-life or width	J π	Qmode(%BR){%Abund}	Principal gammas, alphas
123	Ce	3.8 s	(5/2)	Q ϵ = [8,600](100%)	
				ϵp	
124	Ce	6(2) s	0+	Q ϵ = [5,600](100%)	γ 560
125	Ce	10.2(4) s	(5/2+)	Q ϵ = [7,300](100%)	γ 811
				ϵp	γ 575
126	Ce	51.0(3) s	0+	Q ϵ = [4,400](100%)	γ 188
127	Ce	31(2) s	(5/2+)	Q ϵ = [6,100](100%)	γ 58
128	Ce	3.93(2) m	0+	Q ϵ = [3,200](100%)	γ 147,104,219,545
129	Ce	3.5(5) m	5/2+	Q ϵ = [5,050]($>0\%$)	γ 68
130	Ce	22.9(5) m	0+	Q ϵ = [2,200](100%)	γ 131,220,308,136
131	Ce	10.3(3) m	7/2+	Q ϵ = 4,000(100%)	γ 169,414,119,26
131	Ce(0 + x)	5.4(4) m	(1/2+)	ϵ (100%)	γ 230
132	Ce	3.51(11) h	0+	Q ϵ = [1,290](100%)	γ 182,155
132	Ce(2341.1)	9.4(3) ms	(8-)	IT(100%)	γ 325,533,684
133	Ce	97(4) m	1/2+	Q ϵ = [2,900](100%)	γ 97,77,558
133	Ce(37.1)	4.9(4) h	9/2-	ϵ (100%)	γ 477,510,58,131
134	Ce	3.16(4) days	0+	Q ϵ = 500(100%)	γ 162,130,301,32
135	Ce	17.7(3) h	1/2(+)	Q ϵ = 2,026(100%)	γ 266,300,607,518
135	Ce(445.8)	20(1) s	(11/2-)	IT(100%)	γ 213,150,82,296
136	Ce	$>7E13$ years	0+	2 ϵ	
				{0.185(2)%}	
137	Ce	9.0(3) h	3/2+	Q ϵ = 1,222.1(100%)	γ 447,11,437
137	Ce(254.3)	34.4(3) h	11/2-	IT(99.21%)	γ 254
				ϵ (0.79%)	γ 825,169,762,835

59	138	Ce	> 9E13 years	0+	{0.251(2)%}		
	138	Ce(2129.7)	8.65(20) ms	7−	IT(100%)	γ1038,789,303	
	139	Ce	137.641(20) days	3/2+	Qε = 278(100%)	γ166	
	139	Ce(754.2)	54.8(10) s	11/2−	IT(100%)	γ754	
	140	Ce	Stable	0+	{88.450(51)%}		
	141	Ce	32.508(13) days	7/2−	Qβ− = 580.7(100%)	γ145	
	142	Ce	> 5E16 years	0+	{1.114(51)%}		
	143	Ce	33.039(6) h	3/2−	Qβ− = 1,461.4(100%)	γ293,57,665,722	
	144	Ce	284.91(5) days	0+	Qβ− = 318.7(100%)	γ134,80	
	145	Ce	3.01(6) m	(5/2−)	Qβ− = 2,530(100%)	γ724,63,1148,285	
	146	Ce	13.52(13) m	0+	Qβ− = 1,030(100%)	γ317,218,265,134	
	147	Ce	56.4(10) s	(5/2−)	Qβ− = 3,290(100%)	γ269,93,374,452	
	148	Ce	56(1) s	0+	Qβ− = 2,060(100%)	γ270,292,121,99	
	149	Ce	5.3(2) s	(3/2−)	Qβ− = 4,190(100%)	γ58,380,86	
	150	Ce	4.0(6) s	0+	Qβ− = 3,010(100%)	γ110	
	151	Ce	1.76(6) s	(5/2+)	Qβ− = [5,400](100%)	γ97	
	152	Ce	1.4(2) s	0+	Qβ− = [4,500](100%)	γ115,98	
59	153	Ce	> 100 ns		Qβ− = [6,500]		
	154	Ce	> 150 ns	0+	Qβ− = [5,500]		
	155	Ce	> 300 ns		Qβ− = [7,500]		
	156	Ce	≈ 0.15 s	0+	Qβ− = [6,700]		
	157	Ce	≈ 0.05 s		Qβ− = [8,500]		
		Praseodymium					
	121	Pr	1.4(8) s	(3/2−)	Qp = 840		
	122	Pr	≈ 0.5 s		Qε = [12,700]		
	123	Pr	≈ 0.8 s		Qε = [9,700]		

Table 22.1 (Continued)

A	Element	Half-life or width	J π	Qmode(%BR){%Abund}	Principal gammas, alphas
124	Pr	1.2(2) s		Q ϵ = [11,600](100%)	γ 142
				ϵ p	
125	Pr	3.3(7) s		Q ϵ = [8,700](100%)	γ 180
				ϵ p	
126	Pr	3.14(22) s	(≥ 4)	Q ϵ = [10,400](100%)	γ 170,350,496
				ϵ p	
127	Pr	4.2(3) s		Q ϵ = [7,500](100%)	γ 126,30,243,431
128	Pr	2.84(9) s	4,5,6	Q ϵ = [9,300](100%)	γ 207,400,845
129	Pr	32(3) s	(11/2 $-$)	Q ϵ = [6,300]($>0\%$)	γ 1864
130	Pr(0 + x)	40(4) s	(4,5)+	Q ϵ = [8,100](100%)	γ 254,457,924,581
131	Pr	1.51(2) m	(3/2+)	Q ϵ = 5,250(100%)	γ 266,73,388,324
131	Pr(152.6)	5.73(20) s	(11/2 $-$)	IT(96.4%)	γ 88
				ϵ (3.6%)	γ 138
132	Pr	1.6(3) m	(2)+	Q ϵ = [7,100](100%)	γ 325,497,822,534
133	Pr	6.5(3) m	(3/2+)	Q ϵ = [4,300](100%)	γ 134,316,465,331
134	Pr	17(2) m	2 $-$	Q ϵ = [6,190](100%)	γ 409,966,556,2136
134	Pr(0 + x)	\approx 11 m	(6 $-$)	ϵ (100%)	γ 409,640,215,332
135	Pr	24(1) m	3/2(+)	Q ϵ = 3,720(100%)	γ 296,83,213,538
136	Pr	13.1(1) m	2+	Q ϵ = 5,126(100%)	γ 552,540,1092,461
137	Pr	1.28(3) h	5/2+	Q ϵ = 2,702(100%)	γ 837,434,514,160
138	Pr	1.45(5) m	1+	Q ϵ = 4,437(100%)	γ 789,688,1551
138	Pr(364)	2.12(4) h	7 $-$	ϵ (100%)	γ 1038,789,303
139	Pr	4.41(4) h	5/2+	Q ϵ = 2,129(100%)	γ 1347,1631,255,1376
140	Pr	3.39(1) m	1+	Q ϵ = 3,388(100%)	γ 1596,307
141	Pr	Stable	5/2+	{100%}	

60	142	Pr	19.12(4) h	2−	Qβ− = 2,162.2(99.98%) Qε = 745.3(0.02%)	γ1576 γ642
	142	Pr(3.7)	14.6(5) m	5−	IT(100%)	
	143	Pr	13.57(2) days	7/2+	Qβ− = 933.9(100%)	γ742
	144	Pr	17.28(5) m	0−	Qβ− = 2,997.5(100%)	γ697,2186,1489
	144	Pr(59.0)	7.2(3) m	3−	IT(99.93%) β − (0.07%)	γ59 γ1631,618,1885
	145	Pr	5.984(10) h	7/2+	Qβ− = 1,805(100%)	γ748,676,73,979
	146	Pr	24.15(18) m	(2)−	Qβ− = 4,170(100%)	γ454,1525,736,789
	147	Pr	13.4(4) m	(3/2+)	Qβ− = 2,690(100%)	γ78,315,641,578
	148	Pr	2.29(2) m	1−	Qβ− = 4,930(100%)	γ302,1358
	148	Pr(90)	2.01(7) m	(4)	β − (100%)	γ302,451,698
	149	Pr	2.26(7) m	(5/2+)	Qβ− = 3,397(100%)	γ138,165,109,333
	150	Pr	6.19(16) s	(1)−	Qβ− = 5,690(100%)	γ130,723,853,1141
	151	Pr	18.90(7) s	(3/2−)	Qβ− = 4,100(100%)	γ485,880,495,189
	152	Pr	3.63(12) s	(4−)	Qβ− = [6,400](100%)	γ164,285,1470,1364
	153	Pr	4.28(11) s		Qβ− = [5,500](100%)	γ192,142,50
	154	Pr	2.3(1) s	(3+,2+)	Qβ− = [7,400](100%)	γ162,932,71,563
	155	Pr	> 300 ns		Qβ− = [6,900]	
	156	Pr	> 300 ns		Qβ− = [8,300]	
	157	Pr	≈ 0.3 s		Qβ− = [7,400]	
	158	Pr	≈ 0.2 s		Qβ− = [9,200]	
	159	Pr	≈ 0.1 s		Qβ− = [8,200]	
60		Neodymium				
	124	Nd	(0.5 s)	0+	ε	
	125	Nd	0.60(15) s	(5/2)	ε(100%) εp(> 0%)	

Table 22.1 (Continued)

A	Element	Half-life or width	J π	Qmode(%BR){%Abund}	Principal gammas, alphas
126	Nd	>200 ns	0+	Q ϵ = [7,200]	
127	Nd	1.8(4) s		Q ϵ = [9,000](100%) ϵ p	
128	Nd	5 s	0+	Q ϵ = [6,100](100%) ϵ p	
129	Nd	4.9(2) s	(5/2+)	Q ϵ = [7,800] ϵ p	
130	Nd	21(3) s	0+	Q ϵ = [5,000](100%)	γ 92,141,120,161
131	Nd	25.4(9) s	(5/2+)	Q ϵ = 6,560(100%) ϵ p	γ 87,174,164,668 γ 254
132	Nd	94(8) s	0+	Q ϵ = [3,700](100%)	γ 148,567,137,430
133	Nd	70(10) s	(7/2+)	Q ϵ = [5,600](100%)	γ 403
133	Nd(128.0)	\approx 70 s	(1/2)+	ϵ (100%)	
134	Nd	8.5(15) m	0+	Q ϵ = 2,770(100%)	γ 163,289,217
135	Nd	12.4(6) m	9/2(–)	Q ϵ = [4,750](100%)	γ 204,41,441,502
135	Nd(65.0)	5.5(5) m	(1/2+)	ϵ (>99.97%) IT(<0.03%)	
136	Nd	50.65(33) m	0+	Q ϵ = 2,211(100%)	γ 109,40,575,149
137	Nd	38.5(15) m	1/2+	Q ϵ = 3,690(100%)	γ 76,581,307,782
137	Nd(519.4)	1.60(15) s	11/2–	IT(100%)	γ 234,178,108,286
138	Nd	5.04(9) h	0+	Q ϵ = [1,100](100%)	γ 326,200,342
139	Nd	29.7(5) m	3/2+	Q ϵ = 2,790(100%)	γ 405,1074,917,669
139	Nd(231.2)	5.50(20) h	11/2–	ϵ (88.2%) IT(11.8%)	γ 114,738,982,708 γ 231

140	Nd	3.37(2) days	0+	$Q_{\varepsilon} = 222(100\%)$		
141	Nd	2.49(3) h	3/2+	$Q_{\varepsilon} = 1,823(100\%)$		$\gamma 1127, 1293, 1147, 145$
141	Nd(756.5)	62.0(8) s	11/2–	IT(100%)		$\gamma 757$
				$\varepsilon(<0.05\%)$		$\gamma 1855, 883, 549$
142	Nd	Stable	0+	{27.2(5)%}		
143	Nd	Stable	7/2–	{12.2(2)%}		
144	Nd	2.29(16)E15 years	0+	$Q_{\alpha} = 1,905.2(100\%)$		$\alpha 1852$
				{23.8(3)%}		
145	Nd	Stable	7/2–	{8.3(1)%}		
146	Nd	Stable	0+	{17.2(3)%}		
147	Nd	10.98(1) days	5/2–	$Q_{\beta-} = 896.0(100\%)$		$\gamma 91, 531$
148	Nd	Stable	0+	{5.7(1)%}		
149	Nd	1.728(1) h	5/2–	$Q_{\beta-} = 1,691(100\%)$		$\gamma 211, 114, 270, 655$
150	Nd	> 7.9E18 years	0+	2 β –		
				{5.6(2)%}		
151	Nd	12.44(7) m	3/2+	$Q_{\beta-} = 2,442(100\%)$		$\gamma 117, 256, 1181, 139$
152	Nd	11.4(2) m	0+	$Q_{\beta-} = 1,110(100\%)$		$\gamma 279, 250, 44, 16$
153	Nd	31.6(10) s	(3/2)–	$Q_{\beta-} = 3,336(100\%)$		$\gamma 418, 32, 1966, 105$
154	Nd	25.9(2) s	0+	$Q_{\beta-} = 2,740(100\%)$		$\gamma 152, 800, 181, 84$
155	Nd	8.9(2) s		$Q_{\beta-} = 4,220(100\%)$		$\gamma 181, 419, 955, 67$
156	Nd	5.49(7) s	0+	$Q_{\beta-} = [3,900](100\%)$		$\gamma 150, 157, 85, 274$
157	Nd	> 100 ns		$Q_{\beta-} = [5,700]$		
158	Nd	> 50 ns	0+	$Q_{\beta-} = [4,800]$		
159	Nd	≈ 0.7 s		$Q_{\beta-} = [6,800]$		
160	Nd	≈ 0.3 s	0+	$Q_{\beta-} = [6,000]$		
161	Nd	≈ 0.2 s		$Q_{\beta-} = [7,900]$		

Table 22.1 (Continued)

61	A	Element	Half-life or width	J^{π}	Qmode(%BR){%Abund}	Principal gammas, alphas
		Promethium				
	126	Pm	(0.5 s)		ϵ	
	127	Pm	(1 s)		ϵ	
					p	
	128	Pm	1.0(3) s		$Q_{\epsilon} = [12,000](100\%)$	
					$Q_{\alpha} = [2,500]$	
					ϵp	
	129	Pm	2.4(9) s	(5/2-)	$Q_{\epsilon} = [9,200]$	
	130	Pm	2.6(2) s	(4,5,6)	$Q_{\epsilon} = [10,900](100\%)$	$\gamma 326,159,454,547$
					ϵp	
	131	Pm	6.3(8) s	(11/2-)	$Q_{\epsilon} = [8,100]$	
					ϵp	
	132	Pm	6.2(6) s	(3+)	$Q_{\epsilon} = [9,900](100\%)$	$\gamma 213,397,610,824$
					$\epsilon p(\sim 5.0\epsilon - 5\%)$	
	133	Pm	15(3) s	(11/2-)	$Q_{\epsilon} = [7,000](100\%)$	$\gamma 181,291,272,345$
	134	Pm	≈ 5 s	(2+)	$Q_{\epsilon} = 9,170(100\%)$	$\gamma 294,795,754,459$
	134	Pm(0 + x)	22(1) s	(5+)	$\epsilon(100\%)$	$\gamma 294,495,631,795$
	135	Pm(0 + x)	45(4) s	(11/2-)	$Q_{\epsilon} = [5,940](100\%)$	$\gamma 199,464,978,1177$
	135	Pm(0 + y)	49(3) s	(3/2+,5/2+)	$\epsilon(100\%)$	$\gamma 129,263,208,270$
	136	Pm(x)	47(2) s	(2+)	$Q_{\epsilon} = 7,850(100\%)$	$\gamma 374,862,489,603$
	136	Pm(y)	107(6) s	(5-)	$\epsilon(100\%)$	$\gamma 374,603,858,815$
	137	Pm	2.4(1) m	11/2-	$Q_{\epsilon} = [5,660](100\%)$	$\gamma 178,109,234,286$
	138	Pm	10(2) s		$Q_{\epsilon} = 7,000(100\%)$	
	138	Pm(0 + x)	3.24(5) m		$\epsilon(100\%)$	

138	Pm(0 + y)	3.24 m	(5−)	ε(100%)	
139	Pm	4.15(5) m	(5/2)+	Qε = 4,500(100%)	γ403,463,368,757
139	Pm(188.7)	180(20) ms	(11/2)−	IT(99.94%)	γ189
140	Pm	9.2(2) s	1+	ε(0.06%)	
140	Pm(0 + x)	5.95(5) m	8−	Qε = 6,047(100%)	γ774,477,1205,1139
141	Pm	20.90(5) m	5/2+	ε(100%)	γ774,1028,420
142	Pm	40.5(5) s	1+	Qε = 3,730(100%)	γ1223,886,194,1346
142	Pm(883.2)	2.0(2) ms	(8)−	Qε = 4,870(100%)	γ1576,641
143	Pm	265(7) days	5/2+	IT(100%)	
144	Pm	363(14) days	5−	Qε = 1,041.4(100%)	γ742
145	Pm	17.7(4) years	5/2+	Qε = 2,331.7(100%)	γ696,618,477
				Qε = 163.0(100%)	γ72,67
146	Pm	5.53(5) years	3−	Qα = 2,322(3E − 07%)	α2240
				Qε = 1,472(66%)	γ454,736
147	Pm	2.6234(2) years	7/2+	Qβ− = 1,542(34%)	γ747
148	Pm	5.368(2) days	1−	Qβ− = 224.1(100%)	γ121
148	Pm(137.9)	41.29(11) days	5−,6−	Qβ− = 2,468(100%)	γ1465,550,915
				β − (95.8%)	γ550,630,726,1014
149	Pm	53.08(5) h	7/2+	IT(4.2%)	γ76
150	Pm	2.68(2) h	(1 −)	Qβ− = 1,071(100%)	γ286
151	Pm	28.40(4) h	5/2+	Qβ− = 3,454(100%)	γ334,1325,1166,832
152	Pm	4.12(8) m	1+	Qβ− = 1,187(100%)	γ340,168,275,718
152	Pm(150)	7.52(8) m	4−	Qβ− = 3,500(100%)	γ122,841,961,963
152	Pm(150 + x)	13.8(2) m	(8)	β − (100%)	γ245,122,340,1097
				β − (<100%)	γ230
				IT(>0%)	

Table 22.1 (Continued)

	A	Element	Half-life or width	J^{π}	Qmode(%BR){%Abund}	Principal gammas, alphas
	153	Pm	5.25(2) m	5/2−	Qβ− = 1,881(100%)	γ127,36,120,28
	154	Pm(0 + x)	2.68(7) m	(3,4)	Qβ− = 4,040(100%)	γ185,82,547,1440
	154	Pm	1.73(10) m	(0,1)	β − (100%)	γ2058,1394,82,2140
	155	Pm	41.5(2) s	5/2−	Qβ− = 3,220(100%)	γ779,725,410,762
	156	Pm	26.70(10) s	4−	Qβ− = 5,160(100%)	γ174,1148,117,267
	157	Pm	10.56(10) s	(5/2−)	Qβ− = [4,500](100%)	γ161,188,571,851
	158	Pm	4.8(5) s		Qβ− = [6,200](100%)	γ73
	159	Pm	1.47(15) s		Qβ− = [5,500]	
	160	Pm	≈2 s		Qβ− = [7,300]	
	161	Pm	≈0.7 s		Qβ− = [6,500]	
	162	Pm	≈0.5 s		Qβ− = [8,400]	
	163	Pm	≈0.2 s		Qβ− = [7,600]	
		Samarium				
62	128	Sm	(0.5 s)	0+	ε	
					p	
	129	Sm	0.55(10) s	1/2+,3/2+	ε(100%)	
					p	
	130	Sm	(1 s)	0+	Qε = [7,600]	
	131	Sm	1.2(2) s		Qε = [9,400](100%)	
					εp(>0%)	γ159

132	Sm	4.0(3) s	0+	$Q_{\beta} = [6,600](100\%)$	
133	Sm	3.7(7) s	(5/2+)	$Q_{\beta} = [8,400](100\%)$	
134	Sm	9.5(8) s	0+	$Q_{\beta} = [5,200](100\%)$	$\gamma 119,219,380,161$
135	Sm	10.3(5) s	(3/2+,5/2+)	$Q_{\beta} = [7,200](100\%)$	$\gamma 190,126,286,363$
136	Sm	47(2) s	0+	$Q_{\beta} = [4,500](100\%)$	$\gamma 114,748,485,314$
137	Sm	45(1) s	(9/2-)	$Q_{\beta} = [5,900](100\%)$	$\gamma 381,164,408,531$
138	Sm	3.1(2) m	0+	$Q_{\beta} = [3,800](100\%)$	$\gamma 75$
139	Sm	2.57(10) m	1/2+	$Q_{\beta} = 5,160(100\%)$	$\gamma 274,307,596,782$
139	Sm(457.4)	10.7(6) s	11/2-	$IT(93.7\%)$	$\gamma 190,267,155,112$
140	Sm	14.82(12) m	0+	$\epsilon(6.3\%)$	$\gamma 189$
141	Sm	10.2(2) m	1/2+	$Q_{\beta} = 2,970(100\%)$	$\gamma 225,140,341,1138$
141	Sm(175.8)	22.6(2) m	11/2-	$Q_{\beta} = 4,530(100\%)$	$\gamma 404,438,1293$
142	Sm	72.49(5) m	0+	$\epsilon(99.69\%)$	$\gamma 197,432,777,1786$
143	Sm	8.75(8) m	3/2+	$IT(0.31\%)$	$\gamma 174$
143	Sm(754.0)	66(2) s	11/2-	$Q_{\beta} = 2,090(100\%)$	$\gamma 1243,1345,679,849$
143	Sm	30(3) ms	23/2(-)	$Q_{\beta} = 3,443(100\%)$	$\gamma 1057,1515,1173,1403$
144	Sm	Stable	0+	$IT(99.76\%)$	$\gamma 754$
145	Sm	340(3) days	7/2-	$\epsilon(0.24\%)$	$\gamma 689,963$
145	Sm	340(3) days	7/2-	$IT(100\%)$	$\gamma 1573,208,77,1706$
145	Sm	340(3) days	7/2-	$\{3.07(7)\%$	
145	Sm	340(3) days	7/2-	$Q_{\beta} = 616.4(100\%)$	$\gamma 61$

Table 22.1 (Continued)

A	Element	Half-life or width	$J\pi$	Qmode(%BR){%Abund}	Principal gammas, alphas
146	Sm	1.03(5)E8 years	0+	$Q\alpha = 2,529(100\%)$	$\alpha 2460$
147	Sm	1.06(2)E11 years	7/2−	$Q\alpha = 2,310.5(100\%)$ {14.99(18)%}	$\alpha 2908$
148	Sm	7(3)E15 years	0+	$Q\alpha = 1,986.0(100\%)$ {11.24(10)%}	$\alpha 1932$
149	Sm	>2E15 years	7/2−	$Q\alpha = 1,869.9$ {13.82(7)%}	
150	Sm	Stable	0+	{7.38(1)%}	
151	Sm	90(8) years	5/2−	$Q\beta^- = 76.7(100\%)$	$\gamma 22$
152	Sm	Stable	0+	{26.75(16)%}	
153	Sm	46.284(4) h	3/2+	$Q\beta^- = 808.2(100\%)$	$\gamma 103,70$
153	Sm(98.4)	10.6(3) ms	11/2−	IT(100%)	$\gamma 33$
154	Sm	Stable	0+	{22.75(29)%}	
155	Sm	22.3(2) m	3/2−	$Q\beta^- = 1,626.9(100\%)$	$\gamma 104$
156	Sm	9.4(2) h	0+	$Q\beta^- = 722(100\%)$	$\gamma 88,204,166,23$
157	Sm	8.03(7) m	(3/2−)	$Q\beta^- = 2,730(100\%)$	$\gamma 198,196,394$
158	Sm	5.30(3) m	0+	$Q\beta^- = 1,999(100\%)$	$\gamma 189,364,325,224$
159	Sm	11.37(15) s	5/2−	$Q\beta^- = [3,800](100\%)$	$\gamma 190,862,254,797$
160	Sm	9.6(3) s	0+	$Q\beta^- = [3,000](100\%)$	
161	Sm	4.8(8) s		$Q\beta^- = [4,800](100\%)$	$\gamma 264$
162	Sm	2.4(5) s	0+	$Q\beta^- = [3,900]$	
163	Sm	≈1 s		$Q\beta^- = [5,700]$	
164	Sm	≈0.5 s	0+	$Q\beta^- = [4,900]$	
165	Sm	≈0.2 s		$Q\beta^- = [6,800]$	

63						
	Europium					
130	Eu	0.90(+49–29) ms	1+	p(\approx 100%)		γ 122
131	Eu	17.8(19) ms	3/2+	p(87.9%)		γ 122
				ε (12.1%)		
132	Eu	(100 ms)		Q_{ε} = [12,400]		
133	Eu	\approx 1 s		Q_{ε} = [9,500]		
134	Eu	0.5(2) s		Q_{ε} = [11,500](100%)		
				ε p(>0%)		
135	Eu	1.5(2) s		Q_{ε} = [8,700](100%)		γ 121
				ε p		
136	Eu	3.3(3) s	(7+)	Q_{ε} = [10,400](100%)		
				ε p(0.09%)		
136	Eu(x)	3.8(3) s	(3+)	ε (100%)		γ 255,432,458,713
				ε p(0.09%)		
137	Eu	11(2) s	(11/2–)	Q_{ε} = [7,600](100%)		
138	Eu	12.1(6) s	(6–)	Q_{ε} = [9,200](100%)		γ 347,545,686,399
139	Eu	17.9(6) s	(11/2)–	Q_{ε} = [7,020](100%)		γ 267,155,190,112
140	Eu	1.51(2) s	1+	Q_{ε} = 8,470(100%)		γ 531,1068,460
140	Eu(234)	125(2) ms	(5–)	IT(100%)		γ 175,185
				ε (<1%)		
141	Eu	40.7(7) s	5/2+	Q_{ε} = 5,980(100%)		γ 394,385,383,593
141	Eu(96.4)	2.7(3) s	11/2–	IT(87%)		γ 96
				ε (13%)		γ 394,883,519,804
142	Eu	2.34(12) s	1+	Q_{ε} = 7,640(100%)		γ 768,1658,1754,1671
142	Eu(0 + x)	1.223(8) m	8–	ε (100%)		γ 768,1023,557,1016
143	Eu	2.59(2) m	5/2+	Q_{ε} = 5,275(100%)		γ 1107,1537,1913,108

Table 22.1 (Continued)

A	Element	Half-life or width	$J\pi$	Qmode(%BR){%Abund}	Principal gammas, alphas
144	Eu	10.2(1) s	1+	Q ϵ = 6.315(100%)	γ 1660,818
145	Eu	5.93(4) days	5/2+	Q ϵ = 2.660(100%)	γ 894,654,1659,1997
146	Eu	4.61(3) days	4-	Q ϵ = 3.878(100%)	γ 747,634,633
147	Eu	24.1(6) days	5/2+	Q ϵ = 1.721.3(100%)	γ 197,121,678,1077
				Q α = 2.990(0.0022%)	α 2908
148	Eu	54.5(5) days	5-	Q ϵ = 3.107(100%)	γ 550,630,611,553
				Q α = 2.762(9.4E - 7%)	α 2630
149	Eu	93.1(4) days	5/2+	Q ϵ = 695(100%)	γ 328,277,23,255
150	Eu	36.9(9) years	5(-)	Q ϵ = 2.261(100%)	γ 334,439,584
150	Eu(42.1)	12.8(1) h	0-	Q β - = 971(89%)	
				ϵ (11%)	γ 334,407
				IT(<5.0E - 8%)	
151	Eu	> 1.7E18 years	5/2+	{47.81(3)%}	
152	Eu	13.537(6) years	3-	Q ϵ = 1,874.3(72.1%)	γ 122,1408,964,1112
				Q β - = 1,818.8(27.9%)	γ 344,779
152	Eu(45.6)	9.3116(13) h	0-	β - (72%)	γ 344,1315,970
				ϵ (28%)	γ 842,963,122
152	Eu(147.8)	96(1) m	8-	IT(100%)	γ 90
153	Eu	Stable	5/2+	{52.19(3)%}	
154	Eu	8.593(4) years	3-	Q β - = 1,968.4(99.98%)	γ 123,1274,723,1005
				Q ϵ = 717.3(0.02%)	γ 185,82
154	Eu(145.3)	46.3(4) m	(8-)	IT(100%)	γ 68,101,36,32
155	Eu	4.753(14) years	5/2+	Q β - = 252.1(100%)	γ 87,105
156	Eu	15.19(8) days	0+	Q β - = 2.451(100%)	γ 812,89,1231,1154

64	157	Eu	15.18(3) h		5/2+	$Q\beta^- = 1,363(100\%)$	$\gamma 64,411,371,55$
	158	Eu	45.9(2) m		(1-)	$Q\beta^- = 3,490(100\%)$	$\gamma 944,977,898,79$
	159	Eu	18.1(1) m		5/2+	$Q\beta^- = 2,514(100\%)$	$\gamma 68,79,96,146$
	160	Eu	38(4) s		1	$Q\beta^- = [4,580](100\%)$	$\gamma 173,515,412,822$
	161	Eu	26(3) s			$Q\beta^- = [3,700](100\%)$	$\gamma 314$
	162	Eu	10.6(10) s			$Q\beta^- = [5,600](100\%)$	
	163	Eu	7.8(5) s			$Q\beta^- = [4,900]$	
	164	Eu	4.2(2) s			$Q\beta^- = [6,600]$	
	165	Eu	2.3(2) s			$Q\beta^- = [5,900]$	
	166	Eu	≈ 0.4 s			$Q\beta^- = [7,800]$	
64	167	Eu	≈ 0.2 s			$Q\beta^- = [7,000]$	
		Gadolinium					
	134	Gd	(0.4 s)		0+	ϵ	
	135	Gd	1.1(2) s		(5/2+)	$\epsilon(100\%)$	
						$\epsilon p(18\%)$	$\gamma 163$
	136	Gd	>200 ns		0+	$Q\epsilon = [7,100]$	
	137	Gd	2.2(3) s		(7/2)	$Q\epsilon = [8,800](100\%)$	
	138	Gd	4.7(9) s		0+	$Q\epsilon = [6,100](100\%)$	
	139	Gd	5.8(9) s		(9/2-)	$Q\epsilon = [7,700](>0\%)$	$\gamma 472$
						$\epsilon p(>0\%)$	
64	139	Gd(x)	4.8(9) s			$\epsilon(>0\%)$	$\gamma 904$
						$\epsilon p(>0\%)$	
	140	Gd	15.8(4) s		0+	$Q\epsilon = [5,500](100\%)$	$\gamma 175,750,379,191$
	141	Gd	14(4) s		1/2+	$Q\epsilon = [6,800](100\%)$	$\gamma 216,336,526,121$
						$\epsilon p(0.03\%)$	
64	141	Gd(377.8)	24.5(5) s		11/2-	$\epsilon(89\%)$	$\gamma 351,224,575,361$
						IT(11%)	$\gamma 198,258,113,145$

Table 22.1 (Continued)

A	Element	Half-life or width	J π	Qmode(%BR){%Abund}	Principal gammas, alphas
142	Gd	70.2(6) s	0+	Q ϵ = [4,500](100%)	γ 179,284,526,1260
143	Gd	39(2) s	(1/2)+	Q ϵ = 6,010(100%)	γ 259,205,464
143	Gd(152.6)	110.0(14) s	(11/2-)	ϵ (100%)	γ 272,588,799,668
144	Gd	4.47(6) m	0+	Q ϵ = [3,740](100%)	γ 333,2433,630,347
145	Gd	23.0(4) m	1/2+	Q ϵ = 5,050(100%)	γ 1758,1881,1042,808
145	Gd(749.1)	85(3) s	11/2-	IT(94.3%)	γ 721
				ϵ (5.7%)	γ 330,387
146	Gd	48.27(10) days	0+	Q ϵ = 1,030(100%)	γ 155,115,116
147	Gd	38.06(12) h	7/2-	Q ϵ = 2,187(100%)	γ 229,396,929,370
148	Gd	70.9(10) years	0+	Q α = 3,271.21(100%)	
149	Gd	9.28(10) days	7/2-	Q ϵ = 1,314(100%)	γ 150,299,347,749
				Q α = 3,100(0.00043%)	
150	Gd	1.79(8)E6 years	0+	Q α = 2,809(100%)	α 2726
151	Gd	123.9(10) days	7/2-	Q ϵ = 464(100%)	γ 154,243,175,22
				Q α = 2,653(~8.0E - 7%)	α 2600
152	Gd	1.08(8)E14 years	0+	Q α = 2,204.6(100%)	α 2147
				{0.20(1)%}	
153	Gd	240.4(10) days	3/2-	Q ϵ = 484.4(100%)	γ 97,103
154	Gd	Stable	0+	{2.18(3)%}	
155	Gd	Stable	3/2-	{14.80(12)%}	
155	Gd(121.0)	31.97(27) ms	11/2-	IT(100%)	γ 87,13
156	Gd	Stable	0+	{20.47(9)%}	
157	Gd	Stable	3/2-	{15.65(2)%}	

	158	Gd	Stable	0+	{24.84(7)%}		
	159	Gd	18.479(4) h	3/2–	Q β – = 970.6(100%)	γ 364,58	
	160	Gd	>3.1E19 years	0+	2 β –		
					{21.86(19)%}		
	161	Gd	3.66(5) m	5/2–	Q β – = 1,955.6(100%)	γ 361,315,102	
	162	Gd	8.4(2) m	0+	Q β – = 1,390(100%)	γ 442,403	
	163	Gd	68(3) s	(5/2–,7/2+)	Q β – = [3,100](100%)	γ 1562,1685,1168,633	
	164	Gd	45(3) s	0+	Q β – = [2,300](100%)		
	165	Gd	10.3(16) s		Q β – = [4,200](100%)		
	166	Gd	4.8(10) s	0+	Q β – = [3,300]		
	167	Gd	\approx 3 s		Q β – = [5,100]		
	168	Gd	\approx 0.3 s	0+	Q β – = [4,400]		
	169	Gd	\approx 1 s		Q β – = [6,200]		
65		Terbium					
	135	Tb	0.94(+33–22) s	(7/2–)	p(100%)		
	136	Tb	(0.2 s)		ε		
	137	Tb	(0.6 s)		ε		
					p		
	138	Tb	>200 ns		Q ε = [12,000]		
					p		
	139	Tb	1.6(2) s		Q ε = [9,300]	γ 120	
	140	Tb	2.4(2) s	(7+)	Q ε = [10,800](100%)	γ 328,628	
					ε p(0.26%)		
	141	Tb	3.5(2) s	(5/2–)	Q ε = [8,300](100%)	γ 293,344,198,137	
	141	Tb(0 + x)	7.9(6) s		ε (100%)		
	142	Tb	597(17) ms	1+	Q ε = [9,900](100%)	γ 515,465	
					ε p(0.0022%)		

Table 22.1 (Continued)

A	Element	Half-life or width	J π	Qmode(%BR){%Abund}	Principal gammas, alphas
142	Tb(280.2)	303(17) ms	(5-)	IT(100%)	γ 212,182
143	Tb	12(1) s	(11/2-)	Q ϵ = [7,500](100%)	γ 45,686,463,380
143	Tb(0 + x)	<21 s		ϵ	
144	Tb	\approx 1 s	1+	Q ϵ = [9,100](100%)	γ 743,1144
144	Tb(396.9)	4.25(15) s	(6-)	IT(66%)	γ 284
				ϵ (34%)	γ 743,1002,959,558
145	Tb	\sim 20 m	(3/2+)	Q ϵ = [6,700]	
145	Tb(0 + x)	30.9(7) s	(11/2-)	ϵ (100%)	γ 258,988,537,1447
146	Tb	8(4) s	1+	Q ϵ = 8,270(100%)	γ 1971
146	Tb(0 + x)	23(2) s	5-	ϵ (100%)	γ 1580,1079,1417,441
146	Tb(779.6 + x)	1.18(2) ms	(10+)	IT(100%)	γ 418,343
147	Tb	1.7(1) h	(1/2+)	Q ϵ = 4,609(100%)	γ 1152,694,140
147	Tb(50.6)	1.83(6) m	(11/2)-	ϵ (100%)	γ 1397,1798
148	Tb	60(1) m	2-	Q ϵ = 5,760(100%)	γ 784,489,1079,632
148	Tb(90.1)	2.20(5) m	(9)+	ϵ (100%)	γ 784,395,632,882
149	Tb	4.118(25) h	1/2+	Q ϵ = 3,638(83.3%)	γ 352,165,389,652
				Q α = 4,077.2(16.7%)	α 3967
149	Tb(35.8)	4.16(4) m	11/2-	ϵ (99.98%)	γ 796,651
				α (0.02%)	α 3999
150	Tb	3.48(16) h	(2-)	Q ϵ = 4,656(100%)	γ 638,511,496
				Q α = 3,587(<0.05%)	α 3492
150	Tb(474)	5.8(2) m	9+	ϵ (100%)	γ 638,650,438,827
151	Tb	17.609(1) h	1/2(+)	Q ϵ = 2,565(100%)	γ 287,252,108,587
				Q α = 3,497(0.0095%)	α 3409

151	Tb(99.5)	25(3) s	(11/2 ⁻)	IT(93.4%) ε(6.6%) Q _ε = 3,990(<7.0E – 7%) Q _α = 3,090(<7.0E – 7%)	γ _{49,23} γ _{380,831,522} γ _{344,586,271}
152	Tb	17.5(1) h	2 ⁻	IT(78.8%) ε(21.2%)	γ _{283,160,277,59} γ _{344,411,472,519}
152	Tb(501.7)	4.2(1) m	8 ⁺	Q _ε = 1,569(100%) Q _ε = 3,560(100%) Q _{β⁻} = 250(<0.1%) ε(78.2%) IT(21.8%) β ⁻ – (<0.1%) ε(98.2%) IT(1.8%)	γ _{212,110,102,170} γ _{123,1274,2187,722}
153	Tb	2.34(1) days	5/2 ⁺		
154	Tb	21.5(4) h	0		
154	Tb(0 + x)	9.4(4) h	3 ⁻		γ _{123,248,540,1005}
154	Tb(0 + y)	22.7(5) h	7 ⁻		γ _{248,347,1420,123}
155	Tb	5.32(6) days	3/2 ⁺	Q _ε = 821(100%)	γ _{87,105,180,262}
156	Tb	5.35(10) days	3 ⁻	Q _ε = 2,444(100%) Q _{β⁻} = 434 IT(100%) ε IT Q _ε = 60.1(100%) Q _ε = 1,220.0(83.4%) Q _{β⁻} = 936.7(16.6%) IT(100%) β ⁻ – (<0.6%) ε(<0.01%)	γ _{534,199,1222,89}
156	Tb(49.6 + x)	24.4(10) h	(7 ⁻)		γ ₅₀
156	Tb(88.0)	5.3(2) h	(0 ⁺)		
157	Tb	71(7) years	3/2 ⁺		γ ₈₈ γ ₅₅
158	Tb	180(11) years	3 ⁻		γ _{944,962,80,182} γ _{99,218}
158	Tb(110.3)	10.70(17) s	0 ⁻		γ ₁₁₀

Table 22.1 (Continued)

A	Element	Half-life or width	J π	Qmode(%BR){%Abund}	Principal gammas, alphas
158	Tb(388.4)	0.40(4) ms	7−	IT(100%)	γ 110
159	Tb	Stable	3/2+	{100%}	
160	Tb	72.3(2) days	3−	Q β − = 1,835.3(100%)	γ 879,299,966,1178
161	Tb	6.906(19) days	3/2+	Q β − = 593.1(100%)	γ 26,49,75
162	Tb	7.60(15) m	1−	Q β − = 2,510(100%)	γ 260,808,888,185
163	Tb	19.5(3) m	3/2+	Q β − = 1,785(100%)	γ 351,390,495,422
164	Tb	3.0(1) m	(5+)	Q β − = 3,890(100%)	γ 169,755,688,215
165	Tb	2.11(10) m	(3/2+)	Q β − = [2,960](100%)	γ 1179,539,1292,1665
166	Tb	25.1(21) s	(2−)	Q β − = [4,900](100%)	
167	Tb	19.4(27) s	(3/2+)	Q β − = [4,100](100%)	γ 70
168	Tb	8.2(13) s	(4−)	Q β − = [6,000](100%)	γ 173,227,75
169	Tb	\approx 2 s		Q β − = [5,500]	
170	Tb	\approx 3 s		Q β − = [7,100]	
171	Tb	\approx 0.5 s		Q β − = [6,400]	
66	Dysprosium				
	Dy	(200 ms)	0+	ϵ	
	Dy	0.6(2) s	(7/2+)	ϵ ($>$ 0%)	
				ϵ p($>$ 0%)	
	Dy		0+	ϵ	
	Dy (2166)	7.0(5) μ s	(8−)	IT(100%)	
	Dy	0.9(2) s	(9/2−)	Q ϵ = [9,300](100%)	
				ϵ p	
	Dy	2.3(3) s	0+	Q ϵ = [6,900](100%)	γ 182
				ϵ p(0.06%)	

143	Dy	3.2(6) s	(1/2+)	$Q_{\varepsilon} = [8,500](100\%)$	
				εp	
144	Dy	9.1(4) s	0+	$Q_{\varepsilon} = [6,100](100\%)$	$\gamma 197,299,476,322$
				εp	
145	Dy	6(2) s	(1/2+)	$Q_{\varepsilon} = [7,520](100\%)$	
145	Dy(118.2)	14.1(7) s	(11/2-)	$\varepsilon(100\%)$	$\gamma 40$
146	Dy	29(3) s	0+	$Q_{\varepsilon} = 5,160(100\%)$	$\gamma 2157$
146	Dy(2935.7)	150(20) ms	(10+)	IT(100%)	$\gamma 925,237,683,674$
147	Dy	40(10) s	1/2+	$Q_{\varepsilon} = 6,370(100\%)$	
				$\varepsilon p(>0\%)$	
147	Dy(750.5)	55.7(7) s	11/2-	$\varepsilon(65\%)$	$\gamma 365,253,1388,101$
				IT(35%)	$\gamma 679,72$
148	Dy	3.3(2) m	0+	$Q_{\varepsilon} = 2,682(100\%)$	$\gamma 620$
149	Dy	4.20(14) m	(7/2-)	$Q_{\varepsilon} = 3,812(100\%)$	$\gamma 101,789,1776,654$
149	Dy(2661.1)	0.490(15) s	(27/2-)	IT(99.3%)	$\gamma 1179,1073,299$
				$\varepsilon(0.7\%)$	$\gamma 361,291,787,630$
150	Dy	7.17(5) m	0+	$Q_{\varepsilon} = 1,794(64\%)$	$\gamma 397$
				$Q_{\alpha} = 4,351.1(36\%)$	$\alpha 4233$
151	Dy	17.9(3) m	7/2(-)	$Q_{\varepsilon} = 2,870(94.4\%)$	$\gamma 386,49,546,176$
				$Q_{\alpha} = 4,180(5.6\%)$	$\alpha 4069$
152	Dy	2.38(2) h	0+	$Q_{\varepsilon} = 600(99.9\%)$	$\gamma 257$
				$Q_{\alpha} = 3,727(0.1\%)$	$\alpha 3628$
153	Dy	6.4(1) h	7/2(-)	$Q_{\varepsilon} = 2,1704(99.99\%)$	$\gamma 81,214,100,254$
				$Q_{\alpha} = 3,559(0.0094\%)$	$\alpha 3464$
154	Dy	3.0(15)E6 years	0+	$Q_{\alpha} = 2,947(100\%)$	$\alpha 2870$
155	Dy	9.9(2) h	3/2-	$Q_{\varepsilon} = 2,094.5(100\%)$	$\gamma 227$

Table 22.1 (Continued)

A	Element	Half-life or width	J^{π}	Qmode(%BR){%Abund}	Principal gammas, alphas
156	Dy	Stable	0+	{0.06(1)%}	
157	Dy	8.14(4) h	3/2−	Q ϵ = 1,341(100%)	γ 326
157	Dy(199.5)	21.6(16) ms	11/2−	IT(100%)	γ 37,87,61,148
158	Dy	Stable	0+	{0.10(1)%}	
159	Dy	144.4(2) days	3/2−	Q ϵ = 365.6(100%)	γ 58
160	Dy	Stable	0+	{2.34(8)%}	
161	Dy	Stable	5/2+	{18.91(24)%}	
162	Dy	Stable	0+	{25.51(26)%}	
163	Dy	Stable	5/2−	{24.90(16)%}	
164	Dy	Stable	0+	{28.18(37)%}	
165	Dy	2.334(1) h	7/2+	Q β − = 1,286.1(100%)	γ 95,362,633,715
165	Dy(108.2)	1.257(6) m	1/2−	IT(97.76%)	γ 108
				β − (2.24%)	γ 515,361,154
166	Dy	81.6(1) h	0+	Q β − = 486.2(100%)	γ 82
167	Dy	6.20(8) m	(1/2−)	Q β − = 2,350(100%)	γ 570,259,310,250
168	Dy	8.7(3) m	0+	Q β − = [1,600](100%)	γ 193,487,443,630
169	Dy	39(8) s	(5/2−)	Q β − = 3,200(100%)	γ 1578
170	Dy	≈30 s	0+	Q β − = [2,800]	
171	Dy	≈6 s		Q β − = [4,700]	
172	Dy	≈3 s	0+	Q β − = [4,000]	
173	Dy	≈2 s		Q β − = [5,700]	
	Holmium				
140	Ho	6(3) ms	(6−,0−,8+)	p(100%)	
141	Ho	4.1(3) ms	7/2−	p(100%)	

142	Ho	0.4(1) s	(6,7,8,9)	$Q_{\varepsilon} = [12,700]$	
143	Ho	>200 ns		$Q_{\varepsilon} = [10,100]$	
144	Ho	0.7(1) s	(5-)	$Q_{\varepsilon} = [11,700]$	
145	Ho	2.4(1) s	(11/2-)	$Q_{\varepsilon} = [9,200](100\%)$	$\gamma 340,313,334,402$
146	Ho	3.6(3) s	(10+)	$Q_{\varepsilon} = [10,600](100\%)$	$\gamma 683,925,674,237$
147	Ho	5.8(4) s	(11/2-)	$Q_{\varepsilon} = [8,300](100\%)$	$\gamma 884,189,487,1264$
148	Ho	2.2(11) s	(1+)	$Q_{\varepsilon} = [9,400](100\%)$	$\gamma 1678$
148	Ho(0 + x)	9.59(15) s	(6)-	$\varepsilon(100\%)$	$\gamma 1688,661,504,1678$
148	Ho(694.4 + x)	2.35(4) ms	(10+)	$\varepsilon p(0.08\%)$	
149	Ho	21.1(2) s	(11/2-)	$IT(100\%)$	$\gamma 373,321,180$
149	Ho(48.8)	56(3) s	(1/2+)	$Q_{\varepsilon} = 6,014(100\%)$	$\gamma 1091$
150	Ho	72(4) s	2-	$\varepsilon(100\%)$	$\gamma 1035,1736,372,1754$
150	Ho(800)	23.3(3) s	(9)+	$Q_{\varepsilon} = [7,240](100\%)$	$\gamma 804,591,653$
151	Ho	35.2(1) s	(11/2-)	$\varepsilon(100\%)$	$\gamma 803,653,394,551$
151	Ho(41.0)	47.2(10) s	(1/2+)	$Q_{\varepsilon} = 5,124(78\%)$	$\gamma 527,775$
152	Ho	161.8(3) s	2-	$Q_{\alpha} = 4,695.1(22\%)$	$\gamma 101, \alpha 4522$
152	Ho(160)	50.0(4) s	9+	$\alpha(80\%)$	$\gamma 101, \alpha 4611$
153	Ho	2.01(3) m	11/2-	$\varepsilon(20\%)$	
				$Q_{\varepsilon} = 6,550(88\%)$	$\gamma 614,647,700,613$
				$Q_{\alpha} = 4,507.2(12\%)$	$\gamma 102, \alpha 4386$
				$\varepsilon(89.2\%)$	$\gamma 614,647,684,493$
				$\alpha(10.8\%)$	$\gamma 316, \alpha 4454$
				$Q_{\varepsilon} = 4,130(99.95\%)$	$\gamma 296$
				$Q_{\alpha} = 4,052(0.05\%)$	$\alpha 3910$

Table 22.1 (Continued)

A	Element	Half-life or width	J^{π}	Qmode(%BR){%Abund}	Principal gammas, alphas
153	Ho(68)	9.3(5) m	1/2+	ϵ (99.82%) α (0.18%)	γ 109,366,162,271 α 4011
154	Ho	11.76(19) m	2-	$Q\epsilon = 5,751(99.98\%)$ $Q\alpha = 4,042(0.02\%)$	γ 335,413,873,570 α 3937
154	Ho(0 + x)	3.10(14) m	8+	ϵ (100%) α (<0.001%) $IT(-0\%)$	γ 335,412,477,407 α 3721
155	Ho	48(1) m	5/2+	$Q\epsilon = 3,102(100\%)$	γ 240,136,45,39
156	Ho	56(1) m	4-	$Q\epsilon = [5,060](100\%)$	γ 267,138,366,885
156	Ho(52.4)	9.5(15) s	1-	$IT(100\%)$	
156	Ho(52.4)	7.8(3) m	9+	ϵ (75%) $IT(25\%)$	
157	Ho	12.6(2) m	7/2-	$Q\epsilon = 2,540(100\%)$	γ 280,341,193,87
158	Ho	11.3(4) m	5+	$Q\epsilon = 4,230(100\%)$	
158	Ho(67.2)	28(2) m	2-	$IT(>81\%)$ ϵ (<19%) ϵ (>93%) $IT(<7\%)$	γ 67 γ 218,99,946,949 γ 406,839,1484,166
158	Ho(180)	21.3(23) m	(9+)		
159	Ho	33.05(11) m	7/2-	$Q\epsilon = 1,838(100\%)$	γ 121,132,310,253
159	Ho(205.9)	8.30(8) s	1/2+	$IT(100\%)$	γ 206,166
160	Ho	25.6(3) m	5+	$Q\epsilon = 3,290(100\%)$	γ 728,879,962,645
160	Ho(60.0)	5.02(5) h	2-	$IT(73\%)$ ϵ (27%)	γ 60 γ 728,879,962,966

160	Ho(169.6 + x)	3 s	(9+)	IT(100%)	γ 118,51,107
161	Ho	2.48(5) h	7/2–	Q ε = 859(100%)	γ 26,103
161	Ho(211.2)	6.76(7) s	1/2+	IT(100%)	γ 211
162	Ho	15.0(10) m	1+	Q ε = 2,140(100%)	γ 81,1320,1373
162	Ho(106)	67.0(7) m	6–	IT(62%)	γ 38,58
				ε (38%)	γ 185,1220,283,937
163	Ho	4,570(25) years	7/2–	Q ε = 2,565(100%)	
163	Ho(299)	1.09(3) s	1/2+	IT(100%)	γ 299
164	Ho	29(1) m	1+	Q ε = 986.8(60%)	γ 73
				Q β – = 962.8(40%)	γ 91
164	Ho(139.8)	37.5(+15–5) m	6–	IT(100%)	γ 37,57
165	Ho	Stable	7/2–	{100%}	
166	Ho	26.824(12) h	0–	Q β – = 1,854.9(100%)	γ 81,1379
166	Ho(6.0)	1,200(180) years	7–	β – (100%)	γ 184,810,712,280
167	Ho	3.003(18) h	7/2–	Q β – = 1,007(100%)	γ 347,321
168	Ho	2.99(7) m	3+	Q β – = 2,910(100%)	γ 741,821,816,80
168	Ho(59.0)	132(4) s	(6+)	IT(>99.5%)	
				β – (<0.5%)	
169	Ho	4.72(10) m	7/2–	Q β – = 2,124(100%)	γ 788,853,761,778
170	Ho	2.76(5) m	(6+)	Q β – = 3,870(100%)	γ 258,932,182,890
170	Ho(120)	43(2) s	(1+)	β – (100%)	γ 812,1894,79,1973
171	Ho	53(2) s	(7/2–)	Q β – = 3,200(100%)	γ 903,199,279,532
172	Ho	25(3) s		Q β – = [5,100](100%)	γ 134,178,757,291
173	Ho	\approx 10 s		Q β – = [4,600]	
174	Ho	\approx 8 s		Q β – = [6,300]	
175	Ho	\approx 5 s		Q β – = [5,700]	

Table 22.1 (Continued)

68	A	Element	Half-life or width	J^{π}	Qmode(%BR){%Abund}	Principal gammas, alphas
		Erbium				
	143	Er	(0.2 s)		ϵ	
	144	Er	> 200 ns	0+	$Q\epsilon = [8,300]$	
	145	Er		(1/2+)	$Q\epsilon = [9,900]$	
	145	Er(253)	0.9(3) s	(11/2-)	$Q\epsilon(100\%)$	
					ϵp	
	146	Er	1.7(6) s	0+	$Q\epsilon = [7,500](100\%)$	
					$\epsilon p(100\%)$	
	147	Er	2.5(2) s	(11/2-)	$Q\epsilon = [8,800](100\%)$	
					$\epsilon p(> 0\%)$	
	147	Er (0 + x)	~2.5 s	(1/2+)	$\epsilon(100\%)$	
					$\epsilon p(> 0\%)$	
	148	Er	4.6(2) s	0+	$Q\epsilon = [6,700](100\%)$	$\gamma 1312, 244, 315, 610$
	149	Er	4(2) s	(1/2+)	$Q\epsilon = [7,800](100\%)$	$\gamma 1748, 1578, 172$
					$\epsilon p(7\%)$	
	149	Er(741.8)	8.9(2) s	(11/2-)	$\epsilon(96.5\%)$	$\gamma 1171, 172, 344, 1531$
					$IT(3.5\%)$	$\gamma 631, 111$
					$\epsilon p(0.18\%)$	$\gamma 1688, 661, 1678, 739$
	150	Er	18.5(7) s	0+	$Q\epsilon = 4,108(100\%)$	$\gamma 476$
	151	Er	23.5(13) s	(7/2-)	$Q\epsilon = [5,400](100\%)$	$\gamma 638, 257, 667, 869$
	151	Er(2585.5)	0.58(2) s	(27/2-)	$IT(95.3\%)$	$\gamma 1140, 1099, 289$
					$\epsilon(4.7\%)$	$\gamma 789, 597, 297, 414$
	152	Er	10.3(1) s	0+	$Q\alpha = 4,934.4(90\%)$	$\alpha 4804$
					$Q\epsilon = 3,109(10\%)$	$\gamma 179$

153	Er	37.1(2) s	(7/2-)	$Q\alpha = 4,802.7(53\%)$ $Q\epsilon = 4,563(47\%)$	$\alpha 4674$ $\gamma 351,398,188,378$
154	Er	3.73(9) m	0+	$Q\epsilon = 2,032(99.53\%)$ $Q\alpha = 4,280(0.47\%)$	$\gamma 27$ $\alpha 4168$
155	Er	5.3(3) m	7/2-	$Q\epsilon = 3,840(99.98\%)$ $Q\alpha = 4,120(0.02\%)$	$\gamma 110,242,234,512$ $\alpha 4012$
156	Er	19.5(10) m	0+	$Q\epsilon = [1,220](\sim 100\%)$ $Q\alpha = 3,440(1.7\epsilon - 5\%)$	$\gamma 35,30$
157	Er	18.65(10) m	3/2-	$Q\epsilon = 3,500(\sim 100\%)$ $Q\alpha = 3,340(<0.02\%)$	$\gamma 53,391,121,67$
157	Er(155.4)	76(6) ms	(9/2+)	IT(100%)	
158	Er	2.29(6) h	0+	$Q\epsilon = [900](100\%)$	$\gamma 72,387,249,46$
159	Er	36(1) m	3/2-	$Q\epsilon = 2,768.6(100\%)$	$\gamma 625,649,206,166$
160	Er	28.58(9) h	0+	$Q\epsilon = 330(100\%)$	$\gamma 7$
161	Er	3.21(3) h	3/2-	$Q\epsilon = 2,002(100\%)$	$\gamma 827,211$
162	Er	Stable	0+	{0.14(1)%}	
163	Er	75.0(4) m	5/2-	$Q\epsilon = 1,210(100\%)$	$\gamma 114,436,440,298$
164	Er	Stable	0+	{1.61(3)%}	
165	Er	10.36(4) h	5/2-	$Q\epsilon = 376.0(100\%)$	
166	Er	Stable	0+	{33.61(35)%}	
167	Er	Stable	7/2+	{22.93(17)%}	
167	Er(207.8)	2.269(6) s	1/2-	IT(100%)	$\gamma 208$
168	Er	Stable	0+	{26.78(26)%}	
169	Er	9.392(18) days	1/2-	$Q\beta^- = 351.1(100\%)$	$\gamma 8$
170	Er	Stable	0+	{14.93(27)%}	
171	Er	7.516(2) h	5/2-	$Q\beta^- = 1,490.5(100\%)$	$\gamma 308,296,112,124$

Table 22.1 (Continued)

A	Element	Half-life or width	$J\pi$	Qmode(%BR){%Abund}	Principal gammas, alphas
172	Er	49.3(3) h	0+	$Q\beta^- = 891(100\%)$	$\gamma 610,407$
173	Er	1.4(1) m	(7/2-)	$Q\beta^- = [2,610](100\%)$	$\gamma 895,199,193,122$
174	Er	3.2(2) m	0+	$Q\beta^- = [2,000](100\%)$	$\gamma 100,767,773,152$
175	Er	1.2(3) m	(9/2+)	$Q\beta^- = [3,800](100\%)$	$\gamma 1168,234,121,281$
176	Er	≈ 20 s	0+	$Q\beta^- = [3,100]$	
177	Er	≈ 3 s		$Q\beta^- = [5,000]$	
69	Thulium				
	Tm	1.9(+12-5) μ s	10+	p	
	Tm	3.17(20) μ s	(11/2-)	p(100%)	
	Tm	80(10) ms	(5-)	$Qp = 1,127$	
				$Q\varepsilon = [13,400]$	
	Tm(180.0)	200(10) ms	(8+)	p	
				ε	
	Tm	0.58(3) s	11/2-	$Q\varepsilon = [11,000](85\%)$	
				$Qp = 1,058(15\%)$	
	Tm(0 + x)	0.7(2) s	(10+)	$Q\varepsilon = [12,200](100\%)$	$\gamma 647,877,1003,258$
149	Tm	0.9(2) s	(11/2-)	$Q\varepsilon = [9,800](100\%)$	$\gamma 796,159,417,907$
				$\varepsilon p(0.2\%)$	
150	Tm	2.2(2) s	(6-)	$Q\varepsilon = [11,100](100\%)$	$\gamma 1579,474,208,594$
151	Tm	4.17(10) s	(11/2-)	$Q\varepsilon = [7,400](100\%)$	$\gamma 802,2115,1140,1549$
151	Tm(0 + x)	6.6(20) s	(1/2+)	$\varepsilon(100\%)$	$\gamma 984,1637,2067,1982$
152	Tm	8.0(10) s	(2)-	$Q\varepsilon = [8,600](100\%)$	$\gamma 808,716$
152	Tm(0 + x)	5.2(6) s	(9)+	$\varepsilon(100\%)$	$\gamma 808,673,423,280$
153	Tm	1.48(1) s	(11/2-)	$Q\alpha = 5,248.4(91\%)$	$\gamma 344,\alpha 5103$
				$Q\varepsilon = 6,459(9\%)$	$\gamma 299,766,965$

153	Tm(43.2)	2.5(2) s	(1/2+)	α (92%) ε (8%)	γ 344, α 5096
154	Tm(y)	8.1(3) s	(2-)	$Q\alpha = 5,090(54\%)$ $Q\varepsilon = [8,050](46\%)$	γ 267 α 4956 γ 561
154	Tm(x)	3.30(7) s	(9+)	α (58%) ε (42%)	α 5031 γ 561,601,625,542
155	Tm	21.6(2) s	11/2-	$Q\varepsilon = 5,580(99.11\%)$ $Q\alpha = 4,571(0.89\%)$	γ 227,532,88,1057 α 4452
155	Tm(41)	45(3) s	1/2+	$\varepsilon(>98\%)$ $\alpha(<2\%)$	γ 88,323,507,247 α 4450
156	Tm	83.8(18) s	2-	$Q\varepsilon = 7,440(99.94\%)$ $Q\alpha = 4,340(0.06\%)$	γ 345,453,586,586 α 4232
156	Tm	19(3) s		α	
157	Tm(0 + x)	3.63(9) m	1/2+	$Q\varepsilon = 4,480(100\%)$	γ 455,386,348,110
158	Tm	3.98(6) m	2-	$Q\varepsilon = 6,600(100\%)$	γ 192,335,1150,628
158	Tm (0 + x)	≈ 20 s	(5+)		
159	Tm	9.13(16) m	5/2+	$Q\varepsilon = 3,850(100\%)$	γ 38,85,271,220
160	Tm	9.4(3) m	1-	$Q\varepsilon = 5,600(100\%)$	γ 126,729,264,1369
160	Tm(70.0)	74.5(15) s	5	IT(85%) ε (15%)	γ 264,126,376,739
161	Tm	30.2(8) m	7/2+	$Q\varepsilon = 3,160(100\%)$	γ 46,1648,84,60
162	Tm	21.70(19) m	1-	$Q\varepsilon = 4,840(100\%)$	γ 102,799,228,901
162	Tm(x)	24.3(17) s	5+	IT(82%) ε (18%)	γ 67 γ 812,799,228,901
163	Tm	1.810(5) h	1/2+	$Q\varepsilon = 2,439(100\%)$	γ 104,69,241,1434

Table 22.1 (Continued)

A	Element	Half-life or width	$J\pi$	Qmode(%BR){%Abund}	Principal gammas, alphas
164	Tm	2.0(1) m	1+	$Q_{\alpha} = 3.963(100\%)$	$\gamma_{91,1155,769,208}$
164	Tm(0 + x)	5.1(1) m	6−	$IT(\sim 80\%)$ $\varepsilon(\sim 20\%)$	$\gamma_{208,315,240,547}$
165	Tm	30.06(3) h	1/2+	$Q_{\alpha} = 1.592.5(100\%)$	$\gamma_{243,47,297,806}$
166	Tm	7.70(3) h	2+	$Q_{\alpha} = 3.040(100\%)$	$\gamma_{779,2052,184,1274}$
166	Tm(109.3)	340(25) ms	(6−)	$IT(100\%)$	
167	Tm	9.25(2) days	1/2+	$Q_{\alpha} = 748.4(100\%)$	$\gamma_{208,57}$
168	Tm	93.1(2) days	3+	$Q_{\alpha} = 1,679.1(99.99\%)$ $Q\beta^{-} = 257(0.01\%)$	$\gamma_{198,816,448,184}$ γ_{88}
169	Tm	Stable	1/2+	{100%}	
170	Tm	128.6(3) days	1−	$Q\beta^{-} = 968.0(99.87\%)$ $Q_{\alpha} = 314.4(0.13\%)$	γ_{84} γ_{79}
171	Tm	1.92(1) years	1/2+	$Q\beta^{-} = 96.4(100\%)$	γ_{67}
172	Tm	63.6(2) h	2−	$Q\beta^{-} = 1,880(100\%)$	$\gamma_{79,1094,1387,1530}$
173	Tm	8.24(8) h	(1/2+)	$Q\beta^{-} = 1,298(100\%)$	γ_{399}
174	Tm	5.4(1) m	(4)−	$Q\beta^{-} = 3,080(100\%)$	$\gamma_{366,992,273,177}$
175	Tm	15.2(5) m	(1/2+)	$Q\beta^{-} = 2,390(100\%)$	$\gamma_{515,941,364,982}$
176	Tm	1.9(1) m	(4+)	$Q\beta^{-} = 4,120(100\%)$	$\gamma_{190,1069,382,82}$
177	Tm	90(6) s	(7/2−)	$Q\beta^{-} = [3,500](100\%)$	$\gamma_{105,518}$
178	Tm	≈30 s		$Q\beta^{-} = [5,600]$	
179	Tm	≈20 s		$Q\beta^{-} = [4,800]$	
70	Ytterbium				
	Yb	≈0.25 s	0+	$Q_{\alpha} = [8,600]$	
	Yb	0.7(2) s	(1/2+,3/2+)	$Q_{\alpha} = [10,100]$ $\varepsilon p(\approx 100\%)$	

150	Yb	>200 ns	0+	Q ϵ = [7,800]	
151	Yb	1.6(1) s	(1/2+)	Q ϵ = [9,100](100%)	
151	Yb(0 + x)	1.6(1) s	(1/2-)	ϵp	
				ϵ (~100%)	
				ϵp	
152	Yb	3.04(6) s	0+	IT	
				Q ϵ = 5,470(100%)	γ 482,142
153	Yb	4.2(2) s	7/2-	ϵp	
				Q α = [4,100](60%)	
				Q ϵ = [6,700](40%)	γ 547,674,370,909
154	Yb	0.409(2) s	0+	ϵp (0.08%)	γ 673
				Q α = 5,474.3(92.6%)	α 5331
				Q ϵ = 4,490(7.4%)	γ 133
155	Yb	1.793(19) s	(7/2-)	Q α = 5,337(89%)	α 5200
				Q ϵ = [6,100](11%)	γ 236,175,362,378
156	Yb	26.1(7) s	0+	Q ϵ = 3,580(90%)	γ 115
				Q α = 4,812(10%)	α 4687
157	Yb	38.6(10) s	7/2-	Q ϵ = 5,500(99.5%)	γ 23,242,231,164
				Q α = 4,620(0.5%)	α 4504
158	Yb	1.49(13) m	0+	Q ϵ = [2,670](100%)	γ 74
				Q α = 4,171(~0.0021%)	α 4065
159	Yb	1.67(9) m	5/2(-)	Q ϵ = 4,980(100%)	γ 166,177,390,330
160	Yb	4.8(2) m	0+	Q ϵ = [2,300](100%)	γ 174,216,140,132
161	Yb	4.2(2) m	3/2-	Q ϵ = [4,150](100%)	γ 78,600,631,570
162	Yb	18.87(19) m	0+	Q ϵ = [1,660](100%)	γ 163,119

Table 22.1 (Continued)

A	Element	Half-life or width	J^{π}	Qmode(%BR){%Abund}	Principal gammas, alphas
163	Yb	11.05(35) m	3/2−	Q ϵ = 3.370(100%)	γ 860,64,123,1747
164	Yb	75.8(17) m	0+	Q ϵ = 1,000(100%)	γ 41,675,391,447
165	Yb	9.9(3) m	5/2−	Q ϵ = 2,762(100%)	γ 80,69
166	Yb	56.7(1) h	0+	Q ϵ = 304(100%)	γ 82
167	Yb	17.5(2) m	5/2−	Q ϵ = 1,954(100%)	γ 113,106,176
168	Yb	Stable	0+	{0.13(1)%}	
169	Yb	32.018(5) days	7/2+	Q ϵ = 909(100%)	γ 63,198,177,110
169	Yb(24.2)	46(2) s	1/2−	IT(100%)	γ 24
170	Yb	Stable	0+	{3.04(15)%}	
171	Yb	Stable	1/2−	{14.28(57)%}	
171	Yb(95.3)	5.25(24) ms	7/2+	IT(100%)	
172	Yb	Stable	0+	{21.83(67)%}	
173	Yb	Stable	5/2−	{16.13(27)%}	
174	Yb	Stable	0+	{31.83(92)%}	
175	Yb	4.185(1) days	(7/2−)	Q β − = 470.0(100%)	γ 396,283,114
175	Yb (514.9)	68.2(3) ms	1/2−	IT(100%)	
176	Yb	> 1.6E17 years	0+	2 β −	
				{12.76(41)%}	
176	Yb(1050.3)	11.4(3) s	8−	IT(> 90%)	γ 293,389,190,96
				β − (<10%)	
177	Yb	1.911(3) h	(9/2+)	Q β − = 1,399.2(100%)	γ 151,1080,1241,123
177	Yb(331.5)	6.41(3) s	(1/2−)	IT(100%)	γ 105,227

	178	Yb	74(3) m	0+	Qβ− = 645(100%)	γ391,348
	179	Yb	8.0(4) m	(1/2−)	Qβ− = [2,700](100%)	γ592,612,381,654
	180	Yb	2.4(5) m	0+	Qβ− = [2,300](100%)	γ173,375,420,339
	181	Yb	(1 m)		Qβ− = [3,900]	
71		Lutetium				
	150	Lu	43(5) ms	(2+)	Qp = 1,270(68%)	
					Qε = [13,700](32%)	
	151	Lu	80.6(20) ms	11/2−	Qp = [1,240](63.4%)	
					Qε = [11,100](36.6%)	
	152	Lu	0.7(1) s	(5−,6−)	Qε = [12,500](100%)	γ1531,359,313
					εp(15%)	
	153	Lu	0.9(2) s	11/2−	Qα = [3,200](~70%)	
					Qε = [8,800](~30%)	γ567,1491
	154	Lu	~2 s	(2−)	Qε = [10,100]	
	154	Lu(0 + x)	1.12(8) s	(9+)	ε(~100%)	γ821,695,434,97
	155	Lu	68(1) ms	11/2−	Qα = [5,771](90%)	α5650
	155	Lu(200)	138(8) ms	1/2+	Qε = [7,900](10%)	
					ε	
	155	Lu(1798)	2.71(3) ms	(25/2−)	α(100%)	α5581
	156	Lu(0 + x)	198(2) ms	9+	Qα = 5,590(100%)	α7390
	156	Lu(0 + y)	494(12) ms	(2)−	α(~95%)	α5565
					Qε = [9,400](~5%)	α5453
	157	Lu	6.8(18) s	(1/2+,3/2+)	Qα = 5,096(>0%)	
	157	Lu(26)	4.79(12) s	(11/2−)	Qε = 6,930(94%)	γ968
					α(6%)	α4996

Table 22.1 (Continued)

A	Element	Half-life or width	J π	Qmode(%BR){%Abund}	Principal gammas, alphas
158	Lu	10.6(3) s		Q ϵ = [8,670](99.09%) Q α = 4,790(0.91%)	γ 358,477 α 4669
159	Lu	12.1(10) s		Q ϵ = 6,020(99.9%) Q α = 4,490(0.1%)	γ 151,188,369 α 4419
160	Lu	36.1(3) s		Q ϵ = [7,880](100%) Q α = [4,110]($<0.001\%$)	
160	Lu(0 + x)	40(1) s		ϵ ($<100\%$) α	γ 243,395,577
161	Lu	77(2) s	1/2+	Q ϵ = 5,300(100%)	γ 111,100,44,256
161	Lu(135.8 + x)	7.3(4) ms	(9/2-)	IT(100%)	γ 136
162	Lu	1.37(2) m	1-	Q ϵ = 6,960($<100\%$)	
162	Lu(x)	1.5 m	(4-)	ϵ ($<100\%$)	
162	Lu(y)	1.9 m		ϵ ($<100\%$)	γ 167,632,799,321
163	Lu	3.97(13) m	1/2(+)	Q ϵ = 4,600(100%)	γ 163,54,396,372
164	Lu	3.14(3) m	1	Q ϵ = 6,240(100%)	γ 123,741,262,864
165	Lu	10.74(10) m	1/2+	Q ϵ = 3,920(100%)	γ 132,121,174,204
166	Lu	2.65(10) m	6-	Q ϵ = 5,480(100%)	γ 228,338,368,102
166	Lu(34.4)	1.41(10) m	3(-)	ϵ (58%) IT(42%)	γ 228,102,285,830 γ 34
166	Lu(42.9)	2.12(10) m	0-	ϵ ($>80\%$) IT($<20\%$)	γ 1427,2099,1257,1359
167	Lu	51.5(10) m	7/2+	Q ϵ = 3,130(100%)	γ 30,239,1267,213
167	Lu(0 + x)	>1 m	1/2+	ϵ IT	

168	Lu	5.5(1) m	(6−)	$Q_{\varepsilon} = 4,480(100\%)$	$\gamma 1484,229,112,111$
168	Lu(220)	6.7(4) m	3+	$\varepsilon(>95\%)$	$\gamma 199,979,896,885$
169	Lu	34.06(5) h	7/2+	$IT(<5\%)$	
169	Lu(29.0)	160(10) s	1/2−	$Q_{\varepsilon} = 2,293(100\%)$	$\gamma 961,191,1450,890$
170	Lu	2.012(20) days	0+	$IT(100\%)$	$\gamma 29$
170	Lu(93.0)	0.67(10) s	(4)−	$Q_{\varepsilon} = 3,459(100\%)$	$\gamma 84,1280,2042,985$
171	Lu	8.24(3) days	7/2+	$IT(100\%)$	$\gamma 45,48$
171	Lu(71.1)	79(2) s	1/2−	$Q_{\varepsilon} = 1,478.8(100\%)$	$\gamma 740,19,667,76$
172	Lu	6.70(3) days	4−	$IT(100\%)$	$\gamma 71$
172	Lu(41.9)	3.7(5) m	1−	$Q_{\varepsilon} = 2,519.3(100\%)$	$\gamma 1094,901,182,810$
173	Lu	1.37(1) years	7/2+	$IT(100\%)$	$\gamma 42$
174	Lu	3.31(5) years	(1)−	$Q_{\varepsilon} = 670.8(100\%)$	$\gamma 272,79,101,171$
174	Lu(170.8)	142(2) days	(6)−	$Q_{\varepsilon} = 1,374.3(100\%)$	$\gamma 76,1242$
175	Lu	Stable	7/2+	$IT(99.38\%)$	$\gamma 45,67$
176	Lu	3.76(7)E10 years	7−	$\varepsilon(0.62\%)$	$\gamma 273,992,177,76$
176	Lu(123.0)	3.664(19) h	1−	{97.41(2)%}	
177	Lu	6.647(4) days	7/2+	$Q_{\beta-} = 1,192.8(100\%)$	$\gamma 307,202,88$
177	Lu(970.2)	160.44(6) days	23/2−	{2.59(2)%}	
177	Lu(2700)	6(+3−2) m	(39/2−)	$\beta - (99.91\%)$	$\gamma 88$
178	Lu	28.4(2) m	1(+)	$Q_{\varepsilon} = 106.2(0.09\%)$	$\gamma 82$
				$Q_{\beta-} = 498.3(100\%)$	$\gamma 208,113$
				$\beta - (78.3\%)$	$\gamma 208,228,379,419$
				$IT(21.7\%)$	$\gamma 414,319,122,172$
				$\beta - (<100\%)$	$\gamma 208,228,379,419$
				IT	
				$Q_{\beta-} = 2,099.2(100\%)$	$\gamma 93,1341,1310,1269$

Table 22.1 (Continued)

A	Element	Half-life or width	J π	Qmode(%BR){%Abund}	Principal gammas, alphas
178	Lu(120)	23.1(3) m	(9-)	β^- (100%)	γ 426,326,213,89
179	Lu	4.59(6) h	7/2(+)	$Q\beta^- = 1,406(100\%)$	γ 214
179	Lu(592.4)	3.1(9) ms	1/2(+)	IT(100%)	
180	Lu	5.7(1) m	(3+)	$Q\beta^- = 3,100(100\%)$	γ 408,1200,1107,215
181	Lu	3.5(3) m	(7/2+)	$Q\beta^- = [2,700](100\%)$	γ 652,206,575,806
182	Lu	2.0(2) m	(0,1,2)	$Q\beta^- = [4,300](100\%)$	γ 818,721,808,98
183	Lu	58(4) s	(7/2+)	$Q\beta^- = [3,800](100\%)$	γ 1125,1057,168,248
184	Lu(x)	20(3) s	(3+)	$Q\beta^- = [5,300](100\%)$	γ 368,242,107
72	Hafnium				
	Hf	>60 ns			
	Hf	2(1) s	0+	$Q\epsilon = [6,700](\sim 100\%)$	
				$Q\alpha = [3,400](\sim 0\%)$	
	Hf	0.89(12) s		$Q\epsilon = [7,900](100\%)$	
				$Q\alpha = [4,600]$	
	Hf	23(1) ms	0+	$Q\alpha = 6,033(100\%)$	α 5873
	Hf	110(6) ms	7/2-	$Q\alpha = 5,880(86\%)$	α 5731
				$Q\epsilon = [7,500](14\%)$	
	Hf	2.85(7) s	0+	$Q\epsilon = 5,100(55.7\%)$	
			$Q\alpha = 5,403(44.3\%)$	α 5268	
159	Hf	5.6(4) s	7/2-	$Q\epsilon = [6,900](65\%)$	
				$Q\alpha = 5,220(35\%)$	α 5092
160	Hf	13.6(2) s	0+	$Q\epsilon = [4,370](99.3\%)$	
				$Q\alpha = 4,903(0.7\%)$	α 4780
161	Hf	18.2(5) s		$Q\epsilon = [6,320](> 99.87\%)$	γ 136,276,209,200
				$Q\alpha = 4,720(< 0.13\%)$	α 4599

162	Hf	39.4(9) s		0+	$Q_{\beta} = [3,710](99.99\%)$	$\gamma 174,196,410$
163	Hf	40.0(6) s			$Q_{\alpha} = 4,417(0.008\%)$	$\alpha 4308$
164	Hf	111(8) s		0+	$Q_{\beta} = [5,500](100\%)$	$\gamma 171,62,45,688$
165	Hf	76(4) s		(5/2-)	$Q_{\alpha} = [4,000](< 0.00010\%)$	
166	Hf	6.77(30) m		0+	$Q_{\beta} = [2,990](100\%)$	$\gamma 122,153,314,31$
167	Hf	2.05(5) m		(5/2-)	$Q_{\beta} = [4,600](100\%)$	$\gamma 180$
168	Hf	25.95(20) m		0+	$Q_{\beta} = [2,300](100\%)$	$\gamma 79,342,408$
169	Hf	3.24(4) m		5/2-	$Q_{\beta} = [4,000](100\%)$	$\gamma 315$
170	Hf	16.01(13) h		0+	$Q_{\beta} = [1,800](100\%)$	$\gamma 184,157$
171	Hf	12.1(4) h		7/2(+)	$Q_{\beta} = [1,800](100\%)$	$\gamma 493,370$
171	Hf(21.9)	29.5(9) s		1/2(-)	$Q_{\beta} = [1,100](100\%)$	$\gamma 165,621,120,573$
172	Hf	1.87(3) years		0+	$Q_{\beta} = [2,400](100\%)$	$\gamma 662,122,347,1072$
173	Hf	23.6(1) h		1/2-	IT(<100%)	
174	Hf	2.0(4)E15 years		0+	ϵ	
175	Hf	70(2) days		5/2(-)	$Q_{\beta} = 350(100\%)$	$\gamma 24,126,67,82$
176	Hf	Stable		0+	$Q_{\beta} = [1,610](100\%)$	$\gamma 124,297,140,311$
177	Hf	Stable		7/2-	$Q_{\alpha} = 2,494.8(100\%)$	$\alpha 2500$
177	Hf(1315.5)	1.09(5) s		23/2+	{0.16(1)%}	
177	Hf(2740.0)	51.4(5) m		37/2-	$Q_{\beta} = 684.7(100\%)$	$\gamma 343$
178	Hf	Stable		0+	{5.26(7)%}	
178	Hf(1147.4)	4.0(2) s		8-	{18.60(9)%}	
					IT(100%)	$\gamma 208,228,379,419$
					IT(100%)	$\gamma 277,295,327,312$
					{27.28(7)%}	
					IT(100%)	$\gamma 426,326,213,89$

Table 22.1 (Continued)

	A	Element	Half-life or width	J π	Qmode(%BR){%Abund}	Principal gammas, alphas
	178	Hf(2446.0)	31(1) years	16+	IT(100%)	γ 426,326,574,213
	179	Hf	Stable	9/2+	{13.629(6)%}	
	179	Hf(375.0)	18.67(4) s	1/2–	IT(100%)	γ 214
	179	Hf(1105.8)	25.05(25) days	25/2–	IT(100%)	γ 454,363,123,146
	180	Hf	Stable	0+	{35.08(16)%}	
	180	Hf(1141.7)	5.47(4) h	8–	IT(99.7%)	γ 332,443,215,58
					β – (0.3%)	γ 101
	181	Hf	42.39(6) days	1/2–	Q β – = 1,027(100%)	γ 482,133,346
	181	Hf	1.5(5) ms	(25/2–)	IT(100%)	
	182	Hf	8.90(9)E6 years	0+	Q β – = 373(100%)	γ 270
	182	Hf(1172.9)	61.5(15) m	8–	β – (58%)	γ 943,800,114,340
					IT(42%)	γ 344,224,507,456
	183	Hf	1.067(17) h	(3/2–)	Q β – = 2,010(100%)	γ 784,73,459
	184	Hf	4.12(5) h	0+	Q β – = 1,340(100%)	γ 139,345,181,41
	184	Hf(0 + x)	48(10) s	8–	β – (100%)	
	185	Hf	3.5(6) m		Q β – = [3,000](100%)	γ 165
	186	Hf	2.6(12) m	0+	Q β – = [2,200](100%)	
	187	Hf	(30 ms)		β –	
	188	Hf	(20 ms)	0+	β –	
73		Tantalum				
	155	Ta	2.9(+15–11) ms	11/2–	p(100%)	
	156	Ta	144(24) ms	(2–)	Qp = 1,029(59%)	
					Q ϵ = [11,600](41%)	
	156	Ta(102.0)	0.36(4) s	9+	ϵ (95.8%)	
					p(4.2%)	

157	Ta	10.1(4) ms	1/2+	$Q\alpha = 6,380(96.6\%)$ $Qp = [1,000](3.4\%)$	$\alpha 6117$
157	Ta(22)	4.3(1) ms	11/2–	$\alpha(100\%)$	$\alpha 6214$
157	Ta(1589)	1.7(1) ms	(25/2–)	$\alpha(100\%)$	$\alpha 7744$
158	Ta	55(15) ms	(2–)	$Q\alpha = 6,210(91\%)$ $\varepsilon(9\%)$	$\alpha 5968$
158	Ta(141)	36.7(15) ms	(9+)	$\alpha(95\%)$	$\alpha 6047$
159	Ta	0.83(18) s	(1/2–)	$Q\varepsilon = [10,900](5\%)$ $Q\alpha = 5,660(66\%)$	
159	Ta(64)	0.515(20) s	(11/2–)	$Q\varepsilon = [8,300](45\%)$ $Q\alpha = 5,660(55\%)$	$\alpha 5601$
160	Ta	1.55(4) s		$Q\varepsilon = [8,300](20\%)$ $Q\varepsilon = [9,900](66\%)$	
160	Ta(0 + x)	1.7(2) s		$Q\alpha = 5,450(34\%)$	$\alpha 5408$
161	Ta	2.89(12) s		$Q\varepsilon = 7,490(\sim 95.5\%)$	
162	Ta	3.57(12) s		$Q\alpha = 5,280(\sim 4.5\%)$ $Q\varepsilon = [9,260](99.93\%)$	$\alpha 5148$ $\gamma 285,444$
163	Ta	10.6(18) s		$Q\alpha = 5,010(0.07\%)$ $Q\varepsilon = [6,800](\sim 99.8\%)$	$\alpha 4883$ $\gamma 396,451,449,210$
164	Ta	14.2(3) s	(3+)	$Q\alpha = 4,750(\sim 0.2\%)$ $Q\varepsilon = [8,500](100\%)$	$\gamma 211,376,605,862$
165	Ta	31.0(15) s		$Q\varepsilon = [5,800](100\%)$	$\gamma 311$
166	Ta	34.4(5) s	(2+)	$Q\varepsilon = [7,700](100\%)$	$\gamma 159,312,810,651$
167	Ta	80(4) s	(3/2+)	$Q\varepsilon = [5,000](100\%)$	$\gamma 296$
168	Ta	2.0(1) m	(2–,3+)	$Q\varepsilon = [6,700](100\%)$	$\gamma 124,261,751,907$

Table 22.1 (Continued)

A	Element	Half-life or width	J π	Qmode(%BR){%Abund}	Principal gammas, alphas
169	Ta	4.9(4) m	(5/2+)	Q ϵ = [4,440](100%)	γ 511,29
170	Ta	6.76(6) m	(3+)	Q ϵ = [6,000](100%)	γ 101,221,860,987
171	Ta	23.3(3) m	(5/2-)	Q ϵ = [3,700](100%)	γ 50,506,502,166
172	Ta	36.8(3) m	(3+)	Q ϵ = 4,920(100%)	γ 214,95,1109,1086
173	Ta	3.14(13) h	5/2-	Q ϵ = [2,690](100%)	γ 172,70,90,160
174	Ta	1.14(8) h	3+	Q ϵ = 3,850(100%)	γ 207,91
175	Ta	10.5(2) h	7/2+	Q ϵ = [2,000](100%)	γ 207,349,267,82
176	Ta	8.09(5) h	(1)-	Q ϵ = 3,110(100%)	γ 1159,88,1225,202
176	Ta(103.0)	1.1(1) ms	(+)	IT(100%)	
177	Ta	56.56(6) h	7/2+	Q ϵ = 1,166(100%)	γ 113,208
178	Ta(0 + x)	9.31(3) m	1+	Q ϵ = 1,910(100%)	γ 93,1351,1341
178	Ta	2.36(8) h	(7)-	ϵ (100%)	γ 426,326,213,89
179	Ta	1.82(3) years	7/2+	Q ϵ = 111(100%)	
179	Ta(1317.3)	9.0(2) ms	(25/2+)	IT(100%)	
179	Ta(2639.3)	54.1(17) ms	(37/2+)	IT(100%)	
180	Ta	8.154(6) h	1+	Q ϵ = 854(86%) [0.012(2)%]	γ 93
180	Ta(77.1)	>1.2E15 years	9-	Q β - = 708(14%) [0.012(2)%]	γ 104 β - β -
181	Ta	Stable	7/2+	[99.988(2)%]	
182	Ta	114.43(3) days	3-	Q β - = 1,813.5(100%)	γ 68,1121,1221,1189
182	Ta(16.3)	283(3) ms	5+	IT(100%)	γ 16
182	Ta(519.6)	15.84(10) m	10-	IT(100%)	γ 172,147,185,318
183	Ta	5.1(1) days	7/2+	Q β - = 1,070.0(100%)	γ 246,354,108,161

74	184	Ta	8.7(1) h	(5-)	Qβ- = 2,870(100%)	γ414,253,921,111
	185	Ta	49.4(15) m	(7/2+)	Qβ- = 1,992(100%)	γ178,174,66,244
	185	Ta(1258)	> 1 ms	(21/2)	IT(100%)	
	186	Ta	10.5(5) m	(2-,3-)	Qβ- = 3,900(100%)	γ198,215,511,738
	186	Ta(0 + x)	1.54(5) m		β-	
	187	Ta	≈2 m		Qβ- = [3,000]	
	188	Ta	≈20 s		Qβ- = [4,900]	
	189	Ta	(3 s)	(7/2+)	Qβ- = [4,900]	
	190	Ta	(0.3 s)		Qβ- = [4,900]	
		Tungsten				
74	158	W	1.25(21) ms	0+	Qα = 6,600(100%)	α6438
	158	W(1888)	0.143(19) ms	(8+)	α	
					IT	
	159	W	7.3(27) ms		Qα = 6,440(99.9%)	α6299
					Qε = [8,700][0.1%]	
	160	W	91(5) ms	0+	Qα = 6,072(87%)	α5912
	161	W	409(18) ms		Qα = 5,920(73%)	α5776
	162	W	1.36(7) s	0+	Qε = 5,770(54.8%)	
					Qα = 5,674(45.2%)	α5535
	163	W	2.8(2) s		Qε = [7,700](87%)	
					Qα = 5,520(13%)	
	164	W	6.3(2) s	0+	Qε = [5,000](96.2%)	γ111,402
					Qα = 5,278.8(3.8%)	α5150
	165	W	5.1(5) s	(5/2-)	Qε = [7,000](100%)	
					Qα = 5,030(<0.2%)	α4909
	166	W	19.2(6) s	0+	Qε = [4,200](99.96%)	γ126
					Qα = 4,857(0.04%)	α4739

Table 22.1 (Continued)

A	Element	Half-life or width	J^{π}	Qmode(%BR){%Abund}	Principal gammas, alphas
167	W	19.9(5) s	(+)	Q ϵ = [6,200](99.96%) Q α = 4,670(0.04%)	γ 94,110,233,497
168	W	53(2) s	0+	Q ϵ = [3,800](~100%) Q α = 4,506(0.0032%)	γ 179 α 4399
169	W	74(6) s	(5/2-)	Q ϵ = [5,400](100%)	
170	W	2.42(4) m	0+	Q ϵ = [3,000](100%)	γ 316
171	W	2.38(4) m	(5/2-)	Q ϵ = [4,700](100%)	γ 184,295,479,52
172	W	6.6(9) m	0+	Q ϵ = [2,500](100%)	γ 39,423,90,221
173	W	7.6(2) m	5/2-	Q ϵ = 4,000(100%)	γ 458,130,175,623
174	W	33.2(21) m	0+	Q ϵ = [1,900](100%)	γ 35,429,329,379
175	W	35.2(6) m	(1/2-)	Q ϵ = [2,910](100%)	γ 270,167,149,121
176	W	2.5(1) h	0+	Q ϵ = [790](100%)	γ 100
177	W	132(2) m	1/2-	Q ϵ = [2,000](100%)	γ 116,427,1036,115
178	W	21.6(3) days	0+	Q ϵ = 91.3(100%)	
179	W	37.05(16) m	(7/2)-	Q ϵ = 1,060(100%)	γ 31
179	W (221.5)	6.40(7) m	(1/2)-	IT(99.72%) ϵ (0.28%)	γ 222 γ 239,282,223,214
180	W	1.8(2)E18 years	0+	Q α = 2,516 {0.12(1)%}	
181	W	121.2(2) days	9/2+	Q ϵ = 188(100%)	γ 6
182	W	>8.3E18 years	0+	Q α = 1,774 {26.50(16)%}	
183	W	>1.3E19 years	1/2-	IT(100%) {14.31(4)%}	

75	183	W (309.5)	5.2(3) s	11/2+	IT(100%)	γ 108,99,53,46
	184	W	>2.9E19 years	0+	$Q\alpha = 1,659$ {30.64(2)%}	
	185	W	75.1(3) days	3/2-	$Q\beta^- = 433.0(100\%)$	γ 125
	185	W (197.4)	1.67(3) m	11/2+	IT(100%)	γ 66,132,174,188
	186	W	>2.7E19 years	0+	$Q\alpha = 1,123$ {28.42(19)%}	
	187	W	23.72(6) h	3/2-	$Q\beta^- = 1,311.2(100\%)$	γ 686,480,72,134
	188	W	69.78(5) days	0+	$Q\beta^- = 349(100\%)$	γ 291,227,64
	189	W	10.7(5) m	(3/2-)	$Q\beta^- = 2,500(100\%)$	γ 258,417,550,855
	190	W	30.0(15) m	0+	$Q\beta^- = 1,270(100\%)$	γ 158,162
	191	W	>300 ns		β^-	
	192	W	>300 ns	0+	β^-	
		Rhenium				
76	159	Re	20(4) μ s	11/2-	$p = (92.5\%)$ $\alpha(7.5\%)$	
	160	Re	0.82(+15-9) ms	(2-)	$Qp = 1,290(91\%)$ $Q\alpha = 6,699(9\%)$	α 6543
	161	Re	0.37(4) ms	1/2+	$Qp = [1,400](100\%)$	
	161	Re(123.8)	15.6(9) ms	11/2-	$Q\alpha = 6,440(95.2\%)$ $p(4.8\%)$	α 6270
	162	Re	107(13) ms	(2-)	$Q\alpha = 6,270(94\%)$ $Q\varepsilon = [11,500](6\%)$	α 6119
	162	Re(173.0)	77(9) ms	(9+)	$\alpha(91\%)$ $\varepsilon(9\%)$	
	163	Re	390(72) ms	(1/2+)	$Q\varepsilon = [8,800](68\%)$ $Q\alpha = 6,010(32\%)$	

Table 22.1 (Continued)

A	Element	Half-life or width	J^{π}	Qmode(%BR){%Abund}	Principal gammas, alphas
163	Re(115)	214(5) ms	(11/2-)	α (66%) ε (34%)	α 5920
164	Re	0.53(23) s		$Q\alpha = 5,920(\sim 58\%)$	α 5782
165	Re	~ 1 s	(1/2+)	$Q\varepsilon = [10,600](\sim 4.2\%)$ $Q\varepsilon = 8,120$ $Q\alpha = 5,660$	
165	Re(48.0)	2.1(3) s	(11/2-)	ε (87%) α (13%)	α 5512
166	Re	2.25(21) s		$Q\varepsilon = [10,040](> 76\%)$ $Q\alpha = 5,640(< 24\%)$	γ 252,424,550 α 5522
167	Re	5.9(3) s	(9/2-)	$Q\varepsilon = [7,400](\sim 99\%)$ $Q\alpha = [5,260](\sim 1\%)$	γ 221
167	Re(0 + x)	3.4(4) s		$\alpha(\sim 100\%)$	
168	Re	4.4(1) s	(5+6+7+)	$Q\varepsilon = [9,100](\sim 100\%)$ $Q\alpha = 5,063(\sim 0.005\%)$	γ 199,363,480,558 γ 112, α 4833
169	Re	8.1(5) s	(9/2-)	$Q\varepsilon = [6,600](\sim 100\%)$ $Q\alpha = [5,040](\sim 0.00010\%)$	
169	Re(0 + x)	15.1(15) s	(5/2+3/2+)	$\alpha(\approx 0.2\%)$ ε IT	α 5050
170	Re	9.2(2) s	(5+)	$Q\varepsilon = [8,300](100\%)$	γ 306,413,157,488
171	Re	15.2(4) s	(9/2-)	$Q\varepsilon = 5,670(100\%)$	γ 568,102,1066,435
172	Re(0 + x)	15(3) s	(5)	$Q\varepsilon = [7,300](100\%)$	γ 254,350,123

172	Re(0 + y)	55(5) s	(2)	$\epsilon(100\%)$	$\gamma 123, 254, 743$
173	Re	1.98(26) m	(5/2-)	$Q\epsilon = [4, 900](100\%)$	$\gamma 182, 191, 374$
174	Re	2.40(4) m		$Q\epsilon = [6, 500](100\%)$	$\gamma 244, 112, 1003, 349$
175	Re	5.89(5) m	(5/2-)	$Q\epsilon = [4, 300](100\%)$	$\gamma 185$
176	Re	5.3(3) m	(3+)	$Q\epsilon = [5, 600](100\%)$	$\gamma 240, 109$
177	Re	14(1) m	5/2-	$Q\epsilon = [3, 400](100\%)$	$\gamma 197, 80, 84, 95$
178	Re	13.2(2) m	(3+)	$Q\epsilon = 4, 660(100\%)$	$\gamma 237, 106, 939$
179	Re	19.5(1) m	(5/2)+	$Q\epsilon = 2, 710(100\%)$	$\gamma 430, 290, 1680, 415$
180	Re	2.44(6) m	(1)-	$Q\epsilon = 3, 800(100\%)$	$\gamma 903, 104, 825$
181	Re	19.9(7) h	5/2+	$Q\epsilon = 1, 739(100\%)$	$\gamma 366, 361, 639$
182	Re	64.0(5) h	7+	$Q\epsilon = 2, 800(100\%)$	$\gamma 229, 68, 1121, 1221$
182	Re(0 + x)	12.7(2) h	2+	$\epsilon(100\%)$	$\gamma 68, 1121, 1222, 1189$
183	Re	70.0(14) days	5/2+	$Q\epsilon = 556(100\%)$	$\gamma 162, 46, 292, 209$
183	Re(1906.9)	1.04(4) ms	(25/2)+	$IT(100\%)$	$\gamma 194, 586, 257, 175$
184	Re	38.0(5) days	3(-)	$Q\epsilon = 1, 483(100\%)$	$\gamma 903, 792, 111, 895$
184	Re(188.0)	169(8) days	8(+)	$IT(75.4\%)$	$\gamma 105$
				$\epsilon(24.6\%)$	$\gamma 253, 217, 921, 161$
185	Re	Stable	5/2+	$\{37.40(2)\% \}$	
186	Re	3.7186(5) days	1-	$Q\beta^- = 1, 069.5(92.53\%)$	$\gamma 137$
				$Q\epsilon = 581.6(7.47\%)$	$\gamma 123$
186	Re(149)	2E5 years	(8+)	$IT(100\%)$	$\gamma 59, 40$
187	Re	4.12(10)E10 years	5/2+	$Q\beta^- = 2, 663(100\%)$	
				$\{62.60(2)\% \}$	
				$Q\alpha = 1, 652.8(<0.00010\%)$	
188	Re	17.003(3) h	1-	$Q\beta^- = 2, 120.4(100\%)$	$\gamma 155$
188	Re(171.9)	18.59(4) m	(6)-	$IT(100\%)$	$\gamma 64, 106, 92$

Table 22.1 (Continued)

A	Element	Half-life or width	J^{π}	Qmode(%BR){%Abund}	Principal gammas, alphas
76	189 Re	24.3(4) h	5/2+	Q β^- = 1,009(100%)	γ 217,219,245,186
	190 Re	3.1(3) m	(2)–	Q β^- = 3,140(100%)	γ 187,558,224,569
	190 Re(119 + x)	3.2(2) h	(6)–	β^- – (54.4%)	γ 187,605,558,569
				IT(45.6%)	γ 119
	191 Re	9.8(5) m	(3/2+, 1/2+)	Q β^- = 2,045(100%)	
	192 Re	16(1) s		Q β^- = [4,170](100%)	γ 467,751
	194 Re	> 300 ns		β^- –	
	194 Re(0 + x)	38(37) μ s		IT	
	Osmium				
	162 Os	2.1(1) ms	0+	Q α = 6,780(100%)	α 661 1
	163 Os	5.5(6) ms		Q α = 6,670(\sim 100%)	
				Q ϵ = [9,400]	
	164 Os	21(1) ms	0+	Q α = 6,478(98%)	α 632 1
				Q ϵ = 7,090(2%)	
	165 Os	71(3) ms	(7/2–)	Q α = 6,320(>60%)	α 618 3
				Q ϵ = [8,800]($<$ 40%)	
	166 Os	181(38) ms	0+	Q α = 6,131(\sim 72%)	α 599 3
				Q ϵ = 6,260(\sim 28%)	
	167 Os	0.81(6) s		Q α = 5,980(57%)	
				Q ϵ = [8,400](43%)	
	168 Os	2.1(1) s	0+	Q α = 5,818(40%)	α 567 6
				Q ϵ = [5,800]	
	169 Os	3.43(14) s	(5/2–)	Q ϵ = [7,680](89%)	
				Q α = 5,717(11%)	γ 72, α 5577,5508

170	Os	7.37(18) s	0+	$Q_{\beta} = [5,000](90.5\%)$ $Q_{\alpha} = 5,539(9.5\%)$	$\gamma 216,162$ $\alpha 5407$
171	Os	8.3(2) s	(5/2-)	$Q_{\beta} = [7,000](98.2\%)$ $Q_{\alpha} = 5,370(1.8\%)$	$\gamma 190,705,326$ $\gamma 79, \alpha 5244$
172	Os	19.2(5) s	0+	$Q_{\alpha} = 5,227(0.2\%)$ $Q_{\beta} = [4,500](99.8)$	$\alpha 5104$ $\gamma 63,177,240,1120$
173	Os	22.4(9) s	(5/2-)	$Q_{\alpha} = 5,060(0.4\%)$ $Q_{\beta} = [6,300]$	$\alpha 4940$ $\gamma 177,187,285,276$
174	Os	44(4) s	0+	$Q_{\beta} = [3,700](99.98\%)$ $Q_{\alpha} = 4,872(0.02\%)$	$\gamma 118,325,302,138$ $\alpha 4760$
175	Os	1.4(1) m	(5/2-)	$Q_{\beta} = [5,300](100\%)$	$\gamma 125,181$
176	Os	3.6(5) m	0+	$Q_{\beta} = [3,100](100\%)$	
177	Os	3.0(2) m	(1/2-)	$Q_{\beta} = [4,400](100\%)$	$\gamma 85,125,196,1269$
178	Os	5.0(4) m	0+	$Q_{\beta} = 2,300(100\%)$	$\gamma 969,1331,595,685$
179	Os	6.5(3) m	(1/2-)	$Q_{\beta} = [3,700](100\%)$	$\gamma 65,32,219,594$
180	Os	21.5(4) m	0+	$Q_{\beta} = [1,460](100\%)$	$\gamma 20$
181	Os	105(3) m	1/2-	$Q_{\beta} = 2,990(100\%)$	$\gamma 239,827,118,832$
181	Os(49.0)	2.7(1) m	7/2-	$\epsilon(100\%)$	$\gamma 145,118$
182	Os	22.10(25) h	0+	$Q_{\beta} = 910(100\%)$	$\gamma 510,180,263,56$
183	Os	13.0(5) h	9/2+	$Q_{\beta} = [2,130](100\%)$	$\gamma 382,114$
183	Os(170.7)	9.9(3) h	1/2-	$\epsilon(85\%)$ $\Pi(15\%)$	$\gamma 1102,1108,1035$ $\gamma 171$
184	Os	> 5.6E13 years	0+	$Q_{\alpha} = 2,964$ $[0.02(1)\%]$	
185	Os	93.6(5) days	1/2-	$Q_{\beta} = 1,012.8(100\%)$	$\gamma 646$
186	Os	2.0(11)E15 years	0+	$Q_{\alpha} = 2,822.0(100\%)$ $[1.59(3)\%]$	$\alpha 2761$

Table 22.1 (Continued)

A	Element	Half-life or width	J^{π}	Qmode(%BR){%Abund}	Principal gammas, alphas
187	Os	Stable	1/2−	{1.96(2)%}	
188	Os	Stable	0+	{13.24(8)%}	
189	Os	Stable	3/2−	{16.15(5)%}	
189	Os(30.8)	5.81(6) h	9/2−	IT(100%)	γ 31
190	Os	Stable	0+	{26.26(2)%}	
190	Os(1705.8)	9.9(1) m	(10)−	IT(100%)	γ 617,503,361,187
191	Os	15.4(1) days	9/2−	Q β − = 313.7(100%)	γ 129
191	Os(74.4)	13.10(5) h	3/2−	IT(100%)	γ 74
192	Os	Stable	0+	{40.78(19)%}	
192	Os(2015.4)	5.9(1) s	(10−)	IT(>87%)	γ 569,206,453,302
				β − (<13%)	
193	Os	30.11(1) h	3/2−	Q β − = 1,140.5(100%)	γ 139,460,73,557
194	Os	6.0(2) years	0+	Q β − = 96.6(100%)	γ 43
195	Os	\approx 9 m		Q β − = 2,000	
196	Os	34.9(2) m	0+	Q β − = 1,160(100%)	γ 408,126,315,207
197	Os	2.8(6) m		β − (100%)	
199	Os	5(+4−2) s		β − (100%)	
200	Os	6(+4−3) s	0+	β − (100%)	
77	Iridium				
	Ir	94(27) μ s	(9+)	p	
				α	
				ε	
165	Ir	<1 μ s	(1/2+)	Qp = [1,700]	

166	Ir	10.5(22) ms	(2-)	$Q\alpha = 6,700(93.1\%)$ $Qp = [1,100](6.9\%)$	$\alpha 6562$
166	Ir(172)	15.1(9) ms	(9+)	$\alpha(98.2\%)$ $p(1.8\%)$	$\alpha 6560$
167	Ir	35.2(20) ms	1/2+	$Q\alpha = 6,490(48\%)$ $Qp = 1,110(32\%)$	
167	Ir(175.3)	25.7(8) ms	11/2-	$Q\epsilon = [9,300](20\%)$ $\alpha(80\%)$ $\epsilon(20\%)$ $p(0.4\%)$	
168	Ir	125(40) ms		$Q\alpha = [6,560](82\%)$	$\alpha 6258$
168	Ir(0 + x)	161(21) ms		$\alpha(82\%)$	$\alpha 6323$
169	Ir	0.353(4) s	(1/2+)	$Q\alpha = 6,280(45\%)$ $Q\epsilon = 8,680$ $Qp = 680$	$\alpha 6005$
169	Ir(153)	0.281(4) s	(11/2-)	$\alpha(72\%)$	$\alpha 6106$
170	Ir	0.87(+18-12) s	(3-)	$Q\alpha = 6,170(5.2\%)$ $Q\epsilon = [10,680](94.8\%)$	$\alpha 6027$
170	Ir(0 + x)	811(18) ms	(8+)	$\alpha(38\%)$ $\epsilon(<62\%)$ $IT(<62\%)$	$\alpha 6027$
171	Ir	3.2(+13-7) s	(1/2+)	$Q\epsilon = [8,100]$ $Q\alpha = 6,159(>0\%)$	
171	Ir(0 + x)	1.40(10) s	(11/2-)	$Qp = [360]$ $\alpha(58\%)$ $\epsilon(<42\%)$ $p(<42\%)$	$\gamma 92, \alpha 5920$

Table 22.1 (Continued)

A	Element	Half-life or width	J^{π}	Qmode(%BR){%Abund}	Principal gammas, alphas
172	Ir	4.4(3) s	(3+)	Q ϵ = [9,800](~98%) Q α = 5,991(~2%)	γ 475 γ 123,136,90, α 5510
172	Ir(139)	2.0(1) s	(7+)	ϵ (77%) α (23%)	γ 228,378,448,582 γ 162, α 5828
173	Ir(0 + x)	2.4(9) s	(11/2-)	Q α = [5,840](7%) Q ϵ = [7,400]	α 5670 γ 50,285,295,148
173	Ir(0 + y)	9.0(8) s	(3/2+5/2+)	ϵ (>93%) α (<7%)	γ 50,285,92,148
174	Ir	7.9(6) s	(3+)	Q ϵ = [9,000](99.5%) Q α = 5,624(0.5%)	γ 194,225, α 5275 γ 276,159,343,394
174	Ir(193)	4.9(3) s	(7+)	ϵ (97.5%) α (2.5%)	γ 210,190, α 5478,5316
175	Ir	9(2) s	(5/2-)	Q ϵ = [6,700](99.15%) Q α = 5,709(0.85%)	γ 105,399 α 5393
176	Ir	8.7(5) s		Q ϵ = [8,000](96.9%) Q α = 5,240(3.1%)	γ 260,135,347,630 α 5118
177	Ir	30(2) s	5/2-	Q ϵ = [5,700](99.94%) Q α = 5,130(0.06%)	γ 184,75,148,88 α 5011
178	Ir	12(2) s		Q ϵ = [7,200](100%) Q ϵ = [4,800](100%)	γ 267,132,363,900 γ 98,86,45,100
180	Ir	1.5(1) m	(4,5)	Q ϵ = [6,430](100%) Q ϵ = 4,070(100%)	γ 276,132,699,871 γ 108,1640,319,232
181	Ir	4.90(15) m	5/2-		

182	Ir	15(1) m	(5+)	$Q_{\varepsilon} = 5,530(100\%)$	$\gamma_{274,127,236,912}$
183	Ir	57(4) m	5/2−	$Q_{\varepsilon} = 3,450(100\%)$	$\gamma_{393,229,88,283}$
184	Ir	3.09(3) h	5−	$Q_{\varepsilon} = 4,600(100\%)$	$\gamma_{264,120,390,961}$
185	Ir	14.4(1) h	5/2−	$Q_{\varepsilon} = [2,370](100\%)$	$\gamma_{254,1829,60,97}$
186	Ir	16.64(3) h	5+	$Q_{\varepsilon} = 3,831(100\%)$	$\gamma_{297,137,435,773}$
186	Ir(0 + x)	1.90(5) h	2−	$\varepsilon(\sim 75\%)$	$\gamma_{137,767,630,773}$
				IT($\sim 25\%$)	
187	Ir	10.5(3) h	3/2+	$Q_{\varepsilon} = 1,502(100\%)$	$\gamma_{913,427,401,611}$
188	Ir	41.5(5) h	1−	$Q_{\varepsilon} = 2,809(100\%)$	$\gamma_{155,2215,633,478}$
188	Ir(923.5)	4.2(2) ms		IT(100%)	
189	Ir	13.2(1) days	3/2+	$Q_{\varepsilon} = 532(100\%)$	$\gamma_{245,70,59,36}$
189	Ir(372.2)	13.3(3) ms	11/2−	IT(100%)	$\gamma_{301,187,114}$
189	Ir(2333.2)	3.7(2) ms	(25/2)+	IT(100%)	$\gamma_{546,248,702,466}$
190	Ir	11.78(10) days	(4−)	$Q_{\varepsilon} = 2,000(100\%)$	$\gamma_{187,605,519,558}$
190	Ir(26.3)	1.120(3) h	(1 −)	IT(100%)	γ_{26}
190	Ir(376.4)	3.087(12) h	(11)−	$\varepsilon(91.4\%)$	$\gamma_{617,503,361,187}$
				IT(8.6%)	γ_{149}
191	Ir	Stable	3/2+	{37.3(2)%}	
191	Ir(171.3)	4.899(23) s	11/2−	IT(100%)	γ_{129}
191	Ir(2047.0)	5.5(7) s		IT(100%)	
192	Ir	73.827(13) days	4+	$Q_{\beta^{-}} = 1,459.7(95.13\%)$ $Q_{\varepsilon} = 1,046.2(4.87\%)$	$\gamma_{317,468,308,296}$ $\gamma_{206,485,374,201}$
192	Ir(56.7)	1.45(5) m	1−	IT(99.98%)	γ_{57}
				$\beta^{-} - (0.02\%)$	γ_{612}

Table 22.1 (Continued)

A	Element	Half-life or width	J^{π}	Qmode(%BR){%Abund}	Principal gammas, alphas
192	Ir(168.1)	241(9) years	(11-)	IT(100%)	γ 155
193	Ir	Stable	3/2+	{62.7(2)%}	
193	Ir(80.2)	10.53(4) days	11/2-	IT(100%)	γ 80
194	Ir	19.28(13) h	1-	Q β - = 2,246.8(100%)	γ 328,294
194	Ir(147.1)	31.85(24) ms	(4+)	IT(100%)	γ 112,84
194	Ir(190 + x)	171(11) days	(10,11)	β - (100%)	γ 483,329,601,688
195	Ir	2.5(2) h	3/2+	Q β - = 1,120.0(100%)	γ 99,211,31,130
195	Ir(100)	3.8(2) h	11/2-	β - (95%)	γ 99,433,685,320
				IT(5%)	γ 100
196	Ir	52(1) s	(0-)	Q β - = 3,210(100%)	γ 356,780,447,333
196	Ir(410)	1.40(2) h	(10,11-)	β - (~100%)	γ 394,521,447,356
				IT(<0.3%)	
197	Ir	5.8(5) m	3/2+	Q β - = 2,155(100%)	
197	Ir(115)	8.9(3) m	11/2-	β - (99.75%)	γ 470,431,816,378
				IT(0.25%)	
198	Ir	8(1) s		Q β - = [4,100](100%)	γ 507,407
199	Ir	6(+5-4) s		Q β - = 2,990	
202	Ir	11(3) s	(1-,2-)	β - (100%)	
78	Platinum				
	Pt	300(100) μ s	0+	α (100%)	α 7110
	Pt	0.9(3) ms		α (100%)	
	Pt	2.1(2) ms	0+	Q α = 6,991(<100%)	α 6832
	Pt	7.0(2) ms	(7/2-)	Q α = 6,840(<100%)	α 6684

170	Pt	13.8(5) ms	0+	$Q\alpha = 6,704(98\%)$	$\alpha 6545$
171	Pt	51(2) ms		$Q\alpha = 6,610(\sim 98\%)$	$\alpha 6453$
				$Q\epsilon = [8,800](\sim 2\%)$	
172	Pt	0.096(3) s	0+	$Q\alpha = 6,465(94\%)$	$\alpha 6314$
				$Q\epsilon = [6,300](6\%)$	
173	Pt	382(2) ms	(5/2-)	$Q\alpha = 6,350(83\%)$	$\alpha 6213$
				$Q\epsilon = [8,190]$	
174	Pt	0.889(17) s	0+	$Q\alpha = 6,184(76\%)$	$\alpha 6038$
				$Q\epsilon = [5,600](24\%)$	
175	Pt	2.53(6) s	7/2-	$Q\alpha = 6,178(56\%)$	$\gamma 212, \alpha 5960$
				$Q\epsilon = [7,400]$	
176	Pt	6.33(15) s	0+	$Q\epsilon = [5,100](60\%)$	
				$Q\alpha = 5,886.0(40\%)$	$\alpha 5753$
177	Pt	10.6(4) s	5/2-	$Q\epsilon = [6,800](94.3\%)$	$\gamma 148, 85, 223, 157$
				$Q\alpha = 5,644(5.7\%)$	$\gamma 92, \alpha 5517, 5423$
178	Pt	21.1(6) s	0+	$Q\epsilon = [4,300](92.3\%)$	$\gamma 85, 90, 101, 92$
				$Q\alpha = 5,573(7.7\%)$	$\alpha 5446$
179	Pt	21.2(4) s	1/2-	$Q\epsilon = [5,900](99.76\%)$	$\gamma 172, 193, 100, 1565$
				$Q\alpha = 5,395(0.24\%)$	$\alpha 5172$
180	Pt	56(2) s	0+	$Q\epsilon = [3,690](100\%)$	
				$Q\alpha = 5,275(\sim 0.3\%)$	$\alpha 5157$
181	Pt	52.0(22) s	1/2-	$Q\epsilon = [5,200](100\%)$	$\gamma 112, 289, 230, 243$
				$Q\alpha = 5,150(\sim 0.08\%)$	
182	Pt	3.0(2) m	0+	$Q\epsilon = 2,920(99.96\%)$	$\gamma 136, 146, 210$
				$Q\alpha = 4,952(0.04\%)$	$\alpha 4843$
183	Pt	6.5(10) m	1/2-	$Q\epsilon = [4,600](100\%)$	
				$Q\alpha = 4,820(\sim 0.0013\%)$	$\alpha 4730$

Table 22.1 (Continued)

A	Element	Half-life or width	J^{π}	Qmode(%BR){%Abund}	Principal gammas, alphas
183	Pt(34.6)	43(5) s	(7/2) [−]	$\varepsilon(\sim 100\%)$ $\alpha(<0.00040\%)$ IT	$\gamma 630,316,329,312$
184	Pt	17.3(2) m	0 ⁺	$Q_{\varepsilon} = [2,300](100\%)$ $Q\alpha = 4,602(\approx 0.001\%)$	$\gamma 155,192,548,71$ $\alpha 4502$
184	Pt(1836.0)	1.01(5) ms	8 [−]	IT(100%)	$\gamma 272,361,431,610$
185	Pt	70.9(24) m	9/2 ⁺	$Q_{\varepsilon} = [3,900](100\%)$ $Q\alpha = 4,540$	
185	Pt(103.2)	33.0(8) m	1/2 [−]	$\varepsilon(>98\%)$ IT(<2%) α	$\gamma 230,135,197,255$
186	Pt	2.08(5) h	0 ⁺	$Q_{\varepsilon} = 1,380(100\%)$ $Q\alpha = 4,325(\sim 0.00014\%)$	$\gamma 689$ $\alpha 4230$
187	Pt	2.35(3) h	3/2 [−]	$Q_{\varepsilon} = [2,980](100\%)$	$\gamma 106,202,110,709$
188	Pt	10.2(3) days	0 ⁺	$Q_{\varepsilon} = 506(100\%)$ $Q\alpha = 4,007(0.000026\%)$	$\gamma 188,195,381,423$ $\alpha 3922$
189	Pt	10.87(12) h	3/2 [−]	$Q_{\varepsilon} = 1,971(100\%)$	$\gamma 721,94,569,244$
190	Pt	6.5(3)E11 years	0 ⁺	$Q\alpha = 3,249(100\%)$ {0.014(1)%}	$\alpha 3175$
191	Pt	2.83(2) days	3/2 [−]	$Q_{\varepsilon} = 1,019(100\%)$	$\gamma 539,409,360,82$
192	Pt	Stable	0 ⁺	{0.782(7)%}	
193	Pt	50(6) years	1/2 [−]	$Q_{\varepsilon} = 56.6(100\%)$	
193	Pt(149.8)	4.33(3) days	13/2 ⁺	IT(100%)	$\gamma 136$
194	Pt	Stable	0 ⁺	{32.967(99)%}	

79	195	Pt	Stable	1/2–	{33.832(10)%}		
	195	Pt(259.3)	4.010(5) days	13/2+	IT(100%)	γ99,130,31	
	196	Pt	Stable	0+	{25.242(41)%}		
	197	Pt	19.8915(19) h	1/2–	Qβ– = 718.9(100%)	γ77,191	
	197	Pt(399.6)	95.41(18) m	13/2+	IT(96.7%)	γ347	
					β– (3.3%)	γ279	
	198	Pt	Stable	0+	{7.163(55)%}		
	199	Pt	30.80(21) m	5/2–	Qβ– = 1,703(100%)	γ543,494,317,186	
	199	Pt(424)	13.6(4) s	(13/2)+	IT(100%)	γ392	
	200	Pt	12.6(3) h	0+	Qβ– = 660(100%)	γ76,136,244,60	
	201	Pt	2.5(1) m	(5/2–)	Qβ– = 2,660(100%)	γ1760	
	202	Pt	44(15) h	0+	Qβ– = [1,800](100%)		
	202	Pt(1788)	0.28(+42–19) ms	(7–)	IT(100%)		
	203	Pt	10(1) s	(1/2–)	β– (100%)		
		Gold					
	169	Au	(150 μs)		p		
					α		
	170	Au	286(+50–40) μs	(2–)	p(89%)		
					α(11%)		
	171	Au	17(+9–5) μs	(1/2+)	Qp = [1,510](~100%)		
	171	Au(250)	1.02(10) ms	(11/2–)	Qα = [7,110](54%)	α6996	
					p(46%)		
	172	Au	6.3(15) ms		Qα = 7,020(<100%)		
					Qp = [1,000](<2%)		
	173	Au	25(1) ms	(1/2+)	Qα = 6,900(94%)	α6720	
	173	Au(214.0)	14.0(9) ms	(11/2–)	α(92%)		

Table 22.1 (Continued)

A	Element	Half-life or width	J^{π}	Qmode(%BR){%Abund}	Principal gammas, alphas
174	Au	139(3) ms		$Q\alpha = 6,782(>0\%)$	$\alpha 6532$
174	Au(0 + x)	163(4) ms		$\alpha(>0\%)$	$\gamma 191, \alpha 6546, 6471$
175	Au	(0.1 s)	(1/2+)	$Q\alpha = [6,680](<100\%)$	
175	Au(0 + x)	160(5) ms	(11/2-)	$Q\epsilon = [8,600][6\%]$	
				$\alpha(94\%)$	$\alpha 6439$
176	Au	1.05(1) s	(3-)	$Q\alpha = 6,542$	$\gamma 168, \alpha 6228, 6286$
				$Q\epsilon = [10,500]$	
176	Au	1.36(2) s	(9+)		
177	Au	1.462(32) ms	(1/2+, 3/2+)	$Q\epsilon = [8,200]$	
				$Q\alpha = 6,431(<100\%)$	$\alpha 6110, 6150$
177	Au	1.180(12) ms	11/2-	ϵ	
				$\alpha(<100\%)$	$\alpha 6110, 6150$
178	Au	2.6(5) s		$Q\epsilon = [9,600](<60\%)$	
				$Q\alpha = 6,120(>40\%)$	$\alpha 5920, 5980$
179	Au	3.3(13) s		$Q\epsilon = [7,400][78\%]$	
				$Q\alpha = 6,082(22\%)$	$\alpha 5848$
180	Au	8.1(3) s		$Q\epsilon = [8,600](<98.2\%)$	$\gamma 153, 524, 258, 861$
				$Q\alpha = 5,851(>1.8\%)$	$\gamma 195, \alpha 5497, 5611$
181	Au	13.7(14) s	(3/2-)	$Q\epsilon = [6,300][97.3\%]$	$\gamma 199, 79, 2022, 94$
				$Q\alpha = 5,752(2.7\%)$	$\gamma 148, \alpha 5479, 5626$
182	Au	15.6(4) s		$Q\epsilon = [7,800][99.87\%]$	$\gamma 155, 265, 855, 787$
				$Q\alpha = 5,527(0.13\%)$	$\gamma 55, \alpha 5353$
183	Au	42.8(10) s	(5/2)-	$Q\epsilon = [5,500][99.45\%]$	$\gamma 161, 214, 313, 180$
				$Q\alpha = 5,466(0.55\%)$	$\gamma 193, \alpha 5346$

184	Au	20.6(9) s	5+	$Q_{\varepsilon} = [7,060](100\%)$	
184	Au(69)	48(1) s	2+	$\varepsilon(99.98\%)$	$\gamma 163,273,363,777$
				$Q_{\alpha} = 5,232(0.02\%)$	$\alpha 5172,5108$
				IT	
185	Au	4.25(6) m	5/2-	$Q_{\varepsilon} = 4,710(99.74\%)$	$\gamma 311,243,78,332$
				$Q_{\alpha} = 5,181(0.26\%)$	$\alpha 5067$
185	Au(0 + x)	6.8(3) m		$\varepsilon(<100\%)$	
				IT	
186	Au	10.7(5) m	3-	$Q_{\varepsilon} = 6,120(100\%)$	$\gamma 192,299,765,416$
				$Q_{\alpha} = 4,906(0.0008\%)$	
187	Au	8.4(3) m	1/2+	$Q_{\varepsilon} = [3,730](100\%)$	$\gamma 1332,1408,915,1267$
				$Q_{\alpha} = 4,790(0.003\%)$	
187	Au(120.6)	2.3(1) s	9/2-	IT(100%)	$\gamma 101$
188	Au	8.84(6) m	1(-)	$Q_{\varepsilon} = [5,300](100\%)$	$\gamma 266,340,605$
189	Au	28.7(3) m	1/2+	$Q_{\varepsilon} = [2,850](100\%)$	$\gamma 713,813,448,348$
				$Q_{\alpha} = [4,400](<3.0\text{E} - 5\%)$	
189	Au(247.3)	4.59(11) m	11/2-	$\varepsilon(100\%)$	$\gamma 166,321$
				IT(>0%)	
190	Au	42.8(10) m	1-	$Q_{\varepsilon} = 4,442(100\%)$	$\gamma 296,302,598$
				$Q_{\alpha} = 3,860(<1.0\text{E} - 6\%)$	
190	Au(0 + x)	125(20) ms	(11-)	IT(~100%)	
				ε	
191	Au	3.18(8) h	3/2+	$Q_{\varepsilon} = 1,830(100\%)$	$\gamma 586,278,674,284$
191	Au(267)	0.92(11) s	(11/2-)	IT(100%)	$\gamma 253,241$
192	Au	4.94(9) h	1-	$Q_{\varepsilon} = 3,516(100\%)$	$\gamma 317,296$
192	Au(135.4)	29 ms	(5)+	IT(100%)	
192	Au(431.6)	160(20) ms	(11-)	IT(100%)	$\gamma 60$

Table 22.1 (Continued)

A	Element	Half-life or width	J^{π}	Qmode(%BR){%Abund}	Principal gammas, alphas
193	Au	17.65(15) h	3/2+	Q ϵ = 1,069(100%)	γ 186,256,268,174
193	Au(290.2)	3.9(3) s	11/2–	IT(99.97%)	γ 258
				ϵ (~0.03%)	γ 135
194	Au	38.02(10) h	1–	Q ϵ = 2,492(100%)	γ 329,294,1469
194	Au(107.4)	600(8) ms	(5+)	IT(100%)	γ 45,35
194	Au(475.8)	420(10) ms	(11–)	IT(100%)	γ 171,129,137,162
195	Au	186.098(47) days	3/2+	Q ϵ = 226.8(100%)	γ 99
195	Au(318.6)	30.5(2) s	11/2–	IT(100%)	γ 262
196	Au	6.1669(6) days	2–	Q ϵ = 1,506(92.8%)	γ 356,333
				Q β – = 686(7.2%)	γ 426
196	Au(84.7)	8.1(2) s	5+	IT(100%)	γ 85
196	Au(595.7)	9.6(1) h	12–	IT(100%)	γ 148,188,168,285
197	Au	Stable	3/2+	{100%}	
197	Au(409.2)	7.73(6) s	11/2–	IT(100%)	γ 279
198	Au	2.69517(21) days	2–	Q β – = 1,372.5(100%)	γ 412
198	Au(811.7)	2.27(2) days	(12–)	IT(100%)	γ 215,97,180,204
199	Au	3.139(7) days	3/2+	Q β – = 452.3(100%)	γ 158,208
199	Au(548.9)	0.44(3) ms	11/2(–)	IT(100%)	
200	Au	48.4(3) m	1(–)	Q β – = 2,240(100%)	γ 368,1225,1263
200	Au(962)	18.7(5) h	12–	β – (84%)	γ 498,368,579,256
				IT(16%)	γ 333,146,60,133
201	Au	26.0(8) m	3/2+	Q β – = 1,263(100%)	γ 543,517,613,167
202	Au	28.4(12) s	(1–)	Q β – = 2,950(100%)	γ 440,1125,1306,1204
203	Au	60(6) s	3/2+	Q β – = 2,124(100%)	

204	Au	39.8(9) s	(2-)	$Q\beta^- = [3,940](100\%)$	$\gamma 437,1511,692,723$
205	Au	31(2) s	(3/2+)	$Q\beta^- = [3,300](100\%)$	$\gamma 379,467,946,813$
80	Mercury				
	Hg	59(+36-6) μ s		$\alpha(\approx 100\%)$	
	Hg	0.29(+235-0) ms	0+	$\alpha(\approx 100\%)$	
	Hg	0.6(+5-2) ms		$\alpha(\approx 100\%)$	
	Hg	2.1(+18-7) ms	0+	$\alpha(99.6\%)$	$\alpha 7067$
	Hg	10.8(4) ms	(7/2-, 9/2-)	$Q\alpha = 7,040(100\%)$	$\alpha 6889$
	Hg	20.3(14) ms	0+	$Q\alpha = 6,925(94\%)$	$\alpha 6767$
	Hg	127.3(18) ms	(13/2+)	$Q\alpha = 6,740(85\%)$	$\alpha 6580$
				$Q\epsilon = [8,500](15\%)$	
	Hg	0.269(3) s	0+	$Q\alpha = 6,578(\sim 70\%)$	$\alpha 6430$
179	Hg	1.08(9) s		$Q\epsilon = [6,100](\sim 30\%)$	$\alpha 6288$
				$Q\epsilon = [7,800](\sim 47\%)$	
				$\epsilon p(\sim 0.15\%)$	
180	Hg	2.58(1) s	0+	$Q\epsilon = [5,500](52\%)$	$\gamma 301,381,480,405$
				$Q\alpha = 6,258(48\%)$	$\gamma 443, \alpha 6120$
181	Hg	3.6(1) s	1/2-	$Q\epsilon = [7,300](69\%)$	$\gamma 148,43,1987,185$
				$Q\alpha = 6,287(31\%)$	$\gamma 240, \alpha 6005$
				$\epsilon p(0.02\%)$	$\gamma 150$
				$\epsilon \alpha(0.000011\%)$	
182	Hg	10.83(6) s	0+	$Q\epsilon = [4,800](84.8\%)$	$\gamma 129,218,414$
				$Q\alpha = 5,997(15.2\%)$	$\gamma 251,171, \alpha 5867$
183	Hg	9.4(7) s	1/2-	$Q\epsilon = [6,500](88.3\%)$	$\gamma 61,160,173,305$
				$Q\alpha = 6,039(11.7\%)$	$\gamma 154, \alpha 5904$
				$\epsilon p(0.00026\%)$	

Table 22.1 (Continued)

A	Element	Half-life or width	J^{π}	Qmode(%BR){%Abund}	Principal gammas, alphas
184	Hg	30.9(3) s	0+	Q ϵ = [4,120](98.89%) Q α = 5,662(1.11%)	γ 236,156,295,392 α 5535
185	Hg	49.1(10) s	1/2–	Q ϵ = [5,800](94%) Q α = 5,778(6%)	γ 94, α 5653
185	Hg(99)	21.6(15) s	13/2+	Π (54%) ϵ (46%) α (~0.03%)	γ 65,26 γ 223,259,213,190 γ 106, α 5372,5408
186	Hg	1.38(6) m	0+	Q ϵ = 3,230(99.98%) Q α = 5,206(0.02%)	γ 112,252 α 5094
187	Hg	2.4(3) m	13/2+	Q ϵ = [4,900](100%) Q α = [5,080](>0.00012%)	α 4870
187	Hg(134)	1.9(3) m	3/2–	ϵ (100%) α (>0.00025%)	γ 233,376,240,103 α 5035
188	Hg	3.25(15) m	0+	Q ϵ = [2,300](100%) Q α = 4,710(0.000037%)	γ 67 α 4610
189	Hg	7.6(1) m	3/2–	Q ϵ = [3,950](100%) Q α = [4,400](<3.0E – 5%)	
189	Hg(0 + x)	8.6(1) m	13/2+	ϵ (100%) α (<3.0E – 5%)	γ 321,78,566,435
190	Hg	20.0(5) m	0+	Q ϵ = [1,470](100%) Q α = [3,950](<5.0E – 5%)	γ 143
191	Hg	49(10) m	3/2(–)	Q ϵ = 3,180(100%)	γ 252,196,225,241
191	Hg(0 + x)	50.8(15) m	13/2(+)	ϵ (100%)	γ 253,420,579,274

192	Hg	4.85(20) h	0+	$Q_{\varepsilon} = [700](100\%)$	$\gamma_{275,157,307}$
193	Hg	3.80(15) h	3/2−	$Q_{\varepsilon} = 2,340(100\%)$	$\gamma_{382,861,258,1119}$
193	Hg(140.8)	11.8(2) h	13/2+	$\varepsilon(92.8\%)$	$\gamma_{258,408,573,932}$
				$\Pi(7.2\%)$	γ_{101}
194	Hg	444(77) years	0+	$Q_{\varepsilon} = 40(100\%)$	
195	Hg	10.53(3) h	1/2−	$Q_{\varepsilon} = 1,510(100\%)$	$\gamma_{780,61,585,180}$
195	Hg(176.1)	41.6(8) h	13/2+	$\Pi(54.2\%)$	γ_{37}
				$\varepsilon(45.8\%)$	$\gamma_{262,560}$
196	Hg	Stable	0+	$\{0.15(1\%)\}$	
197	Hg	64.14(5) h	1/2−	$Q_{\varepsilon} = 600(100\%)$	γ_{77}
197	Hg(299.0)	23.8(1) h	13/2+	$\Pi(91.4\%)$	γ_{134}
				$\varepsilon(8.6\%)$	γ_{279}
198	Hg	Stable	0+	$\{9.97(20\%)\}$	
199	Hg	Stable	1/2−	$\{16.87(22\%)\}$	
199	Hg(532.5)	42.67(9) m	13/2+	$\Pi(100\%)$	$\gamma_{158,374}$
200	Hg	Stable	0+	$\{23.10(19\%)\}$	
201	Hg	Stable	3/2−	$\{13.18(9\%)\}$	
202	Hg	Stable	0+	$\{29.86(26\%)\}$	
203	Hg	46.612(18) days	5/2−	$Q_{\beta-} = 491.8(100\%)$	γ_{279}
204	Hg	Stable	0+	$\{6.87(15\%)\}$	
205	Hg	5.14(9) m	1/2−	$Q_{\beta-} = 1,531(100\%)$	γ_{204}
206	Hg	8.32(7) m	0+	$Q_{\beta-} = 1,307(100\%)$	γ_{305}
207	Hg	2.9(2) m	(9/2+)	$Q_{\beta-} = 4,820(100\%)$	$\gamma_{351,997,1637,1756}$
208	Hg	41(+5−4) m	0+	$Q_{\beta-} = [3,700](100\%)$	γ_{474}
209	Hg	35(+9−6) s		$\beta - (100\%)$	
210	Hg	> 300 ns	0+	$\beta -$	

Table 22.1 (Continued)

81	A	Element	Half-life or width	J^{π}	Qmode(%BR){%Abund}	Principal gammas, alphas
		Thallium				
	176	Tl(807)	5.2(+30–14) ms	(3–,4–,5–)	p(100%)	
	177	Tl	18(5) ms	1/2+	Q α = [7,340](73%) Qp = [1,530](27%)	
	178	Tl	≈60 ms		Q α = [7,180] Q ϵ = [11,880]	
	179	Tl	0.42(6) s	(1/2+)	Q α = [6,810](<100%) Q ϵ = [9,000]	α6560
	179	Tl(0 + x)	1.7(2) ms	(11/2–)	α(<100%)	α7200
					IT	
					ε	
	180	Tl	1.5(3) s		εF(∼0.0001%)	
					Q ϵ = [11,100]	
					Q α = [6,820]	
	181	Tl(350)	1.4(5) ms	(1/2+)	Q α = [6,600](<10%)	
	181	Tl(350)	3.2(3) s	(9/2–)	Q ϵ = [8,500]	
	182	Tl	3.1(10) s	(7+)	Q ϵ = [10,100](>96%) Q α = 6,550(<4%)	γ351,261,333,414 α6406
	183	Tl	6.9(7) s	(1/2+)	Q ϵ = [7,600](>0%) Q α = [6,220]	
	183	Tl(630)	53.3(3) ms	(9/2–)	α(2%)	α6343,6378
					ε	
					IT	
	184	Tl(x)	11(1) s	(2+)	Q ϵ = [9,200](97.9%) Q α = 6,300(2.1%)	γ367,287,340,534 α6162,5988

185	Tl	19.5(5) s	(1/2+)	Q ϵ = [6,600]		
185	Tl(454)	1.93(8) s	(9/2-)	Q α = [6,100]	α 5976,6010	
186	Tl(0 + x)	27.5(10) s	(7+)	IT	γ 169	
186	Tl(374.0 + x)	2.9(2) s	(10-)	Q ϵ = [8,500](100%) Q α = 5,890(≈0.006%)	γ 405,403,357,675 α 5760	
187	Tl	≈51 s	(1/2+)	IT(100%)	γ 374	
187	Tl(335)	15.60(12) s	(9/2-)	Q ϵ = [5,900](<100%) Q α = 5,539(>0%) ϵ (<99.9%)	γ 161	
188	Tl	71(2) s	(2-)	IT(<99.9%) α (0.15%)	γ 30 γ 12, α 5524	
188	Tl(0 + x)	71(1) s	(7+)	Q ϵ = [7,800](100%) ϵ (100%)		
188	Tl(268.8)	41(4) ms	(9-)	IT(≈100%) ϵ		
189	Tl	2.3(2) m	(1/2+)	Q ϵ = 5,180(100%)	γ 334,942,451,522	
189	Tl(281)	1.4(1) m	(9/2-)	ϵ (100%) IT(<4%)	γ 318,216,228,445	
190	Tl(0 + x)	2.6(3) m	2(-)	Q ϵ = 7,000(100%)	γ 416,625,684	
190	Tl(0 + y)	3.7(3) m	7(+)	ϵ (100%)	γ 416,625,731,840	
190	Tl(161.9)	0.75(4) ms	(8-)	ϵ (100%)	γ 416,625,731,840	
191	Tl		(1/2+)	Q ϵ = [4,490]		
191	Tl(299)	5.22(16) m	9/2(-)	ϵ (100%)	γ 216,326,265,336	
192	Tl(0 + x)	9.6(4) m	(2-)	Q ϵ = [6,120](100%)	γ 423,635,786,746	
192	Tl(156.0)	10.8(2) m	(7+)	ϵ (100%)		

Table 22.1 (Continued)

A	Element	Half-life or width	J^{π}	Qmode(%BR){%Abund}	Principal gammas, alphas
193	Tl	21.6(8) m	1/2(+)	Q ϵ = [3,640](100%)	γ 324,1045,676,1579
193	Tl(365.0 + x)	2.11(15) m	(9/2-)	IT(75%)	γ 365
194	Tl	33.0(5) m	2-	ϵ (25%)	
				Q ϵ = [5,280](100%)	γ 428,636,645
				Q α = [3,490]($<1.0\epsilon$ - 7%)	
194	Tl(0 + x)	32.8(2) m	(7+)	ϵ (100%)	γ 428,636,749,735
195		1.16(5) h	1/2+	Q ϵ = [2,810](100%)	γ 564,884,1364,242
195	Tl(482.6)	3.6(4) s	9/2-	IT(100%)	γ 384
196	Tl	1.84(3) h	2-	Q ϵ = [4,380](100%)	γ 426,611,635
196	Tl(395)	1.41(2) h	(7+)	ϵ (95.5%)	γ 426,635,695
				IT(4.5%)	γ 120
197	Tl	2.84(4) h	1/2+	Q ϵ = 2,180(100%)	γ 426,152,1411,578
197	Tl(608.3)	0.54(1) s	9/2-	IT(100%)	γ 386,222
198	Tl	5.3(5) h	2-	Q ϵ = 3,460(100%)	γ 412,676,637,1201
198	Tl(543.5)	1.87(3) h	7+	ϵ (54%)	γ 637,412,587
				IT(46%)	γ 283,260
198	Tl(742.3)	32.1(10) ms	(10-)	IT(100%)	γ 199
199	Tl	7.42(8) h	1/2+	Q ϵ = 1,450(100%)	γ 455,208,247,158
199	Tl(749.5)	28.4(2) ms	9/2-	IT(100%)	γ 367,383
200	Tl	26.1(1) h	2-	Q ϵ = 2,456(100%)	γ 368,1206,579,828
200	Tl(752)	34.0(9) ms	7+	IT(100%)	γ 539,213
201	Tl	3.0421(17) days	1/2+	Q ϵ = 483(100%)	γ 167,135
201	Tl(919.1)	2.01(7) ms	(9/2-)	IT(100%)	γ 588,331
202	Tl	12.31(8) days	2-	Q ϵ = 1,365(100%)	γ 440

	203	Tl	Stable	1/2+	{29.524(14)%}		
	204	Tl	3.78(2) years	2-	Qβ- = 763.72(97.1%) Qε = 347.5(2.9%)		
	205	Tl	Stable	1/2+	{70.476(14)%}		
	206	Tl	4.202(11) m	0-	Qβ- = 1,533.5(100%)	γ803	
	206	Tl(2643.3)	3.74(3) m	(12-)	IT(100%)	γ453,687,266,216	
	207	Tl	4.77(2) m	1/2+	Qβ- = 1,423(100%)	γ898	
	207	Tl(1350)	1.33(11) s	11/2-	IT(100%)	γ1000	
	208	Tl	3.053(4) m	5+	Qβ- = 5,001.0(100%)	γ2615,583,511,861	
	209	Tl	2.20(7) m	(1/2+)	Qβ- = 3,982(100%)	γ1567,465,117	
	210	Tl	1.30(3) m	(5+)	Qβ- = 5,489(100%) β - n(0.007%)	γ800,296,1316,1210	
	211	Tl	>300 ns		β-		
	212	Tl	>300 ns		β-		
82		Lead					
	178	Pb	0.23(15) ms	0+	α		
	179	Pb	(3 ms)		α		
	180	Pb	4.5(11) ms	0+	α(100%)	α7230	
	181	Pb(0 + x)	45(20) ms	(13/2+)	Qα = [7,240](<100%) Qε = [9,100](~2%)	α7044	
	182	Pb	55(+40 - 35) ms	0+	Qα = 7,076(<100%)	α6920	
	183	Pb	535(30) ms	(3/2-)	Qα = 7,030(~90%) Qε = [8,600]	α6715,6786	
	183	Pb(97)	415(20) ms	(13/2+)	α(100%)		
	184	Pb	490(25) ms	0+	Qα = 6,775(23%) Qε = [6,000](77%)	α6628	

Table 22.1 (Continued)

A	Element	Half-life or width	J^{π}	Qmode(%BR){%Abund}	Principal gammas, alphas
185	Pb	6.3(4) s	3/2 [−]	Q α = [6,680](34%) ϵ	α 6404,6483
185	Pb(0 + x)	4.3(2) s	13/2 ⁺	Q α = [6,680](50%) ϵ	α 6404,6483
186	Pb	4.82(3) s	0 ⁺	Q α = 6,471(40%) Q ϵ = [5,400](60%)	α 6332
187	Pb	15.2(3) s	(3/2 [−])	Q ϵ = [7,300](93%) Q α = 6,395(7%)	γ 300 γ 276, α 6194,5993
187	Pb(81)	18.3(3) s	(13/2 ⁺)	ϵ (88%) α (12%)	γ 393,331,617,494 α 6077
188	Pb	25.1(1) s	0 ⁺	Q ϵ = [4,800](90.7%) Q α = 6,111(9.3%)	γ 185,758 α 5983
189	Pb	51(3) s	(3/2 [−])	Q ϵ = [6,700](>99%) Q α = [5,860](~0.4%)	α 5730
190	Pb	71(1) s	0 ⁺	Q ϵ = [4,100](99.6%) Q α = 5,698(0.4%)	γ 942,151,598,142 α 5581
191	Pb	1.3398) s	(3/2 [−])	Q ϵ = [5,900](99.99%) Q α = [5,410](0.01%)	α 5290
191	Pb(138)	2.18(8) m	(13/2 ⁺)	ϵ (100%) α (~0.02%)	γ 387,712,614,937
192	Pb	3.5(1) m	0 ⁺	Q ϵ = [3,400](99.99%) Q α = 5,221(0.0059%)	γ 1195,608,168,782 α 5112
193	Pb		(3/2 [−])	Q ϵ = [5,200]	
193	Pb(0 + x)	5.8(2) m	(13/2 ⁺)	ϵ (100%)	γ 392,717,736,756

194	Pb	10.7(6) m	0+	$Q_{\beta} = [2,700](100\%)$ $Q_{\alpha} = 4,738(7.3E - 6\%)$	$\gamma 582,1519,204,368$ $\alpha 4640$
195	Pb	≈ 15 m	3/2-	$Q_{\beta} = [4,500](100\%)$	$\gamma 883,394,871,696$
195	Pb(202.9)	15.0(12) m	13/2+	$\varepsilon(100\%)$	$\gamma 384,394,878,708$
196	Pb	37(3) m	0+	$Q_{\beta} = [2,050](\sim 100\%)$ $Q_{\alpha} = [4,200](< 3.0E - 5\%)$	$\gamma 253,502,192,367$
197	Pb	8.1(17) m	3/2-	$Q_{\beta} = [3,580](100\%)$	$\gamma 386,761,375,1261$
197	Pb(319.3)	42.9(9) m	13/2+	$\varepsilon(81\%)$ $IT(19\%)$	$\gamma 386,388,223,774$ $\gamma 85$
198	Pb	2.4(1) h	0+	$Q_{\beta} = [1,410](100\%)$	$\gamma 290,365,173,865$
199	Pb	90(10) m	3/2-	$Q_{\beta} = 2,880(100\%)$	$\gamma 367,353,1135,720$
199	Pb(424.1 + x)	12.2(3) m	(13/2+)	$IT(< 100\%)$ $\varepsilon(> 0\%)$	$\gamma 424$ $\gamma 367$
200	Pb	21.5(4) h	0+	$Q_{\beta} = 811(100\%)$	$\gamma 148,257,236,268$
201	Pb	9.33(3) h	5/2-	$Q_{\beta} = 1,900(100\%)$	$\gamma 331,361$
201	Pb(629.1)	60.8(18) s	13/2+	$IT(> 99\%)$ $\varepsilon(< 1\%)$	
202	Pb	5.25(28)E4 years	0+	$Q_{\beta} = 50(100\%)$ $Q_{\alpha} = 2,598(< 1\%)$	
202	Pb(2169.8)	3.54(2) h	9-	$IT(90.5\%)$ $\varepsilon(9.5\%)$	$\gamma 961,422,787,657$ $\gamma 490,460,390$
203	Pb	51.92(3) h	5/2-	$Q_{\beta} = 975(100\%)$	$\gamma 279$
203	Pb(825.2)	6.21(11) s	13/2+	$IT(100\%)$	$\gamma 825$
203	Pb(2949.6)	480(7) ms	29/2-	$IT(100\%)$	$\gamma 839,259,874,634$
204	Pb	> 1.4E17 years	0+	$Q_{\alpha} = 1,971.8$ {1.4(1)%}	

Table 22.1 (Continued)

A	Element	Half-life or width	J π	Qmode(%BR){%Abund}	Principal gammas, alphas
204	Pb(2185.4)	67.2(3) m	9–	IT(100%)	γ 899,912,375
205	Pb	1.73(7)E7 years	5/2–	Q ϵ = 51.1(100%)	
205	Pb(1013.8)	5.55(2) ms	13/2+	IT(100%)	γ 1014
206	Pb	Stable	0+	{24.1(1)%}	
207	Pb	Stable	1/2–	{22.1(1)%}	
207	Pb(1633.4)	0.806(6) s	13/2+	IT(100%)	γ 570,1064
208	Pb	Stable	0+	{52.4(1)%}	
209	Pb	3.253(14) h	9/2+	Q β – = 644.2(100%)	
210	Pb	22.20(22) years	0+	Q β – = 63.5(100%)	γ 47
				Q α = 3,792(1.9E – 6%)	α 3720
211	Pb	36.1(2) m	9/2+	Q β – = 1,372(100%)	γ 405,832,427,767
212	Pb	10.64(1) h	0+	Q β – = 573.8(100%)	γ 239
213	Pb	10.2(3) m	(9/2+)	Q β – = [1,980](100%)	
214	Pb	26.8(9) m	0+	Q β – = 1,024(100%)	γ 352,295,242
215	Pb	36(1) s		β –	
83	Bismuth				
	Bi	13(2) ms		α	
	Bi	58(4) μ s	1/2+	Q p = [1,570](90%)	
				Q α = [7,600](10%)	
	Bi	15.0(17) ms	(3+)	Q α = [7,700](100%)	
	Bi(0 + x)	9.8(13) ms	(10–)	α (~100%)	
	Bi	32(3) ms	(9/2–)	Q α = [7,600](>50%)	α 6995
	Bi(0 + x)	60(3) ms	(3+)	Q ϵ = [10,400](<100%)	
				Q α = 7,275(>0%)	

188	Bi(0 + y)	265(15) ms	(10−)	ε	
189	Bi	674(11) ms	(9/2−)	Qα = 7,267(>50%) Qε = [8,000](<50%)	α6672
189	Bi(92)	5.0(1) ms	(1/2+)	α(>50%) ε(<50%)	α7206
190	Bi(0 + y)	6.2(1) s	(10−)	Qα = 6,862(70%) Qε = [9,600](30%)	γ374,α6456 γ846,145,701
190	Bi(0 + x)	6.3(1) s	(3+)	α(~90%) ε(~10%)	γ294,α6431
191	Bi	12.4(35) s	(9/2−)	Qα = 6,781(51%) Qε = [7,300](49%)	α6310
191	Bi(241)	125(13) ms	(1/2+)	α(68%) IT(32%)	α6874
192	Bi	34.6(9) s	(3+)	ε	
192	Bi(0 + x)	39.6(4) s	(10−)	Qε = [8,900](88%) Qα = 6,376(12%) ε(90%) α(10%)	γ185,α6060 γ854,502,504,565 γ34,α6052
193	Bi	63.6(30) s	(9/2−)	Qε = [6,500](96.5%) Qα = 6,305(3.5%) α(84%) ε(16%)	α5899 α6475
194	Bi	95(3) s	(3+)	Qε = 8,200(99.54%) Qα = 5,918(0.46%) ε(99.8%) α(0.2%)	γ672,774,711,1739 γ151,α5644
194	Bi(0 + x)	115(4) s	(10−)		γ272,α5598

Table 22.1 (Continued)

A	Element	Half-life or width	J^{π}	Qmode(%BR){%Abund}	Principal gammas, alphas
194	Bi(0 + x)	125(2) s	(6+,7+)	ε (100%)	γ 965,575,280,421
195	Bi	183(4) s	(9/2-)	Q_{ε} = [5,900](99.97%) Q_{α} = 5,833(0.03%)	α 5420
195	Bi(401)	87(1) s	(1/2+)	ε (67%) α (33%)	γ 808,776,134,695
196	Bi	308(12) s	(3+)	Q_{ε} = [7,360](~100%) Q_{α} = 5,460(0.0012%)	α 6106 γ 1049,689,777
196	Bi(167.0)	0.6(5) s	(7+)	IT	α 5153
196	Bi(269)	240(3) s	(10-)	ε (74.2%) IT(25.8%) α (0.00038%)	γ 1049,372,689,59 γ 102 α 5112
197	Bi	9.33(50) m	(9/2-)	Q_{ε} = [5,200](100%) Q_{α} = [5,390](0.0001%)	γ 855,85,867,828
197	Bi(500)	5.04(16) m	(1/2+)	α (55%) ε (45%) IT(<0.3%)	α 5776 γ 1838,1809,215
198	Bi	10.3(3) m	(2+,3+)	Q_{ε} = [6,560](100%)	
198	Bi(0 + x)	11.6(3) m	(7+)	ε (100%)	γ 1063,198,562,318
198	Bi(248.5 + x)	7.7(5) s	10-	IT(100%)	γ 249
199	Bi	27(1) m	9/2-	Q_{ε} = 4,350(100%)	
199	Bi(680)	24.70(15) m	(1/2+)	ε (>98%) IT(<2%) Q_{α} = [4,960](~0.01%)	γ 425,842,946,837 α 5484

200	Bi	36.4(5) m	7+	$Q_{\beta} = 5.890(100\%)$	$\gamma^{1026,462,420,245}$
200	Bi(0 + x)	31(2) m	(2+)	$\varepsilon(>90\%)$	$\gamma^{1027,462,420}$
				IT(<10%)	
200	Bi(428.2)	0.40(5) s	(10-)	IT(100%)	
201	Bi	103(3) m	9/2-	$Q_{\beta} = 3.840(100\%)$	$\gamma^{629,936,1014,786}$
				$Q_{\alpha} = 4.500(<0.00010\%)$	
201	Bi(846.4)	57.5(21) m	1/2+	$\varepsilon(>91.1\%)$	
				IT(<8.6%)	
				$\alpha(\sim 0.3\%)$	α^{5240}
202	Bi	1.72(5) h	5+	$Q_{\beta} = 5.150(100\%)$	$\gamma^{961,422,657}$
				$Q_{\alpha} = 4.290(<1.0E - 5\%)$	
203	Bi	11.76(5) h	9/2-	$Q_{\beta} = 3.253(100\%)$	$\gamma^{820,825,897,1847}$
				$Q_{\alpha} = 4.150(\sim 1.0E - 5\%)$	
203	Bi(1098.1)	303(5) ms	1/2+	IT(100%)	$\gamma^{909,190,894}$
204	Bi	11.22(10) h	6+	$Q_{\beta} = 4.450(100\%)$	$\gamma^{899,375,984,912}$
204	Bi(2833.6)	1.07(3) ms	(17+)	IT(100%)	$\gamma^{608,367,737,182}$
205	Bi	15.31(4) days	9/2-	$Q_{\beta} = 2.708(100\%)$	$\gamma^{1764,703,988,1044}$
206	Bi	6.243(3) days	6+	$Q_{\beta} = 3.758(100\%)$	$\gamma^{803,881,516,1719}$
206	Bi(1044.8)	0.89(1) ms	10-	IT(100%)	
207	Bi	32.9(14) years	9/2-	$Q_{\beta} = 2.398.2(100\%)$	$\gamma^{570,1064}$
208	Bi	3.68(4)E5 years	(5)+	$Q_{\beta} = 2.879.1(100\%)$	γ^{2610}
208	Bi(1571.1)	2.58(4) ms	10-	IT(100%)	$\gamma^{921,510,650,140}$
209	Bi	Stable	9/2-	{100%}	

Table 22.1 (Continued)

A	Element	Half-life or width	J^{π}	Qmode(%BR){%Abund}	Principal gammas, alphas
210	Bi	5.012(5) days	1−	Qβ− = 1,162.1(100%) Qα = 5,036.0(0.00013%)	γ304,α4656,4694
210	Bi(271.2)	3.04(6)E6 years	9−	α(100%)	γ266,305,α4946,4909
211	Bi	2.14(2) m	9/2−	Qα = 6,750.5(99.72%) Qβ− = 579(0.28%)	γ351,α6623,6278
212	Bi	60.55(6) m	1(−)	Qβ− = 2,254.0(64.06%) Qα = 6,207.14(35.94%) β − α(0.014%)	γ727,1621,785 γ40,453,288,328,α6051,6090
212	Bi(250)	25.0(2) m	(8−,9−)	α(67%) β − (33%) β − α(30%)	α6340,6300 γ275
212	Bi(1910.0)	7.0(3) m	≥16	β − (100%)	
213	Bi	45.59(6) m	9/2−	Qβ− = 1,427(97.80%) Qα = 5,982(2.20%)	γ440 γ324,α5869
214	Bi	19.9(4) m	1−	Qβ− = 3,272(99.98%) Qα = 5,616.8(0.02%)	γ609,1764,1120,1238 γ191,α5452,5516
215	Bi	7.6(2) m	(9/2−)	Qβ− = 2,250(100%)	γ294
215	Bi(1347.5)	36.4 s	(25/2−)	IT β−	
216	Bi(0 + x)	2.25(5) m	(6−,7−)	Qβ− = [4,000](<100%)	γ550,419
216	Bi(0 + y)	6.6(21) m	(3)	β−	
217	Bi	98.5(8) s		β−	
218	Bi	33(1) s		β−	

84	Polonium						
	188	Po	0.40(+20–15) ms	0+		$\varepsilon(<100\%)$	
						$\alpha(>0\%)$	
	189	Po	3.5(3) ms	(7/2–)		$\alpha = (\approx 100\%)$	
	190	Po	2.46(5) ms	0+		$Q\alpha = 7,643(100\%)$	$\alpha 7536$
						$Q_{\varepsilon} = [6,100](0.1\%)$	
	191	Po	22(1) ms	(3/2–)		$Q\alpha = 7,471(100\%)$	$\gamma 375, \alpha 6960, 7333$
	191	Po(130)	93(3) ms	(13/2+)		$\alpha(96\%)$	$\gamma 494, \alpha 7378, 6888$
	192	Po	33.2(14) ms	0+		$Q\alpha = 7,320(\sim 99.5\%)$	$\alpha 7167$
						$Q_{\varepsilon} = [5,700](\sim 0.5\%)$	
	193	Po(0 + y)	245(22) ms	(13/2+)		$Q\alpha = 7,100(<100\%)$	$\alpha 6940$
	193	Po(0 + x)	370(+46–40) ms	(3/2–)		$\alpha(<100\%)$	$\alpha 7000$
	194	Po	0.392(4) s	0+		$Q\alpha = 6,987(100\%)$	$\alpha 6843$
	195	Po	4.64(9) s	(3/2–)		$Q\alpha = 6,750(75\%)$	$\alpha 6609$
						$Q_{\varepsilon} = [6,800](25\%)$	
	195	Po(230)	1.92(2) s	(13/2+)		$\alpha(\sim 90\%)$	$\alpha 6699$
						$\varepsilon(\sim 10\%)$	
						$\Pi(<0.01\%)$	
	196	Po	5.8(2) s	0+		$Q\alpha = 6,657(\sim 98\%)$	$\gamma 769, \alpha 6520$
						$Q_{\varepsilon} = [4,600](\sim 2\%)$	
197	Po	84(16) s	(3/2–)		$Q_{\varepsilon} = [6,200](56\%)$		
					$Q\alpha = 6,410(44\%)$	$\alpha 6281$	
197	Po(204)	32(2) s	(13/2+)		$\alpha(84\%)$	$\alpha 6383$	
					$\varepsilon(16\%)$		
					$\Pi(0.01\%)$		
198	Po	1.77(3) m	0+		$Q\alpha = 6,309.1(57\%)$	$\alpha 6182$	
					$Q_{\varepsilon} = [4,020](43\%)$		

Table 22.1 (Continued)

A	Element	Half-life or width	J^{π}	Qmode(%BR){%Abund}	Principal gammas, alphas
199	Po	5.47(15) m	(3/2-)	Q ϵ = [5,600](92.5%) Q α = 6,074.3(7.5%)	γ 246,846,207,546 α 5952
199	Po(310)	4.17(5) m	(13/2+)	ϵ (73.5%) α (24%) Π (2.5%)	γ 1002,1034,362,500 α 6059 γ 238
200	Po	11.51(8) m	0+	Q ϵ = [3,350](88.9%) Q α = 5,981.5(11.1%)	γ 671,618,434,797 α 5862
201	Po	15.6(1) m	3/2-	Q ϵ = [4,880](98.87%) Q α = 5,799.0(1.13%) Π (56.2%)	γ 890,240,904,1187 α 5683 γ 418
201	Po(424.4)	8.96(12) m	13/2+	ϵ (41.4%) α (2.4%)	γ 967,964,412,538 α 5786
202	Po	44.6(4) m	0+	Q ϵ = [2,820](98.08%) Q α = 5,701.0(1.92%)	γ 689,316,166,790 α 5588
203	Po	36.7(5) m	5/2-	Q ϵ = 4,230(99.89%) Q α = 5,496(0.11%)	γ 909,1091,894,215 α 5383
203	Po(640.9)	45(2) s	13/2+	Π (~100%) α (~0.04%)	γ 641
204	Po	3.53(2) h	0+	Q ϵ = 2,330(99.34%) Q α = 5,484.9(0.66%)	γ 884,270,1016,535 α 5377
205	Po	1.74(8) h	5/2-	Q ϵ = 3,530(99.96%) Q α = 5,324(0.04%)	γ 872,1001,850,837 α 5220
205	Po(880.3)	0.645(20) ms	13/2+	Π (100%)	

205	Po(1461.2)	57.4(9) ms	19/2–	IT(100%)	
206	Po	8.8(1) days	0+	Q ϵ = 1,847(94.55%) Q α = 5,326.5(5.45%)	γ 1032,511,286,807 α 5224
207	Po	5.80(2) h	5/2–	Q ϵ = 2,909(99.98%) Q α = 5,215.9(0.02%)	γ 992,743,912,406 α 5115
207	Po(1383.0)	2.79(8) s	19/2–	IT(100%)	γ 814,268,300
208	Po	2.898(2) years	0+	Q α = 5,215.5(100%) Q ϵ = 1,401.3	α 5115 γ 292,571,603,862
209	Po	102(5) years	1/2–	Q α = 4,979.2(99.52%) Q ϵ = 1,893.3(0.48%)	γ 261,263, α 4883,4885 γ 897
210	Po	138.376(2) days	0+	Q α = 5,407.46(100%)	γ 803, α 5304
211	Po	0.516(3) s	9/2+	Q α = 7,594.5(100%)	γ 898,570, α 7450
211	Po(1462)	25.2(6) s	(25/2+)	α (99.98%) IT(0.02%)	γ 900, α 7275
212	Po	0.299(2) μ s	0+	Q α = 8,954.13(100%)	α 8785
212	Po(2922)	45.1(6) s	(18+)	α (99.93%) IT(0.07%)	γ 2610,570, α 11650
213	Po	3.72(12) μ s	9/2+	Q α = 8,537(100%)	γ 779, α 8376
214	Po	164.3(20) μ s	0+	Q α = 7,833.46(100%)	α 7687
215	Po	1.781(4) ms	9/2+	Q α = 7,526.4(100%) Q β – = 720(0.00023%)	γ 439, α 7386
216	Po	0.145(2) s	0+	Q α = 6,906.5(100%)	γ 805, α 6778
217	Po	1.53(5) s	(9/2+)	Q α = 6,660(>95%) Q β – = [1,440](<5%)	α 6537
218	Po	3.098(12) m	0+	Q α = 6,114.68(99.98%) Q β – = 265(0.02%)	α 6002

Table 22.1 (Continued)

A	Element	Half-life or width	J^{π}	Qmode(%BR){%Abund}	Principal gammas, alphas
219	Po	>300 ns		β^-	
220	Po	>300 ns		β^-	
85	Astatine				
191	At	1.7(+11–5) ms	(1/2+)	α (100%)	
191	At(55.0)	2.1(+4–3) ms	(7/2–)	α (100%)	
193	At	28(+5–4) ms	(1/2+)	Q α = 7,530(100%)	
193	At(5.0)	21(5) ms	(7/2–)	α (100%)	
193	At(39.0)	27(+4–3) ms	(13/2+)	α (24%)	
				IT(76%)	
194	At(0 + x)	~40 ms		Q α = [7,310]	
194	At(0 + y)	~250 ms		α	α 7200
195	At	328(20) ms	1/2+	Q α = 7,360(100%)	α 6957
				Q ϵ = [7,900]	
195	At(0 + x)	147(5) ms	7/2–	α (100%)	α 7115,7190
196	At	0.388(7) s	(3+)	Q α = 7,200(95.1%)	α 7055
				ϵ (4.9%)	
197	At	0.388(6) s	(9/2–)	Q α = 7,100(96.1%)	α 6958
				Q ϵ = [7,200](3.9%)	
197	At(52)	2.0(2) s	(1/2+)	α (<100%)	α 6707
				ϵ	
198	At	4.2(3) s	(3+)	Q α = 6,893(90%)	γ 181, α 6754
				Q ϵ = 8,800(10%)	
198	At(102)	1.0(2) s	(10–)	α (84%)	α 6856
				ϵ (16%)	

199	At	7.03(15) s	(9/2 [−])	Q α = 6,780(90%) Q ε = [6,600](10%)	α 6643
200	At	43(1) s	(3 ⁺)	Q α = 6,596.4(52%) Q ε = [7,970](48%)	α 6464
200	At(112)	47(1) s	(7 ⁺)	ε (<57%) α (43%)	γ 666,611,485,565 γ 102, α 6412
200	At(344)	7.3(+26−15) s	(10 [−])	IT(<89.5%) α (~10.5%) ε (<89.5%)	γ 102, α 6537
201	At	85.2(16) s	(9/2 [−])	Q α = 6,473.3(71%) Q ε = [5,800](29%) Q ε = [7,210](82%) Q α = 6,353.7(18%) ε (91.3%) α (8.7%)	α 6344 γ 139, α 6228 γ 677,572,443 α 6135
202	At	184(1) s	(2,3) ⁺	IT(99.7%) ε (0.25%) α (0.1%)	γ 572,677,443,527 γ 249, α 6227
202	At(0 + x)	182(2) s	(7 ⁺)	Q ε = 5,060(69%) Q α = 6,210.3(31%) Q ε = 6,480(96.2%) Q α = 6,069.9(3.8%)	γ 639,642,738,656 α 6087 γ 684,516,426,609 α 5951
202	At(391.7)	0.46(5) s	(10 [−])	IT(100%) Q ε = 4,540(90%) Q α = 6,019.7(10%) Q ε = 5,710(99.1%) Q α = 5,888.4(0.9%)	γ 587 γ 719,669,629,520 α 5902 γ 701,477,396,734 γ 68, α 5703
203	At	7.4(2) m	9/2 [−]		
204	At	9.2(2) m	7 ⁺		
204	At(587.3)	108(10) ms	(10 [−])		
205	At	26.9(8) m	9/2 [−]		
206	At	30.6(13) m	(5) ⁺		

Table 22.1 (Continued)

A	Element	Half-life or width	J^{π}	Qmode(%BR){%Abund}	Principal gammas, alphas
207	At	1.80(4) h	9/2−	Q ϵ = 3,910(91.4%) Q α = 5,873(8.6%)	γ 814,588,301,467 α 5758
208	At	1.63(3) h	6+	Q ϵ = 4,980(99.45%) Q α = 5,751.1(0.55%)	γ 687,660,178,845 α 5640
209	At	5.41(5) h	9/2−	Q ϵ = 3,486(95.9%) Q α = 5,757.3(4.1%)	γ 545,782,790,195 α 5647
210	At	8.1(4) h	(5)+	Q ϵ = 3,981(99.82%) Q α = 5,631.1(0.18%)	γ 1181,245,1483,1437 γ 83,106,167,140, α 5524,5443
211	At	7.214(7) h	9/2−	Q ϵ = 786(58.2%) Q α = 5,982.4(41.8%)	γ 687 γ 670,743, α 5870
212	At	0.314(2) s	(1−)	Q α = 7,828.9(100%) Q ϵ = 1,754(<0.03%) Q β − = 43(<2.0E − 6%)	α 7679,7616
212	At(222)	0.119(3) s	(9−)	α (>99%) IT(<1%)	γ 63, α 7837,7900
213	At	125(6) ns	9/2−	Q α = 9,254(100%)	α 9080
214	At	558(10) ns	1−	Q α = 8,987(100%)	α 8819
215	At	0.10(2) ms	9/2−	Q α = 8,178(100%)	γ 404, α 8026
216	At	0.30(3) ms	1−	Q α = 7,949(100%) Q β − = 2,003(<0.006%) Q ϵ = 469(<3.0E − 7%)	α 7802
217	At	32.3(4) ms	9/2−	Q α = 7,201.9(99.99%) Q β − = 741(0.01%)	γ 259,593, α 7067

86	218	At	1.5(3) s			$Q\alpha = 6,874(99,9\%)$	$\alpha 6693$
	219	At	56(3) s			$Q\beta^- = 2,883(0,1\%)$	
	220	At	3.71(4) m	3		$Q\alpha = 6,390(\sim 97\%)$	$\alpha 6275$
	221	At	2.3(2) m			$Q\beta^- = 1,700(\sim 3\%)$	
	222	At	54(10) s			$Q\beta^- = [3,650](92\%)$	$\gamma 241,293,422$
	223	At	50(7) s			$Q\alpha = 6,050(8\%)$	$\alpha 5943$
		Radon					
	193	Rn	1.15(27) ms	(3/2-)		$\alpha = (100\%)$	
	194	Rn	0.78(16) ms	0+		$\alpha = (100\%)$	
	195	Rn	6(+3-2) ms	3/2-		$\alpha = (100\%)$	
	195	Rn(59)	5(+3-2) ms	13/2+		$\alpha = (100\%)$	
	196	Rn	4.4(+13-9) ms	0+		$Q\alpha = 7,620(99,9\%)$	$\alpha 7465$
	197	Rn	65(+25-14) ms	(3/2-)		$\varepsilon(\approx 0,06\%)$	
	197	Rn(0 + x)	19(+8-4) ms	(13/2+)		$Q\alpha = 7,410(100\%)$	$\alpha 7261$
	198	Rn	65(3) ms	0+		$\alpha(100\%)$	$\alpha 7370$
	199	Rn	0.59(3) s	(3/2-)		$Q\alpha = 7,352$	$\alpha 7205$
						$Q\varepsilon = [5,600]$	
	199	Rn(x)	0.31(2) s	(13/2+)		$Q\alpha = 7,140(94\%)$	$\alpha 6989$
	200	Rn	1.03(+20-11) s	0+		$Q\varepsilon = [7,200](6\%)$	
						$\alpha(97\%)$	$\alpha 7059$
						$\varepsilon(3\%)$	
						$Q\alpha = 7,043(86\%)$	$\alpha 6902$
						$Q\varepsilon = [5,000](14\%)$	

Table 22.1 (Continued)

A	Element	Half-life or width	J^{π}	Qmode(%BR){%Abund}	Principal gammas, alphas
201	Rn	7.0(4) s	(3/2 ⁻)	Q α = 6.860 Q ϵ = [6,600]	α 6724
201	Rn(280)	3.8(1) s	(13/2 ⁺)	α (~90%) ϵ (~10%) Π (~0%)	α 6772
202	Rn	9.7(1) s	0 ⁺	Q α = 6,773.6(78%) Q ϵ = [4,440](22%)	α 6640
203	Rn	44(2) s	(3/2,5/2) ⁻	Q α = 6,629.9(66%) Q ϵ = [6,000](34%)	α 6499
203	Rn(362)	26.9(5) s	(13/2 ⁺)	α (75%) ϵ (25%)	α 6549
204	Rn	1.17(18) m	0 ⁺	Q α = 6,545.6(73%) Q ϵ = [3,820](27%)	α 6419
205	Rn	170(4) s	5/2 ⁻	Q ϵ = [5,250](75.4%) Q α = 6,390(24.6%)	γ 265,465,620,675 α 6262
206	Rn	5.67(17) m	0 ⁺	Q α = 6,383.8(62%) Q ϵ = [3,320](38%)	α 6260 γ 498,325,387,773
207	Rn	9.25(17) m	5/2 ⁻	Q ϵ = 4,610(79%) Q α = 6,251.0(21%)	γ 345,747,403,674 α 6131
208	Rn	24.35(14) m	0 ⁺	Q α = 6,260.5(62%) Q ϵ = 2,840(38%)	α 6140 γ 427,251,350,287
209	Rn	28.5(10) m	5/2 ⁻	Q ϵ = 3,930(83%) Q α = 6,155.3(17%)	γ 408,746,337,689 γ 143,384, α 6039
210	Rn	2.4(1) h	0 ⁺	Q α = 6,158.5(96%) Q ϵ = 2,374(4%)	α 6041 γ 458,649,571,73

87	211	Rn	14.6(2) h	1/2–	Q ϵ = 2,892(72.6%) Q α = 5,965.2(27.4%)	γ 674,1363,678,442 γ 69,168,236, α 5784,5852
	212	Rn	23.9(12) m	0+	Q α = 6,385(100%)	α 6264
	213	Rn	19.5(1) ms	(9/2+)	Q α = 8,243(100%)	α 8088
	214	Rn	0.27(2) μ s	0+	Q α = 9,208(100%)	α 9036
	215	Rn	2.30(10) μ s	9/2+	Q α = 8,839(100%)	α 8674
	216	Rn	45(5) μ s	0+	Q α = 8,200(100%)	α 8050
	217	Rn	0.54(5) ms	9/2+	Q α = 7,889(100%)	α 7741
	218	Rn	35(5) ms	0+	Q α = 7,263.0(100%)	γ 609, α 7129
	219	Rn	3.96(1) s	5/2+	Q α = 6,946.1(100%)	γ 271,402, α 6819,6553
	220	Rn	55.6(1) s	0+	Q α = 6,404.67(100%)	γ 550, α 6288
	221	Rn	25(2) m	7/2+	Q β – = [1,130](78%) Q α = 6,146(22%)	γ 186,150,217,108 γ 254,265, α 6035,5786
	222	Rn	3.8235(3) days	0+	Q α = 5,590.3(100%)	γ 510, α 5490
	223	Rn	24.3(4) m	7/2	Q β – = [1,900](100%)	γ 593,417,636,655
	224	Rn	107(3) m	0+	Q β – = [800](100%)	γ 261,266,202,328
	225	Rn	4.66(4) m	7/2–	Q β – = [2,600](100%)	γ 207
	226	Rn	7.4(1) m	0+	Q β – = [1,400](100%)	
	227	Rn	20.8(7) s		Q β – = [3,300](100%)	γ 162,739,686,805
	228	Rn	65(2) s	0+	Q β – = [2,200](100%)	γ 125,63,156,112
		Francium				
87	199	Fr	12(+10–4) ms		α (>0%) ϵ	
	200	Fr(x)	49(4) ms	(3+)	Q α = 7,630(100%)	α 7468
	200	Fr(200.0)	0.57(+27–14) s	(10–)	α (100%)	

Table 22.1 (Continued)

A	Element	Half-life or width	J^{π}	Qmode(%BR){%Abund}	Principal gammas, alphas
201	Fr	62(5) ms	(9/2 [−])	Q α = 7,540(100%) Q ε = [7,900]	α 7388
201	Fr(0 + x)	19(+19−6) ms	(1/2 ⁺)	Q α = 7,540(100%)	α 7388
202	Fr	0.30(5) s	(3 ⁺)	Q α = 7,389(100%) Q ε = 9,400	α 7237
202	Fr(102 + x)	0.29(5) s	(10 [−])	α (100%)	α 7237
203	Fr	0.55(2) s	(9/2 [−])	Q α = 7,280(\approx 100%) Q ε = [7,200]	α 7133
204	Fr	1.7(3) s	(3 ⁺)	Q α = 7,170(\sim 80%) Q ε = [8,600](\sim 20%)	γ 113, α 7031
204	Fr(41)	2.6(3) s	(7 ⁺)	α (<100%)	α 6969
204	Fr(316)	\approx 1 s	(10 [−])	α (<100%) IT	γ 231, α 7013
205	Fr	3.80(3) s	(9/2 [−])	Q α = 7,050(\leq 100%) Q ε = [6,500]($<$ 1%)	α 6915
206	Fr	\approx 16 s	(2 ⁺ ,3 ⁺)	Q α = 6,926(\sim 84%) Q ε = [7,760](\sim 16%)	
206	Fr(x)	\approx 16 s	(7 ⁺)	α (84%) ε (16%)	α 6790 γ 575,559,629
206	Fr(531)	0.7(1) s	(10 [−])	α (5%) IT(95%)	γ 392, α 6930
207	Fr	14.8(1) s	9/2 [−]	Q α = 6,900(95%) Q ε = 5,710(5%)	α 6768

208	Fr	59.1(3) s	7+	$Q\alpha = 6,770(89\%)$	$\alpha 6641$
				$Q\beta = 6,990(11\%)$	$\gamma 636,779,325,553$
209	Fr	50.0(3) s	9/2-	$Q\alpha = 6,777(89\%)$	$\alpha 6646$
				$Q\beta = 5,160(11\%)$	
210	Fr	3.18(6) m	6+	$Q\alpha = 6,700(60\%)$	$\alpha 6543$
				$Q\beta = 6,258(40\%)$	$\gamma 644,817,203,901$
211	Fr	3.10(2) m	9/2-	$Q\alpha = 6,660(>80\%)$	$\alpha 6534$
				$Q\beta = 4,605(<20\%)$	$\gamma 540,918,281,983$
212	Fr	20.0(6) m	5+	$Q\beta = 5,130(57\%)$	$\gamma 1275,228,1186,138$
				$Q\alpha = 6,529,0(43\%)$	$\gamma 124,84,72,40,\alpha 6262,6383$
213	Fr	34.82(14) s	9/2-	$Q\alpha = 6,905.1(99.44\%)$	$\alpha 6775$
				$Q\beta = 2,148(0.56\%)$	
214	Fr	5.0(2) ms	(1-)	$Q\alpha = 8,589(100\%)$	$\alpha 8427$
214	Fr(122)	3.35(5) ms	(8-)	$\alpha(100\%)$	$\alpha 8478,8547$
215	Fr	86(5) ns	9/2-	$Q\alpha = 9,540(100\%)$	$\alpha 9360$
216	Fr	0.70(2) μ s	(1-)	$Q\alpha = 9,175(100\%)$	$\alpha 9005$
				$Q\beta = 2,729(<2.0E - 7\%)$	
217	Fr	19(3) μ s	9/2-	$Q\alpha = 8,469(100\%)$	$\alpha 8315$
218	Fr	1.0(6) ms	1-	$Q\alpha = 8,014.3(100\%)$	$\alpha 7867$
218	Fr(86)	22.0(5) ms		$\alpha(<100\%)$	$\alpha 7615,7680$
				IT	
219	Fr	20(2) ms	9/2-	$Q\alpha = 7,448.5(100\%)$	$\gamma 352,517,170,\alpha 7312$
220	Fr	27.4(3) s	1+	$Q\alpha = 6,800.7(99.65\%)$	$\gamma 45,161,106,153,\alpha 6677,6633$
				$Q\beta - = 1,209(0.35\%)$	$\gamma 178,413,235$
221	Fr	4.9(2) m	5/2-	$Q\alpha = 6,457.9(100\%)$	$\gamma 218,\alpha 6341,6126$
				$Q\beta - = 315(<0.1\%)$	
				$^{14}\text{C}(9E - 13\%)$	

Table 22.1 (Continued)

A	Element	Half-life or width	$J\pi$	Qmode(%BR){%Abund}	Principal gammas, alphas
222	Fr	14.2(3) m	2-	Q β^- = 2,033(100%)	γ 206,111
223	Fr	22.00(7) m	3/2(-)	Q β^- = 1,149.1(99.99%) Q α = 5,430(0.006%)	γ 50,80 α 5340
224	Fr	3.33(10) m	1-	Q β^- = 2,830(100%)	γ 216,132,837,1341
225	Fr	3.95(14) m	3/2-	Q β^- = 1,865(100%)	γ 182,32,225,75
226	Fr	49(1) s	1-	Q β^- = 3,670(100%)	γ 254,186,254
227	Fr	2.47(3) m	1/2+	Q β^- = 2,480(100%)	γ 90,586,64,434
228	Fr	38(1) s	2-	Q β^- = [4,340](<100%)	γ 474,474,410,141
229	Fr	50.2(4) s	(1/2+)	Q β^- = [3,400](100%)	
230	Fr	19.1(5) s		Q β^- = [5,100](100%)	γ 711,129,728,677
231	Fr	17.6(6) s	(1/2+)	Q β^- = [3,900](100%)	γ 433,454,96
232	Fr	5.5(6) s	(5)	Q β^- = [5,600](100%)	
88	Radium				
	Ra	1.6(+77-7) ms	13/2+	α (100%)	
	Ra	16(+30-7) ms	0+	α (100%)	α 7860
	Ra	31(+17-9) ms	(3/2-)	Q α = 7,730(100%)	α 7577
	Ra(0 + x)	24(+6-4) ms	(13/2+)	α (100%)	α 7615
	Ra	59(+12-9) ms	0+	Q α = 7,636	α 7486
	Ra	0.21(+6-4) s	(3/2-)	Q ε = [7,000] Q α = 7,500	
	Ra(0 + x)	0.17(+6-4) s	(13/2+)	α	
	Ra	0.24(2) s	0+	Q α = 7,416(100%)	α 7272
	Ra	1.3(2) s	(5/2-,3/2-)	Q α = 7,270(~90%) Q ε = [6,400](~10%)	α 7133

207	Ra(470.0)	55(10) ms	(13/2+)	IT(85%) α (15%) ε (~0.35%) $Q\alpha = 7,273(95\%)$ $Q\varepsilon = [4,320](5\%)$ $Q\alpha = 7,150(\sim 90\%)$ $Q\varepsilon = [5,620](\sim 10\%)$ $Q\alpha = 7,157(\sim 96\%)$ $Q\varepsilon = [3,770](\sim 4\%)$ $Q\alpha = 7,046(>93\%)$ $Q\varepsilon = 5,000(<7\%)$ $Q\alpha = 7,031.9(\sim 85\%)$ $Q\varepsilon = 3,340(\sim 15\%)$ $Q\alpha = 6,861(80\%)$ $Q\varepsilon = 3,890(20\%)$	$\alpha 6548$ $\alpha 7133$ $\alpha 7008$ $\alpha 7019$ $\alpha 6910$ $\alpha 6899$ $\gamma 110,215,\alpha 6624,6731$ $\gamma 546,1063,161$ $\gamma 215,110,105,\alpha 8466,8357$ $\alpha 7137$ $\alpha 8699$ $\alpha 9349$ $\alpha 8992$ $\alpha 8389$ $\gamma 805,\alpha 7678,7988$ $\gamma 465,\alpha 7455$
208	Ra	1.3(2) s	0+		
209	Ra	4.6(2) s	5/2-		
210	Ra	3.7(2) s	0+		
211	Ra	13(2) s	5/2(-)		
212	Ra	13.0(2) s	0+		
213	Ra	2.73(5) m	1/2-		
213	Ra(1770)	2.15(7) ms	(17/2-)		
214	Ra	2.46(3) s	0+		
215	Ra	1.55(7) ms	(9/2+)		
216	Ra	182(10) ns	0+		
217	Ra	1.6(2) μ s	(9/2+)		
218	Ra	25.2(3) μ s	0+		
219	Ra	10(3) ms	(7/2)+		
220	Ra	18(2) ms	0+		

Table 22.1 (Continued)

A	Element	Half-life or width	$J\pi$	Qmode(%BR){%Abund}	Principal gammas, alphas
221	Ra	28(2) s	5/2+	Q α = 6,884(100%) ¹⁴ C(1E – 12%)	γ 149,93,174, α 6613,6761
222	Ra	38.0(5) s	0+	Q α = 6,681(100%) ¹⁴ C(3.0E – 8%)	γ 324, α 6559
223	Ra	11.43(5) days	3/2+	Q α = 5,979.3(100%)	γ 269,154,324,144, α 5716,5607
224	Ra	3.6319(23) days	0+	Q α = 5,788.87(100%) ¹⁴ C(4.0E – 9%)	γ 241, α 5685
225	Ra	14.9(2) days	1/2+	Q β^- = 358(100%)	γ 40
226	Ra	1,600(7) years	0+	Q α = 4,870.63(100%) ¹⁴ C(3.2E – 9%)	γ 186, α 4784
227	Ra	42.2(5) m	3/2+	Q β^- = 1,326.2(100%)	γ 27,300,303,284
228	Ra	5.75(3) years	0+	Q β^- = 45.9(100%)	γ 14,16
229	Ra	4.0(2) m	5/2(+)	Q β^- = 1,760(100%)	
230	Ra	93(2) m	0+	Q β^- = 990(100%)	γ 72,63,203,470
231	Ra	103(3) s	(5/2+)	Q β^- = [2,500](100%)	γ 410,205,469,456
232	Ra	4.2(8) m	0+	Q β^- = [1,600](100%)	γ 471,98,479,105
233	Ra	30(5) s		Q β^- = [3,200](100%)	
234	Ra	30(10) s	0+	Q β^- = [2,000](100%)	
89	Actinium				
	Ac(0 + y)	22(+9 – 5) ms	(3+)	α (100%)	
	Ac(0 + z)	33(+22 – 9) ms	(10–)	α (100%)	
	Ac	27(+11 – 6) ms	(9/2–)	Q α = 7,860	α 7712

208	Ac	95(+24–16) ms	(3+)	$Q_{\varepsilon} = [9,040](1\%)$ $Q_{\alpha} = 7,721$	$\alpha 7572$
208	Ac(506.0)	25(+9–5) ms	(10–)	$IT(<10\%)$ $\varepsilon(1\%)$ α	$\alpha 7758$ $\alpha 7585$
209	Ac	0.10(5) s	(9/2–)	$Q_{\alpha} = 7,730(\sim 99\%)$ $Q_{\varepsilon} = [7,100](\sim 1\%)$	$\alpha 7462$
210	Ac	0.35(5) s		$Q_{\alpha} = 7,610(\sim 96\%)$ $Q_{\varepsilon} = [8,210](\sim 4\%)$	$\alpha 7480$
211	Ac	0.21(3) s		$Q_{\alpha} = 7,620(100\%)$	$\alpha 7379$
212	Ac	0.93(5) s		$Q_{\alpha} = 7,520(\sim 57\%)$ $Q_{\varepsilon} = 7,480(\sim 43\%)$	$\alpha 7364$
213	Ac	738(16) ms		$Q_{\alpha} = 7,500(<100\%)$	$\alpha 7214, 7082$
214	Ac	8.2(2) s		$Q_{\alpha} = 7,350(>89\%)$ $Q_{\varepsilon} = 6,340(<11\%)$	$\alpha 7604$
215	Ac	0.17(1) s	9/2–	$Q_{\alpha} = 7,750(99.91\%)$ $Q_{\varepsilon} = 3,490(0.09\%)$	$\alpha 9072, 8992$
216	Ac	440(16) μ s	(1–)	$Q_{\alpha} = 9,243(100\%)$ $\alpha(100\%)$	$\alpha 9650$
216	Ac	441(7) μ s	(9–)	$Q_{\alpha} = 9,832(100\%)$ $Q_{\varepsilon} = 2,819(<2\%)$	$\alpha 9205$
217	Ac	69(4) ns	9/2–	$Q_{\alpha} = 9,380(100\%)$ $Q_{\alpha} = 8,830(100\%)$	$\gamma 133, 93, 343, 160, \alpha 7855, 7709$
218	Ac	1.08(9) μ s	(1–)	$Q_{\alpha} = 8,350(100\%)$ $Q_{\varepsilon} = 3,480(0.0005\%)$	$\alpha 7645, 7440$
219	Ac	11.8(15) μ s	9/2–		
220	Ac	26.4(2) ms	(3–)		
221	Ac	52(2) ms	(3/2–)		

Table 22.1 (Continued)

A	Element	Half-life or width	J^{π}	Qmode(%BR){%Abund}	Principal gammas, alphas
222	Ac	5.0(5) s	1−	Q α = 7,137.4(99%) Q ε = 2,298(1%)	α 7009
222	Ac(0 + x)	63(3) s		α (>88%) IT(<10%) ε (>0.7%)	α 6810,7000
223	Ac	2.10(5) m	(5/2−)	Q α = 6,783.1(99%) Q ε = 586(1%)	γ 99,191,84,434, α 6647,6662
224	Ac	2.78(17) h	0−	Q ε = 1,403(90.9%) Q α = 6,326.9(9.1%)	γ 216,131 γ 157,141,144,261, α 6142,6060
225	Ac	10.0(1) days	(3/2−)	Q β − = 232(<1.6%) Q α = 5,935.2(100%)	γ 100,150,100,188, α 5830,5793
226	Ac	29.37(12) h	(1)	$^{14}\text{C}(6\text{E} - 10\%)$ Q β − = 1,117(83%) Q ε = 640(17%) Q α = 5,536(0.006%)	γ 230,158 γ 254,186 α 5399
227	Ac	21.772(3) years	3/2−	Q β − = 44.8(98.62%) Q α = 5,042.19(1.38%)	γ 38 γ 100,160,6987, α 4953,4941
228	Ac	6.15(2) h	3+	Q β − = 2,127(100%)	γ 911,969,338,965
229	Ac	62.7(5) m	(3/2+)	Q β − = 1,100(100%)	γ 165,569,262,146
230	Ac	122(3) s	(1+)	Q β − = 2,700(100%)	γ 455,508,1244,1348
231	Ac	7.5(1) m	(1/2+)	Q β − = 2,100(100%)	γ 282,307,221,186

	232	Ac	119(5) s	(1+)	$Q\beta^- = 3,700(100\%)$	$\gamma 665,1899,1959,1948$
	233	Ac	145(10) s	(1/2+)	$Q\beta^- = [2,800](100\%)$	$\gamma 523,540$
	234	Ac	44(7) s		$Q\beta^- = [4,500](100\%)$	$\gamma 1847,1912,689,1954$
	235	Ac	60(4) s		$Q\beta^- = [3,400](100\%)$	
	236	Ac	≈ 2 m		$Q\beta^- = [5,100]$	
90		Thorium				
	209	Th	3.8(+69–15) ms	(5/2–)	α	
	210	Th	9(+17–4) ms	0+	$Q\alpha = 8,053(99\%)$	$\alpha 7899$
					$\varepsilon(1\%)$	
	211	Th	0.04(+3–1) s		$Q\varepsilon = [6,700]$	
					$Q\alpha = 7,940$	$\alpha 7792$
	212	Th	30(+20–10) ms	0+	$Q\alpha = 7,952(100\%)$	$\alpha 7802$
					$Q\varepsilon = [4,760](\sim 0.3\%)$	
	213	Th	144(21) ms		$Q\alpha = 7,840(<100\%)$	$\alpha 7692$
	214	Th	100(25) ms	0+	$Q\alpha = 7,826(100\%)$	$\alpha 7678$
	215	Th	1.2(2) s	(1/2–)	$Q\alpha = 7,666(100\%)$	$\alpha 7395,7524$
	216	Th	26.0(2) ms	0+	$Q\alpha = 8,071(100\%)$	$\alpha 7921$
					$Q\varepsilon = 2,170(\sim 0.01\%)$	
	217	Th	0.241(5) ms	(9/2+)	$Q\alpha = 9,424(100\%)$	$\alpha 9250$
	218	Th	117(9) ns	0+	$Q\alpha = 9,849(100\%)$	$\alpha 9666$
	219	Th	1.05(3) μ s		$Q\alpha = 9,510(100\%)$	$\alpha 9340$
	220	Th	9.7(6) μ s	0+	$Q\alpha = 8,953(100\%)$	$\alpha 8790$
					$Q\varepsilon = 910(2.0\text{E} - 7\%)$	
	221	Th	1.68(6) ms	(7/2+)	$Q\alpha = 8,628(100\%)$	$\alpha 8146,8472$
	222	Th	2.237(13) ms	0+	$Q\alpha = 8,129(100\%)$	$\alpha 7982$

Table 22.1 (Continued)

A	Element	Half-life or width	$J\pi$	Qmode(%BR){%Abund}	Principal gammas, alphas
223	Th	0.60(2) s	(5/2)+	Q α = 7,567(100%)	γ 140,152,114,97, α 7298,7286
224	Th	0.81(10) s	0+	Q α = 7,304(100%)	γ 177, α 7170,7000
225	Th	8.72(4) m	(3/2)+	Q α = 6,921.4(~90%)	γ 246,359,306,53, α 6478,6441
227	Th	18.68(9) days	1/2+	Q α = 6,146.43(100%)	γ 236,50,256,330, α 6038,5978
228	Th	1.9116(16) years	0+	Q α = 5,520.12(100%)	γ 84,216,132, α 5423,5340
229	Th	7.880(120) years	5/2+	²⁰ O(1E – 11%) Q α = 5,167.6(100%)	γ 194,211,86,86, α 4845,4901
230	Th	75,380(300) years	0+	Q α = 4,770.0(100%) SF(<4E – 11%)	γ 68,144, α 4687,4621
231	Th	25.52(1) h	5/2+	Q β – = 389.5(100%) Q α = 4,213.3(~4E – 11%)	γ 26,84
232	Th	1.405(6)E10 years	0+	Q α = 4,082.8(100%) SF(1.2E – 8%) {100%} Ne	γ 64, α 4012,3947
233	Th	21.83(4) m	1/2+	Q β – = 1,245.1(100%)	γ 86,29,459,95
234	Th	24.10(3) days	0+	Q β – = 273(100%)	γ 63,92,93
235	Th	7.2(1) m	(1/2+)	Q β – = 1,930(100%)	γ 417,727,696,645
236	Th	37.3(15) m	0+	Q β – = [1,000](100%)	γ 111,647,196,434

	237	Th	4.7(6) m		(5/2+)	$Q\beta^- = [2,600](100\%)$	
	238	Th	9.4(20) m		0+	$Q\beta^- = [1,600]$	γ_{89}
91		Protactinium					
	212	Pa	5.1(+61–19) ms			α	
	213	Pa	5.3(+40–16) ms			$Q\alpha = 8,390(100\%)$	
	214	Pa	17(3) ms			$Q\alpha = 8,270(100\%)$	
	215	Pa	14(2) ms			$Q\alpha = 8,240(100\%)$	
	216	Pa	0.15(+6–4) s			$Q\alpha = 8,100(\sim 98\%)$	$\alpha_{7865,7812}$
						$Q\epsilon = 7,510(\sim 2\%)$	
	217	Pa	3.6(8) ms			$Q\alpha = 8,490(100\%)$	α_{8340}
	217	Pa(1850)	1.2(2) ms			$\alpha(100\%)$	α_{10160}
	218	Pa	0.11(2) ms			$Q\alpha = 9,790(100\%)$	$\alpha_{9614,9535}$
	219	Pa	53(10) ns	9/2–		$Q\alpha = 10,080(100\%)$	α_{9900}
	220	Pa(0 + x)	0.78(16) μ s			$Q\alpha = 9,830(100\%)$	α_{9650}
	221	Pa	5.9(17) μ s	9/2–		$Q\alpha = 9,250(100\%)$	α_{9080}
	222	Pa	3.3(3) ms			$Q\alpha = [8,850](100\%)$	$\alpha_{8540,8330}$
	223	Pa	5.1(6) ms			$Q\alpha = 8,340(100\%)$	$\alpha_{8178,8011}$
	224	Pa	0.85(2) s			$Q\alpha = 7,694(100\%)$	$\gamma_{195,41,153,165},$ $\alpha_{7488,7405}$
	225	Pa	1.7(2) s			$Q\alpha = 7,390(100\%)$	α_{7245}
	226	Pa	1.8(2) m			$Q\alpha = 6,987(74\%)$	$\alpha_{6864,6824}$
						$Q\epsilon = 2,834(26\%)$	
	227	Pa	38.3(3) m	(5/2–)		$Q\alpha = 6,580.0(85\%)$	$\gamma_{65,110}, \alpha_{6466,6416}$
						$Q\epsilon = 1,019(15\%)$	$\gamma_{204,151}, \alpha_{56,220}$
	228	Pa	22(1) h	3+		$Q\epsilon = 2,148(98\%)$	$\gamma_{911,463,969,965}$

Table 22.1 (Continued)

	A	Element	Half-life or width	J^{π}	Qmode(%BR){%Abund}	Principal gammas, alphas
					$Q\alpha = 6,264.5(2\%)$	$\gamma 308,304,317,$ $\alpha 6076,6104$
	229	Pa	1.50(5) days	(5/2+)	$Q\epsilon = 310(99.52\%)$ $Q\alpha = 5,836(0.48\%)$	$\gamma 119,117,42,148$ $\gamma 40,65,75,116,$ $\alpha 5580,5670$
	230	Pa	17.4(5) days	(2-)	$Q\epsilon = 1,310(91.6\%)$ $Q\beta^- = 564(8.4\%)$ $Q\alpha = 5,439.4(0.0032\%)$	$\gamma 952,918,455,899$ $\gamma 315,367,384,52$ $\alpha 5345,5326$
	231	Pa	32,760(110) years	3/2-	$Q\alpha = 5,149.9(100\%)$ $SF(<3E - 10\%)$	$\gamma 27,300,303,284,$ $\alpha 5014,4951$
	232	Pa	1.32(2) days	(2-)	$Q\beta^- = 1,337(100\%)$ $Q\epsilon = 495(0.003\%)$	$\gamma 969,894,150,454$
	233	Pa	26.975(13) days	3/2-	$Q\beta^- = 570.1(100\%)$	$\gamma 312,300,341$
	234	Pa	6.70(5) h	4+	$Q\beta^- = 2,195(100\%)$	$\gamma 131,946,883,570$
	234	Pa(73.9 + x)	1.159(11) m	(0-)	$\beta - (99.84\%)$ $IT(0.16\%)$	$\gamma 1001,766$ $\gamma 74$
	235	Pa	24.44(11) m	(3/2-)	$Q\beta^- = 1,410(100\%)$	$\gamma 652$
	236	Pa	9.1(1) m	1(-)	$Q\beta^- = 2,900(100\%)$	$\gamma 642,688,1763$
	237	Pa	8.7(2) m	(1/2+)	$Q\beta^- = 2,250(100\%)$	$\gamma 854,865,529,541$
	238	Pa	2.27(9) m	(3-)	$Q\beta^- = 3,460(100\%)$ $SF(<2.6E - 6\%)$	$\gamma 1015,1015,635,680$
	239	Pa	1.8(5) h	(3/2)	$Q\beta^- = [2,600](100\%)$	
	240	Pa	≈ 2 m		$Q\beta^- = [4,100]$	

92	Uranium							
217	U	16(+21–6) ms				α		
218	U	0.51(+17–10) ms	0+			$Q\alpha = 8,786(100\%)$		$\alpha 8625$
218	U(2105)	0.56(+26–14) ms	(8+)			$Q\alpha = 8,786(100\%)$		
219	U	42(+34–13) μ s				$Q\alpha = 9,860(100\%)$		$\alpha 9680$
220	U	≈ 60 ns	0+			$Q\alpha = [10,300]$		
						$Q\epsilon = [2,640]$		
221	U	≈ 0.7 μ s	(9/2+)			$Q\alpha = [9,950]$		
						$Q\epsilon = [4,180]$		
222	U	1.0(+10–4) μ s	0+			$Q\alpha = [9,500](100\%)$		
223	U	18(+10–5) μ s				$Q\alpha = 8,940(100\%)$		$\alpha 8780$
						$Q\epsilon = 3,500(0.2\%)$		
224	U	0.9(3) ms	0+			$Q\alpha = 8,620(100\%)$		$\alpha 8466$
225	U	84(4) ms				$Q\alpha = 8,020(100\%)$		$\alpha 7875$
226	U	0.35(15) s	0+			$Q\alpha = 7,715(100\%)$		$\alpha 7570,7420$
227	U	1.1(1) m	(3/2+)			$Q\alpha = 7,211(100\%)$		$\gamma 247,310,259,209,$ $\alpha 6860,7060$
228	U	9.1(2) m	0+			$Q\alpha = 6,804(>95\%)$		$\gamma 246,187,152,$ $\alpha 6680,6590$
						$Q\epsilon = 307(<5\%)$		
229	U	58(3) m	(3/2+)			$Q\epsilon = 1,311(\sim 80\%)$		$\gamma 123,199,88,248$
						$Q\alpha = 6,475(\sim 20\%)$		$\alpha 6360,6332$
230	U	20.8 days	0+			$Q\alpha = 5,992.7(100\%)$		$\gamma 72,154,230,158,\alpha 5888,5818$
						SF		
231	U	4.2(1) days	(5/2–)			$Q\epsilon = 382(100\%)$		$\gamma 26,84$
						$Q\alpha = 5,577(\sim 0.004\%)$		$\gamma 68,53,64,265,\alpha 5456,5471$

Table 22.1 (Continued)

A	Element	Half-life or width	J^{π}	Qmode(% α R){%Abund}	Principal gammas, alphas
232	U	68.9(4) years	0+	Q α = 5413.55(100%) Ne(9E – 10%) SF(<1E – 12%)	γ 58,129, α 5320,5263
233	U	1.592(2)E5 years	5/2+	Q α = 4,908.6(100%) Ne(7E – 11%) SF(<6E – 11%)	γ 42,97,55,29, α 4824,4784
234	U	2.455(6)E5 years	0+	Q α = 4,858.5(100%) SF(1.6E – 9%) Mg(1E – 11%) Ne(9E – 12%)	γ 53,121, α 4775,4722
235	U(0.08)	7.038(5)E8 years	7/2–	Q α = 4,678.7(100%) SF(7.0E – 9%) {0.7200(51)%} Ne(8E – 10%) IT(100%)	γ 186,144, α 4398,4366
235	U	\approx 26 m	1/2+		
236	U	2.342(4)E7 years	0+	Q α = 4,572.0(100%) SF(9.4E – 8%) ³⁰ Mg	γ 49,113, α 4494,4445
237	U	6.75(1) days	1/2+	Q β – = 518.6(100%)	γ 60,208
238	U	4.468(3)E9 years	0+	Q α = 4,270(100%) SF(0.000054%) {99.274(11)%}	γ 50,114, α 4198,4151
239	U	23.45(2) m	5/2+	Q β – = 1,263.5(100%)	γ 75
240	U	14.1(1) h	0+	Q β – = 388(100%)	γ 44,190,67,169

241	U	≈5 m			Qβ− = [1,900]		
242	U	16.8(5) m	0+		Qβ− = [1,200](100%)		γ68,56,585,573
93	Neptunium						
	Np	>2 μs	(9/2−)		Qα = 8,790(100%)		
	Np	35(10) ms			Qα = 8,200(100%)		α8000,8060
	Np	0.51(6) s			Qα = 7,816(100%)		α7650,7677
	Np	61.4(14) s			Qε = [4,480](60%)		
					Qα = [7,420](40%)		
	Np	4.0(2) m			Qα = 7,010(68%)		α6890
					Qε = 2,560(32%)		
	Np	4.6(3) m			Qε = 3,620(<97%)		
					Qα = 6,780(>3%)		α6660
231	Np	48.8(2) m	(5/2)		Qε = 1,810(98%)		γ371,348,264,485
					Qα = 6,370(2%)		α6258
232	Np	14.7(3) m	(4+)		Qε = [2,750](100%)		γ327,820,867,864
233	Np	36.2(1) m	(5/2+)		Qε = 1,030(100%)		γ312,299,547,507
					Qα = 5,630(<0.01%)		
234	Np	4.4(1) days	(0+)		Qε = 1,810(100%)		γ1558,1527,1602,1435
235	Np	396.1(12) days	5/2+		Qε = 123.7(100%)		
					Qα = 5,191.9(0.0026%)		γ84,81,α5025,5008
236	Np	1.53(3)E5 years	(6−)		Qε = 930(87.3%)		γ160,104
					Qβ− = 480(12.5%)		γ158,103
					Qα = 5,010(0.16%)		
236	Np(60)	22.5(4) h	1		ε(50%)		γ642,688
					β − (50%)		γ45
237	Np	2.144(7)E6 years	5/2+		Qα = 4,959.1(100%)		γ29,86,α4788,4771
					SF(<2E − 10%)		

Table 22.1 (Continued)

A	Element	Half-life or width	J^{π}	Qmode(%BR){%Abund}	Principal gammas, alphas
238	Np	2.117(2) days	2+	$Q\beta^- = 1,292.0(100\%)$	$\gamma 984, 1029, 1026, 924$
239	Np	2.356(3) days	5/2+	$Q\beta^- = 721.8(100\%)$	$\gamma 106, 278, 228, 210$
240	Np	61.9(2) m	(5+)	$Q\beta^- = 2,200(100\%)$	$\gamma 566, 974, 601, 896$
240	Np(x)	7.22(2) m	1(+)	$\beta^- - (99.88\%)$	$\gamma 555, 597$
				IT(0.12%)	
241	Np	13.9(2) m	5/2+	$Q\beta^- = 1,310(100\%)$	$\gamma 175, 133, 519$
242	Np	2.2(2) m	(1+)	$Q\beta^- = [2,700](100\%)$	$\gamma 736, 780, 1473, 1137$
242	Np(0 + x)	5.5(1) m	(6+)	$\beta^- - (100\%)$	$\gamma 786, 945, 159, 265$
243	Np	1.85(15) m	(5/2-)	$Q\beta^- = [2,120](100\%)$	$\gamma 288$
244	Np	2.29(16) m	(7-)	$Q\beta^- = [3,400](100\%)$	
94	Plutonium				
	Pu	1.1(+20-5) s	0+	$Q\alpha = 7,950(100\%)$	$\alpha 7810$
	Pu	90(+71-27) s	(3/2+)	$Q\alpha = 7,590(100\%)$	
	Pu	102(10) s	0+	$Q\alpha = 7,175(\leq 100\%)$	$\alpha 7050$
	Pu	8.6(5) m	(3/2+)	$Q\varepsilon = [2,820](< 99.8\%)$	
				$Q\alpha = [7,000](> 0.2\%)$	
	Pu	33.8(7) m	0+	$Q\varepsilon = [1,010](90\%)$	
				$Q\alpha = 6,716(10\%)$	$\alpha 6600, 6542$
	Pu	20.9(4) m		$Q\varepsilon = 2,100(99.88\%)$	$\gamma 235, 535, 500, 688$
				$Q\alpha = 6,420(0.12\%)$	$\alpha 6300$
	Pu	8.8(1) h	0+	$Q\varepsilon = 388(\sim 94\%)$	
				$Q\alpha = 6,310(\sim 6\%)$	$\alpha 6202, 6151$
235	Pu	25.3(5) m	(5/2+)	$Q\varepsilon = 1,142(100\%)$	$\gamma 49, 756$
				$Q\alpha = 5,951(0.0027\%)$	$\alpha 5850$

236	Pu	2.858(8) years	0+	Q α = 5,867.07(100%) SF(1.9E – 7%)	γ 48,109, α 5768,5721
237	Pu	45.2(1) days	7/2–	Q ε = 220.3(100%) Q α = 5,749.5(0.0042%)	γ 60 γ 280,299,321,229, α 5334,5356
237	Pu(145.5)	0.18(2) s	1/2+	IT	γ 146
238	Pu	87.7(3) years	0+	Q α = 5,593.20(100%) SF(1.8E – 7%)	γ 43,100, α 5499,5456
239	Pu	24,110(30) years	1/2+	Q α = 5,244.50(100%) SF(3E – 10%)	γ 52,39,129, α 5157,5144
240	Pu	6,561(7) years	0+	Q α = 5,255.78(100%) SF(5.7E – 6%)	γ 45,104, α 5168,5124
241	Pu	14,290(6) years	5/2+	Q β – = 20.82(100%) Q α = 5,140.1(0.0025%) SF(>2E – 14%)	γ 149,104,77, α 4896,4853
242	Pu	3.75(2)E5 years	0+	Q α = 4,984.4(100%) SF(0.00055%)	γ 45, α 4902,4858
243	Pu	4.956(3) h	7/2+	Q β – = 582(100%)	γ 84
244	Pu	8.00(9)E7 years	0+	Q α = 4,665.5(99.88%) SF(0.12%)	α 4589,4546
245	Pu	10.5(1) h	(9/2–)	Q β – = 1,205(100%)	γ 327,560,308,377
246	Pu	10.84(2) days	0+	Q β – = 401(100%)	γ 44,224,180,28
247	Pu	2.27(23) days		Q β – = [1,800](100%)	

Table 22.1 (Continued)

95	A	Element	Half-life or width	J^{π}	Qmode(%BR){%Abund}	Principal gammas, alphas
		Americium				
	230	Am	≈17 s		Q ϵ = [4,000](100%)	
	231	Am	≈10 s		Q ϵ = [4,000] Q α = [7,500]	
	232	Am	79(2) s		Q ϵ = [5,000](≈97%) Q α = [7,300](≈3%) ϵ (≈0.07%)	
	233	Am	3.2(8) m		Q ϵ = [3,250] Q α = [7,100]	
	234	Am	2.32(8) m		Q ϵ = [4,180](99.96%) Q α = [6,870](0.04%)	γ 185 α 6460
	235	Am	10.3(6) m		Q α = [6,700](0.4%) ϵ (99.6%)	α 6457
	236	Am	3.6(2) m	5–	Q ϵ = [3,280]	
	236	Am(0 + x)	2.9(2) m	(1 –)	ϵ α	
	237	Am	73.6(8) m	5/2(–)	Q ϵ = 1,460(99.97%) Q α = 6,181(0.03%)	γ 280,438 α 6042
	238	Am	98(2) m	1+	Q ϵ = 2,260(>99.99%) Q α = 6,040(0.0001%)	γ 963,919,561,605 α 5940
	239	Am	11.9(1) h	(5/2)–	Q ϵ = 802.9(99.99%) Q α = 5,923.7(0.01%)	γ 278,228,210,226 γ 49, α 5774,5734
	240	Am	50.8(3) h	(3 –)	Q ϵ = 1,379(100%) Q α = 5,710(0.00019%)	γ 988,889 α 5378,5337

241	Am	432.6(6) years	5/2–	Q α = 5.637.81(100%) SF(4E – 10%)	γ 60, α 5486,5443
242	Am	16.02(2) h	1–	Q β^- = 664.8(82.7%) Q ε = 751.0(17.3%)	γ 42 γ 45
242	Am(48.6)	141(2) years	5–	IT(99.55%) Q α = 5,588.34(0.45%)	γ 49 γ 49,87,110,110, α 5207
242	Am(2200.0)	14.0(10) ms	(2+,3–)	SF(<4.7E – 9%) SF(\sim 100%) α (<0.005%) IT	
243	Am	7.370(40) years	5/2–	Q α = 5,438.1(100%) SF(3.7E – 9%)	γ 75, α 5275,5233
244	Am	10.1(1) h	(6–)	Q β^- = 1,428.1(100%)	γ 744,898,154
244	Am(88)	26(1) m	1+	β^- – (99.96%) Q ε = 76(0.04%)	γ 1084,942,1063,1041
244	Am(0 + x)	0.90(15) ms		SF(\leq 100%)	γ 1084,942,1063,1041
245	Am	2.05(1) h	(5/2)+	Q β^- = 894(100%)	γ 253
246	Am	39(3) m	(7–)	Q β^- = 2,376(100%)	γ 679,205,154,756
246	Am(0 + x)	25.0(2) m	2(–)	β^- – (100%) IT(<0.02%)	γ 1079,799,1062,1036
247	Am	23.0(13) m	(5/2)	Q β^- = [1,620](100%)	γ 285,226
248	Am	\approx 10 m		Q β^- = [3,170](100%)	
249	Am	\approx 2 m		Q β^- = [2,400]	
96	Curium				
	Cm	\approx 1 m	0+	SF(<30.3%)	
	Cm	\sim 1 m		Q ε = [4,000] Q α = [7,500]	

Table 22.1 (Continued)

A	Element	Half-life or width	$J\pi$	Qmode(%BR){%Abund}	Principal gammas, alphas
234	Cm	51(12) s	0+	$Q_{\beta} = [2,300](\approx 20\%)$ $Q_{\alpha} = [7,400](\approx 40\%)$ SF($\approx 40\%$)	
235	Cm	(5 m)		$Q_{\beta} = [3,300]$ $Q_{\alpha} = [7,200]$	
236	Cm		0+	$Q_{\beta} = [1,710]$ $Q_{\alpha} = [7,100]$	
237	Cm	≈ 20 m		$Q_{\beta} = [2,720]$ $Q_{\alpha} = [6,800]$	
238	Cm	2.4(1) h	0+	$Q_{\beta} = 970(>90\%)$ $Q_{\alpha} = 6,620(<10\%)$	$\alpha 6520$
239	Cm	≈ 2.9 h	(7/2-)	$Q_{\beta} = [1,800](100\%)$ $Q_{\alpha} = [6,580](<0.1\%)$	$\gamma 188$
240	Cm	27(1) days	0+	$Q_{\alpha} = 6,397.2(>99.5\%)$ $Q_{\beta} = 215(<0.5\%)$ SF(3.9E – 6%)	$\alpha 6291, 6248$
241	Cm	32.8(2) days	1/2+	$Q_{\beta} = 767.4(99\%)$ $Q_{\alpha} = 6,184.9(1\%)$	$\gamma 472$ $\gamma 146, \alpha 5939, 5927$
242	Cm	162.8(2) days	0+	$Q_{\alpha} = 6,215.56(100\%)$ SF(6.2E – 6%) 345i(1.E – 14%)	$\gamma 44, \alpha 6113, 6069$
243	Cm	29.1(1) years	5/2+	$Q_{\alpha} = 6,168.8(99.71\%)$ $Q_{\beta} = 8.9(0.29\%)$ SF(5.3E – 9%)	$\gamma 278, 228, 210,$ $\alpha 5785, 5742$

97	244	Cm	18.1(1) years	0+	Q α = 5,901.61(100%) SF(0.00014%)	γ 43, α 5805,5763
	245	Cm	8,500(100) years	7/2+	Q α = 5,623.5(100%) SF(6.1E – 7%)	γ 175,133, α 5362
	246	Cm	4,760(40) years	0+	Q α = 5,474.8(99.97%) SF(0.03%)	γ 45, α 5387,5344
	247	Cm	1.56(5)E7 years	9/2–	Q α = 5,353(100%)	γ 402, α 4870,5267
	248	Cm	3.48(6)E5 years	0+	Q α = 5,161.73(91.61%) SF(8.39%)	α 5078,5035
	249	Cm	64.15(3) m	1/2(+)	Q β – = 901(100%)	γ 634,560,369,622
	250	Cm	\approx 8,300 years	0+	SF(\approx 74%)	
					Q α = 5,169(\sim 18%) Q β – = 37(\approx 8%)	
	251	Cm	16.8(2) m	(1/2+)	Q β – = 1,420(100%)	γ 543,530,390,438
	252	Cm	<2 days	0+	Q β – = [500]	
		Berkelium				
	234	Bk	140(+140–50) s		α (<80%) ϵ (<20%)	
	235	Bk	\approx 20 s		Q ϵ = [4,600] Q α = [7,800] Q ϵ = [3,900] Q α = [7,500]	
	237	Bk	\approx 1 m			
	238	Bk	144(5) s		Q ϵ = [4,900](100%) ϵ SF(0.048%) Q α = [7,330]	

Table 22.1 (Continued)

A	Element	Half-life or width	J^{π}	Qmode(% β R)(%Abund)	Principal gammas, alphas
239	Bk	≈ 3 m	(7/2+)	Q ϵ = [3,200]	
240	Bk	4.8(8) m		Q ϵ = [3,940]($\sim 100\%$) ϵ SF	
241	Bk	4.6(6) m	(7/2+)	Q α = [7,130]	
242	Bk	7.0(13) m		Q ϵ = [2,400]	
243	Bk	4.5(2) h	(3/2-)	Q ϵ = [3,000]($< 100\%$) Q ϵ = 1,508($\sim 99.85\%$) Q α = 6,874($\sim 0.15\%$)	γ 755,946,840 γ 187,146, α 6577,6545
244	Bk	4.35(15) h	(1-)	Q ϵ = 2,256(99.994%) Q α = 6,778(0.006%)	γ 892,218,922,491 α 6620,6662
245	Bk	4.94(3) days	3/2-	Q ϵ = 810.2(99.88%) Q α = 6,454.5(0.12%)	γ 253 γ 207,472,166, α 5886,6147
246	Bk(0 + x)	1.80(2) days	2(-)	Q ϵ = 1,350(100%) Q α = 6,070($< 0.2\%$)	γ 799
247	Bk	1,380(250) years	(3/2-)	Q α = 5,889($< 100\%$) Q α = [5,770]	γ 84,265, α 5531,5710
248	Bk	> 9 years		Q β - = [840](70%) Q ϵ = [690](30%)	γ 551
249	Bk	330(4) days	7/2+	Q β - = 124.0(100%) Q α = 5,525.0(0.0014%) SF(4.7E - 8%)	γ 327,308, α 5417,5390
250	Bk	3.212(5) h	2-	Q β - = 1,780(100%)	γ 989,1032,1029

	251	Bk	55.6(11) m	(3/2-)	$Q\beta^- = 1,093(100\%)$	$\gamma 178,130,153$
	252	Bk			$Q\beta^- = [2,500]$	
					$Q\alpha = [5,500]$	
	253	Bk	≈ 10 m		$Q\beta^- = [1,600]$	
	254	Bk	≈ 2 m		$Q\beta^- = [3,100]$	
98		Californium				
	237	Cf	2.1(3) s		SF($\sim 10\%$)	
					$Q\alpha = [8,100]$	
	238	Cf	21(2) ms	0+	SF(100%)	
	239	Cf	39(+37 – 12) s		$Q\epsilon = [3,900]$	
					$Q\alpha = [7,810](\approx 98\%)$	$\alpha 7630$
	240	Cf	0.96(15) m	0+	SF($\approx 2\%$)	
					$Q\alpha = 7,719$	$\alpha 7590$
	241	Cf	3.78(70) m		$Q\epsilon = [3,300](\sim 75\%)$	
					$Q\alpha = [7,660](\sim 25\%)$	$\alpha 7342$
	242	Cf	3.7(5) m	0+	$Q\alpha = 7,516(80\%)$	$\alpha 7392, 7358$
					$Q\epsilon = [1,530](20\%)$	
					SF($< 0.01\%$)	
	243	Cf	10.7(5) m	(1/2+)	$Q\epsilon = [2,250](\sim 86\%)$	
					$Q\alpha = [7,330](\sim 14\%)$	$\alpha 7060$
	244	Cf	19.4(6) m	0+	$Q\alpha = 7,329.1(100\%)$	$\alpha 7209, 7174$
	245	Cf	45.0(15) m	(5/2+)	$Q\epsilon = [1,570](64\%)$	
					$Q\alpha = [7,260](36\%)$	$\alpha 7137$
	246	Cf	35.7(5) h	0+	$Q\alpha = 6,861.6(100\%)$	$\gamma 42,96,147,$ $\alpha 6750, 6708$
					$Q\epsilon = 120(< 0.004\%)$	
					SF(0.00025%)	

Table 22.1 (Continued)

A	Element	Half-life or width	J^{π}	Qmode(%BR){%Abund}	Principal gammas, alphas
247	Cf	3.11(3) h	(7/2+)	Q ϵ = 646(99.96%) Q α = 6,527(0.04%)	γ 294,448,418,407 α 6296
248	Cf	333.5(28) days	0+	Q α = 6,361(100%) SF(0.0029%)	α 6258,6217
249	Cf	351(2) years	9/2–	Q α = 6,295.0(100%) SF(5.0E – 7%)	γ 388,333, α 5813
250	Cf	13.08(9) years	0+	Q α = 6,128.44(99.92%) SF(0.08%)	γ 43, α 6030,5989
251	Cf	898(44) years	1/2+	Q α = 6,175.8(100%) SF	γ 177,227, α 5679,5854
252	Cf	2.645(8) years	0+	Q α = 6,216.87(96.91%) SF(3.09%)	γ 43,100, α 6118,6076
253	Cf	17.81(8) days	(7/2+)	Q β – = 288(99.69%) Q α = 6,126(0.31%)	γ 46 α 5980
254	Cf	60.5(2) days	0+	SF(99.69%) Q α = 5,926(0.31%)	α 5833,5791
255	Cf	85(18) m	(7/2+)	Q β – = [720](100%) SF(100%)	
256	Cf	12.3(12) m	0+	β – (<1%) Q α = [5,600](~1.0E – 6%)	
99	Einsteinium				
	Es	(1 s)		α ϵ	

241	Es	8(+6–4) s		$Q\alpha = [8,320]$	
242	Es	13.5(25) s		$Q\alpha = [8,220](>0\%)$ $Q\epsilon = [5,600](>0\%)$	
243	Es	21(2) s		$Q\epsilon = [3,900](<70\%)$ $Q\alpha = 8,072(>30\%)$	$\alpha 7899,7939$
244	Es	37(4) s		$Q\epsilon = [4,640](96\%)$ $Q\alpha = [8,030](4\%)$	$\alpha 7570$
245	Es	1.1(1) m	(3/2–)	$Q\epsilon = [3,050](60\%)$ $Q\alpha = 7,909(40\%)$	$\alpha 7730,7699$
246	Es	7.7(5) m		$Q\epsilon = [3,880](90.1\%)$ $Q\alpha = [7,740](9.9\%)$ $\epsilon SF(0.003\%)$	$\alpha 7370$
247	Es	4.55(26) m	(7/2+)	$Q\epsilon = [2,480](\sim 93\%)$ $Q\alpha = [7,490](\sim 7\%)$	$\alpha 7323,7275$
247	Es(0 + x)	625(84) days		α	
248	Es	27(5) m	(2–,0+)	$Q\epsilon = [3,060](99.7\%)$ $Q\alpha = [7,160](\sim 0.25\%)$	$\alpha 6870$
249	Es	102.2(6) m	7/2+	$Q\epsilon = [1,450](99.43\%)$ $Q\alpha = [6,940](0.57\%)$	$\gamma 380,813$ $\alpha 6776$
250	Es	8.6(1) h	(6+)	$Q\epsilon = [2,100](>97\%)$ $Q\alpha = [6,880](<3\%)$	$\gamma 829,303,349,384$
250	Es(0 + x)	2.22(5) h	1(–)	$\epsilon (<100\%)$	$\gamma 989,1032,829,1167$
251	Es	33(1) h	(3/2–)	$Q\epsilon = 376(99.5\%)$ $Q\alpha = 6,597(0.5\%)$	$\gamma 178,153,130$ $\alpha 6492,6462$

Table 22.1 (Continued)

A	Element	Half-life or width	J^{π}	Qmode(%BR){%Abund}	Principal gammas, alphas
252	Es	471.7(19) days	(5-)	Q α = [6,790](78%)	γ 52,64,400,419, α 6632,6562
				Q ε = 1,260(22%)	γ 785,139,924,102
				Q β^- = 480(~0.01%)	
				Q α = 6,739.16(100%)	γ 389,387,429,381, α 6633
253	Es	20.47(3) days	7/2+	SF(8.7E – 6%)	
254	Es	275.7(5) days	(7+)	Q α = 6,615.7(~100%)	γ 63, α 6429
				Q β^- = 1,088(0.00017%)	
				SF(<3.0E – 6%)	
				Q ε = 652	
254	Es(80)	39.3(2) h	2+	β^- – (98%)	γ 649,694,689,584
				IT(<3%)	
				α (0.32%)	γ 212,177,71,104, α 6382,6357
				ε (0.08%)	
255	Es	39.8(12) days	(7/2+)	SF(<0.05%)	
				Q β^- = 290(92%)	γ 120
				Q α = 6,436.3(8%)	γ 269, α 6301,6267
				SF(0.0041%)	
256	Es	25.4(24) m	(1+,0-)	Q β^- = [1,700](100%)	
256	Es(0 + x)	7.6 h	(8+)	β^- – (100%)	γ 862,231,173,1093
257	Es	7.7(2) days		Q β^- = [800]	γ 26,46,49
				SF	
258	Es	(3 m)		β^-	

100		Fermium						
	242	Fm	0.8(2) ms		0+		SF(<100%)	
	243	Fm	0.18(+8–4) s		(7/2+)		Q α = 8,690(<100%)	α 8546
							SF(<0.4%)	
	244	Fm	3.3(5) ms		0+		SF(<100%)	
	245	Fm	4.2(13) s				Q α = [8,440](<100%)	α 8150
							SF(<0.1%)	
	246	Fm	1.1(2) s		0+		Q α = 8,374(92%)	α 8237
							SF(8%)	
							Q ε = [2,160](<1%)	
	247	Fm(0 + x)	29(4) s		(7/2+)		Q α = 8,190(>50%)	α 7870,7930
							Q ε = [2,950](<50%)	
	247	Fm(0 + y)	4.3(4) s		(1/2+)		α (<100%)	α 8180
	248	Fm	36(3) s		0+		Q α = 8,002(93%)	α 7870,7830
							Q ε = [1,610](7%)	
							SF(0.1%)	
	249	Fm	2.6(7) m		(7/2+)		Q ε = [2,440](67%)	
							Q α = [7,810](33%)	α 7527
	250	Fm	30(3) m		0+		Q α = 7,557(>90%)	α 7436,7396
							Q ε = [800](<10%)	
							SF(0.0069%)	
	250	Fm(0 + x)	1.8(1) s		0+		IT(>80%)	
							α (<20%)	
							SF(<8.2E – 5%)	
							ε	

Table 22.1 (Continued)

	A	Element	Half-life or width	$J\pi$	Qmode(%BR){%Abund}	Principal gammas, alphas
	251	Fm	5.30(8) h	(9/2-)	$Q_{\text{E}} = 1,474(98.2\%)$ $Q_{\alpha} = 7,425.1(1.8\%)$	$\gamma 881,453,406,350$ $\gamma 425,480,358,$ $\alpha 6834$
	252	Fm	25.39(4) h	0+	$Q_{\alpha} = 7,152.7(100\%)$ SF(0.0023%)	$\gamma 96,42,\alpha 7039,6998$
	253	Fm	3.00(12) days	(1/2)+	$Q_{\text{E}} = 334(88\%)$ $Q_{\alpha} = 7,197(12\%)$	$\gamma 272,\alpha 6943,6673$
	254	Fm	3.240(2) h	0+	$Q_{\alpha} = 7,307.2(99.94\%)$ SF(0.06%)	$\gamma 99,43,\alpha 7192,7150$
	255	Fm	20.07(7) h	7/2+	$Q_{\alpha} = 7,239.7(100\%)$ SF(0.000024%)	$\gamma 81,60,73,131,\alpha 7022$
	256	Fm	157.6(13) m	0+	SF(91.9%) $Q_{\alpha} = 7,027(8.1\%)$	$\alpha 6917$
	257	Fm	100.5(2) days	(9/2+)	$Q_{\alpha} = 6,863.8(99.79\%)$ SF(0.21%)	$\gamma 241,179,62,\alpha 6520$
	258	Fm	370(43) μ s	0+	SF(<100%)	
	259	Fm	1.5(3) s		SF(100%)	
	260	Fm	\approx 4 ms	0+	SF(100%)	
101		Mendelevium				
	245	Md	900(250) μ s	(1/2-)	SF(100%) $Q_{\alpha} = [9,080](0.26\%)$	
	245	Md(100.0)	0.35(+23-16) s		$Q_{\text{E}} = [5,300]$ α	

246	Md	1.0(4) s		SF $Q\alpha = [8,970](>0\%)$ $Q\epsilon = [6,200](>0\%)$	$\alpha 7920$
247	Md	1.22(2) s		$Q\alpha = [8,910](\leq 100\%)$	$\alpha 8428$
248	Md	7(3) s		$Q\epsilon = [5,330](80\%)$ $Q\alpha = [8,700](20\%)$ SF(<0.05%)	$\alpha 8320, 8360$
249	Md	24(4) s		$Q\alpha = [8,460](>60\%)$ $Q\epsilon = [3,700](<40\%)$	$\alpha 8030$
250	Md	52(6) s		$Q\epsilon = [4,600](93\%)$ $Q\alpha = [8,310](7\%)$	$\alpha 7751, 7831$
251	Md	4.0(5) m		$Q\epsilon = [3,120](>90\%)$ $Q\alpha = [8,070](<10\%)$	$\alpha 7550$
252	Md	2.3(8) m		$Q\epsilon = [3,880](<100\%)$	
253	Md	6(+12–3) m	(1/2–)	$Q\epsilon = [1,960](<100\%)$ $Q\alpha = [7,710]$	
254	Md(0 + x)	28(8) m		$Q\epsilon = [2,680](<100\%)$	
255	Md	27(2) m	(7/2–)	$Q\epsilon = 1,043(92\%)$ $Q\alpha = 7,907(8\%)$ SF(<0.15%)	$\gamma 430, \alpha 7328$
256	Md	77(2) m	(1–)	$Q\epsilon = 2,130(90.8\%)$ $Q\alpha = 7,897(9.2\%)$ SF(<3%)	$\gamma 400, \alpha 7221, 7155$
257	Md	5.52(5) h	(7/2–)	$Q\epsilon = 406(85\%)$ $Q\alpha = 7,557.6(15\%)$ SF(<1%)	$\gamma 371, 325, \alpha 7074$

Table 22.1 (Continued)

A	Element	Half-life or width	J^{π}	Qmode(%BR){%Abund}	Principal gammas, alphas
102	258	Md	51.5(3) days	$Q\alpha = 7,271.3(100\%)$	$\gamma 368,448,277,$ $\alpha 6718,6763$
	258	Md(0 + x)	57.0(9) m	SF $Q\varepsilon = [1,260](>70\%)$	
	259	Md	96(3) m	SF($\sim 100\%$) $Q\alpha = [7,110](<1.3\%)$	
	260	Md	31.8(5) days	SF($>42\%$) $Q\alpha = [6,900](<25\%)$ $\varepsilon(<23\%)$ $Q\beta- = [900](<10\%)$	
	261	Md	(40 m)	α	
	262	Md	(3 m)	α	
		Nobelium		SF	
	248	No			
	249	No	$<2\ \mu\text{s}$	SF $Q\varepsilon = [4,500]$	
	250	No		$Q\alpha = [9,170]$	
103	250	No	4.2(+12–9) μs	SF($<100\%$)	
	250	No(1050)	46(+22–19) μs	SF($<100\%$) $Q\alpha = [8,950](0.1\%)$	
				$Q\varepsilon = [2,800](0.001\%)$	

251	No	0.80(1) s	(7/2+)	$Q\alpha = [8,890](84\%)$ $SF(<0.3\%)$ $Q\epsilon = [3,800]$	$\alpha 8593,8661$
251	No(106)	1.02(3) s	(1/2+)	$\alpha(100\%)$	$\alpha 8593,8661$
252	No	2.44(4) s	0+	$Q\alpha = 8,549(>66.7\%)$ $Q\epsilon = [2,180](<1.1\%)$ $SF(32.2\%)$	$\alpha 8415,8372$
253	No	1.62(15) m	(9/2-)	$Q\alpha = [8,400](<100\%)$ $Q\epsilon = [3,100]$	$\alpha 8011,8038$
254	No	51(10) s	0+	$Q\alpha = 8,226(90\%)$ $Q\epsilon = [1,140](10\%)$ $SF(0.17\%)$ $IT(>80\%)$	$\alpha 8093$
254	No(0 + x)	0.28(4) s	0+		$\gamma 187, \alpha 8121, 7927$
255	No	3.1(2) m	(1/2+)	$Q\alpha = 8,442(61\%)$ $Q\epsilon = 2,009(39\%)$	
256	No	2.91(5) s	0+	$Q\alpha = 8,581(99.47\%)$ $SF(0.53\%)$	$\alpha 8448,8402$
257	No	25(3) s	(7/2+)	$Q\alpha = 8,450(<100\%)$ $SF(<1.5\%)$ $SF(<100\%)$	$\alpha 8220,8270$
258	No	1.2(2) ms	0+		
259	No	58(5) m		$Q\alpha = [7,890](75\%)$ $Q\epsilon = [490](25\%)$ $SF(<10\%)$ $SF(100\%)$	$\alpha 7500,7533$
260	No	106(8) ms	0+		
261	No			$\beta-$ $Q\alpha = [7,500]$	

Table 22.1 (Continued)

	A	Element	Half-life or width	J^{π}	Qmode(%BR){%Abund}	Principal gammas, alphas
103	262	No	≈ 5 ms	0+	SF(100%)	
	263	No	(20 m)		SF	
					α	
	262	No	(1 m)	0+	α	
		Lawrencium				
	251	Lr			$Q_{\varepsilon} = [5,000]$	
					$Q_{\alpha} = [9,300]$	
	252	Lr	$0.36(+11 - 7)$ s		$Q_{\alpha} = [9,100](\sim 90\%)$	
					$Q_{\varepsilon} = [5,900](\sim 10\%)$	
					SF(<1%)	
	253	Lr(0 + y)	$0.57(+7 - 6)$ s	(7/2 -)	$Q_{\alpha} = [8,990](98.7\%)$	$\alpha 8794$
					SF(1.3%)	
					$Q_{\varepsilon} = [4,300]$	
	253	Lr(0 + x)	$1.49(+30 - 21)$ s	(1/2 -)	$\alpha(92\%)$	$\alpha 8723$
					SF(8%)	
					ε	
	254	Lr	13(3) s		$Q_{\alpha} = [8,850](76\%)$	$\alpha 8460,8408$
					$Q_{\varepsilon} = [5,300](24\%)$	
	255	Lr	22(4) s		$Q_{\alpha} = [8,610](85\%)$	$\alpha 8370$
					$Q_{\varepsilon} = [3,300](\sim 30\%)$	
					SF(<0.1%)	
	256	Lr	27(3) s		$Q_{\alpha} = [8,880](85\%)$	$\alpha 8430,8517$
					$Q_{\varepsilon} = [4,180](15\%)$	
					SF(<0.03%)	

104	257	Lr	0.646(25) s			Q α = [9,060]($<100\%$) SF($<0.03\%$)	α 8861,8796	
	258	Lr	4.1(3) s			Q α = 8,900($>95\%$) SF($<5\%$)	α 8620,8590	
	259	Lr	6.2(3) s			Q α = [8,670](78%) SF(22%)	α 8439	
	260	Lr	180(30) s			Q α = [8,310](80%) Q ε = [2,740]($<40\%$) SF($<10\%$)	α 8035	
	261	Lr	39(12) m			SF(100%)		
	262	Lr	≈ 4 h			SF($<10\%$) Q ε = [2,000] Q α = [8,100]		
	263	Lr	(5 h)			α		
	264	Lr	(10 h)			SF α		
	265	Lr	(10 h)			SF α		
	266	Lr	(1 h)			α SF		
104		Rutherfordium						
	253	Rf	48(+17 – 10) μ s			SF($\sim 50\%$) α ($\sim 50\%$)		
	254	Rf	23(3) μ s	0+		SF($<100\%$)		
	255	Rf	1.68(19) s	(9/2 –)		Q α = [9,250](52%) SF(48%)	α 8768,8739	

Table 22.1 (Continued)

A	Element	Half-life or width	$J\pi$	Qmode(%BR){%Abund}	Principal gammas, alphas
255	Rf(0 + x)	0.8(+5 – 2) s		$\alpha(<100\%)$	
256	Rf	6.4(2) ms	0+	SF(99.68%)	
257	Rf	4.7(3) s	(1/2+)	Q α = 8,952(0.32%) Q α = [9,150](<100%) SF(<1.4%)	α 8790 α 8779,8738
257	Rf(0 + x)	3.9(4) s		Q ϵ = [3,200](>0%) $\alpha(<100\%)$ SF(<1.4%) $\epsilon(>0\%)$	α 9021,8968
258	Rf	12(2) ms	0+	SF(87%)	
259	Rf	3.2(6) s		Q α = [9,330](13%) Q α = [9,120](92%) SF(8%)	α 8770,8870
260	Rf	21(1) ms	0+	SF(<100%) Q α = [8,900]	
261	Rf	65(10) s		Q α = [8,660](>80%) Q ϵ = [1,690](<15%) SF(<10%)	α 8280
262	Rf	2.3(4) s	0+	SF(<100%)	
263	Rf	10(2) m		SF(~100%) Q α = [8,300]	
264	Rf	(1 h)	0+	α	
265	Rf	\approx 13 h		α	

105	266	Rf	(10 h)	0+	α	
					SF	
	268	Rf	(6 h)	0+	SF	
					α	
		Dubnium				
	255	Db	1.6(+6–4) s		$Q\alpha = [9,700](\sim 80\%)$	
					SF($\sim 20\%$)	
	256	Db	1.6(+5–3) s		$Q\alpha = [9,480](64\%)$	
					SF(0.02%)	
					$Q\varepsilon = [6,500](36\%)$	
	257	Db	0.76(+15–11) s		$Q\alpha = [9,310](\sim 87.4\%)$	$\alpha 9163$
					SF($< 13\%$)	
	257	Db(0 + x)	1.50(+19–15) s		$\alpha(> 94\%)$	$\alpha 8967, 9074$
					SF($< 6\%$)	
	258	Db	4.0(10) s		$Q\alpha = [9,550](67\%)$	$\alpha 9078, 9299$
					$Q\varepsilon = [5,500](33\%)$	
					SF($< 1\%$)	
	258	Db(0 + x)	20(10) s		$\varepsilon(\sim 100\%)$	
	259	Db	0.51(15) s		α	
	260	Db	1.52(13) s		$Q\alpha = 9,370(> 90.4\%)$	$\alpha 9042, 9075$
					SF($< 9.6\%$)	
					$Q\varepsilon = [4,700](\sim 2.5\%)$	
	261	Db	1.8(4) s		$Q\alpha = [9,220](\sim 82\%)$	$\alpha 8930$
					SF($< 18\%$)	
	262	Db	35(5) s		$Q\alpha = [9,010](\sim 67\%)$	$\alpha 8450, 8530$
					SF	

Table 22.1 (Continued)

	A	Element	Half-life or width	J^{π}	Qmode(%BR){%Abund}	Principal gammas, alphas
106	263	Db	27(+10–7) s		SF(55%) Q α = [8,830](41%) ϵ (3%)	α 8355
	264	Db	(3 m)		α	
	265	Db	(15 m)		α	
	266	Db	(20 m)		α	
	267	Db	73(+350–33) m		SF(100%)	
	268	Db	32(+11–7) h		SF(100%)	
	269	Db	(3 h)		α	
					SF	
		Seaborgium				
	258	Sg	2.9(+13–7) ms	0+	SF(<100%) Q α = [9,700]	
	259	Sg	0.48(+28–13) s	(1/2+)	Q α = 9,830(90%) SF(<20%)	α 9620,9030
	260	Sg	3.6(9) ms	0+	Q α = 9,920(50%) SF(50%)	α 9770,9720
	261	Sg	0.23(6) s		Q α = [9,800](~100%) SF(<1%)	α 9560,9520
	262	Sg	6.9(+38–18) ms	0+	SF(>78%) Q α = [9,600](<22%)	
	263	Sg	1.0(2) s		Q α = [9,390](>70%) SF(<30%)	α 9060,9250

107	263	Sg(0 + x)	0.12 s			α	
	264	Sg	37(+27–11) ms	0+		IT	
	265	Sg	8(3) s	(9/2+)		SF(100%)	
	266	Sg	21(+20–12) s	0+		SF(<57%)	
	268	Sg	(30 s)			Q α = [9,050](>43%)	α 8840,8760
	270	Sg	(10 m)	0+		SF(>50)	
	271	Sg	2.4(+43–10) m			Q α = 8,760(>18%)	α 8770
	272	Sg	(1 h)	0+		α	
	273	Sg	(1 m)			SF	
	Bohrium					α	
	260	Bh	(0.3 ms)			SF	
	261	Bh	12(+5–3) ms			SF	
	262	Bh	102(26) ms			Q α = [10,300](<100%)	
	263	Bh	(0.2 ms)			Q α = 10,560(95%)	α 10100,10400
	264	Bh	0.44(+60–16) s			SF(<10%)	
	265	Bh	0.9(+7–3) s			α (<100%)	α 9763,9831
	266	Bh	17(+14–6) s			Q α = [9,970](<100%)	α 9475,9619
	267	Bh	1.7(+82–8) s			α	
						α = [9,600](<100%)	α 9290
						α (<100%)	

Table 22.1 (Continued)

A	Element	Half-life or width	J π	Qmode(%BR){%Abund}	Principal gammas, alphas
108	271 Bh			α	
	272 Bh	10(+12–4) s		α (100%)	
	273 Bh	(90 m)		α	
	274 Bh	(90 m)		SF	
				α	
				SF	
	275 Bh	(45 m)		SF	
	Hassium				
	263 Hs				
	264 Hs	~0.8 ms	0+	Q α = [10,700](~100%) Q α = 10,591 (~50%) SF(~50%)	α 10434
	265 Hs	2.0(+3–2) ms		Q α = [10,430](~100%)	α 10301
				SF(<1%)	
	266 Hs	2.3(+13–6) ms	0+	Q α = [10,200](~100%)	α 10180
	267 Hs	52(+13–8) ms		Q α = [10,110](~80%) SF(<20%)	α 9740,9870
	269 Hs	9.7(+97–33) s		Q α = [9,700](~100%)	α 9170,9230
	270 Hs	3.6(+8–14) s	0+	α (~100%)	
	271 Hs	(40 s)		α	
	272 Hs	(40 s)		SF	
			0+	α	
				SF	
	274 Hs	(1 m)	0+	α	
				SF	

109	275	Hs		0.15(+27–6) s			α (100%)		
	276	Hs		(1 h)	0+		SF		
							α		
		Meitnerium							
	265	Mt		(2 m)			α		
	266	Mt		1.7(+18–16) ms			$Q\alpha = [11,480](< 100\%)$		
	267	Mt		(10 ms)			α		
	268	Mt		21(+8–5) ms			$Q\alpha = [10,700](100\%)$	α 10097,10240	
	270	Mt		5.0(+24–3) ms			α (100%)		
	271	Mt		(5 s)			α		
	272	Mt		(10 s)			SF		
							α		
	273	Mt		(20 s)			SF		
110	274	Mt		0.45(+81–18) s			α (100%)		
	275	Mt		9.7(+460–44) ms			α (100%)		
	277	Mt		0.72(+87–25) s			α (100%)		
	279	Mt		(6 m)			SF		
							α		
		Darmstadtium							
	267	Ds		2.8(+233–12) μ s			$Q\alpha = [11,780](100\%)$		
	268	Ds		(100 μ s)	0+		α		
	269	Ds		179(+245–66) μ s			$Q\alpha = [11,680](100\%)$	α 1112	
	270	Ds		0.10(+14–4) ms			α (100%)		
	270	Ds(1130)		6.0(+82–22) ms			α (> 70%)		
							IT(< 30%)		

Table 22.1 (Continued)

	A	Element	Half-life or width	J π	Qmode(%BR){%Abund}	Principal gammas, alphas
	271	Dy(0 + x)	69(+56–21) ms		α	α 10710
	271	Dy(0 + y)	1.63(+44–29) ms		α (100%)	α 10740,10680
	272	Ds	(1 s)	0+	SF	
	273	Ds	0.17(+17–6) ms		$Q\alpha$ = [11,670](100%)	α 11080,11350
	274	Ds	(2 s)	0+	α	
					SF	
	275	Ds	(2 s)		α	
	276	Ds	(5 s)	0+	α	
					SF	
	277	Ds	(5 s)		α	
	278	Ds	(10 s)		α	
					SF	
	279	Ds	0.18(+5–3) ms		α (\approx 10%)	
					SF(\approx 90%)	
	281	Ds	9.6(+50–25) ms		SF(\approx 100%)	
111		Roentgenium				
	272	Rg	3.8(+14–8) ms		$Q\alpha$ = [11,230](\approx 100%)	α 10820
	273	Rg	(5 ms)		α	
	274	Rg	6.4(+307–29) ms		α (\approx 100%)	
	275	Rg	(10 ms)		α	
	276	Rg	(100 ms)		α	
					SF	
	277	Rg	(1 s)		α	
					SF	

112	278	Rg	4.2(+76–17) ms		$\alpha(\approx 100\%)$	
					SF	
	279	Rg	0.17(+81–8) s		$\alpha(\approx 100\%)$	
	280	Rg	3.6(+43–13) s		$\alpha(\approx 100\%)$	
	281	Rg	(1 m)		α	
					SF	
	282	Rg	(4 m)		α	
					SF	
	283	Rg	(10 m)		α	
					SF	
		Ununbium				
	277	112	0.69(+69–24) ms		$\alpha(100\%)$	
	278	112	(10 ms)	0+	α	
					SF	
	279	112	(0.1 s)		α	
	280	112	(1 s)	0+	SF	
					α	
					SF	
	282	112	0.50(+33–14) ms	0+	SF(100%)	
	283	112	4.0(+13–7) ms		$\alpha(>90\%)$	
					SF(<10%)	
	284	112	101(+41–22) ms	0+	SF(100%)	
	285	112	34(+17–9) s		$\alpha(100\%)$	



Chemical Applications of Nuclear Reactions and Radiations



23 Radiation Chemistry

L. Wojnárovits

Institute of Isotopes, HAS, Budapest, Hungary

23.1	Introduction	1267
23.2	Sources of Radiation	1268
23.2.1	Radionuclide Sources	1268
23.2.2	Machine Sources	1268
23.3	Energy Deposition, Ionization	1270
23.3.1	Energy Deposition	1270
23.3.2	Formation and Decay of Ion Pairs	1274
23.4	Techniques in Radiation Chemistry	1275
23.4.1	Steady-State Techniques	1275
23.4.2	Pulse Radiolysis, Technical Realization, and Detection Systems	1277
23.5	G-Value, Absorbed Dose	1281
23.5.1	G-Value	1281
23.5.2	Dosimetric Quantities	1282
23.5.3	Dosimetry of γ -Ray and Electron Irradiation	1282
23.5.4	Pulse Dosimetry	1283
23.6	Water and Aqueous Solutions	1284
23.6.1	Intermediates and Final Products in Pure Water	1284
23.6.2	Reactions of e_{aq}^- , H, and OH Intermediates with Solutes	1285
23.6.3	Water as Reactor Coolant	1289
23.7	Radiation Chemistry of Inorganic Solids	1291
23.7.1	Ice	1291
23.7.2	Metals, Semiconductors	1292
23.8	Organic Systems	1292
23.8.1	Saturated, Unsaturated, and Aromatic Hydrocarbons	1293
23.8.2	Other Organic Molecules	1299
23.8.3	Ionic Liquids	1300
23.9	Radiation Chemistry of Polymers	1301
23.9.1	Polymerization, Kinetics, and Mechanism	1302
23.9.2	Radiation Effects in Polymers	1306
23.9.2.1	Main Chain Scission	1307
23.9.2.2	Cross-Linking	1307

23.10	<i>Biological Molecules</i>	1310
23.10.1	DNA and Its Constituents	1310
23.10.2	Polysaccharides	1311
23.10.3	Amino Acids, Peptides	1312
23.10.4	Lipids	1312
23.11	<i>Radiation Applications</i>	1313
23.11.1	Radiation Synthesis	1313
23.11.2	Applications of Radiation Chemistry to Nuclear Technology: The Purex Process	1315
23.11.3	Radiation Processing	1317
23.11.3.1	Application of Ionizing Radiation for Environmental Protection	1317
23.11.3.2	Food Irradiation	1323
23.11.3.3	Sterilization of Medical Products and Drugs	1324
23.12	<i>Editors' Note</i>	1326

Abstract: Ionizing radiation causes chemical changes in the molecules of the interacting medium. The initial molecules change to new molecules, resulting in changes of the physical, chemical, and eventually biological properties of the material. For instance, water decomposes to its elements H_2 and O_2 . In polymers, degradation and crosslinking take place. In biopolymers, e.g., DNS strand breaks and other alterations occur. Such changes are to be avoided in some cases (radiation protection), however, in other cases they are used for technological purposes (radiation processing). This chapter introduces radiation chemistry by discussing the sources of ionizing radiation (radionuclide sources, machine sources), absorption of radiation energy, techniques used in radiation chemistry research, and methods of absorbed energy (absorbed dose) measurements. Radiation chemistry of different classes of inorganic (water and aqueous solutions, inorganic solids, ionic liquids (ILs)) and organic substances (hydrocarbons, halogenated compounds, polymers, and biomolecules) is discussed in concise form together with theoretical and experimental backgrounds. An essential part of the chapter is the introduction of radiation processing technologies in the fields of polymer chemistry, food processing, and sterilization. The application of radiation chemistry to nuclear technology and to protection of environment (flue gas treatment, wastewater treatment) is also discussed.

23.1 Introduction

Radiation chemistry implies the study of chemical effects of interactions of ionizing radiation with materials. The term ionizing radiation in a wider sense is applied to photons or particles having sufficient energy to ionize the molecules of the medium: it involves photons with energies ranging from the first ionization energy of the medium (~ 10 eV) up to several MeV, as well as energetic charged particles, electrons, positrons, accelerated heavy ions, etc. The result of the energy absorption is breaking or rearrangement of chemical bonds. High-energy photons, charged species with sufficiently high energy and neutrons may be absorbed by the nuclei and cause nuclear reactions. This is the field of nuclear physics and nuclear chemistry or radiochemistry and these effects are not considered in radiation chemistry (Hummel 1992).

The field of radiation chemistry has been intensively investigated for about 100 years. However, there is a basic change in the approach. Until the 1950s and 1960s the main aim was to know more about the basic processes of absorption of radiation energy and about the chemical consequences of irradiation (Kroh 1989). In recent years, radiation chemistry is more and more becoming a quite generally applicable method of reaction kinetics by which important kinetic parameters can be measured and reaction mechanisms can be clarified (Tabata 1991a, b; Mayer 1999). Irradiation techniques are often applied as essential parts of technology, e.g., in polymer processing, food processing, sterilization, wastewater and flue gas treatment (Spinks and Woods 1990; Woods and Pikaev 1994). In the field of biological applications, the radiotherapy for cancer treatment should be mentioned. Therefore, this chapter is written not only for radiation chemists, but also for those whose main interests are in related fields, e.g., chemical kinetics, photochemistry, polymer science, radiation biology, radiation physics, radiation technology, radiochemistry, or nuclear technology.

23.2 Sources of Radiation

The sources of ionizing radiation used for research or industrial irradiation purposes can be divided into two groups: sources containing radionuclides, such as ^{60}Co , ^{137}Cs , or the ^{90}Sr – ^{90}Y pair, and machine sources of radiation, such as X-ray equipment or electron accelerators. Without going into details, this chapter will briefly mention those characteristics of some of the radioactive nuclides and accelerators, which are important from the point of view of using them for irradiation purposes.

23.2.1 Radionuclide Sources

^{60}Co is most widely used γ -radiation source for experimental and industrial purposes. It has a half-life of 5.27 years and emits two high-energy photons, 1.17 and 1.33 MeV per disintegration. The isotope is produced by neutron irradiation in $^{59}\text{Co}(n,\gamma)^{60}\text{Co}$ reaction in nuclear reactors. ^{59}Co is usually irradiated in the form of pellets and then these pellets are encapsulated in stainless-steel containers. For research purposes, generally 3.7×10^{13} – 3.7×10^{14} Bq (10^3 – 10^4 Ci) activity sources are used. The commercially available irradiation facilities are often self-shielded, portable although they may weigh several tons. In the industrial irradiation facilities the activity is generally in the 1.85×10^{15} – 3.7×10^{16} Bq (5×10^4 – 10^6 Ci) range. These facilities have irradiation chambers of the size of a room, 15–50 m². Shielding is provided by massive concrete walls, and the operators enter the irradiation chamber through a labyrinth. In the industrial irradiation facilities many tons of goods, e.g., medical products and agricultural products are treated every day. There are about 200 industrial γ -facilities worldwide (Machi 1998). The irradiation facilities used in cancer therapy usually have activities around 3.7×10^{14} Bq (10^4 Ci).

Less frequently, the fission product ^{137}Cs is used for γ -irradiation (γ -ray energy: 0.66 MeV, half-life: 30 years). ^{137}Cs is separated from spent fuel by reprocessing. It is usually applied in the form of cesium chloride sealed in stainless steel capsules.

From the β -ray emitters ^{90}Sr should be mentioned. This nuclide is also obtained from spent fuel by reprocessing. It emits β^- rays with 0.545 MeV maximum energy and a half-life of 28 years. ^{90}Sr disintegrates to its daughter nuclide ^{90}Y , which is also β^- emitter with a half-life of 64 h, maximum energy 2.25 MeV.

23.2.2 Machine Sources

In the pioneering period of radiation chemical research, the radiation emitted by X-ray equipment was often utilized for irradiation purposes. Nowadays particle accelerators, and first of all *electron accelerators* are the main machine sources of radiation (Spinks and Woods 1990).

In the *Van de Graaff accelerators*, a high-voltage electric field (up to several million volts) accelerates the electrons emitted by the hot cathode. (See more about Van de Graaff accelerators in ► Sect. 50.2.3.2, Chap. 50, Vol. 5, on “Particle Accelerators.”) The maximum energy of electrons is limited by the high-voltage insulation: most accelerators work between 1 and 5 MeV electron energy. These machines normally produce a continuous beam, but some of the accelerators were modified to deliver pulses in the subnanosecond – microsecond ($1 \text{ ns} = 10^{-9} \text{ s}$, $1 \mu\text{s} = 10^{-6} \text{ s}$) range. Van de Graaff type accelerators are also used to accelerate particles other

than electrons, e.g., protons, He^{2+} , or C^{6+} ions: these accelerators are the principal radiation sources in heavy ion radiolysis studies.

Pulse radiolysis studies in several laboratories are carried out by using pulsed field emission accelerators. In these accelerators that are known as *Febetron accelerators* (brand name, Field Emission Corporation, McMinnville, OR), similarly to the Van de Graaffs, electric field is used for electron acceleration. Charging a large number of high-capacity condensers in parallel and then discharging them in series produces the accelerating voltage. In contrast to most other accelerators, in these machines the electrons are produced at a field emission cathode. The pulse length is generally a few nanoseconds and the system is capable of giving very high electric currents in the 1,000 A range.

In *linear accelerators* (LINAC) a microwave produced by a magnetron or klystron power generator is used to accelerate the electrons entering the accelerator tube after a 50–100 keV preacceleration by static electric field. (Magnetron and klystron are different types of microwave generators. The LINAC mentioned here is basically the same as the diaphragm waveguide used for the acceleration of positrons as shown in [▶ Fig. 27.8 in Chap. 27](#) on “Positron Annihilation Spectroscopies.” The radiofrequency (RF)-based linear accelerator shown in [▶ Fig. 50.17, Chap. 50, Vol. 5](#), on “Particle Accelerators,” is also referred to as LINAC; it is used for the acceleration of protons and still heavier ions.) The accelerator tube is a few meters long segmented waveguide. The electrons injected into the waveguide, after a bunching process, ride on the crest of waves traveling along the guide and are accelerated to high energies up to several times 10 MeV (Spinks and Woods 1990). Two microwave frequencies, $\sim 1,400$ MHz (L-band) and $\sim 2,800$ MHz (S-band) are most commonly used. The accelerated electrons are delivered in pulses of nanoseconds or microseconds duration with a repetition rate of 50–500 Hz. For scientific purposes, low-power accelerators are usually applied, whereas for industrial irradiations high-power machines, 10–100 kW, are also available. In the high-power accelerators used for industrial irradiation, the beam can be magnetically deflected to sweep a larger irradiation area.

In both the S-band and L-band accelerators, the electric pulse exhibits a fine structure due to the bunching of electrons in the microwave field. The bunching results in trains of 10–30 ps ($1 \text{ ps} = 10^{-12} \text{ s}$) electron pulses: the individual pulses are separated by ~ 350 or ~ 710 ps. The individual pulses give a unique possibility to carry out picosecond pulse radiolysis experiments (Jonah 1975; Kobayashi and Tabata 1989). The first picosecond pulse radiolysis experiments were realized using trains of pulses. Combination of the trains of pulses with a stroboscopic detection allowed a time resolution in the 10 ps range. A technique called “subharmonic prebunching” is used to produce single picosecond pulses for pulse radiolysis purposes. With the help of a further technique called pulse compression pulses in the femtosecond range ($1 \text{ fs} = 10^{-15} \text{ s}$) were also produced (Uesaka et al. 2001; Muroya et al. 2001; Aoki et al. 2001). Because it involves more accelerating structures with multiple frequencies and phase relationships, and high-performance electron gun to inject electrons, subharmonic prebunching adds a lot of cost and complexity of operation of the LINAC facility (Wishart 2008). Consequently only a few prebunched LINACs were built for pulse radiolysis purposes.

During the late 1980s and into the 1990s, a new technology was introduced for generation of picoseconds electron beams. Instead of emission from a hot cathode to produce the electron beam, a metal or semiconductor cathode is struck with an ultraviolet (UV) laser pulse to emit electrons via photoelectric effect: the emitted electron pulse is as short as the incident laser pulse. Since the photocathode-based picosecond systems are simpler than the prebunched thermal emission setups, the newer picosecond pulse radiolysis systems are using this technique (Barbara 1998; Aoki et al. 2001; Wishart 2008).

Recently laser plasma LINAC accelerators are under development (Barbara 1998; Uesaka et al. 2001; Wishart 2008). In these systems a very intense terawatt (TW) femtosecond laser pulse hits the gas flow (helium) in a supersonic gas jet. The extremely strong electromagnetic field of the laser radiation strips the electrons off the helium atoms and accelerates them to very high energies in a process called wake-field acceleration. The wave energy is transferred to longitudinal electron momentum. The electrons have a broad energy distribution up to 30 MeV energy. This wide energy range is – at present – a disadvantage, limits the ability to transport the electrons from the point of generation.

The electron accelerators mentioned before, with the exception of LINACs, are used for scientific purposes. For industrial (processing) purposes high-power, 100 kW–1 MW, accelerators, which work with high, 20–80% electrical efficiency, are needed. The type of the accelerator selected for a given task depends on the thickness of the product to be irradiated.

In polymer processing, flue gas treatment, and wastewater treatment, medium-energy (0.5–5 MeV) electron accelerators are usually utilized. (Lower energy electrons are unsuitable because of their lower penetration.) In the medium energy range, very often transformer type accelerators are applied that use direct current voltage for the acceleration. The direct current voltage supplies are based on oil- or gas-filled transformers with rectifier circuits. When the voltage level is less than 700 keV, a high-voltage cable may be used to connect the power supply and the accelerator head. Between 700 keV and 5 MeV, high-voltage generators are utilized. In such generators, inductance and capacitance couplings make it possible to multiply the alternating current voltage up to 5 MeV. These machines work with 100–400 kW power and high electrical efficiency of 60–80%.

As mentioned before, high-power LINACs are also available for industrial purposes. In the accelerator tube of LINACs the electrons gain energy from the high-frequency microwave field in several resonant cavities. The new types of medium and large (>5 MeV) energy, high-power, high-frequency (>100 MHz) industrial accelerators use a single large resonant cavity and the electron passes through the cavity several times. In the case of the compact Rhodotron accelerators, when the electron crosses the resonant cavity, it gains ~1 MeV of energy each time. Ten passes and nine bending magnets are needed to obtain 10 MeV electron beam energy. These types of machines are produced up to 700 kW power and the electrical efficiencies are around 30–40% (Haji-Saeid 2007).

23.3 Energy Deposition, Ionization

Since in the radiation chemical practice mostly accelerated electron irradiation and γ -ray irradiation are applied, a brief summary will follow on the energy absorption of these particles in matter. The basic particle–matter interaction types are discussed in ► Chap. 8 of Vol. 1; that chapter approaches this problem from the side of the particle and concentrates on the question how the particle loses its energy. The main interaction types will also be mentioned here; however, the details will only be discussed in connection with the question of how the molecules gain energy from the energetic particles.

23.3.1 Energy Deposition

When they penetrate matter, the high-energy photons or electrons interact with the molecules of the medium. As a consequence of the inelastic collisions the particles lose energy with

concomitant formation of energy-rich excited or ionized molecules. These excited or ionized molecules will be referred to as activated molecules.

High-energy electrons interact either with the Coulomb field of the nucleus of the atom or with the electron shell in elastic or inelastic interactions. By passing through the electric field of an atomic nucleus, the high-energy electron can be decelerated leading to continuous bremsstrahlung. In interactions with the electron shell characteristic X-rays may form. The absorption of energy of X-rays and bremsstrahlung is similar to the absorption of γ -radiation energy. In inelastic collisions with the electrons of the medium the high-energy electron loses energy and slows down, and ionization or excitation of the absorbing material results. In the course of elastic scattering the direction of motion changes without conversion of kinetic energy into any other form of energy. The electron energy and the nature of absorbing material determine the relative frequencies of the different interactions.

High-energy photons interact with the medium by the photoelectric effect, Compton scattering, and by electron–positron pair production (see [Chap. 8, Vol. 1](#)). The threshold energy of the pair production (1.02 MeV) is twice the rest-mass energy of electron (0.51 MeV). This interaction type has importance at energies considerably higher than the threshold energy and especially in materials containing heavy elements. The photoelectric effect is predominant at low energies. In the latter interaction, an electron is ejected from the atom or molecule with a kinetic energy equal to the energy of photon minus the binding energy of the electron. In the Compton effect only a part of the incident photon energy is used to eject electron from the atom or molecule. The lower-energy photon thus produced may take part in further Compton or photoelectric interactions. As a consequence of energy degradation process of a high-energy γ -photon, a large number of energetic electrons are produced. Activated molecules are mostly produced in the interactions of these fast electrons with the atoms or molecules in the medium (Spinks and Woods 1990; Mozumder 1999, 2004). From the point of view of energy dissipation, four cases may be distinguished:

- Case a**, Activated molecule formation in the interactions of very high-energy particles (photons, electrons) with the atoms and molecules (hard collisions);
- Case b**, Interactions of the so-called fast electrons (electrons with several hundred – several thousand eV energy) with the atoms and molecules of the medium;
- Case c**, Reactions of slow electrons (energy between ca. 5 and 100 eV) with the atoms and molecules;
- Case d**, Scattering of very low-energy electrons (<5 eV) in the medium.

In the interactions of the very high-energy electrons (**Case a**) large amount of energy is transferred to the electron of the interacting molecule. For such energetic charged particle–electron interactions the classical model, which treats the system as a fast-moving charged particle passing along the free electron at rest, gives a good description. As a result of the Coulomb interaction the free electron is set in motion at the expense of the momentum (and the energy) of the fast-moving charged particle. The “probability” dP for a charged particle with charge ze and speed u to transfer energy between Q and $Q + dQ$ to an electron of the medium when passing unit distance is given by the model as

$$dP = NZ \frac{2\pi e^4 z^2}{(4\pi\epsilon_0)^2 m_e u^2} \times \frac{dQ}{Q^2}, \quad (23.1)$$

where m_e is the electron mass. In the equation NZ , the product of the number density of molecules, N , and the number of electrons in one molecule, Z , is the electron number density.

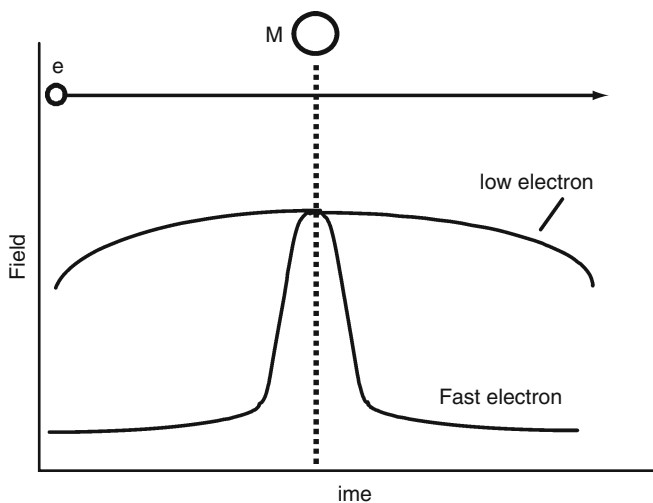
The quantity dP/NZ has a dimension of $(\text{length})^2$ and it is called the differential cross section for the events per electron (Hummel 1992).

For low values of Q , i.e., when Q is comparable to the binding energy of the electron, the picture of a collision with a free electron at rest is not any more correct. For such so-called *soft collisions* a model is applied, which involves resonance-like absorption of energy by the molecules. A visual picture given by Bednar in a conference paper (Bednar 1983) may help to understand the essence of the model. In the gas phase, the fast electron passing by the molecule M induces in the molecule a strongly time-dependent electric polarization (► Fig. 23.1). This time-dependent polarization is experienced by the molecule as electromagnetic waves with a range of frequencies. Some of the electrons of the molecule may start oscillating and a resonant excitation or ionization may occur.

The transit time of a fast electron with a kinetic energy in the 10^2 – 10^4 eV range (**Case b**) nearby the molecule is in the 10^{-18} s range. This is actually similar to the time needed for electric transition induced by the absorption of a photon of ~ 10 eV energy. The impulse action of the fast charged particle is practically equivalent to the absorption of energy from the electromagnetic field. In the charged particle action, like in photolysis, the optical selection rules also have an effect on the nature of the electric transitions. These selection rules determine which transition is symmetry or spin, allowed or forbidden. As regards the spin, according to the general rule, during the transition the multiplicity does not change. Since in the ground state most of the atoms and molecules have singlet multiplicity, after the promotion of an electron to a higher unoccupied atom or molecule orbital, the singlet multiplicity remains. However, there are some important differences between photon absorption and fast electron interactions. In photolysis the total energy of the photon is absorbed by the molecule and usually a given excitation or given ionization occurs. In the fast electron interactions the energy gained by the molecule varies from the energy of the lowest excited state to very high energy.

■ Fig. 23.1

Interaction of a passing electron (e) with a molecule (M). Fast electrons exert an impulse action on the molecule, whereas in the case of slow electrons the effect is elongated



According to Platzman's optical approximation theory (Platzman, 1962) the "probability" of picking up energy between Q and $Q + dQ$ is given by the equation

$$dP = \frac{2\pi e^4 z^2}{(4\pi\epsilon_0)^2 m_e u^2} \frac{df}{dQ} \frac{N}{Q} \ln(2m_e u^2 / Q) dQ, \quad (23.2)$$

In the equation the quantity df/dQ is the so-called *differential oscillation strength*. df/dQ is proportional to the optical absorption coefficient. The logarithmic term varies only slowly with Q , therefore the probability of resonant transition is roughly proportional to the $(df/dQ)/Q$ ratio, i.e., it is proportional to the ratio of optical absorption coefficient and the transition energy. If the optical absorption spectrum is accurately known, this equation gives a possibility for the calculation of the transition probabilities and also the yields of the different excited molecules (Hatano 1968, 1999; Makarov and Polak 1970; Kouchi and Hatano 2004).

The reciprocal energy dependence strongly limits the energy absorption at high energies: most of the energy absorption occurs between 10 and 40 eV. In this energy range there is a high probability for the formation of "superexcited" molecules (Makarov and Polak 1970; Robin 1974, 1975, 1985; Hatano 1999). The "*superexcited*" molecules are neutral excited molecules, but their excess energy is higher than the ionization threshold. The lifetime of the superexcited molecules is generally short. They may disappear in auto ionization, in conversion to lower energy excited molecules or in direct dissociation to fragments (Makarov and Polak 1970; Hatano 1999).

As described previously, the fast electrons slow down gradually losing ~ 10 – 40 eV energy in each interaction. As the kinetic energy of the incident particle drops below a certain value, ~ 100 eV (**Case c**), there is no more possibility of a "sudden" energy transfer like with a fast particle (Bednar 1983). Therefore, the optical approximation loses its validity, and optically not allowed transitions may also occur in the energy transfer process: there is a direct possibility for excitation to triplet excited states.

When the energy of the electron drops below ~ 5 eV (**Case d**) there is no more possibility for energy loss in electron excitation processes. The electron scatters in the medium losing energy in very slow energy transfer processes to the vibration/rotation levels of the molecules.

The total energy lost per unit path length by the primary charged particle is obtained by the sum of integrating over all losses occurring in hard and soft collisions. The total energy lost per unit path is called the *linear energy transfer* (LET). In water, the mean LET for fast electrons is ~ 0.2 eV nm $^{-1}$. When 5.3 MeV α particles are applied for irradiation LET-value is much higher, 43 eV nm $^{-1}$. LET is proportional to the square of the charge of the particle, z^2 , and inversely proportional to the square of its speed, u^2 .

In radiation chemistry, the intermediates form with a strongly nonhomogeneous distribution in the matrix (Freeman 1987). At the beginning of an electron track, when the energy is high, the intermediates are sparsely populated. When, however, the electron slows down to low energies, the local intermediate density is high. The energetic electrons along the track produce also secondary electrons (δ electrons) of lower energy that also cause ionization and excitation in the medium. However, due to the lower energy their tracks are shorter. When the electron energy is ~ 100 eV, its range in condensed phases is short and there is a high probability that the electron transfers excitation or ionization energy to a molecule close to the original ionization. In this way a small cluster or *spur* of ionized or excited molecules forms. (The "spur" concept plays an important role in the "spur model" of positronium formation described by [Eq. \(27.2\)](#) in [Chap. 27](#), on "Positron Annihilation Spectroscopies.") In the spur the intermediates

mutually influence each other's reaction possibilities. According to a more strict definition (Freeman 1968) even a single ionization producing a geminate ion pair create a spur: a spur is a grouping of reactive intermediates in which there is a significant probability that some of the intermediates will react with each other before they can diffuse into the bulk medium. Cloud chamber measurements showed that in water vapor 44% of the spurs contain one, 22% two, and 13% three ion pairs.

In condensed phases there are two to four activated molecules in one spur corresponding to ~ 100 eV energy loss. δ electrons in the 100–500 eV range produce larger spurs that may be called *blobs*. δ electrons in the 500 eV–5 keV range can generate short tracks, or above 5 keV branch tracks.

If a mixture of compounds is irradiated the fraction of the total absorbed energy transferred to each component of the mixture is determined by the mole fraction (x) of the component and by its energy absorption characteristics. To a first approximation the yield of product P, $G(P)$, formed in a mixture of A and B is given by the equation

$$G(P) = G(P)_A \varepsilon_A + G(P)_B \varepsilon_B, \quad (23.3)$$

$$\varepsilon_A = \frac{(1-x)Z_A}{(1-x)Z_A + xZ_B}, \quad (23.4)$$

where $G(P)_A$ and $G(P)_B$ are the yields of P product from A and B, and ε_A and ε_B are the electron fractions of A and B, respectively (*linear mixing rule*). (The radiation chemical yield, or G-value, is defined later by [Eq. \(23.15\)](#).) The electron fraction in a binary mixture is defined by [Eq. \(23.4\)](#), Z_A and Z_B are total numbers of electrons in molecules A and B, respectively.

23.3.2 Formation and Decay of Ion Pairs

As discussed previously, the absorption of the energy of high-energy particles in the medium mostly causes (directly or through a superexcited state) ionization of molecules. In gas phase, the ejected electron can easily escape the Coulomb field of the positive ion. Therefore, the charges become homogeneously distributed in the medium: charge recombination occurs randomly (homogeneous recombination). In contrast to the gas phase, in condensed phases the fate of the ion pairs and the nature of the recombination are strongly dependent on the properties of the medium. In the low-permittivity hydrocarbons, most of the ejected electrons lose the kinetic energy in interactions with the surrounding molecules and return to the geminate ion. Such recombination is called *geminate recombination*.

According to *Onsager's theory* the electron escape probability, $\Phi(r)$, is a function of the permittivity of the solution

$$\Phi(r) = \exp\left(\frac{-e^2}{4\pi\varepsilon_0\varepsilon_r kT}\right), \quad (23.5)$$

where e is the elementary charge, ε_r is the relative permittivity, ε_0 is the vacuum permittivity, and r is the distance between the ion and the electron. The *critical distance*, $r_c = e^2/(4\pi\varepsilon_0\varepsilon_r kT)$, where the energy of Coulomb interaction between electron and positive ion is equal to the thermal energy is 25–32 nm in hydrocarbons. When $r > r_c$ the fate of the electron mainly depends on the thermal diffusion. When $r < r_c$ the Coulomb interactions are predominant. In alkanes, 2–30% of the ejected electrons escape the positive ion and undergo homogeneous recombination (Freeman 1987).

The free ion yields strongly depend on the molecular structure; in linear alkanes the yields are low, the yields increase with the increasing branching. There is a positive correlation between the free ion yields and the mobility of electrons in the hydrocarbons. Since the yield and mobility of electric charge carriers in insulators like hydrocarbons is very important from both theoretical and practical point of view, a large number of papers were devoted to this subject and there are some good review papers as well (Hummel and Schmidt 1974; Holroyd 1987; Holroyd and Schmidt 1989; Holroyd 2004).

In liquid water at room temperature, the critical distance is only $r_c = 0.7$ nm. Most of the ejected electrons (dry electrons) have sufficient kinetic energy to get away from the positive ions. After thermalization, the electron orients the surrounding water molecules and forms the so-called hydrated electron (e_{aq}^-). The properties of this species, the hydrated electron, are now well known. Its reactions with a large variety of solutes were investigated in many hundred papers (Buxton et al. 1988).

➤ Table 23.1 shows the ionization potentials and the mean energies needed for ionization in the gas phase (W -values). The W -values are between 21 and 36 eV, and they are much higher than the ionization potential values. The high difference is partly because a considerable part of energy absorbed is used for excitation and also to the fact that ionization does not solely occur with the lowest energy electron.

23.4 Techniques in Radiation Chemistry

Two main different experimental approaches are used to investigate radiation chemical reactions. One of them is applied to detect, qualitatively or quantitatively determine intermediates and final products that are stable and do not change during the time of measurement. Such intermediates are ions or free radicals “frozen” in solid matrices. The other approach uses time dependent measurement in order to observe intermediates or the build up of final products (pulse radiolysis).

23.4.1 Steady-State Techniques

The final products of radiolysis reactions are analyzed by the usual analytical techniques, like spectrophotometry, gas chromatography, high-performance liquid chromatography (HPLC), and others. In the radiolysis investigations the conversion is generally very low, being on the order of 0.0001–0.01, therefore sensitive analytical techniques are needed. A new generation of techniques, for instance chromatographic and electrophoresis analytical instrumentation based on diode-array technology now makes it possible to examine radiation chemical processes below 10 Gy dose (Barbara 1998).

In radiolysis reactions, excited molecules, cations, free electrons, anions, and radicals are the main intermediates. For the study of radical anions, cations and radicals formed in a solid matrix, e.g., in polymers, electron paramagnetic resonance (EPR) spectroscopy is used since the 1950s. Anion and cation species can also be studied by UV spectroscopy. Absorption spectra of many organic radical anions and cations were measured in tetrahydrofuran or in halogenated hydrocarbon matrices (Shida 1988).

A widespread technique for studying the intermediates is the *scavenger method*. Yields of some of the products decrease, those of others increase or remain unchanged in the presence of

■ Table 23.1

Ionization potentials and the average value of radiation energy spent for producing a single ion pair (W -value) in the gas phase

Molecules	Ionization potential, eV	W -value, eV
Inorganic molecules		
H ₂	15.4	36.5
O ₂	12.1	30.8
CO ₂	13.8	33.0
N ₂ O	12.7	32.6
H ₂ O	12.6	29.6
NH ₃	10.2	26.6
Hydrocarbons		
Methane	12.7	27.3
Ethane	11.7	25.0
<i>n</i> -Hexane	10.17	22.61
3-Methylpentane	10.05	22.67
2,3-Dimethylbutane	10.00	22.80
2,2-Dimethylbutane	10.04	22.88
Cyclohexane	9.88	25.05
Ethylene	10.52	24.6
Benzene	9.25	20.9
Other organic molecules		
Methanol	10.08	
Ethanol	10.5	24.8
Acetone	9.7	

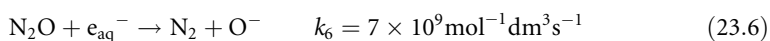
The W values compiled have been measured using electromagnetic radiation; however, the W values are nearly independent of the energy and type of radiation.

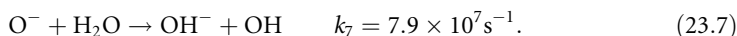
Blaunstein and Christophorou (1971), Christodoulides et al. (1984), Spinks and Woods (1990), Tabata (1991a).

scavengers, and new components appear among the products as a result of the scavenging process (Tabata 1991a). A general problem of the scavenger experiments is the practical impossibility of finding specific additives that react only with one type of intermediate being present during radiolysis. For instance, substances generally used as radical scavengers may also react with electrons, since both radical scavenging and electron scavenging are related to the electron affinity of the substance.

For *scavenging excited molecules* compounds with low excitation energies are used, e.g., aromatic hydrocarbons. These compounds in the excited state exhibit strong fluorescence that can be used to detect excited molecule quenching (Földiák 1981).

Electron scavenging is often carried out using N₂O additive. At room temperature it dissolves in water in 0.025 mol dm⁻³ concentration. In reaction with hydrated electrons, N₂O transforms to N₂ and OH (Schuler and Albarran 2002):





In hydrocarbons N_2 , H_2O , and in small amounts alcohols (e.g., in cyclohexane cyclohexanol) form as a result of electron scavenging. Alkyl halides are often used as electron scavengers in hydrocarbon systems, e.g., methyl bromide:



The methyl radical thus formed may abstract a hydrogen atom in organic solvents and the methane yield represents the electron scavenging yield. In the presence of radioactive I_2 the scavenging yield is calculated from the amount of radioactive methyl iodide formed (Warman et al. 1968, 1969).

It is much more difficult to find good *positive-ion scavengers* than electron scavengers. In ammonia and in hydrocarbons, cyclopropane may be used for this purpose.

Generally, charge scavenging and charge geminate recombination are in competition. It has been found that in saturated hydrocarbons and often in other solvents as well, the scavenged yield can be represented by a simple expression called Warman–Asmus–Schuler equation (Warman et al. 1968, 1969)

$$G(\text{scavenged species}) = G_{\text{fi}} + G_{\text{gi}} \frac{(\alpha c)^n}{1 + (\alpha c)^n}, \quad (23.9)$$

where n is around 0.5. G_{fi} and G_{gi} are the yields of ion pairs undergoing homogeneous (free ion) and inhomogeneous (geminate ion) recombination. The α parameter is a measure of the efficiency of the scavenging reaction.

The *detection of free radicals* and the determination of their yields can be achieved by using unsaturated hydrocarbons (e.g., ethylene) or other substances with unsaturated bonds or with unpaired electron (iodine, oxygen, nitrogen monoxide, benzoquinone, stable free radicals, etc.) as scavengers. The reactions of molecular iodine were often studied by applying radioactive iodine. Iodine reacts with many radicals with diffusion-controlled rate coefficient (LaVerne and Woinárovits 1994)




Radical scavengers are generally applied in $10^{-3} \text{ mol dm}^{-3}$ concentration. This concentration is sufficient to scavenge all the radicals that escape the spur or track; however, at this concentration level the scavenger cannot compete effectively with the reactions taking place in regions where several radical species are in close proximity, or with abstraction, or addition reactions of hot radicals.

23.4.2 Pulse Radiolysis, Technical Realization, and Detection Systems

The intermediates of radiolysis processes can be studied directly by the pulse radiolysis method. In pulse radiolysis experiments a short ps–μs pulse of electrons accelerated to several MeV energy is directed into a cell that contains the sample to be irradiated (Ebert et al. 1965; Baxendale and Busi 1982; Tabata 1991b; Mayer 1999; Wishart 2008). By the method the time dependence of the buildup and decay of intermediates and stable products are followed by

various detection systems. For the observation of intermediate and possibly end products, optical absorption and emission spectroscopy have been used since the early 1960s. In addition to absorption and emission, light scattering, direct current (DC), alternating current (AC), microwave conductivity, polarography, and EPR and nuclear magnetic resonance (NMR) monitoring techniques are also often used for detection. An excellent description of these methods is given in the *Proceedings of the NATO Advanced Study Institute* held at Capri, Italy, 1981 (Baxendale and Busi 1982). Patterson (1987), and more recently Karolczak (1999) also published a book chapter on the different monitoring techniques. The latter works mention some new techniques as well, like detection based on resonance Raman spectroscopy, time-resolved circular dichroism, or time-resolved X-ray absorption measurements. In the book *Pulse Radiolysis* edited by Tabata (1991b), the experts, sometimes inventors of the technique describe some selected pulse radiolysis techniques together with applications. Herkstroeter and Gould (1993) published a detailed description of the optical detection. Recently, Wishart (2008) summarized the ultrafast detection techniques in pulse radiolysis.

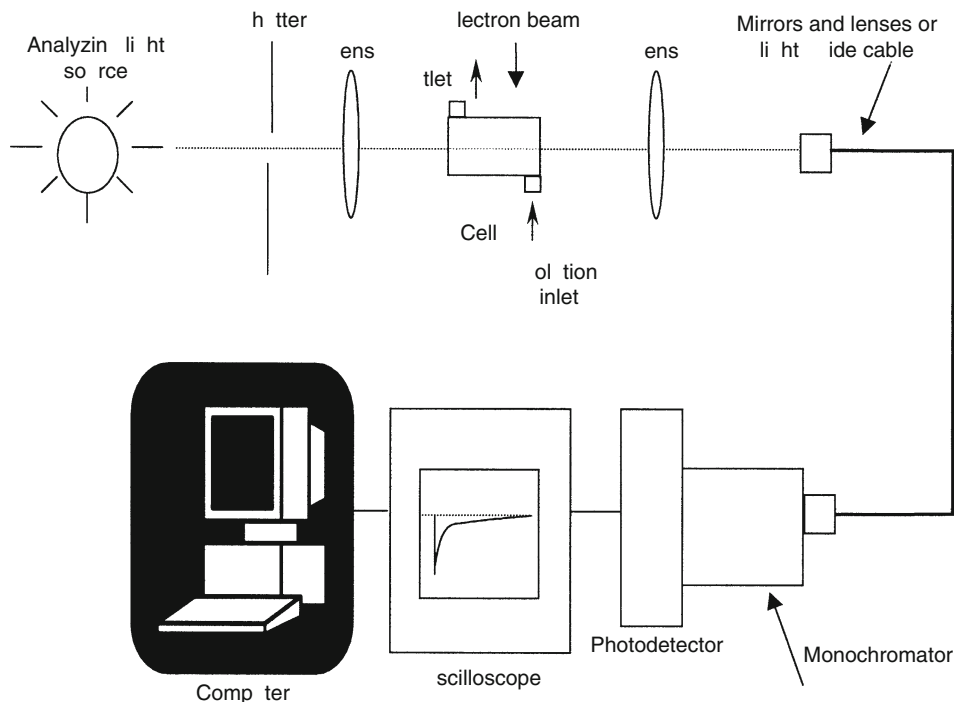
Since optical detection systems are used in most of the pulse radiolysis laboratories (and often the other methods are regarded as subsidiary detection techniques), this subsection only describes the principles and typical implementation of optical systems. The method, also called kinetic spectrophotometry or time-resolved spectrophotometry, differs from the conventional spectrophotometric technique since it uses a single path: the reference level is obtained as the light level passes the sample prior to irradiation. This is the basis for the high sensitivity of kinetic spectrophotometry: changes less than 1% in the transmitted light level are measured accurately. Averaging of a large number of traces is possible when using a computerized data acquisition system. The second important difference as compared to conventional spectrophotometry is the short response time. This setup, without the analyzing light, can also be used for emission measurements, although for the latter simpler systems are also used showing considerable advantages.

A schematic illustration of a pulse radiolysis setup is shown on  Fig. 23.2. In the usual arrangements the measuring system is divided into two parts. The first part, including the light source for the sample illumination, the lens system, the shutter preventing the heating, photolysis of the sample, light filters, and the measuring cell itself, is housed in the irradiation room. The measuring cell should be positioned in the beam so as to achieve an approximately homogeneous irradiation. The other parts of the setup are outside the radiation shielding concrete wall and the Faraday cage protecting against electromagnetic interference. These include the monochromator, the photodetector, the oscilloscope/digitizer, and the computer system for data acquisition and processing. Light is usually transmitted from the irradiation room to the measuring room through a hole in the shielding by means of mirrors and lenses. Less frequently light guide cable is used.

To achieve high sensitivity, the optical system should pass high light intensity at a given wavelength. For this, high-output lamps are needed. As light source, high-pressure xenon lamps are often used, the ones having approximately $1 \times 2 \text{ mm}^2$ illuminating area are the most widespread. Another advantage of the xenon lamps is that their light output can be increased considerably for several milliseconds by pulsing the arc current. During the pulse the arc dimensions do not change appreciably, and the increased power is mainly due to the increased luminosity of the arc. As an additional advantage, light density considerably increases in the ultraviolet part of the spectrum, where, under normal operation, the intensity is rather weak. With commercially available lamps, several thousand pulses can be delivered without substantial deterioration of lamp performance. In practice, mostly 150–1,000 W air-cooled or

■ Fig. 23.2

Schematic representation of pulse radiolysis with kinetic spectroscopic detection



water-cooled xenon lamps are used. The pulsing units contain capacitive pulse forming network; the discharge through the lamp is controlled by a thyristor.

Radiation resistance is an essential requirement for all the optics in the radiation field, this requirement is satisfied by using high purity fused synthetic quartz.

The transient changes of the optical absorption are monitored by photodetectors. The time dependence of the detector signal is monitored on an oscilloscope. Nowadays the signals in the ns–s range are digitized by transient digitizers, or digitizing oscilloscopes. Mostly photomultipliers or photodiodes are used as photodetectors. The photodiodes possess lower noise and higher quantum efficiency as compared to the multipliers, but they require a separate amplifier. Amplification occurs on the dynodes in the photomultipliers. Typical values are in the 10^3 – 10^9 range.

When light strikes the photocathode of a photomultiplier, photoelectrons are continuously produced but the instantaneous rate of production shows a statistical fluctuation because the photons of incident light arrive at random. This fluctuation of photoelectron formation is the reason for the fluctuations known as *shot noise*. The root mean square fluctuation of the cathode current, ΔI_c , is given as

$$\Delta I_c = \sqrt{2eI_c\Delta f}, \quad (23.12)$$

where I_c is the cathode current, e is the elementary charge, and Δf is the bandwidth of the detection system. The multiplier dynodes amplify this noise together with the signal.¹ For ideal

amplifiers $\Delta I_c/I_c$ equals $\Delta I_a/I_a$, where ΔI_a is the root mean square fluctuation of the anode current I_a . The signal at the oscilloscope is given as $I_a R$, where R is the load resistor. The sensitivity of the fast kinetic spectrophotometry is limited first of all by this shot noise. The signal to noise ratio, S/N is given as

$$\frac{S}{N} = \frac{I_c}{\Delta I_c} = \sqrt{\frac{I_c}{2e\Delta f}} \quad (23.13)$$

Decreasing of the shot noise is possible either by increasing the analyzing light intensity or by decreasing the bandwidth of the detection system (but this is practical only for signals in the microsecond range or longer).

As mentioned previously, in order to increase the sensitivity of the measurement, one can use pulsed analyzing light. The resulting small transient signal superimposed to a high DC level can only be measured accurately if it is separated from the DC component. A widespread method for doing this is called “backing-off” (► Fig. 23.3). In this procedure one circuit compensates, the other circuit measures the DC level.

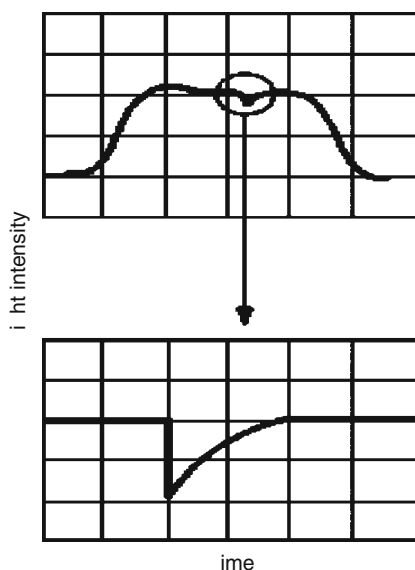
The transient signal, separated from the DC level, is monitored on the oscilloscope and digitized. Several implementations of the backing-off method are described.

By kinetic spectrophotometers, the time-dependent absorbance (A) of the observed species is measured. According to the *Beer–Lambert law*

$$A = \lg \frac{I_0}{I} = \lg \frac{100\%}{T} = \varepsilon_\lambda c l, \quad (23.14)$$

■ Fig. 23.3

Effect of “backing-off” on the light intensity signal. The *upper figure* shows the oscilloscope screen with the pulsed light. The transient light intensity disturbance caused by the light absorption of the intermediate (shown in the circle) is enlarged by the “backing-off” method as shown in the *lower figure*



Where I_0 and I are the intensities of the incident and the transmitted light, respectively, T is the transmission in percentage, ϵ_λ is the molar extinction coefficient at wavelength λ , c is the concentration, and l is the optical path-length in the cell.

In the traditional experiments the time dependence is measured at a given wavelength. The spectrum of the intermediates can be composed from a series of measurements taking the absorbance at a constant time after the pulse. A complete spectrum can be measured in a single step by using gated diode-array detectors. However, their time resolution is not sufficient for very fast measurements. In the 100 ps–100 ns time range streak camera may be used for taking the spectrum. (A streak camera is an instrument making unnecessary the usual process of converting light to electronic signals then converting them back again to light.)

There are two optical detection techniques, which were used to provide picosecond time resolution. One is a system with a very fast photodetector: extremely fast phototube detectors and high-bandwidth oscilloscopes (≥ 6 GHz) offer resolution in the visible range down to 80 ps, which is still slower than the capabilities of the accelerator to produce short electron pulses (Wishart 2008). Detectors in other wavelength regions are slower and have complex responses. The other technique is the stroboscopic pulse radiolysis in which very short electron pulses and very short analyzing light pulses are used. In the latter as the analyzing light Cherenkov radiation may be used. Cherenkov light pulses probe the time profile of the transient produced by electron irradiation by varying the time between electron beam and Cherenkov light pulses. The stroboscopic technique can be combined both with multibunched beams and with single fine structure pulses. In the stroboscopic pulse radiolysis system, since the time response is independent of the time response of the photodetector, detectors with slow time response may be used. In the twin LINAC system operating at the University of Tokyo one accelerator is used for the irradiation and the other one to produce the Cherenkov light for analysis. There are two possibilities for the measurements. When the time interval between electron pulse and Cherenkov light is scanned at a fixed wavelength of Cherenkov light a time profile of an absorbing intermediate can be obtained. On the other hand, when the time interval between electron pulse and Cherenkov light is fixed and the wavelength of analyzing light is scanned a spectrum at a fixed time can be obtained (Tabata 1991b; Muroya et al., 2001; Uesaka et al. 2001; Aoki et al. 2001).

23.5 G-Value, Absorbed Dose

In order to quantify the radiation chemical effects of ionizing radiation one has to know the amount of molecules transformed or produced and the quantity of absorbed radiation energy that caused this effect. The ratio of the two is the radiation chemical yield, also called the G-value.

23.5.1 G-Value

The radiation chemical yield, $G(X)$, is defined as the quotient of the amount $n(X)$ of a substance of a specified entity, X , produced, destroyed, or changed by radiation, by the mean energy imparted, E , to the irradiated matter

$$G(X) = \frac{n(X)}{E}. \quad (23.15)$$

Hence, the SI unit of the G -value is mol J^{-1} . In most of the literature up to the 1990s, the G -value was expressed as the number of molecules produced, destroyed, or changed per 100 eV of energy absorbed. The conversion to SI units is as follows (Spinks and Woods 1990):

$$1 \mu\text{mol J}^{-1} = 9.65 \text{ molecules } (100 \text{ eV})^{-1}, \quad (23.16)$$

$$1 \text{ molecule } (100 \text{ eV})^{-1} = 0.1036 \mu\text{mol J}^{-1}. \quad (23.17)$$

23.5.2 Dosimetric Quantities

Since only the absorbed fraction of the incident radiation flux can induce physical or chemical changes, the absorbed energy, in other words the absorbed dose is an important quantity. The absorbed dose or simply the dose is defined as the mean energy, dE , imparted to an incremental quantity of matter, divided by the mass of that matter:

$$D = \frac{dE}{dm}. \quad (23.18)$$

(See for more details ► Chap. 47, Vol. 5, on “Dosimetry and Biological Effects of Ionizing Radiation”).

The preferred SI unit of the *absorbed dose* is the *gray* (Gy), which expresses in joule per kilogram (J kg^{-1}) the energy imparted to unit mass: $1 \text{ Gy} = 6.24 \times 10^{15} \text{ eV g}^{-1}$. In the radiation safety practice often milligray units are applied ($1 \text{ mGy} = 10^{-3} \text{ Gy}$), whereas in the radiation technological applications kilogray and sometimes megagray units are also used ($1 \text{ kGy} = 10^3 \text{ Gy}$, $1 \text{ MGy} = 10^6 \text{ Gy}$). The former absorbed dose unit, *rad*, was defined as 100 erg g^{-1} or $10^{-2} \text{ J kg}^{-1}$, therefore $1 \text{ Gy} = 100 \text{ rad}$ (Holm and Berry 1970; Kase et al. 1985; McLaughlin et al. 1989).

The energy absorbed by the unit mass in unit time is called the *absorbed dose rate* (\dot{D}); it is expressed in Gy s^{-1} , Gy min^{-1} , or in Gy h^{-1} units:

$$\dot{D} = \frac{dD}{dt}. \quad (23.19)$$

23.5.3 Dosimetry of γ -Ray and Electron Irradiation

The dosimeters developed for measuring absorbed doses are often classified into two groups based on the principle of operation: physical and chemical dosimeters. The physical dosimeters detect some physical effect induced by high-energy particles: e.g., calorimeters measure the part of the absorbed radiation energy transformed to thermal energy.

Most of the chemical dosimeters consist of a bulk component, often a liquid in which practically the total energy imparted by the ionizing radiation is deposited, and a solute that reacts with the radiation-induced species formed by the reaction of the bulk component to produce the observed chemical change.

In the following text, a few dosimeter systems will be mentioned that are commonly used in radiation chemistry. For a more detailed treatment of chemical and physical dosimetry, see ► Chap. 49 in Vol. 5 on “Dosimetry Methods.” However, more attention will be paid to pulse dosimetry that is used in pulse radiolysis investigations.

The most well-known liquid chemical dosimeter, the Fricke solution is based on the radiation-induced oxidation of ferrous ions, Fe(II), to ferric ions, Fe(III), in acidic media (E1026: Fricke Reference Standard Dosimeter, ASTM standard). The standard Fricke solution consists of $0.001 \text{ mol dm}^{-3}$ ferrous ammonium sulfate ($\text{Fe}(\text{NH}_4)_2(\text{SO}_4)_2(6\text{H}_2\text{O})$), or ferrous sulfate ($\text{FeSO}_4(7\text{H}_2\text{O})$), and 0.4 mol dm^{-3} H_2SO_4 in aerated aqueous solution. It is applicable for measuring doses in the 40 to 400 Gy range.

The dose is often measured by the alcoholic chlorobenzene dosimeter (ISO/ASTM 51538: Ethanol-Chlorobenzene Dosimetry System). This system is based on radiolytic formation of hydrochloric acid in aqueous ethanol solution of chlorobenzene. Usually the solution has the composition: 24% monochlorobenzene, 72% ethanol, and 4% water. The chloride ion yield, $G(\text{Cl}^-) = 0.59 \text{ } \mu\text{mol J}^{-1}$, is essentially independent of dose up to $\sim 100 \text{ kGy}$.

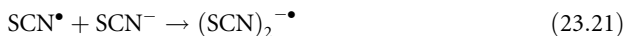
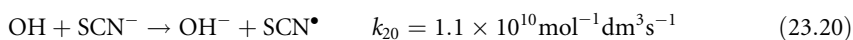
In radiation processing practice the dose is sometimes measured by means of the alanine-EPR ($\text{CH}_3\text{CH}(\text{NH}_2)\text{COOH}$) dosimetry system (ISO/ASTM 51607: Alanine-EPR Dosimetry). The operation of the dosimeter is based on the generation of $\text{CH}_3\text{CH}^\bullet\text{COOH}$ radicals by ionizing radiation. The read-out is made with electron-paramagnetic-resonance analysis. The nominal absorbed dose range is $1\text{--}10^5 \text{ Gy}$, with linear responses up to $\sim 10^4 \text{ Gy}$.

23.5.4 Pulse Dosimetry

In pulse radiolysis, the dose measurement should be carried out in the measuring cell under identical conditions with the experiments. Therefore, for dosimetry purposes it is advisable to use the same detection system that is also utilized in the measurements. In practice mostly the thiocyanate dosimeter and, less frequently, the hydrated electron dosimeter is used in pulse radiolysis studies (Fielden 1982).

The $(\text{SCN})_2^{\bullet-}$ ions produced in the pulse irradiation of potassium thiocyanate (KSCN) aqueous solution show transient optical absorption with a maximum at $\sim 475 \text{ nm}$.

The ions are produced in the reaction



The dosimetry is usually made in 0.01 mol dm^{-3} air- or oxygen-saturated solution. Since the $(\text{SCN})_2^{\bullet-}$ ions disappear in a fairly slow bimolecular reaction with a rate coefficient of $3 \times 10^9 \text{ mol}^{-1} \text{ dm}^3 \text{ s}^{-1}$, this system is applicable for measuring high-dose pulses. The dose can be calculated from the increase of absorbance at 475 nm , ΔA , using $G\varepsilon = 2.6 \times 10^{-4} \text{ m}^2 \text{ J}^{-1}$ (Buxton and Stuart 1995)

$$D = \frac{\Delta A}{G\varepsilon l \rho}, \quad (23.22)$$

where ε is the molar absorption coefficient at the wavelength of measurement, l is the light path in the optical cell, and ρ is the density. For long pulses with high dose, corrections are to be applied, since a fraction of the $(\text{SCN})_2^{\bullet-}$ ions reacts during the pulse. The correction amounts to 8% for $2.6 \text{ } \mu\text{s}$, 100 Gy pulses.

Hydrated electrons, e_{aq}^- , are produced in the radiolysis of water. Their broad optical absorption exhibits a maximum at 720 nm . Dosimetry is usually carried out in a solution containing $10^{-4} \text{ mol dm}^{-3}$ of sodium hydroxide and $10^{-2} \text{ mol dm}^{-3}$ of ethanol (Fielden 1982).

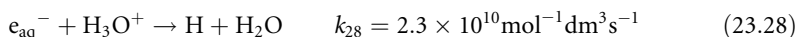
Hydrated electron is reactive toward most solutes, and for this reason the concentrations of hydroxonium ion, oxygen, and other contaminants should be kept at a low level. Due to the large value of $G\epsilon = 5.2 \times 10^{-4} \text{ m}^2 \text{ J}^{-1}$ in the ns domain doses as low as 0.05 Gy can be measured.

23.6 Water and Aqueous Solutions

Due to the intensive investigations more is known about radiation chemistry of water than any other liquid (Buxton 1987). Many of the principles of radiation chemistry as applied to the liquid phase have been developed in the course of studies on the radiation chemistry of water and aqueous solutions. Water and aqueous solutions have been studied because of the part they play in chemistry in general and in radiochemistry in particular, because they are readily available and not too difficult to work with, and because water is a polar liquid that responds in characteristic ways to radiation. A practical motivation for the studies has been the desire to understand the effect of radiation on biological systems. Irradiation of water and several aqueous systems is an important consideration in various aspects of nuclear technology (Swallow 1973).

23.6.1 Intermediates and Final Products in Pure Water

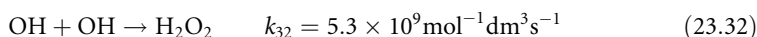
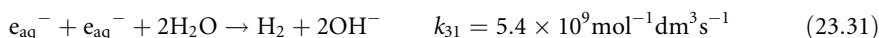
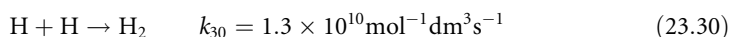
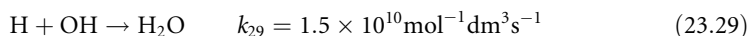
In the radiolysis of pure water the intermediates, hydrated electron (e_{aq}^-), hydroxyl radical (OH), and hydrogen atom (H) are well characterized. The intermediates mainly form as a consequence of ionization of water molecules. There is no unequivocal evidence that excited-state water molecules play any significant role in radiolysis (Draganic and Draganic 1971; Buxton 1982, 1987; Swallow 1982):



The radical cation $\text{H}_2\text{O}^{+\bullet}$ formed in reaction (23.23) may migrate over a distance of a few water molecules by resonance electron transfer, but since $\text{H}_2\text{O}^{+\bullet}$ is a strong acid within 10^{-14} s it gives a proton to one of the surrounding water molecules according to Eq. (23.25). The electron released in reaction (23.23) loses its kinetic energy in collisions with surrounding water molecules (dry electron) and in less than 10^{-12} s is localized in a potential energy well as a result of molecular dipoles rotating under the influence of the negative charge. Thus in reaction (23.26) the smallest anion, the solvated (hydrated) electron forms. In the recent publications the hydrated electron is sometimes called aqueous electron.

The excited water molecules, H_2O^* , formed in reaction (23.24), decompose to OH radical and H atom in reaction (23.27). The latter species also forms in hydrated electron reaction with hydroxonium ions in reaction (23.28).

The final products H_2 and H_2O_2 (and in its decomposition product O_2) form in the reactions of the intermediates

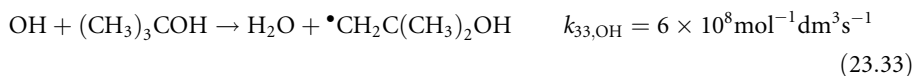


These reactions partly occur in the spur and there is a strong competition between spur reactions and diffusion out of the spur. This process, the so-called spur expansion, is finished in about 10^{-7} s. Scavengers being present in 10^{-4} – 10^{-3} mol dm^{-3} concentration react only with those intermediates that escape spur reactions. The yields of the e_{aq}^- , OH, and H intermediates in neutral and slightly alkaline solutions are usually taken as 0.28, 0.28, and $0.057 \mu\text{mol J}^{-1}$. In order to efficiently interfere with the spur processes scavenger concentrations in the mol dm^{-3} range should be applied.

The OH radical is a strongly oxidizing species, while e_{aq}^- and H show strongly reducing character. In research investigations, it is of special interest to have a more restricted radical source than the mixture of the three intermediates. This can be achieved by using special additives, as it will be shown below.

23.6.2 Reactions of e_{aq}^- , H, and OH Intermediates with Solutes

The *hydrated electron* is strong reducing agent with a standard reduction potential (vs. NHE) of $E^\circ = -2.9$ V. When the OH radicals disturb the observation of e_{aq}^- reactions, the OH radicals are eliminated using saturated H-atom-containing compounds, like *tert*-butanol



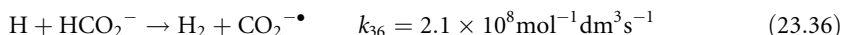
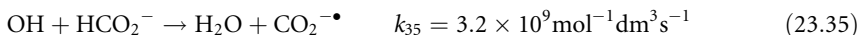
An advantage of alcohols is their good water solubility. The radical formed from *tert*-butanol is a nonreducing radical; it is rather inert in reactions with most organic solutes. This can be verified by saturating the *tert*-butanol-containing solution with N_2O . In such solution the *tert*-butanol radicals are the major radicals present. A disadvantage of *tert*-butanol is that $\bullet\text{CH}_2\text{C}(\text{CH}_3)_2\text{OH}$ may react with the radical under investigation.

The radicals formed from primary or secondary alcohols are reducing radicals. For instance, the α -hydroxyisopropyl radical that is produced by hydrogen abstraction from the secondary alcohol isopropanol is a powerful reducing agent:



This radical may transfer an electron with a high rate coefficient: the reaction often gives the same radical as formed by the e_{aq}^- attack (Buxton 1982; Swallow 1982).

A further possibility of eliminating OH radicals is their reaction with formate ions. These ions also eliminate the H atoms:



$CO_2^{\bullet-}$ has a similar reducing capacity as the α -hydroxyisopropyl radical. The hydrated electrons have a very wide and intense visible infrared (IR) light absorption band centered at $\lambda \approx 720 \text{ nm}$, $\epsilon_{720\text{nm}} \approx 1,850 \text{ m}^2 \text{ mol}^{-1}$. The band is asymmetric; it has a long tail on the high-energy side. Thousands of rate coefficients of hydrated electron attack were measured following the decay of hydrated electrons in pulse radiolysis experiments (Buxton et al. 1988). These coefficients are often high, and for many compounds they are in the diffusion-controlled region (► Table 23.2).

For instance, in the case of e_{aq}^- reactions with metal ions



the rate coefficients (k_{37}) are very often above $10^{10} \text{ mol}^{-1} \text{ dm}^3 \text{ s}^{-1}$. When S^{n+} and $S^{(n-1)+}$ are Ag^+ and Ag^0 , respectively, $k_{37} = 3.7 \times 10^{10} \text{ mol}^{-1} \text{ dm}^3 \text{ s}^{-1}$. For the Cd^{2+}/Cd^+ pair k_{37} is $5.4 \times 10^{10} \text{ mol}^{-1} \text{ dm}^3 \text{ s}^{-1}$. Such reactions are used to produce metal ions with unusual valence state (e.g., dispersed atoms), which, in some cases are not accessible by other methods. The atoms aggregate forming a colloid, which, when stabilized by surfactant, may show unusual catalytic properties (Belloni et al. 1998; Belloni and Mostafavi 2004).

► Table 23.2

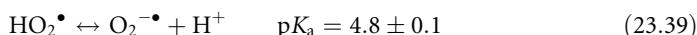
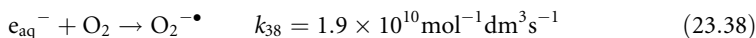
Rate coefficients of e_{aq}^- , H atom and OH radical reactions with some molecules, ions, and radicals, $\text{mol}^{-1} \text{ dm}^3 \text{ s}^{-1}$

	e_{aq}^-	H	OH
e_{aq}^-	5.5×10^9	2.5×10^{10a}	3×10^{10}
H	2.5×10^{10}	7.8×10^9	7×10^9
OH	3×10^{10}	7×10^9	5.5×10^9
Fe^{2+}	1.6×10^8	7.5×10^6	3.2×10^8
H_2O_2	1.1×10^{10}	9×10^7	3×10^7
Benzene	1.1×10^7	9.1×10^8	7.8×10^9
Ethanol	$<10^5$	1.7×10^7	1.9×10^9
Acrylamide	1.7×10^{10}	7.5×10^9	5.9×10^9
Tryptophan	3×10^8	2×10^9	1.3×10^{10}
Thymine	1.8×10^{10}	5.7×10^8	5.4×10^9

^a $e_{aq}^- + H + H_2O \rightarrow H_2 + OH^-$.

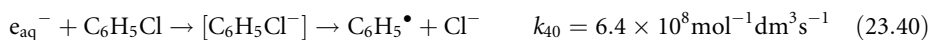
Buxton (1982, 1987, 2001), Buxton et al. (1988), <http://www.rcdc.nd.edu>.

Among the e_{aq}^- reactions one should also mention the reaction with nitrous oxide, N_2O that gives N_2 molecule, hydroxyl radical, and hydroxyl ion (► Eqs. (23.6) and (► 23.7)). In reaction of e_{aq}^- with dissolved O_2 superoxide anion, a reducing radical with $E^\circ(O_2/O_2^{\bullet-}) = -0.33$ V forms



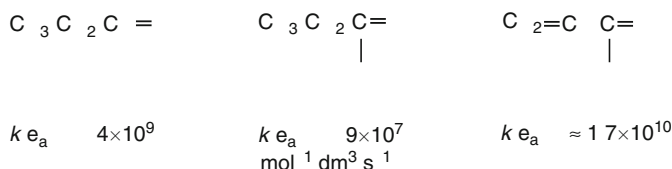
where $O_2^{\bullet-}$ is the anionic form of perhydroxyl radical (HO_2^{\bullet}). In living organisms the $O_2^{\bullet-}$ anion is of considerable importance where it can form in enzymatic reactions that do not involve ionizing radiation (von Sonntag 1987a, 2006).

In reactions with organic molecules e_{aq}^- reacts as nucleophilic reagent: it attacks molecules with low-lying molecular orbital, like aromatic hydrocarbons, conjugated olefinic molecules, carboxyl compounds, and halogenated hydrocarbons (Swallow 1982; Buxton 1982, 1987; Buxton et al. 1988). In the latter case, addition is usually followed by halide ion elimination, so the reaction can be considered as a dissociative electron capture. For instance, the reaction with chlorobenzene yields phenyl radical and chloride ion



Hydrated electron reacts with aldehydes and ketones with high rate coefficients of several times $10^9 \text{ mol}^{-1} \text{ dm}^3 \text{ s}^{-1}$. The electron is accommodated on the carbonyl oxygen. However, in reaction with carboxylic acids and esters or amides, the rate coefficient is low, $\sim 10^7 \text{ mol}^{-1} \text{ dm}^3 \text{ s}^{-1}$. The low rate coefficient is attributed to a mesomeric effect, which creates a new reaction center with low reactivity (Hart et al. 1967) (► Fig. 23.4).

For acrylate type compounds, in which there is a double bond in α position relative to the carboxylic group, the rate coefficient is again high. It shows that the conjugation between the vinyl and carbonyl group destroys the mesomeric effect (Bíró et al. 1996):



The yield of *hydrogen atoms* in neutral or alkaline solutions is very low, $G = 0.057 \mu\text{mol J}^{-1}$. In acidic solutions due to the conversion of hydrated electrons to H atoms in reaction (► 23.28) the yield can be as high as $G = 0.34 \mu\text{mol J}^{-1}$. Therefore, the H atom reactions are

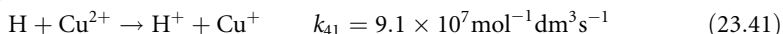
■ Fig. 23.4

Mesomeric effect in carboxylic acid esters and amides

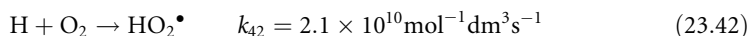


mostly studied in acidic *tert*-butanol-containing solutions. This additive is used to convert the OH radicals to the less reactive *tert*-butanol radicals in reaction (23.33); the reactivity of H atoms with *tert*-butanol is very low. The H atoms (and also the OH radicals) do not absorb the light in a readily accessible region of the spectrum. Therefore, in pulse radiolysis experiments the reaction product of the H atom reaction or competitive techniques are used to determine the rate coefficients.

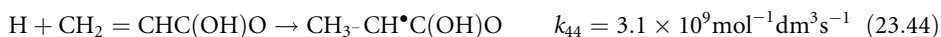
The H atom is slightly less powerful reducing agent than e_{aq}^- ($E^\circ = -2.4$ V and -2.9 V, respectively). It reduces the metal ions with lower reduction potentials, e.g., in reaction with Cu^{2+} Cu^+ forms



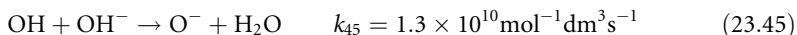
The H atom reacts (with diffusion-controlled rate coefficient) with dissolved oxygen according to Eq. (23.42) forming perhydroxyl radical



There are two main reaction types of H atom reactions with most organic molecules: H atom abstraction (from saturated molecules) and H atom addition (to the double bonds of unsaturated molecules). For instance:



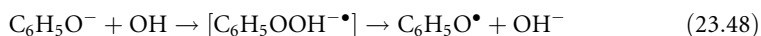
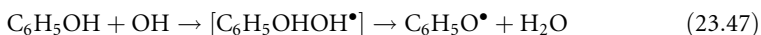
The *hydroxyl radical* is the main oxidizing radical in irradiated aqueous solution. In N_2O saturated solution (see reactions (23.6) and (23.7) also) the yield of OH radicals reacting with a solute of $10^{-3} \text{ mol dm}^{-3}$ concentration is usually taken as $G \approx 0.57 \mu\text{mol J}^{-1}$. In these solutions the H atoms are not eliminated and they also contribute to the reactions in the solution with a yield of $0.057 \mu\text{mol J}^{-1}$. In strongly alkaline solution OH converts to O^- ion with a pK -value of 11.9 (Buxton 1987):



In reactions with inorganic ions generally hydroxyl ion and the oxidized form of the inorganic ion is produced, e.g., Fe^{2+} transforms to Fe^{3+} (Eq. (23.46)). Very often, both with inorganic and organic ions, the reaction takes place with a two-step addition/elimination mechanism due to the large solvent reorganization energy in the formation of the hydrated hydroxide ion. For instance, the reaction with Fe^{2+} probably also occurs through an adduct intermediate



The reaction between OH radicals and phenols and phenolates also takes place with addition/elimination mechanism. The intermediate, a cyclohexadienyl-type radical, decomposes in acid/base catalyzed H_2O/OH^- elimination to phenoxyl radical (Land and Ebert 1967; Steenken 1987, 1996; Ashton et al. 1995; Roder et al. 1999)



With organic compounds, which do not contain double bond, the OH radicals usually react with hydrogen atom abstraction; see, e.g., reactions (23.33) and (23.34).

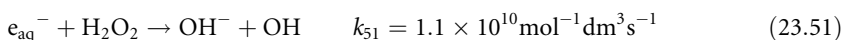
The OH reactions are usually studied in N_2O saturated solutions. In such solutions the conversion of hydrated electrons to hydroxyl radicals is a two-step process with the formation of intermediate O^- ions (reactions (23.6) and (23.7)). At higher solute concentrations, above $10^{-3} \text{ mol dm}^{-3}$, the intermediate O^- ions may also react with the solute to not negligible extent and some fraction is not converted to OH radical in reaction (23.7). When the rate coefficient of the OH reaction is measured with the usual thiocyanate competitive technique (see also reactions (23.20) and (23.21)), this reaction may cause an artifact, causing overestimation of the rate coefficient (Schuler and Albarran 2002)



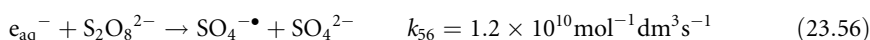
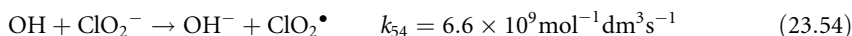
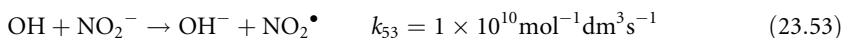
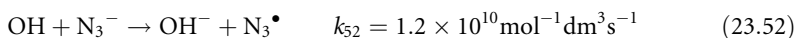
$$\frac{1}{[(\text{SCN})_2^{-\bullet}]} = \frac{1}{[(\text{SCN})_2^{-\bullet}]_0} + \frac{1}{[(\text{SCN})_2^{-\bullet}]_0} \frac{k_{49}}{k_{20}} \frac{[\text{S}]}{[\text{SCN}^-]}, \quad (23.50)$$

where S is the solute molecule and the radical OHS^\bullet is the product of the $\text{OH} + \text{S}$ reaction. In Eq. (23.50) $[(\text{SCN})_2^{-\bullet}]_0$ and $[(\text{SCN})_2^{-\bullet}]$ are the concentrations of $(\text{SCN})_2^{-\bullet}$ ions produced by a constant pulse in the absence and presence of the solute S. $[\text{S}]$ and $[\text{SCN}^-]$ are the concentrations of the solute and thiocyanate ion. If O^- reacts also with the solute S, $[(\text{SCN})_2^{-\bullet}]$ becomes smaller yielding a formally higher k_{49}/k_{20} ratio. In the older literature k_{49} values above $1.5 \times 10^{10} \text{ mol}^{-1} \text{ dm}^3 \text{ s}^{-1}$ were also published (Buxton et al. 1988). Nowadays it is generally accepted that the upper limit is smaller. The reaction between OH radicals and phenols or some other aromatic hydrocarbons is suggested to be truly diffusion controlled, so it shows the upper limit. According to Roder et al. (1999) the upper limit is $\sim 1.4 \times 10^{10} \text{ mol}^{-1} \text{ dm}^3 \text{ s}^{-1}$. Ashton et al. (1995) measured $\sim 1.2 \times 10^{10} \text{ mol}^{-1} \text{ dm}^3 \text{ s}^{-1}$, whereas Schuler and Albarran (2002) suggested a k_{max} of $\sim 1 \times 10^{10} \text{ mol}^{-1} \text{ dm}^3 \text{ s}^{-1}$.

For the conversion of e_{aq}^- to OH sometimes hydrogen peroxide is used. The rate coefficient determined in the presence of H_2O_2 is somewhat smaller than that determined in N_2O saturated solutions (Schuler and Albarran 2002):



The OH radical is a strongly oxidizing species with a reduction potential of $E^\circ(\text{OH}/\text{OH}^-) = 1.9 \text{ V}$. Often milder and more selective oxidants are needed. The techniques producing oxidants with lower reduction potentials are worked out very well. Some examples (see also Table 23.3) are shown below:



23.6.3 Water as Reactor Coolant

Water is the most widespread coolant in nuclear reactors because of its low cost, good thermal properties, high moderating capacity, etc. However, it has two serious disadvantages, in its

■ **Table 23.3**

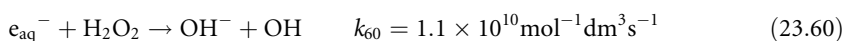
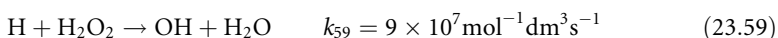
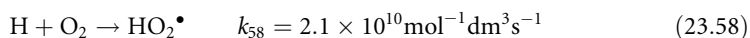
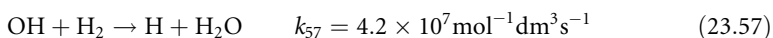
Standard reduction potentials vs. normal hydrogen electrode (NHE) of some radicals used in radiation chemical studies

Pair	E°, V
$\text{aq}/\text{e}_{\text{aq}}^-$	−2.9
$\text{H}_{\text{aq}}^+/\text{H}$	−2.4
$\text{CO}_2/\text{CO}_2^{\bullet-}$	−1.9
$\text{O}_2/\text{O}_2^{\bullet-}$	−0.33 ^a
$\text{C}_6\text{H}_5\text{O}^\bullet/\text{C}_6\text{H}_5\text{O}^-$	0.79
$\text{ClO}_2^\bullet/\text{ClO}_2^-$	0.94
$(\text{SCN})_2^{\bullet-}/2\text{SCN}^-$	1.33
$\text{BrO}_2^\bullet/\text{BrO}_2^-$	1.33
$\text{N}_3^\bullet/\text{N}_3^-$	1.33
OH/OH^-	1.9
$\text{SO}_4^{\bullet-}/\text{SO}_4^{2-}$	2.4

^aThis reduction potential relates, by definition, to O_2 saturated solution. For comparison with other values that are based on molarities, a value of −0.179 V should be taken (von Sonntag 2006).

Steenken (1985a), Neta et al. (1988), Wardman (1989), <http://www.rcdc.nd.edu>.

decomposition explosive mixture of H_2 and O_2 forms, and it is corrosive.² The yield of products (H_2 , O_2 , H_2O_2) strongly depends on the radiolysis conditions and also on the solutes present in water. When these products remain in the water, the decomposition yield is very low due to back reactions that reform water molecules from radiolysis products (Földiák 1986; Woods and Pikaev, 1994)



Reaction (23.58) removes oxygen from the system thus decreasing the corrosion and the radioactivity in the cooling water. The rate coefficients given above refer to room temperature reactions. Nowadays a large number of rate coefficients are available on higher temperature reactions in liquid water up to 300°C (Buxton 2001; Katsumura 2004; Baldacchino and Hickel 2008). By increasing the temperature the rate coefficients change according to the Arrhenius law up to 200°C–300°C. The radiolysis yields of the radical species are similarly increasing with the temperature. This increase is probably due to the acceleration of diffusion with the temperature.

Above 374°C and 22.1 MPa, the liquid and gas phases of water are merged in a single phase called supercritical water. The properties of supercritical water are very much different from that of the liquid water: the density of supercritical water is low and it is pressure dependent.

The permittivity in supercritical water is much less than in liquid water, therefore inorganic acids, bases, salts have low dissociation constants in it. Because supercritical water as coolant has been proposed for Generation IV reactors, there is an increasing interest in its radiation chemistry. Due to the extreme conditions, high temperature, and high pressure, special irradiation cells are needed for the investigations and work in the field is still at the beginning steps. The available experimental results show a strong pressure dependence of the yields. It is not clear yet whether this dependence is related to the change of the density of the medium or to the pressure activation of the reactions. The absorption spectrum of the hydrated electron shifts to longer wavelength with the temperature; above 300°C, the absorption maximum is around 1,200 nm. Since the extinction coefficient also varies with the pressure, the yield determination is rather complicated. As for the rate coefficients above 300°C, little experimental results have been published, again not only temperature, but also pressure dependence was reported (Katsumura 2004; Baldacchino and Hickel 2008).

23.7 Radiation Chemistry of Inorganic Solids

The radiation chemistry of inorganic solids may be regarded as a branch of solid-state physics to which subject it has made substantial contribution (Grigoriev and Traktenberg 1996). The study of radiation effects in solids is of vital importance for nuclear technology, and also relevant to several other fields, e.g., semiconductor technology. The irradiation effect in polymers is discussed in [Sect. 23.9.2](#).

23.7.1 Ice

Radiation chemistry of ice, i.e., solid water, is described in two newer book chapters (Kroh 1991; Wypych 1999), but it was also discussed in many former books on radiation chemistry. Here also, as with liquid water fast kinetic spectroscopic techniques were used to identify the early processes. Pulse radiolysis measurements have been carried out mostly with single crystal ice, which is sufficiently transparent. As it is common in solid-state radiation chemistry some of the intermediates remain trapped in the matrix and can be studied by means of standard spectroscopic techniques like optical absorption and EPR spectroscopy: using these techniques hydroxyl radicals, hydrogen atoms, and trapped electrons were identified at low temperature. The intermediates disappear upon warming up the solid sample. The hydrogen atoms formed at -269°C completely disappear when the solid is warmed to -196°C . The hydroxyl radicals produced at the latter temperature decay between -170°C and -140°C .

By means of pulse radiolysis, two types of localized excess electrons were identified in the irradiated ice. One of them has a visible absorption band with a maximum at $\sim 630\text{ nm}$ (e_{vis}^-); the other has an intense band in the infrared region with $\lambda_{\text{max}} \approx 2,350\text{ nm}$ (e_{ir}^-). The two bands have different decay times and show different sensitivities to the experimental conditions. Buxton et al. (1977) suggested that the electron trap, which leads to e_{vis}^- is vacancy produced by irradiation. The other band, e_{ir}^- , represents an electron localized at a natural cavity in the ice.

The yield of radiation chemical decomposition of water molecules is lower in ice than in liquid or gaseous state. For instance in neutral water the G -value of water decomposition is $G(\text{H}_2\text{O}) = 0.43\text{ }\mu\text{mol J}^{-1}$ at 20°C , whereas it is $0.1\text{ }\mu\text{mol J}^{-1}$ in ice at -10°C . Excited molecules

were not detected in solid water. It is assumed that the excitation energy is dissipated in the solid without producing any net chemical change (Spinks and Woods 1990).

23.7.2 Metals, Semiconductors

Since metals consist of a regular array of positive ions with a pool of mobile, loosely bound electrons, an electron rapidly fills the positive hole left by ionization. For this reason in metals, and also in similar inorganic ordered solid systems, excitations and ionizations are without any significant effect. Radiation effects in metals and semiconductors are interpreted in terms of displacement of atoms, i.e., in terms of radiation-induced dislocations in the ordered system. Such dislocations may cause embrittlement in metals used in nuclear reactor technique. In semiconductors, irradiation produces additional crystal defects, in this way the irradiation changes the concentration, mobility, and lifetime of charge carriers, and thus the electrical behavior of the material. In several countries electron accelerators are used to manufacture diodes and thyristors with short switching times. The radiation-induced centers are annealed at temperatures (250°C–300°C) higher than the usual working temperature of these devices (Spinks and Woods 1990; Woods and Pikaev 1994).

During irradiation of alkali halide crystals, different F centers form and the transparent crystals become colored (Robinson and Chandratillake 1987; Kroh 1991). During annealing these crystals, and also annealing irradiated aluminum oxide, fluorescence photons are emitted. This phenomenon is utilized in thermoluminescence dosimetry (TLD). (See [Sect. 49.3.2.2 in Chap. 49, Vol. 5](#), on “Dosimetry Methods.”) The thermoluminescence of irradiated quartz crystals is used for dating archeological objects.

23.8 Organic Systems

High-energy particle-induced reactions of organic molecules have been intensively studied since the beginning of radiation chemical investigations. In the field of alkane radiolysis, the interest was mainly due to their application as insulators in electric devices or components of lubricants in machines working in radiation field. Alkanes were often used as model compounds in studying inherent problems of radiolysis processes (e.g., spur reactions) or the processes taking place during radiation processing of polymers. The radiolytic reactions of olefins were often studied from the point of view of polymer chemistry. The main reason for the very frequent investigation of aromatic hydrocarbons is their high radiation resistance and their ability to protect other organic substances from decomposition. Several books, book chapters, or review articles were published on the radiolysis of hydrocarbons (Williams 1963; Topchiev 1964; Freeman 1968; Gäumann and Hoigné 1968; Földiák 1981; Hummel 1992; Shkrob et al. 2001). The vacuum ultraviolet (VUV) photochemistry of many of these compounds was also investigated both in gas and liquid phases and these studies are of great help to understand their radiolysis decomposition (Ausloos and Lias 1974; Ausloos et al. 1983; Wojnárovits 2004).

Radiation chemistry of several other classes of organic compounds, e.g., alkyl halides, alcohols, aldehydes, and carboxylic acids was also thoroughly investigated. A reason for the work in the field is that simple organic compounds provide models for polymers and for the

generally more complex compounds, which are of biological interest (Swallow 1973; Milinchuk and Tupikov 1989).

23.8.1 Saturated, Unsaturated, and Aromatic Hydrocarbons

The lowest ionization energies of alkanes in the gas phase are around 10 eV, in the liquids these values are ca. 1.5 eV lower. The lowest singlet excitation energies are 6.5–7.0 eV, and the lowest triplet energies are ca. 1 eV lower (Rothman et al. 1973; Wojnárovits and Földiák 1991). At the same time the energies of C–C bonds and C–H bonds are in the 3.5–4 eV and 3.8–4.5 eV ranges, respectively, i.e., the bond energies are much lower than the lowest excitation and ionization energies. Therefore, practically all activated molecules undergo chemical decomposition. Polymerization type reactions, albeit they were detected, have a minor role in alkane radiolysis (Földiák 1981).

The excited singlet states of alkanes show a weak fluorescence with wavelength of maximum around 200–230 nm and a quantum yield of $\phi = 0.001$ –0.02 (Rothman et al. 1973). The lifetimes of the excited states are generally around 1 ns (Hermann et al. 1985). In gas phase, the lifetime decreases with the decreasing pressure probably due to decreased collisional deactivation of vibrationally excited S_1 molecules. In liquid phase, a characteristic temperature dependence of the fluorescence lifetime was detected (Flamigni et al. 1982; Dellonte et al. 1984; Wickramaaratchi et al. 1985).

The radiation chemistry of *gaseous methane* was often studied. Radiolysis decomposition results in the formation of hydrogen, ethane, and ethylene as main products; longer chains and even polymer-like products also form in low yields (► Table 23.4) (Yang and Manno 1959; Hummel 1970; Lias and Ausloos 1975; György 1981).

The yield of ethylene and those of the higher-molecular-weight products show a strong dependence on the experimental conditions, first of all on the conversion. This is due to the higher reactivity of intermediates with final products than with methane itself. By applying a large variation of techniques, such as VUV photolysis, high-pressure mass spectroscopy, pulse radiolysis, ion–cyclotron resonance spectroscopy, and scavenger experiments, neutral (H , CH_2 ,

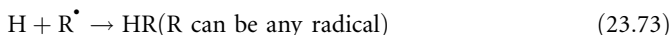
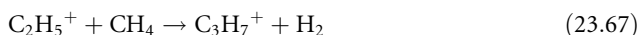
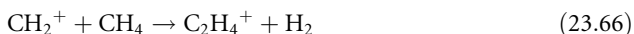
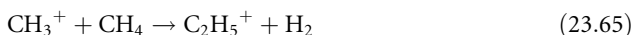
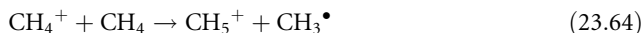
► Table 23.4

Yields of final products in the radiolysis of methane at a pressure of ~1 bar

Product	Yield, $\mu\text{mol J}^{-1}$
H_2	0.59
C_2H_6	0.23
C_2H_4	0.145
C_3H_8	0.037
$n\text{-}C_4H_{10}$	0.011
$C_5\text{--}C_6$	0.003
"Polymer" in CH_4 units	0.21

Hummel (1970), György (1981), Hummel (1992).

CH_3^\bullet , $\text{C}_2\text{H}_5^\bullet$) and charged intermediates (e^- , CH_3^+ , CH_4^+ and CH_5^+) were identified. The proposed reaction scheme is rather complicated



The high reactivity of ethylene in radical reactions explains its conversion sensitivity. The polymer with an approximate composition of $\text{C}_{20}\text{H}_{40}$ is proposed to form in subsequent ion-molecule reactions like (23.65) and (23.67).

Cyclohexane at room temperature may be regarded as a typical liquid alkane. In the molecule all of the C–C bonds and all of the C–H bonds are identical and consequently the product distribution is relatively simple. Hydrogen, hydrogen-deficient cyclohexene, and bicyclohexyl form as main degradation products (Ho and Freeman 1964; Holroyd 1968; Wojnárovits 1981; Ausloos et al. 1983; LaVerne and Wojnárovits 1994) (Table 23.5). The

■ Table 23.5

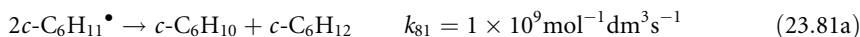
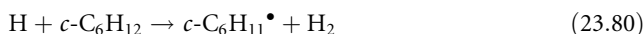
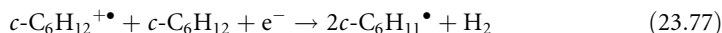
Product yields in the radiolysis of cyclohexane, $\mu\text{mol J}^{-1}$

Temperature, K	373	295	195
Phase	Gas	Liquid	Solid
H ₂	0.49	0.58	0.49
Cyclo-C ₆ H ₁₀	0.105	0.33	0.182
(Cyclo-C ₆ H ₁₁) ₂	0.08	0.182	0.139
Ring decomp. ^a	~0.25	~0.08	~0.025

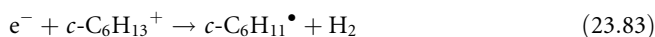
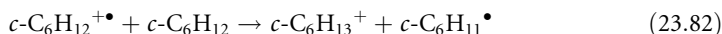
^aMolecules decomposed by C–C scission.

Theard (1965), Burns and Reed (1970), Bouillot (1970), Wojnárovits (1981).

yield of ring decomposition products in condensed phases is little, but the yields are higher in gas phase irradiation especially at low pressures. As intermediates of reactions in condensed phases several research groups identified free electrons, cyclohexyl radical cations, and cyclohexyl radicals. Radical scavenging experiments indirectly reveal also the formation of thermal H atoms:



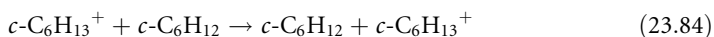
Reaction (► 23.79), the unimolecular H₂ elimination is a typical decomposition mode of the alkane excited molecules in the S₁ excited state: the yield is ~0.12 $\mu\text{mol J}^{-1}$. The cyclohexyl radical yield is much higher, 0.56 $\mu\text{mol J}^{-1}$, more than twice the yield of scavengeable hydrogen atoms ($G \approx 0.15 \mu\text{mol J}^{-1}$). Therefore, cyclohexyl radicals should be produced in reactions, which do not involve thermal hydrogen atoms. In the earlier literature reaction (► 23.77) was suggested to proceed via “hot” hydrogen atoms. Later works suggest the $c\text{-C}_6\text{H}_{13}^{+\bullet}$ cation as the intermediate that forms in an ion–molecule reaction (Shkrob et al. 2001)



The cyclohexyl radicals in liquid phase disappear in self-termination reactions (LaVerne and Wojnárovits 1994) forming cyclohexene and bicyclohexyl in 1.1/1 ratio via the reactions (► 23.81a) and (► 23.81b) (Cramer 1967). In solid cyclohexane, the cyclohexyl radicals, as EPR evidences show, remain trapped in the matrix. They disappear during the phase transition when the solid is warmed up.

In the radiolysis of liquid cyclohexane and a few other cyclic alkanes high mobility cations form (Zador et al. 1973; De Haas et al. 1975, 1976; Shkrob et al. 2001). Their mobility is approximately one order of magnitude higher than the molecular diffusion. During the 35 years that have passed since the discovery lot of papers were devoted to the problem. These papers discussed the questions: (a) the nature of the fast-moving species and (b) whether all of the cations that form in radiolysis of these cyclic alkanes have high mobility or only a part of them. As regards the second question, nowadays most of the papers agree that in cyclohexane radiolysis not all of the cations have high mobility (Shkrob et al. 1996). The high-mobility charge carrier may be the $c\text{-C}_6\text{H}_{12}^{+\bullet}$ radical cation (according to some suggestions this species is supposed to be in vibrationally excited state), which moves with a resonance-like transfer from ion to molecule (without losing the excess energy, Brede et al. 1978).

Other papers suggest the $c\text{-C}_6\text{H}_{11}^+$ or the $c\text{-C}_6\text{H}_{13}^+$ ion as the fast-moving species (Shkrob et al. 2001). In the case of the $c\text{-C}_6\text{H}_{13}^+$ ion a proton transfer may explain the experimental findings:



In the radiolysis of *liquid n-alkanes* both the yields of hydrogen ($G \approx 0.5 \mu\text{mol J}^{-1}$) and C–C bond decompositions ($\sim 0.17 \mu\text{mol J}^{-1}$) remain essentially constant when the carbon atom number increases from C_4 to C_{17} . It should be noted that neither the C–H nor the C–C breaks occur randomly. The frequency of C–H decompositions at the secondary carbon atoms is ~ 3 times more frequent than at the primary carbons. The fragmentation of the carbon skeleton occurs preferentially in its central region, elimination of the methyl group is relatively infrequent (Holroyd 1968; György 1981; Wojnárovits and Schuler 2000).

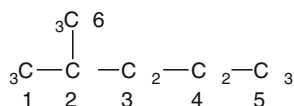
In the radiolysis of *crystalline n-alkanes* preferred H-atom elimination from the penultimate position was observed. This is attributed to ion–molecule reaction that is promoted by the crystalline structure. An interesting even–odd alteration of the yields was also reported (Ichikawa and Yoshida 1992).

In the radiolysis of *liquid branched alkanes*, the C–H decomposition yields are smaller than in the radiolysis of *n-alkanes*, and this decrease is compensated by the increase in the yields of C–C breaking products. Radical scavenging experiments revealed that in branched alkanes a tertiary C–H bond decomposes ~ 14 times more frequently than a primary C–H bond. The decomposition of a secondary C–H bond is ~ 3 times more frequent than that of a primary C–H bond (Földiák et al. 1976; Hummel 1992; Wojnárovits and Schuler 2000; Schuler and Wojnárovits 2003). C–C bonds attached to tertiary or quaternary carbons also have high decomposition frequencies. In *2-methylpentane* (► Fig. 23.5) the C–C bond between carbon atoms 2 and 3 decomposes 3 times more frequently than the bond between 3 and 4, and 6 times more frequently than the bond between 4 and 5.

The summarized yields of primary C–H and C–C decompositions are nearly constant in the radiolysis of liquid alkanes with a yield of $0.67 \pm 0.06 \mu\text{mol J}^{-1}$. Primary decomposition yields do not contain the yields of molecules decomposed in secondary reactions like H atom abstraction (see reaction (► 23.80)) (György 1981; Wojnárovits 1981).

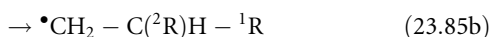
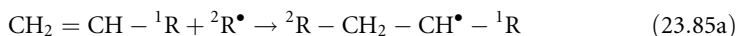
■ Fig. 23.5

2-Methylpentane



In *alkenes* the lowest energy excitations and ionizations are strongly localized in the vicinity of the double bond (Hirayama and Lipsky 1975). Their lowest energy singlet and triplet excitations are ~ 6 and 4 eV, i.e., these values are much smaller than the corresponding values in the *n*-alkanes. The double bonds help to stabilize the molecule against radiolysis, and the primary decomposition yields of alkenes are all smaller than the yields of alkane primary decompositions. Hydrogen yields in the radiolysis of alkenes are ca. one order of magnitude smaller than in the radiolysis of alkanes (Meisels 1970; Cserép 1981; Alfassi 1989). The low yield is partly attributed to the fact that the double bonds can easily scavenge H atoms (and also other radicals). According to Hatano (1968) the H_2 in alkene radiolysis originates from hot H atom reactions. These hot H atoms may form in direct decomposition of superexcited molecules.

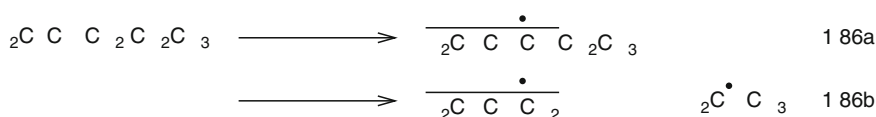
In the case of chain-end olefins, the terminal radical addition is strongly preferred to the nonterminal addition



Allylic interaction has a special importance in the chemistry of alkenes (Cserép 1981). By splitting the C–H or the C–C bond in β position to the double bond, a resonance-stabilized allylic radical forms (► Fig. 23.6). The allylic C–H and C–C decompositions have higher yields than the other C–H and C–C decompositions. Allylic radicals mostly disappear from the solution in very slow combination reactions.

■ Fig. 23.6

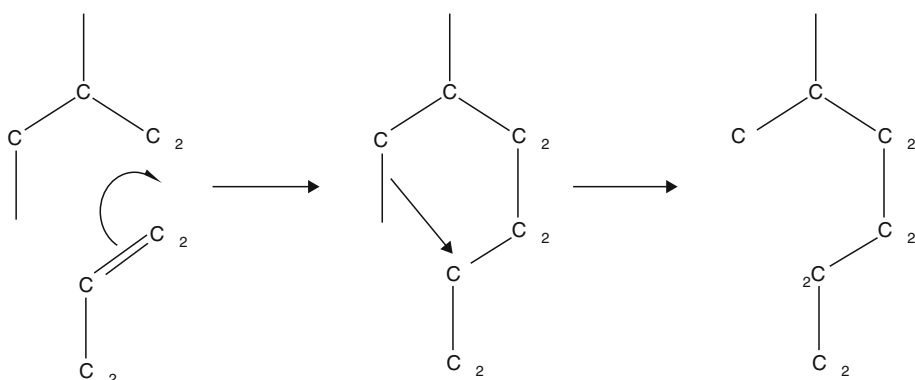
Allylic radical formation in alkene radiolysis



Several groups investigated the reactions of radical cations in liquid alkenes. In pulse radiolysis studies the radical cations show a strong absorption band around 280 nm, which is attributed to the $\pi-\pi^*$ transition of the alkene monomer radical cation. Monomer radical cations “dimerize” with diffusion-controlled rate coefficients with the olefin molecules: the dimer cations have broad absorption bands in the 600–800 nm range (Mehnert et al. 1981, 1985; Alfassi 1989). Dimerization may proceed via a hydride ion (H^-) transfer in the transition-state of radical–molecule reaction (► Fig. 23.7):

Monoalkene dimers form after neutralization. This mechanism explains the experimental finding that in the radiolysis of 1-alkenes mostly linear monoalkene dimers are produced. The

■ Fig. 23.7

Dimerization of alkene radical cations

further condensation reactions are much slower and may yield trimers, tetramers, etc. Oligomerization may also proceed with a radical chain mechanism; the initiating radicals can form in reaction (1.86a and 1.86b). However, under the usual radiation chemical conditions the reactions mostly terminate in dimers or oligomers and real macromolecular polymers practically do not form (Alfassi 1989).

The buildup reactions dominate the radiation chemistry of *acetylenes*: in acetylene radiolysis benzene and the oligomer cuprene are the main products (Cserép 1981).

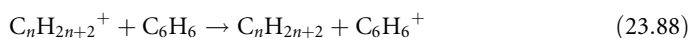
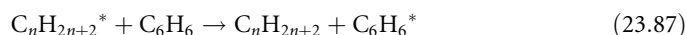
Aromatic hydrocarbons have extraordinarily high radiation resistance in condensed phases (Hoigné 1968; Roder 1981), which is attributed to the conjugated π electron structure. This conjugated system redistributes the energy absorbed over the whole molecule. Thus, the probability of energy localization on a single bond is very low. The energies of the lowest singlet excited and triplet states are low, 4–5 and 3–4 eV, respectively, and the excited state lifetimes are long. The lowest singlet states have lifetimes in the 1–500 ns range, the triplets live up to seconds (Birks 1970; Berلمان 1971). The long lifetimes give a possibility for losing the excess energy in fluorescence/phosphorescence or in quenching processes. The bond dissociation energies in aromatics are relatively high, in benzene $D(\text{C}-\text{C}) \approx 8$ eV and $D(\text{C}-\text{H}) \approx 4.8$ eV.

The yield of H_2 in the γ -radiolysis of benzene is only $0.004 \mu\text{mol J}^{-1}$, i.e., it is ca. 100 times smaller than the $G(\text{H}_2)$ of liquid cyclohexane. It should be noted, however, that the H_2 yield is much higher when instead of γ rays high LET α rays or accelerated heavy ions are used for irradiation (LaVerne and Schuler 1984). The major products from benzene and also from other aromatic hydrocarbons are dimers and higher-molecular-weight compounds that are called “polymer.” The yield of dimers and the “polymer” in γ -radiolysis of benzene is $\sim 0.08 \mu\text{mol J}^{-1}$.

Biphenyl and its higher homologues and the polynuclear hydrocarbons are extremely radiation resistant and they were tested as coolants and moderators in nuclear reactors. For these purposes, different mixtures of aromatic hydrocarbons and hydrogenated aromatic hydrocarbons were applied.

The aromatic rings can act as energy sinks for energy absorbed by other parts of the molecule and therefore in condensed phases the radiolytic yields from alkylbenzenes are not much higher than from benzene itself. Although some increase in the side-chain

decomposition is found as the chain became longer. This protecting effect of aromatic rings is exerted not only on side chains attached to aromatic rings, but it is also observed in mixtures of aromatic hydrocarbons and *n*-alkanes. Practically there is not much difference between the so-called intramolecular and intermolecular protecting effect (Zeman and Heusinger 1966). The intermolecular protecting effect is interpreted in terms of energy and/or charge transfer from the saturated molecule to the aromatic molecule



23.8.2 Other Organic Molecules

In *alkyl chlorides, bromides, and iodides* the carbon–halogen bonds (C–X) are weaker than either the C–C or the C–H bonds. During irradiation mostly carbon–halogen dissociation occurs forming alkyl radical and X or X[−] (Spinks and Woods 1990). Reaction (23.90) is due to the high electron affinity of Cl, Br, and I atoms, 3.61, 3.36, and 3.06 eV, respectively.



The primary decomposition yields in the radiolysis of alkyl halides are probably similar to the yields observed in the radiolysis of saturated hydrocarbons: *G*(primary decomposition) $\approx 0.6\text{--}0.7 \mu\text{mol J}^{-1}$. However, the yields of the measured products often reflect smaller primary decomposition yield due to “back” reactions, these reactions reform the structures of the original molecules. Typical examples are the radiolysis of iodomethane and carbon tetrachloride, for instance. In the radiolysis of the former in liquid phase, both through the neutral and ionic decomposition channels methyl radical and iodine atoms are produced. During the subsequent reactions, due to “back” reactions, only small amounts of ethane and molecular iodine form (*G* ≈ 0.12 and $0.13 \mu\text{mol J}^{-1}$)



Similar products as in the radiolysis of CH₃I, C₂H₆ and I₂ also form in the decomposition of CCl₄, *G*(C₂Cl₆) $\approx G$ (Cl₂) $\approx 0.07 \mu\text{mol J}^{-1}$.

An interesting aspect of the radiolysis of longer-chain alkyl bromides and chlorides is the high yield of isomerization (*G*(isomer) $\geq 6 \mu\text{mol J}^{-1}$: e.g., 1-chloroalkane isomerizes to 2-chloroalkane). These reactions are attributed to free-radical chain reactions, which involve intramolecular shift of a halogen atom.

From the *oxygen-containing* compounds much attention was paid to the radiolysis of alcohols. Their relative permittivities are between those of the hydrocarbons (~ 2) and water (~ 80). The behavior of alcohols in radiation chemistry is in many respects similar to that of water. The electrons ejected from alcohol molecules can be trapped in solid alcohol matrices and can be observed by optical absorption techniques. In liquids, pulse radiolysis measurements confirmed the presence of solvated electrons, for instance in methanol $\lambda_{\max} = 630$ nm, $\epsilon_{\max} = 1,700$ m² mol⁻¹, $G(e_{\text{solv}}^-) \approx 0.5$ $\mu\text{mol J}^{-1}$ in the picosecond time range. On the other hand, as main product of decomposition, H₂ gas forms with a yield comparable to the yield observed in liquid *n*-alkane radiolysis ($G(\text{H}_2) \approx 0.5$ $\mu\text{mol J}^{-1}$) (Freeman 1970, 1974; Spinks and Woods 1990).

Radiolysis of liquid methanol gives hydrogen, formaldehyde, and glycol as major products with yields (liquid phase) 0.55, 0.21, and 0.38 $\mu\text{mol J}^{-1}$, respectively. In the radiolysis of ethanol, hydrogen, acetaldehyde and 2,3-butan diol are the main products. The diols are mainly α -diols indicating that a common radiation chemical reaction of alcohols is loss of an α -hydrogen atom to give α -hydroxyalkyl radical.

In the radiolysis of aliphatic carboxylic acids, carboxylic acid esters and amides preferred formation of α -carboxyalkyl type radicals (e.g., $\text{R}^1\text{CH}^\bullet\text{COOR}$) are observed.

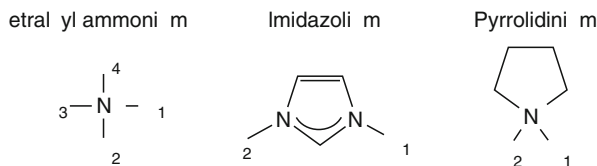
23.8.3 Ionic Liquids

Ionic liquids (ILs) are a class of organic salts that are liquid at or near room temperature. The cation parts of ILs are tetravalent ammonium ions with asymmetric substitution: tetralkyl ammonium ion, imidazolium ion, or pyrrolidinium ion (► Fig. 23.8). The most widely used ILs have positive ions as asymmetric derivatives of *N,N'*-dialkylimidazolium. As the anion counterpart a great number of negative ions are used including BF_4^- , PF_6^- , or $\text{N}(\text{CN})_2^-$.

The ionic liquids are generally nonvolatile, noncombustible, highly conductive, recyclable, and capable of dissolving a wide variety of materials. Therefore, they have been proposed as “green solvents” for chemical reactions and separation purposes. ILs can be used for extraction of metal species from aqueous media, encouraging the potential use of ionic liquids for the reprocessing of spent nuclear fuel: actually these unusual liquids are being suggested as next-generation diluents for extractions in nuclear cycle separations (Shkrob et al. 2007). The critical mass calculations of Harmon et al. (2001) showed the minimum critical concentrations in

■ Fig. 23.8

Tetralkyl ammonium ion, imidazolium ion, and pyrrolidinium ion



F_4^- PF_6^- $\text{N}(\text{CN})_2^-$ CF_3^- 2^- 2N^- etc

some ionic liquids for Pu are at least one order of magnitude higher than in aqueous solution. Successful use of ionic liquids in radiation-filled environments requires an understanding of ionic liquid radiation chemistry.

Ionic liquids have dramatically different properties compared to conventional molecular solvents. Pulse radiolysis of ionic liquids containing tetralkyl ammonium cation $[R_4N]$ $[(CF_3SO_2)_2N]$, $[R_4N][N(CN)_2]$, and $[R_4N][(CF_3SO_2)_2N]$, $[R_4N][N(CN)_2]$ produce solvated electrons that absorb over a broad range in the near infrared and persisting for hundreds of nanoseconds. Systematic cation variation shows that the spectroscopic properties of solvated electrons depend strongly on the lattice structure of the ionic liquid. The rate coefficients of solvated electron reactions with O_2 , and CO_2 and aromatic acceptors measured in several ionic liquids indicate that the diffusion rate for the solvated electron in ionic liquids can be significantly lower than those of small neutral molecules or radicals such as H-atom, in contrast to the situation in molecular solvents. In general the diffusion constants of charged and neutral reactants differ considerably in ionic liquids, which could lead to a means of controlling reactivity through rational selection of ionic liquid properties (Wishart et al. 2006; Asano et al. 2008).

In ionic liquids containing imidazolium cation, the dry electron produced in ionization before full solvation is rapidly scavenged by the cation forming imidazolyl radicals (Wishart and Neta 2003). Secondary reactions of these radicals may lead to the formation of carbene and imidazolyl dimerization products. According to the work of Berthon et al. (2006) the main radical intermediates due to the transformation of 1-butyl-3-methylimidazolium cation ([bmim]) are the methylimidazolium radical cation arising from the scission of the butyl chain on the N atom, the butylmethylimidazolium radical cation forming in homolytical dissociation of the H-C2 bond attached to the ring and a cation radical formed by loss of an H-atom from the butyl chain. Recombinations of the N atom centered radicals yield aromatic dimers with nitrogen heteroatoms, which have high molar absorption coefficients in the ultraviolet-visible (UV-VIS) optical spectra. This accounts for a significant darkening of the imidazolium type ionic liquids when they are subjected to the effect of ionizing radiation (Qi et al. 2008).

Radiation-induced degradation of the negative ion may lead to different radicals. Fragmentation of $[(CF_3SO_2)_2N]^-$ produces CF_3^\bullet radicals through the dissociation of the $(CF_3SO_2)_2N^\bullet$ “hole” radicals (Grodzowski and Neta 2002).

Generally very small amounts of products form in the radiolysis of ILs. Studying the decomposition of several ILs it was concluded that less than 1% of the liquid underwent decomposition when exposed to a dose of 400 kGy. So the chemical properties are only slightly affected by the irradiation.

On the other hand, radiolysis causes a significant increase in the viscosities of ILs. Generally the conductivity decreases as the viscosity increases.

23.9 Radiation Chemistry of Polymers

The use of high-energy radiation in polymer chemistry is one of the major industrial applications of radiation. Main advantages of ionizing radiation initiation include (Charlesby 1960, 1987; Chapiro 1962) the following:

1. Absence of any residual from the decomposition of chemical catalyst.
2. Very wide range of initiation rates.

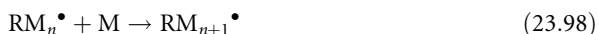
3. Little or no temperature effect, so the temperature can be selected, e.g., to optimize the propagating reaction.
4. There is no danger of runaway reaction due to the energy released in the propagation reacting back to enhance the initiation rate of the catalyst.
5. Unusual features, e.g., initiation in the solid. Polymerization and cross-linking simultaneously.
6. Sometimes sterile end product is synthesized, which is important for biomedical applications.

The explanation for the success of using irradiation techniques for both polymers and biopolymers is usually that they involve macromolecules in which minute chemical changes at the appropriate places have great influence on the morphology. A single bond altered in about 10^5 may convert a free flowing polymer from a fluid to elastic solid. An even smaller change may be lethal in biological systems (Charlesby 1987).

23.9.1 Polymerization, Kinetics, and Mechanism

Polymerization is a synthesis of high-molecular-weight compounds by successive addition of a low-molecular-weight compound to an active site at the end of the growing polymer chain. Monomers are mainly compounds containing multiple bonds (e.g., --C=C-- , $\text{--C}\equiv\text{C--}$). Polymerization of a monomer comprises three major steps, initiation, propagation, and termination. In radiation-induced polymerization, attention is essentially confined to the first step (Charlesby 1960, 1987; Chapiro 1962; Dole 1973; Wilson 1974; Makhliis 1975; Alfassi 1989; Ivanov 1992; Singh and Silverman 1992; Clough and Shalaby 1996; Knolle and Trautman 1999; Clough 2001). During irradiation both charged intermediates (electrons, anions, cations) and neutral radicals form in the matrix. So the radiation-induced polymerization can propagate by anionic, cationic, or radical mechanisms. Sometimes two or three processes occur simultaneously. The relative importance of each mechanism depends on the chemical nature of the monomer, the solvent, the temperature, and the type and concentration of additives. For instance, halogenated solvents facilitate cationic mechanism since the electron capture reaction (see reactions (23.8) and (23.90)) lengthens the lifetime of cations. On the contrary, in amine or amide solvents, the quaternary ammonium-type ion formation act as positive charge stabilizer thus enhancing the possibility of anionic polymerization. More often the radiation-induced polymerization takes place predominantly by free-radical mechanism.

When a monomer or its solution is irradiated with a low-LET (γ or electron) radiation, the radicals formed from the monomer (M) or the solvent (S), to a first approximation, may be assumed to be dispersed essentially uniformly throughout the liquid (Swallow 1973)



The radical R^\bullet adds to the double bond of a monomer molecule initiating by that a polymerization chain reaction. The final step is chain termination, which, in homogeneous

liquid phase, occurs by disproportionation or combination reaction of two radicals giving a “dead” polymer P:



The rate of the stationary free-radical polymerization, R_p , is described by the equation

$$R_p = k_p \sqrt{\frac{R_i}{k_t}} [M], \quad (23.100)$$

where k_p is the rate coefficient of propagation, k_t is the rate coefficient of the termination reaction of two radicals, and R_i is the rate of initiation. Equation (23.100) contains two rates and two rate coefficients. There are several methods for the determination of individual rates or rate coefficients, or their combinations. For instance, by means of radical scavenging techniques, R_i can be determined. Measurement of the monomer consumption may give a possibility for the calculation of R_p . Radical concentration measurement may supply the $k_p/(k_t)^{1/2}$ ratio. Recently for the reliable determination of k_p a technique based on pulsed laser polymerization has been developed (Brandrup et al. 1999).

As mentioned before the temperature has little effect on the rate of radiation-induced radical polymerization. The overall activation energy of the process is calculated by the equation

$$E = \frac{E_i}{2} + E_p - \frac{E_t}{2}, \quad (23.101)$$

In radiation-induced polymerization, the activation energy of initiation, E_i , is close to zero, since the decomposition G -values of forming radicals ($G \approx 0.1\text{--}0.5 \mu\text{mol J}^{-1}$) are practically independent of the temperature. The activation energy of termination, E_t , is generally very low, whereas E_p , the activation energy of propagation in radical polymerization is generally in the $20\text{--}30 \text{ kJ mol}^{-1}$ range (Brandrup et al. 1999).

The rate of initiation R_i is proportional to the G -value of radical formation in the system, i.e., it is proportional to the dose rate. Therefore, the overall rate of polymerization R_p is proportional to the square root of the dose rate (Eq. (23.100)).

The rate coefficient of propagation, k_p , strongly depends on the nature of the monomer (Brandrup et al. 1999). Table 23.6 shows the k_p and k_t rate coefficients for a few monomers that are often polymerized by ionizing radiation initiation.

Table 23.6

Rate coefficients of chain propagation and termination during bulk polymerization of monomers and the G -values of initiation

Monomer	$k_p, \text{mol}^{-1} \text{ dm}^3 \text{ s}^{-1}$	$k_t, \text{mol}^{-1} \text{ dm}^3 \text{ s}^{-1}$	$G, \mu\text{mol J}^{-1}$
Butyl acrylate	6,800	6.4×10^6	
Methyl methacrylate	310	6.6×10^7	0.5–1.0
Acrylamide	18,000	1.5×10^7	
Methacrylamide	80	1.7×10^7	
Vinyl acetate	4,600	2.2×10^8	1.0
Styrene	40	6×10^7	0.07

Temperature $\sim 25^\circ\text{C}$.

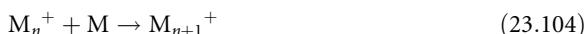
Swallow (1973), Tabata (1991a), Brandrup et al. (1999).

Rates of termination reactions are generally assumed to be strongly influenced by diffusion: most of the rate coefficients are in the $k_t \approx 10^6\text{--}10^8 \text{ mol}^{-1} \text{ dm}^3 \text{ s}^{-1}$ range. This diffusion-limited behavior is also shown by the conversion and solvent dependence of k_t . During polymerization in bulk the viscosity of the liquid gradually increases with the conversion, which results in decreasing diffusivity and decreasing k_t . In solution polymerization k_t decreases with the solvent viscosity.

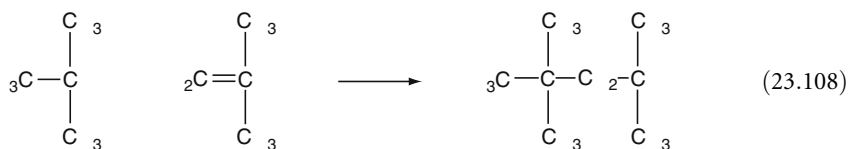
At high conversion, the growth of viscosity hinders the termination by radical–radical reactions, but it has less effect on the propagation reaction, because diffusion of small monomer molecules is not so much affected by viscosity. Hence, both the rate of polymerization and the molecular weight of the polymer show an increase, there is auto acceleration at high conversion. This effect is known as *gel-effect* or *Tommsdorf-effect*, which is usually accompanied by a sudden rise of temperature (Swallow 1973). Such effect was observed in many systems, for instance in the γ -ray induced steady-state bulk polymerization of methyl methacrylate (Luthjens et al. 2001).

Auto acceleration at relatively high conversion can also be caused by formation of free radicals from the polymer that has been produced (Woods and Pikaev 1994). The yield of radicals from the polymer, which is usually a saturated chain, may be higher than the yield from the unsaturated monomer leading to an increase in the rate of polymerization due to the increased radical population. Termination reactions of these radicals with chain-end radicals give rise to branched chains (graft homopolymer), while self-termination of mid-chain radicals brings about cross-links.

Ionic polymerization is understood much less than free radical one and the results are less reproducible due to considerable variations caused by small concentration of impurities (Alfassi 1989). Cationic polymerization can be described by using the scheme



The free electron produced in reaction (23.102) may react to form a non-propagating species. The positive ion can initiate polymerization by adding on another monomer molecule (see reaction (23.103)) or by transferring a proton to a monomer. The latter mechanism is suggested for liquid isobutene polymerization at low temperature (Spinks and Woods 1990)

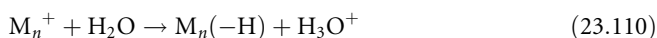


Reaction (23.105) describes a termination reaction with an impurity X present. Impurity termination in free-radical polymerization can also take place, but in free-radical chain

reactions any impurity is generally consumed at the beginning of irradiation. In ionic polymerization, however, the impurity appears to be regenerated in charge neutralization. Based on the scheme, the polymerization rate (R_p) is described by the equation

$$R_p = k_p \frac{R_i}{k_t[X]} [M]. \quad (23.109)$$

An important characteristic of ionic polymerization is that the propagation rate coefficients are several orders of magnitude higher than for free-radical polymerization. In the equation $k_t[X]$ is the bimolecular termination rate coefficient multiplied by the impurity concentration. This equation shows that the rate of polymerization is proportional to the first power of initiation rate, i.e., to the first power of dose rate. Water is a common chain breaker of cationic polymerization since it replaces the cation by a hydroxonium ion. As a proton donor it also inhibits the anionic polymerization



where $(-H)$ indicates removal of a H atom from the n mer.

If during cationic polymerization the impurity concentration is very low, termination reactions between the propagating cation and negatively charged species (e^- , M^- , M_n^-) should also be considered:

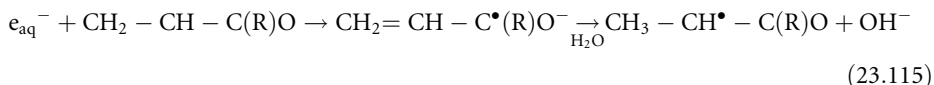
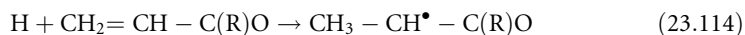


At low impurity content, the polymerization takes place with kinetics that is characteristic of free-radical polymerization (► Eq. (23.100)). Such behavior was observed, for instance, in the cationic polymerization of styrene (Swallow 1973).

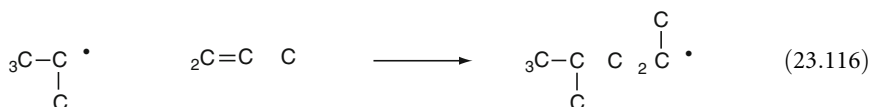
When the monomer is irradiated in a solvent such as water or alcohol, the radical or ionic intermediates formed from both the monomer and the solvent may initiate polymerization. The yield of initiating particles, to a first approximation, is expected to be proportional to the sum of the yields of intermediates in the irradiation of pure monomer or solvent, respectively, multiplied by their electron fractions (linear mixing rule, see ► Eqs. (23.3) and (23.4) in ► Sect. 23.3.1). In practice, however, the yield of initiation may be lower or higher than it is expected assuming linearity. This is due to energy or charge transfer between the components of the mixture. In dilute solutions (e.g., in water) it is commonly assumed that initiation occurs only by the intermediates of the solvent decomposition.

Vinyl monomers are often polymerized in aqueous solutions with the aim of producing hydrogels (Rosiak et al. 2002). Hydrogels are cross-linked hydrophilic polymers (polyvinyl alcohol, polyacrylamide, poly-2-hydroxyethylmethacrylate, methylcellulose, etc.) that can swell (and not dissolve) in water and retain more than 100% water in their volume (Ivanov 1992; Martelli et al. 1999). Because of their high water content, hydrogels usually show good biocompatibility. Some hydrogels show sensitivity to environmental conditions, and respond with high volume changes to small changes in temperature, pH, solute concentration, electrical, magnetic field, etc. For example, the crosslinked polymer of *N*-isopropyl acrylamide (NIPAAm) shows good thermal reversibility. Below the so-called lower critical temperature (LCST) 32°C it absorbs ~10 times more water molecules than the number of monomer units in the polymer. Above LCST the polymer shrinks and expels the water molecules. Hydrogels find a number of practical applications including controlled drug delivery, separation, and surface coatings on artificial organs.

During the usual synthesis conditions in aqueous solutions mainly the OH, H, and e_{aq}^- intermediates of water radiolysis (see ▶ Sect. 23.6.1) initiate the polymerization reaction, e.g., in the case of NIPAAm (Nagaoka et al. 1992; Strauss et al. 1998):



where R is the $-NH-CH(CH_3)_2$ group. The α -carboxyalkyl type radical produced in these reactions adds to a monomer molecule and the chain reaction starts.



With the progress of polymerization, the concentration of monomer molecules in the solution decreases and that of the prepared polymer chains increases. So the probability of forming a radical site on the polymer chain in hydrogen atom abstraction reaction of OH and H is increasing. These intermediates mostly abstract the tertiary H atom of the isopropyl group. The reaction of these mid-chain radicals with each other gives H type cross-links, their reaction with chain-end (propagating) radical yields T type branches. Through these reactions cross-linked polymer network forms.

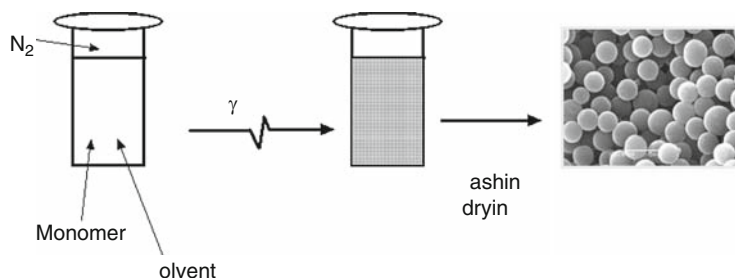
▶ Figure 23.9 shows the synthesis of hydrogel microgels with a diameter of $\sim 2 \mu\text{m}$. Aqueous solution of the monomer (in the figure ethylene glycol dimethacrylate) is irradiated in oxygen-free aqueous solution. The micro-squares are collected by centrifuging. After washing and drying, the micro-squares may be used for chromatographic separation (Graselli et al. 2001).

23.9.2 Radiation Effects in Polymers

As mentioned before, small chemical changes in an irradiated polymer can modify its physical properties substantially. The most important chemical effects are cross-linking, which is

■ Fig. 23.9

Synthesis of hydrogel micro-squares



analogous to dimerization, and degradation, which is analogous to main chain scission. In most polymers, one of these processes predominates. In general, polymers with only secondary and tertiary carbon atoms in the main chain tend to cross-link, while degradation with main-chain scissions occurs if the chain includes quaternary carbon atoms. Polymers that predominantly undergo cross-linking on exposure to ionizing radiation include polyethylene, polyamides, and polyesters. Mainly degradation takes place in polyisobutylene, polymethacrylate, polymethacrylamide, and polytetrafluoroethylene (Swallow 1973; Ivanov 1992).

The changes and yields in polymer irradiation are often similar to those found with lower-molecular-weight compounds with similar structural features. The radiolysis of linear polyethylene is similar to that of the *n*-alkanes, polystyrene resembles the alkylbenzenes, and polymethyl methacrylate behaves like a branched chain ester. Lower-molecular-weight compounds are often used to model processes taking place in polymer irradiation.

23.9.2.1 Main Chain Scission

Radiation-induced degradation of polymers is inherently different from thermal degradation. As it was shown on the example of polyisobutylene in thermal decomposition, which occurs at higher temperature, a chain reaction of depolymerization is involved, releasing considerable amounts of monomer. The radiation-induced degradation is carried out at lower temperature. Since each scission during irradiation is an independent event, this number cannot exceed the number of primary excitations and ionizations. Thus, the degradation can be easily controlled through the dose of irradiation. $G(\text{scission})$ is independent of molecular weight and radiation intensity.

In addition to main chain scission or cross-linking, gas formation is also observed as a result of irradiation. The gas in the hydrocarbon-based polymers mostly consists of hydrogen. The amount of gas produced depends on the nature of the polymer and also on dose, temperature, type of radiation, etc. In the case of polyethylene the G -value of gas production is high, $G \approx 0.32 \mu\text{mol J}^{-1}$, comparable to the gas yields observed in the radiolysis of liquid *n*-alkanes $G \approx 0.5\text{--}0.6 \mu\text{mol J}^{-1}$. In the radiolysis of polystyrene and polymethylstyrene the yield of gaseous products is only $G \approx 0.01 \mu\text{mol J}^{-1}$, that value is typical of aromatic compounds. The benzene rings attached to the main chain exert a protective effect against both the C–H and the C–C decompositions in the chain.

Polytetrafluoroethylene (Teflon) belongs to the group of degrading polymers when irradiated. It is relatively radiation resistant in the absence of oxygen, but rapidly deteriorates in air or oxygen atmosphere. The decomposition takes place with chain mechanism with participation of alkoxy radicals. In practice, radiation-induced degradation is used to produce powdered Teflon. The process requires several hundred kGy dose and the powder is used as lubricant after blending with other materials.

23.9.2.2 Cross-Linking

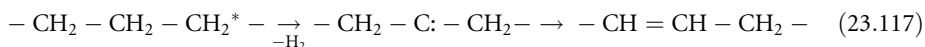
Irradiation of degrading polymers leads to loss of mechanical properties such as strength. On the contrary, irradiation of cross-linking polymers increases the viscosity and also the mechanical strength.

The irradiation of polyethylene and its copolymers has been the most commercially successful of all applications of radiation in the polymer field (Charlesby 1987). Upon warming, the unirradiated polyethylene softens between 70°C to 90°C and turns to a viscous liquid at 115°C–125°C. After irradiation with a dose of ~20 kGy the polymer is form-stable to about 250°C.

Other physical changes consequent on cross-linking include a lower solubility in solvents and several orders of magnitude higher viscosity. The yield of cross-linking is $\sim 0.15 \mu\text{mol J}^{-1}$. It is accompanied by C–H bond rupture with the formation of H_2 gas and vinylene ($-\text{CH}=\text{CH}-$) unsaturation with yields of $G \approx 0.3$ and $\sim 0.15 \mu\text{mol J}^{-1}$, respectively. As intermediates alkyl radicals, radical cations, and trapped electrons are suggested (Brede et al. 1989; Spinks and Woods 1990; Shkrob and Trifunac 1995).

Cross-linking is due to the dimerization of adjacent free radicals (► Fig. 23.10):

Vinylene probably forms in disproportionation reaction, but unimolecular H_2 elimination from an excited state should also contribute to the yield.

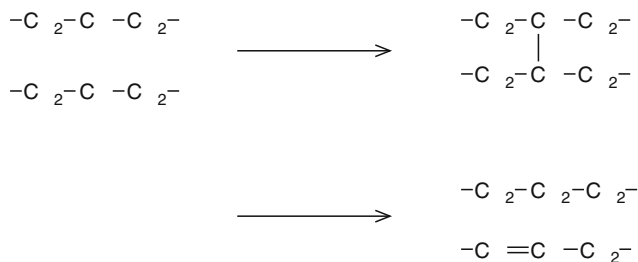


There are several possibilities for the formation of adjacent radical pairs. They may be produced in spurs where in the energy deposition processes at least two activated molecules are populated in each other's vicinity. A radical pair may form if the detached H atom abstracts hydrogen from a neighboring polymer chain, or if a radical center migrates along the polymer chain until it encounters a radical on a neighboring chain. Ion–molecule reactions of the type shown here may also yield neighboring radical pairs (► Fig. 23.11):

Memory effect is a particularly interesting property of irradiated polyethylene and a few other polymers. During processing, polyethylene is irradiated in the required shape, it is then expanded with warming up to the softening temperature, and cooled down in the expanded form. During cooling the crystals reform and hold the polyethylene in this new configuration.

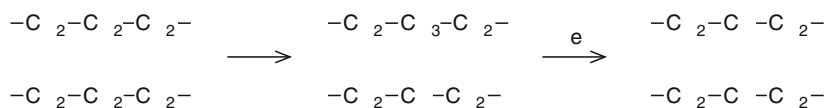
■ Fig. 23.10

Reactions of adjacent free radicals



■ Fig. 23.11

Formation of H_2 molecule in ion–molecule reaction



When warmed up again above its softening temperature, the polymer regains the original size and shape “prescribed” during irradiation. The memory effect has found a lot of practical applications, e.g., shrink film, used for food packaging and, shrinkable connectors in cable and other electrical installations, and other devices in which a controlled shape change is triggered by a simple temperature change.

Irradiation techniques can readily be used to produce grafted copolymers. During grafting, side chains (composed of B monomer units) are attached to the polymer chain formed from monomer units A (► Fig. 23.12).

Several methods are used to produce grafted polymers by irradiation. One of the methods uses simultaneous irradiation of polymer A immersed in monomer B: the radicals formed on A initiate polymerization of B as side chains. During the process some homopolymerization of B and cross-linking or scission also take place. In order to reduce homopolymerization and cross-linking radical scavengers, such as the Mohr-salt, may be applied. In another method, polymer A is irradiated resulting in the formation of radicals on the backbone chain. If this irradiated polymer is now dipped in monomer B, the trapped radicals react with B and provide the initiating centers for the branches. If the irradiation of polymer A is carried out in the presence of oxygen, peroxide groups form on the surface. Then the irradiated polymer A is placed in monomer B and heated to produce the grafted system. These peroxide groups decompose on heating to provide radicals for initiation of the polymerization of B.

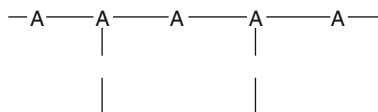
In practice, grafting is often used for making biocompatible surfaces on polymers with good mechanical properties and also for the immobilization of bioactive materials such as enzymes or antigens on a polymer surface.

Radiation-induced curing of polymer coatings is a special field of paint-and-varnish technology. The coatings are applied in the form of a thin film on the corresponding support: paper, cloth, polymer, wood, metal, ceramics, etc. In the industrial use, accelerators with electron energy of 150–600 keV are applied. Apart from the traditional accelerators with beam scanning, a new accelerator family was developed with a hot cathode in the form of 1–2 m long tungsten wire. Advantages of radiation processing are the high rate of polymerization, which is achieved without the application of heat and without the use of solvents. The varnishes used in industrial technology are usually based on oligomer–monomer mixtures. The composition of the mixture basically determines the properties of the surface: hardness, elasticity, etc. Application of acrylates is quite common: apart from monofunctional monomers often di- or trifunctional monomers are also added to the mixture, e.g., 1,6-hexanediolacrylate, triethylene glycol acrylate. In this way during the polymerization, polymer network forms (Takács et al. 1989; Takács and Hedvig 1991; Takács 1992; Ivanov 1992).

In addition to the previously mentioned “classical type” polymer processing technologies a large number of new techniques were also developed. A family of these techniques uses swift

■ Fig. 23.12

During grafting, side chains built from monomer units B are attached to the polymer chain formed from monomer units A



heavy ions with extremely high LET values to irradiate polymer films (polyethylene terephthalate, polycarbonate, polyvinylidene fluoride, and polyamide) perpendicularly to the surface. The high LET radiation strongly degrades the polymer along the particle path (narrow channel). After irradiation the film is etched by wet chemical treatment that reveals pores of which the shape, surface density, and dimensions can be controlled by choosing appropriate conditions. The treated polymer film can be used as micro filter in the desalination process of seawater or in dialysis.

The membrane with the nanometer-sized holes can be used as template of metallic replicas. The holes are filled up with some metal atoms by electrolysis in a galvanic cell, and after deposition, the membrane is removed mechanically or by a suitable solvent. In these ways, little rods with a few μm length and few times 10 nm diameters are produced (Tagawa et al. 2004; Coqueret 2008). By grafting environmental sensitive polymers on the surface of the holes, the permeability of the membrane can be regulated by external signal (temperature, pH, etc.). The operation of such systems may mimic the operation of biological membranes.

23.10 Biological Molecules

Radiation chemistry of biological molecules and radiobiology has been intensively studied since the biological effect of radiation was first observed just after the discovery of ionizing radiation. The books, conference proceedings, review articles, etc., published related to these topics probably could fill a small library (for instance Bensasson et al. 1985, 1993). Excellent books on the subject were published by von Sonntag in 1987 and 2006 with titles *The Chemical Basis of Radiation Biology* and *Free-Radical-Induced DNA Damage and its Repair: A Chemical Perspective*. These books cover practically all aspects of radiation chemistry of biologically important molecules. Besides introducing some basic results in the field, some references will also be mentioned.

Radiation chemistry of biological molecules may be investigated from different aspects. One of the aspects is how to protect living organisms from ionizing radiation, i.e., radiation safety. The other aspect is just the opposite, how the effect of radiation can be enhanced, e.g., in cancer treatment. By using radiation chemical methods it is relatively easy to produce and investigate the reactions of certain reactive short-lived species that are also produced in living organisms, e.g., the superoxide radical anion, $\text{O}_2^{\bullet-}$. In this respect radiation chemistry is a tool for studying biologically important reactions.

Studies on model compounds of biopolymers are usually made in the solid phase that shows the direct effect or in dilute aqueous solutions where the indirect effect is dominating. In the latter case the radicals of water radiolysis, e_{aq}^- , OH and H, induce the chemical changes. In vivo the state of biopolymers is somewhere between the two extremes. Usually the deoxyribonucleic acid (DNA) is regarded as the target molecule whose damage is mostly responsible for the deactivation of irradiated cells (von Sonntag 1987a, 2006; Mae 1987; von Sonntag and Schuchmann 2001).

23.10.1 DNA and Its Constituents

Most of what is known about the mechanisms leading to various types of DNA damages has been obtained by studying low-molecular-weight model systems. In aqueous solutions all the

three water radicals react with high rate coefficients with the four bases of DNA, adenine, cytosine, guanine, and thymine. However, the sugar part, deoxy-d-ribose, is only attacked with higher rate coefficient by OH radicals, as a consequence of which a hydrogen atom is eliminated. Further reactions of this radical may lead to breakage of the sugar–phosphate bond (strand break) or to base release. A large number of rate coefficients on the reactions of water radicals with DNA constituents were compiled in the work of Buxton et al. (1988). In 1986 von Sonntag and Schuchmann (1986), in 1987 von Sonntag (1987b), and von Sonntag and Ross (1987) published updated review and bibliographies on the radiolysis of nucleic acids and their base constituents. Critical evaluation of the results obtained with DNA and its constituents is given in the two books mentioned (von Sonntag 1987a, 2006).

The OH radicals are suggested to be the most damaging species in aqueous solutions, the OH attack may result in multiple lesions, e.g., base damage, sugar damage, DNA + DNA cross-linking, etc. The main reaction of OH with the bases is addition to the double bonds. The radical thus formed in reaction with pyrimidines in the presence of oxygen rapidly converts to peroxy radical. In the subsequent reactions the double bond saturates. Reactions of OH radicals with purine bases lead to the destruction of the imidazole ring. Due to these reactions altered bases form, but they may remain attached to the DNA chain. Other possibility is that the altered bases or their radiation-modified products are released from the polynucleotide chain by rupture of the *N*-glycosidic bond. This reaction may induce a strand breakage.

Any lesion within the DNA, in principle, can be lethal for the cell. In 1987, von Sonntag (1987a) suggested a hierarchy of the various lesions from the point of view of lethality. This hierarchy starts with base damage and single-strand breaks as the least dangerous damages, and finishes with such changes when both strands of the DNA are altered simultaneously, e.g., double-strand breaks, or base damages on opposite strands. The yield of single-strand breaks is estimated in the range $G = 0.02\text{--}0.08 \mu\text{mol J}^{-1}$, whereas the yield of double-strand breaks is an order of magnitude smaller.

23.10.2 Polysaccharides

Cellulose is the most abundant organic compound, comprising at least 50% of all carbon in vegetation. This biopolymer is composed of D-glucose units. The purest source of cellulose is cotton, which contains at least 90% of cellulose. The primary structure of cellulose allows extensive interactions between chains resulting in a highly crystalline supramolecular structure (crystallinity is 60–70%, cellulose I). In order to make available additional surfaces or to alter the crystal structure, cellulose is usually “activated” by various physical and chemical methods (alkali treatment).

The radiation chemistry of cellulose has been investigated mainly with the aim of enhancing the enzymatic degradation. Research work has also been motivated by the possibility of textile improvement by irradiation (dyeability) and also by radiation sterilization of cellulose-containing packaging materials, foodstuffs, etc. A further aspect of the radiation chemistry of cellulose is the production of copolymers: grafting may be carried out by the preirradiation method (► Sect. 23.9.2.2). In this case the radicals produced during irradiation, or by the thermal decomposition of the peroxides formed in radical-oxygen reactions, initiate the polymerization.

Under the effect of irradiation, cellulose may undergo degradation or cross-linking (Charlesby 1960). Above 10 Gy dose the main radiation effect is degradation, which is most likely due to splitting of the glucosidic bond: using a γ dose of 15 kGy the degree of polymerization of cotton–cellulose decreases from ca. 1,200 to 300. Another consequence of radiation treatment is the increase of carbonyl content, which shows oxidative degradation. By EPR method radicals were identified as intermediates of the transformation. The radicals are produced not only in the amorphous region but also in the crystalline region (Hebeish and Guthrie, 1981; Krassig 1996). These radicals, in the presence of vinyl monomers, can initiate reactions to yield grafted cellulosic fibers with special properties.

As mentioned before, chemical changes are observed even after low-dose irradiation, however, up to a dose of 500 kGy no change in the crystalline content was detected. It is assumed that the radiation-induced defects inside the crystallites do not induce destruction of the crystalline structure. However, the defects may change the intermolecular hydrogen bonding system, which keeps together the crystal lattice layers. In this way irradiation causes an increased accessibility, especially to treatments that are able to disrupt highly ordered, hydrogen-bonded cellulose structures. Therefore, when irradiated cellulose substrates are subjected to treatment with chemicals of high swelling power, such as NaOH solutions, increased alkali solubility and transformation of cellulose I crystal structure to cellulose II structure is observed (Dyer and Daul 1998; Takács et al. 2001). This has some technological importance: for instance, irradiation of pulp prior to viscose processing may result in reduced consumption of chemicals and time.

23.10.3 Amino Acids, Peptides

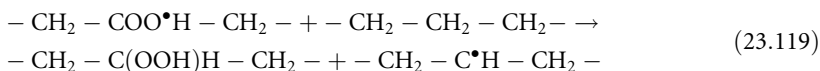
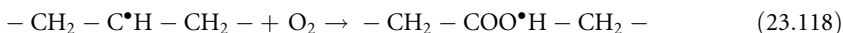
In peptides, amino acids are joined by peptide bonds to form the polypeptide chain. The e_{aq}^- , OH, and H radicals react with the amino acids and with the polypeptide chain with high rate coefficients that are close to the diffusion limit. OH radicals and, less frequently, H atoms abstract a hydrogen atom from the polypeptide chain (from the carbon atoms) or from the side chains, but they can also add to the rings of the aromatic amino acids. The radical site produced on the main chain may move along the chain by an internal hydrogen abstraction mechanism. If the H atom is abstracted from an S–H bond the radical migration stops, since the S–H bond is much weaker than the C–H bonds. This reaction is the basis of repair mechanism. The radicals may terminate in radical–radical reactions.

The hydrated electrons react with the carbonyl groups of the peptide chain or with disulfides and the protonated imidazole ring of histidine. It is assumed that the main sites of electron attachment are the surface peptide groups, and this is followed by internal electron migration into a potential sink, either to histidine or to a disulfide bridge (Mae 1987). As a final result of irradiation action on peptides in aqueous systems (and also in solid state) fragmentation of the peptide chain and cross-linking takes place.

23.10.4 Lipids

During irradiation of lipids in the presence of oxygen, the alkyl-type radicals formed on the fatty-acid chain quickly react with O_2 forming peroxy radicals. By abstracting an H atom from another fatty-acid molecule, the alkyl-type radical is regenerated and the peroxy radical is

converted to hydroperoxide. Thus a chain reaction starts in which lipid hydroperoxides form. The hydroperoxides have low thermal stability and easily decompose to toxic aldehydes and ketones. Antioxidants being present in lipids, for instance vitamin E (tocopherol), inhibit the chain reaction (Mae 1987; von Sonntag 1987a).



23.11 Radiation Applications

As discussed in the previous paragraphs, irradiation brings about physical and chemical changes in the material irradiated, and some of these processes can be applied to solve industrial problems. In [Sect. 23.9](#), some radiation technologies used in polymer chemistry were mentioned; some further industrial applications of irradiation will follow here. Synthetic and radiation processing aspects of irradiations are nicely summarized in the books of Bradley (1984), Spinks and Woods (1990) and Woods and Pikaev (1994). The most important practical applications and their advantages are summarized in [Table 23.7](#).

23.11.1 Radiation Synthesis

In the early period of radiation chemical investigations, the yields of many chemical reactions of industrial importance were determined since the applicability of radiation-induced reactions to synthetic work strongly depends on the yield. For instance, the radiation chemical yields of such reactions as



are low, $G < 0.5 \mu\text{mol J}^{-1}$. Therefore, the industrial application of radiation-induced syntheses of ammonia, hydrazine, and ozone is impractical, in contrast to some suggestions in the 1950s (Woods and Pikaev 1994). When the reaction takes place with a chain mechanism, the G -values can be much higher. Such chain reactions were mentioned before in connection with the isomerization of longer alkyl chlorides or bromides ([Sect. 23.8.2](#)) or with polymerization ([Sect. 23.9.1](#)). Often radiation initiation is advantageous because it can be carried out at lower temperature or without the addition of catalyst or chemical initiator giving a higher purity product.

Many radiation-induced chain reactions of synthetic importance are discussed in the book *Applied Radiation Chemistry* written by Woods and Pikaev (1994), in the *Radiation Chemistry Handbook* edited by Tabata (1991a), and also in a book chapter published by Takamuku and Yamamoto (1991). Earlier reviews on the subject were published by Bansal and Freeman (1971), and also by Chutny and Kucera (1974). A few examples will be mentioned here.

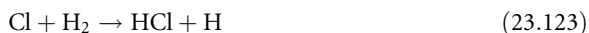
■ Table 23.7

Industrial applications of radiation processing

Product	Product improvements and advantages	Process
Wire and cable insulation; plastic insulating tubing; plastic packaging film	Shrinkability; impact strength; cut-through-, heat-, solvent-, stress-, cracking resistance; low dielectric losses	Cross-linking, vulcanization
Foamed polyethylene	Compression; tensile strength; reduced elongation	
Natural and synthetic rubber	High-temperature stability; abrasion resistance; cold vulcanization; elimination of vulcanizing agents	
Stack gases	Elimination of SO ₂ and NO _x	Chemical reaction
Solid-state semiconductors	Reduced switching time; stabilization of integrated circuit gain; reduced Zener diode noise level	Crystalline alteration
Precious and semiprecious gems, crystal, glass	Permanent coloring	
Adhesives: pressure sensitive, flock, laminate	Increased bonding; chemical-, chipping-, abrasion-, weather resistance; elimination of solvents; 100% convertibility of coating; high-speed cure; flexibility in handling techniques; low energy consumption; room-temperature cure; no limitation on colors	Curing, polymerization
Coatings; paints and inks on woods, metals and plastics		
Wood and organic impregnates	Mar-, scratch-, abrasion-, warping-, swelling-, weather resistance; dimensional stability; surface uniformity; upgrading of softwoods	
Cellulose	Enhanced chemical accessibility	Degradation
Textiles and textile fibers	Soil-release; shrink-, weather resistance; improved dyeability; static dissipation; thermal stability	Grafting
Film and paper	Surface adhesion; improved wettability	
Potatoes; wheat; rice, onions; cod and redfish; chicken; strawberries	Extended storage and shelf life	Sterilization, disinfecting
Wastewater	Safe disposal of wastewater solids; agricultural use of sewage sludge	
Medical supplies and disposable containers	Processing of heat-sensitive materials; high-speed in-line production; low energy consumption	Sterilization

Tabata (1991a), Spinks and Woods (1990), Woods and Pikaev (1994), Machi (1998).

Radiation-initiated chain reaction between H₂ and Cl₂ proceeds with a chain length over 10,000:



Radiation initiation has been used most successfully to induce free-radical chain reactions in organic substrates. The radiation-induced addition of HBr to ethylene is mentioned in many books. This reaction was used by Dow Chemical Company to produce bromoethane for a number of years:



Termination here and also in HCl production takes place with radical–radical reactions or with reaction of the radicals with impurities.

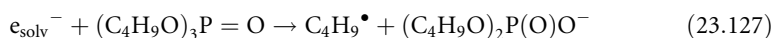
A few other reactions have also been developed to pilot plant or industrial scale including, e.g., chlorination, bromination, or sulfochlorination of hydrocarbons, oxidation of some organic compounds (Spinks and Woods 1990; Woods and Pikaev 1994).

Radiation-initiated cracking of hydrocarbons has been the subject of many studies. Irradiation reduces the temperature needed for chain reactions and also has an effect on the composition of products. The relatively high yield of unsaturated products under suitable conditions make the radiation-initiated process a possible source of feedstock for petrochemical industry (Spinks and Woods 1990; Zaikin and Zaikina 2008).

23.11.2 Applications of Radiation Chemistry to Nuclear Technology: The Purex Process

Some part of the spent fuel of atomic reactors is reprocessed separating uranium, plutonium, and the fission products, in order to produce new fissionable fuel or to collect some part of the valuable fission products. While several reprocessing methods have been proposed, the Purex process is the most widely used all over the world. The process uses 30% tributyl phosphate, TBP, as extractant in dodecane or kerosene solvent that is used to decrease the viscosity and the density of the liquid. The mixture is easily separated from water. The spent fuel is dissolved in concentrated nitric acid and the aqueous solution is mixed with the organic extractant. U and Pu present in the aqueous phase in the forms UO_2^{2+} and Pu^{4+} are extracted to the organic phase, the fission products remain in the aqueous solution. After reduction of Pu^{4+} by chemical or electrochemical method, Pu^{3+} goes back to the aqueous phase, while the uranium remains in the organic phase (Benndict et al., 1981; Choppin et al. 1995; Katsumura 2004).

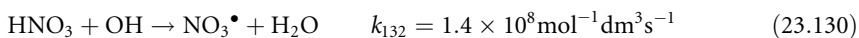
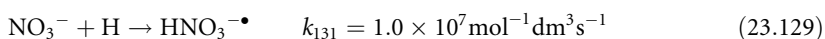
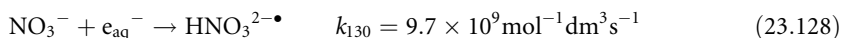
It is obvious that during separation the organic phase is under the effect of intensive γ , β , and α radiation fields. Therefore, radiation resistance is a very important issue. TBP decomposes to products dibutyl phosphate ($G \approx 0.2 \mu\text{mol J}^{-1}$), monobutyl phosphate ($0.02 \mu\text{mol J}^{-1}$), and gaseous hydrogen ($0.15 \mu\text{mol J}^{-1}$). In addition to these main components some minor products, butane, butene, $\text{C}_1\text{--C}_3$ hydrocarbons, butanol, and phosphoric esters are also observed. Dibutyl phosphate is suggested to form in solvated electron reaction



During Purex process thermal degradation and hydrolysis of TBP also takes place. The thermal degradation yields a large number of products including butane, butene, N_2 , NO_2 , CO_2 , NO, and butanol. The specific concern is the dealkylation of the phosphate ester since the dialkyl phosphoric acid ester, formed in the reaction, is capable of nonspecific interactions with metal ions (Katsumura 2004; Shkrob et al. 2007).

The radiolytic decomposition of pure dodecane under oxygen-free conditions takes place with a yield of 0.6–0.7 $\mu\text{mol J}^{-1}$. The decomposition leads mainly to dehydrogenation with a yield of $\sim 0.5 \mu\text{mol J}^{-1}$. In the process hydrogen, dodecenes, and dimers are produced. In addition to the main components, a large number of C_1 – C_{11} fragmentation products and C_{13} – C_{23} buildup products were also observed. The intermediate products are hydrogen atoms, $\text{C}_{12}\text{H}_{23}^\bullet$ parent, and smaller fragment alkyl radicals (Földiák 1981; Wojnárovits and Schuler 2000). In the dodecane-alkyl phosphate system there is an efficient energy and charge transfer from the alkane to the phosphate resulting in radiation protection of the alkane and fragmentation of the phosphate (Shkrob et al. 2007).

In aqueous nitric acid solution, the nitrate ions reacting with hydrated electrons generate NO_2^\bullet radicals through the reactions of $\text{NO}_3^{2-\bullet}$ and HNO_3^\bullet . In the further reactions NO_2 partly transforms to nitrite and nitrate ions. In concentrated nitric acid solution, the reaction of OH radicals gives NO_3^\bullet radicals.



As final products of irradiation of concentrated nitric acid solutions HNO_2 , H_2 , and O_2 form. Their yields strongly depend on the concentration.

Since during the Purex process TBP, alkane, and aqueous nitric acid solution are in mixture or contact condition, the radiation chemical transformations depend on the composition, concentration of nitric acid, contaminant metal ions, irradiation conditions, and oxygen concentration (Tripathi and Ramanujam 2003; Katsumura 2004). Under aerated condition, the organic radicals react with oxygen forming peroxy radicals. After successive reactions a variety of alcohols, ketones, peroxides, and carbonyl compounds form. The ratio of nitration products to oxidation products is ~ 0.8 , and the ratio increases if there is no sufficient supply of O_2 .

Under irradiation there is an increase in the density and viscosity, which is attributed to the polymerization and nitration of the hydrocarbon diluent. The increase in the density becomes more significant with increasing nitric acid content of the solvent and absorbed dose, which leads to much sharper increase in the viscosity. Various possible hydrogen-bonding modes seem to play a major role in enhancing the viscosity of the system (Tripathi and Ramanujam 2003).

As mentioned before (in Sect. 23.8.3) ionic liquids are considered to be the next generation of diluents of TBP in the fuel reprocessing cycle. The ionic liquid diluents of interest consist of large hydrophobic cations and anions that are stable under oxidizing conditions ($1\text{--}2 \text{ mol dm}^{-3} \text{ HNO}_3$) and do not chelate metal ions. Among the investigated ionic liquid diluents are [bmim][PF₆], [bmim][BF₄], and [bmim][(CF₃SO₂)₂N]. In the radiolysis of the ionic liquid–TPB system the yield of radiation-induced fragmentation of the trialkyl phosphate does not exceed 1–4% of that of the solvent, even when the concentration of the solvent is 20–40% by mass. Although the radiation stability of ILs appears to be inferior to the presently used alkane solvents, these IL diluents protect the extractant against radiation damage, unlike such alkane diluents. Dissociative electron attachment (e.g., $\text{PF}_6^- + e^- \rightarrow \text{PF}_5^- + \text{F}^-$) to the extractant and its subsequent dealkylation do occur, but it is a minor reaction, even at the higher end of the concentration range (Shkrob et al. 2007).

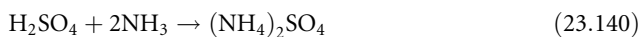
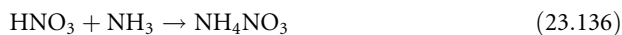
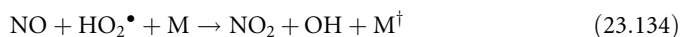
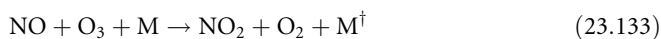
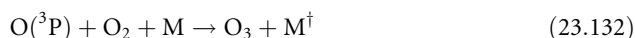
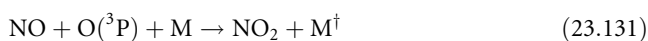
23.11.3 Radiation Processing

Radiation technologies applying gamma sources and electron accelerators for material modification are well-established processes. There are over 160 industrial gamma irradiators and 1,300 industrial electron accelerators in operation worldwide. A new advancement in the field of radiation sources engineering is the development of high-power direct e^-/X conversion sources based on electron accelerators.

23.11.3.1 Application of Ionizing Radiation for Environmental Protection

Strategies to tackle environmental pollution have been receiving increasing attention throughout the world in recent years. Radiation processing using electron beam accelerators and gamma irradiators has shown very promising results in this area.

Electron irradiation of flue gases produced by coal power stations in order to reduce the emission of sulfur and nitrogen oxides after a few pilot plant installations has reached the industrial stage (Chimielewski 2002; Chimielewski et al. 2004; Namba et al. 2004). Before irradiation, water and ammonia are added, the gas stream is cooled to 50°C–100°C, and the ammonium nitrate and sulfate formed during the treatment are separated from the gas stream in electrostatic precipitators: the powdered material collected is used as fertilizer. The reaction mechanism is rather complex, in modeling studies over 100 reactions are considered. In addition to the gas phase reactions, some transformations also take place in water droplets by a solution kinetic mechanism. The primary active species, ions, radicals, excited atoms, and molecules form essentially by interaction of radiation with N_2 , O_2 , and H_2O . The primary species undergo fast neutralization, ion–molecule and dissociation reactions to produce a set of reactive radicals (OH , HO_2^\bullet , and $O(^3P)$ (oxygen atom in triplet state)), which react with the pollutant molecules (Markovic 1986; Busi et al. 1987; Woods and Pikaev 1994; Namba et al. 2004; Haji-Saeid 2007). The most important reactions are as follows:



In the reaction set M and M^\dagger stand for the so-called third molecule in the ground and in some energy-rich state. The colliding third molecule carries away some part of the reaction heat.

Electron beam technology for flue gas treatment was developed in Japan in the early 1970s. The process was later used at pilot plant scale plants in Germany, Japan, the Republic of Korea, and the USA. In Poland the process has been demonstrated to be successful at the Kaweczyn power station in a pilot plant installation with a throughput of $20,000 \text{ Nm}^3 \text{ h}^{-1}$.³ Pilot plant installation with a throughput of $20,000 \text{ Nm}^3 \text{ h}^{-1}$ was also constructed in Bulgaria at the Maritsa East 2 power station.

Industrial scale electron beam gas treatment installations are currently (2007) in operation in coal fired plants in Poland (Pomorzany) and China (Chengdu). The Pomorzany plant treats approximately $270,000 \text{ Nm}^3 \text{ h}^{-1}$ with SO_2 and NO_x removal efficiencies up to 95 and 70%.

A typical installation consists of four main parts:

1. Flue gas conditioning unit,
2. Ammonia storage and feed system,
3. Process vessel with accelerator system,
4. By-product collection and storage unit.

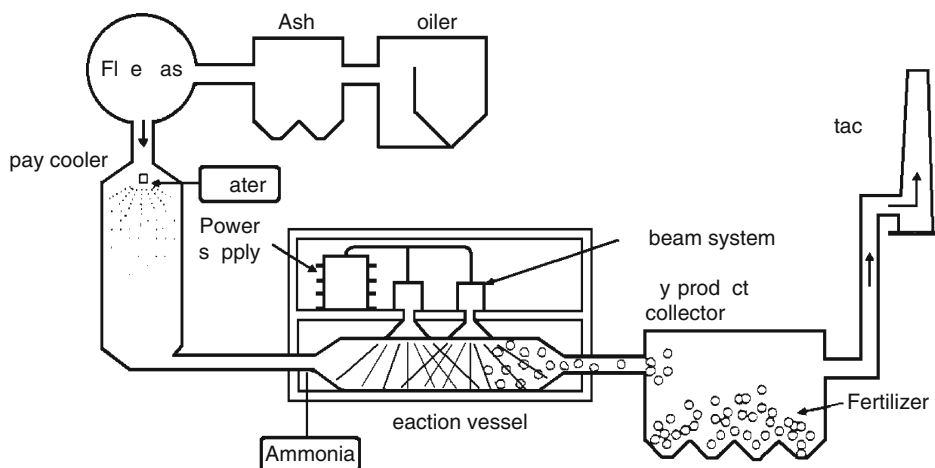
These units and the general schema of the flue gas treating system are shown on [Fig. 23.13](#).

Another possible application of the flue gas treatment technology is for the removal of volatile organic compounds (VOCs) and polycyclic aromatic hydrocarbons (PAHs), e.g., in flue gas treatment facilities of municipal waste incinerator plants.

The recognition that the polluted waters may pose a serious threat to humans has led technologists to look for cost effective technologies for their treatment. A variety of methods based on biological, chemical, photochemical, and electrochemical processes are being explored for decomposing the chemical and biological contaminants in *wastewater treatment*.

■ Fig. 23.13

General scheme of a flue gas purification plant

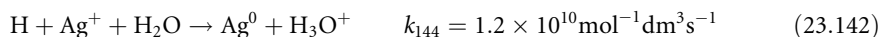
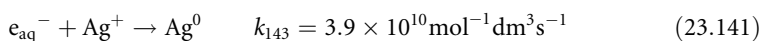


The first studies of the radiation treatment of wastes, principally for disinfection, were carried out in the 1950s. In the 1960s, these studies were extended to purification of water and wastewater. Laboratory research on industrial wastewater and polluted groundwater was conducted in the 1970s and 1980s. In the 1990s, several plants, including mobile electron beam facilities, were built for extended research. Studies in recent years have demonstrated the effectiveness of ionizing radiation such as, gamma rays and electron beams in combination with other treatments, in the decomposition of refractory organic compounds in aqueous solutions, and in the effective removal or inactivation of various microorganisms and parasites. The application of electron beam processing for drinking water, wastewater, and groundwater treatment offers the promise of a cost effective process (IAEA 2008).

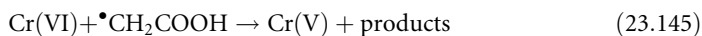
Radiation processing aims at the degradation of pollutants at a faster rate than with conventional processes. Processing of wastewater generally has maximum efficiency at pollutant concentration of 10^{-3} mol dm $^{-3}$ or less. Treatment of such wastewater is simple, requires a low dose (~ 1 kGy) and provides almost complete elimination of odor, color, taste, and turbidity. In general, pollutant transformation involves the following pathways: chain oxidation, formation of insoluble compounds, coagulation of colloids, and enhancement of pollutant biodegradability.

The *toxic metals* present in industrial effluent streams include heavy metals such as silver, lead, mercury, nickel, zinc, and chromium. These heavy metals accumulate in soil and are eventually transferred to the human food chain. In irradiation treatment the general strategy is the reduction of higher oxidation state ions to lower oxidation state ions: in lower oxidation state the solubility is usually lower, so often the reduced ions can be separated by precipitation. The reduction is done by the hydrated electron and hydrogen atom (under oxygen-free conditions) and/or by other reducing-type radicals formed in hydroxyl radical + alcohol or in hydroxyl radical + acetic acid reaction (see for instance reaction (23.34) and (23.144)) (Haji-Saeid 2007; Chaychian et al. 1998; Belloni and Mostafavi 2004; Belloni and Remita 2008).

The hydrated electrons readily reduce the silver ions to silver atoms. The atoms aggregate and finally form a black precipitate

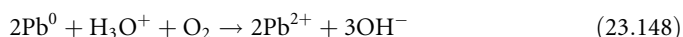


In acidic media, e.g., in the presence of acetic acid, the toxic Cr(VI) compounds can easily be reduced to poorly soluble Cr $^{3+}$ ions. The reduction occurs with a multistep mechanism through the reaction of H atoms. The α -carboxyalkyl radicals formed in OH + acetic acid reaction after forming a complex Cr(VI)-CH $_2$ COOH and dissociation also contribute to Cr(VI) reduction

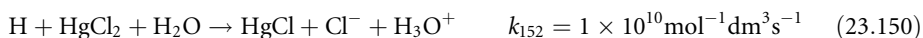
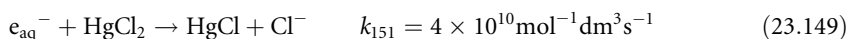


The Pb $^{2+}$ ions reacting with hydrated electrons transform to Pb $^+$ ions: Pb $^+$ ions in disproportionation reaction convert to Pb $^{2+}$ ions and Pb 0 atoms. The H atoms also contribute to the reduction. However, in the presence of dissolved oxygen, the zerovalent lead oxidizes

back to Pb^{2+} , for this reason during the reaction, precipitation and filtering oxygen-free conditions are needed.



Mercury is precipitated in the form of poorly soluble Hg_2Cl_2 : the processes of precipitation will be demonstrated with the example of the aqueous solution of HgCl_2 treated in the presence of small concentrations of isopropanol or ethanol.



The precipitation of metals from $10^{-3} \text{ mol dm}^{-3}$ concentration solutions takes place with 99% efficiency, precipitation of Cr(VI) and Hg(II) needs a few kGy dose; for the elimination of lead ions with the same concentration an order of magnitude higher dose is needed (Chaychian et al. 1998).

Many organic substances such as surfactants, lignin, pesticides, and dyes do not degrade by conventional biochemical methods, or they degrade very slowly. Biodegradation of wastewater depends on the oxidation level and structure of pollutants, preliminary oxidation, and fragmentation of biologically resistant molecules improves their biodegradability (Emmi and Takács 2008; IAEA 2008).

Aqueous effluents that can be degraded by irradiation fall into two categories: industrial wastewater, and natural and contaminated water including effluents from municipal treatment plants. The main differences between the two groups are the concentration of pollutants and the level of microbial infection, both of which are higher in the first group of effluents; however, disinfection is the main focus for the second group. Owing to the great variety of wastewaters generated by the industry, there is no universal treatment process for industrial wastewaters.

After intensive research and pilot plant installations the first full-scale industrial plant was reported for the purification of wastewater generated at the Voronezh (Russia) synthetic rubber plant. Irradiation is used to convert the non-biodegradable emulsifier or Nekal into a biodegradable form. Nekal is a mixture of isomeric isobutyl-naphthalene sulfonates. The installation has two 50 kW capacity electron accelerators and treats 2,000 m^3 effluents per day (Woods and Pikaev 1994).

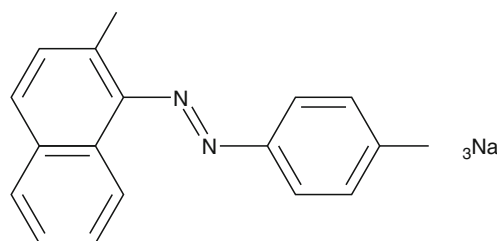
Advances to molecular design of dyes have improved their photostability and stability toward aerobic degradation or common oxidants, for these reasons the removal of dyes from wastewaters is extremely difficult. Effluents of textile dyeing and finishing industries are known to have considerable color, suspended solids, chlorinated organic molecules, surfactants, some heavy metals and to have variable pH, temperature, and chemical oxygen demand (COD). Especially reactive azo dyes cause special environmental concern: their precursors and their degradation products, such as aromatic amines, are considered highly carcinogenic. (Azo dyes are chemical compounds bearing the functional group $\text{R}-\text{N}=\text{N}-\text{R}'$ in which R and R' are aryl groups. Because of the electron delocalization through the $\text{N}=\text{N}$ group these compounds have

vivid colors, such as red, orange, or yellow. Azo dyes generally are bound to the textile fibers through secondary bonds (the structure of a simple azo dye, Acid Orange 7 (AO7) is shown below, ► Fig. 23.14). The reactive dyes have active groups for chemically bonding to the textile). Consequently, dyes have to be removed from industrial wastewater before discharging. Since the traditional elimination methods (e.g., biodegradation) are not efficient enough there is demand for establishing new efficient ways for disposal and treatment of azo dye containing wastewater by new oxidation/reduction processes. Such processes can be initiated by highly reactive radicals. The so-called advanced oxidation processes (AOP) work on this principle and apply highly reactive OH radicals for the reaction produced, e.g., in photo Fenton reaction (UV light-assisted decomposition of H_2O_2), photocatalytic reaction with suspended semiconductor such as TiO_2 (yielding also OH radicals) or ionizing radiation-induced decomposition of water. Due to the intensive research on the field of radiation-induced degradation of azo dyes, the basic processes of the undergoing reactions are now clarified (Wojnárovits and Takács 2008).

The reactive intermediates formed in water radiolysis (e_{aq}^- , H and OH) react with the dye molecules with high, practically diffusion-controlled rate coefficient forming dye radicals. e_{aq}^- and H attack principally the azo bond, whereas the OH radicals mainly react with the aromatic rings. Large number of parallel and consecutive reactions is involved in discoloration and mineralization (degradation to CO_2 , H_2O , N_2 , NO_x , SO_4^{2-}). The products were individually identified in very few cases. As intermediate products, compounds with destroyed $-\text{N}=\text{N}-$ bond, hydroxylated dye molecules, dimers, molecules with opened rings, aldehydes, ketones, and carboxylic acids form. The process of mineralization is usually followed by such techniques as chemical or biological oxygen demand, and total carbon content measurement. Discoloration is highly effective when e_{aq}^- and H are the reaction partners (in the absence of oxygen); however, for mineralization OH radicals and oxygen are required (oxidative degradation).

In order to treat industrial wastewater of dyeing factories the first pilot plant (output $1,000 \text{ m}^3 \text{ day}^{-1}$) was established in the area of Daegu Industrial Complex, Daegu, Republic of Korea. The pilot plant was operating with ELV accelerator (energy 1 MeV, beam power 40 kW) for large-scale test of combined electron-beam and biological treatment of industrial textile dyeing wastewater (Han et al. 2002). According to the pilot-plant investigations of the dyeing complex wastewater equal purification degree corresponds to 17 h of bio-treatment without preliminary irradiation and about 8 h of bio-treatment with preliminary electron-beam treatment and absorbed dose 1–2 kGy. Based on the experiences gained with pilot plant a full-scale electron beam plant was constructed to treat $10,000 \text{ m}^3 \text{ day}^{-1}$ textile wastewater. This full-scale plant, since its start in 2006, has demonstrated that the established radiation

► Fig. 23.14
Acid Orange 7 (AO7)



technology is cost effective when compared to conventional treatment. The regular operation of this facility provides operational data on reliability and additional data for a detailed economic evaluation.

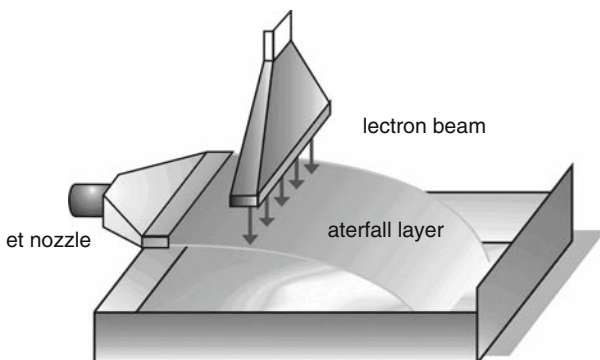
Several reactor types have been suggested for industrial application. One of the best designs is shown in ► Fig. 23.15. The injected wastewater forms a wide continuous layer, which is irradiated by a transverse electron beam. The thickness of the water jet is tied to the beam energy, i.e., to the penetration of the accelerated electrons. The width of the water jet corresponds to the width of the beam window. The water jet type reactor makes possible electron beam treatment at high rates of wastewater flow (Haji-Saeid 2007).

Pilot-and industrial-scale plants for radiation disinfection of *sewage sludge* are in operation in several countries. Sewage is water born waste from domestic premises and industry. Since it carries human waste, it is a source of various human pathogens that need to be controlled for safe disposal. The sludge resulting from municipal wastewater treatment is in the form of a liquid or semisolid liquid that typically contains 1–20% solids by weight, depending on the operations and processes used. Many researchers have shown that sewage sludge can be disinfected by exposure to ionizing radiation, and that irradiation often facilitates dewatering by accelerating sedimentation and filtration. A dose of 2–3 kGy destroys more than 99.9% of the bacteria being present in sewage sludge and leads to the almost complete removal of helminthes eggs and to the inactivation of the agents that cause diseases in animals. Doses of this magnitude are employed for the radiation treatment of sewage sludge at an industrial plant in Geiselbullach, Germany (Lessel and Suess 1984), and slightly higher doses (4 kGy) are used at a pilot plant near Boston in the USA (Trump et al. 1984). Higher doses are needed to inactivate more radiation-resistant organisms. Doses of 10 kGy were used at a sewage treatment plant in Albuquerque, USA (Sivinski 1983), and at an installation in Ukraine (Vysotskaya 1983).

The first plant in Geiselbullach started in 1973 and was used for research and demonstration purposes, not much later an industrial plant went into operation. The pilot plant in Albuquerque operated between 1978 and 1985 and was used for research. In Vadodara, India, a sludge treatment plant for processing 110 m³ of liquid sludge a day has been in operation since 1992 (Rawat et al. 1997; Gautam et al. 2005). The treatment plants mentioned work with ⁶⁰Co or ¹³⁷Cs radionuclides.

■ Fig. 23.15

Wastewater reactor with perfect displacement



A pilot plant using an electron accelerator as radiation source was built in Boston in 1976 and later it was modified to obtain 655 m³ of disinfected sludge per day. In the 1980s, similar facilities were brought into service near Miami (USA), and in Takasaki (Japan, Hashimoto and Kawakami 1984). Construction of an industrial scale plant treating 600 m³ dewatered sludge per day (18% solids content) is planned in Israel (Haji-Saeid 2007).

The operational experiences of the sewage treatment plants using γ - or electron irradiation have shown that the process is simple, effective, and easy to integrate into the existing sewage treatment plants. The irradiated sludge, being pathogen free, after composting can be beneficially used as manure in agricultural fields, as it is rich in soil nutrients. Since the irradiated sludge is free of bacteria, it can also be used as a medium for growing bacteria that are useful for soils to produce biofertilizer that can enhance crop yields (Haji-Saeid 2007).

23.11.3.2 Food Irradiation

Irradiation of food and food components has been the subject of intensive studies since the 1950s and radiation processing of selected foods has been approved by many countries (Elias and Cohen 1983, 1987; Farkas 1988, 2004). During irradiation, the temperature of the irradiated material rises only by a few degree Celsius, therefore irradiation treatment is regarded as isothermal process. Because of the negligible heat effect, irradiation treatment kills the cells of microbes contaminating frozen foods without thawing them up, or, those in fresh food without changing the original physical state of the product. Irradiation needs less energy than thermal treatment; irradiation may be carried out either in bulk or after packaging thus avoiding recontamination or reinfestation of the product. In contrast to the usual chemical treatment processes, no toxic chemicals such ethylene oxide, carcinogens, or mutagens need be used. However, the vitamin content of the food may be reduced due to irradiation, e.g., vitamin C and vitamins A and E may act as radical scavengers. It should be noted, however, that such vitamins are also damaged by other methods of food processing (Mozumder 1999).

The purpose of irradiation can be (a) delaying or preventing sprouting, inactivation of molds and bacteria to prolong shelf life, (b) elimination of insects and parasites, (c) delaying ripening of foods, and (d) production of sterile products, which can be used without refrigeration.

Inhibition of sprouting in onions, potatoes, and the like needs the lowest dose, 0.12–0.15 kGy. Next is the elimination of insects and parasites in cereals, fruits, dried fish, and fresh meat requiring 0.1–1.0 kGy. Delay in physiological processes in fresh fish, meat, and meat products needs ~ 1 kGy. 1.0–5.0 kGy will be needed to prolong the self-life of fresh fish, meat, and meat products. Control of pathogenic microorganisms and spoilage decontamination in seafood, poultry, spices, and animal feed require 3–10 kGy. 10–50 kGy may be needed for sterilization and elimination of viruses in poultry, meat, seafood, prepared foods, hospital diets, and foods for astronauts (radappertization). When meat is irradiated at higher doses there are some flavor changes due to lipid peroxidation. The high-dose treatment must be delivered to a vacuum-packed and deeply frozen (-30°C) product to avoid unwanted changes.

Food processing is usually carried out by ^{60}Co γ rays or less frequently by accelerated electrons. The electron energy should not exceed 10 MeV: below 10 MeV, electrons do not induce appreciable radioactivity in irradiated food. When not the electron itself, but the X-rays generated by electron impact on heavy metals (bremsstrahlung) is used for food treatment, then the electron energy should be kept below 5 MeV. Typical irradiation facilities used for food

irradiation (and also for sterilization of medical products, polymer processing, etc.) consist of a chamber containing the radiation source, some sort of conveyor systems to transport products inside and outside the shielding walls, and sophisticated control and safety system. Irradiation facilities are built with several layers of redundant protection to detect or eliminate equipment malfunctions and protect employees from accidental exposure (Farkas 2004).

The radiobiological effect in foods was first explained by the direct target effect theory. According to the theory, the biological effects are due to direct action of radiation on important molecules on sensitive parts of cells. Later it was shown that a considerable part of biological effects is due to indirect processes, e.g., reactions of reactive intermediates formed in water radiolysis (Elias and Cohen 1983, 1987; Farkas 1988, 2004).

Toxicological, nutritional, and microbiological tests support the safety of irradiated food for consumption and some 50 countries granted national clearances of irradiation of at least one or more food items of food classes (Farkas 2004). Legislator authorities require that irradiated food products be labeled. In general, the international food irradiation symbol, the so-called Radura logo (► Fig. 23.16) is required with a statement that the product has been intentionally subjected to radiation.

Regarding packaging material for irradiated foods, most commonly used food packaging material are suitable for the purpose. However, irradiation of prepackaged food requires approval of its packaging material.

Due to the public concern it is desirable to develop simple methods for the identification of irradiated food products. Because of the low yields of products formed it is a rather complicated problem. One of the standardized methods, electron spin resonance (EPR) technique, permits identification of food that contains a hard dry matrix, e.g., bone (Raffi and Kister 2008). When food containing bone is irradiated, free radicals are produced and trapped in the in the crystal lattice, which can be detected by EPR spectroscopy.

Thermoluminescence measurements observing crystal defects in, e.g., quartz grains being as impurity on the surface of some foods (vegetables) can also be successfully applied (Farkas 2004). Another standardized method is based on the irradiated fat-containing foods using the mass-spectrometric detection 2-alkyl-cyclobutanones after gas chromatographic separation (► Fig. 23.17 (Delincée 2002)).

23.11.3.3 Sterilization of Medical Products and Drugs

One of the most successful applications of radiation technology has been the sterilization of medical supplies. Sterilization was introduced by the mid-1950s, at present, ~30% of all

■ Fig. 23.16
Radura logo



■ Fig. 23.17

2-Alkylcyclobutanone

medical, single-use disposable products are sterilized by irradiation. Of the different kinds of disposables mainly surgical gowns, gloves, syringes, bandages, sutures, dressings, catheters, and transfusion sets are sterilized by irradiation (IAEA 1975, 1990; Woods and Pikaev 1994).

The aim of the irradiation is to kill or inactivate the microorganisms. The exact mechanism of the process is less known, although it is almost certainly connected with the radiation-induced damage of the DNA and perhaps also with the damage of cytoplasmic membranes (Farkas 2004). The radiation sensitivity was shown to increase with the amount of DNA in the nucleus of the microorganism.

In principle there is an exponential relationship between the microorganism survival and the absorbed dose. However, the practically measured survival curves often deviate from the linear relationship on the log survival-absorbed dose plots. At the beginning of the treatment there is a shoulder: initially the survival decreases less steeply than at higher doses. It indicates that more than one lesion is required to kill the microorganism; the shoulder is due to repair processes within the cells.

Generally a reduction of 10^{-6} in microorganism level is required. Since sterilization is equivalent to disruptive action of large biological molecules, relatively small doses are needed for the process making radiation sterilization economically feasible. The minimum absorbed dose required by the authorities in different countries varies somewhat, but it is mostly around 25 kGy. In case of highly radiation resistant microorganisms, higher doses may be required.

When compared with the traditional sterilization methods, such as heating in an autoclave, ethylene oxide, or formaldehyde treatments several advantages of radiation technology should be mentioned

1. Since there is a simple relationship between sterility and, absorbed dose, sterility is controlled by the dose value, which, in turn, is usually controlled by the conveyor speed. Therefore, long-lasting microbiological tests are required only occasionally. It increases the safety of sterilization and simplifies the process. The process is continuous, allowing smooth product flow and requiring minimum human handling.
2. The products can be sterilized after packaging, which gives some flexibility of operation.
3. Irradiation avoids the use of toxic chemicals, e.g., ethylene oxide, or high temperatures in an autoclave.
4. In case of irradiation treatment, new materials can be used for the medical devices (e.g., syringe).

The various materials (often polymers) have to be chosen such that they are sufficiently radiation resistant to withstand the sterilization dose. Under the dose conditions, needed for sterilization some polymers such as polyethylene, polystyrene, poly(ethylene terephthalate), polyurethanes, and epoxides may be stable, whereas others such as polypropylene, poly(methyl methacrylate), polyvinyl chloride (PVC) may not. When the radiation stability of the plastic

material is poor, some additives are included in order to improve the radiation stability (Woods and Pikaev 1994; IAEA 1975, 1990).

Most of the irradiation in the field of sterilization is carried out by ^{60}Co irradiation facilities; however, sometimes electron accelerators are also used for this purpose.

A new field of radiation application is the *radiation sterilization of drugs*. The requirement for sterility of drugs depends on type of administration. It concerns mostly ophthalmic preparations, sterile topical products, and injectable solutions. In some cases, radiation sterilization appears to be an attractive alternative to other types of sterilization, e.g., heat sterilization. For drugs the usual requirement (six orders of magnitude decrease in the microorganism level) is achieved by applying an absorbed dose of 25 kGy.

When drugs in the solid state (tablets, powders, suspensions) are sterilized, the drug molecules are directly ionized and excited by the ionizing radiation: the diffusion of the reactive species is hindered by the solid and they cannot diffuse, except for the mobile deliberated electrons and hydrogen atoms. The reactive species, mostly radicals, are trapped by the solid matrix and they react with high probability with each other reestablishing the initial molecules. For this reason the drug transformation yield is usually very low ($<0.1\%$). In fact, until the 1990s the analytical techniques failed to detect final products present in traces. Due to the development of highly sensitive analytical techniques, nowadays the radiation chemistry research is directed toward the reaction mechanisms and analysis of final products in terms of their potential toxicity. The impurity concentration in drugs is generally higher than the concentration of the newly formed radiolytic products, moreover during radiolysis usually the same products form as the impurities making product determination more difficult (Tilquin 2008).

When the drug is sterilized in aqueous solution most of the energy of ionizing radiation is absorbed by water and the reactive intermediates of water radiolysis, discussed in [Sect. 23.6.1](#), react with the microorganisms and also with the drug molecules. In solutions the drug undergoes decomposition with a high yield, unless by adding a protective agent or by freezing the solution (Woods and Pikaev 1994; Tilquin 2008). As radioprotectors some vitamins or 1,2-propanediol may be used. When an aqueous solution of a pharmaceutical is frozen, the polycrystalline solid contains both ice and solute phases. Since the phases are separate, the indirect effect of the intermediates of water radiolysis on the drug molecules is reduced. So freezing increases the radiation stability of aqueous pharmaceutical preparations. Sterilization of frozen materials is described as cryoradiation sterilization (Woods and Pikaev 1994).

23.12 Editors' Note

1. See [Fig. 9.21 in, Vol. 1 Chap. 9](#), on “Stochastics and Nuclear Measurements,” for a schematic representation of the “smearing” of a signal while it gets amplified by subsequent dynodes (p. 1279).
2. See [Chap. 57 in Vol. 6](#) on “Technical Application of Nuclear Fission.” The problems caused by oxygen formation are commented on in Sect. 57.4.2.1 on “The pressurized water reactor (PWR)” (p. 1290).
3. Nm^3 stands for normal cubic meters, where “normal” refers to standard temperature and pressure of the gas (p. 1318).

References

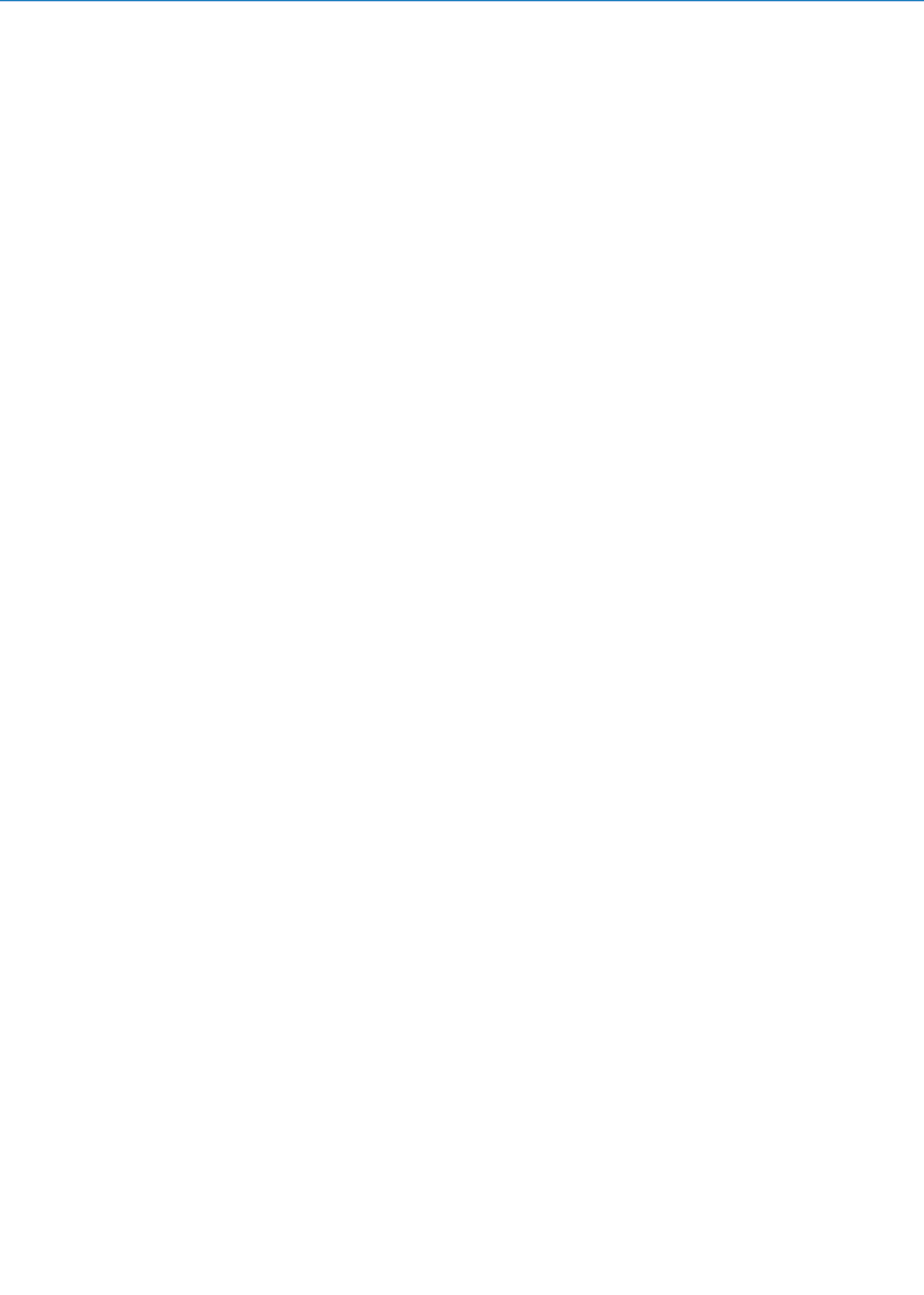
- Alfassi ZB (1989) In: Patai S (ed) *Radiation chemistry of double-bonded compounds, The chemistry of double-bonded functional groups*. Wiley, Chichester, pp 527–565
- Aoki Y, Nakajyo T, Tsunemi A, Yang J, Okada Y, Yorozu M, Hirose M, Sakai F, Endo A (2001) *Res Chem Intermed* 27:689
- Asano A, Yang J, Kundoh T, Norizawa K, Nagaishi R, Akahashi K, Yoshida Y (2008) *Radiat Phys Chem* 77:1244
- Ashton L, Buxton GV, Stuart CR (1995) *J Chem Soc Faraday Trans* 91:1631
- Ausloos P, Lias SG (1974) Far ultraviolet photochemistry of organic compounds. In: Sandorfy C, Ausloos P, Robin MB (eds) *Chemical spectroscopy and photochemistry in the vacuum ultraviolet*. Reidel, Dordrecht, pp 465–482
- Ausloos P, Rebbert FP, Shwartz FP, Lias SG (1983) *Radiat Phys Chem* 21:27
- Baldacchino G, Hickel B (2008) Water radiolysis under extreme conditions. Application to the nuclear industry. In: Spothem-Maurizot M, Mostafavi M, Douki T, Belloni J (eds) *Radiation chemistry: from basics to applications in material and life sciences*. EDP Sciences, Paris, pp 53–64
- Bansal KM, Freeman GR (1971) *Radiat Res Rev* 3:209
- Barbara PF (chair) (1998) Research needs and opportunities in radiation chemistry, Final Report of the Workshop held April 19–22, 1998, Charleston, Indiana
- Baxendale JH, Busi F (eds) (1982) *The study of fast processes and transient species by electron pulse radiolysis*. Reidel, Dordrecht
- Bednar J (1983) Generation of high atomic and molecular Rydberg states. In: Dobó J, Schiller R (eds) *Proceedings of the 5th Tihany symposium on radiation chemistry*. Akadémiai Kiadó, Budapest, pp 21–31
- Belloni J, Remita H (2008) Metal clusters and nanomaterials. In: Spothem-Maurizot M, Mostafavi M, Douki T, Belloni J (eds) *Radiation chemistry: from basics to applications in material and life sciences*. EDP Sciences, Paris, pp 97–116
- Belloni J, Mostafavi M (2004) Charged particle and photon interactions in metal clusters and polarographic systems studies. In: Mozumder A, Hatano Y (eds) *Charged particle and photon interactions with matter: chemical, physicochemical and biological consequences with applications*. Marcel Dekker, New York, pp 579–616
- Belloni J, Mostafavi M, Remita H, Marguier JL, Delcourt MO (1998) *New J Chem* 22:1239
- Benndict M, Pigford TH, Levi HW (1981) *Nuclear chemical engineering*, 2nd edn. McGraw-Hill, New York
- Bensasson RV, Jori G, Land EJ, Truscott TG (eds) (1985) *Primary photo-processes in biology and medicine*. Plenum, New York
- Bensasson RV, Land EJ, Truscott TG (eds) (1993) *Excited states and free radicals in biology and medicine*. Oxford University Press, Oxford
- Berlman IB (1971) *Handbook of fluorescence spectra of aromatic molecules*. Academic, New York
- Berthon L, Nikitenko SI, Bisel I, Berthon C, Faucon M, Saucerotte B, Zorz N, Moisy Ph (2006) *Dalton Trans* 2526
- Birks JB (1970) *Photophysics of aromatic molecules*. Wiley, London
- Bíró A, Takács E, Wojnárovits L (1996) *Macromol Rapid Commun* 17:353
- Blaunstein RP, Christophorou LG (1971) *Radiat Res Rev* 3:69
- Bouillot MS (1970) *Int J Radiat Phys Chem* 2:117
- Bradley R (1984) *Radiation technology handbook*. Marcel Dekker, New York
- Brandrup J, Immergut EH, Grulke EA (1999) *Polymer handbook*, 4th edn. Wiley, New York
- Brede O, Boes J, Naumann W, Mehnert R (1978) *Radiochem Radioanal Lett* 35:85
- Brede O, Hermann R, Wojnárovits L, Stephan L, Taplick T (1989) *Radiat Phys Chem* 34:403
- Burns WG, Reed CRV (1970) *Trans Faraday Soc* 66:2159
- Busi E, D'Angelantonio M, Mulazzani QG, Tubertini O (1987) In: Hedvig P, Nyikos L, Schiller R (eds) *Proceedings of the 6th Tihany symposium on radiation chemistry*. Akadémiai Kiadó, Budapest, pp 741–751
- Buxton CV, Stuart CR (1995) *J Chem Soc Faraday Trans* 91:279
- Buxton G, Gillis H, Klassen NV (1977) *Can J Chem* 54:367
- Buxton GV (1982) Basic radiation chemistry of liquid water. In: Baxendale JH, Busi F (eds) *The study of fast processes and transient species by electron pulse radiolysis*. Reidel, Dordrecht, pp 241–266
- Buxton GV (1987) Radiation chemistry of the liquid state: (1) water and homogenous aqueous solutions. In: Farhataziz, Rodgers MAJ (eds) *Radiation chemistry, principles and applications*. VHC, New York, pp 321–349
- Buxton G, Greenstock CL, Helman WP, Ross AB (1988) *J Phys Chem Ref Data* 17:513, Updated version can be found in the Notre Dame University database, <http://www.rcdc.nd.edu>
- Buxton G (2001) *Stud Phys Theor Chem* 87:145–162
- Chapiro A (1962) *Radiation chemistry of polymeric systems*. Wiley, New York
- Charlesby A (1960) *Atomic radiation and polymers*. Pergamon, New York

- Charlesby A (1987) Radiation chemistry of polymers. In: Farhataziz, Rodgers MAJ (eds) *Radiation chemistry: principles and applications*. VHC Publishers, New York, pp 451–475
- Chaychian M, Al-Sheikhly M, Silverman J, McLaughlin WL (1998) Radiation induced reduction and removal of heavy-metal ions from water. In: Cooper WJ, Curry RD, Shea KE (eds) *Environmental applications of ionizing radiation*. Wiley, New York, pp 353–367
- Chimielewski AG, Licki J, Pawelec A, Tyminski B, Zimek Z (2004) *Radiat Phys Chem* 71:441
- Chimielewski AG (2002) Environmental effects of fossil fuel combustion. In: *Encyclopedia of life support systems (EOLSS)*. EOLSS Publishers, Oxford
- Choppin G, Liljenzin JO, Rydberg J (1995) *Radiochemistry and nuclear chemistry*, 2nd edn. Butterworth-Heinemann, Oxford
- Christodoulides AA, McCorkle DL, Christophorou LG (1984) Electron attachment processes. In: Christophorou LG (ed) *Electron–molecule interaction applications*. Academic, Orlando, pp 477–617
- Chutny B, Kucera J (1974) *Radiat Res Rev* 5:1, 55, 93, 135
- Clough RL, Shalaby SW (eds) (1996) *Irradiation of polymers: fundamentals and technological applications*. American Chemical Society Books, Washington, DC
- Clough RL (2001) *Nucl Instr Meth B* 185:8
- Coqueret X (2008) Obtaining high performance polymeric materials by irradiation. In: Spothheim-Maurizot M, Mostafavi M, Douki T, Belloni J (eds) *Radiation chemistry: from basics to applications in material and life sciences*. EDP Sciences, Paris, pp 131–149
- Cramer WA (1967) *J Phys Chem* 71:1171
- Cserép Gy (1981) Aliphatic alkenes. In: Földiák G (ed) *Radiation chemistry of hydrocarbons*. Amsterdam, Elsevier, pp 253–349; Cycloalkanes. pp 351–392
- De Haas MP, Warman JM, Infelta PP, Hummel A (1975) *Chem Phys Lett* 31:382
- De Haas MP, Hummel A, Infelta PP, Warman JM (1976) *J Chem Phys* 65:5019
- Delincée H (2002) *Radiat Phys Chem* 63:455
- Dellonte S, Flamigni L, Barigelletti F, Wojnárovits L, Orlandi G (1984) *J Phys Chem* 88:58
- Dole M (1973) *The radiation chemistry of macromolecules*. Academic, New York
- Draganic IG, Draganic ZD (1971) *The radiation chemistry of water*. Academic, New York
- Dyer J, Daul C (1998) Rayon fibers. In: Lewin M, Pearce EM (eds) *Handbook of fiber chemistry*. Marcel Dekker, New York, p 738
- Ebert M, Keene JP, Swallow AJ, Baxendale JH (eds) (1965) *Pulse radiolysis*. Academic, London
- Elias PS, Cohen AJ (eds) (1983) *Recent advances in food irradiation*. Elsevier, New York
- Elias PS, Cohen AJ (eds) (1987) *Radiation chemistry of major food components*. Elsevier, New York
- Emmi SS, Takács E (2008) Water remediation by electron-beam treatment. In: Spothheim-Maurizot M, Mostafavi M, Douki T, Belloni J (eds) *Radiation chemistry: from basics to applications in material and life sciences*. EDP Sciences, Paris, pp 87–95
- Farkas J (2004) Food irradiation. In: Mozumder A, Hatano Y (eds) *Charged particle and photon interactions with matter: chemical, physicochemical and biological consequences with applications*. Marcel Dekker, New York, pp 785–812
- Farkas J (1988) *Irradiation of dry food ingredients*. CRC, Boca Raton
- Fielden EM (1982) Chemical dosimetry of pulsed electron and X-ray sources in the 1–20 MeV range. In: Baxendale JH, Busi F (eds) *The study of fast processes and transient species by electron pulse radiolysis*. Reidel, Dordrecht, pp 49–62
- Flamigni L, Barigelletti F, Dellonte S, Orlandi G (1982) *Chem Phys Lett* 89:13
- Földiák G (ed) (1981) *Radiation chemistry of hydrocarbons*. Elsevier, Amsterdam
- Földiák G (ed) (1986) *Industrial application of radioisotopes*. Elsevier, Amsterdam
- Földiák G, György I, Wojnárovits L (1976) *Int J Radiat Phys Chem* 8:575
- Freeman GR (1968) *Radiat Res Rev* 1:1
- Freeman GR (1970) The radiolysis of alcohols. In: Haissinsky M (ed) *Actions Chimiques et Biologiques des Radiations*, vol 14. Masson, Paris, pp 73–134
- Freeman GR (1974) Radiation chemistry of ethanol: a review of data on yields, reaction rate parameters, and spectral properties of transients. *NSRDS-NBS48*, p 43
- Freeman GR (ed) (1987) *Kinetics of nonhomogeneous processes*. Wiley, New York
- Gäumann T, Hoigné J (1968) *Aspects of hydrocarbon radiolysis*. Academic, London
- Graselli M, Smolko E, Hargittai P, Safrany A (2001) *Nucl Instr Meth Phys Res B* 185:254
- Grigoriev EI, Traktenberg LI (1996) *Radiation chemical processes in the solid phase: theory and application*. CRC, Boca Raton
- Gautam S, Shah MR, Sabharwal S, Sharma A (2005) *Water Environ Res* 77:472
- Grodzowski J, Neta P (2002) *J Phys Chem A* 106:9030
- György I (1981) Aliphatic alkanes. In: Földiák G (ed) *Radiation chemistry of hydrocarbons*. Elsevier, Amsterdam, pp 61–176
- Haji-Saeid M (2007) *Radiation processing: environmental applications*. International Atomic Energy Agency, Vienna
- Han B, Ko J, Kim J, Kim Y, Chung W, Makarov IE, Ponomarev AV, Pikaev AK (2002) *Radiat Phys Chem* 64:53
- Harmon CD, Smith WH, Costa DA (2001) *Radiat Phys Chem* 60:157

- Hart EJ, Fielden EM, Anbar M (1967) *J Phys Chem* 71:3993
- Hashimoto S, Kawakami W (1984) *Radiat Phys Chem* 24:29
- Hatano Y (1968) *Bull Chem Soc Jpn* 41:1126
- Hatano Y (1999) *Phys Rep* 313:109
- Hebeish A, Guthrie JT (1981) *The chemistry and technology of cellulosic copolymers*. Springer, Berlin
- Herkstroeter WG, Gould IR (1993) Absorption spectroscopy of transient species. In: Rossiter BW, Baetzold RC (eds) *Determination of electronic and optical properties, vol VIII, Physical methods in chemistry*. Wiley, New York, pp 225–319
- Hermann R, Mehnert R, Wojnárovits L (1985) *J Lumin* 33:69
- Hirayama F, Lipsky S (1975) *J Chem Phys* 62:576
- Ho SK, Freeman GR (1964) *J Phys Chem* 68:2189
- Hoigné J (1968) Aromatic hydrocarbons. In: Gümman T, Hoigné J (eds) *Aspects of hydrocarbon radiolysis*. Academic, London, pp 61–151
- Holm NW, Berry R (1970) *Manual on radiation dosimetry*. Marcel Dekker, New York
- Holroyd RA (1968) Radical yields in hydrocarbons. In: Gümman T, Hoigné J (eds) *Aspects of hydrocarbon radiolysis*. Academic, London, pp 1–32
- Holroyd RA (1987) The electron: its properties and reactions. In: Farhataziz, Rodgers MAJ (eds) *Radiation chemistry: principles and applications*. VCH, New York, pp 201–235
- Holroyd RA, Schmidt WF (1989) *Ann Rev Phys Chem* 40:439
- Holroyd RA (2004) Electrons in nonpolar liquids. In: Mozumder A, Hatano Y (eds) *Charged particle and photon interactions with matter: chemical, physicochemical and biological consequences with applications*. Marcel Dekker, New York, pp 175–206
- Hummel A (1992) Radiation chemistry of alkanes and cycloalkanes. In: Patai S, Rappoport Z (eds) *The chemistry of alkanes and cycloalkanes*. Wiley, Chichester, pp 743–780
- Hummel A, Schmidt WF (1974) *Radiat Res Rev* 5:199
- Hummel RW (1970) *Int J Radiat Phys Chem* 2:119
- IAEA-TECDOC-1598 (2008) Radiation treatment of polluted water and wastewater. International Atomic Energy Agency, Vienna
- IAEA TECDOC-539 (1990) Guidelines for industrial radiation sterilization of disposable medical products (Cobalt-60 gamma irradiation). International Atomic Energy Agency, Vienna
- IAEA (1975) Radiation sterilization of medical products. International Atomic Energy Agency, Vienna
- Ichikawa T, Yoshida H (1992) *J Phys Chem* 96:7661
- Ivanov VS (1992) *Radiation chemistry of polymers*. VSP Publishers, Utrecht
- Jonah CD (1975) *Rev Sci Instrum* 46:62
- Karolczak S (1999) Pulse radiolysis—experimental features. In: Mayer J (ed) *Properties and reactions of radiation induced transients. Selected topics*. Polish Scientific Publishers, Warszawa, pp 5–37
- Kase KR, Bjängard BE, Attix FH (1985) *The dosimetry of ionizing radiation, vol I and II*. Academic, Orlando
- Katsumura Y (2004) Application of radiation chemistry to nuclear technology. In: Mozumder A, Hatano Y (eds) *Charged particle and photon interactions with matter: chemical, physicochemical and biological consequences with applications*. Marcel Dekker, New York, pp 697–727
- Knolle W, Trautman C (eds) (1999) *Conference proceedings of Ionizing radiation and polymers, IRaP98, held in Weinbohl near Dresden*. Nucl Instr Meth B 151:1–4
- Kobayashi H, Tabata Y (1989) *Radiat Phys Chem* 34:447
- Kouchi N, Hatano Y (2004) Interactions of photons with molecules: photoabsorption, photoionization, and photodissociation cross sections. In: Mozumder A, Hatano Y (eds) *Charged particle and photon interactions with matter: chemical, physicochemical and biological consequences with applications*. Marcel Dekker, New York, pp 105–120
- Krassig HA (1996) *Cellulose, structure, accessibility and reactivity*. Gordon & Beach, Amsterdam, p 219
- Kroh J (ed) (1989) *Early developments in radiation chemistry*. The Royal Society of Chemistry, Cambridge
- Kroh J (1991) Pulse radiolysis of glassy solids. In: Tabata Y (ed) *Pulse radiolysis*. CRC, Boca Raton
- Land EJ, Ebert M (1967) *Trans Faraday Soc* 63:1181
- LaVerne JA, Schuler RH (1984) *J Phys Chem* 88:1200
- LaVerne JA, Wojnárovits L (1994) *J Phys Chem* 98:12635
- Lessel T, Suess A (1984) *Radiat Phys Chem* 24:3
- Lias SG, Ausloos P (1975) Ion-molecule reactions. Their role in radiation chemistry. American Chemical Society, Washington DC
- Luthjens LH, Frahn MS, Abellon RD, Hom ML, Warman JM (2001) *Res Chem Intermed* 27:765
- Machi S (1998) *Radiat Phys Chem* 52:591
- Mae LK (1987) Radiation chemistry of biopolymers. In: Farhataziz, Rodgers MAJ (eds) *Radiation chemistry: principles and applications*, VHC, New York, pp 477–499
- Makarov VI, Polak LS (1970) *High Energy Chem* 4:1
- Makhlis FA (1975) *Radiation chemistry of polymers*. Wiley, New York
- Markovic V (ed) (1986) *Electron beam processing of flue gases*. IAEA, Vienna
- Martelli F, Higa OZ, Takács E, Safran J, Yoshida M, Katakai R, Carenza M (1999) *Radiat Phys Chem* 55:155
- Mayer J (ed) (1999) *Properties and reactions of radiation induced transients. Selected topics*. Polish Scientific Publishers, Warszawa

- McLaughlin WL, Boyd AW, Chadwick KH, McDonald JC, Miller A (1989) Dosimetry for radiation processing. Taylor & Francis, London
- Mehnert R, Brede O, Cserép G (1981) Radiochem Radioanal Lett 47:173
- Mehnert R, Brede O, Cserép G (1985) Radiat Phys Chem 26:353
- Meisels GG (1970) The radiolysis of olefins. In: Zabicky J (ed) The chemistry of alkenes, vol 2. Interscience, London, pp 359–410
- Milinchuk VK, Tupikov VI (eds) (1989) Organic chemistry handbook. Ellis Horwood, Chichester
- Mozumder A (2004) Interactions of fast charged particles with matter. In: Mozumder A, Hatano Y (eds) Charged particle and photon interactions with matter: chemical, physicochemical and biological consequences with applications. Marcel Dekker, New York, pp 9–29
- Mozumder A (1999) Fundamentals of radiation chemistry. Academic, San Diego
- Muroya Y, Watanabe T, Wu G, Li X, Kobayashi T, Sugahara J, Ueda T, Yoshii K, Uesaka M, Katsumura Y (2001) Radiat Phys Chem 60:307
- Nagaoka N, Safranji A, Yoshida M, Omichi H, Kubota H, Kataikai R (1992) Macromolecules 26:7386
- Namba H, Tokunaga O, Suzuki R, Aoki J (2004) Electron beam applications to flue gas treatment. In: Mozumder A, Hatano Y (eds) Charged particle and photon interactions with matter: chemical, physicochemical and biological consequences with applications. Marcel Dekker, New York, pp 729–742
- Neta P, Huie RE, Ross AB (1988) J Phys Chem Ref Data 17:1027
- Patterson LK (1987) Instrumentation for measurements of transient behaviour in radiation chemistry. In: Farhataziz, Rodgers MAJ (eds) Radiation chemistry principles and applications. VHC Publishers, New York, pp 65–96
- Platzman RL (1962) The Vortex 23:372
- Qi M, Wu G, Li Q, Luo Y (2008) Radiat. Phys Chem 77:877
- Raffi J, Kister J (2008) Food irradiation: wholesomeness and treatment control. In: Spothem-Maurizot M, Mostafavi M, Douki T, Belloni J (eds) Radiation chemistry: from basics to applications in material and life sciences. EDP Sciences, Paris, pp 165–174
- Rawat KP, Sharma A, Rao SM (1997) Water Res 32:737
- Robin MB (1974, 1975, 1985) Higher excited states of polyatomic molecules, vol I, II, III. Academic, New York
- Robinson VJ, Chandratillake MR (1987) Radiation chemistry of alkali halides. In: Farhataziz, Rodgers MAJ (eds) Radiation chemistry: principles and applications, VHC, New York, pp 439–450
- Roder M (1981) Aromatic hydrocarbons. In: Földiák G (ed) Radiation chemistry of hydrocarbons. Elsevier, Amsterdam, pp 393–468
- Roder M, Wojnárovits L, Földiák G, Emmi SS, Beggiano G, D'Angelantonio M (1999) Radiat Phys Chem 54:475
- Rosiak JM, Janik I, Kadlubowski S, Koziczki M, Kujawa P, Stasica P, Ulanski P (2002) In: Radiation synthesis and modification of polymers for biomedical applications, IAEA-TECDOC-1324. Vienna, Austria, pp 5–47
- Rothman W, Hirayama F, Lipsky S (1973) J Chem Phys 58:1300
- Schuler RH, Albarran G (2002) Radiat Phys Chem 64:109
- Schuler RH, Wojnarovits L (2003) J Phys Chem A 107:9240
- Shida T (1988) Electronic absorption spectra of radical ions. Elsevier, Amsterdam
- Shkrob IA, Trifunac AD (1995) Radiat Phys Chem 46:97
- Shkrob IA, Sauer MC Jr, Trifunac AD (1996) J Phys Chem 100:7237
- Shkrob IA, Sauer MC, Trifunac AD (2001) Stud Phys Theor Chem 87:175
- Shkrob IA, Chemerisov SD, Wishart JF (2007) J Phys Chem B 111:11786
- Singh A, Silverman J (eds) (1992) Radiation processing of polymers. Hanser, Munich
- Spinks JWT, Woods RJ (1990) An introduction to radiation chemistry, 3rd edn. Wiley, New York
- Sivinski JS (1983) Radiat Phys Chem 22:99
- Steenken S (1985) Electron transfer equilibria involving free radicals in aqueous solution. In: Fisher H (ed) Landolt-Börnstein, Neue Serie, Gruppe II, vol 13e. Springer, Heidelberg, pp 147–293
- Steenken S (1987) J Chem Soc Faraday Trans I 83:113
- Steenken S (1996) Top Curr Chem 177:125
- Strauss P, Knolle W, Naumov S (1998) Macromol Chem Phys 199:2229
- Swallow AJ (1973) Radiation chemistry: an introduction. Longman, London
- Swallow AJ (1982) Application of pulse radiolysis to study of aqueous organic systems. In: Baxendale JH, Busi F (eds) The study of fast processes and transient species by electron pulse radiolysis. Reidel, Dordrecht, pp 289–315
- Tabata Y (ed) (1991a) CRC handbook of radiation chemistry. CRC, Boca Raton
- Tabata Y (ed) (1991b) Pulse radiolysis. CRC, Boca Raton
- Tagawa S, Seki S, Kozawa T (2004) Charged particle and photon-induced reactions in polymers. In: Mozumder A, Hatano Y (eds) Charged particle and photon interactions with matter: chemical, physicochemical, and biological consequences with applications. Marcel Dekker, New York, pp 551–578
- Takács E, Czajlik I, Czvikovszky T (1989) Radiat Phys Chem 33:457

- Takács E, Hedvig P (1991) In: Dobo J, Nyikos L, Schiller R (eds) Proceedings of the 7th Tihany symposium on radiation chemistry. Akademiai Kiado, Budapest, pp 261–267
- Takács E (1992) *Radiat Phys Chem* 40:75
- Takács E, Wojnárovits L, Foldvary Cs, Borsa J, Sajo I (2001) *Res Chem Intermed* 27:837
- Takamuku S, Yamamoto Y (1991) Pulse radiolysis study related to organic synthesis. In: Tabata Y (ed) *Pulse radiolysis*. CRC, Boca Raton, pp 431–450
- Theard L (1965) *J Phys Chem* 69:3292
- Tilquin B (2008) Radiosterilization of drugs. In: Spothem-Maurizot M, Mostafavi M, Douki T, Belloni J (eds) *Radiation chemistry: from basics to applications in material and life sciences*. EDP Sciences, Paris, pp 151–163
- Topchiev AV (1964) *Radiation chemistry of hydrocarbons*. Elsevier, Amsterdam
- Tripathi SC, Ramanujam A (2003) *Sep Sci Technol* 38:2307
- Trump J, Merrill EW, Wright KA (1984) *Radiat Phys Chem* 24:55
- Uesaka M, Watanabe T, Kobayashi T, Ueda T, Yoshii K, Wu G, Li X, Saeki A, Kozawa T, Yoshida Y, Tagawa S, Muroya Y, Sugahara J, Kinoshita K, Hafs N, Okuda H, Nishihara T, Terada Y, Nakajima K, Katsumura Y (2001) *Radiat Phys Chem* 60:303
- Vysotskaya NA (1983) Radiation treatment of sewage sludge. In: *Role of chemistry in environmental conservation*, Naukova Dumka, Kiev, p 205, (in Russian)
- von Sonntag C, Schuchmann H-P (1986) *Int J Radiat Biol* 49:1
- von Sonntag C (1987a) *The chemical basis of radiation biology*. Taylor & Francis, London
- von Sonntag C (1987b) *Radiat Phys Chem* 30:313
- von Sonntag C, Ross AD (1987) *Radiat Phys Chem* 30:331
- von Sonntag C, Schuchmann H-P (2001) *Stud Phys Theor Chem* 87:513
- von Sonntag C (2006) *Free-radical-induced DNA damage and its repair: a chemical perspective*. Springer, Heidelberg
- Wardman P (1989) *J Phys Chem Ref Data* 18:1637
- Wickramaarachchi MA, Preses JM, Holroyd RA, Weston RE Jr (1985) *J Chem Phys* 82:4745
- Williams F (1963) *Quart Rev* 17:101
- Wilson JE (1974) *Radiation chemistry of monomers, polymers, and plastics*. Marcel Dekker, New York
- Wishart JF, Funston M, Szeder T (2006) *Radiation chemistry of ionic liquids*. In: Mantz RA et al (eds) *Molten salts*, vol XIV. The Electrochemical Society, Pennington, pp 802–813
- Wishart JF (2008) Tools for radiolysis studies. In: Spothem-Maurizot M, Mostafavi M, Douki T, Belloni J (eds) *Radiation chemistry: from basics to applications in material and life sciences*. EDP Sciences, Paris, pp 17–33
- Wishart JF, Neta P (2003) *J Phys Chem B* 2003(107):7261
- Woods RJ, Pikaev AK (1994) *Applied radiation chemistry: radiation processing*. Wiley, New York
- Warman JM, Asmus K-D, Schuler RH (1968) *Advan Chem Ser* 82:25
- Warman JM, Asmus K-D, Schuler RH (1969) *J Phys Chem* 73:931
- Wojnárovits L, Földiák G (1991) In: Mai H, Brede O, Mehnert R (eds) *Fifth working meeting on radiation interaction*, ZFI, Leipzig, pp 64–74
- Wojnárovits L (1981) *Cycloalkanes*. In: Földiák G (ed) *Radiation chemistry of hydrocarbons*. Elsevier, Amsterdam, pp 177–251
- Wojnárovits L, Schuler RH (2000) *J Phys Chem A* 104:1346
- Wojnárovits L (2004) *Photochemistry and radiation chemistry of liquid alkanes, formation and decay of low energy excited states*. In: Mozumder A, Hatano Y (eds) *Charged particle and photon interactions with matter: chemical, physicochemical, and biological consequences with applications*. Marcel Dekker, New York, pp 365–402
- Wojnárovits L, Takács E (2008) *Radiat Phys Chem* 77:225
- Wypych M (1999) Pulse radiolysis induced transients in frozen aqueous systems at low temperatures. In: Mayer J (ed) *Properties and reactions of radiation induced transients. Selected topics*. Polish Scientific Publishers, Warszawa, pp 5–37
- Yang K, Manno PJ (1959) *J Am Chem Soc* 81:3507
- Zador E, Warman JM, Hummel A (1973) *Chem Phys Lett* 23:363
- Zaikin YA, Zaikina RF (2008) *New trends in radiation processing of petroleum*. In: Camilleri AN (ed) *Radiation physics research progress*. Nova Science Publishers, New York, pp 21–104
- Zeman A, Heusinger H (1966) *J Phys Chem* 70:33



24 Hot Atom Chemistry

H. K. Yoshihara¹ · T. Sekine²

¹Isotope Data Institute, Iwaki city, Japan

²Tohoku University, Sendai, Japan

24.1	<i>Introduction</i>	1334
24.2	<i>Recoil Energy and Charge Distribution</i>	1337
24.2.1	Recoil Energy	1337
24.2.2	Electric Charge Distribution	1340
24.3	<i>Enrichment of Radioisotopes by The Szilard–Chalmers Processes</i>	1342
24.4	<i>Hot Atom Reactions in Gaseous Phase</i>	1348
24.4.1	Tritium	1348
24.4.2	Halogens	1356
24.4.3	Carbon	1359
24.5	<i>Hot Atom Reactions in Liquid Phase</i>	1360
24.6	<i>Hot Atom Reaction in Solid Phase</i>	1362
24.6.1	Appearance Energy	1362
24.6.2	Phosphorus Hot Atom Chemistry	1363
24.6.3	Other Oxyanions	1364
24.6.4	Complexes of Cobalt	1365
24.6.5	Rhenium and Osmium Compounds	1365
24.7	<i>Implantation Reactions</i>	1368
24.7.1	Ion Implantation	1368
24.7.2	Recoil Implantation	1368
24.8	<i>Other Topics in Hot Atom Chemistry</i>	1370
24.8.1	Hot Atom Chemistry in Space	1370
24.8.2	Hot Atom Chemistry for Radiopharmaceuticals	1371
24.8.3	Some New Aspects Related to Hot Atom Chemistry	1371
24.8.3.1	Quantum Mechanical Tunneling Effect	1371
24.8.3.2	Molecular Rocket	1373
24.8.3.3	Fullerenes	1375
24.8.4	Impact of Hot Atom Chemistry on Other Research Fields	1376

Abstract: Various aspects of hot atom chemistry are described, reviewing it from fundamentals to applications. In gas, liquid, and solid systems, recoil atom reactions show characteristic features. Chemical behavior of implanted atoms that is specific to them and somewhat different from that of ordinary recoil atoms is also described. Examples of radioisotope enrichment are included.

24.1 Introduction

It is usually considered that hot atom chemistry deals with chemical effects of nuclear transformations, which result in the formation of “hot atoms” with high kinetic energy or high electric charge. However, in some cases “hot atoms” with high energy can be generated by nonnuclear means (photochemical method, beam acceleration, etc.). These nonnuclear hot atoms are included in up-to-date hot atom chemistry concepts in this chapter.

The recoil phenomenon, which is intimately related to hot atom chemistry, was first observed by H. Brooks (1904) in 1904 at the McGill University (► Table 24.1). She noticed severe contamination with radioactivity of ^{214}Pb and ^{214}Bi in the ionization chamber she used. In 1905, Rutherford (1951) (Nobel Prize 1908) who supervised her work concluded that the phenomenon observed by her was based on the recoil energy of the residual nucleus introduced by α particle emission on the nuclear disintegration of ^{218}Po (in other words, implantation in the wall material occurred). Then the technique using nuclear recoil was successfully employed by Hahn (Nobel Prize 1944) and Meitner (1909) for the separation of short-lived ^{210}Tl (half-life 1.32 min) in 1909. The same technique was absolutely effective to separate a new element Np ($Z=93$) from fission fragments with high kinetic energy when uranium ($Z=92$) was irradiated with neutrons by Mcmillan (Nobel Prize 1951) and Abelson (1940).

Following the above mechanical use of nuclear recoil, purely chemical effects of nuclear recoil were observed by Szilard and Chalmers (1934a, b) in 1934. They used (n, γ) reaction of iodine in ethyl iodide. The product of neutron capture, ^{128}I , could be chemically extracted into an aqueous phase after mixing ethyl iodide with water.

This was the starting point of the so-called hot atom chemistry, which formed a unique branch of nuclear and radiochemistry thereafter.

Although Szilard wrote only two papers on this subject, he was regarded as the father of hot atom chemistry. His finding was further confirmed by Fermi (Nobel Prize 1938) and coworkers (Amaldi et al. 1935) who pointed out that recoil energy of a few hundred eV due to γ emission is enough to break chemical bonds in neutron-irradiated inorganic compounds such as permanganate.

It was then recognized that chemical bond rupture can be caused not only by high kinetic energy, but also by high electric charge. In 1939, Segrè (Nobel Prize 1959), Halford, and Seaborg (Nobel Prize 1951) observed separation of ^{80}Br (the ground-state isomer of $^{80\text{m}}\text{Br}$) from $^{80\text{m}}\text{Br}$ -labeled organic bromide (Segrè et al. 1939). The same kind of ^{80}Br separation was reported by Devault and Libby (1939) (Nobel Prize 1960) independently. The nuclear isomeric transition $^{80\text{m}}\text{Br} \rightarrow ^{80}\text{Br}$ does not produce high kinetic energy but high electric charge by emission of Auger electrons through internal conversion associated with the isomeric transition.

The reason for bond rupture by high electric charge was clarified more clearly later. Snell and Pleasonton (1955) measured charge distribution after nuclear decay by mass spectrometry. Chemical effects of high charge in molecular systems were studied by Wexler (1961a) in detail,

■ Table 24.1

Milestones in the development of hot atom chemistry

Year	Name	Nationality	Discoveries or events
1904	H. Brooks	Canada	Contamination of ionization chamber (attributed to nuclear recoil by E. Rutherford in 1905)
1909	O. Hahn & L. Meitner	Germany	Recoil separation of RaC''
1934	L. Szilard & T. A. Chalmers	Hungary	Chemical separation of recoil ^{128}I from neutron-irradiated $\text{C}_2\text{H}_5\text{I}$
		UK	
1935	E. Amaldi et al.	Italy	Chemical effect of (n,γ) reaction attributed to recoil by γ emission
1939	E. Segrè et al.	Italy, USA	Chemical effect of isomeric transition attributable to high electric charge
	W. F. Libby et al.	USA	
1940	W. F. Libby	USA	Billiard ball collision concepts in hot atom chemical reentry reaction
1949	J. H. Green & A. G. Maddock	UK	Recovery of retention in solids by annealing
1953	J. E. Willard	USA	Random fragmentation model
1955	A. H. Snell & F. Pleasonton	USA	Measurement of charge distribution after nuclear decay
1958	G. Harbottle and N. Sutin	USA	Hot zone model in solid systems
1958	F. Baumgärtner et al.	Germany	Synthesis by recoil implantation
1959		Belgium	International Hot Atom Chemistry Symposium (1st)
1960	IAEA (International Atomic Energy Agency)	Prague	Symposium on "Chemical Effects of Nuclear Transformations" (sponsored by IAEA)
1961	M. Henchman & R. Wolfgang	USA	Kinetic theory analysis of hot tritium reaction (impact model)
1963	E. K. C. Lee and F. S. Rowland	USA	Cushioning collision in hot tritium reaction
1966	T. A. Carlson et al.	USA	Molecular explosion by an initial electron vacancy
1970	K. Yoshihara & H. Kudo	Japan	"Appearance energy" of hot atom reaction in solids
1976	A. P. Wolf & G. Stöcklin	USA	Leading 1st International Symposium on Radiopharmaceutical Chemistry
		Germany	
1992	H. Matsue et al.	Japan	Molecular rocket reaction of ruthenocene included in cyclodextrin
1995	T. Braun et al.	Hungary	Recoil labeling of fullerenes by implosion
1998	T. Miyazaki et al.	Japan	Quantum mechanical tunneling effect for hot tritium reaction

and the "explosion model" proposed by Carlson (Carlson and White 1968) reasonably explained the ruptured product distribution.

After the bond-rupture studies by Szilard and Chalmers (1934a, b) and by Fermi and coworkers (Amaldi et al. 1935), chemists became interested in chemical reactions of recoil atoms. In organic substances, a variety of hot atom chemical products labeled with radiohalogens were detected by Glückauf and Fay (1936). Lu and Sugden (1939) suggested

that the reactions of recoil halogen atoms occurred in an organic liquid cage. They found a scavenger effect on the reaction yield.

Later, Libby (1940) noticed the importance of reentry reaction, that is, the reaction leading to a parent chemical form. In this case, a permanganate fraction (“retention” as he called it) in neutron-irradiated potassium permanganate (KMnO_4) was the main subject of discussion.

Libby (1947) proposed a billiard ball collision model to understand hot atom chemical reaction in solid inorganic compounds. It was, in fact, the first attempt of modeling in the history of hot atom chemistry, even though it is by no means valid in our present knowledge. This model explained the “retention” by assuming that energy loss is maximum for the struck atom of similar mass, and this kind of billiard ball collision leads to the “retention” most effectively. So, the permanganate fraction labeled with ^{56}Mn , for example, was important in neutron-irradiated KMnO_4 according to his model.

However, Libby’s model was criticized by some authors later. Among them, there was Willard (Goldhaber and Willard 1953) who proposed an alternative “random fragmentation model” on the basis of experimental observation of scavenger effect in organic liquids and a variety of products. He thought of an important role of radical scavenger in the cage surrounding the recoil atom concerned.

Instead of using condensed phases, two giants of hot atom chemistry, Wolfgang and Rowland (Nobel Prize 1995) studied hot tritium reaction in a gaseous phase in the 1960s. This reaction system, attractive because of its simplicity (using a radioisotope of hydrogen in a gaseous medium), was suitable to solve the problem of mechanisms of hot reactions. Moderator gas such as helium was available for slowing down hot tritium atoms, and the results could be interpreted similarly to the neutron slowing down process already consolidated in nuclear reactor technology. Wolfgang observed that hot reaction yields could be effectively suppressed by adding the moderator gas helium to the reaction system. The contribution of thermal reaction, which would have disturbed the determination of the reaction yield, could be eliminated in the presence of a scavenger such as oxygen. Wolfgang and coworker (Henchman and Wolfgang 1961) proposed an “impact model” to explain substitution and abstraction yields in rather mechanistic manner.

On the contrary, Rowland and coworkers (Lee and Rowland 1963) inferred that collision of a hot tritium atom with a target molecule to react was relatively “soft” as if cushions were inserted (*cushioning collision model*). He revealed (Root et al. 1965) that the abstraction leading to formation of HT (a molecule consisting of a hydrogen atom and a tritium atom) was remarkably affected by chemical binding energy between carbon and hydrogen atoms in the target molecule.

Wolfgang turned to chemical accelerator work afterward probably because he could not be content with ordinary hot atom chemistry using nuclear reactions. His brilliant papers (Wolfgang 1969) on ADAM and EVA chemical accelerators provoked strong interests among researchers of reaction dynamics in physical chemistry. Especially the latter machine, which was able to specify reaction energy and angle, was much more valuable in obtaining exact information on hot reaction compared to ordinary hot atom chemical experiments using nuclear technique. He was among the constructors of modern chemical dynamics, but he died before his time. While Wolfgang engaged in the study of ion-neutral (molecule) reaction, neutral–neutral reaction was studied by Y.T. Lee (1975) (Nobel Prize 1986) who had been involved in hot atom chemistry.

After the hot tritium reaction studies, Rowland also shifted his interests to atmospheric chemical reactions. He pointed out the danger of the possible destruction of the ozone layer

surrounding the earth by man-made fluorine compounds (Molina and Rowland 1974). His prophetic warning was recognized as a realistic one later by the observations of geophysicists, and the Nobel Prize was awarded to him. It was not in the field of hot atom chemistry; however, without his career in hot atom chemistry, he could not have accomplished his Nobel Prize work.

So, the readers of this chapter should realize that hot atom chemistry was the field in which many Nobel Prize laureates were interested, even though hot atom chemistry itself was not the subject of Nobel Prize.

Some remarks have to be added on hot atom chemistry in solids, which is more or less connected with solid-state physics. Maddock and coworker (Maddock and deMaine 1956) noticed that annealing phenomena occurred in the chemical distribution of neutron-irradiated chromate crystals. This type of study was further extended and elaborated by others, for example, Lindner and Harbottle (1961) studied phosphate compounds. A series of investigations on the appearance (threshold) energy were carried out by Yoshihara et al. (Yoshihara and Kudo 1970) who found that the threshold energy was greater than the energy of Frenkel pair formation in typical crystals. It is worth noting that implantation reactions having similarity to hot atom chemical reactions could be utilized in the synthesis of labeled compounds by Baumgärtner and Reichold (1961). This reaction was interesting for it resulted in enhancement of the reaction yield probably because of shock-wave-like action (Yoshihara et al. 1992). Mixed crystal studies of solid hot atom reactions were performed by Müller and Hagenlocher (1990) who put emphasis on the “lattice disorder” in irradiated crystals.

The International Hot Atom Chemistry Symposium began in 1959 and ended in 1987. Frankly speaking, the boom of hot atom chemistry was over, although still some important works are to be noted. Hot atom chemistry has already gathered lots of information on the chemical effects of nuclear transformations, which may be available for other radio- and nuclear chemists. It is reasonable to believe, however, that hot atom chemistry also has future possibilities in the field of nonnuclear chemical processes.

24.2 Recoil Energy and Charge Distribution

24.2.1 Recoil Energy

To estimate the recoil energy, which is endowed to the hot atom in nuclear transformation, one needs some basic knowledge about nuclear reactions. In the nuclear reaction



where A and B are the reacting nuclei, C and D are the produced nuclei, and Q is the energy released, the energy and momentum are conserved. In nuclear decay processes (including those from compound nuclei), mathematical treatments are rather simple and it is easy to calculate recoil energy.

For nuclear disintegration such as α decay, calculation of recoil energy (E_R) of the residual nucleus is as follows:

$$E_R = M_\alpha E_\alpha / M_R, \quad (24.2)$$

where M_α is the mass of the α particle, E_α is the kinetic energy of the emitted α particle, and M_R is the mass of the residual nucleus. The relation holds good, in principle, in all the cases of

naturally occurring α emitters. In the case of RaA (i.e., ^{218}Po) for which Brooks (1904) observed serious contamination with its daughter nuclides, the calculated result using [Eq. \(24.2\)](#) is 112 keV, which is comparable with or higher than the bombarding energies used in modern implantation technology.

[Equation \(24.2\)](#) can also be applied to other cases of nuclear processes in which compound nucleus formation and subsequent decay are concerned. For the nuclear reaction $^6\text{Li}(n,\alpha)\text{T}$ with the Q -value 4.78 MeV, the recoil energy (E_{T}) of tritium T is as follows:

$$E_{\text{T}} = M_{\alpha}E_{\alpha}/M_{\text{T}} = Q M_{\alpha}/(M_{\alpha} + M_{\text{T}}) \quad (24.3)$$

where E_{α} and M_{α} are α energy and mass, respectively, and M_{T} is the mass of tritium. Similarly, the recoil energy (E_{R}) of the nucleus produced in the (n,p) reaction induced by thermal (i.e., low-energy) neutrons is expressed as

$$E_{\text{R}} = M_{\text{p}}E_{\text{p}}/M_{\text{R}}, \quad (24.4)$$

where M_{p} is the mass of the proton, E_{p} is its energy, and M_{R} is the mass of the recoil atom. In the case of (n, γ) reactions induced by thermal neutrons it is necessary to take the momentum of the photon into consideration. Therefore, the final formula to calculate recoil energy of the recoil atom is

$$E_{\text{R}}/\text{eV} = 537 \frac{(E_{\gamma}/\text{MeV})^2}{M_{\text{R}}/\text{u}}, \quad (24.5)$$

where E_{γ} is the energy of the emitted photon, E_{R} is the recoil energy of the product, and u is the atomic mass unit. For nuclear fission induced by thermal neutrons (or spontaneous nuclear fission), the fragments A and B move to opposite direction with almost equal momentum. So the energy of the fragment A (E_{A}) is expressed as

$$E_{\text{A}} = Q M_{\text{B}}/(M_{\text{A}} + M_{\text{B}}), \quad (24.6)$$

where Q is the total energy generated in fission, and M_{A} and M_{B} are masses of the fragments A and B, respectively. In this case, the contribution of fission neutron in the reaction is neglected for simplicity.

For β -decay processes (both β^{-} and β^{+}) neutrino emission accompanied with electron emission as well as relativistic effects should be taken into account. Thus, the formula for the maximum recoil energy E_{R} is expressed as follows:

$$E_{\text{R}}/\text{eV} = 537 \frac{(E_{\beta}/\text{MeV})(1.02 + E_{\beta}/\text{MeV})}{M_{\text{R}}/\text{u}}, \quad (24.7)$$

where E_{β} is the maximum kinetic energy of the emitted electron and M_{R} is the mass of the recoil atom.

In *electron capture (EC) decay*, recoil by neutrino emission should be considered. Assuming the rest mass of the neutrino is zero, the recoil energy expression is similar to that in the photon emission in (n, γ) reaction in [Eq. \(24.5\)](#).

$$E_{\text{R}}/\text{eV} = 537 \frac{(E_{\nu}/\text{MeV})^2}{M_{\text{R}}/\text{u}}, \quad (24.8)$$

where E_{ν} is the neutrino energy. For the $^{37}\text{Ar} \rightarrow ^{37}\text{Cl}$ decay, Snell and Pleasonton (1955) measured experimentally E_{R} using their mass spectrometer. The measured value (9.63 ± 0.06 eV) was in good agreement with the calculated one.

For isomeric transitions when the excitation energy of the nucleus is carried away by a γ photon, the formula for the recoil energy is the same as in the case of the thermal (n, γ) reaction (2.5):

$$E_R/\text{eV} = 537 \frac{(E_\gamma/\text{MeV})^2}{M_R/\text{u}}. \quad (24.9)$$

However, it should be noted that this is only valid for photon emission. It will be more complicated, if Auger electron emission accompanied with photon emission is taken into account. Calculated recoil energy values for typical nuclear processes are shown in [Table 24.2](#) (Yoshihara 1984).

Assuming isotropic emission of ejected particles in the $A + x \rightarrow B + y + Q$ type reaction, average recoil energy $\langle E_R \rangle$ of B was calculated by Libby (1947). The expression is as follows:

$$\langle E_R \rangle = E_\mu \left\{ \frac{M\mu}{(M+m)^2} + \frac{m(M+m-\mu)}{(M+m)^2} \left[1 + \frac{Q}{E_\mu} \left(\frac{M+m}{M+m-\mu} \right) \right] \right\} \quad (24.10)$$

where E_μ is the kinetic energy of the bombarding particle x with mass μ , M is the mass of the recoiling atom B, m is the mass of the emitted particle y, and Q is the overall mass difference in

Table 24.2

Calculated (maximum) recoil energies for typical nuclear processes

Nuclear process	Examples	E_R (eV)
α decay	$^{238}\text{U}-^{234}\text{Th}$	7.17×10^4
	$^{219}\text{Rn}-^{215}\text{Po}$	1.27×10^5
	$^{218}\text{Po}(\text{RaA})-^{214}\text{Pb}$	1.12×10^5
Thermal neutron (n, α)	$^6\text{Li}(\text{n},\alpha)\text{T}$	2.73×10^6
Thermal neutron (n,p)	$^3\text{He}(\text{n},\text{p})\text{T}$	1.95×10^5
	$^{14}\text{N}(\text{n},\text{p})^{14}\text{C}$	4.5×10^4
	$^{35}\text{Cl}(\text{n},\text{p})^{35}\text{S}$	3.1×10^4
Thermal neutron (n, γ)	$^{31}\text{P}(\text{n},\gamma)^{32}\text{P}$	1.05×10^3
	$^{37}\text{Cl}(\text{n},\gamma)^{38}\text{Cl}$	5.27×10^2
	$^{79}\text{Br}(\text{n},\gamma)^{80}\text{Br}$	4.17×10^2
	$^{127}\text{I}(\text{n},\gamma)^{128}\text{I}$	1.96×10^2
Nuclear fission (thermal neutron, spontaneous)	$^{235}\text{U}(\text{n},\text{f})$	$(6-10) \times 10^7$
β decay	$^3\text{H}-^3\text{He}$	3.6
	$^{32}\text{P}-^{35}\text{S}$	77.5
	$^{36}\text{Cl}-^{36}\text{Ar}$	18.4
	$^{90}\text{Sr}-^{90}\text{Y}$	5.10
	$^{210}\text{Bi}-^{210}\text{Po}$	6.45
Electron capture	$^{37}\text{Ar}-^{37}\text{Cl}$	9.67
Isomeric transition	$^{69\text{m}}\text{Zn}-^{69}\text{Zn}$	1.5

terms of energy (Q -value). For the angle θ between the incident particle x and the emitted particle y , the recoil energy E_R is expressed by the equation

$$E_R = \langle E_R \rangle - A \cos \theta \quad (24.11)$$

where

$$A = \frac{2E_\mu}{(M+m)^2} \left\{ Mm\mu(M+m-\mu) \left[1 + \frac{Q}{E_\mu} \left(\frac{M+m}{M+m-\mu} \right) \right] \right\}^{1/2}. \quad (24.12)$$

In the molecular entity, however, the recoil energy of the recoiling atom is not fully effective to break chemical bonds. This was pointed out by Suess (1940) who calculated the energy available for internal excitation, E_i , as

$$E_i = E_R M_2 / (M_1 + M_2), \quad (24.13)$$

where E_R is the recoil energy of the hot atom with mass M_1 and the mass of the attached atom (or group) is M_2 . Thus, for example, the recoil energy of ^{128}I produced in molecular HI is of poor efficiency in breaking the chemical bond. According to ▶ Eq. (24.13), it is only 0.78%. The maximum energy of the γ quantum in $^{127}\text{I}(\text{n},\gamma)^{128}\text{I}$ is 6.83 MeV, and the recoil energy E_R is 196 eV using ▶ Eq. (24.5). Therefore, E_i (energy available for the chemical bond rupture) for HI is 1.53 eV or 2.45×10^{-19} J. On the other hand, HI bonding energy is 295 kJ/mol, that is, 4.90×10^{-19} J per molecule, which is larger than the energy available. So, it is predicted that the HI bond escapes rupture, in agreement with experimental observation. In the case of ethyl iodide, $\text{C}_2\text{H}_5\text{I}$, in the Szilard–Chalmers experiment, E_i is calculated to be 36.4 eV, which is enough for the rupture of the C–I chemical bond (274 kJ/mol or 1.08 eV per one molecule).

24.2.2 Electric Charge Distribution

Ionization of outer electrons can occur if the moving atom has sufficiently high kinetic energy. The first approach to this problem was demonstrated by Bohr (1940) who postulated that the atom will lose its outermost orbital electron when the speed (u_R) of the atom is greater than that of the orbital electron (u_e). Therefore, the lower limit of the speed, which results in ionization, is determined by the following equation:

$$\frac{1}{2} m_e u_e^2 = I_p, \quad (24.14)$$

where m_e is the electron mass, and I_p is the ionization potential. For the condition $u_R = u_e$ one gets from ▶ Eq. (24.14):

$$I_p = m_e E_R / M, \quad (24.15)$$

where M and E_R are the mass and the (recoil) energy of the atom, respectively. For the atom produced by high-energy reaction, the recoil energy would be in the range of some hundred MeV. Carlson et al. (1970) calculated that the average charge would be between +16 and +17 for iodine at energy of 100 MeV. This estimate was in good agreement with experimental one (+17) obtained by Datz et al. (1971) in gases. However, in solids, the value was much higher (+26). The reason for this was discussed by Betz and Grodzins (1970).

There are other mechanisms for ionization of atoms, when a vacancy in the inner shell of an atom is formed in the moment of electron capture or internal conversion. The initial vacancy in

the inner electron shell is followed by successive electron emission from outer shells (vacancy cascade). In this process, the vacancy in the inner shell is filled by an electron from the adjacent outer shell, and the energy difference of these shells causes the emission of an electron from the same outer shell. The outer shell possesses, therefore, two vacancies, which will be filled by outer electrons. If this process is repeated thereafter, the number of vacancies will be twice. The multiplication of electron vacancies will attain saturation because the atom has only limited number of electrons. This is called the Auger process. The Auger processes may compete with radiative processes, but the probability for Auger processes is greater than radiative processes (X-ray emission) except for K and L shells of heavy elements.

➤ **Figure 24.1** shows a typical example of a vacancy cascade in xenon. Carlson and Krause (1965) compared the charge spectrum obtained by Monte Carlo calculation with experimental results obtained for krypton. The theoretical and experimental results are in agreement as seen in ➤ **Fig. 24.2**.

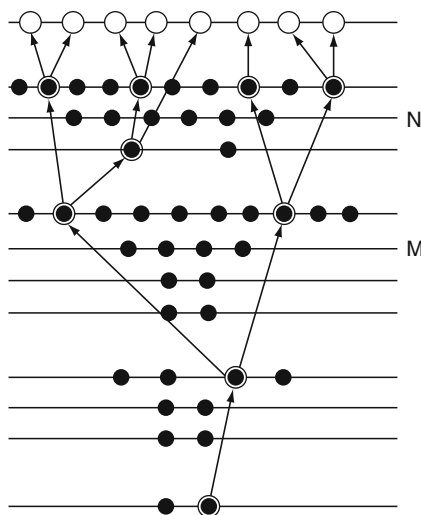
The other cause of ionization is electron shake-off. The charge spectrum observed for this process is entirely different from that for the vacancy cascade.

When the central charge of an atom changes suddenly, for example, as in the case of β^- and β^+ decays, there is a finite probability that an electron in a given orbital goes to an excited level of the continuum. Therefore, the electron will be shaken-off, as if fruits of a tree fall down by shaking. The shake-off probability P_{nlj} for the ionization of an electron from orbital nlj is

$$P_{nlj} = 1 - \left[\left| \int \psi_{nlj}^* \psi_{nlj} d\tau \right|^2 \right]^N \quad (24.16)$$

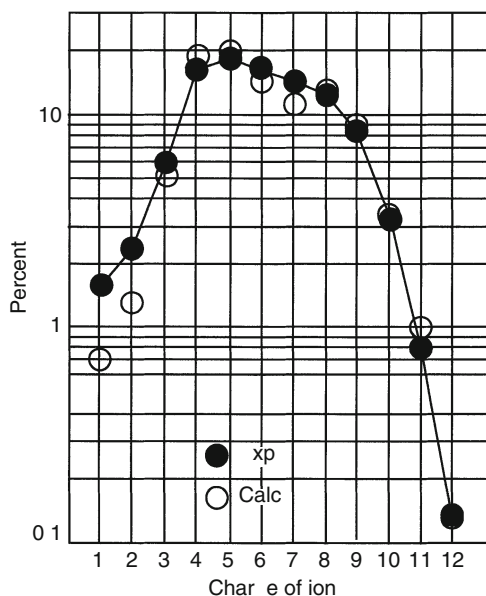
■ **Fig. 24.1**

Typical vacancy cascade in Xe as the result of an initial L vacancy. Black circles represent electrons, white circles represent vacancies, and white circles with black circles show the cases that a subsequent Auger process has filled a vacancy



■ Fig. 24.2

Charge distribution of Kr ions resulting from irradiation of Kr by Mo K X-rays compared with calculated spectrum



where ψ_{nlj} and ψ'_{nlj} are the single-electron wave function for the initial and final states of atomic orbitals nlj , respectively. N is the number of electrons in the orbital of the initial state. The overlap $\psi'^* \psi$ is not unity because the final state has a different central potential. For β^- decay, the nuclear charge changes by +1 and for β^+ decay by -1 (in α decay: -2). Generally speaking, the shake-off probability is not so large: it is usually 10% or less for β^- and β^+ decays.

As a summary of charge distribution after nuclear decay, ▶ Fig. 24.3 shows various cases in monatomic or polyatomic gases (inclusive of solid surface emission for α decay and heavy ion nuclear reaction).

24.3 Enrichment of Radioisotopes by The Szilard–Chalmers Processes

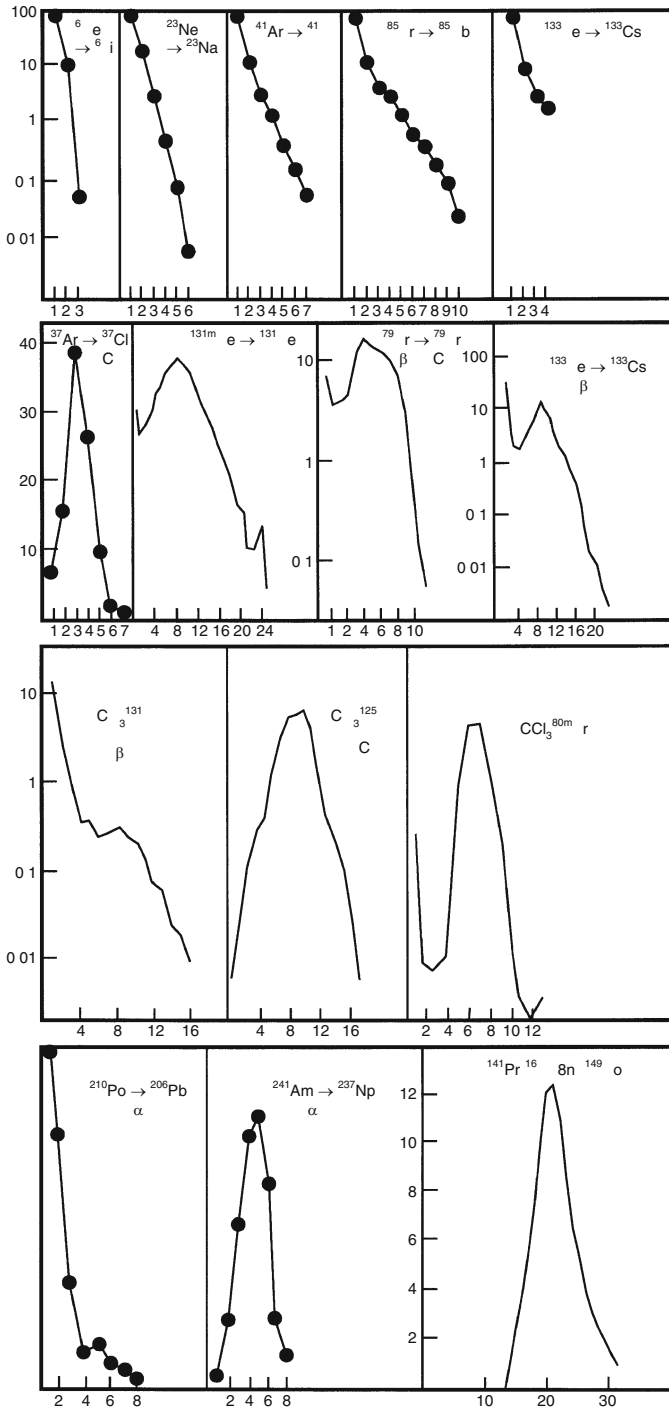
Before nuclear reactors became available for radioisotope production, the Szilard–Chalmers process mentioned in ▶ Sect. 24.1 was very important for its availability to prepare radioisotopes with high specific activity. This unique technique survived for many years after the first nuclear reactor started to operate in 1942. The activity A of a radionuclide produced by activation can be expressed as

$$A = N\sigma f(1 - e^{-\lambda t}) \quad (24.17)$$

where N is the number of the target atoms being irradiated, σ is the nuclear reaction cross section of activation, f is the projectile flux density (in the case of nuclear reactors, neutron flux density), λ is the decay constant of the produced radioisotope, and t is the irradiation time.

■ Fig. 24.3

Charge distribution after nuclear decay



When the atomic number of the produced radioisotope is equal to that of the target element, the specific activity A_s is

$$A_s = A/W \quad (24.18)$$

where W is the mass of the element irradiated. Considering $W = NG/6.02 \times 10^{23}$, where G is the atomic weight of the irradiated element,

$$A_s = 6.02 \times 10^{23} \sigma f (1 - e^{-\lambda t}) / G. \quad (24.19)$$

Equation (24.19) shows that the specific activity of the produced radioisotope is characterized by the curve with a saturation value $A_{\text{sat}} = 6.02 \times 10^{23} \sigma f / G$ with an initial slope $A_{\text{sat}} = 6.02 \times 10^{23} \lambda \sigma f / G$ (Fig. 24.4).

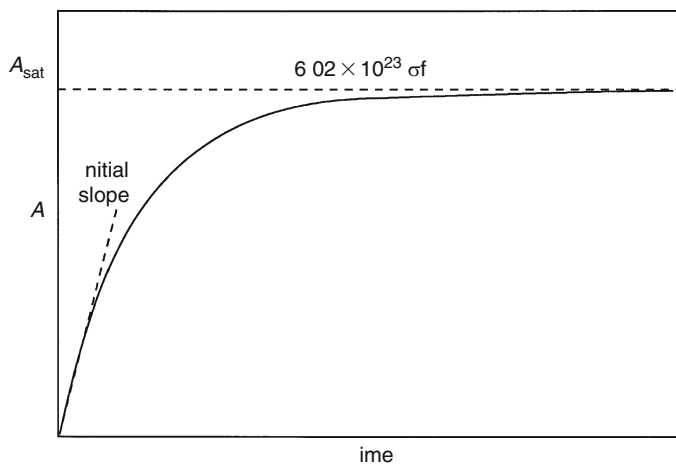
One can use the half-life $T_{1/2}$ instead of λ , which is expressed as

$$\lambda = 0.693 / T_{1/2} \quad (24.20)$$

In the dawn of the history of nuclear science, the neutron flux density (f) of Ra–Be source was only 10^2 – 10^4 n cm $^{-2}$ s $^{-1}$. The total activity produced by such neutron sources via (n, γ) reaction was very low and so was the specific activity of the radionuclides. The Szilard–Chalmers process, however, could dramatically increase the specific activity: the improvement could reach orders of magnitude. In the measurement of β radioactivity, which was a frequent task in early days of nuclear science, samples with low specific activity brought sometimes troublesome problems of self-absorption corrections. By the introduction of the Szilard–Chalmers process, however, this difficulty could be avoided, because the measurement could be performed within small statistical errors using a sample with high specific activity. Therefore, the Szilard–Chalmers process became one of the useful means of preparation of radioisotopes for measurement, as Szilard and Chalmers (1934b) recognized the importance of this technique in their early work.

Fig. 24.4

Radioactivity accumulation curve



In fact, even the very low neutron flux in the upper atmosphere could be measured by $^{80\text{m}}\text{Br}$ radioactivity using this technique by Von Halban Jr et al. (1939) who used ethyl bromide as a target material for the production of the radioisotope from (n,γ) reaction.

It is true, however, that the advent of modern nuclear reactors changed this situation. The neutron flux attained to $10^{11} - 10^{15} \text{ n cm}^{-2} \text{ s}^{-1}$. So, the total activity and the specific activity increased strikingly. Without the Szilard–Chalmers process, the specific activity of the aimed radioisotope was high enough for many purposes.

Even though the specific activity of nuclear-reactor-produced radioisotopes became rather high, users requested still higher levels. For the investigation of living systems involving human beings by radioisotopes of toxic elements, the requested specific activity was beyond that of the ordinary reactor product. Therefore, the Szilard–Chalmers process found its *raison d'être* during the “nuclear age” in the second half of the twentieth century.

A French radioisotope production group provided radionuclides such as ^{51}Cr , ^{59}Fe , ^{64}Cu , ^{65}Zn , and ^{76}As by the Szilard–Chalmers processes (Henry 1957). At the Japan Atomic Energy Research Institute, this process was applied to obtain pure ^{32}P from neutron-irradiated potassium phosphate. Ordinary ^{32}P products using (n,p) reaction in a nuclear reactor contain an impurity isotope ^{33}P in ^{32}P , but ^{32}P produced by (n,γ) reaction in neutron-irradiated phosphate does not contain ^{33}P . Hot atom chemically obtained ^{32}P by (n,γ) reaction was therefore appropriate for some special experiments in which contamination of ^{33}P with different half-life and β -particle energy had to be excluded (Shibata et al. 1963).

Although the Szilard–Chalmers process using nuclear reactors can normally ensure high concentration of the desired radioisotope, it suffers from radiation decomposition problems of the target compound. At higher neutron flux values, radiation decomposition also increases which sets a limit to the enrichment factor (concentration factor). When the enrichment factor (E) is defined by the ratio of the specific activity (S_1) of the separated part of the Szilard–Chalmers process to that (S_2) before separation,

$$E = \frac{S_1}{S_2} = \frac{\gamma m_2}{100 m_1} \quad (24.21)$$

where γ is a radiochemical yield of the separated radioisotope, m_2 is the total mass of the target element, and m_1 is the mass of the separated element. For intense radiation in a nuclear reactor the separable weight of the element (m_1) increases by decomposition, whereas the radiochemical yield (γ) is almost unchanged, and therefore the enrichment of radioisotopes is only practical for materials, which can withstand radiation decomposition in a nuclear reactor.

Generally, the Szilard–Chalmers process is based on valence change of the element, decomplexation, transformation of organic to inorganic compounds, etc. For example, hot atom chemical reactions, $^{50}\text{CrO}_4^{2-}(n,\gamma)^{51}\text{Cr}^{3+}$, $^{63}\text{CuPc}(n,\gamma)^{64}\text{Cu}^{2+}$, and $\text{C}_2\text{H}_5^{79}\text{Br}(n,\gamma)^{80}\text{Br}^-$, are typical cases. In the first reaction, chromate Cr(VI) changes to chromic Cr(III), in the next one copper phthalocyanine complex to noncomplex Cu, and in the last one ethyl bromide to free bromide tagged with radioactivity. Exchange reaction between the mother substance and the product does not occur in either case. ▶ Table 24.3 shows various radioisotopes separated by the Szilard–Chalmers process (Yoshihara 1984).

Note that in ▶ Table 24.3 phthalocyanines are useful target materials. Fe, Co, Cu, Zn, Ga, Mo, Pd, In, Dy, Os, and Pt radioisotopes can be separated from neutron-irradiated metal phthalocyanines. Metal chelate compounds such as metal oxinates are other examples. Ca, V, Mn, Ni, Cu, In, and W are separated by the Szilard–Chalmers process from their oxinates. Salts of oxyacids

■ Table 24.3

Enrichment of radioisotopes by the Szilard–Chalmers process. (ppt: precipitate)

Nuclide	Target material	Separation procedure
^{36}Cl	$\text{NaClO}_3, \text{NaClO}_4$	ppt as AgCl
^{36}Cl	$\text{MXO}_3, \text{MXO}_4$	ppt as AgX , ion exchange
^{38}Cl	Organic halogen compd.	extraction into aqueous phase shaking with active carbon, alumina, metal powder, electrolysis
$^{80\text{m}}\text{Br}$		
^{80}Br		
^{82}Br		
^{128}I		
^{32}P	$(\text{C}_6\text{H}_5)_3\text{PO}_4$	shaking with water, carbon extraction with water
	$(\text{C}_4\text{H}_9)_3\text{PO}_4$	
^{35}S	CS_2	evaporation residue
^{45}Ca	Ca-oxinate	ion exchange from n-butylamine soln.
^{51}Cr	$\text{M}_2\text{CrO}_4, \text{M}_2\text{Cr}_2\text{O}_7$	coppt. with $\text{Fe}(\text{OH})_3, \text{Al}(\text{OH})_3$
	$\text{Cr}(\text{CO})_6$	extraction from CHCl_3 soln.
	$[\text{Cr}(\text{NH}_3)_6](\text{NO}_3)_3$	ion exchange
^{52}V	V-oxinate	extraction into aq. phase
^{56}Mn	$\text{KMnO}_4, \text{K}_2\text{MnO}_4$	MnO_2 ppt.
	inorganic ion exchanger	aq. soln. extract
	Mn-chlorophyl	aq. soln. extract
	Mn-oxinate	extraction from CHCl_3 soln
^{59}Fe (^{55}Fe)	$\text{K}_4[\text{Fe}(\text{CN})_6]$	coppt. with $\text{Al}(\text{OH})_3$
	$\text{H}_4[\text{Fe}(\text{CN})_6]$	ether extraction
	Fe-phthalocyanine	soln. in H_2SO_4 and dilution to ppt. complex
	inorganic ion exchanger	aq. Soln. extract
	ferrocene	solvent extraction
^{60}Co	$\text{Na}_3[\text{Co}(\text{CN})_6]$	extraction with $\text{CH}_3\text{COOC}_3\text{H}_7 + \text{NH}_4\text{SCN}$
	$[\text{Co}(\text{en})_3](\text{NO}_3)_3$	reduction with Zn powder
	inorganic ion exchanger	aq. Soln. extract
	$[\text{Co}(\text{NH}_3)_6](\text{NO}_3)_3$	cation exchange separation electrophoresis
	Co-phthalocyanine	soln. in H_2SO_4 and dilution to ppt. complex
^{65}Ni	Ni-oxinate	extraction from CHCl_3 soln.
^{64}Cu	Cu-phthalocyanine	soln. in H_2SO_4 and dilution to ppt. complex
	Cu-oxinate	extraction from CHCl_3 soln.
^{65}Zn	Zn-phthalocyanine	soln. in H_2SO_4 and dilution to ppt. complex
^{72}Ga	Ga-phthalocyanine	soln in H_2SO_4 and dilution to ppt. complex
	inorganic ion exchanger	aq. Soln. extract

■ Table 24.3 (Continued)

Nuclide	Target material	Separation procedure
⁷⁶ As	AsH ₃	electrode
	cacodylic acid	coppt. with Fe(OH) ₃
	M ₃ AsO ₄	ion exchange, chromatography
	resin-AsO ₄	wash with water
	(C ₆ H ₅) ₃ As	aq. Soln extract
^{81m} Se	M ₂ SeO ₄ , M ₂ SeO ₃	ppt as metallic Se
⁹⁹ Mo	Mo-phthalocyanine derivative	ppt with ferrocyanide
	Mo-carbonyl	aq. Soln. extract from CHCl ₃ soln.
^{104m} Rh	[Rh(en) ₃](NO ₃) ₃	reaction with Zn powder
¹⁰⁹ Pd	Pd-phthalocyanine	coppt. with Fe(OH) ₃
(¹¹¹ Pd)		
¹¹⁵ Cd	Cd-tetraphenylporphine	aq. Soln. extract from CHCl ₃ soln.
^{116m} In	In-phthalocyanine	coppt. with Fe(OH) ₃
	In-oxinate	aq. Soln. extract from CHCl ₃ soln.
	In-edta	ion exchange
¹²¹ Sn	(C ₆ H ₅) ₄ Sn	aq. Soln. extract
¹²⁴ Sb	(C ₆ H ₅) ₃ Sb	aq. Soln. extract
	SbF ₅	evaporation residue
^{127m} Te	M ₂ TeO ₄	metallic Te ppt.
¹²⁷ Te		ion exchange
^{129m} Te		extraction with TBP
¹²⁹ Te		
^{131m} Te		
¹³¹ Te		
¹⁶⁵ Dy	Dy-phthalocyanine	extraction from pyridine soln.
¹⁸⁵ W	W-carbonyl	aq. soln. extract from CHCl ₃ soln.
	W-oxinate	
^{188m} Re	ReCl ₃ , M ₂ ReCl ₆	extraction with ether + 10% benzonitrile
¹⁸⁸ Re		
^{191m} Os	Os-phthalocyanine	soln. in H ₂ SO ₄ and dilution to ppt. complex evaporation
¹⁹¹ Os	M ₂ OsCl ₆	
¹⁹³ Os		
^{193m} Pt	Pt-phthalocyanine	soln. in H ₂ SO ₄ and dilution to ppt. complex
¹⁹⁷ Pt		
¹⁹⁸ Au	Na ₃ AuS ₄ O ₆	shake with Hg
²⁰³ Hg	Hg(C ₂ H ₅) ₂	aq. soln. extract
²³⁹ U	U(SO ₄)·xH ₂ O	CHCl ₃ extraction
	UO ₂ -benzoylacetate	soln. in acetone, shake with BaCO ₃

M_nXO_m are another group of compounds that are available for the process. Two examples of the Szilard–Chalmers processing will be shown to demonstrate the practical use of radioisotopes at 10^8 – 10^{10} Bq levels.

High specific activity ^{51}Cr demand came from the users of blood flow measurements. This radioisotope could be produced either by irradiation of chromium (enriched ^{50}Cr) metal in a high neutron flux ($10^{15} \text{ n cm}^{-2} \text{ s}^{-1}$) for several days or by the Szilard–Chalmers process using potassium chromate (K_2CrO_4) crystals. However, the use of a high flux reactor was not frequently available for ordinary radioisotope production purposes. On the other hand, the Szilard–Chalmers process was practical in any type of nuclear reactor without severe limitations. The following process (Shibata et al. 1969) is used for ^{51}Cr production by the Szilard–Chalmers method as adopted by the Japan Atomic Energy Research Institute. Neutron-irradiated potassium chromate is dissolved in 0.3 M hydrochloric acid containing a small amount of lanthanum chloride. To the solution 1 M sodium hydroxide is added and the mixture is stirred and the formed precipitate is filtered. The precipitate is washed repeatedly, and is dissolved in 0.15 M hydrochloric acid. The precipitation procedure is repeated using 1 M NaOH. The washed precipitate containing chromic and lanthanum hydroxides is submitted to oxidation leaching. This procedure is performed to convert $^{51}\text{Cr(III)}$ to a chemical form of chromate and to separate it from lanthanum using 0.15 M NaOH and hydrogen peroxide.

The leached chromate solution is heated for 30 min to expel hydrogen peroxide. It is filtered and the filtrate is concentrated in a small volume and neutralized with hydrochloric acid. The formed product is distributed to the users. The specific activity of ^{51}Cr ranges between 2×10^6 Bq/mg and 4×10^6 Bq/mg.

The other radioisotope ^{64}Cu has been produced by the Szilard–Chalmers process at the Japan Atomic Energy Research Institute in the 4×10^6 Bq/mg level. This radioisotope is useful for medical purposes, but the total amount of copper should be limited because of its toxicity to biological systems. Therefore, enrichment procedure by the Szilard–Chalmers process using copper phthalocyanine is recommended.

The procedures adopted are as follows. Neutron-irradiated copper phthalocyanine (α -form) is dissolved in concentrated sulfuric acid. The solution is poured on frozen redistilled water, and the mixture of a diluted solution of sulfuric acid and precipitated copper phthalocyanine is filtered using a glass filter. The filtrate of $^{64}\text{CuSO}_4$ in H_2SO_4 is neutralized with 10 M sodium hydroxide. Formed $^{64}\text{Cu(OH)}_2$ is filtered, and washed with water (50°C) three times, and is dissolved in a small volume of acetic acid. The solution is filtered again, and the final product is distributed to the users. Specific activity of ^{64}Cu ranges 1 – 2×10^6 Bq/mg on shipment.

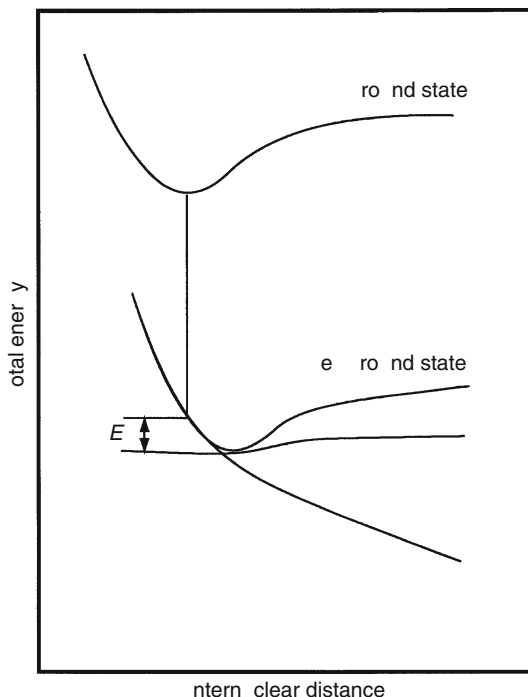
24.4 Hot Atom Reactions in Gaseous Phase

This section describes reactions of recoil atoms in a gaseous phase. Tritium, halogens, and carbon will be involved.

24.4.1 Tritium

First, decay-induced reactions will be considered in simple compounds combined with tritium, RT. The potential energy curve obtained by an ab initio MO calculation (Ikuta et al. 1977)

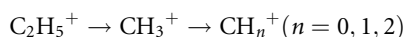
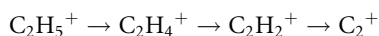
Fig. 24.5

RT \rightarrow RHe⁺ decay and potential energy curves

reveals stability of the RHe⁺ ion decayed from the compound RT in the event of β^- decay of tritium ($T \rightarrow {}^3\text{He}^+$).

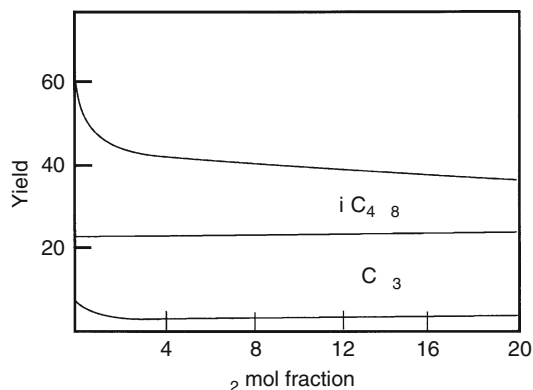
As shown in Fig. 24.5 there are three cases; there exists a potential well for (I) and (II) and there is no well for (III) indicating that chemical bonding is not possible in this case. The transition from the bottom of the potential energy curve of compound RT to the curve of RHe⁺ determines the excess energy E shown in the figure. If E is not beyond the dissociation limit, R–He bonding will be stable (I), but if E is beyond the limit, then the bonding will be broken (II). Calculation shows that HHe⁺, LiHe⁺, and BeHHe⁺ are stable (I) after the β^- decay of HT, LiT, and BeHT, but OHHe⁺ dissociates (II) after the decay of OHT.

As there is no potential well for CH₃He⁺, fragmentation occurs (III). Similarly, after the β^- decay of C₂H₅T dissociation occurs as follows:



■ Fig. 24.6

O₂ scavenger effect on recoil tritium reaction with *i*-C₄H₁₀



These fragmentation paths were confirmed by Wexler (1961b) by means of mass spectroscopy. Hot tritium reactions in a gaseous phase are most interesting because they are relatively simple.

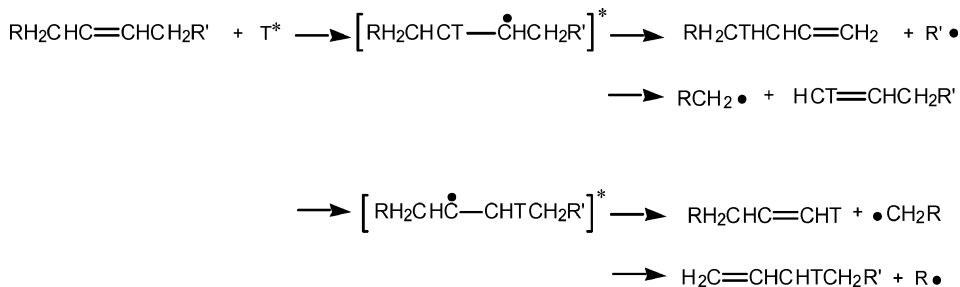
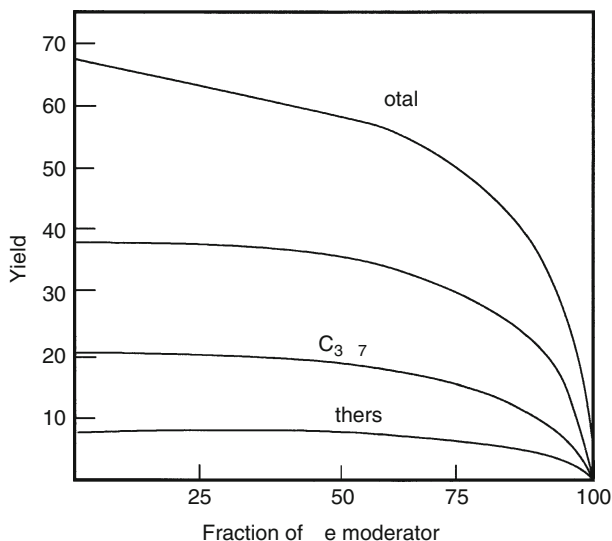
A part of hot tritium atoms produced in the gas phase can escape from the “hot” energy range and react with organics as thermalized ones. In order to study “hot” reactions, therefore, an oxygen scavenger is mixed to the reaction system to exclude thermal tritium atoms. Figure 24.6 shows the scavenger effect of oxygen in recoil tritium reaction with *i*-C₄H₁₀ (Rosenberg and Wolfgang 1964).

A hot reaction yield is not affected by the introduction of a scavenger, but greatly decreases by mixing with moderators such as He, Ne, Ar, Kr, and Xe. These rare gases do not take part in the hot reaction directly, but can contribute to the slowing down of the hot atom. As a result, the hot reaction yield of recoiling tritium decreases with increasing concentration of moderator rare gases. Figure 24.7 reveals a remarkable moderator effect of helium gas in the recoil tritium reaction with propane C₃H₈, especially at the higher concentration region (Rosenberg and Wolfgang 1964). It is clearly seen that the yields of HT, C₃H₇T, and others vanish at the limit of 100% added helium. Hot tritium reactions may be divided into three main types:

1. Hydrogen abstraction reaction: $T^* + RH \rightarrow HT + R$
2. Substitution reaction: $T^* + RX \rightarrow RT^* + X$ ($X = H, Cl, Br, \text{etc.}$)
3. Addition reaction: $T^* + >C=C< \rightarrow [>CT-C<]^*$

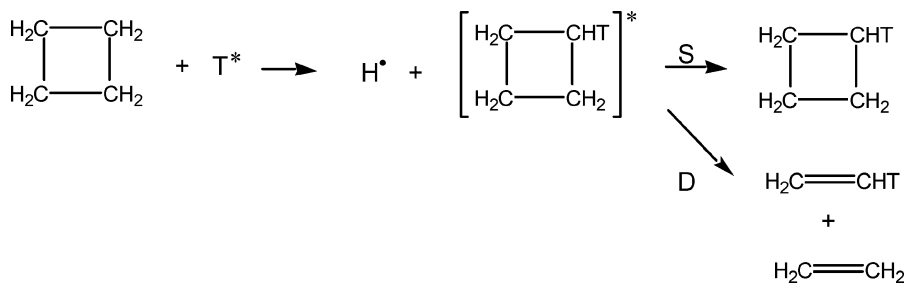
Hydrogen abstraction and substitution reactions usually make up 80–90% of the total reaction yield. The rest (10–20%) is the yield for organic compounds with smaller size. The HT/RT ratio increases with increasing number of carbon atoms in the target organic compound, and as a rule decreases with complexity of branching. Generally, isomerization of the compound does not occur by tritium attack. The yield of substitution of an alkyl radical decreases with an increase of the number of carbon atoms. In the case of recoil tritium reaction with unsaturated organic compounds, addition reaction results in further decomposition leading to the formation of a variety of organic compounds. For example,

■ Fig. 24.7

He moderator effect on recoil tritium reaction with C_3H_8 

Decomposition competes with stabilization (through collision with other molecules), and shows a pressure dependence. The decomposition to stabilization ratio decreases at increased pressure.

It is interesting to see the pressure dependence of hot tritium reaction in cyclobutane C_4H_8 . Recoil tritium attacks this molecule to give tritiated cyclobutane (substitution reaction) in an excited state, which either stabilizes by collision with a third body or decomposes into two molecules of ethylene. This is shown in the following scheme:



where S denotes stabilization and D decomposition. The S/D ratio depends on pressure because the intermediate C_4H_7T molecule de-excites by collision with cyclobutane molecules in the reaction system. An increase of pressure favors stabilization compared with decomposition. Inspection of pressure dependence gives some knowledge on the extent of excitation in the molecule. In this case, average excitation of 5 eV is deduced from the RRK (or RRKM (Rice-Ramsperger-Kassel-Marcus)) theory.

Similar experiments using various organic substances give mean excitation energy in recoil tritium reaction. [▶ Table 24.4](#) lists selected cases for such studies (Tominaga and Tachikawa 1981). Note that the recoil reaction of ^{18}F for fluorine gives the largest values around 10 eV.

In the abstraction reaction of recoil tritium, an important factor is binding energy (Tachikawa and Rowland 1968, 1969). The relation between the H-abstraction yield by recoil tritium (expressed by HT yield per C–H bonding) and the binding energy is shown in [▶ Fig. 24.8](#). It is clear that the higher the binding energy the lower the HT yield. Fluorine substitution of hydrocarbon results in shift of the curve to the higher energy side, but its tendency does not change so much. The same relation is confirmed in the case of Si–H and N–H bonds (Tominaga and Rowland 1969).

For the H substitution reaction of recoil tritium, binding energy also plays an important role. In the $T + CH_3X$ reaction, where $X = SH, NH_2, Cl, OH,$ and F , the yield of substituted CH_2TX increases with binding energy of C–X. This is due to weakening of the C–H bond by introduction of X.

The HT yield linearly correlated (Tang et al. 1971) with proton nuclear magnetic resonance (NMR) chemical shift, indicating the importance of electronic density effect in the reaction.

In the tritium reaction, the following kinds of isotope effects are known:

1. *Moderator isotope effect* due to different moderation efficiency on different molecules
2. *Probability integral isotope effect* due to different reaction probability per collision and different range of reaction
3. *Average energy isotope effect* due to difference of average reaction energy.

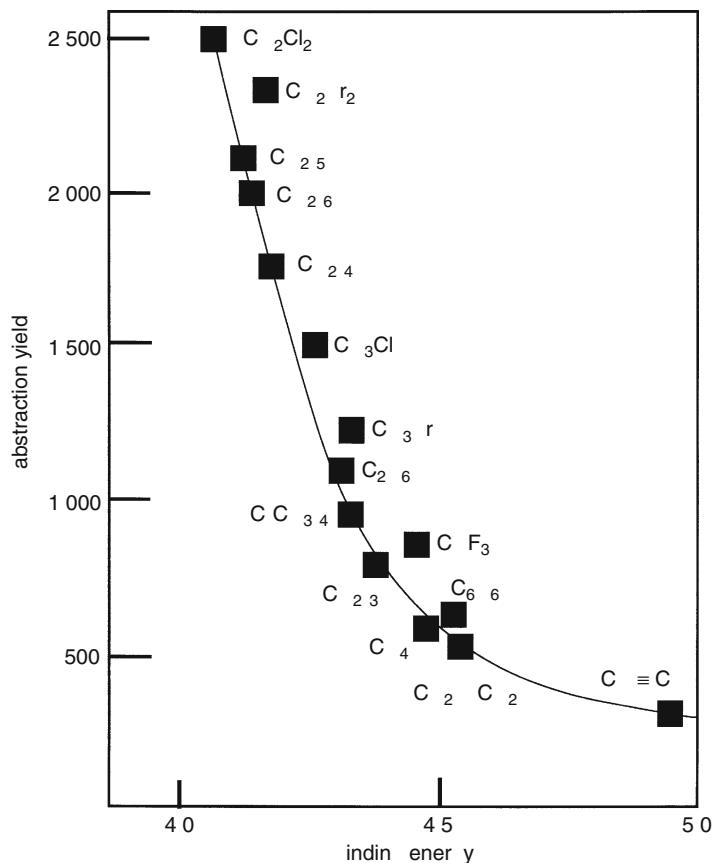
■ **Table 24.4**

Average excitation energy of recoil reaction products

Reaction	Molecule	Primary product	Secondary product	Average excitation energy (eV)
T/H	$c\text{-}C_4H_8$	$c\text{-}C_4H_7T$	C_2H_3T	5 ± 1
	CH_4	CH_3T	CH_2T	3.5 ± 1
	CH_3NC	CH_2TNC	CH_2TNC	> 4
	CH_3CF_3	$CH_2T CF_3$	$CHT=CF_2$	4.7 ± 1
T/D	$c\text{-}C_4D_8$	$c\text{-}C_4D_7T$	C_2D_3T	5 ± 1
T/ CH_3	$C_4H_6(CH_3)_2$	$C_4H_5T(CH_3)_2$	$CH_2=CHT$	6–8
T + olefin	$CH_2CHCH_2CH_3$	$CH_2TCH CH_2CH_3$	$CH_2TCH=CH_2$	≤ 0.5
$^{18}F/F$	CF_4	$CF_3^{18}F$		≥ 10
	CH_3CF_3	$CH_3CF_2^{18}F$	$CH_2=CF_2^{18}F$	8.3 ± 1.5
	$c\text{-}C_4F_8$	$c\text{-}C_4F_7^{18}F$	several	10 ± 2
	$c\text{-}C_3F_6$	$c\text{-}C_3F_5^{18}F$	$CF_2=CF^{18}F$	~ 10
$^{18}F/H$	CH_3CF_3	$CH_2^{18}FCF_3$	$CH^{18}F=CF_2$	6.3 ± 1.0

■ Fig. 24.8

C–H binding energy and HT abstraction yield (per bond)



Of these isotope effects, (1) moderator isotope effect and (3) average reaction energy isotope effect can be eliminated when experiments are performed at a high concentration of rare gas moderator. Therefore, use of a large amount of rare gas moderator (e.g., 90% Ar) is recommended to observe (2) the probability integral isotope effect, which is the most interesting one for hot atom chemists.

In [Table 24.5](#) (Wolfgang 1965; Seewald et al. 1968; Smail and Rowland 1968; Chou and Rowland 1971; Tachikawa and Yanai 1972; Saeki and Tachikawa 1973; Numakura et al. 1973; Numakura and Tachikawa 1973) several examples of the isotope effect experimentally obtained are listed. The effect ranges between 1.25 and 1.41 for recoil tritium substitution reaction, but is much larger (3.1–7.2) for photochemically produced tritium (2.8 eV) in hydrocarbon mixture gases.

In recoil tritium reaction with organic gases, kinetic theory analysis proposed by Estrup and Wolfgang (1960) is worth mentioning. They assumed that the recoil atom slows down through elastic collisions, but in many existing gases elastic collision was recognized to be a rather poor approximation. Therefore, the results obtained from this analysis showed deviations from experiments. The essence of this theory is briefly described in the followings.

Table 24.5

Reactive isotope effect of hot atom reaction

Reacting atom	Type of reaction	Compound	Isotope effect
Recoil T	H(D)-abstraction	CH ₂ D ₂	1.32 ± 0.01
		CH ₃ CD ₃	1.34 ± 0.01
		CH ₃ F-CD ₃ F	1.26 ± 0.05
		CH ₄ -CD ₄	1.28 ± 0.02
		H ₂ -D ₂	1.15 ± 0.04
	H(D)-substitution	(CH ₃) ₃ CH-(CD ₃) ₃ CH	1.41
		CH ₃ F-CD ₃ F	1.33 ± 0.04
		CH ₄ -CD ₄	1.31 ± 0.05
		<i>n</i> -C ₄ H ₁₀ , <i>n</i> -C ₄ D ₁₀	1.31 ± 0.05
		(CH ₃) ₃ CH-(CH ₃) ₃ CD	1.25
	F-substitution	CH ₃ F-CD ₃ F	1.40 ± 0.06
Recoil ⁸² Br	H(D)-abstraction	CH ₄ -CD ₄	2.7 ± 0.3
		C ₂ H ₆ -C ₂ D ₆	1.6 ± 0.2
		C ₃ H ₈ -C ₃ H ₂ D ₆	1.5 ± 0.2
		C ₃ H ₈ -C ₃ D ₂ H ₆	1.5 ± 0.2
2.8 eV T (photochemical)	H(D)-substitution	CH ₄ -CD ₄	7.2 ± 0.2
		C ₂ H ₆ -C ₂ D ₆	5.6 ± 0.2
		CH ₂ D ₂ -CD ₄	3.1 ± 0.3
		CH ₂ D ₂	1.06 ± 0.1
		CHD ₃	1.2 ± 0.3

A recoil atom produced by nuclear reaction undergoes many collisions with surrounding molecules, and loses a great part of its kinetic energy, until the latter drops to E_1 , at which the hot atom is slow enough to get a chance to initiate a hot atom reaction with one of the molecules. If the hot atom escapes reaction, it keeps slowing down by further collisions to energy E_2 below which hot atom reaction is no more possible. In a multicomponent system, the total probability of hot atom reactions (considering all possible reactants and products) is expressed as

$$P = \sum_j \int_{E_2}^{E_1} f_j p_j(E) n(E) dE \quad (24.22)$$

where f_j is the relative collision probability of the hot atom with a molecule of component j , $p_j(E)$ is the reaction probability of the hot atom with the molecule of component j per collision, and $n(E)dE$ is the total collision number of hot atoms with energy between E and $E + dE$. The collision density $n(E)$ is expressed as

$$n(E) = -\frac{1}{\alpha E} \exp \left(-\sum_j \int_E^{E_2} \frac{f_j p_j(E)}{\alpha E} dE \right) \quad (24.23)$$

where α is the *mean logarithmic energy loss* per collision while the hot atom is slowing down.

For a mixture of a *single* reactant and a moderator, the subscript j can be omitted and (using some simplifying assumptions) one gets for the production probability of all possible products:

$$P = 1 - \exp\left(-\frac{f}{\alpha}I\right) \quad (24.24)$$

where I is called the *reactivity integral*:

$$I = \int_{E_1}^{E_2} \frac{p(E)}{E} dE. \quad (24.25)$$

The parameter α is a linear combination of two components:

$$\alpha = f\alpha_{\text{reactant}} + (1-f)\alpha_{\text{moderator}}. \quad (24.26)$$

Inserting [Eq. \(24.26\)](#) into [Eq. \(24.24\)](#), the following formula is obtained:

$$-\frac{1}{\ln(1-P)} = \frac{\alpha_{\text{reactant}}}{I} + \frac{\alpha_{\text{moderator}}}{I} \left(\frac{1-f}{f}\right). \quad (24.27)$$

Using the above equation, the parameters can be determined graphically from experimental data. If, for example, $-1/\ln(1-P)$ is plotted against $(1-f)/f$, then the slope will be equal to $\alpha_{\text{moderator}}/I$ and the intercept to $\alpha_{\text{reactant}}/I$.

Staying with binary mixtures of the moderator-plus-reactant type, in the more general case the hot atom can produce several different products with the reactant. Such products and their characteristic parameters will be identified by the new subscript i . The probability $p(E)$ shown by [Eq. \(24.25\)](#) is now given as the sum of the partial probabilities $p_i(E)$ characterizing the individual reactions: $p(E) = \sum p_i(E)$. After substituting the analogue of [Eq. \(24.23\)](#) into the analogue of [Eq. \(24.22\)](#), series expansion yields for the formation probability P_i of the i th product:

$$P_i = \frac{f}{\alpha} I_i - \frac{f^2}{\alpha^2} K_i + \dots \quad (24.28)$$

where I_i is the *reactivity integral* for the i th product:

$$I_i = \int_{E_1}^{E_2} \frac{p_i(E)}{E} dE \quad (24.29)$$

and K_i is the *ith shadowing parameter*:

$$K_i = \int_{E_1}^{E_2} \frac{p_i(E)}{E} \left(\int_E^{E_2} \frac{p(E)}{E} dE \right) dE. \quad (24.30)$$

Note that the second integral in the shadowing-parameter formula contains $p(E) = \sum p_i(E)$ rather than $p_i(E)$.

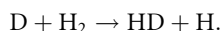
The parameters α , I_i , and K_i can be determined graphically from experimental data in a similar way as mentioned after [Eq. \(24.27\)](#). Using now [Eq. \(24.28\)](#), $\alpha P_i/f$ is plotted against f/α . This graph gives I_i as an intercept and K_i as a slope. Typical I and K (actually I_i and K_i) values are shown in [Table 24.6](#).

■ Table 24.6

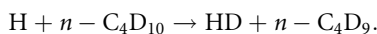
Reactivity integral I and shadowing parameter K in hot tritium reaction with hydrocarbons

Reactant	Product	$I(\text{He})$	$K(\text{He})$	Reactant	Product	$I(\text{He})$	$K(\text{He})$
CH_3	HT	0.35	0.07	$n\text{-C}_4\text{H}_{10}$	HT	2.34	5.10
	CH_3T	0.61	0.35		CH_3T	0.094	0.16
	CH_2T	0.13	0.087		$\text{C}_2\text{H}_3\text{T}$	0.095	0.21
C_2H_6	HT	1.80	3.17		$\text{C}_2\text{H}_5\text{T}$	0.055	0.095
	CH_3T	0.07	0.10		$\text{C}_3\text{H}_7\text{T}$	0.034	0.038
	$\text{C}_2\text{H}_3\text{T}$	0.035	~ 0		$n\text{-C}_4\text{H}_9\text{T}$	0.77	0.25
	$\text{C}_2\text{H}_5\text{T}$	0.57	0.10	$i\text{-C}_4\text{H}_{10}$	HT	3.15	11.3
					$i\text{-C}_4\text{H}_9\text{T}$	1.00	0.25
					others	0.50	0.95

The threshold energy and the excitation function of hot hydrogen reactions are interesting from the physicochemical point of view. Photolysis of DI or DBr gives a hot D atom, which is able to react with hydrogen:

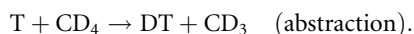
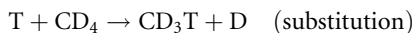


Using this reaction, White and Kuppermann (1966) obtained a threshold energy of 0.33 ± 0.02 eV for the D-abstraction reaction. Similarly, Dubrin and coworkers (Rebick and Dubrin 1970; Gann et al. 1971) studied D-abstraction reaction by photochemically produced H in deuterated butane.



They obtained a threshold energy of 0.35 ± 0.02 eV for the secondary D atom (0.45–0.55 eV for the primary D atom).

Threshold energy for hydrogen substitution reaction is more difficult to measure. Chou and Rowland (1969) used photolysis of TBr to obtain hot tritium atoms for the substitution reaction. They compared the yield of substituted CD_3T in methane to the DT abstraction yield whose threshold energy is known to be smaller. The ratio substitution/abstraction was extrapolated to zero at which the threshold value of energy for substitution was determined to be 1.5 eV.



Wolfgang and his coworker (Menzinger and Wolfgang 1969) studied threshold energy of substitution products in $\text{T}^* + \text{C}_6\text{H}_{12}$ (solid cyclohexane) reaction using a tritium beam accelerator. For simple substitution, the threshold energy is about 0.5 eV. However, for the products (n -hexane-T and hexane-T) for which C–C bond rupture is required, it is about 4.5 eV.

24.4.2 Halogens

In hot atom chemistry of halogens it is known that there exists an interesting case in which electronic charge on the recoil atom plays an important role. Rack and Gordus (1961)

irradiated a mixture of methane and iodine vapor (and moderator gases) with nuclear-reactor neutrons.

The recoil atoms ^{128}I produced by the reaction $^{127}\text{I}(n,\gamma)^{128}\text{I}$ distributed among $\text{CH}_3^{128}\text{I}$ (54.4%), $\text{CH}_2^{128}\text{I}$ (1%), and inorganic species ($\text{H}^{128}\text{I} + \text{I}^{128}\text{I}$, 45%) when no moderator gas was added. Mixing of moderator gases Ne, Ar, or Kr changed the yield of $\text{CH}_3^{128}\text{I}$ to 36% at 100% moderator concentration. On the other hand, mixing of Xe remarkably changed it to the limit of 11% as shown in [Fig. 24.9](#). This specific feature of recoil ^{128}I reaction with methane could be interpreted as follows:

Part A. 18.4% hot reaction affected by moderators.

Part B. 25% thermal reaction of $\text{I}^+(\text{}^1\text{D}_2)$, $^{128}\text{I}^+ + \text{Xe} \rightarrow ^{128}\text{I} + \text{Xe}^+$ (charge transfer reaction)

Part C. 11% thermal reaction of ^{128}I or I^+ ($^3\text{P}_2$, $^3\text{P}_1$, $^3\text{P}_0$).

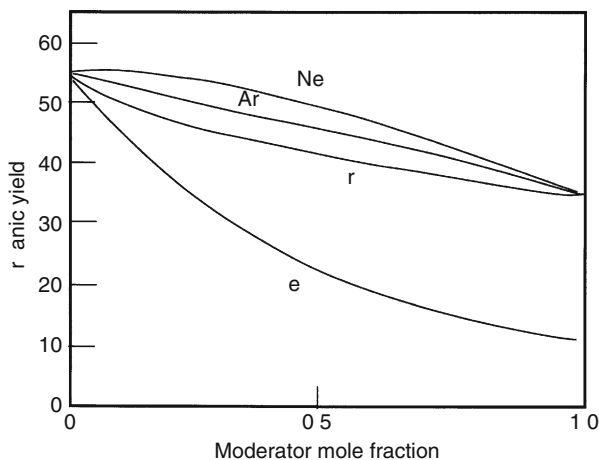
Importance of ion-molecule reaction in a gas phase was recognized in this recoil atom reaction. A similar study on a bromine-methane mixture was performed, but no contribution of charge was found.

An interesting difference of decayed atom behavior between the decays $^{80\text{m}}\text{Br} \rightarrow ^{80}\text{Br}$ and $^{82\text{m}}\text{Br} \rightarrow ^{82}\text{Br}$ was studied using Br_2 and HBr systems. The decay schemes for $^{80\text{m}}\text{Br}$ and $^{82\text{m}}\text{Br}$ are shown in [Fig. 24.10](#).

In $^{80\text{m}}\text{Br}$ decay there are two steps, one having a large conversion coefficient $e_K/\gamma (= 298)$ and the other a small one $e_K/\gamma (= 1.6)$. The first step of decay results in high charge that is then neutralized during the lifetime 7.4 ns of the intermediate level. The cause of the high charge is the Auger process that follows the emission of conversion electron from the radiobromine atom. In the $^{80\text{m}}\text{Br}-\text{Br}(\text{Br}_2)$ system, a part of the charge will be transferred to the partner atom, and the Br-Br bond will be broken by electric repulsion, and $^*\text{Br}$ will acquire kinetic energy. Most of the electric charge will be neutralized during the lifetime of 7.4 ns at the intermediate level, but the kinetic energy will survive. The second decay to the final ^{80}Br level from the intermediate level with a conversion factor $e_K/\gamma (= 1.6)$ produces both charged ^{80}Br and neutral ^{80}Br with kinetic energy. Therefore, ^{80}Br undergoes hot atom chemical reaction with methane to give $\text{CH}_3^{80}\text{Br}$ and therefore the yield will show moderator effect against Kr concentration

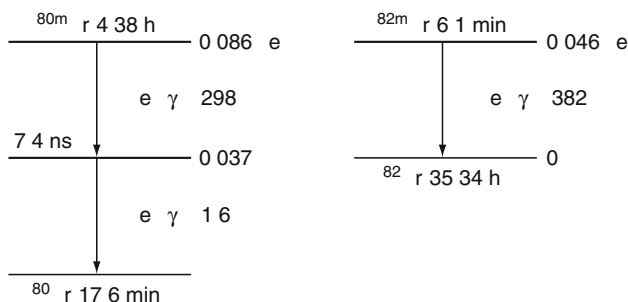
Fig. 24.9

Chemical effects of $^{127}\text{I}(n,\gamma)^{128}\text{I}$ reaction in methane



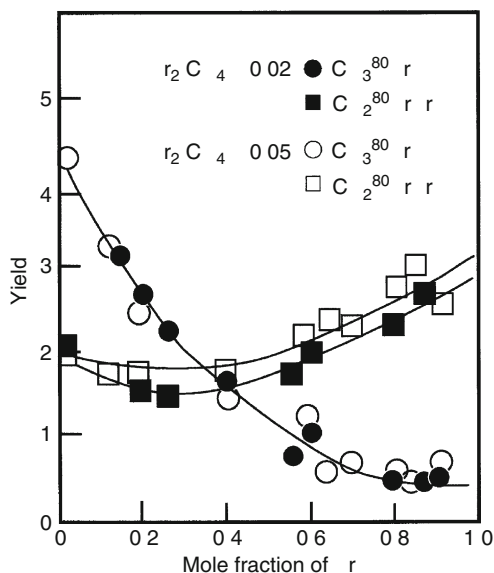
■ Fig. 24.10

Decay schemes for ^{80m}Br and ^{82m}Br . The ratios presented are internal conversion coefficients



■ Fig. 24.11

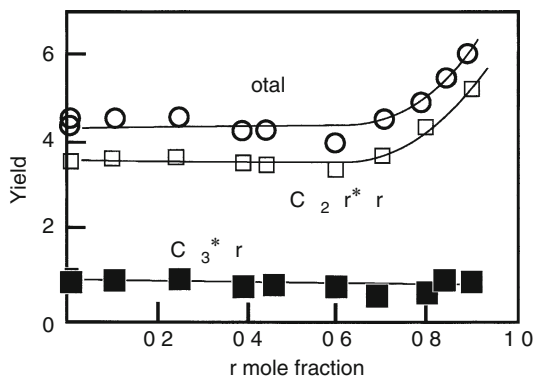
Kr moderator effect on hot atom chemical reaction products in $^{80m}\text{BrBr}-\text{CH}_4$ mixtures



(► Fig. 24.11). A part of ^{80}Br with electric charge reacts with methane to give $\text{CH}_2\text{Br}^{80}\text{Br}$, but no moderator effect is seen in this case.

On the other hand, in H^{82m}Br the decay has only one step (► Fig. 24.10) and the decayed atom ^{82}Br will acquire high charge. But after charge redistribution between H and ^{82}Br , the ^{82}Br has little kinetic energy because of its larger mass compared to H (see ► Sect. 24.2.1), and the charge remains on the ^{82}Br atom. For this reason, ^{82}Br reaction with CH_4 does not show a moderator effect (► Fig. 24.12) for any of the products, that is, $\text{CH}_2\text{Br}^{82}\text{Br}$ and $\text{CH}_3^{82}\text{Br}$ (Yagi et al. 1973). Note, however, that for higher concentration of the Kr moderator, probable formation of krypton clusters involving charged bromine increases the yield of the $\text{CH}_2\text{Br}^*\text{Br}$ component.

Fig. 24.12

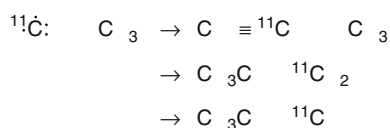
Kr moderator effect on hot atom chemical reaction products in $\text{H}^{82\text{m}}\text{Br-CH}_4$ 

24.4.3 Carbon

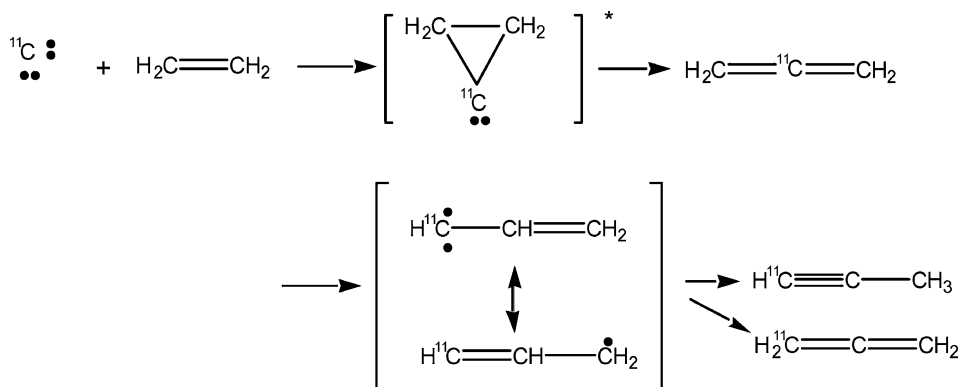
Radioactive carbon can be produced through various nuclear reactions (Stöcklin 1969; Tachikawa 1975). Carbon-11 hot atom reactions are relatively known. Wolfgang (1965) postulated that recoil ^{11}C was obtained by neutron abstraction reaction of carbon ^{12}C , and this energetic carbon could be led into a reaction chamber filled with organic gases. The state of ^{11}C in the reaction region is mostly neutral $\text{C}(^3\text{P})$, but its smaller part consists of $\text{C}(^1\text{D})$ and $\text{C}(^1\text{S})$. ^{11}C reacts with alkanes (e.g., with ethane) as follows.



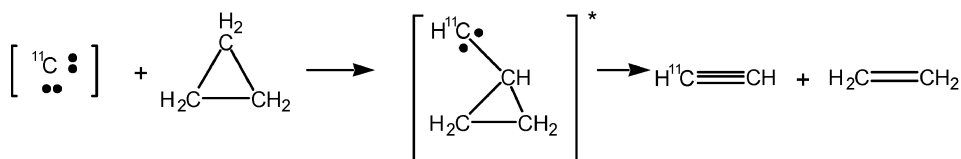
This is known as insertion reaction of a hot carbon atom. The product further changes to alkane and alkyne type compounds.



In the case of insertion of ^{11}C to alkenes, the following reactions take place.



The ^{11}C reaction with cyclopropane gives acetylene and ethylene.



24.5 Hot Atom Reactions in Liquid Phase

Hot atom reaction in a liquid phase may be characterized by the “cage effect,” which increases retention (parent chemical form). The hot atom produced by nuclear reaction interacts with surrounding atoms or molecules that form a cage to confine motion of the recoil atom in a liquid phase.

In ▶ [Table 24.7](#) ^{38}Cl -labeled product distributions of neutron-irradiated propyl chloride ($\text{C}_3\text{H}_7\text{Cl}$) are shown for gaseous and liquid phases. Comparison of the results by gaschromatographic separation showed that the organic yield is considerably larger in the liquid phase than in the gas phase, in particular for the case of retention (Willard 1953).

■ **Table 24.7**

^{38}Cl -labeled compound formation by (n,γ) reaction in isopropyl chloride and normal propyl chloride (%)

	<i>i</i> -C ₃ H ₇ Cl		<i>n</i> -C ₃ H ₇ Cl	
	Gaseous	Liquid	Gaseous	Liquid
Total organic yield	8.9	20.2	10.1	21.6
CH ₃ Cl	1.23	2.79	1.63	2.48
CH ₂ CHCl	1.03	1.09	1.18	1.01
CH ₃ CH ₂ Cl	0.11	0.50	0.35	1.01
CH ₃ CClCH ₂	0.22	0.46	0.04	0.11
CH ₃ CHClCH ₃	<u>2.32</u>	<u>6.75</u>	0.53	1.92
<i>cis</i> -CH ₃ CHCHCl	0.19	0.30	0.1	0.2
CH ₂ Cl ₂	0.52	0.93	1.24	1.66
CH ₂ ClCHCH ₂	0.27	0.61	0.1	trace
CH ₃ CH ₂ CH ₂ Cl	0.14	0.73	<u>1.34</u>	<u>5.03</u>
CH ₃ CHCl ₂	0.21	0.93		0.06
CH ₃ CH ₂ CHCl CH ₃			0.21	0.17
CH ₃ CCl ₂ CH ₃	0.42	0.91		
CH ₂ Cl CH ₂ Cl			trace	0.13
CH ₃ CH ₂ CHCl ₂	0.84	3.45	0.51	2.05
CH ₂ Cl CH ₂ CH ₂ Cl			0.68	2.27
Others	1.34	1.39	1.87	1.54

Retention underlined

This is true for isopropyl chloride and normal propyl chloride. The products are complicated, but can be divided into several groups:

- Shortening of carbon chain: CH_3Cl , $\text{CH}_3\text{CH}_2\text{Cl}$
- Elongation of carbon chain: $\text{CH}_3\text{CH}_2\text{CH}_2\text{CH}_2\text{Cl}$
- Double bond formation: $\text{CH}_2=\text{CHCl}$, $\text{CH}_3\text{CH}=\text{CH}_2$
- Doubly chlorinated compounds: CH_2Cl_2 , etc.
- Isomerization

It is concluded from the results that recoil chlorine ^{38}Cl recombines with its original partner or replaces a chlorine atom of the neighboring molecule (formation of retention); ^{38}Cl attacks a C–C bond to give various kinds of radicals; ^{38}Cl replaces an H atom, and HCl or H_2 elimination occurs from the intermediate in the hot atom reaction.

In the presence of a radical scavenger Br_2 , the thermal reaction component in the hot atom reaction is suppressed. By changing the concentration of Br_2 , the hot reaction component can be obtained as an extrapolated intercept in a scavenger curve as shown in [Fig. 24.13](#) (Milman and Shaw 1957).

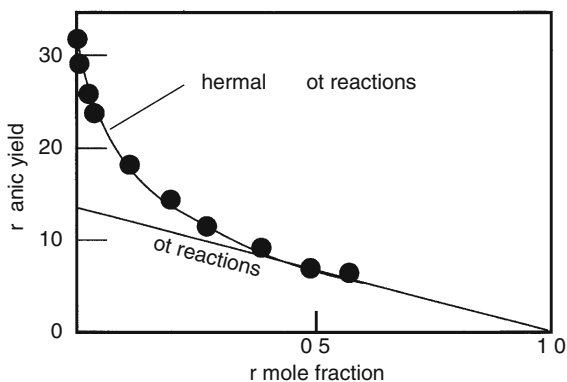
The hot reaction yield, namely, decreases linearly with the concentration of the scavenger added, causing a decrease of concentration of ethyl bromide. On the other hand, thermal reaction drops rapidly by addition of the scavenger Br_2 . [Figure 24.13](#) indicates a large contribution of thermal reaction in ethyl bromide.

When comparing recoil atom reaction yields of (n,γ) and $(n,2n)$ reactions, there is a distinct difference in the thermal reaction yield, whereas little if any difference can be observed in the hot reaction yield. Note that an $(n,2n)$ reaction provides recoil energy $10^2 - 10^3$ times larger than that an (n,γ) reaction. Probably this result indicates a difference of thermal radical concentration in the cages formed along the track of the recoil atom. As hot reactions occur at the end of the recoil track after slowing down and is not affected by recoil energy so much. This is shown in [Fig. 24.14](#) for the $^{82\text{m}}\text{Br}$ recoils produced by (n,γ) and $(n,2n)$ reactions (Cole et al. 1966).

Other examples of scavenger effect are recognized in benzene solutions of cobalt-acetylacetonate complex $\text{Co}(\text{acac})_3$. Addition of FeCl_3 , AlCl_3 , CuCl_2 , NiCl_2 , CoCl_2 , and MgCl_2

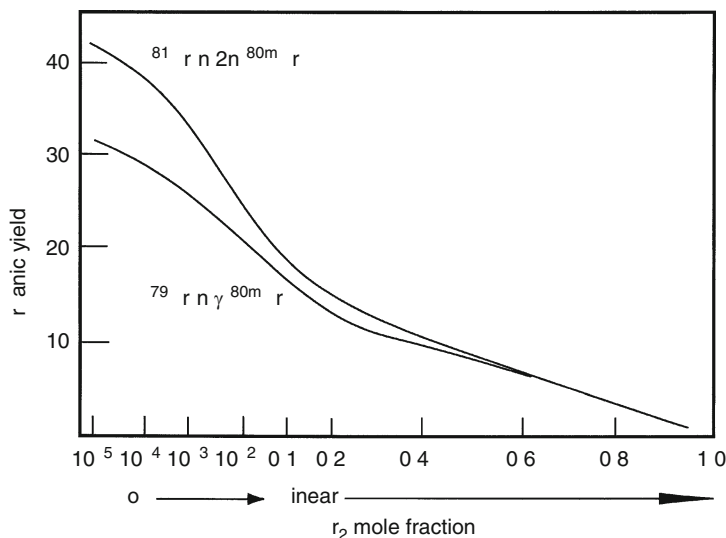
Fig. 24.13

Br_2 scavenger effect on organic yield in neutron-irradiated $\text{C}_2\text{H}_5\text{Br}-\text{Br}_2$ ((n,γ) reaction)



■ Fig. 24.14

Comparison of organic yields of $(n,2n)$ and (n,γ) reactions



as scavenger salts in the complex solutions drastically drop the $^{60}\text{Co}(\text{acac})_3$ yield (retention) (Tominaga 1975).

24.6 Hot Atom Reaction in Solid Phase

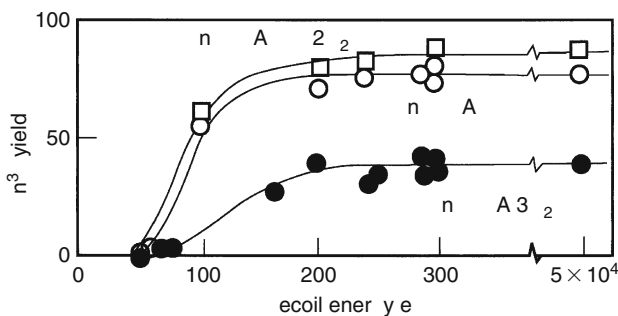
Solid systems are more complicated and more specific in many respects than gaseous and liquid systems. Some special features concerning hot atom chemistry in solids are noted as follows.

1. There is a threshold energy (appearance energy) larger than the typical Frenkel pair formation energy (~ 25 eV).
2. Annealing (thermal or radiational) after irradiation alters chemical form distribution of recoil products. This usually increases the yield of the parent chemical form (retention).
3. Some features specific to solid matrices affect the recoil product distribution; crystal structures, defects introduced into crystals, etc., play important roles in determining chemical fates of recoil atoms.

24.6.1 Appearance Energy

The relation between recoil energy and hot atom reaction yield is a question of fundamental importance in a solid system, but no answer had been given until Yoshihara and Kudo (1970) proposed use of (γ,γ') reaction in an indium complex in 1970. Controlling energy of γ -rays from a linear electron accelerator, a separable yield of $^{115\text{m}}\text{In}^{3+}$ from a bulk of irradiated In-EDTA complex was obtained. As shown in Fig. 24.15, the yield of $^{115\text{m}}\text{In}^{3+}$ rises at a threshold of about 60 eV, increases until 200 eV, and stays almost constant (20%) above 200 eV.

Fig. 24.15

Appearance energy of $^{115m}\text{In}^{3+}$ in various In-complexes

This trend was further confirmed in similar indium and lutetium complexes by the (γ, γ') nuclear excitation (Yoshihara et al. 1970, 1977; Yoshihara and Mizusawa 1972). The threshold energy (appearance energy) larger than Frenkel pair formation (~ 25 eV) indicates participation of chemical factors in the moment of recoil reaction in solids. They proposed a hot atom reaction model involving three reaction zones: (1) the region in which recoil energy is under the appearance energy and the recoil atom always recombines with its original partner, (2) the intermediate region in which recoil energy is above the appearance energy and the recoil atom escapes from recombination reaction to give “retention,” and (3) the region in which the recoil atom attacks surrounding molecules to give a fragmentary component with a constant probability. Namely, region (1) may be regarded as a sink for the recoil atom and in region (3) free attacking of the recoil atom to the surroundings is considered. Saturation of the yield suggests that at the end of its track the recoil atom reacts with its partner in the same manner, irrespective of its (initial) recoil energy. Region (2) is an intermediate one before the recoil energy reaches region (3).

24.6.2 Phosphorus Hot Atom Chemistry

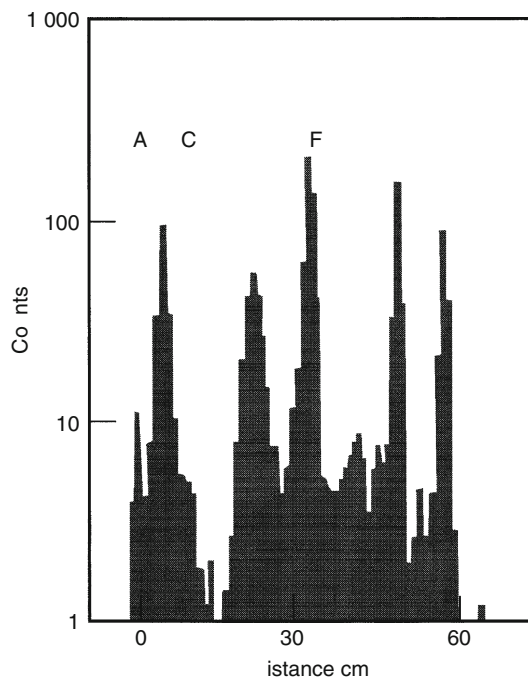
Selected topics will be described on solid hot atom chemistry of phosphorus (^{32}P). The recoil atom produced in phosphate by (n, γ) reaction has relatively large energy (max. 1.05×10^3 eV) and is distributed in a variety of compounds.

Lindner and Harbottle (1961) irradiated various phosphates (K, Na, NH_4 , and Li salts of phosphate, both anhydrous and hydrated) with neutrons at low temperature (-78°C) in a nuclear reactor. After the irradiated phosphates were dissolved in water, the solution was submitted to the analysis using paper electrophoresis. As shown in Fig. 24.16, the recoil products contained many components. (A) tripolyphosphate, (B) $\text{P}^5\text{-O-P}^5\text{-O-P}^5$, (B) pyrophosphate, $\text{P}^5\text{-O-P}^5$, (C) unknown, probably two species, (D) isohypo-phosphate, $\text{P}^5\text{-O-P}^5$, (E) hypophosphate, $\text{P}^4\text{-P}^4$, (F) orthophosphate, P^5 , (G) diphosphate, $\text{P}^4\text{-P}^2$ (and possibly another species), (H) phosphite, P^3 , and (I) hypophosphite, P^1 .

The variety of compounds thus obtained appeared to indicate chemical specialties of the reaction zone. “Hot zone” concept was proposed by Seitz and Koehler (1956) in solid-state physics and it was also discussed by Harbottle and Sutin (1958) from the viewpoint of hot atom chemistry. The interesting phenomena of specific labeling of ^{32}P at the P^3 position of

■ Fig. 24.16

Separation of ^{32}P recoil products in neutron-irradiated $\text{Na}_2\text{HPO}_4 \cdot 7\text{H}_2\text{O}$ by paper electrophoresis. See text for the notation



isohypophosphate $\text{P}^5\text{-O-P}^3$ and at the central position of tripolyphosphate $\text{P}^5\text{-O-P}^5\text{-O-P}^5$ (80%) were inconsistent with a uniformly melting domain around the recoil atom, and with simple sequences of ligand loss.

The reaction zone in ^{32}P hot atom reaction includes at least three phosphorus atoms in the above case. Formation of larger polyphosphates (tetra to hexa) was reported by Nakamura et al. (1970) by ion exchange chromatography in neutron-irradiated phosphate.

In the similar systems, annealing (thermal and radiation) processes were studied by Claridge and Maddock (1963a, b). It was revealed that thermal annealing conversion of $\text{P}^5\text{-O-}^{32}\text{P}^3$ into $^{32}\text{P}^3$ took place at low temperature and polymeric $^{32}\text{P}^5$ species changed into $^{32}\text{P}^3$ at higher temperature. Radiation annealing proceeded somewhat differently from thermal annealing. The most prominent processes were the conversion of $^{32}\text{P}^1$ into $^{32}\text{P}^3$ and $\text{P}^5\text{-O-}^{32}\text{P}^3$ into $\text{P}^5\text{-O-}^{32}\text{P}^5$.

24.6.3 Other Oxyanions

There are many examples of hot atom chemical studies on oxyanions. Among them permanganates, chromates, chlorates, bromates, iodates (and related halogenoxy acid salts) are relatively well known.

After the pioneering work by Libby mentioned in ▶ Sect. 24.1 the valence change of the target element and the appearance of separable fractions were noticed. In the case of

neutron-irradiated permanganate, $^{56}\text{Mn}^{2+}$ and $^{56}\text{MnO}_2$ could be separated from $^{56}\text{MnO}_4^-$ (retention) (Apers 1979). Very careful analytical treatment using double tracer technique disproved the presence of MnO_2 at the recoil event (Collins and Collins 1979). This shows that the chemical species formed at the moment of dissolution.

In the case of ^{51}Cr recoils in neutron-irradiated chromates, most prominent chemical species are chromic Cr(III) and chromate Cr(VI). A review (Collins and Collins 1979) described their chemical behavior from various sides. In spite of apparent simplicity of chromium hot atom chemistry, there are many problems that are not easily solved. The search for the presence of Cr(II) was not successful. In some papers chromium species are classified as Cr(VI), Cr(III)-monomer, Cr(III)-dimer, Cr(III)-trimer, and Cr(III)-polymer, but dissolution before analytical procedure made the initial processes of recoil too much complicated.

Hot atom chemistry of salts of halogen oxyanions has been studied by many authors (Owens 1979) since the Roman group led by Fermi (Amaldi et al. 1935) dealt with it. Boyd and Larson (1968) noticed that the BrO_3^- retention is little dependent on its partner cation but the yield of $^{82}\text{BrO}_2^-$ and $^{82}\text{BrO}^-$ are strongly dependent on the cation. It was found in a variety of bromates that the retention of $^{80\text{m}}\text{Br}$, ^{82}Br , and ^{78}Br was in a good correlation with the electron affinity of the cations (Saito et al. 1965).

24.6.4 Complexes of Cobalt

Hot atom chemistry of cobalt complexes was intensively studied (Tominaga and Saito 1979). Chemical varieties of recoil products found in cobalt complexes of cyano, ammine, and ethylenediamine ligands are worth mentioning. For example, neutron irradiation of hexamminecobalt(III) nitrate $[\text{Co}(\text{NH}_3)_6](\text{NO}_3)_3$ produces $[\text{Co}(\text{NH}_3)_6]^{3+}$, $[\text{Co}(\text{NH}_3)_5\text{NO}_2]^{2+}$, *cis*- and *trans*- $[\text{Co}(\text{NH}_3)_4(\text{NO}_2)_2]^+$, $[\text{Co}(\text{NH}_3)_3(\text{NO}_2)_3]$, $[\text{Co}(\text{NH}_3)_2(\text{NO}_2)_4]^-$, and Co^{2+} , which were detected by paper electrophoresis (Saito et al. 1962).

In neutron-irradiated $[\text{Co}(\text{NH}_3)_5\text{X}]\text{Br}_{2,3}$ a ligand displacement product $[\text{Co}(\text{NH}_3)_5\text{Br}]^{2+}$ was formed, and the yield of this $^{*}\text{Br}$ for displacement correlated with the stability of $[\text{Co}(\text{NH}_3)_5\text{X}]\text{Br}_{2,3}$ as indicated by optical absorption spectra (Saito et al. 1961).

Chemical form distribution of ^{57}Co decayed from ^{57}Ni was compared with that of ^{57}Co produced by $^{58}\text{Ni}(\gamma, p)^{57}\text{Co}$ reaction in the same substance of $[\text{Ni}(\text{NH}_3)_6]\text{Cl}_2$ (Yoshihara 1964). Initial distribution and annealing processes were found fairly different for both cases. This fact suggests that the size of fragmentation zone plays a role in recombination processes.

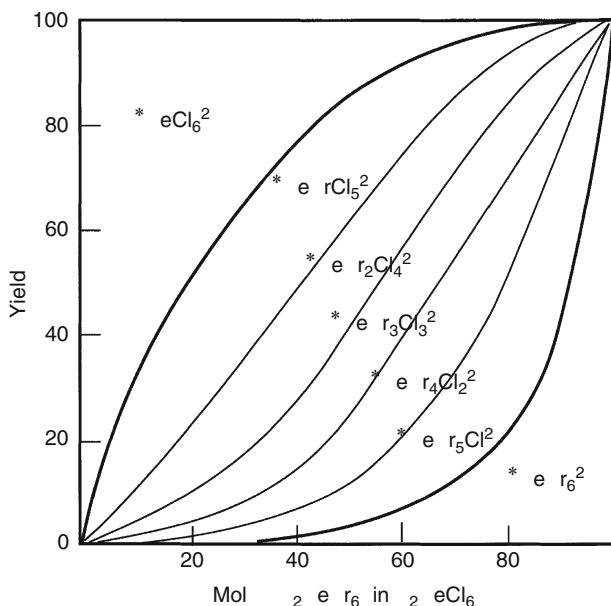
In neutron-irradiated $\text{Co}(\text{acac})_3$, formation of $^{60}\text{Co}(\text{acac})_2$ was confirmed by Sakanoue and his coworker (Amano and Sakanoue 1974) by sublimatography.

24.6.5 Rhenium and Osmium Compounds

An important contribution to solid hot atom chemistry came from H. Müller's laboratory in Freiburg with rhenium (osmium) compounds (Müller 1979). Müller performed his studies on mixed crystal systems involving rhenium, osmium, etc., for many years. An advantage of rhenium (n, γ) recoil reaction is its relatively small recoil energy (E_{max} : 102 eV, average energy may be much lower for ^{186}Re), which results in a reaction zone with a radius of ca. 0.5 nm (one or two unit cells of the crystal lattice).

■ Fig. 24.17

Proportions of the different hexabromochlororhenates resulting from the $^{187}\text{Re}(\gamma, n)^{186}\text{Re}$ reaction as a function of the mixed crystals composition



In the mixed crystal system $\text{K}_2\text{ReBr}_6\text{--K}_2\text{SnCl}_6$, ^{186}Re produced by (γ, n) reaction distributes among various mixed ligand compounds $\text{ReBr}_n\text{Cl}_{6-n}^{2-}$ ($n = 0 \dots 6$) and can be separated by thin layer chromatography. As shown in Fig. 24.17, the distribution is nearly statistical with a slight preponderance of the chloride-containing form. Because of large recoil energy for the (γ, n) reaction (~ 10 keV, recoil range 10 nm) this behavior is not so strange. However, ^{186}Re produced by (n, γ) reaction has a different pattern of the distribution of $\text{ReBr}_n\text{Cl}_{6-n}^{2-}$ ($n = 0 \dots 6$) as seen in Fig. 24.18. It is interesting to see that at the dilution limit (extrapolated to zero) of K_2ReBr_6 with K_2SnCl_6 the $\text{ReBr}_n\text{Cl}_{6-n}^{2-}$ yields are not zero. This fact shows that the reaction zone is very small, and the reaction occurs near the original site where the $^*\text{Re}$ was generated. Müller discussed that this behavior of rhenium recoils could be explained in terms of the disorder model rather than the hot-zone model proposed by Harbottle and Sutin (1958).

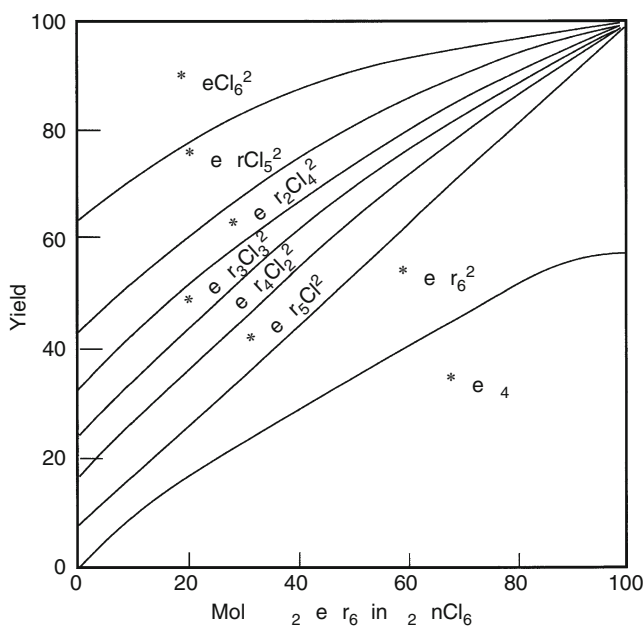
Progressively piling up a huge amount of experimental data on these kinds of mixed crystal systems, Müller created the “*little disorder model*” using central Re recoil. As for halogen ligand recoil, the recoil ranges for (n, γ) reactions for bromine and chlorine are larger than that for rhenium, and its reaction zone is also larger.

He verified that there are two kinds of retention; one is primary retention at the original site and the other is billiard ball secondary retention. For the system $\text{K}_2\text{ReBr}_6\text{--K}_2\text{ReCl}_6$, $^{82}\text{Br}^-$ yield was 12%, primary retention 8%, billiard ball secondary retention 74%, and some products of “larger disorder” $[\text{Re}^{82}\text{Br}_n\text{Cl}_{5-n}]^{2-}$ ($n = 0 \dots 4$) were about 6% altogether.

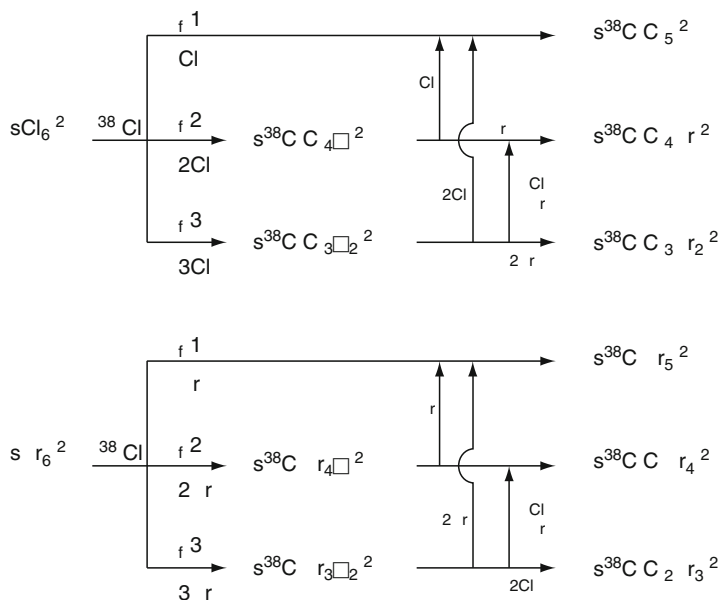
Then he succeeded in interpreting these product yields using a model called “Impact-induced Multiple Ligand Abstraction (IMULA).” Quantitative results were obtained for the system $\text{K}_2\text{OsBr}_6\text{--K}_2\text{SnCl}_6$ (^{82}Br produced by (n, γ) reaction) (Müller et al. 1984) and

■ Fig. 24.18

Yield of mixed hexachlorobromorhenates and perrhenate produced in neutron-irradiated $K_2ReBr_6-K_2SnCl_6$



$K_2OsBr_6-K_2SnCl_6$ (^{36}Cl produced by (n,γ) reaction) (Müller et al. 1986). In the latter case, the production of transient ligand vacancy complexes and their final fates resulting in mixed hexachlorobromometallate species are shown in the following scheme.



Using this scheme the calculated $[\text{Os}^{38}\text{ClCl}_4\text{Br}]^{2-}$ and $[\text{Os}^{38}\text{ClClBr}_4]^{2-}$ yield curves plotted against mixing fraction were in agreement with the experimental ones.

24.7 Implantation Reactions

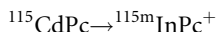
Implantation reactions are interesting because of their similarity as regards reaction mechanisms to hot atom reactions. (However, some features are specific to recoil implantation reactions.) Ion implantation-induced chemical reactions have such features as well, but difficulty lies in keeping surface temperature as low as possible and in obtaining radioactive beams without contamination by other stable isotopes (which may result in severe damage in the target substance). These demerits restricted usefulness of ion implantation. Recoil implantation can be performed simply in the mixture of a recoil source and a catcher (receptor) material. In some cases, thin films of source and catcher could be combined in order to control recoil energy.

24.7.1 Ion Implantation

Ion implantation reaction using a mass spectrometer was first studied by Italian researchers Croatto and Giacomello. Since then implantation of ^{51}Cr in K_2CrO_4 (Andersen and Sørensen 1966), $^{32}\text{P}^+$, and $^{35}\text{S}^+$ in alkali halides (Freeman et al. 1967; Andersen and Ebbesen 1971; Kasrai et al. 1971), ^{57}Co in *trans*- and *cis*- $[\text{Co}(\text{en})_2\text{Cl}_2]\text{NO}_3$ (Andersen and Ostergaard 1968; Wolf and Fritsch 1969) and ^{64}Cu in copper phthalocyanine (Andersen and Ostergaard 1968) were investigated.

Studying chemical effects of ion implantation of ^{35}S into single crystal NaCl , it was found that the same chemical species S^{2-} , S^0 measured as CNS^- , SO_3^{2-} , and SO_4^{2-} were formed as those in $^{35}\text{Cl}(\text{n,p})^{35}\text{S}$ reaction in NaCl , but their percentages showed a little difference. Implantation angles to the crystal axis affected the chemical fate of $^{32}\text{P}^+$ in NaCl single crystals (Andersen and Ebbesen 1971).

In^+ was implanted into copper phthalocyanine, in which new synthesis of indium phthalocyanine was observed (Yoshihara et al. 1974a). The species thus formed was identical with that produced by β -decay synthesis using cadmium phthalocyanine (Yoshihara and Kudo 1969; Kudo and Yoshihara 1970).



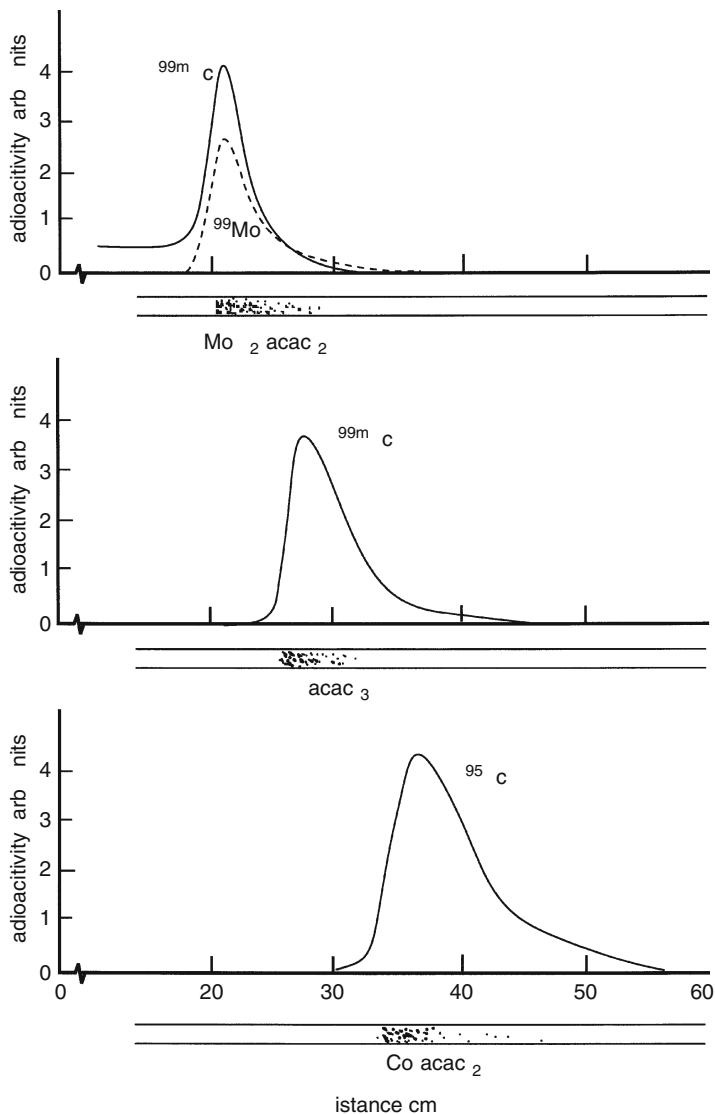
24.7.2 Recoil Implantation

Recoil implantation was first performed by Baumgärtner and Reichold (1961) for fission recoil synthesis of ruthenocene. This technique was applied to the synthesis of new compounds of technetium phthalocyanine (Yoshihara et al. 1974b) and $\text{Tc}(\text{II})(\text{acac})_2$ (Sekine and Yoshihara 1981). In the latter case, sublimatographic separation was effectively employed (► Fig. 24.19).

A “thin film technique” to control implantation energy is introduced in the study of energy dependence of product yield of implantation reaction (Miyakawa et al. 1992). For example, onto a palladium layer deposited on a mylar film, $\text{Rh}(\text{acac})_3$ is evaporated and this set of double layers of $\text{Pd-Rh}(\text{acac})_3$ is irradiated with γ -rays. In the Pd layer, ^{105}Rh is produced by

■ Fig. 24.19

Sublimatograms for (a) $\text{TcO}_2(\text{acac})_2$ produced by (n,γ) reaction in $\text{MoO}_2(\text{acac})_2$, (b) $\text{Tc}(\text{acac})_3$ produced by (γ,p) reaction in $\text{Ru}(\text{acac})_3$, and (c) $\text{Tc}(\text{acac})_2$ produced by recoil implantation of ^{95}Tc into $\text{Co}(\text{acac})_2 \cdot 2\text{H}_2\text{O}$

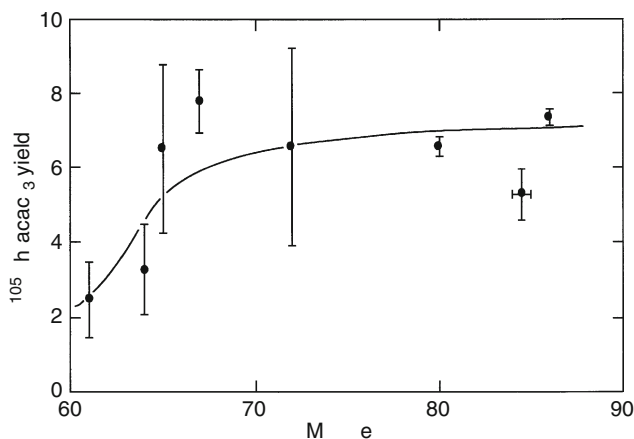


$^{106}\text{Pd}(\gamma,p) ^{105}\text{Rh}$ reaction, while ^{102}Rh is produced by $^{103}\text{Rh}(\gamma,n) ^{102}\text{Rh}$ in the $\text{Rh}(\text{acac})_3$ layer. Average recoil energy of ^{105}Rh is controlled by the thickness of palladium film and ^{105}Rh from the palladium film is implanted into the $\text{Rh}(\text{acac})_3$ layer with variable mean energy.

As shown in Fig. 24.20, the $^{105}\text{Rh}(\text{acac})_3$ yield increases with increasing mean implantation energy (MIE) up to 80 keV. On the other hand, for the inner recoil atom ^{102}Rh , the complex yield $^{102}\text{Rh}(\text{acac})_3$ is unchanged under the same irradiation conditions. Surprisingly,

■ Fig. 24.20

The substitution yield for Rh+Rh(acac)₃ reaction against the mean implantation energy (MIE)



the yield for implanted ^{105}Rh (2–7%) is one order of magnitude larger than that ($\sim 0.65\%$) for the inner recoil atom ^{102}Rh . This shows that implantation reaction yield is more enhanced compared to ordinary hot atom reaction. The reason for the yield enhancement is not fully understood, but a mathematically fitted curve suggests that a shock-wave-like action connected with collision cascades is exerted on the implanted atom at the top of the reaction site (Miyakawa et al. 1993; Matsue et al. 1995a; Yoshihara et al. 1996).

24.8 Other Topics in Hot Atom Chemistry

There have been so many published papers on hot atom chemistry that it is impossible to cover all of them in this section. Therefore, only the most important topics related to hot atom chemistry will be mentioned.

24.8.1 Hot Atom Chemistry in Space

It was pointed out by Rössler (1992) that hot or suprathermal reactions of H, C, N, O, etc., with frozen H_2O , NH_3 , CH_4 , CO, and other substances in space are important. The reactant may be either radioactive or nonradioactive. Hydrogen abstraction is typical of hot hydrogen, resulting in the formation of H_2 . Hot C, N, O can form CH, NH, and OH, and then CH_2 , CH_3 , and NH_2 successively. Hot oxygen can abstract O from oxygen-containing molecules. Replacement takes place in a nearly billiard ball collision manner. Addition can eventually cause fragmentation of the intermediate. Insertion occurs in O–H, N–H, C–C, N–N bonds to give various interesting products as shown in ▶ Table 24.8.

When the reaction takes place in a mixture matrix such as $\text{H}_2\text{O}-\text{CH}_4$ or $\text{H}_2\text{O}-\text{NH}_3-\text{CH}_4$ the products should have more variety. Thus, formation of more complicated large molecules is expected. The key materials of biomolecules can be formed in this manner. It is known that solar wind consists of 1 keV H^+ (95%), 4 keV He^{2+} (4%), 10 keV C^{6+} (0.19%), 13 keV O^{8+}

Table 24.8

Insertion of hot C, N, and O

Reaction to intermediate	Product formation		
	H-elimination	1,2-H transfer	H-uptake
$C + H_2O \rightarrow [HCOH]^*$	<u>CO</u> , COH, HCO	<u>H₂CO</u>	<u>CH₃OH</u>
$C + NH_3 \rightarrow [HCNH_2]^*$	HCN, <u>CN</u> , HNC	<u>CH₂NH</u>	<u>CH₃NH₂</u>
$C + CH_4 \rightarrow [HCCH_3]^*$	<u>C₂H₂</u> , C ₂	<u>C₂H₄</u>	<u>C₂H₆</u>
$N + H_2O \rightarrow [HNOH]^*$	<u>NO</u> , <u>HNO</u>		<u>NH₂OH</u>
$N + NH_3 \rightarrow [HNNH_2]^*$	<u>N₂</u>		<u>N₂H₄</u>
$N + CH_4 \rightarrow [HNCH_3]^*$	HNC, <u>CN</u> , CH ₂ NH		<u>CH₃NH₂</u>
$O + H_2O \rightarrow [HOOH]^*$	<u>O₂</u> , HO ₂		
$O + NH_3 \rightarrow [HONH_2]^*$	<u>NO</u> , <u>HNO</u>		
$O + CH_4 \rightarrow [HOCH_3]^*$	CO, HCO, HOC		

Underlined: experimentally observed

(0.05%), etc. And comets contain ices of H₂O, NH₃, CH₃, CO, CO₂, etc. Meeting of the two (causing ion implantation in solids) can produce various substances both inorganic and organic. Owing to the radiation effects in space, these substances may change further into biomolecule precursors. Although the origin of life has been sought for many years by a number of researchers, the goal of the study seems to be still far. However, its direction is promising. The knowledge accumulated in hot atom chemistry is no doubt important for such studies.

24.8.2 Hot Atom Chemistry for Radiopharmaceuticals

Hot atom chemical techniques are available in production of radiopharmaceuticals labeled with short-lived positron emitters such as ¹¹C, ¹³N, ¹⁵O, and ¹⁸F (Iwata and Wolf 1992). These radionuclides are used for positron emission tomography (PET). They can be easily produced with a small medical cyclotron using protons, deuterons, etc.

Such positron emitters can be produced right in the hospital using a small cyclotron (there exist “baby” cyclotrons!). The hot atom chemical processes are advantageous because the reaction to produce the aimed simple product labeled with a favorable positron emitter takes no time. Of course, for larger, complicated molecules the above products can only serve as starting materials. Examples of labeled compounds (precursors) involving hot atom reactions are listed in ▶ Table 24.9.

24.8.3 Some New Aspects Related to Hot Atom Chemistry

24.8.3.1 Quantum Mechanical Tunneling Effect

It is well known that at very low temperatures quantum mechanical tunneling effect plays a part in the chemical reaction of hydrogen. Miyazaki and coworkers (Fujitani et al. 1991;

■ Table 24.9

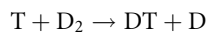
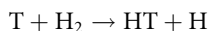
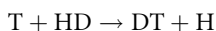
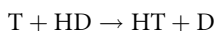
Hot atom chemical production of labeled positron emitters

Compound	Target system	Nuclear reaction
$^{11}\text{CO}_2$	N_2 (+ $\text{O}_2 < 10$ ppm)	$^{14}\text{N}(\text{p},\alpha)^{11}\text{C}$
$^{11}\text{CH}_4$	$\text{N}_2 + 5\% \text{H}_2$	$^{14}\text{N}(\text{p},\alpha)^{11}\text{C}$
H^{11}CN	$\text{N}_2 + 1\% \text{H}_2$ (in flowing)	$^{14}\text{N}(\text{p},\alpha)^{11}\text{C}$
$^{11}\text{CH}_3\text{I}$	$\text{N}_2 + \text{HI}$ (in flowing)	$^{14}\text{N}(\text{p},\alpha)^{11}\text{C}$
H^{11}CCH	CaC_2	$^{12}\text{C}(\text{p},\text{pn})^{11}\text{C}$
	cyclopropane	$^{12}\text{C}(\text{p},\text{pn})^{11}\text{C}$
$^{11}\text{COCl}_2$	$\text{N}_2 + \text{CO} + \text{Cl}_2$	$^{14}\text{N}(\text{p},\alpha)^{11}\text{C}$
$\text{H}_2^{11}\text{CN}_2$	NH_4X ($\text{X} = \text{Cl}, \text{Br}, \text{I}$)	$^{14}\text{N}(\text{p},\alpha)^{11}\text{C}$
$^{11}\text{CN}_2$	Ca_3N_2	$^{14}\text{N}(\text{p},\alpha)^{11}\text{C}$
$(\text{H}_2\text{N})_2^{11}\text{CN}_2$	liq. $\text{NH}_3 + \text{H}_2\text{O}$	$^{14}\text{N}(\text{p},\alpha)^{11}\text{C}$
^{13}NN	CO_2 (trace N_2)	$^{12}\text{C}(\text{d},\text{n})^{13}\text{N}$
	Charcoal (enriched ^{13}C)	$^{13}\text{C}(\text{p},\text{n})^{13}\text{N}$
	$\text{H}_2\text{O} + \text{NH}_3$	$^{16}\text{O}(\text{p},\alpha)^{13}\text{N}$
$^{13}\text{NO}_2$	O_2	$^{16}\text{O}(\text{p},\alpha)^{13}\text{N}$
$^{13}\text{NO}_2^- / ^{13}\text{NO}_3^-$	H_2O	$^{16}\text{O}(\text{p},\alpha)^{13}\text{N}$
$^{13}\text{NH}_3$	CH_4 (flowing)	$^{12}\text{C}(\text{d},\text{n})^{13}\text{N}$
	$^{13}\text{C} + \text{H}_2$	$^{13}\text{C}(\text{p},\text{n})^{13}\text{N}$
	$\text{H}_2\text{O} + \text{H}_2$	$^{16}\text{O}(\text{p},\alpha)^{13}\text{N}$
^{15}OO	$\text{N}_2 + 1 \dots 4\% \text{O}_2$	$^{14}\text{N}(\text{d},\text{n})^{15}\text{O}$
	O_2	$^{16}\text{O}(\text{p},\text{pn})^{15}\text{O}$
	$^{15}\text{N}_2 + 1\% \text{O}_2$	$^{15}\text{N}(\text{p},\text{n})^{15}\text{O}$
C^{15}OO	$\text{N}_2 + 1 \dots 4\% \text{CO}_2$	$^{14}\text{N}(\text{d},\text{n})^{15}\text{O}$
H_2^{15}O	$^{15}\text{N}_2 + 5\% \text{H}_2$ (flowing)	$^{14}\text{N}(\text{d},\text{n})^{15}\text{O}$
	H_2O	$^{16}\text{O}(\text{p},\text{pn})^{15}\text{O}$
^{18}FF	$\text{Ne} + 0.1\% \text{F}_2$	$^{20}\text{Ne}(\text{d},\alpha)^{18}\text{F}$
	$^{18}\text{O}/\text{Ne} + \text{F}_2$	$^{18}\text{O}(\text{p},\text{n})^{18}\text{F}$
H^{18}F	$\text{Ne} + 5\% \text{H}_2$	$^{20}\text{Ne}(\text{d},\alpha)^{18}\text{F}$
$^{18}\text{F}^-$	H_2O	$^{16}\text{O}(\alpha,\text{pn})^{18}\text{F}$
		$^{16}\text{O}(^3\text{He},\text{p})^{18}\text{F}$
	H_2^{18}O (enriched)	$^{18}\text{O}(\text{p},\text{n})^{18}\text{F}$

Kumagai et al. 1998; Aratono et al. 1998) studied this effect in the reaction of H, D, and T with hydrogen molecule (H_2 or D_2) and with mixtures of neopentane and *i*- C_4H_{10} (*c*- C_5H_{10}).

Recoil tritium produced by $^6\text{Li}(\text{n},\alpha)\text{T}$ reaction in enriched ^6LiF reacted with $\text{H}_2\text{-D}_2$ mixture at 4.2 K giving HT and DT as hydrogen abstraction products. From the isotope effect of the rate constants it was deduced that more than 90% of recoil T atoms react with hydrogen in the hot

energy range before thermalization. However, H atoms produced by the photolysis of HI or the radiolysis of *neo*-C₅H₁₂ in the mixture of *neo*-C₅H₁₂ and *i*-C₄H₁₀ react selectively with *i*-C₄H₁₀ in the thermal energy range, in which tunneling abstraction reaction by H atoms occurs. Less energetic T can be obtained from the ³He(n,p)T reaction. They studied the following abstraction reactions in liquid ³He – ⁴He media at 1.3 K:



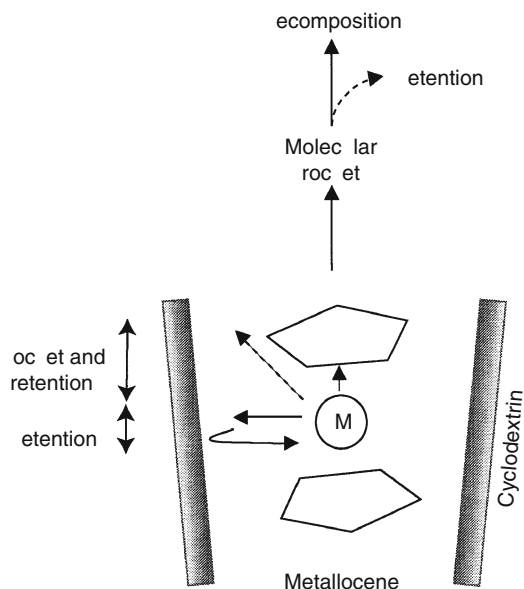
and compared the isotope effects experimentally obtained. It was suggested that quantum mechanical tunneling abstraction dominantly occurs through van der Waals complex.

24.8.3.2 Molecular Rocket

Metallocenes are known to be included in cyclodextrin (CD) and these are called “inclusion complexes.” When neutrons or γ quanta irradiate them, recoil energy is given to the central metal atom of metallocene. The molecules become partly broken to give decomplexed metal,

■ Fig. 24.21

Possible processes occurring in the moment of recoil in metallocene β -cyclodextrin inclusion compounds



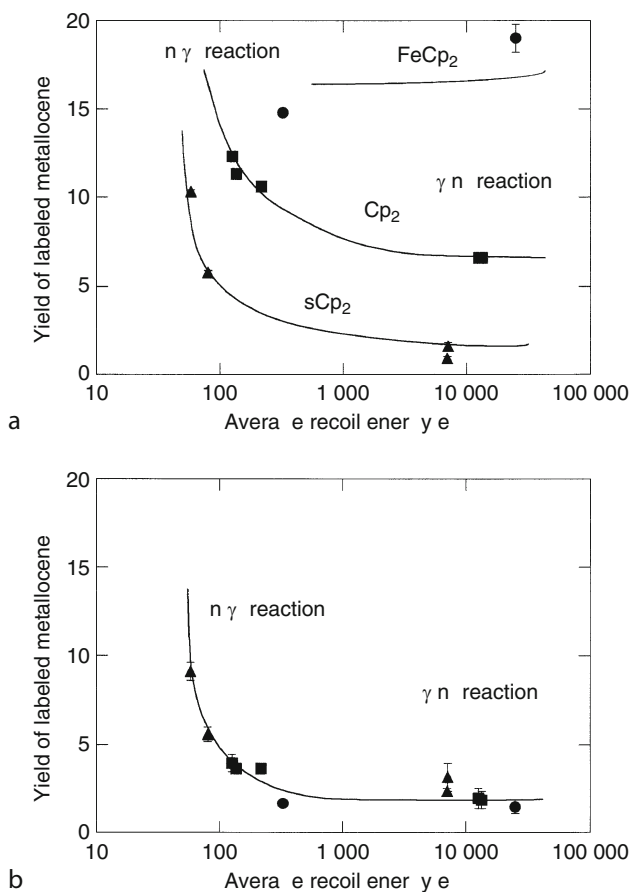
but partly retain their original structure. If excess energy is left in this retained metallocene molecule, it is expected that this molecule dashes out of the cyclodextrin cage just like a rocket.

Matsue et al. (1992, 1993) studied this “*molecular rocket*” phenomenon in metallocene–CD inclusion complex. The yield of unbroken ruthenocene molecules against recoil energy consists of two components of the molecular rocket: one directly ejected outside of the cyclodextrin cage, and the other once broken, but recombined rapidly in the CD cage, and then ejected from the CD cage (► Fig. 24.21). The latter component stays almost energy independent, while the former vanishes at higher energy (Matsue et al. 1995b; Yoshihara and Sekine 1997).

In ► Fig. 24.22a, the retention of metallocene is compared with (► Fig. 24.22b) that of metallocene-CD. Surprisingly, the retention of ferrocene, ruthenocene and osmocene can be plotted on one curve when metallocenes are included in CD (Yoshihara et al. 1994).

■ Fig. 24.22

The relation between retention and recoil energy: (a) metallocenes and (b) their β -cyclodextrin inclusion compounds



24.8.3.3 Fullerenes

The action of recoil atoms on fullerenes (C_{60} , C_{70} , etc.) has been studied recently (Braun and Rausch 2000; Nakahara et al. 2000). Some radionuclides with energy of nuclear recoil easily come to rest inside the fullerene. Braun and Rausch observed the formation of endohedral argon compound of fullerene $^{41}\text{Ar}@C_{60}$ during neutron irradiation of C_{60} in the presence of argon (Braun and Rausch 1995). They attributed their results to endohedral argon compound by implosion of C_{60} in argon nuclear recoil. ▶ Table 24.10 shows endohedral fullerene compounds reported.

Polymer formation of fullerene labeled with radionuclides was also observed. In a multi-tracer study using heavy-ion nuclear reaction of ^{12}C with ^{197}Au formation of new metallofullerenes (Zr, Hf, and Nb included in fullerene) was also reported.

Recently, a great interest was taken to the finding that the half-life of ^7Be in endohedral C_{60} ($^7\text{Be}@C_{60}$) was shortened by about 1% compared to that in Be metal (Ohtsuki et al. 2004).

■ Table 24.10

Labeling of fullerenes by nuclear recoil implosion

Nuclear reaction	Irradiated matrix	Facility	Endohedral fullerene	Reference
(n,γ)	C_{60} + adsorbed Ar	Nuclear reactor	$^{41}\text{Ar}@C_{60}$	Braun and Rausch (1998)
(n,γ)	$\text{Ar}C_{60}$	Nuclear reactor	$^{41}\text{Ar}@C_{60}$	Gadd et al. (1996)
(p,n)	$\text{Li}_2\text{CO}_3 + C_{60}$	Cyclotron	$^7\text{Be}@C_{60}$	Ohtsuki and Masumoto (1996)
(γ,αn)	C_{60}	Linac	$^7\text{Be}@C_{60}$	Ohtsuki and Masumoto (1996)
(n,γ)	Kr_1C_{60} , Xe_1C_{60}	Nuclear reactor	$^{83}\text{Kr}@C_{60}$, $^{125}\text{Xe}@C_{60}$	Gadd et al. (1997)
(n,γ)	Metal oxides + C_{60}	Nuclear reactor	Ho, Pr, La, Zn, $\text{Cu}@C_{60}$	Braun and Rausch (1998)
(d,2n)	$\text{KI} + C_{60}$, C_{70}	Cyclotron	$^{127}\text{Xe}@C_{60}$, $^{127}\text{Xe}@C_{70}$	Ohtsuki et al. (1998)
(d,2n)	$\text{KBr} + C_{60}$, C_{70}	Cyclotron	$^{79}\text{Kr}@C_{60}$, $^{79}\text{Kr}@C_{70}$	Ohtsuki et al. (1998)
(n,γ)	$\text{Xe}_{0.26}C_{60}$	Nuclear reactor	$^{131}\text{Xe}@C_{60}$	Gadd et al. (1998)
(γ,n)	$\text{Sb}_2\text{O}_3 + C_{60}$	Linac	$^{120,122}\text{Sb}@C_{60}$	Ohtsuki et al. (2001)
(d,2n)	"	Cyclotron	$^{121}\text{Te}@C_{60}$	Ohtsuki et al. (2001)
(d,2n)	$\text{As}_2\text{S}_3 + C_{60}$	Cyclotron	$^{75}\text{Se}@C_{60}$	Ohtsuki et al. (2002)
α decay	$^{224}\text{Ra} + C_{60}$	–	$^{212}\text{Pb}@C_{60}$	Diener et al. (2007)
(d,n)	$\text{Bi}_2\text{O}_3 + C_{60}$	Cyclotron	$^{210}\text{Po}@C_{60}$	Ohtsuki and Ohno (2005)
Ion implantation	$^{133}\text{Xe} + C_{76}$, C_{84}	Isotope separator	$^{133}\text{Xe}@C_{76}$, $^{133}\text{Xe}@C_{84}$	Watanabe et al. (2007)

The EC decay rate of ^7Be was further enhanced at 5 K (Ohtsuki et al. 2007). It was explained by the electron density effect at the Be nucleus position inside the C_{60} .

24.8.4 Impact of Hot Atom Chemistry on Other Research Fields

Impact of hot atom chemistry was seen in the study of reaction dynamics in its early days (1970s). See, for example, the international atomic energy agency (IAEA) report written by Y.T. Lee (1975).

Since 1981 (Harris and Kasemo 1981), hot atom reaction concepts have been adopted in the study of adsorption phenomena on surfaces. No radioactivity was used in these studies. Hot atoms of H, D, and O on surfaces have been studied experimentally (Yamanaka et al. 1999) and theoretically (Shalashilin and Jackson 1999).

In muonium chemistry, hot muonium (Mu^*) has been used for its similarity to hot hydrogen. Senba et al. (2000) studied hot atom reaction yield in $\text{Mu}^* + \text{H}_2$, and $\text{T}^* + \text{H}_2$ from quasiclassical trajectory cross sections on the Liu–Siegbahn–Truhler–Horowitz surface. Other examples are described in ► Chap. 28 on “Exotic Atoms and Muonium” in this Volume.

Interaction between energetic deuterium or tritium and wall materials such as graphite has been studied intensively in relation to nuclear fusion technology. For example, Okuno and coworkers (Morimoto and Okuno 2003; Oyaidzu et al. 2003) showed that deuterium implanted in highly oriented pyrolytic graphite revealed two kinds of C–D bonding (in sp^3 and sp^2 hybrid orbitals) as inspected by thermal desorption spectroscopy (TDS) and X-ray photoelectron spectroscopy (XPS).

References

- Amaldi E, D’Agostino O, Fermi E, Pontecorvo B, Rasetti F, Segré E (1935) *Proc R Soc Lond A* 149:522
- Amano R, Sakanoue M (1974) *Radiochem Radioanal Lett* 19:197
- Andersen T, Sørensen G (1966) *Trans Faraday Soc* 62:3427
- Andersen T, Ostergaard P (1968) *Trans Faraday Soc* 64:3014
- Andersen T, Ebbesen A (1971) *Trans Faraday Soc* 67:3540
- Apers D (1979) In: Harbottle G, Maddock AG (eds) *Chemical effects of nuclear transformations in inorganic systems*, North-Holland, Amsterdam, p 123
- Aratono Y, Matsumoto T, Takayanagi T, Kumada T, Komaguchi K, Miyazaki T (1998) *J Phys Chem A* 102:1501
- Baumgärtner F, Fischer EO, Zahn U (1958) *Chem Ber* 91:2336
- Baumgärtner F, Reichold P (1961) *Chemical effects of nuclear transformations*, vol 2. International Atomic Energy Agency, Vienna, p 319
- Betz HD, Grodzins L (1970) *Phys Rev Lett* 25:211
- Bohr N (1940) *Phys Rev* 58:654
- Boyd GE, Larson QV (1968) *J Am Chem Soc* 90:254
- Braun T, Rausch H (1995) *Chem Phys Lett* 237:443
- Braun T, Rausch H (1998) *Chem Phys Lett* 288:179
- Braun T, Rausch H (2000) *J Radioanal Chem* 243:27
- Brooks H (1904) *Nature (London)*, 70:270
- Carlson TA, White RM (1968) *J Chem Phys* 48:5191
- Carlson TA, Nestor CW, Wasserman N, McDowell JD (1970) *Atomic Data* 2:63
- Carlson TA, Krause MO (1965) *Phys Rev* 137A:1655
- Chou CC, Rowland FS (1969) *J Chem Phys* 50:2763
- Chou CC, Rowland FS (1971) *J Phys Chem* 75:1283
- Claridge RFC, Maddock AG (1963a) *Trans Faraday Soc* 59:935
- Claridge RFC, Maddock AG (1963b) *Radiochim Acta* 1:80
- Cole AJ, Mia MD, Miller GE, Shaw PFD (1966) *Radiochim Acta* 6:150
- Collins CH, Collins KE (1979) In: Harbottle G, Maddock AG (eds) *Chemical effects of nuclear transformations in inorganic systems*, North-Holland, Amsterdam, p 163
- Datz S, Moak CD, Lutz HO, Northcliffe LX, Bridewell LB (1971) *Atomic Data* 2:273
- Devault DC, Libby WF (1939) *Phys Rev* 55:322

- Diener MD, Alford JM, Kennel SJ, Mirzadeh S (2007) *J Am Chem Soc* 129:5131
- Estrup PJ, Wolfgang R (1960) *J Am Chem Soc* 82:2665
- Freeman HH, Kasrai M, Maddock AG (1967) *Chem Comm* 19:979
- Fujitani Y, Miyazaki T, Fueki K, Masaki NM, Aratono Y, Saeki M, Tachikawa E (1991) *J Phys Chem* 95:1651
- Gadd GE, Evans PJ, Hurwood DJ, Wood J, Morica S, Blackford M, Elcombe M, Kennedy S, James M (1996) *Chem Phys Lett* 237:221
- Gadd GE, Evans PJ, Hurwood DJ, Wood J, Morica S, Mcorist G, Wall T, Elcombe M, Prasad P (1997) *Sci Technol* 5:871
- Gadd GE, Schmidt P, Bowles C, McOrist G, Evans PJ, Wood J, Smith L, Dixon A, Easey J (1998) *J Am Chem Soc* 120:10322
- Gann RG, Ollison WM, Dubrin J (1971) *J Chem Phys* 54:2304
- Glückauf E, Fay JWJ (1936) *J Chem Soc* 390
- Goldhaber S, Willard JE (1953) *Ann Rev Nucl Sci* 3:193
- Green JH, Maddock AG (1949) *Nature* 164:788
- Hahn O, Meitner L (1909) *Phys Z* 10:697
- Harbottle G, Sutin N (1958) *J Phys Chem* 62:1344
- Harris J, Kasemo B (1981) *Surf Sci Lett* 105:L281
- Henchman M, Wolfgang R (1961) *J Am Chem Soc* 85:897
- Henry R (1957) *Bull. Informations Scientifique et Techniques*, No. 27
- Ikuta S, Yoshihara K, Shiokawa T (1977) *J Nucl Sci Technol* 14:720
- Iwata R, Wolf AP (1992) In: Adloff JP et al. (eds) *Handbook of hot atom chemistry*, Kodansha, Tokyo, p 515
- Kasrai M, Maddock AG, Freeman JH (1971) *Trans Faraday Soc* 67:2108
- Kudo H, Yoshihara K (1970) *J Inorg Nucl Chem* 32:2845
- Kumagai J, Kumada T, Kitagawa N, Morishita N, Miyazaki T (1998) *J Phys Chem A* 102:2842
- Lee EKC, Rowland FS (1963) *J Am Chem Soc* 83:2991
- Lee YT (1975) *Hot atom chemistry status report*, International Atomic Energy Agency, Vienna, p 123
- Libby WF (1940) *J Am Chem Soc* 62:1930
- Libby WF (1947) *J Am Chem Soc* 69:2523
- Lindner L, Harbottle G (1961) *Chemical effects of nuclear transformations*, vol 1. International Atomic Energy Agency, Vienna, p 485
- Lu CS, Sugden S (1939) *J Chem Soc* 1273
- Maddock AG, deMaine MM (1956) *Can J Chem* 34:275
- Matsue H, Sekine T, Yoshihara K (1992) *J Radioanal Nucl Chem Lett* 166:123
- Matsue H, Sekine T, Yoshihara K (1993) *Radiochim Acta* 63:179
- Matsue H, Yamaguchi I, Sekine T, Yoshihara K (1995a) *Shock Waves* 4:267
- Matsue H, Yamaguchi I, Sekine T, Yoshihara K (1995b) *Radiochim Acta* 68:163
- Mcmillan E, Abelson PH (1940) *Phys Rev* 57:1185
- Menzinger M, Wolfgang R (1969) *J Chem Phys* 50:2991
- Milman M, Shaw PFD (1957) *J Chem Soc (London)* 1303
- Miyakawa A, Homma K, Sekine T, Yoshihara K (1992) *Nucl Instrum Methods Phys Res B* 65:452
- Miyakawa A, Sekine T, Yoshihara K (1993) *Radiochim Acta* 60: 87
- Morimoto Y, Okuno K (2003) *J Nucl Mater* 272:467
- Molina MJ, Rowland FS (1974) *Nature* 249:810
- Müller H (1979) In: Harbottle G, Maddock AG (eds) *Chemical effects of nuclear transformations in inorganic systems*, North-Holland, Amsterdam, p 443
- Müller H, Bekk P, Bicheler H (1984) *Radiochim Acta* 36:115
- Müller H, Obergfell P, Hagenlocher I (1986) *J Phys Chem* 90:3418
- Müller H, Hagenlocher I (1990) *J Radioanal Nucl Chem* 140:37
- Nakahara H, Sueki K, Sato W, Akiyama K (2000) *J Radioanal Chem* 243:169
- Nakamura T, Ujimoto K, Yoza N, Ohashi S (1970) *J Inorg Nucl Chem* 32:3191
- Numakura K, Saeki M, Tachikawa E (1973) *Bull Chem Soc Jpn* 46:1
- Numakura K, Tachikawa E (1973) *Bull Chem Soc Jpn* 46:346
- Ohtsuki T, Masumoto K (1996) *Phys Rev Lett* 77:3522
- Ohtsuki T, Maruyama Y, Masumoto K (1998) *Phys Rev Lett* 81:967
- Ohtsuki T, Ohno K, Shiga K, Kawazoe Y, Maruyama Y, Shikano K, Masumoto K (2001) *Phys Rev B* 64: 125402
- Ohtsuki T, Ohno K, Shiga K, Kawazoe Y, Yuki H (2002) *Phys Rev B* 65:073402
- Ohtsuki T, Yuki H, Muto M, Kasagi J, Ohno K (2004) *Phys Rev Lett* 93:112501
- Ohtsuki T, Ohno K (2005) *Phys Rev B* 72:153411
- Ohtsuki T, Ohno K, Morisato T, Mitsugashira T, Hirose K, Yuki H, Kasagi J (2007) *Phys Rev Lett* 98:252501
- Owens CW (1979) In: Harbottle G, Maddock AG (eds) *Chemical effects of nuclear transformations in inorganic systems*, North-Holland, Amsterdam, p 145
- Oyaidzu M, Kimura H, Nakahata Y, Tokitani M, Oya Y, Iwakiri H, Yoshida N, Okuno K (2003) *J Nucl Mater* 367–370, 1522
- Rebeck C, Dubrin J (1970) *J Chem Phys* 53:2079
- Rack EP, Gordus AA (1961) *J Chem Phys* 34:1855
- Root JW, Breckenridge W, Rowland FS (1965) *J Chem Phys* 43:3694
- Rosenberg A, Wolfgang R (1964) *J Chem Phys* 41:2159
- Rutherford E (1951) *Radiation from radioactive substances*. Cambridge University Press, Cambridge, England
- Rössler K (1992) In: Glaser E, Götz G (eds) *Radiation effects in insulators*, North-Holland, Amsterdam, p 55
- Saeki M, Tachikawa E (1973) *Bull Chem Soc Jpn* 46:839

- Saito N, Ambe F, Sano H (1965) *Nature* 206:505
- Saito N, Tominaga T, Sano H (1961) Chemical effects of nuclear transformations, vol 1. IAEA, Vienna, p 541
- Saito N, Tominaga T, Sano H (1962) *J Inorg Nucl Chem* 24:1539
- Seewald D, Gersh M, Wolfgang R (1968) *J Phys Chem* 45:3870
- Segrè E, Halford R, Seaborg GT (1939) *Phys Rev* 55:321
- Seitz F, Koehler JS (1956) In: Seitz F, Turnbull Solid D (eds) *Solid Physics* 2, Academic Press, New York, p 305
- Sekine T, Yoshihara K (1981) *Radiochim Acta* 29:139
- Senba M, Fleming DG, Arseneau DJ, Mayne HR (2000) *J Chem Phys* 112:9390
- Shalashilin DV, Jackson B (1999) *J Chem Phys* 110:11038
- Shibata N, Yoshihara K, Tanaka K, Baba H, Kurosawa K (1963) *Proceedings of the 5th Japan Isotope Conference*, Kyoto, Japan, p 4
- Shibata N, Amano H, Yoshihara K, Ebihara H (1969) *Atompraxis* 15:1
- Smail T, Rowland FS (1968) *J Phys Chem* 72:1845
- Snell AH, Pleasonton F (1955) *Phys Rev* 100:1396
- Stöcklin G (1969) *Chemie Heisser Atome*. Verlag Chemie, Weinheim, p 143
- Suess H (1940) *Z Physik Chem* B45:188
- Szilard L, Chalmers TA (1934a) *Nature (London)*, 134:462
- Szilard L, Chalmers TA (1934b) *Nature (London)*, 134:494
- Tachikawa E, Rowland FS (1968) *J Am Chem Soc* 90:4767
- Tachikawa E, Rowland FS (1969) *J Am Chem Soc* 91:559
- Tachikawa E, Yanai K (1972) *Radiochim Acta* 17:138
- Tachikawa E (1975) In: Mabuchi H (ed) *Nuclear and radiation chemistry*, Maruzen, Tokyo, p 475
- Tang YN, Lee EKC, Tachikawa E, Rowland FS (1971) *J Phys Chem* 75:1290
- Tominaga T, Rowland FS (1969) *J Phys Chem* 73:465
- Tominaga T (1975) In: Mabuchi H (ed) *Nuclear and radiation chemistry*, Maruzen, Tokyo, p 494
- Tominaga T, Saito N (1979) In: Harbottle G, Maddock AG (eds) *Chemical effects of nuclear transformations in inorganic systems*. North-Holland, Amsterdam, p 227.77
- Tominaga T, Tachikawa E (1981) *Modern hot-atom chemistry and its applications*, Springer, Heidelberg, p 50
- Vértes A, Kiss I (1987) *Nuclear Chemistry*. Elsevier, Amsterdam
- Von Halban Jr H, Kowarski L, Magat M (1939) *Compt Rend* 208:572
- Watanabe S, Katabuchi T, Ishioka NS, Matsushashi S, Muramatsu H (2007) *J Radioanal Nucl Chem* 272:467
- Wexler S (1961) *Chemical effects of nuclear transformations*, vol 1. International Atomic Energy Agency, Vienna, p 115
- White JM, Kuppermann A (1966) *J Chem Phys* 44:4352
- Willard JE (1953) *Ann Rev Nucl Sci* 3:193
- Wolf GK, Fritsch T (1969) *Radiochim Acta* 11:194
- Wolfgang R (1965) *Prog React Kinetics* 3:153
- Wolfgang R (1969) *Acc Chem Res* 2:248
- Yagi M, Kondo K, Kobayashi T (1973) *Radiochem Radioanal Lett* 14:123
- Yamanaka T, Inoue Y, Matsushima T (1999) *J Chem Phys* 110:2597
- Yoshihara K (1964) *Nature* 204:1296
- Yoshihara K, Kudo H (1969) *Nature* 222:1060
- Yoshihara K, Kudo H (1970) *J Chem Phys* 52:2950
- Yoshihara K, Yang MH, Shiokawa T (1970) *Radiochem Radioanal Lett* 4:143
- Yoshihara K, Mizusawa T (1972) *Radiochem Radioanal Lett* 9:263
- Yoshihara K, Kishimoto M, Takahashi M, Suzuki S (1974a) *Radiochim Acta* 21:148
- Yoshihara K, Wolf GK, Baumgärtner F (1974b) *Radiochim Acta* 21:96
- Yoshihara K, Fujita A, Shiokawa T (1977) *J Inorg Nucl Chem* 39:1733
- Yoshihara K (1984) *Isotope users guide book*, 3rd edn. Japan Isotope Association, Tokyo, p 73
- Yoshihara K, Miyakawa A, Homma K, Sekine T (1992) In: Takayama K (ed) *Shock waves*, Springer Verlag, Heidelberg, p 753
- Yoshihara K, Matsue H, Sekine T (1994) *Nucl Instrum Methods Phys Res B* 91:103
- Yoshihara K, Miyakawa A, Homma K, Sekine T (1996) *Radiochim Acta* 73:171
- Yoshihara K, Sekine T (1997) *Radiochim Acta* 77:63

25 Mössbauer Spectroscopy

E. Kuzmann¹ · Z. Homonnay¹ · S. Nagy¹ · K. Nomura²

¹Eötvös Loránd University, Budapest, Hungary

²The University of Tokyo, Tokyo, Japan

25.1	<i>Principles of Mössbauer Spectroscopy</i>	1381
25.1.1	Isomeric Transition Between Nuclear Levels	1382
25.1.2	Thermal Broadening: γ Emission and Absorption in Gases	1383
25.1.3	Recoilless γ Emission and Absorption in Condensed Matter, the Mössbauer Effect	1385
25.1.3.1	Conditions of Nuclear Resonance Absorption	1385
25.1.3.2	Lattice Vibrations	1386
25.1.3.3	The Probability of the Mössbauer Effect	1388
25.1.4	The Mössbauer Spectrum	1389
25.1.5	Hyperfine Interactions	1395
25.1.5.1	Electric Monopole Interaction	1396
25.1.5.2	Electric Quadrupole Interaction	1400
25.1.5.3	Magnetic Dipole Interaction	1402
25.1.5.4	Combined Interactions	1403
25.1.5.5	Microenvironment	1404
25.2	<i>Mössbauer Parameters</i>	1404
25.2.1	Isomer Shift	1404
25.2.1.1	Chemical Isomer Shift	1404
25.2.1.2	Second-Order Doppler Shift	1406
25.2.2	Quadrupole Splitting	1407
25.2.3	Magnetic Splitting	1408
25.2.4	Peak Intensity	1411
25.2.5	The f -Factor	1412
25.2.6	Peak Width	1413
25.2.7	Mössbauer Parameters and Experimental Parameters	1414
25.2.7.1	Temperature Dependence	1414
25.2.7.2	Pressure Dependence	1417
25.2.7.3	External Magnetic Field Dependence	1417
25.2.7.4	Radio-Frequency Electromagnetic Radiation	1418
25.2.7.5	Angular Dependence of Peak Areas/Intensities	1418
25.2.7.6	Absorber Thickness	1420
25.2.7.7	Geometric Arrangement	1421
25.3	<i>Analytical Information from Mössbauer Spectra</i>	1421
25.3.1	The Fingerprint Method	1421
25.3.2	Pattern Analysis	1422

25.3.3	Spectrum Evaluation	1424
25.3.4	Quantitative Analysis	1427
25.4	<i>Measurement Techniques in Mössbauer Spectroscopy</i>	1428
25.4.1	Mössbauer Spectrometers	1428
25.4.2	Transmission Geometry	1429
25.4.3	Reflection Geometry	1429
25.4.3.1	Conversion Electron Mössbauer Spectroscopy	1430
25.4.4	Resonance Counters	1433
25.4.5	Emission Mössbauer Spectroscopy	1433
25.4.5.1	Aftereffects	1434
25.4.6	Thermal Scan Method	1435
25.4.7	Mössbauer Polarimetry	1435
25.4.8	Capillary Mössbauer Spectroscopy	1435
25.4.9	Time-Dependent Measurements	1436
25.4.10	Combined Methods	1436
25.4.11	Measurements Using Synchrotron Radiation	1436
25.4.12	Sources and Absorbers	1436
25.4.13	Cryostates, Furnaces, Magnets, and Pressure Cells	1438
25.5	<i>Applications</i>	1438
25.5.1	Applications in Nuclear Sciences	1439
25.5.2	Chemical and Analytical Applications	1440

Abstract: Mössbauer spectroscopy, based on the recoilless resonance emission and absorption of γ photons observed with certain atomic nuclei, is a powerful investigating tool in most disciplines of natural science ranging from physics to chemistry to biology. This nuclear method makes it possible to measure the energy difference between nuclear energy levels to an extremely high resolution (up to 13–15 decimals). This resolution is required to measure the slight variation of nuclear energy levels caused by electric monopole, electric quadrupole, and magnetic dipole interactions between the electrons and the nucleus. Mössbauer nuclides being at different microenvironments act as local probes for the sensitive detection of the hyperfine interactions. Such interactions reflect changes in the electronic, magnetic, geometric, or defect structure as well as in the lattice vibrations, serving as a basis for a variety of applications. In this chapter, the principles and some practical aspects of Mössbauer spectroscopy are described.

25.1 Principles of Mössbauer Spectroscopy

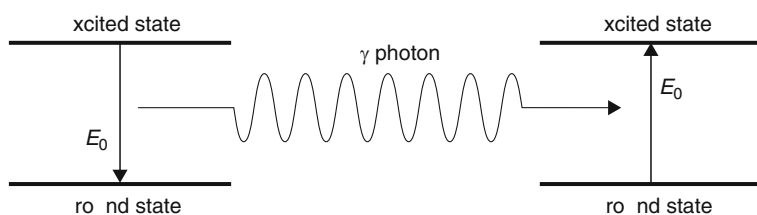
Mössbauer spectroscopy is based on the Mössbauer effect discovered by Rudolf Mössbauer (Mössbauer 1958a, b). The discovery was honored by the Nobel Prize in 1961.

Mössbauer effect is the recoilless (also called: recoil-free) nuclear resonance emission/absorption of γ rays (see Fig. 25.1). In the case of a nuclear transition, the de-excited nucleus is normally recoiled by the momentum of the γ photon emitted, which makes its resonance absorption impossible by another ground-state nucleus of the same type. In solids, however, recoilless photons can be emitted (and reabsorbed by another ground-state nucleus) with some probability.

A number of monographs and articles describe the basic aspects and applications of Mössbauer spectroscopy in detail (see, e.g., Kagan 1962; Goldanskii 1963; Frauenfelder 1962; Wertheim 1964; Abragam 1964; Wegener 1965; Gruverman 1965–1976; Danon 1968; Matthias and Shirley 1968; Goldanskii and Herber 1968; Shpinel 1969; Greenwood and Gibb 1971; Sano 1972; May 1971; Janot 1972; Kaipov 1976; Bancroft 1973; Bhide 1973; Cohen and

■ Fig. 25.1

Schematic representation of nuclear resonance based on the recoilless emission and absorption of a γ photon. The story that goes with the figure is this. A nucleus in excited state emits a γ photon with energy (E_0) equal to the difference between the energies of the excited and ground-state levels, and, subsequently, the same γ photon is absorbed resonantly by another nucleus in the ground state by transforming it to the excited state. This sounds rather trivial but in order to happen both the emission and the absorption of the photon must be a recoilless/recoil-free event (this is called the Mössbauer effect), because recoil of either nucleus would render the energy of the photon insufficient for the resonance to occur



Pasternak 1973; Gruverman and Seidel 1973; Gonser 1975a; Gibb 1976; Cohen 1976; Perlow 1977; Shenoy and Wagner 1978; Gütlich et al. 1978; Vértés et al. 1979; Cohen 1980; Gonser 1981; Mørup 1981; Stevens and Shenoy 1981; Thosar and Iyengar 1983; Long 1984; Herber 1984; Cranshaw et al. 1985; Long 1987, 1989; Vértés and Nagy 1990; Long and Grandjean 1993; Schatz et al. 1996; Long and Grandjean 1996, 1997; Vértés and Homonnay 1997; Fujita 1999). The Mössbauer Effect Reference and Data Index (MERDI) (Muir et al. 1958–1965; Stevens and Stevens 1966–) and Journal (MERDJ) serve as an important data source and contain a compilation of all references in the field.

25.1.1 Isomeric Transition Between Nuclear Levels

With regard to the nuclear resonance effect of γ rays, the (median) energy, E_0 , of the transition and the mean life, τ , of the excited state are very important parameters. The fact that the mean life of the excited state is finite – that the excited state sooner or later “decays” to the ground state according to the exponential law of decay (see [Chap. 7 in Vol. 1](#) on the “Kinetics of Radioactive Decay”) – causes a “blurring” of the supposedly discrete energy of the excited level. The energy of the excited nuclear levels is characterized by a $C(E_0, \Gamma/2)$ Cauchy distribution (see [Chap. 9 in Vol. 1](#) on the “Stochastics and Nuclear Measurements”) whose un-normalized density function is called a *Lorentzian* (or *Breit–Wigner*) curve in physics (Breit and Wigner 1936):

$$L(E) = A \frac{\Gamma}{2\pi} \frac{1}{(E - E_0)^2 + (\frac{\Gamma}{2})^2} = H \left(\frac{\Gamma}{2} \right)^2 \frac{1}{(E - E_0)^2 + (\frac{\Gamma}{2})^2} \quad (25.1)$$

where A is the area under the Lorentzian curve (i.e., for $A = 1$, $L(E)$ is a normalized $C(E_0, \Gamma/2)$ density function), H is the height of the Lorentzian at its maximum (i.e., at $E = E_0$), and $E_0 = E_e - E_g$ is the transition energy, i.e., the median difference between the energies of the excited state and the ground state. (The adjective “median” is used as a technical term here. The reason for avoiding the more usual term “mean” is that the underlying Cauchy distribution does not have a mean in the statistical sense; however, it *does* have a median.) Finally, Γ is the natural line width representing the full width at half maximum (FWHM) of the bell-shaped Lorentzian.

The *natural line width* Γ is also referred to sometimes as the “Heisenberg line width” because it obeys the following equation (see also [Eq. \(2.36\) in Chap. 2, Vol. 1](#), as well as remarks #62–64 in [Chap. 9, Vol. 1](#).):

$$\Gamma \tau = \hbar. \quad (25.2)$$

For the stationary ground state, the mean life is infinite, and [Eq. \(25.2\)](#) shows that such a state is indeed sharp having $\Gamma = 0$. For the excited state, on the other hand, the mean life is finite, so it will result in an energy uncertainty in the range of 10^{-12} to 10^{-5} eV for the states interesting from the point of view of Mössbauer spectroscopy.

Normally, the photons emitted in an isomeric transition will only have the sharp energy distribution of the excited state shown by [Eq. \(25.1\)](#) if the emission is recoilless. In general, however, there will be an energy loss E_R due to the recoil of the body that emits the radiation. (In the case of gases, this body is the nucleus (atom). With solids, the situation is more complex as it will be pointed out later on.)

To calculate E_R , consider an isolated nucleus of mass M that had been at rest before the decay took place and the photon got emitted. It follows from momentum conservation that $p_N = p_\gamma$, where p_N is the magnitude of the momentum of the recoiled nucleus and $p_\gamma = E_\gamma/c$ is that of the photon. The recoil energy can therefore be given as $E_R = (p_N)^2/(2M)$. Since E_R is small compared with E_0 , one can set $E_\gamma = E_0 - E_R \approx E_0$ and thus the *recoil energy* can be expressed as

$$E_R = \frac{E_0^2}{2Mc^2}. \quad (25.3)$$

Considering the excited nuclei of such isolated atoms at rest, the (median) energy of the emitted γ photons (i.e., $E_0 - E_R$) will be less than the transition energy E_0 . For the $\pm 3/2 \rightarrow \pm 1/2$ transition of ^{57}Fe , which is the most frequently used Mössbauer nuclide, one has $E_0 = 14.4 \text{ keV}$, $\Gamma = 4.67 \times 10^{-9} \text{ eV}$, $E_R = 1.92 \times 10^{-3} \text{ eV}$. The energy distribution of the emitted photons – called the emission line that is characterized by a Lorentzian having line width Γ – gets shifted toward the low energies. On the other hand, the energy distribution of the photons, which can be absorbed resonantly by the ground-state nucleus – called the absorption line – is characterized by the same line width, Γ , with a median energy $E_0 + E_R$ due to the recoil of the absorbing nucleus. Resonance absorption can only occur when the absorption and emission lines overlap each other. In other words, the shift between the absorption and emission lines cannot exceed substantially 2Γ . However, in case of recoil, the energy separation between the emission and absorption lines (which is $2E_R$) can be by six orders of magnitude larger than Γ in the case of ^{57}Fe . Thus, there is no overlap between the emission and absorption lines, and, consequently, no resonant absorption occurs in this case.

25.1.2 Thermal Broadening: γ Emission and Absorption in Gases

In the case of gases, one should also consider that the atoms move with relatively large velocities and thus the energy of the emitted γ rays is modified by the Doppler shift. This will cause a smearing out of both the emission and absorption lines and lead to an additional broadening of the spectrum peaks, which is called the *Doppler* or *thermal broadening*.

Let \mathbf{x} refer to the direction of γ emission/observation. The energy of the γ photon emitted by an atom moving at velocity \mathbf{u} is now

$$E_\gamma = (E_0 - E_R) \left(1 + \frac{u}{c} \cos \theta \right) \quad (25.4)$$

where $u = |\mathbf{u}|$ is the speed of the atom, and θ is the angle between \mathbf{u} and the \mathbf{x} -axis as shown in [Fig. 25.2](#).

Since the direction of γ emission is independent of the velocity of the particle, the expected value of the γ energy is easily calculated as

$$\langle E_\gamma \rangle = (E_0 - E_R) \left(1 + \frac{\langle u \rangle}{c} \langle \cos \theta \rangle \right) \quad (25.5)$$

where $\langle u \rangle$ is the mean speed of the atom as calculated from the Boltzmann distribution, and $\langle \cos \theta \rangle$ is calculated with the density function $(\sin \theta)/2$ according to [Fig. 25.2](#).

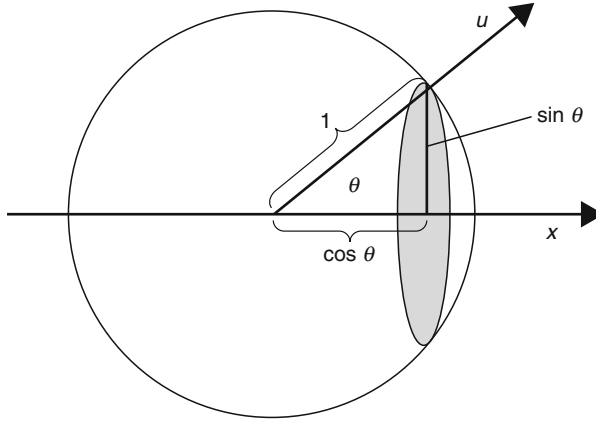
Due to symmetry, $\langle \cos \theta \rangle = 0$ and therefore

$$\langle E_\gamma \rangle = E_0 - E_R \quad (25.6)$$

that is, thermal motion does not affect the mean energy at all.

■ Fig. 25.2

Representation of the notation used in the calculation of Doppler broadening. The density function that is used for averaging out θ (for all possible values between 0 and π) should be proportional to the circumference $2\pi \sin\theta$ of the shaded disc that is perpendicular to the x -axis at $x = \cos\theta$



The variance of the γ energy (i.e., *Doppler broadening*), on the other hand, *does* depend on temperature as one can easily show

$$D^2(E_\gamma) = \langle (E_\gamma - \langle E_\gamma \rangle)^2 \rangle = (E_0 - E_R)^2 \frac{\langle u^2 \rangle}{c^2} \langle \cos^2 \theta \rangle = (E_0 - E_R)^2 \frac{\langle u^2 \rangle}{3c^2} \quad (25.7)$$

where the same density function was used as before for averaging out θ , and $\langle u^2 \rangle$ is the mean square speed of the atoms.

The temperature dependence can be made explicit by using the kinetic theory of gases according to which

$$\frac{M \langle u^2 \rangle}{2} = \frac{3kT}{2} \quad (25.8)$$

Thus, one observes the following formula for the standard deviation of the γ energy:

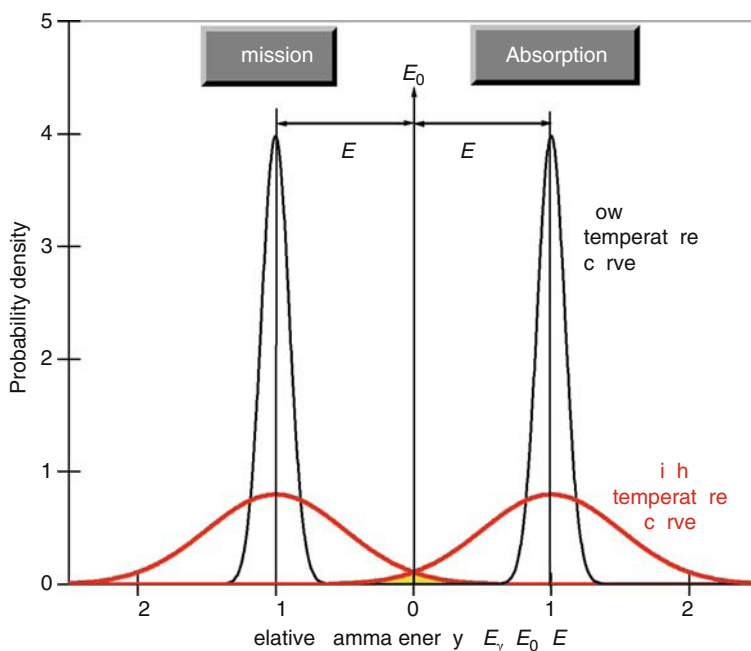
$$D(E_\gamma) = (E_0 - E_R) \sqrt{\frac{kT}{Mc^2}} \approx E_0 \sqrt{\frac{kT}{Mc^2}} = \sqrt{2kTE_R} \quad (25.9)$$

where it was made use of the fact that $E_R \ll E$.

For the $\pm 3/2 \rightarrow \pm 1/2$ transition of ^{57}Fe one has $D(E_\gamma) = 1.0 \times 10^{-2}$ eV at 300 K. Since $D(E_\gamma)$ is commensurable with E_R , one can see that Doppler broadening can cause some overlapping between the shifted emission and absorption lines (► Fig. 25.3), and thus a small yield of nuclear resonance absorption is to be expected (and, indeed, achieved; see Malmfors 1953). However, if the overlap occurs due to such thermal motion, the essence of using resonant nuclear absorption to develop a spectroscopic method with an extremely high-energy resolution is lost.

■ Fig. 25.3

Doppler/thermal broadening in gases. Thermal motion causes blurring of the (normalized) emission and absorption profiles. At high-enough temperatures, the profiles will overlap thus bridging the gap of $2E_R$ between the maxima. Without recoil (and thermal broadening), both the emission and the absorption profile would be represented by a Lorentzian at E_0 , with a full width at half maximum (FWHM) so small that the (normalized) peak would be way out of the vertical scale



25.1.3 Recoilless γ Emission and Absorption in Condensed Matter, the Mössbauer Effect

25.1.3.1 Conditions of Nuclear Resonance Absorption

Before the discovery of the Mössbauer effect, many attempts had been made to improve the chances for γ ray resonance absorption. The idea was to make the overlap between the emission and absorption lines larger by setting the emitter/absorber nuclei in motion (in order to compensate for the energy loss due to recoil) either mechanically (Moon 1950) or thermally (Malmfors 1953).

The key problem, i.e., how to avoid recoil and Doppler broadening at the same time, has been solved by Rudolf Mössbauer (Mössbauer 1958a) when he discovered that γ -ray emitting and absorbing nuclei if embedded in the lattice of a solid give rise to a recoilless line (the so-called Mössbauer line) at the energy E_0 .

The cross section for the resonant absorption depends on the energy E of the γ photons. The energy dependence can be expressed by a Lorentzian shown by ▶ Eq. (25.1) (Frauenfelder 1962):

$$\sigma = \sigma_0 \left(\frac{\Gamma}{2} \right)^2 \frac{1}{(E - E_0)^2 + \left(\frac{\Gamma}{2} \right)^2} \quad (25.10)$$

where σ_0 is the maximum of the resonant cross section for which one has

$$\sigma_0 = 2\pi\lambda^2 \frac{2I_e + 1}{2I_g + 1} \frac{1}{1 + \alpha} \quad (25.11)$$

where I_e and I_g are the nuclear spin quantum numbers of the excited and ground state, respectively, $\lambda \equiv \lambda/(2\pi)$ is proportional to the wavelength λ of the γ ray, and α is the internal conversion coefficient (see [Sect. 2.3.2.1 in Chap. 2, Vol. 1](#)).

25.1.3.2 Lattice Vibrations

Mössbauer effect is unique in that it provides a means of eliminating the destructive effect of recoil and thermal energies. In the Mössbauer domain, recoil energy is much less than the chemical binding energy and also less than the energy needed to excite lattice vibrations (phonons). Since the energy of lattice vibrations is quantized, the relatively low recoil energy cannot be transferred to the solid to increase its internal vibrational energy. It can only be transferred to the lattice, if it suffices to induce a vibrational quantum jump. If no quantum jump occurs (as in the case of the Mössbauer effect), then the recoil energy can be considered as being taken by the whole crystal grain as a rigid object in which the Mössbauer nuclide is embedded. The recoiled mass (M) in the denominator of [Eq. \(25.3\)](#) becomes extremely large (in fact, it becomes equal to the mass of the whole grain), and therefore the recoil energy E_R will be negligibly small in comparison with the natural line width Γ .

In order to understand the interactions between the emitting/absorbing nuclei and the lattice, some basics of the Einstein model and the Debye model of solids are needed.

The *Einstein model* (Kittel 1968) assumes that the solid is composed of a large number of independent linear oscillators each vibrating at the same angular frequency ω_E . (Each atom is represented by three oscillators, one for each dimension.) As the temperature increases, the oscillators keep vibrating with the same frequency, however, the amplitude of vibration – and so the mean square displacement of the atoms – becomes larger. The Einstein frequency ω_E is associated with the Einstein temperature θ_E :

$$\hbar\omega_E = k\theta_E \quad (25.12)$$

and the Einstein energy E_E , which is the minimum of vibrational energy that the lattice can emit or absorb:

$$E_E = \hbar\omega_E = \frac{\hbar c_s}{\lambda_s} = \frac{\pi \hbar c_s}{a} \quad (25.13)$$

where a is the lattice constant, c_s is the speed of the sound waves in the solid, and $2\pi\lambda_s$ is the wavelength of the sound associated with the vibration. The wavelength is supposed to satisfy the condition $\lambda_s = 2a$. For the bcc iron lattice (α -Fe), this yields $E_E = 0.04$ eV.

It is interesting to compare the γ emission of different isotopes of iron embedded in the same α -Fe lattice. Consider, e.g., the 14 keV transition of ^{57}Fe and the 800 keV transition of ^{58}Fe . It is found that the recoil energy of ^{57}Fe ($E_R = 0.002$ eV) is small compared with the Einstein energy ($E_E = 0.04$ eV) and, consequently, recoilless emission can occur. For ^{58}Fe , on the other hand, the recoil energy ($E_R = 6$ eV) is large enough to excite the lattice.

The Einstein model gives a good qualitative agreement with the real behavior of solids, but the quantitative agreement is poor (Cranshaw et al. 1985). A more realistic representation of a solid is given by the *Debye model*. The model describes the lattice vibration of solids as a superposition of independent vibrational modes (i.e., collective wave motion of the lattice, associated with “phonons”) with different frequencies. The (normalized) density function $p(\omega)$ of the vibrational frequencies is monotonically increasing up to a characteristic maximum of ω_D , where it abruptly drops to zero (Kittel 1968):

$$p(\omega) = \begin{cases} 3 \frac{\omega^2}{\omega_D^3} & \text{for } 0 \leq \omega \leq \omega_D \\ 0 & \text{elsewhere} \end{cases} \quad (25.14)$$

It is usual to express the cutoff frequency ω_D with the characteristic Debye temperature θ_D :

$$\hbar\omega_D = k\theta_D \quad (25.15)$$

The energy is quantized for each possible frequency ω :

$$\varepsilon_n = \left(n + \frac{1}{2}\right) \hbar\omega \quad (25.16)$$

where n is a quantum number ($n = 0, 1, 2, \dots$).

The mean energy for a given frequency ω at a given temperature T is calculated as

$$\bar{\varepsilon}(\omega, T) = \frac{\sum_{n=0}^{\infty} \varepsilon_n \exp\left(-\frac{\varepsilon_n}{kT}\right)}{\sum_{n=0}^{\infty} \exp\left(-\frac{\varepsilon_n}{kT}\right)} = \left(\bar{n}(\omega, T) + \frac{1}{2}\right) \hbar\omega \quad (25.17)$$

where $\bar{n}(\omega, T)$, representing the mean of the quantum number n , is called the Bose–Einstein distribution function

$$\bar{n}(\omega, T) = \frac{1}{\exp\left(\frac{\hbar\omega}{kT}\right) - 1} \quad (25.18)$$

In quantum theory, the time-average of the square displacement (and that of the square speed) of an atom doing harmonic oscillation along the x -axis with angular frequency ω is given by

$$\langle x^2 \rangle_{\omega, T} = \frac{\langle \dot{x}^2 \rangle_{\omega, T}}{\omega^2} = \left(\bar{n}(\omega, T) + \frac{1}{2}\right) \frac{\hbar}{M\omega} \quad (25.19)$$

where M is the mass of the atom and the subscripts are to indicate that the time-averages depend on both the frequency and the temperature.

The *mean square displacement* at a given temperature is obtained by averaging the time-average of the square displacement over all frequencies:

$$\langle x^2 \rangle_T = \int_0^{\omega_D} \langle x^2 \rangle_{\omega, T} p(\omega) d\omega = \frac{3\hbar^2}{Mk\theta_D} \left[\frac{1}{4} + \left(\frac{T}{\theta_D}\right)^2 \int_0^{\theta_D/T} \frac{x}{e^x - 1} dx \right]. \quad (25.20)$$

For very low and very high temperatures, [Eq. \(25.20\)](#) can be approximated by the following expressions:

$$\langle x^2 \rangle_T \approx \frac{3\hbar^2}{Mk\theta_D} \left[\frac{1}{4} + \left(\frac{T}{\theta_D} \right)^2 \frac{\pi^2}{6} \right], \quad T \ll \theta_D, \quad (25.21)$$

$$\langle x^2 \rangle_T \approx \frac{3\hbar^2}{Mk\theta_D} \frac{T}{\theta_D}, \quad T \gg \theta_D \quad (25.22)$$

Note that [Eqs. \(25.20\)–\(25.22\)](#) justify the intuitive expectation that the mean square displacement of the vibrating atoms should increase with temperature.

The *mean square velocity* of the lattice vibration, $\langle u^2 \rangle$, at a given temperature can be derived similarly to that of mean square displacement, and obtained as

$$\langle u^2 \rangle_T = \int_0^{\omega_D} \langle u^2 \rangle_{\omega,T} P(\omega) d\omega = \frac{9k\theta_D}{M} \left[\frac{1}{8} + \left(\frac{T}{\theta_D} \right)^4 \int_0^{\theta_D/T} \frac{x^3}{e^x - 1} dx \right] \quad (25.23)$$

25.1.3.3 The Probability of the Mössbauer Effect

The probability of the recoilless emission or absorption is given by the *recoilless fraction* f , meaning the fraction of all γ rays of the Mössbauer transition that are emitted (f_s) or absorbed (f_a) without recoil-energy loss. This is also commonly referred to as the Mössbauer fraction, Debye–Waller factor, Mössbauer–Lamb factor or, simply, the f -factor.

The theory of the *Mössbauer–Lamb factor* has been developed by several authors (Lamb 1939; Mössbauer 1958a; Singwi and Sjolander 1960; Lipkin 1960; Shapiro 1960).

In its most general form, the recoilless fraction is given by the following formulas that are completely equivalent to each other:

$$f = \exp(-k^2 \langle x^2 \rangle_T) = \exp\left(-\frac{\langle x^2 \rangle_T}{\lambda^2}\right) = \exp\left(-\frac{E_0^2}{\hbar^2 c^2} \langle x^2 \rangle_T\right) = \exp\left(-\frac{2ME_R}{\hbar^2} \langle x^2 \rangle_T\right) \quad (25.24)$$

where $k/(2\pi)$ is the wave number of the γ ray:

$$k = \frac{2\pi}{\lambda} = \frac{1}{\lambda} = \frac{E_0}{\hbar c} \quad (25.25)$$

[Equation \(25.24\)](#) carries several important messages for the Mössbauer spectroscopist:

1. The recoilless fraction decreases with increasing γ energy (note that in the recoilless case $E_\gamma = E_0$ except for the energy uncertainty expressed by [Eq. \(25.2\)](#)). This means that isomeric transitions with $E_0 \geq 200$ keV are not practical for the purpose of Mössbauer spectroscopy, since the f -factor would be too small. (The Mössbauer effect has been observed with over 100 transitions of near 50 elements shown in [Fig. 25.4](#). The nuclear data for the Mössbauer transitions are summarized in [Sect. 36.1 of the Appendix of this Volume](#).)
2. Since according to [Eq. \(25.21\)](#) the value of $\langle x^2 \rangle_T$ is supposed to decrease on cooling, the recoilless fraction should increase when the temperature is lowered. This was the crucial and unexpected finding of the first recoilless resonance absorption experiment by Rudolf Mössbauer using ^{191}Ir , which lead to the discovery of the Mössbauer effect (Mössbauer 1958a).

The explicit temperature dependence of the Mössbauer–Lamb factor can be estimated from the Debye model by using [Eqs. \(25.20\)–\(25.22\)](#) and [Eq. \(25.24\)](#):

■ Fig. 25.4

The Mössbauer periodic table. Shaded cells contain elements with no known Mössbauer isotope. Unshaded cells also indicate the mass number(s) of the Mössbauer isotope(s) below the chemical symbol. For brevity's sake no more than two (of the most important) isotopes are indicated for each element. An asterisk "*" after the last mass number means that the full list of the Mössbauer isotopes (see [▶ Sect. 36.1 of the Appendix of this Volume](#)) is longer than shown here

[illegible]

$$f(T) = \exp \left\{ -\frac{6E_R}{k\theta_D} \left(\frac{1}{4} + \left(\frac{T}{\theta_D} \right)^2 \int_0^{\theta_D/T} \frac{x}{e^x - 1} dx \right) \right\}. \quad (25.26)$$

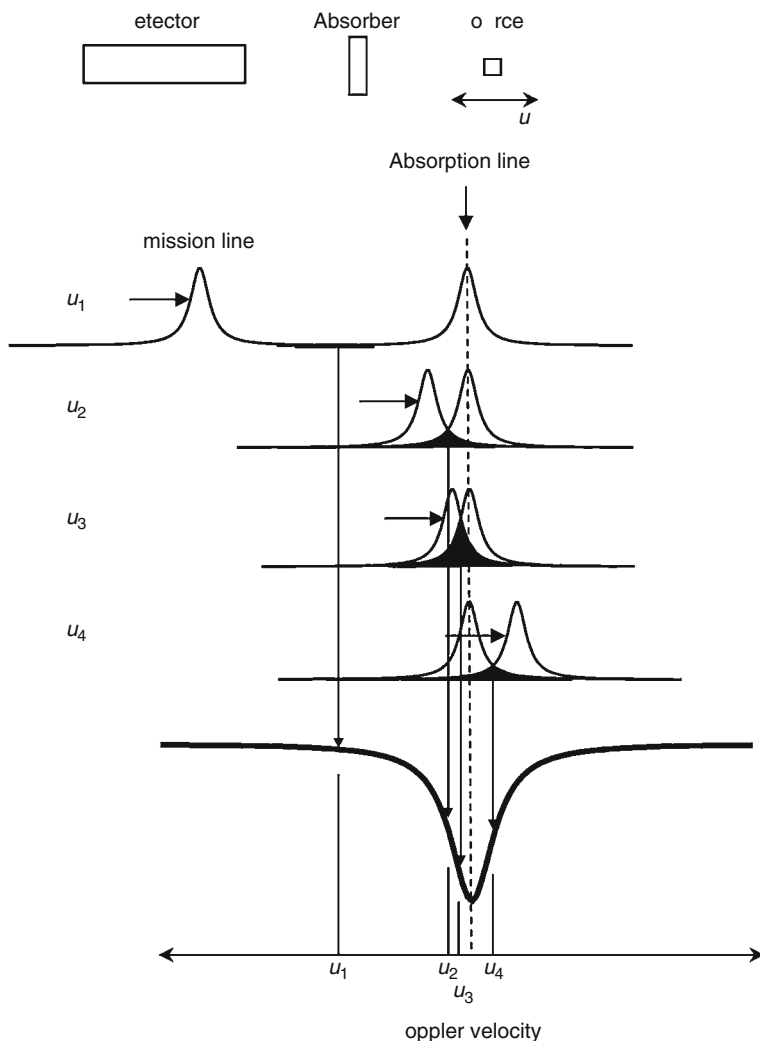
Let us emphasize here, however, that the Debye model had been developed for a monatomic cubic lattice, and thus the quantitative results applied to an arbitrary lattice must be taken with more than a grain of suspicion.

25.1.4 The Mössbauer Spectrum

► **Figure 25.5** shows the schematic arrangement of a typical transmission Mössbauer experiment. The assembly consists of a source, an absorber, and a detector.

■ Fig. 25.5

Schematic arrangement of a transmission type Mössbauer measurement. The scanning of the absorption line with the emission line using the Doppler principle is illustrated. The intensity of the resultant spectrum is proportional to the overlap of the emission and absorption lines (marked at four arbitrarily chosen velocities u_1 to u_4)



The *source* is a body containing the excited-state nuclei of a Mössbauer-active nuclide “frozen” in a solid matrix thus providing the conditions for recoilless γ emission.

The *absorber* is another body that contains the ground-state nuclei of the same Mössbauer-active nuclide also “frozen” in a solid matrix so satisfying the conditions for recoilless absorption.

The γ photons transmitted by the absorber are counted by the detector.

The resonance curve of the absorber (absorption line), however, cannot be measured at all by any existing detector, since it would require an energy resolution (Γ/E_0) of about 13–15 orders of magnitude. Therefore, the Mössbauer nuclei themselves are used to measure the resonance curve in the following way. If both the source and the absorber are at rest, and have the same chemical environment for the Mössbauer nuclei, then there is a maximum overlap of the emission and the absorption lines, and a certain intensity is observed by the detector. This ideal condition for the resonance absorption is destroyed by modifying the energy of the emission line according to the Doppler effect by moving the source with velocity u , relative to the absorber. This action results in a decreased overlap of the emission and absorption lines and therefore an increased count rate of the detector (see [Fig. 25.5](#)). A systematic energy modification of the emission line on the basis of the Doppler effect can be used to scan the absorption characteristics of the absorber very sensitively (with the required resolution). The count rate detected as a function of the Doppler velocity results in the Mössbauer spectrum.

The Mössbauer spectrum itself is usually presented as a plot of counts/percentage/fraction of transmission vs. channel/Doppler velocity.

The transmitted intensity vs. Doppler velocity (i.e., the transmission Mössbauer spectrum) will show a resonance “dip” around the Doppler velocity where the overlap is at its maximum (see [Fig. 25.6](#)).

In the *simplest* (thin-source, thin-absorber) *approximation*, a simple transmission Mössbauer spectrum ([Fig. 25.6](#)) consists of one single *Lorentzian peak* the half width of which corresponds to twice of the natural line width $\Gamma = \hbar \ln 2 / T_{1/2}$ (in energy unit). (The natural line width Γ is characteristic of both the recoilless emission in the source and the resonant absorption in the absorber. So doubling is actually the result of “adding up.”) The peak width $W_0 = 2c\Gamma/E_\gamma$ (in speed unit) thus obtained is an asymptotic minimum to which (normally) actual experimental peak widths are compared. For the $3/2 \rightarrow 1/2$ (see [Fig. 25.7](#)) transition of ^{57}Fe , e.g., $W_0 \approx 0.2$ mm/s is the minimum (or natural) peak width.

In the general case, the peak width will be broadened and the peak shape will be different from Lorentzian.

A general evaluation of the integrated absorption intensity is rather difficult, but a useful result can be obtained under the following conditions (Margulies and Ehrman 1961).

Let both the emission and absorption line be centered at E_0 and have the same natural line width $\Gamma_S = \Gamma_A = \Gamma$. The distribution of the ground-state Mössbauer atoms in question (e.g., ^{57}Fe) is taken to be uniform in both the source and the absorber. The distribution of the parent atoms (e.g., ^{57}Co) producing the excited Mössbauer atoms ([Fig. 25.7](#)) (and thus the γ photons) is described by the density function $\rho(x)$ along the x -axis (see [Fig. 25.6](#) for the notation). In the derivation of the peak shape of the Mössbauer spectrum, nonresonant and resonant absorption processes are to be considered in both the source and the absorber as illustrated schematically in [Fig. 25.6](#).

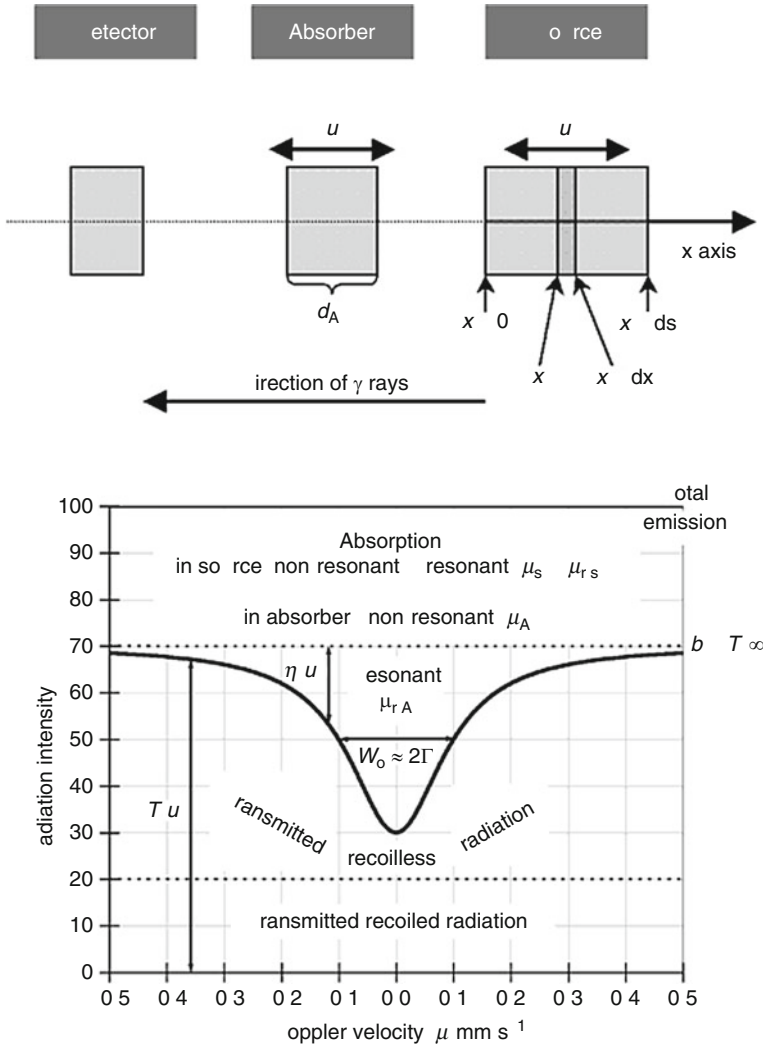
The γ radiation emitted by the excited Mössbauer nuclei will be attenuated by both “electronic” absorption/scattering (mainly due to photoelectric effect) and resonance absorption by ground-state nuclei.

Electronic absorption consumes both the recoiled $(1 - f_S)$ and the recoilless fraction (f_S) of photons. Their attenuation is described by the coefficients μ_S and μ_A for the source and the absorber, respectively. The electronic attenuation coefficients can be considered constant over the whole Doppler-velocity range.

Resonance absorption only concerns the recoilless fraction (f_S) of the radiation. According to [Eq. \(25.1\)](#), the energy distribution of this fraction can be given as

■ Fig. 25.6

Schematic transmission Mössbauer spectrum (*bottom*) with notations for the simplest arrangement (*top*). Either the source or the absorber is vibrated by a transducer. As usual, positive Doppler velocities (u) refer to approaching source and absorber



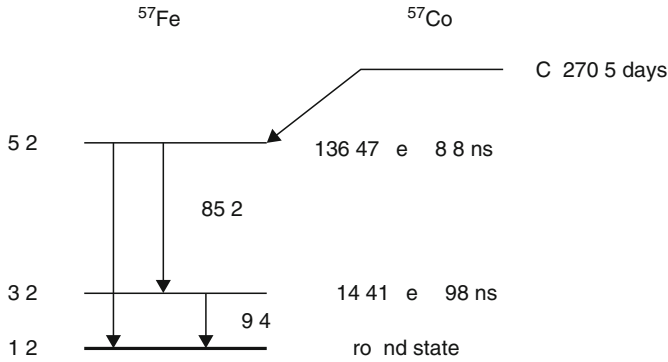
$$L(E) = f_s \frac{\Gamma}{2\pi} \frac{1}{(E - E_0)^2 + \left(\frac{\Gamma}{2}\right)^2}. \quad (25.27)$$

The attenuation coefficients $\mu_{r,s}$ and $\mu_{r,A}$ that characterize the resonance absorption of the recoilless radiation (in the source and in the absorber, respectively) are, however, energy dependent.

Using ➤ Eq. (25.10), for the case when the source is at rest and the absorber is moving with relative velocity u one can write

■ Fig. 25.7

Decay scheme of ^{57}Co to ^{57}Fe . The half-lives of γ transitions are indicated in parentheses



$$\mu_{r,S} = \frac{f_S n_S a_S \sigma_0 (\Gamma/2)^2}{(E - E_0)^2 + (\Gamma/2)^2}, \quad \mu_{r,A} = \frac{f_A n_A a_A \sigma_0 (\Gamma/2)^2}{[E - E_0(1 - u/c)]^2 + (\Gamma/2)^2} \quad (25.28)$$

where f_S and f_A are the Mössbauer–Lamb factors, n_S and n_A are the number densities (unit: number of atoms per volume) of the Mössbauer element (e.g., Fe), a_S and a_A are the fractional abundances of the Mössbauer isotope (e.g., ^{57}Fe in Fe), for the source and absorber, respectively, and σ_0 is the maximum of resonant absorption cross section given by ► Eq. (25.11).

Note that the negative sign before u/c in the second formula means that when the absorber approaches the source, the positive Doppler shift helps lower-energy γ photons to meet the condition of resonance absorption. As a result of this, the absorption line represented by the second formula is shifted to the left by the Doppler term.

The fraction of γ photons reaching the detector (considering only those photons that are emitted in the direction of the detector) can be given as

$$T(u) = \left\{ (1 - f_S) \left[\int_0^{d_S} \rho(x) \exp(-\mu_S x) dx \right] + f_S \left[\int_{-\infty}^{+\infty} \frac{\Gamma}{2\pi} \frac{1}{(E - E_0)^2 + (\Gamma/2)^2} \times \int_0^{d_S} \rho(x) \exp\left(-\frac{f_S n_S a_S \sigma_0 (\Gamma/2)^2}{(E - E_0)^2 + (\Gamma/2)^2} x - \mu_S x\right) dx \times \exp\left(-\frac{\tau_A (\Gamma/2)^2}{[E - E_0(1 - u/c)]^2 + (\Gamma/2)^2} dE \right) \right] \right\} \exp(-\mu_A d_A) \quad (25.29)$$

where d_A is the thickness, and τ_A is the *effective thickness* of the absorber:

$$\tau_A = f_A n_A a_A d_A \sigma_0. \quad (25.30)$$

The first term (line 1) in ► Eq. (25.29) represents the γ radiation emitted with recoil from the source (S) in which it is attenuated by nonresonant absorption via Compton or

photoelectric effect as it proceeds toward the absorber (A). This term is independent of the Doppler shift.

Line 2 contains the $C(E_0, \Gamma/2)$ Cauchy distribution of the γ photons emitted from the source without recoil.

Line 3 describes the resonant and nonresonant (self) absorption within the source for the recoilless γ photons emitted at different depths (x) of the source while they proceed toward the front of the source ($x = 0$) on their way to the absorber.

The first exponential in line 4 expresses the resonant absorption of the recoilless γ photons in the absorber that moves with velocity u toward the source. Finally, the factor $\exp(-\mu_A d_A)$ in the same line accounts for the nonresonant absorption/scattering in the absorber attenuating both the recoiled and the recoilless photons.

In the case of an infinitely thin source – when the radioactive parent forms a monatomic layer on the front of the source at $x = 0$, and therefore $\rho(x) = \delta(x)$, where δ is the Dirac “function” – lines 1 and 3 in [Eq. \(25.29\)](#) are equal to $(1 - f_s)$ and 1, respectively. Therefore, one obtains the following formula, generally called the *transmission integral*:

$$T(u) = \left\{ 1 - f_s + \int_{-\infty}^{+\infty} \frac{\frac{\Gamma f_s}{2\pi}}{(E - E_0)^2 + \left(\frac{\Gamma}{2}\right)^2} \exp\left(-\frac{\tau_A \left(\frac{\Gamma}{2}\right)^2}{[E - E_0(1 - \frac{u}{c})]^2 + \left(\frac{\Gamma}{2}\right)^2}\right) dE \right\} e^{-\mu_A d_A} \quad (25.31)$$

For very large Doppler speeds, there is no resonance absorption at all (note that the exponential part of the integrand is 1 at the limit $|u| \rightarrow \infty$), and therefore, the baseline b can be expressed as

$$b = T(\infty) = e^{-\mu_A d_A}. \quad (25.32)$$

The contour of the transmission peak (see [Fig. 25.6](#)) can be easily determined from the above equations:

$$\eta(u) = \frac{b - T(u)}{b} = f_s \left\{ 1 - \int_{-\infty}^{+\infty} \frac{\frac{\Gamma}{2\pi}}{(E - E_0)^2 + \left(\frac{\Gamma}{2}\right)^2} \exp\left(-\frac{\tau_A \left(\frac{\Gamma}{2}\right)^2}{[E - E_0(1 - \frac{u}{c})]^2 + \left(\frac{\Gamma}{2}\right)^2}\right) dE \right\} \quad (25.33)$$

If the effective thickness of the absorber is very small (i.e., $\tau_A \rightarrow 0$), then the exponential in the integrand of [Eq. \(25.33\)](#) can be replaced by the linear terms of its Taylor series.

As a result, the peak shape can be expressed by the following integral:

$$\eta(u) = f_s \tau_A \int_{-\infty}^{+\infty} \frac{\frac{\Gamma}{2\pi}}{(E - E_0)^2 + \left(\frac{\Gamma}{2}\right)^2} \times \frac{\left(\frac{\Gamma}{2}\right)^2}{[E - E_0(1 - \frac{u}{c})]^2 + \left(\frac{\Gamma}{2}\right)^2} dE. \quad (25.34)$$

Using the residuum theorem, the above formula yields

$$\eta(u) = \frac{f_s \tau_A}{2} \frac{\Gamma^2}{\left(\frac{E_0}{c} u\right)^2 + \Gamma^2} = \frac{f_s \tau_A}{2} \frac{\left(\frac{W_0}{2}\right)^2}{u^2 + \left(\frac{W_0}{2}\right)^2}. \quad (25.35)$$

As it has turned out, the peak shape – in this thin-source, thin-absorber approximation – is indeed Lorentzian, and the FWHM of the peak (W_0), apart from the conversion factor between Doppler speed and energy, is twice the natural line width Γ .

$$W_0 = 2\Gamma \frac{c}{E_0}. \quad (25.36)$$

Note also that the height of the peak is proportional to the effective thickness and, consequently, (through the number density n_A) to the concentration of the Mössbauer species:

$$\eta(0) = \frac{f_S \tau_A}{2} = \frac{f_S f_A n_A a_A d_A \sigma_0}{2}. \quad (25.37)$$

In the general case, one observes a nonlinear formula for the peak height (Mössbauer and Wiedemann 1960):

$$\eta(0) = f_S \left[1 - \exp\left(-\frac{\tau_A}{2}\right) I_0\left(\frac{\tau_A}{2}\right) \right] \quad (25.38)$$

where I_0 is the 0th order modified Bessel function of the first kind (see, e.g., BESSEL 2010). The peak area can be obtained by the integration of [Eq. \(25.33\)](#):

$$A = \int_{-\infty}^{\infty} \eta(u) du = \pi \Gamma f_S \frac{\tau_A}{2} \exp\left(-\frac{\tau_A}{2}\right) \left[I_0\left(\frac{\tau_A}{2}\right) + I_1\left(\frac{\tau_A}{2}\right) \right] \quad (25.39)$$

where I_1 is the first-order modified Bessel function of the first kind.

In the case of a thin absorber ($\tau_A \rightarrow 0$), the Taylor expansion of the exponential and Bessel functions yields a proportional relationship between the peak area and the number of resonant atoms in the absorber:

$$A \approx \frac{\pi \Gamma f_S \tau_A}{2}. \quad (25.40)$$

The latter equation is fundamental in Mössbauer spectroscopy establishing its use as a tool of quantitative analysis.

25.1.5 Hyperfine Interactions

The interaction between the electrons and the nucleus causes a very small perturbation of the nuclear energy levels in comparison with the energy of the nuclear transition. Such interactions are called *hyperfine interactions*. The main hyperfine interactions are the following: electric monopole, electric quadrupole, and magnetic dipole interactions between the nucleus and the electrons (shell electrons, ligands, etc.). Such interactions can be sensitively monitored by Mössbauer spectroscopy. The measurement of hyperfine interactions is the key to the utilization of Mössbauer spectroscopy in a wide range of applications.

Hyperfine interactions shift and/or split the energy levels of the nucleus. The total Hamiltonian can be written as a sum of various contributions:

$$H = H_0 + H_C + H_Q + H_m, \quad (25.41)$$

where H_C , H_Q , and H_m refer to electric monopole (Coulomb) interaction, electric quadrupole interaction, and magnetic dipole interaction, respectively, and H_0 represents all other terms not considered here.

All of the hyperfine interactions may occur together, but only the magnetic and quadrupole interactions are directional thus having a complicated interrelationship.

25.1.5.1 Electric Monopole Interaction

The electric monopole interaction is part of the full electric Coulomb interaction occurring between the nucleus and the surrounding charges. Because of this interaction, the energy levels of the nucleus become shifted. The corresponding energy shift of the ground-state nuclear level may differ from that of the excited state level when the finite size of the nucleus is taken into consideration. (If the nucleus were a point charge, the Coulomb shift due to electrons would be the same for its ground state and its excited state.) Consequently, the electric monopole interaction leads to a change in the energy of the emitted γ ray compared to the case of a bare nucleus that is without any surrounding electric charge (Dunlap and Kalvius 1978).

The full *Coulomb interaction* between the nuclear charge distribution $\rho_N(r_N)$ and the electronic charge distribution $-\rho_e(r_e)$ is given by

$$U = -e^2 \iint \frac{\rho_e(r_e)\rho_N(r_N)}{|r_e - r_N|} dV_e dV_N \quad (25.42)$$

where r_e and r_N are location vectors, and dV_e and dV_N are the volume elements containing the points determined by r_e and r_N , respectively.

The above equation can be rewritten by using the following multipole expansion (Clauser and Mössbauer 1969):

$$\frac{1}{|r_e - r_N|} = \sum_{l=0}^{\infty} \sum_{m=-l}^{+l} \frac{2\pi}{2l+1} \left(\frac{r_{<}^l}{r_{>}^{l+1}} \right) Y_{lm}^*(\theta_N, \phi_N) Y_{lm}(\theta_e, \phi_e) \quad (25.43)$$

where Y_{lm} are the normalized spherical harmonics, $r_{<}$ and $r_{>}$ are the smaller and the larger of $|r_e|$ and $|r_N|$, respectively.

The full Coulomb interaction energy term can be expressed by combining [Eqs. \(25.42\)](#) and [\(25.43\)](#) as the sum of a number of terms with multipole order l . The term for $l=0$ is the electric monopole term. The $l=2$ term gives rise to electric quadrupole interactions and will be discussed later. (All the odd l terms vanish for reasons of symmetry. The very small even terms for $l>2$ can also be ignored.)

For $l=0$, the energy of the interaction is

$$U_0 = -e^2 \iint \frac{\rho_e(r_e)\rho_N(r_N)}{r_{>}} dV_e dV_N. \quad (25.44)$$

In Mössbauer spectroscopy, the only thing that matters is not the energy shift of an individual level, but the energy-shift difference between the ground-state and excited-state levels. Let us consider the energy shifts of the nuclear levels due to the electric monopole interaction and the energy of the γ ray emitted from the source and absorbed by the absorber ([Fig. 25.8](#)).

If the nuclei did not experience any hyperfine interaction, they would have the same energy levels in both the source and the absorber ($E^{S*} = E^{A*}$, $E^S = E^A$, and thus $E^{S*} - E^S = E^{A*} - E^A = E_0$, see [Fig. 25.8](#) for notations). With a finite size nucleus the Coulomb term, U_0 , can be different for the excited state ($U_{0,S}^*$) and the ground state ($U_{0,S}$) in the source, and also for the excited state ($U_{0,A}^*$) and the ground state ($U_{0,A}$) in the absorber.

The energy of the γ ray emitted from the source will be

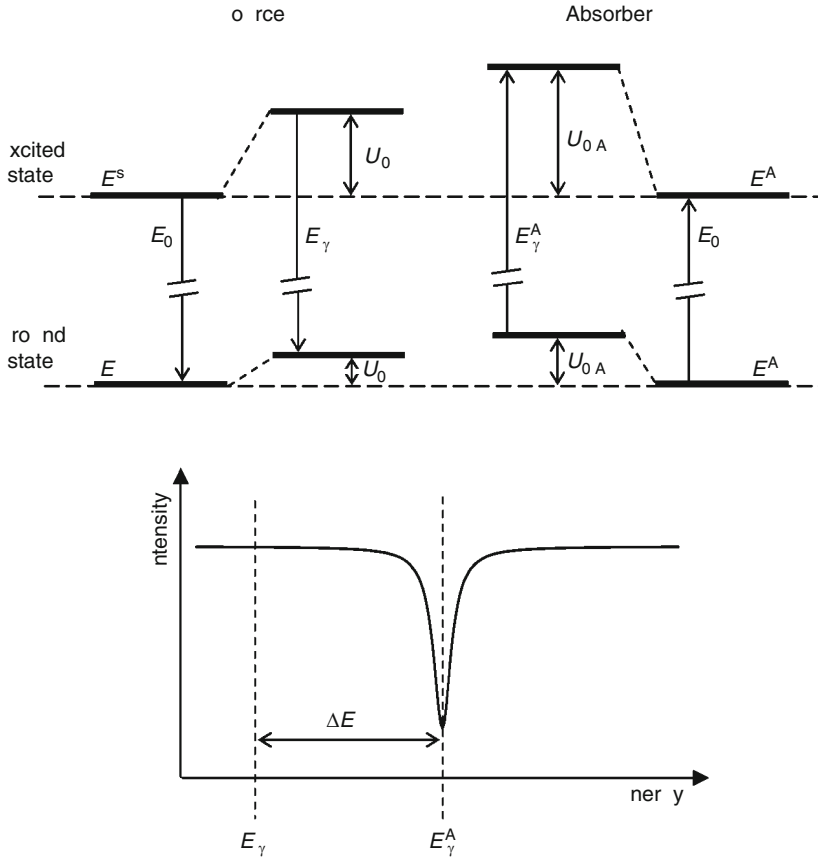
$$E_{\gamma}^S = (E^{S*} - E^S) + (U_{0,S}^* - U_{0,S}) = E_0 + \Delta E_C^S \quad (25.45)$$

where the notation $\Delta E_C^S = (U_{0,S}^* - U_{0,S})$ has been introduced.

■ Fig. 25.8

The shifts of nuclear energy levels in the source and the absorber due to the electric monopole interaction between the nucleus and the electrons, and the resulted Mössbauer spectrum.

According to ► Eq. (25.80), the chemical isomer shift δ_c is proportional to the energy shift ΔE_{IS}



The energy of the γ ray, which can be absorbed by the absorber will be

$$E_\gamma^A = (E^{A*} - E^A) + (U_{0,A}^* - U_{0,A}) = E_0 + \Delta E_C^A \quad (25.46)$$

with the notation $\Delta E_C^A = (U_{0,A}^* - U_{0,A})$.

The energy difference

$$\Delta E_{IS} = E_\gamma^A - E_\gamma^S = \Delta E_C^A - \Delta E_C^S = (U_{0,A}^* - U_{0,A}) - (U_{0,S}^* - U_{0,S}) \quad (25.47)$$

is the missing (or excess) energy of the γ quantum emitted by the source that needs to be compensated in the Mössbauer experiment in order to achieve maximum resonance absorption, i.e., maximum overlap between the emission and absorption lines (► Fig. 25.5). In the corresponding Mössbauer spectrum, the need for this compensation of energy appears as a line shift (see ► Fig. 25.8) that is called the *chemical isomer shift*.

By substituting the Coulomb shifts $U_{0,A}^*$, $U_{0,A}$, $U_{0,S}^*$, and $U_{0,S}$ in [Eq. \(25.47\)](#) with corresponding expressions according to [Eq. \(25.44\)](#) one obtains

$$\Delta E_{\text{IS}} = -e^2 \iint \frac{\rho_{e,A}^*(r_e) \rho_{N,A}^*(r_N) - \rho_{e,A}(r_e) \rho_{N,A}(r_N) - \rho_{e,S}^*(r_e) \rho_{N,S}^*(r_N) + \rho_{e,S}(r_e) \rho_{N,S}(r_N)}{r_{>}} dV_e dV_N \quad (25.48)$$

where the asterisk (*) refers to the excited state of the nucleus in the source (s) and in the absorber (a).

In order to get a simpler expression for the chemical isomer shift, it will be assumed that the electronic charge density around the nucleus is the same whether or not the nucleus is excited:

$$\rho_{e,S}^*(r_e) = \rho_{e,S}(r_e); \rho_{e,A}^*(r_e) = \rho_{e,A}(r_e). \quad (25.49)$$

It is plausible to assume that for a given energy state of the nucleus the nuclear charge density is the same in the source and in the absorber:

$$\rho_{N,S}^*(r_N) = \rho_{N,A}^*(r_N) \equiv \rho_N^*(r_N); \rho_{N,S}(r_N) = \rho_{N,A}(r_N) \equiv \rho_N(r_N). \quad (25.50)$$

Introducing spherically averaged electronic densities

$$\bar{\rho}_e(r_e) = \frac{1}{4\pi} \iint \rho_e(r_e) \sin \theta d\theta d\phi, \quad (25.51)$$

and assuming that the nuclear charge distribution is spherically symmetric one obtains

$$\Delta E_{\text{IS}} = -4\pi e^2 \int_0^\infty (\rho_N^*(r_N) - \rho_N(r_N)) I(r_N) dr_N. \quad (25.52)$$

with

$$I(r_N) = \int_0^{r_N} (\bar{\rho}_{e,A}(r_e) - \bar{\rho}_{e,S}(r_e)) \left(\frac{1}{r_N} - \frac{1}{r_e} \right) r_e^2 dr_e. \quad (25.53)$$

Thus, ΔE_{IS} will depend on the assumptions made for the radial dependence of the average electronic densities in the source and in the absorber within the nuclear volume.

In light atoms (for which $Z \ll 137 \approx 1/\alpha$, where α is the fine-structure constant) relativistic effects are negligible. In such a case, only s electrons (having spherically symmetric distribution) have nonvanishing charge density at the place of the nucleus. Considering also the small size of the nucleus, the electronic density can be taken to be approximately constant over the nuclear volume, and therefore:

$$\bar{\rho}_e(r_e) = \rho_e(r_e) = \rho_e(0) \equiv |\psi(0)|^2 \quad (25.54)$$

where $\psi(0)$ is the nonrelativistic many-electron wave function at the place of the nucleus. Thus, carrying out the integration in [Eq. \(25.53\)](#) one obtains

$$I(r_N) = -\frac{1}{6} r_N^2 |\psi(0)|^2. \quad (25.55)$$

Substituting this result into [Eq. \(25.52\)](#), for the chemical isomer shift one obtains the expression

$$\Delta E_{\text{IS}} = \frac{2\pi e^2}{3} \Delta |\psi(0)|^2 \int_0^\infty \Delta \rho_N(r_N) r_N^2 dr_N = \frac{2\pi Z e^2}{3} \Delta |\psi(0)|^2 \Delta \langle r_N^2 \rangle. \quad (25.56)$$

Note that on the right-hand side of the equation, the *first* Δ (related to the atomic electrons through Ψ) refers to the *difference between absorber and source*, while the *second* Δ (related to the nucleus through r_N) refers to the *difference between the nuclear states*.

In [Eq. \(25.56\)](#) the following expression was used for the *mth* momentum of the nuclear charge distribution:

$$\langle r^m \rangle = \frac{\int r_N^m \rho_N(r_N) dV_N}{\int \rho_N(r_N) dV_N} = \frac{1}{Z} \int r_N^m \rho_N(r_N) dV_N. \quad (25.57)$$

According to [Eq. \(25.56\)](#), one obtains that the energy shift due to electric monopole interaction is proportional to the product of the s electronic density and the second moment of the nuclear charge distribution also called the *mean square nuclear charge radius* (see also [Sect. 2.2.3.1 in Chap. 2, Vol. 1](#)). When the nucleus is considered to be a homogeneously charged sphere with a radius R (often called charge equivalent nuclear radius), then

$$\rho_N(r_N) = \frac{3Z}{4\pi R^3} \quad (25.58)$$

and therefore

$$\langle r_N^2 \rangle = \frac{3}{5} R^2 \quad (25.59)$$

which yields the following expression for the chemical isomer shift:

$$\Delta E_{\text{IS}} = \frac{2\pi Z e^2}{5} \Delta |\psi(0)|^2 \Delta R^2. \quad (25.60)$$

By considering also relativistic effects, in addition to s electrons relativistic $p_{1/2}$ electrons will also turn out to have finite density at the place of the nucleus. Then, for a uniformly charged spherical nucleus of radius R , single-electron approximation gives the following radial density distribution $\rho_e(r)$:

$$\rho_e(r) = \rho_e(0) \left[1 - \frac{\alpha^2 Z^2}{2} \left(\frac{r}{R} \right)^2 + \frac{\alpha^2 Z^2}{10} \left(1 + \frac{9\alpha^2 Z^2}{8} \right) \left(\frac{r}{R} \right)^4 + \dots \right]. \quad (25.61)$$

Hence, the energy corresponding to the chemical isomer shift can be written as

$$\Delta E_{\text{IS}} = \frac{2\pi}{5} Z e^2 S'(Z) \Delta R^2 \Delta |\psi(0)|^2, \quad (25.62)$$

where the numerical factor $S'(Z)$, the so-called *Shirley factor*, corrects the nonrelativistic electron density for relativistic effects. Its value is 1.29 for ^{57}Fe , 2.31 for ^{119}Sn , and 13.6 for ^{237}Np (Shirley 1964).

In the case of a relativistic multi-electron system, further considerations are necessary. The total electron density can be written as

$$\rho_e(r) = \rho_e(0) [1 - a_2 r^2 + a_4 r^4 - \dots] \quad (25.63)$$

which will introduce higher moments of the nuclear charge distribution into the expression of the energy corresponding to the chemical isomer shift:

$$\Delta E_{\text{IS}} = \frac{2\pi}{3} Z e^2 \Delta \rho_e(0) [\Delta \langle r^2 \rangle - b_4 \Delta \langle r^4 \rangle + b_6 \Delta \langle r^6 \rangle - \dots]. \quad (25.64)$$

25.1.5.2 Electric Quadrupole Interaction

A nucleus with nonzero nuclear quadrupole moment is subject to electric quadrupole interaction if it is experiencing an inhomogeneous electric field. The latter is characterized by the electric field gradient (EFG) tensor defined by $\nabla \circ \mathbf{E} = -\nabla \circ \nabla V$, where “ \circ ” indicates dyadic product (the matrix product of a column vector and a row vector resulting in a square matrix). The V_{ij} element of the EFG tensor is given by

$$V_{ij} = -\frac{\partial^2 V}{\partial x_i \partial x_j}(x_i, x_j = x, y, z) \quad (25.65)$$

where V is the electrostatic potential. (Note that from this point on only those charges are considered that are outside the volume of the nucleus.) The EFG tensor can be transformed into its *principal axis system* (PAS) where it is represented by a diagonal matrix with components V_{xx} , V_{yy} , and V_{zz} . One can show that electric charge distributions with spherical symmetry around the nucleus (like s electrons) do not contribute to the electric quadrupole interaction. According to the Laplace equation $\nabla^2 V = V_{xx} + V_{yy} + V_{zz} = 0$ outside the sources of the electric field. Therefore, the EFG at the place of the nucleus is traceless and two independent parameters are enough to specify it completely. The two parameters used in practice are the principal component V_{zz} and the asymmetry parameter η defined as

$$\eta = \frac{V_{xx} - V_{yy}}{V_{zz}}. \quad (25.66)$$

By convention the PAS is chosen such that $|V_{xx}| \leq |V_{yy}| \leq |V_{zz}|$ is satisfied, which ensures $0 \leq \eta \leq 1$.

In operator form, the nuclear quadrupole moment is given by

$$Q_{ik} = \frac{3Q}{2I(2I-1)} \left[I_i I_k + I_k I_i - \frac{2}{3} I^2 \delta_{ik} \right] \quad (25.67)$$

where \mathbf{I} is the nuclear spin operator and δ_{ik} is the *Kronecker delta*. The energy term for the quadrupole interaction, $\frac{e}{6} \sum_{i,k} V_{ik} Q_{ik}$, can be derived by expanding the electrostatic potential into a series at the center of the nucleus (see, e.g., Gütlich et al. 1978). The Hamiltonian for the quadrupole interaction turns out to be

$$\begin{aligned} H_Q &= \frac{e}{6} \sum_i V_{ii} Q_{ii} = \frac{eQ}{2I(2I-1)} \left[V_{xx} I_x^2 + V_{yy} I_y^2 + V_{zz} I_z^2 \right] \\ &= \frac{eQV_{zz}}{4I(2I-1)} \left[3I_z^2 - I^2 + \eta(I_x^2 - I_y^2) \right] \\ &= \frac{eQV_{zz}}{4I(2I-1)} \left[3m_I^2 - I(I+1) + \frac{\eta}{2}(I_+^2 + I_-^2) \right] \end{aligned} \quad (25.68)$$

where \mathbf{I} , \mathbf{I}_x , \mathbf{I}_y , \mathbf{I}_z , $\mathbf{I}_+ = \mathbf{I}_x + i\mathbf{I}_y$ and $\mathbf{I}_- = \mathbf{I}_x - i\mathbf{I}_y$ are the nuclear spin operators ($i^2 = -1$), I and m_I are the quantum numbers belonging to the nuclear spin and its z component, respectively. (The quantity m_I is also called the *magnetic quantum number*.)

In the presence of the quadrupole interaction, represented by the Hamiltonian in [Eq. \(25.68\)](#), the eigenstates of the nucleus will in general be a linear combination of the original orthogonal set of $|I, m_I\rangle$ nuclear states. As H_Q depends on $|m_I|$, the degeneration of

the energy levels of the nuclear states $|I, -I\rangle, |I, -I + 1\rangle, \dots, |I, I - 1\rangle, |I, I\rangle$ is partly removed by the quadrupole interaction. To find the perturbation of the energy levels of the excited (nuclear spin: I_e) and the ground (nuclear spin: I_g) nuclear states, one has to apply the first-order perturbation theory of degenerate states (see, e.g., Raimes 1961 or textbooks on quantum mechanics). In accordance with this theory, the eigenvalues of the matrices $\langle I_e, m_i | H_Q | I_e, m_j \rangle (m_i, m_j = -I_e \dots I_e)$ and $\langle I_g, m_i | H_Q | I_g, m_j \rangle (m_i, m_j = -I_g \dots I_g)$ will provide the energy perturbations of the individual sublevels of the excited state and the ground state, respectively.

As a simple but important example, the energy perturbations of the $I_e = 3/2$ excited state of ^{57}Fe (► Fig. 25.9) experiencing quadrupole interaction are calculated below.

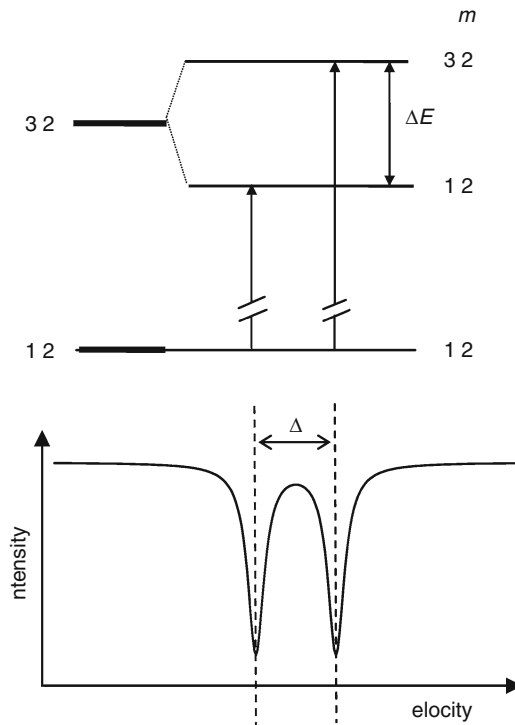
For the calculation of the matrix $\langle 3/2, m_i | H_Q | 3/2, m_j \rangle$ one has to take into account the effect of the I_+ and I_- operators (see ► Eq. (25.68)) on a $|I, m\rangle$ nuclear state:

$$I_+ |I, m\rangle = \sqrt{I(I+1) - m(m+1)} |I, m+1\rangle, \quad (25.69)$$

$$I_- |I, m\rangle = \sqrt{I(I+1) - m(m-1)} |I, m-1\rangle. \quad (25.70)$$

■ Fig. 25.9

Quadrupole splitting of the $I = 3/2$ nuclear level and the resulted Mössbauer spectrum. According to ► Eq. (25.91), Δ is proportional to ΔE_Q



The matrix $\langle 3/2, m_i | H_Q | 3/2, m_j \rangle (m_i, m_j = -3/2 \dots 3/2)$ will then be equal to

$$\left\langle \frac{3}{2}, m_i \left| H_Q \right| \frac{3}{2}, m_j \right\rangle = \frac{eQV_{zz}}{12} \begin{pmatrix} 3 & 0 & \sqrt{3}\eta & 0 \\ 0 & -3 & 0 & \sqrt{3}\eta \\ \sqrt{3}\eta & 0 & -3 & 0 \\ 0 & \sqrt{3}\eta & 0 & 3 \end{pmatrix} \quad (25.71)$$

where increasing row (i) and column (j) numbers correspond to increasing m_i and m_j values, respectively. It can be shown that this matrix has only two different eigenvalues:

$$\lambda_+ = \frac{eQV_{zz}}{4} \sqrt{1 + \frac{\eta^2}{3}} \text{ and } \lambda_- = -\frac{eQV_{zz}}{4} \sqrt{1 + \frac{\eta^2}{3}}. \quad (25.72)$$

Thus, due to the quadrupole interaction, the $I_e = 3/2$ excited state of ^{57}Fe splits giving rise to two sublevels of different energy.

If the EFG tensor has axial symmetry ($\eta = 0$), then the eigenstates $|I_e, m_e\rangle$ of H_0 (see [Eq. \(25.41\)](#)) will also be eigenstates of H_Q , and the $I_e = 3/2$ state will split in two energy sublevels with $\lambda_+ = +eQV_{zz}/4$ and $\lambda_- = -eQV_{zz}/4$ for $m_e = \pm 3/2$ and $m_e = \pm 1/2$, respectively (see [Fig. 25.9](#), where $\Delta E_Q = |\lambda_+ - \lambda_-|$).

At the same time, the ground state of ^{57}Fe has a nuclear spin characterized by $I_g = 1/2$ for which the quadrupole moment $Q = 0$ (see [Sect. 2.2.2.2 in Chap. 2, Vol. 1](#) as well as [Sect. 36.1 of the Appendix of this volume](#)) and therefore the energy of its $m_g = \pm 1/2$ sublevels is not changed by a perturbation of the form described by [Eq. \(25.68\)](#).

For $\eta = 0$, the perturbation of the energy level of a nucleus in the quantum state $|I, m_I\rangle$ can also be given simply by (cf. [Eq. \(25.68\)](#))

$$E_Q = \frac{eQV_{zz}}{4I(2I-1)} [3m_I^2 - I(I+1)]. \quad (25.73)$$

25.1.5.3 Magnetic Dipole Interaction

The nucleus can interact with a magnetic field via its magnetic moment (see [Sect. 2.2.2.3 in Chap. 2, Vol. 1](#)). A magnetic flux density, \mathbf{B} , at the place of the nucleus may be produced by electrons as well as it may be the result of an externally applied magnetic field. The *magnetic hyperfine interaction* can be described by the Hamiltonian

$$H_m = -\boldsymbol{\mu} \mathbf{B} = -g_I \mu_N I_z B \quad (25.74)$$

where $\boldsymbol{\mu}$ is the magnetic moment of the nucleus, μ_N is the nuclear magneton ($eh/4\pi m_p = 5.04929 \times 10^{-27} \text{ Am}^2$), and g_I is the nuclear giromagnetic factor ($g_I = \mu/(\mu_N I)$) of the nuclear state having a nuclear spin I .

In the presence of magnetic hyperfine interaction, the perturbation of energy levels in the excited and in the ground state of the nucleus can be found similarly to the case of the electric quadrupole interaction (see [Sect. 25.1.5.2](#)). The case of ^{57}Fe is considered below.

For the $I = 1/2$ ground state of ^{57}Fe the matrix $\langle 1/2, m_i | H_m | 1/2, m_j \rangle (m_i, m_j = -1/2, 1/2)$ has the form

$$\left\langle \frac{1}{2}, m_i \left| H_m \right| \frac{1}{2}, m_j \right\rangle = -g_{1/2} \mu_N B \begin{pmatrix} -\frac{1}{2} & 0 \\ 0 & \frac{1}{2} \end{pmatrix}. \quad (25.75)$$

And for the excited state ($I = 3/2$) one obtains ($m_i, m_j = -3/2, -1/2, 1/2, 3/2$)

$$\left\langle \frac{3}{2}, m_i \left| H_m \right| \frac{3}{2}, m_j \right\rangle = -g_{3/2} \mu_N B \begin{pmatrix} -\frac{3}{2} & 0 & 0 & 0 \\ 0 & -\frac{1}{2} & 0 & 0 \\ 0 & 0 & \frac{1}{2} & 0 \\ 0 & 0 & 0 & \frac{3}{2} \end{pmatrix}. \quad (25.76)$$

As both matrices are diagonal, it is clear that the original orthogonal $|I, m_I\rangle$ states are eigenstates of H_m and consequently they are also eigenstates of $H_0 + H_m$ (see [Eq. \(25.41\)](#)). The eigenvalues of the diagonal matrices are simply the elements in the diagonal.

For a nuclear state $|I, m_I\rangle$ the energy perturbation due to magnetic hyperfine interaction is thus given by

$$E_m = -g_I \mu_N B m_I \quad (25.77)$$

where m_I is the magnetic quantum number ($m_I = I, I - 1, \dots, -I$).

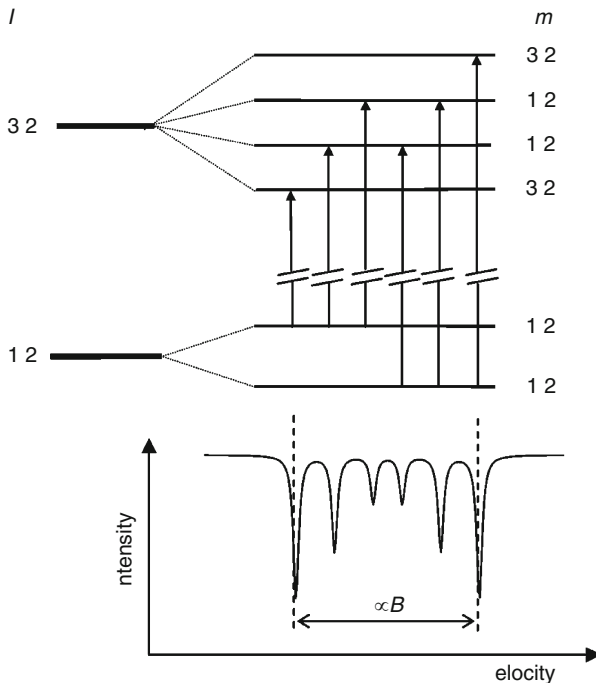
As shown also by [Fig. 25.10](#), the magnetic field splits the nuclear level of spin I into $2I + 1$ equidistantly spaced non-degenerate sublevels with a separation of $g_I \mu_N B$ (*nuclear Zeeman effect*).

25.1.5.4 Combined Interactions

In the general case of combined electric quadrupole and magnetic dipole interactions the peak positions can only be calculated numerically.

Fig. 25.10

Magnetic splitting of the $I = 3/2$ and $I = 1/2$ nuclear levels (of ^{57}Fe) and the corresponding Mössbauer spectrum. The internal magnetic field (induction, B) is proportional to the distance between any two lines of the sextet; the largest such separation is marked



If $|eQV_{zz}| \ll |\mu B|$ first-order perturbation theory may be applied. Let ϑ denote the angle between the z -axis and \mathbf{B} . If the EFG has axial symmetry, the eigenvalue of the Hamiltonian of the combined interaction is given by

$$E_{m_Q} = -g\mu_N B m_I + (-1)^{|m_I|+1/2} \frac{eQV_{zz}}{4} \frac{3\cos^2\vartheta - 1}{2}. \quad (25.78)$$

For more complex cases see Matthias et al. (1963).

25.1.5.5 Microenvironment

The term “microenvironment” is of fundamental importance in Mössbauer spectroscopy. It is directly related to the hyperfine interactions sensed by the nucleus. In a solid studied by Mössbauer spectroscopy, there are a large number of nuclei of the Mössbauer isotope. They all sense local hyperfine interactions, which are determined by the product of a nuclear parameter (charge equivalent nuclear radius, R , nuclear quadrupole moment, Q , and nuclear magnetic moment, μ) and a solid-state parameter (electronic density, ρ , electric field gradient represented by V_{zz} and η , and magnetic flux density, \mathbf{B}) (see [Eqs. \(25.60\)](#), [\(25.68\)](#), and [\(25.74\)](#)).

Normally, the nuclear parameters are the same for all nuclei embedded in a species. However, the solid-state parameters vary from phase to phase in a multiphase species, or may vary within the phase from site to site where the environment of the Mössbauer atom is different. Consequently, there may be assemblies of nuclei sensing different hyperfine interactions in a solid, in general. The microenvironment is a convenient term for the classification of local environments surrounding the Mössbauer atoms. The local environments of two Mössbauer atoms represent the same microenvironment if those atoms experience the same hyperfine interactions there. The correspondence between the microenvironment and hyperfine interactions gives a basis for the analytical use of Mössbauer spectroscopy (see [Sect. 25.3](#)).

25.2 Mössbauer Parameters

25.2.1 Isomer Shift

The isomer shift, denoted by δ , is the most often quoted Mössbauer parameter. It is a peak shift that consists of two terms:

$$\delta = \delta_c + \delta_{\text{SOD}} \quad (25.79)$$

where the first term is the chemical isomer shift δ_c (already mentioned in [Sect. 25.1.5.1](#)) and the second term is the second-order Doppler shift (also called temperature shift). The isomer shift, δ , is measured in velocity units for which the suggested decimal submultiple SI unit is mm/s.

25.2.1.1 Chemical Isomer Shift

The chemical isomer shift, δ_c (measured as Doppler velocity in mm/s units), is related to the electric monopole hyperfine interaction between the nucleus and the electrons. The nuclear energy levels will be shifted as a result of this interaction (see [Fig. 25.8](#), [Sect. 25.1.5.1](#)).

To measure this energy shift in the Mössbauer experiment one should modify the energy of the emitted γ ray by moving the source relative to the absorber by an appropriate Doppler velocity in order to bring the energy of the emitted γ ray into coincidence with the absorption energy in the absorber, when one actually measures the chemical isomer shift.

With the notation introduced in [▶ Sect. 25.1.5.1](#), δ_c can be defined as the Doppler velocity corresponding to the energy shift ΔE_{IS} (see [▶ Eq. \(25.60\)](#)):

$$\delta_c = \frac{c}{E_0} \Delta E_{IS}. \quad (25.80)$$

The name *chemical* isomer shift is related to the fact that the electron density at the place of the nucleus is strongly influenced by the valence state and the chemical bonding of the Mössbauer atom.

The expressions for the chemical isomer shift can be derived by substituting ΔE_{IS} (see [▶ Eqs. \(25.60\)](#), [▶ \(25.62\)](#), and [▶ \(25.64\)](#)) into the formula of δ_c ([▶ 25.80](#)).

All expressions presently used for evaluation of isomer shifts neglect the polarization effects (see [▶ Eqs. \(25.49\)](#) and [▶ \(25.50\)](#)). This introduces an error less than 5%.

By treating the electron density relativistically, the isomer shift can be given by combining [▶ Eqs. \(25.64\)](#) and [▶ \(25.80\)](#) to give

$$\delta_c = C \Delta \rho_e(0) [\Delta \langle r^2 \rangle - b_4 \Delta \langle r^4 \rangle + b_6 \Delta \langle r^6 \rangle] \quad (25.81)$$

where $C = (2/3)\pi Ze^2 c/E_0$, $\Delta \rho_e(0) = \rho_e^A(0) - \rho_e^S(0)$, $\Delta \langle r^m \rangle = \langle r^m \rangle_e - \langle r^m \rangle_g$, and b_4 and b_6 are constants that depend on Z .

In most cases, the terms with order higher than $m = 2$ can be neglected. In this way, one obtains the expression for the chemical isomer shift, which is recommended for general use

$$\delta_c = C \Delta \rho_e(0) \Delta \langle r^2 \rangle \quad (25.82)$$

where with the choice $C = 90.42Z/(E_0/\text{keV})$ and measuring $\Delta \langle r^2 \rangle$ in fm^2 and $\Delta \rho(0)$ in 10^{26} cm^{-3} units, δ_c is obtained in units of mm/s .

The error of using this formula instead of the previous one ([▶ Eq. \(25.81\)](#)) is about 1% to 10%. (The error increases with the mass of the atom.)

By introducing the charge equivalent radius R (see [▶ Eq. \(25.59\)](#)) and by expressing the nuclear parameter as the relative change of this radius one obtains

$$\delta_c = C \Delta \rho_e(0) \frac{\Delta R}{R} \quad (25.83)$$

with $C = (4/5)\pi Ze^2 c(1.2A^{1/3})^2/E_0 = 156.24ZA^{2/3}/E_0$.

The additional error is of the order of a few percentage. This expression has found the most widespread application in the solid state and chemical literature.

If only nonrelativistic electron densities are available a correction by a multiplication factor $S'(Z)$ has to be applied ([▶ Eq. \(25.62\)](#)) and the expression for the chemical isomer shift will be

$$\delta_c = C \Delta |\psi(0)|^2 S'(Z) \frac{\Delta R}{R} \quad (25.84)$$

where $|\psi(0)|^2$ denotes the nonrelativistic s electron density at the place of the nucleus. This is the most commonly used formula of the chemical isomer shift for applications in chemistry.

In the case of ^{57}Fe and ^{119}Sn (which are the most frequently used Mössbauer nuclides), the evaluation of the chemical isomer shift is often performed by using a so-called isomer shift

calibration constant, α or α' , especially in the chemical literature. With the help of these calibration constants, the following expressions can be obtained for the chemical isomer shift:

$$\delta_c = \alpha' \Delta\rho(0) \text{ and } \delta_c = \alpha \Delta|\psi(0)|^2. \quad (25.85)$$

In most chemical applications of Mössbauer spectroscopy, [Eq. \(25.84\)](#) is used. Consequently, from the chemical isomer shift, the charge equivalent nuclear radius (R) and the electron density can be determined. Any of the two can be obtained from a Mössbauer measurement if the other one is determined independently. In most chemical applications, the goal is the determination of the shift in electron density.

In practice, the chemical isomer shift is usually given relative to a standard reference material. In ^{57}Fe Mössbauer spectroscopy, $\alpha\text{-Fe}$ has become the most commonly used standard reference material.

25.2.1.2 Second-Order Doppler Shift

The second-order Doppler shift, δ_{SOD} , which is often called *temperature shift*, is a peak shift related to the relativistic Doppler effect originating from the thermal motion of the nuclei. If the Mössbauer atom has a speed u , and moves in a direction making angle α with the direction of the γ ray it emits, then the ν frequency of the emitted γ ray will differ from the ν_0 frequency it had if the atom had been at rest. The ν frequency is related to ν_0 in the following way:

$$\nu = \nu_0 \frac{\sqrt{1 - \frac{u^2}{c^2}}}{1 - \frac{u}{c} \cos \alpha}. \quad (25.86)$$

As atoms in a solid perform an oscillatory motion with a period in the order of around 10^{-13} s, during the lifetime of the excited state of the Mössbauer nucleus (for the case of ^{57}Fe , e.g., $\tau \approx 10^{-7}$ s) the corresponding atom goes through approximately a million of cycles. As a result, only the time-average of the relativistic Doppler effect can be detected in the Mössbauer spectra. Taking into account that $u \ll c$, time averaging the right-hand side of [Eq. \(25.86\)](#) yields the following equation for the mean frequency of the emitted γ photon (Pound and Rebka 1960):

$$\nu \approx \nu_0 \left(1 - \frac{1}{2} \frac{\langle u^2 \rangle}{c^2} \right), \quad (25.87)$$

i.e., the Doppler effect arising because of the oscillatory motion of atoms in a solid influences the frequency of the emitted γ ray only in the second order of the speed of the atoms.

The corresponding energy shift of the γ ray can be calculated as

$$\Delta E_{\text{SOD}} = h(\nu - \nu_0) = -\frac{h\nu_0}{2} \frac{\langle u^2 \rangle}{c^2} = -\frac{1}{2} \frac{\langle u^2 \rangle}{c^2} E_\gamma \quad (25.88)$$

In the Mössbauer spectrum, the *second-order Doppler shift* is measured as a peak shift in velocity units:

$$\delta_{\text{SOD}} = -\frac{1}{2} \frac{\langle u^2 \rangle}{c}. \quad (25.89)$$

From [Eq. \(25.23\)](#) it follows that δ_{SOD} decreases with increasing temperature.

25.2.2 Quadrupole Splitting

The quadrupole splitting, Δ , is the Mössbauer parameter, which is related to the electric quadrupole hyperfine interaction between the nucleus and the electrons (see [Sect. 25.1.5.2](#)).

In the case of ^{57}Fe and ^{119}Sn , e.g., where the Mössbauer transition occurs between nuclear levels with excited state spin $I_e = 3/2$ and ground state spin $I_g = 1/2$, in the presence of hyperfine quadrupole interaction, the excited state will be split into two sublevels (see [Eq. \(25.72\)](#) and [Fig. 25.9](#)). Resonance absorption can occur between the unsplit ground state and both sublevels of the split-excited state. By performing a Mössbauer measurement (see [Fig. 25.5](#)) one can detect both of the corresponding absorption peaks. The distance between the two peaks, measured in Doppler velocity units as usual in Mössbauer spectroscopy, is called the *quadrupole splitting* Δ . Thus, the quadrupole splitting is proportional to the energy separation (also called the quadrupole splitting energy, ΔE_Q) between the two sublevels of the split-excited state:

$$\Delta \propto \Delta E_Q = \lambda_+ - \lambda_- = \frac{eQV_{zz}}{2} \sqrt{1 + \frac{\eta^2}{3}} \quad (25.90)$$

where λ_+ and λ_- have been defined in [Eq. \(25.72\)](#). The proportionality constant connecting Δ with ΔE_Q depends on the energy of the γ ray (E_0 , see [Fig. 25.1](#)) emitted by the source in a recoilless emission event:

$$\Delta = \frac{c}{E_0} \Delta E_Q. \quad (25.91)$$

The two absorption peaks, appearing in the measured Mössbauer spectrum as a consequence of electric quadrupole hyperfine interaction, are called a *doublet*.

As can be seen from [Eq. \(25.90\)](#), in the case of a $3/2 \rightarrow 1/2$ transition, solely from the knowledge of Δ it is not possible to determine V_{zz} and η independently or to find out the sign of the V_{zz} . It is possible, however, to determine these parameters of the electric field gradient from the angular dependence of the intensity of the peaks when a single crystal is measured. The sign of the V_{zz} can be determined if in addition to electric quadrupole interaction the Mössbauer nuclei experience hyperfine magnetic interaction as well (see [Fig. 25.12](#)).

The connection between the quadrupole splitting energy and the separation of the absorption lines is less obvious if in addition to the excited state, the ground nuclear state is also subject to hyperfine quadrupole interaction. This is the case, e.g., for ^{129}I where the Mössbauer transition occurs between the excited state with $I_e = 5/2$ and the ground state with $I_g = 7/2$. The quadrupole splittings of this transition are treated below by assuming that the asymmetry parameter of the EFG is zero ($\eta = 0$, see [Eqs. \(25.68\)](#) and [\(25.73\)](#)).

In this case, altogether five quadrupole splittings ($\Delta_1 \dots \Delta_5$) can be observed (see [Fig. 25.11](#)). In the excited state the ratio between the splittings $\Delta_1/\Delta_2 = 1/2$, while in the ground state $\Delta_3:\Delta_4:\Delta_5 = 1:2:3$, as can be calculated from [Eq. \(25.92\)](#).

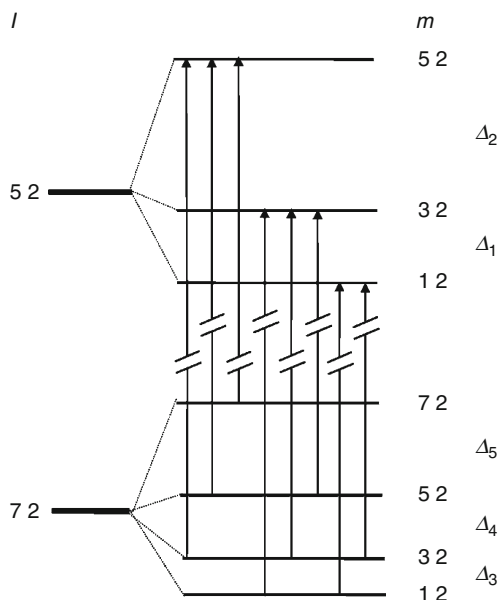
The selection rules for a magnetic dipole (M1) electromagnetic (EM) transition ($\Delta m_I = 0, \pm 1$) allow eight transitions, which result in eight Mössbauer peaks in the spectrum. The positions of the individual peaks (relative to the isomer shift) can be given by

$$\delta_{ij} = \frac{ceV_{zz}Q_g}{4E_0} \left[\frac{Q_e}{Q_g} C(I^e, m_I^e) - C(I^g, m_I^g) \right], \quad \text{where } C(I, m_I) = \frac{3m_I^2 - I(I+1)}{I(2I-1)} \quad (25.92)$$

where Q_e and Q_g are the quadrupole moments of the excited state and the ground state, respectively (Hafemeister 1971).

■ Fig. 25.11

Quadrupole splitting of the $I = 5/2$ (excited state) and $I = 7/2$ (ground state) nuclear levels of ^{129}I . The relative intensities of the allowed transitions indicated are (from the left to the right): 1:6:21:3:10:15:18:10 (May 1971). Note that the $I = 7/2$ levels are indeed lower than the $I = 5/2$ levels in this particular case



From the measured quadrupole splitting, either the nuclear quadrupole moment or the electric field gradient can be determined. Any of the two can be obtained from a Mössbauer measurement if the other can be determined independently. In chemical applications, the determination of the electric field gradient is the goal.

In many cases, not V_{zz} but eQV_{zz} is derived from the measured quadrupole splitting either in velocity or in frequency units. ▶ Table 25.1 shows the corresponding conversion factors for some Mössbauer nuclides.

25.2.3 Magnetic Splitting

The magnetic splitting Δ_m is related to the hyperfine magnetic interaction (see ▶ Sect. 25.1.5.3).

As shown by ▶ Eq. (25.77), the energy levels produced by the nuclear Zeeman splitting can be expressed as a product containing the nuclear magnetic moment μ and the *magnetic flux density*, B , existing at the site of the nucleus.

The magnetic splitting energy ΔE_m means the energy difference between the adjacent Zeeman split sublevels of a nuclear level. Its value derived from ▶ Eq. (25.77) is

$$\Delta E_m = -g_I \mu_N B \Delta m_I = -g_I \mu_N B \quad (25.93)$$

Note that the ΔE_m magnetic splitting energy in the excited state is different from that in the ground state.

■ Table 25.1

Numerical factors that can be used to obtain the value of eQV_{zz} in mm s^{-1} or in MHz units from the value of V_{zz} . In the case of $3/2 \rightarrow 1/2$ transitions (^{57}Fe , ^{119}Sn , ^{125}Te) the conversion factors are calculated with Q referring to the quadrupole moment of the excited nuclear state. For the other nuclides, Q refers to the quadrupole moment of the ground state. The precision of the given numerical factors is limited by the uncertainty of the respective Q values

Mössbauer nuclide ($I_e \rightarrow I_g$)	In order to obtain eQV_{zz} in mm s^{-1} units, $V_{zz}/(10^{21} \text{ V/m}^2)$ should be multiplied by	In order to obtain eQV_{zz} in MHz units, $V_{zz}/(10^{21} \text{ V/m}^2)$ should be multiplied by
^{57}Fe ($3/2 \rightarrow 1/2$)	+0.333(2)	+3.87(2)
^{119}Sn ($3/2 \rightarrow 1/2$)	−0.166(1)	−3.19(2)
^{125}Te ($3/2 \rightarrow 1/2$)	−0.262(17)	−7.5(5)
^{151}Eu ($7/2 \rightarrow 5/2$)	+1.257(14)	+21.83(24)
^{121}Sb ($7/2 \rightarrow 5/2$)	−0.438(9)	−13.13(27)
^{141}Pr ($7/2 \rightarrow 5/2$)	−0.0122(8)	−1.43(10)
^{129}I ($5/2 \rightarrow 7/2$)	−0.537(8)	−12.04(17)
^{237}Np ($5/2 \rightarrow 5/2$)	+1.957(3)	+93.96(15)
^{161}Dy ($5/2 \rightarrow 5/2$)	+2.930(23)	+60.62(48)
^{197}Au ($1/2 \rightarrow 3/2$)	+0.212(6)	+13.23(39)

For a transition between nuclear levels with nuclear spin $I_g = 1/2$ and $I_e = 3/2$, due to hyperfine magnetic interaction, the excited state splits into four sublevels with $m_{3/2} = -3/2, -1/2, +1/2$, and $+3/2$, while the ground state splits into two sublevels with $m_{1/2} = +1/2, -1/2$, as illustrated in [Fig. 25.10](#). According to the selection rule that applies to M1 electromagnetic transitions ($\Delta m_I = 0, \pm 1$), there are six allowed transitions in this case. This results in a six-peak pattern called sextet in the Mössbauer spectrum. The magnetic splitting of the excited state can be determined from the peak separation of the first and second or of the second and third peaks as well as from that of the fourth and fifth or of the fifth and sixth peaks (see [Fig. 25.10](#)). The magnetic splitting of the ground state can be obtained from the peak separation of the second and fourth or of the third and fifth peaks. The peak separation and, consequently, the *magnetic splitting* Δ_m is measured as a Doppler velocity, in mm/s unit:

$$\Delta_m = \Delta E_m \frac{c}{E_0}. \quad (25.94)$$

For the chemical application of Mössbauer spectroscopy, it is not necessary to derive the magnetic splitting explicitly from the Mössbauer spectrum in order to determine the magnetic flux density. As the separation of any two of the peaks in a *magnetic sextet* is also proportional to the magnetic flux density sensed by the corresponding nuclei, the basis of the determination of B is usually the separation of the two outermost peaks of the spectrum.

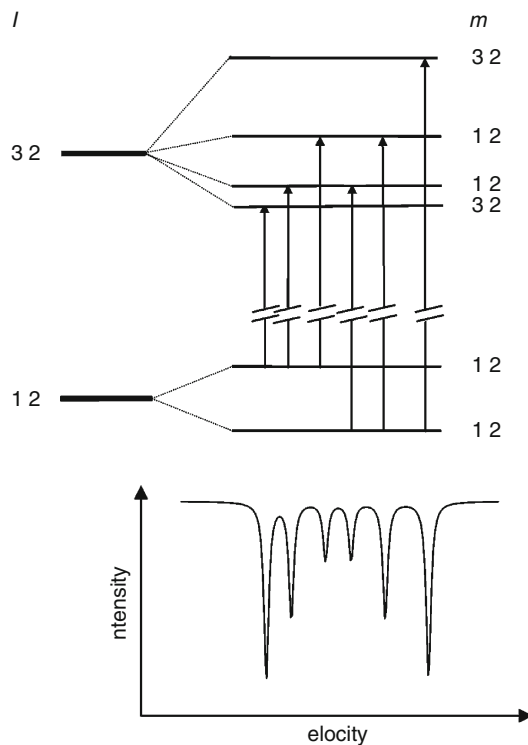
For a transition between nuclear levels with higher nuclear spin values, the magnetic field results in a more complex peak pattern in the Mössbauer spectrum. In the case of ^{151}Eu , e.g., the Mössbauer transition occurs between the $I_g = 5/2$ and $I_e = 7/2$ nuclear levels, and in the presence of magnetic splitting the Mössbauer spectrum consists of 18 peaks (Greenwood and

Gibb 1971). The separation of the peaks will also be proportional to the corresponding magnetic flux density.

In many cases the hyperfine magnetic dipole interaction occurs together with the electric quadrupole interaction. As shown in [Fig. 25.12](#) for the transition $I = 1/2 \rightarrow 3/2$, when $H_Q \ll H_m$, the sublevels of the excited state are no longer equally spaced, but the $m_I = +3/2$ and $m_I = -3/2$ sublevels are raised while the $m_I = +1/2$ and $m_I = -1/2$ sublevels are lowered when $V_{zz} > 0$. (Note that if $V_{zz} > 0$ and $\eta \neq 0$, the eigenstates of $H = H_0 + H_C + H_m$ (i.e., $|I, m_I\rangle$) will no longer be eigenstates of $H' = H_0 + H_C + H_m + H_Q$ – see [Eqs. \(25.41\)](#) and [\(25.68–25.70\)](#) – and therefore the sublevels shifted higher or lower than those belonging to the case $H_Q = 0$ will no longer represent pure $|I, m_I\rangle$ states but linear combinations of several $|I, m_I\rangle$ states as mentioned in [Sect. 25.1.5.2](#).) In the corresponding Mössbauer spectrum, the separation between the centers of the outermost two and of the inner four peaks will be proportional to the quadrupole splitting. From the position of these centers relative to each other, the sign of V_{zz} can be determined. The energies of the individual nuclear sublevels are given by [Eq. \(25.78\)](#) in this case.

Fig. 25.12

Energy shift and magnetic splitting of the $I = 1/2$ and $I = 3/2$ levels in the presence of an electric field gradient with $\eta = 0$, and the corresponding Mössbauer spectrum ($V_{zz} > 0$). Note that due to quadrupole interaction, the symmetry center of the outermost peaks is shifted relative to the inner four peaks in contrast to [Fig. 25.10](#)



25.2.4 Peak Intensity

If no splitting of the nuclear levels occurs, then the Mössbauer peak intensity can be given by [Eq. \(25.31\)](#).

In the case of the electric quadrupole and magnetic dipole interactions, the individual peaks have characteristic intensities relative to each other, which can confirm the assignment of the peaks to the appropriate nuclear transitions, and, in addition to the information provided by δ , Δ , and Δ_m , it helps assigning the various subspectra of the Mössbauer spectrum to lattice sites. The relative intensities can also furnish information on the orientational relationships in the sample/lattice (Schatz et al. 1996).

The relative intensity of a peak is proportional to the *relative* probability of the corresponding nuclear transition. For the *probability of a transition* from a state $|I_e, m_e\rangle$ to the state $|I_g, m_g\rangle$ by electromagnetic (EM) multipole radiation of σl (where $\sigma = E$ for electric and $\sigma = M$ for magnetic multipole character, and 2^l is the multipolarity of the radiation, see [Sect. 2.3.2.2 in Chap. 2, Vol. 1](#)) one can write

$$p(I_g, m_g, M_l^\sigma, I_e, m_e) \propto \left| \langle I_g, m_g | M_{l,m}^\sigma | I_e, m_e \rangle \right|^2 \quad (25.95)$$

where $M_{l,m}^\sigma$ is the multipole operator (for more details see, e.g., Blatt and Weisskopf (1959) or Mayer-Kuckuk (1994)) corresponding to the multipole radiation σl that carries away an angular momentum of $l\hbar$ with a z component of $m\hbar$.

According to the Wigner–Eckart theory (see, e.g., Rotenberg et al. 1959)

$$\langle I_g, m_g | M_{l,m}^\sigma | I_e, m_e \rangle = (-1)^{I_g - m_g} \begin{pmatrix} I_g & l & I_e \\ -m_g & m & m_e \end{pmatrix} \langle I_g | M_l^\sigma | I_e \rangle \quad (25.96)$$

where the term $\langle I_g | M_l^\sigma | I_e \rangle$ (called the *reduced matrix element*) does not depend on m_g , m_e , and m . Consequently, it has the same value for all of the transitions occurring via σl multipole radiation between the excited state and ground state of the nucleus.

As it is only the *relative* value of probabilities of $|I_e, m_e\rangle \rightarrow |I_g, m_g\rangle$ nuclear transitions ($m_e = -I_e, \dots, I_e$, $m_g = -I_g, \dots, I_g$) that can be detected in a Mössbauer measurement, for the probability of a certain $|I_e, m_e\rangle \rightarrow |I_g, m_g\rangle$ transition via σl multipole radiation one can write

$$p(I_g, m_g, M_l^\sigma, I_e, m_e) \propto \left(\begin{pmatrix} I_g & l & I_e \\ -m_g & m & m_e \end{pmatrix} \right)^2 \quad (25.97)$$

where the term on the right side is the so-called “ $3j$ symbol” (see, e.g., Lindner (1984) and Weisstein (2010)). The $3j$ symbols are closely related to the so-called Clebsch–Gordan coefficients. There are numerous Web sites on the Internet where automatic calculators are available for the calculation of $3j$ symbols as a function of I_g , I_e , l , m_g , m_e , and m .

The square of $3j$ symbol values entering the calculations in the case of the Mössbauer transition of ^{57}Fe ($I_e = 3/2$, $I_g = 1/2$, $\sigma l = M1$) are the following:

$$\left(\begin{pmatrix} 1/2 & 1 & 3/2 \\ \pm 1/2 & \pm 1 & \mp 3/2 \end{pmatrix} \right)^2 = \frac{1}{4}, \quad \left(\begin{pmatrix} 1/2 & 1 & 3/2 \\ \pm 1/2 & 0 & \mp 1/2 \end{pmatrix} \right)^2 = \frac{1}{6}, \quad \left(\begin{pmatrix} 1/2 & 1 & 3/2 \\ \pm 1/2 & \mp 1 & \pm 1/2 \end{pmatrix} \right)^2 = \frac{1}{12}. \quad (25.98)$$

To calculate the relative intensities of absorption lines in a Mössbauer spectrum, one also has to take into account that the intensity of the emitted multipole radiation is not isotropic but has a certain angular dependence $F_{lm}(\theta)$ where θ is the polar angle that the direction of observation encloses with the z -axis of the principal axis system (defined, e.g., by the direction

of the hyperfine magnetic field). It follows that the relative intensity of the peak belonging to the transition $|I_e, m_e\rangle \rightarrow |I_g, m_g\rangle$ can be expressed as

$$I(I_e, m_e, I_g, m_g, \sigma lm) \propto \begin{pmatrix} I_g & l & I_e \\ -m_g & m & m_e \end{pmatrix}^2 F_{lm}(\theta). \tag{25.99}$$

For the case of $3/2 \rightarrow 1/2$ magnetic dipole transitions, the angular dependence of the relative peak intensities are tabulated in [Table 25.2](#) together with corresponding values of $3j$ symbol squares.

For an isotropic distribution of \mathbf{B} (e.g., when a powder sample without texture is measured), the term $F_{lm}(\theta)$ describing the angular dependence of the intensity of multipole radiation can be integrated to give a factor of 1 for all the values of m . This means that in the case of powdered samples (and in the absence of additional effects, see [Sect. 25.2.7.5](#)) the relative intensity of the Mössbauer peaks is determined only by the values of $3j$ symbol squares. For $3/2 \rightarrow 1/2$ magnetic dipole transitions, in the case of magnetic splitting this results in a sextet with relative peak intensities of 3:2:1:1:2:3, while in the case of electric quadrupole interaction, assuming an isotropic distribution of the z direction of the EFG's PAS (principal axis system) in this case, a doublet with relative peak intensities of 1:1 is obtained.

The determination of peak intensities becomes a more complicated issue in the case of combined hyperfine magnetic dipole and electric quadrupole interactions (for the case of ^{57}Fe see, e.g., Kündig (1967) and Housley et al. (1969)), or when the Mössbauer transition has a mixed (most often M1 + E2) multipole character (for the case of ^{99}Ru see, e.g., Foyt et al. (1975)). Further factors influencing the relative peak intensities will be discussed in [Sect. 25.2.7.5](#).

25.2.5 The *f*-Factor

The *f*-factor, also called the Mössbauer–Lamb factor, is not only a measure of the probability of recoilless resonance emission/absorption of γ photons as discussed in [Sect. 25.1.3.3](#), but it is

Table 25.2

$3j$ symbols and angular dependent terms determining the relative intensities of peaks in the case of a magnetic dipole transition occurring between nuclear levels with nuclear spins $I = 3/2$ and $I = 1/2$ (which is the case for, e.g., ^{57}Fe and ^{119}Sn)

$m_{3/2}$	$m_{1/2}$	m	Square of corresponding $3j$ symbol	Angular dependence of intensity
			$\begin{pmatrix} 1/2 & 1 & 3/2 \\ -m_{1/2} & m & m_{3/2} \end{pmatrix}^2$	$F_{lm}(\theta)$ ($l = 1$)
3/2	1/2	−1	$\frac{3}{12}$	$\frac{3}{8}(1 + \cos^2\theta)$
1/2	1/2	0	$\frac{2}{12}$	$\frac{3}{4}\sin^2\theta$
−1/2	1/2	1	$\frac{1}{12}$	$\frac{3}{8}(1 + \cos^2\theta)$
−3/2	1/2	2	Not allowed	
3/2	−1/2	−2	Not allowed	
1/2	−1/2	−1	$\frac{1}{12}$	$\frac{3}{8}(1 + \cos^2\theta)$
−1/2	−1/2	0	$\frac{2}{12}$	$\frac{3}{4}\sin^2\theta$
−3/2	−1/2	1	$\frac{3}{12}$	$\frac{3}{8}(1 + \cos^2\theta)$

an important Mössbauer parameter, which can be obtained from the measurement of Mössbauer spectra. The f -factor is defined as the number of recoilless γ events (emission or absorption) divided by the total number of γ events. Since it can be expressed as a function of the mean square displacement, $\langle x^2 \rangle$, of the Mössbauer atom “frozen” in the lattice, (see [Eq. \(25.24\)](#)), it is possible to get important information from the f -factor about the state of lattice vibrations (e.g., to determine the Debye temperature from its temperature dependence).

The Mössbauer–Lamb factors f_S (for the source) and f_A (for the absorber) show up as coefficients to determine the Mössbauer peak intensity (see [Eq. \(25.31\)](#) for the transmission integral). Unfortunately, it is difficult to determine the absolute values of f_S and f_A from the absorption intensity without tedious and difficult experimentation.

The so-called black absorber method may be used for the determination of f_S . This uses the saturation effect of f_S when the effective thickness, τ_A (see [Eq. \(25.30\)](#)), approaches infinity. In this case, the asymptotic form of the spectral peak amplitude can be used to obtain f_S . The measurement of the f -factor of the absorber, f_A , is based on [Eq. \(25.33\)](#) and the corresponding nonlinear dependence of the intensity, amplitude, and width of the Mössbauer spectrum peak on the effective thickness (see later in [Fig. 25.17](#)). This latter is the so-called *blackness effect*. For the determination of f_A , the peak intensity and the peak amplitude should be measured for at least two absorbers of different thicknesses (Vértes and Nagy 1990).

When the Mössbauer nuclides are in different microenvironments, the determination of the relative values of the Mössbauer–Lamb factors belonging to each microenvironment is necessary in order to obtain the correct relative molar quantities.

25.2.6 Peak Width

The Mössbauer peak is characterized by an experimental parameter, the peak width W , which is measured as the full width at half maximum of the peak.

The peak width W for Lorentzian peaks can be derived from [Eq. \(25.31\)](#) (Margulies and Ehrman 1961) as a function of the absorber thickness:

$$W = W_0 \tau \frac{\exp\left(-\frac{\tau}{2}\right) I_0\left(-\frac{\tau}{2}\right) + I_1\left(-\frac{\tau}{2}\right)}{1 - \exp\left(-\frac{\tau}{2}\right) I_0\left(-\frac{\tau}{2}\right)}, \quad (25.100)$$

where $W_0 = 2\Gamma$, and Γ is the natural line width of the given Mössbauer transition. I_0 and I_1 denote the modified Bessel functions (see, e.g., BESSEL 2003) of the first kind (also referred to as having imaginary argument), and τ is the effective thickness of the absorber (which is proportional to the actual surface density d measured in mg/cm^2 , see [Eq. \(25.30\)](#)).

In the case of an ideally thin absorber, the Mössbauer peak width is twice of the natural line width ($W_0 = 2\Gamma$), which gives a possibility to determine the lifetime of the excited states of the Mössbauer nuclei on the basis of [Eq. \(25.2\)](#).

It is possible to observe Mössbauer peak widths narrower than W_0 without violating the uncertainty principle. This can happen, e.g., if γ photons from a nuclear decay are selected in such a way that only those are counted, which are emitted after a certain time of the “birth” of the excited state (*time-dependent Mössbauer spectroscopy*).

Deviations from the expected peak width may arise due to various effects. A number of inherent physical processes cause peak broadening (like diffusion, relaxation processes) and, consequently, a lot of useful information can be obtained from the peak width W .

25.2.7 Mössbauer Parameters and Experimental Parameters

As it was just seen, the main *Mössbauer parameters* that can be derived from a Mössbauer spectrum are as follows: Mössbauer–Lamb factor (f), isomer shift (δ), quadrupole splitting (Δ), magnetic splitting (Δ_m), peak width (W), and the relative area – also called the relative intensity – of the spectrum peaks (A). Sometimes, it is convenient to consider these parameters as the coordinates of the Mössbauer parameter vector \mathbf{P}_M :

$$\mathbf{P}_M = (f, \delta, \Delta, \Delta_m, W, A), \quad (25.101)$$

where the individual symbols between the parentheses may again represent sets of similar parameters (i.e., vectors).

For instance, instead of A one might write \mathbf{A} meaning:

$$\mathbf{A} = (A_1, A_2, \dots), \quad (25.102)$$

where A_1, A_2, \dots represent the spectral areas of different peaks.

The Mössbauer parameters depend on a number of various *experimental parameters* such as temperature (T), pressure (p), external magnetic flux density (\mathbf{B}_{ext}) if any, the polar angles of the sample relative to the direction of the γ rays (θ, ϕ), the frequency (ν) of high-frequency field if any, etc.:

$$\mathbf{P}_M = f(\mathbf{P}_{\text{exp}}), \quad (25.103)$$

where the vector \mathbf{P}_{exp} represents all of the relevant experimental parameters:

$$\mathbf{P}_{\text{exp}} = (T, p, B_{\text{ext}}, \theta, \phi, \nu, c, \dots) \quad (25.104)$$

in which the c concentration of the Mössbauer species in the sample is also included.

Some of the above-listed experimental parameters may have *standard values*. For instance, $T_0 = 293$ K (room temperature, RT), $p_0 = 1$ bar (\sim atmospheric pressure), $\mathbf{B}_{\text{ext},0} = 0$ T (no external magnetic field applied), etc. The measuring conditions specified by such values are called *standard conditions*.

25.2.7.1 Temperature Dependence

The temperature dependence of Mössbauer parameters can be very useful in qualitative analysis. As the temperature dependence of the different spectrum components is usually different, measuring the same sample at different temperatures may help distinguish between species whose “fingerprints” are similar under standard conditions (i.e., at room temperature in the given instance) but different at lower or higher temperatures.

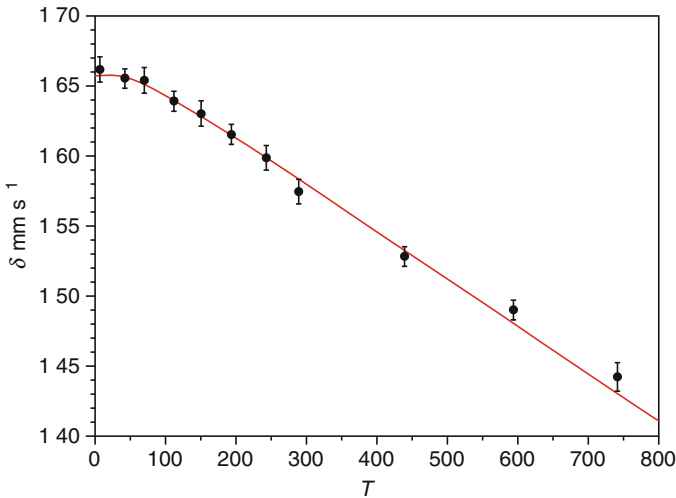
The *temperature dependence of the isomer shift* (see [Fig. 25.13](#)) is mainly determined by that of the second-order Doppler shift and can be obtained by combining [Eqs. \(25.89\)](#) and [\(25.23\)](#):

$$\delta_{\text{SOD}}(T) = -\frac{9k\theta_D}{2cM} \left[\frac{1}{8} + \left(\frac{T}{\theta_D} \right)^4 \int_0^{\theta_D/T} \frac{x^3}{e^x - 1} dx \right]. \quad (25.105)$$

The *temperature dependence of the quadrupole splitting* comes mainly from the temperature-dependent population of the different valence levels of the Mössbauer nuclide, provided that

■ Fig. 25.13

Temperature dependence of the isomer shift of ^{119}Sn in $\text{V}_3\text{Ga}_{0.1}\text{Sn}_{0.9}$, based on the results of Kimball et al. (1974)



the valence contribution to the electric field gradient is not negligible (Ingalls 1964; Eicher and Trautwein 1969; Gütlich et al. 1978).

In the case of ^{57}Fe one has

$$\Delta(T) = \frac{2}{7} e^2 Q \frac{c}{E_\gamma} (1 - R) \langle r^{-3} \rangle \alpha^2 F(E_i, \alpha^2 \lambda_0, T) \quad (25.106)$$

where the temperature sensitive factor F depends on the energy separation of the 3d levels E_p on the isotropic covalency factor α^2 , and on the free-ion spin-orbit coupling constant λ_0 . $\langle r^{-3} \rangle$ means the expectation value of r^{-3} , and R is the antishielding *Sternheimer factor* (Sternheimer 1950, 1951, 1963).

The temperature dependence of quadrupole splitting is illustrated in ► Fig. 25.14 for $\text{Cd}_3[\text{Fe}(\text{CN})_6]_2$.

The temperature dependence of the Mössbauer–Lamb factor (see ► Fig. 25.15) can be calculated in the frame of the Debye model of solids from ► Eq. (25.26). For different temperature regions, the following formulae can be derived (cf. ► Eqs. (25.20)–(25.22) and ► (25.24)):

$$f(T) \approx \exp \left\{ -\frac{6E_R}{k\theta_D} \left(\frac{1}{4} + \left(\frac{T}{\theta_D} \right)^2 \frac{\pi^2}{6} \right) \right\}, \quad \text{if } T \ll \theta_D \quad (25.107)$$

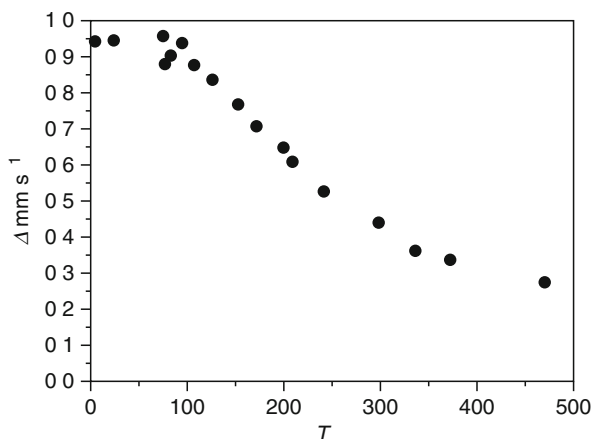
$$f(T) \approx \exp \left\{ -\frac{6E_R}{k\theta_D} \frac{T}{\theta_D} \right\}, \quad \text{if } T \gg \theta_D \quad (25.108)$$

where E_R is the recoil energy and θ_D is the Debye temperature.

The temperature dependence of the magnetic splitting itself depends on the nature of the magnetic interaction in the investigated material.

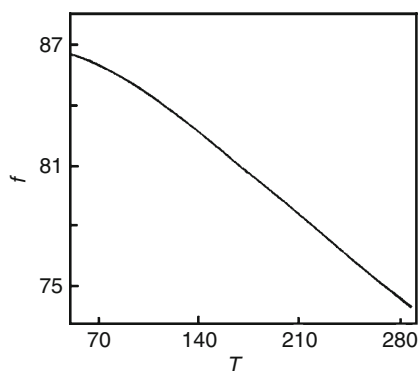
■ Fig. 25.14

Temperature dependence of the quadrupole splitting of ^{57}Fe in $\text{Cd}_3[\text{Fe}(\text{CN})_6]_2$ (Based on Vértés et al. 1979)



■ Fig. 25.15

Typical shape of the temperature dependence of the Mössbauer–Lamb factor



For simple *ferromagnetic* interaction, e.g., when the Bloch law (Kittel 1968) is valid for the field, one obtains

$$\frac{\Delta E_m(T)}{\Delta E_m(0\text{K})} = 1 - CT^{3/2} \quad (25.109)$$

where C is a constant.

In the case of some *paramagnetic* materials exhibiting magnetically split Mössbauer spectra, the magnetic splitting is due to the paramagnetic spin relaxation time τ_{SR} being relatively high in comparison with the *Larmor precession* time of the nucleus. In this case, temperature dependence is governed by that of the spin-lattice relaxation of the material (Vértés and Nagy 1990).

The temperature dependence of the peak width W caused by the diffusive motion of resonant nuclei can be expressed either by the formula

$$\frac{\Delta W}{W} = \exp\left(-\frac{E^*}{kT}\right) \quad (25.110)$$

or by

$$\Delta W = \frac{2c\hbar}{E_0\tau_0} \left[1 - \int e^{i\mathbf{k}\mathbf{r}} h(\mathbf{r}) d\mathbf{r} \right], \quad (25.111)$$

where E^* is the activation energy, \mathbf{k} is the wave vector of the γ photon, $h(\mathbf{r})$ is the probability density of finding an atom after one jump at point \mathbf{r} relative to the origin of the jump, and τ_0^{-1} is the jump frequency (Singwi and Sjolander 1960).

25.2.7.2 Pressure Dependence

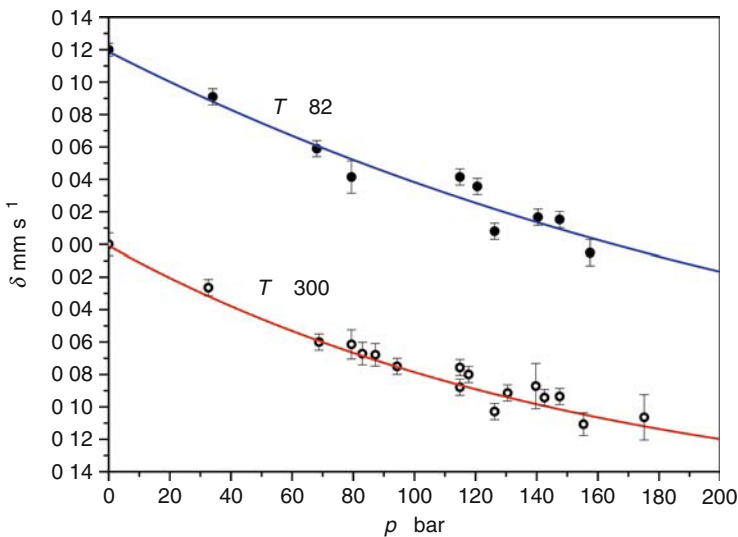
The pressure dependence of Mössbauer parameters follows from that of the physical quantities that determine the values of those parameters. The pressure dependence of the isomer shift (Shenoy and Wagner 1978), e.g., is illustrated in [Fig. 25.16](#).

25.2.7.3 External Magnetic Field Dependence

The external magnetic field dependence of Mössbauer parameters can be very important, because – by choosing an appropriate external magnetic flux density – one often gets a better-resolved spectrum.

Fig. 25.16

Pressure dependence of the isomer shift of ^{57}Fe in $\alpha\text{-Fe}$, based on the results of Williamson et al. (1972)



By applying an external magnetic field, one can produce sources of polarized γ rays. In ^{57}Fe Mössbauer spectroscopy, this can be done by embedding the ^{57}Co parent nuclide in a ferromagnetic host (e.g., in $\alpha\text{-Fe}$) and by magnetically saturating the host material with an appropriate external field. Such a source will emit six lines (instead of just one) which, when overlapping with a simple six-line absorber hyperfine pattern, will lead to 36 (i.e., six times six) possible absorption peaks (Gonser 1975a).

The *effective magnetic flux density* B measured at the nucleus consists of two terms:

$$B = B_{\text{ext}} + B_{\text{int}} \quad (25.112)$$

where B_{ext} is the external magnetic flux density and B_{int} is the *internal magnetic flux density* which, again, consists of a number of components of different origin (Thosar and Iyengar 1983).

The use of external magnetic field makes it possible to determine the sign of the quadrupole splitting from the induced magnetic pattern (Gütlich et al. 1978) in the case of ^{57}Fe and ^{119}Sn spectroscopy of nonmagnetic materials.

The effect of external magnetic field on the magnetic splitting of magnetic materials depends on the nature of magnetic coupling (i.e., whether the material is ferromagnetic, ferrimagnetic, or antiferromagnetic) (Gonser 1975a).

25.2.7.4 Radio-Frequency Electromagnetic Radiation

Radio-frequency electromagnetic radiation can have two kinds of effect on the Mössbauer spectrum (Gonser 1981). It can result in a collapse of the split Mössbauer pattern, but it can also produce side bands in the spectrum on the basis of which a better identification of the atomic species can sometimes be achieved (Kopcewicz 1989).

25.2.7.5 Angular Dependence of Peak Areas/Intensities

The angular dependence of peak areas follows from the angular dependent nature of the intensity of multipole radiations (see [Table 25.2](#) for $F_{lm}(\theta)$ in the case of $l = 1$).

Magnetic sextet. The angular dependence of the relative peak areas of a magnetic sextet (appearing in, e.g., ^{57}Fe and ^{119}Sn Mössbauer spectra, both representing the $I = 3/2 \rightarrow 1/2$ nuclear spin transition), can be calculated by multiplying the $3j$ symbols with the corresponding $F_{lm}(\theta)$ angular dependent terms (both given in [Table 25.2](#)). Apart from a constant factor one obtains

$$A_1(\theta) = A_6(\theta) = 3(1 + \cos^2\theta) \quad (25.113)$$

$$A_2(\theta) = A_5(\theta) = 4\sin^2\theta \quad (25.114)$$

$$A_3(\theta) = A_4(\theta) = \frac{1}{3}A_1(\theta) = \frac{1}{3}A_6(\theta) = (1 + \cos^2\theta) \quad (25.115)$$

where θ is the angle between the respective directions of the γ ray and the effective magnetic flux density, and the area subscripts refer to the peak numbers of the sextet.

In the case of ferromagnetic materials, the direction of the effective magnetic flux density \mathbf{B} can be manipulated by an external field \mathbf{B}_{ext} .

If the direction of the effective magnetic field changes from point to point in a sample so that each direction has the same occurrence, then the relative peak areas (intensities) of the resultant sextet will average out to

$$A_1 : A_2 : A_3 : A_4 : A_5 : A_6 = 3 : 2 : 1 : 1 : 2 : 3, \quad (25.116)$$

which is the typical case for antiferromagnetic powder samples without texture. Bulk ferromagnetic materials (e.g., a not too thin α -iron foil) also have such a tendency, because the magnetic moments of their domains point at random directions.

In the case of magnetic anisotropy, the relative intensity of the second and the fifth lines compared with that of the first and sixth lines depends on θ in the following way:

$$\frac{A_{2,5}}{A_{1,6}} = \frac{4\sin^2\theta}{3(1 + \cos^2\theta)} \quad (25.117)$$

(Note that the intensity ratio of the inner and the outer pairs of lines of a sextet has no angular dependence, it is always equal to 3.)

Quadrupole doublet. In the case of a quadrupole doublet, the relative areas (intensities) of the doublet peaks (one representing the $m_I = \pm 3/2 \rightarrow \pm 1/2$ and the other the $m_I = \pm 1/2 \rightarrow \pm 1/2$ nuclear transitions) apart from a constant factor will have the angular dependences

$$A_{\pm 3/2 \rightarrow \pm 1/2}(\theta) = 1 + \cos^2\theta \quad (25.118)$$

$$A_{\pm 1/2 \rightarrow \pm 1/2}(\theta) = \frac{5}{3} - \cos^2\theta \quad (25.119)$$

where θ is the angle between the respective directions of the γ ray and the main axis of the EFG at the nucleus.

The intensity ratio of the lines of the doublet can also be expressed as (Gütlich et al. 1978)

$$\frac{I_2}{I_1} = \frac{\int_0^\pi (1 + \cos^2\theta) h(\theta) f(\theta) \sin\theta d\theta}{\int_0^\pi (\frac{5}{3} - \cos^2\theta) h(\theta) f(\theta) \sin\theta d\theta} \quad (25.120)$$

where $h(\theta)$ is the probability density of the angle θ , and $f(\theta)$ gives the angular dependence of the Mössbauer–Lamb factor.

In a well-mixed powder sample, where there is a random distribution ($h(\theta) = 1/\pi$) of the electric field gradients, and the Mössbauer–Lamb factor is isotropic, a symmetrical doublet with equal peak areas is expected: $A_{\pm 3/2 \rightarrow \pm 1/2} : A_{\pm 1/2 \rightarrow \pm 1/2} = 1 : 1$

The deviation from the above symmetry in most cases is an indication that the powder sample has some *texture*. If the asymmetry is indeed due to texture, then in accordance with [Eq. \(25.120\)](#) the relative intensity of the peaks should change when the sample is turned around an axis that is perpendicular to the direction of the γ rays. If the preferred orientation of the sample is such that the z -axis of the principal axis system is parallel to the direction of γ rays ($\theta = 0$ in [Eqs. \(25.118\)–\(25.120\)](#)) then a maximum asymmetry of the peaks is observed (relative intensity of the peaks is 3 in this case). If one turns this sample by $\Delta\theta = 54.7^\circ$ (the so-called *magic angle*) then the two peaks in the Mössbauer spectrum will have equal intensity despite the presence of texture.

The other possible reason for the intensity asymmetry ($A_2/A_1 \neq 1$) of the quadrupole split doublet can be the so-called *Goldanskii–Karyagin effect* (Goldanskii et al. 1963), which is caused by the angular dependence of the Mössbauer–Lamb factor due to the anisotropy of lattice vibrations ($f(\theta)$ depends on θ).

For a comparison of the Goldanskii–Karyagin effect with the effect of texture see, e.g., Pfannes and Gonser (1973).

25.2.7.6 Absorber Thickness

The dependence of the experimental peak width (W) on the absorber thickness for Lorentzian peaks is given (Nozik and Kaplan 1967) by the following equations derived from [Eq. \(25.100\)](#):

$$W = W_0(2 + \tau/4 + \tau^2/96 - \tau^3/64) \quad \text{for } \tau < 2, \quad (25.121)$$

and

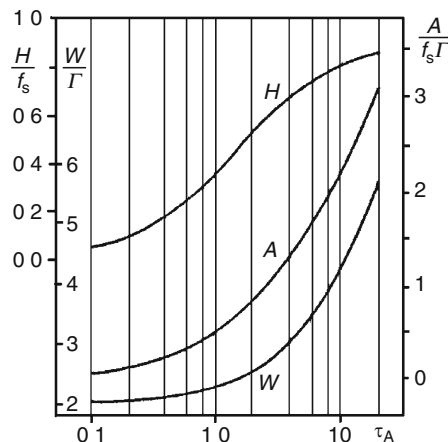
$$W = 2W_0\tau/(\sqrt{\pi\tau} - 1) \quad \text{for } \tau < 2, \quad (25.122)$$

where W_0 is the peak width corresponding to the natural line width of the given Mössbauer transition and τ is the effective thickness of the absorber. The absorber thickness can also be optimized as regards the time necessary to measure a spectrum with satisfactory statistics (Nagy et al. 1975).

[Figure 25.17](#) shows the peak area, peak height, and peak width as the function of effective thickness.

Fig. 25.17


Dependence of the peak area A , peak height H , and peak width W on the effective thickness of the absorber (τ_A). Γ is the natural line width and f_s is the Mössbauer–Lamb factor of the source



25.2.7.7 Geometric Arrangement

The dependence of Mössbauer parameters on geometric arrangements is mainly due to the cosine smearing of the velocity u . Since the Doppler energy shift ΔE_γ is given by

$$\Delta E_\gamma = E_\gamma \frac{u}{c} \cos \theta, \quad (25.123)$$

(where E_γ is the energy of the emitted γ photon) a smearing effect can always be observed on the experimental peak shape, peak width, and isomer shift (Shenoy and Wagner 1978), even under “ideal” conditions when one uses a point source and a circular absorber placed coaxially as illustrated by  Fig. 25.18. (Above, θ is the angle between the γ ray and the direction of motion of the source or the absorber, whichever is moved.)

25.3 Analytical Information from Mössbauer Spectra

25.3.1 The Fingerprint Method

Patterns and physicochemical entities. In general, the fingerprint method operates with patterns (“fingerprints”) characteristic of different phases, compounds, crystallographic sites etc., which will be referred to as physicochemical entities for brevity. The correspondence between individual patterns and such entities is determined by the nature of interactions serving as a basis for the analytical method. In the case of Mössbauer analysis, the basic interactions are the hyperfine interactions.

Since the hyperfine interactions are determined principally by the electron density and the inhomogeneous electric field as well as by the effective magnetic flux density at the nucleus, the Mössbauer spectrum patterns differ from site to site where these physical quantities are different. Thus, a single-phase material may be characterized by a complex Mössbauer spectrum superimposed from a number of simple Mössbauer patterns belonging to resonant atoms experiencing different hyperfine interactions.

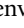
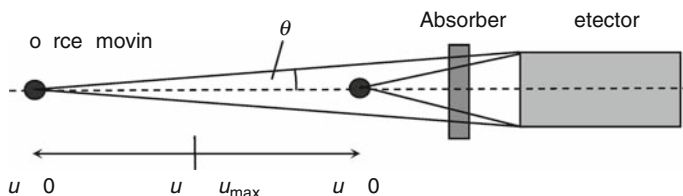
The microenvironment (see  Sect. 25.1.5.5) is of basic importance for analytical purpose. Since there is a one-to-one correspondence between the microenvironment and the hyperfine interactions, a simple Mössbauer pattern is always associated with a microenvironment characteristic of one particular population of Mössbauer nuclei in the studied sample. For brevity, such a population of like Mössbauer nuclei is referred to as a *Mössbauer species*.

 Fig. 25.18

The origin of cosine smearing. u is the velocity of the source relative to the absorber



25.3.2 Pattern Analysis

The basic task of the analysis is to identify the individual Mössbauer species from the corresponding patterns present in the spectrum. Ideally, this can be done if there is an exact correspondence between them.

Unfortunately, such a one-to-one correspondence between Mössbauer species and individual patterns may be nonexistent under the given conditions, i.e., for that particular set of experimental parameters at which the Mössbauer spectrum was recorded. However, when the whole range of the possible conditions is considered, one may find points in the space of experimental parameters at which only one pattern is associated with one species and vice versa and thus one can get round the problem of ambiguity. One can also do simultaneous evaluation of a whole series of Mössbauer spectra taken from the same sample under different conditions. Such a *serial evaluation* is a very effective tool, because the known dependences of the Mössbauer parameters (e.g., isomer shift) on the externally set experimental parameters (e.g., temperature) can be used as constraints for the serial fit.

From the analytical point of view, one can classify *Mössbauer patterns* in the following way (Kuzmann et al. 2003).

According to *experimental conditions* there are *standard patterns* and *induced patterns*.

According to *complexity* there are *elementary patterns* and *superimposed patterns*.

According to *mathematical processing* there are *natural patterns* and *transformed patterns*.

A Mössbauer spectrum can be a simple spectrum (elementary pattern) reflecting only a unique microenvironment/Mössbauer species or a complex spectrum (superimposed pattern), which consists of a number of subspectra.

The *standard pattern* is associated with a Mössbauer spectrum obtained at a standard set of experimental parameters. In most laboratories, e.g., measurements performed at room temperature, under atmospheric pressure and without external magnetic field are considered as standard. The *induced pattern*, however, is obtained under conditions other than standard (e.g., measurements performed in a cryostat or a furnace or in the field of a magnet). In this case, the differences between the induced and standard patterns can give important contribution to the analysis.

The *elementary pattern* is associated with one type of microenvironment/Mössbauer species. The *superimposed pattern* is the superposition of elementary patterns.

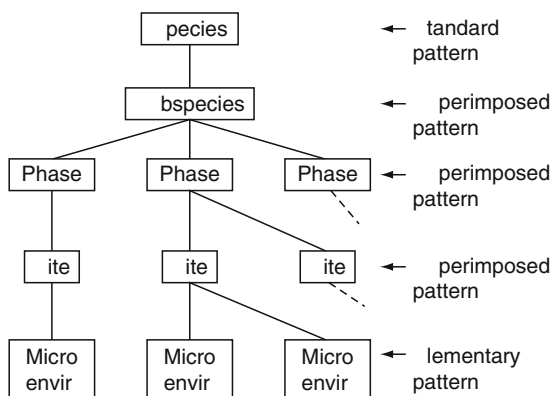
The *transformed pattern* is obtained from the measured Mössbauer spectrum (i.e., from the *natural pattern*) by mathematical transformation (e.g., by Fourier transformation). For instance, the magnetic hyperfine field (i.e., effective magnetic flux density) distribution or the quadrupole splitting distribution are considered transformed patterns. The transformed pattern may give a better resolution for the analysis.

► [Figures 25.19](#) and ► [25.20](#) illustrate the relation between different types of patterns and the object of the analysis as well as the most common strategy followed when doing qualitative analysis in Mössbauer spectroscopy. Generally, the Mössbauer spectrum of a multi-compound/multiphase material is a superposition of superimposed patterns. This is so because each compound/phase can have different crystallographic sites, each site represented by a different pattern. Note that even a single crystallographic site may represent more than one microenvironment due to variations in the hyperfine interactions (e.g., different electronic and spin density and defect arrangement).

In order to give an example, let us consider a steel sample in which ferrite and austenite phases are present. The standard pattern (^{57}Fe Mössbauer spectrum) of the sample is a complex spectrum that is a sum of subspectra (► [Fig. 25.21](#)). The subspectra of the ferromagnetic ferrite

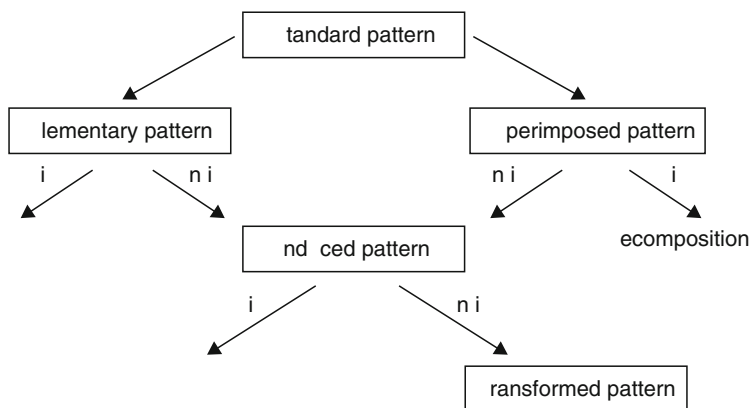
■ Fig. 25.19

Relation between different types of patterns and the object of analysis



■ Fig. 25.20

Simplified strategy of qualitative analysis in Mössbauer spectroscopy (i. and n.i. stand for informative and not informative, respectively)



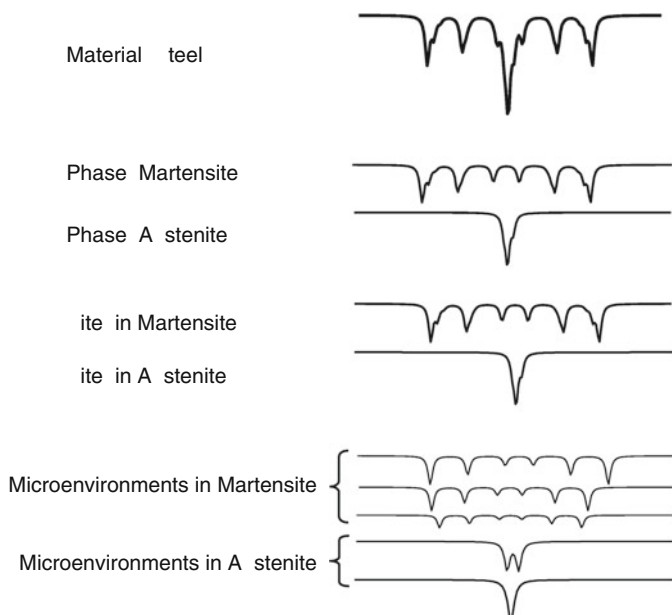
and the paramagnetic austenite are also superimposed from elementary patterns because of the effect of alloying elements.

Very often, when the characteristic subspectra of components are well distinguishable in the standard spectrum, the qualitative analysis can be performed without the need for measuring further nonstandard spectra (induced patterns). In general, however, the subspectra (elementary patterns) overlap each other in the standard spectrum. When the exact decomposition of the spectrum becomes ambiguous, it is still possible to get further analytical information from an induced pattern (e.g., via serial evaluations).

For example, the standard room-temperature patterns of akageneite (β -FeOOH) and lepidocrocite (γ -FeOOH) are paramagnetic doublets with similar parameters. So they cannot be easily differentiated. However, the induced patterns of β -FeOOH taken below the magnetic

■ Fig. 25.21

The standard pattern of a steel in which ferrite and austenite phases are present. The ^{57}Fe Mössbauer spectrum of the sample is a complex spectrum that is a sum of subspectra. The subspectra of the ferromagnetic ferrite with bcc lattice and the paramagnetic austenite with fcc lattice are also superimposed from elementary patterns because of the effect of alloying elements, although the Fe atoms can only occupy one single crystallographic site in each phase



transition temperature (► Fig. 25.22) reflect magnetically split subspectra (sextets). Now, by the help of the induced pattern, the analytical problem can be solved more easily.

In some cases, the natural pattern consists of hundreds of elementary patterns. This is the typical situation with poorly crystallized and amorphous systems. The transformed pattern (► Fig. 25.23) can help get more information about the short-range ordering (by characterizing some of the most probable arrangements), thus it can enhance the analytical applicability.

25.3.3 Spectrum Evaluation

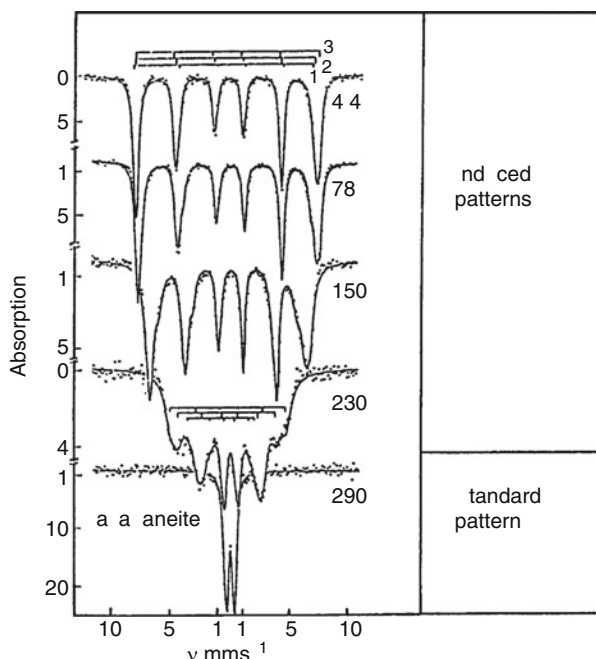
The Mössbauer parameters are derived from the *peak parameters* (base line parameters, peak position, peak width, and peak area/height) via the fitting process by computer evaluation of spectra in the case of the so-called model-dependent evaluation. In this case, an exact a priori knowledge about the spectrum decomposition (peak-shape function, number, and type of subspectra corresponding to the interactions assumed for each microenvironment in the model) is inevitably necessary. (Incorrectly chosen number of peaks renders the analysis itself incorrect.)

The most precise way of fitting is based on the computation of the transmission integral given by ► Eq. (25.31).

Very often, however, the simple Lorentzian peak shape is considered (see also ► Eqs. (25.1) and (► 25.35)):

■ Fig. 25.22

The induced patterns of akagenite (Kuzmann et al. 1994) carry much more information for the analysis than the standard one



$$L(u) = \frac{1}{\pi} \frac{W}{2} \frac{A}{(u - u_0)^2 + \left(\frac{W}{2}\right)^2} = \left(\frac{W}{2}\right)^2 \frac{H}{(u - u_0)^2 + \left(\frac{W}{2}\right)^2} \quad (25.124)$$

where u_0 is the position (in mm/s), W is the width, A is the area (intensity), and H is the height of the peak. This can be a good approximation, if the absorber is sufficiently thin (the effective thickness τ_A should be less than 1) and if the number of overlapping peaks is not very large.

For the analysis of materials whose spectra consist of a large number of overlapping peaks (e.g., amorphous metals), the product (or rather the convolution) of Lorentzian and Gaussian curves (Voigt function) is used to fit the peaks (Seagusa and Morrish 1982).

The spectrum fitting is done by the least-squares method by using an appropriate model function S , e.g., a linear combination of Lorentzians. (See also [Sect. 9.3.6 on Fitting nuclear spectra in Chap. 9, Vol. 1](#), on “Stochastics and Nuclear Measurements.”) In this procedure, the sum

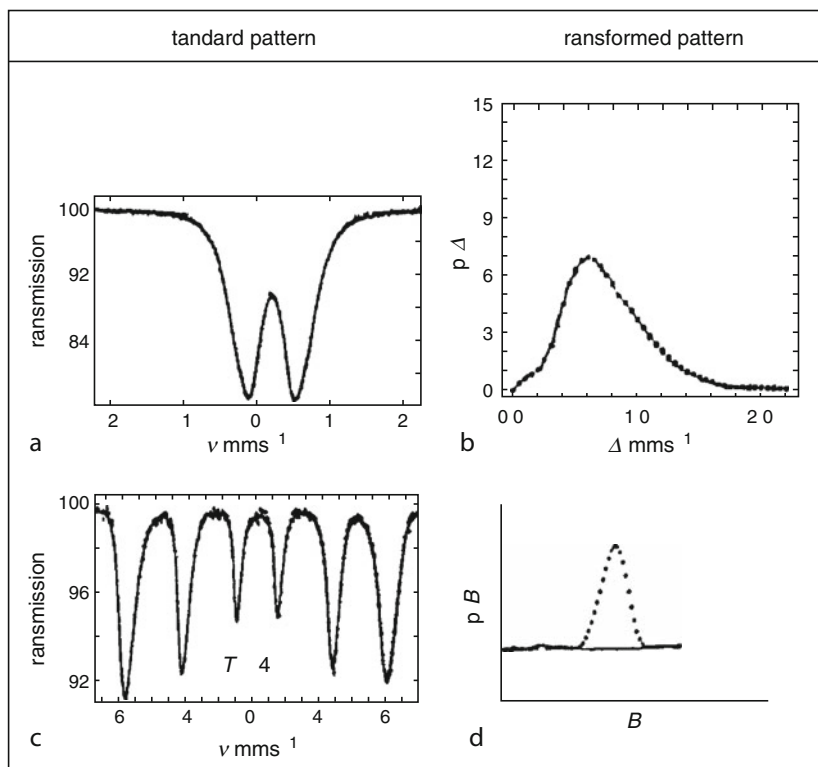
$$\chi^2 = \sum_{i=1}^k \frac{1}{N_i} [N_i - S(i; P_{\text{peak}})]^2 \quad (25.125)$$

is minimized, where N_i is the number of counts stored in the i th channel; k is the total number of channels. The model function S is determined by the vector P_{peak} of the peak parameters that is set up from the individual parameter vectors of the baseline (p_0) and the peaks (p_1, p_2, \dots, p_n):

$$P_{\text{peak}} = (p_0, p_1, p_2, \dots, p_n) \quad (25.126)$$

■ Fig. 25.23

The transformed patterns (graphs on the right side) of poorly crystallized ferrihydrite (Kuzmann et al. 1994). (a) ^{57}Fe Mössbauer spectrum of poorly crystallized ferrihydrite at room temperature, and (b) the corresponding quadrupole splitting distribution. (c) ^{57}Fe Mössbauer spectrum of poorly crystallized ferrihydrite at 4K, and (d) the corresponding hyperfine magnetic field distribution



Each parameter vector \mathbf{p}_j itself represents a set of three parameters characterizing the position, width, and area/height of the j th peak out of n .

In the thin-absorber approximation, an inhomogeneous linear transformation is used to make connection between the vector of the Mössbauer parameters \mathbf{P}_M (set up from isomer shifts, quadrupole splittings, magnetic splittings, etc.) and the vector of the peak parameters \mathbf{P}_{peak} :

$$\mathbf{P}_M^T = \mathbf{T} \mathbf{P}_{\text{peak}}^T + \mathbf{C}^T \quad (25.127)$$

where the constraints are determined by the elements of the transformation matrix \mathbf{T} and the constant vector \mathbf{C} . (The superscript “T” is to indicate that one has column vectors in the formula.)

The a priori knowledge of the matrix \mathbf{T} and the vector \mathbf{C} is normally an essential condition of spectrum evaluation. From the point of view of analytical applications, the a priori determination of the \mathbf{T} matrix is of fundamental importance. Namely, this transformation enables the experimenter to specify a set of peaks as a pattern representing one particular Mössbauer species in the sample.

The assignment of the subspectrum to one particular Mössbauer species is based on the comparison of the derived pattern with a reference spectrum. The *reference spectrum* can be obtained by measuring an etalon material or from the data published in the literature. In some cases, the reference spectrum can be constructed theoretically (computer simulation).

Another, so-called model-independent way of spectrum evaluation is done by obtaining and analyzing transformed patterns. For a thin absorber, the spectrum shape $S(u)$ can be described as the convolution of a density function $f(u)$ with a Lorentzian function $L(u)$:

$$S(u) = \int_{-\infty}^{+\infty} f(v)L(u-v)dv. \quad (25.128)$$

One of the methods for obtaining the distribution of effective magnetic flux density or quadrupole splitting (Campbell and Aubertin 1989; Klencsár et al. 1996) is the *Window method* (Window 1971) that uses a Fourier technique. For instance, the distribution of the effective magnetic flux density (also called *hyperfine field distribution*)

$$p(B) = \sum_i^N a_i \left[\cos \frac{B_i - B_{\min}}{B_{\max} - B_{\min}} - (-1)^i \right] \quad (25.129)$$

can be obtained by fitting the spectrum (B_{\min} and B_{\max} are the minimum and maximum values of the effective magnetic flux density, respectively).

Another way to obtain the distribution of the effective magnetic flux density or the quadrupole splitting is the *Hesse-Rübartsch method* (Hesse and Rübartsch 1974).

25.3.4 Quantitative Analysis

In Mössbauer spectroscopy, as in other spectroscopic methods, quantitative analysis is based upon the determination of peak areas.

In general, the transmission integral (► Eq. (25.31)) can be used to evaluate the peak area that depends nonlinearly on the effective thickness, which, in turn, is proportional to the concentration of the resonant atoms.

In the *thin-absorber approximation* ($\tau_A < 0.1$), the *peak area* is proportional to the Mössbauer atom concentration as shown earlier:

$$A \approx k\tau_A = k\sigma_0 d_A f_A n_A a \quad (25.130)$$

where a is the fractional abundance of the Mössbauer isotope (e.g., that of ^{57}Fe in natural iron) and n_A is the number of atoms of the studied Mössbauer element (e.g., iron) per unit volume of the absorber. The constant k includes other constants and parameters involving the background and matrix effects.

For the determination of concentration n_A all the parameters in the above equation have to be known. However, in most cases, the exact values of the Mössbauer–Lamb factor f_A and the constant k are unknown. In such cases, calibration graphs obtained with etalons are needed. However, the relative f -factors belonging to different microenvironments are usually known. Consequently, Mössbauer spectroscopy has a unique ability for the determination of the relative concentration of individual Mössbauer species in the same sample. The absolute concentration can be determined more accurately using other techniques.

25.4 Measurement Techniques in Mössbauer Spectroscopy

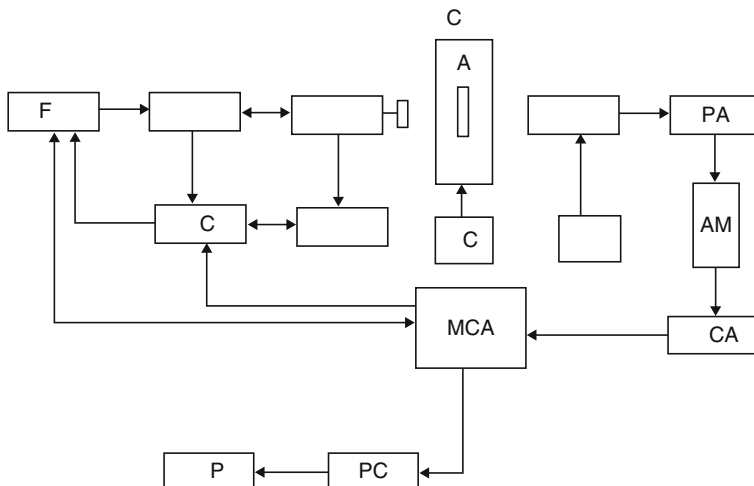
25.4.1 Mössbauer Spectrometers

In order to measure a Mössbauer spectrum one has to detect recoilless absorption or emission of a selected γ radiation as a function of the Doppler velocity of the sample and a reference material relative to each other. In the most common case of transmission geometry, absorption of the γ rays is measured, and the reference material is a standard source, which is moved. Thus, the most important components of a Mössbauer spectrometer are a Doppler velocity drive system and an energy selective γ detection chain with appropriate recording system.

The Mössbauer measurement requires the generation of a precise, controllable relative motion between the source and the absorber. A large variety of drive systems has been developed. The majority of drives work on electromechanical, mechanical, hydraulic, and piezoelectric principle. The spectrometers can be classified into constant-velocity spectrometers and velocity-sweep spectrometers. The mechanical drives, like a lead screw or a cam, move with constant velocity. They have advantages for the thermal scan method and because their absolute velocity calibration is straightforward. The velocity-sweep spectrometers are usually of electromechanical nature (like loudspeaker-type transducers) and normally used in conjunction with a multichannel analyzer. The most commonly used $u(t)$ functions are rectangular (constant velocity), triangular (constant acceleration), trapezoidal, and sinusoidal. A typical Mössbauer spectrometer is shown schematically in [Fig. 25.24](#).

Fig. 25.24

The block scheme of a Mössbauer spectrometer. A, absorber; CR, cryostat with temperature controller TC (optional, for low-temperature measurements); S, source moved by velocity transducer VT of driving unit DR; FG, function generator; VC, velocity calibrator (optional); LI, laser interferometer (optional); DET, detector; HV, high-voltage power supply; PA, preamplifier; AM, amplifier; SCA, single channel analyzer; MCA, multichannel analyzer; and PC, computer, OP, output



The transmitted or scattered radiation is usually detected by scintillation or proportional counters since high resolution is not required. The signals coming from the detector are amplified and gated by a single-channel analyzer set to transmit the Mössbauer transition energy range. These signals are introduced to a multichannel analyzer working in multiscaler regime (multichannel scaling, MCS). The switching (scaling) of channels is synchronized with the moving system so that in every cycle the same velocity is assigned to the same channel. The electromechanical drives move the source relative to the absorber periodically (with 10–100 Hz frequency) according to the given wave form. In the most typical case, a triangular wave form is used (constant acceleration). In modern Mössbauer spectrometers the velocity step signal is produced by a digital reference generator. While evaluating, the triangular waveform of velocity (with a maximum velocity in the orders of several mm/s) is approximated by a stepwise function of time, at each step of which (50–100 μ s) the velocity is considered to be constant. The Mössbauer spectra are usually recorded in 512 or 1,024 channels in each of which 10^5 – 10^7 counts are collected over several hours or days. Nowadays a major part of the Mössbauer equipment is a personal computer including an analyzer card (PCA card). This setup can be used for the pulse height analysis (PHA) that is needed to select the Mössbauer γ ray (or other secondary radiation), for the recording of the spectrum in MCS mode as well as for the evaluation of the recorded spectra with an appropriate software.

The Mössbauer spectrum is usually obtained as the transmitted or scattered intensity (in counts) vs. the Doppler velocity (in mm/s). However, the data provided by the analyzer are normally given in the form of counts vs. channel number. The correspondence between channel numbers and velocity is established by velocity calibration.

The *velocity calibration* of the Mössbauer spectrometer is performed either by measuring the Mössbauer spectrum of standard materials or by a calibrator instrument measuring the absolute velocity of the source relative to the absorber. The latter can be achieved by counting the fringes from a Michelson interferometer with a laser source connected to the multichannel analyzer, and thus the velocity for each channel can be obtained.

25.4.2 Transmission Geometry

Mössbauer spectra can be recorded in different ways. In the most frequently used *transmission technique* (➤ [Fig. 25.5](#)) the γ photons are counted after passing through the sample used as an absorber.

In most cases, the commercial source is moved and the absorber (which is the material to be studied) is at rest. In emission experiments, however, where the source is the material to be studied, the reference absorber is usually moved (see ➤ [Fig. 25.6](#) and ➤ [Sect. 25.4.4](#)).

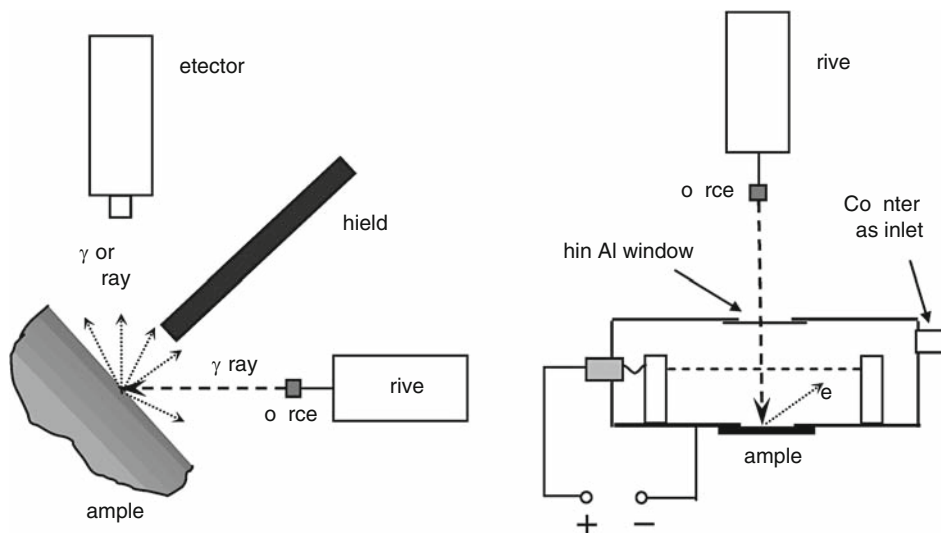
Scintillation detectors with a thin NaI(Tl) crystal are frequently applied for the detection of γ rays for many Mössbauer nuclides depending on the transition energy and the count rate. Various types of proportional counters are also used especially if the count rate is not very high. Semiconductor detectors are also applied occasionally. (For more about γ detectors see ➤ [Chap. 48 in Vol. 5](#).)

25.4.3 Reflection Geometry

In the scattering technique (➤ [Fig. 25.25](#)) the various radiations produced through the de-excitation of the irradiated sample (resonance scatterer) are detected.

■ Fig. 25.25

Scattering techniques. Reflection arrangements for Mössbauer measurements for γ ray or characteristic X-ray detection (*on the left*) and for conversion electron detection, CEMS (*on the right*)



With the *scattering technique*, it is possible to detect γ rays (back-scattering γ -ray Mössbauer spectroscopy), X-rays (X-ray Mössbauer spectroscopy), or conversion electrons (conversion electron Mössbauer spectroscopy, CEMS), which are characterized by different escape depths. Consequently, by the detection of different forms of back-scattered radiation, the surface of the samples can be investigated at different depths. An important advantage of the scattering Mössbauer technique is that it provides a nondestructive way of material testing.


25.4.3.1 Conversion Electron Mössbauer Spectroscopy

Among scattering Mössbauer measurements, the conversion electron Mössbauer spectroscopy (CEMS) is most developed because CEMS provides a unique surface characterization of solid materials. Since in Mössbauer spectroscopy the high Mössbauer–Lamb factor requires low γ energy, it inevitably results in very high electron conversion coefficients (see [▶ Table of Mössbauer Nuclides in Appendix of this volume](#)) and therefore the γ sources work at very high losses. This severe setback is turned to an advantage in CEMS. In this method, the γ rays emitted from the source undergo recoilless absorption in the “CEMS-sample.” The excited Mössbauer nuclei will then de-excite according to a characteristic lifetime and generate the conversion electrons to be detected.

The penetration range of conversion electrons of a few kilo electron volt is limited to a few 100 nm. The depth information of solid surface layers obtained by CEMS depends on the energy of electrons detected. The emitted electron energy corresponds to the photon energy minus the binding energy of the electron. The *conversion coefficient* $\alpha = N_e/N_\gamma$ (where N_e and N_γ are the

numbers of the emitted electrons and photons, respectively) is 8.21 for ^{57}Fe , and 5.1 for ^{119}Sn . The larger the α , the more effective the electron emission. However, not only conversion electrons are emitted, but a large number of Auger electrons can also be expected with substantially lower energies. The emission probability of electrons and photons in the relaxation process following the nuclear absorption in the ^{57}Fe nucleus is 7.3 keV K conversion electrons (80%), 5.6 keV KLL Auger electrons (53%), reemitted 14.4 keV γ rays (10%), and 6.4 keV characteristic $K\alpha$ X-rays (27%). The total number of electrons emitted is 133% of the number of photons absorbed. In the case of ^{119}Sn nuclei, 19.8 keV L conversion electrons (84%), 23.0 keV M conversion electron (13%), 2.8 keV Auger electrons (75%), 23.8 keV γ ray (16%), and 3.6 keV X-ray (9%) are emitted after Mössbauer absorption. The total percent of electrons emitted is 172%. It is clear from the total emission probability of conversion and Auger electrons that the detection of electrons is advantageous for thin films and solid surface studies (Bonchev et al. 1969).

Detectors for CEMS

Gas counter. A simple proportional gas counter is shown in  Fig. 25.25. A backscatter 2π proportional He gas-flow counter has high detection efficiency for low-energy electrons of about 10 keV, because He gas is insensitive to incident X-ray and γ ray (Terrell and Spijckerman 1968). CEMS spectra can be easily recorded by flowing He gas mixed with several % methane or isobutane as a quencher. XM spectra (i.e., when the characteristic X-ray is detected) can also be obtained by using flowing Ar/CH_4 gas mixture and by setting a Lucite plate (3 mm thick) in front of the incident window of the counter in order to filter off the X-rays emitted from the source. Argon, being a relatively light element, can detect 6.3 keV Fe X-rays more efficiently than 14.4 keV incident γ rays. The penetration range of 7.3 keV electrons in He gas at atmospheric pressure is at most 5 mm. The mean energy of electrons emitted is less than 7.3 keV, and the desirable distance between the anode wire and the sample surface is about 2 mm for ^{57}Fe CEMS. The detection efficiency of electrons and good signal-to-noise ratio are crucial to improve the count rate, and they sensitively depend on the actual design of the detector. A good electric contact between the sample (for which it is advisable to be a good conductor) and the body of the detector is very important.

The parallel-plate avalanche counter (PPAC) (Weyer 1976), which consists of flat-plate electrodes of graphite and sample, is advantageous for insulating materials. Any organic polyatomic gas can be used as *counting gas*. Usually acetone vapor is preferred. Depth selective CEMS (DCEMS, see later on) using PPAC is also possible by discriminating electron energy and controlling gas pressure (Weyer 1990). However, the mounting of a sample and the control of pressure in PPAC are rather difficult.

When a proportional counter is operated at low temperature, the gas multiplication decreases, and some quenchers mixed in the He gas get condensed on the cold surface of the sample. A gas counter filled with He + 5% CO at atmospheric pressure showed good performance at 77 K (Isozumi et al. 1983; Cook and Agyekum 1985; Nomura and Ujihira 1985; Meisel 1994). Purified He, H_2 , Ne, and mixtures of two gases such as He + 5% N_2 or He + several % CO may be used from temperatures as low as 15–300 K (Fukumura et al. 1991).

For high-temperature CEMS measurements, a gas-flow counter was installed in a furnace by Isozumi et al. (1979). Another type of gas counter was developed to heat only the sample; it was tested up to 740 K (Inaba et al. 1981). At even higher temperatures, low recoilless fraction, reaction of the quenching gas with the sample surface, and intense thermal electron emission made the measurement impossible. However, the gas reactivity can be utilized to monitor in

situ gas sensing of sensor materials because various gases can be mixed into He gas as a quenching gas (Nomura et al. 1993).

Electron multipliers and other counters. Channeltrons and channelplates have relatively large efficiency for low-energy electrons (below a few kilo electron volt). These types of counters have inherently no energy resolution, and need to work in a vacuum chamber. Both the sample and the channel electron multiplier installed are directly cooled in a conventional vessel by liquid He or liquid N₂ for CEMS (Sawicki et al. 1981).

The avalanche photodiode detector (APD), which is able to detect conversion electrons with very high intensity can also be useful in special applications (Weyer 1976; Gruverman 1976).

Depth Selective CEMS

Since the conversion electrons emitted from the sample surface have different energies depending on the depth they were generated in, it is theoretically possible to record Mössbauer spectra characteristic of selected surface layers of the sample at different depths. Geometric effects and the relatively wide energy spectrum of the various kinds of emitted electrons (K- and L-conversion, Auger, etc.) result in rather poor depth resolution.

To achieve depth selectivity, the Mössbauer setup should be combined with an electron spectrometer. A magnetic wedge spectrometer was first used for the detection of 30.5 keV K shell conversion electrons produced by the 100.1 keV γ transition in ¹⁸²W (Kankeleit 1961). DCEMS was proposed by Baverstam et al. (1973); DCEMS spectra were first measured with ¹¹⁹Sn (Bonchev et al. 1977) and ⁵⁷Fe (Shigematsu et al. 1980) by selecting electrons with a specific energy range.

Practice and theory of DCEMS were further developed by several authors (Liljequist 1981; Kajcsos et al. 1988; Klingelhofer and Kankeleit 1990; Klingelhofer and Meisel 1990; Belozerskii 1993).

Depth selectivity may also be achieved by using normal CEMS (for better distinction sometimes referred to as *ICEMS*, i.e., Integral CEMS) if the sample surface layers are removed stepwise with an appropriate technique like, e.g., noble gas ion sputtering or etching (Smit and van Staple 1982). However, this is already a destructive analytical method.

A pronounced depth selectivity of CEMS spectra is achieved by selecting the angle of the incident γ ray in addition to selection of the energy of the emitted electrons. On the other hand, depth information changes depending on the applied voltage (Kuprin and Novakova 1992). The layer-by-layer analysis of rough structures is possible by selecting the energy of detected electrons and by changing the voltage supplied using a He gas-flow counter.

Glancing angle CEMS (*GACEMS*) is useful to analyze the orientation of thin films. The influence of surface roughness on the surface selectivity in ⁵⁷Fe *GACEMS* is small provided that the electron-emission angle relative to the surface is larger than the average surface inclination angle associated with the surface roughness (Ismail and Liljequist 1986). According to the theory of CEMS at total external reflection (Andreeva and Kuzmin 1984; Topalov and Proikova 1985), the selective observation of a surface layer with a mean depth <10 nm is possible at glancing angles of less than 10 mrad ($\sim 0.6^\circ$).

Grazing incident ⁵⁷Fe CEMS (*GICEMS*) spectra were first observed by Frost et al. (1985), and *GICEMS* equipments were improved to have higher precision (Irakaev et al. 1993).

These techniques are rather time consuming, and the application of monochromatic photon beams of synchrotron sources may reduce the necessary measuring time in the future.

25.4.4 Resonance Counters

The most specific type of detectors used in Mössbauer spectroscopy is the so-called resonance detector. In this type of detectors, mainly conversion electrons are detected in a gas-filled chamber in which an ^{57}Fe -enriched standard target is placed. As conversion electrons can only form after the recoilless absorption of the γ rays in the standard target, the nonresonant radiation is very effectively filtered off, and the resultant Mössbauer spectrum has hardly any background (baseline). Therefore, the signal-to-noise ratio becomes excellent and the required measuring time (or the source activity that is needed) drastically decreases.

Since in this simple case, the detector itself contains a Mössbauer standard, the investigated material is in the source, i.e., one has to perform an emission experiment (see [Sect. 25.4.5](#)).

A “regular” transmission (absorption) experiment can also be carried out using a resonance detector, if the detector and the source are mounted on the same rigid frame and the standard matrix for the source and the target matrix containing the enriched ^{57}Fe (or other Mössbauer nuclide) are the same. The investigated sample should be placed in between. Either the detector + source system or the sample should be moved, which is not simple to realize technically.

A gas-filled resonance counter had been set up, e.g., by installing enriched ^{57}Fe stainless steel foils in a He gas chamber or parallel plate avalanche gas counter by Mullen and Stevenson (1978). An extremely light detector ($\text{K}_2\text{Mg}^{57}\text{Fe}(\text{CN})_6$ in Poly-Vinyl-Xylene scintillator) has also been developed for a movable resonance counter (Budakovski et al. 1999) to replace heavy gas-filled detectors.

Resonance detectors are also useful for Coulomb-excited nuclear experiments and for in situ implantation experiments using short-lived ^{57}Mn as parent nuclide to produce ^{57}Fe (Kobayashi et al. 2000).

25.4.5 Emission Mössbauer Spectroscopy

In an *emission experiment*, the radioactive excited-state Mössbauer nuclide is introduced into the sample to be investigated. In a Mössbauer experiment only the relative velocity of the source and the sample matters. Therefore, the emission experiment may be considered as a simple mirror image of the transmission experiment. This is well reflected by the upper panel of [Fig. 25.6](#), where the “ u ” axes for the (moving) source and absorber point in opposite directions. Instead of a standard source, one can use, in this case, a standard absorber, which consists of a single-peak compound (i.e., no quadrupole splitting and no magnetic splitting is allowed in the absorber). The most commonly used reference material is potassium hexacyanoferrate(II), $\text{K}_4[\text{Fe}(\text{CN})_6] \cdot 3\text{H}_2\text{O}$.

However, the source, which is supposed to be a material doped with a Mössbauer nuclide in its excited state cannot be prepared because the half-life is so short that the source would completely decay before one would start the experiment (for ^{57}Fe , $\tau_{1/2} \approx 10^{-7}$ s). Thus, one has to find a parent nuclide with a reasonably long half-life, which produces the excited Mössbauer level by nuclear decay. This has the consequence that in an emission experiment the dopant element may be different from the Mössbauer active one. In ^{57}Fe Mössbauer spectroscopy, this parent nuclide is ^{57}Co , which decays by electron capture, $^{57}\text{Co}(\text{EC})^{57}\text{Fe}$, with a half-life of ~ 9 months.

The doping with a parent element different from the Mössbauer one needs further considerations. The microenvironment of the parent nuclide in the doped sample may be different from that of its daughter element, the Mössbauer nuclide. (That is, the lattice site occupied and the coordination number or the valence state can all be different.) More importantly, the radioactive decay of the parent nuclide can trigger a relaxation process that alters the microenvironment of the Mössbauer dopant, which, in turn, affects the Mössbauer spectrum. These effects are called “aftereffects” (see [Sect. 25.4.5.1](#)), and in many cases these are the primary targets of this kind of Mössbauer studies in order to explore the hot-atom reactions triggered by the radioactive decay.

A substantial advantage of emission Mössbauer spectroscopy in comparison with the transmission technique is that if the material to be investigated contains heavy elements, then the required dopant concentration (e.g., ^{57}Co) may be 1–2 orders of magnitude lower in the emission experiment than the ^{57}Fe concentration in an analogous transmission experiment. This is in connection with the intensity loss of the Mössbauer radiation due to electronic absorption, which is always *self absorption* in the source and *regular absorption* in the absorber (Vértés and Homonnay 1997). Low dopant concentration is very important in *impurity Mössbauer spectroscopy*, where the investigated material does not contain a Mössbauer element; thus, a conveniently measurable Mössbauer nuclide is introduced artificially as an impurity with a potential risk of perturbing the physicochemical properties of the host phase.

25.4.5.1 Aftereffects

Aftereffects (Spiering et al. 1990; Nagy 1994) show up in the Mössbauer spectra if the relaxation process, which might have been triggered by the nuclear decay of the parent nuclide, is not finished by the time of the decay of the Mössbauer level, or, if it has caused an irreversible change in the microenvironment of the Mössbauer nuclide.

In the case of ^{57}Co , the electron capture triggers an Auger cascade with high probability, in which electrons, mostly in the energy range 0.6–6 keV, will be produced. The resultant highly charged iron ion (up to Fe^{7+}) starts then to recapture electrons and may reach the original oxidation state of the parent nuclide. This neutralization is accompanied by deposition of large excitation energy that has to dissipate fast and smoothly in order to save the microenvironment of the Mössbauer nuclide. If all these processes are completed in $\sim 10^{-9}$ s, then they will be invisible in the Mössbauer spectrum. The probability of this fast relaxation depends most of all on the electronic conduction properties of the host material.

In metals, electronic relaxation is fast and no aftereffects can be detected by Mössbauer spectroscopy. (This is why ^{57}Co can be built in metallic matrices in commercial sources for ^{57}Fe Mössbauer spectroscopy.)

In insulators and semiconductors, aftereffects show up in most cases in the form of *aliovalent charge states* (when the charge state of the nucleogenic ^{57}Fe is different from the equilibrium charge state of iron in that particular host material). The aliovalent charge states are typically higher than the equilibrium charge state (e.g., observation of Fe^{3+} in ^{57}Co -doped CoO , see Harami et al. 1984), but they can also be lower (e.g., Fe^+ in Co^{2+} -doped ZnS , see Garcin et al. 1980). In these ionic or ionic/covalent lattices, the formation of aliovalent charge states is explained mostly by the *competing acceptors model* (Helms and Mullen 1971; Perfiliev et al. 1976).

Aliovalent Fe^{3+} charge states can be observed in frozen aqueous solution of Co(II) -salts, where the formation of Fe^{3+} can be explained by the *radiolysis model*. In this model, oxidation of the nucleogenic Fe^{2+} to Fe^{3+} is assumed by OH radicals, which form during the radiolysis of water molecules coordinated to the parent Co^{2+} ion, by Auger electrons (Friedt and Danon 1980).

Excited electronic states due to aftereffects have been found and verified in only a few cases but in various compounds like in ^{57}Co -doped LiNbO_3 (Doerfler et al. 1984) and $^{57}\text{Co}/\text{Co}(\text{phen})_3(\text{ClO}_3)_2 \cdot 2\text{H}_2\text{O}$ (Ensling et al. 1970).

Bond rupture and complete *fragmentation* of the host molecule due to the deposited large excitation energy during the neutralization of the Auger-ionized Fe^{n+} ion has also been suggested in certain coordination compounds. It was observed that the higher the degree of delocalization in the ligands coordinated to the ^{57}Co center, the higher is the chance to avoid the (supposed) fragmentation (Srivastava and Nath 1976).

Time-differential Mössbauer emission spectroscopy (see Alflen et al. 1989) has also been applied to explore aftereffects.

25.4.6 Thermal Scan Method

In the case of the *Mössbauer thermal scan method*, the spectrum point belonging to zero (or a given constant) velocity is only measured at different temperatures (in the case of zero velocity without Doppler moving). By this simple technique, phase transition temperatures can be detected.

25.4.7 Mössbauer Polarimetry

The principle of *Mössbauer polarimetry* is similar to that of optical polarimetry. In this case, the polarization and the analysis can be performed by appropriately oriented external magnetic fields. Using ^{57}Fe polarization spectroscopy 36 lines, rather than six, are observed with magnetic materials (Gonser and Fisher 1981).

25.4.8 Capillary Mössbauer Spectroscopy

Normally, in liquid state, the recoil of the nucleus at the γ -ray emission hampers the nuclear resonance absorption. However, Mössbauer spectra of liquids can be observed even at room temperature if the molecules of liquids are trapped in the cavities of a special porous silicate glass of a mean pore diameter of ~ 4 nm. This type of Mössbauer spectroscopy is called capillary Mössbauer spectroscopy (Burger and Vértés 1983).

Three different types of behavior were experienced in various systems. It was concluded from the comparison of the Mössbauer parameters of samples obtained in liquid phase and in frozen solution that, in the case of aqueous solution of the Mössbauer active salts, only the solvent molecules were in chemical interaction with the wall of the capillaries in the glass. The microenvironments of the Mössbauer active species were the same both in liquid state and in the frozen solution.

In another case, when the Mössbauer parameters observed for the liquid state were different from those in frozen solution (e.g., SnI_4 in carbon tetrachloride) the Mössbauer atoms were in direct chemical interaction with the wall of the pores of the carrier.

In the third case, when two Mössbauer subspectra were observed in the liquid state and only one of them corresponded to the frozen solution, a fraction of the Mössbauer species was bound to the wall of pores, and the other part exhibited parameters characteristic of the free species.

It was found that high donicity of the solvent is required to keep the Mössbauer solute off the wall of the cavities, which enables one to study the bulk structure of solutions with Mössbauer spectroscopy in liquid phase.

25.4.9 Time-Dependent Measurements

Time-differential Mössbauer spectroscopy (Kajcsos et al. 1986; Alflen et al. 1989; Kobayashi 1989; Nakada et al. 1994) presents a unique tool for the study of chemical aftereffects and relaxation processes following the electron capture of ^{57}Co incorporated into various matrices. The principle of this method is as follows.

Using two detectors simultaneously, one has to detect the 122 keV γ quanta coming from the Mössbauer source as a start signal. This actually marks the birth of the 14.4 keV Mössbauer excited level (see the decay scheme in ► Fig. 25.7). Then, with the other detector, the 14.4 keV γ quantum is detected, and the elapsed time measured (stop signal). With this method, Mössbauer spectra can be recorded in any time interval after the nuclear decay of ^{57}Co . Recording characteristic X-rays following the electron capture, part of the aftereffect events can be filtered off. Due to the coincidence technique, very low activities can only be used, and therefore these measurements are rather time consuming (several weeks or months).

25.4.10 Combined Methods

A number of techniques also use Mössbauer spectroscopy combined with other methods like X-ray diffractometry (Parak et al. 1976; Faigel and Tegze 1994; Kriplani et al. 2002) and electron spectroscopy (Hisatake et al. 1974; Klingelhofer and Meisel 1990).

25.4.11 Measurements Using Synchrotron Radiation

Synchrotron radiation can also be used instead of radioactive sources for the nuclear resonance scattering (Ruby 1974; Gerdau et al. 1985). Since the already achieved results and the future perspectives of this method are very promising, a separate Chapter (see ► Chap. 26 in this Volume) is devoted to this topic.

25.4.12 Sources and Absorbers

The *Mössbauer source* is a solid material containing (or rather continuously generating) the excited-state nuclei of the studied nuclide and thus emitting the γ radiation characteristic of

the nuclear transition in question. Although Mössbauer transition has been observed with more than 48 nuclides (► Fig. 25.4), only a few of them are widely used – those having a relatively long-lived parent nuclide making it possible to produce a source lasting for at least a couple of months. The most common Mössbauer nuclides (and their share from the Mössbauer literature) are as follows: ^{57}Fe (82%), ^{119}Sn (6%), and ^{151}Eu (3%). The remaining 9% is divided among 45 nuclides. The commercial source for the 14.4 keV transition of ^{57}Fe is ^{57}Co diffused into a thin metallic matrix (e.g., Pd, Pt, and Rh) in which the emitted Mössbauer line is sufficiently narrow (to make it possible to produce experimental spectrum peaks as narrow as $W = 0.21$ mm/s). The activity of such sources is typically about 200 MBq to 10 GBq.

The isomer shifts are usually given relative to $\alpha\text{-Fe}$. If the isomer shift is given relative to a particular source matrix, conversion is possible with the help of ► Table 25.3.

If a proper parent nuclide cannot be found for an otherwise promising (e.g., low-energy) isomeric transition for source preparation, the Mössbauer nuclide may be generated continuously by (n, γ) reaction. In such a situation, prompt or slightly delayed γ quanta are used for Mössbauer purpose. The basic requirement is that, for the potential $^A_{Z+1}\text{N}$ Mössbauer nuclide, there should exist an $^A_Z\text{N}(n, \gamma)^{A+1}_Z\text{N}$ reaction with high cross section, and one should have access to a nuclear reactor with high neutron flux capability. A few tens more possible Mössbauer transitions become available with this method; however, the technical background is rather complex.

Normally, the studied sample is used either as an absorber or a scatterer. The *absorber* has to contain the ground-state nuclei of the nuclide responsible for the Mössbauer radiation of the source. Mössbauer absorbers used for transmission experiments can be sheets or powders of solids. Frozen solutions can also be measured.

The ideal sample has uniform thickness, circular shape, texture-free homogeneous distribution of material, and optimum surface density of the Mössbauer nuclide as well as an optimum thickness (Nagy et al. 1975).

For example, in the case of a natural α -iron foil 7 mg/cm² natural iron content (i.e., a linear thickness of 9 μm) is the optimum; however, 0.2 mg/cm² samples can also be measured with some difficulty. From the point of view of the Mössbauer resonant transition, only the ^{57}Fe

■ Table 25.3

^{57}Fe isomer shift conversion for some frequently used standard matrices. To obtain isomer shift values relative to $\alpha\text{-Fe}$, one has to add the corresponding value in column 2 to the isomer shift measured relative to the standard material in column 1

Source matrix/standard material relative to which the isomer shift δ is given	Correction (in mm s ⁻¹) to be added to δ to get the isomer shift relative to $\alpha\text{-Fe}$
Sodium nitroprusside (SNP)	−0.257
Chromium (Cr)	−0.147
Stainless steel (SS)	−0.092
α -Iron (reference)	0.000
Rhodium (Rh)	+0.109
Palladium (Pd)	+0.170
Copper (Cu)	+0.227
Platinum (Pt)	+0.344

content is important (which has a 2.14% abundance in natural iron), and therefore, a significant lowering of the minimum iron content (down to a factor of 1/45) can be achieved by enrichment with that isotope. Thus, e.g., the spectrum of an aluminum sample containing 20 ppm of ^{57}Fe can be easily measured by a conventional modern spectrometer.

Powders to be measured are usually spread out with uniform thickness between thin foils of Mylar or aluminum. Sometimes, in order to avoid vibrational effects, the powder is embedded in a matrix with low atomic absorption (e.g., paraffin, granulated organic, and polymer). It is important that neither the matrix nor the foil should contain any traces of the resonant nuclide (which can happen with aluminum in the case of ^{57}Fe measurements).

For samples used in *scattering experiments*, there is no essential demand other than the available surface density of the Mössbauer nuclide.

25.4.13 Cryostates, Furnaces, Magnets, and Pressure Cells

Different kinds of *cryostats* and *furnaces* are used to determine the temperature dependence of Mössbauer spectra. A simple *cold-finger* cryostat can be designed to measure at the temperature of solid CO_2 or liquid nitrogen. In this case, the precooled sample can be immediately put into the cryostat. This is important, e.g., with frozen solution samples. Temperature-controlled evacuated cryostats are generally applied between the millikelvin and a few hundred kelvin temperature range. They have to be supplied with special coolants (e.g., liquid helium or nitrogen). Nowadays closed circuit *refrigerator* cryostats operating between 12 to 400 K are also used frequently because they do not require liquid helium.

Temperature-controlled *furnaces* operate between room temperature and 1,500 K. *Cryofurnaces* can operate both below and above room temperature.

External magnetic fields are generated by *magnets* producing a field from 1 mT or so to 15 T. High fields are obtained by superconducting magnets. The magnet is usually placed around the cryostat or the furnace.

Cryostats are sometimes combined with *pressure chambers*, which can produce the required pressure on the sample. The high-pressure chambers are capable of pressures up to 200 kbar without disturbing the Mössbauer measurements.

25.5 Applications

Mössbauer spectroscopy has been used to solve problems in a variety of fields. Here is a list of a few examples: archeology (Kostikas et al. 1976), art (Keisch 1976), biochemistry and biology (Moshkovskii 1968; May 1971; Kuzmann 1979; Mössbauer et al. 1981), chemistry (Goldanskii and Herber 1968; Greenwood and Gibb 1971; Gütlich et al. 1978; Vértés et al. 1979; Long 1984; Long 1987; Vértés and Nagy 1990), electronics (Langouche 1989), magnetism (Grant 1975; Long and Grandjean 1993, 1996, 1997), materials sciences, solid-state physics and engineering (Gonser 1971, 1975b; Zemcik 1971), mineralogy and geology (Bancroft 1973; Mitra 1992; Kuzmann et al. 1998), nuclear physics and nuclear chemistry (Hafemeister 1971), physical metallurgy (Fujita 1975), and relativity (Pound 1981).

Shortly after the discovery of recoilless nuclear resonance emission/absorption on ^{193}Ir by Rudolf Mössbauer (Mössbauer 1958a) the Mössbauer effect was shown with ^{57}Fe (Shiffer and Marshall 1959; Pound and Rebka 1959; Hanna et al. 1960; de Pasquali et al. 1960) and

somewhat later with ^{119}Sn (Bartaloud et al. 1960; Deljagin et al. 1960), which nuclides are till now the most frequently used Mössbauer isotopes. The verification of the gravitational red shift of electromagnetic radiation (Pound and Rebka 1960) draws widespread scientific attention to Mössbauer spectroscopy.

More than 40,000 publications are available on various applications. The yearly number of publications is still growing. Bibliographic and other information about all these applications can be found in the Mössbauer Effect Reference Data Index (MERDI) and Mössbauer Effect Reference Data Journal (MERDJ). Many applications are discussed in monographs and in the proceedings of Mössbauer conferences (ICAME, ISIAE, LACAME, and other meetings of Mössbauer spectroscopists).

Accurate knowledge of the physical properties of the nuclei to be used for Mössbauer purpose opens the way for Mössbauer spectroscopy to become a really powerful tool in various research fields. In the followings, a few applications from the field of nuclear sciences are presented along with a list about the important chemical and analytical application areas.

25.5.1 Applications in Nuclear Sciences

Nuclear parameters can be determined and decay aftereffects can be studied with the help of Mössbauer spectroscopy (Hafemeister 1971; Burgov and Davidov 1968; Speth et al. 1978).

Nuclear parameters especially those of the excited state can be obtained from the hyperfine split Mössbauer spectrum.

The *nuclear spin* quantum number of excited state can be derived from the hyperfine spectra, but this is usually known before the Mössbauer experiment.

The fractional *change in the nuclear radius* $\Delta R/R$ can be obtained from the expression of isomer shift (Eq. (25.83)). For this reason, the accurate knowledge of the difference in the electronic density at the site of nucleus of source and absorber is necessary. Because of the difficulties in the estimation of electronic densities at the nucleus, the values of $\Delta R/R$ have considerable uncertainty (Shenoy and Wagner 1978).

The *nuclear magnetic moment* or the *g-factor* of the excited state can be determined with high accuracy from the magnetic splitting (Eq. (25.93)) since the ground-state values are previously known. In certain cases, large external magnetic field is needed to resolve the magnetically split lines (deWaard and Heberle 1964).

For a nucleus with ground-state nuclear spin higher than 1/2, the energy differences between the states in the quadrupole splitting will contain the ratio of the *quadrupole moments* of the excited state and the ground state. If the value of the quadrupole moment of the ground state is known from an independent experiment, then the quadrupole moment of the excited state is obtained from the corresponding ratio (Hafemeister et al. 1964).

For nuclei with ground-state spin $I_g = 1/2$, the determination of quadrupole moment from the expression of quadrupole splitting energy (Eq. (25.90)) can be performed with a relatively large error (Ingalls 1964; Artman et al. 1968; Chappert et al. 1969).

The *internal conversion coefficient* for ^{57}Fe has been accurately determined from the transmission integral (see Eqs. (25.11), (25.30), and (25.31)) by using a series of iron absorbers all having the same thickness of iron atoms but the enrichment in ^{57}Fe varied by a factor of as much as 37 (Hanna and Preston 1965).

Basically, the *lifetime of the excited state* can be determined from the line width (Eq. (25.2)). However, several broadening effects influence the exact determination of the

nuclear lifetime (Hafemeister and Shera 1966), which can be obtained within the range of 10^{-7} and 10^{-10} s. Mössbauer spectroscopy is a unique tool for this application.

A Mössbauer experiment was successfully performed to confirm the *parity nonconservation* in β decay. The Mössbauer spectrum was recorded in a β – γ coincidence experiment and an unequal population of the excited state sublevels was observed when the nuclei in the source were polarized by a large magnetic field in the direction of the β radiation (DeWaard et al. 1968).

The *multipole mixing ratio* δ of mixed M1+E2 radiation ($\delta = |E2/M1|$) as well as the phase angle between E2 and M1 components can be obtained from the relative areas of the corresponding peaks (Kistner 1968; Wagner et al. 1968; Atac et al. 1968). The value of the phase angle has a relevance in testing the time reversal in electromagnetic interaction. No violation of time reversal was found in Mössbauer experiments (Kalvius et al. 1968; Mullen 1986).

25.5.2 Chemical and Analytical Applications

The application of Mössbauer spectroscopy in chemistry is based on the utilization of information obtained mainly from the isomer shift, quadrupole splitting, and magnetic splitting.

The chemical isomer shift is a direct function of the s-electron density at the nucleus (see [Eqs. \(25.83\)–\(25.85\)](#), Shenoy and Wagner 1978), but shows secondary induced effects due to changes in shielding (i.e., electron–electron repulsion) of the s-electrons by p-, d-, or f-electrons. It is therefore sensitive to most changes of orbital occupation in the valence shell of the atom. Since there are well-established monotonous correlations between the electronic density and the oxidation and spin state of the Mössbauer atom, the isomer shift can be used for the *determination of the oxidation and spin state* of Mössbauer nuclides. Isomer shift scales as a function of the oxidation state are now available for a large number of Mössbauer nuclides, and they are helpful in characterizing unknown materials and identifying different species of a certain Mössbauer nuclide in a mixture in wide areas of inorganic chemistry, organic chemistry, biochemistry, and geochemistry.

The quadrupole splitting ([Eqs. \(25.90\)–\(25.91\)](#), see, e.g., Travis (1971), Gütlisch et al. (1978)) is caused by the asymmetric occupation of the nonspherical p-, d-, or f-electron orbitals, and its magnitude and sign can also be used to *determine the asymmetry of the charge distribution with respect to chemical bond*.

The variation of the coordination number in compounds results primarily in a change in the symmetry of the coordination sphere; therefore, the quadrupole splitting can serve as an indicator of such a change. At the same time, the contraction or expansion of the coordination sphere also affects the bond strength between the ligands and the central Mössbauer atom, which will be reflected in the isomer shift values.

One can obtain information about the molecular geometry mainly from the *electric field gradient* data derived from the quadrupole splittings. The principal component of electric field gradient can be written as (Gütlisch et al. 1978)

$$V_{zz} = (1 - \gamma_{\infty})(V_{zz})_L + (1 - R)(V_{zz})_{VAL} = (1 - \gamma_{\infty})(V_{zz})_L + (1 - R)[(V_{zz})_{CF} + (V_{zz})_{MO}] \quad (25.131)$$

where $(V_{zz})_L$ is the *ligand contribution* arising from the aspherical charge distribution in the ligand sphere and/or lattice surroundings with a symmetry lower than cubic, $(V_{zz})_{VAL}$ is

the *valence electron contribution* due to the aspherical distribution of electrons in the valence orbitals. $(V_{zz})_{\text{VAL}}$ can be divided into two parts due to nonspherical population of the *d*-orbitals according to crystal field splitting $(V_{zz})_{\text{CF}}$ and due to anisotropic population of molecular orbitals $(V_{zz})_{\text{MO}}$. The parameters γ_{∞} and R are the Sternheimer factors (Sternheimer 1963).

In the case of compounds where the ligand contribution determines the V_{zz} , the *point-charge model* can be applied to calculate the electric field gradient as the sum of independent contributions of each ligand. Based on the point-charge model, the calculation of V_{zz} for trans and cis isomers of mixed octahedral complexes (Travis 1971) results $(V_{zz})_{\text{trans}} = -2(V_{zz})_{\text{cis}}$. This makes Mössbauer spectroscopy very sensitive to distinguish between *cis* and *trans* isomers by measuring the corresponding quadrupole splitting values.

When the *valence contribution* determines the V_{zz} , the *crystal fields* in the complex compounds (e.g., in the case of high-spin iron(II) or low-spin iron(III) compounds with D_{4h} symmetry) can be determined (Gütlich et al. 1978) by measuring the temperature dependence of the quadrupole splitting (► Eq. (25.106)). In these cases, the change in the thermal

■ Table 25.4

Characteristic applications of Mössbauer spectroscopy considered as fundamental studies of compounds

Fundamental studies of compounds
<i>Electronic structure</i> Determination of oxidation and spin states of the Mössbauer atom, spin transitions (spin crossover)
<i>Bond properties</i> σ and π interactions between the Mössbauer atom and ligands, influence of electronegativity of ligands
<i>Structural properties</i> Molecular geometry, determination of cis- and trans isomers, distortion from cubic symmetry (Jahn–Teller effect), effect of polymerization, finding the right structure of polynuclear complexes, identification of possible structural position occupied by the Mössbauer atom, determination of distribution of Mössbauer atoms among the sites, determination of site preference, determination of coordination number, effect of neighbors
<i>Crystal structure</i> Determination of crystalline and amorphous states, determination of crystal anisotropy, defects and defect structures, characterization of quasicrystalline, microcrystalline, nanocrystalline and amorphous materials
<i>Magnetic properties</i> Diamagnetism, paramagnetism, temperature-dependent spin-changes, spin relaxations, cooperative phenomena, ferromagnetism, ferrimagnetism, antiferromagnetism, determination of transition temperature, determination of magnetic structure
<i>Dynamic processes</i> Phonon mode changes, determination of Debye temperature, determination of effective mass, determination of anisotropy of lattice vibration, electron hopping in spinels, diffusion, determination of jump frequency and diffusion coefficient, paramagnetic spin relaxation, spin–spin relaxation, spin–lattice relaxation, superparamagnetism, determination of grain size

electronic population of the low-lying orbitals is taken into consideration in the temperature dependence of $(V_{zz})_{CF}$.

Bonding properties of complex compounds can be obtained by using data both from isomer shift and quadrupole splitting together, since the electronic density and the electric field gradient at the Mössbauer nucleus are influenced differently by σ donor and π acceptor strengths of surrounding ligands, covalency effects, oxidation/reduction processes, difference in electronegativity of ligands coordinated to the Mössbauer atom, etc.

Magnetically split Mössbauer spectra can be obtained not only with ferro-, ferri-, and antiferromagnetic materials but with paramagnetic compounds, too, when the electronic spin orientation changes slowly as compared to the Larmor precession of the Mössbauer nucleus (paramagnetic spin relaxation, see Wickman et al. 1966). In these cases the internal magnetic flux density at the site of nucleus, B_{int} , is determined from the magnetic splitting (see [Eqs. \(25.93\)](#) and [\(25.94\)](#)). The internal magnetic flux density originates from several terms. In the absence of an external field, $B_{int} = B_c + B_{orb} + B_{dip}$, (Watson and Freeman 1961). The Fermi-contact term B_c arises from the unbalanced spin density of s electrons at the nucleus, the orbital term B_{orb} is from the orbital angular momentum of the ion, while the dipolar term B_{dip} is the field produced at the nucleus by the arrangement of atomic moments through the crystal. By measuring the dependences of the magnetic splitting either on temperature or on concentration of Mössbauer atoms, the *spin-lattice* and *spin-spin relaxation* can also be studied.

As a conclusion, one can distinguish between two main characteristic kinds of applications of Mössbauer spectroscopy in chemistry. It can be applied to study *fundamental properties* of compounds as well as it serves as an *analytical tool* for identifying chemical species. In the latter case it is usually used as a fingerprint method (see [Sect. 25.3.3](#)). In [Tables 25.4](#) and [25.5](#) characteristic applications of Mössbauer spectroscopy in various fields of chemistry are collected.

■ **Table 25.5**

Characteristic applications of Mössbauer spectroscopy considered as analytical studies

Analytical studies
<i>Phase and chemical analysis in compounds and alloys</i>
<i>Surface studies</i> Corrosion, determination of corrosion products on iron and steel surfaces, adsorption properties of ion exchangers, catalysis, surface reactions on catalysts, coatings, effect of the preparation parameters on the phase composition and the short-range order
<i>Solid-state reactions</i> Ligand exchange in transition metal complexes, thermal and radiation-induced decomposition, pressure-induced reactions, electron exchange reactions, substitutional effects in sophisticated oxides
<i>Frozen solution studies</i> Hydration and solvation effects, electron exchange reactions, polymerization
<i>Phase transformation</i> Change in crystal structure, crystallization of amorphous materials, magnetic ordering

References

- Abragam A (1964) *L'Effect Mössbauer*. Gordon & Breach, New York
- Alflen M, Hennen C, Tuzek F, Spiering H, Gütlich P, Kajcsos Zs (1989) *Hyperfine Interact* 47–48:115
- Andreeva MA, Kuzmin RN (1984) *Phys Stat Sol B* 125:461
- Artman JO, Muir AH, Wiedersich H (1968) *Phys Rev* 173:337
- Atac M, Crisman B, Debrunner P, Frauenfelder H (1968) *Phys Rev Lett* 20:691
- Bancroft GM (1973) *Mössbauer spectroscopy*. McGraw Hill, London
- Bartaloud R, Picou JL, Tsara C (1960) *C R Acad Sci Paris* 250:2705
- Baverstam U, Bohm C, Ringstrom B, Ekdahl T (1973) *Nucl Instr Meth* 108:439
- Belozerskii GN (1993) *Mössbauer studies of surface layers*. Elsevier, Amsterdam
- BESSEL (2010) <http://www.efunda.com/math/bessel/bessel.cfm> Accessed 2nd October, 2010
- Bhide VG (1973) *Mössbauer effect and its applications*. Tata McGraw-Hill, New Delhi
- Blatt JM, Weisskopf VF (1959) *Theoretische Kernphysik*. Teubner, Leipzig
- Bonchey T, Jordanov A, Minkova A (1969) *Nucl Instr Meth* 70:36
- Bonchey Ts, Minkova A, Kushev G, Grozdanov M (1977) *Nucl Instr Meth* 147:481
- Breit G, Wigner E (1936) *Phys Rev* 49:519
- Budakovski SV, Iliassov AZ, Lavrov AO, Rogozev BI (1999) *Proceedings of the conference on ICAME99, T9/22*. Garmisch-Partenkirchen, Germany
- Burger K, Vértés A (1983) *Nature* 306:353
- Burgov NA, Davidov AV (1968) In: Goldanskii VI, Herber RH (eds) *Chemical applications of Mössbauer spectroscopy*. Academic, New York, London
- Campbell SJ, Aubertin F (1989) In: Long GJ (ed) *Mössbauer spectroscopy applied to inorganic chemistry, Vol 3*. Plenum, New York
- Chappert J, Frankel RB, Misetich A, Blum NA (1969) *Phys Rev B* 28:406
- Clauser MJ, Mössbauer RL (1969) *Phys Rev* 178:559
- Cohen RL (1976) *Applications of Mössbauer spectroscopy I*. Academic, New York, San Francisco, London
- Cohen RL (1980) *Applications of Mössbauer spectroscopy II*. Academic, New York, San Francisco, London
- Cohen SG, Pasternak M (1973) *Perspectives in Mössbauer spectroscopy*. Plenum, New York, London
- Cook DC, Agyekum E (1985) *Nucl Instr Meth B* 12:515
- Cranshaw TE, Dale BW, Longworth CO, Johnson CE (1985) *Mössbauer spectroscopy and its applications*. Cambridge University Press, Cambridge
- Danon J (1968) *Lectures on the Mössbauer effect*. Gordon & Breach, New York
- De Pasquali G, Frauenfelder H, Margulies S, Peacock RN (1960) *Phys Rev Lett* 4:71
- Deljagin NN, Shpinel VS, Bryukhanov VA, Zwenglinski B (1960) *Zh Exp Theor Fiz* 39:894
- deWaard H, Heberle J (1964) *Phys Rev* 136:1615
- DeWaard H, Heberle J, Schurrer PJ, Hasper H, Koks WWJ (1968) In: Matthias E, Shirley DE (eds) *Hyperfine structure and nuclear reactions*. North Holland, Amsterdam
- Doerfler R, Nagy DL, Pfannes H-D, Putzka A, Ritter G, Zeman N (1984) *Phys Stat Sol B* 124:767
- Dunlap BD, Kalvius GM (1978) In: Shenoy GK, Wagner FE (eds) *Mössbauer isomer shifts*. North Holland, Amsterdam, New York, Oxford
- Eicher H, Trautwein A (1969) *J Chem Phys* 50:2540
- Ensling J, Fitzsimmons BW, Gütlich P, Hasselbach KM (1970) *Angew Chem* 82:638
- Faigel Gy, Tegze M (1994) *Hyperfine Interact* 92:1137
- Foyt DC, Good ML, Cosgrove JG, Collins RL (1975) *J Inorg Nucl Chem* 37:1913
- Frauenfelder H (1962) *The Mössbauer effect*. Benjamin, New York
- Friedt JM, Danon J (1980) *At Energy Rev* 18:893
- Frost JC, Cowie BCC, Chapman SN, Marshall JF (1985) *Appl Phys Lett* 47:581
- Fujita FE (1975) In: Gonser U (ed) *Mössbauer spectroscopy*. Springer, New York
- Fujita FE (ed) (1999) *Introduction to the Mössbauer spectroscopy – principles and applications*. Agune Gijutsu Center, Tokyo
- Fukumura K, Nakanishi A, Kobayashi T, Katano R, Isozumi Y (1991) *Nucl Instr Meth Phys Res A* 301:482
- Garcin C, Imbert P, Jehanno G, Gerard A, Danon J (1980) *J Phys Chem Solids* 41:969
- Gerdau E, Rüffer R, Winkler H, Tolksdorf W, Klages CP, Hannon JP (1985) *Phys Rev Lett* 54:835
- Gibb TC (1976) *Principles of Mössbauer spectroscopy*. Chapman & Hall, London
- Goldanskii VI (1963) *The Mössbauer effect and its application to chemistry*. Izd. Akademii Nauk, Moscow
- Goldanskii VI, Herber RH (1968) *Chemical applications of Mössbauer spectroscopy*. Academic, New York, London
- Goldanskii VI, Makarov EF, Khrapov VV (1963) *Phys Lett* 3:334
- Gonser U (1971) In: May L (ed) *An introduction to Mössbauer spectroscopy*. Adam Hilger/Plenum, London, New York
- Gonser U (ed) (1975a) *Mössbauer spectroscopy*. Springer, New York

- Gonser U (1975b) Proceedings of the conference ICAME, 113. Cracow, Poland
- Gonser U (ed) (1981) Mössbauer spectroscopy II – the exotic side of the method. Springer, Berlin
- Gonser U, Fisher H (1981) In: Gonser U (ed) Mössbauer spectroscopy II – the exotic side of the method. Springer, Berlin
- Grant RW (1975) Mössbauer spectroscopy in magnetism. In: Gonser U (ed) Mössbauer spectroscopy. Springer, New York
- Greenwood NN, Gibb TC (1971) Mössbauer spectroscopy. Chapman & Hall, London
- Gruverman IJ (ed) (1965) Mössbauer effect methodology, Vol 1. Plenum, New York
- Gruverman IJ (ed) (1966) Mössbauer effect methodology, Vol 2. Plenum, New York
- Gruverman IJ (ed) (1967) Mössbauer effect methodology, Vol 3. Plenum, New York
- Gruverman IJ (ed) (1968) Mössbauer effect methodology, Vol 4. Plenum, New York
- Gruverman IJ (ed) (1970) Mössbauer effect methodology, Vol 5. Plenum, New York
- Gruverman IJ (ed) (1971a) Mössbauer effect methodology, Vol 6. Plenum, New York
- Gruverman IJ (ed) (1971b) Mössbauer effect methodology, Vol 7. Plenum, New York
- Gruverman IJ (ed) (1974) Mössbauer effect methodology, Vol 9. Plenum, New York
- Gruverman IJ (ed) (1976) Mössbauer effect methodology, Vol 10. Plenum, New York
- Gruverman IJ, Seidel CW (eds) (1973) Mössbauer effect methodology, Vol 8. Plenum, New York
- Gütlich P, Link R, Trautwein A (1978) Mössbauer spectroscopy and transition metal chemistry. Springer, Berlin
- Hafemeister DW (1971) In: May L (ed) An introduction to Mössbauer spectroscopy. Adam Hilger, Plenum, London, New York
- Hafemeister DW, Shera EB (1966) Nucl Instr Meth 41:133
- Hafemeister DW, dePasquali D, deWaard H (1964) Phys Rev B 135:1089
- Hanna SS, Preston RS (1965) Phys Rev Lett 139:A722
- Hanna SS, Heberle J, Littlejohn C, Perlow GJ, Preston RS, Vincent DJ (1960) Phys Rev Lett 4:177 and 513
- Harami T, Look J, Huenges E, Fontcuberta J, Obradors X, Tejada J, Parak FG (1984) J Phys Chem Solids 45:181
- Helms WR, Mullen JG (1971) Phys Rev B 4:750
- Herber RH (ed) (1984) Chemical Mössbauer spectroscopy. Plenum, London, New York
- Hesse J, Rübarsch A (1974) J Phys E Sci Instrum 7:526
- Hisatake K, Toriyama T, Kigawa M, Fujioka M (1974) J Jpn Appl Phys 2:733
- Housley RM, Grant RW, Gonser U (1969) Phys Rev 178:514
- Inaba M, Nakagawa H, Ujihira Y (1981) Nucl Instr Meth 180:131
- Ingalls R (1964) Phys Rev A 133:787
- Irakae SM, Andreeva MA, Semrenov VG, Belozerskii GN, Grishin OV (1993) Nucl Instr Meth B 74:545
- Isozumi Y, Kurakado M, Katano R (1979) Nucl Instr Meth 166:407
- Isozumi Y, Kurakado M, Katano R (1983) Nucl Instr Meth 204:571
- Ismail M, Liljequist D (1986) Hyperfine Interact 29:1509
- Janot C (1972) L'Effect Mössbauer et ses Applications, a la Physique du Solide et la Metallurgie Physique. Masson, Paris
- Kagan Yu (1962) The Mössbauer effect. Izd. Inostrannoi Literatury, Moscow
- Kaipov DK (1976) Nuclear gamma resonance and its related processes. Nauka, Alma Ata
- Kajcsos Zs, Alfien M, Spiering H, Gütlich P, Albrecht R, Schulze R, Kurz R (1986) Hyperfine Interact 29:1551
- Kajcsos Z, Sauer Ch, Holzwarth A, Kurz R, Zinn W, Ligtenberg MAC, Van Aller G (1988) Nucl Instr Meth Phys Res B 34:384
- Kalvius GM, Sprouse GD, Hanna SS (1968) In: Matthias E, Shirley DE (eds) Hyperfine structure and nuclear reactions. North Holland, Amsterdam
- Kankeleit E (1961) Z Phys 164:442
- Keisch B (1976) In: Cohen RL (ed) Applications of Mössbauer spectroscopy. Academic, New York, San Francisco, London
- Kimball CW, Taneja SP, Weber L, Fradin FY (1974) In: Gruverman IJ (ed) Mössbauer effect methodology, Vol 9. Plenum, New York
- Kistner OC (1968) In: Matthias E, Shirley DE (eds) Hyperfine structure and nuclear reactions. North Holland, Amsterdam
- Kittel Ch (1968) Introduction to solid state physics. Wiley, New York
- Klencsár Z, Kuzmann E, Vértés A (1996) J Rad Nucl Chem 210:105
- Klingelhofer G, Kankeleit E (1990) Hyperfine Interact 53:1905
- Klingelhofer G, Meisel W (1990) Hyperfine Interact 57:1911
- Kobayashi T (1989) Bull Chem Soc Jpn 62:576
- Kobayashi Y, Yoshida Y, Yoshida A, Watanabe Y, Hayakawa K, Yukihiro K, Shimura F, Ambe F (2000) Hyperfine Interact 126:417
- Kopcewicz M (1989) In: Long GJ (ed) Mössbauer spectroscopy applied to inorganic chemistry, Vol 3. Plenum, New York
- Kostikas A, Simopoulos A, Gangas NH (1976) In: Cohen RL (ed) Applications of Mössbauer spectroscopy. Academic, New York, San Francisco, London
- Kriplani U, Regehr MW, Fultz B (2002) Hyperfine Interact 139:667
- Kündig W (1967) Nucl Instr Meth 48:219
- Kuprin AP, Novakova AA (1992) Nucl Instr Meth Phys Res B 62:493

- Kuzmann E (1979) Mössbauer effect in biological research. In: Vértés A, Korecz L, Burger K (eds) Mössbauer spectroscopy. Akadémiai Kiadó, Elsevier, Amsterdam, Oxford, New York, Budapest
- Kuzmann E, Nagy S, Vértés A (1994) *J Radioanal Nucl Chem Lett* 186:463
- Kuzmann E, Nagy S, Vértés A, Weisburg T, Garg VK (1998) In: Vértés A, Nagy S, Süvegh K (eds) *Nuclear methods in mineralogy and geology*. Plenum, New York, London
- Kuzmann E, Nagy S, Vértés A (2003) *Pure Appl Chem* 75:801
- Lamb WE Jr (1939) *Phys Rev* 55:190
- Langouche G (1989) In: Long GJ (ed) *Mössbauer spectroscopy applied to inorganic chemistry*, Vol 1. Plenum, New York
- Liljequist D (1981) *Nucl Instr Meth* 179:617; 185:599
- Lindner A (1984) *Drehimpulse in der Quantenmechanik*. Teubner, Stuttgart
- Lipkin HJ (1960) *Ann Phys* 9:332
- Long GJ (ed) (1984) *Mössbauer spectroscopy applied to inorganic chemistry*, Vol 1. Plenum, New York
- Long GJ (ed) (1987) *Mössbauer spectroscopy applied to inorganic chemistry*, Vol 2. Plenum, New York
- Long GJ (ed) (1989) *Mössbauer spectroscopy applied to inorganic chemistry*, Vol 3. Plenum, New York
- Long GJ, Grandjean F (eds) (1993) *Mössbauer spectroscopy applied to magnetism and materials science*, Vol 1, *Modern inorganic chemistry*, Plenum, New York
- Long GJ, Grandjean F (eds) (1996) *Mössbauer spectroscopy applied to magnetism and materials science*, Vol 2, *Modern inorganic chemistry*, Plenum, New York
- Long GJ, Grandjean F (eds) (1997) *Mössbauer spectroscopy applied to magnetism and materials science*, Vol 3, *Modern inorganic chemistry*, Plenum, New York
- Malmfors KG (1953) *Arkiv Fysik* 6:49
- Margulies S, Ehrman JR (1961) *Nucl Instr Meth* 12:131
- Matthias E, Shirley DE (1968) *Hyperfine structure and nuclear reactions*. North Holland, Amsterdam
- Matthias E, Schneider W, Steffen RM (1963) *Arkiv Fysik* 24:97
- May L (1971) *An introduction to Mössbauer spectroscopy*. Adam Hilger, Plenum, London, New York
- Mayer-Kuckuk T (1994) *Kernphysik*. Teubner, Stuttgart, p 93
- Meisel W (1994) *Hyperfine Interact* 92:1213
- Mitra S (1992) *Applied Mössbauer spectroscopy, physics and chemistry of earth*, Vol 18. Pergamon, Oxford, New York, Seoul, Tokyo
- Moon PB (1950) *Proc Phys Soc* 63:1189
- Mørup S (1981) *Paramagnetic and superparamagnetic relaxation phenomena studied by Mössbauer spectroscopy*. Polyteknisk Forlag, Lyngby
- Mössbauer RL (1958a) *Z Physik* 151:124
- Mössbauer RL (1958b) *Naturwissenschaften* 45:538
- Mössbauer RL, Wiedemann W (1960) *Z Physik* 159:33
- Mössbauer RL, Parak F, Hoppe W (1981) In: Gonser U (ed) *Mössbauer spectroscopy II – the exotic side of the method*. Springer, Berlin
- Moshkovskii Yu Sh (1968) In: Goldanskii VI, Herber RH (eds) *Chemical applications of Mössbauer spectroscopy*, Academic, New York and London
- Muir A, Ando KJ, Coogan HM (1958–1965) *Mössbauer effect data index*. Inter Science, New York, London, Sydney
- Mullen JG (1986) *Hyperfine Interact* 29:1513
- Mullen JG, Stevenson J (1978) *Nucl Instrum Meth* 153:77
- Nagy DL (1994) *Hyperfine Interact* 83:3
- Nagy S, Lévy B, Vértés A (1975) *Acta Chim Acad Sci Hung* 85:273
- Nakada M, Makaki M, Saeki M, Sagawa C, Aratono Y, Endo K (1994) *Hyperfine Interact* 92:183
- Nomura K, Ujihira Y (1985) *Bunseki Kagaku* 34:T5
- Nomura K, Sharma SS, Ujihira Y (1993) *Nucl Instr Meth Phys Res B* 76:357
- Nozik AI, Kaplan M (1967) *J Chem Phys* 47:2960
- Parak F, Mössbauer RL, Hoppe W (1976) *J Phys* 37: C6–703
- Perfiliev YuD, Kulikov LA, Bugaenko LT, Babeshkin AM, Afanasov MI (1976) *J Inorg Nucl Chem* 38:2145
- Perlow JG (1977) *Workshop on new directions in Mössbauer spectroscopy*. AIP, New York
- Pfannes H-D, Gonser U (1973) *Appl Phys* 1:93
- Pound RW (1981) In: Gonser U (ed) *Mössbauer spectroscopy II – the exotic side of the method*. Springer, Berlin
- Pound RV, Rebka GA Jr (1959) *Phys Rev Lett* 3:554
- Pound RV, Rebka GA Jr (1960) *Phys Rev Lett* 4:337
- Raimes S (1961) *The wave mechanics of electrons in metals*. North Holland, Amsterdam
- Rotenberg M, Bivins R, Metropolis N, Wooten JK Jr (1959) *The 3j and 6j symbols*. MIT Press, Cambridge
- Ruby SL (1974) *J Phys* 35:C6–209
- Sano H (1972) *Mössbauer spectroscopy: the chemical applications*. Kodansha, Tokyo
- Sawicki JA, Tylicszczak T, Gzowski O (1981) *Nucl Instr Meth* 190:433
- Schatz G, Weidinger A, Gardner JA (1996) *Nuclear condensed matter physics, Nuclear methods and applications*. Wiley, Chichester, New York, Brisbane, Toronto, Singapore
- Seagusa N, Morrish AH (1982) *Phys Rev B* 26:10
- Shapiro FL (1960) *Usp Fiz Nauk* 72:685
- Shenoy GK, Wagner FE (eds) (1978) *Mössbauer isomer shifts*. North Holland, Amsterdam, New York, Oxford
- Shiffer JP, Marshall V (1959) *Phys Rev Lett* 3:556
- Shigematsu T, Pfannes HD, Keune W (1980) *Am Phys Soc* 45:1206
- Shirley DA (1964) *Rev Mod Phys* 36:339

- Shpinel VSh (1969) Resonance of gamma rays in crystals. Nauka, Moscow
- Singwi KS, Sjolander A (1960) Phys Rev 120:1093
- Smit PH, van Staple RP (1982) Appl Phys A28:113
- Speth J, Henning W, Kienle P, Meyer J (1978) In: Shenoy GK, Wagner FE (eds) Mössbauer isomer shifts. North Holland, Amsterdam, New York, Oxford
- Spiering H, Alflen M, Gütlich P, Hauser A, Hennen C, Manthe U, Tuzcek F (1990) Hyperfine Interact 53:113
- Srivastava TS, Nath A (1976) J Phys Chem 80:529
- Sternheimer RM (1950) Phys Rev 80:102
- Sternheimer RM (1951) Phys Rev 84:244
- Sternheimer RM (1963) Phys Rev 130:1423
- Stevens JG, Shenoy GK (1981) Mössbauer spectroscopy and its chemical applications in: advances in chemistry series, Vol 194. American Chemical Society, Washington DC
- Stevens JG, Stevens VE (1966) Mössbauer effect data index (MERDI). Adam Hilger, London
- Terrell JH, Spijkerman JJ (1968) Appl Phys Lett 13:11
- Thosar BV, Iyengar PK (eds) (1983) Advances in Mössbauer spectroscopy. Elsevier, New York
- Topalov P, Proikova A (1985) Nucl Instr Meth Phys Res A 236:142
- Travis JC (1971) In: May L (ed) An introduction to Mössbauer spectroscopy. Adam Hilger, Plenum, London, New York
- Vértes A, Homonnay Z (1997) Mössbauer spectroscopy of sophisticated oxides. Akadémiai Kiadó, Budapest
- Vértes A, Nagy DL (1990) Mössbauer spectroscopy of frozen solutions. Akadémiai Kiadó, Budapest
- Vértes A, Korecz L, Burger K (1979) Mössbauer spectroscopy. Akadémiai Kiadó, Elsevier, Amsterdam, Oxford, New York, Budapest
- Wagner FE, Kaindl G, Kiennle P, Korner HJ (1968) In: Matthias E, Shirley DE (eds) Hyperfine structure and nuclear reactions. North Holland, Amsterdam
- Watson RE, Freeman AJ (1961) Phys Rev 123:2027
- Wegener H (1965) Der Mössbauer Effect und seine Anwendung. Bibliographisches Institut AG, Mannheim
- Weisstein EW (2010) Wigner 3j-Symbol (MathWorld: A Wolfram Web Resource), <http://mathworld.wolfram.com/Wigner3j-Symbol.html>. Accessed 2nd October, 2010
- Wertheim GK (1964) Mössbauer effect: principles and applications. Academic, New York
- Weyer G (1976) Mössbauer Effect Meth 10:301
- Weyer G (1990) Hyperfine Interact 58:2561
- Wickman HH, Klein MP, Shirley DA (1966) Phys Rev 152:345
- Williamson DL, Bukshpan S, Ingalls R (1972) Phys Rev B 6:4194
- Window B (1971) J Phys E Sci Instrum 4:40
- Zemcik T (1971) Proceedings of the conference ICAME. Dresden, Germany

26 Mössbauer Excitation by Synchrotron Radiation

M. Seto

Kyoto University, Osaka, Japan

<i>26.1 Isomeric Mössbauer Excitation By Synchrotron Radiation</i>	<i>1448</i>
<i>26.2 Nuclear Resonant Elastic Scattering</i>	<i>1449</i>
<i>26.3 Nuclear Resonant Inelastic and Quasi-Elastic Scattering</i>	<i>1454</i>

Abstract: The use of synchrotron radiation has opened up new areas in nuclear resonant scattering studies. It has permitted measurements that are difficult with conventional radioactive sources, such as the measurement of element-specific dynamics. Recent progress in studies using nuclear resonant scattering of synchrotron radiation is reviewed in this chapter.

26.1 Isomeric Mössbauer Excitation By Synchrotron Radiation

Synchrotron radiation has many distinct properties, such as high brilliance, energy tunability, and pulse structure (For more details on synchrotrons, see [Sect. 50.3.2.4](#) of [Chap. 50](#), Vol. 5, on “Particle Accelerators”). Because of these properties, synchrotron radiation has enabled new types of nuclear resonant excitation experiments. One straightforward use is as an alternative excitation source, which is particularly important for parentless Mössbauer nuclides. The use of synchrotron radiation as a Mössbauer source was first proposed by Ruby (1974). Cohen et al. (1978) reported the first attempt to observe nuclear resonant excitation with synchrotron radiation. Following these pioneering experiments, Gerdau et al. (1985) reported clear observation of nuclear Bragg scattering of synchrotron radiation by ^{57}Fe in a single crystal. In 1991, Hastings et al. (1991) observed nuclear resonant forward scattering by ^{57}Fe in iron foil in the time domain. This experiment showed that examining polycrystalline samples with this method is meaningful and led to an extension of traditional Mössbauer spectroscopy. In addition, other spectroscopic methods using nuclear resonant forward scattering have been developed. One method is the heterodyne (stroboscopic) detection method (Coussement et al. 1996, 1999; Callens et al. 2003); spectra are obtained in the energy domain using this method. A spectroscopic method using the “nuclear lighthouse effect” was developed by Röhlberger et al. (2000); the time evolution of decaying nuclei in a rotating sample is translated into an angular deviation through this method. By contrast, Mössbauer spectra can be obtained in a straightforward manner from synchrotron Mössbauer sources obtained through pure nuclear Bragg scattering (Smirnov et al. 1969; 1997; Smirnov 1999; Mitsui et al. 2005; 2007), although ^{57}Fe is the only available nuclide so far. Recently, another method that yields Mössbauer absorption-type spectra was developed, and this method is applicable to many Mössbauer nuclides (Seto et al. 2009).

Unlike traditional Mössbauer spectroscopy, which is based on recoilless nuclear resonance absorption, the use of synchrotron radiation allows information to be gained from nuclear scattering events that involve the creation or annihilation of quanta of lattice vibrations, i.e., phonons. This was shown in 1994, when the phonon energy spectrum of ^{57}Fe in iron foil was measured (Seto et al. 1995). Following this result, the method of using nuclear resonant inelastic scattering experiments to gain information on phonon spectra found widespread applications. An important feature of this method is that the element-specific phonon density of states can be obtained. Furthermore, the combination of electronic- and phonon-state measurements makes possible to measure site-specific phonons (Seto et al. 2003). Note that this method allows studying diffusion dynamics (Zhang et al. 1995).

At present, *nuclear resonant excitation spectroscopy* performed by synchrotron radiation has two major aspects: (1) it serves as an extended or alternative method of Mössbauer spectroscopy by providing information on hyperfine interactions, and (2) it is used for element-specific local vibration and diffusion studies. These aspects are introduced in the following [Sects. 26.2](#) and [26.3](#). Other applications in fundamental physics and nuclear physics,

such as nuclear excitation by electronic transfer (NEET; see Kishimoto et al. 2000), have also been explored and promising results have been obtained.

Although synchrotron radiation has distinct features, the accessible photon energy range depends on the storage ring and insertion devices installed; it is usually limited to values on the order of 10^5 eV. Moreover, observation of resonant excitation of nuclei using synchrotron radiation is limited by several factors such as the intensity of the radiation, the time resolution of the detector, and the detection efficiency without loss of time resolution. ➤ Table 26.1 shows nuclides with the appropriate properties (excited-state half-life >0.5 ns, energy <100 keV, and ground-state half-life >10 years) for excitation at the nuclear resonant scattering beamline BL09XU at SPring-8, which is a third-generation synchrotron radiation facility.

26.2 Nuclear Resonant Elastic Scattering

One of the main purposes of Mössbauer spectroscopy is the investigation of hyperfine interactions that reflect the electronic state of the resonant nuclei. Compared with traditional Mössbauer spectroscopy, the use of synchrotron radiation for studying hyperfine interactions is advantageous as it is also applicable to nuclides with no appropriate mother nuclide, such as ^{40}K (Seto et al. 2000a, 2002). However, when synchrotron radiation is used as an excitation source (excluding one method discussed later), the energy width is much broader (>0.1 meV) than that of conventional Mössbauer sources. Therefore, special measuring techniques are needed to obtain information on the hyperfine interactions when using synchrotron radiation.

One possibility is to make use of the pulsed structure of synchrotron radiation by measuring the hyperfine interactions in the *time domain* (Trammell and Hannon 1978, 1979). If the nuclear energy levels of the resonant nuclei are split due to hyperfine fields and the energy width of the synchrotron radiation is much broader than the splitting, a coherent superposition of the nuclear sublevels is formed by pulsed excitation of the nucleus. X-rays are then scattered from an excited nucleus decaying with a certain lifetime, and *quantum beats*, whose oscillating cycles reflect the energies of splitting, are measured as the time evolution of the (delayed) scattering, which is called a *time spectrum*. An example of a time spectrum with quantum beats is shown in ➤ Fig. 26.1. Nuclear resonant Bragg scattering can be observed by using a single crystal containing a certain amount of resonant nuclei. Even if the sample is polycrystalline (not a single crystal), scattering can be observed in the forward direction (Hastings et al. 1991). This kind of measurement requires a special timing mode for the pulse bunch structure of the storage ring; the interval between pulse bunches should be longer than the lifetime of the excitation state. In most nuclear resonant scattering measurements, Si avalanche photodiode (APD) detectors (Kishimoto 1991) are used, which have the typical time resolution of 100–1000 ps.

There are also suitable measuring methods applicable in the energy domain, one of which is the *heterodyne* (stroboscopic) *detection method* (Coussement et al. 1996, 1999; Callens et al. 2003). This method uses the interference effect between a sample and a reference moved with respect to the sample. Coherent forward scattering is detected, and the spectrum is obtained as a function of the velocity of the reference. This method is especially useful for the measurement of nuclides with longer excited-state lifetimes compared with measurements in the time domain; this is because the time domain measurement is restricted by the pulse interval of the storage ring, although it is simple and has better efficiency for simple hyperfine interaction measurements. Therefore, measurements of nuclides with longer excited-state lifetimes under

■ Table 26.1

Nuclides for which resonant excitation is expected to be observed at the nuclear resonant scattering beamline (BL09XU) of SPring-8 (Firestone and Shirley 1996; Dunford and Kinsey 1998)

Nuclide	$a(\%)$ [$T_{1/2}$ (years)]	E_γ (keV)	$T_{1/2}$ (ns)	I_g	I_e	α
⁴⁰ K	0.0117(1) [$1.277 \times 10^9(8)$]	29.8299(6)	4.24(9)	4—	3—	0.2982
⁵⁷ Fe	2.2(1)	14.412497(3) ^a	98.3(3)	1/2—	3/2—	8.56(26)
⁶¹ Ni	1.140(1)	67.413(3)	5.34(16)	3/2—	5/2—	0.139
⁶³ Ni	0 [100.1(20)]	87.15(11)	1.67×10^3 (3)	1/2—	5/2—	0.998
⁶⁷ Zn	4.1(1)	93.312(5)	9.16×10^3 (3)	5/2—	1/2—	0.873
⁷³ Ge	7.73(1)	13.275(17)	2.95×10^3 (2)	9/2+	5/2+	1120
⁷³ Ge	7.73(1)	68.752(7)	1.74(13)	9/2+	(7/2)+	0.227
⁸¹ Kr	0 [2.29×10^5 (11)]	49.55(3)	3.9(4)	7/2+	9/2+	1.3(6)
⁸³ Kr	11.5(1)	9.4035(18) ^b	147(4)	9/2+	7/2+	17.09(5)
⁹⁹ Ru	12.7(1)	89.68(5)	20.5(1)	5/2+	3/2+	1.498(9)
¹¹⁹ Sn	8.59(4)	23.8795(5) ^c	18.03(7)	1/2+	3/2+	5.22(1)
¹²¹ Sb	57.36(8)	37.1298(2) ^d	3.46(3)	5/2+	7/2+	11.11
¹²⁵ Te	7.139(6)	35.4922(5)	1.48(1)	1/2+	3/2+	14
¹²⁷ I	100	57.608(11)	1.95(1)	5/2+	7/2+	3.77(1)
¹²⁹ I	0 [1.54×10^7 (4)]	27.80(2)	16.8(2)	7/2+	5/2+	5.0(4)
¹²⁹ Xe	26.4(6)	39.578(2)	0.97(2)	1/2+	3/2+	12.31(1)
¹³³ Cs	100	80.9974(13)	6.28(2)	7/2+	5/2+	1.72
¹³³ Ba	0 [10.51(5)]	12.322(5)	7.0(3)	1/2+	3/2+	70.3
¹³⁷ La	0 [6×10^4 (2)]	10.56(5)	89(4)	7/2+	5/2+	122.3
¹³⁸ La	0.0902(2) [1.05×10^{11} (2)]	72.57(3)	116(5)	5+	(3)+	6.41
¹⁴⁵ Nd	8.30(6)	67.22(2)	29.4(10)	7/2—	3/2—	9.61
¹⁴⁵ Nd	8.30(6)	72.50(1)	0.72(5)	7/2—	5/2—	3.64
¹⁴⁵ Pm	0 [17.7(4)]	61.25(5)	2.64(6)	5/2+	7/2+	6.514(13)
¹⁴⁹ Sm	13.8(1)	22.507(6)	7.12(11)	7/2—	5/2—	29.2(9)
¹⁵¹ Sm	0 [90(8)]	4.821(3)	35(1)	5/2—	3/2—	920(120)
¹⁵¹ Eu	47.8(15)	21.54149(16) ^e	9.6(3)	5/2+	7/2+	28(2)
¹⁵² Eu	0 [13.516(6)]	65.2969(4)	940(80)	3—	1—	12.3
¹⁵² Eu	0 [13.516(6)]	77.2593(4)	38(4)	3—	3—	3.99(2)
¹⁵² Eu	0 [13.516(6)]	89.8496(4)	384(10)	3—	4+	0.381
¹⁵³ Eu	52.2(15)	83.36720(17)	0.793(17)	5/2+	7/2+	3.82(4)
¹⁵⁴ Sm	22.7(2)	81.976(18)	3.02(4)	0+	2+	4.94
¹⁵⁵ Gd	14.80(5)	86.5460(6)	6.5(4)	3/2—	5/2+	0.434
¹⁵⁶ Gd	20.47(4)	88.9666(14)	2.21(2)	0+	2+	3.93
¹⁵⁷ Gd	15.65(3)	63.917(5)	460(40)	3/2—	5/2+	0.971
¹⁵⁸ Gd	24.84(12)	79.510(2)	2.52(3)	0+	2+	6.02
¹⁵⁸ Dy	0.10(1)	98.9180(10)	1.66(3)	0+	2+	2.86

■ Table 26.1 (Continued)

Nuclide	α (%) [$T_{1/2}$ (years)]	E_γ (keV)	$T_{1/2}$ (ns)	I_g	I_e	α
^{160}Gd	21.86(4)	75.26(1)	2.69(3)	0+	2+	7.44
^{160}Dy	2.34(6)	86.7882(4)	2.026(12)	0+	2+	4.69
^{161}Dy	18.9(2)	25.65150(7)	29.1(3)	5/2+	5/2–	2.35
^{161}Dy	18.9(2)	43.8211(7)	0.83(6)	5/2+	7/2+	8.0(4)
^{161}Dy	18.9(2)	74.56710(13)	3.14(4)	5/2+	3/2–	0.679
^{162}Dy	25.5(2)	80.6598(7)	2.2(3)	0+	2+	6.22
^{163}Dy	24.9(2)	73.4448(4)	1.51(5)	5/2–	7/2–	8.4
^{164}Dy	28.2(2)	73.392(5)	2.39(3)	0+	2+	9
^{164}Er	1.61(2)	91.40(2)	1.47(3)	0+	2+	4.2
^{166}Er	33.6(2)	80.577(7)	1.82(3)	0+	2+	6.88
^{168}Er	26.8(2)	79.804(1)	1.88(2)	0+	2+	7.14
^{168}Yb	0.13(1)	87.73(1)	1.47(3)	0+	2+	5.43
^{169}Tm	100	8.4103(3)	4.08(8)	1/2+	3/2+	285
^{170}Er	14.9(2)	78.591(22)	1.891(23)	0+	2+	7.59
^{170}Yb	3.05(6)	84.25468(8)	1.605(13)	0+	2+	6.37
^{171}Yb	14.3(2)	66.721(7)	0.81(17)	1/2–	3/2–	13
^{171}Yb	14.3(2)	75.878(5)	1.64(16)	1/2–	5/2–	9.73
^{172}Yb	21.9(3)	78.7427(6)	1.65(5)	0+	2+	8.4
^{174}Yb	31.8(4)	76.471(1)	1.79(4)	0+	2+	9.43
^{174}Hf	0.162(3) [2.0×10^{15} (4)]	90.985(19)	1.66(7)	0+	2+	5.21
^{176}Yb	12.7(2)	82.13(2)	1.76(5)	0+	2+	7.06
^{176}Hf	5.206(5)	88.351(24)	1.43(4)	0+	2+	5.86
^{178}Hf	27.297(4)	93.180(1)	1.48(2)	0+	2+	4.74
^{180}Hf	35.100(7)	93.326(2)	1.5(2)	0+	2+	4.71
^{181}Ta	99.988(2)	6.214(2) ^f	6.05×10^3 (12)	7/2+	9/2–	70.5(25)
^{183}W	14.3(1)[$>1.1 \times 10^{17}$]	99.0793(4)	0.77(4)	1/2–	5/2–	4.12
^{187}Os	1.6(3)	9.746(24)	2.38(18)	1/2–	3/2–	264(33)
^{187}Os	1.6(3)	75.04(3)	2.16(16)	1/2–	5/2–	14.8
^{189}Os	16.1(8)	36.202(16)	0.53(3)	3/2–	1/2–	21
^{189}Os	16.1(8)	69.537(15)	1.62(4)	3/2–	5/2–	8.48(22)
^{191}Ir	37.3(5)	82.420(12)	4.08(7)	3/2+	1/2+	10.9
^{193}Ir	62.7(5)	73.044(5)	6.09(15)	3/2+	1/2+	6.24
^{193}Pt	0 [50(6)]	1.642(2)	9.7(3)	1/2–	3/2–	12000
^{197}Au	100	77.351(2)	1.91(1)	3/2+	1/2+	4.36(14)
^{201}Hg	13.18(8)	26.269(20)	0.630(50)	3/2–	5/2–	76.7(3)
^{226}Ra	0 [1600(7)]	67.67(1)	0.63(2)	0+	2+	61.9
^{227}Ac	0 [21.773(3)]	27.37(1)	38.3(3)	3/2–	3/2+	4.5(6)
^{231}Pa	0 [32760(110)]	84.216(3)	45.1(13)	3/2–	5/2+	2.5(25)

Table 26.1 (Continued)

Nuclide	a (%) [$T_{1/2}$ (years)]	E_{γ} (keV)	$T_{1/2}$ (ns)	I_g	I_e	α
^{235}U	0 [7.038 $\times 10^8$ (5)]	13.040(2)	0.50(3)	7/2−	3/2+	~1000
^{237}Np	0 [2.144 $\times 10^6$ (7)]	59.5412(1)	67(2)	5/2+	5/2−	1.16(7)
^{243}Am	0 [7370(40)]	84.0(2)	2.34(7)	5/2−	5/2+	0.218
^{243}Cm	0 [29.1(1)]	87.4(1)	1.08 $\times 10^3$ (3)	5/2+	1/2+	36.0

a , natural abundance [half-life of ground state]; E_{γ} , excited-state energy; $T_{1/2}$, half-life of excited state; I_g , ground-state nuclear spin quantum number (parity); I_e , excited-state nuclear spin quantum number (parity); and α , internal conversion coefficient.

^aShvyd'ko et al. (2000)

^bBaron et al. (1995)

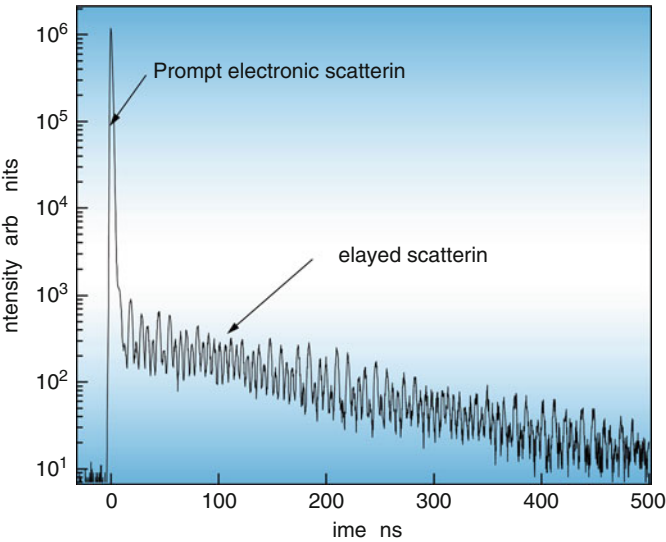
^cKikuta (1994)

^dWille et al. (2006)

^eKoyama et al. (1996)

^fChumakov et al. (1995).

Fig. 26.1
Nuclear resonant scattering measured in the time domain



extreme conditions that require synchrotron radiation are promising candidates for the heterodyne detection method, although the excitation of a longer excited-state is difficult in general.

Another method with nuclear resonant forward scattering adopts the *nuclear lighthouse effect* (Röhlsberger et al. 2000). When nuclei in a rotating sample are coherently excited, the radiative decay of the excited states proceeds in the tangential direction. The time spectrum of nuclear decay is mapped onto an angular scale, and the delayed signals can be detected with a position-sensitive detector without time resolution in the ideal case. By rotating the sample at an appropriately high frequency (on the order of 1 kHz), this method makes it possible to

detect time spectra of nuclides whose excited states have very short lifetimes and high energies (Röhlsberger et al. 2001b; Roth et al. 2005).

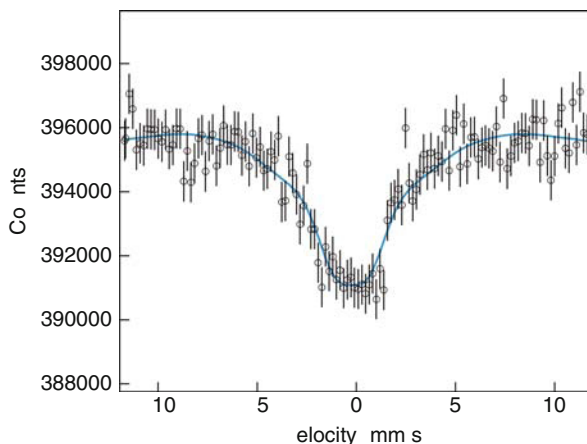
Mössbauer spectroscopy with synchrotron radiation can be used in a straightforward manner with single-line ^{57}Fe Mössbauer sources obtained using iron borate (FeBO_3) single crystals set under diffraction conditions at the Néel temperature (75.3°C) (Smirnov et al. 1969, 1997; Smirnov 1999; Mitsui et al. 2005, 2007). In this method, the spectrum obtained using synchrotron Mössbauer sources is basically identical to that obtained using conventional radioactive sources. This approach, therefore, is easily applicable and beneficial for a wide range of Mössbauer research. However, ^{57}Fe is the only available nuclide so far.

Recently, a new method has been developed that yields Mössbauer absorption type spectra using synchrotron radiation and is applicable to almost all Mössbauer nuclides (Seto et al. 2009). In this method, two samples containing the same resonant Mössbauer nuclide are used: one is used as a transmitter, and the other as a scatterer, which is placed behind the transmitter in the path of the synchrotron radiation. To obtain the Mössbauer spectra in the energy domain, the transmitter or scatterer is moved by a conventional velocity transducer, i.e., a relative energy scan is performed. When the relative resonance energies of the scatterer and transmitter are equal, the nuclear resonant scattering from the scatterer is suppressed compared with that when the relative resonance energies are different. This suppression is due to nuclear resonance absorption in the transmitter. If the resonance energies are different, photons with the resonance energy of the scatterer are not absorbed in the transmitter except for electronic processes such as a photoelectric effect; suppression of the scattering in the scatterer does not occur in this case. Therefore, one can observe a local minimum in the intensity spectrum of the scattering from the scatterer when the relative energy is zero. This velocity-dependent scattering intensity yields a Mössbauer absorption type spectrum in the energy domain. In this method, one of the two samples (the transmitter and the scatterer) is usually the sample under investigation, while the other is a reference sample whose properties are well known. The sample under investigation can be measured as a transmitter or scatterer depending on the sample condition. Note that this method detects not only γ -rays but also fluorescent X-rays and internal conversion electrons, which are emitted at de-excitation. The detection of fluorescent X-rays is easier than γ -rays with a silicon APD detector because the energies of fluorescent X-rays are lower than the energies of γ -rays. Moreover, electron detection is not difficult with APD detectors. Therefore, this method is relatively favorable for high-energy excited state nuclides compared with the method that detects only γ -rays with Si-APD. In fact, the Mössbauer spectrum of the third excited state of ^{73}Ge , which is difficult to measure with RI sources, was obtained by using synchrotron radiation (Seto et al. 2009) as shown in ► Fig. 26.2.

Until now, a considerable number of hyperfine interaction studies using nuclear resonant scattering of synchrotron radiation have already been carried out. Examples to be mentioned here include the use of synchrotron radiation in studying the spin structures of thin films, interfaces, and surfaces (Johnson et al. 1995; Röhlsberger 1999a; Röhlsberger et al. 2001a; Couet et al. 2009) in a superconductor (Kamihara et al. 2008) and in high-pressure experiments (Nasu 1994; Lubbers et al. 1999; Barla et al. 2004). The application of external perturbation synchronized to the pulse timing of synchrotron radiation is a unique method (Shvyd'ko et al. 1995, 1996; Mitsui et al. 1997) and seems to be useful for studying the time evolution of hyperfine interactions caused by light or magnetic fields synchronized to the incident pulse. This kind of experiment is rather difficult to handle using conventional Mössbauer methods.

■ Fig. 26.2

Mössbauer spectrum of ^{73}Ge measured by nuclear resonant scattering of synchrotron radiation. A powder sample of Li_2GeO_3 was used as the transmitter, and a powder sample of $^{73}\text{GeO}_2$ was used as the scatterer (Seto et al. 2009)



Studies on slow dynamics have been performed so far with the conventional method known as *quasi-elastic Mössbauer spectroscopy*. Using synchrotron radiation, the dynamics of glasses (Franz et al. 1999) and the diffusion of atoms in solids (Vogl and Sepiol 1999) can also be studied.

Although hyperfine interaction studies with both radioactive sources and synchrotron radiation have their respective advantages, new techniques based on synchrotron radiation widen the possibilities for studying hyperfine interactions and open up new prospects to perform studies that are out of the reach of conventional Mössbauer spectroscopy.

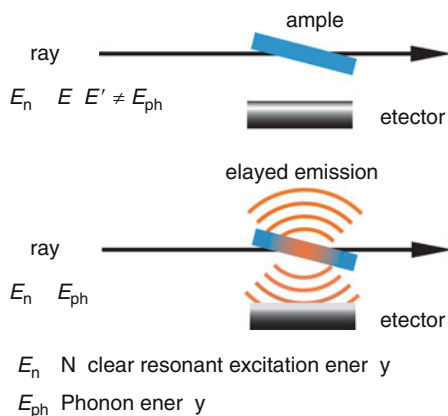
26.3 Nuclear Resonant Inelastic and Quasi-Elastic Scattering

The nuclear resonant inelastic and quasi-elastic scattering method has distinct features favorable for studies concerning the microscopic dynamics (i.e., lattice vibration, diffusion, and molecular rotation) of materials. One advantageous feature is the ability to measure the *element-specific* dynamics of condensed matter. For example, in solids the *partial phonon density of states* can be measured. Furthermore, measurements under exotic conditions – such as high pressure, small samples, and thin films – are possible because of the high brilliance of synchrotron radiation. (For the definition of brilliance, see 🔗 Sect. 50.3.4.5 of Chap. 50, Vol. 5, on “Particle Accelerators.”) This method is applicable not only to solids but also to liquids and gases, and there is no limitation concerning the sample temperature.

Nuclear resonant excitation accompanied by phonon excitation (🔗 Fig. 26.3) can occur when the nucleus is hit by a gamma photon whose energy is equal to the sum of the energy required for recoilless nuclear resonant excitation and the energy of the phonon. If nuclear resonant excitation occurs, delayed photon(s) (e.g., fluorescence X-ray) or electron(s) (e.g., conversion electron) are emitted at de-excitation. The intensity of the delayed emission as

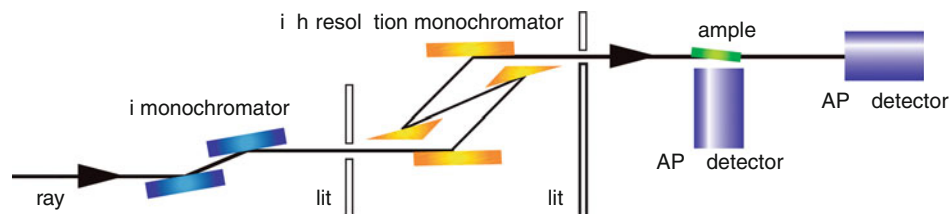
■ Fig. 26.3

Schematic for the measurement of nuclear resonant excitation accompanied by phonon creation or annihilation



■ Fig. 26.4

Schematic for measurement of the nuclear resonance excitation accompanied by phonon excitation. The avalanche photodiode (APD) detector placed below the sample detects inelastic scattering, and another APD detector in the forward direction detects forward scattering for the energy reference

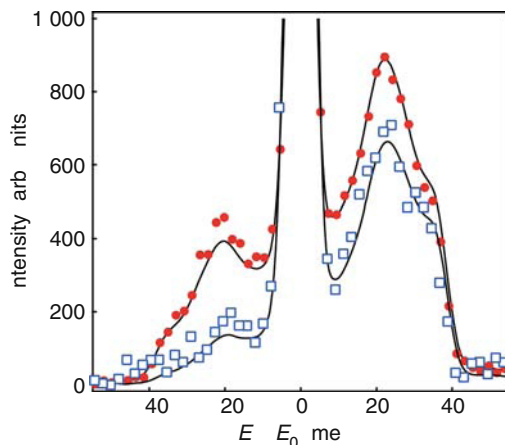


a function of the energy of the incident radiation gives the *phonon energy spectrum*. Therefore, the nuclear resonant *inelastic scattering* spectrum is measured by scanning the incident radiation energy; this is usually done by changing the Bragg angle of the monochromator. The energy resolution attained with a Si high-resolution monochromator is typically 1–10 meV (in special cases, about 0.1 meV can be achieved; see Yabashi et al. 2001). As material for the monochromator, in addition to Si, sapphire ($\alpha\text{-Al}_2\text{O}_3$) has begun to be used, particularly for high-energy nuclides (Shvyd'ko 2004; Wille et al. 2007). A schematic of the nuclear resonant excitation accompanied by phonon excitation and the detection of delayed emission is shown in ▶ Fig. 26.4. The nuclear resonant inelastic scattering spectra of ^{57}Fe at 150 and 300 K are shown in ▶ Fig. 26.5.

A phonon density of states can be obtained from the measured phonon energy spectrum; for compounds, the partial phonon density of states for the specific element can be obtained. It should be noted that since the direction of the conversion electron and the direction of the

■ Fig. 26.5

Nuclear resonant inelastic scattering spectra of ^{57}Fe at 150 K (open squares) and 300 K (closed circles) (Seto et al. 1996). Lines correspond to spectra calculated from results of neutron inelastic scattering measurements (Minkiewicz et al. 1967)



corresponding characteristic X-ray emitted are independent of each other, the position and solid angle of the APD detector do not affect the shape of the phonon energy spectrum.

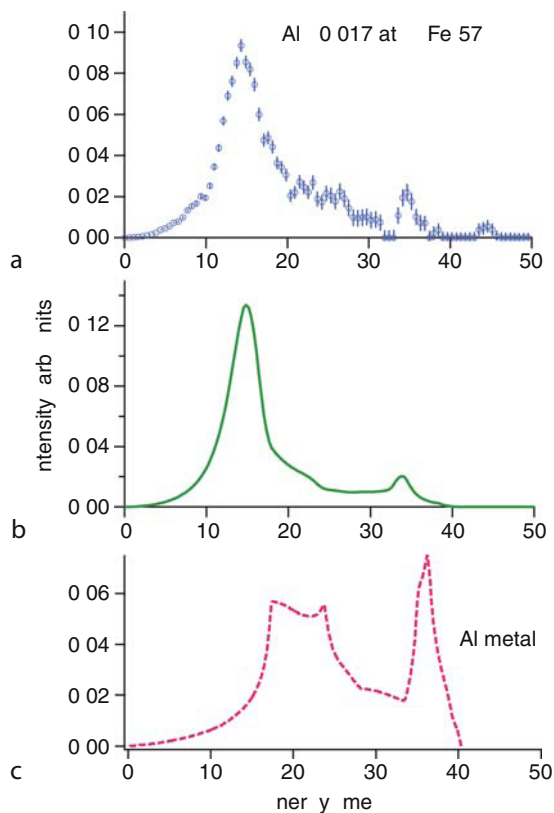
The high brilliance of synchrotron radiation makes possible the phonon density of states to be measured even for small samples. The measurement of the phonon density of states under high pressures using a diamond anvil cell (DAC), where the sample size is usually below 1 mm^2 , is effective for studying the core of earth and has been performed by Lübbbers et al. (2000), Mao et al. (2001), and Lin et al. (2005).

Phonons are quasiparticles, which are quantized lattice vibrations of all atoms in a solid material. Oscillating properties of the individual atoms in nonequivalent positions in a compound, however, are not necessarily equivalent. The dynamics of certain atoms in a compound influence characteristics such as the vibration of the impurity or doped atoms in metals and the rare-earth atom oscillations in filled skutterudite antimonides. Therefore, the ability to measure the *element-specific phonon density of states* is an advantageous feature of the method based on nuclear resonant inelastic scattering. Element-specific studies on the atomic motions in filled skutterudites have been performed (Long et al. 2005; Wille et al. 2007; Tsutsui et al. 2008).

Moreover, it is possible to study the dynamics of specific impurity or doped atoms in metals and semiconductors. The local vibrational density of states of highly dilute Fe (0.017 at%) in Al metal measured by nuclear resonant inelastic scattering of synchrotron radiation is shown in ► Fig. 26.6a (Seto et al. 2000b). The phonon density of states of Al metal, obtained from a neutron inelastic scattering experiment, is also shown in ► Fig. 26.6c for comparison (Gila and Nicklow 1966). The partial phonon density of states of ^{57}Fe in Al clearly differs from the phonon density of states of the Al metal host (compare ► Fig. 26.6a and c). Given the phonon density of states of the host metal, the partial phonon density of states of Fe can be calculated by using the Green function method (Mannheim 1968) along with information on the coupling between Fe and Al. The phonon spectrum calculated this way is shown in ► Fig. 26.6b.

■ Fig. 26.6

(a) Vibrational density of states of ^{57}Fe in Al-0.017 at.% Fe. (b) Response function of the impurity Fe atom to the phonon density of states of Al metal calculated on the basis of Mannheim's impurity theory. (c) Unperturbed phonon density of states of Al (Seto et al. 2000a)

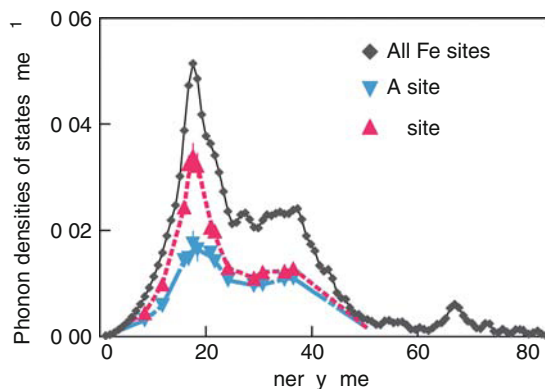


The calculation reproduces the measured (▶ Fig. 26.6a) partial phonon density of states of Fe remarkably well. The characteristic vibrational modes of Fe in Al were found to be modes that vibrate resonantly with the host Al phonons.

The *element-specific dynamics of ions in solutions* can be investigated by nuclear resonant *quasi-elastic scattering* spectroscopy (Zhang et al. 1995). In this case, element-specific diffusion constants of ions can be obtained even in a complex solution. The dynamics of Fe ions in Nafion membranes, which are used as ion-exchange membranes, was studied using this method (Haruki et al. 2000, 2001). In addition, many important studies using the features of nuclear resonant inelastic scattering spectroscopy have been performed, e.g., on nanoparticles (Fultz et al. 1997; Pasquini et al. 2002), very thin films (Keune and Sturhahn 1999; Röhlberger et al. 1999b; Sturhahn et al. 1999; Ruckert et al. 2000; Cuenya et al. 2001), quasi crystals (Brand et al. 1999), low-dimensional material (Kitao et al. 1998), clathrates (Hermann et al. 2005; Tse et al. 2005), superconductors (Higashitaniguchi et al. 2008), macromolecules (Rüffer and Chumakov 1996; Chumakov and Rüffer 1998; Grünsteudel et al. 1998; Keppler et al. 1997; Harami et al. 1998; Parak and Achterhold 1999; Sage et al. 2001; George et al. 2008).

■ Fig. 26.7

Phonon densities of states of ^{57}Fe in the Fe_3O_4 . The phonon density of states of all Fe is shown by closed circles and the partial phonon densities of states of the A and B sites are shown as downward and upward triangles, respectively. Lines are guides for the eye (Seto et al. 2003)



The nuclear resonant inelastic scattering method surely offers element-specific phonon energy spectra. However, for compounds with two or more different atomic states for the same element – such as magnetite, which is a mixed valent Fe compound – even this element-specific method cannot distinguish the “site-specific” vibrational properties. Moreover, no general method is known that could provide the site-specific phonon densities of states (PDOS). However, hyperfine interactions between the nuclei and surrounding electronic states make such measurements possible (Seto et al. 2003). If there are some different electronic states for a certain element in a compound, their hyperfine interactions are different. Therefore, by extracting the information for hyperfine interactions from the time evolution of delayed inelastic scattering by observing the quantum beat pattern, one can get the contributions of the respective sites in the inelastic scattering. Carrying out this procedure at different phonon energies permits the observation of the partial PDOS as distinguished by electronic states. As a mixed valent compound, magnetite (Fe_3O_4) was measured using the site-specific nuclear resonant inelastic scattering method. Magnetite forms a cubic spinel structure at room temperature, and the Fe atoms are located in two nonequivalent positions in the unit cell; one third of the Fe ions (Fe^{3+}) occupy the A sites tetrahedrally coordinated by four oxygen ions, and the remaining two-thirds of the Fe ions ($\text{Fe}^{2.5+}$) occupy the B sites octahedrally surrounded by six oxygen ions. Below $T_N = 858\text{ K}$, magnetite is ferrimagnetic with A sites moments aligned antiparallel to the B sites moments. The measured spectra of partial PDOS for all Fe sites and the site-specific PDOSs of the A and B sites are shown in ► Fig. 26.7.

Although element- and site-specific measurement is one of the advantages of nuclear resonant inelastic and quasi-elastic scattering, available nuclides on which nuclear resonant inelastic scattering has been measured is limited to those whose excitation energy is below about 30 keV. However, the development of a back-scattering type monochromator using high-quality sapphire single crystals has made it possible to extend the available energy range higher; studies using the advantages of this method will be performed widely and will extend the possibility of phonon studies.

References

- Barla A, Sanchez AP, Haga Y, Lapertot G, Doyle BP, Leupold O, Rüffer R, Abd-Elmeguid MM, Lengsdorf R, Flouquet J (2004) *Phys Rev Lett* 92:066401
- Baron AQR, Chumakov AI, Ruby SL, Arthur J, Brown GS, Smirnov GV, van Bück U (1995) *Phys Rev B* 51:16384
- Brand RA, Coddens G, Chumakov AI, Calvayrac Y (1999) *Phys Rev B* 59:14145
- Callens R, Coussement R, Kawakami T, Ladrière J, Nasu S, Ono T, Serdons I, Vyvey K, Yamada T, Yoda Y, Odeurs J (2003) *Phys Rev B* 67:104423
- Chumakov AI, Baron AQR, Arthur J, Ruby SL, Brown GS, Smirnov GV, van Bück U, Wortmann G (1995) *Phys Rev Lett* 75:549
- Chumakov AI, Rüffer R (1998) *Hyperfine Interact* 113:59
- Cohen RL, Miller GL, West KW (1978) *Phys Rev Lett* 41:381
- Couet S, Schlage K, Rüffer R, Stankov S, Diederich Th, Laenens B, Röhlberger R (2009) *Phys Rev Lett* 103:097201
- Coussement R, Cottenier S, L'abbé C (1996) *Phys Rev B* 54:16003
- Coussement R, Odeurs J, L'abbé C, Neyens G (1999) *Hyperfine Interact* 123/124(Pt II):113
- Cuenya BR, Keune W, Sturhahn W, Toellner TS, Hu MY (2001) *Phys Rev B* 64:235321
- Dunford CL, Kinsey RR (1998) NuDat system for access to nuclear data, IAEA-NDS-205 (BNL-NCS-65687), IAEA, Vienna, Austria. (The NuDat data base, version of 23-Feb-2000)
- Firestone RB, Shirley VS (eds) (1996) *Table of isotopes*, 8th edn. Wiley, New York
- Franz H, Petry W, Baron AQR (1999) *Hyperfine Interact* 123/124(Pt I):865
- Fultz B, Ahn CC, Alp EE, Sturhahn W, Toellner TS (1997) *Phys Rev Lett* 79:937
- George SJ, Igarashi RY, Xiao Y, Hernandez JA, Demuez M, Zhao D, Yoda Y, Ludden PW, Rubio LM, Cramer SP (2008) *J Am Chem* 130:5673
- Gerdau E, Rüffer R, Winkler H, Tolksdorf W, Klages CP, Hannon JP (1985) *Phys Rev Lett* 54:835
- Gila G, Nicklow RM (1966) *Phys Rev* 143:487
- Grünsteudel H et al (1998) *Hyperfine Interact* 113:311
- Harami T, Miyazaki G, Seto M, Mitsui T, Yoda Y, Kobayashi Y, Kitao S, Zhang XW (1998) *Hyperfine Interact* 3:61
- Haruki R, Seto M, Kitao S, Yoda Y, Maeda Yu (2000) *J Phys Soc Jpn* 69:4049
- Haruki R, Seto M, Kitao S, Kobayashi Y, Yoda Y, Mitsui T, Maeda Yu (2001) *J Phys Soc Jpn* 70:445
- Hastings JB, Siddons DP, van Bück U, Hollatz R, Bergmann U (1991) *Phys Rev Lett* 66:770
- Hermann RP, Schweika W, Leupold O, Rüffer R, Nolas GS, Grandjean F, Long GJ (2005) *Phys Rev B* 71:174301
- Higashitaniguchi S, Seto M, Kitao S, Kobayashi Y, Saito M, Masuda R, Mitsui T, Yoda Y, Kamihara Y, Hirano M, Hosono H (2008) *Phys Rev B* 78:174507
- Johnson DE, Siddons DP, Larese JZ, Hastings JB (1995) *Phys Rev B* 51:7909
- Kamihara Y, Hiramatsu H, Hirano M, Kobayashi Y, Kitao S, Higashitaniguchi S, Yoda Y, Seto M, Hosono H (2008) *Phys Rev B* 78:184512
- Keppeler C, Achterhold K, Ostermann A, van Bück U, Potzel W, Chumakov AI, Baron AQR, Rüffer R, Parak F (1997) *Eur Biophys J* 25:221
- Keune W, Sturhahn W (1999) *Hyperfine Interact* 123/124(Pt I):847
- Kikuta S (1994) *Hyperfine Interact* 90:335
- Kishimoto S (1991) *Nucl Instr Meth Phys Res A* 309:603
- Kishimoto S, Yoda Y, Seto M, Kobayashi Y, Kitao S, Haruki R, Kawachi T, Fukutani K, Okano T (2000) *Phys Rev Lett* 85:1831
- Kitao S, Mitsui T, Harami T, Yoda Y, Seto M (1998) *Jpn J Appl Phys* 38(suppl 38-1):535
- Koyama I, Yoda Y, Zhang XW, Ando M, Kikuta S (1996) *Jpn J Appl Phys Pt 1* (35):6297
- Lin JF, Sturhahn W, Zhao J, Shen G, Mao HK, Hemley RJ (2005) *Science* 308:1892
- Long GJ, Hermann RP, Grandjean F, Alp EE, Sturhahn W, Johnson CE, Brown DE, Leupold O, Rüffer R (2005) *Phys Rev B* 71:140302 (R)
- Lubbers R, Wortmann G, Grünsteudel HF (1999) *Hyperfine Interact* 123/124(Pt I):529
- Lubbers R, Grünsteudel HF, Chumakov AI, Wortmann G (2000) *Science* 287:1250
- Mannheim PD (1968) *Phys Rev* 165:1011
- Mao HK et al (2001) *Science* 292:914
- Minkiewicz VJ, Shirane G, Nathans R (1967) *Phys Rev* 162:528
- Mitsui T, Shimizu T, Imai Y, Yoda Y, Zhang XW, Takei H, Harami T, Kikuta S (1997) *Jpn J Appl Phys* 36:6525
- Mitsui T, Seto M, Kikuta S, Hirao N, Ohishi Y, Takei H, Kobayashi Y, Kitao S, Higashitaniguchi S, Masuda R (2007) *Jpn J Appl Phys* 46:821
- Mitsui T, Takei H, Kitao S, Seto M, Harami T, Zhang XW, Yoda Y, Kikuta S (2005) *Trans Mater Res Soc Jpn* 30:7
- Nasu S (1994) *Hyperfine Interact* 90:59
- Parak F, Achterhold K (1999) *Hyperfine Interact* 123/124(Pt I):825
- Pasquini L, Barla A, Chumakov AI, Leupold O, Rüffer R, Deriu A, Bonetti E (2002) *Phys Rev B* 66:73410
- Röhlberger R (1999a) *Hyperfine Interact* 123/124 (Pt I):455

- Röhlsberger R, Sturhahn W, Toellner TS, Quast KW, Alp EE, Bernhard A, Metge J, Ruffer R, Burkel E (1999b) *Physica B* 263–264:581
- Röhlsberger R, Toellner TS, Sturhahn W, Quast KW, Alp EE, Bernhard A, Burkel E, Leupold O, Gerdau E (2000) *Phys Rev Lett* 84:1007
- Röhlsberger R, Bansmann J, Senz V, Jonas KL, Bettac A, Leupold O, Ruffer R, Burkel E, Meiwes-Broer KH (2001a) *Phys Rev Lett* 86:5597
- Röhlsberger R, Quast KW, Toellner TS, Lee PL, Sturhahn W, Alp EE, Burkel E (2001b) *Phys Rev Lett* 87:47601
- Roth T, Leupold O, Wille H-C, Ruffer R, Quast KW, Röhlsberger R, Burkel E (2005) *Phys Rev B* 71:140401(R)
- Ruby SL (1974) *J Phys (Paris) Colloq* 35:C6-209
- Ruckert T, Keune W, Sturhahn W, Hu MY, Sutter JP, Toellner TS, Alp EE (2000) *Hyperfine Interact* 126:363
- Ruffer R, Chumakov AI (1996) *Hyperfine Interact* 97/98:589
- Sage JTS, Durbin M, Sturhahn W, Wharton DC, Champion PM, Hession P, Sutter J, Alp EE (2001) *Phys Rev Lett* 86:4966
- Seto M, Yoda Y, Kikuta S, Zhang XY, Ando M (1995) *Phys Rev Lett* 74:3828
- Seto M, Yoda Y, Kikuta S, Zhang XY, Ando M (1996) *Nuovo Cimento D* 18:381
- Seto M, Kitao S, Kobayashi Y, Haruki R, Mitsui T, Yoda Y, Zhang XW, Maeda Yu (2000a) *Phys Rev Lett* 84:566
- Seto M, Kobayashi Y, Kitao S, Haruki R, Mitsui T, Yoda Y, Nasu S, Kikuta S (2000b) *Phys Rev B* 61:11420
- Seto M, Kitao S, Kobayashi Y, Haruki R, Mitsui T, Yoda Y, Zhang XY, Kishimoto S, Maeda Yu (2002) *Hyperfine Interact* 141/142:99
- Seto M, Kitao S, Kobayashi Y, Haruki R, Yoda Y, Mitsui T, Ishikawa T (2003) *Phys Rev Lett* 91:185505
- Seto M, Masuda R, Higashitaniguchi S, Kitao S, Kobayashi Y, Inaba C, Mitsui T, Yoda Y (2009) *Phys Rev Lett* 102:217602
- Shvyd'ko YuV, Hertrich T, Metge J, Leupold O, Gerdau E, Rüter HD (1995) *Phys Rev B* 52:711
- Shvyd'ko YuV et al (1996) *Phys Rev Lett* 77:3232
- Shvyd'ko YuV et al (2000) *Phys Rev Lett* 85:495
- Shvyd'ko YuV (2004) *X-Ray Optics*, Springer series in optical sciences Vol. 98. Springer, Berlin
- Smirnov GV, Sklyarevskii VV, Voskanyan RA, Artem'ev AN (1969) *Pis'ma Zh Eksp Teor Fiz* 9:123
- Smirnov GV, van Bürc U, Chumakov AI, Baron AQR, Ruffer R (1997) *Phys Rev B* 55:5811
- Smirnov GV (1999) *Hyperfine Interact* 123/124(Pt II):91
- Sturhahn W, Röhlsberger R, Alp EE, Ruckert T, Schrör T, Keune W (1999) *J Magn Magn Mater* 198–199:590
- Trammell GT, Hannon JP (1978) *Phys Rev B* 18:165
- Trammell GT, Hannon JP (1979) *Phys Rev B* 18:3835
- Tse JS, Klug DD, Zhao JY, Sturhahn W, Alp EE, Baumert J, Gutt C, Johnson MR, Press W (2005) *Nat Mater* 4:917
- Tsutsui S et al (2008) *J Phys Soc Jpn* 77:033601
- Vogl G, Sepiol B (1999) *Hyperfine Interact* 123/124 (Pt I):595
- Wille H-C, Shvyd'ko YuV, Alp EE, Rüter HD, Leupold O, Sergueev I, Ruffer R, Barla A, Sanchez JP (2006) *Europhys Lett* 74:170
- Wille H-C, Hermann RP, Sergueev I, Leupold O, van der Linden P, Sales BC, Grandjean F, Long GJ, Ruffer R, Shvyd'ko YuV (2007) *Phys Rev B* 76:140301(R)
- Yabashi M, Tamasaku K, Kikuta S, Ishikawa T (2001) *Rev Sci Instrum* 72:4080
- Zhang XW, Yoda Y, Seto M, Maeda Yu, Ando M, Kikuta S (1995) *Jpn J Appl Phys* 34:L330

27 Positron Annihilation Spectroscopies

K. Süvegh¹ · T. Marek²

¹Eötvös Loránd University, Budapest, Hungary

²Hungarian Academy Sciences, Budapest, Hungary

27.1	<i>Introduction</i>	1462
27.1.1	What Is a Positron?	1462
27.1.2	Where to Find It?	1463
27.1.3	Positrons in Materials	1464
27.1.3.1	Thermalization of Positrons	1464
27.1.3.2	Positron States	1465
27.2	<i>The Positronium</i>	1467
27.2.1	Physical Properties of the Positronium Atom	1467
27.2.2	The Formation of the Positronium Atom	1468
27.2.3	Reactions of the Positronium Atom	1469
27.2.3.1	The Pick-Off Annihilation	1469
27.2.3.2	The Ortho-Para Conversion	1470
27.2.3.3	Chemical Reactions	1470
27.2.3.4	Localization of Ps	1471
27.3	<i>Experimental Methods</i>	1471
27.3.1	Construction of Positron Sources	1471
27.3.2	Measurable Quantities	1472
27.3.3	Methods of Measurements	1473
27.3.3.1	Positron Lifetime Spectroscopy	1473
27.3.3.2	Angular Correlation of Annihilation Radiation	1475
27.3.3.3	Doppler-Broadening Spectroscopy	1477
27.3.3.4	Variable-Energy Positron Beams	1479
27.3.3.5	AMOC	1480
27.4	<i>Recent Trends</i>	1481
27.4.1	Crystal Defects and Surfaces	1481
27.4.2	Polymers	1482
27.4.3	Fluids and Molecular Solids	1482
27.5	<i>Editors' Notes</i>	1483

Abstract: This chapter demonstrates the applicability of positrons in nuclear chemistry and material sciences. From the very basics to highly developed spectroscopic methods, a brief outline of positron annihilation spectroscopies is given. The possibilities of these methods are emphasized, and the characteristic applications are outlined for every one of them.

27.1 Introduction

As positron annihilation spectroscopies are not conventional methods in studying materials, this chapter might need a more basic introduction than others. Consequently, the very basics of positron annihilation spectroscopies, along with most variations of spectroscopies applying positrons as probes for material properties, are explained below.

27.1.1 What Is a Positron?

The positron is the antiparticle of the electron. It was theoretically deduced by Dirac (1930) and later observed by Anderson (1932) in cosmic rays. As any other antiparticle, the positron reflects its particle counterpart in every respect, their physical properties are equivalent. The masses of the two particles are identical and so are the absolute values of electric charges, spins, and magnetic moments. However, the electric charge of the positron is positive causing its magnetic moment to point in the direction of its spin.

In a vacuum, the positron is a stable particle, but in materials, it annihilates with an electron rapidly. The particle/antiparticle pair disappears in the annihilation process producing gamma photons. The number of photons and their energies are determined by the most basic laws of physics. The conservation of energy guarantees that the summed energy of all the photons must be 1.022 MeV, the rest energy ($2m_e c^2$) of the electron and positron together, while the spin conservation law (and the conservation of momentum) determines the number of photons. If the overall spin of the annihilating particle/antiparticle pair is zero, the number of photons is even. On the other hand, if the summed spin of the pair is equal to one, odd numbers of photons are formed. There is another important rule governing the photon production. Every excess photon, even if other probabilistic factors are ignored, decreases the annihilation probability by a factor of $1/137$, that is, by the fine structure constant. Consequently, combining the spin conservation law and this rule, the most probable way of annihilation is the formation of two gamma photons from an $S = 0$ state. Although the smallest odd number is one, the one-photon annihilation is usually hindered by the law of momentum conservation. (As the proposed single annihilation photon possesses a non-zero momentum, a third “inert” particle is required besides the annihilating pair to compensate the photon’s momentum by recoil. The case is similar for zero photon annihilation from the $S = 0$ state, but two “inert” particles are required for this rare process.) So, from an $S = 1$ state, the annihilation of a positron–electron pair most likely produces three gamma photons. (For a more detailed description of annihilation probabilities, see, for example, Schrader and Jean (1988) and the references therein.)

The momentum conservation law rules the direction of photons, as well. In the case of two-photon annihilation, photons must depart collinearly and the three-photon annihilation determines a plane in which photons should stay. This strict rule is usually altered slightly by

the momentum of the annihilating electron, thus providing a great opportunity to construct a momentum-sensitive spectroscopy.

In the case of two-photon annihilation, the energy conservation law has one more serious consequence on photons. Both should have an energy of 0.511 MeV. This energy is so uniquely characteristic to electron–positron annihilation that Anderson (1932) proved the existence of positrons by the detection of this annihilation radiation. Although the above rule is rather strict, it is altered, again, a little by the momentum of the electrons.

27.1.2 Where to Find It?

Positrons are not normally present in our world, they are not building blocks of ordinary matter. Even so, one can find annihilation radiation here and there indicating the former presence of positrons. The 0.511 MeV radiation was found in hot galactic cores and even among everyday cosmic rays. These positron sources, however strange and rare, serve as models for the production of antiparticles in a world of particles. The common physical process behind all the observed annihilation radiation sources is the well-known pair production.¹

In gamma ray spectroscopy, positron–electron pair production is a frequent, although unwelcome, side effect. On the other hand, under well-designed conditions, pair production might serve as a positron source. Usually, synchrotron radiation or high-energy **Bremsstrahlung** from accelerated electrons stopping in a heavy metal target (Howell et al. 1985) is used to produce positron–electron pairs in “industrial” quantities by pair production. This is how positrons are “made” for large accelerators and positron–electron colliders.

Under laboratory conditions, the most convenient way of producing positrons is the use of positron emitting radionuclides. Some useful nuclides undergoing positive beta decay are listed in ▶ Table 27.1. Although PET, that is, positron emission tomography, is an important field applying positron sources, it is rather a diagnostic method than a spectroscopy, and therefore it will not be discussed further here. For those interested in it, a vivid description is given by McCarthy et al. (1994).²

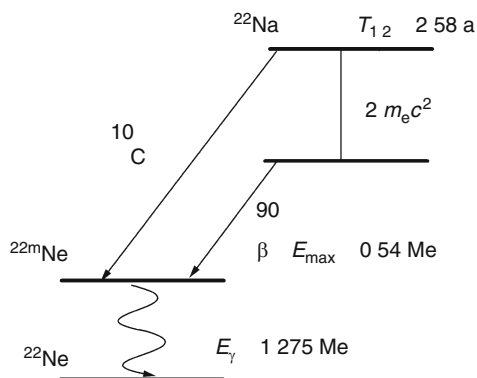
For spectroscopic purposes ²²Na is the most popular radionuclide. Its decay scheme is given in ▶ Fig. 27.1. It has several advantages: its half-life is convenient, the positron energy is not too high and after the emission of the positron it emits a gamma photon within 10^{−11} s.

■ Table 27.1
Some positron emitting radionuclides

Nuclide	Half-life	Positron energy (E_{\max} in MeV)	Probability of positive beta decay (%)	Application
¹¹ C	20.3 min	0.87	>99	PET
¹⁵ O	2.03 min	1.7	>99	PET
¹⁸ F	109.7 min	0.64	97	PET
²² Na	2.6 years	1.83	0.06	Spectroscopy
		0.54	89	
⁶⁴ Cu	12.7 h	0.66	19	Spectroscopy

■ Fig. 27.1

The decay scheme of ^{22}Na



This “prompt gamma” photon marks the moment of positron formation, making positron lifetime measurements possible.

In some special cases also the short-lived ^{64}Cu is used as a positron source, particularly if high specific activity is needed. Sometimes the short half-life of the applied positron source requires an intricate design. In some particular cases, due to the short half-life, the positron source is produced *in situ* using a nuclear reactor (Kaufmann et al. 1997).

27.1.3 Positrons in Materials

Although stable in a vacuum, any positron will eventually annihilate in normal matter with an electron. Thus its effective lifetime is very short ($\tau = 10^{-12} - 10^{-7} \text{ s}$), however, this incredibly short period is still enough for the positron to react with matter in several ways. These physical (and sometimes even chemical) reactions alter from material to material providing a number of unique possibilities to study materials through their annihilation characteristics.

27.1.3.1 Thermalization of Positrons

Positrons, no matter how they have been produced, usually have considerable kinetic energies initially. If these energetic positrons are injected into a material, the probability of their annihilation is much smaller than that of collisions with the atoms and molecules of the substance (Dirac 1930). The continual collisions decrease the kinetic energy of the positron and slow it down to thermal energies ($\sim 0.1 \text{ eV}$). Obviously, the thermalization takes place differently in different materials, but some common features can be easily identified even in so entirely distinct materials as gasses and metals (➤ Table 27.2).

At the beginning of the thermalization process, inelastic collisions dominate almost totally. At this stage, positrons slow down to about 100 eV very rapidly. It takes only $\sim 1 \text{ ps}$ (10^{-12} s) in metals (Brandt 1983), but $\sim 10 \text{ ns}$ (10^{-9} s) in gasses at atmospheric pressure (Green 1966). In the second stage, both elastic and inelastic collisions take place, together with some negligible

■ Table 27.2

A rough outline of the thermalization of positrons (Green 1966; Brandt 1983). The time is measured from the “birth” of positron till the end of the stage

Stage	Final energy of the positron / eV	Slowing down mechanism	Duration time		The fate of positron
			in Lead	in Argon	
I	~100	Bremsstrahlung, electromagnetic ionization, inelastic collisions	1 ps	7 ns	Slowing down
II	~10	Elastic and inelastic collisions			Slowing down, negligible free annihilation
		Plasmon and phonon excitation			
III	~0.1	Elastic collisions, phonons			Slowing down, free annihilation, reactions
IV	Thermal equilibrium is reached	Elastic collisions	45 ps	110 ns	Free annihilation, reactions

free (or direct) annihilation. In the third stage, when the kinetic energy of the positron decreases below the lowest electronic excitation level (~ 10 eV), elastic scattering becomes dominant. From then on, free annihilation becomes more and more significant. At the end, positrons get to thermal equilibrium with their surroundings, and their further fate depends very much on the material. The whole process takes place in only 45 ps in lead (Brandt 1983), but it takes more than 100 ns in argon at 1 bar (Green 1966).

From a material-centered point of view, the thermalization of positrons is a process very similar to that of electrons. The initial stage of inelastic collisions and the electromagnetic slowing down process form the usual radiation products. In fluids and molecular or atomic solids, these are excited and ionized molecules, free radicals, and electrons. In metals, however, plasmon and phonon excitation also play significant roles in the thermalization of positrons.

27.1.3.2 Positron States

Free annihilation is only one of the possibilities for thermalized positrons to stop existing. In some substances it does not happen at all. In most materials, some or all of the originally free positrons “react” somehow with their surroundings. The consequence of the “reaction” is the formation of new positron states. Such positron states differ from each other and from free positrons in their annihilation characteristics. Moreover, although the possible states are the same for similar materials, their exact annihilation properties depend on local conditions. Consequently, these states make positrons a valuable tool in studying the structure of materials.

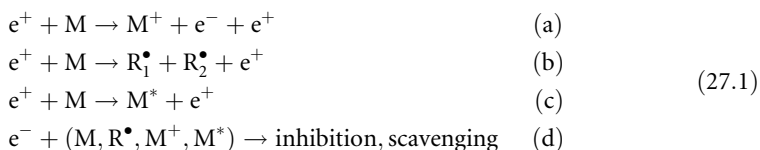
It is the easiest to understand positron states in the case of metals. In a perfect, defectless single crystal, thermalized positrons are in Bloch-states similar to those of electrons (Kittel 1979; Mijnenrends 1983). They are called free positrons. Before their annihilation, these

positrons scan expanded regions of the crystal and have a chance to meet both the electrons of ionic cores and the Bloch-state conducting electrons.

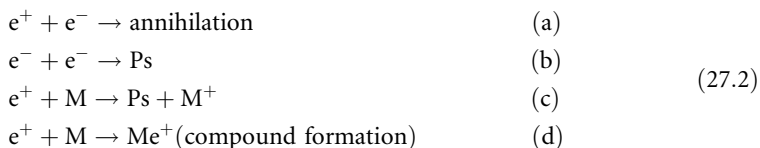
Another positron state is formed when free volume-type crystal defects are present in the metal crystal. The positively charged ionic cores are missing from these defects, so, usually they are effective traps for any positive particle, including the positron in our case. Thus, in most metals, vacancies, vacancy clusters, dislocations, and grain boundaries localize some or all of the free positrons and produce another positron state, the trapped positron. These localized positrons still can meet conducting electrons, but ionic cores are out of their reach. Accordingly, their annihilation characteristics differ from those of free positrons significantly. Different kinds of traps all have their own characteristic annihilation parameters but these parameters are very close to each other.

A positron state of lesser importance is also formed in the case of some metals. The existence of this state is connected with the fact that the work function of positrons is positive in several metals (Lynn 1980). In that particular case, a potential well is formed on the surface of the metal, which can localize positrons reaching the surface eventually during or after their thermalization.

The formation of positron states takes place in a much more complicated way in molecular solids and fluids. The structures of these materials are more complex than those of metals, and diverse radiation products are formed in the thermalization process. Consequently, any theory explaining the behavior of positrons in these materials needs the use of radiation chemistry. The so-called spur model (Mogenssen 1974) does exactly this and states that the thermalized positron reacts with the particles of its own radiation track. The spur contains ground-state (M) and excited molecules (M^*), ions (M^+), free radicals (R^\bullet), and electrons (e^-). These species react with the positron and, parallel, with each other. Some possible reactions are given in ► Eq. (27.1):



Positrons, being antiparticles, ignite some special spur reactions, first of all annihilation. However, positrons are positive particles and, thus, they can replace protons under certain conditions. A positron and an electron are able to form the most specific positron state, a hydrogen-like system called positronium (Ps). Some of the special spur reactions are given in ► Eq. (27.2):



The statistical weights of the above reactions vary in a wide range in different materials. Positronium formation can be as significant as 30%. A positronium atom, being similar to hydrogen atoms, is a reactant particle. Thus, the list of spur reactions should be elongated by its reactions. On the other hand, most of the chemical applications of positrons are based on the use of positronium atoms, consequently these reactions are treated separately in ► Sect. 27.2.3.

27.2 The Positronium

The possibility of a positron–electron bound system was suggested by Mohorovicic (1934) on the basis of theoretical considerations. Several years later, it was given its present name (Ruark 1945), but its actual existence was proved by delayed coincidence measurements only in 1954 (Deutsch 1954). The symbol Ps was introduced by McGervey and De Benedetti (1959) to denote positronium as a chemical element. In a certain sense, Ps is definitely an atom; it can be regarded as an isotope of hydrogen.

27.2.1 Physical Properties of the Positronium Atom

Positronium is a system very similar to a hydrogen atom but its mass is 920 times smaller, because the proton is substituted by the much lighter positron. Because of its lightness, the positronium atom has a smaller binding energy than a hydrogen atom, that is, 6.8 eV instead of 13.6 eV. The smaller binding energy generates a two times larger distance between the positron and the electron in positronium than the ground-state proton–electron distance in a hydrogen atom. However, this does not mean that the Ps atom is larger than a hydrogen atom. Strangely enough, they have the same size. This seeming contradiction can be easily resolved by considering that the proton is located in the center of the hydrogen atom, while the positronium is a totally symmetric entity. In the Ps, the positron and the electron wave functions are identical, at least their spatial part. Metaphorically speaking, the hydrogen atom is a planetary system with a heavy sun at its center (the proton) and a light planet around it (the electron). On the other hand, the positronium is a binary system of two stars of the same mass circling around their center of mass.

The size paradox is only one of the unusual properties of the positronium atom caused by the fact that it is constructed of a particle–antiparticle pair. Some physical properties, not too significant in the case of hydrogen atoms, gain unusual importance in the case of Ps atoms. Most books do not even mention that two kinds of ground-state hydrogen atoms exist that are distinguished by their spins. This seeming ignorance is understandable considering the fact that one should perform very sophisticated measurements to find the differences between *ortho*-H and *para*-H (the effect is well known in, e.g., high-resolution NMR spectroscopy).

In the case of positronium atoms the spin plays a more significant role and distinguishes ground states much more significantly. Determined by the relative orientation of the spins of the constructing electron and positron, the spin of a Ps atom is either 0 or 1 \hbar . The former is called singlet or *para*-Ps (1S_0 , 1Ps), while the latter is the triplet or *ortho*-Ps (3S_1 , 3Ps). According to the magnetic quantum number m , *para*-Ps exists only in one state ($m = 0$), while *ortho*-Ps occurs in three states ($m = +1, 0, -1$). Therefore, the statistical weight of the triplet state is three times larger than that of the singlet. Although both states should be considered ground states, the energy of *para*-Ps is significantly lower. The detailed comparison of the energy levels of hydrogen and positronium was given, for example, by Berko and Pendleton (1980) and Rich (1981).

Beside their energy, the lifetimes of the two states differ significantly as well. Although the expression is similar for the two states, it gives quite distinct lifetimes for *ortho*- and *para*-positronium:

$$\lambda_i^0 = \frac{1}{\tau_i^0} \propto \sigma_i |\psi(0)|^2 \quad (27.3)$$

where i stands for singlet or triplet states, λ is the corresponding decay constant, τ is the mean lifetime, and $\psi(\mathbf{r})$ is the wave function of the positronium. The symbol σ_i denotes the “cross section” of the annihilation from the corresponding spin state. It is determined by fundamental constants of quantum electrodynamics (Schrader and Jean 1988). ➤ Equation (27.3) yields $\tau_S = 1.25 \cdot 10^{-10}$ s for the mean lifetime of free *para*-Ps in a vacuum and $\tau_T = 1.42 \times 10^{-7}$ s for *ortho*-Ps (Asai et al. 1995).

These lifetime values are, seemingly, very short. However, in comparison with the vibration period of atoms in a molecule (10^{-14} s) they are long enough to enable the positronium to take part in interactions with the substance.

27.2.2 The Formation of the Positronium Atom

The formation of positronium atoms is affected by many factors but first of all, as ➤ Eqs. (27.1) and ➤ (27.2) suggest, by the material itself. According to the mentioned spur model (Mogenssen 1974), thermalized positrons compete with molecules of the material and with radiation products for available electrons. Sometimes, these species are such effective inhibitors or scavengers that they prevent positronium formation totally. Even if the inhibition is negligible, not all of the positrons can form Ps. Positronium formation reactions given by ➤ Eqs. (27.2b) and ➤ (27.2c) require positrons of some particular energies.

The energy range most favorable for positronium formation is called Ore gap after its Norwegian discoverer (Ore 1949). The theory was developed for gasses, but, with some restrictions, it applies to liquids and solids as well. Ore has shown that there is a minimum energy, E_{\min} , at which positronium formation is still possible:

$$E_{\min} = V - 6.8 \text{ eV} \quad (27.4)$$

where V is the ionization potential of the gas and the value 6.8 eV is the binding energy of the positronium. This is the minimum energy that still enables the positron to pick up an electron from a gas molecule to form a bound system with it according to ➤ Eq. (27.2c).

The higher energy limit for positronium formation is provided by the requirement that the kinetic energy of Ps cannot be higher than its binding energy; otherwise, it should decompose in a very short time. Kinetic conditions lower this limit. Usually, the positron energy should not exceed the ionization potential of the gas ($V = 15.8$ eV in argon) because, in that case, ionization is a more probable process than Ps formation. Even at this decreased energy limit, the probability of positronium formation is small. It reaches considerable values only if the positron energy is lower than the lowest excitation energy of gas atoms (E_e , which is 11.6 eV for argon). Above this limit, positrons are likelier to excite the atoms of the substance than to form positronium. Thus the width of the **Ore gap** becomes:

$$\Delta = E_e - (V - 6.8 \text{ eV}). \quad (27.5)$$

According to Ore, the **probability of positronium formation** (P_{Ps}) can be estimated as follows:

$$\frac{E_e - (V - 6.8 \text{ eV})}{E_e} < P_{Ps} < \frac{6.8 \text{ eV}}{V}. \quad (27.6)$$

For the special case of argon, the inequality becomes $0.22 < P_{Ps} < 0.43$ and the experimental values measured by different authors are between 0.27 and 0.36 (Green 1966).

Although the Ore model is more quantitative than the spur model, it works without serious errors only for gasses. In a condensed phase, conditions determining Ps formation are much more complicated. Usually, even some crucial parameters (e.g., ionization potential, solvating effect, etc.) are known with insufficient accuracy. Consequently, for condensed phases, one should use the spur model instead. Usually, it does not supply quantitative data, and its list of equations changes from material to material, but, even so, its results are impressive.

Independently of what one thinks of their formation mechanism, Ps atoms need space to be formed. In gasses, there is an enormous empty space between gas molecules, so space (or the shortage of it) is not a limiting factor of Ps formation. In fluids, however, Ps creates a small empty space, a bubble around itself. The **bubble model** was developed a long time ago (Ferrel 1957) and has been modified continually. Its present form tries to synthesize the results of the spur model and modern physical chemistry (Stepanov et al. 2000). In solids, structural free volumes might serve the empty space needed for positronium formation.

In metals and semiconductors Ps formation is negligible. The low excitation energy of electrons, as [Eq. \(27.5\)](#) shows, hinders this process. However, a special kind of positronium might form even in these cases. This is the so-called surface positronium. As mentioned above, some positrons can reach the surface during their thermalization. These antiparticles are reemitted into the vacuum or get trapped on the surface. Some of them form Ps at the solid–vacuum interface.

27.2.3 Reactions of the Positronium Atom

In a material with a random orientation of spins, three quarters of positronium atoms are formed in triplet state (*o*-Ps) and the remaining $\frac{1}{4}$ is *para*-positronium. Usually, the mathematical handling of the annihilation of *p*-Ps is so inconvenient that it is ignored during the interpretation of annihilation data. Ignoring 25% of available signals seems to be too much waste but the separability of *o*-Ps signals compensates for this seeming disadvantage. Consequently, only the reactions of *o*-Ps are discussed below. A more detailed description of the reactions of *o*-Ps was given by Vértés and Kiss (1987). The monograph also gives the radiation chemistry background needed to understand *o*-Ps reactions.

The interaction-free annihilation of an *o*-Ps atom produces three γ photons. According to quantum electrodynamics, the probability of 3γ -annihilation is much smaller than that of 2γ -annihilation, but the spin conservation rule prevents 2γ -annihilation from an $S = 1$ state. Thus, the self-annihilation of *o*-Ps is a relatively slow process, and *ortho*-positronium atoms have enough time to take part in different interactions with the particles of the substance. As a result, *o*-Ps usually escapes self-annihilation because it is forced by its surroundings to undergo quick 2γ -annihilation.

27.2.3.1 The Pick-Off Annihilation

The most general interaction between Ps and materials is the so-called “pick-off” annihilation. It occurs in every material, although sometimes together with other *o*-Ps interactions. This interaction is based on the fact that the positron of the triplet positronium atom can undergo 2γ -annihilation with an opposite-spin electron of a colliding molecule. Thus, the positron–electron pair, which annihilates at the end, is in singlet state ($S = 0$) instead of the original $S = 1$

state. As a result of this interaction, the lifetime of *ortho*-positronium shortens considerably, but, owing to the shielding effect of the Ps-electron, it is still longer than it would be in the case of free annihilation. Pick-off annihilation is especially common in condensed phases.

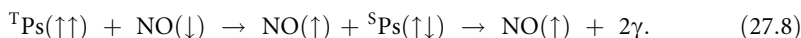
The pick-off annihilation rate constant λ_p can be described (Hyodo 1985) by the overlap between the wave function of *o*-Ps $\varphi(r_-, r_+)$ and that of surrounding “alien” electrons $\psi_v(r)$:

$$\lambda_p = \frac{r_0^2 c \pi}{4V} \sum_i \sum_v n_i n_v \int \int |\varphi_i(r_-, r) \psi_v(r)|^2 dr dr_- \quad (27.7)$$

where r_0 is the classical electron radius, V is the volume of the sample and n_p , n_v are the occupation probabilities of the Ps and electron states, respectively. (The symbols r_- and r_+ indicate that the wave function is dependent on the positions of both the electron and the positron. Note that in the overlap integral, r_+ is replaced by r since the “alien” electron and the positron should be at the same place at the moment of the annihilation.)

27.2.3.2 The Ortho-Para Conversion

Another important interaction of positronium is the *ortho-para* conversion. It occurs when the substance contains paramagnetic particles with unpaired electrons. When colliding with such a particle, the orientation of one of the parallel spins of *ortho*-positronium may be reversed, simultaneously with the reversion of the spin of the unpaired electron of the colliding molecule. This interaction takes place via electron exchange between the molecule and *o*-Ps. The *para*-positronium formed by this process annihilates very rapidly, according to its short mean lifetime. Consequently, this effect also leads to the decrease of the lifetime of positronium. *Ortho-para* conversion can be demonstrated by the following reaction scheme (vertical arrows show the directions of the spins):

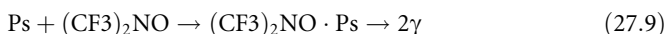


Converters are usually free radicals and transition metal ions having unpaired electrons. However, there is no close relation between the number of unpaired electrons and the “strength” of the converter.

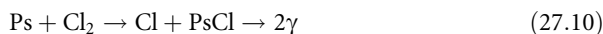
27.2.3.3 Chemical Reactions

The chemical reactions of positronium constitute the third and, with respect to chemistry, the most important group of interactions. (It should be noted that certain types of *ortho-para* conversion reactions, e.g., the interaction with radicals, are also of chemical character.) The most important types of positronium reactions are demonstrated by the following examples:

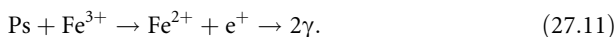
(a) Addition reactions:



(b) Exchange reactions:



(c) Oxidation reactions:



(d) Reduction reactions:



The common result of such reactions is that Ps senses a more electron-rich environment. Thus, its annihilation resembles the pick-off annihilation. The outcome is a shortened lifetime and an annihilation into two γ -quanta, as denoted.

27.2.3.4 Localization of Ps

The next interaction of Ps is a reaction in a wider sense only, however, it modifies the lifetime of Ps considerably. It is the localization (or trapping) of Ps atoms in free volumes of the material. Consequently, this reaction is characteristic of solids, where structural free volumes are stable. If the free volume behaves as a potential well for Ps atoms, *o*-Ps can be localized in it. From then on, the annihilation is determined by local physical properties of the free volume. The size and the electron density of the free-volume affect the Ps lifetime through the pick-off process.

On the other hand, without this trapping, Ps “diffuses” from one free-volume site to another in amorphous materials (Brandt et al. 1960) or gets into Bloch-state in crystalline materials (Brandt et al. 1969). In these cases the annihilation parameters are determined by a larger volume of the substance.

27.3 Experimental Methods

27.3.1 Construction of Positron Sources

Most popular positron sources are based on the use of ^{22}Na . This nuclide has a lot of advantageous properties; for example, the prompt gamma provides an easy way to solve the timing problem of lifetime measurements. On the other hand, handling of sodium is rather complicated; therefore, sources are prepared from sodium compounds, mainly from sodium chloride.

Sodium chloride is soluble in water, which suggests its *in situ* application in aqueous solutions. However, *in situ* measurements raise serious problems. A large fraction of positrons annihilates in the walls of the sample holder modifying annihilation spectra. Moreover, Na^+ ions get easily adsorbed on different surfaces contaminating the equipment with radioactivity. Consequently, the positron source ^{22}Na should be separated from the sample and the sample holder, but in a way allowing positrons to penetrate the sample.

Usually, the positron source $^{22}\text{NaCl}$ is sealed between very thin metal (Ni, Ti) or polymer (kapton, Mylar) foils. The thickness (i.e., surface density) of these foils is around 1–2 mg/cm², but several percents of positrons annihilate in this wrapping even in the case of the thinnest foil. During spectrum evaluation, positrons annihilated in the source foil should be taken into account.

In the study of liquids, the application of thin foils to wrap the active material is, at least, dubious. The foil and its sealing should be absolutely free of leaks and, in the case of polymers the foil must not swell considerably in the studied liquid. Therefore, in the case of liquid samples, special sources are prepared from ^{22}Na diffused into thin (1.2–2 mg/cm²) sodium

glass foil by thermal ion exchange. The foil is then placed in a platinum or glass frame to gain a handy source.

Some applications use more complex sources in which positrons of a well-defined energy are created in more than one step. As these methods bear only particular interest from a chemical point of view, only an outline of them is given below in ▶ Sects. 27.3.3.4 and ▶ 27.3.3.5.

27.3.2 Measurable Quantities

The parameter of a positron experiment that most obviously carries information on the chemistry of the substance is the positronium formation intensity. This value informs about the relative fraction of positrons forming Ps. For example, by completing the list of reactions in ▶ Eqs. (27.1) and ▶ (27.2) with equations containing solute molecules, a system is gained in which positronium formation sensitively depends on the solute concentration. Moreover, the rate constants connected with this equation system depend on the changes of the electron structure of the molecules very sensitively. Thus, also the Ps formation intensity reflects these changes.

As discussed in the previous section, all the possible interactions of *o*-Ps decrease its lifetime. The degree of this lifetime decrease is another parameter that can be related to physical and chemical properties of a system. The connection is quite obvious in the case of chemical reactions and *ortho-para* conversion. In the case of pick-off annihilation, the effects of the substance on positronium lifetime are expressed indirectly through the overlap integral in ▶ Eq. (27.7). Any change in ψ_v (e.g., changes of electron orbits) or in the overlap integral (e.g., free-volume changes) is reflected in the lifetime of *o*-Ps.

The overlap integral (or rather the physical overlap behind it) supplies another measurable quantity besides *o*-Ps lifetime and intensity. This quantity is the momentum distribution of annihilation gamma rays. Due to the momentum conservation law, annihilation gammas should carry the momentum of the annihilating positron–electron pair. In the case of pick-off annihilation, the conserving momentum, where $\hat{\mathbf{P}}$ is the momentum operator, is the combined momentum of e^+ and the electron of the surrounding material:

$$\mathbf{p} = C_1 \int_V \psi_+^* \psi_v^* \hat{\mathbf{P}} \psi_+ \psi_v dV \quad (27.13)$$

where C_1 is a constant and ψ_v indicates electrons in a given state around the positron. The symbol ψ_+ refers to positrons or positronium atoms depending on the previous history of the positron.

So, any change in the electron structure of the studied material is reflected by the momentum distribution of annihilation γ photons.

Beside momentum distribution, one can also measure the energy distribution of annihilation γ photons. This parameter is also connected with the momentum distribution of electrons of the substance through the Doppler effect. As the resultant velocity of the annihilating positron–electron pair is usually larger than zero, the frequency of annihilation γ photons is shifted. This so-called Doppler shift of the frequency is reflected in the energy distribution. Consequently, although one measures energy distribution in this case, the measured physical quantity is momentum. Note that measuring energy distributions is a rather convenient method

(its required equipment is only a standard gamma spectrometer). Therefore, this method is applied more widely than direct momentum distribution measurements.

Usually not just positronium atoms but also positrons are sensitive to changes in the composition or the structure of materials. If the wave function of positronium is replaced with that of the positron in [Eqs. \(27.7\)](#) and [\(27.13\)](#), one obtains the theoretical foundation of the above statement. Positrons even participate in spur reactions. Consequently, positrons are sensitive to the changes of free volume, structural changes of materials, and chemical composition. Thus, there are usually several distinct positron states in a material, all of them being sensitive to any change in electron density. The pieces of information provided by the annihilation characteristics of these states complete each other.

27.3.3 Methods of Measurements

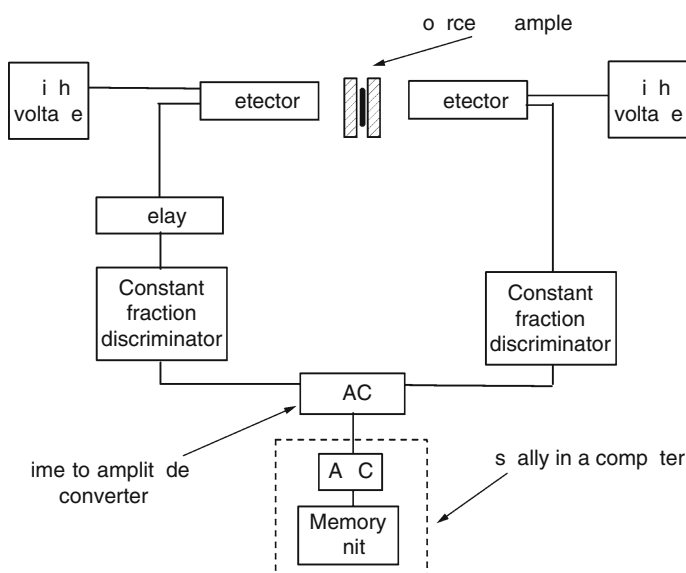
27.3.3.1 Positron Lifetime Spectroscopy

Nowadays positron lifetime spectra are almost exclusively measured by fast-fast coincidence systems ([Fig. 27.2](#)).

[Figure 27.2](#) outlines a general scheme of fast-fast coincidence systems. For positron lifetime measurements, several special requirements should be fulfilled. In positron lifetime spectroscopy, the whole system should be very fast because of the expected very short lifetimes (from ~ 100 ps to ~ 100 ns). Thus, the response of detectors ([Leo 1987a](#)) should be as fast as possible (rise time ~ 2 ns). To ensure the sharp response signal, fast plastic scintillators

Fig. 27.2

The scheme of a fast-fast coincidence system. TAC indicates the “clock”, that is, a time-to-amplitude converter. ADC is an analog–digital converter which is sometimes built into a computer-based multichannel analyzer card



(Ne102, Ne111) or BaF₂ are applied instead of the conventional NaI(Tl), and photomultiplier tubes are chosen accordingly.

The strict timing conditions call for constant fraction discriminators instead of normal leading-edge systems. (A leading-edge discriminator produces its output signal when the incoming signal reaches certain amplitude. The rise times of these input signals vary with their amplitude and the delay of output signals varies accordingly. Even differential discriminators accept a range of incoming amplitudes, so, the output signals are scattered in time. Constant fraction discriminators eliminate this problem by making the delay of output signals to be independent of the rise time input signals.) The time-to-amplitude converter should be linear almost totally and the A/D converter fast (1 MHz) and stable (McKenzie 1983). (The time-to-amplitude converter measures the time elapsed between the detection of a start and a stop signal and produces a proportional electric signal as an output. In the case of positron lifetime spectroscopy, the start signal is provided by the prompt gammas of the decay of ²²Na and the stop signals by the annihilation γ rays.) Fortunately, several firms provide standard electronic units, the properties of which meet these requirements. Even with the best available configuration, the time resolution of a fast-fast coincidence system is about 190 ps for ²²Na. This value is comparable with the shortest lifetimes to be measured, and therefore the resolution curve of the equipment plays a serious role in positron lifetime spectroscopy. The measured spectrum (P) is a convolution of the resolution curve (G) and the actual lifetime spectrum (S):

$$P(t) = G(t) * S(t) = \int_{-\infty}^{+\infty} G(\tau)S(t - \tau)d\tau. \quad (27.14)$$

$G(t)$ is usually approximated by a Gaussian function. $S(t)$ is the “decay curve” of positrons. In most of the materials, several positron states coexist (e.g., free annihilation, p -Ps, o -Ps), so the combined decay curve is formed by a sum of exponentials:

$$S(t) = \sum_{i=1}^n \lambda_i A_i \exp(-\lambda_i t) \quad (27.15)$$

where A_i denotes the relative weight of the i th positron state. Theoretically, n is the number of coexisting states, but in practice, it is not considered larger than four. This restriction is needed because exponential functions are not orthogonal. Consequently, a sum of exponentials cannot be evaluated into more than four components reasonably (Lánczos 1957). A characteristic positron lifetime spectrum is given in [Fig. 27.3](#).

In special cases, instead of the above sum, the lifetime spectrum is approximated by a continuous distribution of exponentials:

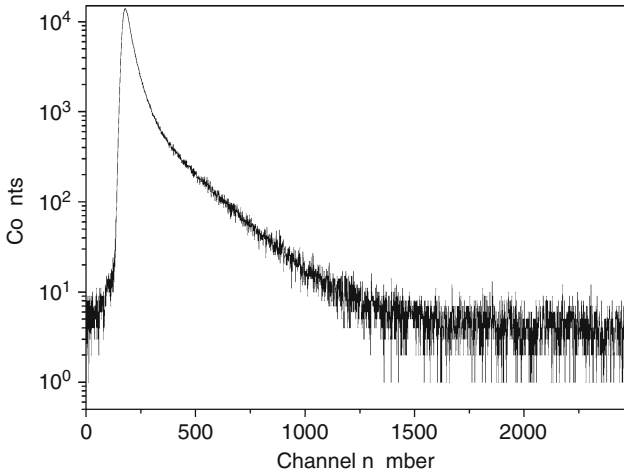
$$S(t) = \int_{\lambda} h(\lambda) \exp(-\lambda t) d\lambda \quad (27.16)$$

where $h(\lambda)$ is the density function of states over λ .

The most characteristic example of continuous distribution of states is supplied by polymers. In an amorphous polymer, the size of the structural free volume (the “hole” between chains) varies randomly and so does the electron density in these free volumes. If Ps atoms are trapped by the “holes,” their lifetimes reflect the size distribution of free volumes (Tao 1974; Eldrup et al. 1981).

■ Fig. 27.3

Semilogarithmic presentation of a characteristic positron lifetime spectrum. The left side of the peak characterizes the equipment resolution and the right side is the “decay” curve of positrons



The evaluation of positron lifetime spectra is usually performed by commercial computer codes. POSITRONFIT and RESOLUTION programs (Kirkegaard et al. 1981) work on the basis of Eqs. (27.14) and (27.15) supplying the lifetimes and relative intensities of the assumed states as final results. Positronium lifetime distributions are obtained applying the CONTIN (Gregory and Zhu 1990) algorithm or the MELT (Shukla et al. 1993) code for lifetime spectra.

27.3.3.2 Angular Correlation of Annihilation Radiation

The momentum distribution of annihilation γ photons are measured by one- or two-dimensional angular correlation spectrometers. The angular correlation of annihilation radiation (ACAR) spectrum is determined by the momentum conservation law; that is, the initial momentum of the annihilating positron–electron pair should be reflected in the angular distribution of γ photons. For a zero-momentum pair, in the case of 2γ -annihilation, the angle between the directions of photons is 2π radians (i.e., 180°). For realistic electron energies, this angle is modified by several milliradians. This modification is approximately:

$$\Theta \approx \frac{p_{\perp}}{m_e c} \quad (27.17)$$

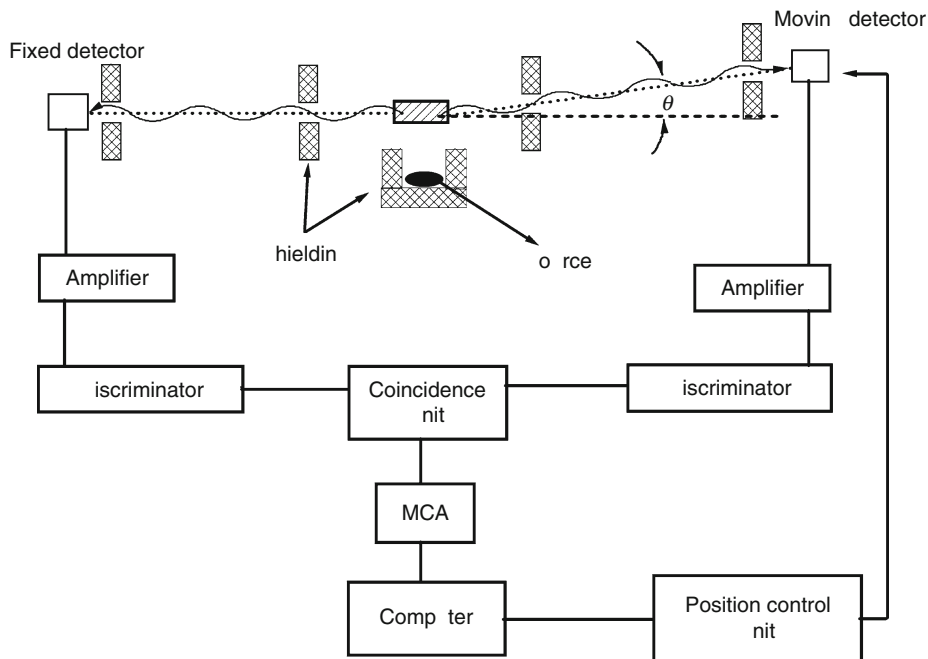
where p_{\perp} indicates the momentum component perpendicular to the axis of the spectrometer, m_e is the electron mass, and c is the speed of light.

The one-dimensional angular correlation “spectrometer” is a relatively simple equipment (Fig. 27.4). It is constructed from two scintillation detectors, several slits, a coincidence unit, and a storage unit.

Although the scheme of an angular correlation spectrometer is simple, due to the very small angles measured, its actual construction is intricate. Very narrow slits, long source/detector distances (several meters), precise positioning of the mobile detector, and an intense source

■ Fig. 27.4

The scheme of a one-dimensional angular correlation equipment. In two-dimensional spectrometers, the mobile detector is moved in two perpendicular directions to map photon distribution. Sometimes the mobile detector is replaced by a position-sensitive gamma camera



(10–20 mCi) should be used to obtain optimum performance. Usually NaI(Tl) or BGO scintillators are applied to optimize detection efficiency (Leo 1987b). However, the complex design and the required preciseness of construction have their advantages; that is, ACAR spectra provide precise and detailed information on the momentum distribution of electrons. In crystals, complete Fermi surfaces are mapped by this method regularly (e.g., Alam et al. 1997).

The measured angular correlation spectrum is a projection of the momentum density function of the sample. In the case of one-dimensional spectra, for example, the density function is integrated over two coordinates:

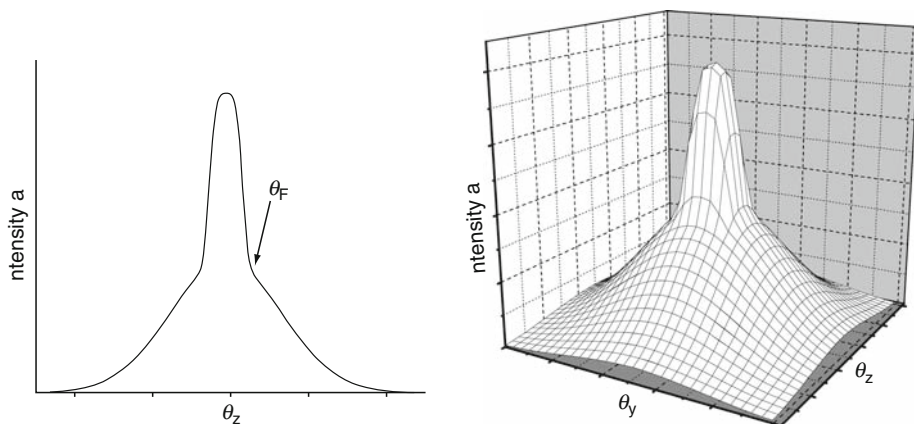
$$N(p_z) = A \int \int \lambda(\mathbf{p}) dp_x dp_y \quad (27.18)$$

where $\lambda(\mathbf{p})$ is the momentum density function and $N(p_z)$ is the transformed angular correlation function. Obviously, two-dimensional mapping decreases the integration coordinates to one. Two characteristic spectra are shown in Fig. 27.5.

There are commercially available computer programs for the evaluation of ACAR spectra (Kirkegaard et al. 1981). Even complicated calculations supplying Fermi surfaces (Dobrzynsky and Holas 1996) or positron distributions (Lock et al. 1973) are well documented in the literature.

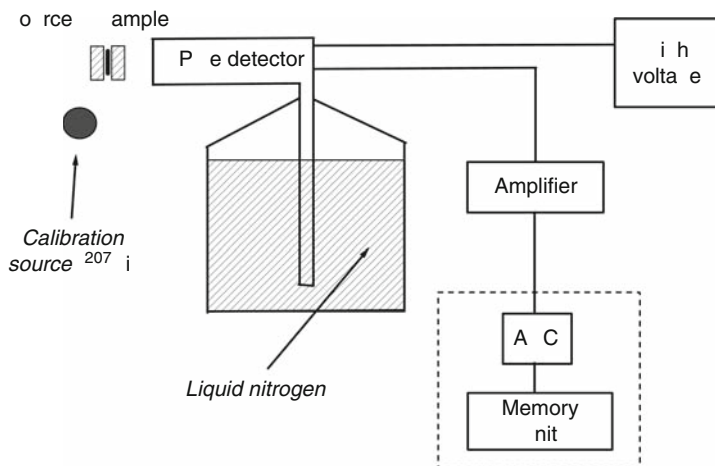
■ Fig. 27.5

One- and two-dimensional ACAR spectra. Note the indication of Fermi energy



■ Fig. 27.6

The scheme of a Doppler-broadening spectrometer. It is a normal gamma spectrometer with some twists. The calibration source is usually applied during measurements to stabilize amplification. Due to large count rates, the amplifier should contain a pile-up rejector unit



27.3.3.3 Doppler-Broadening Spectroscopy

The energy distribution of annihilation photons is studied with standard gamma spectrometers (➡ Fig. 27.6).

The basics of this method are very similar to that of ACAR spectroscopy. For an electron-positron pair of zero kinetic energy, 2γ -annihilation results in two identical photons of

0.511 MeV propagating into opposite directions. If the pair has a momentum component parallel with the direction of photons, the 0.511 MeV energy of photons deviates a little up or down. The phenomenon is called **Doppler-broadening of annihilation radiation**.

The energy deviation is proportional to the momentum component $p_{||}$ of the annihilating electron, which is parallel to the propagation direction of photons:

$$\Delta E \approx mc^2 \frac{v_{||}}{c} = p_{||}c \quad (27.19)$$

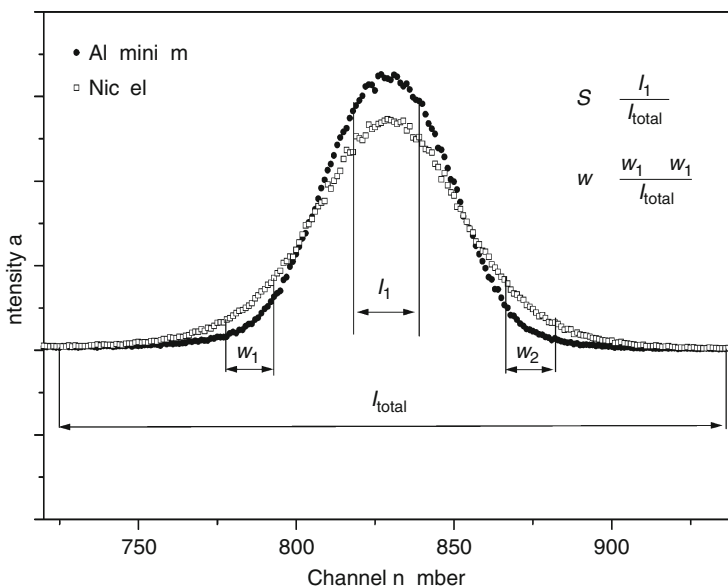
ΔE is on the order of a kiloelectronvolt, that is, comparable with the energy resolution of the best gamma spectrometers. Therefore one cannot expect such detailed information on the electron structure as in the case of ACAR spectra.

The evaluation of Doppler-broadening spectra is a crude method. Usually, only the central region of the annihilation peak is compared with the total area of the peak. Their quotient is called *S*-parameter, and it indicates the low-kinetic-energy part of electrons (► Fig. 27.7). Sometimes, another parameter (*w*) is also determined to describe the high-momentum regions of the spectrum (i.e., high- and low-energy tails of the energy spectrum).

Another possibility suggested several years ago was the use of high-energy part of Doppler-broadening spectra (Lynn et al. 1977). Two detectors were placed in 180° geometry, and coincidence measurements were performed together with the Doppler-broadening measurement. The spectral background was decreased by this method considerably. Under these conditions, the high-energy region could be described by the elemental contributions of the studied mixture (Asoka-Kumar et al. 1996).

■ Fig. 27.7

The definition of *S*- and *w*-parameters used to evaluate Doppler-broadening spectra. The symbols I_1 , I_{total} , w_1 , and w_2 denote areas (intensities) under specific sections of the Gaussian peak



27.3.3.4 Variable-Energy Positron Beams

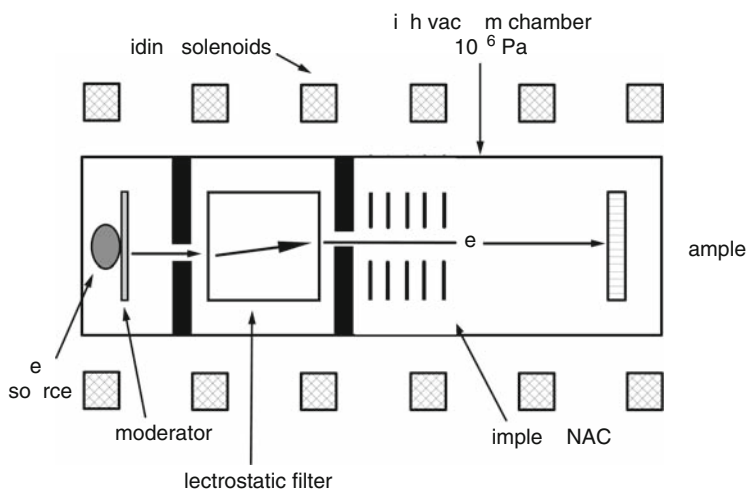
Positrons usually have considerable kinetic energy and, therefore, penetrate materials deeply. The implantation profile is exponential and, using a ^{22}Na source, relatively thick samples are required to stop all the positrons. To be exact, at least a thickness of 100 μm is needed in the case of polymers of $\rho \approx 1 \text{ g/cm}^3$ (Süvegh 1987), but the application of 30 μm of chromium ($\rho = 5.6 \text{ g/cm}^3$) can achieve the same goal (Süvegh et al. 1998). Because of this high penetration depth, positron annihilation spectroscopies provide information on the bulk of materials. To make positrons useful in surface studies and depth-dependent measurements, variable-energy positron beams have been developed.

Any equipment producing monoenergetic positron beams contains a simple linear accelerator (LINAC) in which the polarity is the opposite compared with those accelerating electrons. This is not surprising because, in this respect, positrons are just positively charged electrons. If, for a start, one has a bunch of low-energy positrons, one can do the same things with them as with electrons. They can be accelerated to a certain energy, and the beam can be focused or bent by electrostatic and magnetic fields. The most serious problem is to have low-energy positrons with a narrow-energy distribution and, at the same time, with a high efficiency (Schultz and Lynn 1988).

To obtain low-energy monoenergetic beams, positrons of a continuous energy distribution are injected into a moderator. Most of the injected positrons annihilate in the moderator, but some of them are reemitted into the vacuum. The moderator is usually made of tungsten (W), but sometimes, such exotic materials as solid Ne are used (Schultz and Lynn 1988). Most of the positrons leaving the moderator have low-kinetic energies spread over a narrow range, now useful to make a beam. Moreover, a simple electrostatic filter with an additional shielding is able to produce a very narrow-energy distribution. After the energy filter, everything works as in a LINAC. The beam is accelerated by an electrostatic field and focused by magnets. The outline of a positron beam is given in [Fig. 27.8](#).

■ Fig. 27.8

The outline of a variable-energy positron beam



The energy of positrons is usually varied between 0 and 30 keV, sometimes in a 0–60 keV range. The positrons of such beams penetrate materials only up to several nanometers. Consequently, positron beams are ideal for studying surfaces and near-surface states. However, they are rarely used to solve chemical problems. Their usual application is the investigation of semiconductor surfaces (Schultz and Lynn 1988). Defect structures, oxide layers, interfaces, and absorption processes are frequently studied by variable-energy positron beams. Some of the rare chemical applications of these beams are represented by measurements demonstrating the decomposition of a molecular crystal (Marek et al. 2000), studying Langmuir–Blodgett films (Marek et al. 1999; Koshimizu et al. 2000), and investigating alumina formation on an aluminum substrate (Mills et al. 1983).

The limited application of positron beams is explained by the fact that Doppler-broadening spectroscopy is the only detection method that works with beams without any difficulty. Although angular correlation measurements are possible with positron beams, it requires a very high efficiency beamline. Only very few beams fulfill the requirements of ACAR measurements, but their results are very impressive. The combination of low-energy positron beams and 2D-ACAR measurements is the only possibility to gain direct information on the momentum distribution of electrons at the surface of metals and semiconductors (Chen et al. 1987).

The case is even worse with lifetime spectroscopy. The moderation process erases the information on the “birth” of positrons; thus, performing lifetime spectroscopy is almost impossible. Although this problem was resolved by the construction of pulsed beams (Mills 1980), the time resolution of these systems has only reached that of a normal lifetime spectrometer recently (Hamada et al. 2000; Bauer-Kugelmann et al. 2001).

27.3.3.5 AMOC

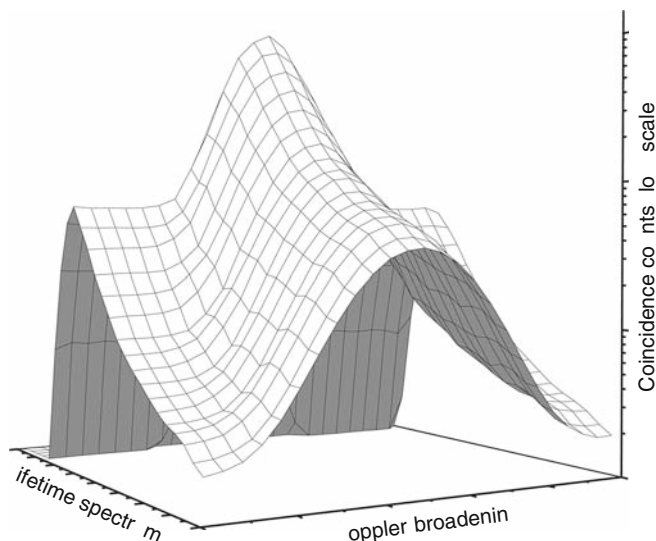
The 2γ -annihilation of positrons produces two correlated photons. On the other hand, both lifetime spectroscopy and Doppler-broadening measurements need only one of them. This suggests an evident possibility, that is, the combination of the two measurements. To achieve this goal, a three-photon coincidence system is required. In the system, one of the detectors measures the energy of an annihilation photon, and the other two determine the lifetime of the corresponding positron.

The first age-momentum correlation (AMOC) measurements were performed more than 20 years ago (McKenzie and McKee 1976; Kishimoto et al. 1982a, b). Those measurements applied ^{22}Na sources and measured, in fact, the energy dependence of lifetime spectra. The electronics of those days resulted in a much worse resolution of these age-momentum correlation spectrometers than that of individual lifetime and Doppler-broadening spectrometers. In spite of the bad resolution, these measurements provided valuable information about, for example, the structure of certain solutions (Kishimoto et al. 1982b).

The idea of age-momentum correlation measurements have been raised again recently (Stoll et al. 1992). The system is more complicated now but modern electronics and computer technique improved its resolution significantly. Nowadays, usual AMOC equipment applies high-energy positron beam (above 1 MeV) instead of ^{22}Na . The beam usually passes through a thin plastic scintillator before it reaches the sample. The signal of this plastic scintillator serves as the starting point for the lifetime measurement. The stop signal is measured with a fast scintillation detector, while the energy spectrum is usually provided by an HPGe detector. The evaluation method has also changed. In modern AMOC measurements, the momentum

■ Fig. 27.9

A simulated AMOC spectrum



distribution is calculated as a function of time, just oppositely as before. Sometimes, the entire two-dimensional function (● Fig. 27.9) is handled as a whole to gain more detailed information (Seeger 2000).

27.4 Recent Trends

Today, the field of positron annihilation spectroscopies is so vast that one can only try to give some hints to help the interested reader. The recent trends are briefly scanned below on the basis of the conference proceedings of Ito et al. (1999) and Triftshäuser et al. (2001). The examples are chosen arbitrarily from the two proceedings and other sources, and they do not cover the whole field.

27.4.1 Crystal Defects and Surfaces

The study of defects in metals and semiconductors is still the largest subsection of the applications of positron annihilation spectroscopies demonstrating the use of these methods in metal and semiconductor physics. Both bulk measurements with ^{22}Na sources and surface studies with low-energy beams are frequent.

Pure metals and dilute alloys have been studied in the past 30 years, thoroughly. Positron states have been described theoretically in these materials by the help of the so-called trapping model (West 1973) and even positron distributions have been determined in numerous cases by *ab initio* calculations (e.g., Gupta and Siegel 1980). Moreover, a vast number of experimental data proved the calculations experimentally during the years of extensive studies.

Nowadays, the interest turns more and more toward three-component alloys and inter-metallic compounds. Studies of vacancy formation in an AlPdMn single crystal (Baier et al. 2001), aging of AlCuMg alloys (Reich et al. 2001), and lattice relaxation in polycrystalline Ni₃Al represent this trend.

Very similar tendencies can be observed in the case of surface studies. Now, the basics are well-known, which provides the possibility to investigate complicated systems. Defects near the surface are studied in ion implanted MgO (van Huis et al. 2001), in BF₂ implanted Si (Akahane et al. 2001), and in bioactive ceramic coatings (Härting et al. 2001). As regards beams, both their efficiency and their electronic background have been improved greatly in recent years. Due to this development, “new” methods become available for everyday practice. Although most of these methods were worked out and some kinds of equipment built more than 20 years ago, they are new in the sense that now they are not exotic possibilities but useful spectroscopic methods.

27.4.2 Polymers

Among chemistry-related applications, the study of polymers is undoubtedly the most frequent. Free volume, glass transition, swelling, radiation damage, and aging are just a few examples of phenomena studied by positrons in polymers. However, radiation effects on Ps formation at low temperature have attracted notable attention in the last few years (e.g., Hirade et al. 2000; Suzuki et al. 2000).

This interest in polymers is due to a simple model connecting *o*-Ps lifetime with the size of free-volume holes in the material. The so-called free-volume model (Brandt et al. 1960; Tao 1972; Eldrup et al. 1981) works very well for polymers making *o*-Ps a unique tool in studying free volume. The model provides, at the end, a simple equation to calculate free-volume size from *o*-Ps lifetime:

$$\tau = \frac{1}{2} \left[1 - \frac{R}{R_0} + \frac{1}{2\pi} \sin \left(\frac{2\pi R}{R_0} \right) \right]^{-1} \quad (27.20)$$

where τ is the *o*-Ps lifetime and R is the radius of the hole that trapped Ps before the annihilation. $R - R_0$ is the depth the Ps penetrates the bulk, its value is assumed to be 1.66 Å for solids.

In recent years the field of studies has shifted towards complicated systems and phenomena in the case of polymers as well. Composites (Debowska et al. 2000), doped polymers (Huang et al. 2000), and membranes (Bi et al. 2000) were studied and self-irradiation effects caused by positrons (Balcaen et al. 2000) were observed.

With more and more data/experiments having been collected, positron lifetime spectroscopy might become a unique characterization method for polymers, that can even give qualitative results on the free-volume hole distribution of polymers.

27.4.3 Fluids and Molecular Solids

Fluids, molecular solids, and porous materials received more and more attention in the last few years. This is due to the continuous development of models and calculation methods (Stepanov et al. 2000; Paiziev 2000) supplying the possibility of a more accurate interpretation

of annihilation data in these complicated materials. The determination of such fundamental parameters as positronium mobilities in fluids (Wang et al. 2000) might also benefit structural studies in fluids.

Materials investigated by annihilation methods were chemically varied. Porous Y-zeolite (Kajcsos et al. 2000), organo-metallic compounds (Ito and Suzuki 2000), and cement-based materials (Consolati et al. 2000) were all studied in the last few years.

27.5 Editors' Notes

1. See [Section 8.4 in Chap. 8, Vol. 1](#), on the “Interaction of Radiation with Matter” (p. 1463).
2. See also [Chaps. 41 and 42 in Vol. 4](#) for such applications of ^{11}C and ^{18}F labeling (p. 1463).

References

- Akahane T, Fujinami M, Ohnishi K, Sawada T (2001) *Mater Sci Forum* 363–365:469
- Alam MA, Fretwell HM, Dugdale SB, Rodriguez-Gonzalez A, Major AG (1997) *Mater Sci Forum* 255–257:161
- Anderson CD (1932) *Phys Rev* 41:405
- Asai S, Orito S, Sinohara N (1995) *Phys Lett B* 357:475
- Asoka-Kumar P, Alatalo M, Ghosh VJ, Kruseman AC, Nielsen B, Lynn KG (1996) *Phys Rev Lett* 77:2097
- Baier F, Müller MA, Sprengel W, Grushko B, Sterzel R, Assmus W, Schaefer H-E (2001) *Mater Sci Forum* 363–365:179
- Balcaen N, de Baerdemaeker J, Dauwe C, Cosaert K, Goethals E, du Prez F (2000) *Rad Phys Chem* 58:497
- Bauer-Kugelmann W, Sperr P, Kögel G, Triftshauser W (2001) *Mater Sci Forum* 363–365:529
- Berko S, Pendleton HN (1980) *Ann Rev Nucl Part Sci* 30:543
- Bi J, Simon GP, Yamasaki A, Wang CL, Kobayashi Y, Griesser HJ (2000) *Rad Phys Chem* 58:563
- Brandt W (1983) In: Brandt W, Dupasquier A (eds) *Positron solid state physics*, Chapter 1. North-Holland, Amsterdam, pp 1–31
- Brandt W, Berko S, Walker WW (1960) *Phys Rev* 120:1289
- Brandt W, Coussot G, Paulin R (1969) *Phys Rev Lett* 23:522
- Chen DM, Berko S, Canter KE, Lynn KG, Mills AP Jr, Roellig LO, Sferlazzo P, Weinert M, West RN (1987) *Phys Rev Lett* 58:921
- Consolati G, Dotelli G, Quasso F (2000) *Rad Phys Chem* 58:727
- de Hosson JTM (2001) *Mater Sci Forum* 363–365:448
- Debowska M, Rudzinska-Girulski J, Jezierski A, Paternak A, Pozniak R (2000) *Rad Phys Chem* 58:575
- Deutsch M (1951) *Phys Rev* 82:455
- Dirac PAM (1930) *Proc Cambridge Phil Soc* 26:361
- Dobrzynsky L, Holas A (1996) *Nucl Instr Meth A* 383:589
- Eldrup M, Lightbody D, Sherwood JN (1981) *Chem Phys* 63:51
- Ferrel RA (1957) *Phys Rev* 108:167
- Gregory RB, Zhu Y (1990) *Nucl Instr Meth Phys Res A* 290:172
- Gupta RP, Siegel RW (1980) *J Phys F* 10:L7
- Hamada E, Oshima N, Suzuki T, Kobayashi H, Kondo K, Kanazawa I, Ito Y (2000) *Rad Phys Chem* 58:771
- Härting M, Hempel A, Hempel M, Bucher R, Britton DT (2001) *Mater Sci Forum* 363–365:502
- Hirade T, Maurer FHJ, Eldrup M (2000) *Rad Phys Chem* 58:465
- Howell RH, Fluss MJ, Rosenberg IR, Meyer P (1985) *Nucl Instr Meth B* 10/11:373
- Huang CM, Yuan J-P, Cao H, Zhang R, Jean YC, Suzuki R, Ohdaira T, Nielsen B (2000) *Rad Phys Chem* 58:571
- Ito Y, Suzuki T (2000) *Rad Phys Chem* 58:743
- Ito Y, Suzuki T, Kobayashi Y (1999) (eds) *Rad Phys Chem* 58:403–795. *Proc. 6th Int. Workshop on positron and positronium chemistry*
- Kaufmann A, Sperr P, Kögel G, Trifithäuser W (1997) *Mater Sci Forum* 255–257:680
- Kajcsos Z, Duplatre G, Liskay L, Billard I, Bonnenfant A, Azenha E, Lázár K, Pál-Borbély G, Caullet P, Patarin J, Lohonyai L (2000) *Rad. Phys Chem* 58:709
- Kirkegaard P, Eldrup M, Mogensen OE, Pedersen NJ (1981) *Comput Phys Commun* 23:307
- Kishimoto Y, Tanigawa S, Morinaga H, Matsuoka Y (1982a) In: Coleman PG, Scharma SC, Diana LM (eds) *Positron annihilation*. North-Holland, Amsterdam, pp 168–170

- Kishimoto Y, Ito K, Tanigawa S, Tsuda N (1982b) In: Coleman PG, Scharma SC, Diana LM (eds) *Positron annihilation*. North-Holland, Amsterdam, pp 843–845
- Kittel CH (1979) *Introduction to solid state physics*. Wiley, New York, p 87
- Koshimizu M, Asai K, Ishigure K, Iwai T, Shibata H, Ito Y (2000) *Rad Phys Chem* 58:633
- Lánczos C (1957) *Applied analysis*. Prentice-Hall, Englewood Cliffs, pp 272–280
- Leo WR (1987a) *Techniques for nuclear and particle physics experiments*. Springer, Berlin, pp 111–112
- Leo WR (1987b) *Techniques for nuclear and particle physics experiments*. Springer, Berlin, pp 113–114
- Lock DG, Crisp VHC, West RN (1973) *J Phys F* 3:561
- Lynn KG, MacDonald JR, Boie RA, Feldman LC, Gabbe JD, Robbins ME, Bonderup E, Golovchenko J (1977) *Phys Rev Lett* 38:241
- Lynn KG (1980) *Scripta Metall* 14:9
- Marek T, Szeles CS, Süvegh K, Kiss É, Vértés A, Lynn KG (1999) *Langmuir* 15:8189
- Marek T, Szeles CS, Molnár G, Borossay J, Vértés A, Lynn KG (2000) *J Radioanal Nucl Chem* 245:329
- Maurer FHJ, Schmidt M (2000) *Rad Phys Chem* 58:509
- McCarthy TJ, Schwartz SW, Weich MJ (1994) *J Chem Edu* 71:830
- McGervy J, De Benedetti S (1959) *Phys Rev* 114:495
- McKenzie IK, McKee BTA (1976) *Appl Phys* 10:245
- McKenzie IK (1983) In: Brandt W, Dupasquier A (eds) *Positron solid state physics*, Chapter 5. North-Holland, Amsterdam, p 196
- Mijnarends PE (1983) In: Brandt W, Dupasquier A (eds) *Positron solid state physics*, Chapter 4. North-Holland, Amsterdam, pp 146–195
- Mills AP Jr (1980) *Appl Phys* 22:273
- Mills AP Jr, Pfeiffer L, Platzman PM (1983) *Phys Rev Lett* 51:1085
- Mogenssen OE (1974) *J Chem Phys* 60:998
- Mohorovicic S (1934) *Astron Nachr* 253:94
- Paiziev AA (2000) *Rad Phys Chem* 58:433
- Reich L, Süvegh K, Lendvai J, Vértés A (2001) *Phyl Mag Lett* 81:145
- Rich A (1981) *Rev Mod Phys* 53:127
- Ruark AE (1945) *Phys Rev* 68:278
- Schrader DM, Jean YC (1988) *Positron and positronium chemistry*. Elsevier, Amsterdam, pp 1–20
- Schultz PJ, Lynn KG (1988) *Rev Mod Phys* 60:701
- Seeger A (2000) *Rad Phys Chem* 58:411
- Shukla A, Peter M, Hoffmann L (1993) *Nucl Inst Meth A* 335:310
- Stepanov SV, Wang C-L, Kobayashi Y, Byakov VM, Hirata K (2000) *Rad Phys Chem* 58:403
- Stoll H, Wesolowski P, Koch M, Maier K, Major J, Seeger A. (1992) *Mater Sci Forum* 105–110:1989
- Suzuki T, Ito Y, Kondo K, Hamada E (2000) *Rad Phys Chem* 58:485
- Süvegh K (1987) *J Radioanal Nucl Chem Lett* 117:183
- Süvegh K, Domján A, Vértés A, El-Sharif M, McDougal J, Chisolm CU (1998) *J Electroanal Chem* 455:69
- Tao SJ (1972) *J Chem Phys* 56:5499
- Triftshäuser W, Kögel G, Sperr P (eds) (2001) *Mater Sci Forum* 363–365:1–719. Proc. 12th International conference on positron annihilation
- van Huis MA, Fedorov AV, van Veen A, Labohm F, Schut H, Mijnarends PE, Kooi BJ, Hyodo T (1985) In: Jain PC, Singru RM, Gopinatan KP (eds) *Positron annihilation*. World Scientific, Singapore, p 643
- van Petegem S, Kuriplach J, Hou M, Zhurkin EE, Segers D, Morales AL, Ettaoussi S, Dauwe C, Mondelaers W (2001) *Mater SciForum* 363–365:210
- Vértés A, Kiss I (1987) *Nuclear chemistry*, Chapter 1. Elsevier, Amsterdam, pp 190–229
- Wang CL, Kobayashi Y, Hirata K (2000) *Rad Phys Chem* 58:451
- West RN (1973) *Adv Phys* 22:263

28 Exotic Atoms and Muonium

D. Horváth

KFKI Research Institute for Particle and Nuclear Physics, Budapest,
Hungary

Institute of Nuclear Research (ATOMKI), Debrecen, Hungary

28.1	<i>Introduction</i>	1487
28.2	<i>Experimental Methods</i>	1488
28.3	<i>Studies with Polarized Muons</i>	1489
28.3.1	Muonium	1489
28.3.2	Muon Polarization, Surface Muons	1489
28.3.3	The μ SR Method	1490
28.3.4	Applications in Solid-State Physics and Chemistry	1491
28.3.5	The Anomalous Magnetic Moment of the Muon	1494
28.4	<i>Theory of Exotic Atoms</i>	1494
28.4.1	Formation of Exotic Atoms	1494
28.4.2	Coulomb Capture Ratios	1495
28.4.3	Deexcitation of Isolated Exotic Atoms	1495
28.4.4	Exotic Atoms in Condensed Media	1497
28.4.5	Exotic Hydrogen Atoms	1498
28.4.6	Muon Capture in Nuclei	1499
28.4.7	Strong Interaction Effects in Hadronic Atoms	1499
28.4.8	Doubly Exotic Atoms	1500
28.5	<i>Muonic Atoms</i>	1500
28.5.1	Muonic Hydrogen	1500
28.5.2	Muon-Catalyzed Fusion	1500
28.5.3	Heavy Muonic Atoms	1501
28.6	<i>Hadronic Atoms</i>	1502
28.6.1	Study of Nuclear Structure	1502
28.6.2	Pionic Hydrogen Atoms	1503
28.6.2.1	Principle of Study	1504
28.6.2.2	Large Mesic Molecules	1504
28.6.2.3	Pion Capture in Hydrogen-Bonded Liquids	1504
28.6.2.4	Development of the LMM Model	1506
28.6.3	Antiprotonic Atoms	1507

28.6.3.1 Antiprotonic Hydrogen 1507

28.6.3.2 Long-Lived Antiprotonic Helium 1507

28.7 *Antihydrogen* 1509

Abstract: In exotic atoms, one of the atomic electrons is replaced by a negatively charged particle, whereas muonium consists of a positive muon and an electron. After a general review of the theoretical and experimental aspects, the present knowledge of this field is summarized. These include muonium and the application of the muon spin resonance method in solid-state physics and chemistry, muonic hydrogen atoms, muonic molecules and muon-catalyzed fusion, pionic hydrogen atoms and their use in chemistry, testing quantum electrodynamics on heavy muonic atoms, measuring particle and nuclear properties using hadronic atoms, and testing basic symmetry principles with antiprotonic helium atoms and antihydrogen.

28.1 Introduction

When a particle with a negative charge and long-enough lifetime slows down and stops in matter, it “replaces” an atomic electron and gets bound on an atomic orbit. The *exotic atoms* formed this way are named after the constituent particle: the most common ones are presented in [Table 28.1](#). According to the particle, one speaks about *muonic*, *pionic*, *kaonic*, *antiprotonic*, or sometimes *mesonic* or *hadronic* atoms.

The atoms formed by a positive particle and an electron (such as positronium, $\text{Ps} = e^-e^+$ or muonium, $\text{Mu} = \mu^+e^-$) also belong to the family of exotic atoms, and owing to the wide applications of positron annihilation and muon spin research in solid-state physics and chemistry, their study is much more intensive than that of the exotic atoms with negative particles. Also, the physical processes are quite different for exotic atoms with negative and positive particles. As positron annihilation and spectroscopy are treated separately in [Chap. 27](#), this chapter is restricted to exotic atoms with negative particles and with the positive muon.

The research of exotic atoms is or has been pursued at all major, intermediate energy accelerators where low-energy charged particles are or were produced.

The “www” pages of the laboratories (in parentheses) give a lot of useful information on the experiments conducted therein, including those on exotic atoms:

Table 28.1

Properties of *exotic* particles as compared to those of electrons. The particle mass m is rest mass. The strongly interacting particles, the integer spin *mesons* and the half-integer spin *baryons*, are together called *hadrons*. The data are taken from Amsler et al. (2008)

Particle	Spin (\hbar)	Lifetime (s)	m/m_e	mc^2/MeV	Class
e^-	1/2	∞	1	0.511	Lepton
μ^-	1/2	2.197×10^{-6}	207	105.7	Lepton
π^-	0	2.603×10^{-8}	273	139.6	Meson
K^-	0	1.237×10^{-8}	966	493.6	Meson
\bar{p}	1/2	∞	1,836	938.3	Baryon
Σ^-	1/2	1.48×10^{-10}	2,343	1,197.4	Baryon

- At the Alternating Gradient Synchrotron of Brookhaven National Laboratory (<http://www.bnl.gov/bnlweb/facilities/AGS.asp>)
- At the Antiproton Decelerator (AD) of CERN, Geneva (<http://psdoc.web.cern.ch/PSdoc/acc/ad/>)
- At KEK, Tsukuba, Japan (<http://www.kek.jp/intra.html>)
- At PSI, the Paul Scherrer Institute, Switzerland (<http://www.psi.ch/psi-home>)
- At ISIS of the Rutherford Appleton Laboratory, England (<http://www.isis.rl.ac.uk/>)
- At the Sankt-Petersburg Nuclear Physics Institute, Russia (<http://www.pnpi.spb.ru/>)
- At DAFNE, the electron–positron collider of INFN Frascati Laboratory, Rome, Italy (<http://www.lnf.infn.it/>)
- At TRIUMF, Vancouver, Canada (<http://www.triumf.ca/>).

This field has an extensive literature. The older papers published prior to 1983 are all collected by Horváth and Lambrecht (1984). Later developments are well presented in the proceedings of the conferences and schools on the various fields of exotic atoms (Simons et al. 1989; Benedek and Schneuwly 1992; Froelich 1993; Petitjean et al. 1999) and also in reviews on specific topics (Ponomarev 1975; Brewer and Crowe 1978; Horváth 1981; Hughes 1988; Roduner 1988; Charlton et al. 1994; zu Putlitz 1996; Batty et al. 1997; Eades and Hartmann 1999; Eides et al. 2001; Yamazaki et al. 2002).

The present review first discusses the studies with positive muons and then the research of exotic atoms with negative particles.

28.2 Experimental Methods

All the particles in [Table 28.1](#) are produced in collisions of high-energy protons with nuclei. The protons must have a kinetic energy much higher than the mass of the particle. The *meson factories* (Paul Scherrer Institute, TRIUMF) use proton energies of 500–1,000 MeV to produce charged pions ($m_{\pi^\pm} = 139.9\text{ MeV}$). The pions are then directly used for studies, or they are allowed to decay to muons via reaction:

$$\pi^+ \rightarrow \mu^+ + \nu_\mu. \quad (28.1)$$

Proton–nucleus collisions at high energies (5–20 GeV) create particle–antiparticle pairs, which then can be separated by charge in a magnetic field. (In particle physics, the usual units are $\text{GeV} = 10^9 \text{ eV}$ for energy E , GeV/c for momentum p , and GeV/c^2 for mass m . When expressed in natural units with $\hbar = 1$ and $c = 1$, one gets for the total energy $E^2 = p^2 + m^2$.) Antiproton is the only stable heavy negative particle, and so it has a special treatment. At CERN’s Antiproton Decelerator (AD) antiprotons are produced with a momentum of 3.5 GeV/c when the 26 GeV proton beam of the Proton Synchrotron hits an iridium target.

In order to form exotic atoms the particles have to be stopped in the target material. In principle, a sufficiently thick target can do the trick alone. However, a thick target will also

swallow some of the information to be gained (e.g., X-rays or Auger electrons); thus, it is better to decelerate the particle beam first while keeping it as monochromatic as possible. There are several methods proposed and used to do that, the most successful ones being the radiofrequency quadrupole decelerator (Lombardi et al. 2001) and the cyclotron trap or anticyclotron (Simons 1988).

Once exotic atoms are formed, one can use various methods to gain experimental information:

- Measure transition energies and level populations via detecting X-rays from atomic transitions with semiconductor, *charge-coupled device* (CCD) detectors or bent crystal spectrometers (spherically bent single crystals (e.g., Si and SiO₂) can be used to analyze the energy of X-rays by making use of the fact that X-rays of wave length λ (i.e., of energy $E = hc/\lambda$) are reflected from lattice planes with a spacing of d into a direction given by the reflection angle θ in accordance with the Bragg reflection condition $n\lambda = 2d\sin\theta$, where the integer n is called the order of reflection) or via laser spectroscopy.
- Measure the lifetime of the exotic atom by detecting the incoming particle and the decay products with scintillators, Cherenkov detectors, gas chambers, etc.
- Detect and analyze the products of the reactions after nuclear capture.

28.3 Studies with Polarized Muons

28.3.1 Muonium

Muonium is the atomic bound state of a positive muon and an electron, and thus it can be considered as a light “hydrogen isotope,” with a mass 1/9 of that of hydrogen. It has a wide interest for both physics and chemistry. In particle physics, it is treated as a “laboratory animal” to test the basic symmetries of matter (zu Putlitz 1996), and in solid-state physics, as a probe to measure local magnetic fields (Brewer and Crowe 1978), and in chemistry as a well-traceable light hydrogen atom (Roduner 1988). The laws governing the formation of muonium in gases and condensed systems are similar to those of positronium, the e^+e^- bound state. In gases, muonium is formed mostly in ionization processes, whereas in condensed systems, the spur mechanism, i.e., muonium formation in the ionization track of the muon, can also be significant (Brewer and Crowe 1978).

From the point of view of field theory, muonium is the bound state of two point-like leptons, so it is an ideal system to study quantum mechanical effects. Several such experiments are described by Jungmann (2000): search for muonium–antimuonium conversion, which should be a violation of lepton number conservation; precise measurement of spectroscopic transitions, which can be very well calculated and so provide a sensitive test of theories; and direct tests of symmetry principles of field theory such as CPT invariance, which predicts the equivalent properties of particles and antiparticles.

28.3.2 Muon Polarization, Surface Muons

The use of positive muons in solid-state physics and chemistry is based on the fact that due to the parity violation of the weak interaction (see ➤ Chap. 10 in Vol. 1 on “Standard Model of

Elementary Particles”), in decay (➔ 28.1) of positive pions, the outgoing muons are polarized against the direction of their momentum and in the muon decay reaction,

$$\mu^+ \rightarrow e^+ + \bar{\nu}_\mu + \nu_e \quad (28.2)$$

the positron is preferentially emitted in the direction of the muon spin (i.e., of the polarization of the muon). Thus, when muons are stopped in matter, their polarization at the time of decay can be measured by detecting the momentum direction of the positrons.

Muons are produced at proton accelerators. Protons of 0.5–1 GeV energy are scattered on a target. Depending on where they are produced, one calls them *surface*, *subsurface*, and *cloud* muons. Surface muons originate from pions stopped close to the surface of the target; they have kinetic energies around 4.1 MeV (momenta about 28 MeV/c). Subsurface muons originate from pions stopped in the bulk of the target, thus losing some energy on their way to the surface (momentum range 5–28 MeV/c). Cloud muons originate from pions decaying outside the target (momentum 10–280 MeV/c). For cloud muons, the pion beam line is frequently equipped with a superconducting solenoid to make sure that all pions travel long enough to decay (the pion’s mean life is 26 ns). At present, mostly surface muons are used for studies in materials science. Negative muons cannot be produced on the surface because negative pions – as soon as they stop – get absorbed by nuclei well before they could decay.

28.3.3 The μ SR Method

μ SR stands for muon spin rotation, relaxation, and resonance. As mentioned before, positive muons are used to measure local magnetic fields. When polarized muons are stopped in a sample material with some magnetic field, the muons will precess around the field lines and the positrons will be preferentially emitted along the muon spin (➔ Fig. 28.1).

Thus, if one measures the time between the muon stops and then decays (this can be done by using a positron detector set at a given angle to the beam direction), one shall have an exponential decay curve of the muon’s 2.2 ns lifetime with a superimposed sinusoidal whose frequency will be the *Larmor precession* frequency of the muon spin:

$$\nu = \frac{2\mu_\mu B}{\hbar} = 1.355 \frac{\text{MHz}}{T} B \quad (28.3)$$

where B is the magnetic flux density and μ_μ is the magnetic moment of the muon.

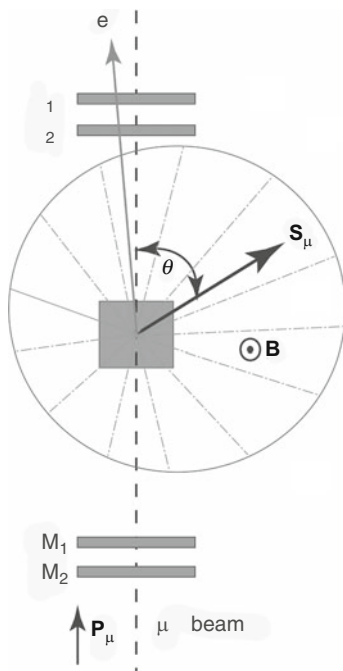
The time distribution of the recorded positron counts will be of the form:

$$\frac{dN(t)}{dt} \propto \frac{1}{\tau_\mu} e^{-\frac{t}{\tau_\mu}} \left[1 + \bar{a}P(t) \int f(\omega) \cos(\omega t + \varphi) d\omega \right] \quad (28.4)$$

where $\tau_\mu = 2.2 \mu\text{s}$ is the lifetime of the free muon, $f(\omega)$ is the distribution of the $\omega = 2\pi\nu$ angular Larmor frequencies, φ is the angle of the axis of the positron detector (usually a series of scintillation counters) to the original muon polarization and \bar{a} is the observed average amplitude of the asymmetry. If all positrons were detected with the same efficiency \bar{a} would be 1/3; in practice $\bar{a} > 1/3$ due to the lower detection efficiency of the lower energy positrons. A typical μ SR spectrum (Kojima 1995) is presented in ➔ Fig. 28.2.

■ Fig. 28.1

Scheme of the μ SR method. The incoming polarized muon passes two-beam detectors (M_1 , M_2), and after stopping in the target, it precesses in the local magnetic field of its environment. The positron is emitted preferentially toward the S_μ spin direction of the decaying muon at an angle $\theta = \phi + \omega t$ and produces an oscillating signal in the positron counters (E_1 , E_2) with a frequency $\nu \propto B = |\mathbf{B}|$, where \mathbf{B} is the magnetic flux density vector



The degree of polarization of the decaying muon, $P(t)$, may assume an exponential time dependence,

$$P(t) = e^{-\frac{t}{T_1}} \quad (28.5)$$

where T_1 is the longitudinal or spin-lattice relaxation time.

In the case of muonium formation, the integral in ► Eq. (28.4) can be approximated by an exponential decay of the muonium frequency ω_0 :

$$\int f(\omega) \cos(\omega t + \phi) d\omega \approx e^{-\frac{t}{T_2}} \cos(\omega_0 t + \phi) \quad (28.6)$$

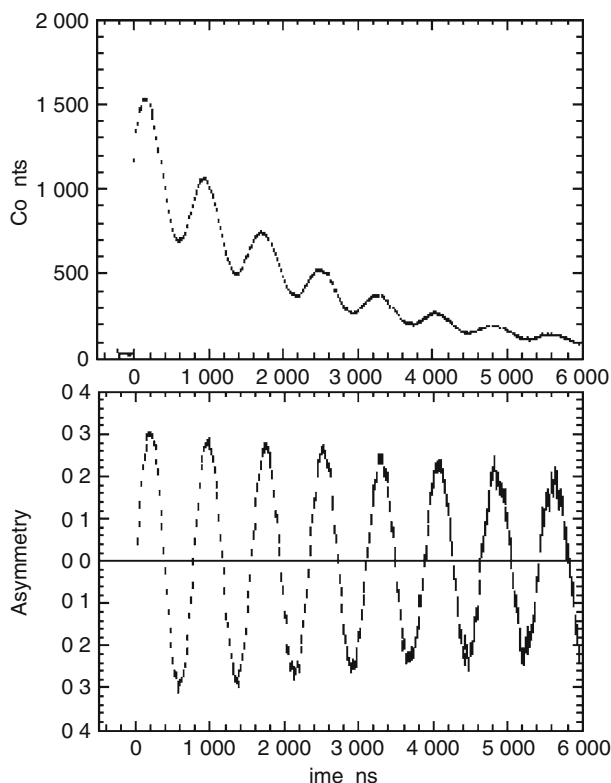
where T_2 is the transverse or spin-spin relaxation time.

28.3.4 Applications in Solid-State Physics and Chemistry

Applications of the μ SR method can be followed by the regular μ SR conferences (μ SR conferences from 1990 onward), and one can consult the home page of International Society for μ SR Spectroscopy (<http://musr.triumf.ca/~isms/>) for recent developments in the field.

■ Fig. 28.2

Typical μ SR spectrum (number of detected positrons against muon lifetime). The exponential muon decay is superposed (*upper spectrum*) by a signal oscillating with the muon precession frequency $\nu \propto B$. The lower spectrum shows the slowly relaxing asymmetry curve with the exponential removed



The formation of various muonic species in a system can be investigated by observing the characteristic precession frequencies and determining their initial amplitudes and decay rates. Three types of muonic species can be identified by their precession signals:

- Free muons in a diamagnetic environment give rise to Larmor precession according to Eq. (4.3).
- In weak magnetic fields ($B \leq 1$ mT), half of the free Mu atoms precess at $14 B$ MHz/mT the other frequency being too high to resolve experimentally.
- In strong magnetic fields ($B \approx 0.1$ T), several muonic radicals were observed because of their characteristic *split muonium* frequencies.

The measured amplitudes are usually scaled to give fractional diamagnetic, muonium, and muonic radical polarizations, directly related to the formation probabilities of the species.

Muonium, similarly to positronium, can be considered a light hydrogen isotope with almost the same binding energy and Bohr radius as hydrogen (see [Table 28.2](#)) and may be

■ Table 28.2

Properties of exotic hydrogen atoms (Horváth and Lambrecht 1984)

Exotic atom	Ground-state binding energy (eV)	Reduced mass (m_e units)	Bohr-radius (fm)
$H = pe^-$	13.6	1.0	5.3×10^4
$Ps = e^+e^-$	6.8	0.5	10.6×10^4
$Mu = \mu^+e^-$	13.5	0.995	5.3×10^4
$p\mu^-$	2,531	186.0	285
$p\pi^-$	3,236	237.9	222
pK^-	8,618	633.4	84
$p\bar{p}$	12,498	918.6	58
$p\Sigma^-$	14,014	1,030.0	51

expected to undergo similar chemical reactions with some isotope effects. For a review on muonium chemistry, see, e.g., Roduner (1988).

In solid-state physics, positive muons are used to measure the local magnetic induction at the site of the muon. Constant fields are measured via the (28.3) precession frequency, whereas fluctuating fields via relaxation. This makes μ SR a method analogous to nuclear magnetic resonance (NMR) or electron paramagnetic resonance (EPR) with the advantages that no radiofrequency field or macroscopic populations of the resonant species are needed. Muons are also easy to use in a cryogenic environment as both the fast muon and the decay positron easily traverse vacuum separation windows.

As a rule, in solids, muons occupy sites of positive ions, e.g., proton sites as demonstrated by comparing NMR and μ SR spectra of gypsum (Brewer and Crowe 1978). In metals, there are no ion sites where the muon could be electrically equivalent, so the positive muon must be either interstitial or trapped at vacancies, dislocations, or other defect centers. The motion of the muon is governed by thermally activated hopping between sites, showing slower spin relaxation at higher temperatures, which is analogous to the motional narrowing effect in NMR. Muon diffusion in solids is one of the major topics of μ SR studies.

Measuring the Larmor precession one can determine the local magnetic flux density at the muon site, which in solids can be described as

$$B_\mu = B_{\text{ext}} + B_{\text{dm}} + B_L + B_{\text{dip}} + B_{\text{hf}}. \quad (28.7)$$

In order to produce a slow, monochromatic muon beam, muons can be decelerated down to ~ 10 eV using a foil moderator and then reaccelerated to the desired energy. For experimental studies of solid surfaces and thin films, however, very slow muons can be produced by stopping surface muons in a thin layer of van der Waals-bound solid like solid nitrogen deposited on a properly microstructured metal substrate (Morenzoni 1999) in ultra-high vacuum. The slow muons cannot ionize or produce muonium, and, as a result of soft muon–atom elastic collisions, they are scattered out of the surface at epithermal energies (i.e., between ~ 0.5 eV and ~ 100 eV). The total efficiency of conversion from an energetic surface muon to an epithermal one is about 10^{-5} – 10^{-4} . Such an apparatus is described by Morenzoni et al. (2001).

28.3.5 The Anomalous Magnetic Moment of the Muon

Polarized muons provide a sensitive tool to test field theory as well. The magnetic moment of a charged particle is $gS\mu_{\text{part}}$ where g and S are the g factor and the spin of the particle, respectively, and μ_{part} is the particle magneton. The theory of the electromagnetism, quantum electrodynamics (QED), predicts that a charged particle is “swimming” in a medium of virtual particle–antiparticle pairs that blink in and out of existence. Without those, the g factor of the magnetic moment of the electron and muon would be the same, i.e., $g = 2$, but the QED contributions from the virtual particles make it $g = 2(1 + a_\mu)$ for the muon, where a_μ measures the relative anomaly of the magnetic moment. Muons are two orders of magnitude heavier than electrons, so the possibilities of having particle–antiparticle pairs in a muon field are much more favorable than for the electron. Thus, measuring the anomalous magnetic moment of the muon (see [Table 10.3 of Chap. 10](#), Vol. 1, on “Standard Model of Elementary Particles”) can hint at new phenomena in physics if the results are different from those predicted by the theory.

In a not too strong magnetic field, the muon has two different movements around the field lines: a cyclotron motion with an angular frequency $\omega_c = eB/(m_\mu c)$, and a Larmor precession with a frequency $\omega_s = g_\mu eB/(2m_\mu c)$. Longitudinally polarized muons moving in a toroidal magnetic field of a storage ring will precess at the difference $\omega_a = \omega_c - \omega_s$, which is proportional to the anomalous part of the magnetic moment containing a_μ . This kind of experiment is called $(g - 2)$ measurement (Hughes [1988](#); Brown et al. [2001](#)). The precision is increased if one uses relativistic muons with $\gamma^2 = 1/(1 - v^2/c^2) \gg 1$ in a magnetic storage ring,

$$\omega_a = -\frac{e}{m_\mu} \left[a_\mu \mathbf{B} - \left(a_\mu - \frac{1}{\gamma^2 - 1} \right) \boldsymbol{\beta} \times \mathbf{D} \right]. \quad (28.8)$$

where ω_a , \mathbf{B} , $\boldsymbol{\beta}$, and \mathbf{D} are the three-dimensional vectors of the Larmor frequency, magnetic flux density, relative velocity, and electric displacement, respectively. The increased precision is due to three things: (1) the relativistic longevity of the muon, (2) at the magic momentum 3.094 GeV/c, where $\gamma = 29.3$, the second term of [Eq. \(28.8\)](#) vanishes, and so (3) the focusing electric fields will not affect the muon motion. Such experiments were performed earlier at CERN and recently at BNL (Hughes [1988](#); Brown et al. [2001](#)). The results do not quite agree with the predictions of the Standard Model (see [Table 10.3 of Chap. 10](#), Vol. 1), although the difference is not statistically significant.

28.4 Theory of Exotic Atoms

28.4.1 Formation of Exotic Atoms

The negative particle entering an absorber (gas or condensed matter) loses its kinetic energy via ionization in collisions with atoms of the medium and in the *last* collision gets stuck in a binding orbit. The higher the overlap between the wave functions of the ejected electron and the particle, the more probable the formation of the exotic atoms. Thus, the initial bound state will be geometrically close to that of the ejected electron. This and the equality of the binding energies of the captured antiproton and the released electron (Massey conditions, Mott

and Massey 1965) mean that the freshly formed exotic atom will be in a highly excited state, with a principal quantum number of the order of

$$n = \sqrt{\frac{m}{m_e}} \quad (28.9)$$

where m and m_e are the masses of the particle and the electron, respectively.

For details of the theory of atomic capture see, e.g., Fermi and Teller (1947), Ponomarev (1975), Cohen (1989), Hartmann (1999), and Yamazaki et al. (2002).

The energy levels of an isolated exotic atom in a state of principal quantum number n and angular momentum j for a point-like nucleus are given by Measday (2001)

$$E_{n,j} = \frac{mc^2}{1 + m/m_N} \frac{(Z\alpha)^2}{2n^2} \left[1 + \left(\frac{Z\alpha}{n} \right)^2 \left(\frac{n}{j + 1/2} - \frac{3}{4} \right) \right], \quad (28.10)$$

where Z and m_N are the atomic number and the nuclear mass ($\sim A$ where A is the mass number), and α is the fine structure constant.

28.4.2 Coulomb Capture Ratios

Numerous models have been proposed for describing the formation of exotic atoms via Coulomb capture. The muons in atoms do reach the atomic ground state (as opposed to hadronic atoms), and the lack of strong interaction effects makes them good probes to study Coulomb capture. One of the most important experimental methods is measuring *Coulomb capture ratios*. In a mixture of two elemental gases (e.g., $N_2 + O_2$) or in binary compounds, one can determine the amount of muons captured in the different elements by summing up the amplitudes of the muonic Lyman series, the ($n p \rightarrow 1s$) transitions.

The main difficulty when comparing experiment with theory is created by the chemical effects: chemical bonds are shown to distort the atomic cascade. As the possibility of studying binary atomic mixtures of elements is restricted to mixtures of noble gases, two attempts were made to overcome the dispersion of individual measurements. All experimental Coulomb capture ratios, measured in binary systems to date, were collected and compared with theoretical predictions by Horváth and Entezami (1983). Average Coulomb capture ratios were deduced by von Egidy et al. (1984) using all measurements made in binary oxides. None of the models agrees well with experiment, although those which assume the weaker-bound electrons to be more efficient in capture (Schneuwly et al. 1978) seem to be better. This conclusion has been recently confirmed by classical trajectory Monte Carlo and Fermi molecular dynamics calculations (Cohen 1997, 2000, 2002).

28.4.3 Deexcitation of Isolated Exotic Atoms

The deexcitation will start via Auger processes, while the level spacing is small (as its rate weakly depends on the ΔE transition energy) and there are electrons to be ejected, and then via radiative transitions as the probability of the latter is roughly proportional to $(\Delta E)^3$. The initial population of the atomic states will be related (though not exactly proportional) to the available density of states, so for any given principal quantum number n the higher orbital momenta will be more populated.

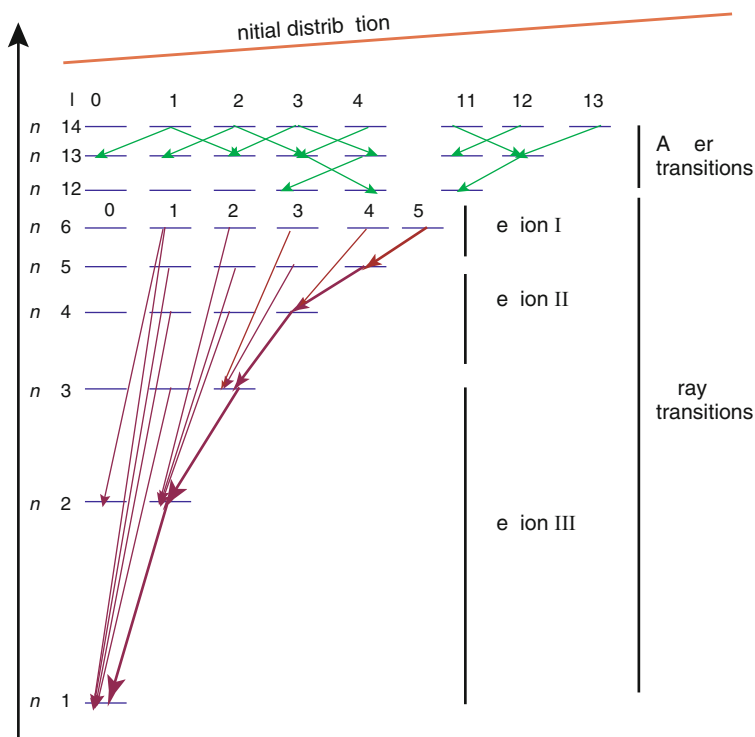
As the Auger transitions do not change the shape of the angular momentum distribution, the particle quickly reaches the ($l = n - 1$) orbits (Hartmann 1989) and from those – owing to the $\Delta l = \pm 1$ rule – can make circular, $(n, l = n - 1) \rightarrow (n - 1, l = n - 2)$ transitions only (► Fig. 28.3). Typical exotic-atoms X-ray spectra are presented in ► Fig. 28.4: note that the spectra are dominated by circular transitions from highly excited states.

There are several cascade codes developed for reproducing the cascade decays of exotic atoms (see, e.g., Borie and Leon 1980; Markushin 1999; Jensen and Markushin 2002). The cascade process is studied by detecting X-rays and Auger electrons from transitions in all exotic atoms and via laser spectroscopy in metastable antiprotonic helium (see ► Sect. 28.6.3.2). It was experimentally observed that medium-heavy muonic atoms such as $\mu^- \text{Ar}$ lose all atomic electrons via Auger effect by the time the muon reaches the ground state (Bacher et al. 1988).

The decay of the exotic atom can be a simple decay of the exotic particle in the case of light muonic atoms; however, due to the strong nuclear interaction in hadronic atoms, the negative hadron can be absorbed by the nucleus leading to nuclear reaction (► Fig. 28.5).

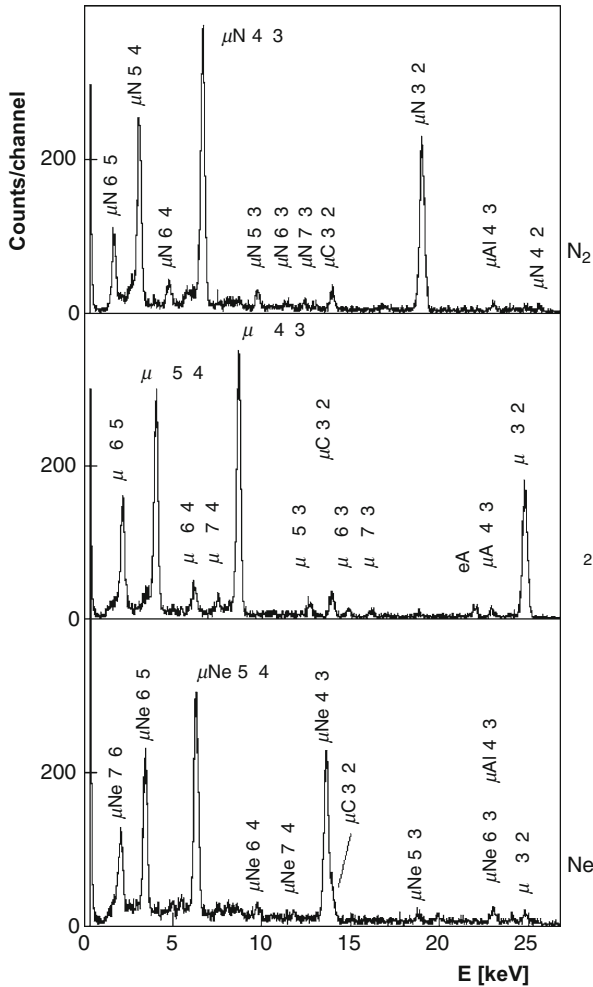
■ Fig. 28.3

Deexcitation of a muonic atom. From highly excited states Auger transitions prevail, in the lower region X-ray emission. The X-ray region can be divided into three subregions: (I) strong electron screening effect, (II) low electron screening, negligible nuclear interaction, (III) interaction with the nucleus



■ Fig. 28.4

X-ray spectra from muonic atoms as measured in nitrogen, oxygen, and neon using a Si(Li) detector (Kirch et al. 1999). The spectra are dominated by circular transitions from highly excited states. The spectra show lines of muonic aluminum and carbon from muons stopping in the container wall of the gas target and in scintillators around it



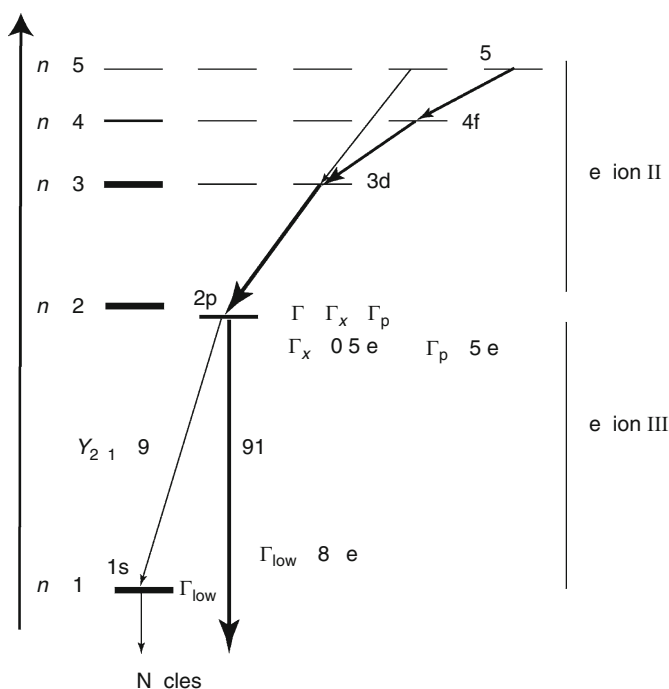
The above picture was theoretically assumed by Fermi and Teller in 1947 and experimentally proven in the 1990s by a measurement of the initial state populations of antiprotonic helium (Yamazaki et al. 2002; Hayano et al. 2007).

28.4.4 Exotic Atoms in Condensed Media

In media of not too low densities the deexcitation process is dominated by collisions. Collisions can cause external Auger effect when the exotic atom loses excitation energy by ejecting an

■ Fig. 28.5

Deexcitation of the pionic oxygen atom. For the highly excited states, see ► Fig. 28.3. In the lower X-ray region, strong interaction with the nucleus shifts and broadens the states with low orbital momentum, and there is strong nuclear absorption from the lowest ns states. Y is the yield of a transition, Γ is the level width



electron from another atom of the medium, or Stark mixing when the energetically degenerate states of various orbital momenta mix in the external electric field of another atom, thereby enabling the exotic atom to make an otherwise forbidden high- Δn radiative transition from a circular state.

28.4.5 Exotic Hydrogen Atoms

The exotic hydrogen atoms, systems consisting of a proton and a negative particle, or a positive particle and an electron, are special in many aspects (Eides et al. 2001). Their basic properties are summarized in ► Table 28.2.

Exotic hydrogen atoms are created when a negatively charged particle is captured in an atomic orbit on a proton. Because normally hydrogen is always bound in molecules, the negative particle must replace a binding electron to form exotic hydrogen. The latter is small, electrically neutral, and has no electrons to feel Pauli repulsion, so it can penetrate the electron shells of other atoms. This can lead to *transfer* when the negative particle moves from the exotic hydrogen atom to another, heavier atom.

The theory of transfer has been developed by Gershtein (1963). He has shown that at small distances between $p\mu^-$ and a heavier nucleus Z , the ground state of muonic hydrogen transforms into a state of a *united atom* $pZ\mu^-$ and the level crossing of $p\mu^-$ and $Z\mu^-$ makes adiabatic transfer possible in slow collisions. Gershtein's theory had an immediate success as it had predicted that muon transfer to helium cannot go this way, and a great suppression of muon transfer to helium was observed, indeed.

Exotic hydrogen atoms have no atomic electrons so their deexcitation is different: at the highest levels Coulomb deexcitation in atomic collisions dominates, then external Auger transitions, i.e., ejection of electrons of other atoms in collisions, before X-ray transitions take over (Jensen and Markushin 2002). Coulomb deexcitation can lead to acceleration thereby producing a hot exotic hydrogen atom as observed experimentally for pionic hydrogen. The atomic cascade in muonic hydrogen is measured to study QED effects and nuclear properties: the Lamb shift, i.e., the energy difference between the 2s and 2p states, e.g., depends on r_p^2 , where r_p is the charge radius (see “Charge Radii” in [Chap. 2](#), Vol. 1) of the proton (Eides et al. 2001).

28.4.6 Muon Capture in Nuclei

In its atomic ground state, the exotic particle has a Bohr radius that is close to or even smaller than the nuclear radius, so it will interact with the nucleus. Muon capture in nuclei (Measday 2001) is governed by the weak interaction between a lepton and a proton (*semi-leptonic process*):

$$\mu^- + p \rightarrow n + \nu_\mu \quad (28.11)$$

This reaction most frequently leads to nucleons or nuclear fragments to be ejected from the nucleus, while most of the released kinetic energy is taken away by the neutrino.

28.4.7 Strong Interaction Effects in Hadronic Atoms

Due to a strong interaction with the nucleus, hadrons cannot reach ground state in exotic atoms as they are captured by the nucleus via strong absorption from higher n s levels where their orbit is closest to the nucleus. As a result of the strong interaction, the hadronic energy levels are broadened and shifted more and more as they get closer to the nucleus.

Using exotic atoms, one can separately study the distributions of protons and neutrons in the nucleus by comparing muon and pion absorption. Muons are absorbed by the protons only, whereas the strong interaction is independent of the electric charge, so hadrons (pions, kaons, and antiprotons) interact equally with protons and neutrons.

Nuclear capture of hadrons can lead to fission of heavy nuclei because the reaction of a negative hadron with a nucleon releases as much energy as the mass of the particle, which is an order of magnitude more than that binding the nucleus.

Muons bound in an atomic orbit in transuranium elements can also cause nuclear fission, but that mechanism is quite involved (Measday 2001). There are two types of fission events, prompt and delayed. The prompt events are induced by energy from the atomic cascade of the muon, whereas the delayed events are from muon capture via the weak interaction.

28.4.8 Doubly Exotic Atoms

In decays of heavy unstable particles many charged mesons can be emitted simultaneously. If two of them are oppositely charged and have close trajectories, they can form a bound state. Nemenov (2000) quotes the experimental study of $\pi^+\mu^-$, $\pi^+\pi^-$, and π^+K^- atoms from which scattering lengths were deduced for the two-particle systems involved.

28.5 Muonic Atoms

28.5.1 Muonic Hydrogen

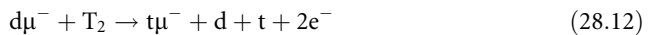
As hydrogen gives up its only atomic electron in order to establish its chemical bond, the exotic particle first *replaces* its molecular binding electron before it can settle on the proton. As proposed by Ponomarev (1975), this means a temporary formation of a *large mesic molecule*, and as a heavy atom provides a lot more available states for the particle than hydrogen, the probability that the particle will eventually form exotic hydrogen with a proton (and not be captured by the heavier atom) is roughly proportional to Z^{-2} , where Z is the atomic number of the atom binding the hydrogen atom.

The exotic hydrogen isotopes (see [Table 28.2](#)) provide numerous interesting processes, like the transfer of the exotic particle from a hydrogen isotope to a heavier nucleus; the formation of exotic molecules, which makes the muon catalysis of nuclear fusion possible; or measuring the electron density on the hydrogen in molecules using the pionic hydrogen atom.

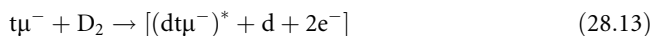
As mentioned before, the neutral exotic hydrogen atom (having neither Coulomb nor Pauli repulsion) can penetrate other atoms and lose its exotic particle to a heavier nucleus. As the rate of this reaction is proportional to the number of collisions, it can be detected for hadronic atoms but it is really dramatic for muonic hydrogen as its lifetime is many orders of magnitude longer: in the muon-catalyzed fusion measurements, for example, the concentration of heavy impurities has to be below 10^{-8} to avoid the distortion of the results by transfer. This feature was used to study muon capture in rare gas isotopes as it is sufficient to have less than 1% krypton in hydrogen to have all muons ended up in muonic krypton states.

28.5.2 Muon-Catalyzed Fusion

The muon, entering, e.g., a deuterium + tritium ($D_2 + T_2$) mixture, forms a $d\mu^-$ or $t\mu^-$ atom. From the former, in a collision, the muon gets transferred to tritium:



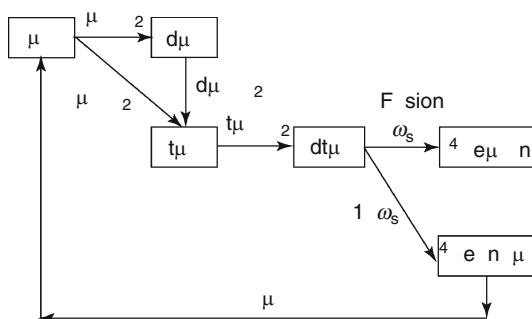
as it is more favorable energetically, and this way practically all of the muons end up in $t\mu^-$ even in mixtures with a small amount of tritium only. The most important process is the formation of a muonic molecule in a collision:



in such a highly excited state that the vibration states of the molecule in the square brackets, consisting of the positive $dt\mu^-$ molecule ion and the deuteron as nuclei with the two electrons,

■ Fig. 28.6

Scheme of muon-catalyzed fusion in a deuterium–tritium mixture. As a result of the fusion 17.6 MeV is released per ${}^4\text{He}$ atom (ω_s is the sticking probability)



can absorb the tiny binding energy of the $(dt\mu)^{-*}$ molecule ion. The process mentioned above has a resonance as a function of ambient temperature through the kinetic energy of the $d\mu^{-}$ atom. With the deexcitation of the $dt\mu^{-}$ molecule ion, the muon *compresses* the two nuclei inducing thereby a nuclear fusion process (with 17.6 MeV energy release) and then it becomes available to restart the whole cycle as a real catalyst (► Fig. 28.6).

After the prediction (Vesman 1967) and first observation (Bystritskii et al. 1979) of the resonant formation of muonic molecules in Dubna, muon-catalyzed fusion (μCF) became the leading field in exotic atoms research (Petitjean 1989), with its own journal and biennial conferences (see MuCF07 (2007) for the latest one). Although there were attempts to propose possible uses of muon-catalyzed fusion in energy production, at present nobody expects reactors to produce fusion energy using muon catalysis soon. Nevertheless, μCF research gave an enormous impetus to the research of basic processes of exotic atoms and of atomic physics in general.

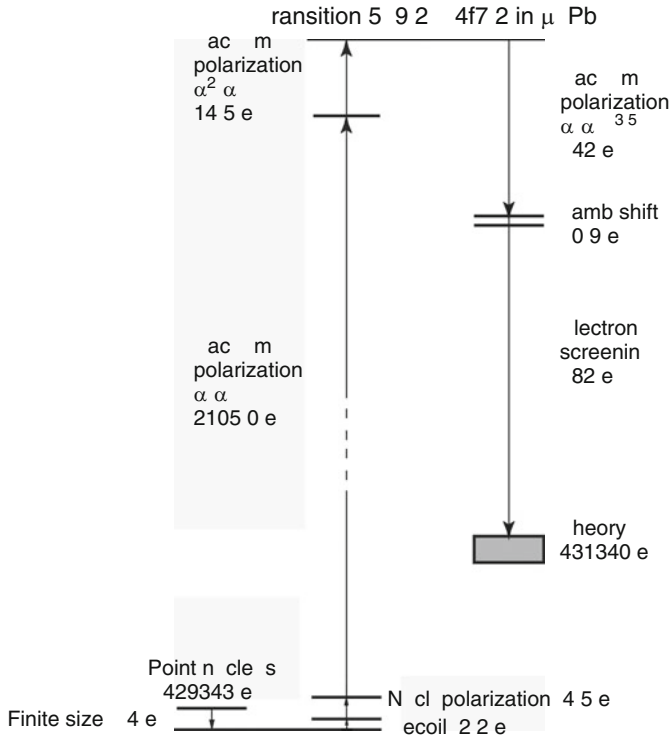
28.5.3 Heavy Muonic Atoms

As shown in ► Fig. 28.3, in the upper region of the X-ray transitions, the particle may interact with and thus probe the electronic shell, while in the lower one it already probes the atomic nucleus as its wave function partially penetrates it. The region between is also interesting as those transitions are weakly influenced both by the remaining or recombined electrons and by the field of the nucleus; there one can get information on the properties of the captured particle or test the effects of quantum electrodynamics. As an example, ► Fig. 28.7 presents (Horváth and Lambrecht 1984) the various energy terms in the $5g\ 9/2 \rightarrow 4f\ 7/2$ transition in muonic lead; here the contribution of the Lamb shift, which is the dominant such term in ordinary atoms, is quite small as compared to the other vacuum polarization effects.

As the X-ray transition energies are proportional to the reduced mass of the system and may be split due to spin–orbit and spin–spin interactions, studies in the intermediate region of the atomic cascade are used to measure the mass, charge, and the magnetic moment of certain negative particles. Such an example will be shown later for the case of the antiproton.

■ Fig. 28.7

Test of quantum electrodynamics in muonic lead: contributions of higher-order processes to the energy levels as predicted by field theory. The height of the shaded block on the right shows the uncertainty of the theoretical value



28.6 Hadronic Atoms

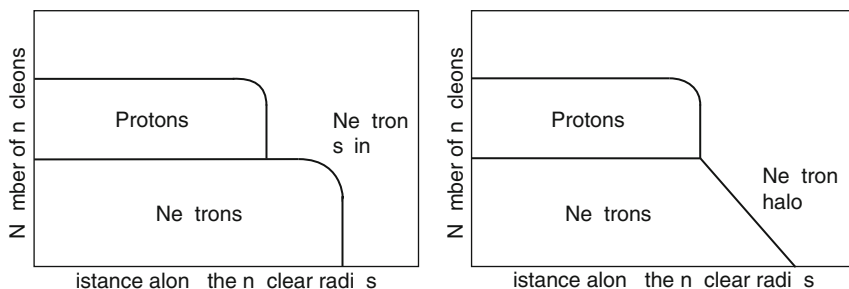
28.6.1 Study of Nuclear Structure

Hadronic atoms provide an excellent tool for studying the nuclear structure and nuclear matter. This is very important as one cannot apply perturbative approximations to the theory of strong interactions (quantum chromodynamics) at low kinetic energies. The particles used, i.e., π^- , K^- , Σ^- , and \bar{p} have much longer natural lifetime (the antiproton is even stable) than the typical slowing down times in condensed media and the atomic timescales. Therefore, after stopping a negatively charged hadron in matter, well-defined atomic states are established. The overlap of the atomic orbitals with the nucleus covers a large range of nuclear densities, and thus the density-dependence of the hadronic interaction can be directly studied (Batty et al. 1997).

Strong interaction between the captured hadron and the nucleus shifts and broadens the energy levels; this makes it possible to study strong interaction effects using X-ray spectroscopy. The shift and broadening of the atomic s and p levels in the antiproton–proton system are

■ Fig. 28.8

Neutron skin and neutron halo in heavy nuclei. The neutron radius of heavy nuclei is observed to be larger than the proton radius. A uniformly *overhanging* neutron distribution is called neutron skin (*on the left*), whereas a gradually diminishing one is a neutron halo



directly related to the complex scattering length and the volume of the antiproton–nucleon system; thus spectroscopy of hadronic atoms is equivalent to scattering experiments at the energy threshold (Gotta 1999).

Physical information can be obtained, e.g., by measuring the shift and broadening of the energy levels of the hadron in the atom due to nuclear interactions as compared to a purely electromagnetic case. The shifts and widths can be measured for one or two levels only in each kind of hadronic atom as the strong nuclear absorption – which causes the level broadening – terminates the atomic cascade at a certain principal quantum number n_{\min} . This lowest n sensitively depends on the mass of the particle and on the atomic number of the nucleus: $n_{\min} = 1$ for pionic oxygen and 8 for antiprotonic nickel.

In heavy nuclei with more neutrons than protons the neutron distribution is observed to have a larger radius than that of the protons. This is in agreement with the observation that nuclear mass radii tend to be larger than charge radii (see Sect. 2.2.3.1 in Chap. 2, Vol. 1, on the “Basic Properties of the Atomic Nucleus”). Hadronic atoms are very sensitive to this: in heavy antiprotonic atoms the antiproton interacts with the outermost part of the nucleus only and it annihilates predominantly in interaction with neutrons rather than protons (Trzcinska et al. 2001) as seen from the summary charge of the decay products. There is a general disagreement, however, about the shape of the neutron distribution, whether it is a *neutron skin* or a *neutron halo* (see Fig. 28.8). Radiochemical experiments definitely prefer a neutron halo (Trzcinska et al. 2001), pionic X-rays seem to disagree with it (Batty et al. 1997), whereas according to Wycech (2001) from the antiproton data one can reject or confirm neither.

As pionic hydrogen atoms found important applications in chemistry most of this chapter is devoted to that particular topic and the rest of hadronic atoms is only briefly summarized.

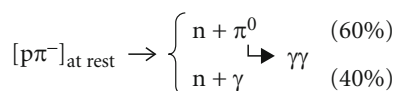
28.6.2 Pionic Hydrogen Atoms

Pion chemistry, i.e., the use of pionic hydrogen in physical chemistry, was invented in Dubna more than 40 years ago (Petrukhin et al. 1967). As shown by the experimental studies of Petrukhin et al., the probability, W_Z , that a pion stopped in a compound containing Z–H groups will be absorbed by a proton, i.e., hydrogen bound by Z atoms, depends on the

properties of the Z–H group, and particularly on the electron density at the hydrogen atoms. Pion capture measurements were performed on various chemical systems at various laboratories: JINR, Dubna; LNPI, Gatchina; TRIUMF, Vancouver; and KEK, Tsukuba. For earlier references see the reviews published by Ponomarev (1975), Gershtein et al. (1970), Horváth (1981, 1984a), Measday (1990), and Armstrong (1991); the more recent work at KEK is summarized by Shinohara et al. (1999).

28.6.2.1 Principle of Study

Experimentally, the two-photon decay of neutral pions from the charge-exchange reaction following π^- capture in proton:



is studied by detecting the two photons using total-absorption Cherenkov counters or large NaI detectors. As π^0 production from stopped π^- has 60% probability for protons, 15% for ^3He , and negligible ($<10^{-4}$) for every other nuclide, the upper one of the above reactions is a unique signal to identify the decay (and therefore the formation) of pionic hydrogen atoms.

28.6.2.2 Large Mesic Molecules

The pionic hydrogen measurements were interpreted using the *model of large mesic molecules* (LMM) proposed by Ponomarev (1975). As the hydrogen atom gives up its only electron to establish the Z–H molecular bond, the negative pion, in order to form a $p\pi^-$ atom, must replace first a binding electron. Its initial orbit is geometrically similar to that of the replaced electron, so it is very large on the pionic scale, hence the name of the model.

According to the original LMM model, the probability W that the pion is captured on the proton can be described as the product of three probabilities (Fig. 28.9),

$$W = PQR, \quad (28.14)$$

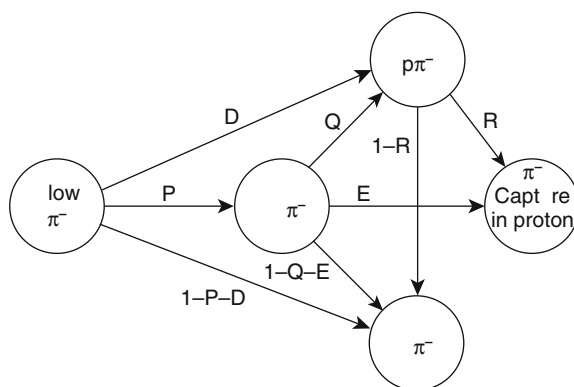
those of the formation of a $Zp\pi^-$ molecule (P), of the transition of the pion from the molecular orbit to a $p\pi^-$ atomic state (Q), and the probability R that from the pionic hydrogen atom the pion will be absorbed by a proton (not necessarily the original one) and not transferred to a heavier nucleus.

28.6.2.3 Pion Capture in Hydrogen-Bonded Liquids

An excellent example for the application of pions in chemistry is the study of the relation between hydrogen bonds and electron density using the pion capture method. This research work began in Dubna (Kachalkin et al. 1979; Horváth et al. 1991b) by a measurement of pion capture in water as a function of temperature from ice to supercritical fluid. As shown in Fig. 28.10, the W probability of pion capture is constant in ice, i.e., below the melting point, T_m , then steeply increases in the liquid phase, and levels off again above the critical temperature, T_c .

■ Fig. 28.9

The fate of a slow negative pion in matter containing hydrogen bound to atom Z (Horváth 1984b). The pion can be captured in a molecular orbit with probability P or in atomic orbits on Z or H (the latter, D , is negligible), from the molecular orbit it goes to H or Z, and from the $p\pi^-$ it can be transferred to a heavier atom or captured in the proton. The probability that a slow pion gets absorbed in a proton is $W = PQR$, because E is also negligible in comparison with QR



The overall temperature dependence of the probability $W(T)$ showed a remarkably good agreement with the so-called *bond-breaking* or *mixture* model of water structure (Haggis et al. 1952; Luck 1979) with one adjustable parameter only,

$$Q = \frac{W(T > T_c)}{W(T < T_m)} \quad (28.15)$$

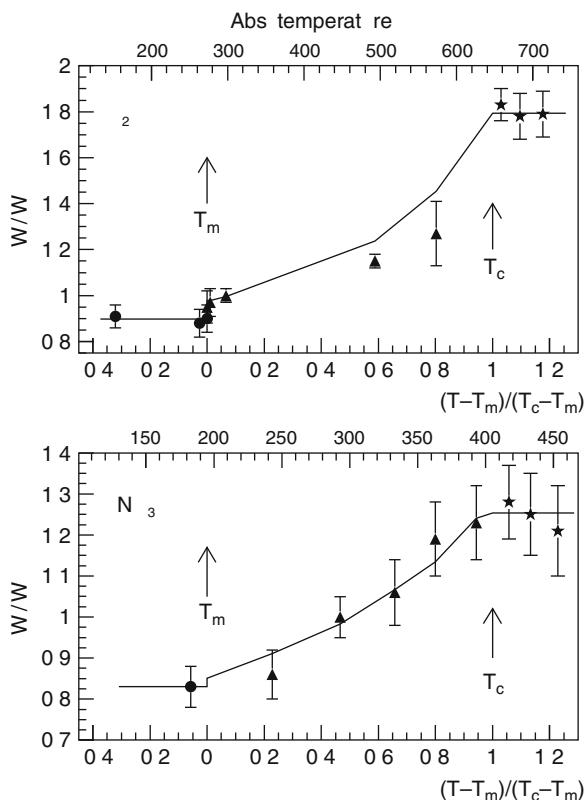
which had a surprisingly high value, $Q(\text{H}_2\text{O}) = 2.0 \pm 0.1$, indicating a large difference between the probabilities of pion capture in ice and in supercritical water.

It is generally assumed that in ice, all protons are bound in hydrogen bonds, while above the critical temperature, there are very few hydrogen bonds; thus the value of $Q(\text{H}_2\text{O})$ should reflect a difference between the proton states inside and outside of hydrogen bonds. However, reliable theoretical estimations predict only about 10% difference between the electron densities of the two proton states (Schuster 1976). This led to the conclusion that unless the measured $Q(\text{H}_2\text{O}) = 2$ value is a “magic” number connected with the existence of two equivalent oxygen atoms near the proton of the hydrogen bond (as suggested by Ponomarev), the pion capture method somehow *magnifies* the electron density effect.

To clarify the above question the Dubna group studied pion capture in solid, liquid, and supercritical ammonia (Horváth et al. 1982) as well, with results very similar to water (► Fig. 28.10). The hydrogen bond effect was smaller, $Q(\text{NH}_3) = 1.51 \pm 0.12$, but still somewhat “magically” connected to the molecular composition, as there are three protons to two nitrogen atoms in the hydrogen bond network. The pion capture measurement made it possible to estimate the model parameter, the fraction of broken $\text{N}-\text{H}\cdots\text{N}$ bonds, as a function of temperature (Horváth et al. 1982). At TRIUMF, yet another family of hydrogen-bonded liquids with strong $\text{O}-\text{H}\cdots\text{O}$ bonds was studied: alcohols (Luck 1979). For this measurement, one had to separate pion capture in hydrogen atoms bound to oxygen and to carbon using partially deuterated compounds. The result was $Q(\text{CD}_3\text{OH}) = 1.79 \pm 0.11$, close to that of water (Horváth et al. 1991a).

■ Fig. 28.10

Temperature dependence of pion capture probability in water (Kachalkin et al. 1979) and ammonia (Horváth et al. 1982). The probability is normalized to that measured at room temperature. The temperature is expressed as $\Theta = (T - T_m)/(T_c - T_m)$, where T , T_m , and T_c are the temperatures of measurement, melting point, and critical point, respectively. Ordinary temperature scales are also shown above the boxes. The curves represent fits using the bond-breaking (mixture) model of hydrogen-bonded liquids (Haggis et al. 1952; Luck 1979)



28.6.2.4 Development of the LMM Model

It is evident that the LMM picture is an extremely simple and rough approximation: the processes involved are not independent and, as shown by ▶ Fig. 28.9, ▶ Eq. (28.14) reflects just one of the possible paths for the pion to follow in a simple system of hydrogen bound by a heavier Z atom. For the correct interpretation of pion-chemistry results, the primordial populations of pionic bound states and pion transfer to heavier atoms were studied in gas mixtures with and without hydrogen (Horváth 1984b; Muroyama et al. 1999). On the basis of these data several efforts were made to improve on the LMM model, the latest and most successful ones were that by Imanishi et al. (1988) and Shinohara et al. (1996).

28.6.3 Antiprotonic Atoms

28.6.3.1 Antiprotonic Hydrogen

Several protonium ($p\bar{p}$) experiments were performed at the antiproton facilities of CERN (Gotta 1999) in order to estimate the strong interaction parameters from atomic X-ray spectra. Experiment PS207 (a Jülich–Geneva–Ioannina–Islamabad–Neuchatel–Paris–Villigen collaboration) has done that with very high precision using a two-arm bent-crystal spectrometer at CERN (Gotta 1999; Augsburg et al. 1999).

28.6.3.2 Long-Lived Antiprotonic Helium

As mentioned in the introduction, the usual lifetime of the strongly interacting hadrons in condensed media is in the order of 10^{-12} s. However, about 3–4% of the antiprotons stopped in gaseous or liquid helium form metastable states that survive for a time of the order of several microseconds. The metastable state is a three-body system of an antiproton, a helium nucleus, and an electron. When the antiproton is located in an ($n \approx 38$, $\ell \geq 35$) orbit of a neutral $\bar{p}ze^-$ atom, those states from which Auger transitions are suppressed due to high angular momentum exchange ($\Delta\ell > 3$) will become metastable as the electron removes the ℓ -degeneracy of the levels with the same principal quantum number n and also screens the $\bar{p}\alpha$ system from collisions.

The energy levels and populations of antiprotonic helium atoms have been thoroughly investigated both theoretically (Korobov 1996, 1999, Korobov and Bakalov 1997) and experimentally, the results are summarized in reviews (Horváth 1997; Eades and Hartmann 1999; Yamazaki et al. 2002; Hayano et al. 2007). The experiments were performed using laser resonance spectroscopy in the following way: stop a bunch of antiprotons in helium, wait until the promptly annihilating states disappear, and then stimulate the transition from a long-lived state to a short-lived one with a tunable laser. At the resonant frequency corresponding to the transition energy of the antiproton, the laser shot will be followed by immediate annihilation creating a peak in the decay-time spectrum.

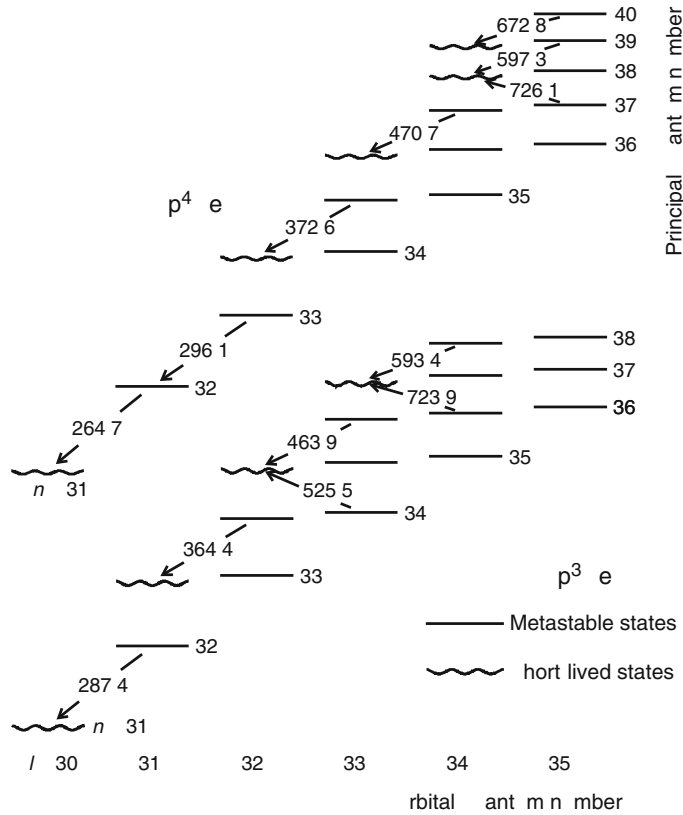
The antiproton is the only stable and heavy antiparticle and thus it is used to test the symmetry of matter and antimatter. This symmetry is the consequence of one of the most fundamental principles of field theory, *CPT invariance* (see [Sect. 10.3 in Chap. 10](#) of Vol. 1 for more detail), which states that the physical properties of a free system do not change when one simultaneously switches three kinds of signs: (1) the signs of the charges (C), i.e., replacing particles by antiparticles; (2) the signs (directions) of the spatial coordinates, which means changing the parity P of the system; and finally (3) changing the sign (direction) of time T . Thus, according to the CPT invariance, an antiparticle is equivalent to its ordinary particle counterpart going *backward* in space and time. In spite of its not really plausible nature, CPT invariance is so far supported by all available experimental evidence in the microworld; nevertheless, serious experimental and theoretical efforts are undertaken to study its possible limits (Kostecký 1997; Kostecký and Lehnert 2001).

Antiprotonic helium was used to test the CPT invariance by measuring the difference of charge and mass between proton and antiproton (Hayano et al. 2007). The charge/mass ratio of the proton and the antiproton was determined at LEAR (Gabrielse et al. 1999) by

measuring cyclotron frequencies in a Penning trap. The charge and mass information was separated via studying antiprotonic transition energies in the $\bar{p}\text{He}^+$ as those are proportional to $m(\bar{p})q(\bar{p})^2$.

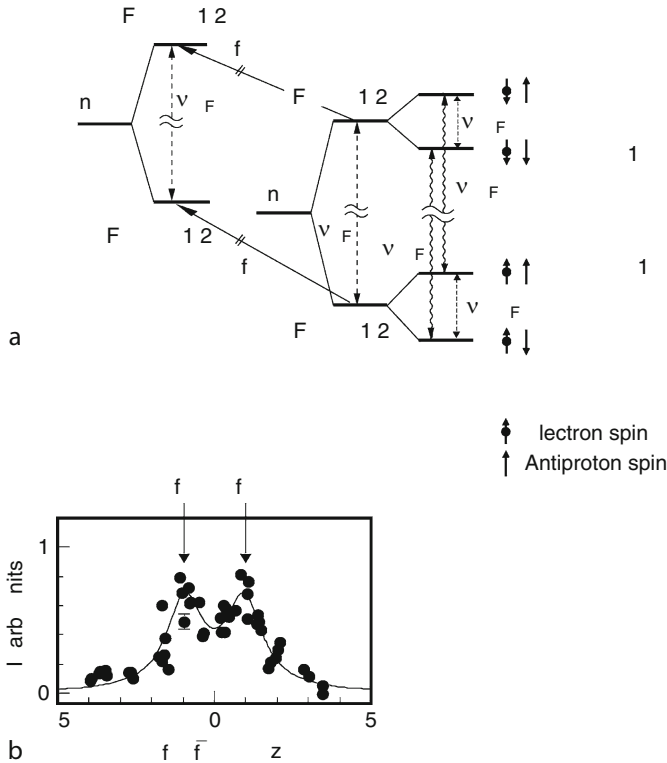
The transitions in antiprotonic helium isotopes studied to obtain a limit on the antiprotonic mass and charge are illustrated in Fig. 28.11. In order to get precise results, one had to minimize the laser bandwidth and the collisional effects by using low temperatures and target densities. The latest result was $|m_p - m_{\bar{p}}|/m_p < 2 \times 10^{-9}$ for the relative mass difference and $|q_p - q_{\bar{p}}|/q_p < 2 \times 10^{-9}$ for the charge difference (Hori et al. 2006). Further plans of the ASACUSA group include using two-photon spectroscopy to eliminate the first-order Doppler broadening of the measured transitions. To date this is the only experimental method to limit the charge and mass difference of protons and antiprotons (Amsler et al. 2008).

Fig. 28.11
Transitions in the $\bar{p}^3\text{He}^+$ and $\bar{p}^4\text{He}^+$ atoms studied using laser spectroscopy in order to measure the mass and charge of the antiproton (Hori et al. 2006). The horizontal lines denote long-lived states, the wavy lines short-lived ones. The arrows indicate experimentally studied transitions with wavelengths in nanometers



■ Fig. 28.12

Hyperfine transitions in the $\bar{p}^3\text{He}^+$ and $\bar{p}^4\text{He}^+$ atoms studied using combined laser and microwave spectroscopy in order to measure the magnetic moment of the antiproton (Widmann et al. 2002) in the atomic bound state: (a) level splitting; (b) the measured spectrum: number of forced antiproton annihilations against the microwave frequency



Another CPT test was done by the same group by measuring the magnetic moment of the antiproton in antiprotonic helium atoms (Widmann et al. 2002). One half of an antiprotonic state, split as a result of the interaction between the electron spin and the total angular momentum of the antiproton in the three-body system, was first partially depopulated using a suitably tuned laser, then repopulated with a microwave of varied frequency, and finally depopulated again with the same laser frequency as first. The relative yield of the second laser resonance was maximum when the microwave frequency corresponded to the hyperfine splitting of the state from which the antiproton magnetic moment could be determined (► Fig. 28.12).

28.7 Antihydrogen

Antihydrogen, the bound system of an antiproton and a positron, stands in the middle of attention of the low-energy antiproton community. The reason is that antihydrogen

spectroscopy offers to test several fundamental principles of physics, the most important ones being CPT symmetry and the weak equivalence principle of gravity (Charlton et al. 1994). According to the CPT invariance an antiproton should accelerate the same way in the gravitational field of an anti-Earth as protons do in that of Earth. The weak equivalence principle states that protons and antiprotons accelerate equally in the gravitational field of Earth. Unfortunately, it is very hard to test experimentally as the gravitational force on an antiproton at the surface of Earth is about the same as the electric force of a point charge (of $1e$) from a distance of 10 cm. Such a test is proposed using the effect of the different gravitational force of the Sun at perihelion (i.e., in the winter in the Northern Hemisphere) and at aphelion (i.e., in the summer) on the atomic transitions of antihydrogen (Charlton et al. 1994).

Antihydrogen atoms were created the first time at CERN in 1995 by crossing a relativistic antiproton beam with a xenon jet target in the LEAR ring (Baur et al. 1996). The antiproton created electron–positron pairs in the field of the Xe nucleus and if the direction of the positron momentum coincided with that of the antiproton, having the same speed near c , they could form an antihydrogen atom that then left the ring through a straight beam line. The antihydrogen atoms were stripped in thin Si detectors; the positron annihilations were detected in NaI X-ray detectors, whereas the freed antiprotons led to a magnetic spectrometer for identification. Eleven antihydrogen atoms were detected with a possible background of 2 ± 1 events.

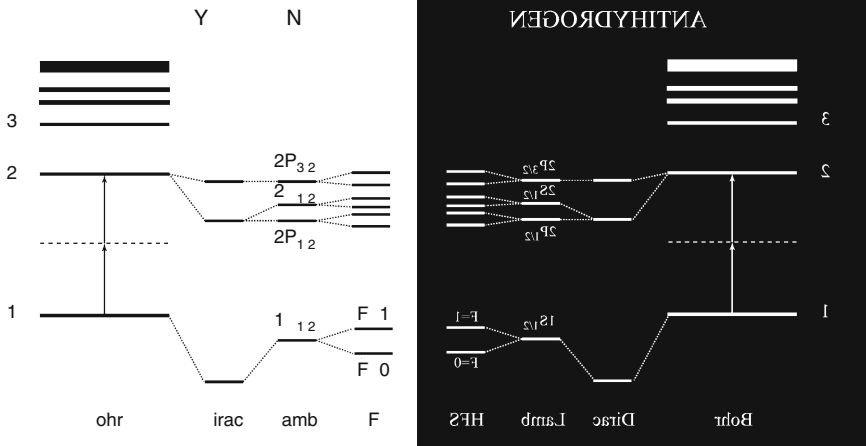
In order to conduct spectroscopic studies, one needs slow, confined, ground-state antihydrogen atoms. Several schemes have been proposed to produce trapped antihydrogen atoms for spectroscopy in order to take momentum away and increase the production rate. Most of them involve a third colliding partner: another positron, an electron, a resonant photon, or an external radiofrequency field (Charlton et al. 1994). Spontaneous radiative two-body recombination is generally considered to be slow. The antihydrogen atoms are to be formed in a quadrupole (or combined quadrupole–octupole) magnetic field in order to confine half of them: those with the correct orientation of the positron spin. Such traps can only confine cold antihydrogen atoms of temperatures below 1 K and therefore they have to be cooled after formation, for which optical (laser) cooling seems to be feasible at present (Charlton et al. 1994).

The extremely small line width (1 Hz) corresponding to the long lifetime of the metastable $2S$ state makes the $2S$ – $1S$ transition (► Fig. 28.13) the most promising candidate for high-precision measurements; a Doppler-free excitation is possible in the case of simultaneous absorption of two photons from opposite directions. This transition has been measured in hydrogen with a relative precision of 1.8×10^{-11} (Andreae et al. 1992) yielding the most precise up-to-date value of the Rydberg constant. A new apparatus is being developed in Garching, at the Max Planck Institute for Quantum Optics (Haensch 2008).

CERN has built a dedicated machine to study the CPT invariance using antiprotons, the AD, which includes two antihydrogen experiments. Quite recently, both of them managed to produce cold antihydrogen atoms in large quantities (Amoretti et al. 2002; Gabrielse et al. 2002). They used the same method for antihydrogen production: a *nested Penning trap* was loaded with positrons and then with antiprotons. With the help of a nested Penning trap one can confine particles of opposite electric charge (in the present case positrons and antiprotons) in a finite volume defined by two electromagnetic potential wells. The outer, larger potential well traps antiprotons and the smaller one, inverted and nested inside the outer, traps positrons. The two kinds of particles can exchange kinetic energy by collisions. The positron cloud *cools* itself (i.e., loses kinetic energy) with synchrotron radiation in the magnetic field of

■ Fig. 28.13

Atomic levels in hydrogen and antihydrogen. CPT symmetry requires them to be exactly equivalent



the trap, and the relatively high-energy antiproton introduced into the outer well will “cool down” in collisions with the cold positrons to the temperature of the positron cloud in seconds. The presence of “cold” interacting particles of opposite charge enables the study of low-temperature recombination processes (Hall and Gabrielse 1996). The ATHENA collaboration (Amoretti et al. 2002) proved the creation of antihydrogen by reconstructing the space–time coordinates of the annihilation of positrons and antiprotons for cold and hot mixing of the constituents – in a hot mix the recombination is suppressed. The ATRAP group (Gabrielse et al. 2002) re-ionized the freshly formed antihydrogen atoms, deducing thereby their quantum states as well. Since then, large numbers of antihydrogen atoms were produced and studied by the two collaborations at the AD, ATRAP and ALPHA (the latter replaced ATHENA), but the problem of confinement of the antihydrogen atoms is not solved yet. A new AD experiment, AEGIS intends to measure the gravitational mass of antihydrogen at a 1% precision. Although CPT invariance states the equivalence of the gravitational force of antimatter to an anti-Earth only, the weak equivalence principle relates them to the gravity of antimatter to Earth.

Acknowledgments

This work was supported by the Hungarian National Science Foundation and the National Office for Science and Technology under contracts NK67974 and K72172.

References

- Amoretti M et al (2002) *Nature* 419:456
- Amsler C et al (2008) *Phys Lett B* 667:1, <http://pdg.lbl.gov>
- Andreae T et al (1992) *Phys Rev Lett* 69:1923
- Armstrong DS (1991) In: Benedek and Schneuwly 1990, p 175
- Augsburger M et al (1999) *Hyperfine Interact* 118:59

- Bacher R et al (1988) *Phys Rev A* 38:4395
- Batty CJ, Friedman E, Gal A (1997) *Phys Rep* 287:385
- Baur G et al (1996) *Phys Lett B* 368:251
- Benedek G, Schneuwly H (eds) (1992) *Exotic atoms in condensed matter, Proceedings of the Erice Workshop, 1990*, Springer, Berlin
- Borie E, Leon M (1980) *Phys Rev A* 21:1460
- Brewer JH, Crowe KM (1978) *Ann Rev Nucl Part Sci* 28:239
- Brown HN et al (Muon g-2 Collaboration) (2001) *Phys Rev Lett* 86:2227
- Bystritskii VM et al (1979) *Sov Phys JETP* 49:232
- Charlton M et al (1994) *Phys Rep* 241:65
- Cohen JS (1989) In: Simons et al (1989) p 1
- Cohen JS (1997) *Phys Rev A* 56:3582
- Cohen JS (2000) *Phys Rev A* 62:022512
- Cohen JS (2002) *Phys Rev A* 65:052714
- Eades J, Hartmann JF (1999) *Rev Mod Phys* 71:373
- Eides MI, Grotch H, Shelyuto VA (2001) *Phys Rep* 342:63
- Fermi E, Teller E (1947) *Phys Rev* 72:399
- Frøelich P (ed) (1993) *Proceedings of the international workshop on muon catalysed fusion, Uppsala, Sweden, 1992*, Hyperfine Interact 82
- Gabrielse G et al (1999) *Phys Rev Lett* 82:3198
- Gabrielse G et al (2002) *Phys Rev Lett* 89:213401
- Gershtein SS (1963) *Sov Phys JETP* 16:50; also in Petitjean et al (1999) p 169
- Gershtein SS et al (1970) *Sov Phys Uspekhi* 12:1
- Gotta D (1999) *Hyperfine Interact* 118:35
- Haensch TW (2008) <http://www.mpg.de/~haensch/hydrogen/index.html>
- Haggis GA, Hasted JB, Buchanan G (1952) *J Chem Phys* 20:1452
- Hall DS, Gabrielse G (1996) *Phys Rev Lett* 77:1962
- Hartmann FJ (1989) In: Simons et al (1989) p 23, 127
- Hartmann FJ (1999) In: Petitjean et al (1999) p 157
- Hayano RS, Hori M, Horváth D, Widmann E (2007) *Rept Prog Phys* 70:1995
- Hori M et al (2006) *Phys Rev Lett* 96:243401
- Horváth D (1981) *Radiochim Acta* 28:241
- Horváth D (1984a) *Hyperfine Interact* 17–19:679
- Horváth D (1984b) *Phys Rev A* 30:2123
- Horváth D (1997) *Radiochimica Acta* 77:75
- Horváth D, Entezami F (1983) *Nucl Phys A* 407:297
- Horváth D, Lambrecht RM (1984) *Exotic atoms. A bibliography 1939–1982*, Elsevier, Amsterdam, p 628
- Horváth D et al (1982) *Chem Phys Lett* 87:504
- Horváth D et al (1991a) *Phys Rev A* 44:1725
- Horváth D, Lévy B, Yutlandov IA (1991b) *Struct Chem* 2:451
- Hughes VW (1988) *Physica Scripta* T22:111
- Imanishi N et al (1988) *Phys Rev A* 37:43
- Jensen TS, Markushin VE (2002) *Eur Phys J D* 21:261, 271
- Jungmann K-P (2000) In: Karshenboim et al (eds) p 81
- Kachalkin AK et al (1979) *Sov Phys JETP* 50:12
- Karshenboim SG et al (eds) (2000) *The hydrogen atom – precision physics of simple atomic systems, Lecture Notes in Physics*. Springer, Berlin
- Kirch K et al (1999) *Phys Rev A* 59:3375
- Kojima K (1995) PhD thesis, University of Tokyo, <http://musr.triumf.ca/theses/Kojima/>
- Korobov VI (1996) *Phys Rev A* 54:R1749
- Korobov VI (1999) *Hyperfine Interact* 119:185
- Korobov VI, Bakalov DD (1997) *Phys Rev Lett* 79:3379
- Kostelecký VA (1997) In: *Flavor-changing neutral currents, Proceedings of the international symposium, Santa Monica, 1997*, p 334
- Kostelecký VA, Lehnert R (2001) *Phys Rev D* 63:065008
- Lombardi AM, Pirkel W, Bylinsky Y (2001) First operating experience with the CERN decelerating RFQ for antiprotons, Report CERN/PS 2001-064
- Luck WAP (1979) *Angew Chem Int Ed Engl* 18:350; (1980) 19:28
- Markushin VE (1999) *Hyperfine Interact* 119:11
- Measday DF (1990) In: Simons et al (1989) p 53
- Measday DF (2001) *Phys Rep* 354:243
- MuCF07 (2007) *Proceedings of the International Conference on Muon Catalyzed Fusion and Related Topics*, JINR, Dubna, Russia
- Morenzoni E (1999) *Physics and applications of low energy muons*. In: Lee S, Kilcoyne SH, Cywinski R (eds) *Muon science*. IOP, Bristol
- Morenzoni E et al (2001) *Hyperfine Interact* 133:179
- Mott NF, Massey HSW (1965) *The theory of atomic collisions*. Oxford University Press, Oxford
- Muroyama T et al (1999) *J Radioanal Nucl Chem* 239:159
- Nemenov L (2000) In: Karshenboim et al (2000) p 223
- Petitjean C (1989) In: Simons et al (1989) p 231
- Petitjean C, Schaller LA (eds) (1999) *Exotic atoms, molecules and muon catalyzed fusion (EXAT98)*, Proceedings of the international conference, Monte Verità, Ascona, Switzerland, 1998; *Hyperfine Interact* 118–119
- Petrushin VI, Ponomarev LI, Prokoshkin YuD (1967) *High Energy Chem (USSR)* 1:180
- Ponomarev LI (1975) *Ann Rev Nucl Sci* 23:395
- Roduner E (1988) *The positive muon as a probe in free radical chemistry*, vol 49, *Lecture Notes in Chemistry*. Springer, Berlin
- Schneuwly H, Pokrovsky VN, Ponomarev LI (1978) *Nucl Phys A* 312:419
- Schuster P (1976) In: Schuster P, Zundel G, Sandorfy C (eds) *The hydrogen bond*. North-Holland, Amsterdam
- Shinohara A et al (1996) *Phys Rev A* 53:130
- Shinohara A et al (1999) Summary of PiAX studies, KEK-PS-1999.8, Tsukuba, Japan
- Simons LM (1988) *Phys Scripta* T22:90
- Simons LM, Horváth D, Torelli G (eds) (1989) *Electromagnetic cascade and chemistry of exotic atoms*,

- Proceedings of the 5th course of physics of exotic atoms, Erice, Italy, 1989, (Plenum, New York, 1990)
- Trzcinska A et al (2001) *Phys Rev Lett* 87:082501; *Nucl Phys A* 692:176c
- Vesman E (1967) *JETP Lett* 5:91
- von Egidy T, Jakubassa-Amundsen DH, Hartmann FJ (1984) *Phys Rev A* 29:455
- Widmann E et al (2002) *Phys Rev Lett* 89:243402
- Wycech S (2001) *Nucl Phys A* 692:29c
- Yamazaki T et al (2002) *Phys Rep* 366:183
- zu Putlitz G (1996) *Hyperfine Interact* 103:157
- μ SR Conferences (1990–2002) Proceedings of the latest international conferences on muon spin rotation/relaxation/resonance, Williamsburg, Virginia, 2002, *Physica B*, 326; Les Diablerets, Switzerland, 1999, *Physica B*, 289–290, (2000); Nikko, Japan, 1996, *Hyperfine Interact* 104–106, (1997); Maui, Hawaii, 1993, *Hyperfine Interact* 85–87, (1994); Oxford, 1990, *Hyperfine Interact* 63–65, (1990)



29 Neutron Scattering Methods in Chemistry

L. Pusztai

Research Institute for Solid State Physics and Optics, HAS, Budapest, Hungary

29.1	<i>The Neutron as a Probe</i>	1517
29.1.1	Important Properties of the Neutron	1517
29.1.2	Comparison with X-ray Scattering	1518
29.2	<i>Scattering of Neutrons by Condensed Matter</i>	1518
29.2.1	Single Atom Scattering	1518
29.2.1.1	Elastic and Inelastic Scattering	1519
29.2.1.2	Nuclear Scattering	1519
29.2.1.3	The Scattering Length	1519
29.2.2	Scattering by Collections of Nuclei	1520
29.2.2.1	Scattering Cross Sections	1521
29.2.2.2	Coherent and Incoherent Scattering	1522
29.2.2.3	Correlation Functions for Nuclear Scattering	1523
29.2.3	Refractive Index and “Neutron Optics”	1525
29.3	<i>Neutron Scattering by Crystalline Materials</i>	1525
29.3.1	Determination of the Crystalline Structure	1526
29.3.1.1	Coherent Elastic Scattering, Bragg’s Law	1526
29.3.1.2	Single-Crystal Neutron Diffraction, “Ab Initio” Structure Determination	1527
29.3.1.3	Neutron Powder Diffraction, Refinement of the Structure	1528
29.3.1.4	Time-of-Flight (TOF) Variants of Neutron Diffraction Methods	1531
29.3.2	Dynamical Studies of Crystals	1531
29.4	<i>Neutron Scattering by Liquids</i>	1533
29.4.1	Structure	1533
29.4.1.1	Description of the Liquid Structure, Based on Experimentally Available Quantities	1534
29.4.1.2	Determination of the Radial Distribution Function from Neutron Diffraction of Liquids	1535
29.4.2	Microscopic Dynamics in Liquids	1537
29.4.2.1	Quasi-Elastic Neutron Scattering	1538
29.4.2.2	Detecting Very Small Exchanges of Energy: Neutron Spin-Echo	1538
29.4.3	Looking at Mesoscopic Length Scales: Small Angle Neutron Scattering	1539
29.4.4	Looking at Liquid Surfaces: Neutron Reflectometry	1541

29.5	<i>Neutron Scattering Instrumentation</i>	1542
29.5.1	Neutron Sources	1542
29.5.1.1	Reactor Sources	1542
29.5.1.2	Spallation Sources	1543
29.5.2	Optical Elements	1543
29.5.2.1	Collimators	1544
29.5.2.2	Neutron Guides	1544
29.5.2.3	Monochromator Crystals	1544
29.5.2.4	Velocity Selectors and Choppers	1545
29.5.2.5	Polarizers	1546
29.5.3	Detection of Neutrons	1546
29.5.4	Examples of Complete Neutron Scattering Instruments	1547
29.5.4.1	Neutron Powder Diffractometer	1547
29.5.4.2	Neutron Spin Echo Spectrometer	1548

Abstract: Starting with basic properties of the neutron, this chapter reviews the most important neutron scattering methods that provide valuable information for a chemist. The range of such methods is amazingly wide, from standard methods of crystallography to neutron spin echo spectroscopy. Experimental techniques like neutron reflectometry and small angle neutron scattering are able to probe large-scale structures on the surface and in the bulk, thus providing access to the “nano-world.” Apart from traditional areas of solid-state physics, like studying phonons, a particular emphasis is placed on the microscopic and mesoscopic structure and dynamics in the liquid state. Practical aspects, such as main components of the instrumentation, are also touched upon.

29.1 The Neutron as a Probe

29.1.1 Important Properties of the Neutron

Before going into details of the scattering of neutrons in condensed phases, some basic properties of this elementary particle should be recalled, as these characteristics play a central role in the scattering process (for more details, see Dianoux and Lander (2001)).

The neutron is a particle of mass 1.675×10^{-27} kg, magnetic moment of $-1.913 \mu_N$ (μ_N being the nuclear magneton, 5.05×10^{-27} J/T) and possessing no electric charge. These properties (particularly the electric neutrality) make the neutron one of the most suitable probes for atomic scale structure and dynamics: neutrons can penetrate deep into the bulk of condensed phases without destroying chemical bonds. Since neutrons do not interact with the electrons via Coulomb forces, they are scattered by the nuclei.

The *wavelength* of thermal (and “cold”) neutrons from reactor or accelerator sources varies between about 0.1 and 20 Å (1 Å = 0.1 nm = 10^{-10} m), which corresponds to atomic scale distances. As it will be shown later, for the study of the structure of condensed phases it is the interference of the scattered radiation that is most important: interference effects, in turn, easier to detect if the scattering angle is sufficiently large. In order to achieve sufficiently large scattering angles, the wavelength of the radiation has to be comparable with the distance between scattering centers.

The most probable speed of a thermal neutron is about 2,200 m/s, which means that its *kinetic energy* is about 25 meV (1 eV $\approx 1.602189 \times 10^{-19}$ J); neutron energies between 0.1 meV and 1 eV can routinely be achieved. (Note that the most probable speed u_{mp} of thermal neutrons is the “mode” (See [Chap. 9, Vol. 1](#), on “Stochastics and Nuclear Measurements”) of the Maxwell distribution at 20°C). The average (mean) speed \bar{u} is somewhat greater at any temperature due to the asymmetry of the Maxwellian density function: $\bar{u} = 1.128 u_{mp}$. As the energy of hydrogen bond stretching is around 100 meV, it is obvious that for processes of chemical interest, neutrons provide an excellent probe for the microscopic dynamics in condensed matter: the energy change during the scattering event is easily detectable.

Since the neutron possesses a *magnetic moment*, the study of magnetic materials/properties is also possible using neutron scattering. Although it is not at the forefront of interest of chemists, it has to be mentioned that understanding (and tailoring) the behavior of high-tech instruments, such as magneto-optic devices, has greatly benefited from the application of neutron scattering.

29.1.2 Comparison with X-ray Scattering

Although this chapter is about neutron scattering techniques, one cannot avoid the comparison of their capabilities to available X-ray scattering methods.

First, it has to be noted that X-rays are scattered not by the nuclei, but by their interaction with the electronic cloud; as a consequence of this, the amplitude of the scattered radiation is affected by the distribution of the electrons and therefore, the “strength” of the scattering will be angle-dependent.

As far as *structural studies* are concerned, X-ray diffraction, in general, provides a comparatively cheap and fast complementary means of investigation. Note, however, that for light nuclei, in the presence of heavier ones, X-rays are still not sensitive enough. (This particular issue will be elaborated further later.)

The energy of an X-ray photon with a wavelength of 1 Å is about 12 keV, roughly five orders of magnitude higher than that of a neutron of the same wavelength. This implies that if the H-bond stretching mentioned above is to be investigated by X-rays, the sensitivity of the detection must be five orders of magnitude better than that for neutron scattering. For this reason, studying the *dynamics of condensed phases* by X-ray scattering can be carried out only at the very few (at the moment of writing, three) third-generation synchrotron X-ray sources available. Also note that many of the delicate chemical/biological samples simply cannot stand the bombardment by such energetic particles.

Until very recently, magnetism was an area where X-ray scattering could not be used at all. The situation now is changing but it is expected that neutron scattering applications will dominate the study of magnetic materials.

On the other hand, synchrotron X-rays have a distinct advantage, which is the relatively high *flux density of radiation*. Synchrotron X-ray beams can routinely deliver six orders of magnitude more (monochromatic) X-ray photons (per unit area per unit time) than the best neutron sources available at present. With the advent of free electron laser facilities, the flux difference is expected to grow even larger.

29.2 Scattering of Neutrons by Condensed Matter

In this section, the basics of the scattering process will be discussed. After describing single atom (nucleus) scattering, the formalism suitable for treating (large) collections of scattering centers is introduced.

It is worth mentioning in advance a major difficulty that occurs while establishing the connection between the measured signal and the quantities of interest: while the scattering process can only be treated quantum mechanically, the desired – and tractable – quantities (like the static and dynamic structure factor) are classical statistical averages.

29.2.1 Single Atom Scattering

While passing through matter, neutrons can be scattered by the atoms in two ways: either by the nucleus or by electrons of unpaired spin. This latter way can only happen in magnetic materials and hence the process has the distinct name “magnetic scattering.” In this chapter, magnetic

scattering will not be discussed in detail and therefore, it will only be mentioned if it is absolutely unavoidable.

The other process, “nuclear scattering,” occurs for all atoms and therefore it is the most significant microscopic event from the point of view of this section.

29.2.1.1 Elastic and Inelastic Scattering

Both nuclear scattering and magnetic scattering can be either elastic or inelastic. The former refers to an event where there is no energy exchange between the scatterer and the scattered neutron, whereas the latter signifies microscopic events with exchange of energy. Elastic scattering dominates the signal of diffraction studies, which aim at the determination of the atomic level structure of materials (with the exception of some liquid structures). Inelastic scattering is made use of while investigating microscopic dynamics. The distinction between the two types cannot be made sharp: in general, all events are inelastic, although during some of them, the energy exchange is, indeed, very small. Note that for microscopic events with small, but measurable energy exchanges the word quasi-elastic scattering is used: this type of description is useful, for instance, for the characterization of diffusion processes in liquids.

29.2.1.2 Nuclear Scattering

When a neutron beam, which can be represented by a plane wave of wavelength λ , falls on a single nucleus then the scattering of the wave depends on the interaction potential $V(r)$ that acts between the neutron and the nucleus being at distance r from each other. The value of $V(r)$ becomes zero rapidly beyond nuclear dimensions that are of the order of 10^{-14} m. Since neutron wavelengths are usually of the order of 10^{-10} m (or greater), the nucleus can be considered as a point-scatterer that yields a scattered beam of amplitude $-b/r$ at a distance r from the nucleus (for an incoming beam with a magnitude of unity).

29.2.1.3 The Scattering Length

The constant b determines the “strength” of the scattering from an individual nucleus; it has the dimensions of length and therefore, it is called the (nuclear) scattering length (or scattering amplitude). Since nuclei are point-scatterers, the value of b does not change noticeably over atomic length scales and therefore, there is no angular dependence of it: this greatly simplifies the evaluation of neutron data. (On the other hand, complicated angular dependence *does* occur for the X-ray scattering form factor).

What remains to be seen is that how the scattering length varies over different atoms, or more precisely, over different nuclei. As it may be expected, there is a (rather weak) size dependence (the larger the radius, the larger the value of b), but there is another effect that almost completely disguises the size dependence: this is called *resonance scattering*. There are very few examples where thermal neutrons can excite nuclear resonance energy levels; when this happens, *anomalous scattering* takes place (see, e.g., ^{113}Cd , or ^{149}Sm). However, even

a more remote resonance level influences the actual value of b so much that if the nuclides are arranged according to their Z and N values then their b 's vary seemingly at random from one nuclide to its neighbors.

In ▶ [Table 29.1](#), scattering lengths of some important nuclei are given. A full listing of the most up-to-date values was given by Koester et al. (1991) and Sears (1992), and scattering length values are also available on the Internet (Munter 2003). There are two more points to emphasize: (a) different isotopes of the same chemical element may possess very different scattering length values, which feature is exploited heavily in the practice of neutron scattering (see ▶ [Sects. 29.4.1](#) and ▶ [29.4.3](#)); (b) most scattering length values are positive but some (notably, that of the proton) are negative. Negative values mean that the phase of the neutron “wave” does not change during the scattering whereas a positive b implies a 180° phase alteration.

29.2.2 Scattering by Collections of Nuclei

Phenomena that occur in connection with scattering from a large number of scattering centers, and quantities that characterize them are introduced in the following pages.

■ [Table 29.1](#)

Scattering lengths (b) of nuclei. If more than one isotope is indicated for an element then the average value for the element is also shown

Element	Isotope	$b/10^{-14}$ m	Element	Isotope	$b/10^{-14}$ m
H		−0.374	Ti		−0.34
	^1H	−0.374		^{46}Ti	0.48
	^2H	0.667		^{48}Ti	−0.58
He	^4He	0.30		^{49}Ti	0.08
Li		−0.214	Ni		1.03
	^6Li	$0.18 + 0.025 i$		^{58}Ni	1.44
	^7Li	−0.233		^{60}Ni	0.28
B	^{11}B	0.60		^{62}Ni	−0.87
C	^{12}C	0.665	Cu		0.76
N		0.936		^{63}Cu	0.67
	^{14}N	0.94		^{65}Cu	1.11
	^{15}N	0.65	I	^{127}I	0.53
O	^{16}O	0.58	Dy		1.69
F	^{19}F	0.56		^{160}Dy	0.67
Na	^{23}Na	0.36		^{162}Dy	−0.14
Al	^{27}Al	0.35		^{164}Dy	4.94
Cl		0.96	U		0.842
	^{35}Cl	1.18		^{235}U	1.05
	^{37}Cl	0.26		^{238}U	0.840

29.2.2.1 Scattering Cross Sections

In an ideal neutron scattering experiment, a beam of (thermal) neutrons of identical energy E would fall on a target (sample), with the latter being a general collection of scattering centers (atoms). A neutron scattering measurement concerns the scattered neutrons and relevant results can be given in terms of various scattering cross sections. The *total scattering cross section* is defined as

$$\sigma_{\text{tot}} = \frac{\aleph_{\text{tot}}}{\Phi} \quad (29.1)$$

where \aleph_{tot} (pronounce: aleph) is the total number of neutrons scattered per second in all directions, and Φ is the incident neutron flux density, i.e., the number of incident neutrons passing through unit area per second. It can be shown that for a single nucleus $\sigma_{\text{tot}} = 4\pi b^2$ (see, e.g., Squires 1996).

The *differential cross section*, to which the static structure factor – the physical quantity describing the static microscopic structure (see [Sect. 29.2.2.3](#)) – can be related, is defined as

$$\frac{d\sigma}{d\Omega} = \frac{\aleph_{d\Omega}(\theta, \varphi)}{\Phi d\Omega} \quad (29.2)$$

where $\aleph_{d\Omega}(\theta, \varphi)$ is the number of neutrons scattered per second into a small solid angle element $d\Omega$, which is in the direction of (θ, φ) , θ and φ being the polar and azimuthal angle coordinates relative to the original direction of the neutron beam (taken as the z -axis for the usual interpretation of spherical coordinates r, θ , and φ). Further, if the energy of the scattered neutrons is analyzed then one arrives at the *partial (double) differential cross section*, which is related to the dynamics (“instantaneous structure”) of the sample system as

$$\frac{d^2\sigma}{d\Omega dE'} = \frac{\aleph_{d\Omega, dE'}(\theta, \varphi)}{\Phi d\Omega dE'} \quad (29.3)$$

where $\aleph_{d\Omega, dE'}(\theta, \varphi)$ is the number of scattered neutrons per second into a solid angle element $d\Omega$ with final energy between E' and $E' + dE'$. The total and differential cross sections are related to each other as

$$\sigma_{\text{tot}} = \int \left(\frac{d\sigma}{d\Omega} \right) d\Omega = \int \left(\frac{d^2\sigma}{d\Omega dE'} \right) d\Omega dE' \quad (29.4)$$

Much of the theory of neutron scattering concern the elaboration of expressions (closed formulas) for the partial differential cross section, starting from (model) interaction potentials between the neutron and the nucleus (see, e.g., Squires 1996; Lovesey 1987). The final result of these calculations for nuclear scattering will be outlined below.

Taking into account the quantum mechanical probability of the transition of a neutron from a state characterized by wavevector \mathbf{k} and energy E to another state characterized by wavevector \mathbf{k}' and energy E' , caused by scattering from a target-system via potential V (taken as the extremely short ranged Fermi-pseudopotential), one arrives at the following expression for the partial differential cross section (see, e.g., Squires 1996):

$$\frac{d^2\sigma}{d\Omega dE'} = \frac{k'}{k} \frac{1}{2\pi\hbar} \sum_{jj'} b_j b_{j'} \int_{-\infty}^{\infty} \left\langle e^{-i\mathbf{Q}\mathbf{R}_{j'}(0)} e^{i\mathbf{Q}\mathbf{R}_j(t)} \right\rangle e^{-i\omega t} dt \quad (29.5)$$

where $Q = k - k'$, is the so-called *scattering vector*, and the $\mathbf{R}_j(t)$ symbols represent the time-dependent Heisenberg operators (see Squires 1996), defined by

$$\mathbf{R}_j(t) = e^{iHt/\hbar} \mathbf{R}_j e^{-iHt/\hbar}. \quad (29.6)$$

In the latter equation $\mathbf{R}_j [\equiv \mathbf{R}_j(0)]$ describes the position of the j th scattering nucleus and H , the Hamiltonian of the neutron + nucleus system, contains the properties of the scattering system. That is, [Eq. \(29.5\)](#) has to be evaluated individually for each scattering system. For example, crystalline materials behave quite differently from liquids, etc.

29.2.2.2 Coherent and Incoherent Scattering

Even in a scattering system of a single chemical element, the scattering length changes (randomly, but taking well-defined values) from atom to atom, because of the presence of isotopes or/and the variation of the individual nuclear spin. The average values of b and b^2 are

$$\bar{b} = \sum_i f_i b_i \quad \bar{b^2} = \sum_i f_i b_i^2 \quad (29.7)$$

where f_i is the frequency of a given value of b (normalized to unity). Considering [Eq. \(29.5\)](#) again, it is apparent that the right-hand side can be split into two parts, one that contains the sum where $j = j'$ and the other that contains the sum where $j \neq j'$. The first case is termed as *incoherent*, while the second is called *coherent cross section*; these terms possess particular emphasis in neutron scattering. The usual expressions for the coherent and incoherent cross sections are

$$\sigma_{\text{coh}} = 4\pi \bar{b}^2 \quad \sigma_{\text{inc}} = 4\pi (\bar{b^2} - \bar{b}^2) \quad (29.8)$$

Coherent scattering can be considered as scattering coming from a system of equal nuclei with the average (see [Eq. \(29.7\)](#)) scattering length; incoherent scattering is the term that has to be added for recovering the total scattering of the actual system. Incoherent scattering may be thought as arising from the random distribution of the deviations of the scattering length from the average of b_i . In fact, the right-hand side of [Eq. \(29.8\)](#) expresses a simple proportionality between σ_{inc} and the variance of b . (See [Eq. \(9.25\) in Chap. 9, Vol. 1](#), on “Stochastics and Nuclear Measurements.”)

According to the above, if all nuclei are of the same isotope with zero nuclear spin then the scattering is entirely coherent. Pure *isotope incoherence* (or rather, it should be called “disordering”) occurs when the scattering system contains several different isotopes of a single element, with all isotopes having zero nuclear spins and the distribution of the different isotopic nuclei is random. *Spin incoherence* occurs if the system consists of a single isotope with a (nonzero) nuclear spin I and – because unpolarized neutrons can have a spin either $+1/2$ or $-1/2$ – this leads to two different b values, b^+ and b^- . If these values are very different, such as in the case of hydrogen (^1H), and the f_i weighting factors have unfavorable values, then the incoherent scattering cross section can be orders of magnitude larger than the coherent counterpart (see, e.g., Bacon 1977). This is a very unfortunate situation when collective properties, such as the structure of hydrogenous materials, are studied.

It should also be noted that coherent scattering depends on the correlations of the positions of different nuclei, whereas incoherent scattering reflects only correlations between positions of the same nuclei at different times. In other words, *interference effects* occur only for coherent

scattering, which then will be characteristic of collective properties (such as the atomic structure, or collective excitations). On the other hand, incoherent scattering describes the motion of individual atoms (such as, e.g., diffusion).

29.2.2.3 Correlation Functions for Nuclear Scattering

This is a very important section where the connection between experimental data (measurable by neutron scattering) and thermal averages (that are fundamental properties of the scattering system) is established. Thermal averages can be expressed in terms of correlation functions. The distinction between coherent and incoherent parts of the scattering is a basic concept in relating neutron scattering results to well-known physical properties. Following Van Hove (1954) and using the notation of [Eq. \(29.5\)](#), it is customary to define the intermediate scattering function, $I(\mathbf{Q}, t)$ as

$$I(\mathbf{Q}, t) = \frac{1}{N} \sum_{jj'} \left\langle e^{-i\mathbf{Q}\mathbf{r}_{j'}(0)} e^{i\mathbf{Q}\mathbf{r}_j(t)} \right\rangle \quad (29.9)$$

where N is the number of scattering centers (nuclei) in the system. Note that $I(\mathbf{Q}, t)$ does not depend on the actual scattering process. The *Van Hove correlation function* (or time-dependent pair correlation function) is then defined in real space as

$$G(\mathbf{r}, t) = \frac{1}{(2\pi)^3} \int I(\mathbf{Q}, t) e^{-i\mathbf{Q}\mathbf{r}} d\mathbf{Q} \quad (29.10)$$

where $d\mathbf{Q}$ is the volume element in \mathbf{Q} -space and \mathbf{r} denotes particle coordinates. The scattering function or dynamic structure factor can be obtained as

$$S(\mathbf{Q}, \omega) = \frac{1}{2\pi\hbar} \int I(\mathbf{Q}, t) e^{-i\omega t} dt \quad (29.11)$$

that is sometimes referred to as the “scattering law.” From the above equation it is obvious that $G(\mathbf{r}, t)$ and $S(\mathbf{Q}, \omega)$ are Fourier transform pairs related to each other as

$$G(\mathbf{r}, t) = \frac{\hbar}{(2\pi)^3} \int S(\mathbf{Q}, \omega) e^{-i(\mathbf{Q}\mathbf{r} - \omega t)} d\mathbf{Q} d\omega \quad (29.12)$$

and

$$S(\mathbf{Q}, \omega) = \frac{1}{2\pi\hbar} \int G(\mathbf{r}, t) e^{-i(\mathbf{Q}\mathbf{r} - \omega t)} d\mathbf{r} dt \quad (29.13)$$

where $d\mathbf{r}$ is the volume element in real space, normally denoted by dV . It has to be noted, again, that the scattering function depends only on the structure and dynamics of the scattering system and not on the neutron–nuclei interaction – in fact, it does not depend on any particular experimental technique. From [Eqs. \(29.5\)](#), [Eq. \(29.8\)](#), [Eq. \(29.9\)](#), and [Eq. \(29.11\)](#), one arrives at the relation between the partial differential cross section (which is the result of a neutron scattering experiment) and the physics of the scattering system:

$$\left(\frac{d^2\sigma}{d\Omega dE'} \right)_{\text{coh}} = \frac{\sigma_{\text{coh}}}{4\pi} \frac{k'}{k} N S_{\text{coh}}(\mathbf{Q}, \omega) \quad (29.14)$$

The relation of the incoherent scattering cross section with the incoherent scattering function is analogous (see, e.g., Squires 1996).

The classical form of $G(\mathbf{r}, t)$ can be expressed as follows. Ignoring that the Heisenberg operators $\mathbf{R}_{j'}(0)$ and $\mathbf{R}_j(t)$, in general, do not commute and supposing that all nuclei are equivalent (so that the sum over j' can be taken as N times the value for $j' = 0$):

$$G^{\text{cl}}(\mathbf{r}, t) = \sum_j \langle \delta[\mathbf{r} - \mathbf{R}_j(t) + \mathbf{R}_0(0)] \rangle \quad (29.15)$$

where the superscript “cl” stands for “classical” and δ is the Dirac delta (or δ function).

As regards the physical interpretation of $G^{\text{cl}}(\mathbf{r}, t)d\mathbf{r}$, it gives the probability that particle j will be found in volume element $d\mathbf{r}$ (at position \mathbf{r}) at time t provided that any of the particles (including j) was at the origin at time $t = 0$.

For the incoherent scattering part, the Van Hove correlation function becomes a self-correlation function:

$$G_{\text{self}}^{\text{cl}}(\mathbf{r}, t) = \sum_j \langle \delta[\mathbf{r} - \mathbf{R}_0(t) + \mathbf{R}_0(0)] \rangle \quad (29.16)$$

where $G_{\text{self}}^{\text{cl}}(\mathbf{r}, t)d\mathbf{r}$ is the probability that a particle is in volume element $d\mathbf{r}$ (at position \mathbf{r}) at time t provided that the *same* particle was at the origin at $t = 0$. From these interpretations, it can be deduced that

$$\int G_{\text{self}}^{\text{cl}}(\mathbf{r}, t)d\mathbf{r} = 1 \quad \int G^{\text{cl}}(\mathbf{r}, t)d\mathbf{r} = N \quad (29.17)$$

It can be shown that not only the classical, but also the general forms obey the above “sum rules.” If, furthermore, $t = 0$ is taken, then one arrives at a most useful correlation function that characterizes the static structure:

$$G(\mathbf{r}, 0) = \sum_j \langle \delta(\mathbf{r} - \mathbf{R}_j + \mathbf{R}_0) \rangle = \delta(\mathbf{r}) + g(\mathbf{r}), \quad (29.18)$$

where $\mathbf{R}_j = \mathbf{R}_j(0)$ and $g(\mathbf{r})$ is the (static) *pair distribution function* (pdf), which yields the average particle density with respect to any particle at the origin (ratio of the local density at \mathbf{r} and the macroscopic density of the system):

$$g(\mathbf{r}) = \sum_{j \neq 0} \langle \delta(\mathbf{r} - \mathbf{R}_j + \mathbf{R}_0) \rangle. \quad (29.19)$$

Important limits for $g(\mathbf{r})$ are

$$g(\mathbf{r}) = 0 \quad |\mathbf{r}| \rightarrow 0; \quad g(\mathbf{r}) = 1 \quad |\mathbf{r}| \rightarrow \infty \quad (29.20)$$

It is helpful to define the Fourier transform pair of $g(\mathbf{r})$, the so-called *static structure factor*, via the “0th energy moment” of the dynamic structure factor:

$$S_0(\mathbf{Q}) = \int_{-\infty}^{\infty} S(\mathbf{Q}, \omega) d(\hbar\omega) = I(\mathbf{Q}, 0) = \frac{1}{N} \sum_{jj'} \langle e^{i\mathbf{Q}(\mathbf{R}_j - \mathbf{R}_{j'})} \rangle = 1 + \int g(\mathbf{r}) e^{i\mathbf{Q}\mathbf{r}} d\mathbf{r} \quad (29.21)$$

In the following discussion the subscript “0” will be omitted. The static structure factor can be expressed in relation to the differential cross section as

$$\left(\frac{d\sigma}{d\Omega} \right)_{\text{coh}} = \frac{\sigma_{\text{coh}}}{4\pi} N S_{\text{coh}}(\mathbf{Q}) \quad (29.22)$$

where the “static approximation” ($k = k'$) has also been made use of (where $k = |\mathbf{k}|$). It is the main goal of a generic scattering experiment to determine $S(\mathbf{Q}, \omega)$ over a scattering vector and energy range as wide as possible; arguably, among the available experimental techniques, neutron scattering provides the widest access to the dynamic structure factor. Unfortunately, the instrumentation is cumbersome, neutron fluxes are very limited and furthermore, very different types of instruments have to be built for accessing different parts of $S(\mathbf{Q}, \omega)$.

29.2.3 Refractive Index and “Neutron Optics”

So far, the interaction of neutrons with (collections of) point-like scatterers, with δ -function-like neutron-nucleus interaction potential, has been considered. However, provided that the magnitude of the momentum transfer, $Q = |\mathbf{Q}| \ll 1/R_0$ (where R_0 is on the order of the distance between nuclei), i.e., $Q \ll 1 \text{ \AA}^{-1}$, then the sample may be considered as a potential that is “smeared out” homogeneously. This is how optical phenomena, like total reflection, diffraction by a slit, etc., can be explained for neutron beams.

The *refractive index* can be expressed as (Squires 1996; Scherm 1972)

$$n = 1 - \frac{1}{2\pi} \rho \lambda^2 \bar{b} \quad \left(= 1 - \frac{2\pi N \bar{b}}{k_{\text{inc}}^2} \right) \quad (29.23)$$

where ρ is the number of scattering centers (nuclei) per unit volume (“number density”), λ is the wavelength of incident neutrons, \bar{b} is the mean value of the scattering lengths of the nuclei, k_{inc} is the wavenumber (magnitude of the wavevector) of the incident neutrons, and N is the number of nuclei. With typical values of these parameters, the refractive index takes the value of about 0.99995, very close to unity.

However, even this minute deviation from one gives the possibility of making use of the critical mirror angle (see ▶ Sect. 29.5.2.2) for the fabrication of neutron guides. Another important application is *neutron reflectometry*, used extensively for the investigation of (solid and liquid) surfaces (see ▶ Sect. 29.4.4). Neutron reflection can also be used for the accurate determination of the scattering length (Maier-Leibnitz 1962; Koester et al. 1991).

29.3 Neutron Scattering by Crystalline Materials

Chemical crystallography (or “crystal chemistry”) is one of the oldest areas of using neutron scattering in chemical applications: the atomic structure of a material is arguably its most basic property and therefore once a new material is synthesized, its crystalline structure has to be known. X-ray diffraction (mostly laboratory based) is thus a well-known technique to most synthetic chemists. However, there are quite a few cases where neutron diffraction lends itself as the only experimental technique for the determination of the microscopic structure: this happens when the positions of “light” atoms are of particular interest but X-ray scattering from “heavy” atoms dominate the signal. One such best-known situation is obviously when hydrogen positions have to be determined, although oxygen may also be hard to “see” by X-rays in some high-temperature superconductors, for instance.

Note, however, that hydrogenous materials, in general, have to be (at least partially) deuterated before neutron diffraction experiments, since the huge incoherent inelastic cross section of ^1H would hide the structurally relevant information otherwise.

Although magnetism has been deliberately left out from the scope of this chapter, it must be mentioned that the determination of magnetic structures takes probably the largest proportion of neutron diffraction today; this type of investigation was initiated by the Nobel Prize-winning work of C. Shull (1963).

29.3.1 Determination of the Crystalline Structure

Although the correlation function formalism introduced in the previous section (see ▶ Sect. 29.2.2.3) is entirely valid for crystalline materials, it is very rarely applied explicitly. The reason is, as it has been established long time ago (Bragg 1928), that long-range periodic ordering of identical structural units, the unit cells, makes it possible to determine the position of each scattering nucleus in the scattering system. The tools for doing so are well known from crystallography textbooks (see, e.g., Woolfson 1997), or the “International Tables for Crystallography” series (Prince and Wilson 1999; Shmueli 2001; Hahn 2002) and therefore, they are not discussed here. Textbooks on X-ray diffraction may also provide useful sources of information (see, e.g., Warren 1969).

29.3.1.1 Coherent Elastic Scattering, Bragg’s Law

The concept of the *reciprocal lattice* (see, e.g., Ashcroft and Mermin 1976; Woolfson 1997) is central to understanding crystallography. Here it may suffice to remind the reader that each point in the reciprocal lattice refers to a given set of lattice planes of the crystal (in real space), with a well-defined orientation and spacing. A reciprocal lattice vector \mathbf{H} is normal to the corresponding plane in real space and its length is the reciprocal value of the interplanar spacing.

It can be shown (see, e.g., Squires 1996) that coherent elastic (neutron) scattering from a crystal occurs only when the scattering vector is equal to a valid reciprocal lattice vector (note that for arbitrary arrangements, this requirement is not fulfilled and therefore, the special – eligible – orientations of the crystal have to be found):

$$\mathbf{Q} = \mathbf{k} - \mathbf{k}' = \mathbf{H} \quad (29.24)$$

The above condition is an alternative expression of Bragg’s law, known originally from X-ray scattering (Bragg 1928), which means that coherent elastic scattering of neutrons is Bragg scattering. Following a few straightforward steps, one arrives at the familiar form of Bragg’s law:

$$n\lambda = 2d \sin \frac{\theta}{2} \quad (29.25)$$

where λ is the wavelength of incident neutrons, n is an integer, d is the spacing of lattice planes (in real space), and θ is the angle between the incident beam and the scattered beam. ($\theta/2$, also known as the Bragg angle, is actually the angle between the incident beam and the crystal planes; quite frequently, the Bragg angle is noted as θ .)

Bragg’s law (and therefore, the coherent elastic differential cross section) can be exploited for determining the precise crystalline structure. Obviously, neutron scattering from crystals is not restricted to the coherent elastic contribution: scattering observed in between Bragg peaks is called *diffuse scattering*, which is generally connected to some sort of disorder (thermal,

positional, etc.). A recent monograph (Nield and Keen 2001) deals with problems concerning this increasingly important area.

29.3.1.2 Single-Crystal Neutron Diffraction, “Ab Initio” Structure Determination

Structural studies of single crystals were among the earliest applications of neutron scattering in chemically interesting systems (Bacon and Lowde 1948; Bacon 1951; Peterson and Levy 1951). The general aim of investigating single crystals is to explore the largest possible volume of the reciprocal lattice, so that the reconstruction of the original (real space) lattice could be made unequivocally. Experimental results are Bragg intensities in three dimensions, at the appropriate reciprocal lattice points. The diffracted intensity, in turn, is proportional to the square of the amplitude of the scattered wave for each individual Bragg peak (or “Bragg reflection,” as crystallographers call it frequently):

$$I(\mathbf{Q}) \propto |F(\mathbf{Q})|^2 \quad (29.26)$$

where $F(\mathbf{Q})$ is the (static) structure factor. Note that the (static) structure factor $F(\mathbf{Q})$ means basically the same as $S_0(\mathbf{Q})$ defined by Eq. (29.21), but from this point on notations better known in the area of crystallography are adhered to.

Further, the structure factor can be written as the product of its modulus and a “phase factor”:

$$F(\mathbf{Q}) = \sum_j b_j e^{i\mathbf{Q}\mathbf{R}_j} e^{-W_j} = |F(\mathbf{Q})| e^{i\varphi(\mathbf{Q})} \quad (29.27)$$

where W_j is the so-called *Debye–Waller factor* that accounts for the instantaneous displacement of nucleus j from its equilibrium position. The phase factor incorporates everything that cannot be included in the modulus of $F(\mathbf{Q})$.

As the measured intensities provide (after the necessary corrections for background, instrumental resolution, etc.) the moduli of the structure factor, but not the phase factor, the Fourier synthesis (inverse Fourier transformation) cannot be applied to the determination of the nuclei in the unit cell: this is the well-known “*phase problem*” of crystallography.

However, due to the cheap computer power available, evaluation of single-crystal neutron diffraction data (at the level of atomic coordinates in the unit cell and the Debye–Waller factors associated with them) is a routine task nowadays. The trick is to apply “direct methods” of phase determination – methods that depend on the many mutual relationships (inequalities and probabilities) between structure factors and their phases. The simplest such constraint is that scattering power in solids is concentrated on atoms, which are well-defined regions by their size and shape. (For pioneering applications, see the works published by Karle and Karle (1966), Bernal and Watkins (1972) and Jonsson and Hamilton (1972).) Similar conditions cannot be cast into exact mathematical equations, but computer algorithms can easily cope with them.

Naturally, because of the lack of exact relationships between measured data and the desired information, and also, because measured data contain errors, it is of utmost importance to determine the structure factor at as many reciprocal lattice points as possible. It is quite accepted to measure the intensity of several thousand Bragg reflections and therefore,

traditional single-crystal neutron diffractometry is one of the most time-consuming neutron scattering applications.

There are two basic methods for measuring diffracted intensities at well-defined reciprocal lattice points: one is the rotating crystal method and the other is the so-called *Laue method*. The *rotating crystal method* employs a monochromatic beam of neutrons (of wavevector \mathbf{k}) that is incident on a single crystal that can be rotated, so that all orientations can be realized. (For this purpose, most frequently, a 4-circle goniometer is used – for this reason, single-crystal instruments are sometimes also called “4-circle diffractometers.”) At reactor-based neutron sources (see ▶ Sect. 29.5), the majority of single-crystal diffractometers make use of the rotating crystal technique.

The *Laue method*, in contrast, applies a “white beam” of neutrons, containing a continuous spectrum of wavevectors; the sample orientation is kept fixed. Bragg reflections may be detected at several Bragg angles simultaneously. For quite a long period of time, Laue diffraction has mainly been used for the monochromatization of neutron beams (see ▶ Sect. 29.5); lately, however, single-crystal diffractometers have been built that exploit this method.

As for applications, the study of hydrogen bonding in crystalline materials may seem to be the most attractive for a chemist (Peterson and Levy 1952; Williams and Schneemeyer 1973; Preisinger et al. 1982; Nelmes et al. 1985). Determining the structure of materials of biological relevance is still a fast-growing area of research; for an early example, see the single-crystal analysis of sucrose (Brown and Levy 1963, 1973). The enormous power of combining X-ray and neutron single-crystal diffraction must not be left unmentioned: this “X-N synthesis” seems to be the most fruitful approach toward determining electron density maps experimentally (Coppens 1974).

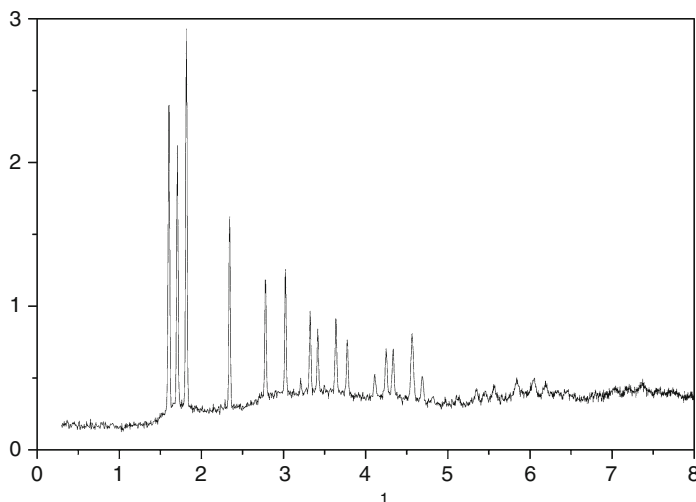
29.3.1.3 Neutron Powder Diffraction, Refinement of the Structure

In contrast to a good single crystal, a good crystalline powder consists of a large number of small crystallites that are oriented randomly with respect to each other. Fulfilling these conditions, there would always be some crystallites that would satisfy the orientation requirements necessary for Bragg scattering the beam of fixed direction. Too big crystallites, or/and nonrandom (“preferential”) orientation cause severe distortion of the signal, many times making proper interpretation impossible – therefore, these are arguably the most problematic aspects of this type of experiment. (This preferential orientation of crystallites is called “texture” as opposed to perfectly random orientation.)

In the standard realization of the powder diffraction experiment, a monochromatic neutron beam, with wavevector \mathbf{k} , falls on a powder sample. For a specified value of $|\mathbf{H}|$, the \mathbf{k}' wavevector of the scattered beam will form a cone, known as the *Debye–Scherrer cone*. Only microcrystals with \mathbf{H} vectors lying on the cone and with axis along \mathbf{k} (satisfying also an angle-constraint, see, e.g., Squires 1996) will contribute to the scattering. (The requirement for randomly oriented microcrystals can now be understood: preferred orientation(s) would corrupt true peak intensities.) According to Bragg’s law, (▶ Eq. 29.25), differences in lattice plane spacing can be measured by moving the detector over the angular range available for the given instrument. This procedure provides an intensity curve as a function of the scattering angle – traditional neutron powder diffraction is a “fixed wavelength (thus fixed energy), angle dispersive technique.” As an example of a powder spectrum, the $S(Q)$ structure factor of “high temperature” D_2O ice (close to the melting point) is shown in ▶ Fig. 29.1.

■ Fig. 29.1

Neutron powder diffraction spectrum of (hexagonal) D_2O ($^2\text{H}_2\text{O}$) ice (phase Ih) at 260 K, close to the melting point. Note the large amount of diffuse scattering under the Bragg peaks, indicating effects of structural disorder (Pusztai and McGreevy 1997, unpublished data)



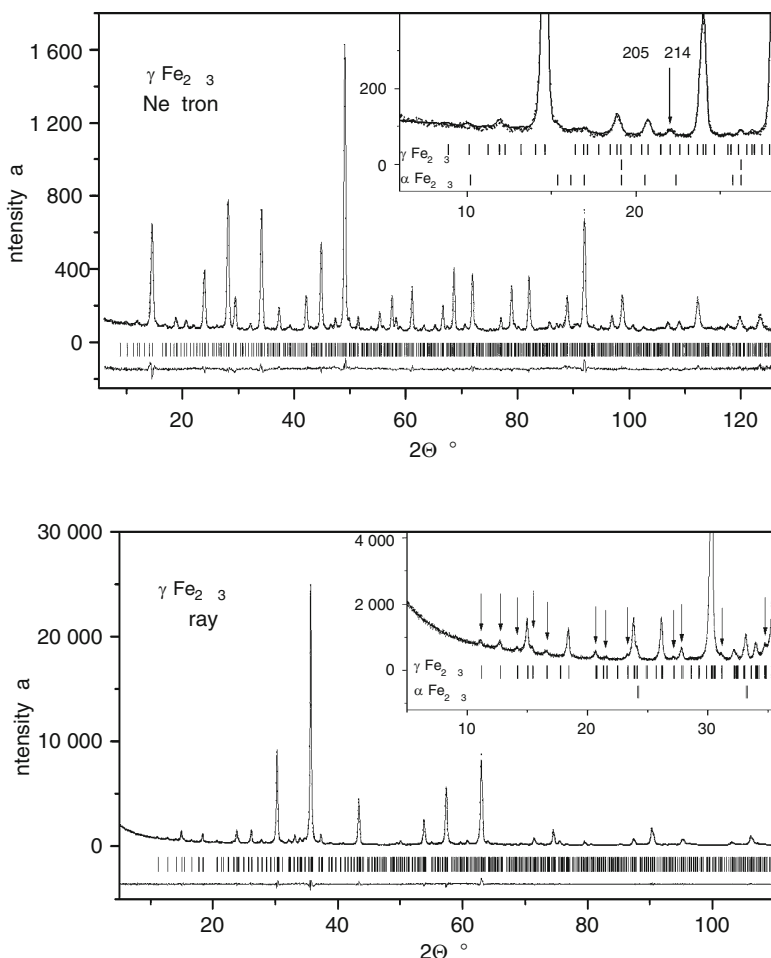
Note that the resulting function depends only on $|\mathbf{H}|$ – which means that the three-dimensional information, available in single-crystal diffraction, is lost, or rather, averaged over the orientations of the crystallites. Since many different \mathbf{H} s may have the same magnitude, peaks (maxima) of the powder spectrum may well receive contributions from more than one reciprocal lattice point (thus the “multiplicity” of the reflections have to be established).

Instead of considering Bragg reflections one by one, evaluation of powder spectra these days is done almost exclusively by a kind of “whole profile fitting structure refinement,” or *Rietveld refinement* (Rietveld 1969; Loopstra and Rietveld 1969). The Rietveld algorithm fits entire observed diffraction patterns using parameters for instrumental characteristics (resolution, etc.), as well as for structural features (cell constants, atomic coordinates, and displacements). The fitting is done by least-squares methods, minimizing the differences between measured and calculated intensities at each experimental point. Although this procedure is extremely powerful, it has to be emphasized that Rietveld refinement is not a method for structure determination since all (including structural) parameters require reasonably good initial values. Simultaneous refinement of neutron and X-ray powder patterns is performed more and more frequently. ▶ Figure 29.2 shows, e.g., X-ray and neutron powder diffraction results obtained in this way for maghemite, $\gamma\text{-Fe}_2\text{O}_3$ (Somogyvári et al. 2002a).

Following the idea of “interpretation-by-fitting-a-model-to-data,” two more methods for the evaluation of powder patterns have to be reported briefly, both with elements of Monte Carlo simulations (for Monte Carlo methods, see, e.g., Allen and Tildesley 1987; Binder and Heermann 1992). One of them, the so-called pair distribution function (PDF) analysis, uses the pair distribution function, (▶ Eq. 29.19), for fitting (in real space) with a model containing as small a number of atoms as possible (Billinge and Egami 1993; Proffen and Billinge 1999). The other, called Reverse Monte Carlo (RMC) modeling (McGreevy and Pusztai 1988),

■ Fig. 29.2

Neutron (upper part) and X-ray (lower part) powder diffraction spectra of maghemite. The two patterns were simultaneously refined by the Rietveld method (the difference between model and measurement can be seen as the bottom curves of both parts). The arrows (in both parts) indicate extra reflections, due to tetrahedral ordering of vacancies in the crystal



employs large models (many thousands of atoms), in order to be able to describe Bragg- and diffuse-, nuclear and magnetic scattering in reciprocal space; the special algorithm for powders is called reverse monte carlo for powder patterns (RMCPOW) (Møllergård and McGreevy 1999). It is expected that with further increase of cheap computer power, these Monte Carlo based methods will be widely used.

There are a number of reasons why the powder technique may be preferred to single-crystal diffraction. The most important are the unavailability of suitable single crystals (catalysts, zeolites, fullerenes, etc.); data taking, handling and interpretation is straightforward and relatively fast, making the method available also to non-crystallographers. Also, in many cases, the powder pattern is exploited as a “fingerprint” of a given material (no two

powder patterns are exactly the same), which approach yields the fastest way of phase identification for materials that may appear in different crystallographic phases as well as for composite samples.

Details of the powder technique can be found, e.g., in the work of Bish and Post (1989) and Young (1993). Up-to-date applications are easiest to find in recent proceedings of the European Powder Diffraction Conference series (Delhez and Mittemeijer 1998, 2000, 2001).

29.3.1.4 Time-of-Flight (TOF) Variants of Neutron Diffraction Methods

Pulsed (mostly spallation) neutron sources (see [Sect. 29.5](#)) are becoming more and more important for the whole area of neutron scattering and therefore, it is essential to develop/improve experimental techniques that are well suited for exploiting features of pulsed beams. In a white beam, neutrons with different wavelengths travel at different speeds. Instead of varying the scattering angle, one measures the *time-of-flight* of neutrons when pulsed beams are applied. This is possible because the time $t = 0$ is naturally signaled by the start of the pulse. For a continuous – reactor based – neutron source, pulsing requires extra instrumentation, the inclusion of beam choppers (see [Sect. 29.5](#)).

For neutron diffraction one substitutes the (de Broglie) neutron wavelength $\lambda = h/p$ (p is the momentum of the neutron, h is the Planck constant) in Bragg's law, ([Eq. 29.25](#)), which (after expressing the lattice plane spacing d for $n = 1$) yields

$$d = \frac{t}{2 \frac{m}{h} L \sin \frac{\theta}{2}} \quad (29.28)$$

where m is the mass of the neutron, L is the total length of the source-to-sample-to-detector flight path, and t is the total time-of-flight. According to the above equation, a whole range of plane spacings can be measured at fixed scattering angle θ ; hence TOF neutron diffraction is called a “fixed angle, wavelength (and energy) dispersive” technique. The resulting powder pattern is the scattered intensity as a function of d -spacing; the corresponding Rietveld refinement algorithm therefore is different from that used for “angle dispersive” patterns.

For single-crystal diffraction, the white-beam-based Laue method can be applied on a TOF instrument. By making use of large-area detectors, covering possibly almost the full solid angle range around the sample, substantial volume of the reciprocal lattice (many reciprocal lattice points) can be explored simultaneously. In this way, the duration of single-crystal structure determinations may be reduced enormously.

Further information on time-of-flight neutron diffraction (and other time-of-flight neutron scattering methods) can be obtained from the Web site of the ISIS Pulsed Neutron and Muon Facility, Rutherford Appleton Laboratory, UK (ISIS 2003).

29.3.2 Dynamical Studies of Crystals

Elementary excitations (“dynamics”) in condensed matter systems may be studied by inelastic neutron scattering. A large proportion of solid-state physics concerns dynamical phenomena (“collective excitations”) in crystalline materials, such as lattice vibrations (phonons), or spin waves (magnons) (see, e.g., Ashcroft and Mermin 1976). These phenomena have been

investigated by neutron scattering for decades – see, for instance, early works considering one-phonon absorption by time-of-flight (Squires 1956) and crystal (“triple axis”) spectrometers (Brockhouse 1960). Browsing through the proceedings of recent neutron scattering conferences (see, e.g., Petry 2002), one quickly realizes that, at the beginning of the twenty-first century, a massive part of all neutron scattering investigations deal with some sort of dynamics in crystals. In this subsection, focus is put on dynamics in crystals that are particularly interesting from the chemical point of view.

As it was discussed in [Sect. 29.2](#), incoherent (inelastic) neutron scattering accounts for the individual motions of atoms. Thus, in the crystalline solid state, in the absence of diffusion, most of the incoherent signals originate from molecular vibrations. Most chemical applications have something to do with the role of hydrogen to which neutrons are more sensitive than any other probe. The reason for this can be understood by looking at the incoherent inelastic cross section, which can be related to the (vibrational, “one-phonon” approximated) density of states distribution function $Z(\omega)$ as (see, e.g., Marshall and Lovesey 1971; Bacon 1977)

$$\left(\frac{d^2\sigma}{d\Omega dE'}\right)_{\text{incoh}} = \frac{\kappa'}{\kappa} \sum_j \left(b_j^2 - \bar{b}_j^2\right) \frac{Q^2 U_j^2}{2M_j} e^{-2W_j} \left(\frac{1}{e^{\varepsilon/kT} - 1} + \frac{1}{2} \pm \frac{1}{2}\right) N \frac{Z(\omega)}{\omega} \quad (29.29)$$

where κ s replace the usual k s, used previously (see [Eq. 29.5](#)) etc.) for denoting wavevector moduli; k now denotes the Boltzmann constant, ω is angular frequency, and $\varepsilon = E - E' = \hbar\omega$ is the change in neutron energy due to the scattering process. The \pm sign is to be replaced by $+$ or $-$ depending on whether the neutrons lose or gain energy. The subscript j runs over the atoms in a molecule. The above expression shows that each vibration is “weighted” by the different atoms taking part in it, according to their incoherent scattering lengths (the term following the summation sign, see [Eq. \(29.8\)](#)), their atomic displacements U_j , and the reciprocal value of their atomic masses M_j . Due to this weighting, neutron spectra will always contain larger contributions arising from hydrogen atoms than their “fair share” considering their number. This is because of the small mass, large displacements, and huge incoherent scattering characterizing hydrogen atoms.

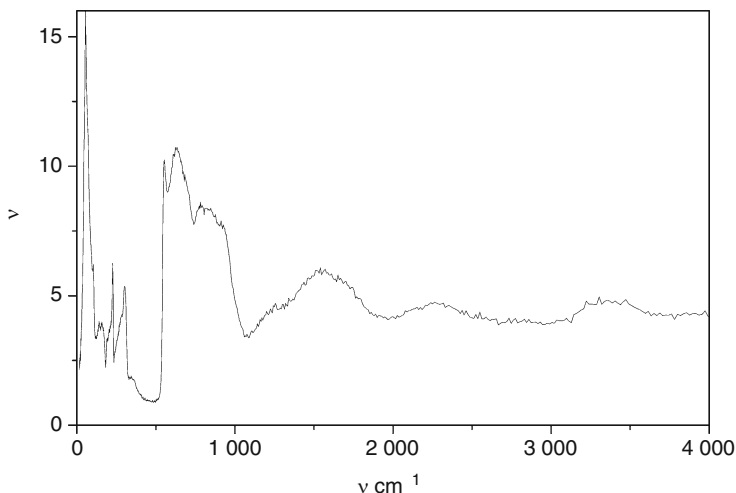
Note that deuteration will decrease enormously the amplitude of peaks related to hydrogen, whereas in infrared (IR) spectroscopy there would only be a change in the vibrational frequency. That is, the information on molecular-scale dynamics can be multiplied if IR, Raman, and neutron spectroscopies are applied together.

As far as applications are concerned, the investigation of the hydrogen bond seems a natural choice, since the bending vibration, for reasons mentioned above, is the most intense band in the spectrum. Indeed, crystalline compounds with strong H-bond have long been subjects of incoherent inelastic neutron scattering studies: substances like KHF_2 (Boutin et al. 1963), CHCl_2 and CDCl_2 (Stirling et al. 1970), and HCrO_2 (Rush and Ferraro 1966) or HCoO_2 (Delaplane et al. 1969) have been considered. As an example, incoherent inelastic neutron scattering data are shown for H_2O ice Ih in [Fig. 29.3](#) (Li 1996).

On the instrumental side, most inelastic neutron scattering setups are capable of molecular spectroscopic experiments; perhaps TOSCA, installed at the ISIS Pulsed Neutron and Muon Facility (UK), should be mentioned as it is dedicated to such studies (ISIS 2003). Data analysis most often includes quantum chemical calculations of the vibrational density of states, which are compared to experiment (see, e.g., Line and Kearley 2000; Fernández-Liencres et al. 2001).

■ Fig. 29.3

Dynamic structure factor S of (hexagonal) H_2O ($^1\text{H}_2\text{O}$) ice (phase Ih), obtained from incoherent inelastic neutron scattering (Li 1996) vs. wave number ν . Note the similarity of the above curve to results of conventional vibrational spectroscopic methods (IR, Raman)



29.4 Neutron Scattering by Liquids

For a chemist, the liquid state holds a special status: most of “traditional” chemistry and a large proportion of “modern” chemistry take place in solutions of some sort. For this reason, neutron scattering by liquids is treated with a particular emphasis here.

Due to its essential role, determining the microscopic properties of water has long been central to neutron scattering studies. As is well known, water behaves anomalously in many respects (see, e.g., Eisenberg and Kauzmann 1969) and, unfortunately, it presents quite a few experiment-related difficulties that make the understanding of the anomalies harder. Neutrons provide a unique opportunity to study hydrogenous materials, such as water. However, as it will be shown below, what was a great help in studying individual atomic dynamics in the solid may turn into an even greater obstacle when studying the liquid structure.

Before going into details, an important general property of neutron scattering from liquids should be noted. As was derived by Squires (1996), true elastic scattering from a liquid occurs only when $Q = 0$, i.e., for forward scattering. This finding applies to coherent and incoherent scattering alike, which corresponds to the general view that there is no “static” structure for a liquid, in the sense that the atoms have no equilibrium positions around which they oscillate; there is no Bragg scattering, either.

29.4.1 Structure

Again, the main feature of the liquid structure is the lack of structural units and long-range ordering (translational symmetry). Therefore, there is no sense in pursuing the determination of all nuclear coordinates (it is also impossible).

29.4.1.1 Description of the Liquid Structure, Based on Experimentally Available Quantities

Theoretical approaches to the structure of liquids are well developed (see, e.g., Gray and Gubbins 1984; Hansen and McDonald 1986). However, by considering only what is available strictly from diffraction experiments, one has to rely on the pair distribution function given by [Eq. \(29.19\)](#).

Liquids (at least the ones concerned with here) are isotropic, and therefore the correlation function depends only on the magnitude of \mathbf{r} (r), and the structure factor (static and dynamic) depends only on the magnitude of \mathbf{Q} (Q). The relations between the static structure factor and the radially symmetric pair distribution function (also known as the *radial distribution function*, rdf) then can be expressed as (compare [Eq. \(29.21\)](#))

$$S(Q) = 1 + \frac{4\pi\rho}{Q} \int_0^\infty r(g(r) - 1) \sin(Qr) dr \quad (29.30)$$

and

$$g(r) = 1 + \frac{1}{2\pi^2\rho r} \int_0^\infty Q(S(Q) - 1) \sin(Qr) dQ \quad (29.31)$$

It is $g(r)$ that has to be considered as the final result of a neutron diffraction experiment, which means that instead of particle coordinates, only a “distance spectrum” can be obtained. In other words, diffraction experiments can only access two-particle distribution functions of a liquid (and the same applies, naturally, to amorphous solids, as well). The calculation of $g(r)$ from nuclear coordinates can be carried out as follows:

$$g(r) = \frac{dN(r)}{4\pi r^2 \rho dr} \quad (29.32)$$

where $dN(r)$ is the number of atoms in the spherical shell between r and $r + dr$, so that the above equation gives the ratio of local and average number densities directly.

For a multicomponent liquid that consists of at least two different chemical elements, the desired information would be the (possibly complete) set of *partial pair* (or *partial radial distribution functions* (ppdf/prdf)); if there are k different types of scattering centers (nuclei) then there are $k(k+1)/2$ of these partials. For the case of liquid water, which can be considered as a guiding example throughout this section, there are two types of scatterers, H (or D) and O, and the number of prdfs is three: it is possible (and important) to distinguish between O–O, O–H, and H–H partial correlations. What can be measured by diffraction is the total (or “composite”) structure factor, defined as

$$S(Q) = \sum_{i=1}^k \sum_{j=1}^k c_i c_j \bar{b}_i \bar{b}_j S_{ij}(Q) \quad (29.33)$$

where c_i is the molar fraction of component i , $S_{ij}(Q)$ are the partial structure factors whose sine Fourier transforms are the $g_{ij}(r)$ prdfs, according to [Eq. \(29.31\)](#).

For water, the knowledge of the O–H partial radial distribution function is crucial; since it can provide the most decisive piece of information on hydrogen bonding (similar statement

can be made for other liquids with H-bonding). It is obvious, however, that from one measurement, three pdfs cannot be derived unambiguously; possible solutions to this problem will be outlined in the next subsections.

Another related point to note is that direct information on molecular orientations (and on their correlations) *cannot* be obtained from a diffraction experiment. One may speculate about possible orientations that may or may not be consistent with experimental data. In other words, very different *higher order correlation functions* (like those describing mutual orientations of two or more molecules) may average out and provide identical two-particle correlation functions (that can be measured). That is, diffraction data are inherently ambiguous in describing detailed atomic level structural arrangements in liquids; a fact that has to be kept in mind when interpreting the results of neutron diffraction experiments.

29.4.1.2 Determination of the Radial Distribution Function from Neutron Diffraction of Liquids

Although instrumental requirements are very similar, a liquid diffraction experiment is much less a routine task than taking the powder pattern. The reason is that when Bragg scattering is present then Rietveld refinement can work with just the ratio of the Bragg-reflection amplitudes; there is no need for precise absolute values. In a powder diffraction measurement, most frequently only the coherent elastic scattering is important. On the other hand, in the absence of true elastic scattering, the total coherent scattering is measured, so that for being able to carry out the transformation to real space with sufficient accuracy the absolute scale must be established. Also, scattering amplitudes are much lower without Bragg scattering, so that data correction procedures are crucial; therefore, they need to be described at this point briefly.

Generally speaking, the aim of data correction is to convert neutron counts (as received by the detectors) into properly normalized scattering cross sections. For achieving this goal, six measurements have to be made for a total scattering experiment: the sample, the empty container, the empty sample environment (for high/low temperature and or high/low pressure, etc.), a standard incoherent scatterer (usually vanadium) for the absolute normalization, the instrumental background and, finally, a standard sample (usually Ni powder) for the calibration of the instrumental geometry.

Based on the above measurements, the following correction steps are taken (see, e.g., Egelstaff 1994; Nield and Keen 2001):

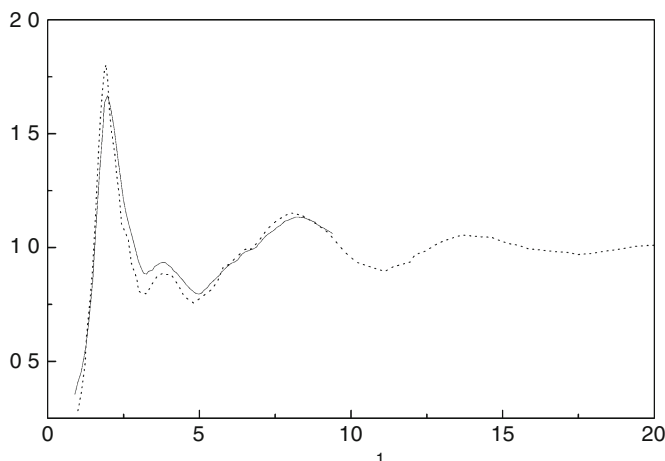
Attenuation corrections. Scattering from the sample is modified by (instrumental and general) background, container and environment scattering, by attenuation in the sample, the container and the sample environment and also, by multiple scattering of the sample, the container and sample environment.

Normalization. This step is done by dividing the sample scattering intensity by the vanadium standard scattering intensity. The idea behind is that a sample that is almost entirely incoherent scatterer sets the proper “zero level” for the coherent part.

Inelasticity. When measuring total scattering, the integration over energy transfer (see ► Eq. (29.4)), which is done automatically by the instrument, is not done at constant values of Q , but at best at constant angle. Corrections to this problem are instrument dependent and can only be approximated, see (Placzek 1952; Howe et al. 1989). However, these analytical approximations do not work for light atoms, like hydrogen. For hydrogenous materials, inelasticity corrections are the most important, and unfortunately, they are the ones that can

■ Fig. 29.4

Static structure factor of liquid D_2O . Solid line: reactor source (Thiessen and Narten 1982); dots: pulsed source (Soper et al. 1997)



only be handled with great difficulties (if at all). ▶ Figure 29.4 shows the corrected structure factor for liquid heavy water, as measured at a reactor source (Thiessen and Narten 1982) and at a pulsed source (Soper et al. 1997); differences observed between the two curves do not seem to influence the interpretation significantly in this particular case.

Calculating the radial distribution function. This step is, to date, most frequently carried out by simple “forward” transform, according to ▶ Eq. (29.31). For this reason, it is generally believed that a very wide scattering vector range, extending possibly over 20 \AA^{-1} , is necessary when measuring the structure factor (see, e.g., Wright 1994). (The lower limit of Q is usually not smaller than 0.3 \AA^{-1} , due to instrumental restrictions.) Note that there are “inverse” Monte Carlo based modeling methods also available, like monte carlo evaluation of the G of R (MCGR) (Pusztai and McGreevy 1997), which can overcome some of the difficulties concerning truncation errors during Fourier transformations.

If one wishes to determine all the three partial radial distribution functions of a two-component material, like water, then three independent total structure factors must be measured for (chemically) the same material. In this way, the coefficients of the partial structure factors $S_{ij}(Q)$, ▶ Eq. (29.33), will be different, because the scattering lengths will be different. As shown by ▶ Table 29.1, different isotopes of the same element do possess different scattering amplitudes for neutrons. This property made possible the development of the technique called *isotopic substitution* (North et al. 1968). For a two-component system, three different isotopic samples have to be prepared, so that the coefficients of the partial structure factors should differ sufficiently well for being able to solve a set of three linear equations, of the form of ▶ Eq. (29.33), for the three unknown partial structure factor.

Unfortunately, there are no suitable isotopes for each element; “good” elements are, for instance, chlorine and nickel. In many cases, differences between coefficients are not big enough for the matrix inversion; i.e., the set of equations is “ill defined.” Sometimes, application of the Reverse Monte Carlo modeling method can help in separating partial structure

factors, as was the case for molten CuBr (Pusztai and McGreevy 1998). (For synchrotron X-rays, an emerging similar method is anomalous X-ray scattering (Waseda 2002), where it is the Q -dependent atomic form factors, equivalents of b values, that can be varied.)

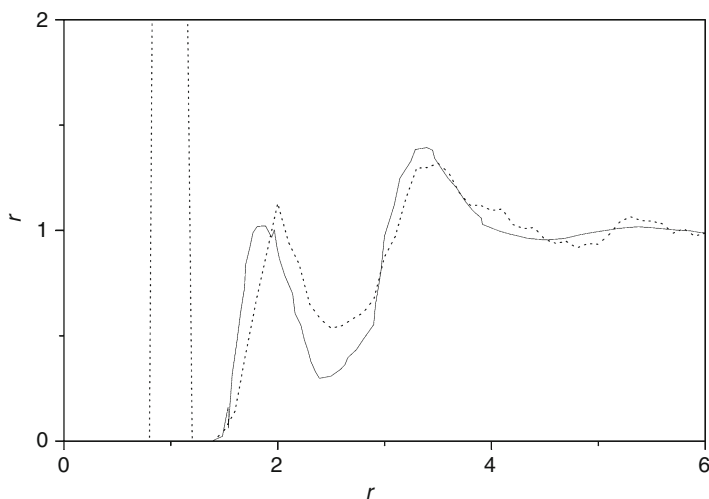
For a chemist, undoubtedly the best-known isotopic substitution is that of ^1H by ^2H (H to D): neutron diffraction studies of water (Thiessen and Narten 1982; Soper et al. 1997) are the most cited examples of that. Exploiting the substantial difference between the scattering lengths of H and D (Table 29.1), at least three samples (most frequently with 0, 50, and 100% of H_2O) are measured (the rest is D_2O). The huge inelastic incoherent cross section of ^1H has already been mentioned. As a result of this, in the case of the neutron diffraction intensity measured for pure H_2O , less than 5% of the signal contains information on the structure (i.e., more than 95% has to be treated as “background”). Another problem is that H_2O and D_2O are two (although only slightly, but noticeably) different liquids, with different melting points, etc., so that the “identity” of the samples is questionable. For these reasons, there are still controversial issues concerning details of the microscopic structure of pure liquid water (see, e.g., Pusztai 1999), which is demonstrated in Fig. 29.5. This is a really unfortunate situation, since a lot of interesting chemistry, including solutions, complexes, polymers, biological samples, etc., could benefit enormously from a well-established H–D substitution practice.

29.4.2 Microscopic Dynamics in Liquids

In many cases, neutron scattering studies of microscopic dynamics in the liquid state pursue remnants of solid-like behavior, like phonons (see, e.g., Pusztai and McGreevy 1989). Concerning chemical properties, this approach is not relevant. “Molecular spectroscopy,”

Fig. 29.5

O–H partial radial distribution functions of liquid water. *Solid line:* from Soper et al. (1997); *dots:* Reverse Monte Carlo analysis from Pusztai (1999). Note the significant deviation in terms of the position of the first intermolecular maximum, which is characteristic of the hydrogen bond



making use of incoherent inelastic scattering as described briefly in ► Sect. 29.3.2, can also be used in the liquid state. For instance, liquid hydrogen sulfide was investigated by Andreani et al. (2001) using the TOSCA time-of-flight spectrometer mentioned earlier. This approach is useful when local (as opposed to “collective”) vibrational modes are probed. There are, however, further areas, specific to (or at least, more frequent for) liquids; these will be the subjects of the next subsections.

29.4.2.1 Quasi-Elastic Neutron Scattering

Elementary excitations also include “single particle diffusive excitations” beside quantized vibrations (i.e., molecular vibrations and vibrations of the crystal as a whole associated with phonons/magnons). Consider the incoherent dynamic structure factor $S_{\text{inc}}(Q, \omega)$, which is the Fourier transform pair of the time-dependent self-correlation function, $G_{\text{self}}(r, t)$, compare ► Eqs. (29.12), (► 29.13), and (► 29.16), around the elastic ($\Delta E = 0$) peak (measured at a number of Q values). This is the range where for large Q , $S_{\text{inc}}(Q, \omega)$ exhibits a very broad maximum, and for low Q values, below about 1 \AA^{-1} , it peaks sharply (see, e.g., Sköld et al. (1972) for the case of liquid argon). A qualitative explanation can be given on the basis of the properties of Fourier transform pairs: at small values of r and t (large values of Q and ω), the liquid behaves as a perfect (ideal) gas (“free movement”), whereas at the other extreme, large values of r and t , diffusion dominates (many collisions with other atoms). This latter type of behavior is being investigated rather heavily in liquids (which means high demand for beamtime on suitable instruments, like IRIS at ISIS, UK), therefore some of the related basic formulas are given below.

Fick’s (second) law, which is the basic equation of diffusion, reads as (see, e.g., Atkins 1994)

$$\frac{\partial n(\mathbf{r}, t)}{\partial t} = D \nabla^2 n(\mathbf{r}, t) \quad (29.34)$$

where $n(\mathbf{r}, t)$ is the number density at point \mathbf{r} and D is the diffusion coefficient. Owing to its probabilistic interpretation, $G_{\text{self}}(r, t)$ must satisfy the above equation (Squires 1996). Following some algebra, one ends up with the following expression for $S_{\text{inc}}(Q, \omega)$:

$$S_{\text{inc}}(Q, \omega) = \frac{1}{\hbar \pi} \frac{D Q^2}{D^2 Q^4 + \omega^2}. \quad (29.35)$$

The above function has a Lorentzian shape with a maximum at $\omega = 0$, where

$$S_{\text{inc}}(Q, 0) = \frac{1}{\hbar \pi D Q^2}. \quad (29.36)$$

That is, information on the diffusion constant is available directly. Up-to-date information on the current use of quasi-elastic neutron scattering can be obtained from the work of McGreevy (1999).

29.4.2.2 Detecting Very Small Exchanges of Energy: Neutron Spin-Echo

In standard inelastic (coherent or incoherent; time-of-flight) scattering experiments, increasing the resolution (the precision of the determination of energy transfers) by a given factor x costs

reducing the available intensity by a factor of x^2 . This is because one loses a factor of x of the intensity on both the speed selection and speed analysis, before and after the sample. This rate quickly makes the experimenter losing all the intensity around the energy resolution of about 0.1 μeV (which is well into the range of diffusion “excitations”). However, there are important processes, like chain relaxation in polymers, whose study would require even better an energy resolution, since extremely low energy excitations have to be maintained. For that, one has to replace the direct measurement of neutron speed by a more sophisticated method, which is achieved in the technique of *neutron spin-echo spectroscopy* (Mezei 1972, 1979).

A set of polarized particles with a magnetic moment and spin $\frac{1}{2}$ will behave similarly to a small (classical) magnetic moment: when entering a region where the magnetic field is perpendicular to its magnetic moment, Larmor precession (see, e.g., Ashcroft and Mermin 1976) will occur. If a polarized neutron beam (with spins only either “up” or “down”) enters a region of length l with a magnetic flux density \mathbf{B} , the total precession angle will be

$$\varphi_1 = \frac{\gamma B l}{u_1} \quad (29.37)$$

where u_1 is the speed of neutrons and γ is the gyromagnetic ratio of the neutron. Such a beam, with precession angle φ_1 , is incident on the sample and then, the scattered beam passes another region of length l and magnetic flux density $-\mathbf{B}$. If the scattering is elastic then the total precession angle is 0 and at the end of this second region, the original polarized neutron beam is recovered. If, however, the scattering is inelastic and there is a (small) energy exchange $\hbar\omega$, then there will be a net precession angle and the detector signal will be a transmission function. The probability that a neutron is transmitted (at a specific analyzer geometry) is $\cos \varphi$. Remember that at a given value of Q , the probability of scattering with energy exchange $\hbar\omega$ is $S(Q, \omega)$. Taking the expectation value by integrating over all values of ω one obtains

$$\langle \cos \varphi \rangle = \frac{\int \cos\left(\frac{\hbar\gamma B l}{mu^2} \omega\right) S(Q, \omega) d\omega}{\int S(Q, \omega) d\omega} = S(Q, t). \quad (29.38)$$

That is, the measured beam polarization is in a direct relation to the intermediate scattering function at a given value of Q . Details of the instrumentation can be found in ▶ Sect. 29.5 (see also Monkenbusch and Zorn 2000). Applications, mostly for dynamics of polymer melts and solutions, can be browsed in the work of Ewen and Richter (1997).

29.4.3 Looking at Mesoscopic Length Scales: Small Angle Neutron Scattering

As it was mentioned before, when doing standard neutron diffraction, the lowest available value of Q is usually not smaller than about 0.3 \AA^{-1} . Since the purpose of these “wide angle” diffraction measurements is to resolve atomic scale distances, this lower limit is actually sufficient (perhaps with the exception of high-resolution powder diffraction studies of magnetic materials). However, there may be structural features that are manifest at superatomic length scales; examples are colloids, polymers, gels, and precipitations in alloys. Neutron scattering does provide means for investigating such systems, by detecting scattering at the scattering vector range between about 10^{-3} \AA^{-1} and 10^{-1} \AA^{-1} : this technique is the *small angle neutron scattering* (SANS).

If the scattering vectors are limited to below about π/d , where d is a general interatomic distance, about 3 Å, then the discrete positions of scattering centers (nuclei, as point-like scatterers) cannot be resolved; instead, the distribution of scattering lengths can be represented by a continuously varying *scattering length density*, $\rho_b(\mathbf{r})$. If ρ_b is uniformly distributed beyond atomic length scales then there is no small angle scattering signal observable; for this reason, pure liquids normally are not studied by SANS.

Fluctuations of $\rho_b(\mathbf{r})$ can be caused by density or concentration fluctuations. Real density fluctuations in simple (one-component) fluids occur near the critical point, where the isothermal compressibility of the liquid diverges. In multicomponent fluids, the concentration fluctuations can be observed when (at least one of) the components “want” to demix. Naturally, in more complex samples, like colloids in some solvents, fluctuations are present because, on the atomic length scale point of view, there are several (at least two) different phases present. SANS (and also, its X-ray counterpart SAXS) can be applied with success in these latter instances.

Concerning scattering-length densities, contrast is a useful concept when dealing with SANS: it refers to scattering-length density differences between parts of the sample. These parts can be various objects: big molecules, or even parts of very big molecules, associations of particles of a kind, etc. The point to note is that by isotope substitution (► Sect. 29.4.1), the contrast can be varied without changing the chemistry of the system. This powerful methodology has the name of *contrast variation* in the area of SANS.

The SANS scattering function, which is analogous to the structure factor (► Eq. (29.21)), can be written as follows:

$$F_{\text{SANS}}(\mathbf{Q}) = \int_V (\rho_b(\mathbf{r}) - \rho_0) e^{i\mathbf{Q}\mathbf{r}} d\mathbf{r} \quad (29.39)$$

where the integration is over the volume V of the sample, and ρ_0 is the macroscopic (“average”) scattering length density of the system. (In liquid and crystalline powder samples, for their isotropic nature, the vector notation of \mathbf{Q} and \mathbf{r} can be changed to their magnitudes, Q and r). According to the above equation, the SANS scattering function of model structures can be calculated. However, because of the very limited experimental information concerning the Q -space, the distribution of scattering length density cannot be reconstructed directly. For this reason, several approximations have been developed (and are in use) for the interpretation of SANS data.

For all shapes of scattering objects, the equation of Guinier and Fournet (1955) yields the low- Q behavior of the SANS $F(Q)$ for a set of monodisperse, spherical (or at least, not too anisometric) particles:

$$F_{\text{SANS}}(Q) = c_p V^2 (\rho_b(r) - \rho_0)^2 e^{-Q^2 R_g^2} \quad (QR_g < 1) \quad (29.40)$$

where c_p is the concentration and R_g is the *radius of gyration* of the scattering particles. R_g is often considered as a finding of primary interest, since it can be calculated, by taking the slope of the $\log F_{\text{SANS}}(Q)$ vs. Q^2 plot at small Q values, even when only the un-normalized scattering intensity is known. (A word of warning may be appropriate here, since the above relation is usually applied automatically: R_g can be obtained so simply only if all the conditions, particularly the monodispersity and the sphericity, of the Guinier approximation are fulfilled.)

At the high Q end of the SANS region, another approximation, due to Porod (1951), can be used: the signal there is dominated by the interface between the different scattering particles (or regions of different scattering length densities):

$$F_{\text{SANS}}(Q) = 2\pi\Phi(\rho_b(r) - \rho_0)^2 Q^{-4} \quad (Q > 0.1 \text{ nm}^{-1}) \quad (29.41)$$

where Φ is the total interface area per unit volume. By using the above equation, one can calculate Φ from just the intensity curve, but only at the upper limit of Q , and if a clear straight section can be found in the $F_{\text{SANS}}(Q)$ vs. Q^{-4} curve. Porod's law proves to be extremely useful when studying catalysts or other porous materials. Between the Porod and Guinier regions one often finds a power law behavior, reflecting possible fractal nature (i.e., self-similarity over a given size range) of the sample (see, e.g., Teixeira 1987).

The variety of properties that can be investigated by SANS is tremendous: from the determination of the radii of gyration, it extends to the description of fractal behavior. For a general overview of the technique and its application, one can consult the works of Feigin and Svergun (1987) and Brumberger (1995). Detailed information on the appropriate instrumentation can be found on the Internet (see Munter 2003 for reactor sources, and ISIS 2003 for pulsed sources).

29.4.4 Looking at Liquid Surfaces: Neutron Reflectometry

As it was introduced in Sect. 29.2.3, neutrons of sufficiently long wavelength can bring about optical phenomena when encountering boundaries of condensed phases: they, as waves, interact with the continuous potential represented by densely packed atoms. Reflection does occur (although only for very small incident angles, due to the very nearly unity value of the refractive index of most materials for neutrons), which can be exploited for studying liquid (and solid) surfaces (and interfaces) by neutron *reflectometry*.

The specular reflection (for which the incident angle is equal to the outgoing angle) of neutrons can be measured as a function of the scattering vector \mathbf{Q} perpendicular to the liquid surface. The reflection pattern is related to the neutron refractive index profile normal to the surface (or interface), which profile, in turn, is related to the scattering length density profile (see Eq. (29.23), where $\rho_b = \rho b$). Any *off-specular scattering* must come from potential gradients present in the plane of the surface. In this way, the reflectivity pattern provides information on composition and/or density variations at surfaces.

The analysis of reflectivity data is usually done by constructing a model of the interface, containing parallel homogeneous layers. Each layer is characterized by its thickness, d_b , and scattering length density, ρ_b . These parameters (and also, if desired, further ones describing the roughness of the interfaces) are used to calculate the reflectivity profile for the model, according to the “optical matrix” method (Born and Wolfe 1989). The transmission and the reflection from layer to layer are described as a matrix multiplication product for the two adjacent layers. Retrieving the distribution of the scattering length density from the reflectivity curve is obviously a complex problem. Note also that different model profiles can produce the same reflectivity curve within errors. This is sometimes called the “phase problem.” It has a similar origin to what was mentioned while discussing single-crystal diffraction in Sect. 29.3.1.3: measured intensities give information only on the magnitude, but not the phase factor, of the wave function of the scattering system. A review of inversion techniques is available in the work of Zhou and Chen (1995).

The instrumentation of neutron reflectometry can be realized by both monochromatic (angle dispersive) and time-of-flight (wavelength dispersive) methods. The former is capable of measuring smaller reflectivity values due to its lower background, whereas the latter has the advantage of the fixed angle setup. Signal-to-noise ratios of higher than 10^5 can be routinely reached and reflectivities as low as 10^{-7} are measured frequently. As usual, the H/D isotopic substitution gives outstanding opportunities for answering rather specific problems, as the refractive index of hydrogenous and deuterated layers are different while the underlying chemistry remains essentially the same. See the work of Penfold and Thomas (1990) for more details concerning the experimental side.

Applications in the area of surface chemistry are abound. For instance, adsorbed layers of surfactants (Simister et al. 1992) or polymers (Henderson et al. 1993) can be studied in great detail. Finally, it should be noted that the most important solid-state physics/materials science application is *polarized neutron reflectometry*, by which magnetic multilayers are studied (see, e.g., Huang et al. 1993). The current status of neutron reflectometry can be checked in the proceedings of the conference series “Surface X-ray and Neutron Scattering” (Norman and Webster 1998).

29.5 Neutron Scattering Instrumentation

In this section, essential parts of the instruments that can serve for the determination of parts of the $S(\mathbf{Q},\omega)$ function are introduced briefly.

29.5.1 Neutron Sources

As it was already emphasized, maximizing the available flux density of thermal neutrons, including the “cold” as well as the “hot” regions, is vital for neutron scattering applications.

29.5.1.1 Reactor Sources

Nuclear reactors with relatively low thermal power (usually few tens of megawatts), but optimized for neutron yields, serve as reactor sources of thermal neutrons. Most of them exploit the fission process of ^{235}U nuclei, initiated by one thermal neutron and yielding on average 2.5 fast neutrons. These latter have to be moderated to thermal energies for neutron scattering applications. This is done by light or heavy water, which result in different energy distributions of the usable neutrons. An “average” 20 MW reactor source provides a thermal neutron flux of about 10^{14} neutrons $\text{cm}^{-2} \text{s}^{-1}$.

The high flux reactor at the Institut Laue Langevin (ILL) in Grenoble, France, has been recognized as the best steady-state source available for the past 3 decades (Munter 2003). Its single fuel element contains highly enriched (93%) ^{235}U (about 8.5 kg), which is controlled by one central rod and surrounded by D_2O as the reflector medium (diameter: 2.5 m). Outside the reflector vessel is a moderator tank of H_2O , which contains three specific moderator cells (one “hot,” at 2,500 K, one “cold,” at 20 K, and one “ultra cold” at even lower temperature), in order to extend the energy (wavelength) spectrum of neutrons available for the instruments. As a result, neutron wavelengths between 0.5 and 30 Å are routinely available. The thermal flux

density is around 2×10^{15} neutrons $\text{cm}^{-2} \text{s}^{-1}$, which (as both calculations and practice indicate) is about the highest that can be reached by a reactor source. The number of neutron scattering instruments at ILL is about 50.

There are a number of nice features of reactor sources that make data handling in general easier and neater than what must be done at pulsed sources. On the other hand, reactors represent technologies and apply techniques that have been used up to their limits already. This, combined with the fact that beam intensities cannot be increased substantially, suggests that it is not the reactor sources where major breakthroughs can be expected in the future.

29.5.1.2 Spallation Sources

Neutrons can also be produced by a process called *spallation*, in which high-energy particles bombard heavy nuclei (the threshold energy for the incident particle is around 10 MeV; usual bombarding energies are well above 100 MeV). By capturing the high-energy particle, the heavy nucleus gets excited and, by an intranuclear cascade, it emits fast neutrons. Finally, when de-excitation takes place, the target nucleus evaporates various nucleons, including slow neutrons. The total neutron production per incident particle is about 20–30 and, what is also important, the energy released is low compared to that of the fission process. Therefore, in principle, there is no upper limit for the available neutron flux.

Protons are the particles that are most frequently applied as bombarding particles. The usual realization of a spallation neutron source consists of a source of H^- ions, a linear accelerator (LINAC), a synchrotron ring, and finally, a target station that contains heavy nuclei. (The mentioning of H^- ions here is no mistake. H^- ions namely are produced with higher efficiency than H^+ ions, i.e., protons (see [Sect. 50.1.6.2 in Chap. 50, Vol. 5](#), on “Particle accelerators”). The H^- ions are directly accelerated by a LINAC, and then, after “stripping” them, the fast protons thus obtained are further accelerated by a synchrotron. Beam channels are connected via suitable moderator cells that set the required energy range of neutrons.

The brightest spallation neutron source at the moment is ISIS ([ISIS 2003](#)) at the Rutherford Appleton Laboratory (Didcot, UK), where a 52-m diameter synchrotron accelerates protons to their final 800 MeV energy (reaching an average current of 200 μA). The tantalum target is bombarded in pulses, at a frequency of 50 Hz. The target is surrounded by four moderator cells; two of them are light water, one is liquid methane at 110 K, and one is fluid hydrogen at 25 K. An extended beryllium reflector concentrates the neutrons to the regions of the moderators. The effective neutron flux is comparable to that available at the best reactor sources.

Spallation sources have the disadvantage that they must use time-of-flight methods constrained by the frequency of the source. Also, for several technical reasons, data evaluation is much more demanding and less transparent than at reactor sources. However, spallation sources with a projected flux of about an order of magnitude higher are being built, which means that in about 10 years they are likely to change the present neutron scattering landscape dramatically.

29.5.2 Optical Elements

After leaving the moderator, neutrons have to be guided to the sample and then, to the detector. During this process, the state of the neutron, or the shape/size of the beam may have to be changed. Pieces of instrumentation that serve these purposes may be called (neutron) optical devices.

29.5.2.1 Collimators

A collimator defines the shape and divergence of the neutron beam. The most basic collimator is a pair of slits, for which the (maximum) beam divergence is defined as $(a_1 + a_2)/L$, where a_1 and a_2 are the widths of the slits, and L is the collimating distance between the slits.

In order to collimate a beam of larger cross section in one dimension, within a reasonable L , Soller-type collimators have to be applied. Such a collimator is composed of a number of equidistant neutron-absorbing blades, separated by spaces. Blades should be as flat and as thin as possible. The theoretical maximum value for the transmission of a Soller collimator with 10° divergence is 96%.

Soller collimators are most frequently used in combination with single-crystal monochromators (see below), for defining the wavelength resolution of the instrument.

29.5.2.2 Neutron Guides

The principle of *mirror reflection* can be exploited for transmitting neutron beams as far as more than 100 m away from the source. As the refractive index for neutrons is very close to, but slightly less than unity for most materials, total reflection can take place for sufficiently smooth surfaces (at grazing incidence) only. The critical angle, γ_c depends on the neutron wavelength and scattering length of the material as $\gamma_c = \lambda(\rho b_{\text{coh}}/\pi)^{1/2}$ where ρ is the number density of atoms. The value of γ_c for nickel, which was the first material used for fabricating neutron waveguides, is 0.1 \AA^{-1} .

A standard neutron guide element is made of boron glass (boron is used for absorbing neutrons that would leave the guide), assembled into a rectangular cross section of dimensions of max. 200 mm (height) \times 50 mm (width). The reflecting (inner) surface of the guide is coated with a thin layer (of the order of 100 nm) of Ni, ^{58}Ni , or a multilayer structure called a “supermirror” (Mezei 1976). This latter structure consists of appropriately chosen pairs of highly uniform thin layers, with the result of extending the total mirror reflection beyond the critical angle. The extension is commonly described by the factor m that refers to multiples of the critical angle of nickel; the best mirrors have m values of 3 to 4 nowadays. Note that the flux gain (as compared to standard Ni coating) is proportional to m^2 .

Modern neutron guides are evacuated in order to minimize absorption and scattering by air. Neutron guides are frequently curved with a curvature radius of a few thousand meters, so that background radiation would be minimized at the location of the instrument. In addition to this, it is not necessary to pack all the instruments tightly around the source. Several guide systems make extensive use of multiplexing, i.e., putting more than one instrument on a guide sequentially. This technique needs careful planning and the use of high quality optical elements such as monochromator crystals.

29.5.2.3 Monochromator Crystals

Neutron sources provide neutrons with a rather wide energy spectrum, almost like a “white beam.” Bragg reflection from single crystals is the most frequently applied means of selecting a well-defined wavelength (band) from the spectrum, which is used extensively at reactor sources.

The price one has to pay for a wavelength selection (that makes the beam suitable for, e.g., crystal structure determination) is that only a maximum of about 1% of the thermal neutron intensity can be used; the rest is scattered into (and absorbed by) the monochromator shielding. It is essential that monochromator crystals possess high scattering length density and low absorption (and incoherent and inelastic) cross section(s). Most frequently, Cu and Ge are applied. It is also for the optimization of the monochromatic intensity that instead of perfect crystals either mosaic crystals, consisting of small crystallites, or mosaic blocks, with orientation parallel to the crystal surface, or mechanically deformed (large) single crystals are used. This means that a wavelength band broadening of up to about 0.5° is “built in” the monochromator crystal, which is consistent with typical neutron beam divergencies.

It can be shown (Sears 1997) that higher intensities can be obtained in reflection geometry than in transmission geometry. (Note that this “reflection” has nothing to do with the phenomenon of mirror reflection, which was concerned in the previous subsection (see Sect. 29.5.2.2), but it just refers to a particular geometrical arrangement, which utilizes Bragg scattering.) By making use of highly sophisticated crystal fabrication technologies, both horizontal and vertical focusing is possible for investigating small samples. In favorable cases, the intensity gain factor can be as high as five for vertical focusing (Riste 1970; Currat 1973).

29.5.2.4 Velocity Selectors and Choppers

These devices make the wavelength-band selection by taking advantage of measuring the neutron flight time; selectors and choppers are usually chosen if the desired band is fairly wide. A “typical” thermal neutron speed is about 2,000 m/s, which means that it takes about 5×10^{-3} s for a neutron to travel 1 m; this, in turn, makes it possible to determine the time-of-flight very accurately over just a few meters.

Mechanical velocity selectors can be used when a continuous beam is required, with a coarse energy (wavelength) resolution. Consequently, they find their main application in the area of small angle neutron scattering (SANS). Modern selectors are made of lightweight neutron-absorbing blades that are slotted into helical grooves on the rotation axis, while the axis is fixed parallel to the beam direction (Wagner et al. 1992). The neutron wavelength can be tuned by setting the speed of rotation: neutrons that are slower or faster than required will hit the blades and will be absorbed. The best wavelength resolution, $\Delta\lambda/\lambda$, that can be achieved with velocity selectors is about 5%.

Choppers, in contrast to selectors, are used for generating pulsed neutron beams. They are essential whenever time-of-flight instruments are built at a reactor source, as there is no other way of knowing when neutrons start their flight path but pulsing the beam. Up-to-date devices are disc choppers rotating about an axis parallel to the beam direction, with a maximum speed of about 20,000 rpm. The discs are made of neutron-absorbing material and contain slits (apertures) that are transparent to neutrons. The pulse frequency is determined by the number of slits and rotation speed. Two disc choppers, working in phase, are sufficient for pulsing and simultaneously monochromating the beam; the wavelength resolution is limited by the rotation speed. In high-precision instruments, single choppers are routinely replaced by two counter-rotating discs, thus increasing the energy resolution. Note that in practice almost always more than two pairs of choppers are installed, to avoid “time-frame overlaps” between incident and scattered beams.

29.5.2.5 Polarizers

Although in this chapter polarization has only been considered very briefly (mostly because of its limited use in chemical applications so far), it is obvious that its importance is growing extremely fast nowadays. The underlying reason for this development is that the *specificity* of the interaction of nuclei with neutrons can be greatly enhanced if polarized beams (and/or polarized samples, where applicable) are put into use.

The two spin states of the neutron can be distinguished by considering their response to an external magnetic field: a spin “+” would be aligned parallel to the field direction (**B**), whereas a spin “−” would be antiparallel to it. In a non-polarized beam of neutrons the frequency of “+” (and of “−”) spins is 50%. The polarization of a neutron beam (in the direction of **B**), as well as the polarizing efficiency of a polarizer, may be characterized by the parameter *P* defined as $P = (N_+ - N_-)/(N_+ + N_-)$, where N_+ and N_- are the numbers of neutrons with spin “+” and “−,” respectively.

Polarizing a neutron beam requires the removal of neutrons in one of the spin states. This can be achieved via several methods, all of which make use of the (sometimes extremely subtle) difference of some quantity for the two spin states. Ferromagnetic single crystals immersed in a magnetic field that can saturate the atomic moments will diffract neutrons with parallel and antiparallel (to the direction of **B**) spins with different intensities at a given angle. The most widely used such monochromating/polarizing material is the so-called Heusler-alloy, Cu_2MnAl (Delapalme et al. 1971). Polarizing (super)mirrors are made of multilayers, in which one of the layer types is ferromagnetic (e.g., the alternation of Fe and Si thin layers would serve the purpose). The critical mirror reflection angles for spins parallel and antiparallel to **B** differ. Perhaps the most promising variation is the application of polarizing filters in which neutrons in one of the spin states absorb preferentially (Tasset and Resouche 1995). Using ^3He , for instance, $P > 0.95$ can be reached, with acceptable transmission.

Handling a polarized beam is not a trivial matter either, since in zero magnetic field the beam becomes depolarized quickly; the application of a “guide field” over the entire flight path is the most common solution to this particular problem.

29.5.3 Detection of Neutrons

The distinct advantage that neutrons can penetrate deeply in most materials becomes a distinct disadvantage when, as a final stage of any neutron scattering experiment, they have to be detected. Namely, since neutrons are scarce (and therefore, expensive), they have to be detected with a good efficiency. Detection of neutrons always means ceasing their free existence (absorption), by involving them in nuclear reactions. This, in turn, means that it is impossible to measure the energy of a neutron directly: characteristic energy transfers during scattering processes are at most of the order of meV, whereas energies characteristic of suitable nuclear reactions are of the order of MeV. This is one of the important reasons why time-of-flight methods had to be invented in the field of neutron scattering.

Nuclear reactions that are most frequently applied for detecting neutrons are listed in [Table 29.2](#). The resulting particles are all highly energetic and possess electric charge. This latter property can be exploited in the actual detection process.

A *proportional counter* designed to detect neutrons consists of an anode, surrounded by pressurized ^3He or $^{10}\text{BF}_3$ gas. The charged particles, produced by the absorption of neutrons,

■ Table 29.2

Nuclear reactions for neutron detection

Reaction	Cross section/ <i>b</i> (for 25 meV neutrons)	Particles generated	Total energy/MeV
$n + {}^3\text{He}$	5,333	Proton, ${}^3\text{H}$ (triton)	0.77
$n + {}^6\text{Li}$	941	${}^3\text{H}$, ${}^4\text{He}$	4.79
$n + {}^{10}\text{B}$	3,838	${}^4\text{He}$, ${}^7\text{Li}$ (+ γ photon)	2.30
$n + {}^{235}\text{U}$	681	Fission neutrons	1–2

ionize the gas and then, the emitted electrons are accelerated toward the anode and ionize more gas. This avalanche-like process initiates a discharge at the high voltage (1–5 kV) anode. The charge is proportional to the total energy of the reaction, so that neutrons can easily be discriminated against gamma-photons. Proportional counters can reach efficiencies up to about 80% depending on the neutron wavelength. Following the invention of Charpak (1968), large, position-sensitive area detectors could be fabricated by installing more (up to hundreds of) anode wires within one gas chamber. Perhaps the most promising development in this area is the “micro pattern gas counter” (Oed 2001). The best spatial resolution is about 1 mm, and the highest count rate is roughly 20 kHz/mm².

Another possibility is to make neutron-sensitive *scintillation detectors*, in which neutrons are absorbed by ${}^6\text{Li}$ (mixed with ZnS and located within a glass matrix) and the light quanta emitted are collected usually by photomultipliers.

For a more detailed account on radiation detection, see the work of Knoll (1999).

29.5.4 Examples of Complete Neutron Scattering Instruments

Having been acquainted with the components of neutron scattering instruments, two types of complete instruments will be described briefly here: one is “simple,” a standard powder diffractometer, while the other is one of the most complicated, a neutron spin echo spectrometer.

29.5.4.1 Neutron Powder Diffractometer

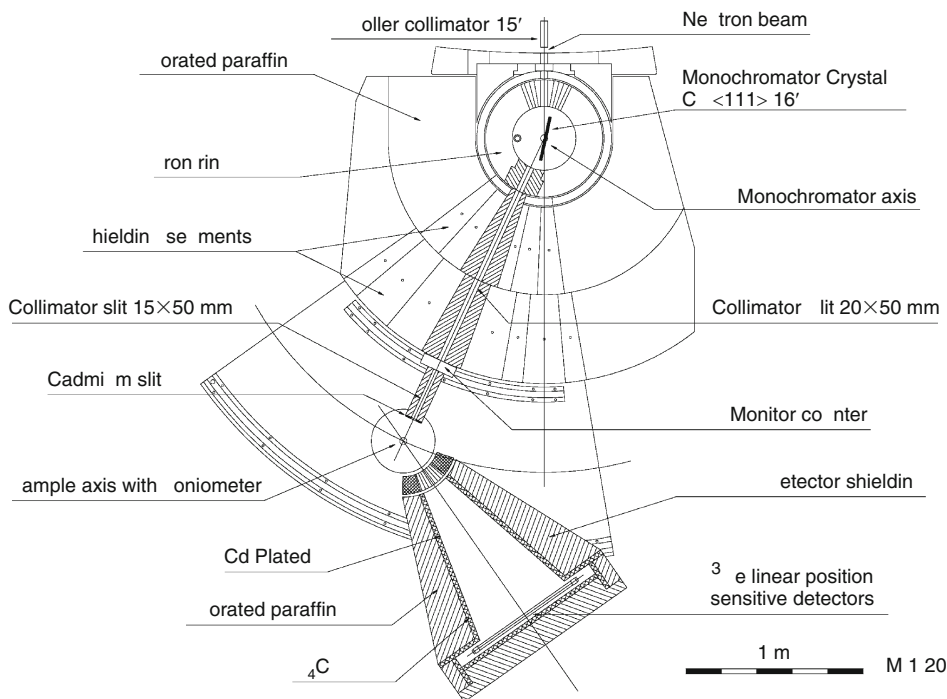
This section is restricted to the description of an “angle dispersive” device (see ▶ Sect. 29.3.1.4). The instrument that is capable of recording neutron powder diffraction patterns is also called “two axis” neutron spectrometer, after the two principle axes “monochromator-sample” and “sample-detector”; the original design is due to Hewat and Bailey (1976).

This is a very popular and useful instrument and therefore virtually every reactor source has at least one of them. Here the “PSD” powder diffractometer, installed at the Budapest Research Reactor (Hungary), is introduced briefly (Sváb et al. 1996). A top view of PSD is shown in ▶ Fig. 29.6.

The PSD diffractometer is placed on a tangential thermal neutron beam of a medium flux reactor source. Primary collimation is done before the monochromator. The wavelength most

■ Fig. 29.6

Schematic view of the “PSD” neutron powder diffractometer, installed at the 10 MW Budapest Research Reactor (Sváb et al. 1996)



frequently selected from the primary neutron spectrum is around 1 \AA , for which, in the case of a Cu(111) monochromator single crystal (with a mosaic spread of $16'$), a neutron flux density of about $10^6 \text{ n cm}^{-2} \text{ s}^{-1}$ can be achieved at the sample position.

Scattered neutrons are detected at a distance of 1.2 m from the sample by 60 cm position-sensitive ^3He detectors (placed within appropriate shielding), which span a scattering angle range of 25° . In order to cover the whole scattering-angle range up to 110° , data are collected at five different positions of the detector system. The resolution that can be routinely achieved by such a setup is about 10^{-2} , in terms of $\Delta d/d$.

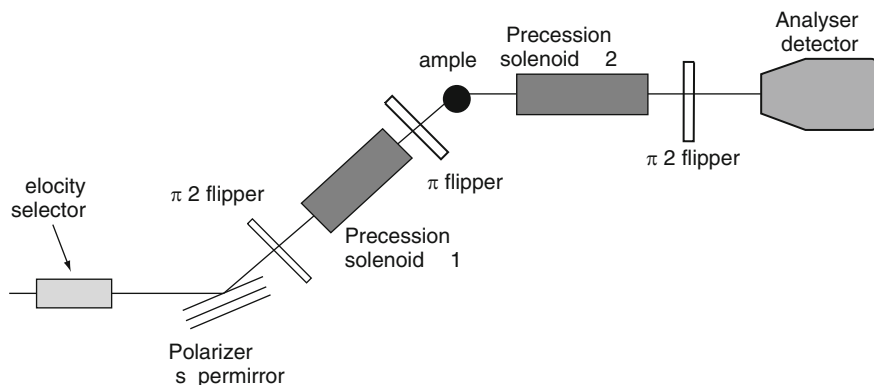
The PSD diffractometer can be used for either standard powder diffraction studies (see, e.g., Somogyvári et al. 2002b), but also, its design allows studying liquids and amorphous materials (see, e.g., Jóvári et al. 2001).

29.5.4.2 Neutron Spin Echo Spectrometer

The main point about neutron spin echo is the manipulation with neutron spins, which has to be carried out rather precisely; this requirement dominates the instrumental realization. (Note that neutron spin echo spectrometers, at present, can only be found at reactor sources.) A schematic drawing of a “generic” spin echo instrument is given in Fig. 29.7.

■ Fig. 29.7

Schematic view of a neutron spin echo spectrometer



Initial wavelength selection is done by a mechanical (rotating) velocity selector, since energy resolution is not an important issue here. Polarized neutrons may be produced by reflection by a magnetic multilayer mirror. Essential parts are the so-called “flippers.” These devices, consisting of flat coils, can change the direction of the neutron spin (which is extremely sensitive to external magnetic fields).

The first ($\pi/2$) flipper rotates the spin to be orthogonal to the first (longitudinal) precession field; the aim of this step is to define the exact initial spin state. During the travel over the first precession coil (which, ideally, is as long as possible, operating at as high a magnetic field as possible), neutron spins acquire a total precession angle. This precession angle is turned round (by 180°) by a π -flipper, situated at (or at least, as close as physically possible to) the sample. Then comes the second precession field, exactly the same as the first one was; as a result, neutrons that travel at the same velocity as they did before the sample (elastic scattering, no energy exchange between the neutron and the sample) will arrive at the end of the second precession coil in the same spin state as they were before entering the first precession coil. Longitudinal polarization is recovered by a final $\pi/2$ flipper that is followed by the analyzer; the analyzer accepts neutrons of one longitudinal spin state, which neutrons then hit the detector. The count rate is proportional to the cosine of the total (cumulative) precession angle.

Acknowledgment

The author wishes to thank Dr. Erzsébet Sváb for her critical reading of the manuscript and suggestions.

References

- | | |
|--|--|
| <p>Allen MP, Tildesley DJ (1987) Computer simulation of liquids. Oxford University Press, Oxford</p> <p>Andreani C, Degiorgi E, Senesi R, Cilloco F, Colognesi D, Mayers J, Nardone M, Pace E (2001) J Chem Phys 114:387</p> | <p>Aschcroft NW, Mermin ND (1976) Solid state physics. Harcourt Brace College Publishers, Fort Worth</p> <p>Atkins PW (1994) Physical chemistry, 5th edn. Oxford University Press, Oxford</p> <p>Bacon GE (1951) Proc Roy Soc A209:397</p> |
|--|--|

- Bacon GE (1977) Neutron scattering in chemistry. Butterworths, London
- Bacon GE, Lowde RD (1948) *Acta Cryst* 1:303
- Bernal I, Watkins SF (1972) *Science* 178:1282
- Billinge SJ, Egami T (1993) *Phys Rev B* 178:1282
- Binder K, Heermann DW (1992) Monte Carlo simulation in statistical physics: an introduction, 2nd edn. Springer, Berlin
- Bish DL, Post JE (eds) (1989) Reviews in Mineralogy and Geochemistry. Mineralogical Society of America, Chantilly (VA)
- Born M, Wolfe E (1989) Principles of optics. Pergamon, Oxford
- Boutin H, Safford GJ, Brajovic V (1963) *J Chem Phys* 39:3135
- Bragg WH (1928) An introduction to crystal analysis. G. Bell, London
- Brockhouse BN (1960) *Bull Amer Phys Soc* 5:462
- Brown GM, Levy HA (1963) *Science* 141:921
- Brown GM, Levy HA (1973) *Acta Cryst* B29:790
- Brumberger H (ed) (1995) Modern aspects of small-angle scattering, vol 451, NATO ASI Series C. Kluwer Academic, Dordrecht
- Chapak G (1968) *Nucl Instr Meth* 62:262
- Coppens P (1974) *Acta Cryst* B31:1946
- Curat R (1973) *Nucl Instr Meth* 107:1
- Delapalme A, Schweizer J, Couderchon G, Perrier de la Bathie R (1971) *Nucl Instr Meth* 95:589
- Delaplane RG, Ibers JA, Ferraro JR, Rush JJ (1969) *J Chem Phys* 50:1920
- Delhez R, Mittermeijer EJ (eds) (1998) European powder diffraction: proceedings of EPDIC-5, Materials Science Forum, Transtech Publications, Stafa-Zurich Switzerland, pp 278–281
- Delhez R, Mittermeijer EJ (eds) (2000) European powder diffraction: proceedings of EPDIC-6, Materials Science Forum, Transtech Publications, Stafa-Zurich Switzerland, pp 321–324
- Delhez R, Mittermeijer EJ (eds) (2001) European powder diffraction: proceedings of EPDIC-7, Materials Science Forum, Transtech Publications, Stafa-Zurich Switzerland, pp 378–381
- Dianoux A-J, Lander G (2001) Neutron data booklet. Institut Laue-Langevin, Grenoble
- Egelstaff PA (1994) An introduction to the liquid state, 2nd edn. Clarendon, Oxford
- Eisenberg D, Kauzmann W (1969) The structure and properties of water. Clarendon, Oxford
- Ewen B, Richter D (1997) Advances in polymer science, vol 134. Springer, Berlin
- Feigin LA, Svergun DI (1987) Structure analysis by small angle X-ray and neutron scattering. Plenum, New York
- Fernández-Liencres MP, Navarro A, López-González JJ, Fernández-Gómez M, Kearley GJ (2001) *Chem Phys* 266:1
- Gray CG, Gubbins KE (1984) Theory of molecular fluids. Clarendon, Oxford
- Guinier A, Fournet G (1955) Small angle scattering of X-rays. Wiley, New York
- Hahn T (ed) (2002) International tables for crystallography volume A: space-group symmetries, 5th edn. Kluwer Academic, Dordrecht
- Hansen J-P, McDonald IR (1986) Theory of simple liquids. Academic, London
- Henderson JA, Richards RW, Penfold J, Thomas RK (1993) *Macromolecules* 26:65
- Hewat AW, Bailey I (1976) *Nucl Instr Meth* 137:463
- Howe MA, McGreevy RL, Howells WS (1989) *J Phys Cond Matt* 1:3433
- Huang YY, Liu C, Felcher GP (1993) *Phys Rev B* 47:183
- ISIS (2003) <http://www.isis.rl.ac.uk> (accessed 26 May 2010)
- Jonsson P-G, Hamilton WC (1972) *J Chem Phys* 56:4433
- Jóvári P, Mészáros G, Pusztai L, Sváb E (2001) *J Chem Phys* 114:8082
- Karle J, Karle IL (1966) *Acta Cryst* 21:849
- Knoll GF (1999) Radiation detection and measurement, 3rd edn. Wiley, New York
- Koester L, Rauch H, Seymann E (1991) Atomic Data and Nuclear Data Table 49:65
- Li J-C (1996) *J Chem Phys* 105:6733
- Line CMB, Kearley GJ (2000) *J Chem Phys* 112:9058
- Loopstra BO, Rietveld HM (1969) *Acta Cryst* B25:787
- Lovesey SW (1987) Theory of neutron scattering from condensed matter. Oxford University Press, Oxford
- Maier-Leibnitz H (1962) *Z Angew Phys* 14:738
- Marshall W, Lovesey SW (1971) Theory of thermal neutron scattering. Oxford University Press, Oxford
- McGreevy RL (ed) (1999) Quasi-elastic neutron scattering. In: Proceedings of the 4th international workshop, Physica B, 266, Elsevier, Amsterdam, pp 1–2
- McGreevy RL, Pusztai L (1988) *Mol Simul* 1:359
- Mellergård A, McGreevy RL (1999) *Acta Cryst* A55:783
- Mezei F (1972) *Z Phys* 255:146
- Mezei F (1976) *Commun Phys* 1:81
- Mezei F (ed) (1979) Neutron spin echo, vol 128, Lecture Notes in Physics. Springer, Berlin
- Monkenbusch M, Zorn R (2000) Neutron scattering. In: Brückel T, Heger G, Richter D (eds) Lectures of a laboratory course at Forschungszentrum Jülich, Chap 11. Forschungszentrum Jülich GmbH, Jülich, pp 11.1–11.18
- Munter (2003) <http://www.ncnr.nist.gov/resources/n-lengths/>
- Nelmes RJ, Kuhs WF, Howard CJ, Tibballs JE, Ryan TW (1985) *J Phys C Solid State Phys* 18:L711
- Nield VM, Keen DA (2001) Diffuse neutron scattering. Clarendon, Oxford
- Norman D, Webster JRP (eds) (1998) Proceedings of the conference on surface X-ray and neutron scattering, vol 248, Physica B. Elsevier, Amsterdam

- North DM, Enderby JE, Egelstaff PA (1968) *J Phys C Solid State Phys* 2:1075
- Oed A (2001) *Nucl Instr Meth A* 471:109
- Penfold J, Thomas RK (1990) *J Phys Cond Matt* 2:1369
- Peterson SW, Levy HA (1951) *J Chem Phys* 19:1416
- Peterson SW, Levy HA (1952) *J Chem Phys* 20:704
- Petry W (ed) (2002) *Proceedings of the international conference on neutron scattering, Munich, 2001, Applied Physics A*, vol 74, Suppl 1. Springer, Heidelberg
- Placzek G (1952) *Phys Rev* 86:377
- Porod G (1951) *Kolloid-Z* 124:83
- Preisinger A, Mereitner K, Baumgartner O, Heger G, Mikenda W, Steidl H (1982) *Inorg Chem Acta* 57:237
- Prince E, Wilson ACJ (eds) (1999) *International tables for crystallography volume C: mathematical, physical and chemical tables*, 2nd edn. Kluwer Academic, Dordrecht
- Proffen Th, Billinge SJ (1999) *J Appl Cryst* 32:572
- Pusztai L (1999) *Phys Rev B* 60:11851
- Pusztai L, McGreevy RL (1989) *J Phys Cond Matt* 1:2369
- Pusztai L, McGreevy RL (1997) *Physica B* 234–236:357
- Pusztai L, McGreevy RL (1998) *J Phys Cond Matt* 10:525
- Rietveld HM (1969) *J Appl Cryst* 2:65
- Riste T (1970) *Nucl Instr Meth* 86:21
- Rush JJ, Ferraro JR (1966) *J Chem Phys* 44:2496
- Scherm R (1972) *Annales de Physique* 7:349
- Sears VF (1992) *Neutron News* 3:26
- Sears VF (1997) *Acta Cryst A* 53:35
- Shmueli U (ed) (2001) *International tables for crystallography volume B: reciprocal space*, 2nd edn. Kluwer Academic, Dordrecht
- Shull CG (1963) *Phys Rev Lett* 10:297
- Simister EA, Lee EM, Thomas RK, Penfold J (1992) *J Phys Chem* 96:1373
- Sköld K, Rowe JM, Ostrowski G, Randolpfs PD (1972) *Phys Rev A* 6:1107
- Somogyvári Z, Sváb E, Mészáros Gy, Krezhov K, Nedkov I, Sajó I, Bourée F (2002a) *Appl Phys A* 74(Suppl):S1077
- Somogyvári Z, Mészáros Gy, Sváb E, Krezhov K, Konstantinov P, Nedkov I, Bourée F (2002b) *J Appl Phys* 91:6185
- Soper AK, Bruni F, Ricci MA (1997) *J Chem Phys* 106:247
- Squires GL (1956) *Phys Rev* 103:304
- Squires GL (1996) *Introduction to the theory of thermal neutron scattering*. Dover, Mineola
- Stirling GC, Ludman CJ, Waddington TC (1970) *J Chem Phys* 52:2730
- Sváb E, Mészáros Gy, Deák F (1996) *Mater Sci Forum* 228–231:247
- Tasset F, Resouche E (1995) *Nucl Instr Meth A* 359:537
- Teixeira J (1987) *J Appl Cryst* 21:781
- Thiessen WE, Narten AH (1982) *J Chem Phys* 77:2656
- Van Hove L (1954) *Phys Rev* 95:249
- Wagner V, Friedrich H, Wille P (1992) *Physica B* 180–181:938
- Warren BE (1969) *X-ray diffraction*. Dover, Mineola
- Waseda Y (2002) *Anomalous X-ray scattering for materials characterisation*. Springer, Berlin
- Williams JM, Schneemeyer LF (1973) *J Amer Chem Soc* 95:5780
- Woolfson MM (1997) *An introduction to X-ray crystallography*, 2nd edn. Cambridge University Press, Cambridge
- Wright AC (1994) In: Baruchel J, Hodeau JL, Lehmann MS, Regnard JR, Schlenker C (eds) *Neutron and synchrotron Radiation for condensed matter studies*, vol II, Chap VIII. Springer, Berlin, pp 167–196
- Young RA (1993) *The Rietveld method*. Oxford University Press, Oxford
- Zhou X-L, Chen S-H (1995) *Phys Rep* 257:223



30 Activation Analysis

R. Zeisler¹ · N. Vajda² · G. Kennedy³ · G. Lamaze¹ · G. L. Molnár^{†4}

¹National Institute of Standards and Technology, Gaithersburg, MD, USA

²RadAnal Ltd, Budapest, Hungary

³Nuclear Engineering Institute, Ecole Polytechnique de Montreal, Montreal, QC, Canada

⁴Institute of Isotope and Surface Chemistry, CRC HAS, Budapest, Hungary

30.1	<i>Introduction</i>	1555
30.2	<i>Principles of Activation Analysis</i>	1555
30.2.1	Activation Reactions	1555
30.2.2	Activation Equation	1559
30.2.3	Standardization	1561
30.2.4	Advantages and Disadvantages of Activation Methods	1562
30.3	<i>Types of Activation Analysis</i>	1563
30.3.1	Neutron Activation Analysis (NAA)	1564
30.3.1.1	Neutron Sources	1564
30.3.1.2	Thermal Neutron Activation Analysis (TNAA)	1564
30.3.1.3	Epithermal Neutron Activation Analysis (ENAA)	1565
30.3.1.4	Fast Neutron Activation Analysis (FNAA)	1565
30.3.1.5	Neutron-Induced Prompt Gamma Activation Analysis (PGAA)	1565
30.3.1.6	Comparison of NAA Methods	1566
30.3.1.7	In Vivo Neutron Activation Analysis	1567
30.3.2	Charged Particle Activation Analysis (CPAA)	1567
30.3.3	Photon Activation Analysis (PAA)	1568
30.4	<i>Instrumental Neutron Activation Analysis (INAA)</i>	1569
30.4.1	Sample Preparation	1569
30.4.1.1	Solid Samples	1569
30.4.1.2	Biological Tissues and Fluids	1569
30.4.1.3	Liquid Samples	1570
30.4.2	Irradiation	1570
30.4.2.1	Automated Systems	1570
30.4.2.2	“In Core” Irradiation	1571
30.4.2.3	External Systems	1571
30.4.3	Gamma-Ray Spectrometry	1572
30.4.3.1	Detector Systems	1573

[†]Deceased

30.4.3.2	Analyzer Systems	1574
30.4.3.3	Software	1575
30.4.4	Quantitation	1575
30.4.4.1	Comparator Method	1576
30.4.4.2	The k_0 Method and Other Parametric Methods	1577
30.5	<i>Radiochemical Activation Analysis (RAA)</i>	1583
30.5.1	Major Types of RAA	1584
30.5.2	Main Features of RAA	1584
30.5.3	Application of RNAA in Materials Science	1586
30.5.3.1	Removal of the Main Activity and Separation of Element Groups	1586
30.5.3.2	Separation of a Single Element	1588
30.5.4	RNAA of Biological, Environmental, and Geological Samples	1589
30.5.4.1	Removal of the Main Interfering Activities	1589
30.5.4.2	Separation of a Single Element and Groups of Chemically Similar Elements	1590
30.5.4.3	Separation of Several Elements and Various Groups of Elements	1595
30.5.5	Application of RNAA for the Determination of Radionuclides	1597
30.5.5.1	Determination of ^{129}I by PC-RNAA	1597
30.5.5.2	Determination of ^{237}Np by PC-RNAA	1598
30.5.5.3	Determination of ^{99}Tc by PC-RNAA	1598
30.5.5.4	Determination of ^{135}Cs by PC-RNAA	1599
30.5.6	Application of NAA for Speciation Studies	1599
30.6	<i>Quality Assurance and Control in NAA</i>	1600
30.6.1	Sources of Uncertainty	1600
30.6.1.1	Nuclear Reaction Rate and Sample Integrity	1600
30.6.1.2	Geometry Uncertainties in Irradiation and Counting	1601
30.6.1.3	Timing Uncertainties	1602
30.6.1.4	Uncertainties in Signal Detection and Processing	1602
30.6.1.5	Gamma-Ray Spectrum Evaluation and Software	1603
30.6.1.6	Interferences	1604
30.6.2	Uncertainty Budget	1605
30.6.3	Validation	1607
30.7	<i>Location Sensitive Analysis</i>	1608
30.7.1	Fundamentals of the Technique	1608
30.7.2	Elemental Detection Limits	1609
30.7.3	Concentration Determination	1609
30.7.4	Depth Determination	1610
30.7.5	Sources of Uncertainty	1611
30.8	<i>Editors' Notes</i>	1612

Abstract: This chapter presents the basic principles of activation analysis and details its different types. Emphasis is given to instrumental neutron activation analysis and radiochemical separations for the determination of trace and ultra-trace elements. Location sensitive analysis is also included.

30.1 Introduction

In their early experiments with rare earth elements, Georg Hevesy and his student Hilde Levi observed that some elements became highly radioactive when irradiated with neutrons. Hevesy recognized that this method could be used for the qualitative detection of the rare earth elements, and he and Levi were the first to report on the new method of activation analysis (Hevesy and Levi 1936). At that time, element discrimination was based on the half-life rather than the energy of the emitted radiation.

However, the neutron activation analysis (NAA) method was not used much after its discovery. Only when the developing reactor technology of the 1950s made more neutron sources available did a rapid growth in NAA occur. It should be noted that the initial development was combined with skillful advancements in radiochemistry since the radionuclides of interest had to be separated from interfering activities. This growth was further enhanced when proportional counters were replaced with energy-resolving gamma-ray detectors, first scintillation detectors, and later high-resolution semiconductor diode-type detectors coupled to multichannel pulse height analyzers.

By the early 1960s, NAA was an accepted method for highly sensitive single and multielement determinations in many applications and had expanded to the use of other activation methods for many investigations. The developments in activation analysis; their impact on analytical chemistry and trace element research; and the applications of activation analysis in environmental sciences, biology, medicine, archeology, criminology, geo- and cosmochemistry, and industry are well documented in the series of conferences on Modern Trends in Activation Analysis (MTAA), the first held in 1961 at the Texas A&M University in College Station (Brown 1961). However, in recent years, its unique position has been challenged by increasingly sensitive and versatile elemental analysis techniques, such as atomic absorption spectrometry, inductively coupled plasma optical emission spectrometry (ICP-OES), and mass spectrometry (ICP-MS), which are widely used today in applications that had previously been a domain for NAA.

Nevertheless, a variety of activation analysis techniques have emerged that complement classical NAA and increase its capabilities. Consequently, activation analysis (AA) techniques still occupy a solid niche in analytical chemistry because of the nuclear principle of analysis with its specific advantageous characteristics as presented in this chapter.

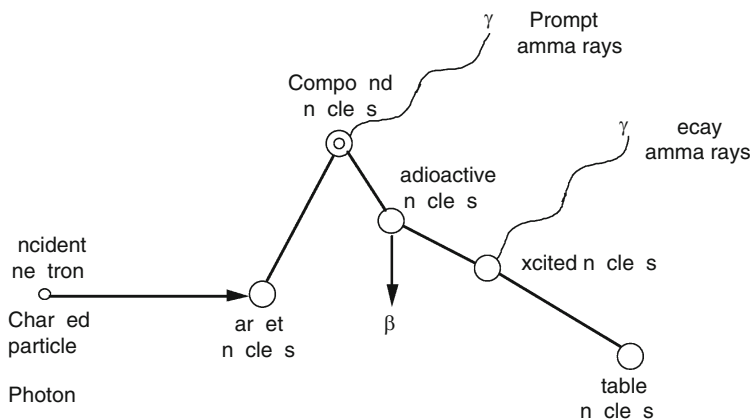
30.2 Principles of Activation Analysis

30.2.1 Activation Reactions

The basic idea of activation analysis is that irradiation by appropriately chosen penetrating radiation induces nuclear reactions in the nuclei of the analyte, and the reaction products (which usually are radioactive) emit radiations characteristic of the identity and quantity of the

■ Fig. 30.1

The activation analysis principle



elements to be determined. This process is depicted schematically in Fig. 30.1, which shows the possibilities with respect to the type of inducing radiation, the mode of decay, and the type of induced radiation.

While neutrons, charged particles, and gamma photons can be equally used for irradiation, the most frequent choice is the irradiation by neutrons. Since the neutron lacks an electric charge, it is more penetrating and makes the analysis of bulk samples possible. Additionally, the high cross-sections of neutron-induced reactions offer extremely high analytical sensitivities for many elements.

The product nuclide can be either stable or radioactive. In the former case, only gamma de-excitation occurs, resulting in an essentially prompt emission of discrete gamma radiation of usually high energy, up to 8–10 MeV. In the latter case, the radioactive reaction product undergoes one or more decays, and is eventually transformed into a stable nuclide. The radioactive decay is characterized by its half-life, which can be anywhere from a fraction of a second to many years. Although the continuous spectrum of beta electrons or positrons can also be utilized for activation analysis, it is most practical to observe the discrete gamma radiation of the reaction product. This is due to the higher selectivity and penetration of the gamma decay radiation.

The number of radioactive nuclides formed per unit time in a nuclear reaction is determined by the reaction rate:

$$R = \int_{E_{\min}}^{E_{\max}} N_0 \sigma(E) \phi(E) dE \quad (30.1)$$

where $\sigma(E)$ is the *differential cross section* (cm^2), $\phi(E) dE$ is the flux or *fluence rate* of particles with kinetic energy between E and $E + dE$ impinging on the sample (the differential flux $\phi(E)$ is measured in units of $\text{cm}^{-2} \text{s}^{-1} \text{eV}^{-1}$), and N_0 is the number of target atoms of the nuclide that take part in the given reaction. The latter is connected with the mass m (g) of the given element in the sample:

$$N_0 = \frac{m}{M} N_A \quad (30.2)$$

where M is the molar mass of the element (g mol^{-1}), θ is the isotopic abundance and N_A is Avogadro's constant:

$$N_A = 6.02214179(30) \times 10^{23} \text{mol}^{-1}. \quad (30.3)$$

For *thermal neutrons*, the absorption cross section is usually inversely proportional to the neutron speed ("1/v" law), and [Eq. \(30.1\)](#) is reduced to the simple product:

$$R_{\text{th}} = N_0 \bar{\sigma}_{\text{th}} \Phi_{\text{th}} = \frac{2}{\sqrt{\pi}} N_0 \sigma_0 \Phi_{\text{th}} \quad (30.4)$$

where σ_0 is the cross section for the most probable speed of $2,200 \text{ m s}^{-1}$ (neutron energy of 0.0253 eV) that corresponds to the maximum of the Maxwellian speed distribution at room temperature ($T = 293.15 \text{ K}$), and Φ_{th} is the thermal neutron flux. The average neutron energy at room temperature is 0.038 eV . Sometimes, Maxwellian averages for a certain equilibrium temperature (usually 300 K) are given, which are obtained by integration of energy-differential cross sections between the limits of 10^{-5} and 10 eV .

At energies higher than about 1 eV , the reaction cross sections exhibit huge variations with the incident neutron energy and are called resonances.¹ Up to about 0.1 MeV , however, the differential flux, $\Phi(E)$, of partially thermalized neutrons is approximately proportional to $1/E$. Hence, an analogous expression can be derived for epithermal neutron activation:

$$R_{\text{epi}} = N_0 I_0 \Phi_{\text{epi}} \quad (30.5)$$

where I_0 is the integral over all resonances:

$$I_0 = \int_{E_{\text{Cd}}}^{\infty} \frac{\sigma(E)}{E} dE \quad (30.6)$$

and Φ_{epi} is the epithermal flux per unit $\ln(E)$. The lower limit of integration is the effective cut-off energy for a Cd filter, usually about 0.5 eV , which is used to absorb the thermal part of the neutron spectrum, while the practical upper limit is 0.1 MeV .

The *thermal neutron cross section*, σ_0 , and the *resonance integral*, I_0 , are conveniently measured in barn (b) units:

$$1 \text{ b} = 10^{-24} \text{cm}^2. \quad (30.7)$$

This unit for the atomic cross section is very convenient because the molar cross section becomes

$$\sigma N_A \approx 0.602(\sigma/\text{b}) \frac{\text{cm}^2}{\text{mol}}. \quad (30.8)$$

The ratio of the thermal cross section to the resonance integral

$$Q_0 = \frac{I_0}{\sigma_0} \quad (30.9)$$

is used to correct for epithermal neutron activation. For certain nuclides, its value is much larger than unity.

For thermal and epithermal neutrons, the most important activation reactions are neutron capture (n, γ) and fission (n, f); for fast neutrons, other reactions, such as (n, n'), (n, p), (n, α), ($n, 2n$), and (n, pn) reactions, dominate. These fast reactions can occur only if the neutron energy exceeds the threshold E_T . The individual rate for a given type of reaction depends on

$\sigma(E)$, which is also called the excitation function in this range. For a non-monochromatic beam, the reaction rate is obtained by numerical integration of [Eq. \(30.1\)](#).

For a *fission neutron spectrum*, it is possible to define an average cross section:

$$\bar{\sigma}_f = \frac{\int_{E_T}^{\infty} \sigma(E) \phi(E) dE}{\int_{E_T}^{\infty} \phi(E) dE} \quad (30.10)$$

which can be used to calculate the reaction rate of fission neutrons the same way as for thermal neutrons:

$$R_f = N_0 \bar{\sigma}_f \Phi_f. \quad (30.11)$$

Tabulated values of thermal cross sections, resonance integrals, ^{235}U fission-averaged cross sections, and 14 MeV neutron cross sections are available in the literature (Mughabghab et al. 1981; Mughabghab 1984; IAEA 1987; OECD 1994). Recommended data for the most important nuclides can be found in the Appendix of this volume.

The reaction rate for charged particle-induced reactions can be calculated in a similar way, i.e., according to [Eq. \(30.1\)](#), but the flux is usually substituted by the beam intensity I .² The charged particles penetrating the sample continuously lose energy due to their interaction with the atomic electrons. Since the cross section is energy dependent, the reaction rate will vary accordingly. This energy loss per unit path length along direction x is called the *stopping power*³

$$S = -\frac{dE}{dx}. \quad (30.12)$$

Hence, an average cross section can be introduced to take into account the effect of energy loss:

$$\bar{\sigma}_f = \frac{\int_{E_0}^0 \sigma(E) \frac{dx}{dE} dE}{\int_{E_0}^0 \frac{dx}{dE} dE} = \frac{\int_{E_0}^{E_0} \sigma(E) \frac{dE}{S}}{r}. \quad (30.13)$$

Here E_0 is the initial particle energy and

$$r = \int_0^{E_0} \frac{dE}{S} \quad (30.14)$$

is the range of penetration, defined as the integral of the inverse stopping power, [Eq. \(30.12\)](#).⁴ The peculiarities of charged-particle reactions are discussed in more detail in [Chap. 32](#) of this Volume.

In all cases, the reaction rate is proportional to the amount of material to be determined, some value of the effective reaction cross section, and the fluence rate. Taking into account [Eq. \(30.2\)](#), the following expression is obtained for the reaction rate R (s^{-1}):

$$R = N_0 \sigma \Phi = m \left(\frac{\theta}{M} N_A \right) \sigma \Phi. \quad (30.15)$$

This expression is valid, however, only for thin irradiated targets where absorption is negligible. Since all nuclides in the sample contribute to the absorption, this effect can be accounted for by introducing a macroscopic absorption cross section (cm^{-1}):

$$\Sigma_a = \sum_i n_i \sigma_{a,i} \quad (30.16)$$

where n_i is the number density (cm^{-3}) of the i th component, and $\sigma_{a,i}$ is the corresponding microscopic (i.e., atomic) absorption cross section (cm^2), which accounts for all reactions leading to absorption or scattering out of the beam.⁵ For a collimated beam, the attenuation follows the exponential law, hence:

$$R = R_0(1 - e^{-\Sigma_a l}) \quad (30.17)$$

where l is the linear target thickness (cm), and R_0 is the reaction rate for an ideally thin target.

It is customary to introduce a *self-shielding factor*, G , which is the ratio of thick target-to-thin target rates. For a thick foil or slab in a collimated beam, this self-shielding factor is given by:

$$G_{\text{coll}} = \frac{1 - e^{-\Sigma_a x}}{\Sigma_a x}. \quad (30.18)$$

For a foil in a diffused isotropic radiation field, the self-shielding factor is given by:

$$G_{\text{isotr}} = \frac{1 - e^{-\Sigma_a x}(1 - \Sigma_a x) + (\Sigma_a x)^2 \text{Ei}(-\Sigma_a x)}{2\Sigma_a x} \quad (30.19)$$

$$\text{Ei}(-\Sigma_a x) = - \int_{\Sigma_a x}^{\infty} \frac{e^{-z}}{z} dz$$

where Ei is the exponential integral. For more complex cases, convenient formulae can be found, e.g., in De Corte (1987a).

30.2.2 Activation Equation

The activation process and the resulting decays of excited nuclear states are controlled by the laws of nuclear physics and can be fully described by mathematical equations. In the activation reaction, a radionuclide is formed and subsequently decays, as depicted in [Fig. 30.1](#).

The rate of change of the number of radioactive atoms N is thus determined by the differential equation:

$$\frac{dN}{dt} = R - \lambda N \quad (30.20)$$

which accounts for simultaneous production and decay.

Integration gives:

$$N(t) = R(1 - e^{-\lambda t})/\lambda \quad (30.21)$$

where R is the reaction rate from [Eq. \(30.15\)](#), and λ is the decay constant (s^{-1}), giving the probability of decay per unit time. The directly observable quantity is the activity, which is the number of disintegrations per unit time:

$$\begin{aligned} A(t) &= \lambda N(t) = R(1 - e^{-\lambda t}) \\ &= m \left(\frac{\theta}{M} N_A \right) \sigma \Phi (1 - e^{-\lambda t}) \\ &= A_S (1 - e^{-\lambda t}). \end{aligned} \quad (30.22)$$

where A_S denotes the saturation activity, which is given by:

$$A_S = R = m \left(\frac{\sigma \theta}{M} N_A \right) \Phi \quad (30.23)$$

and the expression in brackets is the so-called saturation term. Saturation is reached only when the irradiation time, t_A , is long compared to the decay half-life:

$$T_{1/2} = \frac{\ln 2}{\lambda}. \quad (30.24)$$

For prompt gamma rays, the nuclear levels involved have extremely short half-lives, typically 10^{-15} – 10^{-9} s. Hence this term vanishes and the activity $A(t)$ is always at its saturation value, which is simply equal to the constant reaction rate R according to [Eqs. \(30.22\)](#) and [Eq. \(30.23\)](#).

The induced activity must be measured in order to determine the elemental composition of the sample. This is usually done after the irradiation. The sample will be irradiated for a time, t_A ; the nuclide in the sample will decay for some time, t_D , and will be counted for some time, t_C .

The number of counts accumulated by the detector will be:

$$\begin{aligned} N_c(t_C) &= \varepsilon P A(t_A) e^{-\lambda t_D} \int_0^{t_C} e^{-\lambda t} dt \\ &= \varepsilon P A_S (1 - e^{-\lambda t_A}) e^{-\lambda t_D} (1 - e^{-\lambda t_C}) / \lambda \\ &= A_0 e^{-\lambda t_D} (1 - e^{-\lambda t_C}) / \lambda \\ &= m \left(\frac{P \sigma \theta}{M} N_A \right) \varepsilon \Phi S D C t_C \end{aligned} \quad (30.25)$$

where A_0 is the observed activity, i.e., count rate right after activation referred to later as decay-corrected counting rate; P is the emission probability per decay of the observed radiation (usually gamma or beta); and ε is the corresponding detection efficiency. In [Eq. \(30.25\)](#), terms for the saturation (S), decay (D), and counting (C) correction terms were introduced by using [Eq. \(30.15\)](#):

$$\begin{aligned} S &= (1 - e^{-\lambda t_A}) \\ D &= e^{-\lambda t_D} \\ C &= (1 - e^{-\lambda t_C}) / (\lambda t_C). \end{aligned} \quad (30.26)$$

As shown in [Eq. \(30.25\)](#), the number of counts is directly proportional to the mass of the analyte. The quantities in brackets are characteristic of the observed isotope of the analyte element, and ε and Φ are the features of the detector and the irradiation facility, respectively. The correction factors S , D , C have to be optimized to obtain the highest possible statistics at the lowest possible integral value of background counts.

It is instructive to examine the limits of long and short half-lives with respect to the measurement time for the case $t_D = 0$ (i.e., $D = 1$). Substituting λ with $T_{1/2}$ in [Eq. \(30.25\)](#), one obtains:

$$\begin{aligned}\lim_{T_{1/2} \rightarrow \infty} N_c(t_C) &= \varepsilon PR \frac{t_A t_C}{T_{1/2}} \ln 2 \\ \lim_{T_{1/2} \rightarrow 0} N_c(t_C) &= \varepsilon PR \frac{T_{1/2}}{\ln 2}.\end{aligned}\quad (30.27)$$

Hence, for long half-lives the counting statistics can be improved by increasing the activation and counting times; for short half-lives, the best statistical accuracy is limited by the half-life itself even if the counting immediately follows the activation ($D = 1$). In a real situation, of course, additional limitations arise due to the background count rate.

The induced activity can also be instantaneously measured during the activation. In this case, the irradiation and counting times are equal and the number of counts is governed by a simpler equation:

$$\begin{aligned}N_c(t_C) &= \varepsilon P \int_0^{t_C} A(t) dt \\ &= \varepsilon P A_0 \left(1 - \frac{1 - e^{-\lambda t_C}}{\lambda t_C} \right) t_C \\ &= m \left(\frac{P \sigma \theta}{M} N_A \right) \varepsilon \Phi (1 - C) t_C.\end{aligned}\quad (30.28)$$

For short half-lives, C approaches zero and the counting increases linearly with the measurement time. This is automatically the case when prompt radiation is detected instead of decay radiation. For this reason, prompt gamma activation analysis is inherently more sensitive than delayed gamma activation analysis.

30.2.3 Standardization

[Equations \(30.25\)](#) and [\(30.28\)](#) provide the basis for quantitative activation analysis, hence the unknown mass m_x of analyte x can be determined if all other parameters are accurately known. This is seldom the case, so a comparative analysis with a standard sample containing a known mass, m_s , of the same element is usually performed. If the standard matches the size and composition of the unknown sample, the ratio of counts $N_{c,x}/N_{c,s}$ can be used for the calculation of the unknown mass. Applying [Eq. \(30.25\)](#) one obtains:

$$m_{x(\text{unk})} = m_{x(\text{std})} \frac{(N_{x(\text{unk})}/t_{C(\text{unk})})}{(N_{x(\text{std})}/t_{C(\text{std})})} \frac{(P \sigma \theta / M)_{x(\text{std})}}{(P \sigma \theta / M)_{x(\text{unk})}} \frac{\varepsilon_{\text{std}} \Phi_{\text{std}}}{\varepsilon_{\text{unk}} \Phi_{\text{unk}}} \frac{S_{\text{std}} D_{\text{std}} C_{\text{std}}}{S_{\text{unk}} D_{\text{unk}} C_{\text{unk}}}. \quad (30.29)$$

If the conditions for both irradiation and counting are identical, all parameters cancel, and the ratio of masses becomes equal to the ratio of counts:

$$m_{x(\text{unk})} = m_{x(\text{std})} \frac{N_{c(\text{unk})}}{N_{c(\text{std})}}, \quad (30.30)$$

which is the basis of relative standardization.

It may be difficult and/or time consuming to prepare accurate standards for all possible elements; hence, a monostandard method has been introduced in neutron activation analysis. The so-called k_0 -standardization method is based on the recognition that the ratio of nuclear constants for analyte x and a chosen standard s in [Eq. \(30.29\)](#) can be combined into a single constant (Simonits et al. 1975):

$$k_{0,s}(x) = \frac{(P\sigma\theta/M)_x}{(P\sigma\theta/M)_s}. \quad (30.31)$$

This constant can either be calculated or measured accurately with respect to an adopted standard, which practically serves as the fluence monitor. If the monitor, s , which is usually a gold foil, is co-irradiated with the sample, the mass of the analyte is determined as:

$$m_x = m_{\text{Au}} \frac{(N_{\text{c(unk)}}/t_{\text{C(unk)}})}{(N_{\text{c(Au)}}/t_{\text{C(Au)}})} \frac{1}{k_{0,s}(x)} \frac{\varepsilon_{\text{Au}}\Phi_{\text{Au}}}{\varepsilon_{\text{unk}}\Phi_{\text{unk}}} \frac{S_{\text{Au}}D_{\text{Au}}C_{\text{Au}}}{S_{\text{unk}}D_{\text{unk}}C_{\text{unk}}}. \quad (30.32)$$

The above formulas only illustrate the underlying principles. The practical realization is more complicated and is discussed in the context of the various methods of activation analysis in the following sections.

30.2.4 Advantages and Disadvantages of Activation Methods

All nuclear activation methods have several distinct advantages and disadvantages inherent in the underlying physical principle of the method with some unique strengths and weaknesses attributable to the individual activation and measurement technique. They are methods for the determination of the amount of an element, or more correctly, the amount of an isotope representing the element of interest.

The generation of the analytical signal through a nuclear reaction makes the determinations virtually independent of the chemical form of the elements and their chemical environment. The determinations are, to a certain degree, independent of the sample matrix, and in most cases, can be made free of any blank. The blank-free attribute is aided by the fact that the methods require much less sample manipulation than other techniques and they are not as susceptible to reagent and laboratory contamination. The reduction or elimination of blank contributions includes radiochemical processing performed after irradiation (see [Sect. 30.5](#)), where inadvertent chemical contamination would add only nonactivated analyte that would not contribute to the measured signal.

The range of elements accessible to analysis by nuclear activation methods covers virtually all elements with most of their natural and some artificial isotopes. The nuclear methods, NAA, CPAA, and PAA (see [Sect. 30.3](#)), through their variety of techniques, provide very high sensitivities for a large number of elements. This resulted in the early application of nuclear methods in trace and ultra-trace element analysis. In many instances, nuclear methods have been and continue to be at the forefront of analytical developments concerning the determination of elements at trace and ultra-trace levels. This includes developments in biological, medical, and environmental research, as well as in industrial development, such as in high-tech materials. However, these sensitivities are not equally distributed for the elements in the periodic table or for their isotopes used in the assays. Instrumental neutron activation analysis (INAA) using thermal neutrons can determine two thirds of the elements in the periodic table with sensitivities at the mg/kg (ppm) levels or below, including a number of elements

approaching ng/kg levels. However, INAA is not suitable for many light elements; it is also not suitable for tin and lead, which represent two important examples of heavy elements (although the latter can be determined by CPAA).


Another outstanding feature of activation analysis is the selectivity of the methods. Not only can the decay characteristics of the activation product be used for unique identification and quantitation, but selection and exploitation of a variety of physical parameters in activation, decay, and measurement can optimize the sensitivity and selectivity for the desired determination. Moreover, optimization of the physical parameters is well predicted by virtue of the known activation and measurement relationships.

A prominent feature of nuclear analytical methods is the capability of simultaneous multielement analysis. Activation of a sample will induce activity in many elements contained in the sample. Optimized irradiation and counting cycles involving a combination of various NAA procedures applied to a sample of coal have produced results for more than 50 elements (Germani et al. 1980). The analysis of 20–25 elements in biological and environmental materials can be regarded as routine for INAA (Becker et al. 1994).

In some cases, activation analysis may be regarded as a nondestructive method, i.e., the sample is not significantly altered, neither visually nor chemically. This attribute is obviously exploited in the aforementioned sequential multielement determinations. It is a valuable characteristic for situations where the sample needs to be preserved, such as forensic objects or irreplaceable historical samples, such as ancient coins or paintings. For general analytical practice, this valuable feature can allow reactivation for the determination of additional elements or for full reanalysis, as well as the use, with appropriate precautions, of another analytical method.

Some often cited disadvantages of activation analysis include the requirements of dedicated facilities, high equipment cost, and long turn-around time. These cannot be discounted as myth or as misguided competitive arguments. Many activation analysis procedures are capable of rapid analysis with analysis times ranging from seconds for chlorine (Grass et al. 1994) or oxygen (James and Zeisler 2001), to several minutes for oligo-element determinations in air particulate filters offering 100 sample capacities in an 8 h shift (Heller-Zeisler et al. 1999). The measurement of a full complement of elements with longer-lived activation products requires longer analysis times due to the required irradiation, decay, and measurement times (Greenberg et al. 1984). These long analysis times have kept activation analysis out of most industrial processes, with a few exceptions that exploit PGAA and short-lived nuclides, such as coal conveyor belt monitoring and borehole logging (Clayton and Wormald 1983; Borsaru et al. 2001). The cost involved in operating a neutron source, such as a reactor, is generally not solely charged to the activation analysis users and is usually for multielement determinations in an array of samples at a nominal per unit amount. Other activation sources may be operated at costs comparable to nonnuclear instrumentation. The capital and operational costs for nuclear spectroscopy equipment are certainly at or below the cost of many of today's analytical spectrometry instruments. However, the requirements for a dedicated laboratory facility that meets regulations for radiological safety may be a formidable obstacle to the use of activation analysis.

30.3 Types of Activation Analysis

It is probably easiest to classify activation analysis according to the type of nuclear reaction used to generate the analytical signal. As shown in  Fig. 30.1, the commonly used activation

particles are neutrons of various energy, charged particles, and photons. The following sections will summarize the many forms of activation analysis and discuss some of their advantages and disadvantages. A brief description of the sources of activation particles is included in the respective sections.

30.3.1 Neutron Activation Analysis (NAA)

NAA is the most common form of activation analysis. The activation reaction is induced by the interaction of a neutron with the nucleus of an analyte element. Depending on the energy of the incident neutron and the reaction cross sections of the target elements, different types of reactions can take place, leading to activation products as described in ▶ Sect. 30.2. This reaction is commonly followed by the measurement of a nuclide-characteristic de-excitation step (radioactive decay). It is this characteristic gamma-ray decay that is commonly used in the detection and determination of the element of interest.

30.3.1.1 Neutron Sources

The most practical neutron source for NAA is a nuclear reactor, which produces neutrons via the nuclear fission process (see ▶ Chap. 57 in Vol. 6). Many research reactors are equipped with irradiation facilities that provide a stable, well-tailored, isotropic neutron field with sufficiently high flux. Low-energy (thermal) neutrons comprise the most important part of the reactor spectrum; hence the degree of moderation is an important parameter. The irradiation channels are usually created in moderator layers, such as a thermal column or a Be reflector blanket.

When a reactor is not available, or a portable neutron source is required, isotopic sources (Shani 1990), small mobile reactors (Chung 1990), or neutron generators (Csikai 1987) are possible alternatives. The attainable neutron fluence rates of the various neutron sources are compared in ▶ Table 30.1.

30.3.1.2 Thermal Neutron Activation Analysis (TNAA)

Thermal neutrons, also called slow neutrons because their most probable speed is low ($v \approx 2,200 \text{ m/s}$) with a mean energy of 0.038 eV. Due to the $1/v$ -dependence of the capture cross

■ Table 30.1
Important types of neutron sources used in NAA

Source	Usable neutron flux or production rate	
	Thermal	Epithermal or fast
Large research reactor (>10 MW)	$(10^{14}\text{--}10^{15}) \text{ cm}^{-2} \text{ s}^{-1}$	$(10^{11}\text{--}10^{12}) \text{ cm}^{-2} \text{ s}^{-1}$
Small research reactor (>100 kW)	$(10^{12}\text{--}10^{13}) \text{ cm}^{-2} \text{ s}^{-1}$	$(10^{11}\text{--}10^{12}) \text{ cm}^{-2} \text{ s}^{-1}$
Neutron generator		$(10^9\text{--}10^{12}) \text{ s}^{-1}$
Alpha sources		10^6 s^{-1}
^{252}Cf fission source		$2.34 \times 10^9 \text{ s}^{-1} \text{ mg}^{-1}$

section, thermal neutrons have the greatest probability of interacting with most target elements. For this reason, thermal NAA is the most simple and universal activation analysis technique and remains the workhorse in the activation analysis laboratory.

The nondestructive instrumental (INAA) and destructive radiochemical (radiochemical neutron activation analysis – RNAA) procedures of this method are discussed later in this chapter. Specific problems, such as chain decays, cyclic activation, and interferences, as well as typical applications have recently been discussed by Alfassi (2001) and the references therein.

30.3.1.3 Epithermal Neutron Activation Analysis (ENAA)

Neutrons with slightly higher energies (1 eV to 100 keV) than thermal neutrons are called epithermal neutrons. They serve as activation particles in this special type of NAA, which is based on the selective activation of certain nuclides the cross sections of which exhibit strong individual resonances in the lower part of this energy range. Special facilities to enhance ENAA reactions over thermal NAA are employed in the irradiation location. To suppress the thermal neutron activation of the matrix elements, the sample is covered with a thermal neutron absorber, such as cadmium or boron. As a result, high sensitivities can be attained despite the relatively low activity induced by the epithermal neutrons. Specific problems and typical applications of ENAA have been discussed by Alfassi (2001).

30.3.1.4 Fast Neutron Activation Analysis (FNAA)

Neutrons with energies greater than 0.1 MeV are called fast neutrons. The fission spectrum of a light-water-moderated reactor provides as many fast neutrons as thermal neutrons. Therefore, fast neutron activation of certain elements via (n,p) reactions is a very selective technique, complementary to thermal and epithermal NAA. A typical example is Fe, for which the $^{56}\text{Fe}(\text{n,p})^{56}\text{Mn}$ activation reaction produces a better gamma-ray emitter than the thermal capture reaction.

A common and particularly useful form of FNAA is the instrumental analysis with 14 MeV neutrons that are produced by small accelerators known as neutron generators (14 MeV INAA). This technique is discussed in detail in [Chap. 32](#) of this Volume.

30.3.1.5 Neutron-Induced Prompt Gamma Activation Analysis (PGAA)

PGAA is an instrumental procedure that makes use of the prompt gamma-ray emissions that occur immediately after neutron capture during the de-excitation of the newly formed compound nucleus. The capture can produce nuclear states with energies up to about 11 MeV above the ground state, which usually decay through a cascade of gamma rays. The complexity and broad energy range of these spectra distinguishes PGAA from most other NAA procedures (Molnár and Lindstrom 1998).

The main advantage of PGAA is the ability to obtain gamma-ray spectra from the neutron capture of nuclides that do not produce radioactive isotopes through the (n, γ) reaction. PGAA favorably complements NAA through efficient reactions with the light elements that generally do not produce radionuclides, and also a number of higher *Z* elements with high cross sections

the normal decay products of which may be difficult to measure in the presence of high activities induced in certain matrices. The light elements most often investigated are H, B, C, N, Si, P, S, and Cl, and the heavier elements are Cd, Sm, and Gd. Recent advances and a detailed description of the technique of PGAA can be found in the works of Yonezawa (2001) and Molnár (2003). Specific features of the technique are discussed in [▶ Chap. 31](#) of this Volume.

30.3.1.6 Comparison of NAA Methods

NAA procedures are applicable to most element analysis problems, but are most broadly used to determine trace elements in biological, environmental, geological, and industrial materials. Since many factors, such as chemical composition of the sample and irradiation, decay, and measurement procedures determine the achievable sensitivity for a specific element, [Fig. 30.2](#) shows a “typical” sensitivity for the elements determined by INAA and PGAA in biological and environmental matrices. These numbers have been obtained by a survey of the authors’ analytical experience. Depending on the elemental composition and optimization opportunities as well as restrictions by dominant matrix activities, the quoted sensitivities can be better or worse by orders of magnitude.

As a rule of thumb, it can be stated that thermal NAA is the most sensitive, ENAA the most selective, while PGAA is the most universal of the neutron activation techniques discussed in the present section. There are ways to further enhance the analytical sensitivity and selectivity of NAA via radiochemical separations as discussed in [▶ Sect. 30.5](#).

■ Fig. 30.2

Typical instrumental sensitivities in mg/kg (E + 4 denotes 10^4 , etc.) for thermal NAA of elements in light element matrix (e.g., organic, silicate) biological and environmental samples

[illegible]

30.3.1.7 In Vivo Neutron Activation Analysis

The successful establishment of nondestructive NAA as an analytical technique for the study of the elemental composition of biological materials promoted the evaluation of its feasibility for determining some elements in living subjects by *in vivo* NAA (Anderson et al. 1964). From this first demonstration, the technique rapidly evolved (Ellis 1990). Currently, it is possible to measure total-body H, N, O, Na, P, Cl, K, and Ca and to determine most of the same elements in parts of the body, such as a limb or an organ. In special cases, additional important elements such as I (in thyroid), Cd (in kidney), as well as Mn, Fe, and Cu have been reported. The results of the measurements are used in clinical studies of mineral metabolism, nutrition, body physiology, and alterations in composition from clinical or environmental causes and diseases such as osteoporosis.

The principle of *in vivo* NAA is simple and comparable to the other forms of NAA discussed here. The subject or part of the body is exposed to neutrons from a suitable source and prompt gamma rays, as summarized by Morgan (2000), or delayed gamma rays, as for example described by Ma et al. (2000), are measured. The desired results are calculated by comparison with similar measurements on phantoms with known composition. Neutron sources are most often the radionuclidic type (see Sect. 30.3.1.1), but accelerator-based (cyclotron, 14 MeV generator) sources and thermal neutrons from reactors are also used. The induced activities are measured with whole-body counters or other high-efficiency gamma-ray detection systems. Of course, the applicability of the technique is determined not only by the physical NAA parameters, but also by required radiation exposure limits of the subjects. In general, the dose delivered to the subjects, i.e., in the 1 mSv (100 mrem) range, can be as small as that encountered in an X-ray examination.

The majority of clinical applications of *in vivo* NAA have related to the determination of total-body and partial-body Ca to obtain invaluable clinical data on losses of calcium resulting from diseases such as osteoporosis, osteomalacia, and chronic renal diseases, as well as on the potential effect of drugs or therapy programs attempting to stem these losses (Krishnan 2000). Improvements in the technique, which mainly result in lower doses, allow applications to total-body Ca studies in population groups (Ellis et al. 2001). Other elements of clinical interest, such as Na, Cl, and I have been investigated in conjunction with various human diseases and disorders, while the clinical value of the measurement of major elements such as H, N, O, and P remains uncertain. Ellis (2000) recently reviewed the role of *in vivo* NAA among the *in vivo* methods for the measurement of human body composition.

30.3.2 Charged Particle Activation Analysis (CPAA)

In CPAA, particle accelerators generate activation particles such as protons, deuterons, tritons, ^3He (helions), α , and heavier charged particles. The type of nuclear reaction induced in the sample nuclei depends on the identity and energy of the incoming charged particle. Protons are selected in many instances because they can be easily accelerated and have low Coulomb barriers. The (p,n) and (p, γ) reactions are usually induced by protons up to about 10 MeV in energy. Higher energy protons may also induce (p, α), (p,d), or (p,2n) reactions. Larger incident particles require higher energies to overcome the Coulomb barrier. They then deposit higher energies in the target nucleus during reaction, which leads to a greater variety of pathways for the de-excitation of the activated nucleus. Therefore, a great variety of reactions and measurement options are available to the analyst in CPAA.

CPAA can be regarded as a good complement to NAA since the elements that are easily analyzed are quite different from those ordinarily determined by NAA. The low Coulomb barriers and low neutron capture cross sections of light elements make CPAA the choice for the nuclear analysis of B, C, N, O, etc. Because charged particles may not penetrate the entire sample as neutrons do, CPAA is often used for determinations in thin samples or as a surface technique. The interaction of the charged particle with the sample requires a modification of the activation equation, introduced in [Sect. 30.2](#). The particles passing through a sample lose energy; hence, the cross section for the nuclear reaction changes with depth. The expression for the produced activity, [Eq. \(30.22\)](#), has to be modified to account for this effect:

$$A = nI \int_0^r \sigma(x) dx. \quad (30.33)$$

Here I is the beam intensity (replacing the neutron flux Φ), n is the number density of target atoms of the given nuclide, and r is the penetration range determined by the stopping power of the medium according to [Eq. \(30.14\)](#).

As with NAA, the fundamental equation is not directly used in practice, but a relative standardization (comparator) method is used. A working equation for the comparator method is:

$$m_{x(\text{unk})} = m_{x(\text{std})} \frac{A_{0(\text{unk})} I_{\text{std}} r_{\text{std}}}{A_{0(\text{std})} I_{\text{unk}} r_{\text{unk}}}. \quad (30.34)$$

Here the saturation, decay, and counting factors are omitted; they should be applied the same way as in the case of NAA in [Eq. \(30.29\)](#).

Like in NAA, it is also possible to measure the prompt gamma rays emitted following the charged particles' reaction with the target nucleus. This technique is referred to as particle-induced gamma-ray emission (PIGE), and is discussed in [Chap. 33](#) of this Volume. PIGE is most useful for the determination of light elements ($Z < 15$) and is often used as a complementary technique to particle-induced X-ray emission (PIXE).

There are additional considerations for CPAA. The requirement for an accelerator essentially limits the use to some substantial facilities the primary applications of which are in other research fields, and CPAA must obtain a share of the beam time. Generally, only one beam is available, i.e., only one sample or one comparator standard is irradiated at a time. These disadvantages may be outweighed by combining the quantitative information with spatial and depth information, which can be obtained using focused particle beams and modulation of particle energy to change reaction depth. CPAA has been discussed in more detail by Strijckmans (1994).

30.3.3 Photon Activation Analysis (PAA)

Photons may be used as activation particles. The nuclear reactions depend on the atomic number of the target and on the energy of the photons used for irradiation. The source of photons for PAA is nearly always the bremsstrahlung radiation (synchrotron radiation) produced with electron accelerators. The photon energies are commonly 15–20 MeV, predominantly inducing the (γ, n) reaction. Other reactions that can be used include (γ, p) , $(\gamma, 2n)$, and (γ, α) . The method is complementary to INAA, and the determination of light elements C, N,

O, and F are good examples of PAA where detection limits of $<0.5\ \mu\text{g}$ are possible. One reaction with lower energy photons is the ${}^9\text{Be}(\gamma, n){}^{10}\text{Be} \rightarrow 2\ {}^4\text{He} + 2n$ reaction because of the low neutron-binding energy of the Be. The reaction can be induced by the 2.1 MeV gamma rays from ${}^{124}\text{Sb}$ and measured through the detection of the neutrons. (The same reaction is also used as a neutron source.)

PAA is very similar to NAA in that the photons can completely penetrate most samples. Thus, procedures and calculations are similar to those used in NAA. The method has constraints due to the stability and homogeneity of the photon beam with inherent limitations to the comparator method. Recent developments in bremsstrahlung target technology have improved the photon sources, which greatly benefit the precision and accuracy of the method (Goerner et al. 2001). A detailed discussion of PAA has been given by Kusehevsky (1990).

30.4 Instrumental Neutron Activation Analysis (INAA)

Although this section focuses on INAA, most of the discussed steps in the analytical procedure are applicable to all other forms of activation analysis.

30.4.1 Sample Preparation

Sample preparation for INAA can be limited to the physical treatment of a sample in order to obtain a suitable and representative test portion for irradiation and measurement. The goal of obtaining results from an unaltered portion of the investigated sample can be reached in most instances. Factors that alter the analyte content of a sample, such as increases through contamination or decreases through volatilization or precipitation in chemical sample preparation, are minimized or excluded in INAA. Ideally, the test portion is weighed and directly placed into an irradiation container.

30.4.1.1 Solid Samples

Solid samples are commonly analyzed “as received” by weighing and packaging a suitable test portion into an irradiation container. Frequently it is desirable to remove the test portion from the irradiation container after irradiation to minimize blank corrections. For easier handling of this sample transfer, it has become common practice to prepare pellets from powdery samples with a suitable die. If sample masses must be corrected for moisture, the moisture content is commonly determined in a separate portion following prescribed protocols.

30.4.1.2 Biological Tissues and Fluids

Biological samples can also be analyzed “as received,” although handling can be difficult and removal from irradiation containers for measurement is frequently impossible. Biological samples are often converted to “solid” samples by lyophilization; this may allow treatment like the aforementioned solid samples. Frequently, it is necessary to consider the alteration of biological matrices during irradiation through temperature and radiolysis. The resulting

partial destruction of the sample may cause analyte loss and increase blank contributions by the irradiation container from which the decomposed sample cannot be removed. To minimize losses and contamination, biological tissues are often directly sampled into high-purity quartz vials. After irradiation, they can be measured in these vials, or, if required, extracted in a dissolution procedure.

30.4.1.3 Liquid Samples

Liquid samples are generally prepared 'as received' or they are concentrated and/or lyophilized. Liquids with low concentrations of the elements of interest, such as seawater are often pre-concentrated, sometimes with chemical processing, such as ion exchange. The resulting products are then subjected to INAA or RNAA. It should be noted that many liquid samples are more efficiently analyzed by other techniques, such as ICP-MS.

A special case of liquid samples are elemental solutions prepared as single- or multielement comparator standards for INAA. These calibrants commonly contain higher levels of the analytes of interest. This permits quantitative dispensation onto a "carrier" medium such as a filter paper, drying of the solution, followed by preparation as a solid sample.

30.4.2 Irradiation

The task of placing the sample into and retrieving from the field or beam of activation particles has been solved with many different experimental approaches; sometimes very unique solutions have been implemented to cater to a particular task. Some of the more widely used approaches in NAA will be discussed here, with special emphasis on utility for INAA.

30.4.2.1 Automated Systems

INAA lends itself to the possibilities of implementing a fully automated system that carries out the analytical procedure without operator interaction once the sample has been introduced into the analytical system. Examples of such systems can be found throughout the development of NAA procedures. For reasons of flexibility and optimization for greatly varying analytical tasks, automation is often exploited only in parts of the INAA procedure. One key part concerns the irradiation.

Virtually all research reactors offer pneumatic tube systems for transport of sample capsules to the high flux regions near the core. Similar systems are also used with other irradiation sources. The encapsulated samples are placed into a larger irradiation capsule, commonly called a "rabbit." This rabbit then is moved with a flow of carrier gas (N_2 , CO_2 , or others) to the irradiation position with a system of pneumatic tubes. Sensors determine the arrival at the irradiation position, timers control the irradiation time and the retrieval from the irradiation position, and hence the activation time parameters can be determined with a high degree of precision and accuracy. Transfer times have been reported down to the tens of millisecond range; more common are times in seconds to minutes, depending on the distance the samples are moved to the receiving station(s). Obviously, transfer times influence the feasibility of assays via short-lived radionuclides. Depending on the design of the tube system,

the rabbits, and the conditions in the irradiation position, i.e., thermal, gamma-ray, and neutron field density, the use of these transfer systems may be limited to shorter irradiation times, often in the tens of minutes range. Therefore, pneumatic systems are predominantly used for assays via short-lived nuclides where individual samples, together with flux monitors or primary comparator standards, are irradiated one-at-a-time and returned for counting. This is in contrast to assays via longer-lived nuclides where many samples and standards are irradiated simultaneously. Some pneumatic transfer systems allow longer irradiation times and assays via long-lived nuclides are carried out after irradiation in these facilities.

After irradiation, samples are commonly separated from the rabbit and, if feasible, also from their primary packaging containers to minimize blank contributions from the container materials or external contamination encountered in the irradiation facility. For the measurement of ultrashort-lived nuclides ($T_{1/2} \ll 30$ s) facilities have been designed that automatically separate the sample from the rabbit by mechanical means. Usually these systems are implemented in a fully automated irradiation and counting process (Brätter et al. 1977; Ismail et al. 2001).

30.4.2.2 “In Core” Irradiation

To offer the highest possible neutron fluxes, research reactors often have locations in the fuel assembly grid in which encapsulated samples can be placed, often for prolonged exposure covering an operation cycle or longer times. It should be noted that sample encapsulation for such irradiations must meet very specific requirements. Due to the radioactivity of the substantial encapsulation materials, prolonged decay (“cooling”) times are necessary before the samples can be retrieved for the assays.

Many reactors offer “near core” irradiation positions where mechanical devices can be used during operations for the retrieval of sample capsules; insertion is generally done during reactor shutdown. These devices can include the capability of rotating samples around an axis perpendicular to the flux gradient (Lazy Susan) for homogeneous activation of a large number of samples or of a large individual sample. It should be noted that all these irradiations are subject to considerable variations in the activation parameters, from timing precision to flux density, which will require full complements of monitors, standards, etc. with each irradiation set.

30.4.2.3 External Systems

Irradiation positions in neutron beams extracted from reactors are most commonly used for PGAA. These positions offer a major advantage; namely the samples do not require packaging to withstand mechanical and irradiation stresses, i.e., containment can be minimal or is not required at all. In principle, samples are not limited to a certain size and shape, except by the physical space in the irradiation position, which commonly has shielding elements put in place to protect personnel. Nevertheless, irradiation of entire paintings has been demonstrated (Fischer et al. 1987).

Of course, the distance to the source of neutrons, the reactor core, leads to a significant decrease in the available neutron flux of an external irradiation position. During the past 2 decades, considerable developments have been implemented to increase the available neutron

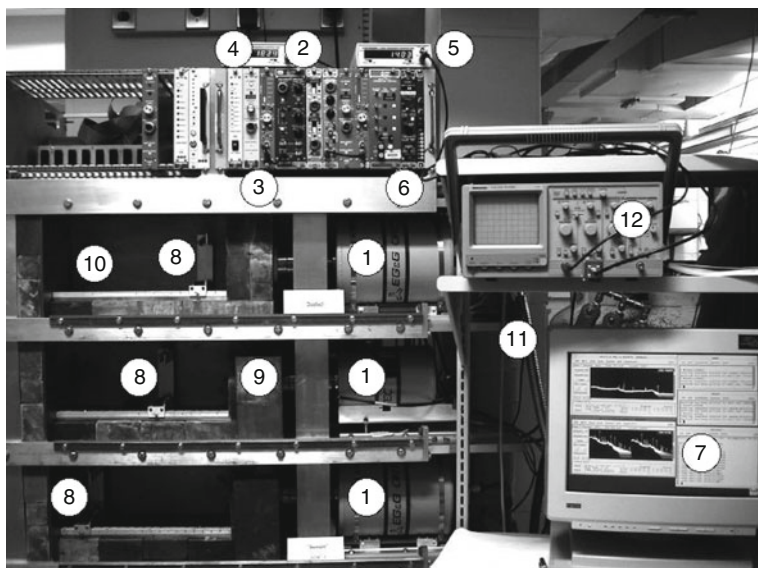
flux in external positions. Various types of cold sources have been installed in research reactors, which provide sufficiently slow (“cold”) neutrons the long wavelength of which allow effective transport along total-reflecting neutron guides to locations away from the core. Cold beams of neutrons offer fluxes of $10^9 \text{ cm}^{-2} \text{ s}^{-1}$, providing 10–30-fold increases in the sensitivity of PGAA, including the thermal shift to higher activation cross sections of the cold neutrons.

30.4.3 Gamma-Ray Spectrometry

Today, activation analysis procedures rely almost exclusively on the detection of gamma rays for simultaneous qualitative identification and quantitative recording of the decay of the activation products. Exceptions are in the use of purely or predominantly β^- -emitting activation products, such as ^{32}P or ^{31}Si , in conjunction with radiochemical separation to achieve specificity (see ▶ Sect. 30.5). INAA procedures utilize a variety of gamma-ray spectrometry systems the principal components of which are illustrated in ▶ Fig. 30.3. In this section, the components and characteristics of gamma-ray spectrometers used for INAA will be briefly described. More technical details can be found in the excellent monographs available (Knoll 2000; Gilmore 2008; Debertin and Helmer 1988) and in ▶ Chap. 48 of Vol. 5 on radiation detectors.

■ Fig. 30.3

Triple detector system as installed at the NIST Center for Neutron Research, Gaithersburg, MD, USA. (1) HPGe-detectors with 48 h dewars; (2) amplifier and bias supplies; (3) ADC with LFC module; (4) network acquisition interface (MCA); (5) rate meter; (6) LN_2 fill system controller; (7) display terminal; (8) sample holders; (9) 10 cm lead shielding; (10) 6 mm copper lining; (11) LN_2 supply line; (12) oscilloscope



30.4.3.1 Detector Systems

Gamma-ray spectrometry is efficiently carried out with solid-state semiconductor detectors, such as high-purity germanium (HPGe) detectors from about 40 keV energy, and silicon Si(Li) detectors for the X-ray region. Occasionally inorganic scintillation detectors such as NaI(Tl) or bismuth germanate (BGO) detectors are used because of their higher efficiencies. It should be noted that solid-state detectors are operated at 77 K to reduce the noise, and thus require supplies of liquid nitrogen (LN₂) or electromechanical cooling apparatus.

Gamma-ray detectors are commonly set up surrounded with heavy shielding against background radiation, i.e., radiation fields near a reactor and natural background radiation in locations more remote from the neutron source. The shielding is often a 10 cm thick lead castle in 4 π geometry, lined with absorbers for secondary Pb X-rays, such as 5 mm electrolytic Cu, and with neutron absorbers where appropriate. These shielding structures somewhat limit the access to the detectors, but automated sample changers are available.

The key characteristics of a gamma-ray detector system are the detection efficiency, the energy resolution, the signal-to-background ratio, and the throughput capabilities.

Detection efficiency is to a significant degree a function of the size of the detector; hence the active volume is specified by the manufacturer. In addition, detection efficiency for the ⁶⁰Co gamma ray at 1,332.5 keV relative to a standard 3' \times 3' (7.5 \times 7.5 cm) NaI(Tl) detector is given, i.e., 100% efficiency means the same analytical signal intensity can be obtained with the detectors that are compared in this manner. Of course, size is an essential price factor. Economically valuable HPGe detectors today have 30–40% efficiencies.

The *energy resolution*, which is important for a detector's ability to discriminate among close gamma-ray energies, is defined as the full width at half maximum (FWHM) of the 1,332.5 keV gamma ray, ranging from as low as 1.65 keV to some 2 keV; better resolution being more costly. Low-energy resolution and peak shape properties are additional criteria for the quality of a detector.

The *signal-to-background ratio of a detector system* is determined (1) by its peak-to-Compton ratio, (2) by the quality of shielding and construction materials used, and (3) by the location of the detector. Measures that go to the limits in the improvement of the latter have been described (Lindstrom et al. 1990). The peak-to-Compton ratio of a manufactured detector is determined by its volume and its geometry; good detectors offer values of 60:1 or better. The peak-to-Compton ratio can be significantly improved by the addition of a Compton suppressor annulus, commonly made of BGO or NaI(Tl), that surrounds the central principal detector and registers the Compton-scattered gamma rays escaping from the central detector. Anticoincidence circuitry prevents the registration of such events in the gamma-ray spectrum. Peak-to-Compton ratios exceeding 400:1 are routinely achievable. Landsberger and Peshev (1996) describe the application of anti-Compton (also called anticoincidence) counting in NAA, which greatly increases the detection limit due to the suppression of continuous spectral background (see also Knoll 2000; Alfassi 2001). However, when the sample is not shielded from the Compton suppression annulus surrounding the detector, problems with coincidence summing may occur (Debertin and Helmer 1988).

Further components of a high-performance gamma-ray spectrometer include the high-voltage bias supply, preamplifier, amplifier, and analog-to-digital converter (ADC). Several components can limit the overall performance of the gamma spectrometer in INAA due to the processing times required to convert the charge collected in the detector to a digital signal. The first limiting step occurs in a (conventional) resistive feedback preamplifier, where the required

time for the return to the baseline for processing the next pulse may be undercut by the frequency of the events. The preamplifier will be “saturated” and only few events will be registered. This happens at input count rates of 100 kHz or so. High-rate spectrometers, however, rely on transistor-reset preamplifiers the count rate capabilities of which by far exceed 1 MHz. Still, all other components in the signal-processing chain have their own limitations regarding the signal-processing frequency and the occurrence of pulse pile-up; hence all contribute to the overall dead time of the system. Thus, the count rate affects the quantitative relationship between the emitted activity of the source and the registered quantity, the gamma-ray peak, as well as the quality of the accumulated spectrum. Modern signal-processing technologies such as digital signal processing can reduce the count rate effects. In addition, technologies for the compensation of suppressed signals have been readily available and are currently augmented by so-called loss-free counting (LFC) or zero dead-time spectrometry systems. Accurate determinations utilizing high activity sources have been demonstrated with these systems (Zeisler 2000). Grass et al. (2001) have described comprehensive NAA systems incorporating the digital technology.

30.4.3.2 Analyzer Systems

Storage of the detector pulses is accomplished with a multichannel analyzer (MCA). An MCA, in its most basic form, is an instrument that sorts and counts events in real time. This sorting is based on some characteristics of these events, and events with the same characteristics are grouped together into bins, called channels, for counting purposes. In gamma-ray spectrometry, the MCA performs pulse height analysis (PHA), where signal pulses from a detector (this refers to the combination of the initial transducer and all subsequent electronics) are sorted into channels. The classifying characteristic is the pulse height or voltage that is proportional to the energy deposited in the detector. An analog-to-digital converter (ADC) is used to convert each pulse into a channel number so that each channel corresponds to a narrow range of pulse heights or voltages, i.e., energy increments. As pulses arrive over time, the MCA will collect a histogram of the count of pulses with respect to pulse height in its own nonvolatile memory. This distribution, arranged in order of increasing energy, is commonly referred to as a spectrum. The acquired spectrum is displayed on an x–y diagram (counts per channel against the channel number representing the gamma-ray energy) and is available for storage and/or analysis.

Modern MCAs offer up to 64 K ($= 2^{16} = 65,536$) channels for PHA. Depending on the requirements, frequently determined by the resolution of the detector and the type of radiation measured, smaller increments (512, 1,024, 2,048, etc. channels) may be used, and are often arranged in adjacent groups in the MCA. When energy resolution is not a requirement, single channel analyzers (also called differential discriminators) have their place when a certain energy range is cumulatively registered or used for coincidence–anticoincidence gating purposes.

As instruments, MCAs exist in many forms – as stand-alone analyzers, modular components, and computer interface cards. Obviously the latter, but in most instances all, are supported by a computer system. The philosophy of a stand-alone analyzer that can display spectra, calculate results, store data, etc., has given way to the flexibility of computer-supported MCA systems, frequently not needing more than a conventional PC with communication capabilities and appropriate data acquisition and spectrometry software. Recently, digital

spectrum analyzers have become available. In addition to the increased throughput capability, these devices replace the entire analog signal processing chain, as they directly digitize and store the pulses from the detector's preamplifier (Knoll 2000).

30.4.3.3 Software

Data acquisition software is chiefly concerned with the handling of the MCA system and its components. The programs will link the hardware of the spectrometry system with the storage memory for the data. Critical physical parameters such as starting time, duration, and dead time of the acquisition are recorded with sufficient resolution (best commercially available is 0.01 s) together with the spectral data. Other data, such as the energy calibration (e.g., kiloelectron volt per channel and zero offset), and user information on irradiation, detector system, and sample are often included with the spectral data or linked to it. The acquisition software can also take care of controlling sample changers, advancing storage file names, sequential counting of decaying sources, and many other related tasks. Display packages provide the necessary visual interface with the human operator. Displayed data can be manipulated (expanded, overlapped, subtracted), allowing the operator to clearly identify and evaluate components of the acquired spectral data, also during acquisition. Some MCA and detector systems are controllable in their settings (bias, gain, etc.) from the acquisition software. Quality assurance packages interface with the spectroscopy system for required record keeping.

The tasks of the spectrometry software packages are to identify energy peaks and to accurately evaluate the number of counts associated with the energy peak. Two philosophies are being used: (1) a mathematical model discovers the occurrence of a peak and models a shape to the peak to calculate the peak area in terms of number of counts, and (2) the gamma-ray energies are obtained from nuclide libraries and matched to the actual spectral data, where again a peak model is used to determine the number of counts. Packages clearly vary in the reliability of the process as shown in a number of intercomparisons (Blaauw et al. 1997). Add-on packages provide lists of nuclides, decay corrections, and activities when calibrated and for INAA quantitative results in mass fractions of elements either by comparison with spectra of standards analyzed under identical conditions or with calibration functions. One of the most robust combinations of data acquisition, peak search, and activation analysis routines have been available for workstation computers operating under VMS. Commercial activation analysis packages are also available for PC-based gamma-ray spectrometry systems, but none have gained in popularity or reputation.

30.4.4 Quantitation

The determination of an element is based on the activation equations of [Sect. 30.2.2](#), which offer the possibility for a direct “absolute” quantitative determination to the activation analyst. However, difficulties in accurately determining the flux distribution within a sample, as well as uncertainties in physical parameters such as cross section, half-life, and decay branching ratios would introduce large components of uncertainty.

Therefore, two methods are routinely employed: (1) a “comparator” standard with known elemental content is irradiated and measured under the same conditions as the sample, or

(2) in a parametric method the values for flux and detection sensitivities are obtained for the irradiation facility and spectrometry equipment through calibration, and tabulated experimental parameters are used for the determination of each individual element.

30.4.4.1 Comparator Method

The measurement process for the determination of the mass fraction of an element by INAA in a blank-free environment can be described by the following equation:

$$C_{x(\text{unk})} = C_{x(\text{std})} \frac{m_{\text{std}}}{wm_{\text{unk}}} \frac{(A_{0(\text{unk})})}{(A_{0(\text{std})})} R_{\theta} R_{\phi} R_{\sigma} R_{\epsilon} \quad (30.35)$$

where $C_{x(\text{unk})}$ is the element content in the unknown sample (in $\mu\text{g/g}$), $C_{x(\text{std})}$ is the element content in the primary assay standard (in $\mu\text{g/g}$), m_{std} is the mass of the primary assay standard used (in g), m_{unk} is the mass of the sample used (in g), w is the dry mass correction factor, $A_{0,\text{unk}}$ is the decay-corrected counting rate for indicator gamma-ray of the unknown, $A_{0,\text{std}}$ is the decay-corrected counting rate for indicator gamma-ray of the standard. A_0 , for a measured nuclide is calculated as:

$$A_0 = \frac{N_x \lambda e^{\lambda t_D}}{1 - e^{-\lambda t_C}} \quad (30.36)$$

where N_x is the number of counts in the indicator gamma-ray peak, λ is the decay constant for the indicator nuclide, t_D is the time elapsed between the end of activation and the start of counting, and t_C is the live time of counting.

The ratio factors R in Eq. (30.35) are ideally unity, but small deviations and their uncertainties must be considered. R_{θ} is the ratio of isotopic abundances for the unknown and standard, R_{ϕ} is the ratio of neutron fluences (including fluence drop off, self-shielding, and scattering), R_{σ} is the ratio of effective cross sections if the shape of neutron spectrum differs from the unknown sample to standard, R_{ϵ} is the ratio of counting efficiencies (differences due to geometry, γ -ray self-shielding, and dead-time effects).

Standards for comparison have been prepared in all conceivable forms, using solids or liquids containing a single element of interest or complex multielement mixtures. Solid standards are commonly made from high purity metals and compounds, certified reference materials, or other materials with known content of the element(s) of interest. Frequently solutions of high purity elements or compounds are prepared as single- or multielement standards, or commercial products such as liquid standards for spectrometry techniques are used for INAA. Care is usually taken that specifically prepared (multielement) standards minimize interferences and allow approaching the unity condition for comparison of the unknown with the standard.

An example for the continuous use of a certified reference material (NIST SRM 1633 Fly Ash) as standard in the multielement comparator INAA is reported by Blackman and Bishop (2007). They have analyzed 32,000 samples in 1,750 irradiations over 29 years, looking for 35 elements. A standard clay co-analyzed as a control sample 311 times showed a 1% coefficient of variance for several elements.

The comparator method has been shown to deliver highest accuracy with standards prepared from chemicals of known purity. A combined uncertainty of $<0.2\%$ was achieved in the determination of implanted As in Si (Greenberg et al. 2000). Other examples of high

quality INAA measurements achieving uncertainties of $\ll 0.5\%$ based on the comparator method were reported by Lindstrom et al. (1978), Fleming and Lindstrom (1987), and Zeisler et al. (2005). Similar small uncertainties have become routine quality features of the results reported by the INAA comparator method in recent CCQM key comparison exercises, e.g., CCQM-K49 Key Comparison Essential and Toxic Elements in Bovine Liver (CCQM 2008).

30.4.4.2 The k_0 Method and Other Parametric Methods

The possibility of using a single element as a comparator for multielement INAA is very attractive since every radioisotope observed in the gamma-ray spectrum can be related to a quantity of the parent element in the sample. A number of schemes have been devised to accomplish this; the one that is most widely accepted is called the k_0 method. This method is discussed in more detail below.

Even before 1970, several researchers had devised standardization techniques for various projects, where calibration factors, sometimes called k -factors, were measured for the gamma rays of the desired elements for specific irradiation and counting conditions. It was very convenient to continue using these k -factors as long as the conditions did not change. These simpler but less robust procedures have been used in many applications where one or several element standards provided an experimental calibration function for an irradiation facility and counting efficiencies for multielement analysis. Usually counting rates of elements were measured and tabulated in spreadsheets as ratios to the counting rate of the monitor element(s). Examples can be found in air particulate monitoring with several elements evaluated against a cobalt monitor (Ondov et al. 1990), and in PGAA analysis where elements in biological materials are assayed against a titanium monitor (Mackey et al. 1998).

Development of the k_0 Method

The development of the k_0 method was motivated by the need for a standardization method that was more convenient than the classical relative method, where a standard of each element had to be prepared to match the specific conditions of every analysis.

In the early 1970s, Simonits proposed the development of a standardization method using universal k -factors. In this method, the essential information for a gamma ray emitted by any nuclide produced by neutron activation would be contained in a universal constant, the k_0 factor, and all factors depending on the specific irradiation and counting conditions would be calculated by models. The inventors of the k_0 method envisioned that for each sample analyzed at least one neutron flux monitor would be co-irradiated and counted, and all other parameters of the models would be measured once and only remeasured when irradiation conditions changed. Thus, multielement analysis could be performed with the same amount of work needed for single-element analysis.

After the k_0 method was introduced (Simonits et al. 1975), the development of the method required many years of hard work. The k_0 values were accurately measured for the gamma rays of 112 nuclides (Simonits et al. 1980; Moens et al. 1984; De Corte et al. 1989a) produced by neutron irradiation, as were other activation and decay properties (De Corte et al. 1989a; De Corte and Simonits 1989; De Corte et al. 1989b). The model for the activation process needed to take into account the complex neutron spectrum of any research reactor. Initially, the k_0 method was seen mainly as a method for modeling the activation process. Of course, the gamma-ray detection process is equally important and the models for it are much more

complex. The gamma ray emission–transmission–detection process was originally modeled by Moens et al. (1981).

A detailed description of the k_0 method can be found in the habilitation thesis of Frans De Corte (1987).

Details of the k_0 method

To understand the k_0 method, it is useful to compare the formula used for calculating the mass fraction or concentration of an element with the one used in the classical relative method:

$$C_{x(\text{unk})} = C_{x(\text{std})} \frac{\left(\frac{N_x/t_c}{\text{SDCW}}\right)_{\text{unk}} \Phi_{\text{std}} \varepsilon_{\text{std}}}{\left(\frac{N_x/t_c}{\text{SDCW}}\right)_{\text{std}} \Phi_{\text{unk}} \varepsilon_{\text{unk}}} \quad (30.37)$$

In the relative method, the mass fraction of the analyte element in the unknown sample is obtained using the mass fraction of the same element in the standard. The equation takes into account the peak areas obtained in the unknown and in the standard; the sample weight (mass), W ; the decay factors S , D , and C (see ► Eq. (30.26)); differences in neutron flux; and differences in detection efficiency due to slightly different counting geometries.

With the k_0 method, the mass fraction of an element is calculated by the formula:

$$C_{x(\text{unk})} = C_m \frac{\left(\frac{N_x/t_c}{\text{SDCW}}\right)_{\text{unk}} k_{0,m} \Phi_m \frac{1 + Q_{0,m}(\alpha)/f}{1 + Q_{0,x}(\alpha)/f} \varepsilon_m}{\left(\frac{N_m/t_c}{\text{SDCW}}\right)_m k_{0,x} \Phi_{\text{unk}} \varepsilon_{\text{unk}}} \quad (30.38)$$

This equation, first written by Simonits et al. (1980), has the same structure as the equation used with the classical relative method, but contains additional correction factors because the analyte nuclide is different from the monitor nuclide. The subscript “m” refers to the monitor, f is the ratio of thermal flux to epithermal flux, and Q_0 is the ratio of the resonance integral to the thermal neutron cross section (see ► Eq. (30.9)).

This equation calculates the mass fraction by comparing the peak area, N_x , measured for a given gamma ray in the unknown sample to the peak area measured in the monitor. The decay correction factors for irradiation (S), decay (D), and counting (C) are simple for the more common exponential decay, but they have been formalized in the k_0 method for more complicated cases (De Corte et al. 1989a), including daughter activity growth and activation and decay schemes with several delayed branches.

In the equation, it is assumed that the peak areas have been corrected for count-rate-dependent random counting losses, whether they are caused by pulse pile-up or by analog-to-digital converter (ADC) dead time. Since modern spectrometers have very accurate live-time clocks, this correction is usually achieved simply by using the spectrometer live-time in the factor N_x/t_c . In the case of a highly varying count rate and significant decay of the analyte nuclide during the counting period, it may be more accurately achieved by a real-time correction method, such as loss-free counting.

All the nuclear factors are contained in the compound nuclear constant, k_0 . For a given gamma ray, γ_x , of a given product nuclide, the k_0 factor is proportional to the isotopic abundance of the target nuclide, the thermal neutron activation cross section, and gamma ray emission probability, and inversely proportional to the atomic mass:

$$k_{0,m}(x) = \frac{(\theta \sigma P_\gamma / M)_x}{(\theta \sigma P_\gamma / M)_m} \quad (30.39)$$

In practice, the k_0 factor is not determined using [Eq. \(30.39\)](#), because the thermal neutron activation cross-section, σ , and the gamma ray abundance, P_γ , are often not known with sufficient accuracy; instead the k_0 factor is measured experimentally. It is expressed relative to a monitor element, “m,” which is usually gold; the k_0 value for the ^{198}Au 411.8 keV gamma ray is defined as unity. The Au activation cross section is 98.7 barns and the 411.8 keV gamma-ray abundance is 95.5%. All other published k_0 values have been measured relative to ^{198}Au . Over the years, accurate k_0 values have been measured for more than 500 gamma rays emitted by more than 144 nuclides, which are essentially all the gamma rays used in NAA. As an aid to understanding the concept, a k_0 value can be thought of as the number of gamma rays emitted per unit mass of the element and unit thermal neutron fluence.

The factor, Φ_m/Φ_{unk} , in [Eq. \(30.38\)](#) corrects for thermal neutron flux differences due to the flux gradient at the positions of the monitor and the unknown sample. In cases where the monitor is irradiated before or after the unknown sample, which is often the case with short irradiations, Φ_m/Φ_{unk} corrects for the possible change in flux between the two irradiations. With the exception of this correction factor, the thermal neutron flux does not directly appear in [Eq. \(30.38\)](#); however, the quantity calculated with the flux monitor (the product of all the factors containing “m”) is proportional to the thermal flux. Thus, when using this equation, it is commonly understood that the quantity measured with the unknown sample is divided by the thermal neutron flux measured with the monitor.

In [Eq. \(30.38\)](#), the term $Q_0(\alpha)/f$ in the factor $(1 + Q_0(\alpha)/f)$ corrects for activation by epithermal neutrons. This factor is the heart of the k_0 method and was the key innovation that made the method possible. It was necessary to predict, with high accuracy, the relative reaction rates for two different (n,γ) reactions in any reactor neutron spectrum. For each reaction, the Q_0 value, the ratio of the resonance integral to the thermal neutron activation cross section, and f , the ratio of thermal flux to epithermal flux for the irradiation channel used, is needed.⁶

This simple method for calculating reaction rates in a mixed thermal–epithermal spectrum is called the Hogdahl convention (Hogdahl, 1965). It assumes that in the thermal neutron region the activation cross section varies with neutron energy as $E^{-1/2}$, the $1/v$ law. This is important because the neutron temperature varies from reactor to reactor, and, as a result, the mean energy of the thermal neutrons varies. However, since the reaction rates for all (n,γ) reactions vary by the same amount, any reaction rate relative to an ^{197}Au monitor remains constant. The Hogdahl convention also assumes that the neutron spectrum varies with energy as $1/E$ in the epithermal neutron region. A small variation from $1/E$ is accommodated by assuming the spectrum varies as $1/E^{1+\alpha}$. The shape parameter, α , is usually measured at the same time as the thermal to epithermal flux ratio, f . The resonance integral, and thus the Q_0 value, varies with α . It varies most for reactions that have resonances at high neutron energies. In the Hogdahl convention, the calculation of $Q_0(\alpha)$ is simplified by using the concept of mean resonance energy, where the contribution to the resonance integral of all the resonances is approximated by one resonance situated at the effective mean resonance energy E_r . Once α is known, $Q_0(\alpha)$ can be calculated using a simple formula:

$$Q_0(\alpha) = (Q_0(0) - 0.429)(E_r/\text{MeV})^{-\alpha} + \frac{0.429}{(2\alpha + 1)0.55^\alpha} \quad (30.40)$$

The mean resonance energies were calculated by Jovanovic et al. (1987) by integrating over all the resonances for all the (n,γ) reactions used in neutron activation analysis.

The assumption that the activation cross section varies with neutron energy as $1/\nu$ in the thermal neutron region is valid for most (n,γ) reactions. The two reactions that deviate the most from the $1/\nu$ assumption are $^{176}\text{Lu}(n,\gamma)^{177}\text{Lu}$ (typically $+0.4\%/K$) and $^{151}\text{Eu}(n,\gamma)^{152}\text{Eu}$ (typically $-0.1\%/K$). The reaction rates for these two reactions, relative to a monitor reaction like $^{197}\text{Au}(n,\gamma)^{198}\text{Au}$, will depend on the thermal neutron temperature in the irradiation channel used. A new set of equations, the Westcott formalism (Westcott 1955), was developed to account for these cases and used the Westcott $g(T_n)$ factor, which is a measure of the variation of the effective thermal neutron activation cross-section relative to that of a $1/\nu$ reaction. In the modified Westcott formalism, the following differences are also included: the $Q_0(\alpha)$ value of the Hogdahl formalism is replaced by the $s_0(\alpha)$ value, and the thermal to epithermal flux ratio, f , is replaced by the modified spectral index, $r(\alpha)(T_n/T_0)^{1/2}$. To use this formalism with the k_0 method (De Corte et al. 1994), it is necessary to measure the neutron temperature, T_n , for each irradiation and a Lu temperature monitor should be irradiated. The Westcott formalism needs to be implemented only when analyzing for Lu and Eu. There are several other non- $1/\nu$ nuclides: ^{103}Rh , ^{115}In , ^{164}Dy , ^{168}Yb , ^{191}Ir , and ^{193}Ir , but for these the error that results from using the simpler Hogdahl formalism will always be less than 1%, except for neutron temperatures far from those normally found in research reactor irradiation channels. One can question the usefulness of the Westcott formalism; when it is used, Lu is measured relative to the Lu monitor, i.e., not by the k_0 method, and the Westcott formalism gives significantly more accurate results for only one element, Eu. A more user-friendly correction method for Lu and Eu has been proposed by St-Pierre and Kennedy (2007), thus eliminating the need for the Westcott formalism.

De Corte et al. (1989a) emphasized the need to take into account neutron self-shielding in the k_0 method for both thermal and epithermal neutrons. With the self-shielding correction factors, the basic equation becomes:

$$C_{x(\text{unk})} = C_m \frac{\left(\frac{N_s/t_c}{\text{SDCW}}\right)_{\text{unk}}}{\left(\frac{N_m/t_c}{\text{SDCW}}\right)_m} \frac{k_{0,m} \Phi_m}{k_{0,x} \Phi_{\text{unk}}} \frac{G_{\text{th},m} + G_{\text{ep},m} Q_{0,m}(\alpha)/f}{G_{\text{th},x(\text{unk})} + G_{\text{ep},x(\text{unk})} Q_{0,x(\text{unk})}(\alpha)/f} \frac{\epsilon_m}{\epsilon_{\text{unk}}} \quad (30.41)$$

The thermal and epithermal self-shielding factors, G_{th} and G_{ep} , are very close to unity for activation reactions in most samples, such as biological materials, and can be ignored. However, the self-shielding effect is important for samples containing large amounts of nuclides with high neutron absorption cross sections. It is also important for many of the neutron spectrum monitors used, such as wires, foils, and pellets. Historically, G_{th} and G_{ep} were extremely difficult to calculate and required Monte Carlo calculations in the case of resonance neutrons; moreover it was recommended to dilute the samples to avoid self-shielding. Now, G_{th} and G_{ep} can be calculated easily and accurately with analytical formulae (Chilian et al. 2008).

Practical Considerations

Users of the k_0 method must determine the thermal neutron flux, the ratio of thermal flux to epithermal flux for the irradiation channel used (f), the shape parameter (α), and detection efficiencies for all counting geometries used. Since the calculations for the derivation and the use of these parameters are extensive, a software package is needed. Some new users begin a collaboration with one of the many laboratories using the k_0 method and adopt their methods of calculation and their software. Two complete software packages are now readily available to all potential users. The KAYZERO/SOLCOI Software (Van Sluijs et al. 1997), now called KayWin, performs the calculations in the well-understood classical manner. It is widely used

and has been well tested over many years. The k_0 -IAEA Software (Rossbach et al. 2007) uses a holistic approach, making use of all available information, and benefits from the support of the International Atomic Energy Agency (IAEA). The maintainers of both packages also provide training.

The instructions with the software packages indicate how to determine f and α , how to measure the parameters of the efficiency calibration of the detector and convert it to specific counting geometries, and how to convert the peak areas into the mass fractions of the elements. The software packages have libraries of k_0 values, Q_0 values, mean resonance energies, half-lives, decay types, and the details of the decay schemes needed for true coincidence summing calculations.

Measuring f and α

Many methods have been developed to measure f and α . They all involve the activation and counting of a number of nuclides having a range of Q_0 values and mean resonance energies. The most accurate measurements of α use irradiations under cadmium cover to activate only with epithermal neutrons. However, many laboratories may not require such high accuracy or may not be permitted to irradiate under cadmium cover. Bare irradiations have been shown to give sufficient accuracy if carefully done. Since the parameters are determined by subtraction of the thermal neutron-produced activity from the total activity – two possibly similar quantities – accurate element masses, peak areas, and detection efficiencies are needed. The minimum number of monitors that need to be irradiated for the simultaneous determination of the thermal neutron flux, the factor f , and α is three.

One of the most convenient trios of monitor elements is Cr, Au, and Mo (Koster-Ammerlaan et al. 2008). The $^{50}\text{Cr}(n,\gamma)^{51}\text{Cr}$ reaction has a low Q_0 value and is primarily produced by thermal neutrons. The $^{197}\text{Au}(n,\gamma)^{198}\text{Au}$ reaction is produced by thermal and low-energy epithermal neutrons, and the $^{98}\text{Mo}(n,\gamma)^{99}\text{Mo}$ reaction is produced by thermal and high-energy epithermal neutrons. Along with samples to be analyzed, the irradiation of a pellet containing well-known quantities of Cr, Au, and Mo, typically 500, 4, and 1,000 μg , respectively, gives the thermal neutron flux, f and α after a simple calculation.

► Figure 30.4 illustrates a Cr, Au, and Mo pellet ready for irradiation next to a sample of ceramic material. They are irradiated in a polyethylene irradiation vial using a pneumatic transport system and 5 days after irradiation, the Cr, Au, Mo pellet is counted to measure the

■ Fig. 30.4

Next to an open polyethylene irradiation vial is an assembly consisting of a 150 mg sample of ceramic material to the left and a smaller diameter neutron-spectrum monitor (in the form of a Cr, Au, Mo pellet) ready for irradiation



thermal neutron flux, f , and α . The sample is counted after 5 and 15 days and the mass fractions of up to 50 elements are determined by the k_0 method. To achieve the same results using the relative method would require irradiating the ceramic material along with the standards of 50 elements. This would be a daunting task even if suitable multielement standards were available.

Detection Efficiency ϵ

Detection efficiencies appear to occupy only a minor part of [Eq. \(30.38\)](#), but in fact their accurate determination is by far the most difficult aspect of the k_0 method. With the relative method, the counting geometry for the unknown sample is maintained almost identical to that of the standard, and only a small correction factor needs to be calculated. With the k_0 method, the counting geometry for the unknown sample may be completely different from that of the monitor and the comparison is between two different nuclides. The fact that monitor and samples may be counted with any geometry is a major advantage of the k_0 method.

It may be straightforward to determine a relative efficiency curve of efficiency versus gamma-ray energy for a point source far from the germanium detector, but what is needed are efficiencies for small or large samples, which may be counted very close to the detector. The efficiency calculation routine, a major part of any k_0 software package, may use a physical or parametric model that considers the gamma ray detection probability as a function of the position of the emitting atom relative to the center of the face of the detector. The calculation includes integration over the volume of the sample and takes into account attenuation in the sample and its support. Using calibrated and uncalibrated sources for absolute and relative efficiencies, respectively, the user will perform the measurements necessary to determine the parameters of the model; the measured dimensions of the detector may also be used. Finally, the parameters of the model are fine-tuned using further measurements in typical counting geometries.

A huge complication is coincidence summing of gamma rays. This is negligible with the relative method because the standard and the unknown contain the same nuclide, they are at the same distance from the detector, and the effect is the same for both. With the k_0 method, the software must have the decay schemes of all the nuclides used, to determine the probability of each decay path involving the gamma ray of interest. Then, for each gamma ray of interest and each counting geometry, the software calculates the probability of summing with the gamma rays emitted simultaneously along each decay path. Many routines have been developed to perform coincidence summing calculations. Three of the routines used with the k_0 method were compared for the case of a small sample counted close to the detector (Van Sluijs et al. 2000). The reduction in detection efficiency due to summing-out was as high as 30% for some nuclides. Discrepancies between the three routines were usually less than 1%, but as high as 10% in some cases. When the reasons for the discrepancies, programming bugs, outdated decay schemes, and neglect of summing with X-rays, were understood they were corrected in all the routines.

Not all routines accurately correct for coincidence summing with X-rays. This may be important, especially for heavy nuclides, but it is difficult to accurately correct because it varies greatly with detector window thickness and sample thickness. For this reason, detectors with thin beryllium windows should not be used with k_0 -NAA unless samples are counted at distances of 10 cm or more. None of the routines correct for coincidence summing with beta rays. This may be important for some short-lived light nuclides that emit high-energy betas in coincidence with gamma rays. In these cases, a 4 mm thick plastic absorber should be placed between sample and detector.

Accuracy

In 1987, it was estimated that the uncertainty of analytical results using the k_0 method was typically 3.8% (De Corte et al. 1987), and included 1% from k_0 values, 1% from Q_0 values, 2.5% from f and α , and 2.5% from detection efficiencies, all combined in quadrature. Since then, several expert laboratories have made a considerable effort to completely understand the method and to determine and eliminate the causes of uncertainty. These laboratories now routinely achieve 2% accuracy under favorable conditions, such as counting the samples far from the detector and using an irradiation channel with high f value. However, for new laboratories adopting the method, a large number of papers comparing results with the accurately known mass fractions in certified reference materials show many deviations between 5% and 10%. These papers did not identify the likely causes of these deviations, and they were not able to resolve them. Thus, it may be concluded that new laboratories adopting the method should expect accuracies between 2% and 5%, depending on the resources available to fully develop the method.

An important step toward improved quality assurance is the development of the synthetic multielement standards (SMELS) material (Vermaercke et al. 2006). There are three types of material, SMELS I, SMELS II, and SMELS III, that produce nuclides with short, medium, and long half-lives when activated. In each of the three spectra, many clear gamma-ray peaks, emitted by at least a dozen nuclides that are produced by (n,γ) reactions with low and high Q_0 values, over the entire energy range are obtained. These stable, homogeneous materials with well-known mass fractions of all the elements are very useful in verifying the method. In spite of their popularity, the three materials are still available from the developer. SMELS I and SMELS II can be recycled after the decay of the activated nuclides. The intended use of this material is to verify that the k_0 method is being correctly used. If discrepancies with the expected mass fractions are observed, the user determines the reason and makes corrections.

There is a continuing effort to improve the nuclear database (De Corte and Simonits 2003) that contains the recommended k_0 values, Q_0 values, mean resonance energies, and half-lives for 144 nuclides. This will make a difference for a few nuclides for which the currently used k_0 and Q_0 values may be in error by as much as 10% (St-Pierre and Kennedy 2006 and references therein). The international committee updating the database hopes to identify all the nuclides for which the current k_0 values may be in error by more than 2% and to publish new recommended values.

30.5 Radiochemical Activation Analysis (RAA)

In radiochemical activation analysis (RAA), the various techniques of activation analysis (AA), i.e., neutron activation analysis (NAA), photon activation analysis (PAA), and charged particle activation analysis (CPAA) are combined with radiochemical separation procedures with the intention of extending the capabilities offered by the purely instrumental methods.

The primary objective of RAA is to increase the sensitivity and/or the accuracy of the analysis, while preserving the main advantage of the instrumental techniques, their multi-element character. The instrumental modes of activation analysis are widely used analytical techniques for the nondestructive and simultaneous determination of trace element mass fractions or concentrations. As a result of chemical separation, interferences caused by other elements/radionuclides are removed; thus additional elements of low concentration become detectable and/or the accuracy of the determination is improved. In this sense, RAA complements instrumental AA methods.

Radiochemical methods can be successfully applied to separate elements and/or radionuclides that cannot be directly analyzed in the radioactive matrix by instrumental methods, e.g., pure beta emitters, short-lived nuclides in the presence of long-lived matrix components. In this case, there is no instrumental alternative to RAA.

A recently defined and new objective has been trace element speciation, which provides information about the physical/chemical state of the trace elements. Species separated by chemical methods are subsequently determined by instrumental or radiochemical activation analysis.

30.5.1 Major Types of RAA

The term RAA is used for the conventional form of radiochemical activation analysis with post-irradiation chemical processing, as well as – in a broad sense – for all types of AA involving chemical and radiochemical operations.

In conventional RAA, chemical separations are carried out *after* the irradiation of samples. The well-known advantages of this technique over other types of trace element analysis where chemical treatment is involved are the reduction of contamination risks and uncontrolled losses of trace elements during processing. These are the beneficial consequences of postirradiation treatment of radioactive samples and the addition of carriers after the irradiation.

Pre-irradiation chemical treatment of samples cannot be always avoided. Samples of large volume or mass have to be concentrated before being analyzed. In the literature this technique is referred to as pre-concentration activation analysis (PCAA). This treatment considerably increases the concentration of the elements to be determined. It may provide a tool for chemical separation of the interfering elements/isotopes at once, thus greatly increasing the sensitivity of AA.

In some extremely demanding cases, pre-irradiation chemical concentrations are carried out together with postirradiation separations, combining the advantages and the drawbacks of both techniques. This method, referred to as PC-RAA, can provide the highest possible sensitivity of trace element analysis among the AA techniques.

Pre-irradiation chemical separations followed by activation analysis are also performed for speciation studies. Speciation cannot be done after irradiation, since the chemical form can be changed due to recoil effects under the drastic conditions of nuclear reactions. This type of analysis is called chemical or molecular activation analysis (CAA).

The most common form of RAA is its use with neutron activation and is called RNAA.

30.5.2 Main Features of RAA

Radiochemical separations involved in conventional postirradiation RAA have some special characteristics that distinguish them from separation procedures used in classical trace element analysis.⁷

Chemical processing usually contains the following steps: Irradiated samples, after the addition of tracers and/or carriers, are dissolved by one of the following destruction/dissolution methods: dry ashing in open or closed systems, wet ashing with mineral acids in open or closed systems, or alkaline fusion. Thermal and microwave ovens or hot plates are often used as heat

sources. The main methods for separation involve precipitation, ion exchange, solvent extraction, and distillation. Chromatographic techniques in the form of ion exchange, extraction chromatography, or thermochromatography are often applied for the separation of single elements as well as groups of elements or for the removal of the matrix interference. Separated sources are usually counted by high-resolution gamma spectrometers and, in some cases, by beta detectors or liquid scintillation counters (LSC).

The major pitfall of chemical separations is the varying and unavoidable loss of material. Nonetheless, there are several ways of controlling the losses by calculating the chemical recoveries for the whole procedure. The amount of carrier can be determined in the measurement source at the end of separation and compared with the initial value. Recovery should be corrected for the presence of the element in the original sample. The amount of carrier can be determined by classical analytical methods, such as gravimetry or by nuclear techniques. In the case of short-lived nuclides, reactivation is an appropriate technique.

Recovery measurements are often performed with the addition of radiotracers, which are most likely analyzed together with the analyte in the measurement source. Since the tracers should not be produced in the sample during irradiation, cyclotron-produced tracers are preferred in NAA, e.g., Co analysis by NAA in the presence of cyclotron-produced ^{56}Co yield tracer. High accuracy in the analysis can only be assured if recovery for each analyte in each sample is determined.

There are several other advantageous features of RAA techniques, such as:

1. The reduction or elimination of contamination hazards of the sample during processing unless the laboratory is contaminated by radionuclides.
2. Chemical losses of the analytes due to formation of radiocolloids and adsorption on the vessels' surfaces are minimized by the addition of carriers to the samples after irradiation and before chemical processing. Using stable isotopes of the analyte of interest increases the overall concentration of the analyte and the carrier beyond the trace level, hence better separation yields can be achieved. Similarly, the addition of stable interfering matrix elements aids the separation efficiency.
3. The multielement character of AA implies that trace elements do not have to be individually separated; it is sufficient to separate them into several groups or just remove the interfering components. Thus, chemical separation schemes are relatively simple and extremely high decontamination factors are not attained. When the recoveries are well controlled, separations need not necessarily be quantitative, although high yields are always desirable. For the determination of short-lived nuclides, fast separation procedures are of major concern.⁸
4. Matrix components generally do not interfere with trace element determination, e.g., C, H, O, and N contained in organic materials do not affect the detection of trace metals in NAA. On the other hand, minor or trace elements that are easily activated, e.g., ^{24}Na , may significantly influence the detection limits for trace elements. Matrix activities are frequently eliminated by selective chemical removal, thus increasing the sensitivity for many trace elements.
5. Since RNAA is applied as a complementary method to INAA, it is most frequently used to analyze single elements that are difficult to determine, e.g., I, Th, and U in biological materials. In this case, chemical separations are designed for the removal of the analyte as a single element or a group of elements that behave chemically similarly, e.g., rare earth elements; thus, separation chemistry can be relatively simple.

An obvious disadvantage of RAA separations is that samples often have to be treated in shielded facilities or in hot cells because of the radioactivity.

General RAA trends have been discussed by various authors (de Bruin 1998; de Goeij 1999; Guinn 1999; Heydorn 1999; Parr 1999) and several excellent reviews on RAA of geological, biological, and environmental samples have been published (Alfassi 1994a, b; Balla et al. 1998; Zeisler and Guinn 1990). Examples from the last 10–20 years are given in the following sections.

30.5.3 Application of RNAA in Materials Science

Neutron activation analysis, including nondestructive as well as radiochemical techniques, has been successfully used for the determination of trace elements in metals, especially high purity metals. In the past, radiochemical separations were extensively used for the removal of matrix interferences. Later this procedure was extended to the group separation of trace elements. Radiochemical methods are also applied to the accurate and sensitive determination of single “difficult-to-determine” elements.

30.5.3.1 Removal of the Main Activity and Separation of Element Groups

The demand for high purity metals has tremendously increased due to needs in the information technology and telecommunications industries. High purity Al is used in various micro-electronic devices and semiconductor detectors are made of hyperpure Ge and Si, etc. Impurity levels depend upon both the raw material and the purification method and may influence the function of the device. For example, in semiconductor materials, alpha particle emission creates damage causing the so-called soft error effect. For this reason, U and Th levels are strictly limited in these applications.

The main activity induced by neutrons in an aluminum matrix is ^{28}Al , which is a short-lived radionuclide ($T_{1/2} = 2.25$ min) that decays within an hour. However, fast neutrons, also present in a nuclear reactor spectrum, react with Al yielding ^{24}Na via the $^{27}\text{Al}(n,\alpha)^{24}\text{Na}$ reaction. Because of the relatively long half-life ($T_{1/2} = 15$ h) and the high-energy photons that cause significant increase of the background due to Compton interaction, ^{24}Na becomes a major interference in the determination of trace elements in Al.

One method (Egger and Krivan 1986) was developed to separate ^{24}Na from irradiated Al using hydrated antimony pentoxide (HAP) in hydrochloric/hydrofluoric acid (HCl/HF) solution. Eighteen trace elements with mass fraction levels of 0.1 ng/g were determined, and another 20 elements could be determined above the 1 ng/g mass fraction level. As shown by Girardi and Sabbioni (1968), HAP retains Na almost quantitatively from concentrated HCl and HF helps elute some slightly adsorbed elements from the column (Ta, As, Se).

Discarding simplicity, the sensitivity of the method was further improved by integrating chromatographic group separation steps into the procedure using ion-exchange columns (Egger and Krivan 1988). Ten groups of elements were formed allowing the determination of 43 trace elements below the 10 ng/g level. After the removal of Na by HAP, the elements were separated into five groups by elution chromatography using an anion-exchange column. U and Th were determined by separating the indicator radionuclides (^{239}Np and ^{233}Pa) using another anion exchange resin; and finally, a cation-exchange resin was used to divide the rest of the elements into four groups.

A sequential group separation method was developed also by Zaidi et al. (1999a) to determine 32 trace elements in high purity Al. The sample was digested, then dissolved in 10 mol/l HCl and passed through an anion-exchange resin column. Non-retained elements were divided into two groups by co-precipitating some of them with calcium oxalate, while others remained in the filtrate. A third group was formed by stripping the retained anions with dilute nitric acid. Low mass fractions of U and Th were determined by retaining the indicator radionuclides, ^{239}Np and ^{233}Pa , from the HCl solution on an additional anion-exchange resin column and preparing a co-precipitated source with LaF_3 .

Comparing the three methods for the determination of trace elements in high purity Al, it can be said that the more complicated the separation, the greater is the number of elements that can be analyzed.

Zaidi et al. (1999b) have successfully adopted the same chemical procedure for the analysis of nickel-based alloys. Nickel was concentrated from the effluent of the anion-exchange resin column by precipitating it with dimethylglyoxime followed by an oxalate precipitation in the same manner as the Al analysis and 40 elements could then be determined. Besides nickel, the other major components were Fe, Cr, Ca, Mg, Ce, Mn, Na, and V, while the rest of the elements were present in minor and trace quantities. Nickel-based alloys are extensively used in the electronics and telecommunications industries as well as in the chemical industry and aircraft production.

Zaidi et al. (2002) adopted the same radiochemical procedure for the determination of minor and trace elements in high purity Ti and W. (Later the procedure was also successfully applied to the analysis of milk samples (Gill et al. 2003).) After acid destruction, Ti and W are precipitated as H_2TiO_3 and H_2WO_4 , respectively. Next, a separation procedure based on anion exchange and precipitation of the rare earth oxalates is applied. Thirty-six elements were determined with high chemical yields and improved sensitivity compared to that of INAA. Due to its light weight, high strength, chemical resistance, and biocompatibility, titanium is used in air- and spacecraft industry and in medical structures such as implants. High purity tungsten has also many applications, e.g., in light bulbs as filament; in electronic equipment as seals, contacts, electrodes; and, more recently (in alloyed form), in sporting equipment.

A simple postirradiation radiochemical procedure has recently been developed at the Jozef Stefan Institute in Slovenia for the selective removal of iron from iron minerals and iron-based reference materials (Makreski et al. 2008, Jacimovic et al. 2008). Iron chlorocomplexes were extracted with di-*i*-propyl ether (DIPE) or *i*-amyl acetate (IAA). After Fe elimination, the distribution of 35–39 elements in the extraction systems was determined. Twelve to fourteen elements, particularly the lanthanides, could be detected with increased sensitivity, while Sb, Mo, Au, Se and Te were co-extracted with Fe, which prevented the determination of these elements.

Single-step separation procedures for the removal of major interferences are scarcely applied, but removal of the matrix activity is often combined with a relatively simple group separation scheme. Chromatographic techniques offer this convenience by eluting or stripping the retained elements sequentially according to the different distribution ratios. Ion-exchange chromatography was very often used. Because of its high capacity, it can be applied to the removal of the matrix as well as to trace element separations. Recently, extraction chromatography has been favored, especially in combination with other separation procedures.

Several procedures have been developed for the determination of trace elements in molybdenum and tungsten that take advantage of the anionic character of both elements. Park et al. (1988) studied the mass fraction of 13 trace elements in Mo by separating them from Mo

and W, which were responsible for the matrix activities. Sequentially eluted cation- and anion-exchange resin columns were used to obtain three groups of elements. Mo and W passed through the cation column and were eluted from the anion column with 7 mol/l nitric acid. The anion exchange served to separate Np and Pa selectively allowing the determination of U and Th traces. In the modified procedures of Theimer and Krivan (1990), 20 elements were determined in high-purity molybdenum using anion-exchange separations from HF media. One of the procedures has the advantage of high sensitivity for Th determination. Caletka et al. (1988) developed a procedure for the determination of 19 trace elements in tungsten. Tungsten was retained by anion-exchange resin and trace elements were eluted into two groups. In order to analyze Ta and Sb, they were selectively extracted as diantipyrimethane (DAM) complexes with an organic solvent before the ion-exchange separation took place. The pure beta emitter, ^{32}P , was also determined after sub-stoichiometric extraction, a method described by Suzuki (1990).

Caletka et al. (1982) analyzed 26 trace elements in niobium by irradiating and processing two sample aliquots. The first aliquot was for the determination of medium-lived nuclides and the second one was for the analysis of long-lived indicator isotopes. In both procedures, solvent extractions were followed by column chromatographic separations. Niobium was removed by extracting its diantipyrimethane (DAM) complexes with dichloroethane. The procedures involve solvent extraction, anion-exchange chromatography, and in the first case sorption on HAP, and in the second case, extraction chromatography on an HDEHP column.⁹

Fifteen trace elements were determined at ng/g mass fraction levels in high purity Sn by Kolotov et al. (1996) using extraction chromatography on Teflon-supported tributylphosphate (TBP). Tin, together with Sb and In radionuclides, which are formed in secondary nuclear reactions of Sn during irradiation, were retained from 6 M HCl on the column. The ^{24}Na was removed from the eluted trace element fraction by sorption on hydrated antimony pentoxide (HAP). Gas phase impurities of N, C, and O were also analyzed in the same material by radiochemical photon activation analysis via ^{13}N , ^{11}C , and ^{15}O detection.

The major disadvantage of group separation procedures is the lack of a chemical recovery determination for each element in each sample.

30.5.3.2 Separation of a Single Element

A few important examples were selected for discussion, i.e., analysis of silicon in high purity metals, phosphorus, and sulfur in steel, molybdenum, and tungsten in geo- and cosmochemical samples.

Silicon. The difficulty with the determination of Si by NAA lies in the fact that the $^{30}\text{Si}(n,\gamma)^{31}\text{Si}$ reaction has a small cross section, the isotope abundance of ^{30}Si , as well as the gamma-ray emission probability of ^{31}Si are small, and the half-life of the latter is short ($T_{1/2} = 2.62$ h). To increase the sensitivity, detection of the emitted β^- radiation is preferred to traditional gamma-ray spectrometry. In this case, ^{31}Si has to be separated from other radionuclides in the sample.

Rouchaud et al. (1977) determined Si in Mo by concentrating it from dilute acid on an anion-exchange resin column and separating it by elution. Silicon was further purified and concentrated using an aluminum oxide column. Silicon was determined by the same author (Rouchaud et al. 1980) in iron and aluminum, but used cation-exchange resins since they offered better separation by retaining the matrix elements than the anion-exchange resins.

Schmid and Krivan (1986) separated Si based on the volatility of SiF_4 by distillation from an $\text{HF} + \text{HCl}$ solution. Silicon was determined in vanadium and niobium using this method.

Phosphorous. The presence of trace amounts of phosphorus in metals and semiconductors is known to affect material properties. The ^{32}P produced in the (n,γ) reaction is a pure β^- emitter and has to be separated and rigorously purified. Paul (1998, 2000) developed a method for P determination in steels and other high-temperature refractory alloys of interest to the aircraft industry. Irradiated samples were dissolved; passed through cation-exchange columns to remove Co, Ni, and Cr; followed by repeated precipitations of magnesium ammonium phosphate and ammonium phosphomolybdate. One of the major advantages of this technique is the determination of the chemical yield by gravimetry. Phosphorus was determined by INAA in matrices other than metals, e.g., polymers. In this case, the beta spectrum was corrected for interferences and self-absorption (St-Pierre and Kennedy 1998). A modified version of this procedure has been used to certify implanted phosphorus in silicon (Paul et al. 2003).

Sulfur. Sulfur is determined by measurement of ^{35}S produced via the $^{34}\text{S}(n,\gamma)^{35}\text{S}$ reaction. It is a pure beta-emitting isotope that can be detected with high counting efficiency by liquid scintillation (LS) counting, but a highly selective separation is required to remove other radionuclides that could interfere with ^{35}S . The chemical separation is often based on the ion exchange of sulfates. According to Paul (2008), sulfate is reduced to sulfide and collected as H_2S in a basic solution that is mixed with LS cocktail. Since the reaction is specific for sulfate, a clean separation of ^{35}S is obtained. The chemical yield of the postirradiation procedure is determined by iodometric titration for the individual samples. To achieve high accuracy, the Cl content of the sample is also determined by RNAA by separating chlorine as AgCl precipitate and correcting the result for the ^{35}S content produced via the $^{35}\text{Cl}(n,p)^{35}\text{S}$ reaction.

Molybdenum and tungsten. Oura et al. (2007) applied postirradiation RNAA to determine trace amounts of Mo and W in geo- and cosmochemical samples. Samples were fused and Mo and W were separated from other elements by an anion resin. Chemical recoveries were determined by ICP-OES for both elements in each sample. To correct the Mo results for fissiogenic ^{99}Mo resulting from fission of ^{235}U , another fission product, i.e., ^{133}I in each sample solution was determined by RNAA. Iodine was separated as PdI_2 precipitate. Under the given experimental conditions, detection limits of about 100 ppb for Mo and W were achieved.

Several other valuable publications have recently appeared on the use of RNAA for trace elements in metals, e.g., the analysis of Na and K in W-Ti alloys by Kim et al. (1998) and trace elements in ancient gold objects by Olariu et al. (1999). Postirradiation RNAA methods separating a single element have the advantages that low detection limits as well as high analytical accuracy can be achieved when results are corrected for chemical losses and all possible interferences are taken into consideration.

30.5.4 RNAA of Biological, Environmental, and Geological Samples

30.5.4.1 Removal of the Main Interfering Activities

The main activities of irradiated biological samples are ^{24}Na ($T_{1/2} = 15$ h), ^{42}K ($T_{1/2} = 12$ h), ^{32}P ($T_{1/2} = 14$ d), and occasionally ^{82}Br ($T_{1/2} = 35$ h). They are produced by neutron capture reactions in Na, K, P, and Br, respectively. When analyzing short-lived radionuclides, ^{38}Cl ($T_{1/2} = 37$ min) contributes significantly to the total activity. In geological and environmental samples, the same nuclides are usually responsible for the matrix activities.

There were many semi-successful attempts to remove these radionuclides by selective chemical separations. A historically important development was the discovery of the high-retention properties of hydrated antimony pentoxide (HAP) by Girardi and Sabbioni (1968). The removal of Na by HAP is quantitative and fast. This discovery contributed to the widespread application of the NAA technique by allowing trace element determinations even before the appearance of semiconductor detectors when NaI(Tl) scintillation detectors were used to register gamma-ray spectra. Investigations were initiated all around the world to find inorganic sorbents that had high selectivity for other elements like that of HAP for Na (Amphlett 1964; Clearfield 1982): removal of phosphate by acidic aluminum oxide or zirconium phosphate, retention of K on titanium dioxide, distillation or extraction of Br and Cl as acid vapors and elemental halogens, respectively, etc. Most of these methods failed to some extent or did not have a long-lasting career because the required high selectivity was not attained. In contrast, many papers were published about the application of HAP for Na removal, either as single-step procedures or as part of sophisticated separation schemes (Schuhmacher et al. 1977; Samsahl 1966).

30.5.4.2 Separation of a Single Element and Groups of Chemically Similar Elements

Single-element separation usually allows the determination of very small amounts, thus providing a highly sensitive analytical method. The activity of the separated radionuclide can be measured by an efficient but less-selective nuclear measuring technique, such as scintillation counting. This technique was used in the past before semiconductor detectors were available and its application is justified at present by the demands of high sensitivity and accuracy in trace analysis in bioassay and other fields studying the role of trace elements. In the following section, examples of the large number of procedures will be given based on recent research revealing new tendencies in RNAA. Other valuable procedures will be cited occasionally to indicate the wealth of this field. A detailed literature review and summary on RNAA until 1994 was prepared by Alfassi (1994a).

Determination of Essential Elements by RNAA

Selenium. It has been recognized that Se plays a seemingly contradictory role in biology as an essential micronutrient for several organisms and a toxic element. It can be determined via the short-lived ^{77m}Se ($T_{1/2} = 17.4$ s) as well as the long-lived ^{75}Se by RNAA (as well as by INAA). Elemental Se can be precipitated after reduction using ascorbic acid (Damsgaard et al. 1973; Alamin et al. 2006), 1-amido-2-thiourea (Itawi and Turrel 1973), or cysteine (Czauderna 1985, Czauderna 1996) as reducing agents. The latter procedure is based on the counting of the precipitated Se without further purification. This was the preferential procedure by many authors in the past when complexes of Se (2-mercaptobenzothiazole, *o*-phenylenediamine, ammonium pyrrolidine dithiocarbamate) were formed followed by solvent extraction or precipitation.

Iodine. Iodine is an essential trace element, which forms an indispensable part of thyroid hormones. Hence, the constant supply of I via the food chain is necessary. Iodine is determined via the $^{127}\text{I}(n,\gamma)^{128}\text{I}$ reaction. A comparative evaluation of INAA and two different methods of RNAA was given by Kucera et al. (2001). In the radiochemical procedures, irradiated samples were digested by alkaline-oxidative fusion to avoid losses of volatile I. According to the first

RNAA procedure, elemental I_2 was extracted with chloroform; in the second procedure, it was precipitated as AgI. The lowest I detection limit of 1 ng/g was achieved by the first procedure. AgI contained some traces of impurities increasing the detection limit, while the detection limit of INAA was two orders of magnitude higher. The chemical yield of the procedure was determined using a ^{131}I radiotracer. The procedure was used by Kucera et al. (2004, 2007) for the determination of I in Asian diets. The iodine extraction procedure was applied with slight modifications by several others (Dermelj and Byrne 1997). I_2 was also separated by distillation from the sample and retention on MnO_2 followed by purification via distillation according to Pietra et al. (1986).

Iodine and bromine. Trace amounts of halogens were determined in silicate rock samples by Ozaki and Ebihara 2007. Activated samples were fused with NaOH and dissolved in water. Metal impurities were removed with hydroxide precipitate. Iodine was separated as PdI_2 , and then a mixed AgCl–AgBr precipitate was formed. Chemical yields determined by the reactivation method varied between 70% and 80%.

Determination of Toxic Elements by RNAA

Mercury. Mercury is an important toxic element of health concern in many materials including coal stack gases and food products. Mercury can be determined by NAA via the 77 keV gamma line of the 2.7 days ^{197}Hg , but in RNAA it is typically analyzed through the longer-lived 47 days ^{203}Hg isotope. INAA data proved to be unsuitable for the determination of low Hg content in the environment. RNAA can be performed by the combustion method that was introduced by Kosta (1969) and applied by several laboratories, e.g., Norman and Becker 1999. The sample was ignited with an oxygen-natural gas torch and the condensed and dissolved Hg was directly counted. The procedure was effective in producing analytical data at the ng/g mass fraction level in biological and coal matrices. An RNAA method based on pyrolysis was developed by Blanchard and Robertson (1997); Hg was collected by double gold amalgamation. The detection limit for Hg in coal was 5 ng/g. Lindstrom (2005) introduced a modification to the combustion method in order to separate selenium from mercury to avoid the interference of ^{75}Se with the 279 keV gamma-ray of ^{203}Hg . Mercury was separated from Se by precipitating mercuric periodate, $Hg_5(IO_6)_2$. Chemical recovery was determined by gravimetry. The method of high accuracy and sensitivity was applied for the certification of Hg content in standard reference materials. Jacimovic and Horvat (2004) determined Hg in environmental and biological samples via the ^{197}Hg isotope where there was no Se interference. Fast combustion separation was performed and ^{197}Hg was detected with a high-efficiency NaI detector.

Hg was often separated by wet chemical procedures containing solvent extraction and precipitation steps in the form of HgI_2 , $Hg(SCN)_2$, HgS , or elementary Hg (Grimanis and Kanas 1982; Biso et al. 1983; Pietra et al. 1986).

According to Goncalves et al. (1998, 2000), irradiated samples were leached with aqua regia in a microwave oven with subsequent selective Hg extraction with bismuth diethyldithiocarbamate. In the organic phase, ^{203}Hg and ^{197}Hg were counted. Mercury mass fractions in soil and sediment samples taken around a gold mine in Brazil were determined above the detection limit of 10–50 $\mu g/kg$. Kucera (2007) described a procedure where Hg was extracted with nickel diethyldithiocarbamate, $Ni(DDC)_3$, into chloroform followed by its stripping with HCl/H_2O_2 solution. Mercury was determined via ^{203}Hg and parallel to Hg. Se was analyzed by INAA and RNAA. Alamin et al. (2006) applied the combined method for the determination of trace amounts of Hg and Se in Libyan food items.

Cadmium. Cadmium is a toxic heavy metal and a main elemental pollutant in the environment originating from metallurgical industry; the production of batteries; anticorrosive coatings of metals, pigments, burning of coal; etc. It is detected via ^{115}Cd in secular equilibrium with its daughter $^{115\text{m}}\text{In}$ by gamma-spectrometry. Bedregal and Montoya (2002) performed postirradiation RNAA of Cd after separation of the chlorocomplexes on an anion-exchange resin column. Ions retained on the resin, i.e., phosphates, iron, zinc, and cadmium were sequentially eluted with 6 mol/l HCl, 0.25 mol/l HCl, 0.024 mol/l HCl, and $\text{NH}_3\text{-NH}_4\text{Cl}$ buffer (pH 10), respectively. The detection limit was about 0.04 mg/kg. Samczynski and Dybczynski (2002) developed a pre- and postirradiation radiochemical procedure for the determination of Cd and Zn that was based on the retention of the analytes on the amphoteric ion-exchange resin Retardion 11A8. Samples are loaded from 2 mol/l HCl on the column. In the pre-concentration step, Cd and Zn are eluted together, during the postirradiation procedure Zn is stripped with an NH_4Cl buffer first, and finally Cd is stripped with 9 mol/l HNO_3 –1 mol/l NH_4Cl . The detection limit of the method was 37 mg/kg and 25 mg/kg for Cd and Zn, respectively.

Arsenic. Arsenic is a well-known toxic element with toxicity depending on the chemical species. On the other hand, sublethal doses of arsenic trioxide can be administered to patients for cancer treatment. INAA is often used to determine As in biological samples. A postirradiation RNAA method of increased sensitivity has been developed at the Jozef Stefan Institute, Slovenia by Byrne and Vakselj (1974). The separation procedure is based on acid destruction of the organic matrix followed by the extraction of AsI_3 into chloroform. The method was used successfully for the determination of the total As content of blood fractions of cancer patients (Slejkovec et al. 2008) with As mass fractions of blood samples in the ng/g range. Speciation studies were performed using HPLC. RNAA was applied for the determination of As in total diet samples from various Iranian provinces (Gharib et al. 2001).

Determination of Elements of Radiological Importance

Strontium. There is a growing interest for the determination of trace elements, which have radiologically important radioactive isotopes in the environment. Biokinetic data about Sr will help predict the behavior of ^{90}Sr in the environment and in human beings. Complementing data provided by INAA, Sr was analyzed by RNAA in total diet samples (Dang et al. 2000, 2001). After acid digestion, Sr was simply co-precipitated with calcium oxalate, thus obtaining a detection limit of 50 ng for Sr in the samples. The dietary intake of Sr by adult Indian population was determined. For Sr RNAA, after the anion-exchange separation of rare earth elements, a sulfate precipitation was performed (Tian et al. 2001).

Thorium and uranium. To study the behavior of alpha-emitting thorium and uranium isotopes in bioassay samples, ultra-sensitive measuring methods are required.

Dang et al. (2000) increased the sensitivity of NAA for Th by separating the indicator radionuclide, ^{233}Pa , using co-precipitations with manganese dioxide and barium sulfate and determined Th in total diet samples. A similar postirradiation procedure was coupled to the following pre-irradiation separation and concentration of Th (PC-RNAA) by Höllriegel et al. (2005) to increase the sensitivity of the method for the determination of urinary Th excretions. The pre-concentration procedure consisted of phosphate and calcium oxalate co-precipitations. The detection limit of Th in the urine sample was about 10 pg (0.04 μBq).

Glover et al. (1998, 2001) developed an ultra-sensitive method for the analysis of ^{232}Th in bioassay and environmental samples and pre-concentration radiochemical neutron activation analysis (PC-RNAA) was applied. In the pre-irradiation procedure, Th was concentrated using

an ion-exchange resin. In the course of the postirradiation chemistry, ^{233}Pa was separated either by ion exchange or by extraction chromatography. For the latter purposes, a TEVA/TRU tandem column containing organic amine (TEVA) and phosphate and phosphine oxide derivatives (TRU) was used (TEVA and TRU are the trade names of the products of Eichrom Co.). (Note: Certain commercial equipment and materials are identified in this work for the purpose of adequately describing experimental procedures. Such mention does not imply endorsement by the National Institute of Standards and Technology.) Finally, the electrodeposited source of Pa was counted. Chemical recoveries were determined both in the pre-concentration and postirradiation processes using the radiotracers ^{229}Th and ^{231}Pa , respectively. The detection limit of 3.5×10^{-7} Bq for ^{232}Th was almost three orders of magnitude lower than for alpha spectrometry.

An ultra-sensitive method was developed for U and Th as well as for ^{40}K determination in liquid scintillators used for neutrino and dark matter experiments. In the RNAA procedure, 250 ml of irradiated cocktail was chemically processed and indicator nuclides of U and Th, namely, ^{239}Np and ^{233}Pa were extracted with tributylphosphate (TBP). Using coincidence techniques, a sensitivity for U down to 10^{-16} g/g was realized (Goldbrunner et al. 1998).

A fast postirradiation separation procedure for the simultaneous determination of V and U in biological (total diet) samples was reported by Repinc and Benedik (2005). Samples were destroyed with mineral acids, V was extracted with BPHA (see above), and U was extracted with TBP. The chemical yield for U was determined by γ spectrometry of the added natural U carrier.

Single-element separations for RNAA purposes have recently been carried out more frequently than before. A detailed bibliography is given in the book by Alfassi (1994a) about the separations of V, Cr, Mn, Cu, As, Zn, Ag, Cd, and Cs. RNAA methods for single element determination and separation are occasionally used for intercomparison purposes. Such procedures of intended high accuracy have been developed, e.g., by Dubczinskij (1996) for the analysis of Cu, Co, Mo, Cd, and Ni in biological materials.

Determination of Other Elements

The role of many trace elements, e.g., V, Sn, Si, Ag, etc. in the environment and biology is not well understood and is often due to the lack of high accuracy analytical data. Recently, several RNAA procedures have been developed/applied for the determination of such elements. Some examples are discussed below.

Vanadium. Vanadium is released to the environment by emission from coal- and oil-fired power plants. Little information is available on natural levels and the role of V on human health. Vanadium can be determined via the short-lived (3.75 min) ^{52}V isotope produced via the $^{51}\text{V}(\text{n},\gamma)$ reaction. Analytical sensitivity has been increased by a rapid postirradiation chemical separation (Repinc et al. 2005). In the separation, biological or environmental samples are destroyed in a Kjeldahl flask; V is oxidized to pentavalent state and extracted with *N*-benzoyl-*N*-phenylhydroxylamine (BPHA). Chemical recovery is determined by detecting the violet complex by spectrophotometry. Nanogram levels of V were determined in selected food and total diet samples from Slovenia (Repinc et al. 2005) and Iran (Gharib et al. 2001).

Silver. Silver has a variety of applications, e.g., in photographic industry, electronics, and jewelry. It can be released to the environment where it can accumulate in biological organisms, including human beings. A postirradiation RNAA procedure has been developed for the determination of Ag in biological reference materials in ng/g mass fractions at the Nuclear Physics Institute, Rez, Czech Republic (Mizera et al. 2008). Samples were irradiated in a Cd

shield to obtain ^{110m}Ag via the nuclear reaction with epithermal neutrons of ^{109}Ag . The simple separation is based on fast fusion of the biological matrix using NaOH and Na_2O_2 followed by the precipitation of Ag as a hydroxide and AgCl . Chemical yields were determined by gravimetry or tracers studies using ^{106m}Ag or ^{105}Ag .

Silicon. It is assumed that Si is an essential element for humans. A postirradiation RNAA method of sufficiently high sensitivity for biological studies has been reported by Kucera and Zeisler (2005). The postirradiation separation consists of fusion, followed by sequential evaporation of Cl , Br , and the distillation of Si as SiF_4 that is absorbed in a boric acid and ammonium molybdate-containing solution. The beta radiation emitted by ^{31}Si produced with thermal neutrons via the $^{30}\text{Si}(\text{n},\gamma)^{31}\text{Si}$ reaction was measured by liquid scintillation counting (LSC). Detection limits as low as $0.5\text{ }\mu\text{g/g}$ could be achieved.

Tin. Tin is used not only as metal alone or alloying component of bronze, but also as a heat and light stabilizer for PVC, pesticides, and fungicides. Radiochemical NAA methods have been reported for the determination of Sn in aquatic biota (Armer and Shawky 2002) and in daily diet samples (Gharib et al. 2001).

There are two groups of chemically similar elements that attract much attention especially in geological and environmental samples, although interest has been raised for presence in bioassays as well: the platinum group elements and the rare earth elements.

Platinum group elements (PGE). PGEs consist of Ru , Rh , Pd , Os , Ir , and Pt . They represent a coherent group of siderophil elements (PGEs extended by Re and Au) from which conclusions can be drawn on the history of rocks. The release of PGEs to the environment has increased because of their applications in the catalysts of cars and pharmaceutical products.

Two methods have been developed for the sensitive determination of PGEs and gold in geological materials by Garuti et al. (2000): an RNAA procedure and pre-concentration NAA. In the RNAA procedure, irradiated samples were subjected to acid destruction in a microwave bomb; Os and Ru were separated by extraction of the tetraoxide compounds into CCl_4 , the remaining noble metals were retained as chlorocomplexes on an anion-exchange column, and divided into two groups by means of elution. In the PC-NAA method, concentration of PGEs and Au in a nickel sulfide bead by a fire assay technique was followed by INAA determination. Detection limits in the range of $0.001\text{--}0.015\text{ ng}$ were derived for both methods. Separation procedures for PGEs based on fire assays have previously been reported (Hillard 1987; Parry et al. 1988).

For the determination of Ir in aerosol particulate samples, Heller-Zeisler et al. (2000) compared three methods, INAA, RNAA, and thermal-ionization mass spectrometry. In the RNAA procedure, Ir was separated from the digested sample on an anion-exchange resin as a chlorocomplex. The sensitivities of INAA and RNAA were comparable, i.e., $60\text{--}100\text{ fg}$ and both of them were superior to mass spectroscopy.

When Au or Pt are determined by RNAA, the ^{198}Au and ^{199}Au indicator radionuclides have to be separated, e.g., by retention as a chlorocomplex on an anion-exchange resin, by precipitation as a reduced metal, by electroplating, or by solvent extraction. For samples containing both Au and Pt , it has to be kept in mind that ^{199}Au is formed from both elements (Zeisler and Greenberg 1982).

Other methods for PGE and noble metal separations have also been published. Chai reviewed the RNAA of PGEs (Chai 1988) and Alfassi prepared a summary (Alfassi 1994a). For group separation purposes, chelating ion-exchange resins (Nadkarni and Morrison 1977; Chai et al. 1987), solvent extraction with long-chain primary amines (Chai et al. 1987), and the combinations of different separation procedures obtaining complicated separation schemes

have been applied. Kucera et al. (2006) has recently published two radiochemical methods for the sensitive and accurate determination of the siderophil element, Re, by RNAA. Rhenium is separated either by extraction with tetraphenylarsonium chloride or by extraction chromatography with trioctylmethylammonium chloride (Aliquat 336, trademark of Cognis Corp.).

Rare Earth Elements (REE). Several radiochemical procedures are based on the chemical similarities of the rare earth elements, especially those of lanthanides.

A simple and accurate chemical separation procedure was applied to the determination of seven REEs in fossil shells by Ohde (1998). REEs were co-precipitated with ferric hydroxide and chemical yields were determined by reactivation of Gd and Yb. Detection limits in the range of 0.1–10 ng/g were attained. Lanthanides were co-precipitated as mixed hydroxides and carbonates followed by their co-precipitation as oxalates in the postirradiation RNAA procedure of Kucera et al. (2006). Chemical yields typically around 80–90% were determined individually for each sample by reactivation of the Pr, Er, and Lu carriers. Detection limits for most lanthanides in agricultural crops were at the level of ng/g. One of the most sensitive analytical procedures for the determination of REEs in geological and cosmochemical samples (1–10 pg) was developed by Minowa and Ebihara (2003), Minowa et al. (2007). After irradiation, REEs were concentrated by co-precipitation as hydroxides and fluorides, then anion-exchange resin was used to remove chloride complexes, e.g., Fe, Co, Cr. Extraction chromatography using TRU resin, an organic phosphorous extractant was applied to separate Sc from the REEs. Thus, the most seriously interfering isotope, ^{46}Sc was removed ($<0.005\%$ ^{46}Sc). Chemical yields determined for 11 REEs by ICP-OES varied between 20% and 60%.

Separations of REEs using anion or cation exchangers, anhydrous manganese dioxide, organic complexes (ammonium pyrrolidone dithiocarbamate), precipitations with hydroxides, fluorides, and the development of combined separation schemes based on these procedures have also been reported and a short review was given by Alfassi (1994a).

Recently, Takeda et al. (2007) and Minowa et al. (2007) introduced a complex RNAA procedure for the determination of trace siderophil elements and REEs in rock and meteorite samples. After irradiation, samples were subjected to alkaline oxidative fusion. Osmium and Ru were removed sequentially by evaporation and the remaining siderophil elements were retained on the chelating resin SRAFION NMRR. REEs, Au, and Pt, and finally, Re and Ir were sequentially stripped from the column with 0.05 mol/l HCl, 5% thiourea, and 7 mol/l NH_4OH , respectively. Although chemical yields determined by the reactivation method widely varied, the method seems to be promising for the sensitive determination of several PGEs (Ru, Os), Re, and lanthanides.

30.5.4.3 Separation of Several Elements and Various Groups of Elements

The literature in this field has grown tremendously during the last 50 years, but most of the publications appeared before the end of the 1980s. When semiconductor detectors became available, INAA almost entirely replaced radiochemical applications. The latest generation of high-purity Ge detectors has not only high resolution, but also high efficiency. At present, the general trend in RNAA is the application of simple and fast separation procedures that allow for the analysis of short-lived nuclides and the exploitation of the inherent multielement nature of the method. The procedures, including chemistry as well as nuclear measurement techniques, should be under total quality control. Fardy (1990) summarized the studies from 1980 to 1988 in table form. The review by Alfassi (1994a) covers the literature to 1994. To illustrate

the major tendencies that determined the research in RNAA to the end of the 1980s, some examples are given below.

Samples were often divided into many groups to enable detection with NaI(Tl) scintillators that had relatively low resolution but high efficiency. The separation scheme was based on the application of a set of columns filled with selective or semi-selective sorption materials that retained certain groups of elements. In the ideal case, the same load solution was passed through consecutively joined columns, thus offering a chance for automation of the procedure.

Pietra et al. (1986) developed several procedures for the separation of as many elements as possible. The most extended procedure is applicable to the analysis of 50 elements in biological materials. In this method, volatile components (Cl, Br, I) are removed by distillation, followed by the chromatographic separation of the condensate using anion exchange (AG1 \times 8: Sb, Sn, Hg, Au) and titanium dioxide: As, Se, Ge columns; Re and Ru are found in the effluent. Nonvolatile components are passed through the following sets of columns: hydrated antimony pentoxide (HAP: Rb, K, Na, Ta), anion-exchange resin (AG1 \times 8: Ga, Fe, Zn, Cd, Pd, Bi, Mo, Au), copper sulfide (CUS), tin dioxide (TDO: Hf, Pa, W, Zr, I), acidic aluminum oxide (AAO: P, Ir), and cation-exchange resin (AG50: Co, Cr, Cs, Mn, Ca, Ba, Sr, Sc, REE). Neptunium and Ag appear in the final effluent. In another procedure for geological and biological samples, 39 elements were separated into five groups using five consecutive columns in the following order: AAO, TDO, CUS, CDO (cadmium oxide) and HAP. Pietra and his coworkers (Pietra et al. 1986) developed altogether 22 RNAA procedures for environmental and biological samples. Several of those, intended for the separation of only a limited number of elements, are less complicated.

Several studies were devoted to the construction of automated equipment for rapid and remote-controlled operation. In 1966, Samsahl (1966) published a paper about the development of an automated system that was based on ion-exchange column separation.

Although automation has not been successfully applied in many laboratories, chromatographic separations using a limited number of columns form the basis of the present investigations and are routinely used in many laboratories. Ion exchange and extraction chromatographic (EC) procedures are available for more and more applications. EC materials were prepared and applied for group separation purposes at the Nuclear Physics Institute, Rez, Czech Republic. Supported CYANEX 301 extractant was applied for the separation of Cu, Cd, As(III), Sb(III), while supported Zn-DDC₂ extractant retained Mo as well as Cu, Cd, As, and Sb (Lucanikova et al. 2006). The general tendency of using selective organic compounds of standard quality, instead of the irreproducible inorganic sorbents of high selectivity, can be recognized.

The general tendency to apply RNAA for the determination of trace elements when high sensitivity and precision are required can be confirmed. Methods have also been developed for multielement determinations by RNAA. These methods are generally based on complicated separation schemes and usually combine several individual procedures. Randa et al. (2003) reported a method for the determination of REEs, Cs, and Rb combining the REE separation based on oxalate precipitation with the Cs–Rb separation using ammonium molybdophosphate (AMP). Tian et al. (2001) published an RNAA method for the determination of REEs, U, and Ba consisting of a fluoride precipitation of REE and U, and a Ba sulfate precipitation. According to another RNAA method, U and Th determination was based on fluoride precipitation of the analyte nuclides (Np and Pa), while Sr was precipitated as sulfate. Combined procedures of Zaidi were briefly reviewed in [Sect. 30.5.3.1](#) (see also Zaidi et al. 2001).

30.5.5 Application of RNAA for the Determination of Radionuclides

Because of its high sensitivity, RNAA has been used to study the behavior of some long-lived radionuclides present in the environment. Strictly speaking, the analysis of uranium and thorium belongs in this field because neither of these elements have stable isotopes, but due to the billion-year long half-lives they are commonly treated like stable elements. There are some isotopes of anthropogenic origin that have some orders of magnitude shorter half-lives (“only” in the range of millions of years) and thus have higher specific activities and are found in nature in ultra-trace levels. Some of these radionuclides were released to the environment during the atmospheric bomb tests of the 1950s and 1960s, as well as during normal and accidental emissions from the nuclear energy industry. These radionuclides represent a potential hazard for the population due to possible leaks in nuclear facilities and waste-disposal sites, not only in the near-term but far into the future as well. ^{129}I ($T_{1/2} = 1.6 \times 10^7$ a) is one of the major representatives of this group, but ^{99}Tc ($T_{1/2} = 2.1 \times 10^5$ a), ^{237}Np ($T_{1/2} = 2.1 \times 10^6$ a) and ^{135}Cs ($T_{1/2} = 2.1 \times 10^6$ a) can also be mentioned.

An excellent review paper was recently written and published by Hou (2008). To express and quantify the advantage of activation analysis with respect to direct radiometric detection of radionuclides, an advantage factor AF was defined by Byrne and Benedik (1999):

$$AF = \frac{A_2}{A_1} = ((\Phi)_{\text{th}}\sigma_{\text{th}} + \Phi_{\text{epi}}I_0) \frac{(1 - e^{-\lambda_2 t_i})}{\lambda_1} \quad (30.42)$$

where $A_1 = N\lambda_1$ is the original activity of the target nuclide, and A_2 is the activity of the new radionuclide produced by irradiation over the period t_i .

Advantage factors of NAA for some long-lived radionuclides under selected irradiation conditions ($\Phi_{\text{th}} = 10^{13} \text{ n cm}^{-2} \text{ s}^{-1}$, $\Phi_{\text{epi}} = 5 \times 10^{11} \text{ n cm}^{-2} \text{ s}^{-1}$, $t_i = 15 \text{ h}$) have been calculated and are given in the paper by Hou (2008). The AF for ^{129}I , ^{99}Tc , ^{237}Np , and ^{135}Cs are 1.3×10^6 , 2.1×10^4 , 3.6×10^5 , and 3.9×10^3 , respectively.

30.5.5.1 Determination of ^{129}I by PC-RNAA

Excellent examples of the determination of ultra-trace levels are provided by the analysis of ^{129}I in environmental and biological samples. The short-lived ^{130}I is produced in the (n, γ) reaction and is easily detected by gamma-ray spectrometry, while the stable ^{127}I undergoes the $(n, 2n)$ reaction-forming ^{126}I that can be used to monitor the chemical recovery. Recovery can also be monitored with radiotracers, e.g., ^{125}I and ^{131}I . To achieve the highest sensitivity, postirradiation radiochemical separation and pre-irradiation chemical concentration are also applied.

For the analysis of ^{129}I and the determination of the $^{129}\text{I}/^{127}\text{I}$ ratio, various separation procedures have been developed. Parry et al. (1995, 2001) used anion-exchange resin for pre-concentration of iodine from milk, vegetation, and atmospheric samples. After irradiation, iodine was eluted and precipitated as AgI . Detection limits below 10 mBq/kg (or mBq/l) for the ^{129}I activity concentration and 10^{-7} for the $^{129}\text{I}/^{127}\text{I}$ ratio were achieved.

Aumann and Güner (1999) used PC-RNAA to determine ^{129}I in soil. The combustion technique was used to pre-concentrate iodine that was collected on charcoal, then removed by heat and finally trapped in a quartz vial. Postirradiation purification consisted of solvent extraction and distillation. Szidat et al. (2000) used the same pre-concentration technique

followed by postirradiation chemistry and precipitation of AgI. Iodine could be separated from solid samples by alkaline fusion and oxidative I_2 extraction and by reductive back-extraction. Frechou et al. (2001) applied PC-RNAA for the measurement of ^{129}I including pre-irradiation separation leading to lead iodate and final evaluation according to the k_0 method. For pre-concentration of large-volume water samples, an anion-exchange resin was used by Szidat et al. (2000) and AgCl co-precipitation technique was applied by Kabai and Vajda (2002). Hou et al. (2002, 2003) determined ^{129}I in various environmental samples collected from the Baltic Sea and from Chernobyl. The PC-RNAA analytical procedure consisted of pre-concentration, extraction of elemental iodine, and conversion to MgI_2 or LiI . During postirradiation separation, iodine was extracted again and finally precipitated as PdI_2 . Osterc and Stibilj (2008) used a similar radiochemical procedure for the determination of ^{129}I and the $^{129}I/^{127}I$ ratio in marine algae from the North Adriatic Sea.

RNAA for ^{129}I is an old technique, used in 1962 by Studier (1962), but its capabilities have significantly been improved. Among the competitive techniques regarding the sensitivity for the $^{129}I/^{127}I$ ratio, accelerator mass spectrometry (AMS) appears to be superior to RNAA. AMS is sensitive enough to determine pre-nuclear environmental ratios in the range of 10^{-10} (Szidat et al. 2000). ICP-MS may also provide results of high sensitivity (Farmer et al. 1998).

RNAA can also be successful for the determination of other long-lived radionuclides, although ICP-MS and AMS are often possible better alternatives.

30.5.5.2 Determination of ^{237}Np by PC-RNAA

In the irradiation of ^{237}Np with thermal neutrons, the 2.1-day ^{238}Np isotope is produced and can be detected by γ spectrometry. Because ^{237}Np is produced both from ^{238}U by (n,2n) reaction and from ^{235}U by consecutive neutron capture, uranium has to be separated from the samples in a PC procedure before irradiation. Three techniques are used to separate Np from the matrix and interfering elements: hydroxide precipitation, solvent extraction, and ion exchange. Postirradiation chemical separation is performed by solvent extraction, ion exchange, or extraction chromatography. In the procedure of Chen et al. (2001), soil samples are destroyed by evaporation with aqua regia, Np is preconcentrated by repeated co-precipitations as hydroxide, extracted with tert-octylamine (TOA) from HCl solution, and purified on an anion-exchanger column. Postirradiation separation is necessary to remove activated impurities. Byrne (1986) used TTA extraction, Germain and Pinte (1990) applied anion-exchange chromatography, and Kalmykov et al. (2004) used UTEVA extraction chromatography. UTEVA is the trade name of the resin produced by Eichrom Co. that contains dipentylpentyl phosphonate on an inert support material. Typically, ^{239}Np is used as a tracer for chemical yield determination.

Neptunium-237 has also been determined by alpha spectrometry, RIMS, AMS, and ICP-MS. RNAA can be regarded as the most sensitive analytical technique for ^{237}Np .

30.5.5.3 Determination of ^{99}Tc by PC-RNAA

In the irradiation of ^{99}Tc with thermal neutrons, the short-lived (15.8 s) ^{100}Tc isotope is produced and can be detected by either gamma spectrometry or a low-background beta counter. Analysis can be performed only with a fast sample transfer system. Both pre- and

postirradiation separations are required to get sufficient purity. Many procedures have been developed for the pre-concentration and separation of Tc. It can be co-precipitated with tetraphenylarsonium perrhenate, retained on an anion exchanger as TcO_4^- anion, separated as a metal cation on a cation exchanger, extracted with cyclohexanone, tert-butyl phosphate, or separated as pertechnetate using TEVA extraction chromatographic material. Chen et al. (1990) used a hydroxide scavenger to remove metals and then retained Tc on an anion-exchange resin. Technetium eluted from the resin was purified by extraction chromatography on TEVA resin. Cyclic activation is preferred if postirradiation separation is not possible. Foti et al. (1972) developed a fast RNAA procedure based on the removal of metal impurities with hydroxide precipitation and precipitation of Tc with tetraphenylarsonium perrhenate. The best detection limit by PC-RNAA (2.5 mBq) is similar to that of the radiometric method (Chen et al. 1990). Lower detection limits can be achieved by ICP-MS.

30.5.5.4 Determination of ^{135}Cs by PC-RNAA

In the neutron capture reaction of ^{135}Cs , the 13-day isotope, ^{136}Cs , is produced and emits a gamma ray of relatively low abundance. The sensitivity of the gamma spectrometric determination is further reduced by the presence of other γ -emitting Cs isotopes, i.e., ^{137}Cs , ^{136}Cs , and ^{134}Cs . There have been a few attempts to determine ^{135}Cs by PC-RNAA. In the procedure by Chao et al. (1996), Cs is pre-concentrated with ammonium molybdophosphate (AMP) and purified by cation-exchange chromatography. In the postirradiation procedure, Cs is removed from the cation exchanger and co-precipitated with AMP or purified with cation-exchange chromatography. A detection limit of 10^{-4} Bq has been reported. Because of the spectral interferences, mass spectrometric techniques seem to be more promising for the determination of ^{135}Cs .

30.5.6 Application of NAA for Speciation Studies

Speciation studies about the chemical nature of trace elements have recently attracted much attention. Chemically separated fractions can be analyzed by NAA (both INAA and RNAA). Out of the increasing number of publications, two examples are mentioned here, one for biological investigations and the other for environmental investigations.

Shoop et al. (1998) studied the behavior of aluminum in urine to understand the role of Al in diseases, such as dialysis, dementia, and osteomalacia, which are of major concern to patients with end-stage renal failure. Non-protein- and protein-bound Al species were separated using a cation-exchange resin followed by NAA of Al. The total Al content was determined by RNAA. It was concluded that the majority of Al is bound to protein.

Pre-separation neutron activation analysis was used to determine the contribution of iodide and iodate to the total iodine content of seawater (Hou et al. 2000). Iodine species were separated by means of an anion-exchange resin that preferentially retained the iodide. Iodate in the effluent was reduced to iodide and passed through another anion exchange column. Both fractions were analyzed by NAA. Urine and milk samples were also analyzed.

30.6 Quality Assurance and Control in NAA

Nuclear analytical techniques have been demonstrated many times to be reliable and under complete statistical control. Nevertheless, a continuous effort by the practitioners is necessary to maintain the accuracy and precision of the analytical results and make these results acceptable in the modern quality environment of a testing laboratory.

This section highlights the common sources of uncertainties in NAA, the resulting uncertainty budgets, and the means of validation. Similar principles are applicable to all forms of activation analysis having in common many of the fundamental considerations regarding the uncertainty of nuclear measurements.

30.6.1 Sources of Uncertainty

As in all analytical determinations, the potential for uncertainties affecting results of a testing laboratory from sources outside the laboratory and outside the applied method must be understood and may not be underestimated (Iyengar 1981; Zeisler 1986). According to the ISO terminology, the uncertainties can be divided into Type A (uncertainties evaluated by statistical methods) and Type B (all other). The Type A terms are dependent mostly on the amount and the reaction cross section of the analyte. In the context of this chapter, only the method-specific sources of uncertainty will be treated, with the main emphasis on NAA.

30.6.1.1 Nuclear Reaction Rate and Sample Integrity

The rate of the nuclear reaction is not constant within a bulk sample. With neutrons, and more predominantly with charged particles, the energy distribution will change within the sample as will the overall density of the activating particles due to the interaction with the sample. In NAA, matrix or sample size and shape effects have been observed with PGAA procedures in an external neutron beam (Mackey et al. 1991), but cannot be studied easily in the isotropic neutron fields of internal irradiation sites. However, the flux in a sample can be significantly affected by the absorption of neutrons. Components of the sample with high neutron absorption cross sections and/or high neutron scattering cross sections, combined with high material density, will result in considerable self-absorption effects, even in rather small samples.

The exact calculation of neutron self-absorption and scattering requires complex numerical calculations. Nevertheless, a set of analytical approximations has been established and proven to be very useful to correct for these effects. These solutions are accurate for spherical samples, infinite and defined length cylinders, and infinite slabs or foils. (As an example, expressions for the self-shielding for a foil in collimated and isotropic neutron fields are given by [Eqs. \(30.18\)](#) and [\(30.19\)](#), respectively.) Many sample shapes approach one of these models and spreadsheets have been made available that calculate an absorption factor, i.e., an average fraction of the sample that has been activated (Fleming 1982, Blaauw 1996). The spreadsheets include tables of all known cross-section values to calculate a macroscopic cross section depending on the composition of the sample that is entered by the analyst. The spreadsheets then resolve the shape function to provide the absorption factor according to the selected shape model. For high-accuracy analysis the selection and exact definition of a sample shape will limit the uncertainty of these corrections. Prudent analysis strategies will limit these absorption corrections to a few percent.

The integrity of sensitive samples with somewhat volatile components cannot be assumed for most irradiation procedures. Thermal mobilization and/or radiative mobilization, recoil effect, and radiolysis can cause the volatile components to leave the sample during irradiation. Containment in quartz vials will prevent loss of the elemental species, but the analyte may be distributed over the whole volume of the container instead of the sample only. Therefore it is required that Hg is determined with the samples sealed in quartz and that provisions are taken to correctly assay the content regardless where the radioactive species are located in the container.

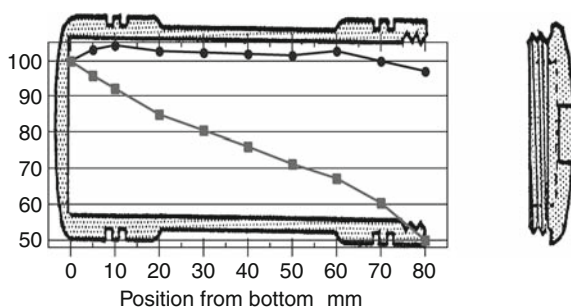
30.6.1.2 Geometry Uncertainties in Irradiation and Counting

A basic requirement for accurate NAA is the correct characterization of the irradiation facility (Becker 1987). Local and temporal neutron flux density gradients as well as gradients in the neutron energy spectrum of the irradiation position must be well understood and known for each irradiation. [Figure 30.5](#) illustrates the gradients in an irradiation capsule as measured by flux monitor foils. A difference of 1 mm in sample positioning will result in a 0.6% relative difference in the measured concentration.

It must be noted that this example presents a rather ideal situation since axial rotation of the irradiation capsule during the irradiation eliminates lateral gradients and the central linear gradient allows for elimination of the gradient through 180° inversion of the capsule at the midpoint of irradiation. Other mechanical devices for minimizing flux gradients in sample irradiation positions include rotators (Abugassa et al. 1999) positioned next to the reactor core for large numbers of samples or larger-size samples (Bode et al. 1997; Lin and Henkelmann 2002). An effective means for quality control of the irradiation are flux monitor foils. It is highly recommended to use these with each irradiation of samples and standards to verify the assumptions about the accurate irradiation geometry. Foils or wires of metals such as titanium, cobalt, zinc, copper, etc., or Al–Au alloy wires can be used for this purpose.

■ Fig. 30.5

Flux gradient within an irradiation capsule in the NIST CNR reactor RT-4 pneumatic tube irradiation facility (mean flux: $3.4 \times 10^{13} \text{ cm}^{-2} \text{ s}^{-1}$). The vertical axis was determined using Zn foils as monitors, where values are percent Zn found when compared to a foil in position 0 cm. The essentially linear drop-off in neutron flux between positions 20 mm and 60 mm provides a roughly even effective flux (see upper curve) when the capsule is turned halfway around its vertical axis (i.e., by 180°) at the midpoint $t_A/2$ of the irradiation



Uncertainties due to counting geometry can be controlled much more reliably, since in principle only geometry factors must be considered. Extensive references can be found regarding gamma-ray spectrometry of various source shapes (Debertin and Helmer 1988) and software is available for appropriate calculations (e.g., KAYZERO/SOLCOI 1996).

Other uncertainties in the gamma-ray detection yield, unrelated to counting geometry, are matrix effects that can suppress some gamma rays by self-absorption. These effects are gamma-ray energy dependent, and can be mathematically or experimentally corrected.

For narrow collimation, the self-absorption correction factor for a slab of thickness d is obtained by integrating the exponential attenuation function:

$$f_T = \frac{1 - e^{-\mu d}}{\mu d}. \quad (30.43)$$

Calculations according to [Eq. \(30.43\)](#) require the knowledge of the photon attenuation coefficients μ of the sample matrix (see [Sect. 11.5.1 in the Appendix of Vol. 1](#)). Experimental calibrations are readily conducted by placing an unirradiated sample between the activated sample and the detector, thus determining the attenuation coefficients for an unknown or unlisted matrix. By using an irradiated standard identical to the sample, as is possible in the comparator method, the need for geometry, self-shielding, and self-absorption corrections is eliminated, and thus the potential errors are reduced.

30.6.1.3 Timing Uncertainties

An accurate time base is essential for the accurate calculation of decay factors for different counting and decay times during the measurement. For the determination of indicator nuclides with less than 300 s half-life, an order of 0.1 s or even 0.01 s timing resolution may become crucial. The recording of real time and live time of a count with this precision is standard in many modern MCA systems. Unfortunately, some “advances” in computer operating systems, e.g., the user-friendly Windows surfaces, do not guarantee the immediate implementation of a MCA command. The range of differences in reading time tags and implementing, e.g., the start of acquisition, has caused manufacturers of PC-based MCAs to report only full seconds for the start of acquisition, a significant source of uncertainty when measuring fluorine using ^{19}Ne with $T_{1/2} = 17.22$ s.

More important to consider are uncertainties in the published half-life of the indicator nuclides. Determinations that rely on experiments with significantly different irradiation and counting times, as well as decay times, are too susceptible to uncertainties in the published values and may require a re-evaluation of the indicator nuclide’s half-life to assure accuracy (Greenberg et al. 2000; Lindstrom et al. 2007). Other methods of minimizing this type of uncertainty are of course irradiation and counting procedures that are exactly the same throughout a measurement cycle.

30.6.1.4 Uncertainties in Signal Detection and Processing

Relevant mechanisms that cause loss of counts from the photopeak include partial conversions of the incident energy event with part of the energy escaping the detector, true coincidence summing, random summing of pulses, also known as pile-up, and dead time. While the first two effects are part of the detector’s efficiency and are the same for all sample and standard counts, random summing and dead time are dependent on a sample’s activity.¹⁰

Dead time is the time required in each of the measurement components to process a single event; additional events arriving during this time cannot be processed. All MCAs exhibit counting losses due to the dead time required to process pulses from any given source of radioactivity. Many algorithms, both electronic and computational, are available to determine the amount of time during which those losses occur. When count rates of the sample being measured are practically constant over the counting period, then the standard method for calculating this time is the use of live-time clocks (LTC). The well-proven Gedcke–Hale live-time extension method (Jenkins et al. 1981) is employed in most nuclear spectroscopy systems. The fundamental problem with this method is that changing dead times during the counting will result in measurements during extended live-time periods when the measured activity can be significantly different from the one at the beginning of the counting period. This results in an underestimation of the activity by the LTC method.

The *loss-free counting* (LFC) method of correcting for dead time losses, as introduced by Harms (1967) and improved by Westphal (1981) gives much better results than LTC techniques in cases where the counting rate changes significantly during the measurement. The LFC method estimates the number of counts lost during a dead time interval and adds this number to the channel of the just processed pulse. This dynamic add-on process is capable of presenting a loss-corrected spectrum, but because of this process, the data no longer obey Poisson statistics. Consequently, the calculation of the resulting activity uncertainty is not easy, or not thought to be possible (Pomme et al. 1999).

A different method of loss-free counting has been implemented in the zero dead time method (ZDT) of a commercial digital signal processor. The ZDT correction is dynamically calculated by the processor to produce both the corrected data spectrum and the channel-by-channel variance spectrum. Upp et al. (2001) have shown that this digital method allows correct estimates of the uncertainty.

Recently Westphal and Lemmel (2008) summarized the correction methods and gave a recommended method for calculating the uncertainty.

The *pile-up losses* are corrected by electronic or computational means. Most spectroscopy amplifiers employ a pile-up detection and rejection circuit, which simply blocks further processing of the event and adds the dead time. The aforementioned dead-time correction principles apply. If pile-up events are not rejected, a calibration of the spectrometer for the losses in dependence of the dead time can be used. For more accurate results injection of events from a highly stable pulser provide a measure with the spectral data with the assumption that these events are subject to the same degree of pile-up as the photopeak events.

Summing of events, either a result of coincident emission of gamma rays in the decay chain of the nuclide of interest or of random coincident emissions, can lead to significant losses or potential additions to an otherwise “clean” peak (De Bruin and Blaauw 1992; Becker et al. 1994). While coincidence losses are not an issue for comparator NAA, calibration, and/or computational correction must be applied (Debertin and Helmer 1988; Blaauw and Gelsema 1999) to arrive at “true” peak areas for other methods of calibration.

30.6.1.5 Gamma-Ray Spectrum Evaluation and Software

The tendency toward fully automated gamma-ray spectrum evaluation can introduce errors. The degree of the potential for error varies among the software packages, nevertheless, there are some common risk factors that must be checked and evaluated by the user. These factors lie in

the peak-shape and peak-background functions used and the quality of the calibration of the functions' parameters as well as the quality of the spectrometry system performing within certain bounds of these calibrations. Since these factors are controlled by the user and the working spectroscopy system, it is suggested here that the analyst should evaluate the bounds of uncertainty introduced in this step. The analyst may resort to forms of interactive peak evaluations, including simple summing routines between visually established peak area boundaries (Lindstrom 1994), or apply different software packages to the evaluation of the collected gamma-ray spectra for quality assurance. The IAEA regularly conducts intercomparisons of software packages with respect to statistical performance (Blaauw et al. 1997). Depending on the individual spectrum, the analyst may find no additional uncertainty discernible from the counting statistics to tenths of percent differences for statistically well-defined peaks.

30.6.1.6 Interferences

There are potential interferences in activation analysis that must be considered and corrected for; these include interfering activation reactions and gamma-ray spectral interferences. Several well-known cases for NAA will be discussed; other forms of AA will need an assessment according to each experiment.

A given radionuclide can often be produced in more than one way. If the indicator nuclide used in the analysis is produced from an element other than the analyte, then a *primary interfering reaction* occurs. The magnitude of many of the primary interferences in NAA depends on the fast-to-thermal flux ratios in a reactor. The analytical reaction $^{50}\text{Cr}(n,\gamma)^{51}\text{Cr}$ with thermal neutrons is subject to the interfering reaction $^{54}\text{Fe}(n,\alpha)^{51}\text{Cr}$ with fast neutrons. For this reason, the determination of Cr in the presence of high Fe content can lead to erroneous results without corrective action. In some cases, corrections can be experimentally determined; in other cases the presence of the interfering reaction may preclude the determination of the analyte. The determination of Cr in whole blood suffers from the above interference, where the apparent Cr content can exceed the natural levels. This interference can be minimized by irradiation in a well-thermalized neutron flux (Zeisler and Young 1987). Recently the RNAA determination of silicon via $^{30}\text{Si}(n,\gamma)^{31}\text{Si}$ in biological materials has been successful through the use of a well-thermalized flux in a thermal column to minimize the primary interference from phosphorus (Kucera and Zeisler 2005). A rather ubiquitous primary interference occurs from uranium fission products in geological, environmental, and, sometimes, biological materials. Again, calibration and correction may be possible, but the apparent mass fraction of the interfering elements (^{99}Mo , ^{131}Ba , ^{140}La) is typically equal to or larger than the common levels of the trace elements when uranium is present at those levels.

A *secondary interfering reaction* is the result of interaction of an activation product with the activating particles. An example of this type of reaction is the activation of ^{198}Au produced from gold in a sample. In this case the reaction $^{198}\text{Au}(n,\gamma)^{199}\text{Au}$ directly interferes with the NAA of Pt via ^{199}Au . This interference can prohibit the determination of platinum in the presence of gold (Zeisler and Greenberg 1982; Rietz and Heydorn 1993). Another possibility is that the product particles interact with the element of interest. Activating particles are preferentially produced in higher-energy activation reactions. For example, in the determination of nitrogen by 14 MeV FNAA via $^{14}\text{N}(n,2n)^{13}\text{N}$ in an organic matrix, the fast neutrons scattering on hydrogen induce a flux of protons that results in the interfering reaction

$^{13}\text{C}(\text{p},\text{n})^{13}\text{N}$. In most instances the latter type of interference is not a serious problem since the secondary particle fluxes are relatively low.

Gamma-ray spectral interference means that two radionuclides emit gamma rays with the same or nearly the same energy. For instance, ^{51}Ti and ^{51}Cr formed in thermal neutron activation decay to the same final nuclide ^{51}V , emitting a single 320.08 keV gamma ray. For these two nuclides, however, a separation via the half-life is in all practical instances possible. In some instances a spectral separation is difficult even with the best-resolution detectors when the count rates are high and the peaks get broadened. An illustrative example is interference between the 846.77 keV line of ^{56}Mn ($T_{1/2} = 2.56$ h) and the 843.74 keV line of ^{27}Mg ($T_{1/2} = 9.45$ min). This interference can be resolved through the use of other gamma-ray lines of ^{27}Mg , or by utilizing the different half-lives. In other situations the difference in half-lives may not be very significant or the nuclide of interest has even a somewhat shorter half-life than the interfering nuclide. One well-known case is the interference for the determination of mercury via the 279.19 keV line of ^{203}Hg ($T_{1/2} = 46.6$ days), which is overlapped by the 279.54 keV line of the selenium indicator nuclide ^{75}Se ($T_{1/2} = 119.77$ days). This case can be resolved because ^{75}Se emits several gamma rays and the interference is corrected by measuring the ratio of the interfering photopeak to a “clean” peak. In this instance, the ratio of the 279.54 to 264.66 keV line of ^{75}Se is typically 0.46 and a corresponding number of counts is calculated based on the “clean” peak and subtracted from the combined peak to arrive at the ^{203}Hg peak. It should be mentioned that in complex matrices care must be taken not to have the “clean” peak interfered by another nuclide, in this instance, e.g., by ^{182}Ta . It can be stated that essentially all spectrometric interferences can be resolved by one of the discussed means. Improvement of detector resolution may help in some cases, or anti-coincidence or coincidence counting can either reduce the interfering photopeaks or allows selection of a nuclide’s gamma rays.

When the interference cannot be resolved by the aforementioned means, the option of selecting a different indicator nuclide may lead to a solution, but sometimes a radiochemical separation may become necessary. Radiochemical separations are discussed in [Sect. 30.5](#). (It should be noted that additional uncertainties are encountered with RNAA.) More examples of interferences can be found in the review by Alfassi (2001).

30.6.2 Uncertainty Budget

An uncertainty budget for NAA can be developed on the basis of [Eq. \(30.35\)](#), or for k_0 -INAA by using [Eq. \(30.37\)](#). All parameters are essentially independent, therefore the combined standard uncertainty in C_x can be obtained from the well-known differential expression for the combination of individual uncertainties.¹¹

$$u_{C_{x(\text{unk})}}^2 = \sum_i \left(\frac{\partial C_{x(\text{unk})}}{\partial p_i} \right)^2 u_{p_i}^2 \quad (30.44)$$

where p_i is the i th parameter on the right-hand side of [Eq. \(30.35\)](#) or [Eq. \(30.37\)](#) (some of which are listed in the first column of [Table 30.2](#)) and u is the uncertainty associated with the parameters.

The following example of a high-accuracy INAA determination of Cr in SRM 1152a Stainless Steel illustrates the use of an uncertainty budget and the resulting observation of a satisfactory measurement outcome (Zeisler et al. 2005). The experiment had been designed to

Table 30.2

Uncertainty analysis for SRM 1152a stainless steel

Uncertainty budget					
Parameter (p_i)	Typical value	Standard uncertainty	Type A/B	n	Description
C_s (g/g)	1.0	0.00022	B		Analyte mass fraction contained in primary assay standard
m_x (g)	0.8?	0.00002	A	8	Mass of sample used
m_s (g)	0.8?	0.00002	A	5	Mass of primary standard used
N_x	1.2×10^7	2,710	A	8	Number of counts in indicator gamma-ray peak for sample
N_s	2×10^7	5,859	A	5	Number of counts in indicator gamma-ray peak for standard
λ (d^{-1})	0.0250211	0.0000022	B		Decay constant
$t_{D,x}$ (d)	10	0.00006	B		Decay time until start of measurement for sample
$t_{D,s}$ (d)	10	0.00006	B		Decay time until start of measurement for standard
$t_{C,x}$ (d)	0.16667	1.16×10^{-7}	B		Elapsed time of measurement for sample
$t_{C,s}$ (d)	0.16667	1.16×10^{-7}	B		Elapsed time of measurement for standard
R_θ	1	0 ^a	B		Ratio of isotopic abundances for sample and standard
R_φ	1	0.0087	B		Ratio of neutron fluences (including fluence gradient, neutron self-shielding and scattering)
R_σ	1	0.001	B		Ratio of effective cross sections if neutron spectrum shape differs for sample and standard
R_ϵ	0.9975	0.0025	B		Ratio of counting efficiencies (including geometry, gamma-ray self-shielding and counting effects)
Results					
C_x (g/g)	0.17776				Analyte mass fraction contained in the sample
u_C (g/g)	0.00175				Combined uncertainty
$U(=ku_C)$	0.0035				Expanded uncertainty ($k = 2$)

^aSet to zero because no natural variations have been reported by the IUPAC Commission of Atomic Weights and Isotopic Abundances (Rosman and Taylor 1998); measurement based on ⁵¹Cr decay.

illustrate that uncertainties comparable to those of other methods can be obtained by INAA. As shown in Table 30.2, the certified value for Cr in the SRM is given as 17.76% with an uncertainty of 0.04% (0.23% relative); the measurement resulted in an expanded uncertainty of 0.17% relative. Examination of the budget shows that the largest relative component of

uncertainty was in the ratio of neutron fluxes between sample and standard because the sample could not be cut to a foil with very uniform thickness. The resulting uncertainty in the fluence gradient corrections determined this component of uncertainty. Obviously, more uniform and correctly measurable foil thickness would minimize this problem, and other uncertainty components, such as weighing, may become the more significant and limiting sources of uncertainty.

The ability to formulate uncertainty budgets directly relating to all components of the measurement equation is a tremendous bonus offered by the AA procedures. Analysts can easily obtain estimates for each of the components of uncertainty for each individual sample measurement. This detailed knowledge not only provides realistic estimates of the overall combined uncertainty, but also provides the information needed for a reduction of these uncertainties for a particular measurement problem.

30.6.3 Validation

Practitioners of AA have paid explicit attention to the quality of their analytical output, not only since the new quality culture has become a common staple of an analytical laboratory but practically since the inception of the procedures. The tools for validating the performance of an AA procedure have been and still are determinations in an interlaboratory comparison exercise, comparisons of the procedures' results with those obtained from a different analytical method, and determinations in certified reference materials (CRM) as well as determinations traceable to an accepted standard (e.g., a CRM).

Interlaboratory comparison exercises, by voluntary participation or by mandate from a quality system requirement, will usually give the analyst a sense of the procedures' performance relative to some average or even all results of a measurement. Recent examples range from NAA-only round-robin analyses (Becker 1993) to multi-method comparisons among national metrological laboratories (CCQM 2008).¹² Sometimes z-scores are given to highlight the degree of agreement or disagreement with the defined reference value, e.g., the mean of the data population. Preferentially, this reference value is established by an authoritative measurement laboratory, such as those participating in the CCQM efforts.

The ability to conduct direct comparisons with another analytical method may be limited because of existing capacities within or outside a laboratory, and frequently the special nature of the AA determination in terms of sensitivity or selectivity for the analyte of interest does not allow determinations with another technique. In these instances as well as a general substitute for a comparison on the investigated sample, the AA of a CRM will provide the desired information. Due to the advantages of being relatively matrix- and amount-independent, it is normally not difficult to demonstrate the accurate performance of nuclear analytical techniques. Of course, it must be noted that the user's result will always have a larger uncertainty than the uncertainty stated for the CRM.

Based on the discussed advantages, it is also relatively easy for the users of AA to include the concept of "traceability" in the quality statements on results from the users' laboratory. Traceability is defined in the international vocabulary on metrology (VIM 2007) as "*The property of a result of a measurement or standard whereby it can be related to a stated reference, usually national or international standards, through an unbroken chain of comparisons all having stated uncertainties.*" AA procedures have generally little problem to demonstrate the unbroken chain of comparison (see ► Eq. (30.35)) and can provide a complete uncertainty budget (see ► Sect. 30.6.2).

30.7 Location Sensitive Analysis

Neutron depth profiling (NDP) is a method of near surface analysis for nuclides that undergo neutron-induced charged particle reactions, e.g., (n,α) , (n,p) , with a positive Q -value. NDP combines nuclear physics with atomic physics to provide information about near-surface concentrations of certain light elements. The technique was originally applied in 1972 by Ziegler et al. (1972) and independently by Biersack and Fink (1973). Fink has produced an excellent report giving many explicit details of the method (Fink 1996). NDP is based on measuring the energy loss of the charged particles as they exit the specimen. Depending on the material under study, depths of up to 10 μm can be profiled and depth resolutions of the order of 10 nm can be obtained. The most studied analytes have been boron, lithium, and nitrogen in a variety of matrices, but several other analytes can also be measured. Because the incoming energy of the neutron is negligible and the interaction rate is small, NDP is considered a nondestructive technique. This allows the same volume of sample to receive further treatment for repeated analysis, or be subsequently analyzed using a different technique that might alter or destroy the sample.

30.7.1 Fundamentals of the Technique

Lithium, boron, nitrogen, and a number of other elements have an isotope that upon absorbing a neutron, undergoes an exoergic charged particle emission. In the low energy region, the cross sections are inversely proportional to the speed, i.e., to the square root of the neutron energy. That is, the lower the neutron energy, the greater the reaction rate. The charged particles produced are protons or alpha particles and an associated recoil nucleus. The energy of the particles is determined by the conservation of mass-energy and is predetermined for each reaction (for thermal neutrons, the added energy brought in by the neutron is negligible). As the charged particle exits the material, its interaction with the matrix causes it to lose energy and this energy loss can be measured and used to determine the depth of the originating reaction. Because only a few neutrons undergo interactions as they penetrate the sample, the neutron fluence rate is essentially the same at all depths. The depth corresponding to the measured energy loss is determined by using the characteristic stopping power of the material. The chemical or electrical state of the target atoms has an inconsequential effect on the measured profile in the NDP technique. Only the mass fraction of the major elements in the material is needed to establish the depth scale through the relationship of stopping power.

Mathematically, the relationship between the depth and residual energy can be expressed as

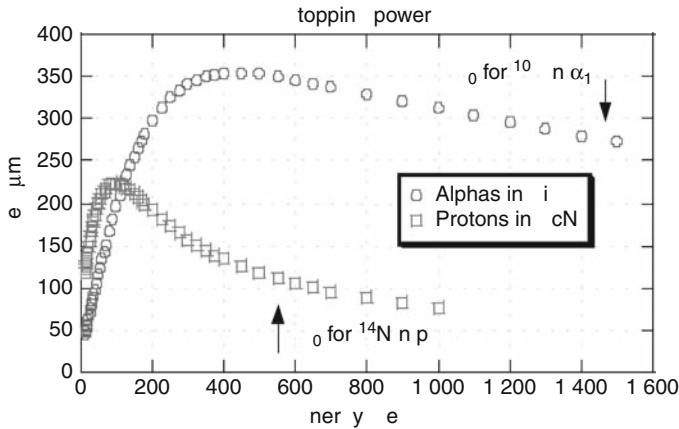
$$x = \int_{E(x)}^{E_0} \frac{dE}{S(E)} \quad (30.45)$$

where x is the path length traveled by the particle through the matrix, E_0 is the initial energy of the particle, $E(x)$ is the energy of the detected particle, and $S(E)$ is the stopping power of the matrix. This expression is equivalent to [Eq. \(30.14\)](#) defining the range r (usually denoted by R) of the particles, i.e., the distance traveled until they are fully stopped in the medium. Examples of the relationship between $S = -dE/dx$ and E are displayed in [Fig. 30.6](#) for $^{10}\text{B}(n,\alpha)$ in silicon and $^{14}\text{N}(n,p)$ in ScN.

For the boron reaction, $^{10}\text{B}(n,\alpha)^7\text{Li}$, there are two outgoing alphas with energies of 1.472 MeV (93% branch) and 1.776 MeV (7% branch), and two corresponding recoil ^7Li

■ Fig. 30.6

Stopping power in units of keV/ μm for alpha particles in silicon and ScN¹³



nuclei with energies of 0.840 and 1.014 MeV. For the nitrogen reaction, $^{14}\text{N}(\text{n,p})^{14}\text{C}$, there is a 584 keV proton and a 42 keV ^{14}C recoil. Particles escaping from the surface of the sample are detected by a silicon surface barrier detector. The charge deposited in the detector is directly proportional to the energy of the incoming particle.

30.7.2 Elemental Detection Limits

The elemental detection limit is directly related to the reaction cross section of the isotope of interest. Only a limited number of elements can be determined by NDP and as a result very few interfering reactions are encountered. Furthermore, since the critical parameters in the technique are nuclear in origin, there is no dependence upon the chemical or optical characteristics of the sample. Consequently, measurements are possible at the outer few atomic layers of a sample or through a rapidly changing composition such as at the interface between insulating and conducting layers, and across chemically distinct interfaces. In contrast, measurement artifacts occur with surface techniques such as secondary ion mass spectrometry (SIMS) and Auger electron spectrometry (AES) when the sample surface becomes charged and the ion yields vary unpredictably. ▶ Table 30.3 lists the major reactions of the NDP method, important parameters and typical detection limits based on a neutron intensity of $6 \times 10^9 \text{ s}^{-1}$ and a 24 h counting interval.

30.7.3 Concentration Determination

To compare concentration profiles among samples, both the charged particle spectrum and the neutron fluence that passes through each sample is monitored and recorded. The area analyzed on a sample is defined by placing an aperture securely against the sample surface. This aperture prevents the charged particle from reaching the detector and can therefore be very thin. Neutron collimation is used to reduce unwanted background, but it does not need to be precise. The

Table 30.3

NDP parameters

Reaction	Abundance (%)	Energy of emitted particles (keV)		Useful range in silicon (μm)	Cross section (b)	Detection limit* (at./cm ²)
³ He(n,p) ³ H	0.00014	572	191	5.7	5,333	1.5 × 10 ¹²
⁶ Li(n,α) ³ H	7.5	2,055	2,727	40	940	9.0 × 10 ¹²
¹⁰ B(n,α) ⁷ Li	19.9	1,472	840	3.8	3,837	2.1 × 10 ¹²
¹⁴ N(n,p) ¹⁴ C	99.6	584	42	5.0	1.83	4.5 × 10 ¹⁵
¹⁷ O(n,α) ¹⁴ C	0.038	1,413	404	3.6	0.24	3.5 × 10 ¹⁶
³³ S(n,α) ³⁰ Si	0.75	3,081	411	11	0.19	6.0 × 10 ¹⁶
³⁵ Cl(n,p) ³⁵ S	75.8	598	17	5.2	0.49	1.7 × 10 ¹⁶

*Detection limit based on 0.1 c/s, 0.1% detector solid angle, and a neutron intensity of 6 × 10⁹ s⁻¹

absolute area defined by the aperture need not be accurately known as long as the counting geometry is constant between samples. The neutron fluence recorded with each analysis is used to normalize data from different samples. In practice, a run-to-run monitor that has a response proportional to the total neutron fluence rate is sufficient to normalize data taken at differing neutron intensities and time intervals. If one of the spectra was obtained using a sample of known isotopic concentration, the true concentration for all the samples can be determined.

30.7.4 Depth Determination

The total sample depth that can be probed using NDP is fixed by both the stopping power of the host material and the energy and charge of the emitted particle. The rate of energy loss for a charged particle is a function of the atomic number of the elements of the matrix, the instantaneous energy of the particle, and its charge.¹⁴ As the charged particle travels through the sample it interacts with the electronic structure of the matrix, which results in incremental losses in the charged particle energy. Ziegler (1977) discusses the physics of stopping power and its calculation in detail. Once the particle emerges from the sample, it is traveling through a vacuum and therefore no longer loses energy until reaching the detector. The detector is typically a surface-barrier detector or other high-resolution charged-particle detector.

The difference between the initial energy of the particle (determined by the neutron reaction kinematics) and its measured energy is equal to the energy loss and, according to ▶ Eq. (30.45), yields the depth of origin. The depth resolution varies from a few nanometers to a few hundred nanometers. ▶ Table 30.3 lists the useful probing depth in a silicon substrate for the tabulated nuclides. For substrates other than silicon the maximum range of analysis will differ. Information from deeper in the sample can sometimes be obtained by carefully etching off a portion of the surface and measuring the area again using NDP. Under optimum conditions the depth resolution for boron in silicon is approximately 8 nm.

Stopping powers for individual elements are given in compilations like that of Ziegler (1977). For compounds such as LiNbO₃, stopping powers are closely approximated by using Bragg's law of addition of the stopping power of individual elements. Because the analytical results are obtained in units of areal number density (atoms/cm²), a linear depth scale can be assigned only if the volume number density (atoms/cm³) of the material remains constant and

is known. Consequently, the conversion of an energy loss scale to a linear depth axis is only as accurate as the knowledge of the volume number density. By supplying a few physical parameters, customized computer programs are used to convert the charged particle spectrum to a depth profile in units of concentration and depth. A Monte Carlo program, SRIM (Ziegler et al. 2008), can also be used to provide stopping power and range information. Even if the density is not well known, mass percent concentration profiles can be accurately determined even through layered materials of different density. In many cases, it is the mass percent composition that is the information desired from the analysis.

30.7.5 Sources of Uncertainty

As is the case in all measurements, the uncertainties from NDP can be divided into Type A (statistical) and Type B (all other). The Type A terms are dependent mostly on the concentration and the neutron cross section of the analyte. While the statistical precision can always be improved by increasing the irradiation time, there are some practical limits. Beam time is in high demand and rarely more than a day can be devoted to a single sample, with 1 h being more typical. There is always some background present and the background subtraction increases the statistical uncertainty. For typical samples of boron in semiconductor materials, the Type A uncertainty is usually about 1% at 1 σ confidence level.

Type B uncertainties are more sample dependent and therefore more difficult to generalize. All samples will have an uncertainty due to the uncertainties of the stopping power of the matrix elements. If the exact composition of the matrix is unknown, this will amplify the uncertainty. Stopping powers are most accurately described in terms of energy loss per atom/cm² of stopping material.¹⁵ To convert to energy loss per linear depth the density of the matrix must be known. The linear depth uncertainty will be proportional to the uncertainty of the density. At all depths, the energy of the outgoing particles will have dispersion due to the energy straggling and this dispersion will be greater as the depth increases. Additional smaller uncertainties derive from such details as the reproducibility of the sample and counter geometry, inscatter and outscatter of the outgoing particle, and accuracy of the energy calibration of the detector. Type B uncertainties are typically of the order of 2% (1 σ). The quadratic sum of Type A and Type B uncertainties yields therefore a resultant uncertainty of the order of 2.5% (1 σ) and in more optimum cases of the order of 2% (1 σ). Interpretation of NDP charged-particle spectra is not always single valued. It is important to obtain as much knowledge about the sample as practical to simplify the analysis and reduce ambiguity. This includes information about lateral variations in surface roughness, which would be averaged within the beam spot of an NDP analysis.

When determining an NDP profile, it should be remembered that only the isotopic concentration is actually determined and that the elemental profile is inferred. While natural isotopic abundances are usually present, anthropogenic activities can severely distort isotopic ratios, especially for boron and lithium. Natural processes can also perturb isotopic proportion, however this is both rare and small in magnitude. Materials prepared by ion implantation will be isotopically different from natural materials. ¹¹B is more abundant (80.1%) and consequently more economical to implant than ¹⁰B. As a result, boron-implanted samples must be especially prepared for NDP analysis. ⁶Li is less abundant in nature and historically has been separated from natural lithium for nuclear applications. This provided a relatively inexpensive source of ⁶Li-depleted, i.e., purified, lithium available for chemical applications.

This not only invalidated simple assumptions for calculating total lithium abundance but also significantly changed the atomic weight of lithium for gravimetric chemical procedures.

30.8 Editors' Notes

1. See [Fig. 3.10 \(left diagram\)](#) in [Chap. 3](#), Vol. 1, on “Nuclear Reactions.” The diagram also shows the “ $1/\nu$ ” law mentioned that appears as a sloping line in the log–log presentation (p. 1557).
2. See [Eq. \(50.33\)](#) as well as [Chap. 50](#), Vol. 5, on “Particle Accelerators” (p. 1558).
3. See more about stopping power in [Chap. 8](#), Vol. 1, on “Interaction of Radiation with Matter,” starting with [Eq. \(8.1\)](#) (p. 1558).
4. The range is normally denoted by R ; however, it has been changed to r , which cannot be confused with the reaction rate (p. 1558).
5. The “macroscopic cross section” is an analogous quantity to the “linear attenuation coefficient” that is used in the exponent of the “Beer–Lambert law” describing the attenuation of γ radiation (p. 1559).
6. The Q value often mentioned in this chapter is a dimensionless number. It is not to be mixed with the Q value of nuclear reactions, which has energy dimension (p. 1579).
7. See more about radiochemical separations in [Chaps. 52](#) and [53](#), Vol. 5, on “Solvent Extraction and Ion Exchange in Radiochemistry” and “Radiochemical Separations by Thermochromatography,” respectively (p. 1584).
8. The separation techniques described in [Chaps. 52](#) and [53](#) of Vol. 5 are really fast. Fast separation is also a crucial requirement for the identification of transuranic/transactinide and superheavy elements as discussed in [Chaps. 18–21](#) of Vol. 2 (p. 1585).
9. HDEHP is di(2-ethylhexyl)orthophosphoric acid. It is used in SISAK equipment, e.g., for the identification of ^{243}Np and ^{244}Np . See [Fig. 18.10](#) in [Chap. 18](#), Vol. 2, on “Production and Chemistry of Transuranium Elements” (p. 1588).
10. The term “photopeak” means the same as the “full-energy peak” used in [Chap. 48](#), Vol. 5, on “Radiation Detection.” The reason for the longer expression is that in a voluminous detector the photopeak is not necessarily connected with a single photoelectric effect. It can also be the result of a sequence of Compton scatterings etc. within the sensitive volume (p. 1602).
11. See [Eq. \(9.58\)](#) in [Chap. 9](#), Vol. 1, on “Stochastics and Nuclear Measurements” (p. 1605).
12. For the benefit of those who are not familiar with American idioms it should be mentioned that the adjective “round-robin” means here that the analysis is done on samples taken from the same material sent to different NAA labs (p. 1607).
13. Although the dimensions are different, the peculiar shapes of the curves can be traced back to that of the Bragg curve shown in [Fig. 8.5](#) of [Chap. 8](#), Vol. 1, on “Interaction of Radiation with Matter” (p. 1609).
14. As regards the rate of energy loss of charged particles and its dependence on different parameters see, e.g., [Eqs. \(8.1\)](#) and [\(8.3\)](#) in [Chap. 8](#), Vol. 1, on “Interaction of Radiation with Matter” (p. 1610).
15. Regular (mass) surface density (in g cm^{-2}) gives essentially the same accuracy as a real number density (in atoms/cm^2). This is why the stopping power expressions in [Chap. 8](#), Vol. 1, contain x as a measure of sample thickness in surface density units (e.g., in g/cm^2) rather than a linear distance (in cm) (p. 1611).

Acknowledgments

The authors wish to thank Donna O'Kelly, NIST Analytical Chemistry Division, and David F. R. Mildner, NIST Center for Neutron Research, for their critical reading of the manuscript and valuable suggestions.

References

- Abugassa I, Sarmani SB, Samat SB (1999) *Appl Radiat Isot* 50:989
- Alamin MB, Beje AM, Kucera J, Mizera J (2006) *J Radioanal Nucl Chem* 270:143
- Alfassi ZB (ed) (1994a) *Chemical analysis by nuclear methods*. Wiley, Chichester
- Alfassi ZB (1994b) *Determination of trace elements*. Balaban Publication, Rehovot
- Alfassi ZB (2001) In: Alfassi ZB (ed) *Non-destructive elemental analysis*, Chapter 1. Blackwell Sciences, Oxford, pp 4–57
- Amphlett CB (1964) *Inorganic ion exchangers*. Elsevier, Amsterdam
- Anderson J, Osborn SB, Tomlinson RWS, Newton D, Rundo J, Salmon L (1964) *Lancet* II:1201
- Armer HA, Shawky S (2002) *Radiochim Acta* 90:350
- Aumann DC, Güner D (1999) *J Radioanal Nucl Chem* 242:641
- Balla M, Keömléy G, Molnár Zs (1998) In: Vértés A, Nagy S, Süvegh K (eds) *Nuclear methods in mineralogy and geology*, Chapter 2. Plenum Press, New York, pp 115–143
- Becker DA (1987) *J Radioanal Nucl Chem* 111:393
- Becker DA (1993) *J Radioanal Nucl Chem* 168:169
- Becker DA, Anderson DL, Lindstrom RM, Greenberg RR, Garrity KM, Mackey EA (1994) *J Radioanal Nucl Chem* 179:149
- Bedregal PS, Montoya EH (2002) *J Radioanal Nucl Chem* 254:363
- Biersack JP, Fink D (1973) *Nucl Instrum Meth* 108:397
- Biso JN, Cohen IM, Resnizki SM (1983) *Radiochem Radio Lett* 58:175
- Blaauw M (1996) *Nucl Sci Eng* 124:431
- Blaauw M, Gelsema SJ (1999) *Nucl Instrum Meth A* 422:417
- Blaauw M, Osorio Fernandez V, Van Espen P, Bernasconi G, Capote Noy R, Manh Dung H, Molla NI (1997) *Nucl Instrum Meth A* 387:416
- Blackman MJ, Bishop RL (2007) *Archaeometry* 49:321
- Blanchard LJ, Robertson JD (1997) *Analyst* 122:1261
- Bode P, Overwater RMW, de Goeij JJM (1997) *J Radioanal Nucl Chem* 216:5
- Borsaru M, Biggs M, Nichols W, Bos F (2001) *Appl Radiat Isot* 54:335
- Brätter P, Gatschke W, Gawlik D, Klatt S (1977) *Kerntechnik* 19:225
- Brown ME (ed) (1961) *Proceedings of the international conference modern trends in activation analysis*. Texas A&M College, College Station
- Byrne AR (1986) *J Environm Radioactivity* 4:133
- Byrne AR, Benedik L (1999) *Czechoslovak J Phys* 49:265
- Byrne AR, Vakselj A (1974) *Croat Chem Acta* 46:225
- Caletka R, Faix WG, Krivan VJ (1982) *J Radioanal Nucl Chem* 72:109
- Caletka R, Hausbeck R, Krivan VJ (1988) *J Radioanal Nucl Chem* 120:305
- CCQM (2008) *Key Comparison Data Base (KCDB)*. Bureau International des Poids et Mesures, Sèvres, France. Published on the internet: <http://kcdb.bipm.org/default.asp>
- Chai CF (1988) *Isotopenpraxis* 24:257
- Chai CF, Ma SL, Mao XY, Liao KN, Liu WC (1987) *J Radioanal Nucl Chem* 114:281
- Chao JH, Tseng CL (1996) *Nucl Instruments Methods Phys Res A* 272:275
- Chen QJ, Dahlgaard H, Hansen HJM, Aarkrog A (1990) *Anal Chim Acta* 228:163
- Chen QJ, Dahlgaard H, Nielsen SP, Aarkrog A (2001) *J Radioanal Nucl Chem* 249:527
- Chilian C, St-Pierre J, Kennedy G (2008) *J Radioanal Nucl Chem* 278:745
- Chung C (1990) In: Alfassi ZB (ed) *Activation analysis*, Chapter 6, vol 2. CRP Press, Boca Raton, pp 299–320
- Clayton CG, Wormald MR (1983) *Int J Appl Radiat Isot* 34:3
- Clearfield A (1982) *Inorganic ion exchanger materials*. CRC Press, Boca Raton
- Csikai J (1987) *CRC handbook of fast neutron generators*, vol 1 and 2. CRC Press, Boca Raton
- Czauderna M (1985) *J Radioanal Nucl Chem* 89:13
- Czauderna M (1996) *Appl Radiat Isot* 47:735
- Damsgaard E, Ostergaard K, Heydorn K (1973) *Talanta* 20:1
- Dang HS, Jaiswal DD, Pullat VR, Mishra UC (2000) *J Radioanal Nucl Chem* 243:513
- Dang HS, Jaiswal DD, Nair S (2001) *J Radioanal Nucl Chem* 249:95
- de Bruin M (1998) *J Radioanal Nucl Chem* 234(1–2):5

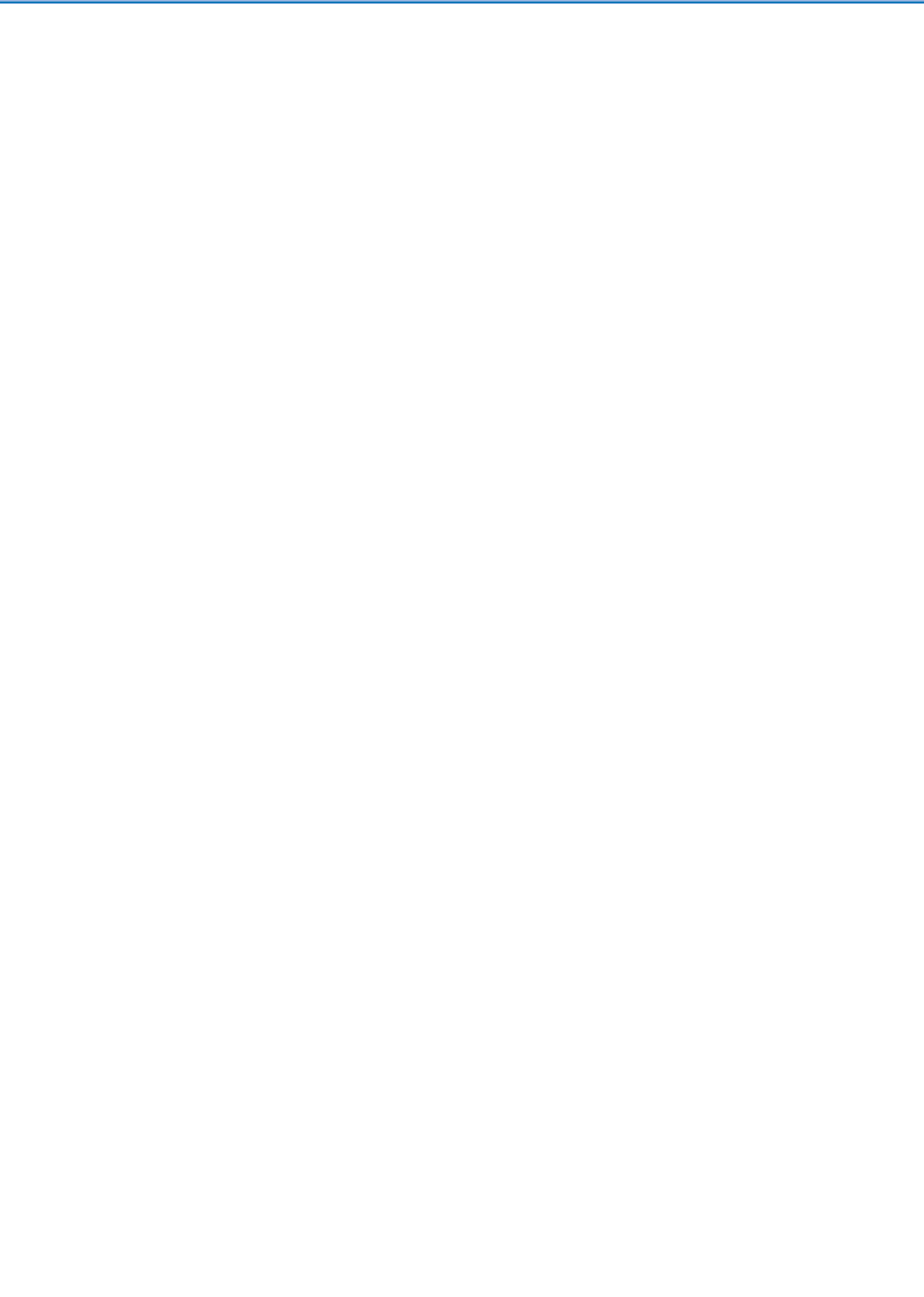
- de Bruin M, Blaauw M (1992) *Analyst* 117:431
- De Corte F (1987) The k_0 -standardization method, a move to the optimization of neutron activation analysis. Rijksuniversiteit, Gent
- De Corte F, Simonits A (1989) *J Radioanal Nucl Chem Art* 133:43
- De Corte F, Simonits A (2003) *At Data Nucl Data Tables* 85:47
- De Corte F, Simonits A, De Wispelaere A, Hoste J (1987) *J Radioanal Nucl Chem* 113:145
- De Corte F, Simonits A, De Wispelaere A (1989a) *J Radioanal Nucl Chem Art* 133:131
- De Corte F, Simonits A, De Wispelaere A, Elek A (1989b) *J Radioanal Nucl Chem* 133:3
- De Corte F, Bellemans F, De Neve P, Simonits A (1994) *J Radioanal Nucl Chem Art* 179:93
- de Goeij JJM (1999) *J Radioanal Nucl Chem* 245:5
- Debertin K, Helmer RG (1988) Gamma- and X-ray spectrometry with semiconductor detectors. North-Holland, Amsterdam
- Dermelj M, Byrne AR (1997) *J Radioanal Nucl Chem* 216:13
- Dubczinskij R (1996) *Zs Anal Him* 51(12):1328, in Russian
- Egger KP, Krivan V (1986) *Fresen J Anal Chem* 323:827
- Egger KP, Krivan V (1988) *Fresen J Anal Chem* 331:394
- Ellis KJ (1990) In: Alfassi ZB (ed) *Activation analysis*, Chapter 10, vol 2. CRP Press, Boca Raton, pp 407–426
- Ellis KJ (2000) *Physiol Rev* 80:649
- Ellis KJ, Shypailo RJ, Hergenroeder AC, Perez MD, Abrams SA (2001) *J Radioanal Nucl Chem* 249:461
- Fardy JJ (1990) In: Alfassi ZB (ed) *Activation analysis*, Chapter 5, vol 1. CRC Press, Boca Raton, pp 62–96
- Farmer OT, Barinaga CJ, Koppelaar DW (1998) *J Radioanal Nucl Chem* 234:153
- Fink D (1996) In: Hahn-Meitner Inst Rep HMI-B 539, Berlin, pp 307–311
- Fischer CO, Kelch J, Laurenze C, Leuthe RW, Slusallek K (1987) *Kerntechnik* 51:9
- Fleming RF (1982) *Int J Appl Radiat Isot* 33:1263
- Fleming RF, Lindstrom RM (1987) *J Radioanal Nucl Chem* 188:35
- Foti S, Delucchi E, Akamian V (1972) *Anal Chim Acta* 60:261
- Frechou C, Calmet D, Bouisset P, Piccot D, Gaudry A, You F, Raisbeck G (2001) *J Radioanal Nucl Chem* 249:133
- Garuti G, Meloni S, Oddone M (2000) *J Radioanal Nucl Chem* 245(1):17
- Germain P, Pinte G (1990) *J Radioanal Nucl Chem* 138:49
- Germani MS, Gokmen I, Sigleo AC, Kowalczyk GS, Olmez I, Small AM, Anderson DL, Failey MP, Gulovali MC, Choquette CE, Lepel EA, Gordon GE, Zoller WH (1980) *Anal Chem* 52:240
- Gharib AG, Fatemi K, Madadi M, Rafiee H, Darabi-zadeh Sh (2001) *J Radioanal Nucl Chem* 249:551
- Gill KP, Zaidi JH, Ahmed S (2003) *Radiochim Acta* 91:547
- Gilmore G (2008) *Practical gamma-ray spectrometry*, 2nd edn. Wiley, Chichester
- Girardi F, Sabbioni E (1968) *Nucl Chem* 1:169
- Glover SE, Filby RH, Clark SB (1998) *J Radioanal Nucl Chem* 234:65
- Glover SE, Qu H, LaMont SP, Grimm CA, Filby RH (2001) *J Radioanal Nucl Chem* 248:29
- Goerner W, Berger A, Ecker KH, Haase O, Hedrich M, Segebade C, Weidemann G, Wermann G (2001) *J Radioanal Nucl Chem* 248:45
- Goldbrunner T, Hentig R, Angloher F, Feilitzsch F (1998) *J Radioanal Nucl Chem* 234:43
- Goncalves C, Favaro DIT, De Oliveira MD, Boulet R, Vasconcellos MBA, Saiki M (1998) *J Radioanal Nucl Chem* 235:267
- Goncalves C, Favaro DIT, Melfi AJ, De Oliveira MD, Vasconcellos MBA, Fostier AH, Guimaraes JRD, Boulet R, Forti MC (2000) *J Radioanal Nucl Chem* 243:789
- Grass F, Bichler M, Dorner J, Holzner H, Ritschel A, Ramadan A, Westphal GP, Grass F, Lemmel H, Westphal GP, Gwozdz R (2001) *J Trace Microprobe T* 19:211
- Grass F, Lemmel H, Westphal GP (1994) *Biol Trace Elem Res* 43:33.
- Greenberg RR, Fleming RF, Zeisler R (1984) *Environ Int* 10:129
- Greenberg RR, Lindstrom RM, Simons DS (2000) *J Radioanal Nucl Ch* 245:57
- Grimanis AP, Kanas GD (1982) *J Radioanal Nucl Chem* 72:587
- Guinn VP (1999) *J Radioanal Nucl Chem* 244:23
- Harms J (1967) *Nucl Instrum Meth* 53:192
- Heller-Zeisler SE, Ondov JM, Zeisler R (1999) *Biol Trace Elem Res* 71–72:195
- Heller-Zeisler SE, Borgoul PV, Moore RR, Smoliar M, Suarez E, Ondov JM (2000) *J Radioanal Nucl Chem* 244:93
- Hevesy G, Levi H (1936) *Math Fys Medd* 14:34
- Heydorn K (1999) *J Radioanal Nucl Chem* 244:7
- Hillard HT (1987) *J Radioanal Nucl Chem* 113:125
- Hogdahl OT (1965) *Proceedings Symposium Radiochemical Methods of Analysis*, IAEA, Vienna, pp 23–40
- Höllriegl V, Oeh U, Röhmuss M, Gerstmann U, Roth P (2005) *J Radioanal Nucl Chem* 266:441
- Hogdahl OT (1965) *Proceedings Symposium Radiochemical Methods of Analysis*, IAEA, Vienna, pp 23–40
- Hou XL, Dahlggaard H, Rietz B, Jacobsen U, Nielsen SP (2000) *J Radioanal Nucl Chem* 244:87
- Hou XL, Dahlggaard H, Nielsen SP, Kucera J (2002) *J Environm Radioactivity* 61:331
- Hou XL, Fogh CL, Kucera J, Andersson KG, Dahlggaard H, Nielsen SP (2003) *Sci Total Environm* 308:97

- IAEA (1987) Handbook of nuclear activation data, Technical report 273. International Atomic Energy Agency, Vienna
- Ismail SS, Brezovits K, Klikovich W (2001) *Instrum Sci Technol* 29:255
- Itawi RK, Turrel ZR (1973) *J Radioanal Nucl Chem* 106:81
- Iyengar V (1981) *J Pathol* 134:173
- Jacimovic R, Horvat M (2004) *J Radioanal Nucl Chem* 259:385
- Jacimovic R, Makreski P, Stribilj V, Stafilov T (2008) *J Radioanal Nucl Chem* 278(3):795
- James WD, Zeisler R (2001) *J Radioanal Nucl Chem* 248:233
- Jenkins R, Gould RW, Gedcke D (1981) *Quantitative X-ray spectrometry*. Marcel Dekker, New York, pp 208–287
- Jovanovic S, De Corte F, Simonits A, Moens L, Vikotic P, Hoste J (1987) *J Radioanal Nucl Chem* 113:177
- Kabai É, Vajda N (2002) In: *Proceedings of the 14th radiochemical conference*. Czech Technical University, Mariánské Lázně, p 121
- Kalmykov StN, Aliev RA, Sapozhnikov DY, Sapozhnikov YuA, Afinogenov AM (2004) *Appl Rad Isotopes* 60:595
- KAYZERO/SOLCOI (1996) PC software package (DSM Research, POB 18, NL-6160 MD Geleen, The Netherlands)
- Kim NB, Raulerson MR, James WD (1998) *J Radioanal Nucl Chem* 234:71
- Knoll GF (2000) *Radiation detection and measurement*, 3rd edn. Wiley, New York
- Kolotov VP, Dogadkin NN, Tsapiznikov BA, Karandashev VK, Sadikov II, Saveljev BV (1996) *Zh Anal Himii* 51(12):1315, in Russian
- Kosta L (1969) *Talanta* 16:1297
- Koster-Ammerlaan MJJ, Bacchi MA, Bode P, De Nadai Fernandes EA (2008) *Appl Radiat Isot* 66:1964
- Krishnan S (2000) *J Radioanal Nucl Chem* 244:209
- Kucera J (2007) *J Radioanal Nucl Chem* 273:273
- Kucera J, Zeisler R (2005) *J Radioanal Nucl Chem* 263:811
- Kucera J, Randa Z, Soukal L (2001) *J Radioanal Nucl Chem* 249:109
- Kucera J, Iyengar GV, Randa Z, Parr RM (2004) *J Radioanal Nucl Chem* 259:505
- Kushelevsky AP (1990) In: Alfassi ZB (ed) *Activation analysis*, Chapter 4, vol 2. CRP Press, Boca Raton, pp 219–237
- Landsberger S, Peshev S (1996) *J Radioanal Nucl Chem* 202:201
- Lin X, Henkelmann R (2002) *J Radioanal Nucl Chem* 251:197
- Lindstrom RM (1994) *Biol Trace Elem Res* 43–44:597
- Lindstrom RM (2005) *J Radioanal Nucl Chem* 263:787
- Lindstrom RM, Harrison SH, Harris JM (1978) *J Appl Phys* 49:5903
- Lindstrom RM, Lindstrom DJ, Slaback LA, Langland JK (1990) *Nucl Instrum Meth A* 299:425
- Lindstrom RM, Zeisler R, Greenberg RR (2007) *J Radioanal Nucl Chem* 271:311
- Lucanikova M, Kucera J, Sebesta F, John J (2006) *J Radioanal Nucl Chem* 269:463
- Ma R, Stammatelatos IE, Yasumura S (2000) *Ann NY Acad Sci* 904:148
- Mackey EA, Gordon GE, Lindstrom RM, Anderson DL (1991) *Anal Chem* 63:288
- Mackey EA, Anderson DL, Chen-Mayer H, Downing RG, Greenberg RR, Lamaze GP, Lindstrom RM, Mildner DFR, Paul RL (1998) *J Radioanal Nucl Chem* 203:413
- Makreski P, Jacimovic R, Stribilj V, Stafilov T, Jovanovski G (2008) *Radiochim Acta* 96:855
- Minowa H, Ebihara M (2003) *Anal Chim Acta* 498:25
- Minowa H, Takeada M, Ebihara M (2007) *J Radioanal Nucl Chem* 272:321
- Mizera J, Randa Z, Kucera J (2008) *J Radioanal Nucl Chem* 278(3):599
- Moens L, De Donder J, Lin X, De Corte F, De Wispelaere A, Simonits A, Hoste J (1981) *Nucl Instrum Meth* 187:451
- Moens L, De Corte F, De Wispelaere A, Hoste J, Simonits A, Elek A, Szabo E (1984) *J Radioanal Nucl Chem* 82:385
- Molnár GL (ed) (2003) *Handbook of prompt gamma activation analysis with neutron beams*. Kluwer Academic, Dordrecht
- Molnár GL, Lindstrom RM (1998) In: Vértés A, Nagy S, Süvegh K (eds) *Nuclear methods in mineralogy and geology*, Chapter 3. Plenum Press, New York, pp 145–164
- Morgan WD (2000) *Ann NY Acad Sci* 904:128
- Mughabghab SF (1984) *Neutron cross sections*, vol 1, part B. Academic, New York
- Mughabghab SF, Divadeenam M, Holden NE (1981) *Neutron cross sections*, vol 1, part A. Academic, New York
- Nadkarni RA, Morrison GH (1977) *J Radioanal Nucl Chem* 38:435
- Norman BR, Becker DA (1999) *J Radioanal Nucl Chem* 245:91
- OECD (1994) *Table of simple integral neutron cross section data from JEF-2.2, ENDF/B-VI, JENDL-3.2, BROND-2 and CENDL-2*, JEF Report 14. OECD Nuclear Energy Agency, Paris
- Ohde S (1998) *J Radioanal Nucl Chem* 237:51
- Olariu A, Constantinescu M, Constantinescu O, Badica T, Popescu IV, Besliu C, Leahu D (1999) *J Radioanal Nucl Chem* 240:261
- Ondov JM, Dodd JA, Tuncel G (1990) *Aerosol Sci Technol* 13:249
- Osterc A, Stibilj V (2008) *J Environm Radioactivity* 99:757
- Oura Y, Motohashi T, Ebihara M (2007) *J Radioanal Nucl Chem* 271(2):305

- Ozaki H, Ebihara M (2007) *Anal Chim Acta* 583:384
- Park KS, Kim NB, Kim YS, Lee KY, Choi HW, Yoon YY (1988) *J Radioanal Nucl Chem* 123:585
- Parr RM (1999) *J Radioanal Nucl Chem* 244:17
- Parry SJ, Asif M, Sinclair IW (1988) *J Radioanal Nucl Chem* 123:593
- Parry SJ, Bennett BA, Benzing R, Lally AE, Birch CP, Fulkner MJ (1995) *Sci Total Environ* 173(174):351
- Parry SJ, Glover SE, Qu H, LaMont SP, Grimm CA, Filby RH (2001) *J Radioanal Nucl Chem* 248(1):137
- Paul RL (1998) *J Radioanal Nucl Chem* 234:55
- Paul RL (2000) *J Radioanal Nucl Chem* 245:11
- Paul RL (2008) *J Radioanal Nucl Chem* 276:243
- Paul RL, Simons DS, Guthrie WF, Lu J (2003) *Anal Chem* 75:4028
- Pietra R, Sabbioni E, Gallorini M, Orvini E (1986) *J Radioanal Nucl Chem* 102:69
- Pomme S, Alzetta JP, Uyttenhove J, Denecke B, Arana G, Robouch P (1999) *Nucl Instrum Meth Phys Res A* 422:388
- Randa Z, Kucera J, Soukal L (2003) *J Radioanal Nucl Chem* 257:275
- Repinc U, Benedik L (2005) *J Radioanal Nucl Chem* 264:77
- Repinc U, Benedik L, Stibilj V (2005) *J Radioanal Nucl Chem* 264:39
- Rietz B, Heydorn K (1993) *J Radioanal Nucl Chem* 174:49
- Rosman KJR, Taylor PDP (1998) *J Phys Chem Ref Data* 27:1275–1287
- Rosbach M, Blaauw M, Bacchi MA, Lin X (2007) *J Radioanal Nucl Chem* 274:657
- Rouchaud JC, Fedoroff M, Revel GJ (1977) *J Radioanal Nucl Chem* 38:185
- Rouchaud JC, Fedoroff M, Revel G (1980) *J Radioanal Nucl Chem* 55:283
- Samczynski Z, Dybczynski R (2002) *J Radioanal Nucl Chem* 254:335
- Samsahl K (1966) *Nukleonik* 8:252
- Schmid W, Krivan V (1986) *Anal Chem* 58:1468
- Schuhmacher J, Maier-borst W, Hauser H (1977) *J Radioanal Nucl Chem* 37:503
- Shani G (1990) In: Alfassi ZB (ed) *Activation analysis*, Chapter 5, vol 2. CRP Press, Boca Raton, pp 239–297
- Shoop DM, Blotzky AJ, Rack EP (1998) *J Radioanal Nucl Chem* 236(1–2):103
- Simonits A, De Corte F, Hoste J (1975) *J Radioanal Chem* 24:31
- Simonits A, Moens L, De Corte F, De Wispelaere A, Elek A, Hoste J (1980) *J Radioanal Chem* 60:461
- Slejkovec Z, Falnoga I, Goessler W, van Elteren JT, Raml R, Podgornik H, Cernelc P (2008) *Anal Chim Acta* 607:83
- St-Pierre J, Kennedy G (1998) *J Radioanal Nucl Chem* 234:51–54
- St-Pierre J, Kennedy G (2006) *Nucl Instrum Meth A* 564:669
- St-Pierre J, Kennedy G (2007) *J Radioanal Nucl Chem* 271:283
- Strijckmans K (1994) In: Alfassi ZB (ed) *Chemical analysis by nuclear methods*, Chapter 10. Wiley, Chichester, pp 215–252
- Studier MH (1962) *J Inorg Nucl Chem* 24:755
- Suzuki N (1990) In: Alfassi ZB (ed) *Activation analysis*, Chapter 9, vol 1. CRP Press, Boca Raton, pp 146–164
- Szidat S, Schmidt A, Handl J, Jakob D, Michel R, Synal HA, Suter M (2000) *J Radioanal Nucl Chem* 244:45
- Takeda M, Minowa H, Ebihara M (2007) *J Radioanal Nucl Chem* 272:363
- Theimer KH, Krivan V (1990) *Anal Chem* 62:2722
- Tian W, Ni B, Wang P, Nie H, Cao L, Zhang Y (2001) *J Radioanal Nucl Chem* 249:25
- Upp DL, Keyser RM, Gedcke DA, Twomey TR, Bingham RD (2001) *J Radioanal Nucl Chem* 248:377
- Van Sluijs R, Bossus DAW, Konings J, De Corte F, De Wispelaere A, Simonits A (1997) *J Radioanal Nucl Chem* 215:283
- Van Sluijs R, Bossus D, Blaauw M, Kennedy G, De Wispelaere A, Van Lierde S, De Corte F (2000) *J Radioanal Nucl Chem* 244:675
- Vermaercke P, Robouch P, Eguskiza M, De Corte F, Kennedy G, Smoldis B, Jacimovic R, Yonezawa C, Matsue H, Lin X, Blaauw M, Kucera J (2006) *Nucl Instrum Meth A* 564:675
- VIM (2007) *International vocabulary of basic and general terms in metrology*. International Organization for Standardization, Geneva
- Westcott CH (1955) *J Nucl Energy* 2:59
- Westphal GP (1981) *J Radioanal Chem* 61:111
- Westphal GP, Lemmel H (2008) *J Radioanal Nucl Chem* 276:601
- Yonezawa C (2001) In: Alfassi ZB (ed) *Non-destructive elemental analysis*, Chapter 2. Blackwell Sciences, Oxford, pp 58–114
- Zaidi JH, Arif M, Fatima I, Ahmed S, Qureshi IH (1999a) *J Radioanal Nucl Chem* 241:123
- Zaidi JH, Waheed S, Ahmed S (1999b) *J Radioanal Nucl Chem* 242:259
- Zaidi JH, Arif M, Fatima I, Qureshi IH (2001) *J Radioanal Nucl Chem* 253:459
- Zaidi JH, Fatima I, Arif M (2002) *Radiochim Acta* 90:889
- Zeisler R (1986) *J Res Natl Inst Stan* 91:75
- Zeisler R (2000) *J Radioanal Nucl Chem* 244:507
- Zeisler R, Greenberg RR (1982) *J Radioanal Chem* 75:27
- Zeisler R, Guinn VP (1990) *Nuclear analytical methods in the life sciences*. The Humana, Clifton
- Zeisler R, Young I (1987) *J Radioanal Nucl Chem* 113:97
- Zeisler R, Lindstrom RM, Greenberg RR (2005) *J Radioanal Nucl Chem* 263:315

Ziegler JF (1977) The stopping and ranges of ions in matter. Pergamon Press, New York
Ziegler JF, Cole GW, Baglin JEE (1972) J Appl Phys 43:3809

Ziegler JF, Ziegler MD, Biersack JP (2008) SRIM – the stopping and range of ions in matter, LuLu Press. The software package version SRIM-2008.04 is available from www.SRIM.org



31 Neutron-Induced Prompt Gamma Activation Analysis (PGAA)

Z. Révay¹ · R. M. Lindstrom² · E. A. Mackey² · T. Belgya¹

¹Hungarian Academy of Sciences, Budapest, Hungary

²National Institute of Standards and Technology, Gaithersburg, MD, USA

31.1	<i>Introduction</i>	1621
31.2	<i>Fundamentals of Prompt Gamma Activation Analysis</i>	1622
31.2.1	Fundamental Processes	1622
31.2.2	Activation Equations	1623
31.2.2.1	Thin Sample Approximation	1623
31.2.2.2	“Black” Sample Approximation	1624
31.3	<i>Characteristics of PGAA</i>	1625
31.3.1	Analytical Properties	1625
31.3.2	Characterization of Prompt Gamma Spectra	1626
31.3.3	Dynamic Range and Detection Limit	1627
31.4	<i>Neutron Beams and PGAA Facilities</i>	1628
31.4.1	Neutron Beams	1628
31.4.2	Neutron Sources	1628
31.4.3	Shaping and Tailoring Neutron Beams	1631
31.4.4	Neutron Absorbers and Shielding Materials	1632
31.4.5	Neutron Shutter, Beam Tube, Sample Holder, and Beam Stop	1633
31.4.6	Characterization and Monitoring the Neutron Beam	1634
31.4.7	PGAA Facilities	1635
31.5	<i>Samples and Standards</i>	1635
31.5.1	Sample Size and Shape	1635
31.5.2	Standardization	1636
31.6	<i>High-Energy Gamma-Ray Spectroscopy</i>	1637
31.6.1	Fundamental Processes	1637
31.6.2	Instrumentation	1638
31.6.2.1	Detector Selection	1638
31.6.2.2	Electronics and Its Characteristics	1639
31.6.2.3	Response Function of Germanium Detectors	1640
31.6.3	Calibration Procedures	1642
31.6.3.1	Energy Resolution	1642

31.6.3.2	System Nonlinearity	1643
31.6.3.3	Detector Efficiency	1644
31.6.3.4	Determination of Spectral Background	1647
31.6.4	Compton-Suppressed Spectrometers	1648
31.6.5	Other Sophisticated Detection Solutions	1649
31.6.5.1	Composite Germanium Detectors	1649
31.6.5.2	Coincidence Techniques	1650
31.6.5.3	Chopped-Beam PGAA	1650
31.7	<i>Spectrum Evaluation</i>	1650
31.8	<i>Quantitative Analysis</i>	1653
31.8.1	Absolute Approach	1653
31.8.2	Relative Approach	1654
31.9	<i>Applications</i>	1655
31.9.1	Innovations and Advances in PGAA Methodologies	1656
31.9.1.1	In Situ PGAA	1656
31.9.1.2	Neutron Focusing	1656
31.9.1.3	PGAA and Neutron Diffraction and Imaging Methods	1657
31.9.1.4	Chopped Beams	1657
31.9.1.5	PGAA in Highly Absorbing Samples or Containers	1658
31.9.1.6	PGAA of Large Samples	1658
31.9.1.7	Improvements in signal-to-noise ratio	1658
31.9.1.8	Advances and Applications in k_0 PGAA	1659
31.9.2	Measurements of Cross sections, Gamma-Ray Energies, and Emission Probabilities	1659
31.9.3	Identification of Explosives and Fissile Materials	1660
31.9.4	Measurements of Advanced Materials	1661
31.9.5	Analysis of Hydrogen	1661
31.9.6	Analysis of Boron	1663
31.9.7	Biological and Environmental Applications	1664
31.9.8	Archeometry	1664
31.9.9	Characterization of Geological Materials	1665
31.9.10	Quality Assurance and Analysis of Reference Materials	1666

Abstract: This section presents the principles, the practical aspects, and the applications of neutron-induced prompt gamma activation analysis (PGAA). The fundamentals of the method, the characteristics of the analytical technique, and the instrumentation are introduced. The measurements of samples and standards together with the procedures of the quantitative analysis are described. High-energy gamma-ray spectroscopy, enabling reliable chemical analyses, is discussed in detail. A comprehensive section of the most recent applications of the PGAA method is also given.

31.1 Introduction

While investigating the capture reaction of neutrons in hydrogenous materials, the emission of a highly penetrating gamma radiation had already been observed in 1934 (Lea 1934). This was the first prompt gamma radiation ever detected. Now it is known as the prompt gamma ray of 2,223.2487 keV energy from the reaction $H(n,\gamma)^2H$.

Whenever a nucleus absorbs a neutron, its binding energy is released in the form of the so-called prompt gamma radiation. If the product nuclide is stable, the process ends here. If it is radioactive, then it decays away while emitting typically a beta particle, mostly followed by gamma rays, too. Both types of gamma radiation are characteristic of the capturing nucleus, and thus are suitable for elemental analysis. Neutron activation analysis is based on the detection of the decay-gamma radiation (see [Chap. 30 in this Volume](#)), while prompt gamma activation analysis (PGAA) utilizes both, but mainly the prompt radiation.

Both activation analytical techniques require powerful neutron sources. The first reactor-based PGAA measurement was performed by Isenhour and Morrison in 1966 (1966a, b) using a chopped neutron beam from a reactor and detecting the gamma rays with a NaI(Tl) detector. In the late 1960s, a major breakthrough was the introduction of semiconductor detectors, whose energy resolution was more than an order of magnitude better than that of the best scintillators. The performance of the PGAA technique has further increased thanks to the new Ge(Li)–NaI(Tl) Compton-suppressed systems (Orphan and Rasmussen 1967). Neutron guides at research reactors were also introduced to this analytical method: first at the Saclay reactor in 1969 (Comar et al. 1969a, b), and then at the high-flux reactor in Grenoble (Henkelmann and Born 1973), while several facilities have been established at collimated reactor beams (Molnár 2004). The application of the PGAA method has increased thanks to the availability of high-flux thermal and cold beams during the 1990s at National Institute of Standards and Technology (NIST), USA (Lindstrom et al. 1993), at Jülich Research Center, Germany (Rossbach 1991), at Japanese Atomic Energy Research Center (JAERI), Japan (Yonezawa et al. 1993) and at the Budapest Neutron Center, Hungary (Molnár et al. 1997). Several other systems have been put into operation since then.

One of the reasons that PGAA was held back from common use was the lack of a proper analytical database. The first systematic series of measurements of capture-gamma spectra for 75 elements was performed by a group at Massachusetts Institute of Technology (MIT) at the end of the 1960s (Orphan et al. 1970; Rasmussen et al. 1969). The best-known compilation of these data was published by Lone et al. (1981). The “Lone table” and its electronic version have been the only source of spectroscopic data for scientists working in the field of PGAA for more than 20 years. The first complete catalog of prompt gamma lines appeared only in 2004 based on the measurements at the Budapest Research Reactor by Révay et al. (Molnár 2004).

31.2 Fundamentals of Prompt Gamma Activation Analysis

31.2.1 Fundamental Processes

Neutrons are elastically or inelastically scattered, or absorbed when they interact with matter. The most essential reaction induced by neutrons in matter is *radiative neutron capture*, or the **(n,γ) reaction** (see [▶ Chap. 30 in this Volume](#)). Prompt gamma radiation is emitted by the excited nuclei after the capture, releasing the binding energy of the neutron (typically 6–9 MeV) within 10^{-14} s. If radioactive isotopes are produced, delayed gamma radiation can also be detected with energies up to 2–3 MeV. Decay gamma radiation from short-lived nuclides can also be observed in prompt gamma measurements.

Other important competing reactions that can occur in samples, are the neutron-induced emission of charged particles, specifically (n,p), (n,α) reactions, and fission, noted as (n,f) reaction (Molnár 2004). The most important cases are the following:

- (n,p) reactions on: ^3He and ^{14}N
- (n,α) reactions on: ^6Li and ^{10}B
- (n,f) reaction on: ^{235}U

Light nuclides have weak (n,γ) branching, while their charged-particle emission branch is much stronger. In the case of ^{10}B , the emission of the alpha particle is followed by the emission of a gamma ray from the residual ^7Li nucleus with the energy of 478 keV. Because of the recoil of the nucleus, the spectrum peak is characteristically broadened over an energy range of about 15 keV. This strong peak makes possible the unambiguous identification of *boron*.

In the case of fissile nuclides, fission can be the dominant reaction. From among the naturally occurring nuclides, it is ^{235}U whose fission cross section is significant— 583 barn— while the capture cross section is 98 barn. During fission, energy of about 15 MeV is released in the form of gamma radiation, which is more than in the case of neutron capture, for which the binding energy is 6.395 MeV. This action results in a characteristic shape of the spectrum with a much steeper low-energy trend, compared to a spectrum from (n,γ) reactions only.

For bulk samples, elastic scattering of the neutrons before the capture reaction may also play an important role, lengthening the path of the neutrons inside the target. The energy distribution of the neutrons may also be modified by elastic scattering especially in the case of hydrogenous materials.

The neutron-capture cross section of the (n,γ), (n,p), and (n,α) reactions typically follow the **1/v law** for low neutron energy. For these *regular nuclides*, the cross section can be described using the following expressions:

$$\sigma(v) = \sigma_0 \frac{v_0}{v} \quad \sigma(E) = \sigma_0 \sqrt{\frac{E_0}{E}} \quad \sigma(\lambda) = \sigma_0 \frac{\lambda}{\lambda_0} \quad (31.1)$$

where σ_0 is the thermal cross section, $v_0 = 2,200 \text{ m s}^{-1}$, $E_0 = 25.26 \text{ meV}$, $\lambda_0 = 1.80 \text{ Å}$. In the cold energy range (below 10 meV) all nuclides are regular. The 1/v dependence continues until the first resonance (if any). Most resonances appear in the eV – keV neutron kinetic energy range. In some cases, the lowest energy resonances partly overlap with the thermal region (^{113}Cd , ^{149}Sm , etc.), resulting in an increase of the capture cross section. These *irregular nuclides* will have an increased reaction rate in thermal beams relative to the regular ones. This discrepancy can be corrected with the so-called Westcott g factor (Westcott 1955).

31.2.2 Activation Equations

In PGAA, one is interested in the correlation of the characteristic spectral peak areas and the masses of the emitting components. The calculation here is simpler, for many reasons, than in neutron activation analysis (NAA):

- In PGAA, the activation takes place in an almost parallel beam instead of an isotropic neutron field. Thus, the attenuation of neutrons can be calculated in a simpler way.
- The spectrum peaks from prompt gamma radiation are acquired only during the activation; hence, peak areas do not need to be corrected for decay.
- Many neutron beams contain only a small amount of epithermal and fast neutrons, and thus any reaction induced by them can normally be neglected.

The simplest equation for the reaction rate produced by a parallel beam of monochromatic neutrons in an ideally thin and homogeneous sample can be written as follows:

$$R = n \sigma \Phi \quad (31.2)$$

where R is the reaction rate (s^{-1}), n is the number of atoms of the examined nuclide in the neutron beam, σ is the cross section for neutron capture at the given energy (cm^2), and Φ is the neutron flux ($\text{cm}^{-2} \text{s}^{-1}$). For the characterization of a given gamma ray, the so-called partial gamma-ray production cross section is used:

$$\sigma_\gamma = \theta \sigma P_\gamma \quad (31.3)$$

where θ is the natural abundance of the given isotope in the element of interest, σ is the isotopic capture cross section, and P_γ is the emission probability of the gamma ray with the given energy and gives the fraction of the emitted gamma photons per capture. The count rate of a peak at a given energy in the gamma spectrum can be written as

$$\rho_\gamma = \varepsilon(E_\gamma) n \sigma_\gamma \Phi = \varepsilon(E_\gamma) \frac{m}{M} N_A \sigma_\gamma \Phi \quad (31.4)$$

where ρ_γ is the count rate, i.e., the net peak area divided by the measuring time (live time of the counting system) and $\varepsilon(E_\gamma)$ is the counting efficiency of the detector (see later), m is the mass of the element, M is its atomic weight, and N_A is the Avogadro constant.

In many practical cases, the neutrons follow an energy distribution, the cross section is energy-dependent, the sample may not be regarded as ideally thin, and thus the modification of the neutron field and the attenuation of gamma rays within the sample must also be taken into account. Instead of considering all these effects, simplifying assumptions may be introduced. Let us examine two limiting cases in more detail, which can be approximated in reality quite well (Molnár 2004).

31.2.2.1 Thin Sample Approximation

When irradiating a homogeneous and thin sample, the gamma-ray self-absorption, neutron self-shielding, as well as other effects, modifying the counting efficiency and the variation of the internal flux inside the sample can be neglected. Thus the reaction rate, as shown in

► Chap. 30 in Vol. 3, depends on the integral of the product of the partial cross section and the neutron flux. For a regular nuclide (i.e., whose cross section follows the $1/v$ law), this integral can be replaced with the product of two average quantities:

$$\int_0^{\infty} \sigma_{\gamma}(E_n) \Phi(E_n) dE_n = \sigma_{\gamma 0} \Phi_0 \quad (31.5)$$

where $\sigma_{\gamma 0}$ is the partial gamma-ray production cross section measured with monochromatic neutrons having the speed of $v_0 = 2,200 \text{ m s}^{-1}$, which equals the cross section determined in a neutron beam having a thermal distribution with the temperature of 293 K, and Φ_0 (sometimes written as Φ_{th}) is the *thermal equivalent neutron flux*:

$$\Phi_0 = \frac{v_0}{\langle v \rangle} \Phi_r \quad (31.6)$$

where Φ_r is the real flux, i.e., the actual number of neutrons reaching a unit surface of the sample in a second. When activating in a cold neutron beam, the reaction rate becomes higher due to the increase of the cross section, which is inversely proportional to the average speed. In PGAA, however, the use of thermal cross sections is preferred for their conceptual simplicity. The speed dependence is taken into account by using the thermal equivalent flux, which is inversely proportional to the average speed. (As can be seen from ► Eq. (31.1), it is also inversely proportional to the square root of the average energy and is proportional to the average wavelength.) Using Φ_0 , the reaction rate expressions become similar to ► Eqs. (31.2) and ► (31.4):

$$R^0 = n \sigma_0 \Phi_0 \quad \rho_{\gamma}^0 = \frac{m}{M} N_A \sigma_{\gamma 0} \Phi_0 \varepsilon(E_{\gamma}) \quad (31.7)$$

It should be mentioned that in this approximation, the count rate depends only on the mass of the component in the beam, and it does not depend on the sample shape, or even the surface area facing the beam (Molnár 2004).

31.2.2.2 “Black” Sample Approximation

In the other limiting case, one of the major components has an extremely large capture cross section, so all the neutrons are absorbed close to the surface in the sample, and every neutron generates gamma photons according to the emission probabilities of the capturing nuclide. The observed count rate does not depend on the cross section any more, but it is directly proportional to the number of neutrons, i.e., the real flux multiplied by the emission probability:

$$\rho_{\gamma}^{\infty} = S P_{\gamma} \Phi_r \varepsilon(E_{\gamma}) \quad (31.8)$$

where S is the surface area of the sample facing the beam, P_{γ} is the emission probability, and Φ_r is the real flux. If the real flux of two different beams is the same, the count rate for black samples will be the same, too. Using black samples, the real flux becomes a directly measurable quantity. Comparing it with the thermal equivalent flux based on ► Eqs. (31.6) and ► (31.7) the average speed or wavelength of the beam can be determined (Molnár 2004; Révay 2005).

31.3 Characteristics of PGAA

31.3.1 Analytical Properties

The most important characteristic of PGAA is based on the fact that both the neutrons and the emitted gamma radiation are highly penetrating. For example, an iron plate with a thickness of 1 cm transmits 80% of incident thermal neutrons, and about the same percentage of high-energy prompt gamma radiation. For gamma lines above 100 keV self-absorption is typically of minor significance. PGAA can be regarded as a matrix-independent analytical tool for samples up to a few grams. As the neutrons illuminate the samples throughout their whole thickness, the analysis provides the *average composition* of the illuminated *bulk sample*.

There are a few cases, when a special care has to be taken:

- When the sample contains a nuclide with a high neutron-capture cross section in a high concentration, neutron self-shielding may become important. However, in spectra of homogeneous samples all peak areas will be lowered uniformly by the neutron absorption, leaving the peak-area ratios the same.
- When the irradiated material contains mainly high-*Z* elements, gamma self-absorption may become significant, especially for the low-energy gamma rays. However, above the energy of 2 MeV the attenuation of the gamma rays is almost independent of energy, which again means an approximately uniform decrease of the absolute intensities, i.e., area ratios of high-energy peaks can be used for chemical analysis without correcting for self-absorption.

The analytical result is independent of the chemical state of the elements because the analytical signal originates from the excitation of the nuclei, not the electron shells. Hence, PGAA can be used for multi-elemental *panorama analysis* without any prior information on the sample.

Since neutron and gamma fields cannot be separated, as is done in NAA, a more complex shielding is needed in this technique. This requires more construction material in the vicinity of the detector, thus increasing the spectral background induced by the scattered neutrons in these materials. (See later.)

PGAA is *nondestructive* in several ways:

- No sample preparation is necessary.
- The irradiation does not change the elemental composition of the sample. (The converted nuclei are mostly stable isotopes of the same element, and their number is at least ten orders of magnitude less than for the atoms in the sample.)

The radiation damage in the sample caused by the neutrons and gamma rays is normally negligible. If, however, charged-particle emission is induced by the neutrons, the material may undergo minor radiation damage, resulting in modifications in the chemical or crystal structure followed by discolorations. This effect may be remarkable when irradiating lithium-, boron- or nitrogen-containing samples.

Usually, the only problem requiring attention is the formation of *radioactive isotopes*. In the worst case, samples must be cooled for a few weeks until their radiation reaches the background level.

Special care must be taken, when *fissile material* is analyzed. From the gamma radiation of the original material its previous irradiation history can be determined, and this may be distorted by exposure to neutrons.

Every chemical element (except ^4He) can be analyzed with PGAA. However the neutron capture cross sections vary by eight orders of magnitude (from O: 0.00019 barn to Gd: 48,800 barn). Thanks to this fact that high-cross section elements can be determined in low-cross section matrices with high sensitivity.

The main power of the method is the analysis of *light elements* (i.e., Ca and below). Their capture cross sections are characteristically a few tenths of a barn, which allows their assay even in weak neutron beams (e.g., the industrial analysis of raw materials using neutron generators). The most important of them is hydrogen, which can be analyzed with a fairly good sensitivity in almost any kind of matrix. PGAA is a unique tool for the determination of hydrogen or water content even in trace amounts.

In NAA, the samples are irradiated in an isotropic neutron field, and the induced decay gamma radiation can be detected even in contact geometry. In PGAA, neutron beams are used for activation (10^{-4} to 10^{-5} times weaker than the activation in reactor cores), and the detector cannot be placed too close to the sample (10^{-2} to 10^{-3} maximum efficiency). On the other hand, only a fraction of the total number of decay events takes place during the counting in NAA, decreasing the sensitivity of the method by a factor of 10^{-1} to 10^{-3} (Isenhour and Morrison 1966b), while in PGAA all prompt gamma photons can be detected with the above mentioned efficiency. All these effects result in analytical sensitivities of PGAA being lower by a factor of usually 10^{-4} to 10^{-6} compared to NAA. This deficiency can partly be overcome by using longer irradiations and larger samples. This fact, however, predestines PGAA to be primarily a major-component analytical technique (Molnár 2004).

31.3.2 Characterization of Prompt Gamma Spectra

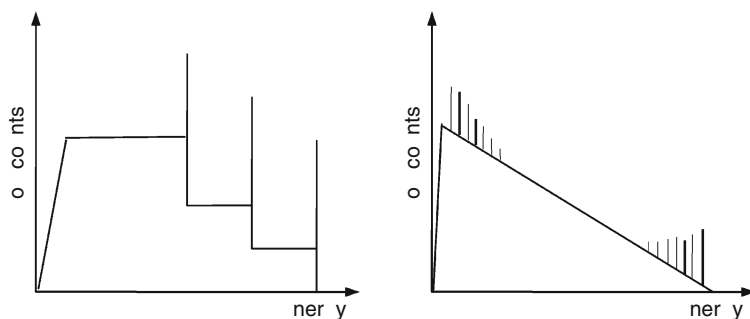
The highest-energy prompt gamma lines are close to 12 MeV, unlike decay lines, which are mostly below 3 MeV. Thus, the energy range of prompt gamma spectra is much wider than that used in NAA. Prompt gamma spectra usually contain several hundred peaks. The largest fraction of the counts appears in the spectral background, not in characteristic peaks.

The complexity of prompt gamma spectra depends on the nuclear level structure of the emitting nuclide. There are two major types of spectra:

1. The lightest nuclides have no energy levels below their capture states; thus, only one prompt gamma peak appears in their spectra corresponding to the transition from the capture state to the ground state (^2H , ^3H , and ^4He product nuclides). The other light nuclides have a couple of levels below their capture states, so besides the direct transitions only a few others appear in the spectra (^7Li , ^8Li , ^{13}C , ^{17}O). These spectra consist of strong prompt gamma lines (the emission probabilities are greater than 10%). The lower energy lines always sit on the Compton plateau caused by the higher-energy lines resulting in an increasing baseline toward low energies.
2. For the heavy elements another spectrum shape is typical because of the large number of possible transitions in the nuclei. The large number of overlapping peaks forms an almost smooth continuum in the mid-energy range and continuously rising with the decreasing energy (the most typical examples are Eu, Tb, and Ir). Identifiable prompt gamma peaks appear only at the low- and high-energy ends of the spectra originating from the primary and the ground-state transitions. The emission probabilities for these lines are typically a few percent only. The basic types of prompt gamma spectra are illustrated schematically in [Fig. 31.1](#).

■ Fig. 31.1

Typical shapes of prompt gamma spectra for the lightest (type 1) and the heaviest nuclides (type 2)



The density of the prompt gamma peaks at the high-energy end is much lower than the density at low gamma energies. Thus, high-energy peaks can be used much more reliably for qualitative analysis. When analyzing multielement samples, one can observe that the upper half of the energy range (6–12 MeV) typically contains peaks from light elements due to the energy dependence of the binding energy (Molnár 2004).

31.3.3 Dynamic Range and Detection Limit

Characteristic peaks always stand on a spectral background originating mainly from the Compton scattering of the higher-energy gamma photons. This Compton continuum usually contains counts that are less by two to three orders of magnitude in each channel than the area of the full-energy peak (FEP) from the gamma ray that generates it. In the case of spectra acquired with high count rates for several hours one can expect a few strong peaks with up to a few million counts, which are standing on a baseline with the height of thousands of counts per channel. In a spectrum like that a peak with the minimum area of a few hundred counts can be detected. In the everyday routine analyses, such high counts are rarely collected, so the area ratio of the strongest and the weakest peaks is typically closer to a thousand. This means that the dynamic range of the prompt gamma spectra, over which the peak areas are detectable, is three to four orders of magnitude.

From these considerations, the detectability of the elements can be estimated. In the case of a sample containing two elements only, the strongest peaks of the minor component can be at least three to four orders of magnitude smaller than those of the dominant component. This is true for the opposite case, too, so the mass ratio of any two elements can vary between six and eight orders of magnitude. For example, 0.1 mg of chlorine can be easily detected in 1 g of water (approximately 0.1 g H), and 0.1 mg of hydrogen (or 1 mg of water) can be analyzed in 0.1 g of carbon tetrachloride (containing 90% chlorine).

In spectra taken on a mixture of elements, the detection limits for components can be estimated efficiently using a few rules of thumb. The efficiency of the detector between 100 keV and 10 MeV drops by two orders of magnitude. Similarly, the minimum detectable peak area varies from a few hundreds of counts at low energies to a few counts at the highest energies. These peak areas corrected with the counting efficiency can be approximated as being constant

all over the spectrum, and that equals the minimum detectable peak area at the maximum of the detector efficiency. For the case of a high-purity germanium (HPGe) detector, the efficiency function has its maximum around 100 keV, and its value equals the geometric efficiency (see later). Based on ► Eq. (31.4), the *detection limit* is the following:

$$DL/g = \frac{A_{\min} M / g \text{ mol}^{-1}}{0.6 \sigma_{\gamma 0} \Phi_0 \varepsilon_{\text{geom}} t_{\max} / \text{mol}^{-1}} \quad (31.9)$$

where A_{\min} is the minimum detectable peak area at 100 keV, M is the atomic weight of the element, 0.6 is the rounded Avogadro constant times 10^{24} (its unit is mol^{-1}), $\sigma_{\gamma 0}$ is the partial gamma-ray production cross section in barns (10^{-24} cm^2), Φ_0 is the thermal equivalent flux ($\text{cm}^{-2} \text{ s}^{-1}$), $\varepsilon_{\text{geom}}$ is the geometric efficiency (the fraction of detected solid angle), and t_{\max} is the maximum possible measurement time (s). For instance, if the minimum detectable peak area is 600 (a typical value) and the collimated detector is at a distance of about 25 cm away from the sample, then the geometric efficiency will be approximately 0.001. If the maximum measurement time is taken 100,000 s (a little longer than 1 day) and the flux $10^8 \text{ cm}^{-2} \text{ s}^{-1}$, then using the above values and a constant with the proper unit, the estimated detection limit in micrograms can be estimated as follows (► Table 31.1; Molnár 2004):

$$DL/\mu\text{g} = \frac{M / g \text{ mol}^{-1}}{10 \sigma_{\gamma 0} / \text{b}} \quad (31.10)$$

31.4 Neutron Beams and PGAA Facilities

31.4.1 Neutron Beams

A PGAA instrument consists of a source of neutrons, a collimating beam tube to shape and direct a beam of neutrons onto a sample, a shutter to turn the beam on and off, a target assembly to position the sample reproducibly in the neutron beam, a gamma-ray detector, a beam stop to absorb the neutrons that are not absorbed by the sample, and shielding to protect the detector and personnel from neutron and gamma radiation. Each of these components will be considered in turn. The construction of a recent system illustrates clearly many of the choices involved (Robinson et al. 2009). More detailed information on the issues can be obtained in the PGAA Handbook (Molnár 2004).

To make the best analytical measurements, the PGAA beam should be both bright and clean. The neutron flux at the sample position should be high enough to obtain good counting statistics for the elements of interest in a reasonable time. Moreover, the beam should be temporally stable, spatially uniform, and contain few epithermal and fast neutrons and gamma rays so as to minimize interfering reactions and background. There should be a permanent scientist in charge of the instrument, which should be accessible to users from outside the host institution. These desiderata follow from the fundamental considerations in the previous sections.

31.4.2 Neutron Sources

The dominant neutron sources in laboratory PGAA are beams extracted from *research reactors*. Other neutron sources, based on radioactive nuclides or neutron generators, commonly used

Table 31.1

Energy, cross section, and detection limit values according to Eq. (31.10) for the most important gamma-ray lines of each element. Decay lines are marked with an asterisk*

El	E (keV)	σ_{γ}	DL (μg)
H	2,223	0.3326	0.3
Li	2,032	0.0381	18
Be	6,810	0.0058	160
B	478	716.0	0.00150
C	4,945	0.00261	500
N	1,885	0.01470	100
O	871	0.000177	9,000
F	1,634*	0.0096	200
Ne	2,036	0.0245	80
Na	472*	0.478	5
Mg	585	0.0314	80
Al	1,779*	0.232	12
Si	3,539	0.1190	24
P	637	0.0311	100
S	841	0.347	10
Cl	1,951	6.33	0.6
Ar	167	0.53	8
K	770	0.903	4
Ca	1,943	0.352	11
Sc	147	6.08	0.7
Ti	1,382	5.18	0.9
V	1,434*	4.81	1.1
Cr	835	1.38	4
Mn	847*	13.10	0.4
Fe	7,631	0.653	9
Co	230	7.18	0.8
Ni	8,998	1.49	4
Cu	278	0.893	7
Zn	1,077	0.356	18
Ga	834	1.65	4
Ge	596	1.100	7
As	559	2.00	4
Se	614	2.14	4
Br	245	0.80	10
Kr	882	20.8	0.4
Rb	557	0.0913	90
Sr	1,836	1.030	9

Table 31.1 (Continued)

El	<i>E</i> (keV)	σ_{γ}	<i>DL</i> (μg)
Y	6,080	0.76	12
Zr	934	0.125	70
Nb	99	0.196	50
Mo	778	2.02	5
Tc	172	16.60	0.6
Ru	540	1.53	7
Rh	181	22.6	0.5
Pd	512	4.00	3
Ag	199	7.75	1.4
Cd	558	1,860	0.006
In	273	33.1	0.3
Sn	1,294	0.1340	90
Sb	564*	2.700	5
Te	603	2.46	5
I	134	1.42	9
Xe	668	6.7	2.0
Cs	176	2.47	5
Ba	627	0.294	50
La	1,596	5.84	20
Ce	662	0.241	60
Pr	177	1.06	13
Nd	696	33.3	0.4
Sm	334	4,790	0.003
Eu	90	1,430	0.010
Gd	182	7,200	0.0022
Tb	154	0.44	40
Dy	184	146	0.11
Ho	137	14.5	1.1
Er	184	56	0.30
Tm	204	8.72	2.0
Yb	515*	9.0	1.9
Lu	150	13.8	1.3
Hf	213*	29.3	0.06
Ta	270	2.60	7
W	146	0.970	19
Re	208	4.44	4
Os	187	2.08	9
Ir	352	10.9	1.8
Pt	356	6.17	3

■ Table 31.1 (Continued)

El	E (keV)	σ_{γ}	DL (μg)
Au	412*	94.0	0.21
Hg	368	251	0.08
Tl	348	0.361	60
Pb	7,368	0.137	150
Bi	4,171	0.0171	1,200
Th	472	0.165	140
U	4,060	0.186	130

in industrial applications are discussed in detail elsewhere (Alfassi and Chung 1995). Reactor neutrons originate in fission reactions at high energy, and are slowed to thermal energies by scattering from light atoms in a moderator, typically water or heavy water, surrounding the fuel. The beam is a mixture of three components: a high-energy ($\sim\text{MeV}$) fission source distribution, a near-Maxwellian ($\sim\text{meV}$) thermal spectrum at the moderator temperature, and an epithermal ($\sim\text{eV}$) slowing-down region with a spectrum being approximately inversely proportional to the neutron energy. Because most neutron cross sections are inversely proportional to the neutron speed, the thermal portion is the most effective in producing (n,γ) neutron capture reactions used in PGAA. *Cold neutrons* from a cryogenic moderator are especially desirable, not only because the reaction rate per neutron is several times that of a room-temperature spectrum but also because cold neutrons can be efficiently transported by neutron guides, as will be discussed below.

The flux of neutrons normally is proportional to the inverse square of the distance from the source, so for the greatest analytical sensitivity, the sample irradiation position should be near the reactor. This is also where the gamma-ray and neutron backgrounds are highest, so care in optimizing the shielding is needed for good results. Published fluxes of reactor beams that have been used for PGAA range from $10^5 \text{ cm}^{-2} \text{ s}^{-1}$ to over $10^{10} \text{ cm}^{-2} \text{ s}^{-1}$, although $10^7\text{--}10^8 \text{ cm}^{-2} \text{ s}^{-1}$ is most common.

31.4.3 Shaping and Tailoring Neutron Beams

Thermal neutron beams are produced by geometrical collimation, with absorbing apertures at each end of a long flight path. A collimator does not affect the neutron energy, so the beam at the sample often contains more fast neutrons and gamma rays than desired. To improve this, the beam may pass through a filter that preferentially removes the fast neutron component and also absorbs gamma radiation. For example, 5.3 cm of sapphire in the thermal PGAA beam at NIST reduced the epithermal neutron background fivefold and the low-energy gamma ray background by an order of magnitude (Mackey et al. 2004). A number of different filter materials used in PGAA systems are listed in the PGAA Handbook (Molnár 2004).

Epithermal and fast neutrons can be eliminated entirely by using diffraction to extract a narrow range of wavelengths from the beam (Byun et al. 2002). Several orders of diffraction can be summed to increase the flux. The best beams are those from *neutron guides*, which operate by total internal reflection in a narrow channel. Neutrons incident on a surface at

angles below a characteristic critical angle are totally reflected, removing the $1/r^2$ loss with distance from the source. The critical angle depends on the material comprising the surface, and is inversely proportional to the neutron wavelength; for this reason, the guide acts as a low-pass filter. The critical angle for natural nickel is 0.7° at 6.8 \AA (the most probable wavelength at the normal boiling point of hydrogen, 20 K) and 0.2° at 1.8 \AA (the most probable wavelength at 300 K). Larger critical angles increase by severalfold, and hence greater transmission efficiency (which is proportional to the square of the critical angle) can be obtained with multilayer *supermirror* reflectors. Curved guides are used to avoid direct sight of the neutron source that emits also fast neutrons and gamma radiation. Reflective optical elements can increase the flux by concentrating the beam into a smaller area (Copley and Majkrzak 1989), at the expense of increased divergence. Capillary optics has been used to create a high-flux submillimeter analytical probe (Mildner et al. 2002).

31.4.4 Neutron Absorbers and Shielding Materials

The perfect neutron shielding material does not exist. Ideally, a shield should absorb all neutrons of all energies in a short distance without generating secondary radiation or producing residual radioactivity (Table 31.2). In practice, the most important absorbers are ^6Li , ^{10}B , and ^{113}Cd , via the (n,α) and (n,γ) reactions. Only ^6Li (and ^3He) absorb neutrons efficiently without producing gamma rays. Although metallic Cd is easily shaped and an excellent absorber, neutron irradiation produces substantial residual radioactivity in addition to the strong prompt 559-keV capture gamma rays, so B and Li are preferred for high-flux tasks such as shutters and beam stops.

Boron has a high cross section and most of the 2.8-MeV reaction energy from neutron capture is carried by an alpha particle and ^7Li recoil nucleus. However, 94% of absorbed neutrons produce a gamma ray of 478 keV. This energy is readily shielded, requiring only 4 mm of lead to reduce the radiation by half. With lithium, there is no gamma ray from the $^6\text{Li}(n,t)^4\text{He}$ reaction, but the high-energy tritons produce about 10^{-4} energetic secondary neutrons per incident neutron from light elements by (t,n) reactions (Lone et al. 1980). If the

Table 31.2

Characteristics of neutron-absorbing materials

Nuclide	Isotopic abundance, %	Cross section, b	Reaction	Product half-life and decay	Chemical forms
^3He	0.00014	5,330	$(n,p)^3\text{H}$	12 years, β^-	Gas
^6Li	7.5	941	$(n,\alpha)^3\text{H}$	12 years, β^-	LiF , Li_2CO_3 , metal, glass
^{10}B	19.9	3,838	$(n,\alpha)^7\text{Li}$	Stable	B_4C , H_3BO_3 , $\text{Na}_2\text{B}_4\text{O}_7$
^{113}Cd	12.22	20,600	$(n,\gamma)^{114}\text{Cd}$	Stable	Metal
^{114}Cd	28.73	0.23	$(n,\gamma)^{115}\text{Cd}$	53 h, β^-,γ	
^{155}Gd	14.8	60,900	$(n,\gamma)^{156}\text{Gd}$	Stable	Metal
^{157}Gd	15.6	255,000	$(n,\gamma)^{158}\text{Gd}$	Stable	
^{160}Gd	21.7	1.51	$(n,\gamma)^{161}\text{Gd}$	3.7 min, β^-,γ	

flux is high, the tritium produced may be hazardous. Isotopically enriched ^6Li and ^{10}B are sometimes used; 100% enrichment improves the stopping power over natural Li and B by a factor of 13 or 5, respectively.

Lithium carbonate and fluoride are inert and can be shaped into machinable forms. A ^6Li silicate glass (Stone et al. 1994) has been used with success for collimators, beam stops, and shielding. Both carbonate and the fluoride have been mixed with polymers or paraffin to make castable (Anderson et al. 1981) or flexible neutron absorbers, but hydrogen capture gamma rays from the organic matrix can be excessive for use in the field of view of the gamma detector. The collimating aperture near the neutron source is commonly fabricated from Boral, a mixture of boron carbide and aluminum powder rolled into sheets and clad with aluminum. Where secondary radiation is of no concern (for instance shielding a detector from the last few neutrons), sheets of cadmium or boron-loaded polymer are often used. For large parts of the apparatus and for personnel protection, massive concrete in either poured or block form is cost-effective for both gamma-ray shielding and neutron shielding.

31.4.5 Neutron Shutter, Beam Tube, Sample Holder, and Beam Stop

It is necessary to shut the neutron beam off in order to change samples. Like the first collimating aperture, the shutter is best located close to the neutron source and surrounded by shielding, so as to minimize stray radiation at the sample position. Thermal neutron shutters are commonly made of thick boron- or lithium-containing materials, supplemented by thermalizing material or epithermal absorbers.

Neutrons are lost from the beam by scattering in air in the flight path: in passing through 1 m of air, about 5% of the neutrons are scattered into the surroundings. For this reason, it is desirable to evacuate the beam tube or fill it with helium, especially the portion outside the biological shield of the reactor. Alternatively, the beam tube can be made large in diameter and lined with ^6Li absorber (Mackey et al. 2004).

Ideally, for PGAA the sample should be held in position by a material that neither absorbs nor scatters neutrons. Fluorocarbons such as **Teflon**[™] Tetrafluoroethylene (TFE) or Fluorinated ethylene propylene (FEP) (both with empirical formula CF_2), or Teflon[™] PFA (approximately $\text{C}_4\text{F}_7\text{O}$), are commonly used; in most cases, only fluorine is an important contributor to the blank spectrum. Heat-sealable FEP is available in monofilament fiber or thin film. Thin polyolefin and polyester films are readily heat sealed, but their hydrogen content can be troublesome. Low-mass samples can be suspended in the beam with fluorocarbon strings, which for most purposes add negligible background (Anderson et al. 1981). For more massive samples, a sample holder can be made of any material that does not absorb neutrons strongly or contain the elements of interest. Aluminum, magnesium, vanadium, graphite, quartz, and silicon have been used. The target chamber should be lined with a neutron absorber, preferably ^6Li , to stop the neutrons scattered by the target.

Only a small fraction of the neutrons striking a typical sample are absorbed. The unused neutrons must be disposed of so that they will not endanger the experiment or the experimenters. Like the shutter, an absorber must stop the entire beam for long periods of time. A common configuration contains boron, surrounded by lead or concrete to absorb the 478-keV capture gamma ray and located out of view of the gamma-ray detector. In an unfiltered beam, the gamma rays from the neutron source must be accounted for: this component may be as important as capture in the beam stop itself.

31.4.6 Characterization and Monitoring the Neutron Beam

For reliable analysis, it is necessary to understand the characteristics of the neutron beam, namely its intensity (flux), spectrum, and spatial and temporal uniformity. These issues are discussed at length in the PGAA Handbook (Molnár 2004). *Foil activation* is the simplest, and perhaps the most accurate, method of measuring flux (ASTM 1998; Beckurts and Wirtz 1964). A known mass of a monitor element is irradiated for a known time, and its induced radioactivity measured with a detector of known efficiency. If the reaction rate per atom $R = \Phi\sigma$ is determined, then with the thermal cross section $\sigma = \sigma_0$ measured at $2,200 \text{ m s}^{-1}$ the thermal equivalent flux Φ_0 is obtained. Gold-198 ($T_{1/2} = 2.7$ days) is a convenient indicator nuclide, with the cross section $\sigma_0 = 98.65 \text{ b}$ for the reaction $^{197}\text{Au}(n,\gamma)^{198}\text{Au}$. The epithermal flux is measured by irradiating a monitor bare and another specimen of the same monitor element under a shield of cadmium to absorb the thermal neutrons. Fast-neutron (MeV) monitoring is similar, using threshold reactions that cannot be induced by slow neutrons, such as $^{54}\text{Fe}(n,p)^{54}\text{Mn}$. Spatial mapping can be done quickly by transfer autoradiography. A foil of In, Gd, or other readily activated material is exposed at the sample position and the induced activity detected with an X-ray film or phosphor plate. *Neutron radiography* cameras can also be used for this purpose (Hilger et al. 2006). One of two methods is generally used to measure the time stability of the neutron beam. If the reactor power is known to be stable during an analysis, the capture rate in a known standard (e.g., the 1,381.7 keV peak in a particular specimen of titanium foil) can be measured before and after each sample in order to normalize to separately irradiated standards. If the neutron source is not constant during the irradiation period, the neutron flux must be measured continuously with a neutron monitor during the time the sample is irradiated. This can be done either by measuring scattered neutrons from the beam or with a low-efficiency transmission neutron monitor.

Excellent beam quality and detector shielding can more than compensate for low neutron flux (Maier-Leibnitz 1969; Kobayashi and Kanda 1983; Matsumoto et al. 1984; Molnár et al. 1997). With careful attention to background, the sample-detector distance can be small and thus the gamma efficiency high. As a result, microgram quantities of boron have been determined in tissue with a neutron flux of only $2 \times 10^6 \text{ cm}^{-2} \text{ s}^{-1}$.

Design criteria for the shielding of the gamma-ray detector in PGAA are similar to that for any gamma-ray spectrometer, with some differences due to the presence of neutrons. *Lead* is the most common shielding material for gamma rays, but it is translucent to neutrons. Even though the capture cross section is small, neutrons striking a massive shield will produce the characteristic 7,368 keV lead capture line and its Compton continuum. Reducing thermal neutron background in the detector requires an absorber outside the lead shield. Enriched ^6Li is best in the line of sight between the sample and the detector because it does not produce extra gamma rays, and does not greatly attenuate gamma rays.

The Ge detector itself is the most convenient tool to measure both fast and thermal neutron background rates at the detector (Chung and Chen 1991). The spectrum may show a composite of the sharp 595.9 keV line from capture of slow neutrons in ^{73}Ge and a broad triangular peak from $(n,n'\gamma)$ fast-neutron excitation of the same level of ^{74}Ge . In addition to increasing background, fast neutrons can lead to *detector damage* at a fluence as low as 10^7 cm^{-2} (Chung 1995); n-type germanium is an order of magnitude less sensitive than p-type.

In addition to the quasi-constant background characteristic of the apparatus, a variable background comes from the presence of a sample in the neutron beam. Capture gamma rays from other elements increase the continuum background under the analytical capture peak,

and may also contribute an interfering peak. Neutrons scattered by the sample itself into the apparatus may affect H, B, C, N, F, Al, Fe, Ge, and other elements (Anderson and Mackey 1993).

31.4.7 PGAA Facilities

PGAA has been performed at dozens of research reactors, with varying degrees of success and permanence. Since a comprehensive list was published in 2004 (Molnár 2004), new PGAA instruments have been established in Beijing (Zhang et al. 2005), Forschungreaktor München Research Reactor at Munich (FRM-II) Munich (Kudejova et al. 2008), and Oregon State (Robinson et al. 2009). Systems at Korea Atomic Energy Research Institute (KAERI) Daejeon, (Cho et al. 2005a) Texas (Révay et al. 2007), and Bhabha Atomic Research Center (BARC) Trombay (Acharya 2009) have been upgraded, and a system is under construction in Lisbon (Beasley et al. 2009).

31.5 Samples and Standards

For a given sample material and experimental arrangement, there is an optimum sample size and shape. Samples must be large enough to give a high capture rate for good counting statistics in a reasonable measurement time but small enough to avoid inaccuracies that creep in with high counting rates. In addition, the sample should be small enough that bias from neutron absorption or scattering will be acceptably small. These considerations usually lead preferentially to small samples and long irradiation times. The composition, the experimental conditions, and the required accuracy determine what “small” means in practice.

31.5.1 Sample Size and Shape

Neutron self-shielding (De Soete et al. 1972; Fleming 1982; Martinho et al. 2003) and gamma-ray self-absorption (Debertin and Helmer 1988; Gilmore and Hemingway 1995) are well understood in conventional instrumental neutron activation analysis (INAA) and apply in PGAA as well. As a rule of thumb, if the thickness of the sample multiplied by the macroscopic absorption cross section (the product of element cross section and concentration summed over all components, with dimension cm^{-1}) is less than 0.01, then *self-shielding* will give less than 1% bias in the analytical result. Similarly, if the product of the gamma attenuation coefficient (in $\text{cm}^2 \text{g}^{-1}$) and the mass thickness (in g cm^{-2}) is less than 0.01 then gamma *self-absorption* may be unimportant. Both self-shadowing effects are best avoided by using small samples, usually less than 1 g. However, PGAA can be performed on massive specimens, even larger than the neutron beam. Normalizing to an internal standard such as a matrix element sacrifices one degree of freedom, but need not compromise the measurement when an element ratio or mass fraction is in fact the quantity of interest. The difficult general case of large samples of unknown composition is approachable through a combination of modeling and experiment (Sueki et al. 1996; Degenaar et al. 2004).

The shape of the sample may be important, especially for hydrogenous materials such as polymers and tissues. When a sample is irradiated in a nearly parallel collimated beam of neutrons, the effects of *neutron scattering* in the sample are much greater than in the nearly

isotropic neutron field generally used for irradiations in INAA (Copley and Stone 1989; Mackey and Copley 1993). Scattering by hydrogen affects the path length of the neutrons in the sample, and therefore the probability of absorption. As a result, reaction rate is no longer proportional to the mass of analyte. The greater the scattering power of the sample (the greater the hydrogen content), the greater the bias; for instance, it is as much as 15% for 0.1 g pellets of cellulose (Mackey et al. 1991). For the most accurate work, standards are made to match the shape and hydrogen content. The shape dependence can be reduced or eliminated by making the sample spherical, or nearly so (Mackey and Copley 1993). Scattering of neutrons from the sample also increases the background from capture in the materials of the apparatus (Anderson and Mackey 1993).

31.5.2 Standardization

The simplest situation is a point sample, smaller than the neutron beam and with negligible mass of material to scatter or absorb neutrons or gamma rays. Most applications of reactor-based PGAA approach this ideal. The analytical sensitivity is defined as the counting rate at a certain gamma-ray energy per unit quantity of element under specified standard conditions. If the neutron flux is constant, the geometry of the system is unchanging, and the counting system is stable, the sensitivity is a constant. Two methods are in use to determine the sensitivity: using elemental standards for each element, and using fundamental parameters.

The elemental standard approach is the most straightforward, and the most tedious. A known quantity of the element of interest is irradiated under standard conditions. Standards are best prepared from pure elements or simple compounds known to be stoichiometric (Moody et al. 1988). Usually selected high-purity metals or analytical reagent grade chemicals are adequate, but a useful check is to compare multiple standards from different sources. If a suitable mass of an element cannot be accurately weighed, it may be dissolved in a suitable solvent and evaporated on filter paper. Solid standards can be diluted with an inert material such as high-purity graphite and pressed into pellets. Prepared PGAA standards may be used repeatedly for many years without change. A few exceptions have been noted: e.g., boric acid volatilizes slowly from filter paper although borax does not.

A drawback of this approach is that each element to be determined requires a separate standard. Moreover, if the experimental conditions change, for instance, a new gamma detector is installed, then each standard must be remeasured. A more robust approach is the k_0 standardization method (Molnár et al. 1998), which does not require standard samples.

If element X irradiated simultaneously with a monitor element M, then the flux cancels and the ratio of counting rates per unit mass can be written according to ► Eqs. (31.4) and ◀ (31.5):

$$\frac{\rho_X/m_X}{\rho_M/m_M} = \frac{\sigma_{\gamma,X}/M_X}{\sigma_{\gamma,M}/M_M} \cdot \frac{\varepsilon(E_X)}{\varepsilon(E_M)} = k_0 \frac{\varepsilon(E_X)}{\varepsilon(E_M)} \quad (31.11)$$

where ρ again is the counting rate, m is the mass of the component, M is the atomic weight, and ε is the counting efficiency at the characteristic energies of elements X and M, while k_0 is a constant. Values of k_0 and their uncertainties, relative to the hydrogen capture gamma ray at 2,223 keV, have been tabulated for more than 30,000 capture lines, (Molnár 2004; Choi et al. 2007), and are available at <http://www-nds.iaea.org/pgaa>. For any experimental conditions, to measure any element relative to any other element only the relative detector efficiency needs to

be calibrated. If epithermal capture is important then the equations contain other terms, but the principle is the same. A list of partial gamma-ray production cross sections (σ_γ) can be found in the Appendix of this volume.

Certified reference materials (CRMs), described in the Appendix such as those available from NIST (<http://ts.nist.gov/>), IAEA (<http://www.iaea.org>), BCR (<http://www.irmm.jrc.be>), or other national or international standards bodies, are occasionally used as multielement calibration standards. The chief drawbacks of these materials are the difficulty of selecting an appropriate material for all the elements of interest and the inferior accuracy of certified element content compared with in-house preparations. The most important use of CRMs is to validate the results of a measurement: if the certified value is obtained when a sample is analyzed in the same manner as the unknown, then the measurement is less likely to be in serious error.

As with most nuclear methods of analysis, backgrounds (peaks present in the absence of a sample) are generally small for most elements. A major goal in the design of a PGAA spectrometer is to minimize the spectral background. As with gamma spectrometry in INAA, detection limits and accuracy are impaired by a high baseline under the analyte peak. Unlike INAA, however, capture-gamma spectra contain so many transitions that the baseline can never be certain to be free of interfering peaks. A first-order background correction can be made by subtracting the signal from an empty sample container irradiated in the same manner as the sample.

However, much of the gamma-ray background counting rate is due to neutrons scattered into the apparatus by the sample. Thus, the background depends on the scattering power of the sample. Since hydrogen usually dominates the scattering, the gamma-ray background of components other than H can be estimated from the counts of the H peak. Conversely, the H background in hydrogenous samples can be estimated from the counting rate of other background components such as Al and Pb. A comprehensive listing of background lines and their origins has been published (Belgya et al. 2005).

31.6 High-Energy Gamma-Ray Spectroscopy

31.6.1 Fundamental Processes

The most important part of the PGAA facility is the gamma-ray spectrometer. The main component is the detector, which converts the energy of the gamma ray to an electronic signal. This signal is amplified, shaped, digitized, and stored in a histogram that makes up a spectrum of gamma peaks.

There are three major interactions a gamma photon may undergo in the detector (Knoll 2000):

- In the *photoelectric absorption* process, the gamma photon gives all of its energy to an electron in the detector material. The released high-energy electron creates electron-hole pairs in semiconductors or excited atoms in scintillators.
- In a *Compton scattering*, only a part of the photon energy is transferred to an electron, which then ionizes the material as it slows down, similar to a photoelectron. The Compton-scattered photon left from the scattering may interact again in the detector or may leave it.

- In *pair production*, a high-energy photon creates an electron–positron pair. Both the electron and the positron ionize the atoms of the material. After the positron slows down to thermal energy, it annihilates with an electron, creating most likely two so-called annihilation photons. The two photons have equal energies of 511 keV and fly off in exactly opposite directions. They may have further interactions.

The photoelectric interaction is the most probable process up to a few hundred keV and that is the only interaction that results in a complete absorption of the photon. Compton scattering may occur at all energies, but is the most important between a few hundred keV and a few MeV, while at high energies pair production becomes the most important interaction (see [Fig. 31.4](#)).

Gamma rays deposit their full energy only when the photoelectric absorption is the final step in the sequence of interactions inside the active volume of the detector, thus resulting in the full-energy peak (FEP). In Compton scattering, gamma photons having almost any energy below the initial energy can escape from the detector, causing a continuum (Compton plateau) below the FEP. Compton-scattered or escape events, however, can be identified using a guard detector annulus around the semiconductor detector. In Compton suppression mode of this guarded system the signal of gamma rays, which leave the germanium crystal (see later), are rejected. The most commonly used materials for the guard detector are sodium iodide (NaI) and bismuth germanate (BGO).

31.6.2 Instrumentation

31.6.2.1 Detector Selection

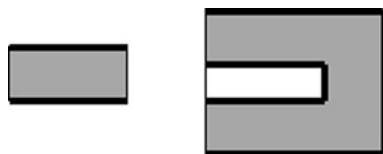
The energy range of prompt gamma radiation extends from a few tens of keV up to 12 MeV. There are two detector types in practice that are able to detect gamma rays over this wide energy range: the solid *scintillation* detector and the germanium semiconductor detector:

- Industrial applications require durable, shock-and vibration-resistant, easy-to-use equipment, which may be operated in a wide range of temperature, humidity, and pressure environments (Johansen and Jackson 2004). These criteria can be better satisfied by scintillation detectors, and such detectors may also be satisfactory for monitoring the composition of nearly identical objects.
- The superior energy resolution of the *high-purity germanium (HPGe) detectors* makes them ideal for high sensitivity analysis of samples having a large variety of compositions (Knoll 2000; Leo 1987).

In this chapter, focus is put on the spectroscopic work with HPGe detectors. There are two types of HPGe crystals; they differ in the donor or acceptor concentration. In the case of n-type detectors, the outer surface is doped with acceptor atoms, typically boron, with a thickness of a few micrometers. They have been shown to have much better resistance against neutron damage than p-type detectors, doped with a thicker layer of acceptor atoms (Knoll 2000). For the measurements of low-energy gamma radiation planar detectors are used, while in PGAA the larger-volume (at least 100 cm³) closed-ended coaxial detectors are preferred (Knoll 2000; Leo 1987) (see [Fig. 31.2](#)). The germanium crystal has to be cooled to liquid nitrogen temperature (77 K) when operated.

■ Fig. 31.2

Schematic shapes of planar and closed-ended types of high-purity germanium (HPGe) detectors. Thick lines show electrode connections



To increase the ratio of the full-energy signal relative to the Compton continuum, the simplest way is to increase the volume of the germanium detector. The suppression, however, is not proportional to the volume as often thought. The peak-to-background ratio improves approximately with the square root of the volume (Heath et al. 1999). There is another serious limitation, too: the width of the active, depleted volume can extend only for about 2–3 cm. The longest crystals commercially available these days are about 9-cm long, which are the best choice for the detection of high-energy gamma rays at present. The efficiency of charge collection of larger detectors is worse than for the smaller ones. Therefore, smaller detectors have better resolutions at low energy; however, at about 1.3 MeV, the difference practically disappears.

31.6.2.2 Electronics and Its Characteristics

Analog electronics. The number of electron–hole pairs produced in the absorption of gamma photons is in the order of hundred thousands. The induced extremely low current has to be amplified before further signal processing. There are two types of *preamplifiers*:

- The Resistive-capacitive feedback (RC-feedback) type produces exponentially decaying signals with decay times of around 50 μs .
- The transistor-reset preamplifiers (TRPs) generate continuously increasing step-like signals, which have to be reset before reaching an upper limiting voltage level. TRPs are supposed to handle high count rates better.

The signal, whose amplitude is carefully maintained to be proportional to the energy of the impinging radiation, is digitized by an analog-to-digital converter (ADC) and the digitized result is sorted in a multichannel analyzer (MCA), then stored in a computer for further analysis. This is the traditional scheme of signal handling.

Digital signal processing (DSP). Digital spectrometers have been available in the market for more than 10 years (Jordanov et al. 1994). The simplest device replaces the spectroscopy amplifier and the ADC. The preamplifier signal enters and digitized data leave the module, which can be directly fed to an MCA. The desktop models integrate the functionality of the high-voltage supply, spectroscopy amplifier, the ADC, and the MCA. The common factor in all of these digital signal processors is that the preamplifier signal is conditioned and a fast sampling ADC digitizes the signal flow in real time. The stream of numbers passes through digital filters, which determines the amplitude and detection time of the signal pulse and the processor generates the corresponding channel numbers for energy or time.

There are two types of digital filters continuously processing the data stream coming from the preamplifier. The filtering process involves the calculation of sums of the digitized data using different weighting factors.

- A fast filter with the total duration of a few hundred nanoseconds is used for the detection of the events, for monitoring pileup, and yields the detection times.
- A slow filter is used to determine the step height of the preamplifier signal, which carries the energy information.

Among other advantages, the DSP manufacturers provide evidence that the temperature and long-term gain stability is much better for the DSP systems than for analog systems. Due to the shorter shaping process, the DSP systems show better high-count rate properties than the analog systems. The throughput and energy resolution also show better characteristics. However, Szentmiklosi et al. (2005) found that in wide energy range applications such as PGAA, there are still problems to be solved.

Dead time and pileup. All detector systems have a certain characteristic time period required to process an event. The detector system may or may not remain sensitive during this period. In the second case, events arriving during this characteristic resolution time will be lost, while in the first case, they may pile up and change the measured value, so generating a count in a different channel, and thus both events will effectively be lost. The time period during which incoming events are lost is called the dead time. To avoid a significant distortion of the number of events occurring, the count rate must be kept sufficiently low. A maximum of a few ten thousand counts per second can be handled by systems available at present. The dead time is influenced by all components of the detector system (Gilmore and Hemingway 1995).

Taking into account the dead time of a detector system is very important when an absolute intensity experiment is performed. All ADCs estimate the dead time, however their accuracy is sometimes questionable. Digital spectrometers are supposed to estimate the dead time accurately, since the time of the signal processing is exactly prescribed.

The simplest way to determine the overall dead time is to measure it using a pulser. The pulser signals should be connected to the preamplifier of the detector, using a pulse amplitude greater than that from any expected capture photon. From the known rate of the pulser and the recorded number of pulser counts, the number lost due to the dead time can be determined. The best performance is obtained with counting a radioactive source or a random time pulser together with the sample (Knoll 2000).

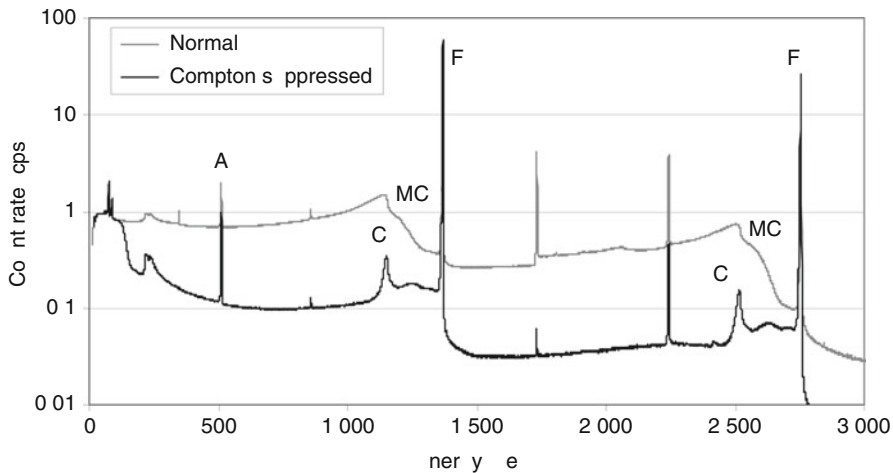
The *pileup* of events occurs when a second signal arrives at the amplifier within its resolution time, i.e., within the shaping width of a single pulse (typically 2–3 times the peaking time for RC-feedback preamplifiers). The piledup pulses then produce one count with an amplitude somewhere between that of the smaller event and the sum of the two event amplitudes (Gilmore and Hemingway 1995) depending on the response of the ADC to the distorted signal. When using an analog amplifier, this effect can be reduced if the *pileup rejection* mode is switched on. When a second event is detected by a fast discriminator during an adjustable inspection interval, a gating pulse is generated to inhibit the storing of the original pulse. This feature can effectively reduce the level of the continuum in the spectrum. DSPs also handle pileups: signals processed by the slow filter are rejected, if the fast filter registers additional events.

31.6.2.3 Response Function of Germanium Detectors

In PGAA, the energy spectrum is collected by a multichannel analyzer (MCA). The spectral shape for a single gamma ray of a given energy is called the response function. Its shape depends on the size of the germanium detector, the spectrometer electronics, the gamma-ray energy

■ Fig. 31.3

The normal and Compton-suppressed spectra of ^{24}Na with the gamma energies of 1,369 keV and 2,754 keV, as measured in Budapest. The features marked with numbers are listed in the text



itself, and the surrounding materials. Figure 31.3 shows the response function in the case of counting ^{24}Na with a 25% HPGe detector in normal and in Compton-suppressed modes.

The following components could be identified in the spectrum. (Some of the events can be more easily identified in a Compton-suppressed spectrum.)

- FE Full-energy peak (FEP), when the photon loses all its energy (E) within the active volume of the detector.
- S Step below the full-energy peak, when the photons lose a small amount of energy in a small-angle Compton scattering in the collimator or in the dead region of the detector followed by full absorption of the scattered photon.
- MC Multiple Compton scattering region below the full energy peak and above the Compton edge.
- CE Compton edge about 220–250 keV below the full energy peak. It is a result of a single Compton-event and corresponds to the highest energy left in the detector in a single scattering. The Compton edge is below the FEP with an energy of $E/(1 + E/255.5 \text{ keV})$, as calculated for free electrons.
- CP Compton plateau is formed, when the Compton photon leaves the detector.
- SE, DE Single and double escape peaks are 511 and 1,022 keV below the full energy peak of high-energy photons that can produce an electron–positron pair. These peaks are produced when one or both annihilation photons leave the detector.
- CF Between the single escape peak and the Compton edge there are events from single escape processes. The escaping 511 keV photons may produce a Compton scattering before leaving the sensitive volume. Even a peak due to back scattering of the annihilation photon from the cold finger can be identified at the energy of $E - 341 \text{ keV}$ (i.e., below the FEP). This component is stronger for high-energy photons.
- AE Between the single escape and double escape peaks there are events from Compton scattering of both escaping 511 keV photons, which leave the sensitive volume. Their

Compton edge is 170 keV below the single escape peak. Sometimes a back-scattered peak of one of the escaping 511 keV photons can be identified at 341 keV below the single escape peak (too weak to see in ► Fig. 31.3).

- A Annihilation peak at 511 keV, when an annihilation radiation produced in the surrounding structural material or the sample is detected.
- BS Back scattering peak at 220–250 keV is produced when back-scattered Compton-photons from the sample chamber and other structural materials in front of the detector are observed. [The exact energy is $E/(1 + E/255.5 \text{ keV})$.] In the special case plotted in ► Fig. 31.3 there are two back scattering peaks according to the two gamma energies, while in the typical prompt gamma spectra it covers a wider region.
- B The strongly increasing background intensity toward low energies comes from the *bremstrahlung* from photo- and Compton-electrons and also from the beta particles emitted by radioactive nuclides. A large amount of shielding material placed next to the detector may also increase the baseline at low energies due to gammas from the multiple Compton scattering in the shield (called buildup). The slope of this region can be especially steep, when the spectrum contains intense high-energy components.
- X Characteristic X-ray peaks also show up below 100 keV from the shielding and other structural materials.

In case of strong pileup or random coincidences, any combinations of the above events can happen, which produce double or higher-order Compton edges or peaks at summed energies of full energy peaks. These random coincidences and peak summing must be distinguished from the true coincidence summing of gamma rays from cascades (Molnár 2004).

31.6.3 Calibration Procedures

The gamma spectrum is a set of counts sorted into channels, which correspond to gamma energies absorbed in the detector. This histogram must be converted into a gamma activity versus energy relationship for the determination of the reaction rate. The activities can be derived from peak areas using the *counting efficiency*. The transformation of channel numbers into energy values is called energy calibration. In the simplest linear energy calibration, one determines the channel positions of two gamma-ray peaks with accurately known energies. To obtain accurate energy data over the whole PGAA spectrum, one usually needs a correction for *nonlinearity* of the counting system. The energy *resolution* is an important quantity giving the peak width as a function of energy. It must be well known to determine the peak areas with high reliability.

31.6.3.1 Energy Resolution

The energy resolution of HPGe detectors is a very important quantity. Its deterioration warns the user of the onset of various problems in the spectrometer system. The peak resolution of a HPGe-based spectrometer depends on three factors (Owens 1989):

- W_d : the statistical fluctuation in the number of electron–hole pairs created by gamma radiation of a given energy. It is a property of the HPGe crystal. Its standard deviation is proportional to the square root of the gamma-ray energy (Knoll 2000).

- W_x : there is a statistical fluctuation in the charge collection, which depends linearly on the gamma-ray energy and is also a property of the HPGe crystal. This term is neglected in most calculations, though experiments with various detectors clearly show that the term is significant, especially at high energies.
- W_e : the electronics has a constant noise, which does not depend on the energy. Part of the electronic noise is superposed on the signals after the amplification and thus, when using a low-gain setting, this component becomes significant (Szentmiklosi et al. 2005).

The total width W_t has the following form:

$$W_t = \sqrt{W_d^2 + W_x^2 + W_e^2} = \sqrt{aE + bE^2 + c} \quad (31.12)$$

For characterization of the width of gamma peaks, the so-called full width at half maximum (FWHM) is used. For a Gaussian peak shape, the FWHM = 2.3548σ , where σ is the standard deviation. Another quantity can be derived in a similar way, the full width at tenth of maximum (FWTM), FWTM = 4.2919σ for Gaussian shapes. Thus, the FWTM/FWHM ratio equals 1.8226 for a pure Gaussian peak. The so-called Gaussian ratio implemented in certain data acquisition programs equals $0.5487 \cdot \text{FWTM}/\text{FWHM}$, which is greater than unity, when the peak has a tailing.

31.6.3.2 System Nonlinearity

The components of the spectrometer have a more-or-less linear response to the energy, which enables the use of a simple two-point energy calibration in most applications. However, there are small deviations from linearity of the order of 10^{-3} , which can be of great importance in PGAA because of the very wide energy range covered. Most data acquisition softwares offer the possibility of a parabolic energy calibration based on three data points; but for precise spectroscopic work over a large energy span, this may not be accurate enough.

The major source of the nonlinearity is the ADC. In fact, it has been observed that the shape of the nonlinearity depends only slightly on the gain settings. The most accurate way of determining the nonlinearity of the spectrometer is based on the measurement of calibration sources with well-known energies (Helmer et al. 1971). The nonlinearity of the spectrometer can be quantified as the difference of the measured peak position, ΔP_p , from a linear function, which is determined by a two-point calibration based on two distinct peaks of the calibration source:

$$\Delta P_i = P_i - P_{\text{low}} - \frac{E_i - E_{\text{low}}}{s} \quad s = \frac{E_{\text{high}} - E_{\text{low}}}{P_{\text{high}} - P_{\text{low}}} \quad (31.13)$$

where E_i is the energy of the i th peak taken from the literature, P_i is the measured channel number for the same peak, and s is the slope of the two-point energy calibration line. The nonlinearity is thus a channel-dependent function, which is zero at the two calibration points by definition. Two nonlinearity functions are regarded as equivalent when they differ only in their constant and linear terms. The same nonlinearity curve can be used for slightly different gains. This is a large advantage compared to the nonlinear energy-dependent functions, (as done with the parabolic energy calibration).

The typical nonlinearities cause only a small energy difference when the amplifier gain is high, which can be neglected in low-energy gamma spectroscopy (e.g., NAA). However,

a typical nonlinearity of one-two channels may cause an energy difference of more than 1 keV at the low gains used in PGAA, which makes the peak identification impossible, and thus the application of the nonlinearity correction is vital.

Radioactive and (n, γ) sources with accurately known energies should be used for the determination of the nonlinearity, e.g., ^{152}Eu , ^{133}Ba , and $^{110\text{m}}\text{Ag}$. The $^{35}\text{Cl}(n,\gamma)$ capture lines extend the energy range up to 8.9 MeV (Krusche et al. 1982). Above this energy, there are no better data than those of $^{14}\text{N}(n,\gamma)$ (Jurney et al. 1997); however, the identification of prompt gamma peaks are not problematic in this energy range. A method has been developed by Fazekas et al. (1999) to fit an overall nonlinearity function with polynomials to separately measured data sets.

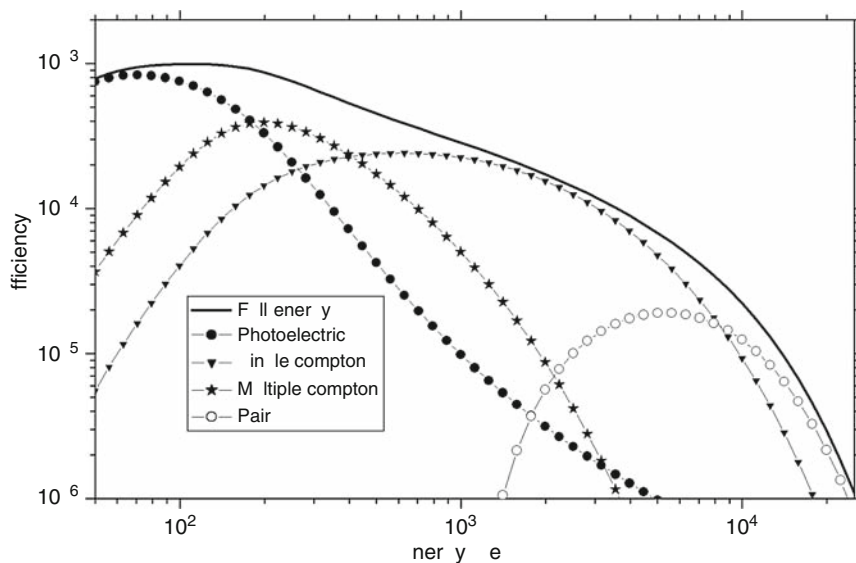
31.6.3.3 Detector Efficiency

To determine reaction rates from the gamma spectrum, the analyst has to know the counting efficiency of the detector, i.e., the ratio of the number of recorded pulses to the number of gamma rays emitted by the source. For germanium detectors, this depends on several factors, the most important of which are the geometry and the gamma-ray energy.

There have been many attempts to determine the absolute detector efficiency ε from various calculations. For instance, a *semiempirical formula* has been derived by Freeman and Jenkins (1966) and has been successfully applied by Owens et al. to HPGe detectors (Owens et al. 1991). This function was successfully fitted to the measured full-energy efficiency data (Molnár et al. 2002b), see Fig. 31.4.

■ Fig. 31.4

The plot of the semiempirical efficiency functions for the Budapest spectrometer. The lines represent the individual effects, which build up the full-energy efficiency



The model has a large number of parameters, so its use in the routine analysis is inconvenient. However, it emphasizes some important characteristics of the efficiency function, e.g., the slight efficiency decrease around 500–600 keV, which explains why the linear approximation on a log–log plot cannot be used in an accurate spectroscopic work.

It is preferable to measure the efficiency using gamma-ray sources with known disintegration rates [activity or reaction rate for (n,γ)-sources]. The corresponding formula is

$$\varepsilon(E_\gamma) = \frac{C_\gamma}{NP_\gamma} K = \frac{R_\gamma}{AP_\gamma} K \quad (31.14)$$

where C_γ is the measured net peak area (counts), R_γ is the count rate, N is the number of disintegrations, A is the activity, P_γ is the emission probability of the corresponding gamma ray, and K contains all the correction factors for losses during the acquisition of gamma-ray events, such as dead time and coincidence summing (Molnár et al. 2002b).

In PGAA, the sample-to-detector distance is usually large, which makes the summing of true and random coincidences negligible.

When determining mass ratios in PGAA, it is sufficient to use only the relative efficiency. During its determination, it is not important to know the accurate source activity, and it is also insensitive to the uncertainty in the source positioning. Thus, the *relative efficiency* can be determined with a higher accuracy.

In [Eq. \(31.14\)](#), ε will depend on the attenuation of gamma rays in the layers between the sample and the detector (e.g., neutron shielding). Therefore, it is important to calibrate the detector system efficiency with the same arrangement that is used for the measurements on unknowns.

Just as in the determination of the nonlinearity, the best way to perform an accurate efficiency calibration is to measure the sources separately. To cover the whole energy range used in PGAA, it is necessary to combine data from several measurements involving both *isotopic multi-gamma sources and capture reactions* (Molnár et al. 2002b). The data sets from different sources must be normalized together at overlapping energy regions. The efficiency at any energy can be interpolated using either nonlinear or linear functions on a log–log scale or polynomials (Kis et al. 1998; Molnár et al. 2002b):

$$\ln \varepsilon(E) = \sum_{i=0}^n a_i (\ln E)^i \quad (31.15)$$

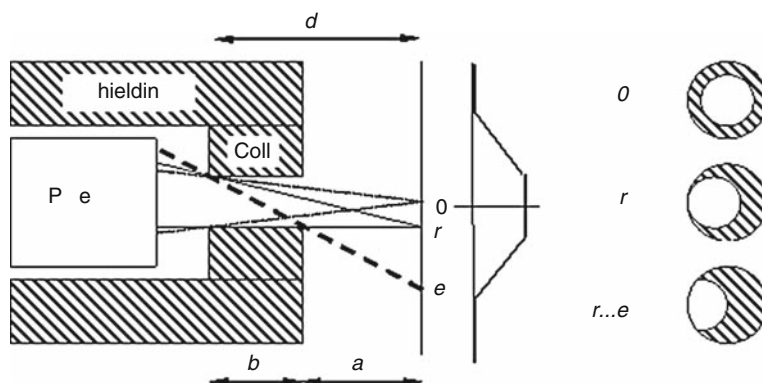
The form of [Eq. \(31.15\)](#) is flexible enough to follow the curvature of the efficiency over a wide energy range (Molnár et al. 2002b). The parameters of the polynomial can be determined from a least-squares fit to the count rates versus energy.

In many cases, the full detector efficiency can be factorized into intrinsic and geometric efficiencies. The *intrinsic efficiency* is the ratio of the number of recorded pulses to the number of gamma rays incident on the detector surface, which depends on the interactions between the gamma photons and the material of the detector, as discussed above, while the *geometric efficiency* equals the fraction of the gamma rays reaching the detector relative to the emitted ones.

Collimated detectors. In contrast to unshielded detectors, collimated detectors show a strong dependence of the counting efficiency on the position of the sample (Debertin and Helmer 1988). The gamma rays can reach a shielded detector only by passing through a *collimator* channel. The range of sample positions over which the detector can be seen from the sample is determined by the dimensions of the collimator a , b , and r (see [Fig. 31.5](#)). The normal viewing solid angle is determined by the radius of the rear collimator hole and the distance $a +$

■ Fig. 31.5

Layout of the collimated detector, and the transmission geometry of the collimator (0 – the geometric center, a – sample-to-shielding distance, b – thickness of the collimator, r – radius of the collimator, e – end of the partial illumination region, d – the distance of the inner aperture to the sample). In the middle, the thick line shows the geometry factor, increasing from 0 to 1 in the transitional regions. The hatched circle represents the view of the front collimator aperture as seen by the source point. The empty circle is the source point view of the rear aperture (drawing is not to scale)



b of this hole from the sample. This result remains valid for any sample position for which the rear aperture is not obscured by the front wall of the shielding, i.e., at sample positions 0 to r . High-energy radiation may also be partially transmitted through the shielding around the apertures, increasing the effective solid angle and thus the geometric efficiency.

If a point source is moved along the line in front of the detector, its detected activity will follow the bold curve (the so-called geometry factor) in the middle of the figure. In the geometrical center ("0"), the point source illuminates the detector with the highest possible intensity (dotted lines in ▶ Fig. 31.5). The source can be moved slightly in the vicinity of the center without changing the illumination of the detector. The observed intensity is constant within the interval from $-r$ to $+r$ (thin lines in ▶ Fig. 31.5). Starting from the position r , the collimator partly shades the detector, and fully covers it at position e (thick dashed line in ▶ Fig. 31.5). The length of the partial illumination zone depends mainly on the ratio of a to b :

$$e = r + 2r \frac{a}{b} \quad (31.16)$$

The geometry factor is unity in the center, and decreases to zero in the interval from r to e . The decrease can be well approximated with a straight line (see the right side of ▶ Fig. 31.5). If the source is further away from the shielding than the thickness of the collimator, the *partial illumination zone* is longer than the constant region in the middle (Molnár 2004).

Active and effective volume of the sample. When measuring bulk (finite size) samples, one detects the different points of the sample with different geometry factors, which may affect the observed intensity. In the case of homogeneous samples, it is useful to introduce two quantities, the active and the effective volumes. The first one is the actual volume of the sample from where photons are emitted and may reach the detector, while the latter one is the integral of the geometry factor over the whole radiating (active) volume of the sample. Because of the

partial illumination zone, these volumes can be significantly different and may be much greater than the volume simply estimated from the projection of the collimator (Molnár 2004).

31.6.3.4 Determination of Spectral Background

The background means any gamma rays that do not arise from the sample under investigation. The lower the background, the lower are the detection limits. That is why it is important to fight for lower background, though it is usually a tedious process.

The origins of the background can be divided into two components. One of them is the *room-background*, which is always present. The other component is present only when the neutron beam is on (the so-called beam-background).

The room-background data discussed here are based on a week-long measurement performed using the Compton-suppressed HPGe detector in Budapest (Belgya et al. 2003; Belgya et al. 1997; Révay et al. 2004). The majority of the peaks originate from the *natural radioactive decay* chains, i.e., the ^{232}Th , ^{238}U , ^{235}U , ^{237}Np series, and ^{40}K . These nuclides are in the construction materials of the building.

The other peaks come from the continuous activation and excitation by the different-energy neutrons induced by the *cosmic rays* of the surrounding shielding and structural materials, like aluminum, fluorine from Teflon and ^6LiF -containing shielding, and even excitation and activation of the germanium in the detector and in the BGO. The evidence for inelastic scattering of fast neutrons in the PGAA detector comes from the presence of the so-called germanium triangles in the room-background spectra. *X-rays* are also observed from the lead shielding and bismuth of the BGO anti-Compton shield surrounding the detector, which are results of the interaction between them and cosmic muons (Nunez-Lagos and Virto 1996).

Some other radiations observed have special explanations for their origin. One part of these radiations is the gamma radiation coming from long-lived ^{207}Bi in the BGO that is an isotopic impurity in the elemental bismuth used in the manufacturing process (Lindstrom 1990). The ^{60}Co gamma rays may originate from activation of ^{59}Co in the iron structure by slow neutrons. Again, the long lifetime makes it a persistent background component.

The total room-background rate for a well-shielded PGAA detector system may be below 1 cps, similar to the performance of a well-shielded low-background experimental set-up (Lindstrom et al. 1990), while the rate is about 100 cps for the unshielded detector.

The *beam-background* can be investigated using a high-purity heavy water (D_2O) sample, as a dummy target. This background spectrum contains peaks from radiation emitted by the nearby structural materials after excitation by the scattered neutrons, as well as the gamma rays from the constituents of the sample holder. The nitrogen capture lines also appear if the sample chamber is not evacuated. The Li and C peaks probably originate from the plastic neutron shielding (which contains ^6Li), while the Al, Pb, Fe, and Sb peaks probably come from the structural materials.

When the germanium detector is not shielded well enough against slow neutrons, the material of the crystal can also be activated. As a result, prompt and decay gamma peaks of germanium isotopes appear in the spectrum. The relative intensities of germanium peaks in this case will be completely different from those of a germanium sample because of the almost complete true coincidence summing of gamma-ray cascades inside the detector. The prompt gamma peak at 596 keV is a clear sign of the prompt activation of the germanium detector by neutrons leaking through the detector shielding (Belgya et al. 2005).

Besides gamma peaks, the β^- spectra from the decays of ^{75}Ge with the maximum energy of 1.2 MeV and with a half-life of 83 min, and of ^{77}Ge ($E_{\beta\text{max}} = 2.2$ MeV, $T_{1/2} = 11.3$ h) can be seen. The β^- particles are in coincidence with the detected decay gammas from the daughter isotopes, partly shifting the **β^- spectrum**. Under steady-state operational conditions one count in the 139.7 keV peak from $^{75\text{m}}\text{Ge}$ indicates about two counts of β^- decay from the 83 min half-life isotope, and similarly one count in the 159.7 keV peak from $^{77\text{m}}\text{Ge}$ accompanies about two counts from the 11.3 h half-life isotope. The conclusion is that one has to wait several days to make low-background measurements with detectors exposed previously to slow neutrons.

Gamma peaks identified as arising from inelastic scattering of fast neutrons on various materials are coming from fast neutrons generated after slow-neutron capture on light elements (Li, B in slow-neutron shielding materials) (Lone et al. 1980). Thus their relative yields depend strongly on the shielding materials. The lowering of this component is the most difficult part of the construction of the shielding, due to the large penetration power of fast neutrons and the diffuse nature of their sources. The most important signals from the (n,n') reaction on the germanium detector (the germanium “triangles”) appear at 596 and 692 keV, and less significant triangles at 834, 563, and 1,039 keV.

31.6.4 Compton-Suppressed Spectrometers

Compton-suppressed spectrometers, as mentioned earlier, are used to decrease the Compton plateau associated with all peaks in the spectrum. The Compton shielding also suppresses the single- and double-escape peaks. The most frequently used setup consists of a main germanium detector, which is surrounded by one or more scintillators, with the exception of an aperture where the radiation enters. (There is also another hole at the back or at the side for the insertion of the germanium detector into the suppressor.) The annulus detects gamma rays scattered out from the germanium detector. To minimize the rate from the external radiation, the detector system should be placed into a thick lead shielding. When, due to a Compton event, the photon transfers only a portion of its energy to the germanium detector, and the resulting Compton photon is caught by the *scintillator*, the registration of the detector signal can be prohibited by an anti-coincidence gating. The most efficient Compton suppressor systems can reduce the Compton plateau by more than an order of magnitude.

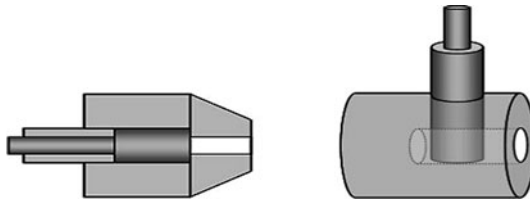
The annulus serves both as an active and a passive shielding for the germanium detector. The annular guard detector is often made of sodium iodide [NaI(Tl)] or *bismuth germanate* ($\text{Bi}_4\text{Ge}_3\text{O}_{12}$ or BGO). The BGO has higher gamma-ray detection efficiency than the cheaper NaI(Tl) , and so is frequently used in PGAA.

There are two basic layouts of Compton-suppressed detector systems.

- In the simpler *coaxial arrangement*, the cylindrical surface of the germanium detector is fully covered by the scintillator. More sophisticated layouts partly cover the flat surfaces in the front and in the back, as well. In the latter geometry, only a small solid angle of the forward and of the backward scattering directions is not shielded (see [Fig. 31.6](#)).
- In the *perpendicular geometry*, the scintillator is placed coaxially with the direction of the detection, while the germanium detector is placed at right angles to it. Thus the detector observes the photons from the side, through the hole in the scintillator facing the source, and the forward scattered photons are caught behind the germanium detector by the scintillator.

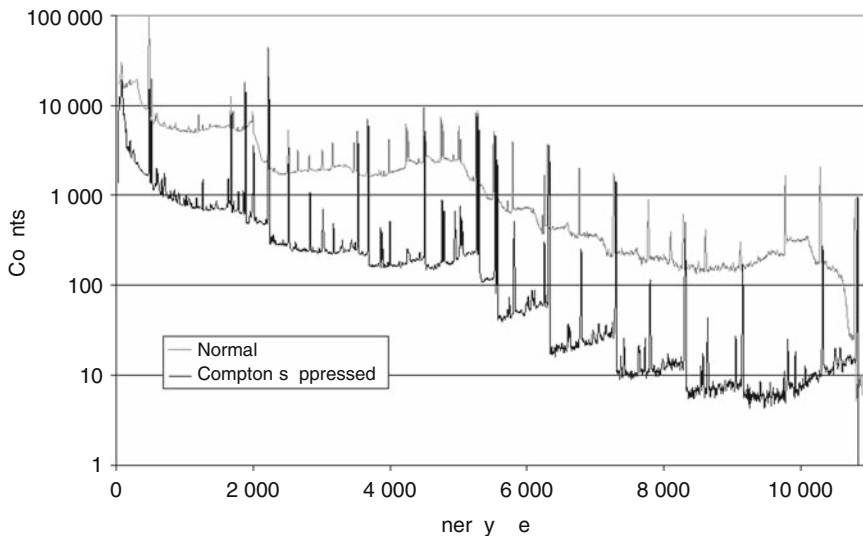
■ Fig. 31.6

Coaxial and perpendicular Compton-suppressed detector systems



■ Fig. 31.7

Normal and Compton-suppressed spectra of a nitrogen-containing compound (deuterated urea)



The perpendicular arrangement preserves more from the shape of the normal spectrum, which may be disadvantageous. The response function of the coaxially arranged HPGe–BGO detector system is simpler by being effective at suppressing the smooth continuum and in many cases the suppression is also better.

Typical normal and Compton-suppressed spectra are shown in ▶ Fig. 31.7.

31.6.5 Other Sophisticated Detection Solutions

31.6.5.1 Composite Germanium Detectors

Composite detectors are relatively new developments in gamma-ray spectroscopy. They make possible the tracking of gamma rays inside the detector. The clover detector has four closely placed germanium crystals arranged like the leaves of a four-leaf clover. The cluster detector has

seven segments; one of them is in the center (Wilhelm et al. 1996). Both of these detector types can also be surrounded by a BGO guard detector. The advantage of this arrangement is that a part of the Compton photons leaving one detector may be detected in a neighboring one. These scattered signals can be used for Compton suppression, but it is better to add them up for the purpose of getting back the original peak energy (Elekes et al. 2003).

31.6.5.2 Coincidence Techniques

The usefulness of γ - γ coincidences in elemental analysis was pointed out by Ehmann and Vance (1991). The simplest coincidence setup consists of two germanium detectors (Ember et al. 2002). In coincidence mode, the two detectors detect two gamma rays that are emitted in fast consecutive decays of an excited nucleus. By doing this, the spectrum can be greatly simplified at the expense of a low coincidence count rate. Single-step (non-cascading) gamma rays can be greatly suppressed together with their Compton continua.

Another way to improve the coincidence detection efficiency is the utilization of gamma-ray detector arrays. This has been proposed and used by the Material Science Group at JAERI (Hatsukawa et al. 2002).

31.6.5.3 Chopped-Beam PGAA

The purpose of a beam chopper is to turn the beam on and off periodically. The separation in time of prompt and decay gamma transitions by means of a beam chopper was suggested in the pioneering work of Isenhour and Morrison (1966a, b), and more recently by Zeisler et al. (2001), with the aim to identify spectral interferences in the prompt spectrum from the decay gammas.

One of the simplest beam choppers is a rotating disk partially covered with neutron-absorbing material. ^6Li -loaded plastic is ideal for prompt gamma measurements because it produces no background gammas resulting in a *pulsed neutron beam*. When a neutron pulse hits the target, it activates the sample just like the continuous beam. The gamma spectra are detected in both the prompt and the pure decay phases. As a result, one can consider the chopped-beam measurement as a combination of PGAA and cyclic NAA (Szentmiklosi et al. 2006a). The decay peaks of certain short-lived nuclides can be measured in a chopped neutron beam with detection limits of about an order of magnitude better than normal PGAA (Szentmiklosi et al. 2005).

31.7 Spectrum Evaluation

Accurate and reproducible evaluation of prompt gamma spectra is of great importance, as the sample composition is determined from the evaluated peak areas. At different energies in a typical prompt gamma spectrum, the height of the baseline and the peak areas may differ by several orders of magnitude. The peaks are asymmetric, their shapes, especially their widths, depend on the energy, and may also depend on the count rate, and the peaks sometimes appear in complex multiplets. It is not infrequent that more than 1,000 peaks can be identified in

a prompt gamma spectrum. The minimum requirement an evaluation software must meet to be applicable in PGAA is the ability to fit at least ten peaks in one region of interest (ROI), and to have the asymmetric built-in function that describes HPGe peaks under extreme conditions. It must be able to evaluate most of the peaks automatically, but it should allow manual fitting whenever needed in difficult cases. Only a few of the evaluation software available on the market can handle this extraordinary task.

Many softwares are capable of fitting only a few peaks in each region. *Peak shapes* are often fit with only the symmetric Gaussian curve, or in some cases with a curve combined from a Gaussian and an exponential decay at the low-energy side, joining smoothly to each other. But many of the features, appearing in typical PGAA spectra cannot be handled using these simple algorithms. One of the most successful approaches is the Hypermet algorithm developed at the Naval Research Laboratory in the 1970s (Phillips and Marlow 1976a, b), which was further developed into PC-based and later into Windows-based, user-friendly programs, and now also involve the calibration routines (energy, efficiency, and nonlinearity correction) (Fazekas et al. 1997).

Peaks are fit in regions wherever the counts exceed the average level of the baseline significantly. The counts in the regions are described as the sum of peaks, peak-dependent background terms, and a parabolic baseline. A peak consists of a symmetric and an asymmetric part, usually a low-energy tailing:

- The symmetric part of the peak is described by a Gaussian. Its width W depends on the energy: $W = (a + bE)^{1/2}$.
- The asymmetric part of the peak, called the *skew term*, is intended to describe the effects of the improper charge collection. It is an exponentially modified Gaussian (EMG) function, i.e., an exponential term with a constant decay parameter convoluted with a Gaussian function having a width of W . The amplitude of the skew term is proportional to the whole peak area (Révay et al. 2001b).

The sum of these two components makes up a peak, while the sum of their integrals equals the peak area.

Peak-dependent background is a step-like shape below the peak, which consists of a rounded step due to small-angle Compton scattering and a tailing component:

- The step is described by the convolution of a Heaviside function (i.e., a unit step function) shifted to the peak and a Gaussian function (with the same width as the peak). This rounded step is thus described with an erf function, whose inflection point is at the peak energy. Full-energy peaks have reverse steps, their height is in the order of a few thousandths of the peak area (Révay et al. 2001b), while the steps below the escape peaks increase toward the high energies. The step height of a single escape peak is almost negligible, and for a double escape peak it is similar to that of the full-energy peak.
- A longer tail is due to surface effects for high-intensity peaks. It is also described by an EMG function, but with a longer decay.

The peaks sit on a baseline described by a second-order parabola. A *right skew* may also appear, especially in the case of strong peaks in the low-energy region. In many cases, this component can be eliminated by adjusting the pole/zero setting of the amplifier (in the case of RC-feedback preamplifiers), at the cost of slightly increasing the easily treatable left skew.

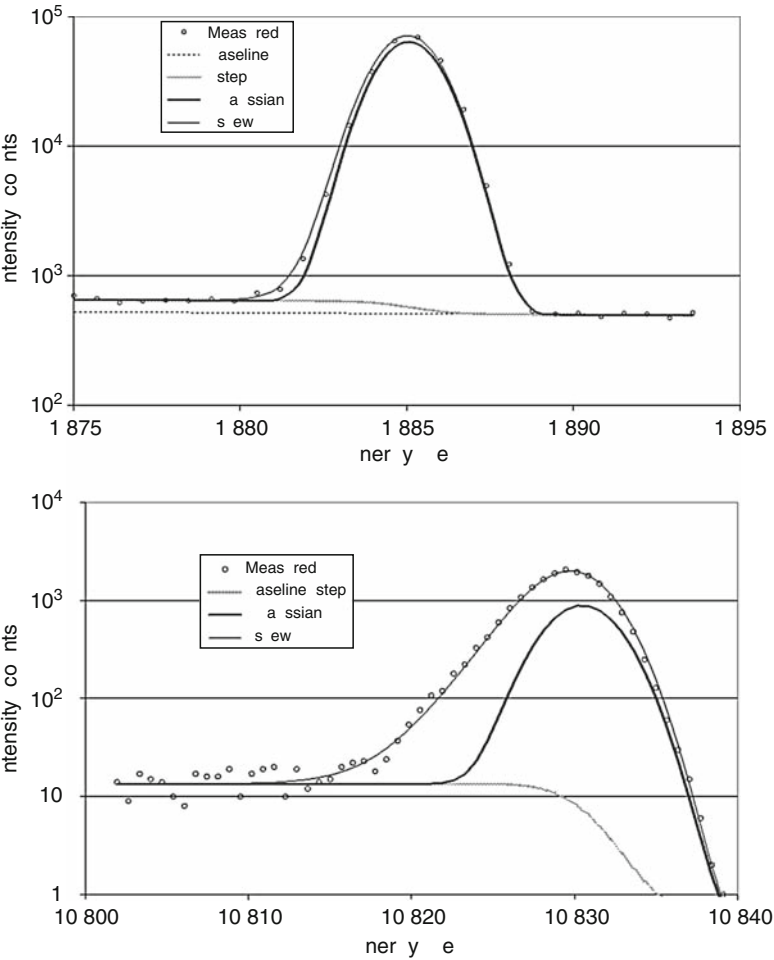
The positions of the peaks can be calculated as the centers of gravity

$$\langle E \rangle = \frac{\int_{-\infty}^{\infty} E(j)P(j) \, dj}{\int_{-\infty}^{\infty} P(j) \, dj} \tag{31.17}$$

where j is the serial number of the channel, $E(j)$ is the energy, while $P(j)$ is the count number in the channel. The above peak shape and its fit to measured data points for two very different single isolated peaks are shown in [Fig. 31.8](#).

The peaks are more asymmetric at high energies, i.e., a substantial fraction of their areas come from the skew. The Gaussian ratio, as defined earlier, is usually about 1.1–1.6 depending on the energy. Low-energy, strong peaks may show further asymmetries compared to the ideal Gaussian shape: e.g., the skew term may increase with increasing count rate.

Fig. 31.8
Prompt gamma peaks of nitrogen at 1,885 and 10,830 keV



The increase in the peak width as well as the amplitude and slope of the skew term over time is a natural consequence of detector *aging*, and can be tracked by the periodic calibration of these parameters. The appearance of a long left skew and a significant, irremovable right skew can be signs of the damage to the semiconductor crystal, which can temporarily be fixed by adjusting the pole/zero in the RC-feedback preamplifier.

In the case of single peaks with shapes that cannot be described using the model built into the evaluation software, the simple *peak summing* method can be used for the determination of their areas. Peak summing (as described in Gilmore and Hemingway 1995) must be performed carefully especially in the case of asymmetric peaks. The region of the summing must be defined symmetrically around the peak maximum, so the background value subtracted using a linear interpolation will not be significantly different from the one using a step function. In the case of peaks with extremely good statistics, peak summing can also be more helpful than fitting, since the minor deviations from the model function may become significant. The uncertainty of peak area determined this way can be simply calculated from the Poisson statistics of the channels involved, i.e., $A \pm \sqrt{A + B}$, where A is the net peak area after background subtraction, B is the background, so $A + B$ equals the total counts in the examined region. This method can be used for single peaks only.

The most important non-electronic process that results in distorted peaks is the *Doppler broadening* of gamma lines due to the recoil of the emitting nucleus (see Sect. 31.2.1). This broadening usually can be corrected with a slightly increased width parameter during the fit; however, in some cases the evaluation programs fit complicated multiplets. The two most prominent representatives of this effect in prompt gamma spectra are the annihilation peak, and the *boron peak* from the $^{10}\text{B}(n,\alpha\gamma)^7\text{Li}$ reaction. While the first one is not used for analysis, the second one is one of the most frequently analyzed peaks in PGAA. Its shape highly depends on the composition of the matrix through the degradation constant (Szentmiklosi et al. 2007a).

31.8 Quantitative Analysis

During quantitative analysis, the masses of certain components and the composition of the sample are determined using peak areas and spectroscopic data. There are two approaches for quantitative analysis: absolute and relative.

31.8.1 Absolute Approach

In the absolute method, the masses of certain components are determined. Assuming thin samples, peak areas are directly proportional to the masses, so the mass can be determined from nuclear constants and the conditions of the measurement based on Eq. (31.4) as follows:

$$m = \frac{M}{N_A} \frac{A}{\varepsilon(E_\gamma) t \sigma_{\gamma 0} \Phi_0} \quad (31.18)$$

where M is the atomic weight, N_A is the Avogadro constant, A is the net peak area, $\varepsilon(E_\gamma)$ is the counting efficiency at a characteristic gamma-ray energy of the given nuclide, t is the measurement time (live time), $\sigma_{\gamma 0}$ is the partial gamma-ray production cross section, and Φ_0 is the thermal equivalent neutron flux. The flux can be determined as described in Sect. 31.4.6, or by measuring a known amount of any element with a known partial cross section.

The analytical sensitivities (count rate per unit mass) can also be determined for any PGAA facility using standards with known masses of components. According to the most frequently used procedure a flux monitor is irradiated first, and the peak area is corrected with the ratio of the monitor values as measured during the analysis and the determination of the sensitivity.

In the case of the absolute method of PGAA the sample has to be weighed, and the concentrations of the detected components can be determined as the ratios of their masses compared to that of the sample. So the accuracy of the final result depends on two measurements, the mass determination with PGAA and the weighing of the sample.

The absolute method can be used with high accuracy, if the following criteria are met:

- The mass of the sample is known accurately. (The sample is chemically stable, and it does not contain unknown amount of absorbed water, etc.)
- The sample has to be close to the ideally thin case, i.e., no significant self-absorption or self-shielding corrections are necessary, and neutron scattering does not affect the result either.
- The flux profile is uniform across the neutron beam and the flux is stable in time.
- The dead-time correction of the spectrometer is accurate in the given count rate range. This is necessary to obtain the accurate live time.
- Samples are measured always in the same geometry using the same detector (i.e., the efficiency does not change).

31.8.2 Relative Approach

In the relative method, the components are determined from a single measurement on one sample. Instead of the masses, the mass ratios of the components are determined to avoid the mentioned corrections and other possible sources of error, whether or not the above criteria are fulfilled. Following the idea of the k_0 standardization (see [Eq. \(31.11\)](#)) the mass ratio can be expressed as

$$\frac{m_1}{m_2} = \frac{A_1 \varepsilon(E_2) \sigma_{\gamma 2} M_1}{A_2 \varepsilon(E_1) \sigma_{\gamma 1} M_2} \quad (31.19)$$

where A is the net peak area, M is the atomic weight, $\varepsilon(E)$ is the counting efficiency, σ_{γ} is the partial gamma-ray production cross section, and subscripts 1 and 2 represent two different chemical elements and their characteristic energies. The equation needs the determination of the peak areas, the counting efficiency, and then the mass ratio can be determined using the partial cross sections from a spectroscopic database (Révay 2009).

The determination of mass ratios is not sensitive to the variation of the neutron flux or the improper dead-time correction. For homogeneous samples, the inhomogeneous flux profile and the neutron self-shielding do not affect the result either. Gamma-ray self-absorption can be neglected in many cases, though it can distort the results when irradiating thick samples and if peak areas at both low and high energies are used in the calculation. When using peaks with the energies above 2 MeV, as mentioned in [Sect. 31.3.1](#) this effect can also be neglected even in the case of bulk samples.

Relative and absolute methods can be used simultaneously, but the analyst has to keep in mind that mass ratios have lower uncertainties than the mass values. The uncertainty calculation is described in detail by Révay (2006).

In many cases, all major and minor components of the sample can be detected using PGAA with a reasonable accuracy. (The total amount of trace elements has to be negligible compared to the uncertainties of the concentration values.) In this case, the concentrations of the constituents can be determined as the ratios of the masses and their sum. The sum of the calculated masses is biased with the same systematic errors as the individual masses; thus, their ratios will be unbiased like the mass ratios (Révay 2009).

Even when it is the dominant component of the sample, oxygen can only be determined with a low accuracy. In the case of minerals, concrete or glasses and many natural inorganic materials the amount of oxygen can be best determined from stoichiometry (Révay 2009).

31.9 Applications

Since the establishment of PGAA in the 1970s as a nuclear method for multielement quantitative analysis, there have been several reviews of PGAA applications; see, e.g., (Deconninck et al. 1981) or more recently (Paul and Lindstrom 2000) and (Yonezawa 2002). In addition, there is a PGAA handbook that includes an excellent application review section by Anderson (Molnár 2004). The last of these is quite thorough and covers reactor-based PGAA applications from 1980 through 2004. Other reviews have focused on measurements of specific elements for which PGAA is highly applicable and widely used such as the review of PGAA hydrogen measurements by Paul (1997), PGAA for boron by Sah and Brown (1997) and Paul (2005), and for cadmium by Grazman and Schweikert (1991). There are also several overviews of applications and developments at specific PGAA facilities. Révay et al. (2008a) has recently published a review of PGAA activities at the Institute of Isotopes, Park et al. (2005) a review of activities at the Korea Atomic Energy Research Institute, Rios-Martinez et al. (1998) and Wehring et al. (1997) reviews of PGAA at the University of Texas, US, Yonezawa (1999) of PGAA at Japan Atomic Energy Research Institute, and Unlu and Rios-Martinez (2005) a review of PGAA at university reactors. To avoid redundancy with or duplication of these very thorough reviews that have preceded this work, this section focuses on PGAA applications developed or implemented during the past decade, focusing primarily on those of the last 5 years and refers the reader to the aforementioned reviews for historical and additional information.

There continues to be development of neutron generator-based PGAA (see, e.g., Park et al. 2009; Reijonen et al. 2004), neutron source-based PGAA (Turhan et al. 2004; Park et al. 2004), and more recently, accelerator-based PGAA (Naqvi and Nagadi 2004; O'Meara et al. 2001; Postma et al. 2007; Postma and Schillebeeckx 2005) in which resonance neutron capture is exploited for quantitative analysis. Applications of PGAA based on the use of these nonreactor neutron sources include: analysis of archeological artifacts (Postma and Schillebeeckx 2005); online bulk analysis of carbon, oxygen, and other elements (see, e.g., Lim and Sowerby 2005); portable-source PGAA detection of explosives or other prohibited materials (Dokhale et al. 2001) and detection of land mines (Miri-Hakimabad et al. 2008). Uses of portable sources include those for borehole logging for coal and ore analysis (e.g., Borsaru et al. 2004; Charbucinski et al. 2004). There has also been recent work using *in vivo* PGAA for determination of nitrogen as it relates to protein status (Ahlgren et al. 1999; Kasviki et al. 2007a, b; O'Meara et al. 2001). See (Morgan 2000) for a review of *in vivo* PGAA applications. The scope of this review has been restricted to PGAA applications using neutron beams extracted from nuclear reactors.

An analysis of recent reactor-based PGAA applications reveals that there have been a number of new developments during the past decade, and that some of the applications that helped to establish the utility of PGAA as a quantitative method continue to be implemented in both traditional and innovative ways. As has been observed for many years, there is a great deal of PGAA work performed in the fields of archeometry and geological sciences, and in the areas of hydrogen and boron analysis. During the past 5 years, innovations have included uses of PGAA in combination with other modes of analysis such as neutron imaging, improvements in instrumentation, innovations based on modifications of the neutron beams, and the development of dynamic in situ PGAA. There has also been an expansion of PGAA applications into the fields of advanced materials analysis, and fissile and explosive materials analysis. This section will begin with a description of new applications and innovations in implementation of PGAA methods, followed by uses of PGAA in fundamental nuclear chemistry, PGAA of advanced materials, element-specific applications, field-specific applications, and finally PGAA for quality assurance and reference material certification.

31.9.1 Innovations and Advances in PGAA Methodologies

31.9.1.1 In Situ PGAA

Perhaps the most noteworthy achievement of the last decade was the work by Révay et al. (2008b) in which the first in situ PGAA measurements of dynamic processes were reported. The challenges presented by dynamic, in situ PGAA measurements are not trivial and include difficulties arising from neutron capture background signals, achieving timing resolution that is consistent with the process, and limitations in amount of signal for a given time window. In this work, uptake of hydrogen by palladium catalysts was observed dynamically by using PGAA to monitor the hydrogen to palladium element ratios. The significance of the new PGAA method has been described as it relates to the process of hydrogenation in catalysts in a recent paper by Teschner et al. (2008).

31.9.1.2 Neutron Focusing

Some of the recent innovations in PGAA involve the use of neutron optics to increase the intensity of the beams used to interrogate the sample. Over the past 2 decades, focused beams of neutrons have been used to provide greater neutron flux density on the sample, thereby enhancing neutron absorption reaction rates (Chen-Mayer et al. 1999; Mildner and Chen-Mayer 1999). Applications of focused beams in PGAA continue to appear in the literature, though are typically limited to analyses of high absorption cross section materials or major element components of a material. Chen-Mayer et al. (2000) achieved threefold PGAA sensitivity gains using multi-capillary lenses. These focused beams combined with prompt gamma-ray spectrometry were used to detect and quantify the amount of a number of elements in a variety of materials, including boron in Standard Reference Material (SRM) 611 Trace Elements in Glass, and iron and chromium in SRM 160b Stainless Steel. For this work, the samples were larger than the focal spot, so the reaction rate gains were not commensurate with the gain in neutron current density. Neutron current density gains of a factor of 40 were

achieved at this same facility using a monolithic lens and the sensitivity for a gadolinium beam enhanced by a factor of 34 (Chen-Mayer et al. 2001). Focused-beam PGAA was used to determine the radial distribution of residual chlorine in high-purity quartz cylinders formed from flame hydrolysis of silicon tetrachloride (Chen-Mayer et al. 2003). This information in combination with NAA results for total chlorine content was used as the basis for comparison with XRF results. Neutron focusing systems at the same facility were used by Swider and Walters (2004) to evaluate the utility of this approach in analysis of paint pigments and metals. Hils et al. (2004) used parabolic guide tube to increase neutron intensity, achieving a sixfold gain in neutron intensity; the authors predicted that gains of several orders of magnitude could be achieved by multiplexing. More recently, Segawa et al. (2008) achieved two-dimensional compositional mapping of cadmium wire figures with spatial resolutions on the order of a millimeter with a focused and collimated neutron beam.

31.9.1.3 PGAA and Neutron Diffraction and Imaging Methods

Additional innovative developments in PGAA, pioneered by scientists from the Institute of Isotopes, Budapest have been achieved through hybridization of PGAA with other neutron-based analytical methods such as neutron imaging and diffraction. Kasztovszky et al. (2007) developed the combination of time-of-flight neutron diffraction and PGAA to provide compositional and structural information on ceramic and metal samples. Pulsed neutrons from a spallation source were used to investigate the utility of performing PGAA to provide compositional information in combination with neutron diffraction studies (Kasztovszky et al. 2008d). This was further developed in a very elaborate combination of neutron and X-ray tomography to locate samples in thick, opaque containers (Kasztovszky et al. 2008c). Belgya et al. (2008) constructed an instrument, which combined PGAA and neutron tomography to provide both compositional information and imaging results.

31.9.1.4 Chopped Beams

Chopped or pulsed neutron beams have been used to improve signal-to-noise ratios in PGAA spectra and to extend the breadth of analytical capabilities by combining PGAA with short-lived NAA, allowing detection and quantification of a larger number of elements from the same experiment. Zeisler et al. (2001) demonstrated the use of coincidence counting with a chopped neutron beam to eliminate the 472-keV gamma-ray interference arising from neutron capture by sodium from the Doppler-broadened gamma ray accompanying neutron capture by ^{10}B , improving the ability to determine boron in biological systems.

More recent work implementing chopped neutron beams includes a number of applications performed at Budapest. Chopped neutron beams were used in conjunction with measurements designed to determine gamma-ray production cross sections (essentially, the neutron absorption cross section multiplied by and gamma yield) and k_0 values for short-lived nuclides used for conventional (delayed) neutron activation analysis (Révay et al. 2003, 2005; Szentmiklosi et al. 2006a). This work was developed further with improvements in the chopper controller to improve the precision and provide simultaneous acquisition of prompt and delayed activation analysis spectra (Szentmiklosi et al. 2007b). The combined PGAA/INAA system was applied to analysis of relatively large samples (several grams) of sodium iodide in

which PGAA and the delayed spectra were used for determination of sodium, iodine, scandium, thorium, and thallium (Szentmiklosi et al. 2008).

31.9.1.5 PGAA in Highly Absorbing Samples or Containers

There has long been utility in performing PGAA for quantitative analysis of materials that cannot be subjected to conventional INAA. A subset of these is strongly absorbing materials. Such materials are typically prohibited from the in-reactor irradiations used for conventional INAA, but not prohibited from neutron beam irradiations. Although, PGAA has very good sensitivities for strong absorbers, these materials present other challenges due to neutron attenuation within the sample. There are two basic approaches to provide accurate results in the PGAA of strong absorbers, one uses experimental data in the form of calibration curves or internal standards contained in the matrices of interest, and the other, calculations to determine correction factors. In recent work by (Acharya 2009), valid results in determination of element content of strongly absorbing samples were obtained by use of a combination of an internal standard and calibration/validation over a large range of mass fraction values of the absorber of interest, boron. A similar approach was used by Harrison and Landsberger (2009) to account for absorption by boron.

When the sample cannot be removed from the container and the container is strongly absorbing, the analysis may be even more complicated as there may be both gamma-ray attenuation and neutron absorption to consider. Révay (2008) described determination of element content of samples in thick containers, specifically the determination of noble gases in aluminum cylinders and uranium compounds in thick lead containers. Two different approaches were applied, one for which gamma-ray attenuation and neutron absorption by the container is minimal, and the other for which attenuation is significant.

31.9.1.6 PGAA of Large Samples

PGAA is an attractive method for determining the average bulk element content of large samples, particularly when the size of the subsamples typically used by other more conventional analytical methods would not be indicative of the bulk composition due to material heterogeneity. However, bulk PGAA measurements present a challenge because both neutron attenuation and gamma-ray attenuation may be significant. A recent approach described by Blaauw and Belgia (2005), to account for neutron attenuation within large samples used a Monte Carlo approach to calculate correction factors for a standard sample geometry based on the absorbing and scattering power of the sample. The results from the Monte Carlo calculations were compared with experimental results for three materials and agreed favorably for correction factors on the order of 5% and 24% but were not in agreement for more strongly absorbing materials.

31.9.1.7 Improvements in signal-to-noise ratio

As with all methods for quantitative analysis, improvements in signal-to-noise ratios are desirable as a means of increasing sensitivities and decreasing limits of detection. Developments

in this area include the use of digital spectrometry, coincidence and anti-coincidence counting, and sophisticated mathematical data manipulation. Improvements in signal-to-noise using Compton suppression were implemented at the PGAA facility at Korean Atomic Energy Research Institute by Cho et al. (2005a) as part of work to optimize the instrument for boron determinations. Coincidence counting was used to improve signal-to-noise in PGAA measurements of liquids containing hydrogen and boron (Ember et al. 2002) and of gadolinium tracers in borosilicate glass samples (Ember et al. 2004). Toh et al. (2008) used coincidence of two or more gamma rays as a means of improving signal-to-noise in analysis of foods and polymer materials. A very innovative approach to improving signal-to-noise was reported by Im et al. (2007), who used principle component analysis to identify and then exclude the noise component of a PGAA spectrum.

31.9.1.8 Advances and Applications in k_0 PGAA

The use of the k_0 method, originally developed for INAA, has come into prominence for use with PGAA during the past decade. This method was originally developed for INAA as a means of standardization for quantitative analysis based on the use of a single comparator, efficiency curves for the detection system, and experimentally determined constants to account for characteristics of the reactor neutron spectrum for a given facility. As applied to PGAA, the k_0 method essentially looks at element sensitivities for a given neutron beam and detection system (efficiency curve) combination. Lindstrom (2003) recently published an overview of k_0 PGAA. Research performed during the past decade has included the work by Sun et al. (2003) at the Korean Atomic Energy Research Institute for determination of k_0 factors for non- $1/\nu$ nuclides (^{113}Cd , ^{149}Sm , ^{151}Eu and ^{155}Gd , ^{157}Gd), and by Sun et al. (2005) for determination of k_0 factors and partial gamma-ray production cross sections for several elements (boron, nitrogen, silicon, phosphorous, sulfur, and chlorine) commonly determined using PGAA.

Applications of the k_0 method in quantitative PGAA are widespread. Some specific examples include the multielement characterization of a National Institute for Environmental Studies (Ibariki, Japan) typical diet reference material (Matsue and Yonezawa 2001) and a collaboration in which scientists used INAA and PGAA for determination of element composition of environmental and food samples (Freitas et al. 2008). In the latter work, k_0 PGAA was performed using the method described by Révay (2006), which includes a very thorough and detailed evaluation of uncertainty. PGAA facilities, particularly those equipped with neutron beam choppers, have also been used for determination of k_0 factors for short-lived products of neutron activation for use in k_0 NAA; see, e.g., (Révay et al. 2003) and (Szentmiklosi et al. 2006a).

31.9.2 Measurements of Cross sections, Gamma-Ray Energies, and Emission Probabilities

The very basis of PGAA, neutron capture followed by de-excitation of the compound nucleus through emission of characteristic gamma rays, provides information on the nuclear properties of the absorbing nuclide. Careful measurements permit determination of the prompt gamma-ray production cross section, which may be decoupled into the gamma yield, and neutron capture cross section. Quantitative PGAA may be based on comparison with element standards

of known composition, or may be based on calculations involving values for the number of neutrons interacting with the sample and values for these cross sections. For this reason, there have been many experiments designed to measure these values. For example, Park et al. (2006) performed high accuracy PGAA to determine the value of the neutron absorption cross section of ^6Li , and Borella et al. (2005) to determine the value for ^{209}Bi .

A great deal of high accuracy, high precision prompt gamma-ray spectroscopy was performed at Budapest to provide values for the partial prompt gamma-ray neutron capture cross sections, as well as gamma-ray energies and intensities (Molnár et al. 2000; Révay et al. 2000, 2001a; Molnár 2004). Their compilation of results represents the most up-to-date and accurate PGAA data available. There are many examples of determinations of partial gamma-ray production cross sections for specific isotopes. For example, thermal neutron capture cross section values were published for ^{99}Tc (Molnár et al. 2002a). In that work, it was also noted that PGAA provided order of magnitude better sensitivity than passive counting for quantitative analysis of this isotope. Extremely careful PGAA measurements to determine the intensities of the prompt gamma rays emitted from neutron capture by chromium were performed to provide more precise values than were available in the literature (Belgya and Molnár 2004). Determinations of the intensities of 36 gamma rays from ^{35}Cl were published in order to enable energy and efficiency calibrations of germanium detection systems over the wide range of energies commonly encountered in PGAA work, i.e., from about 100 keV to 11 MeV (Molnár et al. 2004). Similar work by Belgya (2008) involved determination of the intensities of prompt gamma rays from nitrogen for which the highest energy prompt gamma ray is above 10 MeV, to permit calibration of PGAA detection systems to these energy ranges.

PGAA facilities have also been used to assist in the elucidation of nuclear structure, as de-excitation gamma rays provide information on the level structure of the absorbing nucleus. Swider et al. (1994) used PGAA spectroscopy to observe gamma-ray cascades induced by neutron capture in ^{128}Te , indicating level structure of the ^{129}Te product nucleus. More recent work by Walters (2009) has involved the use of a PGAA gamma-ray spectrometer to provide information on the level structures of several germanium isotopes. Investigations of nuclear parameters involving higher energy, resonant capture phenomenon have been published recently (Pallone and Demaree 2009).

31.9.3 Identification of Explosives and Fissile Materials

Another area in which the number of PGAA applications has grown is that of detection and identification of fissile materials. Neutron-based analytical techniques have the sensitivity and selectivity needed for the investigation of many nuclear materials. Molnár et al. (2004) described the use of chopped beam PGAA to provide both the prompt gamma neutron capture and short-lived decay spectra from uranium isotopes and the use of these values in the determination of uranium and the degree of ^{235}U enrichment. English et al. (2004) described the use of gamma spectrometry and PGAA to characterize *legacy radioactive materials* and subsequently extended the work to include short-lived NAA as well as PGAA (English et al. 2008).

For many years, PGAA has been exploited for use in detection and identification of explosive materials, often based on the use of portable neutron sources and detection of nitrogen. Very recently, Im et al. (2009b) have applied principle components analysis to evaluation of PGAA spectra for identification and classification of explosives. Im and Song (2009a) recently published a review of PGAA applications in the detection of illicit materials.

31.9.4 Measurements of Advanced Materials

Measurement of advanced materials is another area in which the number of PGAA applications has been increasing steadily. The utility of PGAA has kept pace with the needs of the materials science community in the characterization of materials such as the new generations of metal catalysts, ceramics, and biopolymers. In addition, many of the recent PGAA applications have been associated with the study of hydrogen storage materials such as metal hydrides, components of hydrogen fuel cells, hydrogen-selective membranes, and other emerging energy-efficient technologies. Measurements of advanced materials that deal exclusively with determination of hydrogen or boron are covered in the subsequent sections; other recent applications in advanced materials are reviewed here.

PGAA determinations of carbon, nitrogen, and silicon were used to help ascertain the amounts of silicon nitride and silicon carbide formed by high-temperature and high-pressure processes (Balazsi et al. 2004, 2005). Results from PGAA for carbon and hydrogen in fiber epoxy composite samples were used to estimate fiber volumes based on the carbon to hydrogen ratios and comparison with samples of known fiber volume (Dorsey et al. 2004). Kasztovszky et al. (1999) determined impurities in aluminum oxides and Szentmiklosi et al. (2006b) in materials containing calcium-sulfate, as some impurities are known to affect thermoluminescence in materials used for radiation dosimetry. PGAA (together with Fourier-transform infrared spectrometry) was used in the study of another ceramic, barium titanium oxide, to distinguish residual free hydrogen from hydroxyl groups associated with moisture (Atakan et al. 2008). Contaminants also affect magnetic or electrical properties of many metal oxyanion materials; PGAA was used to evaluate levels of both dopant and impurity elements in a variety of these materials (Perry et al. 2008). Similar studies using PGAA to determine rare-earth contaminant elements were carried out on a variety of rare-earth oxides (Perry et al. 2005). In the field of biopolymers, Balazsi et al. (2009) recently used PGAA to determine element composition of biopolymer-apatite structures derived from eggshells with biodegradable coatings. And PGAA was used extensively to determine the chemical composition and water content of synthetic polymer membranes (Young et al. 2003).

Analysis of fullerenes for impurities, especially residual hydrogen has been an important component in the study of the structure and properties of these materials. Révay et al. (2006) determined the amounts of carbon and impurity elements (hydrogen, boron, and nitrogen) in C_{60} and C_{70} fullerenes. In a similar vein, recent work by Paul et al. (2009) involved characterization of carbon nanotube materials to determine levels of residual catalyst metals and hydrogen impurities present in commercially available materials. Other recent applications of advanced materials include the study of proton uptake in un-doped and yttrium-doped $BaPrO_3$ and compared with that in Gd-doped $BaCeO_3$ (Jones et al. 2005).

31.9.5 Analysis of Hydrogen

PGAA is uniquely suited for quantitative analysis of hydrogen due to the large dynamic range of the method and due to the nondestructive nature of the analysis as compared with other analytical methods, which typically rely on combustion of the sample. PGAA has been used to determine hydrogen levels ranging from a few micrograms per gram to several percent. Limits of detection for hydrogen for some representative matrices and facilities include 70 μg for coal and botanical materials at the Oregon State University PGAA facility (Robinson et al. 2009);

15 μg for geological materials at the Japan Atomic Energy Research Institute PGAA facility (Yamazaki et al. 2007); 15 μg for biological materials at the National Institute of Standards and Technology thermal neutron PGAA facility (Mackey et al. 2004); and 5 μg in palladium catalysts in Budapest (Révay et al. 2008b).

Relatively small amounts of hydrogen may affect the properties of metals, ceramic oxides, minerals, and other materials. For example, hydrogen causes embrittlement of metals, alters proton conductivity of ceramics and the physicochemical structures and melting points of minerals. There has been an enormous expansion of PGAA applications for determination of hydrogen in the materials sciences, especially those involving hydrogen storage materials, fuel cells, and other emerging energy-efficient technologies. Recent applications are presented here; for earlier work in hydrogen PGAA applications, see the review by Paul (1997).

PGAA has been used to study a number of materials, particularly light metals, to determine hydrogen storage capacity. Cao et al. (2009) reported using of PGAA to measure hydrogen in thin films that were fabricated to evaluate the H storage capacity of metal and metal alloy hydrides. Materials studied included a series of magnesium hydride thin films that had been exposed to hydrogen for different times and PGAA results were used to evaluate the optimum exposure conditions for maximum hydrogen uptake. To help determine the optimum magnesium-to-titanium ratio for hydrogen uptake, a series of thin films consisting of magnesium–titanium metal alloys with continuously varying composition were exposed to hydrogen to form metal hydrides. PGAA results indicated that the molar fraction of hydrogen increased with increasing magnesium mole fraction. Tompa et al. (2003) used PGAA to determine hydrogen in amorphous alloys containing varying amounts of nickel, copper, and zirconium. Results of PGAA in combination with those from NMR were used to evaluate hydrogen diffusion in alloys of differing compositions and to evaluate residual hydrogen in these materials. Results of PGAA were used together with those obtained from gas chromatography to determine residual hydrogen in aluminum foils and single crystals; gas chromatography was needed to supplement PGAA results due to the presence of hydroxyl–aluminum surface coating (Buckley and Birnbaum 2002).

Other studies have focused on ceramics and other materials that preferentially filter hydrogen, and on engineered catalysts for potential use in hydrogen fuel cells. Some recent PGAA measurements with direct or indirect implications for hydrogen fuel uses include the following examples. PGAA was used to determine hydrogen in platinum catalysts before and after drying to evaluate free hydrogen content, water content, and the hydroxyl component of the support structure (Kasztovszky et al. 2002). Results from quantitative PGAA of hydrogen, combined with qualitative results from other techniques including infrared spectroscopy, neutron vibrational spectroscopy, and small angle X-ray scattering were used to study hydrogen in crystalline and amorphous alumina (Paglia et al. 2004). And similarly, Atakan et al. (2008) used PGAA in combination with Fourier-transform infrared spectroscopy and thermogravimetric analysis to study effects of heat treatments on residual water in ceramic oxides and to help distinguish free hydrogen from hydroxyl groups. PGAA was used to determine amount of hydrogen sequestered by the cage compounds of microporous silicate, clathrasil decadodecasil, finding that results were consistent with those from NMR analyses, which indicated that H was released upon cage decomposition (van den Berg et al. 2007). PGAA has been used extensively by researchers at the University of Texas (US) to study proton exchange in lithium ion batteries (Aghara et al. 2005; Alvarez et al. 2007). At the same facility, Arunkumar et al. (2008) used PGAA for investigations into the structure and proton transfer properties of lithium–manganese–nickel compounds studied for potential use in lithium-type batteries.

A great deal of PGAA work on hydrogen determinations focused on facility characterization and method improvements. Chung et al. (2007) described a very thorough characterization of the PGAA instrument at the Korean Atomic Energy Research Institute, including characterization of the background spectrum and validation of the PGAA method for hydrogen quantification. Validation was accomplished, in part, using SRM 1632c Trace Elements in Coal (Bituminous), SRM 173c Titanium Alloy, and SRM 2453 Hydrogen in Titanium Alloy, demonstrating the large dynamic range for hydrogen measurements. Yamazaki et al. (2007) described a method developed for determination of low levels of hydrogen in geological standards in which samples were measured under helium gas to prevent moisture uptake. This work also involved a very careful hydrogen sensitivity calibration and characterization of hydrogen background count rates for that facility.

31.9.6 Analysis of Boron

PGAA is also uniquely suitable for determination of boron, in this case due to the high neutron capture cross section of ^{10}B , and correspondingly high PGAA sensitivity. Limits of detection for boron using this technique are nearly always submicrogram and often of the order of a few nanograms, depending on the characteristics of facility (Molnár 2004). Robinson et al. (2009b) reported limits of detection of $\leq 0.6 \mu\text{g}$ for botanical materials using a thermal neutron PGAA instrument with a neutron flux of $2.8 \times 10^7 \text{ cm}^{-2} \text{ s}^{-1}$ at Oregon State University, USA. Mackey et al. (2004b) report detection limits of 70 ng for biological materials using a thermal neutron PGAA facility with a neutron flux of $3 \times 10^8 \text{ cm}^{-2} \text{ s}^{-1}$. Byun et al. (2004) report detection limits of 67 ng at the Korean Atomic Energy Research Institute PGAA facility with a flux of $7.9 \times 10^7 \text{ cm}^{-2} \text{ s}^{-1}$ based on evaluation of background and sample container blanks. Detection limits may be even lower for facilities with higher neutron fluxes or more efficient detection systems. Determination of boron is nearly always included in multielement PGAA work; recent work focusing exclusively on PGAA determination of B is described here.

Some recent work determining boron by PGAA has focused on the analytical difficulty, caused by neutron attenuation, of measuring high-content boron materials (Acharya 2009; Harrison and Landsberger 2009). Others have dealt with the difficulty presented by high count rates from highly absorbing, boron-containing materials, such as the work described by Ember et al. (2001) in determining Gd in borated glasses and subsequent work using coincidence counting to improve signal-to-noise in highly absorbing material (Ember et al. 2002). Other PGAA scientists have presented methods for determining the peak area that address the difficulties associated with modeling the shape of the Doppler-broadened peak resulting from the emission of the 472-keV gamma ray from ^7Li following the $^{10}\text{B}(n,\alpha\gamma)^7\text{Li}$ reaction (Sun et al. 2008) or the difficulty encountered when subtracting Gaussian-shaped interfering gamma-ray peaks from the Doppler-broadened boron peak (Szentmiklosi et al. 2007a; Zeisler et al. 2001). Both Sakai et al. (2005) and Yamauchi et al. (2005) interrogated the shape of the broadened boron peak to obtain information on the chemical environment of the capturing nucleus.

PGAA has been employed for quantitative analysis of boron in boron-containing tumor drugs used for boron neutron-capture therapy. To study the distribution of such drugs in the mouse model, Cho et al. (2007) determined boron in tumors and other tissues of mice that had been injected with boronophenylalanine. Accuracy of the boron determinations at this facility had been established by previous work describing the facility, element standards, and the analysis of several certified reference materials (Cho et al. 2005b). Byun et al. (2004)

determined boron in a variety of reference materials as part of work to fully characterize the diffracted polychromatic neutron beam used at the Korean Atomic Energy Research Institute.

31.9.7 Biological and Environmental Applications

PGAA has been used in combination with INAA (or other methods) in biological and environmental studies in which a complete (or nearly complete) compositional characterization is desired. Anderson and coworkers have used both PGAA and INAA for determination of element content of foods for the past 2 decades. Highlights have been described in a 2001 overview of that program (Anderson et al. 2001). A more recent description of quantitative PGAA of 22 elements in a variety of foods, food and dietary supplements was presented by Anderson and Mackey (2005). Similarly, Freitas et al. (2008) used INAA and PGAA for determination of element content of nutritional and environmental samples, and Oura et al. (2007) for the determination of element content of atmospheric particulate matter. Multiple methods were also used to characterize the element content of cosmetics, in which PGAA was used to determine samarium and gadolinium (Furuta et al. 2008). PGAA was used extensively to determine the nutritive elements, carbon, nitrogen, and phosphorus in cattails (Zhao et al. 2008). As part of that research Zhao and Robinson (2009) presented a comparison of results obtained using cold and thermal neutron beams, noting the differences in the effects of hydrogen and sample thickness on element sensitivities.

31.9.8 Archeometry

PGAA has been used extensively over the years, alone or in combination with INAA or other methods, for multielement analysis of archeological specimens or artifacts. In many cases, the artifact or specimen may be unique and, therefore, not expendable. Even when destruction of a portion of the artifact is acceptable, the sample or specimen may be difficult to analyze using methods that require sample dissolution. For either INAA or PGAA, multielement analysis can be achieved without sample dissolution, fusion or other destructive methods used to introduce the sample into the detection device and PGAA has the added advantage of inducing little residual radioactivity. PGAA is often used to provide scientists with information on the element composition without lasting harm to the specimen. And, if necessary, artifacts analyzed by PGAA may be subsequently subjected to further analyses by other methods. Biro (2005) published an overview of PGAA applications in this field; and Lehmann et al. (2007) presented a discussion of neutron-based analytical and imaging techniques for investigation of cultural and archeological artifacts. Selected recent applications of PGAA in archeometry are described here.

In archeometry, element compositional data are often used to determine provenance and to assess artifact age. Results from multielement k_0 PGAA of a variety of artifacts ranging from ceramics to bronzes were used to ascertain provenance and assist in determining specimen ages (Sueki et al. 1998; Oura et al. 1999). PGAA was used to determine metal contents of several bronze and silver artifacts (Kasztovszky et al. 2000) and ancient silver coins (Kasztovszky et al. 2005). The provenance of Iron-Age bronze artifacts was evaluated based on PGAA determinations of major element and selected trace element content (Rogante et al. 2007). Copper-to-zinc ratios and the lead content of organ reed pipes determined by PGAA, combined with historical information concerning the use of these metals in the components of reed

pipes, allowed researchers to estimate the dates of the artifacts (Manescu et al. 2008). Ceramic figurines created by Amerindian peoples in the Los Roques Archipelago prior to the arrival of Europeans were investigated by PGAA; major and minor element contents were used to assist researchers in determining provenance (Kasztovszky et al. 2004). Results from a similar study of Amerindian pottery artifacts from Venezuela were used to ascertain provenance and support the hypothesis that seasonal migration established relationships among communities from different locations (Sajo-Bohus et al. 2005, 2006). A large number of samples from stone tools and associated source materials were analyzed to determine geological classifications of the materials and assess provenance of the tool artifacts (Kasztovszky et al. 2008a, b). Major element and selected trace element contents determined by PGAA of prehistoric stone tools were used to distinguish tools made of green schist from those of blue schist (Szakmany and Kasztovszky 2004).

PGAA has been an integral part of European “ANCIENT CHARM” project (Analysis by Neutron resonant Capture Imaging and other Emerging Neutron techniques: new Cultural Heritage and Archeological Research Methods; <http://ancient-charm.neutron-eu.net/ach>) since its inception in 2006. The research associated with this project has contributed innovations in the method, and the information provided by PGAA measurements has contributed to the knowledge of the art and archeological artifacts studied. Two PGAA instruments, one at the Budapest Research Reactor (Hungary) and the other at the FRM-II Reactor in Garching (Germany), have been used for element determinations in a variety of cultural and archeological objects. Results from PGAA have been used alone or in combination with neutron diffraction for two-dimensional structural information or with neutron tomography for three-dimensional material characterization. The characteristics of the Prompt Gamma Activation Imaging (PGAI), or prompt gamma activation imaging facility at FRM-II reactor were described by Kudejova et al. (2008a). The characteristics of the Budapest PGAA instrument were described by Révay et al. (2004, 2008a). In development of a method to combine PGAA with time-of-flight neutron diffractometry, test samples were fabricated and analyzed as described by Kasztovszky et al. (2008c). Applications of PGAA in the Ancient Charm project have included the analysis of metal-based artifacts such as brass plates, bronze sculpture, tin-lead implements (Kasztovszky et al. 2007), and investigations of copper, limestone, bronze, and glass artifacts (Kasztovszky et al. 2008d).

31.9.9 Characterization of Geological Materials

PGAA has been used extensively over the years for multielement analysis of geological materials, in part, because geological materials may be difficult to analyze using methods that require sample dissolution and because PGAA has very good sensitivity for some elements of interest in these materials such as rare-earth elements, which are often used to distinguish the source or origin of geological materials. For example, (Perry et al. 2002) used PGAA to determine mass fraction values for 25 elements in metal sulfides and silicate rocks formed by processes at oceanic geothermal vents. The rare-earth elements were used to infer the relationship of the materials to specific geothermal field locations. More recently, Cristache et al. (2009) used PGAA and epithermal NAA to determine mass fractions of nine elements in Black Sea sediments, results of which were used to confirm the geological origins of the sediment.

Ebihara and Oura (2001) assessed the use of PGAA at the Japan Atomic Energy Research Institute for element analysis of extraterrestrial materials obtained from space missions; of

particular interest was evaluation of any residual activity and the potential perturbation of isotopic ratios that would interfere with subsequent analysis by other techniques. Evaluation indicated that PGAA was suitable in light of all considerations. More recently, Kudejova et al. (2009) reported on the feasibility of using PGAA for multielement determinations in Allende meteorite specimens.

The presence and amount content of boron in volcanic materials has been determined using PGAA in several studies conducted by Gmeling et al. (2005) and used to infer degree of fluid enrichment in magmatic materials. These researchers investigated both boron and chlorine but found boron to be most suitable as a predictor for fluid enrichment. They followed this work with PGAA studies of volcanic materials from several locations around the globe (Gmeling et al. 2007a) and from the East Carpathian Volcanic Field (Gmeling et al. 2007b). Similarly, Marschall et al. (2005) reported determination of element content of high-pressure metamorphic rocks, finding that results from PGAA compared well with those from other methods. Marschall et al. (2009) also evaluated boron and chlorine as predictors of dehydration in geological materials. Miyoshi et al. (2008) used PGAA for multielement determination of volcanic specimens (basalts) and found that ratios of boron to rare-earth element help to establish geological source information.

31.9.10 Quality Assurance and Analysis of Reference Materials

PGAA data obtained from experiments conducted at well-established facilities have been used routinely as benchmarks against which results from other techniques or newer facilities are evaluated. In the development of newer facilities and instruments in which PGAA is combined with other methods, analytical results were benchmarked against results obtained from the Budapest PGAA facility Kudejova et al. (2005). Sandor et al. (2002) have described a study for determination of major element composition of ancient coins, in which PGAA results were used as the benchmark to evaluate results from a newly developed Energy Dispersive X-Ray Fluorescence (EDXRF) method. In addition, in similar work involving PGAA and EDXRF of Roman silver coins, PGAA results were used as the benchmark (Kasztovszky et al. 2005). Results from PGAA were used by Kvardakov et al. (1998) as a benchmark against which to compare results from neutron incoherent scattering for H determinations. Similarly, hydrogen concentrations in a titanium alloy were determined by neutron incoherent scattering and compared against results obtained from cold neutron PGAA (Perego and Blaauw 2005).

Another of the traditional uses of PGAA has been that of a complementary technique to INAA and other analytical methods in certification of reference materials (Lindstrom 1998; Ihnat 2000). Use of PGAA allows certification of light elements such as hydrogen, boron, nitrogen, and some rare-earth elements such as Gd and Sm that are not easily accessible by other analytical techniques. Depending on levels present, PGAA may contribute results for many more elements in certification campaigns. Some recent applications of PGAA as applied to certification of reference materials are presented here. The materials and elements determined are presented to provide a sense of the breadth and depth of PGAA capabilities. There are no doubt additional instances in which PGAA results were used in the certification of reference materials. However, due to the routine nature of many of these analyses, results of certification analyses are included only in the certificates of analysis, and may not be found in the peer-reviewed literature.

In the analysis of biological materials, PGAA is often used to determine light elements. For example, Anderson (2000) reported use of PGAA to determine mass fractions of H, B, C, N, Na, Cl, K, and S for certification of these elements in SRM 1946 Meat Homogenate. Matsue and Yonezawa (2001) reported use of PGAA to determine H, B, C, N, Na, S, Cl, and K in a National Institute of Environmental Studies (NIES) typical diet reference material. Zeisler et al. (2008) reported on the certification of SRM 1577c Bovine Liver in which PGAA contributed values for H, N, K, and S. Other measurements of certified reference materials include determination of N in a variety of NIST biological and geological Standard Reference Materials (Paul 2001). Both INAA and PGAA data accumulated over more than 10 years were used to assess stability of two biological reference materials, SRM 1566a Oyster Tissue and SRM 1547 Peach Leaves (Mackey and Spatz 2009).

For analyses of geological and environmental reference materials, PGAA may be used to measure both major element constituents (as well as light elements) and trace amounts of boron, cadmium, and rare-earth elements. Dyar et al. (2001) used PGAA to determine boron in a variety of reference minerals. Mackey et al. (2007) reported certification of SRM 695 Multi-Nutrient Fertilizer in which PGAA was one of several techniques used to certify mass fractions for 17 elements and provide reference or information values for another seven elements. PGAA contributed to certified or reference values for B, Cd, Fe, K, Mn, and N in this material. More recently PGAA was used in certification measurements for three soil SRMs (2709a, 2710a, 2711a) contributing results for B, Cd, Fe, Gd, K, Mn, Si, Sm, and Ti in these materials. Paul et al. 2009, Mackey and Spatz 2009, Sieber et al. 2007 reported certification of major and minor element constituents of SRM 57b Silicon Metal for which PGAA was used to provide results for B, Al, Ti, Mn, and Fe. Miura et al. (2008) employed PGAA for determination of boron in National Measurement Institute of Japan ceramic certified reference materials using chlorine and silicon as internal standards in developing calibration curves for boron in this matrix.

References

- Acharya R (2009) *J Radioanal Nucl Chem* 281:291
- Aghara SK, Venkatraman S, Manthiram A, Alvarez E (2005) *J Radioanal Nucl Chem* 265:321
- Ahlgren L, Albertsson M, Areberg J, Kadar L, Linden M, Mattsson S, McNeill F (1999) *Acta Oncol* 38:431
- Alfassi ZB, Chung C (1995) Prompt gamma neutron activation analysis. CRC Press, Boca Raton
- Alvarez E, Biegalski SR, Landsberger S (2007) *Nucl Instrum Meth B* 262:333
- Anderson DL (2000) *J Radioanal Nucl Chem* 244:225
- Anderson DL, Mackey EA (1993) *J Radioanal Nucl Chem* 167:145
- Anderson DL, Mackey EA (2005) *J Radioanal Nucl Chem* 263:683
- Anderson DL, Failey MP, Zoller WH, Walters WB, Gordon GE, Lindstrom RM (1981) *J Radioanal Chem* 63:97
- Anderson DL, Cunningham WC, Capar SG, Baratta EJ, Mackill P (2001) *J Radioanal Nucl Chem* 249:29
- Arunkumar TA, Alvarez E, Manthiram A (2008) *J Mater Chem* 18:190
- ASTM (1998) Standard practice for determining neutron fluence, fluence rate, and spectra by radioactivation techniques (E261), Report E 261-98. ASTM International, West Conshohocken
- Atakan V, Chen CW, Paul R, Riman RE (2008) *Anal Chem* 80:6626
- Balazsi C, Cinar FS, Kasztovszky Z, Cura ME, Yesilcubuk A, Weber F (2004) *Silic Indus* 69:293
- Balazsi C, Cinar FS, Addemir O, Kasztovszky Z, Kover Z, Weber F (2005) Size effects in micro- and nanocarbon added C/Si₃N₄ composite prepared by hot pressing. In: Dusza J, Danzer R, Morrell R (eds) *Fractography of advanced ceramics II*. Trans Tech, Zurich-Uetikon, pp 238–241
- Balazsi C, Bishop A, Yang JHC, Balazsi K, Weber F, Gouma PI (2009) *Compos Interfaces* 16:191
- Beasley DG, Alghamdi A, Freitas MC, Fernandes A, Révay Z (2009) *J Radioanal Nucl Chem* 281:307

- Beckurts KH, Wirtz K (1964) Neutron physics. Springer, Berlin
- Belgya T (2008) *J Radioanal Nucl Chem* 276:609
- Belgya T, Molnár GL (2004) *Nucl Instrum Meth B* 213:29
- Belgya T, Révay Z, Fazekas B, Héjja I, Dabolcsi L, Molnár G, Kis J, Östör J (1997) The new budapest capture gamma-ray facility. In: Molnár GL, Belgya T, Révay Z (eds) *Proceedings of the 9th international symposium capture gamma-ray spectroscopy and related topics*. Springer, Budapest, pp 826–837
- Belgya T, Révay Z, Ember PP, Weil JL, Molnár GL (2003) The cold neutron PGAA-NIPS facility at the Budapest Research Reactor. In: Kvasil J, Cejnar P, Krticka M (eds) *Proceedings of the 11th international symposium on capture gamma-ray spectroscopy and related topics*. World Scientific, Singapore, pp 562–568
- Belgya T, Révay Z, Molnár GL (2005) *J Radioanal Nucl Chem* 265:181
- Belgya T, Kis Z, Szentmiklosi L, Kasztovszky Z, Festa G, Andreanelli L, De Pascale MP, Pietropaolo A, Kudejova P, Schulze R, Materna T (2008) *J Radioanal Nucl Chem* 278:713
- Biro KT (2005) *J Radioanal Nucl Chem* 265:235
- Blaauw M, Belgya T (2005) *J Radioanal Nucl Chem* 265:257
- Borella A, Moens A, Schillebeeckx P, Van Bijlen R, Molnár GL, Belgya T, Révay Z, Szentmiklósi L (2005) *J Radioanal Nucl Chem* 265:267
- Borsaru M, Berry M, Biggs M, Rojc A (2004) *Nucl Instrum Meth B* 213:530
- Buckley CE, Birnbaum HK (2002) *J Alloy Compd* 330:649
- Byun SH, Sun GM, Choi HD (2002) *Nucl Instrum Meth A* 487:521
- Byun SH, Sun GM, Choi HD (2004) *Nucl Instrum Meth B* 213:535
- Cao LR, Hattrick-Simpers JR, Bindel R, Tomlin BE, Zeisler R, Paul R, Bendersky LA, Downing RG (2009) *J Radioanal Nucl Chem*. doi:[10.1007/s10967-009-0058-y](https://doi.org/10.1007/s10967-009-0058-y)
- Charbucinski J, Duran O, Freraut R, Heresi N, Pineyro I (2004) *Appl Radiat Isot* 60:771
- Chen-Mayer HH, Mildner DFR, Lamaze GP, Paul RL, Lindstrom RM (1999) In: Duggan JL, Morgan IL (eds) *Application of accelerators in research and industry (AIP Conference proceedings, Vol. 475)*, Amer Inst Phys, pp 718–721
- Chen-Mayer HH, Mackey EA, Paul RL, Mildner DFR (2000) *J Radioanal Nucl Chem* 244:391
- Chen-Mayer HH, Lamaze GP, Mildner DFR, Zeisler R, Gibson WM (2001) *Anal Sci* 17(Suppl):i629
- Chen-Mayer HH, Heward WJ, Paul RL, Klug FJ, Gao Y (2003) *J Mater Res* 18:2486
- Cho H-J, Chung Y-S, Kim Y-J (2005a) *Nucl Instrum Meth B* 229:499
- Cho HJ, Chung YS, Kim YJ (2005b) *J Radioanal Nucl Chem* 264:701
- Cho HJ, Chun KJ, Park KW, Chung YS, Kim HR (2007) *J Radioanal Nucl Chem* 272:403
- Choi HD, Firestone RB, Lindstrom RM, Molnár GL, Mughabghab SF, Paviotti-Corcuera R, Révay Z, Trkov A, Zerkin V, Zhou C (2007) *Database of prompt gamma rays from slow neutron capture for elemental analysis (STI/PUB/1263)*. IAEA, Vienna
- Chung C (1995) Neutron damage and induced effects on nuclear instruments used for PGAA. In: Alfassi ZB, Chung C (eds) *Prompt gamma neutron activation analysis*. CRC Press, Boca Raton, pp 37–58
- Chung C, Chen YR (1991) *Nucl Instrum Meth A* 301:328
- Chung YS, Moon JH, Cho HJ, Kim HR (2007) *J Radioanal Nucl Chem* 272:391
- Comar D, Crouzel C, Chasteland M, Riviere R, Kellershohn C (1969a) The use of neutron capture gamma radiations for the analysis of biological samples. In: DeVoe JR (ed) *Modern trends in activation analysis (NBS Spec. Pub. 312)*. National Bureau of Standards, Washington, pp 114–127
- Comar D, Crouzel C, Chasteland M, Riviere R, Kellershohn C (1969b) *Nucl Appl* 6:344
- Copley JRD, Majkrzak CF (1989) Calculations and measurement of the performance of converging neutron guides. In: Majkrzak CF (ed) *Thin-film neutron optical devices: mirrors, supermirrors, multilayer monochromators, polarizers, and beam guides (Proc. SPIE 983)*. Society of Photo-Optical Instrumentation Engineers, Bellingham, pp 93–104
- Copley JRD, Stone CA (1989) *Nucl Instrum Meth A* 281:593
- Cristache C, Gmeling K, Culicov O, Frontasyeva MV, Toma M, Dului OG (2009) *J Radioanal Nucl Chem* 279:7
- De Soete D, Gijbels R, Hoste J (1972) *Neutron activation analysis*. Wiley-Interscience, London
- Debertin K, Helmer RG (1988) *Gamma- and X-ray spectrometry with semiconductor detectors*. North-Holland, Amsterdam
- Deconninck G, Demortier G, Bodart F (1981) *Atomic Energy Review, Supplement 2*, IAEA, Vienna, pp 151–234
- Degenaar IH, Blaauw M, Bode P, de Goeij JJM (2004) *J Radioanal Nucl Chem* 260:311
- Dokhale PA, Csikai J, Olah L (2001) *Appl Radiat Isot* 54:967
- Dorsey DJ, Hebner R, Charlton WS (2004) *J Compos Mater* 38:1505
- Dyar MD, Wiedenbeck M, Robertson D, Cross LR, Delaney JS, Ferguson K, Francis CA, Grew ES, Guidotti CV, Hervig RL, Hughes JM, Husler J, Leeman W, McGuire AV, Rhede D, Rothe H,

- Paul RL, Richards I, Yates M (2001) *Geostandard Newslett* 25:441
- Ebihara M, Oura Y (2001) *Earth Planet Space* 53:1039
- Ehmann WD, Vance DE (1991) *Radiochemistry and nuclear methods of analysis*. Wiley, New York
- Elekes Z, Belgya T, Molnár GL, Kiss AZ, Csatlós M, Gulyás J, Krasznahorkay A, Máté Z (2003) *Nucl Instrum Meth A* 503:580
- Ember PP, Révay Z, Belgya T, Molnar G (2001) *Magy Kem Foly* 107:438
- Ember PP, Belgya T, Molnár GL (2002) *Appl Radiat Isot* 56:535
- Ember PP, Belgya T, Weil JL, Molnár GL (2004) *Nucl Instrum Meth B* 213:406
- English GA, Firestone RB, Perry DL, Reijonen J, Ludewigt B, Leung KN, Garabedian G, Molnar G, Révay Z (2004) *Nucl Instrum Meth B* 213:410
- English GA, Firestone RB, Perry DL, Reijonen JP, Leung KN, Garabedian GE, Molnár GL, Révay Z (2008) *J Radioanal Nucl Chem* 277:25
- Fazekas B, Molnár GL, Belgya T, Dabolci L, Simonits A (1997) *J Radioanal Nucl Chem* 215:271
- Fazekas B, Révay Z, Östör J, Belgya T, Molnár G, Simonits A (1999) *Nucl Instrum Meth A* 422:469
- Fleming RF (1982) *Appl Radiat Isot* 33:1263
- Freeman JM, Jenkin JG (1966) *Nucl Instrum Meth* 43:269
- Freitas MC, Révay Z, Szentmiklosi L, Dionisio I, Dung HM, Pacheco AMG (2008) *J Radioanal Nucl Chem* 278:381
- Furuta E, Nakahara H, Hatsukawa Y, Matsue H, Sakane H (2008) *J Radioanal Nucl Chem* 278:553
- Gilmore G, Hemingway JD (1995) *Practical gamma-ray spectrometry*. Wiley, Chichester
- Gmeling K, Harangi S, Kasztovszky Z (2005) *J Radioanal Nucl Chem* 265:201
- Gmeling K, Nemeth K, Martin U, Eby N, Varga Z (2007a) *J Volcanol Geoth Res* 159:70
- Gmeling K, Kasztovszky Z, Szentmiklosi L, Revay Z, Harangi S (2007b) *J Radioanal Nucl Chem* 271:397
- Grazman BL, Schweikert EA (1991) *J Radioanal Nucl Chem At* 152:497
- Harrison RK, Landsberger S (2009) *Nucl Instrum Meth B* 267:513
- Hatsukawa Y, Oshima M, Hayakawa T, Noh T, Shinohara N (2002) *Nucl Instrum Meth A* 482:328
- Heath RL, Helmer RG, Davidson JR, Gehrke RJ (1999) *Gamma-ray spectrum catalogue: Ge and Si detector spectra*, 4th edn. CD-ROM., 4, CD-ROM. INEEL, Idaho Falls
- Helmer RG, Greenwood RC, Gehrke RJ (1971) *Nucl Instrum* 96:173
- Henkelmann R, Born HJ (1973) *J Radioanal Chem* 16:473
- Hilger A, Kardjilov N, Strobl M, Treimar W, Banhart W (2006) *Physica B* 385–386:1213
- Hils T, Boeni P, Stahn J (2004) *Focusing parabolic guide for very small samples*. Elsevier Science, Physica B-Condensed Matter 350:166–168
- Ihnat M (2000) *J Radioanal Nucl Chem* 245:73
- Im HJ, Lee YH, Park YJ, Song BC, Cho J, Kim WH (2007) *Nucl Instrum Meth A* 574:272
- Im HJ, Song K (2009a) *Appl Spectrosc Rev* 44:317
- Im HJ, Song BC, Park YJ, Song K (2009b) *Classification of materials for explosives from prompt gamma spectra by using principal component analysis*. Pergamon-Elsevier Science, *Appl Rad Isot* 67:1458–1462
- Isenhour TL, Morrison GH (1966a) *Anal Chem* 38:162
- Isenhour TL, Morrison GH (1966b) *Anal Chem* 38:167
- Johansen GA, Jackson P (2004) *Radioisotope gauges for industrial process measurements*. Wiley, Chichester
- Jones CY, Wu J, Li LP, Haile SM (2005) *J Appl Phys* 97:114908
- Jordanov VT, Knoll GF, Huber AC, Pantazis JA (1994) *Nucl Instrum Meth A* 353:261
- Jurney ET, Starner JW, Lynn JE, Raman S (1997) *Phys Rev C* 56:118
- Kasviki K, Stamatelatos IE, Kalef-Ezra J (2007a) *Evaluation of spatial sensitivity of a prompt gamma neutron activation analysis facility for the in vivo determination of nitrogen in small animals*. Springer, Berlin, pp 225–231
- Kasviki K, Stamatelatos IE, Yannakopoulou E, Papadopoulos P, Kalef-Ezra J (2007b) *Nucl Instrum Meth B* 263:3
- Kasztovszky Z, Révay Z, Belgya T, Fazekas B, Östör J, Molnár GL, Molnar G, Borossay J (1999) *J Anal Atom Spectrom* 14:593
- Kasztovszky Z, Révay Z, Belgya T, Molnár GL (2000) *J Radioanal Nucl Chem* 244:379
- Kasztovszky Z, Révay Z, Molnar G, Wootsch A, Paal Z (2002) *Catal Comm* 3:553
- Kasztovszky Z, de Antczak MM, Antczak A, Milian B, Bermudez J, Sajo-Bohus L (2004) *Nukleonika* 49:107
- Kasztovszky Z, Panczyk E, Fedorowicz W, Révay Z, Sartowska B (2005) *J Radioanal Nucl Chem* 265:193
- Kasztovszky Z, Visser D, Kockelmann W, Pantos E, Brown A, Blaauw M, Hallebeek P, Veerkamp J, Krook W, Stuchfield HM (2007) *Nuovo Cimento* 30:67
- Kasztovszky Z, Biro KT, Marko A, Dobosi V (2008a) *Archaeometry* 50:12
- Kasztovszky Z, Biro KT, Marko A, Dobosi V (2008b) *J Radioanal Nucl Chem* 278:293
- Kasztovszky Z, Kis Z, Belgya T, Kockelmann W, Imberti S, Festa G, Filabozzi A, Andreani C, Kirfel A, Biro KT, Duzs K, Hajnal Z, Kudejova P, Tardocchi M (2008c) *J Radioanal Nucl Chem* 278:661
- Kasztovszky Z, Kockelmann WA, Cippo EP, Gorini G, Tardocchi M (2008d) *Nuovo Cimento* 31:143
- Kis Z, Fazekas B, Östör J, Révay Z, Belgya T, Molnár GL, Koltay I (1998) *Nucl Instrum Methods A* 418:374

- Knoll GF (2000) Radiation detection and measurement. Wiley, New York
- Kobayashi T, Kanda K (1983) Nucl Instrum Meth 204:525
- Krusche B, Lieb KP, Daniel H, von Egidy T, Barreau G, Börner HG, Brissot R, Hofmeyr C, Rascher R (1982) Nucl Phys A386:245
- Kudejova P, Materna T, Jolie J, Turler A, Wilk P, Baechler S, Kasztovszky Z, Révay Z, Belgia T (2005) J Radioanal Nucl Chem 265:221
- Kudejova P, Meierhofer G, Zeitelhack K, Jolie J, Schulze R, Turler A, Materna T (2008) J Radioanal Nucl Chem 278:691
- Kudejova P, Canella L, Schulze R, Jolie J, Turler A (2009) New PGAI-NT and PGAA at FRM II for geological samples: test measurements on allende meteorite. Pergamon-Elsevier Science, Geochim Cosmochim Acta 73(Suppl):A701–A701
- Kvardakov VV, Chen-Mayer HH, Mildner DFR, Somenkov VA (1998) J Appl Phys 83:3876
- Lea DE (1934) Nature 133:24
- Lehmann EH, Vontobel P, Frei G (2007) Nuovo Cimento C 30:93
- Leo WR (1987) Techniques for nuclear and particle physics experiments. Springer, Berlin
- Lim CS, Sowerby BD (2005) J Radioanal Nucl Chem 264:4
- Lindstrom DJ (1990) Nucl Instrum Meth A299:584
- Lindstrom RM (1998) Fresenius J Anal Chem 360:322
- Lindstrom RM (2003) J Radioanal Nucl Chem 257:557
- Lindstrom RM, Lindstrom DJ, Slaback LA, Langland JK (1990) Nucl Instrum Meth A299:425
- Lindstrom RM, Zeisler R, Vincent DH, Greenberg RR, Stone CA, Mackey EA, Anderson DL, Clark DD (1993) J Radioanal Nucl Chem At 167:121
- Lone MA, Santry DC, Inglis WM (1980) Nucl Instrum Meth 174:521
- Lone MA, Leavitt RA, Harrison DA (1981) At Data Nucl Data Tables 26:511
- Mackey EA, Copley JRD (1993) J Radioanal Nucl Chem 167:127
- Mackey EA, Spatz RO (2009) J Radioanal Nucl Chem 281:91
- Mackey EA, Gordon GE, Lindstrom RM, Anderson DL (1991) Anal Chem 63:288
- Mackey EA, Anderson DL, Liposky PJ, Lindstrom RM, Chen-Mayer H, Lamaze GP (2004) Nucl Instrum Meth B226:426
- Mackey EA, Cronise MP, Fales CN, Greenberg RR, Leigh SD, Long SE, Marlow AF, Murphy KE, Oflaz R, Sieber JR, Rearick MS, Wood LJ, Yu LL, Wilson SA, Briggs PH, Brown ZA, Budahn J, Kane PF, Hall WL (2007) Anal Bioanal Chem 387:2401
- Maier-Leibnitz H (1969) Neutron conducting tubes. In: Ryde N (ed) Neutron-capture gamma-ray spectroscopy (STI/PUB/235). IAEA, Vienna, pp 93–103
- Manescu A, Fiori F, Giuliani A, Kardjilov N, Kasztovszky Z, Rustichelli F, Straumal B (2008) J Phys-Condens Mat 20:104250
- Marshall HR, Kasztovszky Z, Gmeling K, Altherr R (2005) J Radioanal Nucl Chem 265:339
- Marshall HR, Altherr R, Gmeling K, Kasztovszky Z (2009) Mineral Petrol 95:291
- Martinho E, Gonçalves IF, Salgado J (2003) Appl Radiat Isot 58:371
- Matsue H, Yonezawa C (2001) J Radioanal Nucl Chem 249:11
- Matsumoto T, Aizawa O, Nozaki T, Sato T (1984) Atomkernenergie 44:566
- Mildner DFR, Chen-Mayer HH (1999) Nucl Instrum Meth At 422: 21
- Mildner DFR, Chen-Mayer HH, Gibson WM (2002) J Appl Phys 92:6911
- Miri-Hakimabad H, Panjeh H, Vejdani-Noghreian A (2008) Nucl Sci Tech 19:109
- Miura T, Matsue H, Kuroiwa T, Chiba K (2008) J Radioanal Nucl Chem 278:653
- Miyoshi M, Shimono M, Hasenaka T, Sano T, Fukuoka T (2008) J Radioanal Nucl Chem 278:343
- Molnár GL (2004) Handbook of prompt gamma activation analysis with neutron beams. Kluwer, Dordrecht
- Molnár G, Belgia T, Dabolcsi L, Fazekas B, Révay Z, Veres Á, Bikit I, Kiss Z, Östör J (1997) J Radioanal Nucl Chem 215:111
- Molnár GL, Révay Z, Paul RL, Lindstrom RM (1998) J Radioanal Nucl Chem 234:21
- Molnár GL, Révay Z, Belgia T, Firestone RB (2000) Appl Radiat Isot 53:527
- Molnár GL, Belgia T, Révay Z, Qaim SM (2002a) Radiochim Acta 90:479
- Molnár GL, Révay Z, Belgia T (2002b) Nucl Instrum Meth 489:140
- Molnár GL, Révay Z, Belgia T (2004) Nucl Instrum Meth B213:389
- Moody JR, Greenberg RR, Pratt KW, Rains TC (1988) Anal Chem 60:1203A
- Morgan WD (2000) In: Yasumura S, Wang J, Pierson RN (eds) Of mermaids and mountains – three decades of prompt activation in vivo., pp 128–133
- Naqvi AA, Nagadi MM (2004) J Radioanal Nucl Chem 260:641
- Nunez-Lagos R, Virto A (1996) Appl Radiat Isot 47:1011
- O'Meara JM, Blackburn BW, Chichester DL, Gierga DP, Yanch JC (2001) Appl Radiat Isot 55:767
- Orphan VJ, Rasmussen NC (1967) Nucl Instrum Meth 48:282
- Orphan VJ, Rasmussen NC, Harper TL (1970) In: Report DASA 2570 (GA 10278), Gulf General Atomic, San Diego, 685
- Oura Y, Nakahara H, Sueki K, Sato W, Saito A, Tomizawa T, Nishikawa T (1999) Czech J Phys Suppl 49:311

- Oura Y, Iguchi H, Nagahata T, Nakamatsu H, Otoshi T, Ebihara M (2007) *J Radioanal Nucl Chem* 272:381
- Owens A (1989) *Nucl Instrum Meth* A274:297
- Owens A, Gehrels N, Pascarella SM, Teegarden BJ (1991) *IEEE Trans Nucl Sci* 38:221
- Paglia G, Buckley CE, Udovic TJ, Rohl AL, Jones F, Maitland CF, Connolly J (2004) *Chem Mater* 16:1914
- Pallone AK, Demaree JD (2009) *Nucl Instrum Meth* B267:2927
- Park CS, Sun GM, Byun SH, Choi HD (2005) *J Radioanal Nucl Chem* 265:283
- Park CS, Sun GM, Choi HD (2006) *Nucl Instrum Meth* B245:367
- Park YJ, Song BC, Chowdhury MI, Jee KY (2004) *J Radioanal Nucl Chem* 260:585
- Park YJ, Song BC, Im HJ, Kim JY (2009) *Nucl Instrum Meth* A606:243
- Paul R, Mackey EA, Zeisler R, Spatz RO, Tomlin BE (2009) *J Radioanal Nucl Chem* 282:945
- Paul RL (1997) *Analyst* 122:R35
- Paul RL (2001) *Analyst* 126:217
- Paul RL (2005) *Analyst* 130:99
- Paul RL, Lindstrom RM (2000) *J Radioanal Nucl Chem* 243:181
- Perego RC, Blaauw M (2005) *J Appl Phys* 97:123533
- Perry DL, Firestone RB, Molnár GL, Révay Z, Kasztovszky Z, Gatti RC, Wilde P (2002) *J Anal Atom Spectrom* 17:32
- Perry DL, English GA, Firestone RB, Molnár GL, Révay Z (2005) *J Radioanal Nucl Chem* 265:229
- Perry DL, English GA, Firestone RB, Leung KN, Garabedian G, Molnár GL, Révay Z (2008) *J Radioanal Nucl Chem* 276:273
- Phillips GW, Marlow KW (1976a) *Nucl Instrum Meth* 72:125
- Phillips GW, Marlow KW (1976b) *Nucl Instrum Meth* 137:525
- Postma H, Schillebeeckx P (2005) *J Radioanal Nucl Chem* 265:297
- Postma H, Perego RC, Schillebeeckx P, Siegler P, Borella A (2007) *Neutron resonance capture analysis and applications*. Springer, Berlin, pp 95–99
- Rasmussen NC, Hukai Y, Inouye T, Orphan VJ (1969) *Thermal neutron capture gamma-ray spectra of the elements*, Report AFCRL-69-0071. Massachusetts Institute of Technology, Boston
- Reijonen J, Leung KN, Firestone RB, English JA, Perry DL, Smith A, Gicquel F, Sun M, Koivunoro H, Lou TP, Bandong B, Garabedian G, Révay Z, Szentmiklósi L, Molnár G (2004) *Nucl Instrum Meth* A522:598
- Révay Z (2005) *J Radioanal Nucl Chem* 264:283
- Révay Z (2006) *Nucl Instrum Meth* A564:688
- Révay Z (2008) *J Radioanal Nucl Chem* 276:825
- Révay Z (2009) *Anal Chem* 81:6851
- Révay Z, Molnár GL, Belgya T, Kasztovszky Z, Firestone RB (2000) *J Radioanal Nucl Chem* 244:383
- Révay Z, Molnár GL, Belgya T, Kasztovszky Z, Firestone RB (2001a) *J Radioanal Nucl Chem* 248:395
- Révay Z, Belgya T, Ember PP, Molnár GL (2001b) *J Radioanal Nucl Chem* 248:401
- Révay Z, Molnár GL, Belgya T, Kasztovszky Z (2003) *J Radioanal Nucl Chem* 257:561
- Révay Z, Belgya T, Kasztovszky Z, Weil JL, Molnár GL (2004) *Nucl Instrum Meth* B 213:385
- Révay Z, Belgya T, Szentmiklósi L, Molnár GL (2005) *J Radioanal Nucl Chem* 264:277
- Révay Z, Belgya T, Molnár GL, Rausch H, Braun T (2006) *Chem Phys Lett* 423:450
- Révay Z, Harrison RK, Alvarez E, Biegalski SR, Landsberger S (2007) *Nucl Instrum Meth* A577:611
- Révay Z, Belgya T, Szentmiklósi L, Kis Z (2008a) *J Radioanal Nucl Chem* 278:643
- Révay Z, Belgya T, Szentmiklósi L, Kis Z, Wootsch A, Teschner D, Swoboda M, Schlögl R, Borsodi J, Zepernick R (2008b) *Anal Chem* 80:6066
- Rios-Martinez C, Unlu K, Wehring BW (1998) *J Radioanal Nucl Chem* 234:119
- Robinson JA, Hartman MR, Reese SR (2009) *J Radioanal Nucl Chem*. doi:10.1007/s10967-009-0358-2
- Rogante M, De Marinis G, Kasztovszky Z, Milazzo F (2007) *Nuovo Cimento C* 30:113
- Rosbach M (1991) *Anal Chem* 63:2156
- Sah RN, Brown PH (1997) *Microchem J* 56:285
- Sajo-Bohus LS, de Antczak MMM, Greaves ED, Antczak A, Bermudez J, Kasztovszky Z, Poirier T, Simonits A (2005) *J Radioanal Nucl Chem* 265:247
- Sajo-Bohus L, Mackowiak deAntczak, M. M., Kasztovszky Z, Greaves ED, Antczak A, Simonits A, Palacios D, Millan B (2006) *J Phys Conference Series* 41:8
- Sakai Y, Kubo MK, Matsue H, Yonezawa C (2005) *J Radioanal Nucl Chem* 265:287
- Sandor Z, Tolgyesi S, Gresits I, Kasztovszky Z (2002) *J Radioanal Nucl Chem* 254:283
- Segawa M, Matsue H, Sekiya Y, Yamada S, Shinohara T, Oku T, Sasao H, Suzuki J, Shimizu HM (2008) *J Radioanal Nucl Chem* 278:647
- Sieber JR, Mackey EA, Marlow AF, Paul R, Martin R (2007) *Powder Diffr* 22:146
- Stone CA, Blackburn DH, Kauffman DA, Cranmer DC, Olmez I (1994) *Nucl Instrum Meth* A349:515
- Sueki K, Kobayashi K, Sato W, Nakahara H, Tomizawa T (1996) *Anal Chem* 68:2203
- Sueki K, Oura Y, Sato W, Nakahara H, Tomizawa T (1998) *J Radioanal Nucl Chem* 234:27
- Sun G, Park C, Choi H (2008) *J Radioanal Nucl Chem* 278:637
- Sun GM, Byun SH, Choi HD (2003) *J Radioanal Nucl Chem* 256:541
- Sun GM, Park CS, Choi HD (2005) *J Radioanal Nucl Chem* 264:603
- Swider JR, Walters WB (2004) *Nucl Instrum Meth* B 226:659

- Swider JR, Mustillo DM, Conticchio LF, Walters WB, Paul RL, Lindstrom RM (1994) In: Kern J (ed) Proceedings of the 8th international symposium on capture gamma-ray spectroscopy and related topic, World Scientific, Singapore, pp 335–337
- Szakmany G, Kasztovszky Z (2004) Eur J Mineralog 16:285
- Szentmiklosi L, Belgia T, Révay Z (2005) J Radioanal Nucl Chem 264:229
- Szentmiklosi L, Révay Z, Belgia T (2006a) Nucl Instrum Meth A 564:655
- Szentmiklosi L, Révay Z, Chobola R, Mell P, Szakacs S, Kasa I (2006b) J Radioanal Nucl Chem 267:415
- Szentmiklosi L, Gmeling K, Révay Z (2007a) J Radioanal Nucl Chem 271:447
- Szentmiklosi L, Révay Z, Belgia T (2007b) Nucl Instrum Meth B 263:90
- Szentmiklosi L, Révay Z, Belgia T, Simonits A, Kis Z (2008) J Radioanal Nucl Chem 278:657
- Teschner D, Borsodi J, Woosch A, Révay Z, Havecker M, Knop-Gericke A, Jackson SD, Schlogl R (2008) Science 320:86
- Toh Y, Oshima M, Kimura A, Koizumi M, Furutaka K, Hatsukawa Y, Goto J (2008) J Radioanal Nucl Chem 278:685
- Tompa K, Banki P, Bokor M, Lasanda G, Vasaros L (2003) J Alloy Compd 350:52
- Turhan S, Yucel H, Demirbas A (2004) J Radioanal Nucl Chem 262:661
- Unlu K, Rios-Martinez C (2005) J Radioanal Nucl Chem 265:329
- van den Berg AWC, Pescarmona PP, Schoonman J, Jansen JC (2007) Chem Eur J 13:3590
- Westcott CH (1955) J Nucl Energy 2:59
- Wehring BW, Unlu K, Rios-Martinez C (1997) Appl Rad Isotopes 48:1343
- Wilhelm M, Eberth J, Pascovici G, Radermacher E, Thomas HG, vonBrentano P, Prade H, Lieder RM (1996) Nucl Instrum Meth A381:462
- Yamauchi S, Sakai Y, Watanabe Y, Kubo MK, Matsue H (2005) In: Proceedings of the 55th annual meeting of the Japan-Wood-Research-Society, Kyoto, Japan, March. Springer, Tokyo, pp 279–281
- Yamazaki S, Oura Y, Ebihara M (2007) J Radioanal Nucl Chem 272:353
- Yonezawa C, Wood AKH, Magara M, Sawahata S, Hoshi M, Ito Y, Tachikawa E (1993) Prompt gamma-ray analysis using JRR-3M cold and thermal neutron guide beams. In: Proceedings of the 5th international symposium advanced nuclear energy research (JAERI-M 93-228), Mito, Japan, vol 2. JAERI, Tokai, pp 854–861
- Yonezawa C (1999) Biol Trace Elem Res 71–2:407
- Yonezawa C (2002) Bunseki Kagaku 51:61
- Young SK, Trevino SF, Tan NCB, Paul RL (2003) J Polym Sci B41:1485
- Zeisler R, Lamaze GP, Chen-Mayer HH (2001) J Radioanal Nucl Chem 248:35
- Zeisler R, James WD, Mackey EA, Spatz RO, Greenberg RR (2008) J Radioanal Nucl Chem 278:783
- Zhang L, Ni B, Tian W, Huang D, Zhang G, Liu C, Wang P, Liu L, Li D (2005) Atom Energy Sci Tech 39:282
- Zhao L, Robinson L (2009) J Radioanal Nucl Chem 282:151
- Zhao L, Robinson L, Mackey EA, Paul RL, Greenberg RR (2008) J Radioanal Nucl Chem 277:275

32 Applications of Neutron Generators

J. Csikai¹ · R. Dóczi²

¹University of Debrecen, Debrecen, Hungary

²Budapest University of Technology and Economics, Budapest, Hungary

32.1	<i>Introduction</i>	1674
32.2	<i>Activation Analysis with 14 and 3 MeV Neutrons</i>	1674
32.3	<i>Prompt Radiation Analysis</i>	1678
32.3.1	Neutron Methods	1678
32.3.2	Gamma-Ray Methods	1680
32.3.3	Specific Applications	1682
32.4	<i>Neutron Imaging and Profiling Systems</i>	1682
32.5	<i>Fast Neutron Irradiation Effects in Solids</i>	1686
32.6	<i>Radiobiology with Fast Neutrons</i>	1687
32.7	<i>Neutron Attenuation and Shielding</i>	1688
32.8	<i>Editors' Notes</i>	1691

Abstract: Miscellaneous applications of low-voltage neutron generators providing 3 and 14 MeV neutrons via the D-D and D-T reactions, respectively, are reviewed. New experimental methods are reported, and emerging applications in the areas of prompt and delayed neutron activation analysis, fast neutron imaging and profiling, irradiation effects, fast neutron radiobiology, and shielding design are highlighted.

32.1 Introduction

In this chapter some applications of low voltage (~ 150 – 200 kV) neutron generators using 3 and 14 MeV neutrons, produced via the $^2\text{H}(\text{d},\text{n})^3\text{He}$ (D-D) and $^3\text{H}(\text{d},\text{n})^4\text{He}$ (D-T) reactions, respectively, are discussed. Principles of operation and output characteristics of neutron generators have been described elsewhere (Csikai 1987, 1989; IAEA 1996, 2000). The nuclear methods based on small neutron generators have a great importance in the development of such new technologies as process and quality-control systems, exploration of natural resources, detection of illicit traffic materials, transmutation of nuclear waste, fusion reactor neutronics, irradiation effects on biological and industrial samples, which can be directly utilized in other sciences, in the economy and society.

32.2 Activation Analysis with 14 and 3 MeV Neutrons

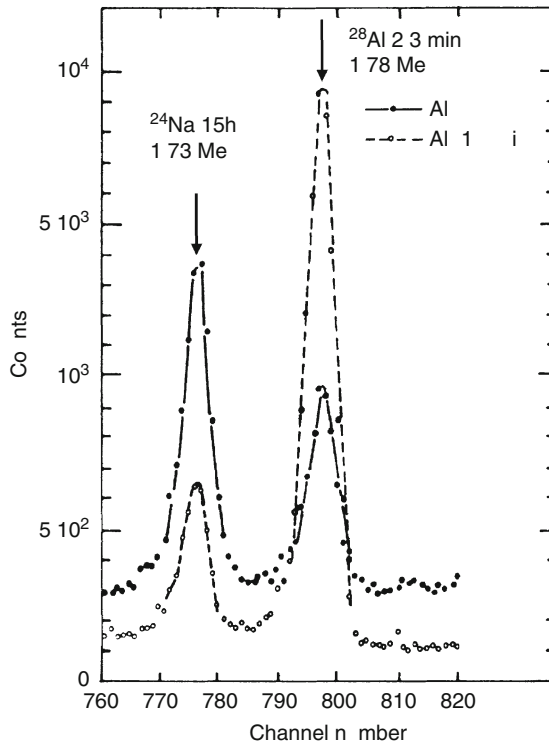
Recently, neutron activation analysis (NAA) has been improved by application of separated isotopes as targets, quick radiochemical separations, corrections for flux perturbation in the case of bulky samples, high-resolution detectors (Ge(Li), HPGe, LEGe, Si(Li), Si-avalanche, etc. – for a summary of the properties of LEGe and other types of Ge detectors see [Fig. 48.9 in Chap. 48, Vol. 5](#), on “Radiation Detection”) and better data acquisition as well as processing systems, in addition to the use of high-efficiency detectors ($\text{Bi}_4\text{Ge}_3\text{O}_{12}$, GSO, CsI, PbWO_4 , BaF_2 , CdTe, etc.) (Proctor et al. 1999; Dokhale et al. 2001; Hlavác 2001). A typical example of the advantages of high-resolution gamma spectrometry in elemental analysis is the determination of Si in Al alloys. (The problems of trace element determination by INNA in aluminum matrix are touched upon in various parts of [Chap. 30 in this Volume](#), on “Activation Analysis”.) The intensity ratio of the 1.73 and 1.78 MeV gamma-lines produced in $^{27}\text{Al}(\text{n},\alpha)^{24}\text{Na}$ and $^{27}\text{Al}(\text{n},\gamma)^{28}\text{Al}$, $^{28}\text{Si}(\text{n},\text{p})^{28}\text{Al}$ reactions, respectively, depends strongly on the Si content in the Al matrix (see [Fig. 32.1](#)). Another example showing the importance of high-efficiency gamma detectors is related to the detection of illicit traffic materials (drugs, explosives) via the determination of carbon and oxygen, using the respective 4.44 and 6.13 MeV gamma rays from the $(\text{n},\text{n}'\gamma)$ reactions.

There are two important new fields of application of fast neutrons in elemental analysis: determination of chemical compounds by measuring the atomic ratios of the composite elements and the correlations between them, and studies of the interaction of secondary energetic charged particles (p, α , t, d) with their chemical environment (hot atom chemistry) and the role of secondary reactions in activation analysis of light elements such as Li, Be, B, and C. Considerable progress has been made in the knowledge of decay data for radioactive products (IAEA 2002) and the possible interfering reactions and gamma-lines from fast neutron reactions, as presented in [Sect. 36.3 of the Appendix of this Volume](#).

The activation expression related to the decay of a single state should be extended to a more general case in which ground and isomeric states are produced and the ground state activity is used for the analysis. Such a typical case is the $^{58}\text{Ni}(\text{n},\text{p})$ reaction in which the $^{58\text{m}+\text{g}}\text{Co}$ isomeric

■ Fig. 32.1

Gamma-ray spectrum of Al and Al + Si mixture. Note that on adding just 1% of Si to Al, the peak ratio $^{24}\text{Na}/^{28}\text{Al}$ changes from about 2/1 to about 1/4



pair is produced and the activation analysis is based on the decay of ^{58}gCo . Some decay modes of the radioactive atoms are demonstrated in ► Fig. 32.2.

If the final nucleus has an isomeric state, which can also populate the ground state via an isomeric transition IT with a branching ratio β , then the differential equations for the two states are as follows:

$$\frac{dN_m}{dt} = \Phi\sigma_m n - \lambda_m N_m \quad \text{and} \quad \frac{dN_g}{dt} = \Phi\sigma_g n - \lambda_g N_g + \beta\lambda_m N_m \quad (32.1)$$

where Φ , n , λ_g , λ_m , σ_g , and σ_m are the neutron flux density, the number of atoms to be determined in the sample, decay constants of the nuclei produced in ground and metastable states, and the corresponding cross sections, respectively.

If the activity is measured via the decay of ground state atoms as a function of cooling time, t_c the $N_g(t_c)$ function is given by

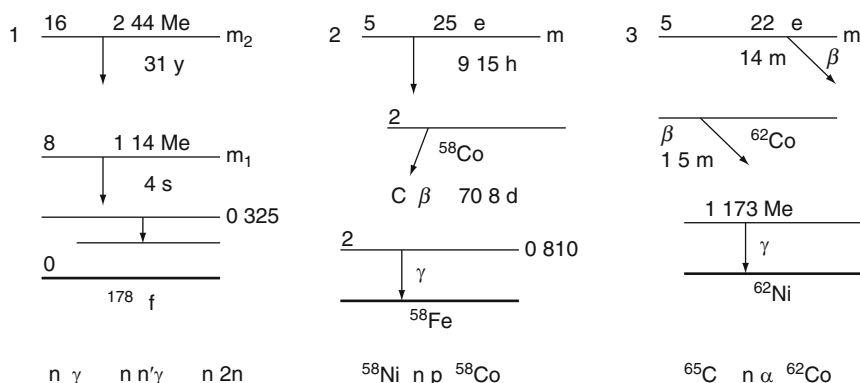
$$N_g(t_c) = \Phi n \left\{ \left(\frac{(\sigma_m \beta + \sigma_g)}{\lambda_g} + \frac{\sigma_m \beta}{\lambda_m - \lambda_g} \right) \times (1 - e^{-\lambda_g t_i}) e^{-\lambda_g t_c} - \frac{\sigma_m \beta}{\lambda_m - \lambda_g} \times (1 - e^{-\lambda_m t_i}) e^{-\lambda_m t_c} \right\} \quad (32.2)$$

where t_c and t_i are the cooling time and the irradiation time, respectively.

For example, in the case of ^{58}mCo $\beta = 1$ and the ground state decays by an 810 keV gamma-line. By measuring the peak area of this line as a function of cooling time, the σ_m/σ_g ratio can be

■ Fig. 32.2

Typical decay modes involving metastable (m) and ground (g) states



deduced. It follows from (32.2) that the intensity function $I_g(t_c)$ is given by the following expression:

$$I_g(t_c) = \Phi n (Ae^{-\lambda_g t_c} + Be^{-\lambda_m t_c}) \quad (32.3)$$

that is, the measured intensity is approximated by the sum of two exponential functions. The pre-exponential constants, A and B , contain the σ_m and σ_g values as unknown parameters. In the knowledge of the isomeric cross sections, the decay parameters, the irradiation, and measuring conditions, the number of atoms of a given element n can be determined. In some cases, if $\lambda_g \ll \lambda_m$ and t_c is high, then $I_g(t_c)$ is given by a single exponential function, that is, by the first term in (32.3).

Investigations on the sensitivity, accuracy, interfering reactions, and gamma-lines lead to the conclusion that neutron activation analysis based on small accelerators requires the use of thermal, resonance, and fast neutrons depending on the element to be determined in different matrices. In this case, the D-D and D-T targets are surrounded with hydrogenous moderators. Thermal (TNAA) and epithermal (ENAA) or resonance neutron activation analysis as well as the capture of gamma-ray techniques are favored over the fast neutron (FNAA) method for the following elements: Dy, Eu, In, Mn, Lu, Au, V; U, Th, Rb, Sr, Mo, Sb, Cs, Ba, Ta, Tb; and H, Be, B, N, O, S, Ni, Cd, Gd, Eu. It should be noted, however, that the method to be chosen for NAA depends also on the type of the detector. The RNAA is favored over TNAA, for example, for Ni, Zn, Rb, Sr, Sb, Cs, Tb, Ta, Th, and Mo, Ba, Gd, Tm, Yb, Hf, U if a GeLi, HPGe and a low energy photon (LEP) detector is used, respectively.

Though there are less interfering reactions and gamma-lines for the reactions induced by the 3 MeV D-D neutrons as compared to the 14 MeV D-T neutron reactions, the latter is recommended for NAA because of the much higher neutron yield and the availability of the multi-elemental analysis via the many open reaction channels. The specific activity expected from the principal reactions at $E_n = 14.5$ MeV was calculated using the recommended nuclear data (Bódy and Csikai 1987). The specific activity in Bq/g was calculated for the reactions of maximum yield of each element, assuming a reasonable flux $\Phi = 10^9 \text{ cm}^{-2} \text{ s}^{-1}$ and irradiation time $t_i = 1 \text{ h}$. Nuclear processes proposed for the determination of each element together with the possible interfering reactions are summarized in Sect. 36.3 of the Appendix of this Volume.

Recently, large efforts have been carried out for the determination of the thermal neutron flux perturbation factor in the case of bulky samples of unknown composition (Csikai et al. 2002b). The flux perturbation factor, F is defined by the following relation $F = \langle \Phi \rangle / \langle \Phi_0 \rangle$, where $\langle \Phi \rangle$ and $\langle \Phi_0 \rangle$ denote the average thermal neutron fluxes in the sample and in a moderator material of similar volume, respectively. It was found that the flux distribution $\Phi(x)$ both in thin (Buczkó and Borbély 1978) and bulk (Csikai et al. 2002b) absorbing samples can be described by the following expression:

$$\Phi(x) = (ax^2 + bx + c)^{-1} \quad (32.4)$$

where x is the distance from the surface of the sample while a , b , and c are fitting parameters. According to (32.4) for the determination of the $\Phi(x)$ function, it is sufficient to measure the flux value only in three positions, for example, at $x = 0$, $x = d/2$, and $x = d$ for a sample of thickness d . In the knowledge of the $\Phi(x)$ function the average neutron flux is given by

$$\langle \Phi \rangle = \frac{1}{d} \int_0^d \Phi(x) dx. \quad (32.5)$$

The unperturbed flux density $\langle \Phi_0 \rangle$ must be measured in the same positions using activation detector foils and replacing the sample with the moderator material. The spatial distribution of the thermal neutron flux around a point source changes significantly for hydrogenous moderators which prevents the use of TNAA for bulky samples. In the case of graphite moderator, the thermal neutron flux distribution changes only slightly, assuring an almost constant flux density for irradiation of bulky samples whose size is on the order of $10 \times 10 \times 10 \text{ cm}^3$.

The semi-log plot of F as a function of thickness d is linear both for graphite and for hydrogenous moderators, that is, the following simple equation

$$F = \frac{\langle \Phi \rangle}{\langle \Phi_0 \rangle} = F_0 e^{-Kd} \quad (32.6)$$

can be used for the determination of the flux perturbation factor, for both thin and bulky absorbing samples of unknown compositions if K is determined by experiment.

After determining F , the corrected activity $\langle A_0 \rangle$ at the end of irradiation time t_i is given by

$$\langle A_0 \rangle = \frac{\langle A \rangle}{F} = \langle \Phi_0 \rangle \sigma n (1 - e^{-\lambda t_i}) \quad (32.7)$$

where $\langle A \rangle$ is the activity of the sample produced by the average activating flux, $\langle \Phi \rangle$. It should be noted that the correction for the flux perturbation can be neglected neither for bulky nor for thin samples if they contain absorbing elements. For the elemental analysis of thin absorbing samples, hydrogenous moderators are recommended. For bulky samples, however, the graphite moderator is better. The attenuation of 3 and 14 MeV neutrons in different samples is discussed in (32.3) of the Appendix of this Volume.

In practice, the $\Phi(E)$ function in a given point inside the sample is determined by the unfolding method using a set of activation threshold detector foils. The most commonly used dosimetry reactions are also summarized in (32.3) of the Appendix of this Volume. With the knowledge of the $\Phi(E)$ and $\sigma(E)$ functions, the differential and spectrum-averaged reaction

rates, $R(E) = \Phi(E)\sigma(E)$ for any element can be determined. A method based on the combination of physical integration and activation threshold detectors was developed by Csikai et al. (1988) to determine the volume-averaged activity produced by neutron-induced reactions.

32.3 Prompt Radiation Analysis

In addition to NAA, neutrons are widely used in prompt radiation analysis for the determination of concentration and spatial distribution of elements in different matrices. For example, a track-etched detector (LR-115, Makrofol KG, CR 39, mica) placed on the polished surface of a sample is irradiated with fast or thermal neutrons then etched with a suitable chemical to deduce the concentration profiles from the track distributions. This method can also be used for the detection of suspended and dissolved U, Th, and Pu in water by (n,f) reactions; N in polymers by the $^{14}\text{N}(\text{n,p})^{14}\text{C}$ reaction; B and Li in semiconductors or glasses by the $^{10}\text{B}(\text{n},\alpha)^7\text{Li}$ and $^6\text{Li}(\text{n},\alpha)^3\text{H}$ reactions, respectively. For the detection of fission fragments the use of mica is recommended.

32.3.1 Neutron Methods

Neutron absorption, moderation, and reflection methods are also widely used in elemental analysis of bulk samples, especially for the determination of hydrogen and moisture content. A systematic study had shown that the relative number of excess neutrons $\eta = (I - I_0)/I_0$, measured with (I) and without (I_0) a reflector (see [Fig. 32.3](#)), depends linearly on the hydrogen content of liquid, powder, and solid samples up to about 1 cm thickness, that is,

$$\eta = sH + \eta(T) \quad (32.8)$$

where H is the hydrogen content in wt%, s is the slope of the η - H calibration function, and $\eta(T)$ is the matrix effect (Buczko et al. 1975). For the determination of the relation expressed by [\(32.8\)](#) and for the given source-sample-detector geometry, a combination of reflector with thin polyethylene (PE, composition: $\text{C}_n\text{H}_{2n+2}$) layers was recommended (Csikai et al. 2002a).

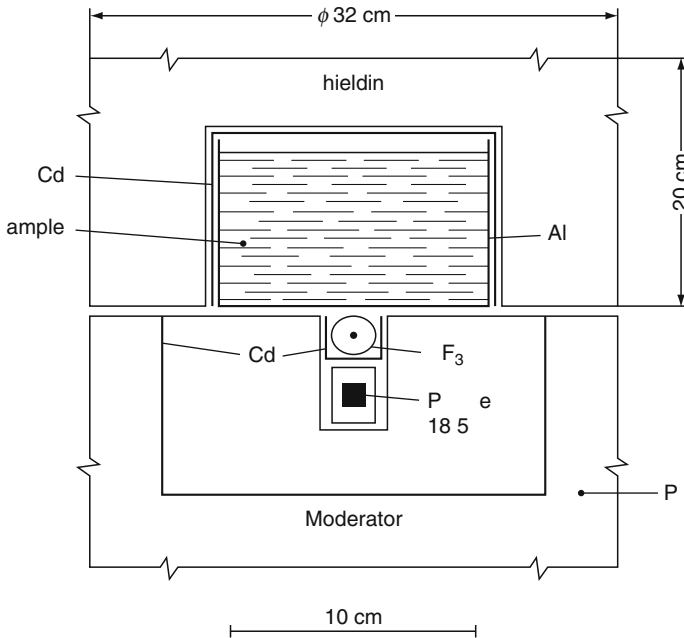
The concept of the reflection cross section of thermal neutrons σ_β as a microscopic parameter for the characterization of the reflection property of substances has been introduced (Csikai and Buczko 1999). The relation between η , σ_β , and the surface density of atoms is given by

$$\eta = Nd\sigma_\beta = \frac{n\sigma_\beta}{S} \quad (32.9)$$

where n is the total number of atoms in the sample, N the number of atoms per cm^3 , S the surface of the sample in cm^2 , and d is the thickness of the sample in cm. The quantity $Nd = mN_A/(MS)$ is obtained from the mass of the sample (m) and the molar mass of the element (M), where N_A is the Avogadro constant (see [Sect. 11.2 in the Appendix of Vol. 1](#)). If the reflector consists of molecules, the following formula can be used:

$$\eta = \frac{n_{\text{molec}}\sigma_{\beta \text{ molec}}}{S} = \frac{n_{\text{molec}} \sum_i v_i \sigma_{\beta i}}{S} \quad (32.10)$$

■ Fig. 32.3

Neutron reflection arrangement

where n_{molec} is the total number of molecules in the sample and v_i is the number of atoms of type i with cross section $\sigma_{\beta i}$ in the molecule. The cross-correlation between the σ_{β} values deduced from the $\sigma_{\beta \text{ molec}}$ data obtained for different compounds has proved that the reflection cross sections are additive. For a mixture of elements, the averaged molar mass of the elements should be used, that is,

$$\langle M \rangle = \frac{\sum_i m_i}{\sum_i \frac{m_i}{M_i}} \quad (32.11)$$

where m_i and M_i are the mass and molar mass, respectively, of the element of type i in the target. The values of cross sections for elements, organic and inorganic compounds, as well as for different combinations of metal layers are given by Csikai and Buczkó (1999), Király and Csikai (2000), and Csikai et al. (2002a). These data are useful for different applications of neutrons, like quality control of organic and inorganic compounds; bulk hydrogen analysis; atomic H/C ratio for the detection of illicit drugs, explosives, and qualification of fossil fuels; assay of nuclear materials in solutions (Mohapatra and Reddy 2001); and validation of neutron data libraries (NEA 1994). For example, it follows from the relation that the measured cross sections for hydrogenous materials, such as crude oil, coal, illicit drugs, normalized to the number of carbon atoms present in the molecule as a function of the H/C atomic ratio exhibit a straight line (Jonah 2001). The calibration equation can also be determined from the excess counts $\eta = s(n_{\text{H}}/n_{\text{C}}) + \eta_0$ measured for different hydrocarbons.

It is worth noting that the determination of hydrogen in bulk materials has great importance in many areas (NEA 2001), for example, hydrogen in metals and alloys causes structural weakness in the components of heavy-duty systems (aircraft, engines, missiles, pipelines of nuclear and chemical plants). Metal hydrides are applied in various fields of science and technology (electricity, propulsion, battery, food, nuclear fusion, etc.).

Both pulsed-neutron backscattering combined with time-of-flight (TOF; see later) measurements and the elastic scattering of neutrons can be used for the detection of light elements. Scattering signatures measured for multi-element samples were analyzed to determine atom fractions for H, C, N, O, and other elements in different objects by using a combination of TOF and pulse height measurement (Buffler et al. 2001). Simple backscattering spectrometry is based on the fact that the broad spectra of neutrons from Pu-Be, ^{252}Cf , and $^9\text{Be(d,n)}$ sources can cover a large energy interval (1.5–10 MeV) of the elastic scattering cross sections (σ_{EL}) of light elements like C, N, and O as the major constituents of a number of organic and inorganic compounds. Therefore, the spectral yields of backscattered neutrons are affected by the structures present in the $\sigma_{\text{EL}}(E_n)$ functions. The measured spectral yields and the calculated energy dependence of the reaction rate, $R(E_n)$ indicate the different structures in the $\sigma_{\text{EL}}(E_n)$ functions for C, N, and O (Csikai and ElAgib 1999). An improved neutron backscattering technique based on the combination of a ~ 1.5 ns wide-pulsed beam of 550 keV and the TOF technique at 150° scattering angle was applied for the detection of C, N, and O from different samples (Aoki et al. 2000).

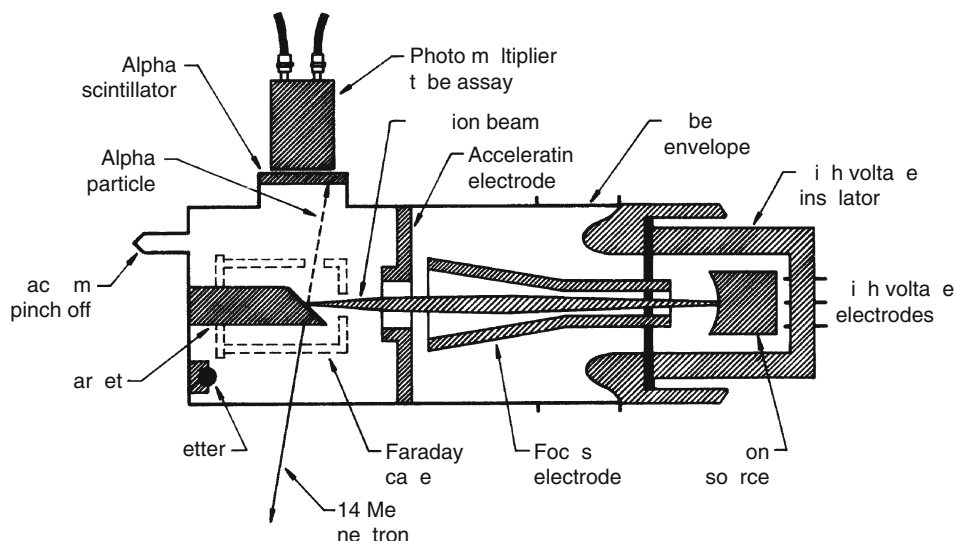
32.3.2 Gamma-Ray Methods

Recently, the neutron induced prompt gamma emission method (also called prompt gamma neutron activation analysis or PGNA) is widely used in online bulk elemental analysis, especially for the identification of explosives and illicit drugs. This method is not restricted to the use of prompt gammas emitted in radiative capture or (n,γ) reaction of slowed-down neutrons, but is extended to the fast-neutron $(n,x\gamma)$ reactions with $x = (n, p, \alpha)$, in which characteristic gamma rays are also produced. Among the $(n,x\gamma)$ type reactions, the inelastic neutron scattering $(n,n'\gamma)$ is the most common in elemental analysis. The (n,γ) and $(n,x\gamma)$ reactions are quite complementary to each other. For example, the (n,γ) cross section is low for Li, Be, B, C, N, O, and also for Na, Mg, Al, and Si, while the $(n,x\gamma)$ reaction yields are very high and the produced gamma rays specific to these elements. Therefore, prompt gamma rays produced in thermal, epithermal, and fast neutron interactions are all used for the elemental analysis of bulk media (Watterson et al. 1995). A typical example is the inspection of waste containers by irradiation with low-energy neutrons. The prompt gamma rays emitted in the de-excitation of fission fragments of actinide materials are measured with an array of HPGe detectors. The actinide isotopes are identified by observing selected gamma rays emitted from the fragments in pair-wise coincidence (Smith and Micklich 2000).

Pulsed 14 MeV neutron generators with neutron pulse width in the μs and ns regions have also been developed for analysis of bulk media and for borehole logging (Clayton and Wormald 1983; Schweitzer et al. 1988). The high penetrability of fast neutrons and energetic gamma rays renders the multi-elemental analysis of bulk ($m \gg 1$ kg, $V \gg 1$ dm³) samples possible. In addition to the identification of explosives and illicit drugs by the detection of the 4.44 and 6.13 MeV gamma rays emitted in the $^{12}\text{C}(n,n'\gamma)$ and $^{16}\text{O}(n,n'\gamma)$ reactions, respectively (Gozani 1994; Vourvopoulos 1994; Viesti et al. 1999), the online analysis is applied, for

■ Fig. 32.4

Combination of the sealed tube accelerator and the associated alpha-particle method (APM)



example, at coal mines, coal preparation plants, and coal-fired power plants. Concentrations of H, C, O, and N give information on caloric value, S on environmental pollution, Cl on corrosion of boiler, Al, Si, Ca, and Fe on ash content.

The combination of the sealed tube accelerator with the associated alpha-particle method (APM), illustrated in [Fig. 32.4](#), has great importance in the analysis of bulk samples, verification of chemical and nuclear weapons, in vivo analysis of human body element contents, and three-dimensional elemental analysis in solids. The time spectrum measured by the APM suggests that about 90% of the gamma rays of interest for prompt gamma-ray analysis are emitted from the 12 cm thick surface layer of solids in less than 10 ns after the neutrons hit the sample. Considering the attenuation of neutrons and gammas in the sample, the PGNA technique can give representative information on a few 10 kg of the samples. Some recommended reactions for bulk-media assay by prompt gamma-ray analysis using thermal and fast neutrons are summarized in [Sect. 36.3 of the Appendix of this Volume](#).

Among the gamma-ray methods, pulsed fast-thermal neutron analysis (PFTNA) plays an important role. The PFTNA method (Gozani 1994; Vourvopoulos 1994) is based on 14 MeV neutrons with 10 μ s pulse duration and 10 kHz frequency produced by a sealed tube D-T generator. The gated signals from the gamma rays, emitted during and between the neutron bursts are routed separately into two channel regions of an MCA. The 4.44 and 6.13 MeV gamma rays are recorded in the prompt region while the 2.23 MeV gamma rays from the $H(n,\gamma)$ reaction induced by the neutrons thermalized in the sample volume are measured between the pulses. Two devices based on this method, namely, PELAN (Pulsed Elemental Analysis with Neutrons) for the detection of explosives and NELIS (pallet inspection system) for the observation of illicit drugs are promising. Advantages and limitations of this technique are discussed in detail in a recent publication (Dokhale et al. 2001).

32.3.3 Specific Applications

The prompt and delayed gamma rays produced in 14 MeV neutron bombardment of rocks were published by Przewlocki et al. (1984). In the case of such complex samples, a number of interfering reactions and gamma-lines are produced. Separation between different elements can be improved by the combination of the D-D and D-T reactions. For example, the $(n, n'\gamma)$ reaction cannot be performed by the 3 MeV D-D neutrons on ^{12}C and ^{16}O . The use of associated particle timing based on the D-D reaction has been demonstrated for elemental analysis of bulk samples such as the human body (Evans et al. 1997). The nanosecond timing of an HPGe detector rendered it possible to identify the spatial origin of the measured gamma rays. The major elements in most rock types are Si, O, Al, Fe, Mg, Ca, Na, K, Ti, and P. Concentrations of these elements in the well-known terrestrial rocks vary from one to four orders of magnitude, therefore, careful investigations are needed to develop the most suitable methods for the elemental analysis of minerals, standard geological materials, lunar soil samples, processing solutions or slurries, and ocean bottom cores (Csikai 1992).

The conventional neutron methods are the neutron-epithermal neutron, neutron-thermal neutron, and the neutron-gamma procedures. In all three cases, rocks are bombarded by fast neutrons and either epithermal or thermal neutrons or gamma rays from radiative capture are registered. Both pulsed and stationary neutron sources are applied to these measurements (Berg and Jacobs 1983; Morris et al. 1983; Tittle et al. 1985; Demény et al. 1988; Mills et al. 1991). The pulsed TOF prompt gamma-ray analysis has been successfully applied by a number of authors, especially to the measurements of light elements (Sawa 1993; Brown et al. 1994; Gozani 1994; Vilaithong et al. 2000).

Nuclear techniques based on neutrons from radionuclides (^{252}Cf , Pu-Be, Am-Be) or small accelerator sources are successfully used in elemental analysis of bulk samples including the detection of illicit traffic materials in airline luggage (suitcases, briefcases, small boxes) by identifying H, C, N, O, Cl as major elements of these objects (Dokhale and Hussein 1997; Evans et al. 1999; Csikai et al. 2001). The atom fractions of these elements, in particular the C/O, C/H, and C/N ratios are quite different for drugs (cocaine $\text{C}_{17}\text{H}_{21}\text{NO}_4$, morphine $\text{C}_{17}\text{H}_{19}\text{NO}_3$, heroine $\text{C}_{21}\text{H}_{23}\text{NO}_5$) and explosives (nitroglycerin $\text{C}_3\text{H}_5\text{N}_3\text{O}_9$, TNT $\text{C}_7\text{H}_5\text{N}_3\text{O}_6$, RDX $\text{C}_3\text{H}_6\text{N}_6\text{O}_6$) as compared to other materials (sugar $\text{C}_{12}\text{H}_{22}\text{O}_{11}$, alcohol $\text{C}_2\text{H}_6\text{O}$, melamine $\text{C}_3\text{H}_6\text{N}_6$). Recently, a comprehensive review on the possible use of neutron methods for the detection and identification of explosives and drugs has been published (Cinausero and Viesti 2000).

There are many more new fields in the utilization of neutrons produced mainly by small D-D and D-T accelerators (IAEA 2000). Some typical fields of activation and prompt radiation analysis are summarized in [Table 32.1](#).

32.4 Neutron Imaging and Profiling Systems

The various applications of neutron radiography (reactor technology; rocket and missile technology; medical and biological investigations; inspection of plastic coating, gaskets, and turbines) have been extended for many new fields during the last 3 decades. The main advantages of neutron radiography (NR) are the ability of revealing many low-density media (water, oil, plastic) inside dense materials such as steel, Pb, Zr, U; high penetrability; high sensitivity for certain elements (H, B); discrimination between elements of similar atomic

■ Table 32.1

Typical applications of neutrons in elemental analysis

Field	Elements (matrices)
Metallurgy	N, O, F (alloys); O (refractory and nonferrous metals); Al, Si, P, Mg (cast iron, Al, Si-compounds); Al, Si, K (tungsten)
Chemistry	N, O, P, Al, Cl (explosives and propellants); N, O, Na, P (organic compounds and polymers); Cl, I (emulsions); N, P, K (fertilizers)
Electronics	N, O, Si, Al, Ti, P, Zn, Cr, Fe, Y, Zr, Eu, Ba, Dy (oxides, circuit boards, thin films)
Biology	N, Na, P, Cl, Ca (whole body); N (proteins, fossil bones); N, O, P, Ca (mixed feeds); N, O, K, Cl, Ca, Fe (plants); F, Na, Si, S, Ca, Fe, Ti, Sr, Ba, Hg, Pb (air-dust, fly ash)
Geology/mining/space sciences	O, Al, Si, Fe (lunar rocks); H, O, Na, S, Cl, V, Mn, Ni (crude oils); U, Th (rocks); O, Mg, Al, Si, Fe (sea cores); H, O, Al, Si (zeolites); H, C, O, Al, Si, Fe (coals)

weight and physical density; discrimination between different isotopes of the same element (^{10}B , ^{11}B , ^{113}Cd , ^{114}Cd); and applicability for highly radioactive objects, for example, fuel elements (Csikai 1987). It is impossible to cover all the new applications in a short review, therefore some results on the neutron depth profiling and imaging systems are intended to be discussed.

The nanosecond pulsed beam with time gating at the detector and the associated particle method (APM) render the three-dimensional (3D) elemental analysis of solids possible (Overley 1987; Rynes et al. 1999). The APM is based mainly on the D-D and D-T reactions by the detection of ^3He and ^4He particles, respectively, emitted at $\sim 180^\circ$ to the neutron direction. The 4–5 cm/ns travel time of the neutrons allows the imaging of the interrogated volume along the direction of the ns pulsed neutrons with a spatial resolution of ~ 5 cm. Some 2D-3D fast neutron imaging principles and techniques are summarized by Gozani (1994), Mikerov et al. (1998, 2001), and Chen and Lanza (2001), while typical thermal neutron radiography systems are demonstrated by Balaskó et al. 1998, 2001) and Shaikh et al. (1998, 2001).

Fast neutron resonance radiography (NRR) used by Chen and Lanza (2001) for elemental mapping is based on a hydrogen-rich plastic scintillator to detect the transmitted neutrons of 2–6 MeV energy. Different energies of neutrons were obtained by rotating the object detector assembly around a D-D source based on a 5 MV Van de Graaff accelerator. Monoenergetic neutrons in the 1.5 and 2.5 MeV ranges could also be obtained from the $^7\text{Li}(p,n)^7\text{Be}$ reaction

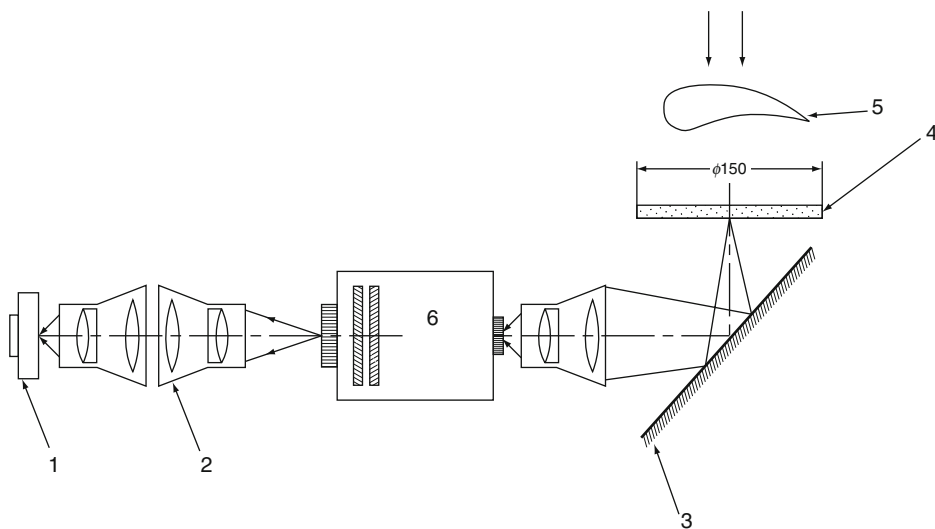
with a 10 μm thin Li target. Light from the scintillator is recorded by a charge coupled device (CCD) camera to form a radiographic image.¹ The structures in the energy dependence of the total cross sections, $\sigma_T(E_n)$, below 6 MeV render the distinction between light elements possible. The 2D images were formed using a 1 cm thick BC-430 plastic scintillator lens-coupled system with a cooled CCD camera which used a $1,242 \times 1,152$ pixel CCD.

Recently, investigations on the realization and prospects of real-time fast neutron radiography with a portable sealed tube D-T neutron generator with a yield up to 10^{10} s^{-1} and a luminescent CCD detector were published (Mikarov et al. 2001). The major components of the detector are shown in [Fig. 32.5](#): fast neutron screen prepared from hydrogenous polymer mixed with powder luminophor ($\text{Gd}_2\text{O}_2\text{S:Tb}$), image intensifier, CCD matrix, and fast lens system. Efficiency of disperse fast neutron screens and the effects of X-ray emission, scattered neutrons, and geometry of measurements on the quality of the image are also described.

Dynamic neutron radiography (DNR) measurements were performed (Balaskó et al. 2001) at the thermal channel of the 10 MW Budapest Research Reactor with a collimator ratio $L/D = 170$. The $10^8 \text{ cm}^{-2} \text{ s}^{-1}$ thermal neutron flux at the sample position of a beam with diameter of 150 mm and the 40 ms imaging cycle rendered the medium speed movements up to about 2.4 m/s possible. The light from an NE 426 converter screen was detected by a high sensitivity video camera. The neutron images of $\sim 200 \mu\text{m}$ resolution were displayed on a monitor and stored by an S-VHS recorder. This neutron imaging system provides a unique possibility to visualize various hydrogen-containing materials inside closed objects. A similar electronic imaging system based on a commercially available image intensifier tube and a low-cost CCD camera has been used (Shaikh et al. 2001) for visualization and analysis of water/air, water/vapor two-phase flow inside metallic pipes under high temperature and pressure conditions. Most of the cladding metals such as aluminum or steel are transparent to neutrons while hydrogenous materials such as water are relatively opaque which makes neutrons a unique tool

■ Fig. 32.5

Fast neutron luminescent CCD-detector on the basis. 1 – CCD-matrix, 2 – lens system, 3 – mirror, 4 – luminescent screen, 5 – sample, 6 – image intensifier



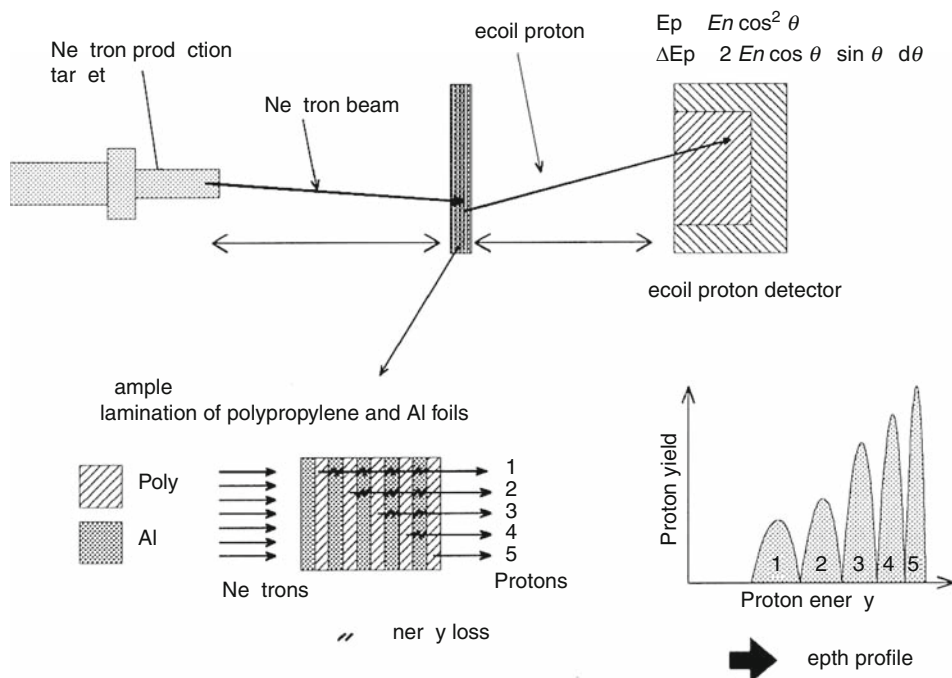
for visualizing the flow pattern. The fully automated neutron radiography system (DIANE) based on a sealed tube neutron generator is commercially available (Cluzeau et al. 1994). The necessary exposure fluence is about $10^{12}/\text{m}^2$ which can be produced at a 3 m source-object distance within 1 min by an intense neutron generator of $5 \times 10^{12}/\text{s}$ output rate.

Associated particle timing based on D-D neutrons was applied successfully (Evans and Mutamba 2002) for imaging an aluminum box. A combination of a Si detector for charged particles and an NaI(Tl) scintillator for induced gamma rays yielded a time resolution of 0.4 ns assuring a spatial resolution of better than 1 cm.

Knowledge of the concentration and spatial distribution of hydrogen in solids is required in many fields of science and technology. Therefore the development of such a hydrogen depth profiling method by which over 100 μm depth can be analyzed is indispensable. The drawback of elastic recoil detection and resonant nuclear reaction methods is that the depth is limited to several micrometers and serious radiation damage may occur. However, a fast neutron beam as a probe via the $\text{H}(n,p)$ reaction is nondestructive and can extend the depth to be analyzed beyond 100 μm . The energy distribution of recoiled protons is related to the depth profile of hydrogen. A fast neutron profiling method is based on the combination of an imaging plate (IP) and a polyethylene film as a converter. An experimental setup for the depth profiling is shown in Fig. 32.6. Using an appropriate neutron energy in the 5–15 MeV interval and a converter thickness close to the proton range, fairly clear images could be obtained (Miura et al. 2000; Sanami et al. 2000).

Fig. 32.6

Schematic view of the experimental setup and principle of NERD used for depth profiling



32.5 Fast Neutron Irradiation Effects in Solids

Recently, both steady-state and pulsed fast neutron generators have been applied to the investigation of radiation damage of metals, alloys, semiconductors, and high T_c ceramics and to nuclear heating of superconductors by prompt reaction products and long-lived radioisotopes. Of the wide range of applications a few typical examples are discussed in this review (Csikai 1995).

The irradiation of solids with fast neutrons results in the displacement of atoms from their lattice sites; the resultant interstitials and vacancies can cause various radiation damage phenomena. In addition, the determination of H and He gas production as well as the neutron multiplication by 14 MeV-neutron-induced (n,p), (n, α) and (n,2n) reactions, respectively, in the construction materials of fusion reactors is very important. Studies on the tritium breeding and outgassing efficiency for different blanket materials are also important tasks.

Some physical parameters related to the radiation effects which can be studied with small neutron generators are as follows:

Determination of the average range of recoil atoms by measuring the activities (A) of catcher foils placed on the surface of a sample of thickness d . (Note that r is used for the range of recoil atoms instead of the usual notation of R . The reason for this is that the latter could be confused with the reaction rate which is also denoted by R .) The mean projected range $\langle r \rangle$ of recoil atoms in forward and backward directions are given by the ratios of the released to the produced radioactive atoms, that is, $\langle r_f \rangle = (A_f/A_t)d$ and $\langle r_b \rangle = (A_b/A_t)d$, where $A_t = A_{\text{sample}} + A_{\text{catcher}}$ while the mean range $\langle r \rangle$ is obtained from $\langle r \rangle = [(A_f + A_b)/A_t]d$. The mean range of recoil atoms is between 10 and 1,000 nm in 14 MeV-neutron-induced reactions. Both the mean range and the value of d are customarily given in mg/cm². These data are also important for the elemental analysis of thin layers at which the released atoms should be taken into account. Therefore, for the elemental analysis of thin layers by neutron-induced reactions the knowledge of the $\langle r \rangle$ versus d function is required.

For the investigations on the release of foreign and lattice atoms by diffusion or evaporation from metals and alloys, the activated sample is placed into a vacuum chamber and the released radioactive atoms are collected by catcher foils. The activity of these foils is measured as a function of time at different sample temperatures. Data on the release of alloying elements from metallic compounds and alloys are required not only by solid state physics but also by high-tech industry and fusion technology.

The diffusion coefficients of tracers and the displacement of lattice atoms and their activation energies can also be measured (Sudár et al. 1977). Using fast neutrons, radioactive tracers can be produced homogeneously in extended samples. For example, the measurement of the diffusion coefficient of the ^{24}Na produced in $^{27}\text{Al}(n,\alpha)$ reaction for different alloys has a great practical importance, because a number of alloys used in reactor technology contain aluminum (e.g., the reactor fuel can).

Production rates of total hydrogen and total helium are important parameters in the evolution of the microstructure during the irradiation of solids, especially for fission and fusion reactor construction materials. These data can be measured by using a vacuum furnace equipment connected to a mass spectrometer for the detection of H and He gases produced in an irradiated bulk sample.

The production rate and the outgassing efficiency of tritium for different Li, Be, B compounds, and alloys used as blanket or structural materials (e.g., lithium–vanadium, lead–lithium and ceramic breeder, TiBe_{12}) can be determined for fusion neutrons by using

small neutron generators, even for the EURATOM fusion project (Gasparotto 2002). Data for the outgassing efficiency as a function of heating time and temperature for different samples are required. In addition, the behavior of hydrogen in metals can also be investigated by using deuterium and tritium as tracers. Studies on deuterium and tritium as substitutes for hydrogen in solids are of considerable interest to a better understanding of the depth profile, trapping, reflection, and diffusion of hydrogen implanted into different samples like metals, semiconductors, metallic glasses, or high T_c ceramics. For deuterium the retention kinetics, concentration profile, and the saturation yield can be determined via the $^2\text{H}(\text{d},\text{p})$ and $^2\text{H}(\text{d},\text{n})$ reactions (Csikai et al. 1997).

Studies of the effect of 14 MeV neutron irradiation on semiconductor electronic components have an essential role, because many electronic instruments are used in intense fast neutron fields. Radiation effects can be observed at a fast neutron fluence in the order of $10^{10}/\text{cm}^2$ at 20°C . Changes in the main characteristics of electronic circuits depend strongly on the type of semiconductor components. For example, definite changes were observed in the operating characteristics of Si(Li) detectors, diodes, transistors, and integrated circuits after the irradiation with 14 MeV neutrons up to $\sim 10^{13}/\text{cm}^2$ fluence. Further investigations are needed to study the effect of self-recovery of the irradiated Si(Li) detectors and integrated circuits.

Irradiations of optical components (laser glasses, fiber optics) to measure any effects of 14 MeV neutrons on light transmission or the index of refraction was carried out in the last decades (Heikkinen 1989). Studies on the effect of fast neutrons on electro-optical components are also required.

Online and off-line investigations are in progress to study the effects of fast neutrons in solids using fluences in the range $\sim 10^{18}$ – $10^{15}/\text{cm}^2$. Samples and physical properties to be studied are as follows: metals and alloys (mechanical, microstructure, electrical resistivity), superconductors (critical current, temperature and field), and insulators (electrical and mechanical properties).

In recent years various types of high T_c superconducting ceramics have been developed. Studies of the effects of fast neutrons on the physical parameters of high T_c superconductors are of interest both for basic research and applications. In the case of multiphase $\text{YBa}_2\text{Cu}_3\text{O}_7$ and $\text{Tl}_2\text{CaBa}_2\text{Cu}_2\text{O}_8$ ceramics a fluence of about $10^{14}/\text{cm}^2$ can cause a definite change in the physical parameters (Bódi et al. 1994), for example, both the specific resistance R/R_{293} and the microwave absorption of the sample decrease significantly. A systematic investigation on the oxygen content of high T_c ceramics is also required. This can be measured with high accuracy by the detection of the 6.13 MeV gamma-line produced in the $^{16}\text{O}(\text{n},\text{p})^{16}\text{N}$ reaction.

32.6 Radiobiology with Fast Neutrons

Neutrons are of interest for cancer therapy because they produce protons and other densely ionizing particles (alphas, recoil nuclei) in tissue. The use of fast neutrons in cancer radiotherapy was stimulated by three radiobiological findings: the oxygen enhancement ratio (OER), the sensitivity of cells at different phases of the cell cycle, and the contribution of sublethal damage to cell reproductive death. Neutrons have advantages to treat those types of tumors which contain anoxic cells. The variation in radio sensitivity of cells in different phases is less for neutrons than for X-rays. The relative biological effectiveness (RBE) of neutrons is generally higher in tumors than in normal tissues. Taking into account the cross sections at 14 MeV and abundances of H, C, N, and O in tissues, about 65% of the absorbed dose is due to

neutron–proton elastic scattering. Therefore, the absorbed dose is proportional to the H content of the organs, that is, it is about 15% higher in fat tissue than in muscle ones, while it is much lower in bones.

The radiation therapy in practice requires from the neutron source a high dose rate, good depth dose, well-defined horizontal and vertical beams movable around the patient, and a variable beam size up to about $20 \times 20 \text{ cm}^2$. In addition, an average neutron yield of $4 \times 10^{12}/\text{s}$, as well as 125 cm specified source–screen distance (SSD), and 2 cm maximum source diameter are needed for cancer therapy. A typical treatment schedule for malignant diseases involves two fractions per week, modal tumor doses of 1.2–1.3 Gy per fraction, and total doses in the range of 14–21 Gy.

In order to estimate the induced activity, the neutron dose value and the effect of interfering reactions, the distributions of thermal, epithermal, and fast neutron flux densities should be determined in a bulk media or a phantom. The most commonly used dosimetry reactions are given in [Sect. 36.3 of the Appendix of this Volume](#). In the case of a phantom, the combination of the activation detectors and the physical integration methods is recommended for the determination of the volume averaged dose equivalent rates and through it the total dose absorbed by a given organ (Csikai et al. 1988).

32.7 Neutron Attenuation and Shielding

Neutron moderators, filters, absorbers, and shielding are used in many devices and facilities of experimental nuclear and high-energy particle physics and in nuclear technology as well. Extended neutron transporting media are considered in some large-scale projects like online analysis of bulky geological samples, such as coal and minerals (Watterson 2000), bulk hydrogen analysis using neutrons (IAEA 1998, 2001), design of blankets of fusion reactors, development of accelerator-driven transmutation of nuclear waste (NEA 2002; Reimer 2002), checking of neutron transport calculations for shielding, effects of nuclear weapons, etc.

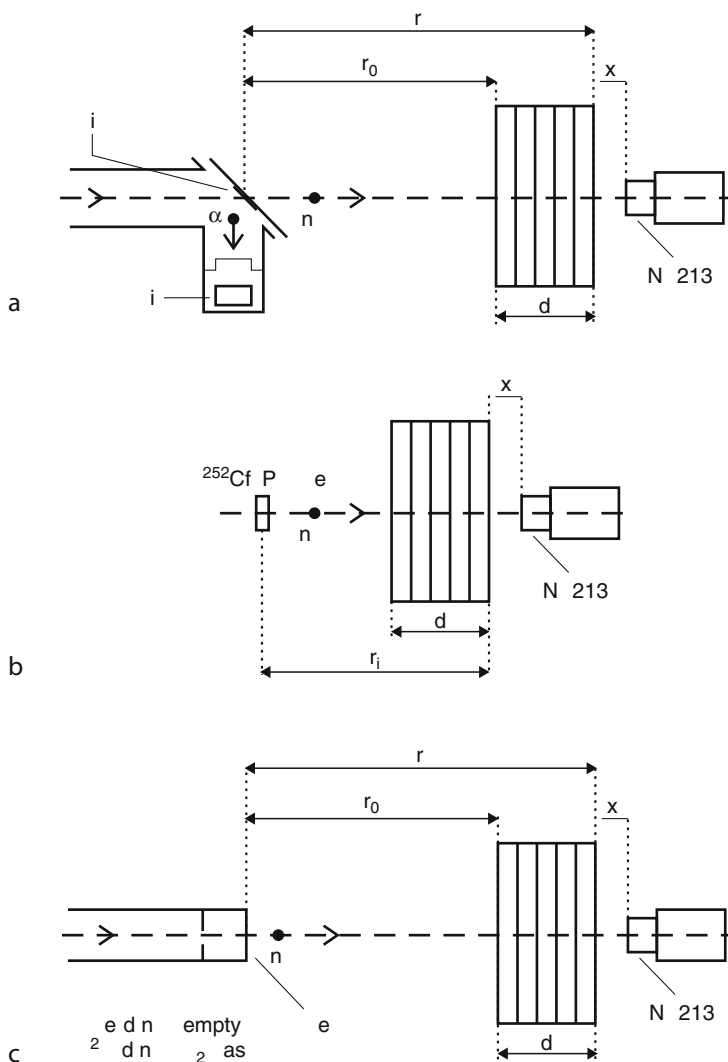
The characterization of the transport and the estimation of the radiation-induced damage and activation inside the medium require the knowledge of the expected neutron spectrum at each point of interest or of the average value over a large volume of the materials to be investigated. The above bulky units are typically planned on the basis of detailed Monte Carlo transport calculations using cross sections taken from different libraries. The consistency of the data used in the calculations can be checked experimentally by leakage spectrum measurements using simple geometries and known spectra of primary neutrons.

The leakage spectra of neutrons depend on the integrated density of the elements present between the neutron source and the detector, and on the interaction cross sections. A pulse height response spectrometer (PHRS) based on a relatively small volume of NE213 liquid scintillator with neutron–gamma discrimination can be used to measure the spectral yield of leakage neutrons in the 1.2–15 MeV range (Oláh et al. 1998), in addition to the multiple foil activation method. The latter has advantages in the determination of the spectral yield especially in the $E_{\text{th}} \leq E_n \leq 3 \text{ MeV}$ interval. Slabs and spheres of the most important shielding, construction, biological, and geological materials are used in these studies. The use of quasi-monoenergetic $^2\text{H}(\text{d},\text{n})$, $^3\text{H}(\text{d},\text{n})$ neutrons, and broad spectra of $^9\text{Be}(\text{d},\text{n})$, ^{252}Cf , Pu–Be source neutrons can assure the integral tests of the differential data. Recently, the backscattering spectrometry as a tool for elemental analysis of bulky samples based on the broad spectrum of Pu–Be neutrons has been investigated (Csikai and ElAgib 1999). The broad spectrum of

Pu-Be neutrons can cover a large energy interval (1.5–8 MeV) of the elastic scattering cross sections (σ_{EL}) of C, N, and O. Therefore, the spectral yields of backscattered neutrons are affected by the structures present in the $\sigma_{\text{EL}}(E_n)$ functions and so the reaction rate versus incident neutron energy is given by $R(E_n) = Y_0(E_n) \sigma_{\text{EL}}(E_n)$, where $Y_0(E_n)$ is the relative yield of the source neutrons while the $\sigma_{\text{EL}}(E_n)$ data are taken from different libraries. The geometrical arrangements used for a neutron leakage and backscattering spectrometries are shown in ► Fig. 32.7. Some typical spectra compared with the calculated values are shown in ► Fig. 32.8.

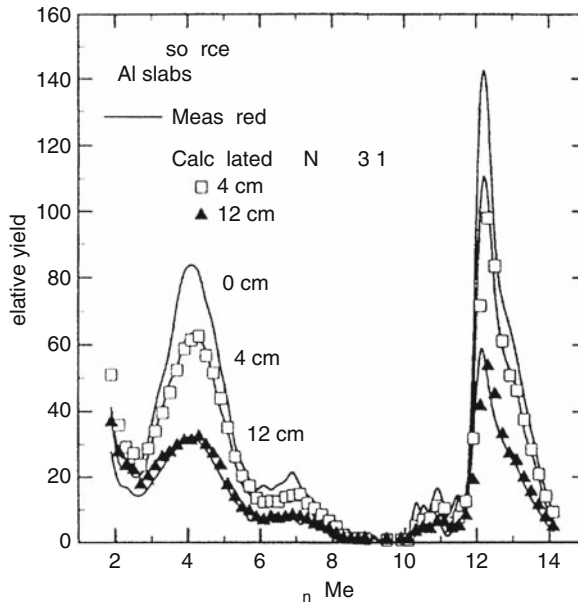
► Fig. 32.7

Setup geometries for leakage spectra measurements ($1.2 \leq E_n \leq 15 \text{ MeV}$)



■ Fig. 32.8

Measured and calculated leakage spectra of $^2\text{H}(\text{d},\text{n})$ source neutrons for Al slabs at $E_d = 9.4$ MeV



Among the neutron sources, the low voltage (100–200 kV) D-T 14 MeV generators play a special role in many applications (standard cross sections, activation and prompt radiation analysis, irradiation effects, radiography, well logging, shielding). Therefore, the flux density distributions of thermal and primary 14 MeV neutrons have been measured in different source-sample-detector geometries and calculated for different configurations of bulk samples (Ali et al. 1995). On the basis of these results, the differential and integrated reaction rates as a function of sample thickness could be determined.

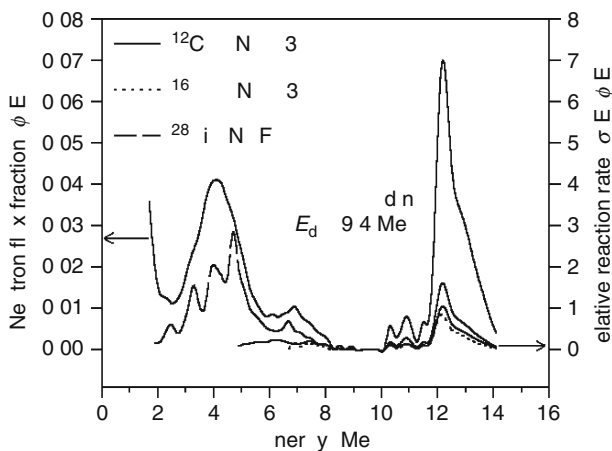
The removal cross section is a useful parameter for the characterization of the attenuation property of shielding materials. The flux of neutrons of energy E from a point source is given by

$$\Phi(x, d, E) = Y \frac{e^{-\Sigma(E)x}}{4d^2\pi} \quad (32.12)$$

where d , Y , x , and Σ are the distance from the source (cm), the source strength (s^{-1}), the shield thickness (cm), and the macroscopic removal cross section (cm^{-1}), respectively. Using either the activation or the PHRS methods, the value of $\ln(\Phi d^2)$ plotted against x results in a straight line from the slope of which Σ can be determined for different geometries and energies. The samples, in general, are slabs with dimensions of $30 \times 30 \text{ cm}^2$ and disks of 30 cm diameter. The thickness is changed in the range $0 \leq x \leq 25$ cm. The values of macroscopic removal cross sections of fission, 14 and 3 MeV neutrons for elements and some compounds are given in the literature (Nargolwalla and Przybyłowicz 1973; Csikai 1987, 1995). A comparison of the Σ values measured by TOF technique indicates the effect of sample-detector geometry on the removal cross section.

In general the three-dimensional Monte Carlo transport codes MCNP-4A, -4B, -4C are used to predict the measured spectra. Point-wise cross sections from FENDL/E-1 are used mainly in

■ Fig. 32.9

Neutron flux fraction and reaction rate versus neutron energy for a $^2\text{H}(\text{d},\text{n})$ source

the calculations. These data were derived by MacFarlane from ENDF/B-VI, JENDL-3.1, and BROND-2 evaluations using the NJOY code system for different elements. The ENDF/B-IV and ENDF/B-V libraries are also used in continuous energy calculations (Jordanova et al. 1999).

As shown in ► Fig. 32.9 the spectrum-averaged integrated reaction rates and through them the possible use of the prompt gamma method for the detection of C, O, and Si depends strongly on the type of the neutron source. The integrated reaction rates, R , can be determined as a function of sample thickness x using the leakage spectra of different source neutrons. The $R(x)$ function is given by

$$R(x) = \int_{E_{thr}}^{\infty} \Phi(E_n, x) \sigma(E_n) dE. \quad (32.13)$$

Recent investigations have shown that the rate function $R(d)$ depends exponentially on the sample thickness, that is,

$$R(d) = \int_0^d R(x) dx = R_0 e^{-bd} \quad (32.14)$$

where the attenuation parameter b is related to the spectrum of the source neutrons and the shielding materials.

32.8 Editors' Notes

1. Charge coupled devices are silicon chips containing a matrix of potential wells that can trap electrons released by radiation. Since the size of the potential wells is only a few micrometers, they have good spatial resolution, a useful feature for electronic imaging (p. 1684).

References

- Ali MY, El-Megrab AM, Jonah SA, Su D, Váradi M, Csikai J (1995) Nucl Geophys 9:203
- Aoki T, Baba M, Ibaraki M, Miura T (2000) Feasibility study on non-destructive analysis of light elements by fast neutron back-scattering technique, radiation detectors and their uses. In: Sasaki S, Shibata T, Takahashi H, Nakazawa M (eds) KEK proceedings 2000-14, KEK, Japan, p 163
- Balaskó M, Sváb E, Körösi F (1998) Neutron radiography imaging of hydrogen containing materials, IAEA/PS/RCM98-2, Bulk hydrogen analysis using neutrons. Report of the Third Research Co-ordination Meeting, International Atomic Energy Agency, Vienna
- Balaskó M, Sváb E, Körösi F (2001) Neutron radiography imaging of hydrogen containing materials, F1-RC-655.3, Bulk hydrogen analysis using neutrons. Report of the Third Research Co-ordination Meeting, International Atomic Energy Agency, Vienna
- Berg RS, Jacobs EL (1983) IEEE Trans Nucl Sci NS-30:1459
- Bódi AC, Csikai J, Kirschner I (1994) Z Phys B95:181
- Bódy Z, Csikai J (1987) Data for 14 MeV neutron activation analysis. Handbook on Nuclear Activation Data Technical Reports 273, International Atomic Energy Agency, Vienna, p 261
- Brown DR, Gozani T, Loveman R, Bendahan J, Ryge P, Stevenson J, Liu F, Sivakumar M (1994) Nucl Instrum Meth A 353:684
- Buczko CsM, Borbély A (1978) J Radioanal Chem 42:393
- Buczko M, Dezső Z, Csikai J (1975) J Radioanal Chem 25:179
- Bufler A, Brooks FD, Allie MS, Bharuth-Ram K, Nchodu MR (2001) Nucl Instrum Meth B 173:483
- Chen G, Lanza RC (2001) Fast neutron resonance radiography for elemental mapping, F1-RC-655.3, Bulk hydrogen analysis using neutrons. Report of the Third Research Co-ordination Meeting, International Atomic Energy Agency, Vienna
- Cinausero M, Viesti G (2000) The EXPLODET project, Progress Report 1999, edited by Cinausero M, Viesti G, DFPD 1/NP/00-January 2000, Padova, Italy
- Clayton CG, Wormald MR (1983) J Appl Radiat Isot 34:3
- Cluzeau S, Huet P, Le Tourneur P (1994) Nucl Instrum Meth B 89:432
- Csikai J (1987) Handbook of fast neutron generators. CRC Press, Boca Raton, FL
- Csikai J (1989) Nucl Instrum Meth A 280:233
- Csikai J (1992) Nuclear data for geology and mining. In: Qaim SM (ed) Nuclear data for science and technology. Springer, Berlin/Heidelberg, pp 656–659
- Csikai J (1995) Use of small accelerator and isotope neutron sources in materials research. In: Vourvopoulos G, Paradellis T (eds) SPIE proceedings, neutrons and their applications, vol 2339. Bellingham, Washington, DC, p 318
- Csikai J, Buczko CsM (1999) Appl Radiat Isot 50:487
- Csikai J, ElAgib I (1999) Nucl Instrum Meth A 432:410
- Csikai J, Váradi M, Buczko CsM, Sudár S (1988) Nucl Instrum Meth A269:287
- Csikai J, Szegedi S, Oláh L, Ibrahim SM, El-Megrab AM, Molla NI, Rahman MM, Miah RU, Habbani F, Shaddad I (1997) Nucl Instrum Meth A 397:75
- Csikai J, Király B, Dóczy R (2001) Application of neutrons to plastic landmines detection, 2nd RCM on Nuclear Demining Techniques. Report IAEA/PS/RC-799-2, International Atomic Energy Agency, Vienna
- Csikai J, Király B, Buczko CsM (2002a) Nucl Instrum Meth A 480:166
- Csikai J, Király B, Sanami T, Michikawa T (2002b) Nucl Instrum Meth A 488:634
- Demény A, Dede KM, Vas L (1988) Nucl Geophys 2:15
- Dokhale PP, Hussein EMA (1997) Appl Radiat Isot 48:973
- Dokhale PA, Csikai J, Oláh L (2001) Appl Radiat Isot 54:967
- Evans CJ, Mutamba QB (2002) Appl Radiat Isot 56:711
- Evans CJ, Pető GC, Al-Lehyani S, Darko JB (1997) Appl Radiat Isot 48:257
- Evans RJ, Jupp ID, Lei F, Ramsden D (1999) Nucl Instrum Meth A 422:900
- Gasparotto M (2002) Tritium breeding and materials, EFDA-STAC-T(02)-1/3.2-Annex 5
- Gozani T (1994) Nucl Instrum Meth A 353:635
- Heikkinen DW (1989) Nucl Instrum Meth B 40/41:1162
- Hlavác S (2001) Application of nuclear techniques to anti-personnel landmine identification. Research Coordination Meeting, St. Petersburg, Report IAEA/PS/RC-799-2, International Atomic Energy Agency, Vienna
- IAEA (1996) Manual for troubleshooting and upgrading of neutron generators. IAEA-TECDOC-913, International Atomic Energy Agency, Vienna
- IAEA (1998) Bulk hydrogen analysis using neutrons. Report of the Third Research Co-ordination Meeting IAEA/PS/RCM98-2, International Atomic Energy Agency, Vienna
- IAEA (2000) Use of accelerator based neutron sources. IAEA-TECDOC-1153, International Atomic Energy Agency, Vienna
- IAEA (2001) Bulk hydrogen analysis using neutrons. Report of the Third Research Co-ordination Meeting, Report F1-RC-655.3, International Atomic Energy Agency, Vienna
- IAEA (2002) Reference neutron activation library. IAEA-TECDOC-1285, International Atomic Energy Agency, Vienna

- Jonah SA (2001) Development of neutron-based facilities for bulk H analysis of energy minerals, Bulk hydrogen analysis using neutrons. Report of the Third Research Co-ordination Meeting, International Atomic Energy Agency, Vienna
- Jordanova J, Oláh L, Fenyvesi A, El-Megrab AM, ElAgib I, Darsono KU, Csikai J (1999) Nucl Instrum Meth A 42:522
- Király B, Csikai J (2000) Appl Radiat Isot 52:93
- Mikarov VI, Andreev AV, Zhitnik IA, Makarov SA, Koshelev AP, Bogolyubov EP, Ryzhkov VI, Tukarev BA, Krutov VV, Kuzin SV, Pertsov AA (1998) The development of fast neutron radiography and laminography methods on the basis of a portable equipment. IAEA/PS/RCM98-2, Bulk hydrogen analysis using neutrons, Report of the Third Research Co-ordination Meeting, International Atomic Energy Agency, Vienna
- Mikarov VI, Zhitnik IA, Barmakov JN, Isakov AI, Bogolubov EP, Ryzhkov VI, Koshelev AP, Tukarev BA, Sosin NP, Waschkowski W (2001) Investigation of prospects of fast neutron radiography on the basis of a portable equipment. F1-RC-655.3, Bulk hydrogen analysis using neutrons, Report of the Third Research Co-ordination Meeting, International Atomic Energy Agency, Vienna
- Mills WR, Stromswold DC, Allen LS (1991) Nucl Geophys 3:1
- Miura T, Hiroisi T, Aoki T, Sanami T, Nakamura T (2000) Development of fast neutron profile method, Radiation detectors and their uses, In: S. Sasaki, T. Shibata, H. Takahashi and M. Nakazawa, (eds) KEK proceedings 2000-14, edited by, (KEK, Japan) p. 102.
- Mohapatra DK, Reddy CP (2001) Appl Radiat Isot 55:693
- Morris GR, Bush CH, Reichardt JW (1983) IEEE Trans Nucl Sci NS-30:1648
- Nargolwalla SS, Przybyłowicz EP (1973) Activation analysis with neutron generators. Wiley, New York
- NEA (1994) Table of simple integral neutron cross section data from JEF-2.2, ENDF/B-VI, JENDL-3.2, BROND-2 and CENDL-2. JEF Report 14, OECD Nuclear Energy Agency, Issy-les-Moulineaux
- NEA (2001) Nuclear production of hydrogen. First Information Exchange Meeting Paris, OECD Nuclear Energy Agency, Issy-les-Moulineaux
- NEA (2002) Accelerator-driven systems (ADS) and fast reactors (FR) in advanced nuclear fuel cycles. Nuclear Development, OECD Nuclear Energy Agency, Issy-les-Moulineaux
- Oláh L, El-Megrab AM, Fenyvesi A, Majdeddin AD, Dóczi R, Semkova V, Qaim SM, Csikai J (1998) Nucl Instrum Meth A 404:373
- Overley JC (1987) Nucl Instrum Meth B 24:1058
- Proctor R, Yusuf S, Miller J, Scott C (1999) Nucl Instrum Meth A 422:933
- Przewlocki K, Mills WR, Givens WW (1984) High resolution gamma-ray spectroscopy for well logging, INDC(NDS)-162/GM. International Atomic Energy Agency, Vienna
- Reimer P (2002) Fast neutron induced reactions leading to activation products: selected cases relevant to development of low activation materials, transmutation and hazard assessment of nuclear wastes. Thesis, D38 Cologne University, Germany, Jül-3980
- Rynes J, Bendahan J, Gozani T, Loveman R, Stevenson J, Bell C (1999) Nucl Instrum Meth A 422:895
- Sanami T, Baba M, Saito K, Hirakawa N (2000) Nucl Instrum Meth A 440:403
- Sawa ZP (1993) Nucl Instrum Meth B 79:593
- Schweitzer JS, Ellis DV, Grau JA, Hertzog RC (1988) J Radiat Appl Instrum Part E 3:175
- Shaikh AM, Sinha A, Rajagopal H (1998) Bulk hydrogen analysis using neutrons. IAEA/PS/RCM98-2, Bulk hydrogen analysis using neutrons, Report of the Third Research Co-ordination Meeting, International Atomic Energy Agency, Vienna
- Shaikh AM, Sinha A, Rajagopal H (2001) Bulk hydrogen analysis using neutrons. F1-RC-655.3, Bulk hydrogen analysis using neutrons, Report of the Third Research Co-ordination Meeting, International Atomic Energy Agency, Vienna
- Smith DL, Micklich BJ (2000) Nuclear data needs for non-intrusive inspection. Advisory Group Meeting on "Long Term Needs for Nuclear Data Development," Vienna, 28 November 1–December 2000
- Sudár S, Csikai J, Buczkó CsM (1977) Z f Metallkunde 68:740
- Tittle CW, Burger C, Mathis G, Veneruso AF (1985) Nucl Instrum Meth B 10/11:1038
- Viesti G, Cinausero M, Cufaro-Petroni N, D'Erasmo G, Fabris D, Fioretto E, Fonte R, Lunardon M, Lazzizzera I, Nardelli G et al (1999) Nucl Instrum Meth A 422:918
- Vilaithong T, Singkarat S, Tippawan U (2000) Utilization of a pulsed D-T neutron generator. IAEA-TECDOC-1153, Use of accelerator based neutron sources, International Atomic Energy Agency, Vienna, p 15
- Vourvopoulos G (1994) Nucl Instrum Meth B 89:388
- Watterson JIW (2000) A review of accelerator based neutron sources and their applications. IAEA-TECDOC-1153, 2000, Use of accelerator based neutron sources, International Atomic Energy Agency, Vienna
- Watterson JIW, Mumba NK, Makhabane JL (1995) Nucl Geophys 4:333



33 Chemical Applications of Ion Accelerators

*E. Koltay*¹ · *F. Pásztí*^{2,†} · *Á. Z. Kiss*¹

¹Institute of Nuclear Research (ATOMKI), Hungarian Academy of Sciences, Debrecen, Hungary

²KFKI Research Institute for Particle and Nuclear Physics, Budapest, Hungary

33.1	<i>Detection of Particle-Induced X-Ray</i>	1697
33.1.1	Characteristics of the Method	1697
33.1.2	Physical Background of PIXE	1698
33.1.3	Instrumental Background	1699
33.1.3.1	Internal Beam PIXE Chambers	1700
33.1.3.2	External Beam PIXE Chambers	1701
33.1.3.3	Micro PIXE Facilities	1703
33.1.4	Quantitative Analysis	1705
33.1.4.1	Spectrum Evaluation	1705
33.1.4.2	Deducing Concentrations	1705
33.1.4.3	Concentrations in Inhomogeneous Samples	1707
33.1.5	Analytical Characteristics of PIXE	1708
33.1.6	Fields of Application	1711
33.2	<i>Analysis by Elastic Scattering of Charged Particles (RBS and ERD)</i>	1712
33.2.1	Theoretical Background	1712
33.2.2	Rutherford Backscattering Spectroscopy, RBS	1715
33.2.2.1	Energies	1715
33.2.2.2	Intensity	1717
33.2.3	Elastic Recoil Detection, ERD	1718
33.2.4	Separation	1718
33.2.5	Channeling Effect	1719
33.2.6	Microbeam	1721
33.2.7	Secondary Effects	1721
33.2.8	Instrumentation	1721
33.2.9	Fields of Application	1722
33.3	<i>Nuclear Reaction Analysis (NRA)</i>	1722
33.3.1	Characteristics of the Method	1722
33.3.2	Physical Background of NRA	1724
33.3.3	Instrumentation	1725

[†]Deceased

33.3.3.1	Ion–Ion Reactions	1725
33.3.3.2	Ion–Gamma Reactions	1726
33.3.4	Quantitative Elemental Analysis	1727
33.3.4.1	Spectrum Evaluation	1727
33.3.4.2	Determination of Concentrations	1729
33.3.4.3	Depth Profiling	1730
33.3.5	Fields of Application	1731
33.4	<i>Editors' Note</i>	1732

Abstract: This chapter discusses the basic principles of analytical methods based on positive ion beams from particle accelerators. The methods, namely, particle-induced X-ray emission (PIXE), Rutherford backscattering spectroscopy (RBS), and nuclear reaction analysis (NRA) are described in detail. Besides the underlying physical processes, methodical questions, analytical capabilities, and typical fields of application are also discussed.

33.1 Detection of Particle-Induced X-Ray

33.1.1 Characteristics of the Method

Particle-induced X-ray emission (PIXE) is a combined process, in which continuum and characteristic X-rays are generated through the recombination of electrons and electron vacancies produced in ion–atom collision events during the slowing down of a beam of charged particles in an object. The unique correspondence between the energies of characteristic X-ray lines and the atomic numbers of the excited atoms makes PIXE a useful method in instrumental analytics. The characteristic features of PIXE as an analytical tool are as follows:

1. Applicability to the determination of absolute concentration of elemental constituents in a wide range of atomic number.
2. Easy sample preparation; practically nondestructive direct analysis of the surface of the original objects.
3. High sensitivity in trace element determination on small-volume samples.
4. High speed in the preparations and measurements.
5. Possibility of obtaining analytical information from microscopic sample areas combined with linear or two-dimensional automatic scanning over the sample surface.
6. Possibility of measuring depth distribution curves for selected elemental constituents below the sample surface.
7. Easy ways for the automation of the measurements and evaluation at an acceptable level of accuracy and precision.

The physical background and the basic processes underlying the PIXE method were first described, in pioneering papers, in the middle of the 1970s (F. Folkmann 1975; Johansson and Johansson 1976).

With the development of methodology, PIXE elemental analysis has become a versatile analytical tool in a continuously broadening field of applications. Detailed introduction to the technique and overviews on its interdisciplinary applications can be found in monographs and review papers (Johansson and Campbell 1988; Koltay 1988; Johansson et al. 1995) as well as in proceedings volumes of the international series of PIXE conferences 1–11 (Johansson 1977; Johansson 1981; Martin 1984; Van Rinveld et al. 1987; Vis 1990; Uda 1993; Moschini and Valkovic 1996; Malmqvist 1999; Campbell 2002. Budnar and Campbell 2005; Miranda and Ruvalcaba-Sil 2008) as well as in proceedings volumes of the International Conferences on Nuclear Microprobe Technology and Applications (Demortier 1982; Grime and Watt 1988; Legge and Jamieson 1991; Lindh 1993; Yang et al. 1995; Doyle et al. 1997; Prozesky et al. 1999; Moretto and Bonin Mosbah 2001; Takai and Kamiya 2003; Jaksic and Bogdanovic Radovic 2005; Osipovicz et al. 2007; Rajta et al. 2009).

33.1.2 Physical Background of PIXE

The PIXE process underlying the present analytical technique can be described in the following way.

The sample to be analyzed is composed of elements $k = 1, \dots, n$ with atomic numbers Z_k present in relative concentrations by weight $C(Z_k)$. It is bombarded by a particle beam of energy E_0 in the range of 10^5 – 10^6 eV delivered by a nuclear particle accelerator. Depending on the purpose of experiment, the bombarding beam is either formed with a diffuser foil and sets of collimator slits to get uniform distribution of current density over a spot of required diameter or focused down to μm size or smaller in an ion-optical particle microbeam channel. Either the sample may be irradiated in the evacuated beam transport channel or the beam can be transported through a thin window to an external irradiation site in the atmosphere. The total number of particles incident during the bombarding time is determined as the time integral of the beam current divided by the electron charge. As the bombarding particles gradually slow down in the subsequent layers of the sample they reach the layer between x and $x + dx$ with energy E , where a set of characteristic X-ray lines with energy $E_X = E_{j,Z_k}^X$ will be induced with the respective cross sections $\sigma_{j,Z_k}(E)$, where j denotes a selected X-ray line emitted by element Z_k . X-ray quanta are detected with an X-ray spectrometer of detection solid angle $\Omega/4\pi$, and the X-ray spectrum is generated by an electronic signal processor. Absorption terms $\exp(-\mu_i x_i)$ representing X-ray absorption between sample and detector as an effect of upper sample layers, energy filter foil, windows of the vacuum chamber and of the X-ray detector, and detector efficiency depending on the X-ray energy should be taken into account in deducing elemental concentrations from the intensities of X-ray lines. The characteristic X-ray lines of intensities Y_{j,Z_k} , which contain the analytical information, are superimposed on an X-ray continuum in the spectrum. This background is partly generated by intrinsic effects during bombardment. A further considerable component is caused by the charging up of the sample by the bombarding beam. Special experimental arrangements can be used for eliminating this effect. Minimum detection limits for the different elements in the sample are mainly determined by the intensity ratio of the characteristic lines to the respective value in background continuum.

The characteristic features of the processes involved are shown in panels (1) to (5) plotted in [Fig. 33.1](#).

1. From the values of the X-ray energies/lines the atomic number of the emitter atom can be uniquely determined. The K_α and K_β lines cover the energy range 0.1–110 keV for elements from lithium to uranium, while for L_α , L_β , and L_γ lines the energy range for elements from zinc to uranium is between 1 and 21.5 keV (Leroux and Think 1977; Sevier 1979). A schematic plot of the X-ray energies is given in panel (1) of [Fig. 33.1](#). A proper selection of K and L lines can result in optimum conditions for elemental analysis in a broad range of atomic numbers.
2. The detector efficiency for a conventional Si(Li) X-ray spectrometer is close to 1 in the energy interval between 1.3 and 20 keV indicated with vertical dotted lines. The low-energy cutoff can be assigned to X-ray absorption in the entrance window of the detector. The actual curves are plotted for two typical thicknesses of the window. Data for calculating the energy-dependent X-ray absorption coefficient can be found in (Berger and Hubbel 1987). At the high-energy side, the silicon detector becomes partly transparent for the X radiation, and the shape of the cutoff depends on the detector thickness. As shown by the crossing of horizontal and vertical dotted lines in panel (2) of [Fig. 33.1](#), elements with atomic

numbers $11 \leq Z \leq 92$ can be detected with high detection efficiency if K and L lines are used for the detection of elements with atomic numbers $Z \leq 47$ and $Z > 47$, respectively. It should be mentioned, however, that the low Z limit can be shifted to $Z \approx 6$ with the application of extra thin windows or even of windowless detectors (Uzonyi et al. 2001).

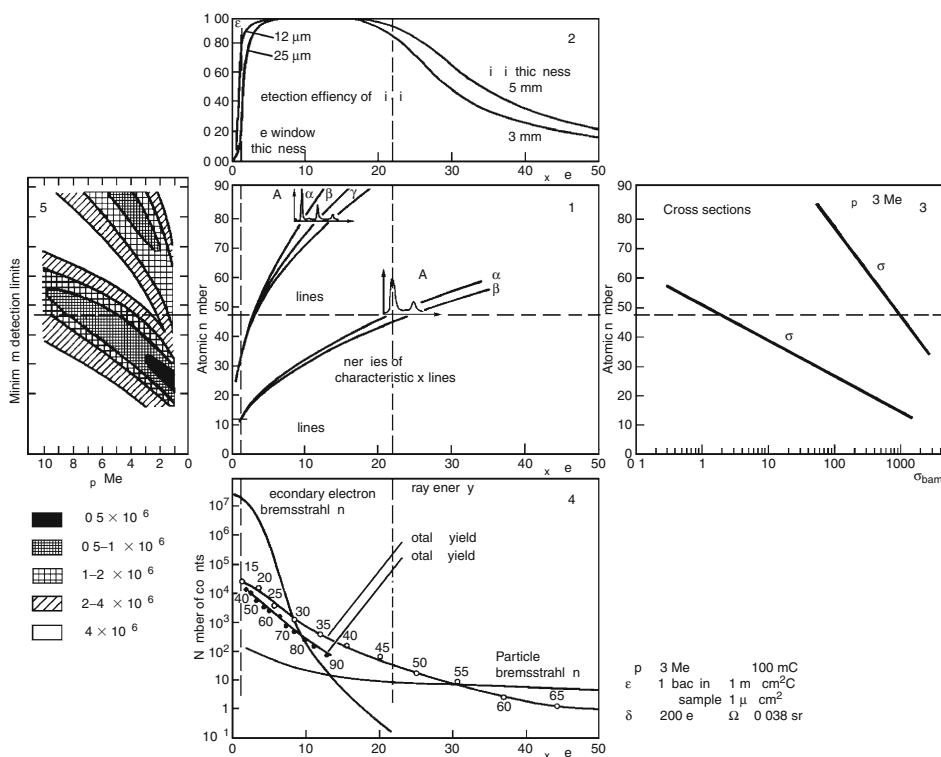
3. The cross sections of the excitation of X-ray lines exhibit a strong decrease with the bombarding energy. The dependence of total cross sections σ_K and σ_L on atomic number is shown for 3 MeV proton bombarding energy (Gardner and Gray 1978; Cohen and Harrigan 1985) in panel (3) of [Fig. 33.1](#). The overall high cross-section values of the excitation process clearly indicate that PIXE can generally be used as a fast, high yield analytical procedure. The strong decrease of σ_K for high Z elements calls again for the application of L lines in the high Z region, in full correspondence with the conclusion drawn in point (2) from the trend of decreasing detector efficiency for high-energy K lines.
4. The continuous X-ray background present in the spectrum is produced in two main processes. On the one hand, the slowing of bombarding particles in the thick (sample + backing) structure of the sample results in a component decreasing with increasing X-ray energy. The physical parameters influencing the differential cross section of the process are the mass numbers and atomic numbers of the bombarding particles and the slowing medium, as well as the bombarding energy. On the other hand, the slowing of secondary electrons released by the bombarding particles from the sample, results in another bremsstrahlung continuum. It has a sharp high-energy cutoff at the maximum kinetic energy of the secondary electron given by a simple kinematic relation for the particle–electron collision event.¹ Calculated curves are presented in panel (4) of [Fig. 33.1](#) for the model case of a series of thin monoelemental samples made of layers of atomic numbers Z with $1 \mu\text{g}/\text{cm}^2$ thickness deposited on a carbon backing of $1 \text{ mg}/\text{cm}^2$ thickness. Here a comparison of total K- and L-line yields is shown for atomic numbers between 15 and 90 with calculated yields of the secondary electron bremsstrahlung and particle bremsstrahlung. The values of the bombarding proton energy E_p , total integrated proton charge q , detector parameters such as efficiency ε , energy resolution δ , and solid angle Ω are given on the right side of the drawing (Folkmann 1975).
5. The detection limit of the method for any given element is determined by the height of the respective characteristic X-ray lines relative to the background level around the lines. Therefore, data like those shown in panel (4) of [Fig. 33.1](#) could be used for the determination of minimum detection limits as the function of atomic number Z and bombarding particle energy E_p . In panel (5) of the figure, the minimum detection limits are plotted as functions of Z and E_p for protons as bombarding particles (Johansson and Johansson 1976).

33.1.3 Instrumental Background

PIXE analytical measurements are based on the use of particle beams generated in a nuclear accelerator covering an energy range of a few MeV. Proper physical conditions for irradiation of the sample and spectroscopic detection of X-rays emitted in PIXE processes can be ensured by special beam transport channels. Here the beam is formed either by a magnetic quadrupole lens system in the conventional beam transport channel of the accelerator or by a microbeam focusing system in a particle microprobe configuration. As passive elements, a beam scatterer foil and a combination of collimator and antiscattering slits are used to get a uniform distribution of current density over the beam spot on the target and to remove any beam halo formed by scattered particles, respectively. Further elements are used for positioning the

■ Fig. 33.1

The characteristic features of the particle-induced X-ray emission (PIXE) process. See text for details



samples and the X-ray spectroscopic detector in well-defined detection geometry, as well as for the accurate measurement of the number of bombarding particles. Furthermore, tools are available for a physical modification of the detected X-ray spectra for minimizing spectrum background and overload of the detection system. With the use of these elements, optimum detection limits can be obtained for selected preferred ranges of atomic numbers in the sample.

The bombarding particle beam is accelerated and transported in the high vacuum system of the accelerator. The X-ray detector unit is encapsulated in a separate clean vacuum system. The irradiation of the sample may be performed in vacuum or under atmospheric conditions, depending on the size, physical state, and other parameters of the sample. To define the physical conditions mentioned above, special PIXE chambers of internal beam and external beam configurations are used for in vacuo and atmospheric irradiations, respectively.

33.1.3.1 Internal Beam PIXE Chambers

In such an arrangement, schematically shown in [Fig. 33.2a](#), the irradiation of the sample takes place in the vacuum of the beam transport channel, while the detector with its separate vacuum volume looks on the sample through the entrance window of the detector formed by a thin foil. The two vacuum volumes are normally separated from each other either by in vacuo

or through-the-window arrangements. In the former case, the detector head penetrates the irradiation chamber, while in the latter case it is separated from the vacuum system of the accelerator by an air gap formed between the entrance window of the detector and a thin foil exit window on the chamber wall.

Detector windows, optional chamber windows, and the air gap formed between chamber and detector windows are X-ray absorbers, which modify the shape of the detected X-ray spectrum in an energy-dependent way. Optionally, additional absorbers can be made use of to optimize the analytical parameters. They are partly to keep away elastically scattered protons from the detector, and partly to improve the detection limits for elements with $Z > 20$ by cutting the background X-ray continuum, which is enhanced at low atomic numbers as shown in panel (4) of [Fig. 33.1](#).

Manually operated or automatic sample changers normally accept a batch of samples arranged in a set to be loaded together in the vacuum chamber. They facilitate a sequential irradiation of the individual samples in a fast serial analysis. Other arrangements permit the measurement of longitudinal or transversal elemental distributions in extended samples through a fine continuous sample advance along an axis perpendicular to the direction of the bombarding beam.

The number of bombarding particles is determined as the time integral of the bombarding current over the total irradiation time divided by the ion charge. Special current measuring methods are needed for two reasons. First, large PIXE cross sections permit the use of particle beam currents as low as 10^{-9} A to decrease the heat load delivered by the beam on the sample. In this way, an almost perfectly nondestructive analysis can be achieved. Second, disturbing effects caused by the bombarding beam through secondary electron emission and charging up of insulating sample material should be diminished to a tolerable level. For thin targets, which are transparent for the beam, the beam current measurement can be performed in a Faraday cup located behind the sample. (Faraday cups are briefly explained at the end of [Sect. 50.1 of Chap. 50, Vol. 5](#), on “Particle Accelerators.”) For thick samples, the whole chamber should be formed as a Faraday cup and kept insulated from the ground to permit current measurements toward the ground. The disturbing effects of secondary electrons can be suppressed by the use of biased collimator elements, which cut the electron trajectories within the chamber as a Faraday cup. An alternative method for the determination of the number of bombarding particles is offered by the monitoring of the current through the yield of particles elastically scattered from a compact beam chopper intermittently cutting a small fraction of the beam near the sample to be analyzed (Bartha and Uzonyi 2000). In this way, all the difficulties of beam-current measurements can be avoided.

The charging up of insulating samples by the particle beam builds up an electrostatic acceleration field in the neighborhood of the sample, which results in an enhanced secondary electron bremsstrahlung. The suppression of this background component can be achieved by the use of a small compact electron gun, which neutralizes the positive charge of the sample (Ahlenberg et al. 1975). The current of the electrons from the source also gets stopped within the Faraday cup formed by the chamber, so it does not interfere with the measurement of the particle beam current.

33.1.3.2 External Beam PIXE Chambers

Technical difficulties may appear in exposing samples to chamber vacuum in the case of large size objects, art treasures, special biological specimens, samples of liquid form, of high volatility

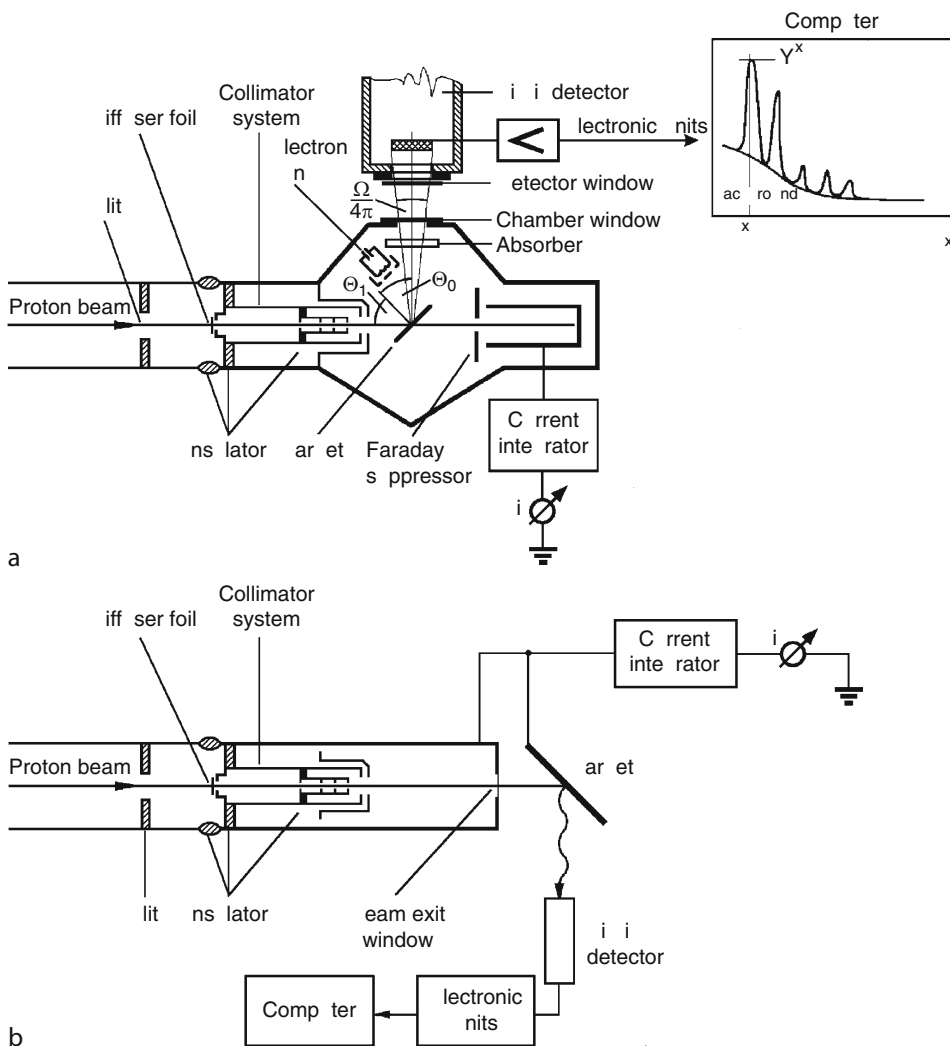
and/or heat sensitivity. Such difficulties may be overcome by the application of an external beam configuration, in which the bombardment takes place under atmospheric pressure (Katsanos et al. 1976; Khan et al. 1979).

In this arrangement, the bombarding beam is led to the air through an exit foil located at the exit of the beam channel behind the collimator set as shown in ▶ Fig. 33.2b. Exit window can be made of thin beryllium, aluminum, or synthetic Kapton foil. Beam bombardment of the metal foils will generate high γ -ray background from nuclear reactions; therefore, Kapton foils are sometimes preferred in spite of their shorter lifetime.

A special source of disturbing background appears in this arrangement when the beam excites the characteristic X-rays of gases present in the gap between the exit foil and the sample.

■ Fig. 33.2

Internal beam and external beam PIXE chambers (a and b, respectively). See text for details



Nitrogen and oxygen are too light elements to be detected in standard cases, but argon contributes with an intense background composed of argon K, argon escape peaks, and argon pileup peak at 2.957, 1.205, and 5.914 keV, respectively. (For atomic-electron binding energies and K X-ray energies see ▶ Sect. 11.4 in Chap. 11 of Vol. 1.) As a result, elements lighter than Cl can hardly be detected. To overcome this limitation, in some external beam configurations the air is replaced by helium gas in the window-to-sample gap.

Local heating in the beam spot on the sample surface is efficiently reduced by the cooling effect of the surrounding gas volume; therefore, the nondestructive character of the PIXE method is improved in this version.

Ionization along the beam trajectory within the gaseous environment has two effects. Firstly, it eliminates the disturbing effect of the charging up of insulating samples. Secondly, however, ionization and the emission of secondary electrons from the exit window render the determination of the intensity of the bombarding beam more difficult. It is conventional to measure the sum of currents on the exit window and on the sample for monitoring the measurements. Alternative methods are to measure the height of the argon X-ray line or the intensity of the particles elastically scattered from the exit window.

33.1.3.3 Micro PIXE Facilities

Elaborate special ion-optical systems of particle accelerators composed of strong focusing and transversal beam scanning elements offer an analytical tool for lateral two-dimensional mapping of elemental constituents in a sample. The ion-optical and technical details of these equipments called scanning particle microprobe (SPM) facilities are briefly described in ▶ Chap. 50 of Vol. 5 on “Particle Accelerators.” Periodic transversal deflections generated in two perpendicular dimensions will drive the fine-focused beam to scan over a selected area of the sample. When equipped with X-ray spectroscopy, elements known from conventional PIXE technique and with data acquisition system arranging spectroscopic information in synchronism with beam scanning in two-dimensional elemental maps, the system permits the application of the PIXE technique with a typical lateral resolution of the order of 1 μm .

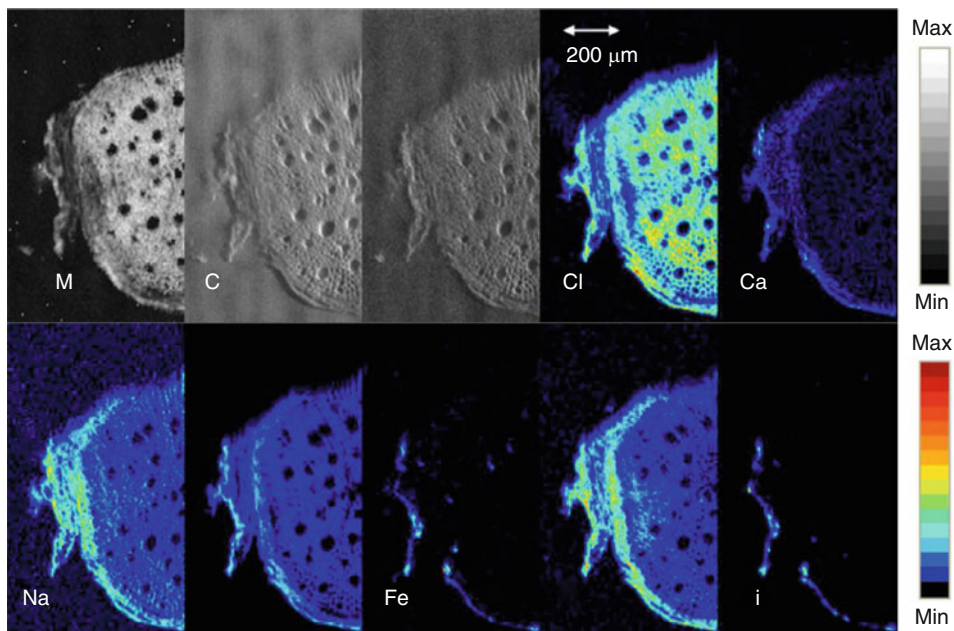
In a similar way, morphological (optical-type) images can be built up from simultaneously acquired counts of secondary electrons released from the sample during ion bombardment. Furthermore, scanning transmission ion microscopic (STIM) images may be obtained by mapping the numbers of ions passed through the scanned pixels in the sample. STIM images give information on the lateral distribution of areal density of the bombarded layer without giving any analytical information (Watt et al. 2009).

The quality of microPIXE maps combined with simultaneously built off-axis STIM image is illustrated in ▶ Fig. 33.3 showing the elemental localization in a root section of the plant *Bidens tripartitus* (Szikszai et al. 2008).

As best performance achieved in PIXE scans, a lateral resolution of <400 nm has been reported (Watt et al. 2002). Further decrease in beam spot size can be expected as a result of ongoing development work. Steps toward nanometer resolution are being taken by several groups (e.g., Watt et al. 2003; Glass et al. 2007; Andersson et al. 2008; Watt et al. 2009). In these nanobeam setups, the beam spot emerging from an above described microbeam system serves as an intermediate image for a second lens system. This system is formed by electron-optically optimized groups of quadrupole-lens configurations (doublets and/or triplets) and provides further demagnification. Several sets of precision-slit devices are arranged in proper positions

■ Fig. 33.3

The scanning transmission ion microscopic (STIM) energy loss image and true elemental PIXE maps of a *Bidens tripartitus* section. The thickness of the section was 20 μm , the scan size was $1,250 \times 1,250 \mu\text{m}^2$



to remove beam halos caused by ions scattered from construction elements of the long beam channel. In state-of-art nanobeam channels, a beam size of a couple of ten nanometers has been achieved.

Scanning particle microbeam facilities are competitive with commercially available electron microprobe analyzers. The replacement of electron beams by ion beams in SPM facilities results in highly improved minimum detection limits for elemental constituents in a sample. In the case of electron microprobe analyzers, characteristic X-rays are superimposed on the strong X-ray continuum from electron bremsstrahlung generated by the bombarding electron beam. This radiation background is orders of magnitude higher than the respective background component released by slowing ions in the PIXE process. Consequently, minimum detection limits determined by signal/background ratio in the spectrum, which amount typically to a few percent for most elements in the case of electron beams, will be improved by more than two orders of magnitude in micro PIXE analyses. The lateral resolution in optical and morphological information to be obtained in the form of maps built up from the intensities of secondary electrons released during beam scanning of the object is inferior in the SPM case due to larger beam sizes at the present normal level of ion beam focusing. However, the optical quality appearing in the X-ray maps in electron microprobes cannot be kept at the high level typical of the corresponding secondary electron image due to the broadening of bombarding electron beam through scattering in the depth of the sample. The interaction volume for the release of characteristic X-rays by bombarding electrons is increased in depth and diameter with respect to the volume participating in the emission of secondary electrons used in forming

the electron image. The lateral resolutions in X-ray elemental maps are comparable in electron and particle microprobe systems.

In recent years, the external beam technique has been subjected to successive steps of improvements to meet the serious requirements with respect to its application in microbeam setups. Among others, the objectives were solving the problems of increased accuracy of beam monitoring, reducing the scattering of the beam in exit windows, and making possible the simultaneous application of PIXE with other ion beam analytical (IBA) methods. A detailed description of one of the latest external microbeam facility can be found in the work of Salomon et al. (2008).

33.1.4 Quantitative Analysis

33.1.4.1 Spectrum Evaluation

The analytical information on the elemental composition of a sample can be deduced from a complex PIXE spectrum, in which characteristic X-ray lines emitted via transitions between different electron shells of the atoms in the sample are superimposed on an energy-dependent X-ray continuum. Yields $Y(Z)$ for a characteristic line of energy $E_{j,Z}^X$ belonging to a transition j in an atom of atomic number Z can be obtained by unfolding the spectra. For this purpose, computer codes have been elaborated. They are based on a least-squares fitting procedure optimizing a number of parameters in a model representing line shapes and background characteristics.² Corrections are also included for treating the dead-time problems and the effects caused by escape and pileup peaks. There are a number of software packages for the evaluation of PIXE spectra. Software packages known under the names of GEOPIXE (Ryan et al. 1990), GUPIX (Maxwell et al. 1989), PIXAN, PIXEKLM (Szabó and Borbély-Kiss 1993, 1999), PIXEKLM-TPI (Uzonyi and Szabó 2005), SAPIX (Sera and Futatsugawa 1996), WINAXIL (Vekemans et al. 1994), and WITSHEX (Lipworth et al. 1993) have been subjected recently to a systematic intercomparison procedure (Blaauw et al. 2002) and have been found to perform reasonably well in deducing peak areas belonging to elemental constituents.

33.1.4.2 Deducing Concentrations

The calibration of a PIXE system, i.e., the determination of sensitivity factors, which assign absolute concentration data to numbers of counts in X-ray peaks, can be performed in two different ways. First, sensitivity factors can be deduced theoretically or in a semiempirical way from calculated cross sections for X-ray excitation and from X-ray absorption data for the absorbents present between the points of emission and detection, in the actual experimental setup. Second, sensitivity factors can be deduced from measurements performed on standard samples consisting of pure elements or pure chemical compounds. The detection solid angle and the energy-dependent detector efficiency should also be determined.

The calibration procedure takes into account the slowing down and the absorption effects. The bombarding particle slows down along the depth of the sample, and thus the cross section of inducing X-ray depends on the depth of the sample. On the other hand, X-rays are absorbed along the thickness of the sample layer between the actual emission point and the entrance window of the X-ray detector.

For a thin uniform homogeneous sample with negligible energy, loss of the bombarding particle and no absorption of the X-rays in the sample, the yield of each X-ray peak can be calculated from the formula

$$Y(Z) = \frac{N_A \sigma_Z(E_0) \omega_Z b_Z \varepsilon_Z}{A_Z} M_a N = K(Z) M_a N, \quad (33.1)$$

where N_A denotes Avogadro's constant, $\sigma_Z(E_0)$ is the ionization cross section at proton energy E_0 , $\omega_Z(E_0)$ and b_Z denote fluorescence yield and branching ratio, respectively, ε_Z is the detection efficiency composed of solid angle $\Omega/4\pi$, absorption factors and absolute detector efficiency ε_{Z^*} for the bare detector, Z and A_Z are atomic number and molar mass, respectively, of the element with areal density M_a , while N stands for the number of bombarding particles. Calibration means the determination of thin target sensitivity factor $K(Z)$ as a function of the atomic number.

For a **thick homogeneous target** in which the bombarding particles are completely stopped and the emitted X-rays are subjected to considerable absorption in the source, the yield of each X-ray peak can be written as follows:

$$Y(Z) = \frac{N_A \omega_Z b_Z \varepsilon_Z}{A_Z} C_Z N \int_{E_0}^0 \frac{\sigma_Z(E) T_Z(E)}{S(E)} dE, \quad (33.2)$$

where C_Z is the concentration of element with atomic number Z , $S(E)$ denotes the stopping power (for its definition see [Eq. \(8.1\) in Chap. 8 of Vol. 1](#)), and

$$T_Z(E) = \exp \left(-\frac{\mu \cos \theta_i}{\rho \sin \theta_0} \int_{E_0}^E \frac{dE}{S(E)} \right) \quad (33.3)$$

gives the photon attenuation in the sample. Symbols θ_i and θ_0 denote the angles of beam incidence and X-ray detection, respectively, measured from the normal to the sample surface. For a sample of more than one bulk element, the resultant μ/ρ attenuation coefficient and stopping power should be deduced by summing over the corresponding data for the basic constituents.

A useful alternative method for calibration in the thick sample case is to perform thick target correction on thin-sample sensitivity factor $K(Z)$ by the help of a calculated function $I(Z)$ to be obtained by rewriting [Eq. \(33.2\)](#) to give

$$Y(Z) = N C_Z K(Z) I(Z) = N C_Z K(Z) \int_{E_0}^0 \frac{\sigma_Z(E) T_Z(E)}{\sigma_Z(E_0) S(E)} dE \quad (33.4)$$

The data should be made use of here on sample composition and thickness.

The above calibration methods are made somewhat inadequate by some effects pertinent to the matrix composition of the sample. They can easily be used in the case of samples the matrix of which is built of bulk elements of known concentrations, and the task is just the determination of trace elements, which do not contribute considerably to the slowing and absorption behavior of the matrix. In the opposite case, when bulk components of unknown

concentrations are to be analyzed, an iterative procedure can be used starting from arbitrary initial concentrations for the major constituents.

Another important matrix effect is the enhancement of X-ray emission through secondary X-ray fluorescence in thick samples. This effect can lead to a significant overestimation of concentration data for some combinations of elements, in which energy differences between the primary X radiation and absorption edge of the lighter component is small. Some numerical and analytical procedures offer more or less appropriate corrections for this effect.

It should be mentioned, that matrix effects disappear with decreasing sample thickness. In the calibration procedure for the thin-sample approximation, i.e., when measuring thin-sample sensitivity factors for K and L lines, standard foils of known areal density (also called surface density) are used regularly as calibration standards.

In the case of thick samples separate thick single-element standards can be made use of for each element to be analyzed with $C_{Z, \text{standard}} = 1$. In this procedure the concentration C_Z of element Z in the sample to be analyzed writes

$$C_Z = \frac{Y(Z) I_s(Z)}{Y_s(Z) I(Z)} \quad (33.5)$$

where the subscript “s” stands for standard.

An alternative way is given by the internal standard method, in which a particular element (most often yttrium) is added in known quantity to the sample to be analyzed. Special care should be taken of homogeneous mixing during addition. In this method an absolute determination of the bombarding particle current is not essential, furthermore matrix effects are well accounted for. The use of thick multielemental standards offers a relatively fast and simple way. However, differences in the composition of standards and samples to be analyzed make matrix corrections necessary if improved accuracy is needed.

Systematic comparison of the theoretical and experimental calibration methods proves that the determination of elemental concentrations can be performed with an overall accuracy of 3–5%; this number includes the errors appearing in spectrum evaluation as well.

33.1.4.3 Concentrations in Inhomogeneous Samples

In many practical cases, correction methods should be applied to allow for nonuniformities and inhomogeneities in the samples. Surface irregularities (Smit et al. 1984), clusterization of the minor components in binary alloys in the form of grains of different sizes (Respaldiza et al. 1987), influence of granular structure of the material (Markowicz et al. 1980), oxide layers appearing on the surface of samples (Rickards 1985) are cases to be treated using improved physical models. In the evaluation of micro PIXE data taken on single granules composing a sample, special care should be taken of the influence of the actual particle shape on slowing down and X-ray absorption processes (Jaksic et al. 1993; Bogdanovic et al. 1994).

The determination of in-depth distribution curves of minor constituents of a bulk may be of importance in the investigation of corrosion, diffusion, oxidation, and annealing processes and in studying surface coating layers. Within an interval of depth coordinate x not exceeding

the range of the bombarding particle such measurements can be evaluated on the basis of [Eq. \(33.2\)](#) by introducing the function $C_Z(x)$ in place of the concentration C_Z . Rewriting [Eq. \(33.2\)](#) with variable x the detected yield of the X-line at bombarding energy E_0 appears in the form

$$Y(Z) = kN \int_0^{R \cos \theta_i} C_Z(x) \sigma[E_0, E(x)] \exp(-\mu x / \cos \theta_0) dx, \quad (33.6)$$

where k is a constant, R is the range of the bombarding particle, $E(x)$ is the particle energy in depth x , and $\sigma[E_0, E(x)]$ is the local mean value of the cross section. Special deconvolution algorithms (Végh et al. 1978; Brissaud et al. 1985), applied to a series of experiments with incident bombarding energies varied over the appropriate energy interval, offer a technique for deducing the depth distribution of detected elements.

33.1.5 Analytical Characteristics of PIXE

Nondestructive character. The PIXE method is practically nondestructive. In many cases, samples can be used in their original form; external beam configuration can accept even large size objects. During analysis, samples are only subjected to a moderate heat load equivalent to the loss of beam energy within the small beam spot on the sample. This effect remains low in thin samples in which case the overwhelming part of the beam energy is dissipated outside the sample in the Faraday cup behind the target. For other sample thicknesses, too, the conventional values of 1–10 nA beam intensity and beam diameter of a few mm in macrobeam mode does not cause an appreciable modification of the state of the sample. However, in microbeam mode, a considerable increase may appear in beam current density in the well-focused beam spot. In internal beam version, the stability of the sample material against warm-up and vacuum environment should be considered. In external beam mode, local warm-up in the beam spot on the sample is efficiently reduced by the cooling effect of the surrounding gas volume; therefore, the nondestructive character of PIXE method is improved in this version.

Range of application. As explained in [Sect. 33.2.2](#), the lower and upper limits of the interval of atomic numbers to be covered by PIXE method are mainly determined by the thickness of detector window and detector crystal, respectively. In typical experimental setups, the lower limit is set at $Z = 13$, but it can be shifted down to $Z = 6$ with the application of extra thin detector windows. The upper limits can reach $Z = 92$. The PIXE method offers simultaneous multielemental analysis for the elements within the named intervals.

Analytical features. As a typical example of the form in which experimental data appear during PIXE analysis, [Fig. 33.4](#) presents an X-ray spectrum obtained on a sample of coarse fraction atmospheric aerosol deposited on a polycarbonate membrane filter of 7 μm thickness. The spectrum was taken with protons of 2 MeV bombarding energy in a run of 1,200 s and beam intensity of 30 nA. The physical conditions in this case correspond to the approximation of the thin uniform homogeneous sample. Full and dashed lines show curves fitted by the spectrum evaluation code to the total spectrum and to its continuous background, respectively. The general features of the spectrum can be well explained on the basis of the simplified diagrams in [Fig. 33.1](#).

The analytical parameters, minimum detection limits, accuracy, and speed, which determine the applicability of the PIXE method and are important from the point of view of its comparison with other competitive methods of instrumental analysis, can be deduced from the

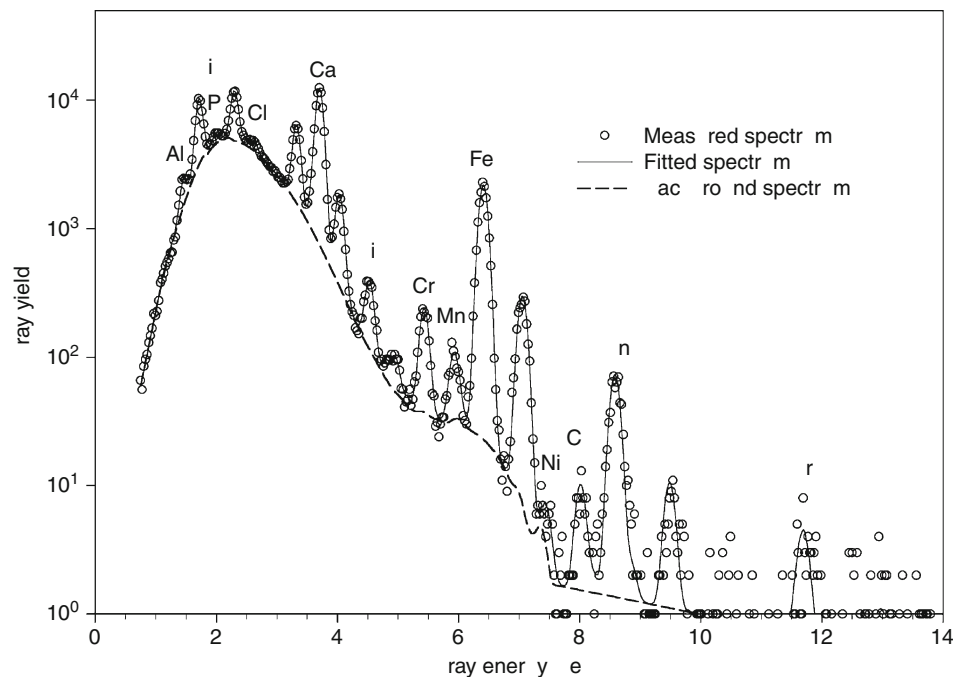
complete evaluation of the experimental data. These parameters are functions of the atomic number of the elemental constituents and may depend on the composition of the sample matrix, the atomic number of the element in question, the detection parameters, and the energy, type, and total number of bombarding particles.

The **minimum detection limit** for a given element in a sample is defined as the minimum concentration at which the X-line intensity equals three times of the standard deviation of the background in the respective interval of the spectrum. Its value is normally expressed in $\mu\text{g/g}$ units and depends on the experimental conditions, mainly through the actual shape of the background and the number of counts in the X-ray line. As shown in panel (5) in [Fig. 33.1](#), calculated for proton beams of 10 μC total collected charge and 1–10 MeV energy in the case of sample thickness (i.e., surface density) of 0.1 mg/cm^2 on carbon matrix, the minimum detection limit is around 1 $\mu\text{g/g}$ for a broad interval of the atomic number. The capabilities of the method in practical applications are illustrated in [Fig. 33.4](#), in which the minimum detectable limits are given in units ng/m^3 air for the case of the spectrum shown in [Fig. 33.5](#).

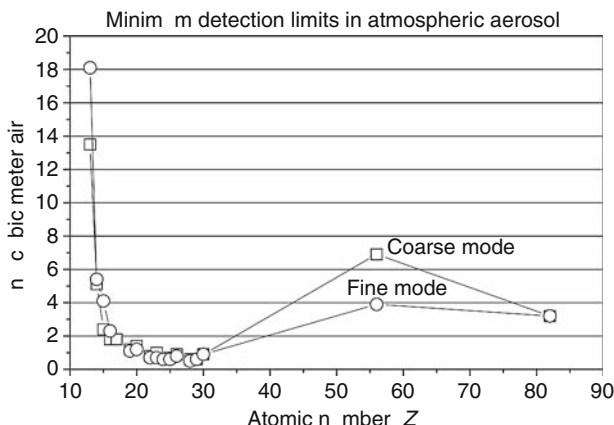
The **accuracy** defined as the deviation of deduced concentrations from the respective true values depends first on the accuracy obtained in the calibration of the measuring configuration. For thin samples, a careful calibration and evaluation procedure can result in the estimated accuracy of 2–3% between $22 \leq Z \leq 30$ and 5% between $11 \leq Z \leq 20$. However, it should be kept in mind that the analytical accuracy in measurements performed on actual thin samples may be degraded by effects pertinent to the applied sampling technique. As described in [Sect. 33.1.4.2](#) special care should be taken with regard to stopping, absorption, and matrix effects in thick sample cases.

Fig. 33.4

PIXE spectrum taken on an aerosol sample of coarse size fraction



■ Fig. 33.5

Minimum detection limits in PIXE analysis of atmospheric aerosol samples

The **speed** of the analysis is a parameter inversely correlated with the detection limits required because an increased statistical accuracy can be achieved by a longer time of spectrum acquisition. A couple of thousand second long measuring time is a typical compromise in most cases.

Selectivity. The good selectivity of PIXE is reduced for some pairs of elements by interference between K and L or M lines, emitted with energies close to each other. The interferences between pairs of sulfur K and lead M, titanium K and barium L, potassium K and indium L lines, respectively, can be mentioned as examples of practical importance. However, the selectivity of the method can be kept at acceptable levels by taking into account the known intensity ratios of K, L, and M lines of the interfering elements.

Chemical specification with high-resolution spectroscopy. The replacement of the commonly used Si(Li) X-ray spectrometer with a high-resolution wavelength-dispersive crystal spectrometer (Petukhov et al. 1999) opens a new field of applications of PIXE by resolving the pattern of satellite lines that is dependent on the chemical state of the atom. In such investigations, beams of multiply charged light heavy ions are preferentially used. The underlying physical processes and the quantitative features of the fine structures in the spectra to be used in chemical state analysis are the subjects of recent investigations.

Combination of PIXE with other analytical techniques. Difficulties connected with the detection of low-energy X-rays characteristic of elements with atomic numbers below $Z \approx 12$ can be avoided by the complementary use of proton induced γ -ray emission (**PIGE**) (Kiss et al. 1985) and/or deuteron-induced γ -ray emission (**DIGE**) (Elekes et al. 2000), processes excited by accelerated particles of the MeV energy range. The combination of these nuclear reaction methods with PIXE may also provide concentration data for light constituents of the samples (e.g., in biological and biochemical applications). Such data, which are not provided by PIXE analyses, are needed in calculating stopping power and X-ray absorption data in the evaluation procedure of PIXE spectra.

The combination of PIXE with Rutherford backscattering spectroscopy (RBS) analysis finds applications mainly in materials science (Ishii and Nakamura 1993).

A combined use of PIXE with polyacrylamide gel electrophoresis (PAGE) provides a new biochemical method in studying separated groups of metalloproteins by permitting in situ

elemental analysis on thin layer electrophoretograms (Szőkefalvi-Nagy et al. 1987). The simultaneous use of PIXE and PAGE on cellulose acetate electrophoretograms makes it possible to determine the metal ion and protein content of samples. (Szőkefalvi-Nagy 1996). A recent application of PAGE method in microPIXE configuration has been reported by Szőkefalvi-Nagy et al. (2009).

Sampling and preconcentration. According to the needs of the application of PIXE in many interdisciplinary fields a broad variety of sample forms and sample preparation methods have been developed. Objects to be analyzed can in special cases be subjected to beam irradiation in their original form (art objects, biological, and biomedical tissues). In other cases, samples can be collected in simple physical processes (e.g., total, size-fractionated, and time-resolved aerosol sampling, lyophilization, and pelletization), prepared by methods of solid-state physics (materials science), separated into different fractions (e.g., erythrocytes, plasma, and serum in blood samples), sliced by microtomes (e.g., plant tissues), with internal standards added (thick biological and biomedical samples). Due to the physical simplicity of the case of differentially thin samples, it is advisable in many cases to prepare samples in this form. A critical compilation of the sample preparation methods specially elaborated for X-ray emission elemental analysis has been published in an International Atomic Energy Agency (IAEC) document (Valkovic 1983). The inherent detection limits of the PIXE procedure can be enhanced if sample preparation is combined with preconcentration of selected analytes.

33.1.6 Fields of Application

As outlined above, the PIXE procedure offers a well-developed, versatile, and useful method of present-day instrumental analysis. While the methodological improvement is still going on to meet all the requirements of accurate routine analysis on large series of various samples, PIXE is already being applied in many different fields. A broad scope of application is documented in the papers presented in the proceedings of the international PIXE and microbeam conferences referred to in [Sect. 33.1.1](#). Details of the investigations performed by using PIXE in different fields of science can be found in special journals of the respective fields.

Within the limits of this chapter, the variety of applications can only be illustrated by a list of most common application fields, arbitrarily selected from the wealth of recent publications.

Biological processes (metal uptake by microorganisms and plants, elemental gradients across membranes, physiological functions and root structure of plants, elemental analysis of lichens, matter exchange between symbiotic partners, and sea grasses).

Biomedical research (analysis of individual cells, essential trace elements and toxic elements, nutrition effects, diagnostic use of elemental concentrations, blood samples, hair samples and history of medical events, body fluids, biopsy samples, deposition and retention of dust in respiratory tract, oral and orthopedic implants, degenerating mechanisms in aging process, calcified tissues, elemental concentrations and processes during healthy and pathologic pregnancies, trace element changes in pathological tissues, penetration of nanoparticles into skin, calcification of carotid arteries, trace element changes in cancer therapy, selenium status in cancer and immune diseases, and trace elements in neurological diseases).

Environmental research (Tree ring analysis, natural and anthropogenic aerosol components, time dependent and sequential measurements of atmospheric aerosols, apportionment of aerosol pollutants to emission sources, global and regional air quality monitoring, desert

dust, aerosols from volcanic eruptions, interregional and intercontinental transport of aerosol, aging and transformation of aerosols during transport, regional signatures as tracers in long-range transport, meteorological effects, elemental constituents of aerosols in cave environment, qualification of individual aerosol particles, acid rains and aerosols, river water analysis, sea-air exchange of materials, marine and lake sediment, aerosols in work environment, respiratory health survey, occupational safety, and contaminated soils).

Materials science (microelectronics analysis, surface layers, multilayers, PIXE channeling of dopants in crystals, depth profiling, binary alloys, impurities deposited in nuclear fusion devices, magnetic relaxation in nanocrystalline iron, insulating materials, radiation-induced segregation, superconductors, catalysts, and diffusion studies).

Geology (cosmochemistry, meteorites and cosmic dust, trace elements in lunar rocks, origin of microspherules, impact material, volcanology, phenocrysts in obsidian glasses, radiolarite, microcrystals and inclusions, grain boundaries, trace element zoning, geogas analysis, dating of ice cores in ice sheets, arid regions as sources of atmospheric aerosol, coastal and river sediments, mixing of salt and fresh water in coastal regions, geochemistry, mineralogy and petrology, and raw materials).

Art and archeology (early development of metallurgy, early development of glassmaking, color additives in glasses, trace elements in bones, numismatics, obsidian tools, archeology of paperlike objects and manuscripts, pottery, ceramics, painting materials, provenance studies of artifacts, prehistoric stone tools, gemstones, jewels, corrosion, and smearing).

Methodology (PIXE evaluation software packages, detector systems [UTWSi(Li), PIN array], μ PIXE chambers with precision goniometer and sample location setup, and nanobeam configurations).

33.2 Analysis by Elastic Scattering of Charged Particles (RBS and ERD)

In the following, the basic principles of ion beam analytical (IBA) methods based on elastic scattering are briefly introduced. To provide hints as to whether or not these methods are suitable for a special problem, their advantages and limits are also shown. More detailed information can be found in the literature (Chu et al. 1978; Tesmer et al. 1990; Tesmer and Nastasi 1995). In case of concrete problems, it is advisable to consult the specialists in the field, since these measurements need rather elaborate technical background.

33.2.1 Theoretical Background

The elastic scattering of nuclei of ionic projectiles on target nuclei can be realized for any ion–target combination. Therefore, one of the most appealing features of the elastic-scattering-based IBA methods is their universality, i.e., through one single measurement, one can obtain almost the whole elemental composition of the target. Depending on which of the colliding partners is detected – the scattered ion or the target atom, which gets recoiled out from the target – the method is called Rutherford backscattering spectroscopy (RBS), or elastic recoil detection (ERD). [ERD is also referred as ERDA (ERD Analysis) or FRES (Forward Recoil Elastic Spectroscopy).] In both methods, the energy distribution, i.e., the spectrum of the particles leaving the target is determined with a suitable experimental setup (see ▶ Sect. 33.2.8), and the spectra are used to determine the composition of the target.

Such spectra are seen, e.g., in ► Figs. 33.6. (In a spectrum, the energy scale is divided into channels, and the numbers of particles with energies corresponding to the various channels are presented in a graph.)

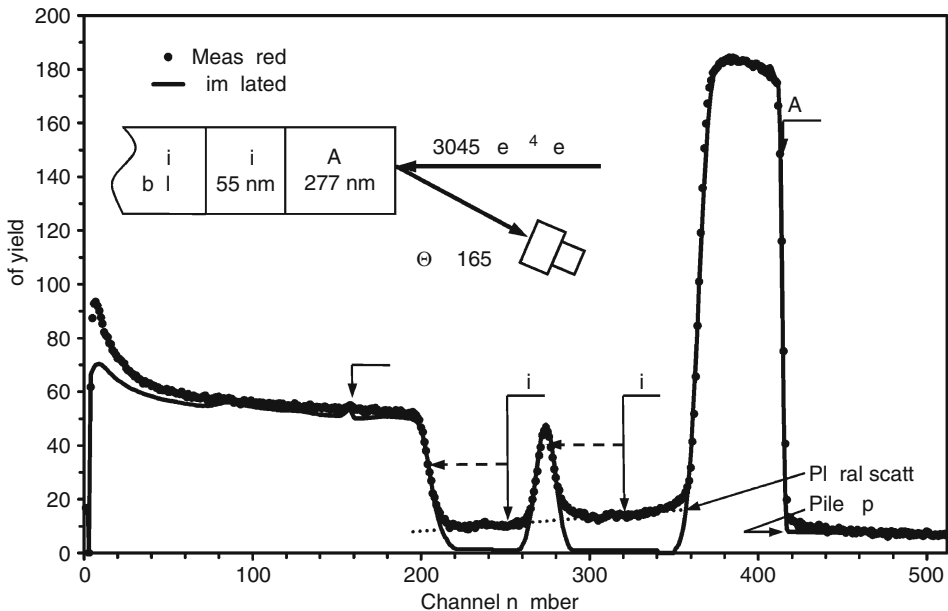
It is worth noting that time-of-flight (TOF) spectra are also frequently used. In these spectra, instead of the energy, the speed of the ions is obtained through the time that they spent to cover a given distance. Actually, TOF spectra are equivalent to energy spectra; they are just reversed in a special way.

In elastic scattering, both the energy and the momentum remain conserved; hence, with the mass and energy of the incident ion, M_1 and E_0 , and the scattering/recoiling angle, Θ/Ψ , one can determine the mass of the scattering nucleus, M_2 , unambiguously from the energy of the detected particle E_d .

The scattering is caused by the electrostatic repulsion between the nuclei of the ion and the target atom; hence, it is called Coulomb scattering. The intensity of this process, i.e., the cross-section σ of the scattering, is precisely given through the formula introduced by Rutherford (see ► Eq. (33.12) in Sect. 33.2.2.2). It also contains the electric charge of the participating nuclei, Z_1 and Z_2 . These methods are absolute, i.e., the number of the scattering atoms is unambiguously given by the number of the observed particles. Since σ is large, the sensitivity of these methods is quite good, especially if one can detect the particles free of background.

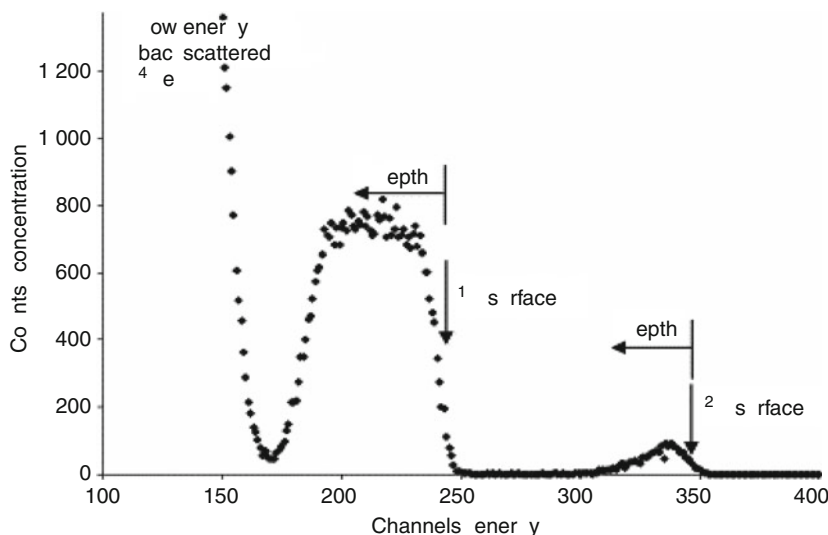
■ Fig. 33.6

Experimental and simulated (RBX) spectra of a sandwich structure. To better see the influence of plural scattering and pileup, the square root of the yield is given on the vertical scale (*Plural scattering*: the ions suffer at least two large-angle scattering. *Pileup*: a signal from the detector arrives so fast after the previous one, that they are treated together as a single signal of higher energy.)



■ Fig. 33.7

Experimental elastic recoil detection (ERD) spectrum from a thin, 200 Å, deuterated polystyrene film (Composto et al. 2002)



Furthermore, the number of ions hitting the sample should not be high, so the sample will be damaged only slightly.

The impinging and outgoing ions continuously hit the electrons of the target and in each encounter they lose a small fraction of energy, i.e., slow down (see ▶ Chap. 8 in Vol. 1). Unfortunately, the intensity of this process cannot be calculated precisely from basic physical principles, however, thanks to precise measurements and detailed compilations, they are known with a precision of 10–20%. If the observed atoms are situated deep in the sample, due to slowing on their way inward and outward, the energy of the observed particles will be smaller than that for surface atoms. The amount of this energy deficit increases monotonically with the depth, so one can also determine the depth of the observed atom. Therefore, in principle, these methods provide, in a single measurement, not only the whole elemental composition, but its depth dependence as well.

Since RBS and ERD are based on nuclear scattering, to penetrate the electronic clouds of the atoms, the ion energy has to be sufficiently large, i.e., a few MeV. However, it may also be a problem if the ions can penetrate the Coulomb barrier of the target nuclei, because in this case σ differs from the Rutherford value because some nuclear reaction channel may open. In such cases, the situation may be too complicated to allow a precise interpretation of the obtained results. The above energy limits, of course, depend strongly on the atomic number of the investigated atoms and the applied ions. Anyway, even if the cross section differs from the Rutherford value, it can be found in the literature or can be determined by some additional measurements, and the methods, with suitable extra care, can still be applied. To be precise, in these cases, RBS used also to be called backscattering spectroscopy, BS.

Results obtained by RBS and ERD are not influenced significantly by low-energy phenomena such as chemical bonds; thus, they can provide the precise elemental composition of the

samples independently of the chemical state. Therefore, combining these methods with those sensitive to chemistry might be especially fruitful.

So far, RBS/ERD have been presented in a rather simplified and idealized way. In the following more detailed description, their drawbacks and limits are also given. Since RBS and ERD are similar to a large extent, first RBS is introduced, and then the main differences between ERD and RBS are pointed out.

33.2.2 Rutherford Backscattering Spectroscopy, RBS

33.2.2.1 Energies

For RBS, the energy of the scattered ion is

$$E_2 = KE_1, \quad (33.7)$$

where K is the kinematic factor,

$$K = \left[\frac{\sqrt{M_2^2 - M_1^2 \sin^2 \Theta} + M_1 \cos \Theta}{M_1 + M_2} \right]^2, \quad (33.8)$$

E_1 and E_2 are the ion energies just before and after the scattering and, as mentioned before, M_1 and M_2 are the mass of the ion and the nucleus, respectively. The scattering angle Θ is measured between the direction of incident and scattered ions. For a detailed description, see the work of Chu et al. (1978) and Leavitt et al. (1995).

In RBS, as indicated by its name, the backward scattered ions are detected in most cases. From [Eq. \(33.7\)](#), one can see that the ion can scatter backward only from atoms that are heavier than itself, i.e., RBS detects only atoms heavier than the ion. The heavier the scattering atom, the larger the energy of the scattered ions will be. The $E_2(M_2)$ function approaches asymptotically the incident energy. While for the light elements the mass resolution is good (even the isotopes can be resolved), the heaviest elements might remain unresolved.

Thin surface layers of known elementary composition can be used to calibrate the energy scale of the applied detector through their kinematic factors.

As was mentioned, if the atoms are situated deep in the sample, the ions lose energy along their inward and outward paths. The rate of the energy loss is given by the so-called stopping power, S (see, e.g., [Eq. \(8.1\) in Chap. 8, Vol. 1](#)), which depends on the following parameters: composition and density of the target, the energy, and the mass and atomic number of the ion. S is available in the literature in the form of tables and semiempirical expressions (Ziegler 1977; Ziegler et al. 1985; Ziegler et al. 2002). Stopping power data can also be found in various figures of [Sect. 11.5 in the Appendix of Vol. 1](#).

If the scattering atom is at a small distance, x , from the surface, then the energy, E_d , of the scattered ion leaving the surface will be

$$E_d(x) = KE_0 - [S] x, \quad (33.9)$$

where

$$[S] = \frac{KS_{\text{in}}(E_0)}{\sin \alpha} + \frac{S_{\text{out}}(KE_0)}{\sin \beta} \quad (33.10)$$

is the cumulative, or the so-called effective stopping power. (E_0 , as mentioned before, is the initial energy of the incident ion.) The quantities S_{in} , S_{out} , α , and β are stopping powers and angles between the ion trajectory and the sample's surface inward and outward, respectively. The angles α and β are often referred to as incident and outgoing angles. For large depths, it must also be taken into account that both the ion energy and/or the composition of the sample may change considerably; therefore, the above simple expression has to be substituted by a numerical integration. In this case, $[S]$ has to be replaced by the more general expression $-dE_d/dx$. The suitable treatment of large depths together with all the other necessary calculations is included in the various computer codes developed to evaluate the RBS measurements (Doolittle 1986; Vízkelethy 1990; Kótai 1994; Szilágyi and Pászti 1994; Barradas et al. 1997; Mayer 1997). Recently IAEA sponsored an intercomparison of seven depth profiling IBA softwares. The results were published by Barradas et al. (2007).

RBS is a direct method. In the simplest cases, an expert eye glancing at an RBS spectrum can see at once the approximate composition of the sample together with the depth profiles of the various elements. The peaks and steps at larger energies correspond to heavier elements, while those at smaller energies are due to the lighter ones. A narrow peak implies that the given element appears in a thin layer while distributions widening into trapezoids are due to thicker layers. If the distribution widens so much that it starts already at the beginning of the spectrum and it stops at the higher-energy side by a step, the considered element appears probably through all the thickness of the sample, i.e., it is a constituent of the bulk. In the first example spectrum (► Fig. 33.6), one can see a double-layered structure on bulk Si. The edges of Si and Ti are shifted to lower energies by the overlaying Au. The surface is slightly contaminated by O.

The heavier constituents of the sample impose a background at energies corresponding to lighter elements. This way, while one can see the heavier elements background-free, the sensitivity for the lighter ones is considerably worsened by an intensive background (see, e.g., the O signal in ► Fig. 33.6).

Due to the slowing of the ions in the sample, from the observed energy alone one cannot decide whether the atom that has scattered the ion is a light one near the surface or a heavier one situated deeper. In spite of this ambiguity, the elementary composition of the sample can still be determined, since, in most cases, the whole spectrum cannot be interpreted in terms of a wrong sample structure. Due to unobservable or weakly observable light elements, the above statement may not always hold. If one cannot exclude the wrong solutions a priori, it is worth repeating the measurement in different ways. For example, one can change the incident or exit angles or the type or energy of the incident ions. To observe the light elements as well, one can turn to ERD or some other method to be mentioned in ► Sect. 33.2.2.2.

Because of the above energy overlaps, the measured spectra frequently become too complicated to be understood without applying suitable computer codes. Of course, if one would like to obtain really precise numerical quantities, the above codes are indispensable. In some of these programs, the user has to construct the model structure of the sample and refine it until the simulated spectrum matches the measured one satisfactorily (Doolittle 1986; Vízkelethy 1990; Kótai 1994; Szilágyi and Pászti 1994; Mayer 1997). The Nuclear Data Furnace code constructs the best model of the sample all by itself; so even beginners might achieve satisfactory results (Barradas et al. 1997). Nevertheless, any of the codes has to be used with special care, since giving imprecise parameters for the measuring setup or neglecting some second-order processes, like plural scattering, might lead to completely wrong conclusions.

33.2.2.2 Intensity

So far, the energy scale (the horizontal extension of the spectra) has been detailed, which is related to the masses and depth positions of the various elements in the sample. The vertical extension of the spectra provides information also on the amount or concentration of these elements. The height, of course (beside the concentration) is also proportional to some other quantities, like the number of incident ions, Φ , and the solid angle $\Delta\Omega$ and effectivity η , of the detector observing the scattered ions.

If a thin layer contains N_t target atoms per surface area (atom/cm² units), the peak area of the corresponding peak is³

$$A = N_t \frac{\Phi \eta \Delta\Omega \sigma}{\sin \alpha}, \quad (33.11)$$

where σ is the differential cross section of the scattering (i.e., the cross section per solid angle), which by the Rutherford expression is⁴

$$\sigma \equiv \sigma_R(E_1, \Theta) = \left(\frac{Z_1 Z_2 e^2}{2E_1} \right)^2 \frac{\left(\sqrt{M_2^2 - M_1^2 \sin^2 \Theta} + M_2 \cos \Theta \right)^2}{M_2 \sin^4 \Theta \sqrt{M_2^2 - M_1^2 \sin^2 \Theta}}, \quad (33.12)$$

where e is the elementary charge and E_1 is the energy of the ion before scattering. (The subscripts 1 and 2 refer to the ion and the atomic nucleus, respectively.) As mentioned before, the cross section can be described by the above expression just in the energy region of pure Coulomb scattering and elsewhere one has to determine σ in separate experiments or get it from the literature. The validity region of [Eq. \(33.12\)](#) together with several $\sigma(E_1)$ graphs can be found in Tesmer and Nastasi (1995). A cross-section collection is also available in SIGMABASE (SIGMA 2003). Most of the evaluation codes either contain the non-Rutherfordian cross sections of interest, or can be made to contain them easily.

For thick layers the peaks widen to trapezoids, whose heights will be

$$H_i \propto \frac{\Phi \eta \Delta\Omega \sigma_i(E_1) n_i \delta E}{[S] \sin \alpha}, \quad (33.13)$$

where δE is the energy width of the measuring channels and n_i is the relative concentration (fraction) of the given element ($\sum n_i = 1$). From the height of the spectral contribution of an element, one can determine the depth dependence of its concentration, i.e., the depth profile. In the spectrum in [Fig. 33.6](#), e.g., Ti is confined in a narrow layer between the thick homogeneous Au layer and the Si substrate.

It can be seen from [Eqs. \(33.11\) and \(33.12\)](#) that, for Rutherford cross sections, the area of the peak of an element is quadratically proportional to its atomic number, so RBS is especially sensitive for heavy elements. Even a few hundredths of a monolayer (about 10^{13} atoms/cm²) or 0.1 atomic% can be easily detected. For light elements, the sensitivity might be worse than even a few atomic%. To enhance the sensitivity, non-Rutherford cross sections are also frequently used. For example, for backscattering of 1,600 keV protons, σ is more or less the same for all the elements lighter than Si, being 100–300 mb/sr. In this way, a simple proton backscattering provides around 1 atomic% sensitivity for all the light elements including deuterium.

It is especially favorable if in the cross section of a light element of interest (or, more precisely, in the cross section of one of its most abundant isotopes), there is a sharp resonance (see, e.g., [Fig. 3.25 in Chap. 3 of Vol. 1](#)), since in this case, a sharp peak corresponding to

the resonance over a more or less smooth background can be unambiguously identified. The resonance is seen only if the energy of the ion coincides with the resonance energy, E_r . Hence, to observe the surface, the incident energy E_0 has to be equal to E_r , while for larger depths $E_0 = E_r + xS_{in}/\sin\alpha$. In this way, by increasing E_0 over E_r , one can map the depth distribution of the investigated element step by step.

33.2.3 Elastic Recoil Detection, ERD

If an atom is not heavier than the incident ion, the corresponding element (or rather nuclide) cannot be observed through RBS. For example, ^1H cannot be observed by RBS; its presence is only indicated by the decreased height of the spectrum. In this case, one can try to observe scattering in the forward direction, where the ions scattered from the given light element appear under a limiting scattering angle. However, if one wants to get rid of the large background of the scattering from heavier elements, it is better to detect, instead of the scattered ions, the recoiled light atoms, i.e., to apply ERD (L'Ecuyer et al. 1976; Barbour and Doyle 1995).

For ERD, the expressions for both the kinematic factor and the cross section differ from those of RBS; furthermore, along the outward path, the stopping formula has to be applied to the recoiled atom. The kinematic factor is now

$$K_{\text{ERD}} = \frac{4M_1M_2\cos^2\Psi}{(M_1 + M_2)^2}, \quad (33.14)$$


where Ψ is the recoil angle measured between the directions of the incident ions and the recoils. The cross section for pure Rutherford scattering is

$$\sigma_{\text{ERD}}(E_1, \Psi) = \left(\frac{Z_1Z_2e^2}{2E_1}\right)^2 \frac{(M_1 + M_2)^2}{M_2^2\cos^3\Psi}. \quad (33.15)$$

As with RBS, the energy scale of ERD spectra can be calibrated by surface elements of a known sample or by observing the same element under various Ψ angles. If all the factors are precisely known, the intensity scale does not need calibration. In practice, however, to achieve better precision, calibration samples are frequently used.

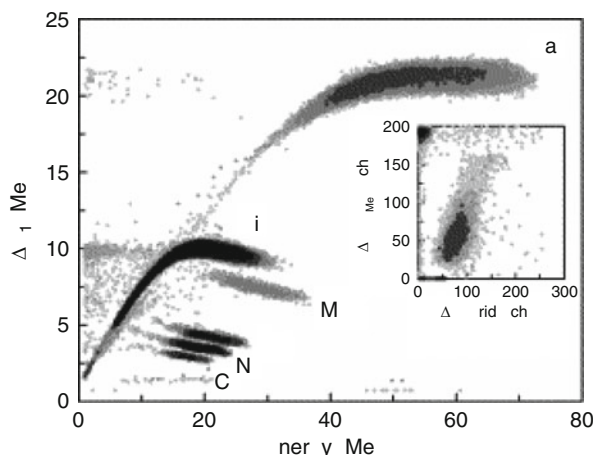
33.2.4 Separation

In the measured spectra, it is necessary to prevent the overlap of recoils with the background of scattered ions. For this purpose, several methods have been developed. The ones most frequently applied are as follows.

The simplest method relies on the fact that the lighter ions lose energy more slowly than the heavier ones. Mounting in front of the detector a foil of suitable thickness, one can stop the scattered ions, while the light recoils can still cross at a tolerable energy loss. The result of such a measurement is shown in  Fig. 33.7. The scattered He ions give only a small background at the lowest energies, while the recoiled D and H atoms are detected background-free. (The He background would disappear for a slightly thicker absorber foil.) The sensitivity of the method is especially remarkable, 0.01–0.1 atomic%. The limit is actually set by the ions scattered from various parts of the setup, which also might contain hydrogen.

■ Fig. 33.8

2D ERD spectra (200 MeV Au ions, ΔE - E gas detector) from a contaminated GaN film on Si (Timmers et al. 2002)



Even better sensitivity can be reached for thin foils, if the recoils and the scattered ions are detected simultaneously in coincidence (Klein 1986; Rijken et al. 1992; Rijken 1993).

The method is widespread, especially for energetic heavy ions, which are not prevented from reaching the detector but, instead, the ions of various kinds are distinguished from each other somehow. For this, one has to determine at least two quantities simultaneously, i.e., spectra of at least two dimensions (2D). One of the dimensions might be the time of flight through a given distance, TOF, while the other might be the energy given to the detector stopping the ions (Gorleau et al. 1983; Thomas et al. 1986; Arai et al. 1992; Gujrathi and Bultena 1992). A ΔE - E telescope, which measures both the energy E and the energy loss ΔE may also be applied to a thin layer. ΔE depends also on the atomic number of the ion. ΔE can be measured, e.g., by a thin detector, which is set just in front of the main detector (Behrooz et al. 1987; Assmann 1992; Arnold Bik et al. 1992; Timmers et al. 2002). During evaluation, the counts corresponding to the various ions in the obtained 2D spectra are first separated, and then the background-free energies or TOF spectra are further processed. Further methods can also be found in the literature, but, owing to lack of space, they have to remain unmentioned.

The 2D methods are especially attractive, since through them, especially in combination with RBS, the full elemental composition can be readily investigated. Such methods can also detect the light elements background-free. The reader can find a sample spectrum in ► Fig. 33.8.

33.2.5 Channeling Effect

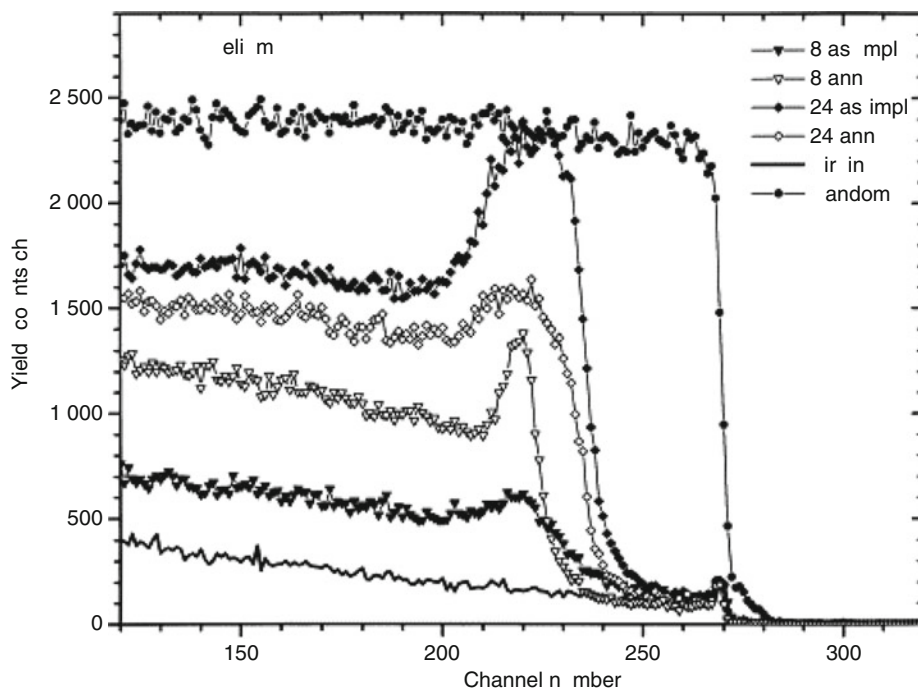
Mainly the RBS, but actually all the IBA methods can be combined with the so-called channeling effect (Chu et al. 1978; Feldman et al. 1982; Swanson 1995). Here one takes advantage of the fact that ions impinging parallel to one of the main axes or planes of a single-crystal target are subject to the following effect. Entering the sample most of them pass by the atoms in the first atomic layer undisturbed and enter the free space between the

atomic rows or planes of the lattice. This space, the channel, contains only electrons. Since both the ions and the atomic nuclei forming the channel walls are positively charged, they repulse each other and the ions are steered to follow trajectories zigzagging inside the channels. In this way, the ions cannot get close enough to the atomic nuclei in the wall to allow any of the processes applied in IBA to happen, i.e., the number of monitored events drastically decreases. This, of course, is true only if there are no extra atoms inside the channels, e.g., impurities sitting in non-substitutional places or interstitial atoms produced during some lattice damage. Extended defects (dislocations, stacking faults) also decrease the channeling effect.

From the picture just described, it is easy to see that by applying channeling, one can observe the lattice damage together with its depth distribution (see, e.g., Manuaba et al. 2001 and ▶ Fig. 33.9). Furthermore, the directions along which impurity atoms are positioned inside the channels can also be determined. This latter observation allows determining their localization in the lattice, i.e., their “lattice localization” (Davies 1973; Rebouta et al. 1992; Swanson 1995). For more precise lattice localization, not only are single spectra along the various channels taken, but one also investigates how the yield from the impurity changes when tilting the crystal axis or plane away from the incident direction step by step. During this process, the ionic distribution in the channels changes gradually: beside the axes or midplanes,

■ Fig. 33.9

Channeling Rutherford backscattering spectra (RBS) of a crystalline Si wafer that was implanted by He ions (10^{16} ion/cm² units) then annealed. Virgin and random spectra are also included (Manuaba et al. 2001)



places closer to the walls get also populated. Performing such “angular scan” measurements one can obtain lattice localization with a typical uncertainty of 0.01 nm.

33.2.6 Microbeam

Like other IBA methods, RBS/ERD can also be combined with a microbeam (e.g., Takai 1995). One has to be aware, however, that especially during longer measurements, besides the quickly appearing lattice damage, a continuously thickening hydrocarbon layer is also deposited over the tiny beam spot. Hence, during such measurements a hydrocarbon-free vacuum is crucial.

33.2.7 Secondary Effects

In RBS/ERD, the situation is never as ideal as it has been assumed above. Some secondary effects might significantly influence the observed spectra. For instance, the shape of the observed features is never sharp; it is smeared out by various effects as follows:

1. Finite detector resolution
2. Direction distribution and energy distribution of the incident ions
3. The exit and scattering/recoil angle fluctuates due to extended beam spot and detector size
4. Energy straggling⁵ in the sample
5. Multiple scattering: both incident and exiting particles suffer numerous small-angle scattering when penetrating the material that leads to continuously curving trajectories and fluctuating angles
6. DOPPLER broadening due to thermal vibrations of atoms

All the above processes are determined and taken into account by the DEPTH code (Szilágyi and Pászti 1994).

Incident ions or exiting particles might suffer additional large angle scattering(s) both in the sample and in the various parts of the measuring setup, especially in the final beam forming slits (plural scattering). As a result, the detected energy might depart from the ordinary one to a rather large extent (especially downward), leading to unwanted background (Moore 1980).

The incident beam is surrounded by a halo of scattered ions, which might involve in the measurement some other objects around the sample.

Spectrum shapes might also be distorted by rough sample surfaces and interfaces.

Although RBS/ERD are not too sensitive to the density or density inhomogeneities of the sample, the latter may give rise to energy spread. Applying suitable measuring arrangements and evaluation methods, one can turn this otherwise disturbing effect into a tool for studying the nanoscopic morphology of the samples, e.g., pore structure (Pászti and Szilágyi 1998).

33.2.8 Instrumentation

As in other IBA methods, it is a must to have fair quality ion beams. The energy stability of the accelerator is especially important in these measurements. For channeling measurements, the angular divergence of the ion beam should be small; this can be ensured by two collimators set far enough from each other.

It is also important to ensure an oil-free vacuum in the scattering chamber, since the hydrocarbon film deposited onto the sample surface gets polymerized gradually under ion bombardment, and, its reevaporation being hindered, grows without limit, influencing the measurements drastically. Therefore, in such measurements one has to consider a liquid-nitrogen cooled trap surrounding the internal wall of the chamber, or use only so-called dry pumps. In practice, oil diffusion pumps may cause serious problems in such systems.

It is useful to have a sample holder tiltable to large angles because with the use of glancing incident/exit angles, the sensitivity and depth resolution can be significantly improved. For channeling, the sample holder should be mounted on a goniometer. For routine measurements, the sample holder has to accept several samples, or it has to be easily changeable through a load-lock system.

The energy distribution of the ions is measured by suitable detectors of which the solid-state particle detectors are the most widely used. When their typically 10–15 keV energy resolution is not enough, a magnetic spectrometer⁶ or TOF system of good resolution is applied. For the latter, the START signal in most cases is generated by the ions crossing a thin carbon foil: the ejected secondary electrons are multiplied by a multichannel plate and their charge pulse is used. The STOP signal might be supplied by a similar unit, but the signal of a solid-state particle detector also may do. In the latter case, the energy may also be obtained, which in 2D ERD spectra is especially important. To reach good resolution for high-energy ions typical in IBA, the STOP detector should be far away from the sample, so large-area detectors are needed. In 2D ERD, the ΔE detector may be a totally depleted solid-state detector. An especially favorable setup is offered by a proportional gas counter divided into two parts, providing both ΔE and E signals simultaneously.

Nowadays, the spectra are collected and evaluated using suitable computer codes.

33.2.9 Fields of Application

RBS and ERD are especially useful when, not only the composition of the samples, but also their depth profiles are to be determined in the first few μm , and the measurements should be performed fast, e.g., in a few minutes. Typical things to study are diffusion, corrosion, solid-phase chemical reactions, and investigation of multilayers.

In many cases, it may be appealing that the sample is damaged only slightly. To examine large-size or vacuum-sensitive samples may be problematic since, although the measuring beam can be extracted to open air, when the ions cross the extraction foil and the air, they suffer significant energy straggling. By microprobes, 3D imaging of the samples may be achieved.

In summary, it can be concluded that RBS and ERD have a rather wide field of applications and, similarly to other IBA methods, there are situations when they are superior to all the other analytical methods.

33.3 Nuclear Reaction Analysis (NRA)

33.3.1 Characteristics of the Method

As was presented in the previous sections, when a beam of energetic ions impinges on a sample, it causes a variety of interactions. This section deals with the case when some particles of the beam interact with the atomic nuclei themselves. As a result, some nuclei are transformed into other nuclei by a nuclear reaction. The interaction between the bombarding particles and the

nuclei of the sample is followed by *prompt* emission of charged particles, neutrons, and/or γ rays. The energies and intensities of these interactions are determined by the internal properties of the nuclei in the sample and the conditions of bombardment. The study of these interactions is the subject of nuclear physics (see [Chap. 3 in Vol. 1](#)). From such studies, it was revealed that with the knowledge of some characteristic features of the emission (the nature and the energy of the outgoing particle or γ radiation and the yields of the nuclear reactions – i.e., the information given by a particle or γ -ray spectrum), the elemental (moreover isotopic) composition of a sample can be determined. Based on the huge amount of knowledge collected in basic nuclear physics, an analytical technique, called **nuclear reaction analysis** (NRA), has been developed. In NRA, the emission is considered *prompt* in the sense that it can only be detected during the irradiation. After the prompt emission, the product nucleus may itself undergo radioactive decay with a characteristic half-life; however, the detection and study of the *delayed* radiation is the basis of another technique called activation analysis (see [Chap. 30](#) in this Volume).

The nuclear reaction analysis technique can be characterized as follows. The particles of the beam have to pass the Coulomb barrier of the nuclei to produce a nuclear reaction with considerably high cross section, thus beam energies of at least several hundred keV are needed from a particle accelerator. The maximum particle energy usable for NRA is only limited by the capability of the particle accelerator itself. The most widely used particle accelerators for IBA are single-ended Van de Graaff and Tandetron machines (see [Fig. 50.15 of Chap. 50, Vol. 5](#), on “Particle Accelerators”), which usually cannot produce more than 5 MeV in the case of protons. The above restrictions have the following consequences:

1. Mostly light particles are used: protons, deuterons, and ^4He ions (A heavier ion, ^{15}N , is applied to special analyses – hydrogen depth profiling – at around 7 MeV.)
2. Mainly light elements can be characterized by NRA due to the increase of the Coulomb barrier height with increasing atomic number.
3. Because of the high energies involved in the process, chemical bonds in the sample material do not interfere; nor is, however, possible to get direct information on them.

Cross sections of nuclear reactions are generally much lower than those of fluorescence or elastic scattering. Moreover, nuclear reaction cross sections depend on atomic or mass numbers and energy rather erratically. Thus, NRA is competitive with PIXE and RBS only for certain light elements, which have increased yields in certain nuclear reactions, and where the difficulties of the detection of light elements due to the low energy of characteristic X-rays in PIXE or the high background from heavier constituents in RBS cause problems.

The main strength of NRA is, however, its capability of highly selective determination of the concentration of isotopes of the various elements. Furthermore, it is a method of determining the absolute areal concentration (atoms/cm²) of light impurities on and below the surface of a sample containing heavy elements and providing an absolute calibration for other surface sensitive techniques. An important advantage of NRA is its capability of high-resolution depth profiling of some elements in the first few micrometers as well.

Other features are the following: (1) the possibility of non-vacuum use, especially in the case of *ion- γ* reactions, where the outgoing γ rays are detected (this feature allows the analysis of volatile samples or those with extended dimensions), (2) the simultaneous applicability with RBS and/or PIXE, (3) the easy preparation of the samples, and last but not least, (4) it is a nondestructive analytical method.

The application of nuclear reactions for analytical purposes started in parallel with the development of low-energy nuclear physics itself, and started to expand in the 1960s, which

expansion is still continuing. Several reviews of the basic principles of the method and its applications can be found in the literature. One of the earliest and most detailed ones was written by Deconninck (1978) in 1978, which was followed by Amsel and Lanford (1984) in 1984, then by Feldman and Mayer (1986) in 1986. Monographs of ion beam analysis also contain detailed descriptions of the technique (Bird and Williams 1989; Tesmer and Nastasi 1995). The latest results and many applications were presented in the proceedings of International Conferences of Ion Beam Analysis (IBA) (1973–2007) and International Conferences on Nuclear Microprobe Technology and Applications (ICNMTA) (1981–2008). The proceedings of the latest IBA and ICNMTA conferences can be found in references Pathak et al. (2008) and Rajta et al. (2009), respectively.

33.3.2 Physical Background of NRA

The probability that a nuclear reaction takes place during bombardment with energetic particles depends on many circumstances and is discussed in detail in nuclear physics.

The energies of the outgoing particles can be determined by the nuclear reaction kinematics based on the energy and momentum conservation law. The case is more complicated than RBS in that in nuclear reactions the energy release of the reaction (*Q*-value) and the spacing between the energy levels of the final nucleus also have to be taken into account. In practice, the choice of the particle groups or γ rays suitable for the identification of an element (isotope) depends on many circumstances. First, on the properties of the ion beam (its type and energy), then on the nuclear reaction occurred, the isotope of the given element and its natural abundance, the cross section, the nuclear parameters of the excited states, etc. Possible interfering reactions in the sample matrix must be known as well.

Due to the complexity of nuclear forces, predictions from nuclear model calculations for the **cross sections** of nuclear reactions and their dependence on energy and detection angle are difficult, and even if it is possible, they are not precise enough for analytical purposes. Thus, one has to rely on measured data. There are many published experimental cross-section data in the basic literature on nuclear physics, but usually the same problem occurs again; neither are the experimental conditions the same, nor are the precisions good enough for NRA. For depth profile measurements, the knowledge of precise resonance parameters is crucial, and often the published experimental data have to be remeasured to fulfill the requirements of the technique.

For convenience, most of the information necessary to perform qualitative or quantitative NRA is collected in handbooks. In the analytical work, it is useful to consult catalogs of prompt nuclear reaction analysis, which give advice on the nuclear reaction and ion energy appropriate for the analysis of a certain element in a given matrix. The energies of the outgoing particles or γ rays to be detected are also given. Remeasured cross-section data at the optimum conditions, which are precise enough for NRA, are also published in those handbooks. The latest compilations for **ion-ion** and **ion- γ reactions** are found in Tesmer and Nastasi (1995). They have been complemented by the thick target yields of deuteron-induced γ -ray emission (DIGE) that were completely missing before (Elekes et al. 2000). Precise cross-section measurements for the reaction $^{19}\text{F}(\text{p}, \text{p}'\gamma)^{19}\text{F}$ were started by Jesus et al. (2000) and continued later by the same authors (see Mateus et al. 2005). In the case of deuteron-induced γ -ray emission analysis, fundamental cross-section data were measured for the reactions $^{14}\text{N}(\text{d}, \text{p}\gamma)^{15}\text{N}$ (Bebber et al. 1996) as well as for $^6\text{Li}(\text{d}, \text{p}\gamma)^7\text{Li}$, $^9\text{Be}(\text{d}, \text{n}\gamma)^{10}\text{B}$, $^{11}\text{B}(\text{d}, \text{p}\gamma)^{12}\text{B}$, $^{16}\text{O}(\text{d}, \text{p}\gamma)^{17}\text{O}$, and $^{19}\text{F}(\text{d}, \text{p}\gamma)^{20}\text{F}$ (Sziki et al. 2006). At present, a new nuclear cross-section database for ion

beam analysis is under development. The intention is to compile and assess existing cross sections and evaluate them (Gurbich et al. 2008).

33.3.3 Instrumentation

As NRA has grown from accelerator-based nuclear physics and expanded after the invention of solid-state detectors (the surface barrier Si detector for the detection of particles and Ge(Li) detectors for the detection of γ rays), its instrumentation is very much similar to those used in particle and γ -ray nuclear spectroscopy. The PIXE method also started to use an existing instrumentation, the Si(Li) X-ray detectors, nearly a decade later. Consequently, this review will refer to the previous [Sects. 33.1](#) and [33.2](#) on PIXE and RBS concerning the acceleration and the formation of energetic ion beams, the internal and external sample chambers, scanning particle microprobe facilities, particle detection, and data acquisition. It will only deal with the characteristic features of the detection of ions and γ rays produced in nuclear reactions. Neutrons are also produced in these reactions, but in practice they are rarely used for NRA. Because of space limitations, that technique (Bird and Williams 1989) will not be discussed.

As for the accelerated ion beams, contrary to PIXE and RBS, in NRA the use of deuterons is favored because of the high yields produced with them. However, the deuteron beam itself can produce more neutrons than any other ion beams; therefore, its use is associated with the possibility of neutron hazard. NRA requires only very small deuteron beam intensities, the orders of 100 pA–10 nA, contrary to basic nuclear physics, where μ A beams are common. Moreover, the energy of the deuteron beam used for analysis is quite low (usually lower than 2 MeV), thus practically no health hazard is expected around the experimental facility (Kiss et al. 1994). Nevertheless, radiation safety rules demand heavy shielding against neutrons for laboratories working with deuteron beams, which is not available around many accelerators. This is a limiting factor for the wide use of deuteron-induced NRA.

It is convenient to consider *ion–ion* and *ion– γ* reactions separately, since the product type determines the detectors and methods required.

33.3.3.1 Ion–Ion Reactions

The particles from nuclear reactions differ from the elastically scattered ions in two respects: their intensity is much lower because of the much lower cross section, but their energy is usually higher because of the mostly positive reaction Q -value. Thus, although the same experimental setup can be used for ion–ion reactions as for RBS, the sensitive depth of the Si surface barrier detector should be high enough to absorb the high-energy reaction products (usually protons) completely. The high-intensity scattered ions cause pileup and damage the detector. There is a need to eliminate them before they can reach the particle detector. Several methods, such as magnetic deflection or electrostatic deflection are used, but the simplest is the use of a uniformly thin foil of metal or Mylar in front of the semiconductor detector, placed usually at backward angles to the beam direction. The thickness of the foil is chosen to be close to the range of the scattered ions, but still allowing the higher-energy reaction products to pass.

High detection efficiency is particularly needed in nuclear microprobes, where the beam intensity is limited; furthermore, beam current density has to be kept below a certain level, depending on the sample material, to avoid irradiation damage. For example, for a $1\text{ }\mu\text{m}^2$ beam spot and 100 pA beam current the determination of ^7Li , ^{11}B , ^{12}C , ^{16}O , and ^{19}F is possible in

metals, alloys, or refractory materials, but for thick polymers and biological samples higher spot size is needed with this current to avoid sample damage (Trocellier et al. 1999). High detection efficiency can be achieved by one or more large surface barrier detectors set close to the sample and connected electronically, or by the use of an annular detector with large solid angle. For example, 1.63 sr was used for the determination of the boron distribution of about 7 ppm average concentration in cells from a rat brain (Sjöland et al. 1997).

More sophisticated methods, like ΔE - E telescopes for the simultaneous measurement of the speed and the energy of the detected particle, have also been applied recently (Trocellier et al. 1999).

33.3.3.2 Ion–Gamma Reactions

To exploit the resonance character of (p,γ) reactions, (see [Sect. 33.3.4.3](#)), one has to detect the γ rays. Similarly, in many (p,α) reactions the α particles have energies too low for efficient detection, thus the γ rays associated with the α particles are worth detecting. In the inelastic proton scattering $(p,p'\gamma)$ and in deuteron-induced reactions, the detection of γ rays instead of the particles also has many advantages. The main advantage of NRA with γ -ray detection is that, due to the very little attenuation of γ rays, it is not necessary to place the detector into the vacuum chamber. The external beam technique can also be easily realized.

The type of the γ -ray detector to be chosen depends on the aim of the analysis to be performed. The “old-fashioned” NaI(Tl) scintillation detector is conventionally applied when light elements in samples of high Z value are profiled using a well-isolated resonance, since here higher efficiency is needed due to the scanning with energy, while energy resolution is not critical. To the analysis of total average concentrations of several elements, Ge detectors are generally applied, because their energy resolution is high enough to distinguish nearby γ rays emerging from different elements, the laboratory background, and from other disturbing background peaks. The large-volume high purity germanium (HPGe) detectors available recently have efficiencies comparable to NaI(Tl) detectors, together with high-energy resolution. This statement is true between 0.1–2.5 MeV, in which region Ge detectors are predominantly used. When very high-energy γ rays (higher than 6 MeV) are to be detected [e.g., F and N determination by $(p,\alpha\gamma)$ and $(d,p\gamma)$ reaction, respectively], high-energy resolution is not needed and the NaI(Tl) scintillation detectors still have a role, although in some laboratories they are replaced by the even more efficient bismuth-germanate-oxide (BGO) detectors. To increase the detected yield, both types of γ -ray detectors are used such that they collect counts not only from the full-energy peaks but also from single- and double-escaped peaks, which are generally quite pronounced at very high γ -ray energies (see [Fig. 48.13 in Chap. 48 of Vol. 5](#)).

The efficiency of γ -ray detectors used in NRA is increased more and more. For example, in Bochum a γ -ray detection system of very high efficiency was built, which includes a 12 in. \times 12 in. (~ 30 cm \times 30 cm) NaI(Tl) bore hole detector. It covers a solid angle close to 4π , it has a good peak to Compton ratio, and there are practically no escape peaks due to the high volume. The total efficiency for the detection of γ rays reached almost 90% (Piel et al. 1996). Another development in NRA is the application of the so-called Clover-Ge-BGO detector system (Elekes et al. 1999), which was originally developed for the large EUROGAM multi-detector γ -ray spectrometer used in nuclear physics. This detector system consists of a so-called clover type composite HPGe detector surrounded by a BGO anti-Compton shield. The **clover detector** is built up from four separate coaxial HPGe crystals (with 20% relative

photo-peak-efficiency of each) packed together in the same cryostat in a four-leaf clover arrangement. In spite of high detection efficiency, the detector system has an improved peak-to-Compton ratio owing to the anti-Compton shield.

The detector used for the detection of γ radiation in NRA is generally placed either 135° or 90° to the direction of the incident beam. Higher count rates can be obtained at forward directions. Nuclear physics experiments often use a detector angle of 55° to obtain a measured yield proportional to that expected from the reaction cross section integrated over 4π angles.⁷ This geometry is suitable for the absolute determination of elemental concentrations from published total cross-section values, but it has no advantage when reference samples are used.

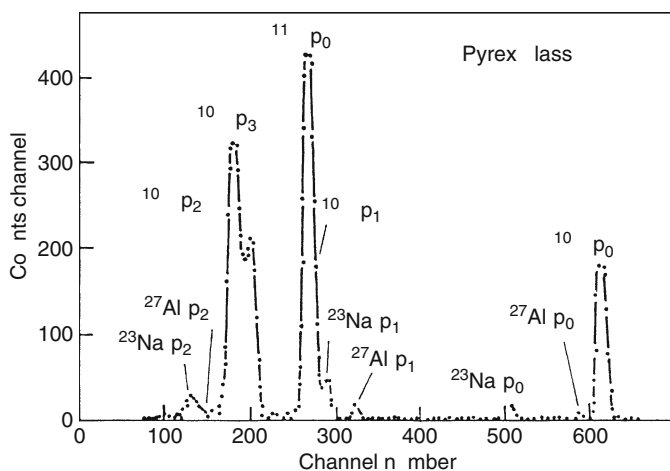
33.3.4 Quantitative Elemental Analysis

33.3.4.1 Spectrum Evaluation

Ion-ion reactions. A particle spectrum in NRA is very similar to a spectrum observed and discussed in RBS. Its advantage is that the particles from a nuclear reaction on a light constituent have higher energies than the elastically scattered particles, thus they are background free. [Figure 33.10](#) shows a typical NRA spectrum obtained by bombardment with 4 MeV α particles of a thin glass sample (with a thickness of 1.1 μm) having high boron content. The backscattered α particles are stopped by a 20 μm Al foil in front of the particle detector, while protons above 1,300 keV can penetrate it. The proton peaks from (α, p) reactions on the nuclei ^{10}B , ^{11}B , ^{23}Na , and ^{27}Al present in the glass appear background free at energies between 1,850 and 5,000 keV. Peaks labeled with p_i refer to protons emitted from the i th level of the corresponding nuclei (Peisach and Pretorius 1973). A general problem of ion-ion reactions is that in the spectrum different types of particles, protons, alphas, or deuterons, may appear due to the more than one open reaction channel. For their separation, one can use

Fig. 33.10

Proton spectrum of a thin glass sample having high boron content irradiated by a 4 MeV α -particle beam (Peisach and Pretorius 1973)



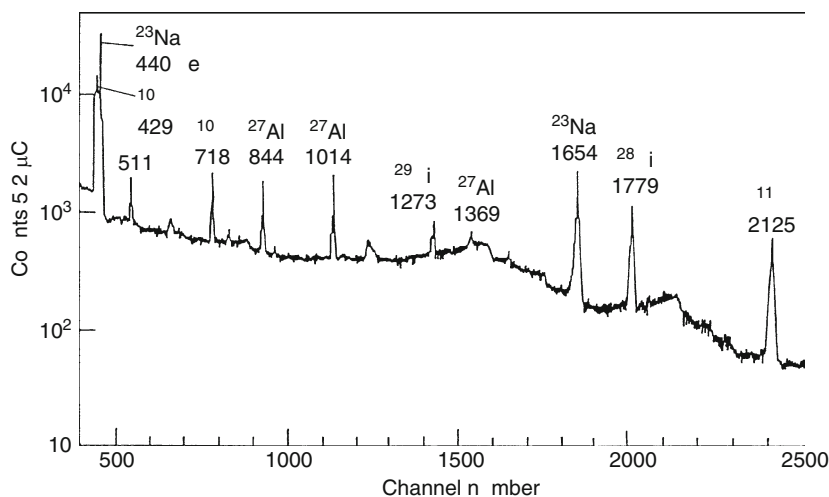
again the absorption foil technique discussed above or a detector of thin sensitive layer (Amsel et al. 1992). For spectrum simulation and deconvolution, the same program packages are available as for RBS (see references therein).

Ion- γ reactions. There is a remarkable difference between ion-ion and ion- γ reactions. In the case of ion-ion reactions, with thickening sample layer, the corresponding particle peaks also broaden like in the case of RBS. In the case of an infinitely thick sample (thicker than the range of the bombarding particle), which contains several light isotopes, the ions emerging from the depth slow down so much that it is a demanding task to separate them from each other. The emerging γ rays from the same thick sample fortunately do not change their energies. In [Fig. 33.11](#), a typical γ -ray spectrum is shown from the bombardment by 3.1 MeV protons of a thick borosilicate glass sample, which is often used as high-voltage insulator. The γ -ray peaks are resolved well, except the 429 keV energy peak from the $^{10}\text{B}(p,\alpha\gamma)^7\text{Be}$ reaction, showing a large kinematic Doppler broadening. The γ rays can penetrate through even the thin wall of the target chamber into the air only with a small attenuation; therefore, it is easy to install the detector out of the vacuum chamber. Moreover, using solid-state detectors, γ rays can be detected with much better energy resolution than particles.

These advantages make the ion- γ reactions a particularly useful elemental analysis technique. Because the detection technique is different from the detection of both X-rays in PIXE and particles in RBS and NRA, the method got in practice a distinctive name: **particle-induced γ -ray emission (PIGE)**, where the word “particle” means mostly proton. PIGE is often used simultaneously with PIXE, and its suitability for the analysis of light elements (mainly Li, B, F, Na, Mg, Al, and Si) complements the performance of PIXE well. Among γ -ray emissions induced by various types of particles, the **deuteron-induced γ -ray emission (DIGE)** deserves the most practical interest, because it is also sensitive to C, N, and O, and its high cross sections

■ Fig. 33.11

Particle-induced γ -ray emission (PIGE) spectrum from a borosilicate glass sample irradiated by a 3.1 MeV proton beam. The peaks are labeled with target nuclides giving the signal and the corresponding γ -ray energies in keV (Borbély-Kiss et al. 1985). Note the large Doppler broadening of the 429 keV peak explained in the text



can be exploited in nuclear microprobe applications. Systematic particle-induced γ yields are available in the literature also for heavier ions (^4He , ^7Li , ^{12}C , etc.) measured at higher beam energies for target elements from Li to Pb. Their possible applicability to NRA was compiled by Räsänen (2001).

Overlapping of γ lines from different reaction channels open on the various constituents of a sample may cause ambiguities in the evaluation of γ -ray spectra. In this case, the appearance of other γ lines can help in the analysis.

Since the yield curves of different reactions have different shapes with varying bombarding energy, a repeated measurement at another bombarding energy could also help. There are γ -ray catalogs containing energies, yields of γ lines, and also complete spectra at different ion energies for the elements to be analyzed, which are helpful in choosing the proper γ peaks for further evaluation (Gihwala and Peisach 1982; Kiss et al. 1985; Elekes et al. 2000).

As the response function for γ -ray detectors is quite complex, various computer programs were developed for the analysis of γ spectra in nuclear physics. Some of them were adapted also for NRA like the program package FORGAMMA (Székely 1985), which is capable of analyzing complex unresolved γ -peaks and special line shapes caused by the kinematic Doppler broadening. In most applications, it is satisfactory to subtract a linear continuum from prominent peaks or to fit overlapping Gaussian distributions and a continuum function to a group of closely spaced peaks in a selected region of interest (ROI) of the spectrum.

33.3.4.2 Determination of Concentrations

For the calculation of concentration from the intensity of a peak observed in an energy spectrum of a nuclear reaction the same rules are valid as for the other ion-induced processes discussed earlier in conjunction with the methods PIXE and RBS with minor differences coming from the particularities of the nuclear processes. Thus, for **thin samples** analyzed by nuclear reactions the considerations for RBS, started with [Eq. \(33.11\) in Sect. 33.2.2.2](#) are also valid, with the difference that σ is the differential cross section of a nuclear reaction. It is supposed that σ changes slowly in the vicinity of the energy of the ion beam. The effect of the increasing sample thickness, including stopping powers and the possibility of resonance behavior of the cross section for ion–ion reactions, is the same as for elastically scattered ions and it has already been discussed in [Sect. 33.1](#). Many experimentally measured cross sections are collected in handbooks of IBA and some of them are available also in digitized form in SIGMABASE mentioned in [Sect. 33.2.2.2](#). Nevertheless, for obtaining very precise results the remeasurement of old data under the actual experimental conditions is recommended.

In **thick samples**, the bombarding particles slow down gradually; thus, if the cross section of a nuclear reaction has resonance structure, the resonances appearing at different energies are summed up and the yield belonging to a particular bombarding energy varies smoothly with the ion energy. To calculate the concentration of a certain element in a sample, one has to integrate the cross-section curve over the energy interval of the slowing down ion by taking into account stopping powers. For nuclear reactions, many different energy dependences are possible. Each cross-section curve needs values measured with sufficient accuracy, and a well-established analytical relation is missing. Hence, the integration cannot be carried out so accurately as in RBS or PIXE. For the integral several approximations exist, with the use of average cross sections, average stopping powers, etc. These features are discussed in detail, e.g., by Bird and Williams (1989). In the case of ion– γ reactions, the energy of γ rays exceeds

100 keV, very often even 1 MeV. The attenuation of such γ rays is significant neither in the sample nor in the detector window. This is an important advantage as no corrections are needed for the absorption of γ rays.

The analysis can be simplified if calibration samples with similar compositions are available. Then, for a certain γ peak whose yield $Y(Z, N)$ is measured on the sample and on a standard will give the concentration $C(Z, N)$ of the nuclide ${}^{Z+N}_{Z}\text{X}_N$ in the sample by the following simple formula (based on the approximation of stopping power ratios, see Deconninck 1978):

$$C(Z, N) = C(Z, N)_{\text{st}} \frac{Y(Z, N)S(E)_{\text{st}}}{Y_{\text{st}}(Z, N)S(E)} \quad (33.16)$$

where st stands for standard.⁸ The stopping power values $S(E)$ can be obtained, e.g., from calculations using the SRIM computer program-package of Ziegler et al. (2002).

Recently, a code was developed for the quantitative PIGE analysis of light elements without standards in thick samples (Mateus et al. 2005). (The code works similarly to what is done for PIXE; via integrating cross sections deduced from precisely measured nuclear reaction excitation functions along the depth of the sample.)

33.3.4.3 Depth Profiling

The relation between the energy of an energetic ion and the depth it penetrates is given by the stopping power formula (see [Chap. 8 in Vol. 1](#)). On the basis of the energy loss process of ions, a powerful method was developed for nondestructive measurement of concentration profiles to depths of the order of 10 μm with a depth resolution better than 20 nm. In practice, the method has many variants, but they can be divided into two main categories according to the shape of the nuclear cross section as a function of energy. The method is called **nonresonant** when the cross section is varying smoothly with energy and the analysis is performed at a fixed energy of the analyzing beam. In this case, the depth profile is derived from the recorded energy spectrum of particles emitted by the reaction. The method is **resonant** when the cross section, as a function of energy, shows a sharp peak, a resonance. Then the depth profile can be obtained from the yield of the nuclear reaction as a function of the beam energy.

Nonresonant Profiling

A medium thick sample is bombarded by the analyzing beam, and the ions hitting the surface lose their energy continuously while penetrating into the depth of the sample. Because the cross section does not change sharply with energy, and the concentration of the examined element does not depend on the depth very strongly, the reaction adds nearly the same amount of counts to the lower energy side of the peak and causes a broadening, as already discussed in the previous [Sect. 33.2.2.1](#) at RBS. There is a minor difference between RBS and NRA in this respect: in the case of a nuclear reaction, the outgoing particle is not the same as the ingoing one and its energy is also different, which means that one has to use a different stopping power value in the calculation of energy loss. For more detail, see [Sect. 33.2.2](#) and references therein.

Resonant Profiling

Both in elastic scattering and in reactions, one can find examples where a strong isolated narrow resonance appears in the cross section as a function of energy. Although the first


application of this technique used the $^{18}\text{O}(\text{p},\alpha)^{15}\text{N}$ reaction (Amsel and Samuel 1962), the best examples can be found in ion- γ reactions, more precisely in (p,γ) reactions. The depth profiling method works as follows.

Consider a reaction with an isolated narrow and strong resonance. This means that reaction products can only be detected if the analyzing beam hits a target nucleus (usually a light element on the surface of a heavier sample) exclusively with the resonance energy E_r . The incident ion energy E_0 is scanned upward from the resonance energy E_r . As the incident ion energy is increasing, the resonance is excited at larger and larger depths in the sample, and the detected γ -ray intensity gives information on the concentration of the considered element at that depth. The depth scale at a certain angle with respect to the surface can be calculated from converting the energy increase $E_0 - E_r$ to the dimension of length by the use of the stopping power characteristic to the main components of the sample material studied: $x = (E_0 - E_r)/\text{d}E/\text{d}x$. The concentration is calculated from the yield and width of the resonance, the stopping power $\text{d}E/\text{d}x$ (assumed to be constant), and the detection efficiency. The depth resolution at the surface is determined by the resonance width and the beam spread. Below the surface, the increasing energy straggling decreases the depth resolution gradually. The scanning of the ion beam can be automatized in different ways, e.g., by modifying the accelerator stabilization system (Amsel et al. 1983) or by applying an acceleration or deceleration voltage on the sample.

To achieve the optimum depth resolution of both nonresonant and resonant nuclear reactions, one must have accurate knowledge of the charged particle stopping process and the energy straggling in solids. To improve depth resolution, these questions are the subjects of continuous research both in RBS and in NRA. The subject has been discussed in more detail, with several examples of applications by Cherniak and Lanford (2001). One of the latest figures is an estimated depth resolution of approximately 0.4 nm near the surface of an ultrathin Al_2O_3 film deposited on Si substrate, which could be obtained using the 404.9 keV resonance (width ≤ 40 eV) in the $^{27}\text{Al}(\text{p},\gamma)^{28}\text{Si}$ reaction. The excellent depth resolution obtained is due to the high-energy stability of the proton beam and the use of glancing incidence (da Rosa et al. 2002).

33.3.5 Fields of Application

Generally speaking, NRA is used in the same fields as the other IBA methods, PIXE and RBS, but their extension is needed down to the lighter elements (H, Li, B, C, N, O, F, and Na) and/or trace elements down to the level of 1–10 $\mu\text{g/g}$. In such a way, NRA is complementary to PIXE (ion- γ reactions) and RBS (ion-ion reactions). The excellent depth resolution (1–10 nm) for nondestructive depth profiling of some light nuclides, ^1H , ^{15}N , ^{19}F , ^{23}Na , and ^{27}Al , is also exploited.

Here is a list of some examples chosen arbitrarily: hydrogen depth profiling by the ($^{15}\text{N},\alpha\gamma$) nuclear reaction was reviewed by Lanford (1992). Recently a particle accelerator was dedicated to high-sensitivity depth profiling accelerating ^{15}N ion beam (Uhrmacher et al. 2005) and in an other work the evaluation of the nonresonant background of this reaction near 13.35 MeV for hydrogen depth profiling was studied (Wilde and Fukutani 2005). For other elements see  Table 33.1.

As an example of the application of NRA in environmental studies, the combined PIXE/PIGE investigations (with the determination of Na, Mg, Al, and Si by PIGE) of Gallien et al. (2001) may be mentioned, where the alteration of glasses by microorganisms were studied. The concentration of the elements Li, Be, F, Na, Mg, Al, and Si, or their lateral and/or depth

■ **Table 33.1**
Examples of materials investigated by depth profiling

Material	Reference
Diamond	Jans et al. 1994
α -quartz samples	Bolse et al. 2000
Silicon dioxide films on silicon	Ecker et al. 2000
Thin films on different metals	Wielunski et al. 2002
Li and B distribution in geological materials	Trompetter et al. 1999
F determination in teeth	Coote et al. 1997
C and O distribution on the surface of micrometeorites	Elekes et al. 2002
^{18}O for oxygen diffusion studies in materials science	Berger et al. 2001
^3He concentration in UO_2 and SiC	Martin et al. 2007

distribution is applied to the characterization of art and archaeological artifacts: obsidians (Murillo et al. 1998), glasses (Jembrih et al. 2001), emeralds (Calligaro et al. 2000), and ancient human bones (Jankuhn et al. 2000).

33.4 Editors’ Note

1. Keeping in mind that the vertical axis of panel (4) in ➤ Fig. 33.1 is logarithmic, one can immediately see by comparing the bremsstrahlung curves why the radiation (bremsstrahlung) term is so important in the stopping power formula of electrons and why the same term is usually neglected for slowing heavy ions (see ➤ Sects. 8.3 and ➤ 8.2, respectively, in Chap. 8, Vol. 1, on “Interaction of Radiation with Matter.”) (p. 1699).
2. See for the statistical bases of fitting nuclear spectra in ➤ Sect. 9.6 of Chap. 9, Vol. 1, on “Stochastics and Nuclear Measurements” (p. 1705).
3. Remember that Φ is just a number here, not a flux density, and therefore the peak area A is again a dimensionless quantity giving the number of scattering events that make up the peak (p. 1717).
4. If the electric charge is measured in SI units, the right-hand side of ➤ Eqs. (33.12) and ➤ (33.15) must be multiplied by $(4\pi\epsilon_0)^{-2}$ to get correct results, where ϵ_0 is the permittivity of vacuum (see under “electric constant” in ➤ Sect. 11.2 in the Appendix of Vol. 1) (p. 1717).
5. “**Straggling**” is a technical term in the field of ionizing radiation – matter interactions. It refers to the fact that the energy (and the momentum) distribution of initially monoenergetic particles gets wider and wider as they penetrate a substance. This “energy straggling” is the result of a series of stochastic interactions (e.g., with electrons), which drain their energy and eventually stop them. Straggling is also reflected in the absorption curve of α particles, for instance, which shows that the individual ranges of particles are different (p. 1721).
6. **Magnetic spectrometers** are based on ➤ Eq. (50.38) in Chap. 50, Vol. 5, stating that a charged particle moving perpendicularly to the magnetic flux density \mathbf{B} will follow a circular path, the radius of which is proportional to the momentum of the particle

($p = qBr$), thus making energy determination possible ($E = p^2/(2m)$) by using a “magnetic sector field” (p. 1722).

7. The angle $\sim 55^\circ$ is used to eliminate the effects of possible “texture” in powder samples and is called the “magic angle” in Mössbauer spectroscopy (see ► Chap. 25 in this Volume) (p. 1727).
8. ► Equation (33.16) is basically the equivalent of ► Eq. (33.5) suggested for PIXE, except that the present one works for nuclides (i.e., isotopes of elements) and not elements (p. 1730).

References

- Ahlenberg M, Johansson G, Malmqvist K (1975) Nucl Instrum Methods 131:377
- Amsel G, D'Artemare E, Girard E (1983) Nucl Instrum Methods 205:5
- Amsel G, Lanford WA (1984) Ann Rev Nucl Part Sci 34:435
- Amsel G, Pászti F, Szilágyi E, Gyulai J (1992) Nucl Instrum Meth B 63:421
- Amsel G, Samuel D (1962) J Phys Chem Solids 23:1707
- Andersson F, Barbaret Ph, Incerti S, Moretto Ph (2008) Nucl Instr Meth B 266:1653–1658
- Arai E, Funaki H, Katayama M, Oguri Y, Shimizu K (1992) Nucl Instrum Meth B 64:296
- Arnold Bik WM, de Laat CTAM, Habraken FHPM (1992) Nucl Instrum Meth B 64:832
- Assmann W (1992) Nucl Instrum Meth B 64:267
- Barbour JC, Doyle BL (1995) In: Tesmer JR, Nastasi M (eds) Handbook of modern ion beam materials analysis, Chapter 5. MRS, Pittsburgh, pp 83–138
- Barradas NP, Jaynes C, Webb RP (1997) Appl Phys Lett 71:291
- Barradas NP, Arstila K, Battistig G, Bianconi M, Dytlewski N, Jaynes C, Kótai E, Lulli G, Mayer M, Rauhala E, Szilágyi E, Thompson M (2007) Nucl Instrum Meth B 262:281
- Bartha L, Uzonyi I (2000) Nucl Instrum Meth B 161–163:339
- van Bebbler H, Borucki L, Farzin K, Kiss AZ, Schultr WH (1998) Nucl Instr Meth B 136:72–76
- Behrooz AM, Headrick RL, Seiberling LE, Zurmuhle RW (1987) Nucl Instrum Meth B 28:108
- Berger MJ, Hubbel M (1987) NBSIR 87-3597. http://physics.nist.gov/cgi/bin/Xcom/xcom3_l-t
- Berger P, Gaillet L, El Tahhann R, Moulin G, Viennot M (2001) Nucl Instrum Meth B 181:382
- Bird JR, Williams JS (1989) Ion beams for materials analysis. Academic, Sidney
- Blaauw M, Campbell JL, Fazinis S, Jaksic M, Orlic I, Van Espen P (2002) Nucl Instrum Meth B 189:113
- Bogdanovic I, Fazinic S, Jaksic M, Grime GW, Valkovic V (1994) Nucl Instrum Meth B 85:732
- Bolse W, Gustafsson M, Harbsmeier F, Roccaforte F (2000) Nucl Instrum Meth B 161–163:641
- Borbély-Kiss I, Józsa M, Kiss ÁZ, Koltay E, Nyakó B, Somorjai E, Szabó G, Seif El-Nasr SJ (1985) Radioanal Nucl Chem 92:391
- Brissaud I, Frontier JP, Regnier P (1985) Nucl Instrum Meth B 12:235
- Budnar MO, Campbell JL (eds) (2005) X-Ray Spectrometry 34(4):263–399
- Calligaro T, Dran J-C, Poirat J-P, Querré G, Salomon J, Zwaan JC (2000) Nucl Instrum Meth B 161–163:769
- Campbell JL (ed) (2002) Nucl Instr Meth B 189:1–519
- Cherniak DJ, Lanford WA (2001) In: Alfasi ZB (ed) Non-destructive elemental analysis, Chapter 8, Blackwell Science Ltd, UK, pp 308–338
- Chu W-K, Mayer JW, Nicolet M-A (1978) Backscattering spectrometry. Academic Press, New York
- Cohen DD, Harrigan M (1985) At Data Nucl Data Tables 33:255–344
- Composto RJ, Walters RM, Genzer J (2002) Mat Sci Eng R 38:107
- Coote GE, Cutress TW, Suckling GW (1997) Nucl Instrum Meth B 130:571
- Da Rosa EBO, Krug C, Stedle FC, Morais IJIR (2002) Nucl Instrum Meth B 190:538
- Davies JC (1973) In: Morgan DV (ed) Channeling: theory, observations and applications. Wiley, New York, p 391
- Deconninck G (1978) Introduction to radioanalytical physics. Akadémiai Kiadó, Budapest
- Demortier G (ed) (1982) Nucl Instr Meth B 197:65–170
- Doolittle LR (1986) Nucl Instrum Meth B 15:227
- Doyle BL, Maggiore CJ, Bench G (eds) (1997) Nucl Instr Meth B B130:1–750
- Ecker KH, Krauser J, Weidinger A, Weise HP, Maser K (2000) Nucl Instrum Meth B 161–163:682
- Elekes Z, Kiss ÁZ, Biron I, Calligaro T, Salomon J (2000) Nucl Instrum Meth B 168:305
- Elekes Z, Kiss ÁZ, Gyürky G, Somorjai E, Uzonyi I (1999) Nucl Instrum Meth B 158:209
- Elekes Z, Szőör G, Kiss ÁZ, Rózsa P, Simon A, Uzonyi I, Simulák J (2002) Nucl Instrum Meth B 190:291
- Feldman LC, Mayer JW (1986) In: Fundamentals of surface and thin film analysis, Chapter 12. North-Holland, New York, pp 283–310

- Feldman LC, Mayer JW, Picraux ST (1982) Materials analysis by ion channeling. Academic, New York
- Folkmann J (1975) *J Phys E Sci Instrum* 8:429
- Gallien J-P, Gouget B, Carrot F, Oriol G, Brunet A (2001) *Nucl Instrum Meth B* 181:382
- Gardner RK, Gray TJ (1978) *At Data Nucl Data Tables* 21:515–536
- Gihwala D, Peisach M (1982) *J Radioanal Chem* 70:287
- Glass GA, Dymnikov AD, Rout B, Zachry DA (2007) *Nucl Instr Meth B* 260:372–377
- Gorleau R, Gujrathi SC, Martin JP (1983) *Nucl Instrum Methods* 218:11
- Grime GW, Watt F (eds) (1988) *Nucl Instr Meth B* B30:227–497
- Gujrathi SC, Bultena S (1992) *Nucl Instrum Meth B* 64:789
- Gurbich A, Bogdanovic-Radovic I, Chiari M, Jaynes C, Kokkoris M, Ramos AR, Mayer M, Rauhala E, Schwerer O, Liqun SHI, Vickridge I (2008) *Nucl Instrum Meth B* 266:1198
- Ishii A, Nakamura K (1993) *Nucl Instrum Meth B* 75:388
- Jaksic M, Bogdanovic I, Cereda E, Eazinic S, Valkovic V (1993) *Nucl Instrum Meth B* 77:505
- Jaksic M, Bogdanovic Radovic I (eds) (2005) *Nucl Instr Meth B* 231:1–556
- Jankuhn S, Vogt J, Butz T (2000) *Nucl Instrum Meth B* 161–163:894
- Jans S, Kalbitzer S, Oberschachtsiek P (1994) *Nucl Instrum Meth B* 85:321
- Jembrih D, Neelmeijer C, Schreiner M, Mäder M, Ebel M, Svagera R, Peev M (2001) *Nucl Instrum Meth B* 181:698
- Jesus AP, Braizinha B, Ribero JP (2000) *Nucl Instrum Meth B* 161:186
- Johansson SAE (ed) (1977) *Nucl Instr Meth* 142:1–338
- Johansson SAE (ed) (1981) *Nucl Instr Meth* 181:1–537
- Johansson SAE, Campbell JL (1988) *PIXE: a novel technique for elemental analysis*. Wiley, Chichester
- Johansson SAE, Campbell JL, Malmqvist KG (1995) *Particle induced X-ray emission spectroscopy (PIXE)*. In: Winefordner JD (ed) *Chemical analysis: a series of monographs on analytical chemistry and its applications*, vol 133. Wiley, New York
- Johansson SAE, Johansson TB (1976) *Nucl Instrum Methods* 137:473–516
- Katsanos A, Xenoulis A, Hadjiantoniou A, Fink RW (1976) *Nucl Instrum Methods* 137:119
- Khan AH, Khaliqzaman M, Husain M, Abdullah M, Katsanos AA (1979) *Nucl Instrum Methods* 165:253
- Kiss ÁZ, Biron I, Calligaro T, Salomon J (1994) *Nucl Instrum Meth B* 85:118
- Kiss ÁZ, Koltay E, Nyakó BM, Somorjai E, Anttila A, Räisänen J (1985) *J Radioanal Chem* 89:123
- Klein SS (1986) *Nucl Instrum Meth B* 15:464
- Koltay E (1988) *Particle induced X-ray emission: basic principles, instrumentation and interdisciplinary applications*. In: Ferreira JG, Ramos MT (eds) *X-ray spectroscopy in atomic and solid state physics*, NATO ASI Series, Series B: Physics, vol 187. Plenum Press, New York, pp 301–334
- Kótai E (1994) *Nucl Instrum Meth B* 85:588
- Lanford WA (1992) *Nucl Instrum Meth B* 66:65
- L'Ecuyer J, Brassard C, Cardinal C, Chabbal J, Deschenes L, Labrie JP, Terreault B, Martel JG, St-Jacques R (1976) *J Appl Phys* 47:881
- Leavitt JA, McIntyre LC Jr, Weller MR (1995) In: Tesmer JR, Nastasi M (eds) *Handbook of modern ion beam materials analysis*, Chapter 4. MRS, Pittsburgh, pp 37–81
- Legge GJF, Jamieson DN (eds) (1991) *Nucl Instr Meth B* 54:1–440
- Leroux J, Think TP (1977) *Revised tables of X-ray mass attenuation coefficients*. Corporation Scientifique Claisse, Quebec
- Lindh U (ed) (1993) *Nucl Instr Meth B* 77:1–547
- Lipworth AD, Annegarn HJ, Kneen MA (1993) *Nucl Instrum Meth B* 75:127
- Malmqvist KG (ed) (1999) *Nucl Instr Meth B* 150:1–682
- Manuaba A, Pásztí F, Ortega C, Grosman A, Horváth ZE, Szilágyi E, Khanh NQ, Vickridge I (2001) *Nucl Instrum Meth B* 179:63
- Markowicz A, Van Dyck P, Van Grieken R (1980) *X-ray Spectrom* 9:52
- Martin B (ed) (1984) *Nucl Instr Meth B* 3:1–699
- Martin G, Sauvage T, Desgardin P, Garcia P, Carlot G, Barthe MF (2007) *Nucl Instrum Meth B* 258:471
- Mateus R, Jesus AP, Ribeiro JP (2005) *Nucl Instrum Meth B* 229:302
- Maxwell JA, Campbell JL, Teesdale WJ (1989) *Nucl Instrum Meth B* 43:218
- Mayer M (1997) *Report IPP*, 9/113, Garching
- Miranda J, Ruvalcaba-Sil (eds) (2008) *X-ray spectrometry* 37(2):94–197
- Moore J (1980) *Nucl Instrum Methods* 174:577
- Moretto PH, Bonin Mosbah M (eds) (2001) *Nucl Instr Meth B* 181:1–759
- Moschini G, Valkovic V (eds) (1996) *Nucl Instr Meth B* 109/110:1–703
- Murillo G, Policroniades R, Tenorio D, Méndez B, Andrade E, Pineda JC, Zavala EP, Torres JL (1998) *Nucl Instrum Meth B* 136–138:888
- Osipovicz T, Breeze MBH, Watt F, van Kan JA, Bettiol AA (eds) (2007) *Nucl Instr Meth B* 158:1–482
- Pásztí F, Szilágyi E (1998) *Vacuum* 50:451
- Pathak AP, Avasthi DK, Dev BN (eds) (2008) *Nucl Instr Meth B* 266:1149–1932
- Peisach M, Pretorius R (1973) *J Radioanal Chem* 16:559
- Petukhov VP, Terasova M, Török I (1999) *Nucl Instr Meth B* 150:103–108

- Piel N, Schulte WH, Berheide M, Becker HW, Borucki L, Grama C, Mehrhof M, Rolf C (1996) Nucl Instrum Meth B 118:186
- PrOzesky VM, Przybylowicz WJ, Pineda CA (eds) (1999) Nucl Instr Meth B 158:1–735
- Räsänen J (2001) In: Alfasi ZB (ed) Non-destructive elemental analysis, Chapter 8. Blackwell Science, UK, pp 276–307
- Rajta I, Kiss ÁZ, Kertész ZS, Szikszai Z, Simon A (eds) (2009) Nucl Instr Meth B 267:1995–2340
- Rebouta L, Soares JC, da Silva MF, Sanz-Garcia JA, Dieguez E, Agullo-Lopez F (1992) J Mater Res 7:130
- Respaldiza MA, Madurga G, Soares JC (1987) Nucl Instrum Meth B 22:446
- Rickards J (1985) Nucl Instrum Meth B 12:269
- Rijken HA (1993) PhD thesis, Technical University of Eindhoven, Eindhoven
- Rijken HA, Klein SS, de Voigt MJA (1992) Nucl Instrum Meth B 64:395
- Ryan CG, Cousens DR, Sie SH, Griffin WL (1990) Nucl Instrum Meth B 49:271
- Salomon J, Dran JC, Guillou T, Moignard B, Pichon L, Walter L, Mathis F (2008) Nucl Instrum Meth B 266:2273
- Sera K, Futatsugawa S (1996) Nucl Instrum Meth B 109/110:99
- Sevier KD (1979) At Data Nucl Data Tables 24:323–371
- SIGMA (2003) <http://www.mfa.kfki.hu/sigmadatabase/data/index.html>
- Sjöland KA, Kristiansson P, Elfman M, Malmqvist KG, Pallon J, Utui RJ, Yang C (1997) Nucl Instrum Meth B 129:101
- Smit Z, Budnar M, Cindro V, Ravnika M, Ramsak V (1984) Nucl Instrum Meth B 4:114
- Swanson ML (1995) In: Tesmer JR, Nastasi M (eds) Handbook of modern ion beam materials analysis, Chapter 10. MRS, Pittsburgh, pp 231–300
- Szabó G, Borbély-Kiss I (1993) Nucl Instrum Meth B 75:123
- Szabó G, Borbély-Kiss I (1999) PIXEKL program package for evaluation of PIXE spectra. ATOMKI, Debrecen, Hungary
- Székely G (1985) Comput Phys Commun 34:423
- Sziki GÁ, Simon A, Szikszai Z, Kertész ZS, Dobos E (2006) Nucl Instrum Meth B 251:343
- Szikszai Z, Kertész ZS, Kocsár I, Oláh V (2008) Acta Biologica Szegediensis 52:81
- Szilágyi E, Pászti F (1994) Nucl Instrum Meth B 85:616
- Szőkefalvi-Nagy Z (1996) Nucl Instrum Meth B 109–110:234
- Szőkefalvi-Nagy Z, Demeter I, Bagyinka C, Kovács KL (1987) Nucl Instrum Meth B 22:156
- Szőkefalvi-Nagy Z, Kocsanya A, Kovács I, Hopff D, Lúthje S, Niecke M (2009) Nucl Instrum Meth B 267:2163
- Takai M (1995) Nucl Instrum Meth B 96:179
- Takai M, Kamiya T (eds) (2003) Nucl Instr Meth B 210:1–563
- Tesmer JR, Maggiore CJ, Nastasi M, Barbour JC, Mayer JW (1990) High energy and heavy ion beams in materials analysis. MRS, Pittsburgh
- Tesmer JR, Nastasi M (1995) In: Handbook of modern ion beam materials analysis. Materials Research Society, Pittsburgh
- Thomas JP, Fallavier M, Ziani A (1986) Nucl Instrum Meth B 15:443
- Timmers H, Weijers TDM, Elliman RG (2002) Nucl Instrum Meth B 190:393
- Trocellier P, Berger P, Berthier B, Berthoumieux E, Gallien JP, Metrich N, Moreau C, Mosbah M, Varela ME (1999) Nucl Instrum Meth B 158:221
- Trompeter WJ, Reyes AG, Vickridge IC, Markwitz A (1999) Nucl Instrum Meth B 158:568
- Uda M (ed) (1993) Nucl Instr Meth B 75:1–592
- Uhrmacher M, Schwickert M, Schebela H, Lieb K-P (2005) J Alloy Compd 404–406:307
- Uzonyi I, Rajta I, Bartha L, Kiss ÁZ, Nagy A (2001) Nucl Instrum Meth B 181:193
- Uzonyi I, Szabó GY (2005) Nucl Instrum Meth B 231:156
- Van Rinvelt H, Bauman S, Nelson JW, Winchester JW, (eds) (1987) Nucl Instr Meth B 22:1–475
- Végh J, Berényi D, Koltay E, Kiss I, Seif-El-Nasr S, Sarkadi L (1978) Nucl Instrum Methods 153:553
- Vekemans B, Jensens K, Vincze L, Adams F, Van Espen (1994) X-ray spectrometry 23:278
- Vis RD (ed) (1990) Nucl Instr Meth B 49:1–580
- Vízkelethy G (1990) Nucl Instrum Meth B 45:1
- Watt F, Rajta I, Ausari K, Bettiol AA, Osipowicz T (2002) Nucl Instr Meth B 90:306–311
- Watt F, Van Kan JA, Rajta I, Bettiol AA, Choo TF, Breese MBH, Osipowicz T (2003) Nucl Instr Meth B 210:14–20
- Watt F, Bettiol AA, van Kann JA, Ynsa MD, Ren Minqin, Rajendran R, Cui Huifang, Sheu Fwo-Shen, Jenner AM (2009) Nucl Instr Meth B 267:2113
- Wielunski LS, Grambole D, Kreissig U, Grötzschel R, Harding G, Szilágyi E (2002) Nucl Instrum Meth B 190:693
- Wilde M, Fukutani K (2005) Nucl Instrum Meth B 232:280
- Yang F, Tang J, Zhu J (eds) (1995) Nucl Instr Meth B 104:1–652
- Ziegler JF (1977) Helium stopping powers and ranges in all elements. Pergamon Press, Oxford
- Ziegler JF, Biersack JP, Ziegler MD (2002) SRIM stopping and range of ions in matter. <http://www.srim.org/SRIM/SRIM2008.htm>
- Ziegler JF, Biersack JP, Littmark U (1985) Stopping and ranges of ions in solids. Pergamon Press, New York



34 Microscopic X-ray Fluorescence Analysis with Synchrotron Radiation Sources

F. Adams¹ · B. Vekemans² · G. Silversmit² · B. De Samber² · L. Vincze²

¹University of Antwerp, Antwerp, Belgium

²Ghent University, Gent, Belgium

34.1	<i>Introduction</i>	1738
34.2	<i>Synchrotron Micro- and Nanoscopic X-Ray Fluorescence Analysis</i>	1739
34.3	<i>Id18f: A Dedicated X-Ray Microprobe End-Station</i>	1744
34.4	<i>Micro-X-Ray Fluorescence Analysis as an Accurate Method of Microanalysis</i>	1745
34.5	<i>Quantitative Elemental Analysis</i>	1746
34.5.1	X-ray Absorption	1746
34.5.2	Quantitative Analysis	1748
34.6	<i>Related Techniques</i>	1750
34.6.1	Three-Dimensional Micro-XRF Methods: X-Ray Fluorescence Computed Tomography (XFCT) and Confocal Imaging	1751
34.6.1.1	Nanoscope X-ray Fluorescence Computerized Tomography (XFCT)	1752
34.6.1.2	Confocal XRF-Imaging	1753
34.6.2	X-Ray Absorption Spectroscopy: XANES and EXAFS	1756
34.7	<i>Summary</i>	1758

Abstract: This chapter deals with the analytical applications of synchrotron radiation sources for trace-level analysis of materials on microscopic and submicroscopic scales. Elemental analysis with X-ray fluorescence is described in detail. Two-dimensional (2D) and three-dimensional (3D) analyses are discussed in their quantitative aspects. Related methods of analysis based on absorption edge phenomena such as X-ray absorption spectrometry (XAS) and near-edge scanning spectrometry (XANES) yielding molecular information, computerized X-ray fluorescence microtomography (XFCT) based on the penetrative character of X-rays, and microscopic X-ray diffraction (XRD) providing structural data on the sample are also briefly discussed. The methodological treatment is illustrated with a number of applications.

Abbreviations AES, Auger emission spectrometry; CRM, Certified reference material; DL, Detection limit; ED, Energy dispersive; ESRF, European Synchrotron Radiation Facility; EXAFS, Extended X-ray absorption fine structure; NEXAFS, Near edge X-ray absorption fine structure; PCI, Phase contrast imaging; RM, Reference material; SR, Synchrotron radiation; SRM, Standard reference material; TXRF, Total reflection X-ray fluorescence; XANES, X-ray absorption near edge structure; XAS, X-ray absorption spectrometry; XDM, X-ray diffraction microscopy; XFCT, X-ray fluorescence computerized microtomography; XPEEM, X-ray photoelectron microscopy; XPS, X-ray photoelectron spectrometry; XRD, X-ray diffraction; XRF, X-ray fluorescence

34.1 Introduction

For a number of decades, X-ray fluorescence analysis (XRF) has established itself as a multielement analytical technique, which is capable of yielding quantitative information on the elemental composition of a variety of materials in a nondestructive manner. In its wavelength-dispersive configuration, it has proved itself as very important for routine analysis and quality control. The energy-dispersive configuration, on the other hand, offers wide potential as a simple tool for various laboratory and field applications in multielement analysis (Van Grieken and Markowicz 2002).

Two important variants of the method have appeared during the last 2 decades. Both variants are based on confining the volume in which the primary X-ray beam interacts with the analyzed material. In total reflection XRF (TXRF), by irradiating a flat sample with a near-grazing X-ray beam below the angle of total reflection, the in-depth penetration of the primary X-rays can be confined to a few tens of a nanometer below the surface allowing very sensitive surface analysis. Alternatively, the method can be exploited for bulk elemental trace analysis of liquids when these are brought on a clean inert surface (Wobrauschek 2007).

The second major variant of the XRF technique, which in the last decade has received a lot of attention, both with respect to the methodological developments and regarding its applications in diverse fields, is micro-XRF (μ -XRF). This microanalytical variant of bulk XRF is based on the localized excitation and analysis of a microscopically (now even submicroscopically) small area on the surface of a larger sample, providing information on the lateral distribution of major, minor, and trace elements in the material under study. The μ -XRF can be exploited with laboratory X-ray sources but found its most important areas of application when combined with a synchrotron radiation (SR) source (Janssens et al. 2000).

The high intensity and directionality of SR sources implies that they are ideally suited for the generation of X-ray microbeams. The polarization of the incident radiation can be used to reduce the relative contribution of scattered radiation reaching the detector, as scattering cross sections are dependent on the polarization state, whereas photo absorption cross sections giving rise to fluorescence radiation are not. In addition, quasi-monochromatic micron size X-ray beams can be generated from the white radiation spectrum using X-ray monochromators, thanks to the high directionality of the radiation.

In what follows the present status of μ -XRF analysis with synchrotron radiation sources with respect to lateral resolution, achievable detection limits and sensitivity will be reviewed. The possibilities of third-generation synchrotron radiation storage rings, especially those of the European Synchrotron Radiation Facility (ESRF) in Grenoble, France, will be discussed in relation to existing second-generation storage rings and newly built synchrotron sources. The analytical characteristics will be discussed as well as the potential in sensitive and accurate elemental analysis by μ -XRF in general. Related methods of analysis based on absorption edge phenomena such as X-ray absorption spectroscopy (XAS), giving molecular information, computerized X-ray fluorescence microtomography (XFCT) based on the penetrative character of X-rays, and microscopic X-ray diffraction (XRD) providing structural data on the sample will be briefly mentioned.

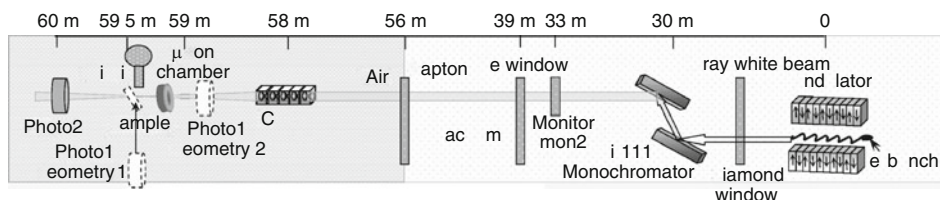
34.2 Synchrotron Micro- and Nanoscopic X-Ray Fluorescence Analysis

Disregarding the inherent complexity of the SR X-ray source problems involved with monochromatization and focusing of the X-rays, the instrumentation for X-ray microanalysis is extremely simple – conceptually. It consists of a mechanical sample stage with precision computer-controlled micro-stepping motors for X, Y, and (optionally) rotational movement of the sample, a semiconductor type detector for the measurement of the fluorescent radiation, different visualization tools for observation of the sample and, finally, a range of diagnostic and control tools.

Figure 34.1 shows the ID18F as a typical setup for SR μ -XRF (Somogyi et al. 2001, 2002). The components are indicated in the figure. The different elements of the μ -XRF instrumentation will be discussed in sequence, starting with the SR source characteristics.

Fig. 34.1

Schematic layout of the ID18 beamline and the ID18F user end-station. Photodiode 1 (photo1) is placed either into the sample position if a sample was measured (geometry 1) or in front of the mini-ionization chamber (geometry 2). For other components, see text (Adapted from Somogyi et al. 2003)



The difficulties in focusing X-rays are the result of the refractive index being very close to unity for hard X-rays. The refractive index is defined as ($\tilde{n} = 1 - \delta - i\beta$) where δ is the refractive index decrement (typically 10^{-6} for hard X-rays) and β is the absorption index. For wavelengths in the X-ray range, the refractive index of materials is very close to (but less than) 1, with the consequence that manufacturing straightforward refractive lenses is difficult. In the soft X-ray range, this problem is compounded by the elevated absorption (attenuation) coefficient for most materials that effectively limits the use of reflective and refractive optical designs. For these reasons, soft X-ray microscopes commonly resort to diffractive optics. Focusing hard X-rays with the help of grazing-incidence on reflecting surfaces is the method mostly used on synchrotron beamlines. A typical example is a toroidal mirror that gives spots several hundreds of micrometers wide. The goal to decrease the spot size to a micrometer or less has triggered technological developments of a specific reflecting system, the so-called Kirkpatrick–Baez (KB) system. Two orthogonal mirrors focus the beam successively in the horizontal and in the vertical planes.

Microfocusing devices that are based on refraction operate in the same way as visible light optics but there are some differences (Schroer et al. 2005). Firstly, the X-ray refractive index of a material is smaller than in vacuum or air and, therefore, an X-ray focusing lens has a double concave shape. Secondly, because the refractive index of all materials is very close to unity for hard X-rays, the deflection is usually very small and many lenses have to be placed in series to achieve reasonably short focal lengths. In order to keep absorption to a minimum, these compound refractive lenses (CRLs) should be made from low-*Z* materials such as beryllium, carbon, aluminum, and silicon. CRLs with parabolic shapes made from polycrystalline aluminum by a pressing technique have proven to be well suited for microanalysis and full field microscopy applications for 20–120 keV X-rays (Lengerer et al. 1998).

In a number of μ -XRF installations (poly)capillary optics are used as focusing devices (e.g., Bilderback et al., 1994; Vincze et al., 2002a, b). These simple (pseudo) focusing devices exploit conditions for total reflection in single glass capillaries or in compound systems of capillary bundles to collimate and focus beams and provide a good lateral resolution but suffer from the short working distance (typically less than few millimeter) between the capillary tip and the sample.

When X-rays interact with matter, three main interaction types are possible: elastic (Rayleigh) scattering, inelastic (Compton) scattering, and absorption due to the photoelectric effect (see also ► Chap. 8 in Vol. 1 on this topic). Most of the X-ray applications during the last 100 years or so have used absorption contrast. In terms of the complex X-ray refractive index ($\tilde{n} = 1 - \delta - i\beta$) this means that the emphasis has been on the imaginary component $i\beta$. During the photoelectric effect, the incoming photon is fully absorbed by an atom and its energy is transferred to a bound electron that will leave the absorbing atom as a photoelectron. Either the measurement of the photoelectron or the fluorescent radiation resulting from the relaxation process can be used for analysis. The first possibility leads to methods of analysis such as X-ray photoelectron microscopy (XPEEM). Combined with a photoelectron microscope with nm lateral/depth resolution, the photoemission technique gives the unique possibility of true nondestructive compositional analysis with nm scale lateral and depth resolution, thus providing new means of measuring 3D morphologies in nanoscience and technology. Third-generation SRs provide beamlines for XPEEM, and thus photoemission measurements at a spatial resolution of better than 50 nm are now possible, and extrapolations indicate a 2 nm resolution to be attainable.

Little or no attention was paid until recently, to the real component δ , which becomes important when dealing with X-ray phase-contrast imaging (PCI). Coherent X-ray diffraction

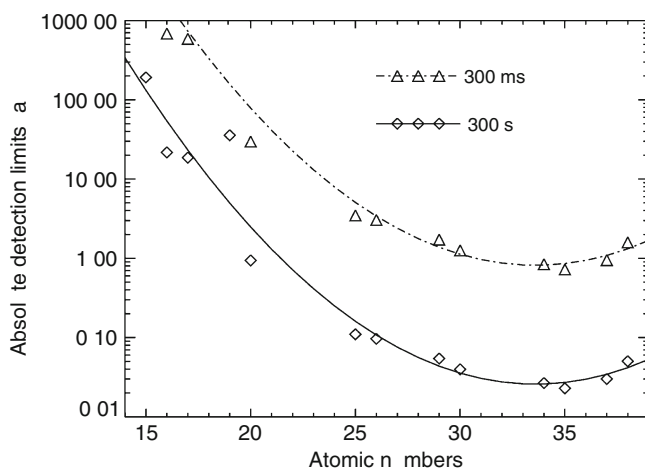
microscopy (XDM) and imaging involves a method of image reconstruction from the coherent X-ray diffraction pattern of a sample. A lensless method is reliant on radiation *coherence* in high-brilliance X-ray sources for 2D or 3D reconstruction of the image of nanoscale structures.

A particular advantage of SR μ -XRF in comparison with the conventional X-ray tube sources is the extremely high brilliance. *Brilliance* is expressed as the number of photons emitted per unit source area over a unit angle of emission and per unit energy (photons $\text{s}^{-1} \text{mm}^{-2} \text{mrad}^{-2}$ per 0.1% of radiation bandwidth). In addition, in the plane of the storage ring the radiation is linearly polarized with the *E*-vector parallel to the ring plane and the *B*-vector normal to it. The radiation is highly collimated along a direction tangential to the movement of the electrons in the ring, which facilitates the delivery of the radiation to a predefined sample area.

The high intensity and directionality imply that SR is ideally suited for the generation of X-ray micro- and nanobeams with very high flux density, exceeding now 10^{13} photons $\text{s}^{-1} \mu\text{m}^{-2}$ by using, e.g., wide bandpass nanofocusing X-ray optics at the largest third-generation SR sources. Such high flux densities are achieved, e.g., at the ESRF ID22NI nanoprobe, where a nanoscopic hard X-ray beam is generated by bent KB multilayer mirrors, producing beam sizes of ~ 90 nm with intensities of approximately 10^{12} photons/s at an energy of 17.5 keV. At this instrument, absolute detection limits below 0.1 ag can be achieved for atomic numbers above 26 using a measuring (live) time of 1000 s (see [Fig. 34.2](#)). The extreme X-ray flux density within the submicron spot results in the possibility of detecting an amount of a few thousand of transition metal atoms. Using a thin Fresnel zone plate with outermost zone widths of 10 nm Kang et al. (2006) demonstrated focal sizes as small as 30 nm and an efficiency of up to 44% at 19.5 keV.

Fig. 34.2

Absolute mass detection limits for elements with atomic number above 14 measured at the European Synchrotron Radiation Facility (ESRF) ID22NI nanoprobe corresponding to a beam size of approximately 100 nm, beam intensity of 6×10^{11} photons/s and measuring times of 300 ms and 300 s



When performing measurements in the plane of the SR source, the polarization of the incident radiation increases the signal-to-background ratios by up to two orders of magnitude. In addition, thanks to the high directionality of the beam, quasi-monochromatic X-ray microbeams can be generated from the polychromatic (white) radiation spectrum using suitable X-ray monochromators. Using these by tuning the energy of the source, the strong energy dependence of the inner shell photoelectric cross sections can be exploited to increase specificity of measurements or to obtain chemically significant information (valence state, molecular information). On the other hand, polychromatic excitation has the advantage that (nearly) all elements in the sample are excited with quite comparable efficiency providing a more uniform spectrometer response over the Z range of interest. Hence, this type of excitation is more appropriate for general-purpose materials characterization. Since losses in flux due to the monochromatization process are excluded, the elemental efficiency of polychromatic setups is also higher than when monochromatic excitation is used. On the other hand, quantification of the detected X-ray intensities is in such circumstances more complicated and error-prone. For quantitative analysis the use of monochromatic radiation is, hence, preferable.

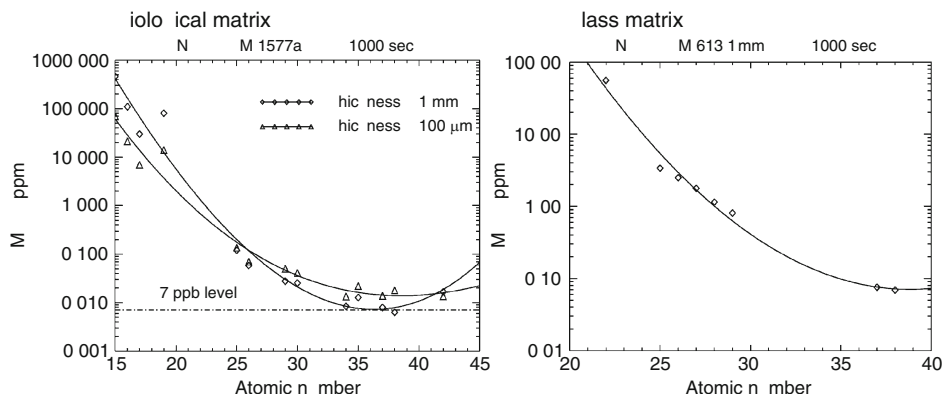
With such characteristics, it is not surprising that a number of existing storage rings have been employed in SR μ -XRF experiments combining the advantages of XRF as an elemental analytical tool with the unique possibilities of the SR. Of special significance are the new so-called third-generation storage rings that are specifically designed to obtain unprecedented intensity and brilliance. A number of these storage rings are now operational – the European Synchrotron Radiation Facility, ESRF; the Advanced Photon Source, APS, Argonne, USA; and the Super Photon ring-8 GeV, SPring-8, Harima, Japan, are the most important examples. Compared to earlier second-generation rings, these SR facilities are characterized by their high energy of 6 to 8 GeV. Significant in these devices also is the systematic use of insertion devices that are placed in the straight sections of the storage ring (wigglers and undulators). *Wigglers* are magnetic structures that create multiple oscillations around the beam path and hence increase both the energy and the intensity of the radiation. *Undulators* are designed to create smaller and more frequent deflections, giving rise to interference effects as a result of which the coherent radiation is concentrated around specific energies. In addition, X-ray optics of increased sophistication amplifies considerably both flux density and brilliance. Other newly built SR sources follow the design characteristics of these sources.

A double crystal monochromator (see [Fig. 34.1](#)) comprising a pair of crystals is a standard item in most μ -XRF setups because the exit direction is kept constant during energy scanning. Furthermore, mechanical systems are adopted to keep the beam height constant during the energy scan. The energy resolution of the double crystal monochromator is of the order of $\Delta E/E = 10^{-4}$ or better, and this is sufficient for XAS and XANES applications. However, in its primary mode of utilization, XRF analysis requires a high photon flux density rather than such high energy resolution, an energy resolution of the order of $\Delta E/E = 10^{-2}$ being sufficient for the purpose. Synthetic multilayers, which are made by vacuum deposition of alternate thin layers of two materials with different electron densities, provide this resolution while yielding a photon flux density one to two orders of magnitude higher than available with a double crystal monochromator. This is due to the wide energy bandpass of the multilayer.

Techniques for the formation of intense X-ray microbeams are readily available using various types of X-ray optics. Bent mirrors, crystals and multilayers, tapered glass monocapillaries, complex polycapillary lens systems, Bragg–Fresnel lenses, one- or two-dimensional waveguides, and refractive lenses have been developed and tested for use in micron (μm) size to

■ Fig. 34.3

Relative detection limits with ID18F (see Fig. 34.1) using a 100 component compound reflective lens set at 21 keV in a biological material (NIST SRM 1577a, bovine liver) and in NIST 613 glass SRM



submicron focusing at synchrotron beam lines. At present, it is possible to obtain sufficient beam intensity on microscale samples to allow reliable sub ppm level determinations of a large number of elements. Figure 34.3 shows relative detection limits obtained at ESRF with the instrument shown in Fig. 34.1 for two reference samples.

The measurement part of the μ -XRF setup is mostly a semiconductor detector, either a conventional Si(Li) or an intrinsic Ge detector or another type of semiconductor detector. Recent technological developments and new topology designs have made semiconductor detectors ideal devices for X-ray detection with reasonably high resolution at high pulse processing rate. The limited energy resolution of the energy-dispersive detection gives rise to complicated spectra with multiple spectral interferences, which need to be resolved through spectral deconvolution. Also, high count rates must be adequately taken into account, e.g., by using digital pulse processing (Adams 2003). To take full profit of the polarization and, hence, to increase signal-to-noise ratios, the X-ray detectors are placed in the plane of the storage ring at typically an angle of 90° to the incident beam direction. Wavelength-dispersive spectrometers are seldom used because of the slow measurement process and the resulting loss in sensitivity.


Techniques have been developed for fast and reliable nonlinear least squares deconvolution of X-ray spectra, which circumvent spectral interferences, e.g., the analysis of X-ray spectra by iterative least squares (AXIL) programme (Vekemans et al. 1994; Janssens et al. 1996). Also, powerful methodologies are now available for modeling by ab initio Monte Carlo simulation both the beam optics and the beam-sample interaction within the sample and the detector (Vincze et al. 1999a, b, c). The combined use of nonlinear least squares deconvolution of X-ray spectra and the powerful methodology for modeling the beam optics and beam-sample interaction allow the optimum use of all spectral information, including the use of Rayleigh and Compton scattering. A number of background effects that were never fully evaluated in XRF appear in the SR spectra, the most important being electron bremsstrahlung in the sample and the detector. Electron bremsstrahlung is able to generate fluorescence radiation from low Z elements and is, hence, an important factor in quantitative analysis. Also, specific spectral artifacts complicate the spectra, e.g., radiative Raman scattering. State-of-the-art multivariate statistical techniques for data reduction of image scans are available (Janssens et al. 1996, 2000).

For the measurement of elemental distribution maps, spectra are taken as the sample is moved over the beam path. Contrarily to t0068e vacuum requirements of most other microprobe methods, samples are normally observed in air, allowing the measurement of samples in their natural (e.g., wet) conditions.

As an example of the many setups available at SR sources, a brief description will be given of the ID18F configuration at ESRF, Grenoble, which is specifically devoted to μ -XRF applications. Some other SR installations exploit μ -XRF as a dedicated beamline, some others use it in combination with other applications.

Total reflection X-ray fluorescence analysis (TXRF) extends XRF down to the ultra-trace element range. Detection limits of picograms or nanograms per gram levels are reached with X-ray tube excitation. Using synchrotron radiation as excitation source, detection limits of femtogram levels are achievable, which is particularly important for the surface analysis of Si wafers. The use of SR as source is an elegant and powerful approach for TXRF to achieve ultimate results in terms of detection limits, reaching the 10^{-18} g levels and, if allowed at dedicated beamlines for low energies, even the determination of extremely light elements down to boron. Applying XANES in combination with TXRF allows the speciation of elements at ultra-trace levels (Ortega et al. 1998; Streli 2006; Streli et al. 2006; Wobrauschek 2007).

34.3 ID18f: A Dedicated X-Ray Microprobe End-Station

ID18F was constructed as a dedicated X-ray microprobe in the third experimental hutch (radiation shielding enclosure) of the ID18 beamline of the ESRF and using its optics infrastructure; the schematic layout is shown in  Fig. 34.1 (Somogyi et al. 2001). The energy of the excitation radiation can be tuned between 6 and 28 keV by changing the undulator gap, and monochromatic radiation of $\Delta E/E = 10^{-4}$ is created by a fixed exit double crystal Si (111) monochromator. The design goal was to improve procedures of μ -XRF in order to reach 5% average accuracy of quantification down to sub-ppm concentration levels for elements of $Z > 13$. To do this it is necessary to insure high reproducibility of the measurement geometry and instrumental parameters of the setup, a very good short- and long-term stability, and precise monitoring ($< 1\%$) of the intensity of the incoming beam.

The entire microprobe setup is positioned on a movable granite table. Compound refractive lenses are used for focusing to a routinely achievable spot size of 1–2 μm vertically and 12–15 μm horizontally. The intensity of the incoming, the focused, and the transmitted beam is monitored by ionization chambers and photodiodes. A miniature ionization chamber with an aperture of 50 μm diameter as an entrance window was developed at the ESRF for measuring the intensity of the focused beam close to the sample (Somogyi et al. 2003). The characteristic X-ray line intensities are detected with a Si(Li) detector of 30 mm^2 active area, 3.5 mm active thickness, and 8 μm thick Be window placed at 90° to the incoming linearly polarized X-ray beam. Fast scanning XRF measurements (> 0.1 s live time/spectrum) are possible.

The analytical characteristics (degree of polarization, absolute and relative limits of detection) of ID18F were determined by measuring a number of existing certified reference materials (CRMs). The degree of polarization is $> 99.5\%$. The available relative detection limits (DL) are < 0.1 ppm for elements of $Z > 25$. Relative DLs down to a few ppb are possible for a number of elements on the basis of 1,000 s live time measurements and ppm DLs can be reached for measurements of a few seconds. The absolute DLs are less than 1 fg for elements of $Z > 25$.

The photon flux in the focused beam is 10^9 – 10^{10} photons/s depending on the energy of the incoming beam (Adams 2003; Vekemans et al. 2003).

The design characteristics of other SR installations can be found in the literature, e.g., the X-26A beamline of the National Synchrotron Light Source in Brookhaven National Laboratory (Smith 1995) and beamline L at HASYLAB (Falkenberg et al. 2001).

34.4 Micro-X-Ray Fluorescence Analysis as an Accurate Method of Microanalysis

Accurate elemental analysis at the microscopic/submicroscopic level is very important in fundamental scientific research and is of growing importance for the characterization at submicron/nanoscale level in various areas of materials technology. All current micro-“beam” methods of analysis are relative, i.e., the signal measured requires either comparison to a reference material or validation through comparison with quantitatively reliable methods of analysis. Most so-called “beam” methods for microanalysis (e.g., electron probe microanalysis, micro-Auger spectroscopy, and secondary ion mass spectrometry) cannot yet be considered as accurate methods of analysis except when applied to compositionally or structurally quite simple samples. Their application to quantitative analysis must rely on the use of CRMs or standard reference materials (SRMs and RMs) for calibration, but, with very few exceptions, these materials are not available at present.

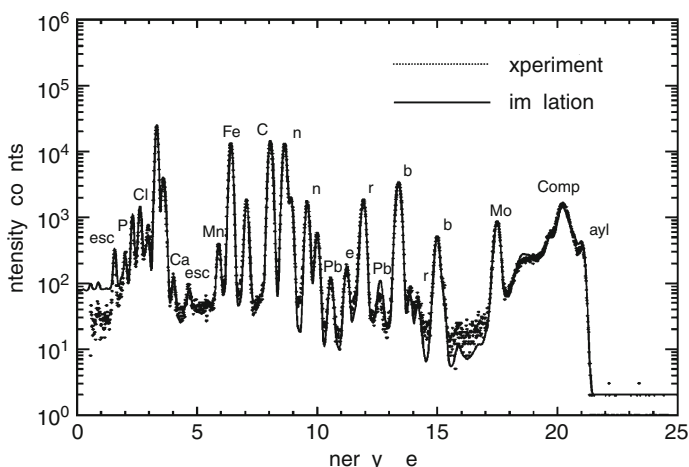
Microscopic methods such as quantitative X-ray photoelectron spectrometry (XPS) and Auger emission spectrometry (AES) are more difficult to apply as a quantitative tool as they require an understanding of the change in energy distribution of electrons as they move in solids. In comparison with XRF, they need to deal with the electron cloud of outer electrons instead of the core electrons. Nevertheless, as demonstrated, e.g., by Tougaard (1997), principles and rules of general validity (universal cross sections) can be defined, which give a reasonably accurate description of the inelastic scattering process and open the way for real quantification. The basic physical processes involved in particle induced X-ray emission (PIXE) and Rutherford backscattering spectrometry (RBS) are also well understood (see previous chapter), and they can also be modeled using readily available software codes (Grime 1996).

The reason for the lack of RMs is the absence of reliable and accurate methods of analysis. Microanalysis is, hence, in need of at least one method that can be used as a reference tool for other techniques and to link RMs or round robin exercises to the international unit of mass. Micro-XRF can be used for this potentially, especially when used for analyzing microscopic samples, where matrix absorption effects are relatively unimportant. At present, XRF is considered to be a rather poor method for certification purposes due to intense matrix effects resulting from intense radiation absorption and enhancement by secondary fluorescence. In wavelength-dispersive XRF, reliable results can only be obtained through calibration with a set of reference samples of closely similar composition to the unknown sample. In the case of energy-dispersive XRF using monochromatic excitation, the correction for matrix effects is simpler but in this case the method suffers from a number of other drawbacks, such as spectral overlap and poor statistics in the spectra.

Despite all these drawbacks, the physical basis of the X-ray – matter interaction is fully understood and the physical parameters governing the interaction and the extent of radiation absorption can be derived accurately from measurements obtained under well-defined

■ Fig. 34.4

Experimental (dots) and simulated (solid curve) synchrotron radiation–X-ray fluorescence (SR–XRF) spectra obtained for the NIST SRM 1577b bovine liver standard, corresponding to 21 keV excitation at the European Synchrotron Radiation Facility (ESRF) ID18F end-station (Adapted from Vincze et al. 2004)



conditions. In principle, it is thus possible to fully correct for deviations from linearity between measured intensities and elemental concentrations, provided time and efforts are spent to make the proper calculations. This is easily performed when the instrumentation is simplified as much as possible, essentially when using a high-intensity monochromatic primary excitation, by employing an energy-dispersive detector, and by using a sample of well-characterized shape and smooth surface.

It has been demonstrated earlier that experimental XRF spectra can be accurately modeled through Monte Carlo simulations starting from first principles (Vincze et al. 1999a, b; Vekemans et al. 2003). As an example, Fig. 34.4 shows a comparison of simulated and experimental SR–XRF spectra corresponding to the biological reference material NIST SRM 1577b (bovine liver). See Fig. 34.3 for the detection limits of these measurements.

Starting from a priori assumptions of the composition of the sample, e.g., on the basis of the measured intensities in the spectrum, it is possible to model spectra and by iteration to arrive at reasonable estimates of the sample composition. Such an approach is by no means easy but with inexpensive computing power available nowadays it becomes well feasible. The following section will review quantitative analysis according to such procedures.

34.5 Quantitative Elemental Analysis

34.5.1 X-ray Absorption

The first issue of concern is radiation absorption of the incoming and the fluorescent radiation.

Assume a monoenergetic X-ray beam with intensity I_0 that travels through a slab of material. The X-ray beam will then be attenuated exponentially with the path length d :

$$I = I_0 e^{-\mu_l d} = I_0 e^{-\mu_\rho \rho d} \quad (34.1)$$

with μ_l the linear absorption coefficient (attenuation coefficient). In practice, the mass absorption coefficient $\mu_\rho = \mu_l / \rho$ (with ρ meaning the density of the material) is being used, as the total absorption of a sample composed of different atom types at a certain photon energy E , can easily be calculated from

$$\mu_{\text{tot}}(E) = \rho \sum_i w_i \mu_{\rho,i}(E) \quad (34.2)$$

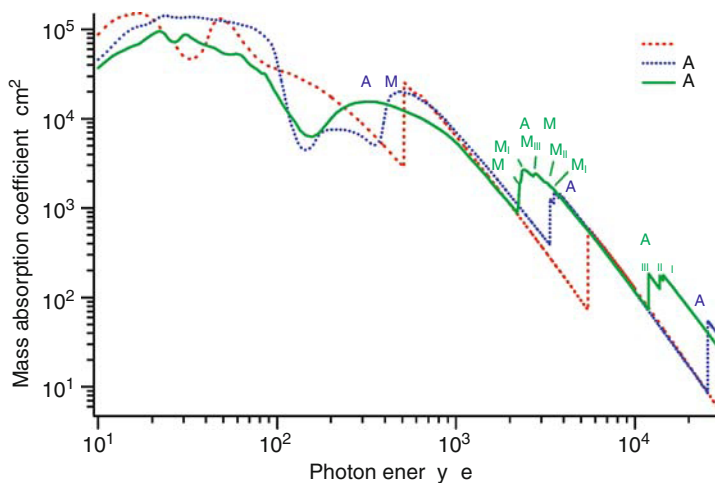
with w_i the weight fraction of element i in the sample. Mass absorption coefficient values for the different elements of the periodic table are given for example in volume III of the International Table for Crystallography.

As an example, the mass absorption coefficients of vanadium, silver, and gold in the 10 eV – 20 keV photon energy range are given in [Fig. 34.5](#).

On a log–log scale, the mass absorption coefficient decreases essentially monotonically from a certain energy value on (which is element specific and larger for higher Z elements; about 200 eV for V and about 1 keV for Au). Matter becomes more and more transparent to X-rays with increasing X-ray energy. Besides this monotonic decrease, a number of discontinuities can be observed at which the absorption increases suddenly. These jumps are called “absorption edges.” The energy positions of the absorption edges for a specific element correspond to the binding energies of electrons occupying different orbitals in that element. Suppose that the energy of the incoming photon beam is increased from just below an absorption edge for a certain element to an energy value just above the edge. As soon as the energy of the photon becomes equal or larger than the binding energy of that particular electron energy level in that atom type, the electrons of that level can contribute to the absorption via the photoelectric effect. A new channel for absorption opens up and the total absorption for that element increases suddenly.

Fig. 34.5

The mass absorption coefficients for V, Ag, and Au as function of photon energy



34.5.2 Quantitative Analysis

Computer modeling can be applied in an iterative manner for the quantitative evaluation of XRF spectra of homogeneous bulk samples and of particles with predetermined shape (Vincze et al. 2002a, b). Errors are mostly due to the uncertainties in the parameters responsible for the interaction process (cross sections, fluorescence yields, and transition probabilities).

The detected characteristic X-ray line intensity $I_{i,\text{meas}}$ of element i is expressed as

$$I_{i,\text{meas}} = I_0 C_i S_i A_i \quad (34.3)$$

where I_0 is the intensity of the primary X-ray beam, C_i is the concentration (fraction) of element i within the particle, S_i is the elemental sensitivity for element i , and A_i is the self-absorption factor of incident and emitted X-rays.

The net-peak intensity $I_{i,\text{meas}}$ can be determined by fitting the experimental spectra using nonlinear least squares fitting (Janssens et al. 1996, 2000). The self-absorption factor A_i depends on the matrix composition and on geometrical factors (size and shape of the sample).

The mass shape and matrix that are relevant to the irradiated part of the sample are not known; it is very difficult to determine these parameters experimentally. Hence, it is necessary to make some a priori assumptions on the basis of independent bulk measurements.

Initial concentration values, necessary to start the iteration, are obtained from the X-ray spectrum neglecting any self-absorption (i.e., $A_i = 1$) and using sensitivity factors (S_i) obtained from thin standard reference materials (e.g., NIST SRM1832, SRM1833 glass calibration standards).

The initial concentration of analyte i , $C_{i,0}$ with detectable X-ray line is calculated as

$$C_i^{(0)} = \frac{I_{i,\text{meas}}/S_i}{\sum_{j=m+1}^n (I_{j,\text{meas}}/S_j)} \times \left(1 - \sum_{j=1}^m C_j \right) \quad (34.4)$$

where n is the total number of elements in the sample and the first m elements are assumed to constitute the so-called *dark matrix*, the elements that do not give rise to detectable radiation. This *dark matrix* can be derived from stoichiometry (e.g., using the known oxygen content by assuming a common oxide form of the elements) or from other (bulk) measurements.

Concentration of low- Z elements ($Z < 14$, dependent on detector window and other windows attenuating the radiation) cannot be estimated from the spectrum: they do not provide detectable X-ray peaks under the experimental conditions used (detector and other windows, air absorption). The second step is to iteratively refine these initial concentration values according to

$$C_i^{(k+1)} = C_i^{(k)} \frac{I_{i,\text{meas}}}{I_{i,\text{calc}} \sum_{j=1}^n C_j^{(k)} \frac{I_{j,\text{meas}}}{I_{j,\text{calc}}}} \quad (34.5)$$

where $C_i^{(k)}$ is the calculated concentration of element i after k iterations. The procedure is terminated when one of the following conditions is met:

$$\left| C_i^{(k+1)} - C_i^{(k)} \right| < \varepsilon \quad (34.6)$$

$$\sum_{i=1}^n \frac{(I_{i,\text{meas}} - I_{i,\text{calc}})^2}{\sigma_{i,\text{meas}}^2} < \delta \quad (34.7)$$

where ε and δ are predefined constants.

It will be necessary to further refine all these methods, to adapt them to the ongoing scientific development and to the fast evolution of technology (both in terms of X-ray optics and computing power) in order to obtain highly accurate analytical data. An intensive effort is also required to take into account secondary effects that affect the precision and accuracy of measurements. These include geometrical factors in the setup, effects that influence the precision and accuracy of measurements in heterogeneous samples, secondary and higher order phenomena of radiation absorption and enhancement, particular artifacts in the X-ray spectra (contribution of resonant Raman scattering and photoelectron bremsstrahlung), effects due to the unique properties of synchrotron radiation (e.g., polarization, time structure), and detector characteristics (e.g., thickness of Be and other detector windows, inactive layers), all of which affect the spectral data obtained.

A systematic comparison of experimentally obtained spectral data with modeling results based on Monte Carlo simulations can pinpoint and show ways to correct for all these effects and eventually bring the measurement accuracy in line with the accuracy of the physical parameters characterizing the X-ray – sample interaction processes. Ultimately, the quality of results that can be reached with this method depends on the accuracy of available physical parameters, mainly the cross sections for X-ray interactions that are, in the most favorable circumstances, 5% for K radiation of elements between $Z = 20$ and 50, 10 – 15% for L radiation between $Z = 50$ and 80 (Elam et al. 2002; Somogyi et al. 2000).

A reasonable goal of this is to reach an average accuracy of quantification in the range of ca 5% for elements above atomic number 12 determined through their K and L fluorescence radiation. ▶ [Table 34.1](#) shows a few results obtained for the standard reference material NIST SRM 1577b bovine liver (see also the related ▶ [Figs. 34.2](#) and ▶ [34.4](#)).

■ **Table 34.1**

Certified and calculated concentrations for the analysis by iterative Monte Carlo calculation of NIST SRM 1577 bovine liver

Element	Certified conc./ppm	Calculated conc./ppm	Rel. deviation/%
Cl	(2,600)	2,300	–12
K	0.97 ± 0.06%	0.92%	–5
Ca	(123)	120	–2
Mn	10.3 ± 1	10.8	+5
Fe	270 ± 20	303	+12
Cu	193 ± 10	183	–5
Zn	130 ± 10	138	+6
Se	1.1 ± 0.1	1.2	+9
Br	—	9	—
Rb	18.3 ± 1	18.4	+0.5
Sr	(0.14)	0.15	+7
Mo	(3.2)	3.4	+6

34.6 Related Techniques

μ -XRF is the most important exploitation mode of X-ray microbeams in chemical analysis. All major SR sources are involved with this type of application with at least one instrumental setup. Detection limits in the ppb region and two-dimensional mapping of the repartition of elements in larger objects than the X-ray beam is possible. Other possibilities for fluorescence analysis based on the interaction of X-rays are less well advanced and are now being developed at several SR sources. In the application of X-ray absorption spectroscopy (XAS), the energy dependence of the inner shell photoelectric cross sections is exploited to increase specificity of measurements or to obtain information on the chemical environment (speciation analysis). X-ray absorption spectroscopy (XAS) is generally applied in the photon energy range of 0.1–100 keV where the scattering processes are 100 to 1000 times less probable than the photoelectric process. The presence or absence of pre-edge structure provides data on the oxidation and coordination state of an element (XANES, “X-ray absorption near edge structure” or NEXAFS, “near edge X-ray absorption fine structure”), while “Extended X-ray absorption fine structure” (EXAFS) analysis provides information on the number and the distance of neighboring atoms by measuring the oscillations from approximately 50 eV above the edge in EXAFS. The word extended is added to the name because the EXAFS oscillations can be found in certain cases up to 1,000 eV above the edge.

The technique is based on irradiation with a highly monochromatic X-ray beam of tunable energy and scanning over an absorption edge of an element of interest while recording either the absorption of the beam (*absorption* XAS), or the fluorescence radiation produced (*fluorescence* XAS) or another shell dependent phenomenon. The possibilities of the utilization of the X-ray absorption structure for obtaining more specific information will be discussed in a later section of this chapter. Recently, there were a number of demonstrations on the use of spatially resolved speciation to distinguish valence states of the elements Cr, Fe, Zn, U, Pu, etc., in geological, cosmo-chemical, and environmental studies.

In addition, the punctual measurement of X-ray diffraction pattern over a complex sample provides information on the variation of its crystallographic structure (XRD) over a heterogeneous object. Micro-XRD is becoming common on many X-ray microprobes. Micro-XRD maps can be obtained together with the maps of elemental information and can assist in characterizing heterogeneous samples.

Computerized X-ray fluorescence microtomography (XFCT) at high spatial resolution with absorption or fluorescence radiation from a spatially confined SR beam is based on the systematic measurement of the fluorescence radiation (and absorption) as it is impinging on the sample. It is then possible to reconstruct three-dimensional shape, density, and composition. By obtaining information on three-dimensional structures, XFCT exploits the penetrative nature of X-rays (which, otherwise, is a drawback for simple μ -XRF). Because of the penetrating nature of X-rays, namely, in the case of a regular scanning micro-XRF instrument, the detected analytical information represents the full line integral along the path where the micro-beam penetrates the sample. A typical scanning XRF experiment therefore results in a two-dimensional (2D) projection of the elemental distributions within the examined sample, without any, or very limited, depth information. The introduction of tomographic techniques, such as XFCT, however, allows the three-dimensional (3D) extension of the scanning XRF method. This computed tomography is one of the emerging methods of providing (potentially 3D) quantitative information on the elemental distribution in the probed sample volume with trace-level detection limits.

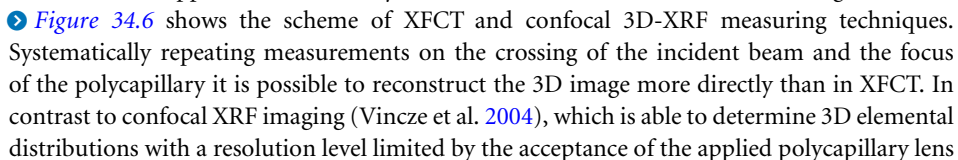
These techniques greatly enhance the capabilities of μ -XRF for the study of heterogeneous materials. Exhaustive recent reviews of applications of μ -XRF and related techniques are available in the literature (Schulze and Bertsch 1995; Potts et al. 2000; Revenko 2000; Bertsch and Hunter 2001; West et al. 2008; Janssens et al. 2000).

This section will discuss these techniques in some detail.

34.6.1 Three-Dimensional Micro-XRF Methods: X-Ray Fluorescence Computed Tomography (XFCT) and Confocal Imaging

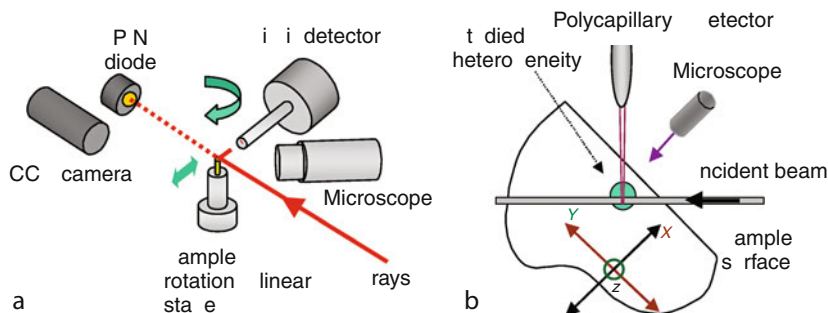
The sample used in XFCT measurements, in addition to being measured, is also rotated over 360° (180° in case of dual-detector setups). For full XRF tomography, repetitive linear scans at a selected height in the sample are recorded for different rotation angles. The different line profiles, as a function of the rotation angle, form the so-called elemental sinograms. The absorption and fluorescence images can then be reconstructed from the combination of the data obtained, yielding elemental cross sections at well-defined heights of the sample. Imaging is possible with the white spectrum as well as with monochromatic radiation. It is now possible to carry out XFCT with volume resolutions better than $1 \mu\text{m}^3$ and with about 10^4 – 10^5 voxels. (Voxels are the 3D versions of pixels.) This information provides possibilities for nondestructive observation of the interior of the sample for the study of, e.g., inclusions, interior pore structures, buried phases, or other features within the sample. The technique is now in full development, the major problems being the complexity of calculations necessary for reconstructing the images, especially when fluorescence radiation is used for reconstructing elemental distributions. In principle, it is possible to combine XAS and XFCT by obtaining the fluorescence or absorption information with two closely spaced excitation energies that are characteristic of the valence states of different ions in the sample.

One of the main limitations associated with the XFCT technique is the lengthy data collection procedure required. Being a first-generation scanning tomography technique, typically 1–5 h of scanning time is needed for obtaining each two-dimensional tomographic slice. With the introduction of fast multielement energy-dispersive (ED) detectors coupled with digital signal processing technology and fast-scanning techniques, in the following years, this limitation is expected to be relaxed considerably or eliminated. Next to the time-consuming data collection procedure, another difficulty of the technique is associated with the quantitative reconstruction of the measured sinograms due to element-dependent self-absorption effects. Recently, generalized XFCT reconstruction algorithms were developed, including accurate correction for self-absorption effects in the matrix material (e.g., Schroer 2001; Golossio et al. 2003). Considerable effort has also been taken to develop a dedicated Monte Carlo simulation procedure for XFCT, based on the detailed modeling of photon–matter interactions (Vekemans et al. 2004).

An alternative approach for the three-dimensional (3D) variant of scanning micro-XRF is based on the excitation with an X-ray micro-beam and confocal detection using a polycapillary half-lens. This approach was recently evaluated at several SR facilities including the ESRF.  **Figure 34.6** shows the scheme of XFCT and confocal 3D-XRF measuring techniques. Systematically repeating measurements on the crossing of the incident beam and the focus of the polycapillary it is possible to reconstruct the 3D image more directly than in XFCT. In contrast to confocal XRF imaging (Vincze et al. 2004), which is able to determine 3D elemental distributions with a resolution level limited by the acceptance of the applied polycapillary lens

■ Fig. 34.6

Schematic representation of a generic XRF tomography setup (a) and of the polycapillary based confocal arrangement for three-dimensional X-ray fluorescence (3D-XRF) (b)



($\sim 10 \mu\text{m}$), the spatial resolution of XRF nanotomography is ultimately limited by the X-ray beam size that is used.

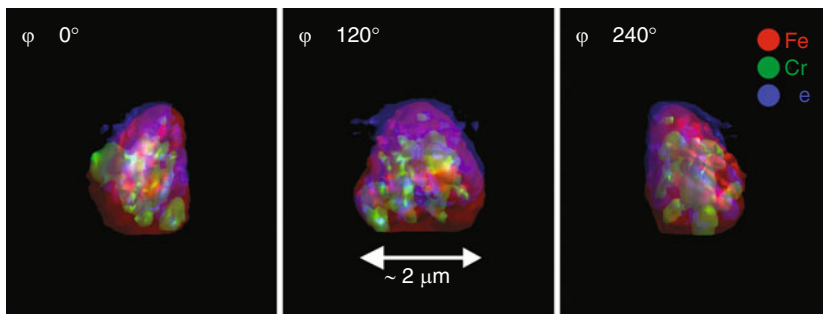
34.6.1.1 Nanoscopic X-ray Fluorescence Computerized Tomography (XFCT)

Submicrometer beam sizes are becoming available at third-generation sources, opening up the possibility of XRF imaging and also XFCT at the nanoscopic level. Using a submicron X-ray beam, full three-dimensional nano-XRF tomography results with a spatial resolution of approximately 200 nm has been demonstrated at the ESRF ID13 instrument (Silversmit et al. 2009a).

The high spatial resolution provided by the beam puts stringent conditions on the accuracy and reproducibility of sample positioning during linear and rotational scans. On the scale of the beam size ($\sim 200 \text{ nm}$), considerable sample displacements can be expected, especially after each rotational movement, because of imperfections of the rotation axis and vertical drifts of the sample stage assembly due to, e.g., gravity. To be able to correct for such instabilities after data collection, instead of analyzing a single sample slice by conventional XRF tomographic (linear) scans, full 2D-XRF projections can be recorded at each observation angle. While more time consuming than linear scans, this method allows for the off-line correction of sample positioning inaccuracies associated with rotational movements, and also gives the possibility of full 3D elemental reconstruction, instead of obtaining elemental distributions only in a single sample cross section. The combination of the reconstructed cross sections (slices) for all heights enables the visualization of the complete 3D view of elemental distributions in the investigated object. An example is given in Fig. 34.7, showing pseudo-color composite images of the low-intensity isosurface distributions of iron (red), chromium (green), and selenium (blue) for different azimuthal viewing angles for a cometary particle returned to Earth in the framework of the NASA Stardust mission (Brownlee and Zolensky 2006; Silversmit et al. 2009a). The heterogeneous nature of the elemental distributions within the terminal particle having a diameter of $2 \mu\text{m}$ could be visualized in a nondestructive manner in 3D on the nanoscopic level (see, e.g., the low-intensity isosurface for chromium).

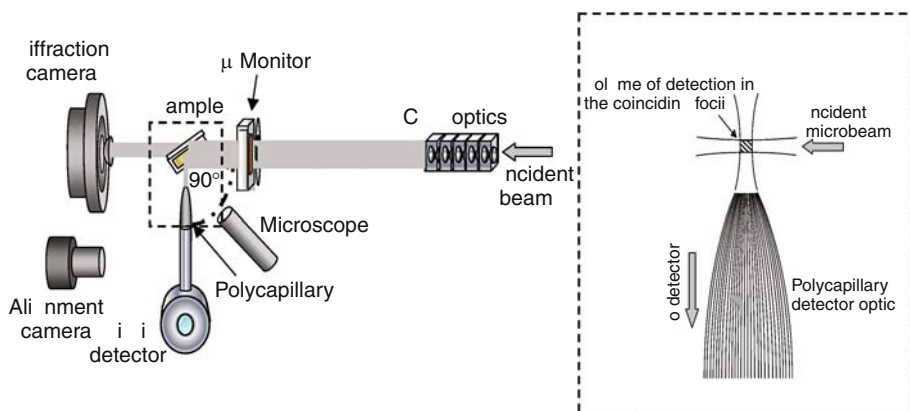
■ Fig. 34.7

Reconstructed low-intensity isosurface composite images for different azimuthal viewing angles: red denotes iron, green represents chromium, and blue indicates selenium (Adapted from Silversmit et al. 2009a)



■ Fig. 34.8

Left panel: Schematic of the experimental set up for confocal 3D-XRF at the European Synchrotron Radiation Facility (ESRF) ID18F end-station. Right panel: Basic principle of confocal X-ray fluorescence analysis using polycapillary detector optics (Adapted from Vincze et al. 2004)



34.6.1.2 Confocal XRF-Imaging

The principle of confocal XRF detection is compared with XFCT in Fig. 34.6 and shown in more detail in Fig. 34.8. The combination of a polycapillary half-lens coupled with an energy-dispersive detector for 3D-XRF has been first proposed in the early 1990s by Kumakhov and coworkers; however, no experimental demonstration was given in this work for the proposed principle (see Romanov 2005 for a recent account on this issue). As the result of the rapid development of monolithic polycapillary optics in recent years, the principle was recently applied in practice by several authors (Kanngiesser et al. 2003; Vincze et al. 2004; Janssens et al. 2004).

Kanngiesser et al. (2003) demonstrated the principle of localized detection and sample depth-scanning for synchrotron radiation-induced XRF. Vincze et al. (2004) gave the full characterization of polycapillary-based confocal XRF and its applications for 3D trace-element analysis.

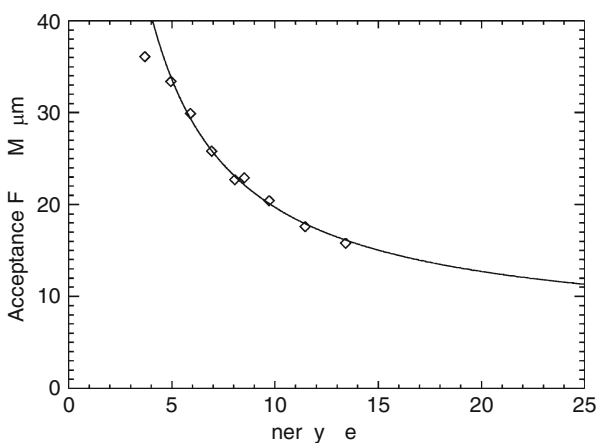
The polycapillary detector lens represents a significant modification to the regular scanning micro-XRF spectrometer, i.e., defining a specific micro-volume from which the XRF signal is detected in the coinciding foci of the detection side polycapillary and the incoming micro-beam. The detection-side polycapillary, which acts as an efficient detector collimator, accepts an energy-dependent section from the incoming beam path as it intersects the sample: this defines a microscopic volume element of detection within the investigated object. As shown here, the polycapillary detector optic accepts a limited section from the path of the penetrating incident beam within the sample, which is determined by the energy dependent focus size of the device. The energy dependence of this acceptance length is governed by the $1/E$ proportionality of the critical angle of total reflection as a function of increasing photon energy. With respect to 3D-XRF analysis, the energy dependent acceptance (depth resolution) of the setup was measured by thin glass calibration standards (NIST SRM 1832/1833), by scanning through the accepted volume with the confocal arrangement.

➤ Figure 34.9 shows the depth resolution (FWHM) expressed as a function of energy, as determined from Gaussian fits to the measured fluorescence line scan profiles. The depth resolution was determined to be about 35 μm at Ca- K_{α} and about 15 μm at the energy of the Sr- K_{α} fluorescent line. Extrapolation of the fitted curve suggests that with this particular polycapillary a depth resolution of 11–12 μm can be achieved in the energy range of 20–25 keV. Above these energies, the collimation properties of the polycapillary break down due to insufficient transmission efficiency and “halo” effects, caused by the penetration of high-energy X-rays through the glass fiber walls.

The energy dependent capillary acceptance has considerable consequence with respect to quantitative analysis of confocal-XRF data sets, since the sampled volume and mass vary with

■ Fig. 34.9

Depth resolution (acceptance) of detection side polycapillary optics as a function of detected fluorescence line energy



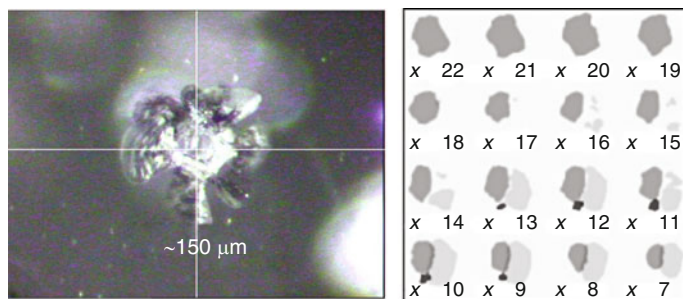
the energy of the measured characteristic lines. In the case of the above experiment, assuming a sample density of 2.20 g/cm^3 corresponding to glass material, the total analyzed sample mass has been estimated to be 0.78 ng at Ca-K $_{\alpha}$, 0.48 ng at Zn-K $_{\alpha}$, and about 0.34 ng at the Sr-K $_{\alpha}$ fluorescent line energy. While it is straightforward to estimate this probed sample volume (and the analyzed mass for a known density) for samples with thickness larger than the acceptance path of the detector optic, this becomes difficult when dealing with thin samples (thickness below $50 \text{ }\mu\text{m}$) where one needs to determine the intersection volume defined by the exciting microbeam, the energy-dependent polycapillary focus, and that of the analyzed thin sample itself. While this is not a fundamental limitation for the quantitative analysis of confocal XRF data, this difficulty is greatly reduced in cases when both the unknown sample and the employed standard have a thickness, which is significantly larger than the polycapillary acceptance path. In such cases, the analyzed volumes can be considered equal for the unknowns and the standards used for quantification.

As an example for confocal 3D-XRF microanalysis, [Fig. 34.10](#) shows the optical image (*left*) and measured elemental distributions (*right*) as a function of depth based on trace levels of Sr-, Zr-, and Th-K $_{\alpha}$ signals within a composite diamond inclusion of ca. $150 \text{ }\mu\text{m}$ diameter. As identified by micro Raman spectroscopy, the Sr-rich phase corresponds to larnite ($\beta\text{-Ca}_2\text{SiO}_4$), while the Zr-rich phase corresponds to CaSiO_3 -walsstromite. The detection of coexisting larnite ($\beta\text{-Ca}_2\text{SiO}_4$)/ CaSiO_3 -walsstromite phases allows constraining possible sources and conditions of formation for the diamond (Brenker et al. 2005).

An exciting direction in the development of nondestructive elemental imaging methods is represented by the combination of synchrotron-based scanning microspectroscopic techniques with complementary X-ray imaging methods, such as X-ray absorption microtomography. X-ray absorption microtomography offers the possibility to facilitate the interpretation and aid the quantification of 2D/3D elemental imaging results by providing a full 3D absorption model, an accurate frame of reference, for the very same sample that is analyzed by SR micro-XRF techniques. Absorption microtomography provides a complementary dataset with density/mass absorption coefficient information, which not only reveals the internal structure/morphology of the examined sample but also aids the quantitative analysis of the measured 2D/3D elemental distributions. By coupling information obtained by synchrotron radiation micro-XRF and absorption microtomography, it is possible to unravel the

■ **Fig. 34.10**

Optical image (*right*) and reconstructed slices at different depth x (measured in steps of $5 \text{ }\mu\text{m}$) of the inclusion based on trace-level Sr, Zr, and Th fluorescent signals. Voxel size: $5 \times 5 \times 6 \text{ }\mu\text{m}^3$



tissue-specific 2D/3D distribution of metals in situ in an essentially nondestructive manner within delicate biological samples. By the application of dynamic (fast) scanning techniques, radiation damage to the illuminated biological samples could be minimized; however, with more intense X-ray nanobeams the use of cryogenic sample stabilization techniques may be necessary for preserving the structural integrity of the sample (De Samber et al. 2008a, b).

The evaluation of μ -XRF images results in data sets that are multidimensional: intensity values for the elements are calculated from the spectra recorded at the positions of the image map (Somogyi et al. 2000). An elegant way to study the properties of such multidimensional data sets is to apply multivariate analysis methods. For example, principal component analysis (PCA) may assist in interpreting the data by the determination of which elements contribute to the principal components, and helps to classify the pixel data on the basis of their elemental properties. Using the set of principal components, one can depict variables (elements) and objects (pixels) with similar or different characteristics. Combining element-specific loading plots with their corresponding pixel-specific score plots, one needs to investigate only a very few graphs, very often those of the most important principal components. In addition to PCA, grouping of objects (pixels) can be done by means of dedicated clustering strategies. In this work, the k -means clustering method is successfully applied to group pixels that provide equal (or similar) compositional information. The additional advantage of this approach is that the resulting sum spectra corresponding to groups of pixels with similar composition feature lower noise levels than the individual pixel spectra (Vekemans et al. 2004).

34.6.2 X-Ray Absorption Spectroscopy: XANES and EXAFS

A close look above the absorption edge reveals that the dependency of μ_ρ as function of X-ray energy such as in [Fig. 34.5](#) is not smooth, but shows a fine structure. Note, that the hypothetical absorption spectrum for an isolated atom, denoted by $\mu_0(E)$, would only have an absorption edge and no fine structure. [Figure 34.11](#) shows the V K absorption edge of a V metal thin-foil sample. The fine structure up to around of the edge (XANES), and the oscillations above the edge (EXAFS) can be used for obtaining structural or chemical information.

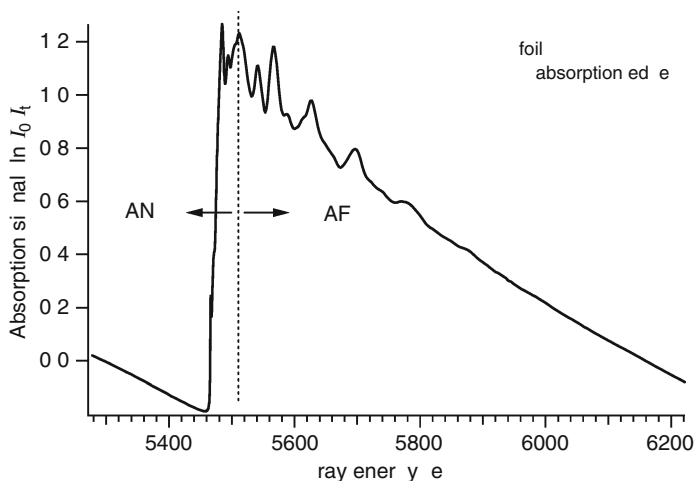
Empirically, one finds that the fine structure around the absorption edge depends on the local structure around the absorbing atom. So, it should be possible to obtain the local structure from an XAS spectrum. The difference between EXAFS and XANES lies in the different kind of information that can be retrieved from them. The EXAFS signal is sensitive to structural parameters such as bond distances and coordination numbers (the number of neighbors at a certain bond distance), while the XANES is more sensitive to electronic properties such as oxidation states, symmetry of the local coordination, and density of states.

In contrast to X-ray diffraction (XRD), the workhorse for structural determination, the sample does not need to contain long-range order in case of XAS: short-range order is already sufficient. This has the advantage that a wide variety of samples can be studied with XAS: gases, solids, liquids, crystalline and amorphous materials, bulk layers, surfaces, adsorbed atoms, and interfaces. Due to the penetrating character of X-rays (of high enough energy) through gases and liquids, XAS can be applied for in situ studies in catalysis, during layer growth, and phase transitions, etc. The obtained information is only applicable to short-range order, so XAS is a complementary technique to XRD.

The simplest and direct way of recording an XAS spectrum is to measure the intensity of the X-ray beam before, I_0 , and after, I , the sample by ionization chambers (see [Fig. 34.12a](#)).

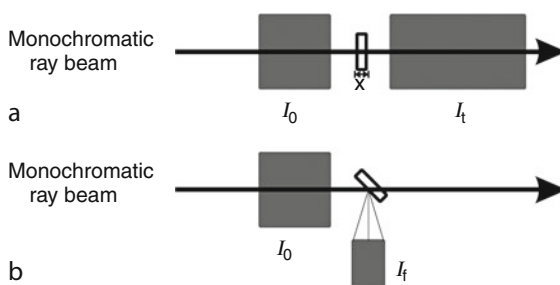
■ Fig. 34.11

Experimental absorption spectrum measured over the V K-edge indicating the relevant energy regions for X-ray absorption near edge structure (XANES) and extended X-ray absorption fine structure (EXAFS) spectroscopy



■ Fig. 34.12

(a) Transmission and (b) fluorescence detection modes for X-ray absorption spectroscopy



This is the transmission mode XAS: for a sample with thickness x and linear absorption coefficient μ_l the absorption is given by

$$\mu_l x = \ln \frac{I_0}{I_t} \quad (34.8)$$

After the absorption of the X-ray photon and emission of the photoelectron, the absorbing atom is in an excited state, as it has a hole in one of its deep core levels. The atom will relax by the emission of a fluorescent X-ray photon or an Auger electron. The fluorescence (fluorescence yield) or Auger (electron yield) intensities are proportional to the absorption in the sample, and the detection of these signals gives an indirect way to measure the absorption.

In the fluorescence detection mode (■ Fig. 34.12b), the incoming X-ray intensity is monitored like in the transmission case and the fluorescence emission, I_f , is recorded at 90° with respect to the incoming beam. The measured absorption is then given by

$$\mu_I x \sim \frac{I_f}{I_0} \quad (34.9)$$

For recording an XAS spectrum, a highly monochromatic X-ray beam tunable over a range of about 1000 eV is needed. The first experiments were performed with rotating X-ray tube laboratory sources. It is only after 1970, with the increasing availability of synchrotron radiation sources, that EXAFS became a practical technique. Thanks to the increased X-ray intensity of synchrotron radiation sources compared to laboratory sources, the measuring time per spectrum has decreased from several days down to the minute time scale for conventional scanning XAS. Nowadays, full XAS spectra can be taken within a few milliseconds using bent polychromators, such as in case of dispersive XAS.

When the employed X-ray beam is focused to micro/nanoscale dimensions, the technique can be used to obtain local information concerning the chemical state and local chemical structure of the absorbing atom on micro/nano scale (e.g., Silversmit et al. 2009b).

34.7 Summary

Synchrotron radiation X-ray fluorescence microbeam techniques using third-generation SR sources offer the potential of nondestructive multielement analysis down to trace concentration levels with unrivaled spatial resolution among X-ray-based analytical techniques (Adams et al. 2005; Adams 2008). For these sources, relative detection limits at the sub-ppm (fg/ng) level can be achieved. With respect to absolute detection limits (DL), submicron-sized X-ray beams can offer DLs below 10 ag for the most efficiently excited transition elements, with a potential lateral resolution level better than 100 nm. There are a number of synchrotron sources in Europe that can be used for basic research on nanoscale analysis and characterization and subsequent applications in problems of materials research. Currently, operational third-generation national sources in Europe such as Bessy II (D) and SLS (CH) have significant activities in micro-focusing and -imaging technologies. Other sources such as Soleil (F) and Diamond (UK) have designated beamlines with micro-focusing capabilities for imaging and analysis. In the ESRF, the construction of eight new beamlines was started to deliver sharply focused beams of X-rays just tens of nanometers in diameter for imaging nanometer-scale features of various materials. Other synchrotrons have achieved similar-sized beams, but the ESRFs will be the first available for general use by scientists.

Within the field of the microanalytical techniques, SR-based μ -XRF emerges as an important new methodology for the characterization and analysis of diverse materials. The simultaneous application of μ -XRF with XAS, XFCT, and XRD greatly enhance the capabilities for the study of microscopically heterogeneous materials, providing three-dimensional elemental information and speciation in a nondestructive manner. The gains in brilliance of SR sources over the past decade and advances in focusing optics during the same period provide spatial resolution at the sub- μ m range while maintaining a high sensitivity.

Thanks to the full understanding of the interaction processes of X-rays with matter, computer techniques, particularly those based on Monte Carlo simulation, are able to predict the spectral response without limitations in approximations or idealizations of the sample geometry. Hence, they allow methods for calibration and correction for radiation absorption, thus opening up the way to perform reliable quantitative analysis.

References

- Adams F (2003) *Nucl Instr and Meth B* 199:375–381
- Adams F (2008) *Spectrochim Acta B* 63:738–745
- Adams F, Van Vaec L, Barrett L (2005) *Spectrochim Acta B* 60:13–26
- Bertsch PM, Hunter DB (2001) *Chem Rev* 101:1809–1842
- Bilderback DH, Hoffman SA, Thiel DJ (1994) *Science* 263:201–203
- Brenker FE, Vincze L, Vekemans B, Nasdala L, Stachel T, Vollmer C, Kersten M, Somogyi A, Adams F, Joswig W, Harris JW (2005) *Earth Planet Sci Lett* 236:579–587
- Brownlee D, Zolensky M (2006) *Science* 314:711–1716
- De Samber B, Silversmit G, Evens R, De Schampelaere K, Janssen C, Masschaele B, Van Hoorebeke L, Balcaen L, Vanhaecke F, Falkenberg G, Vincze L (2008a) *Anal Bioanal Chem* 390:267–271
- De Samber B, Evens R, De Schampelaere K, Silversmit G, Masschaele B, Schoonjans T, Vekemans B, Janssen CR, Van Hoorebeke L, Szaloki I, Vanhaecke F, Falkenberg G, Vincze L (2008b) *J Anal Atom Spectrom* 23:829–839
- Elam WT, Ravel BD, Sieber JR (2002) *Radiat Phys Chem* 63:121
- Falkenberg G, Claus O, Swiderski A, Tschentscher T (2001) *Nucl Instrum Meth A* 467:737–740
- Golossio B, Simionovici A, Somogyi A, Lemelle L, Chukalina MJ (2003) *Appl Phys* 94:145–156
- Grime GW (1996) *Nucl Instrum and Meth B* 109:170
- Janssens K, Vekemans B, Adams F, Van Espen P, Mutsaers P (1996) *Nucl Instr and Meth B* 109/110:179
- Janssens KH, Adams FC, Rindby A (eds) (2000) *Microscopic X-ray fluorescence analysis*. Wiley, Chichester
- Janssens K, Proost K, Falkenberg G (2004) *Spectrochim Acta B* 59(10–11):1637–1645
- Kang HC, Maser J, Stephenson GB, Liu C, Conley R, Macrander AT, Vogt S (2006) *Phys Rev Lett* 96:127401
- Kanngiesser B, Malzer W, Reiche I (2003) *Nucl Instr and Meth Phys Res B* 211:259–264
- Lengrer B, Tummler J, Snigirev A, Snigireva I, Raven C (1998) *J Appl Phys* 84:11
- Ortega L, Comin F, Formosa V, Stierle A (1998) *J Synchrotron Radiat* 5:1064–1066
- Potts PJ, Ellis AT, Holmes M, Kreggamer P, Streli C, West M, Wobraushek P (2000) *J Anal Atom Spectrom* 15:1417
- Revenko AG (2000) *Ind Lab* 66:637
- Romanov A (2005) *Tech Phys Lett* 31(3):200–201
- Schroer CH (2001) *Appl Phys Lett* 79:1912–1914
- Schroer C, Kurapova O, Patommel J, Feldkamp J, Lengrer B, Burghammer M, Riekel C, Vincze L, Vanderhart A, Kuchler M (2005) *Appl Phys Lett* 87:124103
- Schulze DG, Bertsch PM (1995) *Adv Agron* 55:1
- Silversmit G, Vekemans B, Brenker F, Schmitz S, Burghammer M, Riekel C, Vincze L (2009a) *Anal Chem* 81:6107–6112
- Silversmit G, Vekemans B, Nikitenko S, Bras W, Czech V, Zaray G, Szaloki I, Vincze L (2009b) *J Synchrotron Radiat* 16:237–246
- Smith JV (1995) *Analyst* 23:1231
- Somogyi A, Janssens K, Vincze L, Vekemans B, Rindby A, Adams F (2000) *Spectrochim Acta B Atom Spectrosc* 55(1):75–89
- Somogyi A, Drakopoulos M, Vincze L, Vekemans B, Camerani C, Janssens K, Snigirev A, Adams F (2001) *X-ray Spectrom* 30:242
- Somogyi A, Drakopoulos M, Vincze L, Vekemans B, Camerani C, Janssens K, Snigirev A, Adams F (2002) *ESRF Highlights* 2001:96
- Somogyi A, Drakopoulos M, Vekemans B, Vincze L, Simionovici A, Adams F (2003) *Nucl Instr and Meth B* 199:559
- Streli C (2006) *Appl Spectrosc Rev* 41:473–489
- Streli C, Pepponi G, Wobraushek P, Jokubonis C, Falkenberg G, Zaray G, Broekaert J, Fittschen U, Peschel B (2006) *Spectrochim Acta B Atom Spectrosc* 61:1129–1134
- Tougaard S (1997) *Surf Interface Anal* 25:137
- Van Grieken RE, Markowicz A (eds) (2002) *Handbook of X-ray spectrometry*, 2nd edn. Dekker, New York, p 1016
- Vekemans B, Janssens K, Vincze L, Adams F, Van Espen P (1994) *X-Ray Spectrom* 23:278
- Vekemans B, Vincze L, Somogyi A, Drakopoulos M, Kempnaers L, Simionovici A, Adams F (2003) *Nucl Instr and Meth B* 199:396
- Vekemans B, Vincze L, Brenker FE, Adams F (2004) *J Anal Atom spectrom* 19:1302–1308
- Vincze L, Janssens K, Vekemans B, Adams F (1999a) *J Anal Atom Spectrom* 14(3):529
- Vincze L, Janssens K, Vekemans B, Adams F (1999b) *Spectrochim Acta B Atom Spectrosc* 54:1711
- Vincze L, Janssens K, Vekemans B, Adams F (1999c) *J Anal Atom Spectrom* 14:529
- Vincze L, Somogyi A, Osán J, Vekemans B, Török S, Janssens K, Adams F (2002a) *Anal Chem* 74:1128
- Vincze L, Wei F, Proost K, Vekemans B, Janssens K, He Y, Yan Y, Falkenberg G (2002b) *J Anal Atom Spectrom* 17:177
- Vincze L, Vekemans B, Brenker F, Rickers A, Somogyi A, Kersten M, Adams F (2004) *Anal Chem* 76: 6786–6791
- West M, Ellis AT, Kreggamer P (2008) *J Anal Atom Spectrom* 23:1409–1437
- Wobraushek P (2007) *X-Ray Spectrom* 36:289–300



35 Tracer Technique

H. Haba^{1,2} · S. Motomura² · S. Kamino³ · S. Enomoto^{1,2,3}

¹RIKEN Wako Institute, Wako, Saitama, Japan

²RIKEN Kobe Institute, Kobe, Hyogo, Japan

³Okayama University, Okayama, Japan

35.1	<i>Radioactive Tracers</i>	1763
35.1.1	Principles of Radioactive Tracer Technique	1763
35.1.2	Non-Isotopic Tracers	1763
35.1.3	Activable Tracers	1764
35.1.4	Stable Isotopes as Tracers	1764
35.2	<i>Advantages and Disadvantages of Radioactive Tracers</i>	1764
35.3	<i>Essential Points in Using Radioactive Tracers</i>	1765
35.3.1	Carriers	1765
35.3.2	Exchange Reactions	1766
35.3.3	Purity	1766
35.4	<i>Measurement of Radioactive Tracers</i>	1766
35.4.1	General	1766
35.4.2	Gamma-Ray Measurements	1768
35.4.3	Beta-Ray Measurements	1769
35.4.4	Alpha-Ray Measurements	1770
35.4.5	Accelerator Mass Spectrometry	1771
35.5	<i>Selection, Acquisition, and Use of a Radioactive Tracer</i>	1771
35.5.1	Selection of a Radioactive Tracer	1771
35.5.2	Acquisition of a Radioactive Tracer	1772
35.5.3	Use of a Radioactive Tracer	1772
35.6	<i>Radioactive Multitracer Technique</i>	1773
35.6.1	Radioactive Multitracers	1773
35.6.2	Production of Radioactive Multitracers	1773
35.6.3	RI Beam	1775
35.6.4	Measurement of Radioactive Multitracers	1776
35.7	<i>Chemical Application of Radioactive Tracers</i>	1777
35.7.1	Chemical Equilibria	1778
35.7.2	Reaction Kinetics and Mechanisms	1780
35.7.3	Exchange Reactions	1781
35.7.4	Reactions at Equilibrium	1783
35.7.5	Surface and Solid Reactions	1783

35.7.6 Diffusion 1784

35.7.7 Search for Formation of New Compounds 1785

35.8 Analytical Application of Radioactive Tracers 1785

35.8.1 Isotope Dilution Analysis 1786

35.8.2 Radiometric Analysis 1788

35.8.3 Surface-Area Determination 1789

35.9 Biochemical Application of Radioactive Tracers 1789

35.10 Geological Application of Radioactive Tracers 1790

35.11 Industrial Application of Radioactive Tracers 1790

Abstract: In radioactive tracer technique, radioactive nuclides are used to follow the behavior of elements or chemical species in chemical and other processes. This is realized by means of radioactivity measurement. In 1913, Hevesy and Paneth succeeded in determining the extremely low solubility of lead salts by using naturally occurring ^{210}Pb as a radioactive tracer. As various radioactive nuclides became artificially available, this technique has been widely employed in studies of chemical equilibrium and reactions as well as in chemical analysis. It is also an essential technique in biochemical, biological, medical, geological, and environmental studies. Medical diagnosis and industrial process control are the fields of its most important practical application. In this chapter, fundamental ideas concerning radioactive tracers will be described followed by their application with typical examples. Detailed description on their application to life sciences and medicine is given in Vol. 4.

35.1 Radioactive Tracers

35.1.1 Principles of Radioactive Tracer Technique

The fundamental principle of radioactive tracer technique is that the chemical behavior of radioactive isotopes is identical to that of their stable isotopes in any chemical process. Strictly speaking, the difference in atomic mass of radioactive and stable isotopes gives rise to a slight difference in both chemical reaction rate and equilibrium constant. This is the isotope effect (see [▶ Chap. 15 in Vol. 2](#)), which forms the basis of the isotope separation (see [▶ Chap. 51 in Vol. 5](#)). Except for very light elements, however, the isotope effect is negligibly small. This makes the isotope separation very laborious work requiring manifold repetition of a certain process. In ordinary tracer experiments, the isotope effect comes into question only in the case of tritium ^3H , which has an atomic mass approximately three times larger than that of the main stable isotope ^1H . Even in ^3H , however, the isotope effect turns out to be insignificant when the radioactive nuclide is incorporated in a large molecule, as is usually the case in organic chemistry and biochemistry, because the behavior of the molecule depends on the mass of the whole molecule.

The effect of radiation (see [▶ Chap. 23 in this Volume](#)) emitted by the radioactive tracers on a chemical or biological system under study is also usually negligible. The amount of a radioactive tracer necessary for an experiment is normally so small that no detectable radiolysis occurs in the system. However, in long-term storage of radiation-sensitive compounds, one must be cautious of the effect of radiation. And, of course, in application to human body, careful consideration is necessary on the effects of radiation during and after the experiment (see [▶ Chap. 47 of Vol. 5](#)).

35.1.2 Non-Isotopic Tracers

Radioactive nuclides not isotopic with the element to be traced are sometimes employed. In inorganic chemical studies, such non-isotopic tracers are allowed only when the similarity of their chemical behavior with that of the element to be traced is guaranteed as in the case of a pair of lanthanide elements. On the other hand, non-isotopic nuclides are often used for labeling large organic or biochemical molecules (see [▶ Chaps. 42–45 in Vol. 4](#)), because in many cases introduction of a different element to such molecules does not affect significantly their behavior. However, it is recommended to check the effect of labeling on the chemical or biological behavior

of the molecules in each experiment. For example, it is known that unsaturated fatty acids labeled with radioactive iodine do not necessarily show chemical properties expected for unsaturated fatty acids. When the movement of a mass much larger than a molecule is traced, chemical properties of the radioactive tracer do not matter at all and the only requirement is that it is firmly bound to the mass. For example, erythrocytes are easily labeled with $^{51}\text{CrO}_4^{2-}$, and this labeling is utilized in determination of life of erythrocytes in human body. In industrial applications, granules and aerosols labeled with a radioactive nuclide are often used to trace mass flow. This kind of tracer is often referred to as a physical tracer.

35.1.3 Activable Tracers

A version of radioactive tracer technique is the activable tracer method. In this, a stable element is added as a tracer to the system under study and the movement or partition of the tracer element is determined afterward by means of the radiation emitted by a radioactive nuclide produced in activation of the element. The activation is usually done by thermal neutrons in a reactor. The basic requirement for the element employed as an activable tracer is that it has an isotope with high activation cross section for the (n,γ) reaction, that its concentration is negligibly low in the original system to be studied, and that it is harmless to the system. Br, Sm, Eu, Gd, and Dy are frequently used as activable tracers. Activable tracers are especially suitable for environmental studies, where use of radioactive nuclides is often undesirable or not allowed.

35.1.4 Stable Isotopes as Tracers

Stable isotopes are also employed as tracers, though their sensitivity is much lower than that of the radioactive ones. Enriched ^2H , ^{13}C , ^{15}N , and ^{18}O are widely used as stable-isotope tracers. Their measurement is generally done by mass spectrometry, but emission spectrochemical analysis (^{15}N) and nuclear magnetic resonance (^{13}C) can also be used.

35.2 Advantages and Disadvantages of Radioactive Tracers

The advantage of the radioactive tracer technique lies first of all in its high sensitivity. When an appropriate carrier-free tracer is employed, a picogram (10^{-12} g) or less of an element can be easily detected with conventional detectors. In fact, hormones and other biomolecules are routinely determined down to a picogram or less in radioimmunoassay. Therefore, chemical and biological effects of carrier-free tracers on the metabolic system of a living body are insignificant. Tracers of toxic elements such as As and Hg or poisonous compounds such as HCN can be used with no hazardous effects.

Another advantage of radioactive tracers is their ease of detection and determination. The radiating properties of the tracers are not affected at all by the physical and chemical condition of the sample, i.e., temperature, pressure, presence and concentration of chemicals, and so on. This exempts one from laborious preparation and treatment of the sample before measurement. In the measurement of a nuclide emitting a γ ray, all one has to do is to put the sample near a detector and press a button to operate the electronic system. Radioactive tracers are also suitable for continuous-flow detection and some of them further for imaging.

There are applications that can only be performed with the use of an isotopic tracer. Among them are the studies on self-diffusion and isotopic exchange reaction. Examples of such studies are described in detail below.

An unavoidable limitation of the radioactive tracer technique is absence of nuclides suitable as tracers for some elements. For He, Li, B, Ne, for example, there is no radioactive nuclide employable as a tracer in ordinary chemistry. Only short-lived nuclides are available for N ($9.965 \text{ min } ^{13}\text{N}$) and O ($2.037 \text{ min } ^{15}\text{O}$).

The above statement that the radiations from tracers are not affected by the chemical state of the sample means that the radiation carries no chemical information on the tracer. All that the radiations inform about is the location, distribution, and amount of the tracer. Another disadvantage of the radioactive tracer technique is that it requires an experimental facility with the license for the use of a nuclide in the necessary amount.

35.3 Essential Points in Using Radioactive Tracers

35.3.1 Carriers

Radioactive tracers are as a rule accompanied with a certain amount of their stable isotope(s). When the amount of the stable isotope(s) is significant in the sense of ordinary chemistry or for the specific purpose of an experiment, they are called a “*carrier*.” When not, the tracer is “*carrier-free*.” Another term “*no carrier added*” is also used with almost the same meaning. The amount of carrier is expressed by its weight or in terms of the elemental specific activity of the tracer, that is, the activity divided by the mass of the element in question (Bq/g element) or by that of the chemical species in question (Bq/g species).

Carriers can originate in the preparation procedure of the tracers. When the target nuclide employed in the production of a tracer nuclide is its isotope as in (n, γ) and (d, p) reactions, a considerable amount of carrier is inevitable for the product nuclide. Carriers can also result from the impurities in the target material, from nuclear reactions producing the stable isotopes, and also from contamination of the reagents and vessels used for processing the target. Therefore, even when a nuclear reaction changing the atomic number such as (n, p), (p, n), and (γ, n) is used, the tracer is not completely free from its stable isotopes.

In view of the sensitivity of the radioactive tracer, it is desirable that the amount of its carrier is kept minimal. However, presence of a certain amount of carrier is favorable or even essential in many experimental procedures. In separation of a tracer of a metal ion by precipitation and filtration of a sparingly soluble salt, for example, the amount of the carrier must be large enough to exceed the solubility product.

A carrier-free tracer in a solution is sometimes adsorbed on the surface of the vessel or on colloid particles of dust in the solution, or may react specifically with a minute impurity species in the solution. Moreover, the behavior of a carrier-free tracer can be different from that of the same species in ordinary macro chemistry (Guillaumont et al. 1989; Choppin et al. 2002). Therefore, it is desirable in general to add a carrier to the tracer in an amount not disturbing the experiment. The carrier added must be in the same chemical form as, and thoroughly mixed with the tracer. In case of elements stabilized in two or more oxidation states, such as Fe, As, Se, Sb, and I, it is recommended to perform the so-called oxidation–reduction sweep, that is, oxidation of the tracer with the carrier to the highest possible oxidation state followed by reduction down to the lowest possible state preferably in repetition.

Occasionally a non-isotopic carrier is used, namely a carrier that is not isotopic with the tracer but behaves similarly. Usually, an element in the same group of the periodic table is used as a *non-isotopic carrier*. Coprecipitation of Ra with Ba salts is such a case. The non-isotopic carrier has an advantage that it can be removed later by an appropriate chemical technique.

35.3.2 Exchange Reactions

Radioactive tracers sometimes undergo exchange reactions with stable isotopes in a different chemical form. As a result, the chemical form of the tracers changes partly, which certainly disturbs the tracer experiment. Therefore, one must be careful when the system to be studied contains another chemical species having the same element as the tracer. Examples of exchange reactions are described below.

35.3.3 Purity

Two kinds of “purity” must be taken into consideration concerning a radioactive tracer, which are both essential in practice.

Nuclidic purity. The nuclidic purity is the fraction of the total activity due to the stated radioactive nuclide. Even another radioactive nuclide of the same element decreases the nuclidic purity and can disturb activity measurement. However, nuclidic purity turns out not to be essential if different nuclides can be distinguished in measurement as in γ -ray spectrometry with the use of a Ge detector.

Commercial radioactive nuclides are usually available with nuclidic purities exceeding 98%. However, one should remember that the purity decreases gradually when the contaminating nuclide has a longer half-life than that of the stated one. For example, ^{197}Hg (64.14 h) used for scan of kidney and spleen often contains ^{203}Hg (46.61 days) as an impurity. Even if the amount of the latter is 1% at the time of assay, it will exceed that of the former in about 20 days.

Radiochemical purity. The radiochemical purity is the fraction of the stated radioactive nuclide present in the stated chemical form. For tracers of elements stabilized in two or more oxidation states, it is necessary to check their oxidation state by their chemical behavior, ion exchange for example, preferably just before the experiment. In organic compounds labeled with a radioactive nuclide, it is desirable that the number and position of labeling of the radioactive nuclide are unique. However, when the number and position of the nuclide in a compound do not essentially affect its chemical behavior as is often the case in tritium-labeled ones, use of a mixture of a compound labeled with different number of the stated nuclide or labeled at different positions is acceptable. The purity of some labeled compounds decreases gradually due to oxidation, self- or radiolytic decomposition during long storage. Such a labeled compound should be assayed and purified, if necessary, before use.

35.4 Measurement of Radioactive Tracers

35.4.1 General

NaI(Tl) scintillation counters and Ge detectors are most commonly employed for γ rays, and GM counters, proportional counters, and liquid scintillation counters for β rays. A useful table

on the suitability of detectors for various kinds of radiations is given in the textbook of Lieser (2001). Autoradiography is widely used for determination of distribution of β emitters, but imaging cameras are still not in common use at present except in nuclear medicine.

In tracer experiments, determination of absolute activity, that is the total disintegration rate (disintegration per second) of the nuclide used, is rarely necessary. Usually, determination of the relative activities of a series of samples or determination of the ratio of the activity of samples to that of a standard is sufficient. In this relative measurement, the samples are measured under the same geometry, that is spatial disposition against the counter, and the ratio of counting rates (counts per second) is determined. The possible errors due to deviation in the distance between the samples and the counter and in the shape and size of the sample are diminished as the distance increases, though the counting rate decreases. When the geometry inevitably differs in a series of relative measurement, it is possible to correct the effect of this difference by calculation. However, this correction can give rise to an additional error.

The *standard deviation* accompanying a net counting rate of a nuclide depends on the counts accumulated and the *background* (counts due to sources other than the nuclide to be measured). (The error estimation is based on the rules of the error propagation as well as on the – reasonable – assumption that the counts N and N_{bg} follow Poisson statistics: see [Chap. 9 in Vol. 1.](#)) The net counting rate R_{net} and its standard deviation σ_{net} are given by

$$R_{net} = \frac{N}{t} - \frac{N_{bg}}{t_{bg}}, \quad (35.1)$$

$$\sigma_{net} = \sqrt{\frac{N}{t^2} + \frac{N_{bg}}{t_{bg}^2}}, \quad (35.2)$$

where N is the counts accumulated in time t with the sample, and N_{bg} is those accumulated in time t_{bg} without the sample. If $N = 10,000$, then in an ideal case of no background one obtains

$$\frac{\sigma_{net}}{R_{net}} = \frac{\sqrt{10000/t^2}}{10000/t} = 0.01 \quad (35.3)$$

that is the relative standard deviation is 1%. But, if $N = 10,000$ and $N_{bg} = 1,000$ in a measurement where $t = t_{bg}$,

$$\frac{\sigma_{net}}{R_{net}} = \frac{\sqrt{10000/t^2 + 1000/t^2}}{10000/t - 1000/t} = 0.0117. \quad (35.4)$$

The count to be accumulated in order to attain expected precision is estimated in the opposite way. Diminution of background by appropriate shields decreases the necessary duration of counting. Precision of a few percent is easily attainable in ordinary activity measurement.

However, in order to keep the error of counting less than 1%, it is necessary not only to increase the counts accumulated, but also to pay careful attention to other factors such as the geometry of counting, variation of background, and stability of the counter.

Dead time of the counters gives rise to loss of counts. The radiations coming in the detector are not counted during the dead time after a radiation is counted. Dead time can give rise to a serious error in the case of GM counter as described below.

Parent–daughter relationship. When the nuclide employed has a radioactive daughter, one must be cautious in its measurement. Even if the daughter represents the same element as

the parent as in $^{80m}\text{Br} \rightarrow ^{80}\text{Br}$, chemical behavior of the daughter nuclide may not be the same as that of the parent, because the chemical state of the daughter can be quite different due to the hot-atom chemical effects of isomeric transition (see [▶ Chap. 24](#) in this Volume). There are two cases concerning the measurement on a set of parent and daughter. When the parent and daughter nuclides are in radioactive equilibrium in the sample, the radiation of both nuclides is responsible for the behavior of the parent in the experiment. In case of nonequilibrium, however, only the radiation from the parent should be counted.

Decay during counting. It sometimes happens that the duration of counting is not negligible against the half-life of the tracer, when using a short-lived nuclide. In such a case, correction for the decay during measurement is necessary. When the mid-time of the measurement, instead of the starting time, is taken as the nominal time of measurement, the effect of decay is considerably reduced.

35.4.2 Gamma-Ray Measurements

In general, measurement of γ rays is much easier than that of α and β rays because of the much larger range (mean free path) of the γ rays. Moreover, different nuclides can be discriminated by energy analysis, because each γ ray has definite energy. Absolute counting of γ rays is also not difficult using a commercially available calibration source. In addition to IT nuclides (i.e., excited nuclear isomers), a large number of β -decaying nuclides emit γ rays too. The nuclides emitting positrons can be used in a similar manner as γ emitters, as positron emits two 0.511 MeV annihilation radiations (photons) in a short time. Moreover, since the two photons are emitted in the opposite direction, it is possible to locate the nuclides in the sample by detecting both of them. This is the principle of positron emission tomography (PET).

NaI(Tl) scintillation counters and Ge(Li) or pure Ge detectors are most commonly employed for γ counting. The former has a larger counting efficiency than the latter, but the energy resolution of the latter is better.

In γ counting, the requirements on the sample and its vessel and holder are much less demanding than in β counting. Self-absorption is negligible except for low-energy γ rays. Absorption by wall of ordinary plastic vessels is also neglected. So, samples are usually contained in a plastic vessel and put in contact with the detector or at an appropriated distance from it. Liquid samples are often put in a plastic or glass test-tube and mounted in the hole of a “well-type” detector. In relative measurement of liquid samples, the samples are put in plastic vessels of the same type and size (and, of course, the sample volume is also the same for each sample) and measured one by one in the same geometry against the detector. In relative measurement of solid samples of different shape and size, the sample-to-detector distance must be large enough so that the difference in geometry becomes negligible, or it must be corrected by calculation. In any case, a sheet or bag of polyethylene foil should be placed between the detector and the sample to avoid possible contamination. In case of tracers emitting low-energy γ rays around 100 keV or less, absorption especially by heavy elements can be serious. The extent of diminution of γ rays by absorption can be estimated with the help of mass absorption coefficients.

When the tracer emits β rays with a range exceeding the thickness of the vessel wall in addition to γ rays, it is recommended that the β^- or β^+ rays are shielded by an absorber. It is because a part of them can plunge into the detector, contribute to the counts, and bring about annoying problems concerning β counting described below.

A Lucite – poly(methyl methacrylate) – plate of 10 mm thickness is commonly used as an absorber of β rays.

If the purity of a radioactive tracer is guaranteed in ordinary single tracer work, no energy discrimination is necessary. However, when the γ -ray spectrum consists of a main intense peak and other minor ones, use of single channel analyzer set at the main peak will considerably decrease the background of counting and also possible interference by impurity nuclides.

When two or more tracers are used together as in the multitracer technique (see [▶ Sect. 35.6](#)), it is necessary to discriminate them from each other by energy analysis. This is done by means of a Ge detector connected to a multichannel analyzer followed by computer analysis of the observed γ -ray spectrum.

Along with the multitracer technique, a nondestructive analysis method is being developed. A γ -ray imager that employs the principle of Compton cameras has been proposed to realize this, and some successful demonstrations have been performed. This topic is mentioned later in [▶ Sect. 35.6](#).

35.4.3 Beta-Ray Measurements

When a β -emitting tracer is used, it must be born in mind that the energy of β rays is distributed from zero to a maximum and that their range is not large especially in solids.

Beta rays can be attenuated or even completely stopped by the sample itself (self-absorption), by the wall of the sample vessel, by the air layer between the sample and the counter, and by the window material of the counter. On the other hand, β rays can be detected with higher efficiency and lower background than γ rays. Various types of measurement of β rays are described below.

GM counters. For nuclides emitting relatively high-energy β rays, such as ^{32}P (maximum energy 1.711 MeV), ^{89}Sr (1.497 MeV), ^{90}Sr (0.546 MeV), ^{90}Y (2.282 MeV), a GM counter is most frequently used. Each sample for relative measurement must have exactly the same shape, thickness, composition, and also the same backing to eliminate the error caused by self-absorption and backscattering of β rays. The sample should be as thin as possible to minimize self-absorption. A thickness of 1% or less of the range of the β rays is preferable. Alternatively, samples with a thickness exceeding the range of the β rays can be used. In this case, the counting rate does not correspond to the total activity of the sample, but is proportional to the activity in unit volume of the sample. This type of “infinite thickness” sample is also useful in certain experiments.

In using a GM counter, it should be taken to heart that high counting rate results in considerable loss of counts due to long *dead time* of the counter. The dead time differs from one counter to another and is in the range of 100–500 μs . The counting rate should never exceed 10,000 cpm and should preferably be of the order of 3,000 cpm or less when no correction for loss of counts is made. This correction can be made with the help of a series of samples with known intensities.

Liquid scintillation counters. The tracers emitting only low-energy β rays are most conveniently measured by a liquid scintillation counter. The sample is mixed in a vial with an organic scintillator, such as PPO or butyl-PBD, in a solvent like toluene or xylene. A second scintillator is often added to the mixture in order to ensure matching of the wavelength of the scintillation with the photomultiplier tube detecting it. The resulting mixture is commonly called a “*scintillation cocktail*.” The most popular wavelength shifters are POPOP and DMPOPOP. Samples in an organic form are most suitable for this counter. In case of an aqueous solution sample, a second solvent such as alcohols or dioxane is necessary to ensure

mixing. Suspension and emulsion samples can also be measured. The β -emitting tracers frequently employed in organic chemistry and biochemistry, ^3H , ^{14}C , ^{32}P , ^{33}P , ^{35}S , and ^{45}Ca are usually determined by this method. It is also applicable to EC nuclides such as ^{51}Cr , ^{55}Fe , and ^{125}I . For a combination of two or three tracers with largely different maximum energy, ^3H (maximum energy 0.0186 MeV) and ^{14}C (0.156 MeV), for example, simultaneous determination of them in a sample is possible by energy discrimination. Correction for color quenching and chemical quenching is indispensable in liquid scintillation counting.

Proportional counter. Thin-window or windowless gas-flow proportional counter using CH_4 or $\text{CH}_4 + \text{Ar}$ at atmospheric pressure as a counter gas is another choice for tracers emitting low-energy β rays. In the windowless one, the sample is placed inside a counter and the counter is operated after flushing by a counting gas. With sufficiently thin samples, the counting rate is close to 50% (2π counter). The dead time of proportional counters is much shorter than that of the GM counters and the loss of counts is not serious either.

Cherenkov counters. Beta rays traveling in a medium with a speed higher than that of light in the same medium emit Cherenkov radiation, i.e., visible light in the blue region. Nuclides emitting β rays having maximum energy exceeding about 1 MeV can be determined by means of this radiation with high efficiency and low background. A liquid scintillation counter is employed as is to determine ^{32}P in solution samples, for example. No scintillator and, accordingly, no correction for chemical quenching are necessary.

Autoradiography and radioluminography. Autoradiography using a photographic emulsion is a convenient technique for tracers not only in thin or sliced samples, but also for spots of paper or thin-layer chromatograms. In the case of nuclides emitting β rays of 0.2 MeV or less, *microautoradiography* is possible, whose two-dimensional space resolution is comparable to that of an optical microscope. In case of ^3H , *supermicroautoradiography* is possible with the use of extremely thin films with minute particles of silver halide. Supermicroautoradiographs are observable only with the help of an electron microscope.

Radioluminography is a relatively new imaging technique using “*imaging plate*.” The imaging plate is composed of a flexible plastic plate coated with fine “phosphor” crystals. The phosphor is capable of absorbing and storing a fraction of the energy of incident radiations. When irradiated later by visible or infrared rays, it emits photo-stimulated luminescence, whose intensity is proportional to the absorbed energy. Imaging plates have higher resolution, wider dynamic range, and higher detective quantum efficiency compared with photographic emulsion films (Sonoda et al. 1983; Amemiya and Miyahara 1988).

Radiochromatography. Various types of radio-gas chromatographs and radio-high-performance liquid chromatographs are commercially available. They enable automatic separation of different components of a sample and activity measurement on each of them (Roberts 1979). In these instruments, gas or liquid chromatographs are coupled with a detector of β rays such as proportional counter, thin-window GM counter, or plastic or inorganic scintillation counter. Chromatogram scanners are also commercially available, which scan the β rays from spots of paper and thin-layer chromatograms.

35.4.4 Alpha-Ray Measurements

Alpha rays are counted with the use of an ionization chamber, a windowless gas-flow proportional counter, a liquid scintillation counter, or a Si barrier detector. Autoradiography is also effective for α particles. However, α -emitting nuclides are rarely used in ordinary tracer works,

because the range of α rays is very small (a few centimeters in air) and counting of them necessitates an extremely thin sample. Moreover monitoring of contamination during and after the experiment is not simple for α emitters. A unique study on diffusion taking advantage of the short range of an α emitter is described below.

35.4.5 Accelerator Mass Spectrometry

Some long-lived radioactive nuclides can be determined with very high sensitivities down to 10^3 – 10^5 atoms/sample by accelerator mass spectrometry (Liu et al. 1994). This technique, not relying on the radiation emitted, was first used in chronology and has developed in applications to nuclear, geological, environmental, material, and biomedical sciences. Tandem van de Graaff accelerators are most commonly used. Routine determination is made on ^{10}Be , ^{14}C , ^{26}Al , ^{36}Cl , and ^{129}I and many other nuclides are exploited. Because of the high sensitivity, the size of the sample necessary for determination of ^{14}C , for example, is as small as a few milligrams or less in contrast to several grams in conventional low-level β counting.

35.5 Selection, Acquisition, and Use of a Radioactive Tracer

35.5.1 Selection of a Radioactive Tracer

In selection of a radioactive nuclide as a tracer, attention must be paid to the following factors: half-life, radiation emitted, specific activity, chemical form, and purity along with license of use and availability. In the case of a non-isotopic tracer, the element of the tracer must be chosen after due consideration as stated above. In any case, radiation safety and legal regulations have to be carefully followed throughout acquisition, storage, use, and disposal of a radioactive tracer.

Radiations emitted. In general, radioactive nuclides emitting γ rays or positrons are the best choice as radioactive tracers for any element, because γ rays are easy to measure as described above. Quantitative measurement of β rays is not necessarily easy. However, β rays can be detected with high efficiency and low background. Therefore, in certain experiments, β emitters are more suitable than γ emitters. Radiochromatography is such a case. Beta-emitting tracers are in use for quite a number of light elements that are important for both chemistry and biology. For hydrogen, β -emitting ^3H is the sole radioactive nuclide that can be used as a tracer. Carbon has two radioactive isotopes, ^{11}C and ^{14}C , usable as a tracer. The former is a positron emitter convenient in counting, but its half-life is as short as 20.39 min, and therefore β -emitting ^{14}C is widely used. Phosphorus and sulfur only have β -emitting isotopes, ^{32}P , ^{33}P , and ^{35}S , as practical radioactive tracers. Nuclides emitting α rays are not commonly used as a radioactive tracer, because quantitative measurement of α rays is much more difficult than that of β rays and safety control of α emitters is troublesome. However, α emitters emitting γ rays too, ^{241}Am for example, are sometimes used as tracers, the γ rays rather than the α rays being measured.

Half-life. Half-life must of course be long enough so that sufficient counting rate giving required statistics is assured at the time of activity measurement. A half-life longer than at least one third of the passage of time between the beginning of an experiment and the counting will be preferable. Nitrogen and oxygen have only short-lived isotopes, as described above. Use of such short-lived tracers is limited to laboratories equipped with an accelerator producing the tracers or those with a rapid transportation system of the tracers from such an accelerator.

The specific activity of a carrier-free radioactive tracer is inversely proportional to its half-life. This will be problematic only for a tracer with an extremely long half-life in an experiment requiring high specific activity. When a long-lived radioactive tracer is employed, however, careful attention must be paid to contamination during the experiment and also to its storage and disposition afterward.

Necessary amount. The amount of a radioactive tracer to be used in an experiment depends on many factors. Among them are the fraction of the total tracer in each counting sample, the branching ratio of the decay giving the radiation counted, efficiency and background of counting, the precision required, and the time available for counting. When a tracer with the activity A is used in an experiment, the net count N_{net} of a sample in counting for the duration of t s is given by

$$N_{\text{net}} = A \times B \times E \times Y \times t. \quad (35.5)$$

Here, B is the branching ratio of the decay giving the radiation counted, E the efficiency of counting including geometrical factors and diminution by absorption, Y the fraction of the total tracer in the counting sample. When plural radiations emitted in a single decay are counted, N_{net} for each of them are summed. From the necessary precision and the background, N_{net} to be accumulated is estimated on the basis of [Eqs. \(35.1\)](#) and [\(35.2\)](#). Then, the activity A necessary for the experiment is estimated from [Eq. \(35.5\)](#). In biological experiments, Y is often less than 10^{-3} and is the dominating factor.

35.5.2 Acquisition of a Radioactive Tracer

A number of radioactive nuclides are commercially available. For use in organic and biochemical studies, a variety of labeled compounds are supplied. Some short-lived tracers are supplied by generators (see [Chap. 40 in Vol. 4](#)). Detailed information is obtainable from catalogs or home pages of the companies or agencies producing or supplying radioactive nuclides and labeled compounds. See Vol. 4 for customized synthesis of compounds labeled with ^3H , ^{11}C , ^{18}F , $^{99\text{m}}\text{Tc}$, radio-iodines, and radiometals.

For medical purposes, an enormous collection of techniques is accumulated regarding production of short-lived nuclides mainly by cyclotrons. The technique should undoubtedly be useful for application of radioactive tracers to other fields. Such nuclides include ^{11}C , ^{13}N , ^{15}O , ^{18}F , and also many nuclides of metals, halogens, and rare gases. Reactor and cyclotron production of medical radioisotopes is described in [Chaps. 38](#) and [39 of Vol. 4](#), respectively. Basic data for production of short-lived nuclides by cyclotron were compiled with substantial references by Qaim (1982). Another review by Waters and Silvester (1982) emphasizes cyclotron-produced nuclides useful for inorganic studies with many references, too.

35.5.3 Use of a Radioactive Tracer

The radioactive tracer obtained is to be assayed for its nuclidic and chemical purity. Then the tracer is converted to the chemical form used in the experiment, a certain amount of carrier being added when necessary. The tracer is commonly injected into the system to be studied instantaneously (pulse injection). Continuous injection is adopted, however, in certain cases such as process control in industry. Experiments using radioactive tracers are accompanied

with additional problems concerning safety not encountered in ordinary experiments. Therefore, careful and detailed planning of the experiment is indispensable. Moreover, it is recommendable to perform beforehand a cold run, i.e., the same experimental procedure using no tracer, and also a low-level run using a tracer in an amount much smaller than that necessary in the regular experiment. The latter is useful for checking possible contamination, for estimating the optimal amount of the tracer used, and for increasing efficiency of the experiment, which results in decrease of radiation dose to the experimenters.

35.6 Radioactive Multitracer Technique

35.6.1 Radioactive Multitracers

Radioactive tracer technique is not single-elemental anymore. In biochemical studies, two radioactive tracers emitting β rays, ^3H and ^{14}C for example, are often used together to trace the two elements simultaneously. In the case of γ -emitting tracers, literature contains not a few examples of applying up to several tracers together in an experiment. However, such works were sporadic, and there has long been no trial to develop the radioactive tracer technique as a multi-elemental one. Since 1991, the “*multitracer technique*” using heavy-ion reactions has been developed using a number of radioactive nuclides produced by nuclear fragmentation induced by heavy ions (Ambe et al. 1991; Ambe 2000). The nuclides are radiochemically separated from the target material and used together to trace many elements simultaneously. The technique has been applied in chemistry, biology, medicine, engineering, and environmental sciences. Examples of recent application are given in the sections below describing application of radioactive tracers.

Multitracers enable one not only to acquire data for various elements efficiently but also to determine the characteristic behavior of different elements under identical experimental conditions. The results obtained for different elements can be compared free from the peculiarities of the individual samples. This is very advantageous for environmental and biological samples. Multitracers are also useful in the search for an element behaving in a specific way.

35.6.2 Production of Radioactive Multitracers

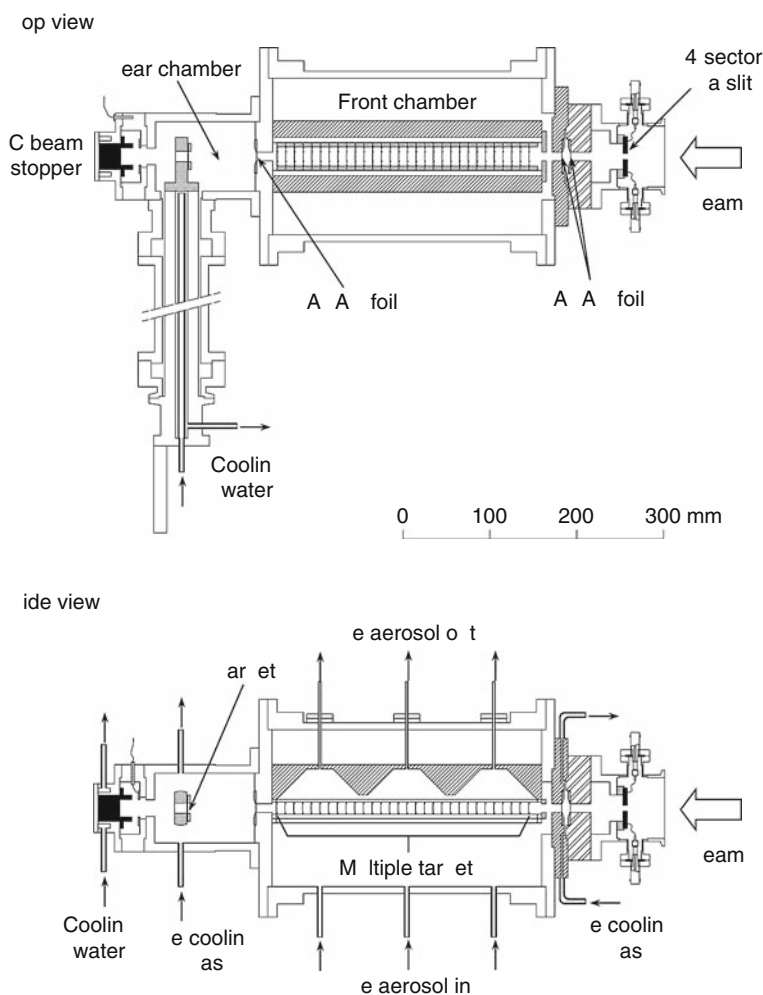
A target is irradiated with heavy ions such as ^{12}C , ^{14}N , or ^{16}O accelerated up to 135 MeV/nucleon, for example. The fragmentation reaction of target nuclei produces a number of radioactive nuclides with proton numbers up to that of the target nuclei (eventually up to that plus one by proton transfer). As a typical example, a schematic of the multitracer production system installed on the beam line of the K540 RIKEN Ring Cyclotron (RRC) is shown in ► Fig. 35.1 (Haba et al. 2005). It consists of a gas-jet-coupled multitarget chamber (front chamber) and a simple gas- and water-cooled target chamber (rear chamber).

The beam diameter from RRC is first collimated to 7 mm in diameter with a four-sector Ta slit. Then, the beam passes through a HAVAR vacuum window of 6 μm thickness and enters 30 multiple targets, each of approximately 1 μm thickness with 10 mm spacing in the front chamber. The recoil nuclei are stopped in helium gas and attached to aerosols such as potassium chloride and carbon. The gas and activity-laden aerosol particles are sucked through

a Teflon capillary (2.0 mm in diameter, 10 m in length) to a chemistry laboratory just beneath the irradiation room by applying vacuum to the downstream end of the capillary, where the aerosol particles are collected on a glass filter. Thus, the multitracer solutions are obtained simply by washing the filter with a suitable solution. The performance of the gas-jet system was first investigated with 50 radionuclides of 18 elements produced in the reaction on ^{nat}Cu induced by 135 MeV/nucleon ^{14}N (Haba et al. 2005). The advantages of the gas-jet system are as follows: (1) The multitracers are separated from the target material without chemical separation and transported to the chemistry laboratory within a few seconds. Thus, radionuclides with short half-lives (less than 1 min) are available for tracer experiments. (2) The targets of almost all the elements can be prepared by electrodeposition or vacuum-evaporation techniques.

■ Fig. 35.1

Schematic of the multitracer production system installed on the beam line of the K540 RIKEN Ring Cyclotron



The composition of the radionuclides in the multitracer can be optimized by changing the target material and its array. (3) The radionuclides of interest are easily concentrated using a gas-jet-coupled liquid chromatography apparatus based on ion exchange or solvent extraction.

In the rear chamber, the beam enters a stack of thick metallic targets such as ^{nat}Ti , ^{nat}Ag , and ^{197}Au , which are each 100–250 μm in thickness, and finally stops in a water-cooled carbon beam stopper. After the irradiation, the targets are dissolved in acid and the target materials are removed leaving as many radioactive nuclides as possible in the final solution as a multitracer. Preparation of the multitracer solution from a silver target is straightforward (Ambe et al. 1995). Dissolution of the target in nitric acid and addition of hydrochloric acid followed by filtration of silver chloride yield a solution containing all the useful radioactive nuclides produced, except for those of silver and halogens. The solution contains almost all the essential elements for humans, animals, and plants. When radioactive tracers of heavier elements are required, a gold target is recommended (Ambe et al. 1995). After heavy-ion irradiation, the target is dissolved in aqua regia. The solution is evaporated under reduced pressure and the residue is dissolved in 1.5 M HCl. Gold is extracted with ethyl acetate, leaving a multitracer solution containing tracers of elements up to mercury. In this case, the number of radioactive nuclides produced is so large that overlap of peaks in their γ -ray spectrum is substantial. Therefore, it is recommended to separate the multitracer into two or more groups of elements (group tracers). Usually, rare earth elements are separated from other elements by cation exchange and used separately. For the production of ^{28}Mg and ^{47}Ca , a Ti target is used (Ambe et al. 2001). The chemical forms of the tracers in the multitracer solutions depend on the preparation procedure employed and can be estimated from the behavior in ion exchange, for example.

35.6.3 RI Beam

In recent years, the advent of radioactive isotope (RI) beams has opened up a number of fascinating new fields (Tanihata 2004). To further develop the new fields of science, the RI Beam Factory (RIBF) has been constructed at RIKEN (Kubo 2003). This new system consists of three ring cyclotrons: the K570 MeV fixed frequency Ring Cyclotron (fRC), the 980 MeV Intermediate-stage Ring Cyclotron (IRC), and the 2,500 MeV Superconducting Ring Cyclotron (SRC). It boosts the energies of the output beams from the existing RRC up to 440 MeV/nucleon for light ions and 350 MeV/nucleon for heavy ions up to ^{238}U . These energetic heavy-ion beams are converted into RI beams via projectile fragmentation or in-flight fission of ^{238}U by the superconducting isotope separator, BigRIPS. Thus, RIBF can derive 3,000 kinds of RI beams with the world's highest intensity. The beam intensities for radioisotopes near the line of stability – which have relatively long half-lives ($> \sim 1$ min) and are practically available for radioactive tracer studies and for radiopharmaceutical diagnosis and therapy – are over 10^{10} atoms s^{-1} . One can catch the RI beams directly with suitable materials such as water, acids, physiological saline, and radiopharmaceuticals. One can select a radionuclide of interest with suitable decay properties for its application. Since they are mass-separated from other fragment isotopes, no chemical separations may be required for preparations of tracer solutions. These tracer solutions should be infinitely pure and carrier-free compared with those produced by conventional cyclotrons or reactors with the aid of chemical separation. As examples, RIBF can generate the isotopes of ^{28}Mg and ^{67}Cu , which are not readily available at present, with intensities of 2.1×10^9 and 4.6×10^{10} atoms s^{-1} , respectively. These result in 1.2 GBq for ^{28}Mg and 11 GBq for ^{67}Cu after 1-day irradiation. Thus, the RI beams derived from the future

RIBF are expected to open new frontiers in nuclear and radiochemistry as next-generation producers of radioactive tracers.

35.6.4 Measurement of Radioactive Multitracers

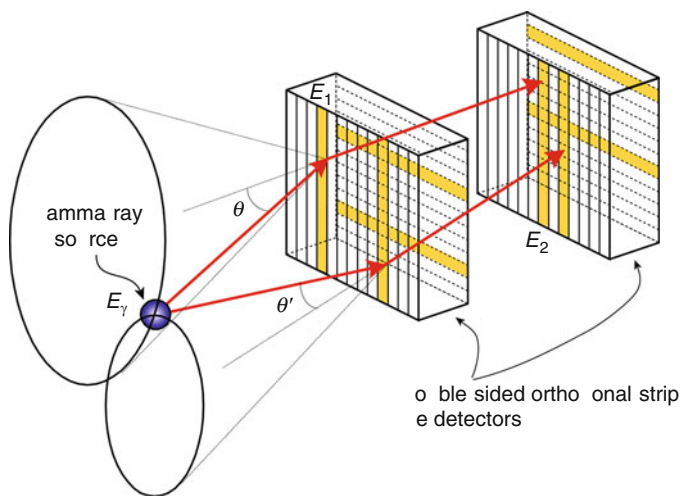
Since the multitracers contain a large number of radioactive nuclides, γ -ray spectrometry using a Ge detector is essential. The kind of elements traceable by the nuclides in the multitracer solution obtained from a target depends on the time elapsed after the irradiation, because radioactive nuclides of different half-lives are produced. Therefore, repetition of measurements increases the number of elements that can be traced. The data obtained are analyzed by means of a computer program and a database of radioactive nuclides.

However, even the method of γ -ray spectrometry performed with Ge detectors in the ordinary manner cannot make full use of the potential of multitracer technology. For example, if one needs to perform time-course analysis of multitracers in living biological samples, one has to prepare the same number of samples as that of the time points. This inherently causes individual differences, while elimination of such differences is one of the significant features of the multitracer technology.

In order to take full advantage of employing multitracer technology, a γ -ray imager for nondestructive analysis of multiple radioactive tracers is being developed (Yang et al. 2001; Motomura et al. 2007, 2009). The imager (► Fig. 35.2), which is called Gamma-Ray Emission Imaging (GREI), employs the principle of the Compton camera, the original idea of which was inaugurated in the early 1970s for γ -ray astronomy (Schoenfelder et al. 1973). GREI adopted position-sensitive Ge detectors to constitute the Compton camera, and succeeded in showing the first successful demonstration of nondestructive and simultaneous imaging analysis of multitracers in biological samples (► Fig. 35.3). After this demonstration, GREI has found an

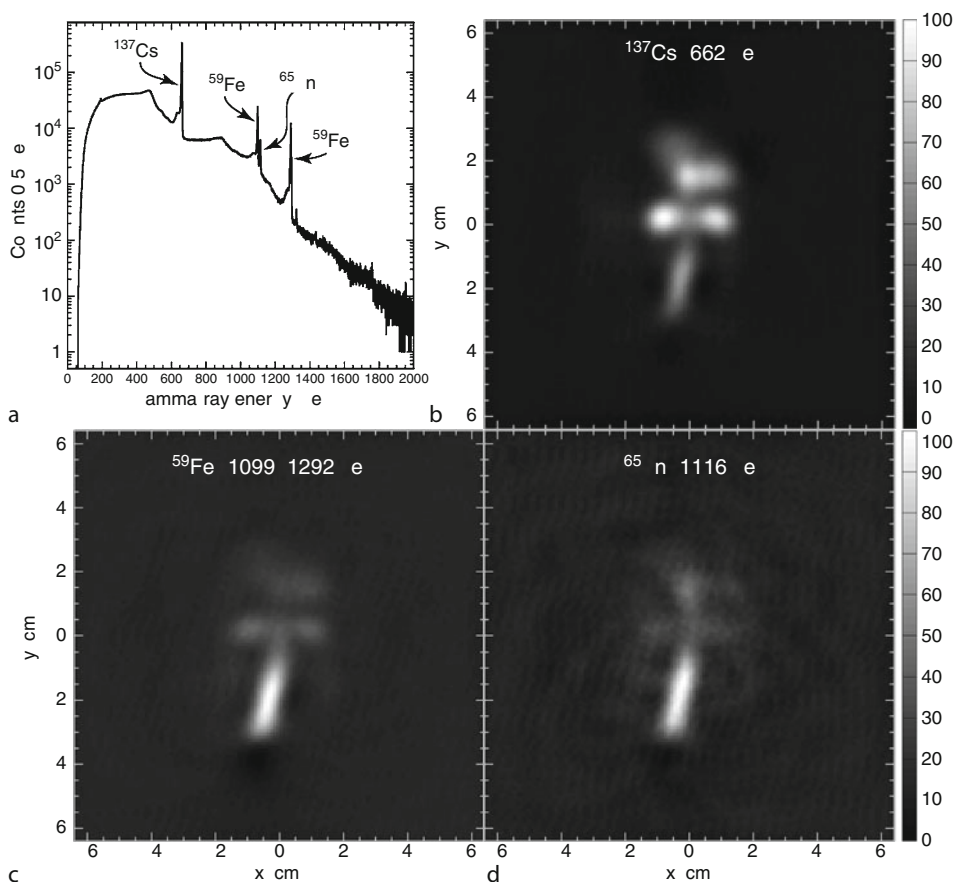
■ Fig. 35.2

Schematic diagram of the principle of γ -ray imaging with the Compton camera GREI (Motomura et al. 2007)



■ Fig. 35.3

Results of the imaging of the radioactive tracers simultaneously administered to a soybean sample. (a) Measured γ -ray energy spectrum; (b)–(d) reconstructed distribution images of the tracers (Motomura et al. 2007)



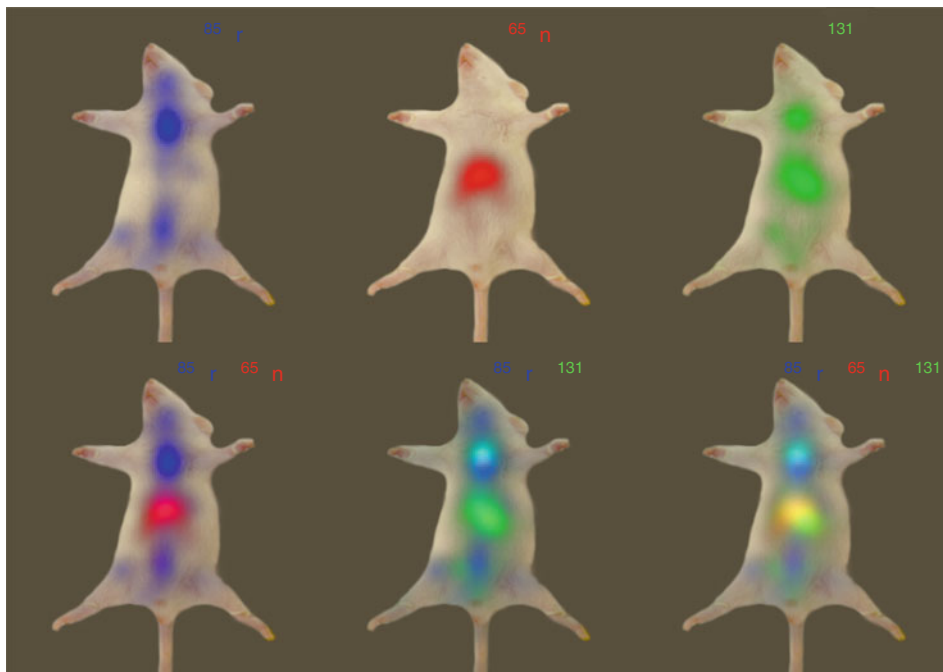
innovative application in nuclear medical molecular imaging, and succeeded in the first proof of the concept (► Fig. 35.4). Multiple molecular imaging, enabled by GREI, results in simultaneous analysis of multiple biological processes within intact living subjects, and will enable exceedingly accurate and early diagnosis of many common diseases.

35.7 Chemical Application of Radioactive Tracers

Radioactive tracers have been used in the study of equilibrium and reactions in various branches of chemistry, including inorganic and organic and also basic and industrial. Solubility, vapor pressure, diffusion, precipitation, deposition, erosion, corrosion, etc., have been extensively studied with the use of radioactive tracers. Early studies were extensively compiled by Wahl and Bonner (1951).

■ Fig. 35.4

Demonstration of multiple molecular imaging in radiopharmaceutical studies. The images clearly show the difference between the reaction processes of iodinated (^{131}I) methyl-norcholestenol (^{131}I -adosterol), strontium chloride ($^{85}\text{SrCl}_2$), and zinc chloride ($^{65}\text{ZnCl}_2$) that were simultaneously injected in a living mouse (Motomura et al. 2008). Reproduced by permission of The Royal Society of Chemistry (RSC)



35.7.1 Chemical Equilibria

Distribution ratios. An example of the determination of distribution ratio in solvent extraction will show the simplicity of application of radioactive tracers to the study of chemical equilibrium.

A hydrochloric acid solution of $^{59}\text{Fe}^{3+}$ is shaken with diisopropyl ether in a separatory funnel. After settling, the two phases are separated and an aliquot of the same volume is pipetted from each of them and put in a plastic vessel of the same shape and size. The γ rays from the samples are counted in the same geometry with a $\text{NaI}(\text{Tl})$ scintillation counter or a Ge detector. The distribution ratio of Fe^{3+} in this system is simply given by

$$K = \frac{c_{\text{org}}}{c_{\text{aq}}} = \frac{A_{\text{org}}}{A_{\text{aq}}}. \quad (35.6)$$

Here, c_{org} and c_{aq} are the concentrations of Fe^{3+} in the organic and aqueous phase respectively, and A_{org} and A_{aq} the activities of the aliquots from both phases. For precise measurement of K , mutual pre-equilibration of both phases and check of equilibrium by back-extraction is necessary.

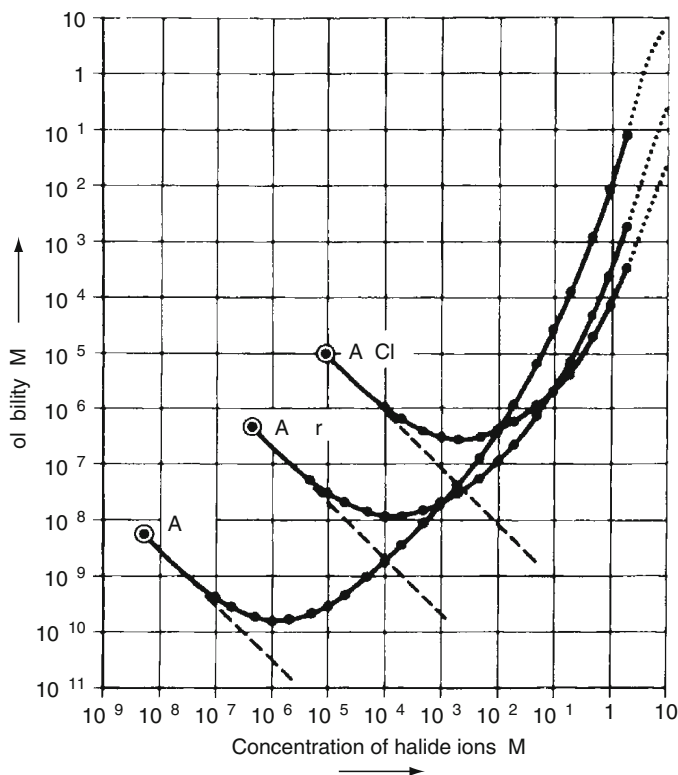
Solubility. The first radioactive tracer study was the determination of the solubility of poorly soluble PbCrO_4 by Hevesy and Paneth (1913). Lead chromate labeled with the naturally occurring ^{210}Pb was prepared, shaken with water, and filtered. The filtrate was evaporated to dryness on a nickel plate and the β activity of ^{210}Bi in equilibrium with ^{210}Pb was measured.

A detailed study on silver halides AgX ($\text{X} = \text{Cl}, \text{Br}, \text{and I}$) was reported by Lieser (1957, 2001). Using ^{110}Ag and ^{111}Ag as tracers, solubility of the halides was determined as a function of the concentration of the corresponding halides, NaCl , NaBr , and NaI up to 2 M. Starting from water, the solubility decreases with the concentration of halide ions as is expected from the solubility product. Then, passing through a minimum, the solubility increases with the halide concentration (Fig. 35.5). The increase of solubility in the higher halide concentration region corresponds to formation of complexes such as $[\text{AgX}_2]^-$ and $[\text{AgX}_3]^{2-}$. The minima are given by the solubility of the undissociated species inaccessible by electrochemical methods.

Water is poorly soluble in hydrocarbons and determination of its solubility by ordinary chemical analysis requires a large amount of hydrocarbon samples. The solubility of water in benzene (Joris and Taylor 1948) and other hydrocarbons (Black et al. 1948) was determined with the use of tritium (^3H , T) as tracer. These studies give an example where correction for the mass difference between an element of natural isotopic composition and its radioactive tracer is necessary. Water labeled with T was prepared by bombardment of heavy water (D_2O) with

■ Fig. 35.5

The solubility of silver halides (Lieser 1957, 2001)



deuterons. A hydrocarbon was saturated with the labeled water by bubbling it with air in a closed system. An aliquot portion of the saturated solution was taken and the labeled water was converted into ethanol. This labeled ethanol was introduced into a GM counter as a part of counting gas and the β activity of T was measured. Since the ratio of T in the labeled heavy water used was of the order of 10^{-12} mol T per mol D, T was essentially all in the form of TDO. Assuming that the Henry's law constant is the same for H_2O and TDO, the solubility determined for TDO was converted to that of H_2O . In this way, the solubility of water in hydrocarbons was determined down to the order of 1 mg water per 100 g hydrocarbon.

35.7.2 Reaction Kinetics and Mechanisms

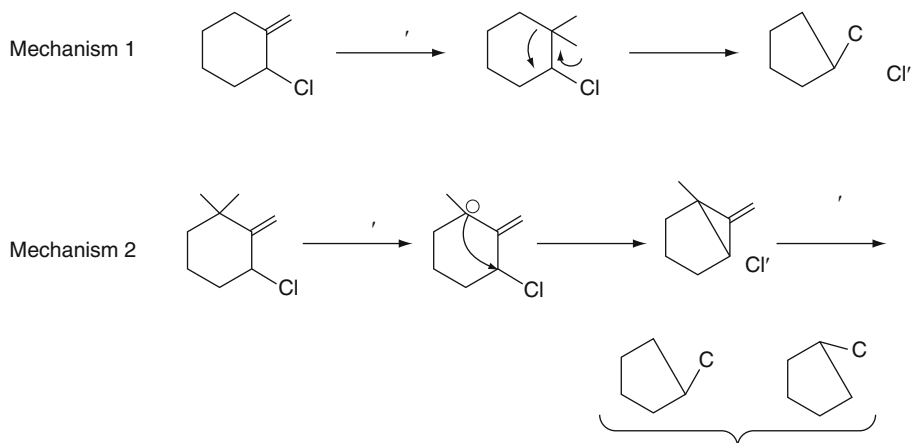
A number of organic reactions were studied by the use of radioactive tracers and their kinetics and mechanism clarified (Arnstein and Bentley 1950; Ropp and Neville 1951). Isotopic-exchange reactions are treated in detail separately in the next section.

In kinetic studies, use of a radioactive tracer is especially advantageous for slow reactions because of its high sensitivity. For example, decarboxylation of alanine was studied using this compound labeled with ^{14}C at C of the carboxyl group (Conway and Libby 1958). This reaction



in aqueous solutions was followed at 298–427 K. The half-time for the reaction at room temperature was found to be about 10 billion years, subtracting the effect of side reactions.

An early study on Favorskii reaction gives a plain explanation how radioactive tracers are used in elucidation of reaction mechanisms (Loftfield 1950). The reaction is the rearrangement of an α -haloketone in alkaline medium. Two mechanisms (1 and 2) had been proposed for the reaction.



Mechanism 1 is closely related to that of the benzilic acid rearrangement. In this case, the chlorine-bearing carbon atom of the 2-chloro-1-cyclohexanone **I** becomes exclusively the α -carbon atom of the cyclopentanecarboxylic acid **II**. In Mechanism 2, which proceeds via

cyclopropanone intermediate, the chlorine-bearing carbon atom of **I** appears in both the α and β positions of **II**. The reaction was studied using α -chlorocyclohexanone labeled with ^{14}C at the chlorine-bearing carbon atom. The results supported strongly Mechanism 2 contrary to expectation of most investigators.

35.7.3 Exchange Reactions

Isotopic tracers are essential in studying exchange reactions, namely exchange of a common component between different molecules or ions. Although the change of enthalpy is negligible in an isotopic-exchange reaction, the entropy term of the free energy drives the reaction to the direction of uniform distribution of the isotopes between the two reactants. A number of exchange reactions have been studied with the use of radioactive tracers, though enriched stable isotopes have also been employed for certain elements.

The simplest case of exchange reactions is that occurring reversibly in a homogeneous system between two chemical species each with only one exchangeable common component.



Here, C and C^* indicate two isotopes of an element. The molar concentration of each molecule and isotopic species in this reaction shall be designated as follows.

$$a = [\text{AC}] + [\text{AC}^*]$$

$$b = [\text{BC}] + [\text{BC}^*]$$

$$x = [\text{AC}^*]$$

$$y = [\text{BC}^*]$$

The rates of the rightward and leftward isotope-exchange reactions above are given by

$$r_{\text{right}} = R \left(\frac{a-x}{a} \right) \frac{y}{b} \quad (35.9)$$

$$r_{\text{left}} = R \frac{x}{a} \left(\frac{b-y}{b} \right) \quad (35.10)$$

where R is the rate of the overall reaction including exchange of C by C and C^* by C^* .

Then, the formation rate of AC^* is

$$\frac{dx}{dt} = r_{\text{right}} - r_{\text{left}} = R \frac{ay - bx}{ab}. \quad (35.11)$$

Designating the values of x and y at equilibrium as x_{eq} and y_{eq} ,

$$\frac{x_{\text{eq}}}{a} = \frac{y_{\text{eq}}}{b} \quad (35.12)$$

and

$$x + y = x_{\text{eq}} + y_{\text{eq}}. \quad (35.13)$$

Then,

$$\frac{dx}{dt} = R \frac{(a+b)}{ab} (x_{\text{eq}} - x) \quad (35.14)$$

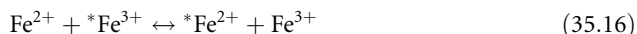
and, by integration, the McKay equation

$$\ln \frac{x_{\text{eq}} - x}{x_{\text{eq}} - x_0} = -R \frac{a+b}{ab} t \quad (35.15)$$

is obtained, where $x_0 = x$ at $t = 0$. The plot of $\ln[(x_{\text{eq}} - x)/(x_{\text{eq}} - x_0)]$ against t yields the value of R .

A lot of exchange reactions fit the above analysis. More complex exchange reactions including multiple and catalytic exchanges were discussed by Logan (1990).

Electron-transfer reactions. Exchange reactions between two chemical species differing only in charge occur through transfer of electrons. The rate of the exchange reaction



was measured in perchloric acid solutions by Dodson (1950). The tracer used was ^{55}Fe and the separation was based on formation of the very stable complex between α , α' -dipyridyl and ferrous ions. The reaction was rapid but still measurable. The reaction half-time is 20 s for 1.1×10^{-3} M Fe^{2+} and 1.0×10^{-3} M Fe^{3+} reactants in 0.4 M HClO_4 at room temperature, for example. The reaction is second order, presumably first order in Fe^{2+} and in Fe^{3+} . Later, the Fe^{2+} – Fe^{3+} -exchange reaction in perchloric and hydrochloric acid solutions was studied (Silverman and Dodson 1952). The reaction is first order in the overall concentration of each oxidation state and the rate increases with decreasing acid concentration and with increasing Cl^- concentration. On the basis of these observations, four reaction paths involving Fe^{2+} with Fe^{3+} , FeOH^{2+} , FeCl^{2+} , and FeCl_2^+ were suggested.

The exchange reaction involving transfer of two electrons



is slow and its rate is also dependent on the first power of both Tl^+ and Tl^{3+} concentrations. Mechanisms of the electron transfer reactions were reviewed by Sutin (1962).

Molecular halogen, halide, halate, and perhalate ions. The exchange rate between halide ions and molecular halogens, namely Cl^- and Cl_2 , Br^- and Br_2 and also I^- and I_2 , in aqueous solutions is too large to be measured by an ordinary radiochemical method.

The exchange between molecular halogen or halides and halates or perhalates is slow. The iodine–iodate-exchange reaction was investigated in detail by Myers and Kennedy (1950). The reaction is complex and a possible mechanism was proposed, which involves two-electron transfer from a chemical species containing I^- to one containing IO_2^+ as a rate determining step.

Metal complexes. Radioactive tracer studies on exchange reactions of metal complexes have greatly contributed to the understanding of the nature of chemical bonding in them and also of the mechanism of their reactions. Exchange of both ligands and central metal ions has been extensively studied. Relative rates of ligand exchange of octahedral complexes of transition metals are related to the electron configuration and ligand field (Taube 1952).

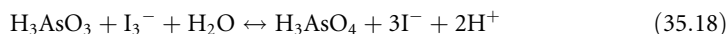
Alkyl halides and halide ions. Halogen atoms of alkyl halides exchange with halide ions in particular solvents such as ethanol and acetone. This substitution reaction occurs ordinarily through *Walden inversion*. The negative halide ion approaches the positive end of the carbon–halogen dipole in the alkyl halide and, displacing the halogen atom, forms a new chemical bond with the carbon atom. When the carbon atom is asymmetric, this exchange reaction leads to optical inversion. This mechanism was confirmed by studies of exchange reaction using radioactive tracers along with optical measurement. For example, Hughes et al. (1935) studied the exchange reaction of radioactive iodine between racemic mixture of *dl*-*sec*-octyl iodide and Na^{128}I in acetone. The reaction was stopped after a suitable time by addition of water and

crushed ice. The *sec*-octyl iodide was extracted with carbon tetrachloride and the activity of the resulting organic and aqueous phases was measured. The observed rate of exchange was found to be the same as the rate of racemization of *d*-*sec*-octyl iodide determined by optical measurement within the experimental error. This agreement confirmed the causal connection between aliphatic substitution and optical inversion. Really, investigations of this type gave a basis for discrimination of the two types of fundamental organic reactions: the first-order nucleophilic substitution (S_N1) and the second-order one (S_N2).

35.7.4 Reactions at Equilibrium

Every textbook of physical chemistry describes that chemical equilibrium is a state where the forward and reverse reactions are taking place at exactly the same rate, and that the equilibrium constant K is the ratio of the forward-rate constant k_f to the reverse one k_r . This universally accepted principle of great importance in chemistry had been conventionally justified on the basis of k_f and k_r determined far from equilibrium since the reactions cannot be followed by conventional chemical methods in the state of equilibrium. This crucial relationship between chemical reaction rate and equilibrium was first proved by the use of radioactive tracers.

A representative study on the reaction rates at equilibrium was made by Wilson and Dickinson (1937) on the exchange reaction between trivalent and pentavalent arsenic, which proceeds in the presence of easily oxidizable or reducible substances like iodine.

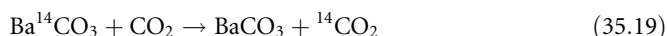


A reaction mixture in this equilibrium was prepared, in which H_3AsO_3 was labeled with ^{76}As . The exchange was quenched by dilution with water and addition of an excess of ammonium hydroxide. The AsO_4^{3-} ions were precipitated as ammonium magnesium arsenate and subjected to activity measurement. The rates of oxidation and reduction measured in this way were in agreement with the kinetic expressions and rate constants, which hold for the same reaction remote from equilibrium.

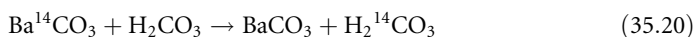
35.7.5 Surface and Solid Reactions

Radioactive tracers, with their high sensitivity and ease of detection, are also an excellent tool for the study of surface reactions. Usually, rapid exchange occurs between a chemical species in a solution or gas and that on a solid. Then follow much slower processes involving species in the deeper layers of the solid, i.e., diffusion and recrystallization. These reactions are easily observed by establishing contact between the solid and a solution of a tracer followed by the separation of the two phases and activity measurement.

A study on the exchange of ^{14}C between carbon dioxide and barium carbonate



was reported by Armstrong and Schubert (1947). This exchange reaction was found to proceed only in the presence of water vapor, and, in the atmosphere saturated with water, more than one third of ^{14}C in $\text{Ba}^{14}\text{CO}_3$ was lost in 65 h. Therefore, a mechanism involving



was proposed for the reaction. This observation is very important for experiments using ^{14}C , because ^{14}C is often supplied or stored in the form of $\text{Ba}^{14}\text{CO}_3$. $\text{Ba}^{14}\text{CO}_3$ loses its radioactivity when it is in contact with humid air, and in the opposite way BaCO_3 in contact with $^{14}\text{CO}_2$ in humid air is contaminated with ^{14}C .

Radioactive tracers have been extensively and successfully applied to the studies of mechanism of precipitation and also aging or ripening of precipitates. Studies of corrosion and erosion using radioactive tracers have greatly contributed to improvement of industrial processes.

Emanation means the release of a radioactive gas, typically a noble gas produced in a solid by radioactive decay or nuclear reaction, from the solid. This phenomenon has been utilized in both basic and industrial studies. The emanation is measured as a function of the temperature and increase of emanation at a certain temperature indicates structural or chemical change in the sample. For example, Zimens (1937) studied emanation of ^{220}Rn from calcite and aragonite, the hexagonal and orthorhombic forms of CaCO_3 . Calcite and aragonite samples doped with ^{224}Ra were prepared and heated in dry CO_2 gas and the activity of ^{220}Rn , the daughter of ^{224}Ra , released from the sample was measured with a flow counter. In the case of aragonite, emanation due to the structural change of CaCO_3 from aragonite to calcite is observed at 530°C as a peak of radioactivity. Then, strong emanation accompanying decomposition of calcite into CaO and CO_2 is observed around 920°C . Finally, emanation increases again above $1,100^\circ\text{C}$, where the Ca^{2+} and O^{2-} ions begin to become mobile in the matrix.

35.7.6 Diffusion

Diffusion is a suitable target of study with radioactive tracers. By ordinary chemical methods, only diffusion occurring in a system with a concentration gradient is observable. However, isotopic tracers enable observation of “self-diffusion,” that is diffusion of atoms or ions in a system having no chemical concentration gradient. Ordinary diffusion and self-diffusion have been extensively studied not only in solid but also in liquid state using radioactive tracers.

Diffusion in solids. In a diffusion study on solids, a layer as thin as possible of a radioactive tracer is formed on the surface of the sample by electroplating, for example. In some cases, an isotope-exchange reaction can be used to prepare a thin layer. Diffusion is allowed to proceed at an elevated temperature for a definite time. Then, the thin sections of the sample surface are removed stepwise by grinding or chemical etching. The activity of the tracer in the sections removed is determined to yield the diffusion constant. Microautoradiography of a section cut vertically against the surface of the sample helps to distinguish between uniform diffusion and that through grain boundaries. An example of geological application is described below.

A historical diffusion study by Hevesy and Obrutsheva (1925) is a unique example of taking advantage of the short range of α particles. Two thin foils of lead, one of inactive lead and the other of lead containing ^{212}Pb , were pressed together. The thickness of the inactive foil was chosen slightly greater than the range of the α particles to be measured. The rate of self-diffusion of lead was determined on the basis of α particles emitted by ^{212}Bi and ^{212}Po (the daughter and granddaughter nuclides of ^{212}Pb) diffused into the inactive foil and observed from the backside of it.


A more elaborate technique in this line was developed by the use of recoil atoms (Hevesy and Seith 1929). Vapor of $^{212}\text{PbCl}_2$ was condensed on the surface of a PbCl_2 disk and the disk was kept at $166\text{--}270^\circ\text{C}$. After waiting for the establishment of radioactive equilibrium in the decay series $^{212}\text{Pb} \rightarrow ^{212}\text{Bi} \rightarrow ^{208}\text{Tl}$, ^{208}Tl atoms recoiled out of the surface as a result of the α

decay of ^{212}Bi were collected and their β activity was measured to yield the diffusion constant of ^{212}Pb in lead halide. The extremely short range of the recoil of ^{208}Tl (about 3×10^{-5} mm in Pb) enabled determination of diffusion constants as small as of the order of $10^{-18} \text{ cm}^2 \text{ s}^{-1}$ and those at a temperature as low as 166°C for PbCl_2 .

Diffusion in liquids. Diffusion in liquids is most commonly measured by the diaphragm cell method. In a self-diffusion study, a radioactive tracer is applied to one of two cells containing a liquid of the same chemical composition and separated by a porous diaphragm. Aliquots taken from one or both of the cells in time sequence are subjected to activity measurement. In the capillary method, a series of uniform capillaries, typically 0.5 mm in diameter and 4 cm long, are filled with the solution containing the radioactive tracer. The capillaries are held in a vertical position below the surface of a circulating bath of a nonradioactive solution for different lengths of time. The activity remaining in the capillaries give the diffusion constant. Isotopic self-diffusion studies on ions in aqueous solutions have an advantage that the diffusion coefficients are determined independent of the diffusion of counter ions, which is inevitable in ordinary determination in solutions with a concentration gradient.

35.7.7 Search for Formation of New Compounds

The multitracer technique is useful in search for new compounds. The formation of metallofullerenes had been established by ordinary chemical methods only for the group 2 elements, Ca, Sr, and Ba; and for the group 3 elements, Sc, Y, and the lanthanide elements. Formation of new metallofullerenes was examined for a number of elements from those in groups 2 through 16 in the periodic table with a multitracer and metallofullerenes with group 4 and 5 elements were successfully discovered (Sueki et al. 1999).

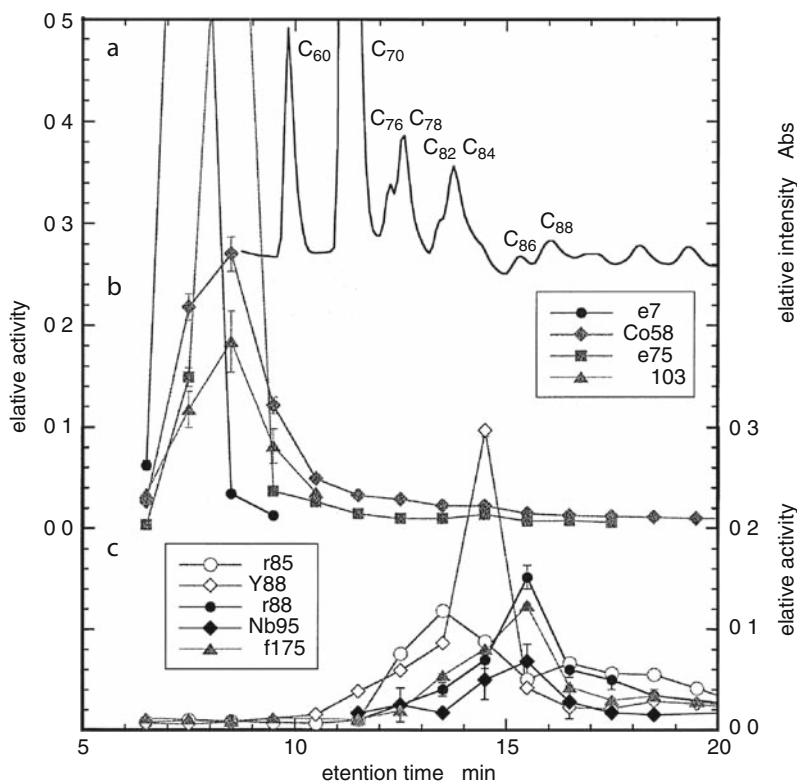
A multitracer containing tracers of 28 elements and macro amount of lanthanum nitrate were dissolved in ethanol and absorbed by a graphite rod. After heat treatment, the rod was used as an electrode for fullerene production by the arc-discharge method in a vacuum chamber. The fullerene-like species in the soot produced inside the chamber were extracted into CS_2 . The CS_2 extract was injected into a High-Performance Liquid Chromatography (HPLC) system with a 5 PBB column and eluted with CS_2 . The elution curves are given in  Fig. 35.6. Thus, formation of metallofullerenes of Zr, Hf (group 4), and Nb (group 5) was radiochemically ascertained. At the same time, it has also been shown that no metallofullerenes are formed for the elements of group 6 and higher ones under the experimental conditions.

35.8 Analytical Application of Radioactive Tracers

Radioactive tracers have shown their usefulness in many aspects of analytical chemistry (Elving 1986). Basic data for separation techniques, solvent extraction, ion exchange, various types of chromatography, etc., have often been obtained by the use of radioactive tracers. Mechanism of coprecipitation and aging of precipitates, important in gravimetric analysis, was also extensively studied.

■ Fig. 35.6

Elution curves of metallofullerenes labeled with a multitracer (Sueki et al. 1999). (a) Shows the UV elution curve of empty fullerenes, (b) radioactivity elution curve of tracers mostly eluted before C_{60} , and (c) that of tracers eluted as metallofullerenes (the elution peaks observed for trivalent La, Ce, Pm, Gd and divalent Eu, Yb are not shown)



Radiometric analysis, or radiometry, is a method of analysis in which a radioactive tracer is employed as an indicator or a reagent. Among them, the most important one is the isotope dilution analysis discussed separately below. Isotope dilution analysis is also used to determine the amount of radioactive elements or compounds (inverse isotope dilution analysis).

35.8.1 Isotope Dilution Analysis

Since the early works of Hevesy in the 1930s, this technique has yielded abundant variations and has been used not only in research but also in industry (Tölgyessy and Braun 1972). Radioimmunoassay is the most developed form of the technique and is routinely used in medicine.

Direct isotope dilution analysis. This method is employed to determine the mass (weight) of an ordinary inactive compound (or an ion) in a solution, being efficacious when quantitative separation of the compound from the mixture is difficult but partial separation of the

compound in the pure state is feasible. The unknown mass of the compound to be determined in the sample solution is taken to be X . To this sample solution is added a solution containing W_0 of the same compound labeled with a radioactive tracer (commonly called a “spike”) with activity A_0 and hence with a specific activity

$$S_0 = \frac{A_0}{W_0}. \quad (35.21)$$

The resulting solution is thoroughly blended so that the original inactive compound and the added radioactive compound attain equilibrium. Now, the specific activity S' of the compound in the solution is given by

$$S' = \frac{A_0}{X + W_0}. \quad (35.22)$$

Then, a portion of the compound is isolated in the pure state. The mass W and the activity A of the portion is measured to yield the specific activity

$$S = \frac{A}{W}. \quad (35.23)$$

As the specific activity remains unchanged during the separation procedure of the compound from the mixed solution,

$$S = \frac{A}{W} = S' = \frac{A_0}{X + W_0}, \quad (35.24)$$

$$X = \frac{S_0 - S}{S} W_0. \quad (35.25)$$

For example, direct isotope dilution analysis is used for mercury inventory in industry (Cowley et al. 1966; Enomoto et al. 1975). The mass X of mercury in electrolytic chlorine cells is determined using ^{197}Hg , ^{203}Hg , or a mixture of them. An aliquot of known mass W_0 and activity A_0 and hence known specific activity S_0 is taken from a stock of mercury labeled with the tracer, added to each electrolytic cell, and left to mix. After homogenization, a sample of mercury is taken from each cell. The samples are shaken with 15–20% HCl to decompose amalgam. The mass W and activity A of the samples are measured to yield to S and, accordingly, X . The accuracy is better than 1%.

Substoichiometric isotope dilution analysis. It is often inconvenient to determine the mass of the isolated compound in the above direct isotope dilution analysis, as is the case for a large number of samples. Substoichiometric isotope dilution analysis is an excellent solution to this problem (Ruzicka and Stary 1968; Stary and Ruzicka 1976). In this method, the same amount of the compound is separated from each of the standard and mixed solutions using a reagent in an amount stoichiometrically less than that of the compound in the solutions. The activity of the portion separated from the standard solution (A_0) and that from the mixed solution (A) are measured. Since the mass of the portions counted are the same, the ratio of their specific activities S_0/S equals the ratio of their activities A_0/A .

Thus, the mass of the compound in the original sample is given as

$$X = \frac{A_0 - A}{A} W_0. \quad (35.26)$$

When the separation is not strictly stoichiometric, a calibration curve determined from a series of known samples is used. Radioimmunoassay is based on this principle of substoichiometric isotope dilution analysis.

Inverse isotope dilution analysis. This variation is a method to determine not an inactive compound but a radioactive one. To be determined is the mass X of a certain radioactive compound (or ion), whose specific activity is known to be S_0 , in a sample. To the sample solution is added a solution containing W of the same but inactive compound (spike). If the specific activity of the compound after this addition and thorough blending is taken to be S , then

$$S_0 X = S(X + W). \quad (35.27)$$

This is so because the total activity of the compound naturally remains unchanged by addition of the inactive one. The specific activity S of a portion of the compound purely isolated from the blended solutions is obtained from its mass and activity. Then, the mass X of the compound in the original sample solution is given by

$$X = \frac{SW}{S_0 - S}. \quad (35.28)$$

The weak point of the above inverse isotope dilution analysis is that the specific activity S_0 of the compound to be determined in the original sample solution must be known. This can be avoided by *double isotope dilution analysis*. In this type of analysis, two portions of exactly the same amount are taken from the sample solution. The mass of the radioactive compound in each portion is taken to be X . To the portions are added different masses W_1 and W_2 of the inactive compound. Taking the specific activities of the compound in the portions after this to be S_1 and S_2 ,

$$S_0 X = S_1(X + W_1), \quad (35.29)$$

$$S_0 X = S_2(X + W_2), \quad (35.30)$$

X and S_0 can be expressed as follows:

$$X = \frac{S_2 W_2 - S_1 W_1}{S_1 - S_2}, \quad (35.31)$$

$$S_0 = S_1 S_2 \frac{W_2 - W_1}{S_2 W_2 - S_1 W_1}. \quad (35.32)$$

35.8.2 Radiometric Analysis

Radiometric methods other than the isotope dilution analysis are not necessarily versatile. But they provide convenient and reliable technique in certain cases (Braun and Tölgyessy 1967). In *radiometric titration*, a radioactive indicator is used to monitor the end-point of the titration. For example, Cl^- ions in an aqueous solution sample are titrated with a standard solution of Ag^+ solution labeled with $^{110\text{m}}\text{Ag}$. Until the equivalence point is attained essentially all the Ag^+ ions are precipitated as AgCl , giving little activity in the supernatant solution. At the equivalence point, the activity begins to increase linearly. Plotting the activity of the solution against the amount of Ag^+ solution added, the equivalence point is clearly determined as the intersection of two lines. This technique is reliable and convenient, if both the separation of the supernatant solution from the precipitate and the activity measurement are made automatically.

Another example of radiometry worth mentioning is determination of a chemical species by precipitation with a radioactive reagent. For example, the amount of K^+ ions in an aqueous solution is determined by the use of ^{60}Co . An excess of a standard solution of $\text{Na}_3[^{60}\text{Co}(\text{NO}_2)_6]$ is added to the sample solution and the precipitate of poorly soluble $\text{K}_2\text{Na}[^{60}\text{Co}(\text{NO}_2)_6]$ is collected by filtration. From the activity of the precipitate, K^+ is determined referring to a calibration curve obtained on samples containing known amounts of K^+ ions. This method is used, for example, to determine 0.1–0.002 mg of K^+ ions in rainwater.

35.8.3 Surface-Area Determination

Area determination of ionic crystals by measurement of exchange reactions of radioactive tracers was established by Paneth and Vorwerk (1922). When a radioactive tracer is uniformly distributed between the solid surface and a solution

$$\frac{N_{\text{surf}}^*}{N_{\text{surf}}} = \frac{N_{\text{sol}}^*}{N_{\text{sol}}} \quad (35.33)$$

where N and N^* designate the number of the total chemical species in question and that of the species labeled with the tracer, and the subscripts “surf” and “sol” refer to solid surface and the solution, respectively. The value of N_{surf} is readily calculated from the measured values of N_{sol} and $N_{\text{surf}}^*/N_{\text{sol}}^*$. The average distance L between the adsorbed species is given by

$$L = \left(\frac{W}{n N_A \rho} \right)^{\frac{1}{3}} \quad (35.34)$$

where W is the molar mass of the solid, n the number of exchangeable species in one formula unit of the solid, N_A the Avogadro constant, and ρ the density of the solid. Then, the surface area S is given by

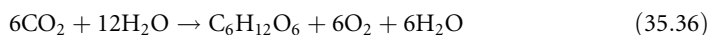
$$S = N_{\text{surf}} L^2 = N_{\text{surf}} \left(\frac{W}{n N_A \rho} \right)^{\frac{2}{3}}. \quad (35.35)$$

On the basis of this principle, Paneth and Vorwerk (1922) measured the surface area of PbSO_4 using ^{212}Pb as the tracer. In this type of measurement, it is necessary to repeat the activity measurement as a function of time and to subtract the component due to the slow processes of diffusion and recrystallization.

35.9 Biochemical Application of Radioactive Tracers

Radioactive tracers have played and are still playing an extremely important role in the fields of biochemistry and other biological sciences. Their application to medicine is described in detail elsewhere (see Vol. 4). Even apart from medicine, the ways of application are too many to mention. Here, the historic study of photosynthesis by Calvin and coworkers is briefly described as the representative one, followed by a recent multitracer study.

The photosynthesis of carbohydrates by plants



was studied by a series of tracer experiments using ^{14}C . Plants were cultivated in atmosphere containing $^{14}\text{CO}_2$. After exposure to light for different periods of time, sections of the plants were digested and organic constituents were separated by paper chromatography and the distribution of ^{14}C among various species was determined by autoradiography (Benson et al. 1950). On the basis of this kind of tracer studies, the well-known mechanism of photosynthesis was established (Bassham and Calvin 1957).

In *positron emission tomography* (PET) of brain tumors, ^{18}F -fluorodeoxyglucose (FDG) is widely used. However, ^{18}F -FDG often fails to detect tumors because of its relatively high uptake in the normal parts of brain. So, a search for a brain tumor-specific element was performed by the multitracer technique (Tamano et al. 2001). A multitracer solution prepared from a silver target was intravenously injected into the rats having C6 glioma in brain. One hour after the injection, the rats were killed and their brain was divided into tumor, cerebral cortex, cerebellum, and the rest, each being subjected to γ -ray spectrometry.

Among radioactive nuclides of 15 elements detected, ^{65}Zn , ^{83}Rb , ^{54}Mn , and ^{22}Na , were found to be preferentially taken up in the tumor. The preferential uptake of ^{65}Zn in C6 glioma is consistent with the result of a single-tracer study and suggests the possibility of imaging of malignant cell proliferation in the brain using relatively short-lived $^{69\text{m}}\text{Zn}$ (13.76 h). Similarly, the above result on ^{54}Mn suggests use of $^{52\text{m}}\text{Mn}$ (21.1 min) for positron emission tomography of brain tumors. The high uptake of ^{83}Rb is suggestive of ^{82}Rb (1.273 min) or ^{81}Rb (4.576 h) in place of ^{201}Tl (72.91 h).

35.10 Geological Application of Radioactive Tracers

Radioactive tracers have been extensively employed in both laboratory and field works of geological studies. Here, only a recent study using a multitracer on diffusion of ions through granite is described.

Diffusion behavior of various elements in micropores of rocks is important from the viewpoint of disposal of radioactive waste in deep underground repository. Diffusion experiments were conducted by the through-diffusion method using a multitracer containing radioactive tracers of 14 elements (Egawa et al. 2001). Granite samples were cut into a 5 mm thick and 40 mm diameter disk. Disks of granite samples were fitted tightly between two cells filled with a 0.10 M NaCl solution (pH 4). The multitracer solution was injected into one of the cells. Activity of the tracers diffusing into the other cell was determined using a Ge detector after various time intervals for about 3 months. Diffusion path of each element in the granite was determined by autoradiograph using an imaging plate.

Diffusion of ^7Be , ^{54}Mn , ^{58}Co , ^{65}Zn , ^{75}Se , ^{83}Rb , ^{85}Sr , and ^{88}Y was observed in the weathered granite, while only ^{54}Mn , ^{75}Se , ^{83}Rb , ^{85}Sr in the fresh one. This difference is attributed to the larger porosity of the former than that of the latter. The autoradiography showed that diffusion paths of the tracers are in the grain boundaries and cleavages of biotite and plagioclase in the granite.

35.11 Industrial Application of Radioactive Tracers

Radioactive tracers are widely used in various fields of industry (Charlton 1986; Földiák 1986). Different ways of application are compiled in a guide published by International Atomic Energy Agency (IAEA; Ferronsky et al. 1990). The present authors rely much on the guidebook

for the following description. An example of industrial application of isotope dilution analysis was described above.

Flow rates of solutions or suspensions are measured with tracers such as ^{82}Br and ^{24}Na . For gas flows, radioactive rare gases, ^{41}Ar , ^{85}Kr , and ^{133}Xe are commonly used. Mixing processes are followed by measuring the tracer concentration. In mixing of solid particles, the best tracer is a fraction of the material itself made radioactive by neutron irradiation.

Radioactive tracers are also used for troubleshooting in industrial processes. Location of a leak is detected by applying a radioactive tracer to the suspected part of a system and monitoring the tracer leaking out of the system. For example, leak problem in a plant is solved by pulse injection of ^{41}Ar and detection of it along the lines of the plant. Leak location of long-buried pipelines with large diameter is economically achieved as follows. The suspected section of a pipeline is filled with water in which $\text{NH}_4^{82}\text{Br}$ is dissolved. The section is pressurized for a while and then thoroughly washed with water. A detector system with recorder mounted on a "pig" is moved through the line by hydraulic pressure to detect ^{82}Br having leaked into the surrounding of the pipe. This method was successfully used to detect five leaks in a 140 km long crude oil pipeline.

Refractory lining wear in blast furnaces is monitored by radioactive tracers. Sources of ^{60}Co are embedded in refractory bricks during lining. The γ rays of ^{60}Co are monitored from outside the furnace and erosion of the bricks is detected as the extinction of the γ rays. Tritiated water ($^3\text{H}_2\text{O}$) provides a very sensitive way of testing watertightness of pieces connected with elastomer joints.

Testing of corrosion resistance of materials is most commonly done with the use of *kryptonates*, i.e., solids into the surfaces of which ^{85}Kr has been incorporated by ion bombardment. Kryptonates of test materials are exposed to corrosive atmosphere and the residual β activity of ^{85}Kr is measured. Surfaces labeled with a radioactive tracer by isotope exchange, electrodeposition, or vacuum deposition are also employed.

An excellent way of measuring the material loss at the surface is use of *thin-layer activation*. A thin layer of radioactive tracer is produced on the surface by irradiation with charged particles. This technique can be applied to all types of iron, steel, nonferrous metals and alloys. It is particularly suitable for metal wear studies, because, if done carefully, the charged-particle activation little alters the mechanical properties of the surfaces of specimens. As the charged particles for irradiation, protons, deuterons, α particles, and occasionally ^3He -particles accelerated by a cyclotron or other accelerators are used. Choosing the kind and energy of the charged particles, a radioactive layer of 10–1,000 μm thickness is produced. Typical nuclear reactions used are as follows.

Iron	$^{56}\text{Fe}(\text{p},\text{n})^{56}\text{Co}$
Nickel	$^{58}\text{Ni}(\text{p},\text{pn})^{57}\text{Ni} \rightarrow ^{57}\text{Co}$
Copper	$^{65}\text{Cu}(\text{p},\text{n})^{65}\text{Zn}$
Molybdenum	$^{95}\text{Mo}(\text{p},\text{n})^{95\text{m}}\text{Tc}$

Loss of surface material due to wear is estimated by measuring the decrease of the activity of the surface or by measuring that of the powder lost from the surface and accumulated in the lubricating oil. The activity is converted to wear depth by a calibration curve obtained on a standard sample. This technique is widely and efficiently used in development of automobile engines, for example, because it is applicable to actual engines and their parts and enables real-time estimation of wear with high sensitivity.

References

- Ambe S, Chen SY, Ohkubo Y, Kobayashi Y, Iwamoto M, Yanokura M, Ambe F (1991) *Chem Lett* 1991:149
- Ambe S, Chen SY, Ohkubo Y, Kobayashi Y, Maeda H, Iwamoto M, Yanokura M, Takematsu N, Ambe F (1995) *J Radioanal Nucl Ch* 195:297
- Ambe F (2000) *J Radioanal Nucl Ch* 243:21
- Ambe S, Ozaki T, Weginwar RG, Enomoto S, Ambe F (2001) *Radiochim Acta* 89:63
- Amemiya Y, Miyahara J (1988) *Nature* 336:89
- Armstrong WD, Schubert J (1947) *Science* 106:403
- Arnstein HRV, Bentley R (1950) *Nucleonics* 6(6):11
- Bassham JA, Calvin M (1957) *The path of carbon in photosynthesis*. Prentice-Hall, New York
- Benson AA, Bassham JA, Calvin M, Goodale TC, Haas VA, Stepka W (1950) *J Am Chem Soc* 72:1710
- Black C, Joris GG, Taylor HS (1948) *J Chem Phys* 16:537
- Braun T, Tölgyessy J (1967) *Radiometric titrations. International series of monographs in analytical chemistry*, vol 29. Pergamon, New York
- Charlton JS (ed) (1986) *Radioisotope techniques for problem solving in industrial process plants*. Gulf Publishing, Houston
- Choppin GR, Liljenzin J-O, Rydberg J (2002) *Radiochemistry and nuclear chemistry*, 3rd edn. Butterworth-Heinemann, Woburn
- Conway D, Libby WF (1958) *J Am Chem Soc* 80:1077
- Cowley WE, Lott B, Brown S (1966) *Chem Engr Lond* 204:345
- Dodson RW (1950) *J Am Chem Soc* 72:3315
- Egawa C, Takahashi Y, Enomoto S, Hirunuma R, Shimizu H (2001) *RIKEN Rev* 35:96
- Elving PJ (1986) *Treatise on analytical chemistry*, part 1: theory and practice, vol 14. Section K, Nuclear activation and radioisotopic methods of analysis. Wiley, New York
- Enomoto S, Kawakami Y, Senoo M, Imahashi T, Tachikawa N, Tominaga H (1975) *Int J Appl Radiat Isot* 26:671
- Ferronsky Y, Guizerix J, Leonhardt J, Niemi A, Przewlocki K, Sevel T (eds) (1990) *Guidebook on radioisotope tracers in industry*. International Atomic Energy Agency, Wien
- Földiák G (ed) (1986) *Industrial applications of radioisotopes*. Elsevier, Amsterdam
- Guillaumont R, Adloff JP, Peneloux A (1989) *Radiochim Acta* 46:169
- Haba H, Kaji D, Kanayama Y, Igarashi K, Enomoto S (2005) *Radiochim Acta* 93:539
- Hevesy G, Paneth F (1913) *Z Anorg Chem* 82:323
- Hevesy G, Obrutshva A (1925) *Nature* 115:674
- Hevesy G, Seith W (1929) *Z Phys* 56(790):869
- Hughes ED, Juliusburger F, Masterman S, Topley B, Weiss J (1935) *J Chem Soc* 1935:1525
- Joris GG, Taylor HS (1948) *J Chem Phys* 16:45
- Kubo T (2003) *Nucl Instrum Meth B* 204:97
- Lieser KH (1957) *Z Anorg Allg Chem* 292:97
- Lieser KH (2001) *Nuclear and radiochemistry*, 2 revised edn. Wiley-VCH, Weinheim
- Liu Y, Guo Z, Liu X, Qu T, Xie J (1994) *Pure Appl Chem* 66:305
- Loftfield RB (1950) *J Am Chem Soc* 72:632
- Logan SR (1990) *J Chem Educ* 67:371
- Motomura S, Enomoto S, Haba H, Igarashi K, Gono Y, Yano Y (2007) *IEEE T Nucl Sci* 54:710
- Motomura S, Fukuchi T, Kanayama Y, Haba H, Watanabe Y, Enomoto S (2009) *IEEE NSS Conference Record* M09-281:3330
- Motomura S, Kanayama Y, Haba H, Watanabe Y, Enomoto S (2008) *J Anal At Spectrom* 23:1089
- Myers OE, Kennedy JW (1950) *J Am Chem Soc* 72:897
- Paneth F, Vorwerk W (1922) *Z Phys Chem* 101:445
- Qaim SM (1982) *Radiochim Acta* 30:147
- Roberts TR (1979) *Radiochromatography: the chromatography and electrophoresis of radiolabelled compounds*. Elsevier, Amsterdam
- Ropp GA, Neville OK (1951) *Nucleonics* 9(2):22
- Ruzicka J, Stary J (1968) *Substoichiometry in radiochemical analysis. International series of monographs in analytical chemistry*, vol 30. Pergamon, New York
- Schoenfelder V (1973) *Nucl Instrum Methods* 107:385
- Silverman J, Dodson RW (1952) *J Phys Chem* 56:846
- Sonoda M, Takano M, Miyahara J, Kato H (1983) *Radiology* 148:833
- Stary J, Ruzicka J (1976) *Substoichiometric analytical methods*. In: Svehla G (ed) *Comprehensive analytical chemistry*, vol 7. Elsevier, Amsterdam, p 207
- Sueki K, Kikuchi K, Akiyama K, Sawa T, Katada M, Ambe S, Ambe F, Nakahara H (1999) *Chem Phys Lett* 300:140
- Sutin N (1962) *Ann Rev Nucl Sci* 12:285
- Tamano H, Enomoto S, Hirunuma R, Takeda A (2001) *RIKEN Rev* 35:57
- Tanihata I (2004) *Nucl Phys A* 734:271
- Taube H (1952) *Chem Rev* 50:69
- Tölgyessy J, Braun T (1972) *Isotope dilution analysis*. Pergamon Press, Oxford
- Wahl AC, Bonner NA (1951) *Radioactivity applied to chemistry*. Wiley, New York
- Waters SL, Silvester DJ (1982) *Radiochim Acta* 30:163
- Wilson JN, Dickinson RG (1937) *J Am Chem Soc* 59:1358
- Yang YF, Gono Y, Motomura S, Enomoto S, Yano Y (2001) *IEEE T Nucl Sci* 48:656
- Zimens KE (1937) *Z Phys Chem* B37:231

36 Appendixes – Reference Data to Part III

Z. Homonnay¹ · Z. Klencsár² · R. B. Firestone³ · Z. Révay⁴ · G. L. Molnár^{4,†} · J. Csikai⁵ · R. Dóczi⁶

¹Eötvös Loránd University, Budapest, Hungary

²Chemical Research Center, HAS, Budapest, Hungary

³Lawrence Berkeley National Laboratory, Berkeley, California, USA

⁴Hungarian Academy of Sciences, Budapest, Hungary

⁵University of Debrecen, Debrecen, Hungary

⁶Budapest University of Technology and Economics, Budapest, Hungary

36.1	<i>Mössbauer Nuclides</i>	1794
36.2	<i>Thermal Neutron Reaction Data</i>	1799
36.2.1	Thermal Neutron Radiative Capture Cross Sections, g-Factors, and Resonance Integrals	1799
36.2.2	Thermal Neutron Capture γ Rays	1810
36.3	<i>Fast Neutron Reaction Data</i>	1834
36.3.1	Status of 14 MeV and 3 MeV Neutron Cross Sections	1835
36.3.2	Recommended Dosimetry Reactions	1845
36.3.3	Recommended Reactions and γ Rays for Activation Analysis	1846

[†]Deceased

36.1 Mössbauer Nuclides

Zoltán Homonnay · Zoltán Klencsár

Table 36.1

Table 36.1
Table of Mössbauer nuclides and isomeric transitions

Nuclide	E (keV)	$T_{1/2}$ (ns)	α	a (%)	I (\hbar)	Q (b)	μ (μ_N)	σ_0 (10^4 b)	W_0 (mm s^{-1})
K-40	0			0.012	4	−0.073	−1.2981		
	29.8299	4.24	6.6		3	–	−1.29	28.7	2.18
Fe-57	0			2.14	1/2	0.0	+0.09044		
	14.4129	98.3	8.21		3/2	+0.16	−0.1549	256	0.1940
	136.4743	8.7	0.142		5/2	–	+0.935	34.5	0.230
Ni-61	0			1.19	3/2	+0.162	−0.75002		
	67.412	5.34	0.135		5/2	−0.20	+0.480	71.2	0.770
Zn-67	0			4.11	5/2	+0.150	+0.87548		
	93.312	9,160	0.89		1/2	0.0	+0.587	4.96	0.000320
Ge-73	0			7.76	9/2	−0.196	−0.87947		
	13.275	2,950	1,095		5/2	–	−0.0941	0.76	0.00698
	68.752	1.86	0.8		7/2	–	–	23	2.14
Kr-83	0			11.55	9/2	+0.259	−0.97067		
	9.396	147	19.6		7/2	+0.507	−0.943	107	0.198
Tc-99	0			–	9/2	−0.129	+5.6847		
	140.5108	0.19	0.15		7/2	–	+3.6	8.6	8.2
Ru-99	0			12.72	5/2	+0.079	−0.641		
	89.68	20.50	1.54		3/2	+0.231	−0.284	8.0	0.1493
Ru-101	0			17.07	5/2	+0.457	−0.7188		
	127.23	0.655	0.16		3/2	–	−0.210	8.7	3.70
Sn-117	0			7.61	1/2	0.0	−1.00104		
	158.562	0.279	0.159		3/2	–	+0.658	16.80	6.23
Sn-119	0			8.58	1/2	0.0	−1.04728		
	23.871	18.03	5.12		3/2	−0.132	+0.633	140	0.647
Sb-121	0			57.25	5/2	−0.543	+3.3634		
	37.133	3.46	11.1		7/2	−0.728	+2.518	19.5	2.10
Te-125	0			7.0	1/2	0.0	−0.88851		
	35.4919	1.48	13.6		3/2	−0.31	+0.605	26.6	5.208
I-127	0			100.00	5/2	−0.696	+2.81327		
	57.606	1.95	3.78		7/2	−0.624	+2.54	20.6	2.49
I-129	0				7/2	−0.498	+2.6210		
	27.78	16.8	5.1		5/2	−0.604	+2.8045	39.0	0.586

■ Table 36.1 (Continued)

Nuclide	E (keV)	$T_{1/2}$ (ns)	α	a (%)	I (\hbar)	Q (b)	μ (μ_N)	σ_o (10^4 b)	W_o (mm s $^{-1}$)
Xe-129	0			26.44	1/2	0.0	−0.77798		
	39.578	0.97	12.3		3/2	−0.393	+0.58	23.5	6.8
Xe-131	0			21.18	3/2	−0.114	0.69186		
	80.185	0.48	1.57		1/2	0.0	−	7.40	6.8
Cs-133	0			100.00	7/2	−0.00343	+2.58203		
	80.997	6.27	1.72		5/2	0.302	+3.45	10.28	0.5350
Ba-133	0				1/2	0.0	−0.77167		
	12.322	7.0	110		3/2	−	+0.51	29.2	2.7
La-139	0			99.91	7/2	+0.200	+2.78305		
	165.86	1.50	0.263		5/2	−	−	5.28	1.100
Pr-141	0			100.00	5/2	−0.059	+4.2754		
	145.44	1.85	0.46		7/2	+0.28	+2.8	10.6	1.017
Nd-145	0			8.30	7/2	−0.33	−0.656		
	67.17	29.4	6.1		3/2	−	−	3.81	0.138
	72.50	0.72	4.9		5/2	−	−0.320	5.9	5.2
Pm-145	0				5/2	−	−		
	61.25	2.64	6.42		7/2	−	−	11.72	1.70
Pm-147	0				7/2	+0.74	+2.58		
	91.10	2.50	2.2		5/2	0.6	+3.22	6.9	1.169
Sm-147	0			14.97	7/2	−0.26	−0.8148		
	121.220	0.80	1.0		5/2	−0.45	−0.449	6.2	2.80
Sm-149	0			13.83	7/2	+0.075	−0.6717		
	22.507	7.12	50		5/2	+1.014	−0.6238	7.1	1.71
Sm-151	0				−	+0.67	−0.363		
	65.83	0.4	5.76		−	−	−	−	0.21
Sm-152	0			26.72	0	0.0	0.0		
	121.7825	1.428	1.17		2	−1.666	+0.84	38.0	1.59
Sm-153	0			$T_{1/2} = 47\text{h}$	3/2	+1.26	−0.0216		
	35.844	< 0.1	0.30		3/2	−	−	146	3.8
Sm-154	0			22.71	0	0.0	0.0		
	81.976	3.02	5.05		2	−1.87	+0.784	30.1	1.11
Eu-151	0			47.82	5/2	+0.903	+3.4717		
	21.541	9.6	28.60		7/2	+1.28	+2.591	23.77	1.31
Eu-153	0			52.18	5/2	+2.412	+1.533		
	83.3671	0.79	3.82		7/2	0.44	+1.81	9.74	4.0
	97.4297	0.20	0.42		5/2	−	−	18.0	13.4
	103.1794	3.88	1.78		3/2	1.254	+2.048	5.46	0.68

Table 36.1 (Continued)

Nuclide	E (keV)	$T_{1/2}$ (ns)	α	a (%)	I (\hbar)	Q (b)	μ (μ_N)	σ_o (10^4 b)	W_o (mm s $^{-1}$)
Gd-154	0			2.15	0	0.0	0.0		
	123.0714	1.186	1.20		2	−1.82	+0.96	36.7	1.9
Gd-155	0			14.73	3/2	+1.27	−0.2591		
	60.0087	0.193	8.72		5/2	−0.44	−	10.48	34
	86.5460	6.50	0.43		5/2	+0.111	−0.525	34	0.499
	105.3109	1.16	0.26		3/2	+0.96	+0.143	16.5	2.22
Gd-156	0			20.47	0	0.0	0.0		
	88.9666	2.21	3.93		2	−1.93	+0.774	31.4	1.42
Gd-157	0			15.68	3/2	+1.35	−0.3398		
	54.533	0.130	11.87		5/2	−0.46	−	9.59	26.8
	63.917	460	0.97		5/2	+2.45	−0.464	23	0.0093
Gd-158	0			24.87	0	0.0	0.0		
	79.510	2.52	6.02		2	−2.01	+0.762	27.6	1.355
Gd-160	0			21.90	0	0.0	0.0		
	75.26	2.69	7.42		2	−2.08	+0.72	25.65	1.346
Tb-159	0			100.00	3/2	+1.432	+2.014		
	58.00	0.0536	9.36		5/2	−	−	10.53	45
Dy-160	0			2.29	0	0.0	0.0		
	86.7882	2.02	4.52		2	1.76	+0.725	29.4	1.547
Dy-161	0			18.88	5/2	+2.507	−0.480		
	25.6514	29.1	2.9		5/2	+2.506	+0.594	95	0.378
	43.8211	0.83	4.32		7/2	+0.53	−0.141	31.9	8.0
	74.56710	3.14	0.65		3/2	+1.45	−0.403	6.8	1.11
Dy-162	0			25.53	0	0.0	0.0		
	80.660	2.20	0.55		2	−	+0.686	121	1.49
Dy-164	0			28.18	0	0.0	0.0		
	73.392	2.39	9.3		2	−2.08	+0.70	22.0	1.56
Ho-165	0			100.00	7/2	+3.58	+4.132		
	94.700	0.022	3.12		9/2	3.43	4.09	8.28	130
Er-164	0			1.56	0	0.0	0.0		
	91.40	1.47	4.18		2	−	0.697	28.3	2.04
Er-166	0			33.41	0	0.0	0.0		
	80.577	1.82	6.93		2	−1.9	+0.632	23.77	1.82
Er-167	0			22.94	7/2	+3.565	−0.56385		
	79.3221	0.119	5.74		9/2	−	−	7.21	29

■ Table 36.1 (Continued)

Nuclide	E (keV)	$T_{1/2}$ (ns)	α	a (%)	I (\hbar)	Q (b)	μ (μ_N)	σ_0 (10^4 b)	W_0 (mm s $^{-1}$)
Er-168	0			27.07	0	0.0	0.0		
	79.804	1.88	7.14		2	−2.17	+0.642	23.60	1.823
Er-170	0			14.88	0	0.0	0.0		
	78.68	1.89	7.33		2	−1.94	0.633	23.35	1.815
Tm-169	0			100.00	1/2	0.0	−0.2316		
	8.4103	4.08	268		3/2	−1.2	+0.5148	25.8	8.1
Yb-170	0			3.03	0	0.0	0.0		
	84.2551	1.60	8.05		2	2.12	+0.674	19.0	2.02
Yb-171	0			14.31	1/2	0.0	+0.49367		
	66.721	0.81	13.0		3/2	1.59	0.350	7.9	4.7
	75.878	1.64	7.83		5/2	2.16	+1.015	14.44	2.2
Yb-172	0			21.82	0	0.0	0.0		
	78.7436	1.65	8.5		2	2.16	+0.669	20.8	1.93
Yb-174	0			31.84	0	0.0	0.0		
	76.471	1.79	9.41		2	2.12	+0.676	20.10	2.03
Yb-176	0			12.73	0	0.0	0.0		
	82.13	1.76	7.07		2	2.22	+0.675	22.47	1.7
Lu-175	0			97.41	7/2	+3.49	+2.2327		
	113.804	0.099	2.51		9/2	−	+2.01	6.73	24.0
Hf-176	0			5.20	0	0.0	0.0		
	88.351	1.43	5.86		2	−2.10	+0.539	22.84	2.23
Hf-177	0			18.50	7/2	+3.365	+0.7935		
	112.9500	0.583	3.0		9/2	1.3	+0.91	6.0	4.8
Hf-178	0			27.14	0	0.0	0.0		
	93.180	1.48	4.6		2	−2.02	+0.48	25	1.96
Hf-180	0			35.24	0	0.0	0.0		
	93.326	1.50	4.71		2	−2.00	+0.533	24.6	1.95
Ta-181	0			99.99	7/2	+3.28	+2.3705		
	6.238	6.050	46		9/2	+3.71	+5.28	167	0.0064
	136.266	0.0395	1.76		9/2	−	+2.57	5.97	50.2
W-180	0			0.14	0	0.0	0.0		
	103.557	1.28	3.44		2	2.12	0.509	25.6	2.08
W-182	0			26.41	0	0.0	0.0		
	100.1065	1.369	3.85		2	−2.13	+0.521	25.2	2.09

Table 36.1 (Continued)

Nuclide	E (keV)	$T_{1/2}$ (ns)	α	a (%)	I (\hbar)	Q (b)	μ (μ_N)	σ_o (10^4 b)	W_o (mm s $^{-1}$)
W-183	0			14.40	1/2	0.0	+0.11778		
	46.4839	0.188	40		3/2	1.77	−0.10	5.5	32.0
	99.0793	0.77	4.12		5/2	1.95	+0.912	8.2	4.01
W-184	0			30.64	0	0.0	0.0		
	111.208	1.251	2.61		2	−1.87	+0.578	27.4	1.92
W-186	0			28.41	0	0.0	0.0		
	122.58	1.036	1.6		2	−1.57	+0.615	31	2.21
Re-187	0			62.93	5/2	+2.07	+3.2197		
	134.243	0.011	2.35		7/2	−	+1.9	5.40	203.8
Os-186	0			1.59	0	0.0	0.0		
	137.155	0.818	1.29		2	−1.63	+0.562	28.4	2.37
Os-188	0			13.30	0	0.0	0.0		
	155.021	0.71	0.82		2	−1.46	+0.584	28.0	2.54
Os-189	0			16.10	3/2	+0.856	+0.65993		
	36.202	0.53	80		1/2	0.0	+0.226	1.15	15.1
	69.537	1.62	8.0		5/2	−0.629	+0.988	8.4	2.40
	95.254	0.23	6.7		3/2	−	−0.32	0.56	12.5
Os-190	0			26.40	0	0.0	0.0		
	186.718	0.363	0.42		2	−1.18	+0.676	24.7	3.11
Ir-191	0			37.30	3/2	0.816	+0.1507		
	82.425	4.08	10.7		1/2	0.0	+0.600	1.54	0.83
	129.430	0.123	2.88		5/2	−	+0.45	5.6	23.8
Ir-193	0			62.70	3/2	+0.751	+0.1637		
	73.041	6.09	6.5		1/2	0.0	+0.519	3.06	0.594
	138.89	0.0819	2.26		5/2	−	+0.528	5.83	24.6
Pt-195	0			33.80	1/2	0.0	+0.60952		
	98.882	0.170	7.2		3/2	−	−0.62	6.11	16.28
	129.777	0.67	1.76		5/2	−	+0.90	7.4	3.40
Au-197	0			100.00	3/2	+0.547	+0.14575		
	77.351	1.91	4.30		1/2	0.0	+0.420	3.86	1.882
Hg-201	0			13.22	3/2	+0.385	−0.56023		
	32.138	0.1	60		3/2	−	−	0.95	42
Th-232	0			100.	0	0.0	0.0		
	49.369	0.345	3.19		2	−	−	1.57	16.1
Pa-231	0			−	3/2	−1.72	2.01		
	84.216	45.1	1.8		5/2	+0.69	−	4.8	0.079
U-234	0			0.060	0	0.0	0.0		
	43.498	0.252	780		2	−2.89	−	0.83	23.6

■ **Table 36.1 (Continued)**

Nuclide	E (keV)	$T_{1/2}$ (ns)	α	a (%)	I (\hbar)	Q (b)	μ (μ_N)	σ_0 (10^4 b)	W_0 (mm s $^{-1}$)
U-236	0			–	0	0.0	0.0		
	45.244	0.234	845		2	–2.96	–	0.71	25.7
U-238	0			99.27	0	0.0	0.0		
	44.916	0.206	660		2	–3.23	0.254	0.92	27
Np-237	0			–	5/2	+3.886	+3.14		
	59.541	67	1.12		5/2	+3.85	+1.68	31	0.0673
Pu-239	0			–	1/2	0.0	+0.203		
	57.276	0.101	223		5/2	–3.345	–	0.77	47
Am-243	0			–	5/2	+4.30	1.53		
	84.0	2.34	0.30		5/2	4.20	+2.74	25.9	1.39

E : energy of the level, $T_{1/2}$: half-life, α : internal conversion coefficient, a : natural abundance, I : nuclear spin, Q : nuclear quadrupole moment, b: barn, μ : nuclear magnetic moment, μ_N : nuclear magneton, σ_0 : nuclear absorption cross section, W_0 : natural line width expressed as Doppler-speed interval. Absence of sign in the Q and μ values means that the sign is undetermined (Cohen and Taylor 1987; Raghavan 1989; Pyykkö 2001, 2008; NuDat 2009).

36.2 Thermal Neutron Reaction Data

Richard B. Firestone · Zsolt Révay · Gábor L. Molnár

36.2.1 Thermal Neutron Radiative Capture Cross Sections, g -Factors, and Resonance Integrals

► **Table 36.2** gives *thermal neutron capture cross sections* from Mughabghab et al. (1981, 1984), and (2003). Atomic abundances are taken from the latest IUPAC compilation (Rosman and Taylor 1998). The Westcott g -factors, which are a measure of the deviation of the cross section from the regular $1/u$ -behavior, were calculated by Trkov (2003) in the framework of a coordinated research project (IAEA 2003). *Resonance integrals* are from Mughabghab (2003), except for those in square brackets that are from the earlier compilation (Mughabghab et al. 1981, 1984) but have been omitted in the later reference. The notations in ► **Table 36.2** are the following:

Column 1: Atomic number and element name.

Column 2: Isotope symbol, followed in parentheses by energy of isomeric level in keV or reaction if not (n, γ).

Column 3: Isotopic abundance (%).

Column 4: Cross section at 2,200 m/s neutron speed (representing the most probable speed at 20°C), in barn (b) or millibarn (mb) units. 1 b = 10 $^{-28}$ m 2 .

Column 5: Westcott g -factor for 300 K Maxwellian flux distribution.

Column 6: Infinite dilution resonance integral, in barn (b) or millibarn (mb) units.

Table 36.2

Thermal neutron radiative capture data

Element	Isotope	Abundance	Cross section	<i>g</i> -factor	Resonance integral
1 Hydrogen	¹ H	99.9885(70)	332.6(7) mb	0.999	149 mb
	² H	0.0115(70)	0.519(7) mb	1.000	0.23 mb
2 Helium	³ He	0.000137(3)	0.031(9) mb	1.000	0.014 mb
	⁴ He	99.999863(3)			
3 Lithium	⁶ Li	7.59(4)	39(3) mb	1.000	17 mb
	⁶ Li(n,α)		940(4) b		
	⁷ Li	92.41(4)	45(3) mb	1.000	20 mb
4 Beryllium	⁹ Be	100	8.8(4) mb	1.000	4.4 mb
5 Boron	¹⁰ B	19.9(7)	300(20) mb	1.000	220 mb
	¹⁰ B(n,α)		3,837(9) b		
	¹¹ B	80.1(7)	6(3) mb	1.000	2.7 mb
6 Carbon	¹² C	98.93(8)	3.53(7) mb	1.000	1.57(5) mb
	¹³ C	1.07(8)	1.37(4) mb	0.998	1.7(2) mb
7 Nitrogen	¹⁴ N	99.632(7)	79.8(14) mb	1.000	34(1) mb
	¹⁴ N(n,p)		1.83(3) b		
	¹⁵ N	0.368(7)	24(8) mb	1.003	0.032 mb
8 Oxygen	¹⁶ O	99.757(16)	0.190(19) mb	1.000	0.085 mb
	¹⁷ O	0.038(1)	0.54(7) mb	0.999	[0.39 mb]
	¹⁷ O(n,α)		235(10) mb		
	¹⁸ O	0.205(14)	0.16(1) mb	1.000	[0.87(4) mb]
9 Fluorine	¹⁹ F	100	9.6(5) mb	1.000	[21(3) mb]
10 Neon	²⁰ Ne	90.48(3)	37(4) mb	1.000	18 mb
	²¹ Ne	0.27(1)	670(110) mb	1.000	0.30 b
	²² Ne	9.25(3)	45(6) mb	1.000	23(3) mb
11 Sodium	²³ Na	100	530(5) mb	1.000	311(10) mb
	²³ Na(472)		400(30) mb		
12 Magnesium	²⁴ Mg	78.99(4)	53.6(15) mb	1.001	32(4) mb
	²⁵ Mg	10.00(1)	200(5) mb	1.001	98(15) mb
	²⁶ Mg	11.01(3)	38.6(6) mb	1.001	26(2) mb
13 Aluminum	²⁷ Al	100	231(3) mb	1.000	140(10) mb
14 Silicon	²⁸ Si	92.2297(7)	177(5) mb	1.001	82 mb
	²⁹ Si	4.6832(5)	119(3) mb	1.003	77(15) mb
	³⁰ Si	3.0872(5)	107(2) mb	1.007	630(30) mb
15 Phosphorus	³¹ P	100	172(6) mb	1.001	140 mb

■ Table 36.2 (Continued)

Element	Isotope	Abundance	Cross section	<i>g</i> -factor	Resonance integral
16 Sulfur	³² S	94.93(31)	548(10) mb	1.000	810 mb
	³³ S	0.76(2)	454(25) mb	1.001	[97 mb]
	³⁴ S	4.29(28)	235(5) mb	1.001	[1.5 mb]
	³⁶ S	0.02(1)	230(20) mb	1.014	[0.17(4) mb]
17 Chlorine	³⁵ Cl	75.78(4)	43.6(4) b	1.000	18(2) b
	³⁷ Cl	24.22(4)	430(6) mb	1.000	295(4) mb
18 Argon	³⁶ Ar	0.3365(30)	5.2(5) b	1.016	
	³⁸ Ar	0.0362(5)	800(200) mb	1.040	
	⁴⁰ Ar	99.6003(30)	660(10) mb	1.002	410(30) mb
19 Potassium	³⁹ K	93.2581(44)	2.1(2) b	1.001	1.1(1) b
	⁴⁰ K	0.0117(1)	30(4) b	1.000	[13(4) b]
	⁴¹ K	6.7302(44)	1.46(3) b	1.001	[1.42(6) b]
20 Calcium	⁴⁰ Ca	96.94(16)	410(20) mb	1.001	220(20) mb
	⁴² Ca	0.647(23)	680(70) mb	1.001	290(40) mb
	⁴³ Ca	0.135(10)	6.2(6) b	1.001	3.93(15) b
	⁴⁴ Ca	2.09(11)	880(50) mb	1.001	580(10) mb
	⁴⁶ Ca	0.004(3)	720(30) mb	1.000	940(40) mb
	⁴⁸ Ca	0.187(21)	1,090(70) mb	1.001	[890(180) mb]
21 Scandium	⁴⁵ Sc	100	27.2(2) b	1.002	12.0(5) b
	⁴⁵ Sc(143)		9.8(11) b		
22 Titanium	⁴⁶ Ti	8.25(3)	590(180) mb	1.001	300(90) mb
	⁴⁷ Ti	7.44(2)	1.52(11) b	1.001	1.5(2) b
	⁴⁸ Ti	73.72(3)	7.88(25) b	1.002	3.9(2) b
	⁴⁹ Ti	5.41(2)	1.79(12) b	1.001	1.2(2) b
	⁵⁰ Ti	5.18(2)	179(3) mb	1.001	118(11) mb
23 Vanadium	⁵⁰ V	0.250(4)	21(4) b	0.999	43(15) b
	⁵¹ V	99.750(4)	4.92(4) b	1.001	2.7(1) b
24 Chromium	⁵⁰ Cr	4.345(13)	15.9(2) b	1.000	7.8(4) b
	⁵² Cr	83.789(18)	760(60) mb	1.000	500(60) mb
	⁵³ Cr	9.501(17)	18.2(15) b	1.000	8.9(9) b
	⁵⁴ Cr	2.365(7)	360(40) mb	1.000	200(30) mb
25 Manganese	⁵⁵ Mn	100	13.36(5) b	1.000	14.0(3) b
26 Iron	⁵⁴ Fe	5.845(35)	2.25(18) b	1.001	1.2(2) b
	⁵⁶ Fe	91.754(36)	2.59(14) b	1.000	1.4(2) b
	⁵⁷ Fe	2.119(10)	2.5(3) b	1.001	1.6(2) b
	⁵⁸ Fe	0.282(4)	1.30(3) b	1.002	1.7(1) b

■ Table 36.2 (Continued)

Element	Isotope	Abundance	Cross section	<i>g</i> -factor	Resonance integral
27 Cobalt	⁵⁹ Co	100	37.18(6) b	1.000	75.9(20) b
	⁵⁹ Co(59)		20.4(8) b		
28 Nickel	⁵⁸ Ni	68.077(9)	4.5(2) b	1.000	2.2(2) b
	⁶⁰ Ni	26.223(8)	2.9(2) b	1.000	1.5(2) b
	⁶¹ Ni	1.1399(6)	2.5(8) b	1.000	1.5(4) b
	⁶² Ni	3.6345(17)	14.5(3) b	1.000	6.6(2) b
	⁶⁴ Ni	0.9256(9)	1.63(7) b	1.000	0.98(15) b
29 Copper	⁶³ Cu	69.17(3)	4.52(2) b	1.001	4.97(8) b
	⁶⁵ Cu	30.83(3)	2.17(3) b	1.002	2.19(7) b
30 Zinc	⁶⁴ Zn	48.6(6)	1.1(1) b	1.001	1.45(6) b
	⁶⁶ Zn	27.9(3)	620(60) mb	1.000	1.8(3) b
	⁶⁷ Zn	4.10(13)	9.5(14) b	1.000	25(3) b
	⁶⁸ Zn(0)	18.8(5)	1,000(100) mb	1.000	3.4(3) b
	⁶⁹ Zn(439)		72(4) mb		
	⁷⁰ Zn(0)	0.62(3)	83(5) mb	1.000	860(60) mb
	⁷⁰ Zn(158)		8.7(5) mb		
31 Gallium	⁶⁹ Ga	60.108(9)	1.68(7) b	1.000	15.6(15) b
	⁷¹ Ga	39.892(9)	4.73(15) b	1.001	31.2(19) b
	⁷¹ Ga(120)		150(50) mb		
32 Germanium	⁷⁰ Ge	20.8(9)	3.45(16) b	1.000	1.5(3) b
	⁷⁰ Ge(198)		280(70) mb		
	⁷² Ge	27.54(34)	950(110) mb	1.000	800(200) mb
	⁷² Ge(67)				
	⁷³ Ge	7.73(5)	14.4(4) b	1.000	64(6) b
	⁷⁴ Ge	36.3(7)	530(50) mb	1.000	1.0(2) b
	⁷⁵ Ge(140)		170(30) mb		
	⁷⁶ Ge(0)	7.61(38)	140(20) mb	1.000	1.8(4) b
	⁷⁶ Ge(160)		100(10) mb		
33 Arsenic	⁷⁵ As	100	4.23(8) b	1.000	61(4) b
	⁷⁴ Se	0.89(4)	51.8(12) b	1.001	560(50) b
34 Selenium	⁷⁶ Se	9.37(29)	85(7) b	1.000	40(4) b
	⁷⁶ Se(162)		22(1) b		
	⁷⁷ Se	7.63(16)	42(4) b	1.000	30(3) b
	⁷⁸ Se(0)	23.77(28)	50(10) mb	1.000	4.0(6) b
	⁷⁸ Se(96)		380(20) mb		
	⁸⁰ Se(0)	49.61(41)	530(50) mb	1.000	1.6(2) b
	⁸⁰ Se(103)		80(10) mb		
	⁸² Se(0)	8.73(22)	5.2(4) mb	1.000	30(4) b
	⁸² Se(228)		39(3) mb		

■ Table 36.2 (Continued)

Element	Isotope	Abundance	Cross section	<i>g</i> -factor	Resonance integral
35 Bromine	⁷⁹ Br	50.69(7)	10.32(13) b	1.000	127(14) b
	⁷⁹ Br(86)		2.4(6) mb		
	⁸¹ Br	49.31(7)	2.36(5) b	1.000	50(5) b
	⁸¹ Br(46)		2.4(4) b		
36 Krypton	⁷⁸ Kr	0.35(2)	4.7(7) b	1.000	19.5(20) b
	⁷⁸ Kr(130)		170(20) mb		
	⁸⁰ Kr	2.25(2)	11.5(5) b	1.000	56.1(56) b
	⁸⁰ Kr(190)		4.6(7) b		
	⁸² Kr	11.6(1)	19(4) b	1.000	130(13) b
	⁸² Kr(42)		14.0(25) b		
	⁸³ Kr	11.5(1)	202(10) b	0.995	183(25) b
	⁸⁴ Kr	57.0(3)	111(15) mb	1.000	2.4(2) b
	⁸⁴ Kr(305)		90(13) mb		
37 Rubidium	⁸⁶ Kr	17.3(2)	3(2) mb	1.000	23(3) mb
	⁸⁵ Rb(0)	72.17(2)	427(11) mb	1.000	5.9(5) b
	⁸⁵ Rb(556)		53(5) mb		
38 Strontium	⁸⁷ Rb	27.83(2)	120(30) mb	1.000	2.7(4) b
	⁸⁴ Sr	0.56(1)	620(60) mb	1.000	8.6(4) b
	⁸⁴ Sr(239)		600(60) mb		
	⁸⁶ Sr(0)	9.86(1)	200(30) mb	1.000	4.80(3) b
	⁸⁶ Sr(389)		840(60) mb		
	⁸⁷ Sr	7.00(1)	17(3) b	1.006	117(30) b
39 Yttrium	⁸⁸ Sr	82.58(1)	5.8(4) mb	1.000	6.5(3) mb
	⁸⁹ Y	100	1.28(2) b	1.005	1.0(1) b
	⁸⁹ Y(682)		1.0(2) mb		
40 Zirconium	⁹⁰ Zr	51.45(40)	11(5) mb	1.000	130(20) mb
	⁹¹ Zr	11.22(5)	1,240(250) mb	1.000	5.2(7) b
	⁹² Zr	17.15(8)	220(60) mb	1.000	630(20) mb
	⁹⁴ Zr	17.38(28)	49.9(24) mb	1.000	270(30) mb
	⁹⁶ Zr	2.80(9)	22.9(10) mb	1.000	5.6(2) b
41 Niobium	⁹³ Nb	100	1.15(5) b	1.002	8.5(5) b
	⁹³ Nb(41)				
42 Molybdenum	⁹² Mo	14.84(35)	19 mb	1.000	810(80) mb
	⁹⁴ Mo	9.25(12)	15 mb	1.001	820(120) mb
	⁹⁵ Mo	15.92(13)	13.4(3) b	0.998	111(5) b
	⁹⁶ Mo	16.68(2)	500(200) mb	1.000	17(3) b
	⁹⁷ Mo	9.55(8)	2.5(2) b	0.998	14(3) b
	⁹⁸ Mo	24.13(31)	137(5) mb	1.000	6.9(3) b
	¹⁰⁰ Mo	9.63(23)	199(3) mb	1.000	3.8(1) b

■ Table 36.2 (Continued)

Element	Isotope	Abundance	Cross section	<i>g</i> -factor	Resonance integral
44 Ruthenium	⁹⁶ Ru	5.54(14)	220(20) mb	1.001	6.5(4) b
	⁹⁸ Ru	1.87(3)	<8 b	1.002	
	⁹⁹ Ru	12.76(14)	7.1(10) b	1.002	160(20) b
	¹⁰⁰ Ru	12.60(7)	5.0(6) b	1.000	11.2(11) b
	¹⁰¹ Ru	17.06(2)	3.4(9) b	1.001	100(20) b
	¹⁰² Ru	31.55(14)	1.21(7) b	1.000	4.2(1) b
	¹⁰² Ru(238)				
	¹⁰⁴ Ru	18.62(27)	470(20) mb	1.000	6.4(5) b
45 Rhodium	¹⁰³ Rh	100	145(2) b	1.023	1,100(50) b
	¹⁰³ Rh(129)		10(1) b		
46 Palladium	¹⁰² Pd	1.02(1)	3.4(3) b	0.997	10.0(20) b
	¹⁰⁴ Pd	11.14(8)	600(300) mb	1.000	16(2) b
	¹⁰⁵ Pd	22.33(8)	21.0(15) b	0.995	98(5) b
	¹⁰⁶ Pd(0)	17.33(8)	290(30) mb	0.999	5.7(6) b
	¹⁰⁶ Pd(242)		13(2) mb		
	¹⁰⁸ Pd	26.46(9)	7.6(4) b	1.000	244(4) b
	¹⁰⁸ Pd(189)		180(30) mb		
	¹¹⁰ Pd(0)	11.72(9)	190(30) mb	1.000	3.1(4) b
	¹¹⁰ Pd(172)		36(6) mb		
47 Silver	¹⁰⁷ Ag	51.839(8)	37.6(12) b	0.998	100(48) b
	¹⁰⁷ Ag(109)		330(80) mb		
	¹⁰⁹ Ag(0)	48.161(8)	86(3) b	1.005	1,400(48) b
	¹⁰⁹ Ag(118)		4.7(2) b		
48 Cadmium	¹⁰⁶ Cd	1.25(6)	~1 b	1.000	4(1) b
	¹⁰⁸ Cd	0.89(3)	720(130) mb	1.001	11(3) b
	¹¹⁰ Cd	12.49(18)	11(1) b	1.000	41(3) b
	¹¹⁰ Cd(396)		140(50) mb		
	¹¹¹ Cd	12.80(12)	24(3) b	0.995	50(5) b
	¹¹² Cd	24.13(21)	2.2(5) b	1.000	12(2) b
	¹¹³ Cd	12.22(12)	20,600(400) b	1.337	390(40) b
	¹¹⁴ Cd(0)	28.73(42)	300(20) mb	1.000	14.1(7) b
	¹¹⁴ Cd(181)		36(7) mb		
	¹¹⁶ Cd(0)	7.49(18)	50(8) mb	1.000	1.6(3) b
	¹¹⁶ Cd(136)		25(10) mb		

■ Table 36.2 (Continued)

Element	Isotope	Abundance	Cross section	<i>g</i> -factor	Resonance integral
49 Indium	¹¹³ In(0)	4.29(5)	3.9(4) b	1.012	310(30) b
	¹¹³ In(190)		8.1(8) b		
	¹¹³ In(502)		3.1(7) b		
	¹¹⁵ In(0)	95.71(5)	40(2) b	1.019	3,300(100) b
	¹¹⁵ In(127)		162.3(7) b		
	¹¹⁵ In(290)		81(8) b		
50 Tin	¹¹² Sn	0.97(1)	860(90) mb	1.000	29(2) b
	¹¹² Sn(77)		300(40) mb		
	¹¹⁴ Sn	0.66(1)	120(30) mb	1.001	5.1(15) b
	¹¹⁵ Sn	0.34(1)	30(7) b	1.000	29(6) b
	¹¹⁶ Sn(0)	14.54(9)	130(30) mb	1.000	11.9(10) b
	¹¹⁶ Sn(314)		6(2) mb		
	¹¹⁷ Sn	7.68(7)	1.32(18) b	1.000	15.7(25) b
	¹¹⁸ Sn	24.22(9)	220(50) mb	1.000	3.4(4) b
	¹¹⁸ Sn(90)		10(6) mb		
	¹¹⁹ Sn	8.59(4)	2.2(5) b	1.000	1.2(3) b
	¹²⁰ Sn(0)	32.58(9)	140(30) mb	1.000	2.9(5) b
	¹²⁰ Sn(6)		1(1) mb		
	¹²² Sn(0)	4.63(3)	1 mb 1	1.000	810(40) mb
	¹²² Sn(25)		138(15) mb		
	¹²⁴ Sn(0)	5.79(5)	4(2) mb	1.000	8.0(2) b
	¹²⁴ Sn(28)		130(5) mb		
51 Antimony	¹²¹ Sb	57.21(5)	5.9(2) b	1.003	205(20) b
	¹²¹ Sb(164)		60(10) mb		
	¹²³ Sb(0)	42.79(5)	4.1(1) b	1.001	127(20) b
	¹²³ Sb(11)		37(10) mb		
	¹²³ Sb(37)		19(10) mb		
52 Tellurium	¹²⁰ Te(0)	0.09(1)	2.0(3) b	1.000	
	¹²⁰ Te(294)		340(60) mb		
	¹²² Te	2.55(12)	3.9(5) b	1.000	89(10) b
	¹²² Te(248)		1.1(5) b		
	¹²³ Te	0.89(3)	418(30) b	1.011	5,630(325) b
	¹²⁴ Te	4.74(14)	6.8(13) b	1.000	5.3(7) b
	¹²⁴ Te(145)		40(25) mb		
	¹²⁵ Te	7.07(15)	1.55(16) b	1.000	21(3) b
	¹²⁶ Te(0)	18.84(25)	900(150) mb	1.000	7.5(10) b

■ Table 36.2 (Continued)

Element	Isotope	Abundance	Cross section	<i>g</i> -factor	Resonance integral
	¹²⁶ Te(88)		135(23) mb		
	¹²⁸ Te(0)	31.74(8)	200(8) mb	1.000	1.6(1) b
	¹²⁸ Te(106)		15(1) mb		
	¹³⁰ Te(0)	34.08(62)	270(6) mb	1.000	300(100) mb
	¹³⁰ Te(182)		20(10) mb		
53 Iodine	¹²⁷ I	100	6.2(2) b	0.999	150(10) b
54 Xenon	¹²⁴ Xe	0.09(1)	165(20) b	1.004	3,600(700) b
	¹²⁴ Xe(253)		28(5) b		
	¹²⁶ Xe	0.09(1)	3.8(5) b	1.000	60(10) b
	¹²⁶ Xe(297)		450(130) mb		
	¹²⁸ Xe	1.92(3)	5.2(13) b	0.998	38(19) b
	¹²⁸ Xe(236)		480(100) mb		
	¹²⁹ Xe	26.44(24)	21(5) b	1.001	250(50) b
	¹³⁰ Xe	4.08(2)	4.8(12) b	0.998	
	¹³⁰ Xe(164)		450(100) mb		[16(4) b]
	¹³¹ Xe	21.18(3)	85(10) b	1.002	900(100) b
	¹³² Xe	26.89(6)	415(50) mb	1.000	4.6(6) b
	¹³² Xe(233)		50(10) mb		
	¹³⁴ Xe	10.44(10)	265(20) mb	0.999	400(100) mb
	¹³⁴ Xe(527)		3.0(3) mb		
	¹³⁶ Xe	8.87(16)	260(20) mb	1.000	700(200) mb
55 Cesium	¹³³ Cs	100	30.3(11) b	1.002	437(26) b
	¹³³ Cs(139)		2.5(2) b		
56 Barium	¹³⁰ Ba(0)	0.106(1)	8.7(9) b	1.000	170(10) b
	¹³⁰ Ba(187)		2.5(3) b		
	¹³² Ba(0)	0.101(1)	6.5(8) b	0.979	33(3) b
	¹³² Ba(288)		500(200) mb		
	¹³⁴ Ba	2.417(18)	1.5(3) b	1.000	22(3) b
	¹³⁴ Ba(268)		158(24) mb		
	¹³⁵ Ba	6.592(12)	5.8(9) b	1.000	97(7) b
	¹³⁵ Ba(2030)		13.9(7) mb		
	¹³⁶ Ba	7.854(24)	680(170) mb	1.000	1.7(3) b
	¹³⁶ Ba(662)		10(1) mb		
	¹³⁷ Ba	11.232(24)	3.6(2) b	1.000	4.3(10) b
	¹³⁸ Ba	71.698(42)	400(40) mb	1.000	320(40) mb

■ Table 36.2 (Continued)

Element	Isotope	Abundance	Cross section	<i>g</i> -factor	Resonance integral
57 Lanthanum	¹³⁸ La	0.090(1)	57(6) b	1.003	362(25) b
	¹³⁹ La	99.910(1)	9.04(4) b	0.999	12.1(6) b
58 Cerium	¹³⁶ Ce(0)	0.185(2)	6.5(10) b	0.999	77(12) b
	¹³⁶ Ce(254)		950(250) mb		
	¹³⁸ Ce(0)	0.251(2)	1.00(24) b	0.991	
	¹³⁸ Ce(754)		15(5) mb		
	¹⁴⁰ Ce	88.450(51)	580(20) mb	0.999	540(50) mb
	¹⁴² Ce	11.114(51)	970(20) mb	0.998	1.15(5) b
59 Praseodymium	¹⁴¹ Pr	100	11.5(3) b	0.999	17.4(20) b
	¹⁴¹ Pr(37)		3.9(3) b		
60 Neodymium	¹⁴² Nd	27.2(5)	18.7(7) b	0.998	9.0(10) b
	¹⁴³ Nd	12.2(2)	325(10) b	0.996	130(30) b
	¹⁴⁴ Nd	23.8(3)	3.6(3) b	1.000	5.4(5) b
	¹⁴⁵ Nd	8.3(1)	42(2) b	1.000	240(35) b
	¹⁴⁶ Nd	17.2(3)	1.41(5) b	0.999	23.2(5) b
	¹⁴⁸ Nd	5.7(1)	2.58(14) b	1.000	14(1) b
	¹⁵⁰ Nd	5.6(2)	1.03(8) b	0.999	14(2) b
62 Samarium	¹⁴⁴ Sm	3.07(7)	1.64(10) b	0.999	2.38(17) b
	¹⁴⁷ Sm	14.99(18)	57(3) b	1.001	775(50) b
	¹⁴⁸ Sm	11.24(10)	2.4(6) b	1.000	35(7) b
	¹⁴⁹ Sm	13.82(7)	40,140(600) b	1.718	3,390(200) b
	¹⁵⁰ Sm	7.38(1)	100(4) b	0.998	358(50) b
	¹⁵² Sm	26.75(16)	206(6) b	1.003	2,970(100) b
	¹⁵⁴ Sm	22.75(29)	8.3(5) b	1.000	36(4) b
63 Europium	¹⁵¹ Eu(0)	47.81(3)	5,900(200) b	0.900	3,300(300) b
	¹⁵¹ Eu(46)		3,300(200) b		
	¹⁵¹ Eu(148)		4(2) b		
	¹⁵³ Eu	52.19(3)	312(7) b	0.966	1,420(100) b
64 Gadolinium	¹⁵² Gd	0.20(1)	735(20) b	0.998	2,020(160) b
	¹⁵⁴ Gd	2.18(3)	85(12) b	1.000	245(30) b
	¹⁵⁴ Gd(122)		49(15) mb		
	¹⁵⁵ Gd	14.80(12)	60,900(500) b	0.843	1,447(100) b
	¹⁵⁶ Gd	20.47(9)	1.8(7) b	1.001	104(15) b
	¹⁵⁷ Gd	15.65(2)	254,000(800) b	0.852	754(20) b
	¹⁵⁸ Gd	24.84(7)	2.2(2) b	1.000	73(7) b
	¹⁶⁰ Gd	21.86(19)	1.4(3) b	1.000	7.4(10) b

■ Table 36.2 (Continued)

Element	Isotope	Abundance	Cross section	<i>g</i> -factor	Resonance integral
65 Terbium	¹⁵⁹ Tb	100	23.3(4) b	1.000	418(20) b
66 Dysprosium	¹⁵⁶ Dy	0.06(1)	33(3) b	1.009	884(80) b
	¹⁵⁸ Dy	0.10(1)	43(6) b	0.989	120(10) b
	¹⁶⁰ Dy	2.34(8)	55(3) b	1.009	1,122(90) b
	¹⁶¹ Dy	18.91(24)	600(25) b	0.991	1,075(80) b
	¹⁶² Dy	25.51(26)	194(10) b	1.005	2,740(270) b
	¹⁶³ Dy	24.90(16)	134(7) b	1.003	1,470(100) b
	¹⁶⁴ Dy(0)	28.18(37)	1,040(140) b	0.988	341(20) b
	¹⁶⁴ Dy(108)		1,610(240) b		
67 Holmium	¹⁶⁵ Ho(0)	100	61.2(11) b	1.002	665(22) b
	¹⁶⁵ Ho(6)		3.5(4) b		
68 Erbium	¹⁶² Er	0.14(1)	19(2) b	1.001	480(50) b
	¹⁶⁴ Er	1.61(3)	13(2) b	1.000	134(10) b
	¹⁶⁶ Er	33.61(35)	16.9(16) b	1.000	95(7) b
	¹⁶⁶ Er(208)		15(2) b		
	¹⁶⁷ Er	22.93(17)	649(8) b	1.069	2,970(70) b
	¹⁶⁸ Er	26.78(26)	2.74(8) b	1.000	37(5) b
	¹⁷⁰ Er	14.93(27)	8.85(30) b	1.000	35.4(59) b
69 Thulium	¹⁶⁹ Tm	100	92(4) b	1.005	1,720(30) b
	¹⁶⁹ Tm(183)		8.2(17) b		
70 Ytterbium	¹⁶⁸ Yb	0.13(1)	2,300(170) b	1.057	21,300(1,000) b
	¹⁷⁰ Yb	3.04(15)	9.9(18) b	1.001	293(30) b
	¹⁷¹ Yb	14.28(57)	58(4) b	0.999	315(30) b
	¹⁷² Yb	21.83(67)	1.3(8) b	1.000	25(3) b
	¹⁷³ Yb	16.13(27)	15.5(15) b	1.001	380(30) b
	¹⁷⁴ Yb	31.83(92)	63.2(15) b	0.999	27(3) b
	¹⁷⁴ Yb(515)				
	¹⁷⁶ Yb	12.76(41)	2.85(5) b	1.000	6.3(6) b
	¹⁷⁶ Yb(332)				
71 Lutetium	¹⁷⁵ Lu(0)	97.41(2)	6.9(13) b	0.976	610(50) b
	¹⁷⁵ Lu(123)		16.2(5) b		
	¹⁷⁶ Lu	2.59(2)	2,090(70) b	1.752	1,087(40) b
	¹⁷⁶ Lu(150)		317(58) b		
	¹⁷⁶ Lu(970)		2.8(7) b		
72 Hafnium	¹⁷⁴ Hf	0.16(1)	549(7) b	0.986	436(35) b
	¹⁷⁶ Hf	5.26(7)	24(3) b	1.002	880(40) b
	¹⁷⁷ Hf	18.60(9)	373(10) b	1.020	7,173(200) b
	¹⁷⁷ Hf(1147)		960(50) mb		
	¹⁷⁷ Hf(2446)		0.2(1) mb		

■ Table 36.2 (Continued)

Element	Isotope	Abundance	Cross section	<i>g</i> -factor	Resonance integral
	¹⁷⁸ Hf	27.28(7)	84(4) b	1.003	1,950(120) b
	¹⁷⁸ Hf(375)		53(6) b		
	¹⁷⁹ Hf	13.629(6)	41(3) b	0.997	630(30) b
	¹⁷⁹ Hf(1142)		445(3) mb		
	¹⁸⁰ Hf	35.08(16)	13.04(7) b	0.997	35.0(10) b
73 Tantalum	¹⁸⁰ Ta	0.012(2)	563(60) b	1.358	1,349(100) b
	¹⁸¹ Ta(0)	99.988(2)	20.5(5) b	1.004	660(23) b
	¹⁸¹ Ta(520)		11(2) mb		
74 Tungsten	¹⁸⁰ W	0.12(1)	<150 b	0.997	214(30) b
	¹⁸² W	26.50(16)	19.9(2) b	1.003	604(90) b
	¹⁸² W(309)				
	¹⁸³ W	14.31(4)	10.3(2) b	0.999	337(50) b
	¹⁸⁴ W	30.64(2)	1.7(1) b	0.999	14.7(15) b
	¹⁸⁴ W(197)		2(1) mb		
	¹⁸⁶ W	28.42(19)	38.5(5) b	1.001	485(15) b
75 Rhenium	¹⁸⁵ Re	37.40(2)	112(2) b	1.004	1,717(50) b
	¹⁸⁷ Re	62.60(2)	76.4(5) b	0.982	300(20) b
	¹⁸⁷ Re(172)		2.8(1) b		
76 Osmium	¹⁸⁴ Os	0.02(1)	3,000(150) b	1.000	601(51) b
	¹⁸⁶ Os	1.59(3)	80(13) b	0.998	280(30) b
	¹⁸⁷ Os	1.96(2)	245(40) b	0.983	500(70) b
	¹⁸⁸ Os	13.24(8)	4.7(5) b	1.002	152(20) b
	¹⁸⁹ Os	16.15(5)	25(4) b	1.004	674(70) b
	¹⁸⁹ Os(1705)		0.26(3) mb		
	¹⁹⁰ Os(0)	26.26(2)	3.9(6) b	0.997	[30(1) b]
	¹⁹⁰ Os(74)		9.2(7) b		
	¹⁹² Os	40.78(19)	3.12(16) b	1.000	4.6(2) b
77 Iridium	¹⁹¹ Ir(0)	37.3(2)	309(30) b	0.996	3,500(100) b
	¹⁹¹ Ir(57)		645(32) b		
	¹⁹¹ Ir(155)		160(70) mb		
	¹⁹³ Ir	62.7(2)	111(5) b	1.017	1,350(100) b
	¹⁹³ Ir(112+y)		5.8(2) b		
78 Platinum	¹⁹⁰ Pt	0.014(1)	122(4) b	0.998	67(5) b
	¹⁹² Pt	0.782(7)	10.0(25) b	1.001	115(20) b
	¹⁹² Pt(150)		2.2(8) b		
	¹⁹⁴ Pt	32.967(99)	580(190) mb	1.000	3.1(1) b
	¹⁹⁴ Pt(259)		98(11) mb		
	¹⁹⁵ Pt	33.832(10)	28.5(12) b	1.000	365(50) b
	¹⁹⁶ Pt(0)	25.242(41)	410(40) mb	1.000	5.1(3) b

■ Table 36.2 (Continued)

Element	Isotope	Abundance	Cross section	<i>g</i> -factor	Resonance integral
	¹⁹⁶ Pt(400)		44(4) mb		
	¹⁹⁸ Pt	7.163(55)	3.66(19) b	1.000	54(4) b
	¹⁹⁸ Pt(424)		350(40) mb		
79 Gold	¹⁹⁷ Au	100	98.65(9) b	1.005	1,550(28) b
80 Mercury	¹⁹⁶ Hg(0)	0.15(1)	3,080(180) b	0.988	472(16) b
	¹⁹⁶ Hg(299)		109(6) b		
	¹⁹⁸ Hg	9.97(20)	2.0(3) b	1.001	71(2) b
	¹⁹⁸ Hg(532)		18(4) mb		
	¹⁹⁹ Hg	16.87(22)	2,150(50) b	0.989	435(20) b
	²⁰⁰ Hg	23.10(19)	<60 b	1.000	2.1 b
	²⁰¹ Hg	13.18(9)	5.7(12) b	1.000	30(3) b
	²⁰² Hg	29.86(26)	4.42(7) b	1.000	4.2(2) b
	²⁰⁴ Hg	6.87(15)	430(100) mb	1.000	
81 Thallium	²⁰³ Tl	29.524(14)	11.4(2) b	1.000	43.0(20) b
	²⁰⁵ Tl	70.476(14)	104(17) mb	1.000	610(150) mb
82 Lead	²⁰⁴ Pb	1.4(1)	660(70) mb	1.001	2.0(2) b
	²⁰⁶ Pb	24.1(1)	26.6(12) mb	1.001	97(14) mb
	²⁰⁶ Pb(1633)		6.3(13) mb		
	²⁰⁷ Pb	22.1(1)	620(14) mb	1.001	390(10) mb
	²⁰⁸ Pb	52.4(1)	0.23(3) mb	1.003	2.0(2) mb
83 Bismuth	²⁰⁹ Bi(0)	100	24.2(4) mb	0.999	190(20) mb
	²⁰⁹ Bi(271)		9.6(8) mb		
90 Thorium	²³² Th	100	7.35(3) b	0.995	85(3) b
92 Uranium	²³⁴ U	0.0055(5)	99.8(13) b	0.990	[660(70) b]
	²³⁵ U	0.7200(51)	98.3(8) b	0.985	[144(6) b]
	²³⁵ U(f)		582.6(11) b		[275(5) b]
	²³⁸ U	99.274(11)	2.68(19) b	1.002	277(3) b

36.2.2 Thermal Neutron Capture γ Rays

The prompt gamma-ray cross sections were derived from a comparison of measurements with the neutron beam at the Budapest Reactor and other data from the literature (Molnár 2004; Choi et al. 2007). In some cases, these values were renormalized to better agree with the adopted total radiative cross section from all measurements. Delayed gamma-ray cross sections were derived from a comparison of Budapest Reactor measurements, corrected for activation and decay times, values derived from the k_0 database, and values adopted from total radiative cross sections and emission probability values from either the “Table of Radionuclides” (Bé et al. 2004) or the ENSDF (2010) nuclear structure and decay database (🔗 Table 36.3).

■ Table 36.3

Energy, half-life and partial gamma-ray production cross section of the most important prompt and decay gamma lines of elements

El	Energy (keV)	Half-life (s)	σ_{γ} (barn)
H	2,223.248		0.3326(7)
Li	2,032.30(4)		0.0409(14)
	980.53(7)		0.00433(12)
	1,051.90(7)		0.00433(12)
	7,245.91(4)		0.0231(14)
	477.595(3)		0.0152(9)
	6,768.81(4)		0.0152(9)
Be	6,809.61(3)		0.0058(5)
	3,367.448(25)		0.00285(22)
	853.630(12)		0.00208(24)
	2,590.014(19)		0.00191(15)
	3,443.406(20)		0.00098(7)
	5,956.53(3)		1.46E-04(12)
B	477.595(3)		715(2)
C	4,945.301(3)		0.0260(5)
	1,261.765(9)		0.00124(3)
	3,683.920(9)		0.00122(3)
N	5,269.159(13)		0.02406(22)
	5,297.821(15)		0.01706(17)
	5,533.395(14)		0.01583(14)
	1,884.821(16)		0.01496(12)
	6,322.428(12)		0.01479(17)
	4,508.731(12)		0.01335(12)
	3,677.732(13)		0.0116(41)
	10,829.120(12)		0.0112(3)
	5,562.057(13)		0.00866(10)
	7,298.983(17)		0.00765(10)
	3,531.981(15)		0.00712(7)
	1,678.281(14)		0.00639(6)
O	870.68(6)		2.00E-4(7)
	2,184.42(7)		1.64E-4(7)
	1,087.75(6)		1.58E-4(7)
	3,272.02(8)		3.54E-5(23)
F	1,633.53(3)	11.2	0.00935(9)
	583.561(16)		0.00360(15)
	656.006(18)		0.00198(10)
	665.207(18)		0.00149(8)

■ Table 36.3 (Continued)

El	Energy (keV)	Half-life (s)	σ_{γ} (barn)
	983.538(20)		0.00116(6)
	6,600.175(16)		0.00094(4)
	1,056.776(17)		0.00094(4)
	6,016.802(16)		0.00094(4)
	1,387.901(20)		0.00083(3)
	1,309.126(17)		0.00076(3)
	3,488.064(18)		0.00072(3)
	5,033.530(23)		0.000620(24)
Ne	439.986(10)	37	0.00101(15)
	2,035.67(20)		0.025(4)
	350.72(6)		0.020(3)
	4,374.13(6)		0.019(3)
	2,793.94(5)		0.0081(13)
	1,931.08(6)		0.0056(9)
	1,071.34(7)		0.0049(8)
	1,979.89(6)		0.0023(4)
	1,017.00(20)		0.0022(4)
	2,895.32(10)		0.0025(4)
	2,203.58(6)		0.0020(4)
	5,688.97(6)		0.0020(3)
	6,760.06(6)		0.0025(4)
Na	1,368.66(3)	53,900	0.541(4)
	2,754.13(6)	53,900	0.541(4)
	472.202(9)	0.0202	0.478(4)
	90.992(10)		0.250(3)
	869.210(9)		0.1120(15)
	6,395.478(15)		0.1005(11)
	874.389(6)		0.0796(13)
	2,517.81(3)		0.0736(7)
	3,981.450(25)		0.0723(8)
	2,752.271(23)		0.0593(10)
	3,587.460(25)		0.0619(17)
	2,025.139(22)		0.0318(3)
Mg	3,916.84(3)		0.0313(6)
	585.00(3)		0.0304(8)
	2,828.172(25)		0.0235(5)
	1,808.668(22)		0.0193(6)
	1,129.575(23)		0.00955(25)
	3,054.00(3)		0.00829(19)

■ Table 36.3 (Continued)

El	Energy (keV)	Half-life (s)	σ_{γ} (barn)
	974.66(3)		0.00640(24)
	3,301.41(3)		0.00610(16)
	389.670(21)		0.00569(24)
	2,438.54(3)		0.00466(13)
	3,831.480(24)		0.00447(12)
	3,413.10(3)		0.00394(13)
	843.76(3)	567	0.00300(6)
	1,014.44(4)	567	0.00117(3)
Al	1,778.92(3)	134	0.232(3)
	30.638(10)		0.080(3)
	7,724.027(4)		0.05236(22)
	3,033.896(6)		0.0178(3)
	4,259.534(7)		0.0149(3)
	4,133.407(7)		0.0147(3)
	3,465.058(7)		0.0145(3)
	4,733.844(11)		0.0123(3)
	4,690.676(5)		0.01047(22)
	3,591.189(8)		0.00982(16)
	1,622.877(18)		0.00987(16)
	982.951(10)		0.00901(14)
Si	3,538.966(22)		0.1187(9)
	4,933.889(24)		0.1080(9)
	2,092.902(18)		0.0334(3)
	1,273.349(17)		0.0289(6)
	6,379.801(21)		0.01915(20)
	7,199.199(23)		0.01173(11)
	3,660.713(23)		0.00692(6)
	5,106.693(22)		0.00609(7)
	2,425.767(23)		0.00508(7)
	3,954.39(3)		0.004113(5)
	8,472.209(23)		0.00363(4)
	752.215(23)		0.00316(7)
	1,266.15(10)	9,438	0.000179(14)
P	512.646(19)		0.079(4)
	78.083(20)		0.059(3)
	636.663(21)		0.0311(14)
	3,899.89(3)		0.0299(9)
	6,785.504(24)		0.0254(7)
	1,071.217(23)		0.0250(12)

Table 36.3 (Continued)

El	Energy (keV)	Half-life (s)	σ_{γ} (barn)
	3,522.59(3)		0.0224(6)
	4,671.37(3)		0.0199(6)
	2,156.90(4)		0.0131(4)
	2,114.47(3)		0.0116(4)
	3,058.17(4)		0.0112(3)
	2,151.52(4)		0.0106(4)
S	840.993(13)		0.346(6)
	5,420.574(24)		0.308(7)
	2,379.661(14)		0.208(3)
	3,220.588(17)		0.1242(21)
	2,930.67(3)		0.0833(14)
	4,869.61(3)		0.0648(14)
	2,753.16(3)		0.0276(5)
	3,369.70(4)		0.0271(5)
	4,430.60(4)		0.0262(5)
	5,047.10(3)		0.0163(4)
	7,799.815(24)		0.0143(5)
	3,723.54(4)		0.0133(3)
Cl	1,164.865(10)		8.92(7)
	517.073(10)		7.43(7)
	6,110.842(18)		7.27(11)
	1,951.1400(20)		6.49(5)
	788.428(10)		5.23(7)
	1,959.346(4)		4.18(5)
	786.302(10)		3.5(5)
	7,413.968(18)		3.53(5)
	7,790.330(18)		2.84(5)
	6,619.615(19)		2.72(4)
	2,863.819(12)		1.83(3)
	5,715.244(21)		1.83(4)
	1,642.43(6)	2,234	0.0349(8)
	2,167.472(9)	2,234	0.0466(7)
	671.355(8)	0.715	0.0130(3)
Ar	167.30(20)		0.439(13)
	4,745.3(8)		0.344(10)
	1,186.8(3)		0.346(10)
	516.0(3)		0.166(5)
	5,582.4(8)		0.075(4)
	3,700.6(8)		0.064(3)

■ Table 36.3 (Continued)

El	Energy (keV)	Half-life (s)	σ_{γ} (barn)
	837.7(3)		0.071(4)
	2,771.9(8)		0.0535(18)
	348.7(3)		0.0474(14)
	1,044.3(4)		0.0421(18)
	2,810.6(8)		0.0369(18)
	2,130.8(8)		0.0355(13)
	1,293.64(4)	6,577	0.62(3)
K	29.83(10)		1.390(18)
	770.3050(20)		0.902(12)
	1,158.887(10)		0.159(3)
	5,380.018(16)		0.149(4)
	2,073.793(19)		0.1371(22)
	1,618.973(10)		0.1295(22)
	1,613.756(10)		0.1194(20)
	7,768.919(14)		0.114(7)
	5,695.442(20)		0.114(3)
	5,751.758(17)		0.109(3)
	1,247.193(11)		0.0784(12)
Ca	1,942.67(3)		0.353(7)
	6,419.59(5)		0.175(5)
	4,418.52(5)		0.0710(17)
	2,001.31(3)		0.0667(15)
	519.66(5)		0.0501(15)
	2,009.84(3)		0.0413(11)
	3,609.80(6)		0.0284(9)
	5,900.02(6)		0.0261(11)
	174.12(7)		0.0181(10)
	2,810.06(5)		0.0167(5)
	4,749.21(7)		0.0133(7)
	727.17(5)		0.0116(4)
	3,084.4(1)	523	0.00191(4)
Sc	227.773(12)		7.11(11)
	147.011(10)		6.05(9)
	142.528(8)	18.8	4.88(7)
	295.243(10)		3.96(10)
	228.716(12)		3.31(5)
	216.44(4)		2.49(4)
	627.462(18)		2.24(5)
	554.44(4)		1.82(4)

■ Table 36.3 (Continued)

El	Energy (keV)	Half-life (s)	σ_{γ} (barn)
	8,175.176(21)		1.94(6)
	584.785(13)		1.78(3)
	6,839.09(4)		0.82(3)
	8,532.122(20)		1.01(4)
Ti	1,381.745(5)		5.18(12)
	6,760.084(14)		2.97(9)
	6,418.426(14)		1.96(6)
	341.706(5)		1.843(21)
	1,585.941(5)		0.624(8)
	6,555.911(14)		0.334(8)
	1,761.974(7)		0.311(4)
	4,881.394(15)		0.308(7)
	1,498.663(7)		0.297(5)
	4,966.802(15)		0.196(5)
	1,793.476(8)		0.1533(24)
	3,026.704(20)		0.145(3)
	320.076(6)	346	0.00858(14)
V	1,434.10(3)	225	4.85(5)
	125.082(3)		1.61(4)
	6,517.282(19)		0.78(3)
	645.703(13)		0.768(16)
	7,162.898(15)		0.599(23)
	6,874.157(19)		0.492(23)
	6,464.887(18)		0.426(19)
	436.627(13)		0.397(10)
	5,515.813(23)		0.378(18)
	5,752.064(22)		0.360(15)
	1,558.843(18)		0.324(8)
	823.184(13)		0.320(8)
Cr	834.849(22)		1.38(3)
	8,884.36(5)		0.78(5)
	749.09(3)		0.569(9)
	7,938.46(23)		0.424(11)
	9,719.06(5)		0.260(18)
	8,510.77(8)		0.233(8)
	2,239.04(8)		0.186(3)
	6,645.61(8)		0.183(13)
	1,784.70(4)		0.1764(20)
	8,482.80(9)		0.169(7)

■ Table 36.3 (Continued)

El	Energy (keV)	Half-life (s)	σ_{γ} (barn)
	7,099.91(6)		0.146(9)
	2,320.8(3)		0.136(3)
Mn	846.754(20)	9,280	13.26(5)
	1,810.72(4)	9,280	3.61(5)
	26.560(20)		3.83(4)
	83.884(23)		3.11(5)
	212.039(21)		2.13(3)
	2,113.05(4)	9,280	1.90(4)
	104.611(23)		1.74(3)
	314.398(20)		1.460(20)
	7,243.52(9)		1.36(3)
	7,057.89(9)		1.22(3)
	5,920.39(8)		1.06(3)
	271.198(22)		0.94(6)
Fe	7,631.136(14)		0.653(13)
	7,645.545(10)		0.549(11)
	352.347(12)		0.273(3)
	6,018.532(20)		0.227(5)
	5,920.449(21)		0.225(5)
	1,725.288(21)		0.181(3)
	1,612.786(18)		0.1529(22)
	14.411(14)		0.1541(20)
	691.960(19)		0.1367(18)
	7,278.838(10)		0.137(4)
	4,218.27(5)		0.099(3)
	122.077(14)		0.096(3)
Co	229.879(17)		6.98(8)
	277.161(17)		6.58(8)
	555.972(13)		5.60(6)
	447.711(19)		3.31(4)
	6,706.01(3)		2.93(6)
	6,877.16(3)		2.93(6)
	5,975.98(4)		2.8(4)
	785.628(21)		2.34(7)
	6,485.99(3)		2.25(5)
	497.269(16)		2.10(4)
	5,660.93(4)		1.84(6)
	1,515.720(25)		1.689(24)
	58.603(7)	628	0.436(6)

Table 36.3 (Continued)

El	Energy (keV)	Half-life (s)	σ_{γ} (barn)
Ni	8,998.414(15)		1.525(20)
	464.978(12)		0.841(9)
	8,533.509(17)		0.681(9)
	6,837.50(3)		0.459(7)
	7,819.517(21)		0.330(3)
	877.977(11)		0.239(2)
	282.917(18)		0.212(3)
	7,536.637(25)		0.188(2)
	339.420(11)		0.1654(20)
	8,120.567(16)		0.1314(20)
	5,817.219(20)		0.1114(12)
	6,583.831(19)		0.0814(9)
	1,115.53(4)	9,061	0.0033(4)
	1,481.84(5)	9,061	0.0050(6)
Cu	278.250(14)		0.893(12)
	7,915.62(4)		0.868(16)
	159.281(5)		0.648(8)
	7,637.40(4)		0.492(8)
	7,306.93(4)		0.304(3)
	608.766(23)		0.269(5)
	185.96(4)		0.244(3)
	343.898(14)		0.215(3)
	202.950(8)		0.194(3)
	7,253.01(5)		0.1462(17)
	465.14(3)		0.1357(18)
	385.77(3)		0.1304(18)
	1,039.24(3)	307	0.0598(6)
	1,673.4(10)	45,724	0.588(4)
Zn	1,077.335(16)		0.356(5)
	115.225(18)		0.167(3)
	7,863.55(7)		0.141(5)
	1,883.12(3)		0.0718(18)
	855.69(3)		0.066(6)
	1,007.809(25)		0.0555(15)
	1,340.14(3)		0.0457(16)
	805.79(3)		0.045(3)
	1,261.15(3)		0.0431(10)
	6,958.8(3)		0.043(3)
	5,474.02(10)		0.0399(4)

■ Table 36.3 (Continued)

El	Energy (keV)	Half-life (s)	σ_{γ} (barn)
	834.77(3)		0.0371(11)
Ga	834.08(3)	50,800	1.766(15)
	2,201.91(13)	50,800	0.478(5)
	629.96(5)	50,800	0.458(4)
	601.21(6)	50,800	0.1023(9)
	145.14(3)		0.465(7)
	894.91(11)	50,800	0.1825(16)
	508.19(3)		0.349(6)
	690.943(24)		0.305(4)
	2,507.40(12)	50,800	0.2360(20)
	192.11(3)		0.194(3)
	2,491.6(3)	50,800	0.1418(12)
	786.17(16)	50,800	0.0591(5)
Ge	595.851(5)		1.097(24)
	867.899(5)		0.553(12)
	608.353(4)		0.250(6)
	175.05(3)		0.161(4)
	499.87(3)		0.155(4)
	1,204.199(6)		0.141(4)
	1,101.282(6)		0.134(3)
	492.933(5)		0.133(3)
	961.055(7)		0.129(4)
	1,471.712(10)		0.083(3)
	708.15(3)		0.0807(23)
As	559.10(5)	94,500	1.95(10)
	165.049(10)		1.030(14)
	86.788(10)		0.615(10)
	44.425(10)		0.98(10)
	6,810.898(8)		0.1656(19)
	120.258(10)		0.410(8)
	46.098(10)		0.301(14)
	657.05(5)	94,500	0.268(18)
	122.247(10)		0.239(5)
	471.00(10)		0.196(3)
	235.877(10)		0.1725(18)
	263.894(10)		0.1624(19)
Se	613.724(3)		2.14(5)
	238.998(10)		2.03(3)
	520.6370(20)		1.261(19)

■ Table 36.3 (Continued)

El	Energy (keV)	Half-life (s)	σ_{γ} (barn)
	161.922(10)	17.4	0.855(21)
	6,600.690(21)		0.624(19)
	139.227(10)		0.546(8)
	249.788(10)		0.536(8)
	694.914(4)		0.443(10)
	7,418.467(21)		0.355(10)
	297.2160(20)		0.331(7)
	439.4510(20)		0.317(8)
	1,308.632(5)		0.317(8)
Br	776.517(3)	127,000	1.016(12)
	554.3480(20)	127,000	0.866(11)
	245.203(4)		0.80(3)
	619.106(4)	127,000	0.530(6)
	271.374(3)		0.462(7)
	314.982(3)		0.460(9)
	244.237(3)		0.45(3)
	195.602(4)		0.434(14)
	37.0520(20)	15,900	1.03(3)
	219.377(3)		0.399(14)
	616.3(5)	1,060	0.228(17)
	698.374(5)	127,000	0.345(4)
Kr	881.74(11)		21.3(10)
	1,213.42(12)		7.8(4)
	1,463.86(6)		7.6(4)
	425.30(11)		2.99(14)
	1,897.79(8)		2.47(12)
	802.62(8)		1.55(7)
	1,124.44(6)		1.52(7)
	6,880.7(7)		1.48(7)
	1,016.2(3)		1.05(5)
	1,979.34(11)		1.05(5)
	943.36(14)		0.84(4)
	190.46(16)	13.1	0.086(8)
Rb	556.82(3)		0.917(3)
	487.89(4)		0.0494(12)
	555.61(3)	61	0.0411(14)
	872.94(4)		0.0321(5)
	1,076.64(20)	1,610,000	0.0312(3)
	421.50(3)		0.0259(5)

■ Table 36.3 (Continued)

El	Energy (keV)	Half-life (s)	σ_{γ} (barn)
	1,032.32(5)		0.0227(4)
	1,026.55(6)		0.0218(4)
	1,304.48(4)		0.0204(5)
	538.66(4)		0.0169(5)
	536.48(4)		0.0167(5)
	1,836.077(21)	1,066	0.0057(2)
Sr	1,836.067(21)		1.030(18)
	898.055(11)		0.702(10)
	850.657(12)		0.275(4)
	388.526(22)	10,100	0.065(10)
	6,266.87(4)		0.077(3)
	585.613(14)		0.0703(14)
	7,527.490(25)		0.0687(24)
	1,717.804(23)		0.0674(15)
	6,660.40(3)		0.0644(23)
	1,218.523(16)		0.0599(13)
	3,009.39(3)		0.0575(15)
	6,941.93(3)		0.0502(20)
Y	6,080.171(22)		0.754(13)
	776.613(18)		0.659(9)
	202.53(3)		0.291(4)
	574.106(20)		0.172(4)
	4,107.68(3)		0.0518(17)
	1,211.573(22)		0.0447(12)
	1,371.124(20)		0.0400(12)
	5,645.236(25)		0.0208(12)
	3,301.23(3)		0.0164(9)
	2,749.181(24)		0.0239(10)
	1,815.15(3)		0.0217(8)
	2,546.68(3)		0.0213(9)
	202.53(3)	11,484	0.0024(3)
	479.51(5)	11,484	0.0023(3)
Zr	934.464(10)		0.125(5)
	1,405.159(3)		0.0301(10)
	560.958(3)		0.0285(5)
	6,295.13(16)		0.0252(18)
Nb	99.407(10)		0.196(9)
	255.9290(20)		0.176(3)
	253.115(5)		0.1320(19)

■ Table 36.3 (Continued)

El	Energy (keV)	Half-life (s)	σ_{γ} (barn)
	113.401(10)		0.117(3)
	309.915(8)		0.0690(17)
	293.206(4)		0.0651(16)
	499.426(8)		0.0648(18)
	17.810(7)		0.0579(14)
	518.113(12)		0.0579(13)
	337.527(7)		0.054(6)
	835.72(3)		0.0376(8)
	562.328(9)		0.0293(11)
	40.94(3)	376	0.079(3)
	871.091(18)	376	0.0052(2)
Mo	778.221(10)		2.02(6)
	849.85(3)		0.43(3)
	847.603(11)		0.324(9)
	719.528(14)		0.31(10)
	1,091.289(20)		0.201(6)
	787.39(3)		0.168(6)
	1,200.10(3)		0.124(4)
	1,497.742(17)		0.122(4)
	608.744(14)		0.121(4)
	736.820(14)		0.119(4)
	6,919.05(9)		0.106(6)
	1,317.35(8)		0.091(6)
	191.92(2)	877	0.00345(6)
Ru	539.538(15)		1.53(13)
	475.0950(20)		0.98(9)
	686.907(17)		0.52(5)
	631.22(4)		0.30(3)
	627.970(22)		0.176(16)
	822.579(22)		0.137(12)
	1,341.50(3)		0.137(12)
	7,792.04(3)		0.132(13)
	1,627.32(3)		0.129(12)
	1,362.111(24)		0.111(13)
	1,046.498(3)		0.103(9)
	724.30(3)	15,984	0.0432(9)
Rh	180.87(3)		22.6(12)
	97.14(3)		20.1(4)
	51.50(3)		14.6(16)

■ Table 36.3 (Continued)

El	Energy (keV)	Half-life (s)	σ_{γ} (barn)
	217.82(3)		7.38(13)
	134.54(3)		6.8(4)
	127.20(3)		5.27(21)
	51.50(3)	260	5.11(15)
	215.340(22)		5.3(3)
	100.74(4)		4.96(10)
	333.44(3)		3.27(8)
	555.81(4)	42.3	3.14(15)
Pd	511.843(20)		4.00(4)
	717.356(22)		0.777(9)
	616.192(20)		0.629(9)
	1,050.31(4)		0.360(8)
	113.401(10)		0.335(5)
	1,128.03(3)		0.323(6)
	1,045.82(3)		0.321(7)
	245.0790(20)		0.250(4)
	325.2840(20)		0.208(3)
	1,572.54(7)		0.207(25)
	339.5290(20)		0.195(3)
	152.942(10)		0.1452(22)
	188.9(1)	281	0.0274(14)
Ag	198.72(4)		7.75(13)
	235.62(4)		4.62(7)
	78.91(4)		4.7(5)
	117.45(8)		3.84(7)
	206.46(3)		2.90(5)
	267.08(3)		2.73(6)
	192.90(3)		1.80(5)
	294.39(3)		1.67(9)
	236.85(4)		1.95(3)
	657.5(10)	24.6	2.36(3)
	632.98(5)	143	0.346(4)
Cd	558.32(3)		1,863(30)
	651.19(3)		358(5)
	805.85(3)		134.0(18)
	1,364.30(4)		123.0(21)
	1,209.65(4)		122.0(19)
	576.04(3)		107.0(17)
	725.19(3)		107.0(13)

Table 36.3 (Continued)

El	Energy (keV)	Half-life (s)	σ_{γ} (barn)
	1,399.54(4)		97.7(15)
	2,455.93(7)		87.3(18)
	5,824.31(16)		69.1(18)
In	1,293.54(15)	3,260	130(3)
	1,097.30(20)	3,260	86.4(17)
	416.86(3)	3,260	42.6(18)
	272.9660(20)		32.9(16)
	186.2100(20)		26.8(14)
	96.062(3)		24.8(12)
	2,112.1(4)	3,260	23.8(6)
	85.5690(20)		20.0(11)
	818.70(20)	3,260	17.7(6)
	60.916(10)		15.5(9)
	162.393(3)	2.18	30(3)
	1,507.40(20)	3,260	15.4(5)
Sn	1,293.591(15)		0.1340(21)
	1,171.28(6)		0.0879(13)
	1,229.64(6)		0.0673(13)
	972.619(17)		0.0158(5)
	2,112.302(16)		0.0152(5)
	463.242(17)		0.0128(3)
	818.721(14)		0.0128(4)
	931.819(23)		0.0111(3)
	925.90(6)		0.0097(3)
	733.89(3)		0.00925(21)
	160.32(5)	2,404	0.0056(3)
Sb	564.24(4)	235,000	2.56(8)
	61.413(10)		0.302(9)
	78.091(10)		0.244(6)
	121.497(10)		0.359(8)
	282.650(10)		0.273(7)
	148.24		0.256(6)
	87.6		0.212(6)
	105.816(10)		0.161(4)
	692.65(4)	235,000	0.151(3)
	332.286(10)		0.101(3)
Te	602.729(17)		2.46(16)
	722.772(25)		0.52(4)
	645.819(20)		0.263(22)

■ Table 36.3 (Continued)

El	Energy (keV)	Half-life (s)	σ_{γ} (barn)
	2,746.92(5)		0.138(11)
	1,488.88(5)		0.120(9)
	353.820(23)		0.100(8)
	6,322.95(8)		0.099(8)
	1,436.55(3)		0.098(9)
	1,720.15(5)		0.083(8)
	1,325.50(3)		0.074(6)
	1,691.06(6)		0.073(7)
	1,579.50(8)		0.072(10)
I	133.611(10)		1.42(4)
	442.901(10)	1,500	0.745(22)
	27.362(10)		0.327(24)
	58.1100(20)		0.282(21)
	153.011(3)		0.178(6)
	160.757(10)		0.150(4)
	124.2810(20)		0.179(6)
	301.906(5)		0.168(3)
	52.385(3)		0.167(9)
	142.1370(20)		0.137(4)
	420.826(7)		0.102(6)
	193.5630(20)		0.0964(24)
Xe	667.79(6)		6.7(5)
	772.72(4)		1.78(14)
	536.17(9)		1.71(24)
	630.29(4)		1.41(11)
	6,467.09(12)		1.33(19)
	1,317.93(8)		0.89(7)
	483.66(10)		0.55(4)
	1,985.71(10)		0.54(5)
	600.19(8)		0.52(4)
	586.17(5)		0.48(7)
	1,136.13(7)		0.45(4)
	505.84(8)		0.40(3)
Cs	176.4040(20)		2.47(4)
	205.615(3)		1.559(25)
	510.795(3)		1.54(3)
	307.015(4)		1.45(3)
	116.612(4)		1.44(12)
	130.2320(20)		1.410(21)

Table 36.3 (Continued)

El	Energy (keV)	Half-life (s)	σ_{γ} (barn)
	116.3740(20)		1.39(12)
	198.3010(20)		1.103(19)
	234.3340(20)		1.066(23)
	450.345(3)		0.99(5)
	113.7650(20)		0.777(15)
	245.8620(20)		0.740(15)
	127.502(3)	10,483	3.80(6)
Ba	1,435.77(4)		0.308(7)
	627.29(5)		0.294(6)
	818.514(12)		0.212(4)
	4,095.84(9)		0.155(4)
	1,261.52(7)		0.095(5)
	454.73(5)		0.0853(22)
	1,444.91(5)		0.0801(20)
	165.857(10)	4,980	0.085(9)
	462.78(4)		0.0660(16)
	5,730.81(6)		0.0617(20)
	3,641.12(9)		0.0562(16)
	2,217.84(8)		0.044(5)
La	1,596.21(4)	145,000	8.64(13)
	487.021(12)	145,000	4.12(4)
	815.772(19)	145,000	2.110(17)
	328.762(8)	145,000	1.84(3)
	218.225(22)		0.780(21)
	288.255(5)		0.728(12)
	5,097.726(6)		0.679(18)
	4,842.695(7)		0.655(17)
	272.306(4)		0.502(8)
	162.659(3)		0.490(13)
	925.189(21)	145,000	0.625(6)
Ce	661.99(5)		0.233(18)
	4,766.10(5)		0.109(9)
	475.04(4)		0.082(7)
	4,291.08(4)		0.053(4)
	1,107.66(5)		0.029(4)
	4,336.46(8)		0.0262(21)
	1,153.97(5)		0.0152(13)
	765.97(5)		0.0151(13)
	3,018.24(7)		0.0112(13)

■ Table 36.3 (Continued)

El	Energy (keV)	Half-life (s)	σ_{γ} (barn)
	3,002.41(6)		0.0106(9)
	808.35(6)		0.0106(9)
	293.266(2)	118,940	0.048(10)
	57.356(7)	118,940	0.0131(4)
Pr	176.8630(20)		1.06(4)
	140.9050(20)		0.479(10)
	1,575.6(5)	68,800	0.412(12)
	5,666.170(6)		0.379(15)
	182.786(4)		0.377(14)
	645.720(24)		0.311(7)
	126.8460(20)		0.307(15)
	4,692.120(22)		0.291(10)
	5,140.72(3)		0.269(11)
	698.65(3)		0.22(6)
	5,096.081(15)		0.208(8)
	84.998(3)		0.207(11)
Nd	696.499(10)		33.3(23)
	618.062(19)		13.4(3)
	814.12(3)		4.98(12)
	864.301(10)		4.27(11)
	742.106(22)		3.8(4)
	6,502.22(17)		3.18(17)
	453.89(5)		3.03(8)
	476.82(5)		1.93(5)
	1,413.16(4)		1.90(5)
	6,255.99(17)		1.50(12)
	980.60(4)		1.21(3)
	863.89(8)		1.07(4)
Sm	333.97(4)		4,794(60)
	439.40(4)		2,860(150)
	737.44(4)		597(8)
	505.51(3)		528(80)
	584.27(3)		480(70)
	712.20(3)		267(4)
	1,170.59(4)		23(10)
	675.83(3)		172(7)
	869.29(3)		119(6)
	1,193.84(4)		106(3)
	1,350.39(5)		94(12)

Table 36.3 (Continued)

El	Energy (keV)	Half-life (s)	σ_{γ} (barn)
	859.86(4)		88(4)
	103.180(12)	167,400	16.2(4)
Eu	89.847(6)		1,430(30)
	77.23(4)		187(13)
	48.31(17)		181(70)
	73.21(9)		106(22)
	221.30(8)		73(3)
	68.23(9)		62(3)
	19.70(10)		34(3)
	206.53(8)		58.7(20)
	52.39(9)		55(3)
	169.28(9)		54.8(22)
	103.34(13)		48(5)
	71.24(12)		45(14)
	344.31(3)	33,522	37.5(20)
	121.777(5)	33,522	110(12)
	841.594(8)	33,522	208(23)
	963.390(12)	33,522	171(19)
Gd	181.931(4)		7,320(400)
	79.510(10)		4,040(110)
	944.174(10)		3,070(80)
	962.104(10)		2,140(50)
	199.213(10)		2,630(190)
	1,107.612(9)		1,850(50)
	1,185.988(9)		1,550(190)
	977.121(10)		1,420(30)
	1,187.122(9)		1,600(190)
	88.967(10)		1,750(120)
	897.502(10)		1,080(50)
	1,119.163(10)		1,180(30)
Tb	75.050(10)		1.78(18)
	63.686(10)		1.46(16)
	64.1100(20)		1.2(2)
	41.890(10)		2.3(5)
	50.869(10)		0.43(17)
	54.129(10)		2.7(3)
	97.503(3)		0.50(6)
	59.643(10)		0.48(6)
	153.6870(20)		0.44(5)

■ Table 36.3 (Continued)

El	Energy (keV)	Half-life (s)	σ_{γ} (barn)
	79.099(6)		0.43(6)
	135.5970(20)		0.39(4)
Dy	184.257(4)		146(15)
	538.609(8)		69.2(19)
	496.931(5)		44.9(11)
	185.19(9)		39.1(12)
	465.416(6)		38.(10)
	5,607.69(3)		35.9(16)
	411.651(5)		35.1(10)
	385.9840(20)		34.8(10)
	50.4310(20)		33.9(15)
	414.985(7)		31(5)
	5,557.26(3)		28.7(14)
	583.982(5)		24(7)
	94.700(3)	8,402	29.1(9)
	108.160(3)	75.4	15.4(4)
	515.467(25)	75.4	7.71(22)
Ho	136.6650(20)		14.5(7)
	116.836(10)		8.1(4)
	80.574(8)	96,500	4.03(6)
	426.012(5)		2.88(15)
	149.309(3)		2.25(12)
	239.132(4)		2.25(12)
	221.186(4)		2.05(11)
	542.780(4)		1.94(13)
	371.772(5)		1.56(8)
	54.240(10)		1.41(4)
	304.617(6)		1.34(7)
	410.265(6)		1.23(7)
Er	184.285(10)		56(5)
	815.9890(20)		42.5(15)
	198.244(10)		29.9(16)
	79.804(10)		18.2(8)
	284.6560(20)		13.7(12)
	730.658(10)		11.6(4)
	631.7050(20)		7.9(3)
	853.481(10)		7.5(3)
	914.942(10)		6.99(24)
	741.3650(20)		6.72(24)

■ Table 36.3 (Continued)

El	Energy (keV)	Half-life (s)	σ_{γ} (barn)
	821.1680(20)		6.2(3)
	829.948(10)		4.12(19)
	207.801(5)	2.27	4.2(7)
	308.291(18)	27,058	0.87(3)
Tm	204.45		8.72(19)
	149.718(10)		7.11(12)
	144.48		5.96(11)
	237.239(10)		5.52(10)
	180.99		3.85(14)
	219.71		3.64(6)
	165.74		3.29(6)
	114.54		3.19(6)
	311.019(10)		2.50(5)
	411.5060(20)		2.37(5)
	512.1370(20)		1.96(5)
	384.0790(20)		1.95(5)
Yb	514.868(7)	0.0682	10.3(6)
	639.261(9)		1.55(10)
	396.329(20)	362,000	2.60(8)
	5,266.3(4)		1.02(16)
	41.2180(20)		1.2(4)
	811.427(9)		1.08(13)
	363.938(6)		0.93(7)
	477.391(5)		0.81(5)
	3,885.0(4)		0.83(16)
	78.743(10)		0.67(10)
	282.522(14)	362,000	0.764(25)
	428.613(12)		0.67(4)
Lu	201.83(4)		0.67(4)
	150.392(3)		13.6(4)
	457.944(15)		8.4(3)
	138.607(5)		6.79(24)
	208.366(10)	581,000	5.88(16)
	162.492(4)		5.28(16)
	121.620(3)		5.8(4)
	147.165(5)		4.4(4)
	71.517(10)		3.96(16)
	319.036(8)		3.83(13)
	112.9498(4)	581,000	3.5(10)

■ Table 36.3 (Continued)

El	Energy (keV)	Half-life (s)	σ_{γ} (barn)
Hf	213.439(7)		29.4(6)
	214.3410(20)	18.7	14.6(13)
	93.182(6)		11.4(4)
	325.559(4)		6.88(15)
	214.3410(20)		20.6(4)
	1,174.635(5)		4.8(7)
	1,229.287(8)		4.26(11)
	1,167.072(6)		3.95(10)
	1,207.213(5)		3.9(3)
	303.9880(20)		4.28(8)
	1,102.824(5)		2.96(8)
Ta	270.4030(20)		5.75(12)
	173.2050(20)		2.66(6)
	402.623(3)		2.60(5)
	133.8770(20)		1.39(15)
	114.315(10)		0.861(20)
	156.0880(20)		0.516(12)
	190.334(3)		0.403(15)
	360.518(3)		0.391(15)
	297.125(3)		1.38(4)
	512.355(4)		0.364(20)
	146.7740(20)		0.311(10)
W	685.73(4)	85,400	3.29(3)
	479.550(22)	85,400	2.64(3)
	72.002(4)	85,400	1.34(2)
	134.247(7)	85,400	1.05(2)
	145.79(3)		1.37(3)
	5,261.68(6)		0.642(23)
	618.26(4)	85,400	0.751(8)
	5,320.72(6)		0.472(17)
	551.52(4)	85,400	0.609(6)
	772.89(5)	85,400	0.480(5)
	6,190.78(3)		0.517(16)
	201.44(5)		0.441(11)
Re	63.5820(20)		7.1(3)
	155.041(4)	61,200	7.25(20)
	59.0100(20)		6.2(6)
	137.157(8)	321,000	3.95(7)
	207.853(4)		4.63(19)

Table 36.3 (Continued)

El	Energy (keV)	Half-life (s)	σ_{γ} (barn)
	290.665(6)		5.0(3)
	214.647(4)		2.58(11)
	316.457(9)		2.30(9)
	144.152(5)		1.83(15)
	251.243(5)		1.47(11)
	227.083(6)		2.03(11)
	105.8620(20)		1.97(8)
Os	186.7180(20)		2.08(5)
	155.10(4)		1.19(3)
	557.978(5)		0.84(3)
	569.344(20)		0.694(25)
	633.14(4)		0.585(16)
	371.261(5)		0.574(14)
	478.04(4)		0.523(14)
	361.137(6)		0.466(15)
	5,146.63(14)		0.409(20)
	635.02(5)		0.405(12)
	527.60(3)		0.30(10)
	272.82(4)		0.242(6)
	74.38(1)	47,160	0.171(5)
Ir	351.689(4)		10.9(4)
	328.448(14)	69,400	9.0(4)
	84.2740(20)		7.7(4)
	48.057(10)		5.7(4)
	216.905(4)		5.57(24)
	58.844(10)		5.3(3)
	77.947(10)		4.8(4)
	226.2980(20)		4.0(4)
	206.220(4)		3.70(18)
	88.734(10)		3.67(24)
	56.71(3)	87	7.48(13)
Pt	355.6840(20)		6.17(6)
	332.985(4)		2.580(25)
	326.353(3)		0.511(10)
	5,254.70(8)		0.41(3)
	521.161(5)		0.338(10)
	779.608(5)		0.227(3)
	1,047.007(11)		0.181(4)
	1,091.334(6)		0.181(4)

■ Table 36.3 (Continued)

El	Energy (keV)	Half-life (s)	σ_{γ} (barn)
	672.894(3)		0.179(4)
	1,978.46(3)		0.163(5)
	1,802.269(10)		0.146(4)
	5,612.62(11)		0.14(3)
Au	411.8	233,000	94.27(14)
	214.971(10)		7.77(8)
	247.573(10)		5.48(6)
	261.404(10)		4.3(3)
	236.045(10)		3.49(13)
	192.392(10)		3.5(3)
	168.334(10)		3.53(4)
	381.199(10)		4.22(6)
	55.181(10)		2.90(12)
	97.250(20)		4.51(6)
	529.165(20)		2.80(17)
Hg	367.947(9)		251(5)
	5,967.02(4)		62.5(15)
	1,693.296(11)		56.2(16)
	4,739.43(5)		30.1(8)
	1,570.273(12)		29.6(7)
	5,658.24(4)		27.5(7)
	2,002.083(13)		24.3(9)
	6,457.98(4)		23.1(8)
	661.403(11)		22.3(5)
	1,262.941(11)		21.5(5)
	4,842.07(6)		20.0(6)
	5,050.07(5)		20.0(6)
Tl	139.94(9)		0.400(7)
	347.96(8)		0.361(10)
	318.88(8)		0.325(6)
	5,641.57(12)		0.316(7)
	5,603.28(13)		0.282(10)
	5,279.86(12)		0.207(6)
	873.16(8)		0.168(4)
	6,166.61(14)		0.166(6)
	4,913.57(11)		0.164(5)
	4,752.24(11)		0.148(5)
	5,404.41(12)		0.147(5)
	5,180.38(12)		0.141(5)

Table 36.3 (Continued)

El	Energy (keV)	Half-life (s)	σ_{γ} (barn)
Pb	7,367.78(7)		0.137(3)
	6,737.62(10)		0.00691(19)
	6,729.38(9)		0.0032(10)
	569.7	0.806	0.00696(19)
Bi	4,171.05(9)		0.0099(13)
	4,054.57(6)		0.0080(11)
	319.78(4)		0.0067(8)
	4,101.76(6)		0.0052(7)
	162.19(11)		0.00094(12)
	673.97(5)		0.00152(23)
	4,256.65(5)		0.00139(19)
	2,505.35(7)		0.00119(16)
	2,828.29(7)		0.00104(14)
	4,165.36(5)		0.00100(14)
	3,396.16(7)		0.00099(14)
	3,356.60(8)		0.00097(14)
Th	583.27(9)		0.279(11)
	566.63(10)		0.19(5)
	472.3(10)		0.165(8)
	968.78(9)		0.132(6)
	578.02(9)		0.105(5)
	522.73(10)		0.102(5)
	256.25(11)		0.093(17)
	77.09(15)		0.09(3)
	335.92(10)		0.089(4)
	665.11(10)		0.084(4)
	86.48(6)	1,338	0.20(3)
	94.68(5)	1,338	0.059(10)
U	4,060.35(5)		0.186(3)
	6,395.16(15)		0.0032(4)

No half-life is given for prompt gamma lines.

36.3 Fast Neutron Reaction Data

J. Csikai · R. Dóczi

The status of available *neutron reaction data* is published regularly in the CINDA (Computer Index of Neutron Data) series. CINDA (see, e.g., CINDA 2003) contains bibliographical references to measurements, calculations, reviews, and evaluations of neutron cross sections and other microscopic nuclear data. It also includes index references to computer libraries of

numerical neutron data available from regional nuclear data centers, such as the International Atomic Energy Agency's Nuclear Data Section (IAEA 2003), the OECD Nuclear Energy Agency's Data Bank (NEA 2003), the US National Nuclear Data Center (NNDC 2003), and the Russian Nuclear Data Center (RNDC 2003). Though the CINDA bibliography allows the users to find the references to specific types of cross-section information on *neutron-induced reactions*, recommended numerical data are indispensable in real applications.

The major fields of application of neutron data, in addition to nuclear theory, are as follows (Csikai 1987): fission reactor technology, fast-reactor design and control calculations, shielding calculations, radiation damage, neutron flux/fluence monitoring, fusion reactor technology, safeguards, neutron therapy, medical physics, activation analysis, prompt radiation analysis, radionuclide production, transmutation of radioactive waste, radiobiology, nuclear geophysics, earth sciences, dosimetry, space sciences, and nuclear astrophysics. Hundreds of requests exist for data at neutron energies up to 20 MeV, with an emphasis on 14 MeV neutrons produced in the $^3\text{H}(\text{d},\text{n})^4\text{He}$ (D-T) reaction. In some cases, however, to avoid the disturbing effects of interfering reactions and gamma-lines the use of $^2\text{H}(\text{d},\text{n})^3\text{He}$ (D-D) reaction is preferred. The IAEA has established a coordinated research project with the objective of providing a library of neutron-activation cross sections for the reactions relevant to a wide range of applications (IAEA 2002).

36.3.1 Status of 14 MeV and 3 MeV Neutron Cross Sections

Low voltage (100–200 kV) neutron generators are widely used for the production of neutrons by the **D-D** ($Q = 3.26$ MeV) and **D-T** ($Q = 17.588$ MeV) reactions. There are about 600 radioisotopes producible by the 14 MeV D-T neutrons on the 290 stable isotopes of the elements via different reactions. The number of nuclei producible by the 3 MeV D-D neutrons via (n,γ) reactions is about 170. Considering the high neutron yield and energy for the D-T reaction as compared to the D-D reaction, the different applications are based almost exclusively on 14 MeV neutrons. In this case, the use of (n,p) , (n,α) , and $(\text{n},2\text{n})$ reactions are recommended. Therefore, the evaluated experimental data are summarized only for these reactions in [Tables 36.4–36.6](#).

Table 36.4

Some recommended (n,p) cross sections at $14.7 \text{ MeV} \pm 0.2 \text{ MeV}$ neutron energy

Target	Z	A	$\sigma \pm \Delta\sigma$ (mb)
B	5	11	4.2 ± 0.2
N	7	14	45.2 ± 6
O	8	18	2.3 ± 0.5
F	9	19	18.6 ± 0.88
Na	11	23	47.0 ± 2
Mg	12	24	183.6 ± 9
		25	88.04 ± 13
		26	39 ± 11
Al	13	27	70 ± 2

Table 36.4 (Continued)

Target	Z	A	$\sigma \pm \Delta\sigma$ (mb)
Si	14	28	261 ± 11
		29	135.33 ± 15
		30	70.04 ± 20
P	15	31	91.85 ± 3.48
S	16	32	237 ± 25
		33	134 ± 22
		34	88 ± 19
Cl	17	35	110 ± 10
		37	25.4 ± 3
K	19	39	314 ± 14
		41	49.8 ± 2.0
Ca	20	40	470.01 ± 50
		42	178.25 ± 12
		43	99.83 ± 13
		44	43.27 ± 6
Sc	21	45	57 ± 8
Ti	22	46	251 ± 13
		47	136 ± 9
		48	57.2 ± 2.7
		50	11.9 ± 6
V	23	51	33.3 ± 1.7
Cr	24	50	294 ± 30
		52	80 ± 4
		53	42 ± 2.1
		54	17.4 ± 1
Mn	25	55	45 ± 10
Fe	26	54	298 ± 22
		56	103.9 ± 2.1
		57	55 ± 4
Co	27	59	47.2 ± 1.6
Ni	28	58	366 ± 19
		60	148 ± 8
		61	64 ± 4
		62	37 ± 4
Cu	29	63	70 ± 13
		65	20.93 ± 4
Zn	30	64	185 ± 10
		66	73.3 ± 8
		67	37.9 ± 6
		68	15.2 ± 2.5

■ Table 36.4 (Continued)

Target	Z	A	$\sigma \pm \Delta\sigma$ (mb)
Ga	31	69	64 ± 5
		71	20.5 ± 1.5
Ge	32	70	74 ± 8
		72	31.6 ± 1.4
		73	19.4 ± 1.1
		74	11.8 ± 0.6
		76	3.7 ± 0.6
As	33	75	18.7 ± 2.1
Se	34	74	134 ± 20
		76	53.7 ± 4.0
		78	20.4 ± 2.2
Br	35	81	21 ± 5
Kr	36	80	45 ± 6
		82	23 ± 5
		84	11 ± 2
		86	5 ± 1.5
Sr	38	84	95 ± 8
		86	44 ± 4
		88	17.4 ± 2
Y	39	89	22.2 ± 4.2
Zr	40	90	37 ± 5
		91	29 ± 4
		92	20.23 ± 2.5
		94	7.5 ± 1.1
Mo	42	95	41.0 ± 3
		96	22.7 ± 1.0
		97	14.6 ± 0.8
Ru	44	96	146 ± 8
		101	21.2 ± 1.2
		104	6 ± 0.7
Rh	45	103	22 ± 0.8
Pd	46	102	93.6 ± 15
		104	58 ± 15
		105	38 ± 2.9
		106	22.5 ± 6
		108	4 ± 1

Table 36.4 (Continued)

Target	Z	A	$\sigma \pm \Delta\sigma$ (mb)
Cd	48	106	130 \pm 24
		111	26.6 \pm 1.9
		112	16.7 \pm 1.7
		113	13 \pm 3
		114	8.5 \pm 1.3
		116	2.96 \pm 0.3
In	49	115	13.26 \pm 2.95
Sn	50	116	14.6 \pm 2
		117	11.7 \pm 0.6
		119	7.1 \pm 0.8
		120	4.5 \pm 0.5
Te	52	122	15.48 \pm 0.98
		126	4.7 \pm 0.2
		128	2.9 \pm 0.1
		130	1.7 \pm 0.1
I	53	127	11.7 \pm 2
Xe	54	128	27 \pm 4
		131	6.1 \pm 0.6
Cs	55	133	10.5 \pm 2
Ba	56	132	15.3 \pm 3.5
		136	4.8 \pm 0.7
		138	2.74 \pm 0.14
La	57	139	4.2 \pm 0.3
Ce	58	140	7.5 \pm 0.4
		142	4.8 \pm 0.8
Pr	59	141	11.5 \pm 0.9
Sm	62	144	19 \pm 4
		148	9.8 \pm 0.8
		150	7 \pm 0.6
Eu	63	153	4.2 \pm 0.4
Gd	64	157	5.4 \pm 1.1
		158	3.2 \pm 1.2
Tb	65	159	5.1 \pm 0.4
Dy	66	158	10.6 \pm 1.2
		160,162	7 \pm 1.5
		164	4.4 \pm 0.4
			2.1 \pm 1.0

■ Table 36.4 (Continued)

Target	Z	A	$\sigma \pm \Delta\sigma$ (mb)
Er	68	166	4.5 ± 0.7
		167	2.8 ± 0.6
		168	4.2 ± 0.8
Yb	70	174	3 ± 0.2
Lu	71	175	4 ± 0.7
Hf	72	180	2.5 ± 0.5
Ta	73	181	3.83 ± 0.4
W	74	182	6.5 ± 0.5
		184	2.96 ± 0.14
		186	1.75 ± 0.22
Re	75	187	3.73 ± 0.28
Os	76	184	9.30 ± 2
		188	4 ± 0.8
		190	2.2 ± 0.5
		192	1 ± 0.03
Au	79	179	2 ± 0.5
Hg	80	196	9.3 ± 1
		198	4.5 ± 0.8
		199	2.5 ± 0.5
Tl	81	203	4.2 ± 0.8
		205	1.9 ± 0.2
Bi	83	209	0.8 ± 0.3

■ Table 36.5

Some recommended (n, α) cross sections at $14.7 \text{ MeV} \pm 0.1 \text{ MeV}$ neutron energy

Target	Z	A	$\sigma \pm \Delta\sigma$ (mb)
Li	3	6	32 ± 3
		7	<2
Be	4	9	11 ± 1.5
B	5	11	31 ± 4
C	6	13	0.241 ± 0.022
N	7	14	55 ± 10
		15	18
O	8	16	98.8 ± 6.4
		17	35.4 ± 6.5
		18	7.6 ± 1.7
F	9	19	25 ± 2
Na	11	23	96 ± 0.9

Table 36.5 (Continued)

Target	Z	A	$\sigma \pm \Delta\sigma$ (mb)
Mg	12	26	56 ± 4
Al	13	27	113 ± 1.5
Si	14	30	69.7 ± 3.9
P	15	31	116 ± 4.7
S	16	34	63 ± 8
Cl	17	35	114 ± 15
		37	67 ± 8
Ar	18	40	11.3 ± 3
K	19	39	159 ± 10
		41	30.4 ± 1.9
Ca	20	40	126 ± 6
		44	28 ± 1.3
		48	1.5 ± 0.4
Sc	21	45	53.7 ± 2.6
Ti	22	46	94 ± 18
		48	31 ± 2
		50	8.6 ± 0.6
V	23	50	40.0 ± 1.6
		51	18.5 ± 0.7
Cr	24	50	93 ± 10
		52	38 ± 4
		54	13.4 ± 1.2
Mn	25	55	23.5 ± 0.9
Fe	26	54	86 ± 5
		56	45.4 ± 1.7
		58	21 ± 2.3
Co	27	59	32.09 ± 0.83
Ni	28	58	105 ± 7
		62	20.1 ± 1.5
		64	5.5 ± 0.8
Cu	29	63	43.2 ± 1.5
		65	11.3 ± 1.5
Zn	30	67	14.8
		68	9.6 ± 0.7
		70	4.0 ± 1.0
Ga	31	69	21.7 ± 1.6
		71	6.5 ± 1.0
Ge	32	72	12.64 ± 0.9
		74	6.1 ± 0.7
		76	2.6 ± 0.3

■ Table 36.5 (Continued)

Target	Z	A	$\sigma \pm \Delta\sigma$ (mb)
As	33	75	11.22 ± 0.66
Se	34	77	11.8 ± 2
		78	10.0 ± 2.0
		80	3.05 ± 0.19
Br	35	79	12.7 ± 1.5
		81	5 ± 2
Rb	37	85	6.43 ± 0.46
		87	4 ± 1
Y	39	89	7.5 ± 1.7
Zr	40	90	15.4 ± 1.6
		92	8.9 ± 1.0
		94	5.3 ± 0.36
		96	2.6 ± 0.5
Nb	41	93	9.0 ± 0.5
Mo	42	92	25.7 ± 1.0
		96	10.6 ± 0.9
		98	6.33 ± 0.31
		100	3.2 ± 0.2
Tc	43	99	6.37 ± 0.30
Ru	44	96	38 ± 4
		102	6.2 ± 0.7
		104	2.6 ± 1.0
Rh	45	103	11.2 ± 1.5
Pd	46	104	9.0 ± 1.0
		106	5.4 ± 0.5
		108	3.25 ± 0.31
Cd	48	112	3.8 ± 1.0
		114	3.8 ± 1.0
		116	0.8 ± 0.13
			0.5
In	49	113	4.7 ± 0.5
		115	2.58 ± 0.2
Sn	50	118	1.3 ± 0.16
		120	0.54 ± 0.12
		122	0.25 ± 0.05
I	53	127	1.4 ± 0.2
Cs	55	133	1.6 ± 0.25
Ba	56	138	2.55 ± 0.17
La	57	139	2.37 ± 0.24

Table 36.5 (Continued)

Target	Z	A	$\sigma \pm \Delta\sigma$ (mb)
Ce	58	136	5.3
		138	4.1 ± 0.5
		140	3.1 ± 0.4
		142	2.3 ± 0.6
Nd	60	142	5.5 ± 0.4
		144	2.2 ± 0.4
		146	3.5 ± 0.3
		148	2.3 ± 0.5
Sm	62	144	14.3 ± 1.1
		150	3.0 ± 0.2
		152	1.7 ± 0.7
		154	0.9 ± 0.1
Eu	63	151	3.5 ± 0.5
		153	1.66 ± 0.19
Yb	70	174	1.23 ± 0.12
Hf	72	178	2.0 ± 0.2
		180	0.90 ± 0.53
Ta	73	181	0.95 ± 0.15
W	74	182	1.25 ± 0.1
		184	0.85 ± 0.09
		186	0.54 ± 0.05
Re	75	185	0.87 ± 0.09
		187	0.56 ± 0.1
Os	76	190	0.82 ± 0.06
Tl	81	203	1.1
		205	0.6 ± 0.1
Pb	82	204	0.88 ± 0.06
		206	0.65 ± 0.05
		207	0.46 ± 0.05
		208	0.35 ± 0.04

Table 36.6

Some recommended (n,2n) cross sections at 14.5 MeV \pm 0.2 MeV neutron energy

Target	Z	A	$\sigma \pm \Delta\sigma$ (mb)
Ca	20	48	767 ± 5
Cr	24	52	315 ± 30
Fe	26	56	540 ± 40
Cu	29	63	464.20

■ Table 36.6 (Continued)

Target	Z	A	$\sigma \pm \Delta\sigma$ (mb)
Zn	30	70	$1,200 \pm 120$
Ge	32	70	605 ± 40
		72	970 ± 75
		76	$1,148 \pm 120$
Se	34	74	320 ± 30
		76	879 ± 70
		78	993 ± 50
		80	$1,132 \pm 60$
		82	$1,050 \pm 50$
Kr	36	80	810 ± 60
Sr	38	84	$1,054 \pm 50$
		86	$1,000 \pm 100$
Zr	40	90	730 ± 35
		96	$1,500 \pm 90$
Mo	42	100	$1,420 \pm 150$
Ru	44	96	700 ± 100
		98	$1,050 \pm 100$
		104	$1,440 \pm 109$
Pd	46	102	$1,100 \pm 100$
		110	$1,850 \pm 120$
Cd	48	106	$1,350 \pm 200$
		108	$1,290 \pm 150$
		110	$1,220 \pm 150$
		116	$1,578 \pm 100$
Sn	50	114	$1,105 \pm 50$
Te	52	120	$1,300 \pm 130$
		128	$1,690 \pm 130$
		130	$1,700 \pm 120$
Xe	54	124	$1,200 \pm 100$
		126	$1,400 \pm 100$
		128	$1,550 \pm 150$
		134	$1,700 \pm 170$
Ce	58	136	$1,600 \pm 140$
		140	$1,630 \pm 90$
		142	$1,760 \pm 80$
Pr	59	141	$1,450 \pm 70$
Nd	60	142	$1,680 \pm 110$
		144	$1,750 \pm 120$
		146	$1,861 \pm 150$

Table 36.6 (Continued)

Target	Z	A	$\sigma \pm \Delta\sigma$ (mb)
Sm	62	148	$1,829 \pm 150$
		150	$1,520 \pm 100$
		144	$1,700 \pm 120$
		148	$1,789 \pm 150$
		150	$1,803 \pm 150$
		152	$1,855 \pm 150$
Gd	64	154	$1,885 \pm 150$
		152	$1,800 \pm 200$
		154	$2,110 \pm 180$
		156	$1,800 \pm 100$
		158	$1,850 \pm 100$
Dy	66	160	$2,100 \pm 500$
		156	$1,850 \pm 150$
		160	$2,000 \pm 200$
		162	$1,900 \pm 130$
Er	68	164	$1,820 \pm 150$
		166	$2,000 \pm 150$
		170	$1,930 \pm 130$
		168	$1,920 \pm 150$
Yb	70	170	$1,940 \pm 150$
		176	$2,150 \pm 230$
		174	$1,900 \pm 150$
Hf	72	176	$2,050 \pm 150$
		180	$1,900 \pm 170$
W	74	184	$2,000 \pm 150$
		186	$1,900 \pm 150$
		184	$2,000 \pm 150$
Os	75	186	$2,000 \pm 150$
		192	$2,200 \pm 150$
		192	$2,030 \pm 100$
Pt	78	198	$1,950 \pm 120$
		196	$2,050 \pm 180$
Hg	80	198	$2,000 \pm 150$
		204	$2,100 \pm 150$
Pb	82	206	$2,232 \pm 130$
		208	$2,000 \pm 100$
		232	$1,259 \pm 50$
Th	90	238	745 ± 30
U	92		

Data available in different activation files were completed with the measurements of Dóczi et al. (1997), Majdeddin et al. (1997), Filatenkov and Chuvaev (1999), Osman and Habbani (2000), Filatenkov and Chuvaev (2001), and Kasugai et al. (2001). The cross section curves change at around 14 MeV; therefore, the data are normalized to 14.7 MeV on the basis of the slopes. Different systematics were established for the estimation of the unknown data and to deduce the *production rate* of long-lived and stable isotopes. Comprehensive reviews of the systematics of (n,p), (n, α), and (n,2n) *reaction cross sections* are given in Dóczi et al. (1997), Majdeddin et al. (1997), and Osman and Habbani (2000).

36.3.2 Recommended Dosimetry Reactions

The knowledge of the flux density spectra, $\Phi(E)$ of neutrons at a given point of a sample or averaged over a large volume is indispensable for various applications of neutrons. The multiple-foil activation method renders possible the determination of the $\Phi(E)$ function with high accuracy especially below the 1–2 MeV region as compared to the time-of-flight (TOF) technique. Further advantage of the activation foil method is that the disturbance of the neutron field can be neglected. In general, about 12 reactions indicated in ► Table 36.7 are used for the unfolding of a given $\Phi(E)$ function with cross sections taken from the International Reactor Dosimetry File (IRDF). A new version of IRDF-90 contains cross sections for 53 *dosimetry reactions*, together with uncertainty information (Zsolnay 1998). The unfolding procedure

► Table 36.7

List of reactions used for the unfolding of a given $\Phi(E)$ function

Reaction	Response energy range (MeV)	Half-life	E_γ (keV)	I_γ (%)
$^{56}\text{Fe}(n,p)^{56}\text{Mn}$	5.4–13.6	2.5785 h	846.812	98.9
$^{115}\text{In}(n,g)^{116\text{m}2+\text{m}1}\text{In}$	0–3.6	54.15 min	416.92	29.2
			1,097.29	56.2
			1,293.59	84.4
$^{115}\text{In}(n,n')^{115\text{m}}\text{In}$	1.5–14.5	4.486 h	336.258	45.8
$^{27}\text{Al}(n,\alpha)^{24}\text{Na}$	7.0–13.4	14.659 h	1,368.598	100
$^{58}\text{Ni}(n,2n)^{57}\text{Ni}$	12.5–15.5	1.503 days	1,377.62	77.9
$^{48}\text{Ti}(n,p)^{48}\text{Sc}$	6.0–15.0	1.821 days	983.501	100.0
			1,037.4961	97.5
			1,312.046	100.0
$^{90}\text{Zr}(n,2n)^{89\text{g}}\text{Zr}$	12.5–15.5	3.268 days	909.15	99.01
$^{47}\text{Ti}(n,p)^{47}\text{Sc}$	2.7–13.2	3.341 days	159.381	68
$^{197}\text{Au}(n,2n)^{196\text{g}}\text{Au}$	9.4–14.4	6.183 days	355.58	87
$^{93}\text{Nb}(n,2n)^{92\text{m}}\text{Nb}$	10.1–14.0	10.15 days	934.53	99.0
$^{58}\text{Ni}(n,p)^{58\text{m}+\text{g}}\text{Co}$	3.3–13.8	70.916 days	810.791	99.5
$^{46}\text{Ti}(n,p)^{46\text{g}}\text{Sc}$	3.1–13.1	83.83 days	889.25	99.984
			1,120.51	99.987

based on the multiple-foil activation method has been described, for example, in Sudár (1989), Zsolnay (1998).

It is well known that the following variables can strongly influence the neutron energy distributions from a given reaction: the types of target atoms, the ratio of atomic to molecular ions, the energy spread of ions, the slowing down, and scattering of projectiles in the target. For absolute normalization of the energy scale mainly the D-T neutrons are recommended accepting a value of (14.00 ± 0.07) MeV at $96\text{--}98^\circ$ emission angles. The measurements of relative activities of ^{89}Zr and $^{92\text{m}}\text{Nb}$ produced in $^{90}\text{Zr}(n,2n)$ and $^{93}\text{Nb}(n,2n)$ reactions, respectively, render the determination of neutron energy with high precision at around 14 MeV possible. A value of (460 ± 5) mb is recommended for the cross section of $^{93}\text{Nb}(n,2n)^{92}\text{Nb}$ *fluence monitor* in the 13.5–15 MeV range. The $^{27}\text{Al}(n,\alpha)$ reaction is also a good *fluence monitor* in the 13.8–14.2 MeV range of D-T neutrons. The $\sigma(E_n)$ curves for $^{90}\text{Zr}(n,2n)^{89}\text{Zr}$ and $^{52}\text{Cr}(n,2n)^{51}\text{Cr}$ energy standards are approximated by the following polynomials:

$$\sigma(E_n)/\text{mb} = -13244.5 + 1668.16(E_n/\text{MeV}) - 48.543(E_n/\text{MeV})^2$$

and

$$\sigma(E_n)/\text{mb} = -2210.0 + 176.32(E_n/\text{MeV}),$$

respectively.

The sensitivity of this activation ratio method between 13 MeV and 15 MeV, on average, is 50%/MeV and 64%/MeV for Zr and Cr, respectively. This method is also applied to determine the mean neutron energy for an extended sample. In this case, the Zr and Nb foils are placed back-to-back in different positions inside the sample. The angular yield of D-D neutrons can be measured either by the $^{238}\text{U}(n,f)$ using a depleted U layer in a fission chamber or by the $^{115}\text{In}(n,n')^{115\text{m}}\text{In}$ reaction. The $\sigma_{n,f}(E_n)$ curve is relatively well known and its change between 2 MeV and 3 MeV is within 2%. For the $^{115}\text{In}(n,n')^{115\text{m}}\text{In}$ reaction the high cross section value of $\sigma = (325 \pm 5)$ mb in this energy range is advantageous; however, this inelastic process is sensitive to the scattered neutrons.

The $^{64}\text{Zn}(n,p)^{64}\text{Cu}$, $^{58}\text{Ni}(n,p)^{58}\text{Co}$, and the $^{31}\text{P}(n,p)^{31}\text{Si}$ reactions are recommended as *energy monitors* for D-D neutrons in the 2–3 MeV range. The product of the latter reaction is a pure beta-emitter. For the D-D reaction, the neutron energy at $\sim 100^\circ$ emission angle is almost constant in the $50 \text{ keV} \leq E_d \leq 500 \text{ keV}$ range. In this case a value of $E_n = (2.414 \pm 0.010)$ MeV can be used for normalization of the energy scale using 100–200 keV incident deuteron energies. The angular dependences of neutron energies and cross sections for monoenergetic neutrons produced by two-body nuclear reactions can be found in Drosch and Schwerer 1987. These data for D-D and D-T neutrons are discussed also in detail in Csikai 1987.

36.3.3 Recommended Reactions and γ Rays for Activation Analysis

In general, the relative method using standards of well-known compositions is preferred in *neutron activation analysis* (NAA). However, the knowledge of decay data and cross sections is indispensable when absolute measurements are performed, and also for choosing the most favorable reaction or estimating the *expected activity* and the role of *interfering reactions*. The *recommended reactions* for NAA with small neutron generators summarized in [Table 36.8](#)

Table 36.8

Recommended reactions for neutron activation analysis (NAA) with small neutron generators; note that (n,γ) relates to thermal energy; other reactions to $E_n = 14.5$ MeV. X stands for X-rays, -annih. for 511 keV annihilation radiation

El.	Reaction	Half-life	E_γ (keV)	R (Bq/g) ($t_i = 1$ h)	Interfering reactions
B	$^{11}\text{B}(\text{n,p})^{11}\text{Be}$	13.81 s	2,124.8	1.47×10^5	–
N	$^{14}\text{N}(\text{n},2\text{n})^{13}\text{N}$	9.963 min	511	2.99×10^5	–
O	$^{16}\text{O}(\text{n,p})^{16}\text{N}$	7.13 s	2,741.2 6,129.2	1.31×10^6	$^{15}\text{N}(\text{n},\gamma); ^{19}\text{F}(\text{n},\alpha); ^{17}\text{O}(\text{n},\text{d})$
F	$^{19}\text{F}(\text{n,p})^{19}\text{O}$	26.76 s	197.1 1,356.8	6.02×10^5	$^{18}\text{O}(\text{n},\gamma)$
Ne	$^{20}\text{Ne}(\text{n,p})^{20}\text{F}$	10.996 s	1,633.7	2.48×10^6	$^{19}\text{F}(\text{n},\gamma); ^{23}\text{Na}(\text{n},\alpha); ^{21}\text{Ne}(\text{n},\text{d})$
Na	$^{23}\text{Na}(\text{n},\alpha)^{20}\text{F}$	10.996 s	1,633.7	3.93×10^6	$^{19}\text{F}(\text{n},\gamma); ^{20}\text{Ne}(\text{n,p}); ^{21}\text{Ne}(\text{n},\text{d})$
Mg	$^{24}\text{Mg}(\text{n,p})^{24}\text{Na}$	14.959 h	1,368.5 2,754.9	1.60×10^5	$^{23}\text{Na}(\text{n},\gamma); ^{27}\text{Al}(\text{n},\alpha); ^{25}\text{Mg}(\text{n},\text{d})$
Al	$^{27}\text{Al}(\text{n,p})^{27}\text{Mg}$	9.462 min	843.7 1,014.43	1.61×10^6	$^{26}\text{Mg}(\text{n},\gamma); ^{30}\text{Si}(\text{n},\alpha)$
Si	$^{28}\text{Si}(\text{n,p})^{28}\text{Al}$	2.2405 min	1,779.0	4.47×10^6	$^{27}\text{Al}(\text{n},\gamma); ^{31}\text{P}(\text{n},\alpha); ^{29}\text{Si}(\text{n},\text{d})$
P	$^{31}\text{P}(\text{n},\alpha)^{28}\text{Al}$	2.2405 min	1,779.0	2.29×10^6	$^{27}\text{Al}(\text{n},\gamma); ^{28}\text{Si}(\text{n,p}); ^{29}\text{Si}(\text{n},\text{d})$
S	$^{34}\text{S}(\text{n},\alpha)^{31}\text{Si}$	2.62 h	1,266.1	2.54×10^4	$^{30}\text{Si}(\text{n},\gamma); ^{31}\text{P}(\text{n,p})$
Cl	$^{37}\text{Cl}(\text{n,p})^{37}\text{S}$	4.99 min	3,103.3	1.15×10^5	$^{36}\text{S}(\text{n},\gamma); ^{40}\text{Ar}(\text{n},\alpha)$
Ar	$^{40}\text{Ar}(\text{n,p})^{40}\text{Cl}$	1.32 min	1,460.8 2,840.2	2.40×10^5	–
K	$^{41}\text{K}(\text{n},\alpha)^{38}\text{Cl}$	37.24 min	1,642.4 2,167.6	2.72×10^4	$^{37}\text{Cl}(\text{n},\gamma); ^{38}\text{Ar}(\text{n,p})$
Ca	$^{44}\text{Ca}(\text{n,p})^{44}\text{K}$	22.15 min	1,157.0 2,150.8	1.22×10^4	–
Sc	$^{45}\text{Sc}(\text{n},2\text{n})^{44}\text{Sc}$	3.927 h	1,157.0	4.08×10^5	–
Ti	$^{48}\text{Ti}(\text{n,p})^{48}\text{Sc}$	43.67 h	983.5 1,312.1	9.63×10^3	$^{51}\text{V}(\text{n},\alpha); ^{49}\text{Ti}(\text{n},\text{d})$
V	$^{51}\text{V}(\text{n,p})^{51}\text{Ti}$	5.752 min	320.1	3.89×10^5	$^{50}\text{Ti}(\text{n},\gamma); ^{54}\text{Cr}(\text{n},\alpha)$
Cr	$^{52}\text{Cr}(\text{n,p})^{52}\text{V}$	3.760 min	1,434.1	7.76×10^5	$^{51}\text{V}(\text{n},\gamma); ^{55}\text{Mn}(\text{n},\alpha); ^{53}\text{Cr}(\text{n},\text{d})$
Mn	$^{55}\text{Mn}(\text{n},\gamma)^{56}\text{Mn}$	2.5785 h	846.8 1,810.7	3.44×10^7	$^{56}\text{Fe}(\text{n,p}); ^{59}\text{Co}(\text{n},\alpha); ^{57}\text{Fe}(\text{n},\text{d})$
Fe	$^{56}\text{Fe}(\text{n,p})^{56}\text{Mn}$	2.5785 h	846.8 1,810.7	2.57×10^5	$^{55}\text{Mn}(\text{n},\gamma); ^{59}\text{Co}(\text{n},\alpha); ^{57}\text{Fe}(\text{n},\text{d})$
Co	$^{59}\text{Co}(\text{n},\gamma)^{60}\text{Co}$	10.47 min	58.6	1.91×10^8	$^{60}\text{Ni}(\text{n,p}); ^{63}\text{Cu}(\text{n},\alpha); ^{61}\text{Ni}(\text{n},\text{d})$
Ni	$^{60}\text{Ni}(\text{n,p})^{60}\text{Co}$	10.47 min	58.6	2.50×10^5	$^{59}\text{Co}(\text{n},\gamma); ^{63}\text{Cu}(\text{n},\alpha); ^{61}\text{Ni}(\text{n},\text{d})$
Cu	$^{63}\text{Cu}(\text{n},2\text{n})^{62}\text{Cu}$	9.74 min	511	3.56×10^6	–
Zn	$^{64}\text{Zn}(\text{n},2\text{n})^{63}\text{Zn}$	38.1 min	669.6	5.21×10^5	–
Ga	$^{69}\text{Ga}(\text{n},2\text{n})^{68}\text{Ga}$	68.1 min	1,077.4	2.25×10^6	–

Table 36.8 (Continued)

El.	Reaction	Half-life	E_{γ} (keV)	R (Bq/g) ($t_i = 1$ h)	Interfering reactions
Ge	$^{76}\text{Ge}(n,2n)^{75}\text{Ge}$	82.80 min	264.6	2.91×10^5	$^{74}\text{Ge}(n,\gamma); ^{75}\text{As}(n,p); ^{78}\text{Se}(n,\alpha)$
As	$^{75}\text{As}(n,p)^{75}\text{Ge}$	82.80 min	264.6	6.09×10^4	$^{74}\text{Ge}(n,\gamma); ^{76}\text{Ge}(n,2n); ^{78}\text{Se}(n,\alpha)$
Se	$^{82}\text{Se}(n,2n)^{81}\text{Se}$	57.28 min	103.1	3.57×10^5	$^{80}\text{Se}(n,\gamma); ^{81}\text{Br}(n,p); ^{84}\text{Kr}(n,\alpha)$
Br	$^{79}\text{Br}(n,2n)^{78}\text{Br}$	6.46 min	613.7	3.72×10^6	$^{78}\text{Kr}(n,p)$
Kr	$^{86}\text{Kr}(n,2n)^{85}\text{Kr}$	4.480 h	151.2	6.24×10^4	$^{84}\text{Kr}(n,\gamma); ^{85}\text{Rb}(n,p); ^{88}\text{Sr}(n,\alpha)$
Rb	$^{85}\text{Rb}(n,2n)^{84}\text{Rb}$	20.5 min	215.6	2.17×10^6	$^{84}\text{Sr}(n,p)$
			248.0		
			463.6		
Sr	$^{86}\text{Sr}(n,2n)^{85}\text{Sr}$	67.66 min	231.9	7.64×10^4	$^{84}\text{Sr}(n,\gamma)$
Y	$^{89}\text{Y}(n,n')^{89\text{m}}\text{Y}$	16.06 s	909.2	2.97×10^6	$^{90}\text{Zr}(n,d)$
Zr	$^{90}\text{Zr}(n,2n)^{89}\text{Zr}$	4.180 min	587.8	2.92×10^5	$^{92}\text{Mo}(n,\alpha)$
Nb	^{93}Nb $(n,2n)^{92}\text{Nb}$	10.150 days	934.5	8.88×10^3	$^{92}\text{Mo}(n,p)$
Mo	^{100}Mo $(n,2n)^{99}\text{Mo}$	66.02 h	181.1	8.94×10^3	$^{98}\text{Mo}(n,\gamma); ^{102}\text{Ru}(n,\alpha)$
			739.4		
Ru	$^{96}\text{Ru}(n,2n)^{95}\text{Ru}$	1.65 h	336.4	7.87×10^4	–
Rh	$^{103}\text{Rh}(n,\gamma)^{104}\text{Rh}$	4.34 min	51.4	6.44×10^7	$^{104}\text{Pd}(n,p); ^{107}\text{Ag}(n,\alpha); ^{105}\text{Pd}(n,d)$
			97.1		
Pd	^{110}Pd $(n,2n)^{109\text{m}}\text{Pd}$	4.69 min	188.9	3.41×10^5	$^{108}\text{Pd}(n,\gamma); ^{109}\text{Ag}(n,p); ^{112}\text{Cd}(n,\alpha)$
Ag	^{109}Ag $(n,2n)^{108}\text{Ag}$	2.37 min	633.0	2.26×10^6	$^{107}\text{Ag}(n,\gamma); ^{108}\text{Cd}(n,p)$
Cd	^{112}Cd $(n,2n)^{111\text{m}}\text{Cd}$	48.6 min	150.8	5.78×10^5	$^{110}\text{Cd}(n,\gamma); ^{114}\text{Sn}(n,\alpha)$
			245.4		
In	$^{115}\text{In}(n,\gamma)^{116}\text{In}$	54.12 min	416.9	9.33×10^8	$^{116}\text{Sn}(n,p); ^{117}\text{Sn}(n,d)$
			1,097.3		
			1,293.5		
Sn	^{124}Sn $(n,2n)^{123}\text{Sn}$	40.08 min	160.3	1.01×10^5	$^{122}\text{Sn}(n,\gamma); ^{123}\text{Sb}(n,p); ^{126}\text{Te}(n,\alpha)$
Sb	^{121}Sb $(n,2n)^{120}\text{Sb}$	15.89 min ^a	1,171.2	2.84×10^6	$^{120}\text{Te}(n,p)$
Te	^{130}Te $(n,2n)^{129}\text{Te}$	69.6 min	459.6	4.18×10^5	$^{128}\text{Te}(n,\gamma); ^{132}\text{Xe}(n,\alpha)$
I	$^{127}\text{I}(n,\gamma)^{128}\text{I}$	24.99 min	442.9	2.35×10^7	$^{128}\text{Xe}(n,p); ^{129}\text{Xe}(n,d)$
Xe	^{136}Xe $(n,2n)^{135}\text{Xe}$	15.6 min	526.6	2.85×10^5	$^{134}\text{Xe}(n,\gamma); ^{138}\text{Ba}(n,\alpha)$
Cs	^{133}Cs $(n,2n)^{132}\text{Cs}$	6.974 days	667.5	3.23×10^4	$^{132}\text{Ba}(n,p)$
Ba	^{138}Ba $(n,2n)^{137}\text{Ba}$	2.5513 min	661.6	3.68×10^6	$^{136}\text{Ba}(n,\gamma); ^{140}\text{Ce}(n,\alpha); ^{138}\text{La}(n,d)$

■ Table 36.8 (Continued)

El.	Reaction	Half-life	E_γ (keV)	R (Bq/g) ($t_i = 1$ h)	Interfering reactions
La	$^{139}\text{La}(n,\gamma)^{140}\text{La}$	40.27 h	328.8	6.80×10^5	$^{140}\text{Ce}(n,p)$
			487.0		
Ce	^{140}Ce (n,2n) ^{139m}Ce	56.44 s	754.2	3.66×10^6	$^{138}\text{Ce}(n,\gamma); ^{142}\text{Nd}(n,\alpha)$
Pr	^{141}Pr (n,2n) ^{140}Pr	3.39 min	511 -annih	7.09×10^6	–
			306.9		
			1,596.5		
Nd	^{150}Nd (n,2n) ^{149}Nd	1.73 h	114.3	1.47×10^5	$^{148}\text{Nd}(n,\gamma); ^{152}\text{Sn}(n,\alpha)$
			211.3		
Sm	^{144}Sm (n,2n) ^{143}Sm	66 s	754.0	8.82×10^4	–
Eu	^{153}Eu (n,2n) ^{152}Eu	96 min	89.8	4.81×10^4	$^{151}\text{Eu}(n,\gamma)$
Gd	^{160}Gd (n,2n) ^{159}Gd	18.56 h	363.6	6.00×10^4	$^{158}\text{Gd}(n,\gamma); ^{159}\text{Tb}(n,p); ^{162}\text{Dy}(n,\alpha)$
Tb	^{159}Tb (n,2n) ^{158}Tb	10.5 s	50.3X	1.71×10^6	$^{158}\text{Dy}(n,p)$
			51.7X		
			110.1		
Dy	^{164}Dy (n, γ) ^{165}Dy	1.257 min	108.2	1.87×10^9	$^{165}\text{Ho}(n,p); ^{168}\text{Er}(n,\alpha)$
Ho	^{165}Ho (n,2n) ^{164}Ho	37.3 min	56.6	2.94×10^6	$^{164}\text{Er}(n,p)$
			99.0		
Er	$^{164}\text{Er}(n,2n)^{163}\text{Er}$	75.1 min	53.8X	4.35×10^4	$^{162}\text{Er}(n,\gamma)$
			436.1		
Tm	^{169}Tm (n,2n) ^{168}Tm	93.1 days	1,113.5	2.29×10^3	$^{168}\text{Yb}(n,p)$
			198.2		
			815.9		
Yb	^{176}Yb (n,2n) ^{175}Yb	4.19 days	282.5	6.63×10^3	$^{176}\text{Lu}(n,p); ^{178}\text{Hf}(n,\alpha)$
			396.3		
Lu	$^{175}\text{Lu}(n,\gamma)^{176}\text{Lu}$	3.684 h	88.3	2.01×10^7	$^{176}\text{Hf}(n,p); ^{177}\text{Hf}(n,d)$
Hf	^{174}Hf (n,2n) ^{173m}Hf	24.0 h	123.7	2.90×10^2	–
			297.0		
Ta	^{181}Ta (n,2n) ^{180}Ta	8.11 h	63.2X	3.03×10^5	$^{180}\text{W}(n,p)$
			93.3		
W	^{186}W (n,2n) ^{185m}W	1.67 min	131.5	6.01×10^5	$^{184}\text{W}(n,\gamma); ^{185}\text{Re}(n,p); ^{188}\text{Os}(n,\alpha)$
			173.7		
Re	^{187}Re (n,2n) ^{186}Re	90.64 h	63.0X	2.65×10^4	$^{185}\text{Re}(n,\gamma); ^{186}\text{Os}(n,p); ^{187}\text{Os}(n,d)$
			137.2		

Table 36.8 (Continued)

El.	Reaction	Half-life	E_{γ} (keV)	R (Bq/g) ($t_i = 1$ h)	Interfering reactions
Os	^{192}Os (n,2n) ^{191}Os	13.105 h	63.0X	7.14×10^4	$^{190}\text{Os}(n,\gamma); ^{191}\text{Ir}(n,p); ^{194}\text{Pt}(n,\alpha)$
			71.3X		
			74.4		
Ir	^{191}Ir (n,2n) $^{190\text{m}}\text{Ir}$	3.25 h	186.7D ^b	4.94×10^4	$^{190}\text{Pt}(n,p)$
			361.1D		
			502.6D		
			616.1D		
Pt	^{198}Pt (n,2n) ^{197}Pt	94.4 min	346.5	7.21×10^4	$^{196}\text{Pt}(n,\gamma); ^{197}\text{Au}(n,p); ^{200}\text{Hg}(n,\alpha)$
Au	^{197}Au (n,n' γ) $^{197\text{m}}\text{Au}$	7.86 s	279.0	8.56×10^5	$^{198}\text{Hg}(n,d)$
Hg	^{200}Hg (n,2n) $^{199\text{m}}\text{Hg}$	42.6 min	158.4	3.41×10^5	–
			374.1		
Tl	$^{203}\text{Tl}(n,2n)^{202}\text{Tl}$	12.23 days	439.6	4.23×10^3	–
Pb	^{204}Pb (n,n' γ) $^{204\text{m}}\text{Pb}$	66.9 min	374.7	9.75×10^2	–
			899.2		
			911.7		
Th	^{232}Th (n,2n) ^{231}Th	25.52 h	84.2	8.76×10^4	–
			163.1		
U	$^{238}\text{U}(n,2n)^{237}\text{U}$	6.752 days	101.1X	7.99×10^3	–
			208.0		

^aMust be separated by half-life from 5.8 days; ^{120}Sb with $\sigma = (427 \pm 20)$ mb.
^bGammas from the 9.9 min daughter, ^{190}Os . The intensities are those observed in transient equilibrium.

were selected on the basis of the specific activity. Using ▶ Eq. (32.7) in Chap. 32 of this Volume, the specific activity $R(t_i)$ becomes

$$R(t_i) = \frac{A(t_i)}{m_i} = N_A \frac{\sigma f \Phi}{M_i} (1 - e^{-\lambda t_i}) \tag{36.1}$$

where $A(t_i)$ is the activity at the end of irradiation time t_i , m_i is the mass of the irradiated element, σ is the reaction cross section, N_A is the Avogadro constant, Φ is the neutron flux density, M_i is the molar mass of the element, λ is the decay constant of the activated product, and f is the abundance (in fraction) of the isotope to be activated. The $R(t_i)$ values in ▶ Table 36.8 were calculated for the reactions of maximum yield for each element, assuming $\Phi = 10^9 \text{ cm}^{-2} \text{ s}^{-1}$ neutron flux and $t_i = 1$ h irradiation time. In addition to the 1 h irradiation time the $R(t_i)$ values have been determined for $t_i = 10$ min and $t_i = \infty$ conditions (Bödy and Csikai 1987). An analysis of these data has indicated that the use of (n,p), (n,2n), (n, γ), (n, α), and (n,n' γ) reactions are recommended for the determination of 22, 57, 13, 8, and 7 elements, respectively. In some cases, there are overlaps in the selected reactions and isotopes. When selecting the most suitable reactions for NAA, the possible overlapping gamma lines were considered in addition to the interfering reactions and the half-lives. The number of interfering

■ Table 36.9

Some recommended reactions for bulk-media assay

Element/ abundance (%)	Reaction	E_{γ} (keV)	I_{γ} (gammas per 100 neutrons absorbed)
H/99.9	$^1\text{H}(n,\gamma)^2\text{H}$	2,223	100
C/98.9	$^{12}\text{C}(n,n'\gamma)^{12}\text{C}$	4,439	100
N/99.6	$^{14}\text{N}(n,\gamma)^{15}\text{N}$	5,269	29.7
	$^{14}\text{N}(n,n'\gamma)^{14}\text{N}$	2,310	100
O/99.7	$^{16}\text{O}(n,n'\gamma)^{16}\text{O}$	6,129	100
Si/92.2	$^{28}\text{Si}(n,n'\gamma)^{28}\text{Si}$	1,779	100
S/95	$^{32}\text{S}(n,\gamma)^{33}\text{S}$	2,380	44.5
		3,221	27.1
Cl/75.8	$^{35}\text{Cl}(n,\gamma)^{36}\text{Cl}$	1,951	21.3
		6,111	20.0
		1,165	19.9
		7,414	10.4
Ca/96.9	$^{40}\text{Ca}(n,\gamma)^{41}\text{Ca}$	1,943	52.5
Fe/91.7	$^{56}\text{Fe}(n,\gamma)^{57}\text{Fe}$	7,645	24.1
		7,631	28.5
Ba/11.9	$^{137}\text{Ba}(n,\gamma)^{138}\text{Ba}$	4,096	16.6
Ba/70.4	$^{138}\text{Ba}(n,n'\gamma)^{138}\text{Ba}$	1,436	100
Hg/23.1	$^{200}\text{Hg}(n,\gamma)^{201}\text{Hg}$	368	81.3
		1,694	14.1
Pb/22.1	$^{207}\text{Pb}(n,\gamma)^{208}\text{Pb}$	7,368	94.8
Pb/52.4	$^{208}\text{Pb}(n,n'\gamma)^{208}\text{Pb}$	2,614	100

gamma lines can be significantly decreased if a high-resolution detector, for example, HPGe is used.

For the estimation of the most suitable reactions in the case of complex geological samples, special attention should be paid to the cross sections, the interfering reactions, and gamma rays. These data including the neutron-induced prompt and nuclear decay gamma rays with intensities higher than 5% are summarized in IAEA 1993. Considering the high penetrating ability of fast neutrons and high-energy gamma rays, the neutron-induced reactions listed in ► Table 36.9 are recommended for the observation and identification of concealed objects (illicit drugs, explosives, and landmines).

References

- Bé MM, Chisté V, Dulieu C, Browne E, Chechev V, Kuzmenko N, Helmer R, Nichols A, Schönfeld E, Dersch R (2004) Table of radionuclides. BIPM, Sévres
- Bódy Z, Csikai J (1987) Data for 14 MeV neutron activation analysis. In: Handbook on nuclear activation data. Technical reports series no. 273, International Atomic Energy Agency, Vienna, pp 261–303

- CINDA (2003) The index to literature and computer files on microscopic neutron data. International Atomic Energy Agency, Vienna. <http://www-nds.iaea.org>
- Choi HD, Firestone RB, Lindstrom RM, Molnár GL, Mughabghab SF, Paviotti-Corcuera R, Révay Z, Trkov A, Zerkov V, Chunmei Z (2007) Database of prompt gamma rays from slow neutron capture for elemental analysis. International Atomic Energy Agency, Vienna
- Cohen ER, Taylor BN (1987) Rev Mod Phys 59:1121
- Csikai J (1987) Handbook of fast neutron generators. CRC Press, Boca Raton
- Dóczi R, Semkova V, Majdeddin AD, Buczkó CsM, Csikai J (1997) Investigations on (n,p) cross sections in the 14 MeV region. Report INDC(HUN)-032/L. International Atomic Energy Agency, Vienna
- Drosg M, Schwerer O (1987) Production of monoenergetic neutrons between 0.1 and 23 MeV. In: Handbook on nuclear activation data. Technical reports series no. 273, International Atomic Energy Agency, Vienna, pp 83–162
- ENSDF (2010) Evaluated Nuclear Structure Data File (ENSDF), a computer file of evaluated experimental nuclear structure data maintained by the National Nuclear Data Center. Brookhaven National Laboratory, <http://www.nndc.bnl.gov/ensdf/>
- Filatenkov AA, Chuvaev SV (1999) Preprint
- Filatenkov AA, Chuvaev SV (2001) Preprint
- IAEA (1993) Handbook on nuclear data for borehole logging and mineral analysis. Technical reports series no. 357. International Atomic Energy Agency, Vienna
- IAEA (2002) Reference neutron activation library, IAEA-TECDOC-1285. International Atomic Energy Agency, Vienna
- IAEA (2003) IAEA nuclear data services. International Atomic Energy Agency, Vienna. <http://www-nds.iaea.org>
- Kasugai Y, Ikeda Y, Uno Y, Yamamoto H, Kawade K (2001) Activation cross section measurement at neutron energy from 13.3 to 14.9 MeV using FNS facility, JAERI-Research 2001-025. Atomic Energy Research Institute, Japan
- Majdeddin AD, Semkova V, Dóczi R, Buczkó CsM, Csikai J (1997) Investigations on (n,α) cross sections in the 14 MeV region. Report INDC(HUN)-031/L. International Atomic Energy Agency, Vienna
- Molnár GL (ed) (2004) Handbook of prompt gamma activation analysis. Kluwer Academic, Dordrecht
- Mughabghab SF (1984) Neutron cross sections, vol 1: neutron resonance parameters and thermal cross sections, part B, Z = 61–100. Academic, Orlando
- Mughabghab SF (2003) Thermal neutron capture cross sections, resonance integrals, and g-factors, report INDC(NDS)-440. International Atomic Energy Agency, Vienna
- Mughabghab SF, Divadeenam M, Holden NE (1981) Neutron cross sections, vol 1: neutron resonance parameters and thermal cross sections, part A, Z = 1–60. Academic, New York
- NEA (2003) NEA data bank. OECD Nuclear Energy Agency, Paris. <http://www.nea.fr>
- NNDC (2003) National nuclear data center. Brookhaven National Laboratory, Upton. <http://www.nndc.bnl.gov>
- NuDat (2009) <http://www.nndc.bnl.gov/nudat2/>
- Osman KT, Habbani FI (2000) On the systematics of the (n,2n) reaction cross sections at 14.5 MeV neutrons. Report INDC(SUD)-004/L0. International Atomic Energy Agency, Vienna
- Pyykkö P (2001) Mol Phys 99:1617
- Pyykkö P (2008) Mol Phys 106:1965
- RNDC (2003) Russian nuclear data center. Fiziko-Energeticheskij Institut, Obninsk
- Raghavan P (1989) At Data Nucl Data Tables 42:189
- Rosman KJR, Taylor PDP (1998) Pure Appl Chem 70:1
- Sudár S (1989) A solution for the neutron spectrum unfolding problem without using input spectrum. Report INDC(HUN)-026/L. International Atomic Energy Agency, Vienna
- Trkov A (2003) Private communication
- Zsolnay ÉM (1998) Multiple foil activation neutron spectrometry and some practical applications. PhD thesis, Kossuth Lajos University of Sciences, Debrecen

Radiochemistry and Radiopharmaceutical Chemistry in Life Sciences



37 Introduction to the Fourth Volume

For the first time, a *Handbook of Nuclear Chemistry* systematically and comprehensively acknowledges the various aspects of radiopharmaceutical chemistry. It thus reflects the significant progress that has been made over the last decades leading to the establishment of an independent field of modern science. The development of radiopharmaceutical chemistry was, nevertheless, a century-long route. It is paved by persons, their ideas and scientific results, being of historical dimensions.

It all began with the discovery of the phenomenon of radioactivity (1903 Nobel prize to H. Becquerel, M. and P. Curie for *the discovery of spontaneous radioactivity... and researches on the radiation phenomena...*). Next in that row were I. Curie and F. Joliot (1935 Nobel prize for *... their synthesis of new radioactive elements...*). Their utilization of nuclear reactions to create artificial radionuclides was in fact applied for the subsequently intensively used “radiopharmaceutical” radionuclides, namely ^{13}N and ^{32}P . In addition to the radionuclides isolated from naturally occurring decay chains, these artificially produced, no-carrier-added radionuclides opened the window for the oncoming tracer concept: The tracer principle applied to biology adopted radionuclides and labeled compounds at a nano-molar scale for the investigation of physiological processes in vivo (1943 Nobel prize to G. Hevesy for his work on *... the use of isotopes as tracers in the study of chemical processes...*). This pioneering application of radioactive nuclides for biochemistry and physiology provided the first insights into the dynamics of reactions in living systems.

In 1938, the experimental and theoretical cognition of nuclear fission by O. Hahn and F. Strassmann, and the theoretical explanation by L. Meitner and O. R. Frisch (1944 Nobel Prize to O. Hahn for *... discovery of the fission of heavy elements...*) made our last century the Uranium century. Radiopharmaceutical chemistry, interestingly, has made a significant and exclusively peaceful profit from this nuclear phenomenon, as the fission of uranium today provides an unrenounceable resource of radionuclides applied in nuclear medicine diagnosis and therapy. The uranium fission product ^{131}I , for example, became a key radionuclide in the 1950s, when R. S. Yalow and S. A. Berson developed the approach of radioimmunoassay for quantitative in vitro analysis of physiological and biochemical processes (1977 Nobel prize to R. S. Yalow for *... the development of radioimmunoassays...*).

The experience in hot atom chemistry, and the bridging of radiochemistry with organic chemistry, for example, further facilitated the production and use of radionuclides and labeled compounds adequate for diagnostic and therapeutic application in vivo. This part of the route of radiopharmaceutical chemistry was accompanied not only by sciences like mathematics, physics, and biology, but also by industry and technology, providing the necessary equipment such as detectors and tomographs, reactors, and cyclotrons. In fact, radiopharmaceutical chemistry shows itself as an excellent example of modern interdisciplinarity in today's world of science and technology. Isn't it breathtaking, that hundreds of thousands of diagnostic procedures are performed every year, with a variety of tracers labeled with $^{99\text{m}}\text{Tc}$, a radioisotope of an element, absolutely non-relevant to our biological nature? Or that a naturally

nonexisting ^{18}F -labeled derivative of glucose is routinely used for the quantification of glucose metabolism of the human brain, the heart and of tumors?

Over the last years, national and international societies of radiopharmaceutical chemistry have been founded. Dedicated national and international journals are devoted to various aspects of radiopharmacy and radiopharmacology. A large number of national and international meetings, symposia, and conferences find the attention of thousands of participants from radiochemistry, radiopharmacy, radiopharmacology and nuclear medicine, attracting particular attention by the new generation of scientists.

Today, radiopharmaceuticals do belong to the standard instrumentation of nuclear medicine in particular, and medicine in general, both in the context of diagnosis and therapy. Parallel to the application of radiopharmaceuticals in hospitals, radiopharmaceutical chemistry demonstrates its capability to contribute to the industrial development of new drugs. Furthermore, radiopharmacy is adding its value to fundamental biochemical and medicinal research. A main focus will be on its unique contribution to brain research, probably the most exciting area of research of this new century.

This Volume 4 of the *Handbook of Nuclear Chemistry* covers the *Radiochemistry and Radiopharmaceutical Chemistry in Life Sciences*. It starts with the radionuclides themselves, that is, their production directly at reactors and cyclotrons or indirectly via radionuclide generator systems. For selected radionuclides, dedicated chapters follow on their individual labeling chemistry and on the correspondingly labeled compounds, the focus being on in vivo application. It begins with the most relevant isotopes used for PET such as ^{11}C or ^{18}F , and for SPECT such as radioiodine and $^{99\text{m}}\text{Tc}$. Other metallic radionuclides are summarized in a separate chapter. The increasing significance of therapeutic applications required a specific discussion. A few other topics might have been covered, such as radiopharmacology or the synthesis of ^{14}C and tritium compounds as the most important representatives of the many labeled compounds used for in vitro application. For the latter aspect, the reader is referred to a recent comprehensive book on “*Preparation of compounds labeled with Tritium and Carbon-14*” by R. Voges, J. R. Heys and T. Moenius, Wiley, Weinheim, Germany, 2009, or comprehensive reviews such as, for example, K. E. MacCarthy, *Recent advances in the design and synthesis of carbon-14 labeled pharmaceuticals from small molecule precursors*, Current Pharmaceutical Design 6, 1057–1083, 2000; M. Saljoughian and P. G. Williams, *Recent developments in tritium incorporation for radiotracer studies*, Current Pharmaceutical Design 6, 1029–1056, 2000; and M. Saljoughian, *Synthetic tritium labeling: reagents and methodologies*, Synthesis, 13, 1781–1800, 2002.

This Volume of the *Handbook of Nuclear Chemistry* reflects the state-of-the-art of radiopharmaceutical chemistry and its own intellectual, apparative, methodological, and logistical structure. With deep routes in basic nuclear chemistry, a solid tribe in hot atom and radio chemistry, with many fruitful trees in radiopharmaceutical chemistry, there are, finally, beautiful leaves and flowers in nuclear medicine and pharmaceutical research. Radiopharmaceutical chemistry is ready today to meet the requirements and challenges of modern life sciences. It will thus continuously contribute to the progress in the understanding of the molecular function of the human body, to the development of new drugs, and will provide in parallel a very strong benefit for patient care.

Frank Rösch
Volume Editor
Mainz, October 15, 2010

38 Reactor-Produced Medical Radionuclides

S. Mirzadeh¹ · L. F. Mausner² · M. A. Garland¹

¹Oak Ridge National Laboratory, Oak Ridge, TN, USA

²Brookhaven National Laboratory, Upton, NY, USA

38.1	<i>Introduction</i>	1859
38.2	<i>Nuclear Reactions</i>	1860
38.2.1	Types of Nuclear Reactions	1860
38.2.2	Nuclear Reaction Models	1860
38.2.3	Energy Considerations in Nuclear Reactions	1861
38.3	<i>Main Production Approaches with Neutrons</i>	1862
38.3.1	Neutron Interactions with Matter	1865
38.3.2	Neutron Transmission and Activation Rates	1869
38.3.3	Neutron Spectrum of Nuclear Reactors	1872
38.3.3.1	Thermal Neutrons	1872
38.3.3.2	Epithermal Neutrons and Resonances	1874
38.3.3.3	Fast Neutrons	1875
38.3.4	Neutron Energy Dependence of Cross Sections	1875
38.3.5	Reaction Rates in Thermal Reactors	1876
38.3.6	Cross Section Measurements and Flux Monitoring	1877
38.3.7	General Equations Governing the Reactor Production of Radionuclides	1878
38.4	<i>Targetry</i>	1879
38.4.1	Physical and Chemical Form	1880
38.4.2	Thermal Properties	1880
38.4.3	Chemical Stability	1880
38.4.4	Purity	1880
38.4.5	Encapsulation	1880
38.4.6	Availability	1881
38.4.7	Target Transport Systems	1881
38.5	<i>Chemical Processing</i>	1882
38.6	<i>Shielded Facilities</i>	1883
38.7	<i>Current Requirements and Challenges</i>	1883

38.8 *Selected Examples* 1883

38.8.1 Molybdenum-99 Produced by Fission and Neutron Capture Reactions 1884

38.8.2 Iodine-131 Produced by Fission and Neutron Capture Reactions 1886

38.8.3 Indium-114m Produced by Neutron Capture Reactions 1888

38.8.4 Lutetium-177 Produced by Neutron Capture Reactions 1889

38.8.5 Iodine-125 Produced by Neutron Capture Followed by β^- Decay 1893

38.8.6 Tungsten-188 Produced by Double Neutron Capture 1896

38.8.7 Tin-117m Produced by Neutron Inelastic Scattering 1897

38.8.8 Copper-67 Produced by fast Neutron-Induced Reactions 1898

38.9 *Conclusion* 1899

Abstract: The therapeutic use of radionuclides in nuclear medicine, oncology, and cardiology is the most rapidly growing use of medical radionuclides. Since most therapeutic radionuclides are neutron rich and decay by β^- emission, they are reactor-produced. This chapter deals mainly with production approaches with neutrons. Neutron interactions with matter, neutron transmission and activation rates, and neutron spectra of nuclear reactors are discussed in some detail. Further, a short discussion of the neutron-energy dependence of cross sections, reaction rates in thermal reactors, cross section measurements and flux monitoring, and general equations governing the reactor production of radionuclides are presented. Finally, the chapter is concluded by providing a number of examples encompassing the various possible reaction routes for the production of a number of medical radionuclides in a reactor.

38.1 Introduction

The majority of radioactive nuclides (radionuclides) are man-made, created by transforming a stable nuclide into an unstable state by irradiation with neutrons, protons, deuterons, alphas, gammas, or other nuclear particles. The source of these particles may be a radionuclide, a nuclear reactor, or a particle accelerator (Van de Graaff, cyclotron, linac, etc.). The tremendous variety of radionuclides discovered in this manner has given rise to many applications in physics, chemistry, biology, and, of course, medicine. The production of those medically useful radionuclides created by exposure to neutrons in a nuclear reactor is discussed in this chapter.

Soon after World War II, the importance of the peaceful use of nuclear reactors for the production of radionuclides for biological research and clinical applications was foreseen. The Graphite Reactors at the Oak Ridge National Laboratory (ORNL) and Brookhaven National Laboratory (BNL) were the first full-scale operating reactor prototypes and were put to use immediately to investigate production of a variety of radionuclides. Carbon-14 was the first reactor-produced radionuclide for clinical use in nuclear medicine, and was produced at ORNL in 1946 for use at the Barnard Free Skin and Cancer Hospital in St. Louis, Missouri. In the first decade following World War II, a variety of reactor-produced radionuclides were distributed for research through the ORNL Radionuclide Development Center and BNL Hot Laboratory Division. This early work, which has been reviewed in a number of publications (see, e.g., Bizzell 1966), included production of carbon-14 and phosphorus-32 and radioisotopes of iodine (^{130}I , ^{131}I , etc.), which rapidly became invaluable tools for application in modern biological research.

Beginning in the 1950–1960s there was also an intensive period of research on *radionuclide generator systems* utilizing reactor-produced parent nuclides (Winsche et al. 1951; Richards 1966a, b; Subramanian 1976). The first strontium-90/yttrium-90 generator and most importantly, the molybdenum-99/technetium-99m ($^{99}\text{Mo}/^{99\text{m}}\text{Tc}$) generator system were developed at BNL (Tucker et al. 1958; Richards 1966c) and marked the beginning of a new era in nuclear medicine. With the availability of generator systems, local production facilities were no longer central factors in providing short-lived radionuclides for clinical use. After a period of evaluation, the utility of the “moly generator” was realized and the $^{99}\text{Mo}/^{99\text{m}}\text{Tc}$ technology was transferred from BNL to industry. Since this early work, $^{99\text{m}}\text{Tc}$ has continued to be the “work horse” for clinical nuclear medicine, and is presently used in approximately 75% of all nuclear medicine procedures. Recent studies have estimated that the annual sale of $^{99}\text{Mo}/^{99\text{m}}\text{Tc}$ generators and associated “kits” for the preparation of various tissue-specific agents exceeds \$200 million in the USA, but the finished radiopharmaceuticals containing $^{99\text{m}}\text{Tc}$ are worth at

least tenfold more. In addition to the $^{99}\text{Mo}/^{99\text{m}}\text{Tc}$ generator system, a variety of other reactor-produced radionuclides, such as ^{131}I , continue to play an important role both in clinical nuclear medicine and in radiopharmaceutical and biological research.

This chapter describes radionuclide production approaches with neutrons. Neutron interactions with matter, neutron transmission and activation rates, and neutron spectra of nuclear reactors are discussed in some detail. Further, a short discussion of the neutron energy dependence of cross sections, reaction rates in thermal reactors, cross section measurements and flux monitoring, and general equations governing the reactor production of radionuclides are presented. Topics such as targetry, chemical processing, and required facilities are only briefly discussed. Finally, the chapter is concluded by providing a number of examples encompassing the various possible reaction routes for the production of a number of medical radionuclides in a reactor.

38.2 Nuclear Reactions

See also [▶ Chap. 3 in Vol. 1.](#)

38.2.1 Types of Nuclear Reactions

Many processes can occur when a neutron strikes an atom. Neutrons carry no charge and their interaction with electrons is negligible, but when an incident neutron comes close enough to the very small atomic nucleus to transfer some kinetic energy to the nucleus as a whole, the nucleus moves but has no internal excitation. This process is called *nuclear elastic scattering* and may be visualized as billiard balls colliding. The energy of nuclear motion eventually dissipates as heat.

More typically, the neutron may be absorbed by the target nucleus to form a new heavier nucleus, sometimes very briefly. The highly excited intermediate nucleus can nearly instantaneously deexcite in several ways. It can emit electromagnetic radiation in the form of γ -rays. These γ -rays are called “prompt” to distinguish this mechanism from γ -ray emission following radioactive decay. This process is called *radiative neutron capture*. If the nuclear excitation energy is concentrated on a few nucleons (i.e., neutrons and protons), either by direct collision with the incident particle or by statistical processes, nucleons can be ejected. If the total excitation energy of the intermediate state is greater than the binding energy of nucleons within the nucleus, nucleon emission is favored. If not, simple prompt γ -ray emission returns the new isotope nucleus to a more stable state. This process of conversion of the original nucleus into a new one is a nuclear reaction, and the residual nucleus is the reaction product. The process in which the reaction product is radioactive is the subject of this chapter.

38.2.2 Nuclear Reaction Models

Initial approaches to understanding reaction phenomena considered the incident particle to be scattered by the nucleus as a whole. Similar to scattering and attenuation of light by a crystal ball, this model was first named the “cloudy crystal ball” and is now known as *the optical model* (reviewed in Hodgson 1967). It represents the reaction process as the interaction of an incident

particle with a potential energy well. It has been successful in calculating elastic scattering results and total reaction probabilities. The optical model is, however, poor in predicting nuclear deexcitation processes or reaction product yields.

An early model useful for radionuclide production reactions was the *compound nucleus model*, introduced by Niels Bohr (1936). An incident particle encountering a nucleus can be absorbed, distributing its kinetic energy and binding energy randomly throughout the nucleus and becoming indistinguishable from other nucleons. The resulting “compound” nucleus is excited and nucleons exchange energy rapidly through many collisions. Due to random statistical fluctuation in energy exchanged in these collisions, enough energy may be concentrated on a nucleon, or a small cluster of nucleons, to cause it to be ejected. Since it is improbable for the total excitation energy to be concentrated on a single nucleon, there may be sequential emission of several particles (protons, neutrons, deuterons, alpha particles), each carrying a fraction of the excitation energy. These emission modes do not proceed with equal probability, since the electrostatic barrier reduces the likelihood of emission of a charged particle compared to a neutron. This process is similar to that of molecules escaping from the surface of a hot liquid and is called nucleon “evaporation.” Thus, the compound nucleus model views the nuclear reaction as two independent steps, projectile capture followed by nucleon evaporation.

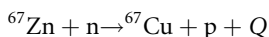
A special mode of nuclear deexcitation in the region of high atomic numbers is fission (see ► Chap. 4 in Vol. 1 for more detail). In *spontaneous fission*, the mutual electrostatic repulsion between protons of a very heavy nucleus can overcome the Coulomb barrier and cause the separation of a heavy nucleus into two lighter positively charged fragments, usually of unequal mass. There are over 60 nuclides known which fission spontaneously. For particle-induced fission, the bombarding particle supplies enough energy to overcome the barrier. In particular, thermal neutron fission of ^{235}U has had great significance for society. The 200 MeV energy release per ^{235}U atom and liberation of an excess of neutrons made possible the development of both the atomic bomb and the nuclear reactor (see ► Chap. 57 in Vol. 6 for details). Over 75 useful radionuclides are produced in this manner and are called *fission products*. Many of these can be separated and purified for medical, industrial, and research applications. Of interest for nuclear medicine are the light fragments resulting from induced fission, especially the radionuclides ^{99}Mo , ^{131}I , and ^{133}Xe .

The production of ^{99}Mo is of paramount importance to nuclear medicine. Molybdenum-99 is not directly used, but serves as the parent radionuclide for the daughter $^{99\text{m}}\text{Tc}$, now used diagnostically in dozens of radiopharmaceuticals. Iodine-131 is widely used to treat thyroid cancer and hyperactive thyroid conditions. Production of both of these nuclides is discussed in some detail in ► Sect. 38.8. Xenon-133 is used for studies of pulmonary ventilation and sometimes for cerebral blood perfusion.

38.2.3 Energy Considerations in Nuclear Reactions

Nuclear reactions, like chemical reactions, release or absorb energy. This energy accounts for the difference in mass of reactants and products and is called the reaction “**Q value**.” Energy is related to mass by Einstein’s famous formula $E = mc^2$, where c is the speed of light in vacuum. Since c is large, a small change in mass equals a large amount of energy. The energy changes in nuclear reactions millions of times greater than in chemical reactions. If the summed reactant mass is greater than the summed product mass, Q is positive and energy is released (exoergic reaction). Conversely, if the product masses are greater, the reaction is endoergic ($-Q$) and

kinetic energy from the incident particle must be supplied to drive the reaction. For example, the production of ^{67}Cu by the neutron capture of ^{67}Zn can be written as



Frequently, the *mass excess* (also called *mass defect*) is used to calculate Q . The mass excess, defined as the difference between the total atomic mass and mass number, $\Delta = M - A$, has been tabulated for all nuclei (Firestone et al. 1996, see also [Sect. 11.6 in the Appendix of Vol. 1](#)). Thus

$$\begin{aligned}\Delta(^{67}\text{Zn}) + \Delta(n) &= \Delta(^{67}\text{Cu}) + \Delta(p) + Q, \\ (-67.877) + (8.071) &= (-67.300) + (7.289) + Q, \\ Q &= 0.205 \text{ MeV, an exoergic reaction.}\end{aligned}$$

However, conservation of momentum requires that some of the incident particles' kinetic energy be transferred to the products and is not available to drive the reaction. For an exoergic reaction ($Q > 0$) such as the above reaction, there is no threshold condition. However, for an endoergic reaction requiring external energy, the minimum or “*threshold*” energy is always higher than the Q value by the factor $(M_t + M_p)/M_t$ where M_t and M_p are the target and projectile atomic masses, respectively.

For charged particle-induced reactions, in addition, the projectile has to have sufficient energy to overcome the *Coulomb barrier*. For a projectile of positive charge Z_2e and radius R_2 , the height of Coulomb barrier V around a nucleus of charge Z_1e and radius R_1 can be estimated as the energy of the Coulomb repulsion, $V = Z_1Z_2e^2/(R_1 + R_2)$, when the two particles are just in contact. Obviously, uncharged neutrons are not affected by the Coulomb barrier of the nucleus. However, there is a Coulomb barrier for charged particles leaving a nucleus during deexcitation even if the reaction was caused by an incident neutron. Therefore, these particles must have substantial energy to penetrate or overcome the barrier and are emitted with considerable kinetic energy (generally > 1 MeV). The Coulomb barrier for a particle of positive charge Z_2e leaving a nucleus of charge Z_1e is $V = Z_1Z_2e^2/r$, where $R_1 < r < (R_1 + R_2)$, and for a first approximation r is typically taken as $1.2 R_1$. Taking the nuclear radius as $1.5 \times 10^{-13} \text{ A}^{1/3} \text{ cm}$ (see [Chap. 2 in Vol. 1](#)), e as $1.602 \times 10^{-19} \text{ C}$ ($1 \text{ C}^2 \text{ cm}^{-1} = 5.61 \times 10^{24} \text{ MeV}$), the barrier height for a proton leaving ^{67}Cu has a value of about 5.5 MeV. Correcting this value to conserve momentum, a proton must have at least $1.02 \times 5.5 = 5.6 \text{ MeV}$ kinetic energy to exit the ^{67}Cu nucleus. Since the energetic threshold for this reaction is 0.21 MeV, the neutron entering the ^{67}Zn nucleus has to provide additional energy. There exists, however, a finite probability for tunneling through the barrier by lower-energy particles, but this probability drops rapidly as the energy of the particle decreases. As shown in [Fig. 38.1](#), when neutron energy is $\sim 6 \text{ MeV}$, the cross section for the above reaction drops to one hundredth of its peak value.

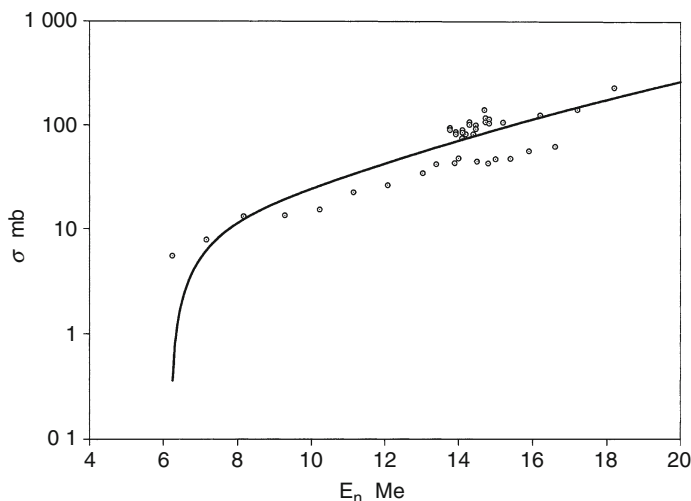
38.3 Main Production Approaches with Neutrons

[Table 38.1](#) lists some examples of reactor-produced radionuclides important to nuclear medicine. There are three general reaction types used: neutron radiative capture (n, γ); neutron capture followed by particle emission, e.g., (n, n'), (n, p), and (n, α); and fission (n, f). The radionuclides in [Table 38.1](#) are arranged in order of mass numbers.

The most widely used route is the (n, γ) reaction with thermal neutrons. The advantage of this production process is its simplicity and high yield. It is straightforward in that, in many

■ Fig. 38.1

$^{67}\text{Zn}(n,p)^{67}\text{Cu}$ cross sections. Data points are from CSISRS (2003); the curve is a cubic polynomial fit of the data



cases, elemental targets may be used and no chemical separation of target and product is required (or possible). Since cross sections tend to be higher than for most other reaction types, yields are generally good. The primary disadvantage of this reaction also relates to the fact that the radioactive product cannot be chemically separated from the target. Thus stable atoms dilute the radioactive atoms and the specific activity will be much lower than that of “carrier-free” radionuclides. Radioimpurities may arise from (n,γ) reactions on other isotopic forms of the target or chemical impurities in the target. The use of isotopically enriched targets can minimize production of impurities and improve yield, but often at high cost. Nevertheless, enriched targets are essential if the natural abundance of the target nuclide is low and significant impurities are produced.

In selected cases, there is a technique that can be utilized to improve the specific activity of (n,γ) -produced radionuclides. This method is known as the *Szilard–Chalmers process* (Szilard and Chalmers 1934). The Szilard–Chalmers process depends upon the fact that, following neutron absorption, prompt γ -rays are emitted, which may cause nuclear recoil and subsequent molecular bond disruption. This excitation sometimes leaves the resulting hot atom in a chemical state different from that of unreacted atoms, which makes it chemically separable. This separated fraction is relatively “enriched” in radioactive atoms and has a specific activity higher than that of the rest of the target.

The enrichment factor (E) is the ratio of specific activity of the recoiled fraction to that of the bulk irradiated target. The target in this case must be a compound that is thermally stable and resistant to radiolytic decomposition by fast neutrons and γ -rays. For example, the Szilard–Chalmers effect has been utilized with tetraphenyl tin to improve the specific activity of $^{117\text{m}}\text{Sn}$ (Mausner et al. 1992). This process can have large enrichment factors in a low flux, but the enrichment factor generally declines in a high flux due to accumulated radiation damage to the target molecule. Therefore, the Szilard–Chalmers effect is often not practiced in modern high flux reactors.

Table 38.1

Examples of reactor-produced radionuclides of current interest to nuclear medicine

Radionuclide ($T_{1/2}$)	Production	Reaction cross section (b) ^a	
		σ	I_0
⁶⁴ Cu (12.7 h)	⁶³ Cu(n,γ)	4.50 ± 0.02	4.97 ± 0.08
⁶⁷ Cu (2.6 days)	⁶⁷ Zn(n,p)	Fast neutrons: (1.07 ± 0.11) × 10 ⁻³ b	
⁹⁰ Y (64.00 h)	⁹⁰ Sr(β ⁻ , 28.79 a)	N/A	N/A
	⁸⁹ Y(n,γ)	1.28 ± 0.02	1.0 ± 0.1
	⁹⁰ Zr(n,p)	Fast neutrons: 0.175 × 10 ⁻³ c	
⁹⁹ Mo (66 h)	²³⁵ U(n,f) (6.07%)	582.6 ± 1.1	144 ± 6
	⁹⁸ Mo(n,γ)	0.13 ± 0.06	6.9 ± 0.3
¹⁰³ Pd (16.99 days)	¹⁰² Pd(n,γ)	3.4 ± 0.3	10.0 ± 2.0
^{114m} In (49.51 h)	¹¹³ In(n,γ)	8.1 ± 0.8	220 ± 15
^{117m} Sn (14.0 days)	¹¹⁶ Sn(n,γ)	(5.8 ± 1.2) × 10 ⁻³ d	(3.50 ± 0.53) × 10 ⁻¹ d
	¹¹⁷ Sn(n,n')	Epithermal neutrons: (2.22 ± 0.16) × 10 ⁻¹ d	
¹²⁵ I (59.4 days)	¹²⁴ Xe(n,γ) ¹²⁵ Xe(β ⁻ , 16.9 h)	165 ± 20	(3.6 ± 0.7) × 10 ³
¹³¹ I (8.02 days)	²³⁵ U(n,f) (2.89%)	582.6 ± 1.1	144 ± 6
	¹³⁰ Te(n,γ) ^{131g} Te(β ⁻ , 25.0 min)	0.27 ± 0.06	0.46 ± 0.05
¹⁵³ Sm (46.28 h)	¹⁵² Sm(n,γ)	206 ± 6	2,970 ± 100
¹⁶⁶ Ho (26.8 h)	¹⁶⁵ Ho(n,γ)	61.2 ± 1.1	650 ± 22
	¹⁶⁴ Dy(n,γ) ¹⁶⁵ Dy (β ⁻ , 2.33 h)	(2.65 ± 0.10) × 10 ³	(3.4 ± 0.2) × 10 ²
	¹⁶⁵ Dy(n,γ) ¹⁶⁶ Dy (β ⁻ , 81.5 h)	(3.6 ± 0.3) × 10 ³	(2.2 ± 0.3) × 10 ⁴
¹⁶⁹ Yb (32.0 days)	¹⁶⁸ Yb(n,γ)	(2.3 ± 0.17) × 10 ³	(2.13 ± 0.1) × 10 ⁴
¹⁷⁷ Lu (6.7 days)	¹⁷⁶ Lu(n,γ)	(2.09 ± 0.07) × 10 ³	(1.09 ± 0.04) × 10 ³
	¹⁷⁶ Yb(n,γ) ¹⁷⁷ Yb (β ⁻ , 1.9 h)	2.85	6.3
¹⁸⁶ Re (3.72 days)	¹⁸⁵ Re(n,γ)	112 ± 2	1,717 ± 50
¹⁸⁸ Re (17.0 h)	¹⁸⁷ Re(n,γ)	76.4 ± 1.0	300 ± 20
¹⁸⁸ W (69.78 days)	¹⁸⁶ W(n,γ) ¹⁸⁷ W (β ⁻ , 23.72 h)	36.48 ^e	290.3 ^e
	¹⁸⁷ W(n,γ)	14.5 ^e	398 ^e
^{191m} Ir (4.94 s)	¹⁹⁰ Os(n,γ) ¹⁹¹ Os (β ⁻ , 15.4 days)	13.1 ± 0.3	30 ± 1
¹⁹⁴ Ir (19.28 h)	¹⁹² Os(n,γ) ¹⁹³ Os (β ⁻ , 30.11 h)	2.0 ± 0.1	4.6 ± 0.2
	¹⁹³ Os(n,γ) ¹⁹⁴ Os (β ⁻ , 6.0 a)	38 ± 10	Unknown
^{195m} Pt (4.02 days)	¹⁹⁴ Pt(n,γ)	(4.2 ± 0.8) × 10 ⁻² d	(5.26 ± 0.79) × 10 ² d
	¹⁹⁵ Pt(n,n')	Epithermal neutrons: (2.87 ± 0.20) × 10 ⁻¹ d	
¹⁹⁹ Au (75.3 days)	¹⁹⁸ Pt(n,γ) ¹⁹⁹ Pt(β ⁻ , 31 min)	3.66 ± 0.19	54 ± 4
	¹⁹⁷ Au(n,γ) ¹⁹⁸ Au	98.7 ± 0.1	1,550 ± 28
	¹⁹⁸ Au(n,γ)	(2.51 ± 0.04) × 10 ⁴	Unknown
²²³ Ra (11.43 d)	²²⁶ Ra(n,γ) ²²⁷ Ra (β ⁻ , 42.2 m) ²²⁷ Ac (β ⁻ , 21.8 y) ²²⁷ Th(β ⁻ , 18.7 d)	12.8 ± 1.5	280

σ: thermal neutron cross section, I₀: resonance integral for epithermal neutrons, defined by Eq. (38.22).

^aAll cross sections from Mughabghab et al. (1981, 1984), except as noted

^bMirzadeh et al. (1986), Mirzadeh and Knapp (1992)

^cJendl (2003)

^dMausner et al. (1985), Mirzadeh et al. (1997b)

^eMughabghab's tungsten cross sections

Another situation occurs as a result of an (n,γ) reaction, in which an intermediate radionuclide decays to the product of interest. This route is followed to make ^{125}I , for example, with the $^{124}\text{Xe}(n,\gamma)^{125}\text{Xe} \xrightarrow{\beta^-} ^{125}\text{I}$ process. The neutron capture product ^{125}Xe beta decays to ^{125}I with a 16.9 h half-life. Because the final product can be chemically separated from the target, specific activity may approach the theoretical value for the pure radionuclide. Obviously, the use of high chemical purity targets and processing reagents is necessary to avoid introducing stable nuclides of the same element as the product. In the ^{125}I example, this means that both the target and reagents should be free of stable iodine. It is also usually desirable to use an enriched target to minimize the coproduction of long-lived or stable isotopes with the desired product. For example, irradiation of ^{124}Xe containing a few percent of ^{126}Xe (0.09% natural abundance) will result in production of stable ^{127}I through the decay of ^{127}Xe , and hence result in lower specific activity of the ^{125}I product. In this case, since target and product are chemically separable, it is possible and may be worthwhile to recover the enriched target material for reuse.

At somewhat higher energies, *neutron inelastic scattering* can be used to produce metastable nuclei. Inelastic scattering is a process in which the emitted particle is the same as the captured particle, but there is loss of kinetic energy in the system, which appears as excitation energy in the product nucleus. In the case of neutron inelastic scattering, it has been shown that the cross section of the $^AZ(n,n')^{Am}Z$ reaction (where the atomic number Z stands for the chemical symbol of the element) is, in some cases, substantially higher than the cross section for the $^{(A-1)}Z(n,\gamma)^{Am}Z$ route (Mausner et al. 1985). For the cases of ^{117m}Sn , ^{119m}Sn , and ^{195m}Pt , the magnitude of gain in the cross section has been shown to compensate for the relatively lower fast neutron flux from a well-moderated fission spectrum in the typical irradiation location of most research reactors (Mirzadeh et al. 1997).

A few useful radionuclides are produced with fast neutrons by (n,p) reactions (e.g., ^{35}S , ^{47}Sc , ^{64}Cu , ^{67}Cu), or by indirect reactions, such as that used for production of ^{18}F . The (n,p) process shares many features with the (n,γ) reaction followed by beta decay process described above, since the target and product are chemically separable. The indirect mechanism involves the use of an outgoing particle from an initial nuclear reaction to cause a second reaction in another target nucleus. Thus the neutron irradiation of ^6Li creates a triton ($^3\text{H}^+$) with sufficient energy to react with a neighboring ^{16}O nucleus (in Li_2CO_3) to form ^{18}F . The product is separable from the target(s).

Neutron-induced fission of ^{235}U creates fission products with atomic numbers ranging predominantly from $Z = 30$ – 66 . The mass distribution of radioactive products from fission of ^{235}U peaks at about mass 100 and mass 140. For the purpose of radionuclide production, targets containing about 25 grams of highly enriched ^{235}U are irradiated and then chemically processed. Fuel rods also contain large amounts of ^{235}U and its fission products, but are not processed for their radionuclide content. Given the large numbers of radionuclides created by the fission process, the chemical procedures to recover the radionuclides of interest may be quite involved. The most important medical radionuclides produced by fission are ^{131}I , ^{133}Xe , and, of course, ^{99}Mo . The special role of ^{99}Mo and its daughter ^{99m}Tc in nuclear medicine must be underscored.

38.3.1 Neutron Interactions with Matter

Due to the fact that a neutron carries no net electrical charge and there is no Coulomb repulsion to hinder its interaction with nuclei, a neutron is able to cross the nuclear boundary

even when moving at very low velocity. Consequently, neutrons of an extremely wide energy range are able to interact with nuclei, and the energy region over which neutrons cause nuclear interactions is much wider than it is for charged particles such as protons. As the neutron's energy increases, its de Broglie wavelength decreases (see ▶ Eq. (38.2)), and at the lowest energy, its wavelength is much larger than the distance between atoms in ordinary matter (see ▶ Chap. 29 in Vol. 3). At the upper energy, neutron wavelength becomes much smaller than the size of the nucleus, eventually reaching a size about the range of nuclear forces. At low energy or long wavelengths, the optical properties of neutrons predominate – resulting in refraction and reflection of neutrons in ordinary matter. The particle characteristics of neutrons become more dominant as neutron energy increases. In this energy range, neutrons can be considered as projectiles colliding with the individual particles that make up the nuclei. The similarity of cross sections for fast neutrons from nuclide to nuclide and the gentle change with energy is a direct result of the fact that for short wavelengths the particle aspects of the neutrons are dominant.

The *cross section* is a measure of the probability of interaction of neutrons with matter. It is measured in units of area, given in “barns” ($1 \text{ barn} = 10^{-28} \text{ m}^2$). The numerical magnitudes of cross sections vary from millions of barns (megabarns) down to millionths of barns (microbarns). The simple concept of cross section in terms of area is applicable to many situations, and in this elementary sense, the cross section is the πR^2 target area displayed by the nucleus to an approaching neutron on a plane perpendicular to the neutron motion. The cross section, however, varies inversely with the velocity of the neutron, whereas the actual size of the nucleus is not dependent on the velocity of the incoming neutron. In classical mechanics, this concept can be explained as decreased residence time near the nuclei as neutron velocity increases and therefore the reaction probability becomes smaller. A better description requires a quantum and wave mechanical analysis of cross sections (Evans 1955). Note that a slow neutron has a longer wavelength than a fast neutron and the reaction probability increases with increasing particle wavelength.

The cross section related to the probability that a neutron will interact with a nucleus regardless of what happens after the collision is called the *total cross section*, being equal to the total probability of all interactions. The total cross section can be subdivided into *partial cross sections*, each equal to the probability of a particular event following the collision of the neutron with the nucleus. For instance, the neutron may collide elastically, it may be captured by the nucleus followed by emission of γ -radiation, it may emerge from the nucleus with its energy decreased (inelastic scattering), or it may cause the nucleus to emit perhaps a proton or an alpha particle or, for several heavy nuclei, it may even cause the nucleus to split (i.e., to fission). The sum of the partial cross sections of course is equal to the total cross section.

The number of interactions taking place per unit time when N_t nuclei with the same total cross section σ_t are bombarded by neutrons of density n (concentration is defined as the number of neutrons per cm^3) and velocity v (cm s^{-1}) is given by

$$N_t n v \sigma_t = N_t \phi \sigma_t \quad (38.1)$$

interactions per second, assuming that N_t is small enough so that the nuclei do not change the neutron density appreciably. The product of neutron density n and velocity v is the neutron flux density, ϕ , or, as is more often called, the *neutron flux*. Thus, a unit cross section gives one interaction per second when a unit neutron flux is incident on a single nucleus. Note in ▶ Eq. (38.1) that the interaction rate depends on the total number of nuclei, N_t , rather than on the number of nuclei per cm^2 , N' . In this model, a target consisting of N_t nuclei is submerged in

a pool of neutrons having a flux of ϕ neutrons per second per unit area. Alternatively, one may consider a case where a beam of neutrons with intensity f per second are incident on a target with a surface density of N' nuclei per unit area.

For high-energy neutrons (for which the wavelength corresponds to the neutron's size), the cross section is about equal to the geometrical cross section of the nucleus itself. For a nucleus of radius R , the geometrical cross section is πR^2 , about $3 \times 10^{-24} \text{ cm}^2$ (3 barns) for a heavy nucleus. Although the total cross section for fast neutrons is typically of the order of a few barns, the partial cross sections may differ greatly from element to element. At lower neutron energy, where the neutron wavelength is larger than the nucleus, the situation becomes much more complicated, as the wave properties begin to emerge. When the neutron wavelength is much larger than the nucleus, the interaction probability is given by the size of the neutron, $\pi\lambda^2$ (where λ is the reduced wavelength, $\lambda/2\pi$) rather than the size of the nucleus, πR^2 . For nonrelativistic velocities (such as those available from nuclear reactors), the neutron wavelength is given by

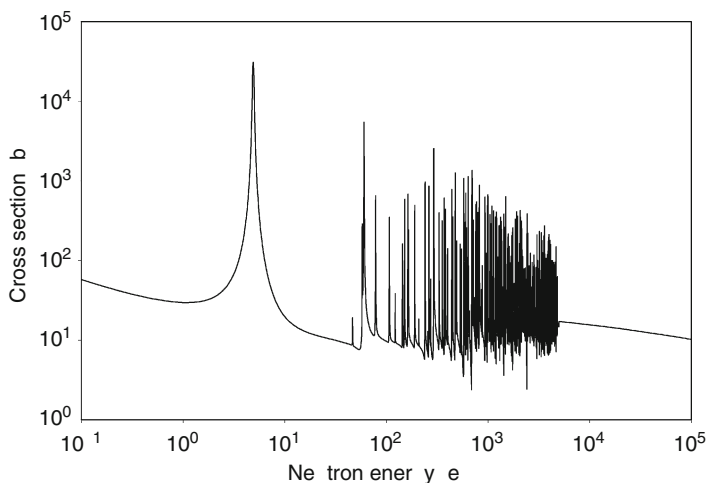
$$\lambda = \frac{h}{mv} = \frac{h}{\sqrt{2mE}} = 2.86 \times 10^{-9} E^{-1/2} \text{ cm} = 0.286 E^{-1/2} \text{ \AA} \quad (38.2)$$

where h is Planck's constant ($\sim 6.626 \times 10^{-34} \text{ J s}$), m is the neutron mass, mv is the momentum of the neutron, and E is the neutron energy measured in eV. For example, the wavelength of a neutron having 1 eV of energy is $2.86 \times 10^{-9} \text{ cm}$ ($\lambda = 4.6 \times 10^{-10} \text{ cm}$), several hundred times larger than a typical nuclear radius. The total cross section for slow neutrons ($<1 \text{ eV}$) is, however, much smaller than $\pi\lambda^2$. The reason for the low cross section values and the rapid variations in energy is that the wave properties of the neutron necessitate a wave-mechanical treatment of the nuclear interaction and the results are not at all what one would expect from a classical view of an object with a cross section of $\pi\lambda^2$ colliding with an area of πR^2 . In addition, the variation in cross section from nuclide to nuclide is very large.

Typically, a cross section is identified with a process as it is manifested experimentally, such as the radiative capture cross section (detection of capture γ -rays), activation cross section (radioactivity of end product), cross section of compound nucleus formation, reaction cross section, etc. The total cross section, which is the sum of all the partial cross sections, represents all the interaction processes that may result from the collision of a neutron with an atom. At lower energies, where the neutron waves scattered by different atoms interfere, the observed scattering cross section may strongly depend on the physical state of the material, for example, whether it is crystalline or liquid. The *scattering cross section* refers to all processes in which the only particle emitted in the interaction is a neutron. When the energy of the emitted neutron is identical with the incoming neutron energy, the scattering is elastic scattering, and in the case that the energy changes it is inelastic scattering. Inelastic scattering is a process in which energy is lost by the neutron and emitted as γ -radiation. The *activation cross section* refers to interactions which were measured by the resulting radioactivity of the nucleus formed. The activation cross section usually is the same as the capture cross section, but activation can sometimes be the result of reactions other than neutron capture, such as the (n,p) and (n,α) reactions. Note that neutron capture can result in a stable nucleus which has a zero activation cross section. The *fission cross section* refers to the case where the heaviest nuclei undergo fission after colliding with neutrons.

In general, below about 0.003 eV, the total neutron cross section rises with decreasing energy; this rising cross section may be a combination of inelastic lattice vibration scattering and simple neutron capture. Above the neutron diffraction region, $\sim 0.03 \text{ eV}$, the cross section

■ Fig. 38.2

Total neutron cross section of ^{197}Au (plot of evaluated nuclear data file)

decreases very slowly with increasing neutron energy due to the capture cross section (although small at this point but still not negligible). An example of a material with a very large neutron capture cross section is ^{197}Au (see ► Fig. 38.2). Here, the capture cross section is so large that it dominates the total cross section.

For neutrons at specific energies, usually in the range of 1–100 eV kinetic energy, some nuclei show very large cross sections, much larger than predicted by the πR^2 geometric cross section area of the target nucleus. This situation can be explained as being due to enhanced neutron capture because the neutron energy exactly matches that of discrete energy levels in the compound nucleus. This phenomenon is called *resonance capture*. Each of the resonances represents an excitation of the compound nucleus to a discrete energy level formed after addition of a neutron to the nucleus. For various atomic masses, resonances become important at different energies. For very heavy elements, the resonances are so closely spaced that they are not distinguishable even in the region of thermal neutrons (~ 0.02 eV). For light elements, on the other hand, such as beryllium and carbon, the resonances are so widely spaced that they are usually not seen until neutron energies of several MeV.

As the neutron energy further increases the resonances seem to disappear (► Fig. 38.2). This effect occurs because the width of the levels increases with increasing neutron energy and eventually attains a value equal to the spacing between levels and at even higher energies it reaches a continuum. Because of the merging of levels, the properties of the neutron cross sections in the continuum region become much simpler and cross sections become relatively smooth with a slow variation with energy; this continuum is known as the *unresolved resonance region*. The energy region where individual resonances have become completely merged occurs at different neutron energies depending on atomic mass. For the lightest elements, resonances occur for neutrons of several MeV, whereas for the heaviest elements individual resonances vanish at energies above about 100 keV. Further, the energy at which resonances merge decreases with increasing atomic mass, with the exception of heavy nuclei containing magic numbers of neutrons which behave as if they were much lighter nuclei.

38.3.2 Neutron Transmission and Activation Rates

The interaction of neutrons with electrons is very weak and therefore primary ionization of atoms by neutrons is negligible. Highly energetic neutrons lose large amounts of energy in inelastic collisions, especially with heavier nuclei. After slowing to intermediate energies, this process is ineffective due to decreasing cross sections of inelastic reactions and most additional slowing proceeds by many successive elastic, “billiard ball” collisions with nuclei. Because of conservation of momentum, a neutron of energy E_0 gives up no more energy than $4AE_0/(A+1)^2$ to the recoil nucleus, where A is the mass number of the target. Clearly, the lighter the nucleus with which a neutron collides, the greater the fraction of its energy that can be lost in a single elastic collision. Thus, hydrogen-containing matter, such as water or paraffin, is most effective at slowing neutrons. Eventually after many collisions, a thermal neutron in a hydrogenous material will be captured by a proton to form a deuteron. For these reasons, shielding for high-energy neutrons usually has layers of steel, graphite, and then water (or paraffin).

The net effect of all these slowing down processes is an exponential attenuation. The rate of transmission of monoenergetic neutrons as they pass through matter is given by

$$\phi_x = \phi_0 e^{-N_t \sigma_t x} \quad (38.3)$$

where ϕ_0 is the incident neutron flux, ϕ_x the flux at thickness x , N_t the number of nuclei per cm^3 , and σ_t the total cross section. The transmission T is defined as ϕ_x/ϕ_0 or $\exp(-N_t \sigma_t x)$. In practice, however, a strictly monoenergetic flux is never available, but the exponential law will still hold if the cross section remains constant over the neutron energy range in the beam. If the cross section changes over the energy range, the transmission will be exponential for each individual energy value, but the net effect will be a gradual depletion of the neutrons of higher cross section.

For a very thin sample, where the neutron transmission is near unity, [Eq. \(38.3\)](#) becomes simply

$$1 - T = N \sigma_t x \quad (38.4)$$

and the term $(1 - T)/Nx$ gives the average total cross section, weighted according to the neutron distribution. In this case, the incident distribution is undistorted by the sample and all atoms in the sample “see” neutrons having a Maxwell distribution of velocities provided that the neutron “gas” is in thermal equilibrium. Subtracting the scattering cross section, which is typically small and rather independent of energy, from the total cross section gives the average absorption cross section for a Maxwell distribution. If the absorption cross section of the sample varies with the reciprocal of neutron velocity, i.e., $\sigma_a = k/v$, one obtains (see [Eq. \(38.15\)](#)):

$$\bar{\sigma}_a = \frac{\int \sigma_a v^2 e^{-\left(\frac{v}{v_{mp}}\right)^2} dv}{\int v^2 e^{-\left(\frac{v}{v_{mp}}\right)^2} dv} = \frac{2}{\sqrt{\pi}} \frac{k}{v_{mp}}, \quad (38.5)$$

$$\bar{\sigma}_a = \frac{2}{\sqrt{\pi}} \sigma_{v_{mp}} = 1.128 \sigma_{v_{mp}}, \quad (38.6)$$

where v_{mp} is the “mode” of the Maxwell distribution of velocities, or the most probable velocity of the “thermalized” neutrons (see [Chap. 9 in Vol. 1](#)).

► Equation (38.6) shows that for a material with $\sigma_a = k/v$, the average cross section obtained from a thin sample transmission measurement (with scattering subtracted) is 1.128 times the cross section at the most probable velocity (it will be shown after ► Eq. (38.14) that $v_{mp} = 2,200 \text{ m s}^{-1}$ for room temperature). The statistical accuracy of the cross section obtained from a thin sample (transmission near unity) is typically very poor, and in practice thick samples must be used, resulting in an increase in distortion of Maxwell distribution. Thus, the cross section measured for a thick sample will be an average over a neutron distribution that changes shape as it penetrates through the absorber.

In the case of reaction or activation rates, for example, when calculating the amount of radioactivity produced in a sample, the fundamental equation is again described by a simple first order differential equation

$$\frac{dN}{dt} = N_t \phi \sigma_{act} \quad (38.7)$$

where dN/dt is the activation rate (per second), N is the number of activated atoms, and N_t is the total number of target atoms that are in the neutron flux ϕ . The activation cross section, σ_{act} , refers to the production of the particular radioactive species regardless of the reaction involved, which is usually (n, γ) but may be (n, p) , (n, α) , $(n, 2n)$, (n, f) , or other reactions. Although the flux in ► Eq. (38.7) is the number of neutrons that cross $1 \text{ cm}^2/\text{s}$, the activation rate, dN/dt , depends on the total number of atoms present, N_t , regardless of the volume over which they are distributed. ► Equation (38.7) holds for isotropic fluxes, such as those within a reactor, equally well. For non-monoenergetic neutrons, an appropriate average flux is used. In practice, whereas the transmission equation, ► Eq. (38.3), often holds extremely well, the activation equation, ► Eq. (38.7), holds only for small targets. The reason is that the neutron flux is often disturbed by the sample itself, the atoms in the center not receiving the full neutron flux. This effect is called *self-absorption* (*self-shielding*), and it is generally difficult to estimate. For accurate measurement of a cross section by reaction rate, it is necessary to use small enough samples so that self-absorption is negligible, but in the case of radionuclide production, for example, a balance must be maintained between self-absorption (which lowers the specific activity, $\lambda N/N_t$) and sample size, which increases the total activity produced, λN , see ► Eq. (38.7).

When the product of activation is radioactive with a *decay constant* of λ ($\lambda = \ln 2/T_{1/2}$), the decay of the activated atoms will decrease the rate of formation as time progresses, and the rate of change of the number of produced or activated atoms per unit time (s) is given by

$$\frac{dN}{dt} = N_t \phi \sigma_{act} - \lambda N. \quad (38.8)$$

The decay rate of activated atoms, or *activity* ($A = \lambda N$), at any time during or at the end of irradiation is then obtained by integration of ► Eq. (38.8):

$$A = \lambda N = N_t \phi \sigma_{act} (1 - e^{-\lambda t}). \quad (38.9)$$

(See also ► Sect. 7.4.2 in Chap. 7, Vol. 1.) In practice, a finite time θ would elapse between the end of irradiation and the actual counting. The activity is then given by

$$A = \lambda N = N_t \phi \sigma_{act} (1 - e^{-\lambda t}) e^{-\lambda \theta}. \quad (38.10)$$

If $\lambda t \ll 1$, for example, because the product nuclei are very long-lived (the decay constant is small, and therefore, the number of activated atoms that have decayed during time t is

negligible), or because the irradiation time is very short, then the term $(1 - e^{-\lambda t}) \approx \lambda t$, and hence [Eq. \(38.9\)](#) will reduce to

$$N = N_t \phi \sigma_{\text{act}} t \quad (38.11)$$

that is, the activation will increase linearly with time. If, however, $\lambda t \gg 1$, for example, because the activated atoms have a relatively large decay constant (very short half-life), or because the irradiation time is very long, the number of activated atoms will increase until the rate of radioactive decay is equal to the rate of formation, $dN/dt = 0$, or the term $(1 - e^{-\lambda t}) \approx 1$, and hence

$$\lambda N = N_t \phi \sigma_{\text{act}}. \quad (38.12)$$

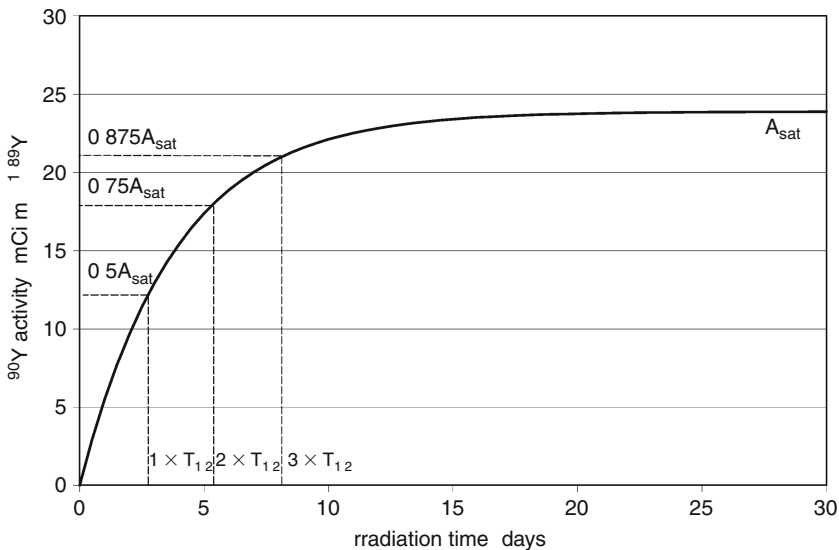
The number of activated atoms will then remain constant on further irradiation. This equilibrium activity is called the saturation activity, and the term $(1 - e^{-\lambda t})$ is called the *saturation factor*. In practice, most irradiations for radionuclide production are for a duration approximately equal to the half-life of the desired product, or half-saturation. As doubling the irradiation time increases the amount of product only by 50%, it becomes increasingly inefficient to irradiate any longer.

The formation of a typical radionuclide, ^{90}Y , as a function of irradiation time is shown in [Fig. 38.3](#). In this example, ^{90}Y is produced by neutron irradiation of an ^{89}Y target, $^{89}\text{Y} (n, \gamma) ^{90}\text{Y}$, at a neutron flux of $1 \times 10^{14} \text{ n cm}^{-2} \text{ s}^{-1}$. The corresponding activation cross section is 1.3 b (Mughabghab et al. 1981).

The half-life of ^{90}Y is 64.00 h and its decay constant is $1.083 \times 10^{-2} \text{ h}^{-1}$. As seen, one half of the final activity is produced in one half-life, three-quarters in two half-lives, etc., and the activity formed approaches the saturation limit of 23.9 mCi mg^{-1} (884 MBq/mg) of ^{89}Y very slowly after the first few half-lives. The general equations governing reactor production of radionuclides are discussed in [Sect. 38.3.7](#).

Fig. 38.3

Reactor production of ^{90}Y via neutron capture by ^{89}Y in a neutron flux of $1 \times 10^{14} \text{ n cm}^{-2} \text{ s}^{-1}$



38.3.3 Neutron Spectrum of Nuclear Reactors

The neutron spectrum from a nuclear reactor is typically divided into two components: a thermalized flux with a Maxwell energy distribution and an epithermal flux whose energy distribution is proportional to the reciprocal of the neutron energy, $1/E_n$.

38.3.3.1 Thermal Neutrons

In most nuclear reactors, *thermal neutrons*, that is, neutrons that are in thermal equilibrium with matter at room temperature, have by far the highest density. The velocity of thermal neutrons exhibits a Maxwell distribution known from the kinetic theory of gases, where the number of neutrons having a velocity between v and $v + dv$ is expressed in terms of the total number of neutrons, temperature, and velocity. Neutron density per unit velocity is given by the equation

$$\frac{dn_v}{dv} = 4\pi \left(\frac{m}{2\pi kT} \right)^{\frac{3}{2}} v^2 e^{\frac{-mv^2}{2kT}} \quad (38.13)$$

where m is the neutron mass, T is the absolute temperature, k is Boltzmann's constant, and n is the total number of neutrons per unit volume, obtained by summing dn_v over all possible velocities between zero and infinity

$$n = \int_{v=0}^{v=\infty} dn_v. \quad (38.14)$$

The most probable velocity, v_{mp} , corresponding to the maximum of the probability curve, as determined from the condition $dn_v/dv = 0$, is $(2kT/m)^{1/2}$. At room temperature (293.6 K), the most probable velocity is $2,200 \text{ m s}^{-1}$, corresponding to a kinetic energy of 0.0253 eV and a wavelength of 1.8 \AA ($1.8 \times 10^{-10} \text{ m}$), which is about the magnitude of interatomic spacing in matter.

By substituting v_{mp}^2 for $(2kT/m)$, [Eq. \(38.13\)](#) can be rewritten as

$$\frac{dn_v}{dv} = \frac{4}{\sqrt{\pi}} \frac{v^2}{v_{mp}^3} e^{\frac{-v^2}{v_{mp}^2}}. \quad (38.15)$$

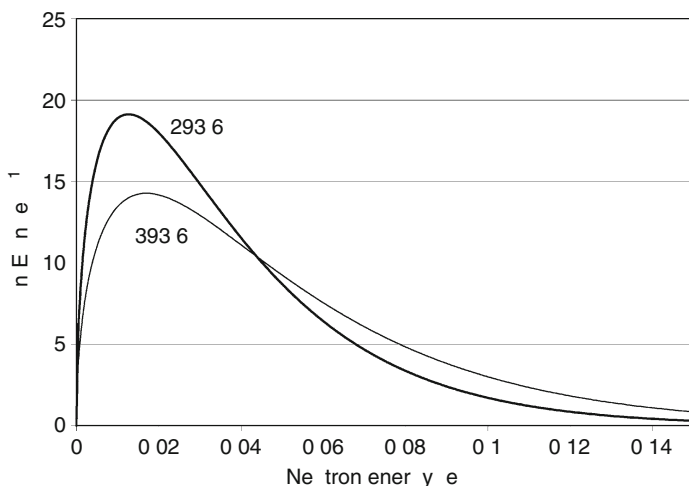
The table of thermal cross sections typically includes values for monoenergetic neutrons, 0.0253 eV (velocity of $2,200 \text{ m s}^{-1}$) rather than cross sections averaged over the entire Maxwell distribution. In practice, however, thermal cross sections are measured or used, not for a single velocity, but for the entire Maxwell distribution of velocities present in a nuclear reactor. In the design of nuclear reactors, for example, neutron flux and cross sections appropriate for the entire Maxwell distribution are of course essential, whereas the monoenergetic neutron flux (ϕ_0) and the corresponding cross sections are most useful in computations of production rates of radionuclides in nuclear reactors.

The velocity distribution, expressed by [Eqs. \(38.13\)](#) and [\(38.15\)](#), can be converted to an energy distribution by replacing v and dv with E and dE , using the energy and velocity relationship ($E = mv^2/2$). Therefore, neutron density per unit energy is given by

$$\frac{dn_E}{dE} = 2\pi n \left(\frac{1}{\pi kT} \right)^{\frac{3}{2}} e^{\frac{-E}{kT}} \sqrt{E} \quad (38.16)$$

■ Fig. 38.4

Thermal neutron density with a Maxwell energy distribution as a function of neutron energy



where dn_E is the number of neutrons per unit volume (neutron density) having kinetic energy between E and $E + dE$. From ► Eq. (38.16), the most probable energy, E_{mp} , corresponding to the maximum of the probability curve, $dn_E/dE = 0$, is $kT/2$, and at room temperature (293.6 K) $E_{mp} = 0.0126$ eV. Note that there is a difference between E_{mp} and the energy corresponding to v_{mp} that was shown to be 0.0253 eV (this energy is equal to kT). This difference is due to the fact that E_{mp} and v_{mp} are derived from different distribution functions given in ► Eqs. (38.13) and ► (38.16), respectively.

► Figure 38.4 shows a graph of the Maxwell energy distributions (► Eq. (38.16)) of thermal neutrons at two temperatures. The normalized functions shown represent the probability of finding a neutron having an energy between E and $E + dE$. (Being normalized means that the area under the curves shown in ► Fig. 38.4 is equal to unity for both temperatures.) ► Equation (38.16) also indicates that an increase in temperature broadens the energy distribution and shifts the maximum to a higher value of E .

The energy-dependent *thermal neutron flux* can be obtained by substituting $n(E)$ from ► Eq. (38.16) in the following equation

$$\begin{aligned}\phi_{th}(E) &= \frac{dn_E}{dE} \frac{dv_E}{dE} \\ &= n(E) v(E) \\ &= \frac{2\pi n}{(\pi kT)^{3/2}} \left(\frac{2}{m}\right)^{1/2} e^{-\frac{E}{kT}}\end{aligned}\quad (38.17)$$

where m is the neutron mass and $v(E) = (2E/m)^{1/2}$.

The one-group thermal flux, ϕ_{th} , is then given by

$$\phi_{th} = \int_{th} \phi_{th}(E) dE \quad (38.18)$$

where the integration is carried out over the thermal range, normally defined to be from zero to about $5kT \approx 0.1$ eV (Lamarsh and Baratta 2001). Since $\phi_{th}(E)$ decreases to very small values above $5kT$, the integration can be taken to infinity and by combining Eqs. (38.17) and (38.18) one obtains

$$\phi_{th}(E) = \frac{2\pi n}{(\pi kT)^{3/2}} \left(\frac{2}{m}\right)^{1/2} \int_0^\infty e^{-\frac{E}{kT}} dE = \frac{2n}{\sqrt{\pi}} \left(\frac{2kT}{m}\right)^{1/2}. \quad (38.19)$$

Let E_T , the neutron energy corresponding to kT , and its associated velocity v_T be defined as $E_T = kT = mv_T^2/2$. The numerical values of E_T and v_T are $8.617 T \times 10^{-5}$ eV and $1.284 T \times 10^4$ cm s⁻¹, respectively, and T is in kelvin. It is important to emphasize that ϕ_{th} is the total neutron flux in the thermal region and is computed by the integral in Eq. (38.19), whereas ϕ_0 (equal to nv_0 , where n is the Maxwellian neutron density, Eq. (38.16)) is a pseudo flux assuming that all the neutrons are monoenergetic with $E_0 = 0.0253$ eV (i.e., that all the neutrons have a velocity equal to the most probable velocity at $T = 20^\circ\text{C}$, namely $\sim 2,200$ m s⁻¹). As defined, ϕ_0 yields the actual reaction rate when used with the corresponding cross section at E_0 , σ_0 , which is typically given in cross section tables.

From rearranging Eq. (38.19), one can deduce the following useful relations between ϕ_{th} and ϕ_0

$$\frac{\phi_{th}}{\phi_0} = \frac{2}{\sqrt{\pi}} \left(\frac{v_T}{v_0}\right) = \frac{2}{\sqrt{\pi}} \left(\frac{T}{T_0}\right)^{1/2}. \quad (38.20)$$

Therefore, the ratio of ϕ_{th} to ϕ_0 depends on the temperature T . If T is equal to the standard temperature T_0 (i.e., 293.60 K), then $\phi_{th}/\phi_0 = 2\pi^{-1/2} \approx 1.128$. In other words, ϕ_{th} will exceed ϕ_0 by 12.8%. In many nuclear reactors where the neutron temperature is considerably higher than 20°C , the difference between ϕ_{th} and ϕ_0 will be significant.

38.3.3.2 Epithermal Neutrons and Resonances

Epithermal neutrons are distinguished from thermal neutrons because many neutron resonances are observed in the epithermal neutron region. Since there is an overlap of the thermal and epithermal fluxes, it is not possible to divide all Maxwellian neutrons from those in the $1/E_n$ distribution. It is generally assumed that the resonance flux goes to zero when the neutron energy is five times kT (Westcott 1955). Because of the rapid decrease in the Maxwellian function with energy (see Eq. (38.16) and Fig. 38.4), only $\sim 1.7\%$ of the Maxwellian neutrons are more energetic than $5kT$. In practice, an effective cutoff determined by the neutron spectrum transmitted through a cadmium filter is used. Such a cutoff varies with the thickness of the filter and for thin filters it also varies with the Maxwellian to epithermal flux ratio.

Epithermal flux is generally assumed to be proportional to $1/E$. In the absence of leakage and epithermal absorption, the $1/E$ assumption is expected to hold rather well for moderators containing hydrogen (e.g., H₂O) from 1 to 2 MeV (the average neutron energies from fission) down to about 1 eV where the scattering cross section is energy-dependent. In practice, however, where the leakage and epithermal absorption in a reactor may not be negligible or where moderators other than water may be used, deviation from $1/E$ dependence would be expected. In general, the resonance flux energy dependence must change at least somewhat

with reactor type and size and with geometrical configuration. Also, at positions very near to any large concentrated absorber, there must be some flux depression at energies close to its resonances.

38.3.3.3 Fast Neutrons

In classifying neutrons according to energy, *fast neutrons* range in energy from about 0.1–20 MeV. From the standpoint of the type of interaction observed, fast neutrons are usually distinguished from epithermal (or resonance) neutrons, because for the great majority of nuclei, apart from the lightest ones, individual resonances are not observed above ~ 100 keV. This distinction between fast and resonance neutrons is extremely vague because the energy at which resonances are observed is a function of the particular resolving power used in the measurement and of the atomic mass of the nucleus investigated. However, one can consider “fast” neutrons as those above 100 keV, for which individual resonances are not resolved in “typical” nuclei. Another criterion appropriate to fast neutrons is the angular momentum involved in collisions. For the majority of the resonances, $l = 0$ is the only angular momentum involved. However, for neutrons with energy in the MeV range, higher angular momentum is transferred to the compound nucleus. The restriction of $l = 0$ for slow neutrons is of course a restriction that changes somewhat with atomic mass. Interactions involving higher angular momentum (e.g., $l = 1$) become appreciable only when the neutron wavelength is equal to the nuclear radius. For example, $l = 1$ collisions become important at about 2.5 MeV for $A = 10$ and 0.33 MeV for $A \approx 200$ (Hughes 1957).

38.3.4 Neutron Energy Dependence of Cross Sections

Many nuclides have absorption cross sections that vary with neutron velocity or energy in the thermal range essentially as $1/v$ or $(1/E)^{1/2}$. All neutron absorption can be formulated in terms of resonance absorption at certain distinct energies. In the region of neutron resonances, the cross section is determined by a few parameters, which are properties of the nuclear excitation level represented by the neutron resonances. These parameters include neutron and radiation widths and the spin of the compound nucleus. In the resonance region, in which only elastic scattering and capture reactions are possible, neutron energies are sufficiently low such that only $l = 0$ interactions are involved, resulting in isotropic angular distributions. The analytical form of a neutron resonance is given by the dispersion formula, analogous to the formula for optical dispersion or for a resonating electrical circuit. The dispersion, or Breit–Wigner formula, gives the cross section as a function of energy, taking into account the contributions of many levels at the same time (Lamarsh and Baratta 2001). When the magnitude of the resonance energy E_r is much greater than the neutron kinetic energy E , the cross section varies essentially as $(1/E)^{1/2}$ or as $1/v$. This situation occurs in the thermal range when the nearest resonance is at an energy considerably higher than thermal. Boron is a good example of an element whose absorption cross section follows the $1/v$ law over a wide energy range, i.e., from about 0.001 to a few hundred eV. The treatment of cross section data when deviating from the $1/v$ law is more complicated (Lamarsh and Baratta 2001). The cross section varies very rapidly with neutron energy and just above a resonance, the radiative capture cross section $\sigma_\gamma(E)$ varies as the inverse square of the difference $E - E_r$. At higher energies, where $E \gg E_r$,

$\sigma_\gamma(E)$ depends on $E^{5/2}$. Because of this great variation of cross section with neutron energy above a resonance, it is possible to use absorbers with resonances near the thermal region to effectively absorb all neutrons below a particular energy E_c and transmit all those above E_c (e.g., cadmium of a given thickness). The cutoff, however, is not very sharp and depends on the thickness of the absorber. For infinitely dilute or very small samples the *resonance integrals* are given by Stoughton and Halperin (1959) as

$$I = \int \sigma(E) \frac{dE}{E} \quad (38.21)$$

where the integration is typically taken from $5kT$ or E_c (the effective cadmium cutoff) to ~ 1 MeV. In order to judge the latter value, note that the average energy of prompt fission neutrons is ~ 2 MeV, while the most probable energy is ~ 0.75 MeV (Lamarsh and Baratta 2001). The lower limit is rather important whereas the upper limit is not. Thus,

$$I_0 = \int_{E_c}^{1 \text{ MeV}} \frac{\sigma(E)}{E} dE \quad \text{and} \quad I'_0 = \int_{5kT}^{1 \text{ MeV}} \frac{\sigma(E)}{E} dE. \quad (38.22)$$

The integrals I_0 and I'_0 are called the *infinitely dilute resonance integrals*, the difference depending on the lower limit of integration (i.e., E_c or $5kT$, respectively). Further, in [Eq. \(38.22\)](#), it is assumed that the resonance flux varies as $1/E$ down to $5kT$ and vanishes below this energy. Values of I_0 and I'_0 can be computed by putting values for $\sigma(E)$ (obtained from the Breit–Wigner formula) into [Eq. \(38.22\)](#) and carrying out the integration from E_c (or $5kT$) to infinity over a particular resonance. Further simplification can also be made by letting $E = E_r$ and then integrating from zero to infinity. The resultant value

$$I_0 \approx I'_0 \approx \frac{\pi \sigma_{r\gamma} \Gamma}{2E_r} \quad (38.23)$$

provides a reasonable approximation of the integral under the $\sigma_\gamma(E)$ vs. $\ln E$ curve at and near a particular resonance “r,” if E_r is a few electron volts or higher (so that the width of the resonance is small compared to the energy E_r). In [Eq. \(38.23\)](#), $\sigma_{r\gamma}$ is the maximum value of the radiative capture cross section at a particular resonance energy E_r and Γ is the total width of the resonance at half the maximum. The contributions to I_0 from all known resonances must then be added to obtain the resonance integral.

An alternative method of determining the resonance integral is to integrate numerically under the cross section vs. $\ln E$ curve if experimental data are available. In principle, the numerical integration should provide a more accurate result.

38.3.5 Reaction Rates in Thermal Reactors

Earlier, it was shown that the reaction rate per atom is the product of the monoenergetic neutron flux and the corresponding cross section. In a reactor, both neutron flux and cross section are functions of neutron energy. The general equation describing the reaction rate is given by

$$R = \int \frac{d(\phi\sigma)}{dE} dE. \quad (38.24)$$

It is customary, however, to divide Eq. (38.24) into two parts (two-group theory), representing the contributions from thermal and epithermal neutrons.

$$R = \int_0^{5kT} \frac{d(\phi\sigma)}{dE} dE + \int_{5kT}^{\infty} \frac{d(\phi\sigma)}{dE} dE. \quad (38.25)$$

As stated earlier, in a reactor, the general reaction rate per atom for a substance at high dilution or very small amount includes contribution from both thermal and epithermal interactions and is given by

$$R = \phi_0 \sigma_0 + \phi_{ep} I_0 \quad (38.26)$$

where I_0 was defined in Eq. (38.22). In Eq. (38.21) it is assumed that the resonance flux varies as $1/E$ down to $5kT$ and vanishes below this energy, and that the Maxwellian neutrons follow Eqs. (38.13), (38.15), and (38.16) at all energies. Thus, just above $5kT$ the flux consists of two components. Typically, Eq. (38.26) is written as

$$R = \phi_0 \left(\sigma_0 + \frac{1}{r} I_0 \right) = \phi_0 \sigma_{eff} \quad (38.27)$$

where r is the $2,200 \text{ m s}^{-1}$ to epithermal flux ratio, ϕ_0/ϕ_{ep} , and σ_{eff} is the effective cross section. It is obvious that the exact values of r and σ_{eff} depend on the position of the sample within a given reactor. If the sample is present in substantial amounts, then the resonance integral may need to be corrected for self-absorption of neutrons at the resonance energies.

An obvious advantage can be seen to using ϕ_0 since cross section tables usually give a list of σ_0 values and since it is necessary to know the temperature corresponding to the Maxwellian velocity in order to determine other fluxes and cross sections. Often, the neutron temperature is not known, and this lack of knowledge is reflected in the uncertainty in any cross section measurement if the species in question is not known to obey the $1/v$ law in and near the thermal region. In any case, it is customary to measure the thermal flux with a $1/v$ absorber of known cross section and then to use the same flux for determining an unknown cross section.

38.3.6 Cross Section Measurements and Flux Monitoring

The problem of measuring an unknown cross section by the activation method involves the determination of ϕ_0 and ϕ_{ep} by choosing appropriate monitors and the determination of R . Usually, the amount of product formed is determined by its radioactivity or by its mass using a mass-spectrometer, making a correction for any product destroyed by other reactions (spontaneous decay or neutron transmutation). A usual procedure is to measure both ϕ_0 and ϕ_{ep} by irradiating one or more monitors with and without cadmium metal covers; or irradiations can be carried out simultaneously at two or more different positions in a reactor if the relations between the fluxes are known. The *cadmium ratio* (CR), that is, the rate of product formed without cadmium to that with a cadmium cover is given by the equation

$$CR = \frac{N(\phi_0 \sigma_0 + \phi_{ep} I_0)}{N \phi_{ep} I_0} = \frac{\phi_0 \sigma_0}{\phi_{ep} I_0} + 1. \quad (38.28)$$

Using one or more monitors of known σ_0 and I_0 , both ϕ_0 and ϕ_{ep} can be determined. If an unknown is irradiated with the monitors, the values of CR for the monitors are measured and used to determine $r = \phi_0/\phi_{ep}$ from [Eq. \(38.28\)](#), the value of CR for the unknown is measured, and then σ_0 and I_0 can be calculated using [Eqs. \(38.26\)](#) and [Eq. \(38.28\)](#).

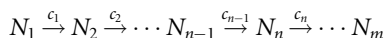
Cadmium shows an effective cutoff of a few tenths of an eV depending on the Cd thickness and flux spectra. Gadolinium with a resonance at 0.03 eV has also been used; with proper thickness an effective cutoff at about 0.10 eV should be obtainable.

It is important to use different monitors for the resonance and thermal fluxes, and to use positions of different ϕ_0/ϕ_{ep} ratios because the error in the measured ϕ_0/ϕ_{ep} ratio is proportional to $(CR - 1)$ (see [Eq. \(38.28\)](#)) and this error will be greater under conditions where CR is near unity (in which case $CR - 1$ approaches 0). In order to minimize the errors in the experimental value of ϕ_0/ϕ_{ep} , it is necessary to use a resonance flux monitor with a large I_0/σ_0 ratio to minimize thermal absorption and the significance of uncertainties in the cutoff. On the other hand, a nearly $1/v$ thermal flux monitor should be used to minimize epithermal absorption. This source of error may also be reduced by irradiating in a position with a higher thermal to resonance flux ratio. For an unknown sample of low cadmium ratio, only this latter approach will minimize the uncertainty. It has been customary to report values of σ_0 and I_0 rather than σ_{th} and I_0' since σ_0 and I_0 are obtained directly from experimental data. These distinctions have not usually been made clear, probably because the difference between σ_0 and σ_{th} is small for a $1/v$ absorber.

38.3.7 General Equations Governing the Reactor Production of Radionuclides

In general, the number of nuclei produced in a nuclear reactor can have several sources and several routes that reduce the number. Direct formation by nuclear reaction and decay of a parent nuclide formed in the bombardment increase the desired product and radioactive decay of the product decreases it. Also, neutron absorption by the radioactive product, transforming it into another species may be significant. An important example of this situation occurs in the production of the medically useful gold isotopes ^{198}Au and ^{199}Au (Hainfeld et al. 1990). The cross section for thermal neutron capture in ^{197}Au is a respectable 98.7 b, but the neutron capture cross section of ^{198}Au going to ^{199}Au is a huge 25,000 b.

Here, it is considered an m -member reaction chain of nuclei undergoing nuclear transmutation by neutron capture in addition to spontaneous decay:



where c_{n-1} is the formation rate constant (λ_{n-1} or $\sigma_{n-1}\phi$) of the n th species from the $(n-1)$ th species and is independent of time or nuclide concentrations.

It is well known that the decay and growth of genetically related species follow a set of simultaneous linear differential equations where the transmutation rate of nuclei of species n , dN_n/dt ($N_n \equiv$ concentration of species n), is governed by a constant coefficient, λ_n , referred to as the “spontaneous radioactive decay constant” (Rutherford et al. 1930). Note that λ_n is independent of time and the concentration of nuclei.

The solution of the corresponding differential equations has been known for a long time, and is referred to as the *Bateman equations* (Bateman 1910, see in [Chap. 7, Vol. 1](#)).

Later Robinson (1949) generalized the equations to include transmutation of nuclei by neutron capture in addition to spontaneous decay. The governing factor in this case is $\sigma_n \phi$, where σ_n is the neutron capture cross section (cm^2) of species n , and ϕ is the neutron flux ($\text{n cm}^{-2} \text{s}^{-1}$).

The exact solution to the corresponding differential equations, the Bateman equations, can be written as

$$N_n(t) = \left(\prod_{i=1}^{n-1} c_i \right) N_1^0 \sum_{i=1}^n a_i e^{-A_i t} \quad (38.29)$$

$$a_i = \prod_{j \neq i} (A_j - A_i)^{-1} \quad (j = 1, 2, \dots, n)$$

where $N_n(t)$ is the number of atoms of the n th species at time t , and N_1^0 is the number of target atoms (which includes appropriate corrections for isotopic mass and enrichment). A_n is the total depletion constant of the n th species, defined as $\lambda_n + \sigma_n \phi$ and t is the irradiation time (s).

► Equation (38.29) only allows for the initial presence of the first species in the chain, N_1^0 . A more general equation accommodating initial quantities of any members of the chain is

$$N_n(t) = \sum_{k=1}^n \left(\prod_{i=k}^{n-1} c_i \right) N_k^0 \sum_{i=k}^n a_i e^{-A_i t} \quad (38.30)$$

$$a_i = \prod_{j \neq i} (A_j - A_i)^{-1} \quad (j = k, k+1, \dots, n).$$

Chains involving more than two species result in lengthy equations that are tedious to evaluate, so computer programs are indispensable for these complex calculations. An algorithm based on the Robinson (1949) approach was used to develop the code LAURA (Mirzadeh and Walsh 1998).

As seen in ► Sect. 38.3.5, care must be taken in using appropriate values for cross sections and fluxes. Since most reported cross sections are $2,200 \text{ m s}^{-1}$ values (σ_0), the thermal flux used in production calculations must be the $2,200 \text{ m s}^{-1}$ flux (ϕ_0) rather than the Maxwellian flux (ϕ_{th}). If necessary, convert ϕ_{th} to ϕ_0 using ► Eq. (38.20). Also, the very definition of the resonance integral, I_0 , requires the use of *epithermal flux per unit lethargy* (lethargy is defined as the natural log of an arbitrary energy divided by a lower energy) rather than total epithermal flux; that is, since I_0 is defined as an integral with respect to energy, the flux used with ► Eq. (38.26) must also be expressed in terms of energy. If necessary, convert total epithermal flux to epithermal flux per unit lethargy by dividing the total epithermal flux by the natural log of the epithermal energy range, i.e., $\ln(E_{\text{upper}}/E_{\text{lower}})$. The appropriate values for cross sections, resonance integrals, and flux ratio (the ratio of $2,200 \text{ m s}^{-1}$ flux to epithermal flux per unit lethargy) can then be used to derive effective cross sections given in ► Eq. (38.27) by substituting ϕ_0 for ϕ in ► Eq. (38.29) or ► (38.30).

38.4 Targetry

Upon determining the production reaction and irradiation conditions, one must select an appropriate target material. Indeed in special cases, for example, when reaching very high specific activity or ultra high purity is the goal, the effort required in target design can be as demanding as the rest of the experiment. There are several general factors to be considered.

38.4.1 Physical and Chemical Form

Pure metals or elements are generally best. If these are not suitable due to the constraints below, favorable materials also include alloys as well as simple compounds such as oxides, carbonates, halides, etc. The form must also be compatible with postirradiation processing. Thus, easily dissolved compounds are sometimes preferable over metal targets.

38.4.2 Thermal Properties

There can be substantial sample heating during irradiation. Incident particles impart energy and some nuclear reactions are exothermic. Although thermal neutrons do not transfer much energy, fast neutrons can. Additionally, some of the energy of prompt γ -rays from (n,γ) reactions generated in the sample, fuel elements, reactor containment, and other nearby samples can be absorbed in the sample. The “gamma heating” is proportional to sample mass and can be substantial for samples in excess of a gram. Target cooling is thus essential in reactors in order to prevent target overheating and possible destruction. In addition, the target material should have good thermal conductivity and a high melting point. For these reasons, organic compounds and aqueous solutions cannot usually be used.

38.4.3 Chemical Stability

The target must not decompose at elevated temperature or evolve gases that would pressurize and rupture the containment capsule. Also, the target material should not react with the encapsulating material or cause corrosion. Finally, the sample must not be substantially decomposed by radiation damage, which is hard to predict in advance. This requirement generally excludes all organic material as a target for large-scale production of nuclides.

38.4.4 Purity

Targets with high chemical purity are often necessary to minimize radiocontaminants due to the activation of impurities. In compounds, the activation of all atoms must be considered, because partner atoms will not lead to the nuclide of interest and thus reduce yield. Sometimes, isotopically enriched material is necessary to suppress competing reactions on other naturally occurring isotopes in the target. To achieve high specific activity, the amount of the final product element in the target is crucial. For example, the Cu content of ZnO targets for ^{67}Cu production must be <0.1 ppm.

38.4.5 Encapsulation

For safety and to prevent cross-contamination, the target is almost always sealed in a primary container and sometimes in a secondary as well. The container should be leak-free and not corrode or overheat during irradiation. For reactor irradiation at low neutron flux and short periods, small plastic tubes (e.g., polypropylene) are useful as they do not activate appreciably

and are inexpensive. At higher neutron flux and longer irradiation time used for most nuclide production, samples are typically encapsulated in high-purity synthetic quartz ampoules. It should be noted that pyrex and soda glass are poor choices because of their boron and sodium content. The $^{10}\text{B}(n,\alpha)^7\text{Li}$ reaction has a large capture cross section and deposits substantial energy in the glass, while the $^{23}\text{Na}(n,\gamma)^{24}\text{Na}$ reaction causes significant activation of the capsule and subsequent handling problems from the high-energy (1,369 keV) γ -ray of ^{24}Na . In practice, it is usually advisable to use gloves when preparing a quartz capsule to minimize depositing sodium from perspiration. Some activation of ^{30}Si (3.1% natural abundance) to ^{31}Si ($T_{1/2} = 2.62$ h, $E_\gamma = 1,266$ keV (0.07%), $\sigma(^{31}\text{Si}) = 0.11$ b) is unavoidable. These quartz ampoules are often placed in aluminum or magnesium holders specific to the irradiation facility. There is some γ -activity produced in these metals, but the formation cross sections of ^{28}Al and ^{27}Mg are small ($\sigma = 0.23$ b and $\sigma = 0.039$ b, respectively) and the half-lives are short ($T_{1/2} = 2.24$ and 9.46 min, respectively).

38.4.6 Availability

The target material should be readily available commercially in high purity. The presence of elements even in trace amounts can degrade product radiopurity if they have large capture cross sections.

38.4.7 Target Transport Systems

Capability for the production of short-lived radionuclides in a nuclear reactor is another important criterion to be considered. Access to the reactor irradiation facilities during normal reactor operation allows for short irradiation periods, which are required for the production of many useful short-lived radionuclides such as ^{64}Cu , ^{67}Cu , ^{105}Rh , ^{109}Pd , ^{153}Sm , ^{166}Ho , ^{165}Dy , and ^{199}Au . These nuclides all have half-lives of about 3 days or less. Production of ^{99}Mo can also be enhanced by on-line access to the targets.

On-line access to the reactor irradiation facilities can be accomplished pneumatically, hydraulically, or mechanically by cables, tubes, or rods. Pneumatic tube facilities are typically used for irradiation of small samples in plastic or graphite capsules for accurate time intervals of a few seconds to 10 min or longer depending on the neutron or γ -heating of the facility. Pneumatic facilities are typically located in the reflector region of the reactor, and the capsule loading and unloading station is located in the experiment room of the neutron activation laboratory. Capsules are inserted into the reactor and returned to the laboratory using compressed air.

A hydraulic “rabbit” permits insertion and removal of samples while the reactor is operating. The water pressure-drops that exist in the primary coolant system are typically utilized as the driving forces for moving the capsules through the system. Normally, the heat flux at the surface of the capsule, due to neutron and/or γ -heating of the capsule and its contents, is limited. For the hydraulic tube facility at ORNL HFIR, for example, this limit is on the order of 200 kW m^{-2} per capsule. In addition, the use of materials with very high thermal neutron capture cross sections is limited such that the reactor is not subjected to a significant reactivity change during the insertion or removal of capsules.

“Thimble” mechanisms allow access to the reactor simply by attaching the irradiation capsule to the end of long aluminum tubing and lowering the capsule into the reactor and withdrawing it after the irradiation. The thimbles are fitted with a set of reentrant tubes connected to a separate cooling system that can circulate cooling water downward through the center and upward through the outer annular region of each tube. Samples can be placed in aluminum cans that are immersed in the cooling water, and thimble tubing can be used to vent the capsule, to fill it with gas in order to enhance heat transfer, and to bring out a pair of thermocouple leads, if desired.

38.5 Chemical Processing

In order to achieve high specific activity, radionuclides require chemical separation from the target material and induced radioactive byproducts.

This is not feasible for neutron capture reactions where there are only subtle differences between the chemical properties of different isotopes of the same element (see ► Chap. 15 in Vol. 2). In principle, however, a mass separator can be used for separation of isotopes of the same element (see ► Chap. 51 in Vol. 5). The standard techniques of analytic separation chemistry are used, such as chromatography, solvent extraction, distillation, and precipitation. Other techniques include electrolysis and electro-deposition, and separations based on sublimation. These processing techniques must then be adapted to the unique requirements of radiochemistry – the hazards of radiation exposure and contamination, rapid separation times in order to minimize decay losses, and the separation of essentially massless (carrier-free) amounts of product from bulk target. A great deal of effort has gone into developing processes suitable for each application. For example, solvent extraction is commonly used for purification of reactor-produced ^{191}Os in the form of OsO_4 which is trapped as perosmate in a NaOH solution (Brihaye et al. 1989). With the proper choice of conditions, ion exchange is very useful for separating carrier-free radionuclides from bulk target (mass ratio $> 10^8$) having significantly lower affinity toward the resin. This method has been particularly successful in separating transition metals from each other and from the rare earth elements. A relevant example is the separation of ^{55}Co from an Fe target (Lagunas-Solar and Jungerman 1979). Ion exchange is also most readily adaptable to remote or automated operation. It can be combined with solvent extraction for better separation factors, as was demonstrated in the case of ^{67}Cu (Dasgupta et al. 1991). More recently, many labs are moving away from the use of solvent extraction for hot cell use because of the difficulty of waste disposal of radioactive toxic organic solvents. It is also readily adaptable to remote or automated operation. High pressure liquid chromatographic (HPLC) systems in combination with cation-exchange resins have been employed for the separation of individual radiolanthanides (Dadachova et al. 1994). Some radiochemical separations can be effected by exploiting differences in volatility in selected cases. For example, ^{131}I can be separated from Te targets by dry distillation at high temperature (Evans and Stevenson 1956) or from a dissolved target (Hupf 1976). One can also distill the target away from the product, as was done to separate ^{32}P from an elemental sulfur target (Evans and Stevenson 1957; Mani and Majali 1966). Alternatively, Re and Os radioimpurities were separated from W targets by dry distillation in air (Mirzadeh et al. 2000). Occasionally, precipitation is useful for a first bulk separation or for low specific activity radionuclides, but precipitation rarely has the desired selectivity for nuclear medicine requirements. Adsorption on walls of glassware and filter paper can be troublesome, and handling precipitates under remote conditions may be difficult.

38.6 Shielded Facilities

The handling and processing of reactor- or accelerator-produced radionuclides usually has to be carried out in specially designed radiochemistry laboratories with controlled ventilation and air conditioning, shielded remote handling facilities, and radioactive waste collection and storage tanks (Mausner 1999). In most cases involving processing of reactor or cyclotron targets, radiation shielding for the personnel is required. At lower dose levels, this may be as simple as some stacked lead bricks inside a standard chemical fume hood, providing some whole body shielding, but no shielding for hands and arms. For pure beta emitters, small lucite disks mounted on tongs to shield the hands are all that is necessary. At higher levels of γ -radiation, a completely enclosed hot box or hot cell will be required. Hot cells usually have 10–20 cm of lead encased in steel panels for the walls or 50–100 cm of concrete, along with lead glass windows and master slave manipulators.

38.7 Current Requirements and Challenges

Specific activity is an important parameter since in many cases, the availability of very high specific activity or carrier-free radionuclides is required for biological applications. One example of the importance of high specific activity is the *radiolabeling* of tumor-specific antibodies or peptides for both diagnostic and therapeutic applications where only very small amounts of the radiolabeled antibodies are administered to ensure maximal uptake at the limited tumor cell surface antigen sites.

Another important need is the use of receptor-mediated radiopharmaceuticals that are potentially very important for the clinical evaluation of neurological diseases. Since the population of neurotransmitter sites is very limited, high specific activity agents are required to evaluate site-specific uptake and not saturate these binding sites with stable cold isotope.

Since the specific activity of a radionuclide produced by particle-induced reactions is a direct function of the incident particle flux, an increase in the incident particle flux results in an absolute increase in the specific activity of the product. This relationship is linear for simple reactions and nonlinear for complex reactions. It is important to note that the half-lives, production and depletion cross sections, and irradiation time are equally important. Several important radionuclides have long physical half-lives and low production cross sections requiring long irradiation periods even in the highest neutron flux available. An example in this category is tungsten-188 (half-life 69 days; parent for rhenium-188).

In addition, the increased flux not only results in higher specific activity products, but can allow utilization of smaller amounts of the enriched (expensive) target material. The limited availability of many enriched materials makes conservation or recycling mandatory.

38.8 Selected Examples

A list of reactor-produced radionuclides of current interest to nuclear medicine is given in [▶ Table 38.1](#) along with modes of production and corresponding nuclear cross sections. From this list, the production and a brief description of chemical processing of the following radionuclides will be discussed:

- Molybdenum-99 produced by fission and neutron capture reactions
- Iodine-131 produced by fission and neutron capture reactions
- Indium-114m produced by neutron capture reactions

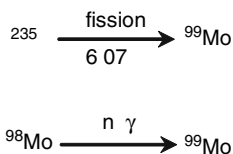
- Lutetium-177 produced by neutron capture reactions
- Iodine-125 produced by neutron capture followed by β^- decay
- Tungsten-188 produced by double neutron capture
- Tin-117m produced by neutron inelastic scattering
- Copper-67 produced by fast neutron-induced reactions

38.8.1 Molybdenum-99 Produced by Fission and Neutron Capture Reactions

Radionuclide uses in diagnostic medicine have increased tremendously in the past several decades, and today, one-third of the annual 40–50 million diagnostic procedures in the United States are performed with radionuclides. The most widely used radionuclide in nuclear medicine is technetium-99m (^{99m}Tc , $T_{1/2} = 6.0$ h), the daughter of 66 h molybdenum-99 (^{99}Mo). Tc-99m is used in 70% of all radionuclide diagnostic procedures with an estimated 16 million medical tests per year (approximately 45,000 per day) and 4–5 billion dollars cost to patients annually in the USA.

Tc-99m decays by $>99\%$ IT to the ground state of ^{99}Tc ($T_{1/2} = 2.1 \times 10^5$ a) with emission of a 140.5 keV γ ray with probability of 89% and about 10% of all IT effects occurs via internal conversion, i.e., by the emission of a K electron of ^{99}Tc . The β^- decay of ^{99}Mo feeds to ^{99m}Tc and ^{99}Tc , 87% and 13% of the disintegrations, respectively. Because Tc does not have a stable isotope in nature, the ^{99m}Tc -specific activity (SpA) approaches $169.5 \text{ GBq } \mu\text{g}^{-1}$ ($4.58 \text{ Ci } \mu\text{g}^{-1}$, 87% of the theoretical value of $195.0 \text{ GBq } \mu\text{g}^{-1}$) in daily elution.

The common sources of ^{99}Mo are the fission of ^{235}U and neutron capture by a ^{98}Mo target (► Table 38.2):



Other reactions for the production of ^{99}Mo include $^{100}\text{Mo}(\gamma, n)^{99}\text{Mo}$, $^{96}\text{Zr}(\alpha, n)^{99}\text{Mo}$, and $^{102}\text{Ru}(n, \alpha)^{99}\text{Mo}$. It may also be possible to produce ^{99m}Tc directly by the $^{100}\text{Mo}(p, 2n)^{99m}\text{Tc}$ reaction. Over the past 40 years, several versions of a $^{99}\text{Mo}/^{99m}\text{Tc}$ generator have been developed. The most common is based on the original generator developed at Brookhaven National Laboratory (Richards 1966a, b, c; Subramanian 1976). In this system, Mo is adsorbed on alumina and separation of ^{99m}Tc is achieved by saline elution. This chromatographic generator has the advantage of being portable and simple to operate. Most commercially available generators provide a sterile vial of saline at the inlet and an evacuated rubber septum sealed vial at the outlet. As soon as the septum is penetrated by a needle on the outlet port, the saline is simply sucked through the column, carrying the nuclide with it. It provides ^{99m}Tc in high efficiency ($\sim 70\%$) and with acceptable quality. Other $^{99}\text{Mo}/^{99m}\text{Tc}$ generators in use include extraction-based and sublimation generators. A review of the latter generators can be found in Boyd (1982) and Mirzadeh and Knapp (1996); cf. also ► Chap. 40 in this Volume.

In North America, ^{99}Mo is solely available from reactors in Canada and is exclusively produced from fission of uranium-235 (^{235}U). The typical yield of fission-produced ^{99}Mo is on

■ Table 38.2

General information on fission-produced ^{99}Mo

Yield	$6.1\%, 5.25 \times 10^3 \text{ GBq g}^{-1} (142 \text{ Ci g}^{-1})$ of ^{235}U ($t_{\text{irr}} = 7 \text{ days at } \phi = 7 \times 10^{13} \text{ n cm}^{-2} \text{ s}^{-1}$)
Maximum SpA	$1.78 \times 10^4 \text{ GBq mg}^{-1} (4.8 \times 10^2 \text{ Ci mg}^{-1})$ of ^{99}Mo
Achievable SpA (at EOB)	$2.66 \times 10^4 \text{ GBq mg}^{-1} (7.2 \times 10^1 \text{ Ci mg}^{-1})$ of Mo ($t_{\text{irr}} = 7 \text{ days at } \phi = 7 \times 10^{13} \text{ n cm}^{-2} \text{ s}^{-1}$)
Required SpA (at EOB)	$37\text{--}74 \text{ GBq mg}^{-1} (1\text{--}2 \text{ Ci mg}^{-1})$
Radioisotopic purity	99.9999%
Chemical purity	99.99%
Other	For each Ci of ^{99}Mo , $3.7 \times 10^3 \text{ GBq} (100 \text{ Ci})$ of other fission products are produced.

EOB: end of bombardment, SpA: specific activity.

the order of 148–370 GBq (4–10 Ci) per g of ^{235}U irradiated for 50–200 h in a neutron flux of $1.5 \times 10^{14} \text{ n cm}^{-2} \text{ s}^{-1}$. This target consisted of 45% enriched ^{235}U in the form of U/Al alloy clad in a $0.45 \times 2 \text{ cm}$ aluminum plate (IAEA Report 2003).

Due to the logistical difficulties associated with ^{99}Mo production and distribution (i.e., short half-lives of ^{99}Mo and $^{99\text{m}}\text{Tc}$, complex chemical processing, status of reactors and processing facilities, and wide distribution of users), only 5–10% of the produced ^{99}Mo typically reaches the users. Since ^{99}Mo cannot be stockpiled, even short-term disturbances in labor situations and interruption of transport systems can have very serious consequences. Multiple production reactor shutdowns have recently impacted ^{99}Mo severely. Among the strategies being considered to replace old reactors is the use of high intensity electron linacs to irradiate a low enriched uranium target to create secondary neutrons which in turn irradiate highly enriched uranium to drive fission.

Another important issue associated with Mo production is the waste and environmental impact of fission-produced Mo. Fission waste contains several radioactive gases, thus requiring dedicated facilities, and highly enriched ^{235}U targets requiring extensive security.

An important alternative non-fission route for production of ^{99}Mo is via neutron capture by ^{98}Mo , a process that does not present any of the disadvantages listed above. A comparison of fission- and neutron-produced ^{99}Mo is given in [Table 38.3](#).

For fabrication of $^{99}\text{Mo}/^{99\text{m}}\text{Tc}$ generators, the principal issue that differentiates fission-produced ^{99}Mo from the direct neutron capture route is specific activity (SpA). Commercial manufacturers of $^{99}\text{Mo}/^{99\text{m}}\text{Tc}$ generators require a SpA of $37\text{--}74 \text{ GBq mg}^{-1} (1\text{--}2 \text{ Ci mg}^{-1})$. Fission-produced ^{99}Mo has a SpA of $\sim 2.6 \times 10^3 \text{ GBq mg}^{-1} (\sim 70 \text{ Ci mg}^{-1})$, whereas the SpA of neutron capture-produced ^{99}Mo , even in the highest available neutron flux (Oak Ridge National Laboratory High Flux Isotope Reactor hydraulic tube), is approximately $1.9\text{--}3.7 \text{ GBq mg}^{-1} (50\text{--}100 \text{ mCi mg}^{-1})$, a factor of 10–20 times lower than required for the traditional single-stage generator system.

In the most widely used generator, ^{99}Mo is loaded onto a column of alumina and $^{99\text{m}}\text{Tc}$ is eluted from the column with normal saline. The required bolus volume for the quantitative elution of $^{99\text{m}}\text{Tc}$ obviously depends on the size of the column which in turn is inversely proportional to the specific activity of ^{99}Mo . Thus the lower SpA of neutron capture-produced ^{99}Mo requires a larger alumina column, resulting in a lower activity concentration of $^{99\text{m}}\text{Tc}$.

Table 38.3
Comparison of fission and neutron-produced ⁹⁹Mo

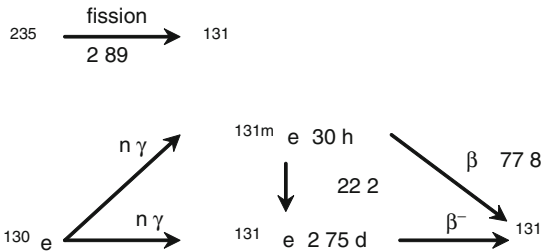
²³⁵ U(n,f) ⁹⁹ Mo	⁹⁸ Mo(n,γ) ⁹⁹ Mo
Produces high specific activity ⁹⁹ Mo	Produces low specific activity ⁹⁹ Mo
Requires highly enriched ²³⁵ U target	Requires highly enriched ⁹⁸ Mo target
Complex chemical processing	Simple chemical processing
Requires dedicated processing facility	Requires high flux nuclear reactor
Generates high-level radioactive waste	Generates minimal waste

(Bq ml⁻¹). One approach to concentrating ^{99m}Tc is by adsorbing TcO₄⁻ on a tandem anion-exchange resin with the subsequent elution of Tc in a small volume with ethylenediamine containing SnCl₂ (Mirzadeh et al. 1998).

38.8.2 Iodine-131 Produced by Fission and Neutron Capture Reactions

Radioactive isotopes of iodine have played a major role in nuclear medicine and a great deal of work has been reported with regard to radioiodination of various biological molecules. Three isotopes of iodine that are in common use are ¹²⁵I, ¹³¹I, and ¹²³I. Two other isotopes of iodine, ¹²²I and ¹²⁴I (both positron emitters), are also of interest as sources for Positron Emission Tomography (PET).

Iodine-131 has a half-life of 8.02 days and decays with 100% β⁻ emission to stable ¹³¹Xe (99%) and to 11.8 days ^{131m}Xe (1%), with an average β⁻ particle energy of 182 keV. The decay of ¹³¹I is followed by emission of an intense γ ray at 364.5 keV (81.2%). Other γ rays include 637.0 keV (7.27%), 284.3 keV (6.06%), 80.2 keV (2.62%), and a number of weaker γ rays. The total equilibrium dose constant of ¹³¹I is 1.21 rad g μCi⁻¹ h⁻¹ or in a more SI-conforming unit 3.3 × 10⁻¹⁰ Gy kg Bq⁻¹ h⁻¹ (see Sect. 10.4.2.3 in Chap. 10). The common sources of ¹³¹I are the fission of ²³⁵U and neutron capture in a ¹³⁰Te target:



The half saturation yield of ¹³¹I from fission is ~2.2 GBq mg⁻¹ (~60 mCi mg⁻¹) of ²³⁵U at a neutron flux of 1 × 10¹⁴ n cm⁻² s⁻¹ (t_{irr} = T_{1/2} = 8 days, and ϕ₀/ϕ_{ep} = 40), with a specific activity of ~0.67 GBq μg⁻¹ (~18 mCi μg⁻¹) at EOB. The theoretical specific activity of ¹³¹I is 4.58 GBq μg⁻¹ (124 mCi μg⁻¹); however, fission-produced ¹³¹I is contaminated with stable ¹²⁷I and ¹²⁹I (T_{1/2} = 1.57 × 10⁷ a) as the fission yields leading to masses 127 and 129 are 0.157% and 0.54%, respectively, vs. 2.89% leading to mass 131. The actual ratio of ¹³¹I to ¹²⁷I and ¹²⁹I, however, will be a function of neutron flux, irradiation time, and postirradiation decay period

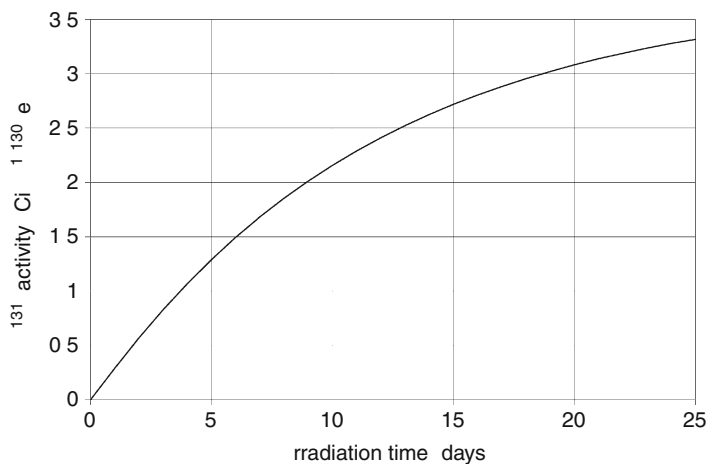
(the age of ^{131}I preparation). Also, fission yields for shorter-lived iodine isotopes are substantial (most importantly mass 133 with a yield of 6.70%), requiring postirradiation decay to increase the radionuclidic purity of ^{131}I (^{131}I has a half-life of 20.8 h). Similar to fission-produced ^{99}Mo , the waste and environmental impact of fission-produced ^{131}I is another important issue associated with ^{131}I production.

Production of ^{131}I by neutron irradiation of a Te target proceeds through β^- decay of 30 h $^{131\text{m}}\text{Te}$ and 2.75 days $^{131\text{g}}\text{Te}$ intermediate radionuclides. The reported reactor cross section to $^{131\text{m}}\text{Te}$ is only 20 mb, more than a factor of 10 smaller than the cross section through the ^{131}Te ground state ($^{131\text{g}}\text{Te}$) path (▶ [Table 38.1](#)). The contribution of both pathways to the theoretical yield of ^{131}I produced by neutron irradiation of a Te target (100% enriched ^{130}Te) is shown in ▶ [Fig. 38.5](#), where the yield of ^{131}I is given as a function of the irradiation time at a neutron flux of $1 \times 10^{14} \text{ n cm}^{-2} \text{ s}^{-1}$. Since the natural abundance of ^{130}Te is 33.8%, the ^{131}I produced from a natural Te target always contains ^{127}I and ^{129}I created by neutron captures by ^{126}Te and ^{128}Te having natural abundances of 19% and 32%, respectively. Similar to fission-produced ^{131}I , the specific activity of Te-produced ^{131}I not only is dependent on neutron flux, irradiation time, and ^{131}I age, but also highly depends on the degree of Te target enrichment. Reported ^{131}I yields from large natural Te metal and oxide targets (20–100 g) range from 22 to 33 GBq g^{-1} (600–890 mCi g^{-1}) of ^{130}Te irradiated for 5–21 days in a flux of $1 \times 10^{14} \text{ n cm}^{-2} \text{ s}^{-1}$ with a specific activity of $\sim 0.74 \text{ GBq } \mu\text{g}^{-1}$ ($\sim 20 \text{ mCi } \mu\text{g}^{-1}$) (IAEA-TECDOC-1340 2003). The experimental yields are 24–57% of the theoretical prediction for thin targets (▶ [Fig. 38.5](#)), with dry distillation processing producing higher yields than wet distillation.

The types of procedures that have been used for the separation of ^{131}I from irradiated U and Te targets include dry distillation methods in which molecular iodine is volatilized from the target at high temperature (600–800°C) and wet methods in which the target is dissolved in an appropriate medium and iodine is converted to the elemental form. Then free iodine is either distilled from acidic or basic solutions containing an oxidizing agent or extracted into a nonpolar solvent such as carbon tetrachloride, benzene, or toluene. In the distillation process, the iodine evolved is trapped in an alkaline Na_2SO_3 solution or on a cold finger. In the extraction process, I_2 is typically back-extracted into an alkaline Na_2SO_3 solution. Several

■ **Fig. 38.5**

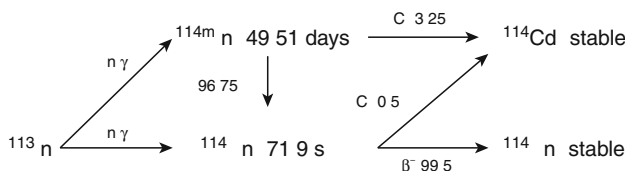
Reactor production of ^{131}I via neutron capture by ^{130}Te ($\phi_0 = 1 \times 10^{14} \text{ n cm}^{-2} \text{ s}^{-1}$, $\phi_0/\phi_{\text{ep}} = 40$)



oxidation–reduction cycles can then be carried out to achieve the desired purity. These general procedures, often with some variation, are still in common use. Oxidation of iodide to elemental form can readily be accomplished by hydrogen peroxide in an HCl medium. An excellent review of the radiochemistry of iodine can be found in Kahn and Kleinberg (1977), and a review of the properties of radioiodine in relation to its use in labeled compounds can be found in Baldwin (1986), and more recently in Finn (2003).

38.8.3 Indium-114m Produced by Neutron Capture Reactions

In-114m is a potential radionuclide for radioimmunotherapy and a potential source for brachytherapy. In-114m has rather complicated nuclear decay properties. It decays with a half-life of 49.51 days with 96.75% isomeric transition to 72 s ^{114}In ground state (3.25% electron capture to ^{114}Cd). In-114g, in turn, decays by 99.5% β^- emission with an end-point energy of 2 MeV to stable ^{114}Sn (0.5% electron capture to ^{114}Cd). In other words, the high energy β^- particle is actually emitted from the very short-lived daughter of $^{114\text{m}}\text{In}$ which is in secular equilibrium with its parent at all times:



The average β^- particle energy of In-114m is 773 keV with a total equilibrium dose constant of $1.66 \text{ rad g } \mu\text{Ci}^{-1} \text{ h}^{-1}$. Isomeric transition of $^{114\text{m}}\text{In}$ to $^{114\text{g}}\text{In}$ takes place with emission of a 190 keV γ -ray with a probability of only 16%; thus, greater than 80% of this transition is internally converted resulting in emission of very short-range secondary electrons and X-rays (approximately 20 keV). A 3.25% branch of the decay of $^{114\text{m}}\text{In}$ takes place by electron capture to stable ^{114}Cd . Although the secondary electrons do not contribute to the total dose in sealed sources used in brachytherapy, they will contribute to the total dose in other potential unsealed applications of this nuclide. Indeed, if $^{114\text{m}}\text{In}$ can be localized on or near a tumor cell nucleus by an appropriate carrier molecule, the high LET Auger electrons can be very effective in cancer therapy, cf. also [Chap. 46](#) in this Volume.

A homogeneous alloy of indium and aluminum can be made up to ~ 17 mass percent indium thus enabling manufacturing of very fine wires of In/Al (~ 0.3 mm in diameter) which are required for brachytherapy sources. Further, In-114m can be produced with high specific activity ($0.37\text{--}3.7 \text{ GBq mg}^{-1}$, $10\text{--}100 \text{ mCi mg}^{-1}$) in a moderate-size nuclear reactor within a short period of time. Alternative production routes via charged particle-induced reactions are also feasible. From the point of view of energy deposition, activation level, manufacturing, and shelf life, the $^{114\text{m}}\text{In}/\text{Al}$ source has advantages relative to other brachytherapy sources.

High-energy beta particle emitters have been recognized as suitable sources for brachytherapy, but to date, only a few radionuclides, ^{90}Y , ^{186}Re , ^{32}P , and ^{188}W ([Table 38.4](#)), have been tried. While ^{90}Y and ^{186}Re suffer from lack of shelf life, ^{188}W has the disadvantage of low specific activity (requiring long irradiation time), manufacturing difficulty associated with the high melting point of tungsten, and availability (only a few nuclear reactors in the world are

■ Table 38.4

High energy β^- particle emitters used in brachytherapy

Radionuclide	$T_{1/2}$	E_{β}^{av} (keV)	$E_{\gamma}(I_{\gamma})$ (keV) (%)	Equilibrium dose constant (rad g μCi^{-1} h $^{-1}$)
^{32}P	14.3 days	695	–	1.48
^{90}Y	64.0 h	934	–	1.99
$^{114\text{m}}\text{In}/^{114\text{g}}\text{In}$	49.51 days/71.9 s	773	190 (16)	1.66
^{186}Re	3.72 days	350	Many low	0.776
$^{188}\text{W}/^{188}\text{Re}$	69.78 days/17.0 h	764	155 (15)	1.78

capable of producing ^{188}W with useful specific activity). Manufacturing ^{32}P sources is time consuming and expensive because of the nonmetallic character of phosphorous.

In contrast, In/Al alloy wire can be manufactured relatively simply employing enriched ^{113}In and the wire can be activated to contain the desired level of radioactivity in a moderate-size nuclear reactor within a rather short irradiation time. The thermal neutron cross section and epithermal resonance integral for $^{113}\text{In}(n,\gamma)^{114\text{m}}\text{In}$ are 8.1 b and 220 b, respectively. The expected yield of $^{114\text{m}}\text{In}$ for 1 week of irradiation at a neutron flux of 1×10^{15} n cm $^{-2}$ s $^{-1}$ is ~ 6.7 GBq mg $^{-1}$ (~ 180 mCi mg $^{-1}$) of ^{113}In . A typical seed wire, 2 cm in length, 0.03 cm in diameter, containing ~ 0.12 mg of ^{113}In (2% In), would contain ~ 0.74 GBq (~ 20 mCi) of $^{114\text{m}}\text{In}$. Experimental results are summarized in [Table 38.5](#). As seen, theoretical calculations are within a factor of 2 of experimental results.

38.8.4 Lutetium-177 Produced by Neutron Capture Reactions

Lutetium-177 (^{177}Lu), attached to biological targeting molecules such as tumor-associated antibodies and peptides, is under active investigations for radioimmunotherapy. Examples of these investigations include ^{177}Lu -labeled peptides (Kwekkeboom et al. 2001, 2005) and DOTA-TOC (Oeksuez et al. 2009) for lung tumors; and ^{177}Lu -labeled antibodies for treatment of prostate cancer (Kelly et al. 2009), for ovarian cancer (Meredith et al. 1996), RS7 for lung cancer (Stein et al. 2001), and for lymphoma (Chakraborty et al. 2008). However, for a number of years, ^{177}Lu radiolabeled receptor-binding somatostatin analogues (octreotide and lanreotide) is routinely used for the treatment of Neuroendocrine tumors constituting a heterogeneous group of tumors that frequently express cell membrane-specific peptide receptors. A review article of the topic is available (Kaltsas et al. 2005).

Lutetium-177 decays with a half-life of 6.647 days to the ground state of stable ^{177}Hf 79.4% of the time ($E_{\beta 1}^{\text{max}} = 0.498$ MeV), to the first excited state 9.0% of the time ($E_{\beta 2}^{\text{max}} = 0.385$ MeV), and to the 0.321 MeV level 11.6% of the time ($E_{\beta 3}^{\text{max}} = 0.177$ MeV). Deexcitation from the first excited state level (0.1129 MeV) provides an imageable γ -ray at 113 keV with an intensity of 6.17%. About 12% of this transition converts at the electronic shell of the Hf providing low range secondary electrons and X-rays (Mirzadeh 1995). Deexcitation from the 0.321 MeV level to the first excited state level provides a γ -ray at 208 keV (10%) suitable for deep-organ imaging. The average β energy of ^{177}Lu is 0.134 MeV and the average equilibrium dose rate constant for ^{177}Lu is estimated to be ~ 0.5 g-rad/ $\mu\text{Ci}\cdot\text{h}$ (0.1342 MeV/Bq-s) (Weber et al. 1989). Some relevant nuclear data for ^{177}Lu and $^{177\text{m}}\text{Lu}$ are given in [Table 38.6](#) (ENSDF 2009; Mughabghab 2006).

Table 38.5

Production of ^{114m}In in the ORNL-HFIR hydraulic tube irradiation facility. Irradiations were performed in hydraulic tube no. 1 at 85 MW power. The thermal neutron flux at this position is $9.0 \times 10^{14} \text{ n cm}^{-2} \text{ s}^{-1}$ with a thermal to epithermal flux ratio of ~40

Target			t_{irr}	Yield at EOB (GBq mg^{-1})	
Mass (mg)	^{113}In enrich. (at%)	Chemical form		Experimental	Experimental/theoretical ^a
1.6	96.26	In_2O_3	24 h	0.39	0.43
a) 1.19	0.043	$\text{In}(2\%)/\text{Al}$	68 h	2.48	
b) 2.55	0.043	$\text{In}(2\%)/\text{Al}$	68 h	2.54	
				Av. 2.51 ± 0.03	0.99
a) 1.00	0.043	$\text{In}(15\%)/\text{Al}$	24 h	0.85	
b) 1.34	0.043	$\text{In}(15\%)/\text{Al}$	24 h	0.62	
c) 1.77	0.043	$\text{In}(15\%)/\text{Al}$	24 h	0.82	
				Av. 0.77 ± 0.13	0.84

^aAs the burn-up cross section of ^{114m}In is not known, a value of 2 b was used in the calculations.

Table 38.6

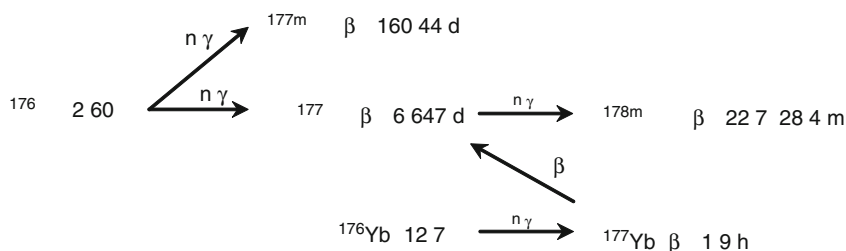
Nuclear data for ^{177}Lu and ^{177m}Lu

Mode of decay					Reaction cross sections (b)			
					Production		Burn-up	
Radionuclide	$t_{1/2}$	E_{β}^{av} (keV)	$E_{\gamma}(I_{\gamma})$ (keV)(%)	Mode of production	σ	I_0	σ	I_0
^{177}Lu	6.647 days	β^- (100%) $E_{\beta}^{\text{av}} = 134$	113(6.17) 208(10.36) Many low	$^{176}\text{Lu}(n,\gamma)$ $^{176}\text{Yb}(n,\gamma)^{177}\text{Yb}$ (β^- , 1.9 h)	2,017 ± 70 2.85	1,087 ± 40 6.3	1,000 ± 300 –	– –
^{177m}Lu	160.4 days	IT (21.4%) β^- (78.6%) $E_{\beta}^{\text{av}} = 40.8$	113(21.9) 208(57.4) 228(37.1) 379(29.9)	$^{176}\text{Lu}(n,\gamma)$	2.8 ± 0.7	4.7 ± 1.4	3.18 ± 0.30	–

The rather longer half-life of ^{177}Lu (6.6 days) is most suited for slow-targeting antibodies, and its lower equilibrium dose rate constant make ^{177}Lu useful for radiotherapy of soft tissues (Mirzadeh 1995; Mirzadeh et al. 1996; Ma et al. 1996). In addition, ^{177}Lu has chemical characteristics suitable for protein labeling with bifunctional chelating agents such as the eight coordinated DTPA, DTPA derivatives, or DOTA. Although Lu is the heaviest member of lanthanides, the ionic radius of Lu^{3+} is comparable to that of Y^{3+} as the result of lanthanides contraction. In coordination number 6, the ionic radius of Lu^{3+} is 89.1 pm, ~4 pm smaller than that of Y^{3+} . At 25°C and 0.1 M ionic strength, the equilibrium constant of Lu-DTPA complex (ML/M·L) is $2.51 \times 10^{22} \text{ M}^{-1}$ in comparison with $1.12 \times 10^{22} \text{ M}^{-1}$ for the Y-DTPA complex (Martel and Smith 1974).

Benefitting from a rather large thermal neutron cross section, high specific activity ^{177}Lu can be obtained directly by the $^{177}\text{Lu}(n,\gamma)$ reaction (the theoretical specific activity of ^{177}Lu is

109.94 mCi/ μg). The natural abundance of ^{176}Lu is only 2.6%, but highly enriched ^{176}Lu is available from the US DOE National Isotope Development Center and Trace Inc. (Russian-made material). Alternatively, ^{177}Lu can be obtained indirectly from β^- decay of 1.9-h ^{177}Yb , which is produced in a fission nuclear reactor via neutron capture by ^{176}Yb (Lebedev et al. 2000). Ytterbium-176 has a natural abundance of 12.7%, but highly enriched ^{176}Yb (up to 99.7%) is available. It is clear that the indirect route yields carrier-free preparations of ^{177}Lu if Lu at a trace level can be separated efficiently from bulk mg amounts of Yb target material. The indirect route produces ^{177}Lu with substantially less contamination from 160-day $^{177\text{m}}\text{Lu}$ which is unavoidably coproduced with ^{177}Lu by the $^{176}\text{Lu}(\text{n},\gamma)$ reaction. The scheme for production of ^{177}Lu in a reactor is shown below (Lederer and Shirley 1978; ENSDF 2009), and a number of reports are available on the production of ^{177}Lu either by direct or indirect route (Lebedev et al. 2000; Hashimoto et al. 2003; Pillai et al. 2003; Mikolajczak et al. 2003; Knapp et al. 2004, 2005; Dvorakova et al. 2007; Zhernosekov et al. 2008).



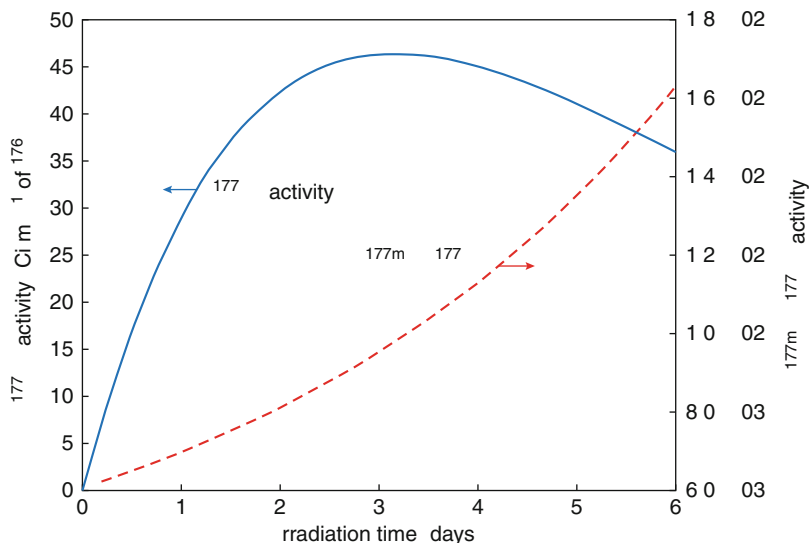
For 1-h irradiation of natural and 43% enriched Lu targets (as Lu_2O_3 , ~ 1 mg target) at the ORNL-HFIR (HT, position 4), the average experimental yields of ^{177}Lu are reported to be $(9.4 \pm 0.8) \times 10^4$ MBq/mg of ^{176}Lu in comparison to the theoretical yield of 6.1×10^4 MBq/mg of ^{176}Lu for an experimental to theoretical ratio of 1.5. The ratio of $^{177\text{m}}\text{Lu}/^{177}\text{Lu}$ was $(4.7 \pm 0.1) \times 10^{-3}\%$.

The theoretical yield of ^{177}Lu as a function of irradiation time is shown in [Fig. 38.6](#). From these data, it is clear that saturation will be reached within 4 days in the ORNL HT#4 or 6 with an expected yield of $\sim 1.7 \times 10^6$ MBq (~ 46 Ci)/mg of ^{176}Lu . As the $^{177\text{m}}\text{Lu}/^{177}\text{Lu}$ ratio will increase with irradiation time ([Fig. 38.6](#)), for a 4-day irradiation, the fraction of $^{177\text{m}}\text{Lu}$ at EOB is expected to be less than 0.012% (Mirzadeh 1995).

The yield from the indirect route (from decay of ^{177}Yb) is 75 ± 5 MBq/mg of ^{176}Yb (2.0 mCi/mg of ^{176}Yb) for 1 h irradiation in the HT #5 using ~ 4 mg of 96% enriched ^{176}Yb . This experimental yield is $\sim 20\%$ lower than the theoretical value (Mirzadeh 1995). In this case, calculations were performed allowing a 12-h decay period postirradiation. The theoretical yield of ^{177}Lu as a function of time is shown in [Fig. 38.7](#). As shown, the yield of ^{177}Lu will reach a saturation value of $\sim 8 \times 10^3$ MBq (217 mCi)/mg of ^{176}Yb within 21 days of irradiation in the HT#5, followed by a 12-h decay. The contribution from the decay of ^{176}Yb to the total activity of ^{177}Lu decreases rapidly as a function of irradiation time. This contribution becomes negligible ($< 1\%$) for irradiation time of more than 20 h. The yield of the indirect route is lower than the direct route by a factor of $\sim 1,300$, but the specific activity of ^{177}Lu from both routes will be roughly the same assuming that carrier-free Lu can be separated from Yb in 1 part per thousand. Separation of ^{177}Lu from macroscopic amounts of Yb (both in the lanthanide family) is not very efficient, although the procedures have been improved (Lebedev et al. 2000; Mirzadeh et al. 2004; Horwitz et al. 2005). In fact, MDS Nordion Inc. distributes ^{177}Lu produced via the “indirect” route with effective specific activity < 45 mCi mg^{-1} of lanthanides

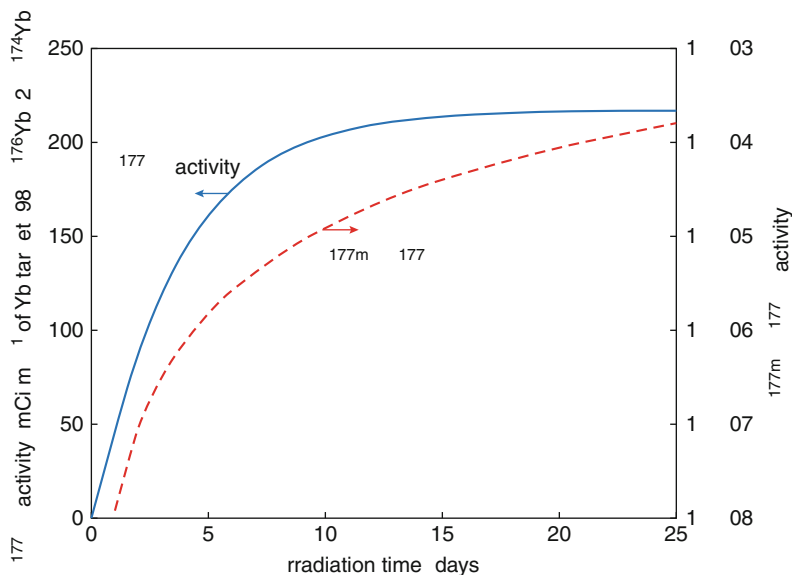
■ Fig. 38.6

Production of ^{177}Lu from a ^{176}Lu target ($\phi_0 = 2 \times 10^{15} \text{ n cm}^{-2} \text{ s}^{-1}$, $\phi_0/\phi_{\text{ep}} = 20$)



■ Fig. 38.7

Production of ^{177}Lu from an ^{176}Yb target ($\phi_0 = 2 \times 10^{15} \text{ n cm}^{-2} \text{ s}^{-1}$, $\phi_0/\phi_{\text{ep}} = 20$)



which is half of the theoretical value (MDSTM NordionTM ^{177}Lu fact sheet, 2004). The main advantage of the indirect route is that the contamination with $^{177\text{m}}\text{Lu}$ is significantly reduced ($<1 \times 10^{-4}\%$) at 12 h postirradiation, but it cannot be totally eliminated due to the presence of a small fraction of ^{174}Yb in the highly enriched ^{176}Yb target (Mirzadeh 1995). Lu-177, produced

via indirect route, with a specific activity of >81 mCi/ μ g is also available from ITG Garching, Germany (ITG Garching 2010).

High energy proton irradiation of natural Ta and Hf targets was very recently attempted (Medvedev et al. 2008) to make no-carrier-added ^{177}Lu . However, the authors concluded that production of ^{177}Lu by this method is not practical mainly because of very low yield and high levels of contamination with ^{171}Lu and ^{172}Lu that have comparable half-lives with that of ^{177}Lu . These radioisotopes are generated through the decay of short-lived W, Ta, and Hf isotopes, which, in turn, are created directly by $^{\text{nat}}\text{Ta}(\text{p},\text{xn})$, $^{\text{nat}}\text{Ta}(\text{p},\text{pxn})$, $^{\text{nat}}\text{Hf}(\text{p},\text{pxn})$, and $^{\text{nat}}\text{Hf}(\text{p},\text{xn})$ reactions. More recently, Siiskonen et al. (2009) investigated the use of low-energy protons on natural Hf to produce ^{177}Lu . They measured excitation functions from 5.6 to 16.7 MeV and calculated cross sections up to 30 MeV. Nevertheless, they conclude that this route is not feasible for producing ^{177}Lu because of very small cross sections below 20 MeV and numerous radioactive Lu contaminants above 20 MeV.

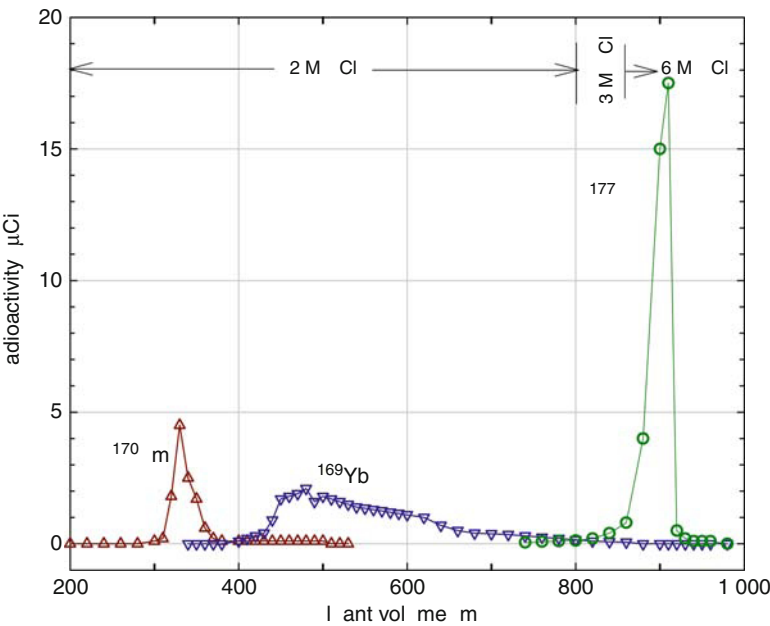
As pointed out, indirect production of ^{177}Lu from an Yb target requires an efficient method of separating trace amounts of Lu from macroscopic amounts of Yb. It is well known that separation of the individual members of the lanthanide series can be achieved by liquid-liquid extraction utilizing organophosphate ligands (e.g., di(2-ethyl hexyl) phosphoric acid, HDEHP) dissolved in organic solvent (e.g., toluene or n-heptane) and dilute mineral acids (Peppard et al. 1957). More conveniently, a similar separation can be conducted by column extraction chromatography using commercial LN resin in dilute nitric acid (Ln resin is manufactured by Eichrom Technologies Inc USA, www.eichrom.com) (Horwitz et al. 2005). A more efficient separation, however, was reported in HCl media (Mirzadeh et al. 2004). In this case, a typical reactor target consisting of ~ 10 mg of Yb target in 10 mL of 2 M HCl was loaded on a 10 mL bed volume (BV) of a LN column (0.7×32 cm, 5 g, ~ 100 mesh). The column was then washed with 800 mL of 2 M HCl at a flow rate of ~ 0.17 mL min^{-1} , followed by 70 mL of 3 M HCl, and finally the purified Lu was stripped off the column by 50 mL of 6 M HCl. The 1st peak in the chromatogram (Fig. 38.8) belongs to ^{170}Tm which is formed by neutron capture by the stable ^{169}Tm impurity in the enriched ^{176}Yb target material. As shown, the Yb target was eluted from the column in a broad peak but under the above conditions, a good separation was achieved between Yb and Lu. The specific activity of ^{177}Lu was found to be >100 Ci mg^{-1} . Alternatively, cementation was used for separation of no-carrier-added ^{177}Lu from macro amounts of Yb. This procedure is based on selective extraction of Lu from bulk of Yb by Na(Hg) amalgam from $\text{Cl}^-/\text{CH}_3\text{COO}^-$ electrolyte, followed by a final cation exchange purification. The process provides a decontamination factor (DF) of >104 for the 1st step and a DF of 102 for the 2nd step. The reported overall yield is $75 \pm 5\%$, and the process can be completed within 4–5 hours (Lebedev et al. 2000).

38.8.5 Iodine-125 Produced by Neutron Capture Followed by β^- Decay

Iodine-125 has a half-life of 59.4 days and decays by 100% electron capture to the first excited state of ^{125}Te (35.5 keV, 1.49 ns). Deexcitation from this level to the ground state of stable ^{125}Te is highly converted, and as a result, the 35.5 keV γ -ray emission occurs in only 6.7% of the total disintegrations (the 35.5 keV emission is just above the 33.2 keV K-absorption edge of iodine). The energy averaged over all photons (X- and γ rays) in the decay of ^{125}I is 26.4 keV.

I-125 is widely used as a tracer in biology and medicine. Some current applications include biodistribution studies of ^{125}I -labeled drugs, peptides and antibodies, and the use of

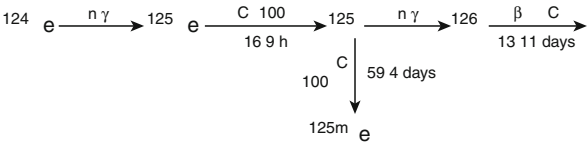
Fig. 38.8
Separation of no-carrier-added ^{177}Lu from Yb target on LN resin in HCl medium. As expected, ^{170}Tm impurity elutes ahead of Yb target



^{125}I -labeled nucleic acid precursors (e.g., ^{125}I -dU, 5'-iododeoxyuridine, a thymidine analog) in cell-targeted therapeutics (Daghighian et al. 1996; Kassis et al. 1987). In this case, the radiotoxicity is due to the fact that the decay of ^{125}I is followed by a shower of short-range secondary electrons of only a few hundred eV and $\sim 1\text{ }\mu\text{m}$ path-length in tissue. Consequently, a significant fraction of the decay energy is deposited in microscopic volumes in the vicinity of nuclear DNA, leading to multiple strand breaks. Such molecular lesions have been shown to have profound biological consequences (Adelstein and Kassis 1987; Howell et al. 1992); cf. also [Chaps. 46](#) and [47](#) of this Volume.

Recently, permanent implants into the prostate with ^{125}I seeds have become increasingly popular. Typical implant seeds (1 mCi of ^{125}I per seed) are designed to deliver a dose of 160 Gy during the full decay. The initial dose rate is 7.72 cGy h^{-1} and 87.5% of the full dose is delivered over a period of 6 months (three half-lives).

Reactor production of ^{125}I involves irradiation of a xenon target, followed by a postirradiation decay time to allow the 16.9 h ^{125}Xe to decay ^{125}I .



The activities of ^{125}I and ^{126}I (mCi mg^{-1} of Xe) as a function of time (100 days irradiation at a neutron flux of $1 \times 10^{14}\text{ n cm}^{-2}\text{ s}^{-1}$, followed by 100 days decay) are depicted in [Fig. 38.9](#). Applicable nuclear data for these calculations are presented in [Table 38.7](#).

Fig. 38.9

Production of ^{125}I from a natural xenon target ($\phi_0 = 1 \times 10^{14} \text{ n cm}^{-2} \text{ s}^{-1}$, $\phi_0/\phi_{\text{ep}} = 40$, $t_{\text{irr}} = 100 \text{ h}$, $t_{\text{decay}} = 100 \text{ h}$)

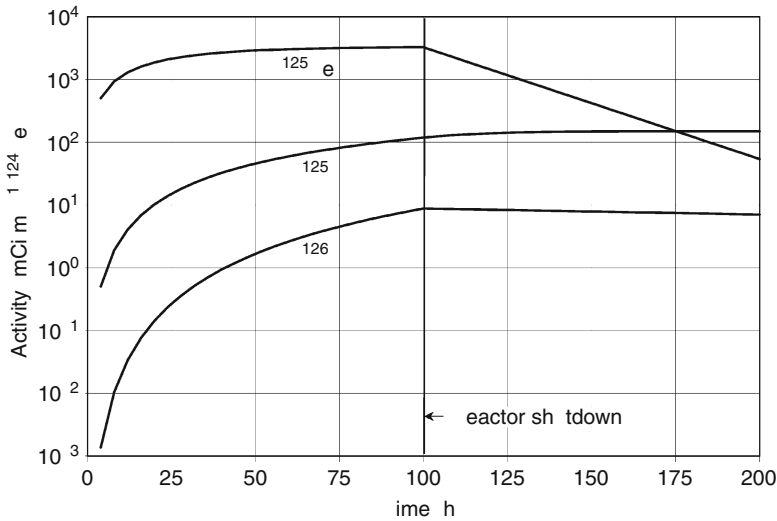


Table 38.7

Nuclear data for neutron irradiation of a natural Xe target for the production of ^{125}I

Nuclide	Natural abundance (%)	$T_{1/2}$	Cross section (b)	
			σ	I_0
^{124}Xe	0.096	Stable	165	3,600
^{125}Xe	–	16.9 h	N/A	N/A
^{125}I	–	59.4 days	894	13,730
^{126}I	–	13.11 days	5,960	40,600
^{126}Xe	0.090	Stable	3.5	60
^{127}Xe	–	36.4 days	N/A	N/A
^{127}I	–	Stable	6.2	147
^{128}I	–	24.99 min	N/A	N/A

N/A – not available

Radionuclidic contamination (defined as the ratio of $^{126}\text{I} + ^{128}\text{I}$ to ^{125}I) is obviously dependent on the enrichment of the ^{124}Xe target (the natural abundance of ^{124}Xe is only 0.096%). A practical complication is that the ^{124}Xe target contains ^{126}Xe ; this leads to additional reactions and radioimpurities that can lower the ^{125}I SpA.

Alternative production routes for ^{125}I include proton- and deuteron-induced reactions in an enriched ^{125}Te target in an accelerator, $^{125}\text{Te}(\text{p}, \text{n})^{125}\text{I}$ and $^{125}\text{Te}(\text{d}, 2\text{n})^{125}\text{I}$, respectively.

Elemental Xe and solid XeF_2 can be used as targets. The elemental Xe can be either in the form of pressurized gas, adsorbed on charcoal, or ion-implanted on synthetic SiO_2 . The melting point of XeF_2 is fairly high (130°C) and large amounts can be irradiated. Owing to

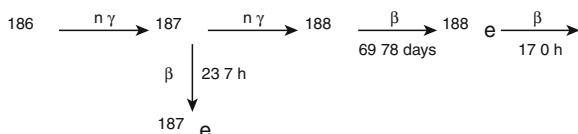
the nuclear properties of fluorine, no radio-contaminants are produced due to the presence of fluorine. After irradiation, the XeF_2 target is dissolved in water at 0°C , and the evolved gaseous Xe is collected in a cold trap at -40°C (isopropyl alcohol/dry ice). After a few days of decay, ^{125}Xe is cryogenically transferred to another cold trap and ^{125}I in the first cold trap is dissolved in a dilute $\text{NaOH}/\text{Na}_2\text{SO}_3$ mixture (Kahn and Kleinberg 1977). Inasmuch as ^{125}I is produced by neutron irradiation of Xe the isotopic impurities are limited to ^{126}I and ^{127}I , which are both made through nuclear reactions, i.e., $^{125}\text{I}(\text{n},\gamma)^{126}\text{I}(\text{n},\gamma)^{127}\text{I}$ and $^{126}\text{Xe}(\text{n},\gamma)^{127}\text{Xe} \xrightarrow{\text{EC}} ^{127}\text{I}$. The total amount of iodine in a ^{125}I preparation is represented primarily by ^{125}I and ^{127}I with only a negligible amount contributed by ^{126}I , which can be experimentally measured by neutron activation analysis (NAA).

High specific activity ^{125}I is available from different manufacturers in an aqueous solution containing NaOH or Na_2SO_3 , with activity claimed to be in the form of I^- . This may be true of freshly prepared solutions, but in the course of a few weeks, significant amounts of this iodide activity are transformed into unidentified species. These species may be volatile and do not exchange with added I^- even after the addition of Na_2SO_3 or $\text{Na}_2\text{S}_2\text{O}_3$.

38.8.6 Tungsten-188 Produced by Double Neutron Capture

Currently, there is considerable interest in rhenium-188 (^{188}Re) for various medical applications (see Lambert and de Klerk 2006; Jeong and Chung 2003; Knapp et al. 1997, and references therein). The convenient 17.0 h half-life and 100% beta emission with high end-point energies ($E_{\beta}^{\text{av}} = 764 \text{ keV}$) make ^{188}Re an attractive candidate for radiotherapy of larger tumors. Rhenium-188 decay provides an imageable γ ray of 155 keV with an intensity of 15%. About 5% of this transition also converts in the electronic shells of the ^{188}Os daughter providing secondary electrons and X-rays of short range. The average equilibrium dose rate constant for ^{188}Re is $1.78 \text{ rad g } \mu\text{Ci}^{-1} \text{ h}^{-1}$. Another major advantage is the availability of ^{188}Re in the carrier-free state from a generator system with a shelf life of many months.

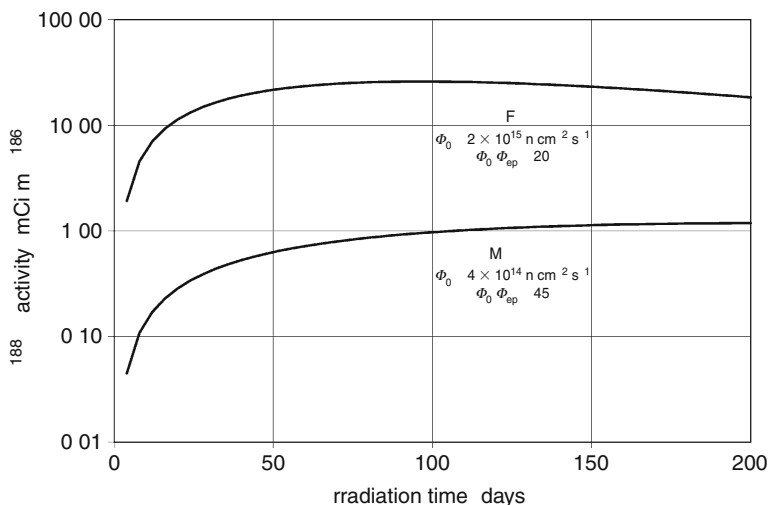
The long-lived (69.78 days) parent nuclide, ^{188}W , is produced in a nuclear reactor by double neutron capture by highly enriched ^{186}W .



Thin-target production yields of ^{188}W as a function of irradiation time at neutron fluxes of $2 \times 10^{15} \text{ n cm}^{-2} \text{ s}^{-1}$ (HFIR) and $4 \times 10^{14} \text{ n cm}^{-2} \text{ s}^{-1}$ (MURR) are shown in [Fig. 38.10](#). The chemical form of the target can be either metallic or oxide. The principal advantage of a metal target is a net increase in the yield per unit target, as a larger amount of the more dense W metal can be packed into an irradiation capsule. This is an important factor for the large-scale production of ^{188}W which has to be balanced against neutron self-absorption by a massive W target. Chemical processing of the neutron-irradiated WO_3 targets involves dissolution in an excess of hot 1 M NaOH in the presence of H_2O_2 or NaOCl or both (Knapp et al. 1994). A favored method to process metallic W is to take advantage of the reactivity of molecular oxygen toward metallic W powder at elevated temperatures, and subsequent dissolution of the WO_3 as above. This approach has an additional benefit in that the technique can be used for simultaneous separation of W from Re and Os which form volatile oxides (Mirzadeh et al. 2000).

■ Fig. 38.10

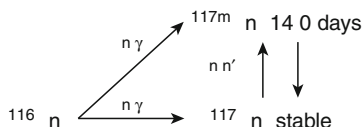
Production of ^{188}W from a ^{186}W target in the Oak Ridge High Flux Isotope Reactor (HFIR) and the Missouri University Research Reactor (MURR)



The elements W and Re are in Groups VIb and VIIb of the periodic table under Mo and Tc, respectively, and similar to the Mo/Tc system, the most common generator is based on adsorption of W on alumina, where selective elution of ^{188}Re is achieved by saline as the eluant (Kadina et al. 1990). The interaction of tungsten ions with alumina has been studied in some detail by Dadachova et al. (1995). The chromatographic generator is portable, simple to operate, and it provides ^{188}Re with a radiopurity of $\sim 75\text{--}85\%$ (Kamioki et al. 1994). Other proposed $^{188}\text{W}/^{188}\text{Re}$ generators include gel-type (Ehrhardt et al. 1990) and sublimation types. A review of the latter can be found in Boyd (1982); cf. also Chap. 40 in this Volume.

38.8.7 Tin-117m Produced by Neutron Inelastic Scattering

Tin-117m has been in Phase II/III clinical trials for palliation of pain caused by breast and prostate cancer metastasized to bone (Atkins et al. 1993, 1995). This isotope of tin can be produced in a reactor by $^{116}\text{Sn}(n,\gamma)^{117\text{m}}\text{Sn}$ and $^{117}\text{Sn}(n,n')^{117\text{m}}\text{Sn}$ reactions. Alternative production routes via proton-induced reactions on Sb isotopes in an accelerator are also possible.



The production of metastable nuclei such as $^{117\text{m}}\text{Sn}$ via neutron radiative capture reactions is characterized by small neutron cross sections and, hence, low production rates. Metastable nuclei typically have excitation energies on the order of 100 keV and large differences in angular momentum from the ground states (most metastable nuclei have high angular momentum which delays de-excitation).

An alternative route for producing metastable nuclei is through neutron inelastic scattering where the cross section of the $^AZ(n,n')^{Am}Z$ reaction is, in some cases, substantially higher than the cross section for the $^{(A-1)}Z(n,\gamma)^{Am}Z$ route. As has been shown for the case of ^{117m}Sn (Mausner et al. 1985), the magnitude of gain in the cross section may compensate for the relatively lower fast neutron flux from a well-moderated fission spectrum in the typical irradiation location of most research reactors. Note that the excitation energies of metastable nuclei represent the thresholds for inelastic scattering. Large research reactors such as HFIR, with significant epithermal and fast neutron fluxes, are well suited for these types of reactions.

A thorough study of the production of ^{117m}Sn in the hydraulic tube (HT) of the HFIR has been reported (Mirzadeh et al. 1997), and it was shown that the yield from the (n,n') reaction was higher than that obtained from the (n,γ) reaction and the relative gain in the specific activity was 3.3. The cross section for the inelastic neutron scattering reaction for the production of ^{117m}Sn was 222 ± 16 mb. A value of 176 ± 14 mb for the cross section of the $^{117}\text{Sn}(n,n')^{117m}\text{Sn}$ reaction obtained at HFBR was reported earlier (Mausner et al. 1985).

The measured thermal neutron capture cross section (σ_{th}) and resonance integral (I_0) for the $^{116}\text{Sn}(n,\gamma)^{117m}\text{Sn}$ reaction are 5.8 ± 1.2 and 350 ± 53 mb, respectively. As demonstrated in this case, in the determination of neutron capture cross sections, the contribution from inelastic neutron scattering to the overall reaction is significant and appropriate corrections are required even when highly enriched target isotopes are used. Consequently, measured cross sections for capture reactions to metastable states are often lower than reported values.

The large-scale production yield of ^{117m}Sn via inelastic scattering reactions was recently measured at the HFIR for a number of targets ranging in mass from 4 to 200 mg with an enrichment of 87–92%. For one reactor cycle (~ 21 days) irradiation at position 5 of the HT facility (corresponding to the reactor midplane), the average yield for 87% enrichment is 0.29 ± 0.03 GBq mg^{-1} (7.9 ± 0.8 mCi mg^{-1}) of Sn (corresponding to 0.34 GBq mg^{-1} of ^{117}Sn). The average yield at saturation is 0.48 ± 0.04 GBq mg^{-1} (12.9 ± 1.2 mCi mg^{-1}) of Sn.

For a one-cycle irradiation, at the end of bombardment (EOB) the radionuclidic impurities in ^{117m}Sn samples include 115 days ^{113}Sn (0.10%), 2.7 days ^{122}Sb (0.22%), 2.7 a ^{125}Sb (0.03%), and 12.4 days ^{126}Sb (0.03%). These values represent the average of nine runs using 84.23% enriched ^{117}Sn . In three runs with a 92% enriched target, the impurities were ^{113}Sn (0.03%), ^{122}Sb (0.13%), ^{125}Sb (0.05%), and ^{126}Sb (0.01%). The more highly enriched target produces a more pure product as expected. Antimony-125 is primarily produced from the β^- decay of 9.5 m ^{125m}Sn . This isotope of Sb can also capture a neutron to form ^{126}Sb . The ^{122}Sb is created by neutron capture of stable ^{121}Sb formed from the beta decay of ^{121}Sn . Two other potential contaminants are 27 h ^{121}Sn (a pure beta emitter and not detectable with γ -ray spectroscopy), and 9.64 days ^{125}Sn (also a parent of ^{125}Sb). The level of ^{121}Sn at 7 days post-EOB is estimated to be $\sim 0.1\%$. No ^{125}Sn was detected in any run and its level was estimated to be $\ll 0.01\%$.

The DTPA complex of ^{117m}Sn very selectively localizes in bone (Srivastava et al. 1985). Its synthesis and use for bone pain palliation has been described by Srivastava et al. (1998).

38.8.8 Copper-67 Produced by fast Neutron-Induced Reactions

There is considerable interest in exploring the potential use of copper-67 (^{67}Cu) for therapeutic applications (DeNardo et al. 1991; Roberts et al. 1989; Green et al. 1988; Roberts et al. 1987). Copper-67 is a pure β^- emitter and decays with a half-life of 67.01 h to the ground state of stable ^{67}Zn in 20% of the disintegrations and to the 93.3 and 184.6 keV excited states in 23%

■ Table 38.8

Reactor production of carrier-free ^{67}Cu

Reactor/position	Fast neutron flux ($E_n \geq 1 \text{ MeV}$) ($\text{n s}^{-1} \text{ cm}^{-2}$)	Sat. yield of ^{67}Cu at EOB (GBq mg^{-1} of ^{67}Zn)	Cross section (mb)
HFIR (85 MW)			
Hydraulic Tube	4.4×10^{14}	4.14 ± 0.37	1.07 ± 0.11^a
HFBR (60 MW)			
In-core, V15	3.0×10^{14}	3.34 ± 0.35	1.23 ± 0.13^b
Core-edge, V11	6.4×10^{13}	0.53 ± 0.01	0.91 ± 0.10^b

^aMirzadeh and Knapp (1992)^bMirzadeh et al. (1986)

and 56% of the disintegrations, respectively. The average β^- particle energy of ^{67}Cu is 142 keV with an equilibrium dose constant of $0.575 \text{ rad g } \mu\text{Ci}^{-1} \text{ h}^{-1}$. The medical interest derives from its convenient several day half-life, medium energy beta emissions, and facile labeling chemistry. The photon energy is also useful for imaging.

The suggested nuclear reactions for the production of ^{67}Cu , in quantities relevant to nuclear medicine applications, include the $^{67}\text{Zn}(\text{n,p})^{67}\text{Cu}$ reaction in a reactor, and the $^{68}\text{Zn}(\text{p},2\text{p})^{67}\text{Cu}$ reaction and spallation of RbBr or As targets in a proton accelerator. Other reactions include $^{68}\text{Zn}(\text{d},2\text{pn})^{67}\text{Cu}$, $^{67}\text{Zn}(\text{d},2\text{p})^{67}\text{Cu}$, $^{64}\text{Ni}(\alpha,\text{p})^{67}\text{Cu}$, and $^{68}\text{Zn}(\gamma,\text{p})^{67}\text{Cu}$ (Mirzadeh et al. 1986, and references therein, Polak et al. 1986).

For the reactor route, the saturation yield of ^{67}Cu from the $^{67}\text{Zn}(\text{n,p})$ reaction at EOB is $4.14 \pm 0.37 \text{ GBq mg}^{-1}$ ($112 \pm 10 \mu\text{Ci mg}^{-1}$) of ^{67}Zn at position no. 5 in the High Flux Isotope Reactor (HFIR) hydraulic tube (reactor midplane). Production data and fast neutron fluxes available in irradiation facilities in HFIR and the High Flux Beam Reactor (HFBR, this reactor was permanently shut down in 1999) are summarized in Table 38.8.

Many approaches for separation of copper at trace concentrations from other metal ions including extraction, ion-exchange (Dasgupta et al. 1991), dry distillation, and electrolytic separation (see Mirzadeh and Knapp 1992, and references therein) have been studied. The application of the *spontaneous electrodeposition technique* for separation of carrier-free radionuclides of copper from proton- or neutron-irradiated zinc targets was reported by Mirzadeh and Knapp (1992). In this process, electrodeposition occurs without an external EMF. The absence of measurable current in this process eliminates hydrogen overvoltage and preserves the nobility of the Pt electrode. Consequently, the highest degree of separation of $^{67}\text{Cu}^{2+}$ from interfering metal ions (i.e., ions of Co, Fe, Ni, etc.) was obtained. Separation factors of $\geq 1 \times 10^7$ were easily achieved from macro amounts (grams) of Zn within 30 min. However, since even trace quantities of stable impurities can compete for binding with a carrier molecule, chelates that are selective for the copper ion are preferred (Srivastava et al. 1995).

38.9 Conclusion

This chapter has summarized a number of approaches to produce medical radionuclides with neutrons in a nuclear reactor. The combination of generally large production cross sections and high neutron flux has made this method the principal route to create medical radionuclides.

Overall demand for the most widely used radionuclides such as ^{99}Mo and ^{131}I continues to grow somewhat, and there is a very large potential demand for newer neutron-rich radionuclides for cancer therapy.

This is occurring in parallel with large increases in demand for short-lived diagnostic radiopharmaceuticals for cancer detection and staging, especially cyclotron produced ^{18}F (fluorodeoxyglucose). While the number of small cyclotrons to supply ^{18}F is increasing rapidly at present, at least one per month in the United States alone, the situation with reactors is not as sanguine. In recent years, the closure of the High Flux Beam Reactor and Brookhaven Medical Research Reactor both at BNL, the closure of the Fast Flux Test Facility at the Hanford Site (Washington State), and the cancelation of the Advanced Neutron Source project at ORNL, have led to a large decline in reactor nuclide production capability in the United States. The most useful remaining reactors for nuclide production are the High Flux Isotope Reactor at ORNL, and the Missouri University Research Reactor. Both are quite old, but very flexible and capable. Outside the US the situation is not dramatically better. Construction of two new production reactors in Canada to replace the aging, unreliable NRU reactor has been canceled and the Petten reactor in Holland has experienced major outages. Fortunately, the new OPAL reactor in Australia has commenced operation, and there is a stable situation in Russia.

Acknowledgments

Research at ORNL was supported by the U.S. DOE under contract DE-AC05-00OR22725 with UT-Battelle, LLC. Research at BNL was supported by the U.S. DOE under Contract DE-AC02-98CH10886 with Brookhaven Science Associates.

References

- Adelstein SJ, Kassis AI (1987) *Nucl Med Biol* 14:165
- Atkins HL, Mausner LF, Srivastava SC, Meinken GE, Strub RF, Cabahug CJ, Weber DA, Wong CT, Sacker DF, Madajewicz S, Park TI, Meek AG (1993) *J Radiol* 186:279
- Atkins HL, Mausner LF, Srivastava SC, Meinken GE, Cabahug CJ, D'Alessandro TD (1995) *J Nucl Med* 36:725
- Baldwin RM (1986) *Appl Radiat Isot* 37:817
- Bateman H (1910) *Proc Cambridge Philos Soc* 15:423
- Bizzell OM (1966) *Isot Radiat Technol* 4:25
- Bohr N (1936) *Nature* 137:344
- Boyd RE (1982) *Radiochim Acta* 30:123
- Brihaye C, Dewez S, Guillaume M, Callahan AP, Rice DC, Knapp FF Jr (1989) *Appl Radiat Isot* 40:183
- Chakraborty S, Dasa T, Sarma HD, Venkatesh M, Banerjee S (2008) *Nucl Med Biol* 35:589
- CSISRS (2003) Experimental nuclear reaction data file (EXFOR[CSISRS]). National Nuclear Data Center, <http://www.nndc.bnl.gov/nndc/exfor/>
- Dadachova E, Mirzadeh S, Lambrecht RM, Hetherington E, Knapp FF Jr (1994) *J Anal Chem* 66:4272
- Dadachova E, Mirzadeh S, Lambrecht RM (1995) *J Phys Chem* 99:10976
- Daghighian F, Barendswaard E, Welt S, Humm J, Scott A, Willingham MC, McGuffie E, Old LJ, Larson SM (1996) *J Nucl Med* 37:1052
- Dasgupta AK, Mausner LF, Srivastava SC (1991) *Int J Radiat Appl Instrum Part A, Appl Radiat Isot* 42:371
- DeNardo G, DeNardo S, Kukuiz D, Diril H, Suny C, Meares C (1991) *Int J Radiat Appl Instrum Part B, Nucl Med Biol* 18:633
- Dvorakova Z, Henkelmann R, Lin X, Turler A, Gerstenberg H (2007) *Appl Radiat Isot* 66:147
- Ehrhardt GJ, Turpin TA, Razavi MS, Vanderheyden JL, Su FM, Fritzberg AR (1990) In: Nicolini M, Bandoli G, Mazzi U (eds) *Technetium and rhenium in chemistry and nuclear medicine 3*. Raven Press, New York, p 631
- ENSDF (2009) Evaluated nuclear structure data file. U.S. National Nuclear Data Center, <http://www.nndc.bnl.gov/ensdf/>
- Evans RD (1955) *The atomic nucleus*. Krieger Publishing, Malabar

- Evans CC, Stevenson J (1956) British Patent 763865
- Evans CC, Stevenson J (1957) British Patent 765489
- Finn R (2003) In: Welch MJ, Redvanly CS (eds) *Handbook of radiopharmaceuticals, radiochemistry and applications*. Wiley, Chichester
- Firestone RB, Shirley VS, Baglin CM, Chu SYF, Zipkin J (1996) *Table of isotopes*, 8th edn. Wiley-Interscience, New York
- Green MA, Klippenstein DL, Tennison JR (1988) *J Nucl Med* 29:1549
- Hainfeld JF, Foley CJ, Srivastava SC, Mausner LF, Feng NI, Meinken GE, Steplewski Z (1990) *Nucl Med Biol* 17:287
- Hashimoto K, Matsuoka H, Uchida S (2003) *J Radioanal Nucl Chem* 255:575
- Hodgson PE (1967) *Annu Rev Nucl Sci* 17:1
- Horwitz EP, McAlister DR, Bond AH, Barrans RE, Williamson JM (2005) *Appl Radiat Isot* 63:23
- Howell RW, Narra VR, Sastry KSR, Rao DV (eds) (1992) In: AAPM symposium series, number 8. American Institute of Physics, Woodbury, pp 1192
- Hughes DJ (1957) *Neutron cross sections*. Pergamon Press, New York
- Hupf HB (1976) In: Tubis M, Wolf A (eds) *Radiopharmacy*. Wiley, New York, p 225
- IAEA-TECDOC-1340 (2003) *Manual for reactor produced radioisotopes*. IAEA
- ITG Garching (2010) <http://www/itg-garching.de>
- JENDL (2003) Japanese evaluated nuclear data library version 3.3. Japan Atomic Energy Research Institute, <http://www.ndc.jaea.go.jp/jendl/jendl.html>
- Jeong JM, Chung JK (2003) *Cancer Biother Radiopharm* 18:707
- Kadina G, Tulskeya T, Gureev E, Brodskaya G, Gapurova O, Drosdovsky B (1990) In: Nicolini M, Bandoli G, Mazzi U (eds) *Technetium and rhenium in chemistry and nuclear medicine 3*. Raven Press, New York, p 635
- Kahn M, Kleinberg J (1977) *Radiochemistry of iodine*. Nuclear science series, National Academy of Sciences-National Research Council NAS-NS-3062
- Kaltsas GA, Papadogias D, Makras P, Grossman AB (2005) *Endocr-Relat Cancer* 12:683
- Kamioki H, Mirzadeh S, Lambrecht RM, Knapp FF Jr, Dadachova E (1994) *Radiochim Acta* 65:39
- Kassis AI, Sastry KSR, Adelstein SJ (1987) *Radiat Res* 109:78
- Kelly MP, Lee ST, Lee FT, Smyth FE, Davis ID, Brechbiel MW, Scott AM (2009) *Prostate* 69:92
- Knapp FF Jr, Callahan AP, Beets AL, Mirzadeh S, Hsieh BT (1994) *Appl Radiat Isot* 45:1123
- Knapp FF Jr, Beets AL, Guhlke S, Zamora PO, Bender H, Palmedo H, Biersack HJ (1997) *Anticancer Res* 17:1783
- Knapp FF, Mirzadeh S, Beets AL, Du M, Garland MA (2004) *Eur J Nucl Med Mol Imaging* 31:S387
- Knapp FF, Mirzadeh S, Beets AL, Du M (2005) *J Radioanal Nucl Chem* 263:503
- Kwekkeboom DJ, Bakker WH, Kooij PP, Konijnenberg MW, Srinivasan A, Erion JL, Schmidt MA, Bugaj JL, de Jong M, Krenning EP (2001) *Eur J Nucl Med* 28:1319
- Kwekkeboom DJ, Teunissen JJ, Bakker WH, Kooij PP, de Herder WW, Feelders RA, van Eijck CH, Esser JP, Kam BL, Krenning EP (2005) *J Clin Oncol* 23:2754
- Lagunas-Solar MC, Jungerman JA (1979) *Int J Appl Radiat Isot* 30:25
- Lamarsh JR, Baratta AJ (2001) *Introduction to nuclear engineering*, 3rd edn. Prentice Hall, Upper Saddle River
- Lambert B, de Klerk JM (2006) *Nucl Med Commun* 27:223
- Lebedev NA, Novgorodov AF, Misiak R, Brockmann J, Rösch F (2000) *Appl Radiat Isot* 53:421
- Lederer CM, Shirley VS (1978) *Table of isotopes*. Wiley, New York
- Ma D, Ketring AR, Ehrhardt GJ, Jia W (1996) *J Radioanal Nucl Chem* 206:119
- Mani RS, Majali AB (1966) *Indian J Chem* 4:391
- Martel AE, Smith RM (1974) *Critical stability constants*, vol 1, amino acids. Plenum Press, New York, pp 281–285
- Mausner LF (1999) McGraw Hill encyclopedia of science & technology, 9th edn. McGraw Hill, New York
- Mausner LF, Mirzadeh S, Ward TE (1985) In: *Proceedings of the international conference on nuclear data for basic and applied science*, Santa Fe, New Mexico, pp 733–737
- Mausner LF, Mirzadeh S, Srivastava SC (1992) *Int J Appl Radiat Isot* 43:1117
- Medvedev DG, Mausner LF, Greene GA, Hanson AL (2008) *Appl Radiat Isot* 66:1300
- Meredith RF, Partridge EE, Alvarez RD, Khazaeli MB, Plott G, Russell CD, Wheeler RH, Liu T, Grizzle WE, Schlom J, LoBuglio AF (1996) *J Nucl Med* 37:1491
- Mikolajczak R, Parus JL, Pawlak D, Zakrzewska E, Michalak W, Sasinowska I (2003) *J Radioanal Nucl Chem* 257:53
- Mirzadeh S (1995) In: Knapp FF Jr (ed) *Nuclear medicine program progress report for quarter ending September 30, 1995*. Oak Ridge National Laboratory, Oak Ridge, TN, ORNL/TM-13107
- Mirzadeh S, Knapp FF Jr (1992) *Radiochim Acta* 57:193
- Mirzadeh S, Knapp FF Jr (1996) *J Radioanal Nucl Chem* 203:471
- Mirzadeh S, Walsh P (1998) *Appl Radiat Isot* 49:379
- Mirzadeh S, Mausner LF, Srivastava SC (1986) *Int J Radiat Appl Instrum Part A, Appl Radiat Isot* 37:29

- Mirzadeh S, Beets AL, Knapp FF (1996) *J Nucl Med* 37:728
- Mirzadeh S, Knapp FF Jr, Alexander CW, Mausner LF (1997) *Appl Radiat Isot* 48:441
- Mirzadeh S, Knapp FF Jr, Collins ED (1998) US Patent no. 5,729,821
- Mirzadeh S, Du M, Beets AL, Knapp FF Jr (2000) *Ind Eng Chem Res* 39:3169
- Mirzadeh S, Du M, Beets A, Knapp FF (2004) US Patent no. 6,716,353B1
- Mughabghab SF (1984) Neutron cross sections, vol 1, part B; Z = 61–100. Academic, New York
- Mughabghab SF (2006) Atlas of neutron resonances. Elsevier, Amsterdam
- Mughabghab SF, Divadeenam M, Holden NE (1981) Neutron cross sections, vol 1, part A; Z = 1–60. Academic, New York
- Oeksuez M, Pfannenberger C, Bares R (2009) *J Nucl Med* 50(Supplement 2):212
- Peppard DF, Manson GM et al (1957) *J Inorg Nucl Chem* 5:141
- Pillai MRA, Chakraborty S, Meera TD, Ramamoorthy V, Ramamoorthy N (2003) *Appl Radiat Isot* 59:109
- Polak P, Geradts J, Van der Vlist R, Lindner L (1986) *Radiochim Acta* 40:169
- Richards P (1966a) In: Radioactive pharmaceuticals. Symposium #6, Conf. 651111, US Atomic Energy Commission, Washington
- Richards P (1966b) In: Radioactive radiopharmaceuticals. Proc. Conf.-651111, National Bureau of Standards, Springfield, pp 323–334
- Richards P (1966c) In: Radioactive radiopharmaceuticals. Proc. Conf.-651111, National Bureau of Standards, Springfield, pp 155–163
- Roberts JC, Figard SD, Mercer-Smith JA, Svitra ZV, Anderson WL, Lavalley DK (1987) *J Immunol Meth* 105:153
- Roberts JC, Newmyer SL, Mercer-Smith JA, Schreyer SA, Lavalley DK (1989) *Int J Radiat Appl Instrum Part A, Appl Radiat Isot* 40:775
- Rubinson W (1949) *J Chem Phys* 17:542
- Rutherford E, Chadwick J, Ellis CD (1930) Radiations from radioactive substances. Cambridge University Press, Cambridge
- Siiskonen T, Huikari J, Haavisto T, Bergman J, Heselius S-J, Lill J-O, Lonnroth T, Perajarvi K, Vartti V-P (2009) *Nucl Instrum Meth B* 267:3500
- Srivastava SC, Meinken GE, Richards P (1985) US Patent no. 4,533,541
- Srivastava SC, Mausner LF, Mease RC, Meinken GE, Joshi V, Kolsky K, Sweet M, Steplewski Z (1995) *Int J Pharmacogn* 33(suppl):92
- Srivastava SC, Atkins HL, Krishnamurthy GT, Zanzi I, Silberstein EB, Meinken GE, Mausner LF, Swailem F, D'Alessandro T, Cabahug CJ, Lau T, Park T, Madajewicz S (1998) *Clin Cancer Res* 4:61
- Stein R, Govindan SV, Chen S, Reed L, Richel H, Griffiths GL, Hansen HJ, Goldenberg DM (2001) *J Nucl Med* 42:967
- Stoughton RW, Halperin J (1959) *Nucl Sci Eng* 6:100
- Subramanian G (1976) In: Tubis M, Wolf W (eds) Radiopharmacy. Wiley, New York, p 556
- Szilard L, Chalmers TA (1934) *Nature* 134:462
- Tucker WD, Greene MW, Weiss AJ, Murrenhoff AP (1958) *T Am Nucl Soc* 1:160
- Weber DA, Eckerman KF, Dillman LT, Ryman JC (1989) MIRD: radionuclide data and decay schemes. Society of Nuclear Medicine, New York
- Westcott CH (1955) *J Nucl Energy* 2:59
- Winsche WE, Stang LG, Tucker R (1951) *Nucleonics* 8:14
- Zhernosekov KP, Perego RC, Dvorakova Z, Henkelmann R, Turler A (2008) *Appl Radiat Isot* 66:1218

39 Cyclotron Production of Medical Radionuclides

S. M. Qaim

Forschungszentrum Jülich GmbH, Jülich, Germany

39.1	<i>Introduction</i>	1904
39.2	<i>Principles, Equipment and Methodology</i>	1905
39.2.1	Types of Cyclotrons	1905
39.2.2	Significance of Nuclear Reaction Cross Section Data	1906
39.2.3	High Current Targetry	1908
39.2.3.1	Targets for Irradiations with Internal Beams	1908
39.2.3.2	Targets for Irradiations with Extracted Beams	1908
39.2.3.3	Targets for Irradiations with Parasitic Beams	1910
39.2.3.4	Recent Developments	1910
39.2.4	Use of Isotopically Enriched Target Material	1911
39.2.5	Chemical Processing of the Irradiated Material	1911
39.2.6	Yield and Purity	1914
39.3	<i>Production of Positron Emitters</i>	1915
39.3.1	Standard Positron Emitters	1915
39.3.1.1	Organic Positron Emitters	1915
39.3.1.2	Generator Produced Positron Emitters	1919
39.3.2	Non-Standard Positron Emitters	1919
39.3.2.1	Alkali Metals	1919
39.3.2.2	Longer-Lived Positron Emitters	1920
39.3.2.3	Positron Emitting Analogs of SPECT and Therapeutic Radionuclides	1923
39.4	<i>Production of Photon Emitters</i>	1924
39.5	<i>Production of Therapeutic Radionuclides</i>	1928
39.6	<i>Conclusions and Perspectives</i>	1930

Abstract: Cyclotron products are gaining in significance in diagnostic investigations via PET and SPECT, as well as in some therapeutic studies. The scientific and technological background of radionuclide production using a cyclotron is briefly discussed. Production methods of the commonly used positron and photon emitters are described and developments in the production of some new positron emitters and therapeutic radionuclides outlined. Some perspectives of cyclotron production of medical radionuclides are considered.

39.1 Introduction

Radionuclides find applications in many fields. Their major use, however, is in medicine, in both diagnosis and therapy. The production of radionuclides is carried out using nuclear reactors as well as cyclotrons. The reactor produced radionuclides are generally neutron excess nuclides. They mostly decay by β^- emission. The cyclotron produced radionuclides, on the other hand, are often neutron deficient and decay mainly by EC or β^+ emission. They are especially suitable for diagnostic studies. The reactor production of radionuclides is described in ► Chap. 38 of this Volume; this chapter treats radionuclide production with cyclotrons. It is worth pointing out that today more than 300 cyclotrons exist worldwide (cf. Directory of Cyclotrons, IAEA-DCRP/CD, 2004), many of them in hospitals; they produce short-lived radionuclides for medical use. Thus, radionuclide production science and technology at cyclotrons has become a very important feature of modern nuclear medicine.

While production of radionuclides at both reactors and cyclotrons has some common features, such as chemical processing of the irradiated material and quality control of the separated product, there are several aspects that are distinctly specific to the production at a cyclotron. These relate to nuclear reaction data and targetry for high current irradiations. As an accelerated charged particle impinging on a material loses energy very sharply, it is not meaningful to use an average cross section of the nuclear process; instead, a full knowledge of the excitation function is required. A second characteristic is that the loss of energy of the charged particle generates a lot of heat in the target material. High current production irradiations thus demand sophisticated methods of heat dissipation.

The application of radionuclides in medicine has been constantly increasing and both reactor- and cyclotron-produced radionuclides are needed. Besides the availability of radionuclides, two other important factors have contributed tremendously to the recent progress. These include radiopharmaceutical chemistry and medical imaging instrumentation. Fast labeling of a molecule with a suitable radionuclide, combined with a stringent quality control of the product, is a prerequisite for any meaningful application of the radioactive material. Similarly, fast and high resolution imaging methods, e.g., positron emission tomography (PET) and single photon emission computed tomography (SPECT), are now commonly available for diagnostic studies. In recent years, radionuclides are also finding increasing applications in internal therapy.

This chapter deals with the production of medically interesting radionuclides using a cyclotron (or an accelerator). Some of the basic aspects of production of radionuclides are discussed in ► Sect. 39.2, while the details on the production of specific groups of radionuclides (positron emitters, photon emitters, therapy related radionuclides) are given in ► Sects. 39.3–39.5. Finally, some perspectives for further use of cyclotrons for production of radionuclides are discussed.

39.2 Principles, Equipment and Methodology

39.2.1 Types of Cyclotrons

Over the last 2 decades several types of cyclotrons and accelerators have been developed to meet the specific demands of radionuclide production; a summary is given in [Table 39.1](#) (cf. Wolf and Barclay Jones 1983; Qaim 2001a; Ruth 2003). The smallest machine is a cyclotron that accelerates deuterons only up to 4 MeV, i.e., below the breakup threshold of the deuteron (to avoid neutron background). It is used exclusively in a hospital environment to produce ^{15}O . A small linear two particle (p, d) accelerator with energies below 3.7 MeV has also been developed, but its use has been limited. The next stage accelerator is a single particle negative ion machine for proton acceleration up to an energy of 11 MeV or 12 MeV. It can be used to produce the four major β^+ emitters, viz. ^{11}C , ^{13}N , ^{15}O and ^{18}F , although the absence of the deuteron beam is somewhat disadvantageous with regard to the production of ^{15}O , and the rather low proton energy gives a low yield of ^{13}N . The next higher group of machines generally comprise two particle machines with $E_p \leq 20$ MeV and $E_d \leq 10$ MeV. It is ideally suited for production of the commonly used PET radionuclides. The even higher energy machines have capabilities of producing many more radionuclides, in particular when, besides p and d, ^3He and α -particle beams are also available. On the other hand, when energies above 100 MeV are under consideration, only the proton beam is of interest.

Table 39.1

Types of accelerators used for radionuclide production

Classification	Characteristics	Energy [MeV]	Major radionuclides produced
Level I	Single particle ^a (d)	<4	^{15}O
Level II	Single particle (p)	≤ 11	^{11}C , ^{13}N , ^{15}O , ^{18}F
Level III	Single or two particle (p, d)	≤ 20	^{11}C , ^{13}N , ^{15}O , ^{18}F , ^{64}Cu , ^{86}Y , ^{124}I (^{123}I , ^{67}Ga , ^{111}In)
Level IV	Single or multiple particle (p, d, ^3He , ^4He)	≤ 40	^{38}K , ^{73}Se , $^{75-77}\text{Br}$, ^{123}I , ^{81}Rb (^{81}Kr), ^{67}Ga , ^{111}In , ^{201}Tl , ^{22}Na , ^{57}Co , ^{44}Ti , ^{68}Ge , ^{72}As , ^{140}Nd
Level V	Single or multiple particle (p, d, ^3He , ^4He)	≤ 100	^{28}Mg , ^{67}Cu , ^{72}Se , ^{82}Sr , $^{117\text{m}}\text{Sn}$, ^{123}I
Level VI	Single particle (p)	≥ 100	^{26}Al , ^{67}Cu , ^{68}Ge , ^{82}Sr , etc.

^a A small linear two particle accelerator (p,d) has also been suggested.


39.2.2 Significance of Nuclear Reaction Cross Section Data



As mentioned above, in cyclotron production of radionuclides, the reaction cross section data play a very important role (for detailed discussion cf. Qaim 1982, 2001a). One needs the full excitation function of the nuclear process to be able to calculate the yield with reasonable accuracy. Another important point is the number of competing reaction channels. At an incident projectile energy of 20 MeV, for example, about six reaction channels with significant cross sections may occur. It is imperative to know the cross sections of all those processes. The demands on the data may thus be extensive. At small-sized cyclotrons, low energy reactions like (p,n), (p, α), (d,n), (d, α), etc., are used. At higher energies, on the other hand, (p,xn) reactions are commonly utilized. In some special cases, the (p,spall) process is applied.

The nuclear reaction cross section data are needed in radioisotope production programs mainly for optimisation of production routes, i.e., to maximize the yield of the desired product and to minimize the yields of the radioactive impurities. From a given excitation function, the expected yield of a product for a certain energy range, i.e., target thickness, can be calculated using the expression:

$$Y = \frac{N_L H}{M} I (1 - e^{-\lambda t}) \int_{E_1}^{E_2} \left(\frac{dE}{d(\rho x)} \right)^{-1} \sigma(E) dE \quad (39.1)$$

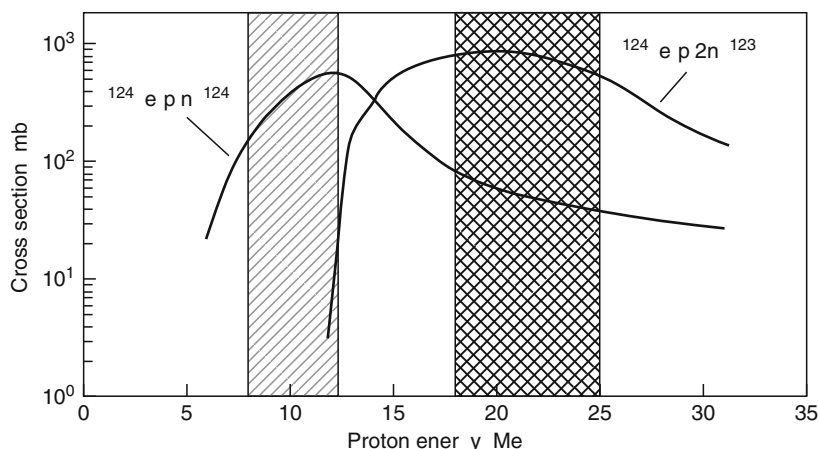
where Y is the activity (in Bq) of the product, N_L the Avogadro number; H , the enrichment (or isotopic abundance) of the target nuclide; M , the mass number of the target element; I , the projectile current; $dE/d(\rho x)$, the stopping power; $\sigma(E)$, the cross section at energy E ; λ , the decay constant of the product; and t , the time of irradiation. The calculated yield value represents the maximum yield that can be expected from a given nuclear process. It should be pointed out that the non-isotopic impurities produced can be removed by chemical separations, whereas the level of isotopic impurities can be suppressed only by using enriched isotopes as target material and/or by a careful selection of the particle energy range effective in the target.

The radioisotope ^{123}I ($T_{1/2} = 13.2$ h), a commonly employed halogen nuclide for labeling organic compounds for diagnostic studies using SPECT, for example, can be produced via various routes. Its production via the $^{124}\text{Te}(p,2n)^{123}\text{I}$ reaction furnishes a good example of the importance of nuclear data. In order to decrease the level of isotopic impurities in the ^{123}I produced, it is essential to use highly enriched ^{124}Te as target material. However, due to the competing $^{124}\text{Te}(p,n)^{124}\text{I}$ reaction it is not possible to eliminate the ^{124}I impurity ($T_{1/2} = 4.2$ days) completely, even if ^{124}Te is 100% enriched.  Figure 39.1 shows that the suitable proton energy range for the production of ^{123}I is $E_p = 25.0 \rightarrow 18.0$ MeV, i.e., the energy of the incident protons should be selected as 25.0 MeV and the thickness of the tellurium target should degrade the incident energy only to 18.0 MeV. Under these conditions, the yield of ^{123}I at the end of bombardment (EOB) amounts to $565 \text{ M Bq } \mu\text{A}^{-1} \text{ h}^{-1}$ and the level of ^{124}I impurity in ^{123}I to about 1%. If a still lower impurity level is desired, the energy window has to be narrowed. Evidently, it is necessary to know the excitation functions of the various competing reactions accurately.

It is worth pointing out that in recent years ^{124}I has gained considerable significance in positron emission tomography for investigating slow metabolic processes (see  Sect. 39.3.2). The data shown in  Fig. 39.1 can be used for the production of pure ^{124}I as well. The suitable energy range then is $E_p = 12 \rightarrow 8$ MeV, the thick target yield of ^{124}I amounting to $16 \text{ M Bq } \mu\text{A}^{-1} \text{ h}^{-1}$.

■ Fig. 39.1

Excitation functions of $^{124}\text{Te}(p,n)^{124}\text{I}$ and $^{124}\text{Te}(p,2n)^{123}\text{I}$ reactions. The suitable energy range for the production of ^{123}I is $E_p = 25.0 \rightarrow 18.0$ MeV (after Qaim 2001a, based on data reported by Kondo et al. (1977) and Scholten et al. (1995)). The same data can be used for the production of pure ^{124}I as well. The suitable energy range then is $E_p = 12 \rightarrow 8$ MeV



The γ -emitting radioactive impurities have a dual effect: first, they adversely affect the line spread function in SPECT-imaging and second, they cause enhanced radiation dose to the patient. If the amount of a longer-lived impurity is too high, it may jeopardize the whole advantage of the short-lived radioisotope used. It may then be necessary to look for an alternative route for production of the desired radioisotope.

Besides isotopic impurities, the awareness of isomeric impurities has also increased, in recent years. Several medically interesting research type radioisotopes have isomeric states that are rather disturbing. A few examples are $^{94\text{m}}\text{Tc}$ ($^{94\text{g}}\text{Tc}$), $^{120\text{g}}\text{I}$ ($^{120\text{m}}\text{I}$), etc. The isomeric impurities cannot be controlled through a careful adjustment of the energy window (as mentioned above). As the isomeric cross section ratio is primarily dependent on the type of reaction involved (cf. Strohmaier et al. 1997), it is essential to investigate all the possible production routes and then to choose the reaction and the energy range giving the best results. Obviously, nuclear data play a very important role here.

The question whether nuclear model calculations can provide cross section data, or only perform tedious measurements is often discussed. Experience has shown that model calculations have so far met with a varying degree of success. The cross sections of the light mass target nuclei can hardly be described by model calculations. In the medium and heavy mass regions, however, both the compound/precompound and precompound/hybrid models (using, for example, the codes STAPRE/GNASH and ALICE-IPPE, respectively) have been partially successful. In recent years, some advanced codes, like EMPIRE and TALYS, have been more successful in reproducing the experimental data. In general, *a priori* calculations do not meet the accuracy requirements needed in radionuclide production programs. Experimental studies are thus often indispensable.

For a detailed discussion of various experimental and theoretical aspects of nuclear reaction cross section data relevant to cyclotron production of radionuclides, the reader is referred to two recent IAEA-coordinated efforts (cf. Gul et al. 2001; Qaim et al. 2008).

39.2.3 High Current Targetry

As mentioned above, one of the major efforts in cyclotron production of medically important radionuclides consists of the development of a suitable target system for irradiations (cf. Qaim 1989; Schlyer 2003). Due to the use of high beam currents, the power density effective at a target is rather high (up to a few kW/cm²). An efficient heat transfer is thus one of the prime requirements in target construction. Some other considerations for target design are: (1) ease of chemical separation of radioactive product; (2) chemical reactivity and specific activity of the product obtained; (3) recovery of the target material, if necessary; and (4) high yield of the product.

In principle, several nuclear reactions may have cross sections that are high enough for use in the production of a radionuclide. In the choice of a target material, however, the mechanical and chemical properties of the substance play an important role, occasionally higher than the role of a nuclear reaction cross section. Solids like metals, alloys or oxides, liquids and gases can all be used, provided they can withstand high beam currents, do not lead to radiation induced strong chemical changes, give rise to a high yield of the radionuclide, and allow its easy chemical separation.

The chemical reactivity of the product is of paramount importance for subsequent labeling of an organic compound with the radionuclide. Often the chemical state of the product isotope is determined by the chemical composition of the target filling and the reaction within the target, especially in the case of gaseous target materials. ¹⁸F production via the ²⁰Ne(d,α)¹⁸F reaction, for example, leads to [¹⁸F]F₂ if a mixture of Ne + 0.1% F₂ is used as target filling (cf. Casella et al. 1980), but to ¹⁸F_{aq}[−] if a mixture of Ne + H₂ is used and the target rinsed with water after irradiation (cf. Blessing et al. 1986). The [¹⁸F]F₂ is suitable for electrophilic labeling and the ¹⁸F_{aq}[−] for nucleophile substitution.

High specific activity of the product is often essential for application in humans, e.g., if receptor-binding ligands are prepared. The recovery of the target material is an important consideration in the case of isotopically enriched isotopes (see below). The high level of radioactivity involved demands the use of remotely controlled or, if possible, automated methods of production. In general, cyclotron targets can be divided into three broad groups described below.

39.2.3.1 Targets for Irradiations with Internal Beams

The use of internal beams generally demands irradiations within the vacuum system of a cyclotron. Materials having high vapor pressure or showing large sputtering effects as a result of irradiation should therefore be avoided. Metals, electroplated targets, and alloys that have high melting points and good thermal conductivity are preferred. As the beam generally falls on the target at a grazing angle, the positioning of the beam on the target may present some difficulty, especially if irradiations with different accelerated particles are envisaged. Use of a temperature sensor may help overcome this difficulty (cf. Blessing and Qaim 1984).

39.2.3.2 Targets for Irradiations with Extracted Beams

Most of the irradiations for medical radioisotope production at cyclotrons are done using extracted beams. There is more versatility in working with the extracted beam than with the internal beam. Through controlled defocusing and wobbling, it is possible to decrease the

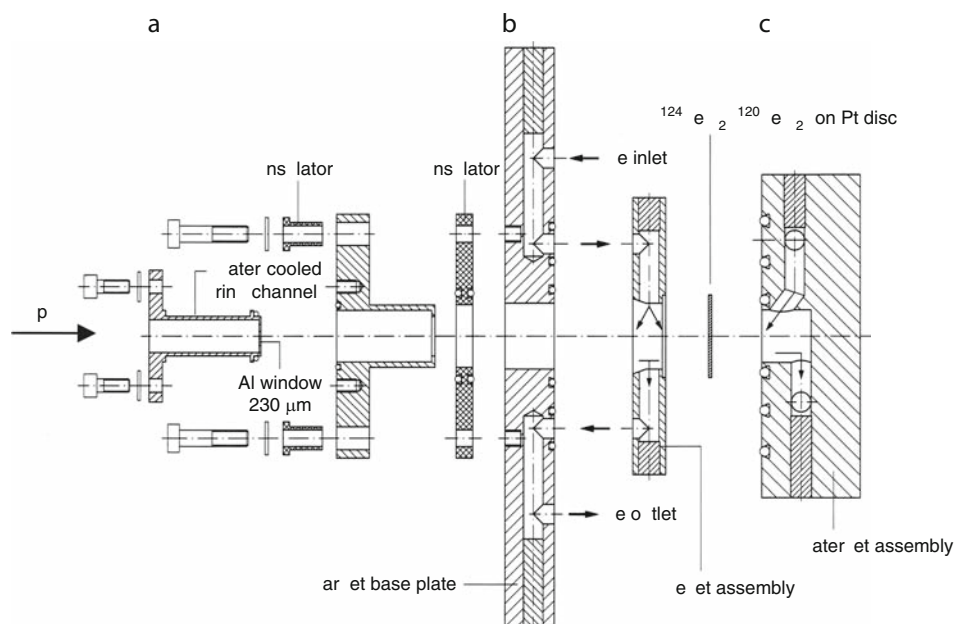
power density effective at a target. Nonetheless, due to the high beam currents used, there is a severe strain on the window foil separating the cyclotron vacuum from the target. Materials like Al, V, Ti, Ni, Cu, Nb, Havar, etc., have found extensive use. The target body (or target holder) has to be a good heat conductor, and materials like Al, Ti, Ni, Cu, Pt, stainless steel, Inconel, etc., have found wide application. The chemical nature of the radioactive product and the method of chemical separation are often deciding factors in the choice of a material of construction.

Irradiations of materials in all the three forms, viz. solid, liquid and gaseous, have been done. In the case of metal targets 2π water-cooling is generally sufficient. In the case of oxides and poor heat conducting materials, however, 4π cooling is often mandatory. In general, the back of the target is cooled by a stream of water and the front by a thin layer of flowing water (cf. Michael et al. 1981) or, more commonly, by a stream of He gas. The latter is in fact a standard technique. A typical irradiation system for the production of ^{124}I utilizing $^{124}\text{TeO}_2$ as target material is shown in Fig. 39.2 (Qaim et al. 2003). Beam currents of up to 20 μA have been used.

For poor thermal-conducting target materials with low melting points, the element is occasionally transformed into a suitable alloy. The thick target yield of the desired product is lower, but the batch yield may be high due to the possibility of use of much higher currents. A typical example is the use of Cu_3As alloy in the production of ^{75}Br and ^{75}Se via ^3He - and p -induced reactions on ^{75}As , respectively (cf. Blessing and Qaim 1984; Blessing et al. 1994). Another example is the use of Cu_2Se for production of radiobromine (cf. Vaalburg et al. 1985; Tolmachev et al. 1998).

Fig. 39.2

Typical target system for irradiation of solid material, in this case $^{124}\text{TeO}_2$ or $^{120}\text{TeO}_2$ withstanding 16 MeV proton wobbled beam of intensity up to 18 μA . Front cooling: helium, 1.5 bar, 10°C , Rear cooling: water jet, 10°C (after Qaim et al. 2003)



Another concept regarding the irradiation of solid targets with extracted beams involves the use of *slanting beams* (cf. Spellerberg et al. 1998; Sheh et al. 2000) (similar to that in the case of internal beam). The target holder is cooled from the back with flowing water. Using a better cooling, for example a chilled system (cf. Sheh et al. 2000), it has been shown that $^{124}\text{TeO}_2$ could withstand proton beam currents of up to 35 μA .

Large-sized liquid targets are not common, mainly on account of hydrolysis and radiation chemical effects. In contrast, small-sized water targets for production of ^{13}N and ^{18}F have attracted considerable attention. Molten salt and flowing-loop liquid targets have found only limited application.

Production of several radionuclides is done using gas targets. Both continuous flow system and batch mode (i.e., irradiation in a closed system and removal of activity at the end) are applied. The target dimensions and the gas pressure are chosen in such a way that the optimum part of the excitation function is utilized. In general, a He-cooled double foil window in front is mandatory to withstand the high beam (up to 50 μA) and high pressure within the target (up to 30 bar when the beam is on). The target body is cooled by air or water. A few measurements show that within the gas target there is a strong density reduction along the beam direction (cf. Wieland et al. 1984; Heselius 1986), and the beam itself becomes broader along its path due to scattering. These effects deserve special consideration while designing a gas target.

If the energy of the extracted particle is sufficiently high, occasionally a series of targets (tandem mode) is irradiated (cf. Ruth 1985). It is then possible to produce two or more radionuclides simultaneously. However, this technique has found only limited application.

39.2.3.3 Targets for Irradiations with Parasitic Beams

At several high energy proton accelerators, only a small fraction of the beam intensity is used for physics experiments, and the rest is diverted to a beam dump. This is of considerable advantage in the production of some longer-lived radionuclides (e.g., $^{68}\text{Ge}/^{68}\text{Ga}$ and $^{82}\text{Sr}/^{82}\text{Rb}$ generators). Because of the long ranges of high energy protons, relatively thick solid targets are used. However, those irradiations are not selective, especially when the spallation process is involved. Due to the formation of a large number of radioactive products, radiochemical separations are rather difficult, and isotopic impurities cannot be completely separated. In a few special cases, mass separation has been applied (e.g., at ISOLDE in Geneva).

39.2.3.4 Recent Developments

As a result of the enhanced use of small cyclotrons and highly enriched isotopes as target material, considerable effort has been devoted in recent years to the development of small-sized high current, liquid and gaseous targets. These developments involve precise nuclear data and sophisticated technology. In particular, for the production of short-lived positron emitters, several efficient and remotely controlled (or even automated) systems are now commercially available (see below). The results of such developments are periodically reported at international Targetry Workshops. During the most recent Workshop in Cambridge (2008), considerable attention was devoted to high-current targets at low-energy machines.

In the case of gas targets, targets of conical shape are preferred for containment of the beam within the gas. An extra advantage of this shape is that the amount of gas required for target

filling is smaller. This is an important consideration in the case of enriched gases (cf. Blessing et al. 1997). As far as liquid targets are concerned, the new thrust is on high pressure design. This reduces radiolytic effect but demands special material and heat dissipation concepts. Regarding solid state targetry, the emphasis in recent years has been on the utilization of extracted high-intensity slanting beams. In particular, for the production of rather commercial radionuclides such as ^{67}Ga , ^{111}In , ^{103}Pd and ^{201}Tl , suitable targets have been developed and beam currents of up to 1 mA are employed. Attempts to use very thin frozen layers of gases or water (e.g., ^{124}Xe , ^{18}O CO₂, H₂ ^{18}O) for high-current irradiations to produce ^{123}I or ^{18}F have not been very successful (cf. Firouzbakht et al. 1993; Mahunka et al. 1996).

39.2.4 Use of Isotopically Enriched Target Material

Highly enriched isotopes as target materials have found considerable use in the production of radionuclides, especially at cyclotrons. In recent years, their utilization has been intensified. About 2 decades ago it was considered uneconomical to bring an isotope of very low natural abundance to ultrahigh enrichment and use it as target material. Today it is a well accepted method, provided it leads to high yield and high purity of the product. The high cost of the enriched material, however, demands very sophisticated target technology. Presently, the most important PET radionuclide (^{18}F) and some of the common SPECT radionuclides (^{67}Ga , ^{111}In , ^{123}I) are produced using highly enriched target isotopes. Similarly the production of most of the research type radionuclides is based on the use of enriched target material (for an overview see Qaim 1989). It should, however, be mentioned that for many of the isotopes under consideration alternative nuclear processes employing natural targets may be available. The development of a method using enriched isotope is necessitated either due to the non-availability of a cyclotron with suitable particles and energy, or due to greater demands on yield and/or purity of the product. On the other hand, for a production process to be economically feasible, it is imperative that the loss of the enriched material during irradiation is minimum, and its recovery after the separation of the desired radioactive product is efficient.

39.2.5 Chemical Processing of the Irradiated Material

In contrast to the reactor production of radionuclides, in cyclotron production, the chemical processing starts in many cases during the irradiation itself. There are two reasons for this: first, the neutron irradiation in a reactor does not cause such intense radiation damage and chemical effects as the charged particle irradiation at a cyclotron, and second, the use of gaseous and liquid targets is much more common in cyclotron production of radionuclides than in reactor production. As expected, in those targets the radiation induced chemical reactions and nuclear recoil effects may lead to the formation of the desired radionuclide in different species (cf. Ferrieri and Wolf 1983). In a nitrogen gas target for the production of ^{11}C via the $^{14}\text{N}(\text{p},\alpha)^{11}\text{C}$ reaction, for example, the product radionuclide occurs as $^{11}\text{CO}_2$ or ^{11}CO , depending on the target filling (see below), the beam current used and the time of irradiation. Similarly, in a water target for the production of ^{13}N via the $^{16}\text{O}(\text{p},\alpha)^{13}\text{N}$ reaction, the radioactive product could occur as $^{13}\text{NO}_2^-$ or $^{13}\text{NO}_3^-$, depending on the radiation dose effective in the target. Also, in solid targets the radioactive product may exist in several oxidation states. The chemical processing to be applied must therefore take all these aspects in consideration.

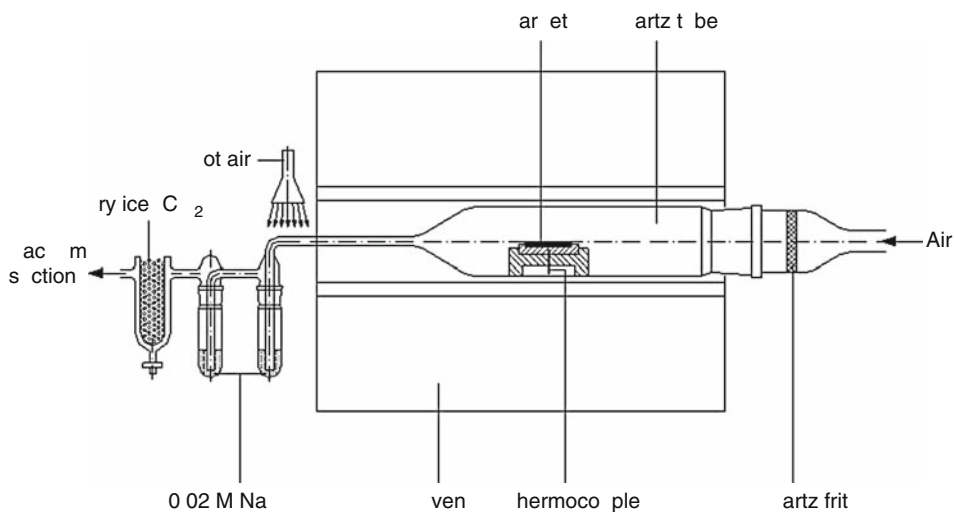
Gaseous and liquid targets are commonly used for the production of short-lived radionuclides, especially positron emitters. The chemical separation techniques of some important positron emitters are described in the next section. It should be pointed out here that the methods used have to be fast and efficient, in terms of the purity of the product as well as the recovery of the enriched target material. Furthermore, the chemical form of the separated radionuclide has to be well defined to allow a convenient synthesis of the desired radiopharmaceutical.

Occasionally, a gas target is also used for the production of a radionuclide, which sticks to the inner walls of the target instead of being removed with the gas. Some typical examples are ^{38}K , ^{81}Rb and ^{123}I , formed via $^{38}\text{Ar}(p,n)^{38}\text{K}$, $^{82}\text{Kr}(p,2n)^{81}\text{Rb}$ and $^{124}\text{Xe}(p,x)^{123}\text{I}$ processes, respectively. Subsequent proper rinsing of the target leads to almost complete removal of the activity (see below).

As regards solid targets, both dry and wet chemical separation methods are used. The dry method involves distillation and thermochromatography. The best example of the dry distillation technique is furnished by separation of radioiodine from irradiated TeO_2 at 755°C and a typical separation apparatus is shown in [Fig. 39.3](#). Optimisation experiments have revealed that above the m.p. of TeO_2 the removal of radioiodine is fast and almost quantitative, and the loss of the target material is negligible (cf. Beyer and Pimentel-Gonzales 2000; Qaim et al. 2003). Furthermore, the target is regenerated for the next production run. Thermochromatography, on the other hand, generally involves the formation of a chemical species of the radioactive product, which allows its removal from the irradiated target, but the vapor pressure is not high enough to allow its transport to large distances, such as in distillation (for a review on thermochromatographic separations see [Chap. 53 in Vol. 5](#)). The activity thus gets deposited in the cooler part of the thermochromatographic tube from where it is removed by rinsing, or is transferred to solid or liquid absorbers. A typical example is depicted in [Fig. 39.4](#).

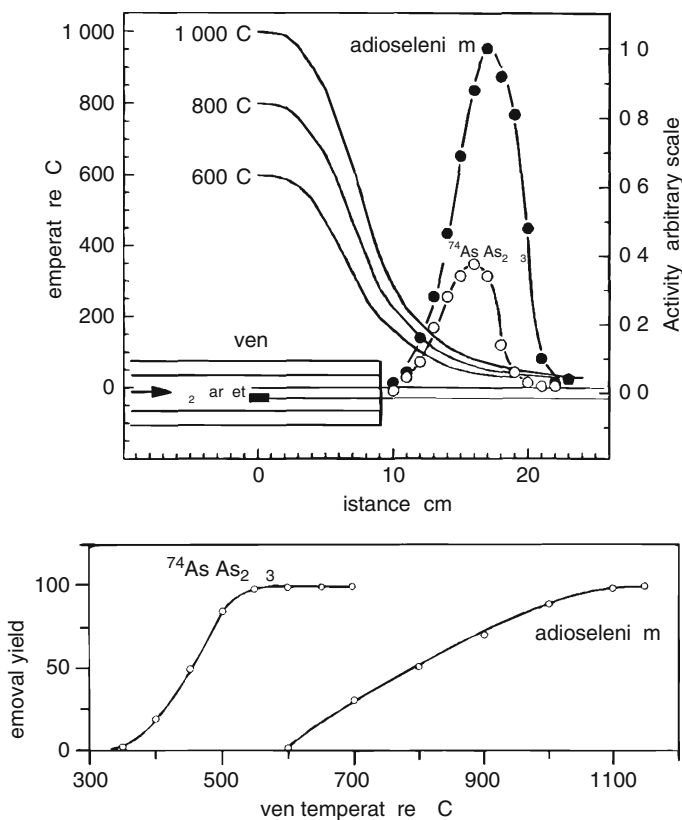
Fig. 39.3

Simplified sketch of quartz distillation apparatus for separation of radioiodine from irradiated $^{\text{nat}}\text{TeO}_2$, $^{124}\text{TeO}_2$ or $^{120}\text{TeO}_2$ target. The tube area outside the oven is heated by a stream of hot air (after Qaim et al. 2003)



■ Fig. 39.4

(Top) Deposition zone of $^{74}\text{AsAs}_2\text{O}_3$ and radioselenium in an O_2 atmosphere for an oven temperature of $>1,000^\circ\text{C}$, after 30 min processing of the irradiated Cu_3As target. (Bottom) Removal of $^{74}\text{AsAs}_2\text{O}_3$ and radioselenium from the Cu_3As target in an oxygen stream as a function of oven temperature (after Blessing et al. 1994)



A Cu_3As target irradiated with protons contains both ^{75}Se and ^{74}As , formed via $^{75}\text{As}(p,n)^{75}\text{Se}$ and $^{75}\text{As}(p,pn)^{74}\text{As}$ reactions, respectively. Detailed removal studies as a function of temperature revealed that $^{74}\text{AsAs}_2\text{O}_3$ is removed at 600°C , whereas for removal of radioselenium, a temperature of about $1,100^\circ\text{C}$ is required. Thus, by a two step thermochromatographic treatment, it is possible to separate radioselenium from the matrix.

It is worth mentioning that a multipurpose vertical thermochromatographic separation module has been developed to separate various target radionuclide systems, including $^{94}\text{MoO}_3/^{94\text{m}}\text{Tc}$, $^{110}\text{Cd}/^{110\text{m}}\text{In}$ and $^{186}\text{WO}_3/^{186}\text{Re}$ (cf. [Chap. 53 in Vol. 5](#) and [Chap. 40](#) in this Volume). On the other hand, it should also be pointed out that thermochromatography serves to concentrate the desired activity at one point and does not necessarily give a very clean separation. For a more clean separation, a subsequent wet chemical step is often necessary. The advantage of this dry separation lies in the easy regeneration and cyclic use of the highly enriched target materials.

In many production processes, a wet chemical procedure is unavoidable. In general, solvent extraction and ion-exchange techniques are commonly used, but occasionally methods like coprecipitation, adsorption, wet distillation, electrodeposition etc., are preferred. The separation procedure finally adopted often depends on the speciality of a laboratory.

39.2.6 Yield and Purity

The yield of a radionuclide from a nuclear process over a certain energy range can be calculated using the excitation function. It is generally expressed as MBq $\mu\text{A}^{-1} \text{h}^{-1}$ or MBq μA^{-1} , i.e., for an irradiation at 1 μA for 1 hour or for saturation, respectively. This calculated thick target yield represents the maximum yield that can be expected via the nuclear process under consideration. In practice, the experimentally obtained yields in high current production runs are invariably lower than the theoretical values. The experimental yield generally decreases as a function of the integrated current. In the case of gaseous targets, the decrease is presumably due to density reduction along the beam direction, and in liquid targets, due to local boiling and bubble formation (cf. Heselius et al. 1989). In solid targets, the decrease in yield is possibly due to inhomogeneity in the incident beam, radiation damage effects, etc. The experimental yields thus reflect a cumulative effect of the specific conditions prevalent during the production process. In general, the negative ion beams can be better homogenized than the positive ion beams. The agreement between theoretical and experimental yields, therefore, tends to be better when cyclotrons with negative ions are used.

In a good production method, besides high yield, a low level of radionuclidic impurities is expected. This is achieved via the choice of a suitable nuclear process and chemical separation scheme. The chemical impurities, on the other hand, are introduced via the reagents used and, to some extent, via radiation induced effects like radiolysis, sputtering from the target body, etc. These inactive impurities may have toxic effects and may also form complexes with the radioactive product, thereby decreasing its chemical reactivity. The product of $^{18}\text{F}_{\text{aq}}^-$ using a small-sized H_2^{18}O target was often associated with this problem. The sputtered metal ions from the target walls possibly formed complexes with $^{18}\text{F}^-$ and rendered it rather unreactive for subsequent labeling work (cf. Kilbourn et al. 1985). A chemical purification step to remove the metal ions was found to be mandatory. The problem is even more acute in the case of metal radionuclides like ^{64}Cu . Even the slightest impurity jeopardizes the formation of metal complexes. Production of the radionuclide under very clean conditions is therefore absolutely necessary.

The radiochemical state of the radionuclide produced deserves special consideration before initiating labeling work. In the case of a solid target, the separated radionuclide is generally brought into a desired radiochemical form through oxidation/reduction cycles. As discussed above, however, in liquid and gaseous targets, the presence of additives and radiation dose effects (i.e., radiation induced chemical reactions) are often deciding factors regarding the chemical state of the product radionuclide.

Whenever high specific activity is demanded, special precautions are required in target construction. For example, the N_2 gas used for target filling in the case of ^{11}C production has to be ultrapure (especially free of CO), and carbon containing seals or joints must be avoided. In the case of ^{18}F production, the presence of Teflon in immediate contact with a water target may give rise to inactive F^- under the impact of radiation and decrease the specific activity of ^{18}F .

39.3 Production of Positron Emitters

39.3.1 Standard Positron Emitters

The number of positron-emitting radionuclides is large. To date, however, PET studies are carried out mostly with the three short-lived organic positron emitters, viz. ^{11}C ($T_{1/2} = 20.4$ min), ^{15}O ($T_{1/2} = 2$ min) and ^{18}F ($T_{1/2} = 110$ min), and to a lesser extent with ^{13}N ($T_{1/2} = 10$ min). The radionuclides ^{11}C , ^{13}N , and ^{15}O are generally used at the site of production. ^{18}F , on the other hand, is extensively employed for transport to nearby PET centers without a cyclotron. For a comprehensive discussion of the ^{11}C - and ^{18}F -labeling chemistry and labeled compounds see [Chaps. 41](#) and [42](#) in this Volume. There is also considerable interest in ^{68}Ga ($T_{1/2} = 68$ min) and ^{82}Rb ($T_{1/2} = 1.3$ min), which are obtained via longer-lived generator parents.

39.3.1.1 Organic Positron Emitters

The common production methods of the short-lived organic β^+ emitters are summarized in [Table 39.2](#) (Qaim et al. 1993; Stöcklin et al. 1995). In general, low energy nuclear reactions like (p,n), (p, α), (d,n), (d, α), etc., are used, and a small-sized cyclotron is adequate for production purposes. The excitation functions have been measured in several laboratories. The cross sections show strong fluctuations with changing incident particle energies, probably due to the population of known discrete levels of the product nucleus. Recently an evaluation of the excitation functions was performed (Qaim et al. 2001). Reliable recommended curves for all the reactions listed in [Table 39.2](#), except for the $^{18}\text{O}(\text{p,n})^{18}\text{F}$ reaction, were made available.

Regarding the $^{18}\text{O}(\text{p,n})^{18}\text{F}$ reaction, only one group had reported the activation cross sections (Ruth and Wolf 1979). A recent detailed study (Hess et al. 2001) established the data base firmly for this production route of the most commonly used PET radionuclide ^{18}F . The results are shown in [Fig. 39.5](#). The yield can now be calculated up to 30 MeV. The resonances at 5.1, 6.1 and 7.2 MeV are in agreement with those found in spectral measurements of emitted neutrons.

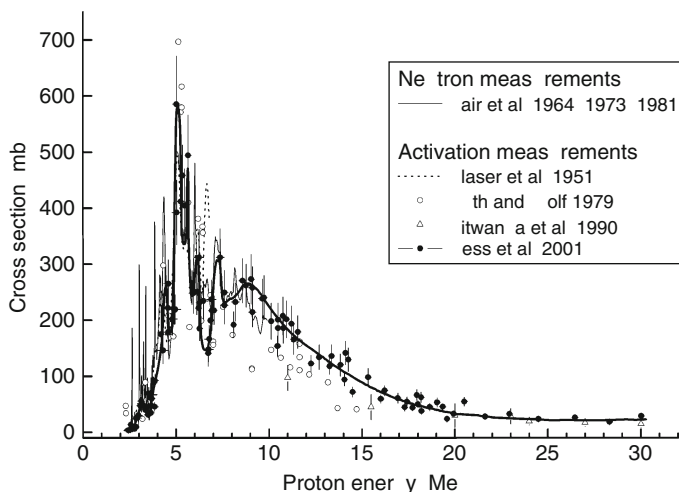
Table 39.2

Common methods of production of short-lived organic positron emitters

Nuclide	$T_{1/2}$ (min)	Mode of decay	Production route	Energy range [MeV]	Thick target yield [$\text{MBq}\mu\text{A}^{-1}\text{h}^{-1}$]	Target	In-target product
^{11}C	20.4	β^+ (99.8) EC (0.2)	$^{14}\text{N}(\text{p},\alpha)$	13→3	3,820	$\text{N}_2(\text{O}_2)$	^{11}CO , $^{11}\text{CO}_2$
^{13}N	10.0	β^+ (100)	$^{16}\text{O}(\text{p},\alpha)$	16→7	1,665	H_2^{16}O	$^{13}\text{NO}_2^-$, $^{13}\text{NO}_3^-$
^{15}O	2.0	β^+ (99.9)	$^{14}\text{N}(\text{d},\text{n})$	8→0	2,368	$^{14}\text{N}_2(\text{O}_2)$	^{15}OO ,
		EC (0.1)	$^{15}\text{N}(\text{p},\text{n})$	10→0	2,220	$^{15}\text{N}_2(\text{O}_2)$	^{15}OO
^{18}F	109.6	β^+ (97)	$^{18}\text{O}(\text{p},\text{n})$	16→3	3,893	H_2^{18}O $^{18}\text{O}_2/(\text{F}_2)$	$^{18}\text{F}_{\text{aq}}^-$, $^{18}\text{F}(\text{F}_2)$
		EC (3)	$^{20}\text{Ne}(\text{d},\alpha)$	14→0	1,110	$\text{Ne}(\text{F}_2)$	$^{18}\text{F}(\text{F}_2)$

■ Fig. 39.5

Excitation function of the $^{18}\text{O}(p,n)^{18}\text{F}$ reaction. Results of both neutron and activation measurements are shown. The rather bold curve is an eye-guide to the activation data (after Hess et al. 2001)



The thick target yield over the optimum energy range for the production of each radionuclide was calculated using the known excitation function. In the case of ^{11}C , ^{13}N , and ^{15}O , the recently evaluated data of Qaim et al. (2001) were utilized and for ^{18}F , the data of Hess et al. (2001). The calculated values are given in Table 39.2.

Considerable effort has been devoted to targetry related to production of short-lived organic positron emitters. For production of ^{11}C and ^{15}O , generally pressurized gas targets in batch mode are used. The product activity is removed from the target by simple expansion and led to vessels where conversion to other chemical forms (known as precursors) suitable for labeling of organic compounds is done. The chemical form of the activity leaving the target depends upon the additive given to the N_2 gas in the target and, in the case of ^{11}C , also on the radiation dose effective in the target. The resulting ^{15}O from an $\text{N}_2(\text{O}_2)$ target, for example, is $[\text{O}_2^{15}\text{O}]$. In the case of ^{11}C production, at high radiation doses mostly $^{11}\text{CO}_2$ is formed. The production of both ^{11}C and ^{15}O is rather simple, and GBq quantities can be easily obtained (cf. Crouzel et al. 1987). There is, however, a problem with ^{11}C if it is to be of high specific activity. Special precautions regarding gas composition, construction material, and chemicals are needed (cf. Crouzel et al. 1987; Suzuki et al. 2000). The most reliable production of ^{15}O demands a deuteron beam at the cyclotron. If it is not available, the (p,n) reaction on highly enriched ^{15}N is utilized. An efficient recovery system for the enriched target gas must then be incorporated in the target system.

The production of **electrophilic** ^{18}F is also carried out using a gas target. However, the removal of the activity from the target demands addition of some F_2 carrier. In the case of $^{20}\text{Ne}(d,\alpha)^{18}\text{F}$ reaction, the F_2 (0.1–0.2%) carrier is added directly to the neon gas target (cf. Bida et al. 1980; Blessing et al. 1986). While using the $^{18}\text{O}(p,n)^{18}\text{F}$ reaction, however, a two-step irradiation is necessary (Nickles et al. 1983). In the first step, highly enriched gaseous O-18 is irradiated with protons, and the ^{18}F formed is deposited on the inner target surface. In

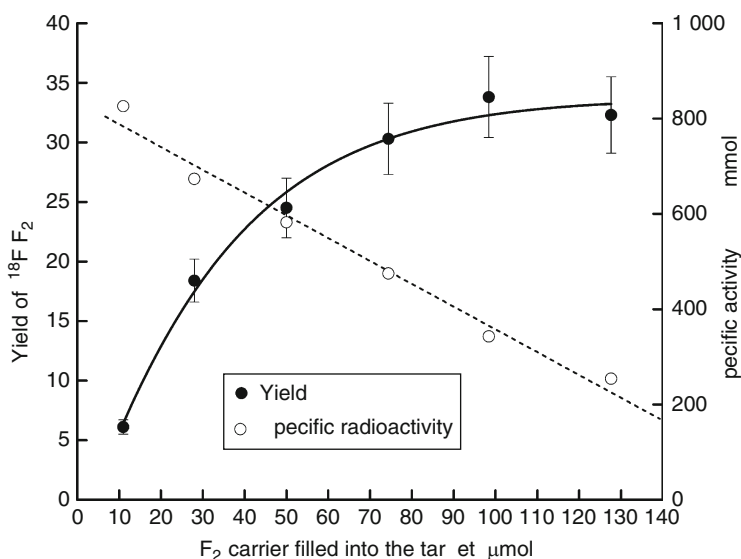
the second step, after cryogenic recovery of oxygen-18 target gas, a mixture of F_2 and Kr is introduced and a short proton irradiation is done, whereby an isotopic exchange between the gaseous F_2 and the deposited ^{18}F occurs. The second step leads to the recovery of radiofluorine as $[^{18}F]F_2$. Optimisation studies show that the yield and the specific activity of the ^{18}F obtained are much higher in the case of the $^{18}O(p,n)$ reaction than in the $^{20}Ne(d,\alpha)$ reaction (Roberts et al. 1995; Bishop et al. 1996; Hess et al. 2000). A correlation between the added F_2 -carrier and the specific activity of ^{18}F is given in ► Fig. 39.6. In many cases, the achieved specific activity of about 600 GBq per mmol may be sufficient. However, it is still about a factor of 50 lower than that needed in preparation of several radiopharmaceuticals, for example, ^{18}F -labeled neuro-receptor ligands.

The radionuclides ^{13}N and ^{18}F are commonly produced using water targets, and several types of water targets have been developed, particularly for ^{18}F production (for reviews cf. Qaim et al. 1993; Schlyer 2003). A typical pressurized water target for medium-scale production is shown in ► Fig. 39.7. It consists of a titanium body, electron-beam welded to two titanium foils (75 μm thick), which act as front and back windows. The target takes 1.3 ml of water with no expansion space and the thickness of the water filling amounts to 3.5 mm. During irradiation, the back window is water-cooled, typically to 8–10°C, and the front window is helium-cooled to –7°C. It withstands pressures of up to 7 bar and proton beam currents of up to 20 μA . A polyethylene-polypropylene copolymer tube with an i.d. of 0.8 mm and a He drive pressure of 1.3 bar is considered a reliable transfer system.

Transfer over 40 m through this tubing from the target to the nearest hot cell takes only 2 min, and >90% of the product activity is recovered. The same target can be used for the production of both ^{13}N and ^{18}F . In the former case, natural water ($H_2^{16}O$) is used, and the proton energy range within the target corresponds to $E_p = 16 \rightarrow 7$ MeV. In the latter case,

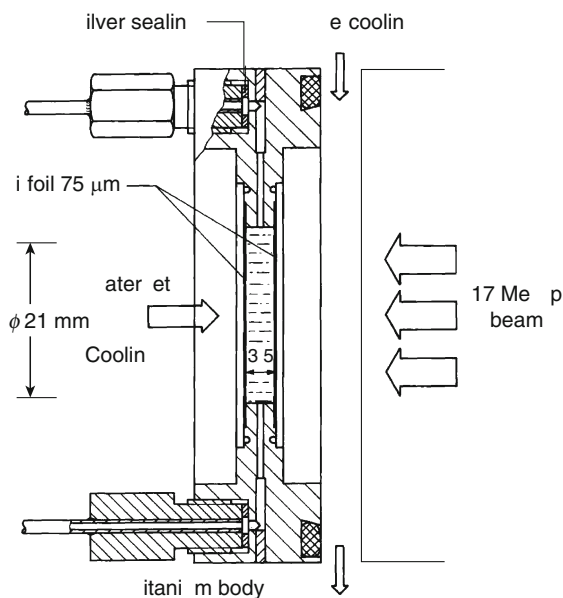
► Fig. 39.6

Yield and specific radioactivity of $[^{18}F]$ fluorine as a function of fluorine carrier; 30 min after end of the activation irradiation (after Hess et al. 2000)



■ Fig. 39.7

Typical medium pressure water target system for production of ^{13}N and ^{18}F (after Qaim et al. 1993)



however, enriched water (H_2^{18}O) is employed and the effective projectile energy is $E_p = 16 \rightarrow 3$ MeV. In high current irradiations, the resulting products are $^{13}\text{NO}_3^-$ and $^{18}\text{F}_{\text{aq}}^-$, respectively. In the latter case, the recovery of the enriched water is essential. This is commonly achieved by transferring the irradiated water to an ion-exchange bed whereby the ^{18}F activity is adsorbed, and the enriched water passes through and is collected. The ^{18}F activity is removed from the column by washing it with a 0.1 M solution of Na_2CO_3 , and the batch yield amounts to about 70 GBq. A recently developed method involves electrolytic separation of $^{18}\text{F}^-$ from the irradiated H_2^{18}O (Hamacher et al. 2002). The defluorinated target water is removed from the electrolytic cell by a gentle stream of helium, and the release of $^{18}\text{F}^-$ from the electrode is effected using a suitable solvent and a low strength electric field.

Due to the increasing significance of ^{18}F in PET, several modified designs of high-pressure (>10 bar) water target have been developed in recent years. They can withstand beam currents of up to about 50 μA . The resulting batch yield of ^{18}F amounts to about 150 GBq. These quantities are desired for producing the most commonly used radiopharmaceutical [^{18}F]2-fluoro-2-deoxy-D-glucose (2-FDG) on an industrial scale. A novel spherical niobium target (Zeisler et al. 2000) has proved to be very effective for use at cyclotrons with proton energies above 20 MeV. A further concept stipulates high current irradiation of ^{18}O gas followed by removal of the ^{18}F activity from the target wall by rinsing (cf. Becker et al. 2001). The full effectivity of the procedure has not been demonstrated as yet.

The radionuclidic and chemical purity of all the four organic positron emitters produced is generally $>99\%$. Reference has been made above to radiochemical purity and specific activity, but they are more relevant to the subsequently labeled product rather than to the radionuclide itself. Thus the production technology of the commonly used PET radionuclides is well established.

39.3.1.2 Generator Produced Positron Emitters

The generator produced positron emitters find application mostly in PET studies at centers without a cyclotron. A discussion of generator preparation is beyond the scope of this article (for a detailed discussion, cf. [Chap. 40](#) in this Volume). Here a very brief account is given of the production of the two long-lived parent radionuclides concerned (cf. Qaim [1987](#); Qaim et al. [1993](#)).

The β^+ emitter ^{68}Ga ($T_{1/2} = 68$ min) is widely used for PET attenuation correction and, to some extent, also for labeling. In recent years, it has been gaining more significance. Some radiopharmacists believe that if suitable labeled compounds are developed, this radionuclide may compete with or even replace ^{18}F . The parent ^{68}Ge is rather difficult to produce. The $^{69}\text{Ga}(p,2n)^{68}\text{Ge}$ reaction has a high cross section, but due to the long half-life of the product, the achievable batch yield is low. The method of choice is thus the spallation process. It is therefore exclusively produced at large accelerators where long irradiations in parasitic positions are possible. The purification of the product involves a multi-step wet chemical process. However, with the availability of modern accelerators that deliver high-intensity 70 to 100 MeV proton beams, the use of the (p,2n) reaction is receiving enhanced attention.

The β^+ emitter ^{82}Rb ($T_{1/2} = 1.3$ min) has found application in myocardial blood flow studies with PET. The possible production methods for the parent ^{82}Sr include the ^3He - and α -particle induced reactions on natural krypton, the (p,4n) reaction on ^{85}Rb and the spallation of molybdenum with high energy protons. In practice, however, the $^{\text{nat}}\text{Rb}(p,xn)^{82}\text{Sr}$ process is commonly used, and the major quantity of ^{82}Sr is presently produced at intermediate energy accelerators (cf. Waters and Coursey [1987](#); Philipps et al. [2000](#)).

Besides the above mentioned generator systems, two other cyclotron produced generators have also found some application. They are $^{62}\text{Zn}/^{62}\text{Cu}$ and $^{122}\text{Xe}/^{122}\text{I}$. The former is clinically established and commercially available, but because of the short half-life of the parent ^{62}Zn ($T_{1/2} = 9.2$ h), its use is rather limited. Due to the difficulty in producing ^{122}Xe ($T_{1/2} = 20.1$ h), the use of the $^{122}\text{Xe}/^{122}\text{I}$ generator system is still more limited.

39.3.2 Non-Standard Positron Emitters

The number of these radionuclides is relatively large. However, they are regarded as research tools and their relative importance keeps on changing. They can be placed under the following categories: (1) alkali metals (e.g., ^{38}K , ^{81}Rb , etc.); (2) longer-lived positron emitters, consisting of halogens and other elements suitable for labeling organic compounds (e.g., $^{75,76}\text{Br}$, ^{124}I , ^{73}Se , etc.), and metals forming complexes with suitable organic ligands (e.g., ^{52}Fe , ^{55}Co , ^{64}Cu , etc.); (3) analogs of SPECT and therapeutic radionuclides (e.g., $^{94\text{m}}\text{Tc}$ for $^{99\text{m}}\text{Tc}$, ^{86}Y for ^{90}Y , $^{120,124}\text{I}$ for ^{123}I and ^{131}I , etc.).

The production of typical radionuclides in each group is discussed in some detail below.

39.3.2.1 Alkali Metals

Three radionuclides, namely ^{38}K ($T_{1/2} = 7.6$ min), ^{81}Rb ($T_{1/2} = 4.6$ h), and $^{82\text{m}}\text{Rb}$ ($T_{1/2} = 6.3$ h), have found some use as blood flow tracers. For production of ^{38}K , three methods have been used, the $^{35}\text{Cl}(\alpha,n)^{38}\text{K}$ process on NaCl, the $^{38}\text{Ar}(p,n)^{38}\text{K}$ reaction on highly enriched ^{38}Ar , and the $^{40}\text{Ar}(p,3n)^{38}\text{K}$ reaction on natural argon (cf. the reviews by Qaim et al. [1993](#); Nagatsu et al. [1998](#)). The $^{81,82\text{m}}\text{Rb}$ tracers are produced via proton irradiation of highly enriched ^{82}Kr : over

the energy range of 20 to 25 MeV, the (p,2n) reaction dominates and the main product is ^{81}Rb ; at lower energies on the other hand, e.g., in the range of 10 to 15 MeV, $^{82\text{m}}\text{Rb}$ is preferentially produced. The enriched gas irradiation technology has been well developed and beam currents up to about 30 μA are commonly used. The gas recovery is efficient and the removal of the alkali metal activity from the inner walls of the target is almost quantitative. A typical system is shown in ► Fig. 39.8.

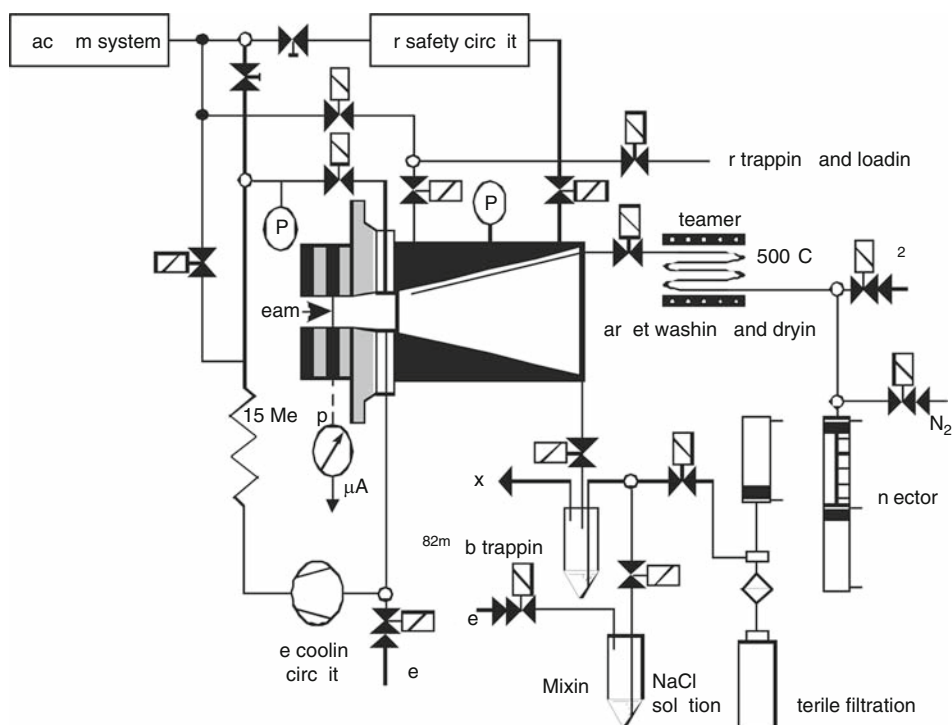
In this particular case, after the recovery of the enriched target gas, the removal of $^{82\text{m}}\text{Rb}$ from the target inner walls was achieved by introducing steam in the target (Blessing et al. 1997). In this way, the radioactivity was collected in about 2.5 mL of water. It may be mentioned here that besides its use as a blood flow tracer, ^{81}Rb is also used as a parent nuclide in the preparation of the $^{81}\text{Rb}/^{81\text{m}}\text{Kr}$ generator system (see below).

39.3.2.2 Longer-Lived Positron Emitters

With increasing significance of PET in diagnostic nuclear medicine, the need for longer-lived β^+ emitters (half-life between a few hours and a few days) is increasing. These radionuclides

► Fig. 39.8

Schematic representation of remotely controlled compact system developed for irradiation, safe handling and recovery of highly enriched rare gas (e.g., ^{82}Kr) and efficient removal of the product alkali metal activity (e.g., ^{81}Rb , $^{82\text{m}}\text{Rb}$) by steam (after Blessing et al. 1997). The system is also used for preparation of ^{83}Sr via the $^{82}\text{Kr}(^3\text{He},2\text{n})$ reaction



could be employed to study slow metabolic processes. Their use could extend to the labeling of organic compounds leading to analog tracers (e.g., with halogens) and the preparation of metal complexes (e.g., with copper). Some of the important or potentially important β^+ emitting radionuclides applied to study slow pharmacokinetics are given in [Table 39.3](#). For each radionuclide, several production routes have been studied. Many more nuclear reactions that use p, d, ^3He and α -particles as projectiles may be possible. In [Table 39.3](#), however, only the most commonly used or the most promising nuclear routes are given, together with the energy ranges over which those processes could be advantageously applied (cf. Qaim 2002, 2008). Some of the radionuclides can already be produced on a medium scale, while for the others, further technical developments are called for. A variety of chemical techniques, involving both wet and dry methods, have been applied in the separation of radioactive products.

In general, investigation of low-energy reactions like (p,n), (p, α), (d,n) etc., on highly enriched target isotopes has been very advantageous in developing production routes of

■ **Table 39.3**

Production routes of some longer-lived β^+ emitters suggested for study of slow pharmacokinetics

Nuclide	Decay data ^a			Useful production route	
	$T_{1/2}$	Positron branching [%]	E_{max} of positron [MeV]	Nuclear reaction	Energy range of interest [MeV]
^{45}Ti	3.1 h	85	1.04	$^{45}\text{Sc}(\text{p},\text{n})$	5–20
^{52}Mn	5.6 days	29	0.57	$^{52}\text{Cr}(\text{p},\text{n})$	5–20
^{52}Fe	8.3 h	56	0.80	$^{55}\text{Mn}(\text{p},4\text{n})$	40–70
				$^{52}\text{Cr}(^3\text{He},3\text{n})$	20–40
^{55}Co	17.6 h	76	1.51	$^{58}\text{Ni}(\text{p},\alpha)$	5–20
				$^{54}\text{Fe}(\text{d},\text{n})$	3–15
^{61}Cu	3.4 h	61	1.20	$^{61}\text{Ni}(\text{p},\text{n})$	5–20
^{64}Cu	12.7 h	17.8	0.66	$^{64}\text{Ni}(\text{p},\text{n})$	5–20
^{66}Ga	9.4 h	57	4.15	$^{66}\text{Zn}(\text{p},\text{n})$	5–20
^{73}Se	7.1 h	66	1.68	$^{75}\text{As}(\text{p},3\text{n})$	20–45
^{75}Br	1.6 h	71	1.74	$^{76}\text{Se}(\text{p},2\text{n})$	10–30
				$^{75}\text{As}(^3\text{He},3\text{n})$	20–40
^{76}Br	16.0 h	58	3.98	$^{76}\text{Se}(\text{p},\text{n})$	5–20
				$^{75}\text{As}(^3\text{He},2\text{n})$	10–30
^{90}Nb	14.6 h	53	1.50	$^{90}\text{Zr}(\text{p},\text{n})$	5–20
^{120}I	1.3 h	56	4.00	$^{120}\text{Te}(\text{p},\text{n})$	5–20
				$^{122}\text{Te}(\text{p},3\text{n})$	20–45
^{121}I	2.1 h	13	1.20	$^{122}\text{Te}(\text{p},2\text{n})$	15–30
^{124}I	4.2 days	22	2.13	$^{124}\text{Te}(\text{p},\text{n})$	5–20
				$^{124}\text{Te}(\text{d},2\text{n})$	5–20
				$^{125}\text{Te}(\text{p},2\text{n})$	15–30

^a Decay data taken mostly from Browne and Firestone (1986) or Qaim et al. (2007).

longer-lived β^+ emitters at small cyclotrons. However, there are a few radionuclides that can be produced only via intermediate-energy reactions. Some of the examples are $^{55}\text{Mn}(p,4n)^{52}\text{Fe}$, $^{75}\text{As}(p,3n)^{73}\text{Se}$, $^{76}\text{Se}(p,2n)^{75}\text{Br}$, etc. Furthermore, ^3He - and α -particle induced reactions are also useful. For example, ^{75}Br was often produced via the $^{75}\text{As}(^3\text{He},3n)$ process.

Out of all the positron emitters listed in [Table 39.3](#), five radionuclides, namely ^{64}Cu , ^{73}Se , ^{76}Br , ^{124}I , and ^{120}gI have attracted considerable interest in recent years, though as yet some of them have not been applied in investigations on humans. The radionuclide ^{64}Cu emits low-energy positrons and has a suitable half-life for slow metabolic studies. It was produced previously via the $^{63}\text{Cu}(n,\gamma)^{64}\text{Cu}$ reaction. Due to the rather low specific activity of the product, the $^{64}\text{Ni}(p,n)^{64}\text{Cu}$ reaction was suggested as an alternative route (Szelecsényi et al. 1993) that can be used at a small cyclotron. Production via this route has been successfully developed, including an efficient recovery of the highly enriched target material (cf. McCarthy et al. 1997). It is now extensively used in radioimmunotherapy.

The radionuclide ^{73}Se is a S-analog. It has been under study for about 3 decades, and several methods have been suggested for its production. The most suitable, however, is the $^{75}\text{As}(p,3n)^{73}\text{Se}$ reaction (cf. Mushtaq et al. 1988). The target material used is of natural isotopic composition, but the process demands a medium-sized cyclotron. Several chemical processing methods have been developed (cf. Mushtaq et al. 1988; Plenevaux et al. 1990) among which thermochromatographic separation of radio-selenium from an irradiated Cu_3As alloy appears to be very promising (Blessing et al. 1994, see also discussion above under [Sect. 39.2.5](#)). The availability and application of this radionuclide are expected to increase.

The radionuclide ^{76}Br has been under discussion for some time, first as an undesirable impurity in ^{75}Br , but lately as a useful longer-lived radionuclide for brominating organic compounds. For its production, originally the $^{75}\text{As}(^3\text{He},2n)^{76}\text{Br}$ reaction was suggested (cf. Qaim 1986; Ločh et al. 1994), and the method is still used in some laboratories, but the reaction $^{76}\text{Se}(p,n)^{76}\text{Br}$ (cf. Kovács et al. 1985; Hassan et al. 2004) appears to be more promising as it can be employed at a small cyclotron. The method has been technically developed (Tolmachev et al. 1998) and is an improved form of a previously reported procedure in connection with the production of ^{75}Br (Vaalburg et al. 1985). It utilizes enriched ^{76}Se in the form of $\text{Cu}_2^{76}\text{Se}$ alloy and the separation of radiobromine is effected via thermochromatography. The yield of ^{76}Br is sufficient for the desired applications.

The radionuclide ^{124}I has also been under discussion for about 30 years, initially as a very disturbing impurity in SPECT investigations with ^{123}I . It was mainly due to this impurity that the very expensive but superior route of ^{123}I production, namely the $^{124}\text{Xe}(p,x)^{123}\text{I}$ process was developed (see below under [Sect. 39.4](#)). About 2 decades ago, however, it was shown that ^{124}I could be advantageously used in slow metabolic and therapeutic studies (Bakir et al. 1990). Since then, its demand has been increasing and hence several production methods have been investigated. Originally, the $^{124}\text{Te}(d,2n)^{124}\text{I}$ reaction was employed (Lambrecht et al. 1988; Sharma et al. 1988; Weinreich and Knust 1996; Knust et al. 2000), but after careful studies of Scholten et al (1995) on the $^{124}\text{Te}(p,n)^{124}\text{I}$ reaction, that reaction is becoming the method of choice for the production of ^{124}I (cf. Sheh et al. 2000; Qaim et al. 2003). Recently, the $^{125}\text{Te}(p,2n)^{124}\text{I}$ process was also studied and it appears to be very promising (Hohn et al. 2001). A summary of the three production routes is given in [Table 39.4](#). The suitable energy ranges, the thick target yields and the impurity levels were deduced from the measured excitation functions (cf. Scholten et al. 1995; Bastian et al. 2001; Hohn et al. 2001). The best route appears to be the $^{124}\text{Te}(p,n)^{124}\text{I}$ process as it can be carried out at a low energy cyclotron and the level of the long-lived ^{125}I impurity is very low. The $^{125}\text{Te}(p,2n)^{124}\text{I}$ reaction, on the other hand, gives

■ Table 39.4

Comparison of production routes of ^{124}I

Nuclear reaction	Suitable energy range [MeV]	Thick target yield of ^{124}I [$\text{MBq}\mu\text{A}^{-1}\text{h}^{-1}$]	Impurity [%]	
			^{123}I	^{125}I
$^{124}\text{Te}(\text{p},\text{n})$	$12 \rightarrow 8$	16	1.0	<0.1
$^{124}\text{Te}(\text{d},2\text{n})$	$14 \rightarrow 10$	17.5	–	1.7
$^{125}\text{Te}(\text{p},2\text{n})$	$21 \rightarrow 15$	81	7.4	0.9

a much higher ^{124}I yield but the ^{125}I impurity level is higher than in the (p,n) reaction. Furthermore, the process demands a medium-sized cyclotron. The final choice of the production process will depend on the tolerable level of the ^{125}I impurity.

The targetry and radiochemical separation related to ^{124}I production (cf. ▶ Sect. 39.2.5 above) are based on established technology for dry distillation of radioiodine from $^{124}\text{TeO}_2$ target (cf. Van den Bosch et al. 1977; Michael et al. 1981). The separated product is either directly led to a 0.01 M solution of NaOH or is first adsorbed on a column and subsequently eluted with dilute NaOH. The final product exists $>98\%$ as iodide and is very suitable for subsequent labeling work.

The batch yield of ^{124}I via the $^{124}\text{Te}(\text{p},\text{n})$ process generally amounts to about 500 MBq; in exceptional cases, yields of about 2 GBq have been reported. These yields are sufficient for local medical use, but not for wide distribution. The increasing demands for this radionuclide call for more development efforts and the production route is now being commercialized.

The radionuclide $^{120\text{g}}\text{I}$ is a recent addition to the list of potentially useful radioisotopes of iodine for tracer applications. It is a positron emitter of suitable half-life. Its positron end-point energy is rather high but PET phantom measurements have shown that it can be used for tomographic studies in man. It can be produced via either the $^{120}\text{Te}(\text{p},\text{n})^{120\text{g}}\text{I}$ or the $^{122}\text{Te}(\text{p},3\text{n})^{120\text{g}}\text{I}$ reaction, but the former route is preferred as it can be used at a low-energy cyclotron and the level of the isomeric impurity is low (Hohn et al. 1998a, b). The major drawback is the high cost of the enriched material. On the other hand, as targetry has been well developed in connection with the production of other radioisotopes of iodine (see above), the expensive target material can be safely handled. A production procedure similar to that for ^{124}I has been developed (Qaim et al. 2003). With the use of a thin target, the batch yield of $^{120\text{g}}\text{I}$ achieved so far has been 750 MBq; with thicker targets, higher yields are expected.

39.3.2.3 Positron Emitting Analogs of SPECT and Therapeutic Radionuclides

A β^+ -emitting analog could be applied for quantification of a SPECT radiopharmaceutical. Similarly, in endotherapy with β^- -emitting particles, therapy planning and dosimetric calculations could be done advantageously using a β^+ -emitting analog.

Some of the important radionuclides that have been developed and used to date under the analog approach are listed in ▶ Table 39.5. In part (A), the β^+ -emitting analogs of the most commonly used SPECT-radionuclides are given and in part (B), the analogs of therapeutic radionuclides. Their commonly used production routes are mentioned. The production

Table 39.5

Positron emitting radionuclides for applying the analog approach

Commonly used radionuclide ($T_{1/2}$)	Analog radionuclide				
	Radionuclide ($T_{1/2}$)	Positron ^a branching [%]	E_{max} of positron [MeV]	Nuclear reaction	Energy range of interest for production [MeV]
A. Analogs of commonly used SPECT radionuclides					
⁶⁷ Ga (78.3 h)	⁶⁶ Ga (9.4 h)	57	4.15	⁶⁶ Zn(p,n)	5–20
^{99m} Tc (6.0 h)	^{94m} Tc (52 min)	70	2.47	⁹⁴ Mo(p,n)	5–20
¹¹¹ In (2.8 days)	^{110m} In (69 min)	62	2.25	¹⁰⁹ Ag(³ He,2n)	15–30
¹²³ I (13.2 h)	^{120g} I (1.3 h)	56	4.00	¹²⁰ Te(p,n)	10–20
B. Analogs of therapeutic radionuclides					
⁸⁹ Sr (50.5 days)	⁸³ Sr (32.4 h)	24	1.23	⁸² Kr(³ He,2n)	15–30
				⁸⁵ Rb(p,3n)	20–50
⁹⁰ Y (2.7 days)	⁸⁶ Y (14.7 h)	33	1.96	⁸⁶ Sr(p,n)	5–20
¹³¹ I (8.0 days)	¹²⁴ I (4.2 days) ^b	22	2.13	¹²⁴ Te(p,n)	5–20

^a Decay data mostly from Browne and Firestone (1986).
^b ¹²⁴I may also be used as a β⁺-emitting analog of the SPECT nuclide ¹²³I, although the half-life of ¹²⁴I is rather long.

methods of ^{120g}I and ¹²⁴I have been given in detail under ▶ Sect. 39.3.2.2. The radionuclides ^{94m}Tc and ⁸⁶Y are drawing considerable interest, and technical efforts are under way to increase their production yields.

The production of ^{94m}Tc has been studied in detail (for a review cf. Qaim 2000). An enriched ⁹⁴MoO₃ target is irradiated with 15 MeV protons in a target assembly similar to that shown in ▶ Fig. 39.1, and ^{94m}Tc formed via the ⁹⁴Mo(p,n) reaction is separated via thermochromatography using moist air as carrier gas (cf. Rösch et al. 1994). Further purification of the product is done using an Al₂O₃ column. The major radionuclidic impurity is ^{94g}Tc ($T_{1/2}$ = 4.9 h) at a level of about 7%. The radionuclide ^{94m}Tc is available in quantities of 5 GBq and is utilized in quantification of new ^{99m}Tc SPECT agents.

The production of ⁸⁶Y was also investigated in detail and the reaction ⁸⁶Sr(p,n)⁸⁶Y was found to be the most suitable (Rösch et al. 1993a). In this case, an enriched ⁸⁶SrCO₃ target is irradiated with 15 MeV protons, and the radioyttrium is separated via one of the wet chemical processes. The separation is done via coprecipitation followed by ion-exchange (Rösch et al. 1993b) or HPLC (Kettern et al. 2002), or separation via electrolysis (Reischl et al. 2002) or chromatography (Gamestani et al. 2002). The radionuclidic purity of ⁸⁶Y is about 97% and its batch yield amounts to about 2 GBq. The radionuclide ⁸⁶Y has become the most suitable β⁺ emitter for quantification of radiation dosimetry of ⁹⁰Y-labeled radiotherapeutics.

39.4 Production of Photon Emitters

A large number of γ-ray emitting radionuclides have found application in diagnostic nuclear medicine using either γ-cameras or, in recent years, mainly SPECT. The most commonly used SPECT radionuclide ^{99m}Tc ($T_{1/2}$ = 6.0 h) is commercially available on a routine basis via the

$^{99}\text{Mo}/^{99\text{m}}\text{Tc}$ generator, the ^{99}Mo being produced using a nuclear reactor; the details are given elsewhere in this Volume. The four major SPECT radionuclides produced at a cyclotron are listed in ▶ [Table 39.6](#). All of them need a medium-sized cyclotron although, in some cases (e.g., ^{67}Ga , ^{111}In and ^{123}I), low-energy machines capable of inducing (p,n) reactions have also been used for producing these radionuclides for local use. For a comprehensive discussion of the $^{99\text{m}}\text{Tc}$ - and ^{123}I -labeling chemistry and labeled compounds see ▶ [Chaps. 43](#) and ▶ [44](#) in this Volume. Similar aspects for ^{111}In are illustrated in ▶ [Chap. 45](#) in this Volume.

The nuclear reaction cross section data for most of the processes are known and have been recently evaluated, using both nuclear model calculations and fitting methods (cf. Hermanne et al. 2001). Surprisingly, the data for the commonly employed $^{124}\text{Xe}(\text{p},\text{x})$ -process for the production of ^{123}I , a widely used SPECT radionuclide, are still somewhat discrepant (cf. Kurenkov et al. 1989; Tárkányi et al. 1991). In recent years, very high intensity medium-sized cyclotrons have been developed with the specific aim of producing medical radioisotopes. Extracted beams of about 0.5 mA are available: they fall slantingly on solid targets (see ▶ [Sect. 39.2.3](#)). Such cyclotrons are now commercially available and allow the production of several SPECT-radionuclides in large quantities.

The metallic radionuclides ^{67}Ga and ^{111}In form strong metal complexes and are of considerable medical interest. Both are produced via (p,2n) reactions, the former on ^{68}Zn and the latter on ^{112}Cd . Targetry and chemical processing problems have been well studied. The medical applications are well documented. For production on a smaller scale, the (p,n) reactions on ^{67}Zn and ^{111}Cd have also been utilized (cf. Tárkányi et al. 1990, 1994).

■ **Table 39.6**

Routine methods of production of some commonly used photon emitters at a cyclotron

Radio-nuclide	$T_{1/2}$	Mode of decay [%]	Main γ -ray energy in keV [%]	Production data		
				Nuclear reaction ^a	Energy range [MeV]	Thick target yield [MBq $\mu\text{A}^{-1} \text{h}^{-1}$]
^{67}Ga	3.26 days	EC (100)	93 (37)	$^{68}\text{Zn}(\text{p},2\text{n})$	26 \rightarrow 18	185
^{111}In	2.8 days	EC (100)	173 (91)	$^{112}\text{Cd}(\text{p},2\text{n})$	25 \rightarrow 18	166
^{123}I	13.2 h	EC (100)	159 (83)	$^{123}\text{Te}(\text{p},\text{n})$	14 \rightarrow 10	130
				$^{124}\text{Te}(\text{p},2\text{n})$	26 \rightarrow 23	392
				$^{127}\text{I}(\text{p},5\text{n})^{123}\text{Xe}^{\text{b}}$	65 \rightarrow 45	777 ^c
				$^{124}\text{Xe}(\text{p},\text{x})^{123}\text{Xe}^{\text{b}}$	29 \rightarrow 23	414 ^c
^{201}Tl	3.06 days	EC (100)	69–82 (X-rays) 166 (10.2)	$^{201}\text{Tl}(\text{p},3\text{n})^{201}\text{Pb}^{\text{d}}$	28 \rightarrow 20	18 ^e

^aEvaluated excitation functions of all the reactions listed here are available (cf. Hermanne et al. 2001).

^b ^{123}Xe decays by EC (87%) and β^+ emission (13%) to ^{123}I .

^cThis is ^{123}I yield expected from the decay of ^{123}Xe over an optimum time of about 7 h.

^d ^{201}Pb decays by EC (100%) to ^{201}Tl .

^eThis is ^{201}Tl yield, expected from the decay of ^{201}Pb over an optimum time of 32 h.

The radionuclide ^{123}I is a very useful analog label for producing radiotracers. Its nuclear properties are also almost ideal for SPECT studies. The radionuclide ^{201}Tl is very broadly used for myocardial blood flow measurements and has a relatively long shelf-life. The production methods of these two important radionuclides are discussed in some detail.

For the production of ^{123}I , about 25 nuclear processes have been investigated. Among them, only the four listed in [Table 39.6](#) are of significance. At low energy cyclotrons, the ^{123}Te (p,n) reaction over $E_p = 14.5 \rightarrow 10$ MeV is applied (cf. Scholten et al. 1989; Hermanne et al. 2001), and at medium energy cyclotrons, the ^{124}Te (p,2n) process over $E_p = 26 \rightarrow 23$ MeV (cf. Kondo et al. 1977; Van den Bosch et al. 1977; Scholten et al. 1995; Hermanne et al. 2001). In either case, highly enriched target material is used. The recovery of ^{123}I is carried out via dry distillation as described above for ^{124}I . The disadvantages of the (p,n) process are the low ^{123}I yield and the relatively high ^{124}I impurity, especially if ^{123}Te of low enrichment is used. The ^{124}I impurity level is still higher in the case of the (p,2n) route.

The third route of ^{123}I -production consists of the ^{127}I (p,5n) ^{123}Xe (EC, $\beta^+/T_{1/2} = 2.1$ h) ^{123}I process (for references cf. Hermanne et al. 2001). The optimum energy range for the process is $E_p = 65 \rightarrow 45$ MeV. Thus it needs a higher energy cyclotron. The removal of radioxenon from the irradiated NaI target is done either on-line, i.e., during the irradiation in a flow system, or off-line, i.e., after the end of the irradiation in a batch mode. The collected radioxenon is allowed to decay for about 7 h during which period the maximum growth of ^{123}I occurs. Thereafter, ^{123}I is removed from the vessel containing radioxenon. This is a relatively high yield process, and the only impurity observed is ^{125}I ($\sim 0.25\%$).

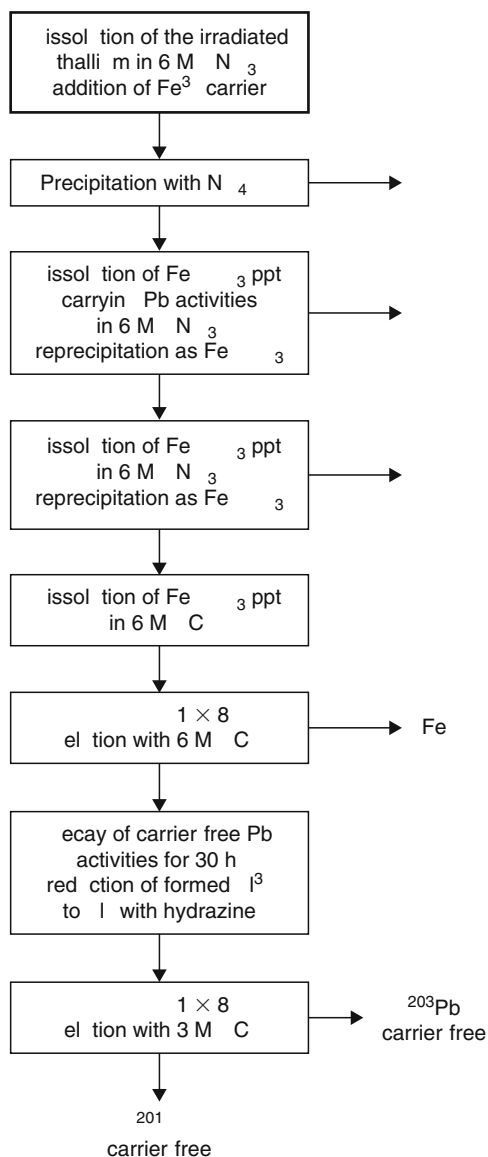
The fourth route of ^{123}I -production consists of the ^{124}Xe (p,x)-process. It involves the use of highly enriched ^{124}Xe , but requires only a medium-sized cyclotron. The development of this process clearly demonstrates the changing demands on the quality of the medically important radionuclides. In contrast to the above mentioned three routes, this process leads to ^{123}I of the highest purity. The natural abundance of ^{124}Xe is only 0.1%; consequently, the highly enriched ^{124}Xe is very expensive. The production method has been well developed. It involves a somewhat similar but more sophisticated target technology than that shown in [Fig. 39.8](#), in particular, checks to avoid loss of the enriched gas. The technology is now commercially available.

For the production of ^{201}Tl also, several methods have been investigated. The most common route, however, consists of the ^{203}Tl (p,3n) ^{201}Pb (EC/ $T_{1/2} = 9.4$ h) ^{201}Tl process. Extensive studies on this route have been done in several laboratories. The optimum energy range for production is $E_p = 28 \rightarrow 20$ MeV (cf. Lagunas-Solar et al. 1978; Qaim et al. 1979). Thus, in this case also, a medium-energy cyclotron is required.

The production of no-carrier-added ^{201}Tl via irradiation of ^{203}Tl or $^{\text{nat}}\text{Tl}$ involves a two step procedure and elaborate wet chemical processing. At first, ^{201}Pb is separated from the matrix activity and inactive Tl. Thereafter, it is allowed to decay for an optimum time of 32 h (cf. Qaim et al. 1979) whereby ^{201}Tl grows in. The removal of the daughter is then effected via anion-exchange chromatography. A flowsheet of the separation procedure is given in [Fig. 39.9](#). In a slightly modified form, it is used for commercial production. Thus, even classical separation methods such as coprecipitation and ion-exchange occasionally find widespread application. It should be mentioned that Tl itself is a toxic heavy metal. The final no-carrier-added ^{201}Tl , therefore, should not contain any measurable quantities of the target material. Furthermore, for medical application, only the product $^{201}\text{Tl}^+$ is of interest. The demands on the chemical, radiochemical and radionuclidic purity of the final product are thus rather stringent.

■ Fig. 39.9

Flow sheet of the separation procedure for the $^{203}\text{Tl}(p,3n)^{201}\text{Pb} \rightarrow ^{201}\text{Tl}$ production process (after Qaim et al. 1979)



Finally, it should be added that a generator system $^{81}\text{Rb}/^{81\text{m}}\text{Kr}$ delivers the short-lived γ -emitter $^{81\text{m}}\text{Kr}$ ($T_{1/2} = 13.1$ s, $E_\gamma = 190$ keV, $I_\gamma = 67\%$), which has found application in lung ventilation studies. The production of the parent cyclotron nuclide ^{81}Rb has been described above. The preparation of the generator is described in [Chap. 40](#) of this Volume.

39.5 Production of Therapeutic Radionuclides

Therapy-related radionuclides are generally produced in a nuclear reactor. The status of nuclear data was recently reviewed (Qaim 2001b). The production technology involved in nuclear reactors is treated elsewhere in this Volume. In recent years, cyclotrons have also been increasingly used to produce some therapeutic radionuclides. The labeling chemistry of the metallic therapeutic radionuclides as well as the aspects relevant to their therapeutic potential are described in detail in ► Chap. 46 in this Volume.

The cyclotron-produced radionuclides ^{64}Cu , ^{124}I , ^{67}Ga , and ^{111}In are diagnostic radioisotopes, but they might also act as therapeutic radionuclides if applied in high activity. The therapeutic use in the first two cases combines PET and low-energy beta particle therapy, and in the case of the next two, SPECT and Auger electron therapy. Their methods of production have been mentioned above (see ► Sects. 39.3.2 and ► 39.4, respectively). Similarly the positron emitters ^{83}Sr and ^{86}Y , which are analogs of the pure β^- -emitting therapeutic radioisotopes ^{89}Sr and ^{90}Y , respectively, are also produced well at cyclotrons and the methods are given above (see ► Sect. 39.3.2.3). The commonly used cyclotron-produced therapeutic radionuclides are given in ► Table 39.7 together with their major production routes. These radionuclides include β^- , α , and Auger electron emitters.

The radionuclide ^{67}Cu emits β^- -particles of ideally suitable energy. It is occasionally produced via the spallation process, but more commonly via the $^{68}\text{Zn}(p,2p)^{67}\text{Cu}$ reaction with protons of energies above 50 MeV. (Mirzadeh et al. 1986; Schwarzbach et al. 1995; Stoll et al. 2002). A recently reported method of production makes use of the $^{70}\text{Zn}(p,\alpha)^{67}\text{Cu}$ reaction over the energy range of 12 to 21 MeV. If highly enriched target material is used, the resulting ^{67}Cu is very pure (Kastleiner et al. 1999).

The calculated integral yields for the latter two processes are given in ► Fig. 39.10a. The targetry with enriched ^{68}Zn or ^{70}Zn is similar to that for production of ^{67}Ga from ^{68}Zn , and so it is well established. The chemical separation of radiocopper is based on a combination of solvent extraction and ion-exchange processes. So far the achievable batch yields of ^{67}Cu , mostly via the $^{68}\text{Zn}(p,2p)$ process, have been limited to about 1 GBq.

The radionuclide ^{103}Pd is almost a pure X-ray and Auger electron emitter. It is being increasingly used in the treatment of prostate cancer, and is therefore in great demand. For its production in a no-carrier-added form, several reactions have been investigated. Their cross section data have been recently reviewed (cf. Hussain et al. 2009). The $^{103}\text{Rh}(p,n)$ reaction is routinely used, the production cross sections of which were measured most accurately by Sudàr et al. (2002). The calculated thick target yield is given in ► Fig. 39.10b. As the target material Rh is rather expensive, a good separation of ^{103}Pd and recovery of Rh are desired. Several methods based on solvent extraction have been worked out. On the other hand, in many cases, ^{103}Pd is not separated. The irradiated Rh in the form of very thin seeds is introduced into the prostate, and the therapy effect is achieved through the X-rays coming out of the seed. In this case, however, it is mandatory that the proton energy does not exceed 13 MeV, so that the reaction $^{103}\text{Rh}(p,pn)^{102}\text{Rh}$ is not induced and the long-lived impurity ^{102}Rh ($T_{1/2} = 207$ days) is avoided. Using slanting beam targets and high current irradiations, batch yields of ^{103}Pd amounting up to 10 GBq have been achieved.

The radionuclide ^{186}Re emits low energy β^- -particles and forms very stable co-ordination compounds (higher homologue of technetium). Therefore, it has great therapeutic potential. Parallel to its production via the $^{185}\text{Re}(n,\gamma)$ process in a nuclear reactor, a cyclotron route,

namely $^{186}\text{W}(\text{p},\text{n})^{186}\text{Re}$, has been suggested (cf. Shigeta et al. 1996). The cross sections for this process were measured (cf. Szelecsényi et al. 1999; Zhang et al. 1999). Szelecsényi et al. (1999) and Zhang et al. (2001) also studied the $^{186}\text{W}(\text{d},2\text{n})^{186}\text{Re}$ reaction. The cross section data of both the (p,n) and the (d,2n) processes have been recently reviewed (cf. Qaim et al. 2008). The yields for the two reactions are shown in [Fig. 39.10c](#). Evidently, above 12 MeV, the yield of ^{186}Re via the (d,2n) reaction is significantly higher than via the (p,n) reaction. Nevertheless, in practice, the (p,n) reaction is preferred for production purposes as the available proton beams are generally of much higher intensity than the deuteron beams. The chemical separation is based on a combination of solvent extraction and ion-exchange processes (cf. Shigeta et al. 1996; Zhang et al. 1999).

The last two radionuclides listed in [Table 39.7](#), i.e., ^{211}At and ^{225}Ac are α -emitters. ^{211}At has been in use in endoradiotherapy for about 30 years but, in recent years, with enhanced progress in tumor targeting, the interest in this radionuclide has greatly increased. It is produced via the $^{209}\text{Bi}(\alpha,2\text{n})^{211}\text{At}$ reaction, and the cross sections are known well (cf. Lambrecht and Mirzadeh 1985). The optimum proton energy incident on the target is 28.0 MeV and it must be carefully controlled. At higher energies, the $^{209}\text{Bi}(\alpha,3\text{n})^{210}\text{At}$ reaction occurs, whose decay product leads to the α -emitting ^{210}Po ($T_{1/2} = 138.4$ days) of high radio-toxicity. In general, thin Bi targets for slanting beams are used. The separation of radioastatine is done mostly by distillation techniques, and the radionuclide is achieved in amounts of about 5 GBq.

The radionuclide ^{225}Ac is very promising, both in itself and as generator for ^{213}Bi . It is generally produced from the nuclear waste via an elaborate chemical processing. An interesting new production route is the $^{226}\text{Ra}(\text{p},2\text{n})^{225}\text{Ac}$ reaction. ^{225}Ac is already produced in reasonable quantities at medium-sized cyclotrons.

Table 39.7

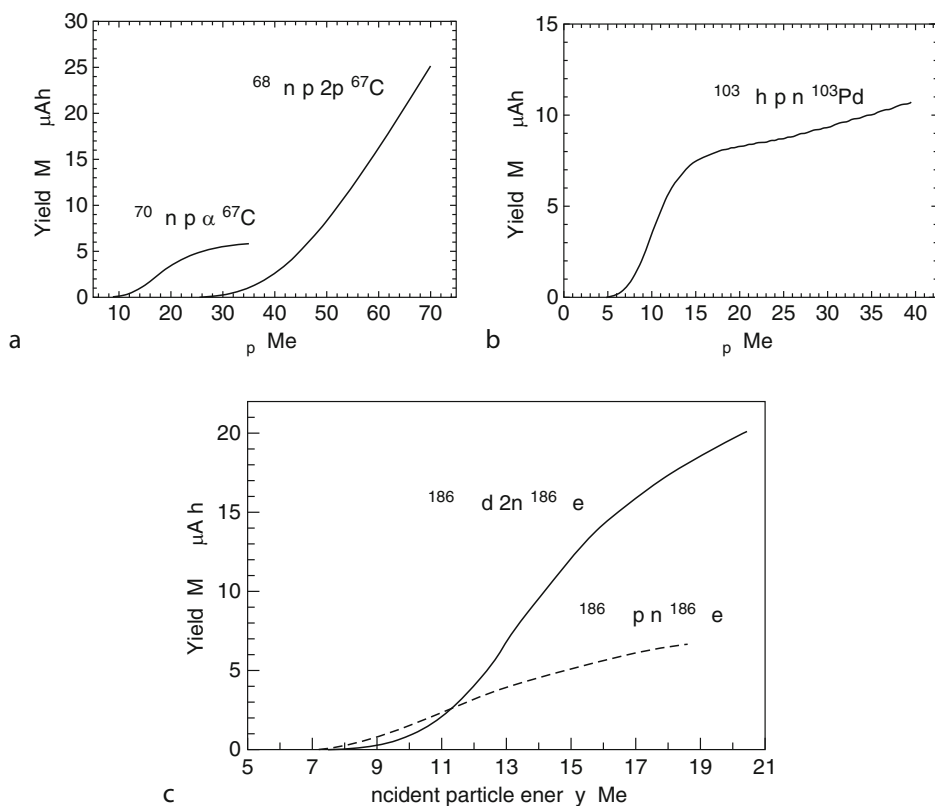
Some therapeutic radionuclides produced at a cyclotron

Radionuclide	$T_{1/2}$	Energy of emitted particle [MeV]	E_{γ} [keV] (I_{γ} in%)	Production route	
				Nuclear reaction	Energy range of interest [MeV]
^{67}Cu	2.6 days	0.6 (β^{-}) ^a	185 (45)	RbBr(p,spall)	800
				$^{68}\text{Zn}(\text{p},2\text{p})$	50–150
				$^{70}\text{Zn}(\text{p},\alpha)$	10–25
^{103}Pd	17.0 days	Auger electrons		$^{103}\text{Rh}(\text{p},\text{n})$	5–15
^{186}Re	3.8 days	1.1 (β^{-}) ^a	137 (8.5)	$^{186}\text{W}(\text{p},\text{n})$	10–20
				$^{186}\text{W}(\text{d},2\text{n})$	10–20
^{211}At (^{211}Po)	7.2 h (0.5 s)	5.9 (α) 7.5 (α)		$^{211}\text{Bi}(\alpha,2\text{n})$	20–28
^{225}Ac	10.0 days	5.8 (α)	100 (1.7)	$^{226}\text{Ra}(\text{p},2\text{n})$ ($T_{1/2} = 1,600$ a)	15–30

^a E_{max} of β^{-} -particle.

■ Fig. 39.10

Integral yields of some therapeutic radionuclides in various nuclear reactions shown as a function of projectile energy: (a) ^{67}Cu , (b) ^{103}Pd , (c) ^{186}Re . The curves for ^{67}Cu were calculated from the excitation functions reported by Kastleiner et al. (1999) and Stoll et al. (2002), and that for ^{103}Pd from the data of Sudàr et al. (2002). The results for ^{186}Re are from Szelecsényi et al. (1999)



In addition to the above mentioned radioisotopes, several other cyclotron-produced, useful or potentially useful, therapeutic radionuclides, e.g., ^{146}Tb ($T_{1/2} = 4.1$ h; $E_{\alpha} = 3.97$ MeV), ^{140}Nd ($T_{1/2} = 3.4$ days, Auger electrons), $^{193\text{m}}\text{Pt}$ ($T_{1/2} = 4.3$ days, Auger electrons), etc., are also receiving attention.

39.6 Conclusions and Perspectives

Radionuclide production technology at cyclotrons has been well developed, especially for short-lived organic positron emitters, commonly used SPECT radionuclides, and a few therapeutic radioisotopes. In this regard, all components of the technology, i.e., special purpose cyclotrons, high current irradiation targets, and automated or remotely controlled chemical processing units can now be purchased. Furthermore, four commonly used cyclotron produced SPECT radionuclides, namely ^{67}Ga , ^{111}In , ^{123}I , and ^{201}Tl , and the generator $^{81}\text{Rb}/^{81\text{m}}\text{Kr}$

are commercially available. Also, the PET radionuclide ^{18}F and the therapeutic radionuclide ^{103}Pd are commercially available in many regions. Some generator systems, which make use of long-lived parents (e.g., $^{68}\text{Ge}/^{68}\text{Ga}$, $^{82}\text{Sr}/^{82}\text{Rb}$), are supplied by several companies, though the parent nuclides are generally produced via intermediate energy nuclear reactions only at a few large research centers.

In contrast to the commonly used radionuclides, a few isotopes that have passed the stage of evaluation and are now in great demand, are not easily available. A few examples are ^{64}Cu , ^{67}Cu , ^{86}Y , ^{124}I , ^{211}At , and ^{225}Ac . Efforts are underway in commercially oriented laboratories to increase the production yields of these radionuclides and thus to ensure their availability on a broader scale.

The number of radionuclides of potential interest for medical applications is relatively large. They are research type radionuclides and the development work needed is rather heavy, calling for investigations in many directions, starting from nuclear data measurements, proceeding via high current target construction and chemical separation, and leading up to quality control and suitability tests for the desired applications. Although in many cases a combination of isotopically enriched target material and a small-sized cyclotron may be sufficient, for production of many new radionuclides, the necessity of an intermediate energy cyclotron may be inevitable. In general, it is concluded that the field of cyclotron production of medical radionuclides is flourishing, and many new impulses are expected within the next few years, especially with regard to new β^+ emitters and therapeutic radionuclides.

Acknowledgments

The author is indebted to many of his colleagues and co-workers for their fruitful co-operation over the years and to Prof. H. H. Coenen for the stimulating discussions.

References

- Bakir MA, Babich JW, Styles JM, Dean CJ, Eccles SA, Lambrecht RM (1990) *J Nucl Med* 31:777
- Bastian Th, Coenen HH, Qaim SM (2001) *Appl Radiat Isot* 55:303
- Becker D, Buckley KR, Chun KS, Hurtado ET, Jivan S, Zeisler S, Ruth TJ (2001) *J Labelled Compd Rad* 44: S122
- Beyer GJ, Pimentel-Gonzales G (2000) *Radiochim Acta* 88:175
- Bida G, Ehrenkauf RL, Wolf AP, Fowler JS, Macgregor RR, Ruth TJ (1980) *J Nucl Med* 21:758
- Bishop A, Satyamurthy N, Bida G, Phelps M, Barrio JR (1996) *Nucl Med Biol* 23:391
- Blessing G, Coenen HH, Franken K, Qaim SM (1986) *Appl Radiat Isot* 37:1135
- Blessing G, Lavi N, Hashimoto K, Qaim SM (1994) *Radiochim Acta* 65:93
- Blessing G, Qaim SM (1984) *Int J Appl Radiat Isot* 35:927
- Blessing G, Tárkányi F, Qaim SM (1997) *Appl Radiat Isot* 48:37
- Browne E, Firestone RB (1986) In: Shirley VS (ed) *Table of radioactive isotopes*. Wiley, New York
- Casella V, Ido T, Wolf AP, Fowler JS, Macgregor RR, Ruth TJ (1980) *J Nucl Med* 21:750
- Crouzel C, Langström B, Pike VW, Coenen HH (1987) *Appl Radiat Isot* 38:601
- Ferrieri RA, Wolf AP (1983) *Radiochim Acta* 34:69
- Firouzbakht ML, Schlyer DJ, Gatley SJ, Wolf AP (1993) *Appl Radiat Isot* 44:1081
- Gamestani K, Milenic DE, Plascjak PS, Brechbiel MW (2002) *Nucl Med Biol* 29:599
- Gul K, Hermanne A, Mustafa MG, Nortier FM, Oblozinsky P, Qaim SM, Scholten B, Shubin Y, Takács S, Tárkányi FT, Zhuang Y (2001) Charged particle cross section database for medical radioisotope production. IAEA-TECDOC-1211, IAEA, Vienna, pp 1–284

- Hamacher K, Hirschfelder Th, Coenen HH (2002) *Appl Radiat Isot* 56:519
- Hassan HE, Qaim SM, Shubin Yu, Azzam A, Morsy M, Coenen HH (2004) *Appl Radiat Isot* 60:899
- Hermanne A, Gul K, Mustafa MG, Nortier FM, Oblozinsky P, Qaim SM, Scholten B, Takács S, Tárkányi F (2001) Photon emitters, in charged particle cross section database for medical radioisotope production. IAEA-TECDOC-1211, IAEA, Vienna, pp 153–233
- Heselius S-J (1986) Studies of density reduction in gas targets, PhD thesis, Abo Akademi, Abo
- Heselius S-J, Schlyer DJ, Wolf AP (1989) *J Labelled Compd Rad* 26:140
- Hess E, Blessing G, Coenen HH, Qaim SM (2000) *Appl Radiat Isot* 52:1431
- Hess E, Tákács S, Scholten B, Tárkányi F, Coenen HH, Qaim SM (2001) *Radiochim Acta* 89:357
- Hohn A, Coenen HH, Qaim SM (1998a) *Appl Radiat Isot* 49:1493
- Hohn A, Nortier FM, Scholten B, van der Walt TN, Coenen HH, Qaim SM (2001) *Appl Radiat Isot* 55:149
- Hohn A, Scholten B, Coenen HH, Qaim SM (1998b) *Appl Radiat Isot* 49:93
- Hussain M, Sudár S, Aslam MN, Shah HA, Ahmad R, Malik AA, Qaim SM (2009) *Appl Radiat Isot* 67:1842
- Kastleiner S, Coenen HH, Qaim SM (1999) *Radiochim Acta* 84:107
- Kettern K, Linse K-H, Spellerberg S, Coenen HH, Qaim SM (2002) *Radiochim Acta* 90:845
- Kilbourn MR, Jerabek PA, Welch MJ (1985) *Int J Appl Radiat Isot* 36:327
- Knust EJ, Dutschka K, Weinreich R (2000) *Appl Radiat Isot* 52:181
- Kondo K, Lambrecht RM, Wolf AP (1977) *Int J Appl Radiat Isot* 28:395
- Kovács Z, Blessing G, Qaim SM, Stöcklin G (1985) *Int J Appl Radiat Isot* 36:635
- Kurenkov NV, Malinin AB, Sebyakin AA, Venikov NI (1989) *J Radioan Nucl Ch Le* 135:39
- Lagunas-Solar MC, Jungerman JA, Peek NF, Theus RM (1978) *Int J Appl Radiat Isot* 29:159
- Lambrecht RM, Mirzadeh S (1985) *Int J Appl Radiat Isot* 36:443
- Lambrecht RM, Sajjad M, Qureshi MA, Al-Yanbawi SJ (1988) *J Radioan Nucl Ch Le* 127:143
- Loch C, Mardon K, Valette H, Bruresco C, Merlet P, Syrota A, Maziere B (1994) *Nucl Med Biol* 21:35
- Mahunka I, Andó L, Gál I, Ido T, Kovács Z (1996) In: Link JM, Ruth TJ (eds) *Proceedings of the 6th workshop on targetry and target chemistry*. Vancouver, Canada, August 1995, TRIUMF, p 192
- McCarthy DW, Shefer RE, Klinkowstein RE, Bass LA, Margeneau WH, Cutler CS, Anderson CJ, Welch MJ (1997) *Nucl Med Biol* 24:35
- Michael H, Rosezin H, Apelt H, Blessing G, Knieper J, Qaim SM (1981) *Int J Appl Radiat Isot* 32:581
- Mirzadeh S, Mausner LF, Srivastava SC (1986) *Appl Radiat Isot* 37:29
- Mushtaq A, Qaim SM, Stöcklin G (1988) *Appl Radiat Isot* 39:1085
- Nagatsu K, Kubodera A, Suzuki K (1998) *Appl Radiat Isot* 49:1505
- Nickles RJ, Hichwa R, Daube ME, Hutchins GD, Congdon DD (1983) *Appl Radiat Isot* 34:625
- Philippis DR, Peterson EJ, Taylor WA, Jamriska DJ, Hamilton VT, Kitten JJ, Valdez FO, Salazar LL, Pitt LR, Heaton RC, Kolsky KL, Mausner LF, Kurczak S, Zhuikov BL, Kokhanyuk VM, Konyakhin NA, Nortier FM, van Derwalt TN, Hanekom J, Sosnowski KM, Carty JS (2000) *Radiochim Acta* 88:149
- Plenevaux A, Guillaume M, Brihaye C, Lemaire C, Cantineau R (1990) *Appl Radiat Isot* 41:829
- Qaim SM (1982) *Radiochim Acta* 30:147
- Qaim SM (1986) *Int J Appl Radiat Isot* 37:803
- Qaim SM (1987) *Radiochim Acta* 41:111
- Qaim SM (1989) *Nucl Instrum Methods* 282:289
- Qaim SM (2000) *J Nucl Med Biol* 27:323
- Qaim SM (ed) (2001a) Nuclear data for medical applications. Special issue of *Radiochim Acta* 89:189–355
- Qaim SM (2001b) *Radiochim Acta* 89:297
- Qaim SM (2002) *J Nucl Sci Tech* (2 Suppl.):1272
- Qaim SM (2008) *Q J Nucl Med Mol Imaging* 52:111
- Qaim SM, Bisinger T, Hilgers K, Nayak D, Coenen HH (2007) *Radiochim Acta* 95:67
- Qaim SM, Capote R, Betak E, Carlson BV, Caldeira AD, Choi HD, Ignatyuk AV, Király B, Menapace E, Nortier FM, Paviotti DE, Corcuera R, Scholten B, Shubin YN, Sublet JC, Tárkányi FT (2008) Production of therapeutic radionuclides. IAEA technical report, in print, available from (<http://www-nds.iaea.org/medportal/>)
- Qaim SM, Clark JC, Crouzel C, Guillaume M, Helmeke HJ, Nebeling B, Pike VW, Stöcklin G (1993) PET radionuclide production. In: Stöcklin G, Pike VW (eds) *Radiopharmaceuticals for positron emission tomography*. Kluwer, Dordrecht, pp 1–42
- Qaim SM, Hohn A, Bastian T, El-Azoney KM, Blessing G, Spellerberg S, Scholten B, Coenen HH (2003) *Appl Radiat Isot* 58:69
- Qaim SM, Tárkányi FT, Oblozinsky P, Gul K, Hermanne A, Mustafa MG, Nortier FM, Scholten B, Shubin YN, Takács S, Zhuang Y (2002) *J Nucl Sci Tech* (2 Suppl.):1281
- Qaim SM, Tárkányi F, Tákács S, Hermanne A, Nortier M, Oblozinsky P, Scholten B, Shubin YN, Zhuang Y (2001) Positron emitters, in charged particle cross section database for medical radioisotope production. IAEA-TECDOC-1211, IAEA, Vienna, pp 234–280
- Qaim SM, Weinreich R, Ollig H (1979) *Int J Appl Radiat Isot* 30:85

- Reischl G, Rösch F, Machulla H-J (2002) *Radiochim Acta* 90:225
- Roberts AD, Oakes TR, Nickles RJ (1995) *Appl Radiat Isot* 46:82
- Rösch F, Novgorodov AF, Qaim SM (1994) *Radiochim Acta* 64:113
- Rösch F, Qaim SM, Stöcklin G (1993a) *Radiochim Acta* 61:1
- Rösch F, Qaim SM, Stöcklin G (1993b) *Appl Radiat Isot* 44:671
- Ruth TJ (1985) *Int J Appl Radiat Isot* 36:107
- Ruth TJ (2003) Accelerators available for isotope production. In: Welch MJ, Redvanly CS (eds) *Handbook of radiopharmaceuticals*. Wiley, Chichester, pp 71–83
- Ruth TJ, Wolf AP (1979) *Radiochim Acta* 26:21
- Scholten B, Kovács Z, Tárkányi F, Qaim SM (1995) *Appl Radiat Isot* 46:255
- Scholten B, Qaim SM, Stöcklin G (1989) *Appl Radiat Isot* 40:127
- Schlyer DJ (2003) Production of radionuclides in accelerators. In: Welch MJ, Redvanly CS (eds) *Handbook of radiopharmaceuticals*. Wiley, Chichester, pp 1–70
- Schwarzbach R, Zimmermann K, Bläuenstein P, Smith A, Schubiger PA (1995) *Appl Radiat Isot* 46:329
- Sharma HL, Zweit J, Downey S, Smith AM, Smith AG (1988) *J Labelled Compd Rad* 26:165
- Sheh Y, Kozirowski J, Balatoni J, Lom C, Dahl JR, Finn RD (2000) *Radiochim Acta* 88:169
- Shigeta N, Matsuoka H, Osa A, Koizumi M, Izumo M, Kobayashi K, Hashimoto K, Lambrecht RM (1996) *J Radioan Nucl Ch Ar* 205:85
- Spellerberg S, Reimer P, Blessing G, Coenen HH, Qaim SM (1998) *Appl Radiat Isot* 49:1519
- Stöcklin G, Qaim SM, Rösch F (1995) *Radiochim Acta* 70(71):249
- Stoll T, Kastleiner S, Shubin YuN, Coenen HH, Qaim SM (2002) *Radiochim Acta* 90:309
- Strohmaier B, Fassbender M, Qaim SM (1997) *Phys Rev C* 56:2654
- Sudár S, Cserpák F, Qaim SM (2002) *Appl Radiat Isot* 56:821
- Suzuki K, Yamazaki I, Sasaki M, Kubodera A (2000) *Radiochim Acta* 88:211
- Szelecsényi F, Blessing G, Qaim SM (1993) *Appl Radiat Isot* 44:575
- Szelecsényi F, Takács S, Tárkányi F, Sonck M, Hermanne A (1999) *J Labelled Compd Rad* 42:912
- Tárkányi F, Szelecsényi F, Kopecky P, Molnár T, Andó L, Míkócz P, Tóth GY, Rydl A (1994) *Appl Radiat Isot* 45:239
- Tárkányi F, Szelecsényi F, Kovács Z, Sudár S (1990) *Radiochim Acta* 50:19
- Tárkányi F, Qaim SM, Stöcklin G, Sajjad M, Lambrecht RM, Schweickert H (1991) *Appl Radiat Isot* 42:221
- Tolmachev V, Löfqvist A, Einarsson L, Schultz J, Lundqvist H (1998) *Appl Radiat Isot* 49:1537
- Vaalburg W, Paans AMJ, Terpstra JW, Wiegman T, Dekens K, Rijkskamp A, Woldring MG (1985) *Int J Appl Radiat Isot* 36:961
- van den Bosch R, de Goeij JJM, van der Heide JA, Tertoolen JFW, Theelen HMJ, Zegers C (1977) *Int J Appl Radiat Isot* 28:255
- Waters SL, Coursey BM (eds) (1987) The $^{82}\text{Sr}/^{82}\text{Rb}$ generator. Special issue of *Appl Radiat Isot* 38:171–240
- Weinreich R, Knust EJ (1996) *J Radioan Nucl Ch Le* 213:253
- Wieland BW, Schlyer DJ, Wolf AP (1984) *Int J Appl Radiat Isot* 35:387
- Wolf AP, Barclay Jones W (1983) *Radiochim Acta* 34:1
- Zeisler SK, Becker DW, Pavan RA, Moschel R, Rühle H (2000) *Appl Radiat Isot* 53:449
- Zhang A, Li W, Fang K, He W, Sheng R, Ying D, Hu W (1999) *Radiochim Acta* 86:11
- Zhang X, Li Q, Li W, Sheng R, Shen S (2001) *Appl Radiat Isot* 54:89



40 Radionuclide Generators

F. Rösch¹ · F. F. (Russ) Knapp²

¹Johannes Gutenberg-University Mainz, Mainz, Germany

²Nuclear Science and Technology Division, Oak Ridge National Laboratory, Oak Ridge, TN, USA

40.1	<i>Introduction</i>	1936
40.1.1	Historical Perspective	1936
40.1.2	Equations of Radioactive Decay and Growth	1937
40.1.2.1	Transient Equilibrium	1938
40.1.2.2	Secular Equilibrium	1939
40.1.2.3	No Equilibrium	1941
40.1.2.4	Decay Chains: Many Successive Decays	1941
40.1.3	Classifications	1941
40.2	<i>Generator-Produced Positron Emitters</i>	1945
40.2.1	Overview	1945
40.2.2	Generators with Potential Medical Application	1945
40.2.3	Key Examples of Generator-Derived Positron-Emitting Radionuclides	1950
40.3	<i>Generator-Produced Photon Emitters</i>	1955
40.3.1	Overview	1955
40.3.2	Key Examples of Generator-Produced Photon Emitters with Proven Medical Applications	1956
40.4	<i>Generator-Produced Particle Emitters for Therapy</i>	1959
40.4.1	Overview	1959
40.4.2	Key Examples of Generator-Derived Therapeutic Radionuclides with Proven Medical Applications	1961
40.5	<i>In Vivo Generators</i>	1966
40.5.1	Concept	1966
40.5.2	Examples of In Vivo Generators	1967

Abstract: Radionuclide generator systems continue to play a key role in providing both diagnostic and therapeutic radionuclides for various applications in nuclear medicine, oncology, and interventional cardiology. Although many parent/daughter pairs have been evaluated as radionuclide generator systems, there are a relatively small number of generators, which are currently in routine clinical and research use. Essentially every conceivable approach has been used for parent/separation strategies, including sublimation, thermochromatographic separation, solvent extraction, and adsorptive column chromatography. The most widely used radionuclide generator for clinical applications is the $^{99}\text{Mo}/^{99\text{m}}\text{Tc}$ generator system, but recent years have seen an enormous increase in the use of generators to provide therapeutic radionuclides, which has paralleled the development of complementary technologies for targeting agents for therapy and in the general increased interest in the use of unsealed therapeutic radioactive sources. More recently, use of the $^{68}\text{Ge}/^{68}\text{Ga}$ generator is showing great potential as a source of positron-emitting ^{68}Ga for positron emission tomography (PET)/CT imaging. Key advantages for the use of radionuclide generators include reasonable costs, the convenience of obtaining the desired daughter radionuclide on demand, and availability of the daughter radionuclide in high specific activity, no-carrier added form.

40.1 Introduction

40.1.1 Historical Perspective

A radionuclide generator is a concept defined as an effective radiochemical separation of decaying parent and daughter radionuclides such that the daughter is obtained in a pure radionuclidic and radiochemical form. Radionuclide generators were historically called “cows” since the daughter radioactivity was “milked” (i.e., removed) from its precursor and the parent then generated a fresh supply of the daughter.

Generator parent radionuclides are obtained from uranium fission products (i.e., ^{99}Mo and ^{90}Sr) or as decay products from ^{233}U ($^{229}\text{Th}/^{225}\text{Ac}$), or are produced directly in nuclear reactors (^{188}W , etc.) or at accelerators (^{82}Rb , ^{62}Zn , etc.).

Compared to in-house radionuclide production facilities such as accelerators or nuclear reactors, the availability of short-lived radionuclides from radionuclide generators provides an inexpensive and convenient alternative. The development of radionuclide generators over the past 3 decades was primarily motivated by the increasing spectrum of applications of radionuclides and labeled compounds in the life sciences, in particular for diagnostic applications in nuclear medicine. In the last years, however, promising applications of generator-derived therapeutic radionuclides have been developed in the fields of nuclear medicine, oncology, and interventions cardiology. This increasing importance of radionuclide generators has initiated a broad development for radionuclide production of the generator parent radionuclide, for sophisticated radiochemical separations as well as reliable technical design of the generator systems.

The first generator for life sciences application was developed in 1920, providing ^{222}Rn ($T_{1/2} = 3.825$ d) to obtain radon seeds for radiation therapy as a daughter of ^{226}Ra ($T_{1/2} = 1.60 \times 10^3$ a) (Failla 1920). However, practical importance of radionuclide generators was achieved in 1951 by the ^{132}Te ($T_{1/2} = 3.26$ d)/ ^{132}I ($T_{1/2} = 1.39$ h) generator (Winsche et al. 1951), and, much more, in 1957 by the pioneering development of the $^{99}\text{Mo}/^{99\text{m}}\text{Tc}$ generator at

Brookhaven National Laboratory (BNL) (Stang et al. 1954, 1957). The technetium daughter radionuclide was soon envisioned for medical use (1960), and indeed its first clinical application was reported in 1961 (Richards 1960; Harper et al. 1962) and has revolutionized radio-pharmaceutical chemistry and nuclear medicine. Since that time, various other generator systems have been developed, and some of them received significant practical application.

The broad use of the $^{99}\text{Mo}/^{99\text{m}}\text{Tc}$ generator system in nuclear medicine is a key example, which has been crucial for more than 2 decades for the hospital or central radiopharmacy preparation of a wide variety of diagnostic agents for applications in nuclear medicine and oncology. Over 35,000 diagnostic procedures are estimated to be currently conducted daily in the USA. (>16 million studies per year) with $^{99\text{m}}\text{Tc}$. This reliance on the availability of $^{99\text{m}}\text{Tc}$ clearly underscores the crucial importance of the continued and reliable ^{99}Mo production and processing facilities to ensure the uninterrupted supply of the generator parent radionuclide required for fabrication of these generator systems.

These developments have been reviewed (Brucer 1965; Stang 1969; Lebowitz and Richards 1974; Lieser 1976; Yano 1978; Boyd et al. 1984; Paras and Thiessen 1985; Boyd 1986; Mani 1987; Lambrecht and Sajjad 1988; Ruth et al. 1989; Knapp et al. 1992; Knapp and Mirzadeh 1994; Mirzadeh and Knapp 1996; Lambrecht et al. 1997). Detailed reviews have addressed the following topics: parent–daughter half-lives (Finn et al. 1983), reactor-produced generators (Mani 1987), accelerator-produced generators (Lambrecht 1983), cyclotron production of generator parent nuclides (Qaim 1987), ultra short-lived generator-produced radionuclides (Guillaume and Brihaye 1986, 1987), generator-derived positron-emitting radionuclides (Knapp et al. 1992), and clinical applications (Knapp and Butler 1984; Knapp and Mirzadeh 1994). In addition to the generators discussed here in a clinical context, a significant number of other generator pairs exist. Many of those cases have been identified by Lieser (1976) for example, but there still may be other parent/daughter radionuclide pairs whose potential feasibility for generators has not yet been considered.

40.1.2 Equations of Radioactive Decay and Growth

The exponential laws of radioactive-series decay and growth of radionuclides were first formulated by Rutherford and Soddy in 1902, to explain their results (Rutherford and Soddy 1902, 1903) on the thorium series of radionuclides. In 1910, Bateman (Bateman 1910) derived generalized mathematical expressions that were used to describe the decay and growth of the naturally occurring actinium, uranium, and thorium series until the discovery of nuclear fission and other new radioactive decay series were found in the 1940s. For the description of half-lives and decay constants, activities and number of radionuclides involved in the decay of two radionuclides, Friedlander et al. (1981) have given a representative overview (see also ► Chap. 5 in Vol. 1).

A radioactive nuclide decays according to an exponential law:

$$N = N_0 e^{-\lambda t} \text{ or } A = A_0 e^{-\lambda t} \quad (40.1)$$

where N and A represent the number of atoms and the activity, respectively, at time t , and N_0 and A_0 the corresponding quantities when $t = 0$, and λ is the decay constant for the radionuclide. The half-life $T_{1/2}$ is related to the decay constant

$$T_{1/2} = \frac{\ln 2}{\lambda} \approx \frac{0.69315}{\lambda}. \quad (40.2)$$

The general case for the generation of a second radioactive nuclide from the decay of a first one must consider the decay parameters of the first radioactive nuclide, denoted by subscript 1 (parent), as well as the parameters of the produced second radioactive nuclide, denoted by subscript 2 (daughter). The behavior of N_1 is

$$-(dN_1/dt) = \lambda_1 N_1, \text{ and } N_1 = N_1^0 e^{-\lambda_1 t} \quad (40.3)$$

where N_1^0 represents the value of N_1 at $t = 0$. The second radionuclide is formed at the rate at which the first decays, $\lambda_1 N_1$, and itself decays at the rate $\lambda_2 N_2$:

$$\frac{dN_2}{dt} = \lambda_1 N_1 - \lambda_2 N_2 \quad (40.4)$$

or

$$\frac{dN_2}{dt} = \lambda_2 N_2 - \lambda_1 N_1^0 e^{-\lambda_1 t} = 0. \quad (40.5)$$

► Equations (40.4) and ► (40.5) represent linear differential equations of the first order and solutions obtained by standard methods lead to

$$N_2 = \frac{\lambda_1}{\lambda_2 - \lambda_1} N_1^0 (e^{-\lambda_1 t} - e^{-\lambda_2 t}) + N_2^0 e^{-\lambda_2 t} \quad (40.6)$$

where N_2^0 is the value of N_2 at $t = 0$. The first group of terms reflects the growth of a “daughter” radionuclide 2 from a “parent” radionuclide 1 and the decay of these “daughter” radionuclides, while the second term gives the contribution at any time from the “daughter” radionuclides initially present.

Radionuclide generations are distinguished according to the half-lives of the parent and daughter radionuclides. Depending on which of the two radionuclides has the longer half-life, three principal cases occur: (1) parent is longer-lived, but not more than by a factor of about 100, i.e., $T_{1/2,2} < T_{1/2,1} < 100 T_{1/2,2}$, *transient equilibrium*, (2) parent is much longer-lived than the daughter ($T_{1/2,1} \gg T_{1/2,2}$, i.e., $\lambda_1 \ll \lambda_2$), *secular equilibrium*, (3) parent is shorter-lived than the daughter ($T_{1/2,1} < T_{1/2,2}$, i.e., $\lambda_1 > \lambda_2$), *no equilibrium*.

Because in some cases daughter radionuclides are relevant, which are generated via one or more intermediate radionuclides from an original parent, also decay chains must be considered.

40.1.2.1 Transient Equilibrium

Suppose the parent is longer-lived than the daughter ($T_{1/2,1} > T_{1/2,2}$, i.e., $\lambda_1 < \lambda_2$), ► Eq. (40.6) reaches the form of ► Eq. (40.7)

$$N_2 = \frac{\lambda_1}{\lambda_2 - \lambda_1} N_1^0 e^{-\lambda_1 t} \quad (40.7)$$

($e^{-\lambda_2 t}$ is negligible compared with $e^{-\lambda_1 t}$ after t becomes sufficiently large, and $N_2^0 e^{-\lambda_2 t}$ also becomes negligible). Since $N_1 = N_1^0 e^{-\lambda_1 t}$, the ratio of the numbers of the two radionuclides is

$$\frac{N_1}{N_2} = \frac{\lambda_2 - \lambda_1}{\lambda_1}, \quad (40.8)$$

and, consequently, the ratio of the absolute activities of the two radionuclides is

$$\frac{A_1}{A_2} = \frac{(\lambda_2 - \lambda_1)}{\lambda_2} = 1 - \frac{\lambda_1}{\lambda_2}. \quad (40.9)$$

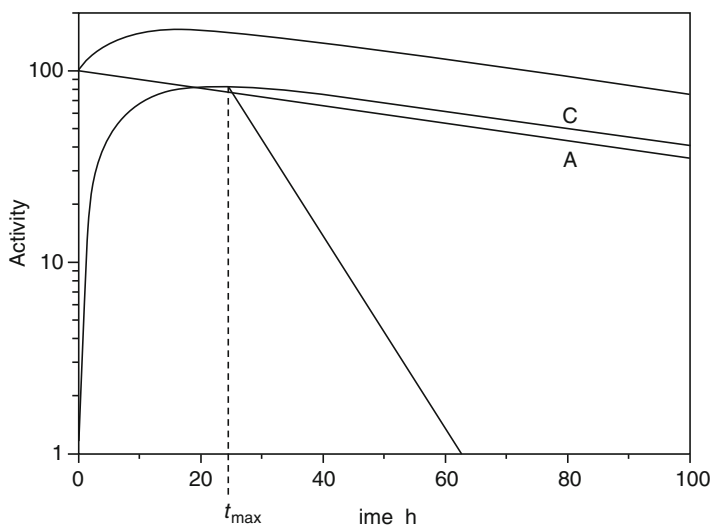
This ratio of the two activities may thus have any value between 0 and 1, depending on the ratio of λ_1 to λ_2 . Consequently, in equilibrium the daughter activity will be greater than the parent activity by the factor $\lambda_2/(\lambda_2 - \lambda_1)$. Starting with an initially pure parent fraction, the sum of the parent and daughter disintegration rates goes through a maximum before transient equilibrium is achieved. In equilibrium, both activities decay with the parent's half-life. The corresponding kinetics are illustrated in ▶ Fig. 40.1, giving an example of the transient equilibrium for the most prominent medical radionuclide generator ^{99}Mo ($T_{1/2} = 65.945 \text{ h}$)/ $^{99\text{m}}\text{Tc}$ ($T_{1/2} = 6.006 \text{ h}$). The ratio between the half-lives is 11. The curves represent variations with time of the parent activity and the activity of a freshly isolated daughter fraction, the growth of daughter activity in a freshly purified parent fraction, and other relations (▶ Fig. 40.2). ▶ Figure 40.2 illustrates the general regime of subsequent separations of the daughter nuclide and shows the ingrowth of the daughter activity within the generators systems after each separation cycle.

40.1.2.2 Secular Equilibrium

The limiting case of radioactive equilibrium at $\lambda_1 \ll \lambda_2$ is called secular equilibrium. In this case, the parent activity does not decrease measurably during many daughter half-lives.

■ Fig. 40.1

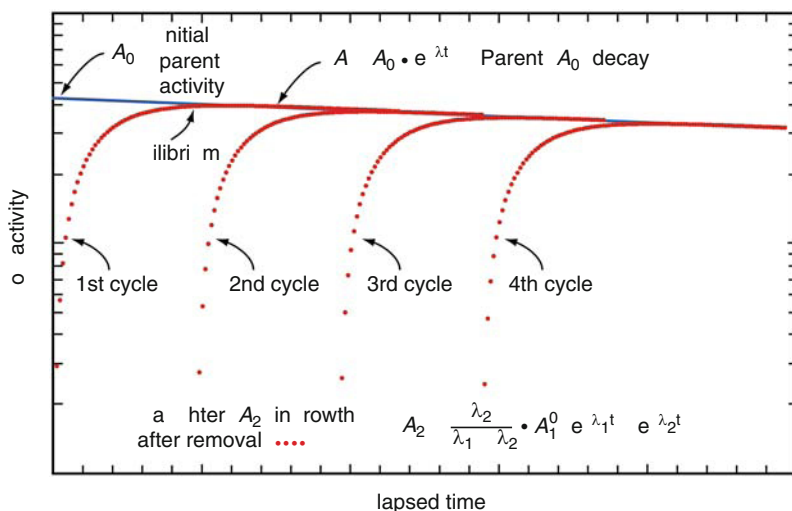
Transient radionuclide generator kinetics for the system $^{99}\text{Mo}/^{99\text{m}}\text{Tc}$. A, independent activity of the parent nuclide; B, growth of cumulative parent and daughter activity in a pure parent fraction; C, growth of daughter activity in a pure parent fraction; D, independent decay of the separated pure daughter fraction at maximum of generated activity



► Equations (40.8) and ► (40.9) reduce to $N_1/N_2 = \lambda_2/\lambda_1$ and $A_1 = A_2$. In these equilibria, the daughter activity will not exceed the parent activity. This characteristic, different from the transient equilibrium shown in ► Fig. 40.1, is illustrated for the $^{68}\text{Ge}/^{68}\text{Ga}$ radionuclide generator in ► Fig. 40.3. The ratio between the mother and daughter half-lives in this case is $270.8 \times 24 \text{ h}/1.135 \text{ h} = 5726$.

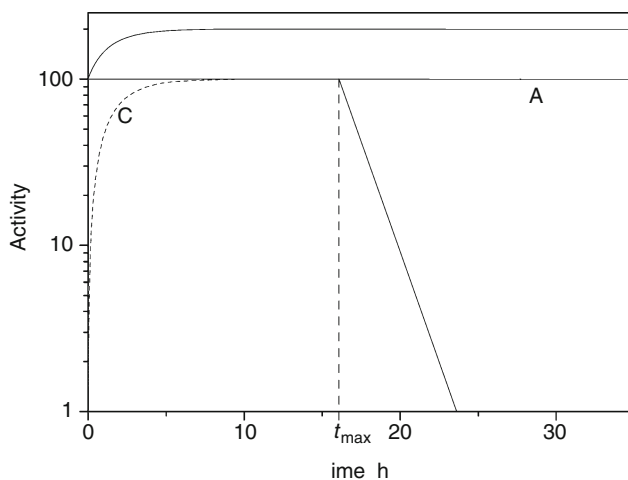
■ Fig. 40.2

Illustration of daughter (A_2) in growth and parent (A_1) decay for four successive elution cycles



■ Fig. 40.3

Secular radionuclide generator kinetics for the system $^{68}\text{Ge}/^{68}\text{Ga}$. A, independent activity of the parent nuclide; B, growth of cumulative parent and daughter activity in a pure parent fraction; C, growth of daughter activity in a pure parent fraction; D, independent decay of the separated pure daughter fraction at maximum of generated activity



In the case of $T_{1/2,1} \gg T_{1/2,2}$ the maximum activity of the daughter occurs at the time, t , which is calculated by ▶ Eq. (40.10):

$$t = \frac{1}{\lambda_2 - \lambda_1} \ln \frac{\lambda_2}{\lambda_1}. \quad (40.10)$$

With the $^{68}\text{Ge}/^{68}\text{Ga}$ system, the theoretical maximum of generated activity is reached after 14.1 h. However, in the case of secular equilibria cyclic separations are performed much more frequently than that, e.g., after three half-lives of ^{68}Ga already (i.e., about 3.4 h after the preceding elution), when about 90% of the theoretical maximum is generated. In a clinical context, this may allow three individual elutions per day.

40.1.2.3 No Equilibrium

If the parent is shorter-lived than the daughter ($T_{1/2,1} < T_{1/2,2}$, i.e., $\lambda_1 > \lambda_2$), it is evident that no equilibrium is attained at any time. If the parent is made initially free of the daughter, then as the parent decays the amount of daughter will rise, pass through a maximum, and eventually decay with the characteristic half-life of the daughter.

40.1.2.4 Decay Chains: Many Successive Decays

The radionuclide of interest might not be produced by a direct generation from a parent radionuclide exclusively. Instead, it might be a product of a decay chain involving more than one parent radionuclide. If a chain of three or more radioactive products needs to be considered, the equations derived for N_1 and N_2 as functions of time are valid as well, and N_3 for example may be found by solving a new differential equation:

$$\frac{dN_3}{dt} = \lambda_2 N_2 - \lambda_3 N_3. \quad (40.11)$$

Mathematical treatments of this equation and for $n \geq 4$ members of a decay chain were developed (Bateman 1910). Moreover, for many decay chains, the case of branching decay needs to be considered. When a nuclide A can decay by more than one mode (e.g., by β^- decay generating the radionuclide B and by α decay generating the radionuclide C) the two partial decay constants λ_B and λ_C must be considered, cf. the generator systems with the ^{213}Bi parent. The considerations for branching decay, of course, are valid as well for a single, i.e., non-decay-chain decay.

40.1.3 Classifications

Generally, the decay of a radioactive nuclide results in a longer-lived or even stable daughter nuclide. In this respect, radionuclide generator systems where the daughter nuclide presents a shorter half-life are a welcome exception from the general properties of β decay. In particular, for a clinical application, a state of a “radioactive equilibrium” is mandatory. Thus, mainly the transient and secular equilibria of radionuclide generations are relevant for

application of the radionuclide pairs discussed in this chapter. There appears to be some relevancy for application of so-called *in vivo* radionuclide generator, which will be discussed as well.

There is another unique property of a “medical” radionuclide generator: The daughter nuclide is generated at a no-carrier-added concentration. It thus ideally meets the criteria of Hevesy’s tracer concept, which entail the application of labeled compounds at almost negligible concentrations, completely irrelevant for pharmacodynamic interactions with the human body.

In addition, radionuclide generators intended for applications in life science, in particular in the context of routine clinical use, must meet strict regulatory and quality control requirements. The production of the radionuclide generator parent, its separation from the target material, the chemical and technical construction of the separation of the radionuclide generator daughter are factors, which in totality shall finally result in an efficient and easy handling. They are discussed below.

1. The production of the radionuclide generator parent: This includes the route of parent nuclide availability, i.e., reactor or accelerator production or usage of decay chains of “naturally” occurring radioisotopes or of reactor-generated ones; the investigation of precise nuclear data, which is mandatory for optimum production parameters providing the corresponding thick target yields and radionuclidic purities; high-flux irradiations with sophisticated target design at adequate irradiation facilities (including cost of irradiations); costs of target materials and if the use of enriched target material is required; specific activity of the parent isotope (no-carrier-added vs. carrier-added). Reactor and cyclotron-based production of the parent nuclides is discussed in detail in [Chaps. 38 and 39](#) of this Volume.
2. The selection of a separation method of the parent nuclide from the target material: Investigation of the optimum chemical form of the target material and the principal separation methods (ion exchange, extraction, volatilization, precipitation, etc.) allowing high chemical yields of the parent nuclide; recovery of enriched target materials, etc.
3. The chemical and technical concept of the separation of the radionuclide generator daughter: Development of the optimum separation method (most often ion exchange or extraction; for in-house use ion exchange chromatography almost exclusively) providing high yield of the daughter nuclide in minimum volumes and highest radionuclidic purity (i.e., lowest breakthrough of parent nuclide); selection of solutions used, etc.
4. The efficient and easy handling: Experimental vs. routine build-up of the final generator, consideration of the activity scale with regard to radiation stability (radiolysis) and radiation safety; regulatory requirements and commercial logistics; eventual recovery of the parent nuclide, etc.

A significant number of generator radionuclide pairs have been discussed over the last decades, most of which are summarized in [Table 40.1](#). This table also indicates the main production route of the parent radionuclide, i.e., whether the parent nuclide is accelerator or reactor produced or is made available via nuclear decay chains. According to their application for PET imaging, single photon emission computer tomography (SPECT), and photon imaging or for therapy, for various individual generators a short review is provided on the medical potential of the generator, the production routes of the parent nuclide, the chemical concepts of generator pair separations, and on some examples of state-of-the-art application of the daughter nuclide.

■ Table 40.1

Radionuclide generator systems relevant for life-sciences application

Generator system	Parent nuclide			Daughter nuclide		
	$T_{1/2}$	Main production route	Main decay	$T_{1/2}$	Main emission	Application
$^{42}\text{Ar}/^{42}\text{K}$	32.9 a	Reactor	β^-	12.36 h	β^-	Chemistry
$^{47}\text{Ca}/^{47}\text{Sc}$	4.536 d	Reactor	β^-	3.341 d	γ, β^-	ERT
$^{44}\text{Ti}/^{44}\text{Sc}$	60.3 a ^a	Accelerator	EC	3.927 h	β^+	PET
$^{52}\text{Fe}/^{52\text{m}}\text{Mn}$	8.28 h	Accelerator	β^+	21.1 min	β^+	PET
$^{66}\text{Ni}/^{66}\text{Cu}$	2.28 d	Reactor	β^-	5.10 min	γ, β^-	in vivo; ERT
$^{62}\text{Zn}/^{62}\text{Cu}$	9.26 h	Accelerator	EC	9.74 min	β^+	PET
$^{68}\text{Ge}/^{68}\text{Ga}$	270.8 d	Accelerator	EC	1.135 h	β^+	PET
$^{72}\text{Se}/^{72}\text{As}$	8.4 d	Accelerator	EC	1.083 d	β^+	PET
$^{77}\text{Br}/^{77\text{m}}\text{Se}$	2.377 d	Accelerator	EC	17.4 s	γ	FPRNA
$^{80\text{m}}\text{Br}/^{80}\text{Br}$	4.42 h	Reactor	IT	17.68 min	γ	Chemistry
$^{81}\text{Rb}/^{81\text{m}}\text{Kr}$	4.58 h	Accelerator	EC	13 s	γ	SPECT
$^{83}\text{Rb}/^{83\text{m}}\text{Kr}$	86.2 d	Accelerator	EC	1.86 h	γ	Chemistry/ RPC
$^{82}\text{Sr}/^{82}\text{Rb}$	25.6 d	Accelerator	EC	1.273 min	β^+	PET
$^{90}\text{Sr}/^{90}\text{Y}$	28.5 a	Reactor, f	β^-	2.671 d	β^-	ERT
$^{87}\text{Y}/^{87\text{m}}\text{Sr}$	3.35 d	Accelerator	EC	2.80 h	γ	Chemistry
$^{89}\text{Zr}/^{89\text{m}}\text{Y}$	3.268 d	Accelerator	EC	16.1 s	γ	Chemistry
$^{97}\text{Zr}/^{97}\text{Nb}$	16.90 h	Accelerator	β^-	1.20 h	γ, β^-	Chemistry
$^{99}\text{Mo}/^{99\text{m}}\text{Tc}$	2.7477 d	Reactor, f	β^-	6.006 h	γ	SPECT
$^{103}\text{Ru}/^{103\text{m}}\text{Rh}$	39.25 h	Reactor, f	β^-	56.12 min	γ, Ae	ERT
$^{103}\text{Pd}/^{103\text{m}}\text{Rh}$	16.97 d	Reactor, Acc.	EC	56.12 min	γ, Ae	Chemistry
$^{112}\text{Pd}/^{112}\text{Ag}$	21.04 h	Reactor, f	β^-	3.14 h	γ, β^-	in vivo, ERT
$^{109}\text{Cd}/^{109\text{m}}\text{Ag}$	1.267 a	Accelerator	EC	39.6 s	γ	FPRNA
$^{115}\text{Cd}/^{115\text{m}}\text{In}$	2.228 d	Reactor	β^-	4.486 h	γ, β^-	Chemistry/ RPC
$^{110}\text{Sn}/^{110\text{m}}\text{In}$	4.1 h	Accelerator	EC	1.15 h	β^+	PET
$^{113}\text{Sn}/^{113\text{m}}\text{In}$	115.1 d	Reactor	EC	1.658 h	γ	Chemistry/ RPC
$^{118}\text{Te}/^{118}\text{Sb}$	6.00 d	Accelerator	EC	3.6 m	β^+	PET
$^{132}\text{Te}/^{132}\text{I}$	3.26 d	Reactor (f)	β^-	2.284 h	γ, β^-	Therapy
$^{122}\text{Xe}/^{122}\text{I}$	20.1 h	Accelerator	EC	3.6 min	β^+	PET

Table 40.1 (Continued)

Generator system	Parent nuclide			Daughter nuclide		
	$T_{1/2}$	Main production route	Main decay	$T_{1/2}$	Main emission	Application
$^{137}\text{Cs}/^{137\text{m}}\text{Ba}$	30.0 a	Reactor, f	β^-	2.552 min	γ	in vivo, Diagnosis
$^{128}\text{Ba}/^{128}\text{Cs}$	2.43 d	Accelerator	EC	3.62 min	β^+	PET
$^{140}\text{Ba}/^{140}\text{La}$	12.75 d	Accelerator	β^-	1.678 d	γ, β^-	Chemistry/ RPC
$^{134}\text{Ce}/^{134}\text{La}$	3.16 d	Accelerator	EC	6.4 min	β^+	PET
$^{144}\text{Ce}/^{144}\text{Pr}$	284.9 d	Reactor, f	β^-	17.3 min	γ	Chemistry/ RPC
$^{140}\text{Nd}/^{140}\text{Pr}$	3.37 d	Accelerator	EC	3.39 min	β^+, Ae	PET
$^{166}\text{Dy}/^{166}\text{Ho}$	3.400 d	Reactor	β^-	1.117 d	β^-	ERT
$^{166}\text{Yb}/^{166}\text{Tm}$	2.362 d	Accelerator	EC	17.70 h	γ	Chemistry/ RPC
$^{167}\text{Tm}/^{167\text{m}}\text{Er}$	9.24 d	Accelerator	EC	2.28 s	γ	Chemistry/ RPC
$^{172}\text{Hf}/^{172}\text{Lu}$	1.87 a	Accelerator	EC	6.70 d	γ	Chemistry/ RPC
$^{178}\text{W}/^{178\text{m}}\text{Ta}$	21.5 d	Accelerator	EC	9.31 min	γ	FPRNA
$^{188}\text{W}/^{188}\text{Re}$	69.4 d	Reactor	β^-	16.98 h	β^-	ERT
$^{191}\text{Os}/^{191\text{m}}\text{Ir}$	15.4 d	Reactor	β^-	4.94 s	γ	FPRNA
$^{194}\text{Os}/^{194}\text{Ir}$	6.0 a	Reactor	β^-	19.15 s	γ, β^-	FPRNA
$^{195\text{m}}\text{Hg}/^{195\text{m}}\text{Au}$	1.73 d	Accelerator	EC	30.5 s	γ	FPRNA
$^{197\text{m}}\text{Hg}/^{197\text{m}}\text{Au}$	2.67 d	Accelerator	EC	7.8 s	γ	FPRNA
$^{212}\text{Pb}/^{212}\text{Bi}$	10.64 h	Decay chain	β^-	1.009 h	β^-, α	ERT
$^{213}\text{Bi}/^{209}\text{Pb}$	45.6 min	Decay chain	β^-, α	3.253 h	β^-	ERT
$^{211}\text{Rn}/^{211}\text{At}$	14.6 h	Accelerator	α, EC	7.21 h	α, ε	ERT
$^{226}\text{Ra}/^{222}\text{Rn}$	1.6×10^3 a	Decay chain	α	3.825 d	α	ERT
$^{225}\text{Ac}/^{213}\text{Bi}$	10.0 d	Decay chain	α	45.6 min	β^-, α	ERT
$^{227}\text{Ac}/^{227}\text{Th}/^{223}\text{Ra}$	21.77 d	Decay chain	α	11.43 d	α	ERT

^a Mean value of most recent various literature data.
EC, electron capture; IT, isomeric transition; β^+ , if EC < 50%; f, fission; Ae, atomic electrons; PET, positron emission tomography; SPECT, single photon emission computer tomography; FPRNA, first-pass radionuclide angiography; RPC, radiopharmaceutical chemistry; ERT, endoradiotherapy.
Nuclear decay data from: Browne and Firestone (1986)

40.2 Generator-Produced Positron Emitters

40.2.1 Overview

Among the generator pairs relevant for quantitative PET (➔ Table 40.2), all parent nuclides are neutron deficient and are thus produced at accelerators. All daughter nuclides are positron emitters and provide a significant positron branching, although in some cases the decay is accompanied by high-energy photons, which might require careful adoption of PET scanners.

The generators can be categorized according to the half-life of the daughter nuclide. The short-lived daughters cover half-lives of a few minutes. As the short half-lives do not allow radiochemical synthesis, these systems are relevant for perfusion imaging exclusively. The generator design must allow for direct application of the separated daughter for human use.

The longer-lived daughter nuclides, on the other hand, provide a potential for the development of labeled radiopharmaceuticals. However, due to the long half-life and the low cross sections, in particular for the parent nuclides ^{44}Ti , ^{68}Ga , and ^{82}Sr , the production rates are relatively low and require long high-current irradiations. Although this results in rather high cost per generator, the number of PET scans achievable lowers the costs per individual patient investigation.

40.2.2 Generators with Potential Medical Application

Some generator pairs have been proposed decades ago and have continuously been improved radiochemically. In many cases, however, there was no parallel development of medical

■ Table 40.2

Generator-produced positron emitters with potential for positron emission tomography (PET) imaging

Generator system	Parent	Daughter			
	$T_{1/2}$	$T_{1/2}$	β_{branch}^+ (%)	E_{β^+} (MeV)	Application
$^{82}\text{Sr}/^{82}\text{Rb}$	25.6 d	1.27 min	95.0	1.41	Perfusion
$^{140}\text{Nd}/^{140}\text{Pr}$	3.37 d	3.39 min	51.0	0.544	Perfusion
$^{118}\text{Te}/^{118}\text{Sb}$	6.00 d	3.6 min	74.0	0.882	Perfusion
$^{122}\text{Xe}/^{122}\text{I}$	20.1 h	3.6 min	77.0	1.09	(Labeling)
$^{128}\text{Ba}/^{128}\text{Cs}$	2.43 d	3.62 min	69.0	0.869	Perfusion
$^{134}\text{Ce}/^{134}\text{La}$	3.16 d	6.4 min	63.0	0.756	Perfusion
$^{62}\text{Zn}/^{62}\text{Cu}$	9.26 h	9.74 min	97.0	1.28	Labeling; Perfusion
$^{52}\text{Fe}/^{52\text{m}}\text{Mn}$	8.28 d	21.1 min	97.0	1.13	Perfusion
$^{68}\text{Ge}/^{68}\text{Ga}$	270.8 d	1.135 h	89.0	0.74	Labeling; Perfusion
$^{110}\text{Sn}/^{110\text{m}}\text{In}$	4.1 h	1.15 h	62.0	0.623	Labeling
$^{44}\text{Ti}/^{44}\text{Sc}$	60.3*a	3.927 h	94.0	0.597	Labeling
$^{72}\text{Se}/^{72}\text{As}$	8.4 d	1.083 d	88.0	1.02	Labeling

*Mean value of most recent various literature data.

application of the generator daughter nuclides due to various reasons, which might have led to a current routine application of the generator. On the other hand, although not yet accepted for routine clinical use, some generator pairs offer a significant potential for application in diagnostic nuclear medicine using PET due to the promising nuclear data of both the parent and daughter.

^{44}Ti ($T_{1/2} = 60 \text{ a}$)/ ^{44}Sc ($T_{1/2} = 3.927 \text{ h}$). Compared to the chemically similar system $^{68}\text{Ge}/^{68}\text{Ga}$, this generator provides a much longer-lived daughter for extended PET/CT measurements. Also for the mother nuclide, the half-life is even longer than for ^{68}Ge . Although ^{44}Ti half-life values found in the literature vary significantly, most recent values average 60 ± 3 years. ^{44}Ti is produced by the $^{45}\text{Sc}(p,2n)$ reaction and by proton-induced spallation on V or Cr targets (Lambrecht and Lynn 1976; Sajjad and Lambrecht 1986; Zaitseva et al. 1994). The production rates are low and require long high-current irradiations. Dowex-1 and 0.1 M oxalic acid in 0.2 M HCl (Greene and Hillman 1967) provided a 60–70% radiochemical yield of ^{44}Sc in 30–50 mL of eluent, while the initial breakthrough of $10^{-3}\%$ increased to $10^{-1}\%$ after eluent volume of up to 2 L. With zirconium oxide as an analogue of Ti(IV) used as the support, and 0.01 M HCl as eluent, Seidl and Lieser (1973) reported a 42–46% radiochemical yield and a decontamination factor of 5×10^4 . A solvent extraction technique with an organic phase of 1% 1-phenyl-3-methyl-4-capryl-pyrazolone-5 in methyl isobutyl ketone led to >90% recovery of Sc in <10 mL with a Ti contamination of $<10^{-6}$ (Mirza and Aziz 1969).

The first 5 mCi high activity level generator was described recently (Filosofov et al. 2010). $^{44}\text{Ti}/^{44}\text{Sc}$ radionuclide generators are of interest for molecular imaging. In this study, 185 MBq of ^{44}Ti were obtained via the $\text{Sc}(p,2n)$ nuclear reaction. The separation of microscopic levels of ^{44}Ti from the macroscopic levels of scandium represents a significant challenge. The ^{44}Ti was separated from 1.5 g of massive scandium targets in multi-step procedures, including exchange chromatography on a cation column (AG 50W-X8, 200–400 mesh, H^+ -form). In order to design a robust $^{44}\text{Ti}/^{44}\text{Sc}$ generator concept, distribution coefficients of Ti(IV) and Sc(III) on both AG 1-X8 (200–400 mesh, Cl^- -form) and AG 50W-X8 (200–400 mesh, H^+ -form) resins eluted with HCl and $\text{HCl}/\text{H}_2\text{C}_2\text{O}_4$ solution of various concentrations were investigated systematically. Optimal conditions for efficient separations of both radionuclides have been determined for AG 1-X8 resin and mixtures of 0.07 M HCl and 0.005 M $\text{H}_2\text{C}_2\text{O}_4$. The 5 mCi generator was prepared on a column ($H = 150 \text{ mm}$, $D = 3 \text{ mm}$, $V_0 = 0.55 \text{ mL}$) made of radiation resistant PEEK polymer (polyetheretherketone). The system achieved elution of 180 MBq ^{44}Sc in 20 mL of eluate solution. The breakthrough of ^{44}Ti was 90 Bq. This corresponds to an excellent separation factor of 2×10^6 . In the context of long-term stability of $^{44}\text{Ti}/^{44}\text{Sc}$ generators, a “reverse” type of washing steps after each elution using 0.07 M HCl/0.005 M $\text{H}_2\text{C}_2\text{O}_4$ mixtures appeared to be essential. To allow efficient ^{44}Sc labeling, a post-elution processing of initial ^{44}Sc generator eluates was investigated in order to reduce its volume, for HCl concentration and to remove the oxalate anions (Pruszyński et al. 2010). The online adsorption of ^{44}Sc on cationic resin AG 50W-X8 (200–400 mesh, H^+ -form) is achieved with >98% efficacy. Subsequently, the purified ^{44}Sc is desorbed by using 3 mL of 0.25 M ammonium acetate ($\text{pH} = 4.0$). The post-processing requires only 10 min. The overall yield of the post-processing reached 90% of the ^{44}Sc obtained from the $^{44}\text{Ti}/^{44}\text{Sc}$ generator. In addition to the chemical purification, the content of ^{44}Ti breakthrough was further reduced by one order of magnitude. The generator finally provides 150 MBq of ^{44}Sc containing <10 Bq of ^{44}Ti ready for radiolabeling chemistry.

Syed and Hosain (1975) proposed ^{44}Sc as a positron-emitting radionuclide for studying bone disease with positron emission tomography. Due to the increasing medical applications

of trivalent radiometals in diagnosis and therapy, the generator could possibly provide an interesting route for PET-imaging using ^{44}Sc -labeled analogues. As a proof-of-principle, ^{44}Sc -DOTA-TOC was synthesized and somatostatin G-protein coupled receptor (GPCR) localization was verified in patient studies (Rösch and Baum 2009, unpublished data). High-quality PET/CT images have been recorded even 18 h post injection. The unique application will focus on the quantitative measurement of uptake kinetics of, e.g., ^{44}Sc -DOTA-TOC in primary and metastatic neuroendocrine tumors in order to estimate the optimum radiation dose the individual patient will receive in a subsequent therapeutic application of biologically and chemically analogue compounds, e.g., ^{90}Y -DOTA-TOC or ^{177}Lu -DOTA-TOC.

^{52}Fe ($T_{1/2} = 8.28\text{ h}$)/ $^{52\text{m}}\text{Mn}$ ($T_{1/2} = 21.1\text{ min}$). Lyster et al. (1982) and Tendov et al. (1988) have reviewed the production and purification of ^{52}Fe by the $^{50}\text{Cr}(\text{}^4\text{He}, 2\text{n})$, $^{52}\text{Cr}(\text{}^3\text{He}, 3\text{n})$, $^{55}\text{Mn}(\text{p}, 4\text{n})$, $^{54}\text{Fe}(\gamma, 2\text{n})$, and $\text{Ni}(\text{p}, \text{s})$ reactions. Experimental thick target yields for the $^{52}\text{Cr}(\text{}^3\text{He}, 3\text{n})$ and the $^{55}\text{Mn}(\text{p}, 4\text{n})$ reactions are 1.85 and $3.6\text{ MBq } \mu\text{A}^{-1}\text{ h}^{-1}$, respectively, while the proton-induced spallation reaction $\text{Ni}(\text{p}, 3\text{pxn})$ provides $24\text{ MBq } \mu\text{A}^{-1}\text{ h}^{-1}$. A projected half-saturation yield of 307 GBq (end of bombardment, EOB) was considered (Grant et al. 1979), and Ku et al. (1979a) reported a yield of 2.6 GBq (EOB) following irradiation of 0.45 g cm^{-2} of Ni at 200 MeV with $70\text{ } \mu\text{A}$ for 15 h . Recent studies thus concentrated on the latter process, also showing lower ^{55}Fe ($T_{1/2} = 2.6\text{ a}$) impurities. Although providing lower yields of 3.7 MBq h^{-1} at $5\text{ } \mu\text{A}$ beam, 0.008% ^{55}Fe and $1.67\text{ MBq } \mu\text{A}^{-1}\text{ h}^{-1}$, the $^{52}\text{Cr}(\text{}^3\text{He}, 3\text{n})$ (Fessler et al. 1994), and $^{50}\text{Cr}(\alpha, 2\text{n})$ processes on enriched chromium targets (Zweit et al. 1988) could be an alternative concerning the radionuclidic impurity of ^{52}Fe . Conventional anion exchange chromatography using 8 M HCl was applied for the isolation of the short-lived daughter onto Dowex 1 columns (Atcher et al. 1978, 1980) or AGI-X8 (Ku et al. 1979b). To avoid hydrochloric solutions either 2 M tartrate solutions were used to eluate $^{52\text{m}}\text{Mn}$ (Schwarzbach et al. 1991) or a 5% glucose solution (Bläuenstein et al. 1997) from Dowex 1, the later approach providing 90% elution yields with a $<0.3\%$ ^{52}Fe contamination. A hydroxamate resin allowed elution of $^{52\text{m}}\text{Mn}$ with acetate buffer or physiological saline (Herscheid et al. 1983). Based on early tissue distribution studies with $^{54}\text{Mn}^{2+}$ (Chauncey et al. 1977), this generator had received some attention because of the high heart uptake of Mn, and the possibility of using $^{52\text{m}}\text{Mn}$ or ^{51}Mn in combination with positron emission tomography for evaluation of myocardial perfusion (Lambrecht and Wolf 1970; Atkins et al. 1979; Atcher et al. 1980).

^{72}Se ($T_{1/2} = 8.4\text{ d}$)/ ^{72}As ($T_{1/2} = 1.083\text{ d}$). This generator could provide a long-lived positron emitter with significant (88%) positron branching. Both deuteron- or proton-induced reactions on arsenic targets and α - or ^3He -induced reaction on germanium targets have been investigated, mainly in the context of ^{73}Se production (Nozaki et al. 1979; Mushtaq et al. 1988; Mushtaq and Qaim 1990). Alternatively, ^{72}Se was obtained via proton-induced spallation of RbBr. Al-Kouraihi and Boswell (1978) were able to obtain a 70% elution yield of ^{72}As from a coagulated form of carrier-added ^{72}Se on a Dowex 50 column in 15 mL of water. Electrolytic generators based on ^{72}Se deposited on Pt electrodes as Cu^{72}Se were reported (Phillips and Nix 1989). Another process using addition of selenium carrier consists of cyclic reduction of selenium to Se^0 and a separation of ^{72}As by filtration with subsequent oxidative dissolution of Se^0 using H_2O_2 . For generators using no-carrier-added ^{72}Se , Novgorodov et al. (2001) described the distillation of AsCl_3 , while Se remains in nonvolatile compounds in the residue. Jennewein et al. (2004) developed a solid phase extraction system with ^{72}Se fixed as metallic Se; the daughter ^{72}As is eluted by protic solvents. Systematic chemical investigations on the labeling chemistry of no-carrier-added radioarsenic, however, are required prior to the application of ^{72}As labeled compounds (Brockmann et al. 1999a, b). In this context, a new method

was developed (Jennewein et al. 2006) for labeling monoclonal antibodies, i.e., proteins, with radioactive arsenic isotopes via the labeling synthon [*As]AsI₃. Arsenic has a high affinity to sulfur and [*As]AsI₃ is able to bind covalently to sulfhydryl groups. In antibodies, the sulfur moieties are mainly associated with dithiol bridges. To increase the number of free thiols, the antibodies were modified with SATA (*N*-succinimidyl S-acetylthioacetate). At least for the mAb (monoclonal antibody) used in this work, this route of radioarsenic labeling does not affect the immunoreactivity of the product. The arsenic label was stable for up to 72 h at the molecular mass of the monoclonal antibody, which is particularly relevant because of the molecular imaging strategy, namely to follow the pharmacology and pharmacokinetics of the labeled mAb for several days. TarvacinTM, a chimeric monoclonal antibody that binds anionic phospholipids in the presence of serum or β 2-glycoprotein 1, was labeled using trivalent radioarsenic and tested for its ability to image Dunning prostate R3227–AT1 tumors growing subcutaneously in rats (Jennewein et al. 2008). [$^{72,74}As$]TarvacinTM localized specifically to tumor vascular endothelial cells after injection into tumor-bearing rats. Clear images of the tumors were obtained using planar γ -scintigraphy and positron emission tomography, confirming the utility of the arsenic radioisotopes for molecular imaging. Biodistribution studies confirmed the specific localization of [$^{72,74}As$]TarvacinTM to the tumors. The tumor-to-liver ratio 72 h after injection was 22 for [$^{72,74}As$]TarvacinTM as compared with 1.5 for an isotype-matched control chimeric antibody of irrelevant specificity, demonstrating the potential merits of this promising approach.

^{110}Sn ($T_{1/2} = 4.1$ h)/ ^{110m}In ($T_{1/2} = 1.15$ h). Positron-emitting ^{110m}In could be a choice for quantitative imaging of analogous ^{111}In SPECT compounds (Tsai et al. 1997, Lubberink et al. 2002b). The direct production of ^{110m}In via $^{110}Cd(p,n)$ -, $^{107}Ag(\alpha,n)$ -, and $^{109}Ag(^3He,2n)$ -processes, however, leads to the co-formation of the ground state isomer ^{110g}In ($T_{1/2} = 4.9$ h). Isotopically pure ^{110m}In could only be prepared via the generator system $^{110}Sn/^{110m}In$ (Tsai et al. 1997). ^{110}Sn was produced via the $^{110}Cd(^3He,3n)$ reaction with $36 \rightarrow 25$ MeV 3He particles and $^{110}SnCl_4$ was isolated thermochromatographically from the enriched target material. The generator itself was designed by adsorption of ^{110}Sn on a small Kieselgel 40 column and ^{110m}In was eluted quantitatively within 1 mL 0.02 M HCl. However, the short half-life of ^{110}Sn resulting in short useful generator shelf life would possibly limit a wide application of the generator system.

^{118}Te ($T_{1/2} = 6.00$ d)/ ^{118}Sb ($T_{1/2} = 3.6$ min). The production of ^{118}Te via $^{123}Sb(p,6n)$ - and $^{121}Sb(p,4n)$ -processes was initially reported by Lindner and Perlman (1950) and Fink et al. (1961), while excitation functions were measured by Lagunas-Solar et al. (1990). Batch yields of ^{118}Te in a Ci-scale, however, would be accompanied by significant $^{119m,g}Te$ impurities resulting in ^{119}Sb ($T_{1/2} = 38.1$ h) impurities. Alternatively, the $^{116}Sn(\alpha,2n)$ reaction holds promise for the production of isotopically more pure ^{118}Te if an enriched ^{116}Sn target would be used (Yano et al. 1989). These authors used SnO_2 and Al_2O_3 type generators to elute ^{118}Sb with tartrate and citrate solutions.

^{122}Xe ($T_{1/2} = 20.1$ h)/ ^{122}I ($T_{1/2} = 3.6$ min). Various positron-emitting nuclides of iodine have been proposed to obtain more precise data on localization, quantification, and dosimetry of these compounds using PET. ^{122}I represents one important example providing a 77% β^+ branching. The availability via the generator was investigated as a by-product during the production of the $^{123}Xe/^{123}I$ generator by the $^{127}I(p,6n)^{122}Xe$ reaction with 70 MeV protons (Diksic and Yaffe 1977; Richards and Ku 1979; Mathis et al. 1986; Lagunas-Solar et al. 1986) or analogously via the (d,7n) channel (Weinreich et al. 1974) and the $^{124}Xe(p,3n)$ process

(Tárkányi et al. 1991). Amphetamine analogues and iodoperidol were successfully labeled with ^{122}I to measure brain blood flow with PET (Braun et al. 1978; Mathis et al. 1985; Moerlein et al. 1987). Not only rapid iodination chemistry is required to make use of the short-lived iodine positron emitter, but also the short physical half-life might not correspond to longer-lasting physiological requirements.

^{128}Ba ($T_{1/2} = 2.43\text{ d}$)/ ^{128}Cs ($T_{1/2} = 3.62\text{ min}$). The accelerator production of ^{128}Ba has been evaluated with the $^{133}\text{Cs}(\text{p},\text{xn})$ reactions at $E_p = 67 \rightarrow 54\text{ MeV}$ (Lagunas-Solar et al. 1982), and 111 MBq $\mu\text{A}^{-1}\text{ h}^{-1}$ experimental thick target yields were reported. The $\text{Xe}(\alpha,\text{xn})$ reactions seem to be possible as well. Elution yields of ^{128}Cs from a Chelex 100 column ranging from 60–80% were obtained with 5–10 mL of 0.9% NaCl pH 9 solutions. Bievelez and Jacquemin (1982) loaded $^{128}\text{Ba}^{2+}$ onto Chelex 100 from a solution of NH_4OH (pH 9.25–9.3) in a buffer of 0.1 M NH_4Cl . Transition between the buffer and an elution medium of 0.1 M NH_4OH and 0.06 M NaCl/HCl at pH 10 was done by successive washings, which resulted in <0.5% loss of the initial ^{128}Ba . ^{128}Cs yields of 75 and 90% were obtained and the breakthrough was $1.1 \times 10^{-3}\%$ per mL. The $^{128}\text{Ba}/^{128}\text{Cs}$ generator is of medical interest, since ^{128}Cs might be applied to blood flow measurements. Bievelez and Jacquemin (1982) attempted to image the heart of rabbits and dogs, but concluded that ^{128}Cs is not compatible with the relatively slow muscle absorption kinetics of Cs.

^{134}Ce ($T_{1/2} = 3.16\text{ d}$)/ ^{134}La ($T_{1/2} = 6.4\text{ min}$). ^{134}Ce is produced via the $^{139}\text{La}(\text{p},6\text{n})$ route within an optimum energy of $61 \rightarrow 53\text{ MeV}$ resulting in a thick target yield of 85 MBq $\mu\text{A}^{-1}\text{ h}^{-1}$. Of several inorganic materials tested, manganese dioxide provided the best adsorption for ^{134}Ce , and ^{134}La was eluted with 85% yield in 1.6 mL of 0.5 M NaCl (Lubberink et al. 2002a). The ^{134}La was proposed as PET perfusion imaging (Zweit et al. 1994). The generator may have, in addition, potential for in vivo application with ^{134}Ce -labeled radiopharmaceuticals.

^{140}Nd ($T_{1/2} = 3.37\text{ d}$)/ ^{140}Pr ($T_{1/2} = 3.39\text{ min}$). This generator also provides a short-lived positron-emitting radiolanthanide nuclide and could have some potential as an in vivo generator. The parent nuclide is produced via the $^{140}\text{Ce}(\alpha,2\text{n})$ or $(^3\text{He},3\text{n})$ reactions (Rösch et al. 1999, 2000) but also via the $^{140}\text{Pr}(\text{p},2\text{n})$ reaction (Zeisler and Becker 1999). The parent nuclide is radiochemically isolated from the target materials by ion exchange chromatography. Chemical isolation of $^{140}\text{Nd}(\text{III})$ from macro amounts of $\text{Ce}(\text{III})$ was performed by cation exchanger chromatography (two purification steps) with an overall separation yield of > 95% ^{140}Nd , overall decontamination factor for cerium of $\sim 10^8$ and with reduction of contaminations of coproduced $\text{Pr}(\text{III})$ isotopes of up to 0.5% (Rösch et al. 2003).

The radiochemical principle of separation of the generator mother and daughter nuclides is based on physical–chemical transitions of ^{140}Pr following the electron capture process. A significant separation effect was observed when the parent nuclide ^{140}Nd was coordinated to a DOTA-conjugated peptide or octylamine, which were absorbed on resins. The thermodynamically and kinetically stable complex binds ^{140}Nd while the released ^{140}Pr is kinetically hindered to form similar complexes with the macrocyclic ligand. The ^{140}Nd -DOTA absorption on the solid phase remains stable within at least three half-lives of ^{140}Nd . ^{140}Pr is eluted with a yield >93% if optimized eluent systems such as 10^{-3} M DTPA are applied with negligible levels of ^{140}Nd breakthrough. For 100 MBq of ^{140}Nd -DOTA-like activity and 0.5 h between two subsequent elutions (half an hour is enough for the accumulation of 100% of ^{140}Pr activity), a breakthrough of about 25 kBq of ^{140}Nd ($\sim 0.025\%$) could be expected (Zhernosekov et al. 2007b).

40.2.3 Key Examples of Generator-Derived Positron-Emitting Radionuclides

^{62}Zn ($T_{1/2} = 9.26\text{ h}$)/ ^{62}Cu ($T_{1/2} = 9.74\text{ min}$). The parent ^{62}Zn can be produced with a significant thick-target yield via the (p,2n) reaction on ^{63}Cu (Robinson et al. 1980) or via the $^{60}\text{Ni}(\alpha,2\text{n})$ process (Neirinckx 1977; Zweit et al. 1992). Anion exchange chromatography is clearly the method of choice for this generator system. To adsorb no-carrier-added $^{62}\text{Zn}^{2+}$, Dowex 1 was used and Cu^{2+} is eluted with hydrochloric acid (Yagi and Kondo 1979; Fujibayashi et al. 1989; Green et al. 1990). CG-120 Amberlite resin provided an elution of ^{62}Cu in 70% yield with a glycine solution (Fujibayashi et al. 1989) allowing subsequent ligand exchange reactions. For elution, other ligands (Okazawa et al. 1994) or HCl/ethanol (Zweit et al. 1992) solutions were also introduced. The ^{62}Cu was chelated to human serum albumin (HSA) (Fujibayashi et al. 1990) and benzyl-TETA-HSA (Mathias et al. 1991b) used for blood pool imaging (Herrero et al. 1996). Several hypoxia and perfusion ^{62}Cu -complexes have been developed and applied for PET studies such as [^{62}Cu]ATSM (diacetyl-bis(N^4 -methylthiosemicarbazone)) (Fujibayashi et al. 1997) and [^{62}Cu]PTSM (pyruvaldehyde bis(N^4 -methylthiosemicarbazone)) (see, e.g., Green et al. 1990; Mathias et al. 1990; Shelton et al. 1989, 1990; Bormans et al. 1992; Taniuchi et al. 1997). Human biodistribution and dosimetry studies of the perfusion agent [^{62}Cu]PTSM were investigated and this tracer was recommended for repeated studies of myocardial imaging in the same patient (Wallhaus et al. 1998) as well as for quantification of the cerebral blood flow (Okazawa et al. 1994). The clinical performance of the $^{62}\text{Zn}/^{62}\text{Cu}$ generator and results of initial evaluation of [^{62}Cu]PTSM in 68 patients have been described (Haynes et al. 2000), and demonstrated that this generator system is easily manufactured and transported, and is an inexpensive source of the ^{62}Cu positron-emitter for in-house radio-pharmaceutical preparation. The compound was also applied for the assessment of angiotensin II-induced blood flow changes in patients with colorectal liver metastases (Flower et al. 2001). The detection of coronary artery disease with [^{62}Cu]PTSM has been reported in 47 patients (Wallhaus et al. 2001). In addition, the successful use of ^{62}Cu liquid-filled angioplasty balloons for the inhibition of coronary restenosis has been reported in a swine coronary overstretch model (Chan et al. 2001). A recent publication (Fukumura et al. 2006), described further refinement of this generator, and focused on high activity (1.8–3.5 GBq) loading of the $^{62}\text{Zn}^{2+}$ on a Sep-Pak™ “plus” CM weak acidic cation exchanger column with a high ^{62}Cu elution yield of ~96% with a low 3 mL volume of 200 mM glycine solution. The Zn parent breakthrough is <0.1%. Semi-automated syringe pump systems were designed for separated hot cell separation system and dispensing systems.

^{68}Ge ($T_{1/2} = 270.8\text{ d}$)/ ^{68}Ga ($T_{1/2} = 68\text{ min}$). The first compilation of the data relevant to $^{68}\text{Ge}/^{68}\text{Ga}$ generator systems was published in 1996 (Mirzadeh and Lambrecht, 1996). The IAEA has recently initiated comprehensive review of the production of several generator mother nuclides including a chapter on ^{68}Ge (Rösch and Filosofov 2009).

Integral ^{68}Ge thick targets yields have been calculated (Horiguchi et al. 1982) for accelerator-based nuclear reactions on natural metallic germanium and zinc, and Ga_2O_3 targets. The yields for the proton-induced reactions on Ga are larger than those on Ge in the region lower than 60 MeV, although the latter become larger above 60 MeV. The thick target yields for the Ga (p,2n) reactions have been recently validated (IAEA 2001). The (p,2n) reaction on gallium targets (Ga_2O_3 or Ga_4Ni) provides significant cross sections. Experimental thick-target yields – calculated for a 1 h irradiation as well as for saturation – amount to 0.96/0.53 MBq $\mu\text{A}^{-1}\text{ h}^{-1}$

at this energy, but reach values of $>2/>1$ MBq $\mu\text{A}^{-1} \text{h}^{-1}$ already at 25 MeV, respectively. Proton-induced spallation reactions on Rb, Br, or As target materials give about one tenth of that yield. The $^{\text{nat}}\text{Zn}(\alpha, \text{xn})$ reactions show similar low cross sections (Hagebo et al. 1984). Due to the long half-life of ^{68}Ge , high-current accelerators are required for sufficient (about 3.7 GBq batch yields) of the parent nuclide. Routine production is established at Brookhaven National Laboratory (BNL) and Los Alamos National Laboratory (LANL), USA, iThemba Laboratories/NAC, Faure, Republic of South Africa, and Obninsk, Russian Federation. These production centers report on production capacities of about 18.5 to 74 GBq (0.5 to 2 Ci) ^{68}Ge per batch. At the Cyclotron Co., Ltd., Obninsk, Russian Federation, gallium–nickel alloys are used as target material, prepared on copper backings. Irradiations are performed at rather high proton beam intensity of several hundred μA at 23 MeV proton energy. ^{68}Ge of high specific activity of >74 GBq (>2 Ci)/mg and 99.8% radionuclidic purity is obtained (Razbash et al. 2005).

Early attempts to adopt liquid–liquid extraction chemistry for the routine generator use were not sustainable (Gleason 1960; Erhardt and Welch 1978). The first column-based generator systems separated ^{68}Ga using 0.005 N EDTA from ^{68}Ge , absorbed on alumina or zirconium oxides (Greene and Tucker 1961; Yano and Anger 1964) and this neutral $[\text{}^{68}\text{Ga}]\text{EDTA}$ solution was directly used in an attempt to image tumors. Analogously, ^{68}Ge was retained on antimony oxide Sb_2O_5 and ^{68}Ga was eluted with oxalate solutions (Arino et al. 1978). Anion exchange resins using dilute hydrofluoric acid solutions as eluents allowed high-purity separations due to the significant differences of distribution coefficients of the elements (Neirinckx and Davis 1980). The breakthrough of ^{68}Ge was $<10^{-4}$ for up to 600 elutions, and the ^{68}Ga yield $>90\%$. In all these cases, however, further application of the generator eluate for ^{68}Ga labeling reactions was not possible.

Consequently, $^{68}\text{Ge}/^{68}\text{Ga}$ generators were developed to avoid the formation of stable ^{68}Ga -ligand complex in the eluate system. This strategy is achieved for eluates providing both $^{68}\text{Ga}(\text{OH})_4^-$ and $^{68}\text{Ga}^{3+}$. Indeed, ^{68}Ga has been eluted in 0.1 M NaOH solution as gallate anion from alumina columns (Lewis and Camin 1960). A comparison of performances of alumina/EDTA, alumina/NaOH, and tin oxide/HCl generators (McElvany et al. 1984), however, indicated superior characteristics for the latter system in terms of ^{68}Ge breakthrough (10^{-6} – $10^{-5}\%$ per bolus) and $^{68}\text{Ga}^{3+}$ elution (70–80%) in 1 M hydrochloric acid (Loc'h et al. 1980). In other cases, ^{68}Ge was absorbed on inorganic matrices such as alumina, $\text{Al}(\text{OH})_3$, and $\text{Fe}(\text{OH})_3$ (Kopecky et al. 1973; Kopecky and Mudrova 1974), SnO_2 , ZrO_2 , TiO_2 (Malyshev and Smirnov 1975), and CeO_2 (Ambe 1988; Bao and Song 1996).

As $\text{Ge}(\text{IV})$ is known to form very stable complexes with phenolic groups (Kurnevich et al. 1974), its adsorption on a 1,2,3-trihydroxybenzene (pyrogallol)-formaldehyde resin was utilized (Schumacher and Maier-Borst 1981; Neirinckx et al. 1982). Average yields of ^{68}Ga of 75% during a period of 250 days were reported (Schumacher and Maier-Borst, 1981). The Ge breakthrough was <0.5 ppm with no detectable radiolytic by-products for a 370 MBq (10 mCi) generator. The pyrogallol-formaldehyde resin was found to be resistant to dissociation from radiation. An organic macroporous styrene-divinylbenzene copolymer containing *N*-methylglucamine groups was developed to provide ^{68}Ga with a solution of a low-affinity gallium-chelating ligand such as citric acid or phosphoric acid. The ^{68}Ge breakthrough was less than 0.0004% of the ^{68}Ge adsorbed on the resin (Nakayama et al. 2003).

For commercial generator productions, however, $\text{Me}(\text{IV})$ -oxide-based matrices were preferred. A modified TiO_2 phase has been used by the pioneers in this field at the Cyclotron Ltd., Obninsk, Russian Federation, since about 2000 (Razbash et al. 2005). These generators are

eluted with 0.1 N HCl and show initial ^{68}Ga elution yields of about 80% with ^{68}Ge breakthrough of about $1 \times 10^{-3}\%$. These values decrease over time (e.g., after about 1 year) or with increasing number of elutions (e.g., 200), approaching values of about 50% of ^{68}Ga elution and about $10^{-2}\%$ of ^{68}Ge breakthrough. A similar generator is available as “IGG 100” providing improved elution characteristics. Another system is produced at iThemba Laboratories, Republic South Africa, using a SnO_2 -based solid phase. Optimum ^{68}Ge elution efficacy is reported at 0.6 N HCl, decreasing at lower HCl concentration.

However, all commercially available generators need further improvement to be acceptable for regulatory approval for routine medical use (Breeman and Verbruggen 2007). The $^{68}\text{Ge}/^{68}\text{Ga}$ radionuclide generator systems used today are not necessarily optimally designed for direct syntheses of radiopharmaceuticals for human use. The eluates still contain measurable activities of long-lived ^{68}Ge . In addition, the rather large volume and the relatively high concentration of hydrochloric acid in many cases prevent the direct use for labeling reactions. Furthermore, labeling yields and specific activities might not reach maximum values due to the presence of metallic impurities. For example, significant amounts of Zn(II) are generated from the decay of ^{68}Ga . For a “fresh” 1110 MBq ^{68}Ge generator, the number of stable ^{68}Zn atoms generated within 1 day after an elution amounts to 9×10^{13} (i.e., 10 ng of Zn(II)) as compared to about 5×10^{12} atoms of ^{68}Ga in 800 MBq of the ^{68}Ga eluted. In the case of “fresh” generators, amounts of stable ^{71}Ga as generated from the ^{71}Ge decay may be one order of magnitude higher than those of stable ^{68}Zn . In addition, Ti(IV) or other residuals from the generator column material and Fe(III) are present in the eluate. All these metallic impurities will adversely affect the ^{68}Ga -labeling yields as well as the specific activity of the labeled product. Thus, dedicated procedures to process the eluate from the radionuclide generator, ideally including labeling and purification of ^{68}Ga radiopharmaceuticals need to be developed.

Anion exchange chromatography: Following the concept of Schumacher and Maier-Borst (1981) of processing 1 N HCl eluates (Meyer et al. 2004) adopted this approach for 0.1 N HCl eluates. The initial volume of 10 mL of the 0.1 N HCl eluate is transferred to a vial containing 15 mL of 9.5 N HCl to obtain a final hydrochloric acid concentration of 5.5 M. Under these conditions ^{68}Ga can be adsorbed on a strong anion exchanger as anionic chloro complexes of $^{68}\text{Ga}(\text{III})$. Following a washing step with 1 mL of 5.5 N HCl, the resin is flushed with a stream of nitrogen and then ^{68}Ga is eluted with H_2O in small volumes. This strategy separates ^{68}Ge , but does not allow *direct* loading of $^{68}\text{Ga}(\text{III})$ on the anion exchange resin from 0.1 N HCl and does not purify Ga(III) from Zn(II) and Fe(III) impurities either. A final yield of $46 \pm 5\%$ for the ^{68}Ga -labeled DOTA-conjugated octreotide is reported (Meyer et al. 2004; Velikyan et al. 2004; Meyer et al. 2005; Decristoforo et al. 2005).

Fractionation (Breeman et al. 2005): The concept utilizes the fact that the eluted ^{68}Ga activity peaks within $\sim 1\text{--}2$ mL, representing about $2/3$ of the total activity. If this fraction is isolated from the eluate, the contents of ^{68}Ge and metallic impurities are lowered because of the lower eluate volume used. When synthesizing ^{68}Ga -labeled compounds, decay-corrected yields of ^{68}Ga radiopharmaceuticals cannot exceed 60–70% and effective yields of labeled DOTA-conjugated peptides like ^{68}Ga -DOTATOC amount to about 50% (Decristoforo et al. 2005).

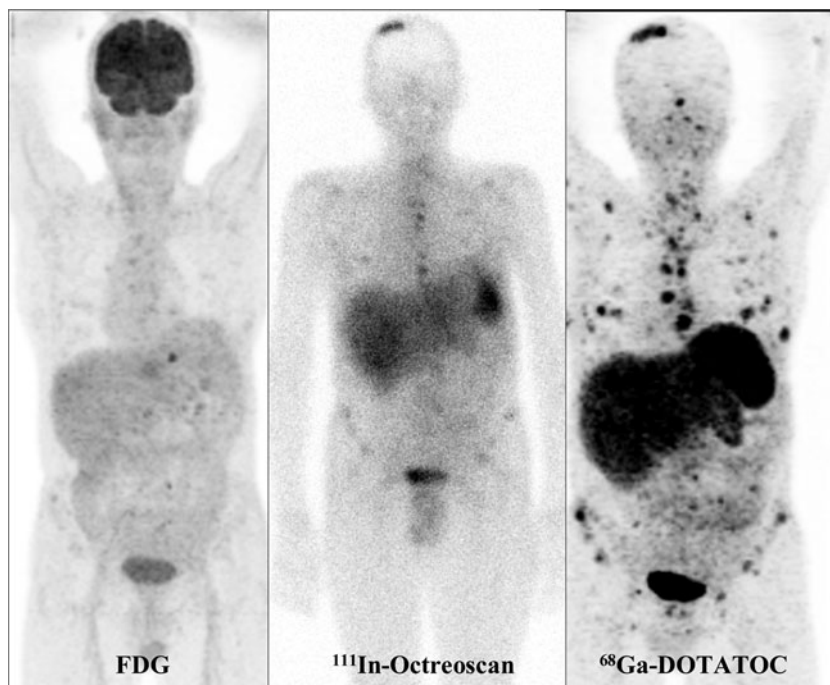
Cation exchange chromatography: The key step in this procedure is the direct transfer of the initial 0.1 N HCl ^{68}Ga eluate to a cation exchanger. Due to high distribution coefficients, ^{68}Ga is quantitatively adsorbed on only about 50 mg of the resin directly from the generator eluate. This effect also occurs with higher concentrations of HCl, e.g., 0.6 N HCl, as used for SnO_2 -based $^{68}\text{Ge}/^{68}\text{Ga}$ generators. Low volumes of 0.4–1.0 mL of hydrochloric acid/acetone mixtures

are applied to purify ^{68}Ga from Ge(IV) , Ti(IV) , Zn(II) , and Fe(III) . This procedure leads to almost complete removal of metallic impurities including ^{68}Ge breakthrough, thus providing the purified ^{68}Ga in a form useful for direct labeling with acceptable pH, volume, and purity. The post-processing takes 4 min with overall ^{68}Ga recovery yields of $97 \pm 2\%$ (Zhernosekov et al. 2007; Asti et al. 2008). The above method is adapted for the preparation of a chemistry module, which is commercially used for the preparation of injectable ^{68}Ga -labeled radiopharmaceuticals.

^{68}Ga had some earlier application as [^{68}Ga]BAT-TECH agent for myocardial perfusion (Mathias et al. 1991a), but significant potential has been developed since about 2000 for imaging neuroendocrine tumors using [^{68}Ga]DOTA-DPhe¹-Tyr³-octreotide ([^{68}Ga]DOTATOC) and PET (Hofmann et al. 2001). This octapeptide shows high affinity to the sstr2 subtype of somatostatin receptor expressing tumors, and the conjugated macrocyclic bifunctional chelator DOTA binds the trivalent $^{68}\text{Ga}^{3+}$ with high thermodynamic and kinetic stability. Despite the short ^{68}Ga half-life, this tracer allows excellent visualization of tumors and small metastases (Al-Nahhas et al. 2007; Decristoforo et al. 2007; Dimitrakopoulou-Strauss et al. 2006; von Falck et al. 2007; Gabriel et al. 2007, 2009; Henze et al. 2004, 2005; Khan et al. 2009; Koukouraki et al. 2006a, b; Lopci et al. 2008; Luboldt et al. 2010; Maecke et al. 2005; Milker-Zabel et al. 2006; Nyuki et al. 2010; Putzer et al. 2009; Win et al. 2007). This diagnosis, in particular if carried out using PET/CT imaging, is superior to any other imaging approach (► Fig. 40.4). Systematic

■ Fig. 40.4

[^{68}Ga]DOTA-DPhe¹-Tyr³-octreotide imaging of neuroendocrine tumors using PET/CT (right) compared to ^{111}In -octreoscan SPECT (middle) and ^{18}F -FDG PET (left) (Courtesy of H. Bihl, Stuttgart)



research continues to develop new ^{68}Ga radiopharmaceuticals. For recent reviews cf. Fani et al. (2008), Rösch and Riss (2010).

Another interesting and potentially important application of ^{68}Ga is the use of ^{68}Ga liquid-filled angioplasty balloons for the inhibition of arterial restenosis following coronary angioplasty (Stoll et al. 2001). This technique with a high-energy positron emitter is similar to the techniques demonstrated using balloons filled with ^{188}Re and other medium and high-energy β emitters (Knapp et al. 2001).

^{82}Sr ($T_{1/2} = 25.6\text{ d}$)/ ^{82}Rb ($T_{1/2} = 1.273\text{ min}$). The ^{82}Rb positron emitter was recognized as a potential PET nuclide due to its analogy to the physiological monovalent potassium cation, which is transported across the cell membrane via the sodium-potassium ATP ion exchange pathway. ^{82}Rb is partially extracted by the myocardium during a single capillary pass. The development of this generator has taken place over the past 25 years and has been intensively discussed in numerous reviews (Waters and Coursey 1987; Vereschchagin et al. 1993). Production routes for ^{82}Sr include $^{85}\text{Rb}(p,4n)$ (Horiguchi et al. 1980; Kastleiner et al. 2002), $^{82}\text{Kr}(^3\text{He},3n)$ (Tárkányi et al. 1988, 1990), and proton-induced spallation processes on Rb, Mo, or Y targets (Erdal et al. 1975; Grütter 1982; Grant et al. 1982). The most common production route is the Mo(p,spall) process (Horlock et al. 1981; Thomas and Barness 1984). The requirement for 600–800 MeV protons, however, limits the production capacities of the generator. As ^{82}Rb is injected intravenously directly from the generator, ^{82}Rb must be obtained from the generator in a sterile pyrogen-free physiological medium. Synthetic resins such as BioRex-70 (Yano and Anger 1968; Yano et al. 1977) and Chelex (Grant et al. 1977; Krizek et al. 1977; Grant et al. 1978) and inorganic ion exchangers such as ZrO_2 (Brihaye et al. 1981) and Al_2O_3 (Neirincx et al. 1982) were developed, with ^{82}Rb eluted with 2% NaCl solutions. Other systems utilize $\alpha\text{-SnO}_2$ (Neirincx et al., 1982), with ^{82}Rb eluted with physiological NaCl solution used either for bolus (Gennaro et al. 1984) or continuous infusion (Brihaye et al. 1987). Commercial generators with up to 3.7 GBq (100 mCi) are available. Corresponding to the flow rate, ^{82}Rb yields range from 10–40%, while the ^{82}Sr breakthrough is in the order of $10^{-6}\%$ per mL (Brihaye et al. 1987).

The automated elution system (Gennaro et al. 1984; Knapp and Butler 1984) provides ^{82}Rb for direct intravenous bolus injection, with an average dose of about 1.9 GBq ($\sim 50\text{ mCi}$) for cardiac PET and sequential rest versus stress studies, is used to identify normal versus abnormal myocardium in patients with suspected myocardial infarction, as well as for the assessment of coronary blood flow, degree of stenosis, viability assessment, and to monitor recovery and maintenance. The generator is routinely used in clinical practice (e.g., Williams et al. 1994; Alvarez-Diez et al. 1999). ^{82}Rb infusion systems for quantitative perfusion imaging were developed (Epstein et al. 2004; Klein et al. 2007).

With commercial generators available, there is a continuous effort to improve its performance concerning PET protocols. A two-dimensional vs. three-dimensional scanning was compared (Votaw and White 2001) and wavelet-based noise reduction (Lin et al. 2001) could assess myocardial flow in humans in regions smaller than 1 cm^3 to the accuracy of that achieved with H_2^{15}O . The use of rubidium-82 for PET evaluation of myocardial perfusion has witnessed continued growth and typical studies involve gated PET for myocardial imaging (Anagnostopoulos et al. 2008; Bateman et al. 2006; Brown et al. 2008; Chander et al. 2008; Chow et al. 2005; Dorbala et al. 2007, 2009; Dorbaia et al. 2009; Eisner and Patterson 2007; El Fakhri et al. 2005; Gibbons and Chareonthaitawee 2009; Javadi et al. 2008; Knesaurek et al. 2003, 2007, 2009; Lertsburapa et al. 2008; Lodge et al. 2005; Lortie et al. 2007; Manabe et al. 2009; Nye et al. 2007; Schuster et al. 2008; Shi et al. 2007; Slomka et al. 2008;

Yoshinaga et al. 2006; Tang et al. 2009; Rahmim et al., 2008; Smith 2008; Schleipman et al. 2006; Parkash et al. 2004; Rosman et al. 2005; Tang et al. 2009).

40.3 Generator-Produced Photon Emitters

40.3.1 Overview

Although the use of ultra short-lived generator-derived radionuclides for first-pass radionuclide angiography (FPRNA) for evaluation of ventricular function (wall motion) is not currently widely practiced, the development and use of generator systems for evaluation of pulmonary ventilation and cardiac function was a major research area in the 1970s and 1980s (see, e.g., Paras and Thiessen (1985)). High count-rate imaging systems and advanced computer technology are required for data acquisition, storage, and analysis. High levels of activity are required for FPRNA, but the short half-lives permit rapid, repeat studies, since the vascular recirculation time is longer than the radionuclide physical half-life. The short radionuclide physical half-lives also ensure greatly reduced radiation burden to both personnel and patients. Generators that provide ultra short-lived daughter radionuclides ($T_{1/2} < 1\text{--}2$ min) for FPRNA include the $^{195\text{m}}\text{Hg}/^{195\text{m}}\text{Au}$ ($T_{1/2} = 30.5$ s) and $^{191}\text{Os}/^{191\text{m}}\text{Ir}$ ($T_{1/2} = 4.94$ s) systems. More recently, the $^{178}\text{W}/^{178\text{m}}\text{Ta}$ ($T_{1/2} = 9.31$ min) generator has been introduced. For pulmonary ventilation studies and evaluation of the right ventricular chamber, the $^{81}\text{Rb}/^{81\text{m}}\text{Kr}$ generator is commercially available and approved for human use in Europe.

Several other generator systems have been developed providing photon-emitting daughter nuclides, but did not receive adequate medical attention. Others were proposed for basic radiochemical and radiopharmaceutical studies rather than for a direct application of the daughter nuclide in nuclear medicine.

^{77}Br ($T_{1/2} = 2.377$ d)/ $^{77\text{m}}\text{Se}$ ($T_{1/2} = 17.4$ s). $^{77\text{m}}\text{Se}$ decays by isomeric transition with the emission of 162 keV photons in 50% abundance and appeared ideal for radionuclide angiocardiology and to study the effects of exercise and pharmaceuticals on hemodynamics (Lambrecht et al. 1977; Norton et al. 1978; Madhusudhan et al. 1979).

^{109}Cd ($T_{1/2} = 1.267$ a)/ $^{109\text{m}}\text{Ag}$ ($T_{1/2} = 39.6$ s). This generator was suggested for FPRNA, although the 88 keV photon emission of $^{109\text{m}}\text{Ag}$ shows a rather low abundance of 3.73% of the ^{109}Cd decay (Steinkruger et al., 1986). While Bartos and Bilewicz (1995) used crystalline antimony acid as absorbent yielding increasing ^{109}Cd breakthrough, Mansur et al. (1995) used cation exchange chromatography, but needed a scavenger column to reduce the ^{109}Cd breakthrough of $10^{-4}\%$.

^{113}Sn ($T_{1/2} = 115.09$ d)/ $^{113\text{m}}\text{In}$ ($T_{1/2} = 1.658$ h). Because of its long shelf life, the $^{113}\text{Sn}/^{113\text{m}}\text{In}$ generator has been proposed for labeling and evaluation of various radiopharmaceuticals with the 392 keV photon-emitting $^{113\text{m}}\text{In}$ as an analogue of ^{111}In (Liu et al. 1989). ^{113}Sn production (Qaim and Döhler 1984) and generators were described (Seidl and Lieser 1973; Rao et al. 1976, 1977; Camin 1977; Al-Janabi and Al-Hashini 1979; Lin et al. 1982).

^{115}Cd ($T_{1/2} = 2.228$ d)/ $^{115\text{m}}\text{In}$ ($T_{1/2} = 4.486$ h). This generator has been considered as an alternative to the $^{113}\text{Sn}/^{113\text{m}}\text{In}$ system. Parent radionuclide production and generator design (Ramamoorthy and Mani 1976; Bhattacharya and Basu, 1979; Erhardt et al. 1981; Yagi et al. 1982) were investigated.

Several radiolanthanides such as $^{140}\text{Ba}/^{140}\text{La}$ (Sakar and Bhattacharya, 1979; Das and Bhattacharya 1982), $^{144}\text{Ce}/^{144}\text{Pr}$ (Skraba et al. 1978), and $^{172}\text{Hf}/^{172}\text{Lu}$ (Daniels et al. 1978, 1987;

Grant et al. 1981, 1985; Thomas 1983; Lebedev et al. 1984; Organessiant et al. 1992; Das et al. 1996; Kueppers, 1999; Novgorodov et al. 2002) are available via generator systems as surrogates for various “medical” radiolanthanides. Some other metallic nuclides are available via generator systems as surrogates for $^{89,90}\text{Sr}$ or ^{90}Nb , for example: $^{87}\text{Y}/^{87\text{m}}\text{Sr}$ (Jannsen et al., 1986) and $^{97}\text{Zr}/^{97}\text{Nb}$ (Bhattacharya and Basu 1979; Das et al. 1993).

40.3.2 Key Examples of Generator-Produced Photon Emitters with Proven Medical Applications

^{81}Rb ($T_{1/2} = 4.58\text{ h}$)/ $^{81\text{m}}\text{Kr}$ ($T_{1/2} = 13\text{ s}$). This generator was introduced in the late 1960s (Yano and Anger 1968; Jones and Clark 1969; Jones et al. 1970; Yano et al. 1970; Colombetti et al. 1974) and was soon made available on a routine scale for clinical use (Clark et al. 1976; Ruth et al. 1980; Finn et al. 1982; Guillaume et al. 1983) for continuous inhalation or infusion studies on regional pulmonary ventilation and perfusion. The short half-life of $^{81\text{m}}\text{Kr}$ and continuous administration enables imaging at high count rates, which results in low patient radiation dose. The common method of production of ^{81}Rb is the $^{82}\text{Kr}(p,2n)$ route on isotopically enriched ^{82}Kr gas targets (Ruth et al. 1980; Acerbi et al. 1981; Kovács et al. 1991; Steyn et al. 1991; Uhlir et al. 1996). ^{81}Rb is typically adsorbed on cation exchange resins such as AG 50W-X8 or BioRad AG MP50. Alternatively, ZrPO_4 has been used as the generator support (Clark et al. 1976; Ruth et al. 1980). $^{81\text{m}}\text{Kr}$ is isolated by either purging the generator with air or oxygen (gas generator, for ventilation studies), or by eluting with normal saline or 5% glucose (solution generator, for perfusion studies). A typical generator consists of a small glass column (4 mm I.D.) filled with resin to the height of 15–20 mm (about 200 mg of resin) and washed with distilled water. A moveable shield with infrared air pump assembly is also available for easy handling. One recent study (Rizzo-Padoni et al., 2001) has reported that the use of the commercial Kryptoscan[®] generator for localization of pulmonary emboli is cost effective and that the cost varied based on the number of patients evaluated with each generator. Bubble type generators were proposed for parallel gas and solution separation (Jannsen et al. 1990, 1992). An online mass separator facility was used to separate ^{81}Rb following $\text{Nb}(p,\text{spall})$ processes at $E_p = 600\text{ MeV}$ with a 2-min collection period providing 0.84 GBq of the parent nuclide. Subsequently, a generator was constructed as Mylar foils implanted with 2×10^{13} atoms of ^{81}Rb (Hanser et al. 1986; Beyer et al. 1991). Although krypton-81m is not widely used currently, some investigators still believe this is an excellent approach for the evaluation of pulmonary perfusion and one recent study described its unique role for lung ventilation scanning in critically ill children on long-term mechanical ventilation (Sundariya et al. 2007).

^{99}Mo ($T_{1/2} = 2.7477\text{ d}$)/ $^{99\text{m}}\text{Tc}$ ($T_{1/2} = 6.006\text{ h}$). This handbook describes in detail the reactor production of ^{99}Mo (► Chap. 1), the radiochemistry of this man-made element and the state-of-the-art of $^{99\text{m}}\text{Tc}$ -radiopharmaceutical chemistry (► Chap. 6). Because of the shortage of fission-produced ^{99}Mo resulting from the undetermined length of the recent NRU reactor shutdown in Canada and the long maintenance outages of other reactors in Europe, the continued availability of ^{99}Mo worldwide for fabrication of the widely used $^{99}\text{Mo}/^{99\text{m}}\text{Tc}$ generators is a major topic of discussion. Several strategies are being discussed to move forward with alternatives to traditional research reactor fission production of ^{99}Mo by irradiation of uranium-235 targets. These strategies include the traditional current fission of ^{235}U targets in research reactors, the use of the *Aqueous Homogeneous Reactor* (AHR) technology originally demonstrated by Enrico Fermi, and the use of high energy accelerators for the $^{238}\text{U}(n,f)\text{ }^{99}\text{Mo}$

and $^{100}\text{Mo}(\gamma, n) ^{99}\text{Mo}$ routes. The AHR technology involves operation of a system where the aqueous ^{235}U salt solution (nitrate or sulfate), which is continuously fissioned, and recycled to remove the ^{99}Mo and off-line separation of other fission products. The advantages of such a system are the low operating temperature, more controlled safety envelope, and compact design, which does not require any specialized/sophisticated cooling or control systems. The expected time is 4–5 years until the new production facility would operate. The regulatory and licensing issues are under discussion and have to be addressed, but such AHR units would presumably not be subject to the complex safety and operational issues that are encountered by traditional research reactors. It is not yet clear which ^{99}Mo production strategy would overcome the recurring severe supply shortages of ^{99}Mo .

The $^{99}\text{Mo}/^{99\text{m}}\text{Tc}$ generator has been described in previous reviews (Boyd 1982; Boyd et al. 1982, 1986). Technetium-99m continues to be the most widely used diagnostic radionuclide in nuclear medicine, and $^{99\text{m}}\text{Tc}$ -labeled tissue-specific radiopharmaceuticals are available for diagnostic studies of essentially all major organs, and represent an estimated 90% of all diagnostic procedures. The widely used chromatographic-type $^{99}\text{Mo}/^{99\text{m}}\text{Tc}$ generator system provides sodium pertechnetate ($\text{Na}^{99\text{m}}\text{TcO}_4$) by elution with saline and uses very high specific activity no-carrier-added ^{99}Mo , produced by the $^{235}\text{U}(\text{n}, \text{fission})^{99}\text{Mo}$ process, which is adsorbed on aluminum oxide. In addition to the chromatographic-type generators, “batch” preparation of $^{99\text{m}}\text{Tc}$ involves solvent extraction (Evans et al. 1982), for instance with methyl ethyl ketone, or sublimation of the low specific activity ^{99}Mo , which can be reactor produced by neutron activation of enriched ^{98}Mo . The latter approach may become more attractive in the future as radioactive waste disposal issues become more crucial.

Two options using low specific activity ^{99}Mo produced by the $^{98}\text{Mo}(\text{n}, \gamma)^{99}\text{Mo}$ for generator fabrication involve the “gel-type” generator or post-elution concentration strategies. The “gel-type” generator approach (Boyd 1982) involves preparation of a molybdenum–zirconium gel. Even if the “gel-type” generator system is used, the specific concentration of the $^{99\text{m}}\text{Tc}$ may be too low for practical use. A useful alternative involves post-elution concentration of $^{99\text{m}}\text{Tc}$ on an anion-exchange column in tandem with the Al_2O_3 generator column, similar to that developed for the $^{188}\text{W}/^{188}\text{Re}$ generator (Knapp et al. 1998a; Guhlke et al. 2000; Sarkar et al. 2001). Although the chromatographic alumina generator is generally considered impractical for use with low specific activity ^{99}Mo because of the significantly larger amounts of alumina adsorbent that are required, the post-elution concentration of the initial low specific volume $^{99\text{m}}\text{Tc}$ provides sufficiently high specific volume activity solutions for labeling.

^{178}W ($T_{1/2} = 21.5 \text{ d}$)/ $^{178\text{m}}\text{Ta}$ ($T_{1/2} = 9.31 \text{ min}$). $^{178\text{m}}\text{Ta}$ decays with the emission of X-rays with energies of 55 keV (K_α , 67.4%) and 64 keV (K_β , 17.7%). The relatively long-lived parent ^{178}W can be produced with the $^{181}\text{Ta}(\text{p}, 4\text{n})^{178}\text{W}$ reaction with yields of $2 \text{ MBq } \mu\text{A}^{-1} \text{ h}^{-1}$ at $40 \rightarrow 32 \text{ MeV}$ proton energy (Neirinckx et al. 1978, 1979; Holman et al. 1978). Neirinckx et al. (1981) evaluated AGI-X8 as the support, and concluded that the generator can operate satisfactorily when eluted with 0.1–0.15 M HCl containing 0.1% H_2O_2 . The ^{178}W breakthrough initially was $10^{-3}\%$, increasing, however, after 100 elutions. The current generator uses a Dowex AG 1-X8 anion exchange column (Lacy et al. 1988a). Elution with 0.03 M HCl provides reproducible $^{178\text{m}}\text{Ta}$ yields with consistently low ^{178}W parent breakthrough.

Preliminary studies explored preparation of $^{178\text{m}}\text{Ta}$ -labeled myocardial perfusion agents (Holman et al. 1979; Layne et al. 1991) and also applications for lung and liver imaging (Neirinckx et al. 1979). High resolution and statistical quality FPRNA studies of ventricular performance were demonstrated in a group of 38 patients in comparison with the traditional $^{99\text{m}}\text{Tc}$ methods (Lacy et al. 1991). Verani et al. (1992a) demonstrated the usefulness of this

system for evaluation of systolic and diastolic left ventricular function in 46 patients undergoing coronary balloon angioplasty. Verani et al. (1992b) reported evaluation of right ventricular performance in 46 patients. The $^{178}\text{W}/^{178\text{m}}\text{Ta}$ generator in combination with a portable multiwire proportional counter gamma camera (MWGC) has recently been shown to be an excellent source of $^{178\text{m}}\text{Ta}$ for the evaluation of ventricular performance (Lacy et al. 2001). These studies clearly demonstrate that the $^{178}\text{W}/^{178\text{m}}\text{Ta}$ generator is the only current system providing a short-lived daughter for the evaluation of FPRNA. In spite of the fact that first-pass ventriculography with ultra-short lived radioisotopes is not currently widely practiced, a recent study described the advantages for the assessment of left ventricular function during upright treadmill exercise using a multiwire gamma camera (Heo et al. 2005).

^{191}Os ($T_{1/2} = 15.4 \text{ d}$)/ $^{191\text{m}}\text{Ir}$ ($T_{1/2} = 4.94 \text{ s}$). The ^{191}Os is produced via the $^{190}\text{Os}(n,\gamma)$ reaction. Radiochemical separations of the generator system were based on ion exchange chromatography (Yano and Anger 1968; Campell and Nelson 1956; Hnatowich 1977; Hnatowich et al. 1977). More recent systems used absorption of $\text{K}_2/^{191}\text{OsO}_2\text{Cl}_4$ or $\text{K}_2/^{191}\text{OsO}_2(\text{OH})_2\text{Cl}_2$ on AGMP-1 anion exchange resin. A second column was required to guaranty radionuclidic purities with a breakthrough of $<10^{-2}\%$ ^{191}Os , while the overall separation yield of $^{191\text{m}}\text{Ir}$ remained relatively low ($<10\%$) (Cheng et al. 1980, 1982). More than 100 patients received injections of $^{191\text{m}}\text{Ir}$ in isotonic saline Na_2HPO_4 buffers. Another system used Os(VI) bound to silica gel impregnated with tridodecylmethylammonium chloride (SG-TDMAC) (Issacher et al. 1989; Hellmann et al. 1989) and provided $^{191\text{m}}\text{Ir}$ in 21–33% yield by elution with acidic (HCl) saline at pH 1 with the final eluate buffered with 1 M succinate solution to pH 9. An activated carbon “scavenger” column was used in tandem with the SG-TDMAC column to remove ^{191}Os parent breakthrough before the eluant is rapidly buffered. Another generator system was also developed for angiocardiology in children which utilized a potassium Os(VI)oxalate species adsorbed on AGMP-1 anion exchange resin (Packard et al. 1986, 1987), which did not require a “scavenger” column. Elution with pH 1 0.9% saline solution provided $^{191\text{m}}\text{Ir}$ in good yields (10% per mL) with low ^{191}Os parent breakthrough ($3 \times 10^{-4}\%$). The use of $^{191}\text{Os(IV)}$ species bound on heat-activated carbon eluted with 0.9% saline at pH 2 containing 0.025% KI was also developed and represented an excellent generator system, providing the daughter nuclide in 16–18% yields with correspondingly low ^{191}Os parent breakthrough ($2\text{--}3 \times 10^{-4}\%$ per bolus). For patient studies, the low-pH bolus was neutralized with 0.13 M TRIS, followed by rapid intravenous administration of the neutralized bolus with physiological saline (Franken et al. 1989, 1991), using a microprocessor-controlled automated elution/injection system.

$^{191\text{m}}\text{Ir}$ was proposed for the evaluation of heart disease and blood flow for various organs (Yano and Anger 1968; Treves et al. 1976, 1980; Thiesson et al. 1983). This first generator provided $^{191\text{m}}\text{Ir}$ for intravenous administration (Yano et al. 1968) and another system was used for quantification of cardiac shunts in children (Treves et al. 1976, 1980) and evaluation of ventricular function in adults (Heller et al. 1986). Studies by Franken et al. (1989, 1991) described rapid sequential multiple view FPRNA for the evaluation of left ventricular ejection fraction and regional wall motion studies in over 600 patients. More recent studies have described the use of $^{191\text{m}}\text{Ir}$ in rabbits via dynamic studies (Kariemo et al. 1994) for renal radionuclide angiograms and continuous infusion for the rapid renal single-photon emission tomographic evaluation of renal blood flow (Treves et al. 1999).

$^{195\text{m}}\text{Hg}$ ($T_{1/2} = 1.73 \text{ d}$)/ $^{195\text{m}}\text{Au}$ ($T_{1/2} = 30.5 \text{ s}$). Like $^{191\text{m}}\text{Ir}$, the short-lived $^{195\text{m}}\text{Au}$ was of interest for first-pass radionuclide angiography (Thiesson and Paras 1983). The parent nuclide

is produced via the $^{197}\text{Au}(p,3n)$ reaction at $34 \rightarrow 26$ MeV proton energies with relatively high thick target yields of $170 \text{ MBq } \mu\text{A}^{-1} \text{ h}^{-1}$ (Birattari and Bonardi 1982; Panek et al. 1985; Guillaume and Brihaye 1986). The $^{195\text{m}}\text{Hg}$ was separated either by solvent extraction (Bett et al. 1981, 1983) or by distillation (Guillaume and Brihaye 1986). Dithiocellulose adsorbents were used showing 1–2% breakthrough of $^{195\text{m}}\text{Hg}$ and 10–20% elution yield of $^{195\text{m}}\text{Au}$ using 10 mM NaCN solution (Bett et al. 1983), while silica gel coated with ZnS showed better retention of the parent nuclide and higher elution yield of 28–30% using $\text{Na}_2\text{S}_2\text{O}_3/\text{NaNO}_3$ solutions (Panek et al. 1984, 1985). For bolus injections, ^{195}Hg was loaded onto a Chelex 100 column, while $^{195\text{m}}\text{Au}$ was eluted with 5% glucose solutions with about 20% yield in mainly ionic form; the ^{195}Hg breakthrough being about $10^{-3}\%$ (Garcia et al. 1981; Brihaye et al. 1982). Some limitations concern the formation of ^{195}Au by isomeric transition of $^{195\text{m}}\text{Au}$, resulting in an increasing absorbed radiation dose. Nevertheless, both cardiac metabolism and function studies have been performed comparing $^{195\text{m}}\text{Au}$ with ^{201}Tl (Mena 1985) and $[^{123}\text{I}]\text{IPPA}$ (Wagner et al. 1990).

40.4 Generator-Produced Particle Emitters for Therapy

40.4.1 Overview

During the last decade there has been a tremendous increase in the development and use of new therapeutic radiopharmaceuticals radiolabeled with radionuclides, which are available from radionuclide generator systems. The availability of generator-derived therapeutic radionuclides is necessary for the development and testing and commercialization of agents with potential for endoradiotherapy (ERT). Just as availability of $^{99\text{m}}\text{Tc}$ from the $^{99}\text{Mo}/^{99\text{m}}\text{Tc}$ has played such a key role in the development of a wide variety of $^{99\text{m}}\text{Tc}$ -labeled radiopharmaceuticals, the availability of generator-derived radionuclides has stimulated the development of an increasing spectrum of therapeutic tracers. It is important to note that in most cases, increased need for and further development of generators, which provide therapeutic radionuclides has been driven by the success in the development of the targeting agents or vectors.

Generator-derived therapeutic radionuclides have a number of characteristic decay processes, and can emit β particles, Auger electrons, low-energy photons, and α particles. Since many therapeutic radionuclides are characterized by β decay, they are often directly produced in a nuclear reactor, since neutron capture by the target nuclide forms a radioactive or unstable product that decays by β emission. Key examples of therapeutic radionuclides obtained from reactor-produced parent radionuclides include ^{166}Ho – from the $^{166}\text{Dy}/^{166}\text{Ho}$ generator, and ^{188}Re – from the $^{188}\text{W}/^{188}\text{Re}$ generator.

Another important source of generator parent radionuclides is recovery of generator parent radionuclides that are produced during nuclear fission. Strontium-90 is the parent for the $^{90}\text{Sr}/^{90}\text{Y}$ generator system and is isolated from fission products. The recent approval by the US Food and Drug Administration (FDA) on February 19, 2002, for “Zevalin” (Ibritumomab tiuxetan) – a ^{90}Y -labeled murine anti CD20 antibody – for the treatment of patients with low grade, follicular, or transformed non-Hodgkin’s lymphoma, represents the first antibody radiolabeled with a therapeutic, generator-derived radionuclide, and would be expected to represent the first of many new therapeutic radiopharmaceuticals for oncologic applications.

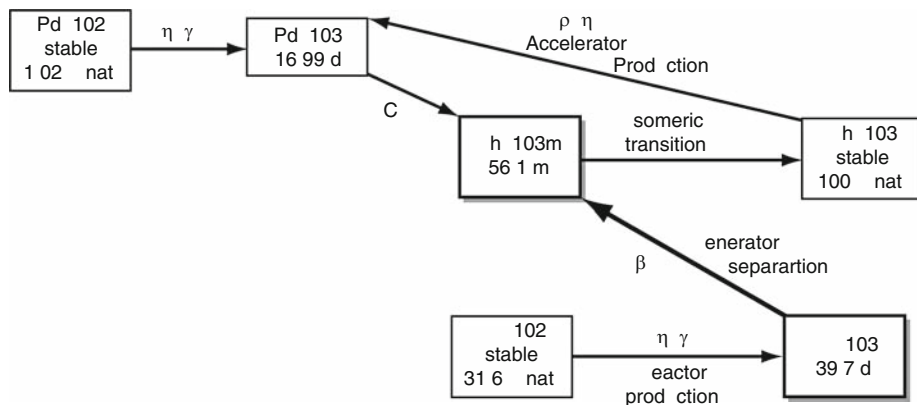
A third source for radionuclide generator systems is the recovery of radioactive parents from “extinct” radioactive decay processes, such as ^{229}Th , which is recovered from ^{233}U decay products. The ^{229}Th represents a convenient, long-lived ($T_{1/2} = 7,340$ years) source from which ^{225}Ac is recovered, which is the parent of the $^{225}\text{Ac}/^{213}\text{Bi}$ generator system.

The α -emitter ^{211}At has great potential for labeling compounds of potential interest in cell biology and endoradiotherapy. Although it is produced mainly via the direct $^{209}\text{Bi}(\alpha, 2n)$ route, it can be produced through the decay of 14.6 h ^{211}Rn (Vachtel et al. 1976; Visser et al. 1979; Mirzadeh and Lambrecht 1980).

^{103}Ru ($T_{1/2} = 39.25$ h)/ $^{103\text{m}}\text{Rh}$ ($T_{1/2} = 56.12$ min). Rhodium-103m is a key example of an Auger-emitting candidate, which can be obtained from decay of reactor-produced ^{103}Ru . Interest for use of $^{103\text{m}}\text{Rh}$ in radioimmunotherapy and other strategies for targeted therapy results from its attractive decay properties (see [Table 40.1](#)) and potential availability from a $^{103}\text{Ru}/^{103\text{m}}\text{Rh}$ generator system for targeted radiotherapy (Bernhard et al. 2001). The 40 keV isomeric decay energy is totally converted in the electronic shells of the stable ^{103}Rh daughter with no measurable γ -rays and results in a “shower” of low-energy electrons and X-rays. Daily elution of equilibrium levels of $^{103\text{m}}\text{Rh}$ is possible from the $^{103}\text{Ru}/^{103\text{m}}\text{Rh}$ generator. Rhodium-103m is expected to exhibit high cytotoxicity resulting from its decay by highly converted isomeric transition and emission of Auger electrons. Availability of a $^{103}\text{Ru}/^{103\text{m}}\text{Rh}$ generator system would offer an opportunity to provide carrier-free $^{103\text{m}}\text{Rh}$ on a routine basis for the assessment of its potential for Auger therapy. Either fission- or reactor-produced ^{103}Ru could be used for the generator system. Although the 3% fission yield of ^{103}Ru from ^{235}U is quite high, fission products are not routinely available. The availability of lower specific-activity ^{103}Ru from reactor irradiation of enriched ^{102}Ru production with sufficient specific activity in many research reactors on an international basis would be expected to be reliable routine source of ^{103}Ru for fabrication of the $^{103}\text{Ru}/^{103\text{m}}\text{Rh}$ generator system. Rhodium-103m can also be obtained by the decay of ^{103}Pd ([Fig. 40.5](#)), and the use of the $^{103}\text{Pd}/^{103\text{m}}\text{Rh}$ in vivo generator has been proposed (Van Rooyen et al. 2008), which may suggest that a $^{103}\text{Pd}/^{103\text{m}}\text{Rh}$ generator for routine availability of $^{103\text{m}}\text{Rh}$ may be feasible. Development of a chromatographic-type $^{103}\text{Ru}/^{103\text{m}}\text{Rh}$ generator would be expected to provide $^{103\text{m}}\text{Rh}$ from

Fig. 40.5

Availability of $^{103\text{m}}\text{Rh}$ from reactor-produced long-lived ^{103}Ru and from decay of ^{103}Pd



separation of Rh from Ru compared to Rh from Pd. In addition, the very low 1.02% natural abundance of ^{102}Pd , coupled with the high costs of enrichment for reactor production of ^{103}Pd , the high costs of accelerator-production of ^{103}Pd from $^{103}\text{Ru}(\text{p},\text{n})$ and the shorter physical half-life of ^{103}Pd compared to ^{103}Ru are other issues.

The separation of Rh from Ru had been described some years ago by solvent extraction techniques (Chiu et al. 1978; Epperson et al. 1976), and these methods with carbon tetrachloride extraction for RuO_4 from Ru/Rh mixtures in HCl have served as the basis for the more recent interest in the availability of $^{103\text{m}}\text{Rh}$. A recent solvent-extraction type $^{103}\text{Ru}/^{103\text{m}}\text{Rh}$ generator, which is based on the earlier extraction work of Epperson et al. (1976) and Chiu et al. (1978), has recently been reassessed (Bartos et al. 2007, 2009; Skarnemark et al. 2009). Recent studies have used both fission- and reactor-produced Ru for these studies (Bartos et al. 2009). The use of batch liquid extraction/post processing of Rh from Ru by liquid extraction technology to routinely provide $^{103\text{m}}\text{Rh}$ may be impractical and could be expected to be primarily centered at a central processing site and not accessible in most research centers. Use of a chromatographic-type generator would be expected to be much more practical and accessible on a routine institutional basis to provide the $^{103\text{m}}\text{Rh}$ Auger emitter for widespread research use.

40.4.2 Key Examples of Generator-Derived Therapeutic Radionuclides with Proven Medical Applications

^{90}Sr ($T_{1/2} = 28.6\text{ a}$)/ ^{90}Y ($T_{1/2} = 64.1\text{ h}$). Yttrium-90 decays with the emission of a high-energy β particle ($E_{\text{max}} = 2.3\text{ MeV}$) and is of broad interest for therapy of solid tumors where deep penetration of radiation is important for cross-fire (cf. [Chaps. 45](#) and [46](#) of this Volume). Although various forms of the $^{90}\text{Sr}/^{90}\text{Y}$ generators have been available for a number of years, broad interest in clinical therapeutic applications of ^{90}Y was stimulated by the development of methods of radiation synovectomy of large synovial joints, and more recently, the development of bifunctional chelating groups that strongly bind the Y^{3+} cation, since the skeletal localization of free trivalent yttrium species would result in significant marrow suppression. The availability of DOTA and the CHX-substituted DTPA chelates provides an opportunity to use ^{90}Y in a predictably safe manner. The availability of the chelates in consort with vectors having very specific cellular targeting, such as the DOTATOC octreotide agent, which binds with high specificity to the somatostatin receptors, provided important agents for the treatment of a wide variety of tumors. Because of the safety issues associated with the use and handling of ^{90}Y and ^{90}Sr , these high-level generators are typically installed in a centralized processing area for preparation of the no-carrier-added ^{90}Y by batch solvent extraction techniques and distribution of the highly purified ^{90}Y product. One method (Bray and Wester, 1996) involves freshly purified HDEHP extraction of ^{90}Y from a nitric acid solution of the purified $^{90}\text{Sr}/^{90}\text{Y}$ mixture. The final $^{90}\text{Y}/^{90}\text{Sr}$ activity ratio of the purified ^{90}Y is $<10^{-7}$ with a concentration of metal impurities of $<10\text{ ppm}$ per Ci ^{90}Y . A generator system has also been described for the separation of ^{90}Y from ^{90}Sr and involves the use of strongly acidic Dowex exchange resin (Chinol and Hnatowich, 1987).

A comparison of solvent extraction, ion exchange, and other radiochemical separation techniques applied to this generator was made by Chuang and Lo (1988). Ion exchange based generators utilize various organic cation exchange resins, but also inorganic compounds, with a particular focus on high radiation resistance (Hsieh et al. 1991; Bielewicz, 1995; Chinol et al. 1996;

Bläuenstein et al. 1996). Because of the limited availability, significant costs of high purity ^{90}Sr and the potential dangers in handling ^{90}Sr , installation of this generator in a hospital-based nuclear pharmacy or a central radiopharmacy is unusual, and high purity ^{90}Y is generally obtained from a central processing approved GMP facility providing both research-grade and sterile, pyrogen-free ^{90}Y for human studies.

^{166}Dy ($T_{1/2} = 3.4\text{ d}$)/ ^{166}Ho ($T_{1/2} = 1.117\text{ d}$). Although ^{166}Ho can be produced with a specific activity of only 8–9 Ci mg^{-1} ($\sim 300\text{ GBq mg}^{-1}$) ^{165}Ho by the $^{165}\text{Ho}(\text{n},\gamma)^{166}\text{Ho}$ reaction even at saturation in a high thermal flux of $2.5 \times 10^{15}\text{ n cm}^{-2}\text{ s}^{-1}$, no-carrier-added ^{166}Ho with a theoretical specific activity of about 700 Ci mg^{-1} ($\sim 26\text{ TBq mg}^{-1}$) is obtained by decay of ^{166}Dy . The ^{166}Dy is reactor produced by the $^{164}\text{Dy}(\text{n},\gamma)^{165}\text{Dy}(\text{n},\gamma)^{166}\text{Dy}$ reaction series. Separation of ^{166}Ho from ^{166}Dy has traditionally been a challenge. Although not a true generator system – since the ^{166}Dy parent is also recovered and requires column reloading for subsequent $^{166}\text{Ho}/^{166}\text{Dy}$ separations following adequate ^{166}Ho in-growth – a method has been described for successful $^{166}\text{Ho}/^{166}\text{Dy}$ separation, which uses an HPLC reversed phase ion-exchange chromatographic method utilizing Dowex AG 50WX12 or Aminex A5 cation exchangers by elution with α -hydroxy-isobutyric acid (α -HIB) of 0.085 M at pH 4.3. This approach provides a Dy/Ho separation factor of approximately 10^3 , with subsequent purification of the $^{166}\text{Ho}^{3+}$ by cation-exchange column chromatography after acid decomposition of the Ho- α -HIB complex (Dadachova et al. 1995a, b). More recently, an apparently simple and efficient method has described separation on the Eichrome Ln resin by elution with dilute nitric acid (Ketrings et al. 2002).

Although ^{166}Ho has attractive radionuclidic properties as a lanthanide for various vector labeling and therapeutic strategies, it has not yet been widely used. Examples are studies of protein labeling with the CHX-B-DTPA ligand system (Dadachova et al. 1997). Animal studies demonstrated that no translocation of the ^{166}Ho daughter radionuclide occurred when the [^{166}Ho]DTPA complex was administered to rats (Smith et al. 1995). The results of these studies may suggest that the $^{166}\text{Dy}/^{166}\text{Ho}$ system may have some promise as an in vivo generator. Clinical applications that have been recently reported include radiation synovectomy with ^{166}Ho -ferric hydroxide (Ofluoglu et al. 2002), the use of [^{166}Ho]DTPA liquid-filled balloons for the inhibition of restenosis following coronary angioplasty (Hong et al. 2002), and use of [^{166}Ho]DOTMP for myeloablative therapy of multiple myeloma (Rajendran et al. 2002). If the availability of no-carrier-added ^{166}Ho becomes a reality, use of this generator system may be a source for these and other applications.

^{188}W ($T_{1/2} = 69\text{ d}$)/ ^{188}Re ($T_{1/2} = 16.9\text{ h}$). Rhenium-188 is currently of broad interest for the development of a wide variety of new therapeutic approaches for applications in nuclear medicine, oncology, and even interventional cardiology, because of the benefits, advantages, and significantly reduced expense of using ^{188}Re in comparison to many other therapeutic radionuclides (Knapp et al. 1997, 1998a, b). There are currently a large number of physician-sponsored clinical protocols in progress. Tungsten-188 is reactor produced by double neutron capture of enriched ^{186}W by the $^{186}\text{W}(\text{n},\gamma)^{187}\text{W}(\text{n},\gamma)^{188}\text{W}$ route. Since the production yield is a function of the square of the thermal neutron flux, even at high thermal neutron flux ($> 2 \times 10^{15}\text{ n cm}^{-2}\text{ s}^{-1}$) ^{188}W is produced with only modest specific activity of 4–5 Ci g^{-1} ($\sim 180\text{ GBq g}^{-1}$) per cycle (Knapp et al. 1994). This is due to the modest neutron capture cross sections and burnup of the ^{188}W product (Mirzadeh et al. 1997). Although the first prototype $^{188}\text{W}/^{188}\text{Re}$ generators were described as early as 1966 using zirconium oxide (Lewis and Eldridge, 1966) and with aluminum oxide in 1972 (Mikheev et al. 1972), in spite of the excellent radionuclidic properties of ^{188}Re , there was no practical use of this therapeutic

radionuclide until nearly 25 years later, when appropriate carrier molecules and targeting agents became available (Knapp et al. 1997, 1998a, b).

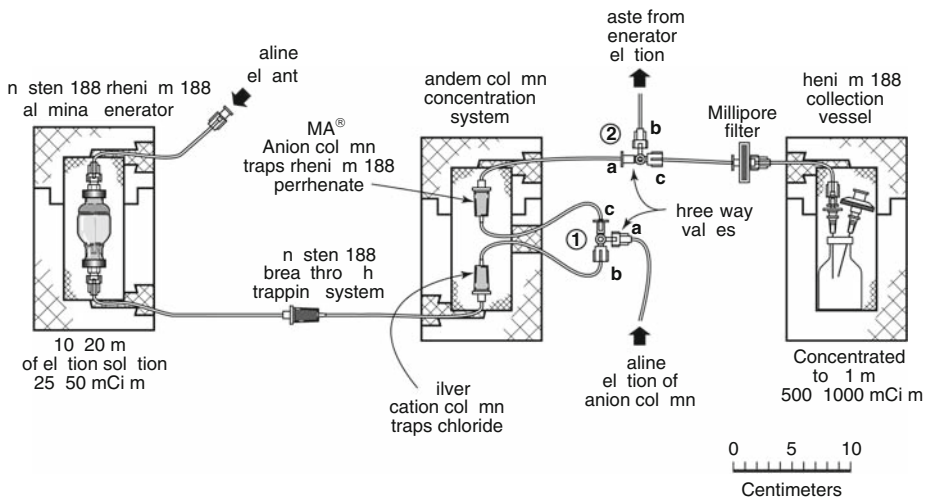
The $^{188}\text{W}/^{188}\text{Re}$ generator systems today are mainly based on separation chemistry similar to that used for the $^{99}\text{Mo}/^{99\text{m}}\text{Tc}$ generator, which includes the adsorption of tungstic acid in the alumina-based generator (Mikheev et al. 1972; Callahan et al. 1989; Knapp et al. 1994) (► Fig. 40.6). In addition to the adsorption column chromatographic separation on alumina, zirconium oxide (Dadachova et al. 1994) and gel-type generators (Erhardt et al., 1992) have been reported. For batch separation of ^{188}Re a thermochromatographic technique was described (Novgorodov et al. 2000).

The adsorption type generator is most practical, since it is easy to prepare, has long-term stability with high ^{188}Re yields and consistently low ^{188}W breakthrough. The availability of effective and inexpensive post-elution tandem column-based concentration systems (Guhlke et al. 2000; Knapp et al. 1997, 1998a) provides a useful method for ^{188}Re concentration to very high specific volumes (<1 mL total volume).

There are presently a large number of physician-sponsored clinical trials in progress using the Oak Ridge National Laboratory (ORNL) alumina-based $^{188}\text{W}/^{188}\text{Re}$ generator system. ^{188}Re -labeled HEDP (Palmedo et al. 2000; Savio, et al. 2001) and DMSA (Blower et al. 2000) have proven to be effective agents for the palliative relief of bone pain from skeletal metastases in patients with prostatic carcinoma, and may represent a more cost-effective alternative to

■ Fig. 40.6

Scheme of the $^{188}\text{W}/^{188}\text{Re}$ generator. Post-elution concentration after saline elution of the alumina-based $^{188}\text{W}/^{188}\text{Re}$ generator system conveniently provides high specific volume ^{188}Re perrhenate solutions. The generator is eluted with physiological saline (for instance, 25–50 mL) at a flow-rate of 1–2 mL min⁻¹ through the disposable, one time use tandem cation/anion exchange system, with stopcocks (SC) 1 and 2 in the following positions: SC 1, position b–c and SC 2, position a–b. After generator elution, the ^{188}Re perrhenate trapped on the QMA anion column is then eluted with a small volume (1–2 mL) of saline with SC 1, in position a–c and SC 2, in position a–c



other radionuclides used for this application. In addition, the use of liquid-filled angioplasty balloons for the inhibition of hyperplastic restenosis after coronary balloon angioplasty using ^{188}Re -perrhenate (Hoeher et al. 2000; Kotzerke et al. 2000; Makkar et al. 2000; Schuelen et al. 2001; Kropp et al. 2002), ^{188}Re -MAG3 (Weinberger and Knapp 1999; Weinberger et al. 1999; Park et al. 2001) and [^{188}Re]DTPA (Hong et al. 2002) are in progress, and the use of the ^{188}Re -labeled anti-CD66 has also been reported (Nowak et al. 2001). The use of the ^{188}Re -labeled anti-CD66 antibody (anti-NCA95) has been found to be a useful new method for marrow ablation using combinational preconditioning in leukemia patients (Bunjes et al. 2000; Reske et al. 2001; Buchman et al. 2002). The use of the $^{188}\text{W}/^{188}\text{Re}$ generator in developing regions has been demonstrated to be of particular usefulness because of its cost-effectiveness, and multi-center trials supported by the International Atomic Energy Agency are in progress for restenosis therapy with ^{188}Re -perrhenate and for the treatment of liver cancer (Sundram et al. 2002) with ^{188}Re -labeled lipiodol analogues (Jeong et al. 2001a, b). A ^{188}Re -labeled antibody has been used for treatment of bladder cancer (Murray et al. 2001) and use of the ^{188}Re -labeled P2045sstr-targeting peptide for the treatment of lung cancer has also been reported (Bugai et al. 2002) and is now in clinical trials in the USA.

Several new generator prototypes for the separation of nca ^{188}Re from ^{188}W have been recently described, which use a new high-capacity adsorbent consisting of synthetic alumina functionalized with sulfate moieties prepared from a sol-gel process (Lee et al. 2009). This material is reported to have a tungsten loading capacity of >450 mg/g, allowing preparation of a 3 Ci generator using only 1 g of adsorbent, which is a much higher loading capacity than reported for acid-washed alumina. Elution with 5 mL of saline at 1 mL/min results in ^{188}Re yields of 70–90%. In this manner, a 1 Ci generator can provide ^{188}Re solutions with a specific volume of >200 mCi/mL saline. In addition, a simple electrochemical separation technique has been reported using platinum electrodes immersed in $^{188}\text{W}/^{188}\text{Re}$ equilibrium mixture by applying a constant 7 V potential difference at 80°C for 60 min. The ^{188}Re is stripped as perrhenic acid from the platinum cathode with warm 0.1 N HCl (Chakravarty et al. 2009). Decay-corrected ^{188}Re yields of $>70\%$ have been reported in preliminary studies using 30 mCi of ^{188}W . There are several examples of recent clinical applications with ^{188}Re which include use of the ORNL $^{188}\text{W}/^{188}\text{Re}$ generator for preparation of the HDD agent for liver cancer therapy (Jeong and Knapp 2008). Results of the recent multicenter clinical trial with this agent coordinated through the IAEA have demonstrated the efficacy of ^{188}Re -labeled HDD/Lipiodol for the transarterial palliative treatment in patients with non-resectable/non-transplantable liver tumors (Padhy et al. 2008). Further assessment of the initial use of ^{188}Re liquid-filled angioplasty balloons for the inhibition of hyperplasia following PCTA of the coronaries has now been demonstrated for the peripheral arteries (Wohlgemuth et al. 2008).

^{225}Ac ($T_{1/2} = 10$ d)/ ^{213}Bi ($T_{1/2} = 45.6$ min). Because of the very high linear energy transfer (LET) in the 50–90 μm range, α particles are very suitable for therapy of microscopic or subclinical disease, such as for the treatment of micrometastatic disease (cf. [▶ Chap. 46](#) of this Volume). The attachment of α emitters to cellular-targeted carrier molecules such as antibodies or peptides is the most common approach. For this reason, interest in the $^{225}\text{Ac}/^{213}\text{Bi}$ generator system has rapidly increased in the last few years. The ^{225}Ac is generally obtained as a decay product of ^{229}Th , which is extracted as a radioactive decay product of the ^{233}U , a member of the “extinct” ^{237}Np decay chain (see [▶ Fig. 5.5 in Chap. 5, Vol. 1](#)). Production has also been proposed via accelerators, as an example, by the $^{226}\text{Ra}(\text{p},\text{n})^{225}\text{Ac}$ reaction. The ^{229}Th can be obtained from processing of the ^{233}U stockpile, which had originally been produced in a proposed molten salt breeder reactor program at ORNL. From a complex series of

ion-exchange and extraction chromatographic steps for recycling of $^{229}\text{Th}(\text{IV})$, the $\text{Ra}(\text{II})$ decay product is separated at optimal timing, and the ^{225}Ac then separated. A variety of chromatographic-type $^{225}\text{Ac}/^{213}\text{Bi}$ generators have been described (Geerlings et al. 1993; Lambrecht et al. 1997; Wu et al. 1997; Boll et al. 1997; Mirzadeh 1998; Hassfjell and Brechbiel 2001).

At ORNL, the ^{225}Ac in 1 M HNO_3 solution is provided to investigators with generator components for on-site generator loading, to minimize the effects of radiolysis. This solution is loaded onto a small AG 50W-X4 strong cation exchange resin with elution of the ^{213}Bi daughter with 0.15 M HI solution. Several other $^{225}\text{Ac}/^{213}\text{Bi}$ generator systems have also been described. One example (Geerlings et al. 1993) used two successive Dowex 50W-X8 cation exchange columns, with initial separation of ^{225}Ac from $^{224/225}\text{Ra}$ with subsequent separation of the desired ^{213}Bi from the ^{225}Ac formed from radon decay. Wu et al. (1997) reported a generator using the inorganic AC-Resin ion exchanger. The ^{213}Bi was eluted with 1 M HCl in a continuous elution mode, diluted to 0.2 M HCl and then loaded on a second small AGMP-50 cation exchange resin and eluted with 0.1 M HI. A similar column is being used (McDevitt et al. 1999a) where ^{213}Bi is being applied for the clinical treatment of acute myeloid leukemia (AML) under physician-sponsored protocols (McDevitt et al. 1999b; Sgoruos et al. 1999; Jurciv et al. 2002). Another variation proposed by Bray et al. (1999) passes a ^{225}Ac solution through a disc containing a thin film of the Anex (3M Company) strong anion-exchange resin that binds the ^{213}Bi , which is subsequently eluted with pH 5.5 solution of 0.05 M NaOAc.

As discussed later in the *in vivo* generator section, in addition to its utilization in a generator system to provide ^{213}Bi for α -targeted therapy, interest is increasing in using the ^{225}Ac parent for targeted therapy, because of the emission of four α particles and the long half-life (Chang et al. 2008; Miederer et al. 2008; Sofou et al. 2007; Antczak et al. 2006). The current major clinical application of bismuth-213 is for treatment of myelogenous leukemia and use of actinium-225 is gaining interest for α therapy because of the longer physical half-life (McDevitt et al. 2001).

^{224}Ra ($T_{1/2} = 3.66\text{ d}$)/ ^{212}Pb ($T_{1/2} = 10.64\text{ h}$)/ ^{212}Bi ($T_{1/2} = 1.01\text{ h}$). Bismuth-212 has been of interest for some time and is available from decay of ^{212}Pb . The traditional generator involves loading a cation exchange resin with ^{224}Ra with subsequent elution of the ^{212}Bi with HCl or HI (Atcher et al. 1988), which requires replacement of the generator every 3–6 days. More recently, a generator based on gaseous ^{222}Ra emanating from thin films of ^{228}Th barium stearate has been described (Hassfjell and Brechbiel 2001), which involves collecting the gaseous ^{224}Ra in a trap containing an organic solvent such as methanol or hexane or a methanol/hexane mixture, at temperatures lower than -72°C . The ^{212}Pb decay product can be obtained in about 70% yield and this system has the advantage of an indefinite shelf life of the long-lived ^{228}Th ($T_{1/2} = 1.913\text{ a}$) source.

^{227}Ac ($T_{1/2} = 21.77\text{ d}$)/ ^{223}Ra ($T_{1/2} = 11.43\text{ d}$). Because of availability from decay of ^{227}Ac , localization of ionic radium in growing bone and the high LET, radium-223 has emerged as a promising new candidate for routine use for palliative treatment of bone pain from tumor metastases to the skeleton (Bruland et al. 2008; Nilsson et al. 2005, 2007). Radium-223 can be conveniently repeatedly obtained from separation from the ^{227}Ac parent. The ^{227}Ac is obtained from decay of ^{235}U and decays to ^{227}Ac through ^{227}Th , or can be reactor produced by neutron irradiation of ^{226}Ra (Larsen et al. 2007) or from α irradiation of protactinium-231 targets. The availability of beryllium/actinium neutron sources often used for well logging can provide a ready source of ^{227}Ac . The purified $^{227}\text{Ac}/^{227}\text{Th}$, purified by traditional ion exchange methods, can be adsorbed on 1 M HCl preconditioned P,P' -di(2-ethylhexyl)

methanediphosphonic acid/silica (Dipex-2) extraction resin (Hendricksen et al. 2001). The ²²³Ra then eluted with 1 M HCl or HNO₃. Further purification of the ²²³Ra is accomplished using a small AG 50W-X12 cation resin by elution with 1 M nitric acid. Although there are no practical complexing/chelating agents for ionic radium, the targeting of Ra²⁺ to metabolically active bone, allows the simple administration of radium chloride. In this manner, the generator can be eluted, the ²²³Ra eluant evaporated, then dissolved in saline/sodium citrate buffer, and dispensed by sterile filtration. It is then ready for administration precluding any complex radiolabeling and purification procedures normally encountered for radiopharmaceutical administration.

40.5 In Vivo Generators

40.5.1 Concept

A relatively recent and potentially useful approach is based on the concept of an in vivo generator (Mausner et al. 1989). The concept involves labeling of various molecular carriers (complexes, peptides, mcAb, mcAb-fragments, etc.) with intermediate half-life generator parents, which after accumulation in the desired tissue generate much shorter half-life daughter radionuclides (Table 40.3). These in vivo generated daughter radionuclides can act either as imaging agent (if decaying via single-photon or positron emission) or as therapeutic agent (if decaying via α, β[−], or Auger electron emission). In particular, for therapy, since the daughter will be in equilibrium in vivo with the parent, formation of the particle-emitting daughter will add in situ a significant radiation dose. This concept of targeting the parent radionuclide will

Table 40.3

Potential parent/daughter pairs for the in vivo generator concept

Generator system	Parent		Daughter			Application
	T _{1/2}	decay	T _{1/2}	Emission (%)	E _{β/α} (MeV)	
⁶⁶ Ni/ ⁶⁶ Cu	2.275 d	β [−]	5.10 min	γ, β [−]	1.076	ERT
¹¹² Pd/ ¹¹² Ag	21.04 h	β [−]	3.14 h	γ, Auger-e, β [−]	1.380	ERT
¹³⁴ Ce/ ¹³⁴ La	3.16 d	EC	6.45 min	γ, Auger-e, β ⁺ (63%)	0.756	PET
¹⁴⁰ Nd/ ¹⁴⁰ Pr	3.37 d	EC	3.39 min	γ, Auger-e, β ⁺ (51%)	0.544	ERT, PET
¹⁶⁶ Dy/ ¹⁶⁶ Ho	3.400 d	β [−]	1.117 d	γ, Auger-e, β [−]	0.711	ERT
²¹² Pb/ ²¹² Bi	10.64 h	β [−]	1.01 h	γ, Auger-e, α (64%), β [−] (36%)	2.170	ERT
					0.492	
²¹³ Bi/ ²⁰⁹ Pb	45.6 min	β [−] , α	3.253 h	β [−]	0.198	ERT
²²⁵ Ac/chain	10.6 d	α	Various	α	Various	ERT
²²⁷ Th/ ²²³ Ra	18.7 d	α	11.4 d	α	Various	ERT

assist to focus the therapeutic efficacy to the tumor cells, which is of particular importance, since the potential usefulness of radiotherapy is often limited by the irradiation of radiation-sensitive non-target tissues. The in vivo generator is thus a potential alternative to minimize exposure.

However, the concept implies that the chemical binding of the daughter nuclide is analogous to the parent one and the daughter radionuclide is thus not released from the original position. If not, i.e., if released from the targeted tracer due to various factors, which are well known from hot atom chemistry processes, the decay product will be bound in the near surrounding environment of the parent due to other chemical or biochemical binding (such as intracellular trapping effects) or is released from the target site.

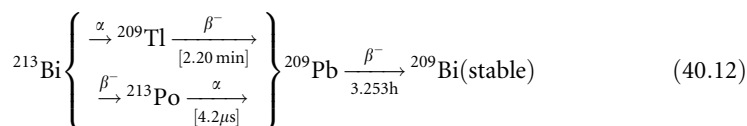
40.5.2 Examples of In Vivo Generators

Several generator pairs could potentially be utilized as in vivo systems, presuming the parent nuclide offers the adequate chemical properties for synthesis of labeled compounds and a half-life adequate to the biochemical/physiological process the labeled compound is involved. In this context, stable labeling with ^{66}Ni and ^{112}Pd , for instance, is not yet established, whereas there are reliable bifunctional chelators available to bind trivalent parent nuclides such as ^{134}Ce , ^{140}Nd , ^{166}Ho , and ^{213}Bi . The most intensively studied pair as in vivo generator is $^{166}\text{Ho}/^{166}\text{Dy}$ (Ma et al. 1993; Mirzadeh et al. 1994; Smith et al. 1995). After intravenous injection of [^{166}Dy] DTPA and accumulation of the parent nuclide in bone, no translocation of the daughter ^{166}Ho was observed subsequent to the β^- decay of ^{166}Dy .

Issues related to the possible in vivo use of the ^{103}Pd ($T_{1/2} = 16.99$ d)/ $^{103\text{m}}\text{Rh}$ ($T_{1/2} = 56.1$ min) generator have also recently been discussed on a theoretical basis (Suzcs et al. 2009; Van Rooyen et al. 2008).

Interest in the use of the in vivo generator concept for tumor therapy has reemerged with increased focus on ^{225}Ac ($T_{1/2} = 10$ days), which decays to the ^{213}Bi ($T_{1/2} = 45$ min) daughter. Although the dose rate is much lower, the integrated delivered radiation dose is much higher for administered levels of radioactivity. The use of complexed ^{225}Ac as an in vivo generator has also been evaluated by McDevitt et al. (2001), where it is described as a “nano generator.” Other studies with ^{225}Ac have demonstrated that select carboxylate-derived calixarene agents have an ionophore cavity capable of highly selective complexation of Ac^{3+} in weak acid and neutral solution. Successful functionalization of these molecules may provide other candidate chelate approaches for use of ^{225}Ac for the in vivo generator approach.

The ongoing clinical application of ^{213}Bi -radiotherapeutics themselves may already be considered as a version of an in vivo generator, as the various nuclides of the decay chains



probably stay in the vicinity of the parent nuclide cellular environment and do significantly contribute to an enhanced radiation dose in the target tissue.

However, as investigated for the $^{140}\text{Nd}/^{140}\text{Pr}$ generator system, the daughter (^{140}Pr) may quantitatively be released from initial (^{140}Nd -DOTA) complexes in, e.g., (^{140}Nd)-DOTA-octreotide compounds despite the very high thermodynamic and kinetic stability of the

trivalent lanthanide with the macrocyclic chelator (Zhernosekov et al. 2007b). This dramatic effect – different to the $^{166}\text{Ho}/^{166}\text{Dy}$ system – is explained by the difference in the radioactive decay. The electron capture $^{140}\text{Nd} \rightarrow ^{140}\text{Pr}$, namely, ruptures the initial chemical bonds of the mother radionuclide and releases a daughter atom in situ, which is not able to form complexes with DOTA-like compounds at room temperature. Thus, nuclide pairs connected by EC and ligands involved with kinetically determined complex formation characteristics are not useful as in vivo generators.

In addition, in vivo generators have been discussed in the context of radiation therapy seeds and of diagnostic tests with ultra-short-lived daughters (Lambrecht et al. 1997).

Acknowledgments

The authors thank their many colleagues and collaborators for their support and interest. Research at the Oak Ridge National Laboratory (ORNL) supported by the US Department of Energy (DOE), under contract DE-AC05-00OR22725 with UT-Battelle, LLC.

References

- Acerbi E, Birattari C, Bonardi M, Martinis CD, Salomone A (1981) *Int J Appl Radiat Isot* 32:465
- Al-Janabi MAA, Al-Hashini HF (1979) *J Radioanal Chem* 53:321
- Al-Kouraiishi SH, Boswell GGJ (1978) *Int J Appl Radiat Isot* 29:607
- Al-Nahhas A, Win Z, Szyszko T, Singh A, Nanni C, Fanti S, Rubello D (2007) *Anticancer Res* 27:4087
- Alvarez-Diez TM, deKemp R, Beanlands R, Vincent J (1999) *Appl Radiat Isot* 50:1015
- Anagnostopoulos C, Almonacid A, El Fakhri G, Curillova Z, Sitek A, Roughton M, Dorbala S, Popma JJ, Di Carli MF (2008) *Eur J Nucl Med Mol Imaging* 35:1593
- Ambe S (1988) *Appl Radiat Isot* 39:49
- Arino H, Skrabala WJ, Kramer HH (1978) *Int J Appl Radiat Isot* 29:117
- Antczak C, Jaggi JS, Lefavre CV, Curico MJ, McDewitt MR, Scheinberg DA (2006) *Bioconjug Chem* 17:1551
- Asti M, De Pietri G, Fraternali A, Grassi E, Sghedoni R, Fioroni F, Roesch F, Versari A, Salvo D (2008) *Nucl Med Biol* 35:721
- Atcher RW, Friedman AM, Huizenga JR, Rayudu GVS, Silverstein EA, Turner DA (1978) *J Nucl Med* 19:689
- Atcher RW, Friedman AM, Huizenga JR, Rayudu GVS, Silverstein EA, Turner DA (1980) *J Nucl Med* 21:565; *Int J Nucl Med Biol* 7:75
- Atcher R, Friedman AM, Hines JJ (1988) *Appl Radiat Isot* 39:238
- Atkins LH, Som P, Fairchild RG, Hui J, Schachner E, Goldman A, Ku TH (1979) *Radiology* 133:769
- Bao B, Song M (1996) *J Radioanal Nucl Chem* 213:233
- Bartos B, Bilewicz A (1995) *J Radioanal Nucl Chem Lett* 201:89
- Bartos B, Kowalska E, Bilewicz A, Skarnemark G (2007) *J Lab Compds Radiopharm* 50:S94
- Bartos B, Kowalska E, Bilewicz A, Skarnemark G (2009) *J Radioanal Nucl Chem* 279:655
- Bateman H (1910) *Proc Cambridge Philos Soc* 15:423
- Bateman TM, Heller GV, McGhie AI, Friedman JD, Case JA, Bryngelson JR, Hertenstein GK, Moutray KL, Reid K, Cullom SJ (2006) *J Nucl Cardiol* 13:24
- Bett R, Coleman GH, Cunningham JG, Sims HE, Elliot AT, Stone DL (1981) *J Nucl Med Comm* 2:75
- Bett R, Cunningham JG, Sims HE, Willis HH, Dymond DS, Flatman W, Stone DL, Elliot AT (1983) *Int J Appl Radiat Isot* 34:959
- Beyer GH, Raun HL (1991) *Appl Radiat Isot* 42:141
- Bhattacharya DK, Basu S (1979) *J Radioanal Chem* 52:267
- Bievelez P, Jacquemin R (1982) *Proceedings of the 3rd world congress of nuclear medicine and biology, vol I, 29 August–2 September, Paris, Pergamon Press, Oxford, p 621*
- Bielewicz A (1995) *Radiochim Acta* 69:127
- Birattari C, Bonardi M (1982) *Proceedings of the 3rd world congress nuclear medicine biology, vol I, 29 August–2 September, Paris, Pergamon Press, Oxford, p 1119*
- Bläuenstein P, Schwarzbach R, Zimmermann K, Schubiger PA (1996) *J Radioanal Nucl Chem* 204:94
- Bläuenstein P, Pellikka R, Schubiger PA (1997) *Appl Radiat Isot* 48:1097

- Blower PJ, Kettle AG, O'doherty MJO, Coakley AJ, Knapp FF Jr (2000) *Eur J Nucl Med* 27:1405
- Boll RA, Mirzadeh S, Kennel SJ (1997) *Radiochim Acta* 79:145
- Bormans G, Janssen A, Adriaens P, Crombez D, Wisenboer A, De Goeij J, Morelmans L, Verbruggen A (1992) *Appl Radiat Isot* 43:1437
- Boyd RE (1982) *Radiochim Acta* 30:123
- Boyd RE, Moore PW, Shying ME, Sodeau JM (1982) *Proceedings of the 3rd world congress nuclear medicine biology*, vol II, 29 August–2 September, Paris, Pergamon Press, p 1592
- Boyd RE, Heterington ELR, Moore PW (1984) Radionuclide generator technology. Status and prospects. In: *Proceedings of the international conference on radiopharmaceuticals and labeled compounds*, IAEA, October 1984, Tokyo, CN 45/102
- Boyd RE (1986) In: *Seminar on radionuclide generator technology*, Paper 21, IAEA-Sr.131
- Braun G, Shulgin AT, Sargent T III (1978) *J Lab Compds Radiopharm* 14:767
- Bray LA, Wester DW (1996) Method of preparation of yttrium-90 from strontium-90, U.S. Patent # 5,512,256, April 30, 1996
- Breeman WAP, de Jong M, de Blois E, Bernard BF, Konijnenberg M, Krenning EP (2005) *Eur J Nucl Med* 32:478
- Breeman WAP, Verbruggen AM (2007) *Eur J Nucl Med* 34:978
- Brihaye C, Guillaume M, Cogneau M (1981) *Radiochem Radioanal Lett* 48:157
- Brihaye C, Guillaume M, Lavi N, Cogneau M (1982) *J Nucl Med* 23:1114
- Brihaye C, Guillaume M, O'Brien HA Jr, Raets D, De Landesheere CH, Rigo P (1987) *Int J Appl Radiat Isot* 38:213
- Brockmann J, Schmidt A, Rösch F (1999a) *J Lab Compds Radiopharm* 42:759
- Brockmann J, Schmidt A, Rösch F (1999b) *J Lab Compds Radiopharm* 42:303
- Brown TL, Merrill J, Hill P, Bengel FM (2008) *Nuklearmedizin* 47:255
- Browne E, Firestone RB (1986) In: Shirley VS (ed) *Table of radioactive nuclides*. Wiley, New York
- Brucer M (1965) *Isot Radiat Tech* 3:1
- Bruland OS, Jostein D, Olsen DR, Larsen RH (2008) Targeted high-LET therapy of bone metastases. Chapter 10 In: Stigbrand T (et al.) (ed) *Targeted radionuclide tumor therapy*. Springer-Science, pp 181–184
- Buchman I, Bunjes D, Kotzerke J, Martin H, Glatting G, Seitz U, Rattat D, Buck A, Doehner H, Reske SN (2002) *Cancer Biother Radiopharm* 17:151
- Bugai JE, Bickel EM, Azure MT, Friebe M, Lister-James J, Dean RT, Dinkelborg LM (2002) *J Nucl Med* 43:123
- Callahan AP, Rice DE, Knapp FF Jr (1989) *Nuc Compact Eur Am Commun Nucl Med* 20:3
- Camin LD (1977) *Int J Appl Radiat Isot* 28:973
- Campbell EC, Nelson F (1956) *J Inorg Nucl Chem* 3:233
- Chakravarty R, Dash A, Kothari K, Pillai MRA, Venkatesh M (2009) *Radiochim Acta* 97:309
- Chan RC, Lacy JL, Bhargava B, Collins SD, Cates P, Cottin Y, Kollum M, Yang N, Haynes NG, Martin CA, Nayak N, Vodovotz Y, Kim H, Waksman R (2001) *Int J Radiat Biol Phys* 48:584
- Chander A, Brenner M, Lautamäki R, Voicu C, Merrill J, Bengel FM (2008) *J Nucl Med* 49:1643
- Chang MY, Siderman J, Sofou S (2008) *Bioconj Chem* 19:1274
- Chauncey EA, Chauncey DM, Schelbert HR, Halpern SE, Delano F, McKegney LM, Ashburn WL, Hagan PL (1977) *J Nucl Med* 18:933
- Cheng C, Treves S, Samuel A, Davis MA (1980) *J Nucl Med* 21:1169
- Cheng C, Treves S, Samuel A, Davis MA (1982) In: Lambrecht RM, Morcos N (eds) *Applications of nuclear and radiochemistry*. Pergamon Press, New York, p 73
- Chinol M, Hnatowich DJ (1987) *J Nucl Med* 28:1465
- Chinol M, Franceschini R, Pecorale A, Paganelli G (1996) *J Nucl Med* 37:195
- Chiu JH, Landolt RR, Kessler WV (1978) *Analyt Chem* 50:670
- Chow BJ, Wong JW, Yoshinaga K, Ruddy TD, Williams K, deKemp RA, DaSilva J, Beanlands RS (2005) *J Nucl Med* 46:1095
- Clark JC, Horlock PL, Watson IA (1976) *Radiochem Radioanal Lett* 25:245
- Colombetti LG, Mayrose LW, Kaplan E, Barnes WE, Friedman AM, Gindler JE (1974) *J Nucl Med* 15:868
- Dadachova E, Lambrecht RM, Hetherington E (1994) *J Radioanal Nucl Chem Lett* 188:267
- Dadachova E, Mirzadeh S, Lambrecht RM, Hetherington E, Knapp FF Jr (1995a) *Anal Chem* 66:4272
- Dadachova E, Mirzadeh S, Lambrecht RM, Hetherington EL, Knapp FF Jr (1995b) *J Radioanal Nucl Chem Lett* 199:115
- Daniels RJ, Grant PM, O'Brien HA Jr (1978) *Nucl Med Biol* 5:11
- Daniels RJ, Grant PM, O'Brien HA Jr (1987) *J Nucl Med Biol* 36:326
- Das NR, Bhattacharya SN (1982) *Int J Appl Radiat Isot* 33:171
- Das NR, Singh K, Lahiri S (1993) *Radiochim Acta* 62:213
- Das SK, Nair AGC, Chatterjee RK, Guin R, Saha SK (1996) *Appl Radiat Isot* 47:643
- Decristoforo C et al (2005) Radioactive isotopes in clinical medicine and research. In: 27th international symposium, Bad Gastein, Austria, 11–14 January 2006, *Nuklearmedizin*, 6:A191

- Decristoforo C, Knopp R, von Guggenberg E, Rupprich M, Dreger T, Hess A, Virgolini I, Haubner R (2007) *Nucl Med Commun* 28:870
- Dimitrakopoulou-Strauss A, Georgoulis V, Eisenhut M, Herth F, Koukouraki S, Mäcke HR, Haberkorn U, Strauss LG (2006) *Eur J Nucl Med Mol Imaging* 33:823
- Diksic M, Yaffe L (1977) *J Inorg Nucl Chem* 39:1299
- Dorbaia S, Hachamovich R, Curillova Z, Thomas D, Vangala D, Kwong RY, Di Carli MF (2009) *JACC Cardiovasc Imaging* 2:846
- Dorbala S, Vangala D, Sampson U, Limaye A, Kwong R, Di Carli MF (2007) *J Nucl Med* 48:349
- Dorbala S, Hachamovitch R, Curillova Z, Thomas D, Vangala D, Kwong RY, Di Carli MF (2009) *JACC Cardiovasc Imaging* 2:846
- Eisner RL, Patterson RE (2007) *J Nucl Med* 48:1912
- El Fakhri G, Sitek A, Guérin B, Kijewski MF, Di Carli MF, Moore SC (2005) *J Nucl Med* 46:1264
- Epperson CE, Landolt RR, Kessler WV (1976) *Analyt Chem* 48:979
- Epstein N, Benelfassi A, Beanlands R, DeKemp RA (2004) *Appl Radiat Isot* 60:921
- Erdal BR, Grant PM, Casella VR, Ogard AE, O'Brien Jr HA (1975) *Proceedings of the conference on nuclear cross sections and technology*, NBS-Special Publication, Washington, DC, p 425, 492
- Erhardt GJ, Welch MJ (1978) *J Nucl Med* 19:925
- Erhardt GJ, Volkert W, Goeckeler WF (1981) *J Lab Compds Radiopharm* 18:65
- Erhardt GJ, Ketrang AR, Liang Q (1992) *Radioact Radiochem* 3:38
- Fani M, André JB, Maecke H (2008) *Contrast Media Molecular Imaging* 3:67
- von Falck C, Boerner AR, Galanski M, Knapp WH (2007) *Eur J Nucl Med Mol Imaging* 34:812
- Failla G (1920) U.S. Patents 1-553-794; 1-609-614
- Fessler A, Alfassi ZB, Qaim SM (1994) *Radiochim Acta* 65:207
- Filosofov DV, Loktionova NS, Rösch F (2010) *Radiochim Acta* 98:149
- Fink RW, Andersen G, Kantele J (1961) *Ark Fys* 19:323
- Finn R, Vora M, Boothe T, Campbell J, Carroll S, Clark K (1982) *Int J Appl Radiat Isot* 33:349
- Finn RD, Molinski VJ, Hupf HB, Kramer H (1983) In: *Nuclear science series – nuclear medicine*, NAS-NS-3202 (De83016360), U.S. DOE
- Flower MA, Zweit J, Hall AD, Burke D, Davies MM, Dworkin MJ, Young HE, Mundy J, Ott RJ, McCreedy VR, Carnochan P, Allen-Mersh TG (2001) *Eur J Nucl Med Mol Imaging* 28:99
- Franken PR, Dobbeler A, Ham HR, Brihaye C, Guillaume M, Knapp FF Jr, Vandevivere J (1989) *J Nucl Med* 30:1025
- Franken PR, Dobbeler A, Ham HR, Ranquin R, Lieber S, Van Den Branden F, Van Den Heuvel P, Brihaye C, Guillaume M, Knapp FF Jr, Vandevivere J (1991) *Nucl Med Commun* 12:473
- Friedlander G, Kennedy JW, Macias ES, Miller JM (1981) *Nuclear and radiochemistry*, 3rd edn. Wiley, New York
- Fujibayashi F, Matsumoto K, Konishi J, Yokoyama A (1989) *J Nucl Med* 30:1838
- Fujiyabasyi Y, Matsumoto K, Arano Y, Yonekura Y, Konishi J, Yokohama A (1990) *Chem Pharm Bull* 38:1946
- Fujibayashi Y, Taniuchi H, Yonekura Y, Ohtani H, Konishi J, Yokoyama A (1997) *J Nucl Med* 38:1155
- Fukumura T, Okada K, Suzuki H, Nakaro R, Mukai K, Szelecesenyi F, Kovacs Z, Suzuki K (2006) *Nucl Med Biol* 33:821
- Gabriel M, Decristoforo C, Kendler D, Dobrozemsky G, Heute D, Uprimny C, Kovacs P, Van Guggenburger E, Bale R, Virgolini IJ (2007) *J Nucl Med* 48:508
- Gabriel M, Oberauer A, Dobrozemsky G, Decristoforo C, Putzer D, Kendler D, Uprimny C, Kovacs P, Bale R, Virgolini IJ (2009) *J Nucl Med* 50:1427
- Garcia E, Mena I, Dejong R (1981) *J Nucl Med* 22:71
- Geerlings MW, Kaspersen FM, Apostolidis C, Van Der Hout R (1993) *Nucl Med Commun* 14:121
- Gennaro GP, Neirinx RD, Bergner B, Muller WR, Waranis A, Haney TA, Barker SL, Loberg MD, Yarnais A (1984) In: Knapp FF Jr, Butler TA (eds) *Radionuclide generators: new systems for nuclear medicine applications*, vol 241, ACS symposium series. American Chemical Society, Washington, DC, p 135
- Gleason GI (1960) *Int J Appl Radiat Isot* 8:90
- Gibbons RJ, Chareonthaitawee P (2009) *JACC Cardiovasc Imaging* 2:855
- Grant PM, Erdal BR, O'Brien HA Jr (1977) *J Nucl Med* 16:46
- Grant PM, Whipple RE, O'Brien HA Jr, Kultrathipanja SJ (1978) *J Nucl Med* 19:1250
- Grant PM, O'Brien HA Jr, Bayhurst BP, Gilmore RJ, Prestwood RJ, Whipple RE, Wanek PM (1979) *J Lab Compds Radiopharm* 16:213
- Grant RM, Daniels RJ, Daniels WJ, Bentley GE, O'Brien HA Jr (1981) *J Lab Compds Radiopharm* 18:61
- Grant PM, Millers DA, Gilmore JS, O'Brien HA Jr (1982) *Int J Appl Radiat Isot* 33:415
- Grant PM, Daniels RJ, Daniels WJ, Bentley GE, O'Brien HA Jr (1985) *J Radioanal Nucl Chem Lett* 96:629
- Green MA, Mathias CJ, Welch MJ, McGuire AH, Perry D, Fernandez-Rubio F, Perlmutter JS, Raichle ME, Bergmann SR (1990) *J Nucl Med* 31:1989
- Greene MW, Tucker WD (1961) *Int J Appl Radiat Isot* 12:62
- Greene MW, Hillman M (1967) *Int J Appl Radiat Isot* 18:540
- Grütter A (1982) *Int J Appl Radiat Isot* 33:725
- Guhlke S, Beets AL, Mirzadeh S, Biersack H-J, Knapp FF Jr (2000) *J Nucl Med* 41:1271
- Guillaume M, Czichosz R, Richard P, Fagard E (1983) *Bull Soc Roy Liège* LII:213

- Guillaume M, Brihaye C (1986) *Int J Appl Radiat Isot* 13:89
- Guillaume M, Brihaye C (1987) *Radiochim Acta* 41:119
- Hagebo E, Haldorsen IR, Mostue MB, Pettersen J, Scheidemann O (1984) *Radiochim Acta* 35:133
- Harper PV, Andros G, Lathrop K (1962) USAEC report ACRH-18, p 788
- Hassfjell S, Brechbiel MW (2001) *Chem Rev* 101:2019
- Haynes NE, Lacy JL, Nayak N, Martin CS, Dai D, Mathias CJ, Green MA (2000) *J Nucl Med* 41:309
- Heller GC, Treves ST, Parker JA, Duke LA, O'Brien GM, Davis RT, Fitzgibbon C, Pakcard AB (1986) *J Am Coll Card* 7:1295
- Hendricksen G, Hoff P, Alstad J, Larsen RH (2001) *Radiochemica Acta* 89:661
- Henze M, Schuhmacher J, Dimitrakopoulou-Strauss A, Strauss LG, Mäcke HR, Eisenhut M, Haberkorn U (2004) *Eur J Nucl Med Mol Imaging* 31:466
- Henze M, Dimitrakopoulou-Strauss A, Milker-Zabel S, Schuhmacher J, Strauss LG, Doll J, Mäcke HR, Eisenhut M, Debus J, Haberkorn U (2005) *J Nucl Med* 46:763
- Heo J, Htay T, Mehata D, Sun L, Lacy J, Iskandrian AE (2005) *J Nucl Card* 12:560
- Herrero P, Hartmann J, Green MA, Anderson C, Welch MJ, Markham J, Bergmann J (1996) *J Nucl Med* 37:1294
- Herscheid JDM, Vos CM, Hoeckstra A (1983) *Int J Appl Radiat Isot* 14:883
- Hnatowich DJ (1977) *Int J Appl Radiat Isot* 28:169
- Hnatowich DJ, Kulprathiapanya S, Treves S (1977) *Radiology* 123:189
- Hoehner M, Woerle J, Wohlfrom M, Hanke H, Voisard R, Osterhaus HH, Kochs M, Reske SN, Hombach V, Kotzerke J (2000) *Circulation* 101:2355
- Hofmann M, Maecke H, Börner R, Weckesser E, Schöffski P, Oei L, Schumacher J, Henze M, Heppeler A, Meyer J, Knapp H (2001) *Eur J Nucl Med* 28:1751
- Holman BL, Harris GI, Neirinckx RD, Jones AG, Idoine J (1978) *J Nucl Med* 19:510
- Hong YD, Park KB, Jang BS, Choi SJ, Choi SM, Kim YM (2002) *Nucl Med Biol* 29:833
- Horiguchi T, Noma H, Yoshizawa Y, Takemi H, Hasai H, Kiso Y (1980) *Int J Appl Radiat Isot* 31:141
- Horiguchi H, Kumahora H, Inoue H, Yoshizawa Y, Noma H, Yoshizawa Y (1982) *Int J Appl Radiat Isot* 34:1531
- Horlock PL, Clark JC, Goodier IW, Barnes JW, Bentley GE, Grant PM, O'Brien HA Jr (1981) *J Radioanal Chem* 62:257
- Hsieh BT, Hsieh TH, Tsai ZT, Ting G (1991) *Nucl Sci* 28:413
- IAEA (2001) Charged particle cross section database for medical radioisotope production: diagnostic radioisotopes and monitor reactions, IAEA-TECDOC-1211, International Atomic Energy Agency, Vienna, <http://www-nds.iaea.or.at/medical/Gap68Ge0.html>
- Issacher D, Abrashkin S, Weiniger J, Zemach D, Lubin E, Hwllman C, Trumper D (1989) *J Nucl Med* 30:538
- Jannsen AGM, Claessens RAMJ, van den Bosch RLP, de Goeji JMM (1986) *Int J Appl Radiat Isot* 37:297
- Jannsen AGM, De Goeji JMM, Witsenboer AJ, Van den Broek JFCM (1990) *Appl Radiat Isot* 41:847
- Jannsen AGM, Witsenboer AJ, De Goeji JMM, Wijnhoven GPJ (1992) *J Lab Compds Radiopharm* 30:478
- Javadi M, Mahesh M, McBride G, Voicu C, Epley W, Merrill J, Bengel FM (2008) *J Nucl Cardiol* 15:783
- Jennewein M, Schmidt A, Novgorodov AF, Qaim SM, Rösch F (2004) *Radiochim Acta* 92:245
- Jennewein M, Hermanne A, Mason RP, Thorpe PE, Rösch F (2006) *Nucl Instr Methods A* 569:512
- Jennewein M, Lewis MA, Zhao D, Tsyganov E, Slavine N, He J, Watkins L, Kodibagkar VD, O'Kelly S, Kulkarni P, Antich PP, Hermanne A, Rösch F, Mason RP, Thorpe PE (2008) *Clin Cancer Res* 14:1377
- Jeong JM, Kim YJ, Lee YS, Ko JI, Son M, Lee DS, Chung J-K, Park JH, Lee MC (2001a) *Nucl Med Biol* 48:197
- Jeong JM, Kim YJ, Lee YS, Chung JC, Cho JH, Suh YG, Lee MC (2001b) *J Lab Compds Radiopharm* 44(Suppl 1):532
- Jeong J-M, Knapp FF Jr (2008) *Sem Nucl Med* 38:S19
- Jones T, Clark JC (1969) *Brit J Radiol* 42:237b
- Jones T, Clark JC, Hughes JM, Rosenzweig DY (1970) *J Nucl Med* 11:118
- Kariemo KJ, Kestila MS, Savolainen S, Hiltunen J, Svahn RI, Korppi-Tommola ET, Knapp FF Jr, Brihaye C (1994) *J Nucl Med Biol* 4:86
- Kastleiner S, Qaim SM, Nortier FM, Blessing G, Van Der Walt TN, Coenen HH (2002) *Appl Radiat Isot* 56:685
- Ketring AR, Ehrhardt GJ, Embree MF, Bailey KD, Tyler TT, Gawenis JA, Jurisson SS, Englebrecht HP, Smith CJ, Cutler CS (2002) *Revista Medicina Nuclear Alasbimn* J 5:1
- Khan MU, Khan S, El-Refaie S, Win Z, Rubello D, Al-Nahhas A (2009) *Eur J Surg Oncol* 35:561
- Klein R, Adler A, Beanlands RS, Dekemp RA (2007) *Phys Med Biol* 7:659
- Knapp FF Jr, Butler TA (eds) (1984) *Radionuclide generators: new systems for nuclear medicine applications*, vol 241, ACS symposium series. American Chemical Society, Washington, DC
- Knapp FF Jr, Mirzadeh S, Callahan AP (eds) (1992) *Symposium on radionuclide generator systems for nuclear medicine applications*, August 1992, American Chemical Society, Washington, DC, *Radioact Radiochem (Special Issue)*:3
- Knapp FF Jr, Callahan AP, Betts AL, Mirzadeh S, Hsieh B-T (1994) *Appl Radiat Isot* 45:1123
- Knapp FF Jr, Mirzadeh S (1994) *Eur J Nucl Med* 21:1151

- Knapp FF Jr, Betts AL, Guhlke S, Zamora PO, Bender H, Palmedo H, Biersack H-J (1997) *Antican Res* 17:1783
- Knapp FF Jr, Beets AL, Guhlke S, Giedd KN, Marboe C, Amols H, Weinberger J (1998a) *J Nucl Med* 39:48
- Knapp FF Jr, Guhlke S, Beets AL, Lin WY, Stabin M, Amols H, Weinberger J (1998b) *Cardiovasc Rad Med* 1:86
- Knapp FF Jr, Spencer R, Kropp J (2001) *J Nucl Med* 42:1384
- Knesaurek K, Machac J, Krynyckyi BR, Almeida OD (2003) *J Nucl Med* 44:1350
- Knesaurek K, Machac J, Ho Kim J (2007) *BMC Nucl Med* 22:4
- Knesaurek K, Machac J, Zhang Z (2009) *BMC Med Phys* 29:2
- Koukouraki S, Strauss LG, Georgoulas V, Schuhmacher J, Haberkorn U, Karkavitsas N, Dimitrakopoulou-Strauss A (2006a) *Eur J Nucl Med Mol Imaging* 33:460
- Koukouraki S, Strauss LG, Georgoulas V, Eisenhut M, Haberkorn U, Dimitrakopoulou-Strauss A (2006b) *Eur J Nucl Med Mol Imaging* 33:1115
- Kopecky P, Mudrova B, Svoboda K (1973) *Int J Appl Radiat Isot* 24:73
- Kopecky P, Mudrova B (1974) *Int J Appl Radiat Isot* 25:263
- Kotzerke J, Hanke J, Hoher M (2000) *Eur J Nucl Med* 27:223
- Kovács Z, Tárkányi F, Qaim SM, Stöcklin G (1991) *Appl Radiat Isot* 42:329
- Krizek H, Harper PV, Grant PM, Barnes HA, O'Brien HA Jr (1977) *J Nucl Med* 18:609
- Kropp J, Reynen K, Koeckeritz U, Wunderlich G, Schmeisser A, Strasse RH, Knapp FF Jr (2002) *World J Nucl Med* 1(Suppl 2):13
- Ku TH, Richards P, Stang LG Jr, Pracht T (1979a) *Radio-pharmaceuticals. Society of Nuclear Medicine, New York*, p 745
- Ku TH, Richards P, Stang LG Jr, Pracht T (1979b) *Radiology* 132:475
- Kueppers G (1999) *J Radionucl Chem* 241:503
- Kurnevich GI, Vishnevskii VB, Loiko EM (1974) *Russ J Inorg Chem* 19:375
- Lacy JL, Ball ME, Verani MS, Wiles HB, Babich JW, Leblanc AD, Stabin M, Bolomey L, Roberts R (1988a) *J Nucl Med* 29:1526
- Lacy JL, Verani MS, Ball ME, Boyce TM, Gibson RW, Roberts R (1988b) *J Nucl Med* 29:293
- Lacy JL, Layne WW, Guidry GW, Verani MS, Roberts R (1991) *J Nucl Med* 32:2158
- Lacy JL, Nanavaty T, Dai D, Nayak N, Haynes N, Martin C (2001) *J Nucl Card* 8:171
- Lagunas-Solar MC, Little FE, Moore HA Jr (1982) *Int J Appl Radiat Isot* 33:619
- Lagunas-Solar MC, Carvacho OF, Liu B-L, Jin Y, Sun ZX (1986) *Int J Appl Radiat Isot* 37:823
- Lagunas-Solar MC, Carvacho OF, Yang S-T, Yano Y (1990) *Appl Radiat Isot* 41:521
- Lambrecht RM, Wolf AP (1970) *J Lab Compds Radiopharm* 16:129
- Lambrecht RM, Lynn KG (1976) *Proceedings of the 4th international conference on positron annihilation, Helsingør, Denmark, 23–26 August, H17*
- Lambrecht RM, Norton E, Wolf AP, Treves S (1977) *J Lab Compds Radiopharm* 12:245
- Lambrecht RM (1983) *Radiochim Acta* 34:9
- Lambrecht RM, Sajjad M (1988) *Radiochim Acta* 43:171
- Lambrecht RM, Tomiyoshi K, Sekine T (1997) *Radiochim Acta* 77:103
- Larsen SH, Borrebaek J, Dahle J, Melhus KB, Krogh MH, Valan MH, Bruland OS (2007) *Can Biother Radiopharm* 22:431
- Lebedev NA, Herrmann E, Echn L (1984) *Radiochimija* 26:223
- Lee JS, Lee J-S, Park U-J, Son K-J, Han H-S (2009) *Appl Radiat Isot* 67:1162
- Lebowitz E, Richards P (1974) *Sem Nucl Med* 4:257
- Lewis RE, Camin LL (1960) *J Lab Compds Radiopharm* 18:164
- Lewis RE, Eldridge JS (1966) *J Nucl Med* 7:804
- Lertsburapa K, Ahlberg AW, Bateman TM, Katten D, Volker L, Cullom SJ, Heller GV (2008) *J Nucl Cardiol* 15:745
- Lieser KH (1976) *Radiochim Acta* 23:57
- Lin T-K, Tsai Z-T, Campbell J, Carroll S, Clark J (1982) *Int J Appl Radiat* 33:349
- Lin J-W, Sciacca RR, Chou R-L, Laine AF, Bergmann SR (2001) *J Nucl Med* 42:201
- Lindner M, Perlman I (1950) *Phys Rev* 73:1124
- Liu BL, Kung HF, Jin YT, Meng M (1989) *J Nucl Med* 30:367
- Loc'h C, Maziere B, Comar D (1980) *J Nucl Med* 21:171
- Lodge MA, Braess H, Mahmoud F, Suh J, Englar N, Geyser-Stoops S, Jenkins J, Bacharach SL, Dilsizian V (2005) *J Invasive Cardiol* 17:491
- Lopci E, Nanni C, Rampin L, Rubello D, Fanti S (2008) *Minerva Endocrinol* 22:277
- Lortie M, Beanlands RS, Yoshinaga K, Klein R, Dasilva JN, DeKemp RA (2007) *Eur J Nucl Med Mol Imaging* 34:1765
- Lubberink M, Lundqvist H, Tolmachev V (2002a) *Phys Med Biol* 47:615
- Lubberink M, Tolmachev V, Widström C, Bruskin A, Lundqvist H, Westlin J-E (2002b) *J Nucl Med* 43:1391
- Luboldt W, Zöphel K, Wunderlich G, Abramuk A, Luboldt HJ, Kotzerke J (2010) *Mol Imaging Biol* 12:78–79
- Lyster DM, Thaller R, Vincent JS, Dougan H, Morrison RT (1982) In: Lambrecht RM, Morcos N (eds)

- Application of nuclear and radiochemistry. Pergamon, New York, pp 45–56
- Ma D, Jurisson SS, Erhardt GJ, Yelon WB, Ketrang AR (1993) *J Nucl Med* 34:231
- Madhusudhan CP, Treves S, Wolf AP, Lambrecht RM (1979) *J Radioanal Chem* 53:299
- Maecke HR, Hofmann M, Haberkorn U (2005) *J Nucl Med* 46:172S
- Makkar R, Whiting JA, Hidehiko H, Fishbien MC, Knapp FF Jr, Litvack F, Eigler NL (2000) *Circulation* 102:3117
- Malyshev KV, Smirnov VV (1975) *Sov Radiochim* 17:137
- Manabe O, Yoshinaga K, Katoh C, Naya M, deKemp RA, Tamaki N (2009) *J Nucl Med* 50:68
- Mani RS (1987) *Radiochim Acta* 41:103
- Mansur MS, Mushtaq A, Muhammad A (1995) *J Radioanal Nucl Chem Lett* 201:205
- Mathias CJ, Welch MJ, Raichle ME, Mintun MA, Linch LL, McGuire AH, Zinn KR, John E, Green MA (1990) *J Nucl Med* 31:351
- Mathias CA, Kung HF, Budinger TF, Wong PJ, Coxson PG, Brennan KM (1991a) *J Nucl Med* 32:974, abstract
- Mathias CJ, Welch MJ, Green MA, Til H, Meares CF, Gropler RJ, Bergman SR (1991b) *J Nucl Med* 32:475
- Mathis CA, Sargent T III, Shulgin AT (1985) *J Nucl Med* 26:1295
- Mathis CA, Lagunas-Solar MC, Sargent T III, Yano Y, Vuletic A, Harris LJ (1986) *Appl Radiat Isot* 37:258
- Mausner LE, Straub RF, Srivastava SC (1989) *J Lab Compds Radiopharm* 26:177
- McDevitt MR, Finn RD, Sgorous G, Ma D, Scheinberg DA (1999a) *Appl Radiat Isot* 50:895
- McDevitt MR, Finn RD, Ma D, Larson SM, Scheinberg DA (1999b) *J Nucl Med* 40:1722
- McDevitt MR, Ma D, Lai LT, Simon J, Borrrhardt P, Frank RK, Wu K, Pelligrini V, Curcio MJ, Miederer M, Rander NH, Scheinberg DA (2001) *Science* 294:1537
- McElvany KD, Hopkins KT, Welch MJ (1984) *Int J Appl Radiat Isot* 35:521
- Mena I (1985) In: Paras P, Thiessen JW (eds) Single-photon ultrashort-lived radionuclides, Proceedings of the symposium held in Washington, DC, 9–10 May 1983, US DOE, Nat. Tech. Inform. Service, Conf-830504 (De 83017017), 19
- Meyer G-J, Mäcke HR, Schuhmacher J, Knapp WH, Hofmann M (2004) *Eur J Nucl Med* 31:1097
- Meyer G-J, Gielow P, Börner ARJ, Hofmann M, Knapp WH, (2005) *Eur J Nucl Med* 31:1097; 27th international symposium on radioactive isotopes in clinical medicine and research, 11–14 January 2006, Bad Gastein, Austria. *Nuklearmedizin*, 6:A192
- Miederer M, Seidl S, Buck A, Scheidhauer K, Wester HJ, Schwaiger M, Perren A (2009) *Eur J Nucl Med Mol Imaging* 36:48
- Milker-Zabel S, Zabel-du Bois A, Henze M, Huber P, Schulz-Ertner D, Hoess A, Haberkorn U, Debus J (2006) *Int J Radiat Oncol Biol Phys* 1:222
- Mikheev NB, Popovich VB, Rumer IA, Savel'ev GI, Volkova NL (1972) *Nuclidenpraxis* 8:248
- Mirza MY, Aziz A (1969) *Radiochim Acta* 11:43
- Mirzadeh S, Lambrecht RM (1980) *Int J Appl Radiat Isot* 31:351
- Mirzadeh S, Dibartolo N, Smith SV, Lambrecht RM (1994) 10th International symposium radiopharmaceutical chemistry, 25–28 October 1994, Kyoto, J Lab Compds Radiopharm 276
- Mirzadeh S, Knapp FF Jr (1996) *J Radioanal Nucl Chem* 203:471
- Mirzadeh S, Lambrecht RM (1996) *Radioanal Nucl Chem* 202:7
- Mirzadeh S, Knapp FF Jr, Lambrecht RM (1997) *Radiochim Acta* 77:99
- Mirzadeh S (1998) *Appl Radiat Isot* 49:345
- Moerlein SM, Mathis CA, Brennan KM, Buddinger TF (1987) *Int J Appl Radiat Isot* 14:91
- Mushtaq A, Qaim SM, Stöcklin G (1988) *Appl Radiat Isot* 39:1085
- Mushtaq A, Qaim SM (1990) *Radiochim Acta* 50:27
- Nakayama M, Haratake M, Ono M, Koiso T, Harada K, Nakayama H, Yahara S, Ohmomo Y, Arano Y (2003) *Appl Radiat Isot* 58:9
- Neirinckx RD (1977) *Int J Appl Radiat Isot* 28:808
- Neirinckx RD, Jones AG, Davis MA, Harris GI, Holman BL (1978) *J Nucl Med* 19:154
- Neirinckx RD, Ku T, Holman BL, Jones AG, Richards P (1979) *Int J Appl Radiat Isot* 30:341
- Neirinckx RD, Davis MA (1980) *J Nucl Med* 21:81
- Neirinckx RD, Davis MA, Holman BL (1981) *Int J Appl Radiat Isot* 32:85
- Neirinckx RD, Kronauge JE, Gennaro GP, Loberg MD (1982) *J Nucl Med* 23:245
- Nilsson S, Franzen L, Parker C, Tyrell C, Blom R, Tennevall J, Lenners B, Petersson U, Johannessen DC, Sokail M, Pigott K, Yachnin J, Garkavij M, Strang P, Harmenberg J, Bolstad B, Bruland OS (2007) *Lancet Oncol* 8:587
- Nilsson S, Larsen RH, Fossa SD, Balteskard L, Borch KW, Westin JE, Solberg G, Bruland OS (2005) *Clin Can Res* 11:4451
- Norton EF, Kondo K, Lambrecht RM, Wolf AP, Treves S (1978) *J Radioanal Chem* 44:207
- Novgorodov AF, Bruchertseifer F, Brockmann J, Lebedev NA, Rösch F (2000) *Radiochim Acta* 88:163
- Novgorodov AF, Schmidt A, Brockmann J, Qaim SM, Rösch F (2001) *J Lab Compds Radiopharm* 44:778
- Novgorodov AF, Filossofov DV, Zernosekov KP, Korobeinikov A, Lebedev NA, Korolev NA, Beyer G-J, Rösch F, the ISOLDE collaboration (2002) COST D18 workshop on lanthanide chemistry for diagnosis and therapy, 23–25 July 2002, Heidelberg, abstracts, p 29

- Nowak B, Meyer JMA, Goergen T, Fluehs D, Block S, Guenther RW, Howecker H, Buell U (2001) *Cardiovasc Rad Med* 2:246
- Nozaki T, Itoh Y, Ogawa K (1979) *Int J Appl Radiat Isot* 30:595
- Nye JA, Esteves F, Votaw JR (2007) *Med Phys* 34:1901
- Nyuki F, Plotkin M, Graf R, Michel R, Steffen I, Denecke T, Geworski L, Fahdt D, Brenner W, Wurm R (2010) *Eur J Nucl Mol Imaging* 37:310
- Ofluoglu S, Schwameis E, Zehetgruber H, Havlik E, Wanivenhaus A, Schweeger I, Weis K, Sinzinger H, Pirich C (2002) *J Nucl Med* 43:1489
- Okazawa H, Yonekura Y, Fushibayashi Y, Nishizawa S, Magata Y, Ishizu K, Tanaka F, Tamaki N, Konishi J (1994) *J Nucl Med* 35:1910
- Organessiant YuTa, Karamian SA, Gangrski YP, Gorski B, Markov BM, Szieglowski Z, Briancon Ch, Ledu D, Meunier R, Hussannois M, Constantinescu O, Subbotin MI (1992) *J Phys G Nucl Part Phys* 18:393
- Packard AB, O'Brien GM, Treves T (1986) *Nucl Med Biol* 13:519
- Packard AB, Treves T, O'Brien GM (1987) *J Nucl Med* 28:1571
- Padhy AJ, Raoul J-L, Zanzonica PB, Stare J (2008) *Sem Nucl Med* 38:55
- Palmedo H, Guhlke S, Bender H, Sartor J, Schoeneich G, Risse J, Grünwald F, Knapp FF Jr, Biersack H-J (2000) *Eur J Nucl Med* 27:123
- Panek KJ, Lindeyer J, Van Der Vlugt HC (1984) In: Knapp FF Jr, Butler TA (eds) *Radionuclide generators – new systems for nuclear medicine applications*, vol 242, ACS symposium series. American Chemical Society, Washington, DC, p 3
- Panek KJ, Lindeyer J, Van Der Vlugt HC (1985) In: Paras P, Thiessen JW (eds) *Single-photon ultrashort-lived radionuclides*, Proceedings of the symposium held in Washington, DC, 9–10 May 1983, U.S. DOE, Nat. Tech. Inform. Service, Conf-830504 (De 83017017), 202
- Paras P, Thiessen JW (eds) (1985) In: *Single-photon ultrashort-lived radionuclides*, Proceedings of the symposium held in Washington, DC, May 1983, U.S. DOE Symp. Ntis Conf-830504 (De 83017017)
- Park SW, Hong MK, Moon DH, Oh SJ, Lee CW, Kim JJ, Park SJ (2001) *J Amer Coll Card* 38:631
- Parkash R, deKemp RA, Ruddy TD, Kitsikis A, Hart R, Beauchesne L, Williams K, Davies RA, Labinaz M, Beanlands RS (2004) *J Nucl Cardiol* 11:440
- Phillips DR, Nix DA (1989) *CONF-891206*, p 608
- Phillips DR, Hamilton VT, Taylor MD, Farnham JE, Emran AM, Rowe RW, Pattel D (1992) *Radioact Radiochem* 3:53
- Pruszyński M, Loktionova NS, Filosofov DV, Rösch F (2010) *Appl Radiat Isot* 68:1636
- Putzer D, Gabriel M, Henninger B, Kendler D, Uprimny C, Dobrozemsky G, Decristoforo C, Bale RJ, Jaschke W, Virgolini I (2009) *J Nucl Med* 50:1213
- Qaim SM, Döhler H (1984) *Int J Appl Radiat Isot* 35:645
- Qaim SM (1987) *Radiochim Acta* 41:111
- Rahmim A, Tang J, Lodge MA, Lashkari S, Ay MR, Lautamäki R, Tsui BM, Bengel FM (2008) *Phys Med Biol* 53:5947
- Rajendran JG, Eary JF, Bensinger W, Durack LD, Vernon C, Fritzberg A (2002) *J Nucl Med* 43:1383
- Rao SA, Chandra R, Braunstein P (1976) *Int J Appl Radiat Isot* 27:589
- Rao SA, Chandra R, Braunstein P (1977) *Int J Appl Radiat Isot* 28:973
- Razbash AA, Sevastianov YuG, Krasnov NN, Leonov AI, Pavlikhin VE (2005) *Proceedings of the 5th international conference on isotopes (5ICI)*, Brussels, Belgium, 25–29 April 2005, Bologna, Medimond 2005, 147
- Ramamoorthy N, Mani RS (1976) *Radiochem Radioanal Lett* 27:175
- Richards P (1960) A survey of the production at Brookhaven National Laboratory of radioisotopes for Medical research in V congresso nucleare “Rome”, comitato nazionale ricerche nucleari 2:223–244
- Richards P, Ku TH (1979) *Int J Appl Radiat Isot* 30:250
- Rizzo-Padoni N, Farina A, Le Pen C, Duet M, Mundler O, Leverage R (2001) *Nucl Med Commun* 22:375
- Robinson GD Jr, Zieleinski FW, Lee AW (1980) *J Appl Radiat Isot* 31:111
- Rösch F, Brockmann J, Lebedev NA, Qaim SM (1999) *J Lab Compds Radiopharm* 42:927
- Rösch F, Brockmann J, Lebedev NA, Qaim SM (2000) *Acta Oncologica* 39:727
- Rösch F, Brockmann J, Grimm J (2003) *Annual report*, Institute of Nuclear Chemistry, University Mainz
- Rösch F, Filosofov DV (2009) *Radionuclide generators using long parent radionuclides for medical applications*. In: IAEA-TEC-DOC Production, radiochemical processing and quality evaluation of Ge-68 suitable for production of a $^{68}\text{Ge}/^{68}\text{Ga}$ generator, International Atomic Energy Agency, Vienna
- Rösch F, Riss P (2010) *Current topics in medicinal chemistry* (in press)
- Rosman J, Hanon S, Shapiro M, Schweitzer P, Van Tosh A (2005) *Am J Cardiol* 96:42
- Ruth TJ, Lambrecht RM, Wolf AP (1980) *Int J Appl Radiat Isot* 31:51
- Ruth TJ, Pate BD, Robertson R, Porter JK (1989) *Nucl Med Biol* 16:323
- Rutherford E, Soddy F (1902) *Philos Mag* 4:370; Part II 4:569
- Rutherford E, Soddy F (1903) *Radioactive Charge* 5:576
- Sajjad M, Lambrecht RM (1986) *Anal Chem* 58:667
- Sakar S, Bhattacharya SN (1979) *J Radioanal Chem* 54:355

- Sarkar SK, Arjun G, Saraswathy P, Ramamoorthy N (2001) *Appl Radiat Isot* 55:561
- Savio E, Gaudiano J, Robles AM, Balter H, Paolino A, López A, Hermida JC, De Marco E, Martinez G, Osinaga E, Knapp FF Jr (2001) *BMC Nucl Med* 1(23):1471
- Schleipman AR, Castronovo FP Jr, Di Carli MF, Dorbala S (2006) *J Nucl Cardiol* 13:378
- Schuelen H, Eigler N, Whiting JS, Haubner R, Hausleiter J, Dirschinger J, Kastrati A, Schwaiger M, Schömig A (2001) *Amer J Cardiol* 87:463
- Schumacher J, Maier-Borst W (1981) *Int J Appl Radiat Isot* 32:31
- Schuster DM, Halkar RK, Esteves FP, Garcia EV, Cooke CD, Syed MA, Bowman FD, Votaw JR (2008) *Mol Imaging Biol* 10:201
- Schwarzbach R, Smith-Jones PM, Leenders KL, Weinreich R, Mäcke M, Tschidin P, Blauenstein P, Schubiger PA (1991) *Proceedings of the 4th European symposium on radiopharmaceuticals, Baden*, p 106
- Seidl VE, Lieser KH (1973) *Radiochim Acta* 19:196
- Shelton ME, Green MA, Mathias CJ, Welch MJ, Bergmann SR (1989) *J Nucl Med* 30:1843
- Shelton ME, Green MA, Mathias CJ, Welch MJ, Bergmann SR (1990) *Circulation* 82:990
- Shi H, Santana CA, Rivero A, Sanyal R, Esteves FP, Verdes L, Ornelas M, Folks RD, Lerakis S, Halkar RK, Garcia EV (2007) *Nucl Med Commun* 28:859
- Skarnemark G, Odegaard-Jense A, Nilsson J, Bartos B, Kowalska E, Bilewicz A, Bernhardt P (2009) *J Radioanal Nucl Chem* 280:371
- Skraba WJ, Arino H, Kramer HH (1978) *Int J Appl Radiat Isot* 29:575
- Slomka PJ, Le Meunier L, Hayes SW, Acampa W, Oba M, Haemer GG, Berman DS, Germano G (2008) *J Nucl Med* 49:1992
- Smith MF (2008) *Curr Cardiol Rep* 10:135
- Smith SV, Di Bartolo N, Mirzadeh S, Lambrecht RM, Knapp FF Jr, Hetherington EL (1995) *Appl Radiat Isot* 46:759
- Sofou S, Kappel BJ, McDevitt MR, Scheinberg DA, Sgorous G (2007) *Bioconjug Chem* 18:2061
- Stang LG Jr, Tucker WD, Doering RF, Mills TH (1954) *Nucleonics* 12:22
- Stang LG Jr, Tucker WD, Doering RF, Weiss AJ, Greene MW, Banks HO Jr (1957) *Development of methods for the production of certain short-lived radionuclides. Proceedings of the first UNESCO international conference, vol 1, Paris*, p 50
- Stang L (1969) *Radionuclide generators: past, present and future*, BNL 50186, T-541. Brookhaven National Laboratory, New York
- Steinkruger FJ, Wanek PM, Moody DC (1986) *Seminar on radionuclide generator technology, Vienna, Austria, 13–17 October 1986, Symposium IAEA-Series 131/08*
- Steyn GF, Mills SJ, Nortier FM, Haasbroek FJ (1991) *Appl Radiat Isot* 42:361
- Stoll H-P, Hutchins GD, Winkle W, Nguyen AT, Appeldorn CR, Janzen I, Seifert H, Rübe C, Schieffer H, March KL (2001) *J Nucl Med* 42:1375
- Sundariya S, Kayani I, Bionsoni L, Gordon I (2007) *Eur J Nucl Med* 34:1516
- Sundram FX, Yu S, Somanesan S, Jeong JM, Bernal P, Osorio M, Esguerra R, Chau TCM, Long HD, Hoa NDS, Onkhuudai P, Lamjay T, Zanzonica P, Padhy AJ, Saw MM, Rooland YA, Knapp FF Jr (2002) *World J Nucl Med* 1:5
- Syed IB, Hosain F (1975) *Applied Radiology/NM* 82
- Szucs Z, Van Rooyen J, Zeevaert JR (2009) *Appl Radiat Isot* 67:1401
- Tang J, Rahmim A, Lautamäki R, Lodge MA, Bengel FM, Tsui BM (2009) *Phys Med Biol* 54:3161
- Taniuchi HH, Fujibayashi Y, Yonekura Y, Konishi J, Yokoyama A (1997) *J Nucl Med* 38:11130
- Tárkányi F, Qaim SM, Stöcklin G (1988) *Appl Radiat Isot* 39:135
- Tárkányi F, Qaim SM, Stöcklin G (1990) *Appl Radiat Isot* 41:91
- Tárkányi F, Qaim SM, Stöcklin G, Sajjad M, Lambrecht RM (1991) *Appl Radiat Isot* 42:229
- Tendov Y, Hashizume A, Ohkubo Y, Kitao K, Sueki K (1988) *Report INDC (NDS) – 195/Gz, P. 180, IAEA, Vienna*
- Thiesson J, Paras P (eds) (1983) *International symposium on single photon ultra-short lived generators, 9–10 May, Oak Ridge National Laboratory*
- Thomas KE (1983) *Radiochim Acta* 34:135
- Thomas KE, Barness JW (1984) In: Knapp FF Jr, Butler TA (eds) *Radionuclide generators: new systems for nuclear medicine applications, vol 241, ACS symposium series. American Chemical Society, Washington DC*, p 123
- Treves S, Kulprathipanya S, Hnatowich DJ (1976) *Circulation* 54:275
- Treves S, Cheng C, Samuel A, Lambrecht R, Babchuck B, Zimmermann R, Norwood W (1980) *J Nucl Med* 21:1151
- Treves ST, Fung L, Packard AB (1999) *Eur J Nucl Med* 26:489
- Tsai Y-M, Rösch F, Novgorodov AE, Qaim SM (1997) *Appl Radiat Isot* 48:19
- Uhlir V, Gasper H, Helus F (1996) *Radioanal Nucl Chem* 204:423
- Vachtel VM, Vinel GV, Vylov T, Gromova II, Novgorodov AE, Norseev YuV, Chumin VG, Khalkin VA (1976) *Radiokhimiya* 18:886
- Van Rooyen J, Szucs Z, Zeevaert JR (2008) *Appl Radiat Isot* 66:1346
- Velikyan I, Beyer GJ, Langström B (2004) *Bioconj Chem* 15:554

- Velikyan I, Beyer GJ, Bergström-Pettermann E, Johansen P, Bergström M, Langström B (2008) *Nucl Med Biol* 35:529
- Verani MS, Lacy JL, Guidry GW, Nishimura S, Mamarian JJ, Athanasoulis T, Roberts R (1992a) *J Amer Coll Card* 19:297
- Verani MS, Guidry GW, Mahmarian JJ, Nishimura S, Athanasoulis T, Roberts R, Lacy JL (1992b) *J Amer Coll Card* 19:1490
- Vereschagin YuI, Zagrydskiy VA, Prusakov VN (1993) *Nucl Instr Meth A* 334:246
- Visser J, Brinkman GA, Bakker CNM (1979) *Int J Appl Radiat Isot* 30:745
- Votaw JR, White M (2001) *J Nucl Med* 42:701
- Wagner RK, Schad N, Bontenbal B (1990) *Nuc Compact Eur Am Commun Nucl Med* 21:118
- Wallhaus TR, Lacy J, Stewart R, Bianco J, Green MA, Nayak N, Stone CK (2001) *J Nucl Card* 8:67
- Wallhaus TR, Lacy J, Whang J, Green MA, Nickles RJ, Stone CK (1998) *J Nucl Med* 39:1958
- Waters SL, Coursey BM (eds) (1987) *Appl Radiat Isot* (Special Issue):38
- Weinberger J, Giedd KN, Simon AD, Marboe C, Knapp FF, Trichter F, Amols H (1999) *Cardiovasc Rad Med* 1:252
- Weinberger J, Knapp FF Jr (1999) In: Waksman R (ed) *Vascular brachytherapy*, 2nd edn. Futura Publishing, Armonk, pp 521–535. ISBN 0-87993-4131
- Weinreich R, Schult O, Stöcklin G (1974) *Int J Appl Radiat Isot* 25:535
- Williams BR, Mullani NA, Jansen DE, Anderson BA (1994) *J Nucl Med* 35:1586
- Win Z, Al-Nahhas A, Rubello D, Gross MD (2007) *Q J Nucl Med Mol Imaging* 51:244
- Winsche WE, Stang LG Jr, Tucker WD (1951) *Nucleonics* 8:14
- Wohlgemuth WA, Leissner G, Wengenmair H, Bohndorf K, Kirchof K (2008) *Cardiovasc Intervent Radiol* 31:698–708
- Wu C, Brechbiel MW, Gansow OA (1997) *Radiochim Acta* 79:141
- Yagi M, Kondo K (1979) *Int J Appl Radiat Isot* 30:569
- Yagi M, Amano R, Izawa G (1982) *J Radioanal Chem* 68:261
- Yano Y, Anger HO (1964) *J Nucl Med* 5:484
- Yano Y, Anger HO (1968) *J Nucl Med* 9:1
- Yano Y, McRae J, Anger HO (1970) *J Nucl Med* 11:674
- Yano Y, Chu P, Budinger TF, Grant PM, Ogard AE, Barnes JW, O'Brien HA Jr, Hoop JB (1977) *J Nucl Med* 18:46
- Yano Y (1978) In: Sunramniam G, Rhodes BA, Cooper JF, Sood VJ (eds) *Radiopharmaceuticals*, Society of Nuclear Medicine, Reston, Virginia, USA, p 2
- Yano Y, Lagunas-Solar MC, Maurer H, Carvacho OF (1989) *J Nucl Med* 30:849
- Yoshinaga K, Chow BJ, Williams K, Chen L, deKemp RA, Garrard L, Lok-Tin Szeto A, Aung M, Davies RA, Ruddy TD, Beanlands RS (2006) *J Am Coll Cardiol* 48:1029
- Zaitseva NG, Ruraz E, Tchikalov MB, Vobecky M, Khalkin VA, Popinenkova LM (1994) *Radiochim Acta* 65:157
- Zeisler SK, Becker DW (1999) *J Lab Compds Radiopharm* 42:921
- Zhernosekov KP, Filosofov DV, Baum RP, Aschoff P, Bihl H, Razbash AA, Jahn M, Jennewein M, Rösch F (2007a) *J Nucl Med* 48:1741
- Zhernosekov KP, Filosofov DV, Qaim SM, Rösch F (2007b) *Radiochim Acta* 95:319
- Zweit J, Downey S, Sharma H (1988) *Appl Radiat Isot* 39:1197
- Zweit J, Goodall R, Cox M, Babich JW, Potter GA, Sharma HL, Ott RJ (1992) *Eur J Nucl Med* 19:418
- Zweit J, Cornachan P, Doyley M, Kacperek A, Ott RJ (1994) *Eur J Nucl Med* S21:S130

41 ^{11}C : Labeling Chemistry and Labeled Compounds

G. Antoni · T. Kihlberg · B. Långström
Uppsala University, Uppsala, Sweden

41.1	Introduction	1979
41.2	Radiotracer Synthesis	1979
41.2.1	Technical Considerations	1979
41.2.2	Synthetic Considerations	1980
41.2.2.1	Position-Specific Labeling	1980
41.2.2.2	Reaction Kinetics	1981
41.2.3	Specific Radioactivity	1982
41.2.3.1	Isotopic Dilution – Radionuclide Production	1982
41.2.3.2	Isotopic Dilution – Labeling Synthesis	1982
41.3	Methods for ^{11}C-Syntheses	1983
41.3.1	Labeled Precursors	1983
41.3.1.1	Primary Precursors – Target Produced One-Carbon Compounds	1983
41.3.1.2	Secondary Precursors	1983
41.3.2	^{11}C –C Bond Formation	1993
41.3.3	Transition Metal–Mediated Reactions	1993
41.3.3.1	General	1993
41.3.3.2	Cyanations	1994
41.3.3.3	Cross-Couplings	1994
41.3.3.4	Carbonylations	1996
41.3.3.5	Copper-Mediated Reactions	1999
41.3.4	Enzymes as Catalysts in ^{11}C -Labeling Synthesis	2000
41.4	Examples of ^{11}C-Labeled Compounds	2002
41.4.1	Amino Acids	2002
41.4.2	Carbohydrates, Steroids, Fatty acids and Nucleosides	2004
41.4.3	Compounds for Study of Enzymes and Receptors	2005
41.5	PET in Drug Development	2010
41.5.1	General Considerations	2010
41.5.2	PET Microdosing	2010
41.5.3	^{11}C -Tracers in Drug Development	2011

41.6	<i>Quality Control of ^{11}C-Compounds</i>	2012
41.7	<i>^{11}C as a Tool in Chemistry Research</i>	2014

Abstract: Methods for the synthesis of compounds labeled with the short-lived positron emitting radionuclide ¹¹C are described. Important aspects on how to achieve high specific radioactivity and the need for technical solutions to establish a reproducible routine tracer production are pointed out. Examples of positron emission tomography (PET) as a tool in drug development are also included.

41.1 Introduction

The possibility to quantify in vivo biochemistry noninvasively using compounds labeled with radioactive isotopes is a milestone in medical imaging. The first production of the short-lived positron emitting radionuclide ¹¹C was performed in 1934 (Crane and Lauritsen 1934). It was found that ¹¹C decays with a half-life of 20.4 min by positron emission to the stable nuclide ¹¹B. Due to its favorable decay characteristics (98.1% by β^+ emission, 0.19% by electron capture), it was recognized as a useful tool in medical imaging. The first biological experiment using ¹¹C was performed by Ruben in 1939 who studied the photosynthesis in plants using [¹¹C]carbon dioxide (Ruben et al. 1939). This was followed by Tobias who in 1945 investigated the fixation of [¹¹C]carbon monoxide by red blood cells in humans (Tobias et al. 1945). The possibility to prepare more complex molecules and to choose labeling position has significantly contributed to the versatility of the positron emission tomography (PET) technique. In this chapter, the most important labeling methods are presented with focus on recent improvements. For a comprehensive review with references to the earlier work in this field of research see Fowler and Wolf (1986). A catalog of references to ¹¹C-labeled compounds is available on the Internet (Cyril 2003).

PET has during the last 10 years evolved into a valuable tool in drug development. Compounds labeled with positron emitting radionuclides are currently used in different phases in the drug development process using preclinical methods as well as PET investigations both in animals and in man. One of the major research fields that have contributed to establish PET as a useful and in some cases a necessary tool in drug development is radiochemistry. Especially developments in ¹¹C chemistry have opened up new perspectives for the use of PET in drug development.

41.2 Radiotracer Synthesis

41.2.1 Technical Considerations

A limiting factor that has to be considered when planning syntheses with ¹¹C is the short physical half-life. It is thus important to use rapid synthetic methods and to avoid reaction sequences that may require lengthy purification processes. The short half-life requires high amounts of starting radioactivity in order to obtain a tracer with enough radioactivity for a PET study. Radiation protection and safe handling of radioactive reactants is thus important. Examples of technical approaches that can be applied when working with short-lived radionuclides and high levels of radioactivity are as follows.

Remote or processor-controlled automated device. Remote or processor-controlled automated devices, mainly developed for radiation protection purposes, also have other advantages such as increasing the reproducibility in the tracer production. This also facilitates

development of standardized procedures, which is important with respect to quality assurance and the implementation of Good Manufacturing Practice (GMP) in PET-related work.

One-pot and online procedures. Transfer of small volumes between reaction vessels may reduce the radiochemical yield and increase the risk of introducing carrier carbon. The uses of one-pot and online procedures are thus important means to facilitate the technical handling.

Miniaturization. Miniaturization of synthesis equipment makes it possible to reduce the amounts of reagents. This feature can facilitate purification or even omit the need of a purification step and may increase the specific radioactivity. Especially when working with [^{11}C]carbon dioxide this is important since reduction of the amount of reagent might increase the specific radioactivity by lowering the amount of carrier carbon present. The gas volume in a reaction vial may have some impact on the alkylation yield using [^{11}C]methyl iodide, since a large gas volume together with high temperature will distribute a significant portion of the [^{11}C]methyl iodide to the gas phase and thus lower the reaction yield.

On-column preparations and closed loops. The use of on-column preparations and closed loops as an alternative to reaction vials is another technical solution (Jewett et al. 1985; Iwata et al. 1995). An example of this approach is the synthesis of [^{11}C]cyclohexanecarbonyl chloride where [^{11}C]carbon dioxide is reacted with cyclohexylmagnesium bromide coated on the internal surface of polypropylene tubing, followed by treatment of the complex with thionylchloride (McCarron et al. 1996).

Sonication and microwaves. Sonication (Le Breton et al. 1991) or microwaves (Niisawa et al. 1984; Hwang et al. 1987; Stone-Elander et al. 1994; Thorell et al. 1992) can be used to speed-up a reaction. The selectivity in the reaction may in some cases also change when microwave heating is used (Elander et al. 2000).

Solvation parameters. Increased control of the solvation parameters by performing the synthesis in a supercritical media may also offer advantages such as high reproducibility (Jacobson et al. 1994a, b, 1996).

41.2.2 Synthetic Considerations

For the production of ^{11}C -labeled tracers, four main approaches have been employed: (1) Biosynthetic methods, (2) Recoil labeling, (3) Organic synthetic methods, and (4) Enzyme catalysis.

Biosynthetic methods using plant leaves or algae (Lifton and Welch 1971) and recoil labeling (e.g., via the spallation reaction $^{16}\text{O}(\text{p},3\text{p}3\text{n})^{11}\text{C}$) are today of little importance. Presently, the only labeling methods of practical interest are organic synthesis and enzymatic catalysis.

The requirement for a rapid tracer production means that the synthesis should be designed in such a way that the ^{11}C atom is introduced as late as possible. This approach is exemplified by alkylation of carbon, nitrogen, oxygen, and sulfur nucleophiles with [^{11}C]methyl iodide, a synthetic route that provides a general method for the labeling of many biomedically interesting compounds.

41.2.2.1 Position-Specific Labeling

The development of rapid labeling syntheses is conditioned on the availability of suitable labeled precursors. A few useful target-produced primary precursors are available such as

[¹¹C]carbon dioxide and [¹¹C]methane. Much work has been devoted to the development of methods for the routine production of secondary precursors to be used as building blocks in the production of PET tracers.

Most biomolecules contain several carbon atoms, which opens up the possibility to select the labeling position (i.e., position-specific labeling). Since heteroatom-bound methyl groups are common in many biomolecules and pharmaceuticals, [¹¹C]methyl iodide has, so far, been the most used labeling reagent. Another general synthetic approach that has been adopted is to label in the carbonyl position using [¹¹C]carbon dioxide, [¹¹C]carbon monoxide, or [¹¹C]phosgene. This has a primary value in PET-tracer synthesis since biologically active substances often contain carbonyl groups or functionalities that can be derived from a carbonyl group.

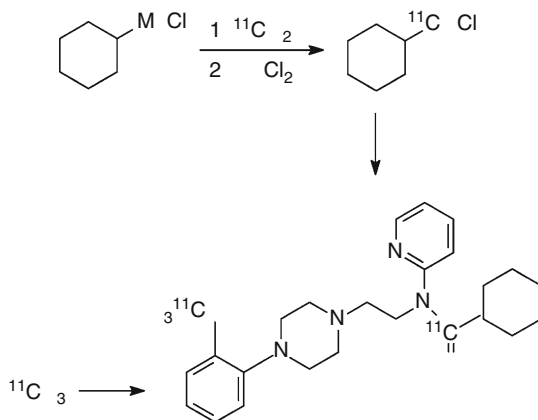
It is important to select a labeling position that does not give rise to labeled metabolites that interfere with the measurement of the process to be studied. It is thus essential to establish synthetic strategies that give access to a variety of labeling positions. This concept is illustrated with the 5-HT_{1A} receptor antagonists WAY100635 (● Fig. 41.1). Labeling in the methoxy position (Mathis et al. 1994) resulted in the formation of the labeled lipophilic metabolite WAY100634 that also penetrated the blood-brain barrier (BBB) and added to the nonspecific binding in the brain (Osman et al. 1996). With the label in the carbonyl group [¹¹C]cyclohexane carboxylic acid was the main labeled metabolite, and since that compound is not transported over the BBB, interpretation of the PET data was simplified.

41.2.2.2 Reaction Kinetics

The kinetic aspect needs special attention when a synthetic strategy is selected. The significance of time as a reaction parameter is of equal importance, as chemical yield has to be considered in the planning of a labeling synthesis. Since the radiochemical yield is a function of chemical yield and radioactive decay, the maximum radiochemical yield is attained before the reaction has proceeded to completion. This relation between time and concentration of reactants with respect to kinetics is described in some of the initial works on ¹¹C-chemistry (Långström and

■ Fig. 41.1

Synthesis of methoxy-¹¹C and cyclohexyl-¹¹C-labeled WAY100635



Bergson 1980; Långström et al. 1981a; Berger et al. 1981). The stoichiometric relationships in labeling synthesis with radionuclides of high specific radioactivity need special attention. The small amounts of labeled compound mean that the ratio between unlabeled precursor and labeled reagent can be very high. This usually increases the conversion rate of the labeled reactant to product to give satisfactory radiochemical yield within 5–10 min. A special case is the aforementioned alkylation of amines with [¹¹C]methyl iodide. Alkylation of amines with methyl iodide in stoichiometric amounts typically results in product mixtures with quarternarized amines as end product. This is due to the increased nucleophilicity from the primary to the secondary and tertiary amines. However, in ¹¹C-labeling synthesis the amount of [¹¹C]methyl iodide is very low and a concentration ratio amine/methyl iodide of 50–500 can be achieved. Due to the resultant change from second-order kinetics to pseudo-first order kinetics, the problem with polyalkylation is minimized and the monoalkylated product is obtained. An example where the large excess of unlabeled reagent is disadvantageous is the synthesis of [1–¹¹C]acetate by the reaction of [¹¹C]carbon dioxide with methylmagnesium bromide. A too high concentration of methylmagnesium bromide results in the formation of labeled acetone and tert-butanol. The use of a solid support for the Grignard reagent instead of performing the reaction in solution is one way of minimizing this problem.

41.2.3 Specific Radioactivity

The theoretical specific radioactivity of ¹¹C is 3.4×10^5 GBq/μmol, a limit that is considerably higher than the 1,500–2,500 GBq/μmol typically obtained at end of radionuclide production (Harada and Hayashi 1993).

41.2.3.1 Isotopic Dilution – Radionuclide Production

It is practically impossible to completely avoid isotopic dilution by stable carbon isotopes from the target material (e.g., nitrogen/oxygen, nitrogen/hydrogen gas mixtures) and target holder, usually aluminum (Heselius et al. 1987). The major isotopic dilution by stable carbon is obtained during the radionuclide production. The amount of carbon isolated in the form of carbon dioxide or methane following radionuclide production is typically in the order of 1–100 nmol.

41.2.3.2 Isotopic Dilution – Labeling Synthesis

The degree of isotopic dilution during production of a PET tracer is also determined by the choice of primary precursor and the quality of the reagents used in the chemical transformations. It is important to remember that products formed from reaction with atmospheric carbon dioxide usually contaminate chemicals such as lithium aluminum hydride and Grignard reagents (Iwata et al. 1988).

In some special cases, an isotopic dilution can occur by exchange (see ► Chap. 15 in Vol. 2) between the labeled reagent and the solvent or reagents used. Dimethyl sulfoxide, a commonly used solvent in alkylation reactions, might react with [¹¹C]methyl iodide to form labeled oxo-trimethyl-sulfonium iodide. This intermediate can transfer any of the three methyl groups to

another nucleophile in the reaction mixture and thus reduce the radiochemical yield and the specific radioactivity (Klein and Holschbach 2001). Other similar problems are the exchange reaction between [¹¹C]cyanide and the cyano group in acetonitrile in the presence of a phase transfer catalyst (Jay et al. 1980) and the transfer of methyl groups in Stille couplings using trimethylstannanes. In spite of all precautions, the amount of carrier carbon introduced during the synthesis is in the range of 10–100 nmol.

41.3 Methods for ¹¹C-Syntheses

41.3.1 Labeled Precursors

41.3.1.1 Primary Precursors – Target Produced One-Carbon Compounds

The limited access to labeled precursors is a restriction in the choice of synthetic route. Development of new precursors for labeling synthesis is thus an important field of research.

Primary precursors are prepared in the target and secondary by further chemical processing of a primary product (usually by online or one-pot procedures). [¹¹C]Carbon dioxide and [¹¹C]methane are the most commonly prepared primary precursors (Bida et al. 1978; Christman et al. 1975). The production method usually employed is the ¹⁴N(p,α)¹¹C reaction. [¹¹C]Carbon monoxide is formed simultaneously with [¹¹C]carbon dioxide but can easily be separated cryogenically from the latter. [¹¹C]Methane is obtained if a nitrogen/hydrogen gas mixture is used. Other precursors available directly in the target are hydrogen [¹¹C]cyanide (Lamb et al. 1971), [¹¹C]cyanamide (Iwata and Ido 1983), [¹¹C]guanidine (Iwata et al. 1981), and [¹¹C]methyl iodide (Wagner et al. 1981).

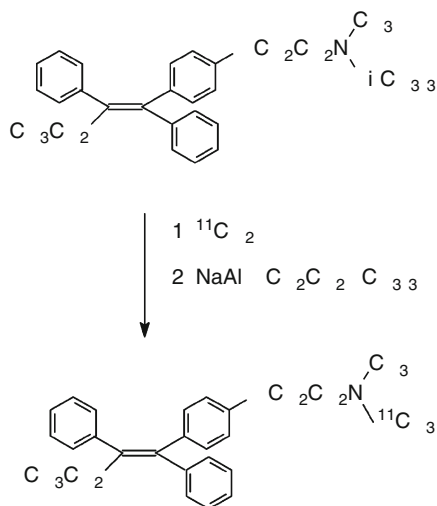
In conclusion, [¹¹C]carbon dioxide is the most versatile primary precursor with respect to production yield, ease of separation from target gas, and prospect for chemical transformations. Furthermore, of the primary precursors only [¹¹C]carbon dioxide has been used directly as a labeling agent to any greater extent. It can be used as a substitute for phosgene in the formation of ureas (Schirbel et al. 1999) or in reactions with alkyl lithium compounds and Grignard reagents. The latter reaction gives access to important tracers such as acetate (Pike et al. 1982) and palmitate labeled in the carboxylic position. Another possibility is to perform a direct incorporation of [¹¹C]carbon dioxide to produce a label in the *N*-methyl position by reaction with a *N*-trimethylsilyl derivative as shown in ► Fig. 41.2 (Ram et al. 1986; Ram and Spicer 1989).

41.3.1.2 Secondary Precursors

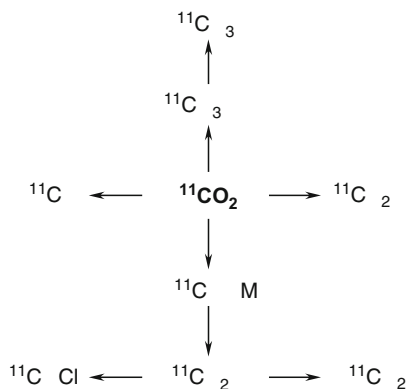
Several reactive molecules have been prepared by simple online or one-pot procedures from [¹¹C]CO₂. Some of the most important secondary precursors obtained from [¹¹C]CO₂ are shown in ► Fig. 41.3. [¹¹C]Methane, the other main primary precursor, is also a useful source for the preparation of more reactive labeling reagents (► Fig. 41.4).

[¹¹C]Methyl iodide (► Fig. 41.5) has been the most versatile of the secondary precursors (Bolton 2001). It can be prepared by reduction of [¹¹C]carbon dioxide with lithium aluminum hydride in tetrahydrofuran or diethyl ether, followed by reaction with hydroiodic acid (Långström and Lundqvist 1976; Crouzel et al. 1987a).

■ Fig. 41.2

Synthesis of [^{11}C]tamoxifen

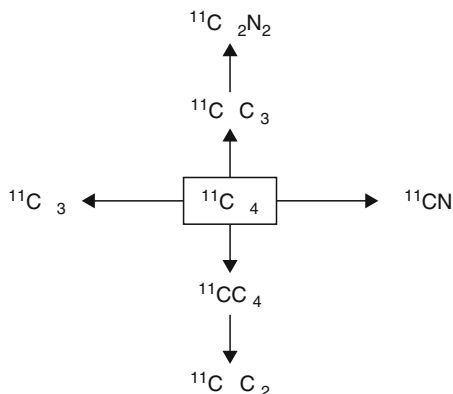
■ Fig. 41.3

Examples of secondary precursors obtained from [^{11}C]CO $_2$ 

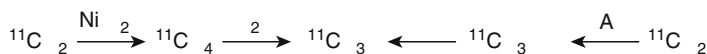
This method is very reliable but suffers from the drawback that the lithium aluminum hydride contains carrier carbon that reduces the specific radioactivity. A solid phase technique has also been reported for the synthesis of [^{11}C]methyl iodide (Sarkadi et al. 1997, 1998). In an alternative method, that gives higher specific radioactivity, [^{11}C]methane undergoes a free radical iodination in a circulating gas phase while the [^{11}C]methyl iodide formed is continuously trapped on a solid phase to prevent further iodination (Larsen et al. 1997).

In order to achieve maximum specific radioactivity, in target production of [^{11}C]methane followed by iodination is the method of choice. Alkylation reactions on oxygen, nitrogen, phosphorus, and sulfur nucleophiles as well as on carbanions indeed cover a large variety of

■ Fig. 41.4

Examples of secondary precursors prepared from [^{11}C]methane

■ Fig. 41.5

Methods for the synthesis of [^{11}C]methyl iodide

possible reactions with [^{11}C]methyl iodide. Alkylation on ionic nucleophiles, e.g., carboxamide anions and carboxylates, generated by the addition of alkali metal hydroxides are usually accompanied by the formation of [^{11}C]methanol. This can be minimized by isolation of the preformed anionic salt either in the form of a tetrabutylammonium salt or as a benzo-5-crown-5 sodium complex. The latter is exemplified by the synthesis of [^{11}C]diazepam (Sassaman et al. 1999).

The reactivity of [^{11}C]methyl iodide can be increased by conversion to [^{11}C]methyl triflate ([^{11}C]methyl trifluoromethanesulphonate) by an online process (Jewett 1992) using silver triflate absorbed on graphite. Methyl triflate is more reactive than methyl iodide, is less sensitive to excess of metal hydroxides and usually gives higher radiochemical yields (Någren et al. 1995). Furthermore, the use of [^{11}C]methyl triflate increases the selection of solvents suitable for alkylation reactions. An alternative method for [^{11}C]methyl triflate synthesis is from [^{11}C]methyl bromide via [^{11}C]methane (Mock et al. 1999). [^{11}C]Methyl bromide can be prepared either by passing [^{11}C]methane through liquid bromine or by recirculation over pyridiniumtribromide. Use of liquid bromine typically results in a mixture of mono and dibromomethanes. The reported conversion from halomethanes to triflate was higher using [^{11}C]methyl bromide than [^{11}C]methyl iodide (Steel et al. 1998).

The reactivity can be further increased using [^{11}C]methyl nona-fluorobutyl-1-sulfonate (Jolly et al. 2007).

Conversion of the electrophilic methyl iodide to the nucleophilic methyl lithium (Reiffers et al. 1980) and lithium [^{11}C]methyl(2-thienyl)cuprates (Kihlberg et al. 1997) broadens the spectrum of functionalities that may be labeled in a methylation reaction. Transformation of [^{11}C]methyl lithium to trimethylsilyl chloride is a method for labeling of aryl trimethylsilyl

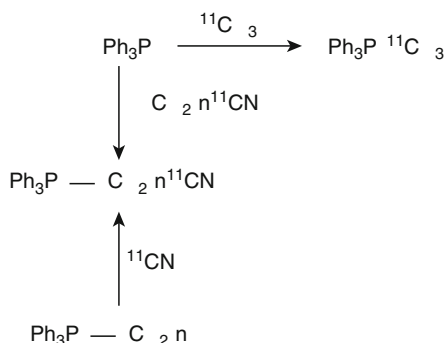
compounds (Roeda et al. 1999). [^{11}C]Diazomethane is a useful but not easily accessible methylating agent (Crouzel et al. 1987b). Other labeling agents that can be prepared from [^{11}C]methyl iodide are Wittig reagents (Kihlberg et al. 1990; Hörnfeldt and Långström 1994a, b, c, see also ▶ Fig. 41.6) useful in alkene syntheses, triphenylarsonium [^{11}C]methylide, used in ring-closure reactions (Zessin et al. 1999), [^{11}C]methylhypofluorite for the formation of enolmethyl ethers (McCarthy et al. 1993) and [^{11}C]methylmagnesium iodide (Elsinga et al. 1995) for Grignard reactions.

A difficulty in the synthesis of the phosphorylide in the Wittig reaction is to add an equimolar amount of base to the alkyl halide. The use of epichlorohydrine, which forms one equivalent of base in situ by the reaction with iodide ions, obtained from the reaction of a ^{11}C -labeled alkyl iodide with triphenyl phosphine is one method to overcome the problem. Some examples of useful precursors prepared from [^{11}C]methyl iodide are shown in ▶ Fig. 41.7.

^{11}C -Labeled ethyl-, allyl-, propyl-, cyclopropyl-, isopropyl-, butyl-, isobutyl-, benzyl-, and some substituted benzyl halides are examples of other alkylating agents prepared from [^{11}C]carbon dioxide and Grignard reagent (Långström et al. 1986; Fasth et al. 1990b; Antoni and Långström 1987a, b, c; Lasne et al. 1991; Luthra et al. 1985) as shown in ▶ Fig. 41.8.

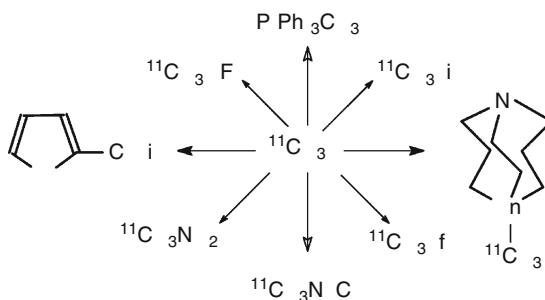
■ Fig. 41.6

Examples of labeled Wittig reagents



■ Fig. 41.7

Examples of precursors obtained from [^{11}C]methyl iodide



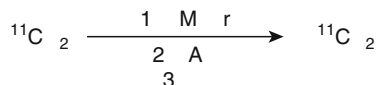
These precursors suffer from the typical isotopic dilution problems encountered with the use of Grignard reagents and lithium alkyl compounds. Another problem encountered when reacting high specific activity [^{11}C]carbon dioxide with Grignard reagents is the formation of products from reaction of two or three Grignard reagents per [^{11}C]carbon dioxide molecule. The synthesis of [^{11}C]ethyl iodide from methylmagnesium bromide and [^{11}C]carbon dioxide is an example of that and both methyl and isopropyl iodide are formed in substantial amounts. This is, however, less problematic when longer alkyl chain Grignard reagents are used such as in the synthesis of carboxylic-labeled fatty acids. On the other hand, di-coupling of the Grignard reagent can be an advantage since precursors such as [$2\text{-}^{11}\text{C}$]acetone (Berger et al. 1980a) and [^{11}C]isopropyl iodide (Antoni and Långström 1987c) can be prepared from methylmagnesium bromide. Alkyl lithium reagents can also be used to achieve di-couplings, and acetone and isopropyl iodide are preferentially prepared from these reagents. Difunctional precursors such as 1,2-dibromo[^{11}C]ethane (► Fig. 41.9) and [^{11}C]chloroethyltriflate synthesized from [^{11}C]ethylene obtained via [^{11}C]ethanol (Shah et al. 1994a; Shah et al. 1997; Prenant et al. 1995b) are also interesting as labeling tools.

Nitro[^{11}C]alkanes have been obtained from labeled methyl-, ethyl-, and propyl iodide by reaction with silver nitrite by the online process presented in ► Fig. 41.10 (Schoeps et al. 1989; Schoeps and Halldin 1992).

Nitroalkanes can be reacted with aldehydes in a Knoevenagel-type condensation reaction; amphetamine and phenethylamine are examples of compounds labeled using this methodology (► Fig. 41.11).

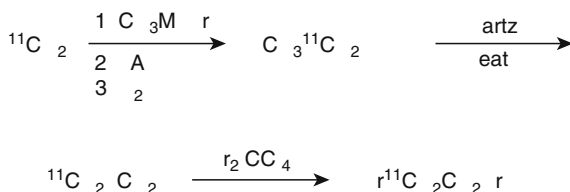
■ Fig. 41.8

Synthesis of [^{11}C]alkyl halides



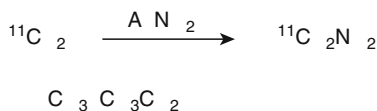
■ Fig. 41.9

Synthesis of 1,2-[^{11}C]dibromoethane



■ Fig. 41.10

Synthesis of [^{11}C]nitroalkanes

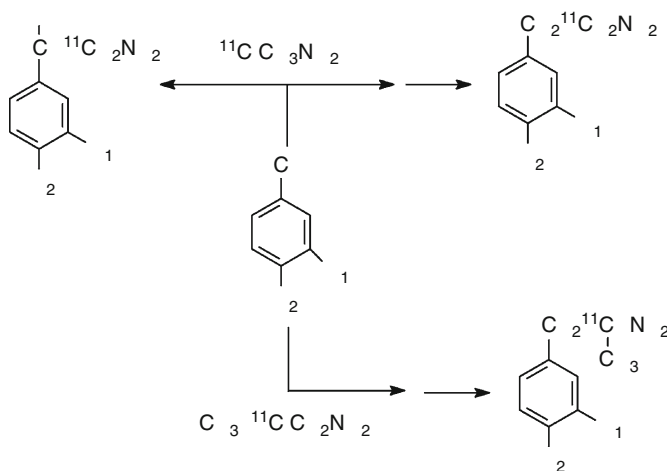


The products obtained are racemic since the addition of nitromethane is not stereospecific. It is possible to modify the reaction conditions to obtain either the nitroalcohol or the dehydrated product.

Labeling of a carbon in an aromatic ring may give access to useful structural units with the label in a metabolically stable position. The synthesis of some aromatic compounds including heterocycles from ^{11}C nitromethane is shown in ► Fig. 41.12 (Zessin et al. 1999; Mäding et al. 1997; Mäding and Steinbach 1998, 2000; Steinbach et al. 1995).

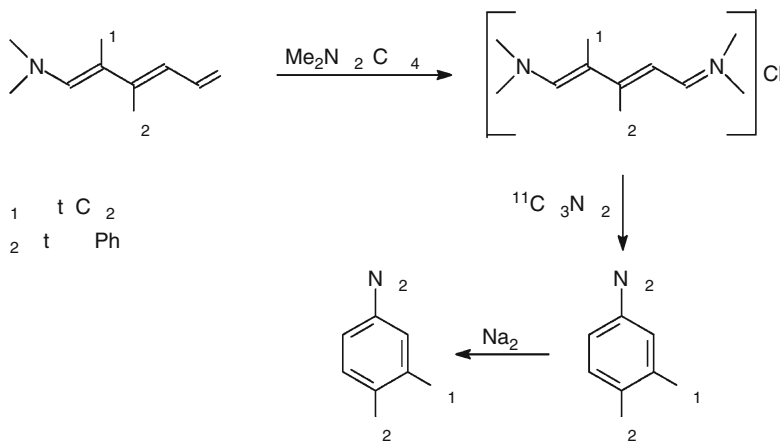
■ Fig. 41.11

Synthesis of amines using ^{11}C nitroalkanes



■ Fig. 41.12

^{11}C Labeling of aromatic compounds in the ring structure. The labeled carbon is indicated by an asterisk



Ethyl nitro[2-¹¹C]acetate, obtained from [¹¹C]nitromethane, could potentially be used for labeling of amino acids and heterocycles (Kato et al. 2007).

In the synthesis of sulphonamides and methane sulphonates [¹¹C]methane sulphonyl chloride has been used (McCarron et al. 1999).

[¹¹C]Methyl azide can be used in rapid and mild reactions, i.e., click chemistry, to label peptides containing an ethynyl-terminal (Schirrmacher et al. 2008).

Formaldehyde is a versatile one-carbon precursor and should thus be an attractive tool in labeling chemistry. Due to lack of reliable and simple production method it has not been used to the same degree as [¹¹C]methyl iodide. The main applications have so far been reductive formylations of amines. [¹¹C]Formaldehyde can be obtained by enzymatic catalysis or organic synthetic approaches (Christman et al. 1971; Hughes and Jay 1995). The most applied methods rely on the formation of [¹¹C]methanol from [¹¹C]carbon dioxide, followed by oxidation by silver wool, ferric molybdenum oxide, or xenon difluoride (Marazano et al. 1977; Berger et al. 1980b; Nader et al. 1997). Reduction of [¹¹C]carbon dioxide with metal hydrides at temperatures below -50°C (Nader et al. 1998; Roeda and Crouzel 2001) is another possibility. In the latter method, the low temperature minimized the reduction of formaldehyde to methanol but formic acid has been identified as a by-product. Recently a simple, robust, and high yielding method was developed where [¹¹C]formaldehyde is obtained from [¹¹C]methyl iodide via a reaction with trimethyl amine *N*-oxide (Hooker et al. 2008).

A procedure for ¹¹C-labeling of the 4-imidazolyl group using [¹¹C]formaldehyde is shown in Fig. 41.13. The 4-imidazolyl group is a commonly found structural unit in histamine receptor ligands (Roeda et al. 1997).

Substituted benzaldehydes have been prepared from [¹¹C]carbon dioxide and Grignard reagents via the corresponding carboxylic acids and reduction to the alcohol followed by selective oxidation (Halldin and Långström 1984a; Kutzman et al. 1980).

The carbonyl functionality is a prevalent structure in many biomolecules. Labeling in this position can be achieved by reaction with [¹¹C]phosgene (Roeda et al. 1978; Roeda and Westera 1981; Nishijima et al. 2002, see also Fig. 41.14) and acyl chlorides such as acetyl- (Luthra et al. 1990), cyclohexanecarbonyl-, (McCarron et al. 1996), and furoyl chloride (Ehrin et al. 1988).

Fig. 41.13

Synthesis of 4-imidazolyl derivatives

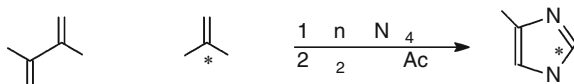
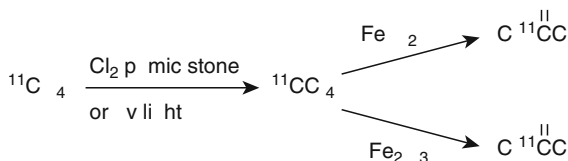


Fig. 41.14

Synthesis of [¹¹C]phosgene



The specific radioactivity of [^{11}C]phosgene has been relative low, probably due to carrier carbon in the chlorine gas.

Labeling in the carbonyl position can be also accomplished by the use of [^{11}C]propyl ketene (Imahori et al. 1989, 1991) obtained by pyrolytic decomposition of [^{11}C]butyric acid. [^{11}C]methylisocyanate (Bonnot-Lours et al. 1993; Brown et al. 1994; Crouzel et al. 1995) prepared either from [^{11}C]acetyl chloride or [^{11}C]phosgene, and [^{11}C]methylchloroformate (Ravert et al. 1995) synthesized from [^{11}C]methanol and phosgene are other examples of useful reactive precursors (► Fig. 41.15).

Phosgenation of *N,N*-bis(trimethylsilyl)amine is superior to the use of methylamine. The Curtius rearrangement reaction effectively produces the labeled methylisocyanate but is very time consuming and results in a low radiochemical yield.

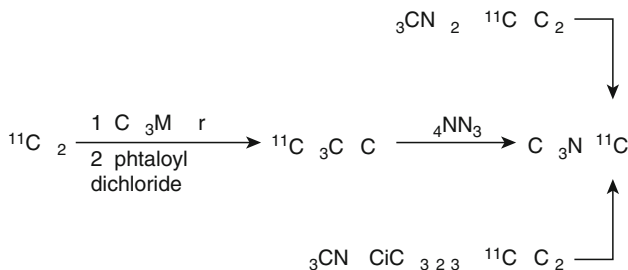
Reacting [^{11}C]methyl iodide with silver cyanate gives methylisocyanate with the label in the methyl group. Other organo-isocyanates have been synthesized from *N*-sulfinylamines or *N,N'*-organo ureas as shown in ► Fig. 41.16 (Brown et al. 2001). The organosulfinylamines give the highest radiochemical yield.

[^{11}C]Urea has been synthesized by several methods starting either with [^{11}C]cyanide (Emran et al. 1985) or with [^{11}C]carbon dioxide (Chakraborty et al. 1997).

A versatile precursor is hydrogen [^{11}C]cyanide prepared from [^{11}C]methane by a platinum catalyzed reaction with ammonia (Christman et al. 1975; Iwata et al. 1987). Hydrogen [^{11}C]cyanide is obtained with a specific radioactivity higher or similar to that of [^{11}C]methyl iodide prepared by the gas phase method. From [^{11}C]cyanide other labeled reagents can be prepared such as $\text{Cu}[^{11}\text{C}]\text{CN}$ (Ponchant et al. 1997), halonitriles (Hörnfeldt et al. 1992), acrylonitrile (Antoni and Långström 1992), [^{11}C]cyanomethyl pivalate (Thorell et al. 1994), and [^{11}C]trifluoroacetone nitrile (Roeda et al. 1999a) as schematically shown in ► Fig. 41.17.

■ Fig. 41.15

Synthesis of methylisocyanate



■ Fig. 41.16

Synthesis of organo-isocyanates



The multistep synthesis of the putative glycine antagonist Licostinel may serve as an example of the use of [¹¹C]cyanide in labeling synthesis. The synthesis of [¹¹C]diethyloxalate and the following ring closure to produce the [¹¹C]quinoxaline ring structure, is shown in ▶ Fig. 41.18 (Thorell et al. 1993b, 1995, 1998).

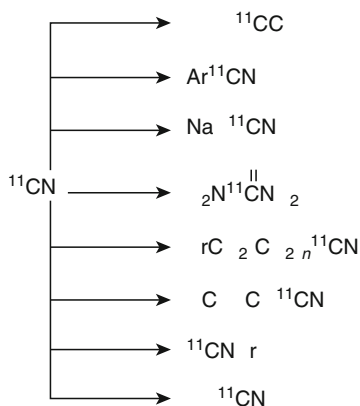
In cyanogen bromide, the carbon has reversed polarity as compared with cyanide and is accordingly used as an electrophilic equivalent of the nucleophilic cyanide. This, so-called, “umpolung” offers new alternatives in labeling synthesis for the introduction of a cyano group. [¹¹C]Cyanogen bromide is prepared by reaction of hydrogen [¹¹C]cyanide with bromine or perbromide (Westerberg and Långström 1993, 1997a, b). Some examples of possible synthetic transformations from [¹¹C]cyanogen bromide are shown in ▶ Fig. 41.19 (Westerberg and Långström 1994a).

The influenza virus neuraminidase inhibitor GG167 labeled with ¹¹C in the guanidine group has been synthesized from [¹¹C]cyanogen bromide (Westerberg et al. 1996) as shown in ▶ Fig. 41.20.

[¹¹C]Cyanogen bromide can also be used for unspecific labeling of macromolecules. The reactions can be performed at near physiological conditions, with respect to temperature and pH.

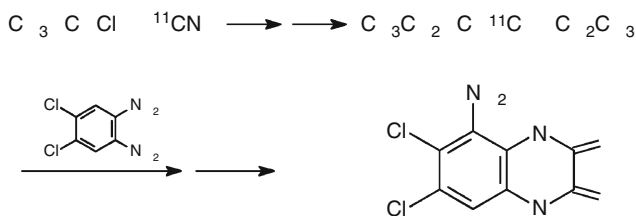
■ Fig. 41.17

Some examples of possible synthetic transformations from [¹¹C]cyanide

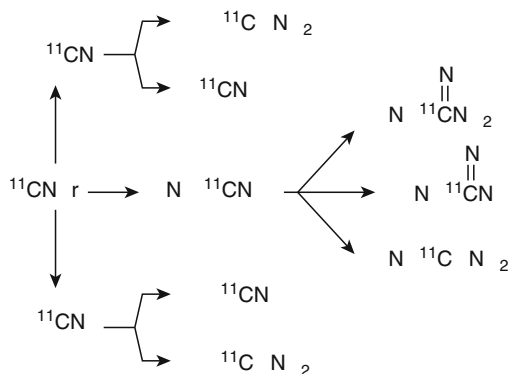


■ Fig. 41.18

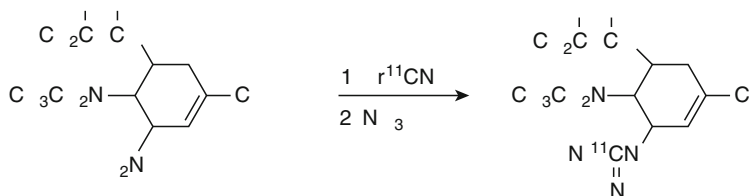
Synthesis of [¹¹C]Licostinel



■ Fig. 41.19

Possible synthetic transformations from $[^{11}\text{C}]$ cyanogen bromide

■ Fig. 41.20

Synthesis of $[^{11}\text{C}]$ GG167

Proteins such as transferrin and albumin as well as the polysaccharide hyaluronan have been labeled by this method (Westerberg and Långström 1994b; Westerberg et al. 1995). The label in the form of a ^{11}CN group is either attached to a free amino group in the protein or to a hydroxyl in a carbohydrate. Other methods used for unspecific labeling of macromolecules include reductive methylation with $[^{11}\text{C}]$ formaldehyde and direct alkylation with methyl iodide (Straatman and Welch 1974; Marche et al. 1975; Turton et al. 1984). Labeling with formaldehyde and methyl iodide suffers from the drawbacks that either a reducing agent or alkaline conditions are needed in the synthesis that may be deleterious to the protein.

$[^{11}\text{C}]$ Carbon monoxide was until recently rarely used as a precursor due to its low reactivity and low solubility in most solvents. It can be prepared by reduction of $[^{11}\text{C}]$ carbon dioxide using Zn (Christman et al. 1975), charcoal (Al-Qahtani and Pike 2000), or molybdenum (Zeisler et al. 1997). The use of solid phase supports for the concentration of $[^{11}\text{C}]$ carbon dioxide and $[^{11}\text{C}]$ carbon monoxide and a micro-autoclave for the transition metal-mediated carbonylation reactions have solved some of the earlier problems that restricted the use of this easily prepared precursor (Kihlberg and Långström 1999; Kihlberg et al. 2001). The earlier discussed problems with low specific radioactivity of alkyl halides prepared from Grignard or alkyllithium reagents may be circumvented by applying a newly presented method where

[¹¹C]ethyl iodide is synthesized with higher specific radioactivity and radiochemical purity from [¹¹C]carbon monoxide by a palladium catalyzed reaction with methyl iodide followed by reduction and iodination (Eriksson and Långström 2001).

41.3.2 ¹¹C–C Bond Formation

In organic chemistry C–C bond formations are among the most essential reactions. In ¹¹C-chemistry, the common method for introduction of the label has been heteroatom alkylations. However, ¹¹C–C bond formations are important complements for compounds lacking a heteroatom-bound alkyl group, or when other labeling positions are needed due to the metabolic fate of the tracer. In tracer synthesis, the following ¹¹C–C bond forming reactions have been applied.

- Alkylation on a stabilized carbanion using a ¹¹C-labeled alkyl iodide (e.g., malonic ester alkylation, see Gee and Långström 1991).
- Carbonation of an organometallic reagent with [¹¹C]carbon dioxide (e.g., [1–¹¹C]acetate, see Pike et al. 1981; Oberdorfer et al. 1992; Iwata et al. 1995).
- Reactions of [¹¹C]cyanide with electrophilic carbons (e.g., [1–¹¹C]glucosamine, see Thorell et al. 1993).
- Reactions with the anion of a ¹¹C-labeled nitroalkane (e.g., [1–¹¹C]norepinephrine, see Schoeps and Halldin 1992).
- Cuprate-mediated coupling reactions using a ¹¹C-labeled alkyl iodide or a ¹¹C-labeled methyl cuprate. (e.g., methyl ¹¹C-labeled fatty acids, ¹¹C-labeled steroids, see Kihlberg and Långström 1994a, b; Lidström et al. 1997; Neu et al. 1998).
- Alkene-synthesis using [¹¹C]methylenetriphenylphosphorane (e.g., ¹¹C-labeled monosaccharides, see Grierson et al. 1993; Ögren et al. 1995b, 1997).

Recently, transition metals and particularly palladium have found an increased use in ¹¹C-synthesis. Reactions such as aromatic cyanation, the Stille-coupling reactions, and palladium-mediated carbonylation reactions using [¹¹C]carbon monoxide are opening up new labeling pathways.

41.3.3 Transition Metal–Mediated Reactions

41.3.3.1 General

Organo transition metallic reagents differ from other organo metallic reagents in several aspects. They are not strongly basic or nucleophilic, they easily coordinate a variety of different compounds and have a low energy barrier between different oxidation states. Thus, mild and selective syntheses can be developed using substrates with relative low reactivity. This is particularly valuable in ¹¹C-labeling synthesis, since it implies that protective groups can be omitted.

In organic chemistry, the reactions are usually performed in a catalytic fashion. In ¹¹C-labeling synthesis, however, all reagents including the transition metals are used in large excess compared to the labeled precursor. For this reason, the term “mediated” is more appropriate than “catalyzed.”

Among the transition metals palladium has been most useful. The organo palladium reagents can be conveniently made in situ, which has a practical value in the context of tracer synthesis. The reactions are very mild and often give high yields using short reaction times. One limitation is encountered with organohalides having β -protons bound to sp^3 -carbons, these usually give low yields due to the competing β -hydride elimination reaction. (Collman et al. 1997; Stille 1986)

Organocuprates are much less prone to β -hydride elimination reaction and rapidly couple with alkyl halides. In this respect, they complement the palladium reagents. A disadvantage is their basicity and that their most common sources are the strongly basic and nucleophilic alkyl lithium and Grignard reagents, which require protection of sensitive functionalities.

41.3.3.2 Cyanations

The ^{11}C -cyano group can be attached to aromatic rings using palladium as exemplified by the labeling of an analogue of the NMDA receptor antagonist MK-801 (3-cyano-MK-801) by cyanation of 3-iodo-MK-801 (Andersson et al. 1998). By the same Pd-mediated cyanation reaction followed by selective hydrolysis to the corresponding amides (Andersson et al. 1994) ^{11}C -benzamides, as potential tracers for poly (ADP-ribose) synthetase, have been obtained.

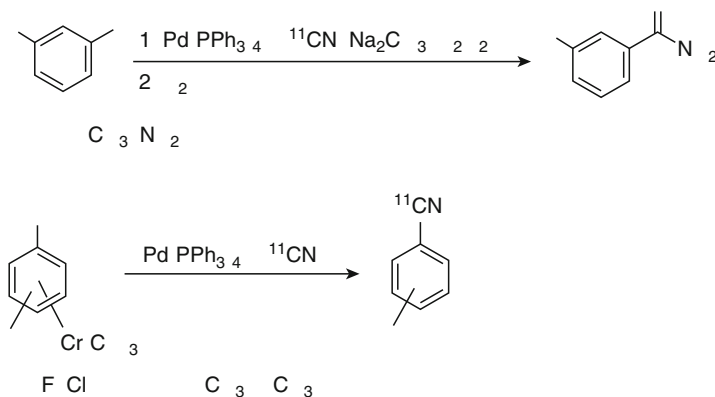
Attaching the strongly electron-withdrawing group tricarbonylchromium to the aromatic ring can further increase the rate of the cyanation reactions. Thus, also deactivated substrates can be labeled in high radiochemical yield with this method (Balatoni et al. 1989; Andersson and Långström 1994, see also [Fig. 41.21](#)).

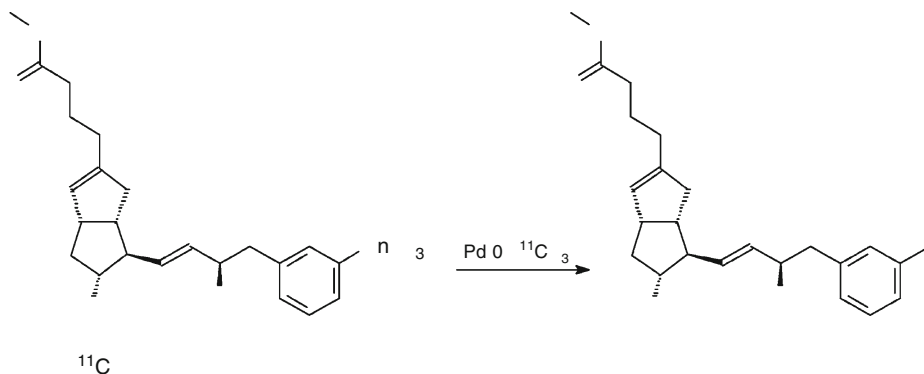
41.3.3.3 Cross-Couplings

Palladium(0)-complex can mediate the cross-coupling of organic halides or triflates to organo-metallic reagents with high regio- and stereoselectivity. Due to the possible β -hydride

■ Fig. 41.21

Transition metal-mediated cyanation reactions





undecane (► Fig. 41.24), was prepared for these reasons and used in Stille couplings (Vedejs et al. 1992; Forngren et al. 2001).

The Heck reaction, i.e., the palladium-promoted coupling of organoelectrophiles with alkenes, is another mild and versatile method for C–C bond formations. Its value for ^{11}C -labeling has been investigated using ^{11}C -labeled alkenes obtained via a Wittig reaction from [^{11}C]methyl iodide (Björkman and Långström 2000). This approach permitted the incorporation of ^{11}C into the backbone of carbon structures inaccessible by other methods (► Fig. 41.25).

41.3.3.4 Carbonylations

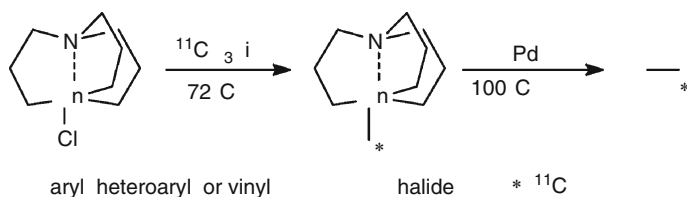
Insufficient trapping caused by low reaction rates and low solubility has hitherto precluded the practical use of [^{11}C]carbon monoxide in tracer synthesis. Examples of early investigations are the carbonylations of lithium dialkylamides (Kilbourn et al. 1983) and the insertion of [^{11}C]CO into a carbon–boron bond (Tang et al. 1979). There are, however, several principal advantages of using [^{11}C]carbon monoxide in tracer synthesis (Långström et al. 2007).

The rich chemistry of carbonylative coupling, developed through the advent of transition metal reagents, offers pathways to a broad range of carbonyl compounds. (1) Carbonyl groups are common among biologically active compounds. (2) Complex building blocks can be assembled in the carbonylation step to yield the target compound, which means short production times.

The low reactivity and the low concentration of carbon monoxide in the environment make prerequisites for high levels of specific radioactivity.

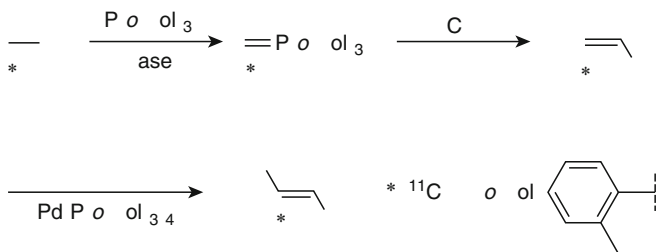
■ Fig. 41.24

Synthesis of ^{11}C -labeled 1-aza-5-stannabicyclo[3.3.3] undecane



■ Fig. 41.25

^{11}C -Labeling with the Heck reaction

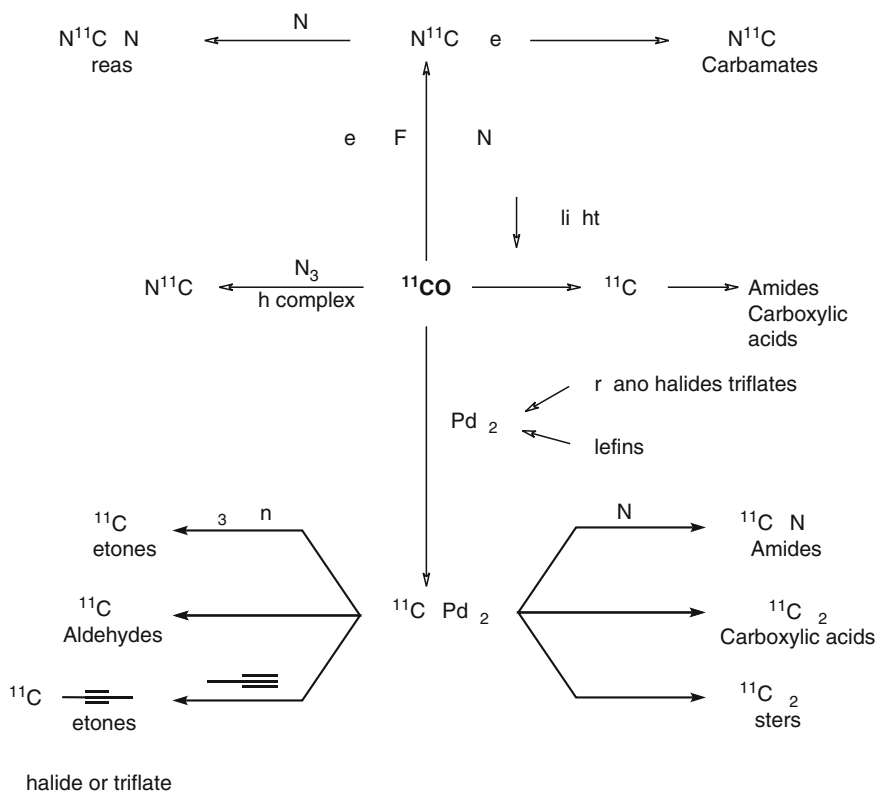


Recent technical innovations, where the $[^{11}\text{C}]$ carbon monoxide is either concentrated and pressurized with the reagent in a micro-autoclave or recycled through the reaction mixture, have greatly diminished the trapping problem (Lidström et al. 1997; Kihlberg and Långström 1999; Burns and Hostetler 2002). The autoclave method gives higher trapping efficiency than the recycling method and allows the use of volatile solvents at high temperature (e.g., THF at 180°C). Another possibility is to trap the $[^{11}\text{C}]$ carbon monoxide as a complex with BH_3 , or a copper(I) scorpionate. This method requires less sophisticated apparatus but is less general and efficient than the autoclave method (Audrain et al. 2004; Long et al. 2008). A microfluidic technology solution is to use a microtube reactor loaded with a silica supported palladium catalyst (Miller et al. 2007).

Compounds where the carbonyl group is bound to carbon have been synthesized using palladium, rhodium, or free radical chemistry and compounds where the carbonyl group is bound to two heteroatoms by using selenium or rhodium (Kihlberg and Långström 1999; Långström et al. 2007; Itsenko 2005; Kihlberg et al. 2002; Doi et al. 2004). The palladium-mediated carbonylations proceed via a palladium acyl complex, which reacts with nucleophiles to form a wide range of carbonyl compounds. Some chemical transformations that have been performed with $[^{11}\text{C}]$ carbon monoxide are shown in Fig. 41.26.

■ Fig. 41.26

Possible chemical transformations using $[^{11}\text{C}]$ carbon monoxide



In most of the palladium-mediated reactions, aryl halides have been used although several other types of electrophiles or alkenes may be employed. Aryl triflates give somewhat lower radiochemical yields and require the presence of lithium bromide. Diaryliodonium salts (e.g., diphenyliodonium bromide) have shown to be an interesting alternative in the synthesis of ^{11}C -labeled ketones (Al-Qahtani and Pike 2000).

The labeling of amides usually runs smoothly and is probably the most useful reaction since amides are common among biologically active compounds (Kihlberg and Långström 1999). In some cases, due to sterical hindrance or weak nucleophilicity, the use of lithium amides is needed, as in the case of the WAY-100635 analogues (► Fig. 41.27). This example shows the convenience by which a large number of derivatives of a lead compound can be labeled using the same carbonylation method. Depending on which part carries the main biological activity, either the organohalide or the nucleophile part is kept unchanged.

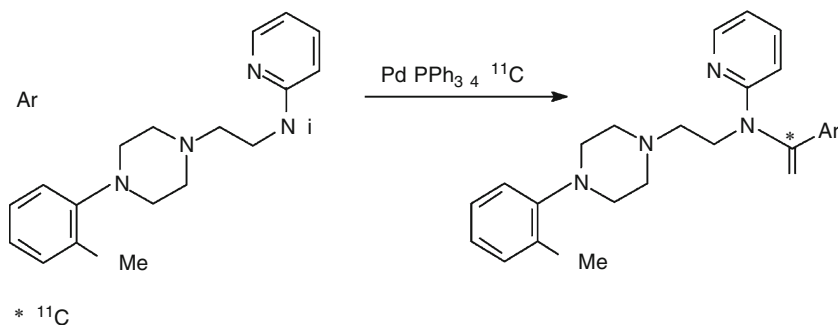
The labeling of open esters gives significantly lower yields due to the weaker nucleophilicity of alcohols compared to amines. The yields can be increased up to threefold by employing the acylation catalyst *N,N*-dimethyl amino pyridine (Kihlberg et al. 2001). Aldehydes are efficiently labeled at relatively low temperatures using different hydride donors as the source of nucleophile (Björkman et al. 2000b). Labeled aldehydes and ketones provide another route to obtain functionalized alkenes via the Heck reaction (Björkman et al. 2000b). Flavones and phthalimides can be synthesized by ^{11}C -carbonylations in ring-closure reactions (Kihlberg et al. 1999; Karimi et al. 2001).

The problem with β -hydride elimination that usually precludes the transition metal-mediated labeling of carbonyl groups bound to sp^3 carbons, can be circumvented by the use of free radical chemistry (Itsenko et al. 2004).

^{11}C -labeled carbamoyl compounds can be prepared by using a selenium-mediated reaction with $[^{11}\text{C}]$ carbon monoxide. The urea formation works excellent in the case of cyclizations but in other cases satisfactorily only with primary amines (Kihlberg et al. 2002). Since selenium is practically insoluble in most solvents the use of primary alkyl amines or tetrabutylammonium fluoride is necessary for the formation of soluble and reactive complexes with selenium. Except for ring closures, rhodium-promoted carbonylations are probably more useful than the corresponding selenium reactions (Ohad et al. 2009).

■ Fig. 41.27

Synthesis of ^{11}C -labeled substituted aryl analogues of WAY-100635






The zerovalent cuprates can also be used for synthesis of lithium [^{11}C]methyl(2-thienyl) cuprates from [^{11}C]methyl iodide (Kihlberg et al. 1997). These nucleophilic alkyl reagents have been employed in the synthesis of [21- ^{11}C]progesterone and [1 α -methyl- ^{11}C]mesterolone (► Fig. 41.29) (Lidström et al. 1997; Neu et al. 1998).

* ¹⁴C

41.3.4 Enzymes as Catalysts in ^{11}C -Labeling Synthesis

The use of enzymes in labeling synthesis, either free in solution or immobilized on a solid support, is an efficient way of synthesizing compounds that would otherwise be difficult to label in the desired position. Enzymes usually exhibit high regio-, chemo-, stereo-, and substrate selectivity. Two different types of enzymatic transformations can be distinguished: carbon–carbon bond formations and functional group transfer or transformation. The latter can be exemplified by transaminations or oxidations of amino groups to ketones (Barrio et al. 1982a; Halldin and Långström 1986).

Examples of the use of enzymes in ^{11}C -labeling are given below. Pyruvate and acetyl coenzyme A (acetyl CoA), are two generally useful precursors, available by enzymatic ^{11}C -labeling. Acetyl coenzyme A (Mannens et al. 1988) can be used as a general acetylating agent as is exemplified in the synthesis of $[^{11}\text{C}]$ acetyl-L-serotonin, *N*-acetyl-D- $[^{11}\text{C}]$ glucosamine (Mannens et al. 1990a, b), and acyl-L-carnitines (Spolter et al. 1979; Holsbach et al. 1991; Davenport et al. 1997; Jacobson et al. 1997; Angelini et al. 1999).  Figure 41.30 shows the multi-enzymatic synthesis of acetyl-L-carnitine labeled in two positions. Acetyl-CoA is formed as an intermediary product that is further used in the multienzymatic synthesis to the product, acetyl carnitine.

Pyruvate can be labeled either in the carboxylic (Hwang et al. 1986; Takahashi et al. 1990) or in the 3-position (Bjurling et al. 1988; Ropchan and Barrio 1984; Cohen et al. 1980). Pyruvate is a versatile compound for further transformations to aromatic amino acids and to lactic acid (Kloster and Laufer 1980; Bjurling and Långström 1989; Cohen et al. 1980). Some aliphatic amino acids have been labeled with ^{11}C employing enzymatic and combined chemo-enzymatic methods (Antoni et al. 1997, 2001; Barrio et al. 1982b; Cohen et al. 1982; Kaneko et al. 1999; Svård et al. 1990) as exemplified in  Fig. 41.31 and  41.32.


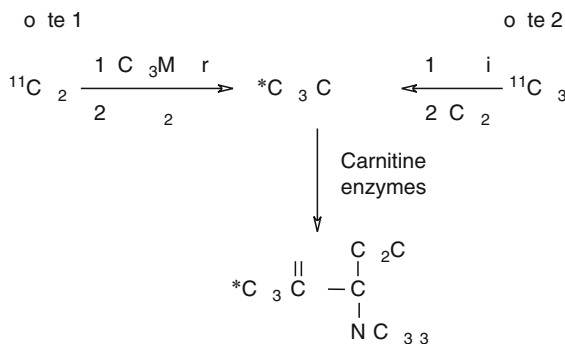
The chemo-enzymatic syntheses ( Fig. 41.33) of the aromatic amino acids, 3,4-dihydroxy-L-phenylalanine (DOPA), L-tyrosine, L-tryptophan, 5-hydroxy-L-tryptophan (5-HTP), and analogues thereof, ^{11}C -labeled either in the carboxylic- or β -position (Bjurling and Långström 1989; Bjurling et al. 1990a, b; Sasaki et al. 1999; Harada et al. 1999; Ikemoto et al. 1999) are other important achievements.

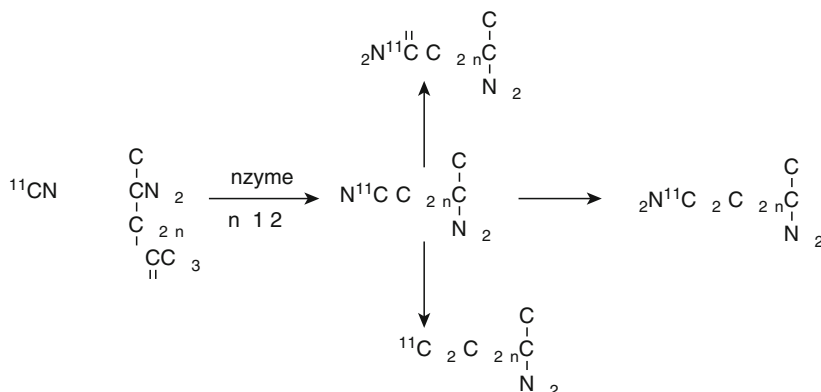
 Fig. 41.30

Synthesis of acetyl-L-carnitine labeled either in position 1 (route 1 *) or 2 (route 2 #) in the acetyl group



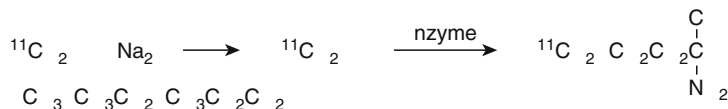
■ Fig. 41.31

Chemo-enzymatic syntheses of aliphatic amino acids by C–C bond formation

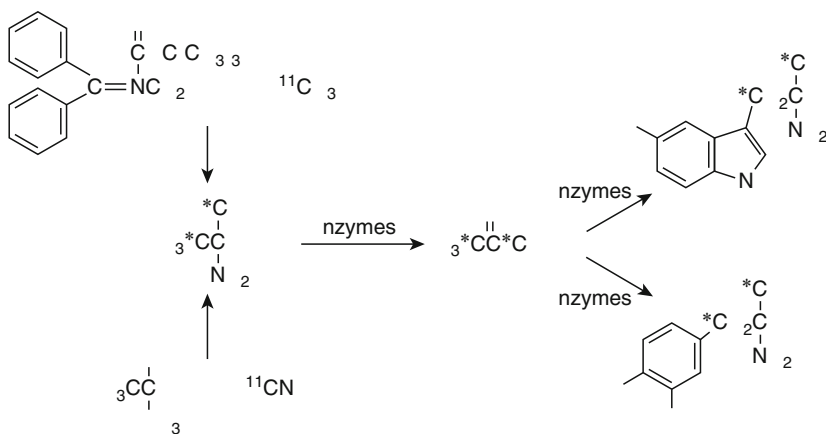


■ Fig. 41.32

Chemo-enzymatic syntheses of aliphatic amino acids by C–S bond formation



■ Fig. 41.33

Chemo-enzymatic synthesis of aromatic L-amino acids ^{11}C -labeled in two positions

The importance of the labeling position is shown in ► Fig. 41.34 where DOPA (3,4-dihydroxy-L-phenylalanine) labeled either in the carboxylic position or the β -position is used to visualize endocrine tumors (Bergström et al. 1996).

Some neuroendocrine tumors overexpress the enzyme aromatic amino acid decarboxylase (AADC). This can be used to visualize the tumor and at the same time gain information about the type of tumor. In these tumors L- $[\beta\text{-}^{11}\text{C}]\text{DOPA}$ is converted to $[\text{}^{11}\text{C}]\text{dopamine}$, which is trapped in the tumor whereas L- $[\text{carboxy-}^{11}\text{C}]\text{DOPA}$ gives unlabeled dopamine and $[\text{}^{11}\text{C}]\text{carbon dioxide}$. In ► Fig. 41.34, the tumor is clearly visualized after administration of L- $[\beta\text{-}^{11}\text{C}]\text{DOPA}$ indicating that AADC is overexpressed. Labeled carbon dioxide is washed out from the tumor, which is demonstrated in the right image.

Enzymatic catalysis is also used in the synthesis of 1- ^{11}C -labeled D-fructose and D-glucose from mannitol and glucitol, respectively (Ögren and Långström 1998). The preparation of S-adenosyl-L- $[\text{}^{11}\text{C}]\text{methionine}$ (Guegen et al. 1982), $[\text{}^{11}\text{C}]\text{epinephrine}$ (Soussain et al. 1984), and $[\text{}^{11}\text{C}]\text{daunorubicin}$ (Eriks-Fluks et al. 1998) are other examples of enzyme catalysis. The nucleosides $[\text{}^{11}\text{C}]\text{thymidine}$ and $[\text{}^{11}\text{C}]\text{-2'-arabino-2'-fluoro-}\beta\text{-5-methyl-uridine}$ have been prepared by enzymes immobilized on hollow fiber membranes using $[\text{}^{11}\text{C}]\text{formaldehyde}$ as the labeled precursor (Hughes and Jay 1995).

41.4 Examples of ^{11}C -Labeled Compounds

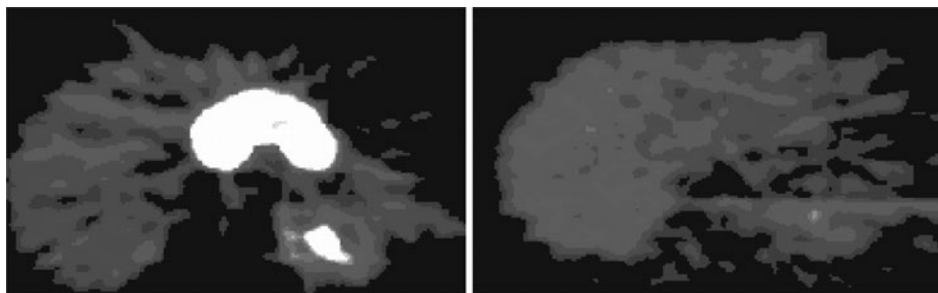
41.4.1 Amino Acids

The labeling position in the amino acids needs to be considered when designing the synthesis. Different positions may be preferred depending on the intended biological application as shown in ► Fig. 41.34. A complication is the chirality of the amino acids. Three synthetic methods have been used: (1) Establishing the stereochemistry in the precursor and introducing the label in a position that does not involve the chiral center. (2) Performing an asymmetric synthesis. (3) Separating the enantiomers of a racemic synthesis by chromatographic (Washburn et al. 1982) or enzymatic methods (Barrio et al. 1982a).

The main synthetic strategies that can be adopted for the synthesis of ^{11}C -labeled amino acids are (1) Bucherer–Strecker synthesis using $[\text{}^{11}\text{C}]\text{cyanide}$ or $[\text{}^{11}\text{C}]\text{aldehydes}$.

► Fig. 41.34

Positron emission tomography (PET) images over the abdomen in a patient with a neuroendocrine tumor (gastrinoma) after administration of L- $[\beta\text{-}^{11}\text{C}]\text{DOPA}$ (left) and L- $[\text{carboxy-}^{11}\text{C}]\text{DOPA}$ (right)



(2) Carboxylation reactions using [¹¹C]carbon dioxide. (3) Condensation reactions using [¹¹C]aldehydes. (4) Alkylation reactions using [¹¹C]alkyl halides. (5) Enzymatic methods.

In the Bucherer–Strecker synthesis, hydrogen [¹¹C]cyanide is reacted with the bisulfite adduct of an aldehyde (Hayes et al. 1978; Casey et al. 1981; Barrio et al. 1982) to produce neutral amino acids labeled in the carboxylic position. Labeled aromatic aldehydes have also been applied in the Bucherer–Strecker synthesis (Halldin and Långström 1984b) as well as in condensation reactions with oxazolones (Halldin and Långström 1984c, d, 1986) for labeling in the α - or the β -positions, respectively.

Carboxylation of lithiated carbanions of isonitriles with [¹¹C]carbon dioxide (Vaalburg et al. 1976; Bolster et al. 1986a; Hamacher and Hanus 1989) is an alternative synthetic approach to racemic amino acids labeled in the carboxylic position. Labeling in the 3-position (or β in the case of aromatic amino acids) can be achieved by alkylation using aliphatic or aromatic alkyl halides (Långström and Stridsberg 1979; Kilbourn et al. 1984; Antoni and Långström 1987).

This approach has also been applied in asymmetric syntheses of aliphatic [¹¹C]amino acids using different glycine derivatives such as [(+)-2-hydroxypinanyl-3-idene]glycine *tert*-butyl ester (Antoni and Långström 1986, 1987b), the nickel complex of the Schiffs base of (S)-*o*-(*N*-benzylpropyl)amino]benzophenone and glycine (Fasth et al. 1989, 1990a; Fasth and Långström 1990). The enantiomeric purity obtained is 80–98% enantiomeric excess (e.e.). The most promising methods, which give nearly enantiomerically pure [¹¹C]amino acids, used an imidazolidinone derivative (► Fig. 41.35) (Fasth et al. 1995; Plenevaux et al. 1994). These amino acid syntheses utilizing [¹¹C]alkyl halides in alkylation reaction on stabilized carbanions are efficient ways of forming C–¹¹C bonds.

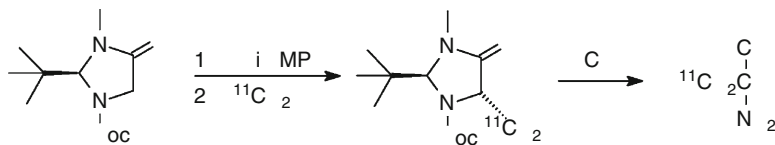
The preparation of L-[¹¹C]methionine (Comar et al. 1976; Långström et al. 1987; Schmitz et al. 1995) and L-[4-¹¹C]ornithine (Ding et al. 1989) from [¹¹C]methyl iodide and hydrogen [¹¹C]cyanide, respectively, are examples of syntheses where the chiral center is established before introduction of the label (► Fig. 41.36).

Labeling of peptides can be accomplished by methylation of the corresponding sulphide anion of a homocysteine residue (Franzén et al. 1987, 1988; Långström et al. 1981b; Någren et al. 1986, 1988) similar to the L-[¹¹C]methionine synthesis. Some dipeptides have also been labeled using a reaction between [1-¹¹C]glycine and the carboxyanhydrides of phenylalanine and leucine (Bolster et al. 1986b).

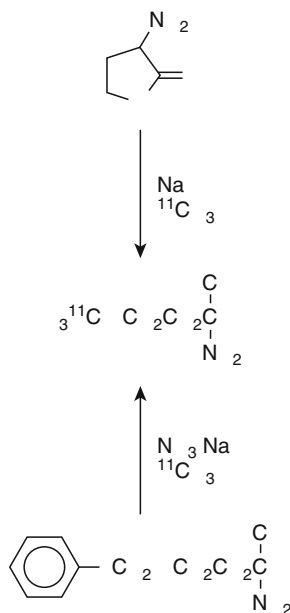
Some amino acid analogues such as α -[methyl-¹¹C]methylphenylalanine and α -[¹¹C-methyl]methyltyrosine have been synthesized by alkylations of malonic esters (Gee and Långström 1991) as well as α -[methyl-¹¹C]methyltryptophan (Bourne et al. 1991; Pulak et al. 1996). α -aminoisobutyric acid, labeled in either the carboxylic position (Dunzendorfer et al. 1981) or 2-position (Prenant et al. 1995a), or the 3-position (Oberdorfer et al. 1993; Schmall et al. 1996) and β -aminoisobutyric acid (Alauddin et al. 1997) are other examples. Other

► Fig. 41.35

Asymmetric synthesis of [¹¹C]amino acids by alkylations of imidazolidinone



■ Fig. 41.36

Methods for the synthesis of L-[methyl- ^{11}C]methionine

non-proteinogenic amino acids that have been prepared are 1-aminocyclopentane carboxylic acid (Hayes et al. 1976; Iwata et al. 1995) and *para*-[^{11}C]boronophenylalanine. The latter was synthesized as a tracer for treatment planning in connection with boron neutron captures therapy (Kabalka et al. 2001).

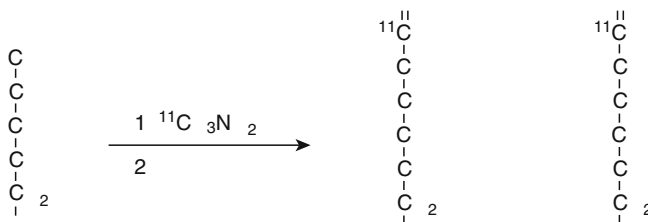
41.4.2 Carbohydrates, Steroids, Fatty acids and Nucleosides

Labeled carbohydrates such as glucose have been important tools for in vivo studies of energy metabolism. Several methods employing [^{11}C]cyanide, [^{11}C]methyl iodide, or [^{11}C]nitromethane have been developed for the specific labeling of glucose in positions 1 and 6 (Shiue and Wolf 1981; Tada et al. 1989; Schoeps et al. 1991; Grierson et al. 1993; Ögren et al. 1995b; Ögren et al. 1997). ➤ Figure 41.37 shows the synthesis of D-glucose and D-mannose labeled in position 1 using [^{11}C]nitromethane. The two sugars could be separated by HPLC.

Labeled 2-deoxy-glucose was developed to acquire metabolic trapping (Reivich et al. 1998; Padgett et al. 1982a). 2-Deoxy-D-[1- ^{11}C]glucose can, e.g., be obtained by a Wittig reaction followed by a PdCl_2 catalyzed oxidation (Ögren et al. 1997).

Saturated and unsaturated fatty acids have been labeled in the carboxylic position using [^{11}C]carbon dioxide and Grignard reagents (Pike et al. 1981; Padgett et al. 1982b; Piette et al. 1989; Oberdorfer et al. 1992; Channing and Simpson 1993; Ishiwata et al. 1995). Branched fatty acids such as β -[^{11}C]methyl heptadecanoic acid (Livni et al. 1982), 3,3-[^{11}C]dimethyl-heptadecanoic acid (Jones et al. 1988), and other fatty acids that do not participate in the β -oxidation have also been developed. Labeling in the 2-position of some β -methyl fatty acids

■ Fig. 41.37

Synthesis of D-[1- ^{11}C]glucose and D-[1- ^{11}C]mannose

was achieved by alkylation of malonic ester with [^{11}C]methyl iodide (Ogawa et al. 1997). Another example is the synthesis of a ^{11}C -leukotriene derivative, a potent metabolite of arachidonic acid, from acetyl chloride (Oberdorfer et al. 1992). The copper-mediated labeling of fatty acids is presented in ▶ Sect. 41.3.3.5.

The steroid structure is difficult to build up from simple labeled intermediates within the time frame allowed for ^{11}C synthesis. However, some examples of successful ^{11}C -labeling include 17- α -[^{11}C]methyltestosterone (Berger et al. 1981b), 17 α -[^{11}C]methylestradiol, and 11 β -ethyl-17 α -[^{11}C]-methylestradiol (Dence et al. 1994). In these syntheses [^{11}C]methyl iodide was converted to [^{11}C]methyllithium and was further reacted with the carbonyl functionality to give the corresponding alcohols. Examples of different labeling strategies are the syntheses of the adrenocortical steroid, triamcininolone acetone, prepared by reaction with [^{11}C]acetone (Berridge et al. 1994) and [*carbonyl*- ^{11}C]estramustine phosphate (Lidström et al. 1998) synthesized using [^{11}C]phosgene (▶ Fig. 41.38). The copper-mediated synthesis of mestrelone and progesterone are presented in ▶ Sect. 41.3.3.5.

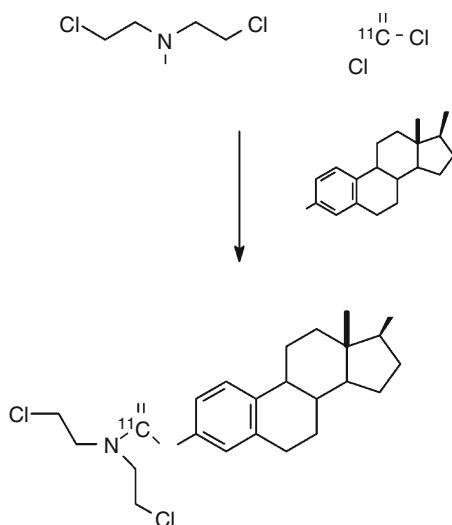
The development of tracers for the study of cell proliferation is an important area of research. The labeling of thymidine in different positions (▶ Fig. 41.39) is such an example (Goethals et al. 1992; Alauddin et al. 1995). The methyl position is not optimal since it gives rise to labeled metabolites interfering with the interpretation of the PET data. Labeling in any of the carbonyl positions may be advantageous since [^{11}C]carbon dioxide is the most prominent labeled metabolite using this labeling position. This has been achieved by using [^{11}C]urea or [^{11}C]phosgene in ring-closure reactions (Labar and Vander Borgh 1991; Borgh et al. 1991; Steel et al. 1993, 1999).

Other potentially useful tracers for the study of cell proliferation are uracil (Chakraborty et al. 1997), the uracil analogue [^{11}C]FMAU (Conti et al. 1995), 6-[methyl- ^{11}C]methyl-2'-deoxyuridine (Goethals et al. 1997), and [*methyl*- ^{11}C] β -pseudothymidine (Grierson et al. 1995). Another nucleoside analogue that was prepared by a ring-closure reaction is 1,3,6-trimethyl [2- ^{11}C]uracil prepared from 1,3-dimethyl [2- ^{11}C]urea (Castro-Ibarra et al. 1997).

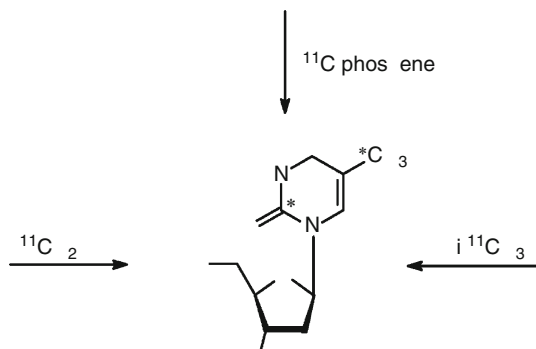
41.4.3 Compounds for Study of Enzymes and Receptors

A comprehensive list of synthesized ^{11}C -labeled receptor ligands is outside the scope of this chapter. Most attention has been focused on ligands for the dopamine- D_1 and D_2 receptors.

■ Fig. 41.38

Synthesis of [*carbonyl*- ^{11}C]estramustine phosphate

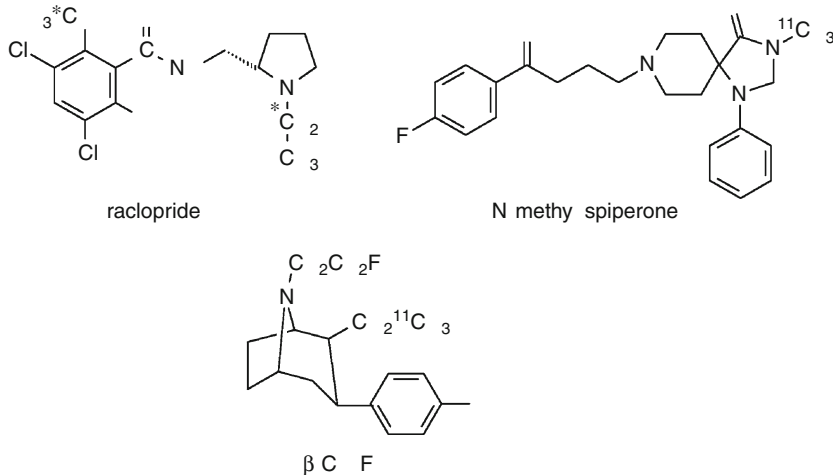
■ Fig. 41.39

Syntheses of [^{11}C]thymidine

The first example of a dopamine- D_2 antagonist that could visualize striatal dopamine receptors was *N*-[methyl- ^{11}C]methylspiperone (Wagner et al. 1983, see also ▶ Fig. 41.40). This compound also has affinity for the 5-HT $_{\text{A}2}$ receptors. [^{11}C]Raclopride is a more selective (Ehrin et al. 1986) D_2 antagonist and has become the golden standard for the investigation of dopamine D_2 receptors. It has been labeled in the methoxy group or in the *N*-ethyl group (▶ Fig. 41.40). The former labeling position being the preferred. The dopamine transporter has also been studied using, e.g., the cocaine analogue β -CIT-FT (Halldin et al. 1996, see also ▶ Fig. 41.40).

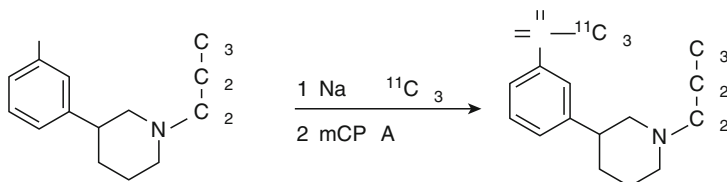
■ Fig. 41.40

Compounds for the dopaminergic system, ^{11}C -labeled raclopride, *N*-methylsipiperone, and β -CIT-FE



■ Fig. 41.41

Synthesis of ^{11}C -labeled OSU6162

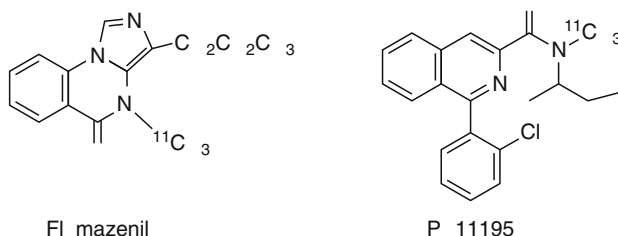


The presynaptic dopamine receptor antagonist (–)-OSU6162 has been labeled with ^{11}C and used to investigate the dopaminergic system (Neu et al. 1997b). OSU6162 has been claimed to be a drug that modulates the dopaminergic system in terms of minimizing on/off effect in late Parkinson's disease. ➤ Figure 41.41 shows the synthesis of OSU6162.

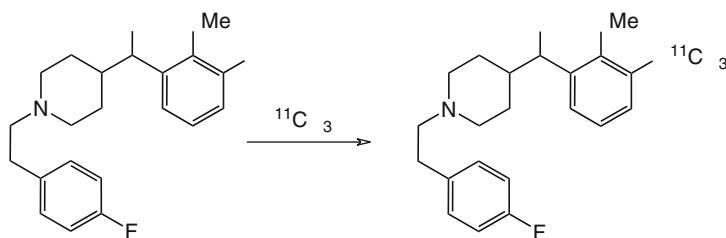
Benzodiazepine receptors, both central and peripheral have been investigated using the benzodiazepine receptor antagonists [^{11}C]flumazenil (Samson et al. 1985) and (+)PK11195 (Shah et al. 1994), respectively (➤ Fig. 41.42).

The serotonergic system has been studied using, e.g., the earlier presented $\text{HT}_{1\text{A}}$ antagonist [^{11}C]WAY100635 (McCarron et al. 1996). The selective 5-HT $_{2\text{A}}$ antagonist [^{11}C]MDL100907 (Lundkvist et al. 1996) is an alternative to *N*-methylsipiperone (➤ Fig. 41.43). The labeling position in MDL100907 is of importance. The methoxy group in the 3-position is preferred since the 3-OH analogue (MDL10575) had been identified as a metabolite. Labeling in position 2 should thus give a labeled compound with unknown biological properties that may disturb interpretation of PET data.

■ Fig. 41.42

Examples of ^{11}C -labeled benzodiazepine receptor ligands

■ Fig. 41.43

Synthesis of ^{11}C -labeled MDL100907

$[^{11}\text{C}]$ Nicotine has been used for the study of nicotinic cholinergic receptors. It is not an ideal tracer and other compounds have been used as alternatives such as analogues of the naturally occurring alkaloid epibatidine, a potent nicotine receptor antagonist (Spang et al. 1999, 2000). The muscarinic acetylcholine receptor has been investigated using, e.g., *N*-methyl-4-piperidyl benzilate and the corresponding ethyl- and propyl analogues (Mulholland et al. 1988; Nishiyama et al. 2000).

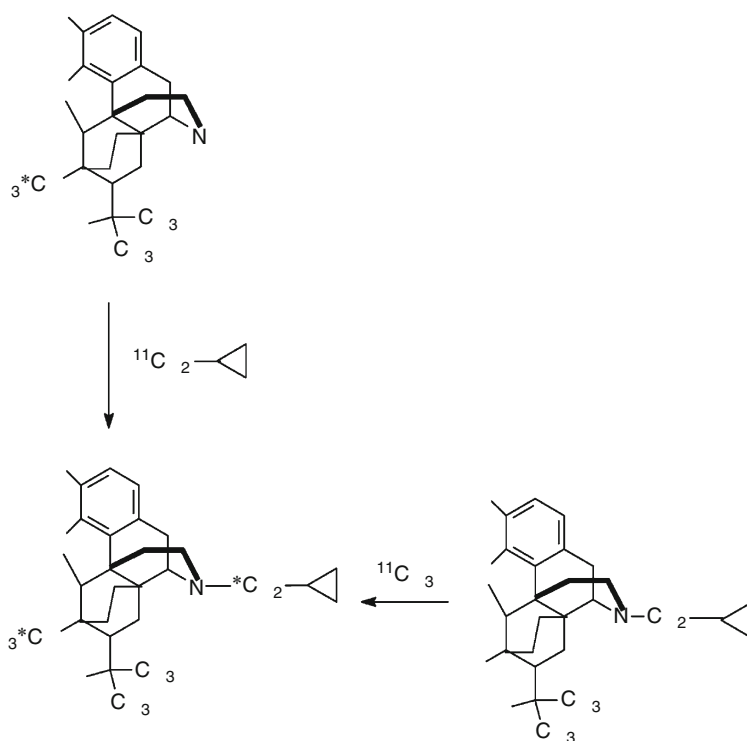
Some tracers for the different subclasses of opioid receptors are also available such as the μ -selective carfentanil and the nonselective diprenorphine (► Fig. 41.44). The latter is either labeled in the cyclopropyl- (Luthra et al. 1985) or the 6-methoxy group (Luthra et al. 1994).

The monoamine oxidase type B enzyme (MAO-B) has attracted much attention. A double-isotope labeling approach has been employed for the determination of MAO-B concentration in the heart and the brain using $[^{11}\text{C}](\text{--})\alpha,\alpha\text{-dideuterophenylephrine}$ (De Rosario and Wieland 1995) and $\alpha,\alpha\text{-dideutero-L-}[^{11}\text{C}]\text{deprenyl}$, respectively (Fowler et al. 1995). A kinetic isotope effect (KIE) (see ► Chap. 15 in Vol. 2) is observed when the deuterated compounds are used indicating that the C–D bond is involved in the rate limiting step with the enzyme. MAO-B has also been investigated using *N,N*-dimethylphenethylamine labeled either in the methyl or phenethyl group (Halldin et al. 1989).

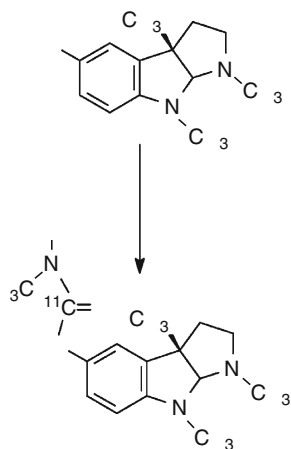
The acetylcholine esterase inhibitor physostigmine has been labeled from $[^{11}\text{C}]\text{methyl isocyanate}$ (► Fig. 41.45).

Other example of useful acetylcholine esterase inhibitors are *N*-methylpiperidine-4-yl acetate (Iyo et al. 1997) and propionate (Kilbourn et al. 1998).

■ Fig. 41.44

Synthesis of diprenorphine ^{11}C -labeled in two positions

■ Fig. 41.45

Synthesis of ^{11}C -labeled physostigmine

41.5 PET in Drug Development

41.5.1 General Considerations

The exploration of new chemical entities as potential drug candidates is a very expensive process and the failure rate, as late in the process as in clinical trials, is around 75%. A shift from the present empirical paradigm to a mechanistic one based on in vivo characterization of biochemical and physiological parameters should increase the scientific impact in the drug development process. Thus, to speed up the development process, achieve more accurate information for decision-making, and reduce the cost for the benefit of patients and the society, the noninvasive PET technology in combination with preclinical methods may be used. The use of labeled compounds to evaluate biological properties of new drug candidates early in the process and to select the lead candidates to be further investigated is a key process in drug development. PET is especially useful in the drug development process for the study of the following.

Pharmacokinetics – labeling of a potential drug candidate. This study includes distribution studies of drug passage over the blood-brain barrier and selective accumulation in critical organs. Apart from intravenous administration, oral and nasal administration routes are other important applications employed for quantification of the deposition and disposition of a drug formulation.

Pharmacodynamics – use of a labeled tracer to monitor drug effect. An evaluated tracer can be used in standard dose-response studies, e.g., to measure receptor occupancy as a function of increasing dose or to follow up treatment effects. Especially in cancer treatment is the use of a surrogate marker for tumor metabolism or proliferation rate of great value since other imaging modalities such as computed tomography (CT) and magnetic resonance imaging (MRI) only can distinguish a reduction in size of the tumor, which usually has a time span of several months from start of treatment, whereas a change in metabolism or proliferation may be observed within days or even hours. The use of L-[methyl-¹¹C]methionine for the differential diagnosis between non-responding pituitary tumors and those tumors that show nearly immediate effect on bromocryptine treatment (Bergström and Muhr 1991; Bergström et al. 1992) is a good example of PET in the evaluation of a therapeutic agent.

41.5.2 PET Microdosing

PET microdosing is a concept consisting of a first-time-in-man (FTIM) application of a labeled drug candidate in a PET study (Bergström et al. 2002). This requires high specific radioactivity of the labeled compound to assure that the given dose is in the nanomolar range and that the study is performed at true tracer conditions. Crucial information about distribution and kinetics can be gained from such investigations aiming at an in vivo characterization of biochemical and/or physiological parameters of the new drug candidate. The PET-microdosing concept is based on the use of trace amount of a drug that has been qualified for a FTIM study by a reduced safety toxicology investigation using a preclinical package that includes assessment of the following.

Acute toxicity. One species should be used to study the acute effect of the new drug. If a significant difference of free fraction of the drug in plasma is found between human and animal plasma, the drug dose is modified in accordance with the results from plasma protein

binding. Acute toxic effects are investigated by inspection and histological evaluation of the organs after different intervals from dosing. Acute effects are investigated using a dose that is at least 100 times the expected administered dose in a human PET study.

Primary pharmacology. Information that suggests that the new drug candidate has affinity and some specificity for the target organ or receptor.

Secondary pharmacology. Clinical observation of acute effects in rats after dosing with 100 times of the expected dose in a human PET study followed by a similar study in monkeys.

Genotoxicity. Potential genotoxicity of the new drug is evaluated using classical methods such as AMES test in bacteria and mammalian cells. The amount of drug used is typically much lower than in the standard test methods.

Metabolism. PET can only measure radioactivity and in order to be able to evaluate those PET data, information about the chemical form of the measured radioactivity is important. Determination of the fraction of intact tracer in plasma and in the target organ in animal experiments can give the required information. The occurrence of labeled metabolites should be assessed at different time points in the human microdosing study.

Dose linearity. In a microdosing study, the drug concentration is significantly lower than at the expected therapeutic level. It cannot be taken for granted that metabolic patterns and the biodistribution are similar at these very different conditions. High-affinity binding sites and saturation of transport and enzyme systems at high doses may result in a nonlinear dose-dependent drug distribution. This can be evaluated by a few PET studies in monkeys where different doses of the new drug are given together with the labeled drug.

Plasma protein binding. Plasma protein binding should be assessed in the same species used for acute toxicity and secondary pharmacology. The main objective is to assure that binding is stable and the risk for a sudden concentration rise in plasma due to an unexpected release of bound tracer is unlikely.

Radiotoxicity. Animal ex vivo studies to evaluate the biodistribution of the labeled compound are performed to exclude selective accumulation of radioactivity in organs that could lead to radiation-induced tissue damage.

The information gained from a human PET-microdosing study can be very helpful in deciding whether or not to continue the drug development process. Vital information about drug pharmacokinetics is obtained such as high accumulation in an organ that could give rise to unwanted side effects. The microdosing study can be performed using small amounts of the new drug candidate and a time-consuming and expensive up-scaling of the synthesis is thus not needed.

41.5.3 ¹¹C-Tracers in Drug Development

A smoke cessation device that simulates a cigarette by inhalation of nicotine from a plastic tube containing a porous plug impregnated with nicotine was labeled with S-[¹¹C]nicotine and the deposition pattern and the appearance of nicotine in plasma were investigated (Bergström et al. 1995; Lunell et al. 1996). As a comparison, a cigarette was impregnated with S-[¹¹C]nicotine and the distribution pattern studied. ▶ [Figure 41.46](#) shows the S-[¹¹C]nicotine deposition.

The use of the vaporizer device resulted in high levels of S-[¹¹C]nicotine in the oral cavity, the esophagus, and the stomach. No activity could be detected in the lungs. Smoking a cigarette gave the expected results with high amounts in the lungs. These findings correlate well with the observed slow increase of blood radioactivity from the vaporizer and the very rapid blood

Fig. 41.46

Lung deposition of S -[^{11}C]nicotine in a healthy volunteer after pulmonary inhalation from the device (left). Deposition of S -[^{11}C]nicotine after smoking a cigarette in a normal way (right)



radioactivity increase from the cigarette. The use of the vaporizer is thus unlikely to give the subject a nicotine effect that maintains the addiction.

Another example of an inhalation study is the investigation of pulmonary distribution of the anti-inflammatory steroid triamcinolone acetonide. Drug deposition following inhalation of [^{11}C]triamcinolone using the Azmacort inhaler was investigated with PET (Berridge et al. 2000).

Another educational example is the quantification of the inhibition of the enzyme monoamino oxidase type A (MAO-A) in the brain using PET. A new reversible MAO-A inhibitor, esuprone, was promoted as an antidepressive drug and a correct assignment of treatment regimes such as dosage and dose intervals was evaluated using PET (Bergström et al. 1997). The pharmacodynamic property of the drug was measured as percentage inhibition of MAO-A in the brain. The duration of the inhibition of the enzyme was an important parameter to determine. Several putative MAO-A inhibitors were investigated and [*methyl*- ^{11}C]harmine was found to be a useful tracer for the assessment of the pharmacodynamics of esuprone (Bergström et al. 1997). [Figure 41.47](#) shows the uptake of [^{11}C]harmine in the brain before and after esuprone treatment.

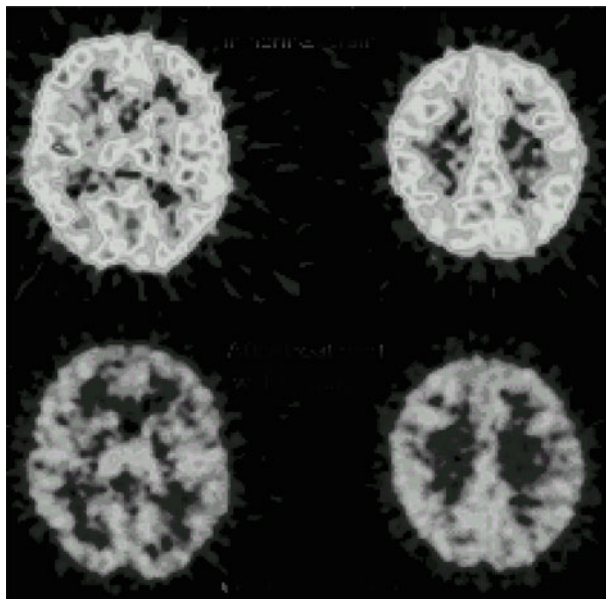
High uptake of [^{11}C]harmine was found in the brain with kinetics indicating trapping of the tracer. After dosing with the study drug, a clear washout was observed. The antidepressant drug esuprone had a half-life of 3.5 h in plasma and 14.8 h at the target enzyme in the brain. The plasma pharmacodynamics was thus significantly different from that on the effector system. This is crucial information with respect to dosing since the drug concentration in plasma is the main input for determining dose and dose interval. The PET data on the other hand give the true drug concentration and enzyme inhibition at the pharmacological target. This information suggests a longer dose interval, which may reduce unwanted side effects from the drug.

41.6 Quality Control of ^{11}C -Compounds

The quality control of radiopharmaceuticals labeled with short-lived radionuclides has to rely on indirect methods for the identification of the compound. Direct methods such as nuclear magnetic resonance (NMR) and infrared spectroscopy cannot be used. Some tests, such as measurement of pH and LC-analysis, can be performed before the radiopharmaceutical is released for use. The radiopharmaceutical is mixed with authentic reference substance and if

■ Fig. 41.47

Brain uptake of [^{11}C]harmine before and after esuprone treatment indicating expression of monoamino oxidase type A (MAO-A) (*upper images*) and after treatment with esuprone a marked inhibition (*lower images*)



identical peak shape and retention times are obtained for the radioactive peak and the response from the mass detector, usually UV-absorbance detector, the identity is verified.

Radiochemical purity is usually determined by a HPLC analysis complemented by another chromatographic method, e.g., TLC. This gives the option of using two distinct chromatographic methods and the risk of coincidental identical retention times is minimized. The recovery of the injected radioactivity from the chromatographic column must be determined in order to validate that the chromatogram obtained is representative of the injected sample.

Liquid chromatography mass spectrometry has evolved as a nearly direct method for the verification of the identity of a labeled compound. A combined $^{11}\text{C}/^{13}\text{C}$ labeling synthesis can be used to further ascertain the identity of the product. After decay of ^{11}C , the ^{13}C -compound is analyzed with NMR and the shift of the ^{13}C -enriched position in the sample can be compared with that of authentic reference substance.

The concept of parametric release has to be adopted since the analyses that are used to ascertain the absence of viable microorganisms or bacterial endotoxins cannot be completed before the radioactivity has decayed. However, it should be emphasized that a strict GMP protocol should be used in routine production of compounds for human use. A validation program should be practiced where randomized sampling of used batches is applied for analysis of presence of microorganisms or endotoxins.

Since most PET radiopharmaceuticals are purified by chromatographic methods using organic solvent, a residual solvent analysis should be performed as a routine validation of a certain number of used batches.

41.7 ¹¹C as a Tool in Chemistry Research

Kinetic isotope effect studies. Kinetic isotope effect (KIE) measurements are a powerful approach for the elucidation of reaction mechanism and the quantification of rate constants. This gives insight into molecular mechanisms and increases one's understanding of molecular interaction. The KIE is dependent on the mass difference between the isotopes and the largest practical value for a carbon KIE ratio is obtained using ¹¹C/¹⁴C (Axelsson et al. 1990; Matsson et al. 1999).

A KIE may occur as a result of an isotopic substitution in a position in the molecule that is involved in a rate-limiting step of the reaction. The magnitude of the effect gives information about the transition state (TS) structure such as if the TS is reactant–product-like or symmetric. KIE can, e.g., be used to determine which step is rate limiting, if the process is stepwise or concerted. The method has been applied to investigate incoming group KIE using [¹¹C]cyanide (Matsson et al. 1996) to study rearrangements in the methyldiene ring system (Axelsson et al. 1990) and enzyme mechanism investigations (Axelsson et al. 1992).

References

- Alauddin MM, Ravert HT, Musachio JL, Mathews WB, Dannals RF, Conti P (1995) Nucl Med Biol 22:791
- Alauddin MM, Fissekis JD, Conti PS (1997) Nucl Med Biol 24:771
- Al-Qahtani MH, Pike VW (2000) J Chem Soc Perkin Trans 1(6):1033
- Andersson Y, Långström B (1994) J Chem Soc Perkin Trans 1395
- Andersson Y, Långström B (1995a) J Chem Soc Perkin Trans 1:287
- Andersson Y, Långström B (1995b) J Lab Comp Radiopharm 37:84
- Andersson Y, Bergström M, Långström B (1994) Appl Radiat Isot 45:707
- Andersson Y, Cheng A, Långström B (1995) Acta Chem Scand 49:683
- Andersson Y, Tyrefors N, Sihver S, Onoe H, Watanabe Y, Tsukada H, Långström B (1998) J Labeled Compd Radiopharm 49:567
- Angelini G, Carnavaletti F, Margonelli A, Corsi G, Ragni P, Fazio F, Toodde S, Tinti O (1999) Appl Radiat Isot 50:303
- Antoni G, Långström B (1986) Acta Chem Scand B 40:152
- Antoni G, Långström B (1987a) J Labeled Compd Radiopharm 24:125
- Antoni G, Långström B (1987b) Acta Chem Scand B 41:511
- Antoni G, Långström B (1987c) Appl Radiat Isot 38:655
- Antoni G, Långström B (1992) Appl Radiat Isot 43:903
- Antoni G, Omura H, Bergström M, Furuya Y, Moulder R, Roberto A, Sundin A, Watanabe Y, Långström B (1997) Nucl Med Biol 24:595
- Antoni G, Omura H, Ikemoto M, Moulder R, Watanabe Y, Långström B (2001) J Labeled Compd Radiopharm 44:285
- Audrain H, Martarello L, Gee A, Bender D (2004) Chem Commun 558
- Axelsson S, Engdahl KÅ, Långström B, Matsson O (1990) J Am Chem Soc 112:6656
- Axelsson S, Bjurling P, Långström B, Matsson O (1992) J Am Chem Soc 114:1502
- Balatoni JA, Adams MJ, Hall LD (1989) J Labeled Compd Radiopharm 27:1429
- Barrio JR, Phelps ME, Huang SC, Keen RE, MacDonald NS (1982a) J Labeled Compd Radiopharm 19:1271
- Barrio JR, Egbert JE, Henze A, Schelbert HR, Baumgartner FJ (1982b) J Med Chem 25:93
- Berger G, Maziere M, Prenant C, Comar D (1980a) Int J Appl Radiat Isot 31:577
- Berger G, Maziere B, Sastre J, Comar D (1980b) J Labeled Compd Radiopharm 17:59
- Berger G, Maziere M, Godot JM, Prenant C, Comar D (1981a) J Labeled Compd Radiopharm 18:1649
- Berger G, Maziere M, Prenant C, Sastre J, Comar D (1981b) Int J Appl Radiat Isot 32:811
- Bergström M, Muhr C (1991) J Endocrinol Inv 14:509
- Bergström M, Muhr C, Jossan S, Lilja A, Nyberg G, Långström B (1992) Neurosurgery 30:855
- Bergström M, Nordberg A, Lunell E, Antoni G, Långström B (1995) Clin Pharmacol Ther 57:309
- Bergström M, Eriksson B, Öberg K, Sundin A, Ahlström H, Lindner KJ, Bjurling P, Långström B (1996) J Nucl Med 37:32
- Bergström M, Westerberg G, Kihlberg T, Långström B (1997) Nucl Med Biol 24:381

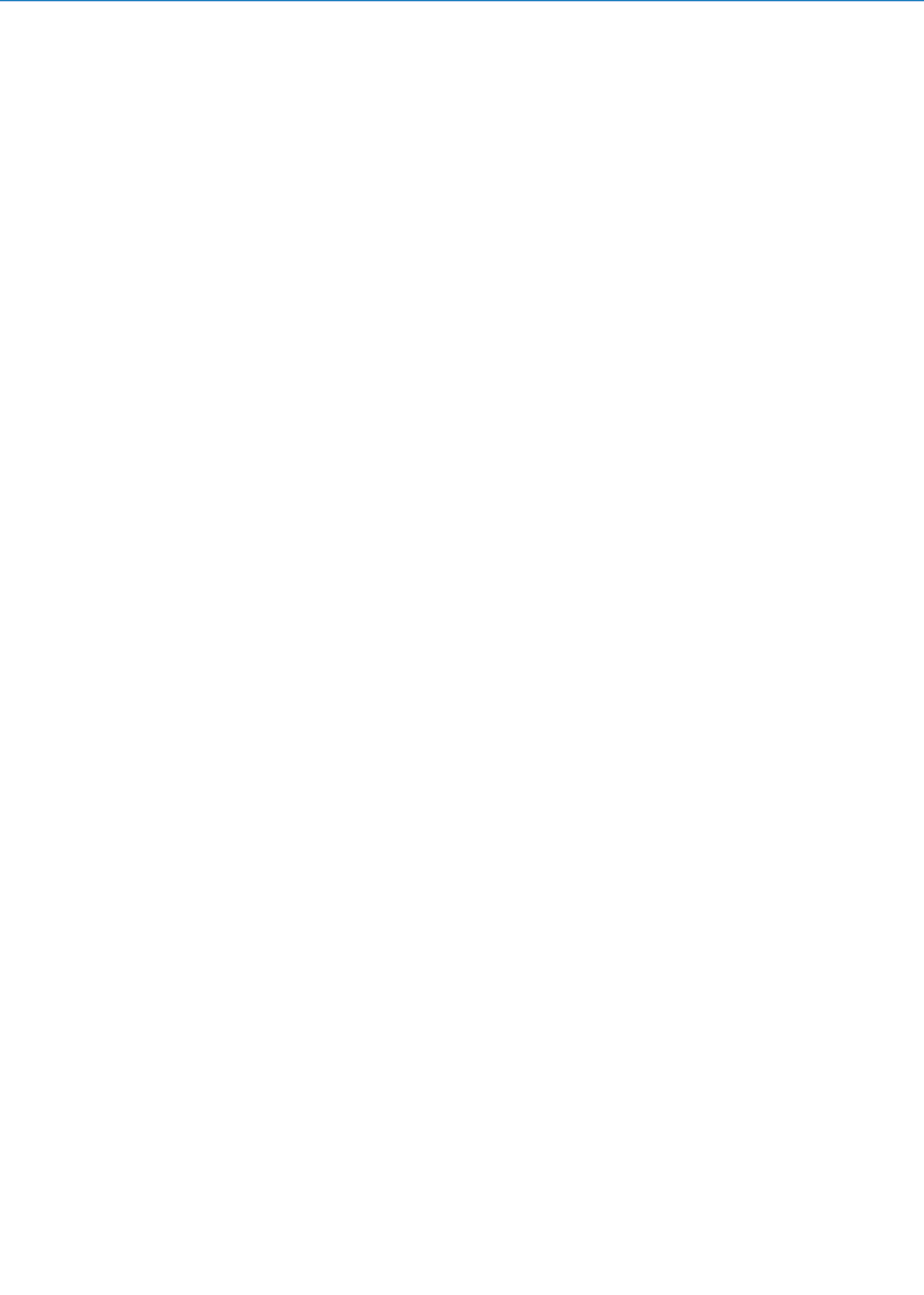
- Bergström M, Westerberg G, Nemeth G, Traut M, Gross G, Greger G, Muller-Peltzer H, Safer A, Bergström M, Grahnén A, Långström B (2002) *Eur J Clin Pharmacol* Berridge MS, Cassidy EH, Bordeaux KG (1994) *Appl Radiat Isot* 45:91
- Berridge MS, Lee Z, Heald DL (2000) *J Nucl Med* 41:1603
- Bida GT, Ruth TJ, Wolf AP (1978) *Radiochim Acta* 27:181
- Björkman M, Långström B (2000) *J Chem Soc Perkin Trans* 1:3031
- Björkman M, Andersson Y, Doi H, Kato K, Suzuki M, Noyori R, Watanabe Y, Långström B (1998) *Acta Chem Scand* 52:635
- Björkman M, Doi H, Resul B, Suzuki M, Noyori R, Watanabe Y, Långström B (2000a) *J Labeled Compd Radiopharm* 43:1327
- Björkman M, Kihlberg T, Långström B (2000b) Manuscript in: M. Björkman: Doctoral Thesis, Acta Universitatis, Upsaliensis, No. 564, Uppsala, 2000
- Bjurling P, Långström B (1989) *J Labeled Compd Radiopharm* 38:427
- Bjurling P, Watanabe Y, Långström B (1988) *Appl Radiat Isot* 39:627
- Bjurling P, Watanabe Y, Tokushige M, Oda T, Långström B (1989) *J Chem Soc Perkin Trans* 1331
- Bjurling P, Watanabe Y, Oka S, Nagasawa T, Yamada H, Långström B (1990a) *Acta Chem Scand* 44:183
- Bjurling P, Antoni G, Watanabe Y, Långström B (1990b) *Acta Chem Scand* 44:178
- Bolster JM, Vaalburg W, Paans AM, van Dijk TH, Elsinga PH, Zijlstra JB, Piers DA, Mulder NH, Woldring MG, Wynberg H (1986a) *Eur J Nucl Med* 12:321
- Bolster JM, Vaalburg W, Elsinga PH, Woldring MG, Wynberg H (1986b) *Appl Radiat Isot* 37:985
- Bolton R (2001) *J Labeled Compd Radiopharm* 44:701
- Bonnot-Lours S, Crouzel C, Prenant C, Hinnen F (1993) *J Labeled Compd Radiopharm* 33:277
- Borghet TV, Labar D, Pauwels S, Lambotte L (1991) *Appl Radiat Isot* 42:103
- Bourne GT, Crich D, Davies JW, Horwell DC (1991) *J Chem Soc Perkin Trans* 1:1693–1699
- Brown GD, Turton DR, Luthra SK, Price P, Jones T, Stevens MFG, Baghurst DR, Mings DMP, Osman S, Waters SL, Brady F (1994) *J Labeled Compd Radiopharm* 35:100
- Brown GD, Henderson D, Steel C, Luthra SK, Price PM, Brady F (2001) *Nuc Med Biol* 28:991
- Burns HD, Hostetler ED (2002) *Nucl Med Biol* 29:845
- Casey DL, Digenis GA, Wesner DA, Washburn LC, Chaney JE, Hayes RL, Callahan AP (1981) *Int J Appl Radiat Isot* 32:325
- Castro-Ibarra A, Weber K, Oberdorfer F (1997) *J Labeled Compd Radiopharm* 40:810
- Chakraborty PK, Manger TJ, Chugani HT (1997) *Appl Radiat Isot* 48:619
- Channing MA, Simpson N (1993) *J Labeled Compd Radiopharm* 33:541
- Christman DR, Crawford EJ, Finn RD, Friedkin M, Wolf AP (1971) *Proc Natl Acad Sci USA* 69:988
- Christman DR, Finn RD, Karlström K, Wolf AP (1975) *Int J Appl Radiat Isot* 26:435
- Cohen MB, Spolter L, Chang CC, Cook JS, MacDonald NS (1980) *Int J Appl Radiat Isot* 31:45
- Cohen MB, Spolter I, Chang CC, Behrendt D, Cooks J, MacDonald N (1982) *Int J Appl Radiat Isot* 33:613
- Collman JP, Hegedus LS, Norton JR, Finke RG (1987) *Organotransition metal chemistry*. University Science Books, Mill Valley
- Comar D, Carton JC, Maziere M, Marazano C (1976) *Eur J Nucl Med* 1:11
- Conti PS, Alauddin MM, Fissekis JR, Schmall B, Watanabe KA (1995) *Nucl Med Biol* 22:783
- Crouzel C, Långström B, Pike VW, Coenen HH (1987a) *Appl Radiat Isot* 38:601
- Crouzel C, Amno R, Fournier D (1987b) *Appl Radiat Isot* 38:669
- Crouzel C, Hinnen F, Maitre E (1995) *Appl Radiat Isot* 46:167
- Cyric (2003) www.rencyric@cyric.tohoku.ac.jp
- Davenport RJ, Pike VW, Dowsett K, Turton DR, Poole K (1997) *Appl Radiat Isot* 48:917
- De Rosario RB, Wieland DM (1995) *J Labeled Compd Radiopharm* 36:625
- Dence CS, Napolitano E, Katzenellenbogen JA, Welch MJ (1994) *Nucl Med Biol* 23:491
- Ding YS, Antoni G, Fowler JS, Wolf AP, Långström B (1989) *J Labeled Compd Radiopharm* 27:1079
- Doi H, Barletta J, Suzuki M, Noyori R, Watanabe Y, Långström B (2004) *Org Biomol Chem* 2:3063
- Dunzendorfer U, Schmall B, Bigler RE (1981) *Eur J Nucl Med* 6:535
- Eckernas SA, Grahner A, Långström B (1997) *Eur J Clin Pharmacol* 52:121
- Ehrin E, Gawell L, Högberg T, de Paulis T, Ström P (1986) *J Labeled Compd Radiopharm* 24:931
- Elsinga PH, Keller DE, Groot TJ, Visser GM, Vaalburg W (1995) *Appl Radiat Isot* 46:227
- Emran AM, Boothe TE, Finn RD, Vora MM, Kothari PJ, Wooten JT (1985) *Int J Appl Radiat Isot* 36:739
- Eriks-Fluks E, Elsinga PH, Hendrikse NH, Franssen EJE, Vaalburg W (1998) *Appl Radiat Isot* 49:811
- Eriksson JPL, Långström B (2001) *J Labeled Compd Radiopharm* 44:S132
- Fasth KJ, Långström B (1990) *Acta Chem Scand* 44:720
- Fasth KJ, Antoni G, Långström B (1989) *J Chem Soc Perkin Trans* 1:3081
- Fasth KJ, Antoni G, Långström B (1990a) *Acta Chem Scand* 44:527
- Fasth KJ, Antoni G, Långström B (1990b) *Appl Radiat Isot* 6:611
- Fasth KJ, Hörnfeldt K, Långström B (1995) *Acta Chem Scand* 49:301

- Forngren T, Samuelsson L, Björkman M, Långström B (2001) *J Labeled Compd Radiopharm* 44:S1011
- Fowler JS, Wolf AP (1986) In: Phelps M, Mazziotta J, Schelbert H (eds) *Positron emission tomography and autoradiography: principles and applications for the brain and heart*. Raven, New York
- Fowler JS, Wang GJ, Logan J, Xie S, Volkow ND, Macgregor RR, Schlyer DJ, Pappas N, Alexoff DL, Patlak C, Wolf AP (1995) *J Nuc Med* 36:1255
- Franzén HM, Ragnarsson U, Långström B (1987) *J Chem Soc Perkin Trans* 1:2241
- Franzén HM, Nägren K, Grehn L, Långström B, Ragnarsson U (1988) *J Chem Soc Perkin Trans* 1:497
- Gee AD, Långström B (1991) *J Chem Soc Perkin Trans* 1:215
- Goethals P, Sambre J, Coene M, Casteleyn K, Poupeye E (1992) *App Radiat Isot* 43:952
- Goethals P, Volders F, Van der Eycken J (1997) *Nucl Med Biol* 24:713
- Grierson JR, Biskupiak JE, Link JM, Krohn K (1993) *Appl Radiat Isot* 44:1449
- Grierson JR, Shields AF, Zheng M, Kozawa SM, Couter JH (1995) *Nucl Med Biol* 22:671
- Guegen P, Maziere B, Berger G, Comar D, Morgat JL (1982) *J Labeled Compd Radiopharm* 19:157
- Halldin C, Långström B (1984a) *Acta Chem Scand B* 38:1
- Halldin C, Långström B (1984b) *J Labeled Compd Radiopharm* 22:631
- Halldin C, Långström B (1984c) *Int J Appl Radiat Isot* 35:779
- Halldin C, Långström B (1984d) *Int J Appl Radiat Isot* 35:945
- Halldin C, Långström B (1986) *J Labeled Compd Radiopharm* 23:715
- Halldin C, Bjurling P, Stålnacke CG, Sukhinder SJ, Orelund L, Långström B (1989) *Appl Radiat Isot* 40:557
- Halldin C, Farde L, Lundkvist C, Ginovart N, Nakashima Y, Karlsson P, Swahn CG (1996) *Synapse* 22:386
- Hamacher K, Hanus J (1989) *J Labeled Compd Radiopharm* 27:1275
- Harada N, Hayashi N (1993) *Appl Radiat Isot* 44:629
- Harada N, Nishiyama S, Sata K, Tsukada H (1999) *Appl Radiat Isot* 52:845
- Hayes RH, Washburn LC, Wieland BW (1976) *J Nucl Med* 17:748
- Hayes RL, Washburn LC, Wieland BW, Sun TT, Anon JB (1978) *Int J Appl Radiat Isot* 29:186
- Heselius SJ, Malmberg P, Solin O, Långström B (1987) *Appl Radiat Isot* 38:49
- Holsbach M, Hamkens W, Roden W, Feindegen LE (1991) *J Labeled Compd Radiopharm* 29:599
- Hooker JM, Schoenberger M, Shchierstein H, Fowler JS (2008) *Angew Chem Int Ed* 47:5989
- Hörnfeldt K, Långström B (1994a) *Acta Chem Scand* 48:665
- Hörnfeldt K, Långström B (1994b) *J Labeled Compd Radiopharm* 35:86
- Hörnfeldt K, Långström B (1994c) *J Labeled Compd Radiopharm* 34:707
- Hörnfeldt K, Antoni G, Långström B (1992) *Acta Chem Scand* 46:87
- Hughes JA, Jay M (1995) *Nucl Med Biol* 22:105
- Hughes JA, Hartman NG, Jay M (1995) *J Labeled Compd Radiopharm* 36:1133
- Hwang DR, Kilbourn MR, Welch MJ (1986) *J Labeled Compd Radiopharm* 23:1064
- Hwang DR, Morlein L, Welch MJ (1987) *J Chem Soc Chem Commun* 1799
- Ikemoto M, Sasaki M, Haradahira T, Yada T, Omura H, Furiya Y, Watanabe Y, Suzuki K (1999) *Appl Radiat Isot* 50:715
- Imahori Y, Fujii R, Ido T, Hirakawa K, Nakahashi M (1989) *J Labeled Compd Radiopharm* 27:1025
- Imahori Y, Fujii R, Ueda S, Ido T, Nishino H, Moriyama Y, Yamamoto LY, Nakahashi H (1991) *J Nucl Med* 32:1622
- Ishiwata K, Ishii SI, Senda M (1995) *Appl Radiat Isot* 46:1035
- Itsenko O (2005) *Photoinitiated radical carbonylation using [¹¹C]carbon monoxide: ¹¹C-labeling of aliphatic carboxylic acids, esters, and amides*. Dissertation, The Faculty of Science and Technology, vol. 106, Uppsala University; ISBN 91-554-6375-4
- Itsenko O, Kihlberg T, Långström B (2004) *J Org Chem* 69:4356
- Iwata R, Ido T (1983) *Int Appl Radiat Isot* 34:973
- Iwata R, Ido T, Tominaga T (1981) *Int J Appl Radiat Isot* 32:303
- Iwata R, Ido T, Takahashi T, Nakanishi H, Iida S (1987) *Appl Radiat Isot* 38:97
- Iwata R, Tatsuo I, Ujie A, Takahashi T, Ishiwata K, Hatano K, Sugahara M (1988) *Appl Radiat Isot* 39:1
- Iwata R, Ido T, Tada H (1995) *Appl Radiat Isot* 46:899
- Iyo M, Namba H, Fukushima K, Shinotoh H, Nagatsu S, Suhara T, Sudo Y, Suzuki K, Irie T (1997) *Lancet* 349:1805
- Jacobson G, Markides K, Långström B (1994a) *Acta Chem Scand* 48:428
- Jacobson G, Markides K, Långström B (1994b) *J Labeled Compd Radiopharm* 35:111
- Jacobson G, Westerberg G, Markides KE, Långström B (1996) *J Am Chem Soc* 118:6868
- Jacobson GB, Watanabe Y, Valind S, Kuratsune H, Långström B (1997) *Nucl Med Biol* 24:471
- Jay M, Layton JW, Digenis G (1980) *Tetrahedron Lett* 21:2621
- Jewett DM (1992) *Appl Radiat Isot* 43:1383
- Jewett DM, Ehrenkaufer RL, Ram S (1985) *Appl Radiat Isot* 36:672
- Jolly D, Lakhrii Y, Kovacevic MM, Chertkow H, Schirmacher R (2007) *J Labeled Compd Radiopharm* 50:1230

- Jones GS, Livni E, Straus HW, Hanson RN, Elaleh DR (1988) *J Nucl Med* 29:68
- Kabalka GW, Nichols TL, Akula M, Langford CPD, Miller L (2001) In: Pleiss U, Voges R (eds) *Synthesis, application of isotopically compounds, Proceedings of the seventh international symposium, Dresden, Germany, 18–22 June 2000*, vol. 7, Wiley, New York, p 329
- Kaneko S, Ishiwata K, Ishii SI, Omura H, Senda M (1999) *Appl Radiat Isot* 50:285
- Karimi F, Kihlberg T, Långström B (2001) *J Chem Soc Perkin Trans* 1:1528
- Kato K, Zhang MR, Suzuki K (2007) *Mol Bio Syst* 4:53
- Kihlberg T, Långström B (1994a) *Acta Chem Scand* 48:570
- Kihlberg T, Långström B (1994b) *J Labeled Compd Radiopharm* 34:617
- Kihlberg T, Långström B (1999) *J Org Chem* 64:9201
- Kihlberg T, Gullberg P, Långström B (1990) *J Labeled Compd Radiopharm* 10:1115
- Kihlberg T, Valind S, Långström B (1994a) *Nucl Med Biol* 21:1067
- Kihlberg T, Valind S, Långström B (1994b) *Nucl Med Biol* 21:1053
- Kihlberg T, Neu H, Långström B (1997) *Acta Chem Scand* 51:791
- Kihlberg T, Karimi F, Långström B (1999) *J Labeled Compd Radiopharm* 42(Suppl 1):86
- Kihlberg T, Karimi F, Långström B (2002) *J Org Chem* 67:3687
- Kilbourn MR, Welch MJ (1982) *Int J Appl Radiat Isot* 33:359
- Kilbourn MR, Jerabek PA, Welch MJ (1983) *J Chem Soc Chem Commun* 16:861
- Kilbourn MR, Nguyen TB, Snyder SE, Sherman P (1998) *Nucl Med Biol* 26:543
- Klein ATJ, Holschbach M (2001) *Appl Radiat Isot* 55:309
- Kloster G, lauer P (1980) *J Labeled Compd Radiopharm* 17:889
- Kutzman RS, Meyer GJ, Wolf AP (1980) *Xenobiotica* 10:281
- Labar D, Vander Borcht T (1991) *J Labeled Compd Radiopharm* 30:342
- Lamb JE, James RW, Winchell HS (1971) *Int J Appl Radiat Isot* 22:475
- Långström B, Kihlberg T, Bergström M, Antoni G, Björkman M, Forngren BH, Forngren T
- Långström B, Bergson G (1980) *Radiochem Radioanal Lett* 43:47
- Långström B, Lundqvist H (1976) *Int J Appl Radiat Isot* 27:357
- Långström B, Stridsberg B (1979) *Int J Appl Radiat Isot* 30:151
- Långström B, Obenius U, Sjöberg S, Bergson G (1981a) *J Radionnal Chem* 64:273
- Långström B, Sjöberg S, Ragnarsson U (1981b) *J Labeled Compd Radiopharm* 18:479
- Långström B, Antoni G, Gullberg P, Halldin C, Någren K, Rimland A, Svärd H (1986) *Appl Radiat Isot* 37:1141
- Långström B, Antoni G, Gullberg P, Halldin C, Malmberg P, Någren K, Rimland A, Svärd H (1987) *J Nucl Med* 28:1037
- Långström B, Itsenko O, Rahman O (2007) *J Labeled Compd Radiopharm* 50:794
- Larsen P, Ulin J, Dahlström K, Jensen M (1997) *Appl Radiat Isot* 48:153
- Lasne MC, Cairon P, Barrè L, Moreau B, Pike VW (1991) *J Labeled Compd Radiopharm* 30:129
- Le Breton C, Crouzel C, Bonnot S, Prenat C (1991) *J Labeled Compd Radiopharm* 30:174
- Lidström P, Neu H, Långström B (1997) *J Labeled Compd Radiopharm* 39:695
- Lidström P, Bonasera TA, Marquez M, Nilsson S, Bergström M, Långström B (1998) *Steroids* 63:228
- Livni E, Elmalch DR, Levy S, Brownell HL, Strauss WH (1982) *J Nucl Med* 23:169
- Long NJ, Kealey S, Miller PW, Gee AD, Audrain H, Bender D (2008) *Abstracts of Papers, 236th ACS National Meeting, August 17–21, 2008, Philadelphia*
- Lundkvist C, Halldin C, Ginovart N, Nyberg S, Swahn CG, Carr AA, Brunner F, Farde L (1996) *Life Sci* 58:187
- Lunell E, Bergström M, Antoni G, Nordbegr A, Långström B (1996) *Clin Pharmacol Ther* 59:593
- Luthra SK, Pike VW, Brady F (1985) *J Chem Soc Chem Commun* 1423
- Luthra SK, Pike VW, Brady F (1990) *J Appl Radiat Isot* 41:471
- Luthra SK, Brady F, Turton DR, Brown DJ, Dowsett K, Waters SL, Jones AKP, Matthews RW, Crowder JC (1994) *Appl Radiat Isot* 45:857
- Mäding P, Steinbach J (1998) *J Labeled Compd Radiopharm* 41:647
- Mäding P, Steinbach J (2000) *J Labeled Compd Radiopharm* 43:557
- Mäding P, Steinbach J, Johannsen B (1997) *J Labeled Compd Radiopharm* 39:585
- Mäding P, Steinbach J, Johannsen B (2000) *J Labeled Compd Radiopharm* 43:565
- Mannens G, Slegers G, Lambrecht R, Goethals P (1988) *J Labeled Compd Radiopharm* 25:695
- Mannens G, Slegers G, Goethals P (1990) *J Labeled Compd Radiopharm* 28:311
- Marazano C, Mazière M, Berger G, Comar D (1977) *Int J Appl Radiat Isot* 28:49
- Marche P, Marazano C, Mazière M, Morgot JL, De La Costa P, Comar D, Fromageot P (1975) *Radioanal Lett* 21:53
- Matsson O, Persson J, Axelsson S, Långström B, Fang Y, Westaway KC (1996) *J Am Chem Soc* 118:6350
- Matsson O, Axelsson S, Hussénius A, Ryberg P (1999) *Acta Chem Scand* 53:670

- McCarron JA, Turton DR, Pike VW, Poole KG (1996) *J Labeled Compd Radiopharm* 38:941
- McCarron JA, Wikström H, Pike VW (1999) *J Labeled Compd Radiopharm* 42:S132
- McCarthy T, Bonasera TA, Welch MR, Rozen S (1993) *J Chem Soc Chem Commun* 561
- Miller PW, Long NJ, De Mello AJ, Vilar R, Audrain H, Bender D, Passchier J, Gee A (2007) *Angew Chem Int Ed* 46:2875
- Mock BH, Mulholland GK, Vavrek MT (1999) *Nucl Med Biol* 26:467
- Nader MW, Oberdorfer F (1999) *J Labeled Compd Radiopharm* 42:121
- Nader M, Theobald A, Oberdorfer F (1997) *J Labeled Compd Radiopharm* 40:730
- Nader MW, Zeisler SK, Theobald A, Oberdorfer F (1998) *Appl Radiat Isot* 49:1599
- Nägren K, Ragnarsson U, Långström B (1986) *Appl Radiat Isot* 37:537
- Nägren K, Ragnarsson U, Långström B (1988) *J Labeled Compd Radiopharm* 25:149
- Nägren K, Muller L, Halldin C, Swahn CG, Leuhkoinen P (1995) *Nucl Med Biol* 22:254
- Neu H, Kihlberg T, Långström B (1997a) *Labeled Compd Radiopharm* 39:509
- Neu H, Hartvig P, Torstenson R, Fasth KJ, Sonesson C, Waters N, Carlsson A, Tedroff J, Långström B (1997b) *Nucl Med Biol* 24:502
- Neu H, Bonasera T, Långström B (1998) *J Labeled Compd Radiopharm* 41:227
- Niisawa K, Ogawa K, Saio J, Taki K, Karazawa T, Nozaki T (1984) *Int J Appl Radiat Isot* 35:29
- Nishijima KI, Kuge Y, Seki KI, Ohkura K, Motok N, Nagatsu K, Tanaka A, Tsukamoto E, Tamaki N (2002) *Nucl Med Biol* 29:345
- Oberdorfer F, Siegel T, Guhlman A, Keppler D, Maier-Borst W (1992) *J Labeled Compd Radiopharm* 31:903
- Oberdorfer F, Zobeley A, Weber K, Prenant C, Haberkorn U, Mair-Borst W (1993) *J Labeled Compd Radiopharm* 33:345
- Ogawa K, Sasaki M, Nozaki T (1997) *Appl Radiat Isot* 48:623
- Ögren M, Långström B (1997) In: *Comprehensive summaries of Uppsala Dissertations from the Faculty of Science and Technology*, 292, ISBN, 91-554-4000-2
- Ögren M, Omura H, Furuya Y, Långström B (1997) In: *Comprehensive summaries of Uppsala Dissertations, from, the Faculty of Science and Technology*, 292, ISBN, 91-554-4000-2
- Ögren M, Långström B (1998) *Acta Chem Scand* 52:1137
- Ögren M, Hörnfeldt K, Fasth KJ, Långström B (1995a) *Appl Radiat Isot* 46:771
- Ögren M, Fasth KJ, Långström B (1995b) *J Labeled Compd Radiopharm* 37:184
- Ohad I, Åberg O, Långström B, Mishani E (2009) *J Labeled Compd Radiopharm*, available online, doi:10.1002/jlcr.1582
- Padgett HC, Barrio JR, MacDonald NS, Phelps M (1982a) *J Nucl Med* 23:739
- Padgett HC, Robinson GD, Barrio JR (1982b) *Int J Appl Radiat Isot* 33:1471
- Piette JL, Pardon MC, Delfiore G, Quaglia L, Peters JM, de Landsheere C, Rogo P (1989) *J Labeled Compd Radiopharm* 26:402
- Pike VW, Eakins MN, Allan RM, Selwyn AP (1981) *J Radioanal Chem* 64:291
- Pike VW, Eakins MN, Allan RM, Selwyn AP (1982) *Int J Appl Radiat Isot* 33:505
- Plenevaux A, Al-Darwich MJ, Lemaire C, Gulfiore G, Comar D (1994) *Appl Radiat Isot* 45:361
- Ponchant M, Hinnen F, Demphel S, Crouzel C (1997) *Appl Radiat Isot* 48:755
- Prenant C, Sastre C, Crouzel C, Syrota A (1986) *J Labeled Compd Radiopharm* 24:227
- Prenant C, Theobald A, Siegel T, Joachim J, Weber K, Haberkorn U, Oberdorfer F (1995a) *J Labeled Compd Radiopharm* 36:579
- Prenant C, Shah F, Brady F, Luthra SK, Pike VW, Burke PJ, Price PM (1995b) *J Labeled Compd Radiopharm* 37:95
- Ram S, Spicer LD (1989) *J Labeled Compd Radiopharm* 27:661
- Ram S, Ehrenkauf RE, Jewett DM (1986) *Appl Radiat Isot* 37:391
- Ravert HT, Mathews WB, Musachio JL, Dannals RF (1995) *J Labeled Compd Radiopharm* 36:365
- Reiffers S, Vaalburg W, Weigman T, Wynberg H, Wolrding MG (1980) *Int J Appl Radiat Isot* 31:535
- Reivich M, Alavi A, Wolf AP, Greenberg JH, Fowler JS, Christman DR, MacGregor R, Jones SC, London J, Shiue C, Yonekura Y (1998) *J Cereb Blood Flow Metab* 2:307
- Roeda D, Crouzel C (2001) *Appl Radiat Isot* 54:935
- Roeda D, Westera G (1981) *Int J Appl Radiat Isot* 32:931
- Roeda D, Crouzel C, van Zanten B (1978) *Radiochem Radioanal Lett* 33:175
- Roeda D, Bramoullé Y, Richards C, Jegou J, Dollé F, Crouzel C (1999a) *J Labeled Compd Radiopharm* 42:119
- Roeda D, Bramoullé Y, Richard C, Dollé F, Crouzel C (1999b) *J Labeled Compd Radiopharm* 42:126
- Ropchan JR, Barrio JR (1984) *J Nucl Med* 25:887
- Ruben S, Hassid WZ, Kamen MD (1939) *J Am Chem Soc* 61:661
- Samson Y, Hantraye P, Baron JC, Soussaline F, Comar D, Maziere M (1985) *Eur J Pharmacol* 110:247
- Sarkadi E, Kovács Z, Andó L, Szelecsényi F (1997) *Radiochim Acta* 76:197
- Sarkadi E, Kovács Z, Horváth G, Lehtikainen P (1998) *Radiochim Acta* 83:49

- Sasaki M, Ikemoto M, Mutoh M, Haradahira T, Tanaka A, Watanabe Y, Suzuki K (1999) *Appl Radiat Isot* 52:199
- Sassaman MB, Danico M, Schmall B, Eckelman WC (1999) *J Labeled Compd Radiopharm* 42:1229
- Schirbel A, Holschbach MH, Coenen HH (1999) *J Labeled Compd Radiopharm* 42:537
- Schirmmayer R, Lakhrissi Y, Jolly D, Goodstein J, Lucas P, Schirmmayer E (2008) *Tetrahedron Lett* 49:4824
- Schmall B, Conti S, Alauddin MM (1996) *Nucl Med Biol* 23:263
- Schmitz F, Plenevaux A, Del-Fiore G, Lemaire C, Comar D, Luxen A (1995) *Appl Radiat Isot* 46:893
- Schoeps KO, Halldin C (1992) *J Labeled Compd Radiopharm* 31:891
- Schoeps KO, Stone-Elander S, Halldin C (1989) *Appl Radiat Isot* 40:261
- Schoeps KO, Långström B, Stone-Elander S, Halldin C (1991) *Appl Radiat Isot* 42:877
- Shah F, Pike VW, Dowsett K, Aigbirhio FI (1994a) *J Labeled Compd Radiopharm* 35:83
- Shah F, Hume SP, Pike VW, Ashworth S, McDermott J (1994b) *Nucl Med Biol* 21:573
- Shah F, Pike VW, Dowsett K (1997) *Appl Radiat Isot* 48:931
- Shiue CY, Wolf AP (1981) *J Nucl Med* 22:58
- Soussain R, Gueguen P, Morgat JL, Mazière B, Berger G, Comar D (1984) *J Labeled Compd Radiopharm* 21:203
- Spang JE, Patt JT, Westera G, Schubiger PA (1999) *J Labeled Compd Radiopharm* 42:761
- Spang JE, Patt JT, Westera G, Schubiger PA (2000) *Nucl Med Biol* 27:239
- Spolter L, Cohen MB, Chang CC, McDonald NS (1979) *J Nucl Med* 20:662
- Steel CJ, Brown GD, Dowsett K, Turton DR, Luthra SK, Tochan-danguy H, Waters SL, Price P, Brady F (1993) *J Labeled Compd Radiopharm* 32:178
- Steel CJ, Prenant C, Shah F, brown G, Henderson D, Brady F, Luthra SK, Pike VW (1998) *J Nucl Med* 39:237
- Steel CJ, Brady F, Luthra SK, Brown G, Khan I, Poole KG, Sergis A, Jones T, Price P (1999) *Appl Radiat Isot* 51:377
- Steinbach J, Mäding P, Fuchtnier F, Johannsen B (1995) *J Labeled Compd Radiopharm* 36:33
- Stille JK (1986) *Angew Chem Int Ed Engl* 25:508
- Stone-Elander S, Elander N, Thorell JO, Solås G, Svennebrink J (1994) *J Labeled Compd Radiopharm* 34:949
- Straatman MG, Welch MJ (1974) *J Nucl Med* 16:425
- Svård H, Nägren K, Malmberg P, Sohn D, Sjöberg S, Långström B (1982) *J Labeled Compd Radiopharm* 19:1519
- Tada M, Oikawa H, Matzuzawa T, Itoh M, Fukuda H, Kubota K, Kawai H, Abe Y, Ugiyama H, Ido T, Ishiwata K, Iwata R, Imahori Y, Sato S (1989) *J Labeled Compd Radiopharm* 27:1
- Takahashi T, Nägren K, Aho K (1990) *Appl Radiat Isot* 41:1187
- Tang DY, Lipman A, Meyer GJ, Wan CN, Wolf AP (1979) *J Labeled Compd Radiopharm* 16:435
- Thorell JO, Stone-Elander S, Elander N (1992) *J Labeled Compd Radiopharm* 31:207
- Thorell JO, Stone-Elander S, Elander N (1993) *J Labeled Compd Radiopharm* 33:995
- Thorell JO, Stone-Elander S, Elander N (1994) *J Labeled Compd Radiopharm* 34:383
- Tobias CA, Lawrence JH, Roughton FJW, Root WS, Gregersen MI (1945) *Am J Physiol* 145:253
- Turton DR, Brady F, Pike VW, Selwyn AP, Shea MJ, Wilson RA, De Landshere CM (1984) *Int J Appl Radiat Isot* 35:337
- Vaalburg W, Beerling-van der Molen HD, Reiffers S, Rijskamp A, Woldring MG, Wynberg H (1976) *Int J Appl Radiat Isot* 27:153
- Vedejs E, Haight AR, Moss WO (1992) *J Am Chem Soc* 114:6556
- Wagner R, Stöcklin G, Schaak W (1981) *J Labeled Compd Radiopharm* 18:1557
- Wagner HN, Burns HD, Dannals RF, Wonf DF, Långström B, Duelfers T, Frost JJ, Ravert HT, Links JM, Rosenbloom SB, Lukas SE, Kramer AV, Kuhar MJ (1983) *Science* 221:1264
- Washburn LC, Sun TT, Byrd BL, Callahan AP (1982) *J Nuc Med* 23:29
- Westerberg G, Långström B (1993) *Acta Chem Scand* 47:974
- Westerberg G, Långström B (1994a) *J Labeled Compd Radiopharm* 34:545
- Westerberg G, Långström B (1994b) *Appl Radiat Isot* 45:773
- Westerberg G, Långström B (1997a) *App Radiat Isot* 48:459
- Westerberg G, Långström B (1997b) *J Labeled Compd Radiopharm* 39:525
- Westerberg G, Bergström M, Gustafsson S, Lindqvist U, Sundin A, Långström B (1995) *Nucl Med Biol* 22:251
- Westerberg G, Bamford M, Daniel MJ, Långström B, Sutherland DR (1996) *J Labeled Compd Radiopharm* 38:585
- Wust F, Dence CS, McCarghy TJ, Welch MJ (2000) *J Labeled Compd Radiopharm* 43:1289
- Zeisler SK, Nader M, Theobald A, Oberdorfer F (1997) *Appl Radiat Isot* 48:1091
- Zessin J, Steinbach J, Johannsen B (1999) *J Labeled Compd Radiopharm* 42:752



42 ^{18}F : Labeling Chemistry and Labeled Compounds

T. L. Ross¹ · H. J. Wester²

¹Johannes Gutenberg-University Mainz, Mainz, Germany

²Klinikum rechts der Isar, Technische Universität München, München, Germany

42.1	<i>Introduction</i>	2022
42.2	<i>Special Characteristics of ^{18}F-Fluorine</i>	2023
42.2.1	Physical Properties and Production	2023
42.2.2	Chemical Properties and Fluorine Substituent Effects	2024
42.3	<i>Methods of ^{18}F-Fluorination</i>	2026
42.3.1	Electrophilic ^{18}F -Fluorination	2026
42.3.1.1	Direct Fluorination	2026
42.3.1.2	^{18}F -Fluorodemetalation	2029
42.3.1.3	Electrophilic $^{18}\text{F}[\text{F}_2]$ from n.c.a. $^{18}\text{F}[\text{F}]^-$	2030
42.3.2	Nucleophilic ^{18}F -Fluorination	2032
42.3.2.1	Nucleophilic Aromatic Substitutions	2034
42.3.2.2	Nucleophilic Aromatic Substitution of Small Synthons	2035
42.3.2.3	Nucleophilic Heteroaromatic Substitutions	2040
42.3.2.4	Nucleophilic Aliphatic Substitution	2041
42.3.3	Prosthetic Group Labeling	2046
42.3.3.1	Introduction of ^{18}F -Fluorine by Fluoromethylation	2046
42.3.3.2	Introduction of ^{18}F -Fluorine by Fluoroethylation	2047
42.3.3.3	Introduction of ^{18}F -Fluorine by Other Secondary Precursors	2049
42.3.3.4	Introduction of ^{18}F -Fluorine by Click Chemistry	2050
42.4	<i>^{18}F-Labeling of Peptides and Proteins</i>	2051
42.5	<i>Miscellaneous</i>	2059
42.5.1	Microwave Applications in Radiolabeling	2059
42.5.2	Silicon-Based ^{18}F -Chemistry	2059
42.5.3	Enzymatic Reactions	2061
42.5.4	Electrochemical Cells	2063
42.5.5	Automated Radiosyntheses and Flow Chemistry	2063

Abstract: Positron emission tomography (PET) is a unique tool for the investigation, localization, and quantification of physiological activities in vivo by tracing the involved or accompanying biochemical processes. Because of its nuclear and chemical properties, fluorine-18, which is commonly produced by a cyclotron using the $^{18}\text{O}(\text{p},\text{n})^{18}\text{F}$ or the $^{20}\text{Ne}(\text{d},\alpha)^{18}\text{F}$ nuclear process, is a nearly ideal positron emitting radionuclide. Its half-life of 109.7 min permits tracer syntheses and imaging protocols extending over hours and allows distribution of ^{18}F -radiopharmaceuticals to hospitals and facilities lacking a cyclotron. The low maximum positron energy of 635 keV results in low radiation doses, short ranges in tissue, and therefore in excellent imaging resolution. Introduction of ^{18}F -fluorine, either via nucleophilic strategies using $[\text{}^{18}\text{F}]\text{F}^-$ or electrophilic routes using molecular $[\text{}^{18}\text{F}]\text{F}_2$, permits the synthesis of a broad spectrum of compounds within a time compatible with the half-life. Although fluorine is only slightly larger than a hydrogen atom, changes in the physiological behavior of bioactive compounds as a result of alteration in metabolic stability, lipophilicity, affinity to the target, or other structures, etc., are often observed even after F-for-H or F-for-OH substitutions. In this chapter, an overview of the scope and limitations of the ^{18}F -chemistry is given. Fluorination strategies, routes, and synthetic aspects are exemplified, as far as possible, by established and selected ^{18}F -radiopharmaceuticals with clinical relevance or with potential for further clinical application.

Further Reading: A review of the clinical use and the potential of ^{18}F -labeled radiopharmaceuticals are by far beyond the scope of this chapter. Excellent reviews have been published, e.g., on PET tracers for mapping cardiac nervous system (Langer and Halldin 2002), on the production (Stöcklin 1995) and future of clinical ^{18}F -labeled radiopharmaceuticals (Stöcklin 1998; Shiue and Welch 2004) for the heart and brain (Stöcklin 1992; Halldin et al. 2001), for the 5-HT system (Crouzel et al. 1992), on targeting peptide receptors by PET (Lundquist and Tolmachev 2002; Okarvi 2001, 2004; Schottelius and Wester 2009; Tolmachev and Stone-Elander 2010) on general aspects in “working against time” during rapid radiotracer synthesis (Fowler and Wolf 1997), on radiotracers for endogenous competition (Laruelle and Huang 2001), on molecular imaging of cancer with PET (Gambhir 2002), on hypoxia PET tracers (Grierson and Patt 1999), on ^{18}F -fluorine chemistry (Lasne et al. 2002; Stöcklin and Pike 1993; Stöcklin 1995; Ametamey et al. 2008; Miller et al. 2008; Cai et al. 2008), on microwave heating (Stone-Elander and Elander 2002), or on fluorinase-based ^{18}F -labeling (Onega et al. 2009), to mention only a few.

42.1 Introduction

Physiological and pathophysiological activities are evolved and are accompanied by biochemical processes and by factors that affect these processes, such as the supply of bioenergetic substrates and enzymes. In 1913, George de Hevesy invented the *tracer principle*, a concept that allows to investigate and to quantify pathways by radiolabeled compounds (*tracer*) (Nobel Prize 1943). On the basis of the coincidence detection of two 511 keV photons, emitted upon positron annihilation in nearly opposite directions, modern *Positron Emission Tomography* permits to measure and quantify the distribution of a tracer labeled with a positron emitting radionuclide noninvasively in living organism with high imaging resolution. PET-radiopharmaceuticals have been developed to quantify molecular processes, e.g., enzyme activities, drug-receptor interactions, energy metabolism or substrate transport, and to

correlate biochemical alterations with the extent of diseases. The choice of the appropriate radionuclide, i.e., its half-life in relation to the kinetics of the process to be monitored, the position of label, the lipophilicity of the tracer, plasma protein binding, clearance kinetics, excretion routes, unspecific uptake in nontarget tissues, affinity to and retention at the locus of interest, and, since PET cannot distinguish between an intact tracer and labeled metabolites, the fate of the label is an aspect among a variety of factors of crucial importance for successful imaging and high target to background ratios.

In contrast to a broad spectrum of drugs with well evaluated and defined in vivo behavior useful for isotopic labeling with ¹¹C, ¹³N, or ¹⁵O (► [Table 42.1](#)), fluorine-containing bioactive probes or drugs are comparatively rare and most of the ¹⁸F-labeled radiopharmaceuticals developed and evaluated so far are non-isotopic analogs of the corresponding drugs or have been designed especially for PET. Even when an ¹⁸F-compound closely resembles the parent structure (e.g., F-for-H or F-for-OH substitutions), alteration of pharmacokinetics and pharmacodynamics cannot be excluded. Thus, an extensive and detailed evaluation process on the characteristics of a new compound using suitable in vitro and in vivo models is generally necessary prior to the first human application. In this chapter, basic aspects of the *¹⁸F-labeling chemistry*, strategies for secondary *precursor synthesis*, and multistep syntheses are summarized, exemplified and discussed.

42.2 Special Characteristics of ¹⁸F-Fluorine

42.2.1 Physical Properties and Production

With regard to its use for PET, the nuclear properties of *fluorine-18* are excellent. The positron energy of $E_{\beta^+ \text{ max}} = 633.5 \text{ keV}$ is the lowest of the commonly used PET nuclides and results in

► **Table 42.1**

Nuclear properties of commonly used positron emitters (Data taken from Brown and Firestone 1986 and from the Brookhaven National Laboratory internet data base, BNL 2003)

Isotope	Half-life	Decay mode	$E_{\beta^+ \text{ avg.}}$ (keV)	Maximum (average) range in H ₂ O (mm)	Maximum specific activity (GBq μmol^{-1})
¹¹ C	20.39 min	β^+ (99.8%)	385	3.8 (1)	3.4×10^5
		EC (0.24%)			
¹³ N	9.965 min	β^+ (99.8%)	491	5 (1.5)	7.0×10^5
		EC (0.2%)			
¹⁵ O	122.24 s	β^+ (99.9%)	735	7.6 (2.7)	3.4×10^6
		EC (0.01%)			
¹⁸ F	109.77 min	β^+ (96.73%)	242	2.2 (0.3)	6.3×10^4
		EC (3.3%)			
⁶⁸ Ga	67.629 min	β^+ (89.1%)	740	13.6 (3.7)	1.0×10^5
		EC (11.0%)			
¹²⁴ I	4.1760 days	β^+ (22.8%)	188	9.7 (3)	1.2×10^3
		EC (11.0%), e^-			

low radiation doses. Furthermore, the short maximum range in tissue of only about 2.2 mm (average range of about 0.3 mm) does not exceed the inherent resolution of state-of-the-art clinical PET scanners (clinical PET: ≥ 4 mm, animal PET: ≥ 1 mm). Compared with ^{11}C ($T_{1/2} = 20.4$ min) the half-life of 109.7 min of ^{18}F allows more flexibility in tracer production (as a rule of thumb < 3 half-lives), transport of tracers to PET facilities without an on-site cyclotron and scanning procedures extending over several hours. ^{18}F -Fluorine can be produced in high yields even with small “baby cyclotrons” (e.g., Qaim and Stöcklin 1983; Guillaume et al. 1991; Stöcklin and Pike 1993; Qaim et al. 1993; cf. also ► Chap. 39 of this Volume) allowing to prepare, e.g., 2- ^{18}F]fluoro-deoxy-D-glucose on the Ci-scale.

Among the four main production routes listed in ► Table 42.2, the $^{18}\text{O}(\text{p},\text{n})^{18}\text{F}$ nuclear process on highly enriched H_2^{18}O is the most effective. This process and the alternative route via $^{16}\text{O}(^3\text{He},\text{n})^{18}\text{F}$ leads to ^{18}F -fluoride ($^{18}\text{F}]\text{F}_{\text{aq}}^-$) suitable for nucleophilic substitutions in high specific activities. To recycle and thus to minimize the quantities of enriched H_2^{18}O to be used and to eliminate cationic impurities from the target material, $^{18}\text{F}]\text{F}_{\text{aq}}^-$ is trapped after irradiation on suitable anion exchange resins (Schlyer et al. 1990; Jewett 1991; Hamacher et al. 1990) and subsequently eluted. $^{18}\text{F}]\text{F}_2$, the corresponding primary species for electrophilic fluorination, can only be obtained in lower specific activities and lower thick target yields. For a detailed discussion about the production of ^{18}F see ► Chap. 39 of this Volume.

42.2.2 Chemical Properties and Fluorine Substituent Effects

- As a substituent, fluorine is never boring, always good for a surprise but often completely unpredictable (Schlosser 1998).

With perhaps the exception of fluorine steric interactions, substituent effects on reactive intermediates that underlie the chemical reactivity of fluorinated compounds are now rather well understood and fairly predictable (see Smart 2001 and references therein). In contrast, *fluorine substituent effects* on the physical properties that can impact pharmacokinetics and pharmacodynamics (e.g., absorption, transport, binding, and pharmacological effect) are often less predictable or at least “always good for a surprise.” The replacement of a hydrogen atom or a hydroxy group by a fluorine atom is not only a strategy used in PET radiotracer development, but also widely used in drug development to alter biological function (Smart 2001; Park et al. 2001;

■ Table 42.2

Production routes to $^{18}\text{F}]\text{fluoride}$ and $^{18}\text{F}]\text{fluorine}$ (Stöcklin 1995; cf. also ► Chap. 39, this volume)

Nuclear reaction	$^{18}\text{O}(\text{p},\text{n})^{18}\text{F}$	$^{16}\text{O}(^3\text{He},\text{n})^{18}\text{F}$	$^{20}\text{Ne}(\text{d},\alpha)^{18}\text{F}$	$^{18}\text{O}(\text{p},\text{n})^{18}\text{F}$
Target	H_2^{18}O	H_2O	Ne (0.1–0.2% F_2 , 18 atm)	$^{18}\text{O}_2$ 20 atm
Energy range of bombarding particle (MeV)	$16 \rightarrow 0$	$36 \rightarrow 0$	$11.2 \rightarrow 0$	$10 \rightarrow 0$
Chemical form	$^{18}\text{F}]\text{F}_{\text{aq}}^-$	$^{18}\text{F}]\text{F}_{\text{aq}}^-$	$^{18}\text{F}]\text{F}_2$	$^{18}\text{F}]\text{F}_2$
Thick target yield ($\text{MBq } \mu\text{A}^{-1} \text{ h}^{-1}$)	2.200	250	350–450	~350
Specific activity ($\text{GBq } \mu\text{mol}^{-1}$)	40×10^3	40×10^3	0.04–0.4	0.04–2

Müller et al. 2007; Hagmann 2008). The van der Waals radius of fluorine (147 pm) lies between hydrogen (120 pm) and oxygen (152 pm) and thus fluorine appears to have a particular close isosteric relationship to oxygen while being larger than hydrogen. Despite the differences in size, numerous studies have demonstrated that fluorine is a reasonable hydrogen mimic. However, due to their quite different electronic properties, resulting changes in the electron distribution in a molecule by F-for-H replacement can alter the pK_a , the dipole moments, lipophilicity, hydrogen bonding, the chemical reactivity, the oxidative stability, the chemical reactivity of neighboring groups, or metabolic processes (► Table 42.3).

As a rule of thumb, fluorination usually but not always increases lipophilicity. Aromatic fluorination always increases lipophilicity, fluorination adjacent to atoms with π -bonds increases lipophilicity, with exceptions for some fluorinated α -carbonyl compounds (Smart 2001 and references therein). Whereas β -fluorination always increases C–H acidity, α -fluorination is less acidifying than other α -halogenations.

The replacement of a hydroxy group is usually based on the premise that fluorine is a hydrogen bond acceptor in a manner similar to the oxygen of a hydroxy function. Ab initio calculations revealed that the $C(sp^3)$ –F fluorine in fluoromethane is a better hydrogen bond acceptor and can enter into stronger hydrogen bonds (optimum distance: 1.9 Å, 2.38 kcal mol^{−1}) than $C(sp^2)$ –F of fluoroethene (1.48 kcal mol^{−1}). However, the $C(sp^3)$ –F⋯H–O bond is less than half the strength of a C–O⋯H–O bond, conservatively estimated to be about 5 kcal mol^{−1} (Howard et al. 1996).

High in vivo stability against defluorination is obviously a major focus in the development of ¹⁸F-PET tracers. However, fluoride is a good leaving group. This aspect is utilized for pharmaceutical design of “lethal drugs” and “suicide substrates” forming stable covalent bonds with their binding sites, receptors, or enzymes. Thus, a careful selection of the labeling position is imperative. Based on the premise, that the C–F bond is much more resistant to cytochrom P450 attack, alteration of the rate, route, and extent of tracer metabolism can not only be achieved by fluorine substitution at the site of metabolic attack, but also by substitution adjacent to the site of attack (Rietjens et al. 1997). Whereas in simple saturated systems the inductive effect of fluorine should reduce susceptibility of adjacent groups to P450 enzymes, the presence of fluorine *ortho* to a phenolic group might increase its reactivity in methylation and glucuronidation reactions (Park et al. 2001).

■ Table 42.3

Physicochemical data of fluorine compared to other halogens, oxygen, and hydrogen

	Fluorine	Chlorine	Bromine	Iodine	Hydrogen	Oxygen
Ionization enthalpy (kJ mol ^{−1})	1,681	1,251	1,139	1,008	1,312	1,314
Electron affinity (kJ mol ^{−1})	328	348	324	295	73	141
van der Waals radius (pm)	147	175	185	198	120	152
Atomic radius	42	79	94	115	53	48
Electronegativity	3.98	3.16	2.96	2.66	2.20	3.44
Atomic polarizability	0.5	2.2	3.1	4.7	4.5	–
Bond energy (kJ) aliphatic	444	–	285	222	398	–
Aromatic	523	–	335	268	460	–

42.3 Methods of ^{18}F -Fluorination

42.3.1 Electrophilic ^{18}F -Fluorination

Electrophilic ^{18}F -fluorination is characterized by the reaction of highly polarized fluorine with an electron rich reactant, e.g., an aromatic system, an alkene, or a carbanion. $[^{18}\text{F}]\text{F}_2$, the simplest electrophilic fluoro-species, is obtained directly from the irradiated target. Other reagents have to be prepared in subsequent steps, either from carrier-added (c.a.) $[^{18}\text{F}]\text{F}_2$ or no-carrier-added (n.c.a.) $[^{18}\text{F}]\text{fluoride}$. $[^{18}\text{F}]\text{XeF}_2$ can be obtained in-target via the $^{19}\text{F}(\text{p,pn})^{18}\text{F}$ process on XeF_2 , by the reaction of Xe and $[^{18}\text{F}]\text{F}_2$ or by isotopic exchange of XeF_2 with $[^{18}\text{F}]\text{HF}$. Synthesis of another important reagent, $[^{18}\text{F}]\text{acetylhypofluorite}$ ($[^{18}\text{F}]\text{AcOF}$) can be carried out by passing dilute fluorine-18 gas through a solution of ammonium acetate in glacial acetic acid (Shiue et al. 1982), or via an on-column gas–solid phase reaction by passing F_2 diluted in N_2 through columns containing complexes of alkali metal acetates with acetic acid (Jewett et al. 1984; Ehrenkaufer et al. 1984; Bida et al. 1984).

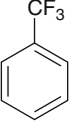
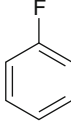
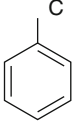
The theoretical maximum radiochemical yield for fluorination with electrophilic reagents is only 50%, because only one of the fluorine atoms in the $[^{18}\text{F}]\text{F}_2$ molecule is labeled and typically only one of them is incorporated. This also applies to all other electrophilic reagents, because they are either produced via $[^{18}\text{F}]\text{F}_2$ or by isotopic exchange. Furthermore, the products are c.a. with maximum specific activities in the range of $0.04\text{--}0.4\text{ GBq }\mu\text{mol}^{-1}$. Consequently, this method is limited to the production of a tracer (a) which competes to a high concentration of endogenous analogs in vivo, e.g., amino acids, or (b) which bind to molecular targets of low saturability, e.g., enzymes or transporter substrates. Nevertheless, the amount of inactive carrier can influence the pharmacokinetics, uptake, and binding to the target. Furthermore, pharmacological or even toxic effects have to be considered.

42.3.1.1 Direct Fluorination

Although the direct electrophilic substitution of electron rich compounds (aryls and alkenes) with $[^{18}\text{F}]\text{F}_2$ is a straightforward method, its major disadvantage is its lack of *regioselectivity* (Coenen et al. 1988, cf. [Fig. 42.1](#)).

■ Fig. 42.1

Selectivity and reactivity of $[^{18}\text{F}]\text{F}_2$ (without brackets) and $[^{18}\text{F}]\text{acetylhypofluorite}$ ($[^{18}\text{F}]\text{AcOF}$) (in brackets) toward monosubstituted benzenes. The radiochemical yields (%) are given for each position

				
		11 10 30 32	15 12 6 3	32 30 05 05
		18 16	58 70	35 39
bstit tion	$^{18}\text{F F}_2$	32 3	34 3	48 2
	$^{18}\text{F Ac F}$	55 2	74 5	85 3

Furthermore, the oxidizing strength of fluorine can lead to the formation of side products. To reduce side reactions, the reactivity of $[^{18}\text{F}]\text{F}_2$ is moderated by dilution with inert gas (neon) at low temperatures (Casella et al. 1980). The solvent has to be inert as well. Freon, trifluoroacetic acid, carbon tetrachloride, and hydrogen fluoride are used.

Cis-addition of $[^{18}\text{F}]\text{F}_2$ on the double bond of 2,4,6-tri-O-acetyl-D-glucal was the first method used for production of 2- $[^{18}\text{F}]$ fluoro-2-deoxy-D-glucose at the Brookhaven National Laboratory (Ido et al. 1978, cf. [Fig. 42.2](#)). Two epimers, 2- $[^{18}\text{F}]$ fluoro-2-deoxy-D-glucose ($[^{18}\text{F}]\text{FDG}$) and 2- $[^{18}\text{F}]$ fluoro-2-deoxy-D-mannose ($[^{18}\text{F}]\text{FDM}$) were formed and separated after hydrolysis ($[^{18}\text{F}]\text{FDG}$: 10% radiochemical yield).

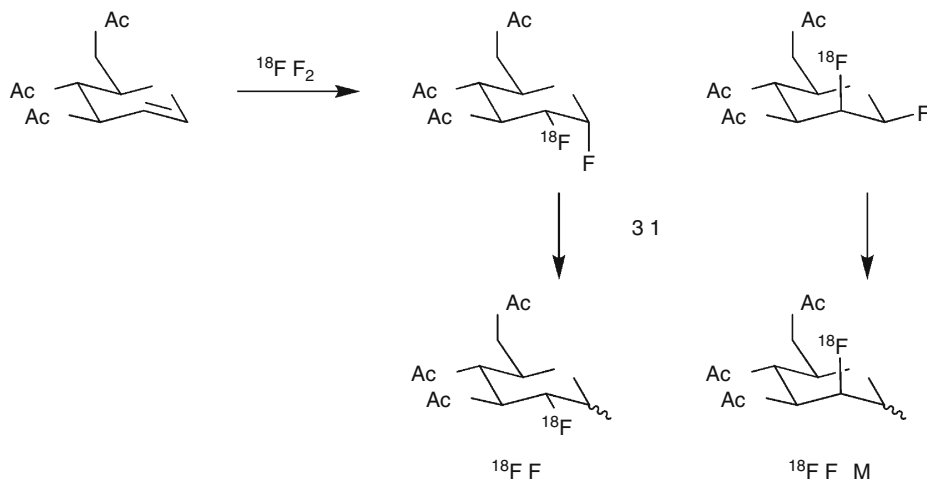
The synthesis was improved (20% yield) by using $[^{18}\text{F}]\text{AcOF}$ instead of $[^{18}\text{F}]\text{F}_2$ (Shiue et al. 1982) and unprotected glucal in water (Ehrenkaufer et al. 1984). Nevertheless, varying amounts of the epimer $[^{18}\text{F}]\text{FDM}$ are formed via the electrophilic route. These disadvantages were overcome by an alternative strategy allowing high-yield production of no-carrier-added $[^{18}\text{F}]\text{FDG}$ with high radiochemical purity via the *nucleophilic substitution* reaction on 1,3,4,6-tetra-O-acetyl-2-triflate- β -D-mannose (Hamacher et al. 1986a). Fowler and Ido (2002) provide a comprehensive overview reflecting the history and different approaches of $[^{18}\text{F}]\text{FDG}$ production.

The addition of elemental $[^{18}\text{F}]$ fluorine to 2-(2-nitro-1[H]-imidazol-1yl)-*N*-(2,3,3-trifluoroallyl)-acetamide in trifluoroacetic acid to form $[^{18}\text{F}]\text{EF}_5$ represents a more recent example of an aliphatic electrophilic fluorination (Dolbier et al. 2001, cf. [Fig. 42.3](#)). EF_5 as well as EF_1 (Kachur et al. 1999) and EF_3 (Josse et al. 2001), which are prepared via nucleophilic routes, have been suggested for PET imaging of tumor hypoxia.

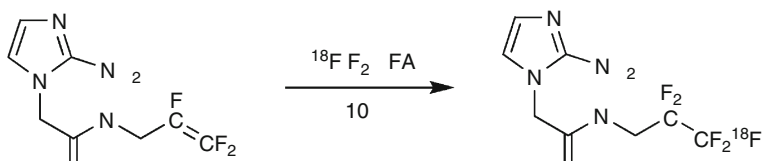
The substitution of hydrogen by ^{18}F -fluorine has also been used for the production of 5- $[^{18}\text{F}]$ fluoro-DOPA (Firnaeu et al. 1973) and 6- $[^{18}\text{F}]$ fluoro-L-DOPA (3,4-di-hydroxy-6- $[^{18}\text{F}]$ fluoro-L-phenylalanine; 6- $[^{18}\text{F}]\text{FDOPA}$) (Garnett et al. 1983a, b; Firnaeu et al. 1980, 1984; Adam et al. 1986; Coenen et al. 1988) (cf. [Fig. 42.4](#)). 6- $[^{18}\text{F}]\text{FDOPA}$ is transported across the blood-brain barrier, where it is decarboxylated to produce 6- $[^{18}\text{F}]$ fluoro-dopamine.

Fig. 42.2

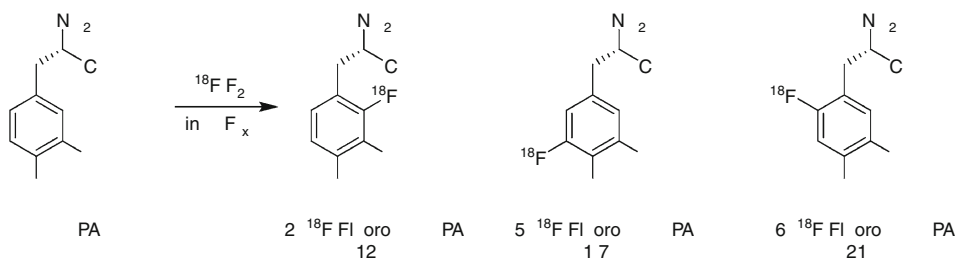
Synthesis of $[^{18}\text{F}]$ fluoro-2-deoxy-D-glucose ($[^{18}\text{F}]\text{FDG}$) and $[^{18}\text{F}]$ fluoro-2-deoxy-D-mannose ($[^{18}\text{F}]\text{FDM}$) via fluorination with $[^{18}\text{F}]\text{F}_2$ (Ido et al. 1978)



■ Fig. 42.3

Synthesis of [^{18}F]EF5 (Dolbier et al. 2001)

■ Fig. 42.4

Synthesis of [^{18}F]FDOPA by [^{18}F]F₂ in (HF)_x (Firnau et al. 1984)

The rate of uptake reflects decarboxylase activity, suitable to assess presynaptic dopaminergic function (Leenders et al. 1986). Direct fluorination was carried out on protected and unprotected DOPA. Labeling of DOPA ([^{18}F]F₂ in HF) yields the three possible regioisomers: 2-, 5-, and 6-[^{18}F]FDOPA. Both regioselectivity and overall radiochemical yields are strongly dependent on the solvent systems used. Using the same methodology, fluorinated analogs of L-tyrosine and L-phenylalanine were also obtained (for review cf. Lemaire 1993).

In 1999, Chirakal et al. investigated the effect of different acidic solvents on the selectivity and reactivity of the [^{18}F]fluorination of L-DOPA. While the orientation of electrophilic fluorination of L-DOPA in weak acids (trifluoroacetic acid, 10% TFA in glacial HOAc and HCOOH) is influenced by the electron donating OH groups on the ring, the orientation in strong acids (HF and HF/BF₃) is mainly influenced by the side chain.

For imaging and monitoring of new techniques in *gene therapy* 8-[^{18}F]fluoroguanines were prepared. The fluorination of *gancyclovir* with [^{18}F]F₂ was carried out in absolute ethanol in the presence of tetraethylammonium hydroxide at room temperature to give 8-[^{18}F]fluorogancyclovir (► Fig. 42.5a) in about 1% radiochemical yield. Similarly, 8-[^{18}F]fluoropencyclovir (B), 8-[^{18}F]fluoroacyclovir (C), and 8-[^{18}F]fluoroguanosine (D) were synthesized from pencyclovir (Barrio et al. 1996; Namavari et al. 2000).

The cytostatic agent 5-[^{18}F]fluorouracil (5-[^{18}F]FU) has been prepared by electrophilic addition of [^{18}F]F₂ (Fowler et al. 1973) and [^{18}F]AcOF (Fowler et al. 1982; Diksic et al. 1986; Visser et al. 1986) to uracil. Subsequent elimination of the 6-fluoro or 6-acetoxy groups results in high regioselectivity for the five positions (see ► Fig. 42.6). Laborious purification methods to separate 5-[^{18}F]FU from unreacted uracil have been overcome by using a single column method reported by Brown et al. (1993). Radiochemical yields >20% are obtained using this method.

Fig. 42.5

Synthesis of 8-¹⁸F]fluoroguanines for gene therapy monitoring (Namavari et al. 2000)

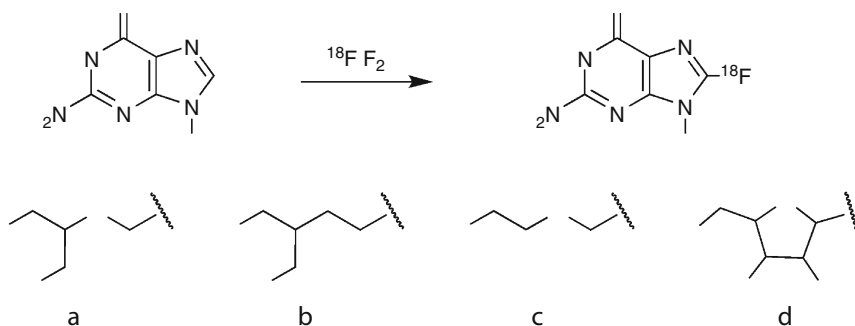
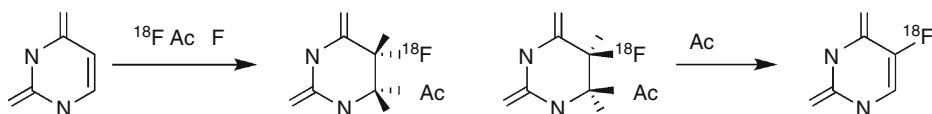


Fig. 42.6

Synthesis of 5-¹⁸F]fluorouracil (5-¹⁸F]FU) from [¹⁸F]acetyl hypofluorite (X = Na, K, NH₄)



Among a variety of other rarely used reagents suggested for electrophilic fluorinations are [¹⁸F]perchloryl fluoride (Ehrenkauf and McGregor 1983), nitrosyl fluoride, N-fluoro-N-alkylsulfonamides (Satyamurthy et al. 1990), or 2-¹⁸F]fluoro-2-pyridone (Oberdorfer et al. 1988a). Fluorination of carbanions, such as, aryllithium and aryl Grignard reagents can be obtained in 60–70% yields with N-¹⁸F]fluoro-N-alkylsulfonamides (Barnette 1986; Satyamurthy et al. 1984) as a source of “positive” [¹⁸F]fluorine. This labeling reagent is prepared from [¹⁸F]F₂ and N-*endo*-norbornyl(p-tolyl)sulfonamide in up to 45% yield. Similarly, [¹⁸F]fluorobenzene can be obtained in 60% yield using N-¹⁸F]fluoro-2-pyridone, a reagent prepared by reaction of N-trimethylsilylpyridinium triflate and [¹⁸F]F₂ (Oberdorfer et al. 1988b). Starting from methyl lithium (MeLi), [¹⁸F]fluoromethane can be prepared using N-¹⁸F]fluoro-2-pyridone in quantitative yields (10 min, −80°C), thus demonstrating the suitability not only for the synthesis of arylfluorides.

42.3.1.2 ¹⁸F-Fluorodemetallation

¹⁸F-fluorodemetallation is the method of choice to introduce fluorine into a predefined position of an aromatic ring and to avoid formation of possible regioisomers. Here, regioselective electrophilic aromatic substitution is accomplished by displacement of a metallic substituent, e.g., alkylated species of Sn, Hg, Si, or Ge by [¹⁸F]F₂ or [¹⁸F]AcOF. In an early comparative study (Coenen and Moerlein 1987), tin compounds appeared to be better leaving groups than the corresponding Si- and Ge-derivatives (cf. Table 42.4). Whereas no or low yields were observed using hydrogen-containing solvents, e.g., CH₂Cl₂, dimethyl sulfoxide (DMSO), or

Table 42.4

Effect of substituent and metal on the chemical yields of demetallation reactions (Data from Coenen and Moerlein 1987)

Ar-X	Sn		Ge		Si	
	[¹⁸ F]F ₂	[¹⁸ F]AcOF	[¹⁸ F]F ₂	[¹⁸ F]AcOF	[¹⁸ F]F ₂	[¹⁸ F]AcOF
X = OCH ₃	70 ± 7%	66 ± 4%	35 ± 1%	–	20 ± 3%	–
X = CH ₃	78 ± 6%	–	41 ± 6%	16 ± 2%	22 ± 4%	9 ± 1%
X = F	74 ± 7%	–	56 ± 4%	–	30 ± 3%	–
X = H	64 ± 7%	68 ± 6%	40 ± 4%	9 ± 1%	23 ± 4%	4 ± 1%
X = CF ₃	35 ± 3%	36 ± 2%	10 ± 2%	–	3 ± 1%	–

MeCN; satisfactory yields were obtained with perhalogenated methane, e.g., CFC₃. Low yields were also obtained in the presence of electron withdrawing groups (NO₂, CF₃).

For synthesis of 6-[¹⁸F]FDOPA via demetallation, a variety of precursors were studied (Adam et al. 1983; Adam and Jivan 1988; Luxen et al. 1990; Namavari et al. 1992; Szajek et al. 1998; Dollé et al. 1998a; de Vries et al. 1999). 6-[¹⁸F]FDOPA can be prepared by demercuration (Adam et al. 1983; Adam and Jivan 1988; Luxen et al. 1990) in solution and in a solid–liquid phase reaction (precursor on solid support, 23% yield) (Szajek et al. 1998) or via destannylation (Namavari et al. 1992). For destannylation, the use of [¹⁸F]F₂ is preferred (30% yield) (Dollé et al. 1998a; de Vries et al. 1999). Hess et al. (2002) described the synthesis of 2-[¹⁸F]fluoro-L-tyrosine via regiospecific destannylation of O,N-di-Boc-2-trimethylstannyl L-tyrosine ethylester in 42% radiochemical yield (► Fig. 42.7).

The radiolabeled catecholamine tracer 6-[¹⁸F]fluorometaraminol (► Fig. 42.8b) for mapping cardiac sympathetic neurons is another example for the introduction of ¹⁸F-fluorine by demetallation. It has been prepared by fluorination of 6-acetoxymercuro-N-t-BOC-metaraminol with acetyl hypofluorite followed by removal of the BOC group in about 30% radiochemical yield (Mislankar et al. 1988). In 2000, Ermert et al. have used an n.c.a. nucleophilic ¹⁸F-for-N(CH₃)₃ exchange on an N,N-dibenzyl protected α-aminopropiophenone derivative, followed by a stereoselective reduction and deprotection step to prepare 4-[¹⁸F]fluorometaraminol in 15–20% radiochemical yield. Another four-step strategy was described by Langer et al. (2001).

The alternative n.c.a. catecholamine analog (–)-6-[¹⁸F]fluronorepinephrine (► Fig. 42.8a) was synthesized by a nucleophilic aromatic ¹⁸F-for-nitro substitution on a protected benzaldehyde precursor (Ding et al. 1991) followed by a multistep procedure. Three-step syntheses starting with a nucleophilic ¹⁸F-for-N(CH₃)₃ exchange are also required to prepare the guanidine-derived catecholamine analogs 4-[¹⁸F]fluoro-3-iodobenzylguanidine (► Fig. 42.8c) (Vaidyanathan et al. 1994) and 4-[¹⁸F]fluorobenzyl guanidine (► Fig. 42.8d) (Garg et al. 1994) (► Table 42.5).

42.3.1.3 Electrophilic [¹⁸F]F₂ from n.c.a. [¹⁸F]F[–]

In order to improve the specific activity of [¹⁸F]F₂ and thus to exploit the electrophilic fluorination also for the production of neuroreceptor ligands, recent studies have addressed the conversion of [¹⁸F]fluoride to [¹⁸F]F₂ with high specific activity, cf. ► Fig. 42.9.

Fig. 42.7

Synthesis of 2-[¹⁸F]fluoro-L-tyrosine via destannylation (Hess et al. 2002)

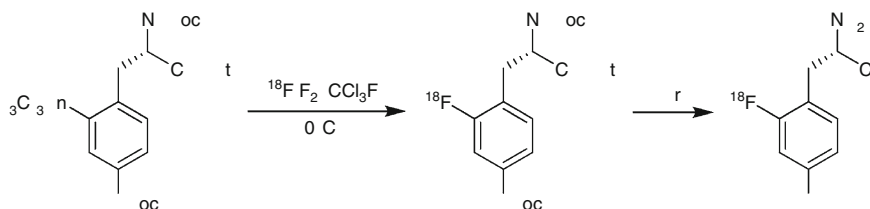


Fig. 42.8

(-)-6-[¹⁸F]Fluoronorepinephrine (a), 4- and 6-[¹⁸F]fluorometaraminol (b), 4-[¹⁸F]fluoro-3-iodobenzylguanidine (c), and 4-[¹⁸F]fluorobenzylguanidine (d)

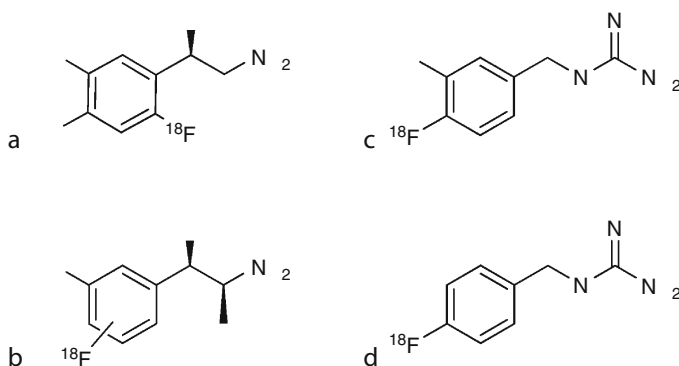


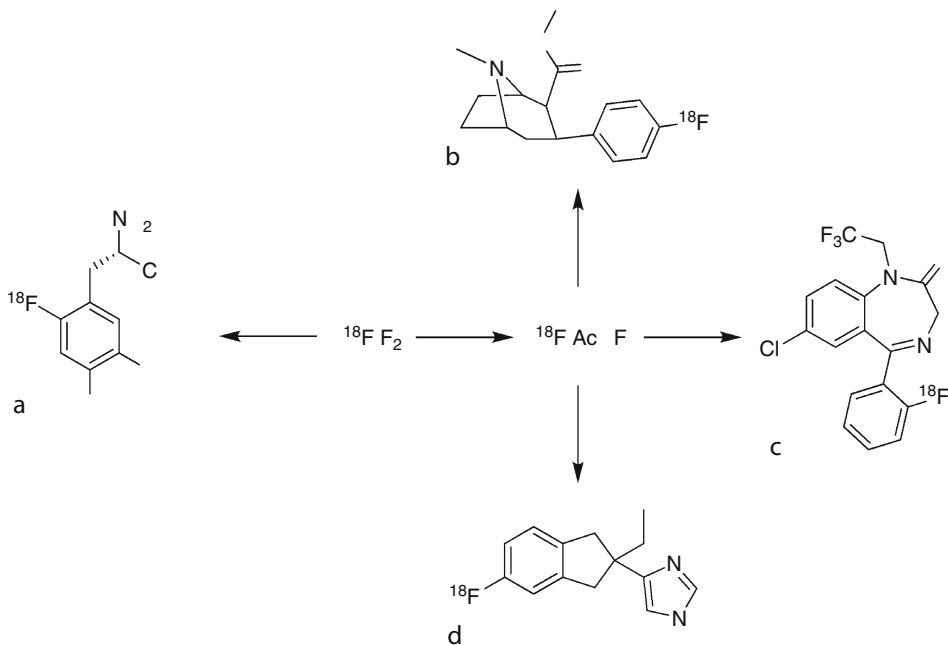
Table 42.5

Selected radiopharmaceuticals prepared via electrophilic ¹⁸F-fluorination

Radiopharmaceutical	Synthesis	Biochemical target	References
6-[¹⁸ F]Fluoro-L-DOPA	Direct	Dopamine metabolism	Adam et al. (1986)
	Demetallation		Namavari et al. (1992)
[¹⁸ F]Fluorometaraminol	Demetallation	Cardiac adrenergic innervation	Matsson et al. (1999)
2-[¹⁸ F]Fluorophenylalanine	Demetallation	Amino acid transport	Coenen et al. (1988), Murakami et al. (1988)
2-[¹⁸ F]Fluoro-L-tyrosine	Demetallation	Amino acid transport	Coenen et al. (1988)
5-[¹⁸ F]Fluorouracil	Direct	Tumor imaging	Fowler et al. (1973)
[¹⁸ F]CFT ([¹⁸ F]WIN 35,428)	Demetallation	Dopamine transport	Haaparanta et al. (1996)
8-[¹⁸ F]Fluoroguanine	Direct	HSV-Tk activity	Namavari et al. (2000)

■ Fig. 42.9

Synthesis of 6- ^{18}F FDOPA (a), ^{18}F CFT (b), ^{18}F oxoquazepam (c), and ^{18}F fluoroatipamezole (d)



In a procedure described by Bergman and Solin (1997), $^{18}\text{F}\text{CH}_3\text{F}$ was synthesized from $^{18}\text{F}\text{F}^-$ in an inert neon matrix. Following atomization in an electric discharge, after which a rearrangement and ^{18}F -for- ^{19}F exchange took place, $^{18}\text{F}\text{F}_2$ was obtained with a specific activity of up to $55\text{ GBq }\mu\text{mol}^{-1}$ (Bergman and Solin 1997). Using the aforementioned methodology, the authors succeeded in the syntheses of 6- ^{18}F FDOPA (● Fig. 42.9a) from N-formyl-3,4-di-*t*-butoxycarbonyloxy-6-(trimethylstannyl)-L-phenylalanine ethyl ester, ^{18}F CFT (B) (a dopamine transport marker) from 2- β -carbomethoxy-3- β -(4-trimethylstannyl-phenyl)tropane, ^{18}F fluoroatipamezole (D) ($\alpha 2$ adrenergic antagonist) from 4-(2-ethyl-2,3-dihydro-5-tributylstannyl-1H-2-indenyl)-1-acetyl-imidazole, and the benzodiazepine ^{18}F fluoro-oxoquazepam (C) from 7-chloro-1-(2,2,2-trifluoroethyl)-1,3-dihydro-5-(2-trimethyl-stannylphenyl)-2H-1,4-benzodiazepine-2-one). The specific activities of the compounds have been about $15\text{ GBq }\mu\text{mol}^{-1}$. All tracers are further examples for the importance of destannylations for the introduction of ^{18}F -fluorine into nonactivated aromatic systems.

42.3.2 Nucleophilic ^{18}F -Fluorination

At present, the aromatic and aliphatic *nucleophilic fluorination* starting with n.c.a., ^{18}F fluoride is the only way suitable for preparing high specific activity ^{18}F -labeled tracers. The ^{18}F fluoride, commonly produced by the $^{18}\text{O}(\text{p},\text{n})^{18}\text{F}$ nuclear reaction on highly enriched $^{18}\text{O}\text{H}_2\text{O}$, is in aqueous solution. Because of the high charge density of the fluoride ion, it is highly solvated in aqueous solution ($^{18}\text{F}\text{F}_{\text{aq}}^-$) and a poor nucleophile. As a strong base, it is

protonated in the presence of acidic protons to form [¹⁸F]HF. Furthermore, n.c.a. [¹⁸F]fluoride has the tendency to adhere or to get absorbed on the reaction vessel walls. Thus, several major aspects have to be considered for successful nucleophilic fluorinations. The fluoride ion has to be activated to increase its nucleophilicity and solubility. Dipolar aprotic solvents are used to avoid protonation. Furthermore, absorption losses may occur when unsuitable reaction vessels are used. High-purity chemicals, precursors, and solvents are strongly recommended and often even small traces of water dramatically impair or even preclude the radiochemical yield.

The reactivity and solubility can be increased by using large and soft cations, such as Rb⁺ and Cs⁺. Although these M[¹⁸F] salts are more soluble in dipolar aprotic solvents than K[¹⁸F], the use of cryptate complexes of potassium or tetraalkylammonium salts as phase transfer catalysts is the method of choice making the fluoride to a “naked” anion with high nucleophilicity. Thus, the *Kryptofix* 2.2.2 (4,7,13,16,21,24-hexaoxa-1,10-diazabicyclo[8.8.8]hexacosane) potassium carbonate system ([K/2.2.2]⁺ carbonate) (Coenen et al. 1986; Block et al. 1986b) has become the most often used phase transfer system in ¹⁸F-fluorination chemistry. For activation, the [¹⁸F]fluoride obtained in [¹⁸O]H₂O from the target is passed through an anion exchange resin. While the [¹⁸F]fluoride is retained, cationic contaminations from the target body are eluted and [¹⁸O]H₂O is recovered. [¹⁸F]Fluoride is then eluted with an aqueous solution of K₂CO₃ and transferred into a vessel. *Kryptofix* 2.2.2 is added, followed by successive azeotropic drying with at least three portions of acetonitrile. In contrast to the less basic carbonate, hydroxide, which is nucleophilic and strongly basic, is also often used as anion with R₄N⁺. If milder conditions are required, substitution of part of the carbonate by the non-nucleophilic and less basic oxalate allows fluorination of base-sensitive compounds. Polymeric-resin bound fluoride was also shown to be an efficient alternative in n.c.a. nucleophilic ¹⁸F-fluorinations. Lemaire et al. (2010) tested a set of strong organic bases, which enabled a sufficient elution of [¹⁸F]fluoride from the exchanger resin with a acetonitrile solution containing 500–10,000 ppm of water. Furthermore, the strong bases allowed effective ¹⁸F-labeling (aliphatic and aromatic) of different tracers directly in the elution volume still containing traces of water.

Nucleophilic ¹⁸F-fluorination has been performed in a variety of solvents. Because of their ability to solubilize the fluoride salts and most of the organic compounds, the dipolar aprotic solvents acetonitrile (MeCN), dimethyl sulfoxide (DMSO), dimethyl formamide (DMF), and dimethyl acetamide (DMAA) are most commonly used. Other solvents successfully used are tetrahydrofuran (THF), *ortho*-dichlorobenzene (DCB), and dichloromethane (DCM). For high temperature reactions, DMSO, DCB, nitrobenzene, or DMAA have been superior in some cases. In some studies, the use of ionic liquids such as [bmim][BF₄] or 1-butyl-3-methylimidazolium trifluoromethanesulfonate (BMI) showed promising results as cosolvents with the major advantages of tolerating the presence of water in the ¹⁸F-labeling step and enhancing the radiochemical yields (Kim et al. 2002; Kim et al. 2004). More recently, an unusual cosolvent of protic tertiary alcohols was found beneficial for ¹⁸F-fluorinations (Kim et al. 2006). The use of tertiary alcohols in a mixture with MeCN was reported to reduce side product formation and to enable higher and very reliable radiochemical yields at lower temperatures and shorter reaction times. Although, the beneficial effect of tertiary alcohol cosolvent system was thought to be limited to aliphatic ¹⁸F-labeling, a first example for an aromatic system was recently reported by Olberg et al. (2010).

As a general aspect of chemistry at the n.c.a. level, the reagents used are added in great excess. When typically 10–100 μmol of reagent are reacted with nmol amounts of the radioactive component, rates of reaction and reaction kinetics can be different from those expected from the “normal” organic chemistry. Although this difference can open routes to tracers not

available in the equimolar range, it also can result in unexpected pitfalls at the n.c.a. level. Thus, surprising results often can be avoided by a careful survey of the proposed reaction mechanism.

42.3.2.1 Nucleophilic Aromatic Substitutions

Finger and Kruse reported the first use of fluoride in *nucleophilic aromatic substitutions* in 1956. Twenty years later this methodology was applied to ¹⁸F-labeling, and introduction of [¹⁸F]fluoride into electron deficient aromatic systems is widely used (Stöcklin 1995; Lasne et al. 2002; Miller et al. 2008; Cai et al. 2008).

A variety of leaving groups, e.g., Y = NO₂, F, Cl, Br, I, (CH₃)₃N⁺, (CH₃)₂S⁺, has been investigated in the presence of activating groups, such as CN, CHO, COR, COOR, and NO₂ in small and complex molecules with different substitution patterns using different phase transfer catalysts and solvents. Radiochemical yields up to 80% are obtained. Variations in temperature, time, solvent, catalyst, and counter ions (for (CH₃)₃N⁺ and (CH₃)₂S⁺) render a direct comparison difficult. High yields are obtained with trimethylammonium salts (preferably triflate) or NO₂ as leaving groups and NO₂, CN, CHO, COR, or COOR as activating groups in *ortho*- or *para*-position (50–85%). Although activation is maximum in *ortho*- and *para*-position, high yields are also observed in some cases in 1,3-disubstituted benzenes, e.g., 3-[¹⁸F]fluoronitrobenzene from 1,3-dinitrobenzene (84%). Although comparable yields are obtained with NO₂ and the cationic leaving group (CH₃)₃N⁺, the latter is superior with respect to precursor separation, both via cartridge systems or HPLC. Demethylation and formation of [¹⁸F]FCH₃ are often reported as limitations when the aromatic system is not sufficiently activated by electron-withdrawing substituents, and indeed, this side reaction was exploited for synthesis of [¹⁸F]fluoromethane. Nevertheless, the high yields for the aromatic nucleophilic substitution reveal that this process can be tolerated.

Fluorine-for-halogen exchange has also been described in DMSO/[K/2.2.2]⁺ systems using 4-haloacetophenones and 4-halobenzonitriles. In both series, ¹⁸F-for-F exchange was the most efficient (70–75%). This process, however, is only suitable when high specific activities are not needed.

Complex molecules have been labeled with [¹⁸F]fluoride by direct aromatic nucleophilic substitution. The serotonin receptor ligands [¹⁸F]altanserin (Lemaire et al. 1991) (► Fig. 42.10a) and the D₂-like receptor ligand N-[¹⁸F]methylspiperone (Hamacher et al. 1986a) were successfully prepared by aromatic ¹⁸F-for-NO₂ and ¹⁸F-for-Cl exchange.

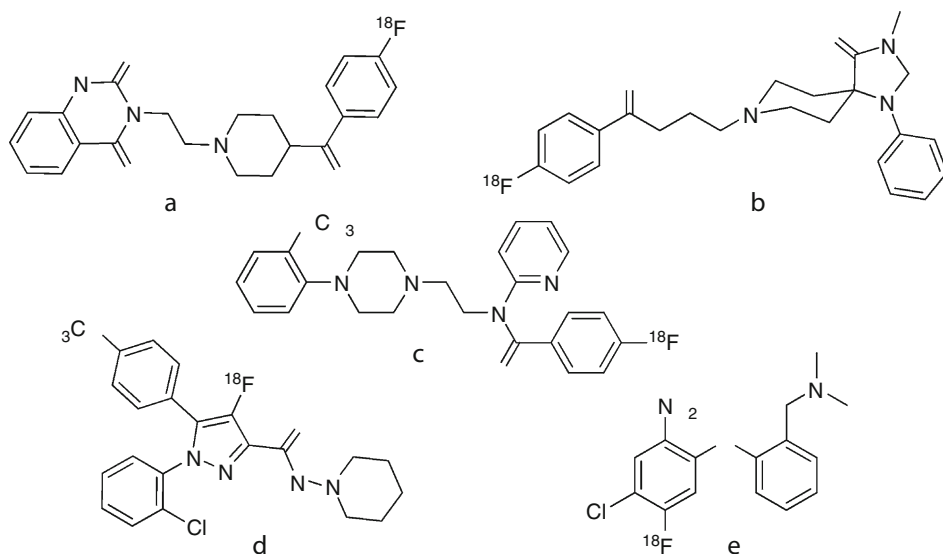
For labeling of the latter compound and other analogs of a series of *butyrophenone neuroleptics* the basicity of the [K/2.2.2]⁺ ¹⁸F[−] was reduced by using the less basic *oxalate* and only traces of carbonate (Hamacher et al. 1986a; Katsifis et al. 1993). Another example for a direct nucleophilic substitution is *p*-[¹⁸F]MPPF (Shiue et al. 1997), a 5-HT_{1A} receptor antagonist (► Fig. 42.10c). [¹⁸F]fluoride-for-bromide displacement on the pyrazole backbone of a CB1 cannabinoid receptor ligand yielded the potential CB1 cannabinoid receptor ligand in only 6% (Katoch-Rouse and Horti 2003) (► Fig. 42.10d).

The new ¹⁸F-labeled phenylthiophenyl derivative, specific for imaging of serotonin reuptake transporters (SERT), was synthesized by ¹⁸F-for-NMe₃ substitution and subsequent combined borane and stannous chloride reduction of the nitro and amido group in the precursor (Oya et al. 2002) (► Fig. 42.10e).

With the aim to obtain 6-[¹⁸F]FDOPA with high specific activity, “nucleophilic” routes were also investigated (Ding et al. 1990; Reddy et al. 1993; Lemaire et al. 1994; Lemaire et al. 2004;

Fig. 42.10

The serotonin receptor ligand [^{18}F]altanserin (**a**), the D_2 -like receptor ligand N-[^{18}F]methylspiperone (**b**), the $5\text{-HT}_{1\text{A}}$ receptor antagonist *p*-[^{18}F]MPPF (**c**), the CB1 cannabinoid receptor ligand (**d**), and a ^{18}F -labeled phenylthiophenyl derivative (**e**), specific for imaging of serotonin reuptake transporters (SERT)



Wagner et al. 2009). [▶ Figure 42.11](#) summarized the asymmetric syntheses of 6-[^{18}F]FDOPA, 2-[^{18}F]fluoro-L-tyrosine, and 4-[^{18}F]fluoro-*meta*-L-tyrosine starting with the nucleophilic aromatic ^{18}F -for- NO_2 -exchange on the aldehydes. Diiodosilane was used to prepare the corresponding benzyl iodides in about 35% radiochemical yield. Alkylation of (S)-1-Boc-2-*tert*-butyl-3-methyl-4-imidazolidinone (S-Boc-BMI) and hydrolysis with hydrogen iodide led to the tracers after purification within about 125 min and 11–16% radiochemical yield (Lemaire 1993).

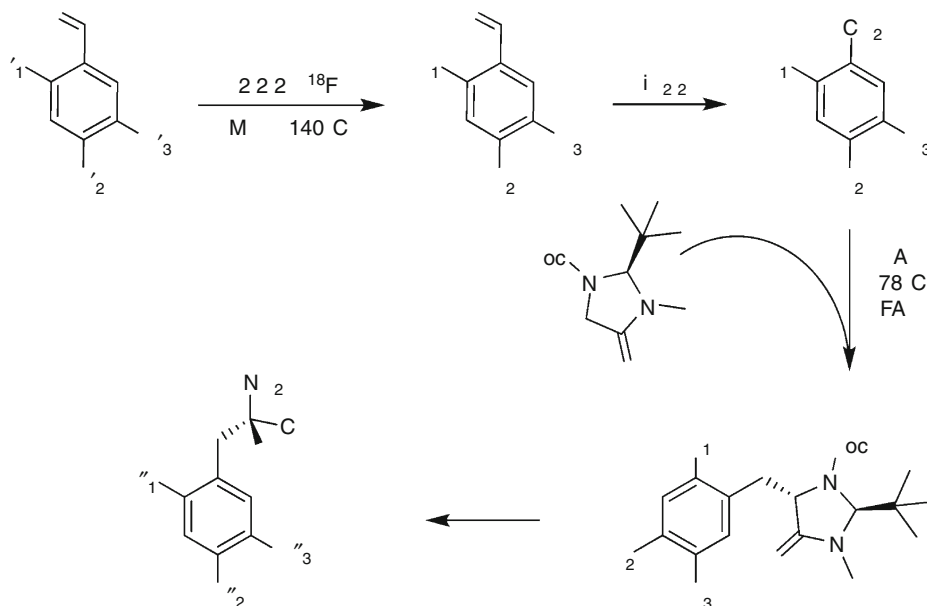
In an enantioselective multistep approach using asymmetric phase-transfer-catalysts, the radiochemical yield of n.c.a. 6-[^{18}F]FDOPA could be increased to 20–30% and the isolated product was obtained with an enantiomeric excess of $\geq 96\%$ (Lemaire et al. 2004). Recently, a direct precursor for nucleophilic ^{18}F -labeling of 6-[^{18}F]FDOPA by isotopic exchange was developed (Wagner et al. 2009). The ^{18}F -introduction is facilitated by an activating aldehyde function in *para*-position ([▶ Fig. 42.12](#)). After Bayer–Villiger oxidation of the aldehyde and subsequent acid hydrolysis, 6-[^{18}F]FDOPA was achieved in good radiochemical yields of 22% within 105 min.

42.3.2.2 Nucleophilic Aromatic Substitution of Small Synthons

Obviously, one-step fluorinations are not always possible or even rare. For the majority of compounds, competing nucleophilic and acidic groups in a molecule have to be protected. For other compounds, labeling can only be achieved in multistep syntheses starting with small labeled synthons.

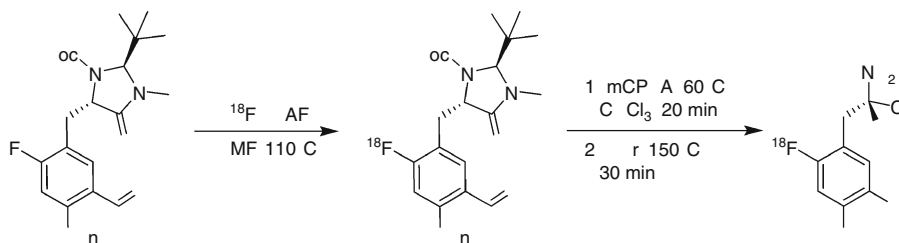
■ Fig. 42.11

Multistep synthesis of no-carrier-added (n.c.a.) 2- ^{18}F fluoro-L-tyrosine (^{18}F FTyr), n.c.a. 6- ^{18}F fluoro-L-DOPA (6- ^{18}F FDOPA) and n.c.a. 4- ^{18}F fluoro-meta-L-tyrosine (4- ^{18}F mTyr) (Lemaire 1993). 2- ^{18}F FTyr: $\text{R}_1' = \text{NO}_2$ or $\text{Me}_3\text{N}^+ - \text{SO}_3\text{CF}_3$; $\text{R}_1 = \text{R}_1'' = ^{18}\text{F}$; $\text{R}_2 = \text{R}_2' = \text{OCH}_3$; $\text{R}_2'' = \text{OH}$, $\text{R}_3 = \text{R}_3' = \text{R}'' = \text{H}$ 6- ^{18}F FDOPA: $\text{R}_1' = \text{NO}_2$ or $\text{Me}_3\text{N}^+ - \text{SO}_3\text{CF}_3$; $\text{R}_1 = \text{R}_1'' = ^{18}\text{F}$; $\text{R}_2 = \text{R}_2' = \text{R}_3 = \text{R}_3' = \text{OCH}_3$; $\text{R}_2'' = \text{R}_3'' = \text{OH}$ 4- ^{18}F mTyr: $\text{R}_2' = \text{NO}_2$ or $\text{Me}_3\text{N}^+ - \text{SO}_3\text{CF}_3$; $\text{R}_2 = \text{R}_2'' = ^{18}\text{F}$; $\text{R}_3 = \text{R}_3' = \text{OCH}_3$; $\text{R}_3'' = \text{OH}$, $\text{R}_1 = \text{R}_1' = \text{R}'' = \text{H}$



■ Fig. 42.12

Radiosynthesis of 6- ^{18}F FDOPA by isotopic exchange and subsequent Bayer–Villiger oxidation and acidic hydrolysis (Wagner et al. 2009)



Although most of the precursors in Fig. 42.13 are shown as substituted NO_2 -compounds, the corresponding trimethylammonium salts (triflates and perchlorates) often lead to comparable or even higher yields (see Table 42.6).

Nonactivated ^{18}F -labeled aromatic systems, such as 4- ^{18}F fluorobenzene and 4- ^{18}F fluoroiodobenzene can be prepared in good yields (30–50%) by symmetrically and

Fig. 42.13

Some synthons obtained by nucleophilic aromatic substitution in *para*-position and transformations studied for the multistep synthesis of ^{18}F -labeled tracers

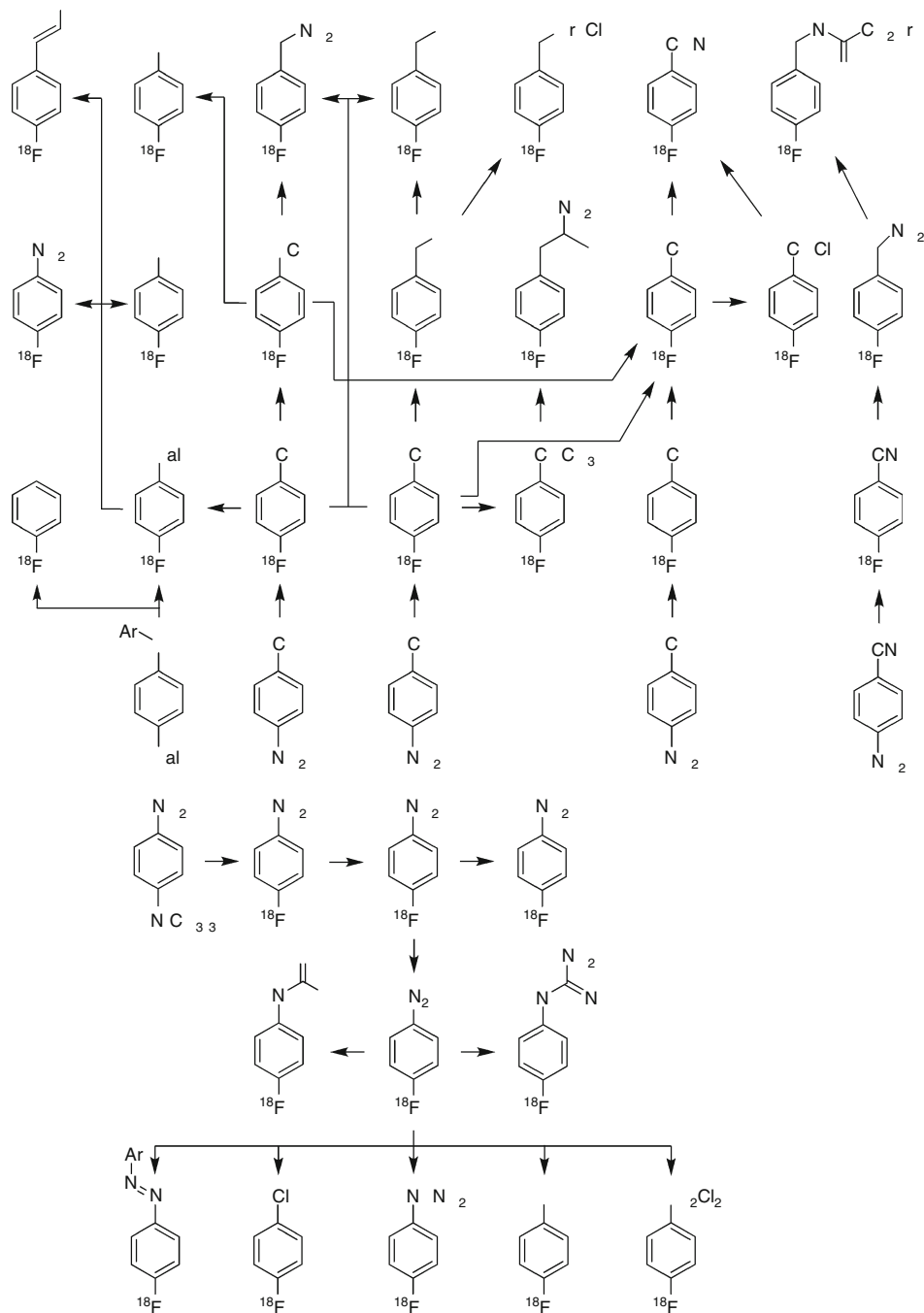


Table 42.6

Radiochemical yields in the aromatic nucleophilic substitution

Activating group	Leaving group	Other substituents	Yield (%)	Activating group	Leaving group	Other substituents	Yield (%)
NO₂	4-NO ₂	–	70–95	CHO	4-NO ₂	–	65–70
	3-NO ₂	–	50–80		4-NO ₂	2-OCH ₃	50–60
	2-NO ₂	–	60–90		3-NO ₂	–	0
	4-Br	–	30		2-NO ₂	–	65–80
	4-Cl	–	35–50		2-NO ₂	5-OCH ₃	5
	4-N(CH ₃) ₃ ⁺	3-Cl	30–90		2-NO ₂	4,5-di-OCH ₃	20
	4-N(CH ₃) ₃ ⁺	3-Br	75–80		Br	–	<5
	4-N(CH ₃) ₃ ⁺	–	70–80		Cl	–	<5
	3-N(CH ₃) ₃ ⁺	2-CH ₃	40		N(CH ₃) ₃ ⁺	–	75
CN	4-NO ₂	–	70	COCH₃	4-NO ₂	–	30–40
	4-Br	–	30		4-Br	–	5–10
	4-F	–	70		4-F	–	75
	4-Cl	–	25		4-Cl	–	30
	4-N(CH ₃) ₃ ⁺	–	75–80		4-N(CH ₃) ₃ ⁺	–	30–40

unsymmetrically substituted *diaryliodonium salts* (e.g., triflates) (Pike and Aigbirhio 1995; Gail et al. 1997; Shah et al. 1998; Wüst and Knieß 2003, 2004). In addition, diaryliodonium salts were used for the radiofluorination of nonactivated heteroaromatic systems and enabled convenient ¹⁸F-labeling of 3-[¹⁸F]fluoropyridines and 3-[¹⁸F]fluoroquinolines, cf. Table 42.7 (Carroll et al. 2007a). Diaryliodonium salt precursors have been applied to ¹⁸F-labeling in microreactors and yielded various *ortho*-substituted [¹⁸F]fluoroarenes in high yields (Chun et al. 2010). In case of symmetrical diaryliodonium salts, the reaction with [¹⁸F]fluoride yields only one ¹⁸F-labeled product. The unsymmetrical diaryliodonium salts lead generally to two ¹⁸F-arenes with a preference for the less electron-rich system. This fact provides an electronic control of the regioselectivity of this ¹⁸F-labeling procedure. Furthermore, also a steric effect of *ortho*-substituents allows an influence on the direction of the nucleophilic attack (*ortho* effect) (Gail et al. 1997; Shah et al. 1998). The use of a very electron-rich heteroaromatic ring to direct the nucleophilic ¹⁸F-attack exclusively toward the desired ¹⁸F-anisoles was investigated using the 2-thienyl moiety (Ross et al. 2007). No 2-[¹⁸F]fluorothiophene was observed in this study and only ¹⁸F-anisoles were found. However, recent investigations on the (radio)fluorination of 2-thienyl(phenyl)iodonium salts reported the detection of 2-fluorothiophene and the 2-thienyl ring revealed not to be an optimal choice due to the extremely problematic detection, isolation, and characterization of 2-fluorothiophene (Carroll et al. 2007b). Nonetheless, the 2-thienyl group in combination with 4-halobenzene rings gave good radiolabeling yields (50–60%) of the corresponding 4-[¹⁸F]fluorohalobenzenes (Ross et al. 2007). Especially the 4-[¹⁸F]fluoroiodobenzene can further undergo palladium-mediated cross coupling reactions, e.g., Sonogashira, Suzuki, Stille, Hartwig-Buchwald or Heck, and presents an attractive intermediate for multistep syntheses (Wüst and Knieß 2003, 2004; Ermert et al. 2004).

Table 42.7
Radiochemical yields for nucleophilic aromatic substitution of pyridines

Leaving group (LG)	Other substituent's	Yields (%)	Leaving group	Other substituent's	Yields (%)
2-I	3-OR	40	2-I	–	20
2-NO ₂	3-OR	70–80	2-Cl	–	60
2-N(CH ₃) ₃ ⁺	3-OR	80–95	2-Br	–	90
6-I	3-OR	30	2-NO ₂	–	90
6-NO ₂	3-OR	20–30	2-N(CH ₃) ₃ ⁺	–	90–95
6-N(CH ₃) ₃ ⁺	3-OR	40–50	3-I(4-MeOC ₆ H ₄) ⁺	–	55–63
6-Br	3-R	25–35	3-NO ₂	6-CO-NHR	37
6-NO ₂	3-R	10–20	3-I(4-MeOC ₆ H ₄) ⁺	“Quinoline”	22–25
6-N(CH ₃) ₃ ⁺	3-R	70			

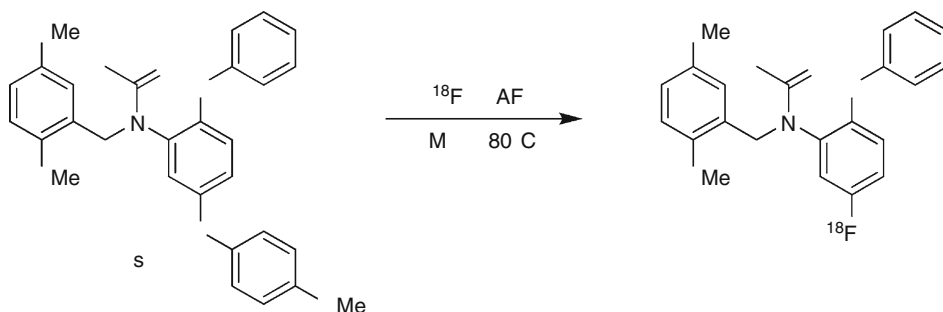
Using Pd-catalysis, reaction of RSnBu₃ with 4-[¹⁸F]fluoroiodo- and 4-[¹⁸F]fluorobromobenzene yielded the corresponding alkyl- and aryl- substituted 4-[¹⁸F]fluorobenzenes (Allain-Barbier et al. 1998; Plevenaux et al. 1992). RP62203, a serotonin receptor antagonist, was successfully synthesized by Pd-catalyzed 4-[¹⁸F]fluorophenylation of a piperazine precursor (Marrière et al. 1999). Via the formation of [¹⁸F]fluorophenyllithium from 4-[¹⁸F]fluorobenzene, a variety of other compounds, which do not lend themselves to nucleophilic aromatic substitution, can be obtained (Ludwig et al. 2001; Ermert et al. 2007). Generally, examples for ¹⁸F-labeling of more complex structures by the use of diaryliodonium salts are rare (Hostetler et al. 1999b; Wüst and Knieß 2003). The most successful example of which is the PBR ligand [¹⁸F]DAA1106, which was labeled in radiochemical yields of 46% within 20 min from the corresponding *para*-anisole iodonium tosylate precursor, cf. Fig. 42.14 (Zhang et al. 2007).

[¹⁸F]Fluorobenzaldehyde, another versatile labeled intermediate, is obtained via the NO₂ or trimethylammonium precursors in good to high yields. The aldehyde is transformed to the [¹⁸F]fluorobenzylhalides (Br, Cl, I) either after the reduction to [¹⁸F]fluorobenzyl alcohol and subsequent halogenation or in one step using di-iodosilane (Hatano et al. 1991; Damhaut et al. 1992; Najafi et al. 1993; Mach et al. 1993; Lemaire et al. 1994; Halldin et al. 1994; Dence et al. 1997; Iwata et al. 2000a, b; Hwang et al. 1991).

Although [¹⁸F]fluoroalkoxyphenols can also be obtained by oxidation of the corresponding [¹⁸F]fluorobenzaldehydes (Chakraborty and Kilbourn 1991b), Bayer–Villiger oxidation of [¹⁸F]fluoroaryketones seems to be the most favorable route to more complex molecules (Ekaeva et al. 1995; Ludwig et al. 2002; Stoll et al. 2004). [¹⁸F]fluorobenzaldehyde was also used to prepare ¹⁸F-labeled activated esters for peptide labeling via oxidation to [¹⁸F]fluorobenzoic acid and esterification (Vaidyanathan and Zalutsky 1992), although labeling of nonactivated (ethyl, butyl, anthrylmethyl) esters and subsequent hydrolysis seems to be the most straightforward approach to the acids, acid chlorides, and activated esters (Guhlke et al. 1994a; Wester et al. 1996). [¹⁸F]fluorobenzaldehydes are also important intermediates for the synthesis of [¹⁸F]fluorobenzylamines by reductive amination (Choe et al. 2000).

■ Fig. 42.14

Radiosynthesis of the PBR ligand [^{18}F]DAA1106 via nucleophilic ^{18}F -labeling of a diaryliodonium salt precursor (Zhang et al. 2007)



For synthesis of ^{18}F -labeled deprenyl (MAO inhibitor), 4- ^{18}F -fluorobenzaldehyde was converted to 4- ^{18}F -fluorobenzylmethylketone (Cooke et al. 1982), followed by reductive amination (Plevenaux et al. 1991).

Decarbonylation of 2- ^{18}F -fluorobenzaldehydes has been used to synthesize labeled arenes with nonactivated substituents, e.g., 4-bromo- ^{18}F -fluorobenzene from 3-bromo-6-nitrobenzaldehyde (Chakraborty and Kilbourn 1991a). This methodology was also applied to ^{18}F -fluoroarylketones (Allain-Barbier et al. 1998; Forngren et al. 1998) and to mono- to tetra-methoxy-substituted ^{18}F -fluorobenzenes from the corresponding 2-nitro(methoxy)benzaldehydes (Shen et al. 2009). In the latter study they identified side products, which derived from demethylation of methoxy groups and intramolecular redox processes that reduced the radiochemical yields.

Similar to most of the other aromatic intermediates discussed before, 4- ^{18}F -fluorocyanobenzene can be obtained both by ^{18}F -for- NO_2 or ^{18}F -for- $(\text{CH}_3)_3\text{N}^+$ -exchange in good to high yields. Reduction led to 4- ^{18}F -fluorobenzylamine (Shiue et al. 1989), which was used as an intermediate in the syntheses of prosthetic groups for peptide (4- ^{18}F -fluorophenacyl bromide (Kilbourn et al. 1987), protein (N-(*para*- ^{18}F -fluorophenyl)maleimide, Shiue et al. 1989), and oligonucleotide labeling (Dollé et al. 1997; Kuhnast et al. 2000a, b).

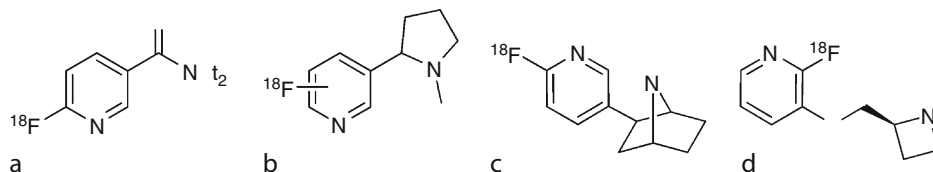
Ortho-, *meta*-, and *para*- ^{18}F -fluoronitrobenzenes are other interesting intermediates. They can be obtained in high yields from the corresponding trimethylammonium nitrobenzenes or dinitrobenzenes. Reduction yields the ^{18}F -fluoroanilines (Feliu 1988; Olma et al. 2006), suitable precursors for labeled piperazines (Collins et al. 1992; Das and Mukherjee 1993; Lasne et al. 1994). Conversion of ^{18}F -fluoroaniline to the diazonium salt opens synthetic routes to 4- ^{18}F -fluorochlorobenzene, 4- ^{18}F -fluorohydrazinobenzene (Feliu 1988), 4- ^{18}F -fluorophenol (Livni et al. 1992), or 4- ^{18}F -fluorobenzenesulfonylchloride. Recently, a 4- ^{18}F -fluorobenzenediazonium salt was successfully employed for ^{18}F -fluoroarylation of 4- ^{18}F -fluorophenyl substituted α -, β -, and γ -amino acids (Höfling et al. 2008) and also suggested as a prosthetic group for peptide labeling (Patt and Patt 2001).

42.3.2.3 Nucleophilic Heteroaromatic Substitutions

Nucleophilic aromatic substitution was also extended to the labeling of *heteroaromatic systems*, such as thiophenes (Kilbourn 1989) or pyridines (Knust et al. 1982; Dollé 2005). Typically, high

Fig. 42.15

2-^{[18}F]fluoropyridines: (a) 6-^{[18}F]fluoronicotinic acid diethylamide (¹⁸F-for-Cl, 40% RCY), (b) 2- and 6-^{[18}F]fluoronicotine (¹⁸F-for-BR, 30–40% RCY), (c) [¹⁸F]norchloro-fluoroeipibatidine (¹⁸F-for-NME₃, 70% RCY), and (d) [¹⁸F]-A-85380 (¹⁸F-for-NO₂, 50% RCY)



temperatures are required, and DMSO is the solvent of choice. Direct fluorination of 6-chloronicotinic acid diethyl amide led to the 6-^{[18}F]fluoronicotinic acid diethylamide in about 40% yield (Knust et al. 1982). Some other substitution reactions are listed in [Table 42.7](#) (Ballinger et al. 1984; Beer et al. 1995; Horti et al. 1996, 1998; Ding et al. 1997, 2000; Dollé et al. 1998b, 1999; Dolci et al. 1999a, b; Koren et al. 2000; Dollé 2005; Carroll et al. 2007a). Highest yields were obtained with trimethylammonium triflates, both for synthesis of the 2- and 6-^{[18}F]fluorinated pyridines, with the 6-position being less reactive than the 2-position in 3-OR substituted pyridines, cf. [Fig. 42.15](#). As mentioned above, the nonactivated 3-position of pyridines and quinolines can be ¹⁸F-fluorinated via the corresponding aryl (heteroaryl)iodonium salt precursors (Carroll et al. 2007a).

42.3.2.4 Nucleophilic Aliphatic Substitution

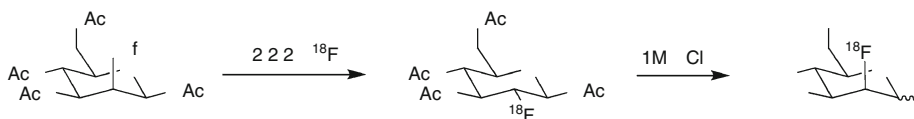
The second broad class of radiopharmaceuticals is opened by *nucleophilic aliphatic substitutions*. Typical leaving groups are iodide, bromide, chloride, tosylate, triflate, mesylate, or nosylate. Epoxides, cyclic sulfonates, or cyclic sulfamides (Brady et al. 1989; De Groot et al. 1994; Lim et al. 1996; Van Dort et al. 1995; Wängler et al. 2009a) were also found to be useful precursor structures for introduction of [¹⁸F]fluoride. Further approaches based on nucleophilic opening of aziridines as precursors have already been reported in 1984 (Farrokhzad et al. 1984) and were successfully readopted in the last decade (Lehel et al. 2000; Kiesewetter and Eckelman 2004; Röhn et al. 2009; Vasdev et al. 2009). In most cases, the [K/2.2.2]⁺ ¹⁸F[−]/acetonitrile system (Block et al. 1986b) is used with K₂CO₃ being the source of potassium and DMSO as an alternative for acetonitrile when higher temperatures are required.

Recently, the cosolvent system of *tertiary alcohols* such as *tert*-butanol, *tert*-amylalcohol, and acetonitrile has shown very promising results for ¹⁸F-fluorination in the presence of TBA⁺ ((C₄H₉)₄N⁺) salts, e.g., hydroxide or carbonate (Kim et al. 2006). Other functionalities with acidic protons (e.g., hydroxyls, phenols, thiols, or amides) or nucleophilic character (e.g., amines, carboxyls) have to be protected. Side products formed by elimination or the formation of the corresponding alcohols by hydrolysis of the high excess of precursor may coelute during HPLC purification and thus contaminate the product (pseudo carrier).

Without a doubt, 2-^{[18}F]fluoro-2-deoxy-D-glucose is the most useful PET radiopharmaceutical. The development of [¹⁸F]FDG, labeled and used to measure regional glucose utilization with PET by Phelps et al. (1979) and Reivich et al. (1979) about 25 years ago were based on observations of Warburg (1930, 1956). He found that tumor cells are characterized by a high

■ Fig. 42.16

Synthesis of [^{18}F]FDG via nucleophilic aliphatic substitution on tetraacetyl mannosyl-2-triflate (Hamacher et al. 1986a)



increase in *glycolytic metabolism*. Sokoloff et al. (1977) used ^{14}C -labeled deoxyglucose and autoradiography for measurement of local cerebral glucose utilization using a simple compartment model. In 1999, about 85% of all PET studies in Germany were carried out using [^{18}F]FDG (Brix et al. 2002), and this even seems to be a low percentage compared to other countries.

[^{18}F]FDG is taken up by the cells by specific glucose transporters (GluT) and is then phosphorylated by hexokinase. Since [^{18}F]FDG-6-phosphate is not a substrate for the glucose-6-phosphate isomerase, it is metabolically trapped in the intracellular compartments.

A comprehensive review of the different approaches for [^{18}F]FDG production has been published by Fowler and Ido (2002) (cf. Table 42.8). [^{18}F]FDG is produced nowadays by a two-step process developed by Hamacher et al. (1986a) (Fig. 42.16). The procedure consists of a nucleophilic aliphatic substitution of tetra-acetyl-trifluoromethanesulfonyl- β -D-mannopyranose (tetraacetylated mannosyl-2-triflate) by ^{18}F -fluoride-for-triflate exchange with $[\text{K}/2.2.2]^+ \text{ } ^{18}\text{F}^-$ in acetonitrile (up to 95% incorporation of ^{18}F -fluoride).

The reaction occurs with Walden inversion, giving rise to the enantiomerically pure no-carrier-added glucose compound. After deprotection by acidic (Hamacher et al. 1986a) or alkaline hydrolysis (Füchtner et al. 1996, Lemaire et al. 2002), the product is purified and neutralized by passing the solution through an ion retardation column with a small volume of isotonic saline, formulated and filtered to sterilize. The overall synthesis including purification proceeds in about 50–70% yields, depending on further modifications implemented. One of them is the use of 4-(4-methyl-1-piperidino)pyridine immobilized on a chloromethylated polystyrene matrix. This anion exchange resin is used in the carbonate form for the fixation of ^{18}F -fluoride, recovery of [^{18}O]H $_2$ O, and subsequent fluorination. In a competing displacement reaction during hydrolysis with 1 M HCl 2-chloro-deoxy-glucose (CIDG) (typically <20–50 $\mu\text{g ml}^{-1}$) is formed. Although CIDG does not present a toxic problem in [^{18}F]FDG preparations, its formation can be avoided by alkaline hydrolysis of tetra-acetyl-2-[^{18}F]fluoro-2-deoxy-D-glucose with NaOH. Though epimerization at C-2 position is a known reaction of aldoses under basic conditions, epimerization can be limited to 0.5% by using 0.33 M NaOH (<40°C, 5 min). To avoid defluorination and epimerization at higher temperatures and higher NaOH concentrations, tetra-acetyl-[^{18}F]FDG was hydrolyzed on solid phase, allowing the use of 2 M NaOH for fast (2 min) and efficient (>99%) deprotection at room temperature (Lemaire et al. 2002).

The use of radiolabeled nucleosides, taken up into proliferating cells and incorporated into DNA, is a well-known approach for the determination of cell proliferation, e.g., utilizing [^3H]thymidine or fluorinated compounds (Shields et al. 1996). Nucleosides are taken up into cells by facilitated diffusion controlled by equilibrative and concentrative transporters. From the two groups of equilibrative transporters (*es* and *is*), the *es*-transporter is mainly expressed in human cell lines investigated so far.

■ Table 42.8

Synthesis of [¹⁸F]fluoro-2-deoxy-D-glucose ([¹⁸F]FDG): major approaches (From Fowler and Ido 2002)

Labeling precursor	Substrate
Electrophilic methods:	
[¹⁸ F]F ₂	3,4,6-tri-O-acetyl-D-glycal
[¹⁸ F]F ₂ → [¹⁸ F]AcOF	3,4,6-tri-O-acetyl-D-glycal
[¹⁸ F]F ₂ → [¹⁸ F]AcOF	D-glycal
[¹⁸ F]F ₂ → [¹⁸ F]XeF ₂	3,4,6-tri-O-acetyl-D-glycal
Nucleophilic methods:	
[¹⁸ F]HF → [¹⁸ F]CsF	Methyl-4,6-O-benzylidene-3-O-methyl-2-O-trifluoromethanesulfonyl-β-D-mannopyranoside
[¹⁸ F]HF → [¹⁸ F]CsF	Methyl- or vinyl 4,6-benzylidene-α-D-mannopyranoside-2,3-cyclic sulfate
[¹⁸ F]HF → [¹⁸ F]CsF	1,2-anhydro-3,4,5,6-di-isopropylidene-1C-nitro-D-mannitol
[¹⁸ F]HF → [K/2.2.2] ⁺ ¹⁸ F [−]	1,3,4,6-tetra-O-acetyl-2-trifluoromethanesulfonyl-β-D-mannopyranose

In 1969, a fluorinated derivative of thymidine, 3'-deoxy-3-fluorothymidine (FLT) was reported to be a new and selective inhibitor of DNA synthesis (Langen et al. 1996) and has been investigated as antiviral agent later. Preparation of the c.a. ¹⁸F-labeled compound was first described in 1991 (Wilson et al. 1991) for noninvasive imaging of drugs against AIDS. After protection of the 5'-hydroxy group with a trityl group, the 3'-hydroxy group was substituted with a mesyl group in the *lyxo*-configuration. Treatment with [¹⁸F]potassium fluoride and crown-18 ether yielded the ¹⁸F-labeled fluoro-derivative, which on detritylation afforded [¹⁸F]FLT with 7% labeling efficiency (Wilson et al. 1991). The n.c.a. synthesis was first presented by Grierson and Shields (2000) using 3-*N*-(2,4-dimethoxybenzyl)-1-[5-*O*-(4,4'-dimethoxytrityl)-3-*O*-nosyl-2-deoxy-β-D-*lyxo*-furanosyl]thymidine as precursor (► Fig. 42.17). To improve work-up and yields, several other methods have been tested (Machulla et al. 2000; Wodarski et al. 2000; Blocher et al. 2002; Martin et al. 2002; Mier et al. 2002; Windhorst et al. 2008). So far, nucleophilic ¹⁸F-fluorination of 3-*N*-Boc-1-[5-*O*-(4,4'-dimethoxytrityl)-3-*O*-nosyl-2-deoxy-β-D-*lyxo*furanosyl]thymidine followed by deprotection with HCl seems to be the most suitable method. In 2003, this approach was optimized to give [¹⁸F]FLT in high radiochemical yields of up to 54% and radiochemical purity of ≥97%, sufficient for clinical applications (Yun et al. 2003).

The synthesis of *O*-(2-[¹⁸F]fluoroethyl)-*L*-tyrosine ([¹⁸F]FET) (Wester et al. 1999), an amino acid transport tracer for tumor imaging (Weber et al. 2000) is another example for a direct nucleophilic introduction of [¹⁸F]fluoride. Initially, a three-step procedure including the ¹⁸F-fluoroalkylation of unprotected *L*-tyrosine was used for evaluation of the biochemical characteristics of the tracer. The promising in vivo data (Wester et al. 1999; Weber et al. 2000) prompted Hamacher and Coenen (2002) to design a more convenient routine synthesis via a direct ¹⁸F-fluorination of the protected precursor (► Fig. 42.18). As an alternative to the HPLC purification of [¹⁸F]FET, Wang et al. (2005) suggested a solid-phase extraction method. Recently, a precursor based on a Ni(II)-complex of a *L*-tyrosine Schiff base was developed for [¹⁸F]FET (Krasikova et al. 2008). The Ni(II)-complex was especially designed to avoid racemization of the amino acid during the ¹⁸F-labeling step.

Fig. 42.17

Approaches to [¹⁸F]FLT (see Griersen and Shields 2000; Machulla et al. 2000; Blocher et al. 2002; Wodarski et al. 2000; Martin et al. 2002; Yun et al. 2003; Windhorst et al. 2008)

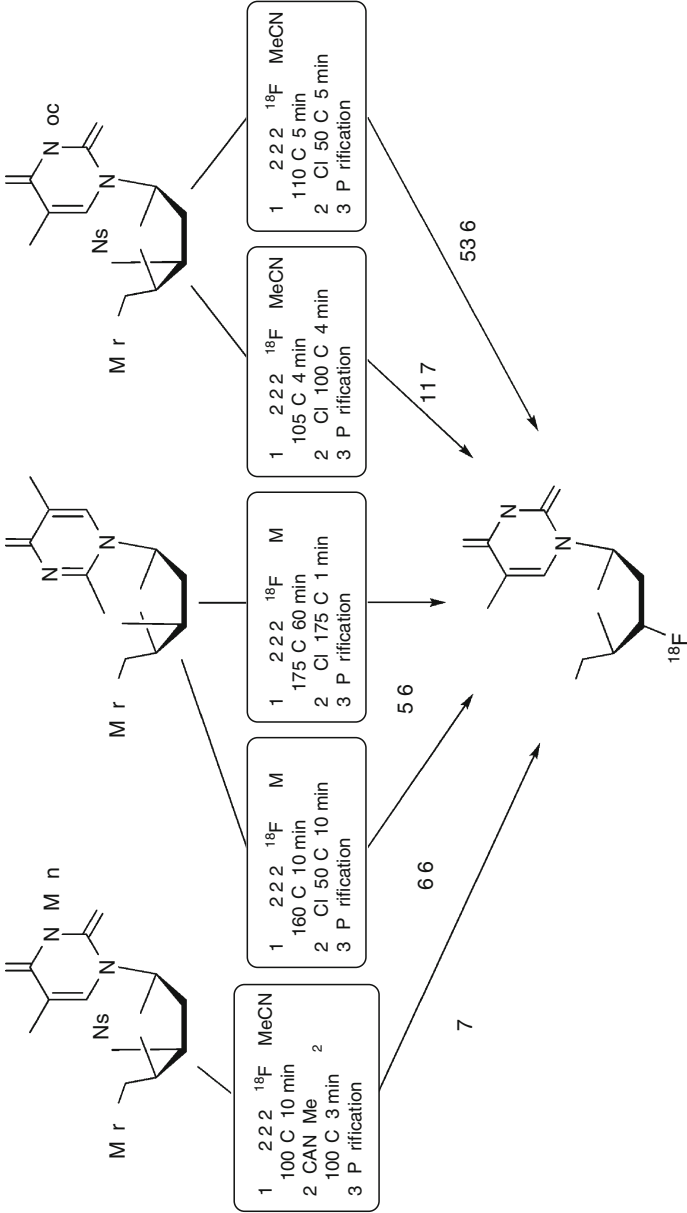
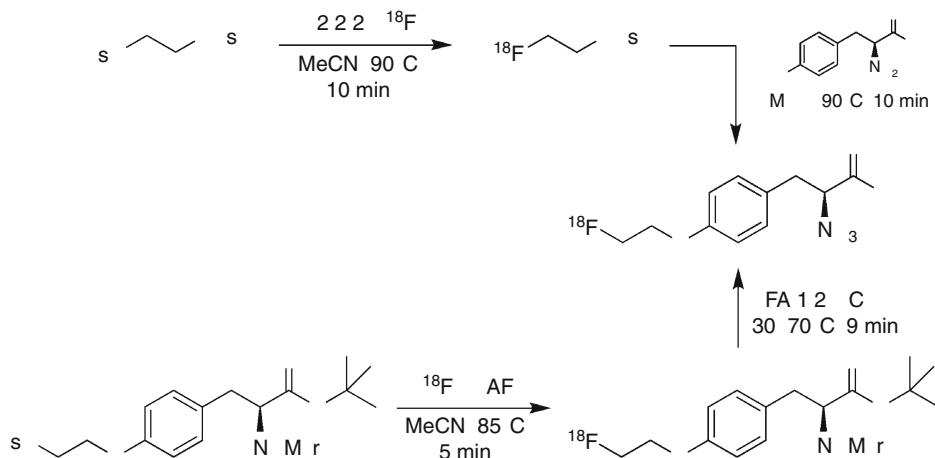


Fig. 42.18

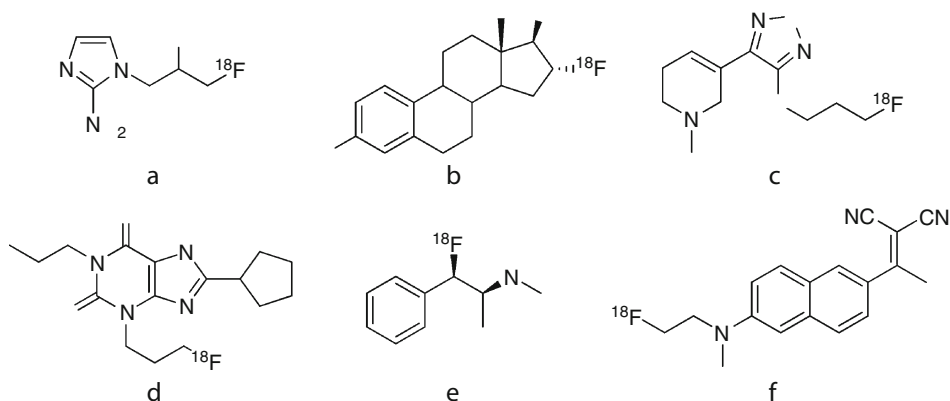
Approaches to [^{18}F]fluoroethyl-L-tyrosine ([^{18}F]FET)

Some other examples for the nucleophilic aliphatic fluorination are given in Fig. 42.19. [^{18}F]FMISO, a tracer for quantification of *tumor hypoxia*, was originally labeled by a two-step procedure: ^{18}F -for-tosylate displacement on (2R)-(-)-glycidyl tosylate leading to [^{18}F]epifluorohydrin and reaction with imidazole to [^{18}F]FMISO (Grierson et al. 1989) (Fig. 42.19a). Lim and Berridge (1993) investigated the use of four different sulfonate-protected precursors for direct displacement with ^{18}F -fluoride. After deprotection, they obtained [^{18}F]FMISO in 55–80% radiochemical yield.

A variety of steroids was investigated for the early detection and staging of prostate and breast cancer. The selective estrogen receptor ligand 16- α -[^{18}F]fluoro-17 β -estradiol ([^{18}F]FES) (Fig. 42.19b) was labeled by displacement of a triflate group of the protected precursor followed by reduction of the fluoroestrone intermediate by LiAlH_4 (43%) (Kiesewetter et al. 1984). A modified procedure utilized 3-methoxymethyl-16 β , 17 β -epiestriol-O-cyclic sulfone for the production of FES (Lim et al. 1996). [^{18}F]FP-TZTP (Fig. 42.19c), a M2 selective muscarinic ligand, has been produced in >20% overall yield by ^{18}F -for-mesylate displacement (Kiesewetter et al. 2003). Recently, Holschbach et al. (2002) described the radiosynthesis of the A_1 adenosine receptor antagonist 8-cyclopentyl-3-(3-[^{18}F]fluoropropyl)-1-propylxanthine ([^{18}F]CPFPX) (Fig. 42.19d). ^{18}F -for-tosylate displacement on the 7-pivaloyloxymethyl protected precursor and subsequent alkaline deprotection gave rise to an overall radiochemical yield of 45%. [^{18}F]FDE (Fig. 42.19e) ((1R,2S)-1-[^{18}F]fluoro-L-deoxyephedrine) was prepared as a model compound to explore the biomimetic potential of F-for-OH substitution in β -phenethanolamines (Van Dort et al. 1995). The synthesis was achieved in high radiochemical yields (62%) by reaction of [^{18}F]fluoride with the chiral cyclic sulfamidate precursor. Radiofluorinated 6-dialkylamino-2-naphthylethylidene derivatives, and especially [^{18}F]FDDNP (Fig. 42.19f) as imaging probes for β -amyloid plaques in Alzheimer's disease, are prepared by simple ^{18}F -for-tosylate exchange in about 25% yield (Agdeppa et al. 2001, 2003). Recently, an automated synthesis for [^{18}F]FDDNP was developed to make this radiotracer available for the clinical routine (Vercouillie et al. 2010).

■ Fig. 42.19

$[^{18}\text{F}]\text{FMISO}$ (a), a tracer for imaging of hypoxia, the selective estrogen receptor ligand 16- α -fluoro-17 β -estradiol $[^{18}\text{F}]\text{FES}$ (b), the M2 selective muscarinic ligand $[^{18}\text{F}]\text{FP-TZTP}$ (c), the A_1 adenosine receptor antagonist $[^{18}\text{F}]\text{CPFPX}$ (d), the model compound (1R,2S)-1- $[^{18}\text{F}]\text{fluoro-1-deoxyephedrine}$ ($[^{18}\text{F}]\text{FDE}$, see text) (e), and $[^{18}\text{F}]\text{FDDNP}$ (f), an imaging probe for β -amyloid plaques in Alzheimer's disease



A novel and very effective strategy for the isolation and separation of ^{18}F -labeled compounds from their precursor molecules by “fluorous detagging” was reported (Bejot et al. 2009). The sulfonate leaving groups on precursor molecules were additionally derivatized with polyfluorinated tags, which allowed a very fast and efficient separation from precursors by fluorous solid-phase extraction. Several prosthetic groups as well as $[^{18}\text{F}]\text{fluoroethylcholine}$, $[^{18}\text{F}]\text{FMISO}$, and *cis*-4- $[^{18}\text{F}]\text{fluoro-L-proline}$ were successfully produced in good to high radiochemical yields and simply purified by this new methodology.

42.3.3 Prosthetic Group Labeling

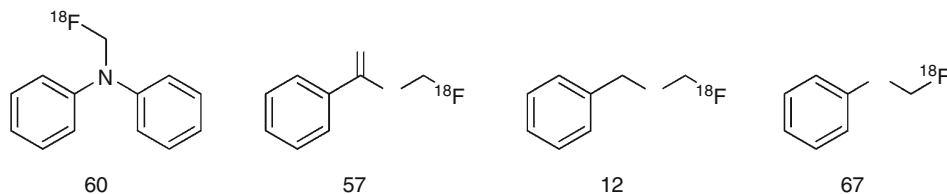
A variety of compounds cannot be prepared by direct nucleophilic ^{18}F -fluorination. When high specific activity is required and electrophilic fluorination thus is impossible, labeling is often carried out by a multistep route using small reactive intermediates, often named *secondary labeling precursors* or *prosthetic groups*. A whole battery of these ^{18}F -labeled intermediates was investigated and prepared, such as amines, alcohols, aldehydes, ketones, carboxylic acids, esters, and halides. Since a quantitative overview about these synthons is outside the scope of this chapter, only some examples are discussed.

42.3.3.1 Introduction of ^{18}F -Fluorine by Fluoromethylation

When approaches to direct introduction of ^{18}F -fluorine by nucleophilic displacement fail, ^{18}F -alkylation procedures are often the alternative of choice. Nevertheless, compared to the battery of tracers produced by ^{11}C -methylation, only a few ^{18}F -labeled tracers prepared via this route are used clinically.

■ Fig. 42.20

Radiochemical yields for the ^{18}F -fluoromethylation of some model compounds (selected nucleophiles) with $[^{18}\text{F}]\text{FCH}_2\text{I}$



On the basis of the aforementioned isosteric relations, production of suitable tracers by ^{18}F -fluoromethylation of precursors in analogy to standard $[^{11}\text{C}]$ methylation seems to be a straightforward method. Unfortunately, most of the compounds prepared by this assumption show low metabolic stability and are extensively defluorinated in vivo (resulting in high $[^{18}\text{F}]$ fluoride bone uptake). The most prominent exception is $[^{18}\text{F}]$ choline, a tracer developed for tumor imaging, i.e., imaging of metastatic prostate cancer. Several attempts have been made to prepare $[^{18}\text{F}]$ halofluoromethanes as methylating agents (Coenen et al. 1986; Zheng and Berridge 2000; Bergman et al. 2001).

$[^{18}\text{F}]\text{FCH}_2\text{I}$, the closest analog of methyl iodide, can be prepared in $(40 \pm 8)\%$ radiochemical yield by F-for-I exchange of CH_2I_2 (Zheng and Berridge 2000; Zhang et al. 2004) (cf. ► Fig. 42.20). Best results are obtained at room temperature using MeCN as solvent and $[\text{K}/2.2.2]^+ ^{18}\text{F}^-$. At elevated temperature, the reaction yield decreased due to decomposition. The product is co-distilled with the reaction solvent under a helium stream. Although being somewhat less reactive, production of $[^{18}\text{F}]\text{FCH}_2\text{Br}$ exhibits the advantage to optionally allow online conversion to $[^{18}\text{F}]\text{FCH}_2\text{OTf}$ (Iwata et al. 2002). $[^{18}\text{F}]\text{FCH}_2\text{Br}$ can be prepared using the $[\text{K}/2.2.2]^+$ carbonate system (4 min, reflux) in $>50\%$ radiochemical yield. After passing all volatile compounds through a batch of silica cartridges by a helium flow, subsequent alkylations can be carried out either with $[^{18}\text{F}]\text{FCH}_2\text{Br}$ or $[^{18}\text{F}]\text{FCH}_2\text{OTf}$ formed by passing $[^{18}\text{F}]\text{FCH}_2\text{Br}$ through a second column filled with AgOTf on solid support (Iwata et al. 2002). Using this methodology, $[^{18}\text{F}]$ choline was prepared either in solution or on-column. The analogs $[^{18}\text{F}]\text{FCH}_2\text{OTos}$ and $[^{18}\text{F}]\text{FCH}_2\text{OMs}$ were already developed in 1987 (Block et al. 1987). Recently, the preparation of $[^{18}\text{F}]\text{FCH}_2\text{OTos}$ from bis(tosyloxy)methane was reexamined and used for the ^{18}F -fluoromethylation of several tracers in high radiochemical yields (Neal et al. 2005).

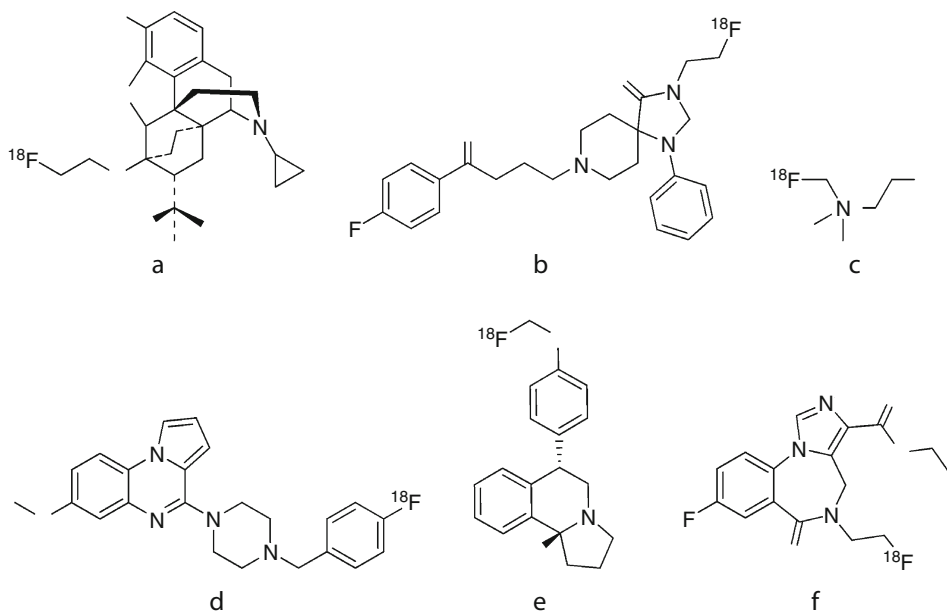
A number of applications were tested (Zheng and Berridge 2000) and first tracers, such as S-([^{18}F]fluoromethyl)-(+)-McN5652 (► Fig. 42.21e), as a potential radiotracer for PET imaging of the 5-HT transporters (Brust et al. 2003), have been evaluated.

42.3.3.2 Introduction of ^{18}F -Fluorine by Fluoroethylation

^{18}F -Fluoroethylation represents another useful way of inserting ^{18}F into molecules containing -NH-, -SH, or -OH groups (Block et al. 1987, 1988; Chi et al. 1986; Zijlstra et al. 1993). Applications and preparations of agents for ^{18}F -fluoroethylation and ^{18}F -fluoroalkylation have been recently reviewed by Wadsak et al. (2007) and Zhang and Suzuki (2007), respectively. An often-applied route to ^{18}F -fluoroethylation or longer ^{18}F -fluoroalkylation reagents was

■ Fig. 42.21

The nonselective (μ , κ , δ) opioid receptor ligand [^{18}F]FDPN (a), the α D_2 -like receptor antagonist [^{18}F]FESP (b), the prostate cancer imaging agent [^{18}F]fluorocholine [^{18}F]FCH (c), the 5-HT $_3$ receptor partial agonist [^{18}F]MR18445 (d), [^{18}F]McN5652 (e), and the central benzodiazepine receptor ligand 5-(2'-[^{18}F]fluoroethyl)flumazenil [^{18}F]FEF (f)



introduced by Block et al. 1987. Symmetrical bis-halide or bis-toxyloxyalkanes are fluorinated in high yields ($\text{Br} < \text{mesyl} < \text{tosyl}$, Block et al. 1987). The ^{18}F -fluoroethylation agent [^{18}F]FCH $_2$ -CH $_2$ OTos ([^{18}F]FETos) can be prepared in automated systems (Tang et al. 2003a). The purification of [^{18}F]FETos can be either done by HPLC (Wester et al. 2000) or by a solid-phase extraction on cartridges (Tang et al. 2003a). Preparation of [^{18}F]fluoroethyl iodide by ^{18}F -fluorination of the corresponding di-iodide gives only negligible radiochemical yields.

Zhang et al. (2002) described an automated system for synthesis, purification, and subsequent ^{18}F -fluoroethylation via 1-bromo-2-[^{18}F]fluoroethane [^{18}F]FCH $_2$ -CH $_2$ Br. Using nitrobenzene and *ortho*-dichlorobenzene as less volatile solvents, [^{18}F]FCH $_2$ -CH $_2$ Br was produced by phase transfer-mediated nucleophilic ^{18}F -fluorination (130°C, 5 min) of Br-CH $_2$ -CH $_2$ -OTos and Br-CH $_2$ -CH $_2$ -OTf in radiochemical yields of 30–55%. Again, the product can be purified by distillation (He, 90–100 ml min $^{-1}$, 130°C, 5 min) and condensation in a cooled trap. Alternatively, isolation of [^{18}F]CH $_2$ -CH $_2$ Br is achieved using more convenient cartridge systems (Comagic et al. 2002). An improved radiochemical yield of ^{18}F -ethylation compounds could be achieved in the presence of alkali iodides (Bauman et al. 2003).

Some selected ^{18}F -compounds prepared by alkylation are shown in Fig. 42.21. Whereas 6-O-(2-[^{18}F]fluoroethyl)-6-O-desmethyldiprenorphine (Fig. 42.21a), a nonselective (μ , κ , δ) opioid receptor ligand, was prepared by [^{18}F]fluoroethylation with [^{18}F]FETos and subsequent 3-O-deprotection (trityl) in about 20% radiochemical yield (Wester et al. 2000), no protection was required to alkylate 3-N-(2'-[^{18}F]fluoroethyl)sipiperone (Fig. 42.21b),

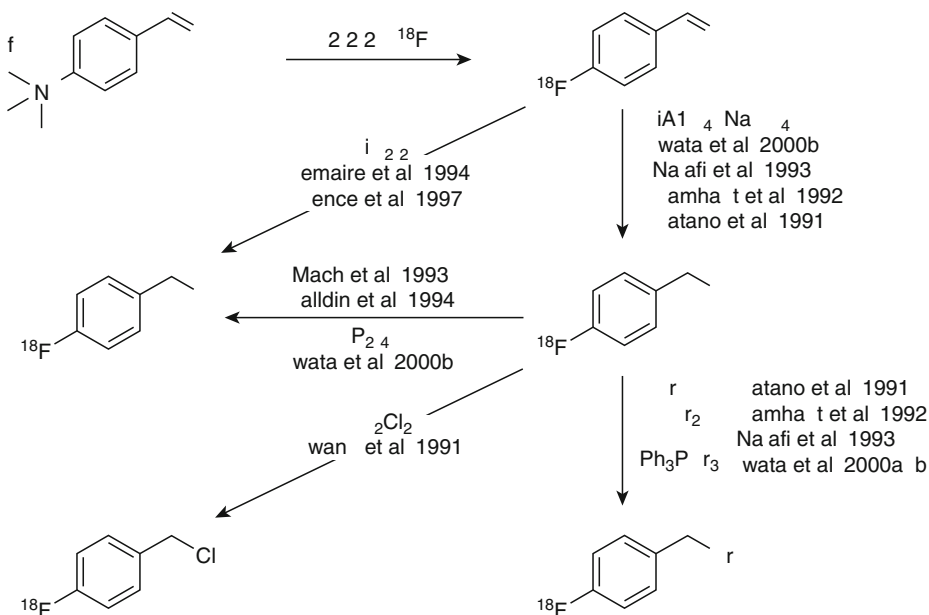
a D₂-like receptor antagonist (Chi et al. 1986; Block et al. 1986a). Both, [¹⁸F]fluoromethylcholine (FCH) (Fig. 42.21c) (DeGrado et al. 2001) and [¹⁸F]fluoroethylcholine (Hara et al. 2002; Piel et al. 2007; Zuhayra et al. 2008) are employed for imaging metastatic prostate cancer. [¹⁸F]Fluorobenzyl iodide, prepared via labeling of the benzaldehyde followed by reduction and halogenation (HI) was used to label [¹⁸F]MR18445 (Fig. 42.21d), a 5-HT₃ receptor partial agonist (Katounina et al. 1998). S-([¹⁸F]fluoromethyl)-(+)-McN5652 has been synthesized as a new radiotracer for PET imaging of 5-HT transporter (Brust et al. 2003). Zessin et al. (2001) prepared the compound by reaction of normethyl-(+)-McN5652 with the fluoromethylation agent [¹⁸F]bromofluoromethane in about 5% overall yield. 5-(2'-[¹⁸F]fluoroethyl)flumazenil ([¹⁸F]FEF) (Fig. 42.21f) (Moerlein and Perlmutter 1992) was synthesized as a longer-lived alternative to [¹¹C]flumazenil.

42.3.3.3 Introduction of ¹⁸F-Fluorine by Other Secondary Precursors

3-[¹⁸F]fluoropropyl bromide and 3-[¹⁸F]fluoropropyl iodide are also useful alkylation reagents and were used to label various receptor ligands, like opioidergic or dopaminergic ligands (Chesis and Welch 1990; Oh et al. 1999; Bai et al. 1990; Teng et al. 1990). The tosyl analog, 3-[¹⁸F]fluoropropyl tosylate (Block et al. 1987) again provides an alternative ¹⁸F-fluoroalkylation agent, which was employed for the synthesis of O-(3-[¹⁸F]fluoropropyl)-L-tyrosine (Tang et al. 2003b). Due to the high stability against defluorination in vivo, ¹⁸F-labeled phenyl groups are often used as structural mimetic for the corresponding non-fluorinated correlates (cf. Fig. 42.22). If direct fluorination fails, multistep synthesis via alkylation reagents can open an alternative strategy. Thus, 4-[¹⁸F]fluorobenzyl

Fig. 42.22

Syntheses of 4-[¹⁸F]fluorobenzylhalides from 4-[¹⁸F]fluorobenzaldehyde



bromide (Hatano et al. 1991; Damhaut et al. 1992; Najafi et al. 1993; Iwata et al. 2000a, b), 4-[¹⁸F]fluorobenzyl iodide (Mach et al. 1993; Halldin et al. 1994; Katounina et al. 1998; Iwata et al. 2000b) and 4-[¹⁸F]fluorobenzyl chloride (Hwang et al. 1991) were prepared and used for the multistep production of radiopharmaceuticals, such as [¹⁸F]fluoropropyfan, [¹⁸F]MR18445 (► Fig. 42.21d), [¹⁸F]fluorotroprapride, [¹⁸F]NCQ 115, and [¹⁸F]fluorodexetimide. The most straightforward synthesis so far seems to be the on-column reduction of the benzaldehyde with NaBH₄ and subsequent halogenation with P₂I₄ or Ph₃PBr₂ (Iwata et al. 2000a, b).

Reductive amination has been found to be a valuable method for a variety of tracers. The fluoro-substituted analog of (*S*)-CGP 12388 (► Fig. 42.23a) was prepared by reacting (*S*)-4-(3-amino-2-hydroxypropoxy)-2*H*-benzimidazol-2-one with [¹⁸F]fluoroacetone in the presence of NaCNBH₃ and glacial acetic acid (Elsinga et al. 1997). [¹⁸F]fluorocarazolol (► Fig. 42.23b) can be produced either by reductive amination (Kindsey et al. 1992; Zheng and Berridge 1992) or by alkylation of the desisopropyl precursor with 1-[¹⁸F]fluoroisopropyl tosylate (De Groot et al. 1992).

42.3.3.4 Introduction of ¹⁸F-Fluorine by Click Chemistry

The Cu(I)-catalyzed version of the 1,3-dipolar Huisgen cycloaddition of alkynes and azides (formation of 1,4-disubstituted 1,2,3-triazoles) became the most prominent example of the so-called click chemistry. Click reactions show certain characteristics such as fast kinetics, wideness in scope, high selectivity, and high yields. In case of the Cu(I)-catalyzed click cycloaddition, these facts are additionally accompanied by orthogonality to most other functional groups and high conversions under (very) mild reaction conditions. These benefits are particularly suitable for ¹⁸F-labeling chemistry (► Fig. 42.24). Different aliphatic ω-[¹⁸F]fluoro-alkynes were purified by co-distillation with the solvent (MeCN) and then coupled to unprotected azide-functionalized peptides under Cu(I)-catalyzed click cycloaddition conditions (Marik and Sutcliffe 2006). The ¹⁸F-labeled peptides were purified by simple cartridge-based solid-phase extraction and obtained in good-to-high radiochemical yields from 20% to 81%.

After the first examples of ¹⁸F-click cycloadditions on ¹⁸F-alkynes (Marik and Sutcliffe 2006; Sirion et al. 2007; Li et al. 2007), this approach was also rapidly extended to ¹⁸F-labeled azides as click-coupling agents (Sirion et al. 2007; Glaser and Årstad 2007; Thonon et al. 2009). In both ¹⁸F-click versions, it is noteworthy that the Cu(I)-catalyzed click step, forming the 1,4-disubstituted 1,2,3-triazoles, succeeded with similarly high efficiency. A clickable version of the established prosthetic group *N*-succinidyl-4-[¹⁸F]fluorobenzoate carrying an aromatic ¹⁸F-label was designed to provide enhanced in vivo stability (Ramenda et al. 2007). Also

► Fig. 42.23

The β-adrenoceptor ligands [¹⁸F]CGP 12388 (a) and [¹⁸F]fluorocarazolole (b)

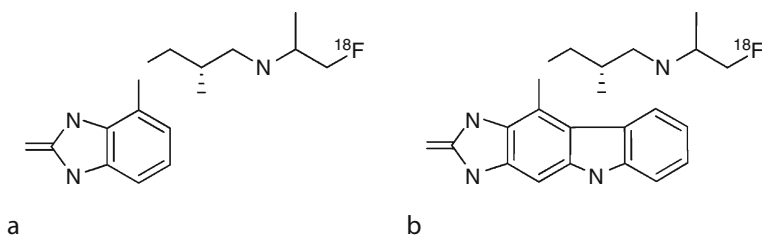
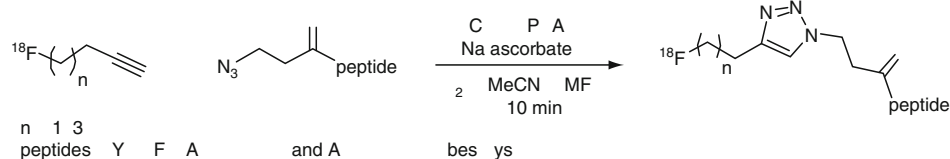


Fig. 42.24

¹⁸F-Click labeling of peptides via Cu(I)-catalyzed 1,3-dipolar Huisgen cycloaddition

alkyne-functionalized ¹⁸F-pyridines were developed as clickable aromatic ¹⁸F-compounds (Kuhnast et al. 2008; Inkster et al. 2008). Recently, an ¹⁸F-labeled azido-glucose was developed as clickable prosthetic groups, which was ¹⁸F-labeled in high radiochemical yields of ~70% and additionally brings extra polarity for improved pharmacokinetics into the final product (Maschauer and Prante 2009). Especially the mild conditions and the inertness to other functional groups made this approach very attractive for the ¹⁸F-labeling of peptides (Marik and Sutcliffe 2006; Ramenda et al. 2007; Li et al. 2007; Inkster et al. 2008; Glaser et al. 2009a; Lei et al. 2010). Accordingly, this convenient method was also applicable for the ¹⁸F-labeling of small molecules and provided new ¹⁸F-derivatives of biomolecules such as thymidine and glucose (Sirion et al. 2007), folic acid (Ross et al. 2008), amino acids (Glaser and Årstad 2007; Thonon et al. 2009), isatin (Smith et al. 2008), and quinazoline (Kobus et al. 2009). The attractiveness and wide applicability of the ¹⁸F-click cycloaddition encouraged many colleagues adopting this efficient and convenient ¹⁸F-labeling method for their needs (Mamat et al. 2009; Glaser and Robins 2009; Ross 2010; Wängler et al. 2010).

42.4 ¹⁸F-Labeling of Peptides and Proteins

For the development of strategies to prepare ¹⁸F-labeled peptides and proteins, which are interesting tracers for receptor mapping, diagnosis, therapy planning, dosimetric calculations, and therapy control, two major limitations have to be considered: (1) the presence of acidic functionalities (e.g., hydroxyls, amides, alcohols, amines, and thiols) does not allow for direct nucleophilic ¹⁸F-fluorination; (2) electrophilic fluorination, as exemplified by Hebel et al. (1990), can only be achieved in the presence of carrier. To overcome these limitations, the commonly used methodology includes the preparation of ¹⁸F-labeled synthons (prosthetic groups), which are subsequently activated or, in only few cases, conjugated without activation to the peptide or protein.

Among the methods listed in Table 42.9, acylation is the commonly used strategy. The isolated N-succinimidyl 4-[¹⁸F]fluorobenzoate (Vaidyanathan and Zalutsky 1992, 1994, 2006; Gohlke et al. 1994a; Wester et al. 1996; Hostetler et al. 1999a; Sutcliffe-Goulden et al. 2000; Marik and Sutcliffe 2007; Glaser et al. 2009b) and 4-nitrophenyl 2-[¹⁸F]fluoropropionate (Gohlke et al. 1994a; Wester et al. 1996) allow to couple small aliphatic (e.g., 2-[¹⁸F]fluoropropionyl) or aromatic (4-[¹⁸F]fluorobenzoyl, 4-([¹⁸F]fluoromethylbenzoyl) groups under mild basic condition (pH 8–9) predominantly to the N-terminus and Lys-side chains of the peptides and proteins. N-succinimidyl 4-([¹⁸F]fluoromethyl)benzoate can be prepared in one step by nucleophilic ¹⁸F-fluorination of the highly activated nosylate precursor (Lang and Eckelman 1994, 1997) (35 min, 18%). In other cases, direct nucleophilic fluorination of the activated ester failed and led to the formation of the acyl-[¹⁸F]fluoride. Nevertheless,

■ Table 42.9

Syntheses of prosthetic groups for ¹⁸F-labeling of peptides and proteins. DCC = 1,3-dicyclohexylcarbodiimide; DSC, *N,N'*-disuccinimidyl carbonate; HATU = *N*-[(dimethylamino)-1*H*-1,2,3-triazolo[4,5-*b*]pyridin-1-yl-methylene]-*N*-methyl-methanaminium hexafluorophosphate *N*-oxide; HOAt, 1-hydroxy-7-azabenzotriazole; TSTU, *O*-(*N*-succinimidyl)-*N,N,N'*-tetramethyluronium tetrafluoroborate; NH S = *N*-hydroxy succinimide

¹⁸ F-labeled prosthetic group used for coupling	Steps/time/RCY	Comments	Reference
Method: acylation			
<i>N</i> -succinimidyl 4-([¹⁸ F]fluoromethyl)benzoate	1/30–35/18	Low yield, moderate stability	Lang and Eckelman (1994, 1997)
methyl 2-[¹⁸ F]fluoropropionate	1/15/90	Low reactivity	Block et al. (1988)
4-[¹⁸ F]fluorobenzoic acid (for subsequent coupling via DCC/HOAt)	2/20/50–60		Hostetler et al. (1999a)
4-[¹⁸ F]fluorobenzoic acid (for subsequent coupling via HATU/DIPEA)	2/~10/not reported		Sutcliffe-Goulden et al. (2000, 2002)
4-nitrophenyl 2-[¹⁸ F]fluoropropionate/KOBt	3/90/60	High in vivo stability	Guhlke et al. (1994a, b) Wester et al. (1997)
<i>N</i> -succinimidyl-8-[4'-[¹⁸ F]fluorobenzyl]amino]suberate	3/55/25–40	Bulky group	Garg et al. (1991)
<i>N</i> -succinimidyl 4-[¹⁸ F]fluorobenzoate (DCC-activated)	3/100/25		Vaidyanathan and Zalutsky (1992)
<i>N</i> -succinimidyl 4-[¹⁸ F]fluorobenzoate (DSC-activated)	3/55/35	High in vivo stability	Vaidyanathan and Zalutsky (1994)
<i>N</i> -succinimidyl 4-[¹⁸ F]fluorobenzoate (TSTU-activated)	3/35/50–60		Wester et al. (1996)
6-[¹⁸ F]fluoronicotinic acid 2,3,5,6-tetrafluorophenyl ester	1/10/60–70	One-step synthesis	Olberg et al. (2010)
Method: amidation			
1-[4-([¹⁸ F]fluoromethyl)benzoyl]-aminobutane-4-amine	2/80/52	Bulky group	Shai et al. (1989)
2-[¹⁸ F]fluoroethylamine	2/30–45/46	Needs protected peptides or peptides without amines	Jelinski et al. (2002)
Method: amidination			
3-[¹⁸ F]fluoro-5-nitrobenzimidate	3/45/20–33	Low reactivity	Kilbourn et al. (1987)
Method: alkylation			
4-[¹⁸ F]fluorophenacyl bromide	3/75/28–40	Low reactivity	Kilbourn et al. (1987), Downer et al. (1997)
<i>N</i> -(4-[¹⁸ F]fluorobenzyl)-2-bromoacetamide	3/90/20–25	Useful for thiols (oligonucleotides)	Dollé et al. (1997) Tavittian et al. (1998)

■ Table 42.9 (Continued)

^{18}F -labeled prosthetic group used for coupling	Steps/time/RCY	Comments	Reference
Method: photochemical conjugation			
4-acidophenacyl [^{18}F]fluoride	1/15/71	Unselective, high unspecific binding	Wester et al. (1996)
[^{18}F]-3,5-difluorophenyl azide (and five derivatives) (*)	1/80/1–12	Carrier added	Hashizume et al. (1995)
3-azido-5-nitrobenzyl-[^{18}F]fluoride	1/45/30–40		Lange et al. (2002)
Method: oxime formation			
4-[^{18}F]fluorobenzaldehyde	1/20/60–80	Fast and efficient, chemoselective, high yields	Poethko et al. (2004)
Method: thiol formation			
N-(4-[^{18}F]fluorophenyl)maleimide	4/100/15		Shiue et al. (1989)
m-Maleimido-N-(4-[^{18}F]fluorobenzyl)-benzamide	3/70/10	Multiple steps	Shiue et al. (1989)
4-[^{18}F]Fluorobenzylidene)aminoxy] butylmaleimide	2/60/37	With impurities	Toyokuni et al. (2003)
	2/90/23	Pure	Li et al. (2008)
1-[3-(2-[^{18}F]fluoropyridin-3-yloxy)-pyrrole-2,5-dione	3/110/37		De Bruin et al. (2005)
N-[2-(4-[^{18}F]fluorobenzamido)ethyl] maleimide	3/150/13		Cai et al. (2006)
	3/~100/23		Kramer-Marek et al. (2008)
Method: FDG-based conjugation			
1,3,4,6-tetra-O-acetyl-2-deoxy-2-[^{18}F] fluoroglucopyranoside	1/30/93	High polarity, OH-selectivity	Maschauer et al. (2005)
3,4,6-tri-O-acetyl-2-deoxy-2-[^{18}F] fluoro-glucopyranosyl phenylthiosulfonate	3/90/33	High polarity, yields and (thiol)-selectivity	Prante et al. (2007)
[^{18}F]FDG-maleimidehexyloxime	1/45/45–70 (from [^{18}F] FDG)	High yields, thiol-selective	Wüst et al. (2008)
[^{18}F]FDG	"[^{18}F]FDG synthesis"	High polarity, direct oxime formation	Wüst et al. (2009a) Namavari et al. (2009)

probably due a somewhat higher in vivo stability against defluorination, most of the ^{18}F -peptides used in preclinical studies were prepared using N-succinimidyl 4-[^{18}F]fluorobenzoate ([^{18}F]SFB) (3 steps, 35 min, 55%) (Wester et al. 1996) and 4-nitrophenyl 2-[^{18}F]fluoropropionate ([^{18}F]NFP) (3 steps, 90 min, 60%) (Guhlke et al. 1994b). Very recently, 6-[^{18}F]fluoronicotinic acid 2,3,5,6-tetrafluorophenyl ester was develop and enabled a direct aromatic ^{18}F -labeling of the activated ester trimethylammonium triflate precursor under mild conditions (Olberg et al. 2010).

[¹⁸F]fluorobenzoic acid can be activated by DCC/NHS (Vaidyanathan and Zalutsky 1992), DSC (Vaidyanathan and Zalutsky 1992; Gohlke et al. 1994a), or TSTU (Wester et al. 1996) prior to coupling or conjugated in situ to the peptide on solid-phase support by HATU/DIPEA (diisopropylethylamine) (Sutcliffe-Goulden et al. 2000, 2002; Marik and Sutcliffe 2007), TBTU/DIPEA (Sutcliffe-Goulden et al. 2000), or DCC/HOAt (Hostetler et al. 1999a). Acylation yields are generally high (see, e.g., [¹⁸F]SFB: Vaidyanathan and Zalutsky 1997; Bergmann et al. 2002; Fredriksson et al. 2002; Johnstrom et al. 2002; Marik and Sutcliffe 2007; [¹⁸F]NFP: Gohlke et al. 1994a, b; Wester et al. 1997, 2003; Haubner et al. 2001).

In order to overcome the increase in lipophilicity especially observed on small peptides after ¹⁸F-fluoracylation, newer approaches combine *carbohydration* with acylation.

This methodology was successfully applied for the synthesis of an ¹⁸F-labeled sugar amino acid derivative of cyclo(Arg-Gly-Asp-DPhe-Lys) (Haubner et al. 2001, 2004) and N^α-(1-deoxy-d-fructosyl)-N^ε-(2-[¹⁸F]fluoropropionyl)-Lys⁰-Tyr³-octreotate ([¹⁸F]FP-Gluc-TOCA) (Schottelius et al. 2004; Wester et al. 2003, 2004). This approach was further developed to [¹⁸F]FDG-based prosthetic groups for chemoselective ¹⁸F-glycosylation of peptides using 1,3,4,6-tetra-O-acetyl-2-deoxy-2-[¹⁸F]fluoroglucopyranoside under Königs–Knorr conditions (Maschauer et al. 2005) or 3,4,6-tri-O-acetyl-2-deoxy-2-[¹⁸F]fluoroglucopyranosyl phenylthiosulfonate (Ac₃-[¹⁸F]FGlc-PTS) for thiol functions (Prante et al. 2007). Ac₃-[¹⁸F]FGlc-PTS was produced in three steps with a radiochemical yield of ~33% and gave excellent conjugation yields of 90% with a model pentapeptide (CAKAY) and c(RGDfC). The sugar-based prosthetic group, [¹⁸F]FDG-maleimidehexyloxime ([¹⁸F]FDG-MHO) was also designed for chemoselective conjugation to thiol groups (Wüst et al. 2008). Starting from routinely produced [¹⁸F]FDG, [¹⁸F]FDG-MHO was prepared in one step by oxime formation and was obtained in radiochemical yields of 45–70% after HPLC purification. [¹⁸F]FDG-MHO was chemoselectively coupled to glutathione and annexin A5 with conjugation efficiencies of ~95% and ~60%, respectively (Wüst et al. 2008). Recently, direct conjugations of [¹⁸F]FDG to aminooxy-functionalized peptides, such as RGD-peptides (Hultsch et al. 2009; Namavari et al. 2009) and neurotensin(8–13) peptides (Wüst et al. 2009a) by oxime formation were developed and yielded [¹⁸F]FDG-labeled peptides in radiochemical yields of 40–88%.

To avoid hydrolysis of the no-carrier-added ¹⁸F-labeled active esters in aqueous buffered solution, the acylation route can be inverted, i.e., radiolabeled amines are prepared and coupled with activated carboxyls at the peptide (► Table 42.9, amidation). Oxytocin was successfully coupled with 2-[¹⁸F]fluoroethylamine in yields >90% by both preactivation (NHS, 4-nitrophenyl and pentafluorophenyl esters) and in situ activation of the C-terminus (TBTU) (Jelinski et al. 2002).

Reactions of imidates with proteins have been shown to be specific for ε-amino groups of lysines, forming a stable amidine, which is protonated under physiological conditions. Thus, and in contrast to acylation and amidation strategies, the net charge of the target molecule is not affected. In a comparative study Kilbourn et al. (1987), [¹⁸F]fluoro-5-nitrobenzimidate was utilized for labeling of human transferrin, IgG, hemoglobin, red blood cells, human platelets, etc. Conjugation yields ranged from 15% to ~60% at 1 h, based on the benzimidate (1 h, 30–65%).

Even being presumably the most applied labeling reaction for synthesis of radiopharmaceuticals, alkylation reactions for peptides are rare. α-Haloketones are known to alkylate various heteroatoms. Thus, 4-[¹⁸F]fluorophenacyl bromide was suggested to be a more indiscriminate labeling agent. Although fibrinogen was successfully labeled (25–30% yield) (Kilbourn et al. 1987), conjugation of *octreotide* failed (Downer et al. 1997). Further studies

suggest the use of 4-¹⁸F]fluorophenacyl bromide only for peptides with free thiols or carboxylic acids. Antibody labeling was carried out using N-*p*-(¹⁸F]fluorophenyl)maleimide and *m*-maleimido-N-(4-¹⁸F]fluorobenzyl)-benzamide with conjugation yields of about 50%. A 18mer *peptide nucleic acid* (PNA), bearing a cysteine at the C-terminus (Kuhnast et al. 2000a) and oligodeoxynucleotides, containing a single phosphothioate monoester (Dollé et al. 1997; Kuhnast et al. 2000b) were labeled using N-(¹⁸F]fluorobenzyl)-2-bromoacetamide and N-[3-(2-¹⁸F]fluoropyridin-3-yloxy(propyl)-2-bromoacetamide (Kuhnast et al. 2004).

In recent years, several maleimide-carrying prosthetic groups have been developed for the chemoselective conjugation to peptidic thiol functionalities; most of which have been synthesized from [¹⁸F]fluorobenzaldehyde ([¹⁸F]FBA) by reacting with aminooxy-maleimides under oxime formation. Accordingly, 4-¹⁸F]Fluorobenzylidene)aminooxy]butylmaleimide ([¹⁸F]FBABM) (Toyokuni et al. 2003; Hultsch et al. 2007; Li et al. 2008) and some derivatives were produced and successfully applied for chemoselective conjugation to peptidic cysteine groups (Berndt et al. 2007; Wüst et al. 2009b). Excellent chemoselectivity was obtained by the use of the ¹⁸F-labeled pyridine derivative 1-[3-(2-¹⁸F]fluoropyridin-3-yloxy)-pyrrole-2,5-dione ([¹⁸F]FPyME), which was obtained from a three-step synthesis in radiochemical yields of 37% within 110 min (de Bruin et al. 2005). N-[2-(4-¹⁸F]fluorobenzamido)ethyl]maleimide ([¹⁸F]FBEM) is another thiol-reactive prosthetic group, which was synthesized from [¹⁸F]SFB by conversion with the N-(2-aminoethyl)maleimide and used for the conjugation to thiolated cRGD peptides (Cai et al. 2006). The synthesis of [¹⁸F]FBEM could be optimized by starting from protected 4-¹⁸F]fluorobenzoic acid instead of [¹⁸F]SFB (Kramer-Marek et al. 2008) (► Table 42.10).

In order to overcome the time-consuming preparation of the ¹⁸F-prosthetic groups, alternative routes have been investigated. Photochemical conjugation agents, such as 4-azidophenacyl [¹⁸F]fluoride (Wester et al. 1996), 3,5-¹⁸F]difluorophenyl azide (Hashizume et al. 1995), or 3-azido-5-nitrobenzyl-¹⁸F]fluoride (Lange et al. 2002) can be prepared in one step. The “masked” electrophilic aryl nitrenes can be generated from the azides by UV-irradiation. Studies on photochemical conjugation of human serum albumin, transferrin, avidin, fibrinogen (Wester et al. 1996), and an *oligonucleotide* aptamer (Lange et al. 2002) have shown that labeling predominantly occurs at primary amines (lysine side chain or hexylamine modified 5'-aptamer terminus). This assumption is in accordance with the general proposed reaction pathways of aryl nitrenes: phenyl nitrenes mainly react by nucleophilic addition, while polyfluorinated aryl nitrenes mainly react by unspecific insertion (Bayley and Staros 1984; Doering and Odum 1966). Radiochemical conjugation yields of up to 30% can be obtained when using protein concentrations of 0.1–1 mg per 100 µl.

Two studies were carried out on the Pd-catalyzed Sonogashira coupling of alkynes with aryl halides: (1) one-step preparation of an ¹⁸F-labeled alkyne for conjugation of iodoaryl-modified peptides (Poethko, personal communication) and (2) one-step preparation of 4-¹⁸F]iodobenzene for coupling with alkyne-modified compounds (Wüst and Knieß 2003).

Conjugation of N-methyl-N-propargyl-¹⁸F]fluoroacetamide with acetyl-4-iodo phenylalanine as a model for peptides conjugated with, e.g., 4-iodobenzoic acid or bearing 4-iodo-Phe within the peptide chain could only be carried out on the carrier-added level using Pd(OAc)₂/tris(*m*-dimethylguanidinephenyl)phosphine/CuI (molar ratio 1:2:5) in yields up to 80%. Addition of carrier was necessary to enter the catalytic cycle after quantitative formation of a reactive Pd/N-methyl-N-propargyl-¹⁸F]fluoroacetamide intermediate. Thus, the use of Pd(0)-catalysts may overcome this limitation. In contrast, C–C bond formation on the n.c.a. level was achieved by Sonogashira coupling following the reverse route, i.e., coupling of

■ **Table 42.10**

Examples for ¹⁸F-labeled peptides. [¹⁸F]SFB = N-succinimidyl 4-[¹⁸F]fluorobenzoate, [¹⁸F]NFP = 4-nitrophenyl 2-[¹⁸F]fluoropropionate, [¹⁸F]FEA = 2-[¹⁸F]fluoroethylamine. [¹⁸F]Bal = 4-[¹⁸F]fluorobenzaldehyde

Principal application	Prosthetic Group	Peptide	References
Somatostatin receptor imaging of neuroendocrine tumors	[¹⁸ F]NFP	(2-[¹⁸ F]fluoropropionyl)-DPhe ¹ -octreotide	(Guhlke et al. 1994b, Wester et al. 1997)
	[¹⁸ F]SFB	(4-[¹⁸ F]fluorobenzoyl)-DPhe ¹ -octreotide	(Hostetler et al. 1999a)
	[¹⁸ F]NFP	N ^α -Glucose-N ^ε -(2-[¹⁸ F]fluoropropionyl)-Lys ⁰ -DPhe ¹ -Cys-Tyr-DTrp-Lys-Thr-Cys-Thr	(Wester et al. 2003)
	[¹⁸ F]BAI	2-(Glu-thiopropionyl)-3-oxyaminoacyl-TOCA cyclo(-Arg-Gly-Asp-D-Phe-Lys((¹⁸ F)Fprop)SAA)	(Poethko et al. 2004, Schottelius et al. 2004)
Imaging of angiogenesis	[¹⁸ F]NFP	[¹⁸ F]Galacto-RGD cyclo(-Arg-Gly-Asp-D-Phe-Lys((¹⁸ F)fluoropropionyl)SAA)	(Haubner et al. 2001)
	[¹⁸ F]FB	N ^α -[¹⁸ F]Fluorobenzoyl-Lys-Pro-Gln-Val-Thr-Arg-Gly-Asp-Val-Phe-Thr-Glu-Gly-NH ₂	(Sutcliffe-Goulden et al. 2002)
Melanoma Imaging	[¹⁸ F]SFB	[Nle ⁴ ,DPhe ⁷ ,Lys ¹¹ ([¹⁸ F]FB)-α-MSH	(Vaidyanathan and Zalutsky 1997)
Pancreatic tumors, Colon cancer	[¹⁸ F]SFB	N ^α -[¹⁸ F]fluorobenzoyl-[Arg ⁸ Ψ(CH ₂ NH)Arg ⁹]NT(8–13)	(Bergmann et al. 2002)
Basic research	[¹⁸ F]SFB	(4-[¹⁸ F]Fluorobenzoyl)-Glu ¹ -C-peptide	(Fredriksson et al. 2001, 2002)
Basic Research	[¹⁸ F]SFB	N ^ε -[¹⁸ F]Fluorobenzoyl-Lys ⁹ -ET-1	(Johnstrom et al. 2002)
Infection/inflammation	[¹⁸ F]SFB	N-formyl-Nle-Leu-Phe-Nle-Tyr-Lys (4-[¹⁸ F]fluorobenzoyl)	(Vaidyanathan and Zalutsky 1995)
Basic research	[¹⁸ F]FEA	Oxytocin-2-[¹⁸ F]fluoroethylamide	(Jelinski et al. 2002)

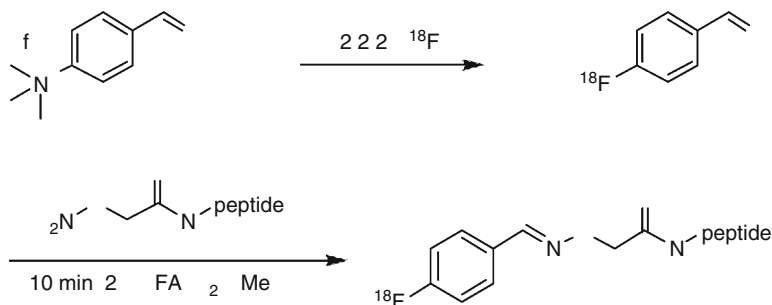
4-[¹⁸F]iodobenzene to alkynes (Wüst and Knieß 2003). However, the reverse route has not been used for peptide labeling so far.

Chemoselective conjugation of unprotected peptides in aqueous systems by oxime formation was suggested (Poethko et al. 2004; Schottelius et al. 2004; Thumshirn et al. 2003) as a very effective, time-saving, high yield ¹⁸F-labeling method, which is also adaptable to radiohalogenation in general (*radioiodination*, *radiobromination*, and *radioastatination*) (► Figs. 42.25 and ► 42.26).

4-[¹⁸F]fluorobenzaldehyde ([¹⁸F]FBA) was prepared within about 30 min in preparative yields of about 50% using solid-phase extraction cartridges for purification. Conjugation of various oxyamine acetate conjugated peptides (► Figs. 42.25 and ► 42.26) was carried out in H₂O/MeOH (pH 2) in 60–80% yield (10 min) and peptide concentrations of 0.5 mm.

Fig. 42.25

^{18}F -Labeling of unprotected peptides using [^{18}F]fluorobenzaldehyde (Poethko et al. 2004; Schottelius et al. 2004; Thumshirn et al. 2003)



Carbohydrylation and polyethylene glycol linkers were combined with chemoselective conjugation to optimize the pharmacokinetics of the peptides investigated. Oxime formation was successfully adopted for chemoselective ^{18}F -labeling of an aminoxy-modified affibody (Namavari et al. 2008) and a suitable derivative of the hormone leptin (Flavell et al. 2008). Recently, the [^{18}F]FBA synthesis was automated and yielded [^{18}F]FBA after 45 min in radiochemical yields of 54% and radiochemical purity of $\geq 99\%$ after automated cartridge purification (Speranza et al. 2009).

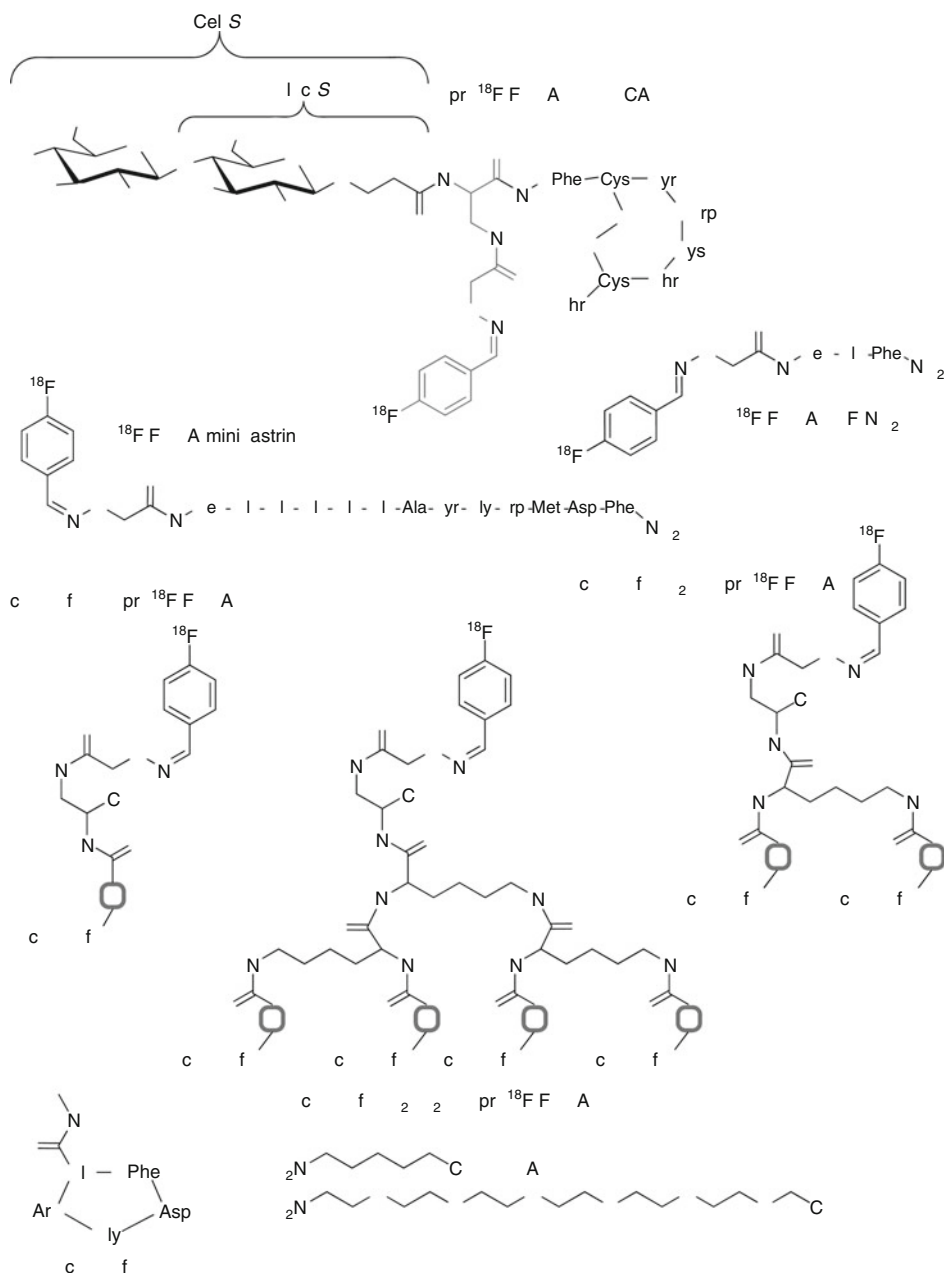
[^{18}F]FBA was also employed for couplings to hydrazine-functionalized peptides and proteins under hydrazone formation (Chang et al. 2005; Bruus-Jensen et al. 2006; Lee et al. 2006). Applied to octreotide and substance P HYNIC-conjugates, this variant gave conjugation yields of the ^{18}F -labeled peptides of up to 85% within 10 min (Bruus-Jensen et al. 2006).

Small ^{18}F -thiols such as the aliphatic [^{18}F]fluoropropane-1-thiol, a PEG3-derivative ([^{18}F]fluoro-PEG3-thiol) and an aromatic system, 4-[^{18}F]Fluoromethyl-N-(2-mercaptoethyl) benzamide, are also useful prosthetic groups, which allow an efficient chemoselective conjugation to N-chloroacetylated peptides (Glaser et al. 2004).

Proteins and peptides generally preclude a direct ^{18}F -labeling approach, due to the load of (unprotected) functional groups and the sensitivity to harsh reaction conditions, such as in ^{18}F -labeling steps usually employed. Nonetheless, Becaude et al. (2009) developed a successful direct ^{18}F -labeling method based on conventional ^{18}F -introduction into model peptides and *bombesin* peptides bearing highly activated aromatic systems such as 3-cyano-trimethyammoniumbenzoyl triflates. The highly activated aromatic systems facilitated an efficient and direct ^{18}F -labeling of the peptides with radiochemical yields of up to 92% under mild reaction conditions. However, this methodology is limited to peptides lacking acidic side chain functionalities.

Recently, a novel ^{18}F -labeling strategy for peptides was developed by McBride et al. (2009). After reacting aqueous [^{18}F]fluoride with aluminum trichloride, the formed [^{18}F]AlF $^{2+}$ was chelated by a NOTA(1,4,7-triazacyclononane-N,N',N''-triacetic acid)-functionalized peptide. The aluminum [^{18}F]fluoride complex showed excellent *in vivo* stability and PET imaging characteristics. This approach was further employed for *NOTA-octreotide*, which allowed fast and efficient ^{18}F -labeling in 45 min by chelator-based radiolabeling with a radiochemical yield of 50% (Laverman et al. 2010). The ^{18}F -labeled *NOTA-octreotide* showed a high stability and no *in vivo* loss or release of either [^{18}F]AlF $^{2+}$ or [^{18}F]F $^{-}$.

¹⁸F-Labeling of unprotected peptides using aldehydes or ketones (here [¹⁸F]fluorobenzaldehyde) for the formation of aldoximes and ketoximes by chemoselective conjugation of oxyamine modified peptides ([¹⁸F]FBOA = 4-[¹⁸F]C₆H₄-CH = NH-O-CH₂-CO) (Poethko et al. 2004; Schottelius et al. 2004; Thumshirn et al. 2003)



42.5 Miscellaneous

42.5.1 Microwave Applications in Radiolabeling

With the aim to reduce reaction times in organic transformations, *microwave dielectric heating* (Gedye et al. 1986; Giguere et al. 1986) is rapidly increasing worldwide. Besides the time gains from simply performing reactions faster, other advantages have been noted, e.g., cleaner reaction mixtures due to decreased sample decomposition and altered product distributions as well as improved chemical flexibility due to the ability to accelerate typically sluggish reactions of less-activated substrates. A review on the use of microwave applications in radiolabeling with short-lived PET radionuclides clearly indicates the advantages compared with conventional heating. The authors of this excellent and comprehensive review (Stone-Elander and Elander 2002) are looking forward to the day when access to application optimized microwave devices in the chemical and radiochemical laboratory is as unquestioned as it is today for applications in the home.

42.5.2 Silicon-Based ¹⁸F-Chemistry

The first study on ¹⁸F-Si compounds was published in 1985 when Rosenthal et al. reported the reaction of chlorotrimethylsilane with [¹⁸F]fluoride in aqueous acetonitrile yielding the corresponding ¹⁸F-Si-compound in radiochemical yields of 65%. Unfortunately, [¹⁸F]fluorotrimethylsilane was found to be hydrolyzed very fast in vivo, and the authors suggested to use sterical hindered ¹⁸F-Si-compounds to avoid hydrolytic loss of [¹⁸F]fluoride. In 2005, Ting et al. described the syntheses of ¹⁸F-labeled biotin derivatives by direct labeling of biotinylated p-aminophenylboronypinacolate and (aminopropyl)triethoxysilane in aqueous solution using target water in the presence of [¹⁸F]KHF₂ in nearly quantitative yields. In aqueous fluoride solution, the ¹⁸F-tetrafluorosilicate was found to be moderately stable whereas the ¹⁸F-trifluoroborate displayed high stability also in serum and blood.

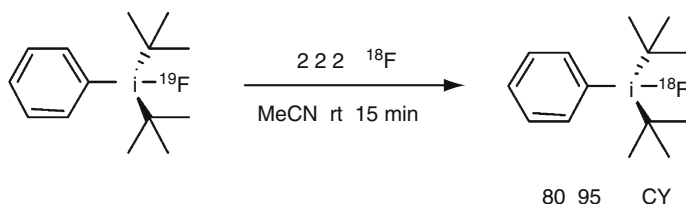
Recently, the concept of isotopic ¹⁹F–¹⁸F exchange at a silicon core was introduced (Schirmacher et al. 2006). The stability of the silicon-¹⁸F bond against hydrolysis was substantially enhanced by connecting bulky substituents such as tert-butyl groups to the ¹⁸F-bearing silicon atom. Di-tert-butyl-phenyl[¹⁸F]fluorosilane, synthesized by reacting the corresponding chlorosilane with [¹⁸F]fluoride in acetonitrile, was found to be extremely stable under physiological conditions.

Since chlorosilanes are unstable and readily hydrolyzed when subjected to aqueous conditions an isotopic exchange reaction using nanomolar quantities of di-tert-butyl-phenyl-¹⁹F-fluorosilane as precursor was tested and evaluated to result at room temperature within 15 min in high radiochemical yields (► Fig. 42.27).

This *silicon-based fluorine acceptor* (SiFA) strategy was transferred to the ¹⁸F-labeling of peptides, e.g., to the N-aminoxy derivatized peptide Tyr3-octreotate coupled to p-(di-tert-butylfluorosilyl) benzaldehyde (95–97% RCY, 10–15 min, rt) with specific activities of 3–5 GBq μmol^{−1}. For the first time, Schirmacher et al. (2007) could demonstrate an unexpectedly efficient isotopic ¹⁹F–¹⁸F exchange, yielded the ¹⁸F-synthon p-(di-tert-butyl[¹⁸F]fluorosilyl) benzaldehyde ([¹⁸F]SiFA-A) in almost quantitative yields in high specific activities between 225 and 680 GBq μmol^{−1} (6,081–18,378 Ci/mmol) without applying HPLC purification (► Fig. 42.28).

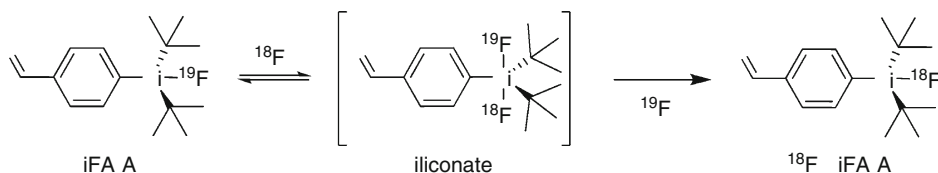
■ Fig. 42.27

Silicon-based ^{18}F -Labeling via isotopic ^{19}F – ^{18}F exchange (Schirmacher et al. 2006)



■ Fig. 42.28

Isotopic ^{19}F – ^{18}F exchange for the production of the ^{18}F -labeling synthon $[\text{}^{18}\text{F}]\text{SiFA-A}$ via a silicate intermediate (Schirmacher et al. 2007)



Using this synthon and chemoselective ligation, different N-terminal amino-oxy (N-AO) derivatized peptides, such as AO-Tyr3-octreotate (AO-TATE), *cyclo*(fK(AO-N)RGD), and N-AO-PEG2-[D-Tyr-Gln-Trp-Ala-Val- β Ala-His-Thi-Nle-NH₂] (AO-BZH3, a bombesin derivative) were prepared in high radiochemical yields. The high efficient exchange was explained by a pentacoordinate silicate intermediate dissociating immediately to form the radiolabeled $[\text{}^{18}\text{F}]\text{SiFA-A}$.

Subsequently, ^{18}F -labeled bombesin analogs were prepared using a silicon-based one-step n.c.a. radiolabeling method (Höhne et al. 2008; Mu et al. 2008). Radiolabeling of the peptide precursors conjugated with the di-tert-butyl silyl building block as labeling moiety proceeded smoothly under acidic conditions (34–85% conversion). 2-(4-(di-tert-butyl- $[\text{}^{18}\text{F}]$ fluorosilyl)phenyl)acetyl-Arg-Ava-Gln-Trp-Ala-Val-NMeGly-His-Sta-Leu-NH₂ showed no significant degradation *ex vitro* and *in vitro*.

Further ^{18}F -labeled bifunctional triorganofluorosilane synthons, allowing for the introduction of $[\text{}^{18}\text{F}]$ fluoride and conjugation to peptides or proteins, such as *t*Bu₂-(*p*-HS-C₆H₄)Si ^{18}F , the corresponding isothiocyanato, isocyanato, aniline, maleimide, and activated ester derivatives were synthesized and evaluated, e.g., on model proteins (Iovkova et al. 2009).

By means of one of these synthons, 4-(di-tert-butyl $[\text{}^{18}\text{F}]$ fluorosilyl)benzenethiol (Si $[\text{}^{18}\text{F}]$ FASH), prepared by isotopic exchange in 40–60% radiochemical yield and subsequent coupling to a maleimide conjugate of serum albumin, an overall radiochemical yield of 12% was obtained within in overall synthesis time of 20–30 min (Wängler et al. 2009b).

Since, as mentioned before, the hydrolytic stability of the silicon–fluorine bond is determined by the nature of the substituents on silicon, a theoretical model of organofluorosilane hydrolysis was developed by means of density functional theory (DFT) methods. As concluded by the authors (Höhne et al. 2009), the calculation of the difference of Si–F bond lengths between optimized structures of the starting material and the intermediate structure allows the

estimation of the hydrolytic stability of newly designed compounds and thus will facilitate the development of improved building blocks for the synthesis of novel ^{18}F -silyl-modified biomolecules (Höhne et al. 2009).

Bohn et al. (2009) reported on a first study on the design of “small-sized” tracers for imaging tissue hypoxia. Using formal alkyloxy-trialkyl and alkoxy-alkyl-diarylsilane precursors of misonidazole, and a mixture of K^{18}F and Kryptofix 2.2.2 in acetonitrile, the ^{18}F -labeled silicon-based misonidazole analogs were easily synthesized (Bohn et al. 2009).

In conclusion, the next years will show whether the silicon-based ^{18}F -labeling approach and the very promising results obtained during the last 3 years will open a new class of radiopharmaceuticals.

42.5.3 Enzymatic Reactions

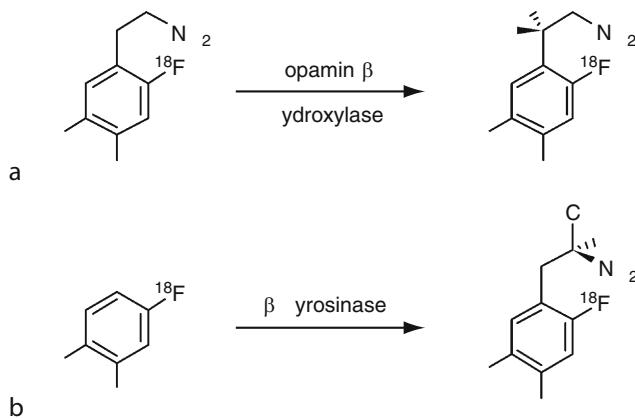
Although a variety of approaches to the *enzymatic synthesis* of ^{11}C -labeled compounds were described in the literature, only a few examples were investigated so far with respect to ^{18}F -labeled radiopharmaceuticals. Enzymatic reactions mostly occur under mild conditions with high efficiency and selectivity, and enzymes can be immobilized on appropriate solid phase for easy recovery and labeled products and for repeated use of the enzymes.

Liu et al. (1998) used dopamine- β -hydroxylase ($\text{D}\beta\text{H}$) to stereospecifically synthesize R-(-)-6- ^{18}F fluoronorepinephrine (6- ^{18}F FNE) (► Fig. 42.29a) from 6- ^{18}F fluorodopamine in the presence of ascorbate, sodium fumarate, and catalase in 2 M sodium acetate buffer at 37°C .

Koneko et al. (1999) developed a synthesis for 6- ^{18}F FDOPA (► Fig. 42.29b). The 4- ^{18}F fluorocatechol was prepared by nucleophilic aromatic substitution of the nitro group on 6-nitroveratryl aldehyde followed by decarbonylation with tris(triphenylphosphine) rhodium(I) chloride and hydrolysis (9.2% yield). 6- ^{18}F FDOPA was then prepared from the 4- ^{18}F fluorocatechol by a β -tyrosinase catalyzed reaction in the presence of ammonium, pyruvate, and ascorbate in an ethanolic Tris-HCl buffer within 5 min in about 60% radiochemical yield without any isomers.

■ Fig. 42.29

Enzymatic synthesis of R-(-)-6- ^{18}F fluoronorepinephrine (6- ^{18}F FNE) (a) and 6- ^{18}F FDOPA (b)

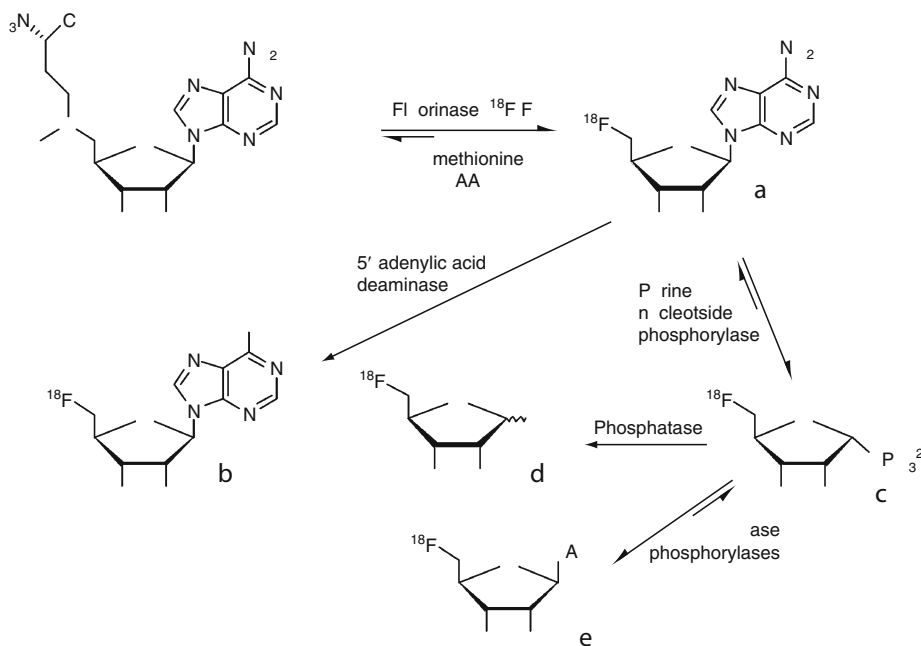


The enzyme *fluorinase* (5'-fluoro-5'-deoxyadenosine synthase) was applied to convert S-adenosyl-L-methionine (SAM) and [^{18}F]fluoride directly into 5'-[^{18}F]fluoro-5'-deoxyadenosine (5'-[^{18}F]FDA) (► Fig. 42.30a) and L-methionine, which was the first example where a radionuclide was enzymatically introduced into an organic molecule (Martarello et al. 2003). In this approach, the native wildtype fluorinase deriving from *Streptomyces cattleya* was employed in low concentrations ($\mu\text{g ml}^{-1}$) and generated only very low radiochemical yields of $\sim 1\%$. Better conversions of $\sim 20\text{--}25\%$ were achieved by the use of higher fluorinase concentrations (mg/ml), which became available by fluorinase over-expressing cloned *Escherichia coli* (Deng et al. 2006).

The aspect of a reversible reaction of fluorinase was of major importance for further optimizations and by addition of the enzyme L-amino acid oxidase (L-AAO) the oxidative removal of formed L-methionine was enabled. In this way, the equilibrium of the reaction was pulled toward 5'-[^{18}F]FDA and allowed very high radiochemical yields of 95% within 1–2 h. Accordingly, the ^{18}F -labeled compounds 5'-[^{18}F]fluoro-5'-deoxyinosine (5'-[^{18}F]FDI) (► Fig. 42.30b), 5'-[^{18}F]fluoro-5'-deoxyribose phosphate (► Fig. 42.30c), and 5'-[^{18}F]fluoro-5'-deoxyribose (► Fig. 42.30d) were successfully produced from 5'-[^{18}F]fluoro-5'-deoxyadenosine (Deng et al. 2006, Onega et al. 2009, 2010). In the “base-swap” strategy, the 5'-[^{18}F]fluoro-5'-deoxyribose phosphate (► Fig. 42.30c) could be further transformed into

■ Fig. 42.30

Direct enzymatic ^{18}F -labeling of 5'-[^{18}F]fluoro-5'-deoxyadenosine (5'-[^{18}F]FDA) (a) using the enzyme fluorinase and subsequent enzymatic conversions into 5'-[^{18}F]fluoro-5'-deoxyinosine (5'-[^{18}F]FDI) (b), 5'-[^{18}F]fluoro-5'-deoxyribose phosphate (c), 5'-[^{18}F]fluoro-5'-deoxyribose (d), and diverse ^{18}F -labeled pyrimidine nucleosides (e) (Deng et al. 2006; Winkler et al. 2008; Onega et al. 2009, 2010)



various ¹⁸F-labeled pyrimidine nucleosides by the use of the appropriate pyrimidine phosphorylase and the pyrimidine base in a one-pot procedure (Winkler et al. 2008).

42.5.4 Electrochemical Cells

Especially with respect to the use of no-carrier-added amounts of radioisotopes (fmol to nmol range), radionuclide “extraction” by means of an electrical field, e.g., the *anodic disposition* of [¹⁸F]fluoride from irradiated ¹⁸O-water seems to be a promising experimental approach. Alexoff et al. (1989) obtained good results concerning the deposition of [¹⁸F]fluoride, but only moderate yields were found for the subsequent recovery. Hamacher and Blessing (1995) designed a more convenient cell, which allows to absorb [¹⁸F]fluoride at the cylindrical surface of a glassy carbon electrode at field strength beyond 100 V/cm. While maintaining a lower electrical field of about 10 V/cm, the fluoride can be dried easily by washing the cell with dry aprotic solvents, making azeotropic drying steps under strong basic conditions unnecessary.

Thus, nucleophilic fluorinations can be carried out under milder conditions in the presence of the less basic cryptate systems such as [K/2.2.2]oxalate and [K/2.2.2]triflate. Nearly quantitative desorption of activity is reached at field strengths of ~8 V/cm (DMF, [K/2.2.2]carbonate system). Using this methodology, the authors synthesized 4-[¹⁸F]fluorobenzaldehyde, 4-[¹⁸F]fluoronitrobenzene, 2-[¹⁸F]fluorotosyloxyethane, and 1,3,4,6-tetra-O-acetyl-2-[¹⁸F]FDG in radiochemical yields of 97%, 98%, 56%, and 85%, respectively ([K/2.2.2]carbonate system) (Hamacher et al. 2002).

42.5.5 Automated Radiosyntheses and Flow Chemistry

Semiautomated and automated processes have always been tried to be implemented into ¹⁸F-labeling methods or syntheses. Such systems allow keeping the radiation dose to the operative personnel at a minimum and allow routine productions for clinical applications to comply with General Manufacturing Practise (GMP) regulations. Furthermore, automated reaction steps or procedures generally are more reliable and thus more reproducible than manual radiosyntheses. In addition, automated processes often save time and therefore enhance product yields and efficiency. Today, the radiosyntheses of almost all routine ¹⁸F-tracers are fully automated and are performed in commercially available modules or systems (Satyamurthy et al. 1999; Alexoff 2003).

In recent years, new approaches using *microreactors* and *microfluidic flow chemistry* have been employed for ¹⁸F-labeling (Lu et al. 2004; Lee et al. 2005; Gillies et al. 2006; Steel et al. 2007; Elizarov 2009). Such microscale reactions especially benefit from very small amounts of precursors, fast reaction kinetics, and very high radiochemical yields. The first systems have proven applicability and have shown promising results for the production of [¹⁸F]FDG and some other ¹⁸F-labeled compounds and tracers (Lu et al. 2004; Lee et al. 2005; Gillies et al. 2006; Steel et al. 2007; Wester et al. 2008; Elizarov 2009). One special challenge of such system is the drying and activation of the [¹⁸F]fluoride from the target water. In several systems, the [¹⁸F]fluoride was dried externally in conventional reaction vessels, mixed with an appropriate phase transfer catalyst and solvent, and then transferred into a microreactor or flow chemistry device for the ¹⁸F-labeling and subsequent reaction steps. Some miniaturized devices already

include a drying system such as a miniaturized anion exchanger column (Lee et al. 2005) or an electrochemical microreactor system based on electrochemical separation and drying (Elizarov et al. 2010).

The development of miniaturized devices for ¹⁸F-labeling is still in progress, but the proof-of-principle has already been made with several systems. The obvious advantages of such approaches will promote the development toward routinely running microreactors or microfluidic devices for routine ¹⁸F-labeling.

References

- Adam MJ, Jivan S (1988) *Appl Radiat Isot* 39:1203
- Adam MJ, Berry JM, Hall LD, Pate BD, Ruth T (1983) *Can J Chem* 61:658
- Adam MJ, Ruth TJ, Grierson JR, Abeysekera B, Pate BD (1986) *J Nucl Med* 27:1462
- Agdeppa ED, Kepe V, Liu J, Flores-Torres S, Satyamurthy N, Petric A, Cole GM, Small GW, Huang SC, Barrio JR (2001) *J Neurosci* 21:RC189
- Agdeppa ED, Kepe V, Liu J, Small GW, Huang S-C, Petric A, Satyamurthy N, Barrio JR (2003) *Mol Imaging Biol* 5:404
- Alexoff DL (2003) In: Welch MJ, Redvanly CS (eds) *Handbook of radiopharmaceuticals: radiochemistry and application*. Wiley, Chichester, p 283
- Alexoff D, Schleyer DJ, Wolf AP (1989) *Appl Radiat Isot* 40:1
- Allain-Barbier L, Lasne M-C, Perrio-Huard C, Moreau B, Barré L (1998) *Acta Chem Scand* 52:480
- Ametamey SM, Honer M, Schubiger PA (2008) *Chem Rev* 108:1501
- Bai LQ, Teng RR, Shiue CY, Wolf AP, Dewey SL, Holland MJ, Simon EJ (1990) *Int J Radiat Appl Instrum B* 17:217
- Ballinger J, Bowen BM, Firna G, Garnett ES, Teare FW (1984) *Int J Appl Radiat Isot* 35:1125
- Barnette WE (1986) *J Am Chem Soc* 106:452
- Barrio JR, Namavari M, Phelps ME, Satyamurthy N (1996) *J Org Chem* 61:6084
- Bauman A, Piel M, Schirmacher R, Rösch F (2003) *Tetrahedron Lett* 44:97
- Bayley H, Staros JV (1984) In: Scriven EFV (ed) *Azides and nitrenes*. Academic, Orlando, p 433
- Becaud J, Mu L, Karramkam M, Schubiger PA, Ametamey SM, Graham K, Stellfeld T, Lehmann L, Borkowski S, Berndorff D, Dinkelborg L, Srinivasan A, Smits R, Koksche B (2009) *Bioconjug Chem* 20:2254
- Beer H-F, Haerberli S, Ametamey S, Schubiger PA (1995) *J Labelled Comp Radiopharm* 36:933
- Bejot R, Fowler T, Carroll L, Boldon S, Moore JE, Declerck J, Gouverneur V (2009) *Angew Chem Int Ed* 48:586
- Bergman J, Eskola O, Lehtikoinen P, Solin O (2001) *Appl Radiat Isot* 54:927
- Bergman J, Solin O (1997) *Nucl Med Biol* 24:677
- Bergmann R, Scheunemann M, Heichert C, Mading P, Wittrisch H, Kretzschmar M, Rodig H, Tourwe D, Iterbeke K, Chavatte K, Zips D, Reubi JC, Johannsen B (2002) *Nucl Med Biol* 29:61
- Berndt M, Pietzsch J, Wüst F (2007) *Nucl Med Biol* 34:5
- Bida GT, Satyamurthy N, Barrio JR (1984) *J Nucl Med* 25:1327
- Blocher A, Kuntsch M, Wei R, Machulla HJ (2002) *J Radioanal Nucl Chem* 251:55
- Block D, Coenen HH, Laufer P, Stöcklin G (1986a) *J Labelled Comp Radiopharm* 23:1042
- Block D, Klatte B, Knöchel A, Beckmann R, Holm U (1986b) *J Labelled Comp Radiopharm* 23:467
- Block D, Coenen HH, Stöcklin G (1987) *J Labelled Comp Radiopharm* 24:1029
- Block D, Coenen HH, Stöcklin G (1988) *J Labelled Comp Radiopharm* 25:201
- BNL (2003) <http://www2.bnl.gov/ton/>
- Bohn P, Deyine A, Azzouz R, Bailly L, Fiol-Petit C, Bischoff L, Fruit C, Marsais F, Vera P (2009) *Nucl Med Biol* 36:895
- Brady F, Luthra SK, Pike VW (1989) *Appl Radiat Isot* 40:325
- Brix G, Noßke D, Glatting G, Minkov V, Reske SN (2002) *Eur J Nucl Med* 29:1091
- Brown E, Firestone RB (1986) In: Shirley VS (ed) *Table of radioactive isotopes*. Wiley, New York
- Brown GD, Khan HR, Steel CJ, Luthra SK, Osman S, Hume SP, Tilsey DWO, Waters SL, Poole KG, Price P, Brady F (1993) *J Labelled Comp Radiopharm* 32:521
- Brust P, Zessin J, Kuwabara H, Pawelke B, Kretzschmar M, Hinz R, Bergman J, Eskola O, Solin O, Steinbach J, Johannsen B (2003) *Synapse* 47:143
- Bruus-Jensen K, Poethko T, Schottelius M, Hauser A, Schwaiger M, Wester HJ (2006) *Nucl Med Biol* 33:173
- Cai W, Zhang X, Wu Y, Chen X (2006) *J Nucl Med* 47:1172
- Cai L, Lu S, Pike VW (2008) *Eur J Org Chem* 17:2853
- Carroll MA, Nairne J, Woodcraft JL (2007a) *J Labelled Comp Radiopharm* 50:452
- Carroll MA, Jones C, Tang S-L (2007b) *J Labelled Comp Radiopharm* 50:450

- Casella VR, Ido T, Wolf AP, Fowler JS, MacGregor RR, Ruth TJ (1980) *J Nucl Med* 21:750
- Chakraborty PK, Kilbourn MR (1991a) *Appl Radiat Isot* 42:1209
- Chakraborty PK, Kilbourn MR (1991b) *Appl Radiat Isot* 42:673
- Chang YS, Jeong JM, Lee Y-S, Kim HW, Rai GB, Lee SJ, Lee DS, Chung J-K, Lee MC (2005) *Bioconjug Chem* 16:1329
- Chesis PL, Welch MJ (1990) *Appl Radiat Isot* 41:259
- Chi DY, Kilbourn MR, Katzenellenbogen JA, Brodack JW, Welch MJ (1986) *Appl Radiat Isot* 37:1373
- Chirakal R, Vasdev N, Schrobilgen GJ, Nahmias C (1999) *J Fluorine Chem* 99:87
- Choe YS, Oh SJ, Shim I, Naruto S, Chi DY, Kim SE, Lee K-H, Choi Y, Kim B-T (2000) *Nucl Med Biol* 27:263
- Chun J-H, Lu S, Lee Y-S, Pike VW (2010) *J Org Chem* 75:3332
- Coenen HH, Moerlein SM (1987) *J Fluorine Chem* 36:63
- Coenen HH, Colosimo M, Schueller M, Stöcklin G (1986) *J Labelled Comp Radiopharm* 23:587
- Coenen HH, Franken K, Kling P, Stöcklin G (1988) *Appl Radiat Isot* 39:1243
- Collins M, Lasne M-C, Barré L (1992) *J Chem Soc Perk Trans* 1:3185
- Comagic S, Piel M, Schirmacher R, Höhnemann S, Rösch F (2002) *Appl Radiat Isot* 56:847
- Cooke F, Roy G, Magnus P (1982) *Organometallics* 1:893
- Crouzel C, Guillaume M, Barre L, Lemaire C, Pike VW (1992) *Int J Radiat Appl Instrum B* 19:857
- Damhaut P, Cantineau R, Lemaire C, Plenevaux A, Christiaens L, Guillaume M (1992) *Appl Radiat Isot* 43:1265
- Das MK, Mukherjee J (1993) *J Labelled Comp Radiopharm* 35:497
- De Bruin B, Kuhnast B, Hinnen F, Yaouancq L, Amessou M, Johannes L, Samson A, Boisgard R, Tavitian B, Dollé F (2005) *Bioconjug Chem* 16:406
- De Groot TJ, Elsinga PH, Visser GM, Vallburg W (1992) *Appl Radiat Isot* 43:1335
- De Groot TJ, Braker AH, Elsinga PH, Visser GM, Vaalburg W (1994) *Appl Radiat Isot* 45:811
- De Vries EFJ, Lurtsema G, Brüssermann M, Elsinga PH, Vaalburg W (1999) *Appl Radiat Isot* 51:389
- DeGrado TR, Coleman RE, Wang S, Baldwin SW, Orr MD, Robertson CN, Polascik TJ, Price DT (2001) *Cancer Res* 61:110
- Dence CS, John CS, Bowen WD, Welch MJ (1997) *Nucl Med Biol* 24:333
- Deng H, Cobb SL, Gee AD, Lockhart A, Martarello L, McGlinchey RP, O'Hagan D, Onega M (2006) *Chem Comm* 652
- Diksic M, Farrokhzad S, Colebrook LD (1986) *Can J Chem* 64:424
- Ding YS, Shiue CY, Fowler JS, Wolf AP, Plenevaux A (1990) *J Fluorine Chem* 48:189
- Ding YS, Fowler JS, Gatley SJ, Dewey SL, Wolf AP (1991) *J Med Chem* 34:767
- Ding YS, Liang F, Fowler JS, Kuhar MJ, Caroll FI (1997) *J Labelled Comp Radiopharm* 39:827
- Ding YS, Liu N, Wang T, Marecek J, Garza V, Ojima I, Fowler JS (2000) *Nucl Med Biol* 27:381
- Doering WVE, Odum RA (1966) *Tetrahedron* 22:81
- Dolbier WR, Li AR, Koch CJ, Shiue CY, Kachur AV (2001) *Appl Radiat Isot* 54:73
- Dolci L, Dollé F, Jubeau S, Vaufrey F, Crouzel C (1999a) *J Labelled Comp Radiopharm* 42:975
- Dolci L, Dollé F, Valette H, Vaufrey F, Fuseau C, Bottlaender M, Crouzel C (1999b) *Bioorg Med Chem* 7:467
- Dollé F (2005) *Curr Pharm Des* 11:3221
- Dollé F, Hinnen F, Vaufrey F, Tavitian B, Crouzel C (1997) *J Labelled Comp Radiopharm* 39:319
- Dollé F, Dempfel S, Hinnen F, Fournier D, Vaufrey F, Crouzel C (1998a) *J Labelled Comp Radiopharm* 41:105
- Dollé F, Valette H, Bottlaender M, Hinnen F, Vaufrey F, Guenther I, Crouzel C (1998b) *J Labelled Comp Radiopharm* 41:451
- Dollé F, Dolci L, Valette H, Hinnen F, Vaufrey F, Guenther I, Fuseau C, Coulon C, Bottlaender M, Crouzel C (1999) *J Med Chem* 42:2251
- Downer JB, McCarthy TJ, Edwards WB, Anderson CJ, Welch MJ (1997) *Appl Radiat Isot* 48:907
- Ehrenkaufer RE, McGregor RR (1983) *Int J Appl Radiat Isot* 34:613
- Ehrenkaufer RE, Potocki JE, Jewett DM (1984) *J Nucl Med* 25:333
- Ekaeva I, Barré L, Lasne M-C, Gourand F (1995) *Appl Radiat Isot* 46:777
- Elizarov AM (2009) *Lab Chip* 9:1326
- Elizarov AM, van Dam RM, Shin YS, Kolb HC, Padgett HC, Stout D, Shu J, Huang J, Daridon A, Heath JR (2010) *J Nucl Med* 51:282
- Elsinga PH, van Waarde A, Jaeggi KA, Schreiber G, Heldoorn M, Vaalburg W (1997) *J Med Chem* 40:3829
- Ermert J, Hamacher K, Coenen HH (2000) *J Labelled Comp Radiopharm* 43:1345
- Ermert J, Hocke C, Ludwig T, Gail R, Coenen HH (2004) *J Labelled Comp Radiopharm* 47:429
- Ermert J, Ludwig T, Gail R, Coenen HH (2007) *J Organomet Chem* 692:4084
- Farrokhzad S, Diksic M, Yamamoto LY, Feindel W (1984) *Can J Chem* 62:2107
- Feliu AL (1988) *J Labelled Comp Radiopharm* 25:1245
- Finger GC, Kruse CW (1956) *J Am Chem Soc* 78:6034
- Firna G, Nahmias C, Garnett ES (1973) *Appl Radiat Isot* 24:182
- Firna G, Chirakal R, Garnett ES (1980) *Can J Chem* 58:1449
- Firna G, Chirakal R, Garnett ES (1984) *J Nucl Med* 25:1228

- Flavell RR, Kothari P, Bar-Dagan M, Synan M, Vallabhajosula S, Friedman JM, Muir TW, Ceccarini G (2008) *J Am Chem Soc* 130:9106
- Forngren T, Andersson Y, Lamm B, Langström B (1998) *Acta Chem Scand* 52:4475
- Fowler JS, Ido T (2002) *Semin Nucl Med* 32:6
- Fowler JS, Wolf AP (1997) *Acc Chem Res* 30:181
- Fowler JS, Finn RD, Lambrecht RM, Wolf AP (1973) *J Nucl Med* 14:63
- Fowler JS, Shiue CY, Wolf AP, Salvadori PA, MacGregor RR (1982) *J Labelled Comp Radiopharm* 19:1634
- Fredriksson A, Johnström P, Stone-Elander S, Lonasson P, Nygren PA, Ekberg K, Johansson BL, Wahren J (2001) *J Labelled Comp Radiopharm* 44:509
- Fredriksson A, Ekberg K, Ingvar M, Johansson BL, Wahren J, Stone-Elander S (2002) *Life Sci* 71:1361
- Füchtner F, Steinbach J, Mäding P, Johannsen B (1996) *Appl Radiat Isot* 47:61
- Gail R, Hocke C, Coenen HH (1997) *J Labelled Comp Radiopharm* 40(suppl 1):50
- Gambhir SS (2002) *Nat Rev Cancer* 2:683
- Garg PK, Garg S, Zalutsky MR (1991) *Bioconjug Chem* 2:44
- Garg PK, Garg S, Zalutsky MR (1994) *Nucl Med Biol* 21:97
- Garnett ES, Firnaui G, Nahmias C, Chirakal R (1983a) *Brain Res* 280:169
- Garnett ES, Firnaui G, Nahmias C (1983b) *Nature* 305:137
- Gedye R, Smith F, Westaway L, Humera A, Baldisera L, Laberge L, Rousell J (1986) *Tetrahedron Lett* 27:279
- Giguere RJ, Bray TL, Duncan SM, Majetich G (1986) *Tetrahedron Lett* 27:4945
- Gillies JM, Prenant C, Chimon GN, Smethurst GJ, Perrie W, Hamblett I, Dekker B, Zweit J (2006) *Appl Radiat Isot* 64:325
- Glaser M, Årstad E (2007) *Bioconjug Chem* 18:989
- Glaser M, Karlsen H, Solbakken M, Arukwe J, Brady F, Luthra SK, Cuthbertson A (2004) *Bioconjugate Chem* 15:1447
- Glaser M, Robins EG (2009) *J Labelled Comp Radiopharm* 52:407
- Glaser M, Karlsen H, Solbakken M, Arukwe J, Brady F, Luthra SK, Cuthbertson A (2007) *Bioconjug Chem* 15:1447
- Glaser M, Solbakken M, Turton DR, Pettitt R, Barnett J, Arukwe J, Karlsen H, Cuthbertson A, Luthra AK, Årstad E (2009a) *Amino Acids* 37:717
- Glaser M, Årstad E, Luthra SK, Robins EG (2009b) *J Labelled Comp Radiopharm* 52:327
- Griersen FR, Shields AF (2000) *Nucl Med Biol* 27:143
- Grierson J, Patt M (1999) In: Machulla HJ Jr (ed) *Imaging of hypoxia: tracer developments*. Kluwer, Amsterdam, p 75
- Grierson JR, Shields AF (2000) *Nucl Med Biol* 27:143
- Grierson JR, Link JM, Mathis CA, Rasey JS, Krohn KA (1989) *J Nucl Med* 30:343
- Guhlke S, Coenen HH, Stöcklin G (1994a) *Appl Radiat Isot* 45:715
- Guhlke S, Wester HJ, Bruns C, Stocklin G (1994b) *Nucl Med Biol* 21:819
- Guillaume G, Luxen A, Nebeling B, Argentini M, Clark J, Pike VW (1991) *Appl Radiat Isot* 42:749
- Haaparanta M, Bergman J, Laakso A, Hietala J, Solin O (1996) *Synapse* 23:321
- Hagmann WK (2008) *J Med Chem* 51:4359
- Halldin C, Högborg T, Farde L (1994) *Nucl Med Biol* 21:627
- Halldin C, Gulyas B, Langer O, Farde L (2001) *Q J Nucl Med* 45:139
- Hamacher K, Blessing G (1995) *J Labelled Comp Radiopharm* 37:739
- Hamacher K, Coenen HH (2002) *Appl Radiat Isot* 57:853
- Hamacher K, Coenen HH, Stöcklin G (1986a) *J Nucl Med* 27:235
- Hamacher K, Coenen HH, Stöcklin G (1986b) *J Labelled Comp Radiopharm* 23:1047
- Hamacher K, Blessing G, Nebeling B (1990) *Appl Radiat Isot* 41:49
- Hamacher K, Hirschfelder T, Coenen HH (2002) *Appl Radiat Isot* 56:519
- Hara T, Kosaka N, Kishi H (2002) *J Nucl Med* 43:187
- Hashizume K, Hashimoto N, Miyake Y (1995) *J Org Chem* 60:6680
- Hatano K, Ido T, Iwata R (1991) *J Labelled Comp Radiopharm* 29:373
- Haubner R, Wester HJ, Weber WA, Mang C, Ziegler SI, Goodman SL, Senekowitsch-Schmidtke R, Kessler H, Schwaiger M (2001) *Cancer Res* 61:1781
- Haubner R, Kuhnast B, Mang C, Weber WA, Kessler H, Wester HJ, Schwaiger M (2004) *Bioconjug Chem* 15:61
- Hebel D, Kirk KL, Cohen LA, Labroo VM (1990) *Tetrahedron Lett* 31:619
- Hess E, Sichler S, Kluge A, Coenen HH (2002) *Appl Radiat Isot* 57:185
- Höfling SB, Hultsch C, Wester HJ, Heinrich MR (2008) *Tetrahedron* 64:11846
- Höhne A, Mu L, Honer M, Schubiger PA, Ametamey SM, Graham K, Stellfeld T, Borkowski S, Berndorff D, Klar U, Voigtman U, Cyr JE, Friebe M, Dinkelborg L, Srinivasan A (2008) *Bioconjug Chem* 19:1871
- Höhne A, Yu L, Mu L, Reiher M, Voigtman U, Klar U, Graham K, Schubiger PA, Ametamey SM (2009) *Chem Eur J* 15:3736
- Holschbach M, Olsson RA, Bier D, Wutz W, Shiver W, Schüller M, Palm B, Coenen HH (2002) *J Med Chem* 45:5150
- Horti A, Ravert HT, London ED, Dannals RF (1996) *J Labelled Comp Radiopharm* 38:355

- Horti AG, Koren AO, Ravert HT, Musachio JL, Mathews WB, London ED, Dannals RF (1998) *J Labelled Comp Radiopharm* 41:309
- Hostetler ED, Edwards WB, Anderson CJ, Welch MJ (1999a) *J Labelled Comp Radiopharm* 42(suppl 1): S720
- Hostetler ED, Jonson SD, Welch MJ, Katzenellenbogen JA (1999b) *J Org Chem* 64:178
- Howard JAK, Hoy VJ, O'Hagan D, Smith GT (1996) *Tetrahedron* 52:12613
- Hultsch C, Berndt M, Bergmann R, Wüst F (2007) *Appl Radiat Isot* 65:818
- Hultsch C, Schottelius M, Auernheimer J, Alke A, Wester HJ (2009) *Eur J Nucl Med Mol Imaging* 36:1469
- Hwang D-R, Dence CS, McKinnon ZA, Mathias CJ, Welch MJ (1991) *Nucl Med Biol* 18:247
- Ido T, Wan CN, Casella V, Fowler JSD, Wolf AP, Reivich M, Kuhl DE (1978) *J Labelled Comp Radiopharm* 14:175
- Inkster JAH, Guérin B, Ruth TJ, Adam MJ (2008) *J Labelled Comp Radiopharm* 51:444
- Iovkova L, Wängler B, Schirmacher E, Schirmacher R, Quandt G, Boening G, Schürmann M, Jurkschat K (2009) *Chem Eur J* 15:2140
- Iwata R, Horváth G, Pascali C, Bogni A, Yanai K, Kovacs Z, Ido T (2000a) *J Labelled Comp Radiopharm* 43:873
- Iwata R, Pascali C, Bogni A, Furumoto S, Terasaki K, Yanai K (2002) *Appl Radiat Isot* 57:347
- Iwata R, Pascali C, Bogni A, Horváth G, Kovacs Z, Yanai K, Ido T (2000b) *Appl Radiat Isot* 52:87
- Jelinski M, Hamacher K, Coenen HH (2002) *J Labelled Comp Radiopharm* 45:217
- Jewett DM (1991) *Appl Radiat Isot* 42:519
- Jewett DM, Potocki JE, Ehrenkaufer R (1984) *J Fluorine Chem* 24:477
- Johnstrom P, Harris NG, Fryer TD, Barret O, Clark JC, Pickard JD, Davenport AP (2002) *Clin Sci* 103(suppl 48):4S
- Josse O, Labar D, Georges B, Gregoire V, Marchand-Brynaert J (2001) *J Bioorg Med Chem* 9:665
- Kachur AV, Dolbier WR, Evans SM, Shiue CY, Shiue GG, Skov KA, Baird IR, James BR, Li AR, Roche A, Koch CJ (1999) *Appl Radiat Isot* 51:643
- Katoch-Rouse R, Horti AG (2003) *J Labelled Comp Radiopharm* 46:93
- Katounina T, Besret L, Dhilly M, Petit-Taboue NC, Barbeliven A, Baron JC, Dauphin F, Barre L (1998) *Bioorg Med Chem* 6:789
- Katsifis A, Hamacher K, Schnitter J, Stöcklin G (1993) *Appl Radiat Isot* 44:1015
- Kiesewetter DO, Eckelman WC (2004) *J Labelled Comp Radiopharm* 47:953
- Kiesewetter DO, Kilbourn MR, Landvatter SW, Katzenellenbogen JA, Welch MJ (1984) *J Nucl Med* 25:1212
- Kiesewetter DO, Vuong BK, Channing MA (2003) *Nucl Med Biol* 30:73
- Kilbourn MR (1989) *Int J Radiat Appl Instrum B* 16:681
- Kilbourn MR, Dence CS, Welch MJ, Mathias CJ (1987) *J Nucl Med* 28:462
- Kim DW, Song CE, Chi DY (2002) *J Am Chem Soc* 124:10278
- Kim HW, Joeng JM, Lee Y-S, Chi DY, Chung K-H, Lee DS, Chung J-K, Lee MC (2004) *Appl Radiat Isot* 61:1241
- Kim DW, Ahn D-S, Oh Y-H, Lee S, Oh SJ, Lee SJ, Kim JS, Ryu J-S, Moon DH, Chi DY (2006) *J Am Chem Soc* 128:16394
- Kindsey BM, Barber R, Tewson TJ (1992) *J Labelled Comp Radiopharm* 31:298
- Knust EJ, Machulla HJ, Millos M (1982) *J Labelled Comp Radiopharm* 19:1638
- Kobus D, Giesen Y, Ullrich R, Backes H, Neumaier B (2009) *Appl Radiat Isot* 67:1977
- Koneko S, Ishiwata K, Hatano K, Omura H, Ito K, Senda M (1999) *Appl Radiat Isot* 51:1025
- Koren AO, Horti AG, Mukhin AG, Gündisch D, Dannals RF, London ED (2000) *J Labelled Comp Radiopharm* 43:413
- Kramer-Marek G, Kiesewetter DO, Martiniova L, Jagoda E, Lee SB, Capala J (2008) *Eur J Nucl Med Mol Imaging* 35:1008
- Krasikova RN, Kuznetsova OF, Fedorova OS, Maleev VI, Saveleva TF, Belokon YN (2008) *Bioorg Med Chem* 16:4994
- Kuhnast B, Dolle F, Vaufrey F, Hinnen F, Crouzel C, Tavitian B (2000a) *J Labelled Comp Radiopharm* 43:837
- Kuhnast B, Dolle F, Terrazzino S, Rousseau B, Loc'h C, Vaufrey F, Hinnen F, Doignon I, Pillon F, David C, Crouzel C, Tavitian B (2000b) *Bioconjug Chem* 11:627
- Kuhnast B, de Bruin B, Hinnen F, Tavitian B, Dollé F (2004) *Bioconjug Chem* 15:617
- Kuhnast B, Hinnen F, Tavitian B, Dollé F (2008) *J Labelled Comp Radiopharm* 51:336
- Lang L, Eckelman WC (1994) *Appl Radiat Isot* 45:1155
- Lang L, Eckelman WC (1997) *Appl Radiat Isot* 48:169
- Lange CW, VanBrocklin HF, Taylor S (2002) *J Labelled Comp Radiopharm* 45:257
- Langen P, Etzold G, Hintsche R, Kowolik G (1996) *Acta Biol Med Ger* 23:759
- Langer O, Dollé F, Valette H, Halldin C, Vaufrey F, Fuseau C, Coulon C, Ottaviani M, Nagren K, Bottlaender M, Maziere B, Crouzel C (2001) *Bioorg Med Chem* 9:677
- Langer O, Halldin C (2002) *Eur J Nucl Med* 29:416
- Laruelle M, Huang Y (2001) *Q J Nucl Med* 45:124
- Lasne M-C, Barré L, Huard C, Le Secq B, Collins M (1994) *Appl Radiat Isot* 45:1085
- Lasne MC, Perrio C, Rouden J, Barre L, Roeda D, Dolle F, Crouzel C (2002) *Top Curr Chem* 222:201

- Laverman P, McBride WJ, Sharkey RM, Eek A, Joosten L, Oyen WJG, Goldenberg DM, Boerman OC (2010) *J Nucl Med* 51:454
- Lee C-C, Sui G, Elizarov A, Shu CJ, Shin Y-S, Dooley AN, Huang J, Daridon A, Wyatt P, Stout D, Kolb HC, Witte ON, Satyamurthy N, Heath JR, Phelps ME, Quake SR, Tseng H-R (2005) *Science* 310:1793
- Lee Y-S, Jeong JM, Kim HW, Chang YS, Kim YJ, Hong MK, Rai GB, Chi DY, Kang WJ, Kang JH, Lee DS, Chung J-K, Lee MC, Suh Y-G (2006) *Nucl Med Biol* 33:677
- Leenders KL, Palmer AJ, Quinn N, Clark CJ, Firnau G, Garnett ES, Nahmias C, Jones T, Marsden CD (1986) *J Neurol Neurosurg Psychiatry* 49:853
- Lehel S, Horvath G, Boros I, Mikecz P, Marian T, Szentmiklosi AJ, Tron L (2000) *J Labelled Comp Radiopharm* 43:807
- Lei M, Tian M, Zhang H (2010) *Curr Med Imag Rev* 6:33
- Lemaire C (1993) Production of L-^[18F]fluoroamino acids for protein synthesis. In: PET studies on amino acid metabolism and protein synthesis. Kluwer, Dordrecht, p 89. Edited by Mazoyer BM, Heiss WD, Comar D, Cox PH (series eds), Development in nuclear medicine, vol 23
- Lemaire C, Cantineau R, Guillaume R, Plenevaux A, Christiaens L (1991) *J Nucl Med* 32:3266
- Lemaire C, Damhaut P, Plenevaux A, Comar D (1994) *J Nucl Med* 35:1996
- Lemaire C, Damhaut P, Lauricella B, Mosdzianowski C, Morelle JL, Moncus M, Van Naemen J, Muelleneers E, Aerts J, Plenevaux A, Brihaye C, Luxen A (2002) *J Labelled Comp Radiopharm* 45:435
- Lemaire C, Gillet S, Guillout S, Plenevaux A, Aerts J, Luxen A (2004) *Eur J Org Chem* 2899
- Lemaire CF, Aerts JJ, Voccia S, Libert LC, Mercier F, Goblet D, Plenevaux AR, Luxen AJ (2010) *Angew Chem Int Ed* 49:3161
- Li ZB, Wu Z, Chen K, Chin FT, Chen X (2007) *Bioconjug Chem* 18:1987
- Li X, Link JM, Stekhova S, Yagle KJ, Smith C, Krohn KA, Tait JF (2008) *Bioconjug Chem* 19:1684
- Lim JL, Berridge MS (1993) *Appl Radiat Isot* 44:1085
- Lim JL, Zheng L, Berridge MS, Tewson TJ (1996) *Nucl Med Biol* 23:911
- Liu E, Chirakal R, Firnau G (1998) *J Labelled Comp Radiopharm* 41:503
- Livni E, Fischman AJ, Ray S, Sinclair I, Elmaleh DR, Alpeert NM, Weiss S, Correia JA, Webb D, Dahl R, Robeson W, Margouleff D, Liss R, Strauss HW, Rubin RH (1992) *Nucl Med Biol* 19:191
- Lu SY, Watts P, Chin FT, Hong J, Musachio JL, Briard E, Pike VW (2004) *Lab Chip* 4:523
- Ludwig T, Gail R, Ermer J, Coenen HH (2001) *Syn Appl Isot Lab Compds* 7:358
- Ludwig T, Ermer J, Coenen HH (2002) *Nucl Med Biol* 29:255
- Lundquist H, Tolmachev V (2002) *Biopolymers* 66:381
- Luxen A, Perlmutter M, Bida GT, Van Moffaert G, Cook JS, Satyamurthy N, Phelps ME, Barrio JR (1990) *Appl Radiat Isot* 41:275
- Mach RH, Elder ST, Morton TE, Nowak PA, Evora PH, Scripko JG, Luedtke RR, Unsworth CD, Filtz T, Rao AV, Molinoff PB, Ehrenkaufer RLE (1993) *Nucl Med Biol* 20:777
- Machulla HJ, Blocher A, Kuntzsch M, Piert M, Wei R, Grierson JR (2000) *J Radioanal Nucl Chem* 243:843
- Mamat C, Ramends T, Wüst FR (2009) *Mini-Rev Org Chem* 6:21
- Marik J, Sutcliffe JL (2006) *Tetrahedron Lett* 47:6681
- Marik J, Sutcliffe JL (2007) *Appl Radiat Isot* 65:199
- Marrière E, Chazalviel L, Dhilly M, Toutain J, Perrio C, Dauphin F, Lasne M-C (1999) *J Labelled Comp Radiopharm* 42(suppl 1):S69
- Martarello L, Schaffrath C, Deng H, Gee AD, Lockhart A, O'Hagan D (2003) *J Labelled Comp Radiopharm* 46:1181
- Martin SJ, Eisenbarth JA, Wagner-Utermann U, Mier W, Henze M, Pritzkow H, Haberkorn U, Eisenhut M (2002) *Nucl Med Biol* 29:263
- Maschauer S, Pischetsrieder M, Kuwert T, Prante O (2005) *J Labelled Comp Radiopharm* 48:701
- Maschauer S, Prante O (2009) *Carbohydr Res* 344:753
- Matsson O, Axelsson S, Hussenius A, Ryberg P (1999) *Acta Chem Scand* 53:670
- Maziere B, Crouzel C, Venet M, Stulzaft O, Sanz G, Ottaviani M, Sejourne C, Pascal O, Bisserbe JC (1988) *Int J Radiat Appl Instrum B* 15:463
- McBride WJ, Sharkey RM, Karacay H, D'Souza CA, Rossi EA, Laverman P, Chang CH, Boerman OC, Goldenberg DM (2009) *J Nucl Med* 50:991
- Mier W, Haberkorn U, Eisenhut M (2002) *Eur J Nucl Med Mol Imaging* 29:165
- Miller PW, Long NJ, Vilar R, Gee AD (2008) *Angew Chem Int Ed* 47:8998
- Mislankar SG, Gildersleeve DL, Wieland DM, Massin CC, Mulholland GK, Toorongan SA (1988) *J Med Chem* 31:362
- Moerlein SM, Perlmutter JS (1992) *Eur J Pharmacol* 218:109
- Mu L, Höhne A, Schubiger PA, Ametamey SM, Graham K, Cyr JE, Dinkelborg L, Stellfeld T, Srinivasan A, Voigtmann U, Klar U (2008) *Angew Chem Int Ed* 47:4922
- Müller K, Faeh C, Diederich F (2007) *Science* 317:1881
- Murakami M, Takahashi K, Kondo Y, Mizusawa S, Nakamichi H, Sasaki H, Hagami E, Iida H, Kanno I, Miura S, Uemura K (1988) *J Labelled Comp Radiopharm* 25:573
- Najafi A, Peterson A, Buchsbaum M, O'Dell S, Weihmuller F (1993) *Nucl Med Biol* 20:549
- Namavari M, Bishop A, Satyamurthy N, Bida G, Barrio JR (1992) *Appl Radiat Isot* 43:989

- Namavari M, Barrio JR, Toyokuni T, Gambhir SS, Cherry SR, Herschman HR, Phelps ME, Satyamurthy N (2000) *Nucl Med Biol* 27:157
- Namavari M, de Jesus OP, Cheng Z, De A, Kovacs E, Levi J, Zhang R, Hoerner JK, Grade H, Syud FA, Gambhir SS (2008) *Mol Imaging Biol* 10:177
- Namavari M, Cheng Z, Zhang R, De A, Levi J, Hoerner JK, Yaghoubi SS, Syud FA, Gambhir SS (2009) *Bioconjug Chem* 20:432
- Neal TR, Apana S, Berridge MS (2005) *J Labelled Comp Radiopharm* 48:557
- Oberdorfer F, Hofmann E, Maier-Borst W (1988a) *Appl Radiat Isot* 39:685
- Oberdorfer F, Hofmann E, Maier-Borst W (1988b) *J Labelled Comp Radiopharm* 25:999
- Oh SJ, Choe YS, Chi DY, Kim SE, Choi Y, Lee KH, Ha HJ, Kim BT (1999) *Appl Radiat Isot* 51:293
- Okarvi SM (2001) *Eur J Nucl Med* 28:929
- Okarvi SM (2004) *Med Res Rev* 24:357
- Olberg DE, Arukwe JM, Grace D, Hjelstuen OK, Solbakken M, Kindberg GM, Cuthbertson A (2010) *J Med Chem* 53:1732
- Olma S, Emert J, Coenen HH (2006) *J Labelled Comp Radiopharm* 49:1037
- Onega M, Winkler M, O'Hagan D (2009) *Future Med Chem* 1:865
- Onega M, Domarkas J, Deng H, Schweiger LE, Smith TAD, Welch AE, Plisson C, Gee AD, O'Hagan D (2010) *Chem Commun* 46:139
- Oya S, Choi SR, Coenen HH, Kung HF (2002) *J Med Chem* 45:4716
- Park BK, Kitteringham NR, O'Neil PM (2001) *Annu Rev Pharmacol Toxicol* 41:443
- Patt JT, Patt M (2001) *J Labelled Comp Radiopharm* 44:154
- Phelps ME, Huang SC, Hoffman EJ, Selin CE, Sokoloff L, Kuhl DE (1979) *Ann Neurol* 6:371
- Piel M, Bauman A, Baum RP, Höhnemann S, Klette I, Wortmann R, Rösch F (2007) *Bioorg Med Chem* 15:3171
- Pike VW, Aigbirhio FI (1995) *J Labelled Comp Radiopharm* 37:120
- Plevenaux A, Fowler JS, Dewey SL, Wolf AP, Guillaume M (1991) *Appl Radiat Isot* 42:121
- Plevenaux A, Lemaire C, Palmer AJ, Damhaut P, Comar D (1992) *Appl Radiat Isot* 43:1035
- Poethko T, Schottelius M, Thumshirn G, Hersel U, Herz M, Henriksen G, Kessler H, Schwaiger M, Wester HJ (2004) *J Nucl Med* 45:892
- Prante O, Einsiedel J, Haubner R, Gmeiner P, Wester HJ, Kuwert T, Maschauer S (2007) *Bioconjug Chem* 18:254
- Qaim SM, Stöcklin G (1983) *Radiochim Acta* 34:25
- Qaim SM, Clark JC, Crouzel C, Guillaume M, Helmeke HJ, Nebeling B, Pike VW, Stöcklin G (1993) In: *Radiopharmaceuticals for positron emission tomography*. Kluwer, Dordrecht. Edited by Stöcklin G, Pike VW, Cox PH (series eds) Development in nuclear medicine, vol 24
- Ramenda T, Bergmann F, Wüst F (2007) *Lett Drug Des Discovery* 4:279
- Reddy GN, Haeberli M, Beer HF, Hasler P, Schubiger AP (1993) *Appl Radiat Isot* 44:993
- Reivich M, Kuhl D, Wolf AP, Greenber J, Phelps M, Ido T, Casella V, Fowler JS, Hoffman E, Alavi A, Som P, Sokoloff L (1979) *Circ Res* 44:127
- Rietjens IMCM, Besten C, Hanzlik RP, Bladeren PJ (1997) *Chem Res Toxicol* 10:629
- Röhn U, Becaud J, Mu L, Srinivasan A, Stellfeld T, Fitzner A, Graham K, Dinkelborg L, Schubiger AP, Ametamey SM (2009) *J Fluorine Chem* 130:902
- Rosenthal MS, Bosch AL, Nickles RJ, Gateley SJ (1985) *Int J Appl Radiat Isot* 36:318
- Ross TL, Ermert J, Hocke C, Coenen HH (2007) *J Am Chem Soc* 129:8018
- Ross TL, Honer M, Lam PYH, Mindt TL, Groehn V, Schibli R, Schubiger PA, Ametamey SM (2008) *Bioconjug Chem* 19:2462
- Ross TL (2010) *Curr Radiopharm* 3:202
- Satyamurthy N, Bida GT, Barrio JR, Phelps ME (1984) *J Nucl Med* 25:23
- Satyamurthy N, Bida GT, Phelps ME, Barrio JR (1990) *Appl Radiat Isot* 41:733
- Satyamurthy N, Phelps ME, Barrio JR (1999) *Clin Posit Imag* 2:233
- Schirmacher R, Bradtmoeller G, Schirmacher E, Thews O, Tillmanns J, Siessmeier T, Buchholz HG, Bartenstein P, Waengler B, Niemeier CM, Jurkschat K (2006) *Angew Chem Int Ed* 45:6047
- Schirmacher E, Wängler B, Cypryk M, Bradtmöller G, Schäfer M, Eisenhut M, Jurkschat K, Schirmacher R (2007) *Bioconjug Chem* 18:2085
- Schlosser M (1998) *Angew Chem Int Edit* 110:1496
- Schlyer DJ, Bastos MAV, Alexoff D, Wolf AP (1990) *Appl Radiat Isot* 41:531
- Schottelius M, Wester HJ (2009) *Methods* 48:161
- Schottelius M, Poetko T, Herz M, Kessler H, Schwaiger M, Wester HJ (2004) *Clin Cancer Res* 10:3593
- Shah A, Pike VW, Widdowson DA (1998) *J Chem Soc Perk Trans* 1:2043
- Shai Y, Kirk KL, Channing MA, Dunn BB, Lesniak MA, Eastman RC, Finn RD, Roth J, Jacobson KA (1989) *Biochemistry* 28:4801
- Shen B, Löffler D, Reischl G, Machulla H-J, Zeller K-P (2009) *J Fluorine Chem* 130:216
- Shields AF, Grierson JR, Kozawa SM, Zheng M (1996) *Nucl Med Biol* 23:17
- Shiue CY, Welch MJ (2004) *Radiol Clin N Am* 42:1033
- Shiue C-Y, Salvadori PA, Wolf AP, Fowler JS, MacGregor RR (1982) *J Nucl Med* 23:899
- Shiue CY, Wolf AP, Hainfeld JF (1989) *J Labelled Comp Radiopharm* 26:287

- Shiue CY, Shiue GG, Mozley PD, Kung MP, Zhuang ZP, Kim HJ, Kung HF (1997) *Synapse* 25:147
- Sirion U, Kim HJ, Lee JH, Seo JW, Lee BS, Lee SJ, Oh SJ, Chi DY (2007) *Tetrahedron Lett* 48:3953
- Smart BE (2001) *J Fluorine Chem* 109:3
- Smith G, Glaser M, Perumal M, Nguyen QD, Shan B, Årstad E, Aboagye EO (2008) *J Med Chem* 51:8057
- Sokoloff L, Reivich M, Kennedy C, Des Rosiers MH, Patlak CS, Pettigrew KD, Sakurada O, Shinohara M (1977) *J Neurochem* 28:897
- Speranza A, Ortosecco G, Castaldi E, Nardelli A, Pace L, Salvatore M (2009) *Appl Radiat Isot* 67:1664
- Steel CJ, O'Brien AT, Luthra SK, Brady F (2007) *J Labelled Comp Radiopharm* 50:308
- Stocklin G (1992) *Eur J Nucl Med* 19:527
- Stöcklin G (1995) Fluorine-18 compounds. In: Wagner HN Jr, Szab Z, Buchanan JW (eds) *Principles of nuclear medicine*. W. B. Saunders, Philadelphia, pp 178–193
- Stöcklin G (1998) *Eur J Nucl Med* 25:1612
- Stöcklin G, Pike VW (eds) (1993) In: *Radiopharmaceuticals for positron emission tomography*. Kluwer, Dordrecht. Cox PH (series ed), *Development in nuclear medicine*, vol 24
- Stoll T, Ermert J, Oya S, Kung HF, Coenen HH (2004) *J Labelled Comp Radiopharm* 47:443
- Stone-Elander S, Elander N (2002) *J Labelled Comp Radiopharm* 45:715
- Sutcliffe-Goulden JL, O'Doherty MJ, Bansal S (2000) *Bioorg Med Chem Lett* 10:1501
- Sutcliffe-Goulden JL, O'Doherty MJ, Marsden PK, Hart IR, Marshall JF, Bansal SS (2002) *Eur J Nucl Med Mol Imaging* 29:754
- Szajek LP, Channing MA, Eckelman WC (1998) *Appl Radiat Isot* 49:795
- Tang G, Tang X, Wang M, Luo L, Gan M, Huang Z (2003a) *J Labelled Comp Radiopharm* 46:661
- Tang G, Tang X, Wang M, Luo L, Gan M (2003b) *Appl Radiat Isot* 58:685
- Tavitian B, Terrazzino S, Kuhnast B, Marzabal S, Stettler O, Dolle F, Deverre JR, Jobert A, Hinnen F, Bendriem B, Crouzel C, DiGiambardino L (1998) *Nat Med* 4:467
- Teng RR, Bai LQ, Shiue CY, Dewey SL, Arnett CD, Wolf AP, Hitzemann RJ (1990) *Int J Radiat Appl Instrum B* 17:811
- Thonon D, Kech C, Paris J, Lemaire C, Luxen A (2009) *Bioconjug Chem* 20:817
- Thumshirn G, Hersel U, Goodman SL, Kessler H (2003) *Chem Eur J* 9:2717
- Tolmachev V, Stone-Elander S (2010) *Biochim Biophys Acta* 1800:487
- Toyokuni T, Walsh JC, Dominguez A, Phelps ME, Barrio JR, Gambhir SS, Satyamurthy N (2003) *Bioconjug Chem* 14:1253
- Vaidyanathan G, Zalutsky MR (1992) *Nucl Med Biol* 19:275
- Vaidyanathan G, Zalutsky MR (1994) *Bioconjug Chem* 5:352
- Vaidyanathan G, Zalutsky MR (1995) *Nucl Med Biol* 22:759
- Vaidyanathan G, Zalutsky MR (1997) *Nucl Med Biol* 24:171
- Vaidyanathan G, Zalutsky MR (2006) *Nat Protoc* 1:1655
- Vaidyanathan G, Affleck DJ, Zalutsky MR (1994) *J Med Chem* 37:3655
- Van Dort ME, Jung Y-W, Sherman PS, Kilbourn MR, Wieland DM (1995) *J Med Chem* 38:810
- Vasdev N, van Oosten EM, Stephenson KA, Zadikian N, Yudin AK, Lough AJ, Houle S, Wilson AA (2009) *Tetrahedron Lett* 50:544
- Vercouillie J, Prenant C, Maia S, Emond P, Guillouet S, Deloye JB, Barr L, Guilloteau D (2010) *J Labelled Comp Radiopharm* 53:208
- Visser GWM, Boele S, van Halteren BW, Knops GHJN, Herscheid JDM, Brinkman GA, Hoekstra A (1986) *J Org Chem* 51:1466
- Wadsak W, Mien LK, Ettlinger DE, Eidherr H, Hausler D, Sidelar KM, Keppler BK, Dudczak R, Kletter K, Mitterhauser M (2007) *Nucl Med Biol* 34:1019
- Wagner FM, Ermert J, Coenen HH (2009) *J Nucl Med* 50:1724
- Wang H-E, Wu S-Y, Chang C-W, Liu R-S, Hwang L-C, Lee T-W, Chen J-C, Hwang J-J (2005) *Nucl Med Biol* 32:367
- Wangler C, Schirmacher E, Lucas P, Schirmacher R (2009a) *J Labelled Comp Radiopharm* 52:S22
- Wangler B, Quandt G, Iovkova L, Schirmacher E, Wangler C, Boening G, Hacker M, Schmoeckel M, Jurkschat K, Bartenstein P, Schirmacher R (2009b) *Bioconjug Chem* 20:317
- Wangler C, Schirmacher R, Bartenstein P, Wangler B (2010) *Curr Med Chem* 17:1092
- Warburg O (1930) *The metabolism of tumours* (trans: Dickens F, German edn). Constable and Co, London
- Warburg O (1956) *Science* 123:309
- Weber W, Wester HJ, Grosu LA, Herz M, Drewas B, Feldmann B, Molls HJ, Stöcklin G, Schwaiger M (2000) *Eur J Nucl Med* 27:542
- Wester HJ, Hamacher K, Stöcklin G (1996) *Nucl Med Biol* 23:365
- Wester HJ, Brockmann J, Rosch F, Wutz W, Herzog H, Smith-Jones P, Stolz B, Bruns C, Stocklin G (1997) *Nucl Med Biol* 24:275
- Wester HJ, Herz M, Weber W, Heiss P, Senekowitsch-Schmidtke R, Schwaiger M, Stöcklin G (1999) *J Nucl Med* 40:205
- Wester HJ, Willoch F, Tölle T, Munz F, Herz M, Oye I, Schadrack J, Schwaiger M, Bartenstein P (2000) *J Nucl Med* 41:1279

- Wester HJ, Schottelius M, Scheidhauer K, Meisetschlager G, Herz M, Rau FC, Reubi JC, Schwaiger M (2003) *Eur J Nucl Med Mol Imaging* 30:117
- Wester HJ, Schottelius M, Poethko T, Bruus-Jensen K, Schwaiger M (2004) *Cancer Biother Radiopharm* 19:231
- Wester HJ, Schoultz BW, Hultsch C, Henriksen G (2008) *Eur J Nucl Med Imaging* 36:653
- Wilson IK, Chatterjee S, Wolf W (1991) *J Fluorine Chem* 55:283
- Windhorst AD, Klein PJ, Eisenbarth J, Oeser T, Kruijer PS, Eisenhut M (2008) *Nucl Med Biol* 35:413
- Winkler M, Domarkas J, Schweiger LE, O'Hagan D (2008) *Angew Chem Int Ed* 47:10141
- Wodarski C, Eisenbarth J, Weber K, Henze M, Haberkorn U, Eisenhut M (2000) *J Labelled Comp Radiopharm* 43:1211
- Wüst F, Knieß T (2003) *J Labelled Comp Radiopharm* 46:699
- Wüst F, Knieß T (2004) *J Labelled Comp Radiopharm* 47:457
- Wüst F, Berndt M, Bergmann R, van de Hoff J, Pietzsch J (2008) *Bioconjug Chem* 19:1202
- Wüst F, Hultsch C, Berndt M, Bergmann R (2009a) *Bioorg Med Chem Lett* 19:5426
- Wüst F, Köhler L, Berndt M, Pietzsch J (2009b) *Amino Acids* 36:283
- Yun M, Oh SJ, Ha H-J, Ryu JS, Moon DH (2003) *Nucl Med Biol* 30:151
- Zesslin J, Escola O, Brust P, Bergmann J, Steinbach J, Lehtikainen P, Solin O, Johannsen B (2001) *Nucl Med Biol* 28:857
- Zhang MR, Suzuki K (2007) *Curr Top Med Chem* 7:1817
- Zhang MR, Tsuchiyama A, Haradahira T, Yoshida Y, Furutsuka K, Suzuki K (2002) *Appl Radiat Isot* 57:335
- Zhang MR, Ogawa M, Furutsuka K, Yoshida Y, Suzuki K (2004) *J Fluorine Chem* 125:1879
- Zhang MR, Kumata K, Suzuki K (2007) *Tetrahedron Lett* 48:8632
- Zheng L, Berridge MS (1992) *J Labelled Comp Radiopharm* 31:296
- Zheng L, Berridge MS (2000) *Appl Radiat Isot* 52:55
- Zijlstra S, Visser GM, Korf J, Vaalburg W (1993) *Appl Radiat Isot* 44:651
- Zuhayra M, Alfteimi A, Papp L, Lützen U, Lützen A, von Forstner C, Meller B, Henze E (2008) *Bioorg Med Chem* 16:9121



43 ^{99m}Tc : Labeling Chemistry and Labeled Compounds

R. Alberto¹ · U. Abram²

¹University of Zurich, Zürich, Switzerland

²Freie Universität Berlin, Berlin, Germany

43.1	<i>Introduction</i>	2074
43.2	<i>General Requirements for the Application of ^{99m}Tc-Radiopharmaceuticals</i>	2077
43.2.1	Requirements from Chemistry/Physics	2077
43.2.2	Requirements from Routine Applications	2078
43.2.3	Requirements from the Market	2080
43.3	<i>Commercial ^{99m}Tc-Radiopharmaceuticals</i>	2081
43.3.1	Myocardial Imaging Agents	2081
43.3.2	Cerebral Blood Flow Agents	2084
43.3.3	Agents for Renal Function	2087
43.3.4	Agents for Other Applications	2089
43.4	<i>Different Types (Generations) of ^{99m}Tc-Radiopharmaceuticals</i>	2090
43.4.1	Perfusion Agents	2090
43.4.2	Receptor-Specific Molecules	2091
43.4.3	Inhibitors	2091
43.5	<i>Strategies for the Labeling of Targeting Molecules</i>	2092
43.5.1	Bifunctional Chelator Approach	2092
43.5.2	Direct Labeling Approach	2100
43.5.3	Integrated Approach	2101
43.6	<i>Developments in the Labeling of Targeting Molecules</i>	2102
43.6.1	Antibodies/Peptides	2102
43.6.2	Neuroreceptor Targeting Molecules	2104
43.6.3	Myocardial Imaging Agents	2108
43.6.4	Vitamins: Folate, Biotin, and B12	2110
43.6.5	Multidrug Resistance	2112
43.7	<i>Recent Developments and Future Role of ^{99m}Tc-Radiopharmaceuticals</i>	2113

Abstract: This chapter reviews the radiopharmaceutical chemistry of technetium related to the synthesis of perfusion agents and to the labeling of receptor-binding biomolecules. To understand the limitations of technetium chemistry imposed by future application of the complexes in nuclear medicine, an introductory section analyzes the compulsory requirements to be considered when facing the incentive of introducing a novel radiopharmaceutical into the market. Requirements from chemistry, routine application, and market are discussed. In a subsequent section, commercially available ^{99m}Tc-based radiopharmaceuticals are treated. It covers the complexes in use for imaging the most important target organs such as heart, brain, or kidney. The commercially available radiopharmaceuticals fulfill the requirements outlined earlier and are discussed with this background. In a following section, the properties and perspectives of the different generations of radiopharmaceuticals are described in a general way, covering characteristics for perfusion agents and for receptor-specific molecules. Technetium chemistry for the synthesis of perfusion agents and the different labeling approaches for target-specific biomolecules are summarized. The review comprises a general introduction to the common approaches currently in use, employing the N_xS_{4-x}, [3+1] and 2-hydrazino-nicotinic acid (HYNIC) method as well as more recent strategies such as the carbonyl and the TcN approach. Direct labeling without the need of a bifunctional chelator is briefly reviewed as well. More particularly, recent developments in the labeling of concrete targeting molecules, the second generation of radiopharmaceuticals, is then discussed and prominent examples with antibodies/peptides, neuroreceptor targeting small molecules, myocardial imaging agents, vitamins, thymidine, and complexes relevant to multidrug resistance are given. In addition, a new approach toward peptide drug development is described. The section has a focus on coordination and labeling chemistry, but biological results are briefly summarized as well. The last (and shortest) section finally intends to give a (subjective) outlook for the future role of ^{99m}Tc-based radiopharmaceuticals. Critical comments are spread over the whole article but are concentrated in this section. Despite the increasing competition of diagnostic radiopharmacy by other commonly applied methods in medicine such as magnetic resonance imaging (MRI) or ultrasound, the authors are convinced that ^{99m}Tc will play a key role also in future if novel approaches are added and the requirements from chemistry biology and the market considered in research to a stronger extent.

43.1 Introduction

The reason for the strong interest in technetium chemistry is essentially based not only on the very favorable decay characteristics of ^{99m}Tc, but also on the very convenient availability of this radionuclide from so-called ⁹⁹Mo/^{99m}Tc generator systems. Favorable decay properties such as half-life time and energy of radiation is an absolute prerequisite for routine application, but price and availability have to be considered more and more as limiting factors. At present, about 80% of all routine applications in diagnostic nuclear medicine are performed with ^{99m}Tc. For many investigations, radiopharmaceuticals can be produced at a reasonable price and the radionuclide ^{99m}Tc is readily available at the moment of demand from a generator. This online availability is a strong “pro” for ^{99m}Tc over cyclotron-produced positron emission tomography (PET) nuclides that are in general not readily available. Such ⁹⁹Mo/^{99m}Tc generators can commercially be purchased from several sources. They allow the physicians to prepare the radiopharmaceutical for a particular diagnostic study in an instant kit when required.

Furthermore, the generators are inexpensive and the price for an investigation is low, a feature becoming more and more important in contemporary health care. The principle of the ⁹⁹Mo/^{99m}Tc generator and some physicochemical aspects will be described in this section.

Historically, the first injection of [^{99m}TcO₄][−] was performed as early as 1961. This was followed by the development of the so-called Brookhaven generator, a principle that has already been described earlier (Richards 1960; Tucker et al. 1958). Subsequently, the use of ^{99m}Tc in diagnostic medicine increased exponentially. The Brookhaven generator, a principle still maintained, consists of a column that contains activated alumina as the stationary phase. This alumina is acidified and loaded with a solution of ⁹⁹Mo in the form of molybdate. In slightly acidic solution, the molybdate anion polymerizes to form a stable heteropolymer Al[Mo₆O₂₄]^{9−} that is strongly adsorbed on the column (Cotton and Wilkinson 1988; Lebedeva and Kyong 1968). This molybdate contains the parent radionuclide ⁹⁹Mo, which upon decay generates ^{99m}Tc. If the molybdate is a fission product, the total amount of molybdenum loaded onto the column is very small and very high specific activities in the range of 10⁴ Ci/g (370 TBq/g) are present. To produce no-carrier-added ⁹⁹Mo generators from products of ²³⁵U fission, many purification steps are required to make sure complete separation from other fission products. An alternative and cheaper method consists in the neutron activation of ⁹⁸Mo-enriched targets in a reactor with thermal neutrons. However, since the thermal neutron cross section of ⁹⁸Mo is only 0.13 barn, the specific activity of ⁹⁹Mo produced in that way is as low as a few Ci/g (100 GBq/g). Many milligrams of carrier ^{98/99}Mo have to be loaded onto the column, but still result in comparably low activity generators.

The ⁹⁹Mo decays with a half-life of 67 h to ^{99m}Tc. The decay yields about 87% of ^{99m}Tc and about 13% decays directly to ground state ⁹⁹Tc. About 10% of the photons are furthermore lost by internal conversion yielding electron emission from the electron shells instead of γ-quanta. Since the half-life of ^{99m}Tc is about 6 h, the system ⁹⁹Mo/^{99m}Tc is a classical parent–daughter system that can quantitatively be treated as a transient equilibrium. The activity of ^{99m}Tc approaches the one of ⁹⁹Mo left in the generator and is at equilibrium about 96.25% of that of ⁹⁹Mo. The radionuclide ^{99m}Tc is present in the form of [^{99m}TcO₄][−] and remains adsorbed on the column. It could be expected that ^{99m}Tc changes its chemical composition by the recoil received upon decay of ⁹⁹Mo but the β-decay is of not sufficient energy to change the chemical environment as is for example the case in Szilard–Chalmers (n,γ) reactions. It has even been shown with low-valency ⁹⁹Mo complexes, that the β-decay gave in very good yield the corresponding ^{99(m)}Tc complex (Baumgärtner 1961; Baumgärtner et al. 1962). In the past, problems with the amount of ^{99m}Tc elution from the generator occurred since [^{99m}TcO₄][−] was reduced to [^{99m}TcO₄]^{2−} by the ubiquitous electrons from the β-decay. The dianion [^{99m}TcO₄]^{2−} remained adsorbed on the column and significantly reduced the amount of activity but these problems are nowadays essentially eliminated in the products offered by the companies. Before or at saturation, [^{99m}TcO₄][−] is then displaced by the anions from an electrolyte that is flushed through the column and eluted into a corresponding vial, “milking the generator” is a common expression for this procedure. Since [^{99m}TcO₄][−] does not form polymers (in contrast to molybdate), it is replaced on the stationary phase by the monoanions from the electrolyte. Typically, the electrolyte is saline (0.9% NaCl in bidistilled water), which allows quantitative removal of [^{99m}TcO₄][−]. Other electrolytes are possible as well, but special attention has to be paid that the electrolyte does not induce release of molybdate from the column.

The eluate contains, beside [^{99m}TcO₄][−], the ground state [⁹⁹TcO₄][−] as a carrier, which is produced from the 13% direct decay but also from decay of [^{99m}TcO₄][−] → [⁹⁹TcO₄][−].

The longer the time period between two elutions, the higher is the content of “cold” $[\text{}^{99}\text{TcO}_4]^-$. In general, the eluate is considered as “no carrier added” (*n.c.a.*), but the direct decay to ^{99}Tc and the decay of $^{99m}\text{Tc} \rightarrow ^{99}\text{Tc}$ leads to a certain dilution with the carrier ^{99}Tc . This has to be considered in the calculations of the specific activity of ^{99m}Tc . Depending on the time period since the last elution, the concentration of the carrier ^{99}Tc can be several factors higher than the actual ^{99m}Tc concentration (see later in this section). These eluates are then the material for the subsequent syntheses of radiopharmaceuticals. The exclusive availability of $[\text{}^{99m}\text{TcO}_4]^-$ in saline explains why any useful chemistry has ultimately to be carried out in this media.

Generators are available in many sizes and activities as high as 37 GBq/ml are possible. Appropriate use of the generators yields products according to international standards. Problems are mainly encountered by so-called breakthrough of ^{99}Mo or by contamination with alumina from the column materials. Eluates have furthermore to be sterile and pyrogen-free. The maximum contaminants in a typical eluate have been regulated under the assumption that ^{99m}Tc is applied within 12 h after the elution.

A very important issue in the application of ^{99m}Tc radiopharmaceuticals is the analysis of the synthesized compound not only in terms of radiochemical purity, but also in regard of its chemical characterization. A novel compound needs to be thoroughly analyzed and characterized in order to be approved by the governmental agencies. As mentioned earlier, the absolute concentration of ^{99m}Tc in a typical eluate is between 10^{-8} and 10^{-6} M. For example, eluting 1 Ci (37 GBq) of ^{99m}Tc in 10 ml of saline 12 h after the last elution results in a solution that is about 0.2 μM in ^{99m}Tc and 0.35 μM in ^{99}Tc , corresponding to about 0.6 μg of Tc in total. For such a small amount of material (and compound) it is essentially impossible to perform a classical chemical analysis. The only way to assess the chemical structure of a novel radiopharmaceutical is then by chromatographic comparison with a surrogate prepared either with rhenium or with long-lived ^{99}Tc . Comparison is performed by chromatography such as thin-layer chromatography (TLC) or high performance liquid chromatography (HPLC). If coinjection of macroscopic amounts of cold compound and the corresponding *n.c.a.* complex ^{99m}Tc exhibits the same retention time, it is accepted that the two compounds are chemically identical. It is, however, not always possible to synthesize (and characterize) the cold complex for thermodynamic or kinetic reasons. This is for instance the case with the important class of technetium-labeled diethylenetriamine pentaacetate (Tc-DTPA) complexes (see ▶ Sect. 43.3.3), which chemical identity could still not be deciphered unambiguously. In the context of peptide labeling by the HYNIC method (see ▶ Sect. 43.5.1) a similar situation is encountered. The structure of the label is unknown and can only be anticipated on experience with related model systems. Clearly, the non-applicability of classical chemical analysis in the context of ^{99m}Tc chemistry is a disadvantage but is also found with other radiopharmaceutically relevant radionuclides. Chromatographic comparison is the only way of indirect analysis. For a few examples, it was possible to detect the mass of a complex directly by means of electrospray ionization liquid chromatography-mass spectrometry (LC-MS). Electrospray ionization-mass spectrometry (ESI-MS) is a very powerful tool to analyze small amounts of material and it was indeed possible to apply the method for unknown radiopharmaceuticals. Still, mass spectrometry is not a quantitative method and it is difficult to conclude unambiguously for the composition of a complex based on its mass number only.

In conclusion, the availability of generators in the context of ^{99m}Tc is a relevant requirement for future development of novel radiopharmaceuticals. Since costs have to be considered, online availability at a very cheap price might define in future, which radionuclides will remain on the market. Though the chemistry is likely to be successful, it is not always available, but is

ideal for ^{99m}Tc. Generator systems are also available for a number of other radionuclides. These are discussed elsewhere in this book.

43.2 General Requirements for the Application of ^{99m}Tc-Radiopharmaceuticals

This section focuses on recent developments in the coordination chemistry of technetium as relevant for radiopharmaceutical applications either for the labeling of biomolecules or for the preparation of radiopharmaceutically active complexes. The radionuclide ^{99m}Tc is still the workhorse in nuclear medicine clearly due to its favorable decay properties and its low price and its availability from generators. These advantages are combined with the disadvantages that result from the transition element nature of technetium, which means that it has to be applied in combination with a chelating agent. Obviously, a basic understanding of coordination chemistry or organometallic chemistry of technetium is a very important requirement for the design of novel radiopharmaceuticals.

43.2.1 Requirements from Chemistry/Physics

The position of technetium in the periodic table allows easily the prediction that it has an extremely rich coordination chemistry with compounds available in many oxidation states and with all type of ligands depending on the particular valency. Technetium is approximately in the middle of the transition metal series, and, according to its position, does so far not have an aquo-ion as in case of indium for instance. Technetium for radiopharmaceutical syntheses is furthermore exclusively available in one of its thermodynamic most stable form as [^{99m}TcO₄][−]. Therefore, the application of ^{99m}Tc radiopharmaceuticals always requires a reduction to a lower oxidation state. The reduction can go along with the concomitant labeling or the formation of a particular complex or can comprise the intermediate formation of a stabilized complex that is then substituted by the final chelator. Both pathways are known in radiopharmaceutical chemistry and very often both pathways might occur concertedly in the application of ^{99m}Tc radiopharmaceuticals. Lower oxidation states tend to disproportionate, which is the major pathway of decomposition of a complex. At the carrier-added level with ^{99g}Tc, Tc(VI) disproportionates to Tc(VII) and Tc(V) and the latter one decomposes to Tc(VII) and Tc(IV). Tc(IV) forms in general polymeric TcO₂ (with a rutil-type structure). Obviously disproportionation is not very likely in case of ^{99m}Tc since the solutions are in general too dilute. However, in these dilute systems, oxidation to [^{99m}TcO₄][−] with traces of O₂ is the general decomposition process if the metal is not sufficiently stabilized with a chelator. Even a chelator is sometimes not enough since decomposition pathways are not only a thermodynamic but also a mechanistic question. TcO₂ for instance is very stable with ⁹⁹Tc in the presence of air, whereas supposed ^{99m}TcO₂ is rapidly reoxidized. The same is true for coordination compounds, although some are very stable against decomposition and find application as radiopharmaceuticals. Chemical stability is a clear requirement. As a consequence, it is obvious that kinetic stability is superior over thermodynamic stability. At high dilution and under nonequilibrium conditions, a very slow decomposition reaction is crucial for applicability of the corresponding compound. Thermodynamically stable but kinetically unstable compounds are produced, in particular if follow-up reactions are coupled to the fast equilibrium, which

interfere with the reverse reaction. The design of closed shell complexes is probably an important physicochemical requirement for a successful development and application of ^{99m}Tc radiopharmaceuticals. Some of the most successful radiopharmaceuticals discussed later in this chapter clearly demonstrate the impact of this argument. High thermodynamic stability combined with low activation barrier is not possible for a radiopharmaceutical, whereas low (even very low) thermodynamic stability in combination with a very robust nature is a preferable combination.

A further requirement beside chemical stability under biological conditions is chemical purity. To be applied as a radiopharmaceutical, the reaction must end up with reproducible purity of better than 98%. This has some impact on the complexes and ligands to be chosen. Since the conditions for the preparation of a radiopharmaceutical in routine use can change, the compound must be formed reliably on a range of parameters. Therefore, the product should be in general a thermodynamic or kinetic trap. This limits the type of ligands considered as useful to multidentate chelators with donating groups matching the valency to be stabilized or the electronic state to d^3 or d^6 . These requirements do not let an extended choice in combinations and indeed the ligands applied so far are more or less similar. The exceptions to this rule are again kinetically stable compounds in which monodentate ligands are sufficient for stabilization. Still, ligands of lower denticity have to fit the aimed valency – isocyanides, carbonyls, and thioether are examples. Although the first ligand type is known to thermodynamically stabilize a broader range of oxidation states, only the one in which most robust complexes are formed is found.

Redox inactive behavior is a further requirement although this characteristic is sometimes not easily to be satisfied. Reduction processes are a particular problem. This essential demand turned out to be a problem in the development of cationic complexes for heart imaging. It could be shown with some Tc(III) phosphine complexes that they are not decomposed in a chemical sense but are reduced to a lower oxidation state and correspondingly been deactivated. Thus, it is highly important that the redox chemistry of technetium complexes is investigated in detail prior to biological studies. Sometimes even a good redox potential does not prevent from being reduced by certain enzymes.

Finally, the occurrence of one and only one stereoisomer is an important chemical requirement. The formation of isomers upon, e.g., the reconstitution of cold kits can be connected to the properties of the metal fragment the ligand coordinates to and/or to the ligand as such. It is difficult to predict whether different complex isomers such as stereoisomers, enantiomers, diastereomers, and others will exhibit a comparable biological behavior and, thus, lead to a useful radiopharmaceutical. It has been shown and will be discussed later in this text that even enantiomers can alter the bioactivity of the vectors they are linked to in a significant way.

43.2.2 Requirements from Routine Applications


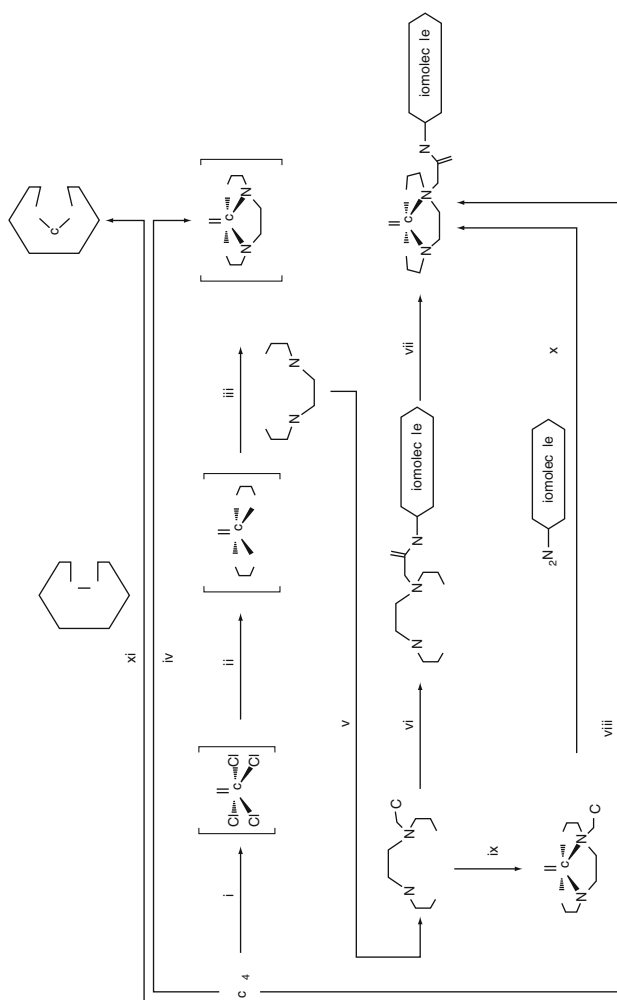
The preparation of a radiopharmaceutical in routine application is usually done in a one- or two-step procedure.  [Figure 43.1](#) gives in the context of coordination chemistry later an overview of the different processes for the production of a radiopharmaceutical in relation to the required fundamental coordination chemistry. Perfusion agents such as pure complexes can be prepared in most cases in one single step upon kit reconstitution. The kit is a vial that contains all the ingredients necessary for performing the chemical reaction to form the

Fig. 43.1

Major pathways toward new complexes and radiopharmaceuticals (i) synthesis of reactive precursor complexes, any condition; (ii) coordination chemistry, new compounds, any condition; (iii) synthesis, characterization of stabilized complexes, water/air stability, serum stability, in vivo behavior, if promising; (iv) one pot kit-based preparation in saline \rightarrow nontargeting perfusion agent; (v) bifunctionalization, if favorable in vivo behavior; (vi) covalent coupling to targeting biomolecule; (vii) labeling under any condition, purification, assessment of in vivo behavior, affinity, stability, etc. (viii) if good biological properties, labeling in one step in saline \rightarrow new targeting radiopharmaceutical with pendant metal complex (pendant, postlabeling approach) (ix) if (viii) not possible, synthesis of complex and coupling to biomolecule, not preferred but possible, two-step prelabeling approach. (xi) Functionalities in the biomolecule are used for labeling, i.e., disulfide bridges are reduced and coordinate to Tc \rightarrow integrated approach, structure often not very well known. Steps (i) through (v) are crucial prerequisites from coordination or organometallic chemistry for the development of novel radiopharmaceuticals



complex in >98% yield. The preparation can be done at room temperature or in boiling water, while other conditions are not convenient for routine application. Obviously, the preparation of the complex or the labeled biomolecule must be performed in aqueous solution, since the generator elute is a saline solution. Other solvents in the cold kit are not feasible. The full preparation from water limits the possibilities of complexes that could be provided by the coordination chemistry. The cold kits contain reductant, antioxidants, buffers, ligands, and stabilizers that must be either destroyed after the preparation or being nontoxic. After the reconstitution of the cold kit with $[\text{}^{99m}\text{TcO}_4]^-$, the product should in principle be ready to be administered to the patient.

The situation presents slightly differently in the case of labeling biomolecules to yield then the corresponding radiopharmaceutical vectors. Here the composition of the cold kit and the biomolecule are often not compatible. A reducing agent such as Sn^{2+} interferes, e.g., with the disulfide bond often encountered in antibodies or peptides. Higher temperatures to be applied for complex formation are not compatible as well since certain biomolecules retain their bioactivity only in a small temperature and pH range. In such cases it is feasible that a precursor complex is prepared separately in a first step according to the requirements outlined above and is then mixed with the biomolecule to be labeled in a second step. For this second vial the same requirements are valid. Again, like in simple complex formation, the labeling must occur in >98% yield and the labeled biomolecule must have the same properties as the corresponding complex. Such “precursor kits” are for instance the glucoheptonate kits in which Tc(V) is stabilized by some weak ligands, which are present in large excess to sufficiently stabilize the Tc(V) center for a convenient time period during which the actual labeling process occurs. These different approaches are depicted in ► Fig. 43.1.

Quality control of the once prepared radiopharmaceutical is important, in particular for therapeutic agents. A chromatographic system must be available that allows a quantitative characterization of the compound. This is usually a TLC method that allows assessment of quality within a reasonable short period of time.

43.2.3 Requirements from the Market

Requirements from the market are not only a scientific aspect but to a large extent also commercial. Following this philosophy, only radiopharmaceuticals that target at diseases concerning a large number of patients will seriously be introduced in the market. This concerns in particular all types of radiopharmaceuticals for cancer diagnosis and therapy, and also myocardial imaging agents. Inflammations and infections represent also an important field in which ^{99m}Tc radiopharmaceuticals could play a future role. Commercial radiopharmaceutical must be cheap and provide an added value over other more and more competing techniques such as MRI or ultrasound although the latter two are not particular methods for functional imaging.

The most important requirement that has to be met before ^{99m}Tc -radiopharmaceuticals can be used routinely in Nuclear Medicine is to have a registration file approved. For all radiopharmaceuticals, extensive information on the “active ingredient” (=the ^{99m}Tc -compound) is to be provided, including data on the exact chemical structure, the analytical methods to proof its purity and identity, the method to produce it from the precursor “kit,” batch data, etc. Another very important aspect of the registration file is the ADME (administration, distribution, metabolism, excretion) part, where especially the metabolic fate of the

^{99m}Tc compound after administration may need major analytical-chemical studies. Furthermore, toxicological (including carcinogenicity and mutagenicity) studies are warranted; although the extent of these studies is clearly less than with “normal” drugs, the different aspects of the administration of a radioactive compound needs to be discussed extensively. The clinical section (including the dosimetry of the compound after administration) needs to contain proof that the ^{99m}Tc compound is a safe and effective compound for the diagnostic uses envisioned. Total costs of these investigations, plus the administrative effort to present it in a readable format, are often several million euros; the sheer costs of the registration effort may therefore hamper the possible registration of ^{99m}Tc compounds for a clinical indication where relatively few patients are involved. Often it takes 3–6 years before a new ^{99m}Tc-radiopharmaceutical is fully accepted by all users.

43.3 Commercial ^{99m}Tc-Radiopharmaceuticals

A number of excellent reviews on radiopharmaceuticals appeared recently covering some of the topics outlined in the following sections (Dilworth and Parrott 1998; Jurisson and Lxdon 1999; Liu and Edwards 1999).

43.3.1 Myocardial Imaging Agents

The biological behavior of myocardial imaging agents has excellently been reviewed in particular in respect of the mechanism of myocardial uptake, the relationship between myocardial blood flow and radiotracer uptake, and redistribution of the tracers (Jain 1999).

Radiopharmaceuticals with ^{99m}Tc for the noninvasive diagnosis of myocardial diseases have significantly progressed during the past decade. This is due to the fact that some excellent and convenient radiopharmaceuticals (see below) are commercially available and in addition there is a large market for such compounds. Myocardial perfusion agents such as sestamibi (*Cardiolite*[®] DuPont) provide important prognostic information about diagnostic evaluation or prognostic stratification for patients with known or suspected coronary artery disease. Although some excellent compounds are on the market, there are still limitations for these compounds and ongoing research in this field mirrors the high interest and potential of developing novel radiopharmaceuticals for the diagnosis of myocardial diseases. Originally, it was postulated that monocationic and lipophilic metal complexes or cations should accumulate in the heart tissue, following the Na⁺/K⁺ATPase mechanism as K⁺ mimics. This conceptual framework seemed to be confirmed by the fact that ²⁰¹Tl⁺, introduced in the mid-1970s, allowed for the first time to image patients with coronary artery disease (Kaul et al. 1986; Wackers et al. 1976). The mechanism of uptake into the myocytes is indeed via the Na⁺/K⁺ATP pump (Sands et al. 1985). Despite this success, ²⁰¹Tl⁺ has rather unfavorable decay characteristics: its half-life is 73 h and the decay energy is 70–80 keV, far from being optimal for good imaging. Furthermore, due to the long physiological half-life of about 10 days, a high dose is burden to the patient. The search for monocationic agents mimicking K⁺ was even more stimulated when it was found that Tc(III) complexes with phosphine ligands showed good accumulation in the heart of animals (Deutsch et al. 1981a, b; Hom et al. 1996; Kung et al. 1997), (Meegalla et al. 1997). Unfortunately, images obtained with these compounds were of very poor quality in humans and not suitable for reasonable imaging. This

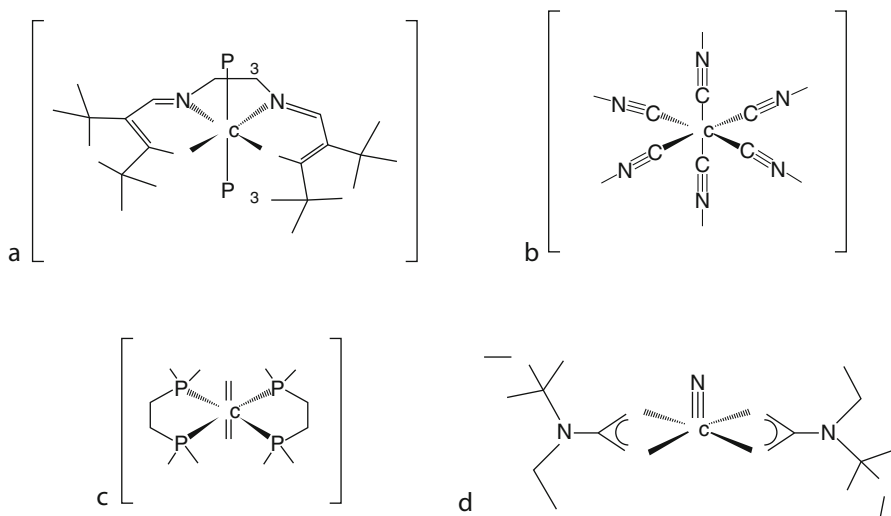
behavior was later explained by the conversion of the cationic Tc(III) complex into a neutral Tc(II) complex through in vivo reduction (Deutsch et al. 1989). The reduced form is washed out rapidly from the heart and accumulates in the liver. After these early findings, many approaches were pursued to reduce the oxidation potential of Tc(III) compounds and a number of other cationic complexes have been investigated. Loss of susceptibility toward reduction was achieved by, e.g., exchanging the phosphines in $[\text{Tc}(\text{P}(\text{O})\text{P})_2\text{Cl}_2]^+$ by diars (diars = o-phenylenebis(dimethylarsine)) and the halides by thiولات to yield complexes of the form $[\text{Tc}(\text{diars})_2(\text{SR})_2]^+$. A wide range of such cationic complexes has been investigated. Although many of them showed reasonable myocardial uptake, they failed from sufficiently rapid washout from the other organs, resulting in images of bad quality and high heart/background ratio. Beside the phosphines and arsine complexes tested for this purpose, organometallic bis-arene and hexakis phosphite Tc(I) complexes are worthwhile to be mentioned (Wester et al. 1987). A real breakthrough in the development of myocardial imaging agents was achieved by changing from redox active oxidation states +V or +III to redox inactive oxidation state +I. Compounds of composition $[\text{}^{99\text{m}}\text{Tc}(\text{CN-R})_6]^+$ have six identical isonitrile ligands, and can be synthesized in one step from $[\text{}^{99\text{m}}\text{TcO}_4]^-$. The original synthesis goes back to 1984 and the compound is commercially available and in extensive clinical use since about 1992 (Abrams et al. 1983; Jones et al. 1984). This complex lead structure $[\text{}^{99\text{m}}\text{Tc}(\text{CN-R})_6]^+$ allows very convenient fine-tuning of the biological properties and a wide variety of residues have been subjected to structure–activity relationships (Holman et al. 1987; Sia et al. 1986). Among the compounds tested, the ligand methoxy-isobutyl-isonitrile (MIBI) showed the most favorable behavior and the complex $[\text{Tc}(\text{MIBI})_6]^+$ (sestamibi, *Cardiolite*®, DuPont) has nowadays replaced $^{201}\text{Tl}^+$ completely and became the market leader (Holman et al. 1987; Sia et al. 1986; Wackers et al. 1989). The preparation of $[\text{Tc}(\text{MIBI})_6]^+$ clearly mirrors the requirements from routine application. Since the isonitriles are usually very volatile compounds, they cannot be lyophilized. Instead, MIBI is coordinated in the kit formulation to Cu(I) to form $[\text{Cu}(\text{MIBI})_4]^+$, a complex that stabilizes the free ligand and makes the kit lyophilizable. SnCl_2 serves as the usual reducing agent in this composition. The kit needs boiling to afford quantitative formation of the radiopharmaceutical. After injection, sestamibi rapidly clears from the blood pool and the organs resulting in a good organ-to-background ratio. One percent heart uptake is observed 1 min postinjection, and less than 5% after 5 min. The residence time is reasonable to allow good images and remains at about 1% after 4 h (Narahara et al. 1990).

Attempts to develop non-reducible and cationic Tc(III) complexes with a reasonable in vivo behavior were finally successful with the preparation of a tetradentate Schiff-base (SB4)-containing complex. These compounds of general composition $[\text{Tc}(\text{SB4})(\text{P})_2]^+$ are referred to as Q compounds, a wide series of which were investigated varying in SB4 as well as in the phosphines. The most promising candidate of this series is Tc-Q12; cf. Fig. 43.2. The radiopharmaceutical has undergone clinical evaluation and is known as Tc-*furifosmin* (*Technecard*®, Mallinckrodt Med.). This complex localizes in the heart according to blood flow (Rossetti et al. 1994). The furanone group in the ligand is believed to support rapid blood clearance. The overall in vivo behavior of *Technecard* was found to be similar to sestamibi but shows a faster hepatobiliary clearance (Deutsch et al. 1989). A very nice feature of the kit formulation is the fact, that additional reducing agents such as SnCl_2 are not required since the phosphines are reduced enough to bring the technetium to the oxidation state +III.

From the series of cationic complexes investigated for myocardial imaging a Tc(V) complex containing the $[\text{O}=\text{Tc}=\text{O}]^+$ moiety has been introduced into the market. The study of complexes of general composition $[\text{TcO}_2(\text{P})_4]^+$, where P is an aliphatic phosphine, based on

■ Fig. 43.2

Myocardial imaging agents: (a) Tc-Q12 ($R=CH_2CH_2OCH_3$), (b) *Cardiolite*[®] ($R=CH_2C(CH_3)_2(OCH_3)$), (c) *Myoview*[®] ($R=CH_2CH_2OC_2H_5$), and (d) TcNNOEt



early observation that they accumulate in heart (Kelly et al. 1990). Subsequently, many phosphines were studied, and it turned out that those bearing an ether residue show the most favorable in vivo properties (Nunn 1992). Among several ether groups containing phosphines, the one called tetrofosmin-encoded P53 was finally found to have the best properties (Lahiri et al. 1989; Libson et al. 1990). The ligand P53 is a bidentate phosphine containing a total of four ether groups per ligand. The complex $[TcO_2(P53)_2]^+$ was launched into the market under the trade name *Myoview*[®] (Nycomed Amersham). In contrast to other phosphine-containing radiopharmaceuticals, reduction takes place in the kit formulation through $SnCl_2$ and the complex forms slowly at room temperature. Good images are recorded 5 min p.i. The major activity is in the gall bladder, whereas liver retention is low (Jain et al. 1993). Consequently, the gall bladder is burdened with the highest radiation dose of all organs. *Myoview* turned out to be one of the most promising myocardial imaging agents. Comparative studies between *Cardiolite* and *Myoview* showed, in particular, that the two compounds are rather complementary than competing since each of the two has special features. Whereas *Cardiolite* allows better differentiation between high and low flow regions, the lower retention time of *Myoview* enables investigation of the same day a patient at stress and at rest (Higley et al. 1993).

A mono-positive charge is not an absolute prerequisite for designing a potential myocardial imaging agent. In fact, the first approved compound was a neutral and highly lipophilic BATO (BATO = boronic acid adducts of technetium dioximes)-type Tc(III) complex. A number of such complexes has been described and the one with cyclohexanedione-bis-dioxime (CDOH2) has been approved and is known as ^{99m}Tc-teboroxime (*CardioteC*[®], Bristol Myers Squibb) (Jurisson et al. 1993; Linder et al. 1990; Linder et al. 1991; Treher et al. 1989). The complex has the formula $[TcCl(CDO)(CDOH)_2(BMe)]$ and is seven-coordinate. The structure comprises three vicinal dioximes. One end of the three dioximes is capped by a B-Me unit which forms a boronic acid ester to the -OH groups of three oximes. The seventh site is coordinated in the solid-state structure by a chloride. Although seven-coordinate Tc(III) complexes are not

uncommon, this unusual composition is reliably produced also on the ^{99m}Tc level by simple reduction of [^{99m}TcO₄][−] with SnCl₂ in the presence of the ligand and methyl-boronic acid. *CardioteC* showed considerable potential for myocardial and brain imaging, and has been registered in Europe and the United States (Jurisson et al. 1993). The in vivo behavior of ^{99m}Tc-teboroxime differs significantly from those of the cationic myocardial imaging agents. It shows very high and rapid accumulation in heart (2.2% after 5 min) via an unknown mechanism but the following clearance is rapid as well. The fast washout from the heart requires a fast imaging protocol but again allow images at rest and at stress to be taken the same day. Good Single Photon Emission Computed Tomography (SPECT) and planar images can be acquired, but for full performance the use of multihead SPECT for image acquisition is recommended due to the rapid heart washout (Seldin et al. 1989).

A new class of neutral myocardial imaging agents is [^{99m}TcN(NOEt)₂], which comprises the [Tc≡N]²⁺ core as a central moiety (Pasqualini and Duatti 1992; Pasqualini et al. 1994). Compounds of this general compositions with various substituents on the nitrogen can be prepared in high yield and radiochemical purity directly from [^{99m}TcO₄][−] (Bolzati et al. 2000b). In a first step, the nitrido precursor is generated by methyldithiocarbamate with water-soluble phosphines as a reducing agent. Subsequently, the addition of dithiocarbamates generates the complex [^{99m}TcN(S₂CNR₂)₂] in general and [^{99m}TcN(NOEt)₂] in particular in very high yield (Ghezzi et al. 1995). Studies for the biological behavior of [^{99m}TcN(NOEt)₂] showed that it is localized predominantly in the cell membrane fraction of myocardial tissue and there was no evidence for chemical decomposition of the complex (Colombo et al. 2001; Riou et al. 1998; Uccelli et al. 1995). The in vivo behavior is quite different to the cationic myocardial imaging agents: the clearance from the blood pool is significantly slower; the myocardial washout is faster. Although the initial uptake is high, the myocardial activity decreases by about 50% after 60 min (Johnson et al. 1997; Vanzetto et al. 2000; Vanzetto et al. 1997).

It remains a major challenge to develop novel myocardial imaging agents with improved pharmacokinetics and biodistribution. The examples shown above are very promising and the chemistry behind inspires future work. As an interesting fact, these examples show in particular that the same ligand can be selected for different metal cores. Thus, improving the biological behavior can not only be done by (an often tedious procedure) variations of the ligand, but also by altering the metal core bound to the same chelator.

Many studies have been performed in order to compare the mode of action, retention kinetics in the myocardium, and the way of excretion of these different cationic and neutral species for both cell cultures as well as in whole heart preparations. Even ⁹⁹Tc NMR spectroscopy has been used to characterize in vivo the nature of the compounds for sestamibi. A recent comparative kinetic study between the different cations can be taken as a base for the clinical interpretation of the different perfusion imaging findings (Narahara et al. 1990; Schaefer et al. 2002).

43.3.2 Cerebral Blood Flow Agents

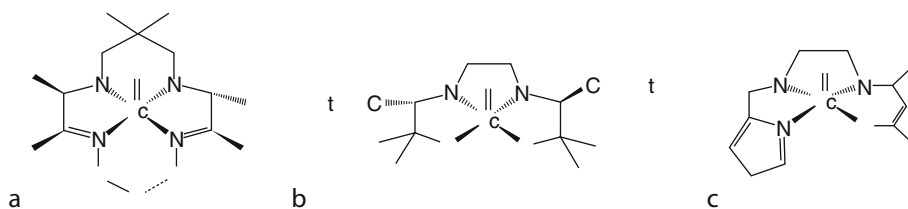
Brain imaging is still an active field of research in radiopharmaceutical chemistry. The compounds for brain imaging can be divided into two classes, one of which is discussed in this section. For the evaluation of the brain, one can apply either regional blood flow agents or receptor specific agents. Currently, the only Food and Drug Administration (FDA)-approved ^{99m}Tc radiopharmaceuticals are from the first class, so-called perfusion agents, but substantial efforts for the introduction of radiopharmaceuticals of the second class are currently

undertaken (see later in this section). The constraints for a ^{99m}Tc based-cerebral blood flow agents are quite high. The complex should be in vivo stable, be extracted to a high extent into the brain, and in proportion to the blood flow over a wide range, cross the blood-brain barrier (BBB) passively, should show no redistribution in the brain and should ideally be trapped in the brain by some change of the chemical composition to prevent rapid washout from the brain (Brodie and Hogben 1957). In addition, to pass easily the BBB, they have to be of low molecular weight, preferentially <500 Da, and the log P value (defined as the distribution coefficient between octanol and water) has to be between 0.5 and 2.5 (Dischino et al. 1983). Cerebral blood flow imaging agents represent a good example for the complementarity of other diagnostic methods such as CT or MRI with nuclear medicine. Although these techniques are highly developed and well established for visualizing structural changes, functional deficiencies causing no or few structural changes are hard to detect. Therefore, the development of corresponding tracers is of great importance and it was indeed possible to develop at least two of them which are nowadays in routine clinical application.

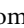
In the earlier stages of technetium chemistry, it was found that tetradentate ligands of the amine-oxime type formed neutral and highly lipophilic complexes with the [Tc=O]³⁺ core. One of the first was the complex with the ligand PnAO (3,3,9,9-tetramethyl-4,8-diazaundecane-2,10-dione). The structure comprises a tetradentate N₄ ligand in which the two aliphatic amines are deprotonated. Together with one deprotonated oxime and the terminal oxo function the overall charge is neutral and the complex due to the methyl substituents of high lipophilicity (Troutner et al. 1984). Many variants of derivatives were tested keeping the structural framework of coordination intact but changing the substituents at the periphery. The original complex [TcO(PnAO)] was very well able to traverse the BBB but was not retained and washed out very fast (Chaplin et al. 1985; Hoffman et al. 1985; Holmes et al. 1985). Further developments of this class of complexes at Amersham was finally successful with the ligand (RR,SS)-4,8-diaza-3,6,9-tetra-methyl-undecane-2,10-dione dioxime (*d,l*-HM-PAO, see ► Fig. 43.3). The ligand is also called hexametazime, and loses again three protons upon coordination to the [Tc=O]³⁺ core. The proligand has two chiral centers, therefore a *meso* and a *d,l*-form exist. The complexes with the *meso* and the *d,l*-form of the ligand show both trapping in the brain, however to a different extent and the brain uptake is dependent on the blood flow in animals (Hoffman et al. 1985; Neirinckx et al. 1987) as well as in humans (Ell et al. 1985; Leonard et al. 1986). The complex with the *d,l*-form of the ligand is better retained in the brain. Although the exact mechanism of retention is not known, it seems that the complexes are converted by enzymatic processes to hydrophilic species. The conversion of [TcO(*d,l*-HMPAO)] is faster, hence, retention is better (Nowotnik et al. 1985; Sharp et al. 1986). The complex with *d,l*-HMPAO is nowadays commercially available and in clinical use

■ Fig. 43.3

Brain perfusion agents: (a) *d,l*-TcO(HMPAO), *Ceretec* (b) Tc-ECD *Neurolite*, (c) Tc-MRP20




(Ceretek[®], Amersham Int.). Its faster transformation to hydrophilic species goes along with a lower stability of the complex [TcO(*d,l*-HM-PAO)]. After preparation it should be applied within 30 min, otherwise too many decomposition products are present. On the other hand, the complex with the *meso*-form of the ligand is significantly more stable and does not decompose within this time period. In principle, the complex with the *meso*-ligand could also have two different stereoisomers, one with the methyl groups *syn* to the oxo group and *anti*, respectively. In fact, only the one with the *syn* conformation has been observed and isolated. Ceretek is a very interesting example since it clearly shows that stereochemical characteristics are essential and can influence the in vivo behavior to a significant extent. This is not surprising, considering the stereoselectivity of enzymes involved in the metabolism of small molecules but is unexpected in the sense that nonbiological molecules are treated the same way. Stereochemical differences clearly fine-tune biological parameters such as biodistribution and pharmacokinetics even in small artificial complexes. Thus, stereochemistry has seriously to be considered in the design of novel perfusion agents and or targeting radiopharmaceuticals.

A similar stereoselective reaction is the base for the use of certain (diamino-dithiol (DADS) ligands in the context of brain perfusion agents. DADS ligands stabilize the [Tc=O]³⁺ core by coordination through the two deprotonated thiol groups and one deprotonated aliphatic amine. The second aliphatic amine remains protonated and coordinates as a normal tertiary amine. In total, the complex is uncharged and, depending on the substituents, of medium to high lipophilic character. The basic complex composition is shown in  Fig. 43.3. Furthermore, the DADS framework has been used for many purposes and in particular in the context of brain imaging agents. An excellent and critical review has recently been published by Johannsen and coworkers (Johannsen and Pietzsch 2002). The complex that is nowadays routinely applied in brain imaging is built up from the dimerization of two cysteines through an ethylene bridge to yield so called ethylene–cysteine dimere (ECD). It is essentially based on earlier efforts to produce neutral [TcO(N2S2)] complexes (Epps et al. 1987; Kung et al. 1990; Kung et al. 1989; Lever et al. 1985). Most of the complexes based on the N2S2 ligands are sufficiently lipophilic to pass the BBB but they are not trapped. ECD on the other hand contains two ester functionalities, which can be subject to hydrolysis, thus, due to strongly increased hydrophilicity, expected to be trapped, which is indeed the case. Esterases hydrolyze the ester groups with surprising stereoselectivity (Vallabhajosula et al. 1989; Walovitch et al. 1989; Walovitch et al. 1988). The complex with the *d,d*-form of the ligand is relatively insensitive for hydrolysis, whereas the *l,l*-form is readily trapped in the brain by fast hydrolysis. These in vivo results were confirmed in vitro with monkey brain homogenate in which the *d,d*-form was clearly much slower hydrolyzed than the *l,l*-form (Walovitch et al. 1994). The partially or fully hydrolyzed species in the blood are readily excreted through the kidneys. It could be shown that the metabolites contained the basic coordination framework intact and no decomposition took place (Walovitch et al. 1994). The complexes are retained in the brain only and no back-diffusion was observed. Apart of the easier preparation, this remarkable stability is also a clear advantage of Tc-ECD over Tc-HM-PAO. Byproducts that still form in the case of HM-PAO can accumulate in the soft tissue around the brain and decrease the quality of the images.

Beside such practical consideration, it should also be emphasized in the case of Tc-ECD that stereochemical behavior is very important. In the case of ECD, clearly an unidentified esterase is responsible for the crucial trapping of the metal complex in the brain.

Beside the two discussed “market leaders” in brain imaging, a number of other coordination compounds has been investigated with respect to practical application. One of these are

complexes of the already mentioned class of BATO compounds. BATO-type complexes are very lipophilic ($\log P > 3.8$), which results in longer residence time in blood due to hydrophobic interaction with serum proteins. This clear disadvantage goes along with a slow but significant washout from the brain, which is unique among brain imaging agents (Narra et al. 1989; Narra et al. 1990). It is anticipated that an equilibrium between a cationic and a neutral complex is responsible for the reversible trapping. In a basic study, it could be shown that in vitro the seventh ligand in the BATO complexes, usually a Cl^- exchanges for water, to give a monocationic complex that is trapped. Equilibrium with the form in which water is again replaced by Cl^- yields a neutral species that is washed out (Jurisson et al. 1991). This illustrates an interesting (chemical) form of interconverting a complex to yield an activated species. A further example of a brain perfusion complex is based on an N3O ligand. The ligand MRP-20 is depicted in  Fig. 43.3. It stabilizes the $[\text{Tc}=\text{O}]^{3+}$ moiety. The pyrrol nitrogen, the aliphatic amine, and the hydroxo group are deprotonated to afford an overall neutral complex. The complex $[\text{TcO}(\text{MRP-20})]$ did not exhibit significant advantages over the other two discussed above and was not pursued any longer (Bossuyt et al. 1991; Morgan et al. 1991).

43.3.3 Agents for Renal Function

Imaging of the kidney function is a very thoroughly investigated field of ^{99m}Tc radiopharmaceuticals. In case of the kidneys it is important to study both function as well as morphology. Significant research has therefore been invested to the design and syntheses of complexes that allow imaging those two features. A number of complexes are nowadays commercially available and a recent excellent review covered not only the chemistry of such ^{99m}Tc complexes but also some physiological aspects of kidney as such (Nosco and Beaty-Nosco 1999). Originally simple $\text{Na}[\text{}^{99\text{m}}\text{TcO}_4]$ was used as kidney imaging agent, but due to rapid clearance through the liver, it was never seriously considered to be a viable renal imaging agent. This is unexpected since $[\text{}^{99\text{m}}\text{TcO}_4]^-$ met the criteria of hydrophilicity, rapid clearance from the blood stream (>98% through kidneys), in vivo and in vitro stability, and other conditions that are considered to be essential for a functional renal imaging agent for potential application. Soon after the investigations on $[\text{}^{99\text{m}}\text{TcO}_4]^-$, two coordination compounds were introduced, exhibiting the required physicochemical properties. One complex used DTPA as a ligand, while a second one took DMSA (dimercaptosuccinic acid) (Blaufox 1991; Eshima et al. 1990; Fritzberg 1984; Ponto et al. 1990; Verbruggen and Deroo 1992; Villa et al. 1986). ^{99m}Tc-DTPA is one of the early radiopharmaceuticals the structure of which is still unknown. Although many attempts were done to properly characterize the complex on the ⁹⁹Tc level, its structure is not unambiguously clear. Oxidation states +III, +IV, and +V have been proposed and complexes with DTPA in these different valencies partially were confirmed to exist (Bandoli et al. 1982; Eckelman et al. 1972; Kempf et al. 1980; Seifert et al. 1982).

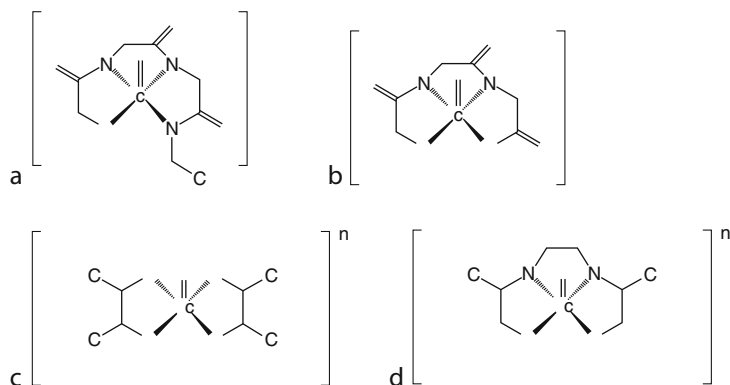
However, the product formation is dependent upon the pH and the amount of SnCl_2 used for reduction. Despite the lacking structure of Tc-DTPA, kits (^{99m}Tc-pentetate) are commercially available from different companies and in extensive use, mainly due to the low-cost and the low-radiation dose delivered to the patient. ^{99m}Tc-DTPA allows the measurement of the glomerular filtration rate. Since the extraction efficiency is only about 20% for each path through the kidneys, a relatively high background harms the quality of the images (Harbert et al. 1996). An increase in rate of clearances from the circulation can be achieved by parallel or exclusive excretion through the renal tubules. This is an active process, which is about four

times more efficient than glomerular excretion. One of the latest ^{99m}Tc complexes that is actively excreted by tubular secretion is ^{99m}Tc -MAG3 (Fritzberg et al. 1986). MAG3 (mercaptoacetyl-triglycine) is a peptide-like ligand that stabilizes the metal center in the oxidation state +V, cf. ► Fig. 43.4.

Different from the DTPA agent, structure and composition of $[\text{}^{99m}\text{TcO}(\text{MAG3})]^-$ are well established. Originally developed by Fritzberg and coworkers (Eshima et al. 1987), it has been demonstrated earlier that tetradentate diamido-dithiolato ligands proved to form physiologically stable complexes with the $[\text{Tc}=\text{O}]^{3+}$ moiety (Davison et al. 1981). Although the basic framework was given, problems arose from the presence of different stereoisomers when the charged acetyl functionality was attached to the five-membered ring. *Syn* and *anti* conformations in respect of the $[\text{Tc}=\text{O}]^{3+}$ moiety were found. The two conformers excreted differently. Fritzberg moved this group to the terminal amido group and circumvented this problem elegantly by eliminating the chiral center but keeping the overall hydrophilicity essentially unchanged. The thiol group in the free ligand is somewhat problematic since it tends, even when stored under N_2 , to form disulfide bridges. Therefore, in the commercially available kits, this group is protected with a benzyl group, which is released during the 10 min process of heating when reconstituting the kit. Labeling efficiency is very high, would even be higher if the ligand was available in its free form not requiring concomitant deprotection (Rao et al. 1990). Furthermore, SnCl_2 is a reasonably strong reducing agent to switch $\text{Tc}(\text{VII})$ to $\text{Tc}(\text{III})$ when heated (and to even lower valencies), thus, relatively few SnCl_2 are in the kit, which is destroyed prior to administration by ventilating the kit with air to destroy excess SnCl_2 . At physiological pH, the free carboxylate is deprotonated, making the complex monoanionic. After administration, the complex binds to a large extent by non-covalent forces to plasma proteins. To be excreted, it seems that the free carboxylate is essential in order to be recognized by the corresponding receptors in the kidney, which entails active excretion through tubular secretion (Despopoulos 1965). About 50% of the radioactivity is excreted for each blood pass through the kidneys. This is less than in case of o-iodohippuran (the golden standard of kidney radiopharmaceuticals), but sufficient to obtain good images for this function of the kidneys. Nowadays, *Technescan*[®] MAG3 (Mallinckrodt Med) has mostly replaced o-iodohippuran.

► Fig. 43.4

(a) Tc -MAG3, *Technescan*[®], (b) Tc -MAG2, and (c) $[\text{TcO}(\text{dmsa})_2]^{n-}$, (d) Tc -EC



The purpose of a third kind of renal imaging agent is to measure the actual renal mass. To achieve this objective, the metal complex now needs to have different characteristics. Typically, it should have high affinity for the proteins localized in the tubular walls or be thermodynamically weak, allowing transmetalation into renal tubule proteins. Two commercially available ^{99m}Tc complexes fall in this class. The first one is the Tc(V) complex with dimercaptosuccinic acid (dmsa) and the other one is with glucoheptonate. The structure for the first one is quite well known, whereas for the second one a structure is assumed, cf. [Fig. 43.4](#).

These two complexes behave in the kidneys in a biological way that it is not well understood (Blaufox 1987; Nosco and Beaty-Nosco 1999). The complex with glucoheptonate, tentatively formulated as $[\text{TcO}(\text{gh})_2]^-$, is not stable once released from the conditions in the kit. Decomposition leads to retention in the kidneys with up to 15% of the injected dose still present after 4 h (Harbert et al. 1996). This retention is a useful measure for the determination of the effective renal plasma flow. The composition of the dmsa complex is most likely to be $[\text{TcO}(\text{dmsa})_2]^-$. Several stereoisomers are possible. Using the *meso*-form of the ligand, three isomers (*syn-endo*, *syn-exo*, and *anti* conformation of the $-\text{COOH}$ groups with respect to the $[\text{Tc}=\text{O}]$ group) are possible, which have been identified indeed for the synthesis of the corresponding ¹⁸⁶Re complexes. It has been shown by ¹H-NMR studies that they all are interconverting rapidly (Spies and Johannsen 1981). Since more precise information on the morphology of kidneys can nowadays be acquired from alternative methods such as ultrasound, CT, or MRI, both compounds are rarely used.

Beside the agents mentioned in this section, it is worthwhile to describe to further agents that are under development and show promising properties for renal imaging. The Tc(V) complex with ethylene–dicysteine shows also promise and contains the same coordination unit as already described in the section on cerebral blood flow agents (ECD) (Verbruggen et al. 1992). A structure of the complex is depicted in [Fig. 43.4](#). The complex is hydrophilic and bears an overall charge of 2−. It has been shown that this complex is actively excreted through the renal tubules with a rate of clearance that is about 40% higher than the one of Tc-MAG3 (Gupta et al. 1995). Another very interesting compound is a homoleptic Tc(I) complex with six monoanionic-charged ligands to afford an overall charge of 5−. Although of more academic interest, the complex is prepared from the ligand present in the ester form and subsequent hydrolysis in the free or coordinated form (Kronauge et al. 1993). The complex has shown promise for the measurement of effective renal plasma flow.

43.3.4 Agents for Other Applications

Attempts have been made to introduce ^{99m}Tc-based radiopharmaceuticals for the imaging of various other functions and diseases as well. Among the most successful ones are bone and liver imaging agents, some of which have been commercialized. Since for most of the corresponding compounds the structure is not clear, they shall not be discussed at this place. Among the recent trends in diagnostic nuclear medicine, imaging of hypoxia is a major development and complexes containing a nitroimidazole group play an important role in this field. Nitroimidazole is reduced in hypoxic cells to compounds that cannot diffuse out of the cell or remain bound in the cell to unknown molecules inside the cytoplasm. The gold standard for imaging hypoxia is the fluorinated compound ¹⁸F-misonidazole (Martin et al. 1992). Basically two approaches have been chosen to develop a useful ^{99m}Tc-based hypoxia radiopharmaceutical. One of the ligands to stabilize Tc is a PnAO-type ligand as depicted in

► **Fig. 43.5.** The ligand is derivatized with nitroimidazole at the oxime group. It is trapped in hypoxic tissue. However, due to the high lipophilicity, it clears too slowly, affording images of poor quality. Some derivatizations have been performed to increase hydrophilicity through the introduction of oxygen in the backbone (Dirocco et al. 1993; Linder et al. 1994). Certain variations in the ligand type have been pursued and the tridentate amine-phenol ligand bis (amine-phenol)nitroimidazole (► **Fig. 43.5**) was introduced (Johnson et al. 1998; Pillai et al. 1990; Ramalingam et al. 1994). A further variation included the extension of the propylene backbone in PnAO to butylene in BnAO. The variation is very interesting from the background that PnAO forms a mono-oxo core, whereas a pentylene backbone gives the dioxo-core $[\text{O}=\text{Tc}=\text{O}]^+$. The behavior of the butylene is not unambiguously clear but from the behavior in hypoxic tissue it seems likely that the complex is reduced to a lower oxidation state complex. It is remarkable that the complex without a nitroimidazole group proved to be more effective than the complex with the nitroimidazole group.

A very recent approach used the [3+1] strategy (see also ► **Sect. 43.4.1**) to introduce a redox active methyl-pyridinium derivative into the $[\text{Tc}=\text{O}]^{3+}$ core, cf. ► **Fig. 43.5**. The redox-active moiety is derivatized with a thiol that acts as the monodentate ligand, whereas the tridentate ligand is represented by a thioether-dithiol framework (Kniess et al. 1998).

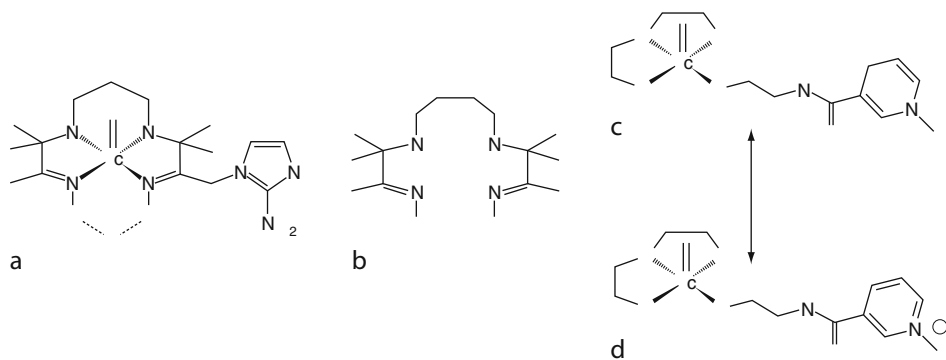
43.4 Different Types (Generations) of ^{99m}Tc -Radiopharmaceuticals

43.4.1 Perfusion Agents

Perfusion agents are the most commonly used radiopharmaceuticals containing ^{99m}Tc . They are also referred to as first-generation radiopharmaceuticals or technetium-essential radiopharmaceuticals. As described in the preceding chapters, they have been developed over the past decades with great success and are in manifold clinical use for the diagnosis of, e.g., renal and heart function, cerebral blood flow, and many others. The radiopharmaceutical is “ ^{99m}Tc essential” since it would obviously not work without technetium: The pharmaceutical has to be considered as an entity in which the Tc-center plays the role of an important structure and

► **Fig. 43.5**

Compounds for imaging of hypoxia (a) Tc-PnAO (BMS181321), (b) alternative ligand BnAO, and (c/d) 3+1 approach with dihydropyridin



physicochemical imposing part. The ligands on the other hand are mono- or multidentate, designed for the particular purpose that the complex is intended to be applied. Essentially any technetium complex could be a perfusion agent, provided that it fulfills the very basic requirements outlined. For the in vivo behavior of the perfusion agent, predictions are difficult to make and the design remains finally a trial-and-error approach as obvious from the development of many of the successful perfusion agents. Some characteristics may help in designing a novel radiopharmaceutical, but, at the end, only the biological experiments will tell the usefulness of a particular compound. Sometimes even animal experiments in mammals are not conclusive for the behavior of the compounds in human as impressively shown with the development of the first myocardial imaging agents based on cationic Tc(III) complexes. An interesting feature that merits probably more consideration in future is the processing of “innocent” radiopharmaceuticals by enzymes. In the case of [TcO(HM-PAO)], for instance, the conversion to a more hydrophilic compound is crucial for the in vivo behavior. It can be concluded that the administered compound is rather a prodrug that is converted at the organ into the actual drug. This working hypothesis, although very demanding for the design of novel perfusion agents, is challenging not only for the chemist but also for the biochemist. It has to be emphasized that perfusion agents are not “out of fashion” although the major actual research efforts focus on the second generation of radiopharmaceuticals. The motivation to further research in this field is of course on one hand to yield improved quality images paralleled by a lower radiation dose to the patient, but is clearly also a question of the market.

43.4.2 Receptor-Specific Molecules

The major actual research efforts are in the development of ^{99m}Tc-labeled vectors, also called targeting biomolecules. Such radioconjugates are referred to as second-generation radiopharmaceuticals. While radiopharmaceuticals of the first generation are technetium essential, those of the second generation are not. It can even be anticipated that the metal complex affects the biological behavior of the biomolecule, although the precise fate of the unlabeled molecule is in most of the cases completely unknown. A second-generation radiopharmaceutical consists of the biologically active molecule, in general an organic molecule such as a peptide, an antibody, or a central nervous system (CNS) receptor binding small molecule that carries at its periphery the metal complex. The metal complex should be “innocent,” not influence the physicochemical properties of the biologically active molecule, and not interfere with receptor binding, requirements that are at least in the case of very small molecules difficult to achieve. A ^{99m}Tc metal complex attached to anyone of these vectors allows monitoring the biodistribution of the biomolecule and, even in case where the receptor affinity is fully maintained, exhibits often unfavorable biological behavior.

43.4.3 Inhibitors

A perspective for the development of novel radiopharmaceuticals is a molecule in which the complex is part of the topology required for the recognition and binding by a particular receptor. After receptor binding, the receptor should be blocked and its function be inhibited. The inhibitor might act as an agonist or an antagonist. So far there is no example in ^{99m}Tc chemistry in which this situation occurs. Katzenellenbogen recently described examples

pointing in the direction of a ^{99m}Tc complex that is able to interfere with the estradiol receptor. The structures of these complexes are depicted in ► Fig. 43.6 (Chi and Katzenellenbogen 1993; Chi et al. 1994; Hom and Katzenellenbogen 1997a; Hom et al. 1996).

The approach, as outlined above, to mimic a naturally occurring structure shows also that it is important to copy not only the actual surface of the molecule but also its electronic properties. The later point is by far more challenging (if possible at all) than just the consideration of topological properties. Although for the coordination chemist a real challenging task, it remains at least doubtful if a de novo inhibitor can ever be achieved and transferred into a versatile product for routine use.

43.5 Strategies for the Labeling of Targeting Molecules

43.5.1 Bifunctional Chelator Approach

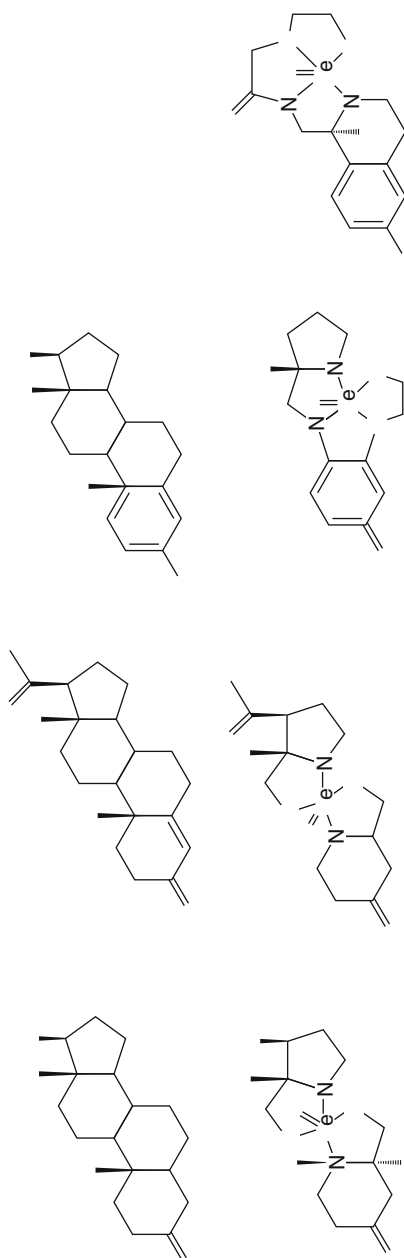
The labeling of targeting molecules entails the question of tightly binding the metal center to the biologically active molecule without affecting its physiological properties. This means in concrete that the metal center in its particular oxidation states needs to be stabilized and covalently linked to the vector. The ligand, an organic molecule, has thus two functions. It is called a bifunctional chelator (BFC). One part of the molecule, the first function, coordinates the technetium, whereas the second function is to covalently bind the ligand to the targeting vector via a suitable spacer. The coordinating part can be chosen from the armory of known ligands as discussed above (i.e., MAG3). The connecting functionality to the biomolecule is usually a carboxylate or an amine group that can conveniently be activated with known strategies from organic chemistry.

Labeling of targeting molecules requires a chelator that is strong enough (1) to coordinate to the technetium center at low concentration (to avoid subsequent purification from cold material), (2) to give one single product, and (3) to stabilize the metal under in vivo conditions (Brenner et al. 1984; Davison et al. 1981; Edwards et al. 1990; Grummon et al. 1995; Jurisson et al. 1986; Wong et al. 1997). In principle, these requirements hold also true for the first-generation radiopharmaceuticals but these also need to be subject of well-controlled metabolic processing, whereas the pendant metal complex in the second-generation radiopharmaceuticals clearly should not. The chelator should afford an innocent metal complex. The most widely applied BFC are those based on a combination of nitrogen and sulfur donors to give the class of tetradentate N_xS_{4-x} ligands. The donor S is in general a thiol group, more rarely a thioether, whereas N represents an amide, an aliphatic amine, or an imine in which case additional sulfur donors are rare. A number of examples for such chelators is given in ► Fig. 43.7.

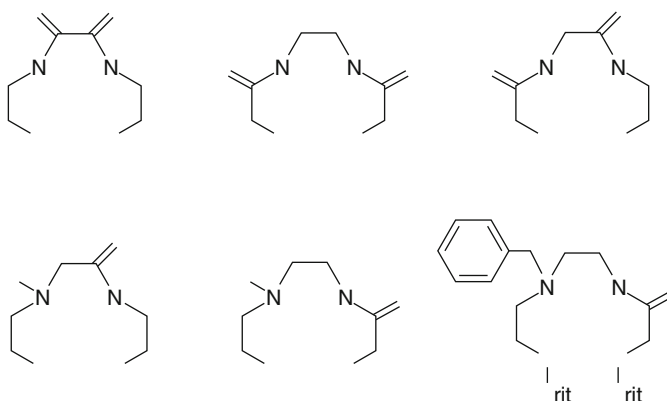
The basic N_xS_{4-x} framework yields neutral or anionic complexes depending on the type and combination of the nitrogen donors. Since amide functions cannot coordinate without deprotonation, an amide in the ligand framework counts for one negative charge in the coordinated form. The ligands coordinate the [Tc=O]³⁺ moiety very efficiently and at low concentration. For labeling, the thiol groups are in general protected (mostly as benzoyl or trityl) since the free thiol groups are susceptible to disulfide formation, and the complex formation gives then often mixtures of products. Protecting the thiol on the other hand results in one well-defined product but requires boiling in order to cleave the protecting groups. The basic ligand framework can now be further derivatized with the second functionality required for binding to the vector. Several strategies have been used for that purpose and some examples are depicted in ► Fig. 43.8.

■ Fig. 43.6

Rhenium complexes that mimic the structure of steroids, upper row dihydrotestosterone, progesterone, and estradiol, lower rows are the corresponding complexes



■ Fig. 43.7

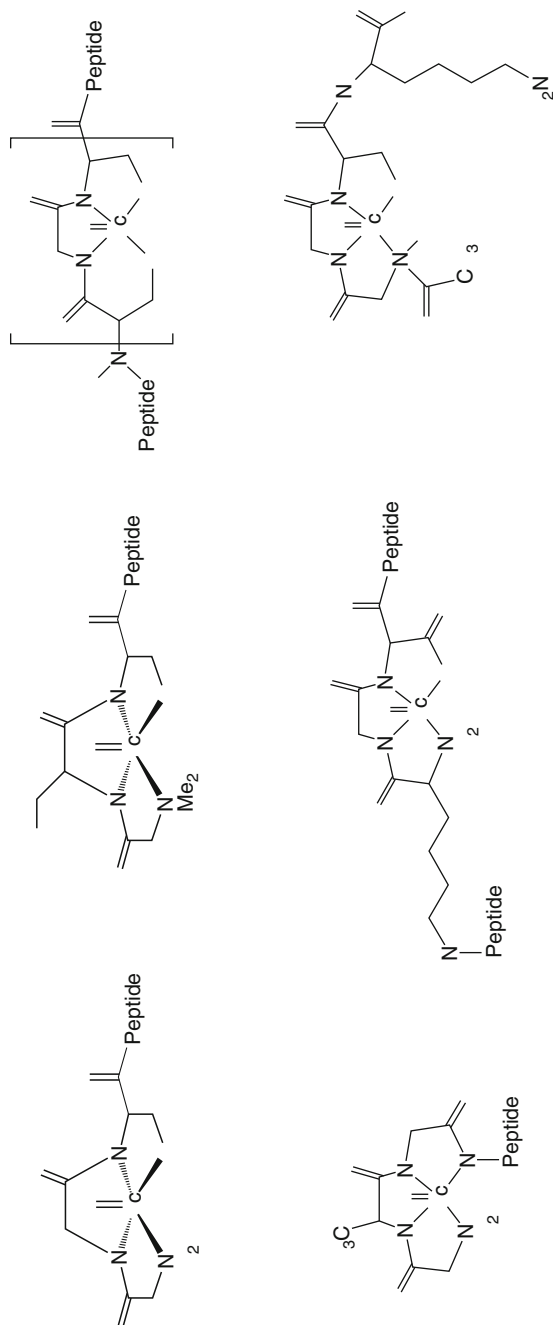
A selection of N2S2 ligands that form anionic and neutral Tc(V) complexes

The linking group can either be attached to one of the aliphatic amines resulting in a tertiary amine if the nitrogen is in the chain or in a secondary amine if the linking amine group is terminal. It can also be attached to one of the carbon atoms in the ligand backbone. This is usually the case if the ligand is built up of a sequence of amino acids or pseudo amino acids. The carboxylic group represents then the C-terminus of such a peptide sequence. The same strategy is also applied to yield an amine group as a second function. The advantage of good stability and high labeling yield is often compensated by the formation of stereoisomers. Any optical active center in the backbone of the ligand gives rise to the formation of a complex with the side chain in *syn* or *anti* orientation in respect of the Tc=O group. Fortunately, one of the possible products is usually thermodynamically preferred and one product only (in general the *syn* stereoisomer) is formed.

A pseudo peptide sequence such as found in MAG_3 may contain a variety of other amino acids instead of the glycines. This allows structure–activity relationships of the biodistribution characteristics by substituting one of the glycines in MAG_3 by another naturally occurring amino acid (Bormans et al. 1992; Hansen et al. 1992; Hansen et al. 1994; Verbruggen et al. 1989). Introduction of, e.g., an alanine instead of the central glycine residue (MAAG) resulted in the *syn* conformation of the structurally analogous complex $[\text{TcO}(\text{MAAG})]^-$ with the same coordination sphere as $[\text{TcO}(\text{MAG}_3)]^-$. Decreasing the number of available amido groups for coordination as in the mercaptoacetyl-glycine-glycine (MAG_2) ligand significantly diminishes the ability of the ligand to stabilize the $[\text{Tc=O}]^{3+}$ core. Nevertheless reaction of $^{99m}\text{Tc(V)}$ -gluconate with MAG_2 gave $[\text{TcO}(\text{MAG}_2)]$. The terminal carboxylato group is now engaged in coordination yielding an N_2SO ligand donor set with an overall square pyramidal geometry (Johannsen et al. 1993). In the presence of excess ligand, additional uncharacterized anionic species were found. It is assumed that these represent 2:1 and probably 4:1 complexes as a consequence of the dominance of the thiol groups over other donors in coordination to the Tc(V) center. In general, it has, however, been found that peptide-based ligands different from the MAG_3 set sometimes suffer of lacking stability (apart the stereochemical problems). Hence, glycine-based peptide sequences still remain the most widely used chelators. The free terminal carboxylate group provides a coupling site for the N-terminus of a receptor binding peptide.

■ Fig. 43.8

Sequences of amino acids that are terminal or integrated parts of a longer sequence



In principle, such chelators cannot only be tagged to a targeting vector but can even be an integrated part of it. A clear drawback of the introduction of MAG₃ as a chelator was the possibility of ^{99m}Tc complex formation by peptide sequences (Brandau et al. 1988; Fritzberg et al. 1986; Fritzberg et al. 1982; Verbeke et al. 1995; Visser et al. 1993).

It is appropriate to introduce here a peptide-based ligand, which has a unique chemical behavior and the perspectives of which has so far not been used to an even nearly sufficient extent. It was recently found that a linear peptide based on four coupled alanines (L-ala)₄ formed, as expected, a tetradentate chelate, wrapping around the [Tc=O]³⁺ core. After coordination, a metal-templated ring closure in (L-ala)₄ took place through amide formation between the terminal amino and carboxylate group and the complex [TcO(cyc-ala₄)][−] formed (Bormans et al. 1996). The ring closure reduces the number of potential coordinating atoms from five to four and provides additional macrocyclic stabilization. The alanine methyl groups are *syn* in relation to the oxo-core. This type of reaction is relatively rare but does indicate a potential for analogous complexes and for the formation of cyclic peptides. It is in particular remarkable that attempts to get complexes directly with cyclic tetrapeptides were unsuccessful. Attempts to increase the denticity of N,S-based ligands as in the (L-ala)₄ ligand often results in intermolecular reactions. Several approaches in respect of peptides have shown that this might be a promising way of labeling bioactive peptides (Wong et al. 2001).

Various alternatives to tetradentate N_xS_{4−x} ligands exist. In terms of flexibility, the so-called mixed ligand [3+1] approach is convenient. The approach is based on the [Tc=O]³⁺ moiety and applies a tridentate and a monodentate ligand. In general, [3+1]-mixed ligand complexes of the type [TcO(SXY)(SR)] (X=O,N,S and Y=N or S) are prepared by the reaction of a potentially dianionic tridentate ligand H₂L and a monodentate monoanionic thiolate coligand with a suitable oxo-technetium precursor (Pietzsch et al. 1989) (Pietzsch et al. 1990; Spies et al. 1990; Spies et al. 1995). The targeting molecule can be attached to the monodentate ligand, which is in general an −SH group or to the middle donor in the tridentate ligand, which is then a tertiary amine. Various combinations of the tridentate ligand have been studied but it seems that the combination of HS−N−SH is the most promising one. This mixed ligand approach has found interest in particular for the labeling of CNS receptor binding molecules. In this case the receptor binding part is in general derivatized with an additional monodentate thiol group. A review on CNS receptor ligands in the context of the [3+1] approach has recently been published (Johannsen and Pietzsch 2002). Actually, the interest in the [3+1] approach is decreasing for biomolecules different from CNS receptor ligands since it was shown that some of the complexes are of limited serum stability (Seifert et al. 1999; Seifert et al. 2000; Syhre et al. 1998). The stability strongly depends on the tridentate ligand and there in particular on the substituent attached to the middle nitrogen donor. Improvements of this situation are currently studied. The [3+1] approach was applied to many biomolecules and model complexes. One of the major problems related to mixed ligand approaches is the feasibility of the synthesis of the final complex. With CNS receptor ligands, the product still needs to be extracted into an organic solvent (often chloroform) to separate it from byproducts. For practical reasons this approach is less convenient for other biomolecules such as peptides or antibodies. Recently, an *n.c.a.* preparation has been introduced which is based on a convenient HPLC separation at the end of the preparation (Seifert et al. 1997).

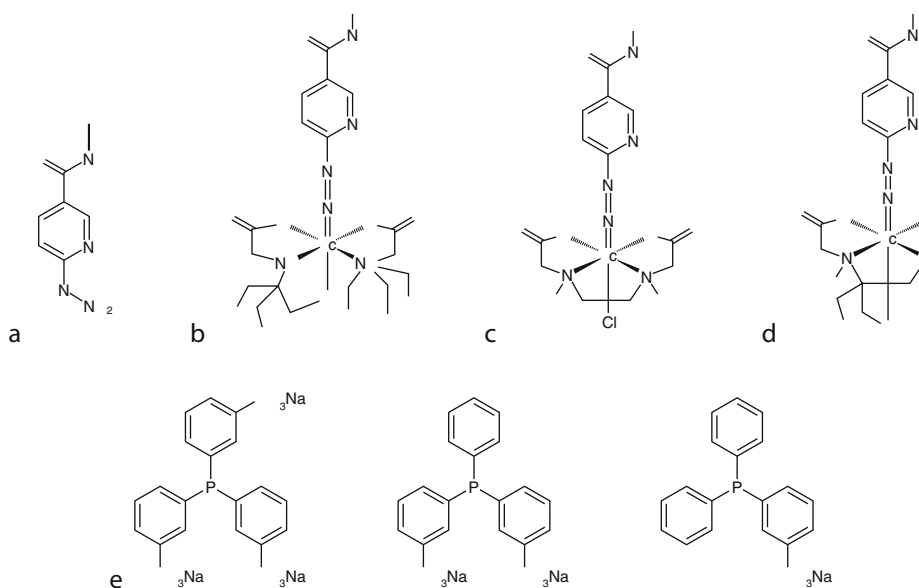
A different approach that is subject of intense developments is the HYNIC approach. Originally, this method was applied for the labeling of polyclonal IgG with ^{99m}Tc for imaging focal sites of infections (Abrams et al. 1990; Larsen et al. 1995; Schwartz et al. 1991). The HYNIC technology has recently been reviewed extensively in the context of small peptide

labeling (Liu and Edwards 1999). Although HYNIC (2-hydrazino-nicotinic acid) is widely used in the labeling of peptides and antibodies, its chemistry is not well understood. The HYNIC is linked through the carboxylic acid to an amine group in the targeting vector. The coordination chemistry of the hydrazine group has been investigated with HYNIC but also with surrogates, however, despite the elucidation of at least three X-ray structures, still does not allow a distinct formulation of the coordination with ^{99m}Tc (Hirsch-Kuchma et al. 1997; Hirsch-Kuchma et al. 1997; Nicholson et al. 1996a, b; Rose et al. 1998). It is believed that the bond to the hydrazine in HYNIC is in fact a Tc==N double bond, as depicted in Fig. 43.9, the so-called diazenido form of a coordinated hydrazine. This formulation is rationalized on the basis of a need for auxiliary ligands to stabilize the overall complex with additional multidentate chelators. The labeling studies with HYNIC chelates are therefore performed in conjunction with additional ligands such as tricine or EDDA. It is believed that the pendant complex can be formulated as [Tc(HYNIC)(EDDA)] or [Tc(HYNIC)(tricine)₂]. The application of these binary systems were associated with disadvantages such as formation of side products, complex instability, and binding to plasma proteins by coligand exchange (Liu et al. 1996; Ono et al. 2001). It was elegantly shown that one additional monodentate ligand would improve these stability disadvantages. Such ternary systems were investigated with phosphines and aromatic amines (Liu et al. 1998a, b). It is likely that the composition of the complexes in the ternary system is [Tc(HYNIC)(tricine)L], where L represents the aromatic amine or the phosphine.

A more recent approach employs the coupling of tridentate or bidentate BFC to target vectors for the application of the [^{99m}Tc(CO)₃]⁺ moiety in the second-generation radiopharmaceuticals. The complex [^{99m}Tc(OH₂)₃(CO)₃]⁺ can conveniently be synthesized from a kit formulation (Isolink[®], Mallinckrodt) in which the three water ligands are replaced by

Fig. 43.9

HYNIC technology (a) hydrazine–nicotinic acid, (b) [Tc(HYNIC)(tricine)₂], (c) [Tc(HYNIC)(edda)], (d) [Tc(HYNIC)(tricine)L], where L is a monodentate ligand such as (e)



incoming ligands. Complexes of high kinetic stability are formed (Alberto et al. 2001; Alberto et al. 1994; Alberto et al. 1996). It is remarkable that essentially all kinds of donors can be used since the stability of complexation is purely kinetic (Schibli et al. 1999; Schibli et al. 2000). Mono-, bis-, and tridentate ligands are cleaved only under highly acidic conditions and at high temperature. The advantage of this method is the fact that the pendant metal complexes are well defined and their structures are known. The $[\text{}^{99m}\text{Tc}(\text{CO})_3]^+$ moiety shows in particular a high affinity for aromatic amines such as imidazoles or pyridine. Several complexes have been prepared on that base and the concept has proven useful for the direct labeling of his-tagged recombinant single chain variable Fragments (scFv) (Waibel et al. 1999). More recently, the introduction of bifunctional histidine derivatized at N^{ϵ} was published. Histidine is a highly efficient ligand and enables the labeling of a model peptide at very low concentrations (Egli et al. 1999; La Bella et al. 2002; Schibli et al. 2002; Wust et al. 1998). Different neurotensin analogues have been labeled with the same approach and biologically tested (Garcia-Garayoa et al. 2002; Garcia-Garayoa et al. 2001). The approach of preparing second-generation radio-pharmaceuticals based on the $[\text{}^{99m}\text{Tc}(\text{CO})_3]^+$ moiety is relatively recent and under extensive investigation. Procedures and some structures are depicted in [Fig. 43.10](#).

Half sandwich complexes of the type $[(\text{Cp})\text{M}(\text{CO})_3]$ (Cp =cyclopentadienyl, $[\text{C}_5\text{H}_5]^-$) are very useful complexes since they are small and highly lipophilic and therefore of high interest in the context of labeling, i.e., estradiol (Jaouen et al. 2000; Jaouen et al. 2001; Top et al. 1995). To bifunctionalize cyclopentadienyl is not routine, and Cp has in general not been introduced as a classical BFC but coupled in the course of a normal organic synthesis. Jaouen and coworkers showed that half sandwich complexes attached to a biomolecule affected its receptor affinity the least, whereas the introduction of N_xS_{4-x} chelator significantly reduced the binding constant. The preparation of $[(\text{R-Cp})^{99m}\text{Tc}(\text{CO})_3]$ found much attention in particular for attempted labeling of CNS receptor ligands. Wenzel originally proved the principle but the double ligand transfer reaction is far from being useful for routine (Wenzel 1992; Wenzel and Klinge 1994). Some improvements were realized and the cyclopentadienyl ligand was even attached to peptides (Minutolo and Katzenellenbogen 1998; Minutolo and Katzenellenbogen 1999). Only recently it could be demonstrated that the introduction of an acetyl functionality at the cyclopentadienyl ring does stabilize the water- and air-sensitive cyclopentadienyl significantly. A potential vector could be coupled to this BFC. The C-acidity increased by several

Fig. 43.10

Preparation of $[\text{}^{99m}\text{Tc}(\text{OH})_2(\text{CO})_3]^+$ and reaction with histidine and ethylenetriamine, respectively

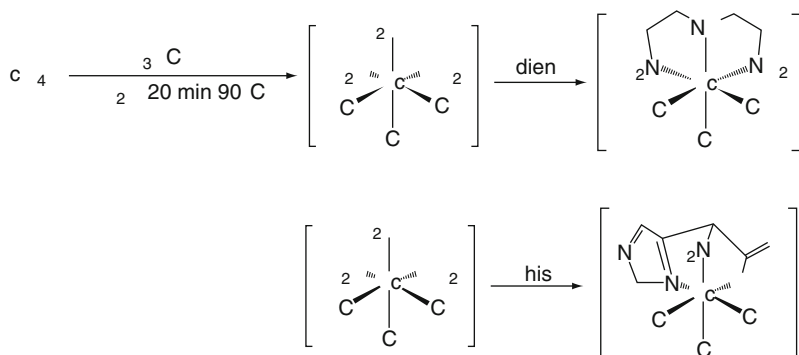
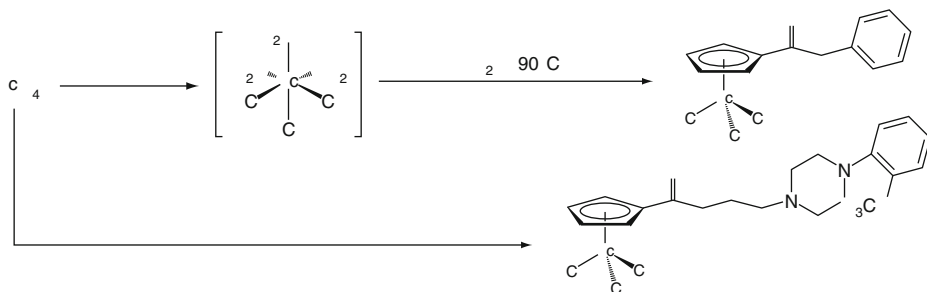


Fig. 43.11

Preparation of cyclopentadienyl Tc(I) complexes directly from water



orders of magnitude, which now enabled the synthesis of $[(R-Cp)^{99m}Tc(CO)_3]$ in one single step directly from water (Wald et al. 2001). The synthetic procedures are depicted in Fig. 43.11.

A relatively recent approach with promise for the labeling of targeting molecules is based on the nitrido core $[Tc \equiv N]^{2+}$. In the well-established complexes $[TcN(PS)_2]$ (where PS is, i.e., $R_2PCH_2CH_2SH$ (R =phenyl, methoxypropyl)), the changing of the connectivity in $[TcN(PS)_2]$ to $[TcN(P_2)(S_2)]$ was expected to give asymmetric complexes with comparable stabilities. The S_2 or SO could then act as bidentate BFC's. The reaction of $[Ph_2P(CH_2)_2O]$ (pop) with a nitrido precursor gave $[TcNCl_2(pop)]$ in which the two P donors are both *cis* and *trans*. The further substitution chemistry, which would allow the coordination of a BFC was investigated with bidentate OSH_2 ligands such as 2-mercaptoethanol or mercaptoacetic acid. The *cis* isomers reacted readily with these ligands forming complexes of general composition $[TcN(PXP)(OS)]$ ($X=O,N$) (Bolzati et al. 2000a). Hence, conveniently available precursors of the type $[^{99m}TcNCl_2(PXP)]$ can be used to label biomolecules by the replacement of the chlorides with an appropriate bifunctional ligand (Boschi et al. 2001).

In conclusion, there are two strategies available for this purpose, the so-called postlabeling and the prelabeling methods. The bifunctional chelator can be coupled to the biomolecule before the labeling reaction. The derivatized biomolecule is then purified and lyophilized prior to labeling. Coupling might occur through amide formation between an activated carboxylic acid pendant of the BFC and the ϵ - NH_2 group of lysin or by the introduction of additional $-SH$ groups in the biomolecule (i.e., by the reaction with iminothiolane) and subsequent reaction with maleinimide derivatized BFC. The labeling reaction is performed by transmetalation from, e.g., a reconstituted Tc-glucoseheptonate kit or directly by reduction and concomitant complexation/labeling. Depending on the biomolecule, high labeling yields can be achieved in which the radiopharmaceutical does not require further purification. However, a drawback might be minor amounts of unspecific labeling, in particular for antibodies that contain other potentially chelating groups. In any case, the postlabeling approach is the most convenient one in particular when considering future routine application (Verbruggen 1990).

The second method of indirect labeling through a BFC consists in the prelabeling strategy. This method includes the preparation of a ^{99m}Tc complex in a first step that enables the preparation at very different conditions which would sometimes not be compatible with the biomolecule. Subsequently, the second function which is not involved in coordination can be activated by a common method in water and reacted with the vector to afford the final targeting

radiopharmaceutical. Clearly, the advantage of this approach is the preparation of the complex at high purity and yield; however, the coupling process to the biomolecule is limiting since covalent coupling is very often not going to completion since hydrolysis of the activated function represents the major competing reaction. Therefore, prelabeling requires in most of the cases purification after the actual labeling, and is not the method of choice for routine application unless it is possible to achieve close to 100% labeling yield.

43.5.2 Direct Labeling Approach

The direct labeling approach is defined as the labeling of a biomolecule by ligand atoms, which are already an integral part of the structure of the biomolecule. For a direct labeling, no additional atoms (donors) are required. It is therefore in principle possible to use functional side chains bearing donor atoms directly as ligands for coordination to the ^{99m}Tc moiety. Considering the position of Tc in the periodic table it is obvious that thiols, thioether groups, and aliphatic or aromatic amines are preferential binding sites. Sulfur donors provide in general high thermodynamic stability to a variety of oxidation states. Therefore it is difficult to predict a preferred valency. On the other hand, the thermodynamic stability provided by the other groups is in general weak, and it is not sufficient to stabilize a metal center under biological conditions, as undesired transmetalation will be the consequence. A direct labeling must be based on kinetics and is suitable for lower valencies. Two feasible approaches for direct labeling have been described – one of them even applied in clinical studies with a number of peptides, antibodies, and antibody fragments. The first successful method, the so-called pretinning method, was introduced in the late 1980s and commercially applied in, e.g., an *anti-melanoma* antibody. Antibodies contain a considerable number of disulfide groups, which stabilize their tertiary structure. These disulfide groups in intact antibodies, F(ab')₂ and in F(ab') fragments, can carefully be incubated with Sn²⁺, which results in the reduction of the disulfides to two thiol groups. Depending on time and Sn²⁺ concentration, the fragments are even created by themselves through such a process. These reactive antibody species are then incubated with [^{99m}TcO₄][−]. Excess Sn²⁺ and/or the thiol groups do reduce Tc(VII) to an unknown oxidation state and bind the Tc very tightly. Since the labeling yield is in general not quantitative, purification is required. The pre-tinning method, if carefully performed, allows a good and stable labeling of antibodies under retention of the bioactivity. Many studies have been performed applying this method. Some variations have been developed for a similar labeling methodology.

The reducing agent Sn²⁺ represents a problem since it tends to form colloids and to stick itself on functionalities of the antibody. Therefore, the well-known mild reducing agent dithiothreitol (DTT) has been employed as well for the same purpose. DTT can be used to reduce an intact antibody to the Fab' state, which is then reacted with, e.g., a reconstituted Tc-glucoheptonate kit. Transmetalation results in high radiochemical yield after a short period of time. The high reactivity and the fast reaction rationalize the assumption that in all of these preparations the oxidation state of Tc is +V. From model complexes, it is well known that thiols stabilize this valency very well (see previous section). Another even milder technique uses 2-mercaptoethanol as a reducing agent. This reagent generates under well-controlled conditions thiol groups. Different kits like Tc-MDP or Tc-glucoheptonate are then reacted with the reduced antibody to give within a short period of time quantitatively labeled antibody that does not require additional purification.

Many antibodies have been labeled in one or the other way and kits for patient studies are commercially available. The method is difficult to apply for smaller molecules. Despite the fact that some important (cyclic) peptides have at least one disulfide bridge in their structure, the coordination affects the structure of this small molecules resulting frequently in the loss of bioactivity. The indirect labeling method is essentially limited to antibodies.

A more recent but yet less-well-developed approach for the direct labeling of antibodies employs the $[\text{Tc}(\text{CO})_3]^+$ moiety. This moiety has a high preference to bind to aromatic amines by substituting one or more water ligands from its coordination sphere. This is in particular true for imidazole. Once an amine is bound to the technetium center, it is only cleaved very slowly if ever. Recombinant scFv have a histidine tag, comprising a peptide sequence made out of histidins only. This tag is used for affinity column purification, but has no biological relevance. It could be shown that this tag is excellent for the direct labeling with $[\text{Tc}(\text{OH})_2(\text{CO})_3]^+$ (Waibel et al. 1999). No additional ligands were required. Although the exact coordination sphere at the metal center remains unknown, the method is convenient for the labeling of such proteins. This is in particular important since no alternatives are available due to the lack of disulfide bridges to be cleaved according to the pre-tinning method.

43.5.3 Integrated Approach

The third approach to incorporate ^{99m}Tc in a receptor targeting molecule is the so-called integrated approach. This is by far the most demanding approach since it does not use a bioactive molecule as vector but attempts to mimic physicochemically and topologically the properties of a lead structure, thereby using the Tc center itself as an important part of the overall structure. The design of such a de novo biomolecule comprises the metal center that coordinates different chelators giving a structure that roughly surrogates the “parent” molecule or the origin. Resulting lipophilicity and dipole moments are important properties of such a new construction. The few examples have already been depicted in [Fig. 43.6](#).

Of particular interest are steroid hormones since they contain five- and six-membered rings that can be considered as chelate rings. These purely structural analogy prompted investigations for the synthesis of Tc(V) complexes, which once coordinated to the appropriate ligands resemble an androgen or progesterone receptor binding steroid (Hom and Katzenellenbogen 1997a; Hom et al. 1996; Katzenellenbogen et al. 1997). Two principle approaches have been described, one using an integrated tetradentate ligand and the other one two asymmetric bidentate ligands of the N,S type. The bidentate ligands are critical for several reasons. The synthesis must carefully be carried out in order to get only one complex out of the three possibilities and, more critically, the in vivo stability of a Tc(V) complex with bidentate ligands only. In one example, the synthetic conditions resulted predominantly in one species of the mixed ligand complex for the examples shown in [Fig. 43.6](#). The complex exhibited only a very weak affinity for the receptor, and the stability was too low to be of practical relevance (Chi and Katzenellenbogen 1993; Chi et al. 1994).

The second complex was designed with a tetradentate chelator based on N2S2 donor set and one of the rare examples of a chelator containing a thioether group. Two diastereomers are possible, and both were found in fact and characterized. The relative binding affinity were again low (Hom and Katzenellenbogen 1997a). Taking the difficulties encountered for the integrated approach into account, it is remarkable that the lead structures in these early examples could be mimicked quite reasonably. The integrated approach is demanding possibly not only due the

design of chelator around an (octahedral) metal center, but also for the design of a novel metal core not containing a dominant group like the $[\text{Tc}=\text{O}]^{3+}$ moiety. It would be of high interest to apply a Tc precursor that is for electronic reasons four-coordinate.

43.6 Developments in the Labeling of Targeting Molecules

The different approaches for the labeling of targeting molecules described in the previous section are routinely applied. Depending on the bioactive molecule, one or the other might be more promising in respect of a particular target. Thus, the following chapter will highlight the developments in the labeling of peptides which experienced an exponential growth. Peptide labeling still relies on one or two approaches only and most of the labeling techniques employ the N_xS_{4-x} approach. It can be more or less easily combined with solid phase chemistry applied in the synthesis of the peptides.

43.6.1 Antibodies/Peptides

Some recent papers reviewed the clinical implications of labeled peptides and antibodies in respect of the targeting molecule and the actually applied radioisotope (Banerjee et al. 2001; Fichna and Janecka 2003; Virgolini et al. 2001; Weiner and Thakur 2002). Peptides are furthermore attractive since they have in general a high affinity for receptors that are overexpressed on malignant mammalian cells. In contrast to antibodies, they penetrate the tumors rather well but are excreted rapidly from the blood stream. On the other hand, susceptibility toward enzymatic degradation is high and requires stabilization by, e.g., the introduction of nonnatural amino acids or the replacement of certain highly sensitive sequences. Stabilization can also be achieved by chemically modifying the original sequence. It is not the issue of this chapter to discuss the implication of particular peptides but rather give an overview for the employed labeling techniques related to the peptides.

The detection of thrombi is a long-standing issue in radiopharmaceutical chemistry. The biochemical events following a rupture in a vessel are well understood. After activation of the clotting process, the glycoprotein IIb/IIIa is exposed to which the fibrinogen will bind. Bridging different platelets will result in aggregation and formation of plugs. This simplified view entails that radioiodinated fibrinogen was the most commonly used radiopharmaceutical. Since this radiopharmaceutical had some inconvenient implications it is not in use anymore. Extensive research efforts have been made, mainly in developing and labeling peptides for clot detection. A successful agent is ^{99m}Tc-apticide (*AcuTect*[®] P280, *Diatide*, Nycomed Amersham), which has recently been FDA-approved. The peptide is a homodimer that contains an RGD (Arg–Gly–Asp) sequence. The labeling uses a glucoheptonate kit for reconstitution, and the labeling takes place at 100°C for 15 min. The glucoheptonate can also be given directly to the peptide solution. The ligand consists of an $\text{N}_x\text{S}_{(4-x)}$ -type located remote in the backbone of the peptide but peptide sequences as chelators have been applied as well (Jackson et al. 1994; Muto et al. 1995; Pearson et al. 1996; Xue and Degrado 1995). To minimize the effect of labeling on the affinity of the peptides, spacers have been introduced between the BFCA and the vector. Newer work with peptidomimetics comprise modified RGD sequences, which are designed to contain in the triple amino acid sequence an N2S2 unit that is able to coordinate directly to ^{99m}Tc (Ali et al. 1994; Lister-Jones et al. 1996; Pearson et al. 1996).

Peptides containing the RGD sequence can also be used in cancer diagnostics due to their ability of interacting with integrins that are responsible parts for platelet adhesion, activation, and leukocyte mobility and for cancer cell dissemination. As a consequence, RGD peptides and RGD mimetics bind to cancer cells and can be used for diagnosis (Sivolapenko et al. 1998).

Neurotensin is another peptide of oncological relevance. Neurotensin analogues are used for the diagnosis of carcinomas such as pancreas, prostate lung, and colon (Reubi et al. 1999; Reubi et al. 1998). Neurotensin has been derivatized with DTPA and more recently with chelators convenient for labeling with the [^{99m}Tc(CO)₃]⁺ moiety. Neurotensin and analogues suffer from fast degradation and various methods have been used for stabilization. Affinity, biodistribution, and labeling conditions for some of these stabilized neurotensin analogues are excellent and preclinical studies currently underway (Garcia-Garayoa et al. 2002). Another peptide in this context is neuropeptide Y (NPY), which is a 36 amino acid peptide from the pancreatic polypeptide family. It is one of the most abundant peptides in the brain (Tatemoto 1982). Its receptors are expressed in a number of neuroblastoma making them optimal targets for tumor scintigraphy. Modified NPY's have been labeled with the [Tc(CO)₃]⁺ approach. The radioconjugates showed high binding affinities that made them good candidates for further studies (Langer et al. 2001).

Bombesin is a further peptide that has been the subject of intensive investigations. Bombesin is a 14 amino acid linear peptide and an analogue of the human gastrin-releasing peptide (GRP). It binds with high affinity and specificity to the corresponding receptors (Mahmoud et al. 1991; Qin et al. 1994; Qin et al. 1995). The synthesis and characterization of radiolabeled BBN have been reported by different groups and various methods of labeling have been applied including all common methods ranging from N_xS_{4-x} to the labeling with the [Tc(CO)₃]⁺ moiety (Baidoo et al. 1998; Breeman et al. 1999a, b; Gali et al. 2001; Hoffman et al. 2001; Karra et al. 1999; La Bella et al. 2002; Moody and Perry 1989; Rogers et al. 1999; Rogers et al. 1997; Van de Wiele et al. 2000). In a recent work, structure–activity relationships of bombesin analogues comprising aliphatic spacers of variable lengths between the chelator and the peptide demonstrated that all compounds with a C3, C5, or C8 tether have high binding affinities and good biodistribution (Smith et al. 2003). As a chelating group, an N3S ligand has been employed, which allowed post-conjugation via the ^{99m}Tc-glucoheptonate intermediate in very good yields. A recent approach used demobesin, a novel linear bombesin analogue that was derivatized at the N-terminus through a spacer with a linear tetramine ligand. Labeling occurs according to a convenient method and gave the relatively rare Tc(V) complex containing the central [O=Tc=O]⁺ moiety (Nock et al. 2003).

Somatostatin is the peptide that has attracted most attention for the labeling of peptides. Receptors for somatostatin are expressed on numerous tumors, which is basic for its application as a radiopharmaceutical. Analogues for somatostatin have been developed and the cyclic octapeptide octreotide is a convenient compound that is reasonably stable toward enzymatic degradation while having similar bioactivity (Anderson et al. 2001; Lamberts 1988). In addition, many derivatives of octreotide have been synthesized. The labeling strategies are essentially based on conjugates with DTPA and DOTA (De Jong et al. 1999; De Jong et al. 1998; Heppeler et al. 2000; Krenning et al. 1993; Otte et al. 1997) and most important with the HYNIC approach discussed earlier in this section (Vallabhajosula et al. 1996).

A further class of peptides is the so-called tat-peptides, which are permeation peptides. It has been observed that tat peptides have rapid translocation properties seemingly independent of receptor-mediated endocytosis. Since membrane translocation is an important feature in drug delivery, tat-peptides are useful also for imaging and probably for therapeutic purposes

(Liu and Edwards 1999; Schwarze et al. 2000). In a recent study, a tat-peptide was tagged and labeled by the $[\text{Tc}(\text{CO})_3]^+$ approach. The conjugate was of excellent stability but accumulated in the liver. It could be shown in the radio assay that cell accumulation is occurring and it was confirmed with a dual labeled tat-peptide that the measured activity in the cell was largely due to peptide translocation into the cell, both in vivo and in vitro, confirming that the function of the peptide was fully retained (Bullok et al. 2002).

Finally, a newer methodology for the labeling of peptides shall be presented. Ligands and complexes are decisive for labeling and for the biological behavior of the tagged vectors. The same ligand but with a different ^{99m}Tc core does normally show very different biological behavior. Parallel studies of equal ligands and biomolecules but with different cores are feasible for chelators designed for the $[\text{Re}(\text{CO})_3]^+$ and the $[\text{Tc}(\text{CO})_3]^+$ core. An alternative strategy would be to keep the ligand constant, while altering the biomolecule. This strategy has been chosen with, e.g., the MAG3 ligand system or the hynic approach with the rationale of high complex stability and convenient labeling. To keep the ligand constant might not be justified when attempting to improve, e.g., biodistribution, but is justified when additional properties are introduced by the ligand or the complex. This is the case with the so-called single amino acid chelate (SAAC) approach. The basic ligands used in this approach are based on bis-methylpyridylamine, a very stable ligand for the $[\text{Tc}(\text{CO})_3]^+$ core. The central aliphatic amine is linked via an alkyl spacer to an α -amino acid group, which can be introduced in peptide chains at any place. Since the formed complexes are very robust, incorporation of the corresponding rhenium complexes can already be done during the automated peptide syntheses on solid phases. This allows for an easy and rapid preparation of libraries of peptides with the SAAC at various positions. Along this line an optimal peptide can be synthesized and selected for ^{99m}Tc labeling studies (Banerjee et al. 2005; Banerjee et al. 2003; Bartholoma et al. 2009).

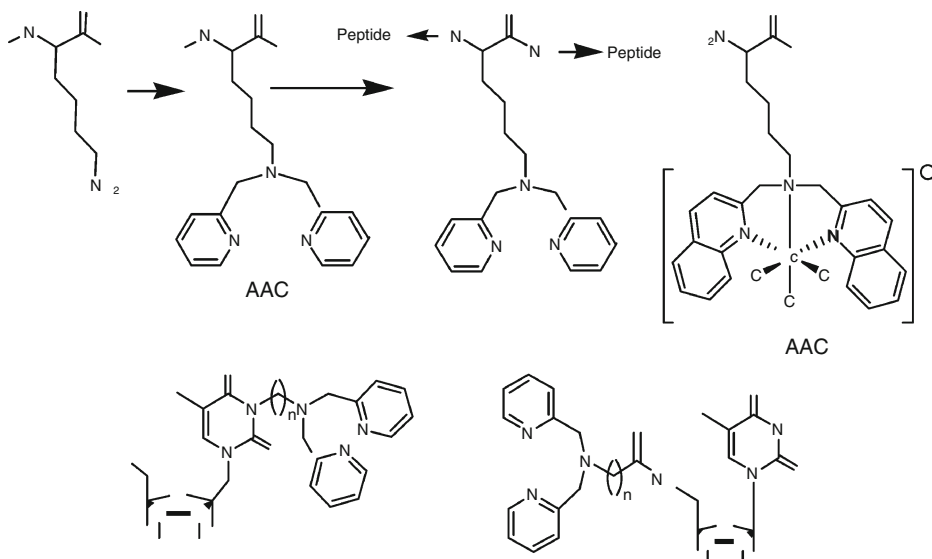
If the pyridine ligands in bis-methylpyridylamine are replaced by quinolines (SAACQ), the important feature of fluorescence is introduced after coordination to the $[\text{Re}(\text{CO})_3]^+$ core. It is not possible to monitor the radioactivity distribution of a radiopharmaceutical on the cellular or subcellular level, but fluorescence microscopy allows for this option. Accordingly, the accumulation of the “cold,” rhenium-bearing pharmaceutical can be visualized via luminescence and, due to the matched pair Re and Tc, one can conclude for the behavior of the ^{99m}Tc analogue. This procedure has successfully been applied for peptides and biotin by the groups of Zubietta and Valliant (James et al. 2006a, b; Stephenson et al. 2004). Equally, isostructural compounds were applied for monitoring neural stem and progenitor cell transplants with fluorescence microscopy and radioactivity (Schaffer et al. 2008). The SAAC approach was used for the labeling of many different biomolecules according to the strategy of keeping the ligand constant, while altering the biomolecule. Besides the aforementioned peptide libraries, there are amyloid plaques (Stephenson et al. 2008), nucleosides (Wei et al. 2005; Wei et al. 2006), carbohydrates, and others (► Fig. 43.12).

43.6.2 Neuroreceptor Targeting Molecules

‘Some excellent reviews about neuroreceptor targeting agents recently appeared covering many important aspects of this field (Banerjee et al. 2001; Johannsen and Pietzsch 2002; Jurisson and Lxdon 1999; Kung et al. 2003). In the context of small receptor binding ^{99m}Tc-labeled biomolecules and pharmacophores, central nervous system (CNS) receptor targeting radiopharmaceuticals are most prominent, a vital need, and under active pursuit. A successful CNS

Fig. 43.12

The general design of SAAC(Q)-type ligands (top) (Bartholoma et al. 2009) and two examples of labeled thymidine with the bis-methylpyridineamine ligand (bottom) (Wei et al. 2005)

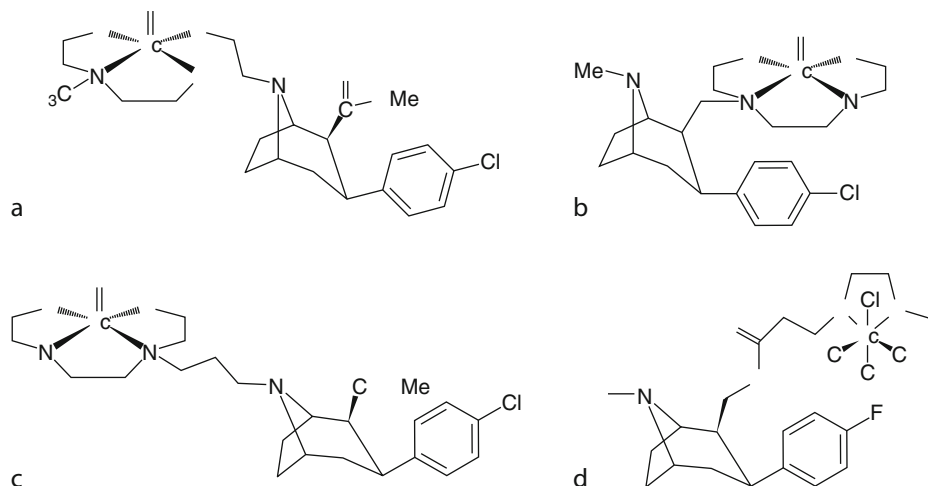


receptor targeting ^{99m}Tc radiopharmaceutical should have a small size ($\text{mw} < 600$), appropriate lipophilicity, and high specificity and selectivity for the particular receptor. Furthermore, for practical application, the labeling process with ^{99m}Tc should take place at low ligand concentration in order to prevent saturation of the receptors. This requirement is sometimes not an issue since the unlabeled vector is often not able to pass the BBB due to the presence of protonated amines and the resulting charge. Despite many efforts only a very limited number achieved the stage of preclinical investigations. Considerable effort is actually directed toward the use of dopamine transporter agents (DAT). They are useful in the evaluation of changes in the presynaptic DAT sites in vivo and in vitro. Several disorders such as Parkinson's disease are characterized by loss of dopamine neurones in basal ganglia or substantial nigra. The successful DAT imaging agents are based on tropane derivatives and some reviews have been dedicated to these compounds (Hom and Katzenellenbogen 1997b; Kung 2001). A relevant number of these derivatives and radiopharmaceuticals are depicted in Fig. 43.13.

The pioneering work in that respect was performed with DAT antagonist β -CIT (2-beta-carboxymethoxy-3-beta(4-iodophenyl)tropane) by Kung and coworkers who developed a potential DAT imaging agent possessing a tropane analogue derivatized with an N2S2 ligand. The ligand is linked through a tertiary amine to the lead structure that gives after labeling a neutral and highly lipophilic Tc(V) complex comprising the $[\text{Tc}=\text{O}]^{3+}$ moiety. This compound is generally referred to as TRODAT-1 (Kung et al. 1997; Meegalla et al. 1996, 1997). A second and similar approach was introduced by Madras who derivatized at the bridging nitrogen in the tropane framework. An aliphatic spacer links to an N2S2 ligand that contains one amido group and leads also to a neutral complex as required for a brain imaging agent (Madras et al. 1996). This compound is called ^{99m}Tc -Technepine.

■ Fig. 43.13

^{99m}Tc -based DAT radiopharmaceuticals: (a) [3+1] approach, (b/c) N2S2 approach (B=TRODAT-1), and (d) $[\text{Tc}(\text{CO})_3]^+$ approach TROTEC-1



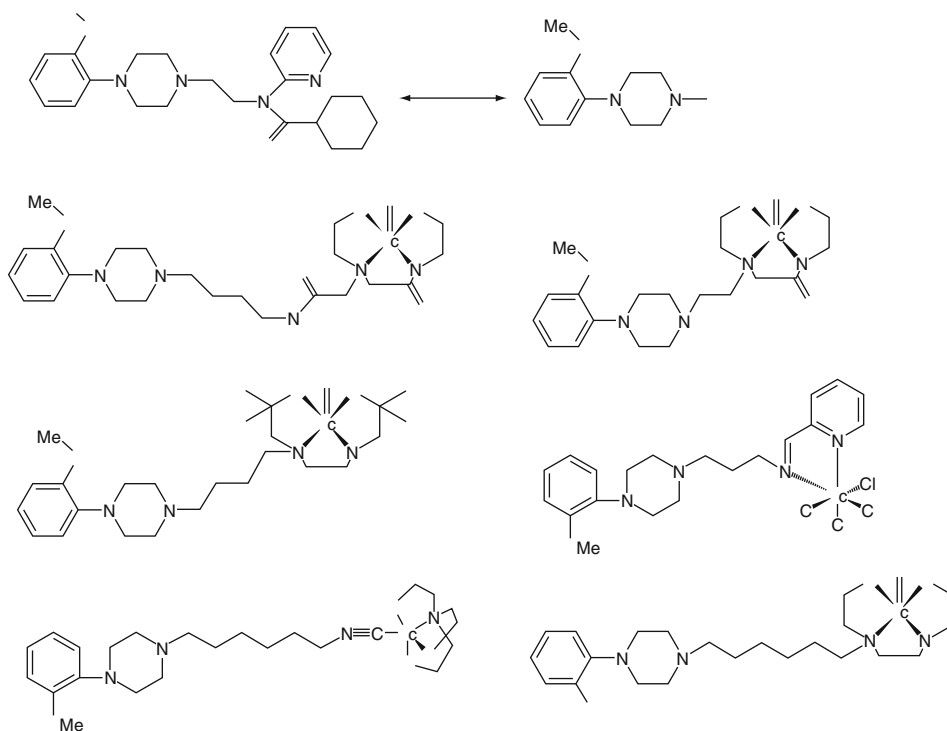
The affinity constant of TRODAT-1 displays a K_i of about 10 nM/L, sufficiently high for excellent binding. (The determination of K_i values for all compounds is in general performed with the corresponding homologues containing cold rhenium instead of radioactive Tc isotopes.) As found with other compounds of the DADT type, two diastereomers exist, both of which are formed at the same time in about equal yields. Interestingly, both show about the same affinity and displayed selective uptake in the striatum, suggesting that the localization is consistent with the DAT distribution (Meegalla et al. 1998). Phase I clinical studies with TRODAT-1 have been performed for practical reasons with the mixture of the diastereomers. This is reasonable based on the available physicochemical and biological data of the compound (Mozley et al. 1998, 1999). Beside the approach described here, there are at least three different other approaches for the labeling of DAT, including the use of NS3 systems, cyclopentadienyl coordination, the [3+1] mixed ligand system, and others (Cesati et al. 1999; Fischmann et al. 1999; Hoepping et al. 1998; Meegalla et al. 1995; Meegalla et al. 1996; Meltzer et al. 2000). The importance of tiny alteration in, e.g., linker length has impressively been shown by introducing an ethyl spacer between tropane and the ligand in contrast the methylene spacer in TRODAT-1. The extension of only one carbon atom resulted in complete lack of brain uptake (Zhuang et al. 1999).

A further brain receptor targeting vector is WAY 100635, which is directed toward 5-HT_{1A} receptor, one of the most thoroughly studied serotonergic receptors. The lead structure has been reduced as shown in Fig. 43.14 and derivatized with various chelators.

The derivatization include MAMA (*monoamino-monoamido*) and DADT (*diamino-dithiol*)-type chelators, dithioethers for the labeling with the $[\text{Tc}(\text{CO})_3]^+$ moiety, the mixed ligand [3+1] approach, and, more recently, monodentate isocyanides for application in the mixed ligand [4+1] approach (Alberto et al. 1999; Baidoo 1995; Drews et al. 2001; Drews et al. 2002; Heimbold et al. 2002; Mahmood et al. 1999; Mallo et al. 1999; Oya et al. 1996; Plössl et al. 1995). Despite the engaged efforts, no valuable candidate is clinically evaluated.

Fig. 43.14

Different structures of ^{99m}Tc labeled-WAY, a serotonergic 5-HT_{1A} ligand



Most of the CNS receptors targeting radiopharmaceuticals mentioned before show high to very high affinity to the receptors, however, brain uptake and specificity remain a problem that represent an incentive for chemists. Penetration and high in vitro affinity is obviously not a guarantee for a successful radiopharmaceutical. The failure of receptor binding in brain of candidates with a comparable brain uptake to TRODAT-1 (~0.4%) might be due to the lack of the pyridine ring in the reduced version of the ligand, which is on the other hand not required for affinity. It has been argued that this structural feature is required for action as antagonist since no agonist has so far resulted in specific in vivo binding to the 5-HT_{1A}.

Beside these two important brain receptors, a number of others such as D₁, D₂, and D₃ as well as 5-HT_{2A} have been the subject of studies with ^{99m}Tc-labeled receptor ligands. Many efforts are not really successful so far and apart from TRODAT-1 only one other compound has entered phase I clinical trials (Callahan et al. 2001). This failure is however not a principle behavior of ^{99m}Tc compounds since the above-mentioned excellent candidates exists. A thorough analysis of the present situation indicates that inconsistent conceptual conditions in the evaluation of the biological behavior and structure–activity relationships between different groups hardly allow guiding the design of new compounds (Johannsen and Pietzsch 2002). Furthermore, the low or absent brain uptake of many high affinity ^{99m}Tc compounds is a main obstacle in the development of novel radiopharmaceuticals, a feature that must challenge the chemists since this is in fact a chemical problem that can probably be overcome

with the introduction of other smaller moieties of high lipophilicity and less influence on the topological features of the receptor-binding part.

The major approaches applied so far for the labeling of CNS receptor ligands are summarized in ► Fig. 43.15.

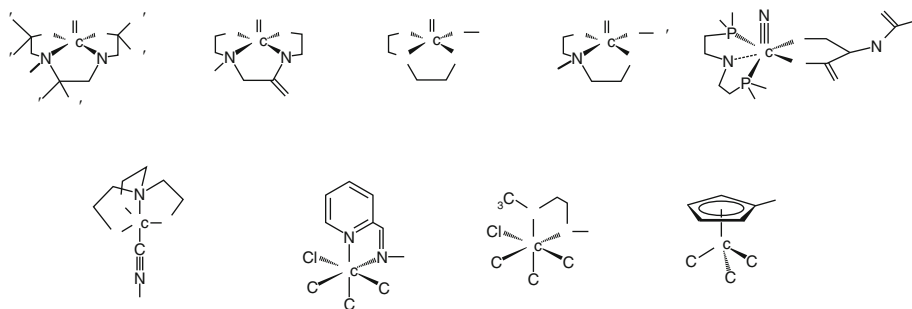
43.6.3 Myocardial Imaging Agents

Beside these established approaches, there has been progress toward novel myocardial imaging agents based on the so-called new cores. The nitrido approach mentioned before has been extended by introducing cyclic crown ethers to the thiocarbamate ligand bound to the $[\text{}^{99m}\text{TcN}(\text{PNP})]^{2+}$ moiety introduced by Duatti et al. (Liu 2007; Liu et al. 2006). The key finding of this study is that crown ether groups are very useful for modifying the biological properties of cationic compounds. In rats, some of these compounds had heart/liver ratios four to five times better than Sestamibi. The crown ether approach was extended with the same ligand also to the $[\text{}^{99m}\text{Tc}(\text{CO})_3]^+$ core. It could again be shown that the corresponding complex had biological properties superior to Sestamibi and was about identical to the complex with the respective complex with the $[\text{}^{99m}\text{TcN}(\text{PNP})]^{2+}$ core (He et al. 2006). A further significant improvement was achieved by Santos et al. who applied tris(pyrazolyl)methane-based ligands with the $[\text{}^{99m}\text{Tc}(\text{CO})_3]^+$ core (Maria et al. 2007, 2009). They received within very short time a stable heart uptake and a liver clearance rate that has not achieved by any of the other ^{99m}Tc complexes for myocardial imaging. These results provide an impetus for pursuing the search for novel radiopharmaceuticals to yield faster and more accurate diagnosis of coronary artery disease in humans (► Fig. 43.16).

To develop novel myocardial imaging agents with improved pharmacokinetics and biodistribution remains a major challenge in radiopharmaceutical chemistry. The previous examples are promising and the chemistry behind inspires future work. As an interesting fact, these examples show in particular that the same ligand can be selected for different metal cores. Thus, improving the biological behavior can not only be done by variations of the ligand (an often tedious procedure), but also by altering the metal core bound to the chelator.

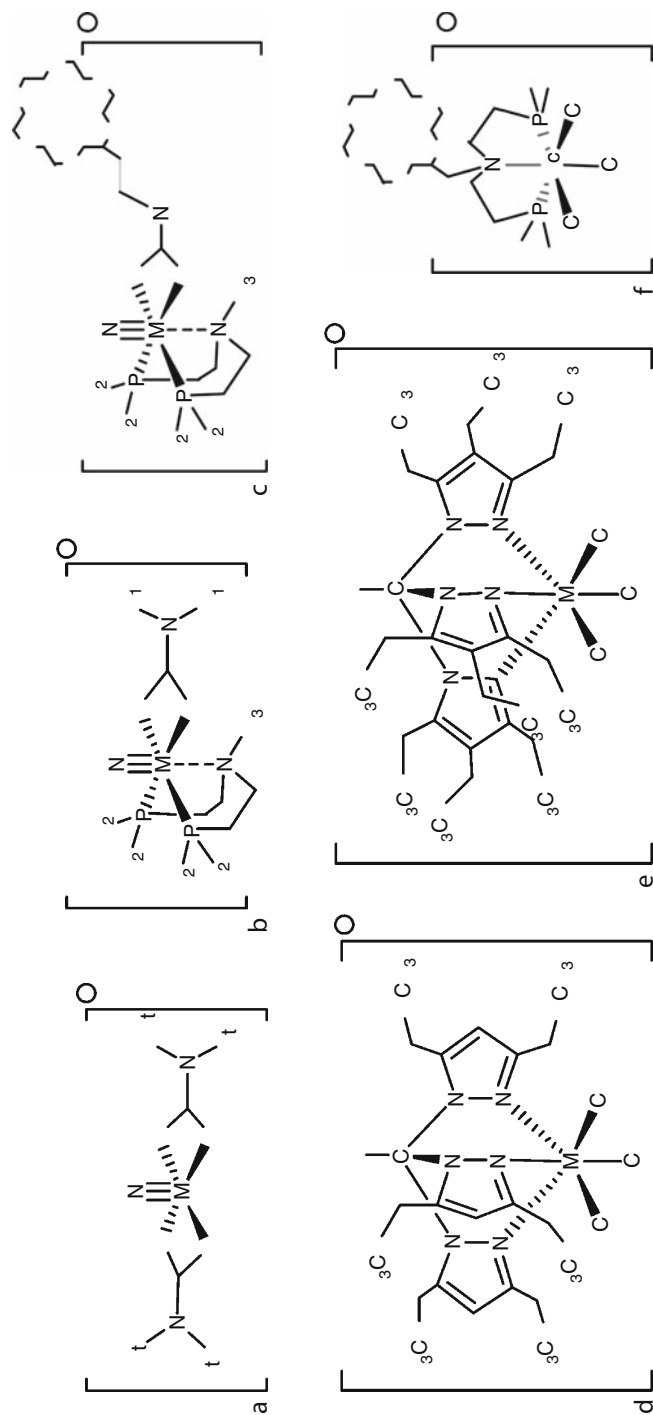
► Fig. 43.15

Major approaches for the labeling of CNS receptor ligands



■ Fig. 43.16

Lead compounds for myocardial imaging based on the $[\text{}^{99m}\text{Tc}\equiv\text{N}]^{2+}$ and the $[\text{}^{99m}\text{Tc}(\text{CO})_3]^+$ core: (a) TcN-NOEt , (b) TcNDBODC5 $\text{R}_1=-(\text{CH}_2)_2\text{O-Et}$, $\text{R}_2=-(\text{CH}_2)_3\text{O-Me}$, $\text{R}_3=-(\text{CH}_2)_2\text{O-Et}$, (Boschi et al. 2003), (c) a nitrido complex with additional crown ethers (Liu 2007), (d) and (e) tris-pyrazolylmethane-based complexes (Maria et al. 2007; Maria et al. 2009) and (f) P2N ligand bearing a crown ether with the $[\text{}^{99m}\text{Tc}(\text{CO})_3]^+$ core (Liu 2007)



43.6.4 Vitamins: Folate, Biotin, and B12

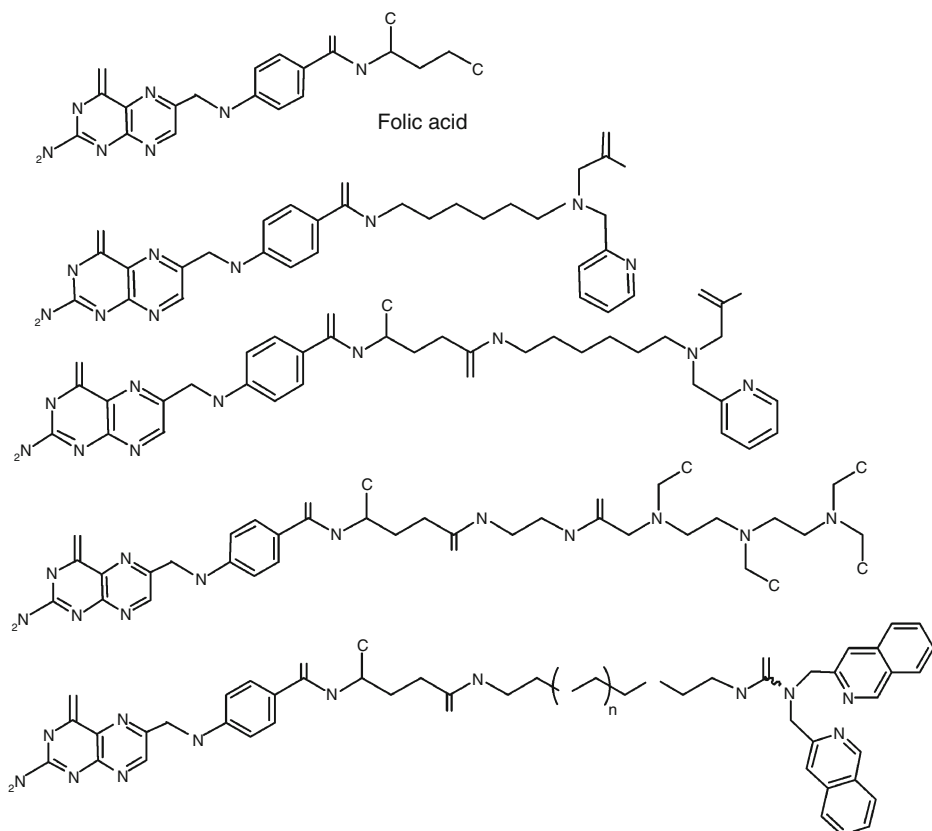
Vitamins are essential lead compounds for the development of novel radiopharmaceuticals. Many vitamin receptors such as the folate receptor are overexpressed on different tumor cell lines (Parker et al. 2005). Biotin labeled with ^{99m}Tc is under investigation since many years in different settings. A vitamin that has not found as much interest as biotin is vitamin B12. Since it is a relatively large molecule, it has been proposed to use B12 as a Trojan horse since rapidly proliferating cells and some bacterial stems show a high demand for this growth essential vitamin. While research toward labeled folate and B12 has intensified over the past couple of years, research with biotin rather slowed down. The biochemical pathways of folate and B12 are interlinked since folate delivers the –CH₃ group to the apoenzyme in order to activate it toward its function in the methionine synthase cycle.

Most attempts to label folate are based on the [^{99m}Tc=O]³⁺ core. BFC were usually DTPA- or MAG3-type chelators. More recently, chemistry with the [^{99m}Tc(CO)₃]⁺ core moved in (Liu et al. 2005; Okarvi and Jammaz 2006). Since DTPA can also be labeled with the [^{99m}Tc(CO)₃]⁺ core, Green et al. used the folate–DTPA conjugate (originally designed for [Tc=O]³⁺) for exploring its in vivo behavior with [^{99m}Tc(CO)₃]⁺ (Trump et al. 2002). Although it is not clear through which donors of DTPA the [^{99m}Tc(CO)₃]⁺ core coordinates, they received one single product in very good yield. The labeled conjugate underwent receptor-mediated uptake in KB cells in vitro. In vivo, the tracer showed accumulation in tissues with high levels of folate receptors but was not superior as compared to other compounds due to accumulation in nontarget tissue. Schibli et al. extended the field by systematically varying folate-bound chelators. At the same time, they administered antifolates together with the ^{99m}Tc-labeled folate. According to this strategy, they stated that parallel application of, e.g., methotrexate suppressed the kidney uptake of ^{99m}Tc-folate in the α-folate receptor positive kidneys. On the other hand, this method left uptake in other α-folate receptor positive neoplastic tissue unaltered opening new perspectives for the diagnosis and treatment of cancer patients (Muller et al. 2007; 2006a, b). Zubieta et al. finally applied folate derivatized with a bis-quinoline amine ligand via a PEG spacer. In vitro imaging and cytotoxic properties of these compounds were tested in detail. The conjugates were internalized by receptor-mediated endocytosis and exerted a substantial cytotoxic action. This behavior implied a concerted therapeutic action of the cold compounds and the ^{99m}Tc-labeled compounds for diagnosis (Viola-Villegas et al. 2008). Derivatives of folic acid are displayed in ► Fig. 43.17.

In the context of biotin, a chemically interesting approach was the combination of this vitamin with a luminescent complex based on a polypyridine ligand sphere bound to the [Re(CO)₃]⁺ core. Such complexes are also feasible for ^{99m}Tc, which would again enable the important combination of light and radioactivity (Lo and Hui 2005). It was found that the K_d value decreased by 4–6 log units upon conjugation of the complex and that the affinity was strongly spacer-dependent. The longer the spacer, the higher is the affinity, an observation which has been made several times in other studies with radiolabeled biotin and which is rationalized by the bulkiness of the complexes (► Figs. 43.17 and ► 43.18).

Studies toward ^{99m}Tc-labeled B12 have been reinforced over the past few years. B12 offers several sites to which a ligand and a complex may be bound. These sites are the propionato groups at the central corrin ring or the 2'-OH group in the ribose of the back loop. Both sites have extensively been derivatized with functionalities mainly for binding to ^{99m}Tc(V) or ¹¹¹In³⁺ (Collins and Hogenkamp 1997; Collins et al. 1999). Kidney and liver are critical and in vivo studies showed often high accumulation in these organs. More recently, B12 was also labeled

Fig. 43.17

Different folic acid derivatives used for labeling with ^{99m}Tc 

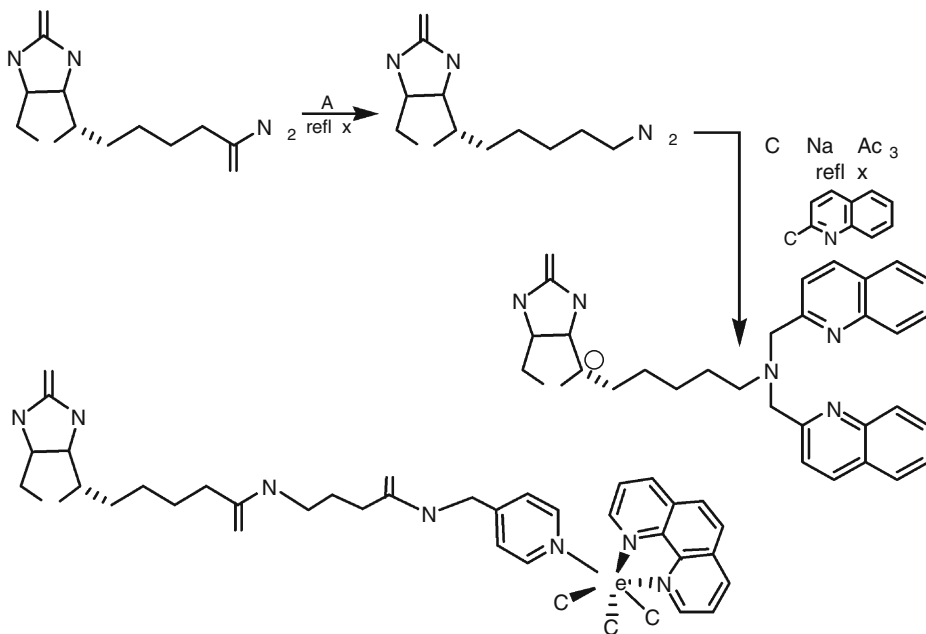
with the $[\text{}^{99m}\text{Tc}(\text{CO})_3]^+$ core using different ligands such as PAMA or histidine and bound to the b- or d-propionato groups via amide formation (► Fig. 43.19) (Alberto et al. 2004; Spingler et al. 2007; van Staveren et al. 2004a, b).

Some of these conjugates did not bind anymore to transcobalamin II (TCII), the transport protein for B12. Waibel et al. showed that TCII non-binders were still taken up in vivo by various cancer cell lines but showed only little retention in the kidneys. This approach resulted in excellent imaging opportunities in mice. Although it is not yet fully understood how these B12 derivatives are taken up by cancer cells, the results are very promising justifying studies in patients (Waibel et al. 2008).

In an uncommon approach, Mundwiler et al. introduced a different way of labeling vitamin B12 by coordinating various $[\text{}^{99m}\text{Tc}(\text{CO})_3]^+$ -core-based compounds directly to the cyanide in B12. According to this methodology, B12 acts as a simple (although structurally rather complex) ligand for the $[\text{}^{99m}\text{Tc}(\text{CO})_3]^+$ core. Despite the relative sterical bulk of these conjugates, these B12 derivatives did still bind to TCII. This is in agreement with the observation that many β -axial derivatives of B12 are tolerated by TCII (Kunze et al. 2004). Since some cancer cell lines and bacteria are high vitamin B12 consumers, B12 certainly merits more consideration as a radiopharmaceutical. Chemistry and biology of B12 are relatively complex.

■ Fig. 43.18

Synthetic strategy toward a biotin derivative with fluorescence properties after coordination of a tridentate ligand to the $[\text{Re}(\text{CO})_3]^+$ core (James et al. 2006a) and a [2+1] mixed ligand system (Lo and Hui 2005)



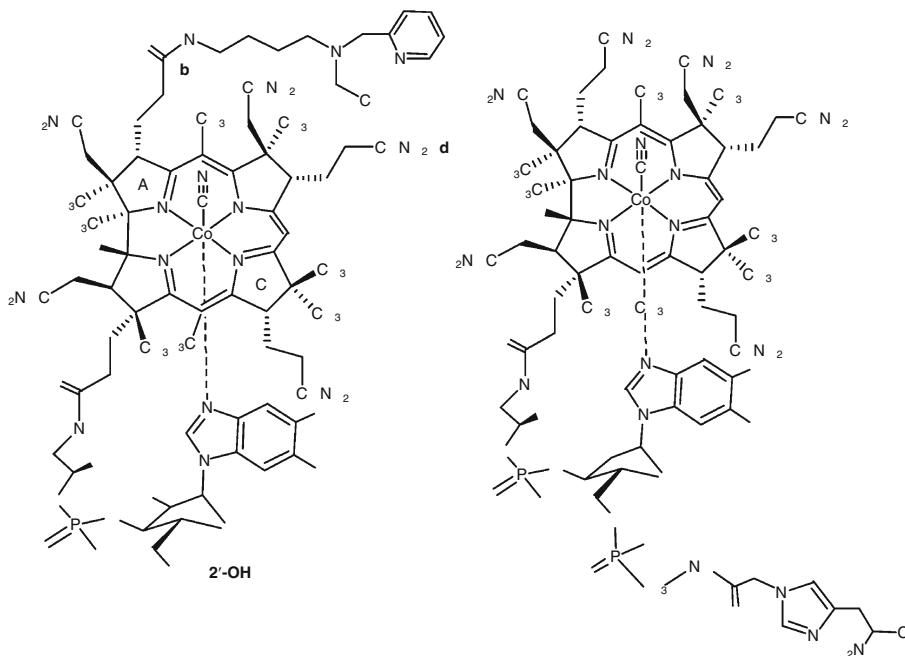
Still, the biological importance of B12 as a proliferation tracer merits endeavors to step into this field, which is justified by the unique authenticity of B12.

43.6.5 Multidrug Resistance

Tumors that are initially sensitive to cytotoxic agents often become refractory to multiple chemotherapeutic drugs. Cells grown in the presence of a specific cytotoxic drug can develop cross-resistance to this and other drugs in the same class and to other classes of drugs entirely. This phenomenon is related to the overexpression of the multidrug resistance (MDR1) transmembrane P-glycoprotein (Pgp). It is an objective of pharmaceutical research to develop molecules called modulators that are able to block the action of Pgp in order to re-establish chemotherapy. A noninvasive method to detect MDR in tumors would be an important diagnostic assay for management and prognostic stratification of cancer patients and a number of ^{99m}Tc coordination compounds have been tested for their ability to indicate the Pgp level in tumor cells. These are cationic and/or highly lipophilic complexes such as ^{99m}Tc -sestamibi (Wackers et al. 1989), ^{99m}Tc -tetrafosmin (Higley et al. 1993), and ^{99m}Tc -furifosmin (Q-compounds) (Crankshaw et al. 1998; Rossetti et al. 1994). The structures of these compounds have been discussed under the section on myocardial imaging agents, since they fall in this class of radiopharmaceuticals. These compounds have been tested as transport substrates

Fig. 43.19

Vitamin B12 derivatives with the chelators at two different sites: bound to the b-acid position (left) and to the 2'-OH group of the ribose in the back loop (right) (Collins and Hogenkamp 1997; Collins et al. 1999)



for Pgp for a variety of multidrug resistant cells in humans (Piwnicaworms et al. 1993). It was shown that the net cellular accumulation is inversely proportional to the amount of Pgp expressed and was significantly enhanced after the administration of modulators.

43.7 Recent Developments and Future Role of ^{99m}Tc -Radiopharmaceuticals

Fundamental technetium chemistry plays an essential role in the development of future radiopharmaceuticals. Although a number of reliable techniques for high-yield and high-stability labeling of targeting biomolecules exist, the possibility of variations is still limited. The metal complex plays an important role in the biological behavior of a radiopharmaceutical and is decisive for success or failure. This implies that more efforts have to be undertaken in the field of basic technetium chemistry, which is actually essentially limited to application in order to develop novel moieties and compounds that allow a convenient and reliable labeling of biomolecules while considering the other limitations given by future clinical application. These aspects have recently lead to the development of two different approaches based on the $[\text{TcN}]^{3+}$ moiety and the $[\text{Tc}(\text{CO})_3]^+$ core. Both concepts have one feature in common, which is probably essential for having extended possibilities in the selection of chelators and therefore in the properties of

the radiopharmaceutical. They represent a water-stable precursor that has two and three coordination sites left that can be substituted by a variety of incoming ligands. New radiopharmaceuticals are therefore not any longer restricted to more or less fixed ligands but allow a choice according to biological considerations. This is an important development that should inspire similar concepts but probably with other novel and even more convenient cores.

A concept which has not been explicitly described in here is the integration of technetium in the topology of the binding part of a biomolecule. Only a very limited number of such attempts have been described so far and are currently not under intense investigations. It is challenging to mimic a structure of a compound comprising main group element only with in general tetrahedral coordination by a transition metal element with octahedral or square pyramidal structure. Thus, it is compulsory to either find *de novo* receptor ligands based on technetium complexes or to introduce a tetrahedral technetium in an existing framework, both highly difficult objectives to be faced by the coordination chemist.

These novel cores mentioned above have already been subjected to the labeling of biomolecules. These approaches represent the only recent developments in ^{99m}Tc labeling chemistry. Since only a limited amount of biological data is available so far, it cannot be yet compared to the existing procedures. Clearly, the labeling chemistry is of comparable convenience and yield or characterization of the compounds much easier than in, e.g., the HYNIC approach. Again, only the development of new cores will also allow the introduction of new labeling techniques more convenient than the existing ones.

Despite the fact that methods such as MRI, ultrasound, and others become more and more competitive in fields previously reserved to radiopharmaceuticals, ^{99m}Tc will continue to play an important role in nuclear medicine because of the possibility of true functional diagnostics on the molecular level. PET also can substitute SPECT (and therefore ^{99m}Tc) in certain aspects, and the more and more cyclotrons built in hospitals underline this tendency. However, the price argument and availability are becoming more and more important factors in diagnostic medicine considering the costs of public health care. Last but not least radiotherapy is a strong factor of nuclear medicine. Probably ^{99m}Tc can act as a surrogate of processes and compounds produced in future with ¹⁸⁸Re, or ¹⁸⁶Re become active as a therapeutic radionuclide as such, again a role that cannot be taken over by the other methods. To keep ^{99m}Tc-based radiopharmaceuticals competitive it is clearly required that more techniques and labeled targeting molecules become available in near future; the first aspect concerns the innovation of the chemist and the second one the biologist and the physician.

References

- Abrams MJ, Brenner D, Davison A, Jones AG (1983) *Inorg Chim A-Lett* 77:L127
- Abrams MJ, Juweid M, Tenkate CI, Schwartz DA, Hauser MM, Gaul FE, Fuccello AJ, Rubin RH, Strauss HW, Fischman AJ (1990) *J Nucl Med* 31:2022
- Alberto R, Ortner K, Wheatley N, Schibli R, Schubiger AP (2001) *J Am Chem Soc* 123:3135
- Alberto R, Pak JK, van Staveren D, Mundwiler S, Benny P (2004) *Biopolymers* 76:324
- Alberto R, Schibli R, Egli A, Abram U, Herrmann WA, Schubiger PA (1994) Low CO pressure synthesis of (NEt₄)(MXX₃(CO)₃) (M=Tc,Re) and its substitution behaviour in water and organic solvents. In: Nicolini M, Mazzi U (eds) *Technetium in chemistry and nuclear medicine*, vol 4. Cortina International, Milano
- Alberto R, Schibli R, Schubiger AP, Abram U, Pietzsch HJ, Johannsen B (1999) *J Am Chem Soc* 121:6076
- Alberto R, Schibli R, Abram U, Hubener R, Berke H, Kaden TA, Schubiger PA (1996) *J Chem Soc Chem Comm* 1291
- Ali FE, Bennett DB, Calvo RR, Elliott JD, Hwang SM, Ku TW, Lago MA, Nichols AJ, Romoff TT, Shah DH, Vasko JA, Wong AS, Yellin TO, Yuan CK, Samanen JM (1994) *J Med Chem* 37:769

- Anderson CJ, Dehdashti F, Cutler PD, Schwarz SW, Laforest R, Bass LA, Lewis JS, McCarthy DW (2001) *J Nucl Med* 42:213
- Baidoo KE (1995) *J Nucl Med* 42:S150
- Baidoo KE, Lin KS, Zhan YG, Finley P, Scheffel U, Wagner HN (1998) *Bioconjug Chem* 9:218
- Bandoli G, Mazzi U, Roncari E (1982) *Coordin Chem Rev* 44:191
- Banerjee S, Pillai MRA, Ramamoorthy N (2001) *Semin Nucl Med* 31:260
- Banerjee SR, Maresca KP, Francesconi L, Valliant J, Babich JW, Zubieta J (2005) *Nucl Med Biol* 32:1
- Banerjee SR, Lazarova N, Wei L, Levadala MK, Maresca KP, Valliant JF, Babich JW, Zubieta JA (2003) *J Nucl Med* 44:50p
- Bartholoma M, Valliant J, Maresca KP, Babich J, Zubieta J (2009) *Chem Commun* 5:493
- Baumgärtner F (1961) *Kerntechnik, Isotopentechnik und Chemie* 297
- Baumgärtner F, Fischer EO, Zahn U (1962) *Naturwissenschaften* 49:156
- Blaufox MD (1987) *Contrib Nephrol* 56:31
- Blaufox MD (1991) *J Nucl Med* 32:1301
- Bolzati C, Boschi A, Duatti A, Prakash S, Uccelli L (2000a) *J Am Chem Soc* 122:4510
- Bolzati C, Uccelli L, Boschi A, Malago E, Duatti A, Tisato F, Refosco F, Pasqualini R, Piffanelli A (2000b) *Nucl Med Biol* 27:369
- Bormans G, Peeters OM, Vanbilloen H, Blaton N, Verbruggen A (1996) *Inorg Chim Acta* 35:6240
- Bormans GM, Cleyndyck BJ, Deroo MJK, Verbruggen AM (1992) *Eur J Nucl Med* 19:271
- Boschi A, Bolzati C, Benini E, Malago E, Uccelli L, Duatti A, Piffanelli A, Refosco F, Tisato F (2001) *Bioconjug Chem* 12:1035
- Boschi A, Uccelli L, Bolzati C, Duatti A, Sabba N, Moretti E, Di Domenico G, Zavattini G, Refosco F, Giganti M (2003) *J Nucl Med* 44:806
- Bossuyt A, Morgan GF, Deblaton M, Pirotte R, Chirico A, Clemens P, Vandenbroeck P, Thornback JR (1991) *J Nucl Med* 32:399
- Brandau W, Bubeck B, Eisenhut M, Taylor DM (1988) *Appl Radiat Isot* 39:121
- Breeman WAP, Hofland LJ, de Jong M, Bernard BF, Srinivasan A, Kwekkeboom DJ, Visser TJ, Krenning EP (1999a) *Int J Cancer* 81:658
- Breeman WAP, de Jong M, Bernard BF, Kwekkeboom DJ, Srinivasan A, van der Pluijm ME, Hofland LJ, Visser TJ, Krenning EP (1999b) *Int J Cancer* 83:657
- Brenner D, Davison A, Listerjames J, Jones AG (1984) *Inorg Chem* 23:3793
- Brodie BB, Hogben CAM (1957) *J Pharm Pharmacol* 9:345
- Bulluk KE, Dyszlewski M, Prior JL, Pica CM, Sharma V, Piwnica-Worms D (2002) *Bioconjug Chem* 13:1226
- Callahan RJ, Dragotakes SC, Barrow SA, Burkner MA, Tokareva EA, Fischman AJ (2001) *J Nucl Med* 42:268
- Cesati RR, Tamagnan G, Baldwin RM, Zoghbi SS, Innis RB, Katzenellenbogen JA (1999) *J Labelled Compd Rad* 42:S150
- Chaplin SB, Oberle PO, Hoffman TJ, Volkert WA, Holmes RA, Nowotnik DP, Pickett RD, Neirinckx R (1985) *J Nucl Med* 26:P18
- Chi DY, Katzenellenbogen JA (1993) *J Am Chem Soc* 115:7045
- Chi DY, Oneil JP, Anderson CJ, Welch MJ, Katzenellenbogen JA (1994) *J Med Chem* 37:928
- Collins DA, Hogenkamp HPC (1997) *J Nucl Med* 38:717
- Collins DA, Hogenkamp HPC, Gebhard MW (1999) *Mayo Clin Proc* 74:687
- Colombo FR, Torrente Y, Casati R, Benti R, Corti S, Salani S, D'angelo MG, Deliso A, Scarlato G, Bresolin N, Gerundini P (2001) *Nucl Med Biol* 28:935
- Cotton FA, Wilkinson G (1988) *Advanced inorganic chemistry*, 5th edn. Wiley-Interscience, New York, p 817
- Crankshaw CL, Marmion M, Luker GD, Rao V, Dahlheimer J, Burleigh BD, Webb E, Deutsch KF, Piwnica-Worms D (1998) *J Nucl Med* 39:77
- Davison A, Jones AG, Orvig C, Sohn M (1981) *Inorg Chem* 20:1629
- De Jong M, Breeman WAP, Bernard HF (1999) *Q J Nucl Med* 43:356
- de Jong M, Bernard BF, de Bruin E, van Gameren A, Bakker WH, Visser TJ, Macke HR, Krenning EP (1998) *Nucl Med Commun* 19:283
- Despopoulos A (1965) *J Theor Biol* 8:163
- Deutsch E, Ketring AR, Libson K, Vanderheyden J-L, Hirth WW (1989) *Nucl Med Biol* 16:191
- Deutsch E, Glavan KA, Sodd VJ, Nishiyama H, Ferguson DL, Lukes SJ (1981a) *J Nucl Med* 22:897
- Deutsch E, Bushong W, Glavan KA, Elder RC, Sodd VJ, Scholz KL, Fortman DL, Lukes SJ (1981b) *Science* 214:85
- Dilworth JR, Parrott SJ (1998) *Chem Soc Rev* 27:43
- Dirocco RJ, Kuczyński BL, Pirro JP, Bauer A, Linder KE, Ramalingam K, Cyr JE, Chan YW, Raju N, Narra RK, Nowotnik DP, Nunn AD (1993) *J Cerebr Blood F Met* 13:755
- Dischino DD, Welch MJ, Kilbourn MR, Raichle ME (1983) *J Nucl Med* 24:1030
- Drewns A, Heimbold I, Hall H, Halldin C, Pietzsch HJ, Syhre R, Seifert S, Brust P, Johannsen B (2001) *J Labelled Compd Rad* 44:S544
- Drewns A, Pietzsch HJ, Syhre R, Seifert S, Varnas K, Hall H, Halldin C, Kraus W, Karlsson P, Johnsson C, Spies H, Johannsen B (2002) *Nucl Med Biol* 29:389
- Eckelman WC, Richards P, Meinken G (1972) *J Nucl Med* 13:577
- Edwards DS, Cheesman EH, Watson MW, Maheu LJ, Nguyen SA, Dimitre L, Nason T, Watson AD,

- Walovitch R (1990) In: Nicolini M, Bandoli G, Mazzi U (eds) *Technetium in chemistry and nuclear medicine*, vol 3. Cortina International Raven Press, Verona/New York, p 433
- Egli A, Alberto R, Tannahill L, Schibli R, Abram U, Schaffland A, Waibel R, Tourwe D, Jeannin L, Iterbeke K, Schubiger PA (1999) *J Nucl Med* 40:1913
- Ell PJ, Jarritt PH, Cullum I, Hocknell JML, Costa DC, Lui D, Jewkes RF, Steiner TJ, Nowotnik DP, Pickett RD, Neirinx RD (1985) *Lancet* 2:50
- Epps LA, Burns HD, Lever SZ, Goldfarb HW, Wagner HN (1987) *Appl Radiat Isot* 38:661
- Eshima D, Fritzberg AR, Taylor A (1990) *Semin Nucl Med* 20:28
- Eshima D, Taylor A, Fritzberg AR, Kasina S, Hansen L, Sorenson JF (1987) *J Nucl Med* 28:1180
- Fichna J, Janecka A (2003) *Bioconjug Chem* 14:3
- Fischmann AJ, Meltzer P, Hillier S, Barrow SA, Callahan RJ, Bonab AA, Madras BK (1999) *Eur J Nucl Med* 26:982
- Fritzberg A (1984) *J Nucl Med Technol* 12:177
- Fritzberg AR, Kasina S, Eshima D, Johnson DL (1986) *J Nucl Med* 27:111
- Fritzberg AR, Kuni CC, Klingensmith WC, Stevens J, Whitney WP (1982) *J Nucl Med* 23:592
- Gali H, Hoffmann TJ, Sieckman GL, Owen NK, Katti KV, Volkert WA (2001) *Bioconjug Chem* 12:354
- Garcia-Garayoa E, Blauenstein P, Bruehlmeier M, Blanc A, Iterbeke K, Conrath P, Tourwe D, Schubiger PA (2002) *J Nucl Med* 43:374
- Garcia-Garayoa E, Allemann-Tannahill L, Blauenstein P, Willmann M, Carrel-Remy N, Tourwe D, Iterbeke K, Conrath P, Schubiger PA (2001) *Nucl Med Biol* 28:75
- Ghezzi C, Fagret D, Arvieux CC, Mathieu JP, Bontron R, Pasqualini R, Deleiris J, Comet M (1995) *J Nucl Med* 36:1069
- Grummon G, Rajagopalan R, Palenik GJ, Koziol AE, Nosco DL (1995) *Inorg Chem* 34:1764
- Gupta NK, Bomanji JB, Waddington W, Lui D, Costa DC, Verbruggen AM, Ell PJ (1995) *Eur J Nucl Med* 22:617
- Hansen L, Cini R, Taylor A, Marzilli LG (1992) *Inorg Chem* 31:2801
- Hansen L, Marzilli LG, Eshima D, Malveaux EJ, Folks R, Taylor A (1994) *J Nucl Med* 35:1198
- Harbert JC, Andrich MP, Peller PJ (1996) In: Harbert JC, Eckelman WC, Neumann RD (eds) *Nuclear medicine: diagnosis and therapy*. Thieme Medical Publishers, New York, p 713
- He Z, Hsieh W-Y, Kim Y-S, Liu S (2006) *Nucl Med Biol* 33:1045
- Heimbold I, Drews A, Syhre R, Kretzschmar M, Pietzsch HJ, Johannsen B (2002) *Eur J Nucl Med* 29:82
- Heppeler A, Froidevaux S, Eberle AN, Maecke HR (2000) *Curr Med Chem* 7:971
- Higley B, Smith FW, Smith T, Gemmell HG, Dasgupta P, Gvozdanovic DV, Graham D, Hinge D, Davidson J, Lahiri A (1993) *J Nucl Med* 34:30
- Hirsch-Kuchma M, Nicholson T, Davison A, Jones AG (1997) *J Chem Soc Dalton* 3:3189
- Hirschkuchma M, Nicholson T, Davison A, Davis WM, Jones AG (1997) *Inorg Chem* 36:3237
- Hoepping A, Reisgys M, Brust P, Seifert S, Spies H, Alberto R, Johannsen B (1998) *J Med Chem* 41:4429
- Hoffman TJ, Quinn TP, Volkert WA (2001) *Nucl Med Biol* 28:527
- Hoffman TJ, Seger RM, McKenzie EH, Volkert WA, Holmes RA, Pettit RP, Canning L, Cumming SA, Nechvatal G (1985) *J Nucl Med* 26:P129
- Holman BL, Sporn V, Jones AG, Sia STB, Perezbalino N, Davison A, Listerjames J, Kronauge JF, Mitta AEA, Camin LL, Campbell S, Williams SJ, Carpenter AT (1987) *J Nucl Med* 28:13
- Holmes RA, Chaplin SB, Royston KG, Hoffman TJ, Volkert WA, Nowotnik DP, Canning LR, Cumming SA, Harrison RC, Higley B, Nechvatal G, Pickett RD, Piper IM, Neirinx RD (1985) *Nucl Med Commun* 6:443
- Hom RK, Katzenellenbogen JA (1997a) *J Org Chem* 62:6290
- Hom RK, Katzenellenbogen JA (1997b) *Nucl Med Biol* 24:485
- Hom RK, Chi DY, Katzenellenbogen JA (1996) *J Org Chem* 61:2624
- Jackson S, Degrado W, Dwivedi A, Parthasarathy A, Higley A, Krywko J, Rockwell A, Markwalder J, Wells G, Wexler R, Mousa S, Harlow R (1994) *J Am Chem Soc* 116:3220
- Jain D (1999) *Semin Nucl Med* 29:221
- Jain D, Wackers FJT, Mattera J, McMahon M, Sinusas AJ, Zaret BL (1993) *J Nucl Med* 34:1254
- James S, Maresca KP, Babich JW, Valliant JF, Doering L, Zubieta J (2006a) *Bioconjug Chem* 17:590
- James S, Maresca KP, Allis DG, Valliant JF, Eckelman W, Babich JW, Zubieta J (2006b) *Bioconjug Chem* 17:579
- Jaouen G, Top S, Vessières A, Alberto R (2000) *J Organomet Chem* 600:23
- Jaouen G, Top S, Vessières A, Pigeon P, Leclercq G, Laios I (2001) *Chem Commun* 383
- Johannsen B, Pietzsch HJ (2002) *Eur J Nucl Med Mol Imaging* 29:263
- Johannsen B, Noll B, Leibnitz P, Reck G, Noll S, Spies H (1993) *Inorg Chim Acta* 210:209
- Johnson G, Nguyen KN, Pasqualini R, Okada RD (1997) *J Nucl Med* 38:138
- Johnson G, Nguyen KN, Liu ZG, Okada RD (1998) *J Nucl Cardiol* 5:285
- Jones AG, Abrams MJ, Davison A, Brodack JW, Toothaker AK, Adelstein SJ, Kassis AI (1984) *Int J Nucl Med Biol* 11:225
- Jurisson S, Berning D, Jia W, Ma DS (1993) *Chem Rev* 93:1137
- Jurisson S, Schlemper EO, Troutner DE, Canning LR, Nowotnik DP, Neirinx RD (1986) *Inorg Chem* 25:543

- Jurisson SS, Lxdon JD (1999) *Chem Rev* 99:2205
- Jurisson SS, Hirth W, Linder KE, Dirocco RJ, Narra RK, Nowotnik DP, Nunn AD (1991) *Nucl Med Biol* 18:735
- Karra SR, Schibli R, Gali H, Katti KV, Hoffman TJ, Higginbotham C, Sieckman GL, Volkert WA (1999) *Bioconjug Chem* 10:254
- Katzenellenbogen JA, Welch MJ, Dehdashti F (1997) *Anticancer Res* 17:1573
- Kaul S, Boucher CA, Newell JB, Chesler DA, Greenberg JM, Okada RD, Strauss HW, Dinsmore RE, Pohost GM (1986) *J Am Coll Cardiol* 7:527
- Kelly JD, Higly B, Archer CM, Al E (1990) Technetium-^{99m} complexes of functionalised diphosphines for myocardial imaging. In: Nicolini M, Bandoli G, Mazzi U (eds) *Technetium and rhenium in chemistry and nuclear medicine*, vol 3. Cortina International, Verona, p 405
- Kempf CR, Clark HM, Aikens DA, Bailey RA, Bunce SC, Applebaum G (1980) *J Nucl Med* 21:402
- Kniess T, Spies H, Brandau W, Johannsen B (1998) *J Labelled Compd Rad* 41:605
- Krenning EP, Kwekkeboom DJ, Bakker WH, Breeman WAP, Kooij PPM, Oei HY, Vanhagen M, Postema PTE, Dejong M, Reubi JC, Visser TJ, Reijs AEM, Hofland LJ, Koper JW, Lamberts SWJ (1993) *Eur J Nucl Med* 20:716
- Kronauge JE, Barbarics E, Davison A, Jones AG (1993) *J Labelled Compd Rad* 32:62
- Kung HF (2001) *Nucl Med Biol* 28:505
- Kung HF, Ohmomo Y, Kung MP (1990) *Semin Nucl Med* 20:290
- Kung HF, Kung MP, Choi SR (2003) *Semin Nucl Med* 33:2
- Kung HF, Guo YZ, Yu CC, Billings J, Subramanyam V, Calabrese JC (1989) *J Med Chem* 32:433
- Kung MP, Stevenson DA, Plossl K, Meegalla SK, Beckwith A, Essman WD, Mu M, Lucki I, Kung HF (1997) *Eur J Nucl Med* 24:372
- Kunze S, Zobi F, Kurz P, Spingler B, Alberto R (2004) *Angew Chem Int Ed* 43:5025
- La Bella R, Garcia-Garayoa E, Bahler M, Blauenstein P, Schibli R, Conrath P, Tourwe D, Schubiger PA (2002) *Bioconjug Chem* 13:599
- Lahiri A, Highley B, Crawley JCW (1989) *J Nucl Med* 30:818
- Lamberts SWJ (1988) *Endocr Rev* 9:417
- Langer M, La Bella R, Garcia-Garayoa E, Beck-Sickinger AG (2001) *Bioconjug Chem* 12:1028
- Larsen SK, Solomon HF, Caldwell G, Abrams MJ (1995) *Bioconjug Chem* 6:635
- Lebedeva LI, Kyong K (1968) *Vestnik Leningrad Univ* 23:127
- Leonard JP, Nowotnik DP, Neirinckx RD (1986) *J Nucl Med* 27:1819
- Lever SZ, Burns HD, Kervitsky TM, Goldfarb HW, Woo DV, Wong DF, Epps LA, Kramer AV, Wagner HN (1985) *J Nucl Med* 26:1287
- Libson K, Messa C, Kwiatkowski M, Al E (1990) Development of new ^{99m}Tc myocardial perfusion imaging agents. In: Nicolini M, Bandoli G, Mazzi U (eds) *Technetium and rhenium in chemistry and nuclear medicine*. Cortina International, Verona, p 365
- Linder KE, Malley MF, Gougoutas JZ, Unger SE, Nunn AD (1990) *Inorg Chem* 29:2428
- Linder KE, Nowotnik DP, Malley MF, Gougoutas JZ, Nunn AD (1991) *Inorg Chim Acta* 190:249
- Linder KE, Chan YW, Cyr JE, Malley MF, Nowotnik DP, Nunn AD (1994) *J Med Chem* 37:9
- Listerjames J, Knight LC, Maurer AH, Bush LR, Moyer BR, Dean RT (1996) *J Nucl Med* 37:775
- Liu M, Xu W, Xu LJ, Zhong GR, Chen SL, Lu WY (2005) *Bioconjug Chem* 16:1126
- Liu S (2007) *Dalton T* 1183
- Liu S, Edwards DS (1999) *Chem Rev* 99:2235
- Liu S, Edwards DS, Harris AR (1998a) *Bioconjug Chem* 9:583
- Liu S, Edwards DS, Harris AR (1998b) *J Nucl Med* 39:215
- Liu S, He ZJ, Hsieh WY, Kim YS (2006) *Nucl Med Biol* 33:419
- Liu S, Edwards DS, Looby RJ, Harris AR, Poirier MJ, Barrett JA, Heminway SJ, Carroll TR (1996) *Bioconjug Chem* 7:63
- Lo KKW, Hui WK (2005) *Inorg Chem* 44:1992
- Madras BK, Jones AG, Mahmood A, Zimmerman RE, Garada B, Holman BL, Davison A, Blundell P, Meltzer PC (1996) *Synapse* 22:239
- Mahmood A, Kronauge JE, Barbarics E, Freiberg E, Madras BK, Li J, Davison A, Jones AG (1999) Technetium(V) and rhenium(V) analogues of WAY 100,635 5HT_{1A} receptor-binding complexes. In: Nicolini M, Mazzi U (eds) *Technetium, rhenium and other metals in chemistry and nuclear medicine*. SGE Editoriali, Padova, p 393
- Mahmoud S, Staley J, Taylor J, Bogden A, Moreau JP, Coy D, Avis I, Cuttitta F, Mulshine JL, Moody TW (1991) *Cancer Res* 51:1798
- Mallo L, León A, Papadopoulos M, Manta E, Rey A, León E, Pirmettis I, Raptopoulou C, Chiotellis E (1999) Preliminary evaluation of a novel ^{99m}Tc complex for imaging 5ht_{1A} serotonin receptors. In: Nicolini M, Mazzi U (eds) *Technetium, rhenium and other metals in chemistry and nuclear medicine*. SGE Editoriali, Padova, p 503
- Maria L, Cunha S, Videira M, Gano L, Paulo A, Santos IC, Santos I (2007) *Dalton Trans* 28:3010
- Maria L, Fernandes C, Garcia R, Gano L, Paulo A, Santos IC, Santos I (2009) *Dalton Trans* 4:603
- Martin GV, Caldwell JH, Graham MM, Grierson JR, Kroll K, Cowan MJ, Lewellen TK, Rasey JS, Casciari JJ, Krohn KA (1992) *J Nucl Med* 33:2202
- Meegalla S, Plossl K, Kung MP, Svenson DA, Liablesands LM, Rheingold AL, Kung HF (1995) *J Am Chem Soc* 117:11037

- Meegalla S, Plössl K, Kung M-P, Chumpradit S, Stevenson DA, Frederick D, Kung HF (1996) *Bioconjug Chem* 7:421
- Meegalla SK, Plössl K, Kung M-P, Chumpradit S, Stevenson DA, Kushner SA, Mcelgin WT, Mozley PD, Kung HF (1997) *J Med Chem* 40:9
- Meegalla SK, Plossl K, Kung MP, Stevenson DA, Mu M, Kushner S, Liable-Sands LM, Reingold AL, Kung HF (1998) *J Med Chem* 41:428
- Meltzer PC, Blundell P, Madras BK, Fischman AJ, Jones AG, Mahomood A (2000) *European Patent Applications* 56
- Minutolo F, Katzenellenbogen JA (1998) *J Am Chem Soc* 120:4514
- Minutolo F, Katzenellenbogen JA (1999) *Angew Chem Int Ed* 38:1617
- Moody TW, Perry DC (1989) In: Williams M, Glennon RA, Timmermans PBMWM (eds) *Receptor pharmacology and function*. Marcell Dekker, New York, p 527
- Morgan GF, Deblaton M, Clemens P, Vandenbroeck P, Bossuyt A, Thornback JR (1991) *J Nucl Med* 32:500
- Mozley PD, Stubbs JB, Plossl K, Dresel SH, Barraclough ED, Alavi A, Araujo LI, Kung HF (1998) *J Med Chem* 39:2069
- Mozley PD, Acton PD, Barraclough ED, Plossl K, Gur RC, Alavi A, Mathur A, Saffer J, Kung HF (1999) *J Nucl Med* 40:1812
- Muller C, Schubiger PA, Schibli R (2007) *Nucl Med Biol* 34:595
- Muller C, Bruhlmeier M, Schubiger PA, Schibli R (2006a) *J Nucl Med* 47:2057
- Muller C, Hohn A, Schubiger PA, Schibli R (2006b) *Eur J Nucl Med Mol Imaging* 33:1007
- Muto P, Lastoria S, Varrella P, Vergara E, Salvatore M, Morgano G, Listerjames J, Bernardy JD, Dean RT, Wencker D, Borer JS (1995) *J Nucl Med* 36:1384
- Narahara KA, Villanuevameyer J, Thompson CJ, Brizendine M, Mena I (1990) *Am J Cardiol* 66:1438
- Narra RK, Nunn AD, Kuczyński BL, Feld T, Wedeking P, Eckelman WC (1989) *J Nucl Med* 30:1830
- Narra RK, Nunn AD, Kuczyński BL, Dirocco RJ, Feld T, Silva DA, Eckelman WC (1990) *J Nucl Med* 31:1370
- Neirincx RD, Canning LR, Piper IM, Nowotnik DP, Pickett RD, Holmes RA, Volkert WA, Forster AM, Weisner PS, Marriott JA, Chaplin SB (1987) *J Nucl Med* 28:191
- Nicholson T, Cook J, Davison A, Rose DJ, Maresca KP, Zubietta JA, Jones AG (1996a) *Inorg Chim Acta* 252:421
- Nicholson T, Cook J, Davison A, Rose DJ, Maresca KP, Zubietta JA, Jones AG (1996b) *Inorg Chim Acta* 252:427
- Nock B, Nikolopoulou A, Chiotellis E, Loudos G, Maintas D, Reubi JC, Maina T (2003) *Eur J Nucl Med Mol Imaging* 30:247
- Nosco DL, Beaty-Nosco JA (1999) *Coordin Chem Rev* 184:91
- Nowotnik DP, Canning LR, Cumming A, Harrison RC, Higley B, Nechvtal G, Pickett RD, Piper IM, Bayne VJ, Forster AM, Weisner PS, Neirincx RD, Volkert WA, Troutner DE, Holmes RA (1985) *Nucl Med Commun* 6:499
- Nunn AD (1992) Single photon radiopharmaceuticals for imaging myocardial perfusion. In: Nunn AD (ed) *Radiopharmaceuticals: chemistry and pharmacology*. Marcell Dekker, New York, p 97
- Okarvi SM, Jammaz IA (2006) *Cancer Biother Radiopharm* 21:49
- Ono M, Arano Y, Mukai T, Uehara T, Fujioka Y, Ogawa K, Namba S, Nakayama M, Saga T, Konishi J, Horiuchi K, Yokoyama A, Saji H (2001) *Nucl Med Biol* 28:155
- Otte A, Jermann E, Behe M, Goetze M, Bucher HC, Roser HW, Heppeler A, Muellerbrand J, Maecke HR (1997) *Eur J Nucl Med* 24:792
- Oya S, Kung MP, Stevenson DA, Kung HF (1996) *J Nucl Med* 37:870
- Parker N, Turk MJ, Westrick E, Lewis JD, Low PS, Leamon CP (2005) *Anal Biochem* 338:284
- Pasqualini R, Duatti A (1992) *J Chem Soc Chem Commun* 1354
- Pasqualini R, Duatti A, Bellande E, Comazzi V, Brucato V, Hoffschir D, Fagret D, Comet M (1994) *J Nucl Med* 35:334
- Pearson DA, Lister-James J, McBride WJ, Wilson DM, Martel LJ, Civitello ER, Dean RT (1996) *J Med Chem* 39:1372
- Pietzsch HJ, Spies H, Hoffmann S (1989) *Inorg Chim Acta* 165:163
- Pietzsch HJ, Spies H, Hoffmann S, Scheller D (1990) *Appl Radiat Isot* 41:185
- Pillai MRA, John CS, Lo JM, Troutner DE (1990) *Appl Radiat Isot* 41:557
- Piwnicaworms D, Chiu ML, Budding M, Kronauge JF, Kramer RA, Croop JM (1993) *Cancer Res* 53:977
- Plössl K, Zhuang ZP, Meegalla SK, Bradshaw J, Frederick D, Stevenson DA, Kung MP, Kung HF (1995) *J Labelled Compd Rad* 37:306
- Ponto JA, Chilton HM, Watson NA Jr (1990) In: Swanson DP, Chilton HM, Thrall JH (eds) *Pharmaceuticals in medical imaging*. MacMillan, New York, p 501
- Qin YF, Ertl T, Cai RZ, Halmos G, Schally AV (1994) *Cancer Res* 54:1035
- Qin YF, Ertl T, Cai RZ, Horvath JE, Groot K, Schally AV (1995) *Int J Cancer* 63:257
- Ramalingam K, Raju N, Nanjappan P, Linder KE, Pirro J, Zeng W, Rumsey W, Nowotnik DP, Nunn AD (1994) *J Med Chem* 37:4155
- Rao TN, Adhikesavalu D, Camerman A, Fritzberg AR (1990) *J Am Chem Soc* 112:5798
- Reubi JC, Waser B, Schaar JC, Laissue JA (1999) *Int J Cancer* 82:213

- Reubi JC, Waser B, Friess H, Buchler M, Laissue J (1998) Gut 42:546
- Richards P (1960) VII Rassegna Internazionale Elettronica e Nucleare. Roma, Atti Ufficiali, 223
- Riou L, Ghezzi C, Mouton O, Mathieu JP, Pasqualini R, Comet M, Fagret D (1998) Circulation 98:2591
- Rogers BE, Brechbiel MW, Kirkman RL, Clarkson M, Buchsbaum DJ (1999) In vitro binding and internalization of an Indium-111 labeled bombesin derivative to cells expressing the gastrin releasing peptide receptor. In: Nicolini M, Mazzi U (eds) Technetium, rhenium and other metals in chemistry and nuclear medicine. SGE Editoriali, Padova, p 519
- Rogers BE, Curiel DT, Mayo MS, Laffoon KK, Bright SJ, Buchsbaum DJ (1997) Cancer 80:2419
- Rose DJ, Maresca KP, Nicholson T, Davison A, Jones AG, Babich J, Fischman A, Graham W, Debord JRD, Zubietta J (1998) Inorg Chem 37:2701
- Rossetti C, Vanoli G, Paganelli G, Kwiatkowski M, Zito F, Colombo F, Bonino C, Carpinelli A, Casati R, Deutsch K, Marmion M, Woulfe SR, Lunghi F, Deutsch E, Fazio F (1994) J Nucl Med 35:1571
- Sands H, Delano ML, Camin LL, Gallagher BM (1985) Biochim Biophys Acta 812:665
- Schaefer WM, Moka D, Brockmann HA, Schomaecker K, Schicha H (2002) Nucl Med Biol 29:243
- Schaffer P, Gleave JA, Lemon JA, Reid LC, Pacey LKK, Farncombe TH, Boreham DR, Zubietta J, Babich JW, Doering LC, Valliant JF (2008) Nucl Med Biol 35:159
- Schibli R, Katti KV, Higginbotham C, Volkert WA, Alberto R (1999) Nucl Med Biol 26:711
- Schibli R, Bella RL, Alberto R, Garcia-Garayoa E, Ortner K, Abram U, Schubiger PA (2000) Bioconjug Chem 3:345
- Schibli R, Schwarzbach R, Alberto R, Ortner K, Schmalte H, Dumas C, Egli A, Schubiger PA (2002) Bioconjug Chem 13:750
- Schwartz DA, Abrams MJ, Hauser MM, Gaul FE, Larsen SK, Rauh D, Zubietta JA (1991) Bioconjug Chem 2:333
- Schwarze SR, Hruska KA, Dowdy SF (2000) Trends Cell Biol 10:290
- Seifert S, Noll B, Münze R (1982) Int J Appl Radiat Isot 33:1391
- Seifert S, Syhre R, Gupta A, Spies H, Johannsen B (1999) Stability studies on "3+1" mixed-ligand technetium and rhenium complexes. In: Nicolini M, Mazzi U (eds) Technetium, rhenium and other metals in chemistry and nuclear medicine, vol 5. SGE Editoriali, Padova, p 687
- Seifert S, Pietzsch H-J, Scheunemann M, Spies H, Syhre R, Johannsen B (1997) Appl Radiat Isot 49:5
- Seifert S, Drews A, Gupta A, Pietzsch HJ, Spies H, Johannsen B (2000) Appl Radiat Isot 53:431
- Seldin DW, Johnson LL, Blood DK, Muschel MJ, Smith KE, Wall RM, Cannon PJ (1989) J Nucl Med 30:312
- Sharp PF, Smith FW, Gemmell HG, Lyall D, Evans NTS, Gvozdanovic D, Davidson J, Tyrrell DA, Pickett RD, Neirinckx RD (1986) J Nucl Med 27:171
- Sia STB, Holman BL, Mckusick K, Rigo P, Gillis F, Sporn V, Perezbalino N, Mitta A, Vosberg H, Szabo Z, Schwartzkopff B, Moretti JL, Davison A, Listerjames J, Jones A (1986) Eur J Nucl Med 12:333
- Sivolapenko GB, Skarlos D, Pectasides D, Stathopoulou E, Milonakis A, Sirmalis G, Stuttle A, Courtenay-Luck NS, Konstantinides K, Epenetos AA (1998) Eur J Nucl Med 25:1383
- Smith CJ, Gali H, Sieckman GL, Higginbotham C, Volkert WA, Hoffman TJ (2003) Bioconjug Chem 14:93
- Spies H, Johannsen B (1981) Inorg Chim A-Article 48:255
- Spies H, Pietzsch HJ, Syhre R, Hoffmann S (1990) Isotopenpraxis 26:159
- Spies H, Fietz T, Pietzsch HJ, Johannsen B, Leibnitz P, Reck G, Scheller D, Klostermann K (1995) J Chem Soc Dalton 2277
- Spingler B, Mundwiler S, Ruiz-Sanchez P, van Staveren DR, Alberto R (2007) Eur J Inorg Chem 18:2641
- Stephenson KA, Reid LC, Zubietta J, Babich JW, Kung MP, Kung HE, Valliant JF (2008) Bioconjug Chem 19:1087
- Stephenson KA, Zubietta J, Banerjee SR, Levadala MK, Taggart L, Ryan L, Mcfarlane N, Boreham DR, Maresca KP, Babich JW, Valliant JF (2004) Bioconjug Chem 15:128
- Syhre R, Seifert S, Spies H, Gupta A, Johannsen B (1998) Eur J Nucl Med 25:793
- Tatemoto K (1982) P Natl Acad Sci-Biol 79:5485
- Top S, Hafa HE, Vessières A, Quivy J, Vaissermann J, Hughes DD, Mcglinchey MJ, Mornon J-P, Thoreau E, Jaouen G (1995) J Am Chem Soc 117:8372
- Treher EN, Francesconi LC, Gougoutas JZ, Malley MF, Nunn AD (1989) Inorg Chem 28:3411
- Troutner DE, Volkert WA, Hoffman TJ, Holmes RA (1984) Int J Appl Radiat Isot 35:467
- Trump DP, Mathias CJ, Yang ZF, Low PSW, Marmion M, Green MA (2002) Nucl Med Biol 29:569
- Tucker WD, Greene MW, Weiss AJ, Murenhoff AP (1958) T Am Nucl Soc 1:160
- Uccelli L, Giganti M, Duatti A, Bolzati C, Pasqualini R, Cittanti C, Colamussi P, Piffanelli A (1995) J Nucl Med 36:2075
- Vallabhajosula S, Moyer BR, Lister-James J, McBride BJ, Lipszyc H, Lee H, Bastidas D, Dean RT (1996) J Nucl Med 37:1016
- Vallabhajosula S, Zimmerman RE, Picard M, Stritzke P, Mena I, Hellman RS, Tikofsky RS, Stabin MG, Morgan RA, Goldsmith SJ (1989) J Nucl Med 30:599
- Van De Wiele C, Dumont F, Vanden Broecke R, Oosterlinck W, Cocquyt V, Serreyn R, Peers S, Thornback J, Slegers G, Dierckx RA (2000) Eur J Nucl Med 27:1694

- Van Staveren DR, Waibel R, Mundwiler S, Schubiger PA, Alberto R (2004a) *J Organomet Chem* 689:4803
- Van Staveren DR, Mundwiler S, Hoffmanns U, Pak JK, Spingler B, Metzler-Nolte N, Alberto R (2004b) *Org Biomol Chem* 2:2593
- Vanzetto G, Fagret D, Pasqualini R, Mathieu JP, Chossat F, Machecourt J (2000) *J Nucl Med* 41:141
- Vanzetto G, Calnon DA, Ruiz M, Watson DD, Pasqualini R, Beller GA, Glover DK (1997) *Circulation* 96:2325
- Verbeke K, Hjelstuen O, Debrock E, Cleynhens B, Deroo M, Verbruggen A (1995) *Nucl Med Commun* 16:942
- Verbruggen A, Bormans G, Cleynhens B, Hoogmartens M, Vandercruys A, Deroo MJK (1989) *J Labelled Compd Rad* 26:436
- Verbruggen AM (1990) *Eur J Nucl Med* 17:346
- Verbruggen AM, Deroo MJK (1992) In: Nunn AD (ed) *Radiopharmaceuticals: chemistry and pharmacology*. Marcel Dekker, New York, p 365
- Verbruggen AM, Nosco DL, Vannerom CG, Bormans GM, Adriaens PJ, Deroo MJ (1992) *J Nucl Med* 33:551
- Villa M, Saccavini JC, Bardy A (1986) *Dev Nucl Med* 10:351
- Viola-Villegas N, Rabideau AE, Cesnavicius J, Zubieta J, Doyle RP (2008) *Chem Med Chem* 3:1387
- Virgolini I, Traub T, Novotny C, Leimer M, Fuger B, Li SR, Patri P, Pangerl T, Angelberger P, Raderer M, Andreae F, Kurtaran A, Dudczak R (2001) *Q J Nucl Med* 45:153
- Visser GWM, Gerretsen M, Herscheid JDM, Snow GB, Vandongen G (1993) *J Nucl Med* 34:1953
- Wackers FJT, Sokole EB, Samson G, Schoot JBVD, Lie KI, Liem KL, Wellens HJJ (1976) *N Engl J Med* 295:1
- Wackers FJT, Berman DS, Maddahi J, Watson DD, Beller GA, Strauss HW, Boucher CA, Picard M, Holman BL, Fridrich R, Inglese E, Delaloye B, Bischofdelaloye A, Camin L, Mckusick K (1989) *J Nucl Med* 30:301
- Waibel R, Alberto R, Willuda J, Finnern R, Schibli R, Stichelberger A, Egli A, Abram U, Mach JP, Pluckthun A, Schubiger PA (1999) *Nat Biotechnol* 17:897
- Waibel R, Treichler H, Schaefer NG, Van Staveren DR, Mundwiler S, Kunze S, Kuenzi M, Alberto R, Nuesch J, Knuth A, Moch H, Schibli R, Schubiger PA (2008) *Cancer Res* 68:2904
- Wald J, Alberto R, Ortner K, Candreia L (2001) *Angew Chem* 113:3152
- Walovitch RC, Cheesman EH, Maheu LJ, Hall KM (1994) *J Cerebr Blood F Met* 14:S4
- Walovitch RC, Hill TC, Garrity ST, Cheesman EH, Burgess BA, Oleary DH, Watson AD, Ganey MV, Morgan RA, Williams SJ (1989) *J Nucl Med* 30:1892
- Walovitch RC, Makuch J, Garrity ST, Burgess BA, Morgan RA, Williams SJ, Leveille J, Donesuard J, Rigo P, Demonceau G, Cantineau R, Deroo MJK (1988) *Neurology* 38:363
- Wei LH, Babich J, Eckelman WC, Zubieta J (2005) *Inorg Chem* 44:2198
- Wei LH, Babich JW, Ouellette W, Zubieta J (2006) *Inorg Chem* 45:3057
- Weiner RE, Thakur ML (2002) *Appl Radiat Isot* 57:749
- Wenzel M (1992) *J Labelled Compd Rad* 31:641
- Wenzel M, Klinge C (1994) *J Labelled Compd Rad* 34:981
- Wester DW, White DH, Miller FW, Dean RT, Schreifels JA, Hunt JE (1987) *Inorg Chim Acta* 131:163
- Wong E, Bennett S, Lawrence B, Fauconnier T, Lu LFL, Bell RA, Thornback JR, Eshima D (2001) *Inorg Chem* 40:5695
- Wong E, Fauconnier T, Bennett S, Valliant J, Nguyen T, Lau F, Lu LFL, Pollak A, Bell RA, Thornback JR (1997) *Inorg Chem* 36:5799
- Wust F, Carlson KE, Katzenellenbogen JA, Spies H, Johannsen B (1998) *Steroids* 63:665
- Xue CB, Degrado WF (1995) *J Org Chem* 60:946
- Zhuang ZP, Mu M, Kung MP, Plössl K, Kung HF (1999) *J Labelled Compd Rad* 42:S351

44 Radioiodination Chemistry and Radioiodinated Compounds

M. Eisenhut¹ · W. Mier²

¹Cancer Research Center Heidelberg (DKFZ), Heidelberg, Germany

²Radiopharmaceutical Chemistry, University of Heidelberg, Heidelberg, Germany

44.1	<i>Introduction</i>	2122
44.2	<i>Radioisotopes of Iodine for Life Sciences</i>	2122
44.3	<i>Radioiodination of Organic Compounds</i>	2123
44.3.1	Radioiododethallation	2123
44.3.2	Radioiododehalogenation	2125
44.3.3	Radioiododestannylation	2126
44.3.4	Radioiododeboronation	2127
44.3.5	Direct Radioiodination	2128
44.3.6	Other Methods	2131
44.4	<i>Radioiodination of Peptides and Proteins</i>	2131
44.4.1	Chloramine-T	2132
44.4.2	Iodogen	2133
44.4.3	Iodobeads	2133
44.4.4	Lactoperoxidase	2134
44.4.5	Heterobifunctional Reagents	2135
44.5	<i>Rating of Radioiodination Methods</i>	2136
44.6	<i>Examples of Clinical Applications</i>	2140
44.6.1	Radioiododethallation	2140
44.6.2	Radioiododehalogenation	2140
44.6.3	Radioiododestannylation	2140
44.6.4	Direct Radioiodination	2140

Abstract: An overview of the chemistry of radioiodination is presented. The focus is directed on the labeling of iodine-containing radiopharmaceuticals, with emphasis on practical aspects of the various radioiodination methods. The advantages and disadvantages of these methods with respect to efficiency and ease of handling are discussed. Examples of the labeling methods are illustrated by protocols.

44.1 Introduction

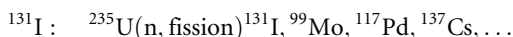
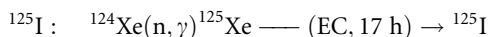
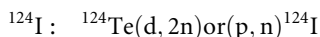
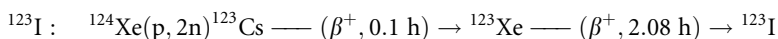
The following paragraphs describe, for the most part, the practical aspects of the radioiodination methods followed, particularly, in radiopharmaceutical chemistry laboratories. Reviews describing the various aspects of radioiodination have been published elsewhere (see, e.g., Coenen et al. 1983; Wilbur 1992). The objective, here, is not so much to cover all the achievements in this field as to provide experimental instructions for routine laboratory work. Thus, a great part of the experimental details stems from experiences acquired in the authors' laboratories. The other experimental details have been taken from the literature.

All manipulations and procedures with radioactive material presented below have to be performed in appropriately shielded fume hoods or glove boxes. In addition, all preparations delivered for human application must meet good manufacturing practice (GMP) standards. Several constraints originating from these conventions should, however, be modified for practicability and radiation safety of personnel.

44.2 Radioisotopes of Iodine for Life Sciences

The Chart of Nuclides summarizes 33 radioactive isotopes of iodine (Pfennig et al. 2006). Four of these isotopes, namely ^{123}I , ^{124}I , ^{125}I , and ^{131}I , are currently applied in the field of life science, either for imaging, therapy, or in vitro studies. In addition, $^{120\text{m}}\text{I}$, $^{120\text{g}}\text{I}$, and ^{121}I are considered as potentially useful positron-emitting iodine isotopes (see also ▶ Chap. 39 in this Volume). ▶ Table 44.1 presents an overview of the physical characteristics of the commercially available radioiodoisotopes ^{123}I , ^{125}I , and ^{131}I . Sources of ^{124}I are mostly academic, but one supplier offers ^{124}I via internet (Ritverc 2003).

The four iodine isotopes are produced in a cyclotron or nuclear reactor (▶ Table 44.1; cf. also ▶ Chaps. 38 and ▶ 39 in this Volume). The nuclear reactions currently used for the commercial production of these isotopes are:



Many more nuclear reactions, which might better apply for other accelerators, are feasible. The irradiated targets have to be processed in order to obtain pure radioiodine isotopes in a solution with high activity concentrations. In case of tellurium-oxide targets, this is generally achieved by dry distillation and trapping of hydrogen iodide in 0.02 M NaOH.

Table 44.1

Radioiodine isotopes used in life sciences

Isotope	Production	Modes of decay	Half-life	E_{γ}/E_{β}^a	Specific activity ^b	Application
¹²³ I	Cyclotron	EC	13.2 h	159/–	>600 ^c	Imaging
¹²⁴ I	Cyclotron	EC/ β^+ (25%)	4.18 days	603/1,530	>30 ^d	Imaging
¹²⁵ I	Nuclear reactor	EC	59.4 days	35/–	>90	In vitro and therapy
¹³¹ I	Nuclear reactor	β^-	8.04 days	364/606	110	Imaging and therapy

^akeV/keV^bGBq μmol^{-1} at time of delivery; theoretic specific activities in GBq μmol^{-1} ^c8,780^d1,147

The *specific activities* summarized in ▶ Table 44.1 indicate differences that might have an impact on the desired application. Especially, radiopharmaceuticals used as receptor ligands are susceptible to a low specific activity of the applied radioisotope. Thus, contamination with stable iodine due to an intrinsic low specific activity and choice of radiolabeling method (*vide infra*) should be a matter of consideration. Another parameter influencing the success of radiolabeling is the activity concentration per volume. This value should also be high in order to obtain sufficiently high radiochemical yields (RCY). In case of diluted [¹²³I]iodide shipments, excess 0.02 M NaOH solution may be concentrated, but the outcome of the labeling is often unpredictable. This may be the result of the concentration of unknown contaminants.

44.3 Radioiodination of Organic Compounds


44.3.1 Radioiododethallation

One of the first reports on the application of *thallium(III) trifluoroacetate* (Tl(TFA)₃) for the radioiodination of organic compounds was given by the synthesis of 15-(4-[¹²³I]iodophenyl)pentadecanoic acid ([¹²³I]IPPA), which was used for the diagnosis of myocardial infarction (Kulkarni and Parkey 1982; Rellas et al. 1983). At the same time, methyl-branched ω -phenyl fatty acids were radiolabeled using the same procedure (Goodman et al. 1982). In the first step, Tl(TFA)₃ was reacted with 15-phenylpentadecanoic acid. This reaction, also called thallation, was performed in situ using trifluoroacetic acid as a solvent. Finally, addition of [¹²³I]iodide admixed with small amounts of carrier iodide (4 mol%) and heating to 50–100°C yielded [¹²³I]IPPA at about 70% yield. The still unresolved reaction mechanism is illustrated in ▶ Fig. 44.1.

In this case, a 4-[¹²³I]iodoaryl derivative is formed as the main product. Depending on the substituent positions, the formation of other derivatives is possible. In each case, this has to be investigated in detail. For more information refer, e.g., to Mekushev (1988).

The original radioiodination conditions have subsequently been changed as far as reactant concentrations, their molar ratios, and reaction temperatures are concerned. The following labeling procedure has been applied to ω -phenyl fatty acids (Eisenhut et al. 2000a).

Radioiododethallation. Twenty microliters of a 10 mM TFA solution of the ω -phenyl fatty acid is mixed with 10 μ l of 10 mM $\text{I}(\text{TFA})_3$ dissolved in TFA. After 10 min at ambient temperature, the solution is mixed with ^{131}I iodide. The volume of the latter solution should not exceed 10% of the total volume, because the solubility and water may impair the RCY. Alternatively, the ^{131}I iodide solution should be evaporated. Five minutes later, the reaction mixture is injected into an analytical RP18-HPLC column and separated with isocratic or gradient elution. The RCY ranges between 70% and 80% (isolated) and the specific activity is 70–90 GBq μmol^{-1} . The RCY drops considerably if no-carrier-added (n.c.a.) iodide solutions are used. This effect can be avoided by the addition of 10 nM carrier iodide/GBq ^{123}I .

Other compounds have also been labeled using the radioiododethallation method: benzamide derivatives (Nicholl et al. 1997; Mohammed et al. 1997; Eisenhut et al. 2000b), the benzoyloxycarbonyl group in zVAD-fmk (Haberkorn et al. 2001), and the nucleoside deoxycytidine. In comparison to previous methods using Chloramine-T, the latter reaction can be improved by the action of thallium(III) (Scherberg 1974; Linz 1982).  Figure 44.2 illustrates this reaction, which uses thallium(III) as an oxidant.

Thallium(III) catalyzed iodination of 2'-deoxycytidine (Mier 2002). In a screw-cap vial, 50 μ l of a solution of 2'-deoxycytidine hydrochloride (2.63 mg in 1 ml 0.5 M acetate buffer pH 5) are mixed with the Na^{131}I -solution. Twenty microliters of a solution of $\text{I}(\text{TFA})_3$ (5.43 mg in 1 ml 0.5 M acetate buffer pH 5) are added and the mixture is heated for 1 h to 60° C. Twenty microliters of a sodium thiosulfate solution (10 mg in 1 ml 0.5 M acetate buffer pH 5) are added and the mixture is separated by RP-HPLC. Elution with a linear gradient of a methanol / Tris-phosphate buffer (pH 2.6) yields no-carrier-added 5- ^{131}I iodo-deoxycytidine.

 Fig. 44.1

The radioiododethallation reaction

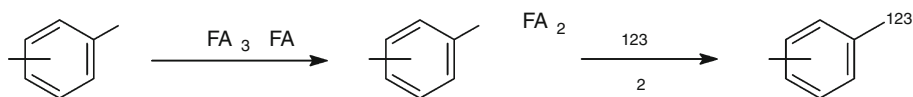
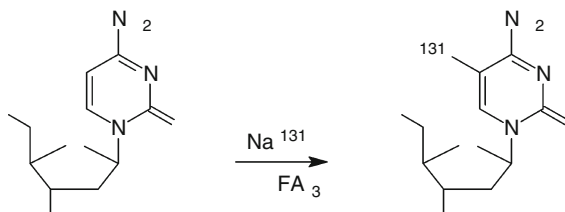


 Fig. 44.2

Radiodination of 2'-deoxycytidine



44.3.2 Radioiododehalogenation

A straightforward method for the introduction of radioiodine into aromatic compounds represents the radioiododehalogenation reaction. Regioselective halogen replacement induced by nucleophilic attack of radioiodide is an energy-demanding process, which is forced at its equilibrium state to the product side by the large molar excess of the starting material. Only the replacement of iodine and bromine by radioiodine is of interest in radiopharmaceutical chemistry. While radioiododeiodination takes place at about 160°C, radioiododebromination is fast enough only above 200°C (Liefhold and Eisenhut 1986). Appropriate solvents or melts providing an acidic environment are necessary to perform this kind of exchange reaction. The impact of energy, however, limits the scope of this method as degradation of the original compound and the product might occur.

An example for the radioiododeiodination reaction represents the preparation of o-[¹²³I] iodo-hippuric acid ([¹²³I]OIH); this preparation method was most often used in the early days of radiopharmaceutical chemistry. OIH (e.g., 15 mg) and [¹²³I]iodide were melted for 10 min at 160°C yielding >99% [¹²³I]OIH (Sinn et al. 1986). Exchange labeling was also applied for the radioiodination of 15-(4-iodophenyl) pentadecanoic acid (IPPA). In order to reduce the amount of starting material (1 mg) and to maintain the acidic environment, benzoic acid was added to the reaction mixture (Eisenhut 1982). A solid phase support was used to radioiodinate meta-iodobenzylguanidine (mIBG). (NH₄)₂SO₄ facilitated the radioiododeiodination reaction, resulting in a lowered exchange temperature (140°C) (Mangner et al. 1982). For radioiodinated benzodiazepines, this method is illustrated by the following procedure (Van Dort et al. 1988).

(NH₄)₂SO₄ facilitated radioiododeiodination. *A mixture of 5 mg (NH₄)₂SO₄ dissolved in 15 µl H₂O, 15 µg 7-iodo-1,3-dihydro-1-methyl-5-(4-chlorophenyl)-2H-1,4-benzodiazepine-2-one in 15 µl of acetone and 300 MBq ¹²³I is heated to dryness at 140°C. Air is then slowly passed through the reaction vial for 1 min and the dry reaction mixture maintained at 140°C for 30 min. The reaction mixture is dissolved in CH₂Cl₂ and separated on a silica cartridge using a series of solvents with 26% RCY.*

The radiochemical yields of all radioiododeiodination reactions strongly depend on the amount of the starting material. Consequently, low specific activities must still be considered as the major drawback of this method. In particular, this problem arose with large dose preparations of [¹³¹I]mIBG needed for therapy purposes. The pharmacological efficacy of mIBG necessitated the load limit of starting material. The various labeling techniques of mIBG have recently been reviewed and discussed (Wafelman et al. 1994).

In contrast to radioiododeiodination, exchange of bromine with radioiodine on aromatic systems is feasible for no-carrier-added syntheses. This method was, e.g., used to label fatty acid derivatives. Thus, 13-(4-[¹²³I]iodophenyl)-3-(p-phenylene)tridecanoic acid ([¹²³I]PHIPA 3-10) was prepared from the 4-bromophenyl derivative in a benzoic acid melt at an exchange temperature of 200°C (Liefhold and Eisenhut 1986). However, the method is laborious because two evaporation steps are needed before exchange can take place.

Radioiododebromination [¹²³I]iodide is evaporated under vacuum in a 1 ml glass ampoule made from a Pasteur Pipette. 10 µl (5 mM) of the bromo precursor and 40 µl 0.2 M benzoic acid are added, both dissolved in EtOH. The solution is shaken in order to dissolve the ¹²³I and evaporated slowly (!) until the precipitating solid appears dry. The ampoule is sealed under vacuum with a gas torch and heated at 200–230°C for 10 min. Then the cold ampoule is opened and the reaction mixture dissolved in 60-µl ethanol. For separation, this solution is injected completely in an analytical RP18-HPLC column. Seventy percent RCY is obtained for [¹²³I]PHIPA 3-10.

Reduction of the exchange temperature is achieved by the addition of catalytic amounts of Cu(I) and Cu(II) salts as well as HAuCl_4 . A series of methods have been published, e.g., mIBG, demonstrating the enhancement of labeling yields and specific activities at 100–140°C (reviewed in Wafelman et al. 1994). Although lower exchange temperatures are feasible, the presence of a transition metal may be another reason for product degradation. The following procedure exemplifies the transition metal-assisted exchange (Kämpfer et al. 1996).

Cu(I) assisted radioiododebromination. Forty microliter 11.5 mM (R,R)BrQNB dissolved in $\text{H}_2\text{O}/\text{EtOH}$ was mixed with 50 μl each of 10 mM Cu(I), Sn(II)SO_4 , and 9 mM ascorbic acid as well as 100 μl [^{123}I]iodide (150 MBq). The closed vial was heated in an autoclave at 132°C for 60 min. The resulting mixture was neutralized and purified over RP-18 cartridges with 57% RCY.

Radioiododehalogenation of aliphatic compounds parallel the experiences with the above mentioned aromatic systems. Due to the 40 kJ M^{-1} smaller bond strength, the exchange is effective at lower temperatures as compared to haloaryl groups. Less energy is, however, also required for the in vivo cleavage of the aliphatic I–C bond. In case of radioiodinated aliphatic long-chain fatty acids, the in vivo cleavage of radioiodine was prominent, mainly induced by the degradation of iodoacetic acid, the final product of β -oxidation. For new compounds, the stability of the aliphatic I–C bond has to be investigated in advance using in vivo experiments on animals.

44.3.3 Radioiododestannylation

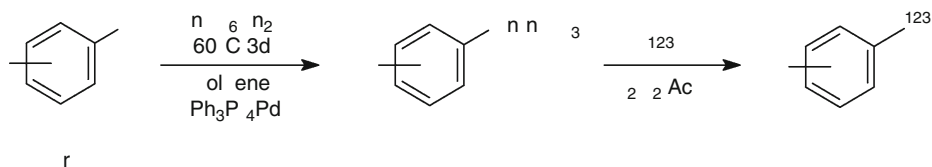
One of the most effective and convenient radioiodination methods represents the radioiododestannylation reaction (Fig. 44.3). The advantages of this technology can be summarized as follows: (1) product formation proceeds with high specific activity, (2) little experimental effort is necessary for a fast reaction, and (3) the regioselectivity of the label is given. In particular, obtaining a high specific activity is attractive for receptor-selective radiopharmaceuticals (e.g., Baldwin et al. 1993) and for the improvement of efficacy of therapeutic agents like mIBG (Vaidyanathan and Zalutsky 1993).

At the beginning, the bromo- or iodoaryl derivative intended for the labeling has to be stannylated. Most often, the $(\text{nBu})_3\text{Sn}$ group is used to replace the aryl halogen, but Me_3Sn groups have also been applied. As an example, the tributylstannylation of 4'-iodococaine illustrates the procedure (Metwally et al. 1992).

Tributylstannylation. A mixture of 4'-iodococaine (429 mg, 1 mM), bis-(tributyl)distannane (1,734 mg, 3 mM), tetrakis(triphenylphosphine)palladium(0) (15 mg, 0.013 mM) and anhydrous toluene (20 ml) was stirred at 60°C for 72 h under dry nitrogen. After cooling to room temperature,

Fig. 44.3

The radioiododestannylation reaction



the reaction mixture was filtered and the solvent was removed in a rotary evaporator. The residue was applied to a column of silica gel (230–400 mesh, 2×20 cm) and eluted with a step gradient of hexane followed by a mixture of hexane, diethyl ether, and isopropylamine (70:30:3). The fractions containing product were pooled and evaporated. The stannylated product was obtained as an oil (350 mg, 60% yield).


The stannylation yields vary considerably. 3β -(4-iodophenyl)tropane-2 β -carboxylate, β -CIT was, e.g., tributylstannylated with only 4% yield (Baldwin et al. 1993). Therefore, to avoid the loss of valuable iodinated starting material column, chromatography should not end after the tributylstannylated product has been separated. More polar solvents may allow to elute the starting material for future stannylation reactions. Great care should be focused on the contamination of the stannylated product with the iodinated starting material, since this would result in a reduction of the specific activity which in turn has an impact on receptor binding. The stannylated precursor should be protected from light and stored in a refrigerator. Aliquots of stock solutions in, e.g., ethanol can be used for months, but the quality has to be checked from time to time by HPLC. A general example is given with the following procedure.

Radioiododestannylation. [^{123}I]iodide (0.4–1 GBq) is mixed with 5 μl of a 10 mM solution of the tributylstannylated precursor. Check for homogeneity of the solution and add ethanol if necessary. Add 10 μl H_2O_2 (4.5% in acetic acid), vortex and let the mixture stand for 10 min at room temperature. Inject the mixture on a RP-18 HPLC column (270×4 mm) and perform either isocratic or gradient elution. Seventy to ninety percent of RCY (isolated) is usually obtained.

It should be noted that volatile [^{123}I]iodomethane was produced during the preparation of 5-[^{123}I]iodo-6-nitroquipazine from the respective trimethylstannylated precursor. In contrast to the procedure described above, heating to about 100°C might explain [^{123}I]iodomethane formation.

The introduction of a tri(*n*-butyl)stannylated vinyl or prop-2-enyl group as prosthetic groups represents another feature of the radioiododestannylation reaction of small organic compounds. (*E*)- and (*Z*)-3-(tri-*n*-butylstannyl)prop-2-en-1-yl *p*-toluenesulfonate were, e.g., used as synthons to form propenyl stannanes of spiperone and diprenorphine (Musachio and Lever 1992). The preparation of the synthon started with propargyl alcohol, tri-*n*-butyltin hydride, and the radical initiator α,α' -azoisobutyronitril. After tosylation, the resulting stannylated alcohols are ready for the synthesis of various stannylated compounds. Similar labeling strategies have been applied to cocaine and quinuclidinylbenzilate derivatives (Goodman et al. 1994; McPherson et al. 1993).

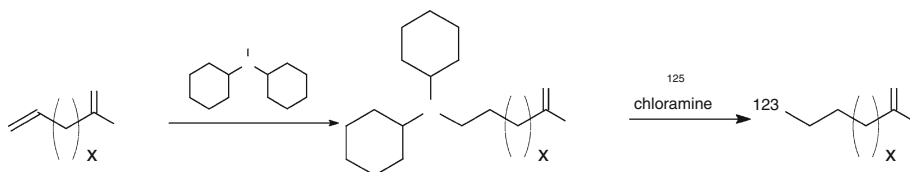
44.3.4 Radioiododeboronation

The oxidative cleavage of the boron–carbon bond with radioiodide/Chloramine-T has been shown to be useful for the radioiodination of various organic compounds (Kabalka et al. 1981). This method is characterized by the reaction sequence in  Fig. 44.4.

After hydroboration, oxidation of radioiodide is performed with Chloramine-T, forming HO-I, which then adds to the C–B bond. The reactivity of the C–B bonds depends on the position of boron, which can either be formed from a terminal double bond or from an internal alkene. While the former case produces two radioiodinated compounds, the latter forms only one. Therefore, dicyclohexylborane is used for the hydroboration step. Both reactions, hydroboration of the alkene and radioiodination can be performed in one sequence without isolating the intermediately formed trialkylborane.

■ Fig. 44.4

The radioiododeboronation reaction



Apart from aliphatic derivatives, radioiodovinyl and radioiodoaryl compounds are obtained from vinylboronic and arylboronic acid intermediates. Thus, catecholborane was used for the hydroboration of alkynes. The following example published for the preparation of 11-cholesterylundec-1-en-1-yl boronic acid (Kabalka et al. 1988) may serve as a generalized hydroboration procedure.

Hydroboration with catecholborane. A solution of ω -undecynyl cholesteryl ether (2.06 g, 3.81 mM), dry THF (15 ml), and catecholborane (1.2 ml, 10.3 mM) was stirred under nitrogen at 60°C overnight. After cooling the solution to room temperature, THF (28 ml) was added, followed by the dropwise addition of water (24 ml). The resulting mixture was stirred for 3 days. Water (150 ml) was added dropwise with vigorous stirring to precipitate the product. The crude product was collected and reprecipitated from THF (15 ml) using water, as described above, to facilitate the removal of catechol. The resulting white precipitate was collected and chromatographed on a silica gel (100 g) column eluting with methanol/dichloromethane to provide the 11-cholesterylundec-1-en-1-yl boronic acid (1.53 g, 69%).

The boronated precursor is stable and may be used from stock for radioiodination as described by the following procedure (Kabalka et al. 1988).

Radioiododeboronation. A solution of 11-cholesterylundec-1-en-1-yl boronic acid (20 μ l of a 0.5 M solution in 50 aqueous THF), THF (85 μ l), and Na¹²⁵I (5 μ l) was mixed in a vial. Chloramine-T (25 μ l of a 0.5 M solution in 50% aqueous THF) was added and the reaction mixture capped and allowed to stand at room temperature for 1 h. The product was extracted into ether (4 \times 1 ml) and concentrated with a stream of nitrogen. The concentrate was spotted equally on two TLC plates and developed with 4% ether/petroleum ether. The radioactive bands corresponding to the product were scraped and extracted with ether (4 \times 1 ml). The radiochemical yield was 17%.

The work-up of the reaction mixture may alternatively be performed with more convenience and higher separation efficiency by using RP18-HPLC technology. The radiochemical yields reported from other boronated compounds amounted up to 61% (Kabalka et al. 2000).

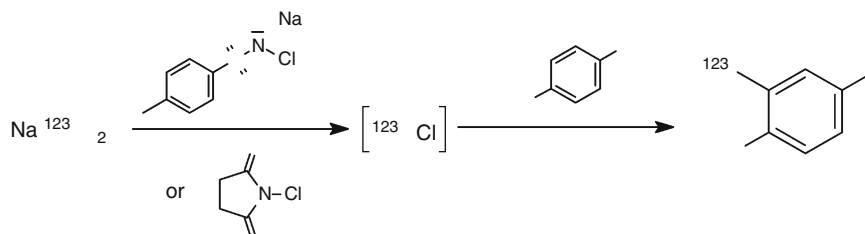
Compared to the radioiododestannylation and radioiododeboronation reactions described above, the radioiododesilylation and radioiododemercuration reactions currently play a minor role in the radioiodination of imaging agents.

44.3.5 Direct Radioiodination

Chloramine-T and *N*-chlorosuccinimide have often been used for the labeling of activated aromatic compounds with radioiodine (see also ▶ Sect. 44.4.1). The reaction is illustrated by the scheme outlined in ▶ Fig. 44.5.

Fig. 44.5

Direct radioiodination by electrophilic aromatic substitution

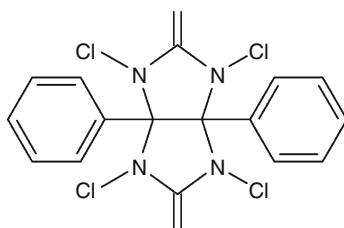


Both agents are widely applied as auxiliary agents for radioiodination. The in situ formed $\text{Cl-}^{123}\text{I}$ or Na^{123}I adds to activated phenyl residues by an electrophilic aromatic substitution reaction. Since tyrosine comprises an activated phenyl residue, the labeling of proteins and peptides is performed with this method (*vide infra*). For smaller organic compounds like 2-hydroxy-6-methoxy-*N*-[(1-ethyl-2-pyrrolidinyl)methyl]benzamide (BZM), Chloramine-T has also been applied for radioiodination (Kung et al. 1988).

Direct radioiodination with Chloramine-T. Chloramine-T solution ($50\ \mu\text{l}$, $1\ \text{mg}\ \text{mL}^{-1}$) was added to a mixture of BZM ($50\ \mu\text{l}$, $1\ \text{mg}\ \text{mL}^{-1}$), sodium [^{125}I]iodide ($10\ \mu\text{l}$, 37–185 MBq [$1\text{--}5\ \text{mCi}$]), no-carrier-added, and phosphate buffer ($0.3\ \text{mL}$, pH 3) in a sealed vial. The reaction was allowed to proceed at room temperature for 1.5 min. The reaction was terminated with the addition of sodium bisulfite ($0.1\ \text{mL}$, $10\ \text{mg}\ \text{mL}^{-1}$) and neutralized with $0.4\ \text{M}$ sodium bicarbonate ($0.5\ \text{mL}$). The product was extracted with ethyl acetate ($3 \times 1\ \text{mL}$). The combined organic layers were dried by passing through an anhydrous sodium sulfate column ($0.2 \times 5\ \text{cm}$). The organic solution was evaporated under a stream of nitrogen, and the residue was dissolved in absolute ethanol ($50\text{--}200\ \mu\text{l}$). The desired product, [^{125}I]BZM, was isolated from the unreacted BZM and a small amount of unknown radioactive impurities by HPLC on a reverse phase column, with an isocratic solvent system 82:18 acetonitrile – pH 7 buffer ($10\ \text{mM}$ 3,3-dimethylglutaric acid). After the appropriate fractions were collected, the solvent was evaporated under a stream of nitrogen, and the product was re-extracted with ethyl acetate ($1 \times 3\ \text{mL}$). The solution containing the no-carrier-added product was condensed to dryness and redissolved in absolute ethanol (radiochemical purity >95%, overall yield 60%).

The orientation of the substitution reaction is sometimes not predictable (► Fig. 44.6). The formation of [^{125}I]BZM may result in two isomers but only the (S)-(–)-3-[^{125}I]iodo-2-hydroxy derivative is formed. The position of the radioiodine can be investigated by ^1H -NMR of the stable iodo derivative. Comparison of the stable and radioiodinated compounds with HPLC is proving the substituent position.

1,3,4,6-Tetrachloro-3,6-diphenylglycoluril (for structure refer to ► Sect. 44.4.2), better known as IodogenTM, has been introduced as an alternative to Chloramine-T for direct radioiodination (Fraker and Speck 1978). The advantage of IodogenTM lies in its stability and sparing solubility in water which has made use of for radiolabeling proteins (*vide infra*). Thus, IodogenTM dissolved in methylene chloride provides a ready-to-use stock solution from which aliquots are transferred into a conical glass vial and evaporated. Addition of the precursor molecule together with radioiodide results in a reaction mixture ready for RP18-HPLC separation. The following procedure exemplifies the procedure for the production of [^{123}I]SCH23982 (dopamine D_1 antagonist) on an industrial scale (Beer et al. 1993).



Chemical structure of 1,3,4,6-tetrachloro-3,6-diphenyl-1,2,3,4-tetrahydro-2H-benzazepine

Direct radioiodination with IodogenTM. [¹²³I]NaI (9.25–18.5 GBq in 0.1 N NaOH) was evaporated to dryness by means of a gentle stream of nitrogen and elevated temperature. Five hundred micrograms of (R)-(+)-2,3,4,5-tetrahydro-3-methyl-5-phenyl-1H-3-benzazepine-7-ol, (R)-(+)-SCH23390, was dissolved in 1 ml of 0.36 M H₃PO₄ and added to the vial with the radioactivity. This mixture was transferred to a vial coated with 500 µg of IodogenTM and stirred for 20 min at room temperature. The reaction mixture was purified using RP-HPLC. The product peak was collected, neutralized with an equal volume of 0.45 N NaOH and passed through a sterile filter.

I-Cl is also formed by the reaction illustrated in [Fig. 44.7](#).

Radioiodination of organic compounds applying this redox reaction has therefore been proven useful in various preparations, e.g., L-3-[¹²³I]iodo-α-methyltyrosine ([¹²³I]IMT). This labeling procedure has been applied to preparations in clinical studies (Henze et al. 2002).

Direct radioiodination with KIO₃. Twenty microliters of 10 mM L-α-methyltyrosine in 1 N HCl and 5 µl 50 mM KIO₃ in water were mixed and transferred to a vial containing 400–1,200 MBq [¹²³I]NaI in 0.02 M NaOH. After 10 min, the mixture was purified using an analytical RP₁₈-HPLC column. The RCY amounted to 80–95%. In order to obtain reproducible high radiochemical yields, 10-µl 0.1 mM NaI solution in water may be added to the radioiodine if

Fig. 44.6

3-[¹²⁵I]iodo- (left) and 5-[¹²⁵I]iodo-IBZM derivative

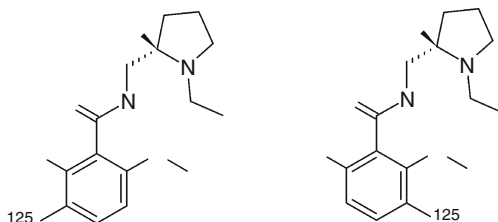
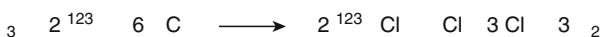


Fig. 44.7

ICI formation from radioiodide/IO₃[−]/HCl mixture



labeling with ^{123}I has to be performed. ^{131}I does not need this addition because intrinsic amounts of stable iodide are present.

An alternative oxidation agent for direct radioiodination is peracetic acid (Kung et al. 1991).

44.3.6 Other Methods

The preparation of radioiodinated arenes from aryl amines by means of the Sandmeyer reaction has proven to be impractical. The unstable diazonium compounds, however, may be converted into stable pyrrolidine triazenes or dialkyltriazenes and used as precursors for labeling. The reaction sequence using pyrrolidine is shown in Fig. 44.8.

For example, the labeling of (*R,S*)-(-)-1-azabicyclo[2.2.2]oct-3-yl-(*R,S*)- α -hydroxy- α -[4-[2-(3-methylpiperidin-1-yl)-1,2-diazaethylen-1-yl]phenyl]- α -phenylacetate (the 4-triazeno derivative of QNB) with ^{123}I using this reaction pathway was accomplished by the following procedure (Rzeszutarski et al. 1984).

One milligram (2.16 μM) of the 4-triazeno derivative of QNB in 100 μl trifluoroethanol (TFE) was added to 407–555 MBq sodium [^{123}I]iodide in 50–120 μl of 0.1 N NaOH. The pH was adjusted to 5.5 ± 0.5 with methanesulfonic acid in TFE. If the need arose, an additional amount of TFE was added to dissolve the reactants. The mixture was sealed in a vial and heated under stirring at 78°C for 50 min. After cooling, the reaction mixture was processed by HPLC. The average specific activity amounted to 20 GBq μM^{-1} and the RCY was 8%.

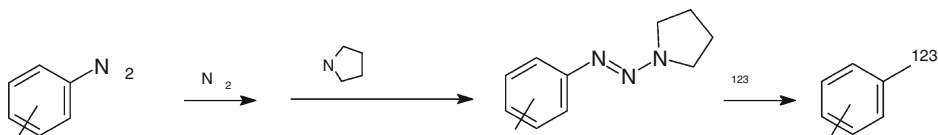
44.4 Radioiodination of Peptides and Proteins

As described in the previous paragraphs, radioiodination of aromatic compounds is usually performed by the electrophilic substitution mechanism. Peptides and proteins containing amino acids with aryl substituents can be labeled with radioiodine using this reaction. While the susceptibility of phenylalanine for electrophilic aromatic substitution is low, the reactivity is strongly increased by additional electron-donating substituents such as hydroxy or amine groups. The increase of the electron density in the aromatic ring leads to an activation for electrophilic attack. Consequently, tyrosine, in particular in its phenolate form at $\text{pH} > 7$, is the main site of protein iodination. In comparison with tyrosine, the electron density of the imidazole ring of histidine is lower. Therefore, electrophilic substitution reactions require higher pH and a higher amount of oxidant.

Most of the other alternatives to incorporate radioiodine into peptides and proteins such as the sulfenyl iodide formation of cysteine are reversible and do not, therefore, lead to stable

Fig. 44.8

The radioiododetriazene reaction



iodinated products. The indole ring of tryptophane can also be radioiodinated. However, iodinated tryptophane undergoes hydrolysis and oxidation reactions, resulting in the formation of an unstable oxindole. This leads to the cleavage of the peptide chain (Alexander 1974).

The addition of one radioiodine atom to large molecules such as antibodies does not usually affect their immunoreactivity. The iodine substituent is too small to induce significant conformational changes of the structure of large molecules. In contrast, the labeling process using oxidation agents as well as the addition of reducing agents to stop the labeling reaction may have destructive effects on sensitive sites of the biomolecules. Depending on the labeling conditions, denaturation can occur due to oligomerization, conformational changes due to the changes of functional groups, or the cleavage of disulfide bonds. Consequently, labeling reactions have to be adapted to the individual proteins or peptides including proof of functional integrity.

Due to the ease of handling and efficiency, the Chloramine-T method is still the most widely used radioiodination procedure and represents an effective way to label a variety of proteins and peptides such as albumins, globulins, neuropeptides, and chemokines. Several other methods, such as the enzymatically catalyzed iodination with lactoperoxidase, have been developed. These methods allow the labeling with mild reaction conditions. In the case of extreme oxidation, sensitive proteins such as pituitary hormones and reactive pre-iodinated compounds such as the Bolton and Hunter reagent can be used to incorporate radioiodine.

44.4.1 Chloramine-T

The sodium salt of *N*-chloro-*p*-toluenesulfonamide, Chloramine-T is a water-soluble reagent with strong oxidizing properties. At pH 7–8, Chloramine-T hydrolyzes and releases hypochlorite (ClO^-), which is an effective oxidizing agent that forms ICl upon contact with radioiodide (for reaction scheme refer to [Fig. 44.5](#), [Sect. 44.3.5](#)).

ICl rapidly undergoes electrophilic substitution predominantly with tyrosine residues of the target molecule. The reaction is fast and finishes within a few seconds. The optimum conditions for the mild incorporation of radioiodine into proteins are a low temperature of 4°C, a pH value in the range of 6–8, and a short reaction time of <1 min. Chloramine-T often degrades sensitive peptides. This has to be prevented by the addition of a reducing agent.

The use of cysteine as a reducing agent is not advisable for peptides or proteins with disulfide bridges. In this case, tyrosine is recommended as it stops the reaction by consuming excess I–Cl, or methionine, which is oxidized. Even though it induces harsher reaction conditions than iodogen, iodobeads, or lactoperoxidase (*vide infra*), Chloramine-T is the most commonly employed agent for radioiodinating peptides and proteins. Iodogen and iodobeads do not allow the labeling of tyrosine residues that are not present on the surface of a protein. Consequently, the amount of iodine that is incorporated into antibodies, e.g., is higher with Chloramine-T. Yields of up to 90% can be obtained with high specific activity. Chloramine-T has to be stored in darkness because it decomposes if exposed to light.

Radioiodination of proteins using Chloramine-T (McConahey and Dixon 1980). In a reaction vial, 10 µg of the protein is mixed with radioiodide in 50-µl 0.25 M phosphate buffer pH 7.5. Five microliters of a freshly prepared solution of Chloramine-T (2 mg ml⁻¹) in 0.25 M phosphate buffer pH 7.5 is added and the solution is mixed. After 30 s, 20 µl of a saturated solution of methionine in 0.25 M phosphate buffer pH 7.5 and 20 ml of a 1% solution

of a suitable carrier-protein (e.g., BSA) is added. The reaction mixture is purified on a size exclusion column or using another appropriate method.

The following example illustrates the procedure for the radioiodination of peptides.

Radioiodination of Tyr³-octreotide using Chloramine-T (modified from Bakker et al. 1990). Twenty-five microliters of 10^{−3} M Tyr³-octreotide is mixed in a reaction vial with 10 MBq ¹²⁵I. 10 μl of a freshly prepared solution of 10^{−2} M Chloramine-T in 0.25 M phosphate buffer pH 7.4 is added. After 30 s, 10 μl of a saturated solution of methionine in 0.25 M phosphate buffer pH 7.4 is added and the reaction mixture is vortexed. Purification is accomplished by reversed-phase HPLC. As Chloramine-T reveals a very similar retention time as the ¹²⁵I labeled Tyr³-octreotide, the eluent system H₂O/acetonitrile containing TFA is not suited for this purpose. Using a gradient of 0% B → 100% B in 30 min (A = Tris-phosphate buffer pH 2.6 and B = methanol), flow rate = 0.7 ml min^{−1}, the radiolabeled peptide can be purified. The ¹²⁵I-labeled peptide can be stored for up to 1 month at −20°C.

44.4.2 Iodogen

Iodogen, 1,3,4,6-tetrachloro-3α,6α-diphenylglycouril, was first described as a mild oxidizing agent for radioiodination by Fraker et al. (see also ▶ Sect. 44.3.5). This *N*-chloro compound is highly insoluble under aqueous conditions and can, therefore, be used as a “solid phase” oxidant.

The reaction mixture is simply separated from the oxidant by decantation. For this purpose, the compound is dissolved, e.g., in chloroform, added to the reaction vial, and coated onto the surface by careful evaporation of the solvent. The coated vials can be prepared in advance and stored in a desiccator. A mixture of the protein and radioiodide is incubated in the reaction vial for a few minutes. Thereafter, the mixture is transferred to a size exclusion or ion exchange column and separated from unbound radioiodide. The reaction proceeds with very little protein denaturation, which may be explained by the reaction on the solid phase (IodogenTM).

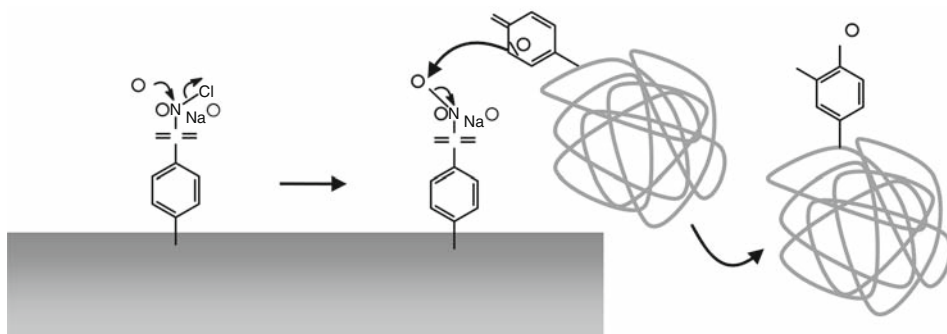
Iodination using IodogenTM (Fukunaga et al. 1990). 18.5 MBq of Na¹²⁵I in 50 μl of distilled water was added to a glass tube coated with 10 μg of IodogenTM and incubated for 7 min on ice. The solution was then transferred to a tube containing 1.5 μg of recombinant mouse G-CSF dissolved in 6 μl of 0.25 M sodium phosphate buffer (pH 7.1) and allowed to react for 10 min at 0°C. The reaction was stopped by adding approximately 1 mg of tyrosine powder, and the labeled G-CSF was separated from free [¹²⁵I]iodide by gel filtration on a PD-10 column (GE Healthcare) equilibrated with Dubbecco's phosphate-buffered saline (PBS) containing 0.1% gelatin, 0.005% Tween 20, and 0.02% NaN₃. The material eluted at void volume was then further purified using a Superose 12 column.

44.4.3 Iodobeads

Iodobeads represent an immobilized form of Chloramine-T (Markwell 1982). This commercially available reagent (Pierce) consists of hydrophilized polystyrene beads labeled with *N*-chlorobenzenesulfonamide. The labeling reaction starts when the beads are added to a mixture of radioiodide and protein to be labeled (▶ Fig. 44.9). The removal of the beads with tweezers or a Pasteur pipette stops the reaction. Consequently, no reducing agent has to be added to terminate the reaction. The method works over a fairly broad pH range (5.5–8.5) with the most favorable pH at 6.5.

■ Fig. 44.9

Reaction sequence for the radioiodination of a protein with Iodobeads. In the first step, the *N*-chloro substituent of the benzenesulfonamide is substituted by radioiodide. The covalently bound iodine reacts subsequently with an activated aromatic side chain of the protein. The degree of damage to the protein is restricted because the reaction only proceeds on the surface of the polymer beads.



Under these conditions, radioiodine incorporation of up to 99% can be achieved at labeled protein recovery rates of >90%. The reaction is more gentle than soluble Chloramine-T because there is less contact between the protein and the immobilized oxidizing agent. If the reaction is conducted at pH values above 8, it is possible to radioiodinate histidine residues. The reaction is believed to proceed in the close proximity of the surface of the polymer beads. An electrophilic iodosulfonamide intermediate species that reacts with either tyrosine or histidine residues of the protein to be labeled is formed.

Iodination using Iodobeads (derived from the manufacturers protocol, Pierce). One Iodobead is rinsed with phosphate buffer (depending on the amount of protein to be labeled, several beads have to be used; the maximum of protein is 500 µg/bead). The bead is placed into the reaction vial containing 100 µl 0.1 M phosphate buffer pH 6.5 followed by a solution of the [¹²⁵I]NaI. After 2 min, a solution of 100 µg of the protein in 100 µl 0.1 M phosphate buffer pH 6.5 is added and the mixture is shaken for 5 min. In order to separate the labeled protein from free iodine, the entire reaction mixture is applied to size exclusion chromatography using Sephadex G-25M. The concentration of protein can be determined by measuring the absorption at 280 nm.

44.4.4 Lactoperoxidase

In search of alternatives to Chloramine-T, Morrison (1980) demonstrated that lactoperoxidase from bovine milk was particularly effective for iodide oxidation and the radioiodination of proteins. The single strand polypeptide lactoperoxidase has a molecular weight of approximately 78 kD. The structure of lactoperoxidase contains a prosthetic heme group which is covalently linked to the protein at the active site of the enzyme. In the presence of minute quantities of hydrogen peroxide, lactoperoxidase oxidizes and binds radioiodide to proteins in the reaction mixture. The pH optimum of iodide oxidation by lactoperoxidase is 4–8.5 with an optimum at pH 5. The reaction is extremely rapid, allowing reaction times of less than 1 min. This provides very mild conditions and denaturation of proteins is low. Yields of up to 85% can be obtained and the method is widely used for labeling proteins and hormones. Lactoperoxidase may itself

become radioiodinated. It is difficult to remove the labeled peroxidase, particularly if the protein of interest is of similar molecular size. Therefore, this method is only suitable if the contamination with labeled lactoperoxidase does not interfere with the application of the labeled protein.

Iodination using lactoperoxidase (derived from the manufacturers protocol, Sigma-Aldrich). Lactoperoxidase is dissolved at a concentration of 10 mg mL^{-1} in 0.1 M sodium acetate buffer at pH 5.6. Aliquots can be stored at -80°C . Care should be taken because the enzyme is sensitive to extraneous substances in the reaction mixture, in particular azide and hydrazides. Ten micrograms of the protein are mixed with radioiodine and 100 ng of lactoperoxidase in $100 \mu\text{l}$ of 0.25 M sodium acetate buffer at pH 5.6. The reaction is started by gently mixing with 100 ng of a freshly prepared hydrogen peroxide solution ($10 \mu\text{g mL}^{-1}$). After standing at room temperature for 20 min , the reaction is stopped by the addition of 0.9 ml of a solution of 0.05 M sodium phosphate buffer at pH 7.4 and the reaction mixture is immediately purified on a Sephadex G-25 column.

The separation of lactoperoxidase from the labeled protein may be avoided by using the immobilized enzyme (David and Reisfeld 1974). This technique applies immobilized lactoperoxidase together with glucose oxidase, which produces H_2O_2 in the presence of glucose.

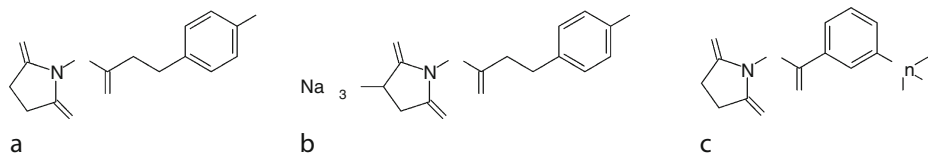
44.4.5 Heterobifunctional Reagents

Heterobifunctional reagents can be used to radioiodinate peptides or proteins, which do not contain a tyrosine residue or peptides whose biological function is impaired by tyrosine iodination. Heterobifunctional reagents typically combine 4-hydroxyphenyl groups with a moiety that is reactive toward, e.g., amine or thiol groups of the target molecule. The reactive groups include succinimidyl or sulfosuccinimidyl esters, which can be coupled to lysine residues; maleimides, which can be coupled to thiols; diazonium salts, which can be coupled to tyrosine; or histidine residues and hydrazides, which can be coupled to oxidized glycoproteins. In most of these heterobifunctional compounds, the moiety susceptible to radioiodination is a phenol derivative. Phenolic groups are, however, iodinated in the *ortho*- and *para*-position, yielding products which are analogous to naturally occurring iodotyrosines such as the thyroid hormone thyroxine. Due to the action of deiodinases and due to the reversibility of the electrophile aromatic substitution, these compounds are unstable in vivo.

As outlined in [Fig. 44.10](#), organotin derivatives have therefore been developed for radioiodination in the *meta*-position of the phenyl residue (Zalutsky and Narula 1987). Organotin derivatives can be iodinated by the radioiododestannylation reaction (see also

Fig. 44.10

Chemical structures of representative heterobifunctional reagents for the radioiodination of proteins. (a) Bolton and Hunter reagent, (b) water-soluble Bolton and Hunter reagent, (c) succinimidyl 3-(tributylstannyl)benzoate



► Sect. 44.3.3) in the presence of hydroperoxide. These compounds proved to be highly resistant to deiodination processes in vivo (Zalutsky et al. 1989).

The radioiodinated Bolton and Hunter reagent (3-(4-hydroxy-3-[125 I]iodo-phenyl)-*N*-succinimidyl-propionate) is the prototype of a heterobifunctional reagent used for the labeling of peptides and proteins (Bolton and Hunter 1973, 1973) (► Fig. 44.10). Proteins lacking tyrosines or proteins sensitive against the denaturing influence of oxidizing agents are labeled via amide bond formation at lysine residues. The optimum condition for the conjugation of the Bolton and Hunter reagent with *N*-terminal amino groups is at a pH of 8.5.

Iodination of Annexin V with water-soluble Bolton and Hunter reagent (Russel et al. 2002). Water-soluble Bolton and Hunter reagent was dissolved in a glass vial in dimethyl sulfoxide at 1.5 mM (0.55 mg mL⁻¹). Ten microliters of Chloramine-T (5 mg mL⁻¹ in PBS) were added to Na¹²⁵I (37 MBq) neutralized in 10 µl PBS, followed by 1 µl water-soluble Bolton and Hunter reagent. The reaction was allowed to proceed for 1 min, stopped by the addition of 10 µl sodium metabisulfite (12 mg mL⁻¹ in PBS), and immediate addition of the Annexin (50 µg protein in 0.5 M borate pH 9.2). After 1 h, the conjugation reaction was stopped by the addition of 300 µl of 0.2 M glycine in 0.2 M borate (pH 8). Annexin V was purified by spinning repeatedly through a Microcon concentrator (Millipore).

44.5 Rating of Radioiodination Methods

For routine labeling of radiopharmaceuticals, the most convenient procedures are recommended because time is a factor barely available for chemists, especially from the physician's point of view. Needless to state, the physical half-life of the more exotic iodine radioisotopes requires similar efforts. Thus, simple pipetting steps are mandatory for the preparation to fulfill the requirements speed and radiation protection. In addition, pipetting steps can be automated and help to optimize the latter aspect.

A key position for radiolabeling is therefore assigned for a suitable labeling precursor, which assures high yields of the expected radiopharmaceutical. The reactions summarized in ► Table 44.2 are in the authors' view the most appropriate radioiodination methods.

The assessment of the radioiododestannylation reaction as the best method relies on the ease of reaction performance giving high radiochemical yields with high specific activity and a predictable regioselective attachment of the radioiodine. This advantage has its price, however: the preceding synthesis of the stannylated precursor is labor intensive. Nevertheless,

■ Table 44.2

Radioiodination methods

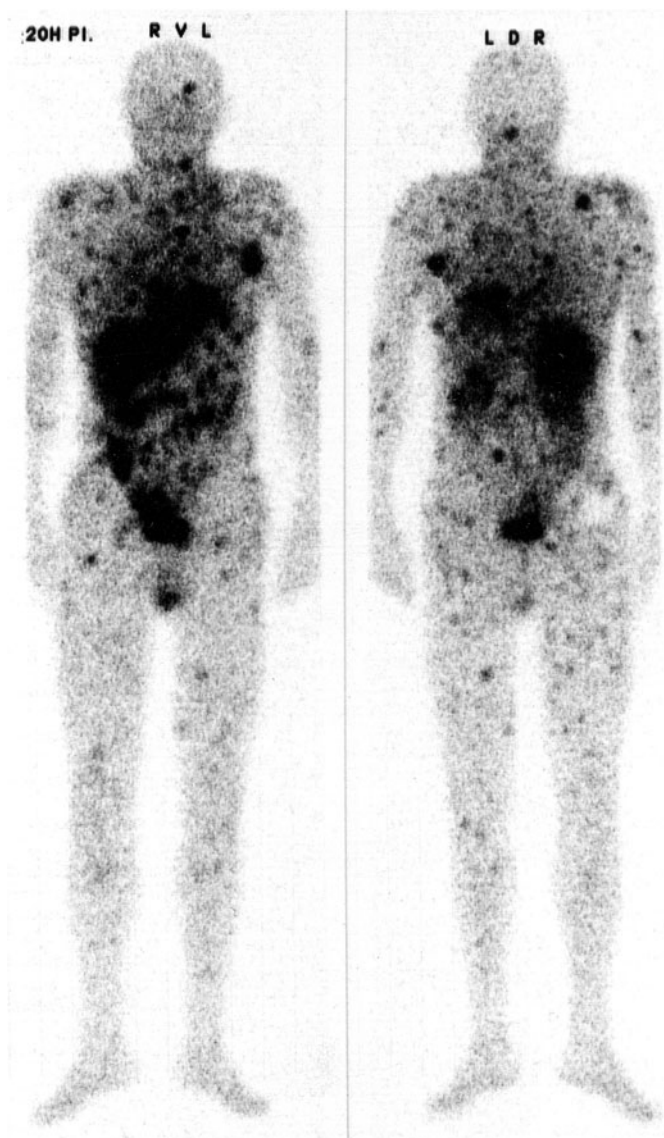
Method	Specific activity ^a	RCY ^b	Position of radioiodine	Rating
Radioiododethallation	Medium/high	High	Varies	Good
Radioiododehalogenation	Medium/high	High	Regioselective	Labor intensive
Radioiododestannylation	High	High	Regioselective	Best
direct radioiodination	Medium/high	High	Varies	Good
heterobifunctional reagents	Low	Low	Varies	Labor intensive

^aHigh: >50 GBq µM⁻¹; medium: between 10 and 50 GBq µM⁻¹; low: <10 GBq µM⁻¹

^bRCY radiochemical yield: high: >60%; low: <30% (isolated final product)

■ Fig. 44.11

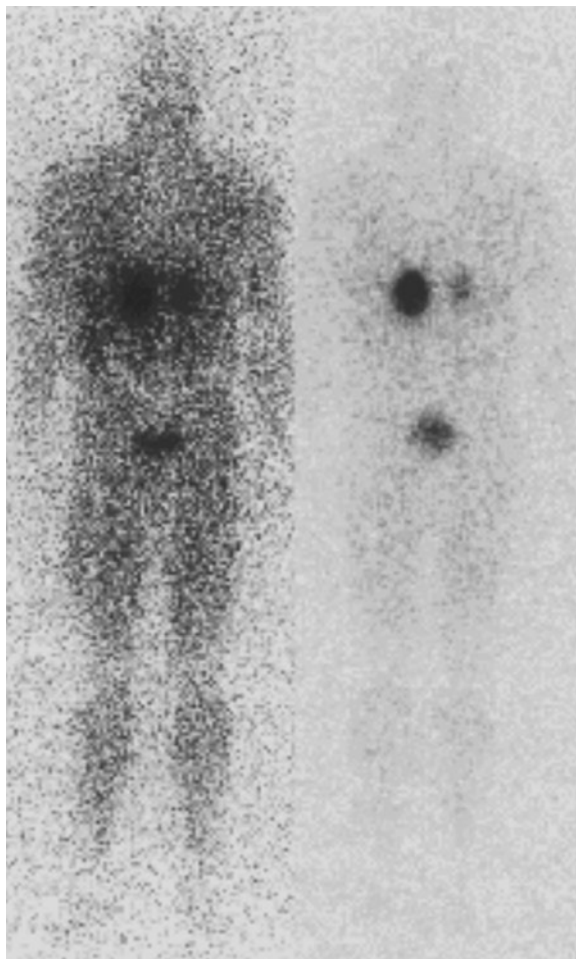
Disseminated visceral, soft-tissue and lymph node metastases 20 h after injection of [^{123}I]IMBA (Image by courtesy of B. Bubeck)



owing to the stability of the stannylated precursors and the very small quantities needed for the radioiododestannylation reaction, this work is worth the effort. The other methods, such as radioiododethallation and direct radioiodination, are also often applied in routine radiolabeling reactions. The only disadvantage of these methods is the potential formation of by-products, which have to be removed from the final product.

■ Fig. 44.12

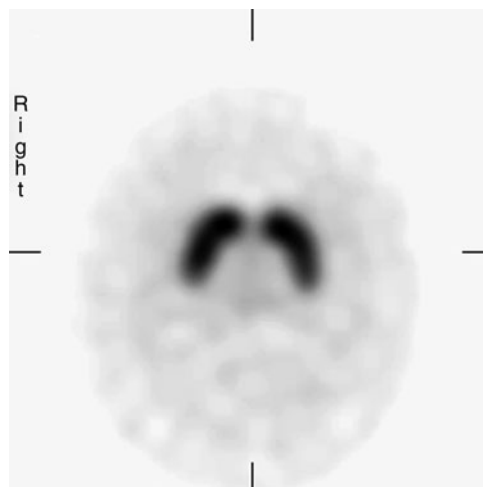
Bilateral pheochromocytoma (M. Recklinghausen), 1 (left) and 24 h post injection of [^{123}I]mIBG (Image by courtesy of U. Haberkorn)



The removal of by-products, precursor, and unreacted radioiodide is mandatory for all radiolabeling reactions. Several chromatographic techniques may be applied to this purpose. Among them, RP_{18} HPLC is currently the most powerful method because it is easy to perform and the separation efficiency is very high under gradient conditions. Evaporation of the organic solvent from the separated radiopharmaceutical may sometimes be time consuming. It should therefore be tested whether ethanol can be used in combination with, e.g., Tris-phosphate buffer for the separation task. This eluate may be formulated for intravenous application without solvent evaporation.

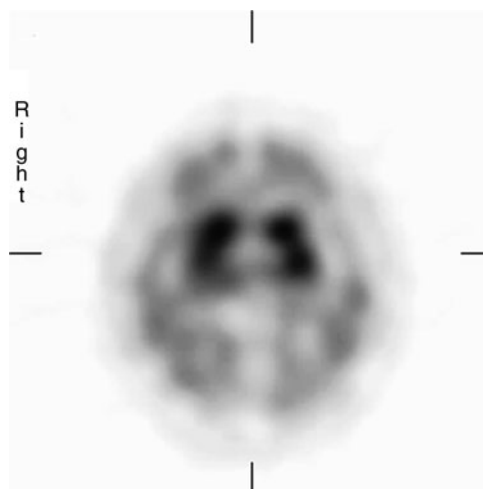
■ Fig. 44.13

Transaxial SPECT image showing striatal accumulation of [^{123}I] β -CIT (Image by courtesy of K. Tatsch)



■ Fig. 44.14

Transaxial SPECT image showing accumulation of [^{123}I]IBZM in the basal ganglia and to a lesser extent in the cortex (Image by courtesy of K. Tatsch)



In case unreacted radioiodide is the only contaminant after, e.g., direct radioiodination, its removal may be accomplished by filtration over AgCl

Dry AgCl of 0.5 g is transferred to a Pasteur Pipette which was tipped before with glass wool. This small column removed quantitatively radioiodide from the reaction mixtures of the

radioiododehalogenation reaction used for [^{123}I]OIH (Sinn et al. 1986) and the direct radioiodination of benzylidenediphosphonates (Eisenhut 1984).

RP₁₈ cartridges (e.g., SepPack, Waters) have also been used for the removal of unwanted reaction products. The efforts to establish reliable separation techniques using cartridge technology are, however, hampered by several drawbacks: (1) The separation efficiency is low because of a small bed volume. (2) The cartridge capacity is too small to separate the labeling mixture. (3) UV and gamma online monitoring is not possible, and (4) the radiation exposure is higher because of the more complicated handling. Compared to the analytical RP₁₈ HPLC columns, RP₁₈ cartridges may be useful only for simple separation steps depending on large lipophilicity differences.

44.6 Examples of Clinical Applications

44.6.1 Radioiododethallation

[^{123}I]IMBA (*N*-(2-diethylaminoethyl)-3-[^{123}I]iodo-4-methoxybenzamide) (► Fig. 44.11)

44.6.2 Radioiododehalogenation

[^{123}I]mIBG (3-[^{123}I]iodo-meta-benzylguanidine) (► Fig. 44.12)

44.6.3 Radioiododestannylation

[^{123}I]β-CIT (3β-(4-[^{123}I]iodophenyl)tropane-2β-carboxylate) (► Fig. 44.13)

44.6.4 Direct Radioiodination

[^{123}I]IBZM ((S)-(-)-3-[^{123}I]iodo-2-hydroxy-6-methoxy-*N*-[(1-ethyl-2-pyrrolidinyl)methyl]benzamide) (► Fig. 44.14)

References

- | | |
|---|---|
| <p>Alexander NM (1974) <i>J Biol Chem</i> 249:1946</p> <p>Bakker WH, Krenning EP, Breeman WA, Koper JW, Kooij PP, Reubi JC, Klijn JG, Visser TJ, Docter R, Lamberts SW (1990) <i>J Nucl Med</i> 31:1501</p> <p>Baldwin RM, Zea-Ponce Y, Zoghbi SS, Laurelle M, Al-Tikriti MS, Sybirska EH, Malison RT, Neumeyer JL, Milius RA, Wang S, Stabin M, Smith EO, Charney DS, Hoffer PB, Innis RB (1993) <i>Nucl Med Biol</i> 20:597</p> | <p>Beer H-F, Lin S, Bläuenstein P, Hasler P, Schubiger PA, Maier A, Lichtensteiger W, Oettli R, Bekir A, Weder B (1993) <i>Nucl Med Biol</i> 20:607</p> <p>Bolton AE, Hunter WM (1973) <i>Biochem J</i> 133:529</p> <p>Coenen HH, Moerlein SM, Stöcklin G (1983) <i>Radiochim Acta</i> 34:47</p> <p>David GS, Reisfeld RA (1974) <i>Biochemistry</i> 13:1014</p> <p>Eisenhut M (1982) <i>Appl Radiat Isot</i> 33:499</p> <p>Eisenhut M (1984) <i>J Nucl Med</i> 25:1356</p> |
|---|---|

- Eisenhut M, Lehmann WD, Hull WE, Just WW, Hoffend J, Zehelein J, Zimmermann R (2000a) *J Nucl Med* 38:1864
- Eisenhut M, Hull WE, Mohammed A, Mier W, Lay D, Just W, Gorgas K, Lehmann WD, Haberkorn U (2000b) *J Med Chem* 43:3913
- Fraker PJ, Speck JC (1978) *Biochem Biophys Res Commun* 80:849
- Fukunaga R, Ishizaka-Ikeda E, Nagata S (1990) *J Biol Chem* 265:14008
- Goodman MM, Kirsch G, Knapp FF Jr (1982) *J Labelled Compd Rad* 19:1316
- Goodman MM, Kung M-P, Kabalka GW, Kung HF, Switzer R (1994) *J Med Chem* 37:1535
- Haberkorn U, Kinscherf R, Krammer PH, Mier W, Eisenhut M (2001) *Nucl Med Biol* 28:793
- Henze M, Mohammed A, Schlemmer H, Herfarth KK, Mier W, Eisenhut M, Debus J, Haberkorn U (2002) *Eur J Nucl Med* 29:1455
- Kabalka GW, Gooch EE, Sastry AR (1981) *J Nucl Med* 22:908
- Kabalka GW, Lambert SJ, Jinaraj VK (1988) *J Labelled Compd Rad* 39:1113
- Kabalka GW, Shoup TM, Daniel GB, Goodman MM (2000) *Nucl Med Biol* 27:279
- Kämpfer I, Heinicke J, Sorger D, Schulze K, Schliebs R, Knapp WH (1996) *J Labelled Compd Rad* 38:1047
- Kulkarni P, Parkey RW (1982) *J Labelled Compd Rad* 19:1319
- Kung HF, Kasliwal R, Pan S, Kung M-P, Mach RH, Guo Y-Z (1988) *J Med Chem* 31:1039
- Kung M-P, Liu B-L, Yang YY, Billings JJ, Kung HF (1991) *J Nucl Med* 32:339
- Liefhold J, Eisenhut M (1986) *J Labelled Compd Rad* 23:1239
- Linz U (1982) *J Labelled Compd Rad* 10:1151
- Mangner TJ, Wu J-L, Wieland DM (1982) *J Org Chem* 47:1484
- Markwell MAK (1982) *Anal Biochem* 125:427
- McConahey PJ, Dixon FJ (1980) *Meth Enzymol* 70:210
- McPherson DW, DeHaven-Hudkins DL, Callahan AP, Knapp FF Jr (1993) *J Med Chem* 36:848
- Mekushev EB (1988) *Synthesis* 923
- Metwally SAM, Gatley SJ, Wolf AP, Yu D-W (1992) *J Labelled Compd Rad* 31:219
- Mier W (2002) unpublished results
- Mohammed A, Nicholl C, Titsch U, Eisenhut M (1997) *Nucl Med Biol* 24:373
- Morrison M (1980) *Meth Enzymol* 70:214
- Musachio JL, Lever JR (1992) *Bioconjug Chem* 3:167
- Nicholl C, Mohammed A, Hull WE, Bubeck B, Eisenhut M (1997) *J Nucl Med* 38:127
- Pfennig G, Klewe-Nebenius H, Seelman-Eggebert W (2006) In: Chart of the nuclides. Kernforschungszentrum Karlsruhe, 7th edn
- Rellas JS, Corbett JR, Kulkarni P, Morgan C, Devous MD, Buja LM, Bush L, Parkey RW, Willerson JT, Lewis SE (1983) *Am J Cardiol* 52:1326
- Ritverc (2003) <http://www.ritverc.com/>
- Russel JS, O'Donoghue JA, Finn R, Koziorowski J, Ruan S, Humm JL, Ling CC (2002) *J Nucl Med* 43:671
- Rzeszutarski WJ, Eckelman WC, Francis BE, Simms DA, Gibson RE, Jagoda EM, Grissom MP, Eng RR, Conklin JJ, Reba RC (1984) *J Med Chem* 27:156
- Scherberg NH (1974) *Biochim Biophys Acta* 340:446
- Sinn H-J, Schrenk HH, Maier-Borst W (1986) *Appl Radiat Isot* 37:17
- Vaidyanathan G, Zalutsky MR (1993) *Appl Radiat Isot* 44:621
- Van Dort ME, Ciliax BJ, Gildersleeve DL, Sherman PS, Rosenspire KC, Young AB, Junck L, Wieland DM (1988) *J Med Chem* 31:2081
- Wafelman AR, Konings MCP, Hoefnagel CA, Maes RAA, Beijnen JH (1994) *Appl Radiat Isot* 45:997
- Wilbur DS (1992) *Bioconjug Chem* 3:433
- Zalutsky MR, Narula AS (1987) *Int J Rad Appl Instrum A* 38:1051
- Zalutsky MR, Noska MA, Colapinto EV, Garg PK, Bigner DD (1989) *Cancer Res* 49:5543



45 Radiometals (non-Tc, non-Re) and Bifunctional Labeling Chemistry

M. Fani¹ · S. Good² · H. R. Maecke¹

¹University Hospital Freiburg, Freiburg, Germany

²University Hospital Basel, Basel, Switzerland

45.1	<i>Introduction</i>	2144
45.2	<i>Choice and Synthesis of Bifunctional Chelators</i>	2146
45.2.1	Role of the Chelator in the Design of Radiopharmaceuticals	2146
45.2.2	Requirements for a BFC	2147
45.2.3	Acyclic Bifunctional Chelators	2149
45.2.4	Macrocyclic Bifunctional Chelators	2152
45.3	<i>Examples of Radiometal–Chelate–Biomolecule Conjugates</i>	2165
45.3.1	Synthesis and Characterization of Chelator–Biomolecule Conjugates	2165
45.3.2	Dependence of Radiometal on Target Binding Affinity and Biodistribution	2169
45.4	<i>Structure and Stability of (Radio) Metal Complexes</i>	2170
45.5	<i>Outlook</i>	2175

Abstract: Radiometals are of increased current interest because of the growing use of targeted radiotherapy for tumors and the development of generators that produce positron-emitting radiometals. In addition, biomedical cyclotrons allow the cheap production of some relevant radiometals. The design of the corresponding radiopharmaceuticals includes the synthesis of bifunctional chelators, which carry a functional unit for the immobilization of the radiometal and a functional group for the covalent attachment to a vector molecule. Radiometals of interest for therapeutic applications are some lanthanides, ^{67}Cu , and ^{90}Y . For diagnostic applications ^{61}Cu , ^{62}Cu , ^{64}Cu , ^{89}Zr , and ^{68}Ga are currently used and corresponding radiopharmaceuticals are being designed. In this chapter, some properties and the synthesis of bifunctional chelators including metal ion selectivity and special aspects of coupling chemistry are being described.

45.1 Introduction

The use of radiometals (non-Tc, non-Re) has increased over the last 10 years and their chemistry and radiopharmacy have received renewed interest. One of the reasons is the development of generators that produce positron-emitting radiometals along with the technological progress, which led to the combination of imaging techniques, such as the positron emission tomography/computerized tomography (PET/CT) instruments, but the main reason is the fast development of clinical targeted radiotherapy in nuclear oncology. In principle, this technique can deliver selectively high linear energy transfer (LET) radiation to the tumor site. The search for an ideal therapeutic radionuclide – which most likely does not exist – has been the driving force to produce radionuclides with different half-lives and energy or even emitting different particles. In addition, efforts to produce some of the interesting carrier-free lanthanides appear to be successful and may lead to new therapeutic radionuclides. The currently most often used therapeutic radiometals are ^{90}Y , ^{177}Lu , and the two Re-isotopes ^{186}Re and ^{188}Re (see [Chap. 46](#) of this Volume).

Of particular interest in this respect is the class of lanthanides including $^{90}\text{Y}^{3+}$; several of them can be produced in high-flux reactors. As they have similar chemical characteristics, their production and use in therapeutic radiopharmaceuticals would allow studying the influence of dose rate and β^- energy on tumor response as it can be assumed that the same labeling chemistry can be applied to all lanthanide-based radiopharmaceuticals. This will most likely result in identical or at least very similar pharmacokinetics. The radiophysical properties of the radiolanthanides under study are compiled in [Table 45.2](#) (ICRP 1983).

Yttrium-90 has similar chemical properties and is usually being considered an analog of the lanthanides (Cotton and Wilkinson 1988). Its major production route is via the $^{90}\text{Sr}/^{90}\text{Y}$ generator (see [Chap. 40](#) of this Volume). All lanthanides in their major oxidation state 3+ can be considered hard Lewis acids and the best way to stabilize them for in vivo use is with macrocyclic chelators like DOTA (1,4,7,10-tetraaza-dodecane-1,4,7,10-tetraacetic acid) and modifications thereof.

The radioisotopes of copper represent another important group. Copper radioisotopes and their radiopharmaceuticals have been discussed in some recent reviews (Wadas et al. 2007; Anderson and Ferdani 2009; Shokeen and Anderson 2009). Radioisotopes of copper offer a variety of potential applications as their radiophysical properties are almost unique ([Tables 45.1](#) and [45.2](#)) (ICRP 1983). They offer a selection of different decay patterns: β^- , electron capture, and positron emission (β^+). Copper-64 combines all three decay modes, which makes it particularly attractive and versatile. It can be produced in large quantities using

Table 45.1

Nuclear properties of some gamma and positron emitting diagnostic radionuclides (ICRP 1983)

Isotope	Half-life [h]	Decay mode	\bar{E}_β [keV] (%)	E_γ [keV] (%)
⁶⁷ Ga	78.3	EC, Auger		93 (38), 185 (21)
¹¹¹ In	67.2	Auger, γ		171 (90), 247 (94)
⁵⁵ Co	17.5	β^+ , EC	650 (46), 437 (27)	931 (75)
⁶⁰ Cu	0.39	β^+ , EC	1,325 (15), 873 (48)	1,792 (45), 1,332 (88)
⁶¹ Cu	3.4	β^+ , EC	527 (50)	656 (10), 283 (13)
⁶² Cu	0.16	β^+ , EC	1,315 (98)	1,173 (0.3)
⁶⁴ Cu	12.9	β^- , β^+ , EC	190 (37) (β^-), 278 (18) (β^+)	1,346 (0.5)
⁶⁶ Ga	9.4	β^+ , EC	1,903 (50), 397 (4)	1,039 (38)
⁶⁸ Ga	1.1	β^+ , EC	836 (88)	1,077 (3)
⁸⁶ Y	14.7	β^+ , EC	550 (13)	1,077 (83), 777 (22)
⁸⁹ Zr	78.5	β^+ , EC	395 (23)	909 (99.9)
⁹⁰ Nb	14.6	β^+ , EC	662 (54)	2,319 (82), 1,129 (92)

Table 45.2

Nuclear properties of some therapeutic radiometals (ICRP 1983)

Isotope	Half-life	Decay mode	\bar{E}_β [MeV] (%)	E_γ [keV] (%)
⁴⁷ Sc	3.35 days	β^- , γ	0.14 (68), 0.20 (32)	159 (68)
⁶⁷ Cu	2.58 days	β^- , γ	0.19 (20), 0.12 (57)	93 (16), 185 (49)
⁹⁰ Y	2.67 days	β^-	0.93 (100)	–
¹¹¹ Ag	7.45 days	β^- , γ	0.36 (93)	342 (6.7)
¹⁹⁸ Au	2.7 days	β^- , γ	0.31 (99)	412 (95)
¹⁹⁹ Au	3.1 days	β^- , γ	0.13 (15), 0.08 (66)	158 (37)
²¹² Bi	1.0 h	α	6.1 (25) (α)	727 (12)
		β^- , γ	0.83 (48) (β^-)	
²¹³ Bi	46 min	α , γ	5.8 (2) (α), 0.49 (65) (α), 0.32 (32) (α)	440 (27)
²²⁵ Ac	10 days	α	5.83 (51) (α)	100 (3.5)
Lanthanides				
¹⁴⁹ Pm	2.21 days	β^- , γ	0.37 (97)	286 (2.9)
¹⁵³ Sm	1.95 days	β^- , γ	0.23 (43), 0.20 (35)	103 (28)
¹⁶⁶ Dy	3.40 days	β^- , γ	0.12 (91)	82.5 (13)
¹⁶⁶ Ho	1.12 days	β^- , γ	0.69 (51), 0.65 (48)	80.6 (6.2)
¹⁷⁷ Lu	6.71 days	β^- , γ	0.15 (79)	208 (11)

biomedical cyclotrons (McCarthy et al. 1997; Obata et al. 2003, see also Chap. 39 of this Volume). It may be used in PET imaging and targeted radiotherapy.

Another attractive aspect of copper radiopharmacy is the fact that the ⁶²Zn/⁶²Cu PET generator can be inexpensively and reliably produced and was shown to be of use in the clinic successfully in the production of the PET perfusion agent ⁶²Cu-PTSM (see Chap. 40 of this Volume).

The coordination chemistry of copper is somewhat more complex than the one of the lanthanides. The most important oxidation state in aqueous solution is Cu^{II} but Cu^{I} is accessible in physiological medium and appears to play a role in the trapping mechanism of copper radiopharmaceuticals used to image hypoxia. Cu^{II} has the electron configuration $[\text{Ar}]3\text{d}^9$, which causes the octahedral and tetrahedral complexes to be distorted by Jahn–Teller effect. This has a profound effect on the stereochemistry and Cu^{II} complexes of planar, distorted tetrahedral, pentacoordinate, and tetragonally distorted octahedral geometry have been characterized. The kinetics of ligand exchange usually is very fast, Cu^{II} complexes are labile, and the design of Cu^{II} radiopharmaceuticals relies on the use of macrocyclic ligands. This condition affords kinetically stable radiocopper complexes.

Another successfully used and commercially available generator system is the $^{68}\text{Ge}/^{68}\text{Ga}$ generator that produces $^{68}\text{Ga}^{3+}$ in 0.1–1 N HCl, which may become an additional incentive to develop radiogallium-based radiopharmaceuticals (Al-Nahhas et al. 2007; Fani et al. 2008, see also [Chap. 40](#) of this Volume). The development of small receptor avid peptides that clear the blood very quickly and show fast target localization are ideally suited for short-lived positron emitters (Hoffmann et al. 2001; Henze et al. 2001; Maecke et al. 2005; Antunes et al. 2007a; Prasad et al. 2010). In addition, ^{66}Ga , a 9.4 h half-life positron emitter, and ^{67}Ga ($T_{1/2} = 78.3$ h) decaying via electron capture with three emissions at 93 keV (38%), 185 keV (24%), and 300 keV (16%) are available. Gallium-67 was also proposed as a therapeutic radionuclide for it is a reasonably efficient Auger-emitter. Ga^{3+} is quite similar to the high-spin Fe^{3+} ion with respect to its coordination chemistry, is also classified as a hard Lewis acid, forming thermodynamically stable complexes with ligands that are hard Lewis bases, such as ligands containing oxygen and nitrogen.

45.2 Choice and Synthesis of Bifunctional Chelators

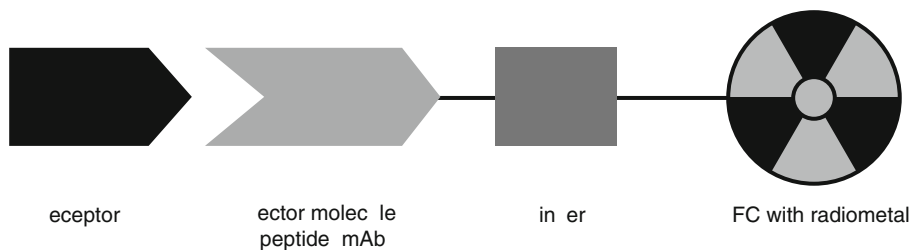
45.2.1 Role of the Chelator in the Design of Radiopharmaceuticals

Within the last decades, much research has been done in the development of new receptor targeting radiometal labeled pharmaceuticals, in particular peptides (Fichna and Janecka 2003; Reubi and Maecke 2008; Eberle and Mild 2009). In general, the design of these pharmaceuticals can be divided into four different parts ([Fig. 45.1](#)):

- A biomolecule (peptide, antibody) that acts as a target specific vector
- A linker

Fig. 45.1

Design of a receptor targeting radiometal labeled radiopharmaceutical



- A bifunctional chelator (BFC)
- A metallic radionuclide

The BFC consists of a chelating moiety to complex the radiometal and a functional group for the covalent attachment of the biomolecule or the linker (Volkert and Hoffmann 1999; Heppeler et al. 2000; Mäcke and Good 2002; Brechbiel 2008; Liu 2008).

While the nature of the vector molecule is determined by the cellular target (i.e., cell surface receptor), the linker is dependent on the pharmacokinetic requirements of the pharmaceutical (Antunes et al. 2007b; Fragozeorgi et al. 2009). It may influence the hydrophilicity of the conjugate and so improve the pharmacokinetics. The linker can also act as a separator between the BFC and the biomolecule to prevent steric influence of the chelator on the binding affinity of the receptor targeting part of the pharmaceutical. The choice of the radiometal is dependent on the following:

- The medical objective (diagnosis, therapy)
- The availability
- The required radiation dose
- The physical half-life
- The cost
- Other factors

(Volkert et al. 1991; Schubiger et al. 1996; Reichert et al. 1999).

The chemical nature of the radiometal then determines the choice of the BFC.

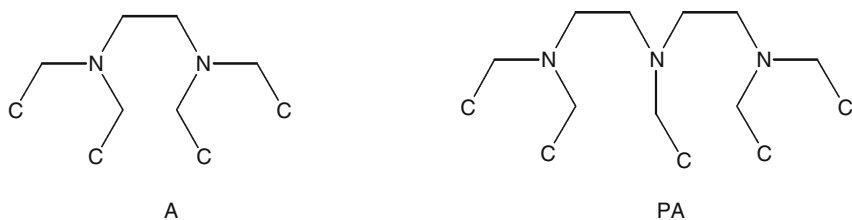
45.2.2 Requirements for a BFC

There is a broad range of requirements for a BFC (Liu and Edwards 2001; Brechbiel 2008; Liu 2008). As mentioned before, a BFC has to form metal chelates with high thermodynamic stability or better kinetic inertness at $5 < \text{pH} < 7.5$. These physicochemical properties are needed because the loss of radiometal would cause undesirable side effects by accumulation in nontarget organs. This is especially important because the free radiometals may show a high toxicity (i.e., $^{177}\text{Lu}^{3+}$, $^{90}\text{Y}^{3+}$, or $^{153}\text{Sm}^{3+}$ are “bone seekers” and would cause bone marrow damage). The BFC is often competing with natural chelators present in the blood stream like transferrin or serum albumin for instance.

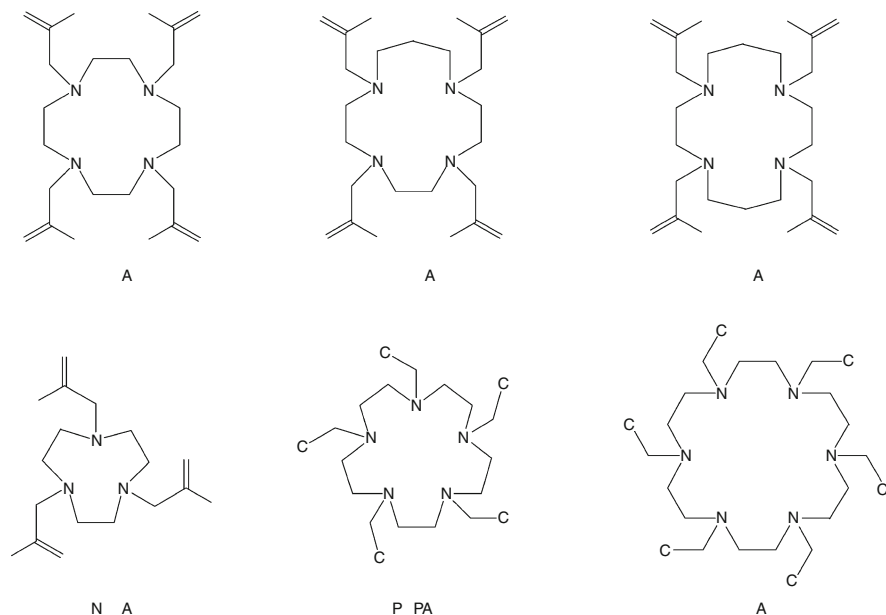
At least as important as the thermodynamic stability is the kinetic inertness because this is the factor that reflects the rate of dissociation of the metal ion from the BFC. Fast dissociation kinetics is often observed in complexes with acyclic chelators or chelators with nonoptimal

■ Fig. 45.2

Selected acyclic chelators based on polyazaalkanes with carboxylate functionalization



■ Fig. 45.3

Selected macrocyclic chelators based on polyazamacrocyclic cores with carboxylate functionalization

denticity (● Fig. 45.2) leading to low in vivo stability. Complexes based on a macrocyclic framework (● Fig. 45.3) often show much higher kinetic inertness.

Unfortunately, macrocyclic BFCs often require harsh labeling conditions (high temperature) to achieve a high labeling yield. Elevated temperature may be problematic especially in the labeling of antibodies because of unfolding of the protein and loss of the binding affinity of the antibody to the desired target receptor. Therefore, for the use with antibodies, it might be of advantage to use acyclic chelators. Finally, the BFC needs to be stable against radiolytic decomposition. This might become a crucial point if radiometals with a high linear energy transfer (LET) like α -emitters or high-energy β^- emitters are used.

The BFC needs to be attached to a biomolecule. There are many functional groups for conjugation available; some will be discussed later in this chapter. The conditions to perform the reaction between biomolecule and BFC have to be compatible with the properties of the two molecules. Undesired modifications of the biomolecule might lead to a loss of binding affinity of the radiopharmaceutical. To introduce a conjugation site to the BFC, the backbone of the chelator may be modified as follows:

- By attaching an additional functional group
- By modifying an existing functional group
- By following a selective protection strategy

While the first route preserves the number of functional groups for complexation of the radiometal, the other two strategies both use one of the complexation functions for coupling to the biomolecule and so potentially reduce the number of offered donors for the metal. The last strategy that provides a prochelator (synthon that becomes a chelator after deprotection) is

Table 45.3

Radiometals of interest (Shannon 1976)

Metal	Ionic radius [pm], octahedral	Nuclides
Sc ³⁺	75	⁴⁷ Sc
Ga ³⁺	62	⁶⁶ Ga, ⁶⁷ Ga, ⁶⁸ Ga
Y ³⁺	90 (105)	⁸⁶ Y, ⁹⁰ Y
In ³⁺	80	¹¹¹ In, ¹¹⁰ In
Dy ³⁺	105	¹⁶⁶ Dy
Ho ³⁺	104	¹⁶⁶ Ho
Lu ³⁺	100	¹⁷⁷ Lu
Bi ³⁺	103	²¹² Bi, ²¹³ Bi
Ac ³⁺	126	²²⁵ Ac
Sm ³⁺	110	¹⁵³ Sm
Cu ²⁺	87	⁶⁷ Cu, ⁶⁴ Cu, ⁶² Cu, ⁶¹ Cu, ⁶⁰ Cu
Ag ⁺	129	¹¹¹ Ag

especially interesting for the conjugation to peptides, which can be performed during solid phase peptide synthesis (SPPS) (Sherry et al. 1989; Albert et al. 1998; Heppeler et al. 1999a; Schottelius et al. 2003). The deprotection, which is required after coupling to the biomolecule, makes this strategy impracticable if antibodies or other sensitive proteins are used as vectors.

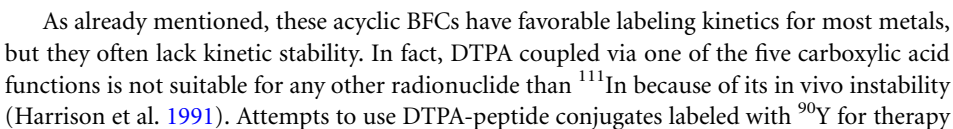
Most of the interesting radiometals are hard acids with 2+ and 3+ as their major oxidation states in aqueous solution. As they are kinetically labile, polydentate BFCs should be used to afford efficient encapsulation and in vivo stabilization. An important aspect of the choice of BFC is the ionic radius of the selected metal, as the metal ion has to fit into the cavity offered by the chelator (Table 45.3). Dependent on its size, the size and denticity of the BFC moiety should be selected (Figs. 45.2 and 45.3).

Apart from the size of the metal ion, it is also important to choose the suitable chelating donor groups for every radiometal. There are several donor groups available like amines, carboxylic acids, thiols, alcohols, phosphonic acids, and so on. The metal–ligand compatibility is dependent on the hard and soft acid and base character of the involved atoms. Oxygen donors have a good affinity to alkali, alkaline earth, and lanthanide atoms; nitrogen donors are favorable for transition metals; and sulfur is a good donor for silver and gold cations.

45.2.3 Acyclic Bifunctional Chelators

While the first BFCs were based on ethylenediaminetetraacetic acid (EDTA) (Sundberg et al. 1974a, b), most of the acyclic bifunctional chelators are based on the structure of diethylenetriaminepentaacetic acid (DTPA) (Fig. 45.4). The first clinically approved peptide-based tumor imaging agent was the DTPA-derivatized somatostatin analog octreotide labeled with ¹¹¹In. For this radionuclide, DTPA is an ideal chelator providing stable chelation and fast chelation kinetics (Maecke et al. 1989). Several analogs of DTPA have been synthesized as BFCs (Krejcarek and Tucker 1977; Hnatowich et al. 1983; Brechbiel et al. 1986; Westerberg et al. 1989; Williams and Rapoport 1993; Safavy et al. 2002a, b; Clifford et al. 2006; Xua et al. 2008).

Synthesis of a backbone-modified DTPA derivative for coupling to biomolecules



(Stolz et al. 1996) have not been as successful as the use of macrocyclic BFC for the labeling of peptides (Otte et al. 1997; De Jong et al. 1997; Stolz et al. 1998; Otte et al. 1998; Kwekkeboom et al. 2001; Waldherr et al. 2002; Chinol et al. 2002; Jamar et al. 2003; Forrer et al. 2006).

To increase the stability, preorganizing groups have been attached to the carbon backbone of EDTA and DTPA (Brechtel et al. 1996; Wu et al. 1997; McMurry et al. 1998; Gouin et al. 2002a, b). Preorganization obviously stabilizes the conformation of the free chelator in a manner that is comparable to the metal chelate (Hancock and Martell 1989; Hancock 1989). The reduction of the entropy, which in general works against the complexation of a metal, leads to faster complexation kinetics. There are BFCs designed this way (Fig. 45.5) (Williams and Rapoport 1994; Brechtel et al. 1991). One of these BFCs is called *tiuxetan* (Cummins et al. 1991; Chinn et al. 2003). Based on this BFC a conjugate with the murine anti-CD20 antibody *Ibritumomab* has been developed. This commercial product *Zevalin*TM is intended to be labeled with ¹¹¹In for imaging as well as with ⁹⁰Y for therapy. It is the first radiolabeled antibody for therapeutic application approved of by the US Food and Drug Administration (FDA).

Further refinements in the preorganization geometry of the DTPA led to BFCs for the labeling of antibodies with ²¹³Bi (Jurcic et al. 2002; Chinn et al. 2003; Abbas Rizvi et al. 2008), while other developments used for the same purpose (Brechtel and Gansow 1991; Nikula et al. 1999) had a peptide as a starting material, where new backbone modifications of the final DTPA derivative may be achieved by simply modifying the starting peptide (Fig. 45.6).

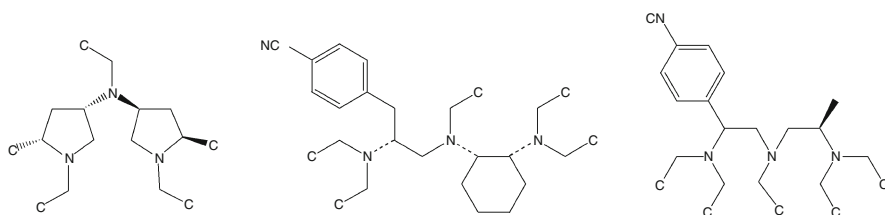
Acyclic BFCs have also been used for inserting Ga³⁺ into peptides and antibodies. One example is Desferrioxamine-B (DFO), which forms stable complexes with Fe³⁺ as well as with Ga³⁺. The stability constant of the Fe–DFO complex is log *K* = 30.4. DFO can be conjugated to a biomolecule via an activated primary amine group or derivatized with succinic acid anhydride as a spacer for coupling to the N-terminus (Mäcke et al. 1993; Smith-Jones et al. 1994; Stolz et al. 1994) (Fig. 45.7).

Interestingly, Desferrioxamine-B appeared to be of particular relevance for the complexation of tetra- and pentavalent radiometals. DFO-conjugated compounds such as DFO-succinyl-D-Phe-octreotide have been successfully labeled with the two longer-lived positron emitting radionuclides ⁸⁹Zr^{IV} (Meijs et al. 1992) and ⁹⁰Nb^V (Busse et al. 1999).

A more recent work on the development of a BFC for Ga³⁺ is based on a S₃N tetra-coordinate chelator (Fig. 45.8) (Luyt and Katzenellenbogen 2002). It shows high stability at neutral aqueous conditions when coupled to an amino acid mimicking a peptidic vector molecule. This could be interesting for the use with gallium labeled diagnostic radiopharmaceuticals.

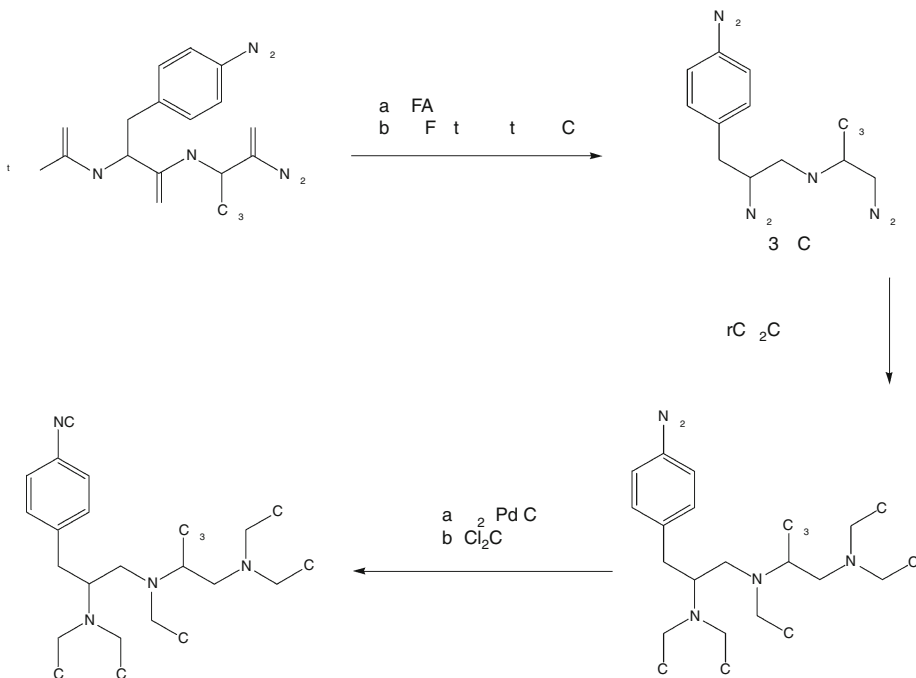
Fig. 45.5

BFCs based on backbone-stabilized DTPA derivatives



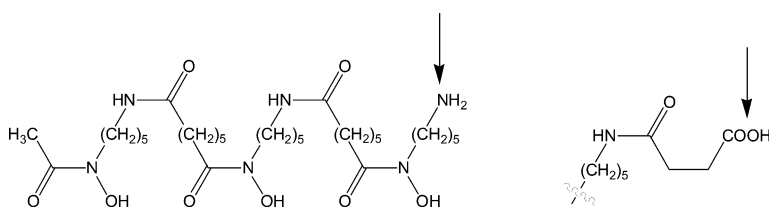
■ Fig. 45.6

Synthesis of 2-pSCNBz-5-Me-DTPA starting from a peptide (Brechtel and Gansow 1991)



■ Fig. 45.7

Structure of Desferrioxamine-B (DFO). Coupling sites to biomolecules may be NH_2 or a succinyl spacer



Additionally, the modified DTPA derivatives have also been used for the labeling of antibodies with ^{68}Ga (Koop et al. 2007).

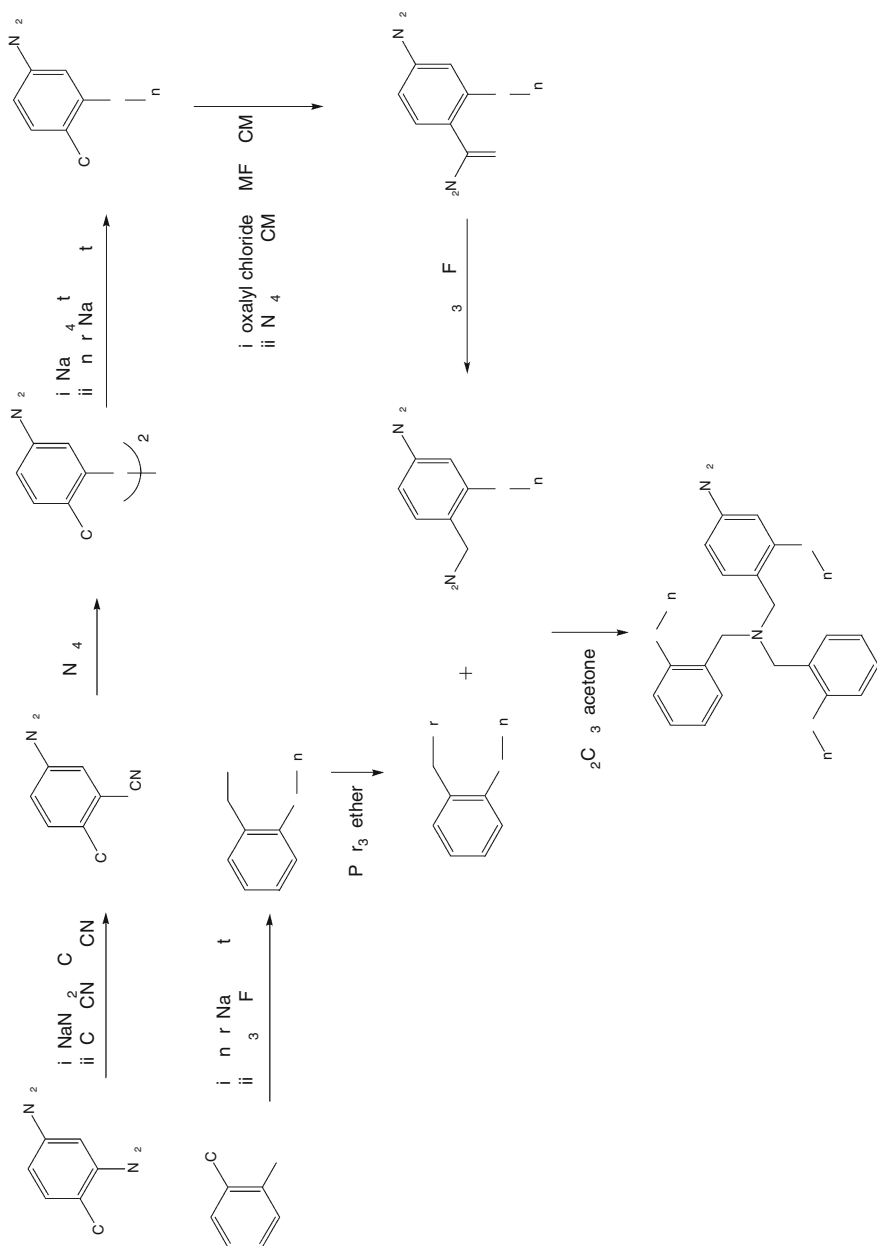
Finally, it should be pointed out again that acyclic BFCs are of special interest when antibodies or short-lived radiometals are used. The fast complexation even at ambient temperature may prevail over the shortcomings of lower stability compared to macrocyclic BFCs.

45.2.4 Macrocyclic Bifunctional Chelators

The labeling of biomolecules with longer-lived radiometals is preferably performed with BFCs based on a macrocyclic core. If peptides are used as vector molecules, the slow kinetic of

Fig. 45.8

Synthesis of a bifunctional prochelator based on S_3N chelation moiety for complexation of Ga^{III} (Luyt and Katzenellenbogen 2002)



formation can be overcome by heating (Breeman et al. 2003) or the use of microwave technology (Velikyan et al. 2004), which usually does not destroy the biomolecule.

One of the most popular macrocyclic frameworks for the design of BFCs is 1,4,7,10-tetraazacyclododecane (cyclen) which – if modified with side arms – results, e.g., in the structure of DOTA (► Fig. 45.3). As DOTA is known to form stable complexes with many radiometals as, e.g. Y^{3+} , In^{3+} or Cu^{2+} , with all the lanthanides as well as with Bi^{3+} and Ac^{3+} , it has been used, modified as BFC, for the radiolabeling of many biomolecules (Heppeler et al. 1999a, b; Cutler et al. 2000; McDevitt et al. 2001; Hu et al. 2002).

The key step in the synthesis of macrocyclic chelators based on linear precursors is the cyclization. There are different strategies for this step. One common route is called the Richman–Atkins method (Richman and Atkins 1974). This method uses tosylated polyamines, reacting with dihalogenides or ditosylates. The yields have been reported to range between 40% and 90% for different sizes of macrocyclic polyamines. Later, an alternative route that uses cheaper starting materials for the synthesis of cyclen has been described (Weisman and Reed 1996). Starting from cyclen, the amines could be functionalized by carboxymethylation, which leads to DOTA or derivatives thereof.

The direct coupling of a biomolecule by one acetic acid function of DOTA leads to a conversion of this group to an amide offering the carbonyl oxygen for potential complexation of the radiometal, which consequently may lead to a decrease in thermodynamic stability compared to the acid. The difference is in one order of magnitude (Good 2006; Heppeler et al. 2008). To prevent this problem, a special coupling moiety should be introduced into the macrocycle.

The first approach in the synthesis of a bifunctional DOTA-derivative is to start with a tetrapeptide. This precursor may be obtained by a peptide route. The treatment with borane to convert the peptide to a linear polyamino alcohol, followed by tosylation and cyclization leads to the macrocycle (► Fig. 45.9). The modification for the coupling of the final BFC to a biomolecule is introduced already at the beginning with the choice of the first amino acid. The final alkylation of the amines of the macrocycle leads to a BFC with four acetic acid groups for the complexation of the radiometal (Moi and Meares 1988).

A different strategy for the formation of the cyclic core of the BFC is based on peptide bond formations (► Fig. 45.10). The macrocycle is formed by an intermolecular reaction of an activated disuccinimido ester with a diamine under high-dilution conditions with a yield of >40%. Reduction of the carbonyl groups and alkylation lead to a BFC, which possesses an attachment function for biomolecules on the carbon backbone of the macrocyclic core (McMurry et al. 1992).

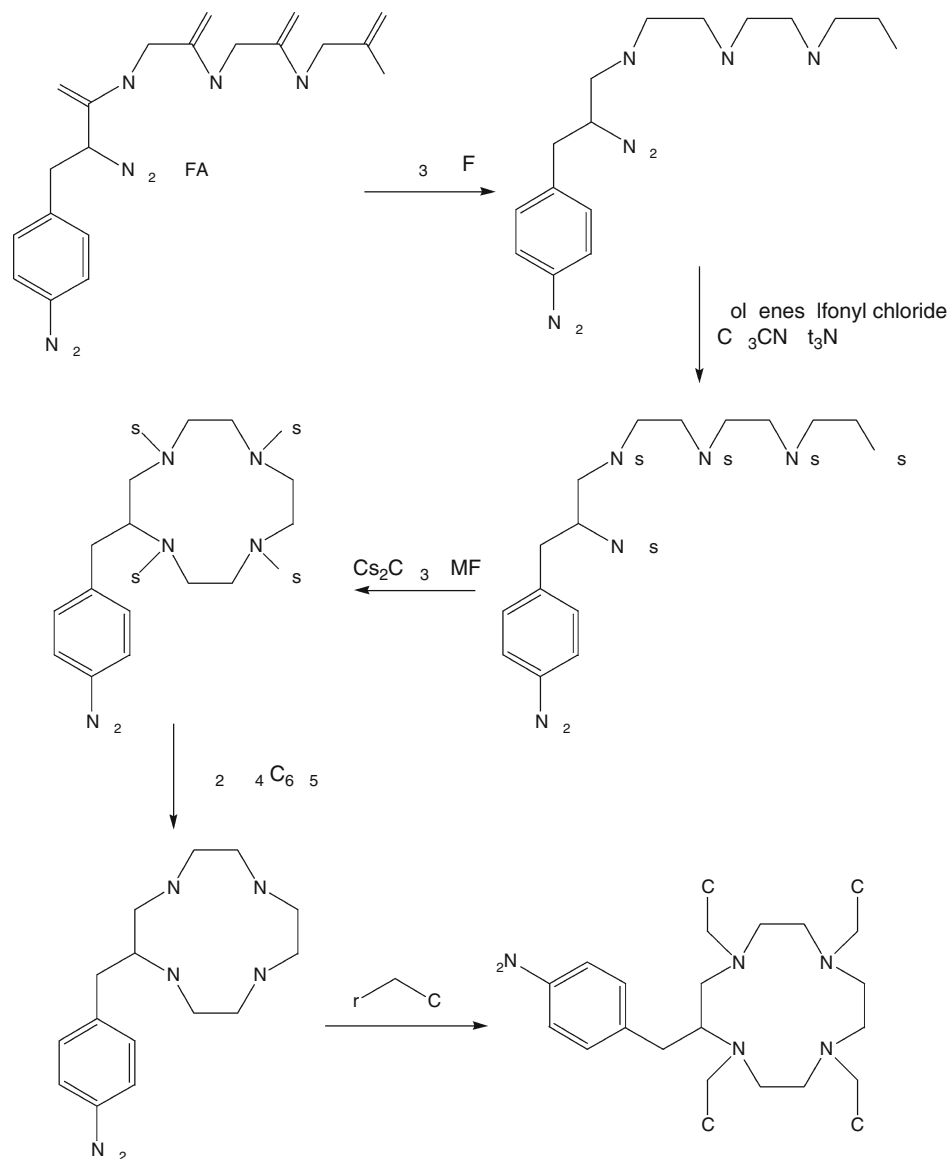
Based on malonic ester synthesis, a bifunctional derivative of 1,4,7,10-tetraazacyclotridecane- N,N',N'',N''' -tetraacetic acid (TRITA) has been developed as well (Ruser et al. 1990). Again, an intermolecular reaction between a diamine and a diester leads to the macrocycle forming peptide bonds (► Fig. 45.11). The final BFCs have been studied as complexation agents for ^{111}In and have shown fast chelate formation, high radiochemical yield, and high stability.

An alternative way to couple a BFC to a vector molecule is to use one of the side chains for the attachment. One example is based on cyclen and alkylation of the amines with orthogonally protected acetic acids. By selective deprotection of only one of the acid functions, a prochelator is achieved, which can also be used in solid phase peptide synthesis protocols; the remaining protecting groups will be cleaved under the same conditions as the protecting groups of the peptide (Heppeler et al. 1999a) (► Fig. 45.12).

Of course, such a prochelator might not be used for attachment to an antibody, as the deprotection needs harsh conditions, which are not compatible with the integrity of the

■ Fig. 45.9

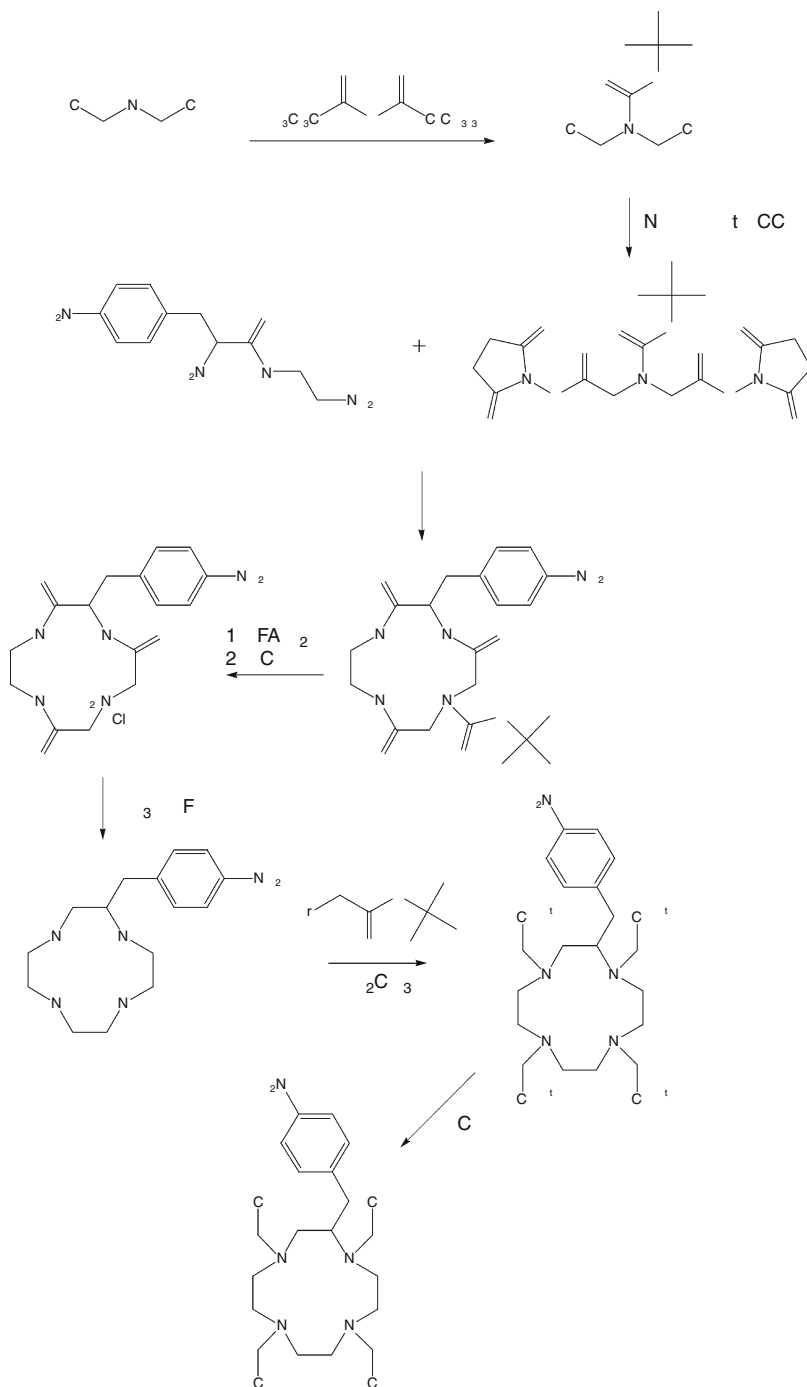
Synthesis of 2-(p-nitrobenzyl)-1,4,7,10-tetraazacyclododecane-N,N',N'',N'''-tetraacetic acid (Moi and Meares 1988)



antibody. For this purpose, DOTA has been activated at a single carboxylate group with N-hydroxysulfosuccinimide. This sulfo-N-hydroxysuccinimide (NHS) active ester of DOTA, which is nowadays a commercially available product, may be coupled to an antibody without subsequent deprotection steps (Lewis et al. 2001). Compared to backbone-modified DOTA derivatives, a disadvantage of this type of BFC may be the loss of one of the carboxylate

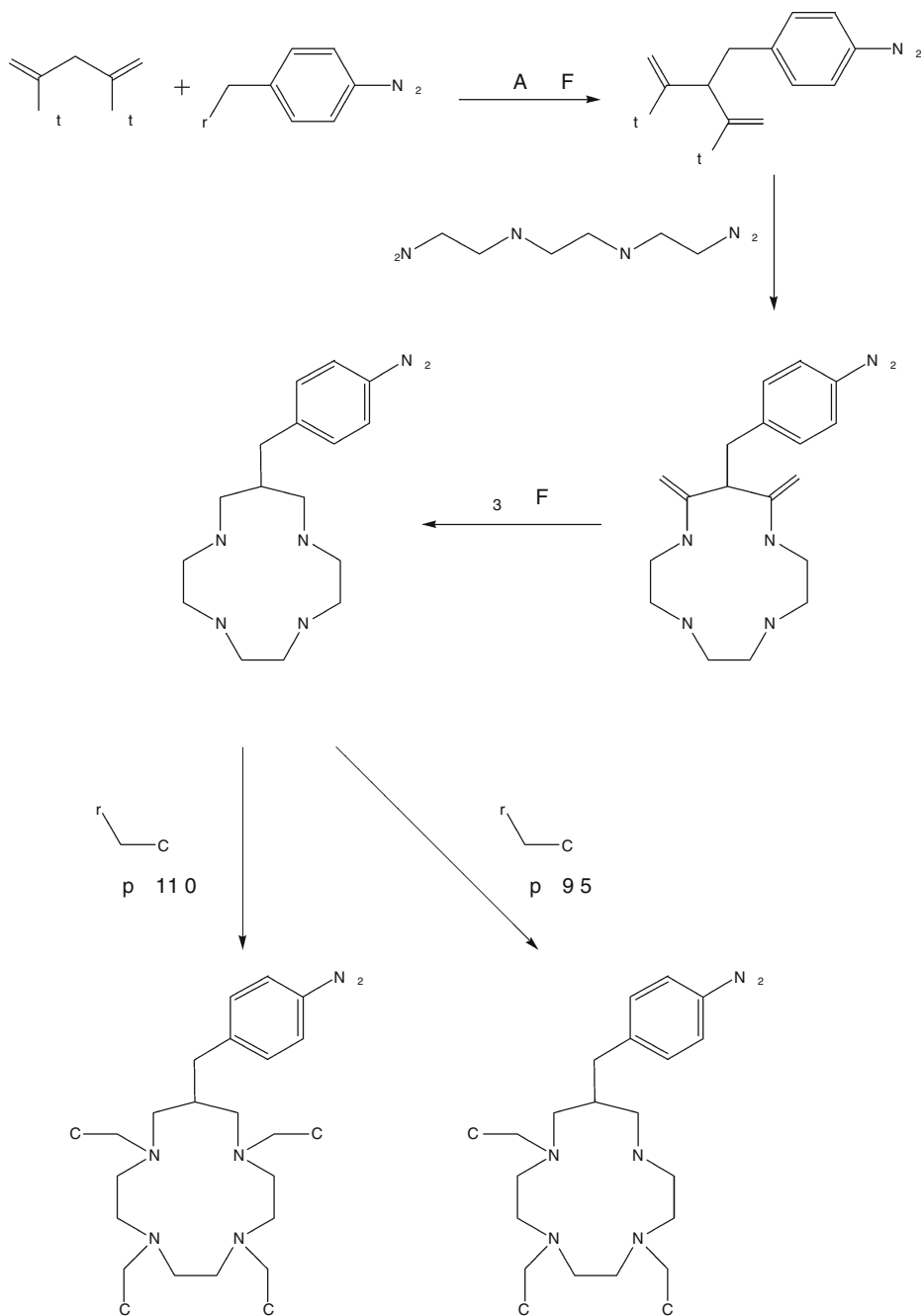
■ Fig. 45.10

Synthesis of 2-(p-nitrobenzyl)-1,4,7,10-tetraazacyclododecane-N,N',N'',N'''-tetraacetic acid (McMurry et al. 1992)



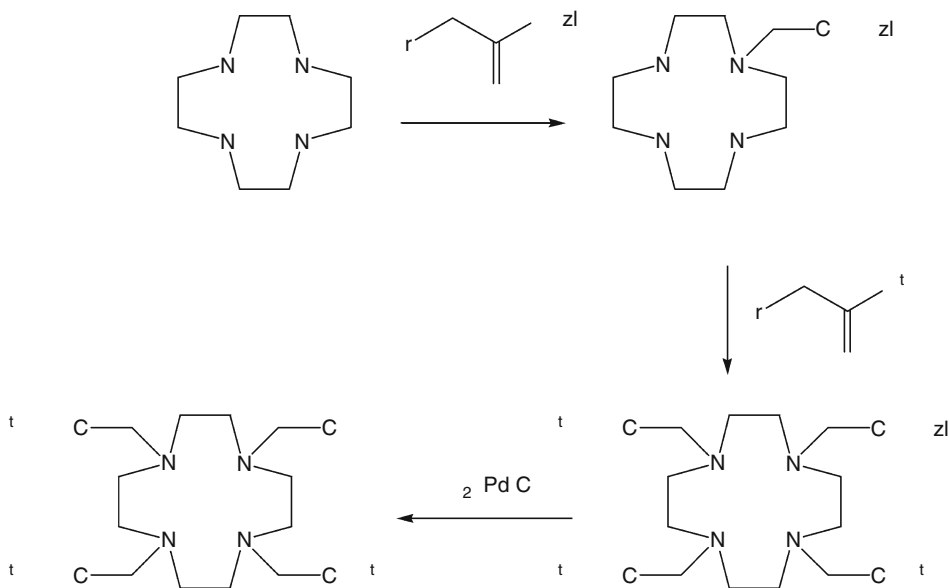
■ Fig. 45.11

Synthesis of a bifunctional derivative of TRITA (Ruser et al. 1990)



■ Fig. 45.12

Synthesis of DOTA-based bifunctional prochelator (4,7,10-tricarboxymethyl-*tert*-butyl ester 1,4,7,10-tetraazacyclododecane-1-acetate) (Heppeler et al. 1999a)



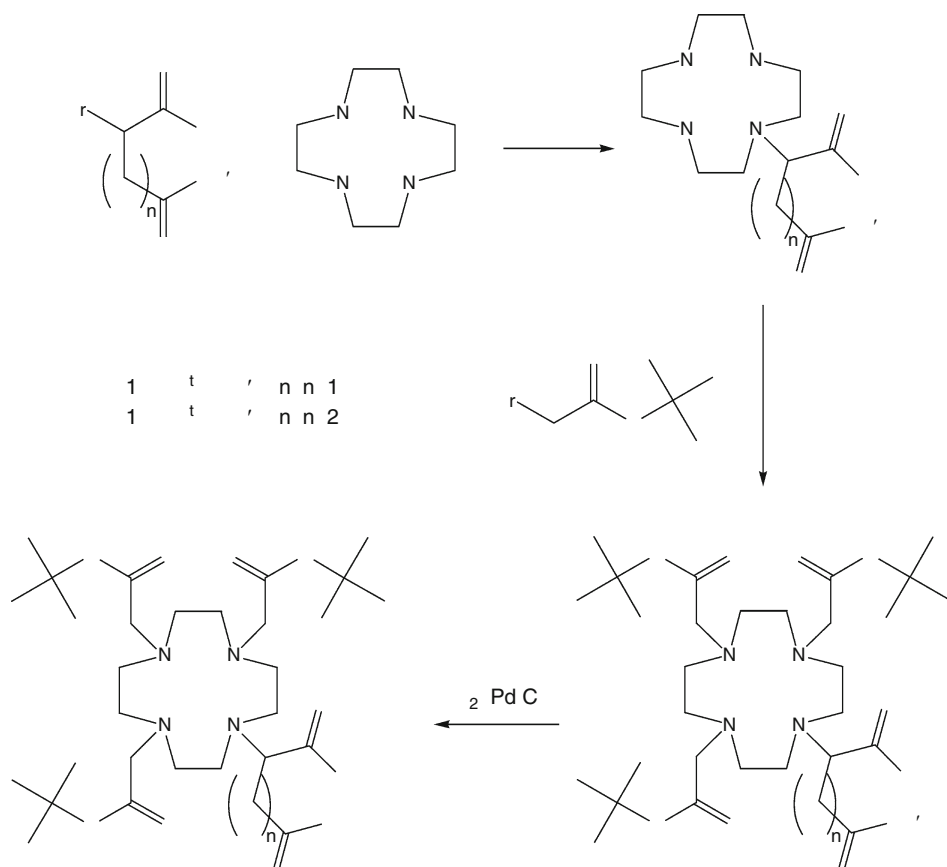
groups for metal bonding. The amide carbonyl oxygen would have to fill the remaining coordination site of the metal.

A strategy to prevent this potential loss of complexation functionality is the introduction of an additional coupling site on a modified acetic acid arm via an alkylation step maintaining the full-fledged functionalities of DOTA (Eisenwiener et al. 2000). Starting from cyclen, an orthogonally protected bis-carboxylic acid is attached to an amino group via alkylation. After carboxymethylation of the three remaining free amines and selective deprotection of the coupling site, a bifunctional prochelator is obtained (► Fig. 45.13). Coupling to a biomolecule and deprotection of the conjugate leads to a BFC designated for the labeling with different radiometals (^{111}In , $^{67/68}\text{Ga}$, ^{90}Y , and ^{177}Lu) (Kneifel et al. 2006; Ginj et al. 2008; Good et al. 2008). This strategy of an additional coupling site might be applied not only to derivatives of DOTA but as a general method to modify chelators based on a polyazaalkyl structure. Such a BFC should show a higher stability because of the higher denticity and possibly also faster complexation kinetics.

One example for the variable applications of this strategy has been demonstrated utilizing a NOTA-based BFC (Eisenwiener et al. 2002) (► Fig. 45.14). 1,4,7-triazacyclononane-1,4,7-triacetic acid (NOTA) has a smaller ring size than DOTA (► Fig. 45.3) and is known to be an excellent chelator for Ga^{3+} . Therefore, NOTA has been modified for coupling to a biomolecule (Cox et al. 1990; Broan et al. 1991; Velikyan et al. 2008). The bifunctional derivative is still a potent chelator for $^{67, 68}\text{Ga}$ (André et al. 1998) and has the additional advantage in regard to DOTA as labeling with radiogallium isotopes can be done at room temperature. It may preferably be coupled in standard peptide synthesis protocols while the proposed preconjugation labeling approach (André et al. 1998) seems to be inferior especially with higher amounts of radioactivity because of the low coupling yields. Other BFCs have been

■ Fig. 45.13

Synthesis of DOTA-based bifunctional prochelators DOTAGA(^tBu)₄ (1) and DOTASA(^tBu)₄ (2) (Eisenwiener et al. 2000)



developed, which do also have an additional coupling site for biomolecules at one carboxylic acid arm but without protecting groups on the free carboxylic acids (Chappell et al. 1999). This type of BFC is proposed for the use of coupling to antibodies.

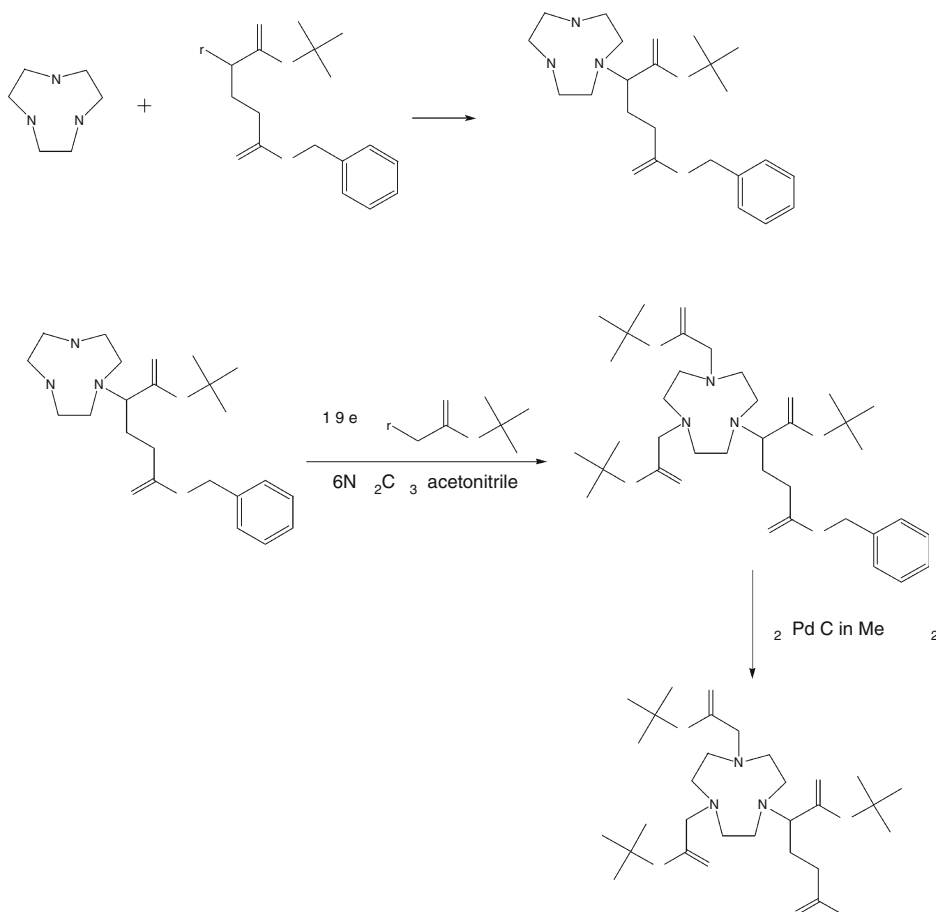
Synthesis starting from a commercially available polyazamacrocycle such as the described strategies (► Figs. 45.12 and ► 45.13) is easier to perform (McMurry et al. 1993).

A common drawback with macrocyclic ligands is their slow complexation rate (Jang et al. 1999). A way to overcome this problem is to increase the ring size. Following this idea, two larger chelators have been developed, one based on a pentaaza macrocycle (PEPA) and the other on a hexaaza macrocycle (HEHA) (► Fig. 45.3). Both these chelators show much faster labeling kinetics with some radiometals (by a factor of about 100 times faster). Still, they have slower labeling kinetics than the acyclic chelator DTPA (by a factor of about 10) (► Table 45.4).

The stability of the PEPA and HEHA complexes is lower than the one of the DOTA complexes, but higher than the one of the acyclic DTPA (Kimura et al. 1985; Kodama et al. 1991)

■ Fig. 45.14

Synthesis of the bifunctional prochelator (1-(1-carboxy-3-carbo-*tert*-butoxypropyl)-4,7-(carbo-*tert*-butoxymethyl)-1,4,7-triazacyclononane (NODAGA(^tBu₃)) (Eisenwiener et al. 2002)



■ Table 45.4

Pseudo first-order rate constants for the complex formation at pH 7.8, 25°C (Kodama et al. 1991)

K_{obs} [min ⁻¹]				
Metal	DOTA	PEPA	HEHA	DTPA
Lu ³⁺	6.3×10^{-3}	9.6×10^{-2}	5.8×10^{-1}	4.6
Y ³⁺	4.6×10^{-3}	2.0×10^{-1}	6.8×10^{-1}	7.3

(► Table 45.5). HEHA has been reported to be a suitable chelator for the use with ²²⁵Ac (Deal et al. 1999; Kennel et al. 2000). Based on these chelators, BFCs have been developed as well.

Again, the most crucial synthetic step is the formation of the macrocycle. In one successful synthesis, the macrocyclic core is formed by an intermolecular reaction forming two peptide

■ Table 45.5

Stability constants (log K_{ML}) of macrocyclic complexes (Alexander 1995)

$K_{ML} = [ML]/[M][L] \text{ (M}^{-1}\text{)}$				
Metal	DOTA	PEPA	HEHA	DTPA
Lu ³⁺	29.2	16.71	24.26	22.4
Y ³⁺	24.9	16.07	24.04	22.1
Sm ³⁺		15.35	21.24	22.3
Ho ³⁺		16.48	23.88	22.8

bonds (► Fig. 45.15) (Ouadi et al. 2000). The yield of the cyclization step is reported to be 50%. Reduction with borane and the following alkylation have been performed as described above.

A different method for the synthesis of the same bifunctional derivative of HEHA has also been reported (Chappell et al. 2000). This BFC has been coupled to an antibody and labeled with the α -emitter ²²⁵Ac. The daughters (²²¹Fr, ²¹⁷At, ²¹³Bi) are α -emitters as well. As the radiation from this metal has a very high linear energy transfer (LET), one should expect a loss of the daughters of actinium by the destructive effect of the radiation on the chelator. Even a rupture of the bond between the chelators and the coupled antibody might be possible. The half-lives of ²²¹Fr and ²¹⁷At are short enough to disable de-complexated radiometals to reach organs and regions far from the tumor but ²¹³Bi has a half-life that is long enough to accumulate thus having a potential negative side effect on organs like the kidneys.

A BFC derived from PEPA has also been developed following the peptide way for cyclization (Garmestani et al. 2001). This chelator was coupled to a monoclonal antibody and labeled with ²⁰⁵, ²⁰⁶Bi. Unfortunately, the results of the biodistribution of this conjugate show that a complex of p-NCS-PEPA is not stable enough in vivo and that even the complexation kinetics at room temperature were not rapid. It appears to be favorable to use backbone-stabilized derivatives of the acyclic chelator DTPA for the application of bismuth (Hassfjell and Brechbiel 2001).

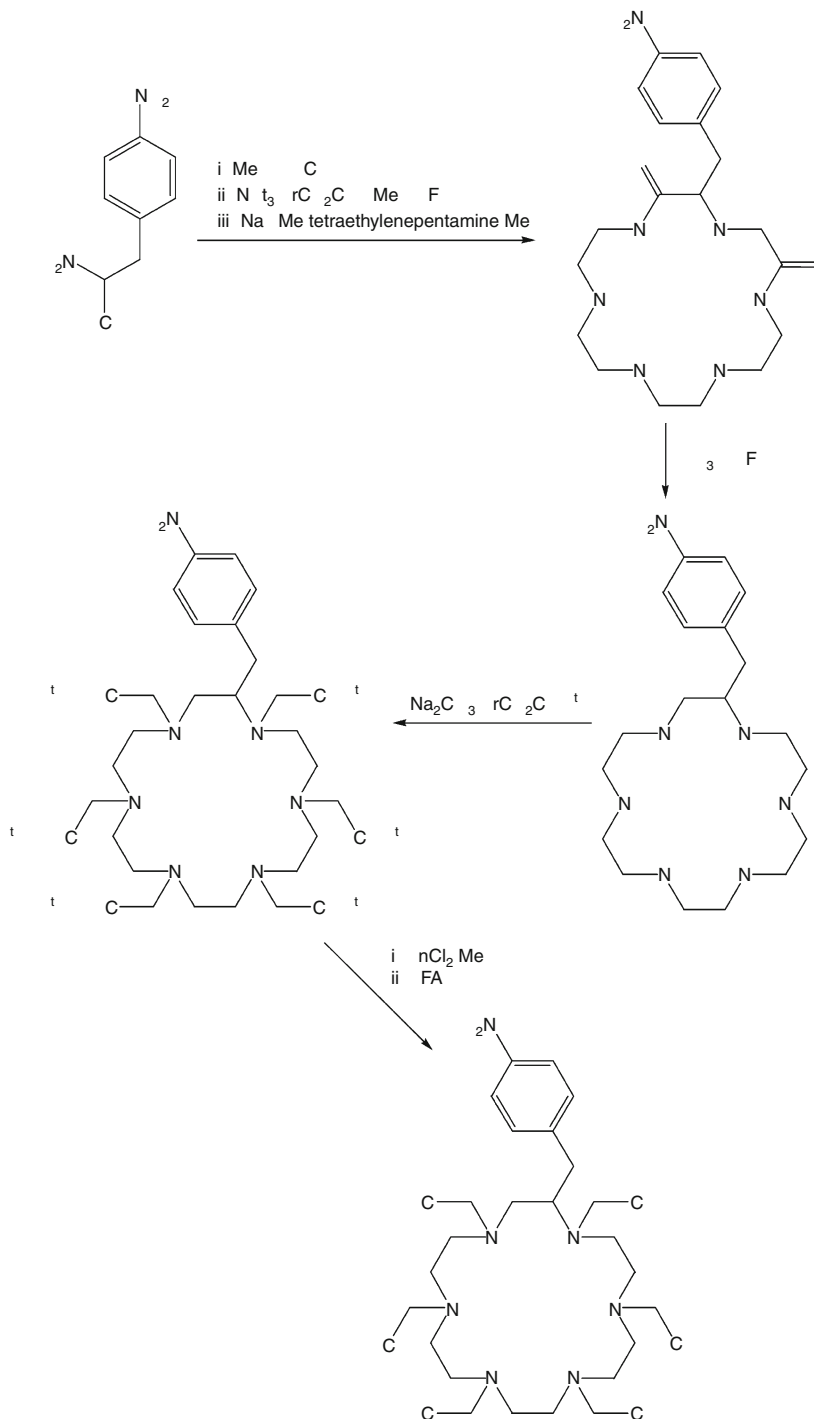
While all syntheses originally presented had been based on the strategy of coupling the biomolecule to a prochelator, a different approach has been presented by Peterson et al. (1999). This new way uses a solid phase bound peptide as anchor to build the chelator step by step (► Fig. 45.16). Solid phase synthesis offers many advantages; one of the major advantages is that by-products may simply be washed away from the solid phase while the desired product stays bound.

A further advantage of this solid phase supported, combined synthesis of biomolecule and chelator is the reduction of purification steps. When using a bifunctional prochelator, this synthon has to be purified prior to the coupling to a biomolecule whereas with the combined strategy only the final product has to be purified.

As Cu²⁺ has many interesting radionuclides for therapeutic as well as for diagnostic applications (► Tables 45.1 and ► 45.2), the development of ideal chelators for this metal is of interest. BFCs used for the coupling of Cu-radioisotopes to biomolecules are based on the 14-membered tetraazamacrocyclic cyclam 14 (1,4,8,11-tetraazacyclotetradecane) (► Fig. 45.17). Two bifunctional versions of cyclam-14, 4-[(1,4,8,11-tetraazacyclotetradec-1-yl)methyl]-benzoic acid (= CPTA) and [6-(p-bromoacetamido)benzyl]-1,4,8,11-tetraazacyclotetradecane-1,4,8,11-tetraacetic acid (= BAT) (► Fig. 45.17), were coupled to monoclonal antibodies and somatostatin analogs (Smith-Jones et al. 1991; Anderson et al. 1995; Wilder et al. 1996). In addition to

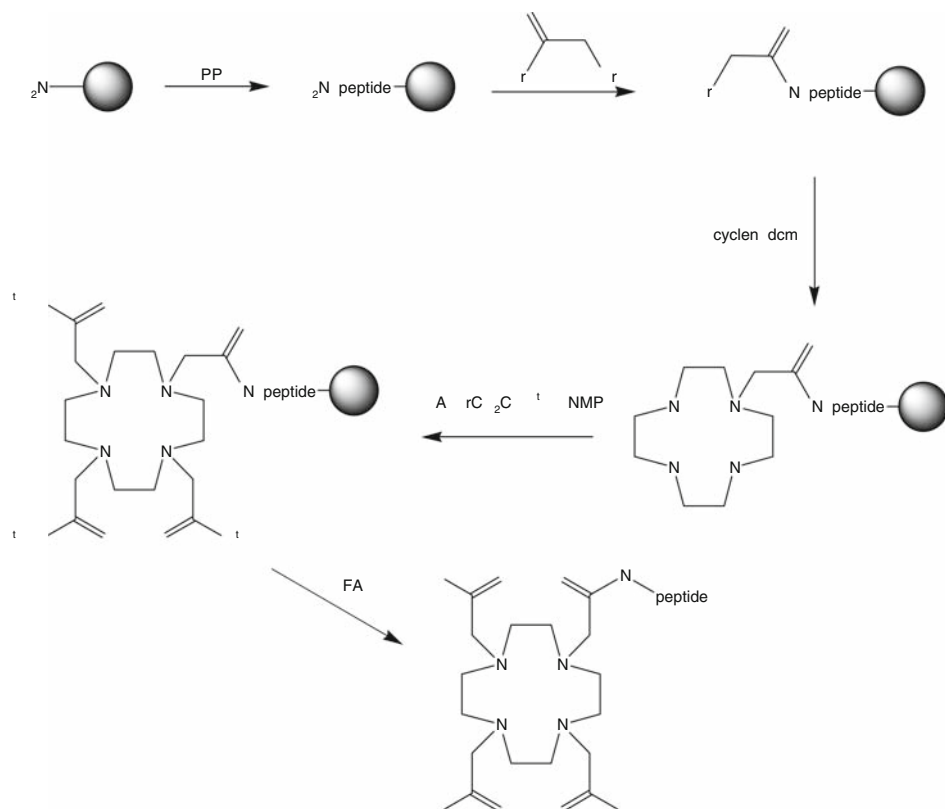
■ Fig. 45.15

Synthesis of p-aminobenzyl hexaaza macrocycle (HEHA) (Ouadi et al. 2000)



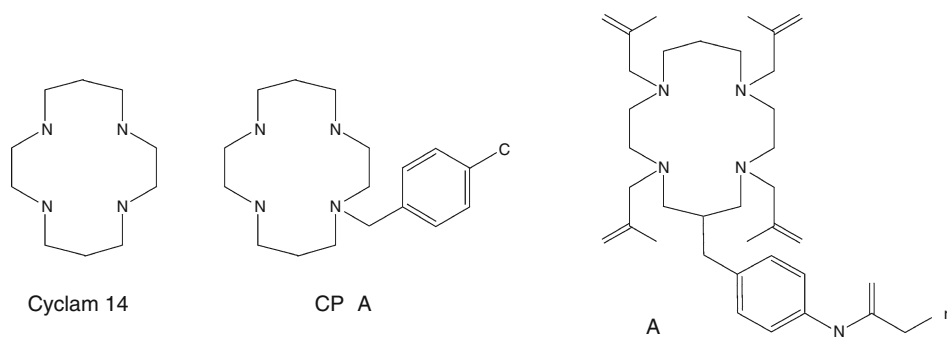
■ Fig. 45.16

Solid phase synthesis of DOTA-peptides (Peterson et al. 1999)



■ Fig. 45.17

Structures of cyclam-14 and bifunctional derivatives CPTA and BAT



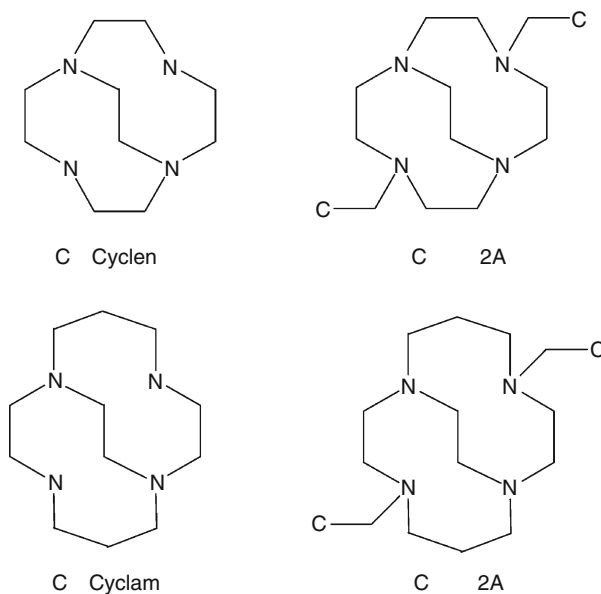
these conjugates, 1,4,8,11-tetraazacyclotetradecane-1,4,8,11-tetraacetic acid (TETA) and DOTA (► Fig. 45.3) as monofunctional versions were shown to be excellent chelators for ^{64}Cu if conjugated to cyclic octapeptides based on octreotide.

Many DOTA and TETA (► Fig. 45.3) derivatives have been used for Cu-complexation to different biomolecules (Anderson et al. 2001; Wu et al. 2005; Parry et al. 2007). Despite the considerable efforts made by researchers to use tetraaza-tetracarboxylate macrocyclic ligands as effective BFCs for Cu, it is evident that the in vivo instability of these Cu complexes emphasizes the need for more stable Cu chelators. The class of ethylene cross-bridged cyclam and its pendant-armed derivatives (► Fig. 45.18), synthesized by Weisman and Wong (Weisman et al. 1990, 1996; Wong et al. 2000) have attracted attention as chelators for radiocopper. Attachment of two carboxymethyl pendant arms to CB-cyclam leads to CB-TE2A, which further ensures complete envelopment of a six-coordinate Cu(II). Studies also focused upon modifying these chelators for the synthesis of BFC (Sprague et al. 2007; Boswell et al. 2008), while ^{64}Cu -labeled peptide-conjugates based on these chelators showed superiority compared to more conventional chelators, such as TETA (Sprague et al. 2004; Wadas et al. 2008). More recently, NOTA (► Fig. 45.3) has been used for labeling of different peptides with ^{64}Cu , exhibiting high in vivo stability (Prasanphanich et al. 2007; Liu et al. 2009).

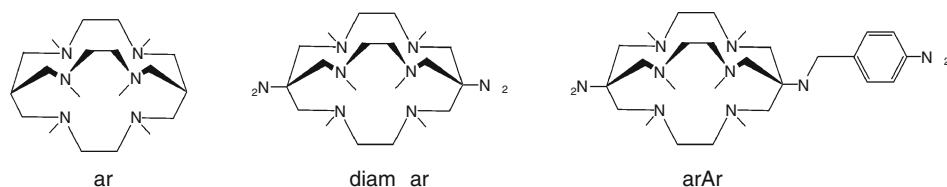
Another class of ligands is the hexaazamacrobicyclic cage type ligands, which are based upon the sepulchrate, or sarcophagine cage motifs shown in ► Fig. 45.19 and whose syntheses were first described by Sargeson and coworkers (Geue et al. 1984; Sargeson 1996). Sarcophagine (Sar) analogs substituted at the apical bridgehead carbons with a variety of functional groups including NH_2 , OH , Cl , and NO_2 or other alkyl or aryl organic groups have also been synthesized. DiBartolo et al. investigated a family of Sar derivatives with various functional groups at the apical sites, such as diamSar and SarAr (► Fig. 45.19) (Di Bartolo et al. 2001).

■ Fig. 45.18

Cross-bridged cyclic polyamine and cross-bridged cyclicpolyaminocarboxylate ligands



■ Fig. 45.19

Sarcophagine and sepulchrate ligands

Different BFCs based on the cage type ligands have been used for ^{64}Cu -labeling of antibodies (Smith 2004; Di Bartolo et al. 2006) and peptides (Ma et al. 2009; Cai et al. 2009).

45.3 Examples of Radiometal–Chelate–Biomolecule Conjugates

45.3.1 Synthesis and Characterization of Chelator–Biomolecule Conjugates

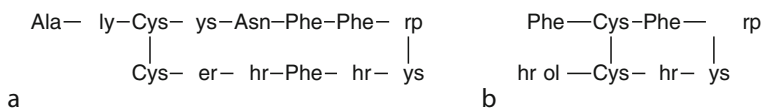
There are many interesting biological targets for radiopharmaceuticals. As already mentioned in Sect. 45.2.1, cell surface receptors of cancer cells allow specific attacks to these cells. This specificity is due to an overexpression of certain receptor types on tumor cells. The biomolecules for this targeting might be antibodies as well as peptides.

Antibodies are proteins to which a varying number of chelators might be coupled. A detailed discussion of antibodies in radionuclide therapy can be found in Chap. 46 of this Volume.

Peptides as biomolecular vectors in radiotherapy are getting more and more popular as a variety of tumors overexpress different peptide receptors as potential targets. They consist of a small number of amino acids (10–50) and may be synthesized quickly and at relatively low cost using solid phase synthesis (Merrifield 1963). The attachment of the chelating moiety to the peptide sequence may be performed at the non-active end of the main chain, mostly the N-terminus of the molecule. As an advantage, the low molecular weight of the conjugate results in a fast diffusion rate. Larger tumors will be penetrated faster than by using radiolabeled proteins and the areas in the center of a spherical tumor will receive a higher radiation dose. Peptides can also withstand harsher conditions for modification and labeling than antibodies, they are less likely to produce immunogenic response, and blood clearance and tumor uptake are faster. The faster clearance of nontarget tissue leads to a better tumor-to-background ratio (better imaging) and therefore to less irradiation of nontarget organs. As a drawback, the used peptides normally play a regulatory role in the human body. Even if the number of receptors on the surface of cancer cells is upregulated, there are receptors on normal tissue that will be attacked as well, and already small amounts of peptides may lead to undesirable side effects. As native peptides are degraded very rapidly by endogenous peptidases and proteases, stabilized derivatives have to be developed. The conjugation of a BFC to a relatively small biomolecule also has a higher potential to influence the binding affinity. To reduce this negative influence, spacers between the peptide and the chelator may be introduced.

The best developed peptides in the field of targeted radiotherapy are analogs of somatostatin. Endogenous somatostatin consists of a family of two forms of 14 (SS-14) or 28 (SS-28) amino acids (Patel et al. 1996). They both show low metabolic stability in human blood with

Structure of native somatostatin SS-14 (a) and its derivative octreotide (b)



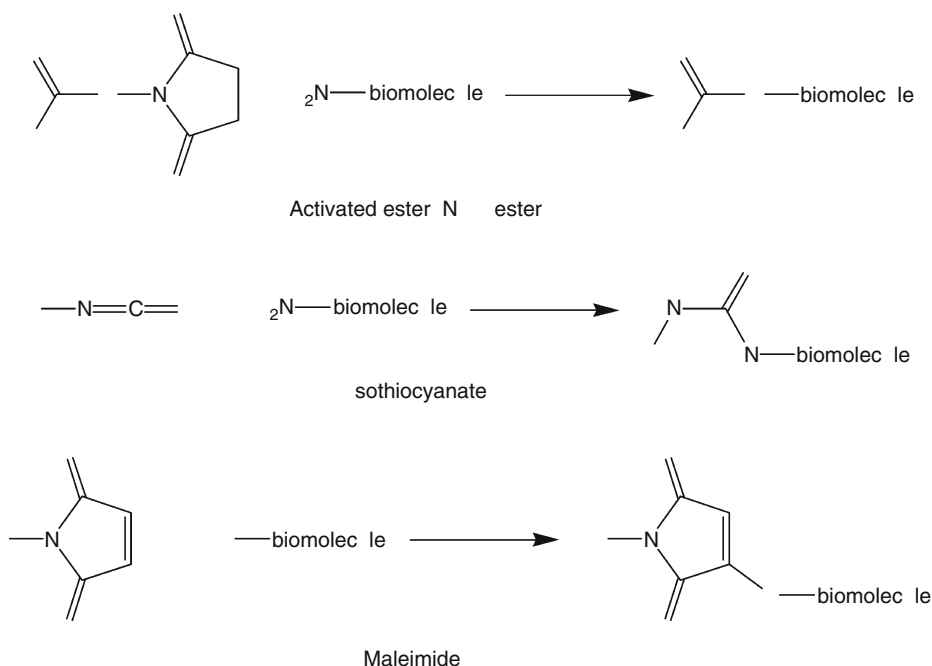
The first radiopeptide used for the localization of tumors was (3-[^{123}I]iodo-Tyr 3)-octreotide. Early results had been very promising (Krenning et al. 1989; Lamberts et al. 1990), but later it has been shown that this compound is not useful as a diagnostic tool because of its low diagnostic sensitivity in the abdomen. As mentioned above the first chelator-conjugate of octreotide, DTPA-octreotide, designed for complexation of $^{111}\text{In}^{3+}$, shows a low in vitro pharmacologic profile (low binding affinity of 22 ± 3.6 nM, slow internalization rate) but the hydrophilic metal complex changes the hydrophilicity of the radiopharmaceutical and its pharmacokinetics dramatically. DTPA-octreotide therefore became the first registered radiopeptide worldwide, its commercial name being *Octreoscan*TM. As DTPA shows favorable labeling kinetics with $^{111}\text{In}^{3+}$, it can be performed in any nuclear medical department whereas iodination needs specially trained personnel.

In the pre-conjugation labeling approach, a metal is encapsulated by a chelator prior to the conjugation of a biomolecule to the chelator. This strategy even allows nonaqueous conditions for the complexation step. It also allows the covalent coupling of a well-defined radiometal complex of high specific activity to a biomolecule. As the conjugation is often not quantitative, a final purification step is needed. In general, after the radionuclide is introduced, the synthesis is time consuming and causes economical and radioecological problems. Both aspects make this strategy unsuitable for routine applications in standard nuclear medicine facilities (Liu and Edwards 2001; Liu 2008).

For the conjugation of the chelator to the biomolecule, the activation of a carboxylate group of the chelator via an active ester and the reaction with a primary amine of the biomolecule (side-chain of a lysine residue or *N*-terminal amine of a peptide) leads to a stable attachment via a peptide bond. This peptide bond is highly stable under physiological conditions. One popular example of activation of the carboxylate is the formation of *N*-hydroxysuccinimide (NHS) esters (► [Fig. 45.21](#)). NHS-activated esters are selective for primary amines in aqueous

■ Fig. 45.21

Conjugation of a bifunctional chelator (R) to a biomolecule



solutions and slightly basic pH as reaction conditions for the conjugation. These esters are useful for reactions with antibodies and peptides (Liu and Edwards 1999).

Isothiocyanates are reactive to amines as well (► Fig. 45.21). They may be formed from nitro groups (► Fig. 45.6) and react in aqueous solutions at pH 9–9.5 with primary amines to form thiourea bonds. This reaction restricts this method to biomolecules, which are not sensitive to alkaline conditions (Fichna and Janecka 2003).

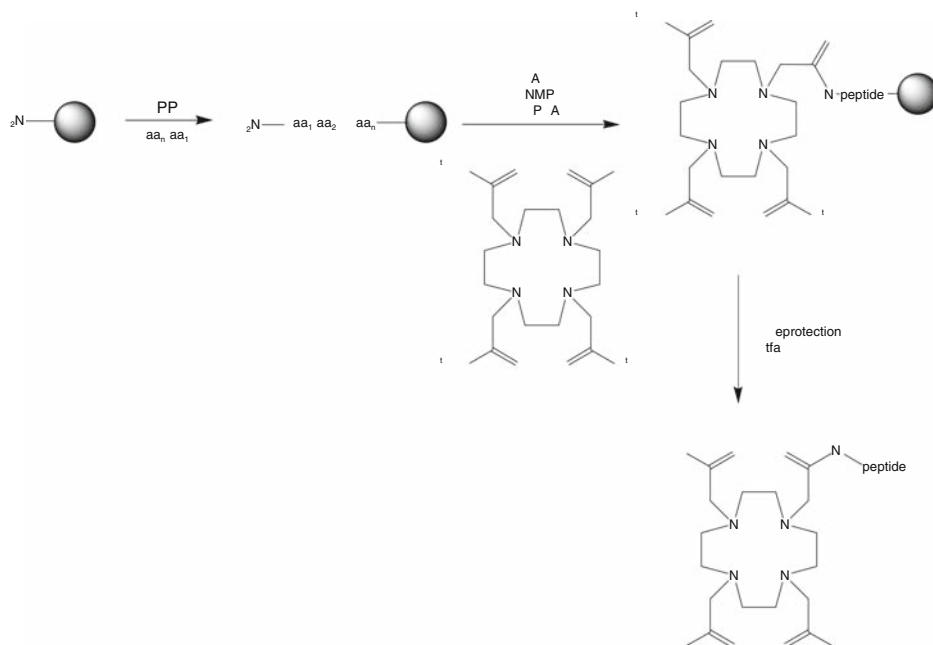
Maleimides are reacting selectively with thiols (► Fig. 45.21). The thiol groups in the biomolecules come from cysteine where a thioether bond with the chelator is formed. The pH for this reaction is close to 7 so that this reaction is ideal for biomolecules (Lewis and Shively 1998).

Anhydrides of the chelator react with primary amines of the biomolecules. Symmetrical dianhydride of DTPA is commercially available and the conjugation may be performed in both aqueous and nonaqueous media. As the dianhydride might react to form a DTPA-monoamide as well as a DTPA-bisamide, cross-linkage of two biomolecules may occur. To circumvent this, asymmetric anhydrides of DTPA but also of DOTA have been developed and used (Sherry et al. 1989; Sieving et al. 1990).

A different approach for the conjugation of a chelator to a biomolecule is the use of monoreactive chelator derivatives. This approach includes the use of protection strategies as shown before (► Figs. 45.12–45.14) and the use of this protected precursors in standard peptide chemistry protocols. The chelator is introduced as a synthon and will be transformed to the final, functional BFC after the coupling to the biomolecule by deprotection of the carboxylic acids (► Fig. 45.22).

■ Fig. 45.22

Solid phase synthesis of DOTA-peptides (Eisenwiener et al. 2000)

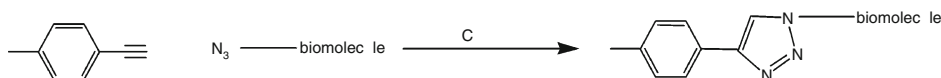


As an example, the prochelator of DOTA, which carries three ^tBu protected carboxylate groups whereas the fourth remains free for coupling to the peptide, is compatible with solid and solution phase peptide chemistry, and was coupled to somatostatin analogs in solution with 65 ± 5% yields after deprotection and purification (Heppeler et al. 1999a, b). DOTA, used unprotected, was also coupled to the same peptide with about 40% overall yield (Albert et al. 1998; Hsieh et al. 1999). Coupling of the unprotected chelator has recently been improved, leading to >98% yield for the coupling of the chelator to a peptide (Schottelius et al. 2003).

Recently, click chemistry has received considerable attention as powerful synthesis approach by utilizing a few practical and reliable reactions with applications in many areas, including drug discovery (Kolb and Sharpless 2003; Mamat et al. 2009). A very popular reaction of click chemistry is the Cu(I)-catalyzed version of Huisgen's dipolar [2 + 3] cycloaddition of terminal alkynes and azides to yield 1,4-disubstituted 1,2,3-triazoles, discovered by the groups of Sharpless and Meldal (Rostovtsev et al. 2002; Tornøe et al. 2002). This new synthetic approach has recently found application in the preparation of bifunctional chelators, bearing the alkyne functionality in their molecule, such as DOTA and DTPA and their conjugation to azido functionalized biomolecules (Fig. 45.23) (Knör et al. 2007; Mindt et al. 2009). This reaction is mild and very efficient, is easy to perform, and is insensitive to oxygen and water. Moreover, it requires no protecting groups, while the azide and alkyne functional groups are largely inert toward biological molecules and aqueous environments. The very mild reaction conditions and the high chemoselectivity and efficiency make this reaction particularly suitable for bioconjugations.

Fig. 45.23

Chemoselective Cu(I)-catalyzed azide-alkyne cycloaddition of an alkyne-bifunctional chelator (R) to an azido-functionalized biomolecule



As the compounds described in this chapter will be applied to humans, quality control is essential. One has to define first a few terms therefore:

Radiolabeling yield	Percentage of radiometal-labeled biomolecule–chelator conjugate
Radiochemical purity	Percentage of total radioactivity in the desired chemical form (as radiopharmaceutical)
Radiolabeling efficiency	Ability of a chelator to form its radiometal complex at a low concentration under mild conditions

The standard technique to check the radiochemical purity of a labeled compound is thin layer chromatography/instant thin layer chromatography (TLC/ITLC) combined with a radioactivity counter. This method is quick and easy to perform. Different isomeric forms of a radiopharmaceutical may not be determined. A more sophisticated method for quality control is high performance liquid chromatography (HPLC) combined with a radioactivity detector. Radiochemical purity as well as isomeric forms and small modifications due to instability, radiolysis, etc., may be determined. To achieve an accurate determination of non-chelated radiometal, a mM solution of DTPA (pH 4–5) has to be added to the HPLC sample to ensure a complexation of the free metal. If DTPA is not added, unchelated metal might bind and stick to the HPLC column and thus indicate a too high radiochemical purity (Smith-Jones et al. 1998).

Radiolabeling efficiency is dependent on the radiolabeling conditions: concentration of the BFC-biomolecule conjugate, concentration of trace metal contaminants, pH, temperature, and reaction time (Brechtel et al. 1996; Breeman et al. 2003; Wu et al. 1997; Williams and Rapoport 1994; Kukis et al. 1998). The conclusions for the labeling of DOTA with ^{90}Y are the following:

- The radiolabeling efficiency is best when the chelator-to-metal ratio is >3
- Increasing amounts of trace metals (Ca^{2+} , Fe^{2+} , Zn^{2+}), present in common commercial ^{90}Y preparations, inhibit the labeling in a concentration-dependent manner
- Higher pH results in faster complexation rate
- Longer reaction time and higher temperature usually enhance the radiolabeling yield

45.3.2 Dependence of Radiometal on Target Binding Affinity and Biodistribution

The binding affinity and the biodistribution are of major importance in the assessment of radiopharmaceuticals (Reubi 1995). The first reflects the potential to fulfill its objective to target a receptor while the second is elementary for reaching the target and avoiding an

undesired radiation of nontarget organs. Both are related to a major advantage of receptor-mediated radiopharmaceuticals, compared to other pharmaceuticals, such as chemotherapeutics: the selectivity.

For evaluation in biodistribution studies, tumor cells for which the bioconjugate is being developed are inoculated to animals (mice, rats) inducing the expression of a tumor. After administration of the labeled radiopharmaceutical, uptake in different organs, especially the receptor-positive organs and in the critical organs concerning toxicity effects, may be determined.

As already exemplified in [Sect. 45.3.1](#), the radiometal bound to the chelator–biomolecule conjugate might influence the binding affinity as well as the biodistribution. It was mentioned there the case of DTPA–octreotide where the non-labeled compound shows poor binding affinity and a bad pharmacological profile while the introduction of the metal influences this behavior positively. The metal itself influences the hydrophilicity of the whole radiopharmaceutical and for that reason the pharmacological profile of the compound.

A good example for the influence of the metal is the somatostatin derivative [DOTA⁰, Tyr³]-octreotide (DOTATOC), which can be labeled with different metals. Binding affinities are determined as IC₅₀ values (Stimmel and Kull 1998). In the case of somatostatin derivatives, ¹²⁵I-[Leu⁸, D-Trp²², Tyr²⁵]-somatostatin 28 is used as radioligand. The nonradioactive metal analogs should behave as the radioactive congeners. [Table 45.6](#) shows the binding affinities to the somatostatin receptor subtype 2 (sstr2).

Co^{II}-DOTATOC shows the best binding affinity of this series, which is even higher than the one of native somatostatin 28. This effect is not yet fully understood. As both Co^{II} and Ga^{III} form hexacoordinated complexes with DOTA, the biomolecule bound carboxymethyl arm remains not coordinated to the metal (Heppeler et al. 1999a). It keeps its flexibility and could play the role of a spacer between the biomolecule and the chelator, reducing the influence of the bulky BFC. In addition, Co^{II} also has a different charge compared to the other metals. Y^{III} shows an octacoordinated structure with DOTA, the biomolecule bound carboxymethyl arm is coordinated to the metal as well; the chelator is more fixed in its position relative to the biomolecule.

45.4 Structure and Stability of (Radio) Metal Complexes

Applications of radionuclides to biological vectors and their use in vivo demands that the radiometal (metallic radionuclide) remains strongly associated with the targeting biomolecule.

Table 45.6

Binding affinities of DOTATOC labeled with different metals

Ligand	IC ₅₀ for sstr2 (nM)
SS 28 (native somatostatin)	2.7 ± 0.3
Co ^{II} -DOTA-[Tyr] ³ -octreotide	0.14 ± 0.1
Ga ^{III} -DOTA-[Tyr] ³ -octreotide	2.5 ± 0.5
Y ^{III} -DOTA-[Tyr] ³ -octreotide	11 ± 1.7
Bi ^{III} -DOTA-[Tyr] ³ -octreotide	30 ± 3

Ligand structure, ligand denticity, thermodynamic and kinetic stability as well as serum stability have been included to rationalize and predict potential in vivo dissociation of radiometals.

Log K -values (1) are usually determined by potentiometric or spectrophotometric methods (McMurry et al. 1998; Kumar et al. 1994; Moore et al. 1989; Jones-Wilson et al. 1995):

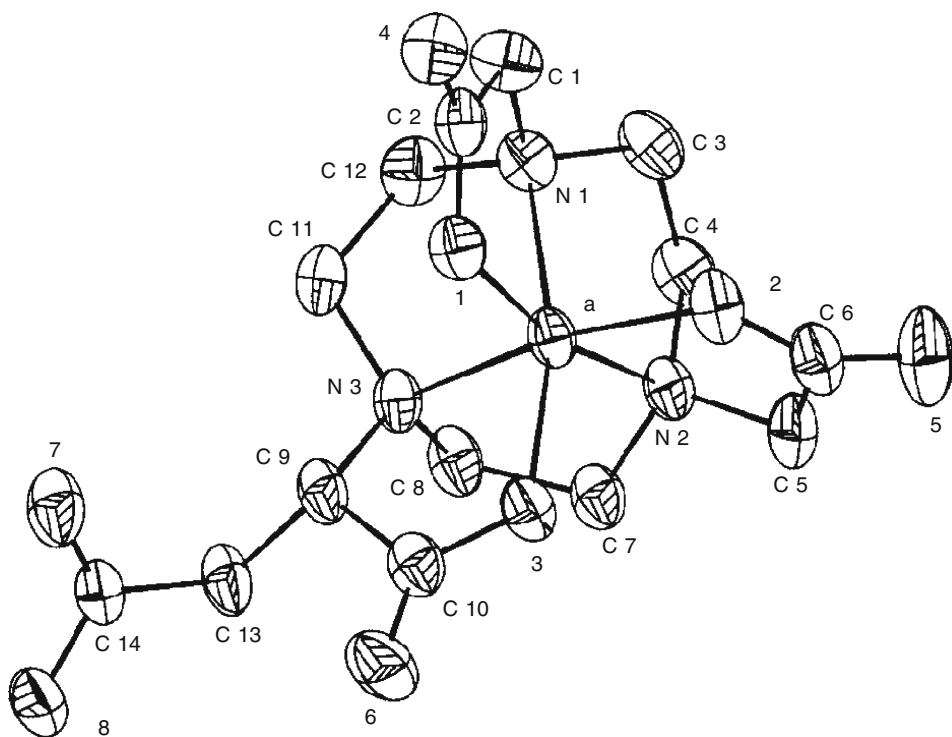
$$K_{ML} = [ML]/[M][L] \quad (45.1)$$

As mentioned before, Copper prefers macrocyclic chelators like cyclam-14 and its derivatives. Cyclam-14 forms thermodynamically stable complexes and its X-ray structure shows a square-plane configuration with four equal Cu–N bonds (Tasker and Sklar 1975). This complex with coordination number four lose less than 0.5% metal when incubated for 24 h in human serum. Open chain chelators do not reach this stability. Its bifunctional derivative CPTA (Fig. 45.17) coupled to an antibody and labeled with ^{67}Cu shows a half-life for copper exchange in phosphate buffer >1,000 days (Smith-Jones et al. 1991).

The polyaminocarboxylate-derivative of cyclam, TETA, forms Cu-complexes with coordination number 6 with involvement of four amino groups and two pendant carboxylates (Moi et al. 1987). Surprisingly, Jahn–Teller distortion involves two amines and not the carboxylates as expected. Again, the Copper-complex coupled to an antibody loses less than 1% of its metal per day when incubated in human serum.

Fig. 45.24

Oak ridge thermal ellipsoid plot (ORTEP) plot of structure Ga(NODASA) (André et al. 1998). Reproduced by permission of The Royal Society of Chemistry



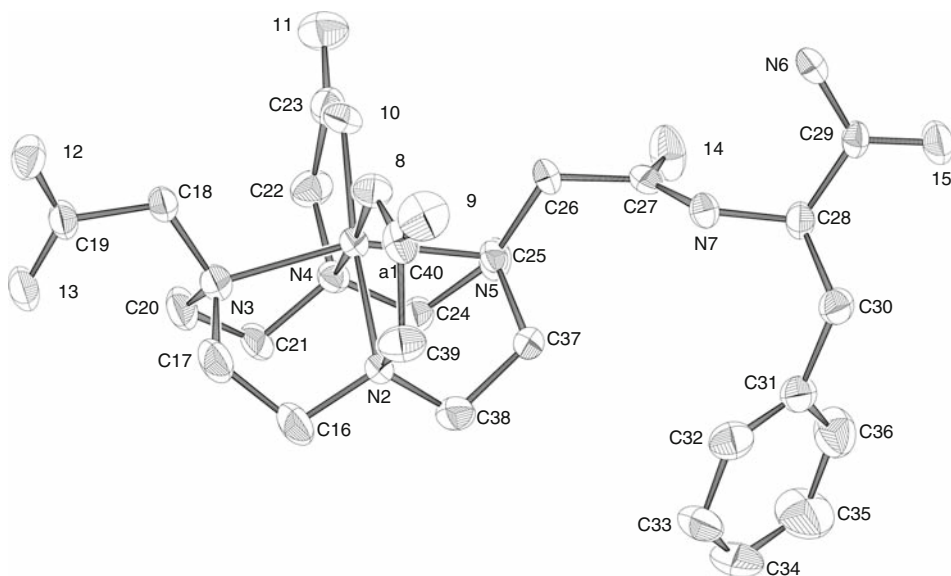
Complexes of Ga^{3+} prefer hexacoordination. An example of a complex with a macrocyclic bifunctional chelator is the structure of $\text{Ga}(\text{NODASA})$ (► Fig. 45.24) (André et al. 1998). It has a slightly distorted octahedral configuration with a plane defined by the amino groups and a second plane defined by three carboxylate oxygens, both in a facial arrangement. The fourth carboxylate (the β -carboxylate) remains free and offers a potential conjugation site in a prelabeling approach. The complex has a high kinetic stability, as it shows no transmetallation to transferrin in blood serum over a period of 5 days.

Ga^{3+} builds complexes with larger chelators as well; it will be shown here the X-ray structure of $\text{Ga}\text{-DOTA-D-Phe-amide}$, where the amino acid serves as model peptide. Again, the complex is hexacoordinated, having *cis*-pseudooctahedral geometry (Heppeler et al. 2000). The polyaza macrocycle is folded and the equatorial plane of the complex is formed by two *trans*-annular nitrogens of the cyclen ring and two corresponding carboxy oxygens (► Fig. 45.25).

When the attachment of a DOTA-based chelator to a biomolecule is performed on one of the acetate arms via an amide bond, the resulting complex with a radiometal also shows a fundamental difference; the radiometal uses a carbonyl oxygen instead of a carboxylate oxygen (► Fig. 45.26). A carbonyl oxygen is a weaker donor than the corresponding carboxylate oxygen. This is reflected in a lower thermodynamic stability of the resulting complex (e.g., $\log K_{\text{Y-DOTA-monoamide}} \approx 21.8$; $\log K_{\text{Y-DOTA}} \approx 23.5$) (Liu and Edwards 2001; Caravan et al. 1999; Sherry et al. 1989). Using a ligand–ligand competition approach performed via potentiometric titration, similar results have been obtained for Y-DTPA-peptides (Brockmann and Rösch 1999). Stability constants $\log K$ decrease from the Y-DTPA complex ($\log K = 22.05$) to Y-DTPA-Phe-Gly-Gly ($\log K = 19.7$), Y-DTPA-Phe-Trp ($\log K = 18.5$), and Y-DTPA-Phe-Tyr

► Fig. 45.25

ORTEP plot of structure $\text{Ga}\text{-DOTA-D-Phe-amide}$ (Heppeler et al. 2000). Reproduced by permission of Bentham Science Publishers Ltd

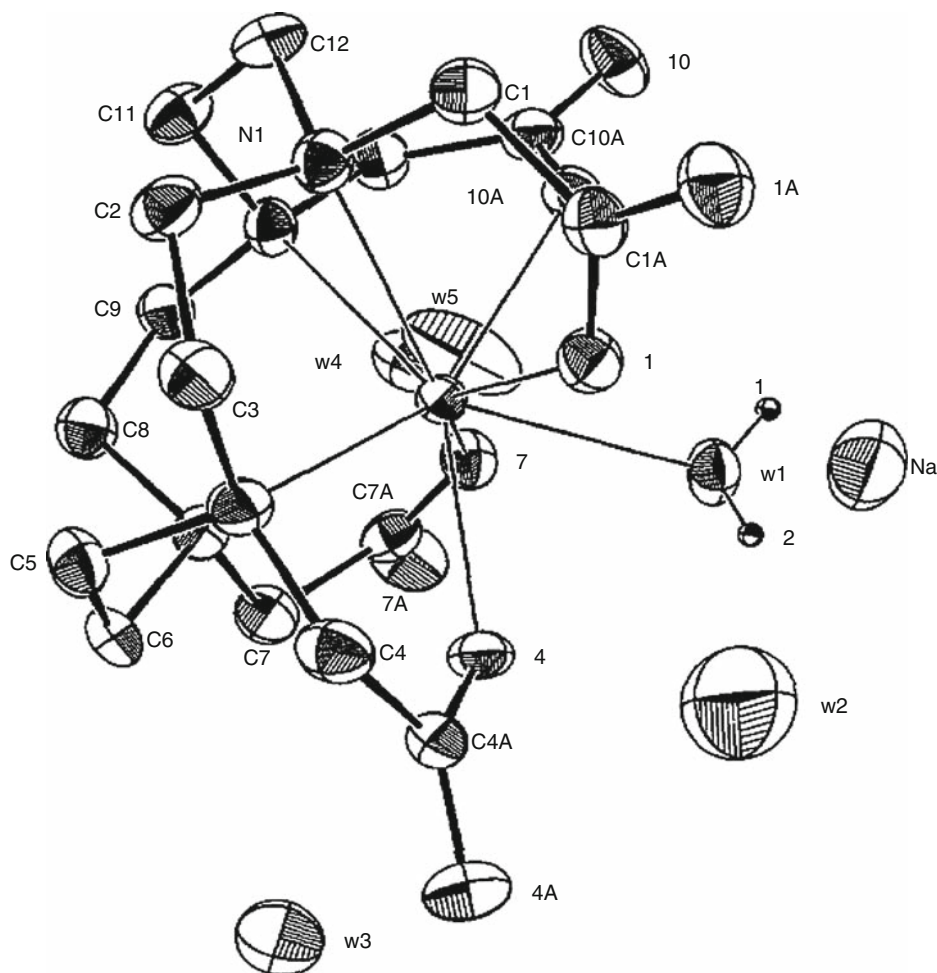


[illegible]

A promising therapeutic radionuclide is ^{111}Ag because of its suitable physical characteristics (▶ [Table 45.2](#)). It also represents an interesting example of how the lack of kinetic and thermodynamic stability prevents its in vivo application. Ag^+ presents one of the most labile coordination spheres. The development of a chelator with high affinity to Ag^+ and introducing high kinetic stability is extremely demanding. A strategy using a polyazamacrocyclic scaffold led to the chelator 1,4,7,10-tetrakis[2-(methylsulfanyl)ethyl]-1,4,7,10-tetraazacyclododecane (DOTETE) (Gyr et al. 1997). While [18]aneS6 (1,4,7,10,13,16-hexathiacyclooctadecane) is known as a strong chelating ligand for Ag^+ with a stability constant $\log K$ of 12.67 ± 0.13

■ Fig. 45.27

X-ray structure $\text{Na}[\text{Lu}(\text{DOTA})(\text{H}_2\text{O})]$ (Aime et al. 1996). Reprinted with permission from Elsevier

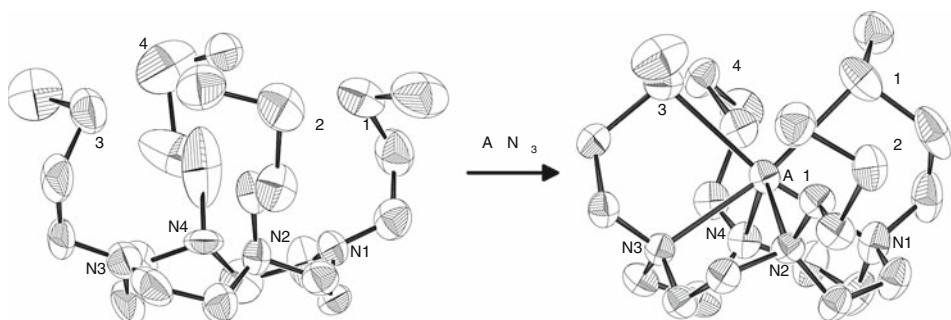


(Alberto et al. 1996), the DOTETE beats this stability by far with $\log K$ of 19.63, which is the highest stability observed for a silver(I) complex (Heppeler et al. 1999b). X-ray crystallographic studies of DOTETE indicate that this high stability is the result of the preorganization of the metal free chelator (► Fig. 45.28). The N4 plane is already visible in the uncoordinated chelator and all sulfur-bearing side chains are *syn* to the N4 plane. The introduction of a silver ion causes only minor changes in the structure of the chelator, leading to a hexacoordinated complex.

An nuclear magnetic resonance (NMR) study of the same complex indicates that the observed hexacoordination in the crystal structure is combined with a fast exchange of the donor thioethers in solution as all carbon atoms of the side chains have equivalent signals. Even at temperatures of 183 K, the signals remain equivalent. This could lead to an extra stability, but despite the high thermodynamic stability the kinetic stability is still too low and slow exchange with serum proteins has been observed.

■ Fig. 45.28

ORTEP plot (at 50% probability) of structures DOTETE and Ag(DOTETE) (Gyr et al. 1997).
Reproduced by permission of WILEY-VCH



45.5 Outlook

It appears that for most radiometals optimal bifunctional chelators have been developed. Improvements may be necessary in cases where very high specific activity labeling is needed, e.g., with pharmacologically active molecules. Strategies to increase the on-rate (rate of labeling) will help in these situations.

An unsolved and hardly to be solved problem appears to be the development of chelators that immobilize α -emitters. The recoil energy will destroy all currently used chelators. Strategies to use fullerenes to encapsulate α -emitters are under way. These and other nanocontainers may finally serve as the ultimate chelators.

References

- Abbas Rizvi SM, Song EY, Raja C, Beretov J, Morgenstern A, Apostolidis C, Russell PJ, Kearsley JH, Abbas K, Allen BJ (2008) *Cancer Biol Ther* 7:1547
- Aime S, Barge A, Botta M, Fasano M, Ayala JD, Bombieri G (1996) *Inorg Chim Acta* 246:423
- Albert R, Smith-Jones P, Stolz B, Simeon C, Knecht H, Bruns C, Pless J (1998) *Bioorg Med Chem Lett* 8:1207
- Alberto R, Nef W, Smith A, Kaden TA, Neuburger M, Zehnder M, Frey A, Abram U, Schubiger PA (1996) *Inorg Chem* 35:3420
- Alexander V (1995) *Chem Rev* 95:273
- Al-Nahhas A, Win Z, Szyzsko T, Singh A, Nanni C, Fanti S, Rubello D (2007) *Anticancer Res* 27:4087
- Anderson CJ, Pajeau TS, Edwards WB, Sherman EL, Rogers BE, Welch MJ (1995) *J Nucl Med* 36:2315
- Anderson CJ, Ferdani R (2009) *Cancer Biother Radiopharm* 24:379
- Anderson CJ, Dehdashti F, Cutler PD, Schwarz SW, Laforest R, Bass LA, Lewis JS, McCarthy DW (2001) *J Nucl Med* 42:213
- André JP, Maecke HR, Zehnder M, Macko L, Akyel KG (1998) *Chem Commun* 12:1301
- Antunes P, Ginj M, Zhang H, Waser B, Baum RP, Reubi JC, Maecke HR (2007a) *Eur J Nucl Med Mol Imaging* 34:982
- Antunes P, Ginj M, Walter MA, Chen J, Reubi JC, Maecke HR (2007b) *Bioconjug Chem* 18:84
- Boswell CA, Regino CAS, Baidoo KE, Wong KJ, Bumb A, Xu H, Milenic DE, Kelley JA, Lai CC, Brechbiel MW (2008) *Bioconjug Chem* 19:1476
- Breeman WAP, De Jong M, Visser TJ, Erion JL, Krenning EP (2003) *Eur J Nucl Med* 30:917
- Brechbiel MW (2008) *Q J Nucl Med Mol Imaging* 52:166
- Brechbiel MW, Gansow OA, Atcher RW, Schlom J, Esteban J, Simpson DE, Colcher D (1986) *Inorg Chem* 25:2772
- Brechbiel MW, Gansow OA (1991) *Bioconjug Chem* 2:187
- Brechbiel MW, Pippin CG, McMurry TJ, Milenic D, Roselli M, Colcher D, Gansow OA (1991) *J Chem Soc Chem Commun* 17:1169

- Brechbiel MW, Gansow OA, Pippin CG, Rogers RD, Planalp RP (1996) *Inorg Chem* 35:6343
- Broan CJ, Cox JPL, Craig AS, Katakly R, Parker D, Harrison A, Randall AM, Ferguson G (1991) *J Chem Soc Perk T* 2:87
- Brockmann J, Rösch F (1999) *Radiochim Acta* 87:79
- Busse S, Brockmann J, Rösch F (1999) *J Labelled Compd Rad* 42:300
- Cai H, Fissekis J, Conti PS (2009) *Dalton Trans* 27:5395
- Caravan P, Ellison JJ, McMurry TJ, Lauffer RB (1999) *Chem Rev* 99:2293
- Chappell LL, Rogers BE, Khazaeli MB, Mayo MS, Buchsbaum DJ, Brechbiel MW (1999) *Bioorg Med Chem* 7:2313
- Chappell LL, Deal KA, Dadachova E, Brechbiel MW (2000) *Bioconjug Chem* 11:510
- Chinn P, Braslawsky G, White C, Hanna N (2003) *Cancer Immunol Immunother* 52:257
- Chinol M, Bodei L, Cremonesi M, Paganelli G (2002) *Sem Nucl Med* 32:141
- Clifford T, Boswell CA, Biddlecombe GB, Lewis JS, Brechbiel MW (2006) *J Med Chem* 49:4297
- Cotton FA, Wilkinson G (1988) In: Cotton FA, Wilkinson G (eds) *Advanced inorganic chemistry*, 5th edn. New York, Wiley
- Cox JPL, Craig AS, Helps IM, Jankowski KJ, Parker D, Eaton MAW, Millican AT, Millar K, Beeley NRA, Boyce BA (1990) *J Chem Soc Perk T* 1:2567
- Cummins CH, Rutter EW, Fordyce WA (1991) *Bioconjug Chem* 2:180
- Cutler CS, Smith CJ, Ehrhardt GJ, Tyler TT, Jurisson SS, Deutsch E (2000) *Cancer Biother Radiopharm* 15:531
- Deal KA, Davis IA, Mirzadeh S, Kennel SJ, Brechbiel MW (1999) *J Med Chem* 42:2988
- De Jong M, Bakker WH, Krenning EP, Breeman WAP, van der Pluijm ME, Bernard BF, Visser TJ, Jermann E, Béhé M, Powell P, Mäcke HR (1997) *Eur J Nucl Med* 24:368
- Di Bartolo NM, Sargeson AM, Donlevy TM, Smith SV (2001) *J Chem Soc Dalton Trans* 15:2303
- Di Bartolo N, Sargeson AM, Smith SV (2006) *Org Biomol Chem* 4:3350
- Eberle AN, Mild G (2009) *J Recept Signal T* 29:1
- Eisenwiener KP, Powell P, Mäcke HR (2000) *Bioorg Med Chem Lett* 10:2133
- Eisenwiener KP, Prata MIM, Buschmann I, Zhang HW, Santos AC, Wenger S, Reubi JC, Mäcke HR (2002) *Bioconjug Chem* 13:530
- Fani M, André JP, Mäcke HR (2008) *Contrast Media Mol Imaging* 3:67
- Fichna J, Janecka A (2003) *Bioconjug Chem* 14:3
- Forrer F, Waldherr C, Mäcke HR, Mueller-Brand J (2006) *Anticancer Res* 26:703
- Fragogeorgi EA, Zikos C, Gourni E, Bouziotis P, Paravatou-Petsotas M, Loudos G, Mitsokapas N, Xanthopoulos S, Mavri-Vavayanni M, Livaniou E, Varvarigou AD, Archimandritis SC (2009) *Bioconjug Chem* 20:856
- Garmestani K, Yao Z, Zhang M, Wong K, Park CW, Pastan I, Carrasquillo JA, Brechbiel MW (2001) *Nucl Med Biol* 28:409
- Geue RJ, Hambley TW, Harrowfield JM, Sargeson AM, Snow MR (1984) *J Am Chem Soc* 106:5478
- Ginj M, Zhang H, Eisenwiener KP, Wild D, Schulz S, Rink H, Cescato R, Reubi JC, Mäcke HR (2008) *Clin Cancer Res* 14:2019
- Good S (2006) PhD thesis, University of Basel, Faculty of Science
- Good S, Walter MA, Waser B, Wang X, Müller-Brand J, Béhé MP, Reubi JC, Mäcke HR (2008) *Eur J Nucl Med Mol Imaging* 35:1868
- Gouin SG, Gustin JF, Joly K, Loussouarn A, Reliquet A, Meslin JC, Deniaud D (2002a) *Tetrahedron* 58:1131
- Gouin SG, Gustin J-F, Reliquet A, Meslin JC, Deniaud D (2002b) *Tetrahedron Lett* 43:3003
- Gyr T, Mäcke HR, Hennig M (1997) *Angew Chem Int Ed Engl* 36:2786
- Hancock RD (1989) *Prog Inorg Chem* 37:187
- Hancock RD, Martell AE (1989) *Chem Rev* 89:1875
- Harrison A, Walker C, Parker D (1991) *Nucl Med Biol* 18:469
- Hassfjell S, Brechbiel MW (2001) *Chem Rev* 101:2019
- Henze M, Schuhmacher J, Hipp P, Kowalski J, Becker DW, Doll J, Mäcke HR, Hofmann M, Debus J, Haberkorn U (2001) *J Nucl Med* 42:1053
- Heppeler A, Friodevaux S, Mäcke MR, Jermann E, Béhé M, Powell P, Hennig M (1999a) *Chem Eur J* 5:1974
- Heppeler A, Froidevaux S, Eberle AN, Mäcke HR (2000) *Curr Med Chem* 7:971
- Heppeler A, Jermann E, Gyr T, Dyson RM, Ruser G, Hennig M, Neuburger M, Neuburger-Zehnder M, Kaden T, Mäcke HR (1999b) In: Nicolini M, Mazzi U (eds) *Technetium, rhenium and other metals in chemistry and nuclear medicine*, vol 5. SGE Editoriali, Padua, pp 65–69
- Heppeler A, André JP, Buschmann I, Wang X, Reubi JC, Hennig M, Kaden TA, Mäcke HR (2008) *Chemistry* 14:3026
- Hnatowich DJ, Layne WW, Childs RL, Lanteigne D, Davis MA, Griffin TW, Doherty PW (1983) *Science* 220:613
- Hoffmann M, Mäcke H, Börner AR, Weckesser E, Schöffski P, Oei ML, Schumacher J, Henze M, Heppeler A, Meyer GJ, Knapp WH (2001) *Eur J Nucl Med* 28:1751
- Hsieh HP, Wu YT, Chen ST, Wang KT (1999) *Bioorg Med Chem* 7:1797
- Hu F, Cutler CS, Hoffman T, Sieckman G, Volkert WA, Jurisson SS (2002) *Nucl Med Biol* 29:423
- ICRP: International Commission on Radiological Protection (1983) *Radionuclide transformations*, ICRP Publication 38. Pergamon Press, Oxford

- Jamar F, Barone R, Mathieu I, Walrand S, Labar D, Carlier P, De Camps J, Schran H, Chen T, Smith MC, Bouterfa H, Valkema R, Krenning EP, Kvols LK, Pauwels S (2003) *Eur J Nucl Med* 30:510
- Jang YH, Blanco M, Dasgupta S, Keire DA, Shively JE, Goddard WA (1999) *J Am Chem Soc* 121:6142
- Jones-Wilson TM, Motekaitis RJ, Sun Y, Anderson CJ, Martell AE, Welch MJ (1995) *Nucl Med Biol* 22:859
- Jurcic JG, Larson SM, Sgouros G, McDevitt MR, Finn RD, Divgi CR, Ballangrud AM, Hamacher KA, Ma D, Humm JL, Brechbiel MW, Molinet R, Scheinberg DA (2002) *Blood* 100:1233
- Kennel SJ, Chappell LL, Dadachova K, Brechbiel MW, Lankford TK, Davis IA, Stabin M, Mirzadeh S (2000) *Cancer Biother Radiopharm* 15:235
- Kimura E, Fujioka H, Yatsunami A, Nihira H, Kodama M (1985) *Chem Pharm Bull* 33:655
- Kneifel S, Cordier D, Good S, Ionescu MC, Ghaffari A, Hofer S, Kretschmar M, Tolnay M, Apostolidis C, Waser B, Arnold M, Mueller-Brand J, Maecke HR, Reubi JC, Merlo A (2006) *Clin Cancer Res* 12:3843
- Knör S, Modlinger A, Poethko T, Schottelius M, Wester HJ, Kessler H (2007) *Chem Eur J* 13:6082
- Kodama M, Koike T, Mahatma AB, Kimura E (1991) *Inorg Chem* 30:1270
- Kolb HC, Sharpless KB (2003) *Drug Discov Today* 8:1128
- Koop B, Sven N, Reske SN, Neumaier B (2007) *Radiochim Acta* 95:39
- Krejcarek GE, Tucker KL (1977) *Biochem Biophys Res Commun* 77:581
- Krenning EP, Bakker WH, Breeman WAP (1989) *Lancet* 1:242
- Kukis DL, De Nardo SJ, De Nardo GL, O'Donnell RT, Meares CF (1998) *J Nucl Med* 39:2105
- Kumar K, Chang CA, Francesconi LC, Dischino DD, Malley MF, Gougoutas JZ, Tweedle MF (1994) *Inorg Chem* 33:3567
- Kumar K, Chang CA, Tweedle MF (1993) *Inorg Chem* 32:587
- Kwekkeboom DJ, Bakker WH, Kooij PP, Konijnenberg MW, Srinivasan A, Erion JL, Schmidt MA, Bugaj JL, De Jong M, Krenning EP (2001) *Eur J Nucl Med* 28:1319
- Lamberts SWJ, Bakker WH, Reubi JC, Krenning EP (1990) *N Engl J Med* 323:1246
- Lewis MR, Kao JY, Anderson AL, Shively JE, Raubitschek A (2001) *Bioconjug Chem* 12:320
- Lewis MR, Shively JE (1998) *Bioconjug Chem* 9:72
- Liu S (2008) *Adv Drug Deliv Rev* 60:1347
- Liu Z, Li ZB, Cao Q, Liu S, Wang F, Chen X (2009) *J Nucl Med* 50:1168
- Liu S, Edwards DS (2001) *Bioconjug Chem* 12:7
- Liu S, Edwards DS (1999) *Chem Rev* 99:2235
- Luyt LG, Katzenellenbogen JA (2002) *Bioconjug Chem* 13:1140
- Ma MT, Karas JA, White JM, Scanlon D, Donnelly PS (2009) *Chem Commun* 14:3237
- Maecke HR, Riesen A, Ritter W (1989) *J Nucl Med* 30:1235
- Mäcke HR, Smith-Jones P, Maina T, Stolz B, Albert R, Bruns C, Reist H (1993) *Horm Metab Res Suppl* 27:12
- Mäcke HR, Good S (2002) In: Nicolini M, Mazzi U (eds) *Technetium, rhenium and other metals in chemistry and nuclear medicine*, vol 6. SGE Editoriali, Padua, pp 35–41
- Maecke HR, Hofmann M, Haberkorn U (2005) *J Nucl Med* 46:172S
- Mamat C, Ramenda T, Wuest FR (2009) *Mini-Rev Org Chem* 6:21
- McCarthy DW, Shefer RE, Klinkowstein RE, Bass LA, Margeneau WH, Cutler CS, Anderson CJ, Welch MJ (1997) *Nucl Med Biol* 24:35
- McDevitt MR, Ma D, Lai LT, Simon J, Borchardt P, Frank RK, Wu K, Pellegrini V, Curcio MJ, Miederer M, Bander NH, Scheinberg DA (2001) *Science* 294:1537
- McMurry TJ, Brechbiel M, Kumar K, Gansow OA (1992) *Bioconjug Chem* 3:108
- McMurry TJ, Brechbiel M, Wu C, Gansow OA (1993) *Bioconjug Chem* 4:236
- McMurry TJ, Pippin CG, Wu C, Deal KA, Brechbiel MW, Mirzadeh S, Gansow OA (1998) *J Med Chem* 41:3546
- Meijs WE, Herscheid JDM, Haisma HJ (1992) *Appl Radiat Isot* 43:1443
- Merrifield RB (1963) *J Am Chem Soc* 85:2149
- Mindt TL, Müller C, Stuker F, Salazar JF, Hohn A, Mueggler T, Rudin M, Schibli R (2009) *Bioconjug Chem* 20:1940
- Moi MK, Meares CF (1988) *J Am Chem Soc* 110:6266
- Moi MK, Yanuck M, Deshpande SV, Hope H, DeNardo SJ, Meares CF (1987) *Inorg Chem* 26:3458
- Moore DA, Fanwick PE, Welch MJ (1989) *Inorg Chem* 28:1504
- Nikula TK, McDevitt MR, Finn RD, Wu C, Kozak RW, Garmestani K, Brechbiel MW, Curcio MJ, Pippin CG, Tiffany-Jones L, Geerlings MW, Apostolidis C, Molinet R, Geerlings MW, Gansow OA, Scheinberg DA (1999) *J Nucl Med* 40:166
- Obata A, Kasamatsu S, McCarthy DW, Welch MJ, Saji H, Yonekura Y, Fujibayashi Y (2003) *Nucl Med Biol* 30:535
- Otte A, Jermann E, Behe M, Goetze M, Bucher HC, Roser HW, Heppeler A, Mueller-Brand J, Maecke HR (1997) *Eur J Nucl Med* 24:792
- Otte A, Mueller-Brand J, Dellas S, Nitzsche E, Herrmann R, Maecke H (1998) *Lancet* 351:417
- Ouadi A, Loussouarn A, Remaud P, Morandeau L, Apostolidis C, Musikas C, Faivre-Chauvet A, Gestin JF (2000) *Tetrahedron Lett* 41:7207

- Parry JJ, Kelly TS, Andrews R, Rogers BE (2007) *Bioconjug Chem* 18:1110
- Patel YC, Greenwood M, Panetta R, Hukovic N, Grigorakis S, Robertson LA, Srikant CB (1996) *Metabolism* 45:31
- Peterson JJ, Pak RH, Meares CF (1999) *Bioconjug Chem* 10:316
- Prasad V, Ambrosini V, Hommann M, Hoersch D, Fanti S, Baum RP (2010) *Eur J Nucl Med Mol Imaging* 37:67
- Prasanphanich AF, Nanda PK, Rold TL, Ma L, Lewis MR, Garrison JC, Hoffman TJ, Sieckman GL, Figueroa SD, Smith CJ (2007) *Proc Natl Acad Sci U S A* 104:12462
- Reichert DE, Lewis JS, Anderson CJ (1999) *Coordination Chem Rev* 184:3
- Reubi JC, Maecke HR (2008) *J Nucl Med* 49:1735
- Reubi JC (1995) *J Nucl Med* 36:1825
- Richman JE, Atkins TJ (1974) *J Am Chem Soc* 96:2268
- Rostovtsev VV, Green LG, Fokin VV, Sharpless KB (2002) *Angew Chem Int Ed* 41:2596
- Ruser G, Ritter W, Maecke HR (1990) *Bioconjug Chem* 1:345
- Safavy A, Smith DC, Bazooband A, Buchsbaum DJ (2002a) *Bioconjug Chem* 13:317
- Safavy A, Smith DC, Bazooband A, Buchsbaum DJ (2002b) *Bioconjug Chem* 13:327
- Sargeson AM (1996) *Coord Chem Rev* 151:89
- Schottelius M, Schwaiger M, Wester HJ (2003) *Tetrahedron Lett* 44:2393
- Schubiger PA, Alberto R, Smith A (1996) *Bioconjug Chem* 7:165
- Shannon RD (1976) *Acta Crystallogr A* 32:751
- Sherry AD, Brown RD, Gerald CFCG, Koenig SH, Kuan KT, Spiller M (1989) *Inorg Chem* 28:620
- Shokeen M, Anderson CJ (2009) *Acc Chem Res* 42:832
- Sieving PF, Watson AD, Rocklage SM (1990) *Bioconjug Chem* 1:65
- Smith SV (2004) *J Inorg Biochem* 98:1874
- Smith-Jones PM, Friedrich R, Kaden TA, Novak-Hofer I, Siebold K, Tschudin D, Maecke HR (1991) *Bioconjug Chem* 2:415
- Smith-Jones PM, Stolz B, Albert R, Ruser G, Briner U, Maecke HR (1994) *J Nucl Med* 35:317
- Smith-Jones PM, Stolz B, Albert R, Ruser G, Briner U, Maecke HR (1998) *Nucl Med Biol* 25:181
- Sprague JE, Peng Y, Fiamengo AL, Woodin KS, Southwick EA, Weisman GR, Wong EH, Golen JA, Rheingold AL, Anderson CJ (2007) *J Med Chem* 50:2527
- Sprague JE, Peng Y, Sun X, Weisman GR, Wong EH, Achilefu S, Anderson CJ (2004) *Clin Cancer Res* 10:8674
- Stimmel JB, Kull FC Jr (1998) *Nucl Med Biol* 25:117
- Stolz B, Smith-Jones PM, Albert R, Reist H, Mäcke H, Bruns C (1994) *Horm Metab Res* 26:447
- Stolz B, Smith-Jones P, Albert R, Tolcsvai L, Briner U, Ruser G, Mäcke H, Weckbecker G, Bruns C (1996) *Digestion* 57(suppl 1):17
- Stolz B, Weckbecker G, Smith-Jones PM, Albert R, Friedrich R, Bruns C (1998) *Eur J Nucl Med* 25:668
- Sundberg MW, Meares CF, Goodwin DA, Diamanti CI (1974a) *J Med Chem* 17:1304
- Sundberg MW, Meares CF, Goodwin DA, Diamanti CI (1974b) *Nature* 250:587
- Tasker PA, Sklar L (1975) *J Cryst Mol Struct* 5:329
- Tornøe CW, Christensen C, Meldal M (2002) *J Org Chem* 67:3057
- Tóth É, Brücher E, Lázár I, Tóth I (1994) *Inorg Chem* 33:4070
- Velikyan I, Beyer GJ, Långström B (2004) *Bioconjug Chem* 15:554
- Velikyan I, Maecke HR, Langstrom B (2008) *Bioconjug Chem* 19:569
- Volkert WA, Goeckeler WF, Ehrhardt GJ, Ketring AR (1991) *J Nucl Med* 32:174
- Volkert WA, Hoffmann TJ (1999) *Chem Rev* 99:2269
- Wadas TJ, Wong EH, Weisman GR, Anderson CJ (2007) *Curr Pharm Des* 13:3
- Wadas TJ, Eiblmaier M, Zheleznyak A, Sherman CD, Ferdani R, Liang K, Achilefu S, Anderson CJ (2008) *J Nucl Med* 49:1819
- Waldherr C, Pless M, Maecke H, Schumacher T, Crazzolaro A, Nitzsche E, Haldemann A, Mueller-Brand J (2002) *J Nucl Med* 43:610
- Weisman GR, Reed DP (1996) *J Org Chem* 61:5186
- Weisman GR, Rogers ME, Wong EH, Jasinski JP, Paight ES (1990) *J Am Chem Soc* 112:8604
- Weisman GR, Wong EH, Hill DC, Rogers ME, Reed DP (1996) *J Chem Soc Chem Commun* 8:947
- Westerberg DA, Carney PL, Rogers PJ, Kline SJ, Johnson DK (1989) *J Med Chem* 32:236
- Wilder RB, DeNardo GL, DeNardo SJ (1996) *J Clin Oncol* 14:1383
- Williams MA, Rapoport H (1993) *J Org Chem* 58:1151
- Williams MA, Rapoport H (1994) *J Org Chem* 59:3616
- Wong EH, Weisman GR, Hill DC, Reed DP, Rogers ME, Condon JS, Fagan MA, Calabrese JC, Lam KC, Guzei IA, Rheingold AL (2000) *J Am Chem Soc* 122:10561
- Wu C, Kobayashi H, Sun B, Yoo TM, Paik CH, Gansow OA, Carrasquillo JA, Pastan I, Brechbiel MW (1997) *Bioorg Med Chem* 5:1925
- Wu Y, Zhang X, Xiong Z, Cheng Z, Fisher DR, Liu S, Gambhir SS, Chen X (2005) *J Nucl Med* 46:1707
- Xua H, Baidoo KE, Wongb KJ, Brechbiel MW (2008) *Bioorg Med Chem Lett* 18:2679

46 Radionuclide Therapy

M. R. Zalutsky

Duke University, Durham, NC, USA

46.1	<i>Introduction</i>	2180
46.2	<i>Design of Targeted Radiotherapeutics</i>	2180
46.2.1	Selection of the Radionuclide	2181
46.2.1.1	Geometrical Considerations	2181
46.2.1.2	Heterogeneity	2183
46.2.1.3	Other Considerations	2185
46.2.2	Selection of the Targeting Vehicle	2186
46.2.2.1	Particulate Carriers	2187
46.2.2.2	Monoclonal Antibodies	2187
46.2.2.3	Peptides as Radionuclide Carriers	2192
46.3	<i>Radionuclides for Targeted Radiotherapy</i>	2194
46.3.1	Beta-Particle-Emitting Radionuclides	2194
46.3.1.1	Short Range β -Particle Emitters	2196
46.3.1.2	Medium Range β -Particle Emitters	2197
46.3.1.3	Long Range β -Particle Emitters	2198
46.3.2	Alpha-Particle-Emitting Radionuclides	2198
46.3.2.1	Terbium-149	2199
46.3.2.2	Astatine-211	2200
46.3.2.3	Bismuth-212	2201
46.3.2.4	Bismuth-213	2202
46.3.2.5	Actinium-225	2202
46.3.3	Low-Energy Electron Emitters	2203

Abstract: Radionuclide therapy utilizes unsealed sources of radionuclides as a treatment for cancer or other pathological conditions such as rheumatoid arthritis. Radionuclides that decay by the emission of β and α particles, as well as those that emit Auger electrons, have been used for this purpose. In this chapter, radiochemical aspects of radionuclide therapy, including criteria for radionuclide selection, radionuclide production, radiolabeling chemistry, and radiation dosimetry are discussed.

46.1 Introduction

The toxic effects of radiation have long been recognized and applied to the treatment of a variety of pathological conditions, notably cancer and rheumatoid arthritis. In its most widely applied manifestation, tumor irradiation is achieved by focusing an external beam of radiation on the malignancy. A less common approach, brachytherapy, involves the implantation of an unsealed source of radiation, usually in the form of a wire or a pellet, in close proximity to the tumor. Although these forms of radiation therapy have been effective in the treatment of many diseases, they have intrinsic limitations that compromise their effectiveness. To be effective, external beam radiation and brachytherapy require knowledge of the precise location and geometrical configuration of the tumor in order to maximize the destruction of cancer cells, while minimizing the radiation dose to neighboring normal tissues. In addition, these treatment modalities are of limited utility for treating multifocal tumors and metastasis cancer sites. In order to circumvent this limitation, a concerted effort has been devoted to developing radionuclide therapy (also known as endoradiotherapy) as an alternative radiation-based treatment strategy.

Targeted radionuclide therapy involves the use of a radiolabeled molecule to selectively deliver a cytotoxic level of radiation to a disease site. The overriding objectives of radionuclide therapy and external beam therapy are the same: obtaining the maximum radiation dose for the tumor while minimizing the irradiation of normal organs. However, the two treatment approaches differ considerably with regard to the impediments that must be overcome to achieve this goal.

Advances in tumor biology, recombinant antibody technology, and radio synthetic chemistry have led to a flurry of activity in the development and clinical application of endoradiotherapeutic agents. However, it is important to bear in mind that radionuclide therapy is actually not a new concept, having been used in patients for more than 60 years. A number of textbooks provide excellent chronicles of early efforts in radionuclide therapy (Spencer 1978; Harbert 1987; Spencer et al. 1987). A notable example is sodium [^{131}I]iodide, which has been utilized for the treatment of hyperthyroidism and thyroid carcinomas and remains the most widely utilized targeted radiotherapeutic in current clinical use. Radiocolloids such as those labeled with either ^{198}Au or ^{32}P have been used for more than 50 years for the treatment of diseases such as malignant pleural effusions and intraperitoneal tumors.

46.2 Design of Targeted Radiotherapeutics

The design of an effective endoradiotherapeutic agent requires a careful optimization of its two components, namely the radionuclide and the carrier system that is used to direct the radionuclide to the tumor, so that the radiation emitted during its de-excitation will have

a high probability of being deposited within the malignant cell population. With physical carriers, barriers created by isolated body cavities are utilized to confine a radiolabeled colloid, particulate, or other inert, nondiffusible substance to that cavity. This approach has been applied in the treatment of rheumatoid arthritis as well as tumors spread throughout the peritoneum or intrathecal space. Biological carriers attempt to exploit a biochemical or metabolic difference between tumor and normal tissue in order to identify a compound that will preferentially localize in the cancer after being injected into the patient. Because they can be applied to a wider variety of disease processes and can be used to treat metastatic cancers, biological carrier systems are particularly attractive for targeted radionuclide therapy.

46.2.1 Selection of the Radionuclide

A number of factors influence the choice of radionuclide for a particular therapeutic application. The first consideration is to ensure that the decay mode and radiation range are well matched to the size, location, and geometry of a tumor. As discussed in subsequent sections of this chapter, the irradiation of tissue volumes with multicellular, cellular, and subcellular dimensions can be accomplished with *radionuclides emitting β particles, α particles, and Auger electrons*, respectively. The ideal radionuclide for treating a large solid tumor such as a hepatoma will be clearly different from that which would be preferred for elimination of metastatic deposits consisting of a few hundred cells. In addition to radiation range, a number of other factors must be considered in selecting a radionuclide for endoradiotherapy. In addition to the characteristics of the emissions, the following parameters should be considered: (1) half-life, (2) production method, (3) chemistry, and (4) biological behavior.

46.2.1.1 Geometrical Considerations

The objective of radionuclide therapy is to deliver a cytotoxic dose of radiation to all the cells within a tumor, while sparing normal tissues. Clearly, the size and geometrical configuration of a particular tumor will be important considerations. The idea of optimizing radiation range for a particular tumor is obviously idealistic because that would necessitate a priori detailed knowledge of tumor volume and configuration for each patient. Furthermore, different radionuclides would be required for different patients and this would be impractical. Nonetheless, generalizations can be made to guide in the selection of a radionuclide that would be best for an individual type of malignancy. Particularly for smaller tumors, even under conditions where the radionuclide is deposited uniformly, the radiation dose received by tumor cells will be dependent upon their position within the lesion. Finally, it must be recognized that the site of decay in subcellular dimensions can have a major effect on the radiation dose received by the cell nucleus, generally considered to be the subcellular target for radiation-mediated cell killing (Hall 2000).

For larger tumors such as a 500-g hepatoma in the liver, radionuclides emitting long-range β particles such as ^{186}Re and ^{90}Y were calculated to be ideal because most of their decay energy would be deposited within the tumor (Wessels and Rogus 1984). However, for smaller tumors, generally considered to be the ideal setting for endoradiotherapy (Sautterbihl et al. 1996), different radionuclides should be used. Humm (1986) compared the fraction of decay energy that would be absorbed for a high-energy β emitter (^{90}Y), a low-energy β emitter (^{131}I), and an

α emitter (^{211}At) when uniformly distributed in spherical tumors. In 1-cm-diameter tumors, the absorbed fractions were calculated to be 0.097, 0.54, and ~ 0.9 , for the particulate emissions of ^{90}Y , ^{131}I , and ^{211}At , respectively; for 0.2-cm-diameter tumors, absorbed fractions of 0.015, 0.17, and ~ 0.5 were calculated. For 1-cm-diameter tumors, more than 90% of the β -particle energy of ^{90}Y is already deposited outside the lesion, resulting in less efficient cell kill, and higher dose to neighboring normal tissues.

Monte Carlo transport simulations have been utilized to calculate the radiation absorbed dose received by normal tissues in close proximity to tumors containing a radiotherapeutic (Sparks et al. 2002). For normal tissues 1 mm from tumors containing ^{90}Y - or ^{131}I -labeled compounds, doses were 24% and 4% of the absorbed dose in the tumor itself. For small structures such as arteries or nerves surrounded by tumor, these doses were 103% and 46%, respectively. Another setting in which the effects of radiation range have been investigated is in the treatment of neoplastic meningitis, a malignancy characterized by free-floating tumor cells in the cerebrospinal fluid (CSF). Direct injection of a labeled compound into the CSF can be effective in irradiating these tumor cells; however, deleterious effects to normal spinal cord must be avoided. Millar and Barrett (1990) calculated that as a consequence of its shorter-range β emissions, CSF-to-normal-spinal-cord dose ratios for ^{131}I were up to nine times higher than those for ^{90}Y .

The above discussion has focused on a comparison of ^{90}Y and ^{131}I because these are the most frequently utilized radionuclides in endoradiotherapy; however, the effect of particle range on therapeutic utility has been evaluated theoretically for other radionuclides as well. For a comprehensive discussion of the relationship between tumor size and therapeutic effectiveness for 22 uniformly distributed β emitters, the reader is referred to a paper by O'Donoghue et al. (1995). In this study, a model was developed that took into account both *tumor radiosensitivity and proliferation* and yielded the diameter of tumor that could be optimally treated by each radionuclide. These ranged from 0.6 mm for ^{33}P to 3.4 cm for ^{90}Y . A tumor control probability model has also been utilized to compare the potential therapeutic efficacy of six β emitters (Nahum 1996).


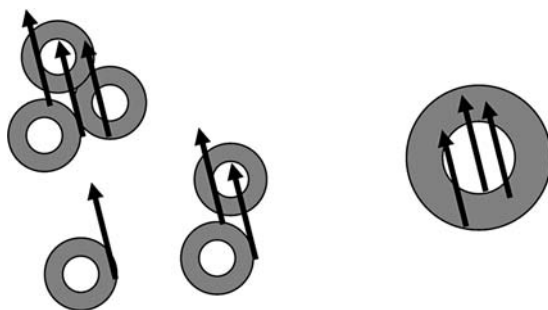
In selecting radionuclides for a particular endoradiotherapeutic strategy, it is important to note that for a given radionuclide, geometrical factors also can result in considerable variation in radiation dose to the radiosensitive cell element, the nucleus.  Figure 46.1 illustrates two

 Fig. 46.1

Radiation dose to the cell nucleus can come from either self-irradiation or cross fire (left) and will vary depending upon whether the site of decay was in the cell membrane, in the cytoplasm, or in the cell nucleus (right)



processes that must be considered: radiation crossfire and the subcellular site of radioactive decay. Even with a uniformly distributed radionuclide, the dose received by individual cells can vary because of differences in crossfire dose and the fraction of the radiation bound to the cell that is deposited in the tumor. This is particularly apparent for micrometastatic disease, which presents as small clusters of tumor cells, magnifying the impact of these factors.

Hartman et al. (2000) utilized numerical integration and a point kernel approach to investigate these effects for cells with diameters of 10, 14, and 20 μm using ^{131}I as the radionuclide. It was found that the dose received under single-cell conditions was about half that which was delivered in cell clusters containing six cells. The regional variation in cell dose also was calculated for larger clusters of tumor cells. For a 100- μm -diameter tumor, the radiation absorbed dose received at the surface of the cluster was only about half that delivered to the center. With regard to the effect of the subcellular site of decay, Hartman et al. (2000) showed that shifting the site of ^{131}I decay from the cell membrane to the nucleus would increase the dose to the cell nucleus by an order of magnitude.

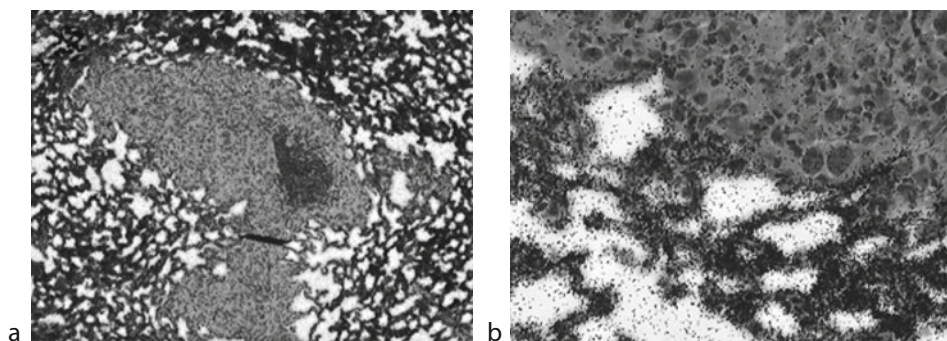
46.2.1.2 Heterogeneity

If the only goal from a radiation range perspective were maximizing absorbed dose fraction to tumor while minimizing irradiation of adjacent normal tissue structures, then it would appear that radionuclides emitting short-range radiation would be preferred. However, the success of radionuclide therapy is also critically dependent upon achieving *homogeneous dose deposition within the tumor*, so that regrowth from an untreated subpopulation will be avoided. Unfortunately, autoradiographic studies have documented the highly heterogeneous distribution of labeled molecules in tumors (Sands et al. 1988; Gridley et al. 1991).

The heterogeneous nature of radionuclide distribution after intravenous injection of a targeted radiotherapeutic compound is illustrated in [Fig. 46.2](#). These autoradiographs are of an EMT-6 lung tumor in a mouse obtained after the intravenous administration of a ^{125}I -labeled monoclonal antibody. In [Fig. 46.2a](#) obtained at $4\times$ magnification, an absence of black grains corresponding to ^{125}I activity in the central region of the tumor is apparent. At $40\times$

Fig. 46.2

Autoradiographs of an EMT-6 lung tumor obtained from a mouse injected with a ^{125}I -labeled monoclonal antibody; (a) $4\times$ and (b) $40\times$ magnification (Akabani et al. unpublished data)



magnification (► [Fig. 46.2b](#)), even in the region that accumulated the labeled antibody, a heterogeneous pattern of radionuclide is observed, with the activity being localized primarily in the extracellular matrix (i.e., the regions between the cells).

There are many impediments to delivering a uniform dose of radiation to tumors from exogenously administered targeted radiotherapeutic compound (Hauck et al. 1995). Some of these are dependent on the nature of the tumor and others on the characteristics of the labeled compound and its molecular target. Because it is often difficult to overcome these heterogeneities by other means, radionuclides emitting longer-range radiation are frequently utilized for radionuclide therapy.

Heterogeneities Related to the Nature of the Tumor

Because most endoradiotherapeutic agents are administered via intravenous injection, tumor hemodynamic factors play an important role in defining the degree of heterogeneity in their delivery. Regional variations in delivery can be influenced by blood flow, vascular density and permeability. Tumor vasculature is arranged differently from that in normal tissues, in that it is more irregular, may lack an endothelial lining, and exhibits variations in blood flow with time (Warren 1979; Jain and Ward-Hartley 1984; Jain 1988). On the other hand, tumor vasculature is generally more leaky than that of normal tissues, and this increased permeability can facilitate the distribution of labeled drugs within the tumor (Sands et al. 1988). Unfortunately, increased permeability in tumor vessels is of little benefit if blood flow to these vessels is compromised, as is often the case (Warren 1979).

Another feature of tumors that can have a major impact on the distribution of targeted radiotherapeutics is *tumor interstitial fluid pressure*. Interstitial fluid pressure results in a pressure gradient that can inhibit the delivery of molecules from the plasma to the extracellular fluid in central regions of a tumor. This pressure gradient is not present in normal tissues because they have a lymphatic system; however, tumors do not, creating an additional barrier that must be overcome. Experimental evidence of an elevated interstitial pressure in murine tumor models has been reported by Boucher et al. (1990). As expected, the effect was most apparent at the tumor periphery. Using a mathematical model, the magnitude of this outward convection fluid flow was predicted to be 0.1–0.2 $\mu\text{m/s}$ (Jain and Baxter 1988).

Heterogeneities Related to the Properties of the Labeled Molecule

The most promising strategies for radionuclide therapy are those that offer the prospect of achieving preferential uptake in tumor compared with normal tissues by binding to a molecule such as an antigen or receptor that is present in high concentrations on tumor cells. If the forward rate constant for binding is very high and the concentration of the endoradiotherapeutic is low, then rapid binding to tumor cells close to the capillary can occur. This *binding-site barrier* can inhibit the penetration of the labeled compound into the interior of the tumor (Weinstein et al. 1987). An additional problem for macromolecules is their slow diffusion; it has been predicted that diffusion of a 150 kDa protein into the center of a 150-m-diameter spherical tumor would take days (van Osdol et al. 1991). Mathematical models have been developed that suggest greater tumor penetration could be achieved with molecules that bound with lower affinity (Baxter and Jain 1991). From a theoretical perspective, the best solution appears to be a molecule that maintains a high affinity constant by combining a relatively slow association rate constant with a slow dissociation rate constant (Fujimori et al. 1989).

An additional factor that must be considered is the uniformity of the concentration of the molecular target within the tumor. The concentrations of tumor-associated antigens (Hayes et al. 1989) and receptors (Wikstrand et al. 1995) among tumors from patients with a particular type of malignancy can vary from over 10^5 molecules per cell to undetectable levels. Furthermore, wide variations in antigen or receptor expression have been reported both within the cells of a particular tumor as well as between different tumors from the same patient (Del Vecchio et al. 1989, Mattes et al. 1990). For targeted radiotherapy, a particularly problematic aspect of heterogeneous target molecule expression is that in many cases, large regions of tumor lack the capacity for binding the targeted radiotherapeutic. As noted above, one strategy for circumventing this problem is to utilize radionuclides with sufficient range to deliver meaningful radiation doses to tumor regions that do not express appreciable levels of the target molecule through radiation crossfire.

46.2.1.3 Other Considerations

The *physical half-life of the radionuclide* is another factor that must be considered in the design of endoradiotherapeutic agents. The half-life should be long enough to permit radio synthesis and quality control and in some cases, distribution to locations distant from the production site of the radiopharmaceutical. More importantly, the half-life should be compatible with the *pharmacokinetics of localization* in tumor and clearance from normal tissues. Finally, it is generally easier to achieve higher radiation dose rates with shorter half-life radionuclides. This is an important consideration because cell culture experiments (Bedford and Mitchell 1973) and clinical studies (Mazeron et al. 1991) have shown that increasing the dose rate for low linear energy transfer radiation can lead to a greater degree of tumor control.

Radionuclide availability also must be considered. Reactors, cyclotrons, and natural decay chains have all been utilized as sources of radionuclides for targeted radiotherapy; cf. ➤ Chaps. 38, ➤ 39 and ➤ 40 in this Volume. A high degree of radionuclidic purity is required for therapeutic radiopharmaceuticals. Depending on the nature of the molecule that will be labeled, *specific activity* (GBq/mmol) may also be an important consideration. For radiocolloids or other agents that are taken up by a nonsaturable process, specific activity is less important, and low specific activity production methods such as (n,γ) reactions on nuclear reactors are acceptable. However, if the targeting mechanism is easily saturated, as is often the case with tumor-associated antigens, receptors or transporters, then no-carrier-added production methods may be required (Eckelman 1995). In any case, cost and availability of the radionuclide must be considered in the development of a practical endoradiotherapeutic agent. Indeed, lack of availability of the radionuclide has sometimes been the largest impediment to the development of promising α-particle emitters such as ^{213}Bi and ^{211}At .

Selection of a radionuclide for targeted radiotherapy must also take into account its chemical-biological properties. Chemical methods must be devised for attaching the radionuclide to the targeting molecule of interest without compromising the tumor localizing capacity of the molecule. In addition, the bond between the radionuclide and the carrier molecule must be stable in the *in vivo* environment over a time period consistent with the physical half-life of the radionuclide in order to minimize damage to normal organs from released activity.

Because some dissociation of radionuclide from the carrier molecule is likely to occur either due to instability or metabolism, it is important to also consider the *in vivo* localization

and clearance properties of the free radionuclide and other labeled catabolic species. For example, radioiodine distributes primarily in the thyroid and the stomach, and for radioiodinated biomolecules, this background activity can be minimized through the administration of blocking doses of potassium iodide (Larsen et al. 1998a). On the other hand, many metallic radionuclides, when released in ionic form, are avidly accumulated in the bone. This can result in irradiation of the bone marrow, one of the most highly radiosensitive normal tissues, and compromise the effectiveness of these agents. This difference between radio metals and radioiodine is illustrated by comparisons of proteins labeled with the β emitters ^{131}I and ^{90}Y , which showed that at the maximum tolerated dose of the radio metal–labeled, protein was considerably lower than that of its radioiodinated counterpart (Sharkey et al. 1990, 1997; Buchsbaum et al. 1993). Clearly, such comparisons are influenced not only by the disposition of the labeled catabolites generated from the radio metal– and radioiodine-labeled proteins (including the free metal ions and halides), but also by the methodologies used to attach the radio metal to the protein.

46.2.2 Selection of the Targeting Vehicle

With the exception of carriers that rely on tumor localization by physical entrapment such as colloids, the development of effective targeting agents for delivering radionuclides to tumors involves two steps: *identification of a molecular target* that is either uniquely expressed or over expressed on tumors, and generation of a molecule that can be radiolabeled and can bind to the tumor-associated target. A wide variety of targeting vehicles have been investigated for radio-nuclide therapy and some of these are summarized in ▶ Table 46.1. After a brief discussion of radiolabeled particulates, the following sections will describe the properties of monoclonal antibodies and peptides because these targeting vehicles are the focus of the majority of current radionuclide therapy research.

■ Table 46.1
Some targeting vehicles utilized for radionuclide therapy

Vehicle	Example	Reference
Colloid	^{165}Dy -labeled ferric hydroxide macroaggregates	Sledge et al. (1986)
Organic molecule	Meta- ^{131}I iodobenzylguanidine	Wieland et al. (1980)
Inorganic complex	^{153}Sm EDTMP	Goeckeler et al. (1987)
Peptide	^{90}Y -labeled DOTA-octreotide	de Jong et al. (2002)
Protein	^{131}I -labeled anti-tenascin antibody 81C6	Zalutsky et al. (1989a)
Drug	^{211}At -labeled Syncovit	Brown and Mitchell (1998)
Steroid	^{125}I -labeled estradiol analogs	Hanson (2000)
Nucleoside	5- ^{125}I iodo-2'-deoxyuridine	Bloomer and Adelstein (1977)

46.2.2.1 Particulate Carriers

Much of the early work with radionuclide therapy involved *radiolabeled particulates* (Spencer 1978; Harbert 1987), and these agents are still routinely used in certain clinical applications. In general, this type of agent is used when the tumor or other disease state is confined to an isolated body cavity. The goal is to obtain a uniformly distributed radiation dose within the cavity, while minimizing *leakage* into the rest of the body. In addition to stability, the most important characteristic of particulate carriers is their size because this dictates not only homogeneity of dose deposition but also leakage from the treatment site.

Perhaps the most frequent current use of radiolabeled particulates is not in the cancer field but in the treatment of rheumatoid arthritis. In this procedure, the goal is to selectively destroy the inflamed joint lining, the hallmark of rheumatoid arthritis, through the intra-articular administration of a radionuclide. This is an attractive alternative to the conventional surgical approach because *radiation synovectomy* is considerably less expensive and requires less extensive hospitalization. Initially, radiation synovectomy was performed using a ^{198}Au colloid; however, leakage of this particulate from the knee joint was excessive, with over 10% of the injected dose generally being taken up in the regional lymph nodes (Virkkunen et al. 1967). A variety of ^{90}Y -labeled colloids were also evaluated, but the leakage from the joint to the lymph node was again problematic (Rekonen et al. 1972; Gumpel et al. 1975). A common characteristic of these colloids was their small size, less than $0.1\text{ }\mu\text{m}$ in diameter.

To circumvent this problem, Sledge et al. (1977) utilized ferric hydroxide macroaggregates as a particulate in tandem with the 3.3-h half-life β emitter, ^{165}Dy , which was produced by a neutron bombardment of natural dysprosium. Leakage rates of this 5–10- μm -diameter particulate from knee joints were considerably lower than that observed with the ^{198}Au and ^{90}Y colloids noted above (Zalutsky et al. 1986). From a practical standpoint, the short half-life of ^{165}Dy limits the utility of this endoradiotherapeutic agent to medical centers that are located in reasonable proximity to a nuclear reactor. This has led to the search for a particulate carrier than can be used for radiation synovectomy that can be labeled with a longer half-life radionuclide. Among the radionuclides that have been investigated for this purpose are ^{188}Re (Wang et al. 2001), ^{169}Er (Ruotsi et al. 1979), ^{32}P (Onetti et al. 1982), ^{166}Ho (Song et al. 2001), and ^{153}Sm (Shin et al. 2001).

46.2.2.2 Monoclonal Antibodies

No advance has done more to resurrect interest in targeted radionuclide therapy than the development of *monoclonal antibody (mAb) technology*. Antibodies are proteins that are generated in response to a specific molecular stimulus, which is known as the antigen. In principle, antibodies can be produced that react with antigenic structures that are present on cancer cells, and this has been possible even when the molecular nature of the antigen has not been determined. As the knowledge on the molecular biology of tumor cells has grown, the ability to define the structure of these antigenic targets has improved, making it easier to generate antibodies that bind with high affinity to tumor cells. Many laboratories throughout the world have attempted to exploit the molecular specificity of antibody binding to tumor-associated antigens in order to selectively target radionuclides to tumors. In the past few years, this form of targeted radiotherapy, known as radioimmunotherapy, has reached the stage of

development that a number of labeled antibodies are commercially available for the treatment of certain types of cancer.

Initially, antibodies first were generated by immunizing goats or rabbits, and these were utilized to demonstrate the feasibility of antibody-mediated targeting of radionuclides to tumors. For example, Primus et al. (1977) showed preferential uptake of radioiodine in human tumors implanted in hamsters after the injection of a radioiodinated antibody reactive with carcinoembryonic antigen, a molecule found on human colorectal cancers. A severe limitation of these animal-generated antisera that compromised their utility as carrier molecules for targeted radiotherapy was their polyclonal nature. Polyclonal antibodies consist of a family of proteins with a range of specificity and affinity for the antigenic target of interest. It was not until the introduction of hybridoma technology by Kohler and Milstein (1975) that it became possible to circumvent this problem. This methodology yields mAbs, which are proteins with a defined amino acid sequence, resulting in a carrier with a defined antigen specificity and affinity. Other advantages of mAbs that have facilitated the development of antibody-based therapeutic radiopharmaceuticals is the fact that large quantities of these proteins can be produced more conveniently, at a lower cost, and in a more reproducible fashion.

Fate of the Antibody–Antigen Complex

The suitability of a particular antigen–mAb system for therapeutic applications depends in part on the biological fate of the antigen–mAb complex (Hayes et al. 1989). The ideal scenario is if the complex remains on the cell membrane or extracellular matrix after binding for a time period compatible with the physical half-life of the radionuclide. In some cases, after antibody binding, the resultant immune complex is rapidly released from the tumor. This process, known as shedding, decreases the radiation dose received by the tumor, and depending on the size of the antigen–antibody complex, can increase the radiation dose received by the blood, bone marrow, and liver.

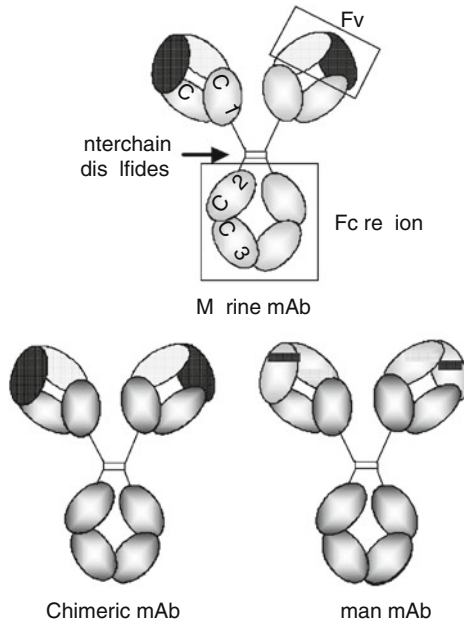
An additional possibility is that the antigen–antibody complex can be internalized into the tumor cell. This is an important consideration from a labeling perspective because in general, internalization exposes the labeled mAb to intracellular catabolic processes. Of primary concern is lysosomal proteolysis, which can lead to rapid loss of the radionuclide from the tumor cell (Press et al. 1990; Geissler et al. 1991), significantly decreasing the efficacy of radioimmunotherapy. This is an important problem for antibody-mediated radiotherapy because many of the most tumor-specific antigenic targets rapidly internalize (Slamon et al. 1989; Press et al. 1994; Wikstrand et al. 1995), exposing labeled mAbs reactive with these molecules to the intracellular environment. Although methods for minimizing the release of radio halogens from internalizing mAbs have been developed recently (Foulon et al. 2000), labeling internalizing mAbs with radio metals generally results in better retention of the radionuclide in tumor cells compared with conventional radioiodination methods (Novak-Hofer et al. 1994).

Antibody Structure

Unlike most other endoradiotherapeutic agents, radiolabeled mAbs are macromolecules. While there are five classes of human immunoglobulins from which this type of agent could be developed, the vast majority of mAbs utilized for radioimmunotherapy are IgG. These molecules have an approximate molecular weight of 150 kDa and are the predominant immunoglobulin class found in the blood. A schematic structure of an IgG molecule is

■ Fig. 46.3

Simplified structure of IgG molecules. Monoclonal antibodies (mAbs) consist of two heavy (H) and light (L) chains composed of a series of constant (C) and variable (V) region domains. Chimeric mAbs are composed of murine V region domains and C domains of human origin, while humanized mAbs only contain the murine amino acid sequences (represented by dotted bars) involved in antigen recognition



illustrated in Fig. 46.3. The IgG molecule is composed of two identical polypeptide heavy (H) and light (L) chains coupled together by multiple disulfide bonds in order to form a $(HL)_2$ dimeric species.

The heavy chain includes five *separate domains* – V_H , C_{H1} , hinge, C_{H2} , and C_{H3} – and has a molecular weight of about 50 kDa, and the L chain is composed of the V_L and C_L domains and has a molecular weight of about 25 kDa.

The binding of an IgG molecule to its antigenic target is controlled by the variable (V) domains, and the specificity of this recognition is controlled by the configuration of only a few amino acid residues within these regions. In contrast, the amino acid sequences of the constant (C) region domains, which are not involved in antigen recognition, are the same for all mAbs of a particular subclass. For human IgG, there are four subclasses – IgG₁, IgG₂, IgG₃, and IgG₄ – that differ with regard to the nature of the hinge region containing the interchain disulfide bonds linking the molecule and the amino acid sequence of the Fc region containing the C_{H2} and C_{H3} domains (Turner 1981). These hinge regions differ with regard to their length, and the number and position of the disulfide bonds linking the HL monomers.

Because of these differences, the four human IgG subclasses bind with different affinities to Fc receptors. The Fc receptor affinity of human IgG₂ is less than 10^5 M^{-1} , while those of the other three IgG subclasses range from 10^8 to 10^9 M^{-1} (Shin 1991). This is important for radioimmunotherapy because Fc receptors are found on many normal tissues such as the liver,

and IgG molecules with a higher binding affinity to these receptors could result in higher radiation-absorbed doses to these organs. Unfortunately, most radioimmunotherapy trials have utilized IgG₁ and IgG₃ mAbs that were originally developed for other antibody-dependent therapeutic approaches, where Fc receptor binding was advantageous.

Most mAbs that have been utilized for radioimmunotherapy are of murine origin because they were produced through the immunization of mice with the antigen of interest. A problem with these mAbs for human use is that patients frequently develop an immune response to murine proteins, compromising their usefulness for targeted radiotherapy, particularly when multiple injections are desired. To circumvent this limitation, two types of mAbs have been developed, chimeric mAbs and humanized mAbs. As shown in [Fig. 46.3](#), chimeric mAbs consist of a combination of murine V domains and human C domains and are constructed by genetic engineering techniques (Morrison 1985). On the other hand, humanized mAbs are essentially human proteins with the exception of the amino acid residues from the murine V domains that make up the antigen recognition site of the original murine parent (Riechmann et al. 1988).

Clinical studies have confirmed that chimeric and humanized mAbs are less immunogenic. However, the half time for clearance of these molecules from the blood pool in humans is much slower than their murine counterparts due to the fact that they have human Fc regions. This feature must be considered in selecting the optimal radionuclide-mAb combination for radioimmunotherapy. Indeed, the ideal radionuclide for labeling a particular mAb may be different depending upon whether the protein is in murine, chimeric, or humanized form.

An additional characteristic of mAb constant regions of importance for radionuclide therapy is that the stability of the molecule is dependent on the characteristics of the constant region. The flexibility of the mAb hinge region may be the critical parameter because it can have a major impact on the accessibility of the molecule to proteases that can rapidly degrade the protein (Tao and Morrison 1989). Rotational correlation studies have shown that the human IgG₂ hinge region is more rigid than other murine and human IgG subclasses (Dangl et al. 1988). A number of chimeric mAbs have been constructed with human IgG₂ constant regions and shown to have prolonged tissue residence times relative to their murine counterparts (Batra et al. 1994; He et al. 1994; Reist et al. 1997). A comparative analysis of the labeled catabolites generated from a radioiodinated human IgG₂ chimeric and a murine IgG_{2b} mAb demonstrated that the chimeric mAb was more resistant to both proteolytic degradation and deiodination (Reist et al. 1998). These results suggest that mAbs containing human IgG₂ constant regions might be the molecules of choice for radioimmunotherapy not only because of their low Fc receptor binding but also because of their enhanced stability in vivo.

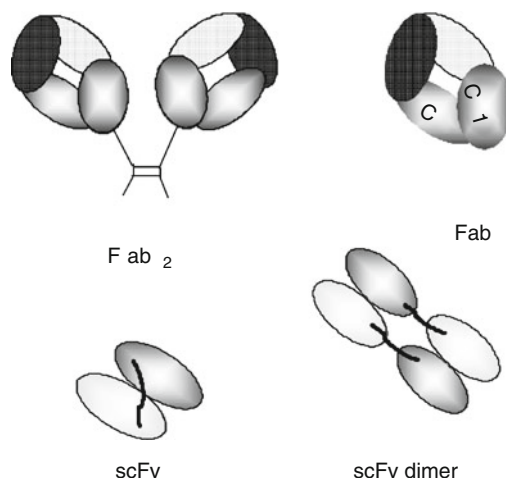
Antibody Fragments

One of the advantages of utilizing mAbs as carriers for targeted radiotherapy is that one can choose to label either an intact, 150-kDa IgG molecule or a smaller mAb fragment that has the same tumor specificity as the whole IgG. mAb fragments clear more rapidly than the intact IgG from normal tissues, and their penetration into the tumor is also more rapid, making it possible to utilize radionuclides with relatively short half-lives. A variety of enzymatically and genetically derived mAb fragments have been investigated for targeting radionuclides to tumors ([Fig. 46.4](#)).

Fab fragments (~50 kDa) and single-chain scFv (~26 kDa) are monovalent species that exhibit rapid clearance from the blood pool and other tissues. On the other hand, both F(ab')₂

■ Fig. 46.4

Schematic structure of some mAb fragments that have been evaluated as molecular carriers for targeted radionuclide therapy



and $(scFv)_2$ dimers have two antigen-binding sites, which increases their functional affinity. Trimeric and tetrameric $scFv$ have also been developed but have yet to be evaluated as molecular carriers for radiotherapeutic applications.

General Considerations for Labeling mAbs and Their Fragments

Unlike most other carrier molecules of potential utility for targeted radiotherapy, mAbs contain multiple sites for labeling. An important consideration is to determine the *number of radionuclides per protein molecule* that will be optimal. Clearly, as the number of labels per IgG increases, the probability of altering the antigen-binding capacity of the mAb also increases. On the other hand, if the number of antigenic sites per tumor cell is relatively low, substitution of multiple radionuclides per mAb may be required in order to deliver sufficient radiation dose to the tumor. This is of particular importance when the specific activity of the radionuclide is relatively low, as is sometimes the case when reactor production methods are used. In general, mAbs can be labeled without significant loss of antigen-binding capacity when the substitution level (i.e., the number of iodines or chelates for radio metal labeling) is below four per molecule. However, with some mAbs, it is necessary to utilize an even lower substitution level.

When deciding whether an intact mAb or mAb fragment would be preferable, radiolabeling issues also must be considered. As will be discussed in other chapters in this volume, the vast majority of mAb labeling strategies involve modification of either tyrosine or lysine residues on the protein through electrophilic iodination and conjugation reactions, respectively. According to the amino acid sequence compilation of Kabat et al. (1991), an intact IgG molecule contains an average of 88 lysine and 54 tyrosine residues per molecule. For the mAb to retain its antigen-binding capacity, substitution of the label into the antigen recognition site must be avoided. The antigen recognition site is also known as the complementary determining regions, i.e., CDRs, located within the V domains shown in ► Fig. 46.3. Because the CDRs are such small portions of the IgG molecule, the probability of labeling an amino acid within the CDRs is quite low, assuming that all tyrosine or lysine residues are equally reactive.

In the followings, the situation with mAb fragments is considered. As the size of the protein decreases, the probability of modifying the CDRs increases because mAb fragments maintain the same CDRs as intact mAbs but exclude one or more C region domains. This issue is particularly important for the labeling of scFv fragments (either monomers or multimers), which are constructed by combining only the V_L and V_H domains from an mAb. In order to select the best mAb fragment and labeling strategy for scFv, it is sometimes necessary to determine the location and number of tyrosine and lysine residues on candidate molecules. Olafsen et al. (1995) have performed this type of analysis for the V domains of two mAbs reactive with osteosarcoma, TP-1 and TP-3. For both mAbs, less than 25% of the lysine residues were in the CDR regions, while about 50% of the tyrosine residues were found in the CDRs. Therefore, a radiolabeling method that involved modification of lysine residues instead of tyrosine residues would be the more prudent approach for labeling the scFv fragments of TP-1 and TP-3 mAbs.

The reactivity of amino acids within a protein actually can vary considerably with regard to their reactivity for labeling due to variations in the microenvironment of the residues. These differences in reactivity are related to a number of factors including proximity to hydrophobic sequences or bulky amino acids such as tryptophan. Accessibility to solvent also must be considered. The relative amino acid reactivity of amino acids toward labeling has not been investigated on mAbs because of their complexity. However, studies with smaller proteins and peptides have documented, for example, that the rate of iodination of tyrosine residues in these molecules can vary by factors of 50–100 (Dube et al. 1966; Seon et al. 1970).

46.2.2.3 Peptides as Radionuclide Carriers

Peptides, like mAbs, are composed of amino acids; however, they are much smaller, generally consisting of 50 amino acids or less. The differences between peptides and proteins have important implications for radionuclide therapy (Weiner and Thakur 2001). Because of the smaller size of peptides, they clear much more rapidly from the blood pool and most normal tissues. In addition, a consequence of their lower molecular weight is more rapid penetration into tumors, offering the possibility of more rapidly achieving homogeneous distribution of the radionuclide in the tumor. Peptides are also considerably less immunogenic than proteins, making radiotherapeutic strategies involving multiple dose administrations possible. Finally, although hybridoma technology has markedly decreased the cost of producing mAbs, the synthesis of peptides is even more convenient, being readily accomplished using automated solid-phase procedures. A recent development is the application of phage display and other combinatorial techniques to provide peptides with improved properties for radiolabeling (Ladner 1999).

Peptides are not without their disadvantages. As will be discussed below, most of the peptides being investigated for targeted radiotherapy are *regulatory peptides*. Although their corresponding receptors are upregulated in certain malignant cell populations, they are also present in some normal tissues, notably, those in the gastrointestinal tract (Warner and O'Dorisio 2002). Furthermore, these regulatory peptides cause physiological effects at very small concentrations, making it important to maximize the specific activity of labeled peptide preparations. Native peptides are rapidly degraded in vivo (Reubi 1997), making it necessary to develop analogs with improved stability. Generally, this can be accomplished by the insertion of D-amino acids at critical locations and the cyclization of a portion of the molecule

(Lamberts et al. 1987). A final issue is that as a consequence of their rapid elimination via urinary excretion, labeled peptides can cause dose-limiting radiotoxicity to the kidneys (Breeman et al. 2001). A potential solution to this problem is the coadministration of basic amino acids to inhibit the tubular reabsorption of glomerularly filtered peptides (Behr and Behe 2002).

Some of the regulatory peptides and corresponding receptors that are being evaluated for radionuclide targeting applications are summarized in [Table 46.2](#). By far the most widely investigated receptor for peptide-mediated targeting of radionuclides to tumors is the somatostatin receptor (Heppeler et al. 2000; Kwekkeboom et al. 2001; de Jong et al. 2002). The concentration of these receptors on tumors is a critical feature in determining their potential as molecular targets for radionuclide therapy. For example, the concentration of somatostatin receptors on different types of tumor is quite different. Medulloblastomas have very high levels of expression, about 2 pmol/mg tumor tissue, while the expression on gliomas is about an order of magnitude lower (Mueller et al. 1998; Cervera et al. 2002). A potential problem with α -melanocyte stimulating hormone receptor targeting is that human melanomas have only a few hundred to a thousand receptors per cell (Tatro et al. 1990; Siegrist and Eberle 1995), requiring very high specific activity-labeled peptides for effective treatment. In evaluating the potential of a receptor system for targeted radiotherapy, it is important to consider that some receptor types, including many listed in [Table 46.2](#), can rapidly recycle to the cell membrane after ligand binding, offering the possibility of a single receptor being able to deliver multiple peptide molecules to the tumor cell.

The fact that peptides are much smaller than mAbs presents different issues that must be addressed in order to develop them as a targeted radiotherapeutic. With peptides, the probability of label substitution in the binding recognition portion of the molecule is much higher

Table 46.2

Peptides and corresponding receptors that are overexpressed on human tumors

Peptide/receptor	Amino acids	Tumors over expressing receptor
Somatostatin	14, 28	Neuroendocrine, small cell lung cancer, medullary thyroid carcinoma, astrocytoma
Vasoactive intestinal peptide	28	Small cell lung cancer, colon carcinoma, pancreatic cancer, stomach cancer
α -melanocyte stimulating hormone	13	Melanoma
Bombesin, gastric releasing peptide	14, 27	Small cell lung cancer, colon carcinoma, glioblastoma
Substance P	11	Glioblastoma, astrocytoma, medullary thyroid carcinoma, breast tumors, small cell lung cancer
Neurotensin	13	Pancreatic cancer, colon carcinoma, small cell lung cancer, prostate cancer
Cholecystokinin B, gastrin	17, 12	Medullary thyroid carcinoma, small cell lung cancer, ovarian cancer, astrocytoma
Epidermal growth factor	53	Glioblastoma, squamous cell carcinoma, breast carcinoma

than with mAbs. However, with peptides, the amino acids involved in receptor recognition generally are known, while in most cases, this information is not available for mAbs. Because of the ease of peptide synthesis, amino acids can be changed or added in order to create a site for labeling that does not interfere with receptor binding.

Native somatostatin binds with high affinity to all five of the *somatostatin receptor* subtypes; however, the affinity of the various stabilized somatostatin analogs for these receptor subtypes varies considerably. *Octreotide*, the most commonly used somatostatin analog, binds with high affinity to receptor subtype-2, with lower affinity to subtype-3 and subtype-5, but does not bind to subtype-1 or subtype-4 (Patel 1999). Reubi et al. (2000) have shown that modifying the nature of the chelate or the radio metal had a significant effect on the affinity profile of a series of octreotide analogs. For example, complexation of yttrium had no effect on the 50% inhibitory concentration of *DOTA-[Tyr³]octreotate* for the human somatostatin subtype-2 receptor; in contrast, complexation with gallium, another Group III metal, increased the affinity for this receptor subtype by about a factor of 7. This illustrates the difficulty in predicting the effect of peptide radiolabeling on affinity and specificity for the intended receptor target.

Peptides bind to their receptors in univalent fashion and are washed out of tissues quite rapidly. Thus, it might seem counterintuitive to consider these molecules as carriers for targeted radiotherapy due to the anticipated difficulty in maintaining adequate levels of radioactivity in tumor over a sufficient time period to deliver an effective radiation absorbed dose. However, prolonged retention of radionuclide in tumors does occur due to the rapid internalization of these labeled peptides after binding to their corresponding receptor. It should be noted that the degree of internalization can vary considerably for different receptor targets and individual peptides.

Translocation of the peptide–receptor complex to the lysosomes is problematic from a labeling perspective because of the exposure of the labeled peptide to proteolysis. For this reason, it is critical to utilize a labeling method that yields labeled catabolites that do not cross the lysosomal or cell membranes. For example, after a somatostatin-receptor-mediated internalization of [¹¹¹In-DTPA]octreotide, the radioactivity was trapped in tumor cells as an ¹¹¹In-DTPA-D-phenylalanine conjugate (Duncan et al. 1997). Evaluation of the retention of radioactivity in tumor cells in vitro after the binding of labeled peptides has emerged as an important predictor of in vivo tumor localizing capacity (de Jong et al. 1998a, b; Hofland et al. 1999).

46.3 Radionuclides for Targeted Radiotherapy

46.3.1 Beta-Particle-Emitting Radionuclides

Radionuclides that decay by the emission of β particles were the first to be utilized in patients for radionuclide therapy. For an excellent review of early studies with [¹³¹I]iodide, various radiocolloids and other compounds, the reader is referred to a book by Harbert (1987). Beta emitters remain the type of radionuclide used most frequently for targeted radiotherapy. When negatively charged electrons are emitted from the nucleus as β particles, their energy spectrum consists of a continuum of energies ranging from almost zero to their maximum energy. The average energy for a β -particle spectrum is about one-third of the maximum energy. For therapeutic applications, an important energy-dependent parameter is the mean and

maximum range of the β particles in tissue. The range of electrons in biologically relevant media as a function of energy can be found in ICRU Report 37 (1984).

There are β -particle-emitting radionuclides available for radionuclide therapy with a wide variety of tissue ranges. In ► [Tables 46.3–46.5](#), the physical properties of some β -particle-emitting radionuclides of potential utility for radionuclide therapy have been arranged into three groups according to range: short range ($<1,000\ \mu\text{m}$; ► [Table 46.3](#)), medium range ($1,000\text{--}2,000\ \mu\text{m}$; ► [Table 46.4](#)), and long range ($>2,000\ \mu\text{m}$; ► [Table 46.5](#)).

As discussed in the previous section, in selecting a radionuclide, it is important to *match the range of the radionuclide with the anticipated size of the tumor target*. The practical advantage of this strategy has been demonstrated in radiotherapy experiments performed in animal models. As would be predicted from the calculations of O'Donoghue et al. (1995), small tumors were more effectively treated by a short-range β emitter, while a higher cure rate could be obtained in larger tumors with a long-range β emitter (de Jong et al. 2002).

■ **Table 46.3**

Selected short-range β -particle-emitting radionuclides for targeted radiotherapy

Radionuclide	Half-life (days)	Mean range (μm)	Average β energy (keV)
^{199}Au	3.1	410	82
^{169}Er	9.3	510	101
^{177}Lu	6.7	670	133
^{67}Cu	2.6	710	141
^{105}Rh	1.5	760	152
^{161}Tb	6.9	770	154
^{47}Sc	3.4	810	162
^{131}I	8.1	910	182

■ **Table 46.4**

Selected medium-range β -particle-emitting radionuclides for targeted radiotherapy

Radionuclide	Half-life (days)	Mean range (μm)	Average β energy (keV)
^{77}As	1.6	1,200	228
^{153}Sm	1.9	1,200	229
^{159}Gd	0.8	1,600	311
^{143}Pr	13.6	1,600	314
^{198}Au	2.7	1,600	315
^{111}Ag	7.5	1,800	360
^{109}Pd	0.5	1,800	361
^{186}Re	3.8	1,800	362
^{149}Pm	2.2	1,800	364

Table 46.5

Selected long-range β -particle-emitting radionuclides for targeted radiotherapy

Radionuclide	Half-life (days)	Mean range (μm)	Average β energy (keV)
^{165}Dy	0.1	2,200	451
^{89}Sr	50	2,500	580
^{166}Ho	1.1	3,200	666
^{32}P	14	2,900	695
^{188}Re	0.7	3,500	764
$^{114\text{m}}\text{In}$	50	3,600	777
^{142}Pr	0.8	3,700	809
^{90}Y	2.7	3,900	935
^{76}As	1.1	5,000	1,000

46.3.1.1 Short Range β -Particle Emitters

All the radionuclides listed in Table 46.3 emit β particles with relatively short tissue ranges. Erbium-169 colloids have found application for the treatment of arthritis in small joints (Menkes et al. 1982). Three other radionuclides that have been explored in clinical radionuclide therapy studies are ^{131}I , ^{67}Cu , and ^{177}Lu . All of the others have not been pursued either due to problems with their production in sufficient specific activity and radionuclidic purity, or lack of suitable chemistry for attaching them to carrier molecules of interest. Nonetheless, all the radionuclides listed in Table 46.3 would be suited, from an energetic perspective, to the treatment of small tumor metastases (O'Donoghue et al. 1995).

Iodine-131

Iodine-131, with a half-life of 8.1 days, has been the most frequently utilized radionuclide for therapeutic applications and has a mean range of 910 μm . Although ^{131}I has a tissue range that is well suited to the treatment of small tumors, it also emits a 364-keV γ ray in 81% abundance. The energy of this γ ray is not ideal for conventional or single photon emission tomographic imaging devices; however, it does permit monitoring of the distribution of ^{131}I -labeled endoradiotherapeutic agents in a semiquantitative fashion. Such procedures are important because they permit the calculation of patient-specific radiation dosimetry (Akabani et al. 1999). In this way, it is possible to attempt to relate the response of a particular patient to the radiation dose delivered to the tumor, or to study the radiation dose dependence of normal tissue toxicities. An additional problem with radionuclides such as ^{131}I that emit medium-energy γ rays is that it complicates the radiotherapy procedure. First, it can increase the radiation dose received by health-care personnel and second, it is frequently necessary to confine the patient to a lead-lined room until body radioactivity has decayed to a reasonable level.

Copper-67

Copper-67 is perhaps the most attractive alternative to ^{131}I as a short-range β emitter. Because of its 2.6-day half-life, it can be considered for use with a variety of molecular carriers including mAbs and peptides. An advantage of ^{67}Cu is that it emits several γ rays with energies ranging

from 91 to 185 keV that are ideal for imaging. The shorter physical half-life and lower γ -ray energies of ^{67}Cu combine to make patient handling easier than with ^{131}I . Unfortunately, use of ^{67}Cu for radionuclide therapy has been rather limited because of the poor availability of this radionuclide due to the fact that its production requires a high-energy accelerator. Furthermore, none of the currently available chelators for Cu(II) are ideal in terms of *in vivo* stability.

Lutetium-177

In recent years, 6.7-day half-life ^{177}Lu has emerged as a *promising short-range β emitter* for targeted radiotherapy. The mean range of ^{177}Lu β particles is 670 μm , making this radionuclide ideal for treating micro-metastatic disease. Because it also emits γ rays (208 keV, 11% abundance), imaging of ^{177}Lu -labeled endoradiotherapeutic agents is possible. Lutetium-177 can be produced by neutron bombardment of lutetium; with high flux reactors and isotopically enriched ^{176}Lu (71%), specific activities of about 740 GBq mg^{-1} can be obtained (Hu et al. 2002). Production of no-carrier-added ^{177}Lu is also possible, and this approach is recommended for applications where very high specific activities of the labeled molecule are needed because of low concentration of receptor or antigen sites on the tumor. To provide no-carrier-added ^{177}Lu , Lebedev et al. (2000) utilized the $^{176}\text{Yb}(n,\gamma)^{177}\text{Yb}$ (1.9-h half-life), which decays by β emission to ^{177}Lu . Isolation of ^{177}Lu from the ytterbium target is then performed via a two-step process.

The therapeutic potential of ^{177}Lu is currently being evaluated in tandem with a variety of molecular carriers. In a comparative study of the somatostatin-avid peptide [DOTA^0 , Tyr^3] octreotate (*DOTA macrocycle = 1,4,7,10-tetraaza-cyclodecane- N,N',N'',N''' -tetraacetic acid*) in rats with CA20948 xenografts, the tumor uptake of the ^{177}Lu -labeled peptide was higher than that of the same peptide labeled with either ^{111}In or ^{90}Y (de Jong et al. 2001). Based on these encouraging results, [^{177}Lu - DOTA^0 , Tyr^3]octreotate is currently being evaluated in patients (Kwekkeboom et al. 2001). Bombesin peptide analogs also have been labeled with ^{177}Lu (Hu et al. 2002).

Lutetium-177 complexes with several polyphosphate ligands have been reported as potential agents for the palliation of pain associated with bone metastasis (Chakraborty et al. 2002). A recent study has compared the potential utility of several macrocyclic and acyclic ligands for labeling mAbs with ^{177}Lu (Milenic et al. 2002). The acyclic ligand $\text{CHX-A}''\text{-DTPA}$ [2-(*p*-isothiocyanatobenzyl)-cyclohexyl-diethylenetriamine-pentaacetic acid] yielded similar *in vivo* behavior of a ^{177}Lu -labeled mAb fragment as was observed with the DOTA conjugate; however, ease of synthesis was an important advantage for $\text{CHX-A}''\text{-DTPA}$. More extensive investigations will be required in order to identify the optimal ligand system for labeling mAbs and peptides with ^{177}Lu .

46.3.1.2 Medium Range β -Particle Emitters

Only a few of the β emitters listed in [Table 46.4](#) have been investigated for therapeutic applications. Many of these radionuclides are reactor produced, limiting the types of carrier molecules for which they are suitable. Several radiocolloids labeled with ^{198}Au have been studied for intracavitary therapies; however, their relatively high degree of leakage from the treatment site has limited their clinical utility (Virkkunen et al. 1967; Spencer 1978; Harbert 1987). Treatment of bone pain with polyphosphate complexes of both ^{153}Sm and ^{186}Re has been investigated. With ^{186}Re , work has focused on the hydroxylethylenediphosphonate complex

(de Klerck et al. 1994; McEwan 1997). The most useful agent for treating bone pain with ^{153}Sm is the ethylenediamine-tetramethylphosphonate complex (Farhanghi et al. 1992) that has progressed to the stage where it is commercially available (Serafini et al. 1998). For a more extensive discussion of the development of these complexes as therapeutic radiopharmaceuticals for treating bone pain, the reader is referred to an excellent review by Volkert and Hoffman (1999).

46.3.1.3 Long Range β -Particle Emitters

Long-range β -particle emitters such as those listed in [Table 46.5](#) have an average range in tissue of more than 2 mm. They offer the prospect of compensating for heterogeneous distribution of the labeled compound within the tumor by the irradiation of non-accumulating cells through radiation cross fire. Radiocolloids and other particulate carriers have been labeled with ^{165}Dy , ^{166}Ho , ^{32}P , and ^{188}Re and utilized for the treatment of rheumatoid arthritis and compartmentally spread neoplasms (Sledge et al. 1977; Harbert 1987; Wang et al. 2001; Song et al. 2001). Strontium-89, in the form of the ionic chloride, was one of the first radiopharmaceuticals utilized for the treatment of painful skeletal metastases, and it is still utilized for this purpose. The long range of ^{89}Sr β particles can be problematic for this purpose because their range is sufficient to cause significant *bone marrow toxicity*, decreasing the dose that can be administered (McEwan 1997).

Yttrium-90 has been the most widely investigated long-range β emitter for radionuclide therapy. This radionuclide is routinely available commercially at reasonable cost in high specific activity. However, because ^{90}Y does not emit γ rays, imaging its distribution in animal models or in patients is difficult. A wide variety of proteins and peptides have been labeled with ^{90}Y using *bifunctional chelates*, molecules that contain a ligand system for metal complexation and a second functionality that permits coupling of the ligand to the molecule of interest. Derivatives of both DOTA and DTPA have been investigated, with macrocyclic ligands generally providing a more stable product (Hnatowich et al. 1988; Kozak et al. 1989; Deshpande et al. 1990; Lewis et al. 1994; Camera et al. 1994). The radiochemistry of ^{90}Y -labeled radiotherapeutics is discussed in depth in [Chap. 45 of this Volume](#).

46.3.2 Alpha-Particle-Emitting Radionuclides

The range of α particles in tissue is equivalent to only *a few cell diameters*, offering the prospect of matching the cell-specific nature of targeted molecular carriers with radiation having a similar range of action (Zalutsky and Vaidyanathan 2000). The short range of α particles also may be ideally suited for minimal residual disease settings, applications in which radionuclide therapy has the greatest chance of making a meaningful clinical impact (Sautterbihl et al. 1996). These include the treatment of micrometastases, residual tumor margins left after surgical debulking, such as gliomas, and tumors present in the circulation such as leukemia and lymphoma. Another type of application that appears to be ideally suited to targeted α -particle therapy is the treatment of malignancies such as neoplastic meningitis and ovarian cancer that spread as thin sheets on body compartment surfaces, frequently accompanied by free floating tumor cells.

■ Table 46.6

Selected α -particle-emitting radionuclides for targeted radiotherapy

Radionuclide	Daughters	Half-life	α -particle energy (MeV)	Yield per 100 decays
^{149}Tb		4.15 h	3.97	17
^{211}At		7.21 h	5.87	42
	^{211}Po	516 ms	7.44	58
^{212}Bi		61 min	6.05	36
	^{212}Po	298 ns	8.78	64
^{213}Bi		45.6 min	5.84	36
	^{213}Po	4.2 μs	8.38	64
^{225}Ac		10 days	5.75	100
	^{221}Fr	4.9 min	6.36	100
	^{217}At	32.3 ms	7.07	100
	^{213}Bi	45.6 min	5.84	2
	^{213}Po	4.2 μs	8.38	98

Utilization of α -particle emitters for radionuclide therapy offers several important advantages from a radiobiological perspective. Alpha particles have higher decay energies than β emitters, generally in the range of 4.0–8.8 MeV for the radionuclides that have been considered for endoradiotherapy (► Table 46.6). This characteristic, in combination with their short range, makes α -particles radiation with high *linear energy transfer* (LET). For example, the α particles from ^{211}At have a mean LET of about $97 \text{ keV } \mu\text{m}^{-1}$ compared with a value of $0.22 \text{ keV } \mu\text{m}^{-1}$ for the high-energy β particles emitted by ^{90}Y . This is a critical distinction for therapeutic purposes because the mean LET for ^{211}At occurs where the relative biological effectiveness of radiation is maximum (Hall 2000). Radiation at $100 \text{ keV } \mu\text{m}^{-1}$ has this quality because at this LET, the distance between ionizing events is nearly identical to that between DNA strands, increasing the probability of creating highly cytotoxic double DNA strand breaks (Kampf 1988). In contrast to low LET radiation such as β emitters, α particles are also cytotoxic in hypoxic regions within a tumor (Langmuir and Sutherland 1988). Finally, the cytotoxicity of high LET radiation is nearly independent of dose rate (Hall 2000). This is an important feature for radionuclide therapy where radiation dose is often delivered at a relatively low dose rate, where repair of DNA lesions can compromise effectiveness.

Although there are approximately 100 radionuclides that decay by the emission of α particles, only a few possess half-lives that are compatible with radionuclide therapy applications (McDevitt et al. 1998). The physical properties of the radionuclides that have been evaluated for this purpose are summarized in ► Table 46.6. In selecting an α emitter for radiotherapy, one must also consider its availability and radionuclidic purity, and the half-life and chemistry of its radionuclide daughters.

46.3.2.1 Terbium-149

Terbium-149 was first proposed as a candidate radionuclide for α -particle radiotherapy by Allen and Blagojevic (1996). This radiolanthanide has a half-life of 4.14 h, and α -particle

emission is associated with 17% of its decays. The production of ^{149}Tb has been accomplished at the CERN spallation source using 600 MeV protons and isolated using the ISOLDE magnetic separator (Allen et al. 1996, 2001a). This group was able to label two mAbs with ^{149}Tb using the DTPA-CHX-A'' chelate and demonstrate the ability of these immunoconjugates to kill human cancer cells (Allen et al. 2001b). The potential utility of ^{149}Tb -labeled mAbs cannot be ascertained at this time because of the lack of information concerning the stability of these labeled mAbs and their tissue distribution in animals.

46.3.2.2 Astatine-211

Astatine-211 has many attractive features for targeted α -particle radiotherapy. It has a half-life of 7.2 h that is long enough to permit multistep labeling strategies. It is also well matched to the biokinetics of a variety of molecular carriers including peptides, mAbs and small organic molecules. Alpha-particle emission is associated with each decay of ^{211}At either by direct α emission to ^{207}Bi (42%) or by electron capture decay to 520 ms ^{211}Po (58%), followed by α emission. As a consequence of the electron capture branch, 77–92-keV polonium x-rays are emitted, and these can be used to monitor ^{211}At distributions in animals or patients using either conventional nuclear medicine planar or single photon emission tomographic imaging devices (Turkington et al. 1993; Johnson et al. 1995).

Astatine-211 is produced by the cyclotron bombardment of natural bismuth metal targets with α particles via the $^{209}\text{Bi}(\alpha, 2n)^{211}\text{At}$ reaction. For radiotherapy applications, it is important to utilize an incident α -particle energy that minimizes the production of 8.1 h ^{210}At . This nuclide is a concern because it decays to ^{210}Po , a 138-day α emitter that could cause bone marrow toxicity. For this reason, incident beam energies for ^{211}At production are generally kept below 29 MeV. Separation of ^{211}At from the bismuth metal target is readily accomplished using a dry distillation procedure (Friedman et al. 1977). Internal cyclotron target systems have been developed that permit the production of clinically useful levels of ^{211}At (Larsen et al. 1996; Schwartz et al. 1998). The highest production level reported to date is 6.6 GBq after a 4-h irradiation with a 55- μA beam of 28-MeV α particles (Zalutsky et al. 2001).

Because astatine is a halogen, radioiodination methods can be adapted for use with ^{211}At , sometimes without significant modification. However, astatine also exhibits metallic properties under certain circumstances (Visser 1989). Direct astatination of proteins is not useful because this results in transient binding to thiol groups, with the activity rapidly released from the protein in vivo. A wide variety of ^{211}At -labeled molecules have been synthesized and evaluated as potential targeted radiotherapeutics (Zalutsky and Vaidyanathan 2000). Some of these approaches are summarized in [Table 46.7](#). Radiotoxicity determinations in cell culture models of human cancers have demonstrated that significant cell killing can be achieved with only 1–10 ^{211}At atoms bound per cell (Strickland et al. 1994; Vaidyanathan et al. 1996; Larsen et al. 1998b).

Studies involving ^{211}At -labeled anti-tenascin mAbs are illustrative of the steps required to develop labeling procedures with an α -particle emitter to the stage where clinical evaluation was possible. The first step was the development of a method for labeling the mAb with ^{211}At , which was accomplished via an *N*-succinimidyl 3- ^{211}At astatobenzoate intermediate, which was synthesized from the corresponding trialkylstannyl precursor (Zalutsky et al. 1989b). The in vivo stability of ^{211}At -labeled 81C6-labeled anti-tenascin 81C6 was then confirmed in mice (Zalutsky et al. 1997). The cytotoxicity of ^{211}At -labeled 81C6 mAb was demonstrated in both in

■ Table 46.7

Some ^{211}At -labeled compounds developed for targeted radiotherapy

Agent	Application	Reference
^{211}At astatine-tellurium colloid	Compartmental tumors	Bloomer et al. (1981a,b, 1984)
6- ^{211}At astato-2-methyl-1,4-naphthoquinol diphosphate	Adenocarcinomas	Brown et al. (1992)
		Brown and Mitchell (1998)
^{211}At -labeled methylene blue	Melanoma	Link and Carpenter (1990, 1992)
Meta- ^{211}At astatobenzyl guanidine	Neuroendocrine tumors	Vaidyanathan and Zalutsky (1992)
		Strickland et al. (1994)
5- ^{211}At astato-2'-deoxyuridine	Various	Vaidyanathan et al. (1996)
		Larsen et al. (1997)
^{211}At -labeled biotin conjugates	Various pretargeting	Foulon et al. (1997, 1998)
^{211}At -labeled octreotide	Somatostatin receptor	Vaidyanathan et al. (2000)
^{211}At -labeled mAbs and fragments	Various	Zalutsky et al. (1989b), Wilbur et al. (1993), Larsen et al. (1994)
^{211}At -labeled bisphosphonates	Bone metastases	Murud et al. (1999)
		Larsen et al. (1999)

vitro and in vivo models of human cancer (Zalutsky et al. 1994; Larsen et al. 1998b). Finally, the toxicity of ^{211}At -labeled human/mouse chimeric 81C6 was determined in normal mice (McLendon et al. 1999).

With these data in hand, permission was obtained from the United States Food and Drug Administration to initiate the first clinical trial of an ^{211}At -labeled therapeutic. This protocol involves the injection of ^{211}At -labeled chimeric 81C6 directly into the surgical tumor resection cavity of patients with recurrent brain tumors (Zalutsky et al. 2001). The results to date have been very encouraging with a median survival of about 60 weeks observed, compared with about 25–30 weeks for recurrent brain tumor patients treated by conventional therapies.

46.3.2.3 Bismuth-212

Bismuth-212 is a 60.6-min daughter of the ^{228}Th natural decay chain. This radionuclide has two decay modes: by the emission of 6.05-MeV α particles (36%) as well as by β decay to 298-ns ^{212}Po , which in turn, decays by the emission of 8.78-MeV α particles. Radionuclide generators have been developed that utilize 3.6-day ^{224}Ra as the parent (Atcher et al. 1988). First, ^{224}Ra is separated from ^{228}Th by isolating the parent on an anion exchange resin in nitric acid. The ^{224}Ra that is eluted is dissolved in 0.1 N HCl and added to a cation exchange column, and this serves as the generator for ^{212}Bi . Separation of ^{212}Bi from ^{224}Ra is accomplished using either 0.15 N HI or 0.5 N HCl as the eluent.

Several mAbs have been labeled with ^{212}Bi via DTPA- or DOTA-coupled bifunctional chelates (Kozak et al. 1986; Junghans et al. 1993). These mAbs were very efficient at killing cancer cells in vitro (Kozak et al. 1986; Black et al. 1988; Kurtzman et al. 1988). Promising results were also observed in some radiotherapy trials in animal models (Macklis et al. 1988; Huneke et al. 1992); however, in other reports, the very short half-life of ^{212}Bi compromised therapeutic utility (Hartmann et al. 1994). An EDTMP complex of ^{212}Bi also has been described as an α -particle emitting agent for the treatment of bone pain (Hassfjell et al. 1994).

In recent years, practical concerns have caused most researchers to abandon ^{212}Bi as a potential therapeutic radionuclide in favor of ^{213}Bi . The ^{224}Ra parent decays to ^{220}Rn , and this gaseous α -emitting radionuclide is of great concern from a radiation safety perspective, and requires that the $^{224}\text{Ra}/^{212}\text{Bi}$ generator be placed in an isolated, gas-tight enclosure. In addition, the ^{208}Tl produced by the β -decay branch of ^{212}Bi emits a 2.6-MeV γ ray, which increases radiation dose to personnel and nonspecific whole body dose to the patient.

46.3.2.4 Bismuth-213

Bismuth-213 has a 45.6-min half-life and α -particle emission is associated with each of its decays, either directly to 2.2-min ^{209}Tl (2%) or after β decay to 4.2- μs ^{213}Po (98%), followed by α emission to 3.25-h ^{209}Pb . A radionuclide generator system has been developed using 10-day ^{225}Ac as the parent that can provide clinically useful levels of ^{213}Bi (McDevitt et al. 1996, 1999b; Ma et al. 2001). The generator consists of an AGMP-50 column and is eluted with 0.1 M HCl/NaI.

Several tumor-specific mAbs have been labeled with ^{213}Bi using the bifunctional *trans*-cyclohexyldiethylenetriaminepentaacetic acid SCN-CHXA"-DTPA and evaluated for their therapeutic potential. The anti-prostate-specific membrane antigen (PSMA) mAb J591 was labeled with ^{213}Bi and shown to be highly cytotoxic for human prostate carcinoma cells grown in culture, as tumor spheroids, and as subcutaneous tumor xenografts grown in athymic mice (McDevitt et al. 2000; Ballangrud et al. 2001). Intraperitoneal injection of a ^{213}Bi -labeled mAb reactive with a tumor-specific mutant E-cadherin molecule was reported to be effective in treating a peritoneally spread gastric cancer in mice (Senekowitsch-Schmidke et al. 2001). And finally, a humanized anti-CD33 mAb, HuM195, has been labeled with ^{213}Bi and is currently being evaluated in patients with leukemia (McDevitt et al. 1999a; Sgouros et al. 1999). This study involves the administration of multiple doses of ^{213}Bi -labeled HuM195. Although it is too early to determine the therapeutic efficacy of this targeted radiotherapeutic, it is important to note that no dose-limiting normal tissue toxicities have been observed.

46.3.2.5 Actinium-225

The short half-life of the α emitters discussed above is problematic for several reasons. First, particularly for 46-min ^{213}Bi , delivery of the endoradiotherapeutic to the tumor must be accomplished very rapidly in order to achieve reasonable tumor-to-normal organ radiation absorbed dose ratios. Second, decay during radionuclide purification, radiolabeling, and transport of the labeled compound to the clinic decreases the activity that is available for use. And third, the short half-life of these α emitters impedes their application at centers distant

from radionuclide production facilities. For this reason, investigators have been searching for a longer-lived α emitter for radionuclide therapy.

Of the radionuclides that have been proposed (Zweit 1996), 10-day ^{225}Ac has received the most attention. As shown in ► Table 46.6, each decay of ^{225}Ac results in the production of four α particles, making it an extremely cytotoxic radionuclide (Davis et al. 1999). There are several relatively long-lived ^{225}Ac daughters such as 4.9-min ^{221}Fr and 46-min ^{213}Bi , and there is considerable concern that the release of these and other daughter radionuclides will result in excessive toxicity to normal organs. The design of a ligand system that will form stable complexes with Ac, Fr, At, and Bi will be a formidable task from a chemical perspective. This will be even more difficult when the effects of the high α -particle recoil energy on the stability of the daughter complex is considered.

A $^{229}\text{Th}/^{225}\text{Ac}$ generator system has been reported that utilizes a two-column system to provide ^{225}Ac in reasonable radionuclidic purity (Geerlings et al. 1993). A number of acyclic chelators have been investigated for ^{225}Ac complex formation; however, their in vivo stability was poor (Davis et al. 1999). A series of ^{225}Ac acyclic and macrocyclic ligands have been evaluated with regard to their in vivo stability (Deal et al. 1999). Excellent stability was reported for ^{225}Ac chelated with 1,4,7,10,13,16-hexaazacyclo-hexadecane-N,N',N'',N''',N''''-hexaacetic acid (HEHA). However, when 2-(4-isothiocyanatobenzyl)-HEHA was utilized to label mAbs with ^{225}Ac , more than half of the ^{225}Ac activity in the serum of mice at 24 h was no longer associated with the mAb (Chappell et al. 2000). Another study using the HEHA chelate concluded that the results suggested that release of ^{225}Ac from the chelate and the radiotoxicity of daughter radionuclides released from the mAb compromised the potential utility of this approach (Kennel et al. 2000).

Recently, McDevitt et al. (2001) described an interesting approach for trapping the daughter radionuclides from ^{225}Ac in the tumor cell that involved labeling mAbs that are rapidly internalized after binding to their antigen or receptor target. A DOTA derivative was utilized for binding ^{225}Ac and excellent therapeutic responses were obtained in several murine tumor models. However, a potential problem with utilizing this tactic in patients is that in most clinical radioimmunotherapy trials, only of the order of 1% of the injected dose of labeled mAb is taken up by the tumor. Thus, one might anticipate that release and redistribution of the daughter radionuclides of ^{225}Ac could occur with 99% of the administered activity.

46.3.3 Low-Energy Electron Emitters

For the purposes of radionuclide therapy, low-energy electrons are considered to be those that deposit their energy in subcellular dimensions. These electrons can arise from two decay processes, internal conversion and electron capture. Internal conversion and electron capture both create inner atomic shell vacancies that are transferred by a series of rearrangements to outer atomic shells. The binding energy difference between the inner and outer shells may then be transferred to other outer shell electrons that are ejected from the atom. These electrons are called *Auger electrons* if they arise from higher shells and are called *Coster-Kronig electrons* if they originate from higher sub shells. Thus, the decay of a single atom by electron capture or internal conversion can result in the emission of a multitude of low-energy electrons, most with ranges in tissue on the order of nanometers (O'Donoghue and Wheldon 1996).

Some of the radionuclides emitting electrons of *subcellular range*, which are of potential utility for radionuclide therapy, are given in ► Table 46.8. Because of this very short range,

■ Table 46.8

Selected radionuclides emitting electrons of subcellular range

Radionuclide	Half-life (days)	Mean electron yield per decay ^a
⁶⁷ Ga	3.3	4.7
⁷⁷ Br	2.4	6.7
¹¹¹ In	2.8	14.7
^{115m} In	4.5	6.1
¹¹⁹ Sb	1.6	4.4
¹²³ I	0.6	14.9
¹²⁵ I	60	24.9
^{193m} Pt	4.3	26.4
^{195m} Pt	4.0	32.8

^aData from Howell (1992)

low-energy electron emitters require targeting strategies that can localize the radionuclide in close proximity to the cell nucleus. The majority of studies evaluating the therapeutic potential of low-energy electron emitters have utilized ¹²⁵I. Although its 60-day half-life is not ideal for most potential therapeutic applications, ¹²⁵I emits about 25 subcellular-range electrons per decay. In addition, it is commercially available and can be readily attached to a wide variety of molecular carriers.

The most widely used approach for targeting low-energy electron emitters to the cell nucleus is to incorporate them into cellular DNA via labeled nucleosides. The thymidine uptake analog 5- [¹²⁵I]iodo-2'-deoxyuridine is rapidly accumulated in proliferating cells and has been shown to be highly cytotoxic (Chan et al. 1976); similar behavior was observed when low-energy-electron-emitting ¹²³I (Makrigiorgos et al. 1989) and ⁷⁷Br (Kassis et al. 1982) were used for labeling. A lack of shoulder at low doses, a feature of high-LET radiation, characterized the cell survival curves obtained with these compounds. When low-energy electron emitters are localized in cellular DNA, their relative biological effectiveness is similar to that observed with α -particle emitters (Howell et al. 1991). A number of studies have confirmed that localization of the decay site in the cell nucleus is required for low-energy electron emitters to exert high-LET cytotoxic effects (Hofer et al. 1975; Warters et al. 1977).

Although 5- [¹²⁵I]iodo-2'-deoxyuridine has served as a useful model compound for investigating the cytotoxicity of low-energy electron emitters, it has several problems that limit its clinical utility. The 60-day half-life of ¹²⁵I is considerably longer than desirable for a targeted radiotherapeutic. Only cells that are rapidly dividing (in S-phase) take up the labeled drug, so quiescent cells are not killed. Finally, 5- [¹²⁵I]iodo-2'-deoxyuridine is rapidly dehalogenated in vivo. This has led to the investigation of other radionuclides and carrier molecules in order to identify an agent that can more effectively exploit the therapeutic potential for low-energy electron emitters.

The estrogen receptor has been evaluated as a means of delivering low-energy electron emitters to the cell nucleus. The nonsteroidal ligand tamoxifen has been labeled with ¹²⁵I and shown to be highly cytotoxic for cells that express the estrogen receptor, but not control cell lines (Bloomer et al. 1980, 1981a,b). Steroidal ligands labeled with ^{80m}Br and ¹²⁵I have also been evaluated (De Sombre et al. 1988, 1992; Holt et al. 1992; Beckman et al. 1993; Hughes et al.

1993). Other steroid hormone receptors have been considered including both the androgen and progesterone receptors (Hanson 2000).

Another method that has been pursued for delivering radionuclides to the cell nucleus is to attach them to DNA intrachelating agents. The synthesis and evaluation of both [^{125}I]iodo-Hoechst 33342 (Kassis et al. 1999a, b) and iodo-Hoechst 33258 (Squire et al. 2000) have been reported. Because growth factors are overexpressed on many types of cancer cells and are rapidly internalized (Zalutsky 1997), they are excellent molecular targets for low-energy electron emitters. Both mAbs (Wikstrand et al. 1995) and growth factors (Lindstron and Carlsson 1993) have been considered. Finally, a recent report suggests that radiolabeled somatostatin receptor-avid peptides are rapidly internalized and translocated to the cell nucleus (Hornick et al. 2000). This approach has been evaluated clinically using [^{111}In -DTPA]octreotide (Kwekkeboom et al. 2000; de Jong et al. 2002).

References

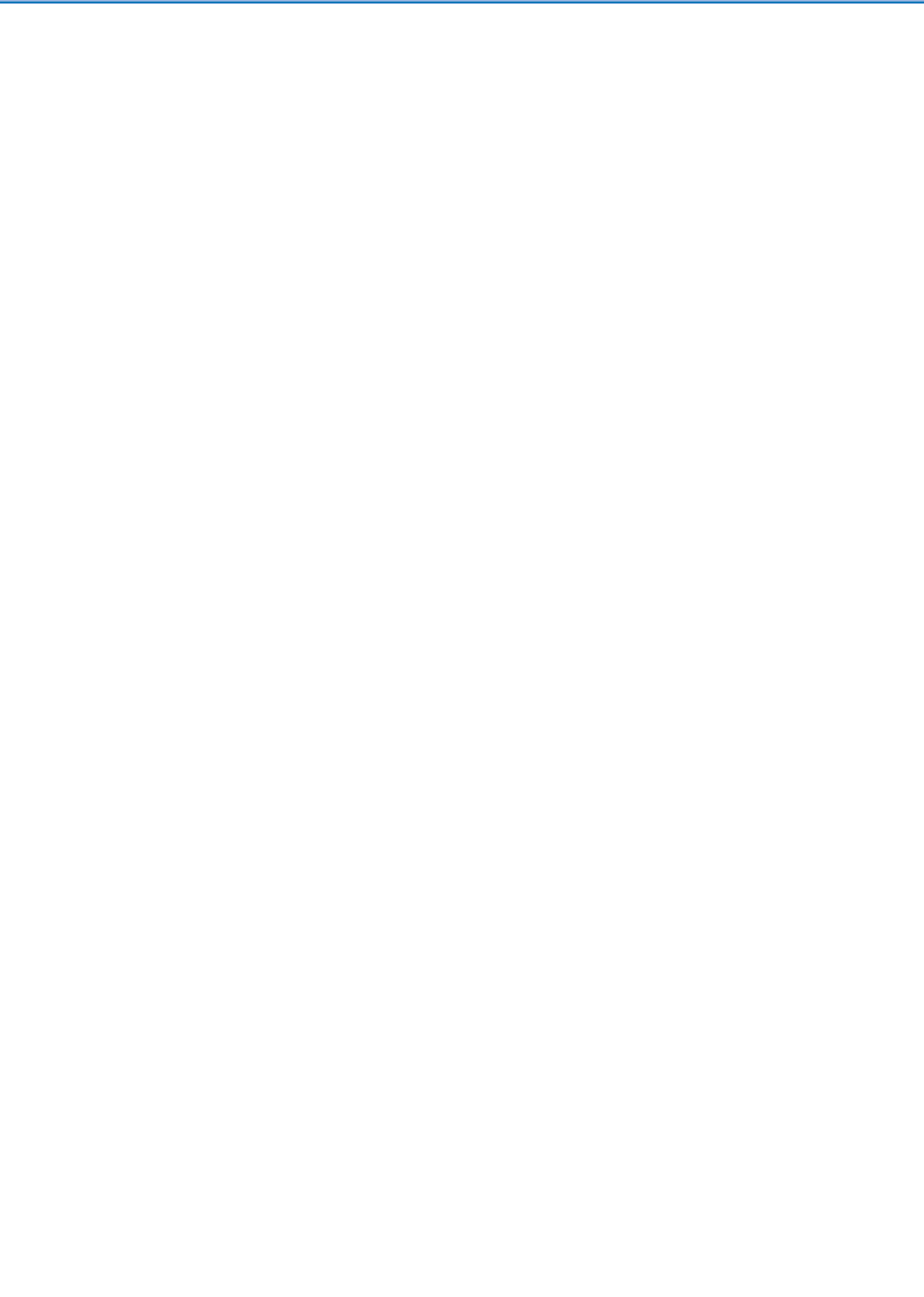
- Akabani G, Reist CJ, Cokgor I, Friedman AH, Friedman HS, Coleman RE, Bigner DD, Zalutsky MR (1999) *J Nucl Med* 40:631
- Allen BJ, Blagojevic N (1996) *Nucl Med Commun* 17:40
- Allen BJ, Goozee G, Iman S, Leigh J, Beyer G (1996) In: *Proceedings of the 6th international conference on radiopharmaceutical dosimetry*, Gatlinburg, pp 392–399
- Allen BJ, Goozee G, Sarkar S, Beyer G, Morel C, Byrne AP (2001a) *Appl Radiat Isot* 54:53
- Allen BJ, Rizvi S, Li Y, Tian Z, Ranson M (2001b) *Crit Rev Oncol Hematol* 39:139
- Atcher RW, Friedman AM, Hines JJ (1988) *Int J Appl Radiat Isot* 39:283
- Ballangrud AM, Yang W-H, Charlton DE, McDevitt MR, Hamacher KA, Panageas KS (2001) *Cancer Res* 61:2008
- Batra SK, Niswonger ML, Wikstrand CJ, Pegram CN, Zalutsky MR, Morrison SL, Bigner DD (1994) *Hybridoma* 13:87
- Baxter LT, Jain RK (1991) *Microvasc Res* 41:252
- Beckman MW, Schnarl A, Rosinsky BJ, Holt JA (1993) *J Cancer Res Clin Oncol* 119:207
- Bedford JS, Mitchell JB (1973) *Radiat Res* 54:316
- Behr TM, Behe MP (2002) *Semin Nucl Med* 32:97
- Black CDV, Atcher RW, Barbet J, Brechbiel MW, Holton OD III, Hines JJ, Gansow OA, Weinstein JN (1988) *Antibody Immunoconj* 1:43
- Bloomer WD, Adelstein SJ (1977) *Nature* 265:620
- Bloomer WD, McLaughlin WH, Weichselbaum RR, Tonnesen GL, Hellman S, Seitz DE, Hanson RN, Adelstein SJ, Rosner AL, Burnstein NA, Nove JL, Little JB (1980) *Int J Radiat Biol* 38:197
- Bloomer WD, McLaughlin WH, Neirinckx RD, Adelstein SJ, Gordon PR, Ruth TJ, Wolf AP (1981a) *Science* 212:340
- Bloomer WD, McLaughlin WH, Weichselbaum RR, Tonnesen GL, Hellman S, Seitz DE, Hanson RH, Adelstein SJ, Seitz DE (1981b) *J Radioanal Chem* 65:209
- Bloomer WD, McLaughlin WH, Lambrecht RM, Atcher RW, Mirzadeh S, Madara JL, Milius RA, Zalutsky MR, Adelstein SJ, Wolf AP (1984) *Int J Radiat Oncol Biol Phys* 10:341
- Boucher Y, Baxter LT, Jain RK (1990) *Cancer Res* 50:4478
- Breeman WA, de Jong M, Kwekkeboom DJ, Valkema R, Bakker WH, Kooij PP, Visser TJ, Krenning EP (2001) *Eur J Nucl Med* 28:1421
- Brown I, Carpenter RN, Mitchell JS (1992) *Int J Radiat Oncol Biol Phys* 23:563
- Brown I, Mitchell JS (1998) *Int J Radiat Oncol Biol Phys* 40:1177
- Buchsbaum DJ, Lawrence TS, Roberson PL, Heidorn DB, Ten Haken RK, Steplewski Z (1993) *Int J Radiat Oncol Biol Phys* 5:629
- Camera L, Kinuya S, Garmestani K, Wu C, Brechbiel MW, Pai LH, McMurry TJ, Gansow OA, Pastan I, Paik CH, Carrasquillo JA (1994) *J Nucl Med* 35:882
- Cervera P, Videau C, Viollet C, Petrucci C, Lacombe J, Winsky-Sommerer R, Csaba Z, Helboe L, Daumas-Duport C, Reubi JC, Epelbaum J (2002) *J Neuroendocrin* 14:458
- Chan PC, Lisco E, Lisco H, Adelstein SJ (1976) *Radiat Res* 67:332
- Chakraborty S, Das T, Unni PR, Sarma HD, Samuel G, Banerjee S, Venkatesh M, Ramamoorthy N, Pillai MR (2002) *Nucl Med Commun* 23:67
- Chappell LL, Deal KA, Dadachova E, Brechbiel MW (2000) *Bioconj Chem* 11:510
- Dangl JL, Wensel TG, Morrison SL, Stryer L, Herzenberg LA, Oi VT (1988) *EMBO J* 7:1989

- Davis IA, Glowienka KA, Boll RA, Deal KA, Brechbiel MW, Stabin M, Bochsler PN, Mirzadeh S, Kennel SJ (1999) *Nucl Med Biol* 26:581
- Deal KA, Davis IA, Mirzadeh S, Kennel SJ, Brechbiel MW (1999) *J Med Chem* 42:2988
- De Jong M, Bakker WH, Breeman WAP, Bernard BF, Hoffland LJ, Visser TJ, Srinivastan A, Schmidt M, B     M, M     H, Krenning EP (1998a) *Int J Cancer* 75:406
- De Jong M, Bakker WH, Breeman WAP, Hoffland LJ, Visser TJ, Srinivasan A, Schmidt M, Kooij PPM, Bernard BF, Visser TJ, Schmidt MA, Erion JL, Bugaj JE, M     HR, Krenning EP (1998b) *Cancer Res* 58:437
- De Jong M, Breeman WAP, Bernard BF, Bakker WH, Schaar M, van Gameren A, Bugaj JL, Erion J, Schmidt M, Srinivastan A, Krenning EP (2001) *Int J Cancer* 92:628
- De Jong M, Valkema R, Jamar F, Kvols LK, Kwekkeboom DJ, Breeman WAP, Bakker WH, Smith C, Pauwels S, Krenning EP (2002) *Semin Nucl Med* 32:133
- De Klerck JMH, Zonnenberg BA, van het Schip AD, van Dijk A, Han SH, Quirijen JMSP, Blijham GH, van Rijk PO (1994) *Eur J Nucl Med* 21:1114
- De Sombre ER, Mease RC, Hughes A, Harper PC, De Jesus OT, Friedman AM (1988) *Cancer Res* 48:899
- De Sombre ER, Shafii B, Hanson RN, Kuivanen PC, Hughes A (1992) *Cancer Res* 52:5752
- Del Vecchio S, Reynolds JC, Carrasquillo JA, Blasberg RG, Neuman RD, Lotze MT, Bryant GJ, Farkas RJ, Larson SM (1989) *Cancer Res* 49:2783
- Deshpande SV, DeNardo SJ, Kukis DL, Moi MK, McCall MJ, DeNardo GL, Meares CF (1990) *J Nucl Med* 31:473
- Dube SK, Roholt OA, Pressman D (1966) *J Biol Chem* 241:4665
- Duncan JR, Stephenson MI, Wu HP, Anderson CJ (1997) *Cancer Res* 57:659
- Eckelman WC (1995) *Eur J Nucl Med* 22:249
- Farhanghi M, Holmes RA, Volkert WA, Logan KW, Singh A (1992) *J Nucl Med* 33:1451
- Foulon CF, Schoultz BW, Zalutsky MR (1997) *Nucl Med Biol* 24:135
- Foulon CF, Alston KL, Zalutsky MR (1998) *Nucl Med Biol* 25:81
- Foulon CF, Reist CJ, Bigner DD, Zalutsky MR (2000) *Cancer Res* 60:4453
- Friedman AM, Zalutsky MR, Wung W, Buckingham F, Harper PVJ, Scherr GH, Wainer B, Hunter RL, Appelmann EH, Rothberg RM, Fitch FW, Stuart FP, Simonian SJ (1977) *Int J Nucl Med Biol* 4:219
- Fujimori K, Covell DG, Fletcher JE, Weinstein JN (1989) *Cancer Res* 49:5656
- Geerlings MW Sr, Kaspersen FM, Apostolidis C, Van der Hout R (1993) *Nucl Med Commun* 14:121
- Geissler F, Anderson SK, Press O (1991) *Cell Immunol* 137:96
- Goeckeler WF, Edwards B, Volkert WA, Troutner DE, Holmes RA, Simon J, Wilson DJ (1987) *J Nucl Med* 28:495
- Gridley DS, Ewart KL, Coa JD, Stickney DR (1991) *Cancer Res* 51:1515
- Gumpel J, Beer T, Crawley J, Farran H (1975) *Brit J Radiol* 48:377
- Hall EJ (2000) Radiobiology for the radiologist. Lippincott Williams and Wilkins, Philadelphia
- Hanson RN (2000) *Curr Pharm Des* 6:1457
- Harbert JC (1987) Nuclear medicine therapy. Thieme Medical Publishers, New York
- Hartmann F, Horak EM, Garmestani K, Wu C, Brechbiel MW, Kozak RW, Tso J, Kosteiny SA, Gansow OA, Nelson DL, Waldmann TA (1994) *Cancer Res* 54:4362
- Hartman T, Lundqvist H, Westlin J-E, Carlsson J (2000) *Int J Radiat Oncol Biol Phys* 46:1025
- Hassfjell SP, Hoff P, Bruland OS, Alstad J (1994) *J Labelled Compd Rad* 34:717
- Hauck ML, Dewhirst MW, Zalutsky MR (1995) In: Torchilin VP (ed) Handbook of targeted delivery of imaging agents, Chapter 20. CRC Press, Boca Raton, pp 337–341
- Hayes DF, Friedman EL, Kufe DW (1989) In: Zalutsky MR (ed) Antibodies in radiodiagnosis and therapy, Chapter 4. CRC Press, Boca Raton, pp 57–81
- He X, Archer GE, Wikstrand CJ, Morrison SL, Zalutsky MR, Bigner DD, Batra SK (1994) *J Neuroimmunol* 52:127
- Heppeler A, Froidevaux S, Eberle AN, Maecke HR (2000) *Curr Med Chem* 7:2000
- Hnatowich DJ, Chinol M, Siebecker DA (1988) *J Nucl Med* 29:1428
- Hofer KG, Harris CR, Smith JM (1975) *Int J Radiat Biol* 28:225
- Hoffland LJ, Breeman WAP, Krenning EP, de Jong M, Waaijers M, van Koetsveld PM, M     HR, Lamberts SWJ (1999) *Proc Am Assoc Physicians* 111:63
- Holt JA, Scharl A, Kullander S, Beckman MW (1992) *Acta Obstet Gyn Scand* 155(Suppl.):39
- Hornick CA, Anthony CT, Hughey S, Gebhardt BM, Espenan GD, Woltering EA (2000) *J Nucl Med* 41:1256
- Howell RW, Rao DV, Hou DY, Narra VR, Sastry KSR (1991) *Radiat Res* 128:282
- Howell RW (1992) *Med Phys* 19:1371
- Hu F, Cutler CS, Hoffman T, Sieckman G, Volkert WA, Jurisson SS (2002) *Nucl Med Biol* 29:423
- Hughes A, Gatley SJ, De Sombre ER (1993) *J Nucl Med* 34:272
- Humm JL (1986) *J Nucl Med* 27:1490
- Huneke RB, Pippin CG, Squire RA, Brechbiel MW, Gansow OA, Strand M (1992) *Cancer Res* 52:5818

- ICRU (1984) Stopping powers for electrons and positrons, Report 47. International Commission on Radiation Units and Measurements, Bethesda, pp 1–267
- Jain RK, Ward-Hartley K (1984) IEEE T Son Ultrason SU31:504
- Jain RK (1988) Cancer Res 48:2641
- Jain RK, Baxter LT (1988) Cancer Res 48:7022
- Johnson EL, Turkington TG, Jaszczak RJ, Gilland DR, Vaidyanathan G, Greer KL, Coleman RE, Zalutsky MR (1995) Nucl Med Biol 22:45
- Junghans RP, Dobbs D, Brechbiel MW, Mirzadeh S, Raubitschek AA, Gansow OA, Waldmann TA (1993) Cancer Res 53:5683
- Kabat EA, Wu TT, Perry HM, Gottesman KS, Foeller C (1991) Sequences of proteins of immunological interest, 5th edn. US Public Health Service, National Institutes of Health, Washington
- Kampf G (1988) Radiobiol Radiother 29:631
- Kassis AI, Adelstein SJ, Haydock C, Sastry KSR, McElvany KD, Welch MJ (1982) Radiat Res 90:362
- Kassis AI, Harapanhalli RS, Adelstein SJ (1999a) Radiat Res 151:167
- Kassis AI, Harapanhalli RS, Adelstein SJ (1999b) Radiat Res 152:530
- Kennel SJ, Chappell LL, Dadachova K, Brechbiel MW, Lankford TK, Davis IA, Stabin M, Mirzadeh S (2000) Cancer Biother Radiopharm 15:219
- Kohler G, Milstein C (1975) Nature 256:495
- Kozak RW, Atcher RW, Gansow OA, Friedman AM, Hines JJ, Waldmann TA (1986) Proc Natl Acad Sci USA 83:474
- Kozak RW, Raubitschek A, Mirzadeh S, Brechbiel MW, Junghaus R, Gansow OA, Waldmann TA (1989) Cancer Res 49:2639
- Kurtzman SH, Russo A, Mitchell JB, DeGraff W, Sindelar WF, Brechbiel MW, Gansow OA, Friedman AM, Hines JJ, Gamson J, Atcher RW (1988) J Natl Cancer Inst 80:449
- Kwekkeboom D, Krenning EP, de Jong M (2000) J Nucl Med 41:1704
- Kwekkeboom DJ, Bakker WH, Kooij PPM, Konijnenberg MW, Srinivastan A, Erion JL, Schmidt MA, Bugaj JL, de Jong M, Krenning EP (2001) Eur J Nucl Med 28:1319
- Ladner RC (1999) Q J Nucl Med 43:119
- Lamberts SW, Koper JW, Reubi JC (1987) Eur J Clin Invest 17:281
- Langmuir VK, Sutherland RM (1988) Antibody Immunoconj 1:195
- Larsen RH, Bruland ØS, Hoff P, Alstad J, Rofstad EK (1994) Br J Cancer 69:1000
- Larsen RH, Wieland BW, Zalutsky MR (1996) Appl Radiat Isot 47:135
- Larsen RH, Vaidyanathan G, Zalutsky MR (1997) Int J Radiat Biol 72:79
- Larsen RH, Slade S, Zalutsky MR (1998a) Nucl Med Biol 25:351
- Larsen RH, Akabani G, Welsh P, Zalutsky MR (1998b) Radiat Res 149:155
- Larsen RH, Murud K, Akabani G, Hoff P, Zalutsky MR (1999) J Nucl Med 40:1197
- Lebedev NA, Novgorodov AF, Misiak R, Brockmann J, Rosch F (2000) Appl Radiat Isot 53:421
- Lewis MR, Raubitschek A, Shively JE (1994) Bioconjug Chem 5:565
- Lindstron A, Carlsson J (1993) Cancer Biother 8:145
- Link EM, Carpenter RN (1990) Cancer Res 50:2963
- Link EM, Carpenter RN (1992) Cancer Res 52:4385
- Ma D, McDevitt MR, Finn RD, Scheinberg DA (2001) Appl Radiat Isot 55:667
- Macklis RM, Kinsey BM, Kassis AI, Ferrara JLM, Atcher RW, Hines JJ, Coleman CN, Adelstein SJ, Burakoff SJ (1988) Science 240:1024
- Makrigiorgos GM, Kassis AI, Baranowska-Kortylewicz J, McElvany KD, Welch MJ, Sastry KSR, Adelstein SJ (1989) Radiat Res 118:532
- Mattes MJ, Major PP, Goldenberg DM, Dion AS, Hutter RVP, Klein KM (1990) Cancer Res 50(Suppl.):880
- Mazeron JJ, Simon JM, Crook J, Calitchi E, Otmeguin Y, Le Bourgeois JP, Pierquin B (1991) Int J Radiat Oncol Biol Phys 21:1173
- McDevitt MR, Nikula TN, Finn RD, Curcio MJ, Gansow OA, Geerlings MW Sr, Larson SM, Scheinberg DA (1996) Tumor Targeting 2:182
- McDevitt MR, Sgouros G, Finn RD, Humm JL, Jurcic JG, Larson SM, Scheinberg DA (1998) Eur J Nucl Med 25:1341
- McDevitt MR, Finn RD, Ma D, Larson SM, Scheinberg DA (1999a) J Nucl Med 40:1727
- McDevitt MR, Finn RD, Sgouros G, Ma D, Scheinberg DA (1999b) Appl Radiat Isot 50:895
- McDevitt MR, Barendswaard E, Ma D, Lai L, Curcio MJ, Sgouros G, Ballangrud AM, Yang W-H, Finn RD, Pellegrini V, Geerlings MW Jr, Lee M, Brechbiel MW, Bander NH, Cordon-Cardo C, Scheinberg DA (2000) Cancer Res 60:6095
- McDevitt MR, Ma D, Lai LT, Simon J, Borchardt P, Frank RK, Wu K, Pellegrini V, Curcio MJ, Miederer M, Bander NH, Scheinberg DA (2001) Science 294:1537
- McEwan AJB (1997) Semin Nucl Med 27:165
- McLendon RE, Archer GE, Larsen RH, Akabani G, Bigner DD, Zalutsky MR (1999) Int J Radiat Oncol Biol Phys 45:491
- Menkes CJ, Ingrand J, Paris MN (1982) In: Kolarz G, Thumb N (eds) Methods of nuclear medicine in rheumatology. Schattauer Verlag, Stuttgart, p 131
- Milenic DE, Garmestani K, Chappel LL, Dadachova E, Yordanov A, Ma D, Scholm J, Brechbiel MW (2002) Nucl Med Biol 29:431
- Millar WT, Barrett A (1990) Cancer Res 50(Suppl.):1043s
- Morrison SL (1985) Science 229:1202

- Mueller HL, Fruhwald MC, Scheubeck M, Rendl J, Warmuth-Metz M, S'ensen N, Kuhl J, Reubi JC (1998) *J Neuro-Oncol* 38:27
- Murud K, Larsen RH, Bruland ØS, Hoff P (1999) *Nucl Med Biol* 26:791
- Nahum AE (1996) *Phys Med Biol* 41:1957
- Novak-Hofer I, Amstutz HP, Morgenthaler JJ, Schubiger PA (1994) *Int J Cancer* 57:427
- O'Donoghue JA, Bardies M, Wheldon TE (1995) *J Nucl Med* 36:1902
- O'Donoghue JA, Wheldon TE (1996) *Phys Med Biol* 41:1973
- Olafsen T, Bruland ØS, Zalutsky MR, Sandlie I (1995) *Nucl Med Biol* 22:765
- Onetti CM, Gutierrez E, Hleba E, Aguirre C (1982) *J Rheumatol* 9:229
- Patel YC (1999) *Front Neuroendocrinol* 20:157
- Press OW, DeSantes K, Angerson SK, Geissler F (1990) *Cancer Res* 56:1243–1250
- Press OW, Howell-Clark J, Anderson S, Bernstein I (1994) *Blood* 83:1390
- Primus FJ, MacDonald R, Goldenberg DM, Hansen HJ (1977) *Cancer Res* 37:1544
- Reist CJ, Batra SK, Pegram CN, Bigner DD, Zalutsky MR (1997) *Nucl Med Biol* 24:639
- Reist CJ, Bigner DD, Zalutsky MR (1998) *Clin Cancer Res* 4:2495
- Rekonen A, Oka M, Ruotsi A (1972) *Rheumatology* 2:53
- Reubi JC (1997) *Q J Nucl Med* 41:63
- Reubi JC, Schär J-C, Waser B, Wenger S, Heppeler A, Schmitt JS, Mäcke HR (2000) *Eur J Nucl Med* 27:273
- Riechmann L, Clark M, Waldmann H, Winter G (1988) *Nature* 332:323
- Ruotsi A, Hypen M, Rekonen A, Oka M (1979) *Ann Rheum Dis* 38:45
- Sands H, Jones PL, Shah SA, Palme D, Vesele RL, Gallagher BM (1988) *Cancer Res* 48:188
- Sautterbühl M-L, Herbold G, Bihl H (1996) *Recent Results Cancer Res* 141:67
- Schwartz UP, Plascjak P, Beitzel MP, Gansow OA, Eckelman WC, Waldmann TA (1998) *Nucl Med Biol* 25:89
- Senekowitsch-Schmidke R, Schuhmacher C, Becker K-F, Nikula TK, Seidel C, Becker I, Miederer M, Apostolidis C, Adam C, Huber R, Kremmer E, Fischer K, Schwaiger M (2001) *Cancer Res* 61:2804
- Seon BK, Roholt OA, Pressman D (1970) *Biochim Biophys Acta* 200:81
- Serafini AN, Houston SJ, Resche I, Quick DP, Grund FM, Ell PJ, Bertand A, Ahmann FR, Orihuela E, Reid RH, Lerski RA, Collier BD, McKillop JH, Purnell GL, Pecking AP, Thomas FD, Harrison KA (1998) *J Clin Oncol* 16:1574
- Sgouros G, Ballangrud AM, Juric JG, McDevitt MR, Humm JL, Erdi YE, Mehta BM, Finn RD, Larson SM, Scheinberg DA (1999) *J Nucl Med* 40:1935
- Sharkey RM, Motta-Hennessy C, Pawlyk D, Siegel JA, Goldenberg DM (1990) *Cancer Res* 50:2230
- Sharkey RM, Blumenthal RD, Behr TM, Wong GW, Haywood LH, Forman D, Griffiths GL, Goldenberg DM (1997) *Int J Cancer* 72:477
- Shin S-U (1991) *Biotherapy* 3:43
- Shin BC, Park KB, Jang BS, Lim SM, Shim CK (2001) *Nucl Med Biol* 28:719
- Siegrist W, Eberle AN (1995) *Trends Endocrinol Metab* 6:115
- Slamon DJ, Godolphin W, Jones LA, Holt JA, Wong SG, Keith DE, Levin WJ, Stuart SG, Udove J, Ullrich A, Press MF (1989) *Science* 244:707
- Sledge CB, Noble J, Hnatowich DJ, Kramer R, Shortkroff S (1977) *Arthritis Rheum* 22:1334
- Sledge CB, Zuckerman JD, Zalutsky MR, Atcher RN, Shortkroff SA, Lionberger DR, Rose HA, Hurson BJ, Lankener PA, Anderson RJ, Bloomer WA (1986) *Arthritis Rheum* 29:153
- Song J, Suh CH, Park YB, Lee SH, Yoo NC, Lee JD, Kim KH, Lee SK (2001) *Eur J Nucl Med* 28:489
- Sparks RB, Crowe EA, Wong FC, Toohey RE, Siegel JA (2002) *J Nucl Med* 43:1110
- Spencer RP (1978) *Therapy in nuclear medicine*. Grune & Stratton, New York
- Spencer RP, Sievers RH, Friedman AM (1987) *Radionuclides in therapy*. CRC Press, Boca Raton
- Squire CJ, Baker LJ, Clark GR, Martin RF, White J (2000) *Nucl Acid Res* 28:1252
- Strickland DK, Vaidyanathan G, Zalutsky MR (1994) *Cancer Res* 54:5414
- Tao M-H, Morrison SL (1989) *J Immunol* 143:2595
- Tatro JB, Atkins M, Mier JW, Hardarson S, Wolfe H, Smith T, Entwistle ML, Reichlin S (1990) *J Clin Invest* 85:1825
- Turkington TG, Zalutsky MR, Jaszczak RJ, Garg P, Vaidyanathan G, Coleman RE (1993) *Phys Med Biol* 38:1121
- Turner MW (1981) In: Glynn LE, Steward MW (eds) *Structure and function of antibodies*, Chapter 1. Wiley, Chichester, pp 1–57
- Van Osdol W, Fujimori K, Weinstein JN (1991) *Cancer Res* 51:4776
- Vaidyanathan G, Zalutsky MR (1992) *Bioconjug Chem* 3:499
- Vaidyanathan G, Larsen RH, Zalutsky MR (1996) *Cancer Res* 56:1204
- Vaidyanathan G, Affleck D, Welsh P, Srinivasan A, Schmidt M, Zalutsky MR (2000) *Nucl Med Biol* 27:329
- Virkkunen M, Krusius FE, Heiskanen T (1967) *Acta Rheum Scand* 13:81
- Visser GM (1989) *Radiochim Acta* 47:97
- Volkert WA, Hoffman TJ (1999) *Chem Rev* 99:2269
- Wang SJ, Lin WY, Chen NM, Chen JT, Ho WL, Hsieh BT, Huang H, Shen LH, Ting G, Knapp FF Jr (2001) *Nucl Med Biol* 28:727

- Warner RP, O'Dorisio TM (2002) *Semin Nucl Med* 32:79
- Warren BA (1979) In: Peterson H-I (ed) *Tumor blood circulation: angiogenesis, vascular morphology and blood flow of human tumors*, Chapter 1. CRC Press, Boca Raton, p 1
- Warters RL, Hofer KG, Harris CR, Smith JM (1977) *Curr Topics Radiat Res Q* 12:389
- Weiner RE, Thakur ML (2001) *Semin Nucl Med* 31:296
- Weinstein JM, Eger RR, Covell DG, Black CDV, Mulshine J, Carrasquillo JA, Larson SM, Keenan AM (1987) *Ann NY Acad Sci* 507:199
- Wessels BW, Rogus RD (1984) *Med Phys* 11:638
- Wieland DM, Wu J, Brown LE, Mangner TJ, Swanson DP, Beierwaltes WH (1980) *J Nucl Med* 21:349
- Wikstrand CJ, Hale LP, Batra SK, Hill ML, Humphrey PA, Kurpad SN, McLendon RE, Moscatello D, Pegram CN, Reist CJ, Traweek ST, Wong AJ, Zalutsky MR, Bigner DD (1995) *Cancer Res* 55:3140
- Wilbur DS, Vessella RL, Stray JE, Goffe DK, Blouke KA, Atcher RW (1993) *Nucl Med Biol* 20:917
- Zalutsky MR, Venkatesan P, English R, Shortkroff S, Sledge C, Adelstein S (1986) *Nucl Med Biol* 12:457
- Zalutsky MR, Moseley RP, Coakham HB, Coleman RE, Bigner DD (1989a) *Cancer Res* 49:2807
- Zalutsky MR, Garg PK, Friedman HS, Bigner DD (1989b) *Proc Natl Acad Sci USA* 86:7149
- Zalutsky MR, McLendon R, Garg PK, Archer GE, Schuster JM, Bigner DD (1994) *Cancer Res* 54:4719
- Zalutsky MR (1997) *Q J Nucl Med* 41:71
- Zalutsky MR, Stabin M, Larsen RH, Bigner DD (1997) *Nucl Med Biol* 24:255
- Zalutsky MR, Vaidyanathan G (2000) *Curr Pharm Des* 6:1433
- Zalutsky MR, Zhao X-G, Alstron KL, Bigner DD (2001) *J Nucl Med* 42:1508
- Zweit J (1996) *Phys Med Biol* 41:1905



Volume 5

**Instrumentation,
Separation Techniques,
Environmental Issues**



47 Dosimetry and Biological Effects of Ionizing Radiation

B. Kanyár¹ · G. J. Köteles²

¹University of Pannonia, Veszprém, Hungary

²National Research Institute for Radiobiology and Radiohygiene,
Budapest, Hungary

47.1	<i>Introduction</i>	2215
47.2	<i>Interaction of Ionizing Radiation with Biological Substances on Molecular, Cellular, and Tissue Levels</i>	2216
47.2.1	Overview of the Effects of Ionizing Radiation on Living Systems	2216
47.2.2	Specific Ionization and Linear Energy Transfer	2217
47.3	<i>Dosimetric Quantities and Units</i>	2218
47.3.1	Dosimetric Quantities and Factors	2219
47.3.1.1	Absorbed Dose, D	2219
47.3.1.2	Equivalent Dose, H_T	2219
47.3.1.3	Effective Dose, E	2220
47.3.1.4	Individual and Collective Doses	2222
47.3.1.5	Dose Rate	2222
47.3.2	Subsidiary Dose Quantities and Units	2223
47.3.2.1	Committed Dose	2223
47.3.2.2	Exposure Dose, X	2223
47.3.2.3	Kerma, K	2224
47.3.2.4	Ambient Dose Equivalent, $H^*(d)$	2224
47.3.2.5	Organ Dose, D_T	2224
47.4	<i>Mechanisms of External and Internal Exposure</i>	2225
47.4.1	External Exposures	2225
47.4.1.1	Point Source	2225
47.4.1.2	Cloud Immersion and Surface Contamination	2227
47.4.2	Internal Pathways	2228
47.4.2.1	Inhalation Pathway	2229
47.4.2.2	Ingestion Pathway	2229
47.4.2.3	The MIRD Methodology	2230
47.4.3	Intervention and Action to Reduce Exposures	2232
47.4.3.1	Factors to Reduce Exposure from External Sources	2232
47.4.3.2	Factors to Reduce Exposure from Internal Sources	2232

47.5	<i>System of Radiological Protection of Humans</i>	2233
47.5.1	Types of Exposure Situations	2233
47.5.2	Categories of Exposures	2233
47.5.2.1	Occupational Radiation Protection	2233
47.5.2.2	Medical Radiation Protection	2236
47.5.2.3	Environmental Radiation Protection	2238
47.5.3	Limitation of Exposure to Ionizing Radiation	2241
47.5.3.1	Action Levels for Radon Concentrations	2243
47.6	<i>Health Hazards of Radiation Exposure</i>	2243
47.6.1	Deterministic Effects	2243
47.6.2	Stochastic (Somatic and Genetic) Effects	2245
47.7	<i>Diagnostic Procedures for Radiation Injuries (Biological Dosimetry)</i>	2247
47.7.1	Hematological Indicators	2248
47.7.2	Cytogenetic Assays	2249
47.7.2.1	Lymphocyte Metaphase Chromosomes	2249
47.7.2.2	Lymphocyte Micronuclei	2250
47.7.2.3	Premature Chromosome Condensation (PCC)	2250
47.8	<i>Management of Overexposures</i>	2250
47.9	<i>Dose–Response Relationships</i>	2252
47.9.1	Biological Effects of Low Radiation Doses	2252
47.9.2	The LNT Theory and Its Critical Review	2254

Abstract: The extension of the use of ionizing radiation and the new biological information on the effects of radiation exposure that is now becoming available, present new challenges to the development of concepts and methodology in determination of doses and assessment of hazards for the protection of living systems. Concise information is given on the deterministic and stochastic effects, on the debate concerning the effects of low doses, the detection of injuries by biological assays, and the radiation sickness.

47.1 Introduction

Soon after the discovery of X-rays and radioactivity at the end of the nineteenth century, biological effects of ionizing radiation were observed. Experience shows that radiation exposure can damage living cells, killing some of them and modifying others. The ultimate damage is related to a number of factors, such as the spatial distribution in the cells of the energy deposition along the radiation tracks, the distribution of the absorbed energy with time, and the radiosensitivity of the cells within the organism. Most tissues in the living body are unaffected by the loss of even a considerable number of cells; however, if the number of cells lost is large enough, there will be observable harm to tissues or organs that may lead to death.

During the first decades following the introduction of ionizing radiation, many serious accidents occurred before there was an adequate understanding of its biological effects. By 1922, approximately 100 radiologists (medical practitioners) had died due to the harmful effects of radiation.

The early deaths and other effects of radiation on man led to the initiation of the second International Congress of Radiology to establish the International X-Ray and Radium Protection Committee in 1928. The Committee forced an international cooperation to introduce protective criteria in the use of X-rays and radium therapy. After the beginning of the nuclear age in the 1940s, the increasing interest and extended fields in radiation were restructured and the Committee was renamed the International Commission on Radiological Protection (ICRP), in 1950. Because of the different conditions that apply in various countries, the Commission sets out recommendations but does not intend to provide a regulatory text.

In general, the Recommendation for the System of Radiological Protection (revised every 15–20 years) updates the former one and develops the additional guidance on the control of exposure from radiation sources. The new recommendation is based on the latest available scientific information of the biology and physics of radiation exposure.

Currently, the international standards, such as International Basic Safety Standards (IBSS) and European Directives on radiological protection, and most national regulations are based on the ICRP-1990 recommendations (ICRP Publication No. 60). New scientific data have been published since 1990, but the concept and philosophy of the system have not been changed. The overall estimates of deterministic effects remain fundamentally the same and the estimates of cancer risk have not changed much either, whereas the estimated risks of heritable effects are currently lower than were before.

The ICRP works closely with the International Commission on Radiation Units and Measurements (ICRU), with UN bodies such as the World Health Organization (WHO), International Atomic Energy Agency (IAEA), and Scientific Committee on the Effects of Atomic Radiation (UNSCEAR), and other special and regional organizations. The most important results of the ICRP are reported in the ICRP Publications, several of them as general recommendations for radiation protection, including dosimetry and health effects (ICRP 1977). The most

recent recommendations concerned with the protection of humans appeared in 2007 (ICRP 2007) and are concerned only with ionizing radiation. On the basis of the recommendations, standards for practical use of the concepts have been issued by the IAEA in collaboration with many other bodies. The last one – based on ICRP 2007 – is in preparation, as are the new EU directives and national regulations.

In the last decades, the advice that all exposures should be kept as low as possible has been modified to the requirement to keep all the exposures “as low as reasonably achievable (ALARA), taking economic and social factors into account.” The new ICRP emphasizes the greater importance of the optimization in the protective procedures, in comparison with the former one.

The practical aim in work with radiation must take into account the protective point of view by the introduction of standards, methods, and measures to protect living systems without unduly limiting the beneficial practices. The aim should be achieved on the bases of both scientific concepts about the biological effects of radiation and judgments about the relative importance of different kinds of risk.

47.2 Interaction of Ionizing Radiation with Biological Substances on Molecular, Cellular, and Tissue Levels

Radiation can interact with the atoms and molecules of the absorbing material while passing through it, producing excitation of molecular vibrations and orbital electrons, and ionization of atoms. Radiation is called ionizing radiation when the energy transferred to the orbital electron is sufficient to eject the electron from the atom, producing a positively charged ion. The positive ion and the electron thus formed are known as an ion pair. The ejected electron may have sufficient kinetic energy to produce further excitations and ionization in the matter, and the processes will continue until the incident particle and all electrons come to rest. Most of the atomic processes that occur are transient ones and take nanoseconds, but others manifestly cause changes in the absorbing matter.

The atomic and molecular effects of radiation depend on many factors, in general on the composition of the absorbing matter and the amount of energy deposited by the radiation. The energy required to produce an ion pair varies with the type of matter, falling in the range of 20–50 eV for most gaseous materials and living tissues. For the same absorbing material, it is nearly independent of the type of radiation and the energy (Choppin et al. 1995).

Radiation with energy less than the ionization energy is called nonionizing radiation (Mosely 1988; Dennis and Stather 1997); this primarily excites the vibrational and rotational spectra of the molecules in absorbing matter, including tissues.

47.2.1 Overview of the Effects of Ionizing Radiation on Living Systems

The process of ionization necessarily changes atoms and molecules, at least transiently, and may rupture chemical bonds in the molecules of the absorbing material, forming various chemical entities.

If the affected molecules are in a living cell, the cell itself may sometimes be damaged, either directly or indirectly, for example, by production of free radicals due to radiolysis, etc. With respect to the life function, one of the most serious types of damage is a strand break in a DNA chain. The direct or indirect effects of the radiation on DNA may result in irreversible damage

or alterations to the genetic code; the responses may be latent or immediately apparent. The damage in DNA may occur in the genes and chromosome, for example, resulting in an increased frequency of aberrations such as dicentric chromosomes. If enough cells in an organ or tissue are killed or prevented from reproducing and functioning normally, there will be a loss of organ function. The loss of function becomes more serious as the number of affected cells is increased.

Radiation exposure has been associated with most forms of cancer in many organs, such as the lung, breast, and thyroid gland. If the cell is only modified by the radiation damage, the damage is usually repaired. In some conditions, the repair mechanism may not be perfect, and the modification will be transmitted to daughter cells. This may eventually lead to cancer in the tissue of the exposed individual. Radiation-induced cancer may manifest itself decades after the exposure and does not differ from cancers that arise spontaneously or are attributable to other factors.

Exposure to radiation also has the potential to cause hereditary effects in the offspring of persons exposed to radiation. However, radiation-induced hereditary effects have yet to be detected in human populations exposed to radiation, although they are known to occur in other species.

47.2.2 Specific Ionization and Linear Energy Transfer

In radiation absorption processes of living tissue, the probability of interaction with electrons is considerably greater than that of nuclear reactions, and the number of electrons produced in secondary ionization is often larger than that of the primary ionization. Therefore, in general, the dominant part of the energy deposited in living tissue results in ionization.

Specific ionization (J) means the total number of ion pairs produced per unit length of the path of the incident radiation. The mathematical definition is

$$J = \frac{dN}{dl}, \quad (47.1)$$

where dN is the number of ion pairs produced along the path of length dl .

For heavy charged particles, the specific ionization increases with decreasing energy of the charged particles because of the increased probability of interaction at low energies. The specific ionization, the number of ion pairs formed per millimeter in normal air, is shown in [Fig. 47.1](#) for electrons, protons, and α particles.

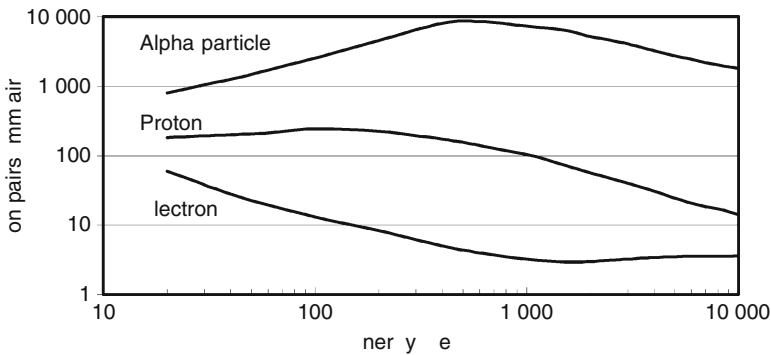
Because γ -rays and neutrons are uncharged radiation, they may ionize the matter only indirectly. A photon imparts a large fraction of its energy to a single electron – mainly by the photoelectric effect, Compton scattering, and pair production – which ionizes and excites many other atoms and molecules along its path. Therefore, the specific ionization of γ -rays is similar to that of electrons.

The neutron interacts primarily with the nucleus of the absorbing atom, by elastic and inelastic scattering. In elastic collisions, the target nucleus is not itself ionized. However, it may produce ionization in other atoms. In inelastic scattering, including nuclear transformation, the newly formed nuclide and the emitted photon or charged particle may produce ions.

The quantity of *linear energy transfer* (abbreviated as LET) is the amount of energy deposited by the radiation per unit length of the path. In mathematical form, it is defined as:

$$\text{LET} = \frac{d\varepsilon}{dl} \quad (47.2)$$

■ Fig. 47.1

Energy dependence of specific ionization in air

where $d\varepsilon$ is the fraction of energy lost to the medium along a section dl of a charged particle's path. The SI unit is J m^{-1} , but the most frequently used unit is $\text{keV } \mu\text{m}^{-1}$. The LET is equivalent to the restricted linear collision stopping power used in particle physics.

47.3 Dosimetric Quantities and Units

According to experience, ionization is the major cause of the biological effects of radiation. Since the microdistribution of the ionizations and excitations in the atoms produced by ionizing radiation cannot be fully quantified at present, approximations are used to assess, for example, the number of ion pairs in cells or in other parts of living tissues. Therefore, the energy imparted to the matter, the absorbed dose, and other specific quantities are used conventionally to express the effects on the living function of the body. These approaches omit consideration of the discontinuous nature of the radiation energy and matter exposed, but are justified empirically by observations that the gross quantities correlate sufficiently well with the resulting biological effects.

Future developments in microdosimetry may indicate use of quantities based on the probability distribution of events in a small volume of material corresponding to the dimensions of biological entities such as the cell nucleus or its molecular DNA (ICRP 1977). Meanwhile, however, use of macroscopic quantities in dosimetry of ionizing radiation is recommended.

To assess exposure, a number of specialized quantities and units are used. The present chapter depends mainly on the bases of quantities introduced in 1980 by the ICRU (ICRU 1980) and on revised terminology and definitions proposed in 1990 by the ICRP (ICRP 1991). Additionally, the recent results and interpretations of the UNSCEAR reports have been included (UNSCEAR 1996, 2000).

Radiation can cause changes in living systems; the effects depend on various factors, such as absorbed energy, dose, dose rate, etc. All the quantities and important factors are to be defined in adequate forms, usable to predict the future outcome of the biological effects and measurable with proper precision.

In general, to assess the delayed effects of current exposure, dose quantities of the ionizing radiations are introduced. The term dose is used in a general sense as a measure of the “quantity of radiation” or the energy deposited by radiation in a target. For the strictest use in dosimetry, the term must be specified as absorbed dose, equivalent dose, organ dose, etc. These quantities may refer to exposed individuals (individual dose) or to a group of people (collective dose).

47.3.1 Dosimetric Quantities and Factors

The fundamental dosimetric quantity used is the absorbed dose. The equivalent dose and the effective dose are also important quantities. Special circumstances might be characterized by committed dose, kerma dose, and some other dose quantities and factors.

47.3.1.1 Absorbed Dose, D

The absorbed dose (D) is defined as:

$$D = \frac{d\varepsilon}{dm} \quad (47.3)$$

where $d\varepsilon$ is the mean energy imparted by ionizing radiation to matter in a volume element, and dm is the mass of matter in the volume element. The energy can be averaged over any defined volume, the average dose being equal to the total energy imparted in the volume divided by the mass in the volume. Usually, the absorbed dose is an averaged dose over a tissue or organ.

The SI unit of the absorbed dose is the gray (Gy); $1 \text{ Gy} = 1 \text{ J kg}^{-1}$. The old unit is the rad (roentgen absorbed dose); $1 \text{ Gy} = 100 \text{ rad}$.

The absorbed dose may be used for any type of ionizing radiation (α , β , X-ray, etc.) and to any type of matter (both living systems and nonliving materials).

47.3.1.2 Equivalent Dose, H_T

The equivalent dose (H_T) to a tissue T is defined as the product of the absorbed dose delivered by radiation type R averaged over tissue or organ T, times the radiation weighting factor w_R for radiation type R. In mathematical form:

$$H_T = w_R D_T, \quad (47.4)$$

where D_T is the absorbed dose over tissue T and w_R is the *radiation weighting factor* for radiation type and energy R. The weighting factor w_R varies between 1 and 20. [Table 47.1](#) contains values of weighting factors recommended by the ICRP (ICRP 1991). The SI unit of the equivalent dose is the sievert (Sv); $1 \text{ Sv} = 1 \text{ J kg}^{-1}$. The equivalent dose has the same fundamental units (J kg^{-1}) as the absorbed dose. However, it is given its own special name, the sievert, in recognition that it is obtained from the gray by multiplying by a dimensionless scale factor.

Usually the values w_R are broadly compatible with the values of the quality factor (Q) and the *relative biological effectiveness* (RBE), used more frequently in the past (ICRP 1977, 1991) and with respect to personal dose measurements, even nowadays (IBSS 1996).

■ Table 47.1

Radiation weighting factors, w_R and LET-values

Type and energy range of radiation	w_R	LET in water (fJ μm^{-1})
Photons, all energies	1	0.03–5
Electrons and muons, all energies	1 ^a	0.03–0.2
Neutrons, energy dependency	🔗 Fig. 47.2)	2–10
Protons, other than recoil protons, energy >2 MeV	5	~2
Alpha particles, fission fragments, heavy nuclei	20	~20

^aExcluding auger electrons emitted from nuclei to DNA, for which special microdosimetric considerations apply.

When the radiation field is composed of different types of radiation with different values of w_R , the equivalent dose is the following sum:

$$H_T = \sum_R w_R D_{TR}. \quad (47.5)$$

The equivalent dose partly corresponds to the formerly used *dose equivalent*, where, instead of w_R , the quality factor (Q) of the radiation type was used. In this case, the values of Q and w_R are identical or nearly identical.

Both the step function and the continuous function in 🔗 Fig. 47.2 had been introduced in the former recommendation (in ICRP 1991). The recently recommended continuous function of radiation weighting factors for neutrons reflects only practical considerations and does not imply the availability of more precise data. Mainly due to the continuous energy spectrum of the neutrons, in calculations the continuous function of the w_R has been used rather than the step function.

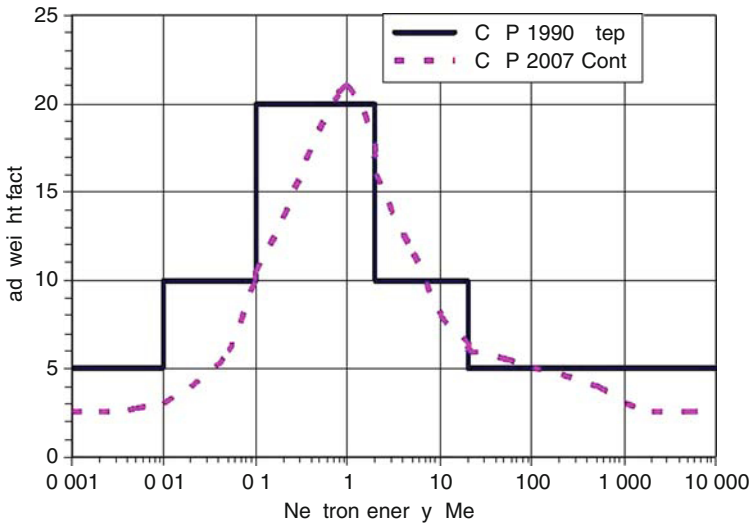
The *directional dose equivalent* $H^*(d, \Omega)$ at a point in a radiation field is defined as the dose equivalent that would be produced by the corresponding expanded field in the ICRU sphere at a depth d on a radius in a specified direction Ω . The depth, $d = 0.07$ mm, is used for weakly penetrating (e.g., β^-) radiation. In personal monitoring of occupational impact, the quantity of *personal dose equivalent* is recommended for use (ICRU 1980). The equivalent dose is defined only for living systems, including biota and man, but strictly, only for man. Steps are made to introduce and determine values of w_R for other living systems too (IAEA-TECDOC 1999). The equivalent dose expresses that the biological effect (more precisely, the *stochastic effect*; see later) depends – in addition to the absorbed dose – on the type and energy of radiation or, more directly, on the value of LET.

47.3.1.3 Effective Dose, E

It is necessary to take into account the different sensitivities of various tissues and organs to the induction of deleterious health effects to the whole organism. The effective dose (E) is defined as a summation of the tissue *equivalent doses* multiplied by the appropriate tissue weighting factor w_T . According to this definition,

$$E = \sum_T w_T H_T, \quad (47.6)$$

■ Fig. 47.2

Radiation weighting factors (w_R) for neutrons versus neutron energy

where H_T is the equivalent dose in organ or tissue T, and w_T is the tissue weighting factor for the organ or tissue T.

Mainly due to the additional experimental data, the concept of tissue weighting factors is to be extended. Based on new data, the improved values of the factors are issued regularly. In general, the w_T -values recommended by the ICRP were based on the risk of fatal cancer and of serious heritable disease. The last concept and the values of w_T are based on the incidence of radiation-induced cancer, rather than on mortality, as well as on the risk of heritable disease over the first two generations.

The recommended values of w_T are given in ▶ Table 47.2. The differences between the corresponding values of the two columns show the development of fundamental knowledge in dosimetry over a short period.

According to the definition of the tissue weighting factor, the summation of the factor over all the tissues results in the value 1, that is

$$\sum_T w_T = 1. \quad (47.7)$$

From the definition of the equivalent dose, it follows that

$$E = \sum_T w_T \sum_R w_R D_{TR}, \quad (47.8)$$

where D_{TR} is the average absorbed dose in the organ or tissue T due to radiation R. ▶ Equation (47.8) indicates that the various doses due to the different types of radiation and different tissues are additive quantities without any cross-contributions or synergism among them. Very probably, this is valid only for sufficiently small doses in the range of occupational exposures.

The Commission is an advisory body that offers its recommendations to regulatory and advisory agencies, mainly by providing development of the ICRP recommendations including weight factors.

■ Table 47.2

Tissue weighting factors, w_T

Tissue or organ	ICRP-1990/IBSS-1996	ICRP-2007
Gonads	0.20	0.08
Bone marrow, red	0.12	0.12
Colon	0.12	0.12
Lung	0.12	0.12
Stomach	0.12	0.12
Bladder	0.05	0.04
Breast	0.05	0.12
Liver	0.05	0.04
Esophagus	0.05	0.04
Thyroid	0.05	0.04
Skin	0.01	0.01
Bone surface	0.01	0.01
Brain	–	0.01
Salivary glands	–	0.01
Remainder	0.05	0.12
Total	1.00	1.00

47.3.1.4 Individual and Collective Doses

The dose incurred by an individual member of the population is an individual dose. More generally, the individual dose can be extended to other living organisms besides man.

The collective dose quantity represents the total consequences of exposures of a population or group. The use should be limited to situations in which the consequences are truly proportional to both the dosimetric quantity and the number of people exposed. The *collective equivalent dose*, S_T , is the average dose to a tissue or organ T in the exposed group multiplied by the number of individuals in the group. If several groups are involved, the total collective quantity is the sum of the collective quantities for each group. The *collective effective dose*, S , has similarly been defined by ICRP:

$$S = \sum_i \bar{E}_i N_i, \quad (47.9)$$

where \bar{E} is the mean effective dose and N_i is the number of individuals in population subgroup i . The unit of both the collective equivalent dose and collective effective dose is man-Sv (or person-Sv).

47.3.1.5 Dose Rate

The dose rate (\dot{D}) expresses the time variation of the dose. It is defined as follows:

$$\dot{D} = \frac{dD}{dt}, \quad (47.10)$$

where D is the dose and t is the time. The SI units are Gy s^{-1} or Sv s^{-1} ; for environmental radiation monitoring, however, the units nGy h^{-1} and nSv h^{-1} are more frequently used.

In radiation protection practice, most of the dose limits correspond to an annual dose (IBSS 1996). The annual dose is the sum of the external exposure in a year and the *committed dose* (see ▶ Sect. 47.3.2.1) the sum of intakes of radionuclides in that year.

47.3.2 Subsidiary Dose Quantities and Units

At the same time that there is a close cooperation among the international commissions and bodies involved in radiation dosimetry, practical problems and changes in concepts involve a mixed use of various derived quantities. The following dose quantities are not primary ones, but for special circumstances, they may become important.

47.3.2.1 Committed Dose

Committed doses are defined in cases of intakes of radioactive materials, mainly by ingestion, inhalation, or absorption through the skin, in terms of internal radiation impact. In most cases, the quantities of *committed absorbed dose*, committed equivalent dose, and committed effective dose are used.

The quantity of *committed effective dose*, $E(\tau)$, is defined as:

$$E(\tau) = \int_{t_0}^{t_0+\tau} \dot{E}(t) dt, \quad (47.11)$$

where t_0 is the time of intake, $\dot{E}(t)$ is the effective dose rate at time t , and τ is the time elapsed since the intake of radioactive substances. When τ is not specified it will be taken as 50 years for adults and 70 years for children.

The SI unit of committed effective dose is Sv, the same as for effective dose. Similarly, one can derive a *committed equivalent dose*. The quantity of *dose commitment* differs from the committed dose only by the upper integration limit. It is defined as the infinite time integral ($\tau = \infty$) of the per caput dose rate (\dot{H}_T or \dot{E}) of the population due to a specified event. The unit of the dose commitment is the same as for committed dose. Both individual dose commitment and collective dose commitment can be defined.

47.3.2.2 Exposure Dose, X

The exposure dose with its unit R (roentgen) was the first defined quantity in radiology, in 1928. It refers to ionization in air by the γ - (or X-) rays, and its determination could be provided by a relatively simple technique, using an air-filled ionization chamber. The quantity X is defined as:

$$X = \frac{dq}{dm} \quad (47.12)$$

where dq is the total electrical charge of the particles produced by the photons in the volume element of air in unperturbed circumstances and dm is the mass of the volume element.

The SI unit is C kg^{-1} , without any special name. The unit roentgen (R) is the photon exposure that produces in air ion pairs with total – either positive or negative – electrical charge per unit mass of $2.58 \times 10^{-4} \text{ C kg}^{-1}$. The unit R is still used in practice, especially in medical fields, in spite of the problems of defining it with respect to the newly introduced quantities recommended by the ICRP. The advantage of its use probably comes from the ease of determining the electrical charge in practical ranges by ionization chambers or other electrical devices.

The unit 1 R corresponds to 1.61×10^{15} ion pairs per kg in air or $8.80 \times 10^{-3} \text{ J kg}^{-1}$ absorbed dose in air and similarly in soft tissues. The corresponding absorbed dose in bones, etc., may be by 20–30% higher.

47.3.2.3 Kerma, K

For indirectly ionizing radiation, the quantity K is defined as:

$$K = \frac{d\varepsilon_{\text{tr}}}{dm} \quad (47.13)$$

where $d\varepsilon_{\text{tr}}$ is the sum of the initial kinetic energies of all charged ionizing particles liberated by uncharged ionizing particles in a material of mass dm .

The expression kerma is an acronym from *kinetic energy released in material*. The SI unit is the gray (Gy), and $1 \text{ Gy} = 1 \text{ J kg}^{-1}$.

47.3.2.4 Ambient Dose Equivalent, $H^*(d)$

This quantity is defined by the ICRU, not by the ICRP, and is used mainly for operational aims in measurement of the radiation impact together with the quantities of *directional dose equivalent* and *personal dose equivalent* (see description of equivalent dose). The quantity $H^*(d)$ at a point in the radiation field is defined as the dose equivalent that would be produced by the corresponding aligned and expanded field in the ICRU-sphere at a depth d on the radius opposing the direction of the aligned field. The depth $d = 10 \text{ mm}$ is recommended for strongly penetrating radiation such as γ - or neutron radiation.

47.3.2.5 Organ Dose, D_T

The mean dose D_T in a specific tissue or organ T of the living body is given by:

$$D_T = \frac{1}{m_T} \int_{m_T} D(m) dm \quad (47.14)$$

where m_T is the mass of the organ and $D(m)$ is the local absorbed dose in the mass element dm . The SI unit is termed the gray (Gy), as with the absorbed dose; $1 \text{ Gy} = 1 \text{ J kg}^{-1}$. Because the radiosensitive cells nearest the skin surface are located at the basal layer of the epidermis, the dose rate in skin is evaluated at $d = 0.07 \text{ mm}$ depth, primarily for external β radiations.

47.4 Mechanisms of External and Internal Exposure

Dose assessments are usually based on both measurements and calculations, taking into account the distribution of the radionuclides and the radiation fields influenced by the absorption, scattering, and other effects of the environment close to the source and to the individual body exposed. Whenever direct measurements are not feasible, or if they must be generalized and extended, dose assessment methods are applied. For example, for discharges from industrial processes, it is not usually possible to measure dose rates and activity concentrations in the environment, and so models are required to calculate the dispersion in the environment.

The choice of the method depends primarily on the type of information available. In general, the determination of dose needs the following two main types of procedures.

1. Assessment of the distribution of the radionuclides both outside and inside the body, including the distance and orientation between the source and detector and kinetic aspects (the transport and transformation of the source of radiation with any radioactive daughter elements produced).
2. Estimation of the dose from a radiation field due to the distribution of the radionuclides or other sources of radiation. The radiation field may be influenced by shielding and by the scattering configuration of the geometry.

Individuals can be exposed from sources of radiation outside the body and by radionuclides incorporated into the body. The radiation pathway from a source outside the body produces an external dose, from incorporated radioactive material an internal dose.

47.4.1 External Exposures

The external dose results primarily from γ radiation arising from the decay of radionuclides at locations outside the specified body. Secondly, the exposures from neutron radiation and to the skin from β radiation may be considered as an external pathway. The α , proton, and ion radiations are to be considered as an external impact only in very special cases, for example, for a geometry extremely close to the eyes.

The external dose is usually determined by the absorbed dose. The effective dose and the other dose quantities are derived by multiplying the absorbed dose by appropriate factors.

Depending on the volumetric distribution of the source of radiation, the following typical geometries may be selected for assessment of external doses: point source, immersion in a plume, and radioactivity deposited on surfaces. In addition, more complex arrangements of sources and geometries can often be described. For those cases, the point-kernel numeric integration method is performed based on calculations as a point source solution (Wood 1982).

47.4.1.1 Point Source

Around a point source, the external absorbed dose rate \dot{D} with an isotropic radiation field can be assessed by

$$\dot{D} = \Gamma \frac{A}{r^2}, \quad (47.15)$$

where A is the source activity (Bq), r is the distance from the source (m), and Γ is the *external dose coefficient*, taking into account the yield of the radionuclide decay and energy of the γ radiation. Values of Γ for several radionuclides are listed in ▶ [Table 47.3](#) together with other types of dose coefficients.

More exactly, the absorbed dose in ▶ [Eq. \(47.15\)](#) refers to the absorption dose in air without any absorption in the material around the point source or any influence by scattering of radiation. In the most realistic situation, the body of the person may affect the radiation field; for example, the dose rate (in units of nGy h^{-1}) measured in a geometry of anterior-posterior (A-P) differs slightly from the posterior-anterior (P-A) measured dose rate (▶ [Fig. 47.3](#)).

By use of shielding layers produced from different materials (lead, copper, iron, etc.), the dose calculation must take into account the buildup of lower energy photons together with attenuation in the shielding materials, including air and self-absorption of the human body (Wood [1982](#)).

Methods for assessing the dose rate from a source with varying volume, size, shape, and distribution, including absorption and scattering of the radiation, usually require numerical approximations with integration in space (Wood [1982](#)). Assessments can take into account the modifying effect of the human body on absorption and scattering of the radiation, and in addition to the effective dose, the equivalent dose to the different organs and tissues may be estimated using various sizes and shapes of anthropomorphic phantoms (Jacob et al. [1990](#)). That kind of calculation is provided primarily for occupational dose assessments.

■ **Table 47.3**

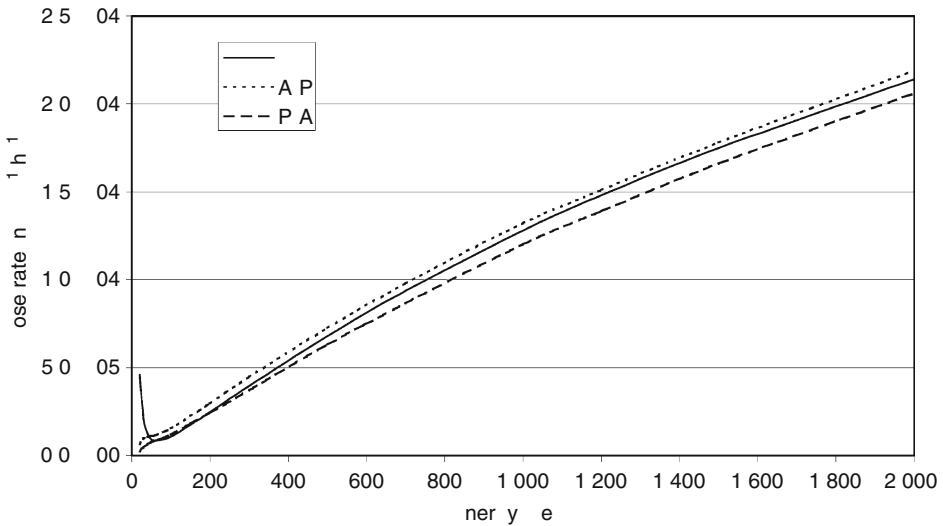
Dose coefficients (Jacob et al. [1990](#); Eckerman and Ryman [1993](#); IBSS [1996](#))

Radio-nuclides	Half-life	Γ	K_B	$K_{\gamma v}$	$K_{\gamma s}$	K_{inh}	K_{ing}
		(nGy h^{-1} per Bq m^{-2})	(nSv h^{-1} per Bq m^{-3})	(nSv h^{-1} per Bq m^{-3})	(nSv h^{-1} per kBq m^{-2})	(nSv per Bq)	(nSv per Bq)
H-3	12.3 a	–	0	–	–	–	0.042 ^a
C-14	5,730 a	–	0.016	–	–	–	0.58
Co-60	5.27 a	0.30	0.53	0.43	5.5	32	3.4
Sr-90	29.1 a	–	0.033	–	–	160	28
Tc-99m	6.02 h	0.013	0.026	0.018	0.28	0.019	0.022
Ag-110m	250 days	0.30	0.57	0.46	6.2	13	2.8
I-131	8.04 days	0.050	0.11	0.060	0.89	7.4	22
Cs-134	2.06 a	0.21	0.34	0.26	3.6	6.6	19
Ba-137m	30.0 a	0.076	0.16	0.098	1.4	4.6	13
Ra-226	1,600 a	0.19	0.0017	9.8×10^{-4}	0.015	7,800	330
Pu-239	24,100 a	–	0.000067	1.3×10^{-5}	1.3×10^{-4}	50,000	250
Am-241	432 a	–	0.0046	0.0024	0.039	41,000	200

^aFor organically bound tritium (OBT).

■ Fig. 47.3

Energy dependency of dose quantities assessed from external γ radiation at a distance of 1 m from a point source of 1 photon s^{-1} (D: absorbed dose rate in air, nGy h^{-1} , A-P: effective dose rate measured by geometry anterior/posterior, P-A: effective dose rate measured posterior/anterior, nSv h^{-1})



47.4.1.2 Cloud Immersion and Surface Contamination

After a release of radionuclides into the atmosphere and deposition to the ground surface, the main exposure pathways are the external doses from the air and from the deposited γ exposure. From the average height of the human body, listed values of dose rates without any special remarks are calculated for a height of 1 m above the soil surface.

Because the range of β particles in air is only 1–2 m, the equivalent dose to the skin from β radiation is determined by the very volume of air very close around the location of the body. For γ radiation of the most common energies (50–1,500 keV), the half thickness in air is 50–200 m; therefore, the local external doses both from the air volume and the ground surface are determined by a distance of several hundred meters. Due to the relatively small ranges of the radiation in the environment, a homogeneous contamination of the air and ground surface may be assumed as a semi-infinite geometry. Dose rates from monoenergetic and semi-infinite volume sources in air and plane sources at the ground can be assessed by

$$H_k = \sum_l K_{kl} F_{kl} C_l \tau_k \quad (47.16)$$

where H_k is the dose quantity (effective dose, equivalent dose to the organ or tissue, etc.) by pathway k (external exposure from air volume, from contaminated surface, etc.), C_l is the radionuclide concentration of the environmental element l (air, surface), K_{kl} is the dose coefficient relevant to pathway k and environmental element l , F_{kl} is a reduction factor relative to the absorption of radiation by buildings, trees, etc. at the location, and τ_k is the duration of exposure at the location due to pathway k . Representative units include the following:

H is usually expressed in Sv, C is expressed in Bq m^{-3} for the air volume or Bq m^{-2} for deposition on the surface, the quantity F is dimensionless, τ is usually expressed in hours or seconds, and K is expressed in Sv h^{-1} per Bq m^{-3} or per Bq m^{-2} , depending on the pathway and units of C .

External irradiation from β -emitters deposited on the ground usually produces a negligible contribution to the skin dose. ➤ Equation (47.16) assumes constant contamination during time τ . In the case of time-dependent contamination in air or on a surface, the product $C\tau$ is replaced by the time-integration of the concentration C . Dose coefficients are listed in ➤ Table 47.3 for frequently used radionuclides, namely for the equivalent dose to skin by β radiation (K_β) and for the effective dose due to the contaminated air volume (K_{air}) and the ground surface (K_{gs}). Dose coefficients K_{inh} and K_{ing} pertain to the internal pathways.

Effective dose from γ -emitters distributed in soil for depth $d > 0$ is less than assessed by the coefficient K_{gs} due to absorption in the soil layer above the radionuclides. The attenuation coefficient and build-up factor in soil depends primarily on the γ energy, depth of distribution, soil composition, and density.

External exposure can be measured by personnel monitoring using film badges or thermoluminescent dosimeters (TLD); in occupational and environmental monitoring, additionally, dose rate meters based on G-M tubes, proportional counters, scintillation detectors, etc., are introduced.

47.4.2 Internal Pathways

Incorporation of radionuclides into the body may occur by inhalation, by ingestion, and, rarely, through the skin. Intake by inhalation and ingestion is determined by the activity concentrations in air, in foods, and in water and by age-specific estimates of breathing rate and food consumption. The ICRP has provided the following representative ages: 3 months (for the 0–1 year age group), 1 year (for the 1–2 year group), 5 years (2–7 years), 10 years (7–12 years), 15 years (12–17 years), and adults (>17 years old).

Following an intake to the body, the retention of the radionuclides depends on the chemical form administered and the metabolism, including uptake by the lung or gastrointestinal tract, transport by blood, and excretion. The dose is influenced by the physical decay of radioactivity, and in the case of a decay series, the metabolism and radiation of daughters as well.

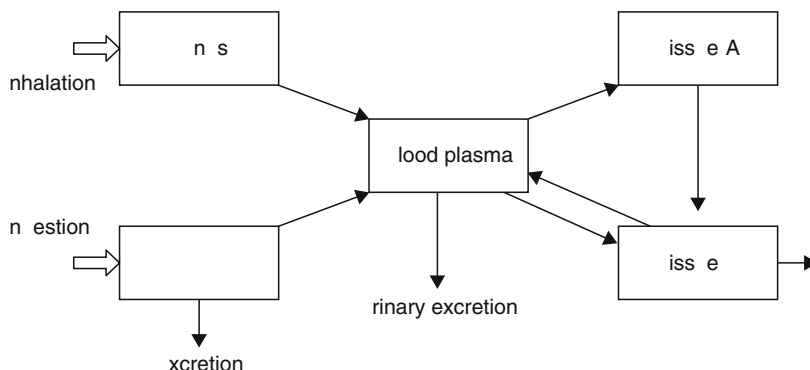
Models taking into consideration the metabolism and time variation of the radionuclide concentrations in man are conceptualized as compartmental systems, including dynamic processes (ICRP 1994; Jacquez 1996; Thorne 2001).

The transport processes in man without any details are illustrated in ➤ Fig. 47.4. Intake of radionuclides through the lungs (inhalation) or gastrointestinal tract (ingestion) produces an increasing concentration in the central circulation system, usually in blood plasma. Depending on the chemical species of the radionuclide in the central circulation, various tissues or organs incorporate the activity, or it may be excreted through the kidney and urinary system.

Recent models tend to be much more complex than previous ones and involve recycling between tissues, taking into consideration the chemical forms of the radionuclides administered and the physiological functions of tissues. A different binding site of a tracer in the same tissue may be represented by a different compartment. Therefore, in internal dose assessments, models with more than 10 compartments are frequently used; only rarely will more than 50 compartments be used.

Fig. 47.4

Compartmental model for illustration of the transport of radionuclides in man (GIT: gastrointestinal tract)



Most of the transport phenomena are described by linear processes, but, for example, the uptake of inorganic iodine by the thyroid from the blood plasma is primarily a zero-order process, and several enzyme kinetic reactions and bindings are second-order processes.

47.4.2.1 Inhalation Pathway

In steady-state conditions, or for a long-time average, the committed dose due to inhalation of contaminated air during time τ may be assessed in the following form:

$$H_k = K_k I C \tau, \quad (47.17)$$

where H_k is the proper dose quantity (committed effective dose, committed equivalent dose to the organ k , etc., in units of Sv), I is the inhalation rate ($\text{m}^3 \text{h}^{-1}$), and C is the activity concentration in air (Bq m^{-3}). The *inhalation dose coefficient*, K_k (Sv Bq^{-1}), concerning either the k th organ or whole body doses, means the dose due to a unit inhalation of activity. Table 47.3 includes the dose coefficient (K_{inh}) for the committed effective (whole body) dose for the adult age group. Similar values can be derived for all the tissues (lung, bone marrow, etc.) as *committed equivalent dose coefficients*, in units of Sv Bq^{-1} .

For most radionuclides, the inhalation dose coefficient is higher for children than for adults, but the inhalation rate (I) is probably lower for children. Therefore, the inhalation dose rates for the same level of air contamination may be even less for children and infants than for adults. The inhalation rate (I), consumption habits, and committed dose conversion coefficients with respect to groups of different ages, species of contamination in air (ionic, aerosol bound, aerosol diameter, etc.) or foodstuffs, and radionuclides are listed in tables of dose assessments (Jacob et al. 1990; IBSS 1996). These values are derived from calculations assuming various types of body phantoms and measurements.

47.4.2.2 Ingestion Pathway

In steady-state conditions, the committed dose from ingested radionuclides may be assessed in a similar way as given for the inhalation pathway. Instead of the inhalation rate I , the

consumption rate is used to assess the total intake of radioactivity from the contamination of the foodstuffs (IAEA-SRS 2001). The uptake and metabolism of the radionuclides also depend on the chemical form administered. Therefore, the *ingestion (committed) dose coefficient* depends on the chemical binding of the radionuclide ingested, uptake by the intestine, and other physiological factors, including age. Coefficient K_{ing} related to the committed effective dose is listed in ► Table 47.3 (last column).

Direct monitoring of incorporated radionuclides is based on whole-body measurement of the penetrating (primarily γ) radiation. Indirect methods are used for those radionuclides, such as tritium, which do not emit a significant amount of penetrating radiation and are based on the determination of activity concentrations in biological materials separated from the body (urine, feces, and breath samples), or in other physical samples taken from the close environment.

To assess the total committed (internal) dose, the results obtained from each pathway (inhalation, ingestion, different foodstuffs, and radionuclides, etc.) are to be summed. In radiation protection, the total committed dose due to a whole year's uptake is determined and monitored systematically.

47.4.2.3 The MIRD Methodology

The technique for estimation of the absorbed dose to organs and tissues from radionuclides inside the human body has been developed by the Medical Internal Radiation Dose (MIRD) Committee of the Society of Nuclear Medicine, USA. The schema and pamphlets issued by the Committee since the 1960s contain measurement and calculation procedures and examples of the use of methodology. The methodology is widely accepted throughout the world (Watson 1994; Zanzonico et al. 1995).

The MIRD techniques are primarily intended for assessment of absorbed radiation doses received by patients who are undergoing nuclear medical tests and not for directly linking the dose to the radiation effects. The population of patients studied with radiopharmaceuticals is not well represented in the determination of tissue weighting factors or committed equivalent or effective doses due to inhalation and ingestion. Therefore, the MIRD schema are prepared to estimate doses for various situations and purposes, to each age-specific and gender-specific body habitus, extending the applicability beyond the original 70 kg adult anthropomorphic “standard man.”

In the MIRD formalism, the mean absorbed dose to a target region r_k from uniformly distributed, cumulative activity in the source region r_h becomes the following:

$$\overline{D}(r_k \leftarrow r_h) = \frac{\overline{A}_h \sum_i A_i \phi_i(r_k \leftarrow r_h)}{M_k} = \overline{A}_h S(r_k \leftarrow r_h), \quad (47.18)$$

where \overline{A}_h is the cumulative activity (e.g., in units MBq h) in the source region r_h , A_i is the equilibrium dose constant (in Gy h⁻¹ per MBq kg⁻¹) for radiation i , $\phi_i(r_k \leftarrow r_h)$ is the absorbed fraction in target region r_k for radiation i emitted in source region r_h , M_k is the mass (in kg) of target region r_k , and $S(r_k \leftarrow r_h)$ is the radionuclide specific S factor (in Gy per MBq h) for target region r_k and source region r_h . The S factor is the absorbed dose to target region r_k per unit of cumulative activity in source region r_h .

The total mean absorbed dose to the target region r_k is calculated by the sum of the absorbed dose contributions from all the source regions r_h :

$$\overline{D}(r_k) = \sum_h \overline{A}_h S(r_k \leftarrow r_h). \quad (47.19)$$

For α and β radiation and a huge volume of tissue, all of the emitted energy would be absorbed within the source region. Therefore the fraction $\phi_i = 1$ for the source region and 0 for any other region outside the source region for all radiation types i , and dose calculations become simple. For penetrating radiation (γ -rays) and the human body, only a fraction of the energy emitted in a source organ is absorbed in that organ, and some of the energy will escape from the body completely. It means that for all targets, $0 < \phi_i < 1$ and ϕ_i depends on the energy of the radiation, volumes and localization of the tissues, and some other parameters characteristic of the body.

To determine absorbed fractions (ϕ_i) for photons, an anatomic model approximating the human body (more generally, the living system being investigated) must be developed. Sizes and shapes that resemble the organs and tissues are defined by mathematical expressions. The volumes and distances of the organs are usually taken into consideration by the age, body weight, sex, and other characteristics of man as represented by the Reference Man initially developed by Snyder (Snyder et al. 1969).

► **Table 47.4** lists examples of absorbed fractions for liver as the source organ. For determination of the absorbed dose by the form (► 47.18) additionally the equilibrium dose constant (Δ_i) is to be used. The constant depends on the γ -yield and -energy emitted by the radionuclide and the value of ^{99m}Tc takes $\Delta = 7.2 \times 10^{-5} \text{ Gy h}^{-1} \text{ per MBq kg}^{-1}$.

The formalism given can be extended to an inhomogeneously distributed source volume, which may be important in radionuclide therapies with markedly nonuniform, spatially accumulated activity within different organs. Radiation dosimetry of sufficient accuracy and precision for radionuclide therapy must be customized to the specific patient being treated, however. Therefore, additional parameters are introduced taking into account the inhomogeneity, including metastases, to be determined by nuclear medicine imaging, transmission computer tomography, etc.

With inhomogeneous energy deposition at the cellular level, it is necessary to consider microdosimetric dose estimates for treatment planning. The total dose from a radionuclide with γ -rays of very different energies is the sum of the separately assessed doses for all the γ energies.

► **Table 47.4**

Absorbed fractions (ϕ) from a uniform γ -ray source in liver to various target organs of reference man (Watson 1994)

Gamma energy	$\phi, \rightarrow \text{liver}$	$\phi, \rightarrow \text{kidney}$	$\phi, \rightarrow \text{lungs}$	$\phi, \rightarrow \text{marrow}$	$\phi, \rightarrow \text{whole body}$
100 keV	0.165	0.0044	0.010	0.021	0.45
140 keV	0.162	0.0042	0.0096	0.017	0.43
200 keV	0.158	0.0039	0.0092	0.013	0.42
500 keV	0.157	0.0039	0.0084	0.011	0.41
1,000 keV	0.144	0.0034	0.0083	0.0094	0.38

47.4.3 Intervention and Action to Reduce Exposures

During an accident or emergency, a source is often out of human control. This necessitates prompt action to mitigate a hazard or to prevent adverse consequences for human health and safety, quality of life, and condition of the environment. In addition, protective action should be taken in some chronic exposures. Intervention and action levels support the decisions regarding the introduction of different preventive procedures.

47.4.3.1 Factors to Reduce Exposure from External Sources

According to the mathematical formulae of external expositions, the exposition time, the distance from the radiation source, and the shielding have important effect on the individual dose. Naturally, the dose is linearly proportional to the intensity of radiation or radioactivity of the source.

- *Time.* The total radiation exposure to an individual is directly proportional to the duration of his/her exposure to the radiation source. The longer the exposure, the higher is the radiation dose. Therefore, it is wise to spend no more time than necessary near sources or in a radiation field.
- *Distance.* The intensity of radiation, and hence the radiation exposure, varies inversely as the square of the distance from the source to the point of exposure. It is recommended that an individual should keep as far away as possible from a radiation source.
- *Shielding.* Because the ranges of α - and low energy β -particles are short in matter, air and clothing provide adequate shielding for these radiation types. Most gamma-radiations, however, are highly penetrating, and therefore highly absorbing material (usually Pb) should be used for shielding. Special shielding is to be used for neutron radiation. Neutrons of high energy (ranges of keV – MeV) are first to be moderated to low energy by absorbers of low atomic number (e.g., water or wax) and then absorbed by nuclear reaction of large cross section, for example, by a Cd plate.

47.4.3.2 Factors to Reduce Exposure from Internal Sources

The most effective way of reducing internal contamination is reducing the intakes of radionuclides through inhalation and ingestion. Less effective and only in special conditions useable procedures are based on the increased excretion of radionuclides by the gastrointestinal and renal systems.

The most frequently used procedure is the iodine prophylaxis. It is based on the zero order absorption of iodine by the thyroid gland from the blood plasma and on the first order kinetics of renal clearance. Therefore, the stable iodine – if administered shortly before the intake of the radioactive one – reduces the radioactive iodine absorption to the thyroid, and most of it is excreted by urine. Depending on the administration time and metabolic parameters of the human body, the effectiveness of reducing might reach 50–90%. Iodine prophylaxis can be an effective method in the early phase of airborne ^{131}I -release from a nuclear installation. In most cases, it is expected that the exposure through ingestion can be avoided or reduced by a proper change on consumption habits, while exposure through inhalation cannot.

47.5 System of Radiological Protection of Humans

For practical control of exposures, the ICRP defines different types of exposure situations and different categories of exposure. Depending on the exposure situations and categories, the control, limitation, and other activities may be different.

47.5.1 Types of Exposure Situations

The ICRP Recommendation is to be applied to all sources and to individuals exposed to radiation but distinguishes three different types of exposure situations.

In the *planned situation*, the sources are under human control. In simple words, it means planned (normal) work with radiation. In the former recommendation, it was named as practice.

The *emergency situation* may occur during normal operation due to malicious act or from any other unexpected situation and require urgent action in order to avoid or reduce undesirable consequences.

The *existing exposure situation* exists when a decision on control and/or protected action has to be taken, including prolonged exposure situations after contamination. A typical example appears during remediation of the close environment after U-mining activity.

Especially in the last two situations, the optimization with respect to the averted dose (risk) and cost of actions should be analyzed.

47.5.2 Categories of Exposures

In the practice of radiation protection, three categories of exposures are generally distinguished: occupational exposure, medical exposure, and public (or environmental) exposure. Regulations, including dose limits, monitoring of the radiation relations, and technical managing can differ in the three categories.

47.5.2.1 Occupational Radiation Protection

Artificial sources of radiation are commonly used in industry, research, medicine, nuclear power plants (NPP), etc. Some workers are exposed to natural sources, for example, in mines and other conditions where the radon concentration in air might be higher than in normal cases. Relatively high dose rates are measured during air travel due to the elevated levels of cosmic rays at high altitudes. This means that many people are exposed in their work. Some of them are monitored individually, for example, by a small photographic film, thermoluminescent material, or portable electronic devices. These types of detectors on the body register the dose due to the external sources and yield an estimate of the dose received by the wearer.

Worldwide there are nearly one million workers in industry and over two million workers in medicine who are exposed by use of nuclear technology or ionizing radiation, including X-rays.

Personnel Monitoring

Personnel monitoring is usually required when (1) workers are likely to receive in 1 year 10% of the annual limit of exposure from the external radiation source, and (2) individuals enter high

radiation areas. Monitoring for occupational intake of radioactive material (e.g., in a nuclear medicine laboratory, in the operations hall of a nuclear power plant, or by production and separation of radioisotopes) is also required if the annual intake by an individual is likely to exceed 10% of the value derived from the annual dose limit.

The most commonly used devices to monitor the personal dose include film badges, thermoluminescent (TL) badges, and pocket-type electronic tools (► Fig. 47.5). The workers should wear the devices only at work, in order to exclude background doses received at home or at other sites.

To monitor the intake, a whole body counter (► Fig. 47.6) can be used to measure the γ -radiation outside the body. Due to the internal contamination by isotopes of pure α - and β -radiation, excreta samples (usually urine) are to be analyzed.

The plastic holder of the film and TL discs are equipped with filters of different metals (aluminum, copper, and cadmium) inside the holder, in front of the film and TL to differentiate exposure from radiations of different types and energies.

Film badges are usually changed monthly for each worker and the exposure duration should be no longer than about 2 months, due to the effects on the film of humidity and other factors. The exposition to TL-discs might be longer. The TL-material can be reused many times after proper reading by thermo heating.

The principle and use of detector materials based on optically stimulated luminescence (OSL) are similar to those of the TL ones, but the reading does not destroy the stored information.

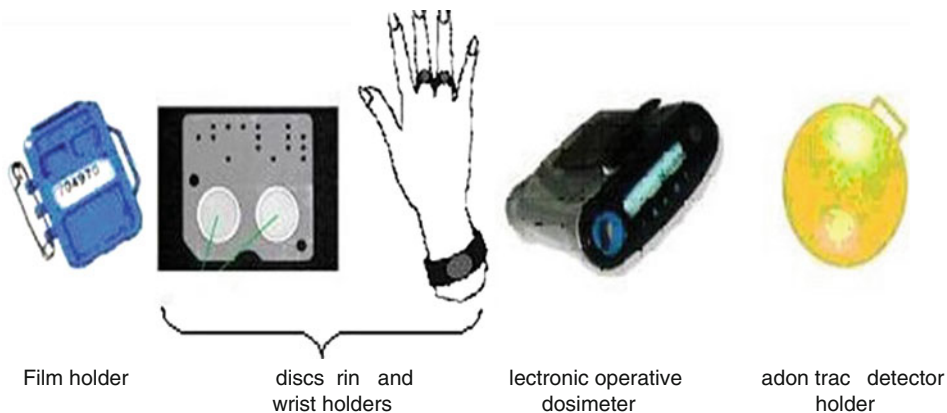
Radon Dosimeter

An organic plate as a track detector is in a domed holder, which allows radon gas to enter but excludes dirt, moisture, and radon decay products (e.g., ^{218}Po , ^{214}Bi) attached to aerosol particles in air (► Fig. 47.5). The number of tracks is proportional to the radon gas concentration in the building. Tracks due to the α -particles from radon are counted by a scanning microscope. Detectors are usually exposed for 1–6 months.

The personal portable (pocket) dosimeter usually contains a gas-filled or a semiconductor radiation detector (e.g., a G-M tube) tailored with an electronic device and a dedicated

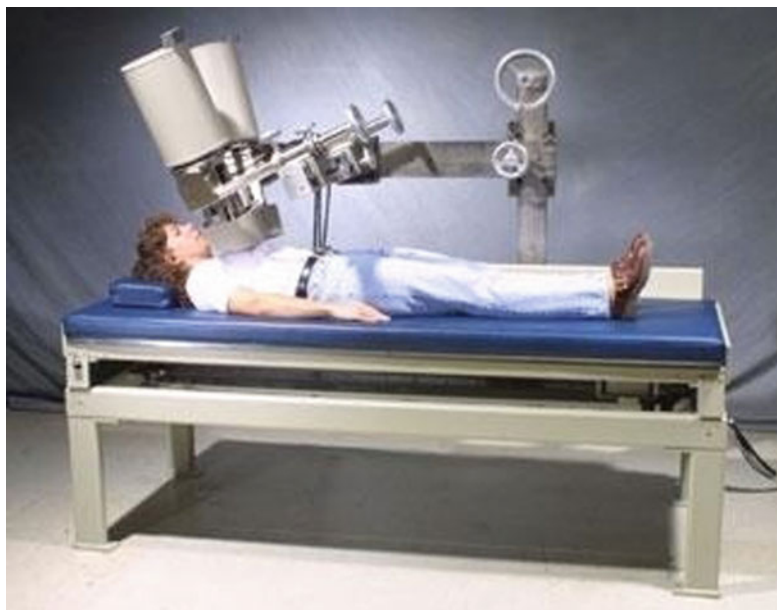
► Fig. 47.5

Film badge holder, thermoluminescent (TL) dosimeters (in the form of discs and rings), electronic and radon dosimeters



■ Fig. 47.6

Whole-body counter with external detectors for γ -ray determination



computer. It measures the dose rate continually, and time integration is provided by the computer, which is equipped with alarm levels and visual and audible signals. The integrated dose can be read any time, and the device can be used as an “operative dosimeter” in an emergency situation.

Whole-Body Counter

The whole-body counter is used to provide measured data on levels of radionuclides in the whole body and/or in organs. Therefore, radiation detectors (scintillation or semiconductor types) facing the whole body or the organs of interest are used in either stable or scanning geometry to determine the intensity of γ -radiation from the radionuclides inside the body. The detectors identify the radionuclides by their γ -energy radiated and the measured intensities can be transferred to dose rates in the body and/or different organs, tissues, by using proper computer software. ● Figure 47.6 shows a scheme of a body counter with two detectors.

Hand-Foot Contamination Monitor

This monitor is designed to monitor radioactive material deposited on clothes, shoes, and body surfaces of a worker in an isotope laboratory. Therefore, the device contains foot and hand detectors. It is usually posted at the exit of the laboratory. The purpose of the monitor is to avoid the spread of radioactive substances and to discover any internal contamination.

Monitoring at Workplaces

Devices equipped with detectors and radiation level monitors are posted inside rooms of a workplace. They usually measure the external radiation continuously. Their alarm levels are

put slightly higher than the background in the laboratory. Any alarm signal of the monitor is to be investigated and interpreted (e.g., due to the opening of a radioisotope container). Contamination of the air and surfaces of furniture is to be controlled by determination of the radioactivity of air filters and rubbed samples.

Transportation of Radioactive Material

Transportation of radioactive material is governed by regulations, with guidelines for packaging, for example, types of packaging material, limits of radioactivity in a package, exposure limits outside the package, and labels on the packages. Employees who ship radioactive material must have proper training, and a record of training must be kept.

Exposure of Workers

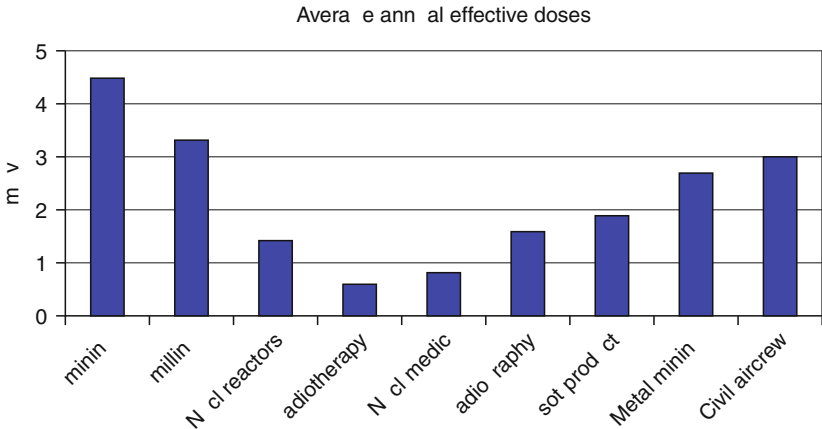
Exposures of workers due to various sources are 3–5 mSv yearly, as reported by the United Nations Scientific Committee on the Effects of Atomic Radiation (UNSCEAR). According to the report in 2000, the average annual effective doses of the most exposed groups in different fields are shown in Fig. 47.7.

The last two groups are exposed to natural sources: in metal mining mainly to radon, the aircrew to cosmic rays. With the exception of mining, the average annual doses from most types of occupational exposure due to artificial sources, including the nuclear industry, are below 2 mSv. Doses have been reduced in recent decades primarily because of the widespread introduction of the ICRP recommendations and control by appropriate authorities.

47.5.2.2 Medical Radiation Protection

The terms “medical exposure” and “medical radiation protection” refer to patients. In addition, members of the family and close friends either in the hospital or at home, who may come close to the patients following administration of radiopharmaceuticals, plus volunteers in biomedical research studies, belong to this category of exposure. The exposure of doctors and

Fig. 47.7
Average annual doses in different highly exposed occupations (UNSCEAR 2000)



other workers, and the proper requirements for their work in the medical stations belong to the occupational category of radiation protection.

The exposed people, the patients, are directly interested in getting better diagnostic results and directed to improved therapy; therefore, the benefits of exposure are realized individually, and public anxiety is less than that due, for example, to a nuclear facility built near a living site. The worldwide average of the number of medical examinations per 1,000 people per year is 330. The annual effective dose is 0.4 mSv per examination. The spread of these data is high. Where the population per physician is less than 1,000, both the frequency and the annual dose are about three times higher than the world averages, mainly due to the often-used CT (computed tomography).

Medical X-Ray Imaging

The average dose contribution from artificial sources is mostly attributable to medical diagnostics by radiographic imaging, including CT. A conventional X-ray investigation produces nearly 0.2 mSv and the CT 1–10 mSv external effective dose, while dental imaging and screening mammography produce less than 0.1 mSv. Although mammography-screening exposures will increase the radiation risk, the potential benefit for women who carry an undetected breast cancer is much higher than the associated risk from radiation.

A relatively high patient dose (10–100 mGy local tissue dose) can be provided by interventional radiology, for example, a series of X-ray imaging during a surgical procedure. In some cases, the doses are high enough to cause deterministic effects; therefore, these procedures should be carefully controlled and optimized.

Nuclear Medicine

Medical procedures involving intake of radioisotopes (e.g., in vivo tests in nuclear medicine for functional and morphological investigations, such as uptake metabolism of tissues, gamma camera, Positron Emission Tomography – PET, etc.) are less frequently used than X-ray imaging. Depending on the type of test, organ investigated, and radioisotope used, the internal dose from a single investigation involves 0.5–5 mSv effective dose to the patient.

Radiotherapy

Radiation of high intensity and dose is used to kill cancerous cells and tumor tissues. Using external radiation, the beam from an external source is directed to the tumor, while sparing the surrounding healthy tissues. Especially for deeply placed tumors, the protection of healthy tissues is incomplete, and the radiation may possibly cause cancer in other tissues. The aim of planning radiotherapy involves maximizing the effectiveness of treatment while minimizing the adverse side effects.

Radiotherapeutical procedures can also be provided by internal sources. Thyroid tumors that are hyperfunctioning are cured by intake of ^{131}I (200–1,000 MBq). The iodine is accumulated nearly 100% in the tumor tissue, and the β -radiation kills the cells within 1–2 mm. The penetrating γ -radiation simultaneously emitted from ^{131}I provides a dose to the healthy tissues, to the whole body, and even to people in the vicinity of the patient.

Release of Patients Administered a Radiopharmaceutical

The decision to hospitalize or release a patient after administration of radiopharmaceuticals should be made on an individual basis, considering the residual activity in the patient, patient's wishes, family considerations (particularly the presence of children at home), environmental

factors, and national regulations. The international recommendation for caregivers and comforters of the patient advises a dose constraint of 5 mSv per episode. Written instructions must be given to the patient on his staying at home (maintain distances from others, have sole use of the bathroom, limit visits by others, drink plenty of water, etc.).

Guidance Level of Medical Exposure

The decision whether to prescribe an X-ray or other radiological examination is a matter of medical judgment made in the best interest of the patient. In medical practice, so-called guidance levels, rather than dose limits, are used. The radiologist locally has to balance the exposure against the advantages of the radiological procedure. The dose contribution to the patient has to be in the range of or less than the guidance level established for the specific procedure or technique by professional bodies. It means that the medical doctor has some flexibility based on the clinical situation and the techniques used. The guidance levels are to be revised as technology and techniques improve. Examples of guidance levels in diagnostic radiography for a chest PA (posterior-anterior) examination is 0.4 mSv, for a lumbar spine AP (anterior-posterior) examination, 10 mSv. Guidance levels of activity for procedures in nuclear medicine are listed in ➤ [Table 47.5](#).

47.5.2.3 Environmental Radiation Protection

Ionizing radiation in the environment arises from both natural and artificial sources. Natural sources include cosmic rays and γ -rays from Earth; artificial sources include X-rays in medicine and discharges of radioactive waste from the nuclear industry. Sometimes the separation between natural and artificial sources involves difficulties; for example, the radionuclides ^3H and ^{14}C in the air can result from both cosmic rays and the nuclear industry.

The dose in the environment – the delivered dose to a human body – depends on many factors, namely, on the spatial distribution of radionuclides (in soils or in the atmosphere), the characteristics of the radiation (energy, type, etc.), the living site of individuals (at sea level or high elevation, indoors or outdoors), including the incorporation of radionuclides into the body through inhalation and food intake. With high local variation, the worldwide average annual effective dose is about 4 mSv, nearly 3 mSv of it from natural sources and 1 mSv from artificial sources (➤ [Table 47.6](#)).

Radon in the Atmosphere

The largest component of the natural dose comes from inhalation of the daughter nuclides of ^{222}Rn ($T_{1/2} = 3.8$ days). The radionuclide ^{222}Rn is an intermediate member in the uranium

■ Table 47.5

Examples of guidance levels in nuclear medicine, for a typical adult patient

Test	Radionuclide	Chemical form	Activity (MBq)
Bone imaging by single-photon emission tomography	Tc-99m	Phosphate compounds	800
Liver and spleen imaging	Tc-99m	Labeled colloid	80
Tumor or abscess imaging	Ga-67	Citrate	300
Lung ventilation study	Xe-133	Gas	400

■ Table 47.6

Worldwide average annual doses in the environment (dose to the human body). The ranges correspond to about a 90% confidence interval

Components or sources	Mean dose and range (mSv)
Natural sources	
Cosmic rays, external effective dose	0.38 (0.3–1.0)
Cosmogenic radionuclides due to inhalation and ingestion (internal, committed effective dose)	0.012 (0.008–0.02)
Terrestrial, external effective dose:	
Outdoor	0.45 (0.3–0.6)
Indoor	0.55 (0.4–0.8)
Terrestrial due to intake (except radon daughters) (internal, committed effective dose)	0.27 (0.2–0.5)
Terrestrial from radon and its daughters (internal, committed effective dose)	1.2 (0.5–5.0)
Terrestrial from radon and its daughters to lungs (internal, equivalent dose of lung tissue)	10
Artificial sources	
Medicine, external (mainly due to X-ray diagnosis)	1.5 (0.1–5)
Nuclear power plant (within 1–5 km)	0.01 (–0.1)
Nuclear weapon in Hiroshima and Nagasaki (in the area of the cities)	100–5,000
Nuclear weapons tests:	
Northern hemisphere	0.1–2
Southern hemisphere	<0.01
Chernobyl nuclear accident:	
In the $r \approx 30$ km circle	1–20
In Middle and West Europe	0.1–2.0
In North America	0.01
In Japan	0.01
In the southern hemisphere	<0.01

decay series (from ^{238}U to the stable ^{206}Pb) and emanates directly from ^{226}Ra in the soil due to α -decay, into a form of noble gas. Most of the radon atoms decay in the soil, but, primarily from the upper 20–50 cm layer, part of them are exhaled into the atmosphere and are distributed in the lower 200–300 m of air to an activity concentration of 5–8 Bq/m³ (the density of the radon is a bit higher than that of air). The ^{222}Rn nuclide decays into radionuclides of ^{218}Po , ^{214}Pb , etc., by α - and β -decays over a short time (in minutes), and the metallic elements of Po, Pb, and Bi are attached to aerosol particles in air very quickly. There is essentially no deposition of inhaled radon atoms – as a noble gas – into the lungs; therefore, the α -radiation due to the decay of ^{222}Rn has no contribution to the body dose. In contrast, the daughter atoms of Po, Pb, and Bi are attached to aerosols, and vapor drops are efficiently deposited into the lung tissues, where they are metabolized by the individual; therefore, a relatively large dose contribution might be provided from the radiation of short-lived

daughters such as ^{218}Po , ^{214}Pb , ^{214}Bi , and ^{214}Po . One daughter element in the series, ^{210}Pb , has a longer half-life ($T_{1/2} = 22$ years); therefore, most of the radioactive ^{210}Pb atoms are already excreted from the body before the decay and emission of radiation; less than 10% is incorporated into the bones, where it stays for a long while.

The radionuclide ^{220}Rn ($T_{1/2} = 56$ s) is an intermediate of the thorium decay series (from ^{232}Th to ^{208}Pb); this radionuclide (another isotope of the *element* radon besides its most common isotope ^{222}Rn) has the special name of thoron. Due to the short half-life, the exhalation rate of ^{220}Th from minerals to the atmosphere is small, and the concentration in air is about 10 times less than that of ^{222}Rn , at equilibrium. Therefore, the dose contribution is negligible, except in the atmosphere where the upper soils are rich in thorium content. The actinium series (from ^{235}U to ^{207}Pb) involves the intermediate of ^{219}Rn ($T_{1/2} = 4$ s). Due to the very short half-life of ^{219}Rn , its exhalation from soil is very small, as is the dose contribution.

Indoor and Outdoor Doses

Because most building materials are extracted from the Earth, walls made from bricks, stones, etc., contribute to the dose received by a person staying in the building, while the external dose from an outside source might be reduced due to the shielding of the γ -radiation by the walls. The external dose, after reduction by shielding, is usually less than the increased dose from the materials in walls.

Indoors, the building material contributes to the radon originating from the soil. In a closed space, with little ventilation, dilution with outside air is less effective, and the radon concentration at equilibrium might be 10–100 times higher than outdoors, causing activity concentrations as high as 100–1,000 Bq/m³. Elevated radon concentrations in air might also be observed in other closed spaces, such as mines, caves, and closed thermal springs.

Due to the inhomogeneous distribution of uranium, thorium, and other radionuclides in materials in the Earth's crust, the doses to humans are affected both by the geological formations of the area and the structure of the buildings in which they live. The world-average dose due to inhalation of radon daughters (annual effective dose, 1.3 mSv; see [Table 47.6](#)) is derived mainly by staying indoors (occupancy: ~80%). This is especially so in temperate and subarctic zones where the isolation that helps maintaining a comfortable temperature inside a building results in an enclosed space for radon. The contribution to dose in winter is usually higher than that in summer, due to the difference in building ventilation rates.

In dwellings, the main source of radon is the soil below the building due to the flux of radon through gaps in the ground. Therefore, the rooms on the ground floor are usually more contaminated than the ones on the upper floors.

Technologically-Enhanced Natural Exposures

Usually, the deeper soil layers contain heavy metals at higher concentrations than the surface layers. By mining and other soil shifting, including replacing coal slag – in other words, by technology – the minerals with higher U and Th contents can come closer to humans, even into the ground and building materials of houses. This kind of technology results in an enhanced exposure to people from natural radionuclides.

Actions to Reduce the Radon Dose in Dwellings

To prevent enhanced radon concentrations in the living spaces of buildings, ground soils and building materials should be tested before their use. To mitigate the radon concentration in an existing house, two main actions can be introduced: (1) increasing the ventilation in rooms that

are occupied, and (2) aspiration of the soil layer under the building. Naturally, the exchange of highly active ground soil is an effective action, but usually it is not a cost-effective procedure.

47.5.3 Limitation of Exposure to Ionizing Radiation

Ionizing radiation and radioactive substances are natural and permanent features of life on the Earth, and thus the risks associated with the radiation can only be restricted, not eliminated. Additionally, sources of ionizing radiation become essential to human practice: in energy supplying, in modern health care including X-ray diagnostics and radiation therapy, etc. The use of artificial radiation is widespread.

The acceptance by society of risk associated with radiation is conditional on the benefits to be gained from using the radiation. Nonetheless, the risk must be restricted and protected against by the application of radiation safety standards established by the national authority that take into account a desirable international consensus.

The general principles of radiological protection recommended by the ICRP (1991) are the following.

1. No practice involving exposures to radiation should be adopted unless it produces sufficient benefit to the exposed individual or to society to offset the radiation detriment it causes. (Justification of a practice.)
2. In relation to any particular source, the magnitude of individual doses, the number of people exposed, and the likelihood of incurring exposures where these are not certain to be received should all be kept as low as reasonably achievable, economic and social factors being taken into account. (Optimization of protection.)
3. The exposure of individuals resulting from the combination of all the relevant practices should be subject to dose limits, or to some control of risk in the case of potential exposures. No individual is exposed to radiation risks that are judged to be unacceptable from these practices in any normal circumstances. (Individual dose and risk limitation.)

Any system of protection should include an overall assessment of its effectiveness in practice. The international standards (IBSS 1996) established on the bases of the ICRP recommendations specify the basic requirements for protection of people against exposure to ionizing radiation and for the safety of radiation sources. In addition to the viewpoints of protection and safety in radiation, the technical developments, economics, and social situations are to be included in the general requirements of the system. Therefore:

1. Any exposure whose magnitude or likelihood is impossible to control is deemed to be excluded from the standards (e.g., the exposure caused by ^{40}K in the body or by cosmic radiation on the surface of the earth).
2. Procedures with and sources of ionizing radiation may be exempted from the requirements of the standards, for example, due to the very low activity and activity concentrations of radionuclides in the material, radiation risk to individuals caused by the exempted practice or source being sufficiently low as to be of no regulatory concern.

The standards for protection and safety differentiate the following circumstances: exemption, practices (formerly referred to as planned impact), and intervention. For exemption, most of the regulative requirements and standards are not applicable; in practices, they are to be applied. The intervention situations to which the standards apply are emergency exposures

requiring protective action to reduce or avert temporary or chronic exposures, including accidents and remediation of contaminated areas.

The requirements for the practices to which the standards shall apply include dose limits recommended by the ICRP and accepted by most of the international, regional, and national organizations; these dose limits are listed in ▶ [Table 47.7](#).

The limits apply to the sum of the relevant doses from the external exposure in the specified period and the 50- (for children 70-) year committed dose from intakes in the same period. The limitation on the effective dose to the public provides sufficient protection for the extremities (hands and feet) against stochastic effects; therefore, no limitations are established for them .

For students 16–18 years of age who are required to use radiation sources in their training and studies, the occupational exposure shall be controlled, and the following annual limits must not be exceeded: effective dose of 6 mSv, equivalent dose of 50 mSv to the lens of the eye, and equivalent dose of 150 mSv to the extremities or the skin.

Additionally, some special circumstances with respect to the regulations and monitoring of the doses are also recommended. Among them, for radon (^{222}Rn) in workplaces, the yearly average activity concentration should be less than $1,000 \text{ Bq m}^{-3}$ in air, as an action level. The ICRP derived radon conversion coefficient based on epidemiological determinations corresponds to $6 \text{ nSv (Bq h m}^{-3})^{-1}$.

Dose limits are to be applied to occupational and public exposures but not to medical exposures to a patient. Medical exposures should be justified by weighing the diagnostic or therapeutic benefits they produce against the radiation detriment they might cause. The medical practitioners are assigned the primary task and obligation of ensuring overall patient protection and safety in the prescription of medical exposure. Medical decisions with respect to potential exposures are supported by guidance levels concerned with different procedures (IBSS 1996). The limits of dose contributions listed in ▶ [Table 47.7](#) may be compared to various sources in planned and other situations.

The world average annual impact from natural sources results in 2–3 mSv effective dose; half of that dose derives from the radon component, due to the inhalation of radon daughters (UNSCEAR 2000). The contribution of cosmic rays to the natural background can be assessed at 0.35 mSv per year. The dose consequence of a transmission computer tomography for a typical adult patient is about 50 mGy of absorbed dose in the head, and the average individual dose due to an in vivo diagnostic test in nuclear medicine involves 2–5 mSv effective dose.

■ **Table 47.7**
Dose limits recommended by the ICRP (2007)

Application		Annual limits	
		Occupational	Public
Effective dose		20 mSv averaged over 5 years, but 50 mSv in any single year	1 mSv
Equivalent dose in	• the lens of the eye	150 mSv	15 mSv
	• the skin	500 mSv	50 mSv
	• the hands and feet	500 mSv	–


In an emergency situation, the intervention dose level recommended for acute exposure is between 10 and 50 mSv effective dose to individual members of the public.


47.5.3.1 Action Levels for Radon Concentrations

To avoid an unacceptably high exposure from radon, many countries have introduced limitations on the radon concentration in dwellings for chronic exposures. Action levels have been designated above which protective actions should be carried out to decrease chronic exposure. In most countries, action levels for dwellings are established between 200 and 600 Bq m⁻³ for the annual average radon concentration, based on representative measurements and other parameters.

Formerly, the principal objective of radiation protection was to achieve appropriately safe conditions for all human individuals engaged in activities involving exposures. This concept has been expressed by “if man is adequately protected, then other living things are also likely to be sufficiently protected.” Recently, it has been recognized that this statement might not apply under all conditions, such as situations where humans are absent. Therefore, new approaches are being developed to specify dose quantities, criteria, standards, and guidance to extend the scope of radiation protection to protect nonhuman biota, ecosystems, or the whole environment with respect to radiation exposure (IAEA-TECDOC 1999; UNSCEAR 2008).

47.6 Health Hazards of Radiation Exposure

The biological effects of ionizing radiation appear in several ways. They depend on the absorbed dose, various dose modifying factors, physical conditions of radiation, and endogenous and exogenous chemical-biochemical-biological circumstances. The possible range of doses of biological-medical interest covers several orders of magnitude.  *Figure 47.8* demonstrates these wide possibilities indicating the average natural level, the dose levels that induce cytogenetic effects detectable by chromosome aberration analyses being one of the most sensitive assays to reveal injuries in cells.

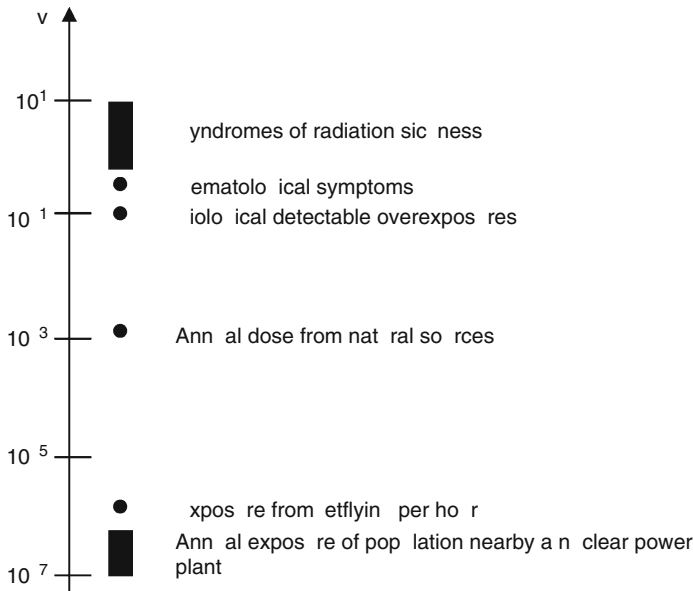
Even higher dose levels induce radiation injuries and illnesses. Below the natural level, a few examples are indicated for population exposure (e.g., normal operation of a nuclear power station with pressurized power reactors and air traveling at about 10–12,000 m). Below the indicated level of inducing chromosome aberrations, only epidemiological investigations are available to score somatic effects like occurrences and frequencies of malignant tumors, that is, cancers. Accordingly,  *Fig. 47.8* indicates that there are differences of several orders of magnitude (approximately 6–7) between doses provoking radiation illnesses and those raising the probability of carcinogenesis.

47.6.1 Deterministic Effects

With respect to radiation protection and radiation hygiene, the biological effects of ionizing radiation are categorized into two groups according to the features of their dose–effect

■ Fig. 47.8

Comparison of dose levels above the natural background provoking radiation injuries and below that population exposure from flying in an airplane or living near a nuclear power plant



relationships, that is, the deterministic and stochastic effects. The deterministic effects appear only above a certain threshold dose, and then the severity increases with dose. This dose–effect relationship is shown in ▶ Fig. 47.9. A few threshold dose-values based on ICRP1984 are shown in ▶ Table 47.8.

Tissue and organ injuries, local injuries, the various syndromes of acute radiation sickness like the bone marrow syndrome, the gastro-intestinal syndrome, the vascular-nervous syndrome, and any other combinations with local radiation burns are the syndromes of deterministic effects (Barabanova et al. 2008).

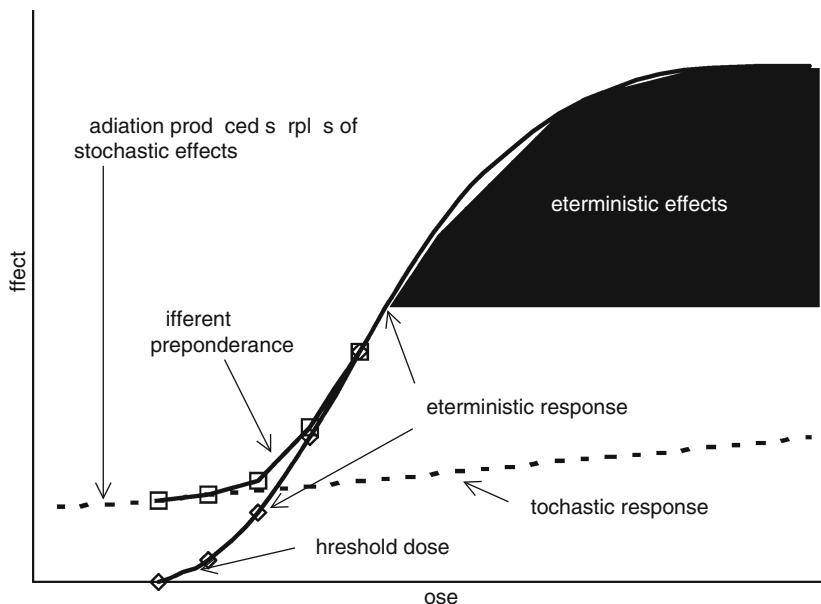
The deterministic effects develop as consequences of injuries or deaths of many cells. Their appearances and severities depend on the radiation sensitivities of the cell components of exposed tissues. The cellular injuries or the radiation-induced functional alterations might serve for the assessment of absorbed doses, too. These parameters are called biological indicators or dosimeters of radiation injury. The radiation sensitivity like mortality of cells can be determined.

For high-LET radiation, the dose-response curve may be exponential, that is, linear on a semi-logarithmic plot. It may be characterized by the slope, which is usually represented by its reciprocal, the dose (D_0) required to reduce survival to 37%.

In the mammalian (including the human) organism, the most sensitive cells are the circulating small lymphocytes and the internal layer of vessels, the endothelial cells. Tissues in decreasing order of radiation sensitivities are the lymphatic tissue, bone marrow, epithelia of stomach and intestines, the gonad cells, the basal layer of skin, the glandular tissues, liver, the connective tissue, muscle, and the nervous tissue.

■ Fig. 47.9

Schematic dose-response curves for the stochastic and deterministic effects of ionizing radiation



47.6.2 Stochastic (Somatic and Genetic) Effects

The stochastic effects are characterized by a linear dose-response without threshold (LNT model) where the probability of the effect is increasing with the dose (see ▶ Fig. 47.9). Accordingly, a certain risk can be attributed to the very low doses, too. The validity of the LNT theory is under wide international debate. The stochastic effects include the carcinogenesis and the hereditary alterations. Hereditary effects, however, in human population could not be shown. Not even on two generations from the survivors of atomic bombing. Hereditary effects exist as demonstrated from radiation biology experiments from lower (microbes) up to higher organisms (plants, mammals). The fortunate lack of effects in human population is probably due to the fact that the injured gonad cells either male or female will not be able to serve as starting points for embryonic developments. It is also possible to consider that the mutations induced by radiation exposure in a population might be rather quickly repaired. Of course, genetic alterations in humans cannot be excluded, though rather large population would be needed for statistically significant evaluation. The nominal risk coefficients for stochastic effects according to ICRP103 are shown in ▶ Table 47.9.

The values for carcinogenesis are average values. The risk of development and lethality of various types of cancers might be different from these average values. In general, the risk of leukemia, lung and breast cancers are 3–5 times larger than that of throat or thyroid. The latency periods are also different: for leukemia, it is approximately 5 years, while for pharyngeal cancer, it is approximately 27 years. Among the survivors in Japan, the leukemia cumulated between 5 and 20 years with an average of 14 years, while for solid cancers, the latency periods were, on average, 25 years.

Table 47.8
Examples of threshold doses for deterministic effects

Tissue and effect	Threshold values for		
	Total equivalent dose received in a single brief exposure (Sv)	Total equivalent dose received in highly fractionated or protracted exposures (Sv)	Annual dose rate if received yearly on highly fractionated or protracted exposures for many years (Sv a ⁻¹)
<i>Testes</i>			
Temporary sterility	0.15	NA ^a	0.4
Permanent sterility	3.5–6.0	NA ^a	2.0
<i>Ovaries</i>			
Sterility	2.5–6.0	6.0	>0.2
<i>Lens</i>			
Detectable opacities	0.5–2.0	5	>0.1
Visual impairment (cataract)	5.0	>8	>0.15
<i>Bone marrow</i>			
Depression of hematopoiesis	0.5	NA ^a	>0.4

^aNA denotes *Not Applicable*, since the threshold is dependent on dose rate rather than on total dose.

Table 47.9
Nominal risk coefficients (10⁻² Sv⁻¹) for stochastic effects

Exposed population	Cancer	Heritable effects	Total
Adult	4.1	0.1	4.2
Whole	5.5	0.2	5.7

Ionizing radiation might induce various types of cancers, and these cannot be distinguished histologically from those induced by other carcinogen exposures. The frequencies depend on genetic factors, the ages of exposed persons, and population groups. The probabilities of cancer induction might be modified by physical and chemical factors either increasing or decreasing it. Among the physical factors, the type of radiation and the dose rates are relevant (the less the dose rate the lower the probability). At high-LET radiation like alpha-radiation the probability of hitting sensitive targets is higher than for low-LET radiation. Among the chemical factors, the presence of sensitizers or protective compounds like antioxidants during irradiation might modify the radiation effect.

47.7 Diagnostic Procedures for Radiation Injuries (Biological Dosimetry)

The biological indicators or biological dosimeters are based on radiation-induced alterations at various levels of biological organization from molecular through subcellular, cellular, tissue, organ to organism level. As there are “protective mechanisms” built-in against all levels of injury, the balance between the injury and biological response will determine the nature and severity of the detectable endpoint. Therefore, the detection of the deterministic effects above the threshold dose and its severity are the main interests for medical points of view in accidental exposures for dose assessment.

The “dose-assessing” function of biological indicators or dosimeters has important roles in the following cases:

1. When physical dose measurement data are not available (e.g., because the injured person has not worn a personal dosimeter).
2. When the dose has been detected and recorded by the personal dosimeter but its reading is not reliable (e.g., due to the nonuniform exposure of the body, the dosimeter was outside the main beam of radiation).
3. When the physical dosimeter was irradiated tentatively or accidentally without the exposure of its owner.
4. When the follow-up is needed in radiation-induced process, including the regeneration. In addition, biological indicators are needed to follow the conditions of radiation-therapy patients.
5. When the compliance has to be assessed for dose limits of radiological protection system for occupational and population categories.

Based on these needs, the general requirements for the indicators are

- Sensitivity to indicate overexposures from acute irradiation in the dose range from dose limits of occupational exposure (>20 mSv) up to accidental overexposures of several grays.
- Proportionality of its changes with the dose absorbed by the cells, tissues, and organisms.
- Ability to react mostly to electromagnetic or particle radiations, that is, possibly no other physical, chemical, or biological factors might provoke the change of the indicator.
- Early appearances of changes – within hours or days – and long duration of signal after irradiation.
- Partial-body exposure should be detectable, preferably with exact localization.
- The method should be applicable to fractionated and chronic exposures.
- All the different radiation qualities should be covered by the method; in particular, exposure due to internal emitters should be measurable.
- The biological material that shows the effect must be readily accessible without extensive invasive methods.
- Evaluation should be either easy and rapid or transferable to machines.
- It has to be easily performable without any further serious burden to the patient.

Until now, however, no such an assay has been developed, that can fulfill all these requirements. Depending on the actual level of scientific knowledge in biology and radiobiology, there were always efforts to use various radiobiological phenomena as biological indicators and it is still an important practical task of radiation biology. It is supposed that no

single indicator will be ever found that will be able to mark the various phases of the complex radiation-induced processes. The solution of the problem probably lies in various observations, tests, and the complex evaluation of several biological signs and symptoms. Therefore, the indicators already existing and those to be developed will form a system for analysis.

In the followings, a brief summary of the presently available techniques is presented.

➤ **Table 47.10** demonstrates the main groups of methods, the combination of which is necessary, as most of them have limited information if alone.

47.7.1 Hematological Indicators

The changes of blood cell counts as hematological indicators in the peripheral blood following irradiation have been studied for many years. The early phase after radiation accident is usually

■ **Table 47.10**
Main groups of biological indicators and dosimeters of radiation effects.

Group	
Hematology	
	Peripheral depletion of cells in the peripheral blood (lymphocytes, granulocytes, platelets, erythrocytes)
	Depletion of cells in the bone marrow
Cytogenetic	
	Development of metaphase chromosome aberrations (dicentrics, rings)
	Increase of numerical aberrations
	Development of interphase aberrations like micronuclei
	Detection of premature chromosome condensation PCC
	Detection of chromosome aberrations by fluorescent in situ hybridization (FISH)
Cytological – molecular	
	Detection of DNA breaks by gel electrophoresis “comet assay”
	Detection of membrane-related phenomena
	● Cell electrophoresis
	● Binding alterations, e.g., lectins
	Detection of loss of gene expressions at glycophorin A locus on erythrocytes
	Detection of altered
	● cellular functions
	● cellular morphology
	● cellular density
	● reproductive capacity

characterized by an initial and temporary granulocyte peak and the early fall in the lymphocyte count. These signs might appear between 0.5 and 1 Gy of low LET irradiation. The sharper the slope of the fall of lymphocyte number and the lower the value of the minimum, the more severe the exposure is. The number of platelets also decreases after about 1 Gy, but this process is more protracted than the decrease of lymphocyte counts. These events, however, can be followed only by rather frequent blood sampling and the dose-dependency shows great differences in various individuals. The hematological data allow judging the individual reactivity both in the acute phase and in the phase of regeneration. The main advantage of blood cell count is that it gives an immediate impression on the severity of an accident particularly during the first 2 days, when no other commonly applicable techniques are available.

47.7.2 Cytogenetic Assays

The chromosome aberration analysis of peripheral blood lymphocytes is a widely recognized tool for assessing the dose (IAEA-TRS 2001). It is especially important to note that at an equivalent dose lower than 1 Sv, the chromosome aberration analysis might be the only possible biological indicator of exposure. It is influenced by the background level of aberrations in the human population and the number of cells that are analyzed per case. Depending on the expertise of the laboratory personnel, sufficiently reliable dose estimates can be made above 0.1–0.15 Gy of low LET radiations or 0.01 Gy fission spectrum neutrons. One of the most important drawbacks of this test is that it is rather time-consuming and due to the need for cell-culturing and scoring, it requires about 3 days to get a result about a person.

47.7.2.1 Lymphocyte Metaphase Chromosomes

The dose–response curve for low-LET induced dicentrics will be a combination of one- and two-track events, with the former being more frequent at low doses and the latter much more frequent at high doses. The dose–response curve is generally assumed to fit the equation

$$Y = A + \alpha D + \beta D^2,$$

where Y is the yield of dicentrics, D is the dose, A is the control background frequency, α is the linear coefficient, and β is the dose squared coefficient. The ratio of α/β of the two coefficients is equal to the dose at which the linear and the quadratic components contribute equally to the formation of dicentrics.

In the further development of chromosome aberration analysis, new results were obtained like the fluorescent in situ hybridization (FISH) technique. Its great potential arises from its unique ability to combine cytological information about chromosome with molecular information about DNA sequence structure. In situ hybridization enables the localization of any particular DNA sequence along metaphase chromosomes. While staining only two or three chromosomes, linear-quadratic dose–effect relationships could be found for stable as well as for unstable chromosome aberrations like translocations and dicentric chromosomes (dicentrics), respectively, in circulating lymphocytes gamma-irradiated in vitro. The main advantage of this new staining technique is that the stable aberrations can be detected long after the irradiation. The yield after a given dose was found to be between 1.5 and 2 times higher than that of dicentrics. Certain limitation of the application might be

that the base value of the population is approximately an order of magnitude higher than that for dicentrics.

47.7.2.2 Lymphocyte Micronuclei

In recent years, a large number of references has been accumulated indicating the scoring of human lymphocytic micronuclei as a source of information for cytogenetic injury following ionizing radiations, as well as chemical toxicants. Well-reproducible dose–effect relationships could be established, which were found to be linear-quadratic in a dose range of 0.25–4 Gy. The data on the base line values in the population are cumulating also, accordingly, the dose assessments are getting more reliable. The relatively simple performance of the test could assist in testing combined effects and it gives a hope to assess individual radiosensitivities.

47.7.2.3 Premature Chromosome Condensation (PCC)

Lymphocytes isolated from irradiated peripheral blood are fused with mitotic Chinese hamster ovary cells using polyethylene glycol. The damage in their prematurely condensed chromosomes is shown to be a sensitive indicator of exposure. Radiation effects manifest themselves as fragments, that is, chromatid material in excess of 46 chromatid chromosomes is counted and used to estimate the cytogenetic damage. PCC can be used as a biodosimeter in non-stimulated human lymphocytes, thus avoiding complication arising from cell cycle delays and interphase death at high doses. The technique is rather efficient to detect proportion of undamaged cells. The initial damage can be determined immediately after exposure. Linear-quadratic dose–effect relationship could be found. A further step was introduced in painting the chromosomes when the FISH technique was combined with PCC. The dose–response curve for fragment induction was linear within a couple of hours after exposure. Later, it became linear-quadratic. The approach indicates that painting the prematurely condensed chromosomes might be useful for biological dosimetry.

There are several other assays in development, which might become in the future proper biological indicators or dosimeters in radiation accidents. These are, for instance, various gene expression profiles, cytological and molecular biomarkers, and clustered DNA lesions.

47.8 Management of Overexposures

The early recognition and a quick initial response to an accidental radiation injury are important in diagnosis, in treatment planning, and assessing the prognosis (🔗 [Table 47.11](#)).

For all of these tasks, properly prepared personnel as well as medical facilities are necessary. The exposure can be

- External to the body, in which case it may affect the whole body or may be limited to a part of the body, or
- Internal due to contamination with radioactive materials, if ingested, inhaled, or deposited in wounds.

■ Table 47.11

Guide for the management of radiation injuries based on early symptoms (IAEA-SRS2 1998)

Clinical signs		Corresponding dose (Gy)		Decision
WBE	LE	WBE	LE	
No vomiting	No early erythema	<1	<10	Outpatient with 5 week surveillance period (blood, skin)
Vomiting 2–3 h after exposure	Early erythema or abnormal sensation 12–24 h after exposure	1–2	8–15	Surveillance in a general hospital (or outpatient for 3 weeks followed by hospitalization if necessary)
Vomiting 1–2 h after exposure	Early erythema or abnormal sensation 8–15 h after exposure	2–4	15–30	Hospitalization in a haematological or surgical (burns) department
Vomiting earlier than 1 h after exposure and/or other severe symptoms, e.g., hypotension	Early erythema, within the first 3–6 h (or less) after exposure of skin and/or mucosa with oedema	>4	>30	Hospitalization in a well equipped haematological or surgical department with transfer to a specialized center for radiopathology

WBE: whole body exposure. LE: local exposure.

Exposure can be acute, protracted, or fractionated. It can occur alone, or be combined with other injury, such as trauma, thermal burn, and toxic effects.

Recognizing radiation injuries can be performed by clinical manifestations and laboratory assays. (For the latter, see the chapter on biological indicators.)

Following a high-level accidental exposure to radiation, injuries evolve over time in distinct phases. The length and time of the occurrences of the phases depend on the dose. Low doses like below 0.2 Gy do not produce observable effects.

A typical course following a whole body exposure to a source of penetrating radiation involves an initial prodromal phase with symptoms such as nausea, vomiting, fatigue, and possibly fever and diarrhoea, followed by a latent period of varying lengths. A period of illness follows, characterized by infection, bleeding, and gastrointestinal symptoms. Problems in this period are due to a deficiency of cells of the haematopoietic system, and with higher doses, to loss of cells lining the gastrointestinal tract.

A local exposure, depending on dose, can produce signs and symptoms in the exposed area such as erythema, oedema, dry and wet desquamation, blistering, pain, necrosis, gangrene, or epilation. Local skin injuries evolve slowly over time – usually weeks to months – may become very painful, and are difficult to treat by usual dermatological methods. Approximately above 20 Gy of local dose, irreversible alterations might occur; below this dose healing can be expected. Partial body exposures result in a combination of varying symptoms as mentioned above, the type and severity of which depend on the dose and volume of the exposed part of the body.

Additional symptoms may be related to location of the tissues and organs involved. There are usually no early symptoms associated with internal contamination unless the intake has been very high, which is extremely rare. If this has occurred, it will normally be obvious to the person concerned.

There are a few important rules to be considered in case of an accident when radiation injury is suspected as follows:

- If the person involved has a conventional injury or illness, save his/her life and treat him/her as normally required. Note that radiation does not produce life threatening early symptoms.
- Be aware that a radiation-injured person does not present a health risk to the personnel handling him/her.
- If contamination is suspected, avoid spread of material by using isolation procedures. The level and contamination should be monitored.
- Do a prompt complete blood count, repeated in 4–6 h within the first day.
- Look for a decrease in the absolute lymphocyte count if exposure was recent. If at the same time, the initial white blood cell and platelet counts are abnormally low, consider the possibility of an exposure 3–4 weeks earlier. Additional daily blood counts will be needed. The cytogenetic biological dosimetry through chromosome aberration analyses should be done as early as possible. A careful differential diagnosis is the task of the physician based on the anamnesis, physical dosimetry data, clinical observation on the patient, and laboratory assays.

An important point in the preparedness is to have satisfactory information on the name, address, and phone number of proper health institution to be called as soon as possible. The main procedures in the therapy (🔗 [Table 47.12](#)) involve antibiotic treatment against bacteria, viruses, and fungi; provision of blood preparations for platelets, red blood cells; application of cytokines for stimulation of blood formation; isolation of the person under aseptic conditions; and feeding the person with sterilized food and water. Provide proper care to the body and soul.

47.9 Dose–Response Relationships

For radiation protection purposes, the biological effects of ionizing radiation are grouped into two main categories, the stochastic and deterministic effects. In both cases, the effects are related to the absorbed doses. Therefore, the knowledge on the dose–response relationships is essential for risk assessment.

47.9.1 Biological Effects of Low Radiation Doses

The effects of low doses are considered by observations in epidemiology, cellular radiation biology, and microdosimetry. The levels according to these views are demonstrated in 🔗 [Table 47.13](#).

Based on epidemiological data of radiation-induced cancer occurrences, various authors agree that low dose is below 200 mGy as under this level the statistical evaluation of data becomes more and more uncertain.

■ Table 47.12

Principal therapeutic measures for acute radiation syndrome (ARS) according to degree of severity (IAEA-SRS2 1998)

Whole body dose (Gy)	1–2	2–4	4–6	6–8	>8			
Degree of severity of ARS	Mild	Moderate	Severe	Very severe	Lethal			
Medical management and treatment	Outpatient observation for maximum of 1 month	Hospitalization						
		Isolation, as early as possible						
		G-CSF or GM-CSF as early as possible (or within the first week)	IL-3 and GM-CSF					
		Antibiotics of broad spectrum activity (from the end of the latent period) Antifungal and antiviral preparations (when necessary)						
		Blood components transfusion: platelets, erythrocytes (when necessary)						
			Complete parenteral nutrition (first week)					
			Metabolism correction, detoxication (when necessary)					
			Plasmapheresis (second or third week)					
			Prophylaxis of disseminated intravascular coagulation (second week)					
				HLA-identical allogene BMT (first week)	Symptomatic therapy only			

BMT: bone marrow transplantation; G-CSF: granulocyte-colony stimulating factor; GM-CSF: granulocyte macrophage-colony stimulating factor; IL-3: interleukin.

Certain cellular reactions like enzyme inductions, DNA-repair processes, adaptive responses, chromosome aberrations, etc., could already be observed between 10 and 100 mGy by various sensitive assay techniques (🔗 Table 47.14). However, this dose range is considered low. In general, the doses causing fully recoverable cellular damages or alterations might be considered low doses in the cell biology. In microdosimetry, the low dose is defined when 20% of targets, that is, cells in tissue are hit.

Among the low dose radiation-induced cellular alterations, special interest has been focused recently toward the hormesis and adaptive responses. Although these phenomena, that is, inducing stimulatory or beneficial effects are more and more targets for research, no direct evidence is available for their possible impact on human radiation protection.

It is also worth mentioning that when individual radiosensitivity of persons was studied through the frequencies of radiation-induced lymphocytic micronuclei following in vitro irradiation of individual blood samples, below 200 mGy the responses were found to be

Table 47.13
Dose ranges considered low by various approaches to biological effects of ionizing radiation

Approaches	mGy, mSv
For stochastic effects as carcinogenicity	200
For gamma and X-rays	200
For neutrons	50
For cellular reactions	10–100
By microdosimetrical consideration	When less than 20% of gross sensitive volume – GSV – will be hit once
For comparison:	
The average natural background	
In a year	3
In the lifetime of a person	50–200
“Insignificant individual dose”	0.01
“De minimis” dose	0.01

unrelated to the absorbed dose. These data suggest the importance of other factors in individual sensitivity besides the dose. On the other hand, the data point to the existence of dose–effect modifying biological factors, making the response statistics uncertain like in epidemiology below the same dose range.

In the foregoing, the dose range was given in mGy. It has to be recalled that the natural background from cosmic and terrestrial sources is approximately 3 mGy on world average. This level means one hit per cell per year for a person. For comparison of considerations on low doses, it has to be noted that earlier the opinion was that 10 μ Sv for an individual is an “insignificant dose.” In other words, 10 μ Sv is a “*de minimis* dose.” The expression comes from the language of jurisprudence, that is, “*De minimis non curat lex*,” – the law does not care about minimal causes or effects. At dose levels when “the collective dose committed by one year of performance of the practice is no more than about 1 man-sievert, or an assessment for the optimization of protection shows that exemption is the optimum option,” the risk assessments based on the collective dose is not justified (IBSS 1996).

47.9.2 The LNT Theory and Its Critical Review

The biological effects of ionizing radiation for radiation protection considerations are grouped into two categories: the deterministic and the stochastic ones (► Fig. 47.9).

The deterministic effects occur when above a certain “threshold”, an appropriately high dose (above 500–1,000 mSv) is absorbed in the tissues and organs to cause the death of a large number of cells and consequently to impair tissue or organ functions early after exposure. The severity of injury depending on the absorbed dose according to an s-shaped dose–response curve might be manifested in the various syndromes of radiation illness, that is, the bone

■ Table 47.14

Examples for cellular responses and alterations provoked by low doses

Response/alteration	Dose-range (mGy)
Free radicals	
Increases of production of granulocyte oxidant	0.1–1
Increases of superoxide dismutase	100
Increases of oxidative stress	50
Cellular responses	
Lymphocyte mitogenic stimulation by lectins increases	10–40
Thymidin kinase activity increases	10
Prospholipase C, increases	
Adenylatecyclase increases	2.5
Spleen colony formation stimulation	6
Mutagenic alternations	
Lymphoblast 6-thioguanin resistance (6-TGr) formation increases	10
Nuclear structure	
Chromatin conformation alteration	40–250
Cytogenetic alterations:	
Increases of micronucleus formation	>100
Increases of dicentric aberrations	
Cell membrane structure and function	
Lipid composition changes	10–100
Antioxidant capacity decreases	10–100
Micromorphological alterations	250
Adaptive response develops	5–10

marrow, the gastro-intestinal, and the central nervous system-vascular syndromes. The effects can be detected by laboratory and clinical techniques.

The stochastic effects might occur following low doses (below several tens or 100–200 mSv). The probability of consequences increases with the dose and the relationship between dose and effect is assumed linear. Accordingly, not having a “threshold” dose a certain risk – albeit very small – can be attributed to any low dose.

Such late effects might be the development of malignant (cancerous) diseases and of the hereditary consequences. Here, it has to be mentioned that in human populations, hereditary effects could not be detected even in the offspring of the large population of A-bomb survivors in the first two generations. The possibility of hereditary alterations is known only from experimental observations in radiation biology.

The model for assessing the detrimental health effects used for the deterministic effects is the nonlinear-threshold (NLT) model, while for the stochastic effects the linear-non-threshold “LNT” model. In the low-dose dilemma, the problem raised is whether the use of the LNT model is justified to attach any health risks to low doses.

The arguments of those who oppose the LNT model can be summarized as follows, though not necessarily including all the available reasoning:

- Below 200 mSv, no cancer cases were found in a significantly increased frequency among the A-bomb survivors.
- No higher risk could be detected at high natural background areas though they might be 3–10 times higher than the average level.
- The carcinogenesis is not a first order kinetic process, that is, the hit of cellular genes at sensitive sites or the malignant transformation of one or a few cells does not lead necessarily to the clinical manifestation of a malignant disease.
- Repairing a few single strand breaks (SSB) or double strand breaks (DSB) following a damage in the DNA caused by low doses does not overload the repair capacity of a cell: the metabolism of cellular DNA and the repair of damages induced by other endogenous or exogenous factors are running with much higher intensity.
- A real threshold might appear when the latency period is long enough compared with the life time of an individual by low dose exposures no detectable biological or health effects are provoked, the LNT model is for regulatory purposes, as a tool for risk assessment, but it is not verified scientifically or statistically in epidemiology.

The arguments of those who are in favor of keeping this model further as valid for the risk assessment are mainly the followings:

- The linearity is known and it has a great tradition in radiation biology since the detection of the genetic effects on *Drosophila*.
- For stochastic effects, the LNT model is recommended by the ICRP and it is widely used in assessment of health detriment.
- In cellular radiation biology including observations on the survival of cells in culture, formation of cytogenetic aberrations and mutations, many results can be fitted to a linear dose–response relationship or linear-quadratic one when the investigations are extended to higher doses, that is, approximately above 1 Gy.
- Recent data indicate significant increase of risk for thyroid cancer, breast cancer, and malignancy following in utero irradiations also in the range between 50 and 100 mGy.
- Even among the A-bomb survivors, the risk of cancer increased already above 50 mGy significantly, though it is obvious that the risk below 100 mGy is really small.
- Among the “liquidators” of the Chernobyl, accident site increases of malignant tumors of the digestive system were observed up to 1995. The average dose of the studied cohort was 108 mGy.
- It is also repeatedly mentioned that the consequences of DSB if not repaired are more serious than the consequences of SSB-s.

It is foreseen that the multisided debate will be continued but at this stage some views can be delineated as *conclusions*: Further research and investigations, on the cell biological as well as on the epidemiological aspects of health consequences of low doses are necessary.

It has to be realized that a biological response itself experienced following rather low doses does not mean detrimental health consequences. The LNT model might be too conservative and unjustified, but at present it seems to be safe enough to ensure the safe application and uses of ionizing radiation and nuclear energy. The rejection of the LNT model and the acceptance of a threshold in cases of stochastic effects would raise many questions concerning the regulatory action. These foreseen questions like the safe thresholds

for late effects, for different population groups, for various practices, etc., are hardly answerable at the moment. It seems to be easier, however, to reach an agreement on the level of acceptable risk instead of the risk threshold dose.

References

- Barabanova A, Baranov A, Bushmanov A, Guskova A (2008) In: Kotenko K, Bushmanov A (eds) *Radiation effects in man*. Medicina Publhaus, Moscow
- Choppin GR, Rydberg J, Liljenzin JO (1995) *Radiochemistry and nuclear chemistry*. Butterworth-Heinemann, Oxford, pp 166–183
- Dennis JA, Stather J (eds) (1997) Non-ionising radiation, special issue. *Radiat Prot Dosim* 92(3/4), pp 84–105
- Eckerman KF, Ryman JC (1993) External exposures to radionuclides in air, water and soil. Federal guidance report no. 12. US Environmental Protection Agency, Washington
- IAEA-SRS 2 (1998) Diagnosis and treatment of radiation injuries. Safety reports series no. 2. International Atomic Energy Agency, Vienna
- IAEA-SRS (2001) Generic models for use in assessing the impact of discharges of radioactive substances to the environment. Safety reports series No 19. International Atomic Energy Agency, Vienna
- IAEA-TECDOC (1999) Protection of the environment from the effects of ionizing radiation. Technical document 1091. IAEA, Vienna
- IAEA-TRS (2001) Cytogenetic analysis for radiation dose assessment, a manual. Technical report series no. 405. International Atomic Energy Agency, Vienna
- IBSS (1996) International basic safety standards for protection against ionizing radiation and for safety of radiation sources. Safety series no. 115. IAEA, Vienna
- ICRP (1977) Recommendations of the International Commission on Radiological Protection (ICRP). ICRP publication no. 26. Pergamon, Oxford
- ICRP (1984) Non-stochastic effects of ionising radiation. *Annals of the ICRP* publication no. 41. Pergamon, Oxford
- ICRP (1991) Recommendations of the International Commission on Radiological Protection (ICRP), ICRP publication no. 60. Pergamon, Oxford
- ICRP (1994) Age-dependent doses to members of the public from intake of radionuclides: part 2. Ingestion dose coefficients, ICRP publication no. 67. Pergamon, Oxford
- ICRP (2007) The 2007 recommendations of the International Commission on Radiological Protection. *Annals of the ICRP* publication 103. Elsevier, Amsterdam
- ICRU (1980) Radiation quantities and units. International Commission on Radiation Units and Measurements (ICRU), ICRU report no. 33. Pergamon, Washington
- Jacob P, Rosenbaum H, Petoussi N, Zankl M (1990) Calculation of organ doses from environmental gamma rays using human phantoms and monte carlo methods: part II. Radionuclides distributed in the air or deposited on the ground, GSF-Bericht 12/90. GSF, Neuherberg, Germany
- Jacquez JA (1996) *Compartmental analysis in biology and medicine*, 3rd edn. BioMedware, Ann Arbor
- Mosely H (1988) Non-ionizing radiation. Adams Hilger, Bristol
- Thorne M (2001) Assessing the radiological impact of releases of radionuclides to the environment. In: Van der Stricht E, Kirchmann R (eds) *Radioecology: radioactivity and ecosystems*, Chapter VII. Fortemps, Liege, pp 391–446
- UNSCEAR (1996) In: United Nations Scientific Committee on the Effects of Atomic Radiation (ed) *Effects of radiation on the environment. Annex to sources and effects of ionizing radiation*. UN, New York
- UNSCEAR (2000) In: United Nations Scientific Committee on the Effects of Atomic Radiation (ed) *Dose assessment methodologies. Sources and effects of ionizing radiation*, vol 1 Annex A. UN, New York, pp 19–82
- UNSCEAR (2008) In: United Nations Scientific Committee on the Effects of Atomic Radiation. *Effects of ionizing radiation on non-human biota*. Annex E. UN, New York (in press)
- Watson EE (1994) The MIRD internal dose methodology. In: Raabe OG (ed) *Internal radiation dosimetry*, Chapter 4. Health Summer School, Madison, pp 335–374
- Wood J (1982) Computational methods in reactor shielding, Chapter 5. Pergamon, Oxford, pp 119–191
- Zanzonico PB, Brill AB, Becker DV (1995) Radiation dosimetry. In: Wagner HN, Szabó Z, Buchman JW (eds) *Principles of nuclear medicine*, Chapter 9. Saunders, Philadelphia, pp 106–134



48 Radiation Detection

H. C. Griffin

University of Michigan, Ann Arbor, MI, USA

48.1	<i>Introduction</i>	2260
48.2	<i>General Properties of Detectors</i>	2261
48.3	<i>Detectors Based on Gas Ionization</i>	2262
48.3.1	Ionization Chambers	2262
48.3.2	Geiger-Müller	2263
48.3.3	Proportional Counters	2263
48.3.4	Avalanche Detectors	2265
48.4	<i>Semiconductors</i>	2265
48.4.1	Si for Alphas	2266
48.4.2	Si for Photons	2267
48.4.3	Ge for Photons	2268
48.4.4	Other Semiconductors	2278
48.5	<i>Scintillators</i>	2278
48.5.1	NaI(Tl)	2280
48.5.2	Plastics	2281
48.5.3	Liquid Scintillators	2281
48.6	<i>Neutrinos and Fission Fragments</i>	2285
48.7	<i>Composite Detectors</i>	2285
48.8	<i>Editors' Notes</i>	2286

Abstract: Most radiation related to nuclear properties is outside the visible part of the electromagnetic spectrum or involves submicroscopic particles, hence is invisible. Detectors – devices to sense the radiation, and perhaps measure its properties – are essential. The emphasis in research has moved from the characterization of radioactivity, through simple nuclear reactions, to explorations of the extremes of nuclear matter, but the central importance of suitable radiation detectors has persisted. This chapter emphasizes detectors associated with measurements of radioactivity, as opposed to nuclear reactions. Thus, much of the current creative work is excluded, but otherwise the scope of these volumes would at least double. Detectors are classified broadly as based on ionization of gases, conduction in semiconductors, or scintillation. The concluding section is an introduction to systems based on two or more components of one of these basic types.

48.1 Introduction

Radiation detectors have played and continue to play an essential role in the study and use of nuclear transformations. The goal of this chapter is to describe the general characteristics of radiation detectors with emphasis on detectors for radiations associated with radioactive decay. These radiations include photons, electrons (both negative and positive), and energetic atomic ions (primarily, but not exclusively, α particles). The detectors can be classed according to the physical form of the detector (gas, liquid, solid), the nature of the signal (ions, current, light), or the purpose (simple detection, spectroscopy, or diverse other roles).

The relevant part of the energy spectrum (for photons and electrons) extends from low energies of a few keV to high energies of about 10 MeV. The upper value is related to alternatives available to excited nuclei. When excitation energies are greater than nuclear binding energies, it is more likely for the nucleus to come apart than for a photon or β particle to be created. The lower value is also related to alternative deexcitation mechanisms. Photon emission is retarded when the size (wavelength) of the photon is large compared with the size of the radiator (nucleus). Electron and neutrino emission are retarded when the momentum phase space is severely limited. There is an effective lower limit for α particles because of the nuclear Coulomb barrier.

For the user, the primary questions may be what radiation to detect and what properties to measure. Is it sufficient to measure the amount of radiation without regard to type? Is it desired to discriminate among types? Is it important to measure the energy of the radiation? Is time dependence important?

Radioactivity was discovered by detecting the radiations emitted by samples of uranium. The detector was photographic film, and the radiations were primarily electrons (β rays) emitted, not by uranium, but by $^{234\text{m}}\text{Pa}$ in equilibrium with ^{234}Th , in turn in equilibrium with the decay of ^{238}U . It is unlikely that these facts would have been discovered without improved detectors – first electroscopes and then Geiger-Müller (GM) detectors. Each of these detectors is still in common use. Electroscopes are used as personal dosimetry devices, such as for a visitor to a facility where exposure to radiation is possible. GM detectors are used to measure ambient radiation levels and to locate surface contamination resulting from radiochemical work. Although new detectors, combinations of detectors, large arrays, on-board logic, etc. are what have carried investigations of nuclear matter to the extreme, they must be understood in terms of basic, simple types. That understanding is the object of this chapter.

Two types of information sources have been used: textbooks, and manufacturers' catalogs and specification sheets. The textbooks include Glenn Knoll's *Radiation Detection and Measurement*, 3rd edn (Knoll 2000) and Debertin and Helmer's *Gamma- and X-ray Spectrometry with Semiconductor Detectors* (Debertin and Helmer 1988). The former describes detectors and their principles so that one might design or modify detectors for specific purposes, as well as use them intelligently; check for a 4th edn. The latter gives the principles and procedures for state-of-the-art metrology with available detector systems. Current manufacturer information should be consulted to find out "what is available." Properties of individual nuclides are taken from current compilations (Browne et al. 1986; Firestone et al. 1996; Baum et al. 2002).

48.2 General Properties of Detectors

A typical detection system consists of the following parts.

Detector. This is the "transducer" that converts the nuclear radiation, such as an energetic α particle, into, for example, a number of electron-hole pairs in a semiconductor. It may also include shields, collimators, spacers, etc.

Power supply. This permits the detection event to trigger the release of a larger, perhaps proportional, amount of energy. In the example of an α particle detected in a semiconductor (Si diode), a voltage is used to sweep out the electrons and holes before they can recombine.

Additional mode converters. These convert current into voltage, step functions into pulses, voltage into a binary number, etc. They include preamplifiers, amplifiers, discriminators, and analog-to-digital converters (ADCs).

Recorder. This might be the product of a chemical reaction, an image on paper, or a complex file of data.

Another way to understand radiation detection is by a case method and the factors that influence the quality of the result. In general, the factors are the following.

Attenuation. If a measurement seeks to identify radionuclides and measure how much of each is present, it is important to know what fraction of the initial radiation reaches the sensitive volume of the detector. This also includes attenuation in the source, the outer parts of the detector system, and the medium between source and detector.

Uncertainties in position. In most cases, nuclear radiation is emitted in all directions from the source, and the fraction reaching the detector depends on relative positions.

Statistics. If each detection event leads to a "count," and the measurement as a whole depends on the relation between a sample and the larger population, precision requires large numbers of events.

Efficiency calibration. What fraction of the radiation would lead to a count if there were no uncertainties in absorption or position?

Dead time. Does the detector ever miss counts, perhaps because it is "busy" processing another event?

Coincidence summing. Some radioactive materials emit two or more radiations in rapid succession, and the detector misses the parts and sees the whole. The missing parts must be accounted for.

Pile-up. When the count rates are high, by chance two radiations may be sensed as one. Again, corrections for the missing parts, and perhaps the unexpected whole, must be made.

In the following sections, various types of detectors are described, and in a few cases the detailed considerations required for accurate quantitative work are given.

48.3 Detectors Based on Gas Ionization

Most nuclear radiation is classified as “ionizing radiation” because interaction with individual atoms or molecules generally transfers enough energy to exceed the ionization potential of the absorber. Some of the earliest replacements of photographic detectors were based on this ionization process, and developments continue.

The main subclasses of detectors depend on how the ions are collected and measured. If a modest voltage gradient is imposed on the gas, some of the electrons and ions produced by radiation will be swept out, and some will recombine and ultimately produce heat. As the gradient is increased, recombination will diminish and the ion current will increase. If and when recombination is negligible and the current approaches an asymptote, the system functions as an ionization chamber.

If the gradient becomes large enough that an electron gains enough energy between collisions with gas molecules to ionize the struck molecule, the number of ions will increase. Under appropriate conditions, the increase will be approximately the same for all initially formed ions, and the system functions as a proportional counter. In this region, an increase in gradient will increase the multiplication factor while maintaining proportionality.

At higher gradients, the proportionality will be lost. This will certainly be the case if there is an electric discharge, a spark. However, some combinations of electrode geometry and gas composition lead to propagation of the discharge so that a nearly constant pulse is produced, regardless of the amount of original ionization. This is the Geiger (or Geiger-Müller) region of operation.

Detectors based on ionization continue to be developed, and they do not always fit these simple categories, but these categories provide a foundation for selecting and using modern ionization detectors.

48.3.1 Ionization Chambers

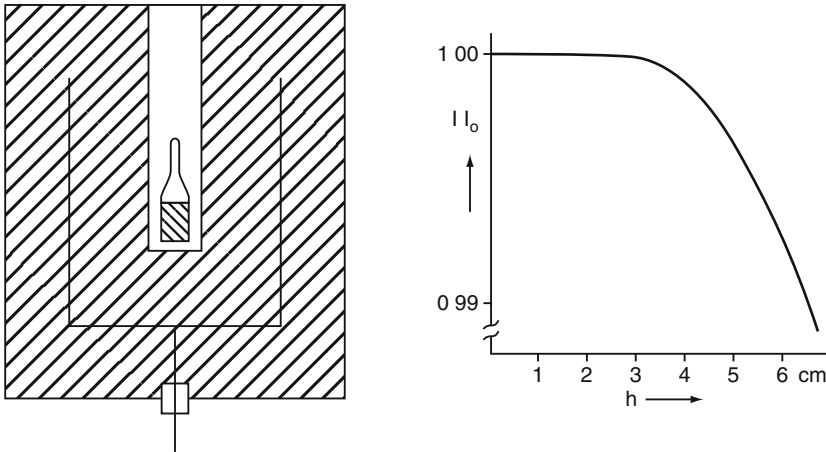
There are few restrictions on the geometry of the gas and electrodes in ionization chambers, but they are less likely to be operated in pulse mode than are the other types. In effect, one measures the electrical resistance of the gas under conditions of saturation current.

This saturation collection current finds two important applications – measurement of high radiation fields without paralysis and measurement of intensities of extended photon emitters. A GM detector (see next section) is a useful survey meter for modest levels of radiation, but in high radiation fields a GM detector becomes paralyzed. Ionization chambers based on continuous current do not have this deficiency and even benefit from the more robust current.

A therapeutic dose of a radiopharmaceutical is too active to count individual decays, but quite sufficient to produce robust continuous ionization current. It is important that amount of radioactive material be known quite accurately. ➤ *Figure 48.1* shows the geometry of an ionization chamber designed to measure the activities of, for example, batches of radioactive material packaged in a standard way. Although the detector can be stable over long periods of time, variations in absorption in the samples must be minimized. The system must be calibrated for each radionuclide and each geometry of container and contents.

■ Fig. 48.1

Schematic of ionization chamber used to measure packaged doses. The textured area shows the volume sensitive to ionization events. The graph shows detection efficiency versus sample position (From Weiss 1973; used by permission of Elsevier)



48.3.2 Geiger-Müller

If the electric field in a cylindrical chamber (see ► Fig. 48.2) is high enough and the gas has appropriate properties (not discussed here), each ionization event in the sensitive volume will lead to discharge the entire length of the anode. The advantage is that a large signal is produced. It can be registered with a simple electronic circuit. The disadvantage is that the discharge in effect enlarges the anode and changes the voltage gradient so that these large discharges cannot occur until the slow positive ions migrate toward the cathode. There is a rather long time ($\gg 10 \mu\text{s}$) during which the detector is dead. This dead time is “paralyzable.” If such a detector is in a very high radiation field, counting can cease entirely – not a good thing if the device is intended to warn of dangerous radiation conditions. However, when used with discretion, GM detectors are inexpensive, effective devices.

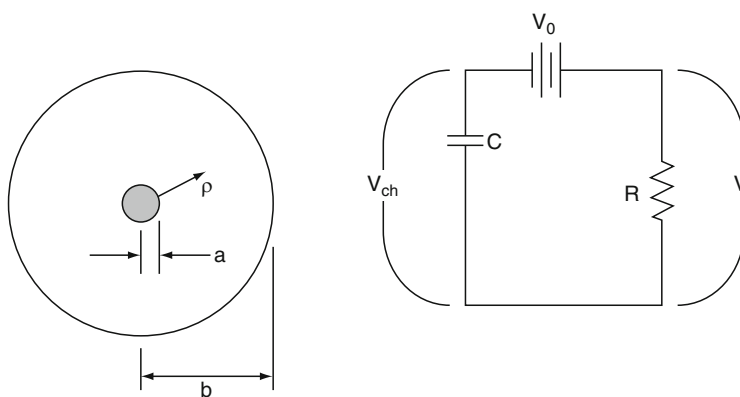
48.3.3 Proportional Counters

The development of proportional counters accelerated when electronic instrumentation permitted realization of the advantages (energy proportionality, fast response, negligible dead time) of these devices. Two (of many) implementations are given in ► Figs. 48.3 and ► 48.4.

Many radioactive materials in the natural decay series and in the nuclear fuel cycle are α emitters for which very little radiation escapes a macroscopic sample. If radiochemistry is used to isolate a particular element, and its mass is small, the solid can be deposited on a metal planchet (e.g., by evaporating a small volume of liquid containing the purified material) and counted with the planchet forming the bottom of the gas chamber such as shown in ► Fig. 48.3. Under these conditions, the α detection efficiency can be about 52% and the β detection efficiency about 80%. (Some β particles that are emitted toward the planchet are scattered into the gas volume.)

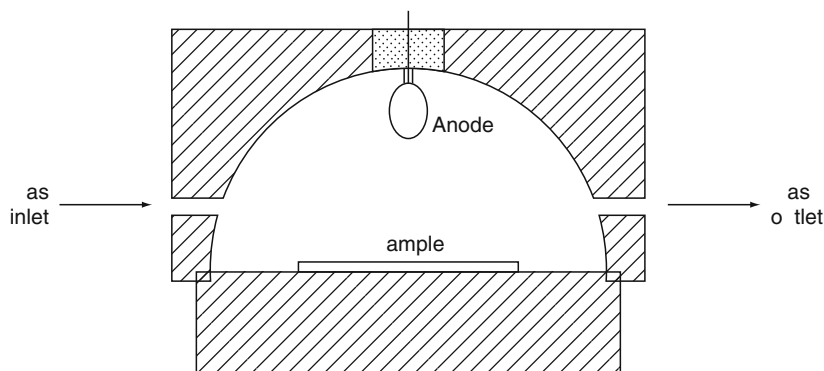
■ Fig. 48.2

Cylindrical geometry for detector based on gas ionization. (This type of design is used both in Geiger-Müller and proportional counters.) The cross section on the left defines the size of the inner and outer electrodes. When a is quite small compared with b , avalanches can be confined to a small volume around the central, positive electrode. Most of the interactions with radiation take place outside this volume, and the primary electrons are swept into the region, where they are subject to the same degree of multiplication, an important property of proportional counters. Hence, at moderate voltages and using an appropriate filling gas, most of the pulse heights are proportional to the number of primary ions. A simplified diagram of the power supply (V_0), detector (capacitor C), and the development of signals (voltage V_R developed when current flows through the detector) is given on the right (From Knoll 2000; used by permission of Wiley)



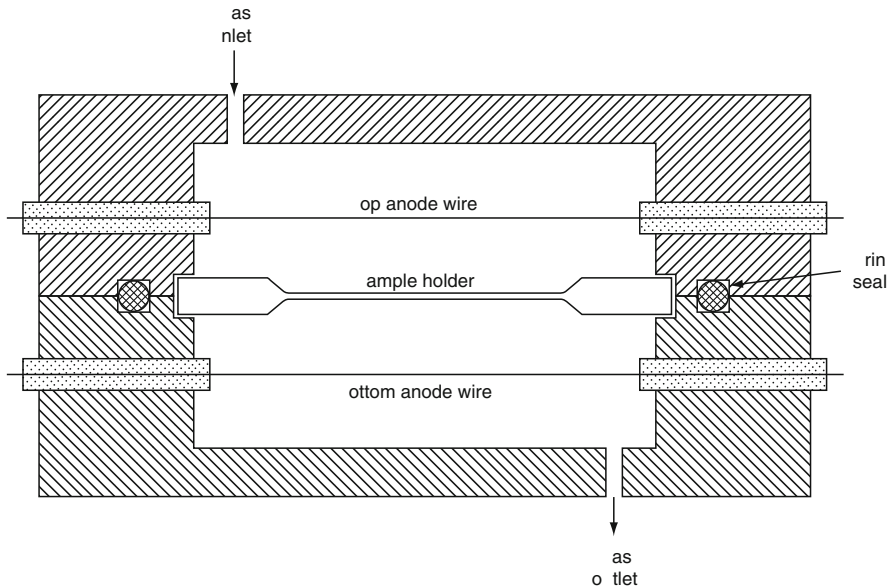
■ Fig. 48.3

Proportional counter with 2π geometry. The electric field near the anode is not as uniform as it could be, and energy resolution is modest. However, effective discrimination between α particles, which deposit most of their considerable energy in the sensitive volume, and γ or β rays can be obtained (From Knoll 2000; used by permission of Wiley)



■ Fig. 48.4

Proportional counter with 4π geometry (From Knoll 2000; used by permission of Wiley)



When it is important to know the total disintegration rate of a sample accurately and the material can be obtained in a thin deposit, it can be counted in a 4π geometry with a detection efficiency close to 100%. This type of detector is shown in ► Fig. 48.4.

Proportional counters filled with BF_3 or ^3He can be used to detect low-energy neutrons. The reaction $^{10}\text{B}(\text{n},\alpha)^7\text{Li}$ has a large cross section for thermal neutrons, and the charged reaction products produce a large, distinctive pulse. The cross section drops as energy increases, but it remains useful to keV neutron energies. Similarly, the $^3\text{He}(\text{n},\text{p})^3\text{H}$ reaction has a large cross section, produces a distinctive pulse, and can be used for spectroscopy.

48.3.4 Avalanche Detectors

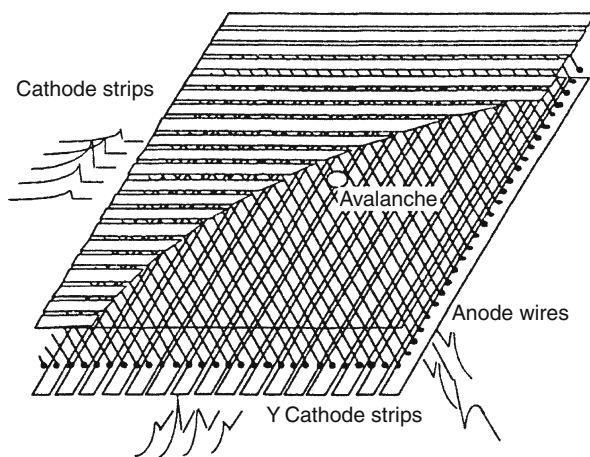
Arrays of proportional counters can be used to measure position as well as energy. Such an array is shown in ► Fig. 48.5. More limited, but useful, amounts of gain can be obtained with the uniform electric field between parallel plates. These PPAC's (parallel plate avalanche counters) are used to detect and time individual particles in beams at accelerators. In this geometry, as usual, the avalanches involve electrons. The gain depends on where the primary electron was created. In typical applications, all particles pass through the gas and have the same path length, so the pulses are proportional to the energy deposited, albeit weighted by the deposits near the cathode.

48.4 Semiconductors

The motivation to produce transistors and integrated circuits led to improvements in semiconductor materials, which led to improved detectors. Semiconductors might be considered

■ Fig. 48.5

Multi-wire proportional counter for energy and 2D spatial resolution (From Sauli 1994)



“solid state ionization chambers” with several advantages over gas devices. The energy required to produce an electron–hole pair in a semiconductor is about a tenth that required to produce an ion pair in a gas. This increase in number of carriers leads to improved statistics and better energy resolution.¹ The efficiency of energy to carrier conversion constrains the relative variation in the number of carriers for a given energy deposit. The absence of windows to contain a gas or of a gas supply is also advantageous.

The most common, and therefore important, semiconductors are silicon and germanium. These materials have good mobilities of carriers, very similar mobilities for electrons and holes, and low trapping. They are chemically stable and can be fabricated in a variety of shapes, including very thin sheets (most commonly for silicon) and large crystals (mainly germanium).

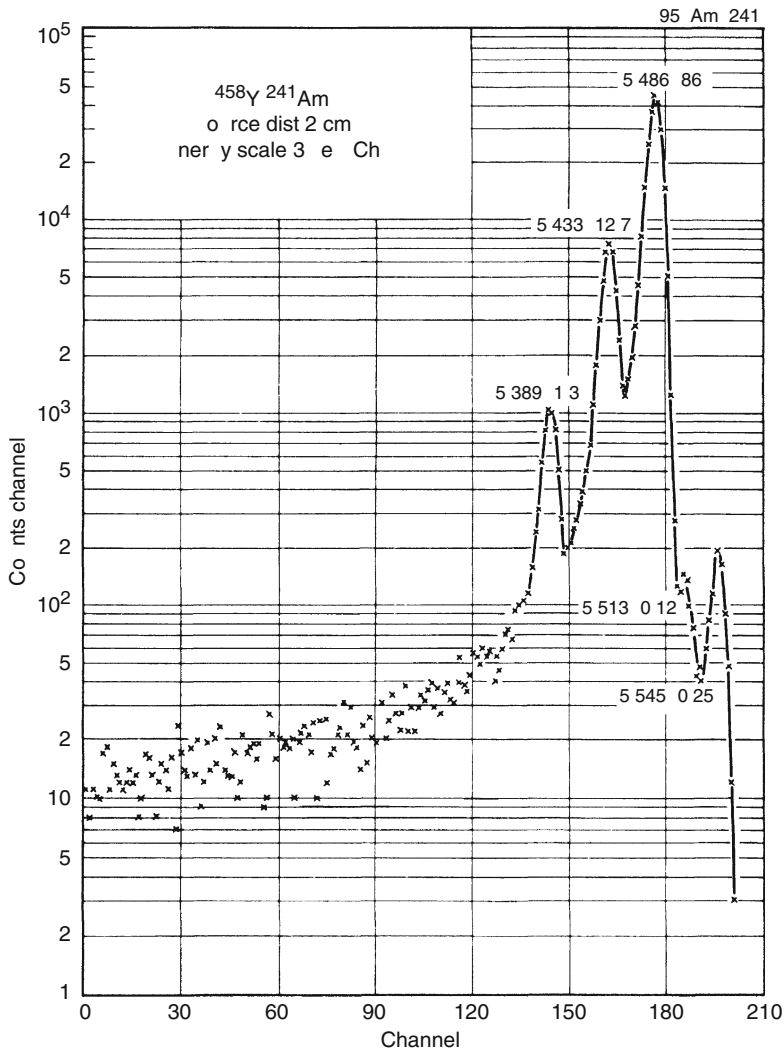
48.4.1 Si for Alphas

Spectroscopy of α particles is used for detecting, identifying, and quantifying components in a mixture of α emitting nuclides. Note that, in contrast to γ -ray detection, α spectroscopy with silicon detectors requires thin sources, which usually involves radiochemical purifications. However, for suitable sources, impressive results can be obtained. Figure 48.6 shows the spectrum obtained for ^{241}Am . Note that the weak 5,512 keV α is resolved from the major peak only 26 keV away. There are many weak α groups with energies below 5,389 keV. Some of them would be discernable with longer counting times; others would require α – γ coincidence measurements.

For use with radioactive samples, relevant parameters of Si detectors are depletion depth (100 μm is sufficient for normal α energies), area (geometrical efficiency), and ruggedness (some electrodes can be damaged by exposure to chemicals and vapors). The decay of heavy elements may include spontaneous fission. The ranges of fission fragments are comparable to the ranges of α ’s from decay, and the same detector criteria apply. However, fission fragments produce many more electron–hole pairs per unit path length, and the high density of carriers

■ Fig. 48.6

Spectrum of α 's emitted by a thin source of ^{241}Am measured with a Si detector (Chanda and Deal 1970)



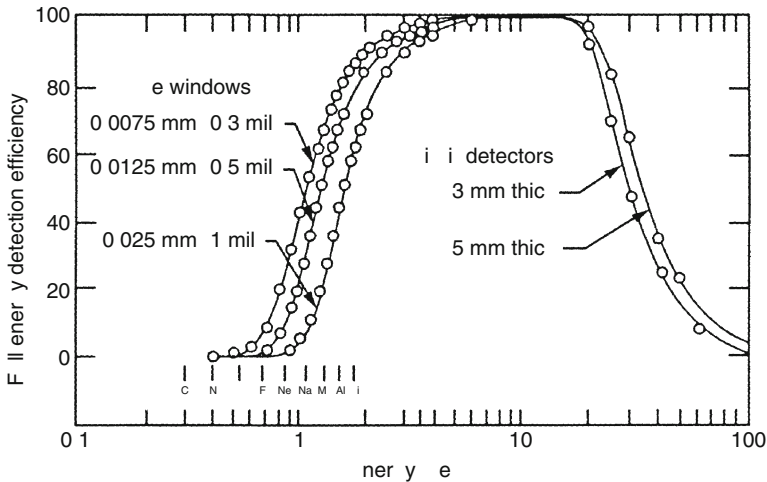
leads to significant recombination (the pulse height defect). For this and other reasons, one need not specify the best energy resolution (at higher cost for the detector) for fission fragments or for α spectroscopy of relatively thick sources.

48.4.2 Si for Photons

The dominant interaction of high-energy photons (>100 keV) with silicon is Compton scattering. For these energies, silicon is not attractive for spectroscopy, which depends on

■ Fig. 48.7

Energy dependence of detection efficiency for photons in a Si(Li) detector (Used by permission of Canberra)



events in which all of the energy is deposited in the detector volume. Below about 50 keV, photoelectric absorption is significant, and silicon can be quite useful. ➤ Figure 48.7 shows the energy dependence of full energy absorption as a function of detector characteristics and of photon energy.

➤ Figure 48.8 shows the low-energy photon spectrum of ^{241}Am . Note that in terms of photons emitted by the source, the intensity of the 59 keV γ ray is more than 15 times that of the 26 keV γ ray. That the peak areas in the spectrum are about the same shows the drop in full energy efficiency of silicon above ~ 50 keV. However, the energy resolution in the range for which the detector is useful is very good. In contrast to silicon, germanium, which can be used in the same energy region, produces a large escape peak about 10 keV (the energy of a Ge K X-ray) below the main peak.

48.4.3 Ge for Photons

All Ge detectors operate at low temperature, generally that of liquid nitrogen. When the first Ge detectors were made, even the purest available material had significant amounts of p-type impurities. These impurities were compensated by diffusing and drifting lithium atoms into the crystal. Unfortunately, the lithium in these Ge(Li) detectors would migrate and the detector characteristics would be destroyed if the crystal warmed to room temperature. Currently, high purity (“intrinsic”) Ge is used, and the lithium compensation is not required. These detectors can be stored at room temperature.

Photon spectrometers fabricated from germanium are available from several manufacturers with a variety of specifications. The technology is highly developed, and it is unlikely that any user would attempt to construct one from raw materials. Some of the available shapes and electrode geometries are shown in ➤ Fig. 48.9. Corresponding detection efficiencies are given

Fig. 48.8

Photon spectrum for ^{241}Am observed in a Si(Li) detector (From Gehrke and Lokken 1971; used by permission of Elsevier)

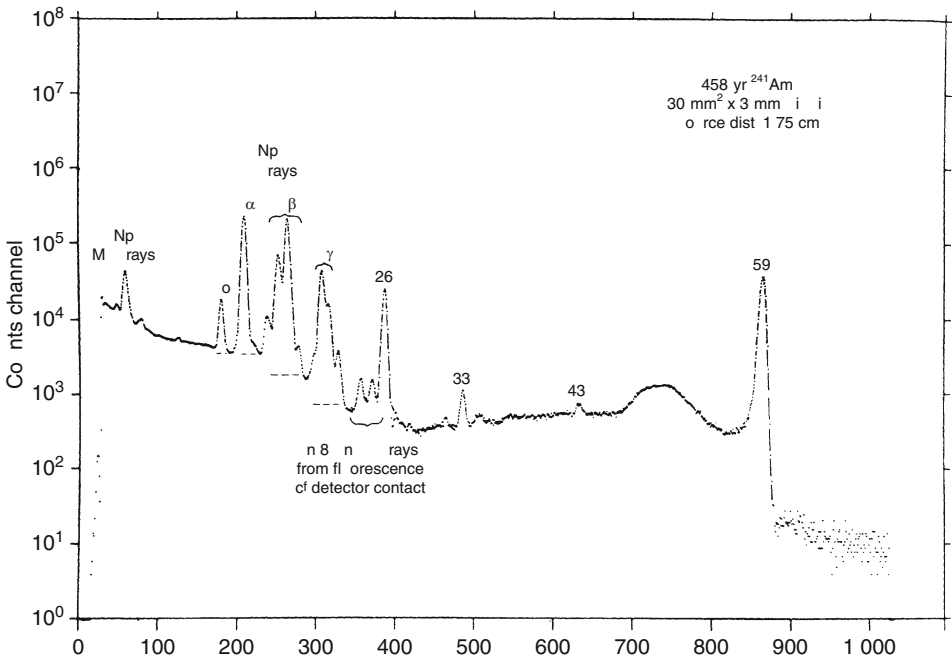
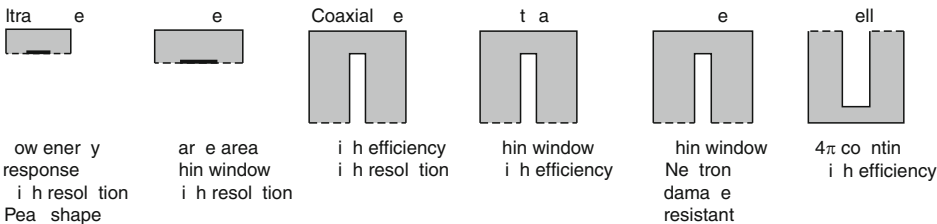


Fig. 48.9

Shapes of Ge detectors. The thick boundaries are thick electrodes that attenuate low-energy radiation (Used by permission of Canberra)



in Fig. 48.10, and resolutions are given in Fig. 48.11. It is apparent from the trends in resolution that small detectors can have superior energy resolution. As shown in Fig. 48.10, these small detectors have low efficiency at high energies.

Figure 48.12 shows the spectrum of L and K X-rays (from ^{207}Bi) observed with a small Ge detector. The efficiency within the display range is nearly constant (except for increasing Ge K X-ray escape at lower energies; see Fig. 48.10). The high resolution results from low electrical capacitance of the small crystal.

Fig. 48.10

Detection efficiencies for various configurations of Ge. Circled numbers refer to types ①, REGe; ②, 10 cm² LEGe; ③, 2 cm² LEGe; and ④, 10% Coaxial Ge (See Fig. 48.9)

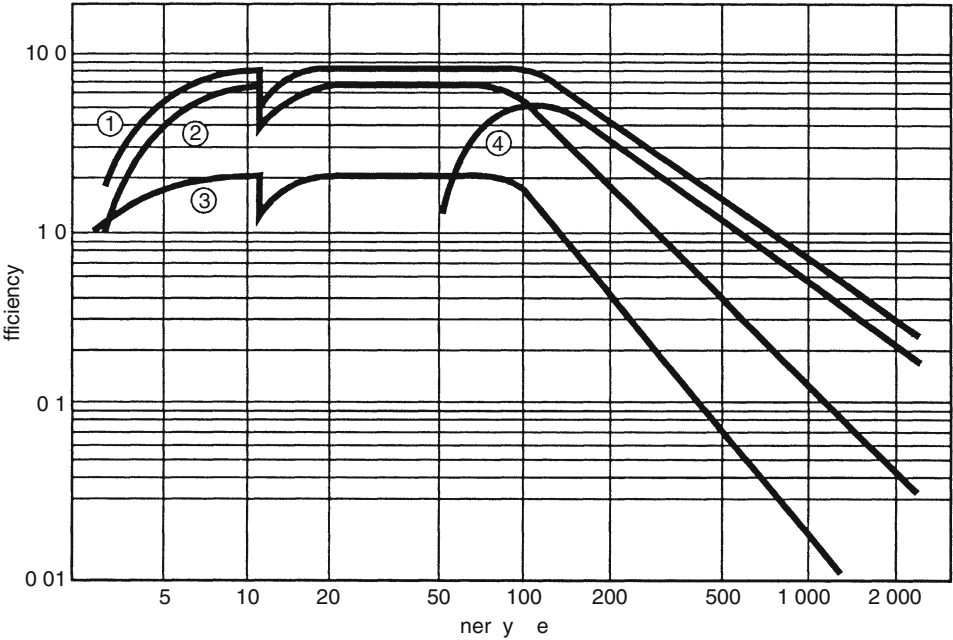
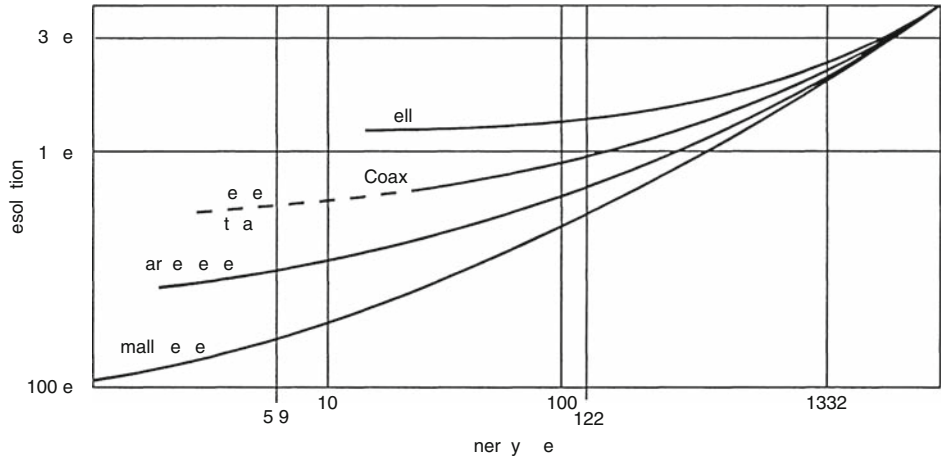


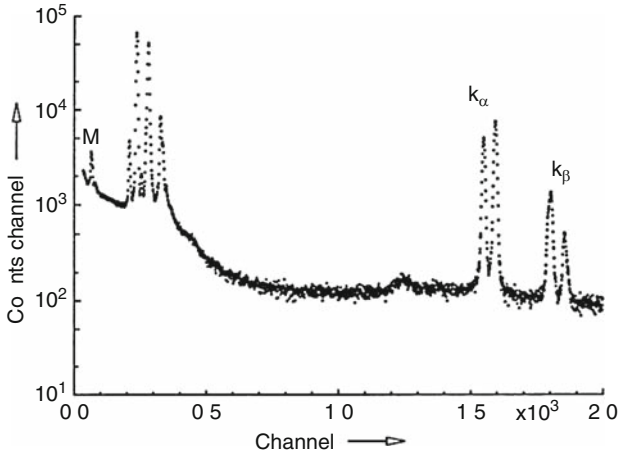
Fig. 48.11

Resolution for various types (See Fig. 48.9) of commercial Ge systems (Used by permission of Canberra)



■ Fig. 48.12

Spectra for Pb L and K X-rays observed in the small, thin-window Ge detector. The region labeled M is more likely to be escape peaks than easily absorbed M X-rays (From Debertin and Helmer 1988; used by permission of the author)



The probability for photoelectric absorption drops below that for Compton scattering at about 150 keV in germanium. That large crystals can be used for energies of many MeV is due to multiple interactions with photons and a sufficient size to absorb the energetic secondary electrons. At energies well above the 1,022 keV threshold, production of electron–positron pairs becomes important.

It is normal to treat empirically the complex mixture of interactions that lead to full energy deposit and to the spectral peak corresponding to that full energy. The trends in spectral features are shown in Fig. 48.13. At energies below about 200 keV the full energy peak is the dominant feature; most of the γ rays that enter the sensitive volume of the detector deposit all of their energy. At higher energies, the Compton continuum (broad plateau extending from 0 to about 250 keV below the peak) becomes more important, in accord with the decreasing probability for photoelectric interaction.

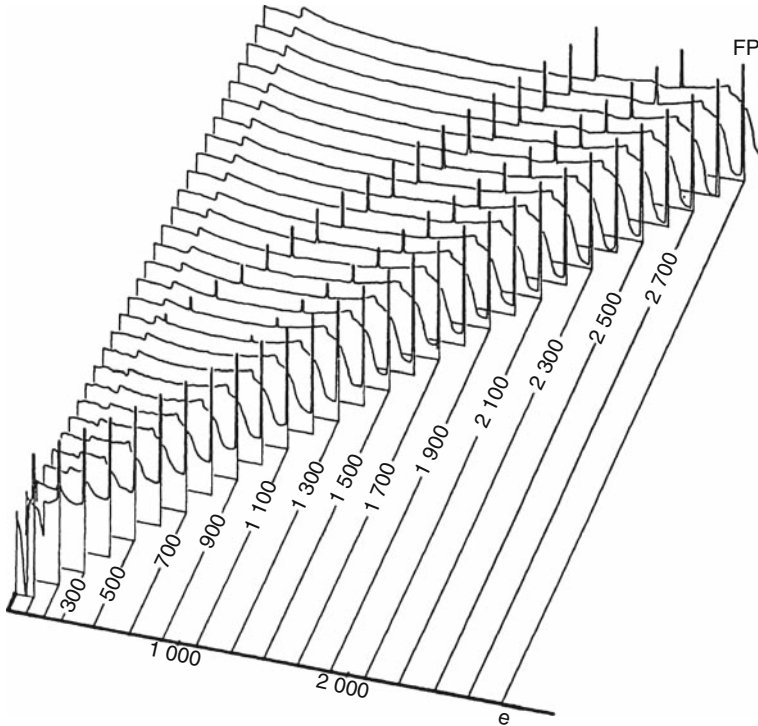
At still higher energies (above 1,022 keV), pair production becomes significant, and there are escape peaks resulting from annihilation of positrons.

The processes that form the escape peaks are as follows. Some of the original, high-energy photons that entered the Ge crystal produced an electron pair (e^+ and e^-) in the first interaction. The electrons were created with, between them, kinetic energies equal to the photon energy less the energy (1,022 keV) required to create two electrons. Unless the process takes place near the surface of the crystal, the electrons are likely to deposit all of their kinetic energies in the crystal. The negative electron is no longer of interest, but the positron is not finished. When the positron reaches approximately thermal energies, it finds an electron and, most often, the matter/antimatter pair annihilates into a pair of photons, each with the energy (511 keV) derived from the mass of an electron. Depending on how much more energy the annihilation quanta deposit, three peaks and additions to the continuum result. (See response functions for high-energy γ rays in Fig. 48.13.)

Real spectra corresponding to intermediate and high-energy γ rays are shown in Fig. 48.14. The upper part shows the spectrum for ^{137}Cs . This source emits β rays and

■ Fig. 48.13

Calculated response functions for monoenergetic γ rays in a Ge crystal. The *bottom row of peaks* shows full-energy peak (FP) when the total γ energy is absorbed by the Ge crystal. The top and the middle rows show double-escape (DE) and single-escape (SE) peaks, respectively. See text for more details (From Meixner 1974; used by permission of Elsevier)

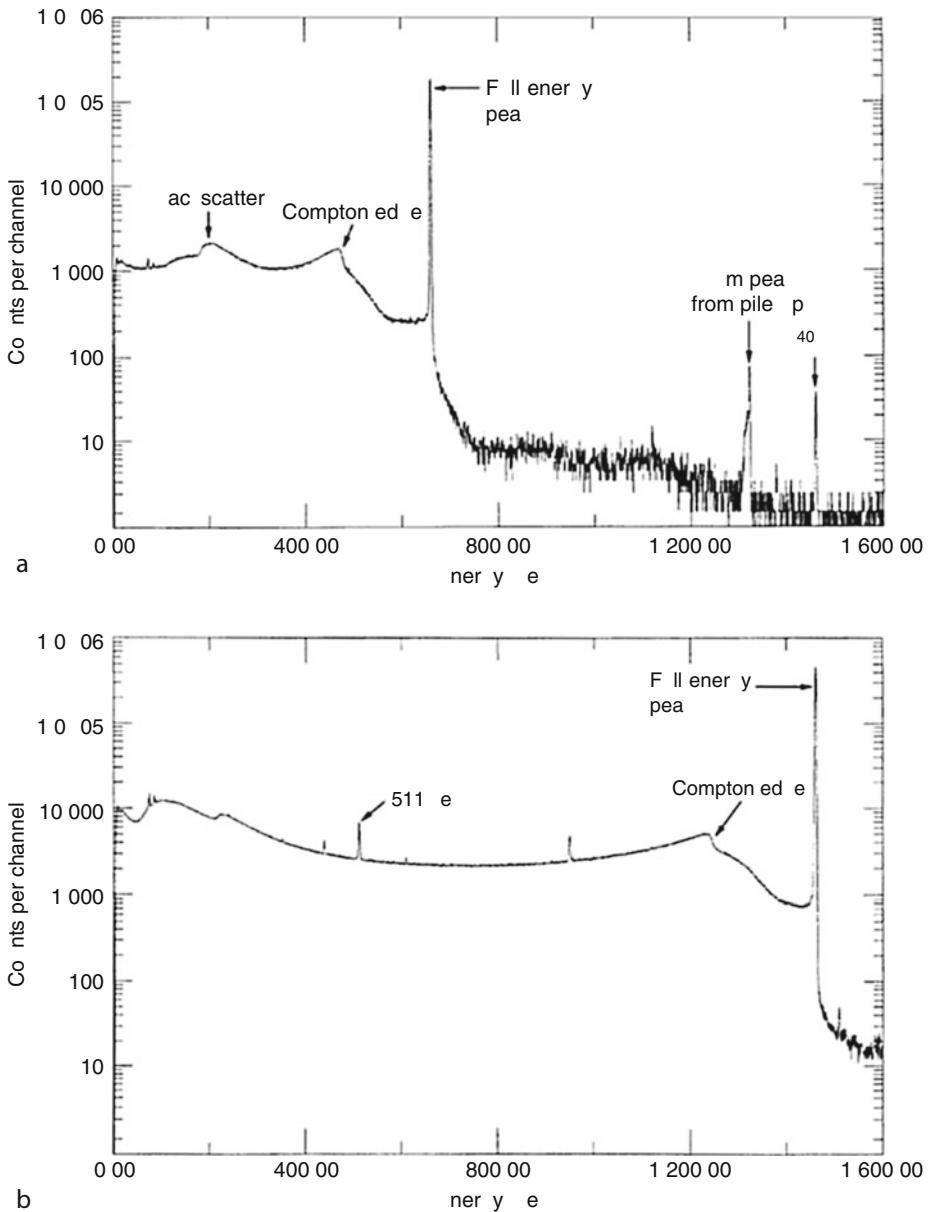


conversion electrons that are almost always absorbed before reaching the sensitive Ge volume. There are also Ba X-rays and 661.6 keV γ rays. Whether the X-rays reach the detector depends on the specific type of electrodes used in the detector. In this case, the p-type high-purity Ge crystal has a thick absorbing layer, and most of the Ba X-rays are absorbed. More energetic Pb K X-rays (from the shield) are detected. The backscatter peak arises from 662 keV γ rays that Compton scatter from electrons in the surroundings. The peak is broad because of the range in scattering angles. The Compton edge shows a rather sharp maximum in the energy transferred to electrons in the Ge crystal. Note that the backscatter peak and the Compton edge are complementary.² Sometimes, two γ rays from separate decays enter the detector at about the same time and give rise to a sum peak.

The lower part shows the spectrum of 1460.8 keV γ rays emitted in the decay of ^{40}K . (Note that a weak ^{40}K γ -ray peak occurs in the upper spectrum due to potassium in materials outside the detector and shield.) Interactions of the γ rays with the detector give annihilation escape peaks (SE for single escape, DE for double escape) in addition to the components seen for the lower energy ^{137}Cs γ ray. The 511 keV peak results from pair production followed by annihilation in the surroundings, most likely in the Pb of the shield. Note again the Pb K X-rays (~ 74 and ~ 85 keV).

■ Fig. 48.14

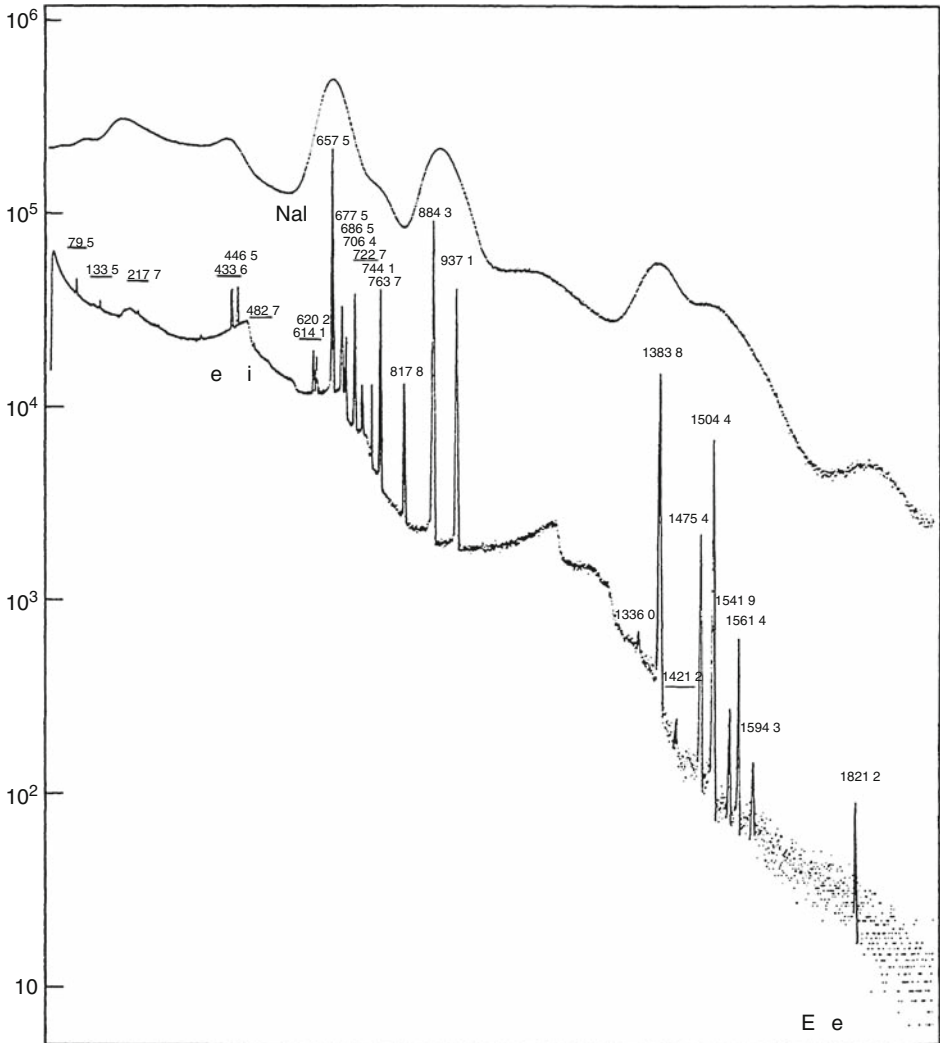
Spectra for monoenergetic γ rays in a large Ge crystal. The radiation source is ^{137}Cs for the upper and ^{40}K for the lower spectrum (Courtesy of the ORTEC Products Group, Oak Ridge, TN)



Real applications generally involve a mixture of radioactive materials, each with many γ rays. ➤ [Figure 48.15](#) shows a spectrum of intermediate complexity from a source of neutron-activated silver. The source is dominated by $^{110\text{m}}\text{Ag}$ but includes a small amount of $^{108\text{m}}\text{Ag}$. The $^{108\text{m}}\text{Ag}$ has a relatively simple spectrum with the major peaks showing up at

■ **Figure 48.15**

Typical spectra for multi-gamma sources with NaI(Tl) and Ge. Energies are in keV. Most of the peaks arise from $^{110\text{m}}\text{Ag}$. A few originate from $^{108\text{m}}\text{Ag}$ (From Philippot 1970; © 1970 IEEE)

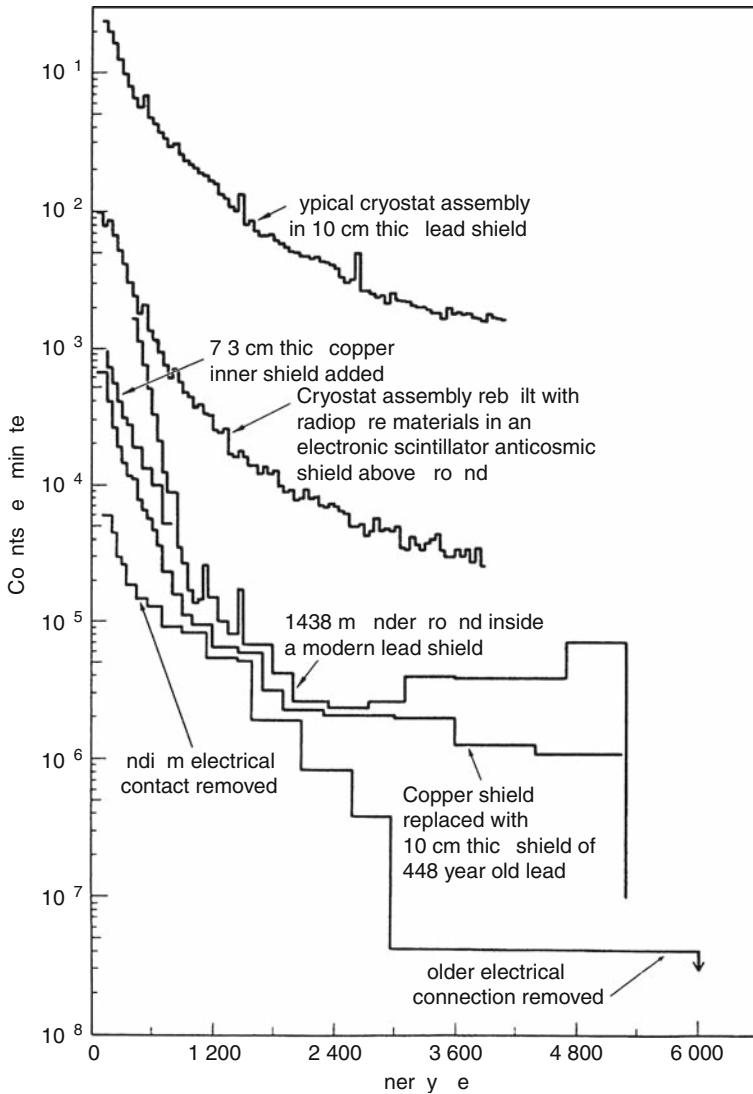


79.5, 433.6, 614.1, and 722.7 keV. The upper trace shows the spectrum obtained with a low resolution detector (NaI(Tl); see ▶ Sect. 48.4.1), which cannot detect $^{108\text{m}}\text{Ag}$ under these conditions. The advantage of the Ge resolution is obvious.

If no $^{110\text{m}}\text{Ag}$ were present, it would be easy to detect the $^{108\text{m}}\text{Ag}$ in the sample, even with NaI(Tl). If there were very little radioactivity of any type in the sample, competition from background radiation would become important, particularly if some of the γ rays of interest in the sample also were in the background. ▶ Figure 48.16 shows various techniques for reducing the background spectrum for a γ -ray spectrometer.

■ Fig. 48.16

Background spectra for a large Ge detector under different conditions (From Brodzinski et al. 1987; used by permission of Elsevier)

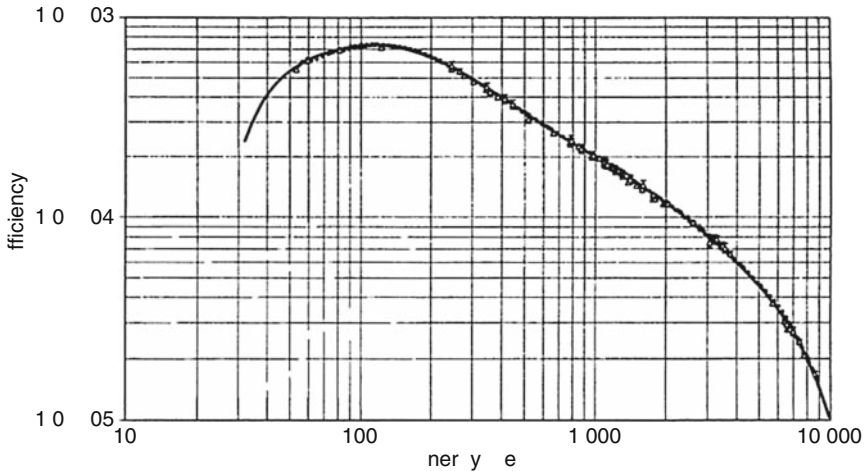


In some cases, the amount of a radioactive material can be determined by comparison with a standard amount of that same material. Details of the detector are unimportant. More often, it is inconvenient to obtain such a standard, and the absolute efficiency of the detector for the relevant energies must be known. (Also, the absolute intensities of the γ rays must be known.)

For precision work ($<10\%$ uncertainties), the detection efficiency for each spectroscopy system must be measured under the conditions of use. ➤ Figure 48.17 shows a (unusually

■ Fig. 48.17

Experimental detection efficiencies for a large Ge detector (From Kis et al. 1998; used by permission of Elsevier)



detailed) calibration curve for a specific detector. The efficiency is maximum at ~ 120 keV; its value reflects the solid angle subtended by the detector from the source position.

The drop in efficiency for lower energies reflects absorption (in the source or parts of the detector system between the source and the active Ge volume). For higher energies, an increasing fraction of interactions fail to deposit all of the energy of the photon in the detector, and the full energy efficiency drops. At the very highest energies, the ranges of the secondary electrons become significant compared to the size of the crystal; efficiency drops more steeply.

Note that in the energy range for common γ rays from radioactive sources (200–3,000 keV) the logarithms of the efficiency and the energy are nearly linearly related.

It is important that the calibration be made under the conditions of use. Choosing those conditions requires balancing many factors. Placing the sources close to the detector increases count rates and peak areas, which reduces statistical uncertainties. Unfortunately, some systematic uncertainties may increase.

Consider what might happen after a given γ ray has deposited all of its energy in the detector. There is nothing to prevent additional radiations from adding energy to the detector and removing the event from the range of pulse heights that would be interpreted as the full energy of the γ ray. If that radiation comes from the decay of the same atom, the effect is called “coincidence summing,” and can be understood in terms of cascade relations (shown by the decay scheme) and detection probabilities. If the radiation is from the decay of another atom, the effect is called “pileup” or “random summing.” These two effects are quite different.

Pileup is a function of the total count rate, the time constants of the amplifier, and (weakly) the energies of the γ rays. Reducing the count rate (at the expense of statistics) or shortening the time constants (at the expense of energy resolution) can reduce pileup.

Coincidence summing depends on the details of the relevant decay scheme. Each nuclide must be evaluated on the basis of its unique scheme. Consider the decay of ^{207}Bi .³ The most likely decay path is (1) electron capture to the 1,633 keV level of ^{207}Pb , the stable end-product of

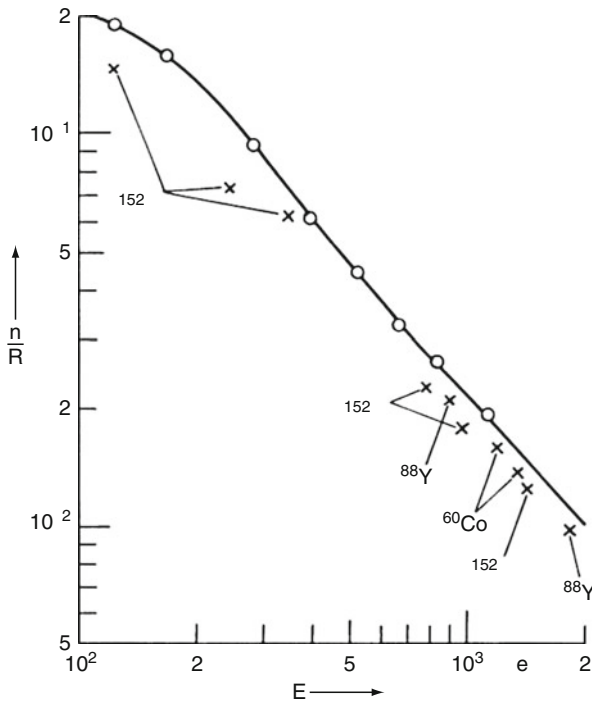
the $4n+3$ series, (2) delayed emission of a 1,064 keV γ ray, and (3) almost immediately after the 1,064 keV γ ray, emission of a 570 keV γ ray. The 1,064 keV γ ray is emitted in 74.5% of the decays. Perhaps, this transition has been chosen as an indicator for ^{207}Bi , and the sample has been counted in a geometry for which both peak and total detection efficiencies are well known. The effective detection efficiency for the 1,064 keV γ ray is the probability that it will deposit all of its energy in the detector times the probability that no other radiation will be detected at the same time. Because of the delay following electron capture, the atomic transitions associated with the vacancy following capture are unlikely to occur at the same time. (The probability of γ -ray emission to occur within 10 μs of the capture is $\sim 7.7 \times 10^{-6}$.) However, any interaction by the 570 keV γ ray will prevent recording a count in the 1,064 keV peak.

The coincidence summing effect is shown in [Fig. 48.18](#). The calibration points were obtained with a mixed source containing, among others, ^{60}Co , ^{88}Y , and ^{152}Eu . Each of these decays has strong cascades for which the apparent efficiencies are considerably below the true efficiencies for individual γ rays of those energies.

Beta detection should not be ignored. Beta rays do not produce features as distinctive as those produced by photons (bremsstrahlung excepted), but if they reach the sensitive volume of the detector they are equally effective in removing a full-energy event from its spectral peak. For many detectors, such as p-type intrinsic Ge detectors, the layer of dead Ge may be sufficient

Fig. 48.18

Coincidence losses in a Ge detector (From Debertin and Helmer 1988; used by permission of the author)



to prevent β detection. A p-type detector might have a dead layer of $\sim 0.3 \text{ g cm}^{-2}$, which is range for $\sim 750 \text{ keV}$ electrons. On the other hand, detectors that are designed for detecting low-energy photons are also sensitive to intermediate energy (several hundred keV) electrons.

48.4.4 Other Semiconductors

The favorable characteristics of Si and Ge notwithstanding, both have low atomic number (hence low photoelectric absorption) and Ge requires cooling. Diamond can function as a detector and has been used, but it is expensive and has even lower atomic number. The most common alternatives to Si and Ge are the compound semiconductors $\text{Cd}_{1-x}\text{Zn}_x\text{Te}$ (CZT, or just CdTe when $x = 0$) and HgI_2 . Their band gaps are sufficiently large for operation at or slightly below room temperature. Interested readers should consult specifications of available commercial devices.

48.5 Scintillators

There are many materials that scintillate – give off visible light when excited by radiation, including the ionizing radiation of interest in nuclear studies. Only a few will be described, but they all depend on some device to convert the light into an electrical signal. Most commonly, a photomultiplier is used. The structure of a typical tube is shown in [Fig. 48.19](#).

An external source of high voltage (perhaps 1–3 kV, depending on the number of stages of amplification) provides the force to draw electrons from the photocathode, which converts the scintillation light into a very small current, down the series of intermediate electrodes called dynodes, increasing the current at each stage.⁴ The composition of the photocathode is chosen to match the spectral characteristics of the scintillator. This matching is illustrated in [Fig. 48.20](#).

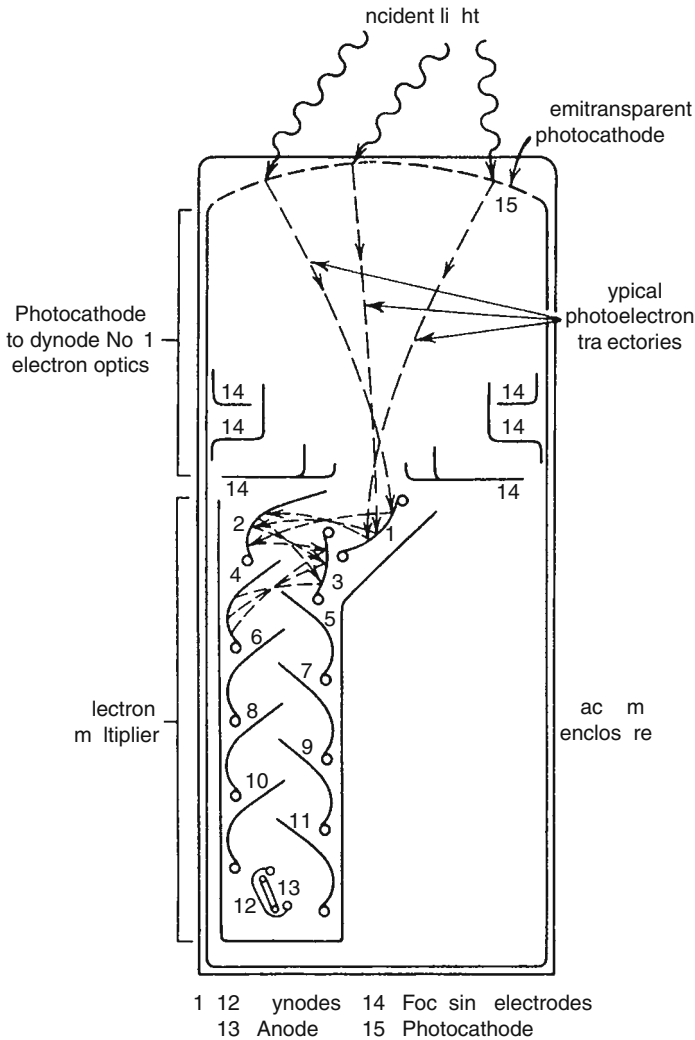
The scintillators are chosen based on the type of radiation to be detected and the desired geometry. For spectroscopy of γ rays, it is generally desirable to have a scintillator with high average atomic number. This enhances the probability of photoelectric absorption, which leads to a full energy deposit. This application is illustrated by thallium-activated sodium iodide – NaI(Tl) . There are scintillators with higher effective atomic number, such as *bismuth germanate* (BGO), but they are slower, much more expensive, or have poorer resolution than NaI(Tl) . Plastics are easy to form into complex shapes that may be needed for a given application. They generally have slightly lower light output than NaI(Tl) , but the emission is generally much faster. Although semiconductors have largely replaced scintillators in many applications, the liquid scintillation spectrometer remains the most important detector for tracers that are pure β emitters.

The mechanisms whereby energy deposited by nuclear radiation is converted into light are quite diverse. Although inorganic scintillators are generally slow (time constants of $\sim 1 \mu\text{s}$) compared with organics, some of the light emitted by BaF_2 is very fast ($< 1 \text{ ns}$). Unfortunately, the yield is low and the emission is in the UV part of the spectrum, requiring special (e.g., quartz) windows and light pipes.

Some materials, such as properly doped salt crystals, store the energy deposited by radiation until they are stimulated (e.g., by warming) to release the energy by emitting light. These TLDs (thermoluminescent dosimeters) have largely replaced film for monitoring

■ Fig. 48.19

Cross section of a typical photomultiplier tube (PMT) (From Knoll 2000; used by permission of Wiley)

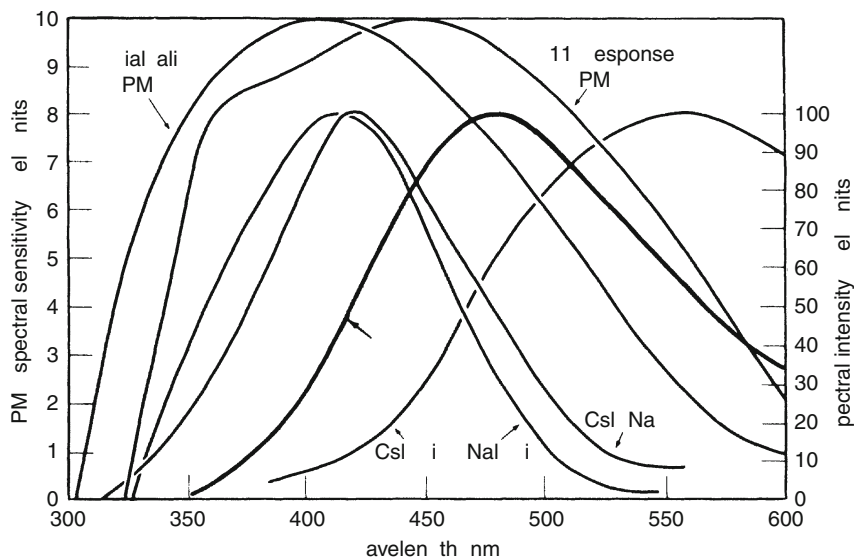


accumulated dose over weeks or months.⁵ There is considerable variation in response among individual chips of salt, but each chip can be characterized and then used many times.

In spite of the variety of scintillators, they are unusual materials. There is a mechanism for emission of light that is quite general for certain types of nuclear radiation. Charged particles moving through a transparent medium (e.g., water or glass) at a speed greater than the speed of light in that medium emit light – Cherenkov radiation. This is the blue glow emitted from the water surrounding the core of an operating reactor. The requirements that the incident radiation be charged and exceed the speed of light in the medium limits application, in the context of radioactive decay, to high-energy β emitters (see ▶ Sect. 48.4.3).

■ Fig. 48.20

Response functions of two photocathode materials used in PMT construction (*left scale*) to spectral characteristics of four inorganic scintillators (*right scale*). See text for details (From Knoll 2000; used by permission of Wiley)



48.5.1 NaI(Tl)

For many years, a “3 × 3 NaI” detector was the standard for routine measurements of γ -active materials. The detector consisted of a cylindrical piece of thallium-activated NaI 7.6 cm (i.e., 3 in.) in diameter and 7.6 cm in height. The hygroscopic crystal was enclosed in an aluminum can (with a glass window on one end) to protect it from moisture. These crystals could be manufactured sufficiently reproducibly that efficiencies could be taken from tabulations. Another useful geometry was similar except for a coaxial well where small samples could be counted at nearly 100% detection efficiency.

All of the details involved in obtaining precision results from γ -ray spectroscopy with Ge detectors apply to NaI(Tl). In fact, the methods were developed with NaI(Tl) and later applied to Ge. NaI(Tl) is superior to Ge in effective atomic number (total energy absorption), operation at room temperature, and size (up to 25 cm linear dimensions for the scintillator). But the vastly superior resolution of Ge dominates all other characteristics for most users. At about 1,000 keV, the energy resolution of a Ge detector is about 1.5 keV, and that of NaI(Tl) is about 60 keV (Fig. 48.15).⁶ Whereas Ge spectra can be analyzed in terms of individual peaks and their areas, NaI(Tl) spectra are usually analyzed in terms of the overall, somewhat indistinct pattern each nuclide produces under the conditions of the measurement. When conditions change and effects such as summing and pileup change, the patterns change.

In spite of these shortcomings, a shielded NaI(Tl) detector, perhaps in a “well” geometry with several external counting positions, is a valuable tool for tracking laboratory processing of radioactive materials.

48.5.2 Plastics

Plastic scintillators can generally be used in any application for which a gas detector might be considered, except where physical damage to the plastic might occur. Plastic can be formed into more complex shapes than can gas chambers with collection electrodes, but shapes are limited by the need to collect the light at the photocathode of a photomultiplier. The material itself is relatively inexpensive, so it is attractive for large volume detectors. Many plastic scintillators emit light on a nanosecond time scale – much faster than most inorganic scintillators.

48.5.3 Liquid Scintillators

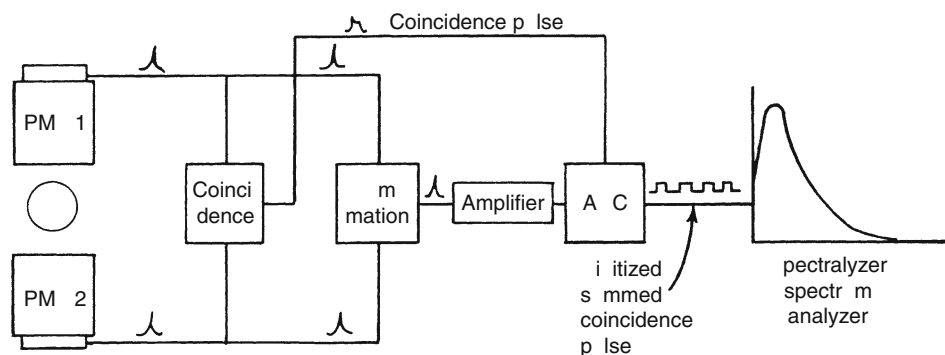
The largest use of radioactive materials is in the life sciences, and most of the nuclides used are pure β emitters. These nuclides include $12.3\text{ y }^3\text{H}$ (18.6 keV), $5,715\text{ y }^{14}\text{C}$ (156 keV), $14.3\text{ d }^{32}\text{P}$ (1,711 keV), $87.2\text{ d }^{35}\text{S}$ (167 keV), and $163\text{ d }^{45}\text{Ca}$ (257 keV; very weak 12.4 keV γ). Users generally are not interested in detectors per se; they just want to measure the amounts of these tracers, sometimes with more than one tracer used at a time. Manufacturers have met their needs with sophisticated systems and explicit protocols based on liquid scintillators into which the sample is dissolved.

► **Figure 48.21** shows the components of a *liquid scintillation spectrometer*. Two photomultipliers are used in coincidence to reduce the counts due to pmt noise. The noise from separate tubes is not correlated in time, but the light from a decay in the sample is. The energy corresponding to the triggers can be low, which reduces the loss of true events from low-energy decays. Once the coincidence condition has been met, the height of the sum of the two pulses is measured in an ADC. After the spectrum is stored, it can be analyzed and reanalyzed for the contributions from the nuclides present.

Light is produced, and sometimes quenched, by processes illustrated in ► **Fig. 48.22**. Since the sample is dissolved in the scintillator, there is no attenuation of the radiation on the way to the detector. Unfortunately, having the sample in the detector may interfere with scintillation. Most commercial systems can sense and correct for this quenching. Typically, a small pellet

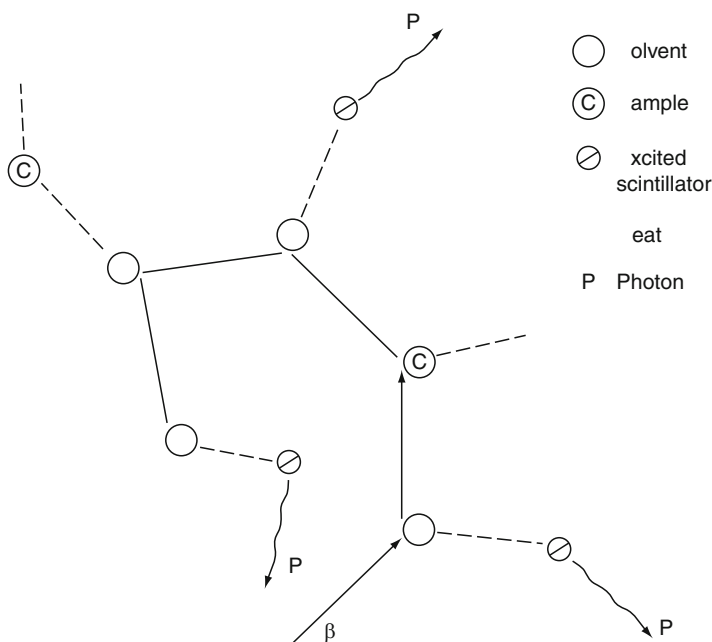
► **Fig. 48.21**

Components of a modern liquid scintillation spectrometer (From Kessler 1989; used by permission of Perkin Elmer)



■ Fig. 48.22

The scintillation process in an organic liquid scintillator (From Kessler 1989; used by permission of Perkin Elmer)



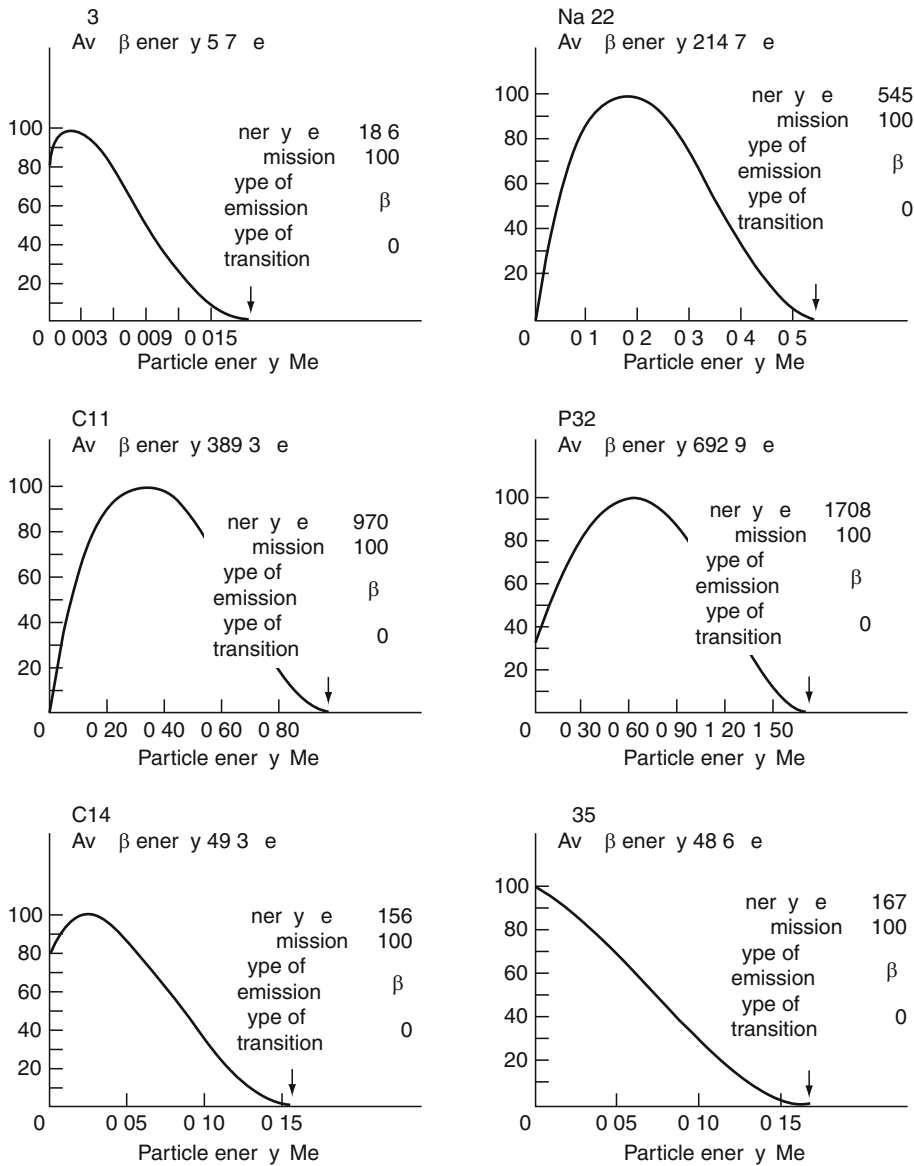
containing a γ emitter is pneumatically moved to the scintillation vial, and the shape of the Compton distribution is used to infer the degree of quenching. This information can be used to correct the energy scale and compensate for additional losses of low-energy events.

► Figure 48.23 shows the pulse height spectra for some commonly used tracers. The main features to note are the importance of very low pulse heights for tritium (^3H), and the smaller number of low pulse heights for positrons (e.g., ^{11}C) vs. negatrons (e.g., ^{14}C). This is explained by the simple fact that positrons (e^+) are accelerated as they leave the positive nucleus, the negatrons (e^-), on the other hand, are retarded. So, in the first case, the low-energy fraction decreases, while in the second it increases. The electrons emitted in β decay share energy with an unseen (anti)neutrino, which sometimes has almost all of the available energy.

Liquid scintillation is particularly attractive for α emitters if discrimination among nuclides is not required. The main advantage is avoiding the need to prepare thin sources or to correct for external absorption. The disadvantage is that only about 10% of the α energy is effective in producing scintillations. For typical systems not optimized for α detection, all α particles fall in a broad peak corresponding to about 500 keV electrons. ► Figure 48.24 show that if volumes are small, light collection is efficient, and quenching agents are avoided, modest α resolution can be obtained. Under these conditions, it is possible to use the shape of the scintillation pulse to distinguish α 's from electrons. Very low backgrounds for α counting can be obtained. Of course, if α decay leads to excited states which subsequently decay by internal conversion (electron emission), the resulting pulse is intermediate in shape. Pulse shape discrimination or α spectroscopy may not be applicable.

Fig. 48.23

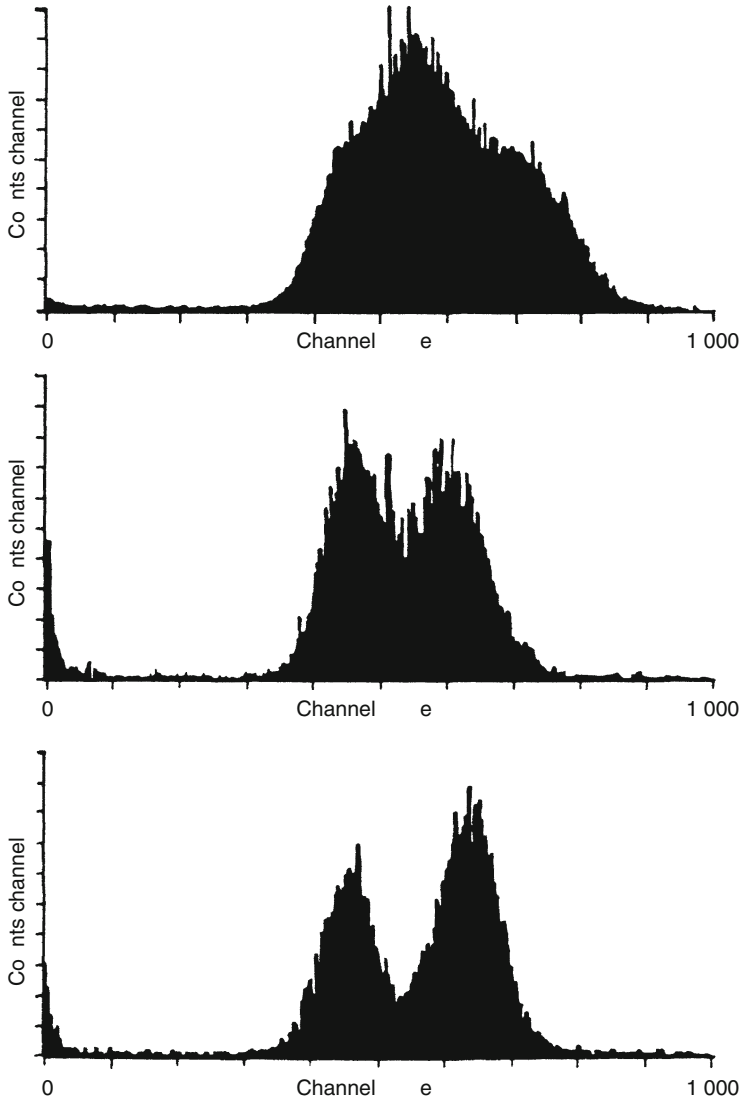
Spectra of typical β emitters (From Mantel 1972; reprinted with permission from Elsevier)



There are many choices among commercial scintillation fluids. Significant parameters include dissolving power (aqueous or organic), flammability, resistance to quenching, and environmental factors (“mixed” wastes containing hazardous chemicals and radioactivity are to be avoided). However, for detecting high-energy β decay by Cherenkov radiation (discussed together with transition radiation in [Sect. 8.3.6, Chap. 8, Vol. 1](#)), normal scintillation processes must be avoided. If water (index of refraction ~ 1.33) is used, Cherenkov radiation

■ Fig. 48.24

Spectra of α particles in liquid scintillators. Samples for the top two spectra contained ^{233}U (4.8 MeV) and ^{241}Am (5.5 MeV). A standard 20 mL vial was used for the top spectrum. A narrow tube, 6 mm in diameter, was used for the middle and bottom spectra. For the bottom spectrum ^{244}Cm (5.8 MeV) replaced ^{241}Am (From Kessler 1989; used by permission of Perkin Elmer)



will be emitted by electrons with speeds greater than $c/1.33$ where c denotes the speed of light in vacuum. This corresponds to energies greater than about 250 keV. These energetic decays can be detected in the presence of large amounts of low-energy β radiation. Note, however, that photons with energies greater than about 500 keV can produce Compton electrons above the Cherenkov threshold.

48.6 Neutrinos and Fission Fragments

Neutrinos are emitted in all β -decay processes and often carry away most of the decay energy. None of the detectors mentioned above is sensitive to neutrinos, which rarely interact with matter except by β interactions. For example, neutrinos (but *not* antineutrinos) with energies >0.82 MeV can react with ^{37}Cl to produce radioactive ^{37}Ar . The cross section is *very* small. In spite of the difficulty in detecting neutrinos, their spectroscopy is an active area of research.

Heavy ions, such as fission fragments, produce tracks of damage in absorbing materials. The damage makes the material more reactive chemically than it otherwise would be, and the tracks can be “developed” by suitable reagents. For example, glass containing damage tracks can be etched to reveal pits where the tracks reach the surface. When the etch conditions are carefully controlled and the absorbing material is uniform, the technique can reveal dE/dx along the path, hence the identity and energy of the particle causing the track⁷.

48.7 Composite Detectors

The possibility of constructing “composite” detectors which combine several individual detectors is open ended. Here, attention is limited to showing why combinations are desirable. In general, the motivation stems from the difference between analyzing small numbers of events directly as opposed to small differences in large numbers.

One of the earliest composites was designed to detect α particles in the presence of relatively large amounts of β and γ radiation. Two scintillators, the first thin and fast and the other thicker and slow, were mounted on a single phototube. Electronic filters were used to separate the fast and slow signals. Because of the short ranges of α particles, a fast signal without an appreciable slow component indicated an α particle, whereas a fast accompanied by a slow component indicated particles with longer ranges (electrons from Compton events, or β particles themselves). Note that the light emission from some scintillators includes more than one time constant and that different types of particles can give different ratios of these components. Similar circuitry (“pulse shape discrimination”) can be used to identify the particle type.

More commonly, the parts are operated separately and the signals are combined to achieve the desired results. For energies above a few 100 keV, relatively few γ -ray events in a Ge crystal lead to the full energy deposit that is required for the distinctive signal on which γ -ray spectroscopy is based. That loss of potential counts in the peak is not as serious as the production of counts at lower pulse heights where one might look for other signals. The height of the Compton continuum can be reduced significantly by nearly surrounding the Ge crystal with, for example, NaI(Tl) or BGO (see [Sect. 48.4](#)). The latter is quite compact and opaque to γ rays; the former is sensitive to low energies. If events in the Ge are accepted only if no photons are detected in the surrounding material, the Compton continuum can be suppressed by a factor of 5–10, except near the Compton edge, where the recoil photon exits along the same path the original photon entered to reach the Ge.

If the process to be studied involves the simultaneous emission of many γ rays (e.g., in-beam spectroscopy of high spin states), individual detectors should subtend small solid angles to avoid excessive coincidence summing. There is room for lots of these detectors, and some implementations include over a 100 Compton-suppressed Ge detectors in a geometry that approaches a “ball” of detectors (4π). Since thin plastic or silicon detectors for charged particles are relatively transparent to γ -rays, there can be a ball within a ball (8π), etc.

An extreme case for needing to select particular events to the exclusion of many others is the study of nuclides far from stability. Even with the availability of radioactive beams, nuclear reactions that lead to products at the extremes of stability have small probabilities compared to those that are more energetically favorable. A particular study might include several thin detectors to identify particles on an event-by-event basis (by dE/dx and time of flight) and track them along a beam.⁸ Individual particles might be caught in a detector with two-dimensional resolution; this detector could signal the arrival of a particle characterized by upstream detectors and its subsequent decay. That decay could be characterized by arrays of suitable detectors that surround the stopping point. And a needle could be found in the haystack.

48.8 Editors' Notes

1. See [Sect. 9.5.1.3 in Chap. 9 of Vol. 1](#) on Stochastics and Nuclear Measurements (p. 2266).
2. This means that the energies represented by them add up to the γ energy represented by the position of the full-energy peak along the horizontal pulse-height axis that is proportional to the energy absorbed. The reason is that the Compton edge represents the maximum of kinetic energy of an electron scattered in the crystal – see [Eq. 8.46 in Chap. 8, Vol. 1](#) – while the backscatter peak represents the minimum of energy of a γ photon scattered outside the crystal (p. 2272).
3. See the Appendix on the [Table of Nuclides in Vol. 2](#) (p. 2276).
4. The “multiplication” of a single photoelectron passing through a sequence of dynodes is represented by [Fig. 9.21 in Chap. 9, Vol. 1](#), as a stochastic process (p. 2278).
5. See [Sect. 49.3.2.2 in Chap. 49](#) of this volume for more details on TLDs (p. 2279).
6. In the case of soft γ radiation, one can make use of the fact that thinner scintillators have better resolution. [Figure 9.20, e.g., in Chap. 9, Vol. 1](#), shows the detector signal of a mere 0.1 mm thick NaI(Tl) scintillator at the 14.4 keV radiation produced by the first excited state of ^{57}Fe , the most common Mössbauer nuclide (p. 2280).
7. See the Bragg curve in [Fig. 8.5 and the related formulae in Chap. 8, Vol. 1](#), on the Interaction of Radiation with Matter (p. 2285).
8. See [Fig. 19.6 in Chap. 19, Vol. 2](#), on Production and Identification of Transactinide Elements (p. 2286).

References

- | | |
|---|---|
| Baum EM, Knox HD, Miller TR (2002) Nuclides and isotopes, 16th edn. KAPL, New York | Gehrke RJ, Lokken RA (1971) Nucl Instrum Methods 97:219 |
| Brodzinski RL et al (1987) Nucl Instrum Meth A 254:472 | Kessler MJ (1989) Liquid scintillation analysis. Packard Instruments, Meriden |
| Browne E, Firestone RB, Shirley VS (1986) Table of radioactive isotopes. Wiley, New York | Kis Z et al (1998) Nucl Instrum Meth A 418:374 |
| Chanda RN, Deal RA (1970) Catalogue of semiconductor alpha-particle spectra, IN-1261. Idaho Nuclear, USAEC | Knoll GF (2000) Radiation detection and measurement, 3rd edn. Wiley, New York |
| Debertin K, Helmer RG (1988) Gamma- and X-ray spectrometry with semiconductor detectors. North-Holland, Amsterdam | Mantel J (1972) Int J Appl Rad Isot 23:407 |
| Firestone RB, Shirley VS, Baglin CM, Zipkin J, Chu SYF (1996) Table of isotopes, 8th edn. Wiley, New York | Meixner Ch (1974) Nucl Instrum Methods 119:521 |
| | Philippot JC (1970) IEEE Trans Nucl Sci NS-17(3):446 |
| | Sauli F (1994) CERN-ppe/94-195 |
| | Weiss HM (1973) Nucl Instrum Methods 112:291 |

49 Dosimetry Methods

W. L. McLaughlin^{1,†} · A. Miller² · A. Kovács³ · K. K. Mehta⁴

¹National Institute of Standards and Technology, Gaithersburg, MD, USA

²Risø-DTU, Technical University of Denmark, Roskilde, Denmark

³Hungarian Academy of Sciences, Budapest, Hungary

⁴Vienna, Austria

49.1	<i>Introduction</i>	2288
49.2	<i>Role of Dosimetry</i>	2288
49.3	<i>Chemical Methods of Dosimetry</i>	2290
49.3.1	Liquid Systems	2290
49.3.1.1	Aqueous Chemical Dosimeters	2290
49.3.1.2	Organic Chemical Dosimeters	2294
49.3.2	Solid Systems	2297
49.3.2.1	Dosimetry Systems Based on the Measurement of Optical Absorption	2297
49.3.2.2	Dosimetry Systems Based on the Measurement of Luminescence	2302
49.3.2.3	Electron Paramagnetic Resonance (EPR) Dosimeters	2305
49.4	<i>Physical Methods of Dosimetry</i>	2308
49.4.1	Calorimetry	2308
49.4.1.1	Principles of Calorimetry	2308
49.4.1.2	Calibration	2310
49.4.1.3	Types of Calorimeters	2310
49.4.1.4	Dosimetry at Low-Energy Electron Irradiation	2312
49.4.2	Semiconductors for Dosimetry	2312

[†]Deceased

Abstract: Chemical and physical radiation dosimetry methods, used for the measurement of absorbed dose mainly during the practical use of ionizing radiation, are discussed with respect to their characteristics and fields of application.

49.1 Introduction

The ionizing radiation quantity, absorbed dose (D) needs to be measured in many applications, and several effective dosimetry systems have been developed over the past century. The main purposes are measurement of (1) the energy imparted in a given mass of a specific material at a certain point of interest, namely dose, in units gray (Gy) where $1 \text{ Gy} = 1 \text{ J/kg}$; (2) absorbed dose rate; (3) the dose distribution over a specified material volume. Dose measurement is of basic significance especially in radiation processing, radiation protection, and in medicine, and the physical and chemical concepts developed for dosimetry are equally relevant for these applications. Although some of these methods are described in other chapters, dosimetry systems used mainly in radiation processing are discussed here, and when dealing with certain groups of dosimeters, other applications characteristic of that group, are also described briefly.

49.2 Role of Dosimetry

The most important practical applications of ionizing radiation in industry have been discussed in Vol. 3 (🔗 Chap. 23, “Radiation Chemistry”) describing the basic characteristics of the various processes. Some of these applications do not need exact doses, but many require knowledge of the dose applied in order to carry out uniform and accurate irradiation to achieve the necessary effect, i.e., the desired property of the product, e.g., sterility of medical devices or pasteurization of certain foods, while avoiding damage to the product. The exact measurement of absorbed dose in the course of the radiation process is critical, since it is used to document the successful execution of the irradiation process. Thus, dosimetry is also important in routine quality control as an independent, inexpensive, and reliable tool to measure and document whether the process was carried out according to specifications. Dosimetry then plays an important role in the transfer of the irradiation process from the laboratory to the industrial stage and in the quality control of radiation processing.

The main application fields of dosimetry in radiation processing include installation, operational and performance qualification, and routine process control. The selection of suitable routine dosimetry systems depends on the actual measurement to be carried out. Various characteristics should be considered, such as accurate and reproducible response, dose and dose rate range, energy of radiation, environmental effects on the response, stability before, during, and after irradiation, and method of evaluation.

In practical radiation processing, i.e., during installation, operational and performance qualification exercises, the selection of the most suitable dosimetry systems requires special care and the use of previous experiences. Some suggestions concerning the applicable dosimetry systems are given below.

Radiation sterilization is radiation process with the most detailed regulations, and the international standard for radiation sterilization, ISO 11137 (2006) specifies the measurements to be carried out in connection with validation of a radiation sterilization process. These requirements can also be applied to other radiation processes. In *installation qualification* (IQ)

of gamma facilities there are no specific dosimetry requirements to verify operation of the plant within specifications, i.e., no dosimetry exercises are needed. In the case of electron irradiation facilities, however, the beam characteristics like the electron energy, the width, and homogeneity of the scanned beam and the beam spot – in the case of pulsed electron accelerators – must be measured.

In the case of *operational qualification* (OQ) exercises like (1) determination of relationship between irradiation time and dose, (2) measurement of dose distribution in reference material, (3) measurement of effects of process interruption, and (4) measurement of beam characteristics have to be performed.

In case (1) in gamma facilities the dose vs. irradiation time (in plants with no product transport system) or the dwell time (in plants with product transport system) can be measured by using different reference standard, transfer standard, or routine dosimeters. In EB facilities, the dose vs. conveyor speed relationship can be measured mainly with process calorimeters, but other dosimetry systems with quick dose evaluation capabilities after irradiation can also be used for this purpose.

The measurement of dose distribution (2) in reference material can be carried out with various liquid or solid phase dosimeters in gamma plants, while mainly with film dosimeters in EB plants taking into account the specific spatial resolution requirements.

The measurement of beam characteristics can be performed the same way as described in the case of IQ exercises.

The basic procedure in *performance qualification* (PQ) exercises is the measurement of dose distribution in real products. In gamma processing, similar dosimetry systems can be applied like in OQ exercises. In electron processing, usually film dosimeters are suggested for use with the restriction of the application of only thin film dosimeters for dose mapping in inhomogeneous products.

Note: The dosimetry systems applicable in gamma processing can also be used in X-ray processing according to the present knowledge.

Reliable dosimetry requires the knowledge of the level of accuracy and precision of the dosimetry system used. All dosimeters need calibration in order to establish measurement traceability. This can be achieved by carrying out suitable calibration procedures – traceable to an appropriate national standard – with respect to both the dosimeter system and the instrumentation used for evaluation. The main aim of dosimeter calibration is to determine the relationship between the response of the dosimeter and the dose absorbed in it. This relationship depends on a number of external factors with respect to irradiation conditions, and therefore calibration procedures should be selected to minimize the effect of these influence factors (e.g., environmental conditions affecting the dosimeter response), thus improving the accuracy of the dose measurement. It can be done by using calibration in-plant (i.e., under processing conditions) whenever possible. The other option is to calibrate dosimeters in a calibration laboratory applying correction factors (e.g., irradiation temperature coefficient), which is followed by calibration verification in the irradiation plant (ASTM 51261, Sharpe and Miller 1999). The calibration of routine dosimeters is usually carried out by irradiating routine dosimeters together with reference or transfer standard dosimeters. Both the reference and transfer standard dosimeter systems require calibration and this is often done by comparison with dosimeters of higher quality. Such systems are categorized as primary-, secondary reference, or transfer standard dosimeters of higher metrological characteristics, namely high accuracy and reproducibility ($\pm 1\text{--}2\%$, $k = 2$), long-term stability and limited – but known – environmental effects on their response (ASTM 2628, McLaughlin et al. 1989).

Uncertainties are usually reported based on either a 95% or a 99% probability that the correct value is within the range. The accurate calculation of such values according to the current practice is to report standard uncertainties multiplied by a coverage factor (k) of either 2 or 3. For most situations, a coverage factor of 2 is very close to a 95% confidence interval, and a coverage factor of 3 is very close to a 99% confidence interval (Sharpe and Miller 1999).

The ASTM Subcommittee E10.01 on “Radiation Processing: Dosimetry and Applications” has under its jurisdiction approximately 30 standard practices and standard guides, collectively known as the E10.01 standards on radiation processing. These practices and guides describe the dosimetry systems most commonly used in radiation processing, and the dose measurements that are required in the validation and routine monitoring of the radiation processes. The development, validation, and routine control of a radiation process comprises a number of activities, most of which rely on the ability to measure the delivered dose accurately. It is therefore necessary that dose is measured with traceability to national standards, and the uncertainty is known, including the effect of influence quantities. The E10.01 standards on radiation processing dosimetry serve to fulfill these requirements.

The scientific basis and historical development of many of the dosimetry systems used in radiation processing can be found in the recently published ICRU Report 80 (ICRU 2008).

49.3 Chemical Methods of Dosimetry

49.3.1 Liquid Systems

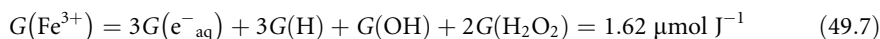
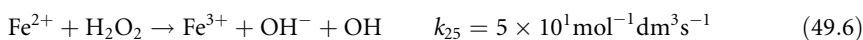
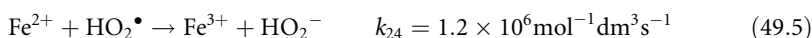
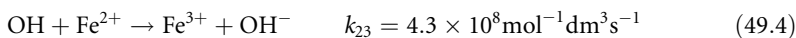
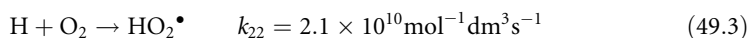
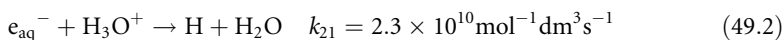
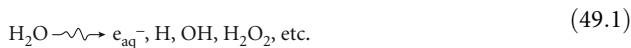
The most significant liquid dosimetry systems used in high-dose dosimetry are aqueous solutions of inorganic solutes, but a few organic systems (i.e., organic solvents containing organic solutes) are also of importance. Most of these systems consist of a bulk liquid component – in which practically all the energy imparted by the ionizing radiation is absorbed – and a solute that reacts with the radiation-induced species formed upon the interaction of the solvent with the ionizing radiation. The radiation chemistry of both components is well documented, and the main processes used for dosimetry are based on a carefully selected chemical change, i.e., the appearance or disappearance of a product or component of the system.

49.3.1.1 Aqueous Chemical Dosimeters

Ferrous Sulfate (Fricke) Dosimeter

The best-known liquid chemical dosimeter, the Fricke dosimeter, is based on the radiation-induced oxidation of ferrous ions, Fe(II), to ferric ions, Fe(III), in acidic media (Sehested 1970). The standard Fricke solution consists of $0.001 \text{ mol dm}^{-3}$ ferrous ammonium sulfate (Mohr's salt: $\text{Fe}(\text{NH}_4)_2(\text{SO}_4)_2 \cdot 6\text{H}_2\text{O}$) or ferrous sulfate ($\text{FeSO}_4 \cdot 7\text{H}_2\text{O}$) and 0.4 mol dm^{-3} H_2SO_4 in aerated aqueous solution. Organic impurities are to be carefully removed since they facilitate excess Fe^{3+} ion formation. Sometimes $0.001 \text{ mol dm}^{-3}$ NaCl is also added to the solution in order to reduce the effect of trace organic impurities (ASTM E 1026-04). The Fe^{3+}

ions form in reactions of the intermediates of water radiolysis with the Fe^{2+} ions (water radiolysis is discussed in ► Sect. 23.6, Chap. 23, Vol. 1).



The dosimeter containers are usually sealed glass ampoules of 2–5 cm³ capacities. Fe^{3+} ion concentration is measured in a spectrophotometer at the absorption maximum of these ions, at 304 nm. The dose is determined from the increase of optical absorbance, ΔA :

$$D = \frac{\Delta A}{G \varepsilon_m l \rho} \quad (49.8)$$

where l is the light path in the optical cell and ρ is the density. The molar linear absorption coefficient ε_m is 219 m² mol^{−1} at 25°C; it increases with the analysis temperature by 0.7% (°C)^{−1}. The response of the system is nearly independent of spectral energy of photon and electron radiation in the range of 0.5–16 MeV (Mattson and Johansson 1982).

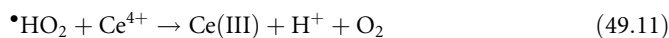
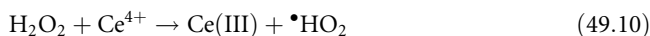
The conventional Fricke dosimeter is applicable for measuring doses in the 40–400 Gy range; actually the consumption of oxygen determines the upper limit. For doses up to 2 kGy, the super Fricke dosimeter can be used, which contains higher Fe^{2+} concentration and is saturated with oxygen (Sehested et al. 1973).

The system is widely used for calibration purposes, but its routine application for irradiation process control is also well known. It is mainly used in gamma and X-ray fields, but the solution can also be used for electron dosimetry.

The calibration of the Fricke dosimeter must be verified by comparison with reference standard dosimeters in order to provide measurement traceability to national standards.

Ceric Sulfate (or Ceric-Cerous Sulfate) Dosimeter

The use of the ceric sulfate dosimeter solution is based on the radiolytic reduction of the ceric ions to cerous ions in an aqueous acidic solution (Weiss 1952).



The response of the dosimeter is based on the difference in ceric ion concentration before and after irradiation. The initial concentration of ceric sulfate (or ceric ammonium sulfate) can be varied between 2×10^{-4} and 5×10^{-2} mol dm^{−3} in an aqueous solution

containing 0.4 mol dm^{-3} sulfuric acid. This system can be used for dose measurement in the range of 1–200 kGy (ISO/ASTM 2002a). The evaluation of the irradiated solutions is carried out with spectrophotometry by measuring the change of absorbance of the ceric ions at 320 nm, which is approximately linear with dose. The molar linear absorption coefficient (ϵ_m) for the ceric ion is $561 \text{ m}^2 \text{ mol}^{-1}$ at 25°C (Matthews 1982).

The ceric sulfate dosimeter is sensitive to impurities, but this effect can be decreased by the addition of scavengers, e.g., cerous ions, or by preirradiation of the solution to a dose of approximately 1 kGy. Other unfavorable characteristics of the solution are its light sensitivity, energy dependence below 0.1 MeV, dose rate dependence above 10^6 Gy s^{-1} , and the need to dilute the irradiated solutions for the spectrophotometric evaluation. The temperature coefficient of the solution during irradiation is not significant in the range of $10\text{--}62^\circ\text{C}$ (Matthews 1982).

Since the addition of cerous ions to the ceric sulfate solution suppresses the effect of impurities, Matthews introduced the modified version of this dosimetry system by using a mixture of the ceric and cerous ions (Matthews 1982). Electrochemical potentiometry is applied to evaluate the irradiated solutions by measuring the redox potential difference between the unirradiated and irradiated solutions. This method can be applied in the dose ranges of 0.5–5 kGy or 5–50 kGy depending on the initial ceric ion concentration chosen. An important advantage of this method compared to spectrophotometry is that no dilution of the irradiated solution is needed.

This dosimetry system has been applied widely for dose mapping and routine process control, especially due to dedicated commercially available instruments such as potentiometric electrochemical cells.

Dichromate Dosimeter

This dosimeter relies on the radiolytic reduction of the dichromate ion $(\text{Cr}_2\text{O}_7)^{2-}$ to chromic ion in aqueous perchloric acid solution. In this aqueous solution the radiolytically produced hydrogen atoms reduce Cr(VI) , while the hydroxyl radicals oxidize Cr^{3+} . Matthews (1981) suggested adding silver ions to the solution, since these scavenge the oxidizing hydroxyl radicals.

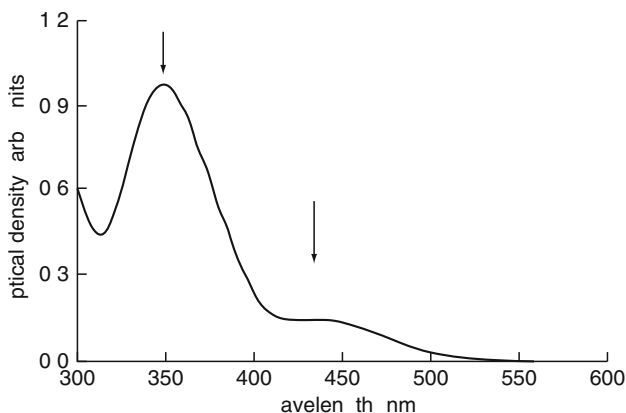
The solution consists of $2 \times 10^{-3} \text{ mol dm}^{-3} \text{ K}_2\text{Cr}_2\text{O}_7$ and $5 \times 10^{-4} \text{ mol dm}^{-3} \text{ Ag}_2\text{Cr}_2\text{O}_7$ in 0.1 mol dm^{-3} perchloric acid. The decrease of dichromate ion concentration is almost linear with dose, which is determined by spectrophotometric measurement of the absorbance on the high wavelength shoulder of the radiation-induced absorption band at 440 nm (► Fig. 49.1). At this wavelength, however, both the dichromate and the chromic ion absorb; therefore, the net molar linear absorption coefficient ($44 \text{ m}^2 \text{ mol}^{-1}$ at 25°C) and the $G((\text{Cr}_2\text{O}_7)^{2-})$ ($0.0395 \times 10^{-6} \text{ mol J}^{-1}$) can be used to calculate the dose.

The dosimetry characteristics of the solution are quite favorable according to Sharpe et al. (1985), who have shown good reproducibility ($\pm 0.5\%$) and almost linear response in the dose range of 5–40 kGy. The irradiation temperature coefficient of the solution is $-0.2\% (^\circ\text{C})^{-1}$ in the temperature range of $25\text{--}50^\circ\text{C}$ (Sharpe et al. 1985). No significant photon and electron energy dependence (Miller 1985), dose rate effect (in the range of $0.7\text{--}500 \text{ Gy s}^{-1}$, Sharpe et al. 1985) or ambient light effect is observed on the response of the dosimeter solution.

By using lower concentration of $\text{Ag}_2\text{Cr}_2\text{O}_7$ ($5 \times 10^{-4} \text{ mol dm}^{-3}$) in 0.1 mol dm^{-3} perchloric acid solution doses down to about 2 kGy can be measured, but in this case the analysis has to be carried out at 350 nm, i.e., at the absorption maximum (Thomassen 1985).

■ Fig. 49.1

Optical absorption spectrum of dichromate ion (measurement wavelengths are shown with arrows)



The dichromate dosimeter solution is of importance mainly for radiation sterilization and food irradiation applications both for gamma and electron dosimetry. Due to its very good reproducibility, the system is classified as a reference standard system (ASTM E 2628-2009) in the 5–50 kGy dose range and used widely also as a transfer standard dosimeter.

Tetrazolium Dosimeter Solutions

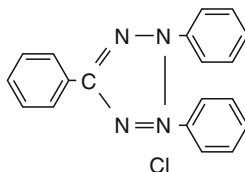
Besides the well-established aqueous dosimeter solutions, new systems are also under development and test; and the introduction of the tetrazolium solutions for dose control in radiation processing is one example of these new dosimeter systems.

Tetrazolium salts are heterocyclic organic compounds (quaternary ammonium compounds) with a significant property of forming water-insoluble, highly colored formazans by reduction. Gierlach and Krebs (1949) observed the appearance of red color upon UV light exposure, as well as α - or X-ray radiation of its aqueous solutions and gelatin emulsions, and this can be utilized for dosimetry purposes. The radiolytic reduction of the tetrazolium salts (e.g., 2,3,5-triphenyltetrazolium chloride, ► Fig. 49.2) is a two-electron process, i.e., the reduction of each tetrazolium molecule needs two reducing species. In the first step a tetrazolinyl radical forms, which is then reduced further to formazan (Kovács et al. 1999). In the case of tetrazolium salts containing two tetrazolium rings (e.g., nitrotetrazolium blue) the formation of diformazan is a four-electron process involving the consecutive reactions of the formation of monotetrazolium radical, monoformazan, monoformazan radical, and the final diformazan product (Bielski et al 1980).

In aqueous solutions of tetrazolium salts, the formation of a precipitate was observed due to the nature of the formazan. In aqueous–alcoholic solutions, however, no precipitation was observed due to the solubility of the formazan in organic solvents. In such solutions (containing primary or secondary alcohols), the radiolytic reduction is found to be more effective, because the α -hydroxyalkyl radicals that form in the reaction of OH radicals and H atoms with the alcohol, also reduce the tetrazolium ion (Kriminskaya et al. 1987).

Different tetrazolium salts have been studied for dosimetry purposes both in solutions and in solid matrices. The 2,3,5-triphenyl-tetrazolium chloride (TTC) solutions and gels are found

■ Fig. 49.2

2,3,5- Triphenyltetrazolium chloride

to be useful for high-dose dosimetry (Krebs 1963; Kovács et al. 1996). The alcoholic solution of $0.045 \text{ mol dm}^{-3}$ TTC has a linear response of absorbance ($\lambda_{\text{max}} = 480 \text{ nm}$) with dose over the range of 1–16 kGy.

The aqueous solution of nitro blue tetrazolium chloride was investigated (Kovács et al. 1999) and it was observed that the NBT^{2+} ions were reduced radiolytically first to monoformazan (MF^+) and then to diformazan (DF) having high linear molar extinction coefficients at the absorption maxima of 522 nm and 570–610 nm. The formation of formazans was found more pronounced in the presence of alcohol and the aqueous-ethanol nitro blue tetrazolium solutions were found useful for high-dose dosimetry in the dose range of 0.1–30 kGy.

The response of the aqueous and aqueous–alcoholic solutions of tetrazolium violet (2,5-diphenyl-3-(1-naphthyl)-2H-tetrazolium chloride, TV) was found useful for dosimetry purposes in the 0.25–60 kGy dose range. The polyvinylalcohol-based TV-containing dosimeter films showed also suitable response in the 1–60 kGy dose range making it useful for radiation process control both in gamma and electron beam radiation processing (Emy-Reynolds et al. 2007a, b).

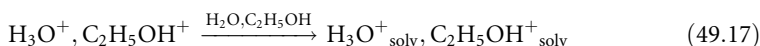
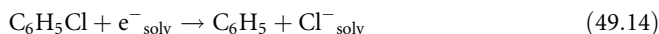
49.3.1.2 Organic Chemical Dosimeters

Ethanol-Monochlorobenzene Dosimeter

This dosimeter system, developed and introduced by Dvornik et al (1966), contains monochlorobenzene ($\text{C}_6\text{H}_5\text{Cl}$) in aerated ethanol–water solution. The original solution contained also small amounts (0.04 vol%) of acetone and benzene in order to inhibit the effect of impurities, but later it was shown (Coninckx et al. 1993) that the use of these minor additives is not essential. In order to match the radiation absorption characteristics of the product to be irradiated, tissue-equivalent dosimetry can be achieved by changing the concentration of monochlorobenzene between 4 and 40 vol% (Razem and Dvornik 1973a). In radiation processing practice, however, the solution containing 24 vol% of monochlorobenzene has achieved wide application and thus the dosimetry characteristics of this system have been thoroughly studied and established.

The dosimeter is based on the formation of hydrochloric acid (HCl) upon irradiation via dissociative electron attachment, since the monochlorobenzene, as a good electron scavenger, reacts both with the “dry” and the solvated electrons. The HCl is in dissociated form in the solution and its formation is shown in the following reaction scheme:





As shown, the chloride ions as well as the positive ions, formed due to ionizing radiation, are in solvated form in the solution, giving rise to formation of hydrochloric acid (Dvornik et al. 1969). The $G(\text{Cl}^-)$ was found to be independent of dose up to about 100 kGy (Razem et al. 1981) (which means that the dose response is linear) and of dose rate up to about 10 Gy s^{-1} (Razem and Dvornik 1973a, b), supporting the above described reaction mechanism. The $G(\text{Cl}^-)$ value is nearly independent of irradiation temperature between 20°C and 90°C (Dvornik 1970) and very little energy dependence was found for photons with energies greater than 50 keV in comparison with energy imparted to water or soft tissue (Miller 1985). The solution is not sensitive to impurities, can be stored both before and after irradiation in the dark for long periods.

The measurement of absorbed dose is carried out by measuring the concentration of HCl using alkalimetric or mercurimetric titration in the dose range of 0.4–400 kGy (Dvornik et al. 1966). The hydrogen ion concentration is determined with alkalimetric titration using bromphenol blue indicator. However, due to the reaction of the hydrogen ion with glass, this method should only be used at doses above 2 kGy. The mercurimetric method can be used in the entire dose range to determine the concentration of chloride ions using diphenyl carbazone indicator.

There are, however, other measurement methods developed mainly for routine process control in radiation processing, such as high-frequency conductivity (oscillometric) analysis, spectrophotometric evaluation, and conductivity measurement.

Dose Measurement Methods

1. *Conductivity methods.* In solutions, the electric current is carried by the ions, which start to migrate under the influence of the electric field strength between the electrodes. The conductivity of a solution is the sum of the conductivity of the electrolyte and that of the solvent. The measurement of conductivity is carried out by measuring the resistance in the solution by immersing a pair of inactive electrodes into the solution. In this way, the direct conductivity of the solution is measured in units of siemens (S).

The measurement of absorbed dose is possible by directly measuring the conductivity (in siemens, ohm^{-1}) of the irradiated dosimetry solutions by immersing a pair of inactive electrodes (e.g., bell electrode consisting of platinum rings) into the solution. The method can cover a wide dose range of 50 Gy to 1 MGy with an accuracy of $\pm 5\%$ and reproducibility of $\pm 3\%$ (Kovács et al. 1985). Due to the temperature dependence of the conductivity of the solutions, a temperature correction of the response with respect to that of the calibration can be carried out by using the Nernst equation (CRC Handbook 1978).

High-frequency conductivity (oscillometric) measurement. Oscillometry (Blaedel and Petitjean 1956), i.e., the high-frequency method of chemical analysis to measure or follow changes in the composition of chemical systems was introduced to measure absorbed dose

by evaluating the irradiated ethanol-monochlorobenzene (ECB) dosimeter solution (Földiák et al. 1973). Since the amount of ions present in the solutions is altered due to irradiation, the conductivity of the solution is changed. Thus, a relative measure of the conductivity of the dosimeter solution is obtained by a high-frequency oscillator circuit, which employs a capacitive cell. An oscillator circuit is characterized by the Q factor as well as by the frequency. Either the shift in the frequency or the change in the Q factor is utilized in the oscillometric measurements. In the case of the oscillometric measurements of the ECB solutions, the change of the Q factor is measured through following the change in conductance. Because there is no galvanic contact between the solution and the electrodes, the measurements can be carried out in sealed ampoules, which are placed in between the electrodes, so that the Q factor of the parallel oscillatory circuit is changed, thus producing a change in the amplitude of the oscillations giving a relative signal.

The oscillometric evaluation method is nondestructive thus making possible the reevaluation of the dosimeters later at any time due to the stability of the solutions. The effect of UV light during storage on the unirradiated and irradiated solutions, however, has to be avoided. In order to decrease the measurement uncertainty, the preselection of the glass ampoules according to their diameter may be needed. The oscillometric evaluation method is applicable in the dose range of 1–300 kGy for dose mapping in gamma processing, for routine process control in gamma, and in electron beam processing, as well as a transfer standard system (ISO/ASTM 2002b).

2. *Spectrophotometric analysis.* This method of analysis requires the addition of ferric nitrate and mercuric thiocyanate to the irradiated ethanol-monochlorobenzene solution (Razem et al. 1981). The radiolytically generated Cl^- ions react with the mercury(II) thiocyanate followed by the reaction of the liberated thiocyanate ions with ferric ions to produce the red colored ferric thiocyanate complex, which is measured at 485 nm. The method is applicable in the dose range of $10\text{--}10^4$ Gy.

Radiochromic Dye Solutions

The measurement of absorbed dose with radiochromic dye solutions is based on the color change induced by radiation. The most important systems are the leucocyanides or leucomethoxides of a number of triphenylmethane dyes, which were first used as dosimeters for UV radiation (Weyde and Frankenburger 1931) and then suggested for ionizing-radiation dosimetry by McLaughlin and Chalkley (1965). Depending on the substitutions on triphenylmethane both organic and aqueous solutions can be prepared. Four compounds have been studied extensively: pararosanine cyanide (McLaughlin and Kosanic 1974), hexa (hydroxyethyl) pararosanine cyanide (McLaughlin et al. 1971), new fuchsin cyanide (Farahani and McLaughlin 1988), and malachite green methoxide (Bobrowski et al. 1985).

In the presence of weak acid and polar organic solvents, the cyanide radical is detached due to ionizing radiation, leaving a deeply colored cation, the carbonium cation, which is stable in polar acidic solution. This phenomenon is utilized for dosimetry, since there is a nearly linear relationship between the increase of absorbance due to cation formation and the absorbed dose in the range of $10\text{--}3 \times 10^4$ Gy. These systems have the advantage of being tissue equivalent with respect to radiation absorption characteristics; their response is independent of impurities and of dose rate up to about 10^{12} Gy s^{-1} . The effect of UV light on the solutions, however, has to be avoided and the irradiation temperature effect ($\sim 0.2\text{--}0.3\%$ /°C) must be taken into account (ISO/ASTM 51540 2002c).

Concerning the practical use of these solutions, the introduction of light waveguides proved to be an important step by increasing significantly the optical pathlength for spectral analysis. These solutions are held in long plastic tubes of inner diameter of 1–2 mm, sealed at both ends with glass or plastic beads. The optical measurements are made with routine densitometers designed for the given application. Absorbed dose measurements can be made in a wide dose range with a reproducibility of about $\pm 3\%$ (Radak and McLaughlin 1984). One of the most important applications of these systems concerns food irradiation due to the applicable dose range and the ruggedness of the system.

The liquid dosimeter systems used most frequently in radiation processing are shown in [Table 49.1](#).

49.3.2 Solid Systems

Many of the solid dosimetry systems used in high-dose dosimetry consist of either ordered organic or inorganic crystalline materials or amorphous or quasi-crystalline materials (such as glasses or plastics). The advantage of using such materials in comparison with liquid systems is, among others, their small size, better spatial resolution for dose distribution measurements, ruggedness, and ease of handling. The evaluation methods of these systems include spectrophotometry, spectrofluorimetry, various types of luminescence measurements, and the analysis of radiation-induced signals via electron-spin resonance spectroscopy. The measurement of electric current or voltage changes in semiconductors and insulators or the variation of conductivity in doped polymer film systems is also utilized for dosimetry purposes.

49.3.2.1 Dosimetry Systems Based on the Measurement of Optical Absorption

The color of many solid-phase systems changes, when they are irradiated. Colorless systems get colored, while originally colored systems become darker or bleach and these changes can be

[Table 49.1](#)

Liquid chemical dosimeters for high doses

Dosimeter system	Method of analysis	Useful dose range (Gy)	Typical precision limits ($k = 2$)	Reference
Fricke solution	UV spectrophotometry	$2 \times 10^{-2} - 4 \times 10^2$	1%	ASTM E 1026-04
Ceric-cerous sulfate	UV spectrophotometry, potentiometry	$10^3 - 10^6$	3%	ISO/ASTM 51205
Potassium dichromate	UV–VIS spectrophotometry	$5 \times 10^3 - 4 \times 10^4$	1%	ISO/ASTM 51401
Ethanol-chlorobenzene	Titration or HF oscillometry	$4 \times 10^2 - 3 \times 10^5$	3%	ISO/ASTM 51538
Radiochromic dyes	Visible spectrophotometry	$10 - 3 \times 10^4$	5%	ISO/ASTM 51540

utilized for the measurement of absorbed dose. In certain transparent, clear solid materials, optical bands absorbing in the UV are produced. The appearance of these bands is due to the changes in the structure of these solid materials, such as the formation of unsaturated chemical bonds (Charlesby 1960; Dole 1972) or color centers occurring as electron-filled negative ion lattice vacancies.

One solid dosimetry system (silver halide emulsions in thin gelatin layer matrixes) undergoes radiation-induced darkening by chemical development of latent photographic images.

Other groups of these dosimeters contain certain dyes mixed into the basic material (in most cases a polymer), and the optical absorption of these dyes changes upon irradiation. These systems are simple to measure and apply, but their response is affected by environmental factors such as humidity, light, and temperature. Some of these systems are preferred in gamma processing, while the main application field of others is electron-beam dosimetry.

Color-Center Systems

Crystalline materials. Pure colorless optical quality LiF in various forms like natural LiF, ^6Li -enriched LiF, or ^7Li -enriched LiF can be used for dosimetry purpose by measuring the increase in their absorbances, ΔA , at the maxima of a number of color center absorption bands. The absorption of these radiation-induced characteristic LiF color centers absorbing in the UV, visible and near IR range allow dosimetry in the dose range of 10^2 – 10^7 Gy (McLaughlin et al. 1980; Baeyens et al. 1985). The dose ranges of these color centers – which are a progression of single (F-center), double (M-center), triple (N- or R-center), etc., electron-filled negative-ion vacancies – overlap, making it possible to measure a continuous wide range of doses provided calibration for each individual dosimeter is established. After 1 day, the radiation-induced absorption is stable for weeks when dosimeters are stored at room temperature (McLaughlin et al. 1979a). The characteristics of the M-center shows a small irradiation temperature coefficient ($+0.1\% (^{\circ}\text{C})^{-1}$), reasonable precision for routine applications ($\pm 5\%$), and negligible dose rate dependence. The radiation absorption properties of LiF differ only slightly from those of water over a wide range of energies (Miller and McLaughlin 1982; Hubbell 1982).

The optical-quality LiF dosimeter can be reused repeatedly if the darkened crystals are bleached to the colorless state by a high-temperature annealing treatment (550°C for 1 h).

Glasses. The potential dosimetric use of several various types of glasses has been studied (Kreidl and Blair 1956, 1959). These materials can be applied for the measurement of absorbed dose by spectrophotometric, densitometric, or fluorimetric analysis of color centers formed upon irradiation in the dose range of 10 – 10^4 Gy. High doses (10^3 – 10^7 Gy) can be measured utilizing the degradation of photostimulated luminescence intensity (Freytag 1971; Becker 1973). Although the routine use of a few systems is possible, the energy and dose rate dependence of their response as well as the fading after irradiation generally limits their application.

Undyed Solid Systems

In certain clear, transparent polymer materials new optical absorption bands – absorbing mainly in the ultraviolet or in the infrared region – form upon irradiation. These radiation-induced changes in the UV region involve (1) main-chain unsaturations of polyene groups (e.g., $-\text{C}=\text{C}-$ in polyolefins) or (2) side-chain unsaturations (e.g., $=\text{C}=\text{O}$ groups in polymethylmethacrylate) as described by Charlesby (1960) and Dole (1972). The increase of absorbance of these absorption bands can be used for dosimetry measurements.

The dosimetry utilization of polyethylene films in the 10^5 – 10^6 Gy dose range is based on ultraviolet at 240 nm (Chen et al. 1980) or infrared measurement of carbonyl or trans-vinylene groups formed upon irradiation and analyzed at 5,800 nm or 10,600 nm, respectively (Charlesby et al. 1964; McLaughlin et al. 1999).

Cellulose triacetate film dosimeter. The use of this dosimeter film is based on the radiation-induced absorbance change at 280 nm, which is linear in the dose range of 30–200 kGy (Puig et al. 1974; Tamura et al. 1981, ISO/ASTM 51650). The spectrophotometric measurement of the irradiated film is made on the steep high-wavelength edge of the absorption band; therefore, accurate setting of the wavelength is essential. The response of the film is lower for electron irradiation than for gamma by about 30% due to the O_2 diffusion during irradiation. The performance of the film is affected by relative humidity during irradiation (Tanaka et al. 1984). These effects were, however, not observed by Tanaka et al. when applying the films in high dose rate ($>1 \text{ MGy h}^{-1}$) electron radiation fields. The irradiation temperature coefficient of the film is about $+0.5\% \text{ } ^\circ\text{C}^{-1}$ (Tamura et al. 1981). The response of the dosimeter changes after irradiation due to the reaction of oxygen and the radicals present in the film (Gehring et al. 1985). The reproducibility of the radiation-induced change in absorbance was measured to be 5% ($k = 1$) by Tanaka et al. (1984).

Polymethylmethacrylate dosimeter. Several types of polymethylmethacrylate are known as potential dosimeters, and one system, clear (HX) Perspex, was developed for routine dose measurement (ISO/ASTM 51276). It is prepared using benzoyl peroxide as polymerization initiator. The irradiated clear Perspex dosimeters are measured by spectrophotometry usually at 314 nm or 315 nm, as the most stable wavelengths for evaluation (Chadwick 1969). The response of the HX Perspex was found to be independent of irradiation temperature in the range of 0–30°C, but at higher temperatures the response was decreasing (Miller and McLaughlin 1981). Miller et al. (1975) observed the effect of dose rate on the response too at values above 10^6 Gy s^{-1} .

Dyed Solid Systems

Polymer films or plates containing certain dyes that change color when irradiated are well known as dosimeters. The thickness of the dosimeters must be taken into account during evaluation, so that the response of each dosimeter is the absorption divided the thickness. In most cases, the radiation-induced response is nonlinear with absorbed dose and it is affected by temperature, humidity, light, and dose rate. Due to the combined effects of these factors and other environmental factors, careful calibration of these systems preferably using in-plant calibration is needed (Miller et al. 1975; McLaughlin 1978).

Some of these systems (like dyed cellulosic materials and indicator dyes in halogenated materials) are not accurate and reproducible enough for absorbed dose measurement, but these systems can be used as dose monitors or indicators to distinguish between irradiated and nonirradiated materials, e.g., in radiation sterilization (McLaughlin et al. 1988).

Dyed polymethylmethacrylate (PMMA) dosimeter. Polymethylmethacrylate dosimeters containing different types of dyes have been developed for routine dosimetry mainly in radiation sterilization and have been used extensively for many decades (Whitaker 1970; ISO/ASTM 2002e). Various types of the PMMA dosimeters are known, but the most popular are the red Perspex, the amber Perspex, and the Gammachrome YR.

When irradiating the red Perspex dosimeter, the appearance of an optical band absorbing between 600 nm and 700 nm can be observed resulting in the darkening of the original red color of the $1 \text{ cm} \times 3 \text{ cm}$ dosimeter (Whitaker et al. 1985). Spectrophotometric evaluation of

the irradiated dosimeter is performed at 640 nm (i.e., not at the absorption maximum), since the postirradiation effects (temperature and storage time) on the response of the dosimeter are the least pronounced at this wavelength. The useful dose range of the red Perspex dosimeter is 5–50 kGy. The amber Perspex is used for measurement of doses in the 3–15 kGy range at 603 nm or 651 nm (Barrett 1982). To measure low doses (0.1–3 kGy) mainly in food irradiation applications, the Gammachrome YR system was developed. It is evaluated after irradiation at 530 nm (Whitaker 1988). This dosimeter is applicable over a wide temperature range during irradiation, thus it is suitable for process control for foods irradiated at low temperatures provided that the dosimeters have been calibrated under these conditions (Biramonti et al. 1996).

The temperature and humidity during and after irradiation, as well as the diffusion of O₂ into the dosimeters, can affect the radiation-induced response of all types of Perspex dosimeters, but the packaging applied (i.e., airtight pouches) minimizes the effects of the latter two factors. The measurement of these dosimeters should be carried out at a specified time after irradiation due to short- and long-term instability. The effect of irradiation temperature becomes significant over 40°C being more pronounced at higher doses, e.g., the temperature coefficient of 1.5% (°C)⁻¹ was determined for a dose of 20 kGy (Miller et al. 1975). Postirradiation heat, on the other hand, changes the response significantly and should therefore be avoided during storage (Barrett et al. 1980).

The Perspex dosimeter “family” is frequently used in radiation processing for process control in a wide dose range mainly in gamma radiation processing. Due to the combined effects of environmental factors, however, they – like most dosimeters used in radiation processing – should be calibrated under conditions of use (Glover et al. 1985).

Film dosimeters. The radiation-induced change of optical absorption in various film systems has been utilized for dosimetry purposes for many decades. Although correct application of films requires controlled conditions because their response is affected by almost all environmental factors, these systems are widely used in both gamma and electron beam radiation processing. They are well suited for dosimetry of electron radiation because of their good spatial resolution characteristics, e.g., for dose distribution measurements as compared to other systems.

1. *Radiochromic film dosimeters.* Many polymer-based film dosimeters have been developed containing various types of dyes, whose color or depth of color changes during irradiation. Certain leucocyanides or leucomethoxides of triphenylmethane dyes are widely applied in the dose range of 10²–10⁶ Gy (McLaughlin 1974, 1977, 1985, ISO/ASTM 51275).

One of the established systems contains hexa(hydroxyethyl)pararosaniline cyanide in a nylon matrix and is available in large batches (McLaughlin 1966; Kantz and Humpherys 1977). This colorless thin film (~50 μm) changes to deep blue upon irradiation and is applicable in the dose range of about 3 kGy up to about 150 kGy. The response of the film is independent of the energy and type of the radiation (electron, gamma, and X-ray radiation) and of the dose rate up to about 10¹³ Gy s⁻¹ resulting in its use for process control for gamma as well as for low- and high-energy electron irradiation. The spectrophotometric evaluation of this film is carried out either at the maximum of the absorption band at 605 nm (dose range: 3–30 kGy) or at the edge of the spectrum at 510 nm (dose range: 30–150 kGy). Similarly to the Perspex dosimeters, the so-called specific absorbance (absorbance divided by thickness) of the irradiated films is used for the evaluation. The relative humidity during storage and irradiation significantly affect the response of the film. It was

found that at around 34% relative humidity the response is least affected by changes in the humidity and, therefore, the dosimeters are suggested to be conditioned and irradiated in such an environment (McLaughlin et al. 1983; Abdel-Fattah and Miller 1996). To ensure this condition and to avoid the effect of light, these dosimeters are sold in airtight pouches similar to the Perspex dosimeters. The response of these dosimeters depends in complex ways on dose, temperature, and humidity. It is therefore not recommended to calibrate them under fixed conditions, and to consider varying conditions by applying correction factors for the differences between calibration conditions and the conditions of use. The dosimeters should be calibrated in-plant at the conditions of use (Abdel-Fattah and Miller 1996). The radiation-induced color increases after irradiation, but this can be eliminated using a 5-min long postirradiation heat treatment at 60°C (Chappas 1980).

Polyhalo-styrene-based films containing similar dyes (e.g., malachite green methoxide) have similar characteristics as mentioned above, but these are free of humidity effects (Bishop et al. 1973).

Miller et al. (1988) have developed a thin (20 μm) polyvinyl butyral film containing the leucocyanide of pararosaniline, which changes from colorless to pink in its useful dose range of 2–100 kGy. The spectrophotometric measurement of the irradiated film is performed at 554 nm at the absorption maximum of the radiation-induced optical band. Another version of the same film contains the same dye and a radiation insensitive additive. Since the optical absorbance measured at 650 nm depends only on the thickness of the film, thus using the difference of the optical absorbance values measured at 554 nm and 650 nm respectively, as response, the measurement of thickness becomes unnecessary. A third version of this type of film is provided with adhesive backing and UV protective cover and it is to be used for reflected light measurement with potential for label dosimetry applications (Kovács et al. 2000b).

Polyvinyl alcohol (PVA) based films containing different tetrazolium salts have been found useful for routine dose measurement in gamma and electron radiation processing. 2,3,5-triphenyl tetrazolium chloride (TTC) dissolved in PVA films (changing from colorless to pink) have been found suitable for dose measurement in the dose range of 1–100 kGy by evaluating the 50 μm thick film at the absorption maximum of 493 nm (Kovács et al. 1996). Dosimeter films containing dissolved nitro blue tetrazolium chloride have a dose range of 5–50 kGy measuring the absorbance of the irradiated films either at the maximum of the absorption peak (540 nm) or at the shoulder of the spectrum (580 nm). To ensure suitable stability, conditioning of the films in the relative humidity range of 34–55% is recommended. Using reflectometric evaluation, this film can be applied as a label dosimeter system (Kovács et al. 2000).

A thin radiochromic film consisting of colorless transparent coatings of polycrystalline, substituted-diacetylene sensor layer on a clear polyester base, called *GafChromic*, was developed both for low- and high-dose determinations (Saylor et al. 1988). With various formulations, the useful dose range extends from 1 Gy up to about 40 kGy. The radiochromic reaction is a solid-state polymerization, whereby the films turn deep blue upon irradiation due to progressive 1,4-trans additions as polyconjugations along the ladder-like polymer chains (McLaughlin et al. 1994). The irradiated films can be evaluated by spectrophotometry at different wavelengths (670 nm, 633 nm, 600 nm, 500 nm, and 400 nm) depending on the absorbed dose. This film dosimeter has broad application in radiographic imaging, nuclear medicine, and dosimetry for blood irradiation, insect population control, food irradiation, and industrial radiation processing, although it has

been designed particularly for measuring radiation therapy absorbed doses (1–100 Gy) (McLaughlin et al. 1996; Niroomand-Rad et al. 1998).

2. *Other film dosimeters.* Colorless PVC foils are used at electron accelerators to monitor the irradiation process and the accelerator parameters (like scan width and beam spot). In these materials unsaturated chemical bonds form upon irradiation and the optical absorption of these new species can be measured by spectrophotometry at 395 nm in the dose range of 0.5–60 kGy (Artandi and Stonehill 1958). It is important to mention, however, that due to various factors (environmental effects on the response, dose rate effects, batch-to-batch variation, etc.) these films should not be considered and used as dosimeters, but only as dose indicators.

49.3.2.2 Dosimetry Systems Based on the Measurement of Luminescence

Thermoluminescent Dosimeters (TLDs)

In many inorganic crystalline materials, electrons are removed from the valence band (ground state) upon irradiation, leaving mobile, positively charged holes. These free charge carriers become localized by the impurities present in the crystal lattice (as defects), i.e., the filling of electron and hole traps between the valence band and the conduction band takes place during irradiation (Cameron 1970). The energy absorbed from ionizing radiation and stored in the crystal lattice can be released in the form of light by several methods, like heating (thermoluminescence), dissolution of the crystals (lioluminescence), excitation by ultraviolet or visible light (optically stimulated luminescence, OSL), and by friction (triboluminescence).

In the case of thermoluminescence during the carefully controlled heating of the irradiated crystalline material, the trapped electrons and holes leave the traps, recombine together with the emission of characteristic light, the amount of which is the measure of absorbed dose (Fowler and Attix 1966; Cameron et al. 1968; Horowitz 1984). The intensity of the emitted light as a function of temperature is known as the glow curve. Its shape, i.e., the position of the peaks, is characteristic of the crystalline material. These characteristic peaks of the glow curve – either the height of the peaks or the area below them – are used for the determination of dose. In the case of certain TL materials there is a linear relationship between the absorbed dose and the amount of emitted light in a given dose range. At higher doses, first supralinearity appears (i.e., the slope of the line gradually decreases) followed by saturation. The evaluation of the irradiated crystalline material (i.e., the heating process) destroys the radiation effect and the dosimeters, if fully annealed at high temperature, can be reused.

The most common materials used in thermoluminescent dosimetry are LiF, CaF₂, CaSO₄, Li₂B₄O₇, Al₂O₃, MgB₄O₇, BeO, and MgSiO₄, which are used either alone or with trace amounts of additives (e.g., rare earths or transition metals), since these additives can significantly influence the formation of imperfections in the crystal lattice, i.e., the formation of the structure of traps and luminescence centers. The TL dosimeters are used in various forms (such as powder, single crystal, and pellet) depending on the field of application.

The TL dosimeters are mainly used for the measurement of low doses, thus these systems are mostly used in radiation therapy, personal dosimetry (Christensen et al. 1982), and environmental monitoring (Deplanque and Gesell 1982). The use of thermoluminescent dosimetry in radiation processing (ISO/ASTM 2002g) where the doses are high is of limited importance due to supralinearity, saturation effects, and radiation damage. Calcium fluoride

(CaF₂) and calcium sulfate (CaSO₄) are used worldwide in different forms like natural and manganese-activated TL phosphors. The CaF₂:Mn system is characterized by a single glow curve (maximum intensity at ~260°C) and by a relatively large useful dose range (10 μGy–10 kGy). Both types of materials have high sensitivity, which allows the detection of very low doses even below 10⁻⁵ Gy (Björngard 1963). Due to their high effective atomic number, however, these materials also present an important over-response at low photon energies (~100 keV). As with silver halide films, this effect can be corrected by using suitable filters. For instance, to get an appropriate correction on energy dependence, a shielding (of about 1.4 mm Cu) is proposed during irradiation. Lithium fluoride (LiF) and lithium tetraborate (Li₂B₄O₇) with an effective atomic number similar to soft tissue are good for measurement of absorbed dose in tissue, water, or air. The useful dose range of LiF covers the range of 10⁻⁵–10³ Gy and its main advantage over CaF₂ is its much better energy response. The manganese- and titanium-activated LiF (LiF:Mg, Ti) is often used in environmental monitoring (Barquero et al. 2002). With respect to measuring mixed fields, it is important to note that due to the difference of the two Li isotopes (⁶Li and ⁷Li) toward neutron detection efficiency these systems can distinguish between radiations of different origin in environmental monitoring. During the past 15 years, various tissue-equivalent phosphors of high sensitivity (e.g., LiF:Mg, Cu, P; Al₂O₃:C) have been developed in different laboratories for environmental applications.

The Al₂O₃:Mg,Y system developed by Osvay and Bíró (1980) has favorable characteristics both for personal and environmental monitoring and for food irradiation control due to its very wide dose range (10⁻³ Gy–10 kGy).

Several investigations have been carried out to extend the dose range of the most common TL phosphors. The use of higher-temperature glow peaks results in saturation at higher doses thus extending the dose range. Applying this approach in the case of LiF at 470°C, the measurement of doses of 10⁶ Gy becomes possible and Li₂B₄O₇:Mn can be used up to about 10⁴ Gy by using the 200°C peak before reaching saturation. Lakshmanan and Bhatt (1979) studied several TL phosphors with respect to high-dose applications using high-temperature glow peaks. The highest dose (~5 × 10⁶ Gy) was reached with CaSO₄:Dy (Lakshmanan and Bhuwanchandra Bhatt 1978). Other systems like CaF₂:Mn, LiF, and Li₂B₄O₇:Mn were used for gamma and X-ray dose determinations up to about 10⁴ Gy.

UV treatment of TL materials irradiated with ionizing radiation releases the deeply trapped charge carriers into shallower traps when followed by the regular thermoluminescent evaluation procedure. Using this method, the Li₂B₄O₇:Mn system can measure doses of about 1 kGy, the LiF:Mg,Ti phosphor is suitable for dose determination of about 10 kGy, while the CaSO₄:Dy dosimeter can measure doses as high as 1 MGy (Christensen 1982). Even higher doses can be measured with the same systems by applying pre-irradiation of the phosphors with gamma rays to the region of saturation followed by the evaluation of loss of emission upon irradiation to higher doses of about 10⁶ Gy (Lakshmanan and Bhuwanchandra Bhatt 1978).

Taking into account all these observations, the use of TL materials for high-dose determination appears possible. The fact that there are very few examples of practical application for high-dose dosimetry can be explained with problems of supralinearity, energy dependence, limited accuracy (> ±5%), and the difficulties originating from the repeated use of the systems (Burgkhardt et al. 1977).

Lyoluminescent Dosimeters

Upon dissolution of certain irradiated crystalline materials in a suitable solvent, light is emitted. The phenomenon – called lyoluminescence (LL) and suggested for dosimetry by

Ettinger and Puite (1982) – is based on the reaction of the solvent (usually distilled water) and free radicals produced by irradiation in the crystal. The luminescence signal during dissolution is integrated over a certain time period (~ 20 – 30 s). The dosimeter material must be carefully weighed and the dissolution must be carried out under controlled conditions. Typical lyoluminescent materials are saccharides (mannose, glucose monohydrate, or trehalose dihydrate) and amino acids (glutamine, valine, phenylalanine, glutamic acid). The useful dose range of lyoluminescence depends on the crystalline material, e.g., it is about 1 – 10^3 Gy for saccharides, while for glutamine it is 10 – 10^5 Gy (Miller and Xie 1985). The lyoluminescent dose response depends on different parameters like temperature, purity of water, O_2 concentration of water, and batch-to-batch variation of the crystalline material. With respect to practical application of the method different lyoluminescent materials were investigated like mannose and alkali halides (NaCl, KCl, LiCl), but their usefulness has been prevented by many factors (Puite and Ettinger 1982).

Glutamine has been found suitable for LL dosimetry. The glutamine system has been developed for high-dose dosimetry as routine dosimeter in radiation processing (Puite and Ettinger 1982; Temperton et al. 1984). The irradiation temperature coefficient for this dosimeter is about $+0.35\%$ $(^\circ\text{C})^{-1}$ in the temperature range of 10 – 40°C . Miller and Xie (1985) found no dose-rate dependence up to about 10^7 Gy s^{-1} .

The widespread application of the method is limited by, e.g., the effect of environmental factors and the lack of commercial readers. It is, however, possible to adapt instruments designed for chemiluminescence investigations as suggested by Temperton et al. (1984).

Radiophotoluminescent Dosimeters

Fluorimetry is the measurement of the intensity and/or spectrum of fluorescent light, when, e.g., an optically excited molecule emits part of its excitation energy in the form of light. Fluorescence is a special type of luminescence characterized such that (usually only a part of) the absorbed energy is emitted micro- or nanoseconds after excitation.

Photoluminescence originating from certain organic or inorganic molecules is a versatile method of dosimetry that is useful in radiation therapy, radiation protection, and radiation processing and covers broad radiation spectra, radiation types, dose ranges, and dose rates. Such types of organic molecules are, e.g., bridged polyphenyl dyes, terphenyls, oligophenylenes, bipyridyls, which can be excited into triplet states and free radicals by ionizing radiation. Some of these compounds undergo efficient proton transfer reactions in phototautomeric triplet states when held in suitable liquid and polymeric solvents resulting in relatively broad separation of excitation and emission bands, which is a basic requirement for dosimetric applications. Inorganic molecules involve mainly alkali halide crystals, e.g., LiF, or metal oxides, e.g., Al_2O_3 . The irradiation of such systems results in the formation of lattice defects (color centers). If the defect being excited by light is itself the color center created by irradiation of the sample, a PL signal that is dependent on the absorbed dose may be obtained. This is termed radiophotoluminescence (RPL) and the RPL signal may be utilized in dosimetry. RPL is significantly different from the OSL method, as here the excitation with light does not result in ionization of the defect. (Botter-Jensen et al. 2003).

The basic advantage of applying fluorimetry for dosimetry purposes is the high sensitivity of the method as compared to, e.g., spectrophotometry. Other advantages are the wide dynamic range, use for both passive and real-time dosimetry and for both low- and high-dose rates, variable geometries of the dosimeters (pellets, films, optical fibers, etc.), and inexpensive multiuse radiation detectors.

Fluorimetry can be used for dosimetry in different ways. In fluorescent compounds such as fluorescein, the fluorescent light intensity decreases due to the radiation damage to the molecule. Anthracene that emits fluorescence at 440 nm was used in this way in pressed powder form or in gelatin (Attix 1959). The other way involves radiolysis products, formed upon irradiation of organic or inorganic molecules that yield optically stimulated luminescence. Collins et al. (1994) published results about the usefulness of the aqueous coumarin-3-carboxylic acid solution for dosimetry purposes in the therapy range. Upon irradiation, oxidation takes place resulting in the formation of a hydroxylated product of the original molecule, which gives fluorescence at 450 nm due to excitation at 388 nm. Other oxidation materials yielding fluorimetric products include calcium benzoate.

Besides oxidative processes, other radiation-initiated reactions like proton transfer, appearance of new absorption bands in the crystal lattice of, e.g., alkali halide molecules, can also lead to the formation of active materials giving optically stimulated luminescence. The use of inorganic microcrystalline solid-state fluorescent materials dispersed in a polymeric medium is a well-established technique for measuring and imaging relatively small radiation absorbed dose (10^{-4} – 10^1 Gy) (Miller et al. 1989a; Miller et al. 1991; Miller and Yoder 1996). Non-flexible photoluminescent glasses and alkali halides have also been used for dosimetry purposes (McLaughlin 1970; Regulla 1972).

The OSL-based *Sunna film* is a new dosimeter utilizing the measurement of fluorescence for high-dose dosimetry (ASTM E 2303-2004, McLaughlin et al. 1999). The film contains a microcrystalline dispersion of LiF in a polymer matrix. It is an opalescent flexible film of uniform thickness and dispersion concentration. Upon irradiation of the LiF crystals, the color centers induced are manifested by discrete optical absorption bands in the near UV and visible spectrum. The F-center in LiF is due to an excess electron trapped at an ionic vacancy, which has a narrow absorption band peaking at 247 nm. With increasing dose, more complex centers are formed absorbing in the visible spectrum, as represented by the M-center with an absorption peak at 443 nm (McLaughlin et al. 1979; McLaughlin 1996). The excitation of the irradiated crystal with light at the wavelength of the color center absorption can raise the electron from the ground state to an excited energy level followed by a temperature-dependent return to the ground state (Mott and Gurney 1948). This process in the ns timescale is accompanied by characteristic luminescence at a significantly higher wavelength. Out of the different color centers, the M-center has been shown to exhibit the strongest OSL with a broad emission band having peaks at 530 nm and 670 nm. This OSL behavior has been utilized at the Sunna film. The film has been found useful for dosimetry at 530 nm with a tabletop routine fluorimeter in the dose range of 50–200 kGy. By measuring the absorbance of the irradiated films at 240 nm, dose determination is also possible with spectrophotometry in the dose range of 5–100 kGy (Kovács et al. 2000, 2002). No humidity effect of the dosimeter was observed, but a significant irradiation temperature effect was found in the temperature range of 0–40°C. To stabilize the OSL signal after irradiation, a heat treatment method was introduced (70°C, 20 min). The film can be applied both for gamma and electron dose measurements.

49.3.2.3 Electron Paramagnetic Resonance (EPR) Dosimeters

In certain solid-phase materials, free radicals – paramagnetic species containing unpaired electrons – form upon irradiation. The concentration of these free radicals can be related to absorbed dose by electron paramagnetic resonance (EPR) analysis, sometimes referred to as

electron spin resonance (ESR). There have been various attempts to introduce, e.g., bone, teeth, saccharides, polymers for reference dose measurements, but due to stability and reproducibility problems the use of these systems are limited (Ostrowski 1974; Brady et al. 1968; Nakayima 1982; McLaughlin et al. 1993). When studying crystalline organic materials (e.g., amino acids), it was found that the concentration of free radicals formed is very stable for long periods. These radicals can be analyzed quantitatively using the EPR spectrum that has suitable resolution. The use of α -L-alanine has shown especially good characteristics for medium- and high-dose measurements as shown by Bradshaw et al. (1962) and by Regulla and Deffner (1982, 1985) (ISO/ASTM 2004).

During room temperature irradiation of α -L-alanine samples, free radicals form as shown in [Fig. 49.3](#).

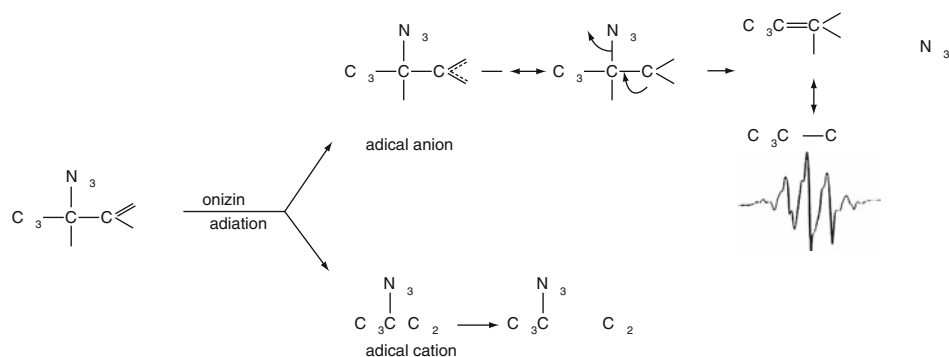
The free radical most important in dosimetry is $\text{CH}_3\text{-CH-COOH}$ whose ESR spectrum is used for dosimetry after suitable calibration (► Fig. 49.4). The signal measured is the increase in the amplitude of the first derivative of the EPR spectrum, which is proportional to the mass of the sample.

The α -L-alanine dosimeter has been developed by Regulla and Deffner (1982). It can be used for dosimetry in the range of 10 – 10^5 Gy with precision of 1% (2σ). The dose response of the dosimeter is almost linear up to 10^4 Gy and reaches saturation at 10^6 Gy (► Fig. 49.4). The dosimeter consists typically of $\sim 90\%$ polycrystalline α -L-alanine powder and $\sim 10\%$ paraffin is added to form small rods of 4.9-mm diameter and 10-mm length. Other formulations are also known using binders such as cellulose, polyvinylpyrrolidone (Hansen 1984; Hansen et al. 1987), and polystyrene (Kojima et al. 1986). Thin polymer films were produced by Kojima et al. (1986), Janovsky et al. (1988), Garcia et al. (2004), Desrosiers and Puhl (2009). An important point when selecting the binder is that it should not show a competitive radiation-induced EPR signal.

The density of the alanine–paraffin dosimeter is 1.2 g cm^{-3} and radiation absorption characteristics are similar to those of biological tissue. The irradiation temperature coefficient varies with the dose level being $+0.015\% (\text{°C})^{-1}$ up to 10 kGy, while this value is $+0.3\% (\text{°C})^{-1}$ at 100 kGy (Desrosiers et al. 2004, 2009a, b; Sharpe et al. 2009a, 2009b). There is little fading when storing or irradiating the dosimeter below 50°C . The response of the dosimeter was found to be independent of dose rate up to 10^8 Gy s^{-1} and energy dependence was observed

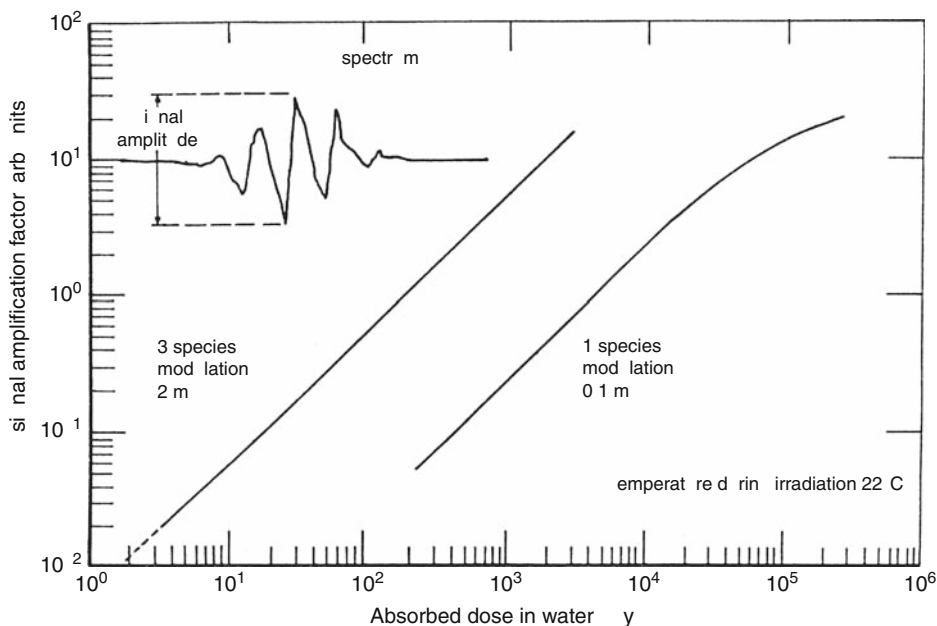
Fig. 49.3

Radiation-induced decomposition of α -L-alanine



■ Fig. 49.4

Typical dose response of the α -L-alanine dosimeter with an insert showing the electron paramagnetic resonance (EPR) signal (Regulla and Deffner 1982)



only below 100 keV (Bartolotta et al. 1985). Humidity and UV light was shown to affect the dosimeter response, but by using hermetically sealed plastic pouches, this problem is avoided.

The high cost of the EPR spectrometer limits the routine application of the method. To overcome this problem there are continuous efforts to develop more compact and less expensive instruments for routine use.

There have been different approaches to use chemical methods to evaluate the irradiated alanine dosimeter. Gupta et al. (1985) introduced the dissolution of irradiated alanine powder in an aqueous sulfuric acid solution of ferrous-ammonium-sulfate and xylenol orange. The free radicals present in irradiated alanine oxidize the ferrous ions to ferric and these form a complex with xylenol orange, which absorbs at 525 nm. The measured absorbance increase is related to absorbed dose. The method can be used in the dose range of 10 Gy–4 kGy, which was later extended by Van Laere et al. (1989) to 12 kGy. Ebraheem et al. (1999) developed another method by dissolving the irradiated alanine powder in aqueous solution of 2,3,5-triphenyl tetrazolium chloride. The radicals produced by irradiation of alanine react during the dissolution with TTC forming pink-colored formazans with absorption maxima around 401 nm and 487 nm. This read-out method can be used in the 2–200 kGy dose range. Another version of the same principle is the use of aqueous solution of 1,4-phenyl diammonium dichloride to dissolve the irradiated alanine powder (Ebraheem et al. 2003). Upon dissolution, a complex of purple color forms showing an increasing absorbance (360 nm or 505 nm) with increasing dose in the range of 1–10 kGy. Beside spectrophotometry, fluorimetric evaluation can also be used by measuring the emission of the complex at 435 nm (1–20 kGy).

The solid dosimetry systems used most frequently for dosimetry in radiation processing are summarized in ▶ Table 49.2.

■ Table 2.2

Solid dosimeters for high doses

Dosimeter system	Method of analysis	Useful dose range (Gy)	Nominal precision limits ($k = 2$)	Reference
Perspex systems	VIS spectrophotometry	$10^3 - 5 \times 10^4$	3%	ISO/ASTM 51276
α -L-alanine	EPR	$1 - 10^5$	0.5%	ISO/ASTM 51607
Cellulose triacetate	UV spectrophotometry	$10^4 - 10^6$	3%	ISO/ASTM 51650
FWT-60 film	VIS spectrophotometry	$10^3 - 10^5$	3%	ISO/ASTM 51275
Risø B3 film	VIS spectrophotometry	$10^3 - 10^5$	3%	ISO/ASTM 51275
Sunna film	OSL	$10^{-3} \times 10^5$	3%	ASTM 2303
$\text{Al}_2\text{O}_3\text{:Mg,Y}$	TLD	$10^{-3} - 5 \times 10^3$	5%	ISO/ASTM 51956

49.4 Physical Methods of Dosimetry

The most common physical methods applied in the dosimetry practice of ionizing radiation are calorimetry and ionization methods. Calorimetry is a primary standard method in dosimetry used both to measure dose rate in various radiation fields and to calibrate standard and routine dosimeters. Ionization chambers are discussed in ► Chap. 48, Vol. 5, thus only calorimetric systems will be shortly described here, with particular respect to those applied mainly in radiation processing.

49.4.1 Calorimetry

Calorimetry is an absolute method of dosimetry, since almost all absorbed radiation energy is converted into heat that can be readily measured as a temperature rise of the calorimetric body. Calorimeters that are used as primary dosimeters do not require calibration and, ideally, their response is independent of dose rate, radiation characteristics, and environmental factors (Domen 1987). The calorimeters that are used in radiation processing for the measurement of absorbed dose are relatively simple and need calibration (ISO/ASTM 2003b). The use of calorimeters as primary standard dosimeters for electron beam irradiation is described by McEwen and Dusatuoy (2009) and for gamma irradiation by Seuntjens and Duane (2009).

49.4.1.1 Principles of Calorimetry

The use of calorimeters is based on the measurement of heat, since the energy deposited in the thermally insulated mass of the absorber is converted to heat. The measured energy per unit mass results directly in the absorbed dose, being the product of the measured temperature rise and the specific heat of the absorber (see ► Eq. 49.18). Thus a calorimeter consists of the absorber (also called calorimeter body or the core of the calorimeter), the instrumentation to

measure temperature, the heat insulation around the absorber (i.e., the surrounding medium), and in certain cases the outer core of the insulation (also called the jacket) (ISO/ASTM 51631). The calorimetric body must be thermally insulated from its surroundings – using, e.g., plastic foam or mounting the absorber with supports of low mass and low thermal conductivity – so that only a minimal heat is lost during and after irradiation.

The temperature rise is usually measured with calibrated thermistors or thermocouples. Thermistors are more sensitive than thermocouples, but the advantages of using thermocouples (consisting of a junction of two metals) are their small size and mass, and the known dependence of the output voltage on temperature.

For an ideal adiabatic case, the radiation-induced temperature rise of the absorber of the calorimeter is a linear function of time during irradiation at constant dose rate. The temperature rise of a semi-adiabatic calorimeter during irradiation as a function of time is shown in

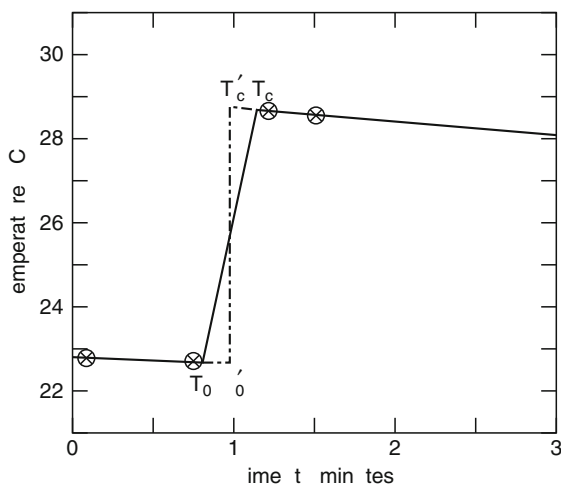
► Fig. 49.5.

The temperature variation of the calorimeter absorber before and after irradiation is shown in region I and III, respectively, while region II illustrates the radiation-induced change. In order to get the correct dose value, the measured temperature difference ($T_c - T_0$) has to be corrected for heat losses by extrapolating the slopes of the temperature changes of regions I and III to the midpoint of irradiation resulting in ($T'_c - T'_0$).

The use of certain materials as absorbers in calorimeters can give rise to a problem, because not all absorbed energy might be converted into heat due to the appearance of endo- or exothermic chemical reactions resulting in erroneous dose determination. This phenomenon, called “heat defect,” has been observed especially in the case of water and polymer calorimeters. When using water calorimeters for measuring doses up to 10 Gy, Domen (1982) observed the production of 3.5% excess heat. Miller (1984) showed that in the case of pulsed electron irradiation doses above 5 kGy, the dose determination is affected by less than 1% by this phenomenon. Endothermic reactions were observed when working with tissue-equivalent plastic calorimeters leading to lower absorbed doses than expected (Bewley et al. 1972). Reaction with dissolved oxygen of radiation-generated free radicals in plastic calorimeters

■ Fig. 49.5

Temperature rise of a semi-adiabatic calorimeter before, during, and after irradiation



can result in exothermic reactions especially in the low-dose region (McDonald et al. 1976). The structure of many radiation-induced polymer changes can result in the change of the specific heat and this effect has to be taken into account too when constructing or using plastic calorimeters.

49.4.1.2 Calibration

Calorimeters can be calibrated in different ways depending on their construction and application. When used as a primary dosimeter, the temperature rise (ΔT) during irradiation is related to the absorbed dose D by

$$D = E/m = C_a \times \Delta T \quad (49.18)$$

where E is the absorbed energy, m is the mass of the absorber, C_a is the specific heat capacity of the absorber, which needs to be measured separately. The calorimeter may also be calibrated by irradiation in a known radiation field or by embedding an electrical heater in the calorimetric absorber (McLaughlin et al. 1989).

The calorimeters used in radiation processing are calibrated by comparison with reference standard dosimeters issued by a calibration laboratory. It is important to ensure that the calorimeter and the reference standard dosimeter receive the same dose during the calibration irradiation.

Calorimeters can be used as in-house standards for the calibration of other dosimeters. It is crucial to pay special attention to the irradiation geometry to ensure the same dose to the calorimeter and to the dosimeter being irradiated. The thickness of the calorimeter (i.e., the absorber) must be chosen so that, for unidirectional perpendicular electron beams, the absorbed dose measurement is the average dose on the ascending part of the depth-dose curve. Phantoms of, e.g., polystyrene have been built of similar size as the water, graphite, or polystyrene calorimeters allowing the secondary dosimeter to be placed at depths of interest to provide the same irradiation conditions both for the absorber and the reference or routine dosimeter.

49.4.1.3 Types of Calorimeters

Calorimetric methods can be classified also as isothermal, adiabatic, and heat-flow type calorimetry (Calvet and Prat 1956; Radak and Markovic 1970). In isothermal calorimetry, the temperature of the calorimeter body remains constant during irradiation, since a phase transformation induced by the absorbed energy of the radiation (e.g., melting or boiling of the absorber) is measured. Ideally, adiabatic calorimetry requires no heat exchange between the absorber and the surroundings. To ensure adiabatic conditions experimentally is always problematic, and thus so-called quasi-adiabatic conditions are achieved resulting in quasi-adiabatic calorimeters designed and used in various fields in radiation dosimetry (Genna et al. 1963). The principle of heat-flow calorimetry allows the heat exchange between the calorimetric body and the jacket by selecting a suitable heat insulation material that surrounds the absorber (Radak and Markovic 1962).

Various calorimetric dosimeters have been designed for use in radiation dosimetry in medical applications and in radiation processing. Calorimetry is often used to calibrate chemical and solid-state dosimeter systems, but, until recently, it was rarely applied for routine

dose monitoring. The increasing application of electron accelerators in radiation processing, however, gave importance to the use of so-called process calorimeters.

In medical applications, it is of basic significance that the radiation absorption characteristics of the medium to be irradiated and that of the calorimetric absorber should be similar. Thus, calorimeters to that purpose have been constructed of water (Domen 1982), graphite (Petree and Lamperti 1967), polystyrene, polyethylene–carbon mixture (Milwy et al. 1958), and A-150 tissue-equivalent plastic (McDonald et al. 1976; Smathers et al. 1977).

Two types of calorimeters are used in radiation dosimetry, i.e., the total energy absorption calorimeters (e.g., to determine the energy or power of a particle beam) and thin calorimeters that are partially absorbing and used to measure absorbed dose. The temperature of the calorimeter can be measured either during irradiation (online) or before and after irradiation (off-line).

Spherical calorimeters (Petree and Lamperti 1967; Murray and Attix 1973) and cylindrical ones (Domen and Ba 1987) have been constructed for use in isotropic fields as reference standards for gamma-ray fields at high dose rates (McLaughlin 1978, 1985, 1988).

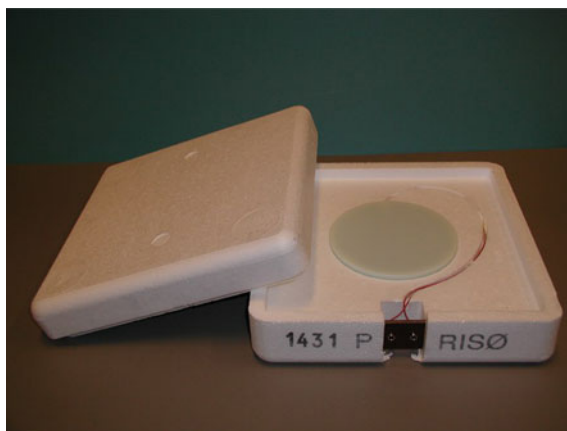
A common design of semi-adiabatic calorimeters contains thin or thick disc-shape absorbers used mainly in monodirectional beams both for low-energy (McDonald et al. 1972) and for higher-energy electron beams (Bewley 1969). Water calorimeters of the same shape were designed by Brynjolfsson et al. (1963) and Fielden and Holm (1970).

Semi-adiabatic calorimeters have been designed for dosimetry at high-energy electron accelerators (1–10 MeV) both for calibration and for routine process control (Humphreys and McLaughlin 1989; Miller and Kovács 1985; Burns and Morris 1988) and also for low energies between 100 keV and 500 keV (Janovsky and Miller 1987). The disc-shape absorber is either water or graphite containing thermistors for temperature measurement placed in the center of the absorber. The absorber is placed in polystyrene foam insulation.

Calorimeters have been designed for use at industrial electron accelerators for dose measurement in the range of 1.5–50 kGy and 4–10 MeV electron energy. (ISO/ASTM 51631 2003b). These calorimeters are made with water, polystyrene (see Fig. 49.6), or graphite calorimetric body and are calibrated by comparison with transfer reference dosimeters

■ Fig. 49.6

The Risø-DTU polystyrene calorimeter



(Miller and Kovács 1985; Humphreys and McLaughlin 1989). The advantage of using graphite instead of water is the lack of thermal defects. Graphite calorimeters can measure lower doses (1.5–15 kGy) compared to the water calorimeter due to the smaller specific heat of graphite. Graphite calorimeters are mainly used for calibration purposes at standard national laboratories (National Institute of Standards and Technology, USA; Risø National Laboratory, Denmark; National Physical Laboratory, UK), and can also be used as routine dosimeters. Polystyrene calorimeters for lower electron energies (1.5–4 MeV) with 2-mm thick absorbers were designed by Miller et al. (2002). Polystyrene was chosen due to its radiation resistance, although its specific heat capacity changes with increasing dose ($\sim +1\%/MGy$) (Miller 1995).

Differential calorimeters consisting of two graphite discs (with separate thermocouples each) have been designed and used mainly for calibration of routine dosimeters (Janovsky 1985). During irradiation, only one of the two graphite discs is irradiated, while the other one is used as reference. The temperature difference measured between the two discs serves to calculate the dose. Radak et al. (1973) designed similar instrument for calibration at low electron energies (400 keV).

49.4.1.4 Dosimetry at Low-Energy Electron Irradiation

The dosimetry discussion in this chapter is generally intended for situations in which there is no significant dose variation within the measuring part of the dosimeter. This is normally the case for gamma and X-ray irradiation and for electron irradiation at energy above approximately 4 MeV, but at lower energies, dose gradients can become significant for thicker dosimeters. This situation might be acceptable if the dosimeter can be irradiated so that an average dose over the thickness of the dosimeter can conveniently be calculated. This is the case if the dosimeter is irradiated at the ascending part of the depth dose curve, but it is difficult if the dosimeter is thicker than approximately 1/3 of the electron range. Three-millimeter alanine pellets, e.g., can be used down to approximately 2.5 MeV. At lower energies, thinner dosimeters must be used, and 130-micrometer alanine films can be used down to approximately 300 keV.

It must be recognized that irradiation of many dosimeters with low-energy electrons (less than 300 keV) will lead to dose gradients through the thickness of the dosimeter. When the dosimeter is measured, this will lead to an apparent dose that is related to the dose distribution. For a given set of irradiation conditions, the apparent dose will depend on the thickness of the dosimeter, i.e., dosimeters of different thickness will measure different apparent doses.

One solution to overcome this problem is that all dose measurements are specified as dose to water in the first micrometer of the absorbing material. This is given the symbol D_w and is independent of dosimeter thickness (Sharpe et al. 2009b).

The relationship between D_w and the apparent dose strongly depends on dosimeter response function, dosimeter thickness, dose, radiation energy, accelerator window material and thickness, distance of the window from dosimeter, and temperature of air between window and dosimeter. The relationship must be calculated for each set of irradiation conditions.

49.4.2 Semiconductors for Dosimetry

Silicon diodes and other types of semiconductors have already been used for decades in radiation dosimetry for the measurement of dose and dose rate. There is a basic difference

between the two types of instruments, since the dose rate measurement is carried out “in situ,” while the diodes used for absorbed dose measurement are evaluated after irradiation.

When measuring dose rate, the basic principle is the generation of electric current upon irradiation through the p-n junction due to diffusion of the electron-hole pairs into the adjacent p and n layers (Muller 1970a, b; Parker 1970; Osvey et al. 1975). Current measurement for dose rate determination can be made in the so-called short-circuit mode. The p-n junction solar cells were found suitable for dose determination in the range of 10 Gy–1 MGy (Muller 1970b). Their use, however, requires individual calibration.

Semiconductor dosimeters cannot be used for dosimetry above 6 MeV photons and 10 MeV electrons due to radiation damage in the semiconductor material (Dixon and Eckstrand 1982) and because of the high-energy bremsstrahlung radiation, which – approaching the threshold energy required for a (γ , n) reaction in silicon – can induce radioactivity in the doped silicon material. Energy and temperature dependence were also observed when using these detectors. Preirradiation to higher doses (>0.1 MGy) was found useful to decrease the effect of radiation damage and to avoid temperature dependence (Dixon and Eckstrand 1982). The advantages of using such detectors for dosimetry involve good sensitivity, low cost, small size, and wide availability.

Semiconductor dosimeters are widely used for dose distribution measurements both in laboratory and at industrial-scale ^{60}Co gamma irradiation facilities (Rageh et al. 1985; Hartsom et al. 1995). Pesek (1985) used also p-n type detectors for the determination of the best irradiation position of objects to be irradiated. Special boron- and phosphorus-doped p-type silicon diodes were developed by Osvey et al. (1975). These systems, sealed against humidity and light effects, showed linear response with dose rate in the range of $1\text{--}10^5$ Gy s^{-1} . These detectors have been proven more resistant against radiation damage as compared to n-type diodes, but more pronounced temperature dependence was observed at higher dose rates (>10 Gy h^{-1}). Semiconductors were also applied to control the dose field of radiation-therapy irradiation facilities (Butson et al. 1996), as well as to follow the radiation-induced changes in electronic instruments (McLaughlin et al. 1989).

Fuochi et al. (1999, 2004, 2006, 2009a, b) have studied the dosimetry performance of bipolar power transistors in gamma and electron radiation fields for routine process control. These transistors have been investigated under laboratory conditions using electron beams of energies from 1.9 MeV to 8.6 MeV and gamma rays from ^{60}Co source and tested in industrial irradiation plants having high-activity ^{60}Co γ -source and high-energy, high-power electron beam. Their results indicated the usefulness of these detectors – after suitable calibration – for absorbed dose measurement in the dose range of 50 Gy to 50 kGy. Linear relationship was found in this dose range of 50 Gy to 5 kGy between the absorbed dose and a measured physical parameter (which is directly related to the charge carrier lifetime). Small semiconductors were suggested for dose control in flow systems like grain irradiation (Ehlermann 1988).

References

-
- | | |
|--|---|
| Abdel-Fattah AA, Miller A (1996) Radiat Phys Chem 47:611 | ANSI (1996) Method for evaluation films for monitoring x-rays and gamma rays having energies up to 3 million electron vpolts. ANSI/NAPM standard no. IT2.10–1996, American National Standards Institute, New York |
| ANSI (1993) Personnel dosimetry performance; criteria for testing. ANSI standard no. N13.11–1993, American National Standard Institute, New York | |

- Artandi C, Stonehill AA (1958) *Nucleonics* 16:118
- ASTM (1995) Standard practice for using the Fricke reference standard dosimetry system. ASTM standard E 1026-1995, American Society for Testing and Materials, <http://www.astm.org>
- ASTM (2004) Standard practice for using of a LiF photo-fluorescent film dosimetry system. ASTM standard E 2304-2004, American Society for Testing and Materials, <http://www.astm.org>
- Attix FH (1959) *Nucleonics* 17(4):142
- Baeyens B, Coninx F, Maier P, Schonbacher H (1985) High-dose dosimetry. In: Proceedings of symposium, IAEA, 1984. STI/PUB/671, International Atomic Energy Agency, Vienna, p 275
- Barquero R, Mendez R, Iniguez MP, Vega HR, Voltchev M (2002) *Radiat Prot Dosim* 101:493
- Barrett JH (1982) *Int J Appl Radiat Isot* 33:1177
- Barrett JH, Sharpe PHG, Stuart IP (1980) Part 1. NPL report RS 49. National Physical Laboratory, Teddington
- Bartolotta A, Caccia B, Indovina PL, Onori S, Rosati A (1985) High-dose dosimetry. In: Symposium proceedings, IAEA, STI/PUB/671, International Atomic Energy Agency, Vienna, p 245
- Becker K (1973) *Solid-state dosimetry*, CRC press, Boca Raton, Florida.
- Bewley DK (1969) *Ann NY Acad Sci* 161:94
- Bewley DK, McCullough EC, Page BC, Sakata S (1972) Neutron dosimetry in biology and medicine. In: Proceedings of first symposium on neutron dosimetry, Munich/Neuherberg, p 159
- Bielski B, SHLUE GG, BAJUK S (1980) *J Phys Chem* 84:830
- Biramontri S, Haneda N, Tachibana H, Kojima T (1996) *Radiat Phys Chem* 48:105
- Bishop WP, Humpherys KC, Randike PT (1973) *Rev Sci Instrum* 44:443
- BjÄrngaard B (1963) *Aktiebolaget Atomenergie report AE-118*, Stockholm, Sweden
- Bjergbakke E (1970) In: Holm NW, Berry RJ (eds) *Manual on radiation dosimetry, part 2*. Marcel Dekker, New York, p 323
- Blaedel WJ, Petitjean DL (1956) In: Berl WG (ed) *Physical methods in chemical analysis*, vol III. Academic, New York, p 107
- Bobrowski K, Dzierzkowska G, Grodkowski J, Stuglik Z, Zagorski ZP, McLaughlin WL (1985) *J Phys Chem* 89:4358
- Boetter-Jensen L, McKeever SWS, Wintle AG (2003) *Optically stimulated luminescence dosimetry*, Elsevier.
- Bradshaw WW, Cadena DC, Crawford EW, Spetzler HAW (1962) *Radiat Res* 17:11
- Brady JM, Aaerestad NO, Swartz HM (1968) *Health Phys* 15:43
- Brynjolfsson A, Holm NW, ThÄrup G, Sehested K (1963) Industrial uses of large radiation sources. In: Symposium proceedings, vol II, International Atomic Energy Agency, Vienna, p 281
- Burghardt B, Singh D, Piesch E (1977) *Nucl Instrum Methods* 141:363
- Burns DT, Morris WT (1988) High-dose calorimetric standard for electron beams. NPL Report RS (EXT) 101, National Physical Laboratory, Teddington
- Butson MJ, Rozenfeld A, Mathur JN, Carolan M, Wong TPY, Metcalfe PE (1996) *Med Phys* 23:655
- Calvet A, Prat H (1956) *Microcalorimetrie*. Masson et Cie, Paris
- Cameron JR (1970) In: Holm NW, Berry RJ (eds) *Manual on radiation dosimetry*, chapter C. Marcel Dekker, New York, p 410
- Cameron JR, Suntharalingam N, Kenney GN (1968) *Thermoluminescent dosimetry*. University of Wisconsin Press, Madison
- Chadwick KH (1969) *Atompraxis* 15:181
- Chadwick KH (1977) In: Casnati E (ed) *Ionizing radiation metrology*. Editrice Compositori, Bologna, p 195
- Chadwick KH, Rintjema D, Broeke WRR (1978) Food preservation by irradiation. In: Proceedings of symposium, vol II, IAEA publication STI/PUB/470, International Atomic Energy Agency, Vienna, p 327
- Chappas W (1980) *Radiat Phys Chem* 18:1017
- Charlesby A (1960) *Atomic radiation and polymers*. Academic, New York
- Charlesby A, Gould AR, Ledbury KJ (1964) *Proc Roy Soc A* 247:348
- Chen W, Haishen J, Xiang D, Dongyuan L, Huaying B (1980) *Radiat Phys Chem* 16:195
- Christensen P (1982) Application of thermoluminescent dosimetry to high-dose measurements. In: Seminar on IAEA high-dose dosimetry in industrial radiation processing, Riso National Laboratory, Roskilde
- Christensen P, Bøtter-Jensen L, Majborn B (1982) *Int J Appl Radiat Isot* 33:1035
- Collins AK, Makrigiorgos GM, Svensson GK (1994) *Med Phys* 21:1741
- Coninx F, Schönbacher H, Tavet M, Paic G, Razem D (1993) *Nucl Instrum Meth Phys Res B* 83:181
- Deplanque G, Gesell TF (1982) *Int J Appl Radiat Isot* 31(11):1015
- Desrosiers MF, Cooper SL, Puhl JM, McBain AL, Calwert GW (2004) *Radiat Phys Chem* 71(1-2):365
- Desrosiers MF, Peters M, Puhl JM (2009a) *Radiat Phys Chem* 78(7-8):465
- Desrosiers MF, Puhl JM (2009b) *Radiat Phys Chem* 78(7-8):461
- Dixon RL, Eckstrand KE (1982) *Radiat Phys Chem* 33:1171
- Dole M (1972) *The radiation chemistry of macromolecules*, vol 1. Academic, New York
- Domen SR (1982) *J Res Natl Bur Stand* 87:211
- Domen SR (1983a) *Int J Appl Radiat Isot* 34:643
- Domen SR (1983b) *J Res Natl Bur Stand* 88:373

- Domen SR (1987) In: Kase KR, Bjärngaard B, Attix FH (eds) *The dosimetry of ionizing radiation*, chapter 4, vol II. Academic, New York, p 245
- Domen SR, Ba WZ (1987) *Nucl Instrum Meth Phys Res B* 24/25:1054
- Domen SR, Lamperti PJ (1974) *J Res Natl Bur Stand A* 78:595
- Dvornik I (1970) In: Holm NW, Berry RJ (eds) *Manual on radiation dosimetry*, part II. Marcel Dekker, New York, p 345
- Dvornik I, Zec U, Ranogajec F (1966) Food irradiation. In: *Proceedings of symposium*, SM-73/15, IAEA, International Atomic Energy Agency, Vienna, p 81
- Dvornik I, Razem D, Baric M (1969) Large radiation sources for industrial processes. In: *IAEA symposium proceedings*, International Atomic Energy Agency, Vienna, p 613
- Ebraheem S, Beshir WB, Kovács A, Wojnárovits L, McLaughlin WL (1999) *Radiat Phys Chem* 55:785
- Ebraheem S, Beshir WB, Eid S, Sobhy R, Kovács A (2003) *Radiat Phys Chem* 67:569
- Ehlermann DAE (1988) In: Bögl KW, Regulla DF, Suess MJ (eds) *Health impact, identification, and dosimetry of irradiated foods*, Institut für Strahlenhygiene, report 125, report of WHO working group, Institut für Strahlenhygiene des Bundesgesundheitsamt, Neuherberg/Munich, p 415
- Emy-Reynolds G, Kovács A, Fletcher JJ (2007a) *Radiat Phys Chem* 76:1515
- Emy-Reynolds G, Kovács A, Fletcher JJ (2007b) *Radiat Phys Chem* 76:1519
- Ettinger RV, Puite KJ (1982) *Int J Appl Radiat Isot* 33:1115
- Farahani M, McLaughlin WL (1988) *Radiat Phys Chem* 32:683
- Fielden EM, Holm NW (1970) In: Holm NW, Berry RJ (eds) *Manual on radiation dosimetry*. Marcel Dekker, New York, p 262
- Földiák G, Horváth Zs, Stenger V (1973) Dosimetry in agriculture, industry, biology, and medicine. In: *International Atomic Energy Agency (ed) Proceedings of symposium*, STI/PUB/311, International Atomic Energy Agency, Vienna, p 367
- Fowler JH, Attix FH (1966) In: Attix FH, Roesch WC (eds) *Radiation dosimetry*, vol II. International Atomic Energy Agency, New York, p 367
- Freytag E (1971) *Health Phys* 20:93
- Fricke H, Hart EJ (1966) In: Attix FH, Roesch WC (eds) *Radiation dosimetry*, chapter 12, vol II. Academic, New York, p 1
- Fuochi PG, Lavallo M, Gombia E, Mosca R, Kovács A, Vitanza A, Patti A (1999) On the use of a bipolar power transistor as routine dosimeter in radiation processing. IAEA-TECDOC-1070, IAEA-SM-356/47. International Atomic Energy Agency, Vienna, p 95
- Fuochi PG, Lavallo M, Corda U, Recupero S, Bosetto A, Bascieri V, Kovács A (2004) *Radiat Phys Chem* 71:385
- Fuochi PG, Corda U, Gombia E, Lavallo M (2006) *Nucl Instrum Meth A* 564:521
- Fuochi PG, Lavallo M, Corda U, Kovács A, Peimel-Stuglik Z, Gombia E (2009a) *Nucl Instrum Meth A* 599:284
- Fuochi PG, Lavallo M, Corda U, Kuntz F, Plumeri S, Gombia E (2009b) *Radiat Phys Chem*. doi:[10.1016/j.radphyschem.2009.10.001](https://doi.org/10.1016/j.radphyschem.2009.10.001)
- Garcia RMD, Desrosiers MF, Attwood JG, Steklenski D, Griggs J, Ainsworth A, Heiss A, Mellor P, Patil D, Meiner J (2004) *Radiat Phys Chem* 71(1–2):375
- Gehringer P, Proksch E, Eschweiler H (1985) High-dose dosimetry. In: *Proceedings of symposium*, IAEA, STI/PUB/671, International Atomic Energy Agency, Vienna, p 333
- Genna S, Jaeger RG, Nagl J, Sanielevici A (1963) *At Energy Rev* 1:239
- Gierlach ZS, Krebs AT (1949) *Am J Roentgenol Radium Ther* 62:559
- Glover KM, King M, Watts MF (1985) High-dose dosimetry. In: *Proceedings of symposium*, IAEA, 1984. STI/PUB/671, International Atomic Energy Agency, Vienna, p 373
- Gupta BL, Bhat RM, Nariyan GR, Nilekani SR (1985) *Radiat Phys Chem* 26:647
- Hansen JW (1984) Risø report R-507. Risø National Laboratory, Roskilde
- Hansen JW, Olsen KJ (1986) *Radiat Phys Chem* 28(5–6):535
- Hansen JW, Olsen KJ, Wille M (1987) *Radiat Prot Dosim* 19:43
- Hartsom A, Mackay G, Spender M, Thomson I (1995) Absorbed dose mapping in self-shielded irradiators using direct reading MOSFET dosimeters. In: *Annual meeting of the health physics society*, July 1995. Available from Thomson and Nielsen Electronics, 25E Northside Road, Nepean, Ontario, Canada K2H8S1
- Horowitz YS (1984) *Thermoluminescence and thermoluminescence dosimetry*, vol I–III. CRC Press, Boca Raton
- Hubbell JH (1982) In: McLaughlin WL (ed) *Trends in radiation dosimetry*. Pergamon Press, Oxford; *Int J Appl Radiat Isot* 33:1269
- Humphreys JC, McLaughlin WL (1989) Radiation processing: state of the art. In: *Proceedings of 7th international meeting on radiation processing*; *Radiat Phys Chem* 35:744
- ICRU (1969) *Radiation dosimetry: X rays and gamma rays with maximum photon energies between 0.6 and 50 MeV*, ICRU report 14. International Commission on Radiation Units and Measurements, Bethesda

- ICRU (2008) Dosimetry systems for use in radiation processing, ICRU report 80. International Commission on Radiation Units and Measurements, Bethesda
- ISO (1994) Personal photographic dosimeters, ISO/DIS report 1757. International Standards Organization, Geneva
- ISO (2006) Sterilization of health care products – radiation – parts 1-2-3, ISO 11137. International Organization for Standardization, Geneva
- ISO/ASTM (2002a) Standard practice for use of a ceric-cerous sulphate dosimetry system. ISO/ASTM standard 51205, American Society for Testing and Materials, <http://www.astm.org>
- ISO/ASTM (2002b) Standard practice for use of the ethanol-chlorobenzene dosimetry system. ISO/ASTM standard 51538, American Society for Testing and Materials, <http://www.astm.org>
- ISO/ASTM (2002c) Standard practice for use of a radiochromic liquid dosimetry system. ISO/ASTM standard 51540, American Society for Testing and Materials, <http://www.astm.org>
- ISO/ASTM (2002d) Standard practice for use of cellulose acetate dosimetry system. ISO/ASTM standard 51650, American Society for Testing and Materials, <http://www.astm.org>
- ISO/ASTM (2002e) Standard practice for the use of a polymethylmethacrylate dosimetry system. ISO/ASTM standard 51276, American Society for Testing and Materials, <http://www.astm.org>
- ISO/ASTM (2002f) Standard practice for use of a radiochromic film dosimetry system. ISO/ASTM standard 51275, American Society for Testing and Materials, <http://www.astm.org>
- ISO/ASTM (2002g) Standard practice for thermoluminescence-dosimetry (TLD) systems for radiation processing. ISO/ASTM standard 51956, American Society for Testing and Materials, <http://www.astm.org>
- ISO/ASTM (2003a) Standard practice for the use of a dichromate dosimetry system. ISO/ASTM standard 51401, American Society for Testing and Materials, <http://www.astm.org>
- ISO/ASTM (2003b) Standard practice for use of calorimetric dosimetry system. ISO/ASTM standard 51631, American Society for Testing and Materials, <http://www.astm.org>
- ISO/ASTM (2004) Standard practice for use of the alanine-EPR dosimetry system. ISO/ASTM standard 51607, American Society for Testing and Materials, <http://www.astm.org>
- Janovsky I (1985) High-dose dosimetry. In: Proceedings of symposium, IAEA, STI/PUB/671, International Atomic Energy Agency, Vienna, p 307
- Janovsky I, Miller A (1987) Appl Radiat Isot 38:931
- Janovsky I, Hansen J, Cernoch P (1988) Appl Radiat Isot 39:651
- Kantz AD, Humpherys KC (1977) Radiat Phys Chem 9:737
- Kojima T, Tanaka R, Morita A, Seguchi T (1986) Appl Radiat Isot 37:517
- Kovács A, Stenger V, Földiák G, Legeza L (1985) High-dose dosimetry. In: Proceedings of symposium, IAEA, STI/PUB/671, International Atomic Energy Agency, Vienna, p 135
- Kovács A, Wojnárovits L, McLaughlin WL, Ebraheem Eid SE, Miller A (1996) Radiat Phys Chem 47:483
- Kovács A, Baranyai M, Wojnárovits L, Moussa A, Othman I, McLaughlin WL (1999) Radiat Phys Chem 55:795
- Kovács A, Baranyai M, Wojnárovits L, McLaughlin WL, Miller SD, Miller A, Fuocho PG, Lavalie M, Slezsák I (2000a) Radiat Phys Chem 57:691
- Kovács A, Baranyai M, Wojnárovits L, Slezsák I, McLaughlin WL, Miller A, Moussa A (2000b) Radiat Phys Chem 57:711
- Kovács A, Baranyai M, Wojnárovits L, Miller SD, Murphy M, McLaughlin WL, Slezsák I, Kovács AI (2002) Radiat Phys Chem 63:777
- Krebs AT (1963) In: Clark GL (ed) The encyclopedia of X-rays and gamma rays. Reinhold Publishing, New York, p 274
- Kreidl NJ, Blair GE (1956) Nucleonics 14:56
- Kreidl NJ, Blair GE (1959) Nucleonics 17:58
- Kriminskaya ZK, Makshanova NP, Dyumaev KM, Pikaev AK (1987) High Energy Chem 22:412
- Lakshmanan AR, Bhatt RC (1979) Phys Med Biol 24:1258
- Lakshmanan AR, Bhuwanchandra Bhatt RC (1978) Nucl Instrum Methods 153:431
- Matthews RW (1981) J Appl Radiat Isot 32:861
- Matthews RW (1982) In: McLaughlin WL (ed) Trends in radiation dosimetry. Pergamon, Oxford; Int J Appl Radiat Isot 33:1159
- Mattson LO, Johansson KA (1982) Acta Radiol Oncol 21:139
- Mcdonald JC, Pinkerton AP, Weiss H, Epp ER (1972) Radiat Res 49:495
- Mcdonald JC, Laughlin JS, Freeman RE (1976) Med Phys 3:80
- McEwen MR, Dusatuoy AR (2009) Metrologica 46:59
- McLaughlin WL (1966) Int J Appl Radiat Isot 17:85
- McLaughlin WL (1970) In: Holm NW, Berry RJ (eds) Manual on radiation dosimetry, chapter 5. Marcel Dekker, New York, p 129
- McLaughlin WL (1974) In: Gaughran ERL, Goudie AJ (eds) Sterilization by ionizing radiation, vol I. Multiscience, Montreal, p 219
- McLaughlin WL (1977) Radiation processing. In: Silverman J, Van Dyken A (eds) Transactions of 1st international meeting, Puerto Rico, 1976, vol I; Radiat Phys Chem 9:147

- McLaughlin WL (1978) National and international standardization in radiation dosimetry. In: Proceedings of symposium Atlanta, 1977, IAEA, STI/PUB/471, vol I. International Atomic Energy Agency, Vienna, p 89
- McLaughlin WL (1983) *Radiat Phys Chem* 21:359
- McLaughlin WL (1985) High-dose dosimetry. In: Proceedings of symposium, IAEA, STI/PUB/671, International Atomic Energy Agency, Vienna, p 357
- McLaughlin WL (1988) In: Bögl KW, Regulla DF, Suess MJ (eds) Health impact, identification and dosimetry of irradiated foods, ISH Report 125, proceedings of WHO workshop, Neuherberg/Munich, 1986, Institut für Strahlenhygiene des Bundesgesundheitsamt, Neuherberg/Munich, p 384
- McLaughlin WL (1996) In: Proceedings of the 11th international conference on solid state dosimetry, Budapest; *Radiat. Prot. Dosimetry* 66:197
- McLaughlin WL, Chalkley L (1965) *Photogr Sci Eng* 9:195
- McLaughlin WL, Kosanic MM (1974) *Int J Appl Radiat Isot* 25:249
- McLaughlin WL, Hussmann EK, Eisenlohr HH, Chalkley L (1971) *Int J Appl Radiat Isot* 22:135
- McLaughlin WL, Humphreys JC, Radak BB, Miller A, Olejnik TA (1979a) Advances in radiation processing. In: Silverman J (ed) Transactions of second international meeting, Miami, 1978, vol II; *Radiat Phys Chem* 14:535
- McLaughlin WL, Lucas AC, Kapsar BM, Miller A (1979b) *Radiat Phys Chem* 14:467
- McLaughlin WL, Miller A, Ellis SC, Lucas AC, Kapsar BM (1980) *Nucl Instrum Methods* 175:17
- McLaughlin WL, Uribe RM, Miller A (1983) Radiation processing. In: Markovic V (ed) Transactions of 4th international meeting, Dubrovnik, 1982, vol II; *Radiat Phys Chem* 22:333
- McLaughlin WL, Ba W-Z, Chappas WJ (1988) Progress in radiation processing. In: Fraser FM (ed) Proceedings of 6th international symposium, Ottawa, 1987, vol II; *Radiat Phys Chem* 31:481
- McLaughlin WL, Boyd AW, Chadwick KH, McDonald JC, Miller A (1989) Dosimetry for radiation processing. Taylor and Francis, London/New York/Philadelphia, pp 81, 113, 140
- McLaughlin WL, Khan HM, Warasawas W, Al-sheikhly M, Radak BB (1989b) *Radiat Phys Chem* 33:39
- McLaughlin WL, Desrosiers MF, Saylor MC (1993) In: Morissey RF (ed) Sterilization of medical products, vol VI. Polysciences Publications, Morin Heights, p 213
- McLaughlin WL, Al-sheikhly M, Lewis DF, Kovács A, Wojnárovits L (1994) *Polym Prepr* 35:920
- McLaughlin WL, Puhl JM, Al-sheikhly M, Christou M, Miller A, Kovács A, Wojnárovits WL, Lewis DF (1996) *Radiat Prot Dosim* 66:263
- McLaughlin WL, Miller SD, Saylor MC, Kovács A, Wojnárovits L (1999) *Radiat Phys Chem* 55:247
- Miller A (1984) *J Indust Irradiat Techn* 2(3-4):367
- Miller A (1985) High-dose dosimetry. In: Proceedings of symposium, IAEA, 1984, STI/PUB/671, International Atomic Energy Agency, Vienna, p 425
- Miller A (1995) In: Proceedings of the 9th international meeting on radiation processing; *Radiat Phys Chem* 46:1243
- Miller A, Kovács A (1985) Applications of accelerators in research and industry '84. In: Proceedings of 8th conference, Denton, Texas, part II; *Nucl Instrum Meth B10/11:994*
- Miller A, McLaughlin WL (1981) High-dose measurements in industrial radiation processing. Technical report series no. 205. IAEA Publication STI/DOC/10/205. International Atomic Energy Agency, Vienna, p 119
- Miller A, McLaughlin WL (1982) In: McLaughlin WL (ed) Trends in radiation dosimetry. Pergamon, Oxford; *J Appl Radiat Isot* 33:1299
- Miller A, Xie L (1985) Food irradiation processing. In: Proceedings of symposium, Washington, 1985. IAEA, STI/PUB/695, International Atomic Energy Agency, Vienna, p 347
- Miller SD, Yoder C (1996) In: Proceedings of the 11th international conference on solid state dosimetry, Budapest; *Radiat Prot Dosim* 66:89
- Miller A, Bjergbakke E, McLaughlin WL (1975) *Int J Appl Radiat Isot* 26:611
- Miller A, Batsberg W, Karman W (1988) Progress in radiation processing. In: Fraser FM (ed) Proceedings of 6th international meeting, Ottawa, 1987, vol II; *Radiat Phys Chem* 31:491
- Miller A, Kovács A, Wieser A, Regulla DF (1989a) In: Proceedings of 2nd international symposium on ESR dosimetry and applications, Neuherberg/Munich, 1988; *Appl Radiat Isot* 40:967
- Miller SD, Stahl KA, Endres GWR, McDonald JC (1989b) *Radiat Prot Dosim* 22:195
- Miller SD, Endres GWR, McDonald JC, Swinth KL (1991) *Radiat Prot Dosim* 35:201
- Miller A, Kovács A, Kuntz F (2002) *Radiat Phys Chem* 63:739
- Milwy P, Genna S, Barr NF, Laughlin JS (1958) In: Proceedings of 2nd international conference, peaceful uses of atomic energy, Geneva, Columbia University Press, New York, p 142
- Mott NF, Gurney RW (1948) Electronic processes in ionic crystals, 2nd edn. Oxford University Press, New York
- Muller AC (1970a) In: Holm NW, Berry RJ (eds) Manual on radiation dosimetry. Marcel Dekker, New York, p 423
- Muller AC (1970b) In: Holm NW, Berry RJ (eds) Manual on radiation dosimetry. Marcel Dekker, New York, p 429

- Murray KM, Attix FH (1973) *Health Phys* 25:169
- Nakayima T (1982) In: McLaughlin WL (ed) *Trends in radiation dosimetry*. Pergamon, Oxford; *Int J Appl Radiat Isot* 33:1077
- Niroomand-Rad A, Blackwell CR, Coursey BM, Gall KP, Galvin JM, McLaughlin WL, Meigooni AS, Nath R, Rodgers JE, Soares CG (1998) *Med Phys* 25:2093
- Ostrowski K (1974) In: Gaughran ERL, Goudie AJ (eds) *Sterilization by ionizing radiation*, vol 1. Multiscience Publications, Montreal, p 325
- Osvay M, Bíró T (1980) *Nucl Instrum Methods* 175:60
- Osvay M, Stenger V, Földiák G (1975) *Biomedical dosimetry*. In: *Proceedings of symposium*, IAEA, STI/PUB/401, International Atomic Energy Agency, Vienna, p 347
- Parker RP (1970) *Phys Med Biol* 15:605
- Pesek M (1985) *High-dose dosimetry*. In: *Proceedings of symposium*, IAEA, STI/PUB/671, International Atomic Energy Agency, Vienna, p 263
- Petree B, Lamperti P (1967) *J Res Natl Bur Stand* 71C:19
- Puig JR, Laizier J, Sundardi F (1974) *Radiosterilization of medical products*. In: *Proceedings of symposium*, Bombay, 1974, IAEA, STI/PUB/383, International Atomic Energy Agency, Vienna, p 113
- Puite KJ, Ettinger KV (1982) *Int J Appl Radiat Isot* 33:1139
- Radak BB, Markovic V (1962) *Int J Appl Radiat Isot* 13:287
- Radak BB, Markovic VM (1970) In: Holm NW, Berry RJ (eds) *Manual on radiation dosimetry*, chapter 3. Marcel Dekker, New York, p 45
- Radak BB, McLaughlin WL (1984) *Radiat Phys Chem* 23:673
- Radak BB, Hjortenbergh PE, Holm NW (1973) *Dosimetry in agriculture, industry, biology and medicine*. In: *Proceedings of symposium*, IAEA, STI/PUB/311, International Atomic Energy Agency, Vienna
- Rageh MS, El-behay AZ, Soliman FAS (1985) *High-dose dosimetry*. In: *Proceedings of symposium*, IAEA, STI/PUB/671, International Atomic Energy Agency, Vienna, p 255
- Razem D, Dvornik I (1973a) *Dosimetry in agriculture, industry, biology, and medicine*. In: *International Atomic Energy Agency (ed) Proceedings of symposium*, Vienna 1972, IAEA STI/PUB/311, International Atomic Energy Agency, Vienna, p 405
- Razem D, Dvornik I (1973b) *Radiation preservation of food*. In: *International Atomic Energy Agency (ed) Proceedings of symposium*, Bombay 1972, IAEA STI/PUB/317, International Atomic Energy Agency, Vienna, p 537
- Razem D, Ocic G, Jamicic J, Dvornik I (1981) *Int J Appl Radiat Isot* 32:705
- Regulla DF (1972) *Health Phys* 22:491
- Regulla DF, Deffner U (1982) In: McLaughlin WL (ed) *Trends in radiation dosimetry*. Pergamon, Oxford; *Int J Appl Radiat Isot* 33:1101
- Regulla DF, Deffner U (1985) *High-dose dosimetry*. In: *Proceedings of symposium*, IAEA, STI/PUB/671, International Atomic Energy Agency, Vienna, p 221
- Saylor MC, Tamargo TT, McLaughlin WL, Khan HM, Lewis DF, Schenfele RD (1988) *Radiat Phys Chem* 31:529
- Sehested K (1970) In: Holm NW, Berry RJ (eds) *Manual on radiation dosimetry*, part 2. Marcel Dekker, New York, p 313
- Sehested K, Bjergbakke E, Holm NW, Fricke H (1973) *Dosimetry in agriculture, industry, biology and medicine*. In: *International Atomic Energy Agency (ed) Proceedings of symposium* Vienna 1972, IAEA STI/PUB/311, International Atomic Energy Agency, Vienna, p 397
- Seuntjens J, Duane S (2009) *Metrologia* 46:39
- Sharpe PHG, Miller A (1999) *Guidelines for the calibration of dosimeters for use in radiation processing*, NPL report CIRM 29, p 1
- Sharpe PHG, Barrett JJ, Berkley AM (1985) *Int J Appl Radiat Isot* 36:647
- Sharpe PHG, Sephton JP, Gouldstone CA (2009a) *Radiat Phys Chem* 78(7–8):477
- Sharpe PHG, Miller A, Sephton JP, Gouldstone CA, Bailey M, Helt-Hansen J (2009b) *Radiat Phys Chem* 78(7–8):473
- Smathers JB, Otte VA, Smith AR, Almond PR, Attix FH, Spokas JJ, Quam WM, Goodman LJ (1977) *Med Phys* 4:74
- Tamura N, Tanaka R, Mitomo S, Matsuda K, Nagai S (1981) *Radiat Phys Chem* 18:947
- Tanaka R, Mitomo S, Tamura N (1984) *Int J Appl Radiat Isot* 35:875
- Temperton DJ, Dixon SM, Shentall GS, Ettinger KV (1984) *J Appl Radiat Isot* 35:139
- Thomassen J (1985) *High-dose dosimetry*. In: *Proceedings of symposium*, IAEA, 1984, STI/PUB/671, International Atomic Energy Agency, Vienna, p 171
- Van Laere K, Buysse J, Berkvens P (1989) *Appl Radiat Isot* 40:885
- Weast RC (ed) (1977–1978) *CRC handbook of chemistry and physics*, 58th edn. CRC Press, Cleveland
- Weiss J (1952) *Nucleonics* 10(7):28
- Weyde E, Frankenburger W (1931) *Trans Faraday Soc* 27:561
- Whitaker B (1970) In: Holm NW, Berry RJ (eds) *Manual on radiation dosimetry*. Marcel Dekker, New York, p 363
- Whitaker B (1988) *Dosimetry and control of radiation processing*. In: *Proceedings of symposium of UK panel on gamma and electron irradiation*, Teddington, 1987. NPL Report RS (EST) 7, National Physical Laboratory, Teddington, p 18
- Whitaker B, Watts M, Mellor S, Heneghan M (1985) *High-dose dosimetry*. In: *Proceedings of symposium*, Vienna, 1984, IAEA, STI/PUB/671, International Atomic Energy Agency, Vienna, p 293

50 Particle Accelerators

S. Biri · E. Koltay · A. Valek

Institute of Nuclear Research of the Hungarian Academy of Sciences
(ATOMKI), Debrecen, Hungary

50.1	<i>Ion Sources</i>	2321
50.1.1	The Plasma Physics of Ion Sources	2321
50.1.1.1	Basic Plasma Parameters	2321
50.1.1.2	Fundamental Processes in the Plasma	2322
50.1.2	Classification of Ion Sources	2325
50.1.3	Traditional and High-Current Ion Sources	2326
50.1.3.1	The Plasmatron Family	2326
50.1.3.2	Penning (PIG) Ion Source	2327
50.1.3.3	The Cusp Family	2328
50.1.3.4	Radio Frequency and Microwave Ion Source	2328
50.1.4	Production of Ions from NonGaseous Materials	2329
50.1.5	Sources of Highly Charged Ions	2330
50.1.5.1	Electron Cyclotron Resonance (ECR) Ion Sources	2330
50.1.5.2	Electron Beam Ion Source (EBIS) and Ion Trap (EBIT)	2333
50.1.6	Other Ion Sources	2334
50.1.6.1	Radioactive-Ion Sources	2334
50.1.6.2	Ion Sources for Negative Ions	2335
50.1.7	Beam Extraction	2336
50.2	<i>Electrostatic Accelerators</i>	2338
50.2.1	Principles of Direct Voltage Accelerators	2338
50.2.2	Accelerator Configurations	2338
50.2.3	Construction Units of the Accelerator	2341
50.2.3.1	Ion Sources	2341
50.2.3.2	Voltage Sources of the Accelerator	2341
50.2.3.3	Terminal and Insulator Stack	2345
50.2.3.4	Acceleration Tubes	2345
50.2.3.5	Energy Analysis and Stabilization	2346
50.2.4	Beam Transport System	2347
50.2.5	Microbeam Channels	2347
50.3	<i>RF-Based and AC-Voltage Accelerators</i>	2348
50.3.1	Basic Principles of Operation	2348
50.3.2	Types of Cyclic and Linear Accelerators	2350
50.3.2.1	Classical Cyclotron	2350
50.3.2.2	Synchrocyclotron	2350
50.3.2.3	Isochronous Cyclotron	2350

- 50.3.2.4 Synchrotron 2352
- 50.3.2.5 Storage Ring 2354
- 50.3.2.6 Linear Accelerators 2354
- 50.3.2.7 Radio Frequency Quadrupoles 2355
- 50.3.2.8 Coupled Accelerators 2356
- 50.3.2.9 Microtrons 2356
- 50.3.2.10 Betatrons 2357
- 50.3.3 Focusing the Particle Beam 2357
- 50.3.3.1 Magnetic Field 2358
- 50.3.3.2 Coupled Resonances 2359
- 50.3.3.3 Electric Field 2360
- 50.3.3.4 Phase Stability 2361
- 50.3.4 Beam Parameters 2361
- 50.3.4.1 Energy 2361
- 50.3.4.2 Intensity 2362
- 50.3.4.3 Emittance and Acceptance 2363
- 50.3.4.4 Luminosity 2364
- 50.3.4.5 Brightness and Brilliance 2364
- 50.4 *Editors' Notes* 2364

Abstract: This chapter is designed to serve as a review and reference for the wide and still-evolving field of particle sources and accelerators. The object of this chapter is to give a comprehensive and easily understandable survey of the field in greater detail to the users of accelerators, nuclear physicists and chemists, as well as students. The field of particle accelerators covers facilities from hand-size mass separators through room-scale cyclotrons to huge storage rings. In spite of their important differences, all of them own a key subsystem, the ion source. The parameters of the ion beam generated in and extracted from the ion source determine the features of the accelerated beam on the target. Therefore, in ➤ Sect. 50.1, the ion sources of particle accelerators are reviewed. ➤ Section 50.2 is devoted to the electrostatic accelerators. The cyclic and linear accelerators are summarized in ➤ Sect. 50.3 where a survey on beam parameters is also given.

50.1 Ion Sources

The field of *ion sources* has grown dramatically in the last decades. New areas of application have evolved, new kinds of ion sources have been developed, and existing types have been improved. This development was symbiotic with the growth of the fields of accelerators and applications. New requirements from the accelerators and applications forced ion source developers to elaborate new ideas and the appearance of a new or upgraded ion source made new experiments and applications possible. The stand-alone usage of ion sources (i.e., without any post-accelerator) is also becoming more and more popular. In many institutes, groups with small laboratories have been formed for ion source development and usage.

This short review cannot deal with all types of ion sources; it will focus on the most popular types used in *linear* and *cyclic accelerators*. The accelerators themselves are described in detail in ➤ Sects. 50.2 and ➤ 50.3 of this chapter. The most relevant ion source literature includes two excellent books (Wolf 1995; Brown 2004) and two of the many review articles (Angert 1994; Wolf 1996) devoted to the large family of ion sources. The proceedings of the biennially organized international ion source conferences contain the most detailed technical information (ICIS 1989–2009). One can also find reviews and useful links on the Internet (LINAC 1996; CASETECH 2005).

50.1.1 The Plasma Physics of Ion Sources

An ion source is a plasma generator from which beam of ions can be extracted. Most ion sources are “**plasma**” sources, that is, the ionization of atoms and ions occurs in a plasma formed in the chamber of the ion source. Thus, the physics of ion sources is mainly based on the physics of the plasma. First, a summary will follow on the most important plasma parameters and the main processes (from the point of view of operation of the ion sources) in the plasma.

50.1.1.1 Basic Plasma Parameters

Plasma density. The term “density” actually means number density here, that is, number of particles per volume. The plasma consists of *ions*, *electrons*, and *neutrals* (atoms, molecules), so one can define plasma neutral density (n_0), plasma electron density (n_e), and plasma ion

density (n_z). The subscript e means “electron” and the subscript z refers to a z-times ionized atom. In ion sources, the plasma is near neutral, that is

$$e \sum_z z n_z - e n_e \approx 0 \quad (50.1)$$

if all the ions are positive. The subscript z runs over the different charge states ($z = 1, 2, 3, \dots, Z$). This equation is not valid close to the plasma boundary. Some authors mean plasma density as simply the density of the plasma electrons. Typical values of the latter in ion sources are 10^{10} – 10^{16} cm^{-3} .

Plasma temperature. Generally, the concept of “temperature” is valid only for Maxwellian energy distributions, which cover most of plasmas but not all. In spite of this, quite often the “plasma temperature” is used also for plasmas of ion sources which are not in equilibrium. The ion temperatures T_z (of z-times ionized ions) and electron temperature T_e are not necessarily equal and in the presence of magnetic field the temperatures parallel and perpendicular to the field may be different, especially for the electrons. It is usual to express the plasma temperature in electron volts (eV) using the relationship $E = kT$, where 1 eV corresponds to 11,600 K. Typical plasma electron and ion temperatures are several tens of electron volts. In some plasmas (e.g., ECR, see in [Sect. 50.1.5.1](#)), however, the T_e electron temperature can be several keV or higher.

Ionization cross section, mean free path. In the plasma, several processes can take place in collisions: excitation, ionization, recombination, and charge exchange. For every process, a corresponding cross section (σ) and mean free path (λ) can be defined. If one of the plasma components has a number density of n , then

$$\sigma \lambda n = 1. \quad (50.2)$$

Confinement time. The average time between the creation and loss of an ion with a particular charge state $z = q/e$ (where q is the charge) is called confinement time or ion lifetime (τ_z). In this particular respect, the only types of losses considered are those caused by diffusion of ions out of the plasma (to the wall of the plasma chamber) or by their extraction using external electrostatic field. The (average) confinement times of every charge state must be large enough if further ionization is required (see in [Sect. 50.1.1.2](#)).

Cyclotron frequency. In a magnetic field, a charged particle moving with speed u in a plane perpendicular to the magnetic flux density B is forced to perform a circular motion (For a more general treatment, see [Sect. 50.3.3.1](#)). The angular frequency of this circulation is the “cyclotron frequency.” For electrons, the cyclotron frequency is

$$\omega_c = 2\pi\nu_c = \frac{e}{m} B, \quad (50.3)$$

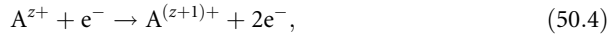
where e is the elementary charge, B is the magnitude of the magnetic flux density, and m is the (relativistic) electron mass. A similar expression is valid for ions. Since the magnetic flux density applied in ion sources is usually $B = 0.1$ – 1 tesla, the frequency ν_c for electrons is 1–30 GHz, and for ions 100 kHz–10 MHz.

50.1.1.2 Fundamental Processes in the Plasma

Ionization. In most ion sources, the ionization of atoms and ions is caused by collisions with energetic electrons. An optimal value of the electron temperature T_e (or the electron energy $E_e = kT_e$, where k is the Boltzmann constant) is necessary for each ionization process. Generally,

E_e should be several times larger than the ionization potential of the subshell of the atom to be ionized. Multiple ionizations can take place in various ways:

1. *Step-by-step single ionization* on a z -times ionized atom A^{z+}



2. *Single ionization by excitation*



where the asterisk means an excited state. Note that many excited ions do not inject electrons but produce a photon when returning back to the ground state. These photons give the *visible light* of ion source plasmas. In [Fig. 50.1](#), typical cross sections of the step-by-step ionization can be seen. The cross section strongly depends on the electron energy. The cross sections of some other processes (double or multiple ionization in one step, Auger ionization, “shake-off,” etc.) are much smaller in most plasma ion sources.

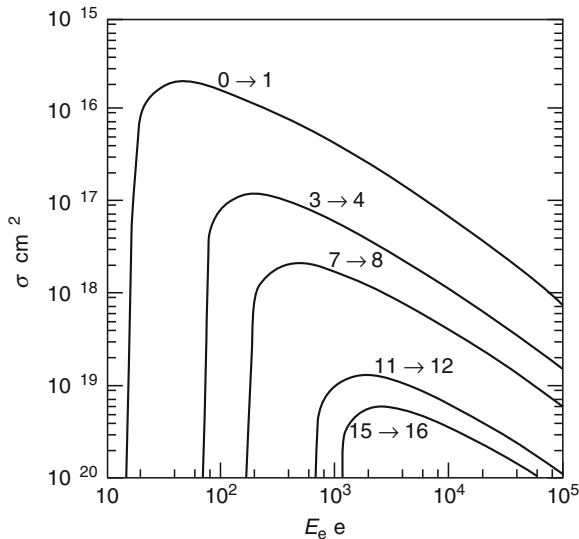
All of the above processes have their effective cross sections. If the cross section of the ionization process $z_1 \rightarrow z_2$ is σ then, as a consequence of [Eq. 50.2](#), the mean time for a transition between the charge states z_1 and z_2 to take place is

$$\tau = \frac{1}{n_e \langle \sigma u_e \rangle}, \quad (50.6)$$

where n_e and u_e are the electron number density and speed, respectively, and $\langle \dots \rangle$ means averaging over temperature. Let τ_z be the confinement time of the z -charged ion (z can be any

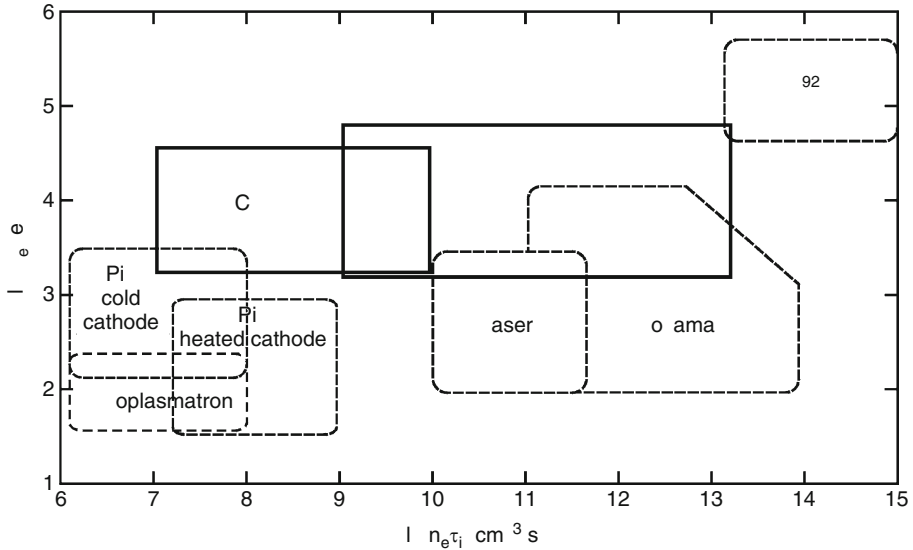
Fig. 50.1

Ionization cross sections for argon (Brown 2004, p 211, reproduced with permission)



■ Fig. 50.2

Some ion sources and fusion facilities in the plasma plane. PIG: Penning Ion Gauge, ECRIS: Electron Cyclotron Resonance Ion Source, EBIS/EBIT: Electron Beam Ion Source or Trap, laser: plasma produced by laser ablation in solids, tokamak: fusion device of light ions, U^{92+} : fully stripped uranium ion



integer between 1 and Z and for simplicity sake, it will be assumed that τ_z does not depend on z). Then for $z_1 \rightarrow z_2$, the condition $\tau_z \geq \tau$ must hold. To produce multiply charged ions, the (average) confinement times must be larger than the (average) ionization times for every particular charge state. With a simple transformation, one obtains

$$n_e \tau_z \geq \frac{1}{\langle \sigma u_e \rangle}. \quad (50.7)$$

The conclusion is that the most important plasma parameters for the ionization are the T_e electron temperature (or the $E_e = kT_e$ electron energy) and the $n_e \tau_z$ factor. These two parameters determine the character of the plasma and the charge states in it. Moreover, the ion sources themselves can be characterized by their positions in the $(n_e \tau_z, E_e)$ plane (● Fig. 50.2). The figure also shows the typical values for $n_e \tau_z$ and E_e .

Ion charge loss processes. In the plasma, the opposite of the ionization process also takes place: ions can be recombined by “electron capture” or charge exchange. All these charge loss processes have their cross sections similarly to the ionization.

The equation of the plasma equilibrium state. The charge state distribution (CSD) in the plasma is a result of the dynamical processes mentioned above. Let n_z be the number density of the z -times charged ions with atomic number Z . Then the following simplified differential equation is valid ($z = 1, Z - 1$):

$$\frac{dn_z}{dt} = I(n_{z-1} \rightarrow n_z) + R(n_{z+1} \rightarrow n_z) - I(n_z \rightarrow n_{z+1}) - R(n_z \rightarrow n_{z-1}) - n_z/\tau_z \quad (50.8)$$

where I and R represent rates of ionization and recombination/charge exchange, respectively. For $z = 0$ and $z = Z$, the equations are simpler. In equilibrium state, the left side is equal to zero. On the right-hand side, the expressions are (from left to right):

(1) ionization (both charge and n_z increase), (2) recombination or charge exchange (charge decreases, n_z increases), (3) ionization (charge increases, n_z decreases), (4) recombination or charge exchange (both charge and n_z decreases), (5) loss due to the limited confinement time of the ions.

The quantities I and R usually depend on the number densities and the relative velocities of the interacting particles and on the cross section of the interaction itself.

The cross section of the charge transfer is usually considered only for the ion-neutral case (the electron transfer between two ions is negligible in most ion source plasmas). The charge state can change by one or (with much smaller cross sections) by two in one such step. The recombination with free plasma electrons is much less important in ion sources.

The challenge for ion source theorists is to formulate [Eq. 50.8](#) more precisely and solve it to get a charge state distribution that fits the experimental data. Several authors (Jongen 1980; Bliman and Chan-Tung 1981; West 1982; Brown 2004; Shirkov 1991, 2000; Wolf 1995; Melin and Girard 1997; Girard et al. 2002; ICIS 1989–2009) tried to write down and solve [Eq. 50.8](#) for a given ion source type. The results are quite satisfactory for some types (e.g., EBIS), but altogether there are still spaces to further explore the elementary processes in most of the ion sources.

50.1.2 Classification of Ion Sources

The parameters of the ion source must match the features of the accelerator, and these parameters strongly influence the final (beam) parameters of the accelerator. The most important ion source characteristics are:

1. Working range (the elements of the periodic table that can be ionized in the source)
2. Charge state distribution of the extracted beam
3. Size, energy spread, and emittance of the extracted beam
4. Electrical efficiency (ion intensity vs. electrical power consumption)
5. Gas efficiency (ion intensity vs. working gas consumption)
6. Maintenance period (replacement time of cathodes or other consumable parts, cleaning, etc.)

The requirements for these parameters are needed for choosing the appropriate type of ion source. There are many ion source types (a rough estimation: between 50 and 100) and they can be classified in several ways.

By working principle, they can be classified as hot filament sources, ion sources based on Penning discharge (PIG), radio frequency (RF) and microwave (MW) ion sources, electron cyclotron resonance (ECR) ion sources, electron beam ion sources (EBIS, EBIT), laser ion sources, cusp and multicusp ion sources, sputtering ion sources.

By application, they can be classified as internal (cyclotron) ion sources, external (cyclotron, synchrotron) sources, ion sources for noncyclic electrostatic accelerators, ion sources for linear accelerators, ion sources for implanters, mass separators, and stand-alone ion sources for atomic physics and applications.

By the ion and its charge state they can be classified as proton ion sources, light-ion sources (atomic number 1–10, charge 1–5), multiply charged heavy-ion sources (charge > 5), highly charged heavy-ion sources (charge > 10), and negative-ion sources.

By the physical condition of the material to be ionized, they can be classified as gas ion sources, solid materials ion sources, ion sources for beams of stable elements, and those of promptly produced radioactive elements.

By the operation mode, they can be classified as continuous working (CW) regime and pulsed mode (PM) regime ion sources.

The above classifications are not strict. In the next sections, the various ion source types will be reviewed.

50.1.3 Traditional and High-Current Ion Sources

This section gives a short overview of most traditional ion sources that deliver single or multiply charged ion beams with medium or high intensity.

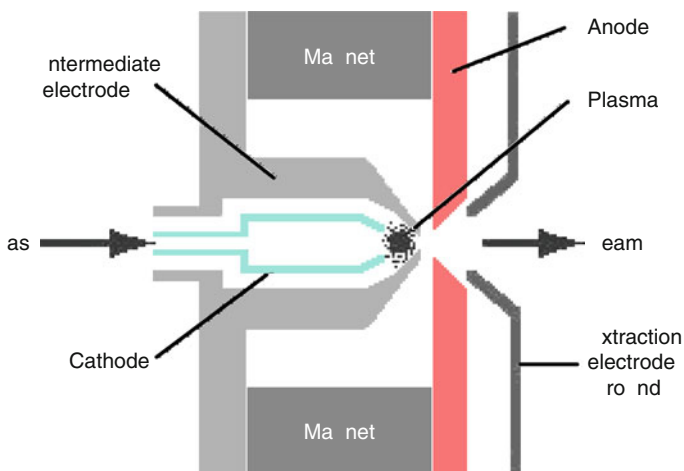
50.1.3.1 The Plasmatron Family

The plasmatron is a family of ion sources that has been used for many years for the production of single- or low-charged beams. In all plasmatron types, the plasma is formed between the cathode and anode plates. Electrons emitted by the cathode gain energy by running the cathode–anode voltage difference and ionize the atoms injected into this volume. The produced ions are extracted through the circular slit of the anode.

The most popular member of the plasmatron family is the *duoplasmatron* (Fig. 50.3). Its idea is that the plasma density between the anode and cathode is greatly increased in a small volume by an intermediate electrode placed between the anode and cathode putting on

Fig. 50.3

Duoplasmatron. Courtesy and copyright of Evans Analytical Group (EAG 2010)



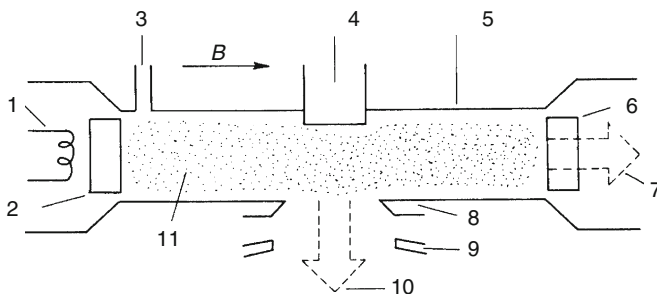
a suitable electrostatic potential. Furthermore, a magnetic field is applied in the volume in question, which partly traps electrons and thus increases the density. The result is a quasi two-stage ion source, where the function of the intermediate electrode is twofold: it is the extractor of the first stage (similarly to the anode it has a slit) and the emitter for the second stage. The ions are extracted through the anode into an expansion region, which can be considered as a third stage. Typical discharge voltages and currents are up to 250 V and 20 A, respectively. The duoplasmatron is able to strip a wide range of ions (from H to U, Keller and Müller 1976) with high intensity (current density: 100 A/cm^2) and medium charge. The gas efficiency is exceptionally good. Sometimes, a subsequent electrode is applied after the anode to form an anticathode (duopigatron).

50.1.3.2 Penning (PIG) Ion Source

The PIG (Penning Ion Gauge) has been the most popular cyclotron ion source for many years. The working principle is applied not only in ion sources, but in vacuum gauges and in ion-getter pumps as well. The principle of the PIG can be understood by [Fig. 50.4](#). The primary electrons emitted by the cathode are accelerated toward the anode wall. Because of the applied axial magnetic field, the electrons usually do not reach the anode. They fly toward the anticathode following a helical path. The circular motion of the electron (mentioned in connection with the cyclotron frequency in [Sect. 50.1.1.1](#)) only applies to the projection plane perpendicular to B . The velocity component parallel to B remains unaffected by the magnetic field, thus resulting in a helical path (see also [Sect. 50.3.3.1](#) for more detail). The electrical potential of the anticathode is close to the potential of the cathode, thus reflecting back most of the electrons. As a result, the electrons oscillate between the cathode and anticathode. The mean confinement time of the electrons will be large and they can perform many collisions with atoms and ions. The atoms injected through the gas inlet slit (or sputtered in the chamber from solids, see [Fig. 50.4](#)) are ionized and an arc discharge is formed in the chamber. The temperature of the mixture of the primary (emitted) and secondary (stripped) electrons is between ten and a few hundred eV. The ions can be extracted axially or radially.


Fig. 50.4

The Penning (PIG) ion source. 1 – cathode, 2 – indirect heating (optional), 3 – gas inlet, 4 – sputtering electrode (optional), 5 – anode, 6 – anticathode, 7 – ion beam (axial extraction), 8 – emission slit, 9 – extraction electrode, 10 – ion beam (radial extraction), 11 – plasma, B – magnetic flux density



Within the PIG family, several subtypes are known: PIG with direct heating (Livingston and Jones 1954; Jones and Zucker 1954), PIG with indirect heating (Morozov et al. 1956; Baumann and Bethge 1981), and PIG with cold cathode (Anderson and Ehlers 1956).

50.1.3.3 The Cusp Family

Placing two solenoids or permanent magnets, with their poles of the same polarity facing each other, a special magnetic field of “**cusp**” shape will be formed in a small volume. Applying many small “cusps” in rows around a rectangular or cylindrical plasma chamber, the arrangement is called “**multicusp**.” The (multi)cusp-shaped magnetic field can confine the electrons very effectively. Using a cathode (filament) and an anode (source chamber walls) in this volume, a discharge can be ignited and a simple, however, effective multicusp ion source is obtained.  Figure 50.5 shows a cusp and a multicusp arrangement.

The discharge in the multicusp source is sometimes maintained by external RF field coupled into the discharge volume by a small induction coil. Usually, but not always, a small starter filament is used to provide electrons to help plasma ignition. This type of ion source can also be called RF ion source (see in the next section).

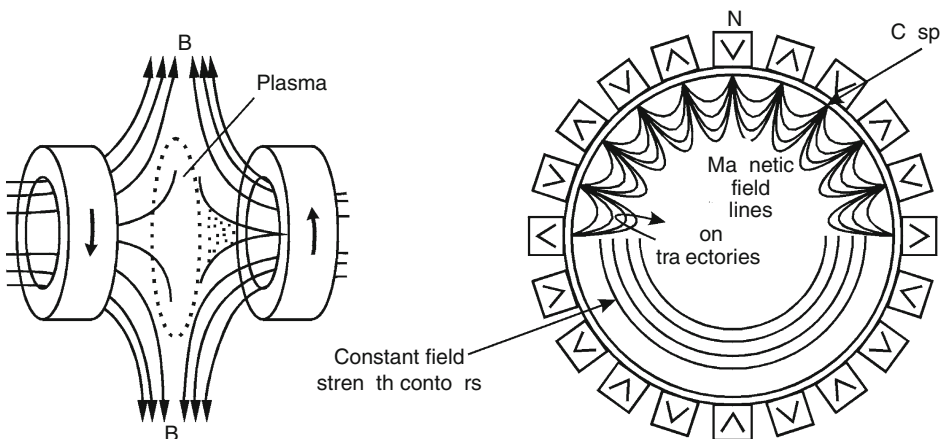
The multicusp ion source (sometimes also called as “bucket” source, Wolf 1995) is nowadays widely used to produce single- or low-charged, high-current (up to some tens of mA) ion beams (Leung 1994). The main advantages of these sources are their stable plasma, the high output beam current, and that they can be made to have almost any size. Types for multicharged and negative-ion production were also developed (Wolf 1995; ICIS 1989–2009).

50.1.3.4 Radio Frequency and Microwave Ion Source

Dense plasmas can be generated by RF or MW discharge in magnetic field. For such discharges, a relatively high gas pressure (about 10^{-3} mbar) is necessary and this condition determines the

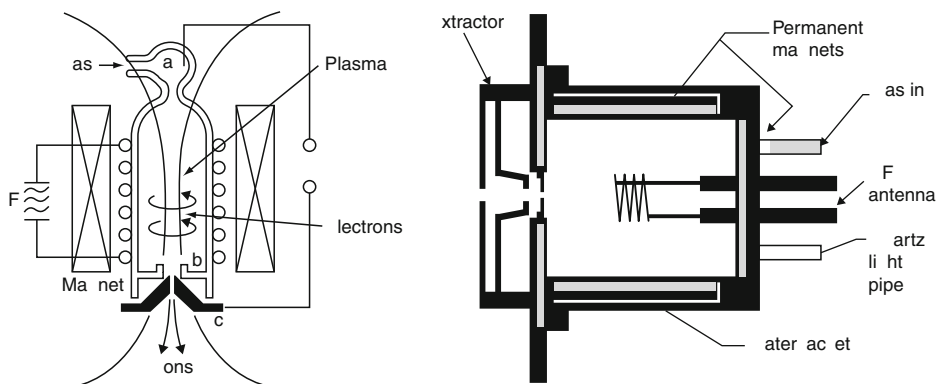
 Fig. 50.5

Mono-cusp (left) and multicusp (right) magnetic geometries



■ Fig. 50.6

Schematic pictures of two RF ion sources. *Left: the original Thonemann design (Thonemann 1953), right: RF multicusp source (Reijonen 2000)*



main features of such ion sources: low ionization degree, high extracted beam current, and stable operation (Angert 1994; Wolf 1995, 1996).

In the case of *RF ion sources*, the discharge is generated by an induction coil. This coil can be either inside or outside the plasma chamber. In the latter case, the wall material (like quartz) must be transparent for electromagnetic waves. An azimuthal RF electric field is generated in the plasma chamber by the alternating magnetic field. The electrons in the gas volume are excited into oscillation by the electric field and quickly gain enough energy to form plasma by ionizing the neutral atoms. The applied RF is usually a few (or a few times 10) MHz and the coupled power is a few hundreds of watts. In ► Fig. 50.6, schematics of two RF sources are shown.

MW ion sources differ from RF sources in frequency, size and magnetic field. Many MW sources work at **2.45 GHz** frequency due to the fact that cheap and reliable MW generators are commercially available (used also in microwave ovens). In MW ion sources (contrary to the RF sources), the size of the plasma chamber is in relation to the MW length in order to form a multimode cavity. In multimode cavities, the energy transfer from the electrical component of the electromagnetic wave to the electrons can be much more effective due to the increased power density in certain local places inside the plasma chamber. In MW sources, a magnetic field is superimposed to improve heating of the electrons. MWs entering the discharge chamber through a waveguide can propagate through the plasma and transfer their energy to free electrons that further ionize the gas atoms and ions. If the magnetic field strength fulfills the ECR condition (see ► Sect. 50.1.5.1 for more details), then the MW source can be considered and called a low-frequency ECR ion source (► Sect. 50.1.5.1).

50.1.4 Production of Ions from NonGaseous Materials

The normal and easiest way to produce plasma in any ion source is to use a gas dosing valve and inject the required element in gas form into the discharge chamber. Many elements of the periodic table, however, are not available in gaseous form. There have been various methods developed for *ion production from solids*. Some methods resulted in new types of ion sources

(e.g., sputtering ion source, laser ion source) many years ago. Nowadays, these methods are more and more applied in different kinds of ion sources. That is why these methods are described in a separate subsection. A very detailed description of these methods is presented by Wolf (1995, 1996). The most important methods for feeding solids into ion sources are summarized as follows.

1. **Evaporation from an external or internal oven.** Different kinds of ovens and mini-ovens have been developed to evaporate solids with melting points up to 2,000°C (Lang et al. 2000; Barué et al. 2002; Kidera et al. 2002; Závodszky et al. 2002). The ovens are usually very close to (or sometimes inside) the plasma chamber. An important requirement is the precise online monitoring of the oven temperature. Because evaporation is a continuous process, ovens are usually used in continuously operating ion sources.
2. **Use of volatile chemical compounds.** The use of chemical compounds that are volatile at room temperature is as easy as the use of a pure gas. The main disadvantage of this method is the amount of unwanted ions of the elements of the compound (usually H, C, N, O, F). The popular name of this method in ECR ion sources is MIVOC (Metal Ions from Volatile Compounds) developed in Finland (Arje et al. 1995; Koivisto 1998). Note that a combination of methods (1) and (2) also exists.
3. **Cathodic sputtering of the solid.** Sputtering is the most generally applicable universal method to feed atoms into an ion source discharge. The sputter electrode (or the end of the electrode) made of the required material is usually negatively biased. The sputter yield depends on the electrode potential, but this potential also affects the discharge and an optimum should be found. A support gas (like argon) is necessary for the stable operation. Sputtering is ideal for materials with high melting point like W, Ta, Mo, etc. The sputtering method is suitable for both continuous and pulsed operation (the bias voltage of the electrode can be switched simultaneously with the accelerator). Nowadays, the method is routinely used in PIG, ECR, RF, and negative-ion sources (Wolf 1996; Kitagawa et al. 2002).
4. **Evaporation by vacuum arc or laser.** Metal evaporation by vacuum arc (MEVVA) is also a method that resulted in a small family of independent ion source types (Brown 1992, 2004). A high voltage vacuum arc creates metal plasma that expands rapidly and can be further ionized. The physical basis of the laser method (or laser ion source) is very similar. If a powerful (power density $> 10^8$ W/cm²) laser beam hits a solid target, high energy can be transferred to a small volume of the solid material and very high charge states can be registered (Wolf 1995; Fournier 2000; Mironov et al. 2001). Both methods make operation in pulsed mode possible.

50.1.5 Sources of Highly Charged Ions

50.1.5.1 Electron Cyclotron Resonance (ECR) Ion Sources

Electron cyclotron resonance ion sources (ECRIS) are nowadays widely used for the production of high-charge-state heavy ions. Development of these sources began in the 1970s (Geller 1976). The conventional ion sources (mostly PIG-types) were inadequate for accelerators requiring highly charged ions. To improve their reliability and to lower their cost, better

sources had to be developed. The particle energy per nucleon (in MeV) delivered by cyclotrons is given by

$$E = K \left(\frac{z}{A} \right)^2, \quad (50.9)$$

where z and A are the charge state (charge number) and the mass number of the accelerated ion, respectively, and K is a factor depending on the size of the machine and its magnetic field. The value of K is generally between 10 and 1,000 MeV. Thus by increasing z by a factor of 2 or 3, one can increase the particle energy by 4 or 9 without changing anything else. The cost of such a change (i.e., replacing a PIG by an ECRIS) is several orders of magnitude lower than the cost of increasing K by a factor of 4 or 9.

Today, most of heavy-ion cyclotrons are equipped with an external ECRIS. Over the last 30 years, ECR ion sources have evolved from a single large, power-consuming, complex prototype (Geller 1976) into a variety of compact, simple, reliable, efficient, and high-performance sources of high-charge-state ions. They are stand-alone devices with their own power supplies, vacuum, and control systems. Altogether, about 100 high-charge-state ECRISs are working all around the world and 10–20 are being developed or upgraded. The “must-have” literature on ECR ion sources is the famous and excellent book by Richard Geller (Geller 1996) who was the inventor of the ECRIS. There are numerous review papers (e.g., Melin and Girard 1997; Hitz et al. 2000; Sortais 2000; Drentje 2003) devoted to the ECR sources. International ECRIS workshops are organized in every second or third year and in 2008 already the eighteenth such meeting was held in Chicago, USA. The proceedings of these workshops contain most detailed information on the ECR ion sources all over the world. The material of the last workshop can be found on the Internet (ECRIS 2008).

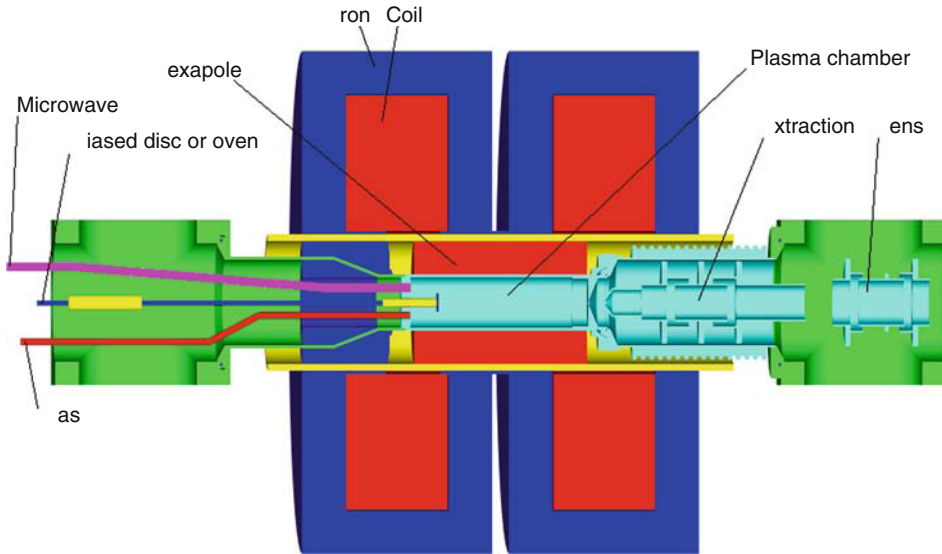
The layout of a typical 14 GHz ECRIS is shown in [Fig. 50.7](#). To get highly charged ions in ECR sources, two tasks have to be solved simultaneously: (1) The ions must be trapped in the chamber for a long time because their inner shells get ionized step by step. (2) A great number of energetic electrons are needed, while the energy of the ion component should be kept as low as possible.

The first condition is fulfilled using the so-called ***B*-minimum geometry** (B is the absolute value of the magnetic flux density in the plasma chamber). The superposition of two axial mirror coils and a radial hexapole magnet (see the magnetic system in [Fig. 50.7](#)) forms a magnetic structure in which the magnetic flux density is increasing in any direction starting from the center of the chamber, that is, it has a minimum there. This results in an effective *magnetic trap* for the electrons and the space charge of the electrons keeps the ions inside the trap (quasi-neutrality). The magnetic trap can be formed in several ways: it can consist of exclusively room-temperature permanent and electro-magnets (Biri et al. 2002), superconducting (SC) solenoids in combination with a room-temperature permanent magnet hexapole (Biri et al. 2000; Nakagawa et al. 2002; ECRIS 2008), SC mirror coils and an SC hexapole (Ludwig et al. 1998; ECRIS 2008), or solely permanent magnets (Muramatsu et al. 2002).

The electrons are heated by external high-power, high-frequency electromagnetic waves. The frequency is usually between 2.45 and 28 GHz (the most often used frequency is 14.5 GHz) and the applied MW power is several hundreds of watts, sometimes up to several kW. The cyclotron frequency of electrons is proportional to the magnetic flux density (see [Eq. 50.3](#)), that is, depends on the time-dependent position of the electron in the plasma. Because the

■ Fig. 50.7

Layout of a typical ECR ion source with room-temperature coils and with permanent magnet hexapole (ECR 2010)



magnetic flux density in B -minimum geometry increases from the center toward the chamber walls, the cyclotron frequency of electrons increases as well.

The geometrical points where the electron's cyclotron frequency equals the frequency of the external electromagnetic wave – in other words where the *ECR condition* is fulfilled – form a closed, “egg-shaped” surface. This surface is often called resonance surface or *resonance zone* and can be characterized by the strength of the magnetic field. For 14.5 GHz ECR ion sources, this value is 0.52 T. The electrons crossing many-many times the resonance surface following a strange, complicated serpentine path (► Fig. 50.8) gain energy by means of resonance (called cyclotron resonance for historical reasons) from the electromagnetic wave. (By a simplified model, resonance means that the electron and the electrical \mathbf{E} -vector of the electromagnetic wave rotate “together” with the same frequency on the resonance surface for a short time.) Some electrons get energies up to tens of keV, so they are able to tear off electrons even from inner shells. The ion component becomes cold because the resonance condition is not fulfilled for them. The gas to be ionized is fed into the plasma chamber by a needle valve.

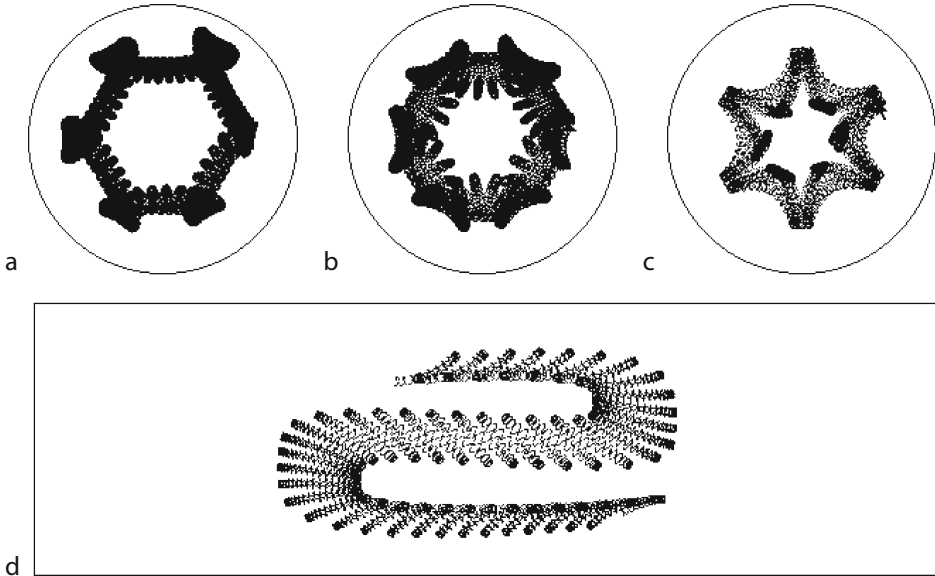
The techniques of producing ions from solids have been mentioned in the previous section. The ions are extracted from the plasma chamber by the electrostatic extraction system (see ► Fig. 50.7) like in all other types of ion sources.

In ► Fig. 50.8, the path of one electron is shown in the cylindrical plasma chamber of an ECRIS. ► Figure 50.8 was made by the TrapCAD code (Vámosi and Biri 1996) which was recently upgraded (Biri et al., 2007). The demo version is available for downloading from the Internet (ECR 2010).

The ECRIS is the most popular ion source today. It is able to produce highly charged plasmas and ion beams from a wide variety of elements with high intensity both in continuous and pulsed modes. The most advanced ECR sources produce more than 1 mA of middle-charged heavy-ion

■ Fig. 50.8

Simulation of the path of a single electron in the ECRIS plasma chamber (Biri et al. 1997). Upper part (a, b, c) end views of the plasma chamber with different electron starting conditions, lower part (d) side view of the plasma chamber



beams (e.g., Ar^{8+}) and several μA of very highly charged beams, for example, Ar^{17+} , Xe^{36+} , U^{50+} (ICIS 1989–2009; Sortais 2000; ECRIS 2008 and references therein). The highest-charged extracted ion beams obtained in ECRIS are, for example, Xe^{44+} , Bi^{50+} , U^{55+} (Xie and Lyneis 1997; ECRIS 2008).

In most ECRIS devices, “tricks” are also applied to increase the intensity of highly charged ions. More information about gas-mixing, biased-disc, special-wall, etc. methods can be found in papers cited in this section.

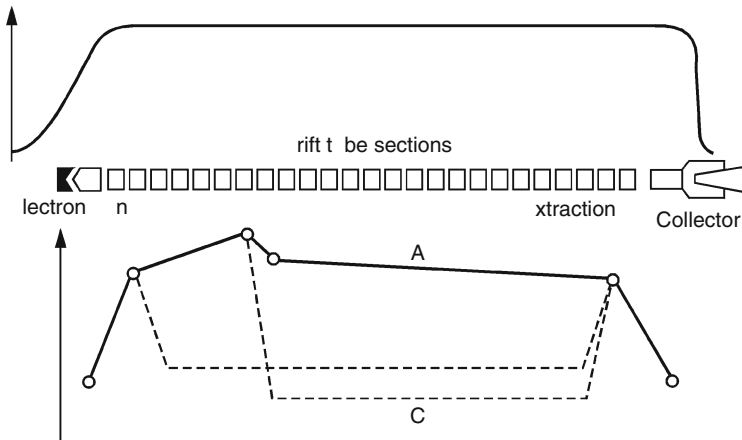
50.1.5.2 Electron Beam Ion Source (EBIS) and Ion Trap (EBIT)

The working principle of the EBIS can be understood from ► Fig. 50.9. An intensive electron beam is collimated by a very strong axial magnetic field. Neutrals are hit and ionized by these electrons. The ions are radially trapped by means of the space charge of the electron beam. The axial trapping of the ions is caused by a special electrostatic profile generated by a number of drift tubes. The potential of the drift tubes can be independently varied, thus different potential shapes can be achieved (► Fig. 50.9A–C).

First, the profile A cleans the electron beam from the positive ions. Then neutrals are injected for a short time, meanwhile the profile B is set in, which traps the ions. The profile C pushes the ions toward the extraction region and prevents the diffusion of low-charged ions into the ionization volume. Finally, the profile A again opens the trap and highly ionized ions are extracted. It is obvious that the EBIS works in pulsed regime only. In this way, very high charges but low intensities can be achieved.

■ Fig. 50.9

Principle of the EBIS. B and U are the axial magnetic flux density and the electrostatic potential, respectively



The first EBIS (Donets et al. 1968) worked at room temperature. In later versions, the very high magnetic field (B is several teslas) is produced by SC coils (Wolf 1995). The EBIT, which is the same as EBIS but contains no extraction, finds its application in atomic and plasma physics studies. It is especially suitable for spectroscopic (X-ray) studies of highly charged ions. Traditionally, the EBIS is a successful injector of fully stripped light ions into synchrotrons, but is also useful for high charge states of heavy ions. Existing EBIS are capable of producing fully stripped Xe^{54+} ions (Donets 1993), while fully stripped uranium (U^{92+}) was detected in an EBIT with an electron energy of 198 keV (Marrs 1996). These high charges exceed those values produced by ECRIS, however the amount of such ultra-stripped ions is extremely low (10^4 Xe^{54+} ions/per pulse and ten U^{92+} ions were detected).

The working mechanism of EBIS is better understood than other ion sources. Because the electron component is a beam in EBIS, usually $j_e \tau_z$ is calculated (where j_e is the current density of electron) instead of the $n_e \tau_z$ factor (described in ▶ Sect. 50.1.1.2). ▶ Figure 50.10 shows the different charge states versus $j_e \tau_z$. In EBIS, the plasma parameters (e.g., electron number density and electron energy) are much better known than in other sources, so the calculations fit experiments better.

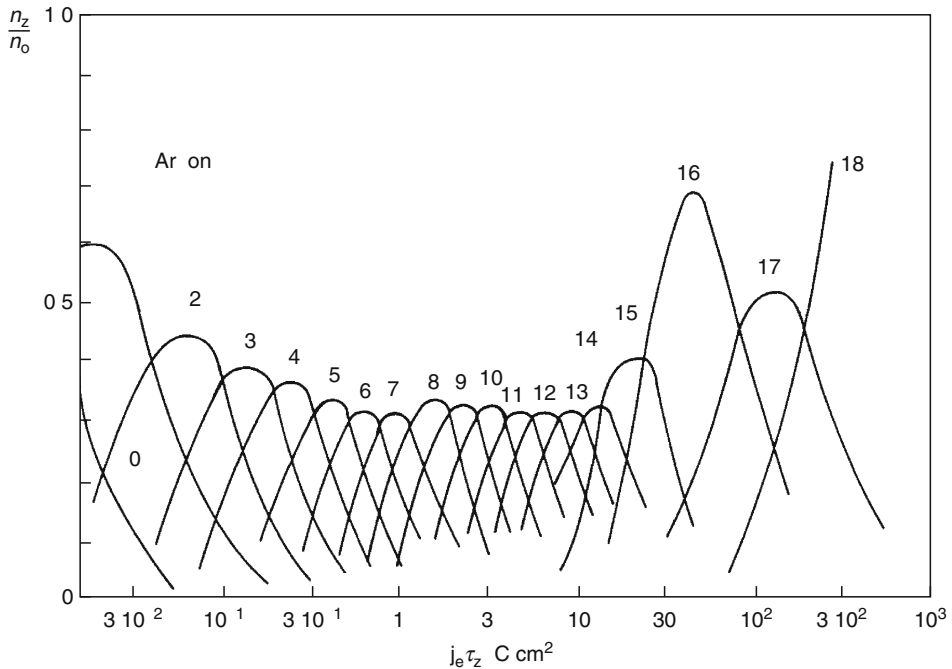
50.1.6 Other Ion Sources

50.1.6.1 Radioactive-Ion Sources

This subsection discusses ion sources in which the radioactive atoms to be ionized are produced online in nuclear reactions. For the ionization of atoms with radioactive nuclei, the key factor is the efficiency of the source, that is, the ratio of the number of ions in the beam with respect to the number of atoms injected into the source. This ratio for the nonradioactive-ion sources is usually between 10% and 90%. If only one required charge state is considered, this ratio is, of course, lower, depending on the nature of the charge-state distribution in the particular ion source.

■ Fig. 50.10

Calculated charge state distribution in EBIS (Arianer et al. 1982)



Two methods will be described briefly; they serve as examples of how to produce radioactive-ion beams. Both of them are connected with ECR ion sources, but other types of ion sources can also be applied to high-efficiency radioactive-ion beam production (Wolf 1995).

The radioactive elements are created by bombarding suitable targets with energetic (usually 30 MeV) cyclotron proton beams (Barué et al. 1998). Those released by the hot target in a neutral gaseous form are transferred by diffusion to an ordinary ECR ion source where they are ionized, extracted, and usually injected into a second accelerator. Production of both single and multicharged ions (of ${}^6\text{He}$, ${}^{13}\text{N}$, ${}^{19}\text{Ne}$, among others) is possible for post-acceleration.

The charge-breeding method is another powerful technology to produce multicharged radioactive beams (Sortais 2000). Two ECRIS units are coupled in such a way that the first one works in a high-pressure mode to produce single-charged ions from radioactive atoms (see the previous paragraph). Then the single-charged ions (called “1+” beam) are transported at a common 10–15 keV potential into another powerful ECRIS where they are decelerated upon entering into the plasma. This second (low-pressure) ECRIS operates as charge accumulator where the captured “1+” ions are multi-ionized into “ $n+$ ” ions (the method is sometimes called the “1+/ $n+$ ” method). The efficiency can reach 50% (Sortais 2000).

50.1.6.2 Ion Sources for Negative Ions

Heavy ions can be negative as well. A whole ion source family exists for the production of negative ions. Originally, these ion sources were able to generate negative H ions only. Nowadays, however,

they produce high-intensity negative (usually single-charged) heavy-ion beams. In such ion sources, electrons and negative ions have the same charge and thus both are extracted from the source together. Elimination of the high-intensity unwanted electron component is one of the major technological problems in designing negative-ion sources. The physical processes in negative-ion sources are still subject to investigations. Two main types of source are generally known: *surface* and *volume* ion sources (Brown 2004; Angert 1994; Wolf 1995).

In experiments with different types of ion sources (duoplasmatron, multicusp, etc.), it was recognized that negative ions were produced near an electrode surface, that is, at the edge of the plasma. Insertion of a floating electrode in the appropriate region of the plasma improved the yield of the negative ions. The addition of an alkaline surface layer (usually cesium) to the electrode, however, dramatically increased the negative ion (and electron) current (Kobayashi et al. 1976). The increase in ion source efficiency from the addition of Cs accelerated the development of negative-ion sources toward higher intensities. The structure of the up-to-date negative-ion sources is very similar to the multicusp ion sources in which the discharge is maintained by RF or MW power and a converter electrode with cesium surface layer generates the negative ions (Wolf 1996). This converter electrode can also act as a sputter electrode to produce (negative) metal ions. Sometimes, such sources are also called sputtering ion sources.

Volume-type negative-ion sources operate simply by virtue of the fact that every plasma contains not only positive ions and electrons, but some negative ions as well. With suitable modifications of the geometry of traditional positive-ion sources (PIG, duoplasmatron, cusp, etc.), these sources can work as negative-ion sources. A magnetic filter is often used inside the plasma chamber to deflect the unwanted electrons from the extraction area (Hahto et al. 2002). The region of the plasma near the extraction is poor in electrons and contains mostly single-charged positive and negative ions. In such plasma, even more H^- ions can be produced by volume processes with high efficiency.

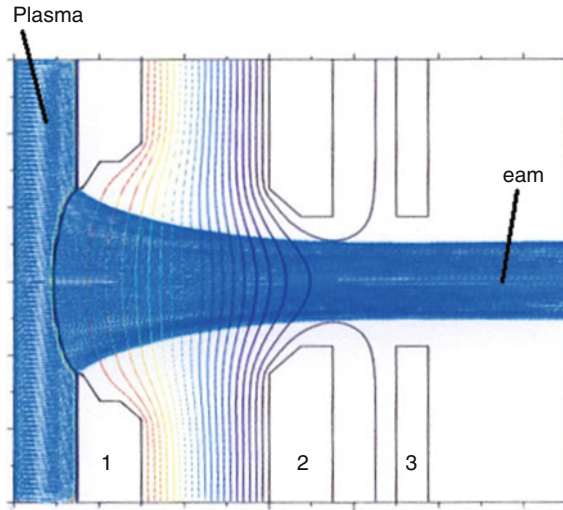
The best negative-ion sources are able to deliver amperes of hydrogen beams and tens of mA of heavy negative-ion beams (Wolf 1995).

50.1.7 Beam Extraction

For further use, the ions must be extracted from the plasma of the ion source. In most cases, electrostatic extraction systems are applied. An electrostatic ion-optical system for a cylindrically symmetric beam consists of several coaxial electrodes with suitable shapes and apertures. The first one of these electrodes (called exit-hole or extraction-slit or plasma electrode) is usually on high positive potential, while the last one is on the ground and serves as an entrance slit to the beam transport channel. Between these electrodes further electrodes can be placed with various potential values. The most common arrangement is the triode system, which consists of three electrodes. Depending on the potential of the middle electrode, “accel-decel” or “accel-accel” potential configurations are obtained. In an “accel-decel” system, the middle electrode (which is often called a puller) has a small negative potential to prevent electrons from backstreaming to the plasma. This solution also has the possibility to change the extraction field strength without changing the beam energy. In [Fig. 50.11](#), a typical three-element extraction system is shown. The ECR ion source in [Fig. 50.7](#) has a four-element extraction system.

■ Fig. 50.11

Typical accel-decel extraction system with calculated equipotential lines and simulated beam trajectories (Spädtke 1998) (1, 2, 3 denote electrodes)



The maximum density j of the extracted current from a plasma is given by the Child–Langmuir law:

$$j = (1.72 \text{ A})(U/V)^{3/2} \frac{\sqrt{z/A}}{d^2}, \quad (50.10)$$

where U is the extraction voltage, A the mass number, z the ion charge state, and d the extraction gap width (distance between the plasma electrode and the puller).

Real extraction systems cannot reach this current density limit because of imperfect geometries. The trajectories of the extracted beam are influenced by the electrostatic field strength, the magnetic flux density (if any) and direction in the extraction region, the space charge density of the beam, and the shape of the plasma in the emission slit. The design of an ion-optical system involves the determination of the number, shapes, and potentials of these electrodes. There are elaborated theories and accepted methods to do that (Angert 1994; Wolf 1995, 1996; Brown 2004). Many efforts were carried out to find rules for the electrode shapes, distances, etc. Today powerful computer codes are available (e.g., Spädtke and Mühle 2000; Dahl et al. 1990; SIMION 2009). Using such codes, one can easily simulate the beam trajectories and find an optimal basic electrode arrangement.

The ion source with the extraction system is connected to the accelerator or directly to the target through a transport system. The transport system consists of several elements. After the extraction optics, an active beam-focusing tool is usually applied (electrostatic einzel lens or solenoid) followed by a charge separator. Diagnostics units are installed in the beam line to measure the beam quality. The most important beam parameters are the ion current, beam profile, and emittance. The beam current is measured by a special cup-shaped metal electrodes (Faraday cups) that convert the intensity of the stopped ion beam into electrical current. The beam profile and emittance can be diagnosed by several methods. The detailed description of different transport systems can be found in the ion source handbooks (Wolf 1995; Brown 2004).

50.2 Electrostatic Accelerators

50.2.1 Principles of Direct Voltage Accelerators

A straightforward method for producing energetic beams of accelerated particles for nuclear reaction experiments is offered by electrostatic accelerators. In these facilities, the ion beams of selected atomic number and atomic mass are either directly extracted from a gas discharge or are generated from a primary beam in subsequent sputtering and/or charge exchange processes. The beams are then accelerated to the energy needed through the equivalent total direct-current acceleration voltage connected to an acceleration tube inside the insulation column, which holds the voltage generator and the high voltage terminal. Since the beam energy is determined by the total acceleration voltage available in a direct current source, the intrinsic stability of the beam energy is guaranteed at high level and a smooth, stepless adjustment of the beam energy can be achieved within a broad energy interval.

Detailed introductions into the physics and technique of electrostatic accelerators can be found in monographs and review papers (Herb 1959; England 1974; Rolfs and Rodney 1988; Takács 1997), as well as in proceedings volumes of the series of Tandem Conferences (Migneco and Vinciguerra 1981; Aitken and Tait 1984; Heyder and Ziegler 1998) and International Conferences on Electrostatic Accelerators and Associated Boosters (Aitken and Tait 1973; Frick 1977; Jones and Martin 1981; Ventura and Thienberger 1986; Frick and Jaeschke 1990; Signorini and Spolaore 1993; Weisser 1996).

The development of electrostatic accelerators during the decades of their history has been motivated by the trends of ongoing and planned basic nuclear research and interdisciplinary applications based on accelerated ion beams.

The primary aim prescribed by former trends in nuclear structure physics was the broadening of the interval of particle energies and of the selection of atomic number and atomic mass of accelerated nuclei. The increase of the maximum voltage of the machines and the multiple use of the acceleration voltage achieved opened the new field of heavy-ion nuclear reactions and led to important results in nuclear structure physics around the middle of the twentieth century. Machines of rated accelerating voltages around 20–30 MV used in multiple acceleration mode offer beam energies in the hundred MeV region today. Due to increased technological difficulties related to the use of extreme high voltages on the one hand, and new technical requirements posed by the latest new trends in the physics of exotic nuclei on the other hand, more ambitious plans for increasing the rated terminal voltage seems to be absent nowadays. At the same time, however, parallel with the applications of large electrostatic accelerators in basic nuclear research, accelerated beams find broad scale interdisciplinary applications in many scientific fields. In most applied research projects, light ions of energies in the range of a few MeV are needed for such accelerator-based investigations. Consequently, along with further intense use of complex nuclear facilities built up around electrostatic accelerators of ~ 20 MV rated terminal voltage, a number of new electrostatic accelerator laboratories equipped with machines of a few MV voltage have been founded for interdisciplinary applications.

50.2.2 Accelerator Configurations

The basic factor influencing the construction and the feasibility limits of electrostatic accelerators is the need for insulating high voltages surpassing those normal for technical applications.

Atmospheric air typically used as insulator in high voltage facilities will break down around a field strength of 30 kV/cm, that is, insulating high voltage by atmospheric air can only be achieved, if field strengths on electrode surfaces are kept below this value through increasing the electrode dimensions accordingly. Due to spatial limitations, open-air accelerators (i.e., those not closed in vessels) are only practical up to a few hundred kV terminal voltages. Above this limit the accelerators should be closed in a steel vessel, in which air as insulator is replaced by pressurized dry electronegative gases with breakdown strength around 150 kV/cm. Even with such improved insulation strengths, voltages in the MV region can only be reached in large-size configurations.

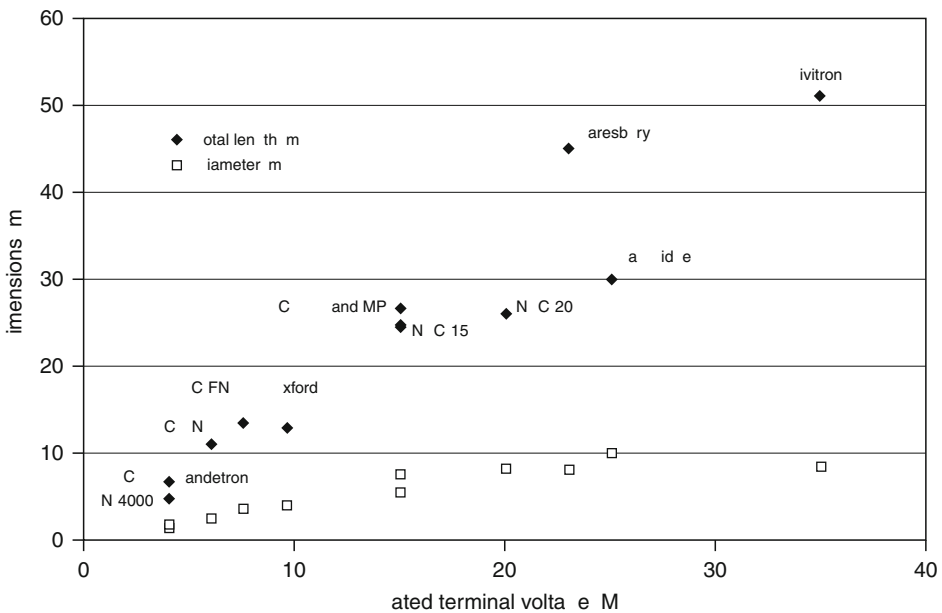
As shown in [Fig. 50.12](#) for some machines, which were important steps in the history of electrostatic accelerators, the total length and diameter of the accelerator vessel are closely correlated with the rated nominal voltages of the machines. The high terminal voltage over the insulator surfaces in the column, used for holding the high voltage terminal and for screening the acceleration tubes and elements of the voltage generation, can be insulated with high-quality glass or ceramic insulators of multisectioned structure. Insulator elements are subjected to the total high-voltage difference in a linear voltage drop.

The limitation in ion energies set by the technical limitations of the terminal voltage in the classical single-ended electrostatic accelerators can be overcome by multiple use of the terminal voltage in the so-called tandem configurations. In [Fig. 50.13](#), a schematic figure of a classical single-ended electrostatic accelerator is compared with those of two typical tandem configurations.

In single-ended machines, positive ions extracted from an ion source in the positive terminal are accelerated through the terminal voltage in a single acceleration tube.

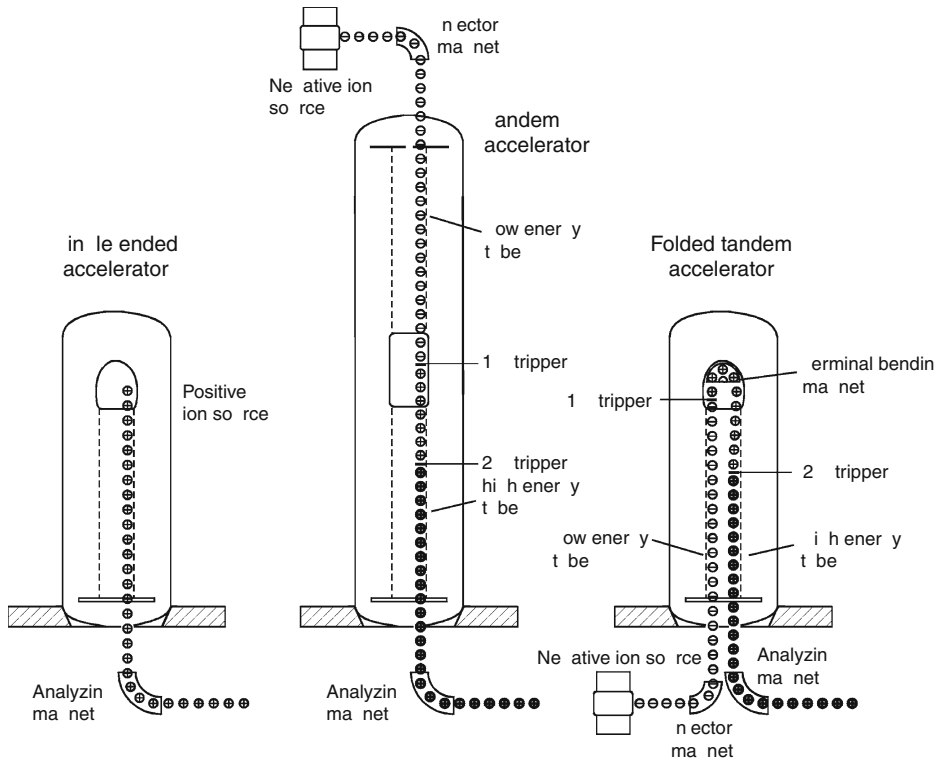
Fig. 50.12

The dependence of the dimensions of electrostatic accelerators on rated terminal voltage shown by vessel length (♦) and diameter (□) of some electrostatic accelerators



■ Fig. 50.13

Schematic pictures of single-ended and two-stage configurations of electrostatic accelerators



Tandem accelerators are equipped with two acceleration tubes called low-energy and high-energy tubes, for the subsequent acceleration of negative ions from earth potential toward the positive terminal and positive ions obtained from the negative ions via charge exchange toward ground potential. The whole acceleration process consists of two or three steps here. In the first step negative ions, extracted from an ion source at earth potential and injected after a charge stage selection by an injection magnet, are accelerated in charge state -1 toward the terminal in the low-energy tube. The charge exchange process in the terminal is generated by transmitting the negative ions through a gas cell or solid charge-stripper target. The charge state of the stripped ions will be distributed around a mean positive value, which depends on the kinetic energy and atomic number of the ion. The multiple-charged positive ions will pick up energy during the next acceleration steps in the high-energy tube according to their charge state and the potential difference passed. Since the equilibrium charge state obtained in the stripping process increases with ion energy, it is useful to apply a second stripper target down in the high-energy tube. In this way, the energy increase obtained in the rest of the tube will be further enhanced by the higher charge states reached in the second stripper.

As shown in [Fig. 50.13](#), the tandem principle can be realized both in the classical straight-line setup and in the more compact folded configuration. In the latter case, both the low-energy and high-energy tubes are contained in a single insulating column, and a 180° magnetic

charge-state analyzer and a beam-inflection sector are used within the terminal for coupling the low- and high-energy tubes.

Tandem accelerators can be used as flexible sources of highly charged heavy-ion beams as injectors of heavy-ion cyclic accelerators. In such applications, the charge state of the beam injected in the cyclic accelerator can further be increased by subjecting it to an additional charge exchange process behind the tandem accelerator. In the following, the charge states resulting from this post-accelerator stripper will be denoted by symbol z_{pa} .

The total energies E_t and post-accelerator charge states z_{pa} to be obtained on foil strippers as the function of the terminal voltage of the accelerator are summarized in [Fig. 50.14](#) for elements S, Fe, I, and U. Here, upper (a) and lower (b) parts relate to configurations with a single terminal stripper and an additional second stripper, respectively. (The latter is placed at one-third of the length of the high-energy tube.) Charge state values are calculated from an approximate model (Nikolaev and Dmitriev 1968), while the energies are given for case (a) and case (b) by the simple relations

$$E_0 = eV_0, \quad (50.11)$$

$$E_t = E_0 + ez_0 V_0, \quad (50.12)$$

and

$$E_0 = eV_0, \quad (50.13)$$

$$E_i = E_0 + ez_0 \frac{V_0}{3}, \quad (50.14)$$

$$E_t = E_i + ez_i \frac{2V_0}{3}, \quad (50.15)$$

respectively, where the subscript “i” refers to the intermediate (second) stripper.

50.2.3 Construction Units of the Accelerator

50.2.3.1 Ion Sources

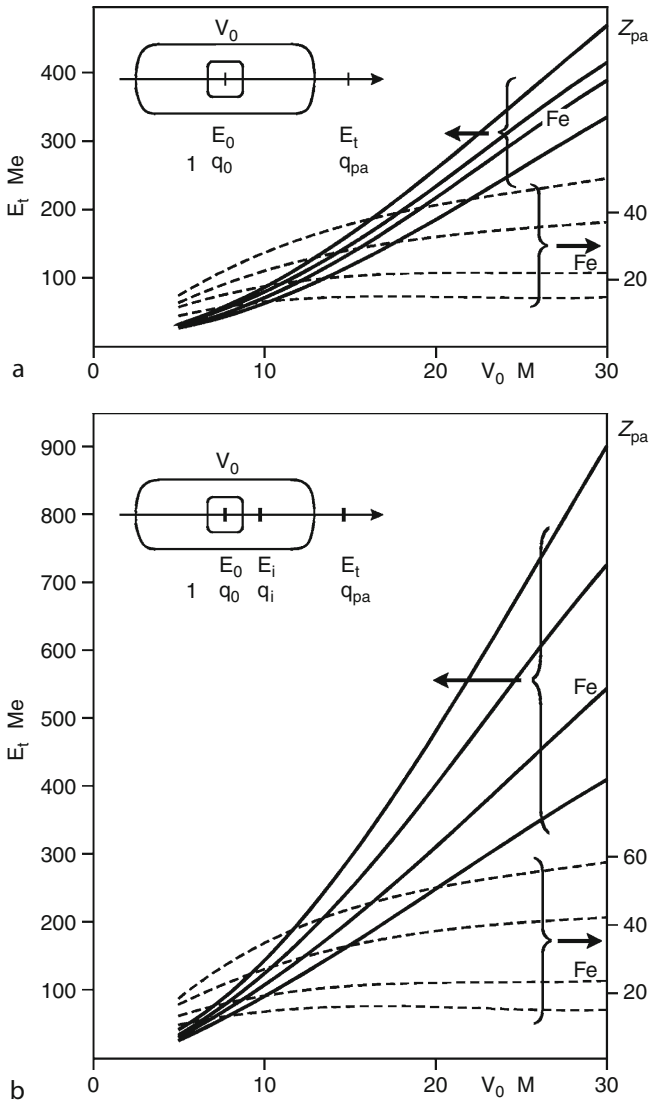
In single-ended electrostatic accelerators, RF ([Fig. 50.6](#)) and Penning sources ([Fig. 50.4](#)) are most often used. In the former case, extraction arrangements of Bayly and Ward and, alternatively, that of Thoneman and Harrison can be applied (Kiss et al. 1977). An improved version of the Penning source (Baumann and Bethge 1981) is especially well fitted to the production of multiple-charged light ions in single-ended machines. In tandem accelerators, duoplasmatron ([Fig. 50.3](#)) is regularly used for the production of light negative ions, while a broad selection of heavy ions can be delivered by sputtering sources (Middleton 1977, 1983).

50.2.3.2 Voltage Sources of the Accelerator

In the electrostatic accelerators, the high acceleration voltage is generated by charging up a capacitor made up by the high voltage terminal and the grounded vessel.

■ Fig. 50.14

Total energies E_t (full lines) and post-acceleration charge states z_{pa} (dashed lines) of sulfur, iron, iodine, and uranium beams obtained from a tandem accelerator as a function of the terminal voltage. Data are shown for the cases of a single terminal foil stripper and a combination of a terminal stripper with a second (intermediate) stripper placed at 1/3 of the length of the high-energy tube in the upper (a) and lower (b) part of the figure, respectively



In the classical arrangement called *Van de Graaff accelerator*, static charge is transferred to the terminal by an endless insulator belt running on pulleys from ground to terminal and back. The charge is deposited to and removed from the belt surface in electric discharges generated in special circuits at the base of the generator column and in the high voltage terminal,

respectively. In order to avoid mechanical and electric instabilities as well as to eliminate dust due to belt wear, the belt in more recent generations has been replaced with a flexible chain of small capacitors formed by metallic elements separated by insulator elements. Here, the metallic conductors are charged by electrostatic induction. In the *pellettron version*, the chain consists of metallic pellets spaced out along an insulating cord. The chain runs on conducting pulleys (Isoya and Nakashima 1970). The maximum transferred charge is limited here by the small surface of the individual pellets. This limitation can be overcome in the *laddertron* charging system, where the small pellets of the pellettron chain are replaced by pairs of small cylinders joined together by an elongated bar. The chain runs on pairs of pulley wheels (Allen and Joyce 1973; Aitken and Leese 1977).

While these arrangements have outstanding characteristics of terminal voltages up to around 20 MV and stabilities in beam energy 10^{-4} or better, the total charge transfer capacities of the moving transfer media limit the charging currents. Furthermore, mechanical wear appearing during service time may cause troubles and makes attendance and adjustments necessary.

Some alternative ways for generating direct voltages in the few MV range are offered by different realizations of the so-called *cascade generators*, in which mechanical charge transfer is replaced by electric or electronic multistage structures of high voltage rectifiers and capacitors. Here, the total accelerator voltage is given by summing up steps of direct voltages, which are obtained through the rectification of alternating voltages and stored in capacitors in individual stages of a power supply chain, respectively. The beam currents available from accelerators of such construction can be orders of magnitude higher than those delivered by machines with mechanical transport media.

The original construction named as *Cockcroft–Walton source* and shown schematically in panel (a) of Fig. 50.15 can be used in the region of a few hundred kV (Baldinger 1959). In this voltage source, N stages composed of a pair of rectifiers and capacitors of C capacitance are fed in series through the chain of capacitors. Due to AC feeding with frequency f of the system, and a load of current I , a ripple of

$$\delta V = \frac{N^2 I}{2fC}, \quad (50.16)$$

will appear on the total acceleration voltage.

At the same time, the total $2NV$ output voltage of the source will be lowered by a *voltage drop* of

$$\Delta V = -\frac{2N^3 I}{3fC}. \quad (50.17)$$

The cubic increase of the output voltage drop sets a limit on the increase of the total output voltage of the source. The number of stages is optimal at

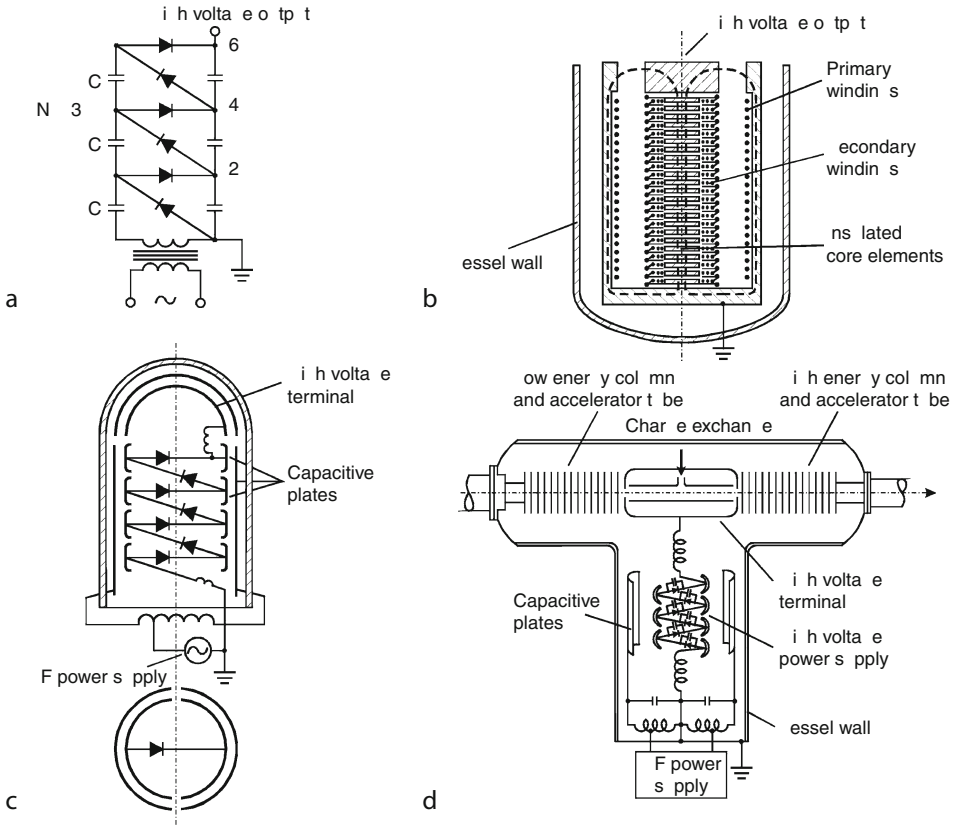
$$N_{\text{opt}}^2 = \frac{VfC}{I}. \quad (50.18)$$

Beyond this limit, the output voltage drop starts decreasing with increasing N .

The limitations caused by serial charging of the DC condensers can be overcome by different arrangements, in which stages of the voltage sources are fed parallel, that is, each of them receive AC voltages to be rectified independently, and only the DC outputs of the stages are connected in series for their voltages to be summed up.


■ Fig. 50.15

Schematic pictures of high-voltage power supplies of cascade multiplier types. (a) Cockcroft–Walton generator, (b) Insulated core transformer (HVEC), (c) Dynamitron (Radiation Dynamics), (d) Tandetron (HVEC)



In *insulated core transformers*, developed by High Voltage Engineering Corporation and shown schematically in part (b) of [Fig. 50.15](#), independent feeding of the individual stages is given by separate secondary coils wound on successive separate segments of the core of a transformer driven by a single primary coil. The segments are insulated from each other to about 30 kV DC. The magnetic flux path penetrates the stack of insulated core elements; the return path from the insulated core is an iron cylinder enclosing the primary coil and is closed through an air gap which withstands the total output DC voltage difference generated by the voltage source. The source can be either directly integrated with the insulation column of the accelerator or housed in a separate pressurized vessel connected to the accelerator.

In *dynamitron* sources, developed by Radiation Dynamics Corporation and shown schematically in part (c) of [Fig. 50.15](#), the chain of high voltage rectifiers is fed by AC voltage at a frequency of around 100 kHz through semicircular capacitive plates that are situated inside a cylindrical liner near the wall of the vessel. The capacitive liner is fed by a powerful high-frequency oscillator. The source is integrated with the accelerator column of the machine, not shown here.

A *tandetron* machine, developed by High Voltage Engineering Corporation, is composed of a single stage or tandem accelerator configuration combined with a high voltage source essentially similar to that in the dynamitron machine. A tandetron accelerator of this type is shown schematically in part (d) of  Fig. 50.15.

50.2.3.3 Terminal and Insulator Stack

The construction elements of the electrostatic accelerators, which are elevated to the total accelerator voltage or to parts of it, should fulfill delicate mechanical and electrostatic requirements. On the one hand, heavy and voluminous elements should be positioned accurately in the pressure vessel over a total length of several tens of meters. A structure called insulating stack is built in the vessel for holding the high voltage terminal and elements of the charge transfer system. On the other hand, all elements should be screened by properly dimensioned smooth metallic electrodes with large enough radii of curvature to keep the local electric field strengths at the rated generator voltage under the breakdown value of the insulating media both in the electrode gaps and over the insulator surfaces. The most important screening elements are the high voltage terminal and the structure of equipotential hoops, which encloses the electrically graded elements of the solid insulators and acceleration tubes.

In an ideal construction, the same absolute field value would exist at every point of the high voltage electrode gaps in order to avoid voltage limitations set by strong local maxima in the field distribution. At the same time, axial field values appearing over insulating surfaces should be kept under surface sparking limits. The general rules to be followed in the optimum construction of the terminal and stack are summarized in the papers of Boag (1953), Kiss et al. (1967).

50.2.3.4 Acceleration Tubes

The ions directly extracted from the ion source in single-ended machines or obtained from charge exchange processes in tandem accelerators are subjected to the accelerating voltage inside the acceleration tubes located in the insulation stack of the accelerator. Tubes are built up of a series of insulating rings separated by metallic electrodes, and are kept under vacuum of the order of 10^{-4} Pa. The total terminal voltage is graded to the tube electrodes by a resistor chain. The tube has to meet serious mechanical, vacuum technical, and electrical requirements. The function of the tube electrodes is proper forming of ion beam trajectories, extracting secondary electrons released from tube construction elements by ion bombardment in the tube, limiting electrode sputtering, and screening the insulator surfaces from scattered ions and secondary electrons. Careful ion-optical design and tube-building technologies are equally important for good voltage holding and stable operation of the machine, limited bremsstrahlung load inside and around the accelerator, as well as for limiting wear. The historical development of electrostatic accelerators toward increased accelerator voltages was supported by new ideas in tube optics and technology (Joy 1990). The following milestones mark the road starting from classical tubes of homogeneous field toward improved ion-optical arrangements with better voltage-holding capabilities:

- Electron-suppressed tubes of *inclined field configuration* (Van de Graaff et al. 1962; Koltay 1963),
- *Spiraling tube configuration* (Allen 1966; Kiss et al. 1981),

- *Magnetically suppressed tube configurations* (Isoya et al. 1977), and
- *Tubes with axial gradient modulation* (Herb 1974; Kiss et al. 1988).

Tube-building technologies got developed through improved cementing methods and better-quality insulator and electrode materials.

50.2.3.5 Energy Analysis and Stabilization

The stabilization of the energy of the beam delivered by an electrostatic accelerator is achieved through the stabilization of the terminal voltage. In the classical electrostatic accelerators, energy adjustment and stabilization can be achieved through the proper control of the balance between charging current and loading currents toward and from the high voltage terminal, respectively. An overview of the systems developed for the energy stabilization of electrostatic accelerators is given in the reference (Takács 1997).

Driving error signals to a two-looped energy stabilization system are taken from a voltage sensing electrostatic device of limited accuracy called generating voltmeter and a high precision beam energy sensing system called magnetic beam analyzer. The *generating voltmeter* is an electromechanical device in which small stationary metallic plates are periodically exposed to and screened from the electric field, generated by the terminal near the wall of the pressure vessel, through sector-shaped windows cut on a rotary disc. The AC voltage to be sensed on a resistor connecting the stationary plates to the ground is proportional to the terminal voltage. The typical accuracy of the device amounts to 1%. With the *magnetic beam analyzer*, the high precision energy signal can be deduced through a comparison of beam current components to be measured on the exit slits of a magnetic deflection sector field used as a momentum analyzer behind the accelerator. The accuracy of the energy determination can be as good as 0.01%. A mixed signal deduced from a combination of the separate error signals is split into slow and fast components, driving a slow-charging current regulator system and a fast-loading current controller, respectively.

A typical actuating element for controlling a loading current component in the voltage stabilization is the *corona triode*. The unit, facing the terminal near the internal wall of the generator vessel, consists of a set of insulated needles centered in circular openings on a grounded screening cup. If the distance of the triode head from the terminal is set properly, a continuous corona discharge will appear on the needles, which represents a load to the terminal. The loading current can be electronically adjusted by the voltage stabilization system through controlling the voltage difference between the needles and the cup.

An alternative fast acting tool in energy stabilization is the so-called *capacitive liner*, which is a large-surface metallic cylinder surrounding the terminal near the vessel wall. High-voltage pulses delivered by the output of an energy stabilizing circuit will be transferred to the terminal through the high-voltage capacitor formed by the terminal and the liner. This stabilization principle can be advantageous in cases of very large accelerators, where multiple electrode configurations may cause complications in using the corona triode as actuating element.

In the case of scientific applications that require extreme beam energy stability, energy ripples originating from sources other than the acceleration voltage of the generator (e.g., ripples on the voltage of power supply feeding the ion source) can be removed by additional energy modulation through an electrode on the beam path. Modulation voltages can be connected to the terminal stripping tube or to the target insulated from the ground.

In parallel fed cascade voltage sources, characterized by high current and low inner resistance, a direct voltage adjustment and stabilization is used in place of voltage stabilization through additional regulated loading current components typical of Van de Graaff machines.

50.2.4 Beam Transport System

The particle beam generated in the accelerator and stabilized by the above-described electronic system may alternatively serve a variety of experiments. They need different types of collision and detection configurations to meet the requirements of the selected atomic and nuclear processes. Therefore, dedicated vacuum chambers are normally set up behind the exit port of the beam-defining and energy-sensing slits of the analyzing magnet. The beam can be directed with a switching magnet of several exit ports along the axes of vacuum transport tubes to any of the required chambers. The beam traveling several meters is confined and focused with magnetic lenses according to the needs of the experiments. Due to their high magnetic rigidity, the ions in the MeV energy range can only be focused by strong transversal magnetic fields. The appropriate elements are the magnetic quadrupole lenses (Hawkes 1970). A single quadrupole unit possesses focusing property in the x -direction, and defocusing property in the y -direction perpendicular to the longitudinal z -axis of the element. In order to achieve focusing in both directions, a second quadrupole lens should jointly be used, which is rotated by 90° with respect to the first lens. The two lenses make a quadrupole doublet.

50.2.5 Microbeam Channels

As treated in [Chap. 32 of Vol. 3](#), fine-focused particle beams find analytical applications in microscale lateral mapping of elemental concentrations in a sample through the detection of characteristic X-rays and/or nuclei released under particle bombardment. The focusing of a particle beam into microspots of sharply cut current density distribution can be achieved in an ion-optical system of high demagnification and minimized aberration effects (Watt and Grime 1995). This system can be composed of a magnetic condenser lens and a micro-focusing lens system. The condenser lens is a quadrupole doublet that forms a crossover of the order of millimeter size over a set of object slits. The short-focal-length second lens system consists of a doublet or triplet of elaborate quadrupole lenses and focuses the crossover as an object to a small-diameter image on the target surface. This can be achieved with a large object distance in the configuration. The average diameter of the beam spot can be as small as $1\text{ }\mu\text{m}$. A further optical element serves for periodic transversal beam deflections in two perpendicular directions for sweeping the beam over pixels covering a preselected area on the target that is placed in the image plane of the lens system. Elemental maps can be built up from the spectroscopic information since the beam deflection and data acquisition can be synchronized. In a similar way, morphological (optical-type) images can be built up from simultaneously acquired counts of secondary electrons released from the sample during ion bombardment. Furthermore, Scanning Transmission Ion Microscopic (STIM) images may be obtained through counting the number of ions transpassed the scanned pixels in the sample. STIM images give information on the lateral distribution of areal density of the bombarded layer without giving any analytical information.

Steps toward nanometer resolution are being taken by several groups (e.g., Watt et al. 2003; Glass et al. 2007; Andersson et al. 2008). In these nanobeam setups, the beam spot emerging from the above-mentioned microbeam system serves as an intermediate image for a second lens system. This is formed by electron-optically optimized groups of quadrupole-lens configurations (doublets and/or triplets) providing further demagnification. Several sets of precision-slit devices are arranged in proper positions to remove beam halos caused by ions scattered from construction elements of the long beam channel. In state-of-the-art nanobeam channels, a beam size of a couple of 10 nm has been achieved.

Detailed introduction to the physics and technique of microbeam channels can be found in the proceedings volumes of the series of International Conferences on Nuclear Microprobe Technology and Applications (Demortier 1982; Grime and Watt 1988; Legge and Jamieson 1991; Lindh 1993; Yang et al. 1995; Doyle et al. 1997; Przesky et al. 1999; Moretto and Bonin Mosbah 2001; Takai and Kamiya 2003; Jaksic and Bogdanovic Radovic 2005; Osipovicz et al. 2007; Rajta et al. 2009).

50.3 RF-Based and AC-Voltage Accelerators

RF-based particle accelerators are either linear, which accelerate particles in a single pass, or circular (i.e., cyclic) which recirculate the particles through an accelerating gap many times. This section is mainly devoted to the cyclic accelerators, and particularly to AVF (azimuthally varying field, see Sect. 50.3.2.3) cyclotrons, but other accelerators using RF or AC voltage for the acceleration will be briefly mentioned. Information about these accelerators can be found in the proceedings of dedicated international conferences (e.g., Strathdee 1985; Dutto and Craddock 1993; Suller and Petit-Jean-Genaz 1994; Duggan and Morgan 1995; Cornell 1996; Myers et al. 1998; Baron and Lieuvin 1999; Gudat and Zimmermann 2000; ACCELCONF 2009); operation principles, physicist's and engineering considerations are presented, for example, in Livingood (1961), Richardson (1965), Harvey (1974), Conte and Mackay (1991a), Weihrer (1996), Margaritondo (1998), Wangler (1998), Chao and Tigner (1999). An amusing review together with historical details about the cyclic accelerators can be found in Boslough (1985).

50.3.1 Basic Principles of Operation

In the *cyclic accelerators*, the acceleration of the charged particles is realized in a magnetic field, bending them to an approximately circular orbit, which is mostly chosen to be horizontal, and an RF electric field repeatedly increases its energy in each gap crossing. A schematic construction of such a system is shown in Fig. 50.16.

The orbit radius r for the particles moving with speed u in the homogenous magnetic field is

$$r = \frac{mu}{qB}, \quad (50.19)$$

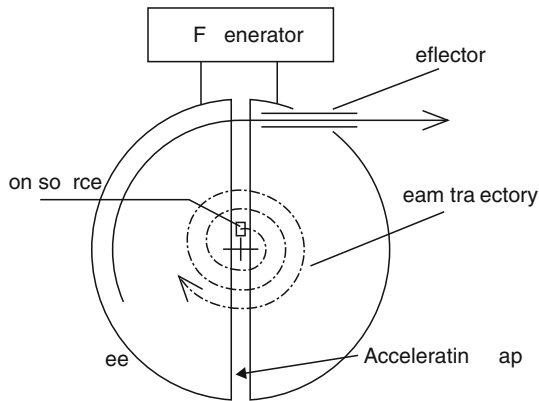
where m and $q = ze$ are the mass and electric charge of the particle and B is the magnitude of magnetic flux density. The angular frequency ω of the circular motion

$$\omega = \frac{u}{r} = \frac{qB}{m}, \quad (50.20)$$

is independent of the radius of the particle orbit (see also Eq. 50.3 for electrons).

■ Fig. 50.16

Layout of cyclic acceleration. The magnetic flux density is perpendicular to the motion of particles



The electrodes are fed with an RF generator of angular frequency ω . A bunch of particles crossing the accelerating gap in the right phase (in which they gain the highest energy at the crossing) will feel accelerating field again when arriving at the next gap. The radius of the orbit is a function of the particle speed; it increases with time and therefore the particles follow a spiral path from the ion source to the edge of the magnet where they are extracted from the accelerator by a so called deflector system.

Equation 50.20 is the so-called *cyclotron equation*, and the accelerator that is based on this principle is the classical cyclotron. The accelerating electrodes are named dees after their D-shape and usually an electrostatic deflector compensating for the bending force of the magnetic field is used to extract the beam.

With this simple arrangement, only moderate energies can be achieved. As the speed of the particles increases, the angular frequency will slowly decrease, because the mass of the particles increases according to the relativistic equation

$$m = m_0 \left[1 - \left(\frac{u}{c} \right)^2 \right]^{-1/2}, \quad (50.21)$$

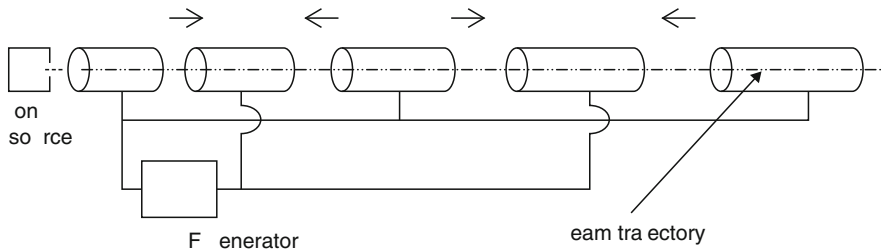
where m_0 is the rest mass and c is the speed of light in vacuum. Another disadvantage is that there is no vertical focusing in homogeneous magnetic field. Due to these facts, there is high loss of the beam intensity during the acceleration. The first cyclotrons accelerated protons and deuterons to the MeV range. To achieve higher and higher energies and to accelerate other particles, this simple machine was substantially modified later.

The *linear accelerator* (also called LINAC) is a series of cylindrical tubes, which are alternately connected to a high-frequency generator, as shown in Fig. 50.17. The charged particles are accelerated in the gaps between the tubes and then they drift inside the tube in a field-free region. While the particles are inside the tube, the direction of the electric field is reversed. If the length of tubes is increased in proportion to the particle speed, the particles will always arrive at the next gap at the correct phase of the RF voltage.

Both in cyclotrons and linear accelerators, particles can only leave the ion source when the voltage in the first gap has the correct sign to accelerate them, thus bunches of particles are accelerated, that is, their beam will have a pulsed structure. At the center of the cyclotrons, there

■ Fig. 50.17

Schematic structure of the linear accelerator. The arrows indicate the local direction of the electric field at a particular value of the RF phase



is room only for a small ion source, and PIG ion sources are mostly used (see Sect. 50.1.3.2). Any more powerful or sophisticated ion source (e.g., ECR or multicusp) can only be installed externally, with the ion beam injected through a beam line to the acceleration plane of the cyclotron.

50.3.2 Types of Cyclic and Linear Accelerators

50.3.2.1 Classical Cyclotron

In classical cyclotrons, the vertical focusing is achieved by decreasing the magnetic flux density at large radii (see Fig. 50.22 and discussion in Sect. 50.3.3.1). This is inconsistent with what is required by the relativistic mass increase. To compensate for the loss due to the phase delay of particles, high accelerating voltages were used. The classical cyclotron was a valuable instrument at one time and machines with pole diameter up to 3 m were built. The maximum energy of deuterons was in the 20–25 MeV region, the typical beam currents would be about 1 mA.

50.3.2.2 Synchrocyclotron

In synchrocyclotrons, (1) the magnetic field falls as a function of the radius giving the necessary vertical focusing of the beam and (2) the RF frequency is gradually reduced in the course of the acceleration so that a group of particles can cross the accelerating gap in the right phase. After each acceleration period, the frequency resumes its initial value and the acceleration of the next group begins. Thus, the beam comes from the synchrocyclotron in macropulses with the repetition rate of the RF system. The final energy of protons would be in the 600–700 MeV range, but the beam intensity is of the order of microamperes.

50.3.2.3 Isochronous Cyclotron

In isochronous cyclotrons, the magnetic field is increased along the radius at the rate of the relativistic increase of the mass of the accelerated particles. The time required for one revolution is constant during the acceleration, and a fixed-frequency RF system can be used. For vertical focusing, the magnetic field is appropriately shaped with radial or spiral sectors

(see ► Fig. 50.18). In recently built cyclotrons, this method is used to overcome the above-mentioned limitations in increasing the particle energy. To emphasize the shape of the magnetic field, this type of cyclotron is sometimes called *sector-focusing cyclotron* or *AVF cyclotron* (where AVF stands for “azimuthally varied field”).

There is a wide variety of AVF cyclotrons in operation regarding the types of the accelerated particles and the construction features. Detailed information can be found in the proceedings of the series of International Conferences on Cyclotrons (Dutto and Craddock 1993; Cornell 1996; Baron and Lieuvain 1999).

Negative-ion cyclotrons accelerate the negative ions of ordinary hydrogen (protium) and deuterium usually with high beam intensities (Jongen et al. 1996) and are used for radionuclide production. Commercial models are also available (Milton 1996; Bogdanov et al. 1999).

Heavy-ion cyclotrons accelerate ions of almost every element of the periodic table. Moreover, “secondary” radioactive ions can also be accelerated (e.g., Loiselet et al. 1996).

As for the construction of isochronous cyclotrons, the magnet of small- and medium-sized machines has the usual H-shape and the magnetic sectors are mounted onto the magnet pole. The large machines contain sector magnets (so-called separated-sector cyclotrons) and the accelerating system and other instrumentation are placed between the sectors. There are cyclotrons where the magnet is excited by SC coils (see, e.g., Goto et al. 1999). The number of the accelerating gaps can be more than two (as in the above simple model) and the so-called *higher-harmonic acceleration* (when the frequency of the RF system is a multiple of the revolution frequency of the beam) can also be used.

Separated-sector cyclotrons accelerate protons up to 600 MeV with beam intensities of the order of 1 mA (Stammbach and Adams 1999). In heavy-ion cyclotrons the particle energy can reach 25–200 MeV/nucleon (Gelbke 1999), and the intensity of the beam depends very strongly on the effectiveness of the production of the ions. The parameters of some well-known machines are summarized in ► Table 50.1. The value K is used at heavy-ion cyclotrons to calculate the maximum energy of the accelerated particle (see ► Eqs. 50.9 and ► 50.41 later).

■ Fig. 50.18

Pole faces of the isochronous cyclotrons: the “hills” are the sectors. Between the hills, the magnetic field is made stronger by reducing the pole gap

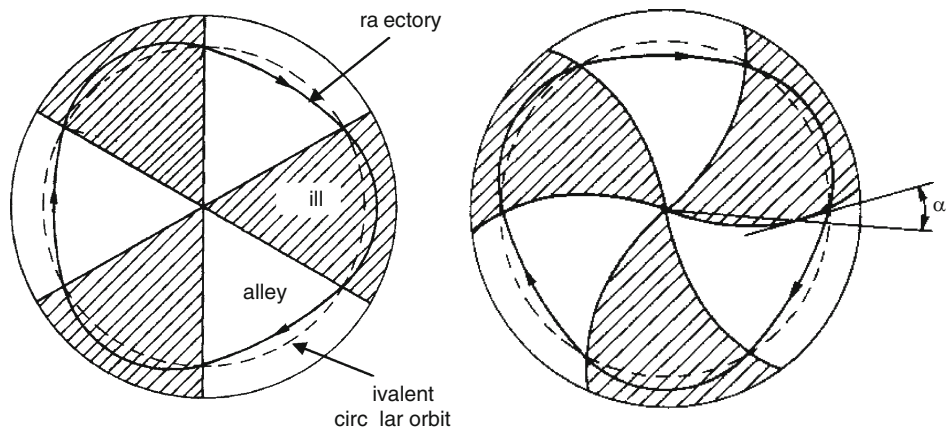


Table 50.1

High-energy cyclotrons and synchrocyclotrons

Name and location	Particle	Energy/ MeV	Intensity	Pole diameter/m	Mass of iron/t	Remarks
Ring cyclotron	Proton	590	1.5 mA	cca. 9 ^a	1,960	Separated sectors, beam power of 1 MW
PSI, Villigen, Switzerland						
U400M	Heavy ions	$K = 450$		4.0	2,100	
JINR-LNR, Dubna, Russia						
K1200	Heavy ions	$K = 1,200$	2.5×10^6 pps ^b	2.197	240	Superconducting (SC) coils
NSCL-MSU, East- Lansing, USA						
Phasotron	Proton	680	5 μ A	6.0	7,000	
JINR-LNP, Dubna Russia						
Synchrocyclotron	Proton	1,000	0.5 μ A	6.85	7,800	
PNPI, St. Petersburg, Russia						

^a Extraction radius: 4.45 m.
^b For $^{238}\text{U}^{39+}$ ions, an example of the intensity of an exotic beam (Gelbke 1999) (K is the constant in [Eqs. 50.9](#) and [50.41](#); pps means particles per second).

50.3.2.4 Synchrotron

It can be seen from [Table 50.1](#) that to increase the energy beyond 1 GeV is technically not sensible by increasing further the pole diameter of a magnet. In the relativistic region at a given magnetic flux density, the mass of the magnet is proportional to the square of the proton energy while its bending radius is linearly proportional to the energy. To build a magnetic ring is more economical (its mass is proportional to the radius) but, in consequence, the acceleration should be completed on a constant or nearly constant radius.

The ring of the synchrotron contains “bending” magnets; between them are the focusing and accelerating RF sections. At the beginning of the acceleration, the particle should have a minimum kinetic energy which is determined by the initial magnetic field and radius of the accelerator. Then the magnetic field is varied during the acceleration. A cycle begins with low magnetic field and finishes with the highest one. The repetition rate and the beam intensity are usually low. The frequency of the accelerating RF field also increases during the cycle. The particle is pre-accelerated by another accelerator up to the injection energy.

Synchrotrons are used to accelerate not only protons and heavier ions, but electrons and positrons as well. The electron is fully relativistic in the GeV region; its speed is close to that of light and is practically unchanged during the acceleration. The main difference between light-charged particles (such as electrons) and much heavier ones (like protons and still heavier ions) is that the circulating (i.e., accelerating)¹ electrons suffer considerable energy loss by producing a substantial amount of electromagnetic radiation, the so-called synchrotron radiation. Some characteristic parameters of synchrotrons are listed in [Table 50.2](#).

■ Table 50.2

Proton and electron synchrotrons

Name and location	Particle	Energy/ GeV	Mean orbit radius/m	Remarks
SPS	Proton ^a	400	1,100	Part of the CERN's accelerator complex
CERN, Geneva, Switzerland (SPS 2009)				
ISIS	Proton	0.8	26	Spallation neutron source
Rutherford Appleton Lab. UK (ISIS 2009)				
DESYII	Electron	7	46	Injector to PETRA and HERA colliders
DESY, Hamburg, Germany (DESY 2009)				
ESRF	Electron	6	48	Injector to the Storage Ring of the ESR Facility
ESRF, Grenoble France (ESRF 2009)				
APS	Positron	7	59	Injector to storage ring, Advanced Photon Source
ANL, Argonne, USA (APS 2009)				
SPring8	Electron	8	63	Injector to storage ring, Super Photon Ring
JASRI, HARIMA Ins. Japan (SPring8 2009)				

^a Also other ions, electrons, and positrons for LEP-II collider.

The synchrotron radiation consists of individual photons with random directions and momenta. The total energy W irradiated during one revolution by one electron is about

$$W/\text{keV} \approx 90 \frac{(E/\text{GeV})^4}{R/\text{m}}, \quad (50.22)$$

where E is the total energy of the electron and R is the radius of the circular path. The energy spectrum of the radiation is characterized by a “critical frequency”

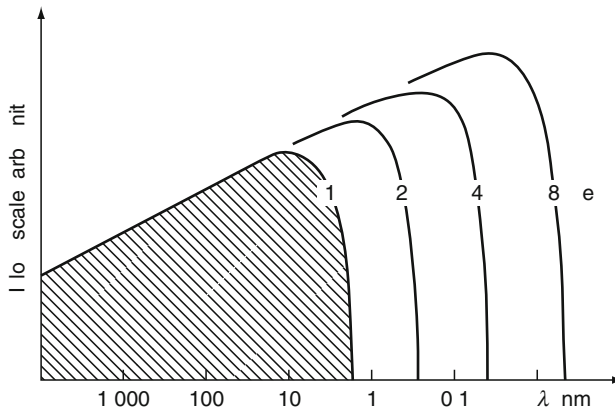
$$\omega_c = \frac{2c}{3R} \left(\frac{E}{E_0} \right)^3, \quad (50.23)$$

where c is the speed of light in vacuum and E_0 is the rest mass energy ($m_e c^2$) of the electron. The energy of the photon is $\hbar\omega$. Half of the energy is emitted by photons carrying less than the critical energy $E_c = \hbar\omega_c$, and the other half by more energetic photons.² Most of the energy is irradiated in the direction of the electron velocity, that is, tangentially. Without energy fed in constantly, the circulating electrons would slow down.

The intensity distribution of the synchrotron radiation is schematically shown in ► Fig. 50.19. The energy of the radiation increases rapidly with the energy of the particles. One can see that the synchrotron is a good transformer of the RF power supplied to the acceleration system into shortwave radiation (visible light and X-rays). A review of synchrotron light sources is given by Eriksson (1994).

■ Fig. 50.19

Spectral distributions (intensity versus wavelength) of the synchrotron radiation for different electron energies



50.3.2.5 Storage Ring

When a particle hits a target, a substantial part of its energy is spent on accelerating the center of mass of the colliding partners. To concentrate all energy on the excitation of the colliding system, two particle beams are driven at each other. In a head-on collision of two 100 GeV protons, the same amount of energy is spent on excitation as if a 20 TeV proton hit another one in a fixed target. (Note the relativistic kinematics.)

The encounter of two particles belonging to two colliding beams has a very low probability, because the number density of the colliding particles is very low. Two beams “see” each other almost transparent, and for one collision event to occur, the beams should be driven at each other many times, that is, the beams should be stored and they should have a suitably long life.

The construction and operating principles of storage rings are the same as those of synchrotrons. The special requirements are:

1. Suitable beam lines and arrangement for the collision experiments.
2. Very good vacuum (order of 10^{-10} Pa), because a major loss of the beam comes from its interaction with the residual gas.
3. The ring is filled via so-called “multi-turn” injection in order to increase the particle number density.
4. The collective motion of the particles should be controlled by beam cooling.

Some parameters of storage rings and colliders are collected in [Table 50.3](#).

50.3.2.6 Linear Accelerators

The structure of the linear accelerator shown in [Fig. 50.17](#) is named *Wideröe* structure or π -mode structure. The reason for the second name is that the configuration of the electric field is repeated in every two gaps. Bunches of particles are not accelerated in every gap, but must be spaced with a free gap between every pair of bunches. In another version, the drift tubes are

■ **Table 50.3**

Storage rings and colliders (A is the mass number of the accelerated ions)

Name and location	Particle	Energy/GeV	Circumference/m	Remarks
CELSIUS	Up to argon	max. 0.47/A	82	Storage ring
TSL, Uppsala, Sweden (TSL 2009)				
Tevatron	Proton	2,000	6,280	Collider
Fermilab, Batavia USA (TEV 2009)				
RHIC	Proton	100	3,860	Collider
Brookhaven NL, NY, USA (RHIC 2009)				
LEP II	Electron positron	47	26,659	Collider
CERN, Geneve Switzerland				
HERA	Electron positron proton	26.6	6,300	Collider
DESY, Hamburg Germany		0.82		

mounted into a resonating tank powered by the RF system. In this structure, the charges oscillate between the ends of the drift tubes. This is the *Alvarez* or 2π -mode structure, where the particles are accelerated simultaneously in each gap.

As the speed of particles increases, the drift tubes get longer. The final energy of the particles is limited by the available RF driver frequencies, the lengths of the drift tubes and that of the whole accelerating system. These types of linear accelerators are used to accelerate protons and heavier particles. To produce higher energy ion beams, such structures are coupled in a synchronized accelerating system.

The relativistic particles, electrons, and positrons require a source of higher frequency. In the MW region, there are high-power sources for feeding linear accelerators of the *cylindrical waveguide* type. A wave traveling in a waveguide can be used to accelerate light particles if its phase velocity is slowed down to a value where the particles can keep in phase with the traveling wave. Then the particles may “surf” along the wave with the phase yielding an accelerating force. Some parameters of a few huge linear accelerators are summarized in [Table 50.4](#).

50.3.2.7 Radio Frequency Quadrupoles

The radio frequency quadrupole (RFQ) is used to accelerate protons and heavier ions. It uses four parallel electrodes around the beam axis as shown in [Fig. 50.20](#). The RFQs operate at high frequencies, typically from tens to hundreds of MHz. The electrodes, which are called “vanes,” are placed in a cavity forming a resonant structure. The adjacent electrodes have opposite charges. From the end, the RFQ looks like an electric quadrupole. This arrangement of electric field focuses the beam in one plane and defocuses it in the other one. Since the electric field oscillates, a net focusing effect can be obtained along the length of the vanes.

A longitudinal field can be created by perturbing the electrodes in a periodic way, that is, a part of the originally transverse field is distorted into the longitudinal direction. A convenient

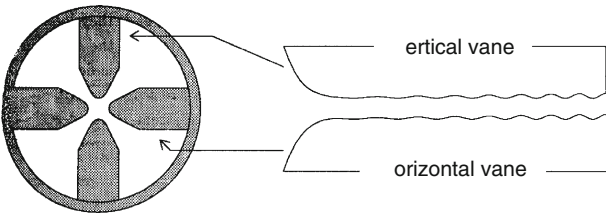
Table 50.4

Linear accelerators

Name and location	Particle	Energy	Length/m	Remarks
UNILAC GSI, Darmstadt Germany (GSI 2009)	Heavy ions	1.4–14 MeV/ nucleon	cca. 80	Part of the GSI accelerator complex
LANSCÉ LNL, Los Alamos, USA (LANL 2009)	Proton	800 MeV	cca. 850	Beam power 1 MW, spallation neutron source
SLAC Stanford Univ., USA (SLAC 2009)	Electron positron	47 GeV	3,050	Injector of PEP-II collider

Fig. 50.20

The RFQ structure



perturbation is the sinusoidal modulation. The sinusoids of the horizontal and vertical electrodes have to be displaced by half a period. The period of the perturbation is adjusted to create synchronism between the “wave” and the particle to be accelerated and, in addition, the transverse RF field provides an alternating gradient focusing. Details of an operating RFQ accelerator is presented, for example, in RFQ (2003).

50.3.2.8 Coupled Accelerators

To produce beams of extreme specifications, for example, very high-energy particles or heavy-ion beams, a chain of accelerators have to be used (see ▶ Tables 50.2–50.4 and the Internet sources referred to there). Generally, the ions coming from the ion source are accelerated in the first step by an electrostatic accelerator and after a bunching system, preparing the DC beam for the acceleration in an RF-based structure, they are accelerated further by cyclic or linear accelerators.

50.3.2.9 Microtrons

For electrons, the relativistic effects are already dominant at relatively low energies, so when increasing their energy, their revolution frequency lags behind. Assume that electrons are

moving cyclically in a plane perpendicular to a magnetic field, and they receive a push in every revolution from an electric field when passing a gap. If the energy of electrons at the gap crossing is changed so that the accelerating frequency is a multiple of the new revolution frequency, then the electrons can resonate with the RF field and can be accelerated (in harmonic mode). For such a system, the RF wavelength must be in the centimeter region and the magnetic field has to be uniform in a relatively wide range. The schematic layout is shown by the left panel in ▶ Fig. 50.21. The circles represent the bunches of electrons accelerated. In this arrangement, electrons can be accelerated to energies of a few MeV. A high-energy portable microtron is discussed by Sobenin et al. (1994).

50.3.2.10 Betatrons

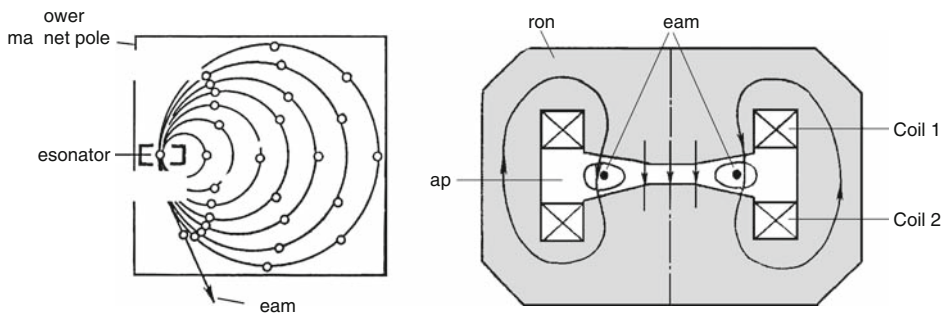
The betatron, like the microtron, is used to accelerate only electrons, but the operation principle differs from that of RF-based accelerators. It is also a circular accelerator. Its schematic layout is shown in ▶ Fig. 50.21. The electromagnet is supplied by an AC current and the changing magnetic flux density in the gap generates an “electromotive” force (e.m.f.), which can accelerate (or decelerate) the electrons along the circular orbit. This e.m.f. is relatively low, so the electrons complete millions of revolutions to get an energy of the order of 10 MeV. The intensity of the electron beam is pulsed according to the frequency of the supplying AC voltage, which is usually 50 Hz (sometimes higher up to 400 Hz). The accelerated electrons are mostly used to hit an internal target and the produced bremsstrahlung is used. Applications and technical information are available on the Internet (BETATRON 2009).

50.3.3 Focusing the Particle Beam

In cyclic accelerators, the beam takes many turns and the particles should keep together in a bunch both longitudinally and transversally. By the action of focusing forces, the particles perform “synchrotron” and “betatron” oscillations around an imaginary “synchronous” particle moving on a stable/smooth “equilibrium orbit.”

■ Fig. 50.21

Layout of the microtron (*left*) and betatron (*right*). Note that the viewpoints of the sketches are different: the beam lies in the plane of the diagram of the microtron, whereas the plane of the beam is perpendicular (horizontal) to that of the cross section of the betatron



50.3.3.1 Magnetic Field

The force \mathbf{F} upon a charged particle moving in a magnetic field is

$$\mathbf{F} = q(\mathbf{u} \times \mathbf{B}), \quad (50.24)$$

where q is the charge of the particle and \mathbf{u} is its velocity, and B is the magnetic flux density. The axial component of \mathbf{B} takes care of the radial focusing of the beam. In a uniform field, \mathbf{B} has no radial component and \mathbf{F} has no axial component. In a field that falls as a function of radius (see [Fig. 50.22](#)) the radial component of \mathbf{B} produces an axial component of \mathbf{F} , which directs particles leaving the median plane of the magnet back to this plane (this is the focusing force in the classical cyclotron). In the median plane, there is no focusing force.

The radial variation of the magnetic field may be described by means of the “**field index**” n defined by

$$n = -\frac{dB/B}{dr/r}. \quad (50.25)$$

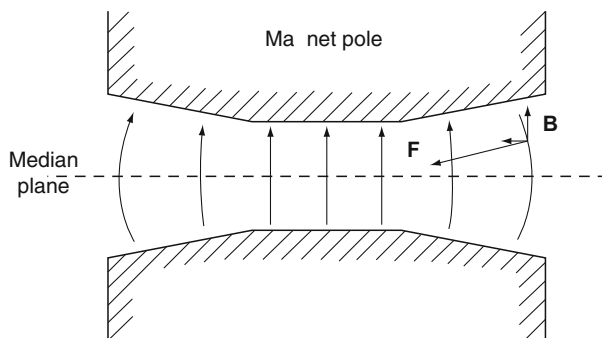
A positive value of n implies a focusing effect. The value of n varies with the radius r (it is zero at the center of the magnet) and it can be used to calculate the motion of particles in the radial and axial directions at a particular radius. Ignoring the detailed discussion, particles displaced axially or radially from their equilibrium orbit will sense a force which is proportional to the displacement (like a simple harmonic oscillator) and will perform stable axial and radial oscillations, which are known as “**betatron**” oscillations. These oscillations are stable when n lies between 0 and 1. Any ion leaving the ion source in a direction not in the median plane and not on the equilibrium orbit will make axial and radial betatron oscillation.

A field increasing with the radius (i.e., when n is negative) will make an axial defocusing effect: if a particle is moving off the median plane, a force pushes it even further off. In isochronous cyclotrons, however, where the magnetic flux density increases with the radius in accordance with the mass of the accelerated particles, the forces arising at the edges of the sectors will cause axial focusing.

By adding sectors to the pole tips as shown in [Fig. 50.18](#), an azimuthal variation is induced in the magnetic field. Since the magnetic field varies with the azimuthal angle, so must

Fig. 50.22

Representation of the axial (vertical arrow) and radial (horizontal arrow) components of \mathbf{B} in a nonuniform magnetic field. The slanted arrow shows the direction of the resultant force \mathbf{F} acting on the charged particle



the radius of the orbit. The particles zigzag inward and outward with respect to a circle, called the “equivalent” orbit, which would be the orbit given by the azimuthally averaged field, enter and leave a sector non-normally. The curvature of the magnetic field lines at the boundaries of the sector, combined with the non-normal motion, is responsible for the axial focusing.

To describe the magnetic field variation, the “**field flutter**” f is defined by

$$B_h = B(1 + f), \quad (50.26)$$

$$B_v = B(1 - f) \quad (50.27)$$

where B_h and B_v are called the hill and valley field, respectively, and B is the magnitude of the magnetic flux density averaged over a complete revolution.

The velocity of a particle moving in the AVF cyclotron has a radial component u_r , which reaches maximum when the orbit crosses the circular orbit (see [Fig. 50.18](#)). Since the field varies as a function of θ , there is an azimuthal component B_θ and therefore there is a force F acting upon the particle. This force can be expressed as

$$F = qu_r B_\theta. \quad (50.28)$$

Again, suppressing the details, this force acts such that a particle always returns toward the median plane and the axial motion is a harmonic oscillation again.

This force alone is able to compensate for the defocusing effect of the radially increasing field up to a limited energy. Additional focusing forces can be obtained by the use of spiral ridges instead of the straight radial ones as shown in [Fig. 50.18](#). The angle α between a tangent to the spiral and the radius vector at the point of tangency is called the “spiral angle.”

The motion in such a composite field shows that the resultant force causes axial oscillations of angular frequency ω_z

$$\omega_z \approx \frac{\omega f}{\sqrt{2}} (1 + 2\tan^2 \alpha)^{1/2}. \quad (50.29)$$

The radial increase of the average magnetic field comes partly from the effect of the hills and partly from the concentric current-carrying coils mounted on the upper and lower poles. The isochronous field B_r is defined as an average of the magnetic flux density over an orbit of radius r . It can be shown that

$$B_r = \frac{m_r}{m_0} B_0 = \left(1 + \frac{T}{E_0}\right) B_0, \quad (50.30)$$

where m_r is the particle mass on the orbit of radius r , B_0 , and m_0 are the values of those at radius zero, and T and E_0 are the kinetic energy and rest mass energy of the particle. The effect of the spiral ridges should counteract the axial instability due to this rising field.

The radial betatron oscillation frequency can be determined by numerical calculations and it is usually close to the revolution frequency of the particle:

$$\omega_r \approx \frac{m_r}{m_0} \omega. \quad (50.31)$$

50.3.3.2 Coupled Resonances

There is a coupling between the axial and radial oscillations, which can cause coupled resonances. Detailed examinations show that they are present when the axial and radial

frequencies are related to each other in certain simple ways. Define the quantities v_z and v_r as the number of axial and radial oscillations per revolution:

$$v_z = \frac{\omega_z}{\omega}, \quad (50.32)$$

$$v_r = \frac{\omega_r}{\omega}. \quad (50.33)$$

Resonance occurs when $v_r = v_z$, $v_r = 2v_z$, etc. If a particle makes many turns at radii close to the resonant value in the course of the acceleration, a disastrous increase in the betatron amplitude may develop.

Imperfections in the magnetic field can induce additional radial and axial oscillations. When v_r and v_z are integers or ratios of integers, the disturbance caused by a field imperfection occurs with same phase in each revolution so that a disastrous increase may result in the amplitude.

50.3.3.3 Electric Field

The particles crossing the gap between the dees are accelerated by a time-dependent force

$$\mathbf{F}_e = q\mathbf{E} = ze\mathbf{E}, \quad (50.34)$$

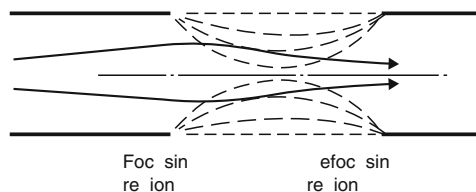
where \mathbf{E} is the electric component of the RF field.

As might be expected, the particles subjected to an accelerating force begin to oscillate around their equilibrium orbit, thus the amplitude of the radial oscillation will be increased. However, in addition to the acceleration, this electric field produces a weak axial focusing force. [Figure 50.23](#) shows two trajectories in the electric field of a gap. The particle beam is at first focused and then defocused. Since the particle is accelerating during the gap crossing, the focusing force acts for a longer time than the defocusing force, so the net result is that the particles tend to return toward the median plane. The force depends also on the time of the crossing with respect to the phase of RF field. If the dee-to-dee potential decreases in time, the defocusing effect will be further weakened.

The electric axial focusing effect is only important in the first few rounds, because it is proportional to the ratio of the energy gain to the kinetic energy of the particle. The almost uniform magnetic field in the center of the magnet (field index n is close to zero) produces at the same time an especially weak axial focusing.

■ Fig. 50.23

Focusing effect of the electric field (*dashed lines*) at gap crossing



50.3.3.4 Phase Stability

The acceleration is continued while the particles gain energy at the gap crossing, that is, they arrive at the dee gap when the RF electric field produces an energy gain rather than an energy loss.

In a perfectly isochronous magnetic field, the particles move fully in phase with the RF field. If a particle loses the “right phase” for any reason, there will be a “phase slip” in one direction or the other. In classical and isochronous cyclotrons, it is not possible to stabilize the phase of the gap crossing and the acceleration continues until the phase error becomes so great that deceleration occurs.

In synchrocyclotrons and synchrotrons, there is a mechanism that guarantees that a particle arriving too early at the dee gap will arrive later in its next revolution. All particles will cross the gap with different phases relative to the RF oscillation, arriving either too early or too late with respect to the synchronous particle. The synchrocyclotron is operated such that the ions pass the gap in the phase of decreasing field strength. In this way, the ions that arrive there too early get a larger-than-average push. That will steer them onto a path of slightly larger radius, which implies a lower revolution frequency. They will thus arrive at the next gap more in phase with the others, that is, its phase will be closer to φ_s as shown in [Fig. 50.24](#). Therefore, the phase of the accelerated particles will perform stable oscillations, known as “**synchrotron**” oscillations, around the stable value φ_s .

50.3.4 Beam Parameters

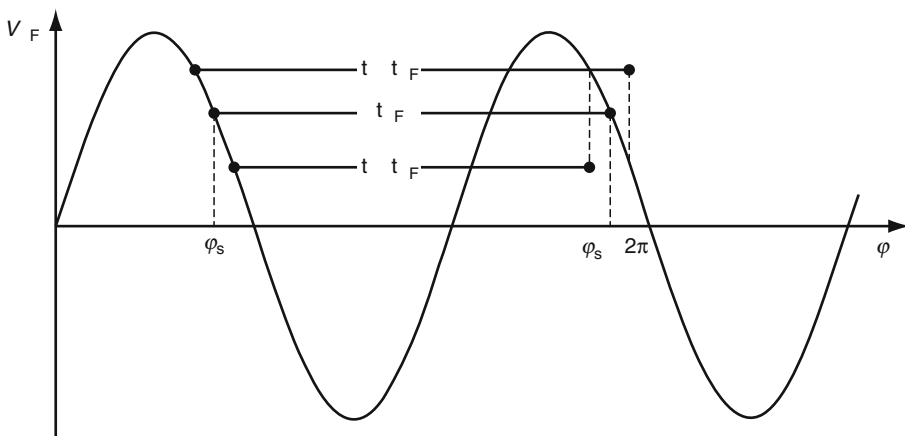
50.3.4.1 Energy

Accelerators can accelerate particles up to *relativistic speeds* where the total energy, momentum, and kinetic energy are the following:

$$E = \gamma m_0 c^2, \quad (50.35)$$

Fig. 50.24

Phase-stability principle in synchrocyclotrons. The symbols t and t_{RF} stand for the periodic time of the particle and the RF field, respectively



$$p = \beta\gamma m_0 c, \quad (50.36)$$

$$T = (\gamma - 1)m_0 c^2, \quad (50.37)$$

where $\beta = u/c$ is the particle speed relative to the speed of light, and $\gamma = (1 - \beta^2)^{-1/2}$ is the Lorentz factor. For a particle moving in a plane perpendicular to the magnetic field, the momentum in terms of the orbital radius r , the magnetic flux density, and charge is

$$p = qBr. \quad (50.38)$$

In the ultra-relativistic case

$$E \approx T \approx pc. \quad (50.39)$$

In the *nonrelativistic region*

$$T = \frac{1}{2} m_0 u^2. \quad (50.40)$$

Note, however, that at nonrelativistic speeds it is much more common to denote the kinetic energy simply by E , which convention will be followed from this point on.

The isochronous cyclotrons can accelerate different particles from protons to the ions of the heaviest elements. The energy of the particles is determined by the setting of the cyclotron, and that can be changed in a wide range. The relativistic behavior of the particles can be neglected for the sake of these considerations. The heavy-ion cyclotron can be specified by the so-called K factor determining the maximum kinetic energy of the ions by the relation

$$E_{\max} = K \frac{z^2}{A} \quad (50.41)$$

where $z = q/e$ and A are the charge state and mass number of the ion, respectively, and E_{\max} is measured in MeV.

50.3.4.2 Intensity

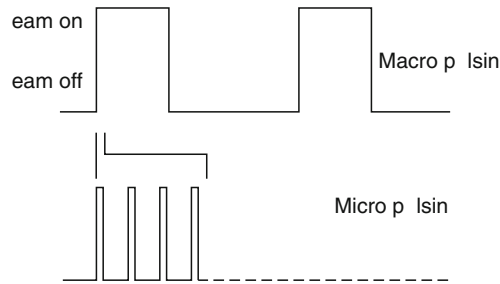
The average intensity of a beam is usually given as an electric current, generated by the charge of moving particles through a cross section of the beam tube. Other usual units are particle electric current (electric current divided by the charge state of the ions of the beam) and the number of particles in unit time (pps meaning particle per second) or in one pulse.

The beams coming from cyclic and linear accelerators consist of short pulses of particles, that is, their beam has a time structure as shown in [Fig. 50.25](#). The repetition frequency of the bunches (“microstructure”) is determined by the RF system, while the “macrostructure” can be varied by switching on and off the acceleration process. Taking into account the *duty factor*, which is the fraction of time when there is current, the peak current is much higher than the measured average current of the beam.

The distribution of the beam intensity in the plane normal to the beam direction (i.e., its cross section) defines the size of the beam. The shape of the beam is usually an ellipse. The horizontal and vertical dimensions have special importance; these values are calculated by ion-optical calculations and, as a rule, they are measured by beam diagnostic devices. The size and shape of the beam vary along the beam line; where the size is small, its angular divergence is large. The distribution of the particles inside the beam is not uniform. To a first approximation,

■ Fig. 50.25

Time structure of the beam



it can be taken to be Gaussian around an axis. In some cases, the particle distribution may show a high peak, which is named a “hot spot” of the beam.

50.3.4.3 Emittance and Acceptance

The beam consists of a large number of particles. Most of them move along orbits that differ from the equilibrium orbit (e.g., the axis of a beam line). This behavior is characterized by the property called the emittance of the beam. This parameter is derived from considerations of the particle motion in the phase space, which is a six-dimensional hyperspace composed of the particle coordinates (x, y, z) and the three momentum components (p_x, p_y, p_z) (Banford 1966).

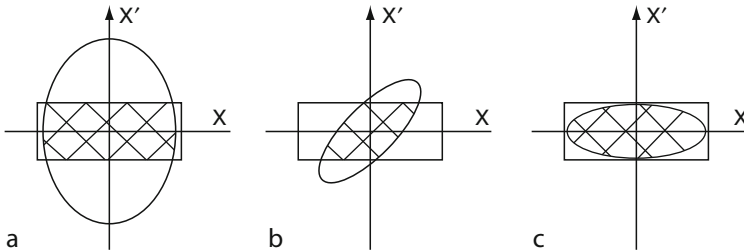
The volume of the hyperspace populated by the particles remains constant (Liouville’s theorem), while the shape and the magnitude of its various cross sections may vary along the beam line. At beam transportation (which is done by steering, bending, and focusing), the motions in the propagation direction (z -axis) and in transverse directions (x - and y -axes) are mutually independent, so the motion in the planes (x, p_x) , (y, p_y) , and (z, p_z) can be treated separately. The axial momentum of the particles can be taken to be constant, and, instead of p_x and p_y , the angular divergence x' and y' can be used to represent the beam in the two-dimensional phase space of (x, x') and (y, y') . The displacement from the axis and the divergence are directly observable quantities. The particles composing the beam cover regions with their (x, x') and (y, y') coordinates in this phase space, which can be circumscribed by ellipses or parallelograms.

The emittance of the beam is the area of this region, which will not change during the transportation. In other words, one of the parameters can be decreased only at the expense of an increase of the other one. If the axes of the ellipse coincide with the coordinate axes x – x' or y – y' , the position of the phase ellipse is normal (“waist” in the beam envelope). The emittance in the horizontal (x, x') and vertical (y, y') planes are used to represent the beam.

The *transportation of a beam* requires manipulation on the phase space regions to arrive at a desired shape. The shape and the orientation of the phase space ellipse can be changed by positioning and setting the optical elements. To decrease the beam loss on the collimating system of an experimental chamber, the emittance of the beam should match the acceptance of the experimental setup (see ► Fig. 50.26). The *acceptance* of a device is the phase space area containing all the points whose input displacement and divergence coordinates are such that the particles having those values will be transmitted. If the acceptance required by the

■ Fig. 50.26

The acceptance of a hypothetical device is represented by the rectangles and the emittance of the input beam by the ellipses. In diagram (a), the beam emittance is too big for complete transmission whatever its shape is. In diagrams (b) and (c), the emittances are equal or less than the acceptance. The beam is correctly shaped and therefore transmitted completely only in diagram (c)



experiment is smaller than the emittance of the beam, then the unused part of the phase space ellipse should be cut (i.e., the particles having the required parameters are selected from the beam, and physical obstacles are used to prevent the passage of the unwanted particles). Therefore, the transportation can be carried out only with some loss. The optimal places of the diaphragms of the collimating system are to be set by considering various points of view (sources of the background radiation, optics, accessibility, etc.).

50.3.4.4 Luminosity

The term luminosity is used in connection with colliding beam experiments to determine the production rate of a collision. The *instantaneous luminosity* is proportional to the overlap integral to the densities of the two beams. The total number of individual collisions in an experiment is given by the cross section of the collision process times the *integrated luminosity*, which is defined as the instantaneous luminosity integrated over the total time of the experiment. More details can be found in the work of Conte and Mackay (1991b).

50.3.4.5 Brightness and Brilliance

These terms are used to characterize the intensities of the synchrotron light sources. The *brightness* is proportional to the number of photons hitting the target per second. It is inversely proportional to the bandwidth of the photon beam. The *brilliance* is defined as the brightness per area of the source. For more details, see the work of Eriksson (1994).

50.4 Editors' Notes

1. There is an apparent contradiction between the constant speed of electrons and their acceleration. Note that a circulating mass constantly changes its velocity even if the angular

frequency is constant. The rate of this velocity change (called centripetal acceleration) is one of the reasons for the production of synchrotron radiation. The energy loss caused by radiation would, of course, decrease the speed of electrons unless they are constantly accelerated, which they indeed are (p. 2352).

2. In other words, ω_c is the median of the frequency/energy distribution (just like the half-life $T_{1/2}$ is that of the lifetime distribution of radionuclides). See ► Chap. 9 in Vol. 1 on “Stochastics and Nuclear Measurements” (p. 2353).

Acknowledgments

The section “Ion Sources” was contributed by S. Biri, “Electrostatic Accelerators” by E. Koltay, and “RF-based and AC-voltage Accelerators” by A. Valek.

References

- ACCELCONF (2009) <http://accelconf.web.cern.ch/AccelConf/>
- Aitken TW, Leese JM (1977) *Rev Phys Appl* 12(10):1391
- Aitken TW, Tait NRS (eds) (1973) Proceedings of the international conference on the technology of electrostatic accelerators, Daresbury, 4–7 May 1973 (Daresbury Nuclear Physics Laboratory) DNPL/NSF/R5
- Aitken TW, Tait NRS (1984) *Nucl Instrum Methods* 220:1–223
- Allen WD (1966) Report NIRL/R21/1966/, Rutherford High Energy Laboratory
- Allen WD, Joyce NG (1973) Proceedings of the international conference on the technology of electrostatic accelerators, Daresbury, 4–7 May 1973 (Daresbury Nuclear Physics Laboratory) DNPL/NSF/R5, pp 242–253
- Anderson CE, Ehlers KW (1956) *Rev Sci Instrum* 27(10):809
- Andersson F, Barberet Ph, Incerti S, Moretto Ph (2008) *Nucl Instrum Meth B* 266:1653
- Angert N (1994) CERN 94-01 II:619–642
- APS (2009) <http://www.aps.anl.gov/>
- Arianer J, Cabrespine A, Goldstein C (1982) *Nucl Instrum Methods* 193:401
- Arje J, Koivisto H, Nurmia M (1995) Status report of the JYFL-ECR ion source. In: Proceedings of the 12th international workshop on ECR ion sources, Sept 1995, Wako-shi, Japan, INS-J-182, pp 136–140
- Baldinger E (1959) Kaskedengeneratoren. In: Flügge S (ed) *Handbuch der Physik* XXLIV. Springer, Berlin, pp 1–63
- Banford AP (1966) *The transport of charged particle beams*. Spon, London
- Baron E, Lieuvain M (1999) In: Baron E, Lieuvain M (eds) Proceedings of the 15th international conference on cyclotrons and their applications. Institute of Physics, Bristol
- Barué C, Biri S, Cherkani-Hassani S, Gaeleus M, Loiselet M, Ryckewaert G (1998) *Rev Sci Instrum* 69:764
- Barué C, Canet C, Dupuis M et al (2002) Metallic ion beam developments, In: Proc. 15th Int. Workshop on ECRIS, Jyväskylä, Finland, June 12–14, 2002. JYFL Research Report 4/2002, pp 219–223
- Baumann H, Bethge K (1981) *Nucl Instrum Methods* 189:107
- BETATRON (2009) http://www.globalxray.com/services_PXRB.asp
- Biri S, Vámosi J, Valek A, Kormány Z, Takács E, Pálinkás J (1997) *Nucl Instrum Meth B* 124:427
- Biri S, Simons L, Hitz D (2000) *Rev Sci Instrum* 71(2):1116
- Biri S, Valek A, Kitagawa A, Muramatsu M (2002) Status of the 14.5 GHz ATOMKI-ECRIS, In: Proc. 15th Int. Workshop on ECRIS, Jyväskylä, Finland, June 12–14, 2002. JYFL Research Report 4/2002, pp 49–52
- Biri S, Derzi A, Fekete É, Iván I (2007) *High Energ Phys Nucl Suppl* 31:165
- Bliman S, Chan-Tung N (1981) *J Phys* 42:1247
- Boag JW (1953) *Proc IEEE* 100 IV, vol 51, pp 63–82
- Bogdanov PV, Galchuk AB, Mudrolyobov VG, Popov AV, Tronov BN, Vorogushin MF (1999) Experience of the MGC-20 operation and its prospects. In: Baron E, Lieuvain M (eds) Proceedings of the 15th international conference on cyclotrons and their applications. Institute of Physics, Bristol, pp 673–676
- Boslough J (1985) *Natl Geogr* 167:634–663
- Brown IG (1992) *Rev Sci Instrum* 63:2351
- Brown IG (ed) (2004) *The physics and technology of ion sources*. Copyright WILEY-VCH Verlag GmbH/Co. KGaA.

- CASETECH (2005) <http://www.casetechnology.com/source.html>
- Chao AW, Tigner M (1999) In: Chao AW, Tigner M (eds) Handbook of accelerator physics and engineering. World Scientific, Singapore/New Jersey/London/Hong Kong
- Conte M, Mackay W (1991a) An introduction to the physics of particle accelerators. World Scientific, Singapore/New Jersey/London/Hong Kong
- Conte M, Mackay W (1991b) An introduction to the physics of particle accelerators. World Scientific, Singapore/New Jersey/London/Hong Kong, p 2, 230
- Cornell J (1996) In: Cornell J (ed) Proceedings of the 14th international conference on cyclotrons and their applications. World Scientific, Singapore/New Jersey/London/Hong Kong
- Dahl DA, Delmore JE, Appelhans AD (1990) Rev Sci Instrum 61:607
- Demortier G (ed) (1982) Nucl Instrum Methods 197:65–170
- DESY (2009) <http://m.desy.de/>
- Donets ED (1993) AIP conference proceedings, HCI-92, 274, pp 663–670
- Donets ED, Ilyushenko VI, Alpert VA (1968) JINR-preprint P7-4124, Dubna, Russia
- Doyle BL, Maggiore CJ, Bench G (eds) (1997) Nucl Instrum Methods B 130:1–750
- Drentje AG (2003) Rev Sci Instrum 74(5):2631
- Duggan JL, Morgan IL (1995) In: Duggan JL, Morgan IL (eds) Proceedings of the thirteenth international conference on the application of accelerators in research and industry; Nucl Instrum Meth B 99:1–888
- Dutto G, Craddock MK (1993) In: Dutto G, Craddock MK (eds) Proceedings of the 13th international conference on cyclotrons and their applications. World Scientific, Singapore/New Jersey/London/Hong Kong
- EAG (2010) Evans Analytical Group. <http://www.eaglabs.com/>
- ECR (2010) <http://www.atomki.hu/ECR/>
- ECRIS (2008) <http://accelconf.web.cern.ch/AccelConf/>
- England JBA (1974) Techniques in nuclear structure physics. MacMillan, London
- Eriksson M (1994) Recent highlights from synchrotron radiation facilities. In: Suller V, Petit-Jean-Genaz Ch (eds) Proceedings of the fourth European particle accelerator conference. World Scientific, Singapore/New Jersey/London/Hong Kong, pp 67–70
- ESRF (2009) <http://www.esrf.eu/Accelerators/Accelerators/>
- Fournier P (2000) Rev Sci Instrum 71(3):1405
- Frick G (ed) (1977) Rev Phys Appl 12(10)
- Frick G, Jaeschke E (eds) (1990) Nucl Instrum Meth A 287:1–336
- Gelbke CK (1999) Data sheet C72. In: Baron E, Lieuvain M (eds) Proceedings of the 15th international conference on cyclotrons and their applications. Institute of Physics, Bristol, p 786
- Geller R (1976) IEEE T Nucl Sci NS-23(2):904
- Geller R (1996) Electron cyclotron resonance ion sources and ECR plasmas. Institute of Physics, Bristol/Philadelphia
- Girard A, Serebrennikov K, Lécot C, Melin G, Hitz D, Sun L, (2002) ECRIS modelling, In: Proc. 15th Int. Workshop on ECRIS, Jyväskylä, Finland, June 12–14, 2002. JYFL Research Report 4/2002, pp 192–195
- Glass GA, Dymnikov AD, Rout B, Zachry DF (2007) Nucl Instrum Meth B 260:372
- Goto A, Okuno H, Kawaguchi T, Misumoto T, Tominaka T, Fujishima S, Kim JW, Ohnishi J, Ikegami K, Sakamoto N et al (1999) The K2500 superconducting ring cyclotron of RIKEN RI beam factory – overview and status. In: Baron E, Lieuvain M (eds) Proceedings of the 15th international conference on cyclotrons and their application. Institute of Physics, Bristol, pp 148–155
- Grime GW, Watt F (eds) (1988) Nucl Instrum Methods B 30:227–497
- GSI (2009) <http://www-inj.gsi.de/>
- Gudat W, Zimmermann P (2000) In: Gudat W, Zimmermann P (eds) Proceedings of the seventh international conference on synchrotron radiation instrumentation; Nucl Instrum Meth A 467–468:1–1632
- Hahto S, Leung K, Persaud A, Reijonen J (2002) Rev Sci Instrum 73:967
- Harvey BS (1974) In: Cerny J (ed) Nuclear spectroscopy and reactions, part A. Academic, New York/London, pp 35–77
- Hawkes PW (1970) Quadrupoles in electron lens design. Academic, New York/London
- Herb RG (1959) Van de Graaff generators. In: Flüge S (ed) Handbuch der Physik XLIV. Springer, Berlin, pp 64–104
- Herb RG (1974) Nucl Instrum Methods 122:267
- Heyder HRMc, Ziegler K (1998) Nucl Instrum Meth A 268:285–588
- Hitz D, Melin G, Girard A (2000) Rev Sci Instrum 71(2):839
- ICIS (1989–2009) In: Proceedings of the international conferences on ion sources (ICIS), 1989, 1991, 1993, 1995, 1997, 1999, 2001, 2003, 2005, 2007; Rev Sci Instrum 61(1), 63(4), 65(4), 67(3), 69(2), 71(2), 73(2), 75(5), 77(3), 79(2), 81(2), respectively
- ISIS (2009) <http://www.isis.stfc.ac.uk/>
- Isoya A et al (1977) Rev Phys Appl 12:1315
- Isoya A, Nakashima T (1970) Nucl Instrum Methods 88:33
- Jaksic M, Bogdanovic Radovic I (eds) (2005) Nucl Instrum Methods B 231:1–556
- Jones CM, Martin JA (1981) Proceedings of the 3rd international conference on electrostatic accelerator

- technology, IEEE Catalog 81CH1639-4, IEEE, New York
- Jones RJ, Zucker A (1954) *Rev Sci Instrum* 25(6):562
- Jongen Y (1980) Laboratoire du Cyclotron, UCL, LC-8001, Louvain-la-Neuve
- Jongen Y, Vandeplasse D, Cohilis P (1996) High intensity cyclotrons for radioisotope production or the comeback of the positive ions. In: Cornell J (ed) *Proceedings of the 14th international conference on cyclotrons and their applications*. World Scientific, Singapore/New Jersey/London/Hong Kong, pp 115–119
- Joy T (1990) *Nucl Instrum Meth A* 287:48
- Keller R, Müller M (1976) *IEEE T Nucl Sci NS-23*(2):1049
- Kidera M, Nakagawa T, Higurashi Y, Aihara T, Kase M, Yano Y (2002) Development of RIKEN 18 GHz ECRIS, In: *Proc. 15th Int. Workshop on ECRIS, Jyväskylä, Finland, June 12–14, 2002*. JYFL Research Report 4/2002, pp 74–76
- Kiss ÁZ, Koltay E, Szalay A (1967) *Nucl Instrum Methods* 46:130
- Kiss ÁZ, Koltay E, Szabó Gy (1981) In: Jones CM, Martin JA (eds) *Proceedings of the 3rd international conference on electrostatic accelerator technology*. IEEE Catalog 81CH1639-4, IEEE, New York, pp 103–106
- Kiss ÁZ, Koltay E, Papp I, Szabó Gy, Félsszerfalvi J, Nyilas I (1988) *Nucl Instrum Meth A* 268:382
- Kiss I, Koltay E, Bornemisza-Pauszpertl P (1977) *Rev Phys Appl* 12(10):1481
- Kitagawa A, Muramatsu M, Sasaki M et al (2002) Trial for extension of the range of ion species at HIMAC, In: *Proc. 15th Int. Workshop on ECRIS, Jyväskylä, Finland, June 12–14, 2002*. JYFL Research Report 4/2002, pp 70–73
- Kobayashi M et al (1976) *Rev Sci Instrum* 47:1425
- Koivisto H (1998) The MIVOC method for the production of metal ion beams. PhD dissertation, University Jyväskylä, Finland
- Koltay E (1963) *Phys Lett* 4:66
- Lang R, Bossler J, Schulte H, Tinschert K (2000) *Rev Sci Instrum* 71:651
- LANL (2009) <http://lansce.lanl.gov/>
- Legge GJF, Jamieson DN (eds) (1991) *Nucl Instrum Methods B* 54:1–440
- Leung KN (1994) *Rev Sci Instrum* 65(4):1165
- LINAC (1996) <http://linac2.home.cern.ch/linac2/seminar/seminar.htm>
- Lindh U (ed) (1993) *Nucl Instrum Methods B* 77:1–547
- Livingood JJ (1961) *Principles of cyclic particle accelerators*. D. Van Nostrand, Toronto/Princeton/New York
- Livingston RS, Jones RJ (1954) *Rev Sci Instrum* 25(6):552
- Loiselet M, Berger G, Breyne D, Daras Th, Goffaux H, Postiau N, Ryckwaert G, Ryckwaert J (1996) Production and acceleration of radioactive beams at Louvain-la-Neuve. In: Cornell J (ed) *Proceedings of the 14th international conference on cyclotrons and their applications*. World Scientific, Singapore/New Jersey/London/Hong Kong, pp 629–633
- Ludwig P et al (1998) *Rev Sci Instrum* 69(12):4082
- Margaritondo G (1998) *Introduction to Synchrotron Radiation*. Oxford University Press, Oxford
- Marrs RE (1996) *Rev Sci Instrum* 67(3):941
- Melin G, Girard A (1997) In: Shafroth SM, Austin JC (eds) *Accelerator-based atomic physics techniques and applications*. AIP, Woodbury/New York, Chapter 2, pp 33–66
- Middleton R (1977) *Rev Phys Appl* 12(10):1435
- Middleton R (1983) *Nucl Instrum Methods* 214:139
- Migneco E, Vinciguerra D (1981) *Nucl Instrum Methods* 184:1–284
- Milton BF (1996) Commercial compact cyclotrons in the 90s. In: Cornell J (ed) *Proceedings of the 14th international conference on cyclotrons and their applications*. World Scientific, Singapore/New Jersey/London/Hong Kong, pp 99–106
- Mironov V, Runkel S, Stiebing KE, Hohn O, Shirkov G, Schmidt-Böcking H, Schempp A (2001) *Rev Sci Instrum* 72(5):2271
- Moretto Ph, Bonin Mosbah M (eds) (2001) *Nucl Instrum Methods B* 181:1–759
- Morozov PM, Makov BN, Ioffe MS (1956) *Atomnaya Energiya* 3:272
- Muramatsu M, Kitagawa A, Suda M, Yamada S, Hanagasaki M, Ogawa Hiroyuku, Ogawa Hirotsugu, Biri S, Hattori T, Drentje AG, (2002) In: *Proc. 15th Int. Workshop on ECRIS, Jyväskylä, Finland, June 12–14 2002*. JYFL Research Report 4/2002, pp 59–62
- Myers S, Liljebj L, Petit-Jean-Genaz Ch, Poole J, Rensfelt K-G (1998) In: Myers S, Liljebj L, Petit-Jean-Genaz Ch, Poole J, Rensfelt K-G (eds) *Proceedings of the sixth European particle accelerator conference*. Institute of Physics, Bristol/Philadelphia
- Nakagawa T, Kurita T, Imanaka M, Arai H, Kidera M, Higurashi Y, Lee SM, Kase M, Yano Y (2002) Recent progress of liquid-He-free-SC-ECRISs (SHIVA and RAMSES), In: *Proc. 15th Int. Workshop on ECRIS, Jyväskylä, Finland, June 12–14, 2002*. JYFL Research Report 4/2002, pp 25–28
- Nikolaev VS, Dmitriev IS (1968) *Phys Lett A* 28:277
- Osipovitch T, Breeze MBH, Watt F, van Kan JA, Bettiol AA (eds) (2007) *Nucl Instrum Methods B* 158:1–482
- Przcsesky VM, Przybylowicz WJ, Pineda CA (eds) (1999) *Nucl Instrum Methods B* 158:1–735
- Rajta I, Kiss AZ, Kertész Zs, Szikszai ZA, Simon A (eds) (2009) *Nucl Instrum Methods B* 267:1995–2340
- Reijonen J (2000) Plasma and ion beam generation using RF and microwave ion sources. PhD dissertation, University Jyväskylä, Finland
- RFQ (2003) <http://hsbpc1.ikf.physik.uni-frankfurt.de/ezr/rfq.htm>

- RHIC (2009) <http://www.bnl.gov/RHIC/>
- Richardson JR (1965) In: Farley FJM (ed) Progress in nuclear techniques and instrumentation. North Holland, Amsterdam, pp 1–101
- Rolf CS, Rodney WS (1988) Cauldrons in the cosmos. University of Chicago Press, Chicago, pp 192–208
- Shirkov GD (1991) Nucl Instrum Meth A 302:1
- Shirkov GD (2000) Rev Sci Instrum 71(2):850
- Signorini C, Spolaore P (1993) Nucl Instrum Meth A 328:1–383
- SIMION (2009) <http://simion.com>
- SLAC (2009) <http://www2.slac.stanford.edu/vvc/>
- Sobenin NP, Karev AI, Melekhin VN, Shvedunov VI, Trower WP (1994) Design of a compact 70 MeV multi-purpose pulsed race-track microtron. In: Suller V, Petit-Jean-Genaz Ch (eds) Proceedings of the fourth european particle accelerator conference. World Scientific, Singapore/New Jersey/London/Hong Kong, pp 512–514
- Sortais P (2000) Status and developments of ECR ion sources. In: Proceedings of the EPAC-2000, EPAC-2000, Vienna, Austria, 26–30 June 2000, pp 78–82, <http://accelconf.web.cern.ch/AccelConf/e00/PAPERS/TUZF203.pdf>
- Spädtke P (1998) AXCEL-INP user manual v.3.42. INP, Wiesbaden, Germany
- Spädtke P, Mühle C (2000) Rev Sci Instrum 71:820
- SPRING8 (2009) <http://www.spring8.or.jp/en>
- SPS (2009) <http://ab-dep-op-sps.web.cern.ch/ab-dep-op-sps/>
- Stammbach T, Adams S (1999) Data sheet C60. In: Baron E, Lieuvain M (eds) Proceedings of the 15th international conference on cyclotrons and their applications. Institute of Physics, Bristol, p 775
- Strathdee A (1985) In: Strathdee A (ed) Proceedings of the particle accelerator conference; IEEE T Nucl Sci NS-32(5)
- Suller V, Petit-Jean-Genaz Ch (1994) In: Suller V, Petit-Jean-Genaz Ch (eds) Proceedings of the fourth European particle accelerator conference. World Scientific, Singapore/New Jersey/London/Hong Kong
- Takács J (1997) Energy stabilization of electrostatic accelerators. Wiley, Chichester
- Takai M, Kamiya T (eds) (2003) Nucl Instrum Methods B 210:1–563
- TEV (2009) <http://www-bd.fnal.gov/public/>
- Thonemann PC (1953) Progress in nuclear physics. Pergamon Press, London, p 219
- TSL (2009) <http://www4.tsl.uu.se/>
- Vámosi J, Biri S (1996) Comput Phys Commun 98:215
- Van de Graaff RJ, Rose PH, Wittkower AB (1962) Nature 195:1292
- Ventura E, Thienberger P (eds) (1986) Nucl Instrum Meth A 244:1–322
- Wangler T (1998) Principles of RF linear accelerators. Wiley, New York
- Watt F, Grime GW (1995) The high energy ion microprobe. In: Johansson SAE, Campbell JL, Malmqvist KG (eds) Particle induced X-ray emission spectroscopy. Wiley, New York, pp 101–165
- Watt F, van Kan JA, Rajta I, Bettiol AA, Choo TF, Breese MBH, Osipowicz T (2003) Nucl Instrum Meth B 210:14–20
- Weihreter E (1996) Compact synchrotron radiation sources. World Scientific, Singapore/New Jersey/London/HongKong
- Weisser DC (1996) Nucl Instrum Meth A 382:1–365
- West HI (1982) UCRL-53391 (internal report), Lawrence Livermore National Laboratory, USA. Available from National Technical Information Service, Springfield, USA
- Wolf BH (ed) (1995) Handbook of ion sources. CRC Press, New York/London/Toronto
- Wolf BH (1996) Nucl Instrum Meth B 112:30
- Xie ZQ, Lyneis CM (1997) Performance of the upgraded LBNL AECL ion source. In: May DP, Ramirez JE (eds) Proceedings of the 13th international workshop on ECRIS. Texas A&M University, College Station, Texas USA, pp 16–21
- Yang F, Tang J, Zhu J (eds) (1995) Nucl Instrum Methods B 104:1–652
- Závodszy P, Cole D, Miller P, Moskalik J (2002) Metallic ion beam production at NSCL/MSU, In: Proc. 15th Int. Workshop on ECRIS, Jyväskylä, Finland, JYFL Research Report 4/2002, pp 178–178

51 Isotope Separation

W. A. Van Hook

University of Tennessee, Knoxville, Tennessee, USA

51.1	<i>Introduction</i>	2371
51.2	<i>Theory of Cascades: Terminology</i>	2372
51.3	<i>Types of Separations: Cascades</i>	2373
51.3.1	Rayleigh Separation	2373
51.3.2	Simple and Countercurrent Cascades	2373
51.3.3	The Ideal Cascade	2375
51.3.4	Equilibrium Time	2377
51.4	<i>Isotope Separation Processes</i>	2377
51.4.1	Electromagnetic Separation	2378
51.4.2	Thermal Diffusion	2379
51.4.3	Large-Scale Separations, Energy Demands, and Comparisons	2380
51.4.4	Gaseous Diffusion	2382
51.4.5	Centrifugation	2382
51.4.6	Aerodynamic Isotope Separation	2383
51.5	<i>Distillation and Exchange Distillation: Large-Scale Production of Deuterium</i>	2384
51.5.1	Monothermal Isotope Exchange, the ^{15}N Example	2386
51.5.2	Dual Temperature Exchange: The GS Process	2387
51.5.3	Distillation	2389
51.5.4	Specific Examples, Isotope Separation by Distillation	2390
51.5.4.1	Hydrogen	2391
51.5.4.2	Carbon Monoxide	2391
51.5.4.3	Nitrous Oxide	2392
51.5.5	Exchange Distillation	2392
51.6	<i>Chromatography</i>	2393
51.6.1	Gas Chromatography	2394
51.6.2	Isotope Separation by Redox Ion-Exchange Chromatography	2396
51.7	<i>Photochemical and Laser Isotope Separation</i>	2397
51.7.1	Outline of a Laser Isotope Separation (LIS) Scheme	2398
51.7.2	LIS of Deuterium	2399
51.7.3	LIS for Uranium	2400
51.7.3.1	AVLIS	2400
51.7.3.2	LIS of UF_6	2400

51.8 *Other Isotope Separation Processes* 2401

51.9 *Editors' Notes* 2401

Abstract: Methods of isotope enrichment and isotope separation are reviewed. Several examples of commercially important or historically important separative processes are discussed.

51.1 Introduction

The small differences in chemical and physical properties of the isotopes of all but the lightest elements make their separation from each other unusually difficult. That difficulty is often compounded by the fact that the desired *isotopic molecules* (isotopologues) are often present at low or very low concentration in the starting material.¹ These factors, taken together, imply the processing of very large amounts of feedstock, at high reflux, through numerous separative stages. This, in barest outline, accounts for the high cost of samples of most separated isotopes.

Over the past 50 or more years, the nuclides of greatest industrial and/or military importance have been ^{235}U , the heavy isotopes of hydrogen, $^2\text{H}(\text{D})$ and $^3\text{H}(\text{T})$, and in greatly reduced amount, ^6Li and ^7Li , ^{10}B , ^{13}C , ^{15}N , and ^{18}O . Samples of many other enriched isotopes, chiefly for medical or research use, have been or are available. Very often, these have been obtained by electromagnetic separation, a process which is too expensive for large-scale separations.

During peak production, on the order of \$1 billion of ^{235}U was enriched per year from the natural abundance level (0.7%) to 1.5–4% for use in graphite- or water-moderated power reactors, or at higher enrichment for military purposes. Again, at its peak, worldwide production of deuterium (>99%) from water or other natural abundance feeds (0.015%) was on the order of several thousand metric tons per year. These rates of production demanded large-scale expensive industrial efforts.

A variety of processes have been used to separate isotopes on industrial or large pilot plant scales. These include (for U) gaseous diffusion, gas centrifugation, thermal diffusion, electromagnetic separation, laser-based methods, and various nonequilibrium vapor expansion processes. Because the properties of ^{235}U and ^{238}U are so very similar, the enrichment per separative unit (stage) is very small (except for laser-based methods), and it is necessary to multiply the effect by repeating it many times in a cascade. For enrichment of lighter isotopes (D from H, or ^{13}C from ^{12}C) separation factors are larger and the list of practical processes broadens to include chemical exchange, distillation, electrolysis, and similar methods. Even then, however, enrichment factors are close enough to unity that production of highly enriched samples requires partial separations carried out many times over in a multistage cascade. So far as the basic theory of cascade design is concerned, the particular process or type of separating unit is irrelevant. Once a given separative process has been selected, the design of the individual separative unit completed, and the separation factor per separative stage established, the problem of isotope separation reduces to an understanding of the principles of cascade design. In [Sect. 51.2](#), those principles are reviewed. The theory, originally due to Cohen (1951), was developed for uranium separation during the Manhattan Project (1942–1945). The highly abbreviated version below follows Benedict et al. (1981). Other reviews include those of London (1961), Spindel and Ishida (1990), Villani (1976), and Vértés and Kiss (1987).

51.2 Theory of Cascades: Terminology

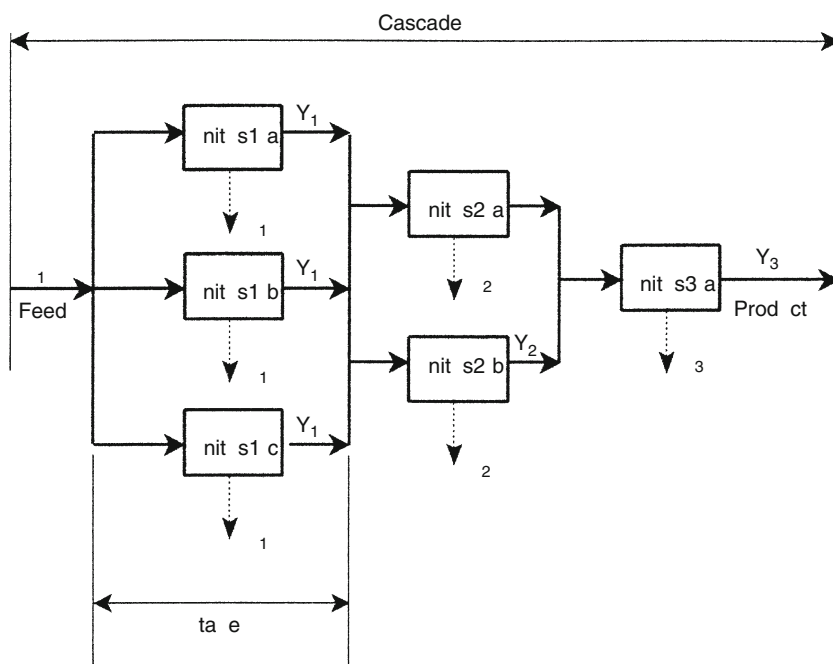
The relation between a separation unit, a stage, and a cascade is outlined in [Fig. 51.1](#).² The smallest element in a separation plant is a unit that might be a single plate in a distillation or chemical-exchange column, a gas centrifuge, a single laser separator, one membrane separative unit, etc. A group of such units, connected in parallel, all taking feedstock of the same chemical and isotopic composition, and producing a partially enriched product stream of different composition is called a stage. Sometimes a single unit serves as a stage, but more often single units have low capacity and many units in parallel are required. Because the separation per stage is generally less than the total required enrichment, stages are usually connected in series; the resulting assembly is called a cascade. A cascade with the same number of units in each stage is “*squared-off*,” while one in which the number of units per stage decrease as the product (or waste) end is approached is a “*tapered cascade*.”

In further discussion, it will be useful to employ the idea of an “ideal” stage, one where the feed stream is acted on to produce two exit streams (one product, one waste) that are in equilibrium with one another. Because actual stages always involve various inefficiencies, the number of stages in a real plant is always larger than the ideal number.

Examination of [Fig. 51.1](#) shows that each separating unit gains feedstock at a rate Z (mol/s) of material of isotopic composition z , and produces an enriched product stream at rate

Fig. 51.1

Relationships between separative units, stages (s), and cascades. The cascade shown is tapered; see text for other definitions



Y and isotopic composition y , and a waste stream at rate X and composition x . Material balance demands $Z = X + Y$ and $Zz = Xx + Yy$.

It follows that $Y/Z = \theta = (z - x)/(y - x)$ and $X/Z = (y - z)/(y - x)$. Y/Z , the ratio of heads to feed flow rates, is known as the “cut,” θ . The fraction of desired component in the heads stream is the “recovery,” $r = (yY)/(zZ) = y\theta/z$. The overall “separation factor,” α , is the ratio of head to tail isotopic ratios.

$$\alpha = \frac{y/(1 - y)}{x/(1 - x)}. \quad (51.1)$$

It is also convenient to define head-to-feed or tail-to-feed separation factors, β and γ .

51.3 Types of Separations: Cascades

51.3.1 Rayleigh Separation

Consider a separating unit where the heads, enriched in one component, are slowly removed (at zero feed) so the material remaining in the stage is progressively depleted in that component. A one-plate batch distillation from an unreplenished pot is a good example; the problem is equivalent to a differential separator fed with a continuously varying feed of tails composition. Equations governing such a separation were first deduced by Lord Rayleigh (1902), who found

$$\ln\left(\frac{X}{Z}\right) = \int \frac{1}{\alpha' - 1} \left[\frac{\alpha'}{1 - x} + 1 - x \right] dx, \quad (51.2)$$

where α' is the instantaneous or “local” separation factor.

For the case $|\alpha' - 1| \ll 1$, remembering that $X/Z = (1 - \theta)$, one obtains:


$$\alpha_{\text{overall}} - 1 = (\alpha' - 1) \left(1 + \frac{\theta}{2} + \dots \right). \quad (51.3)$$

► Equation (51.3) demonstrates that the overall separation factor (i.e., the ratio of isotopic compositions of the material remaining in the pot to that stripped away, and which is the parameter of practical usefulness) is greater than the instantaneous (single stage) α' and becomes much greater as the cut, θ , approaches unity. None of this is particularly surprising. The equations simply state that if one starts with a mixture and slowly strip away the more volatile component, at the end one will be left with a pot containing a sample highly enriched in the less volatile component. This multiplicative feature of Rayleigh distillation has tempted many workers into using it to determine single-stage separation factors, α' , but this is dangerous because experimental errors are multiplied as the stripping ratio increases. The assumption of an unvarying long-term state of equilibrium throughout is hard to meet, and the method is not recommended as a method for determining single-stage separation factors.

51.3.2 Simple and Countercurrent Cascades

A simple cascade is one where the feedstock for each stage, say the i th, is the heads cut from the $(i - 1)$ th stage. The $(i - 1)$ th tails are sent directly to waste as they have insufficient value to

warrant reprocessing. Thus, successive stages process progressively smaller amounts in the ratio of the cuts, θ_i . In a simple cascade, it is impossible to obtain a high recovery of the desired component because of the losses in the tails stream. The method can only be employed when the feedstock is abundant and cheap.

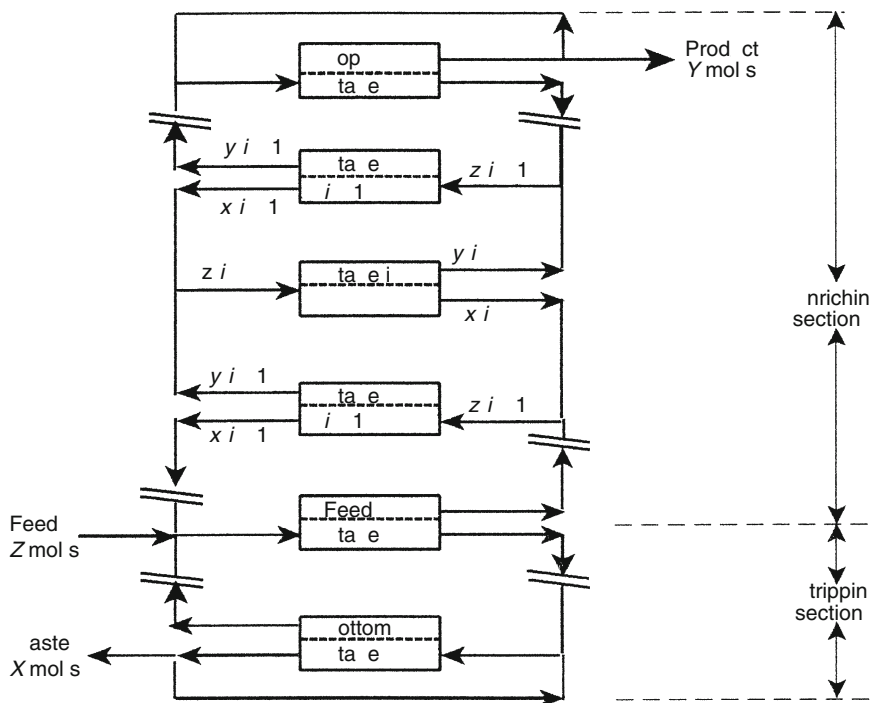
The countercurrent recycle cascade,  Fig. 51.2, is more commonly encountered because costs are usually such that tails warrant reprocessing. Here each stage, say the i th, is fed by a mixture of the heads stream from the $(i - 1)$ th, and tails stream from the $(i + 1)$ th, stages. A distillation column is a good example. Feed is introduced around the midpoint of the cascade. The portion between feed and product end is designated the “enriching” section, and the portion between feed and waste withdrawal, the “stripping” section. The enriching section is essential to give the desired product, the stripping section only serves to reduce the amount of feed required per unit amount of product.

If feed is cheap, e.g., natural water fed to a deuterium separation plant, the stripping section might be dispensed with. The countercurrent streams moving from product or waste ends back to the feed point are known as “reflux” streams. Materials balance requires the sum of product and waste withdrawal rates to equal the feed rate.

The processing rate, however, is much larger because countercurrent reflux material is being continually processed and reprocessed.

 Fig. 51.2

Separative stages arranged in a countercurrent recycle cascade



In short, one finds

$$y_i - x_{i+1} = \frac{(y_p - y_i)}{X_{i+1}/P}. \quad (51.4)$$

Here y_p is the isotopic composition at the top stage, P is the product withdrawal rate, and, as before, X_{i+1} is the tails withdrawal rate at the $(i + 1)$ th stage. The ratio (X_{i+1}/P) is the reflux, which for a simple countercurrent cascade is independent of stage number (i.e., such a cascade is squared off). Note that y_i and x_{i+1} approach each other as X_{i+1}/P approaches infinity, which happens at total reflux. In that case, the number of stages required to carry out a given overall separation is a minimum and is given by the *Fenske equation* (Fenske 1932):

$$n_{\min} = \frac{\ln \left[\frac{y_p/(1 - y_p)}{x_w/(1 - x_w)} \right]}{\ln \alpha}, \quad (51.5)$$

where x_w is the isotopic composition of the waste.

Equation (51.5) shows n_{\min} increases as the overall separation is increased and as the separation factor α gets closer and closer to unity. For the latter reason, the minimum number of stages required for isotope separation can be very large. To cite a practical example, in a ^{235}U diffusion plant with $\alpha = 1.0043$, producing 90% enriched product, and rejecting 0.3% tails, from natural uranium (0.7%) feedstock, $n_{\min} \approx 1,870$. Of course, under the conditions of total reflux no product is withdrawn, it is all held in the cascade as inventory. For finite product withdrawal, even more stages will be required.

With infinite (total) reflux, the concentration ratios on successive stages reach their maxima. Conversely as the reflux ratio decreases the concentration ratios follow. They reach unity (no enrichment) at minimum reflux. Material balance considerations yield an expression for the minimum reflux ratio (Eq. (51.6)).

$$\left[\frac{X_{i+1}}{P} \right]_{\min} = \frac{x_p(\alpha x_{i+1} + 1 - x_{i+1}) - \alpha x_{i+1}}{(\alpha - 1)x_{i+1}(1 - x_{i+1})} \quad (51.6)$$

When α is close to 1 the minimum reflux ratio is large. At the feed point in the uranium plant enriching to 90% ^{235}U , the minimum reflux ratio is 29,100, but at the product end of the cascade, it approaches zero.

Clearly a practical separation plant can operate at neither minimum reflux (where the separation is zero, but the rate of production is high), nor at minimum number of stages (where the rate of production is zero, but the separation is high). A compromise is required. Because for given separation the optimum reflux varies with stage number, it is usual to design “tapered” cascades for isotope separation. This results in marked savings in material hold-up in the cascade, and in plant size and investment, but at the cost of a more complicated design and increased operating complexity.

51.3.3 The Ideal Cascade

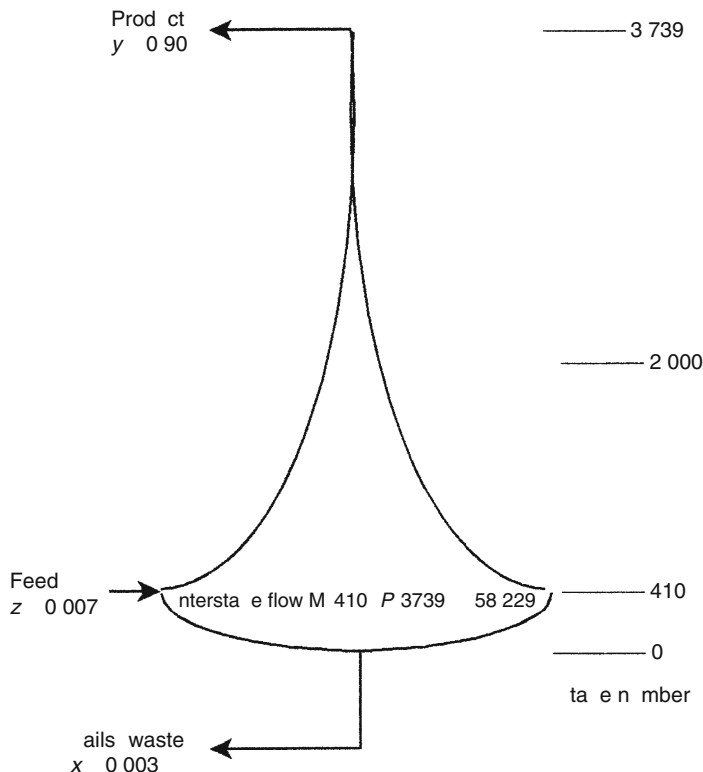
An ideal cascade is one which is tapered to yield minimum interstage flow and thus minimum operating cost. In an ideal cascade, the heads stream from the $(i - 1)$ th and the tails stream from the $(i + 1)$ th stages are mixed to form the feed to the i th stage. Obviously for best efficiency the two streams should be of identical isotopic composition, otherwise some separative work is

being used to no good purpose. Materials and isotope balance considerations lead to the result that the number of stages in an ideal cascade is just twice the minimum number of stages at total reflux, less one. Expressions for the ratio of the numbers of stages in the stripping to enriching sections are available (Benedict et al. 1981). The function that describes the tapering depends sensitively on the single-stage separation factor and the overall separation required. For the presented illustration (^{235}U separation with $y_p = 0.9$, $x_w = 0.003$, $z_f = 0.007$, and $\alpha = 1.0043$, where z_f is the feed composition), one finds that 213.6 moles of feed results in 212.6 moles of depleted tails (waste). The number of stages is twice the minimum less one, or 3,738, with 410 stages in the stripping section and the rest in the enriching section. The figures are characteristic of uranium enrichment using gaseous diffusion and natural abundance feedstock. The interstage flow at the feed point, $i = 410$, is enormous, $M_{410}/P = 58,229$, but decreases rapidly as one moves away from the feed point. ▶ Figure 51.3 represents this schematically.

Figure height is proportional to stage number, and width to interstage flow. A proportionality between interstage flow and capital investment and energy demand is expected. Once feed product and waste isotopic abundances are set, the plant size diverges to infinity with α approaching 1 according to $1/(1 - \alpha)^2$. It is therefore of the utmost importance to select a practical process with the largest possible α in order to minimize plant size and capital investment. Still, α is small for many isotope separations and this accounts for the

■ Fig. 51.3

Ideal cascade for uranium isotope separation



enormous size (cost) of industrially important isotope separation plants. For the presented example of gaseous diffusion enriching uranium, about 42×10^6 moles of UF_6 must be processed for every mole of 90% $^{235}\text{UF}_6$ product.

51.3.4 Equilibrium Time

This section is concluded with brief remarks on the time required to bring the cascade from start to first withdrawal of product. Due to their large size, many isotope separation plants have inventories that correspond to many days of normal production. [Equation \(51.7\)](#) is an approximate relation between the time to first production, t_p , feed and product isotopic compositions at equilibrium, single-stage separation factor, α , and the residence time per stage, h , for a cascade like that in [Fig. 51.3](#). The behavior of t_p is similar to that for plant size, i.e., t_p diverges to infinity proportionally to $1/(1 - \alpha)^2$.

$$t_p = \frac{8h}{(1 - \alpha^2)} \left[\frac{y_p - 2y_p z_f + z_f}{y_p - z_f} \ln \frac{y_p - z_f}{z_f(1 - y_p)} - 2 \right]. \quad (51.7)$$

For the 90% ^{235}U example, and taking $h = 1$ s, $t_p \approx 30$ days. In cascades that are not tapered, t_p will be even longer because of the increased inventory of enriched material in upper stages.

Long time to production implies the necessity for safeguards against stage-to-stage remixing in the event of power failure or other problems. In a distillation plant a power failure causes the column to drain and results in isotope remixing in the boiler. It is then necessary to start over at considerable economic and emotional cost.

51.4 Isotope Separation Processes

The selection of a particular separative process including the design of individual units and their incorporation into a cascade depends principally on engineering and economic considerations. These must take account of the desired output, available starting material, energy demands, etc. It comes as no surprise, then, that a wide variety of methods have been used for isotope separation. The more important of these are listed in [Table 51.1](#), and, in the balance of this chapter some will be briefly discussed.

Table 51.1

Commonly used methods for isotope separation

Electromagnetic	Electrolysis
Thermal diffusion	Electromigration
Gaseous diffusion	Chromatography
Gas centrifuge	Ion exchange
Chemical exchange	Supersonic nozzle expansion
Distillation	Mass or sweep diffusion
Exchange distillation	Membrane pervaporation
Photochemical and laser	

The aim is to illustrate the principles above, and not to give an exhaustive review of methods of isotope separation, nor a detailed treatment of any one method. Useful reviews of isotope separation have been given by Kistemaker et al. (1958), London (1961), Bigeleisen (1969), Spindel (1975), Rae (1978), Benedict et al. (1981), and Spindel and Ishida (1990), among others.

While the single-stage factor α is the best single measure of separative ease, a process cannot be optimized on that basis alone. Engineering considerations, and convenience, are also important. Even for a given isotope there is no single best method, but experience over the past half century or more demonstrates that *electromagnetic separation* is the most versatile means for the production of small quantities of isotopes of moderate to heavy mass. Alternatively, the simplest and most inexpensive method for small-scale separation of isotopes of light to moderate mass is the *thermal diffusion column* (Clusius and Dickel 1938). However, for large-scale separation of light elements, distillation and/or chemical exchange or exchange distillation are the best. For heavy elements (read uranium), gaseous diffusion and gas centrifugation have been employed on large scale, together (more recently) with various separative processes based on laser technology.

51.4.1 Electromagnetic Separation

Electromagnetic separators (large-scale mass spectrometers, also known as “*Calutrons*” because they were originally developed at the California cyclotron laboratory), were constructed at Oak Ridge in the early 1940s to separate ^{235}U from natural abundance feed in kilogram quantities. This method of uranium isotope separation was discontinued in 1945 because of high cost. Under high vacuum conditions, it is possible to obtain genuinely large separation factors in an electromagnetic separator (high resolution in the language of the mass spectroscopist), but this important advantage is offset with a number of difficulties. To begin, the source must be chemically treated to provide compounds of appropriate volatility and chemical purity. More importantly, the electromagnetic process has inherent high losses. First, only a small fraction of feed is ionized and then extracted through the electrical accelerating slits. There are scattering losses in the beam, and space charge effects result in high loss and degradation of separation factors as ion current increases. These factors work against electromagnetic separation for large-scale isotope production, although the method is well suited for preparing small quantities (milligram to gram) of separated isotopes for research and specialized medical purposes. As an example, consider the medical products company “*Theragenics*,” which produces a “rice-sized” implantation seed of ^{103}Pd used for the treatment of prostate cancer. The separated isotope is currently produced using cyclotrons, but the company plans to employ a new production facility using refurbished plasma separation equipment purchased from the Department of Energy, Oak Ridge. Also, it will soon expand operations and produce isotopes for other medical therapies. Another, and apparently more versatile facility designed for the electromagnetic preparation of small amounts of separated (usually high mass) isotopes is the ISOLDE online isotope separator at the European accelerator facility CERN. This facility has been recently described in detail by Kugler (2000) and Habs et al. (2000).

Many of the problems in electromagnetic separation are rooted in the technology of handling plasmas at high charge density. They are analogous to the ones experienced in the controlled thermonuclear fusion program. Developments there might result in a new look at large-scale electromagnetic isotope separation.

51.4.2 Thermal Diffusion

When a gas mixture is subjected to a temperature gradient, diffusion occurs and a concentration gradient is established. Enskog (1911) and Chapman (1916) deduced the transport equation, which relates separation factor, θ , to the temperature gradient.

$$\ln \theta = g \ln \frac{T_2}{T_1}. \quad (51.8)$$

The thermal diffusion factor, g , can be obtained from the kinetic theory of gases if the intermolecular potential is known. In first order, it is proportional to $(m_2 - m_1)/(m_2 + m_1)$. Momentum transport vanishes for particles following an inverse sixth power potential. If the potential falls off with a power greater than six, the lighter molecule concentrates in the high-temperature region, and if less than six it concentrates in the cold region. Calculation shows that g is small for mixtures of isotopes (order 10^{-2}), but Clusius and Dickel (1938) successfully developed an elegant countercurrent apparatus that multiplies the elementary effect.

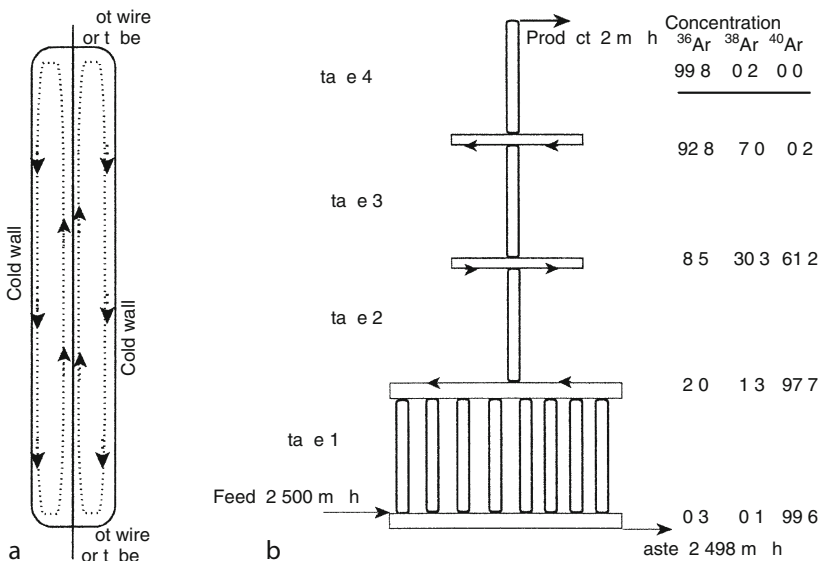
A schematic diagram of a Clusius–Dickel column is shown in Fig. 51.4a. An electrically heated wire or tube runs down the axis of a cylinder with a refrigerated wall.

The resulting temperature gradient establishes thermal diffusion in the radial direction and the consequent mass gradient causes convection. Molecules near the center move up the tube with respect to gas near the cold wall. The countercurrent flow thus established leads to multiplication of the elementary separation factor. The theory of such columns has been developed in detail, but will not be reviewed here (Jones and Furry 1946; London 1961).

In practical application a number of individual thermal diffusion columns, each about 3 m long, are connected in a cascade. Fig. 51.4b shows a cascade of 11 columns used to

Fig. 51.4

(a) Hot Wire Thermal Diffusion Column (Clusius–Dickel column). (b) Four-stage thermal diffusion cascade for argon isotope separation



separate argon isotopes at Mound Laboratories USDOE (or its commercial heir, Isotec Corp.). Separations and production rates are indicated (notice that ³⁸Ar concentrates in the middle of the cascade, which in this case is operated without a stripping section). Thermal diffusion dissipates large amounts of power, and for that reason, it is primarily of interest for laboratory-scale separations. Results illustrating the versatility of the method are given in ▶ [Table 51.2](#).

51.4.3 Large-Scale Separations, Energy Demands, and Comparisons

Sections 0 and 0 demonstrate that almost any desired isotope can be separated by thermal diffusion or electromagnetic methods on a small scale. For large-scale separation, enormous amounts of material must be processed and energy consumption, cascade design, and other such factors become important. ▶ [Tables 51.3](#) and ▶ [51.4](#) list theoretical upper limits of single-stage separation factors for H/D, ¹²C/¹³C, and ²³⁵U/²³⁸U for several different separative methods.

■ [Table 51.2](#)

Isotopes separated by K. Clusius and coworkers by thermal diffusion (Clusius and Dickel [1938](#); Clusius and Starke [1949](#))

Year	Isotope	Abundance (%)	Separation factor	Final purity
1939	³⁵ Cl	75.7	53	99.4
1939	³⁷ Cl	24.3	775	99.6
1942	⁸⁴ Kr	57.1	45	98.3
1942	⁸⁶ Kr	17.5	940	99.5
1950	²⁰ Ne	90.5	210	99.95
1950	¹⁵ N	0.37	135,000	99.8
1953	¹³ C	1.09	45,000	99.8
1955	¹³⁶ Xe	8.9	810	99.0
1956	²¹ Ne	0.275	96,500	99.6
1959	¹⁸ O	0.204	200,000	99.75
1959	³⁸ Ar	0.064	9,750,000	99.98
1960	²² Ne	9.21	12,500	99.92
1962	³⁶ Ar	0.37	3,300,000	99.99

■ [Table 51.3](#)

Comparison of separation factors for some isotopes using different methods

Method	H/D	¹² C/ ¹³ C	²³⁵ U/ ²³⁸ U
Chemical exchange	3	1.02	1.001
Distillation	1.05–1.7	1.01	1.0000
Gaseous diffusion	1.2	1.03	1.004
Centrifuge, 250 m/s	1.01	1.01	1.026

■ Table 51.4

Some H/D separation factors for distillation

Compound	T/K	P/kPa	Separation factor
Hydrogen	24	250	1.5
Methane	112	100	1.0036
Ammonia	239	100	1.036
Water	378	120	1.024

It has been shown that α values of a few tenths percent or so, lead to reflux ratios at the feed point of 10^4 or greater. In gaseous diffusion, UF_6 diffuses from high to low pressure through a porous membrane. The upper limit of the separation factor is given by Knudsen theory of molecular flow. In an ideal cascade with $(\alpha - 1) \ll 1$, theory optimizes the cut at each stage, $\theta = 0.5$. The minimum reflux energy is therefore the work of ideal recompression, $RT \ln 2 = 1.9 \text{ kJ/mol}$ at 333 K. The real compression is not isothermal and warms the gas by about 5%. That heat must be removed at each stage, which increases the compressor bill from ~ 1.9 to $\sim 2.0 \text{ kJ/mol}$ of gas processed. If, roughly, one assumes the equipment operates at one half the ideal efficiency, the energy cost increases to $\sim 4 \text{ kJ/mol}$. For the example of the uranium plant that was discussed approximately 42×10^6 moles are processed for each mole of 90% ^{235}U product (Benedict et al. 1981). Thus the energy demand, just for reflux, is estimated at an enormous $17 \times 10^{10} \text{ J/mol}$ product. A more realistic calculation based on a 1972 DOE estimate for its then most efficient plant gives almost 2.5 times that $45 \times 10^{10} \text{ J/mol}$ total energy demand. In 1975, at or near the peak of production, installed gaseous diffusion capacity for ^{235}U was $\sim 3.2 \times 10^5$ moles/year (Spindel 1975), which if completely used would have required a power input of $\sim 4,500 \text{ MW}$.

Of course, at any given time, a large fraction of the separative capacity was not being used, or was only being used for partial enrichment (from 0.7 to 3.5% or 4% as required for fueling nuclear power plants). However, even the scaled down demand was enormous. It was almost certainly responsible for the decision to phase out gaseous diffusion enrichment replacing it with gas centrifugation or laser separation processes (*vide infra*).

Now compare the energy demand for reflux in gaseous diffusion with that required for distillation. In an ideal distillation, heat must be added only at the boiler, and extracted only at the condenser. In between there are many separating units (plates or stages) where vapor is continually condensing and liquid continually evaporating. However, the heat of vaporization is exactly the negative of the heat of condensation, so if the column is perfectly adiabatic, the plates in the column do not contribute to the energy demand. A well-designed laboratory distillation column has on the order of 100 plates in a 1 or 2 m length, so the energy cost per stage is around a percent or so of the heat of vaporization, and the reflux cost is several tens rather than several thousands of joules per mole processed. When chemical exchange is compared with distillation, the reflux energy increases by about a factor of ten, i.e., it is now proportional to the heat of chemical reaction rather than to the heat of vaporization. The height equivalent per theoretical plate (HETP) also increases, and energy demand per stage rises from several tens to several hundreds of joules per mole processed.

One can now appreciate the reasons for the high cost of enriched uranium. The single-stage separation factors are low, as is the natural abundance. This leads inexorably to a high reflux

demand and a large number of stages. Additionally, the historically practical processes have a large reflux cost, and the result is an extremely expensive product. The world is now blessed (?) or cursed (?) with a large oversupply of enriched uranium. Consider how much sooner this might have occurred were there a practical uranium distillation process with cheap reflux.

51.4.4 Gaseous Diffusion

The examples discussed in earlier sections were chosen to illustrate principles of cascade design for gaseous diffusion in a UF_6 separation plant because of historical and engineering interest in that process. Design details are classified or confidential, but in essence the gas is fed at the higher pressure into a set of parallel tubes with porous walls. The process is simplified by virtue of the fact that there is only one natural isotope of fluorine, so all enrichment is due to uranium isotope effects. The diffusion through the pore structure can be described in the limit by the laws of Knudsen flow. UF_6 is extremely reactive, and much of the technology focuses on the handling of this dangerous material in quantity. Design details of the diffusion tubes are not available but presumably the walls are constructed from a spongy alloy of high nickel content. To appreciate the genuinely large scale of the operation, one should note that the Portsmouth, Ohio facility (now closed) involved a production facility that covers 93 acres ($\sim 0.38 \text{ km}^2$), but has a floor area nearly three times larger than that ($\sim 1 \text{ km}^2$), since much of the plant has several stories.

51.4.5 Centrifugation

The use of centrifuges for isotope enrichment was suggested as early as 1919 by Lindemann and Aston (1919), but successful experiments awaited the development of vacuum centrifuges by Beams and coworkers in the late 1930s (Beams 1938). The devices rotate in vacuum chambers suspended on metal capillaries through which gas is introduced and withdrawn. Thorough discussions have been given by London (1961) and Benedict et al. (1981).

In a centrifugal field, the energy per mole at distance r from the axis is $M(\omega r^2)/2$, where M is molar mass and ω angular velocity. The ratio of partial pressures (p) for two isotopologues (primed and unprimed) at the wall, r_w , and on the axis, r_0 , yields the elementary separation factor.

$$\alpha = \frac{p'(r_w)/p(r_w)}{p'(r_0)/p(r_0)} = e^{\frac{(M'-M)(\omega r_w)^2}{2RT}}. \quad (51.9)$$

► Equation (51.9) shows α to be a simple function of the absolute (molar) mass difference, $(M' - M)$. This is in contrast to most methods of isotope separation where α depends on the ratio of masses, or the ratio raised to some power. Centrifuge α' values for $^{235}\text{UF}_6/^{238}\text{UF}_6$ at several peripheral speeds are shown in ► Tables 51.5 and ► 51.6. The values are far above those for gaseous diffusion.

► Figure 51.5 is a schematic diagram of a countercurrent gas centrifuge separation unit with externally pumped streams. Important problems of shaft and bearing design, frictional loss, vibrational damping, materials of construction, and strength of materials are relevant. Already in 1961, London (1961) compared maximum peripheral velocities of thin wall steel,

■ Table 51.5

Separation factors α for $^{235}\text{U}/^{238}\text{U}$ in a centrifugal field as a function of the peripheral speed (ωa) and relative radial position (r/a), where $a = r_w$ is the rotor radius

r/a	400 m/s	500 m/s	700 m/s
0	1.101	1.162	1.343
0.5	1.075	1.119	1.247
0.8	1.035	1.056	1.112
0.9	1.018	1.029	1.058
1.0	1.0	1.0	1.0

■ Table 51.6

Pressure ratios $p(r)/p(a)$ for UF_6 in a centrifugal field. See ▶ Table 51.5 for further details

r/a	400 m/s	500 m/s	700 m/s
0	1.3×10^{-5}	2.2×10^{-8}	1×10^{-15}
0.5	2.1×10^{-4}	1.8×10^{-6}	5×10^{-12}
0.8	1.7×10^{-2}	1.7×10^{-3}	4×10^{-6}
0.9	1.2×10^{-1}	3.5×10^{-2}	1.4×10^{-3}
1.0	1.0	1.0	1.0

titanium, and glass fiber rotors (318, 427, and 527 m/s, respectively). More recent materials have moved this level beyond 700 m/s where the UF_6 separation factor is in excess of 1.3.

It is interesting to compare the economics of gas centrifugation to gaseous diffusion, albeit crudely. London (1961) divides enrichment cost into two principal categories: (1) specific investment, i.e., capital cost per separative work unit (SWU) amortized over the plant life, and (2) power cost per SWU. (SWU, which is a function of quantities and concentrations of feed, product, and waste provides a quantitative measure of the isotope separation task for any conceivable process.) The latter comprises the bulk of operating costs. The estimates, which are crude, clearly demonstrate an advantage for gas centrifugation.

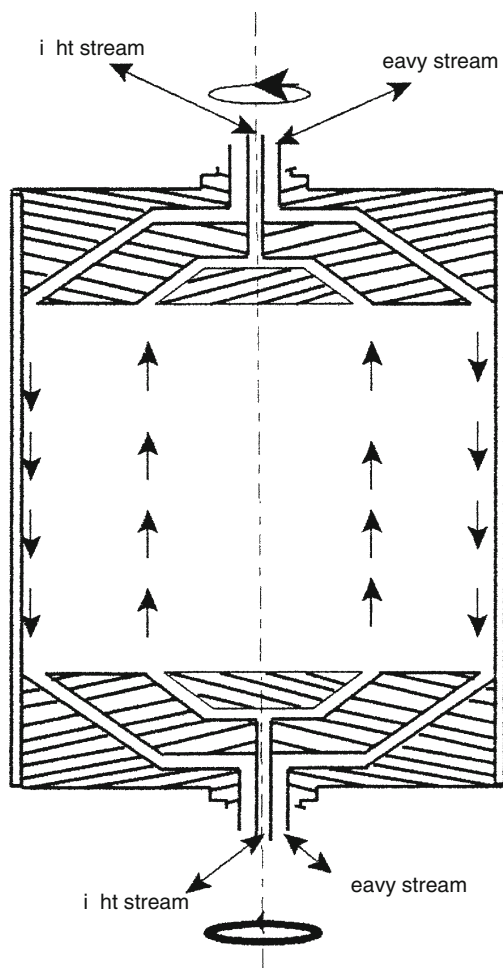
These considerations led the European community to elect gas centrifuge production for enriched uranium to be used in its power production facilities. The United States also turned away from gaseous diffusion because of its high cost. Its diffusion plants have been retired. After extensive development a large gas centrifuge facility was constructed, but that in turn was abandoned in favor of even more economical laser separation processes (see below). In around 2002, the laser separation plants have also been closed, presumably due to present day oversupply of enriched uranium.

51.4.6 Aerodynamic Isotope Separation

The basic idea of aerodynamic isotope separation is illustrated in ▶ Fig. 51.6a. Feed, such as UF_6 , diluted with light gas, H_2 or He , to a total pressure ~ 2.5 kPa, is fed through a slit-shaped

■ Fig. 51.5

Gas centrifuge isotope separation unit



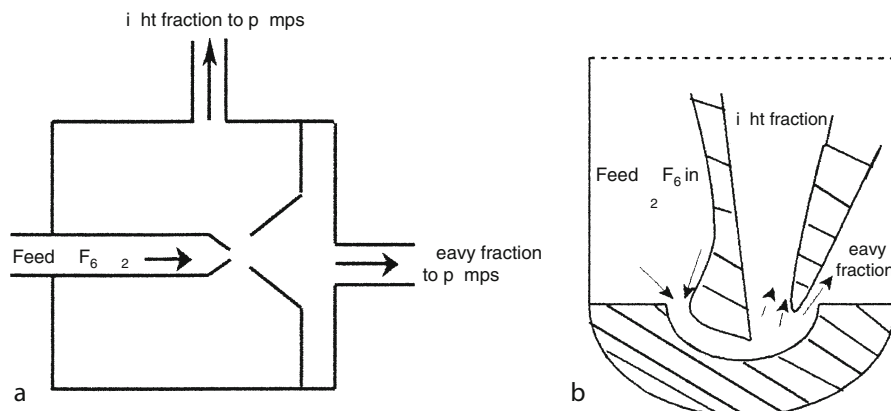
nozzle into a region of much lower pressure. The flow is such that the velocity in the forward direction is supersonic. Because of kinetic-molecular effects a certain fraction, θ , diverges from the feed jet (~ 0.05 mm) enriched in the lighter isotope, while the rest of the jet passes through a second and somewhat wider “skimming” slit (~ 0.2 mm). An alternate radial design, [Fig. 51.6b](#), yields significantly larger separations.

51.5 Distillation and Exchange Distillation: Large-Scale Production of Deuterium

It is instructive to use the case of enriched deuterium production to describe distillation and exchange distillation isotope separation. To begin, the historical background of the need for

■ Fig. 51.6

(a) Schematic of a crude nozzle aerodynamic separator. (b) An improved nozzle separator



deuterium, the magnitude of world demand, and related questions will be commented on. Historically, the principal demand for deuterium was in the form of heavy water, D_2O , for use as a moderator in certain types of nuclear reactors. Deuterium is an excellent neutron moderator, and more importantly, has a low-absorption cross section for slow neutrons. Therefore, a reactor moderated and cooled with D_2O can be fueled with natural uranium and thus avoid the problems of uranium isotope enrichment. This was the route chosen by Atomic Energy of Canada for its nuclear electric power program. Their CANDU reactors (CANada Deuterium Uranium) require approximately 0.8 t D_2O per megawatt (McAlpine and Evans 1985), and cumulative Canadian production exceeds 11,000 t. American production ended in 1981 after cumulative production of $\sim 7,000$ t. That material had been mostly used as a moderator in reactors breeding plutonium from uranium fuel. The United States, and most worldwide nuclear power programs, use pressurized normal water reactors. There are no large-scale commercial uses of deuterium except as a moderator in power production or breeder reactors. One can assume that deuterium and tritium were used in weapons programs, but that activity is tapering off, and hopefully will soon end. In spite of the large number of bombs in military stockpiles, 1945 to present, this should not have amounted to any significant fraction of world deuterium production. Also, although deuterium is widely employed in scientific research, this does not consume any large fraction of the available stockpile.

The very low D/H natural abundance ratio (0.015%, 150 ppm) is the factor responsible for the high cost of heavy water. Materials balance shows it to be necessary to process a minimum of 8,000 mol feed per mol of product, and even more for reasonable values of tails analysis (for more recent GS plants the feed/product ratio reached nearly 40,000 to 1).³ At peak, Canadian production is ~ 800 t/year, which means feed quantities approaching 2.4×10^6 t/year. Such amounts demand cheap and easily accessible feed (i.e., water), or alternatively, require D production to be parasitic on some other large industrial process, e.g., NH_3 used for fertilizer production or petrochemical processing. However, very often even large-scale industrial facilities are not large enough to be a practical source of deuterium on the scale described above.

► Table 51.7 contains a partial list of possible processes for heavy water production. Distillation, while the simplest, is prohibitively expensive (except for low-temperature

■ Table 51.7

Possible processes for heavy water production (Rae 1978)

Process	Remarks
Distillation	Size excessive, except for H ₂
Chemical exchange	Most promising
Diffusion	Barrier or membrane cost excessive
	High energy demand
Electrolysis	Excessive energy cost
Gravitational	Excessive energy cost
Adsorption	High absorbent volume
Biological	Excessive volume
Crystallization	Impractical on large scale
Selective photochemical	Promising if selectivity approaches 10 ⁴

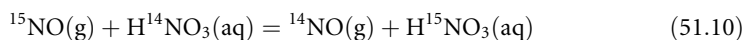
distillation of H₂/HD) because the α values are too close to 1. This implies high reflux, and large capital investment. A small-scale Indian plant used water electrolysis followed by hydrogen distillation (~ 14 t/year D₂O), and several somewhat larger plants (~ 65 t/year), parasitic to fertilizer production, and based on ammonia distillation or ammonia–hydrogen exchange have been described (Galley 1983).

In view of the enormous quantities of methane processed in the petroleum and natural gas industries, it is unfortunate that the separation factor for CH₃D/CH₄ is unattractively small. Of the other processes in ■ Table 51.7, most have high energy or large capital cost per SWU. Laser and photochemical methods continue to be investigated but have not proven economical for H/D separation, even on small scale (McAlpine and Evans 1985). Historically, and still at present, the most promising methods are those based on chemical exchange (H₂S/H₂O, H₂/H₂O, H₂/NH₃). These equilibria have large separation factors that are pronounced functions of temperature. This allows the design of dual temperature processes, which provide efficient thermal refluxing and yield decided economic advantage. Other exchange processes employ chemical refluxing, normally much more expensive.

Because of the very large enrichments required in heavy water production, cascades must taper markedly. In the upper stages the relative advantage of chemical exchange over water distillation vanishes. Most heavy water plants carry out the last portion of the enrichment by distillation (from 20 to 30 atom percent D to 99.85%). Accordingly both exchange and distillation will be briefly treated in this section.

51.5.1 Monothermal Isotope Exchange, the ¹⁵N Example

Taylor and Spindel (1958) described the preparation of 99.8% ¹⁵N using the reaction,

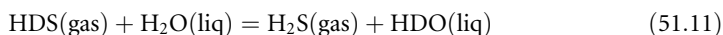


The reaction occurs at acceptable rate for $[\text{HNO}_3(\text{aq})] = 10$ M, $T = 298$ K, with $\alpha = (^{15}\text{N}/^{14}\text{N})_{\text{aq}}/(^{15}\text{N}/^{14}\text{N})_{\text{gas}} = 1.055$. The value calculated from the theory of isotope effects⁴ and

spectroscopic data is 1.096, so there appears to be an exchange between species other than NO(g) and HNO₃(aq). In the actual process, aqueous acid flows downward through a packed column countercurrent to an uprising gas stream containing the NO. A two-column cascade was employed in which 4% of the acid flow was shunted to the upper stages, and the remaining 96% decomposed to NO for recycle by treatment with SO₂. The depleted NO from the lower section is mixed with air and water to generate a waste HNO₃(aq) flow. Thus, the Spindel–Taylor process based on ▶ Eq. (51.10) separates a nitric acid feed stream into a highly enriched nitric acid product and a slightly depleted nitric acid waste, while converting SO₂(g) and air to H₂SO₄(aq). The minimum ratio of H₂SO₄ to ¹⁵N is 1.5 times the minimum reflux, so for product at 0.998 ¹⁵N generated from feed at 0.00365, with $\alpha = 1.055$, $n(\text{SO}_2) = (3/2)[(\gamma_p - z_f)/z_f][\alpha/(\alpha-1)] = 7,930$. This is a high-reflux requirement. The cost of the consumption of $\sim 8 \times 10^3$ moles SO₂ per mole product is partly offset by the fact that H₂SO₄ is a more valuable commodity than SO₂. It is important to note that even though the cascade is tapered, the amount of reflux chemical required is unchanged from the “squared-off” cascade because reflux demand is proportional to interstage flow at the feed point. The principal advantage of tapering is that it results in much lower holdup of valuable enriched ¹⁵N, and a corresponding reduction in time to production from startup.

51.5.2 Dual Temperature Exchange: The GS Process

To avoid the high cost of chemical reflux, Geib (1946) and Spevack (1957) independently suggested a dual temperature process. Consider application to the H₂S/H₂O exchange known as the GS (Geib–Spevack, Girdler–Sulfide) process. The method exploits the fact that the isotope-exchange equilibrium constant is temperature-dependent. The scheme which results is illustrated in ▶ Fig. 51.7. Here the isotope of interest, D, concentrates in the liquid.



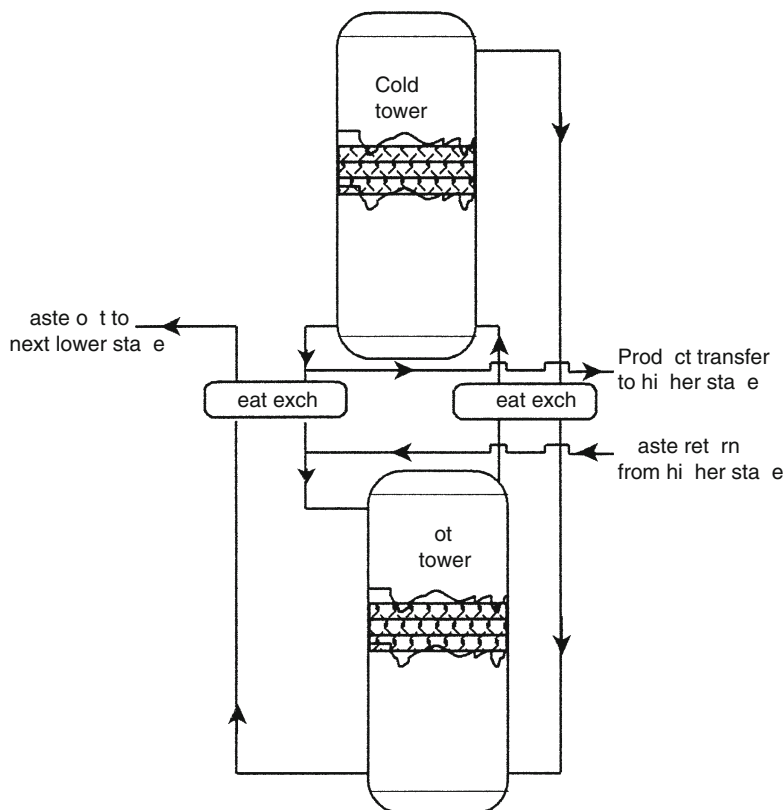
The feed (H₂O) is introduced at the top of a *cold tower* where it equilibrates in a countercurrent multiplate column against a gas stream (mostly H₂S). The D concentration builds toward its maximum at the bottom of the cold tower. The essential distinction between the GS process and standard chemical reflux is that in the GS process, the reflux is carried out thermally. The hot tower serves as refluxer for the cold tower. At the top of the cold tower, an intermediate point in the plant, the D content of the gas stream, u_g , is set by equilibration against the cold feed, the separation factor is α_c , $\alpha_c = [z_f/(1 - z_f)]/[u_g/(1 - u_g)]$. Next, that gas is introduced to the bottom of the hot tower where it equilibrates with the waste flow, $\alpha_h = [x_w/(1 - x_w)]/[u_g/(1 - u_g)]$. (The symbols have been defined in earlier sections.) The overall separation, S , in a stage containing both a hot and a cold tower is $S = \alpha_c/\alpha_h$. Notice that S is an effective separation factor.

Both the hot and cold towers contain a number of plates, so S is much larger than it would be for single equilibrations at the hot and cold temperatures. If the feed abundance is small, the fraction of isotope extracted can be approximated as $(1 - \alpha_h/\alpha_c)$. For the GS process (hot tower temperature = 138°C, $\alpha_h = 1.80$; cold tower temperature = 32°C, $\alpha_c = 2.32$) the recovery of deuterium is 0.224 fraction.

A very large industrial scale GS plant (100 kg/h 99.8% D₂O) operated by Ontario Hydro has been described in some detail by Rae (1978). The GS part of the plant consisted of three stages of hot/cold towers with a total enrichment from natural abundance to 20% D₂O. Each tower

■ Fig. 51.7

Schematic of dual temperature GS plant. First stage steel towers are ~7 m diameter, and 60 m high



contained a hot and cold section. Deuterium is carried forward to the second and third stages only in the gas phase. Any deuterium not extracted is returned to waste (Lake Huron) after removal of H_2S (i.e., there is an H_2S stripper to satisfy environmental regulations, but there is no deuterium stripping).

The plant tapers markedly between towers 1 and 2, and 2 and 3. Because deuterium recovery increases with increasing α_c/α_h , it might be supposed the hot tower should run at as high a temperature as possible, and the cold tower at as low a temperature as possible, and this would be so in the absence of complications. The selection of 30°C – 32°C for t_c is necessary in order to avoid precipitation of solid hydrate H_2S – H_2O . In GS pilot plant operations, freeze-ups regularly occurred until t_c was raised above 30°C . The optimum t_h , 130°C – 140°C , is determined by balancing the improvement in overall separation (S) as t_h increases against higher heating costs.

The discussion of the GS process will be closed with the comment that it is dangerous. A GS plant requires a large inventory of highly toxic H_2S , which is employed at elevated temperature and pressure in a corrosive environment. Safety of operating personnel and of the population in the area surrounding the plant is a major concern.

Bigeleisen (1958, 1969) has discussed the separation factors for a number of exchange reactions that involve hydrogen. The ones with the highest separation factors also have the largest temperature coefficients; see ► Fig. 51.8.

It is interesting to note that the GS process, which has one of the smallest separation factors of those shown, appears to be the most practical large-scale industrial process. That is because the kinetics of the exchange are favorable, even in the absence of a catalyst. That factor, combined with the further advantage that an abundant and cheap feedstock (water) is employed, and that the process is nonparasitic (i.e., not coupled to a large-scale production plant for some chemical commodity), accounts for the dominance of the GS method.

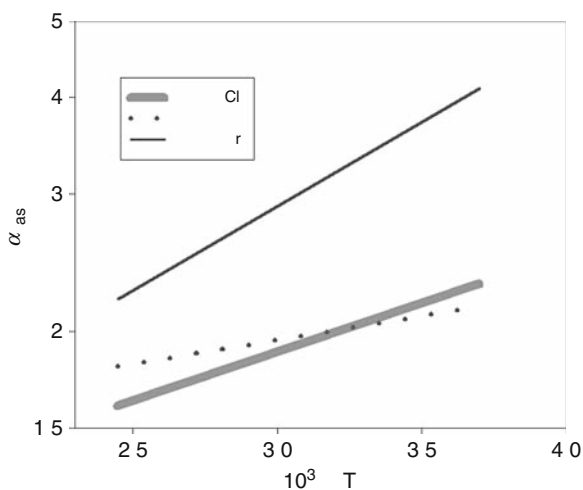
Even so, a good deal of effort has been applied to other systems that show larger separation factors. Could they be efficiently implemented, plant size and capital investment per product unit would drop significantly. To that end, Butler et al. (1978) described nonwetting catalysts that allow efficient H_2O –HD exchange. Delmas et al. (1969) reported work on amide catalyzed NH_3 /HD exchange at low temperature. Note that separation factor is ~ 8 at liquid ammonia temperatures. Galley (1983) has reviewed work on catalyzed exchanges between hydrogen and methyl amines. This process is designed to be parasitic on Haber–Bosch ammonia synthesis plants.

51.5.3 Distillation

Distillation is a countercurrent process in which equilibrium is maintained between liquid and vapor, normally in a vertical column containing packing, thin wetted walls, or bubble cap plates. The single-stage separation factor for distillation is given by the vapor pressure isotope effect.⁵ Because mixtures of isotopic molecules show little or no nonideality in either liquid or vapor phase (Jancsó et al. 1993), liquid vapor separation factors should be virtually independent of isotope enrichment (plate number), and the analysis of the distillation process is

■ Fig. 51.8

Semilog-plot of deuterium fractionation factor (α_{gas}) vs. the reciprocal of temperature for some compounds of hydrogen (Bigeleisen 1969)



simplified. In large-scale plants, however, there is usually an appreciable pressure drop along the column and thus a change in boiling temperature. In that case, α can no longer be assumed to be independent of plate number.

For most separations of interest the required enrichment usually cannot be managed using a single column and it is necessary to place several columns in series. This can be rather a convenience instead of an annoyance, since in that case the plant can be tapered at column interconnections.

The properties of a fractionating column that are important for isotope separation are (1) the throughput that determines production rate, (2) height equivalent per theoretical plate (HETP) that determines column length, (3) the hold-up per plate that determines plant inventory and time to production, and (4) the pressure drop per plate that should be as small as possible. The choice of a particular column is invariably a compromise between these factors. A voluminous literature concerning the design of columns, packings, and staging is available.

The energy consumption of a distillation plant is an important consideration. In the limit, as for any separative process, it is only necessary to introduce an amount of energy equivalent to the entropy of mixing, $E = T\Delta S_{\text{mix}} = RT[z_f \ln(z_f) + (1 - z_f) \ln(1 - z_f)]$. In practice, however, many irreversibilities arise. To approach the ideal value the column would have to be lengthened to infinity (for complete separation), the boil-up rate varied according to plate number, and the pressure drop made infinitesimally low. This is impossible. If, instead, one elects the common simplification of boiling all liquid in the pot, and condensing all vapor in the head, it follows that to separate one mole of component having abundance z_f from a mixture, at least $1/[z_f(\alpha - 1)]$ moles of the mixture must be boiled and recondensed, even if the column perfectly adiabatic (London 1961). Since the heat of vaporization of a liquid at its normal boiling point is typically $\sim 10RT$ (*Trouton's rule*) the quantity of heat put into the boiler and extracted from the condenser is $q \approx 10RT/[z_f(\alpha - 1)]$ per mole. To take a specific example, consider $^{14}\text{N}_2/^{14}\text{N}^{15}\text{N}$ separation by distillation with $\alpha = 1.0038$, $T = 78\text{ K}$, and $z_f = 0.0074$, in which case $q \approx 2.3 \times 10^8\text{ J/mol}$ of $^{14}\text{N}^{15}\text{N}$. This contrasts with the value of 28 J/mol for the perfectly reversible process. The difference is striking.

Even though the energy demand for distillation is many times the minimum reversible energy for separation, it is still small compared to the energy demand of most irreversible processes. On a laboratory scale the power costs of distillation are almost always low compared to the cost of building and operating the equipment. As the scale of operations increase, however, power costs become proportionally more important; this is because they rise approximately in direct proportion to production rate, but other costs increase more slowly. As a consequence at some point it becomes economic to consider staged columns employing vapor recompression and heat exchangers. In the best case, London suggests energy demand can be reduced significantly, perhaps by as much as a factor of ten. This is well worth a significant increase in capital cost and vapor recompression, or other energy-saving schemes should be (are) an essential feature of industrial-scale isotope separation distillation plants.

51.5.4 Specific Examples, Isotope Separation by Distillation

Distillation plants have been or are being operated for the separation of the following isotopes: (1) D by distillation of hydrogen, water, or ammonia; (2) ^{10}B by distillation of BF_3 or exchange distillation of BF_3 : ether complexes; (3) ^{13}C by distillation of carbon monoxide; (4) ^{15}N by

distillation of NO; (5) ^{17}O and ^{18}O by distillation of water or NO; (6) ^{22}Ne by distillation of neon; (7) ^{36}Ar by distillation of argon. There may be others not listed.

Single-stage factors, $\alpha = P'/P$, the prime referring to the lighter isotopologue, are given to good approximation by the vapor pressure ratios of the separated isotopologues, although there may be corrections for excess free energies of mixing in both liquid and vapor phases. Also, to good approximation, $\ln \alpha = A/T^2 - B/T$. The positive constant A is characteristic of each particular isotopologue pair, and B can be either positive or negative depending on the details of molecular interaction in the condensed phase (Jancsó and Van Hook 1974; see also [► Eq. \(15.22\) in Chap. 15, Vol. 2](#)). In certain cases, A and B may be available from theory or spectroscopic measurements. Most often it is advantageous to distill at as low a temperature as possible (except when B is positive and large, as it is for hydrocarbons). Of course, as temperature drops, so does vapor pressure, and at low enough temperature throughput falls to unacceptable values. It is impractical to design isotope production plants, even on a laboratory scale, for vapor pressures less than about 0.05–0.1 bar.

51.5.4.1 Hydrogen

Distillation of hydrogen for deuterium production is attractive because of the large vapor pressure isotope effect ($P(\text{H}_2)/P(\text{HD}) = 1.7$ at 21 K), although this is somewhat offset by corrections for liquid and vapor nonideality (Bigeleisen 1963). The production of D by distillation of hydrogen (parasitic to industrial-scale ammonia production) has been employed in moderate-sized plants (Galley 1983), but high concentrations of nitrogen and other impurities in ammonia synthesis gas introduce complications. A design of a hydrogen distillation unit was described by Clusius and Starke (1949). Natural hydrogen cooled to its dew point is fed to a primary tower where it is split into a bottom fraction of 5–10% HD and a top fraction of essentially pure H_2 . The bottoms are fed to a second tower where separation to nearly pure HD is completed. This intermediate product is warmed, and then fed to a catalytic exchanger where it disproportionates to the room temperature equilibrium mixture (in which the ratio of concentrations of H_2 , HD, and D_2 is 1:2:1), which is fed to the bottom of yet another distillation tower. Here the mixture fractionates to a top mixture of HD and H_2 , and a bottom product fraction that is essentially pure D_2 . The light fraction is fed to the top of tower 2 for recovery of HD. A 1983 report (Galley 1983) mentioned the Nangal, India, plant with an estimated capacity of 14 t/year of D_2O using this process.

A special problem that occurs in the distillation of hydrogen is the need to minimize the conversion of ortho to para hydrogen. At room temperature the equilibrium ortho/para ratio is close to 3, but that ratio drops rapidly with temperature, and at the boiling point (20 K) it is essentially zero. The reaction of ortho to para releases about 1.5 times the heat of vaporization. This would significantly increase power consumption if allowed to occur. The ortho–para reaction is catalyzed by paramagnetic and ferromagnetic materials, including oxygen and certain steels, and accordingly, these materials must be carefully excluded from the low-temperature portions of the equipment.

51.5.4.2 Carbon Monoxide

A plant for the production of ^{13}C via CO distillation was described by London (1961). CO is easy to distill. Its vapor pressure curve follows N_2 closely and liquid nitrogen can be used as

a convenient refrigerant. At the boiling point of nitrogen, 77.4 K, $(\alpha - 1)$ for $^{12}\text{C}^{16}\text{O}/^{13}\text{C}^{16}\text{O}$ is 0.0078 and for $^{12}\text{C}^{16}\text{O}/^{12}\text{C}^{18}\text{O}$ is 0.0057. At 72 K the vapor pressure is ~ 0.25 bar and the α values are 0.0096 and 0.0070, respectively (Jancsó and Van Hook 1974). This increase in α makes it well worthwhile to operate the plant at reduced pressure. The triple point of CO (68 K, 0.15 bar) establishes a lower limit for the operating temperature. Natural abundances of ^{13}C and ^{18}O are 1.1% and 0.2%, respectively.

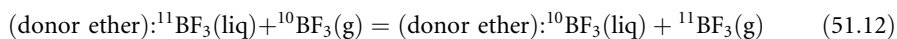
The CO distillation plant used a two-section vacuum-insulated column packed with wire gauze rings. The upper section was 5.2 m long with a diameter of 3.2 cm, the lower 4.6 m \times 1.9 cm. The column contained about 600 plates. An intermediate boiler re-evaporated part of the downward flowing liquid at the junction. Note that this plant accumulates product in the liquid and enriches toward the bottom. Enriched CO (0.4 g/day with $\sim 65\%$ ^{13}C content and 0.05 g/day with $\sim 5\%$ ^{18}O content) is withdrawn from the bottom of the column and converted to CH_4 and H_2O by catalytic reaction with hydrogen. Arrangements were made to automatically collect the contents of the different sections of the column in the event of power failure; the isotope inventory corresponded to about 2 months of production.

51.5.4.3 Nitrous Oxide

Macinteer et al. (1965, 1979, 1989) described production of ^{18}O , ^{17}O , and ^{15}N by low-temperature distillation of NO. The isotope effects are some three to five times larger than those for other diatomic molecules with similar boiling points. The large α values imply marked efficiencies. They reduce the number of plates required for a given separation and markedly decrease time to production. Even so, these advantages are offset in part by the relatively high cost of the feed material, and its chemical instability and toxicity. A theoretical analysis of NO separation factors established the fact that the abnormally large α values are due to the formation of dimers that are negligibly dissociated in the boiling liquid, but completely dissociated in the vapor (Bigeleisen 1960).

51.5.5 Exchange Distillation

Exchange distillation takes advantage of the fact that condensed phase–vapor phase separation factors can be enhanced (as compared to liquid–vapor factors) by association–dissociation equilibria in one or the other phase. A good example is found in $^{10}\text{B}/^{11}\text{B}$ separations. At the normal boiling point of 173 K, the vapor pressure isotope effect for BF_3 , $\ln \alpha \approx \ln [P(^{10}\text{BF}_3)/P(^{11}\text{BF}_3)] = -0.0075$, is sufficiently large for useful separation by distillation (Neetley et al., 1958). Compare this effect, however, with association–dissociation constants (K_{eq}) for reactions of the type



At the convenient operating temperature 298 K values for $\ln K_{\text{eq}}$ lie between 0.02 and 0.03 (Palko and Drury 1969). Obviously a distillation plant based on the larger separation factor, and operating at a more convenient temperature, promises superior performance.

51.6 Chromatography

Chromatography is a widely used separative process employing exchange between a stationary phase and a mobile fluid phase. It thus differs from distillation or liquid–liquid extraction that employs two mobile phases. There are a number of distinctly different chromatographic processes. If the moving phase is a vapor carried along in a stream of permanent gas and the stationary phase is a suitably supported liquid film, one speaks of *gas–liquid chromatography*. If, alternatively, the stationary phase is a solid of high absorptive capacity, one has *gas–solid chromatography*. If the moving phase is a solution at low concentration in a liquid solvent or a high-temperature–high-pressure fluid solvent of liquid or near-liquid density, one speaks of liquid chromatography, or super-critical fluid chromatography, as appropriate. In yet another mode, the stationary phase might be an ion-exchange resin and the moving phase an aqueous (or nonaqueous) solution. A general discussion of chromatography as applied to isotope separation has been given by Glueckauf (1961). Some years ago Van Hook (1969) reviewed the field of gas chromatographic isotope separation and more recently he commented on other chromatographic separations of isotopes (Van Hook 1985).

The essential feature of any chromatographic process is that it offers opportunity for multiple equilibrations between the mobile and stationary phases. By straightforward analogy with distillation where the single-stage separation factor is given by the vapor pressure isotope effect, one defines the single-stage chromatographic factor in terms of the equilibrium distribution coefficient between mobile and stationary phases. This accounts for one of the great advantages of chromatography, i.e., the possibility of tailoring the separation factor to fit the problem (within limits) by varying the chemical nature of the stationary phase, the solvent for the mobile phase, the temperature, etc.

Another advantage of chromatography is the fact that it offers columns containing large numbers of theoretical plates (in excess of 10^6 for gas chromatography, 10^5 or more for liquid elution chromatography). Therefore, it can achieve complete or substantially complete enrichments even for cases where separation factors are small enough to limit the applicability of other methods. Still, this advantage is offset by serious difficulties. In chromatographic experiments, a small amount of adsorbate (isotopic mixture in the present case) is placed on the first plate, or the first few plates, and subsequently washed through the chromatographic column using an eluent mobile phase. The more strongly adsorbed isotope lags the less strongly adsorbed one(s). As elution proceeds, separation increases, but so do band widths. The technical problem is to adjust conditions to optimize separation for given band broadening.

Throughout any chromatographic process it is easy to see that not all plates are carrying out separative work. In fact separation only takes place at the front and rear of the moving band. At any given instant, most of the column is empty of adsorbate. A direct comparison between the number of plates in chromatography, where there are a very large number indeed, but only a few of them are working at a given time, and the number in reflux distillation, where there are far fewer plates, but all are working, is inappropriate. It can even be misleading. Another important difficulty in chromatography is that band broadening and other diffusive inefficiencies increase dramatically (and nonlinearly) with column loading. The result, except in special cases, is that it is difficult to scale-up chromatographic separations to produce useful amounts of separated isotopes. Most often, chromatography is better suited to the analysis of isotopic mixtures than it is to the production of separated isotopes.

51.6.1 Gas Chromatography

To illustrate gas chromatography is chosen first. ▶ [Figure 51.9](#) shows an idealized chromatogram plotting detector response versus time. Here t_0 is time from injection to elution of inert nonadsorbed material, and t_1 and t_2 are retention times for components of interest. For difficult separations $t_0 \ll t_1 \approx t_2$. The resolution, R , between component bands is related to the band width (w), $R = (t_2 - t_1)/(2w)$, and the number of plates (assumed to be the same for both isotopes) is $n = 4(t/w)^2$.

The separation factor is $\alpha = t_2/t_1$, and the *Henry's Law* constant characterizing the equilibrium is $K_H = (V_c/V_g)(t/t_0 - 1)$. V_c and V_g are the volumes of condensed and vapor phases in the column (i.e., for gas-liquid chromatography, V_c is the volume of the liquid film on the supported packing or open tubular wall, and V_g the volume of void space, respectively. If the column is in the linear range (small loading), the resolution is given

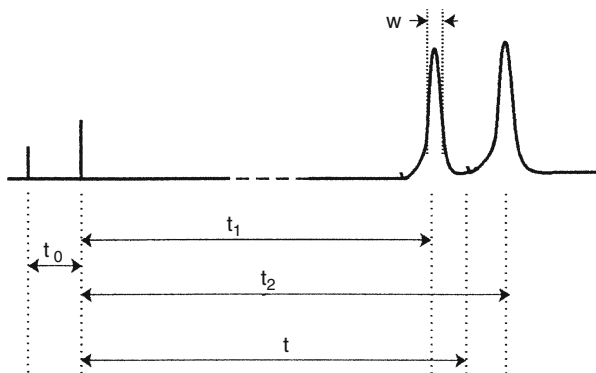
$$\frac{R^2}{t} = \frac{1}{16} \frac{V_g}{V_c} \frac{C}{K_H} \left(\frac{\alpha - 1}{\alpha} \right)^2 \quad (51.13)$$

where C is a constant characterizing the apparatus. ▶ [Equation \(51.13\)](#) can be employed to optimize the separation (see, e.g., Bruner et al. 1966; Matucha 1989). Usually, C , α , and K_H are temperature dependent, but α and K_H much more than C . Also, α most often increases as temperature falls according to $1/T$ or $1/T^2$ (Jancsó and Van Hook 1974), and K_H , $K_H \approx K_H^0 \exp(b/T)$, normally increases exponentially as temperature falls. These two criteria conflict for the best choice of temperature and it is necessary to determine the optimum compromise. With α and K_H set by the selection of operating system and temperature, resolution is proportional to V_g/V_c . For maximum resolution, the vapor volume is increased by electing open tubular columns, i.e., wetted wall columns with minimal liquid loading, and therefore minimal capacity. The result is the expected one.

Examples of gas chromatographic isotope separation are shown in ▶ [Figs. 51.10](#) and ▶ [51.11](#). The gas chromatographic trace of a separation of a mixture of protio and deuterio-acetylenes is shown in ▶ [Fig. 51.10](#) (Phillips and Van Hook 1967). The separation is interesting, all known preparations of these acetylenes lead to a disproportionated mixture of C_2H_2 , C_2HD ,

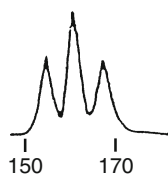
■ [Fig. 51.9](#)

An idealized chromatogram. The ordinate shows detector response, the abscissa is time



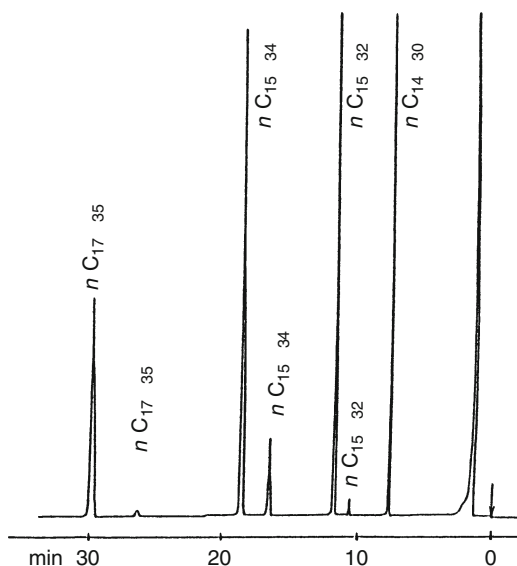
■ Fig. 51.10

Gas-liquid chromatographic separation of deuterated acetylenes at -78°C using triethyl-amine liquid phase supported on Chromosorb-P. Elution (min, left to right) is in the order C_2H_2 – C_2HD – C_2D_2 . The broadening is a consequence of strong amine-acetylene interaction (Phillips and Van Hook 1967)



■ Fig. 51.11

High-resolution gas-liquid chromatographic separation of perdeutero-perprotio *n*-alkanes on an open tubular fused silica column coated with cross-linked phenylmethyl-silicone (140°C , $0.5\ \mu\text{m}$ film, $\sim 1.5 \times 10^5$ theoretical plates); see Matucha (1989)



and C_2D_2 . Consequently, pure C_2HD can only be obtained by separation of the ternary mixture.

Distillation is inappropriate because the triple point lies above 1 atm, and not only is the compressed gas dangerous but it also tends to polymerize except when dilute. The authors attempted to scale-up chromatographic separation, but resolution deteriorated with column loading and the method was found to be impractical except for preparation of very small amounts of C_2HD .

■ **Table 51.8**

Gas chromatographic separation factors for C_2H_6/C_2D_6 for several different liquid phases on firebrick at two temperatures (Phillips and Van Hook 1966)

Column	Gas liquid separation factor, $\ln[(t(H)/t(D))]$	
	150 K	200 K
15% w/w acetaldehyde	0.03	0.01
33% w/w ethanol	0.06	0.07
15% w/w methylcyclopentane	0.08	0.10
Vapor pressure ratio, $\ln[P(C_2D_6)/P(C_2H_6)]$	0.065	0.075

► **Table 51.8** shows the dependence of gas–liquid chromatographic separation factors for C_2H_6/C_2D_6 on temperature and liquid phase. Significant differences are obtained by varying the polarity of the liquid loading of column substrate, and the temperature. The results clearly demonstrate that careful attention must be paid to both factors when optimizing chromatographic separations. ► **Figure 51.11** is an example of a more recent high-resolution separation using an open tubular liquid film capillary column. Again, it nicely demonstrates the power of gas chromatography for small-scale (analytical) separations.

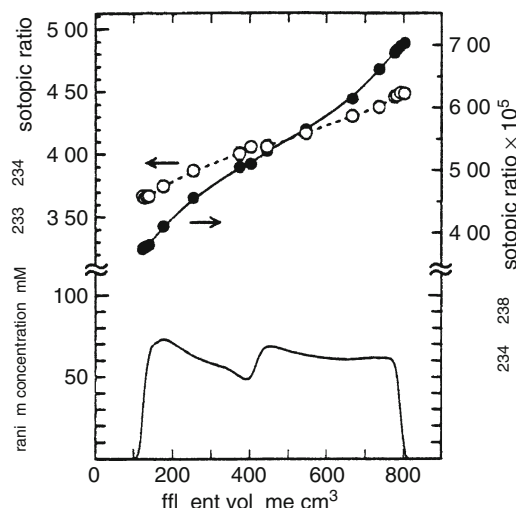
51.6.2 Isotope Separation by Redox Ion-Exchange Chromatography

Fujii and coworkers (Fujii et al. 1989; Nomura et al. 1996; Nakanishi et al. 1996) have reported on the use of anion redox chromatography applied to the U(IV)–U(VI) couple and utilizing Ti (III) as reducing agent and Fe(III) as oxidizing reagent to separate uranium isotopes. In an intensive development process, Asahi Chemical Industries in collaboration with Tokyo Institute of Technology refined the process enabling recovery of the reducing and oxidizing reagents (Sego 1992). This is an obvious requirement for practical implementation of this separation method. In a typical set of experiments (Nomura et al. 1996), a 0.1 M U(VI) solution in 3.6 M HCl was fed to a column packed with a highly porous strongly basic anion exchanger supported on 50 μ m porous silica beads to form a uranium adsorption band. The band was then eluted with a solution containing 3.5 M HCl, 0.6 M V(IV), a reducing reagent, and 1 M Fe (II), a catalyst for the U(VI)–U(IV) exchange. A cyclic process utilizing two 1 m columns was employed with intermittent addition of the redox reagents after each band pass. After a total migration of ~ 192 m, the uranium band, now 1.4 m long was extracted from the column and fractions collected for elemental and isotope ratio analysis. Results from one such experiment are shown in ► **Fig. 51.12**.

It is interesting to note that these data (amply confirmed with many additional experiments on uranium and other systems) show that the temperature dependence and the odd–even mass ratios of isotope-exchange fractionation factors of uranium and other metals differ significantly from the predictions of the well-established theory of isotope effects based on vibrational properties (Bigeisen and Mayer 1947). That observation, one of theoretical importance, has been shown to be a consequence of the large nuclear isotope field shifts found in the heavy elements. The field shifts introduce new mechanisms for understanding the

■ Fig. 51.12

Uranium concentration profile and isotope separation factors for a U(VI)–U(IV) sample eluted from an ion-exchange column; see text (Nomura et al. 1996)



physical basis of the unusual temperature dependences and large mass-independent isotope effects now well established in exchange equilibria of the heavy elements (Bigeleisen 1996).⁶

51.7 Photochemical and Laser Isotope Separation

The idea of using selectively absorbed radiation to effect isotope separation is an old one. Hartley et al. (1922) proposed synthesis of HCl from a mixture of H_2 and Cl_2 , where only one Cl_2 isotopologue would be photoexcited, then go on to react preferentially. The actual experiment, using white light filtered through natural chlorine, failed, but for the incidental reason that the reaction involves a lengthy chain mechanism, a fact not appreciated in 1922. A later photochemical experiment succeeded in separating mercury isotopes by exciting gas phase Hg atoms with light from a mercury arc made from a pre-separated mercury isotope. The method succeeded, first because mercury has a relatively simple spectrum with widely separated lines, and second because a monoisotopic light source was available.

The essential conditions for photochemical isotope separation are (1) the existence of a significant isotope shift in the absorption spectrum of the element or compound being irradiated (i.e., larger than the band width of the incident radiation), (2) a rapid reaction of the excited state that leads to production of some atom or molecule readily separable from the mixture, and (3) a light source with spectral band narrow enough to excite only one isotopic species, and intensity large enough to carry out that excitation efficiently. It was the invention of the laser that provided a convenient source of intense radiation of narrow band width and made photochemical isotope separation practical. The first laser isotope separation (on bromine) was reported in 1967 (Tiffany et al. 1967), and since that time, a large amount of development work has been carried out, and small-scale separations have been reported for

many elements. An enormous literature dealing with the theoretical and experimental aspects of laser pumped processes has developed. There will be made no effort to review this material but, below, the conceptual basis of laser isotope separation will be simply indicated in broadest outline.

51.7.1 Outline of a Laser Isotope Separation (LIS) Scheme

McAlpine and Evans (1985) divide any LIS scheme into five parts:

1. Exchange with bulk feed. Usually, it will not be possible to apply LIS directly to cheap bulk feed (e.g., water or methane for H/D separation), and the desired isotope must be chemically exchanged into a “working” molecule. If the isotope of interest is rare, it will be important that the working material be recyclable. Although step (1) involves conventional chemistry, its cost may dominate the overall LIS.
2. Selective excitation. The working molecule is irradiated with a laser tuned to a frequency that excites only the desired species.
3. Excited state molecules are converted to some new and isotopically enriched chemical species (molecules, free radicals, ions, etc.).
4. Capture of the secondary species before it converts to a form where enrichment will be lost by decay or exchange.
5. Final conversion of the secondary species to useful chemical or physical form.

Note that it is only in step (2), above, that technology based on laser physics is involved. Nonetheless in the overall LIS process each and every step is important, and may be critical. In the actual lasing step, it may be advantageous to employ long wavelength lasers because they have relatively good efficiency and low-energy cost per photon. An important parameter in step (2) is the photon efficiency, ε , which gives the fraction of absorbed photons that yield excited species containing the desired isotope. This is approximately

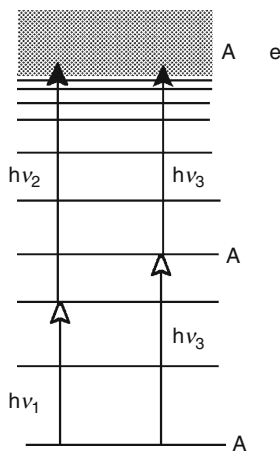
$$\varepsilon = \frac{1}{1 + \frac{1}{\delta S}} \quad (51.14)$$

S is the selectivity ratio for photon absorption under the experimental conditions, and δ is the relative abundance of the desired isotope. ▶ Equation (51.14) demonstrates, for example, that S values on the order of 10^3 are required before more than about 10% of photons are used to excite D in natural abundance H/D mixtures ($\delta \approx 1.5 \times 10^{-4}$). The selectivity required for uranium separation is less because $\delta(\text{D}) < \delta(^{235}\text{U})$, but in a real sense that is misleading because the density of spectroscopic states for molecules containing heavy atoms (or for the isolated atoms themselves) is orders of magnitude larger than for light species. Hence the spectroscopic requirements are much more difficult to implement.

Practical LIS schemes usually involve the absorption of more than one photon. It is convenient to refer to a schematic energy level diagram like the ones sketched in ▶ Fig. 51.13. Provided laser fluence is sufficiently high, a species will absorb enough photons to decompose if the pulse is sufficiently short so that collisions (which lead to deactivation) do not occur during the pulse. As the molecule absorbs photons, it is said to be “pumped” up the excitational ladder. In the low-energy region, the density of states is small and radiationless processes leading to deexcitation are slower than pumping. In this region, the states are isotopically well separated, and with proper laser tuning, the desired isotope is preferentially

■ Fig. 51.13

Two-photon photoionization using lasers of the same (*right*) or different frequency (*left*)



excited. As pumping continues, the level spacing decreases (in vibrational spectroscopy because of anharmonic effects, for example), and the laser becomes increasingly “off-resonance.”

This results in a drop or “bottle-necking” in pumping efficiency, but once this intermediate region is passed, the level density increases dramatically as dissociation is approached, and pumping efficiency once again increases. However, near dissociation, the level density for undesired species is also high, and in this region, pumping does not lead to isotope discrimination, but only to dissociation. Also, the high density of states near dissociation leads to an increase in the efficiency of radiationless decay and exchange, which may cause isotopic scrambling or recycling to the ground state. One finds that short pulse lasers of high fluence are necessary for efficient separations.

51.7.2 LIS of Deuterium

The ideas in the last section are nicely illustrated with one of the many LIS schemes proposed for H/D enrichment. The multiphoton dissociation of fluoroform, CHF_3 , will be considered first. Certain vibration/rotation bands of CHF_3 , CDF_3 , and CTF_3 are spectroscopically well separated, and selective excitation of the heavier isotopologue is practical. For $\text{CDF}_3/\text{CHF}_3$ the selectivity is greater than 2×10^3 when a CO_2 laser is tuned to the ν_5 *R* branch in the vicinity of 980 cm^{-1} . Dissociation occurs primarily via the reaction, $\text{CDF}_3 \rightarrow \text{CF}_2 + \text{DF}$. Heads enrichment as high as 2×10^4 have been reported (Herman and Mailing, 1980) and there is little or no anharmonicity bottle-necking. Because of the high cost of CHF_3 , recycling would have to be incorporated into any practical process. A possibility is the exchange, $\text{CHF}_3 + \text{HDO} \rightarrow \text{CDF}_3 + \text{H}_2\text{O}$, but without a catalyst this reaction is too slow to be practical. The overall economics of LIS H/D enrichment will be determined by the details of the feedstock and exchange reaction selected (Bigeisen et al. 1983).

An alternative LIS scheme is one in which a vibrationally excited molecule reacts preferentially with another species. An example is the hydrogen halide–olefin addition reaction, $\text{HX}^* + \text{R}_1\text{R}_2\text{C} \rightarrow \text{CH}_2=\text{R}_1\text{R}_2\text{CXCH}_2\text{D}$ (Mailing et al. 1978). The reaction involves sequential

absorption of several quanta from a CO₂ laser near 5 μm which selectively excites DX to a vibrational quantum number of 3 or more. Successful implementation of this scheme would be expensive because of the highly corrosive nature of the halogen acids.

51.7.3 LIS for Uranium

Uranium isotope enrichment by LIS has been exhaustively studied and the conceptual outlines of two separate programs have made their way into the open literature. These methods are multiphoton dissociation of UF₆ and LIS of monatomic uranium vapor (atomic vapor laser isotope separation, or AVLIS). AVLIS was selected by the United States DOE as the process to be used in its separation plants during the 1980s and 1990s, but, once again due to the present oversupply of separated uranium, the plant has recently been closed.

51.7.3.1 AVLIS

The spectrum of uranium metal vapor is complex with over 3×10^5 lines in the visible region. Still, many of these are very sharp and show sufficient isotope separation to permit selective excitation. The basic idea of AVLIS is to irradiate uranium metal vapor at a concentration around 10^{13} atoms cm^{-3} (higher concentrations destroy the separation due to collisional broadening). Uranium is a refractory metal, and vaporization is difficult. Electron bombardment under high vacuum yields an atomic beam that passes through the laser radiation field where ^{235}U is selectively excited.

The isotope shift $^{235}\text{U}/^{238}\text{U}$ is only $\sim(1/5) \times 10^4$ and it is necessary to select a very narrow ^{235}U line, and to carry the ionization process out in two steps (because line widths in the ionization region are broad and hence not selective). In the first step ^{235}U is excited from its ground state to some state well below the 6.18 eV ionization potential. That is followed by a less-selective absorption into the ionization continuum (using another laser). The ionized uranium atoms are then swept to a charged plate and collected. Even though selectivity is high, Benedict, Pigford, and Levi writing in 1981 state that the charge exchange that occurs during atomic collisions deflects enough ^{238}U to the collector to lower the heads enrichment factor to about 10. At that time, the single-stage product of $\sim 6\%$ ^{235}U was the highest yet obtained from natural abundance uranium. Presumably enrichment factors have now improved. Even for the earlier figure, however, nearly complete stripping of ^{235}U was claimed. This is a valuable feature because the feed is expensive. In summary, AVLIS has a sufficient single-stage enrichment factor to produce uranium of high enough ^{235}U content to power light water reactors. Furthermore, because AVLIS is an excellent stripper, it can be used to produce 2–3% ^{235}U from the large stockpile of tails now available from earlier gaseous diffusion or gas centrifuge separations. This confers an additional economic advantage.

51.7.3.2 LIS of UF₆

Although UF₆ has a conveniently high vapor pressure at room temperature, its absorption spectrum is much more complex than that of the metal because of the large number of vibrational and rotational states superposed on each electronic state. Moreover, at room temperature these bands are broadened sufficiently to preclude selective absorption.

However, if the molecules are cooled, the population of thermally excited vib-rot states falls drastically and the spectrum simplifies. Thus, at 77 K, 69% of UF_6 is in its lowest vibrational state, and this increases to 85% at 55 K. However, the vapor pressure is untenably low at such temperatures (7×10^{-3} Pa at 77 K), and equilibrium cooling is out of the question. Still by cooling in a nonequilibrium expansion nozzle, uranium vapor concentration can be kept at a useful level and LIS is possible. None of this changes the fact that molecular LIS was abandoned in favor of AVLIS.

51.8 Other Isotope Separation Processes

A number of other processes for separating isotopes are documented. A partial list includes membrane pervaporation, thermal diffusion of liquids, mass diffusion, electrolysis and electro migration, differential precipitation, solvent extraction, biological microbial enrichment, and more. Although not discussed in this chapter, some are suitable for small-scale laboratory separations, and others have been applied on reasonably large scale to D/T, H/T, and $^6\text{Li}/^7\text{Li}$ and presumably to other pairs of isotopes.

51.9 Editors' Notes

1. Isotopic molecules – or isotopologues – mean molecules of the same compound that only differ in isotopic composition. Related terms such as isotopomers are explained in [▶ Sect. 15.1 of Chap. 15, Vol. 2](#), on “Isotope Effects,” a topic closely associated with isotope separation (p. 2371).
2. The Author uses the terms “separation unit,” “separative unit,” and “separating unit” interchangeably (p. 2372).
3. The GS process is described in [▶ Sect. 51.5.2](#). See also [▶ Fig. 51.7](#) (p. 2385).
4. See [▶ Sect. 15.4 in Chap. 15 of Vol. 2](#) on “Isotope Effects” (p. 2386).
5. See the theory of vapor pressure isotope effect in [▶ Sect. 15.5.1, Chap. 15, Vol. 2](#) (p. 2389).
6. See more about mass-independent isotope effects in [▶ Sect. 15.8 of Chap. 15, Vol. 2](#) (p. 2397).

References

- Beams JW (1938) *Rev Mod Phys* 10:245
- Benedict M, Pigford M, Levi HW (1981) *Nuclear chemical engineering*, 2nd edn. McGraw Hill, New York
- Bigeleisen J (1958) *Proceedings of the international symposium on isotope separation*. Amsterdam, North Holland, p 121
- Bigeleisen J (1960) *J Chem Phys* 33:1775
- Bigeleisen J (1963) *J Chem Phys* 39:769
- Bigeleisen J (1969) *Adv Chem Ser* 89:1
- Bigeleisen J (1996) *Proc Natl Acad Sci USA* 93:9393
- Bigeleisen J, Mayer MG (1947) *J Chem Phys* 15:261
- Bigeleisen J, Hammond WB, Tuccio S (1983) *Nucl Sci Eng* 83:473
- Bruner F, Cartoni GP, Liberti A (1966) *Anal Chem* 38:298
- Butler JP, Rolston JA, Stevens WH (1978) *ACS Symp Ser* 11:93
- Chapman S (1916) *Proc Roy Soc Ser A* 216:279
- Clusius K, Dickel G (1938) *Naturwissenschaften* 26:546
- Clusius K, Starke K (1949) *Z Naturforsch* 4A:549
- Cohen K (1951) *The theory of isotope separation*. McGraw Hill, New York

- Delmas R, Courvoisier P, Ravoire J (1969) *Adv Chem Ser* 89:25
- Enskog D (1911) *Z Physik* 12(56):533
- Fenske MR (1932) *Ind Eng Chem* 24:482
- Fujii Y, Nomura M, Okamoto M, Onitsuka H, Kawakami F, Takeda K (1989) *Z Naturforschung* 44A:395
- Galley MR (1983) Future trends in heavy water production, AECL # 7547
- Geib E (1946) See Clusius K et al *Fiat review of German science (1939–1946)*, Physical Chemistry.
- Glueckauf E (1961) In: London H (ed) *Separation of isotopes*. George Newnes, London, p 209
- Habs D et al (2000) *Hyperfine Interact* 129:43
- Hartley H, Pondon AO, Bowen EJ, Merton TR (1922) *Phil Mag* 43:430
- Herman IP, Mailing JB (1980) *J Chem Phys* 72:516
- Jancsó G, Van Hook WA (1974) *Chem Rev* 74:689
- Jancsó G, Rebelo LP, Van Hook WA (1993) *Chem Rev* 93:2645
- Jones RC, Furry WH (1946) *Rev Mod Phys* 18:151
- Kistemaker J, Bigeleisen J, Nier AOC (1958) *Proceedings of the international symposium on isotope separation*. North Holland, Amsterdam
- Kugler E (2000) *Hyperfine Interact* 129:23
- Lindemann FA, Aston FW (1919) *Phil Mag* 37:530
- London H (ed) (1961) *Separation of isotopes*. George Newnes, London
- Macinteer BB, Potter RM (1965) *Ind Eng Chem Process Des Dev* 4:35
- Macinteer BB, Armstrong DE, Mills TR, Montoya E (1979) In: Klein ER, Klein PL (eds) *Proceedings of the 3rd international conference on stable isotopes*. Academic, New York, p 175
- Macinteer BB, Mills TR, Garcia MG, Vandervort RC (1989) *Sep Sci Technol* 24:415
- Mailing JB, Simpson JR, Miller MM (1978) *ACS Symp Ser* 68:134
- Matucha M (1989) *Chromatographia* 27:552
- McAlpine RD, Evans DK (1985) *Adv Chem Phys* 60:31
- Nakanishi T, Higuchi N, Nomura M, Aida M, Fujii Y (1996) *J Nucl Sci Technol* 33:341
- Neetley PT, Cartwright DK, Kronberger H (1958) *Proceedings of the international symposium on isotope separation*. Amsterdam, North Holland, p 385
- Nomura M, Higuchi N, Fujii Y (1996) *J Am Chem Soc* 118:9127
- Palko AA, Drury JS (1969) *Adv Chem Ser* 89:40
- Phillips JT, Van Hook WA (1966) *J Phys Chem* 70:1515
- Phillips JT, Van Hook WA (1967) *J Chromatography* 30:211
- Rae HK (ed) (1978) *Separation of hydrogen isotopes*, vol 68, ACS symposium series., p 134
- Rayleigh L (1902) *Phil Mag* 4:51
- Sego M (1992) *Bull Res Lab Nucl React* 1:176
- Spevack JS (1957, 1959) US Patent #2,787,526, #2, 895, 803
- Spindel W (1975) *ACS Symp Ser* 11:77
- Spindel W, Ishida T (1990) *Isotope separation*. In: Lerner RG, Trigg GL (eds) *Encyclopedia of physics*, 2nd edn, VCH, New York
- Taylor TI, Spindel W (1958) *Proceedings of the international symposium on isotope separation*. Amsterdam, North Holland, p 158
- Tiffany WB, Moos NW, Schawlow AL (1967) *Science* 157:40
- Van Hook WA (1969) *Adv Chem Ser* 89:99
- Van Hook WA (1985a) *J Chromatography* 328:333
- Van Hook WA (1985b) *J Liquid Chromatog* 8:2699
- Vértés A, Kiss I (1987) *Nuclear chemistry*, Chap 11. Akadémiai Kiadó, Budapest
- Villani S (1976) *Isotope separation*. American Nuclear Society, Hinsdale

52 Solvent Extraction and Ion Exchange in Radiochemistry

G. Skarnemark

Chalmers University of Technology, Göteborg, Sweden

52.1	<i>Introduction</i>	2404
52.1.1	Solvent Extraction Theory	2405
52.1.2	Extraction Systems	2407
52.1.3	Equipment	2408
52.1.4	Ion-Exchange Theory	2409
52.1.5	Equipment	2410
52.2	<i>Solvent Extraction and Ion Exchange in Small-Scale Nuclear Chemistry</i>	2410
52.2.1	Nuclide Production	2410
52.2.2	Isolation of Exotic Radionuclides	2411
52.2.3	Studies in Complex Chemistry	2414
52.2.4	Studies of Plutonium Speciation	2415
52.2.5	On-Line Determination of Iodine Speciation in Reactor Water	2416
52.2.6	Radioanalytical Chemistry	2417
52.2.7	Production of ^{234}Th Tracer	2421
52.2.8	Production of ^{239}Np Tracer	2421
52.3	<i>Solvent Extraction and Ion Exchange in the Nuclear Industry</i>	2422
52.3.1	Uranium Production	2422
52.3.2	Thorium Production	2422
52.3.3	Uranium Isotope Enrichment	2422
52.3.4	Reprocessing of Nuclear Fuel	2423
52.3.5	Partitioning and Transmutation	2424
52.3.6	Water Clean-Up in Nuclear Power Stations	2425
52.3.7	Final Storage of Radioactive Waste	2425
52.4	<i>Acronyms</i>	2426

Abstract: In 1805, Bucholz extracted uranium from a nitric acid solution into ether and back-extracted it into pure water. This is probably the first reported solvent-extraction investigation. During the following decades, the distribution of neutral compounds between aqueous phases and pure solvents was studied, e.g., by Peligot, Berthelot and Jungfleisch, and Nernst. Selective extractants for analytical purposes became available during the first decades of the twentieth century. From about 1940, extractants such as organophosphorous esters and amines were developed for use in the nuclear fuel cycle. This connection between radiochemistry and solvent-extraction chemistry made radiochemists heavily involved in the development of new solvent extraction processes, and eventually solvent extraction became a major separation technique in radiochemistry. About 160 years ago, Thompson and Way observed that soil can remove potassium and ammonium ions from an aqueous solution and release calcium ions. This is probably the first scientific report on an ion-exchange separation. The first synthesis of the type of organic ion exchangers that are used today was performed by Adams and Holmes in 1935. Since then, ion-exchange techniques have been used extensively for separations of various radionuclides in trace as well as macro amounts. During the last 4 decades, inorganic ion exchangers have also found a variety of applications. Today, solvent extraction as well as ion exchange are used extensively in the nuclear industry and for nuclear, chemical, and medical research. Some of these applications are discussed in the chapter.

52.1 Introduction

The origin of solvent extraction is shrouded in mystery, but the method might have been used already by the Persian alchemist al-Razi who is believed to have used extraction to separate metals (Al-Razi ~900, Heym 1938).

In 1805, almost a century before radioactivity was discovered, Bucholz extracted uranium from a nitric acid solution into ether and back-extracted it into pure water (Bucholz 1805). In his pioneering work, Bucholz performed extraction as well as strip and he concluded that the degree of extraction depends on the phase volume ratio as well as the salt concentration in the aqueous phase. His work was not only the first well-documented solvent extraction experiment but also, in fact, the first application to radiochemistry. During the following decades, the distribution of several neutral compounds between aqueous phases and pure solvents was studied experimentally as well as from a theoretical point of view (Peligot 1842; Berthelot and Jungfleisch 1872; Nernst 1891). Selective extractants for analytical separation of several elements became available during the first decades of the twentieth century. Between 1940 and the early 1950s, extractants like organophosphorous esters and amines were developed for use in the nuclear fuel cycle. This connection between radiochemistry and solvent extraction chemistry made radiochemists heavily involved in the development of new solvent extraction processes, and eventually solvent extraction became a major separation technique in radiochemistry.

The first description of an ion-exchange separation may be the passage in Exodus, where Moses purified the brackish water of Marah with a piece of wood (Exodus). Another ancient reference to the use of ion exchangers is given by Aristotle, who described that seawater loses its salt contents if it is passed through certain types of sand (Aristotle ~330 BC).

About 150 years ago it was observed that soil can remove potassium and ammonium ions from an aqueous solution and release calcium ions (Thompson 1850; Way 1850). This is probably the first scientific reference to an ion-exchange separation. Surprisingly, the discovery

of Thompson and Way antedates the ionic dissociation theory (Arrhenius 1887) that explains the chemistry behind the ion-exchange process. The first synthesis of the type of organic ion exchangers that are used today was reported by Adams and Holmes (1935). Since then, ion-exchange techniques have been used extensively for separations of various radionuclides in trace as well as macro amounts. During the last 4 decades, inorganic ion exchangers like manganese dioxide and hydrated antimony pentoxide have also found a variety of applications.

Extensive information about solvent extraction and ion exchange can be found, e.g., in refs. Rydberg et al. (1992), Walton and Rocklin (1990), Harland (1994), and Moyer (2009).

52.1.1 Solvent Extraction Theory

The simplicity, speed, and versatility of solvent extraction make it an excellent radiochemical separation method. Even simple equipment like a test tube or a separation funnel allows radiochemists to perform elaborate studies within a few minutes. The method works for a wide concentration range, from the rather concentrated solutions in uranium production or nuclear fuel reprocessing to one-atom-at-a-time separations of the heaviest elements.

According to International Union of Pure and Applied Chemistry (IUPAC; Rice et al. 1993), the definition of *solvent extraction* is “the process of transferring a substance from any matrix to an appropriate liquid phase.” If the substance is initially present as a solute in an immiscible liquid phase, the process is synonymous with *liquid–liquid extraction*. In the following, IUPAC nomenclature (Rice et al. 1993) will be used if not otherwise stated. The solutes discussed in this chapter are usually metal ions or, in some cases, acids. As liquid phases only aqueous and organic phases will be considered, although other types of liquid–liquid systems exist as well, e.g., molten salts or liquid metals.

Most inorganic species are only slightly soluble in inert organic solvents. Consequently, the extraction can occur only through interaction with an organic molecule, the *extractant*. The organic phase sometimes consists of a pure extractant, but more commonly, the extractant is dissolved in an inert organic *diluent*. In industrial extraction, the diluent is often a hydrocarbon-like kerosene or toluene. In small-scale extraction a variety of diluents is used, e.g., chloroform, carbon tetrachloride, and many others. The extractant is defined as “the active component(s) primarily responsible for transfer of a solute from one phase to the other” (Rice et al. 1993), but usually the word denotes all components of the solvent that are involved in the extraction. Usually the term “extraction” is reserved for the transfer from an aqueous to an organic phase, while the opposite transfer direction is called *strip* or *back-extraction*.

As mentioned above, solvent extraction is based on the distribution of a solute between two immiscible phases. Gibbs’ phase rule (Gibbs 1876) can be applied, namely:

$$P + F = C + 2 \quad (52.1)$$

where P is the number of phases, F the number of degrees of freedom, and C the number of components. Thus, a system consisting of two immiscible solvents and one solute distributed between them has one degree of freedom at constant temperature and pressure. Consequently, if the solute concentration in one phase is constant, the concentration in the other phase is also constant. The relationship between these concentrations led to Nernst’s distribution law (Nernst 1891). This law can be expressed as

$$k_d = \frac{c_{\text{org}}}{c_{\text{aq}}} \quad (52.2)$$

where c_{org} is the concentration of an extractable species in the organic phase and c_{aq} the concentration in the aqueous phase. Thus, k_d , referred to as the distribution factor, is dimensionless. From ▶ Eq. (52.2) it follows that the distribution factor does not depend on the total solute concentration or the phase volumes. Nernst proved that his equation was valid for a number of organic acids, if taking dimerization and dissociation into account. A decade later, Morse extended the validity of Nernst's equation to metal salts (Morse 1902).

It is also possible to derive the Nernst distribution law from thermodynamic considerations using the concept of free energy (Lewis and Randall 1923). At equilibrium, the chemical potential of a solute X has to be the same in the aqueous and the organic phase, i.e.,

$$\mu_X(\text{aq}) = \mu_X(\text{org}) \quad (52.3)$$

For each phase $\mu_X = \mu_X^0 + RT \ln a_X$, which gives

$$\mu_X^0(\text{aq}) + RT \ln a_X(\text{aq}) = \mu_X^0(\text{org}) + RT \ln a_X(\text{org}) \quad (52.4)$$

In this equation μ_X^0 is the standard chemical potential in the (given) phase and a_X is the chemical activity of X. It is defined as

$$a_X = f_X[X] \quad (52.5)$$

where f is the activity coefficient.

If ▶ Eq. (52.5) is combined with ▶ Eq. (52.4) the result can be written

$$\frac{a_X(\text{org})}{a_X(\text{aq})} = e^{[\mu_X^0(\text{aq}) - \mu_X^0(\text{org})]/RT} = K_d \quad (52.6)$$

K_d is sometimes called the thermodynamic partition ratio. It is related to the concentration partition ratio via the ratio between the activity coefficients, i.e.,

$$k_d = K_d \cdot \frac{f_X(\text{aq})}{f_X(\text{org})} \quad (52.7)$$

The expressions given for k_d and K_d are valid if there is only one species that distributes between the phases. Usually the situation is more complicated; e.g., in metal ion extraction, the metal can be present in the aqueous phase as free metal ion as well as positive, neutral, or negative complexes. In the organic phase, it is present as an uncharged complex. For such cases, the *distribution ratio* is used. It is abbreviated D and it is defined as:

$$D = \frac{c_{\text{org}}}{c_{\text{aq}}} \quad (52.8)$$

where c_{org} is the total analytical concentration of, e.g., a metal in the organic phase and c_{aq} the corresponding total analytical concentration in the aqueous phase. D is easy to determine by radiometric methods since it is equal to the ratio between the specific activities of the phases. This is one reason why liquid–liquid extraction is a common method in radiochemistry.

The extracted fraction of an element can be calculated using the expression

$$\%E = \frac{D\Theta}{(1 + D\Theta)} \cdot 100 \quad (52.9)$$

where $\Theta = V_{\text{org}}/V_{\text{aq}}$

Another useful definition is that of the *separation factor*, SF_{AB} , between the elements A and B in a liquid–liquid system. It is simply defined as

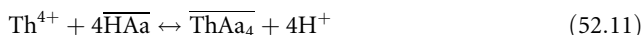
$$SF_{AB} = \frac{D_A}{D_B} \quad (52.10)$$

52.1.2 Extraction Systems

There are four major types of extraction systems that can be used for separation procedures:

Extraction of simple inorganic compounds can be exemplified by the classical distribution of iodine between water and carbon tetrachloride or by the extraction of, e.g., RuO_4 , OsO_4 , or AsI_3 into an organic solvent. Such extraction procedures are usually rapid, selective, and well suited for radiochemical separations.

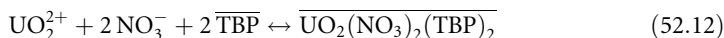
A metal ion, M^{v+} , may also form a complex with an organic anion A^- to form a neutral, hydrophobic complex MA_v . The organic reagent often is an acid, HA, and the anion A^- a bidentate chelating agent. The mechanism is therefore often referred to as *chelate extraction*. An example is the extraction of thorium with acetylacetone, HAa:



In this case, the bidentate ligand saturates the eight coordination sites of thorium, i.e., the complex contains no water at all. This makes it hydrophobic and gives high D values.

Chelate extraction was used more than a century ago (Cazaneuve 1900). Many of the important chelating agents were developed during the first half of the twentieth century, e.g., cupferron (Bandish and Fürst 1917), dithizone (Fischer 1933, 1934), and thenoyltrifluoroacetone (Reid and Calvin 1950). Many of these extractants are important in analytical chemistry since they provide a possibility to perform extremely selective separations and preconcentrations.

Another possibility to extract a metal ion is to replace its hydrate water by a *solvating* reagent. This makes the metal species less hydrophilic and it can be transferred to an organic phase. The solvating reagent can be the organic phase or it can be dissolved in a diluent. A well-known example is the extraction of uranium by tri-*n*-butyl phosphate from nitric acid:



Solvate extraction, which is also known as adduct extraction, became really important during the Manhattan Project when there was a need to produce uranium, plutonium, and other elements. Thus, tri-*n*-butyl phosphate was introduced for uranium and plutonium extraction (Flanary 1956). Trioctylphosphine oxide and bis-2-ethylhexyl phosphoric acid were also developed at this time (Mason and Peppard 1963; Siddall 1959; McKay 1956). These reagents are used not only in the nuclear fuel cycle but also for production of lanthanides and many other metals.

As discussed in [Sect. 52.3.5](#), the extractants now developed for actinide partitioning in partitioning and transmutation processes employ the solvate-extraction mechanism.

In *ion pair extraction* the concentration of the inorganic anion L^- is high enough to form the complex $\text{ML}_n^{(v-n)-}$. This complex usually is an inner sphere complex that is more weakly hydrolyzed than the uncomplexed metal ion. It can therefore be extracted as an ion pair with the organic cation Q^+ . Metal anions like TcO_4^- and ReO_4^- can, of course, be extracted without any extra inorganic anions. Q often is a primary, secondary, or tertiary amine or a quaternary

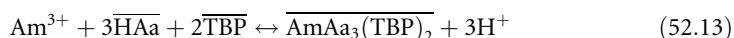
ammonium salt. These types of extractants are often referred to as liquid ion exchangers because of the similarity between the ion-pair formation process and an ion-exchange process. Negatively charged ion-pair extractants (e.g., sulfonic acids) that directly extract metal ions also exist. They are not, however, of great importance because of their poor selectivity.

Cationic alkylamine extractants were introduced in 1948 (Smith and Page 1948) for uranium production on an industrial scale. A few years later similar reagents based on phosphorous or arsenic, e.g., tetraphenylphosphonium and tetraphenylarsonium cations were introduced (Tribalat 1949). Today tertiary amines like trioctylamine extractants play a very important role in uranium production. Amines and quaternary ammonium salts are also used for production of many other metals, e.g., rare earth metals.

Ionic liquids are somewhat related to ion-pair extractants but they might nevertheless be regarded as a separate class of extractants. An ionic liquid is a salt that forms a stable liquid. In recent years, ionic liquids with melting point below 100°C, also called room temperature ionic liquids or RTIL, have been of great interest for separations. In the nuclear industry, RTIL are of interest as potential extractants of, e.g., uranium and lanthanides as well as useful fission products such as palladium, rhodium, and ruthenium. An example of such a reagent is protonated betaine bis(trifluoromethanesulfonyl) imide that has been used to separate the uranium oxides UO_3 , UO_2 , and U_3O_8 from each other (Jagadeeswara Rao et al. 2008)

There are also other types of extractants such as *crown ethers* that have a ring structure that fits an atom with a certain ionic radius, thus forming a hydrophobic and extractable species. These reagents have been used, e.g., for isolation of cesium and strontium. Many extractants also combine several of the mechanisms mentioned above.

Sometimes a mixture of two extractants gives a higher distribution ratio than the extractants separately. This is referred to as *synergy*. The reason for synergy is that one extractant neutralizes the charge of the metal ion while the other replaces remaining hydrate water molecules, e.g.,



52.1.3 Equipment

Small-scale solvent extraction is often done batchwise in separation funnels or test tubes. However, for more elaborate extraction studies and industrial processes continuous extraction is usually preferred. All continuous solvent extraction equipment consists of a *mixer* for phase contact and mass transfer and a *separation part* for phase disengagement. The main types of continuously working apparatus are:

- *Mixer-settlers*: stepwise phase contactors with conditions close to equilibrium in each step and pure outgoing phases.
- *Columns*: differential phase contactors without equilibrium in each step (“bottom”) and continuous phase contact without total phase disengagement.
- *Centrifuges and centrifugal extractors*: usually no equilibrium and phase disengagement in a centrifugal field.

Mixer-settlers consist of a mixing chamber, usually with an impeller that also pumps the liquid through the system, and a separation chamber in which the phases are separated by gravity. The size ranges from laboratory equipment with a volume of a few milliliters per step to

industrial settlers with a volume of several thousand cubic meters. The main advantages of mixer-settlers are that they are easy to construct, cheap, easy to run, need very little service, have well-defined steps, and also that it is easy to add more steps to an existing facility. The disadvantages are that they contain a large organic phase volume (= high capital costs) and also that it takes a rather long time to reach steady-state after start-up of the plant. On the other hand steady-state is not destroyed if halting the system, i.e., restart is very simple. In the nuclear industry, the large volumes make mixer-settlers less suitable for elements that may cause criticality problems.

Columns are either dynamic (e.g., pulse columns) or static, i.e., without mechanical mixing of the phases. The size and capacity cover a wide range, from a few centimeters diameter and about 50 cm length to 4 m diameter and 60 m height. The main advantage of columns is that a large number of steps can be contained in one column. The disadvantages are that they are more difficult to design and scale-up than mixer-settlers and also that they are sensitive to load variations and crud (e.g., solid particles in the solutions). They cannot be halted without losing steady-state and it is also impossible to add more steps once the column has been constructed. An advantage in the nuclear industry is that it is easy to construct columns that are safe against criticality (the maximum volume is well defined) provided that the concentration of fissile material is kept within the design limits.

Centrifuges or centrifugal contactors are used when rapid phase disengagement is necessary to prevent chemical or radiolytical degradation of an extractant or an extracted compound. They are also an attractive alternative if the requirements on the phase purity are high. The liquid holdup volumes are often small, and therefore this type of equipment is also suitable if expensive reagents are used. The difference between a centrifuge and a centrifugal contactor is mainly that the centrifuge has an external mixer and each centrifuge is one well-defined step, while a centrifugal extractor has internal mixing and several steps integrated within one unit. The advantages of centrifuges and centrifugal extractors are that they have high capacity despite their rather small volumes and that they give a good and rapid phase separation. The disadvantages are that they are mechanically complicated, difficult to scale up or down and sensitive to solid entrainment. Centrifuges are used for nuclear science but not very much in the nuclear industry. This may change in the future, when partitioning and transmutation processes may require extraction with short contact times to avoid problems with radiolysis.

Practically all of the industrial extraction processes are run in the counter-current mode, i.e., the fresh solvent meets an aqueous solution that has already been through all extraction steps except the last one. In such a counter current battery the fraction of the element of interest that remains in the aqueous phase is

$$\varphi_n = \frac{P - 1}{P^{n+1} - 1} \quad (52.14)$$

where P is the *extraction factor* ($P = D \cdot \Theta$; Θ is the phase volume ratio) and n = the number of steps. The extracted fraction is

$$\psi_n = 1 - \varphi_n \quad (52.15)$$

52.1.4 Ion-Exchange Theory

Ion-exchange resins are either cation or anion exchangers. The former group may be classified as strong, moderate, or weak acid cation exchangers, while the anion exchangers are classified

into weak and strong base exchangers. There are also other types of ion exchangers, e.g., chelating resins and bifunctional resins. A typical ion exchanger consists of functional groups attached to a polymer matrix. As an example, a strong acid type cation exchanger typically consists of sulfonic acid groups bound to a cross-linked polystyrene matrix. The exchange reaction can be written as:



where M^+ is a metal ion and X^- an anionic ligand.

Moderately strong cation exchangers contain $-\text{PO}(\text{OH})_2$ as a functional group, while weak acid cation exchangers contain the functional group $-\text{COOH}$. Strong base anion exchangers contain the group $-(\text{CH}_2\text{NR}_3)\text{Cl}$, while weak base anion exchangers contain $-(\text{CH}_2\text{NHR}_2)\text{Cl}$ or $-(\text{CH}_2\text{NH}_2\text{R})\text{Cl}$. In these formulas, R represents an alkyl chain.

For the exchange reaction given in [Eq. \(52.16\)](#) a *selectivity coefficient* can be defined as

$$K_s = \frac{[\text{R-SO}_3\text{M}] \cdot [\text{HX}]}{[\text{R-SO}_3\text{H}] \cdot [\text{MX}]} \quad (52.17)$$

The selectivity coefficient depends on several parameters, e.g., on the type of ion exchanger, the charge of the exchanged ion, and the conditions of the solution.

It is also possible to define a *distribution ratio* for the ion exchanger. This ratio is expressed as

$$K_D = c_{\text{res}} / c_{\text{aq}} \quad (52.18)$$

where c_{res} is the equilibrium concentration of the exchanged ion in the resin (mol/kg) and c_{aq} the concentration in the aqueous solution (mol/m³). Thus, the SI unit of K_D is m³/kg.

In radiochemistry, the distribution ratio is more useful than the selectivity coefficient. It can be determined easily by using radioactive tracers.

52.1.5 Equipment

Ion exchangers are always solid and operated as columns, membranes, or surfaces covered with ion exchanger (liquid ion exchangers are solvent extraction reagents, e.g., ion-pair reagents). The size of such columns ranges from a few millimeters up to several cubic meters, and the flow capacities from a few milliliters per minute to several cubic meters per hour (the latter range covered by a scaling factor of about 17,000).

52.2 Solvent Extraction and Ion Exchange in Small-Scale Nuclear Chemistry

52.2.1 Nuclide Production

Solvent extraction and ion exchange are widely used to produce various radionuclides from irradiated targets. The common routine is that the target is dissolved in an aqueous phase, often a mineral acid, and then treated with a suitable extractant or ion exchanger to isolate the nuclide of interest. Several steps are often applied to obtain the desired radiochemical purity.

A well-known example is actinide or lanthanide separation when the individual trivalent metal ion can be isolated from a bombarded target by multistage solvent extraction or ion-exchange chromatography.

52.2.2 Isolation of Exotic Radionuclides

The distribution of a species between two immiscible phases may be extremely specific and the process itself very fast. This makes solvent extraction well suited for isolation of exotic nuclides from complex nuclear reaction product mixtures (in this context “exotic” refers to nuclides with a half-life shorter than ~ 60 s and nuclides that can be produced only at a one-atom-at-a-time scale). Under ideal conditions, the transport through a liquid interface can be completed within fractions of a second; a measured value for transfer of nitric acid from water to tributylphosphate is 12 ms (Lunes and Wishow 1985). Phase separation can also be obtained within a few milliseconds if applying a centrifugal field on the mixture of the two solvents. Another possibility to get an efficient phase separation is to sorb the extractant onto a solid material and thus using one liquid and one solid phase; this technique is utilized in liquid–liquid partition chromatography (LLPC) and high-performance liquid chromatography (HPLC).

More thorough descriptions of the techniques outlined below can be found, e.g., in refs. Trautmann (1995), Kratz (1999), and Skarnemark (2000) together with several references to applications of the methods and the results obtained.

Solvent extraction techniques employed for fast separations are either continuous (when chemical separation and nuclear measurements are performed online during irradiation) or batchwise. There are also combinations of the techniques, e.g., collection of a continuously produced nuclide followed by batchwise separation and measurement. The batch and online approaches both have advantages and disadvantages when studying short-lived nuclides. Generally, batchwise techniques are the best when performing measurements that do not require constant source strength, e.g., half-life determinations, while continuous techniques (or batch techniques with a high repetition frequency) are more convenient when performing long-term measurements that require a comparatively constant source strength. Such measurements include $\beta\gamma$ - and $\gamma\gamma$ -coincidences, as well as $\gamma\gamma$ -angular correlations.

The original technique for batchwise solvent extraction separations consisted of dissolving the irradiated sample in an aqueous phase, mixing the aqueous phase with an organic solution in a funnel, shaking for some time, and waiting until the phases had settled. If necessary, consecutive back-extractions and re-extractions were performed until the radiochemical purity of the product was acceptable. The method was time-consuming and required a lot of manpower, and it was difficult to obtain separation times shorter than ~ 30 s. Nevertheless, the method has been used with good results for studies of several rather short-lived fission products as well as for studies of chemical properties of the transactinide elements rutherfordium and dubnium, using $78\text{ s }^{261}\text{Rf}$ and $34\text{ s }^{262}\text{Db}$ as tracers.

Batch experiments are hampered by the time needed for phase separation and the need to repeat the experiments a large number of times to get sufficient counting statistics. To overcome these limitations the group at the Institut für Kernchemie, University of Mainz (Germany) has developed an apparatus (Trautmann 1995), where the extraction agent is sorbed onto a plastic powder. Thus, the phase separation problem is taken care of by using a solid organic phase. The apparatus was operated by an electronic programmer, which decreased the need for manual work and made it possible for a single person to perform

hundreds of experiments in a comparatively short time. The technique also took advantage of the possibility to pulse the Mainz TRIGA reactor, i.e., each pulse irradiation was followed by an automatic batch separation.

This type of solvent extraction procedure was developed for several elements and used very successfully in nuclear spectroscopy investigations of nuclei in the area around $A = 100$. The technique has also been used for fission yield determinations.

Automated Rapid Chemistry Apparatus (ARCA) is another successful technique using solid organic phases and computer control. It was developed at the Gesellschaft für Schwerionenforschung (GSI), Darmstadt (Germany). ARCA is an HPLC system based on fast repetitive chromatographic separations in micro columns. Depending on the separation procedure to be performed, the columns can be filled either with an organic extractant adsorbed on an inert supporting material, or with ion exchanger.

The ARCA II system (Schädel et al. 1989) consists of

1. A section for collecting activity from the gas-jet and for carrying out the chemical separations
2. An HPLC section of pumps, valves, and solvent reservoirs
3. An electropneumatic valve system
4. A control unit

All parts in contact with solutions are made of inert materials. The chemical separation section is symmetrical and operated in an alternating mode between left and right. Simultaneously three operations are performed: activity from the gas-jet (Stender et al. 1980) is collected on a polyethylene frit, previously collected activity is dissolved and transported to a column for chemical separation on one side, and the next column is washed and conditioned on the other side. The products of interest are eluted from the columns onto preheated tantalum or titanium disks and the eluent is evaporated. After flaming and cooling, the disk is placed in the measuring position. Typical times from the end of irradiation to the start of measurements are 50 s, which makes it possible to study nuclides with a half-life down to 10–15 s.

ARCA was constructed mainly to study chemical and nuclear properties of the transactinide elements. It has been used successfully to obtain data on the chemical behavior of rutherfordium, dubnium, and seaborgium.

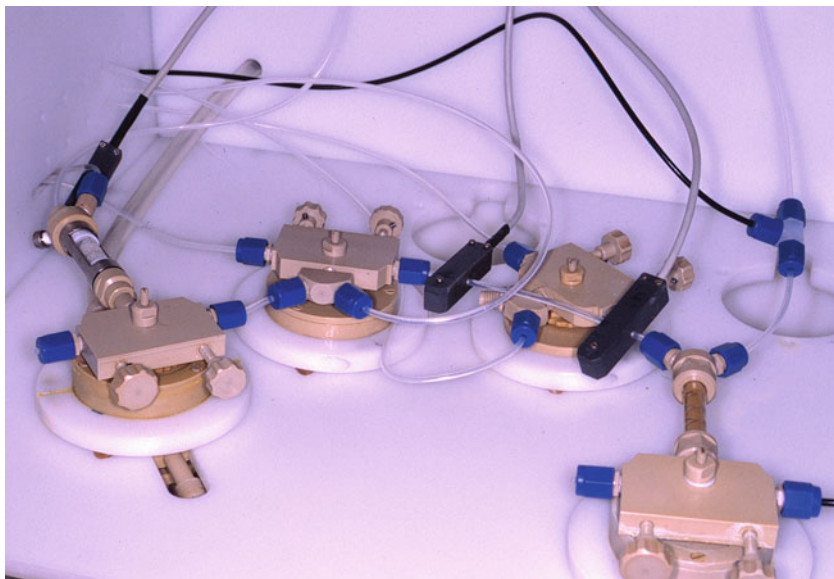
At the Department of Nuclear Chemistry, Chalmers University of Technology, a new type of liquid–liquid separation centrifuge, the H-centrifuge, (Rydberg 1969) was developed in the late 1960s. The centrifuge was designed for studies of solvent extraction equilibria, but the holdup time was so short that it could be used also for investigations of short-lived nuclides. Therefore multistage solvent extraction equipment based on the centrifuge was developed. The equipment is called Short-lived Isotopes Studied by the AKUFVE technique (SISAK); AKUFVE is a Swedish acronym for Apparatus for Continuous Investigation of Distribution Coefficients in Solvent Extraction. SISAK is the only fully continuous solvent extraction technique that is used for studies of exotic nuclides.

The SISAK version presently in operation, SISAK 3 (Persson et al. 1989) uses centrifuges with a holdup volume of ~ 0.3 ml/phase and maximum flow rates of 3 ml/s per phase.

In a typical SISAK experiment, see ► Fig. 52.1, radionuclides are continuously transported from the production site in an accelerator or a research reactor to the SISAK equipment via a gas-jet transport system (Trautmann 1995; Skarnemark 2000). The nuclides carried by the gas-jet are dissolved in an aqueous phase in a static mixer, and then a specially designed degassing centrifuge (Skarnemark 2000) is used to separate the carrier gas and volatile products

■ Fig. 52.1

A SISAK set-up used for liquid-liquid extraction of rutherfordium from heavy-ion reaction products



from the liquid. The temperature of the solution is usually $\sim 70^{\circ}\text{C}$ to enhance the dissolution of the aerosol particles (clusters) delivered by the gas-jet, to increase the efficiency of the degassing centrifuge and to speed up the solvent extraction kinetics in the subsequent separation steps. The solution leaving the degasser is fed into a centrifuge battery that consists of 1–4 H-centrifuges. The transport time from the target site to the detection system depends on the number of centrifuge steps and the flow rate. For a one-step chemistry, i.e., a degassing centrifuge and a single centrifuge for extraction, and maximum flow rates, the overall transport time is around 2.5 s, including ~ 1 s for the gas-jet. This fast transport has allowed detailed γ -spectroscopic studies of nuclides with half-lives down to ~ 1 s. The shortest-lived nuclide so far observed with SISAK is 0.57 s ^{114}Ru .

From the last centrifuge, the solution containing the element to be studied is pumped to a flow-through measuring cell installed at the nuclear detection system. The volume of the cell is chosen to enhance the count-rate of the isotope(s) under investigation. γ measurements are performed directly on the measuring cell that could be filled with ion-exchange resin or extraction chromatography material to increase the holdup time in front of the detectors. $\beta\gamma$ coincidence measurements are performed on a small, thin-walled cell using plastic scintillators for β detection. α measurements are performed using a specially developed liquid scintillation system (Wierczinski et al. 1996).

Rapid SISAK solvent extraction procedures have so far been developed for 20 elements. The SISAK technique has mainly been used for nuclear spectroscopic studies of short-lived fission products in the regions with deformed nuclei around $A \approx 110$ and $A \approx 150$ and to characterize previously unknown nuclei, e.g., ^{116}Pd and $^{243,244}\text{Np}$. Attempts have also been made to use SISAK for fission yield measurements. Recently the technique was successfully applied to one-atom-at-a-time studies of rutherfordium (Omtvedt et al. 2002, 2007).

52.2.3 Studies in Complex Chemistry

Solvent extraction is an excellent method to study complex equilibria and to determine complex formation constants. Suppose that an organic acid distributes between an organic and an aqueous phase with the distribution ratio k_D and also that the fraction of A^- present in the aqueous phase dissociates with the dissociation constant k_a . The anion A^- present in the aqueous phase can form complexes with the metal ion M^{v+} . The uncharged complex MA_v will distribute with the distribution ratio λ . The stability constants of the complexes are β_{1ij} where 1 is the number of metal ions in the complex (only mononuclear complexes are considered), i is the number of A^- ions in the complex, and j is the number of hydroxyl ions. Usually the β_{1i0} constants are determined under conditions where hydrolysis, and thus the concentration of OH^- , is negligible. Knowing these constants, the β_{10j} constants can be determined under less acidic conditions where all HA is dissociated into A^- , i.e., $[A^-]$ is constant if $[OH^-]$ is varied.

It can be shown that in such a system, the distribution ratio of the metal ion (D_M) can be written as

$$D_M = \frac{\lambda_v \beta_{1v0} [A^-]^v}{1 + \sum_{i=1}^v \beta_{1i0} [A^-]^i + \sum_{j=1}^{\omega} \beta_{10j} [OH^-]^j} \quad (52.19)$$

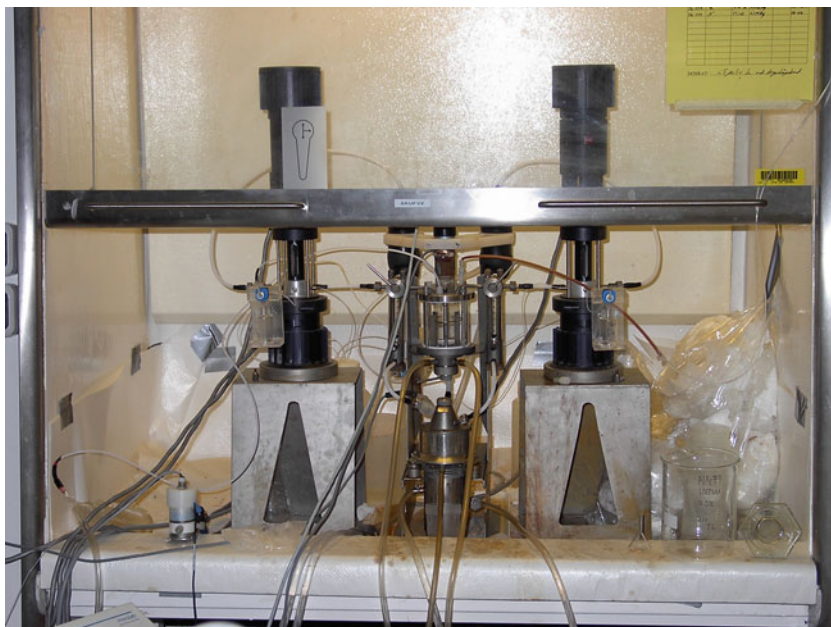
where v is the maximum number of A^- and ω the maximum number of OH^- in the complex.

Equation (52.19) requires (1) that no mixed complexes containing A^- and OH^- are formed and (2) that the metal is present in trace amounts, i.e., the metal ion concentration does not affect the concentration of the complexing agent. If D_M is measured as a function of $[A^-]$, the stability constants β_{1i0} and β_{10j} can be determined. To minimize the uncertainty of the constants at least 10–20 points are required. The distribution ratio value determinations can be done in funnels or test tubes, but to speed up the work and make the chemical conditions well defined, the AKUFVE apparatus was developed (Rydberg 1969). The AKUFVE (see Fig. 52.2) consists of a mixing chamber connected to a centrifuge for continuous, absolute phase separation, i.e., under ideal conditions no phase contains more of the other phase than the amount that corresponds to the solubility. The outgoing phases are pumped to a sampling device where samples are taken for subsequent radiometric or ICP-MS analysis. Online radiometric measurements are also possible. The phases are then pumped back to the mixing chamber. The aqueous phase contains cells for online measurements of the hydrogen ion concentration as well as a reducer to keep redox sensitive elements in the desired charge state. Chemicals to change, e.g., pH are added into the mixing cell. Temperature is measured at several points in the system. The centrifuge is made of palladium-passivated titanium or polyetheretherketone (PEEK).

The AKUFVE can be used to determine D values in the range $10^{-5} < D < 10^5$. The time needed for determination of a complete extraction curve is about 1 day. A typical AKUFVE extraction curve is shown in Fig. 52.3. This curve shows how to determine complex stability constants if the formed complex is not extractable. In such a case, it is possible to start with the metal tracer extracted into a suitable organic solvent. With the increasing concentration of the complexing agent in the aqueous phase, the extraction will decrease. By plotting the ratio between D_0 (without complexing agent) and D versus the concentration of the complexing agent it is possible to calculate the complex stability constants.

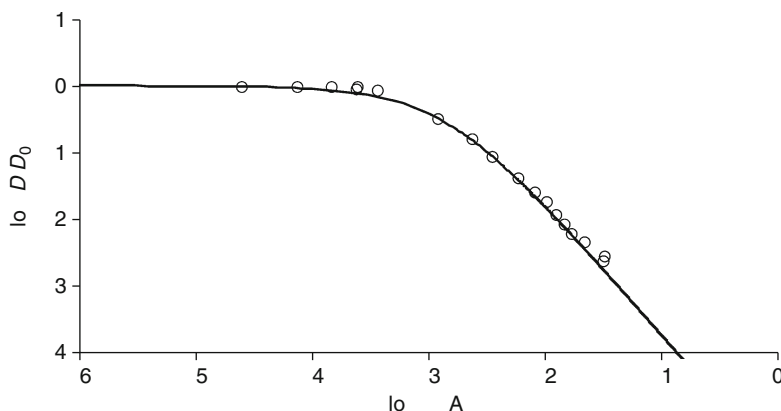
■ Fig. 52.2

AKUFVE unit



■ Fig. 52.3

AKUFVE extraction curve for the system americium in 1 M NaClO_4 with varying concentration of α -D-isosaccharinic acid//TBP (from Allard et al. 2008)



52.2.4 Studies of Plutonium Speciation

Plutonium is a difficult element to investigate since its redox potentials make possible four oxidation states – Pu(III), Pu(IV), Pu(V), and Pu(VI) – to coexist in solution at the same time. Thus, it is important to have experimental methods to determine the speciation. At high

concentrations, e.g., spectrophotometry can be used. However, since most experiments are performed at tracer-level concentrations, there is also a need for radiochemical methods. One such method is solvent extraction with HTTA (thenoyltrifluoroacetone) as reported by Choppin et al. (1997).

In this method Pu(IV) is extracted below pH 1, Pu(VI) in the pH range 1–2, Pu(III) above pH 3, while Pu(V) is poorly extracted even at pH 5. The method has limitations, e.g., because pH adjustments may perturb the redox equilibria. Other extractants used for plutonium speciation include tri-*n*-butyl phosphate (TBP), bis-2-ethylhexyl phosphoric acid (HDEHP).

52.2.5 On-Line Determination of Iodine Speciation in Reactor Water

Another application of solvent extraction to redox speciation studies is the method developed for iodine (Malmbeck and Skarnemark 1995). It was used for online speciation of iodine in the Forsmark BWR power plant in Sweden. Iodine can enter the reactor water in two ways, either by fission of “tramp” uranium (uranium that is adsorbed on the outer surface of the fuel pins) or via leaking fuel pins. In this method, a tiny stream of water was withdrawn from the reactor system and used as feed for a 20 stage mixer–settler battery. The mixer–settlers were arranged in four batteries with 4, 4, 6, and 6 mixer–settler units. Part of such a mixer–settler battery is shown in ► Fig. 52.4.

In the first four-stage mixer–settler battery, elementary iodine and organic iodides like CH_3I are extracted into an aliphatic kerosene. In a second four-stage mixer–settler battery, the

► Fig. 52.4

Small mixer-settler battery of the type used for iodine speciation experiments



organic phase is contacted with an aqueous phase containing NaI carrier, Na_2SO_3 as reductant and H_2SO_4 . The organic iodides remain in the organic phase, while iodine is reduced to iodide and stripped to the aqueous phase. The aqueous phase from the first extraction step is mixed with NaI carrier, HNO_3 and NaNO_2 to oxidize iodide to iodine. This iodine is then extracted into kerosene in a six-stage mixer-settler battery together with iodine that has been present in the reactor water as HIO. After these steps, the aqueous phase only contains iodine as iodate and periodate. The aqueous phase from this extraction battery is first mixed with KIO_3 carrier and H_2SO_4 , and then with Na_2SO_3 to reduce IO_3^- and IO_4^- to I^- . Then NaNO_2 is added and the formed iodine is extracted in a further six-stage mixer-settler battery. The aqueous phase from this step only contains a residual fraction with a few percent of the incoming iodine, probably as colloids.

Thus, in total, the method continuously produces fractions that represent the reactor-water contents of elementary iodine, organic iodides, iodide + hypiodous acid, and iodate + periodate. By comparing the specific activity of different iodine isotopes, it is also possible to determine the relative age of the iodine species in the different fractions.

52.2.6 Radioanalytical Chemistry

During the last decades methods such as Inductively Coupled Plasma Optical Emission Spectroscopy (ICP-OES), Inductively Coupled Plasma Mass Spectroscopy (ICP-MS), and Resonance Ionization Mass spectrometry (RIMS) have decreased the need for selective radiochemical procedures. Many long-lived radionuclides today have lower detection limits if using, e.g., ICP-MS than if performing radiometric measurements with reasonable measuring times. At present, the half-life limit is a few hundred years, i.e., nuclides with longer half-life (e.g., ^{99}Tc , ^{235}U , ^{238}U , ^{237}Np , or ^{239}Pu) should preferably be measured by ICP-MS and more short-lived nuclides (e.g., ^{90}Sr , ^{137}Cs , ^{238}Pu or ^{244}Cm) should be measured by radiometric methods. Thus, the main applications for modern radioanalytical methods are:

1. Determination of nuclides with half-life less than a few hundred years
2. Preconcentration of samples where the analyte is below the detection limit, e.g., the determination of ^{99}Tc in seawater.
3. Pretreatment of samples to be determined by ICP-MS to reduce the influence of interfering masses. An instructive example is the measurement of ^{99}Tc , where a separation from ^{99}Ru is imperative. Other examples are $^{238}\text{U}/^{238}\text{Pu}$ and $^{241}\text{Pu}/^{241}\text{Am}$. This pretreatment is not necessary if using a high-resolution ICP-MS, as such an instrument is capable of resolving the small mass differences within an isobar.

There is an enormous number of radioanalytical procedures based on solvent extraction and here it is only possible to give a few examples. The examples chosen have been taken from the analysis of samples from the European PHEBUS project performed at the Nuclear Chemistry, Chalmers University of Technology. Very briefly, the Phebus reactor was used to study the products formed in severe reactor accidents. The released gases and aerosols were collected in filters and in water at different positions in the experimental setup.

The unseparated samples were characterized by a high concentration of $^{134,137}\text{Cs}$ that made direct γ -spectroscopic determination of other nuclides impossible as well as by presence of fission product elements with a nonnatural isotopic composition. Thus, radiochemical separations were a prerequisite for successful radiometric and ICP-MS measurements.

The quantitative analyses were performed on acid solutions resulting from the leaching of filter cartridges. One set of samples contained 1 M HNO_3 + $\sim 2 \times 10^{-5}$ M HF and another, with a higher nuclide concentration 1 M HNO_3 and 0.002 M HF. The samples also included iodine trap samples in 4 M NaOH.

Cobalt: The separation procedure for Co was based on the extraction of Co(II) by Cyanex 272 (bis(2,4,4-trimethylpentyl) phosphinic acid) in toluene. First, the pH of the solution was adjusted to ~ 5 by addition of NH_3 . Then cobalt was extracted into Cyanex 272 in toluene. In separate experiments, the yield of the extraction step was determined to be $40 \pm 3\%$. After phase separation, the extract was contacted with 1 M HNO_3 to strip the cobalt. The yield of the strip step was measured to be $>99\%$ in separate experiments.

After phase separation, the HNO_3 solution was used for γ -spectrometry and ICP-MS measurements. No interfering elements could be seen.

Nickel: An equal amount of 10% sodium citrate solution was added to the sample. The acidity of the samples was then adjusted to $\text{pH} > 7.5$ by addition of NH_3 . Thereafter, 2 ml 1% dimethyl-glyoxime (DMG) was added to the solution. The nickel-DMG complex was extracted into pure chloroform. The extraction was repeated with fresh chloroform to improve the yield. The combined organic phases were then washed with 0.5 M NH_3 to remove impurities. Nickel was then back-extracted into 0.5 ml HNO_3 . The back-extraction was repeated once to improve the yield. The HNO_3 solution was then used for ICP-MS and liquid scintillation measurements. γ -spectrometry showed no contamination that could disturb the LSC measurements. The overall yield of this standard procedure is $>99\%$.

Zinc: First NH_3 was added to the sample until the pH was ~ 2.5 . Then zinc was extracted into 0.3 M Cyanex 302 (bis(2,4,4-trimethylpentyl)-monothiophosphinic acid) in toluene. The extract was then contacted with 5 M HNO_3 to strip the zinc. 1.5 ml of the HNO_3 solution was used for γ -spectrometry and ICP-MS measurements. It contained no other radionuclides and no elements that could interfere with the ICP-MS measurement. The chemical yield of the extraction and strip steps has been determined to be $>99\%$ in separate experiments.

Rubidium: The stable isotopes ^{85}Rb and ^{87}Rb were determined by direct ICP-MS measurements. It should be pointed out that the original intention was to isolate the individual alkali and alkaline earth metals by using cation and ion-exchange columns. The radioactive rubidium and barium isotopes had, however, decayed before dissolution of the samples and therefore only stable isotopes of these elements were determined (by ICP-MS), with the exception of ^{90}Sr , ^{134}Cs , and ^{137}Cs .

Strontium: The stable isotopes ^{84}Sr , ^{86}Sr , and ^{88}Sr were determined by direct ICP-MS measurements on the sample solutions. ^{87}Sr was not determined because it is shielded by its β -decay precursor ^{87}Rb , i.e., there should be no ^{87}Sr from fission present in the samples. ^{90}Sr has been determined indirectly via growth-and-decay of its daughter ^{90}Y , using the following standard procedure:

Sample solutions measuring 50 μl were mixed with 350 μl 5 M HNO_3 and 2.4 ml 0.1 M $\text{Al}(\text{NO}_3)_3$. The aluminum nitrate was used to complex fluoride ions. ^{90}Y and disturbing nuclides (mainly lanthanides) were extracted into 1.0 M HDEHP (bis-2-ethylhexyl orthophosphoric acid) in Solvent 70 (an aliphatic kerosene); 2.0 ml of the aqueous phase was taken out, and ^{90}Y was allowed to grow for 115 h, which gave about 72% of the equilibrium activity of ^{90}Y . The grown-in ^{90}Y was then extracted into 1.0 M HDEHP in toluene. The organic phase was washed twice with 1 M HNO_3 to remove any traces of the rather radioactive aqueous phase. ^{90}Y was then measured by Cerenkov counting directly on the organic phase. The decay of ^{90}Y was followed for approximately nine half-lives, and then the sample activity at the time of

separation was determined by a simple extrapolation of the decay curve. The decay curve gave the correct half-life of 64.1 h, which implies that the ^{90}Y sample did not contain any interfering β -emitters. The chemical yield of this procedure is known from earlier work to be $95 \pm 1\%$.

Zirconium: The sample solution was mixed with 1 M HNO_3 and 0.1 M $\text{Al}(\text{NO}_3)_3$ to complex fluoride ions and to keep the acidity high. Zr was then extracted into 0.5 M HTTA (thenoyltrifluoroacetone) in xylene. It is essential that the contact time is at least 15 min to assure complete extraction. At 1 M HNO_3 HTTA is very selective and only tetravalent elements like Zr are extracted. The organic phase was then washed with 1 M HNO_3 to remove impurities. γ -spectrometry was performed directly on the organic phase. For ICP-MS measurements zirconium can be back-extracted using 10 M HNO_3 .

Technetium and rhenium: 100 μl of the sample solution was diluted to 5 ml by addition of 0.1 M KBrO_3 . The bromate assured that technetium was present as TcO_4^- . Then TcO_4^- and ReO_4^- were extracted into 5 ml 0.05 M TOA (tri-*n*-octylamine) in toluene. The organic phase also contained 2.5% (by volume) *n*-dodecanol to prevent third phase formation. For further analysis 4 ml of the organic phase was taken out. Finally, TcO_4^- and ReO_4^- were back-extracted into 1 ml of 10 M HNO_3 . This solution was diluted and fed into the ICP-MS system.

The final fraction was also measured γ -spectrometrically. As expected, no γ -emitters could be observed, except a slight contamination of $^{134,137}\text{Cs}$. This contamination did not interfere with the ICP-MS measurements.

In separate experiments the yield of the extraction step has been determined to be $>99\%$ for Tc and $>98.6\%$ for Re. The back-extraction yield is $>99\%$ for both elements.

Molybdenum and tungsten: 1 ml of the sample solution was diluted to 20 ml with 1 M lactic acid. The acid was not treated to break up the esters that are known to form. In a separate experiment, the degree of esterification was determined to be about 10%. This does not affect the yield of the separations. In order to complex the fluoride ions ($\sim 10^{-6}$ M) in the solution, $\text{Al}(\text{NO}_3)_3$ was added to a final concentration of ~ 0.01 M. Mo and W were then extracted into 20 ml of 0.05 M TOA in toluene. The organic phase also contained 2.5% 1-dodecanol to prevent third phase formation. Finally, Mo and W were back-extracted into 10 ml of 1 M HNO_3 . This solution was diluted and measured by ICP-MS.

The final fraction was also measured γ -spectrometrically. As expected no γ -emitters could be observed.

In separate experiments, the yield of the extraction step was determined to be $>99.5\%$ for Mo and W. The back-extraction yield was $>99\%$ for both elements.

Ruthenium: 5.0 ml of the samples were made ~ 5 M with respect to HNO_3 and 0.1 M with respect to H_5IO_6 . The aqueous solutions were heated to $\sim 75^\circ\text{C}$ for 1 h to oxidize Ru to RuO_4 . The heating was performed in a closed vessel to prevent gaseous RuO_4 from escaping. RuO_4 was then extracted into 2 ml of toluene. The organic phase was measured by γ -spectrometry.

Antimony: In the direct γ -measurement of the samples, the four strongest peaks of ^{125}Sb could be observed and used for determination of the concentration. Chemical separation was also successfully performed as follows. 2 ml of the sample solution was converted from nitrate to chloride medium by repeated evaporations with concentrated hydrochloric acid. After dissolution in 3 M HCl , antimony can be extracted into pure chloroform (or another organic solvent). It can then be back-extracted into 0.1 M HCl . The extraction step is not quantitative, and three to four extractions with fresh solvent are required to obtain an acceptable yield. The back-extraction step is quantitative. The γ -spectrometric investigation showed that neither the organic nor the final aqueous phase contained anything but antimony isotopes.

Iodine: The samples contained no radioactive iodine isotopes other than ^{129}I and they were therefore analyzed only by ICP-MS and without chemical separation. However, the following radiochemical method was also developed for the samples. Some Na_2SO_3 was added to the solution to reduce iodine to iodide. Then iodide carrier was added in a concentration of $\sim 10^{-3}$ M. An equal amount of 0.1 M NaNO_2 was added to oxidize iodide to I_2 . The elementary iodine was then extracted quantitatively into pure kerosene. It could then be back-extracted into an aqueous phase containing 0.2 M H_2SO_4 and 0.05 M Na_2SO_3 . The back-extraction is not quantitative and thus it has to be repeated at least twice with a fresh aqueous phase.

Cesium: ^{133}Cs and ^{135}Cs were determined by direct ICP-MS measurements of the sample solutions. ^{134}Cs was determined by γ -spectrometry and ^{137}Cs by γ -spectrometry and ICP-MS, which gave an opportunity for intercalibration of the methods. The results agreed within the error limits.

Lanthanides: 0.2 ml of the nitric acid solutions were diluted to 20 ml with a 0.1 M $\text{Al}(\text{NO}_3)_3$ solution. The $\text{Al}(\text{III})$ ions were present to complex fluoride ions. Then the $\text{Ln}(\text{III})$ ions were extracted into 20 ml 1 M HDEHP (bis-2-ethylhexyl orthophosphoric acid) in Solvent 70. The organic phase was washed with 2 ml 0.01 M HNO_3 . Thereafter the lanthanides were back-extracted with 2.2 ml 5 M HNO_3 . The strip solutions were combined and used for ICP-MS measurements. A contact time of 60 s was used for extraction as well as for back-extraction.

In separate experiments the yield of the extraction step has been determined to be $>99\%$ for all lanthanides. In the washing step $>99.9\%$ of the lanthanides stay in the organic phase. The total yield of the two-step back-extraction is $>99\%$.

Neptunium, plutonium, americium, and curium: To improve the sensitivity, neptunium, plutonium, americium, and curium were measured after chemical separation. For americium and curium, chemical separation and radiometric measurement were the only alternative; due to the short half-lives, α -spectrometry is more sensitive than ICP-MS.

200 μl of the sample solutions were mixed with 0.4 ml 0.4 M $\text{Al}(\text{NO}_3)_3$ and 3.6 ml 1 M HNO_3 . The resulting $\text{Al}(\text{III})$ concentration was ~ 0.01 M. This measure was taken to complex the fluoride ions present in the solution ($\sim 10^{-5}$ M). 0.3 ml 10 M HNO_3 and 0.3 ml 3.1 M $\text{NH}_2\text{O}\cdot\text{HCl}$ was added to the samples to reduce Pu to Pu(III). Thereafter the samples were heated to $80\text{--}85^\circ\text{C}$ for 15 min and 8 ml 2.1 M NaNO_2 was added to oxidize Pu(III) to Pu(IV). After cooling to room temperature, Pu and Np were extracted into an equal amount of 0.5 M HTTA in xylene. The contact time was 20 min to get close to equilibrium. The resulting organic phase was used for the Pu and Np determination and the aqueous for Am and Cm. The organic phase was washed with 10 ml 1 M HNO_3 . Then Pu and Np were back-extracted into 0.5 ml 10 M HNO_3 , using 5 min contact time. The acid concentration was adjusted to 1 M, and Pu and Np re-extracted into 0.5 M HTTA in xylene. The contact time was 20 min. Pu and Np were back-extracted with 1 ml 10 M HNO_3 . The aqueous phase was diluted to 1 M HNO_3 and measured with ICP-MS and α -spectrometry.

The pH of the aqueous phase from the first HTTA extraction was then adjusted to 1. When adjusting it is important not to exceed $\text{pH} \sim 2$, because a too high pH will cause an irreversible sorption of trivalent actinides on the walls of the extraction vessel. Am and Cm were then extracted into 2.5 ml 1 M HDEHP in kerosene. The extraction was repeated with 2.5 ml of fresh HDEHP solution to increase the yield. The contact time was 60 s. Then Am and Cm were back-extracted into 1 ml 7 M HNO_3 . The acid was diluted to 1 M HNO_3 , and used for α -spectrometry.

The total yield of Np, Pu, Am, and Cm is known to be $>99\%$ in these separations.

52.2.7 Production of ^{234}Th Tracer

In chemical investigations, thorium is often used as an analog for tetravalent actinides. The reasons are that it has only one, stable valence state and also that it is more easy to handle than, e.g., Pu(IV). ^{232}Th is, however, not always suitable because of its low specific activity. In, e.g., solvent extraction experiments ^{234}Th ($T_{1/2} = 24.1$ days) is more convenient because the chemical concentration can be kept at a tracer level. ^{234}Th is formed in the decay of ^{238}U and, thus it can be isolated from uranium. Here one procedure will be described in more detail.

The procedure (Albinsson et al. 2002) involves one cation-exchange column with Dowex 50 W X-8 (C1) and one column with Dowex 50 W X-4 (C2). The ^{234}Th is formed by growth from natural or depleted uranium in an ether solution. This ether solution is contacted with a few milliliters of water. In this step, thorium will be stripped while uranium stays in the ether solution. The aqueous phase is then transferred to column C1. Since the solution has an almost neutral pH, thorium will be strongly sorbed onto the column. The column is then washed with water to remove traces of uranium.

In the next step, oxalic acid is added to the column to elute thorium as an oxalate complex. The solution is then evaporated to dryness. After cooling ~ 15 ml concentration HNO_3 and ~ 4 ml concentration HClO_4 are added to the evaporation residue. The solution is evaporated again to remove the oxalic acid by wet combustion.

The evaporation residue is dissolved in 6 M HCl and transferred to column C2 where thorium is sorbed. Remaining traces of uranium and other decay products pass through the column. The column is washed with 6 M HCl and then thorium is eluted with 0.5 M oxalic acid. The wet combustion procedure is repeated to remove all oxalic acid and then the residue is dissolved in water while heated. The dissolution step is repeated and then the ^{234}Th tracer solution is ready for use.

Theoretically, ~ 12 MBq of ^{234}Th can be produced from 1 kg of aged ^{238}U . The chemical yield of the procedure is $>90\%$ and the specific activity of the ^{234}Th tracer is 1–3 PBq/mol Th.

52.2.8 Production of ^{239}Np Tracer

^{239}Np is often a good alternative to ^{237}Np in experiments that can be performed in a few days, e.g., investigation of solvent extraction properties. It is a β -emitter with short half-life (2.3 days), i.e., it does not create any significant amount of long-lived radioactive waste. One way to produce ^{239}Np is via the α -decay of ^{243}Am ($T_{1/2} = 7,370$ a). ^{243}Am can easily be sorbed on a cation-exchange column. In the production procedure used at Nuclear Chemistry, Chalmers University of Technology, ^{239}Np is first eluted from the column with 0.6 M HCl and 0.1 M H_5IO_6 . The periodic acid oxidizes neptunium to NpO_2^+ that does not stick to the column at this HCl concentration. Americium remains in its trivalent state and is strongly sorbed on the column.

When the neptunium has been eluted, the eluate is evaporated to dryness. Iodine disappears as I_2 gas, i.e., there is no solid evaporation residue. Neptunium is then dissolved in a suitable acid.

The amount of ^{243}Am sorbed on the column is 370 MBq, and thus it is possible to obtain 370 MBq of ^{239}Np at each elution if allowing maximum growth. Since almost no longer-lived isotopes of neptunium are present (only 0.05% of the americium is ^{241}Am that decays to ^{237}Np) the specific molar activity of ^{239}Np is ~ 2 EBq/mol if the column is eluted more often than a few times per year.

52.3 Solvent Extraction and Ion Exchange in the Nuclear Industry

52.3.1 Uranium Production

Solvent extraction is used extensively for production of uranium with every uranium atom passing at least one solvent extraction process on its way from the uranium mine to the fuel element factory. In the most common process, uranium ore is leached with sulfuric acid containing an oxidizing agent, e.g., chlorate, to oxidize uranium to U(VI). In this environment, uranium forms the complex $\text{UO}_2(\text{SO}_4)_2^{2-}$, while the unwanted daughter product radium remains in the sludge as insoluble RaSO_4 . The aqueous phase is then contacted with a tertiary amine (R_3N) and the anionic uranium complex is extracted, probably as $(\text{R}_3\text{NH})_4\text{UO}_2(\text{SO}_4)_3$. Uranium is then back-extracted to an aqueous phase that contains either chloride or carbonate ions. If the leachate contains molybdenum, it is advantageous to back-extract with chloride since this procedure is selective and retains molybdenum in the organic phase. In this case, the organic phase has to be regenerated from time to time by treatment with ammonium carbonate to back-extract the accumulated molybdenum. The aqueous phase containing uranium is treated with NH_3 to precipitate uranium as ammonium diuranate, also referred to as yellowcake. Finally, the yellowcake is purified to the product U_3O_8 .

52.3.2 Thorium Production

In nature thorium is commonly present as monazite, a lanthanide phosphate mineral that contains 1–15% ThO_2 and usually 0.1–1% U_3O_8 . Thus, thorium is often produced as a by-product together with rare earth metals and uranium. There are several production methods (see, e.g., Ritcey 2006). The choice of method depends not only on the composition of the ore but also on whether thorium is the main product or a by-product.

A common procedure begins with a treatment of monazite sand with 50–70% sodium hydroxide at $\sim 1,400^\circ\text{C}$ to convert thorium oxide to hydroxide. The filtered hydroxide is then dissolved in hydrochloric acid and the pH adjusted to 5–6 to precipitate thorium but not the main fraction of the rare earth elements. After dissolution of the hydroxide in nitric acid, thorium is extracted with methyl isobutyl ketone (MIBK) or TBP in kerosene. Thorium is then stripped from the solvent using an alkali solution.

There are also thorium recovery processes based on extraction from sulfuric acid solutions, e.g., with primary, secondary, or tertiary amines or alkyl phosphorous acids such as bis-2-ethylhexyl phosphoric acid (HDEHP) or dibutylbutyl phosphonate (DBBP). Thorium is then stripped into a nitric acid solution. The alkyl phosphorous acid processes are often employed when recovering thorium as a by-product in uranium production.

Finally, thorium is precipitated as oxalate and calcined to ThO_2 .

52.3.3 Uranium Isotope Enrichment

Neither solvent extraction nor ion exchange has become common methods for enrichment of ^{235}U but processes based on both techniques have been developed and successfully tested. They are based on chemical separations involving redox couples like U(IV)/U(VI) or U(III)/U(IV). The isotope ^{235}U shows a very slight preference for the higher valence and by combining a large number of steps a separation can be obtained.

The solvent extraction process was developed in France and is commonly referred to as the CHEMEX process (Pesme 1982). It uses the exchange reaction that takes place between tetravalent and trivalent uranium ions in an aqueous solution, in this case concentrated hydrochloric acid. The heavier isotope ^{238}U has a tendency to concentrate in the trivalent species, while the tetravalent one becomes enriched in ^{235}U . A catalyst is used to speed up the rate of exchange. If using a solvent that extracts U(IV) it is possible to obtain a fraction that is slightly enriched in ^{235}U . As extractant, TBP in an aromatic diluent was chosen. The extraction is performed in a pulse column. In a plant for high-enriched uranium (HEU) centrifugal contactors might be used especially for the higher assay sections. By doing so, the stage times and corresponding specific uranium inventory could be reduced significantly. After passing through the column, the enriched and depleted uranium streams must be chemically treated so that they can be recirculated through the column again (refluxed) or sent to another column for additional enrichment.

The ion-exchange process, also referred to as the Asahi process, was developed in Japan. It is based on the chemical isotope effect between tetravalent and hexavalent uranium. The aqueous phase flows through an ion-exchange column, and the net effect of all the chemical reactions is a “band” of uranium that moves through the ion-exchange column. In this continuous separation system, ^{235}U and ^{238}U tend to accumulate at the entrance and exit ends of the adsorption band, respectively. The adsorbent is an anion-exchange resin with high separation efficiency and an exchange rate over 1,000 times faster than the rates obtained in most commercially available resins.

The two exchange processes discussed here are representative of alternative enrichment processes that have been under study in several countries. At present, however, no country has built or operated a full-scale uranium enrichment plant based on an exchange process. The CHEMEX process has, however, been tested in pilot scale. The primary proliferation concern is that these processes are based on standard chemical engineering technology.

52.3.4 Reprocessing of Nuclear Fuel

Some countries, e.g., France, Japan, Russia, and the United Kingdom have chosen to reprocess their spent nuclear fuel to recycle uranium and plutonium as nuclear fuel and to obtain a high active waste (HAW) fraction that is less radiotoxic than the spent fuel itself. In this process, very high separation factors are necessary. The fission product activity has to be reduced by a factor of $>10^7$ and the separation factor between uranium and plutonium must be at least 2×10^4 . All full-scale reprocessing processes are based on solvent extraction, and today the plutonium uranium redox extraction (PUREX) process dominates the market completely.

In a modern PUREX plant, the fuel pins are first cut into pieces that are 3–5 cm long. The fuel is then dissolved in 6–11 M nitric acid, while the cladding hulls do not dissolve. Sometimes $<0.05\text{ M AlF}_3$ is added to the nitric acid to improve dissolution of, e.g., zirconium by complex formation. The solution is then diluted to 3–4 M and nitrite is added to assure that plutonium is present as Pu(IV) and uranium as U(VI). Plutonium and uranium are then selectively extracted into TBP in aliphatic kerosene. Fission products and trivalent actinides remain in the aqueous phase. The extract is scrubbed with nitric acid to remove all contaminants except traces of ruthenium, neptunium, and zirconium.

Plutonium is then back-extracted into an aqueous phase by reduction to Pu(III) by U(IV) or Fe(II) sulfamate. Uranium is not reduced and remains in the organic phase. Later on, it is back-extracted to an aqueous phase containing very dilute (0.01 M) nitric acid.

The plutonium fraction is then purified by several cycles comprising oxidation to Pu(IV), extraction, scrub, and back-extraction by reduction to Pu(III). This purification removes neptunium and the last traces of fission products. Finally, Pu(IV) is back-extracted into ~ 0.2 M nitric acid. The plutonium nitrate is then converted to PuO₂ or Pu metal.

The uranium fraction is concentrated by evaporation and nitric acid is added to ~ 3 M. Uranium is then extracted into a TBP solution that is scrubbed with a reducing solution to remove traces of plutonium and neptunium. This process is repeated twice. Then uranium is back-extracted into 0.01 M nitric acid and converted to uranium oxide.

The fission product solution is vitrified and stored in a final repository. More information about reprocessing can be found, e.g., in ref. Choppin et al. 2002.

The aim of the present improvement work on the PUREX process is to make the separations more selective and to create effluent streams of high purity. Thus, modifications are performed to make neptunium end up in a fraction for later transmutation in a reactor or accelerator-driven system. This can be achieved by a better control of redox conditions in the process. Today neptunium is partially co-extracted with plutonium and uranium. There are also suggestions to withdraw product streams with ⁹⁹Tc and ¹²⁹I, respectively, i.e., long-lived nuclides that might be of interest for transmutation.

52.3.5 Partitioning and Transmutation

Spent nuclear fuel can either be reprocessed (see ► Sect. 52.3.4) or put directly into a deep underground repository like in, e.g., Sweden or Finland. In both cases, the material stored in the repository contains long-lived radionuclides like ²³⁷Np and ²⁴³Am as well as varying amounts of plutonium. Therefore, the storage facility has to fulfill strict safety requirements for a very long time, typically several hundred thousand years for unprocessed fuel.

In partitioning and transmutation (P/T) the most radiotoxic elements will be removed from the waste fraction and “burned” in specially designed reactors or accelerator-driven systems. The advantages of P/T are the removal of long-lived, radiotoxic elements from the waste, which decreases the time necessary for a safe storage from several hundred thousand to ~ 700 years, and the possibility to utilize almost 100% of the energy contents of the fuel, to be compared to $\sim 3\%$ in an once-through fuel cycle with direct disposal. In a long time perspective, accelerator-driven P/T would also make it possible to produce energy from natural uranium or thorium instead of using thermal reactors.

The P/T process will be coupled after an improved PUREX process that puts all technetium, iodine, and neptunium into the waste fraction or into special fractions. Thus, the waste will contain fission products and minor actinides (americium and curium). The process will probably be a solvent extraction process although molten salt systems are also studied as an alternative. The main issue will be to obtain pure Am and Cm fractions for subsequent destruction, i.e., fractions that do not contain any lanthanides. Some of the lanthanides, which are chemically very similar to trivalent actinides, have very high neutron cross sections. Therefore, they must be removed to make actinide burning possible. In some cases, it may also be desirable to transmute some long-lived fission products, e.g., ⁹⁹Tc and ¹²⁹I, to more short-lived nuclides.

The development of P/T processes in the European Union, Japan, and the United States has created a new interest in solvent extraction chemistry. The process has to be extremely efficient and it should preferably be based on extractants and diluents containing nothing but carbon,

hydrogen, oxygen, and nitrogen (the CHON principle). By doing so, the organic phase will be completely incinerable after use, without creating additional waste. The CHON principle also means that many traditional extractants cannot be used for P/T since they contain phosphorous, sulfur, or other non-CHON elements.

During the last 15 years, several EU framework programs have been dedicated to the partitioning of nuclear waste for nuclear transmutation. The liquid–liquid extraction projects have been NEWPART between 1996 and 1999 (Madic et al. 2000), PARTNEW between 2000 and 2003 (Madic et al. 2004), EUROPART between 2004 and 2007 (Hill et al. 2007), and at present ACSEPT. The running project started in 2008 and was planned to continue till 2011. In the United States, much effort is put into the UREX (Law et al. 2001) and TRUEX (Alexandratos et al. 1993) processes, and in Japan into ARTIST (Tachimori et al. 2002).

It is impossible to give a summary of all work that is performed in this field. The European projects, however, started with the, at that time, almost impossible task of separating trivalent actinides from trivalent lanthanides with high separation factors. A few years later the separation factors had increased from 5–6 to $\sim 1,000$. This was far too high since it made stripping difficult. Today the work has arrived at new molecules that have an appropriate separation factor, i.e., around 100, and appropriate distribution ratios. Too high separation factors are not useful since the phase separation in the equipment used in industrial liquid–liquid extraction processes does not allow higher separation factor than 10–20. This development, which has been achieved by using nitrogen donor ligands that have a higher affinity for trivalent actinides than for trivalent lanthanides, is described in Ekberg et al. (2008).

No P/T exists today, apart from reprocessing and production of mixed oxide (MOX) fuel (an embryo of P/T), but it is likely that demonstration facilities will be built within the next decades.

52.3.6 Water Clean-Up in Nuclear Power Stations

In a nuclear power station, there are several ion-exchange systems for water clean-up. In a typical BWR there are purification circuits after the steam condenser, in a small stream from the reactor vessel and for the water in the fuel storage pool. In a pressurized water reactor (PWR), part of the coolant in the primary circuit is withdrawn, cooled, and pumped through an ion-exchange filter. As indicated by the word “filter,” these ion exchangers are also used to remove particles from the liquids. They often consist of mixed cation and anion exchangers that are very finely ground; bead sizes of ~ 400 mesh are common.

The ion exchangers become very radioactive, and for organic ion exchangers a limit is set at an absorbed dose of $\sim 10^6$ Gy. Remotely controlled systems are used to backwash the filters and change the resin when too much activity leaks through or the pressure drop becomes too large.

52.3.7 Final Storage of Radioactive Waste

Ion-exchange processes are also of utmost importance in the Swedish concept for final storage of nuclear fuel. According to this method, the spent nuclear fuel will be placed in copper canisters that are disposed into bentonite-filled shafts at about 500 m depth in the granite bedrock close to the Forsmark nuclear power plant. In this concept there are four barriers that will prevent radionuclides from leaking into the groundwater: (1) the fuel itself is very insoluble in water, (2) the copper canister is chemically stable, (3) bentonite clay (sodium montmorillonite) is

a good ion exchanger, and (4) the bedrock itself is an excellent ion exchanger that makes most cations sorb strongly. The Swedish groundwater is strongly reducing, i.e., long-lived elements like plutonium and technetium will be reduced to Pu(IV) and Tc(IV) that are strongly retained on the “ion-exchange column” formed by the rock surfaces.

A similar repository is under construction in Finland, close to the Olkiluoto nuclear power plant.

52.4 Acronyms

ACSEPT	European P/T project
AKUFVE	Apparatus for continuous determination of distribution ratios in solvent extraction
ARCA	Automated Rapid Chemistry Apparatus
ARTIST	Japanese P/T project
BWR	Boiling Water Reactor
CHEMEX	French uranium enrichment process based on solvent extraction
CHON	Contains only carbon, hydrogen, oxygen or nitrogen
EUROPART	European P/T project
HAW	High Active Waste
HEU	High-Enriched Uranium
HPLC	High-Performance Liquid Chromatography
ICP-MS	Inductively Coupled Plasma Mass Spectrometry
ICP-OES	Inductively Coupled Plasma Optical Emission Spectrometry
IUPAC	International Union of Pure and Applied Chemistry
LLPC	Liquid-Liquid Partition Chromatography
MOX	Mixed OXide fuel
NEWPART	European P/T project
PARTNEW	European P/T project
PHEBUS	European reactor safety project
P/T	Partitioning and Transmutation
PUREX	Plutonium Uranium Redox EXtraction
RTIL	Room Temperature Ionic Liquid
SISAK	Short-lived Isotopes Studied by the AKufve technique
TRIGA	Research reactor constructed by General Atomics
TRUEX	TRansUranium EXtraction process
UREX	URanium EXtraction process

References

- Adams BA, Holmes EL (1935) J Soc Chem Ind 54:1
 Alexandratos SD, Trochimczuk AQ, Crick DW,
 Horwitz EP, Gatrone RC, Chiarizia R (1993) In:
 Emerging separation technology for metallic
 fuels, Proc Symp, p 111
 Al-Razi ~900, Kitab Al-Asrar (The book of secrets)

- Albinsson A, Ekberg C, Holgersson S, Jakobsson A-M, Landgren A, Skarnemark G (2002) *Appl Radiat Isot* 56:681
- Allard S, Ekberg C, Jolsterå R, Knutsson A, Ödegaard-Jensen A (2008) *Proceedings of ISEC 2008*, p 1133
- Arrhenius S (1887) *Z Phys Chem* 1:631
- Aristotle, 330 B.C., *Works*, 7, 933b
- Bandish O, Fürst R (1917) *Chem Ber* 50:234
- Berthelot M, Jungfleisch E (1872) *J Ann Chim Phys* 26:396
- Buchholz CF (1805) *Neues allgem J der Chemie* 4:157
- Cazaneuve P (1900) *Compt Rend* 131:346
- Choppin GR, Bond AH, Hromadka PM (1997) *J Radioanal Nucl Chem* 219(2):203
- Choppin GR, Liljenzin JO, Rydberg J (2002) *Radiochemistry and nuclear chemistry*. Butterworth-Heinemann, Woburn, p 605
- Ekberg C, Fermvik A, Retegan T, Skarnemark G, Foreman MRS, Hudson MJ, Englund S, Nilsson M (2008) *Radiochim Acta* 96:1
- Exodus 15:25–25
- Fischer H (1933) *Angew Chemie* 46:442
- Fischer H (1934) *Angew Chemie* 47:685
- Flanary JR (1956) *Proc Int Conf Peaceful Uses At Energy* 9:528
- Gibbs JW (1876) *Trans Conn Acad Arts Sci*
- Harland CE (1994) *Ion exchange: theory and practice*, 2nd edn. Royal Society of Chemistry, Cambridge
- Heym G (1938) *Ambix* 1:184
- Hill C, Arnaud-Neu F, Espartero AG, Desreux J-F, Modolo G, Bourg S, Malmbeck R, Caravaca C, Harrison M, de Angelis G, Uhlir J, Ouvrier N, Madic C (2007) *EUROPART – Final Activity Report*, (Contract Number : F16W-CT-2003–508 854)
- Jagadeeswara Rao CH, Venkatesana KA, Nagarajana K, Srinivasan TG (2008) *Radiochim Acta* 96(7):403
- Kratz J (1999) Chemical properties of the transactinide elements. In: Greiner W, Gupta RK (eds) *Heavy elements and related new phenomena*. World Scientific, Singapore
- Law JD, Herbst RS, Todd TA, Romanovsky VN, Babain VA, Esimantovsky VM, Smirnov IV, Zaitsev BN (2001) *Solvent Extr Ion Exc* 19(1):23
- Lewis GN, Randall M (1923) *Thermodynamics and the free energy of chemical substances*. McGraw-Hill, New York
- Lunes KK, Wishow RP (1985) *USAEC Report TID-11414*
- Madic C, Hudson MJ, Liljenzin J-O, Glatz JP, Nannicini R, Facchini A, Kolarik Z, Odoj R (2000) *New partitioning techniques for minor actinides*. Final report, NEWPART European Union project FI4I-CT-96-0010, European Commission Project report EUR 19149
- Madic C, Testard F, Hudson MJ, Liljenzin J-O, Christiansen B, Ferrando M, Facchini A, Geist A, Modolo G, Gonzalez-Espartero A, de Mendoza J (2004) *PARTNEW new solvent extraction processes for minor actinides*. Final report, European Union project FIKW-CT-2000-00087, Report CEA-R-6066
- Malmbeck R, Skarnemark G (1995) *Radiochim Acta* 68:169
- Mason GW, Peppard D (1963) *Nucl Sci Eng* 17:247
- McKay HAC (1956) *Proc Int Conf Peaceful Uses At Energy* 7:314
- Morse H (1902) *Z Phys Chem* 41:709
- Moyer BA (2009) *Ion exchange and solvent extraction*, vol 19. CRC Press, Boca Raton
- Nernst W (1891) *Z Phys Chem* 8:110
- Omtvedt JP, Alstad J, Breivik H, Dyve JE, Eberhardt K, Folden CM III, Ginter T, Gregorich KE, Hult EA, Johansson M, Kirbach UW, Lee DM, Mendel M, Nähler A, Ninov V, Omtvedt LA, Patin JB, Skarnemark G, Stavsetra L, Sudowe R, Wiehl N, Wierczinski B, Wilk PA, Zielinski PM, Kratz JV, Trautmann N, Nitsche H, Hoffman DC (2002) *J Nucl Radiochem Sci* 3(1):121
- Omtvedt JP, Alstad J, Björnstad T, Düllmann ChE, Gregorich KE, Hoffman DC, Nitsche H, Opel K, Polakova D, Samadani F, Schulz F, Skarnemark G, Stavsetra L, Sudowe R, Zheng Z (2007) *Eur Phys J* 45(1):91
- Peligot E (1842) *Ann Chim Phys* 5(3):7
- Pesme L (1982) *Echos CEA Groupe. French Atomic Energy Commission*
- Persson H, Skarnemark G, Skållberg M, Alstad J, Liljenzin JO, Bauer G, Haberberger F, Kaffrell N, Rogowski J, Trautmann N (1989) *Radiochim Acta* 48:177
- Rice NM, Irving HMNH, Leonard MA (1993) *Pure & Appl Chem* 65(11):2373
- Reid JC, Calvin M (1950) *J Am Chem Soc* 72:2948
- Ritcey GM (2006) *Solvent extraction - principles and applications to process metallurgy*, Revised 2nd edn. Ritcey and Associates, Ottawa, Canada
- Rydberg J (1969) *Acta Chem Scand* 23:647
- Rydberg J, Musikas C, Choppin GR (1992) *Principles and practices of solvent extraction*. Marcel Dekker, New York
- Schädel M, Brüchle W, Jäger E, Schimpf E, Kratz JV, Scherer UW, Zimmermann P (1989) *Radiochim Acta* 48:171
- Siddall TH (1959) *Proc Int Conf Peaceful Uses At Energy* 17:339
- Skarnemark G (2000) *J Radioanal Nucl Ch* 243(1):219
- Smith EL, Page JE (1948) *J Chem Soc Ind Lond* 67:48
- Stavsetra L, Gregorich KE, Alstad J, Breivik H, Eberhardt K, Folden CM III, Ginter T, Johansson M, Kirbach UW, Lee DM, Mendel M, Omtvedt L, Patin JB, Skarnemark G, Sudowe R, Wilk PA, Zielinski PM, Nitsche H, Hoffman DC, Omtvedt JP (2005) *Nucl Instrum Meth A* 543:509

- Stender E, Trautmann T, Herrmann G (1980) *Radiochem Radioa Let* 42:291
- Tachimori S, Sasaki Y, Morita Y, Suzuki S (2002) Recent progress of partitioning process in JAERI: development of amide-based ARTIST process. In: 7th information exchange meeting on actinide and fission product partitioning and transmutation, Jeju, Republic of Korea, Oct 2002
- Thompson HS (1850) *J Roy Agr Soc Engl* 11:68
- Trautmann N (1995) *Radiochim Acta* 70(71):237
- Tribalat S (1949) *Anal Chim Acta* 4:228
- Walton H, Rocklin R (1990) Ion exchange in analytical chemistry. CRC Press, Boca Raton
- Way TJ (1850) *J Roy Agr Soc Engl* 11:313
- Wierczinski B, Eberhardt K, Herrmann G, Kratz JV, Mendel M, Nähler A, Rocker F, Tharun U, Trautmann N, Weiner K, Wiehl N, Alstad J, Skarnemark G (1996) *Nucl Instrum Meth A* 370:532

53 Radiochemical Separations by Thermochromatography

A. F. Novgorodov¹ · F. Rösch² · N. A. Korolev¹

¹Joint Institute of Nuclear Research, Dubna, Russian Federation

²Johannes Gutenberg-University of Mainz, Mainz, Germany

53.1	<i>Introduction</i>	2430
53.2	<i>Equipment and Techniques</i>	2431
53.3	<i>Theory</i>	2433
53.3.1	Transport of Volatile Species Along the Column	2433
53.3.2	The Potential of Thermochromatography for Radiochemical Separations	2435
53.4	<i>Systematic Experiments</i>	2439
53.5	<i>Preparative Radiochemistry</i>	2449
53.6	<i>Investigation of New Transactinide Elements</i>	2451
53.7	<i>Conclusion</i>	2454

Abstract: The history, theoretical fundamentals, and practical application of thermochemistry are briefly reviewed. The main advantages of the method – the speed and selectivity of chemical separation of complex mixtures of short-lived radionuclides, including transactinide ones – are analyzed. Prospects of thermochemistry in production of radionuclides widely used in science and technology are considered on the basis of the performed systematic investigations of the thermochemical behavior of volatile compounds of the elements of the periodic table.

53.1 Introduction

The increasing interest in studying short-lived radionuclides, including transactinide ones, in the early 1960s created a demand for improved or newly created methods allowing fast and highly selective separation of various radioelements.

The analysis of the trends in development of analytical and radiochemical methods showed that the simplest and most effective way to satisfy this demand was through high-temperature gas chemistry. The already gained experience in using a variety of gas chromatography versions logically led to the choice of thermochemistry (TC), i.e., stationary non-isothermal gas–solid chromatography based on thermal variation of the interaction between the volatile radioactive species (atoms or molecules) and the adsorbent. In this method, a negative temperature gradient is produced in the direction of the carrier gas flow or, alternatively, in vacuum. It is, consequently, this temperature gradient that retards the transport of species in the column. If the slowing-down is different for different species, they are separated. Thus, it becomes possible to concentrate components of complex mixtures supplied to the thermochemical column even continuously (in contrast to ordinary gas chromatography).

Historically, the term “thermochemistry” was first applied to the method for separation of mainly volatile organic compounds in which the temperature field with a negative gradient moves along the column, so that the outlet temperature gradually increases ousting the separated substances from the column. In this case the thermochemical diagram is a curve expressing the time (t) or temperature (T) dependence of the outlet concentration, i.e., $c = f(t)$ or $c = f(T)$.

In radiochemistry, the most popular version is TC with a stationary temperature gradient, in which the concentration of a substance and its local distribution depend on the distance or temperature, i.e., $c = f(x)$ or $c = f(T)$. This means that the volatile compounds remain in the thermochemical column. In the literature this method was previously referred to by various jargon terms, e.g., “horizontal distillation,” “separation on the gradient tube,” “separation on the temperature gradient,” etc.

It is particularly noteworthy that Marie and Pierre Curie used the method in question as far back as the end of the nineteenth century when they discovered Ra and Po (Curie and Curie 1898). Polonium sulfide was distilled in a carbon dioxide flow into a tube with a negative temperature gradient, where it was precipitated in a narrow zone. Unfortunately, this experience and method has long been forgotten. What may also be considered the first publication on the use of TC in radiochemistry is the paper by Merinis and Bouissieres (1961) on separation of noncarrier-added spallogenic products: radioactive Hg, Pt, Ir, Os, and Re isotopes have been separated from macroscopic gold targets bombarded with medium-energy protons. Another important work of those, which stimulated the further development of TC, was an attempt to

separate and identify the artificial element 104 (now named rutherfordium), an analog of Hf, which clearly showed advantages of the method in the study of short-lived radionuclides (Zvara et al. 1971).

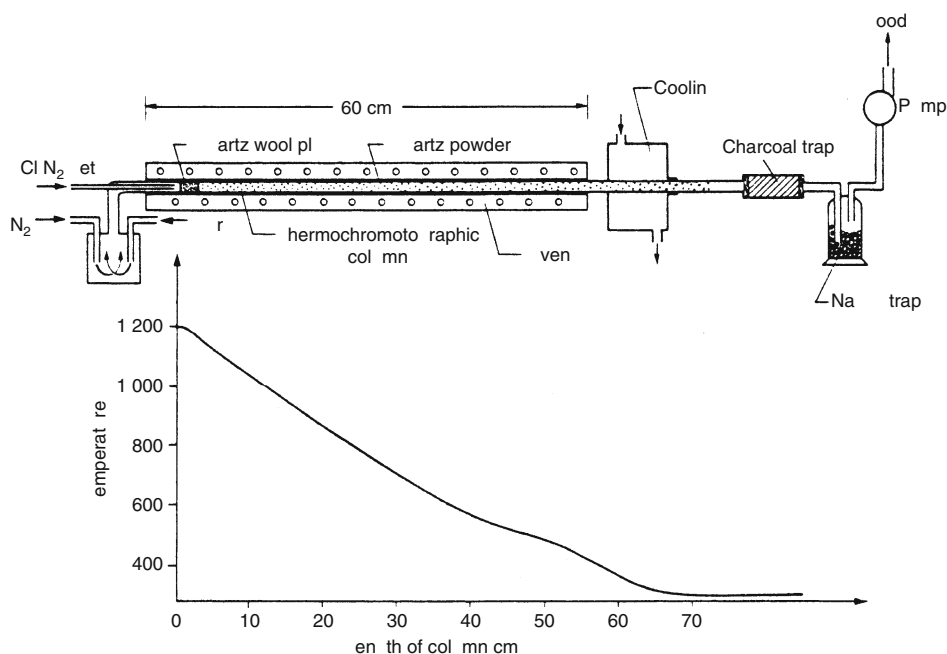
The simple equipment required and the high efficiency of the method stimulated its rapid theoretical and practical development in the 1960s, marked with some outstanding results, as for example, the characterization of previously unknown isotopes of many elements from the periodical system and even more – the discovery of new transactinide elements. Much has been contributed for the increasingly wide use of TC by a group of radiochemists (I. Zvara, B. Eichler, Yu. T. Chuburkov, V. P. Domanov, S. Hübener, A. B. Yakushev, et al.) from the Flerov Laboratory of Nuclear Reactions (JINR Dubna, Russian Federation). This and another group (H.W. Gäggeler, A. Türlér, R. Eichler, et al.) from the Paul Scherrer Institut, Villigen, Switzerland, still successfully continue the development of thermochemistry.

53.2 Equipment and Techniques

Thermochemical set-up: Figure 53.1 displays a typical thermochemical apparatus (Hickmann et al. 1993), the main part representing a gradient oven providing the required temperature field along the column. The oven may be made of a large number of short sections or by winding a heat-releasing wire (nichrome, superkanthal, platinum, etc.) on an insulating tube (quartz, porcelain, alundum, etc.) in a varying mode. To smooth the temperature field of the oven, it has a heat-conducting tube inside and a thermal-insulating

Fig. 53.1

Thermochemical setup and typical profile of temperature along the column (Reproduced with permission from Radiochimica Acta, Hickmann et al. 1993)



coating outside. The simplest design is an oven heating at one end of a long heat-conducting tube surrounded with a vacuum enclosure. This design ensures almost linear temperature distribution along the apparatus. The “cold” end of the tube is usually cooled with water or even liquid nitrogen.

The thermochromatographic apparatus also comprises

- A system for carrier gas (and/or reactant gas) supply, purification, and flow rate control; or, alternatively, an appropriate vacuum system.
- A system for injection of substances to be separated (periodic or continuous).
- A system for trapping outgoing reactant gases and possible radioactive gases or aerosols.

Thermochromatographic columns (TCC) are usually made of glass, quartz, porcelain, or metallic tubes, chemically resistant to reactant gases. They may be open (hollow) or filled with various substances (metals, oxides, halides, etc.). Probes, containing the radionuclides of interest, are inserted into the TCC at places of maximum temperature (T_S) in a batch mode before the experiments (off-line) or continuously (online) using gas jets with the radionuclides of interest adsorbed on microdisperse aerosol particles (KCl, MoO₃, etc.).

Temperature profiles: A method for determining the profile of the distribution of separated substances in the column is of major importance in thermochromatographic experiments. Most of them are carried out with radionuclides emitting radiation that penetrates through the columns walls (relatively “hard” β and γ rays), which allows the radioactivity within the column sections to be measured off-line either by cutting the column into small parts or by collimating the detector used and screening the column. Mixtures of radionuclides usually require the use of HPGe detectors because of the high-energy resolution. If sufficient activities of radionuclides decaying with emission of high-energy γ -quanta are used, it is in principle possible to monitor the substance distribution in the column online during the thermochromatographic experiment by using one or several well-collimated movable detectors.

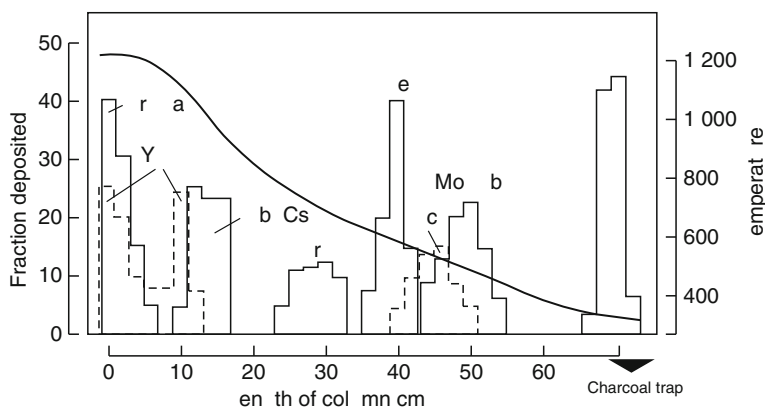
The situation becomes much more complicated when the radionuclides used undergo α decay or spontaneous fission, i.e., if non-penetrating radiation needs to be detected. If these radionuclides are long-lived, the column is cut into small sections, the substances adsorbed on its inner surface are washed off with appropriate solutions, and the resulting solutions are analyzed. In the case of short-lived radionuclides, e.g., transactinide elements, semiconductor or track detectors (mica, quartz) placed inside the column are used. They allow single decays to be determined at each point of the column. In principle, other methods may be used to determine the distribution of substances in the column, e.g., photospectrometry and X-ray fluorescence.

The experiment result is a thermochromatogram. An example is given in [Fig. 53.2](#) (Hickmann et al. 1993), which displays the distribution of bromides of uranium fission products continuously supplied to the column for 15 min. The thermochromatogram for each chemical species allows the determination of the basic parameter T_a , the adsorption temperature (center of gravity of distribution of the substance in the column).

Numerous experiments have shown that this quantity depends first of all on the chemical composition of the volatile substance and on the column material (adsorbate–adsorbent interaction). In addition, it depends on the starting temperature of the column, the period of the thermochromatography procedure, the temperature gradient, the diameter of the column, type and flow-rate of carrier gas (or gas-reagent), and some other parameters. Thus, the adsorption temperature T_a is not a constant and, for example, varies inversely with the duration of the thermochromatography procedure of a particular experiment. Therefore, it is

■ Fig. 53.2

Element distribution in a thermochematographic column with 9 vol% hydrogen bromide as reactive additive to the carrier gas nitrogen, together with the temperature profile along the column. Quartz-powder column, 15 min exposure time (Reproduced with permission from *Radiochimica Acta*, Hickmann et al. 1993)



essential for researchers to try to find ways of transferring the variable T_a to standard constants $\Delta \overline{H}_a^0$ and $\Delta \overline{S}_a^0$, enthalpy and entropy, respectively, used in ordinary gas chromatography.

53.3 Theory

53.3.1 Transport of Volatile Species Along the Column

All theoretical treatments of the thermochematographic process (Merinis and Bouissieres 1969; B. Eichler and Zvara 1975; Steffen and Bächmann 1978b; Novgorodov and Kolatchkowski 1979), beginning with papers by Merinis and Bouissieres (1969), are based on the fact that the species' (atom, molecule) transfer time within the TCC breaks into two components – the residence time in the gaseous phase and the residence time on the surface of the column. The latter is governed by the average lifetime of the species in the adsorbed state τ_a (s) related to the temperature by the Frenkel equation (Frenkel 1924):

$$\tau_a = \tau_0 \cdot \exp\left(\frac{Q}{RT}\right), \quad (53.1)$$

where τ_0 is the period of oscillation of the species in the adsorbed state perpendicularly to the surface (s); Q is the adsorption heat ($\text{J} \cdot \text{mol}^{-1}$); R is the gas constant ($\text{J} \cdot \text{mol}^{-1} \cdot \text{K}^{-1}$); T is the absolute temperature (K).

The total time of the species transfer (transport) in the column from the starting temperature T_s to the adsorption temperature T_a is most comprehensively described by B. Eichler and Zvara (1975):

$$t = \frac{T_0}{gu_0} \ln \frac{T_a}{T_s} + \frac{sT_0 \frac{V}{A} \exp\left(\frac{\Delta \overline{S}_a^0}{R}\right)}{vgu_0} \int_{T_s}^{T_a} \frac{1}{T} \exp\left(-\frac{\Delta \overline{H}_a^0}{RT}\right) dT \quad (53.2)$$

where T_0 is the standard temperature, 298.15 K; g is the gradient of the temperature for its linear distribution along the column ($\text{K} \cdot \text{cm}^{-1}$); u_0 is the linear velocity of the carrier (reagent) gas in the column under standard conditions ($\text{cm} \cdot \text{s}^{-1}$); s and v are the open surface and the open volume of the column per its unit length, (cm) and (cm^2) respectively; V/A is the ratio of the standard molar volume to the standard molar surface (cm); $\Delta\overline{H}_a^0$ is the adsorption enthalpy ($\text{J} \cdot \text{mol}^{-1}$); $\Delta\overline{S}_a^0$ is the adsorption entropy ($\text{J} \cdot \text{mol}^{-1} \cdot \text{K}^{-1}$).

This equation is derived on the assumption that the main characteristic parameters of the adsorption interaction ($\Delta\overline{H}_a^0$ and $\Delta\overline{S}_a^0$) are independent of the temperature, that there is no surface diffusion, and that the carrier (reagent) gas adsorption is negligibly small. Solution of this equation, i.e., finding $\Delta\overline{H}_a^0$ is virtually reduced to solution of the integral in expression (53.2). This may be done either numerically or by replacing the integral by the difference of the so-called integral exponential function represented in the tabulated form:

$$\int_{T_s}^{T_a} \frac{1}{T} \exp\left(-\frac{\Delta\overline{H}_a^0}{RT}\right) dT = \left[E_i^*\left(-\frac{\Delta\overline{H}_a^0}{RT_a}\right) - E_i^*\left(-\frac{\Delta\overline{H}_a^0}{RT_s}\right) \right] \quad (53.3)$$

Analyzing (53.2) B. Eichler and Zvara (1982) considered the effect of various standard state models (V/A) and values of $\Delta\overline{S}_a^0$, calculated on the basis of the molecular-kinetic concepts as the loss of degrees of freedom of the particle (atom) on its transition from the gas phase to the adsorbed state, on $\Delta\overline{H}_a^0$. With given mobile and localized adsorption and five standard states, the theoretically calculated values of $\Delta\overline{S}_a^0$ for absorption of Po on the Cu surface vary in a very wide range from -31.10 to $-512.27 \text{ J} \cdot \text{mol}^{-1} \cdot \text{K}^{-1}$ (B. Eichler and Zvara 1982). Naturally, this strongly affects the values of $\Delta\overline{H}_a^0$ calculated by expression (53.2). In the case of polyatomic molecules, when one has to take into account the entropy variation due to variation of internal degrees of freedom, rotation of the molecule, and probably chemical bond of molecules with the surface, a theoretical calculation of $\Delta\overline{S}_a^0$ becomes much more complicated. Thus, the uncertainty in evaluation of $\Delta\overline{S}_a^0$ results in approximate values of $\Delta\overline{H}_a^0$ only. Several attempts have been made to calculate empirically $\Delta\overline{S}_a^0$ and $\Delta\overline{H}_a^0$ for various compounds, e.g., chlorides and oxides (B. Eichler 1976), and to determine experimentally these two main parameters of the adsorption interaction, but their values obtained for a majority of adsorbate–adsorbent pairs are still estimates. Therefore, it is desirable to cite these values together, no matter how they were obtained.

The generally accepted theoretical value of $\Delta\overline{S}_a^0$ is the one obtained for the mobile adsorption model and the standard state $V/A = 1 \text{ cm}$ (B. Eichler and Zvara 1982)

$$\Delta\overline{S}_a^0 = R \cdot \ln\left(\frac{1}{(1 \text{ cm}) \cdot v_B} \sqrt{\frac{kT_a}{2\pi m}}\right) + \frac{1}{2}R, \quad (53.4)$$

where R is the gas constant; v_B is the characteristic adsorbent frequency equal to $5 \times 10^{12} \text{ s}^{-1}$ for quartz; k is the Boltzmann constant; T_a is the adsorption temperature (K) (B. Eichler et al. 2002); m is the mass of the molecule (g).

The key question about the values of $\Delta\overline{S}_a^0$ and $\Delta\overline{H}_a^0$ and, if possible, about their dependence on the temperature may be eventually solved by carrying out quite systematic series of experiments with several experimental conditions, e.g., experiment period, starting temperature, gas composition and velocity, column diameter, etc., varied over a wide range for one and the same adsorbate–adsorbent pair (Steffen and Bächmann 1978b; Chuburkov et al. 1993). Provided that $\Delta\overline{S}_a^0$ and $\Delta\overline{H}_a^0$ are temperature-independent, dependence of $\ln \frac{-\lg v_0}{sT_a \cdot (1 \text{ cm})}$ on $\frac{1}{T_a}$

Table 53.1

Values of ΔS_a^0 ($\text{J} \cdot \text{mol}^{-1} \cdot \text{K}^{-1}$) obtained by various methods

Compound	Experiment (Steffen and Bächmann 1978b)		Empirical dependence (Chuburkov et al. 1993)	Equation 10.4
	Isothermal chromatography	Thermo-chromatography		
ReO_3	-187.0 ± 5.0	-147.3 ± 17.0	-150 ± 5	-166.3
HReO_4	-206.4 ± 3.4	-114.8 ± 11.0	-133 ± 3	-168.9
IrO_3	-191.0 ± 6.2	-137.0 ± 15.3	-150 ± 5	-168.1

(v_0 is the volume gas flow under standard conditions) yields a straight line with a slope $-\Delta H_a^0/R$ and an intercept on the x -axis at $\ln \frac{RT_0}{-\Delta H_a^0} + \frac{\Delta S_a^0}{R}$.

► Table 53.1 illustrates the different approaches of determination of ΔS_a^0 in the case of adsorption of volatile Re and Ir compounds with oxygen-containing carrier gas systems on TCC quartz surfaces. Undoubtedly, experiments are of primary importance in determining the entropy values.

53.3.2 The Potential of Thermochemistry for Radiochemical Separations

In analytical chemistry the quality of separation is characterized by the criterion for separation of two substances ($R_{1,2}$), expressed in TC as:

$$R_{1,2} = \frac{T_{a1} - T_{a2}}{2(\sigma_1 + \sigma_2)} \quad (53.5)$$

where T_{a1} and T_{a2} are the temperatures of the centers of gravity of the distribution of substances 1 and 2 (K); σ_1 and σ_2 are the standard deviations of their distribution (K).

Two theoretical contributions have focused on the distribution of the substance in the course of its motion along the TCC (Novgorodov and Kolatchkowski 1979; Zvara 1985). In one of them the general relations of gas chromatography are adopted. The height equivalency to the theoretical plate (HETP), H (cm), for the laminar flow in an open straight tube column, is (Giddings and Seager 1960)

$$H = \frac{2D_{\text{gas}}}{u_x} + \frac{d^2 u_x}{96D_{\text{gas}}} \quad (53.6)$$

where D_{gas} is the diffusion coefficient of the substance under study in the carrier gas ($\text{cm}^2 \cdot \text{s}^{-1}$); u_x is the linear velocity of the carrier gas defined as

$$u_x = u_0 \cdot \frac{T}{T_0} = \frac{4v_0 T}{\pi d^2 T_0} \quad (53.7)$$

where u_0 is linear velocity of the carrier gas under standard conditions ($\text{cm} \cdot \text{s}^{-1}$); d is the diameter of the column (cm); T is the temperature of the column (K). The diffusion coefficients correlate according to the molecular-kinetic concepts:

$$D_{\text{gas}} = D_{\text{gas}}^0 \left(\frac{T}{T_0} \right)^{3/2} \quad (53.8)$$

where D_{gas}^0 is the diffusion coefficient under standard conditions. Considering (53.7) and (53.8), expression (53.6) takes the following form

$$H = \frac{aT + b}{\sqrt{T}} \quad (53.9)$$

where $a = \frac{\pi D_{\text{gas}} d^2}{2v_0 \sqrt{T_0}}$ and $b = \frac{v_0 \sqrt{T_0}}{24\pi D_{\text{gas}}}$.

For isothermal gas chromatography the dispersion (σ^2) of the substance distribution in the column increases with the coordinate x (i.e., the zone is expanded) as

$$\sigma_{\text{exp}}^2 = xH \quad (53.10)$$

As described above, an advantage of TC over ordinary gas chromatography is that the decrease in the temperature of the column slows down the motion of the zone of the substance to be separated. In addition, the delayed part of the zone meets a higher temperature and is speeded up while the leading part, on the contrary, is slowed down. Thus, the distribution of the substance formed at each moment of the process, i.e., at each individual adsorption temperature, is determined by the fact that the expanding of the zone is equal to its compression

$$d\sigma/dt = (d\sigma/dt)_{\text{exp}} + (d\sigma/dt)_{\text{comp}} = 0 \quad (53.11)$$

As follows from (53.9) and (53.10) and in view of $T = T_s + gx$, the dispersion causing the expanding of the zone is

$$\sigma_{\text{exp}}^2 = \frac{a(T_s + gx) + b}{\sqrt{T_s + gx}} \cdot x \quad (53.12)$$

Differentiation of this expression results in the expression

$$\left(\frac{d\sigma}{dt}\right)_{\text{exp}} = \frac{1}{4\sigma\sqrt{T}} [a(3T^2 - TT_s) + b(T + T_s)] \cdot w_{\text{zone}} \quad (53.13)$$

where w_{zone} is the velocity of the moving center of gravity of the zone ($\text{cm} \cdot \text{s}^{-1}$). The compression component can be expressed, according to Ohline and Deford (1963), as

$$\left(\frac{d\sigma}{dt}\right)_{\text{comp}} = -g\sigma\Delta\overline{H}_a^0 \frac{w_{\text{zone}}}{RT^2} \quad (53.14)$$

Substituting (53.13) and (53.14) into (53.11) yields

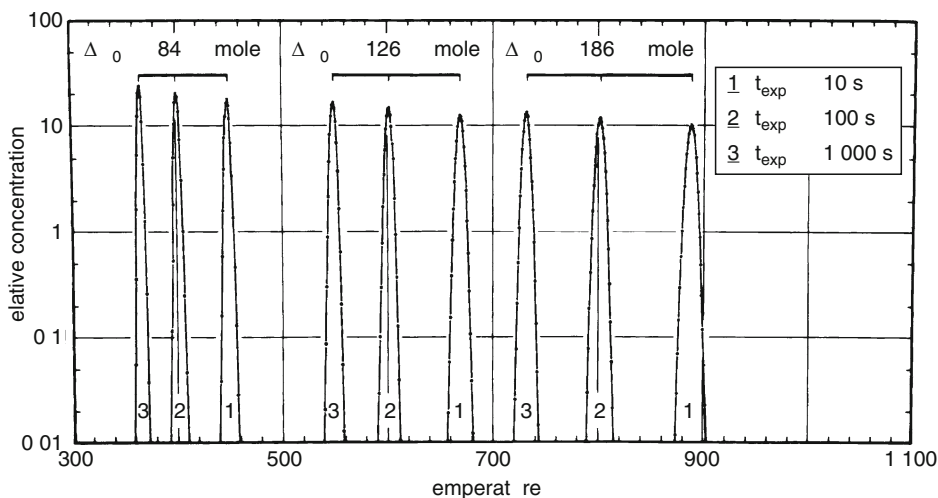
$$\sigma^2 = \frac{R\sqrt{T_a}[aT_a(3T_a - T_s) + b(T_a + T_s)]}{4g\Delta\overline{H}_a^0} \quad (53.15)$$

By using the derived basic equations of TC (Novgorodov and Kolatchkowski 1979), the distribution of a substance along the column was calculated for the simplest case, i.e., when the substance is injected in the column in the form of a δ -function [$c = f(s, t) = \infty$].

Figure 53.3 displays the computed thermochematogram of three hypothetical substances with $\Delta\overline{H}_a^0 = -84, -126, \text{ and } -168 \text{ kJ} \cdot \text{mol}^{-1}$ for three process periods of 10, 100 and 1,000 s. The calculation was carried out with the parameters $d = 0.3 \text{ cm}$; $v_0 = 0.5 \text{ cm}^3 \cdot \text{s}^{-1}$; $D_{\text{gas}}^0 = 0.1 \text{ cm}^2 \cdot \text{s}^{-1}$; $T_s = 1,100 \text{ K}$, and $g = -16 \text{ K} \cdot \text{cm}^{-1}$. Not only retarding but also compression of the zone of the hypothetical substances is obvious. Note that the calculations

Fig. 53.3

Distribution of three hypothetical substances in the TCC for three exposure times (see explanation in the text)



were carried out for the carrier gas velocity close to the optimum velocity, the expression for which was derived from (53.6)

$$v_{0(\text{opt})} = \pi D_{\text{gas}}^0 d \sqrt{\frac{6(T_s + T_a)}{T_0}} \quad (53.16)$$

The standard deviation σ for the substance with $\Delta \overline{H}_a^0 = -126 \text{ kJ} \cdot \text{mol}^{-1}$ and $T_a = 500 \text{ K}$ is 3.6 K under the conditions considered.

A slightly different approach to determine the distribution of a substance in no carrier amounts (n.c.a.) was introduced by Zvara (1985). Using the Monte Carlo method and assuming that species leaving the surface of the column with an adopted probability immediately start moving at the carrier gas velocity, the author calculated the extent of the “jump” ($\overline{\eta}$) of the species to the next adsorption event, which is on the average equal to

$$\overline{\eta} = \frac{11 v_0}{48 \pi D_{\text{gas}}} \quad (53.17)$$

The calculations for the case like the one considered above yielded $\sigma = 21 \text{ K}$ for $T_a = 476 \text{ K}$ (Zvara 1985).

The calculations of the standard deviation σ were experimentally checked (Nguyen et al. 1984a) with chlorides of n.c.a. radiolanthanides. The reactant gas was an $\text{H}_2 + \text{HCl}$ (1:1) mixture thoroughly purified of O_2 and H_2O . The starting temperature was $1,373 \text{ K}$. The thermochematographic quartz column with the inner diameter of 1.25 mm was thoroughly cleaned and treated with the reactant gas at the starting temperature of $1,373 \text{ K}$. The experiments lasted for 1 h and volatilization of the chlorides was 95% in 2 min , i.e., their injection in the column was close to the “instant” (near to δ -function) mode. The optimum gas flow rate of $0.33 \text{ cm}^3 \cdot \text{s}^{-1}$ was provided. The average value of T_a for the lanthanide (La, Ce, Nd, Sm, Eu, Gd,

Yb, Lu) chlorides was 840 K and $\sigma = 5\text{--}6.5$ K. Calculation by (53.16) for $D_0 = 0.795 \text{ cm}^2 \cdot \text{s}^{-1}$ (Bretshneider 1966) and $\Delta \overline{H}_a^0 = -200 \text{ kJ/mol}$ (B. Eichler 1976) yielded $\sigma = 8.7$ K. A slight discrepancy between experiment and theory is probably due to stronger temperature dependence of D_{gas} : the real exponent in Eq. (53.8) is not 1.5 but 1.8 (Bretshneider 1966).

Gas-thermochromatographic separation techniques found wide application in radiochemistry because here, as pointed out above, the quality of separation is much less dependent on the duration and mode of sample injection in the column than in isothermal gas chromatography. The problems arising from the effect of the size of samples as well as time and mode of their injection in ordinary isothermal gas-chromatographic columns on the separation efficiency are discussed in textbooks and monographs. This issue, however, requires particular consideration in the case of gas TC. On the basis of Eqs. (53.2) and (53.15), substance distributions along the TCC were calculated for a prolonged injection mode, in particular for cork injection (Nogare and Juvert 1962), i.e., in the most often occurring case in radiochemistry, when substances are supplied into column continuously (online operation in conjunction with a reactor or an accelerator). In these computer-aided calculations the injection profile was divided into 100 pseudo- δ -functions. The response, i.e., the distribution of the substance in the thermochromatographic column, was determined for each of the input models first, and all the responses were summed subsequently. The computing parameters were the same as in the calculation shown in Fig. 53.3.

Figure 53.4 displays the distribution of a substance with $\Delta \overline{H}_a^0 = -84 \text{ kJ/mol}$ via cork injection. The ordinate shows the relative concentration, namely per cent of the injected substance, over the column length corresponding to $\Delta T = 1 \text{ K}$. Curves 1, 2, and 3 are for the sample injection times t_{in} equal to 0.1, 0.5, and 1.0 of the experiment time t_{exp} . The peaks, which result from the infinite number of divisions (100) of the injection profile, clearly show the motion of the substance in the TCC and the gradual compression (concentration) of the adsorption zone. For example, at the experiment period $t_{\text{exp}} = t_{\text{in}} = 100 \text{ s}$ the extreme right peak corresponds to the transfer time 0.5 s, the next one to 1.5 s, then to 2.5 s, 3.5 s, etc. Accordingly, at $t_{\text{exp}} = t_{\text{in}} = 10 \text{ s}$ the peaks (right to left) correspond to the transfer times 0.05, 0.15, 0.25 s, etc.

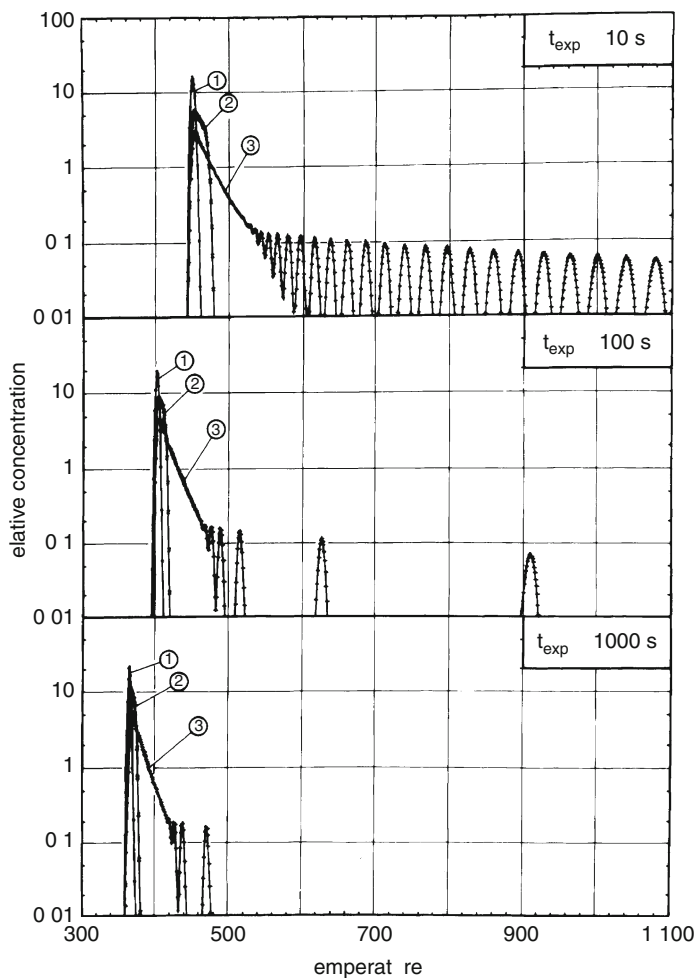
It is also illustrated, that at $t_{\text{exp}} = 10 \text{ s}$ and $t_{\text{in}} = 5 \text{ s}$ the adsorption peak is already formed 5 s after the initiation of the thermochromatographic process. The calculations were carried out for the optimum carrier gas flow rate (53.16). This flow rate might be appreciably larger, e.g., in the study of very short-lived radionuclides (with $T_{1/2} \approx 1\text{--}3 \text{ s}$) (Zvara et al. 1998), but this will result in an increased σ , i.e., in worse separation.

The separation criteria in the case of continuous sample injection in the TCC ($t_{\text{in}} = t_{\text{exp}}$) over a period of 10, 100, and 1,000 s for two pairs of substances with $\Delta \overline{H}_a^0 = -84$ and -126 kJ/mol and $\Delta \overline{H}_a^0 = -126$ and -168 kJ/mol are 0.43, 1.05, and 2.26 and 0.84, 1.27, and 1.66, respectively. Hence, satisfactory separation of the hypothetical substances under consideration is attained as soon as after 100 s.

These theoretical considerations of the thermochromatographic process presume that the adsorption entropy and enthalpy do not depend on the temperature. It was also postulated that the adsorbent was homogeneous, its surface was not saturated with the adsorbate (monolayer or less), and the carrier (reagent) gas was “unsorbable.” Diffusion in the solid phase (adsorbent) and surface diffusion were ignored. Furthermore, in the theoretical considerations the effect of the carrier (reagent) gas pressure on the substance transport was not taken into account, which, however, should be considered in the case of TC at reduced reactant gas pressures and vacuum TC or with densely filled columns.

■ Fig. 53.4

Distribution of a substance in TCC for cork injection: (1) – $t_{in} = 0.1 t_{exp}$, (2) – $t_{in} = 0.5 t_{exp}$, (3) – $t_{in} = t_{exp}$ (see explanation in the text)



53.4 Systematic Experiments

Thermochematographic investigations in radiochemistry deal with volatile (as a rule, at temperatures up to 1,500 K) radioactive elements or their compounds. At the above-mentioned temperatures most elements form one or more volatile compounds: hydrides, halides, oxides, sulfides, oxyhalides, hydroxides, organic derivatives, etc. Radionuclides used in TC are produced in various nuclear reactions. They are mainly fission products of uranium and transuranium elements, spallogenic products of reactions involving medium-energy particles, and radionuclides produced at accelerators of low-energy charged particles (p, d, ^3He , α) or of heavy ions (^{18}O , ^{22}Ne , ^{48}Ca , etc.). The latter occupy a prominent place in

thermochromatographic experiments as they are used for synthesizing atoms of new elements. The rapid development of TC was significantly due to the study and realization of the potency of this method for discovering new elements, the isotopes of which are characterized by half-lives from a few seconds to tens of seconds, too small for “usual” chemical investigations. To attain these objectives and to plan efficient work on synthesis, purification, and detection of new elements, a lot of experiments have been carried out to study the behavior of not only analogues of new elements of the periodic table but also impurity elements.

Hydrogen, air, oxygen, water vapor, halogens, hydrohalogens, CCl_4 , BBr_3 , SOCl_2 , sulfur vapor, and mixtures of some of them were used as reagent gases. The choice of the reagent gas is dictated by the conditions to be created. They must allow domination of only one volatile compound of the element under study for correct interpretation of its behavior. Most experiments were carried out with relatively long-lived radionuclides, whose volatile compounds were injected in the thermochromatographic column either directly from the pre-irradiated target or from a specially prepared sample. In this case the speed at which the volatile compound is supplied into the column depends on the diffusion speed in the sample and the rate of interaction with the reagent gas, and the injection profile usually has a decreasing exponential form. In some experiments volatile compounds were supplied into the TCC in a continuous mode immediately after production of the desired radionuclide in the reactor or at the accelerator.

Below, a brief review of the volatile compounds of most chemical elements at n.c.a. amounts, which were used in thermochromatographic experiments, will follow. The adsorption temperature was taken as the volatility criterion, which allows planning of thermochromatographic separations in preparative radiochemistry. As this quantity is not constant, its variation within traditional duration times of the thermochromatographic process (15–60 min) shall be taken into account. In addition, this variation applies to the adsorption temperatures of each component of the mixtures under separation. A particular contribution to systematic thermochromatographic investigations has been made by B. Eichler, who published a remarkable review of mainly his own works more than 30 years ago (B. Eichler 1976).

Group 1: The main compounds of alkali elements relevant for thermochromatography are the chlorides. B. Eichler and Malzeva (1976) separated Cs and Fr chlorides in a column filled with quartz sand as is described. The adsorption temperatures T_a at a chlorine flow of $t_{\text{exp}} = 1,800$ s were 670 and 590 K, respectively. According to other authors (Rudstam and Grapengiesser 1973), T_a for NaCl and RbCl are 720 and 680 K, respectively, while Merinis and Bouissieres (1969) give a T_a for CsCl of 620 K. Alkali bromides and iodides show similar behavior. The alkali elements may also be studied in the form of metals, e.g., in vacuum thermochromatographic columns of high-melting metals (Hübener and Zvara 1979).

Group 2: Ca, Sr, and Ba chlorides were investigated, and their adsorption temperatures turned out to be equal to approximately 1,200 K (B. Eichler and Domanov 1974). For Ra dichloride, T_a is slightly lower (1,130 K) (Merinis et al. 1970). The thermochromatographic investigations of these metals are described systematically (Hübener and Zvara 1982).

Group 3: The most completely studied compounds in thermochromatography are the lanthanide and actinide chlorides. Their temperatures of adsorption on quartz are presented in [Table 53.2](#). The behavior of bromides is similar to that of the chlorides (Hickmann et al. 1993). The adsorption temperatures of La and Tb trichlorides (Kim et al. 1987b) are 30 K higher than for their tribromides. High-temperature thermochromatographic investigations of volatile hydroxides of hexavalent U and Pu (probably W analogues) started recently (Hübener et al. 2001). Interesting results were obtained in thermochromatographic studies

Table 53.2

Volatile compounds of elements of group 3 of the periodic table

Probable compound	Adsorption temperature on quartz, K	Probable compound	Adsorption temperature on quartz, K
EuCl ₂	1,180 (Nguen et al. 1984b)	AcCl ₃	1,120 (Merinis et al. 1970)
YbCl ₂	1,180 (Nguen et al. 1984b)	UCl ₃	820 (Merinis et al. 1970)
ScCl ₃	739 (B. Eichler 1976)	NpCl ₃	850 (Merinis et al. 1970)
YCl ₃	903 (B. Eichler 1976), 1,050 (Hickmann et al. 1980)	PuCl ₃	820 (Merinis et al. 1970)
LaCl ₃	920 (Merinis and Bouissieres 1969), 1,120 (B. Eichler 1976), 846 (Nguen et al. 1984a)	AmCl ₃	850, 880 (Merinis et al. 1970) 900 (B. Eichler et al. 2002) 890 (Adams et al. 1998)
CeCl ₃	893 (B. Eichler 1976), 843 (Nguen et al. 1984a)	CmCl ₃	860 (Merinis et al. 1970)
PrCl ₃	900 (Merinis and Bouissieres 1969)	BkCl ₃	820, 880 (Merinis et al. 1970) 920 (Yakushev et al. 2003)
NdCl ₃	920 (Merinis and Bouissieres 1969), 838 (Nguen et al. 1984a)	CfCl ₃	840, 860 (Merinis et al. 1970)
PmCl ₃	890 (Merinis and Bouissieres 1969)	EsCl ₃	895 (Adams et al. 1998) 920 (B. Eichler et al. 2002) <853 (Yakushev et al. 2003)
SmCl ₃	843 (Nguen et al. 1984a)	EsBr ₃	730 (Graf et al. 1999)
EuCl ₃	890 (Merinis and Bouissieres 1969), 858 (Nguen et al. 1984a)	CeCl ₄	720 (Merinis and Bouissieres 1969)
GdCl ₃	843 (Nguen et al. 1984a)	ThCl ₄	700 (Merinis et al. 1970)
TbCl ₃	790 (Merinis and Bouissieres 1969), 943 (B. Eichler 1976)	UCl ₄	630 (Merinis et al. 1970)
YbCl ₃	903 (B. Eichler 1976), 838 (Nguen et al. 1984a)	NpCl ₄	620, 640 (Merinis et al. 1970)
LuCl ₃	790 (Merinis and Bouissieres 1969), 873 (B. Eichler 1976), 835 (Nguen et al. 1984a)	PuCl ₄	640 (Merinis et al. 1970)
		BkCl ₄	<648 (Yakushev et al. 2003)
		PaCl ₅	370 (Merinis et al. 1970)
		UCl ₆	390 (Gärtner et al. 1997)

of plutonium in moist oxygen (Domanov et al. 2002). Observed adsorption zones with $T_a \approx 720, 520, 400,$ and 170 K were attributed to plutonium compounds PuO_2 , PuO_3 , $\text{PuO}_x(\text{OH})_y$, and PuO_4 , respectively.

The study of metals or lanthanide and actinide suboxides using thermochemical columns of high-melting metals (Ti, Zr, Ta, Mo, W) is particularly promising. The experiments were carried out in vacuum (Beyer and Novgorodov 1976) or in inert helium atmosphere with Na and Ca vapor added as a reducing agent (Hübener and Zvara 1979). Adsorption of metals on metal surfaces was heretically treated (Roßbach and Eichler 1984), with both the adsorption enthalpy and entropy calculated for 63 adsorbates on 22 adsorbents. Lanthanide (B. Eichler et al. 1985b) and actinide (B. Eichler et al. 1985a) adsorbates were considered analogously. The

potential of vacuum thermochemistry for the separation of lanthanides was demonstrated (Beyer and Novgorodov 1976), where Lu, Yb, and Tm as well as Gd, Eu, and Sm were satisfactorily separated in a tantalum column with no more than 50 theoretical plates. Particularly noteworthy are the experiments with the excellent separation of Cf–Md achieved in a molybdenum TCC (Hübener and Zvara 1982), and Cm–Bk in a niobium TCC (Taut et al. 2000). The behavior of heavy actinides in TCC made of Ti, V, Nb, and Ta has been studied by Taut et al. (1998, 2001).

Group 4: The thermochemical behavior of the elements of this group received special consideration because they are assumed to be lighter analogues of the first transactinide element 104 (Rf). Zr and Hf chlorides and bromides have been studied carefully, but the results were extremely discrepant. While in early investigations the adsorption temperature of the Ti, Zr, and Hf tetrachlorides was found to be 438, 463, and 453 K, respectively (B. Eichler 1976), parallel investigation of T_a for the Zr and Hf tetrachlorides yielded 393 and 373 K, respectively (Kim et al. 1987b). Evidently, the uncontrolled oxygen content of the reactant gas led to very high T_a for ZrCl₄, e.g., 550 K (Bayar et al. 1978a) and even 840 K (Hickmann et al. 1993). This effect was carefully studied (Domanov and Kim 1988; Domanov et al. 1988), who assumed existence of volatile oxychlorides ZrOCl₂ and HfOCl₂, thermally stable in the gas up to the temperature of approximately 700 K. Their T_a values are slightly higher than the T_a of the analogue tetrachlorides (383 and 373 K) and are equal to 423 K (for ZrOCl₂ and HfOCl₂). The behavior of hafnium and zirconium bromides is similar to chlorides. Thermochemistry of Hf and Zr chlorides and bromides have also been performed in columns filled with NaCl, KCl, CsCl, and KBr. The T_a increase considerably (to about 850 K) because of chemical interaction resulting in formation of compounds like (Na,K,Cs)₂(Zr,Hf)(Cl,Br)₆ (Tsalas and Bächmann 1978; Kim et al. 1987a). Stability of these compounds increases in the series Na→Cs.

Group 5: Elements of this group form two well-known types of volatile compounds: halides and oxyhalides. Noteworthy vanadium compounds are VCl₄ (or VOCl₃) with T_a = 298 K (B. Eichler and Domanov 1974) and VCl₃ (or VCl₂) with T_a = 684 K (Novgorodov et al. 1986a). The adsorption temperatures of Nb and Ta pentachlorides on quartz were found to be 410 and 770 K, respectively (B. Eichler and Domanov 1974). The value of T_a for tantalum is unexplainably overestimated. This is confirmed by the fact that the adsorption temperatures for pentabromides of the two elements are similar and are equal to approximately 330 K (Belov et al. 1974; Zvara et al. 1975). Carefully performed experiments (Domanov and Kim 1988) yielded close T_a values for Nb pentachloride and oxychloride on quartz, 333 and 373 K, respectively. The adsorption temperatures of Nb and Ta pentachlorides in the columns filled with KCl and CsCl increase to approximately 530 and 660 K for the respective adsorbents, which is due to formation of compounds like (K,Cs)(Nb,Ta)Cl₆ (Tsalas and Bächmann 1978).

Group 6: High-melting elements of this group form a variety of volatile compounds whose adsorption temperatures on quartz are listed in ▶ Table 53.3. It is, however, difficult to interpret the composition and properties of oxychlorides because of their close T_a values. In TCC filled with KCl or CsCl, molybdenum chloride forms two approximately equal peaks at T_a = 533 and 453 K or 653 and 573 K, respectively (Tsalas and Bächmann 1978).

Group 7: The main volatile compounds formed by the elements of this group are halides, oxides, oxyhalides, and hydroxides. ▶ Table 53.4 shows that many experiments have been carried out, there is a large difference between the adsorption temperatures of the compounds as, for example, ReO₃ and HReO₄.

■ Table 53.3

Volatile compounds of elements of group 6 of the periodic table

Probable compound	Adsorption temperature on quartz, K
CrCl_2	883 (Novgorodov et al. 1986a)
CrCl_4 (CrO_2Cl_2)	293 (B. Eichler and Domanov 1974)
MoBr_4	370 (Hickmann et al. 1993), 370 (Belov et al. 1974)
MoJ_4	680 (Hickmann et al. 1993)
MoCl_5	358 (B. Eichler and Domanov 1974), 290 (Hickmann et al. 1993), 353 (Helas et al. 1978), 360 (Bayar et al. 1978d), 323 (Chuburkov et al. 1996)
MoOCl_3	413 (Helas et al. 1978), 378 (Chuburkov et al. 1996)
MoOCl_4	<300 (Helas et al. 1978), 373 (Bayar et al. 1978d), 310 (Chuburkov et al. 1996)
MoO_2Cl_2	320 (Bayar et al. 1978d), 330 (Helas et al. 1978), 340 (Chuburkov et al. 1996) <440 (Türler et al. 1996)
MoO_3	1,260 (B. Eichler 1976)
H_2MoO_4	623 (Helas et al. 1978) 700 (Vahle et al. 1995) 650 (Vahle et al. 1997)
WCl_6	353 (B. Eichler and Domanov 1974), 448 (Helas et al. 1978)
WOCl_4	328 (Helas et al. 1978), 400 (Belov et al. 1972), 373 (Chuburkov et al. 1996)
WO_2Cl_2	448 (Helas et al. 1978), 570 (Belov et al. 1972), 423 (Chuburkov et al. 1996), 423 (Yakushev et al. 1993)
WO_3	>1,300 (Bayar et al. 1975)
H_2WO_4	830 (Bayar et al. 1975), 650 (Vahle et al. 1999)

The adsorption temperatures of Tc and Re chlorides in the columns filled with KCl or CsCl increase to 813 or 873 K and to 613 or 643 K, respectively (Tsalsas and Bächmann 1978). When Mg and Ca oxides were used as adsorbents (Zhuikov 1982a), this leads to a considerable increase in the adsorption temperatures. These solid phases very likely might be considered as effective filters in preparative radiochemistry.

■ Table 53.4

Volatile compounds of elements of group 7 of the periodic table

Probable compound	Adsorption temperature on quartz, K
MnCl ₂	773 (Novgorodov et al. 1986a), 733 (Kim et al. 1987b)
TcCl ₄	320 (Hickmann et al. 1993)
TcCl ₅	408 (B. Eichler and Domanov 1974)
TcBr _x	430 (Hickmann et al. 1993)
ReCl ₅	283 (Merinis and Bouissieres 1969), 313 (B. Eichler and Domanov 1974)
ReO	1,300 (Adilbish et al. 1977)
TcO ₂	~1,000 (Steffen and Bächmann 1978a) , ~1,000 (Steffen and Bächmann 1978b)
TcO ₃	470 (Steffen and Bächmann 1978b), 610–730 (B. Eichler and Domanov 1975), ~750 (Häfeli et al. 2000)
ReO ₂	950 (Bayar et al. 1973), 900 (Adilbish et al. 1977)
ReO ₃	670 (Merinis and Bouissieres 1961), 813 (Steffen and Bächmann 1978b), 823 (R. Eichler et al. 1999), 660 (Bayar et al. 1974), 593 (Bayar et al. 1973), 653 (Bayar et al. 1974), 423, 673, 783 (Bayar et al. 1978b), 780, 870 (B. Eichler and Domanov 1975), 663 (Domanov et al. 1981)
HTcO ₄	483 (Bächmann et al. 1976), 588 (Steffen and Bächmann 1978b), ~350 (Häfeli et al. 2000)
HReO ₄	373 (Bayar et al. 1978b), 503 (Bächmann et al. 1976), 390 (Zvara et al. 1982), 346 (R. Eichler et al. 1999), 620 (Steffen and Bächmann 1978b), 443 (Bayar et al. 1975), 353 (Bayar et al. 1978b), 353 (Domanov et al. 1981), 243 (B. Eichler and Domanov 1975), 375 (B. Eichler et al. 1999)

Group 8: Interest in this group of elements arises first of all from the existence of very volatile osmium tetroxide, with osmium being an analogue of element 108 (Hs). ▶ Table 53.5 presents absorption temperatures for various volatile compounds of group 8 elements. The T_a value of Ru and Os chlorides on KCl or CsCl surfaces is 873 K (Tsalas and Bächmann 1978). Osmium tetroxide adsorbs on a CaO surface at 733 K (Zhuikov 1982a).

Table 53.5

Volatile compounds of elements of group 8 of the periodic table

Probable compound	Adsorption temperature on quartz, K
FeCl ₂	677 (Novgorodov et al. 1986a)
FeCl ₃	433 (Merinis and Bouissieres 1969), 433 (B. Eichler and Domanov 1974)
RuCl ₄	583 (B. Eichler and Domanov 1974), 708 (Davydov 1973)
OsCl ₄	333 (Merinis and Bouissieres 1969), 333 (Merinis and Bouissieres 1961), 393 (B. Eichler and Domanov 1974)
OsO	1,250 (Adilbish et al. 1977)
RuO ₂	1,430 (B. Eichler et al. 1992), 1,270 (Adilbish et al. 1979)
RuO ₃	600, 690, 730 (B. Eichler and Domanov 1975), 563 (Steffen and Bächmann 1978b), 625 (B. Eichler et al. 1992), 833 (Adilbish et al. 1979), 398 (Domanov and Zvara 1983), 580 (Düllmann et al. 1999)
OsO ₃	373 (Adilbish et al. 1977)
RuO ₄	453 (Steffen and Bächmann 1978b), 241 (B. Eichler et al. 1992)
OsO ₄	173 (Domanov and Zvara 1983), <298 (Steffen and Bächmann 1978b), <293 (Bayar et al. 1974), <191 (Düllmann et al. 2002)
RuO _x Cl _y	438 (Bayar et al. 1978e)

Group 9: The behavior of chlorides, oxides, and hydroxides of the elements from this group has been studied in thermochemical experiments (► Table 53.6). It is, however, very difficult to interpret the composition of these compounds, as is evident, for example, from T_a values for IrO₃ and H₂IrO₄.

Group 10: Elements of this group form relatively volatile dichlorides, the adsorption temperatures of which on quartz are 763, 863, and 803 K for NiCl₂, PdCl₂, and PtCl₂, respectively (B. Eichler and Domanov 1974). For the latter compound values of 543 and 663 K are (Merinis and Bouissieres 1969; Merinis and Bouissieres 1961), which is probably due to the presence of macro amounts of more volatile gold chloride. Compounds with oxygen are known only for platinum (Domanov et al. 1982; Domanov and Zvara 1983). The adsorption temperatures on quartz for PtO₂, PtO₃, and “platinum acid” PtO_x(OH)_y are estimated to be 573, 373, and 293 K, respectively. According to a later work (Zude et al. 1993), the adsorption temperatures of Pt on quartz in a flow of dry and humid air are 535 and 550 K, respectively.

■ Table 53.6

Volatile compounds of elements of group 9 of the periodic table

Probable compound	Adsorption temperature on quartz, K
CoCl ₂	771 (Novgorodov et al. 1986a), 658 (B. Eichler et al. 1976), 653 (Rudstam and Grapengiessser 1973)
RhCl ₃	883 (B. Eichler et al. 1976)
IrCl ₄	848 (Merinis and Bouissieres 1961), 823 (Merinis and Bouissieres 1969), 1,008 (B. Eichler and Domanov 1974)
IrO ₂	673 (Steffen and Bächmann 1978b)
RhO ₃	373 (Domanov and Zvara 1983)
IrO ₃	530 (B. Eichler and Domanov 1975), 523 (Domanov et al. 1982), 353 (Domanov and Zvara 1983), 493 (Steffen and Bächmann 1978b), 520 (B. Eichler et al. 1993)
H ₂ IrO ₄	433 (Domanov et al. 1982), 288 (Domanov and Zvara 1983), 580 (B. Eichler et al. 1993)

The high volatility of “platinum acid” arouses special interest and calls for further investigations. In addition, Pt forms thermochromatographically promising volatile carbonyl halogenides (Herrmann and Denschlag 1969).

Group 11: In this group of elements it is difficult to identify a single type of compound, which could be used in systematic investigations. The most stable valence states for Cu, Ag, and Au are +2, +1, and +3. The most volatile compound is gold trichloride with the adsorption temperature on quartz of approximately 463 K (Merinis and Bouissieres 1961). Silver chloride is reported with $T_a = 893$ K (B. Eichler and Domanov 1974) or 823 K (Rudstam and Grapengiessser 1973). Behavior of elemental Ag and Au was investigated and their adsorption temperatures were found to be very high, 1,133 and 1,403 K (B. Eichler 1976), respectively. Volatile sulfides show more promise in this group – the adsorption temperatures of ¹⁹⁵Au and ¹¹¹Ag sulfides in a sulfur vapor flow were found to be 770 and 650 K, respectively (Korotkin et al. 1988).

Group 12: Elements of this group are among the most intensively ones studied. T_a of quartz for Zn, Cd, and Hg are approximately 660, 600, and 300 K, respectively (B. Eichler 1976). The adsorption temperatures for their chlorides are also relatively low: 580, 630, and 350 K, respectively (B. Eichler 1976). Sulfide adsorption temperatures are slightly higher, namely 830 and 880 K for ZnS and CdS (Korotkin et al. 1988). Mercury sulfide, like mercury oxide, is unstable at high temperature and shows the behavior of the element. With copper or nickel used as adsorbents, T_a sharply increases (approximately 1,000 K) only for zinc (B. Eichler 1976). The adsorption temperatures of Zn, Cd, and Hg on quartz surface in vacuum are about 1.5 lower than in a hydrogen atmosphere: 460, 350, and 200 K, respectively (B. Eichler 1976). Adsorption of Hg on different surfaces (Cu, Ag, Au, Ni, Pd, Pt) has been studied by Niklaus et al. (2003).

Group 13: Adsorption temperatures for elements of this group on quartz surface in a hydrogen atmosphere are quite low: 830, 580, and 610 K for Ga, In, and Tl, respectively (B. Eichler 1976). Strong absorption on copper and nickel surfaces is observed only for Ga (B. Eichler 1976), as in the case of Zn (see above). In vacuum, T_a on quartz is slightly lower: 455 K for In and 420 K for Tl. For chlorides of HCl and H_2O gas mixtures, absorption peaks are found which correspond to InOCl, InCl, and InCl₃ with T_a = 655, 475, and 385 K, respectively (Novgorodov et al. 1986b). For InCl₃, a value of T_a = 313 K was found (Rudstam and Grapengiesser 1973). Thallium reveals increased volatility in the oxygen atmosphere; the adsorption temperature is approximately 500 K (Bayar et al. 1978c). An interesting observation is the volatility of thallium micro amounts in sulfur vapor; the adsorption temperature is 450 K (Kim et al. 1988). An even more unexpected result was obtained in thermochromatographic experiments at a reduced HF vapor pressure. The adsorption temperatures of Ga, In, and Tl monofluorides or oxyfluorides were 460, 350, and 340 K, respectively (Novgorodov et al. 1987a, b, 1988).

Group 14: The best-studied compounds among the group 14 elements are Ge, Sn, and Pb dichlorides. Their absorption temperatures on quartz are 840, 590 (Rudstam and Grapengiesser 1973), and 588 K (B. Eichler and Domanov 1974). For the highly volatile GeCl₄ and SnCl₄, T_a is estimated to be approximately 300 K (B. Eichler and Domanov 1974). The metals show low volatility, their adsorption temperatures on quartz in a hydrogen flow are 1,050, 1,060, and 780 K for Ge, Sn, and Pb, respectively (B. Eichler 1978). The effect of the carrier gas on Pb adsorption is shown: its adsorption temperature is 950 K in an argon gas flow compared to 730 K in a hydrogen gas flow (Fan and Gäggeler 1982). Adsorption of these elements in metallic TCC (Ni, Mo, Au) is also strong, and T_a varies from 900 to 1,200 K (B. Eichler 1978). Tetravalent lead may form highly volatile tetraalkyl (methyl-, ethyl-) compounds, which might be considered in thermochromatography.

Group 15: As, Sb, and Bi trichlorides are adsorbed on quartz at 300, 330, and 420 K, respectively (B. Eichler and Domanov 1974). A similar adsorption temperature (300 K) was found for SbCl₃ (Hickmann et al. 1993). The adsorption temperature of antimony pentachloride was only mentioned (Rudstam and Grapengiesser 1973), and T_a for SbCl₃ and SbCl₅ were found to be 840 and 590 K, respectively. The T_a for BiOCl was found to be 580 K (R. Eichler et al. 2000). TC of the elements in the form of metals yields similar values of T_a ≈ 830 K on quartz surfaces for all three elements (B. Eichler 1976). If copper or nickel is used as an adsorbent instead of quartz, the As- and Bi-adsorption temperatures increase to approximately 1,100 K (B. Eichler 1976). Ultramicro amounts of Bi show interesting behavior in sulfur vapor: T_a on quartz is 590 K (Korotkin et al. 1988). For BiO(OH) hydroxide a T_a ≈ 770 K was observed (R. Eichler et al. 1999).

Group 16: The data on the thermochromatographic behavior of the elements from this group are difficult to systematize. Tellurium and polonium in the elemental state are adsorbed on quartz in hydrogen flow at T_a ≈ 730 and 520 K, respectively; and in vacuum at 575 and 370 (B. Eichler 1976). With copper and nickel used as adsorbents, T_a significantly increases, reaching 1,088 K for Se(Ni), 823 K for Po(Cu), and 943 K for Po(Ni) (B. Eichler 1976). Polonium adsorption on various surfaces under isothermal conditions is considered (Gäggeler et al. 1985), where it was found to be very strongly adsorbed on the palladium surface (T_a > 1,300 K). Volatile Te and Po tetrachlorides are adsorbed on quartz at T_a = 448 and 563 K (B. Eichler and Domanov 1974); a value of T_a for PoCl₄ was reported to be 450 K (Gärtner et al. 1999). A similar value for TeCl₄ (T_a = 450 K) was obtained (Hickmann et al. 1993),

where T_a for tellurium tetrabromide and tetraiodide are also given, which are 560 and 480 K. With KCl and CsCl used as adsorbents, tellurium tetrachloride adsorbs at $T_a = 473$ and 713 K, respectively (Tsalsas and Bächmann 1978). For PoOCl_2 , the T_a value was determined to be 320 K (R. Eichler et al. 2000) or 530 K (Gärtner et al. 1999). Adsorption of TeO_2 on quartz at approximately 900 K was also mentioned (B. Eichler 1976).

Group 17: All halogens and interhalogens are highly volatile. Their temperatures of adsorption on quartz lie within the range from 241 to 473 K (Merinis et al. 1972). Interestingly, monatomic iodine is adsorbed at 473 K, while molecular iodine is adsorbed at 268 K. Compounds of Br, I, and At with oxygen in air flow have $T_a = 273$, 263, and 280 K (B. Eichler and Domanov 1975). For compounds of iodine with oxygen (IO_x) a value of $T_a = 573$ K is given (Rudstam and Grapengiesser 1973). The adsorption temperatures of iodine and astatine on quartz in vacuum (B. Eichler 1977) are 275 and 230 K. With various metals used as adsorbents, T_a substantially increases because of formation of more stable chemical compounds. For example, the adsorption temperatures of iodine and astatine on silver are very different, 1,200 and 663 K, respectively. Bromine and iodine adsorb on the platinum adsorbent at 873 and 798 K (Rudstam and Grapengiesser 1973). The adsorption temperature of astatine on the Pd surface is 515 K (B. Eichler and Chun 1985).

Group 18: There is no study on the adsorption of noble gases in open thermochemical quartz columns available because of the difficult set-up for adequate experiments. It is safe to suggest that the Xe adsorption temperature should be below 100 K (B. Eichler et al. 1995). With palladium as an adsorbent, Rn was adsorbed at 168 K (B. Eichler and Chun 1985). This indicates that elements of this group must be purified of all other elements to a very high degree.

The brief review of volatile compounds of the elements of the periodic table used in thermochemical experiments in some cases reveals discordance of adsorption temperatures. This inconsistency, sometimes quite substantial, is probably due to incorrect experimental condition and interpretation which results first of all from the following:

- Insufficient purification of the carrier (reactant) gas
- Inadequate purification of the adsorbent
- Variation in the chemical form of substances injected in the starting zone of thermochemical columns for formation of volatile compounds
- Limited information on the kinetics of formation and dissociation of volatile compounds
- Variation in the sample injection profile (“online” or “off-line” experiments)
- Some above-mentioned variation in the period of experiments

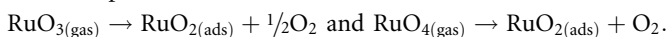
Naturally, most investigators studied or took into account the effect of these factors on the adsorption temperature, though not fully and accurately, perhaps. Most important for the accurate characterization of volatile compounds and their T_a are, in the authors' opinion, experiments with various pure reactant gases or their mixtures (Domanov and Kim 1988; Domanov et al. 1988; Nguyen et al. 1984a), with significantly different periods of duration of the TC experiments (Fan and Gäggeler 1982), and with different initial starting compounds (Chuburkov et al. 1996; Steffen and Bächmann 1978b). These approaches will be adequate, when compounds, transferred through the TCC, are chemically stable both in the gas phase and on the surface of the adsorbent. The picture considerably complicates if the transfer of the substance under study is accompanied by chemical reactions resulting in decomposition and formation of the initial and secondary volatile compounds on the surface of the adsorbent. This is most conspicuous in the case of polyvalent elements of groups 6–9. For example, the

Fig. 53.5

Dissociative character of ruthenium oxide adsorption on the SiO₂ surface

scheme on [Fig. 53.5](#) is accepted for transfer of ruthenium compounds with oxygen (Steffen and Bächmann 1978a).

Developing this assumption, B. Eichler et al. (1992) determined the enthalpy and entropy of the dissociative adsorption for the reactions



Thorough investigation of noncarrier-added amounts of ^{183,184}Re in dry and humid oxygen allowed (R. Eichler et al. 1999) to conclude that there was no volatile ReO₂ in the temperature range considered (up to 1,400 K) and that the peaks previously ascribed by other authors to ReO₂, ReO₃, and HReO₄ actually corresponded only to the latter two compounds formed in different ways.

Far more complications arise when volatile Mo and W oxychlorides are dealt with. Even in pure chlorinating reactant gases, tetra-, penta-, and hexavalent states of Mo and W may exist in the form of not only chlorides but also oxychlorides due to chemical reactions involving the adsorbent (SiO₂). In these complicated cases useful information can be probably gained in thermochemical experiments at reduced reactant gas pressures (about 0.1 Pa) (Adilbish et al. 1977), i.e., when the stepped nature of formation of volatile oxidation products is particularly conspicuous. It should be mentioned that the volatility of monomeric molecules, such as MoO₃, PdCl₂, FeCl₃, RhCl₃, is very small. Experimental values of *T_a* for these compounds most probably correspond to their polymer species such as (MoO₃)₃, (PdCl₂)₅, (FeCl₃)₂, etc.

53.5 Preparative Radiochemistry

The rapid development of thermochemistry in the 1960–1970s was stimulated first of all by the desire of researchers to discover new short-lived radionuclides and to investigate their nuclear-physical and chemical properties. Various methods for fast chemical separation in both liquid and gaseous phases were described in a review (Herrmann and Denschlag 1969), allowing investigation of radionuclides with half-lives of about 1 s. New radionuclides produced at reactors (neutron-rich radionuclides) and at medium-energy particle accelerators (neutron-deficient radionuclides) have been discovered and investigated. For gas chemistry, chemically stable substances were utilized as targets, from which the produced radionuclides were transferred under controllable conditions into known volatile compounds for their subsequent thermochemical separation. The most comprehensively studied targets were UF₄ (Weber et al. 1971), U₃O₈ (Röder and Herrmann 1966; Wolf 1973), AgCl (Novgorodov 1982), Au (Adilbish et al. 1977; Bayar et al. 1974), and others. The most widely used source of neutron-rich radionuclides was ²⁵²Cf (Bögl and Bächmann 1975).

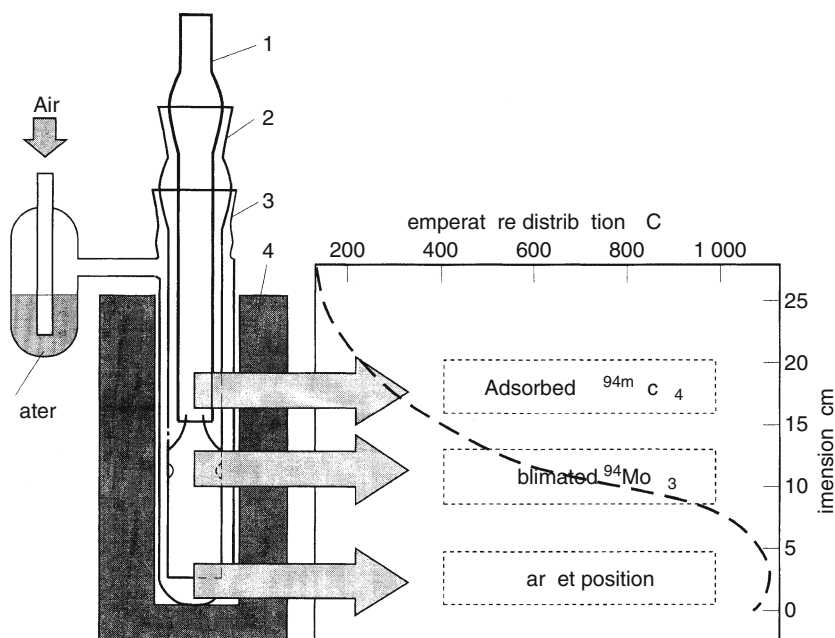
TC remained advantageous for these investigations until the advent of ISOL (isotope separator online) facilities operating online with reactors or medium-energy accelerators (Talbert 1970). Radioisotopes of known elements with half-lives well below 1 s (^{11}Li , ^{35}Na , ^{74}Rb , ^{150}Lu , Hg isotopes, and others) were discovered and investigated at these facilities with targets composed of metal melts or finely dispersed powder (Beyer et al. 1989). The tubular connection of the target to the ion source may in principle be regarded as a TCC.

Consideration was also given to potentialities of TC for separation and concentration of relatively large amounts of radionuclides used in science and technology (Khalkin et al. 1979). The data given in ▶ Sect. 53.4 of this review described conditions of thermochemical separations to be selected for virtually any target-product pair. This may be distillation of macro amounts of the target elements, e.g., Zn (Novgorodov et al. 1990), Cd, and Hg (B. Eichler and Domanov 1974) in vacuum or Au via chlorination (Merinis and Bouissieres 1961). Of interest is scenario in which the irradiated target is burnt in the reactant gas (O_2 , Cl_2 , and others) with the formation of a nonvolatile residue, while the nuclear reaction product is transferred by the gas flow further to the TCC (Bayar et al. 1978b; Vakhtel et al. 1976). These separations were usually carried out in a horizontal apparatus similar to that displayed in ▶ Fig. 53.1, but recently the vertical arrangement of the TCC is believed to be more rational (Rösch et al. 1994) (▶ Fig. 53.6).

This arrangement greatly decreases the carry-away of gaseous products against the direction of incoming reactant gas flow and allows the process to be easily automated. The target is

■ Fig. 53.6

Apparatus for routine separation of $^{94\text{m}}\text{Tc}$ from irradiated ^{94}Mo targets: (1) – TCC-inner quartz tube for adsorption of $^{94\text{m}}\text{Tc}$; (2) – middle quartz tube for condensation of $^{94}\text{MoO}_3$; (3) – outer quartz tube; (4) – electric resistance oven (Rösch et al. 1994)



loaded in bottom of the open apparatus, the apparatus is closed using inserted smaller quartz tubes, the reactant gas is passed through it, and then the assembly is placed in the vertical oven with the required temperature distribution. After the termination of the separation process the assembly is taken out of the oven, cooled, and from it the inner TCC is removed with the adsorbed product, which can be washed off with a minimum volume of an appropriate solution. This apparatus, first developed to separate the positron emitter ^{94m}Tc from the irradiated molybdenum oxide in 25 min (Rösch et al. 1994), was subsequently used more universally for separations of the systems $^{110}\text{Sn}/^{111}\text{In}$ (Rösch et al. 1997), $^{186}\text{W}/^{186}\text{Re}$, $^{188}\text{W}/^{188}\text{Re}$ (Novgorodov et al. 2000), and $^{72}\text{Se}/^{72}\text{As}$ (Novgorodov et al. 2001).

Multiple use of the target material, when separation of nuclear reaction products does not entail changes in its chemical composition, holds the greatest promise for production of some radionuclides. ▶ Table 53.7 presents examples of using such targets for producing radionuclides relevant for nuclear medicine. The ^{67}Ga , ^{111}In , and ^{201}Tl separation procedure consists in merely heating massive targets at controllable pressure of the reactant gas. The target material loss does not exceed 0.1% in one cycle of radiochemical separation, but it is easily restored after 20–30 target irradiation-radionuclide separation cycles. In addition, multiple use of the target material gradually leads to a high specific activity of the produced radioactive samples due to periodic separation of impurities. Moreover, the use of gaseous reactants at lowered pressure (1–10 Pa) allowed the application of the thermochemical columns for ISOL setups (*Isotope Online Separations*) as a chemical transport between target and mass separators, cf. ▶ Table 53.7 and Adilbish et al. (1977, 1979).

It should be noted that thermochemistry might be used for construction of generator systems (B. Eichler 1976). By now the parent–daughter radionuclide pairs $^{188}\text{W}/^{188}\text{Re}$ (Novgorodov et al. 2000) and $^{72}\text{Se}/^{72}\text{As}$ (Novgorodov et al. 2001) have been comprehensively studied.

53.6 Investigation of New Transactinide Elements

Thermochemistry entered into wide use for the identification of new elements due to the assumption that transactinide elements ($Z = 104\text{--}118$) belong to groups 4–18 of the periodic table, where lighter homologues are known to form volatile compounds. The crucial

■ Table 53.7

Separation of medical radionuclides from massive targets

Radionuclide	Target	Reaction	Separation conditions	References
^{67}Ga	^{70}Ge	(p,xpyn)	1,375 K, (HF+H ₂ O 1:1), 1.5 Pa	(Novgorodov et al. 1988)
^{111}In	Ag	(α ,2n)	1,150 K, (HCl+H ₂ O 10:1), 7 Pa	(Schomächer et al. 1988) (Novgorodov et al. 1986b)
^{111}In	^{112}Sn	(γ ,n)EC	1,225 K, (HF+H ₂ O 1:1), 0.4 Pa	(Novgorodov et al. 1987a)
^{201}Tl	$^{204,206,208}\text{Pb}$	(p,xn)EC, EC	825 K, (HF+H ₂ O 1:1), 0.4 Pa	(Novgorodov et al. 1987b)

feature of the method was its “high speed,” i.e., the time needed to transfer accelerator-produced atoms of the elements under study from the target to the detectors, which was a few tenths of a second, according to various estimates (Belov et al. 1974). Chemical studies of new elements is an extreme challenge, because the lifetime – even of comparatively long-lived ones of their isotopes – is of the order of a few seconds or tens of seconds only and the rate of their production at modern accelerators is very low (an atom per a few hours or even days). Other problems are laborious measurements of decay events and incomplete knowledge of the decay properties (half-lives, ratios of spontaneous fission, alpha decay, and electron capture), though chemical identification is normally preceded by elaborate physics experiments on determining the yield of the desired isotope of the new element, its decay mode, and half-life. The experiments are carried out with varying combinations of target nuclei and accelerated ions, the energies of which also vary. To achieve a high yield of the desired isotope of the new element, neutron-rich isotopes of both the target and the accelerated ion are used, e.g., ^{238}U , ^{244}Pu , ^{248}Cm and ^{18}O , ^{22}Ne , ^{26}Mg , ^{48}Ca , respectively. Using accelerated ions of neutron-rich radionuclides like ^{90}Kr , ^{132}Sn , or ^{140}Xe has been suggested, but not reported for the production of the heaviest elements so far.

During the experimental studies of chemical properties of transactinides early approaches exploited the possibility to detect spontaneous fission in thermochromatographic columns by mica or quartz track detectors at temperatures below 400°C , while more modern setups employ Si detectors to register α decay or spontaneous fission at room temperature and below (liquid nitrogen). Then, the technique, however, is limited to the study of highly volatile atoms or compounds.

The history of discovery of the first transactinide elements is closely associated with the rivalry for priority of their discovery and identification and with mutual criticism of the researchers (Flerov and Zvara 1971; Hyde et al. 1987; Flerov and Ter-Akopian 1987). Now these matters are no longer acute owing to establishment and joint work of international collaborations.

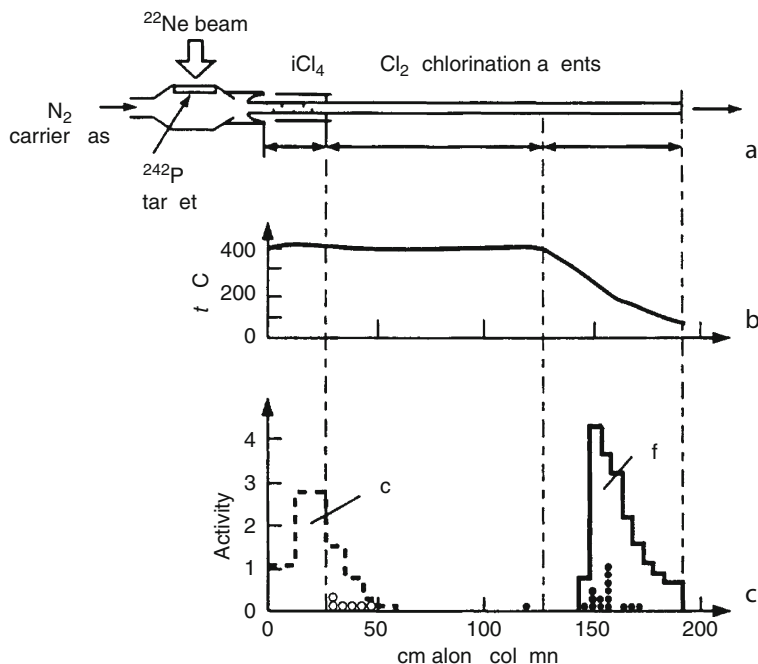
On the assumption of analogy between transactinide elements and group 4–18 elements halides, oxyhalides, and oxides of the first transactinide elements were expected to have increased volatility, which might allow good selectivity of their separation and concentration by gas chemistry methods (IC and TC). The first identifications of Rf (element 104) were carried out by isothermal chromatography of its most volatile compound, the chloride (Zvara et al. 1969a, b; Chuburkov et al. 1969). It was shown that the behavior of Rf chloride was analogous to the behavior of Hf tetrachloride. Thermochemistry was first used in investigations of transactinide elements in 1971 (Zvara et al. 1971). ▶ Figure 53.7 shows a schematic diagram of the apparatus used and the results obtained, i.e., the distribution of spontaneous fission events.

The measured distribution of decay events over the thermochromatographic column is a basis for evaluating the adsorption enthalpy ΔH_a^0 . Evaluation of ΔH_a^0 for a single decay event is performed by the method proposed by Zvara (1985), who developed a microscopic model of TC. On its basis the migratory process of individual atoms in the column is simulated by the Monte Carlo method with allowance made for their radioactive decay.

Similar setups were used to study chemical properties of volatile compounds of elements 105–108 (Db, Sg, Bh, Hs) at different laboratories. Recently, a monograph (Zvara 2008) in detail covered theoretical considerations related to the thermochromatographic behavior of single atoms of transactinide elements. A remarkable contribution (Türler 1999) most

■ Fig. 53.7

(a) Schematic of the experimental apparatus to investigate the volatility of ^{259}Rf and $^{170,171}\text{Hf}$ chlorides; (b) temperature profile in the column; (c) distribution of spontaneous fission tracks (circles) and distribution of γ -activity $^{44\text{m}}\text{Sc}$, $^{170,171}\text{Hf}$ (lines) (reproduced with permission from Dissertation B., Türlér 1999)



comprehensively describes gas chemistry of halides of the first two transactinides, Rf and Db, and oxychlorides of the third one, Sg. Sg was shown to form volatile oxychlorides (Schädel et al. 1998; Türlér et al. 1999) as well as oxyhydroxides (Hübener et al. 2001). Considering the high volatility of rhenium hydroxide HReO_4 , many researchers (Belov et al. 1972; B. Eichler 1976) planned to use and used (Zvara et al. 1984) an analogous compound for the identification of element 107 (Bh). However, HReO_4 turned out to partially decompose in the TCC at a temperature of about 600 K (R. Eichler et al. 1999) with formation of ReO_3 . Evidently, this is why Bh was chemical identified with its oxychloride BhO_3Cl (R. Eichler et al. 2000b), though under isothermal conditions. High volatility of HsO_4 , expected in analogy to OsO_4 , has motivated the development of thermochemistry setups where the TCC consists of detectors suitable for the registration of α -particles and fission fragments emitted by species adsorbed within the TCC (Kirbach et al. 2002). This technique has first been used to compare adsorption of OsO_4 and HsO_4 (Düllmann et al. 2002). It appears that the volatility of HsO_4 , though high, is somewhat lower than that of OsO_4 . This highly efficient radiochemical separation technique has since found application in studies of nuclear aspects related to the production of Hs isotopes (Dvorak et al. 2006, 2008).

The lack of isotopes with half-lives long enough for their chemical investigation of elements 109–111 (Mt, Ds, Rg) prevented chemistry experiments with these elements to date. However,

the closed-shell element 112 – for which the name *copernicium* (Cn) has recently been approved – has been the focus of a series of experiments. Following initial experiments (Yakushev et al. 2001, 2002), recent studies suggest (R. Eichler et al. 2007) that the trend in sublimation enthalpies established in group 12 by the lighter homologues is fully preserved (R. Eichler et al. 2008).

It should be noted that all experiments on the study of properties of transactinide elements aim at finding first of all the distinctions between the properties of the analogue elements under study. As for elements with high Z electrons close to the nucleus have relativistic velocities, “relativistic effects,” which are proportional to Z^2 , strongly affect their chemical properties. These effects are expected to be most pronounced in transactinide elements and their compounds. Theoretical investigations in this area (Pershina 1996) showed, for example, that elements with larger Z are more noble and more volatile (B. Eichler et al. 1995). Analogy of Rf (as a p-element) and Pb was predicted (Glebov et al. 1988), but experiments disproved the prediction (Zhuikov et al. 1989). At present the series of relative volatilities of some analogue elements or compounds have been established in ascending order:

$\text{HfCl}_4 < \text{RfCl}_4 \approx \text{ZrCl}_4$
$\text{HfBr}_4 < \text{RfBr}_4 \approx \text{ZrBr}_4$
$\text{DbOCl}_3 < \text{NbOCl}_3$
$\text{DbBr}_5 < \text{TaBr}_5 \approx \text{NbBr}_5$
$\text{SgO}_2\text{Cl}_2 \approx \text{WO}_2\text{Cl}_2 < \text{MoO}_2\text{Cl}_2$
$\text{BhO}_3\text{Cl} < \text{ReO}_3\text{Cl} < \text{TcO}_3\text{Cl}$
$\text{HsO}_4 < \text{OsO}_4$
$\text{Hg} < \text{element 112 (Cn)}$

Scarce experimental data on chemical behavior of transactinides gained for many years emphasize enormous difficulties of the investigations, on the one hand, and their scientific importance for further study of the periodical table and structure of matter, on the other hand.

53.7 Conclusion

The relatively short time of development of thermochemistry and the value of the results obtained with it allow the lines of its further development to be outlined as follows:

- Theory and experimental investigations of the gas–solid interaction of a variety of adsorbent–adsorbate systems.
- Study of physicochemical properties of transactinides to find distinctions between their behavior and the behavior of the analogue lighter elements. Obviously, thermochemistry compares favorably with isothermal gas chromatography in the study of extremely rare events of formation and decay of isotopes of new elements.
- Use of thermochemistry in production of radionuclides for science and technology (first of all for nuclear medicine). It should be noted that this method holds promise too for development of generator systems.

Acknowledgments

The authors are grateful to Dr. A. B. Yakushev and Dr. S. N. Timokhin for providing information and important comments that helped to complete this review. The authors acknowledge contribution by Dr. Ch. Düllmann concerning the recent developments related to the transactinide elements.

References

- Adams J, Eichler B, Türlér A, Gäggeler HW, Peterson J (1998) Annual report 1997 PSI, Labor für Radio- und Umweltchemie, 16
- Adilbish M, Zaitseva NG, Kovacs Z, Novgorodov AF, Sergeev YuYa, Tikhonov VI (1977) Preprint JINR, P12-10584
- Adilbish M, Zaitseva NG, Kowalev A, Kovacs Z, Novgorodov AF, Fominykh MI (1979) Preprint JINR, P6-12746
- Bächmann K, Matschoß V, Rudolph J, Steffen A, Tsalas S (1976) Nucl Instr Meth 139:343
- Bayar B, Novgorodov AF, Zaitseva NG (1973) Radiochem Radioa Let 15:231
- Bayar B, Novgorodov AF, Vocilka I, Zaitseva NG (1974) Radiochem Radioa Let 19:43
- Bayar B, Novgorodov AF, Vocilka I, Zaitseva NG (1975) Radiochem Radioa Let 22:53
- Bayar B, Vocilka I, Zaitseva NG, Novgorodov AF (1978a) Radiochem Radioa Let 34:63
- Bayar B, Vocilka I, Zaitseva NG, Novgorodov AF (1978b) Radiochem Radioa Let 34:75
- Bayar B, Zaitseva NG, Novgorodov AF (1978c) Radiochem Radioa Let 34:89
- Bayar B, Novgorodov AF, Vocilka I, Zaitseva NG (1978d) Radiochem Radioa Let 35:109
- Bayar B, Vocilka I, Zaitseva NG, Novgorodov AF (1978e) J Inorg Nucl Chem 40:1461
- Belov VZ, Zvara I, Korotkin YuS, Shalaevsky MR, Shchegolev VA, Domanov VP (1972) Preprint JINR, P6-6685
- Belov VZ, Zvarova TS, Shalaevsky MR (1974) Preprint JINR, P12-8216
- Beyer GJ, Novgorodov AF (1976) Zfk-305, Dresden
- Beyer GJ, Novgorodov AF, Rösch F, Ravn HL (1989) Isotopenpraxis 25:2
- Bögl W, Bächmann K (1975) J Inorg Nucl Chem 37:1115
- Bretshneider S (1966) Svojstva gasov i zhidkostei. Moskow-Leningrad
- Chuburkov YuT, Zvara I, Shilov BV (1969) Radiokhimija 11:174
- Chuburkov YuT, Nam HS, Alpert LK, Zvara I (1993) Preprint JINR, P6-93-289
- Chuburkov YuT, Kim SC, Timokhin SN, Belov AG, Alpert LK (1996) Preprint JINR, P12-96-425
- Curie P, Curie M (1898) C R Acad Sci Paris 127:1215
- Davydov AV (1973) J Radioanal Chem 14:285
- Domanov VP, Kim UJ (1988) Preprint JINR, P6-88-56
- Domanov VP, Zvara I (1983) Preprint JINR, P6-83-245
- Domanov VP, Hübener S, Shalagaevsky MR, Timokhin SN, Petrov DV, Zvara I (1981) Preprint JINR, P6-81-768
- Domanov VP, Eichler B, Zvara I (1982) Preprint JINR, P6-82-859
- Domanov VP, Kim UJ, Berdonosov SS, Kopylova IA, Lebedev VJa (1988) Preprint JINR, P6-88-633
- Domanov VP, Buklanov GV, Lobanov YuV (2002) Abstracts 14th Radiochem Conf Marianske Lazne 188
- Düllmann ChE, Eichler B, Gäggeler HW, Türlér A (1999) Annual report 1998 PSI, Labor für Radio- und Umweltchemie, 4
- Düllmann ChE, Bruchle W, Dressler R, Eberhardt K, Eichler B, Eichler R, Gäggeler HW, Ginter TN, Claus F, Gregorich KE, Hoffman DC, Jäger E, Jost DT, Kirbach UW, Lee DM, Nitsche H, Patin JB, Pershing V, Piguet D, Qin Z, Schädel M, Schausten B, Schimpf E, Schött H-J, Soverna S, Sudowe R, Thörle P, Timokhin SN, Trautmann N, Türlér A, Vahle A, Wirth G, Yakushev AB, Zielinski PM (2002) Nature 418:859
- Dvorak J, Bruchle W, Chelnokov M, Dressler R, Düllmann ChE, Eberhardt K, Gorshkov V, Jäger E, Krücken R, Kuznetsov A, Nagame Y, Nebel F, Novackova Z, Qin Q, Schädel M, Schausten B, Schimpf E, Semchenkov A, Thörle P, Türlér A, Wegrzecki M, Wierczinski B, Yakushev A, Yereimin A (2006) Phys Rev Lett 97:242501
- Dvorak J, Bruchle W, Chelnokov M, Düllmann ChE, Dvorakova Z, Eberhardt K, Jäger E, Krücken R, Kuznetsov A, Nagame Y, Nebel F, Nishio K, Perego R, Qin Z, Schädel M, Schausten B, Schimpf E, Schubert R, Semchenkov A, Thörle P, Türlér A, Wegrzecki M, Wierczinski B, Yakushev A, Yereimin A (2008) Phys Rev Lett 100:132503
- Eichler B (1976) Dissertation B, Technische Universität Dresden

- Eichler B (1977) ZfK-346, Dresden
- Eichler B (1978) ZfK-374, Dresden
- Eichler B, Chun KS (1985) Isotopenpraxis 21:180
- Eichler B, Domanov VP (1974) Preprint JINR, P12-7775
- Eichler B, Domanov VP (1975) J Radioanal Chem 28:143
- Eichler B, Malzeva NS (1976) Preprint JINR, P12-9959
- Eichler B, Zvara I (1975) Preprint JINR, P12-8943
- Eichler B, Zvara I (1982) Radiochim Acta 30:233
- Eichler B, Domanov VP, Zvara I (1976) Preprint JINR, P12-9454
- Eichler B, Hübener S, Roßbach H (1985a) ZfK-560, Dresden
- Eichler B, Hübener S, Roßbach H (1985b) ZfK-561, Dresden
- Eichler B, Zude F, Fan W, Trautmann N, Herrmann G (1992) Radiochim Acta 56:133
- Eichler B, Zude F, Fan W, Trautmann N, Herrmann G (1993) Radiochim Acta 61:81
- Eichler B, Baltensperger U, Ammann M, Jost DT, Gäggeler HW, Türlér A (1995) Radiochim Acta 68:41
- Eichler B, Adams J, Eichler R, Gäggeler HW, Peterson J (2002) Radiochim Acta 90:895
- Eichler R, Eichler B, Gäggeler HW, Jost DT, Dressler R, Türlér A (1999a) Radiochim Acta 87:151
- Eichler R, Gäggeler HW, Eichler B, Türlér A (1999) Annual report 1998 PSI, Labor für Radio- und Umweltchemie, 5
- Eichler R, Eichler B, Gäggeler HW, Jost DT, Pignet D, Türlér A (2000a) Radiochim Acta 88:87
- Eichler R, Brüchle W, Dressler R, Düllmann ChE, Eichler B, Gäggeler HW, Gregorich KE, Hoffman DC, Hübener S, Jost DT, Kirbach UW, Laue CA, Lavanchy VM, Nitsche H, Patin JB, Piguet D, Schädle M, Shaughnessy DA, Strellis DA, Taut S, Tobbler L, Tsyganov YS, Türlér A, Vahle A, Wilk PA, Yakushev AB (2000b) Nature 407:63
- Eichler R, Aksenov NV, Belozero AV, Bozhikov GA, Chepigina VI, Dmitriev SN, Dressler R, Gäggeler HW, Gorshkov VA, Haenssler F, Itkis MG, Laube A, Lebedev VYa, Malyshev ON, Oganessian YuTs, Petrushkin OV, Piguet D, Rasmussen P, Shishkin SV, Shutov AV, Svirikhin AI, Tereshatov EE, Vostokin GK, Wegrzecki M, Yeregin AV (2007) Nature 447:72
- Eichler R, Aksenov NV, Belozero AV, Bozhikov GA, Chepigina VI, Dmitriev SN, Dressler R, Gäggeler HW, Gorshkov AV, Itkis MG, Haenssler F, Laube A, Lebedev VYa, Malyshev ON, Oganessian YuTs, Petrushkin OV, Piguet D, Popeko AG, Rasmussen P, Shishkin SV, Serov AA, Shutov AV, Svirikhin AI, Tereshatov EE, Vostokin GK, Wegrzecki M, Yeregin AV (2008) Angew Chem Int Ed 47:3262
- Fan W, Gäggeler H (1982) Radiochim Acta 31:95
- Frenkel J (1924) Z Phys 26:117
- Gäggeler H, Dornhöfer H, Schmidt-Ott WD, Grenlich N, Eichler B (1985) Radiochim Acta 38:103
- Gärtner M, Boettger M, Eichler B, Gäggeler HW, Grantz M, Hübener S, Jost DT, Pignet D, Dressler R, Türlér A, Yakushev AB (1997) Radiochim Acta 78:59
- Gärtner M, Dressler R, Eichler B, Türlér A, Gäggeler HW (2000) Annual report 1999 PSI, Labor für Radio- und Umweltchemie, 18
- Giddings JC, Seager SL (1960) J Chem Phys 33:1579
- Glebov VA, Kasztura L, Nefedov VS, Zhuikov BL (1988) Preprint JINR, P6-88-201
- Glebov VA, Kasztura L, Nefedov VS, Zhuikov B (1989) Radiochim Acta 46:117
- Graf U, Eichler B, Türlér A, Gäggeler HW, Hairl RG (1999) Annual report 1998 PSI, Labor für Radio- und Umweltchemie, 12
- Häfeli T, Gäggeler HW, Eichler B, Düllmann ChE (2000) Annual report 1999 PSI, Labor für Radio- und Umweltchemie, 11
- Helas G, Hoffmann P, Bächmann K (1978) J Radioanal Chem 47:159
- Herrmann G, Denschlag HO (1969) Ann Rev Nucl Sci 19:1
- Hickmann U, Greulich N, Trautmann N, Gäggeler H (1980) GSI 80-3, Darmstadt, S.154
- Hickmann U, Grenlich N, Trautmann N, Herrmann G (1993) Radiochim Acta 60:127
- Hübener S, Zvara I (1979) Preprint JINR, E12-12753
- Hübener S, Zvara I (1982) Preprint JINR, E12-82-103
- Hübener S, Taut ST, Vahle A, Faughänel TH (2001) GDCh-Jahrestagung Chemie 2001, Universität Würzburg, S.15
- Khalkin VA, Novgorodov AF, Kolaczowski A (1979) Report IFJ N-1073/c, Krakow
- Kim UJ, Timokhin SN, Domanov VP, Chuburkov YuT (1987a) Preprint JINR, P6-87-158
- Kim UJ, Timokhin SN, Zvara I (1987b) Preprint JINR, P6-87-159
- Kim UJ, Timokhin SN, Domanov VP, Korotkin JuS (1988) Preprint JINR, P6-88-635
- Kirbach U, Folden CM III, Ginter T, Gregorich KE, Lee DM, Ninov V, Omtvedt JB, Patin JB, Seward NK, Strellis DA, Sudowe R, Türlér A, Wilk PA, Zielinski PM, Hoffman DC, Nitsche H (2002) Nucl Instrum Meth A 484:587
- Korotkin YuS, Kim UJ, Timokhin SN, Orelobitch OL, Altynov VA (1988) Preprint JINR, P6-88-595
- Merinis J, Bouissieres G (1961) Anal Chim Acta 25:498
- Merinis J, Bouissieres G (1969) Radiochim Acta 12:140
- Merinis J, Legoux Y, Bouissieres G (1970) Radiochem Radioa Let 3:255
- Merinis J, Legoux Y, Bouissieres G (1972) Radiochem Radioa Let 11:59
- Nguen CT, Novgorodov AF, Kaskevitch M, Kolatchkowski A, Chalkin VA (1984a) Radiokhimija 26:60

- Nguyen CT, Kolatchkowski A, Novgorodov AF (1984b) Preprint JINR, 6-84-849
- Niklaus J-P, Eichler R, Soverna S, Gäggeler HW, Tobler L (2003) Scientific report 2002 PSI, VI, 70
- Nogare SD, Juvert RS (1962) Gas-liquid chromatography. Wiley Interscience, New York/London
- Novgorodov AF, Kolatchkowski A (1979) Preprint JINR, P6-12457
- Novgorodov AF (1982) Dissertation, Preprint JINR 6-82-839
- Novgorodov AF, Kolatchkowski A, Nguyen CT, Zelinski A, Kaskevitch M (1986a) Radiokhimija 28:380
- Novgorodov AF, Buklanov GV, Zielinski A, Kolachkovski A, Rösch F, Schomäcker K (1986b) Appl Radiat Isot 37:445
- Novgorodov AF, Belov AG, Zelinski A, Kolatchkowski A (1987a) Radiokhimija 29:254
- Novgorodov AF, Belov AG, Zelinski A, Kolatchkowski A, Ageev VA, Kljutchnikov AA, Mikecs P, Mikulski JA, Misiak R, Sazhenjuk AD, Sobezka M (1987b) Radiokhimija 29:549
- Novgorodov AF, Zelinski A, Kolatchkowski A, Misiak R, Sobezka M, Ageev VA, Belov AG, Kaskevitch M, Kljutchnikov AA, Odinzov AA, Mikulski JA (1988) Radiokhimija 30:672
- Novgorodov AF, Rösch F, Zielinski A, Misiak P, Kolaczkowski A, Beyer GJ, Schomäcker K (1990) Isotopenpraxis 26:118
- Novgorodov AF, Bruchertseifer F, Brockmann J, Lebedev NA, Rösch F (2000) Radiochim Acta 88:163
- Novgorodov AF, Schmidt A, Brockmann J, Qaim SM, Rösch F (2001) J Labelled Compd Rad 44:778
- Ohline RW, DeFord DD (1963) Anal Chem 35:227
- Pershina VG (1996) Chem Rev 96:1977
- Röder E, Herrmann G (1966) Z Anal Chem 219:93
- Rösch F, Novgorodov AF, Qaim SM (1994) Radiochim Acta 64:113
- Rösch F, Qaim SM, Novgorodov AF, Tsai Y-M (1997) Appl Radiat Isot 48:19
- Roßbach H, Eichler B (1984) ZfK-527, Dresden
- Rudstam G, Grapengiesser B (1973) Radiochim Acta 20:97
- Schädel M, Brüchle W, Dressler R, Eichler B, Gäggeler HW, Günther R, Gregorich KE, Hoffman DC, Hübener S, Jost DT, Kratz JV, Paulus W, Schumann D, Timokhin S, Trautmann N, Türler A, Wirth G, Yakushev A (1997) Nature 388:55
- Schomäcker K, Schwarzbach R, Beyer G-J, Novgorodov AF (1988) Appl Radiat Isot 39:483
- Steffen A, Bächmann K (1978a) Talanta 25:551
- Steffen A, Bächmann K (1978b) Talanta 25:677
- Talbert WL Jr (1970) CERN 70-30, 1:109
- Taut S, Hübener S, Eichler B, Türler A, Gäggeler HW, Timokhin SN, Zvara I (1998) J Alloy Comp 271-273:316
- Taut S, Vahle A, Hübener S, Eichler B, Jost D, Türler A (2000) Annual report 1999 PSI, Labor für Radio- und Umweltchemie, 17
- Taut S, Hübener S, Eichler B (2001) GDCh-Jahrestagung Chemie 2001, Universität Würzburg, S.60
- Tsalas S, Bächmann K (1978) Anal Chim Acta 98:17
- Türler A (1999) Dissertation B: gas phase chemistry of the transactinide elements Rf, Db and Sg, Universität Bern
- Türler A, Eichler B, Jost DT, Dressler R, Piguet D, Gäggeler HW, Hübener S, Boettger M, Grantz M (1996) Annual report 1995 PSI, Labor für Radio- und Umweltchemie, 28
- Türler A, Brüchle W, Dressler W, Eichler B, Eichler R, Gäggeler HW, Gärtner M, Glatz J-P, Gregorich KE, Hübener S, Jost DT, Lebedev V Ya, Pershina VG, Schädel M, Taut S, Timokhin SN, Trautmann N, Vahle A, Yakushev AB (1999) Angew Chem Int Ed 38:2212
- Vahle A, Hübener S, Eichler B (1995) Radiochim Acta 69:233
- Vahle A, Hübener S, Dressler R, Eichler B, Türler A (1997) Radiochim Acta 78:53
- Vahle A, Hübener S, Funke H, Eichler B, Jost DT, Türler A, Brüchle W, Jäger E (1999) Radiochim Acta 84:43
- Vakhtel VM, Vinel GV, Vylov Z, Gromova II, Novgorodov AF, Norseev JuV, Khalkin VA, Chumin VG (1976) Isotopenpraxis 12:441
- Weber M, Trautmann N, Herrmann G (1971) Radiochem Radioa Let 6:73
- Wolf GK (1973) GSI 73-7
- Yakushev AB, Timokhin SN, Xu H, Zvara I (1993) Scientific Report FLNR 1991-2, E7-93-57, 169
- Yakushev AB, Buklanov GV, Chelnokov ML, Chepigin VI, Dmitriev SN, Gorshkov VA, Hübener S, Lebedev VYa, Malyshev ON, Oganessian YuTs, Popeko AG, Sokol EA, Timokhin SN, Türler A, Vasko VM, Yeregin AV, Zvara I (2001) Radiochim Acta 89:743
- Yakushev AB, Zvara I, Belozarov AV, Dmitriev SN, Eichler B, Hübener S, Sokol EA, Türler A, Yeregin AV, Buklanov GV, Chelnokov ML, Chepigin VI, Gorshkov VA, Gulyaev AV, Lebedev VYa, Malyshev ON, Popeko AG, Soverna S, Szełgowski Z, Timokhin SN, Tretyakova SP, Vasko VM, Itkis MG (2002) Preprint JINR, E12-2002-297
- Yakushev AB, Eichler B, Türler A, Gäggeler HW, Peterson J (2003) Radiochim Acta 91:123
- Zhuikov BL (1982a) Preprint JINR, P12-82-63
- Zhuikov BL (1982b) Preprint JINR, 12-82-736
- Zhuikov BL, Chuburkov YuT, Timokhin SN, Kim UJ, Zvara I, (1988) Preprint JINR, P6-88-109
- Zude F, Fan W, Trautmann N, Herrmann G, Eichler B (1993) Radiochim Acta 62:61
- Zvara I (1985) Radiochim Acta 38:95

- Zvara I (2008) The inorganic radiochemistry of heavy elements. Methods for studying gaseous compounds. Springer, ISBN: 978-1-4020-6601-6
- Zvara I, Chuburkov YuT, Zvarova TS, Tsaletka R (1969a) Radiokhimija 11:154
- Zvara I, Chuburkov YuT, Tsaletka R, Shalaevsky MR (1969b) Radiokhimija 11:163
- Zvara I, Belov VZ, Chelnokov LP, Domanov VP, Hussonois M, Korotkin YuS, Schegolev VA, Shalaevsky MR (1971) Inorg Nucl Chem Lett 7:1109
- Zvara I, Belov VZ, Domanov VP, Shalaevsky MR (1975) Preprint JINR, P12-8740
- Zvara I, Domanov VP, Hübener S, Shalaevsky MR, Timokhin SN, Zhuikov BL, Eichler B, Buklanov GV (1982) Preprint JINR, P6-82-616
- Zvara I, Domanov VP, Hübener S, Shalaevsky MR, Timokhin SN, Zhuikov BL, Eichler B, Buklanov GV (1984) Radiokhimija 26:76
- Zvara I, Yakushev AB, Timokhin SN, Xu H, Pereygin VP, Chuburkov YuT (1998) Radiokhim Acta 81:179

54 Methods of Cosmochemical Analysis

S. Lahiri · M. Maiti

Saha Institute of Nuclear Physics, Kolkata, India

54.1	<i>Introduction</i>	2461
54.2	<i>Accelerator Mass Spectrometry (AMS)</i>	2462
54.2.1	Principle and Components of AMS	2462
54.2.1.1	Ion Injector System	2463
54.2.1.2	Tandem Accelerator	2466
54.2.1.3	High Energy Beam Selector	2467
54.2.1.4	Faraday Cups	2469
54.2.1.5	Ion Detector	2470
54.2.2	Protocols of Sample Preparation and Measurements	2473
54.2.2.1	Pretreatment of Samples	2473
54.2.2.2	Sample Preparation	2474
54.2.2.3	Quality Control Parameters	2474
54.2.3	Importance of Cosmogenic and SN Radionuclides and the Required Chemistry for AMS Analysis	2475
54.2.3.1	^{10}Be	2476
54.2.3.2	^{26}Al	2478
54.2.3.3	^{53}Mn	2479
54.2.3.4	^{129}I	2480
54.2.3.5	^{60}Fe	2481
54.2.3.6	^{146}Sm	2482
54.2.3.7	^{182}Hf	2483
54.2.3.8	^{244}Pu	2484
54.3	<i>Other Mass Spectrometric Techniques Related to Cosmochemical Analysis</i>	2485
54.3.1	Inductively Coupled Plasma-Mass Spectrometer (ICP-MS)	2485
54.3.1.1	Components of ICP-MS	2485
54.3.1.2	Application of ICP-MS in Long-lived Analysis	2491
54.3.2	Resonant Ionization Mass Spectrometry (RIMS)	2492
54.3.2.1	Working Principle	2492
54.3.2.2	Components of RIMS	2492
54.3.2.3	Application of RIMS	2494
54.3.2.4	RIMS and AMS	2495
54.3.3	Thermal Ionization Mass Spectrometry (TIMS)	2495
54.3.3.1	Principle and Components: A Quick Look	2495
54.3.3.2	Application of TIMS in Cosmochemical Analysis	2496

54.3.4 Secondary Ion Mass Spectrometry (SIMS) 2497

54.3.4.1 Principle of SIMS 2498

54.3.4.2 NanoSIMS 50 2498

54.3.4.3 Application of nanoSIMS 2499

54.4 Conclusion and Future Scope 2500

Abstract: Some radionuclides, like ^{10}Be ($T_{1/2} = 1.5$ Ma), ^{14}C ($T_{1/2} = 5,730$ years), ^{26}Al ($T_{1/2} = 0.716$ Ma), ^{53}Mn ($T_{1/2} = 3.7$ Ma), and ^{60}Fe ($T_{1/2} = 1.5$ Ma), ^{146}Sm ($T_{1/2} = 103$ Ma), ^{182}Hf ($T_{1/2} = 9$ Ma), ^{244}Pu ($T_{1/2} = 80$ Ma) are either being produced continuously by the interaction of cosmic rays (CR) or might have been produced in supernovae millions of years ago. Analysis of these radionuclides in ultratrace scale has strong influence in almost all branches of sciences, starting from archaeology to biology, nuclear physics to astrophysics. However, measurement of these radionuclides appeared as a borderline problem exploiting their decay properties because of scarcity in natural archives and long half-life. The one and only way seemed to be that of mass measurement. Accelerator mass spectrometry (AMS) is the best suited for this purpose. Apart from AMS, other mass measurement techniques like inductively coupled plasma-mass spectrometry (ICP-MS), thermal ionization mass spectrometry (TIMS), resonant laser ionization mass spectrometry (RIMS), secondary ionization mass spectrometry (SIMS) have also been used with limited sensitivity and approach.

This chapter gives an essence of measurement of cosmogenic or supernova-produced radionuclides with various mass spectrometric techniques with special emphasis on AMS. The challenges of AMS measurement like isobaric interference, and development of chemical methods for separation of isobars have also been discussed. An abridged discussion has been made on the other techniques like ICP-MS, TIMS, RIMS, and SIMS.

54.1 Introduction

A survey of the Table of Nuclides reveals the presence of few radionuclides with half-lives in the range of thousand to million years. In general sense or in terms of nuclear sciences these radionuclides are named as long-lived radionuclides. Interestingly, cosmologists or astrophysicists designate them as “short-lived” radionuclides comparing their half-lives with the time span of creation of the solar system (Gounelle 2006; Fitoussi et al. 2008b). These radionuclides have important bearings in the astrophysical context as well, answering many hitherto unraveled questions. How the Earth was formed billions of years ago? What is the erosion rate of rocks and soils in the Earth or in the Moon and so on?

These radionuclides are either being produced continuously in the upper atmosphere by the interaction of solar cosmic rays (SCR) or galactic cosmic rays (GCR) or had been produced in supernova (SN) long back and deposited on the Earth millions of years ago. The production cross section of cosmogenic radionuclides (extraterrestrial or terrestrial) is extremely low. The signatures of SN radionuclides are almost faded out. In both cases, these radionuclides are present only in minuscule amounts in the Earth's crust and therefore their detection requires *state-of-art* instrumentation. Even with the availability of very powerful instruments, detection of these radionuclides requires rigorous chemical treatment, from sample collection to ion source preparation. Sometimes chemical separation is mandatory to overcome the problem of isobaric interferences.

Analysis of cosmogenic radionuclides present in ultra trace scale cannot be based on their nuclear decay properties as in the experimental time period only a small fragment of the sample is decayed; therefore, statistically significant result cannot be obtained. The mass measurement is much more precise and sensitive compared to decay counting because in mass measurement, every individual atom is counted and one has not to wait for the decay of the radionuclide.

In Vol. 2 of this handbook, the origin of elements has been discussed in detail. Therefore, the present authors will exclude that part, except for some comments on the importance of particular radionuclides. In this chapter, the principles and instrumentation of accelerator mass spectrometry (AMS), the key player for detection of cosmological radionuclides in ultra trace scale, will be discussed in detail. Detailed discussion of all the research works carried out to date with cosmogenic radionuclides is out of scope. Only the detection of million-year half-life radionuclides in ultra trace concentration will be touched, followed by concise description of the required chemistry. Rather than giving a general description, a few of them have been chosen and described in separate sections. Inductively coupled plasma-mass spectrometry (ICP-MS), thermal ionization mass spectrometry (TIMS), secondary ion mass spectrometry (SIMS), or resonant laser ionization mass spectrometer (RIMS), etc. have also been used for detection of cosmogenic radionuclides. However, these techniques have much lower sensitivity compared to AMS. Brief discussions on these instruments have been appended at the end of this chapter. This chapter ends with a conclusion.

54.2 Accelerator Mass Spectrometry (AMS)

54.2.1 Principle and Components of AMS

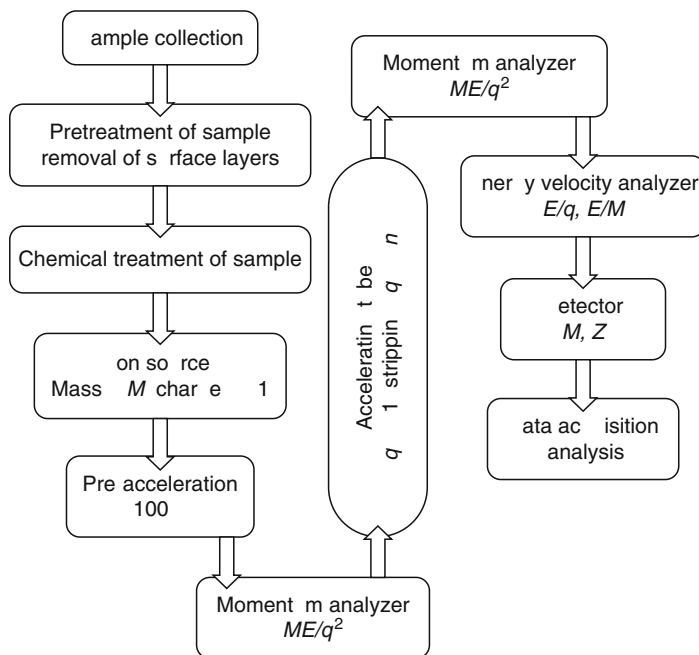
Among various mass measurement techniques, AMS is the best suited and widely used for the analysis of cosmological radionuclides. In AMS, the ratio of the desired nuclide and its more abundant stable isotope is measured. For example, ^{14}C ($T_{1/2} = 5,730$ years) is measured as the ratio of $^{14}\text{C}/^{12}\text{C}$. In AMS measurement, the most common problems are the following: (1) molecular ion interference (e.g., $^{12}\text{CH}_2$ or ^{13}CH have nearly the same mass as ^{14}C). The interfering molecular ion species are much more abundant than the radionuclide of interest. The acceleration of ions in AMS dissociates the molecular ion species and finally only the nuclides of interest enter the detector. (2) isobaric interference (e.g., ^{14}N is trillion times more abundant than ^{14}C in the atmosphere). Even in the presence of a minute amount of ^{14}N , it is impossible to detect ^{14}C . Measurement of the long-lived radionuclides is a big challenge as it suffers from the interference of stable isobars. AMS is capable of measuring the isotopic ratio of certain elements up to the order of 1 in 10^{15} cleverly removing the isobaric interference in different steps (discussed in following sections). This sensitivity is achieved approximately in a 1-h measurement using a sample weighing less than 1 mg. Various factors, for example, efficiency of ion beam production, the control of the background, and minimum level sample contamination, are responsible to achieve the detection limit in AMS. In some favorable cases, it is possible to measure the isotopic abundance ratio even in the order of 10^{-16} .

The various steps of AMS measurement include (1) collection of samples from the possible sources, (2) cleaning and chemical treatment, (3) injection of the sample into the ion source, (4) acceleration of the desired isotopes, and finally (5) measurement of the isotope ratio. Block diagram of various AMS steps has been presented in [Fig. 54.1](#).

The tandem accelerator (in which the ion beam experiences two acceleration stages: one before stripping and one after stripping) is the most often used accelerator in the AMS facilities. Negative ions are injected in the tandem accelerator. Stripping of electrons at the center of tandem converts the negative ion to a positive ion, which is then accelerated and transmitted as positive ion from the accelerator.

■ Fig. 54.1

A pictorial diagram of various accelerator mass spectrometry (AMS) steps



In general an AMS facility consists of the following components that are discussed in the following sections.

1. Ion injector system
2. Tandem accelerator
3. High energy beam selector
4. Faraday cups
5. Ion detector

54.2.1.1 Ion Injector System

The ion injector system consists of three major components: (1) negative ion source, (2) pre-acceleration system, and (3) beam analysis equipment. Commonly, Cs sputter ion source is used to generate negative ions. Sputter-source produced negative ions traverse through the efficient energy and mass analysis equipment before being injected to the accelerator. Molecular interference is significantly reduced in this analyzer, which in turn reduces the background of the unwanted ions.

Ion Source

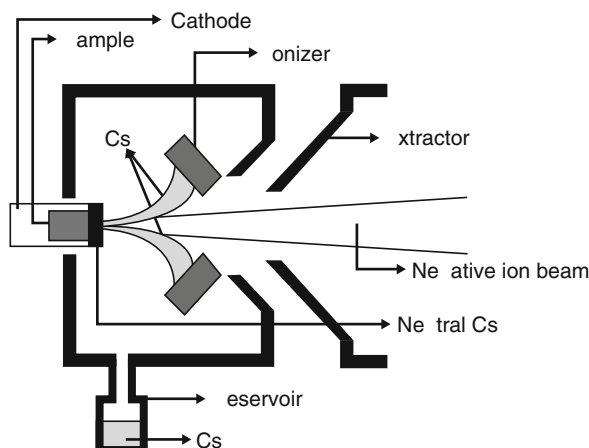
The injection of negative ion beam to the tandem for the first-stage acceleration reduces huge isobaric background of some nuclides at the beginning because their competing isobars do not

form negative ions. Moreover, negative ions of noble gas and some other elements are quite unstable and they often fail to reach the terminal of the tandem accelerator. For example, ^{14}C and its competing isobar ^{14}N have electronic configurations $[\text{He}] 2s^2 2p^2$, and $[\text{He}] 2s^2 2p^3$ respectively. Therefore, $^{14}\text{C}^-$ is highly stable and $^{14}\text{N}^-$ is totally unstable. The unstable $^{14}\text{N}^-$ is suppressed at the very beginning, that is, in the ion source itself. Similarly, for the radionuclides ^{26}Al and ^{129}I , the interfering isobars ^{26}Mg and ^{129}Xe do not form stable negative ions and hence are suppressed. If this is not the case, it is often possible to use appropriate molecules such as oxides, fluorides, or hydrides to reduce the background interference as well as to increase the negative ion current as elemental ion currents found to be low for many elements. For example, ^{41}Ca suffers isobaric interference from ^{41}K . Selection of a molecule like CaH_3^- or CaF_3^- helps to reduce isobaric background because potassium does not form potassium trihydride or trifluoride negative ions. Therefore, the negative ion source helps to get rid of the million times more abundant naturally occurring stable isobars of the long-lived radionuclides. High charge state of ions is also preferred in the tandem accelerator to remove the molecular interference from the desired one because molecular ions become highly unstable for charge $+q \geq 3$ and fragment immediately. This feature of tandem accelerators eliminates the need for high mass resolution to resolve the molecular interference.

The cesium sputtered ion source is an ideal device to generate negatively charged atomic or molecular ions from the solid sample material. Ion sources of this type are operational in AMS facilities across the world because of their low cross contamination probability and reasonable negative ion yields for almost all the radionuclides measured by AMS. Moreover, reliability of this device can be improved by simple modifications. A schematic diagram of a Cs sputtered ion source is shown in [Fig. 54.2](#). The cathode is a metallic cylindrical body made of silver, copper, or aluminum, having a small cavity inside along the cylindrical axis. Chemically treated sample containing the desired nuclides, mainly in the form of powder, is loaded into the cavity. The cathode then acts as target for the ion source. The sample is sputtered by Cs beam to generate the desired negative ions. The latter are extracted as a negative ion beam for injection

■ Fig. 54.2

A schematic diagram of Cs sputter ion source



into the accelerator. The probable factors determining the negative ion yield are (1) electron affinity of the element, (2) physical condition of the sample, (3) ion–atom collision, and (4) atomic ion current.

Negative ion yield is proportional to the electron affinity of the element. Sputter yield depends on the difference between electron affinity of the desired atom and the effective work function. Work function varies upon the environment of the surface of the sample. Physical conditions of the sample affect the properties of atoms on the surface. The probability of negative ion formation is enhanced by the presence of Cs layer at the surface of the sample and electron cloud near the sample surface. Samples are mixed with metallic powder (e.g., Ag or Nb) to improve the thermal and electrical conductivity. Ion–atom collision kinematics reduces the sputter yield for heavy elements. Production of negative ions is at the maximum for normal incidence of the sputtering beam, but the total sputter rate, which means positive, negative, and neutral emission, increases when the angle of incidence is away from the normal. Atomic ion current is very low or zero for some elements. In that case, selection of one molecular ion out of many possible molecular ions (like oxides, hydrides, or carbides) becomes important (Tuniz et al. 1998).

Apart from the sputter source, gas sources are also used to convert CO₂ directly to negative ion beam, minimizing the effort of sample preparation. However, gas sources are not common in AMS because of two reasons: (1) low negative ion yield in comparison with sputter sources and (2) the cathode needs to be changed frequently. Recent developments are going on gas sources at AMS laboratory in Woods Hole, USA, where the source produces positive ions, which are converted to negative ions by passing through alkali vapor (Tuniz et al. 1998).

Pre-acceleration System

The pre-acceleration system provides definite acceleration to the negative ions extracted from the ion source so that they can be injected to the accelerator. The ions extracted from the ion source carry 10–30 keV energy, which is enough for direct injection in small tandem accelerators (~3 MV). The minimum ion energy required for injection of ions is known as injection energy. In large tandem accelerators (4–15 MV), injection energy of 50–150 keV is required, which is obtained from the pre-acceleration system. Pre-acceleration also reduces the energy spread of the negative ion beam before injection.

Injection Magnet

The negative ion beam extracted from the sample passes through a beam-analyzing magnet and is injected to the accelerator. When the ions pass through the injection magnet of uniform magnetic field B directed perpendicular to the ion path, ions are deflected along different radii depending on their mass (M), energy (E), and charge (q). Radius of curvature, ρ of the ion path is related to M , E , and q as

$$\frac{ME}{q^2} \propto (B\rho)^2 \quad (54.1)$$

Ions having specific mass and well-defined energy are allowed to the accelerator. In case of a big AMS facility, a large magnet is required to deflect ions up to mass 200 or even higher with good resolution. Specific design of the injector magnet may help in achieving good focusing of beam. An insulated vacuum chamber placed between the pole-pieces allows fast switching of nuclides.

54.2.1.2 Tandem Accelerator

Tandem is a class of accelerator that accelerate ions by applying an electrostatic field with a feature of supplying high voltage. A tandem accelerator consists of two accelerating tubes, for low- and high-energy acceleration, along with a metal electrode, known as terminal, kept at the center and in between the two accelerating tubes of the tandem. The terminal is kept at a large positive potential ($V_T \approx 0.2\text{--}15\text{ MV}$) and therefore known as voltage dome. Tandem accelerators achieve two-stage acceleration with a single voltage by converting the electric charge of negative ions at the high-voltage terminal. The accelerator is housed inside a large steel tank that contains insulating gas with significant high pressure (usually a 4:1 mixture of N_2 and CO_2 at $\sim 300\text{ kPa}$ or pure SF_6 at $\sim 100\text{ kPa}$) to prevent electrical discharging of the high-voltage surfaces within the accelerator. Voltage holding capacity may also be improved by the addition of SF_6 to the mixture of N_2 and CO_2 . The steel tank isolates the high-voltage surfaces of the accelerator electrodes from the outside.

The structures within the tank, which support the terminal electrode, are referred to as *columns*. The low-energy column starts from the tank base nearest to the ion source and ends at the center of the terminal. The high-energy column connects the terminal region to the tank base opposite to the ion source. The columns are composed of a series of metal planes, with each plane electrically isolated from the next by glass blocks, which are glued to each plane. There are approximately 200 such planes in each of the low- and high-energy columns. A large spring inside the high-energy tank base compresses both columns with tremendous force, holding the columns and the terminal region suspended within the tank. A controlled charging system is used to hold the terminal voltage constant. The charging system is composed of a rotating rubber belt or metal-plastic chains. Normally, belts are dusty and cause spark affecting the insulating properties. Therefore, chains with alternate metal and plastic cylinders called pelletron are used for most stable charging current, which is a very important parameter for AMS. In tandem accelerators, high voltage is generated by a radio frequency (RF) power supply connected to the accelerator tank that provides high current capacity as well as high stability.

Selection of terminal voltage is crucial and solely depends on the radionuclides under analysis. High energies are more effective in identifying nuclides of interest in some cases (e.g., ^{36}Cl , ^{41}Ca , and ^{59}Ni) where the stable isobar needs to be highly separated. Successful operation of the accelerator for AMS experiments requires constant and stable terminal voltage over a long period of time. This is because change in terminal voltage causes change in beam trajectory through the analyzing magnet. Equilibrium must be established between the charge brought to the terminal by the pelletron chains and that which flows from the terminal to the ground through the column resistors.

Negatively charged ion beam, having energy $E_i = eV_i$, where V_i is the injection voltage, is transported from the injector toward the terminal in vacuum. Negative ions are therefore accelerated to high energy as they approach the terminal kept at positive high voltage. While the beam enters the region that houses the terminal, it passes through an electron stripper, either gas or thin carbon foil, which strips electrons from the ions in the beam, leaving the beam positively charged (charge = $+q$). The function of the stripper is to convert the ions from negative to positive for further acceleration when they leave the terminal. Thin carbon foils of $2\text{--}5\text{ }\mu\text{g}/\text{cm}^2$ thickness or gas or the combination of both serve satisfactorily as stripper. The positively charged beam accelerates away from the high positive potential at the terminal and exits the accelerator at very high energy, E . The energy of ions is

given as follows: $E = E_i + (q + 1)eV_T$, where V_T is the terminal voltage. Molecular ions are dissociated at high energy and filtrated afterward, which in turn reduces the background of the desired ion beam.

54.2.1.3 High Energy Beam Selector

It is an efficient beam-analyzing equipment that analyzes the beam and simultaneously rejects the unwanted ions, at the maximum possible extent before the beam reaches the detector. The use of two different kinds of high-energy analyzers are required to select ions of specific E/q and M/q in the detector. The most popular approach is to use a magnetic analyzer, which selects a beam of required ME/q^2 followed by an electrostatic analyzer to select E/q . Use of velocity analyzer is necessary to remove ambiguities in selecting desired ions in heavy ion AMS measurements. In a nutshell, when high-energy ions are passed through the electric and magnetic field of mass analyzers, they are separated spatially according to their momentum, charge, and energy. Specific window is set to select the ions of interest from the rest of the beam. Individual ions are counted after their proper identification with correct mass and atomic number.

Wien Velocity Filter

The Wien filter uses an electrostatic field E perpendicular to a magnetic field B to disperse ions of different energies. When electrically charged particle of charge q passes through an electric field, it feels an electric force on it. If electric force is expressed as F_e , then $F_e = qE$. In a similar way, when the particle crosses a magnetic field it feels magnetic force, which is given by $F_m = q(\mathbf{v} \times \mathbf{B})$. The net force on the ions will be zero and hence they will be unperturbed as they travel through the crossed fields. This leads to the balance of electric and magnetic force field, that is, $F_e = F_m$; $qE = q(\mathbf{v} \times \mathbf{B})$ and hence the magnitude of ion velocity is $v_{ion} = E/B$. Ions with velocity, $\mathbf{v} = v_{ion}$, pass perpendicularly through the crossed fields along the optical axis without any change in their trajectories because the net force acting on them is zero. All other ions will feel a nonzero force and hence will be deflected from their straight path. By placing a proper slit, only those ions that feel zero force are allowed to pass through the crossed electric and magnetic fields. If a monoenergetic ion beam is passed through a Wien filter, the beam will be separated according to the ion velocities and hence their masses, since $E = Mv^2/2$. The reason is that the electric and magnetic forces cancel each other. Ions with different velocities will be deflected from the optic axis as $\mathbf{v} = v_{ion}(1 + \delta)$, where δ is the deviation in velocity. The radius of the trajectory of the ions with velocity v_{ion} upon action of the magnetic field is given by

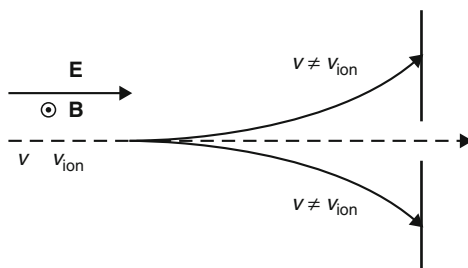
$$\rho = \frac{Mv_{ion}}{qB}. \quad (54.2)$$

The trajectory of ions passing through the Wien velocity filter is shown in  Fig. 54.3.

Magnetic Analyzer

The analyzer magnet is used to select the desired ion species. As the ions travel through the magnetic field whose B is perpendicular to the direction of motion, the magnetic force (Lorentz force) makes the particles to move in a circular path. Kinetic energy of the ions is not affected by the influence of the magnetic field, only the direction of motion changes. Radius of curvature of the path of ions is proportional to the velocity of the ions. Double focusing magnetic analyzer with narrow object and image slits are used to achieve high

■ Fig. 54.3

Wien velocity filter

resolution for ions of known mass and charge. In general, 90° deflecting magnet is used for the good separation of beams of different mass and charge state. If the ions of charge q and energy E from the accelerator pass through a magnetic analyzer, then they are separated according to the atomic mass M in a uniform magnetic field \mathbf{B} directed perpendicularly to the plane of motion. The radius of curvature ρ of the path of each ion depends on M , E , and q following

► Eq. (54.1).

Electrostatic Analyzer

An electrostatic analyzer behaves like a filter. It only allows particles within a certain range of energies and charges to pass through. It consists of two parallel cylindrical or spherical conducting plates that have different voltages. This voltage difference sets up an electric field, which acts on charged particles.

The upper plate of the electrostatic analyzer remains at a positive voltage, and the lower one at a negative voltage. Any positively charged particle coming toward the top plate will be pushed to the bottom plate, because like charges repel each other. When the charged particle enters through the entrance slit of an electrostatic analyzer, it starts to feel the electric force field and moves down toward the bottom plate as it travels. This movement depends on its energy-to-charge ratio, E/q . If the ratio is low, that means either the particle is having low energy E , or the field pushes the particle too hard that is, high q , then it will fall short of the exit. On the other hand, if the ratio is high, that means the particle is with high E , or low q , then it will cross the slit. Therefore, the lucky particles that have just the right ratio of energy and charge pass through the exit slit. These outgoing particles from the slit are the desired particles because they must have a certain energy-to-charge ratio.

The analyzer only measures positively charged particles. In case of measurement of the negatively charged particle instead of positive, one needs just to reverse the voltages of the plates, so that the top plate gets negative voltage and the bottom gets positive voltage.

Gas-Filled Magnet

In a common magnetic analyzer, the path of the ion beam is kept in vacuum. The magnetic rigidity, which is defined by the ratio of the momentum of the ion and its electrical charge, governs the trajectory of the ion in a magnetic field region and is normally a constant throughout the path of the ion in vacuum. When the ion beam passes through the magnetic analyzer, ions having different magnetic rigidities are spatially separated in the focal plane of the apparatus according to their charge state. Ions carrying higher charge are deflected more

than those with lower charge. Therefore, magnetic rigidity can be used in identifying ions along with energy or velocity. The situation becomes more and more complicated for heavy ions. While passing through the matter (like absorber and window foil) heavy ions emerge with a distribution of ionic charge states and follow different trajectories in the magnetic field. The trajectories of the isobaric nuclei will be essentially identical if the ions have the same energy and the same charge state and cannot be separated. Gas-filled magnet is a unique technique used for good isobaric separation.

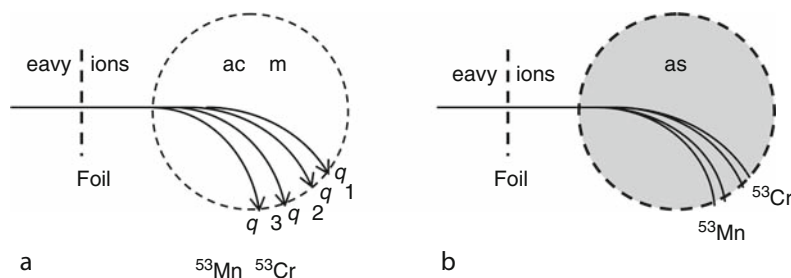
A gas-filled magnet is a special kind of magnetic analyzer, which contains gas instead of vacuum in the region of the beam path. Gas pressure inside the magnet is controlled from outside. Entrance and exit end of the gas-filled magnet is separated by two thin foils from the high vacuum component of the accelerator. While the ion beam passes through a gas-filled magnet, each ion undergoes several interactions with the gas atoms as well as the atoms of the foils. Due to the ion-atom interaction, charge exchange takes place between them. The trajectories of ions in vacuum and in gas-filled magnetic field region are illustrated in [Fig. 54.4](#). If the mean free path of the ions between the charge-changing collisions is short enough, depending on the gas pressure and the atomic collision cross sections, the ions will closely follow the trajectory determined by the mean magnetic rigidity, corresponding to the mean charge state q_m of the ion. The behavior of ions moving in a magnetic field changes largely with the gas pressure, which is of the order of 1–10 torr. For the ions with the same mass number but with different atomic number (isobars), the mean charge state in the gas is different and the corresponding trajectories in the magnetic field are therefore spatially separated. The average charge (q_m) of the ion depends on the atomic number Z and is roughly proportional to its velocity. Therefore, the average magnetic rigidity, $\langle B\rho \rangle \propto Mv/q_m$ is almost independent of the velocity distribution of the ions. The trajectories of the ions will be determined by the mass number A and the atomic number Z of the ion. A gas-filled magnet can therefore direct the isobaric ions along separate paths, and hence separate them. Gas-filled magnets are very useful for ions having high energies so that energy loss within the gas becomes small and that does not affect detector performance (Knie et al. 1999, 2004).

54.2.1.4 Faraday Cups

A Faraday cup is a specially designed metallic cup used to measure current directly from the ion beam in vacuum. The measured current in turn provides the number of ions reaching the

Fig. 54.4

Schematic diagram of the heavy ion trajectories in the magnetic field area (a) in vacuum (b) in gas



conducting cup. If the measured current in the Faraday cup is 1 nA, then 6 billion singly charged ions ($= 10^{-9}/1.6 \times 10^{-19}$) are impinging the cup in each second. When an ion beam strikes the metallic surface, it emits electrons. As a result, an electric current is induced in it. An electrical circuit is attached to the cup to amplify and conduct the current to a measuring device. The design of the cup may be sufficiently complicated to measure small current and high-energy beam, which does not stop in the cup.

54.2.1.5 Ion Detector

The detection of ions coming to the detector is the final step of AMS measurement. Mass, M and atomic number, Z of the ion is inferred measuring the parameters discussed below. (1) Total energy of ion coming into the detector. (2) Rate of energy loss of ions: The rate at which the ion loses energy per unit path length is called the stopping power of the medium. Energy loss is calculated from the Bethe–Bloch formula excluding relativistic effect ($v \ll c$, speed of light) as

$$-\frac{dE}{dx} = \left(\frac{e^2}{4\pi\epsilon_0} \right)^2 \frac{4\pi n Z^2}{m_e v^2} \ln \left(\frac{2m_e v^2}{I} \right) \quad (54.3)$$

where Ze , E , v , and x are the charge, energy, velocity, and the distance traveled by the ion respectively; e and m_e are charge and rest mass of electron; n is the electron density in the medium; and I is the mean excitation potential of the medium. Electron number density n in the medium is calculated as

$$n = \frac{z\rho N_A}{A_s}. \quad (54.4)$$

N_A is Avogadro's number, and A_s , z , and ρ are the mass number, atomic number and density of the stopping material, respectively. The rate of energy loss of the ion increases to a maximum and then abruptly falls to zero beyond the peak, which is known as Bragg peak. (3) Energy loss of the ion at the Bragg peak, which increases linearly with atomic number of ion, z . (4) Range of ion is an important parameter to measure which is calculated as

$$R = \int_E^0 dx = \int_E^0 \frac{dE}{(dE/dx)}. \quad (54.5)$$

Energy loss is obtained from [Eq. \(54.3\)](#) as

$$\frac{dE}{dx} \propto Z^2 f(v), \quad (54.6)$$

where, $f(v)$ is a function that depends on the speed of ion. Combining [Eqs. \(54.5\)](#) and [\(54.6\)](#), range of ion R is calculated as

$$R = \int_E^0 \frac{dE}{(dE/dx)} \propto \frac{m}{Z^2} F(v). \quad (54.7)$$

Since, $dE = d(Mv^2/2) = Mvdv$; M is the mass of the ion and $F(v)$ is a function of the speed of ion. Therefore, the range of ions with same velocity varies inversely proportional to Z^2 .

(5) When an ion passes through a specific thickness of the absorber, residual energy after the absorber is measured to determine atomic number Z of the ion. (6) Flight time of the ions between two detectors determines the speed of the ions and hence mass of the ions are also determined.

Different kinds of detectors are designed to measure these parameters accurately. Sometimes isobar identification appears to be difficult in AMS measurement. Therefore, the best possible combination of ion beam-analysis equipment and a sophisticated detector is required for proper identification of ions. Interfering isobars may come from the sources like (a) angular scattering and energy straggling, (b) variation in electron multiplication and recombination in the detector, and (c) effects of noise and pileup in the electronics. In order to measure the isotope ratios below 10^{-15} or even lower it is necessary to measure background levels to the order of magnitude lower than the isotopic ratio. Ion identification detector also provides a mechanism for rejecting ions with incorrect E , M , or Z only when count rate total is much less. The principles of three types of detectors will be discussed below in brief.

Solid-State Detectors

Solid-state or, more strictly, surface barrier detectors are semiconductor detectors, built usually from a single crystal of either silicon or germanium, which are used to detect charged particles. An electric field gradient is introduced between the front and rear surfaces of the semiconductor crystal. When an energetic ion strikes on a surface barrier detector, it immediately produces one or more energetic electrons. These energetic electrons rapidly achieve thermal equilibrium with other electrons in the medium losing their energy mostly by ionizing atoms. Ionization process leads to the creation of energetic particle-hole pairs, which further promotes the chain of ionization processes. The average energy required to create an electron-hole pair is about 3.6 eV for silicon and 3.0 eV for germanium. As a result, many electron-hole pairs are created whose number will be proportional to the total energy absorbed by the medium from the incident ions. The electrons in the conduction band and the holes in the valence band move under the influence of the applied electric field in the opposite direction toward their respective electrodes. Movement of electrons and holes produces a pulse of current with the arrival of electrons and holes to their respective electrodes without recombination or being trapped at impurity sites in the crystal. The resulting current measured in an outer circuit, will be proportional to the energy of the ion if the thickness of the crystal is greater than the range of the ion. Detectors with thicknesses down to 10 μm or less are available for ΔE measurements. In easy cases, such as with ^{14}C , a relatively simple detector system is sufficient. For example, a thin silicon detector used for determining the rate of energy loss and a thick silicon detector for measuring the residual energy give sufficient information to identify the mass and atomic number of ^{14}C and competing ions. Pulse height defect is the main problem in the use of solid-state detectors for heavy ions.

Gas Ionization Detectors

Gas ionization detectors are popular for identification of heavy ions in AMS measurement. They are simple to design and operate, and come in different shapes and sizes. Such a detector is basically a gas-filled enclosure, which contains two electrodes. The electrodes may be of different types: parallel plate, coaxial cylinder, segmented anode, etc. depending up on the purpose of use. When an energetic heavy ion enters the detector, it ionizes gas atoms during its travel. As a result, electron-ion pairs are generated, which are separated and collected by a transverse electric field. The entrance window of the detector is a thin Mylar film ($\sim 150\text{--}300\text{ }\mu\text{g}/\text{cm}^2$),

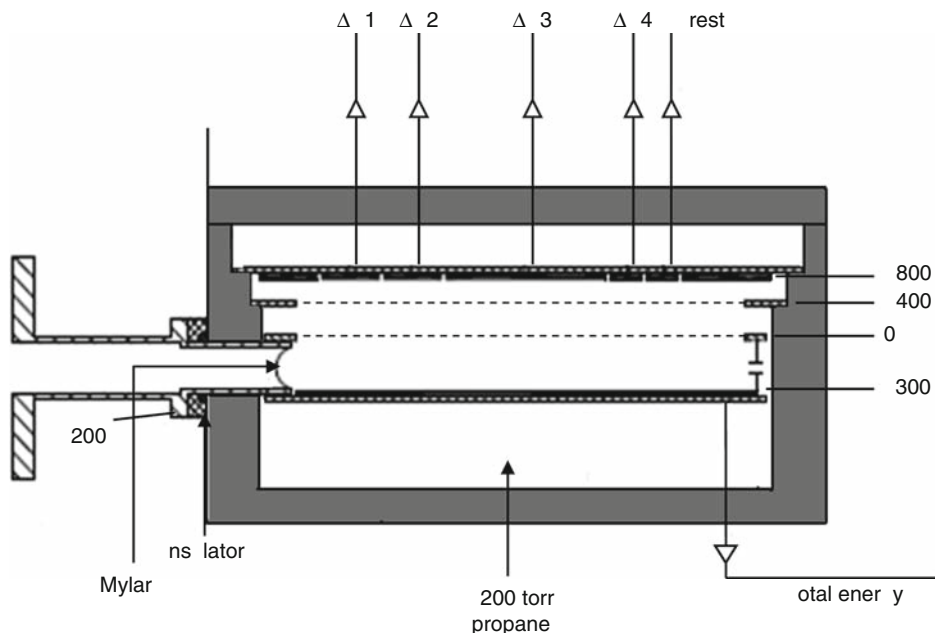
which separates the detector gas from the other components of the ion beam transport system. Ions enter the detector through the thin film, and then travel through a transverse electric field. Electrons and ions are separated by the electric field and induce voltage signals at the cathode and anodes. The choice of operational gas pressure, which usually varies between 10–200 torr, depends on the energy of the incident ion. In general, argon–methane mixture, isobutene, or propane are used as detector gases. Sometimes, impurities like oxygen or other electronegative species delay the collection of electrons by forming O_2^- . This results in smaller pulse height and poor energy resolution. This problem can be minimized by passing the gas through a purifier with controlled flow from the supply cylinder. Precision control of gas pressure is important to avoid peak shifts and to obtain good resolution.

Segmented anode provides a number of independent signals, which correspond to the energy ΔE deposited in each segment over the ion path. The cathode provides a signal proportional to the total ion energy. A coincidence unit is used to make sure that all electrodes have received a signal. A novel approach is to use of a timing signal between the first and last anode plates to reject anomalous events. A diagram of a segmented anode gas ionization detector is shown in [Fig. 54.5](#).

The radionuclide of interest and the isobars enter the gas ionization detector with equal energies but lose energy at different rates due to their different atomic number and hence have different energies in the gas. It is possible to measure the range of each ion taking information of the energy deposited in the last anode segment with optimized gas pressure.

■ Fig. 54.5

Cross-sectional view of a segmented-anode gas ionization detector



Time-of-Flight Detector

The ion goes through the electrostatic and/or magnetic analyzer and then passes through the time-of-flight region separated by two micro-channel plate detectors called start detector and stop detector. Time of flight provides better mass resolution than the other methods like energy loss, total energy, or range measurements. The start detector consists of a very thin carbon foil (\sim a few $\mu\text{g}/\text{cm}^2$) accompanied by a channel plate. When the ion hits the carbon foil, electrons are produced and scattered. These scattered electrons are then sucked down to the positively charged channel plate. A timer clock starts immediately after the electrons hit the plate. At the end of the flight path region there is another similar plate. When the ion hits the second carbon foil, electrons scatter from it again, are sucked down to the positively charged plate, and the clock stops. Time difference between the start and stop detectors is measured. The second detector is a solid-state detector, which measures the energy of the ion.

The distance traveled by the ions between the start and stop time is determined through precise measurements of the space between the two plates. From the time of flight t and from the flight distance d the absolute velocity of the ion is readily calculated using $v = d/t$. When the ion with energy E hits the second plate, the latter measures the kinetic energy of the ion and stops the clock. Since the velocity and energy of the ion is known, its mass is given by $M = 2E/v^2$. The charge of the ion can also be calculated from the relation, $q = E/(q/E)$ as E is known from the solid-state detector and E/q is found from the electrostatic analyzer placed before the time-of-flight region. The electrostatic analyzer determines the type of ion passed through the instrument and ensures that one type of ion was measured because only the ions with exactly the right combination of mass and energy can pass through it. The disadvantage of the time-of-flight technique is that it cannot distinguish between unwanted and desired ions. Moreover, angular spread of ions sometimes reduces transmission.

54.2.2 Protocols of Sample Preparation and Measurements

Indeed AMS is a *state-of-art* ultrasensitive technique for trace analysis, but the success of AMS depends on many crucial steps before the actual measurement in the AMS system. In fact, sometimes expertise from several areas of science is required to make the AMS experiments reliable. Some of the crucial points are *sample collection*, *pretreatment*, *sample preparation for ion source*, *development of separation methods for isobars*, etc. Like all other analytical techniques, it is also necessary to measure *standard*, *blank*, and *background* simultaneously with the sample. Below some of the crucial steps are described in nutshell.

54.2.2.1 Pretreatment of Samples

Before collecting samples, it is of utmost necessity to decontaminate all sampling equipment prior to use, between the two sampling depth intervals and between each sample collection point. The decontamination of collecting equipment may be done by removing gross contamination by brushing and rinsing with water, washing with detergent or soap solution, and rinsing with alcohol and deionized water. Geological sample material is collected with great care from the layer below a certain depth to avoid exposure of the object to the environment. After the collection of the samples, surface layers are removed because these are most

susceptible to contamination. The samples must be sealed and labeled to show the date and time of sample collection. In all cases, pretreatment procedure depends on the type of sample and the specific interest of measurement.

54.2.2.2 Sample Preparation

Sample preparation is the most crucial for all AMS measurements. The samples for cosmochemical analysis can be various types of raw materials, for example, sediment, lava, rocks, manganese crusts, and ice core. Actually, there is no common or absolute method for the preparation of samples for cosmochemical analysis prior to their introduction to the AMS system. Sample preparation techniques are continuously being developed with the philosophy of reducing isobaric interference, cross contamination, and bulk size. Generally, appropriate carrier is added to the pretreated geological samples (especially if the sample material is precious or available in trace amount only, when addition of carrier becomes mandatory to handle the sample). Samples are then dissolved in the appropriate acid (e.g., stony materials are dissolved in a mixture of HF, HNO₃, and HClO₄). This procedure is followed by evaporation of the solution, and taking up the residue in 1 M HCl (Schaefer et al. 2006). Various methodologies have been developed to separate the radionuclide of interest from the solution and to convert it to a suitable chemical form before putting it into the ion source. The separation method of the radionuclide of interest from bulk sample or from its isobars varies on the chemical properties of the particular radionuclide and the corresponding matrix. Therefore, the separation chemistries have been discussed in the following section individually for each radionuclide. The purpose of chemical treatment is to bring the elements of interest to a specific form to generate high negative ion current from the ion source. Appropriate binders, for example, Ag or Nb powder, having high thermal and chemical conductivity, are used to generate high negative current. Sometimes chemical processing brings the desired atoms in such a favorable form that they become open to ionization and leaves the interfering atoms resistant to ionization. Thus, chemical preparation of the sample helps to minimize interfering background.

In spite of all these advantages, chemical processing sometimes carries its own set of problems by introducing various kinds of contamination into the sample. Very low-conductivity water (resistivity $\sim 18 \text{ M}\Omega \text{ cm}$) and extremely high-purity reagents should be used. Sometimes solvents are distilled before use. One should also be careful about addition of carrier while extracting a very small amount of sample. Even with all precautionary measures, contamination is possible as impurities in solvents and reagents are determined with instruments, which have much higher detection limit than AMS. The quality control requires that these errors must be nullified by using *standards* and *blanks* similar to other methods of measurements in trace analysis. Below some terms related to quality control have been defined (Hotchkis et al. 2000).

54.2.2.3 Quality Control Parameters

Standard: In AMS, standard sample is that where the ratio of the long-lived radioactive isotope to stable isotope is known. The standard samples can be diluted to meet the level desired for AMS analysis. Isotope ratios in the range from 1 to 1×10^{-11} are usually convenient for system calibration.

Blank: In a real blank, the radioisotope of interest should be absent. But in practice, very low isotopic ratio (radioactive/stable) is called blank.

Reagent blank: To reduce the background often reagent blanks are measured. When a blank sample is processed with all the similar pretreatment and chemical steps without addition of the isotope of interest is called reagent blank.

Internal standard: Sometimes standards are not available for all the cosmogenic and SN radionuclides. Therefore, many AMS facilities have embarked on elaborate programs to manufacture their own calibrated standards. In most cases, these materials have been prepared locally with the utmost care using conventional radiometric counting, mass spectrometric methods, and/or standard gravimetric dilution techniques to establish their isotopic ratios. Alternatively, some AMS laboratories have prepared standard materials by series dilutions of primary standards.

Interlaboratory standards: These methods are needed to calibrate in-house standards, which are prepared in sufficient quantity for use in every measurement cycle.

Background: There are two types of contribution to the background, which together limit the reliability of the AMS method. First, other ions may be wrongly identified in the detection system as being the radioisotope of interest. The mass, energy, and charge resolution of the beam transport and detection systems may be insufficient to fully distinguish their signals. For example, while detecting ^{36}Cl some ^{36}S atoms may also reach the detector. Second, the sample may become contaminated from another source of the radioisotope of interest during handling, processing, or analysis. Routine assessment of the background, through measurement of blanks, is an essential part of AMS measurements.

Apart from these samples, some other quality control samples such as *duplicate samples* and *equipment field blanks* are used by different laboratories. Duplicate samples are taken from the same collection site to determine the variability of results for the same sample after the AMS analysis. Generally, one duplicate sample should be collected for every 20 samples. Equipment blanks are collected using laboratory-provided water, which has been run over the decontaminated soil sampling equipment. These samples are used to determine the efficiency of cleaning procedures for soil sampling equipment.

Precision and accuracy: As in all other techniques, precision is a measure of reproducibility while accuracy deals with the closeness of the result with the true value. The precision of an AMS measurement is evaluated from the reproducibility or spread of repeat measurements of the isotopic ratio of a sample. In AMS, stable and radioactive isotopes are measured simultaneously. The precision in AMS is limited by the uncertainty of the counts of the ions arriving in the detector. Precision or uncertainty is also dependent on the sample size. To have a more accurate result all the instruments required in various steps of AMS measurement should be calibrated properly (Hotchkis et al. 2000).

54.2.3 Importance of Cosmogenic and SN Radionuclides and the Required Chemistry for AMS Analysis

The measurement of cosmological and SN produced radionuclides down to subpart per trillion or even less have tremendous impact on various fields of basic and applied sciences. The range includes astrophysics, nuclear physics, biology, pharmacology, toxicology, biomedicine, archeology, geology, meteorology, environment, oceanography, and many other areas (Maiti and Lahiri 2008). The use of cosmogenic radionuclide ^{14}C ($T_{1/2} = 5,730$ years) has

increased dramatically in recent years. There are a number of commercial laboratories available worldwide for the detection of ^{14}C . The AMS determination of ^{14}C is used for radiocarbon dating up to 50,000-year-old samples; to understand the intricacies of prehistorical events, like ancient painting and engravings; for serving human health by tracing the metabolic activities of various drugs in minute scale, and by labeling DNA with ^{14}C . However, in the following discussions, applications of ^{14}C have been deliberately excluded as they can be found elsewhere. Discussion will be focused on the applications of other long-lived radionuclides, like ^{10}Be ($T_{1/2} = 1.5 \text{ Ma}$), ^{26}Al ($T_{1/2} = 0.716 \text{ Ma}$), ^{53}Mn ($T_{1/2} = 3.7 \text{ Ma}$), ^{129}I ($T_{1/2} = 15.7 \text{ Ma}$), (cosmogenic radionuclides); and ^{60}Fe ($T_{1/2} = 1.5 \text{ Ma}$), ^{146}Sm ($T_{1/2} = 103 \text{ Ma}$), ^{182}Hf ($T_{1/2} = 9 \text{ Ma}$), ^{244}Pu ($T_{1/2} = 80 \text{ Ma}$), (SN radionuclides). The discussions will be limited mainly to give an essence of their implication for solving cosmological puzzles. A list of cosmogenic radionuclides measured by AMS is presented in [Table 54.1](#).

54.2.3.1 ^{10}Be

The radionuclide ^{10}Be is mainly produced in the Earth's atmosphere through spallation reactions by cosmic-ray particles on atmospheric N and O atoms. Newborn ^{10}Be atoms get readily attached to the ambient aerosols and are transported and deposited to the Earth via wet and dry deposition after its resident time of 1–2 years in the stratosphere. Owing to its long half-life, the measurement of ^{10}Be in natural archives may reveal several scientific aspects. Both ^{10}Be and ^{26}Al are accumulated in exposed quartz surfaces over a geological timescale. Initially, the abundance of cosmogenic radionuclides in quartz increases as a function of cosmic-ray exposure. However, natural enrichment of radionuclides is limited by landscape erosion and their natural radioactive decay processes. ^{10}Be is extensively used in exposure-dating applications. This is mainly so because a $^9\text{BeO}^-$ current of several milliamperes is easily achieved, which makes possible to get a $\sim 3\%$ ^{10}Be counting statistics for a sample with a $^{10}\text{Be}/\text{Be}$ ratio of 5×10^{-13} in just 5 minutes. Be content in natural samples (e.g., quartz) is exceptionally low, and Be carrier is invariably added before dissolution of the quartz sample to get sufficient amount of BeO for AMS measurement. This allows manipulating the $^{10}\text{Be}/\text{Be}$ ratio either by increasing the amount of quartz to 100 g and/or decreasing the quantity of stable ^9Be to 0.25 mg or less (Fifield et al. 2007).

Recently, ^{10}Be in ice cores has been measured to reconstruct the solar activity during the Holocene (McCracken et al. 2004; Muscheler et al. 2007; Vonmoos et al. 2006).

Table 54.1

Cosmogenic radionuclides measured by accelerator mass spectrometry (AMS)

Radio nuclide	Half-life (year)	Stable isotopes	Stable isobars	Chemical form	Detection limit (atom ratio)
^{10}Be	1.51×10^6	^9Be	^{10}B	BeO	$\sim 10^{-15}$
^{14}C	5,730	$^{12,13}\text{C}$	^{14}N	C (graphite)	$\sim 10^{-15}$
^{26}Al	7.2×10^5	^{27}Al	^{26}Mg	Al_2O_3	$\sim 10^{-15}$
^{41}Ca	1.03×10^5	$^{40,42,43,44}\text{Ca}$	^{41}K	CaH_2 , CaF_2	$\sim 10^{-15}$
^{53}Mn	3.7×10^6	^{55}Mn	^{53}Cr	MnO	$\sim 10^{-13}$
^{129}I	15.7×10^6	^{127}I	^{129}Xe	AgI	$\sim 10^{-14}$

The measurement of ^{10}Be from Greenland and Antarctica reveals that in the Maunder Minimum period, 1645–1715, the mean global ^{10}Be production was 32% higher than today due to low solar activity and colder climate. In the Maunder Minimum period, production of ^{10}Be in the stratosphere was high leading to larger ^{10}Be deposition in the subtropics, where stratosphere–troposphere exchange is strong.

It has been found that the concentrations of ^{10}Be in the deep-sea sedimentation cores vary mostly due to the changes in sedimentation rates. However, climatic changes and the variation of Earth's magnetic field may also be responsible for the changes of ^{10}Be contents in sediments. It has been inferred that global production rates of ^{10}Be have been varied by less than $\pm 30\%$ in the past 2.5 Ma when averaged over periods of 10^5 years (Reddy et al. 1983; Somayajulu 1977; Tanaka and Inoue 1979; Sharma and Somayajulu 1982).

The concentrations of cosmogenic radionuclides ^{10}Be , ^{26}Al , and ^{36}Cl in 120–200 ka old coralline matrix from Barbados and Puerto Rico were measured by Lal et al. (2005). The concentrations of ^{10}Be were measured in the range of 2.3×10^6 to 1.0×10^8 atoms/g coral while ^9Be concentrations lie in the range of 1.6×10^{-9} to 1.6×10^{-7} g Be/g coral. The intrinsic ratio of $^{10}\text{Be}/^9\text{Be}$ atoms were measured between 6×10^{-9} and 3×10^{-8} . The group reported cosmogenic ^{10}Be is suitable for determining the ages of old corals up to about ~ 10 Ma.

In order to distinguish the concentration of ^{10}Be in samples from the corresponding blanks, samples must be prepared using stable isotope carrier with low intrinsic radionuclide concentrations. Precise determinations of $^{10}\text{Be}/^9\text{Be}$ at the level of 10^{-14} need sample preparation to produce the highest ^9Be currents in AMS measurements. Measurements of intrinsic isotopic ratio at different AMS facilities conclude that commercially available ^9Be carriers rarely meet the requirement in geological samples. It has been advised therefore to use ^9Be carriers prepared from Be-containing minerals such as beryl aquamarine ($\text{Be}_3\text{Al}_2\text{Si}_6\text{O}_{18}$ with traces of Fe) beryl morganite ($\text{Be}_3\text{Al}_2\text{Si}_6\text{O}_{18}$ with traces of Mn) and phenakite (Be_2SiO_4) (Merchel et al. 2008).

For the precise AMS analysis of ^{10}Be and ^{26}Al , Hunt et al. (2008) reported an efficient sample preparation method, where quartz was separated from rocks following a sequence of pulverization, size fractionation, acid etching and leaching, and liquid density separation. This protocol yields pure quartz mineral phase, however, trace-level contamination is expected. Most of the time quartz is contaminated due to lattice imperfections with some combination of native Al, Fe, Ti, alkalis, and alkaline earth metals.

Stable Be and Al carrier is added to the quartz before dissolution in a multiacid medium, that is, in the mixture of HF, HClO_4 , HNO_3 , HCl at 120°C for 24 h, following standard US Geological Survey methods (Biggs and Meier 2002). Typically, 30 g quartz is dissolved in the mixture of 80 mL HF, 4 mL HClO_4 , 1 mL HNO_3 , and 2 mL HCl at 120°C . Most of the impurities native to the quartz phase, except Ti, are converted to fluoride under this condition. In the interim, the interfering isobar ^{10}B forms BF_3 and is volatilized. The quartz digest is evaporated to dryness leaving a bead of HClO_4 that contains nonvolatile elements. Fluorides are decomposed in concentrated HClO_4 . Repeated HClO_4 evaporations produce perchlorate salts that are again dissolved in HCl. Insoluble TiO_2 is removed by centrifugation. The resulting chloride solution is eluted from an anion exchange resin (BioRad AG 1-X8, 200 mesh), evaporated to dryness, and redissolved in HCl. Two selective precipitations are carried out from this solution (at $\text{pH} < 4.1$ and at < 8.9) to remove metallic and alkaline earth impurities (Tera et al. 1986).

From the resulting solution Be and Al are separated on a cation exchange resin (BioRad AG 50W-X8, 200 mesh) (Ochs and Ivy-Ochs 1997). Be fraction is then eluted by 1.2 M HCl, while the Al fraction is eluted with 3 M HCl. The Be fraction is evaporated to dryness and fumed with

1 mL of concentrated HClO_4 to expel any trace boron impurities remaining in the sample. $\text{Be}(\text{OH})_2$ and $\text{Al}(\text{OH})_3$ are precipitated from the respective Be and Al fractions by NH_4OH ($8.1 < \text{pH} < 8.9$). The supernatant is discarded by centrifugation and the gel is transferred to quartz vials, which are ignited in a gas flame to produce BeO by thermal decomposition. BeO cathodes are prepared for AMS analysis mixing with niobium powder to enhance ion beam currents.

54.2.3.2 ^{26}Al

^{26}Al is produced by spallation of oxygen or silicon atoms and accumulated in exposed quartz surfaces. In the atmosphere, ^{26}Al is produced by spallation of argon. This radionuclide is also present as extraterrestrial material such as interplanetary dust. ^{26}Al provides information indicating the exposure history of a landscape or, with complementary ^{10}Be data, the burial history of a sample (Granger et al. 2001; Hunt et al. 2007). Like ^{10}Be , the production rate of ^{26}Al is also very low, (e.g., 30 atoms/g of quartz per year) and hence the detection of ^{26}Al is only possible by AMS (Hunt et al. 2008). $^{26}\text{Al}/^{10}\text{Be}$ ratio is often used to dating the climate archived like old ice relicts. The age range that can be addressed by this method is in the order of 1×10^6 years to 5×10^6 years. Recently, Vienna group at VERA laboratory started a project to measure atmospheric ^{26}Al (Auer et al. 2007). For the determination of atmospheric ^{26}Al , aerosol samples and large-volume ice samples have been tested. Aerosol filter samples are leached in 1 M HCl for 1 to 2 h and filtered through 0.45 μm pore size cellulose ester filters. For ice samples, the melt water is acidified to pH 1 with HCl, filtered through 0.45 μm pore size filters, and concentrated by adsorption on cation exchange resin. Prior to filtration, the samples are spiked with 1 mg Al carrier. Fe is separated from the sample. Subsequently Al and Be are separated, precipitated as hydroxides, washed several times with double-distilled H_2O , and converted into the respective oxides at approximately 800°C . However, due to very low production rate of atmospheric ^{26}Al (about 100 atoms/ m^3), one must be careful about the contamination from non-atmospheric ^{26}Al .

The measurement of ^{26}Al has several interesting applications. For example, Pavicevic et al. (2004) measured ^{26}Al in quartz to assess the cosmic-ray background for the geochemical solar neutrino experiment. Nishiizumi et al. (2009) concluded solar cosmic-ray records by measuring the cosmogenic radionuclides ^{10}Be and ^{26}Al . Solar energy drives many processes occurring throughout the solar system, including Earth's climate. The lunar surface is an archive of solar cosmic rays, and studies of lunar surface rocks provide important information on past solar activity (Reddy et al. 1983). Cosmogenic nuclides on the surface of the Moon are produced by both solar cosmic rays (SCR) and galactic cosmic rays (GCR). Nishiizumi et al. (2009) studied the lunar rock erosion rate using ^{10}Be , ^{26}Al , and ^{36}Cl .

Both ^{10}Be and ^{26}Al are the key sources of cosmogenic radionuclides and they are often analyzed in the same matrix like quartz. The chemical extraction procedures for beryllium and aluminum are similar. Unlike Be, ^{26}Al is extracted in AMS as Al^- . The isobaric interference from ^{26}Mg does not exist because Mg does not form Mg^- . The stable ^{27}Al is spiked with the sample to generate higher current in the cathode. However, some authors prefer not to add stable carrier for ^{26}Al determination, especially in quartz as the Al content of even highly purified quartz is typically 100 ppm. Therefore, 10–20 g of quartz yields sufficient Al for an AMS target (Fifield et al. 2007). The separation of quartz from rocks by a sequence of pulverization, size fractionation, acid etching, and leaching is similar to the one that has

been described already in beryllium section (Hunt et al. 2008). In most of the AMS systems, for Al measurements Al_2O_3 is mixed with a small amount of metal powder (e.g., Ag, Cu, or Nb) as a heat and charge conductor.

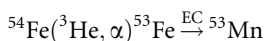
54.2.3.3 ^{53}Mn

The radionuclide ^{53}Mn is produced by nuclear reactions of cosmic rays (mostly protons) on iron present in Earth's surface minerals or in meteorites and cosmic dusts. Measurements of concentrations of ^{53}Mn in rocks might help to understand Earth's surface processes that occurred in time periods not accessible with any other cosmogenic nuclides. ^{53}Mn with its long half-life (3.7 Ma) records cosmic-rays irradiation time up to 11 Ma (Schnabel et al. 2001). Ability to measure ^{53}Mn expanded the dating timescale and improved analytical precision. The important archive of ^{53}Mn (specially, the extraterrestrial ^{53}Mn , which might have been stored in Kuiper and Asteroids belts) is the ferromanganese crusts and sediments. These crusts and sediments may be collected from the Pacific Ocean, the Antarctic Ice, etc. The abundance of ^{53}Mn in the Earth's crust is scanty and the ratio of $^{53}\text{Mn}/^{55}\text{Mn}$ might be $1/10^{14}$, depending on the location. Only AMS can determine such ultratrace levels of ^{53}Mn .

The main interference in the detection of ^{53}Mn by AMS is its stable isobar ^{53}Cr , which is roughly 10^{12} times more abundant in nature (e.g., in manganese crust, sediment, or lava samples). A prerequisite of any AMS measurement of ^{53}Mn in geological samples is therefore chromium separation by an efficient chemistry. Lahiri et al. (2006) developed a method for the separation of chromium and manganese using radiometric technique. They simulated the condition where a particular isotope of manganese is in scanty amounts but chromium is in much larger amounts, a situation near to the abundance ratio of ^{53}Mn and ^{53}Cr in Earth's surface. The ratio of $^{52}\text{Mn}/\text{Cr}$ produced by the nuclear reaction $^{\text{nat}}\text{Cr}(\text{p},\text{xn})^{52}\text{Mn}$ is similar to this. They consecutively irradiated four types of Cr samples (viz., pure Cr metal, $\text{Cr}(\text{NO}_3)_3 \cdot 9\text{H}_2\text{O}$, $\text{K}_2\text{Cr}_2\text{O}_7$, mixture of Cr(III) and Cr(VI)) with a 12 and a 23 MeV proton beam to produce ^{52}Mn , and ^{51}Cr in the matrix, respectively. The separation procedure was monitored by ^{51}Cr ($T_{1/2} = 27.70$ days) and ^{52}Mn ($T_{1/2} = 5.59$ days), the corresponding radiotracers for chromium and manganese. The separation studies were performed by a liquid–liquid extraction (LLX) technique using trioctyl amine (TOA) diluted in cyclohexane. A high separation factor for Mn and Cr was obtained in optimal conditions of 0.8 M TOA and 9 M HCl, in presence of 0.025 mL octanol. As ^{52}Mn is extracted in the organic phase, it is back extracted into the aqueous phase by shaking with 0.001 M NH_3 . Excess AlCl_3 was added to aqueous solution to precipitate $\text{Mn}(\text{OH})_2$ along with $\text{Al}(\text{OH})_3$. The developed method has been found equally applicable for real geological samples such as manganese crusts, lava, and sediment samples. Therefore, the method offers an important tool to improve ^{53}Mn measurements by AMS.

Schnabel et al. (2001) reported separation of Cr from Mn samples by anion exchange chromatography. They took the sample in 10.2 M HCl, added a few drops of H_2O_2 to the solution. The solution was loaded onto an anion-exchange column. Al, Be, Ni, and most of the Cr were eluted by 10.2 M HCl, followed by the elution by 7.1 M HCl to collect Mn^{2+} and remaining Cr. The procedure was repeated for Mn-bearing fractions a number of times to reduce the amount of Cr. After decontamination of chromium, the Mn fraction was evaporated to dryness, dissolved in 7 M HNO_3 and Mn was precipitated as MnO_2 by addition of KClO_3 . The MnO_2 was redissolved and precipitated, and dried, first at 110°C and then at 250°C .

While measuring ^{53}Mn , it is very difficult to get a standard. Therefore, each laboratory makes its internal standard. For example, Munich AMS laboratory made ^{53}Mn standard by irradiating ^{54}Fe by 19 MeV ^3He to produce ^{53}Mn using the following nuclear reaction:



54.2.3.4 ^{129}I

Iodine-129 is a weak β^- emitter with end-point energy of 152 keV and decays to ^{129}Xe that emits 40 keV γ and X-rays. Due to its long half-life, it is difficult to measure ^{129}I by decay counting. The concentration of ^{129}I in natural samples, for example, seawater, is extremely low ($\sim 10^9$ atoms/g) relative to ^{127}I and can only be measured by AMS, the atom counting technique, as INAA and ICP-MS are limited by lower sensitivity.

In the pre-nuclear era, the total quantity of ^{129}I in the oceans was ~ 100 kg (Raisbeck and Yiou 1999), which is believed to have originated from the cosmic-ray interaction on xenon in the atmosphere and by spontaneous fission of ^{238}U (Fabryka-Martin et al. 1985). In the post-nuclear era, concentration of ^{129}I was found to be enhanced by more than one order of magnitude due to nuclear weapons testing, nuclear reprocessing, Chernobyl disaster, marine discharges, etc.

Raisbeck and Yiou (1999) have shown how ^{129}I can be used as *pathway* and *transit time* tracer in the North Atlantic and Arctic oceans. Santschi et al. (1996) measured profiles of ^{129}I in the Deep Western Boundary Current in the Middle Atlantic Bight. The AMS-measured isotopic ratio of $^{129}\text{I}/^{127}\text{I}$ was as high as 1.0×10^{-10} near the surface, while the ratio in the subsurface peaked at 1,000–1,500 m depth of water giving the value 55×10^{-12} . A steady increase in the ratio was observed below 2,000 m water depth reaching maximum of 80×10^{-12} at 2,600 m depth, which is accredited to the Deep Western Boundary Current. The reason is that the Deep Western Boundary Current in the Greenland Sea is more directly connected to the ^{129}I enriched North Sea water than to the Labrador Sea. The minor maximum at 1,000–1,500 m is due to the Labrador Sea water.

The concentration of ^{129}I and the ratios of $^{129}\text{I}/^{127}\text{I}$ were measured by López-Gutiérrez et al. (2000) in rainwater from Sevilla, Spain, and sea sediment core near the Ringhals coast, Sweden, using AMS to study the environmental effects. The typical ^{129}I concentrations in rainwater in Sevilla zone were 10^7 – 10^8 ^{129}I atoms/L. The ^{129}I concentrations were found to be 10^8 – 10^9 ^{129}I atoms/L in rainwater samples in 1996–1997, which corresponds to the measurements in Europe range (Krupp and Aumann 1999). The enhancement of ^{129}I concentrations occurred due to the emissions from large nuclear reprocessing plants (Paul et al. 1987; Wagner et al. 1996; Muramatsu and Ohmomo 1986).

Buraglio et al. (2000) have reported a sample preparation technique for AMS analysis of ^{129}I , which is the modified procedure of Moran et al. (1995), from natural water. Water samples collected from different sources: oceans, seas, freshwater lakes, rivers, and groundwater are stored securely in a cold dark room. The stored samples are equilibrated to room temperature and filtered through 0.45 μm . Potassium iodide (KI) carrier is added (~ 0.25 – 2.0 mg/100 mL water) to the sample. In order to ensure the complete conversion of iodate into iodide, 2 mL of 0.1 M NaHSO_3 is added to the sample. The sample is then acidified (pH 2) by concentrated HNO_3 and the solution is transferred to a separating funnel. The iodide is oxidized to iodine by adding 30% H_2O_2 and extracted into CCl_4 forming a purple color solution. The remaining

iodate in the aqueous phase is further extracted by adding hydroxylammonium chloride and CCl_4 . The iodine extracted to CCl_4 is back extracted into 0.1 M NaHSO_3 . A few drops of 18 M H_2SO_4 are added to remove excess of sulfite during back extraction of iodine. The iodine is precipitated from the aqueous solution by adding 0.01 M AgNO_3 . The precipitated AgI is then washed with NH_3 to get rid of eventual silver-sulfo compounds or AgCl and with double-distilled H_2O and left at 60°C to dry overnight. The sample (AgI) thus prepared is mixed with silver or niobium powder and pressed in a copper holder for the AMS measurements.

54.2.3.5 ^{60}Fe

The radionuclide ^{60}Fe ($T_{1/2} = 1.5$ Ma) is produced inside the solar system only in minute amounts. Because of spallation reactions with cosmic rays, $^{60}\text{Fe}/\text{Fe}$ ratios in the order of only 10^{-14} have been reported for meteorites. On Earth, a much smaller concentration is expected because of the atmospheric shielding from CRs. However, large amounts of ^{60}Fe are produced by stellar nucleosynthesis, as confirmed by the RHESSI satellite (Smith 2004). The presence of ^{60}Fe in interstellar space reflects ongoing nucleosynthesis in the Galaxy on the timescale of the order of 10^6 years (Rugel et al. 2009). In case of a SN sufficiently close to the solar system, this material can be directly deposited on Earth, leaving a ^{60}Fe signal far above the natural terrestrial level. The half-life of ^{60}Fe is long enough to search for such a signal during the past several millions of years (Ellis et al. 1996; Knie et al. 2004). Therefore, ^{60}Fe is a unique indicator for the detection of SN debris on Earth. One of the earliest attempts to detect ^{60}Fe signal in hydrogenetic ferromanganese crust with a growth rate of only a few millimeter per megannum was carried out in Munich by Knie et al. (1999). They collected a crust sample from South Pacific at a depth of about 1,300 m. Knie et al. (2004) also attempted to measure such SNs' distance from the Earth by the quantification of ^{60}Fe obtained from ferromanganese crusts originating from the equatorial Pacific.

From various layers of ferromanganese crust (each layer is 1–2 mm thick) iron was extracted with diisopropyl ether, purified by ion exchange chromatography with AG1X8 resin and was precipitated with NH_3 . To exclude contaminations during sample preparation, different AMS samples have been independently prepared from each layer. Negative FeO^- ions have been produced in a sputter ion source and were accelerated by the Munich tandem accelerator as Fe^{11+} ions up to an energy of 155 MeV. ^{60}Ni is a stable interfering isobar for the detection of ^{60}Fe . Knie et al. got rid of this interfering nuclide employing physical means of separation using a 135° magnet filled with 6 mbar of nitrogen. Because of the interactions with the gas, the ions assume an average charge state depending on their nuclear charge. Therefore, isobaric ions exit the magnet at different positions (Knie et al. 1999). In the ionization chamber, ^{60}Fe can be identified by position, residual energy, differential energy loss, and angle. In 1999, Knie et al. obtained 1 to 14 ^{60}Fe counts in different layers of ferromanganese crust leading to $^{60}\text{Fe}/\text{Fe}$ ratio of $(0.25\text{--}2.1) \times 10^{-15}$. In 2004, the same group obtained in total 69 ^{60}Fe events in various layers, corresponding to an $^{60}\text{Fe}/\text{Fe}$ ratio of 1.9×10^{-15} .

Fitoussi et al. searched for supernova-produced ^{60}Fe in marine sediment using a different chemical treatment (Fitoussi and Raisbeck 2007). The samples were collected from the North Atlantic Ocean. The sediment was leached with 0.04 M $\text{NH}_2\text{OH}.\text{HCl}$ in HOAc (25% v/v) for 6 h, at 100°C . After centrifugation, the solution was separated, evaporated to dryness, and then dissolved in 10 M HCl . To separate Fe from Ni and Al, an anion-exchange column BioRad AG1X8 was used. The elution of the solution was done by 10 M HCl . Mn was then eluted with

7.1 M HCl. Finally, iron was eluted with water. Fe was precipitated as iron hydroxide. The precipitate was redissolved in HCl for purification and reprecipitated with NH_3 , centrifuged and dried at 80°C . The AMS measurement of $^{60}\text{Fe}/\text{Fe}$ ratio shows inconsistency with the traversal of the solar system by a young SN shock wave having the ^{60}Fe -calculated fluence. Therefore, further experiment is required with samples collected from other locations of the globe.

The age of the crust (from where samples are taken to measure ^{60}Fe) is an important parameter since it defines the time span of ^{60}Fe accumulation in the sample. For almost all the measurements discussed above, dating of the crust has been simultaneously done by ^{10}Be measurement (Fitoussi et al. 2008a).

54.2.3.6 ^{146}Sm

Most of the unstable nuclides, present at the beginning in the solar system have faded away. However, some of them with sufficiently long half-lives are still around. Measurement of specific radioactive nuclei on Earth synthesized before the formation of the solar system is a new approach to understanding these processes. ^{146}Sm ($T_{1/2} = 1 \times 10^8$ years), and ^{244}Pu ($T_{1/2} = 82.6 \times 10^6$ years) are such long-lived radionuclides, which have been produced in significant amounts and should still be around in measurable quantities (Wallner et al. 2004).

No measurement or attempted measurement has been performed so far to detect ^{146}Sm in natural samples. The obstacle, until now, is the lack of a method to detect such low concentrations. Because of the long half-life, any attempt to count directly the decay of ^{146}Sm is out of the scope of present detector technology. The measurement of ^{146}Sm through AMS is also a big challenge. Any attempt to measure ^{146}Sm by AMS must ensure that the sample is free from its naturally occurring and million times more abundant stable isobar ^{146}Nd . However, this is a serious problem, because samarium and neodymium, due to their similar chemical properties, always occur together in nature. The phenomenon of lanthanide contraction is mainly responsible for this similarity; introducing a colossal challenge for their mutual decontamination. Therefore as a first step of AMS detection of ^{146}Sm , separation of samarium and neodymium is of utmost importance.

There are many reports on chromatographic techniques describing the separation of samarium and neodymium (Stray and Dahlgren 1995; Arai et al. 2006; Miranda et al. 2002; Pin and Zalduogui 1997; Schwantes et al. 2006; Tsuyoshi and Akiba 2000). Compared to chromatographic techniques LLX is easy to handle, simple and much faster. A larger sample volume can be handled at a time. Recently, a publication coauthored by the senior author of this chapter reported an efficient separation of Sm and Nd with a very high separation factor through LLX so that the result can be directly applied to decontaminate ^{146}Sm from ^{146}Nd for measurement of the former through AMS (Maji et al. 2006b).

The separation of samarium and neodymium was simulated radiometrically using the radioisotopes ^{153}Sm ($T_{1/2} = 46.28$ h) and ^{147}Nd ($T_{1/2} = 10.98$ days). Di-2-(ethylhexyl)phosphoric acid (HDEHP) was used as organic extractant and cyclohexane was used as diluent. As samarium also exhibits a +2 oxidation state, hydroxylamine hydrochloride was added to the radioactive solution containing samarium and neodymium. In optimal conditions, that is, at 0.025 M HCl and 0.1% HDEHP in the presence of hydroxylamine hydrochloride, a separation factor as high as 10^6 has been achieved, where Sm goes to the organic phase along with slight Nd contamination. The metals extracted in the organic phase are stripped back completely into

the aqueous phase with the help of 0.1 M HCl. The aqueous phase was diluted to 0.025 M HCl and the process of extraction was repeated again. After third time extraction, 99% Sm is extracted by the organic phase contaminated with only 0.01% Nd. The developed process for the separation of samarium and neodymium not only offers a very high separation factor but also ensures the suppression of neodymium contamination of samarium by a factor of 10^6 at least after multiple extraction and back extraction processes. Therefore, the developed method might be highly helpful for the pretreatment of samarium samples for the AMS measurement of ultratrace amounts of ^{146}Sm in nature to study nuclear synthesis.

54.2.3.7 ^{182}Hf

Several observations indicate that one or even more supernova (SN) explosions occurred rather close to the solar system during the past several million years. ^{182}Hf ($T_{1/2} = 9 \times 10^6$ years) is believed to be formed by two distinct types of r-process at different rates (Qian 2003) during a supernova explosion. In contrast, according to Meyer and Clayton (2000), a kind of fast “s” process in carbon and helium burning shell is responsible for the production of ^{182}Hf . It is one of the examples of an “extinct” radionuclide with a high abundance in the early solar system, which has led to a powerful application as a geochronometer for dating the formation of objects in the inner solar system (Vockenhuber et al. 2005). ^{182}Hf is expected to be present in the interstellar medium (ISM) as a result of recent nucleosynthesis. Gamma-ray detection of ^{182}Hf through γ -ray telescope is unfeasible due to its overall low activity. However, deposition of ISM grains by accretion onto Earth could make a direct detection of live ^{182}Hf possible in slow-accumulating reservoirs such as deep-sea sediments. Finding of live ^{182}Hf on Earth is also a strong proof for the introduction of material from recent nucleosynthesis, that is, from nearby supernovae.

The average concentrations of hafnium and tungsten in deep-sea sediment are 10 ppm, while the ratio $^{182}\text{Hf}/^{180}\text{Hf}$ has been estimated 1×10^{-12} (Vockenhuber et al. 2004b). The success of an AMS measurement of such minute level of ^{182}Hf relies on two main properties: (1) high mass resolution to separate neighboring isotopes; (2) an efficient suppression of the stable isobar ^{182}W . Because of the natural abundance of ^{182}W , its concentration might be a million times higher in a sample than that of the ultra trace analyte ^{182}Hf . Therefore, prerequisite of ^{182}Hf measurement by AMS is that the sample must be free (until the limits of a chemical separation) of ^{182}W . Again, elements such as hafnium and tungsten, due to lanthanide contraction, always occur together in nature. Their mutual decontamination is always a challenge to the analytical chemist.

There are a few reports available dealing with the decontamination of tungsten from hafnium samples to measure ^{182}Hf by AMS. Attempt was made by Maji et al. (2006a) to develop a method of decontamination of ^{187}W (23.9 h) from ^{175}Hf (70 days) (both produced in a nuclear reactor by irradiating natural tungsten and hafnium salts). The separation studies were performed using LLX technique. Trioctylamine (TOA) dissolved in cyclohexane and HCl were used as organic and aqueous phase respectively. It was observed that tungsten could be quantitatively extracted in the organic phase along with only 2% of hafnium when 6 M HCl in the presence of H_2O_2 and 0.3 M TOA were used as aqueous and organic phase, respectively. The separation factor achieved in this condition was as high as 1.6×10^6 , indicating the possibility of getting ultrapure hafnium without contamination from tungsten. After developing the radiochemical method, the same procedure for stable isotopes of hafnium and tungsten

was checked with AMS facility at Munich. It was found that the developed method alone was responsible for reduction of ^{182}W with a suppression factor of 5–6 orders of magnitude. This finding together with the suppression in the ion source by 3–4 orders of magnitude by using $^{182}\text{HfF}_5^-$ (Vockenhuber et al. 2004a, b), and the additional suppression of 2–3 orders of magnitude by Delta TOF results in a total suppression of around 10^{-11} or 10^{-12} . That value might be further pushed by 2–3 orders of magnitude with an improved chemistry and the appliance of more rigid software cuts at the spectra of the AMS measurements. By this view, a measurement of ^{182}Hf seems to be feasible at an extremely low level as is expected in the case of a supernova-related signal.

Vockenhuber et al. (2007) separated tantalum and hafnium by ion exchange. Strongly basic anion exchange resin Dowex 1X8 (mesh 200–400) was prepared by immersion in a 1:1 mixture of 1 M hydrofluoric and 1 M nitric acid overnight. The same acid mixture was used as eluant and it was possible to eluate out pure Hf fraction free from tantalum.

Earlier the same group (Vockenhuber et al. 2004b) also separated Hf from Ta by dissolving it in HF acid and thereby converting Ta into heptafluorotantalate ions $[\text{TaF}_7]^{2-}$, which could be removed easily by LLX with tributyl phosphate (TBP) in *n*-heptane. The purified Hf solution was mixed with commercial HfF_4 . Finally, HfF_4 was precipitated and dried. The sample material was mixed with silver powder to make the ion source.

Qiu et al. (2007) also followed a similar method to separate Ta and W from hafnium sample. HfO_2 standard sample was dissolved in conc. HF and conc. HNO_3 mixed solution. The sample was roasted in oven for 2 h at 120°C to obtain desiccated HfF_4 powder, which was redissolved in 1 M HF solution. The sample solution was loaded onto an anion-exchange column. Hf was then eluted by 0.01 M HF 9 M HCl, while W and Ta retained on the column. However, through tracer experiments, the author found that the decontamination factors for W and Ta were only in the order of 1,000. The Hf sample purified with this procedure was transformed to HfF_4 powder again and was mixed with 1:1 w/w silver powder and pressed firmly for making ion source. The silver powder served as both an electrical and thermal conductor.

54.2.3.8 ^{244}Pu

After the detection of interstellar ^{60}Fe in deep-sea ferromanganese crust, thrust for searching ^{244}Pu ($T_{1/2} = 8.3 \times 10^7$ years) has been increased many folds (Wallner et al. 2000). ^{244}Pu is produced in recent supernova exclusively by the r-process. They are also present in the interstellar medium. By measuring the current abundance of ^{244}Pu and comparing it to the longer-lived ^{238}U , one may deduce the portion of r-process material from the last nucleosynthesis process that has contributed to the protosolar cloud before the formation of the Earth (Lachner et al. 2009). The Munich AMS group has set up a time-of-flight system for the detection of actinides. This setup was used by Wallner et al. (2004) to measure ^{244}Pu in deep-sea ferromanganese crust. They found about 4,000 atoms/cm² in the surface of such crust, which is believed to be 1–14 Ma old. It should be kept in mind that ^{244}Pu is also generated by atmospheric weapon tests, though it is unlikely to be deposited in deep-sea sediments and crust.

AMS measures the ratio of a long-lived radionuclide to its stable isotope (e.g., $^{14}\text{C}/^{12}\text{C}$). However, in the case of plutonium, there is no stable isotope. Hence, it is necessary to add a “spike” of a known amount of one of the long-lived isotopes, generally ^{242}Pu (3.75×10^5 years) or ^{239}Pu (2.4×10^4 years), to the sample in order to quantify the concentrations of the

isotopes of interest (Fifield 2008). Lack of stable isotopes and stable isobars offers favorable conditions for the AMS measurement of plutonium. As there are no isobaric interferences, it is not required to develop elaborated chemistry for isobar separation. These are the reasons for the success of ^{244}Pu detection by AMS though the production rates of the actinides in supernovae are a few orders of magnitude lower than that of ^{60}Fe .

The chemical extraction of plutonium helps to reduce the matrix (crust) material from kilogram range to below 1 mg. After dissolving the manganese crust in aqua regia, plutonium is recovered by passing the solution through anion exchange resin followed by co-precipitation with calcium oxalate. In the case of plutonium, only picogram quantities of the element are available, whereas the Cs sputter ion sources require sample masses of 1–10 mg. The extra bulk is achieved by dispersing the plutonium in an iron oxide matrix. Typically, 1–2 mg of $\text{Fe}(\text{NO}_3)_3$ is added to the plutonium-containing solution. The solution is then either evaporated to dryness, or precipitated as $\text{Fe}(\text{OH})_3$ by making the solution alkaline. The resulting solid is converted to Fe_2O_3 by baking at 800°C , mixed with a conductor like aluminum, silver, copper, or niobium, and pressed into a sample holder (Wallner et al. 2000, 2004). In the ion source PuO^+ molecular ions are preferred as intensity of this ion is higher than that of the Pu^+ ions.

54.3 Other Mass Spectrometric Techniques Related to Cosmochemical Analysis

AMS is the most reliable and ultra sensitive technique for measuring cosmogenic radionuclides. However, with the advent of analytical sciences, some other mass spectrometric techniques became potential competitors of the AMS system. Nowadays resonance ionization mass spectrometry (RIMS) is also considered as a sensitive and selective method for cosmochemical analysis in ultra trace scale. It provides extremely high isobaric suppression and good overall efficiency. The determination of naturally occurring and cosmogenic radionuclides by inductively coupled plasma-mass spectrometry (ICP-MS) has gained recognition over the last 15 years. With the increase in instrumental sensitivity, it is now possible to measure ultratrace levels (fg range) of many radionuclides by ICP-MS without requiring very complex sample pre-concentration schemes. The abundances and isotopic compositions of some long-lived radionuclides can also be measured by the thermal ionization mass spectrometry (TIMS). In this section, the principle and instrumentation of ICP-MS, TIMS, and RIMS will be discussed briefly together with their use in cosmochemical analysis.

54.3.1 Inductively Coupled Plasma-Mass Spectrometer (ICP-MS)

54.3.1.1 Components of ICP-MS

The most widely used mass spectrometric technique in the last couple of years is the inductively coupled plasma-mass spectrometry (ICP-MS), which is a highly sensitive mass spectrometry and is capable of determining a range of metals and several nonmetals at concentrations below one part in 10^{12} . It is based on coupling together with inductively coupled plasma, a method of producing ions, with a mass spectrometer as a method of separating and detecting the ions. ICP-MS is also capable of monitoring isotopic speciation for the ions of choice. Being a powerful tool, ICP-MS has opened up new applications for isotope ratio measurements of

elements, which are difficult to analyze (e.g., Mo, Hf, and Fe). Because of multielement handling capability, very low detection limits, good accuracy and precision measurements, ICP mass spectrometers are preferred among other comparing mass analysis techniques. A detailed description of the instrument and the functions of each component of ICP-MS can be found in the handbook by Nelms (2005). An ICP-mass spectrometer consists of the following components:

- Sample injection system
- Inductively coupled plasma formation
- Plasma sampling interface
- Mass analyzer
- Detector

A flowchart of the various steps of ICP-MS is given in [Fig. 54.6](#).

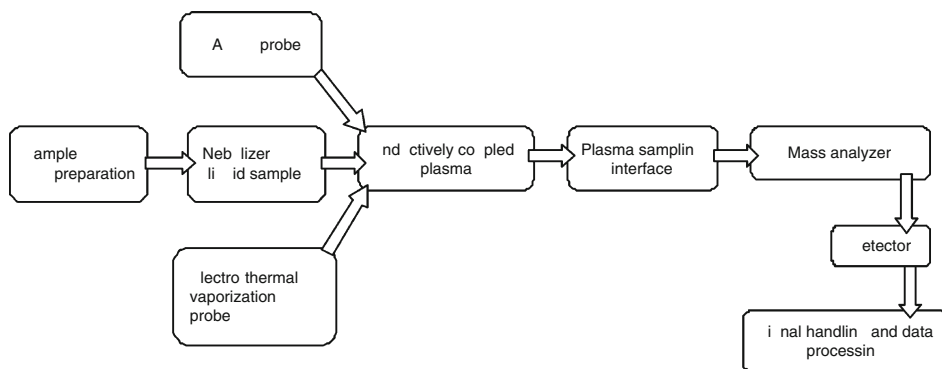
Sample Introduction System

The mostly liquid samples are introduced into an ICP-mass spectrometer by different techniques. Each of these techniques aims to generate fine aerosol of the liquid sample to achieve efficient ionization of the sample atoms in the plasma. However, only 1–2% of the sample can find way into the plasma; hence, the sample introduction system is considered as the weakest component of an ICP-MS. The introduction system works in two steps, namely, aerosol generation using nebulizer and droplet selection by the spray chamber. Most commonly, the liquid sample is pumped into the nebulizer by a peristaltic pump at a speed of ~ 1 mL/min. When the liquid sample enters the nebulizer, it is transformed into fine aerosol under the pneumatic action of the nebulizer gas flow (~ 1 L/min). However, some pneumatic nebulizers do not use a pump. They suck the sample through the tubing through the action of positive pressure of the nebulizer gas.

The spray chamber restricts the movement of large droplets (~ 10 μm in diameter or more) toward the plasma allowing only fine droplets (~ 5 – 10 μm diameter) to enter the plasma. The reason is that the plasma is not efficient enough to dissociate large droplets. The spray chamber also smoothes out the pulses that form during the nebulization process due to the pumping.

■ Fig. 54.6

Block diagram of the sample analysis in inductively coupled plasma-mass spectrometry (ICP-MS)



The fine droplets inserted into the plasma proceed through the process of dissociation, atomization, and finally ionization of the sample elements.

ICP Formation

Inductively coupled plasma forms when argon gas passes through a quartz torch placed in an induction coil, commonly called load coil, where radio frequency (RF) power of 750–1,700 W is applied. As a result, an alternating current oscillates within the field and the frequency of oscillation is governed by the RF generator. These oscillations generate electric and magnetic fields at the top of the torch. A high-voltage spark is introduced in order to strip electrons from the argon atoms. Stripped electrons are trapped in the surrounded magnetic field and accelerated in closed circular loop. Rapidly moving electrons collide again with neutral argon atoms stripping a new set of electrons and thus a chain reaction is sustained. High temperature of the plasma is governed by this collision process. The plasma flame is therefore the assembly of neutral argon atoms, positively charged argon ions, and electrons. Plasma remains alive until the radio frequency power is supplied through the inductive coil. In general, the temperature of plasma varies between 6,000 and 10,000 K, depending on the region of the plasma. The sample aerosol that enters the plasma is immediately de-solvated, vaporized, atomized, and finally partially ionized. It has already been established that most of the elements in the Periodic Table produce predominantly singly charged ions at yields ranging from 5% to 100%.

In most cases, plasmas are formed entirely of argon gas. However, the introduction of alternative gases may also have beneficial effects. For example, nitrogen can be introduced either as coolant gas or as a nebulizer gas flow to overcome various interferences including that of $^{40}\text{Ar}^{35}\text{Cl}^+$ on $^{75}\text{As}^+$ and oxide-based interferences. The introduction of nitrogen has substantial effect on the physical and electrical properties of plasma. If it is introduced as nebulizer gas flow, annular width of the plasma increases significantly though electron temperature decreases to 3,000–5,000 K along with the decrease in the gas kinetic temperature. As a result, interference effect decreases significantly, and at the same time sensitivity of the measurement also decreases.

Plasma Sampling Interface

The sampling interface consists of two sample cones with a small orifice in the center and is designed to extract the analyte ions from the ICP and transport them to the mass spectrometer for analysis. Analyte ions are generated in the ICP at high temperature ($\sim 7,500$ K) and atmospheric pressure. During the transportation, extracted analyte ions travel from the ICP to the mass spectrometer and detector, which are operating at room temperature (~ 300 K) and reduced pressures (10^{-5} – 10^{-9} mbar). Pressure gradient between the plasma and specially designed cone shapes, namely, sample cone and skimmer cone, of the sampling interface strongly influence the analyte sensitivity and the degree of the possible molecular interferences. An expansion chamber operated at 2–5 mbar pressure is located just behind the sample cone. Consequently, a significant portion of the plasma drives through the sample cone aperture into the expansion chamber. Argon ICP is a weakly ionized plasma, and therefore the bulk of the argon gas drawn through the sample orifice remains unionized. The cloud entering the expansion chamber is a mixture of gas atoms, molecules, ions, and electrons. Each constituent of the cloud gains speed quickly and expands outward under the influence of reduced pressure, generating a free jet. The supersonic expansion of gas is observed in the interface region. Rapid increase of gas velocity is due to the conversion of thermal energy of gas into the kinetic energy,

resulting in a reduction of gas temperature to 100–200 K. However, the gas does not attain thermal equilibrium in the interface as the electron temperature remains close to the source temperature, but ion–electron recombination is prevented due to the rapid drop in density. This process is known as adiabatic expansion, which is fundamental to ICP-MS analysis.

Ion Extraction and Ion Optics

ICP-MS is divided into two distinct regions, which are separated from each other by a gate valve. The first part of the instrument combines ICP generation system and expansion chamber, which readily attains atmospheric pressure when ICP is not functioning. The high vacuum, $\sim 10^{-7}$ – 10^{-8} mbar, is maintained for the ion optics, quadrupole, and detector. The gate valve between these two parts only opens when the ICP is operational and the expansion chamber is pumped out to the required operating pressure. Analyte ions travel through the interface region as they tend to achieve high velocity of the bulk argon gas, but the ion kinetic energies (E) exhibit a mass dependence as soon as the ions cross the sampling interface following the equation, $E = Mv^2/2$, where M is the ion mass and v is the ion velocity. The first charge separation takes place just behind the skimmer cone orifice, even in the absence of any applied external electric field. This action leads to a typical energy spread of 0.5–10 eV for the total mass range of Li to U. In the skimmer region, difference in mobilities between ion and electron occurred due to the drop of pressure and relative size difference. The high temperature of electron creates net negative charge diffusion readily toward the inner wall of the skimmer cone and this leaves a net positive charge along the axis with the bulk neutral gas flow. In the ICP, most elements of the Periodic Table efficiently produce positive ions, which survive long enough allowing mass selection and detection in the mass spectrometer. Positive ions are therefore favored for ICP-MS.

Application of an electric field in the interface can enhance the charge separation process and that means positive charge concentration increases largely in a comparatively small volume. Naturally, positive ions in the gas beam start repelling each other. This effect produces a self-defocused beam and the phenomenon is known as space charge effect. The maximum achievable sensitivity is limited by the space charge effect, which not only resists transmission of low-mass ions, but also sometimes suppresses the whole matrix. It strongly influences the operation of the ion optics. The “extraction” of ions usually means the selection of only positive ions applying electric field from the gas beam, which contains positive and negative ions, electrons, and uncharged species. Ions are generally extracted by a circular metal tube placed behind the skimmer cone. A negative voltage is applied to the metal tube to accelerate the positive ions from the gas beam toward the ion optics repelling electrons. Several important factors like plasma operating conditions, pressure of the expansion chamber, skimmer cone shape, ion current are considered to decide the magnitude of extraction voltage to be applied. In general, high extraction voltage helps to achieve high sensitivity for high-mass elements ($A > 80$), while lower extraction voltages favor sensitivity for low-mass elements ($A \leq 80$).

The objective of using ion optics is to transport the positive ions from the rear of the skimmer cone to the quadrupole, where they are separated according to their mass-to-charge ratio for analysis. Ion optics acts as an ion–energy filter, which must be compatible with the range of ion kinetic energies that emerge from the plasma sampling interface.

Mass Analyzer

The nucleus of ICP-MS is the mass separation device, generally called mass analyzer, is positioned between the ion optics and the detector. The task of this device is to separate the

ions of interest from the non-analyte and argon-based ions. Ions are traveling through the mass analyzer are separated according to their mass-to-charge ratio (M/q). However, the mass separation is performed in various ways depending upon the mass separation device used in ICP-MS. Various analyzers are used in the ICP-MS depending upon the application and are named accordingly. Among others, quadrupole (ICP-QMS), magnetic sector combined with electrostatic analyzer (High Resolution, HR-ICP-MS or Multi Collector, MC-ICP-MS), time-of-flight analyzers (TOF-ICP-MS) are commonly used for trace element analysis (Aggarwal 2010). Ions are routinely detected by using either Faraday cups or secondary electron multiplier. However, all above-discussed mass analyzers carry their own advantages and shortcomings.

The most common among the analyzers is the quadrupole mass filter that uses time-varying electric fields. In all these instruments, electric fields are varied rapidly compared to the transit time of the ions, hence these spectrometers are known as *dynamic* mass spectrometers. Potential energy of the ions is governed by the plasma potential. This potential energy is converted to equivalent kinetic energy when the ions are accelerated entering a grounded surface. Ion velocity (v) is calculated equating the potential energy and the kinetic energy expressions.

In ICP-QMS, the quadrupole consists of four cylindrical rods, typically made of stainless steel or molybdenum of equal length (~ 15 – 20 cm) and diameter of about 1 cm, enclosed in a cylinder of fixed radius (r_0). A fixed (DC) potential is applied on one diagonal pair of rods; and a radio frequency field on the opposite pair selects the ions by mass, which are allowed to pass through the quadrupole, while the rest eventually strike the quadrupole rods, where they are neutralized and stay until the rods are cleaned. The potential ϕ in the quadrupole mass filter is expressed as

$$\phi = \phi_0 \frac{(x^2 - y^2)}{2r_0^2} \quad (54.8)$$

The components of electric field along the axes are

$$E_x = -\phi_0(x/r_0^2), \quad E_y = \phi_0(y/r_0^2), \quad E_z = 0 \quad (54.9)$$

The potential, ϕ_0 , consists of a direct and an alternating component as

$$\phi_0 = V_{DC} - V \cos \omega(t - t_0) \quad (54.10)$$

where V_{DC} is the direct potential (constant), V is the amplitude of the RF potential, $\omega = 2\pi f$ is the angular frequency, f is the frequency of the RF supply, t is the time, and t_0 is the initial phase of the RF component. Ion motion can be obtained by solving the differential equation in each direction. There will be no acceleration along the axis of the cylinder; therefore, ions are transmitted with a constant axial velocity. This velocity is obtained from the difference between the ion's kinetic energy and the constant potential along the axis of the quadrupole mass filter. The electric field along the z -axis is zero, but often a constant unipolar potential is superimposed. This is known as fixed axis potential. The fixed axis potential controls the motion of ions (speed up or slow down) within the field, so that they can be transmitted with optimal axial velocity. Ions may speed up or slow down when they cross the intermediate lenses before the quadrupole mass filter. In practice, fringing field, which gives rise to nonzero field components in the axial (z) direction, always exists near the entrance and the exit of the quadrupole mass filter. Ions are lost at the entrance and the exit of the mass filter. Loss of ions is more near the entrance of the mass filter than at the exit end. It is therefore

usual to minimize the loss of ions in the entrance of mass filter by controlling carefully the ion entry conditions.

A set of DC-RF voltage on the rods will steer the analyte ions of interest electrostatically through the center of the quadrupole mass filter until the exit and they will be converted to an electrical pulse by the detector while other ions of different mass-to-charge ratios will stop in the quadrupole. In a multielemental analysis, the mass scan process is repeated one after another for all analyte ions of different mass-to-charge ratio until all the analytes in a multielement analysis have been measured. Quadrupole scan rates are typically on the order of 2,500 atomic mass units (amu) per second and can cover the entire mass range of 0–300 amu in about 0.1 s. However, real-world analysis speeds are much slower than the above.

Detectors

The detection system of ICP-MS counts the number of ions coming out from the mass analyzer. The detector converts the ions into electrical pulses that are counted by the integrated circuitry. The measure of the electrical pulses correlates the concentration of analyte ions in a matrix. The quantification of trace element is obtained comparing the ion signature with respect to the reference standards.

The ultratrace analysis in ICP-MS involves the use of sophisticated detectors such as active film or discrete dynode electron multiplier that efficiently converts the ion current to the electrical signal. The detector is kept off the axis of the mass analyzer in order to minimize the background. Consequently, the ion emerges from the mass analyzer, traverses through a curved path, and hits the first dynode creating lots of secondary electrons. The design of the dynodes is made in such a way that the secondary electrons are accelerated to the next dynode, where they generate more electrons. The electron multiplication process is continued in each dynode creating a pulse of electrons and is collected by the anode placed at the end. Though the discrete dynode detector is in general more sensitive than the old channeltron multiplier, the function of the measurement circuitry is also important in handling the low and high ion count rate.

In general, quadrupole-based ICP-MS allows isotope ratios to be measured in a few minutes with a precision between 0.1% and 0.5% and detection limits in the nanogram per liter range and below in aqueous solutions. The factor, which deteriorates the accuracy and precision of the isotope analysis, is the occurrence of isobaric interferences (atomic ions or molecular ions at the same mass/charge ratio) of analyte ions. The precision of isotope ratio measurements and the detection limits for selected elements (e.g., Ca, Fe, S, I, and Se) were improved by the insertion of a collision/reaction cell in quadrupole-based ICP-MS. Due to the collisions of ions formed in the ICP with gas atoms (He, Xe, Ar) or molecules (H_2 , O_2 , CH_4 , NH_3) introduced into a collision cell (CC), the kinetic energy spread of ions is reduced from several eV to <0.1 eV, which results in an increasing sensitivity of analyte ions. Moreover, isobaric interferences from disturbing atomic or molecular ions are significantly reduced by the interaction between collision gas and ions in the collision cell. For instance, the determination of $^{80}\text{Se}^+$ or $^{40}\text{Ca}^+$ isotope abundance is almost impossible even in a high mass-resolution sector-field ICP-MS. The problem can easily be solved by ICP-QMS with a collision cell, because the interfering Ar dimer ions ($^{40}\text{Ar}_2^{2+}$) are dissociated or atomic plasma gas ions ($^{40}\text{Ar}^+$) are neutralized via collision-induced reactions (Tanner et al. 2002; Boulyga and Becker 2001). Sometimes, molecular ions are also formed in the collision cell to be used as analyte ions to avoid interference. For example, $^{31}\text{P}^+$ or $^{32}\text{S}^+$ determination is carried out via the oxide ions $^{31}\text{P}^{16}\text{O}^+$ and $^{32}\text{S}^{16}\text{O}^+$, which are interference-free at mass/charge = 47 and 48, respectively,

formed with maximum ion intensities in the collision or reaction cell under optimized experimental conditions (Boulyga et al. 2003).

The other type of mass spectrometer that is used in isotope analysis is the double-focusing sector field ICP-MS. It allows a determination of isotope ratios with a precision between 0.02% and 0.2% and detection limits from nanogram per liter to sub-nanogram per liter range.

In order to overcome the limitation of the mass spectrometer having single ion collector, multiple ion collector is used for simultaneous measurements of mass-separated ion currents of several isotopes. Insertion of multiple ion collectors in sector field mass spectrometers improved the precision of isotope ratio measurements down to 0.001–0.002%.

54.3.1.2 Application of ICP-MS in Long-lived Analysis

ICP-MS is advantageous over RIMS and AMS due to fast and relatively inexpensive multielement determination, precise and accurate isotopic analysis at the trace, and ultratrace concentration levels in any material. Another advantage of ICP-MS compared to other atomic mass spectrometric techniques is the simple sample preparation and introduction of aqueous solutions into the normal-pressure inductively coupled plasma ion source.

Measurements of isotopic ratios of certain elements using ICP-MS combined with other attachments are described in the review of Becker (2005). A sensitive analytical technique for ^{129}I determination in soil and sediments was proposed by Izmer et al. (2003). Hot extraction (at 1,000°C with oxygen) of volatile analyte iodine was carried out in an oven coupled to ICP-CC-QMS. Oxygen was used as the extraction and collision gas and also for eliminating the isobaric interference of $^{129}\text{Xe}^+$, which disturbs ^{129}I detection. A cold finger for the collection of iodine between the oven for hot extraction and ICP was introduced and achieved a significant improvement of the detection limit for ^{129}I in sediments (0.4 pg/g instead of 30 pg/g, without cooling). $^{129}\text{I}/^{127}\text{I}$ isotope ratios of about 10^{-6} were measured in sediments at the ultratrace level with a precision <10% (Izmer et al. 2004). The abundance sensitivity for $^{236}\text{U}/^{238}\text{U}$ was also determined by ICP-CC-QMS, using helium as collision gas, as 6.3×10^{-8} (Boulyga and Becker 2002).

An ultratrace level Pu isotope analysis was performed in MC-ICP-MS by Becker et al. (2004) after separation on TEVA resin and enrichment of Pu from 100 L lake water from the Sea of Galilee. Studies of the separation procedure for 2.1 pg ^{242}Pu spiked to 100 L of lake water have resulted in a yield of 62%. The detection limit for Pu measurement by MC-ICP-MS was 3×10^{-20} g/mL. ^{239}Pu was detected in 100 L lake water at a concentration level of about $\sim 3.6 \times 10^{-19}$ g/mL. Hence, the measured $^{240}\text{Pu}/^{239}\text{Pu}$ isotope ratio by MC-ICP-MS of 0.17 is a clear evidence of plutonium contamination from the global nuclear fallout in the 1960s.

A direct determination of plutonium isotopes in soils and sediments was proposed by Boulyga et al. (2004) by Laser Ablation (LA)-ICP-MS. To minimize uranium hydride formation and peak tailing of $^{238}\text{U}^+$ on mass/charge = 239, LA-ICP-MS measurements were carried out at the optimum condition of the spectrometer. Isotope ratio of $^{240}\text{Pu}/^{239}\text{Pu} \approx 0.4$ was measured in contaminated Chernobyl soil samples, wherein the detection limit for Pu was determined as 0.3 pg/g.

Though the above-discussed samples are not directly of cosmogenic origin, the technique used is similar.

Wolfa et al. (2005) have developed a method for the quantification of a large number of trace elements, from moderately volatile to highly volatile (Cu, Zn, Ga, Se, Rb, Ag, Cd, In, Sn,

Sb, Te, Cs, Tl, and Bi) in chondritic meteorites by ICP-MS. The method allows for a rapid and accurate determination of the cosmochemically important volatiles in chondritic meteorites providing the means for an even more comprehensive elemental analysis of a single sample of chondritic material.

54.3.2 Resonant Ionization Mass Spectrometry (RIMS)

Resonant ionization mass spectrometry (RIMS) is a promising analytical technique that can accomplish distinct identification of low elemental concentrations in bulk materials. The technique offers high sensitivity and selectivity, which helps to determine low-concentration elements at and below the parts-per-billion (ppb) level. Moreover, such determinations can be quantitative even in complex matrices.

The high selectivity of the technique is due to sequential optical excitations combined with mass spectrometry coupled with high-efficiency ion detection. Several experimental combinations of RIMS have been studied aiming individual application. Nevertheless all individual techniques share a common goal.

54.3.2.1 Working Principle

Conventional chemical extraction of the sample is carried out before introducing it into an atomic beam source and thermally evaporated into high vacuum ($<10^{-6}$ torr). Single or multistep resonance excitation and ionization takes place upon irradiation with precisely tuned laser light onto individual optical resonance of the selected isotope. In most cases, excitation starts from the atomic ground state, passes through intermediate bound states, and ends at high-lying or auto-ionizing states for the final ionization. The resulting ions are accelerated in an electric field and transmitted through a mass spectrometer to a low-background ion detector. The overall isotopic selectivity is achieved through proper optimization of the instrumental parameters, suppressing neighboring masses by as much as a factor of 10^8 .

54.3.2.2 Components of RIMS

The simplest version of RIMS is composed of a source of atoms or molecules, one or more tunable lasers, and a mass analyzer or detector. A detail of instrumentation is discussed by Young et al. (1989).

Atom Source

Atoms are generated in gas phase using thermal sources, heated filament, and graphite furnace. Atom generation by a filament or in furnace is normally continuous in time, which may yield coupling inefficiency between such an atom source and a pulsed laser. In order to overcome the problem, two types of pulsed atom sources have been developed that use either a pulsed laser or a pulsed particle beam to generate an atom cloud. Either of these types of atom sources is coupled to pulsed-laser excitation. Glow discharge is another useful atom-generating source used in RIMS.

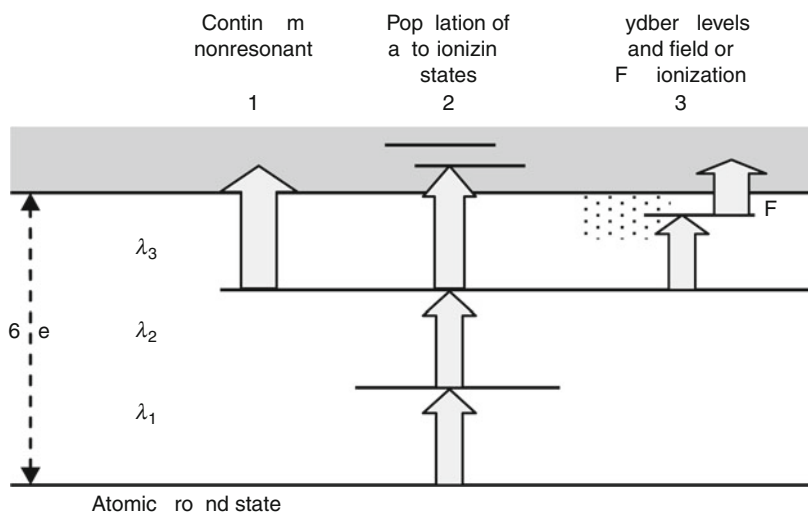
Lasers

Commonly, either of two types of lasers, continuous-wave or pulsed, have been applied to RIMS. Resonant optical processes have typically included one, two, or more laser energies delivered by one or more lasers. For analytical simplicity, one laser is desirable. Application of one laser wavelength (single-color RIMS), requires the absorption of two or more photons, of which at least one transition must be a bound-bound transition. All kinds of tunable lasers are commercially available and the wavelength ranges available to tunable lasers are very broad. Among them, dye lasers pumped by a Nd:YAG laser, excimer laser, flash-lamp laser, and semiconductor diode lasers are easy to operate. Continuous-wave or pulsed lasers are used alone or in a variety of combinations to produce ionization. An ideal arrangement that was found to be satisfactory is the use of relatively low-power continuous-wave lasers for the bound-bound steps and a high-power CO₂ laser as additional energy source or electric field for the ionization step. Another combination in RIMS is the use of semiconductor diode laser in combination with another high-power laser for excitation and ionization, respectively.

Optical resonance excitation from the atomic ground state up to final ionization can follow a number of different pathways (► Fig. 54.7). Typical ionization potential is ~ 6 eV for all the alkaline earths, rare earths, and actinides. Due to the high optical cross section ($\sigma = \lambda^2/2\pi$) of the order of $\sim 10^{-10}$ cm², all resonant optical excitation steps between bound atomic states (typical excited state lifetime of 10^{-8} s) can be saturated with continuous-wave as well as pulsed laser systems. Nonresonant ionization into the continuum has a relatively low cross section in the range of $\sim 10^{-17}$ – 10^{-20} cm² and is thus difficult to saturate with continuous-wave lasers. This blockage of the process can often be avoided for elements with more than one valence electron, by tuning the ionization laser to an auto-ionizing state, which decays rapidly within its lifetime of far less than 1 ns into an ion and a free electron. This is particularly effective for lanthanide and actinide elements, which have a high density of auto-ionizing states near the

■ Fig. 54.7

Resonance excitation methods followed in resonant laser ionization mass spectrometry(RIMS)



threshold. Otherwise, efficient excitation into high-lying Rydberg states and subsequent electric field- or infrared-ionization can be used to increase the ionization probability. Even with these additional processes, which increase the ionization probability by 2–3 orders of magnitude, the ionization step still requires the most intense laser light provided by a high-power laser system. As isotope shifts are usually not resolved with pulsed lasers, a compromise between isotopic selectivity (requiring narrow-bandwidth continuous-wave lasers) and efficiency (requiring high repetition rate pulsed lasers) must be done. High isotopic selectivity requires multistep excitation and experimental arrangements capable of avoiding or at least minimizing the Doppler-broadening of optical resonance, which usually overshadows the small effects of isotope shift and hyperfine structure, while isobaric selectivity is obtained in a single optical excitation (Ott et al. 2004; Wendt et al. 2000; Wendt and Trautmann 2005; Becker 2005).

Mass Analyzer/Detector

All kinds of mass analyzers, such as magnetic sector, quadrupole, and time-of-flight instruments, have been used in RIMS studies. Each of these mass analyzers carries its own advantages and disadvantages. The combination of a time-of-flight analyzer with a pulsed laser is an ideal system in terms of matching duty cycle to the characteristics of the mass analyzer. The pulsed laser is capable of generating a burst of ions in a short period suitable for time-of-flight separation. However, in terms of mass resolution, magnetic sector instruments are superior to time-of-flight analyzers. New improved quadrupole mass analyzers are also found efficient with regard to several important mass spectrometric parameters. Moreover, these analyzers are compact and less costly than sector instruments.

The decision of using continuous-wave or pulsed lasers for ion generation depends on the choice of mass analyzer that will be used in RIMS. This is because, compared to the pulsed lasers, the probability of ion generation is poor in continuous-wave lasers and an independent source of energy is required to improve the situation.

In case of pulsed lasers, the probability of ion generation approaches unity per pulse, but detector dead time can result in errors if too many ions arrive at the detector in a short time. However, pulsed-laser approach is ideal in detecting extremely small numbers of atoms.

54.3.2.3 Application of RIMS

A few reports are available till date on cosmochemical analysis using RIMS though the performance of each individual combination has been studied using several laser systems for the atomic excitation and mass analyzers for isotope selection. Commonly it is used in the analysis of environmental and biomedical samples. Wendt et al. (2000) demonstrated the measurement of $^{41}\text{Ca}/^{40}\text{Ca}$ ratio using the promising technique of coherent multistep RIMS, which achieved high isotopic selectivity with values of 10^{13} and higher. Improved method is needed for the cosmogenic analysis, which demands isotopic selectivity greater than 10^{14} . The measurement of $^{236-244}\text{Pu}$ was also reported by Wendt et al. (1999) in environmental samples with experimental detection limit as low as 10^6 per sample.

Lu and Wendt (2003) described the performance of laser-based ionization spectroscopy with quadrupole mass analyzer. The expected neighboring mass suppression factor could not be achieved in the experiment due to backgrounds arising from photo-induced Ca dimmers and Ca hydrides, surface ionized ^{41}K and highly excited neutral Ca that pass through the mass

spectrometer, scattered photons, and detector dark counts. These effects limit the isotopic selectivity of high-resolution RIMS at about 5×10^{12} for ^{41}Ca against ^{40}Ca , and limit the isobaric selectivity at 10^8 for ^{41}Ca against ^{41}K . Environmental, cosmochemical samples, where relative abundances of ^{41}Ca lies in the range of 3×10^{-10} – 3×10^{-11} , were analyzed with a precision of 5% and overall efficiency of 5×10^{-5} .

The expected source of ^{244}Pu is the interstellar medium (ISM) from fresh r-process nucleosynthesis or in direct ejecta from supernovae. Deposition onto Earth may result in traces of live ^{244}Pu in suitable reservoirs. Ofan et al. (2006) developed a method for ^{244}Pu detection based on RIMS. Gd was chosen as a proxy, because its chemical properties, excitation and ionization schemes, and wavelengths are similar to those of Pu. The Pu detection efficiency achieved for by RIMS was found to be smaller than that obtained by AMS (10^{-6} – 10^{-5}) by a factor of $\sim 1,000$. However, a value of the order of 0.5%, as obtained here for Gd, is believed to be feasible for Pu detection as well. This efficiency would allow the determination of the abundance of ^{244}Pu continuously accreted from the ISM or deposited in a single supernova event such as the one occurred 3 Ma before present, as evidenced by the ^{60}Fe anomaly reported in a deep-sea manganese crust.

54.3.2.4 RIMS and AMS

RIMS technique has been established as a well-suited method in determining certain trace and ultratrace isotopes. Isobaric suppression interferences and the ability to effectively combine optical isotopic and mass spectrometric selectivity are the major advantages of RIMS. Measurement of extremely rare isotopes is possible by enhancing the efficiency and hence increasing the effective dynamic range by the easy adjustment of laser intensities. However, the variety of problems tackled by the RIMS is not comparable with the vast application of AMS. Developments are in progress to achieve isotopic selectivity above 10^{13} , detection limits of isotopic ratios below 10^6 atoms, as it is the characteristics of AMS in commonly measured isotopes. Nevertheless, RIMS can be a good alternative technique for many ultratrace isotopes, where AMS encounters fundamental limitations, such as insufficient or no production of negative ions, strong isobaric interferences, or other sources of background. Hence, RIMS should be treated as complementary technique of AMS, rather than as competitive.

54.3.3 Thermal Ionization Mass Spectrometry (TIMS)

54.3.3.1 Principle and Components: A Quick Look

Thermal ionization mass spectrometry (TIMS) is an analytical technique for precise measurements of isotope ratios of elements that can be ionized thermally. TIMS is essentially a magnetic sector mass spectrometer that is used in geochemistry, geochronology, and cosmochemistry. Generally, ions are created on a thin metal ribbon by passing current through the metal ribbon in vacuum. Ions are accelerated across an electric potential gradient up to ~ 10 kV and focused into a beam passing through a series of slits and electrostatically charged plates. The focused ion beam is then allowed to traverse through a bending magnetic field in order to achieve dispersion of the original ion beam into separate beams based on their mass to charge (M/q) ratio. The mass-resolved ion beams are directed to the collectors, where the ion beam is

converted into voltage. Precise isotope ratios are obtained by comparing voltages corresponding to the individual ion beams.

TIMS consists of the following components:

1. Ion source and ion optics: the region where positive or negative ions are produced, accelerated, and focused into a single ion beam.
2. Mass analyzer: the equipment splits a single ion beam into separate ion beams according to the ion's mass/charge ratio.
3. Collector: it measures the ion beams either sequentially or simultaneously. TIMS is able to measure the isotopic ratios with a precision to 0.01–0.001%.

TIMS is able to ionize and evaporate samples at different temperatures by using multiple filament assemblies and allows complete transmission of ions from source to collector that yields highly precise measurement (e.g., Sr and Nd is measured with a precision better than 10^{-5} using sample sizes of a nanogram or less). Switching between positive and negative ion mode is easy; however, the technique is limited by its ionization efficiency for some elements and because rigorous sample preparation is needed to avoid isobaric interference.

54.3.3.2 Application of TIMS in Cosmochemical Analysis

The major application of TIMS is to the geochronology and tracer studies using terrestrial radiometric systems, for example, U–Th–Pb, Rb–Sr, Sm–Nd, and Lu–Hf. Geochronology exploits the radioactive decay in closed systems to obtain the date of a specific geological event. Tracer studies use the growth of daughter nuclides from radioactive decay to evaluate the interaction between geochemical systems and/or reservoirs. The application of TIMS in cosmochemical analysis is limited; however, it is used to measure the isotopic compositions as tracers of nucleosynthesis processes. This includes the measurement of radionuclides observed mainly in meteorites, for example, Mn–Cr, Al–Mg, Fe–Ni, and Ca–K system in addition to the above-mentioned systems.

A few reports are available where TIMS has been used for cosmochemical analysis. The recent report of Yamakawa et al. (2009) deals with sequential chemical separation technique for Cr, Fe, Ni, Zn, and Cu in terrestrial and extraterrestrial silicate rocks for precise and accurate determination of elemental concentration. The chemical technique uses a combination of cation–anion exchange chromatography and Eichrom nickel specific resin. The developed method was tested to a variety of matrixes; bulk meteorite (Allende), terrestrial peridotite (JP-1), and basalt (JB-1b). Concentrations of each element were determined by TIMS. The analytical procedure was further extended to obtain high-precision isotope data for Cr. The method is capable to determine the isotopic ratios of $^{53}\text{Cr}/^{52}\text{Cr}$ and $^{54}\text{Cr}/^{52}\text{Cr}$ with precision of 5×10^{-6} and 1×10^{-5} , respectively. The method can be equally applicable in cosmochemical studies, like Mn–Cr chronology and investigation of nucleosynthetic isotopic anomalies in meteorites. The elemental concentrations measured by TIMS in Allende are, for example, Cr: $3,600 \pm 0.007$ ppm, Fe: $233,400 \pm 0.009$ ppm, Ni: $14,020 \pm 0.006$ ppm, Cu: 107 ± 0.013 ppm, and Zn: 117.8 ± 0.01 ppm. The detection of ^{26}Al (0.7 Ma) in the Allende meteorite proves that nucleosynthesis is still active in the Milky Way as the half-life of ^{26}Al is much less than the timescale of galactic evolution (10^9 years).

Harvey and Baxter (2009) reported very high-precision (<10 ppm) isotopic measurement of Nd using TIMS. Nd isotopic measurements are important in view of geological,

cosmochemical, and environmental materials that yield only a few nanograms of Nd. Nd isotopes are commonly analyzed as oxide (NdO^+) involving an oxygen bleed valve and/or silica gel. The authors reported a method that uses a slurry containing tantalum oxide (Ta_2O_5) and phosphoric acid, which provides the oxygen source. The Ta_2O_5 loading method is of great use in refining Sm/Nd garnet geochronology, making possible the analysis of small garnet samples in which Nd concentrations are very low (<1 ppm). Garnet $^{143}\text{Nd}/^{144}\text{Nd}$ from several field areas was measured with Ta_2O_5 loading method resulting internal precisions of 8–42 ppm with garnet Nd load sizes ranging from 2.3 to 12 ng Nd. Garnet analysis yields age precisions of 0.4–4.6 Ma depending on the $^{147}\text{Sm}/^{144}\text{Nd}$ ratio. With the help of efficient chemistry and sufficiently low blanks, this method allows high-precision (13–21 ppm) analysis of potentially small sample (~ 4 ng) aliquots of Nd separated from natural samples.

Extensive report of Qin et al. (2010) deals with the measurement of Cr isotopic compositions of a broad range of meteorites using TIMS. They reported high-precision survey of the Cr isotopic compositions of primitive chondrites, along with some differentiated meteorites. Carbonaceous chondrites exhibit excesses in $^{54}\text{Cr}/^{52}\text{Cr}$ from $0.4\text{--}1.6 \times 10^{-4}$, and ordinary chondrites display a common $^{54}\text{Cr}/^{52}\text{Cr}$ deficit of $\sim 0.4 \times 10^{-4}$ when measured against the NIST Cr standard (SRM 3112a). This is because carbonaceous and ordinary chondrites share a common ^{54}Cr -enriched carrier, which is characterized by a large excess in $^{54}\text{Cr}/^{52}\text{Cr}$ (up to 200×10^{-4}) associated with a very small deficit in $^{53}\text{Cr}/^{52}\text{Cr}$ ($<2 \times 10^{-4}$). The eucrite and Martian meteorites studied exhibit small deficits in $^{54}\text{Cr}/^{52}\text{Cr}$. The $^{54}\text{Cr}/^{52}\text{Cr}$ variations among different meteorite classes suggest that there was a spatial and/or temporal heterogeneity in the distribution of a ^{54}Cr -rich component in the inner solar system.

They confirmed the excesses in $^{54}\text{Cr}/^{52}\text{Cr}$ and $^{53}\text{Cr}/^{52}\text{Cr}$ for bulk carbonaceous chondrites, which may affect the use of the Mn–Cr chronometer in carbonaceous chondrites, reported by Shukolyukov and Lugmair (2004, 2006). Bulk chondrites have small $\epsilon^{53}\text{Cr}$ (1 ϵ unit is 1 part in 10^4) excesses (up to 0.3) relative to the Earth, most likely reflecting the subchondritic Mn/Cr ratio of the Earth. The $\epsilon^{53}\text{Cr}$ variations in chondrites probably correlate with Mn/Cr and yield an initial solar system $^{53}\text{Mn}/^{55}\text{Mn}$ value of $5.4(\pm 2.4) \times 10^{-6}$, corresponding to an absolute age of $4,566.4(\pm 2.2)$ Ma. Interactions of cosmic rays result in excesses of $\epsilon^{54}\text{Cr}$ and $\epsilon^{53}\text{Cr}$ with $\sim 4:1$ ratio in phases with high Fe/Cr. These are most dramatically verified in the iron meteorite Carbo. Hence, the Mn–Cr chronometer should be used with caution in samples/minerals with high Fe/Cr and long cosmic-ray exposure ages.

54.3.4 Secondary Ion Mass Spectrometry (SIMS)

When the surface of a solid is bombarded by energetic *primary* particles, usually, electrons, ions, neutrals, or photons, and *secondary* particles are emitted. The *secondary* particles are mainly electrons, neutral species, atoms or molecules, atomic and cluster ions. The majority of *secondary* particles are neutral species. The secondary ion mass spectrometry (SIMS) is a kind of mass spectrometry, where only secondary ions are detected and analyzed by the mass spectrometer. The process yields a mass spectrum of a surface and thus the method enables a detailed chemical analysis of a surface or solid. SIMS is such a powerful technique of surface analysis and microstructural characterization of solids that a very low primary particle flux density of ~ 1 nA/cm² or even less can generate spectral data in a timescale, which is very short compared to the lifetime of the surface layer. SIMS is particularly well known for its outstanding sensitivity of chemical and isotopic detection. Quantitative or semiquantitative analysis can

be performed for small concentrations of most elements in the Periodic Table, including the lightest; however, deficiencies exist in the capability of SIMS for quantitative elemental analyses compared to other surface techniques (Auger, X-ray photoelectron spectroscopy, electron microprobe techniques, etc.). Use of high-resolution mass analyzers ($M/\Delta M > 3,000$) may reduce the commonly occurring isotopic and molecular interferences, like, hydrocarbons, oxides, and hydrides, in the mass analysis of secondary ions. A review of Betti (2005) describes SIMS technique in details.

54.3.4.1 Principle of SIMS

The SIMS technique follows three important steps:

1. Bombardment of the sample surface by focused primary ions, with sputtering of the outmost atomic layers;
2. Mass spectrometric separation of the ionized secondary species, which are sputtered atoms, molecules, clusters, according to their mass-to-charge ratios;
3. Collection of separated secondary ions as quantifiable mass spectra, as in-depth or along-surface profiles, or as distribution images of the sputtered surface.

The primary ions are produced in a number of ways, for example, by duoplasmatron gas source (O_2^+ , O^- , N_2^+ , Ar^+); surface ionization (Cs^+ and Rb^+); or by liquid-metal field ion emission (Ga^+ and In^+). The common primary ions used in SIMS are the oxygen ions, Cs^+ , and Ga^+ . Ions are accelerated and focused to a selected impact area on the specimen. The collision of a primary ion results in the implantation of the primary particle on the impact area, reshuffling of ~ 50 – 500 matrix atoms, and emission of neutral or ionized secondary particles. Secondary ions from the specimen are transmitted into the mass spectrometer to be separated according to their mass-to-charge ratio. The mass spectrometer can be either of the following designs: electrostatic/magnetic analyzer; quadrupole; and time-of-flight type. Secondary ions of specific mass-to-charge ratio and having kinetic energy within a certain interval are collected for pulse/current measurement, ion-optic imaging, and data processing.

Generally, SIMS instruments are operated in two modes: microscope mode and microprobe mode. A defocused primary ion beam (~ 5 – $300\ \mu m$) is used for investigating a large surface in the microscope mode. The secondary ions are then transmitted to the mass spectrometer and generally detected by imaging. In the microprobe mode, a focused primary ion beam ($< 10\ \mu m$) is used to investigate a small portion of the surface and detected usually in an electron multiplier.

54.3.4.2 NanoSIMS 50

The name, nanoSIMS 50, stands for a new-generation SIMS instrument. The unique feature of the instrument is that it combines high sensitivity with a high lateral resolution of $\sim 50\ nm$ when operated with the Cs^+ primary beam. This is achieved by using a specific design of ion optics where the primary and secondary ion optics are coaxial and the primary beam hits the sample surface at an angle of 90° . Compared to the old SIMS, the transmission of the new instrument for secondary ions is a factor of ~ 20 – 30 better in typical measurement conditions.

Apart from the design, the nanoSIMS has six detectors, out of which four are movable, for simultaneous ion collection, resulting in the increase in effective detection efficiency. These detectors can cover a wide mass range and therefore, elements with large difference in mass can be analyzed in a single run.

54.3.4.3 Application of nanoSIMS

Various potential applications of nanoSIMS in characterization of solids have already been recognized. Though the technique seems to be promising in cosmochemical analysis, its real application is still limited due to the strong isobaric interference. However, nanoSIMS is a more flexible alternative for elements that are ionized easily (Hoppe et al. 2004; Marhas et al. 2003) when compared with RIMS or TIMS. Hoppe et al. (2004) of MPI for Chemistry, Mainz, reported the measurement of extinct ^{26}Al , ^{53}Mn , and ^{60}Fe in meteoritic minerals formed early in solar system history. They also measured extinct ^{44}Ti and ^{49}V , and s-process Ba in pre-solar silicon carbide grains of supernova origin.

NanoSIMS measurements were carried out for $^{26}\text{Al}/^{27}\text{Al}$ ratio on plagioclase grains in two different ordinary chondrites (Zinner et al. 2002). Polished thin sections, in which the grains were located by automatic energy dispersive X-ray mapping, were analyzed. The size of the grains as found was large; therefore, high spatial resolution of the nanoSIMS proved effective in avoiding numerous tiny Mg-rich grains within the plagioclase during measurement. The $^{26}\text{Al}/^{27}\text{Al}$ ratio of 1.6×10^{-7} is inferred for the time when the feldspar in Forest Vale formed. An absolute age was calculated by comparing this value with the canonical value and found to be in agreement with Pb–Pb ages of phosphates in the same meteorite. Analysis concluded that ^{26}Al was indeed widely and uniformly distributed in the early solar system and can be used as a potential chronometer.

Primitive meteorites, in particular carbonaceous chondrites, show evidence for aqueous alteration. It is of great interest to ascertain when this aqueous activity occurred on the meteorite parent body. I–Xe analyses of halite in ordinary chondrites indicate that this formed very early in solar system history (Whitby et al. 2000); however, the time resolution of the I–Xe chronometer is limited because of its rather long half-life. The Mn/Cr ratios in the carbonate products of aqueous alteration are rather high and therefore, ^{53}Mn – ^{53}Cr can be a superior chronometer. The Mainz nanoSIMS was useful to exclude Cr-rich inclusions and to analyze spots with $^{55}\text{Mn}/^{52}\text{Cr}$ ratios up to $\sim 50,000$ because of the small beam diameter. The inferred $^{53}\text{Mn}/^{55}\text{Mn}$ ratios of $\sim 3 \times 10^{-6}$ found for five carbonate grains from Orgueil correspond to the absolute time of carbonate formation and aqueous activity on the meteorite parent body $\sim 4,563$ Ma.

^{60}Fe is a potential heat source for melting asteroidal bodies in the early solar system like, ^{26}Al . Because of long lifetime it is of special interest to know the early development of solar system bodies. The first demonstration of the existence of ^{60}Fe in the early solar system was obtained by Shukolyukov and Lugmair (1993) while studying the HED meteorites, which were planetary differentiation and therefore relatively young. The measured $^{60}\text{Fe}/^{56}\text{Fe}$ ratio was $\sim 4 \times 10^{-9}$ at the time of their formation. Using nanoSIMS, analyses were performed on one of the most primitive ordinary chondrites, Semarkona (Mostefaoui et al. 2003). The studied mineral was troilite, iron sulfide, which has a suitably high Fe/Ni ratio. The inferred initial $^{60}\text{Fe}/^{56}\text{Fe}$ ratio of $\sim 1 \times 10^{-6}$ is several times higher than the $1\text{--}2 \times 10^{-7}$ found by Tachibana and Huss (2003) in troilite from two other ordinary chondrites.

54.4 Conclusion and Future Scope

Cosmochemical analysis has become easier nowadays than it was in the past due to huge development of instrumentation and technology. Apart from the ultrasensitive AMS technique, several other techniques such as ICP-MS, RIMS, TIMS, nanoSIMS emerged as potential tools to measure cosmogenic radionuclides, though they still could not reach the sensitivity of AMS. However, they are found to be suitable in specific applications, especially when there is a significant amount of radionuclide present in the sample. In isotope analysis, RIMS can be viewed as an alternative of AMS rather than competitive for elements where AMS has limitations, for example, severe chemical treatment of sample, isobaric interference, and negative ion current. Precise and accurate multielemental analysis is possible by ICP-MS and it is the most used mass spectrometer at present. The sector field or collision cell-based ICP-MS can achieve the sensitivity of AMS for some elements. Revolution in technology has already simplified the AMS instrumentation; therefore, it is now a tabletop machine for regular analysis. However, the instrumental development of the technique is still a real challenge. A limited number of radionuclides are measured by AMS. A long list of radionuclides, which may have potential applications in various fields, is still untouched by any of these techniques including AMS. Half-life measurement of long-lived (\sim Ma) radionuclides is also a big challenge, as limited literature is available for them.

Cosmogenic radionuclides have enriched the idea about the surface stability and integral cosmic-ray exposure on the Moon. The exposure history and infall rate of meteorites have been learned from their radionuclide compositions. The measurement of radionuclides in ultra-small samples of Martian atmospheric CO₂, ice, and rock may also become important; hence, refinement of AMS equipment and sample chemistry should be developed in advance of sample-return missions, expected by 2015 (Jull and Burr 2006). *Sample-return missions* from other bodies, as well as Mars, are also expected. Measurement of cosmogenic radionuclides, especially ¹⁴C, in the Martian atmosphere and other reservoirs will be of particular interest because of the recent evidence of water on Mars in the past. Atmospheric samples from Mars, surface sediments, and carbonates, along with polar ice-cap material, would allow developing a good model of the carbon cycle and size of exchangeable reservoirs on Mars. AMS measurements of cosmogenic radionuclides in these materials would allow establishing a *Martian carbon cycle*. Jakosky et al. (1996) have discussed the expected sizes of various reservoirs and using this information, one can devise a prototype Mars carbon cycle. Studies of cosmogenic nuclides (whose production rate is much higher on Mars) may provide information on Martian geomorphology. The discussion on the possibility of measuring radiocarbon by Lorenz et al. (2002) in Titan sample may be helpful in this context.

References

- | | |
|--|--|
| <p>Aggarwal SK (2010) Inductively coupled plasma mass spectrometry for trace analysis. In: Lahiri S (ed) <i>Advance trace analysis</i>. Narosa Publishing House, New Delhi, pp 71–92</p> <p>Arai T, Wei Y, Kumagai M, Horiguchi K (2006) <i>J Alloys Compd</i> 408–412:1008</p> <p>Auer M, Kutschera W, Priller A, Wagenbach D, Wallner A, Wild EM (2007) <i>Nucl Inst Meth Phys Res B</i> 259:595</p> <p>Becker JS (2005) <i>J Anal At Spectrom</i> 20:1173</p> | <p>Becker JS, Zoriy M, Halicz L, Teplyakov N, Mueller C, Segal I, Pickhardt C, Platzner IT (2004) <i>J Anal At Spectrom</i> 19:1257</p> <p>Betti M (2005) <i>Int J Mass Spectrom</i> 242:169</p> <p>Biggs PH, Meier AL (2002) U.S. Geological Survey Open File Report; 02-223-1</p> <p>Boulyga SF, Becker JS (2001) <i>Fresenius J Anal Chem</i> 370:618</p> <p>Boulyga SF, Becker JS (2002) <i>J Anal At Spectrom</i> 17:1202</p> |
|--|--|

- Boulyga SF, Pickhardt CJ, Becker S, Przybylski M, Becker JS (2003) Plasma source mass spectrometry: applications and emerging technologies, 8th international conference on plasma source mass spectrometry, Durham, UK, September 8–13, p 54
- Boulyga SF, Tibi M, Heumann KG (2004) *Anal Bioanal Chem* 342:3478
- Buraglio N, Aldahan A, Possnert G (2000) *Nucl Instrum Meth Phys Res B* 172:518
- Ellis J, Fields BD, Schramm DN (1996) *Astrophys J* 470:1227
- Fabryka-Martin J, Bentley H, Elmore D, Airey PL (1985) *Geochim Cosmochim Acta* 49:337
- Fifield LK (2008) *Quaternary Geochronology* 3:276
- Fifield LK, Tims SG, Gladkis LG, Morton CR (2007) *Nucl Inst Methods Phys Res B* 259:178
- Fitoussi C, Raisbeck GM (2007) *Nucl Inst Methods Phys Res B* 259:351
- Fitoussi C, Raisbeck GM, Knie K, Korschinek G, Faestermann T, Goriely S, Lunney D, Poutivtsev M, Rugel G, Waelbroeck C, Wallner A (2008a) *Phys Rev Lett* 101:121101
- Fitoussi C, Duprat J, Tatischeff V, Kiener J, Naulin F, Raisbeck G, Assuncao M, Bourgeois C, Chabot M, Coc A, Engrand C, Gounelle M, Hammache F, Lefebvre A, Porquet MG, Scarpaci JA, de Sereville N, Thibaud JP, Yiou F (2008b) *Phys Rev C* 78:044613
- Gounelle M (2006) *New Astron Rev* 50:596
- Granger DE, Fabel D, Palmer AN (2001) *Geol Soc Am Bull* 113:825
- Harvey J, Baxter EF (2009) *Chem Geol* 258:251
- Hoppe P, Ott U, Lugmair GW (2004) *New Astron Rev* 48:171
- Hotchkis M, Fink D, Tuniz C, Vogt S (2000) *Appl Radiat Isotopes* 53:31
- Hunt AL, Petrucc GA, Bierman PR, Finkel RC (2007) *Nucl Inst Methods Phys Res B* 260:633
- Hunt AL, Larsen J, Bierman PR, Petrucc GA (2008) *Anal Chem* 80:1656
- Izmer AV, Boulyga SF, Becker JS (2003) *J Anal At Spectrom* 18:1339
- Izmer AV, Zoriy MV, Boulyga SF, Becker JS (2004) *J Anal At Spectrom* 19:1287
- Jakosky BM, Reedy RC, Masarik J (1996) *J Geophys Res Planets* 111:2247
- Jull AJT, Burr GS (2006) *Earth Planet Sci Lett* 243:305
- Knie K, Korschinek G, Faestermann T, Wallner C, Scholten J, Hillebrandt W (1999) *Phys Rev Lett* 83:18
- Knie K, Korschinek G, Faestermann T, Dorfi EA, Rugel G, Wallner A (2004) *Phys Rev Lett* 93:171103
- Krupp G, Aumann DC (1999) *J Environ Radioact* 46:287
- Lachner J, Dillmann I, Faestermann T, Korschinek G, Lierse C, Poutivtsev M, Rugel G, Tuerler A (2009) *Geochim Cosmochim Acta* 73:A713
- Lahiri S, Nayak D, Korschinek G (2006) *Anal Chem* 78:7517
- Lal D, Gallup CD, Somayajulu BLK, Vacher L, Caffee MW, Jull AJT, Finkel RC, Speed RC, Winters A (2005) *Geochim Cosmochim Acta* 69:5717
- López-Gutiérrez JM, García-León M, García-Tenorio R, Schnabel Ch, Suter M, Synal H-A, Szidat S (2000) *Nucl Instrum Meth Phys Res B* 172:574
- Lorenz RD, Jull AJT, Swindle TD, Lunine JJ (2002) *Meteorit Planet Sci* 37:867
- Lu Z-T, Wendt KDA (2003) *Rev Sci Instrum* 74:1169
- Maiti M, Lahiri S (2008) Accelerator mass spectrometry – an ultrasensitive probe for elemental analysis. In: Lahiri S (ed) *Trace analysis*. Narosa Publishing House, New Delhi, pp 145–171
- Maji S, Lahiri S, Wierczinski B, Korschinek G (2006a) *Anal Chem* 78:2302
- Maji S, Lahiri S, Wierczinski B, Korschinek G (2006b) *Analyst* 131:1332
- Marhas KK, Hoppe P, Ott U (2003) *Meteorit Planet Sci* 38:A58
- McCracken K, McDonald F, Beer J, Raisbeck G, Yiou F (2004) *J Geophys Res* 109:A12103
- Merchel S, Arnold M, Aumaitre G, Benedetti L, Bourles DL, Braucher R, Alfimov V, Freeman SPHT, Steier P, Wallner A (2008) *Nucl Instr Meth B* 266:4921
- Meyer BS, Clayton DD (2000) *Space Sci Rev* 92:133
- Miranda P Jr, Máduar MF, Vicentini G, Zinner LB, Moraes NMP, Shihomatsu HM (2002) *J Alloys Compd* 344:46
- Moran JE, Teng RTD, Rao U, Fehn U (1995) *J Chromatogr* 706:215
- Mostefaoui S, Lugmair GW, Hoppe P, El Goresy A (2003) *Lunar Planet Sci* 34:A1585
- Muramatsu Y, Ohmomo Y (1986) *Sci Total Environ* 48:33
- Muscheler R, Joos F, Beer J, Mueller S, Vonmoos M, Snowball I (2007) *Quaternary Sci Rev* 26:82
- Nelms SM (ed) (2005) *ICP mass spectrometry handbook*. Blackwell, CRC, USA
- Nishiizumi K, Arnold JR, Kohl CP, Caffee MW, Masarik J, Reedy RC (2009) *Geochim Cosmochim Acta* 73:2163
- Ochs M, Ivy-Ochs S (1997) *Nucl Instrum Meth Phys Res B* 132:235
- Ofan A, Ahmad I, Greene JP, Paul M, Savina MR (2006) *New Astron Rev* 50:640
- Ott U, Hoppe P, Lugmair GW (2004) *New Astron Rev* 48:165
- Paul M, Fink D, Hollos G, Kaufman A, Kutschera W, Magaritz M (1987) *Nucl Instrum Meth Phys Res B* 29:341
- Pavicevic MK, Wild EM, Amthauer G, Berger M, Boev B, Kutschera W, Priller A, Prohaska T, Steffan I (2004) *Nucl Inst Meth Phys Res B* 223–224:660
- Pin C, Zalduogui JFS (1997) *Anal Chim Acta* 339:79
- Qian YZ (2003) *Prog Part Nucl Phys* 50:153
- Qin L, Alexander Conel MO'D, Carlson RW, Horan MF, Yokoyama T (2010) *Geochim Cosmochim Acta* 74:1122

- Qiu J, Jiang S, He M, Yin X, Dong K, Guan Y, Bao Y, Wu S, Yuan J, Yang B (2007) *Nucl Instrum Meth B* 259:246
- Raisbeck GM, Yiou F (1999) *Sci Total Environ* 237/238:31
- Reddy RC, Arnold JR, Lal D (1983) *Annu Rev Nucl Part Sci* 33:505
- Rugel G, Faestermann T, Knie K, Korschinek G, Poutivtsev M (2009) *Phys Rev Lett* 103:072502
- Santschi PH, Schink DR, Corapcioglu O, Kotay-Marshall S, Fehn U, Sharma P (1996) *Deep-Sea Res* 43:259
- Schaefer JM, Faestermann T, Herzog GF, Knie K, Korschinek G, Masarik J, Meier A, Poutivtsev M, Rugel G, Schluechter C, Serifiddin F, Winckler G (2006) *Earth Planet Sci Lett* 251:334
- Schnabel C, Ma P, Herzog GF, Faestermann T, Knie K, Korschinek G (2001) *Lunar Planet Sci XXXII*:1353
- Schwantes JM, Rundberg RS, Taylor WA, Vieira DJ (2006) *J Alloys Compd* 418:189
- Sharma P, Somayajulu BLK (1982) *Earth Planet Sci Lett* 59:235
- Shukolyukov A, Lugmair GW (1993) *Science* 259:1138
- Shukolyukov A, Lugmair GW (2004) *Geochim Cosmochim Acta* 68:2875
- Shukolyukov A, Lugmair GW (2006) *Earth Planet Sci Lett* 250:200
- Smith DM (2004) *New Astron Rev* 48:87
- Somayajulu BLK (1977) *Geochim Cosmochim Acta* 41:909
- Stray H, Dahlgren S (1995) *Chem Geol* 125:233
- Tachibana S, Huss GR (2003) *Astrophys J* 588:L41
- Tanaka S, Inoue T (1979) *Earth Planet Sci Lett* 45:181
- Tanner SD, Baranov VI, Bandura DR (2002) *Spectrochim Acta B At Spectrosc* 57:1361
- Tera F, Brown L, Morris J, Sacks IS, Klein J, Middleton R (1986) *Geochim Cosmochim Acta* 50:535
- Tsuyoshi A, Akiba K (2000) *Anal Sci* 16:843
- Tuniz C, Bird JR, Fink D, Herzog GF (1998) *Accelerator mass spectrometry: ultrasensitive analysis of global science*. CRC, Boca Raton
- Vockenhuber C, Feldstein C, Paul M, Trubnikov N, Bichler M, Golser R, Kutschera W, Priller A, Steier P, Winkler S (2004a) *New Astron Rev* 48:161
- Vockenhuber C, Bichler M, Golser R, Kutschera W, Priller A, Steier P, Winkler S (2004b) *Nucl Instrum Meth B* 224:823
- Vockenhuber C, Dillmann I, Heil M, Kaeppler F, Winckler N, Kutschera W, Wallner A, Bichler M, Dababneh S, Bisterzo S, Gallino R (2007) *Phys Rev C* 75:015804
- Vockenhuber C, Golser R, Kutschera W, Priller A, Steiera P, Wallner A, Bichle M (2005) *Nucl Phys A* 758:340c
- Vonmoos M, Beer J, Muscheler R (2006) *J Geophys Res* 111:A10105
- Wagner MJM, Dittrich-Hannen B, Synal H-A, Suter M, Schotterer U (1996) *Nucl Instrum Meth Phys Res B* 113:490
- Wallner C, Faestermann T, Gersmann U, Hillebrandt W, Knie K, Korschinek G, Lierse C, Pomar C, Rugel G (2000) *Nucl Inst Meth Phys Res B* 172:333
- Wallner C, Faestermann T, Gersmann U, Knie K, Korschinek G, Lierse C, Rugel G (2004) *New Astron Rev* 48:145
- Wendt K, Trautmann N (2005) *Int J Mass Spect* 242:161
- Wendt K, Blaum K, Bushaw BA, Gruning C, Horn R, Huber G, Kratz JV, Kunz P, Muller P, Nortershauser W, Nunnemann M, Passler G, Schmitt A, Trautmann N, Waldek A (1999) *Fresenius J Anal Chem* 364:471
- Wendt K, Trautmann N, Bushaw BA (2000) *Nucl Instrum Meth Phys Res B* 172:162
- Whitby J, Burgess R, Turner G, Gilmour J, Bridges J (2000) *Science* 288:1819
- Wolfa SE, Unger DL, Friedrich JM (2005) *Analytica Chimica Acta* 528:121
- Yamakawa A, Yamashita K, Makishima A, Nakamura E (2009) *Anal Chem* 81:9787
- Young JP, Shaw RW, Smith DH (1989) *Anal Chem* 61:1271
- Zinner E, Hoppe P, Lugmair G (2002) *Lunar Planet Sci* 33:A1204

55 Environmental Radiation Protection

Y. Maeda¹ · S. Osaki¹ · A. Vincze²

¹Kyushu University, Fukuoka, Japan

²Hungarian Atomic Energy Authority, Budapest, Hungary

55.1	<i>Introduction</i>	2505
55.2	<i>Monitoring Methods of Environmental Radioactivity</i>	2506
55.3	<i>Radionuclides in the Environment</i>	2506
55.3.1	Aquatic Environment (Oceans, Rivers, Lakes)	2507
55.3.1.1	Oceans	2507
55.3.1.2	Sediments	2510
55.3.1.3	Fish	2511
55.3.1.4	River	2513
55.3.1.5	Lakes	2514
55.3.2	Terrestrial Environment	2515
55.3.2.1	Atmosphere	2515
55.3.2.2	Soil	2517
55.3.2.3	Vegetation	2518
55.3.2.4	Foodstuffs and Algae	2518
55.4	<i>Environmental Transport of Radioactive Effluents; Routine and Accidental Releases</i>	2521
55.4.1	Radionuclides Released to Aquatic Systems	2522
55.4.2	Radionuclides in the Food Chain	2524
55.5	<i>Sources of the Effective Dose to the Population in the Environment</i>	2527
55.5.1	Exposure to Natural Sources	2527
55.5.1.1	Cosmic Radiation	2528
55.5.1.2	Terrestrial Radiation	2530
55.5.1.3	Technologically Enhanced Dose Contribution	2533
55.5.1.4	Worldwide Average Exposure from Natural Sources	2533
55.5.2	Medical Exposure	2533
55.5.2.1	Diagnostic Radiology	2535
55.5.2.2	Diagnostic Administrations of Radiopharmaceuticals	2538
55.5.2.3	Teletherapy and Brachytherapy	2538
55.5.2.4	Therapeutic Administrations of Radiopharmaceuticals	2538
55.5.2.5	Estimated Doses to the World Population from Medical Uses of Radiation	2539

- 55.5.3 Global Fallout and Nuclear Facilities 2539
 - 55.5.3.1 Normal Activities 2540
 - 55.5.3.2 Accidents 2547
- 55.5.4 Occupational Exposure 2552
 - 55.5.4.1 The Nuclear Fuel Cycle 2554
 - 55.5.4.2 Medical Uses of Radiation 2555
 - 55.5.4.3 Industrial Use of Radiation 2556
 - 55.5.4.4 Natural Sources of Radiation 2557
- 55.6 Measures in Nuclear Emergency 2558**
 - 55.6.1 Averted Dose and Action Levels 2558
 - 55.6.1.1 Principles for Intervention in Emergency 2558
 - 55.6.1.2 The Concept for Intervention 2558
 - 55.6.2 Categorization of Radiological Emergencies for Planning Intervention 2558
 - 55.6.3 Intervention Levels 2560
 - 55.6.4 Protection of Workers for Intervention 2560
- 55.7 Editors' Notes 2560**

Abstract: The environmental distribution of radionuclides, released from nuclear facilities and other sources, and the principles of the emergency countermeasures for radiation protection of the public and workers are discussed in this chapter. The concentration levels of radionuclides in various aquatic and terrestrial environments and the exposure levels of the population due to the various sources of radiation (natural and artificial radionuclides, cosmic radiation, diagnostic medical examinations, atmospheric nuclear tests, etc.) are presented.

55.1 Introduction

The main objective of the current system of radiation protection is to provide humans with adequate protection from the unacceptable effects of ionizing radiation; therefore, it requires the assessment of pathways leading to their exposure. A certain level of contamination in the environment will imply a certain dose in humans. Environmental radiation protection therefore deals with those pathways that originate from environmental media and edible biota in areas liable to contamination by artificial radionuclides (or enhanced levels of natural radioactive materials).

Since the dose to humans is strictly controlled and there are usually efforts to reduce it further, this practice also results in the control and reduction of contamination in the environment. The system for protecting humans is therefore still believed to implicitly protect other species in the environment as well. This safety measure was outlined in the Publication 60 of the International Commission on Radiological Protection (ICRP): “The Commission believes that the standards of environmental control needed to protect man to the degree currently thought desirable will ensure that other species are not put at risk. Occasionally, individual members of nonhuman species might be harmed, but not to the extent of endangering whole species or creating imbalance between species. At the present time, the Commission concerns itself with mankind’s environment only with regard to the transfer of radionuclides through the environment, since this directly affects the radiological protection of man.” (ICRP 1991)

Although most experts consider that the environment receives a sufficient level of protection against radiation from the nuclear industry, some also believe that the current approach should be reviewed. Although ICRP continues to believe that the standards of environmental control needed in order to protect the public would ensure that other species are not put at risk, ICRP has been revising their recommendations to explicitly cover protection of the environment from ionizing radiation (ICRP 2007). A set of Reference Animals and Plants has been elaborated representing a few types of organisms that are typical of the major environments. They will form the basis of a more structured approach to understanding the relationships between exposures and dose, dose and effects, and the potential consequences of these effects in the environment (ICRP 2008).

Because this is still an ongoing process, this chapter follows the traditional concept of environmental radiation protection; therefore, focus is given on the various sources, the transport of radionuclides in the environment, and the concentration levels of radionuclides in environmental media and edible biota. The exposure levels of the population due to the various sources of radiation (natural and artificial radionuclides, cosmic radiation, diagnostic medical examinations, atmospheric nuclear tests, etc.) are presented and the principles of the emergency countermeasures for radiation protection of the public and workers are briefly discussed based on ICRP Publication 60 and 63 (ICRP 1991, 1991a).

55.2 Monitoring Methods of Environmental Radioactivity

Environmental monitoring must be vigilant with sensitive measurement techniques and is needed for early warning of breaches of containment. Mathematical modeling of processes is used to support decisions related to a response in an emergency, facility design to comply with safety regulations, and selection of a suitable site for a facility. Accurate models are also used to help better understanding of the world and to increase scientific knowledge or processes.

The methods for the collection and pretreatment of environmental and dietary samples and materials are described in several papers (RSDJ 2002; L'Annunziata 2003). To keep reliable data that can be compared with other measurement methods, samples collected by a standardized sampling method and prepared with a standardized pretreatment are necessary. Measurement of the radioactivity of γ -ray emitters is carried out by high-resolution gamma spectrometry (HRGS), using usually a high-purity germanium (HPGe) detector with a lead shield. Spectra are analyzed automatically using a suitable γ -spectrum analysis program provided that counting efficiency (geometry), energy, and resolution calibration are carried out with Standard Reference Materials (SRM) following standard procedures. Radioactivity of β -ray emitters is measured using a low-background anticoincidence β counter.

Accelerator mass spectrometry (AMS) is useful to measure extremely low-abundance nuclides (isotope ratio of 10^{-12} to 10^{-16} relative to its stable isotope), such as ^{10}Be , ^{14}C , ^{26}Al , ^{36}Cl , ^{41}Ca , and ^{129}I , in natural samples. Small amounts of ^{14}C and ^{129}I can be measured by AMS on mg size samples of carbon and iodine extracted from 500-ml seawater samples (Povinec et al. 2000). Neutron activation analysis (NAA), radiochemical neutron activation analysis (RNAA), and inductively coupled plasma mass spectrometry (ICP-MS) are useful for the determination of ultra-trace Th and U in geological and cosmochemical samples, and for determination of the concentration of ^{239}Pu and ^{240}Pu .¹ Reference marine-biological samples are necessary to test the performance of the analytical methods employed in surveying and monitoring radioactive materials in the sea. An ocean shellfish composite material containing 0.1% w/w Irish Sea mussel, 12% w/w White Sea mussel, and 87.9% w/w Japan Sea oyster has been prepared as the NIST SRM 4358 (The National Institute of Standards and Technology, SRM) in the natural-matrix, environmental-level radioactive SRM series (Altitzoglou 2000). This NIST SRM 4358 sample will be useful for the determination of the activity of ^{40}K , ^{137}Cs , ^{210}Pb , ^{226}Ra , ^{228}Th , ^{238}U , and ^{241}Am .

55.3 Radionuclides in the Environment

Chemists are required to solve environmental problems: transport and biogeochemical cycling of stable and radioactive nuclides through the environment, and the effects of ionizing radiation on biota. The knowledge of the biogeochemical cycles is critical to future global development. It is difficult to make decisions concerning the allowable releases of specific radioactive materials without a good knowledge of the fate and transport of nuclides in the environment. The atmospheric nuclear weapon tests and the accident at Chernobyl in 1986 provided important knowledge concerning the transport of radionuclides and the complexity of radionuclide cycling in the environment.

Naturally occurring radionuclides are composed of three distinct chains of ^{238}U , ^{235}U , ^{232}Th , and their daughter nuclides, ^{226}Ra , ^{210}Po , ^{222}Rn , and long-lived radionuclides such as ^{40}K and ^{87}Rb , which were already present at the birth of the earth.² The relative abundance of

the isotopes present on the earth is derived from the isotopic ratios produced shortly after the universe was formed, although all the short-lived isotopes have disappeared by now.³ Furthermore, there are some induced radionuclides such as ^3H , ^7Be , ^{10}Be , ^{14}C , ^{22}Na , ^{32}P , ^{35}S , and ^{39}Cl , which are created by the interaction of cosmic rays with nuclei in the atmosphere. The natural rate of production of ^{14}C over the surface of the earth is estimated to be $1.6 \text{ atoms cm}^{-2} \text{ s}^{-1}$ and the equilibrium specific activity of ^{14}C in living biological substances is estimated to be $(0.28 \pm 0.10) \text{ Bq/g}$ of carbon.⁴

^3H and ^{14}C are very mobile and are readily incorporated into biological materials (Boyera et al. 2009). ^{129}I (16 million years of radiological half-life) is not very radiotoxic, but constitutes a special problem in the disposal of high- and low-level radioactive waste⁵ and is mobile.

The artificial nuclides ^{90}Sr , ^{85}Kr , ^{137}Cs , ^{239}Pu , etc., were released from nuclear facilities and explosions of atomic bombs in the past. The concentration of the radionuclides from nuclear tests in the ocean has decreased to fallout level by now except in special areas (Livingston and Povinec 2000). The most abundant nuclear fission product radionuclide present in the environment is ^{137}Cs , which was generated as a product of the nuclear weapons testing or from nuclear accidents (e.g., Chernobyl). The weapons tests released ^{137}Cs into the stratosphere, which was distributed globally, while the fallout of ^{137}Cs released into the troposphere by nuclear accidents had a more heterogeneous distribution, reflecting the atmospheric circulation and precipitation distribution immediately following the release. In recent decades, ^{137}Cs has been commonly used as a tracer of soil erosion and sedimentation, particularly in the Northern Hemisphere where atomic deposition was three times as great as in the Southern Hemisphere (Mabit et al. 2008). Its mean specific activities in Japan are reported to be $(13 \pm 12) \text{ Bq/kg}$ for soil, $(2.0 \pm 2.1) \text{ Bq/kg}$ for grass, 0.06 Bq/kg for hinoki, and 5.6 Bq/kg for broadleaf trees in 2001.

55.3.1 Aquatic Environment (Oceans, Rivers, Lakes)

55.3.1.1 Oceans

Near-surface water of the oceans, from 100 m to 300 m in depth, undergoes rapid mixing as a result of wind action. The intermediate zone of the ocean may be as much as 1,000 m in depth, being known as the thermocline or pycnocline. The characteristic speed of movement of the ocean surface layer is as much as 14–150 km/day dependent on the current. The movement and characteristic of the oceans have become well known by the development of recent technology such as the Advanced Earth Observing Satellite. Transport, potential vorticity, and related dynamical properties of the Florida Current have been studied by three-dimensional analysis (Wang and Mooers 1997; Stewart et al. 1957). The coupling between the wind stress and the ocean surface currents has also been modeled on the global scale (Deng et al. 2009). Since the first nuclear weapons tests in the 1940s, pulsed inputs of plutonium isotopes have served as excellent tracers for understanding sources, pathways, dynamics, and the fate of pollutants and particles in the marine environment (Lindahl et al. 2009). Activity concentrations of some radionuclides in the oceans are summarized in [Table 55.1](#).

Body burdens of $^{239+240}\text{Pu}$ (i.e., ^{239}Pu and ^{240}Pu together) in zooplankton and juvenile squid collected in the Sea of Japan and in the Northwest Pacific for the period of 1993–1996 have been reported. The specific activity concentration of $^{239+240}\text{Pu}$ in mixed populations of zooplankton living in seawater varies from $(0.08 \pm 0.01) \text{ Bq/kg}$ to $(0.39 \pm 0.08) \text{ Bq/kg}$

■ Table 55.1

Activity concentration of some radionuclides in Ocean (Bq/m³)

	²²⁶ Ra	¹³⁷ Cs	⁹⁰ Sr	⁹⁹ Tc	Reference
Indian and Atlantic Ocean	2.96				
Pacific Ocean		5.55			
Mediterranean Sea		0–36			Sanchez-Cabeza et al. (2002)
Southeastern part of the Baltic Sea			60–92	15–64	Styro et al. (2001)
Spanish Mediterranean coast			4.8		Molero et al. (1999)
Western Irish Sea				21–45	Smith et al. (2001)
South coast of Norway				0–0.44	Smith et al. (2001)
Brazilian coast			1.4	1.8	Cunha et al. (1999)

(dry mass). That in the southwestern part of the East Sea (Sea of Japan) varies from (0.07 ± 0.02) Bq/kg dry wt. to (0.11 ± 0.01) Bq/kg dry wt., being lower than that in the northwestern part of the East Sea. The ²³⁹⁺²⁴⁰Pu specific activity varies from (0.08 ± 0.06) Bq/kg dry wt. to (0.26 ± 0.05) Bq/kg dry wt. for the Sea of Okhotsk and varies from (0.05 ± 0.01) Bq/kg dry wt. to (0.29 ± 0.03) Bq/kg dry wt. in the subarctic region of the Northwest Pacific off the Kamchatka Peninsula. In the Northwestern Pacific, off the central Honshu Island, the ²³⁹⁺²⁴⁰Pu concentration varies from (0.03 ± 0.01) Bq/kg dry wt. to (0.17 ± 0.04) Bq/kg dry wt. ²³⁹⁺²⁴⁰Pu concentration of the samples from the Bransfield Strait of the Antarctic Ocean is very low and constitutes levels due only to atmospheric bomb fallout. In the Northwest Pacific, ²³⁹⁺²⁴⁰Pu specific activity in zooplankton increase at the higher latitudes, and smaller-sized copepods contain the highest body burdens of ²³⁹⁺²⁴⁰Pu. The concentration factor (R_c) of ²³⁹⁺²⁴⁰Pu for zooplankton living in the East China Sea was 2.7×10^3 and that in the Bransfield Strait was 1.4×10^3 (Hong et al. 2002).⁶ The concentration of ¹³⁷Cs for walleye pollock (*Theragra chalcogramma*) was similar to those reported in other studies. The concentration factors of ¹³⁷Cs for fresh squid in the East Sea varies from 1 to 60 and that for fresh walleye pollock was estimated to be 11, 18, and 14 in the East Sea, the Pacific coast off Hokkaido, and the Sea of Okhotsk, these values being within the range of values reported by IAEA (1985).

Seawater samples and sea grass *Posidonia oceanica* were collected along the Spanish Mediterranean coast. The mean activity concentrations for ¹³⁷Cs and ¹³⁴Cs in surface waters collected from the Spanish Mediterranean shoreline were (4.8 ± 0.2) Bq/m³ and (0.27 ± 0.01) Bq/m³ (1987–1991), respectively. Because of its short radioactive decay period, ¹³⁴Cs has not been detectable in the Western Mediterranean waters. From 1987 to 1991, the enhancement of radiocesium levels in the Spanish Mediterranean marine environment was observed after the Chernobyl accident. The ¹³⁴Cs/¹³⁷Cs isotopic ratio in Chernobyl fresh deposition was used to identify the weapon-test fallout and Chernobyl deposition components. The mean isotopic ratio ¹³⁴Cs/¹³⁷Cs is 0.057 ± 0.003 . The mean ¹³⁴Cs/¹³⁷Cs isotopic ratio of *Posidonia oceanica* is 0.20 ± 0.04 . This value is twice that of the ¹³⁴Cs/¹³⁷Cs ratio (0.11 ± 0.01) observed for water samples from the vicinity of Vandellos NPP. The activity concentration of ¹³⁷Cs input into Mediterranean waters as a consequence of the post-Chernobyl deposition is estimated to be (1.16 ± 0.04) Bq/m³, which brought about an increase of $(33 \pm 3)\%$ over the previous levels. Activation and fission products ¹⁰⁶Ru, ^{110m}Ag, ¹³⁴Cs, ¹³⁷Cs, and ¹⁴⁴Ce are detected in all samples of *Posidonia oceanica*. Mean radiocesium levels in the bioindicator were (1.02 ± 0.25) Bq/kg

for ^{137}Cs and $(0.20 \pm 0.03) \text{ Bq/kg}$ for ^{134}Cs , corresponding to a mean isotopic ratio $^{134}\text{Cs}/^{137}\text{Cs} = 0.20 \pm 0.04$ (1987). ^{137}Cs specific activity incorporated by *Posidonia oceanica* after the Chernobyl deposition over the Mediterranean Sea is estimated to be $(0.51 \pm 0.08) \text{ Bq/kg}$ (Molero et al. 1999).

Radioactivities for ^{134}Cs , ^{137}Cs , ^{238}Pu , and $^{239+240}\text{Pu}$ of tissues from seals and porpoises in the marine environment around the UK were measured (Watson et al. 1999). Multifactor analysis of variance indicate that for radiocesium there was no significant difference for harbor seals, gray seals, or porpoises in terms of species or gender; however, activity concentration of the tissue increased with body mass, and decreased with distance from Sellafield. The marine mammals concentrate radiocesium by a factor of 300 relative to the concentration in seawater. The highest activity, 0.037 Bq/kg ($^{239}\text{Pu} + ^{240}\text{Pu}$), was detected in a gray seal stranded at Rathlin Island in Northern Ireland.

There was information that high-level radioactive wastes had been dumped in the shallow waters of the Kara Sea in 1993 and several assessment and research programs were started. The $^{238}\text{Pu}/^{239+240}\text{Pu}$ activity ratio ranged from 0.3 to 0.7, and is over one order of magnitude higher than the global fallout ratio, confirming that the contamination is derived from the waste (Osvath et al. 1999). The maximum activity concentration levels measured in water were 1 kBq/m^3 for ^3H , 2.5 Bq/m^3 for ^{90}Sr , 7 Bq/m^3 for ^{137}Cs , and 5 mBq/m^3 for $^{239+240}\text{Pu}$ in 1994. The latest estimate of the International Atomic Energy Agency (IAEA) indicates that no radiologically significant contamination has occurred outside of the dumping sites in the Novaya Zemlya bays in the Kara Sea. High levels of radioactivity in sediment are observed only in Abrosimov and Stepovoy Bays, very close to the dumped containers. Radionuclide inventories in water and sediment of the open Kara Sea and Novaya Zemlya bays, as well as soil from the shore of Abrosimov Bay are mainly due to global fallout, with smaller contributions from the Sellafield reprocessing plant, the Chernobyl accident run-off from the Ob and Yenisey rivers, and local fallout. From the result of computer modeling, maximum annual doses of approximately 1 mSv are expected for a hypothetical critical group subsisting on fish caught in the Novaya Zemlya bays whereas populations living on the mainland are expected to receive doses at least three orders of magnitude lower than the worldwide average.

$^{129}\text{I}/^{127}\text{I}$ ratios in marine systems were about 10^{-12} before the nuclear era, reflecting natural sources of the long-lived radionuclide ^{129}I from cosmic ray spallation of atmospheric xenon and natural uranium fission.⁷ However, the contribution of ^{129}I to the North Atlantic Ocean from nuclear fuel reprocessing facilities reaches detectable levels. Pacific Ocean burdens of ^{129}I are relatively low in the Pacific-influenced Arctic, particularly compared to high-latitude waters influenced by the North Atlantic. The concentration of ^{129}I for near-surface seawater ranges from $12 \times 10^6 \text{ atoms/kg}$ to $31 \times 10^6 \text{ atoms/kg}$. ^{129}I concentrations in the Bering Strait in 1993 show concentrations of 62×10^6 – $82 \times 10^6 \text{ atoms/kg}$ and that in the Long Strait between the East Siberian and Chukchi Seas is 44×10^6 – $76 \times 10^6 \text{ atoms/kg}$ (Cooper et al. 2001).

Samples collected in the eastern subtropical North Atlantic in 1969 were used in order to measure the impact of weapons-fallout ^{129}I in the oceans (Edmonds et al. 1998). The measured $^{129}\text{I}/^{127}\text{I}$ ratio of the sample was $(0.53 \pm 0.08) \times 10^{-10}$, being ten times higher compared with the pre-anthropogenic ratio of about 10^{-12} . The ratio of ^{129}I to ^{137}Cs was 2.0 ± 0.6 (atom ratio), 1.6 ± 0.6 when corrected for the 7-year radioactive decay from the bomb-input peak.

The ratios $^{129}\text{I}/^{127}\text{I}$, $^{129}\text{I}/^{137}\text{Cs}$, and $^{129}\text{I}/^{99}\text{Tc}$ in seaweeds sampled at two locations along the Norwegian Coastal current from 1990 to 1998 were measured to estimate “transit time” in the thermohaline circulation of the Arctic and North Atlantic oceans (Yiou et al. 2002). ^{129}I , ^{99}Tc , and ^{137}Cs are discharged from nuclear fuel reprocessing facilities into the Irish Sea and the

English Channel. Most of these discharges are transported into the Arctic Ocean by the Norwegian Coastal Current. The ratios $^{129}\text{I}/^{127}\text{I}$, $^{129}\text{I}/^{137}\text{Cs}$, and $^{129}\text{I}/^{99}\text{Tc}$, which vary up to two orders of magnitude over this period, are potentially very interesting for determining “transit times” in the Arctic and North Atlantic oceans.

Surface and bottom seawater samples from three locations in the Kattegat and Baltic Sea were analyzed for ^{129}I and ^{127}I in both iodide and iodate species, and total inorganic iodine by neutron activation analysis using nuclear reactions of $^{129}\text{I}(\text{n},\gamma)^{130}\text{I}$ and $^{127}\text{I}(\text{n},\gamma)^{128}\text{I}$ (Hou et al. 2001). Levels of 2.3×10^{-15} mol/l for ^{129}I and 7×10^{-9} mol/l for ^{127}I are obtained. Therefore, these isotopes of iodine are promising tracers of physical and biochemical process in the ocean, and research about the chemical speciation of ^{129}I and ^{127}I in ocean will be developed.⁸

55.3.1.2 Sediments

The specific activities of radionuclides contained in sediments collected in uncontaminated areas are listed in [Table 55.2](#).

Continental margins are important areas to study concerning the distribution and deposition of pollutants, because coastal sediments accumulate most of those contaminants. The main source of radioactive pollutants is fallout from stratospheric nuclear testing performed from the late 1950s until the early 1960s. Northeastern Spain has also been affected by the 1986 Chernobyl accident, as the $^{134}\text{Cs}/^{137}\text{Cs}$ ratio calculated for seawater samples has proven. However, no sign of ^{134}Cs has been detected in sediments collected in the area. In the Mediterranean Sea, the mean residence times in shallow waters are estimated as 11 years for plutonium and 5.5 years for americium. The $^{239+240}\text{Pu}$ inventory ranges from 9 Bq/m² to 120 Bq/m², ^{241}Am varies from 15 Bq/m² to 44 Bq/m², and cesium accumulation varies from 161 Bq/m² to 727 Bq/m² (Gasco’ et al. 2002).

The marine surface sediments collected in Ghazaouet, a small bay on the western coast of Algeria, contain measurable amounts of radioactivity: from 0.02 Bq/kg ash to 0.05 Bq/kg ash for ^{238}Pu , from 0.3 Bq/kg ash to 0.6 Bq/kg ash for $^{239+240}\text{Pu}$, from 6.9 Bq/kg ash to 8.5 Bq/kg ash for ^{137}Cs , and from 1.4 Bq/kg ash to 7.4 Bq/kg ash for ^{90}Sr (Nouredine and Baggoura 1997).

Table 55.2

The concentration of radionuclides contained in sediments that are collected in uncontaminated areas (Bq/kg)

Radionuclide	Red sea	Ghazaouet	Brazilian coast
^{238}U	29.6 ± 16.3		
^{226}Ra	11.6 ± 15.2	31–133	
^{210}Po	33 ± 29.1		
^{230}Th	6.6 ± 4.6		
^{212}Pb		6–32	
^{228}Th	48.4 ± 20.9		
^{137}Cs	0–10	0.7–9	
^{40}K	158.4 ± 161.9	184–632	0.4–1.8
Reference	Sam et al. (1998)	Nouredine et al. (1998)	Cunha et al. (1999)

Concentration ratios $^{238}\text{Pu}/^{239+240}\text{Pu}$ and $^{137}\text{Cs}/^{239+240}\text{Pu}$ obtained for these samples confirm that these artificial radioactivities are mainly due to nuclear-testing fallout. The radioactivities of ^{238}U , ^{232}Th daughters, ^{40}K , and ^{137}Cs are detected in different types of sediments; fine or muddy sand and mud, and decrease from very fine grain to larger pore-size particles as shown in [Table 55.3](#).

^{210}Po and ^{210}Pb cycling in a hydrothermal vent zone in the coastal Aegean Sea was studied. ^{210}Pb levels in sinking particles from the control site tend to be higher than those measured in the vent zone, as demonstrated by the lower $^{210}\text{Po}/^{210}\text{Pb}$ ratios (3.3–8.5) observed on particles in the control site. These ^{210}Pb levels (0.01–0.23 Bq/g) are comparable with data reported for the northwestern Mediterranean Sea. The hydrothermal emissions in the shallow Aegean Sea off Milos Island do not have any major effect on the biogeochemical cycling of the natural radionuclides ^{210}Po and ^{210}Pb in the water column (Boisson et al. 2001).

The concentration of ^{239}Pu , ^{240}Pu , ^{241}Pu , ^{242}Pu , and ^{237}Np isolated from oceanic estuarine and riverine sediments in the Arctic Ocean Basin indicates that the Pu in these sediments, as well as that in the deep basins (Amerasian and Eurasian) of the Arctic Ocean, has its origin in stratospheric and tropospheric fallout (Cooper et al. 2000).

Activity levels of uranium isotopes, thorium isotopes, ^{226}Ra , ^{210}Po , ^{40}K , and ^{137}Cs were determined in marine surface sediments, sea grass, and algae collected from the Sudanese coastal waters of the Red Sea, 30-km offshore. The anthropogenic and terrestrial influx from the hinterland is negligible. However, values for ^{226}Ra and ^{210}Po are higher in the sediments of Port Sudan harbor relative to those from the adjacent fringing reefs. The $^{228}\text{Th}/^{232}\text{Th}$ ratio in sediments is in disequilibrium, indicating a rapid rate of sedimentation at the sampling sites. The activity levels of ^{137}Cs in sediments collected in the Port Sudan harbor area are fairly high as compared with values in other sampling locations. Specific activity for ^{137}Cs in algae (*Sargassum*) is high, 0.33–1.32 Bq/kg (Sam et al. 1998).

Host phases of fallout $^{239,240}\text{Pu}$ and ^{241}Pu were studied in the surface sediments obtained in 1994 from abyssal basins of the western North Pacific (Haque and Nakanishi 1999). An analytical procedure involving sequential chemical extraction was employed for partitioning the host phases of the nuclides in the sediment into five fractions: (1) exchangeable, (2) bound to carbonate, (3) bound to hydrous Fe–Mn oxides, (4) bound to organic matter, and (5) residual. Decrease of total $^{239,240}\text{Pu}$ concentration with decreasing association of $^{239,240}\text{Pu}$ with organic matter, high $^{241}\text{Am}/^{239,240}\text{Pu}$ activity ratio in the carbonate phase, and somewhat high proportion of oxidized $^{239,240}\text{Pu}$ in the reachable phases suggest the possibility of post-depositional diagenetic remobilization of Pu from the sediment to the water column.

55.3.1.3 Fish

Anthropogenic radioactivity was measured in Cienfuegos Bay in the vicinity of the first Cuban nuclear power station while under construction. In this area, the main contribution to the radiation dose received by marine fauna comes from naturally occurring uranium-series radionuclides accumulated in the body. ^{210}Po belongs to the natural uranium series, being constantly supplied to the marine environment. ^{137}Cs was released mainly during atmospheric nuclear weapon tests in the late 1950s and early 1960s, from nuclear-fuel reprocessing plants and the Chernobyl accident in 1986. The highest value and mean value of ^{210}Po in dissected edible parts of fish, mollusks, and crustaceans are on the order of 25 Bq/kg wet wt. and 19.5 Bq/kg wet wt., respectively. The polonium concentrations found in mollusks are

Table 55.3
Specific activities in Bq/kg dry weight for different classes of sediment (Noureddine et al. 1998)

Sediment	Grain-size/ μm	^{226}Ra	^{214}Pb	^{214}Bi	^{228}Ac	^{212}Pb	^{40}K	^{137}Cs
Sand	800 to 200	32.4 ± 10.5	4.8 ± 0.8	4.8 ± 0.9	5.2 ± 1.1	6.6 ± 0.9	57.4 ± 8.6	0.7 ± 0.2
	200 to 100	23.7 ± 7.7	6.0 ± 0.9	6.4 ± 1.3	6.2 ± 1.3	6.3 ± 0.9	65.6 ± 8.3	0.6 ± 0.2
	<100	59.3 ± 14.6	12.5 ± 2.0	12.4 ± 2.1	14.8 ± 2.9	21.4 ± 2.9	290 ± 41	8.1 ± 1.4
Fine mud, sand	800 to 200	20.7 ± 8.9	4.2 ± 0.8	3.1 ± 0.7	4.1 ± 1.1	5.6 ± 0.8	67.1 ± 10.3	0.5 ± 0.2
	200 to 100	29.3 ± 8.7	6.4 ± 1.0	6.2 ± 1.0	6.3 ± 1.3	8.2 ± 1.1	91.5 ± 13.5	0.5 ± 0.1
	<100	70.9 ± 8.5	23.4 ± 1.7	22.6 ± 1.7	31.9 ± 2.4	32.5 ± 2.0	608 ± 31	11.4 ± 0.8
Mud	800 to 200	42.2 ± 9.8	7.7 ± 1.2	7.6 ± 1.3	5.9 ± 1.2	7.1 ± 0.9	81.6 ± 12.1	1.1 ± 0.2
	200 to 100	39.9 ± 6.9	14.3 ± 1.2	14.5 ± 1.1	13.2 ± 1.5	17.8 ± 1.4	234 ± 13	3.0 ± 0.4
	<100	60.1 ± 8.1	21.6 ± 1.6	17.9 ± 1.4	29.5 ± 2.7	28.3 ± 1.9	364 ± 20	6.3 ± 0.5

comparable to the available data on bivalves inhabiting different marine systems, but the mean concentration of ^{210}Po in fish is high in comparison to those reported by the United Nations Science Committee on the Effects of Atomic Radiation (UNSCEAR 1996). ^{137}Cs levels are in the range from 0.1 Bq/kg wet wt. to 0.9 Bq/kg wet wt., and are in good agreement with ^{137}Cs concentrations of marine species originating only from global fallout. The mean ^{137}Cs activity concentration in edible parts of the analyzed organisms is two orders of magnitude lower than those observed for ^{210}Po (Alonso-Hernandez et al. 2002).

The concentrations of ^{40}K , ^{232}Th , ^{238}U , ^{137}Cs , and ^{134}Cs in different marine fish samples caught in the Bay of Bengal in Bangladesh were determined (Alam et al. 1995). The specific activities for ^{137}Cs ranged from 0.06 Bq/kg (Foli Chanda) to 1.98 Bq/kg (Hail Chanda), being below the detection limit for many of the fish samples. ^{134}Cs was below the detection level for all samples. ^{238}U specific activities ranged from 0.11 Bq/kg (whole Chaka Chingri) to 1.94 Bq/kg (head of Hail Chanda) and ^{232}Th ranged from 0.24 Bq/kg (Rup Chanda) to 0.28 Bq/kg (Bom Maittya).

The concentration of natural and artificial radionuclides in two types of fresh water fish and four types of marine fish consumed by the Hong Kong population were measured (Yu et al. 1997). The two types of fresh water fish are gray mullet (*Mugil cephalus*) and grass carp (*Ctenopharyngodon idellus*), and the four types of marine fish are white pomfret (*Pampus argenteus*), red bullseye (*Priacanthus macracanthus*), golden thread (*Nemipterus*), and naked-headed sea bream or ginkgo (*Gymnocranius griseus*). The concentrations of U and Th chain radionuclides in the samples have values below the minimum detectable activities (MDA) except for positive detection of ^{228}Ra (assuming ^{228}Ra to be in equilibrium with ^{228}Ac) in gray mullet and red bullseye. ^{40}K of 0.01–0.2 Bq/kg and ^{137}Cs of 41.23–111.47 Bq/kg were detected in the samples. Authors say that the different levels of radioactivity in different species of fish are due to differences in metabolism and feeding patterns.

$^{108\text{m}}\text{Ag}$ is detected in oysters (*Crassostrea gigas*) on the Japanese coast and its specific activity decreased from the initial value of about 30 mBq/kg fresh weight (fw) in the early 1980s to the value of about 10 mBq/kg fresh in the early 1990s (Ishikawa et al. 1995).

55.3.1.4 River

The natural radionuclides ^{234}Th and ^7Be are good tracers for the transport and sources of particles in the suspended sediment reservoir. In the Hudson River estuary, ^{234}Th is produced from the decay of dissolved ^{238}U , which varies linearly with salinity, while ^7Be is added directly to the estuary from the atmosphere (Feng et al. 1999). Samples in the Hudson under conditions of low and high river flow show that $^{234}\text{Th}/^7\text{Be}$ activity ratio in suspended sediment increases from low salinity to higher salinity waters. The distribution of heavy metals in the suspended sediment reservoir can be compared with that of $^{234}\text{Th}/^7\text{Be}$ activity ratio by normalizing the metals to Fe, and therefore iron and aluminum in suspended sediments of the Hudson can be used to normalize grain-size effects on specific concentrations of metals.

Concentrations of ^{238}Pu , $^{239,240}\text{Pu}$, ^{137}Cs , and excess ^{210}Pb in biological samples (five isopods, ten bivalves, two amphipods, two mussels, one fish fat, six fish liver, and two worm tubes) from the Ob and Yenisey Rivers and Kara Sea, and sediment samples from the Pechora Sea of the Russian Arctic were measured (Baskaran et al. 2000). In surface sediment samples (upper 3 cm) of the Pechora Sea, the $^{239,240}\text{Pu}$ specific activities ranged from 38 mBq/kg to 877 mBq/kg (mean = 193 mBq/kg). ^{238}Pu concentrations were below the detection limit.

The $^{238}\text{Pu}/^{239,240}\text{Pu}$ activity ratios in the sediment samples of the Pechora Sea vary between 0.015 and 0.056, which shows that there is no detectable input either from the European nuclear effluents or from the dumped nuclear reactors in the Kara and Barents Sea. The specific activities for ^{137}Cs (27 surface sediments of the Pechora Sea) vary between below detection limits and 10.4 Bq/kg (mean = 3.13 Bq/kg). The mean values of ^{137}Cs and $^{239,240}\text{Pu}$ are lower than those for the sediments from the Ob and Yenisey Rivers and Kara Sea.

On the other hand, sediments from the Ob and Yenisey Rivers show the presence of weapons-grade Pu originating from nuclear fuel reprocessing. The data are distinctly different from those of northern-hemisphere stratospheric fallout (see references in Haque and Nakanishi 1999).

Artificial radionuclides in bottom sediments of the Don River Estuary-Azov Sea (Black Sea) were measured to examine the storage and migration of radionuclides within this inland sea and to estimate the annual dose received by individuals in the local population who regularly consume fish (Matishov et al. 2002). The specific activity of surface sediments was 0.5–100 Bq/kg dry wt. [mean = (33.8 ± 25.9) Bq/kg dry wt., the number of samples = 57] for ^{137}Cs , 0.2–5.7 Bq/kg dry wt. [mean = (2.1 ± 1.4) Bq/kg dry wt., the number of samples = 34] for ^{90}Sr and 0.31–0.51 Bq/kg dry wt. (the number of samples = 2) for $^{239,240}\text{Pu}$ in 1997–1999. ^{137}Cs specific activities increase with distance from the mouth of the Don River and correlate negatively with the sediment grain size (square of the correlation coefficient, $r^2 = 0.77$, the number of data points, $n = 21$). The annual ^{137}Cs -derived dose received by an individual through the tropic chain: water–fish–humans (approximately 10^{-6} Sv/a) is well below regulatory recommended limits.

Uranium, plutonium, and americium in fish, mussels, and sediments from the Peconic River system on Long Island, NY were analyzed (Rapiejko et al. 2001). Sediments were cored in four sections to 0.37-m depth, whole fish were analyzed, and mussels were separated into flesh and shells. Radioisotopes of the cited elements were detected in sediments, some of the fish contained ^{137}Cs , ^{241}Am , and uranium, and mussel flesh contained ^{137}Cs and uranium. All of the ^{60}Co , ^{233}U , and enriched uranium, and some of the ^{137}Cs and ^{241}Am , can most likely be attributed to Brookhaven National Laboratory. The other radionuclides (and some of the ^{137}Cs and ^{241}Am) are believed to have either fallout or nature as their origin. The New York State Department of Health (NYSDOH) determined that the added radiation doses, which result from eating such fish are a small fraction of the radiation dose that normally results from radionuclides present in the body.

Aquatic biota in the Rhone River downstream of the Marcoule nuclear complex in France are exposed to natural sources of radiation and to radioactivity released from the Marcoule complex (St-Pierre et al. 1999). Radioactivity of five categories of aquatic organisms, i.e., submerged aquatic plants (phanerogam), non-bottom-feeding fish, bottom-feeding fish, mollusca, and fish-eating birds were studied. The dose rates range over three orders of magnitude, with maximum dose rates of 1–10 $\mu\text{Gy/h}$. These maximum dose rates are a factor of 40 or more below the international guideline intended to ensure the protection of aquatic populations (about 400 $\mu\text{Gy/h}$).

55.3.1.5 Lakes

The distribution of ^{90}Sr and ^{137}Cs in lake ecosystems in the southern Urals, which were affected by the 1957 radiation accident, was studied (Kryshev 1997; Kryshev et al. 1997; Aarkrog et al. 1997). The levels of ^{90}Sr in the most highly contaminated lakes in 1992 were as follow: 17–120 Bq/l in water, 70–110 kBq/kg in fish, and 2.9–5.2 kBq/kg in aquatic plants. At the

present time, the levels of ^{90}Sr have decreased to 0.05–0.5 Bq/l in water and 4–550 Bq/kg in fish. The levels of ^{137}Cs in these lakes have decreased to 0.03–0.06 Bq/l in water and 2–33 Bq/kg in fish. In the first few years following the accident, a dose rate level of 10^{-2} Gy/day to mollusks, bottom-dwelling fish, and aquatic plants exceeded that in the most highly contaminated lakes of Uruskul' and Berdyandish. In 1992, the background exposure level for fish in these lakes is still exceeded by a factor of 1,000. Doses to the population from lake fish consumption do not exceed 10^{-3} Sv/year.

Geochemical coexistence of ^{137}Cs and $^{239,240}\text{Pu}$ in the surface sediments from two oligotrophic and mesotrophic lakes in Japan was studied by sequential chemical extractions (Nagao et al. 1999). The fractions separated were exchangeable and bound to carbonate, bound to oxides, bound to organic matter-sulfides, and residual. The ^{137}Cs and $^{239,240}\text{Pu}$ were mainly associated with the organic matter-sulfides and residual fractions, but exhibited different vertical profiles in both lakes.

55.3.2 Terrestrial Environment

The following three sources of radionuclides in the environment need to be considered.

1. Fallout from the atmospheric bomb tests from the 1950s to the 1960s.
2. Routine emissions to the atmosphere from reprocessing plants and nuclear power stations.
3. Accidents at nuclear facilities, the most prominent being Chernobyl.

The effects of atmospheric bomb tests and the Chernobyl accident are no longer considered to be of radiological importance. The reprocessing plants and nuclear power stations during routine operation release radionuclides in airborne and liquid effluents, the level of which is usually higher for the reprocessing plants than of the power reactors. Radionuclides released from the Calder Hall reactor in 1997 are listed as examples: ^{41}Ar (2.6×10^3 TBq/a), ^{14}C (3.2×10^{-1} TBq/a), ^{60}Co (6.0×10^{-2} TBq/a), ^3H (4.4×10^0 TBq/a), and ^{35}S (8.9×10^1 TBq/a). The total critical group annual effective dose was estimated to be $4.56 \times 10^1 \mu\text{Sv}$. Even this dose is negligible compared to the annual dose received from the natural background (~ 2.4 mSv/a), routine releases from reprocessing and reactor sites require continued monitoring for radiation protection control purposes.

Noble gases are released to the atmosphere, however they are not considered to be biological material. If one considers the radionuclides released from reprocessing plants, ^3H , ^{14}C , ^{35}S , ^{85}Sr , ^{90}Sr , ^{129}I , ^{131}I , ^{134}Cs , ^{137}Cs , and actinides are of potential interest. Fruit Working Group (FWG) in the UK suggests that ^{36}Cl and ^{45}Ca should be added to a group of monitored nuclides in the future because both nuclides are very mobile (Ould-dada et al. 2001).

A little information is available on the chemical forms of radionuclides in routine emissions from nuclear facilities and on chemical speciation in the atmosphere. The chemical identity of radionuclides affecting their mobilities and biological effects in environmental media must be made clear.

55.3.2.1 Atmosphere

Tritium may be released to the atmosphere as HTO, HT, and CH_3T . These species are transferred to other chemical species through many complex processes in atmosphere.

For example, HT released from a plant is rapidly oxidized to HTO. Tritium water may be incorporated in organic matter as organically bound tritium (OBT) within tissues. The specific radioactivity of tritium in the form of CH_3T in the atmosphere is very high, but the reason is not understood. ^{14}C may be released to the atmosphere as CO , CO_2 , CH_4 , HCHO , and COS . $^{14}\text{CO}_2$ released becomes incorporated into crops via photosynthesis leading to enhanced levels of ^{14}C in crops.

The background level of tritium in Cernavoda in Romania, before the nuclear power plant was operational, was measured in 1996. The mean values determined are (7.4 ± 5.5) Bq/l in humid air, (3.1 ± 1.0) Bq/l in water, (3.5 ± 0.7) Bq/l in tissue water from vegetables, and (4.9 ± 1.7) Bq/l in tissue water from cereals. The transfer parameters for deposition from the atmosphere to forage and crops, and for the contamination of land and vegetation by spray-irrigation water found to be $29\text{--}49$ and (0.90 ± 0.27) , respectively (Paunescu et al. 1999). A background level of tritium was measured for rain collected at Fukuoka in Japan between 1984 and 1995 (Hayashi et al. 1999) and Kumamoto, Japan during 2003–2005 (Momoshima et al. 2007) with average results of 0.85 Bq/l and 0.69 Bq/l, respectively. On the other hand, an average tritium activity concentration of atmospheric water vapor is (1.88 ± 0.26) Bq/l, showing a higher level than that of the rain. Surface seawater and water vapor about 10 m above the sea level were collected in the Pacific and Indian Oceans during the expedition of KH-96-5 to examine tritium concentrations in the open sea. The tritium concentration in the water vapor was one order of magnitude higher than that in the surface seawater, attributed to a downward movement of naturally occurring tritium from the stratosphere to the troposphere (Kakiuchi et al. 1999).

^7Be produced by cosmic-ray-induced nuclear reactions is useful for studying atmospheric transport mechanisms. Since the production of ^7Be and other cosmogenic nuclides is directly dependent on the cosmic-ray intensity, a relationship between the production rate of these nuclides and the 11-year solar cycle has been found (Kulan et al. 2006). It is known that the galactic cosmic-ray intensity at the earth's orbit is inversely related to solar activity (Hotzl et al. 1991).

Average ^{35}S levels were $110 \text{ mBq m}^{-2} \text{ d}^{-1}$ for atmospheric deposition, 0.078 mBq/m^3 for aerosol in surface air, and 45 mBq/l for rainwater at Fukuoka in Japan. The $^7\text{Be}/^{35}\text{S}$ ratios are abnormally low, although most of $^{32}\text{P}/^7\text{Be}$ ratios show reasonable values corresponding to residence times of 10–60 days. The excess ^{35}S suggests an external source of ^{35}S (Osaki et al. 1999).

Historical data on radioactivity in air and precipitation samples have been collected and analyzed at study sites in Norway to investigate the correlation between air concentration, precipitation and deposition, and to identify areas with high deposition rates. The base line data are obtained from the measurements of total β -ray activities in air and precipitation on a daily basis for the period 1956–1982. Radioactive fallout correlates strongly with annual precipitation, which varies from 280 mm per year to 4,200 mm per year in Norway. The deposition of ^{137}Cs was calculated to be $(3.23 \pm 1.20) \text{ kBq/m}^2$ per 1,000 mm precipitation for the period 1955–1975. The age of fallout in Norway ranges from 3 months to 9 months during the test periods, which is considerably shorter than the global average, where the mean residence time for debris in the lower stratosphere is estimated to be 1.3 years. There is no evidence of local fallout reaching Norwegian areas from tests on Novaya Zemlya (Bergan 2002).

Atmospheric radioactivity is monitored globally for the verification of the Comprehensive Nuclear-Test-Ban Treaty (CTBT), with xenon isotopes $^{131\text{m}}\text{Xe}$, ^{133}Xe , $^{133\text{m}}\text{Xe}$, and ^{135}Xe serving as important indicators of nuclear explosions. The interpretation of atmospheric concentrations of radioxenon has been enhanced by quantifying radioxenon emissions released from

civilian facilities, which resulted in the first global radioxenon emission inventory for nuclear power plants, based on North American and European emission reports for the years 1995–2005 (Kalinowski and Tuma 2009). Based on new, more sensitive technologies with higher time resolution, recent studies have shown that regions with nuclear facilities have a background of few mBq/m^3 of ^{133}Xe with short spikes up to few hundred mBq/m^3 . These spikes could not in general be explained by normal nuclear power plant operations. Based on several years of measurements, combined with advanced atmospheric transport model results, it was shown that the main source of radioxenon observations are strong and regular batch releases from a very limited number of radiopharmaceutical facilities in the northern and southern hemisphere. These releases can be up to several orders of magnitude above those attributed to nuclear power plants (Saey 2009).

It is customary to concentrate the major gaseous fission products (krypton, xenon, and iodine) by cryogenic adsorption. Schell et al. (1997) made the initial efforts to develop an automated portable system for online separation and concentration, with the potential for measuring environmental levels of radioactive gases, including ^{85}Kr , $^{131,133,135}\text{Xe}$, ^{14}C , ^3H , ^{35}S , and $^{125,131}\text{I}$, without using cryogenic fluids. There is now the ability to measure amounts of fission-produced xenon isotopes that decay by internal conversion electrons and beta radiation with short half-lives, namely ^{131}Xe ($T_{1/2} = 11.8$ days), ^{133}Xe ($T_{1/2} = 2.2$ days), and ^{135}Xe ($T_{1/2} = 9.1$ h).

According to the model proposed by Stewart et al., air enters the stratosphere in the tropical regions where it is heated and rises to an altitude of about 30 km, at which level it begins to move toward the poles. The mean residence time of stratospheric debris depends on altitude, time of year, and latitude. Debris injected into the lower polar stratosphere in Russia has been found to have a mean residence time of less than 6 months, whereas in tropical latitudes residence time has been found to be 2–3 years for the middle stratosphere and 5–10 years for debris injected at 100-km altitude.

55.3.2.2 Soil

The cumulative deposition of anthropogenic radionuclides shows a typical latitudinal distribution, with high levels in the mid-latitude regions of the Northern Hemisphere, reflecting the stratosphere–troposphere exchange of air masses in the mid-latitude region (UNSCEAR 2000a).

Analysis of the 50-year records of the atmospheric deposition of long-lived radionuclides (^{137}Cs , ^{90}Sr , and Pu isotopes) has been carried out in Japan (Hirose et al. 2008). The maximum annual deposition occurred in 1963 after the large-scale atmospheric nuclear weapons testing of 1961–1962. In the 1980s, the fallout from the Chinese nuclear weapons tests was observed and the released radionuclides from the Chernobyl accident affected radioactive deposition in Japan until the early 1990s. The recent deposition samples in Japan showed varying behavior although they all primarily originate from the resuspension of radionuclide-bearing particles deposited on land surfaces. These radionuclides may be useful tracers of environmental changes, such as desertification and erosion, in terrestrial regions. The mean annual deposition of ^{90}Sr and ^{137}Cs is estimated to be $150 \text{ mBq m}^{-2} \text{ a}^{-1}$ and $300 \text{ mBq m}^{-2} \text{ a}^{-1}$ in Japan and are almost the same as observed in England (Igarashi et al. 1999).

The cumulative depositions of ^{137}Cs , ^{90}Sr , and fallout Pu in the volcanic ash soil of Korea were determined. From depth profiles, it was found that ^{137}Cs , ^{90}Sr , and $^{239,240}\text{Pu}$ in the

volcanic soil are more mobile than those in other forest sites of Korea and the downward movement of ^{90}Sr is faster than that of ^{137}Cs and $^{239,240}\text{Pu}$. The activity ratios of $^{238}\text{Pu}/^{239,240}\text{Pu}$ and $^{241}\text{Pu}/^{239,240}\text{Pu}$ in the soils are close to those observed in the cumulative deposit from the global fallout of nuclear weapon testing (Lee and Lee 1999).

Soils in Japan have been monitored by the National Institute of Radiological Science. The average level of ^{90}Sr in rain and dry fallout was 0.01866 MBq/km^2 and that of ^{137}Cs was 0.00895 MBq/km^2 in 1999. The average activity of ^{90}Sr of soils is 0.26 Bq/km^2 and that of ^{137}Cs is 0.8275 Bq/km^2 (RSDJ 2002). The $^{240}\text{Pu}/^{239}\text{Pu}$ atom ratios observed in Japanese soil samples are estimated to be around 0.17 (in the range of 0.15–0.19) (Muramatsu et al. 2001).

The activity concentration of ^{238}Pu , $^{239/240}\text{Pu}$, and ^{241}Pu was also measured recently in Hungary (Varga et al., 2008). The $^{239/240}\text{Pu}$ concentration is in the range of $0.01\text{--}0.84 \text{ Bq/kg}$ dry soil with the average of 0.10 Bq/kg . ^{238}Pu could be detected only in few moss samples and the $^{238}\text{Pu}/^{239/240}\text{Pu}$ ratio is close to the value of the global fallout. The activity concentration of ^{241}Pu was between 0.04 Bq/kg and 3.74 Bq/kg with the average of 0.82 Bq/kg , while in the moss is also similar $0.01\text{--}2.07 \text{ Bq/kg}$ fresh mass with the average of 0.43 Bq/kg . The isotope ratios $^{241}\text{Pu}/^{239/240}\text{Pu}$ prove that the origin of the plutonium in Hungary is the global fallout determined by the atmospheric nuclear weapon tests.

Transport, speciation, and sources of plutonium in the Ob and Yenisey river systems (Siberia, Russia) and the adjacent Kara Sea was studied showing a clear difference in speciation between high $^{240}\text{Pu}/^{239}\text{Pu}$ atom ratio Pu derived from global weapon fallout and low $^{240}\text{Pu}/^{239}\text{Pu}$ atom ratio Pu, presumably originating from weapons grade Pu (Lind et al., 2006). In particular, the $^{240}\text{Pu}/^{239}\text{Pu}$ atom ratios (mean 0.18 ± 0.06) for particles ($>0.45 \mu\text{m}$) could not be distinguished from global fallout Pu ($0.17\text{--}0.19$), whereas for low molecular mass (LMM; $<8 \text{ kDa}$) species the Pu ratio was much lower than for global fallout Pu in both rivers.

55.3.2.3 Vegetation

Activity concentrations of ^7Be , ^{210}Pb , and ^{210}Po in precipitation (rain, throughfall, and stemflow), wood, and soil were determined to estimate the migration behavior of these radionuclides in the forest canopy (Sugihara et al. 1999). Output/input ratios of precipitation for the forest canopy were 0.53 for ^7Be , 0.79 for ^{210}Pb , and 1.5 for ^{210}Po in *Pasania edulis* forest. Mean residence times of the radionuclides were estimated to be 56 days for ^7Be , 765 days for ^{210}Pb , and 653 days for ^{210}Po for *Pasania edulis* forest.

55.3.2.4 Foodstuffs and Algae

Studies of the transfer, uptake, and retention of radionuclides in foodstuffs have been mainly concerned with ^{137}Cs , ^{90}Sr , ^3H , ^{14}C , and ^{35}S because these nuclides have relatively long half-lives and represent biologically important elements.

The concentration and temporal variation of ^{55}Fe in seaweed, shellfish, crab, and lobster collected in Weymouth Bay, adjacent coastal areas, and southern England were measured (WAWICK et al. 2001). Significant quantities of ^{55}Fe have been released into the environment following the atmospheric testing of nuclear weapons as well as through authorized discharges of radioactivity from nuclear power and reprocessing sites. These areas have received authorized discharges of radionuclides originating from the operation of a now-decommissioned

steam-generating, heavy-water-type reactor at AEE Winfrith. The highest activities of ^{55}Fe are found in marine sediments collected near the discharge pipeline and a rapid decline occurs away from the pipeline. This is consistent with rapid sorption of ^{55}Fe by the sediment.

Potted plants were exposed to D_2O vapor in a greenhouse and the uptake of D_2O by leaf and deposition of D_2O in pot soil were examined (Momoshima et al. 1999). Although the variation of D_2O concentration in leaves followed that in air, showing a time delay, D_2O concentration in leaves did not reach the same level as that in air, and veins showed a lower concentration than lamina. The D_2O concentration in the pot soil increased slowly with diffusion to deeper layers.

Edible seaweed products have become popular in the food industry, especially in Japan. Elements of 15 seaweed samples collected on the coasts of British Columbia (Canada), Japan, and Norway were analyzed, and the radioactivity were measured. The iodine content of algae was found to vary widely, with the highest concentrations in wakame from Japan. The analysis shows little activity above background; only traces of ^{137}Cs were found in a product from Norway, and traces of ^{226}Ra were found in a product from Japan. Arsenic levels are found to be elevated (van Netten et al., 2000).

Collective and individual dose rates to humans were estimated from the consumption of seafood harvested in the Arctic Seas. The actual collective dose rates to the world population are estimated to be 2.7–4.5 man-Sv/a due to the consumption of seafood from the Barents Sea, and 0.03 man-Sv/a due to seafood from the Kara Sea. The contribution of ^{137}Cs to the collective dose rate is estimated to be about 90% (Sazykina and Kryshev 1997).

Radioactivity levels of natural ^{210}Po and anthropogenic ^{137}Cs in seawater and biota (fish and shellfish) were estimated for the FAO fishing areas. Collective doses resulting from seafood consumption are calculated for each FAO area using radioactivity data for water and biota. Good agreement is observed between the results calculated by these two methods, with the exception of the doses from ^{210}Po via shellfish consumption. The effective dose due to the anthropogenic ^{137}Cs (mainly originating from nuclear weapons tests) in marine food in 1990 is estimated to be two orders of magnitude less than the corresponding dose from ^{210}Po , the latter being the dominant contribution to the doses due to fish and shellfish and the contribution from ^{137}Cs is negligible (Aarkrog et al. 1996).

The radioactivity of ^{226}Ra in fish, pork, rice, flour, chicken, vegetable, milk, fruit, egg, and water samples in Taiwan was measured. The ^{226}Ra activity concentration of groundwater is 12.0 mBq/l and ^{226}Ra specific activities of the food range from 0.02 Bq/kg fresh to 0.17 Bq/kg fresh. The annual internal dose due to ingestion of ^{226}Ra in food and drinking water per capita is evaluated to be 7.5 μSv (Kuo et al. 1997).

A region between Chelyabinsk and Ekaterinburg in the Southern Urals has been heavily contaminated due to operational and accidental releases from the first Soviet plutonium production facility, Mayak, during the late 1940s and 1950s. Environmental samples were collected in areas affected by the explosion of a fission product storage tank in 1957. Soil, sediments, water, milk, and food samples were analyzed for ^{90}Sr , ^{137}Cs , and plutonium. The highest contamination of an area accessible to the local population is found in the vicinity of the Tcha river around Muslumovo. Specific activity of food samples in 1992–1993 reached 37,000 Bq/kg for ^{137}Cs , 5,600 Bq/kg for ^{90}Sr , and 9.9 Bq/kg for Pu. ^{90}Sr and ^{137}Cs specific activities in vegetables in Muslyumove are listed in [Table 55.4](#). Milk and potatoes in Muslumovo show low levels in the range from 0.7 Bq/kg to 25 Bq/kg for ^{90}Sr , respectively (Winkelmann et al. 1998).

■ **Table 55.4**

⁹⁰Sr and ¹³⁷Cs specific activities in vegetables in Muslyumove

Products	n	⁹⁰ Sr/Bq kg ⁻¹		¹³⁷ Cs/Bq kg ⁻¹	
		Mean ± SD	Range	Mean ± SD	Range
Potatoes	15	0.63 ± 0.59	0.1–2.4	0.57 ± 0.59	0.05–2.8
Beetroot	4	1.50 ± 0.52	0.96–1.92	0.42 ± 0.51	0.07–1.19
Carrots	4	3.2 ± 2.9	1.4–7.1	2.7 ± 2.3	0.6–3.0
Cucumbers	4	0.67 ± 0.29	0.34–0.91	0.74 ± 0.76	0.11–1.59
Tomatoes	1	0.58		1.1	
Peppers	1	1.20		13.0	
Dill	9	29 ± 14	11.3–40.9	4.6 ± 2.0	1.6–6.8
Spring onions	8	49.0 ± 30.2	0.21–92.7	8.4 ± 8.7	0.13–27.4
Onions	1	4.70		0.80	
Garlic	2	4.4 ± 1.8	3.2–5.7	0.85 ± 1.10	0.10–1.65
Currants	3	2.0 ± 0.6	1.39–2.54	1.7 ± 1.0	0.93–2.8

The current radioactive contamination of soil, vegetation, and foodstuffs in the two remaining villages closest to the Mayak site, Muslyumovo, and Brodokalmak were examined. The highest contamination levels in soil are 5.5 MBq/m² for ¹³⁷Cs and 1.0 MBq/m² for ⁹⁰Sr and are found in the floodplain. Radionuclide contamination in the soil of the villages is much lower, but exceeded the level expected from global fallout.

Significantly, higher ¹³⁷Cs activities are found in milk sampled from cows housed in winter period in Muslyumovo compared with the grazing summer period. The highest measured activities in food products for ¹³⁷Cs and ⁹⁰Sr are found in river fish, waterfowl, poultry, and milk. The activity concentrations of ¹³⁷Cs and ⁹⁰Sr in some animal products are higher than that expected for soil and vegetation from fields and pasture in the villages (not including the floodplain). The ¹³⁷Cs specific activity of milk ranges 0.1–174 Bq/kg during May–October and 0.03–200 Bq/kg during November–April in Muslyumove, and 0.1–38 Bq/kg during May–October and 0.01–66 Bq/kg during November–April in Brodokalmak. The ⁹⁰Sr level of milk ranges 0.1–37 Bq/kg during May–October and 0.1–34 Bq/kg fresh weight (fw) during November–April in Muslyumove, and 0.1–5.6 Bq/kg during May–October and 0.1–4.7 Bq/kg during November–April in Brodokalmak (Shutov et al. 2002).

The average specific activity of ⁹⁰Sr (69 samples) of milk produced in Japan is 0.287 Bq/kg fw and that of ¹³⁷Cs of milk is 0.0225 Bq/kg fw. The specific activities related to homologous chemical elements common in milk are as follows. ⁹⁰Sr: 0.02519 Bq per 1 g of Ca, ¹³⁷Cs: 0.01364 Bq per 1 g of K. The specific activities in vegetables are 0.145 Bq/kg fw and 0.00498 Bq/g Ca for ⁹⁰Sr, and 0.0865 Bq/kg fw and 0.03798 Bq/g K for ¹³⁷Cs. The activities in tea (19 samples) are 0.5968 Bq/kg fw and 0.2744 Bq/g Ca for ⁹⁰Sr, and 0.4895 Bq/kg fw and 0.02679 Bq/g K for ¹³⁷Cs. The activities in tea are higher than in other vegetables. The specific activities in fish (12 samples) are 0.00428 Bq/kg fw and 0.00318 Bq/g Ca for ⁹⁰Sr, and 0.1123 Bq/kg fw, and 0.0316 Bq/g K for ¹³⁷Cs. The specific activities in shellfish (six samples) are 0.0041 Bq/kg fw and 0.00505 Bq/g Ca for ⁹⁰Sr, and 0.0222 Bq/kg fw and 0.00937 Bq/g K for ¹³⁷Cs. The specific activities in seaweeds (five samples) are 0.226 Bq/kg fw and 0.0224 Bq/g Ca for ⁹⁰Sr,

and 0.0236 Bq/kg fw and 0.00366 Bq/g K for ^{137}Cs . It should be noted that the activity of ^{137}Cs is higher in fish than in shellfish or seaweed and it is well known that the concentration factor R_c of fish for ^{137}Cs is high (RSDJ 2002).

55.4 Environmental Transport of Radioactive Effluents; Routine and Accidental Releases

The prediction of fluid motions in the atmosphere, ocean, ground water, and surface water is often not accurate enough, showing that these processes are still not completely understood. Beside the knowledge of the physical half-lives of the radionuclides and the basic *physical transport processes*, it is important to understand the general circulation modes of the atmosphere to improve the accuracy of estimations of the transport of all nuclides. In order to understand the chemistry and transport of atmospheric pollutants, it is indispensable that the applied models include coupling between different components of the global environment, such as atmosphere, hydrosphere, cryosphere, and the soil system. One possible solution is the application of *box modeling*, where for instance the dispersion of radionuclides in marine systems relates to instantaneous mixing in each box. A new approach to box modeling, which includes dispersion of radionuclides as a function of time, has been developed by Iosjpe et al. (2002) in order to provide a better and more realistic approximation.

The process of assessing risk to the environment following a given release of radioactivity requires the quantification of activity concentrations in environmental media and in the food chain. In some cases, the radiological impact, i.e., the level and significance of the radiation exposure, can be estimated from measurements of radioactivity concentration in the environment. In many cases however, suitable measured values will not exist, and in these cases models are needed to provide estimates of the values. Some of these models attempt to relate a measured or estimated discharge of a radionuclide from a particular source to the resulting activity concentration of the radionuclide in air at the point of interest and its level of deposition to the ground. These models, known as atmospheric dispersion models, are mathematical representations of the transport and dilution of material in the atmosphere and they are reviewed in detail elsewhere (Mavall 2003).

Similarly, the methodologies implemented in state-of-the-art models for predicting the physical processes of radionuclide migration through the aquatic environment are not discussed here. A review of the methodologies, including transport due to water currents, diffusion, settling, and resuspension has recently been published by Monte et al., where the models are briefly described, model parameter values reviewed, and values recommended (Montea et al. 2009).

The dose to man from radionuclides released to the environment is also assessed with mathematical models that require transfer factors as input parameters to predict the concentration of radionuclides in foodstuffs. For the assessment and management of environmental risks from ionizing contaminants an integrated approach has been developed (ERICA Integrated Approach), which involves the application of concentration ratios and distribution coefficients for aquatic systems (Larsson 2008). Hosseini provides the description of the methodologies applied to derive default transfer parameters, collated within the ERICATool databases (Hosseini et al. 2008).

Because naturally occurring and artificially produced radionuclides in the environment may be present in different physicochemical forms (i.e., radionuclide species) varying in size

(nominal molecular mass), charge properties and valence, oxidation state, structure and morphology, density, and degree of complexation, the understanding of the transfer process becomes more complicated. To assess the environmental impact from radionuclide contamination, information on radionuclide species deposited, interactions within affected ecosystems, and the time-dependent distribution of radionuclide species influencing mobility and biological uptake is essential (Salbu 2009).

55.4.1 Radionuclides Released to Aquatic Systems

The water around Greenland has received radioactive contamination from three major sources: global fallout, discharges from the nuclear fuel reprocessing plant at Sellafield in the UK, and the Chernobyl accident in the former Soviet Union. The *global fallout* peaked in the early 1960s. The radiologically most important radionuclides of this source are ⁹⁰Sr and ¹³⁷Cs. The waterborne discharges from Sellafield, which were at a peak between 1974 and 1981, consist mainly of ¹³⁷Cs. The Chernobyl accident in 1986 was characterized by its substantial atmospheric release of ¹³⁴Cs and ¹³⁷Cs. Other sources may be La Hague, France, and radioactive discharge to the great Siberian rivers (Ob, Yenisey, and Lena) from nuclear activities, local fallout from the Novaya Zemlya nuclear weapons test site, or dumping of nuclear waste in the Kara and Barents Seas. The time integral activity concentrations of seawater were estimated to be (164 ± 18) Bq/m³ for ⁹⁰Sr and (239 ± 32) Bq/m³ for ¹³⁷Cs from 1962 to 1980 and (64 ± 7) Bq/m³ for ⁹⁰Sr and (117 ± 64) Bq/m³ for ¹³⁷Cs from 1980 to 1997. The transport of ⁹⁰Sr and ¹³⁷Cs by the East Greenland Current from the Arctic to the Atlantic Ocean has been calculated to be (24 ± 3) PBq/a and (40 ± 9) PBq/a, respectively (Aarkrog et al. 1999). Concentration factors – R_c as defined by ▶ Eq. (55.3) – for Greenland marine shrimp, fish, and mammals are collected in ▶ Table 55.5.

The civilian nuclear icebreaker facility, RTP “ATOMFLOT,” is located in Kola Bay, Northwest Russia, where several nuclear installations are operated by the Russian Northern Fleet. The Atomflot facility discharges purified nuclear waste into the bay at an annual rate of 500 m³. The mean ¹³⁷Cs activity concentration of seawater at the mouth of the Kola Bay was (8.0 ± 0.8) Bq/m³ at 1994, showing no indication of contamination. In 1986, ¹³⁷Cs levels in seaweed were increased by the Chernobyl release, but in the 1990s, ¹³⁷Cs levels decreased to less than 2 Bq/kg from 8 Bq/kg earlier in the 1980s. However, one exceptional seaweed sample, which shows ¹³⁷Cs level of (46 ± 5) Bq/kg wet wt. and additional radioactivities of ¹³⁴Cs, ¹⁰³Ru, Co, and Eu, is found in the Atomflot area (Matishov et al. 2000).

The quantity of ¹²⁹I in the pre-nuclear age ocean is estimated to be about 10 kg and the quantity increased by one order of magnitude due to various nuclear fuel reprocessing plants.

■ Table 55.5

Concentration factors for Greenland marine shrimps, fish, and mammals (Aarkrog et al. 1999)

Species	⁹⁰ Sr	¹³⁷ Cs
Shrimps	6 ± 3	25 ± 10
Fish	4.6 ± 1.3	78 ± 23
Seal and whales	2.2 ± 0.5	108 ± 23

The two largest commercial reprocessing facilities are at Sellafield (UK) and La Hague (France). A pathway and transit time of tracers in the North Atlantic and Arctic ocean were examined. Atmospheric testing of nuclear weapons is estimated to have produced ~ 50 kg (325 GBq) of ^{129}I , mainly in the early 1960s. Assuming all of this ^{129}I has been deposited and mixed in an ocean surface layer of 100 m depth, it would be expected to raise the $^{129}\text{I}/^{127}\text{I}$ atomic ratio in this layer to $\sim 2 \times 10^{-11}$ (Yiou et al. 2002). At these facilities, special steps have been taken to trap most ($>90\%$) of the iodine, and iodine is discharged to the NE Irish Sea and the English Channel through the steps, respectively, as part of their authorized liquid discharges. The current discharge rates are thus ~ 330 kg/year, with approximately 75% coming from La Hague. The integrated discharge from La Hague is estimated to be $\sim 2,360$ kg (Raisbeck and Yiou 1999).

Iodine and ^{129}I concentrations as well as $^{129}\text{I}/\text{I}$ ratios were measured in lakes and rivers in order to report the global distribution of anthropogenic ^{129}I (Snyder and Fehn 2004). The highest values in ratios and ^{129}I concentrations were found in the mid-latitudes of the Northern Hemisphere, but levels above pre-anthropogenic were found in all samples, including those from the high Arctic and from Antarctica. Low values are observed in equatorial regions, but another maximum is present in the mid-latitudes of the Southern Hemisphere, although it is smaller than that in the Northern Hemisphere. The distribution demonstrates on a global scale the rapid atmospheric transport of ^{129}I from its sources, reprocessing plants located in the Northern Hemisphere. The minimum in ^{129}I concentrations observed at low latitudes probably indicates that the overall remobilization of iodine is a function of regional soil ecosystems.

The International Atomic Energy Agency (IAEA) carried out an international project: "The Study of the Radiological Situation at the Atolls of Mururoa and Fangataufa." Marine radioactivity of present radionuclide concentrations in water, sediment, and biota of the Mururoa and Fangataufa lagoons, and the surrounding ocean were studied. The dominant radionuclide in both lagoons is Pu in sediments (the total inventory is approximately 30 TBq). A decline in radionuclide concentrations has been observed in recent years in lagoon water, with the exception of ^3H and ^{90}Sr . With respect to ^3H and ^{90}Sr , a contribution from underground sources is expected. Radionuclide concentrations in biota from the lagoons and the surrounding ocean are low and consistent with previous measurements. The observed radionuclide concentrations in both lagoons show that no radiological risk exists for hypothetical inhabitants of Mururoa and Fangataufa Atolls (Povinec et al. 1999).

During 1971–1977, the highest specific activities of ^{241}Am and $^{239,240}\text{Pu}$ in Bikini were 2.85 Bq/g and 4.44 Bq/g, respectively, in surface sediments in the northwest part of the lagoon, respectively. Concentrations of soluble and particulate Pu and Am in surface and deep water samples show distributions similar to the sediment samples. Continuous circulation of water in the lagoon and exchange of water with the open ocean results in removal of 111 GBq/a for ^{241}Am and 222 GBq/a for $^{239,240}\text{Pu}$ into the North Equatorial Current (Donaldson et al. 1997).

The behavior and distribution of actinide radionuclides in the estuarine and marine sediments of the NE Irish Sea are significantly influenced by the releases of nonradioactive industrial wastes. There are many industrial activities in the Cumbrian coastal region: hematite mining, diversion-ferric metal extraction industries, coal mining, and a large number of blast furnaces for the manufacture of iron. Large quantities of liquid and solid waste were discharged into the eastern Irish Sea from the Albright & Wilson phosphoric acid production plant between 1954 and 1992, and are a local source of natural series radionuclides entering the eastern Irish Sea. The phosphate ore mix used at the plant before June 1992 contains activity of $(1,377 \pm 34)$ Bq/kg of ^{238}U , (56 ± 4) Bq/kg of ^{235}U , and (13 ± 2) Bq/kg of ^{232}Th .

The radionuclides ^{230}Th and ^{226}Ra are almost in equilibrium $[(1,508 \pm 57) \text{ Bq/kg}$ and $(1,477 \pm 36) \text{ Bq/kg}$, respectively]. ^{210}Pb and ^{210}Po have lower specific activity than ^{226}Ra , but are in equilibrium with each other $[(837 \pm 55) \text{ Bq/kg}$ and $(835 \pm 29) \text{ Bq/kg}$, respectively] (Poole et al. 1995; Hamilton 1999).

The radioactivity in tobacco leaves collected from 15 different regions of Greece was studied. The activities of radium, ^{226}Ra and ^{228}Ra , in the tobacco leaves reflect their origin from the soil by root uptake rather than from fertilizers used in the tobacco cultivation. ^{210}Pb originates from the air and is deposited onto the tobacco leaves and trapped by the trichomes. ^{40}K in the tobacco leaves is due to root uptake either from soil or from fertilizer. ^{137}Cs and ^{134}Cs in the tobacco leaves is due to root uptake and not due to deposition onto the leaf foliage as these isotopes of Cs still remained in the soil 4 years after the Chernobyl reactor accident but were absent from the atmosphere in *rain washout* (precipitation) and *gravitational settling* (Papastefanou 2001).

Results pertaining to ^{226}Ra in thermal and mineral water springs, mostly spas and health resorts, in the Republic of Croatia have been presented. The ^{226}Ra activity concentration of thermal and mineral waters range from 0.07 Bq/l to 4.40 Bq/l. In the spas, water is used both for bathing and for drinking purposes. ^{226}Ra activity concentrations in some springs have been found to exceed the maximal permissible level of 1 Bq/l for drinking water (Marovi et al. 1996). Activity concentrations of naturally occurring alpha-emitter radionuclides, ^{226}Ra , ^{224}Ra , ^{234}U , ^{238}U , and ^{210}Po were determined in 30 frequently visited and regularly consumed spring waters in the Balaton Upland region of Hungary. The average concentration (mBq L^{-1}) was in the range of 2–600, 1–66, 4–742, 0.4–275 and 2–15, respectively. The doses due to the consumption of spring water are in the range $3.5\text{--}167 \mu\text{Sv a}^{-1}$ with an average of $18.2 \mu\text{Sv a}^{-1}$ (Jobbágy et al. 2010). This is well below the $100 \mu\text{Sv a}^{-1}$ reference level of the committed effective dose recommended by World Health Organization (WHO).

55.4.2 Radionuclides in the Food Chain

Brown trout were exposed to ^{32}P in their tank water (7.4 Bq/l) and the uptake to muscle was followed over 6 weeks. A steady-state concentration factor of 1.7 and a biological half-life for clearance of 45 days are calculated (Winpenny et al. 1998).

On the other hand, juvenile rainbow trout (*Oncorhynchus mykiss*) were subjected to a 2-day radioactive pulse of $^{110\text{m}}\text{Ag}$ at 11.9 g/l (as AgNO_3), followed by a 19-day post-tracer exposure to nonradioactive Ag(I) (3.8 g/l). The distribution of $^{110\text{m}}\text{Ag}$ in the gills, liver, intestine, kidney, brain, and remaining carcass was investigated over a 19-day post-tracer period. Initially, the intestine contains the highest proportion of the $^{110\text{m}}\text{Ag}$ burden (34%); however, by day 8, less than 5% of the total radioactivity remains in this tissue. The majority of the $^{110\text{m}}\text{Ag}$ eliminated from the intestine moves to the liver and as much as 65% of the total radioactivity of the $^{110\text{m}}\text{Ag}$ in the fish are found in the liver (Galvez et al. 2002).

Dietary uptake, retention, and tissue distribution of ^{54}Mn , ^{60}Co , and ^{137}Cs in the rainbow trout have been studied, because this fish is widely distributed in European waterways. These radionuclides present a special interest from a biological standpoint, because Cs is biochemically analogous to K; and Mn and Co are classified among the ten vital elements for life. The theoretical values of the steady-state trophic transfer factor (TF) were significantly lower than one for ^{54}Mn and ^{60}Co , indicating that these radionuclides are not being biomagnified in their transfer to trout, while ^{137}Cs showed the opposite. At the end of the uptake phase (42 days), the

highest concentrations of ^{54}Mn were found in the liver, ^{60}Co in the kidneys, and ^{137}Cs in the digestive tract. After 73 days of depuration, the highest concentrations of ^{54}Mn were detected in the fins, ^{60}Co in the kidneys, and ^{137}Cs in the muscles. In general, ^{54}Mn was concentrated in the bony and cartilaginous tissues, ^{60}Co in skin, head, bone, and muscle, and ^{137}Cs in muscle (Baudin et al. 2000).

It is widely believed that iodine in soil is derived from iodine in the ocean rather than from iodine in the rock. This implies that the specific activity of ^{129}I in the iodine of human thyroids should be the same as that in the oceans. If, however, the iodine in soil originates from weathering of rocks (as is the case with other heavy trace elements), then the ^{129}I specific activity in thyroids should be much lower. It now appears that only a small fraction of the iodine in soil is of oceanic origin. Most calculations of very long-term effects of ^{129}I on human health are therefore considered to have resulted in overestimated figures (Cohen 1985).

Rice is a staple food in Japan and other Asian countries. Transfer of ^{137}Cs and stable Cs from paddy soil to polished rice in Aomori, Japan was measured. The specific activity of ^{137}Cs derived from fallout depositions and the mass fractions of stable Cs and K in paddy soils are 2.5–21 Bq/kg, 1.2–5.3 mg/kg, and 5,000–13,000 mg/kg, respectively. The respective values in polished rice are 2.5–8.5 mBq/kg dry wt., 0.0005–0.0065 mg/kg, and 580–910 mg/kg. The geometric mean of soil-to-polished rice *transfer factor* (TF) of ^{137}Cs is estimated to be 0.0016, being approximately three times higher than that of stable Cs, 0.00056. Here, TF is defined as follows:

$$\text{TF} = \frac{C_{\text{pr}}}{C_{\text{s}}} \quad (55.1)$$

where C_{pr} denotes the specific activity/mass fraction of a radionuclide/element in polished rice (Bq/kg dry mass for radionuclide or mg/kg dry wt. for stable element), and C_{s} stands for the specific activity/mass fraction of the same radionuclide/element in soil (Bq/kg dry wt. for radionuclide or mg/kg dry wt. for stable element).


Fallout ^{137}Cs , mostly deposited up to the 1980s, is more mobile and more easily absorbed by plants than stable Cs in the soil. Potassium in the soil is reported to be a competitive factor for the transfers of both ^{137}Cs and stable Cs from soil-to-polished rice. A similar difference between the transfer of ^{137}Cs and stable Cs was reported for polished rice (TF is about 40), wild mushrooms (4), and potato tubers (about 3) (Tsukada et al. 2002).

Radium is similar to calcium in chemical behavior and is absorbed from soil by plants and is passed up the food chain to man. Chemical factors such as the amount of exchangeable calcium in the soil will determine the rate at which radium will be absorbed by plants. The radium in food transferred from soil is known to be as variable as ^{137}Cs contents of food.

It is very important to understand how each radionuclide behaves in passing from the root to the edible portion of the plant and through the body of the stock animal and into the meat and/or milk consumed by man. The metabolisms of ^{90}Sr , ^{137}Cs , and ^{131}I have been studied in detail.

To understand the metabolism of radionuclides in relation to the congeners, the observed ratio (R_{obs}) defined as follows is used:

$$R_{\text{obs}} = \frac{(C_{\text{e}}/C_{\text{c}})_{\text{sample}}}{(C_{\text{e}}/C_{\text{c}})_{\text{precursor}}} \quad (55.2)$$

where C_{e} and C_{c} are the concentrations of the element and its congener, respectively. For the purpose of  Eq. (55.2), the concentration C_{e} can be replaced by the specific activity. For example, if a cow ingests 1,000 Bq of ^{90}Sr activity per 1 g of Ca and the cow's milk contains 100

Bq ^{90}Sr /g Ca, R_{obs} will be 0.1. However, the application of R_{obs} to ^{90}Sr is often not useful because ^{90}Sr is not homogeneously mixed throughout the soils.

Pyle and Clulow have reported the R_{obs} [(Bq ^{226}Ra /g Ca in fish tissue)/(Bq ^{226}Ra /g Ca in water)] in Quirke Lake white sucker (*Catostomus commersoni*) bone (mean = 0.07) and muscle (mean = 3.60), and these values correspond well to those reported by Rope and Whicker and show that bone could discriminate against ^{226}Ra in the water, but muscle does not (Pyle and Clulow 1998).

There are a number of hypotheses concerning the rates of uptake and elimination of radiocesium in fish. The level of radioactive concentration of aquatic biota is commonly defined in terms of a *concentration factor* (R_c) as follows:

$$R_c = \frac{\text{Activity per kg of aquatic biota (wet wt)}}{\text{Activity per liter of water}} \text{ l/kg.} \quad (55.3)$$

Smith et al. (2002) have obtained the following results from a considerable number of data measured for radiocesium in lakes:

1. Fish-water concentration factors are inversely proportional to $[\text{K}^+]$ of the lakes.
2. The uptake rate of ^{137}Cs in fish is negatively correlated with lake $[\text{K}^+]$.
3. The excretion rate of ^{137}Cs in fish is not positively correlated with lake $[\text{K}^+]$.
4. Lake pH or $[\text{Ca}^{++}]$ may reduce accumulation of ^{137}Cs .

It is assumed that the Sellafield plutonium reprocessing plant discharges large amounts of ^{99}Tc : a total of about 3,000 TBq of ^{99}Tc by the year 2015, weighing about 5 tons. Levels of ^{99}Tc in Norwegian coastal waters increased by a factor of ten between 1991 and 1996. ^{99}Tc is concentrated in seaweed, winkles, and mussels. A concentration factor of 120,000 is reported in seaweed and one of 650,000 has been measured in the green gland of lobster (Barnaby and Boeker 1999). Recent studies have shown that accumulation of ^{99}Tc in seabed sediments labeled by authorized radioactive liquid discharges into the NE Irish Sea from the Sellafield reprocessing complex is greater than previously thought. New data on ^{99}Tc concentration profiles in subtidal and intertidal sediments from the eastern and western Irish Sea show that substantial amounts of ^{99}Tc have accumulated in the fine-grained subtidal sediments off the Cumbrian coast, particularly after increased releases from Sellafield following the commissioning of the Enhanced Actinide Removal Plant (EARP) in 1994 (Finegan et al. 2009).

^{99}Tc activity concentration factors were measured in fish in the Irish marine environment. The mean annual ^{99}Tc level in filtered seawater ($<0.45 \mu\text{m}$) is 21–45 mBq/l for seawater from the western Irish Sea in 1995–1998, and 0–0.44 mBq/l from the south and west coasts in 1998. In seawater, technetium exists predominantly as the pertechnetate ion (TcO_4^-), which is highly soluble. Weighted mean ^{99}Tc specific activities in fish, prawns, and mussels landed at northeast ports in 1996–1998 are 0.15–0.37, 63–88, and 18–37 Bq/kg wet weight, respectively. Concentration factors for ^{99}Tc in seafood from the western Irish Sea are 6,850 for lobster (tail meat), 2,800 for prawns (edible), 970 for mussels (edible part), 280 for oysters (edible part), and 12 for fish (edible part) (Smith et al. 2001).

Reported values of ^{137}Cs specific activity (A_{sp}) and concentration factor (R_c) for fish in reservoirs close to the Mayak Production Association (PA) in Russia in 1994 are as follows. A_{sp} = 80 kBq/kg and R_c = 800 for pike (*Esox lucius*) (7.2 kg), A_{sp} = 120 kBq/kg and R_c = 1,200 for perch, A_{sp} = 0.3 and R_c = 240 for roach, and A_{sp} = 1.3 and R_c = 1,000 for pike (1.7 kg). Activity concentrations of ^{137}Cs and ^{90}Sr are reported to be 100 Bq/l and 8.4–14.0 kBq/l, respectively, in

Reservoir 10, and those in Reservoir 11 are in the range of 1.1–1.5 Bq/l for ^{137}Cs , and 1.9–2.4 kBq/l for ^{90}Sr (Strand et al. 1999).

Data on the concentrations of ^{210}Pb in water, sediment, and biota of the Kaveri River ecosystem at Tiruchirappalli in South India are presented. The highest level of ^{210}Pb was observed in the sediment (15.5 Bq/kg dry) and the lowest level in water (2.7 mBq/l). The concentration factors of ^{210}Pb in biotic components range from about 10^1 to about 10^3 . The high R_c is observed for shells and bones (Hameed et al. 1997).

55.5 Sources of the Effective Dose to the Population in the Environment

Everyone is exposed to natural radiation and globally dispersed radionuclides from atmospheric nuclear tests and accidents, and almost all people are exposed to medical radiography. The annual average doses in the world are estimated by the United Nations Scientific Committee on the Effects of Atomic Radiation (UNSCEAR) and listed in [Table 55.6](#).⁹

UNSCEAR has globally and extensively surveyed the sources of radiation, human exposure, and the effects of radiation, and the reports have been published successively since 1958. The most recent report was published in 2008. In this chapter, almost all data come from the UNSCEAR reports, especially those published in 1988, 1993, 2000, and 2008.

55.5.1 Exposure to Natural Sources

As shown in [Table 55.6](#), exposure to natural sources is predominant in all exposures, and covers a wide range. Natural sources are divided into cosmic and terrestrial sources. The external exposures to the two sources are similar as shown in [Table 55.7](#) and the inhalation of radon is the maximum source of human exposure, and varies widely depending on environmental conditions.

Table 55.6

Annual average doses and ranges of individual doses of ionizing radiation by source (UNSCEAR 2008)

Source	Annual per capita effective dose/mSv	Range or trend in exposure
Natural background	2.4	Typical range 1–13 mSv
Medical diagnosis (not therapy)	0.4	Range from 0.04–1.0 mSv
Atmospheric nuclear tests	0.005	Maximum of 0.15 mSv in 1963
Chernobyl accident	0.002 ^a	The average in the northern hemisphere has decreased from a maximum of 0.04 mSv in 1986
Nuclear power production	0.0002 ^a	Doses are up to 0.02 mSv for critical groups at 1 km from some nuclear reactor sites. Decreased with improved practice

^aGlobally dispersed radionuclides.

■ **Table 55.7**
Average radiation dose from natural sources (UNSCEAR 2008)

Source	Worldwide average annual effective dose/mSv	Typical range/mSv
External		
Cosmic rays	0.39	0.3–1.0
Terrestrial gamma rays	0.48	0.3–1.0
Internal		
Inhalation (mainly radon)	1.26	0.2–10
Ingestion	0.29	0.2–1.0
Total	2.4	1–13

55.5.1.1 Cosmic Radiation

Cosmic Rays

Ground level The components of galactic cosmic rays incident at the top of the atmosphere are primary protons (87%), alpha particles (10%), heavier nuclei (1%), and electrons (2%). The high-energy particles impinging on the atmosphere interact with atoms in the air and generate a complex set of secondary charged or uncharged particles. At ground level, the dominant components of the cosmic-ray secondaries are muons with energy mostly between 1 GeV and 20 GeV. About 80% of the absorbed dose rate in free air comes from the directly ionizing radiation of muons, and the remainder comes from electrons produced by the muons. A representative value for ionizing radiation for this dose rate at the sea level is 32 nSv h⁻¹. The geomagnetic latitude effect is about 10%, so that a value of 30 nSv h⁻¹ is appropriate for latitude below 30°. Since the radiation factor of muons is mostly unity, the effective dose rate is 31 nSv h⁻¹ or 270 μSv a⁻¹.

The effective dose rates for cosmic-ray neutrons were measured to be 4 nSv h⁻¹ at 24°N and 9 nSv h⁻¹ at 50°N, and the latitude variation at sea level was estimated from calculations and listed in ► [Table 55.8](#).

There are substantial altitude effects for both the directly ionizing and photon components and the neutron component of cosmic rays. The annual effective doses from cosmic ray for some high altitude cities are listed in ► [Table 55.9](#). At the altitude of 3,900 m of Lapaz, Bolivia, the average effective dose is 2,020 μSv a⁻¹, i.e., 5.3 times higher than the population-weighted average of the world, 380 μSv a⁻¹.

Aircraft altitudes Aircraft passengers and crews are subject to cosmic radiation exposure rates much higher than the rates at ground level. Estimation of doses to passengers and crews depends on the particular path taken through the atmosphere in terms of altitude and geomagnetic latitude, and on the duration of the exposure. For altitude of 9–12 km at temperate latitudes, the effective dose rates are in the range of 5–8 μSv h⁻¹, and at equatorial latitudes, the dose rates are lower and in the range of 2–4 μSv h⁻¹. For a transatlantic flight from Europe to North America, as an example, the route dose would be 30–45 μSv.

■ Table 55.8

Latitude distribution of cosmic ray dose rates outdoors at sea level. Population-weighted average in the world: ionization 30.9 nSv h⁻¹, neutron 5.5 nSv h⁻¹ (UNSCEAR 2000c)

	Latitude	80–90°	70–80°	60–70°	50–60°	40–50°	30–40°	20–30°	10–20°	0–10°
Effective dose rate/ nSv h ⁻¹	Ionization component	32	32	32	32	32	32	30	30	30
	Neutron component	11	11	10.9	10	7.8	5.3	4	3.7	3.6

■ Table 55.9

Cosmic ray dose rates in high altitude areas (UNSCEAR 1993a)

Locality	Population (million)	Altitude/m	Effective dose/μSv a ⁻¹		
			Ionization	Neutron	Total
Lapaz, Bolivia	1	3,900	1,120	900	2,020
Lasa, China	0.3	3,600	970	740	1,710
Quito, Ecuador	11	2,840	690	440	1,130
Mexico City, Mexico	17.3	2,240	530	290	820
Nairobi, Kenya	1.2	1,660	410	170	580
Denver, USA	1.6	1,610	400	170	570
Teheran, Iran	7.5	1,180	330	110	440

■ Table 55.10

Ingestion and effective doses to an average person by cosmic ray-produced radionuclides (UNSCEAR 1993a)

Radionuclides	Production rate PBq a ⁻¹	Ingestion Bq a ⁻¹	Annual effective dose μSv
³ H	72	500	0.01
⁷ Be	1,960	1,000	0.03
¹⁴ C	1.52	2,000	12
²² Na	0.12	50	0.15

Cosmic Radionuclides

The cosmic radionuclides, ³H, ⁷Be, ¹⁴C, ²²Na, etc., are produced by the interaction of cosmic ray particles with the atoms in the atmosphere, and the production rates are 72 PBq a⁻¹, 1,960 PBq a⁻¹, 1.54 PBq a⁻¹, and 0.12 PBq a⁻¹, respectively. The ingestion and the effective doses of an average person are listed in ▶ Table 55.10. Only ¹⁴C contributes slightly to the total effective doses of 2,400 μSv a⁻¹.

55.5.1.2 Terrestrial Radiation

External Exposure

Outdoors Only the ^{238}U series, ^{232}Th series, and ^{40}K contribute significantly to the exposure of the human body to terrestrial radiation. Other long-lived radionuclides, such as the ^{235}U series, ^{87}Rb , ^{138}La , ^{147}Sm , and ^{176}Lu exist in small amounts and do not contribute to the exposure dose. Therefore, the external radiation exposure depends on the abundance of the first group of nuclides in soil and rock. Generally igneous rocks, such as granite, contain much uranium and thorium, while the sedimentary rock contents are lower. The population-weighted average specific activities are 420 Bq kg^{-1} , 33 Bq kg^{-1} , and 45 Bq kg^{-1} for ^{40}K , ^{238}U , and ^{232}Th , respectively. The above values correspond to the absorbed dose rates in air of 18 nGy h^{-1} , 15 nGy h^{-1} , and 27 nGy h^{-1} , respectively, and the average absorbed dose rate calculated from terrestrial radionuclides in soil is 60 nGy h^{-1} . The distribution of terrestrial radionuclides shows large fluctuation in the world, and the average absorbed dose rates in countries range from 18 nGy h^{-1} (Cyprus) to 93 nGy h^{-1} (Australia).

Indoors Indoor exposure to gamma rays depends on the materials of the construction of houses. Some national average indoor exposure rates are listed in [Table 55.11](#). The lower-rate countries such as the USA and Thailand mainly use wood-frame houses, and the higher-rate countries, such as Iran and Sweden, reflect the wide use of stone or masonry materials in buildings. The ratios of indoor and outdoor exposure in the table show these conditions. There are some areas of high natural radiation background as shown in [Table 55.12](#). The higher radiation rates mainly derive from U- and/or Th-rich minerals in the soil. Monazite, (Ce, La, Y, Th) (PO_4), is such a mineral, which tends to concentrate by weathering with a higher density

Table 55.11

External exposure rates from terrestrial gamma radiation in some countries (UNSCEAR 2000e)

Country	Population (10^6)	Absorbed dose rate in air/ nGy h^{-1}		
		Outdoors	Indoors	Ratio I/O
USA	269.4	47	38	0.8
Chile	14.42	51	61	1.2
China	1,232	62	99	1.6
Japan	125.4	53	53	1
Thailand	58.7	77	48	0.6
Iran	69.98	71	115	1.6
Sweden	8.82	56	110	2
Germany	81.92	50	70	1.4
Poland	38.6	45	67	1.5
Greece	10.49	56	67	1.2
Italy	57.32	74	105	1.4
Average (mean)		57	75	1.3
Population-weighted average		59	84	1.4

■ Table 55.12

Areas of high natural radiation background (UNSCEAR 2000f)

Country	Area	Characteristics	Population	Absorbed dose rate/nGy h ⁻¹
Brazil	Guarapari	Monazite sands	73,000	90–170 (Street) 90–90,000 (Beaches)
	Mineas Gerais and Goias Pocos de Caldas Araxa	Volcanic intrusive	350	110–1,300 ave. 340
China	Yangjian	Monazite particles	80,000	ave. 370
Egypt	Nile delta	Monazite sands		20–400
France	Central region	Granite, schistous	7,000,000	20–400
	Southwest	Uranium minerals		10–10,000
India	Kerala and Madras	Monazite sand	100,000	20–4,000
	Ganges delta			260–440
Iran	Ramsar	Spring water	2,000	70–17,000
	Mahallat			800–4,000
Italy	Lazio	Volcanic soil	5,100,000	ave. 180
	Campania		5,600,000	ave. 200
	Oriveto town		21,000	ave. 560
	South Toscana		100,000	150–200
Niue Island	Pacific	Volcanic soil	4,500	1,100 max.
Switzerland	Tessin, Alps, Jura	Ra-226 in karst soil	300,000	100–200

■ Table 55.13

Estimation of average annual effective doses in countries by terrestrial gamma rays (UNSCEAR 1993b, 2008)

Country	Bulgaria	Canada	China	Denmark	Finland	Germany	Japan
Effective dose/mSv	0.45	0.23	0.55	0.36	0.49	0.41	0.32
Country	Norway	Spain	Sweden	UK	USA	Former Soviet Union	Pop. weight. average
Effective dose/mSv	0.48	0.4	0.65	0.35	0.28	0.32	0.48

of 4.6–5.4. The estimation of average annual effective doses in countries by terrestrial gamma rays is listed in ● Table 55.13.

Radon and Its Decay Products

Source of radon Radon and its decay products are the most important for human exposure from natural sources. There are two important radon isotopes, ²²⁰Rn (referred to later as “thoron”) in the ²³²Th series and ²²²Rn (referred to later as “radon”) in the ²³⁸U series.¹⁰ The half-lives of ²²²Rn and ²²⁰Rn are 3.82 days and 55.6 s, respectively. The half-life of ²²⁰Rn is so short that ²²⁰Rn itself does not travel a long time, but ²¹²Pb, one of its descendants, has a rather

long half-life (10.6 h) and can transfer as an attachment of aerosol. ^{222}Rn can migrate for a long time as a gaseous component and change to short-lived decay products, ^{218}Po (3.05 min), ^{214}Pb (26.8 min), ^{214}Bi (19.9 min), and ^{214}Po (164 μs) and then change to a long-lived decay product, ^{210}Pb (21.3 a).

The evaluation of exposures to radon and its decay products must take account of the actual activity concentrations of the various alpha-emitting radionuclides in the two series in the air that is breathed.

The fraction of radon atoms released into rock or soil pore space from a radium-bearing grain is called the emanation coefficient (also called emanation factor or emanating power). Typical emanation coefficients for rocks and soils range from 0.05 to 0.7. The grain size, the shape, and the soil moisture are important factors.

Concentrations of “radon” and “thoron” in air and their doses Diffusion and advection from the ground and building materials, the entry of outdoor air, and radon released from water and natural gas affect the radon entry rates into structures. The estimation of effective doses for indoor and outdoor inhalation of “radon” (^{222}Rn), “thoron” (^{220}Rn), and their decay products by members of the public are shown in [▶ Table 55.14](#).

Their average activity concentrations outdoors are the same (10 Bq m^{-3}), but indoors the average activity concentration of “radon” (40 Bq m^{-3}) is larger than that of “thoron” (3 Bq m^{-3}). Indoors, “radon” is concentrated, but “thoron” decays due to its short half-life. The equilibrium equivalent activity concentrations are the product of the activity concentration of “radon”/“thoron” and the equilibrium factor. The equilibrium factor is defined as the ratio of the actual PAEC (the Potential Alpha Energy Concentration) to the PAEC that would prevail if all the decay products in each series were in equilibrium with the radon present, and is 0.6 outdoors and 0.4 indoors for “radon.” Those factors for “thoron” were obtained from the average of measured values. The global average annual effective dose from “radon” and its daughters is $1,200 \mu\text{Sv a}^{-1}$ and that for “thoron” and its daughters is $73 \mu\text{Sv a}^{-1}$. As shown in [Table 55.14](#), the annual effective doses due to “radon” daughters are very high, especially the indoor value ($1,000 \mu\text{Sv}$).

Table 55.14

Average activity concentration of "radon" (^{222}Rn), "thoron" (^{220}Rn), and their daughters in air, and annual effective doses (UNSCEAR 1993c)

Radionuclides	Place	Activity concentration/ Bq m ⁻³		Effective dose equivalent Concentration factor/ nSv Bq ⁻¹ h ⁻¹ m ³		Annual effective dose/ μ Sv	
		Radon Thoron gas	Equilibrium equivalent	Radon Thoron gas	Equilibrium equivalent	Radon Thoron gas	Equilibrium equivalent
Radon	Outdoors	10	6	0.17	9	3.0	130
	Indoors	40	16	0.17	9	48	1,000
Total (rounded)							1,200
Thoron	Outdoors	10	0.1	0.11	10	1.9	1.8
	Indoors	3	0.3	0.11	32	2.3	67
Total (rounded)							73

■ **Table 55.15**

Annual effective doses from ingestion of uranium and thorium radionuclides (UNSCEAR 2000g)

	Effective dose rate/ $\mu\text{Sv a}^{-1}$						
	$^{238}/^{234}\text{U}$	^{230}Th	^{226}Ra	$^{210}\text{Pb}/^{210}\text{Po}$	^{232}Th	$^{228}/^{224}\text{Ra}$	Total
Dose from body	7	6	7	80	4	18	120
Dose from food intake	0.5	0.6	6	91	0.4	11	110

Other than radon Internal exposures due to sources other than radon arise from the intake of terrestrial radionuclides by inhalation and ingestion mainly due to ^{40}K , the ^{238}U series, and ^{232}Th series nuclides present in foods and drinking water.

The dose rate from ^{40}K can be determined directly and accurately from external measurements of its concentration in the body, and the average dose rate is $170 \mu\text{Sv a}^{-1}$.

The estimation of dose rates from the internal exposure to the ^{238}U series and ^{232}Th series is more difficult. UNSCEAR (2000a) surveyed their contents in the human body and their dietary intake, and estimated annual effective doses from ingestion of the radionuclides from uranium- and thorium- series are shown in ▶ [Table 55.15](#). The exposure due to these radionuclides contained in the body ($120 \mu\text{Sv a}^{-1}$) is almost the same as that from food intake, $110 \mu\text{Sv a}^{-1}$. In the series of ^{238}U and ^{232}Th (disregarding “radon,” “thoron,” and their short-lived daughters) $^{210}\text{Pb}/^{210}\text{Po}$ contributes most to the exposure (about 75%).

55.5.1.3 Technologically Enhanced Dose Contribution

There are many materials containing radionuclides in which radioactivity is not an essential factor. For example, thorium is used as an additive of welding electrodes and in gas mantles. There are many raw materials containing natural radionuclides and discharges from plants and the use of the waste materials may cause exposure to the public. In phosphate processing, metal ore processing, titanium pigment production, fossil fuels, etc., radionuclides are discharged and expose the public. But the exposure rates may be less than the levels of $1\text{--}10 \mu\text{Sv a}^{-1}$, and can be considered negligible compared to other natural rates.

55.5.1.4 Worldwide Average Exposure from Natural Sources

Finally, averaged worldwide exposure to natural radiation sources are listed in ▶ [Table 55.16](#). There is a wide distribution of exposures from many sources; therefore, typical annual effective doses are also distributed over a wide range, from 1 mSv to 13 mSv and the (population-weighted) average is 2.4 mSv of which 0.39 mSv is due to cosmic rays, 0.48 mSv to external terrestrial radiation, and 1.26 mSv to “radon” and “thoron” inhalation, and 0.29 mSv to the ingestion of ^{40}K and uranium and thorium. As shown in the table, “radon” and its daughters constitute the largest contribution to the total exposure.

55.5.2 Medical Exposure

Medical applications of ionizing radiation are the largest artificial sources of radiation exposure, and population exposures from the diagnostic and therapeutic uses of ionizing radiation

■ **Table 55.16**

Average worldwide exposure to natural radiation sources (UNSCEAR 2000c)

Source	Annual effective dose/mSv	
	Average	Typical range
Cosmic radiation		
Direct ionizing and photon component	0.28	
Neutron component	0.1	
Cosmogenic radionuclides	0.01	
Total cosmic and cosmogenic	0.39	0.3–1.0
External terrestrial radiation		
Outdoors	0.07	
Indoors	0.41	
Total external terrestrial radiation	0.48	0.3–1.0
Inhalation exposure		
Uranium and thorium series (except Rn)	0.006	
Radon	1.15	
Thoron	0.1	
Total inhalation exposure	1.26	0.2–10
Ingestion exposure		
K-40	0.17	
Uranium and thorium series	0.12	
Total ingestion	0.29	0.2–1.0
Total	2.4	1–13

■ **Table 55.17**

Radiation exposure from diagnostic medical X-ray examinations (UNSCEAR 2000h)

Health-care level	Population per physician	Annual number of examinations per 1,000 population	Average annual effective dose to population/mSv	Population in 1996 (million)
I	<1,000	920	1.2	1,508
II	1,000–3,000	150	0.14	3,074
III	3,000–10,000	20	0.02	638
IV	>10,000	<20	<0.02	580
Worldwide average		330	0.4	Total 5,800

are likely to be increasing. In order to obtain a worldwide estimation of medical exposure doses, quantitative information on the frequencies and the dose for diagnostic and therapeutic procedures are required. Since there are significant country-to-country variations in medical radiology, all countries are divided into four levels of health care, based on the number of physicians available to serve the inhabitants of a country (► [Table 55.17](#)). The annual number of examinations per 1,000 people, and the average annual effective doses, are significantly

different on the various health-care levels. Global data were estimated from the data on the number of examinations and their dose per capita and from the populations of countries of different health-care levels.

55.5.2.1 Diagnostic Radiology

Average effective doses from diagnostic examinations with X-ray are shown in [Table 55.18](#). The effective dose of a typical examination of the chest is 0.14–1.1 mSv and other examinations such as lumbar spine, abdomen, and pelvis are 0.3–0.6 mSv. The patient effective dose of an X-ray examination for upper GI (gastrointestinal) tract is 3.6 mSv and that for the lower GI tract is 6.4 mSv, and about 3.7 mSv for urography.

Patient doses per procedure from diagnostic angiographic examinations are 2–10 mSv for coronary, 1–12 mSv for cerebral, 2–48 mSv for abdominal, and 1–22 mSv for peripheral scans ([Table 55.19](#)).

The doses for the procedure during interventional radiology are generally very high, e.g., 7.5–57 mSv for PTCA (percutaneous transluminal coronary angioplasty), 2–40 mSv for TIPS (transjugular intrahepatic portosystemic shunt), 17–25 mSv for radiofrequency ablation, 5.7–20 mSv for cerebral embolization, and 0.3–24 mSv for biliary procedure ([Table 55.20](#)).

The doses to patients from computed tomography (CT) depend on the survey regions, and that for the head is low (1.5–2.5 mSv), that for the abdomen is high (10–17 mSv), and others are 5–10 mSv ([Table 55.21](#)).

■ **Table 55.18**

Average effective doses from diagnostic medical X-ray examinations (UNSCEAR 2000i)

Examination	Average effective dose/mSv
Chest radiography	0.14
Chest photofluoroscopy	0.65
Chest fluorography	1.1
Limb and joints	1.8
Lumbar spine	1.8
Pelvis and hip	0.83
Head	0.07
Abdomen	0.53
Upper GI tract	3.6
Lower GI tract	6.4
Cholecystography	2.3
Urography	3.7
Mammography	0.51
CT	8.8
Angiography	12
PTCA	22

GI (gastrointestinal), CT (computed tomography), PTCA (percutaneous transluminal coronary angioplasty).

■ **Table 55.19****Patient dose per procedure from diagnostic angiographic examination (UNSCEAR 2000j)**

Procedure	Coronary	Coronary	Cerebral	Cerebral	Abdominal
Technique	Cine film	Digital cine	Carotid (DSA)	Digital	Hepatic (DSA)
Fluoroscopy time/min	4.3 (1.5–15)	5.7	3.9 (1.2–11.8)	12.1 (2.9–36)	10.3 (2.3–28.6)
Effective dose/mSv	(2–9)	9.4	4 (1–12)	7.4 (2.1–19.6)	23 (4–48)
Procedure	Abdominal	Peripheral	Peripheral	Peripheral	
Technique	Renal (DSA)	Femoral (DSA)	Femoral	Lower limbs	
Fluoroscopy time/min	12.1 (5.5–21)	3.7 (1.2–19)	2.4 (1.3–8.3)	3.7 (± 3.1)	
Effective dose/mSv	16 (6–34)	4 (1–16)	9	6.2	

Numbers in parentheses mean ranges while the rest averages.

DSA stands for digital subtraction angiography.

■ **Table 55.20****Patient dose per procedure during interventional radiology (UNSCEAR 2000k)**

Procedure	PTCA	PTA	TIPS	Radiofrequency ablation
Fluoroscopy time/min	11.5 (2.4–28)	24 (5–45)	59 (26–115)	53 (± 50)
Localized dose to skin/Gy	0.15 (0.05–0.3)	0.3	0.4	1.3 (± 1.3)
Effective dose/mSv	28.9 (7.5–57)	12.5	8 (2–40)	17–25
Procedure	Valvuloplasty	Embolization	Biliary	Stent
Fluoroscopy time/min	31.8	34.1 (15.2–55.8)	7.1 (0.6–26.3)	17 (± 9)
Localized dose to skin/Gy	–	0.34 (0.19–0.66)	0.11 (0.01–0.37)	2 (max)
Effective dose/mSv	29.3	10.5 (5.7–20)	6.9 (0.3–23.9)	5.8

PTCA: Percutaneous transluminal coronary angioplasty, PTA: Percutaneous transluminal angioplasty

TIPS: Transjugular intrahepatic portosystemic shunt.

Dental radiography is also frequently used. The averaged effective dose for one examination is about 1.1–3.3 μSv , and the frequency is 309 times for 1,000 people for group I. The global average exposure dose per examination of dental radiography is calculated to be 16 μSv . Similar investigations show that the surface absorbed doses for mammography, uterus, and bone densitometry are 0.5–10 mGy, but the effective doses are less than 1 μSv .

Averaged (individual) effective doses and collective effective doses from diagnostic medical X-ray examinations in some counties are listed in [▶ Table 55.22](#).

Germany has the highest effective dose both per examination and per capita. The annual effective doses from diagnostic medical examination of Brazil, China, and Malaysia are lower, and these countries are classified as countries of health-care level II. The number of examinations for the countries of health-care level II has been increased and will reach that of the countries of health-care level I; therefore, the average doses from diagnostic radiology are estimated to be globally increasing.

■ Table 55.21

Average doses to patients from computed tomography (CT) in some countries (UNSCEAR 2000l)

Country	Year	Mean effective dose per procedure/mSv							
		Head	Cervical spine	Chest	Abdomen	Liver	Kidneys	Pelvis	Lumbar spine
Australia	1995	2.6	5.2	10.4	16.7	12.7	–	11	5.2
New Zealand	1992	1.8	3.3	8.9	9.7	6.5	7.6	6.9	4.7
Norway	1993	2	–	11.5	12.8	11.9	9.9	9.8	4.5
Sweden	1993	2.1	6	10	10	10	10	10	6
UK	1994	1.6	1.5	9.7	12	10.3	9.1	9.8	3.3

■ Table 55.22

Annual effective doses from diagnostic medical X-ray examination (UNSCEAR 2000j)

Effective dose/mSv			Collective effective dose/man-Sv
Country	Per examination	Per capita	
Australia	1.3	0.8	13,000
Brazil	0.26	0.09	–
Bulgaria	1.28	0.75	6,400
Canada	1.05	0.94	26,200
China, continental	0.57	0.08	91,600
China, Taiwan	0.43	0.23	4,700
Denmark	0.7	0.36	1,820
Finland	0.63	0.45	2,270
France	–	1	57,660
Germany	1.5	1.9	153,360
Malaysia	0.28	0.05	1,000
Netherlands	1	0.6	9,000
Poland	1.2	0.8	32,300
Portugal	0.83	0.71	7,000
Romania	1.35	0.61	13,800
Russian Federation	0.7	0.9	128,000
Sweden	1.2	0.68	6,000
Ukraine	0.83	0.5	26,250
USA	0.5	0.5	13,000

55.5.2.2 Diagnostic Administrations of Radiopharmaceuticals

Administration of radionuclide preparations (radiopharmaceuticals) to patients is widely practiced throughout the world. Many of the diagnostic applications of radionuclides are conducted in vitro and in vivo. Since the in vitro experiments do not give rise to the exposure of patients, only diagnostic in vivo examinations are referred to in this section.

The main diagnostic practices with radiopharmaceuticals are the procedures for bone, cardiovascular, lung perfusion, lung ventilation, thyroid scan, thyroid uptake, renal, liver/spleen, and brain examinations. The effective doses per procedure are considerably higher and are 4.5 mSv, 8 mSv, 1.5 mSv, 1 mSv, 3.4 mSv, 15 mSv, 1.9 mSv, 1.7 mSv, and 6 mSv, respectively, and the number of procedures per 1,000 population are 4.5, 2.7, 1.8, 0.34, 4.1, 0.92, 0.89, 2.1, and 1.3, respectively for countries at health-care level I. But patients near to the end of their lives receive many of these exposures, and thus the doses are not distributed evenly among the population. Therefore, these doses should not be used for the assessment of detrimental effects of radiation exposure.

55.5.2.3 Teletherapy and Brachytherapy

Teletherapy has been used for the therapy of various types of tumor. The most frequent ones are (figures in the parentheses show the annual numbers of treatments per 1,000 population in the health-care level I countries): leukemia (0.01), lymphoma (0.06), breast tumor (0.35), lung/thorax tumor (0.36), gynecological tumor (0.12), head/neck tumor (0.06), brain tumor (0.04), skin tumor (0.05), bladder tumor (0.04), prostate tumor (0.18), tumor of the rectum (0.07) benign disease (0.09), and others (0.09). Brachytherapy has been used for the therapy of head/neck tumor (0.01), breast tumor (0.02), gynecological tumor (0.16), prostate tumor (0.004), and others (0.01).

The average doses to patients undergoing radiation teletherapy for countries of health-care level I are 17 Gy for leukemia, 39 Gy for lymphoma, 48–60 Gy for breast tumor, lung/thorax tumor, gynecological tumor, head/neck tumor, brain tumor, skin tumor, bladder tumor, prostate tumor, tumor of rectum, and 6 Gy for benign disease. The average doses to patients on brachytherapy are 44 Gy for head/neck tumor, 16 Gy for breast tumor, 45 Gy for gynecological tumor, and 35 Gy for prostate tumor. These doses are very high, but should not be used to infer deterministic or stochastic risks for the same reason as described in the previous subsection.

55.5.2.4 Therapeutic Administrations of Radiopharmaceuticals

The average annual numbers of therapeutic treatments with radiopharmaceuticals per 1,000 population for countries of health-care level 1 are 0.038 for thyroid malignancy (radionuclide: ^{131}I), 0.15 for hyperthyroidism (radionuclide: ^{131}I), 0.0046 for polycythemia vera (^{32}P), 0.0063 for bone metastases (^{89}Sr), and 0.098 for synovitis (^{90}Y). The average activities administered in the therapeutic treatments are 4,760 MBq of ^{131}I (iodide) for thyroid malignancy, 415 MBq of ^{131}I (iodide) for hyperthyroidism, 170 MBq of ^{32}P (phosphate) for polycythemia vera, 140 MBq of ^{89}Sr chloride for bone metastases, and 250 MBq of ^{90}Y for synovitis.

55.5.2.5 Estimated Doses to the World Population from Medical Uses of Radiation

The doses from various medical uses of radiation have been discussed above and are summarized in ► [Table 55.23](#).

Thus almost all exposures (>90%) of the medical variety are derived from diagnostic radiology. The number of dental X-ray examination is large (520 millions), but because the effective dose per examination is very low (about 16 μSv), the contribution to the total effective dose is small. In contrast, the number of diagnostical nuclear medicine procedures is small, but because the effective dose per examination is high (about 4 mSv), the collective effective dose is about ten times more than that for dental examinations. The absorbed doses involved in radiotherapy and nuclear medicine therapy procedures are very much higher, but their contribution is not used for the assessment of radiological detriment, because a great part of the exposure is received by patients near the end of their lives. Finally, the effective dose per capita for medical use is estimated to be 0.4 mSv, and this value is one sixth of the dose from natural sources of radiation.

55.5.3 Global Fallout and Nuclear Facilities

The major anthropogenic sources that have lead, or could potentially contribute, to the radionuclide contamination of the environment are the following: (1) the testing and production of nuclear weapons; (2) the normal activities of the nuclear power fuel cycle; (3) the radioisotope production and research reactors; and (4) the nuclear accidents.

In this section, the amounts of radionuclides suddenly released from testing of nuclear weapons and from various accidents and that gradually released from normal operational activities of the nuclear cycle and radioisotope production are reviewed and the corresponding dose effects are estimated.

► [Table 55.23](#)

Estimated annual global practices and doses to the world population (UNSCEAR 2000m) from medical use of radiation (1991–1996)

		Number of procedures/ 10^6	Effective dose per capita/mSv
Diagnosis	Medical radiation use	1,910	0.4
	Dental X-ray examination	520	0.002
	Nuclear medicine procedures	32	0.03
Total		2,500	0.4
Therapy	Radiotherapy treatments	5.1	
	Nuclear medicine procedures	0.4	
Total		5.5	

55.5.3.1 Normal Activities

Testing and Production of Nuclear Weapons

Atmospheric tests From the first test in New Mexico on July 16, 1945, to the last atmospheric test at Lop Nor on October 16, 1980, 543 nuclear tests were carried out in the atmosphere, and enormous amounts of radionuclides were released. The radioactive debris is deposited locally (up to 100–200 km from ground zero), regionally (2,000–3,000 km), or released into the troposphere and/or stratosphere resulting in global dispersion (➤ [Table 55.24](#)).

For refractory radionuclides such as ⁹⁵Zr and ¹⁴⁴Ce, 50% are assumed to be deposited locally and a further 25% is deposited regionally, while for volatile radionuclides such as ⁹⁰Sr, ¹³⁷Cs, and ¹³¹I, 50% of the fission yield is assumed to be deposited locally and regionally. The remainder of the debris and all of the debris from airbursts is widely dispersed in the atmosphere.

The radionuclides of mass numbers about 90–140 have high yields in fission¹¹, very large activities were therefore produced of ⁹¹Y, ⁹⁵Zr, ¹³¹I, ¹⁴⁰Ba, and ¹⁴⁴Ce as shown in ➤ [Table 55.25](#). Tritium was produced in large quantities by ternary fission.¹² Although their yields are smaller,

■ **Table 55.24**

Atmospheric nuclear tests and partitioned fission yield (UNSCEAR 2000n)

Country	Number of tests	Partitioned fission energy/Mt ^a			Test sites
		Local and regional	Troposphere	Stratosphere	
China	23	0.15	0.66	11.4	Lop Nor
France	50	0.23	0.57	5.37	Mururoa, Algeria, etc.
UK	21	0.07	1.76	2.39	Marilinga, Christmas Is., etc.
USA	217	28.2	8.27	44.9	Nevada, Enewetok, Christmas Is., etc.
USSR	219	0.13	4.28	80.8	Semipalatinsk, Novaya Zemlya, etc.
Total	530	29	16	145	

^aThe energy is expressed by the weight (mega ton) of TNT gunpowder.

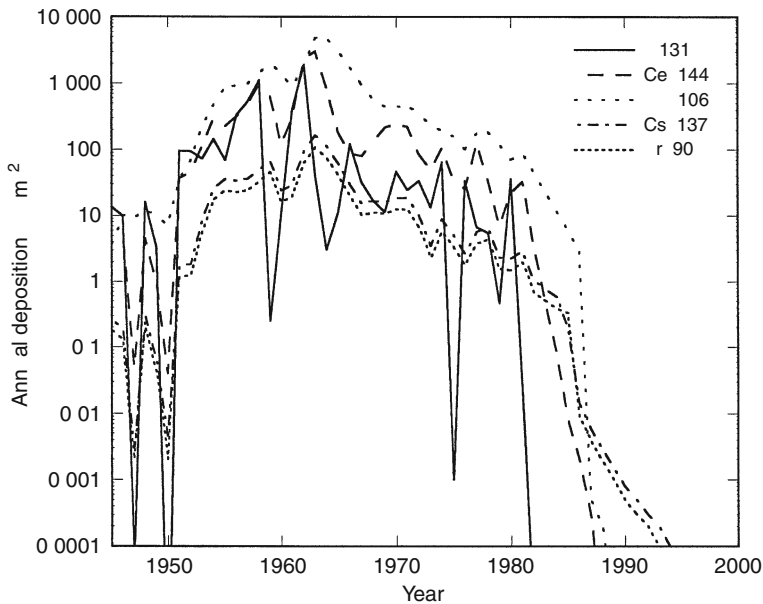
■ **Table 55.25**

Radionuclides produced and globally dispersed in the total of atmospheric nuclear testing (UNSCEAR 2000o)

Radionuclides	³ H	¹⁴ C	⁵⁴ Mn	⁵⁵ Fe	⁹⁰ Sr	⁹¹ Y	⁹⁵ Zr	¹⁰⁶ Ru
Half-life	12.3 a	5,730 a	312 d	2.73 a	28.8 a	58.5 d	64.0 d	374 d
Global release/PBq	186,000	213	3,980	1,530	622	120,000	148,000	12,200
Radionuclides	¹²⁵ Sb	¹³¹ I	¹⁴⁰ Ba	¹⁴⁴ Ce	¹³⁷ Cs	²³⁹ Pu	²⁴⁰ Pu	²⁴¹ Pu
Half-life	2.76 a	8.02 d	12.8 d	285 d	30.1 a	24,110 a	6,563 a	14.4 a
Global release/PBq	741	675,000	759,000	30,700	948	6.52	4.35	142

■ Fig. 55.1

Annual deposition of the radionuclides produced in atmospheric nuclear tests (UNSCEAR 2000r)



the radionuclides of long half-lives, ^{90}Sr (28.8 a), ^{137}Cs (30.1 a), and the plutonium isotopes (^{239}Pu : 24,110 a; ^{240}Pu : 6.536 a; ^{241}Pu : 14.4 a) are important in the exposure of people. Since the atmospheric tests were ended in 1980, and the average mean residence time of particles in the stratosphere is about 2 years, almost all fallouts had been deposited in the 1980s as shown in [Fig. 55.1](#).

The sum of the worldwide average annual effective dose for the period of 1945–1999 caused by relevant radionuclides from atmospheric tests is shown in [Table 55.26](#).

At the beginning of the tests, $^{95}\text{Zr}/\text{Nb}$ dominated the external exposure, but due to the short half-life of ^{95}Zr , ^{137}Cs has been the primary source of this irradiation path since the 1960s. ^{131}I and other nuclides with short half-life significantly contributed to the ingestion dose at the time of their fallout, but on the long term ^{90}Sr , ^{137}Cs , and ^{14}C became the most dominant. Since the half-life of ^{14}C is long and circulates in the biosphere, today ^{14}C contributes 93% of the total ingestion and 70% of the total effective dose commitment. Inhalation dose was primarily determined by ^{144}Ce , the transuranium isotopes, and ^{106}Ru , but after 1985 their concentration significantly dropped in the air and today this contribution is not significant.

The annual effective dose from radionuclides due to atmospheric nuclear testing reached a maximum in 1963 of 113 μSv (37.5 μSv for external, 39.8 μSv for ingestion, and 36.0 μSv for inhalation). In 1999, the effective dose dropped to 5.51 μSv (2.9 μSv for external, 2.61 μSv for ingestion, and 0.0 μSv for inhalation) and decays very slowly due to the significant ^{14}C contribution.

Underground testing The underground tests of nuclear weapons were begun in 1951 by the USA and in 1961 by the USSR. Until 1998, 1,876 underground nuclear tests were carried out in seven countries ([Table 55.27](#)).

■ Table 55.26

Sum of the worldwide average annual effective dose for the period of 1945–1999 from radionuclides produced in atmospheric testing (UNSCEAR 2000p)

Radionuclides	Effective dose commitment/ μ Sv			
	External	Ingestion	Inhalation	Total exposure
H-3		23.7		23.7
C-14		144		144
Mn-54	19.2		0.1	19.3
Sr-90		97	9.2	106.2
Zr-95/Nb	81.3		2.9	84.2
Ru-106	24.5		35.2	59.7
I-131	1.6	64.2	2.6	68.4
Cs-137	166	154	0.3	320.3
Ce-144	7.9		52.5	60.4
Pu and Am			37.8	37.8
Total	353	492	149	994

■ Table 55.27

Underground nuclear tests (UNSCEAR 2000q)

Country	Number	Fission energy/Mt ^a	Period
China	22	1	1969–1996
France	160	3	1961–1996
India	6		1974, 1998
Pakistan	6		1998
UK	24	2	1962–1991
USA	908	46	1955–1992
USSR	750	38	1961–1990

^aThe energy is expressed by the weight (mega ton) of TNT gunpowder.

The release of ^{131}I into the atmosphere at the Nevada underground site was estimated to be 5,000 TBq. If other tests release similar amounts of ^{131}I assuming similar magnitudes of explosions, the total release by underground nuclear tests is estimated to be 15,000 TBq of ^{131}I . The estimated released ^{131}I was about 0.004% of the estimated total production of ^{131}I . If the same rate can be applied to other gaseous radionuclides, 50 PBq of ^{133}Xe and 0.1 TBq of ^3H were released by the underground tests.

The exposure dose does not contribute significantly to the total human exposure since the release is very localized and the half-life of ^{131}I is short (8.02 days).

Production of weapon materials The production rates of nuclear weapon materials have never been published; therefore, they are estimated by the amounts of the long-lived nuclides in

high-level radioactive waste in the USA. These data suggest that the USA and Russian Federation stock about 100 tons of plutonium, each.

Tritium is also produced for weapons, and about 55 kg of tritium are stocked in the USA and maybe 110 kg in the world.

Radionuclides released from the production of nuclear weapon materials and from fabrication plants are not widely published. The exposures from nuclear materials production/processing centers (Chelyabinsk, Krasnoyarsk, and Tomsk) in the Russian Federation were published, and the annual effective doses were 0.0054–0.11 mSv.

Nuclear Power Production

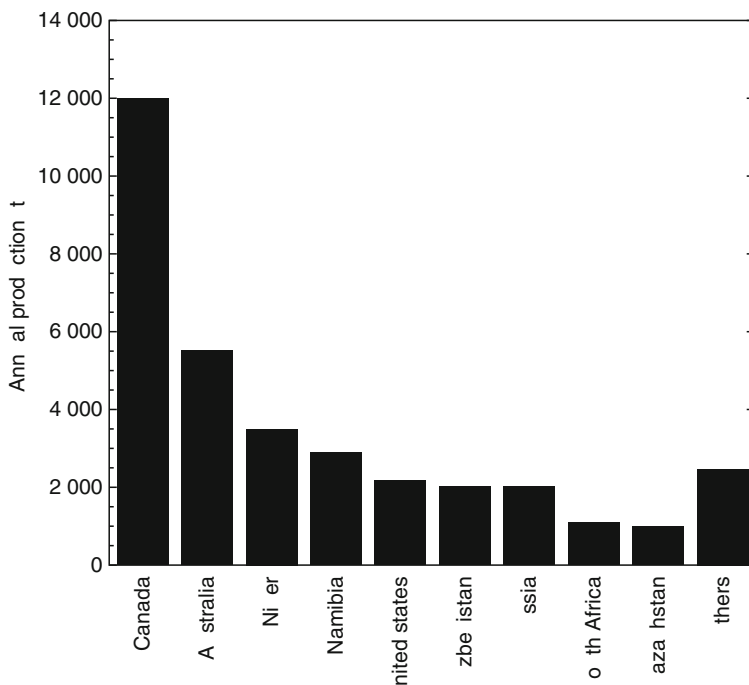
Mining and milling Uranium was produced to the extent of 35.7 kilotons globally in 1997. Canada produces one third of this as shown in [Fig. 55.2](#). The uranium mines are unevenly distributed in the world and 90% of uranium is produced in ten countries.

^{222}Rn is the daughter of ^{226}Ra and a descendant of ^{238}U . While producing 1 ton of uranium, ~ 300 GBq of ^{222}Rn is released during mining and ~ 13 GBq during milling. This means that almost all of the radon is released during mining.

In the 100-km range of a model mining activity producing 4,000 t of uranium annually, the average per capita annual effective dose is estimated to be 40 μSv . The normalized collective effective doses per electrical energy generation are estimated to be 0.19 man-Sv(GW y) $^{-1}$ for mining and 7.54 man-Sv(GW y) $^{-1}$ for milling.

■ Fig. 55.2

Annual production of uranium in various countries in 1997 (UNSCEAR 2000s)



Uranium enrichment and fuel fabrication For light-water-moderated and light-water-cooled reactors (LWRs) and for advanced gas-cooled graphite moderated reactors (AGRs), the uranium processed at the mills needs to be enriched in the fissile isotope ^{235}U . Enrichments of 2–5% are required. Before the enrichment, the uranium oxide (U_3O_8) must be converted to uranium tetra-fluoride (UF_4) and then to uranium hexa-fluoride (UF_6).

In fuel fabrication for LWRs (PWRs and BWRs) and AGRs, the enriched UF_6 is chemically converted to UO_2 . The UO_2 powder is sintered, and formed into pellets. The releases of radioactive materials in the processes of the conversion, enrichment, and fuel fabrication plants are generally small and the exposure to the public is also small.

Nuclear reactor operation The reactors used for electrical energy generation are classified for the most part, by their coolant systems and moderators. PWRs and BWRs are light-water-moderated and cooled-pressurized or boiling water reactors, HWRs are heavy water cooled and moderated reactors, GCRs are gas-cooled and graphite-moderated reactors and LWGRs are light water-cooled, graphite-moderated reactors. Fast breeder reactors (FBRs) have no moderator materials and are cooled by a liquid metal, normally sodium metal, and the fission is induced by fast neutrons. FBRs make a minor contribution to the total energy production by nuclear means.¹³

The energy-normalized releases of radionuclides from various types of nuclear reactors are shown in ▶ [Table 55.28](#). The gaseous release is characterized by the type of reactors: noble gases are released largely from GCRs and LWGRs, tritium gas is largely released from HWRs, ^{131}I is released mostly from LWGRs, and particulates are released largely from BWRs. The average of the worldwide total electrical power generated by these various types of reactors for 1995–1997 is also shown in ▶ [Table 55.28](#).

From the average effluents data UNSCEAR determined the collective doses for a model site based on nuclide specific dose-conversion coefficients, which were calculated applying a simple dispersion model, nuclide specific transport parameters, and population density data of 400 km^{-2} for 1–50 km, 20 km^{-2} for 50–2,000 km. The normalized collective effective doses

■ **Table 55.28**

The average of the energy-normalized releases (TBq/GW_y, with the energy expressed in gigawatt-year) of radionuclides from nuclear reactor (UNSCEAR 2000t) for the period of 1995–1997

Energy and release	PWR	BWR	GCR	HWR	LWGR	FBR
Power generated (GW) ^b	166.3	50.6	8.4	11.6	9.4	0.5
Power capacity (GW)	224.1	72.9	13.9	19.8	15	2.4
Noble gas	13	180	1,200	250	460	210
^3H (gaseous)	2.4	0.86	3.9	330	26	49 ^a
^{14}C	0.22	0.51	1.4	1.6	1.3 ^a	0.12 ^a
^{131}I	0.0002	0.0003	0.0004	0.00011	0.007	0.0002
Particulates	0.0001	0.35	0.0002	0.00005	0.008	0.001
^3H (liquid)	19	0.87	280	340	11 ^a	1.7
Other (liquid)	0.008	0.011	0.70	0.044	0.006	0.023

^aEstimated value.

^bThe amounts of released radionuclides are normalized by the fraction of energy generated by the reactor types.

■ **Table 55.29**

Normalized collective effective doses from radionuclides released from reactors, 1990–1994 (UNSCEAR 2000u)

Reactor type	Collective effective dose per unit electrical energy generated (man-Sv/GW _y)						
	Airborne effluents					Liquid effluents	
	Noble gas	³ H	¹⁴ C	¹³¹ I	Particulates	³ H	Others
PWR	0.003	0.005	0.059	0.0001	0.0004	0.014	0.006
BWR	0.15	0.002	0.14	0.0002	0.36	0.0006	0.014
GCR	1.44	0.01	0.38	0.0004	0.0006	0.14	0.17
HWR	0.23	1.4	0.43	0.0001	0.0001	0.32	0.043
LWGR	0.19	0.05	0.35	0.002	0.028	0.007	0.002
FBR	0.042	0.1	0.032	0.00009	0.024	0.0012	0.016
Power weighted average	0.11	0.075	0.12	0.0002	0.08	0.031	0.016
Total				0.43			

from radionuclides from reactors are shown in ▶ [Table 55.29](#). As shown in the table, noble gases and ¹⁴C mainly contribute to the collective effective doses.

Supposing that all the doses are committed to the population in the 50 km vicinity of a model reactor, the average annual per capita effective dose is 5 μSv for PWR and GCR types, 10 μSv for BWR and HWR types, and 2 μSv, 0.04 μSv for LWGR and FBR types, respectively. Due to the definition and the inappropriate use of the collective dose, these values are somewhat overestimated. This overestimation is well illustrated by the study carried out for European power reactors, where for instance for the 2004 effluents data the annual effective dose for the member of the critical group at 500 m from a PWR or BWR reactor is less than 1 μSv (EUROPEAN COMMISSION 2008).

Fuel reprocessing Fuel reprocessing is carried out to recover uranium and plutonium from spent fuel used in reactors. Most spent fuel from reactors is retained on-site in interim storage, pending decision on ultimate disposal or retrievable storage. Only about 5–10% of fuel is submitted to the reprocessing stage of the nuclear fuel cycle. The plants are operated in France, Japan, and the UK.

The released activities in fuel reprocessing, normalized by the unit of electric energy, are shown in ▶ [Table 55.30](#). In airborne effluents, ⁸⁵Kr is most important, tritium and ¹⁴C are minor, and others are present only as traces. In liquid effluents, tritium is a major component.

Due to the significant decrease of the ¹³⁷Cs activity in liquid effluents, the annual per capita effective dose has decreased from 200–500 μSv in the 1980s to 5–8 μSv in 1997–2004, despite the increase of the amount of reprocessed fuel annually.

Globally dispersed radionuclides Radionuclides that are sufficiently long lived and easily dispersed in the environment can give rise to global doses. The radionuclides of interest are ³H (the half-life: 12.3 a), ¹⁴C (5,730 a), ⁸⁵Kr (10.7 a), and ¹²⁹I (1.6 × 10⁷ a). The estimates of the released radionuclides are shown in ▶ [Table 55.31](#) (UNSCEAR 1993d). The electrical energy generated by nuclear reactors has grown steadily from the start of the industry in 1956 and thus

■ Table 55.30

Normalized release in fuel reprocessing between 1995 and 1997 (UNSCEAR 2000v)

Energy content of reprocessed fuel/GWy	Normalized release, TBq/GWy					
160	Airborne effluents					
	^3H	^{14}C	^{85}Kr	^{129}I	^{131}I	^{137}Cs
	9.6	0.3	6,900	0.006	0.00005	0.0001
	Liquid effluents					
	^3H	^{14}C	^{90}Sr	^{106}Ru	^{129}I	^{137}Cs
	255	0.4	0.8	0.5	0.04	0.2

■ Table 55.31

Globally dispersed activities and corresponding world average effective dose commitments for the period of 1970–1997. The energy produced was 3,860 GWy, the reprocessed fuel was equivalent to 420 GWy

Release radioactivity/PBq				Average annual effective dose commitment/nSv
Radionuclides	Reactor	Reprocessing	Total	
^3H	270	170	440	1
^{14}C	2	1	3	4
^{85}Kr		3,200	3,200	10
^{129}I		0.015	0.015	1
Total				16

the concomitant release of radionuclides has also increased. The noble gas ^{85}Kr , and tritium hydrogen gas are difficult to separate from the exhausting gases. Tritium water is also difficult to separate from the wastewater. Tritium and ^{85}Kr , therefore, are largely released from nuclear facilities, but they are easily dispersed homogeneously in the hydrosphere or atmosphere, then most people in the world are homogeneously exposed to their radioactivity. The world average effective dose commitments from several nuclides are also shown in [Table 55.31](#).

The global collective effective dose estimated for 10,000 years amounts to 50 man-Sv/GWy. The main contribution is from globally dispersed ^{14}C from reactors and reprocessing. The longer-term trends in collective effective doses per unit electrical energy generated show decreases due to reductions in the release of radionuclides from reactors and fuel reprocessing plants.

Solid-waste disposal and transport Solid waste arises at various stages of the nuclear fuel cycle, and is classified as low- and intermediate-level waste (LLW) mainly from reactor operation, and high-level waste (HLW) from fuel reprocessing and from “spent” fuel meant for direct disposal.¹⁴ Low- and intermediate-level wastes are generally disposed of by shallow burial in trenches or concrete-lined structures.

From today’s operating nuclear power plants in 30 countries, over 10,000 metric tons of heavy metal (tHM) are unloaded each year, with annual discharges projected to increase to ~11,500 tHM by 2010. Since less than one third is reprocessed, an additional 8,000 tHM/year, on average, will need to be placed in storage facilities. No geological repository for spent fuel or

HLW has yet been built. The only operating geological repository to date is the Waste Isolation Pilot Plant (WIPP) in the USA. In addition to WIPP, good progress has been made in several countries on repositories for HLW or spent fuel from commercial nuclear power plants.

The radiological impact assessment of the waste disposal sites needs the modeling of the long-term behavior of the waste packages and the migration of released radionuclides near the site. Decommissioning of nuclear facilities gives a huge amount of extra low-level radioactive waste, but the released amounts of radionuclides will be very small.

Radionuclide Production and Research Reactors

Radionuclide production and use Radionuclides are widely used in the fields of industry, medicine, and research. For example, in Japan 5.2 GBq of ^{14}C , 6.1 GBq of ^{125}I , 14 GBq of ^3H , and 34 GBq of ^{131}I are used in hospitals, universities, institutes, and one million people work in this field. The estimates of globally released radionuclides for industry, medicine, and research are 0.13 PBq of ^3H , 0.05 PBq of ^{14}C , 0.02 PBq of ^{85}Kr , 0.7 PBq of ^{123}I , 0.06 PBq of ^{125}I , 0.3 PBq of ^{131}I , and 2.6 PBq of ^{133}Xe . Annual collective doses from these released radionuclides are estimated to be 100 man-Sv. Almost all exposure is derived from ^{14}C . The radionuclides used most widely in medical examinations and in nuclear medicine procedures are ^{131}I and $^{99\text{m}}\text{Tc}$. With the estimated global annual usage of ^{131}I in therapeutic treatments of 600 TBq, a fraction of 5×10^{-4} is released in liquid effluents. The release of $^{99\text{m}}\text{Tc}$ (its half-life is 6.01 h) is reduced by a holdup tank and may be negligible.

Research reactors At the end of 1999, 292 nuclear research reactors had been operated in the world. The annual releases from research reactors are only known from few reactors like that of Obninsk in Russian Federation and are 0.7 PBq of noble gases, 5 GBq of ^{131}I , 0.3 GBq of ^{90}Sr , 0.6 GBq of ^{137}Cs , and 0.1 GBq of plutonium. The annual effective doses to individuals in Obninsk were estimated not to exceed 30 μSv .

The radionuclides released from industry, medicine, and research are limited and localized, and thus the exposure to the public may be negligible.

55.5.3.2 Accidents

Commercial Reactors

Three Mile Island On March 28, 1979, the feed water pumps that supplied the steam generator of Three Mile Island Unit 2 shut down, leading to automatic shutdown of the reactor. Heat from residual radioactivity in the core caused the temperature and pressure of the reactor coolant to rise and a relief valve used to stop the repressurizer, to open. The open valve could not close and since the reactor coolant water was draining, a loss-of-coolant accident was in progress. Large amounts of radionuclides were released in the reactor building basement, but comparatively small amounts of noble gas (mainly ^{133}Xe , 370 PBq) and ^{131}I (550 GBq) were released to the atmosphere and the collective effective dose is estimated to be 40 man-Sv in the surrounding area.

Chernobyl On April 26, 1986, the accident at Chernobyl happened. A water-cooled, pressure tube, graphite-moderated, 1,000 MWe reactor was destroyed. It was the first power reactor accident to result in radiation casualties, the first to result in extensive contamination of the environment, and the first to require the evacuation of nearby residents.

■ **Table 55.32**

Core inventory and estimate of total release of radionuclides from the accident of Chernobyl (IAEA 2006)

Radionuclides	Inventory/EBq	Percent released
^{85}Kr	0.033	100
^{133}Xe	6.5	100
^{131}I	3.2	55
^{137}Cs	0.26	33
^{132}Te	4.2	27
^{134}Cs	0.19	25
^{106}Ru	0.85	8–9
^{90}Sr	0.22	4–5
^{95}Zr	5.85	1–2
^{140}Ba	6.04	4
^{144}Ce	3.92	1
^{239}Pu	0.00096	1
^{242}Cm	0.031	1
^{239}Np	58.1	<1

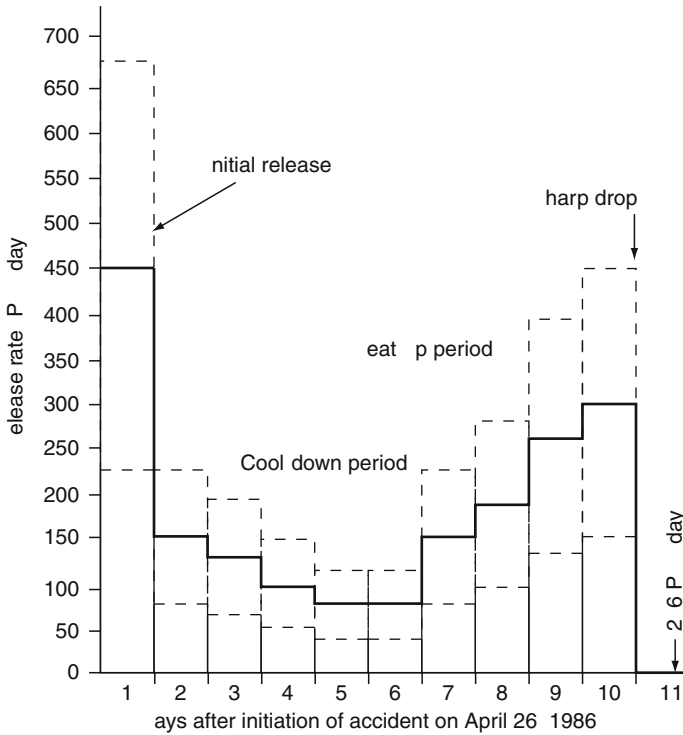
The reactor had operated since 1983, and thus huge amounts of fission products had been stocked in the core and released corresponding to their chemical characteristics (► [Table 55.32](#)). Gaseous and volatile elements such as noble gases, iodine, and cesium were released in large amounts. In contrast, only 2–3% of nonvolatile elements such as cerium and zirconium were released. Fission products in the core of the reactor were released for about 10 days following the destruction of the core before the sharp drop of the releases at May 6 (► [Fig. 55.3](#)).

The total release of radioactive substances was about 14 EBq (as of April 26, 1986), which included 1.8 EBq of ^{131}I , 0.085 EBq of ^{137}Cs and other cesium radioisotopes, 0.01 EBq of ^{90}Sr , and 0.003 EBq of plutonium radioisotopes. The noble gases contributed about 50% of the total release of radioactivity. About 115,000 residents had to be evacuated from the area of around 30 km of the reactor. The fission products had been transported by the plumes by meteorological dynamics and were deposited all over the world. The first plume moved to the north and arrived in Sweden and Finland on the next day. The second plume moved to the east and on April 29 and 30 arrived in Hungary and Austria. The third plume moved to the south and arrived in Greece on May 2 (► [Fig. 55.4](#)). Furthermore, the radionuclides were transferred with global atmospheric dynamics and arrived on May 4 in China, May 5–6 in Canada and the USA (► [Table 55.33](#)).

An area of more than 200,000 km² in Europe was contaminated with radiocesium (above 0.04 MBq of $^{137}\text{Cs}/\text{m}^2$), of which 71% was in the three most affected countries (Belarus, the Russian Federation, and Ukraine). The deposition was highly heterogeneous; it was strongly influenced by rain when the contaminated air masses passed. Most of the strontium and plutonium radioisotopes were deposited close (less than 100 km) to the reactor, due to their being contained within larger (hot) particles.

■ Fig. 55.3

Daily release rate to the atmosphere of radioactive materials during the Chernobyl accident (excluding noble gases) (UNSCEAR 1988b). The dotted lines show a range of uncertainty of $\pm 50\%$



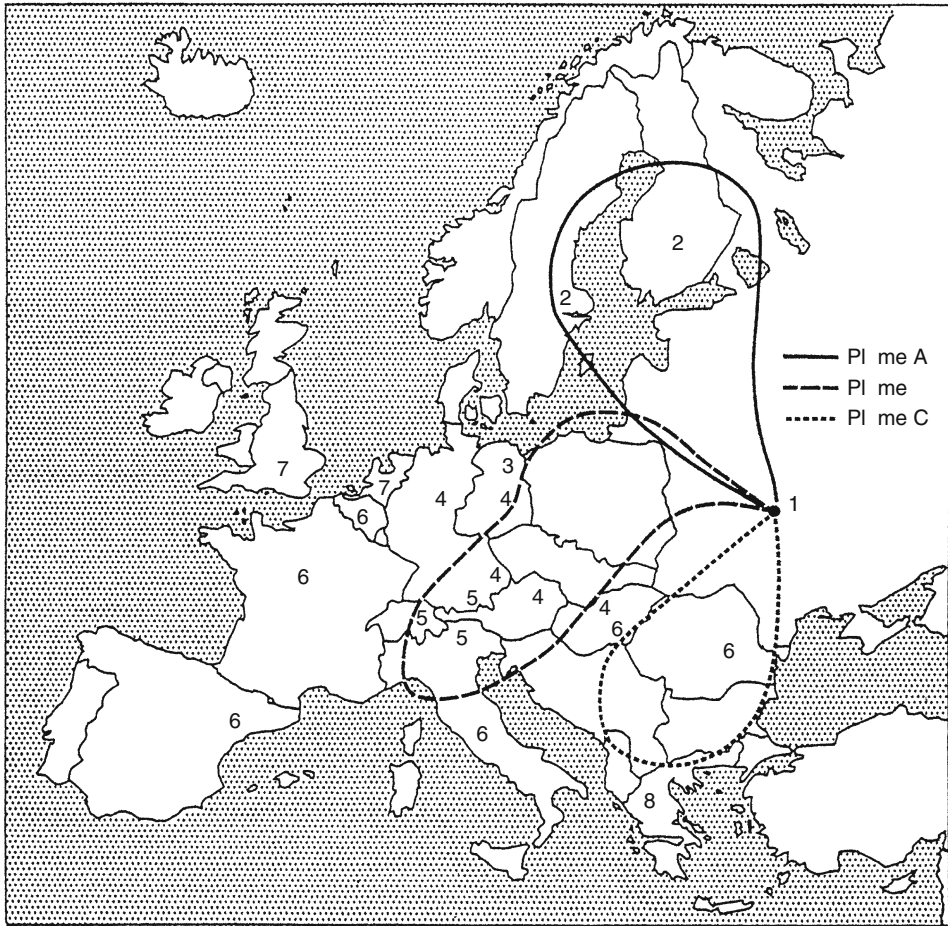
The collective effective dose (not including dose to the thyroid) received by about five million residents living in the areas of Belarus, the Russian Federation, and Ukraine contaminated by the Chernobyl accident (^{137}Cs deposition on soil of $>37 \text{ kBq/m}^2$) was approximately 40,000 man-Sv during the period 1986–1995. The groups of exposed persons within each country received an approximately equal collective dose. The additional amount of collective effective dose projected to be received between 1996 and 2006 is about 9,000 man-Sv. The collective dose to the thyroid was nearly 2×10^6 man-Gy, with nearly half received by persons exposed in Ukraine.

Army Facilities

Kyshtym On September 29, 1957, a 300-m³ tank containing high-level radioactive waste exploded, and about 90% (900 PBq) of the radionuclides in the tank were released and fallen in the area 300 km downwind over the next 11 h. Main released nuclides were $^{144}\text{Ce} + ^{144}\text{Pr}$ (66%), $^{95}\text{Zr} + ^{95}\text{Nb}$ (24.9%), $^{90}\text{Sr} + ^{90}\text{Y}$ (5.4%), $^{106}\text{Ru} + ^{106}\text{Rh}$ (3.7%), ^{137}Cs (0.036%), and trace amounts of ^{89}Sr , ^{147}Pm , ^{156}Eu , and $^{239,240}\text{Pu}$. 1,154 people lived in an area registering 40 MBq m⁻²; 1,500 in an area registering 4 MBq m⁻²; and 10,000 in an area registering 70 kBq m⁻². Within 10 days, 1,154 people escaped from the contaminated area, and in total 10,730 people escaped from that area. The collective dose is estimated to be 2,500 man-Sv in the contaminated area.

■ Fig. 55.4

Descriptive plume behavior and reported initial arrival times of detectable activity in air. Plumes A, B, and C correspond to air mass movements originating from Chernobyl on April 26, April 27–28, and April 29–30, respectively. The numbers 1–8 indicate initial arrival days from April 26 (UNSCEAR 1988c)



Windscale The Windscale (now called Sellafield) Reactor No. 1 was partially consumed by combustion in October 1957, resulting in the release of fission products to the surrounding countryside. The reactor was an air-cooled graphite-moderated natural-uranium reactor employed primarily for plutonium production. The radionuclides ^{131}I (740 TBq), ^{137}Cs (22 TBq), ^{106}Ru (3 TBq), and ^{133}Xe (1.2 PBq) were released. In addition to those fission products, 8.8 TBq of ^{210}Po was also released, because the nuclide was produced by neutron irradiation of bismuth. The released radionuclides moved from Windscale to the south, southeast, and to London, and they contaminated vast grasslands. The collective dose is estimated to be 2,000 man-Sv in the contaminated area.

■ Table 55.33

Deposition densities in some regions of countries (UNSCEAR 1988b)

Country	Deposition density/kBq m ⁻²				
	Ru-103	Ru-106	I-131	Cs-134	Cs-137
USSR, White Russia	41	808	590	21	39
USSR, Ukraine	17	206	480	807	15
Poland	13	1.6	38	2.6	5.2
Romania, Central	52	13	94	8.6	18
Hungary, Eastern	12	2.9	30	2.4	4.8
Bulgaria, Northern	9.9	2.6	4.2	2	3.9
Greece, Northern	33	3	36	4	8
Dem. Rep. Germany, Northern	14	1.8	19	2.9	6.1
Fed. Rep. Germany, NE	20	4.8	100	8	1.6
Austria	31	6.3	120	12	23
Sweden, Central	9.9	3.7	160	17	31
UK, Southern	0.18	0.06	0.8	0.05	0.1
USA	0.062	0.0079	0.15	0.013	0.026
China	0.21	0.044	0.29	0.075	0.15
India	0.073	0.01	0.044	0.01	0.035
Japan	0.45	0.09	1.6	0.087	0.18

Transport of Atomic Weapons

Palomares Four hydrogen bombs were released from a crashed airplane on January 17, 1966, and two fell slowly with a parachute and were recovered without damage. But the remaining two bombs crashed to the earth's surface because the parachute did not open, and their normal gunpowder exploded and considerable amounts of ²³⁹Pu and ²⁴⁰Pu were scattered in an area of 2.26 km² of urban areas and uncultivated farmlands. An area of 22,000 m² was contaminated by above 1.2 MBq m⁻² of alpha-emitting nuclides. Contaminated plants and soil (to a depth of 10 cm) were collected and treated as radioactive waste. The collective dose is estimated to be 3 man-Sv in the contaminated area.

Thule An airplane crashed on Thule in Greenland in January 1968 and four hydrogen bombs were exploded by their gunpowder. About 10 TBq of Plutonium was recovered from the snow surface, and about 1 TBq was estimated to be taken into ice. At about 20 km from the crash point, measurable plutonium was found in the summer of the year. The exposure was not estimated because the point is near the Arctic area and people do not live there.

Re-Entry of Satellites

SNAP-9A A navigator satellite was launched on April 21, 1964, but failed to reach orbital speed and reentered the atmosphere at about 45 km over Indian Ocean. The satellite carried an isotopic power unit known as SNAP-9A, which contained about 6,300 GBq of ²³⁸Pu. The ²³⁸Pu was first detected at an altitude of 30 km after 4 months, and was detected following 4 months.

The plutonium decreased exponentially with the half-life of about 14 months. The sizes of the particles ranged from 5 μm to 58 μm . The ^{238}Pu contents of ground level-air were measured and the collective effective dose from the ^{238}Pu exposure in the world is estimated as 2,100 man-Sv.

Cosmos-954 A satellite of the USSR, Cosmos-954, reentered the atmosphere over Northwest Canada on January 24, 1978. The satellite was believed to have contained 20 kg of highly enriched uranium. Released fission products were estimated since the reactor worked for 128 days at 100 kW. 75% of the particulate radionuclides were estimated to be dispersed in the atmosphere and 25% to be deposited on uninhabited regions in Northeast Canada. The vaporized radionuclides, ^{131}I and ^{137}Cs , were dispersed in the atmosphere. The collective effective dose was 20 man-Sv in the world.

Industrial and Medical Sources

Ciudad Juarez, Mexico A medical source of 16.7 TBq of ^{60}Co was discarded by mistake in December 1983 at Ciudad Juarez in Mexico, and the 6,000 pellets of that source contaminated many products of steel, which were sold in Mexico and the USA. About 1,000 people were exposed by this source and the collective effective dose was estimated to be 150 man-Sv.

Mochmedia, Morocco A ^{192}Ir source for the radiography of welding at construction sites was accidentally dropped in a street in September 1984, and a passenger picked it up and went home with it. All eight people of his household were exposed to 8–25 Sv and died, and the collective effective dose was estimated to be 80 man-Sv.

Goiania, Brazil A medical source of 50.9 TBq of ^{137}Cs was disposed of in September 1987 and was dismantled by a trader of scrap metal. Subsequently, 20 exposed people were hospitalized and 4 people died. For the decontamination, 42 houses were decontaminated and the total volume of 3,500 m^3 waste was produced and the collective effective dose was estimated to be 60 man-Sv.

Tokaimura, Japan A criticality accident took place at the Tokaimura nuclear fuel processing plant in Japan on September 30, 1999, because of improper procedures. During the 24-h event, and because of only limited shielding provided by the building, some direct irradiation was measurable outside the plant site. There was only a trace release of gaseous fission products. The collective effective dose was estimated to be 150 man-Sv. Three workers inside the plant were severely exposed (5.4 Gy of neutrons and 8.5 Gy of gamma-rays for Person A, 2.9 Gy of neutrons and 4.5 Gy of gamma-rays for Person B, and 0.81 Gy of neutrons and 1.3 Gy of gamma-rays for Person C). Person A and B eventually died of multiple organ failure after 82 and 210 days following the accident (Hirama et al. 2003).

55.5.4 Occupational Exposure

The definition of occupational exposure is given in ICRP Publication 103 as all radiation exposure of workers as a result of their work (ICRP 1997). The worldwide occupational exposures are reviewed in [Table 55.34](#).

■ Table 55.34

Worldwide occupational exposure (1990–1994), see UNSCEAR (2000v). Totals include other components as well

Practice	Number of monitored workers	Average annual collective effective dose/man-Sv	Average annual collective effective dose per unit energy generated/man-Sv (GWy) ⁻¹	Average effective dose/mSv	
				For monitored workers	Measurably exposed workers
Nuclear fuel cycle					
Mining	69	310	1.72	4.5	5
Milling	6	20	0.11	3.3	–
Enrichment	13	1	0.02	0.12	–
Fuel fabrication	21	22	0.1	1.03	2
Reactor operation	530	900	3.9	1.4	2.7
Reprocessing	45	67	3	1.5	2.8
Research	120	90	1	0.78	2.5
Total	800	1,400	9.8	1.75	3.1
Medical use of radiation					
Diagnostic radiology	950	470		0.5	1.34
Dental practice	265	16		0.06	0.89
Nuclear medicine	115	90		0.79	1.41
Radiotherapy	120	65		0.55	1.33
Total	2,320	760		0.33	1.39
Industrial use of radiation					
Radiography	106	170		1.58	3.17
Radioisotope production	24	47		1.93	2.95
Other	570	140		0.25	
Total	700	360		0.51	2.24
Natural radiation					
Coal mining	3,910	2,600		0.7	
Other mining	760	2,000		2.7	
Mineral processing, etc.	300	300		1	
Exposure above ground (Radon)	1,250	6,000		4.8	

■ **Table 55.34 (Continued)**

Practice	Number of monitored workers	Average annual collective effective dose/man-Sv	Average annual collective effective dose per unit energy generated/man-Sv (GWy) ⁻¹	Average effective dose/mSv	
				For monitored workers	Measurably exposed workers
Aircrew	250	800		3	
Total	6,500	11,700		1.8	
Defense activities					
Weapons	380	7.5		0.19	
Nuclear ships and support	40	25		0.82	
Total	420	100		0.24	
Miscellaneous uses of radiation					
Education	310	33		0.11	1.1
Veterinary medicine	45	8		0.18	0.62
Total	360	40		0.11	1
Total of all uses					
Man-made	4,600	2,700		0.6	2
Natural	6,500	11,700		1.8	
Total	11,100	14,000		1.26	

The monitoring practices for radiation workers differ from country to country and the dose recording and reporting practices also vary, e.g., the recording of the dose over the minimum detectable level (MDL), the subtraction of background radiation doses, whether or not internal exposures are included or treated separately.

55.5.4.1 The Nuclear Fuel Cycle

Uranium mining and milling The mining and milling of uranium ores can lead to both internal and external exposures of workers. Internal exposure may arise mainly from the inhalation of radon and its decay products. Higher doses from this source would be expected in the milling of ore and the production of yellowcake. Monitored workers number 69,000 men for mining and 6,000 men for milling and their average annual effective doses are 4.5 mSv and 3.3 mSv, respectively. Their doses are the highest except for the exposure by radon above ground. However, the exposure by radon is very obscure.

Uranium enrichment and conversion Yellowcake, U_3O_8 is converted to UF_6 and enriched in ^{235}U . The enrichment is carried out by the diffusion method or by the centrifugation of UF_6 . The occupational exposures occur during both conversion and enrichment, but average annual effective doses are rather small.

Fuel fabrication Enriched uranium gases are converted again to the metallic form or oxide fuels. The worldwide production of fuel has increased steadily and is 11.3 kt per year with equivalent annual energy figures of 210 GWy from 1990 to 1995. The average annual effective dose is 1.03 mSv.

Reactor operation The exposure doses during reactor operation also depend on the reactor types. The average annual effective doses to monitored workers are 1.34 mSv for PWR, 1.57 mSv for BWR, 1.74 mSv for HWR, and 0.54 mSv for GCR (► [Table 55.35](#)).

Fuel reprocessing Commercial-scale reprocessing of irradiated spent fuel from nuclear power facilities to recover uranium and plutonium is performed only in France and the UK. Some other countries such as Japan, India, and the Netherlands have small facilities. The used fuel elements contain high levels of radioactive materials. But remote operations and heavy shielding insure a low annual effective dose of 1.5 mSv for the workers.

Research in the nuclear fuel cycle It is difficult to estimate the level of occupational exposure to workers from research and development in the commercial nuclear fuel cycle, but evaluated from the data on those from 24 countries, the average annual effective dose is 0.78 mSv.

55.5.4.2 Medical Uses of Radiation

Diagnostic radiology Radiography is the most widely used X-ray imaging technique. Although doses to patients from diagnostic radiography may be high, the exposure of staff is usually low. The dose to a radiographer in the control booth area is typically less than 1 μ Sv for a single film taken with a technique of 80 kVp (the pressurized voltage) and 40 mAs

■ **Table 55.35**

Summary of worldwide exposure from reactor operation (1990–1994), see UNSCEAR (2000y)

Reactor type	PWR	BWR	HWR	LWGR	GCR	Total (Ave.)
Average number of reactors	242	90	31	20	38	421
Average annual energy generated/GWy	149	50	12	9.4	8.4	230
Number of monitored workers/1,000	310	160	20		30	530
Average annual collective effective dose/man-Sv	415	240	35	190	16	900
Collective effective dose per reactor/man-Sv	1.7	2.7	1.1	9.4	0.4	(2.1)
Collective effective dose per energy generated/ man-Sv (GWy) ⁻¹	2.8	4.8	3	20.3	2	(3.9)
Average annual effective dose to monitored workers/mSv	1.3	1.6	1.7		0.5	(1.4)
Annual average dose to measurably exposed workers/mSv	2.5	2.9	4.4			(2.7)

(the current). The annual average individual dose for monitored workers in diagnostic radiology is estimated to be 0.50 mSv for 630,000 workers.

Dental practice In almost every dental office, a diagnostic X-ray machine is available and frequently used. Most dental practitioners do not receive a measurable dose. The annual dose for 370,000 monitored workers is probably very low and is estimated to be 0.06 mSv.

Nuclear medicine Radionuclides used for organ imaging emit penetrating gamma radiation and give rise to an exposure of the nuclear medicine staff and other persons in the vicinity of patients undergoing diagnosis or treatment. For example, the dose rate at a distance of 1 m from a typical diagnostic patient is about $10 \mu\text{Sv h}^{-1}$ after the administration of 0.74 GBq of $^{99\text{m}}\text{Tc}$. Therapeutic administrations, e.g., 3.7 GBq of ^{131}I , give rise to a dose rate about $200 \mu\text{Sv h}^{-1}$ at 1 m from the patient. Then the annual average individual dose of 115,000 workers in this field is 0.79 mSv, which is the highest in the group of medical workers.

Radiotherapy Radiotherapy is an important treatment modality for malignant disease. The annual average effective dose to monitored workers in radiotherapy fell over the four 5-year-periods (from 1975 to 1994) consistently with the values of 2.2 mSv, 1.6 mSv, 0.87 mSv, and 0.55 mSv. Some of this decrease will have been due to improvements in radiological protection arrangements, following the replacement of many ^{226}Ra sources by ^{137}Cs and the widespread use of remote handling after loading the equipment.

55.5.4.3 Industrial Use of Radiation

Industrial irradiation There are 160 gamma-irradiation facilities and over 600 electron-beam facilities in operation in the world. Most facilities are for the sterilization of medical and pharmaceutical products, the preservation of foodstuffs, polymer synthesis and modification, and the eradication of insect infestation. Dose rates in the irradiation chamber would be of the order of 1 Gy s^{-1} . Therefore, there is a need for sophisticated engineered safety systems, and during normal usage the exposure of workers should be very low. The average annual effective dose of 57,200 monitored workers in 15 countries is 0.10 mSv.

Industrial radiography Industrial radiography is carried out in two different ways. In the first case, the source is located in a facility and the items to be radio-graphed are brought to the facility. In the second case, the source is brought to the location where the radiography is required. The most common sealed sources are 1.8–4.4 TBq of ^{192}Ir , 0.3 GBq of ^{60}Co , and 0.3–80 GBq of ^{137}Cs .

In fixed radiography facilities, the shielding and engineered safety systems should ensure low doses, but site radiography is often undertaken in remote, difficult, or even hostile environments. In addition, the supervision tends to be poor. The average annual effective dose for monitored workers is 1.58 mSv and that for the measurably exposed workers is 3.17 mSv, which is considerably higher and may be attributed to high exposure rates to workers of site radiography.

Radionuclide production and distribution Radionuclides are produced for a great variety of industrial and medical purposes. This industry is mature and well established, with multinational companies replacing the often nationally focused entities that prevailed in earlier years. In the manufacture and processing of radionuclides there is the potential for both internal and external exposure, but the internal component is not always apparent. In general, the contribution of internal exposure to the total was reported to be a few percents. The monitored workers' dose rate is rather small, but the average annual effective dose is 1.93 mSv, which is larger than that for radiography.

Others In the fields of luminizing, well logging, and accelerator operating, occupational radiation exposures are observed. Radioactive materials have been used in luminizing, but the shift from radium to tritium reduced the occupational dose significantly. Both gamma and neutron sources are used in well logging. The annual effective dose to monitored workers for 1990–1994 is 0.36 mSv. The distribution ratios of the effective doses indicate that the majority get a low dose, but some receive more significant doses.

55.5.4.4 Natural Sources of Radiation

Aircrew An aircrew is exposed to elevated levels of cosmic radiation, and ICRP Publication 60 (ICRP 1991a) recommended that the exposure of the aircrew in a jet aircraft should be treated as an occupational exposure. The effective dose rate at an altitude of 8 km in temperate latitudes is typically up to about $3 \mu\text{Sv h}^{-1}$, and at 12 km about $6 \mu\text{Sv h}^{-1}$. The effective doses in one flight on short-haul routes for 70–190 min are 3–10 μSv , and those on long-haul routes for 450–760 min are 25–70 μSv . The average annual effective dose is typically 1–2 mSv for those on short-haul flight and 3–5 mSv for those on long-haul flights. The average annual effective doses of aircrews in civil aviation are in the range of 2–4 mSv for 27,300 persons, measured mainly in the UK.

Mining and the processing industries The main source of radiation exposure in most mining operations is radon. The levels of radon in workplaces are exceptionally variable. Mining is an extensive industry, and there are about 4.7 million underground miners worldwide, and about 84% of them are engaged in coal mining. The exposure to radon progeny depends on a number of factors, including the type of mine, the geology, and the working conditions, particularly the ventilation. The average effective dose to coal miners from radon was 0.7 mSv in 1990–1994. A survey of non-coal mines that covers about 1,300 miners indicated an average annual dose of 2.7 mSv.

Exposures to radon progeny may be important in some above ground workplaces. Radon exposures are largely determined by the geology underlying the building, its construction, and the ventilation. These exposures are estimated to contribute to the annual average effective dose of 4.8 mSv, which is the largest dose in occupational exposure. But this is clearly very obscure and country-to-country variable such as geology, building material, configurations, and regulations could have a significant effect.

Totally 4.6 million people are exposed to 0.6 mSv from man-made sources and 6.5 million people are exposed to 1.8 mSv from natural sources.

55.6 Measures in Nuclear Emergency

55.6.1 Averted Dose and Action Levels

55.6.1.1 Principles for Intervention in Emergency

In accidents, there is a possibility for deterministic (non-stochastic) and stochastic health effects. The principles for planning intervention in the case of a radiation emergency are set out in ICRP Publication 60 and 63 (ICRP 1991a, b, respectively). Intervention is the term applied to steps taken, in an accident situation, to restrict the exposure of member of the public and to minimize the consequences of unavoidable exposure. The assessment of the radiological situation and the implementation of the individual protection measures make up an overall protection strategy that is recommended to be justified and optimized. In the process of optimization, reference levels are to be applied and particular attention should be given to the prevention of severe deterministic health effects.

Emergency response is a process that develops in time according to the different phases of the emergency exposure situation:

1. *The early phase* is the period from the time when potential for off-site exposure of the public is recognized, to the time when significant amounts of radioactive material are released, and the first few hours after the commencement of that release.
2. The second stage, *the intermediate phase*, covers that period of time from the first few hours to a few days after the onset of the accident. It starts with the cessation of any release and regaining control of the source of releases.
3. The third stage, *the late or recovery phase* is the one in which decisions are made concerning the return to normal living conditions and it may extend over a prolonged period.

55.6.1.2 The Concept for Intervention

The *projected dose* (PD) is the overall exposure to the population, which is projected to occur as a result of the exposure situation if no protective actions are implemented and should first be estimated for each exposure pathway (ICRP 1991b). The dose that would result when the protection strategy is implemented is called the *residual dose* (RD). The difference dose from each pathway (projected dose minus residual dose) is called the *averted dose* (AD). This is the dose saved by implementing a given protective action and is the concept for the optimization of the protective measures that will make up the overall protection strategy.

55.6.2 Categorization of Radiological Emergencies for Planning Intervention

Radiological emergencies are classified according to exposure pathways. Exposure of the public and workers to radiation following an accident may be either external or internal, or both and may be incurred by various pathways. The pathways of external exposure are derived from the source or the facility, the plume, the radionuclide contamination on surfaces, and radionuclide contamination of skin and clothing. Those of internal exposure are the inhalation of radionuclides in a plume, the inhalation of re-suspended radionuclides, the ingestion of

contaminated food and water, the ingestion of radionuclides from contaminated materials, and the absorption through skin and wounds.

The temporal and spatial aspects of radiological emergencies are also important in planning the appropriate emergency response. The protective actions for averting exposure via various pathways are as follows (ICRP 1991c).

Control of access External irradiation from the source, plume, and/or radionuclides (abbreviated as RI from radioisotope) deposited.¹⁵

- Inhalation or ingestion of RI in the plume and/or re-suspended RI.
- External contamination of the individual.

Shielding External irradiation from the source, plume, and/or RI deposited.

Protective clothing External contamination.

Sheltering External irradiation from the source, plume, and/or RI deposited.

- Inhalation of RI in the plume.
- External contamination of individuals.

Evacuation External irradiation from the source, plume, and RI deposited.

- Inhalation or ingestion of RI in the plume and/or re-suspended RI.
- External contamination of individuals.

Stable iodine administration Inhalation of radioiodine in the plume.

Decontamination of individuals and clothing External contamination.

Intervention in food chain and water supply Ingestion of RI.

- Restriction on food and water, banning consumption, processing of food/water.
- Decreasing RI incorporation into the food chain, alternative fodder, binders, deep plowing and other change in agricultural practice, temporary fixation in ground (e.g., spraying): inhalation of re-suspended RI.

Relocation External irradiation from RI deposited on the ground.

- Inhalation and ingestion of re-suspended RI.

Decontamination of materials and controls on use of contaminated materials Inadvertent ingestion.

Decontamination of ground and other surfaces External irradiation

- Inhalation of re-suspended RI.

55.6.3 Intervention Levels

For intervention measures, it is important that subjective judgments are made within a widely agreed framework. For this reason, national and international organizations have published generic guidance on dose criteria for intervention, particularly for intervention following accidents.

They have produced some recommended generic intervention levels, these levels satisfy the basic principles in that deterministic effects are avoided and the intervention is justified in generic terms that the risks of implementing the interventions are less than the risks of the dose that would be received.

The intervention levels of averted doses recommended by ICRP are those at which intervention is almost always justified. In the early phase, these doses are 50 mSv for sheltering, 500 mSv equivalent dose to thyroid for administration of stable iodine, 500 mSv (1 week) whole body dose or 5,000 mSv equivalent dose to skin for evacuation (ICRP 1991d). For the late phase countermeasures 1,000 mSv for relocation (5–15 mSv per month for prolonged exposure), and 10 mSv (in 1 year) for restriction to a single foodstuff (1,000–10,000 Bq kg⁻¹ for beta/gamma emitters and 10–100 Bq kg⁻¹ for alpha emitters) are recommended.

55.6.4 Protection of Workers for Intervention

The working conditions in relation to the actions required following an accident are divided into three categories (ICRP 1991d).

Category 1 (Urgent action at the site of the accident.) Workers in this category must act to save life, to prevent serious injuries, or to prevent a substantial increase in potential doses to members of the public. They should keep the doses below 1 Sv effective dose or 5 Sv equivalent dose to skin for all actions except life-saving action.

Category 2 (Implementing early protective actions and taking action to protect the public.) This group consists of workers who will incur additional exposure in order to avert doses to the public, such as police, medical personnel, drivers, and crews of vehicles used for evacuation and similar group. Ideally, the aim should be to keep the doses below those permitted in normal conditions.

Category 3 (Recovery operation.) The workers of this category undertake recovery operations. The actions required may include repairs to plant and building, waste disposal, decontamination of the site, and the surrounding area. The workers in this group should be subjected to the normal system of radiological protection for occupational exposure.

55.7 Editors' Notes

1. NAA including RNAA is detailed in ➤ Chap. 30 in Vol. 3 on “Activation Analysis” (p. 2506).
2. See ➤ Chap. 13 in Vol. 2 on “Natural Radioactive Decay Chains” (p. 2506).
3. See ➤ Chap. 12 in Vol. 2 on “The Origin of the Chemical Elements” (p. 2507).
4. See ➤ Chap. 17 in Vol. 2 on “Radioactive Dating Methods” (p. 2507).
5. See ➤ Table 61.3 in Chap. 61 in Vol. 6 on “Radioactive Waste Management” (p. 2507).

6. The concentration factor for aquatic biota is defined by [▶ Eq. \(55.3\) in Sect. 55.4.2.](#) (p. 2508).
7. As regards the other nuclide, ^{127}I , it is the only stable isotope of iodine. On the other hand, the time elapsed since the Earth was formed ($\sim 4.5 \times 10^9$ years) leaves about 280 half-lives for ^{129}I to be erased from the planet. Assuming an initial $^{129}\text{I}/^{127}\text{I}$ ratio of 1, the present ratio would be $\sim 5 \times 10^{-85}$ compared to which the value 10^{-12} is really enormous (p. 2509).
8. ^{129}I together with ^{129}Xe could also make a precise geochronometer as mentioned in [▶ Chap. 17](#) in Vol. 2 on “Radioactive Dating Methods” (p. 2510).
9. Exposure in general and dose-related quantities and units are detailed in [▶ Chap. 47](#) in this Volume on “Dosimetry and Biological Effects of Ionizing Radiation” (p. 2527).
10. For the explanation of the historical names of radon isotopes such as “thoron” (^{220}Rn) and “radon” (^{222}Rn) see the introduction of [▶ Chap. 13](#) in Vol. 2 on “Natural Radioactive Decay Chains” (p. 2531).
11. See [▶ Fig. 4.10 in Chap. 4](#) in Vol. 1 on “Nuclear Fission” (p. 2540).
12. Ternary decay is discussed in detail in [▶ Sect. 4.4.4, Chap. 4](#), Vol. 1 (p. 2540).
13. For more details see [▶ Sect. 57.4 in Chap. 57](#) in Vol. 6 on “Technical Application of Nuclear Fission.” See also [▶ Sect. 58.2 in Chap. 58](#) in Vol. 6 on “Developments and Tendencies in Fission Reactor Concepts” (p. 2544).
14. See also [▶ Chap. 61](#) in Vol. 6 on “Radioactive Waste Management” (p. 2546).
15. In various applications, and particularly in nuclear medicine, the term radioisotope is used in the sense “radionuclide” (p. 2559).

References

- Aarkrog A, Baxter MS, Bettencourt AO, Bojanowski R, Bologna A, Charmasson S, Cunha I, Delfanti R, Duran E, Holm E et al (1997) *J Environ Radioactiv* 34:69
- Aarkrog A, Dahlgard H, Nielsen SP (1999) *Sci Total Environ* 237/238:143
- Alam MN, Chowdhury MI, Kamal M, Ghose S (1995) *Appl Radiat Isot* 46:363
- Alonso-Hernandez C, Diaz-Asencio M, Munos-Caravaca A, Suarez-Morell E, Avila-Moreno R (2002) *J Environ Radioactiv* 61:203
- Altiztzioglou T (2000) *Appl Radiat Isotopes* 52:539
- Barnaby F, Boeker E (1999) *Med Confl Surviv* 15:57
- Baskaran M, Shaunna A, Jon S, Peter S, Santschi MA, Champ MA, Brooks JM, Adkinson D, Makeyev V (2000) *Mar Pollut Bull* 40:830
- Baudin JP, Adam C, Garnier-laplace J (2000) *Wat Res* 34:2869
- Bergan TD (2002) *J Environ Radioactiv* 60:189
- Biomovs (1996) Biosphere modeling for dose assessments of radioactive waste repositories. Report of the complementary studies working group, BIOMOVs II Tech. Rept. 12 and 17, Swedish Radiation Protection Institute, Stockholm
- Boisson F, Miquel J-C, Cotret O, Fowler SW (2001) *Sci Total Environ* 281:111
- Boyera C, Vichotb L, Frommc M, Lossetb Y, Tatin-Frouxa F, GUÉTATB P, Badota PM (2009) *Environ Exp Bot* 67:34
- Cohen BL (1985) *Health Phys* 49:279
- Cooper LW, Kelley JM, Bond LA, Orlandini KA, Grebmeier JM (2000) *Mar Chem* 69:253
- Cooper LW, Hong GIH, Beasley TM, Grebmeier JM (2001) *Mar Pollut Bull* 42:1347
- Cunha ILL, Figueira RCL, Saito T (1999) *J Radioanal Nucl Chem* 239:477
- Deng Z, Xie L, Liu B, Wua K, Zhao D, Yu T (2009) *Ocean Model* 29:261
- Donaldson LR, Seymour AH, Nevissi AE (1997) *Health Phys* 73:214
- Edmonds HN, Smith JN, Livingston HD, Kilius LR, Edmond JM (1998) *Deep Sea Res Pt 1* 45:1111
- European Commission (2008) Implied doses to the population of the EU arising from reported discharges from EU nuclear power stations and reprocessing sites in the years 1997 to 2004. Radiation protection no. 153, DG TREN- Directorate H – Nuclear Energy Unit H.4 – Radiation Protection

- Finegan P, Vintró LL, Mitchell PI, Boust D, Gouzy A, Kershaw PJ, Lucey JA (2009) *Cont Shelf Res* 29:1995
- Feng H, Cochran JK, Hirschberg DJ (1999) *Sci Total Environ* 237–238:401
- Galvez F, Mayer GD, Wood CM, Hogstrand C (2002) *Comp Biochem Phys C* 131:367
- Gasco' C, Antón MP, Pozuelo M, Meral J, Gonza'lez AM, Papucci C, Delfaniti R (2002) *J Environ Radioactiv* 59:75
- Hameed PS, Shaheed K, Somasundaram SSN, Iyenger MAR (1997) *J Environ Radioactiv* 37:17
- Hamilton EI (1999) *J Environ Radioactiv* 44:297
- Haque MA, Nakanishi T (1999) *J Radioanal Nucl Chem* 239:565
- Hayashi Y, Momoshima N, Maeda Y, Kakiuchi H (1999) *J Radioanal Nucl Chem* 239:517
- Hirama T, Tanosaki S, Kandatsu S, Kuroiwa N, Kamada T, Tsuji H, Yamada S, Katoh H, Yamamoto N, Tsujii H, Suzuki G, Akashi M (2003) *Brit J Radiol* 76:246
- Hirose K, Igarashi Y, Aoyama M (2008) *Appl Radiat Isot* 66:1675
- Hong GH, Kim YI, Lee SH, Cooper LW, Choe SM, Tkalin V, Lee T, Kima SH, Chung CS, Hirose K (2002) *Mar Pollut Bull* 44:660
- Hou X, Dalgaard H, Nielsen SP (2001) *Mar Chem* 74:145
- Hosseini A, Thørring H, Brown JE, Saxén R, Ilus E (2008) *J Environ Radioactiv* 99:1408
- Hotzl H, Rosner G, Winkler R (1991) *Naturwissenschaften* 78:215
- IAEA (1985) Technical report series no. 247, International Atomic Energy Agency, Vienna
- IAEA (2006) Environmental consequences of the chernobyl accident and their remediation twenty years of experience. Report of the Chernobyl Forum Expert Group "Environment", International Atomic Energy Agency, Vienna
- ICRP (1991) 1990 Recommendations of the international commission on radiological protection. ICRP publication 60. *Ann ICRP* 21(1–3)
- ICRP (1991a) Principles for intervention for protection of the public in a radiological emergency. ICRP publication 63. *Ann ICRP* 22(4):2
- ICRP (1991b) Principles for intervention for protection of the public in a radiological emergency. ICRP publication 63. *Ann ICRP* 22(4):11
- ICRP (1991c) Principles for intervention for protection of the public in a radiological emergency. ICRP publication 63. *Ann ICRP* 22(4):23
- ICRP (1992) Principles for intervention for protection of the public in a radiological emergency. ICRP publication 63. *Ann ICRP* 22(4):25
- ICRP (2007) The 2007 recommendations of the international commission on radiological protection, ICRP publication 103. *Ann ICRP* 37(2–4):83
- ICRP (2008) Environmental protection: the concept and use of reference animals and plants, ICRP publication 108. *Ann ICRP* 38(4–6)
- Igarashi Y, Aoyama M, Miyao T, Hirose K, Tomita M (1999) *J Radioanal Nucl Chem* 239:539
- Iosjpe M, Brown J, Strand P (2002) *J Environ Radioactiv* 60:91
- Ishikawa Y, Kikuchi T, Sekine T, Yoshihara K (1995) *J Radioanal Nucl Chem* 197:343
- Jobbágy V, Norbert Kávási N, Somlai J, Máté B, Kovács T (2010) *Microchem J* 94:159
- Kakiuchi H, Momoshima N, Okai T, Maeda Y (1999) *J Radioanal Nucl Chem* 239:523
- Kalinowski M-B, Tuma MP (2009) *J Environ Radioactiv* 100:58
- Kryshev II (1997) *Fuel Energy Abstr* 38:52
- Kryshev II, Romanov GN, Isaeva LN, Kholina YuB (1997) *J Environ Radioactiv* 34:223
- Kulan A, Aldahan A, Possnert G, Vintersved I (2006) *Atmos Environ* 40:3855
- Kuo YC, Lai SY, Huang CC, Lin YM (1997) *Appl Radiat Isotopes: Including Data, Instrumentation and Methods for use in Agriculture, Industry and Medicine* 48:1245
- L'annunziata MF (2003) *Handbook of radioactivity analysis*, 2nd edn. Academic, New York
- Larsson CM (2008) *J Environ Radioactiv* 99:1364
- Lee MH, Lee CW (1999) *J Radioanal Nucl Chem* 239:471
- Lind OC, Oughton DH, Salbu B, Skipperud L, Sickel MA, Brown JE, Fifield JK, Tims SG (2006) *Earth Planet Sci Lett* 251:33
- Lindahl P, Lee S-H, Worsfold P, Keith-Roach M (2009) *Mar Environ Res* (in press)
- Livingston HD, Povinec PP (2000) *Ocean Coast Manage* 43:689
- Mabit L, Benmansour M, Walling DE (2008) *J Environ Radioactiv* 99:1799
- Marovi G, Senar J, Frani Z, Lokobauer N (1996) *J Environ Radioactiv* 33:309
- Matishov GG, Matishov DG, Namjatov AA, Alexey A, Carroll J, Dahle S (2002a) *J Environ Radioactiv* 59:309
- Matishov GG, Matishov DG, Namjatov AA, Carroll J, Dahle S (2002b) *J Environ Radioactiv* 48:5
- Mavall A (2003) *Radioactiv Environ* 4:13
- McDonald P, Cook G, Baxter MS (1991) *Radionuclides in the study of Marine processes*. Elsevier Applied Science, London/New York
- Molero J, Sanchez-Cabeza JA, Merino J, Mitchell PI, Vidal-Quadras A (1999) *J Environ Radioactiv* 43:357
- Momoshima N, Kakiuchi H, Okai T, Yokoyama S, Noguchi H, Atarashi M, Amano H, Hisamatsu S, Ichimasa M, Ichimasa Y, Maeda Y (1999) *J Radioanal Nucl Chem* 239:459

- Momoshima N, Yamaguchi T, Toyoshima T, Nagao Y, Takahashi M, Takamura M, Nakamura Y (2007) *J Nucl Radiochem Sci* 8:117
- Montea L, Periañez R, Boyerc P, Smith JT, Brittain JE (2009) *J Environ Radioactiv* 100:779
- Muramatsu Y, Yoshida S, Tanaka A (2001) *J Nucl Radiochemical Sci* 2(Suppl):151
- Nagao S, Matsunaga T, Muraoka S (1999) *J Radioanal Nucl Chem* 239:555
- Noureddine A, Baggoura B (1997) *Fuel Energy Abst* 38:52
- Noureddine A, Baggoura B, Hocini N, Boulahdid M (1998) *Appl Radiat Isotopes: Including Data, Instrumentation and Methods for use in Agriculture, Industry and Medicine* 49:1745
- Osaki S, Tagawa Y, Chijiwa T, Sugihara S, Maeda Y (1999) *J Radioanal Nucl Chem* 239:543
- Osvath I, Povinec PP, Baxter MS (1999) *Sci Total Environ* 237/238:167
- Ould-Dada Z, Fairlie I, Read C (2001) *J Environ Radioactiv* 52:159
- Papastefanou C (2001) *J Environ Radioactiv* 53:67
- Paunescu N, Cotarlea M, Galerie D, Margineanu R, Mocanu N (1999) *J Radioanal Nucl Chem* 239:465
- Poole AJ, Allington DJ, Baxter AJ, Young AK (1995) *Appl Radiat Isotopes: Including Data, Instrumentation and Methods for use in Agriculture, Industry and Medicine* 173–174:137
- Povinec PP, Woodhead D, Blowers P, Bonfield R, Cooper M et al (1999) *Sci Total Environ* 237–238:249
- Povinec PP, Oregoni B, Jull AJT, Kieser WE, Zhao X-L (2000) *Nucl Instrum Meth B* 172:672
- Pyle GG, Clulow FV (1998) *J Environ Radioactiv* 40:59
- Raisbeck GM, Yiou F (1999) *Sci Total Environ* 237/238:31
- Rapiejko A, Rosson R, Lahr J, Garcia R, Kahn B (2001) *Health Phys* 81:698
- RSDJ (2002) Radioactivity survey data in Japan, 2002, (Published by National Institute of Radiological Science), (ISSN 0441-2516) references in ref. HAQUE 1999
- Saey PRJ (2009) *J Environ Radioactiv* 100:396
- Salbu B (2009) *J Environ Radioactiv* 100:281
- Sam AK, Ahamed MMO, El Khangi FA, El Nigumi YO, Holm E (1998) *Mar Pollut Bull* 36:19
- Sanchez-Cabeza JA, Ortega M, Merino J, Masqu P (2002) *J Marine Syst* 33–34:457
- Sazykina TG, Kryshev II (1997) *Sci Total Environ* 202:57
- Schell WR, Tobin MJ, Marsan DJ, Schell CW, Vives-batlle J, Yoon SR (1997) *Nucl Instrum Meth A* 385:277
- Shutov VN, Travnikove IG, Bruk GYA, Golikov VY, Balonov MI et al (2002) 61:91
- Smith V, Fegan M, Pollard D, Long S, Hayden E, Ryan TP (2001) *J Environ Radioactiv* 56:269
- Smith JT, Kudelsky AV, Ryabov IN, Daire SE, Boyer L, Blust RJ, Fernandez JA, Hadderingh RH, Voitsekhovitch OV (2002) *J Environ Radioactiv* 62:145
- Snyder G, Fehn U (2004) *Nucl Instrum Meth B* 223–224:579
- St-pierre S, Chambers DB, Lowe LM, Bontoux JG (1999) *Health Phys* 77:313
- Stewart NG et al (1957) United Kingdom Atomic Energy Authority, Research Group, Report MP/R2354
- Strand P, Brown JE, Drozhko E, Mokrov Yu, Salbu B, Oughton D, Christensen GC, Amundsen I (1999) *Sci Total Environ* 241:107
- Styro D, Bumeliene Z, Lukinskiene M, Morkuniene R (2001) *J Environ Radioactiv* 53:27
- Sugihara S, Osaki S, Baba T, Tagawa Y, Maeda Y, Inokura Y (1999) *J Radioanal Nucl Chem* 239:549
- Tsukada H, Hasegawa H, Hisamatsu S, Yamasaki S (2002) *J Environ Radioactiv* 59:351
- UNSCEAR (1988a) Sources, effects and risks of ionization radiation. United Nations, New York, p 344
- UNSCEAR (1988b) Sources, effects and risks of ionization radiation. United Nations, New York, p 313
- UNSCEAR (1988c) Sources, effects and risks of ionization radiation. United Nations, New York, p 314
- UNSCEAR (1988d) Sources, effects and risks of ionization radiation. United Nations, New York, p 350
- UNSCEAR (1993a) Sources and effects of ionizing radiation. United Nations, New York, p 69
- UNSCEAR (1993b) Sources and effects of ionizing radiation. United Nations, New York, p 73
- UNSCEAR (1993c) Sources and effects of ionizing radiation. United Nations, New York, p 80
- UNSCEAR (1993d) Sources and effects of ionizing radiation. United Nations, New York, p 206
- UNSCEAR (1996) Sources and effects of ionizing radiation. United Nations, New York
- UNSCEAR (2000a) Sources and effects of ionizing radiation. United Nations, New York
- UNSCEAR (2000b) Sources and effects of ionizing radiation. United Nations, New York, p 8
- UNSCEAR (2000c) Sources and effects of ionizing radiation. United Nations, New York, p 140
- UNSCEAR (2000d) Sources and effects of ionizing radiation. United Nations, New York, p 113
- UNSCEAR (2000e) Sources and effects of ionizing radiation. United Nations, New York, p 117
- UNSCEAR (2000f) Sources and effects of ionizing radiation. United Nations, New York, p 121
- UNSCEAR (2000g) Sources and effects of ionizing radiation. United Nations, New York, p 130
- UNSCEAR (2000h) Sources and effects of ionizing radiation. United Nations, New York, p 297
- UNSCEAR (2000i) Sources and effects of ionizing radiation. United Nations, New York, p 394
- UNSCEAR (2000j) Sources and effects of ionizing radiation. United Nations, New York, p 393
- UNSCEAR (2000k) Sources and effects of ionizing radiation. United Nations, New York, p 384

- UNSCEAR (2000l) Sources and effects of ionizing radiation. United Nations, New York, p 385
- UNSCEAR (2000m) Sources and effects of ionizing radiation. United Nations, New York, p 464
- UNSCEAR (2000n) Sources and effects of ionizing radiation. United Nations, New York, p 205
- UNSCEAR (2000o) Sources and effects of ionizing radiation. United Nations, New York, p 213
- UNSCEAR (2000p) Sources and effects of ionizing radiation. United Nations, New York, p 224
- UNSCEAR (2000q) Sources and effects of ionizing radiation. United Nations, New York, p 232
- UNSCEAR (2000r) Sources and effects of ionizing radiation. United Nations, New York, p 221
- UNSCEAR (2000s) Sources and effects of ionizing radiation. United Nations, New York, p 235
- UNSCEAR (2000t) Sources and effects of ionizing radiation. United Nations, New York, p 278
- UNSCEAR (2000u) Sources and effects of ionizing radiation. United Nations, New York, p 279
- UNSCEAR (2000v) Sources and effects of ionizing radiation. United Nations, New York, p 282
- UNSCEAR (2000w) Sources and effects of ionizing radiation. United Nations, New York, p 284
- UNSCEAR (2000x) Sources and effects of ionizing radiation. United Nations, New York, p 647
- UNSCEAR (2000y) Sources and effects of ionizing radiation. United Nations, New York, p 577
- UNSCEAR (2008) Report of the United Nations Scientific Committee on the effects of atomic radiation, report to the general assembly fifty-sixth session (10–18 July 2008). United Nations, New York
- van Netten C, Hopton Cann SA, Morleyd DR, van Netten JP (2000) *Sci Total Environ* 255:169
- Varga B, Tarján S, Vajda N (2008) *J Environ Radioactiv* 99:641
- Wang J, Mooers CNK (1997) *Dyn Atmos Oceans* 27:135
- Watson WS, Sumner DJ, Baker JR, Kennedy S, Reid R, Robinson I (1999) *Sci Total Environ* 234:1
- Wawick PE, Cundy AB, Croudace IW, Bains ME, Dale AA (2001) *Environ Sci Technol* 35:2171
- Winkelmann I, Romanov GN, Goloshapov P, Gesewsky P, Mundigl S, Buchrlér H, Thomas M, Brummer C, Burkart W (1998) *Radiat Environ Bioph* 37:57
- Winpenny K, Knowles JF, Smith DL (1998) *J Environ Radioactiv* 38:211
- Yiou F, Raisbeck GM, Christensen GC, Holm E (2002) *J Environ Radioactiv* 60:61
- Yu KN, Mao SY, Young EC, Stokes MJ (1997) *Applied Radiation and Isotopes: Including Data, Instrumentation and Methods for use in Agriculture, Industry and Medicine* 48:515

56 Appendix – Reference Data to Part V

R. B. Firestone¹ · G. L. Molnár^{2,†}

¹Lawrence Berkeley National Laboratory, Berkeley, California, USA

²Chemical Research Center, Budapest, Hungary

56.1	<i>Standards for Detector Calibration</i>	2566
56.1.1	X- and Gamma-Ray Sources	2566
56.1.1.1	Wavelengths and Energies	2566
56.1.1.2	Energy and Intensity Standards	2569
56.1.2	Electron and Alpha Sources	2575
56.2	<i>Fission Product Yields</i>	2575

[†]Deceased

56.1 Standards for Detector Calibration

Richard B. Firestone · Gábor L. Molnár

56.1.1 X- and Gamma-Ray Sources

56.1.1.1 Wavelengths and Energies

The latest values of the fundamental constants for *X-ray standards* are grouped in ▶ [Table 56.1](#). The conversion of wavelengths to energies in keV is done by multiplying the reciprocal wavelength with the conversion factor $1.239841857(49) \times 10^{-9}$ keV m (Mohr and Taylor 1999, 2000; CODATA 2003). The database of X-ray wavelengths for elements (Bearden 1967) has recently been updated, adjusted to the new standards, and compared with new calculations using the Dirac–Fock method (Deslattes et al. 2003a). Their values of X-ray energies for neon ($Z = 10$) to fermium ($Z = 100$) are also available on the Internet (Deslattes et al. 2003b).

The most accurate γ -ray energies have been measured with crystal spectrometers and rely on the Si lattice constant (see ▶ [Table 56.1](#)). In their evaluation of *γ -ray energies for calibration standards*, Helmer and van der Leun (2000) used the 1986 values of the fundamental constants. Using their published data it can be estimated that after the adjustments of lattice parameter and conversion factor the energy of the ^{198}Au decay γ -ray, used as the standard, decreases from 411.80205(17) keV to about 411.80176(12) keV, i.e., by only 0.3 eV (0.7 ppm). This change is less than twice the standard uncertainty, hence the recommended energy values in Helmer and van der Leun (2000), relying on this standard, are practically unaffected.

■ Table 56.1

Fundamental constants for X-ray standards (Mohr and Taylor 1999, 2000)

Quantity	Symbol	Value	Unit	Relative std. uncert. u_r
Cu x unit: $\lambda(\text{CuK}\alpha_1)/1\,537.400$	$xu(\text{CuK}\alpha_1)$	$1.00207703(28) \times 10^{-13}$	m	2.8×10^{-7}
Mo x unit: $\lambda(\text{MoK}\alpha_1)/707.831$	$xu(\text{MoK}\alpha_1)$	$1.00209959(53) \times 10^{-13}$	m	5.3×10^{-7}
Ångstrom star: $\lambda(\text{WK}\alpha_1)/0.2090100$	\AA^*	$1.00001501(90) \times 10^{-10}$	m	9.0×10^{-7}
Lattice parameter ^a of Si (in vacuum, 22.5°C)	a	$543.102088(16) \times 10^{-12}$	m	2.9×10^{-8}
{220} lattice spacing of Si: $a/\sqrt{8}$ (in vacuum, 22.5°C)	d_{220}	$192.0155845(56) \times 10^{-12}$	m	2.9×10^{-8}
Molar volume of Si: $M(\text{Si})/\rho(\text{Si}) = N_A a^3/8$ (in vacuum, 22.5°C)	$V_m(\text{Si})$	$12.0588369(14) \times 10^{-6}$	m ³ /mol	1.2×10^{-7}

^a This is the lattice parameter (unit cell edge length) of an ideal single crystal of naturally occurring Si free of impurities and imperfections, and is deduced from lattice spacing measurements on extremely pure and nearly perfect single crystals of Si by correcting for the effects of impurities.

■ Table 56.2

Some radionuclides recommended for calibration of γ -ray detectors

Nuclide	Half-life ^a	Decay mode	Source type	E_{\min}	E_{\max}
²² Na	2.6027 (10) a	β^+	s	511	1,275
²⁴ Na	14.9574 (20) h	β^-	s	1,369	2,754
⁴⁶ Sc	83.788 (20) d	β^-	s	1,121	1,121
⁵¹ Cr	27.703 (3) d	EC	s	320	320
⁵⁴ Mn	312.13 (3) d	EC	s	835	835
⁵⁶ Mn	2.5824 (48) h	β^-	m	847	2,523
⁵⁵ Fe	2.741 (6) a	EC	s	6	6
⁵⁹ Fe	44.495 (8) d	β^-	m	143	1,292
⁵⁷ Co	271.80 (5) d	EC	s	6	136
⁵⁸ Co	70.83 (10) d	EC	s	511	811
⁶⁰ Co	5.271 (1) a	β^-	s	1,173	1,332
⁶⁵ Zn	244.06 (10) d	EC	s	1,116	1,116
⁷⁵ Se	119.79 (4) d	EC	m	66	401
⁸⁵ Sr	64.851 (5) d	EC	s	514	514
⁸⁸ Y	106.629 (24) d	EC + β^+	s	14	1,836
^{93m} Nb	16.12 (15) a	IT	s	31	31
^{110m} Ag	249.78 (2) d	β^-	m	447	1,562
¹⁰⁹ Cd	461.4 (12) d	EC	s	22	22
¹¹³ Sn	115.09 (3) d	EC	s	24	392
¹²⁵ I	59.407 (9) d	EC	s	27	35
¹³⁷ Cs	30.018 (25) a	β^-	s	32	662
¹³³ Ba	10.54 (1) a	EC	m	31	384
¹³⁹ Ce	137.641 (20) d	EC	s	33	166
¹⁴¹ Ce	32.508 (13) d	β^-	s	36	145
¹⁵² Eu	13.525 (14) a	EC/ β^-	m	40	1,458
¹⁵⁴ Eu	8.601 (4) a	β^- /EC	m	42	1,596
¹⁵³ Gd	240.4 (10) d	EC	m	41	173
¹⁶⁹ Yb	32.018 (5) d	EC	m	50	308
¹⁹² Ir	73.827 (13) d	β^- /EC	m	61	885
¹⁹⁸ Au	2.6948 (4) d	β^-	s	412	412
²⁰³ Hg	46.603 (21) d	β^-	s	71	279
²⁰⁷ Bi	32.9(14) a	EC	m	570	1,770
²⁴¹ Am	432.6 a	α	s	26	60

^a Definition of tropical year: 1 a = 365.242198 d = 31556926 s (CODATA 2003).

Table 56.3

Strong decay γ -rays of simple calibration sources

Nuclide	X-ray type	Photon energy/keV	Photons per 100 disintegrations	Comment
²² Na		511 ^a	179.8 (2) ^a	Primary source
		1,274.537 (7) ^b	99.940 (14)	
²⁴ Na		1,368.626 (5) ^b	99.9935 (5)	
		2,754.007 (11) ^b	99.872 (8)	
⁴⁶ Sc		889.271 (2) ^b	99.9833 (5)	Primary source
		1,120.537 (3) ^b	99.986	
⁵¹ Cr		320.0835 (4)	9.87 (5)	
⁵⁴ Mn		834.838 (5) ^b	99.9746 (11)	Primary source
⁵⁵ Fe	K α_2 (Mn)	5.8877	8.45 (14)	
	K α_1 (Mn)	5.8988	16.56 (27)	
	Σ K α (Mn)	5.895	25.0 (3)	
⁵⁷ Co	K α_2 (Fe)	6.39084	16.8 (3)	Primary source
	K α_1 (Fe)	6.40384	33.2 (5)	
	Σ K α (Fe)	6.4	50.0 (6)	
		14.41295 (31)	9.15 (17)	
		122.06065 (12) ^b	85.51 (6)	
		136.47356 (29) ^b	10.71 (15)	
⁵⁸ Co		511 ^a	30.0 (4) ^a	Primary source
		810.759 (2) ^b	99.45 (1)	
⁶⁰ Co		1,173.228 (3) ^b	99.85 (3)	Primary source
		1,332.492 (4) ^b	99.9826 (6)	
⁶⁵ Zn		1,115.539 (2) ^b	50.60 (22)	Primary source
⁸⁵ Sr		514.0048 (22) ^b	98.5 (4)	Primary source
⁸⁸ Y	K α_2 (Sr)	14.098	17.30 (22)	Primary source
	K α_1 (Sr)	14.1652	33.2 (4)	
	Σ K α (Sr)	14.142	50.5 (5)	
		898.036 (4) ^b	93.90 (23)	
		1,836.052 (13) ^b	99.32 (3)	
^{93m} Nb		30.77 (2)	0.000559 (16)	
¹⁰⁹ Cd	K α_2 (Ag)	21.9906	28.99 (25)	
	K α_1 (Ag)	22.1632	54.7 (4)	
	Σ K α (Ag)	22.103	83.7 (5)	
		88.0336 (11)	3.626 (20)	
¹¹³ Sn	K α_2 (In)	24.002	27.85 (22)	Primary source
	K α_1 (In)	24.2097	52.2 (4)	
	Σ K α (In)	24.138	80.1 (5)	
		391.698 (3) ^b	64.97 (17)	

■ **Table 56.3 (Continued)**

Nuclide	X-ray type	Photon energy/keV	Photons per 100 disintegrations	Comment
¹²⁵ I	K α_2 (Te)	27.202	39.7 (6)	
	K α_1 (Te)	27.4726	74.0 (11)	
	Σ K α (Te)	27.379	113.7 (13)	
		35.4919 (5)	6.67 (17)	
¹³⁷ Cs	K α_2 (Ba)	31.8174	1.95 (4)	Primary source
	K α_1 (Ba)	32.1939	3.59 (7)	
	Σ K α (Ba)	32.063	5.54 (8)	
		661.657 (3) ^b	84.99 (20)	
¹³⁹ Ce	K α_2 (La)	33.0344	22.5 (3)	Primary source
	K α_1 (La)	33.4421	41.2 (4)	
	Σ K α (La)	33.3	63.7 (5)	
		165.857 (3)	79.90 (4)	
¹⁴¹ Ce	K α_2 (Pr)	35.5506	4.74 (11)	
	K α_1 (Pr)	36.0267	8.65 (12)	
	Σ K α (Pr)	35.86	13.39 (16)	
		145.4433 (14) ^b	48.29 (20)	
¹⁹⁸ Au		411.80205 (17) ^b	95.54 (7)	
²⁰³ Hg	K α_2 (Tl)	70.8325	3.75 (4)	Primary source
	K α_1 (Tl)	72.8725	6.33 (5)	
	Σ K α (Tl)	72.112	10.08 (6)	
		279.1952 (10) ^b	81.48 (8)	
²⁴¹ Am		26.3446 (2) ^b	2.40 (3)	
		59.5409 (1) ^b	35.78 (9)	

^a Annihilation peak.

^b Energy from Helmer and van der Leun (2000).

56.1.1.2 Energy and Intensity Standards

For the calibration of γ -ray detectors, easily produced radionuclides with convenient decay half-life and accurately known *photon energies* and *emission probabilities* or intensities are needed. For many years, the X- and γ -ray standards recommended by the International Atomic Energy Agency (IAEA) have been the most widely accepted choice. As a result of a coordinated research project, the 1991 recommendations (IAEA 1991) are being replaced by a new set of standards data for 64 radionuclides as well as nuclear reactions producing high energy γ -rays (IAEA 2002, 2003). This program has greatly benefited from the parallel effort of the Decay Data Evaluation Project (DDEP) involving about 250 radionuclides (Browne et al. 2001). The data presented here are preliminary values for a subset of nuclides. More details and more nuclides can be found on the DDEP Web site (DDEP 2003), part of which has been published (Bé et al. 1999a, b).

■ Table 56.4

Strong decay γ -rays of multi-gamma calibration sources

Nuclide	X-ray type	Photon energy/keV	Photons per 100 disintegrations	Comment
⁵⁶ Mn		846.7638 (19)	98.83 (3)	
		1,810.726 (4)	27.6 (6)	
		2,113.092 (6)	14.8 (4)	
		2,523.06 (5)	1.03 (3)	
⁵⁹ Fe		142.651 (2)	0.972 (15)	
		192.349 (5)	2.918 (29)	
		1,099.245 (3)	56.59 (21)	
		1,291.590 (6)	43.21 (25)	
⁷⁵ Se		66.0518 (8) ^a	1.112 (12)	
		96.7340 (9) ^a	3.42 (3)	
		121.1155 (11) ^a	17.2 (3)	
		136.0001 (6) ^a	58.2 (7)	
		198.6060 (12) ^a	1.48 (4)	
		264.6576 (9) ^a	58.9 (3)	
		279.5422 (10) ^a	24.99 (13)	
		303.9236 (10) ^a	1.316 (8)	
		400.6572 (8) ^a	11.47 (9)	
^{110m} Ag		446.812 (3) ^a	3.65 (5)	
		620.3553 (17) ^a	2.72 (8)	
		657.7600 (11) ^a	94.38 (8)	
		677.6217 (12) ^a	10.56 (6)	
		687.0091 (18) ^a	6.45 (3)	
		706.6760 (15) ^a	16.48 (8)	
		744.2755 (18) ^a	4.71 (3)	
		763.9424 (17) ^a	22.31 (9)	
		818.0244 (18) ^a	7.33 (4)	
		884.6781 (13) ^a	74.0 (12)	
		937.485 (3) ^a	34.51 (27)	
		1,384.2931 (20) ^a	24.7 (5)	
		1,475.7792 (23) ^a	4.03 (5)	
		1,505.028 (2) ^a	13.16 (16)	
		1,562.2940 (18) ^a	1.21 (3)	
¹³³ Ba	K α_2 (Cs)	30.625	34.0 (4)	79.6 keV peak close
	K α_1 (Cs)	30.973	62.8 (7)	
	Σ K α (Cs)	30.852	96.8 (8)	
		53.1622 (6) ^a	2.14 (3)	
		80.9979 (11)	32.9 (3)	

Table 56.4 (Continued)

Nuclide	X-ray type	Photon energy/keV	Photons per 100 disintegrations	Comment
		160.6120 (16) ^a	0.638 (4)	
		223.2368 (13) ^a	0.453 (3)	
		276.3989 (12) ^a	7.16 (5)	
		302.8508 (5) ^a	18.34 (13)	
		356.0129 (7) ^a	62.05 (19)	
		383.8485 (12) ^a	8.94 (6)	
¹⁵² Eu	K α_2 (Sm)	39.5229	20.8 (3)	
	K α_1 (Sm)	40.1186	37.7 (5)	
	Σ K α (Sm)	39.91	58.5 (6)	
		121.7817 (3) ^a	28.41 (13)	
		244.6974 (8) ^a	7.55 (4)	
		295.9387 (17) ^a	0.442 (3)	
		344.2785 (12) ^a	26.58 (12)	
		367.7891 (20) ^a	0.862 (5)	
		411.1165 (12) ^a	2.237 (10)	
		443.965 (3)	3.12 (3)	
		488.6792 (20) ^a	0.4137 (24)	Unresolved doublet
		586.265 (3)	0.462 (4)	
		678.623 (5) ^a	0.470 (4)	
		688.670 (5) ^a	0.841 (6)	
		778.9045 (24) ^a	12.96 (6)	
		867.380 (3) ^a	4.241 (23)	
		919.337 (4) ^a	0.429 (5)	
		963.390 (12)	0.1341 (20)	
		964.079 (18)	14.49 (6)	
		1,085.837 (10) ^a	10.13 (6)	
		1,089.737 (5) ^a	1.73 (1)	
		1,112.076 (3) ^a	13.40 (6)	1,109.2 keV peak close
		1,212.948 (11) ^a	1.415 (9)	
		1,299.142 (8) ^a	1.632 (9)	
		1,408.013 (3) ^a	20.84 (9)	
		1,457.643 (11) ^a	0.498 (4)	
¹⁵⁴ Eu	K α_2 (Gd)	42.3093	7.2 (2)	
	K α_1 (Gd)	42.9967	13.0 (3)	
	Σ K α (Gd)	42.751	20.2 (4)	
		123.0706 (9) ^a	40.4 (5)	
		247.9288 (7) ^a	6.89 (7)	
		591.755 (3) ^a	4.95 (5)	

Table 56.4 (Continued)

Nuclide	X-ray type	Photon energy/keV	Photons per 100 disintegrations	Comment
		723.3014 (22) ^a	20.05 (21)	
		756.8020 (23) ^a	4.53 (5)	
		873.1834 (23) ^a	12.17 (12)	
		996.25 (5)	10.5 (1)	
		1,004.718 (7)	17.86 (18)	
		1,274.429 (4) ^a	34.9 (3)	
		1,494.048 (4) ^a	0.698 (9)	
		1,596.4804 (28)	1.783 (17)	
¹⁵³ Gd	K α_2 (Eu)	40.9024	34.5 (9)	
	K α_1 (Eu)	41.5427	62.2 (15)	
	Σ K α (Eu)	41.318	96.7 (17)	
		69.67302 (13) ^a	2.42 (7)	
		97.43100 (21) ^a	29.0 (8)	
		103.18012 (17) ^a	21.1 (6)	
		172.85307 (21) ^a	0.036 (2)	
¹⁶⁹ Yb	K α_2 (Tm)	49.7731	52.9 (8)	
	K α_1 (Tm)	50.7417	93.5 (13)	
	Σ K α (Tm)	50.39	146.4 (15)	
		63.12044 (4) ^a	44.05 (24)	
		93.61447 (8) ^a	2.571 (17)	
		109.77924 (4) ^a	17.36 (9)	
		130.52293 (6) ^a	11.38 (5)	
		177.21307 (6) ^a	22.32 (10)	
		197.95675 (7) ^a	35.93 (12)	
		261.07712 (9) ^a	1.687 (8)	
		307.73757 (9)	10.046 (45)	
¹⁹² Ir	K α_2 (Os)	61.4873	1.211 (25)	
	K α_1 (Os)	63.0011	2.09 (5)	
	Σ K α (Os)	62.448	3.30 (6)	
	K α_2 (Pt)	65.123	2.66 (5)	
	K α_1 (Pt)	66.833	4.55 (8)	
	Σ K α (Pt)	66.196	7.21 (9)	
		136.3426 (3)	0.199 (25)	
		205.79430 (9) ^a	3.34 (4)	
		295.95650 (15) ^a	28.72 (14)	
		308.45507 (17) ^a	29.68 (15)	
		316.50618 (17) ^a	82.75 (21)	
		468.0688 (3)	47.81 (24)	

■ **Table 56.4 (Continued)**

Nuclide	X-ray type	Photon energy/keV	Photons per 100 disintegrations	Comment
		484.5751 (4) ^a	3.189 (24)	
		588.5810 (7) ^a	4.517 (22)	
		604.41105 (25) ^a	8.20 (4)	
		612.4621 (3)	5.34 (8)	
		884.5365 (7) ^a	0.291 (7)	
²⁰⁷ Bi		569.698 (2) ^a	97.76 (3)	
		1,063.656 (3) ^a	74.58 (49)	
		1,770.228 (9) ^a	6.87 (3)	

^a Energy from Helmer and van der Leun (2000).

■ **Table 56.5**

Conversion electron sources in increasing order of electron energy.

Source nuclide	Decay Mode	Half-life	Atomic shell	Electron energy/keV	Electrons per 100 disintegrations
¹⁵³ Gd	EC	240.4 (10) d	K-Eu	54.6611 (5)	30.6 (11)
¹⁰⁹ Cd	EC	462.6 (7) d	K-Ag	62.5	87
¹⁴¹ Ce	β ⁻	32.508 (13) d	K-Pr	103.453 (2)	18.25 (23)
¹³⁹ Ce	EC	137.641 (20) d	K-La	126.932	17.15 (8)
¹¹³ Sn	EC	115.09 (3) d	K-In	363.758 (3)	28.4 (3)
¹³⁷ Cs	β ⁻	30.018 (25) a	K-Ba	624.2164	7.62 (19)
²⁰⁷ Bi	EC	32.9(14) a	K-Pb	481.695 (2)	1.52 (2)
			K-Pb	975.655 (3)	7.03 (13)

► **Table 56.2** summarizes the main characteristics of the selected *standard radionuclides*. Those labeled with “s” are simple sources emitting one or two γ-rays. Many of them are primary standards with extremely simple decay schemes, for which the relationship between the source activity and the γ-ray emission probability can be derived without any *a priori* knowledge of detection efficiencies. Hence, primary sources with accurately calibrated activity are suitable for absolute *detector efficiency calibrations*. Those sources labeled with “m” are multi-gamma emitters, practical for the calibration of high-resolution detectors, such as Si(Li) and high-purity Ge detectors. The energies and emission probabilities of the strongest X- and γ-rays are presented separately for simple and multi-gamma sources in ► **Tables 56.3** and ► **56.4**, respectively. The data are from the recent evaluation (IAEA 2003; DDEP 2003), unless noted otherwise. For the X-rays the mean energies were obtained by Schönfeld and Rodloff (1999) from the data of Bearden 1967, while the emission probabilities per

Table 56.6

Common alpha-particle standard sources

Nuclide	Half-life	Alpha energy/keV	Percent branching
¹⁴⁸ Gd	74.6(30) a	3,182.680 (24)	100
²¹⁰ Po	138.376(2) d	5,304.38 (7)	100
²³¹ Pa	3.2760(110) × 10 ⁴ a	4,736.0 (8)	8.4
		4,951.3 (14)	22.8
		5,013.8 (14)	25.4
		5,028.4 (10)	20
		5,058.6 (15)	11
²³² Th	1.405(6) × 10 ¹⁰ a	3,947.2 (20)	21.7 (13)
		4,012.3 (14)	78.2 (13)
²³⁴ U	2.455(6) × 10 ⁵ a	4,722.4 (14)	28.42 (9)
		4,774.6 (14)	71.38 (16)
²³⁵ U	7.038(5) × 10 ⁸ a	4,214.7 (19)	5.7 (6)
		4,366.1 (20)	17 (2)
		4,397.8 (13)	55 (3)
		4,596.4 (13)	5.0 (5)
²³⁶ U	2.342(3) × 10 ⁷ a	4,445 (5)	25.9 (40)
		4,494 (3)	73.8 (40)
²³⁸ U	4.468(3) × 10 ⁹ a	4,151 (5)	20.9 (27)
		4,198 (3)	79.0 (27)
²³⁸ Pu	87.7(3) a	5,456.3 (3)	28.98 (10)
		5,499.03 (20)	70.91 (10)
²³⁹ Pu	2.4110(30) × 10 ⁴ a	5,105.5 (8)	11.5 (8)
		5,144.3 (8)	15.1 (8)
		5,156.59 (14)	73.3 (8)
²⁴⁰ Pu	6,564(11) a	5,123.68 (23)	27.1 (1)
		5,168.17 (15)	72.8 (1)
²⁴¹ Am	432.6(6) a	5,442.90 (13)	13.10 (11)
		5,485.60 (12)	84.6 (2)
²⁴³ Am	7,370(40) a	5,233.3 (10)	11.0 (4)
		5,275.3 (10)	87.4 (4)
²⁴² Cm	162.8(2) d	6,069.42 (12)	25.0 (5)
		6,112.72 (8)	74.0 (5)
²⁴³ Cm	29.1(1) a	5,742.1 (9)	11.5 (5)
		5,785.2 (9)	72.9 (10)
		5,991.8 (15)	5.7 (2)
		6,058 (1)	4.7 (3)

■ **Table 56.6 (Continued)**

Nuclide	Half-life	Alpha energy/keV	Percent branching
²⁴⁴ Cm	18.10(2) a	5,762.70 (3)	23.6 (2)
		5,804.82 (5)	76.4 (2)
²⁵³ Es	20.47(3) d	6,592 (2)	6.6 (1)
		6,632.57 (5)	89.8 (2)
²⁵⁴ Es	275.7(5) d	6,428.8 (20)	93.1 (10)

disintegration were calculated by Schönfeld and Janssen (2000). Only the strongest $K\alpha_1$ and $K\alpha_2$ lines are listed. In some cases, these lines cannot be resolved. Therefore, their summed intensity at the mean energy is also included, which is the intensity-weighted sum of $E(K\alpha_1)$ and $E(K\alpha_2)$.

56.1.2 Electron and Alpha Sources

For the calibration of charged-particle detectors, emission characteristics of some convenient *conversion electron* and *alpha decay sources* are presented in ► [Tables 56.5](#) and ► [56.6](#), respectively.

The electron data are extracted from the recent evaluation of X- and γ -ray standard sources (IAEA 2003; DDEP 2003). Only the K conversion electrons are given, since those are the most intensive.

For alpha emitters the energy and branching percentage data come from the latest Table of Isotopes (Firestone et al. 1996). The half-lives were obtained from Tuli 2000. More details about the decay characteristics of these nuclides can be found in the Appendix of Vol. 2.

56.2 Fission Product Yields

Richard B. Firestone

► [Table 56.7](#) lists independent *fission product yields* (England and Rider 1994) per 100 fissions for the most important fissionable nuclides. For ²³⁵U thermal, fast neutron (fission spectrum), and high-energy neutron (14 MeV) induced, for ²³⁸U fast neutron induced, for ²³⁹Pu thermal neutron induced, and for ²⁵²Cf spontaneous fission data are provided. Fission yield measurements from the literature and calculated charge distributions were used to produce this recommended set of yields for the fission products. The full data set can be found in the report by England and Rider (1994), which also serves as the primary documentation for the second evaluation of fission yields in the nuclear data library ENDF/B-VI released in 1993.

Table 56.7
Independent fission product yields

Fission product	Half-life	²³⁵ U Thermal	²³⁵ U Fast	²³⁵ U High	²³⁸ U Fast	²³⁹ Pu Thermal	²⁵² Cf Spontaneous
⁶⁶ Cr	>150 ns	2.41×10^{-12}	4.03×10^{-11}	7.91×10^{-8}	1.71×10^{-9}		1.52×10^{-11}
⁶⁷ Cr	~50 ms		4.88×10^{-12}	1.51×10^{-8}	6.74×10^{-10}		3.07×10^{-12}
⁶⁸ Cr				1.44×10^{-9}	4.48×10^{-11}		
⁷⁰ Cr				5.68×10^{-12}			
⁶⁶ Mn	66 ms	7.20×10^{-10}	9.44×10^{-9}	8.63×10^{-6}	2.02×10^{-7}	3.69×10^{-10}	1.83×10^{-9}
⁶⁷ Mn	42 ms	5.38×10^{-10}	5.31×10^{-9}	3.98×10^{-6}	2.67×10^{-7}	7.58×10^{-11}	1.01×10^{-9}
⁶⁸ Mn	28 ms	6.66×10^{-11}	6.66×10^{-10}	9.27×10^{-7}	5.04×10^{-8}	1.58×10^{-11}	3.88×10^{-10}
⁶⁹ Mn	14 ms	8.03×10^{-12}	8.92×10^{-11}	1.56×10^{-7}	6.03×10^{-9}	2.67×10^{-12}	9.82×10^{-11}
⁷⁰ Mn			5.78×10^{-12}	2.25×10^{-8}	4.45×10^{-10}		1.48×10^{-11}
⁷¹ Mn				2.14×10^{-9}	2.22×10^{-11}		1.73×10^{-12}
⁶⁶ Fe	0.44 s	3.76×10^{-8}	3.95×10^{-7}	1.01×10^{-4}	2.17×10^{-6}	3.63×10^{-8}	2.30×10^{-8}
⁶⁷ Fe	0.47 s	6.87×10^{-8}	5.14×10^{-7}	1.07×10^{-4}	7.40×10^{-6}	1.82×10^{-8}	3.25×10^{-8}
⁶⁸ Fe	0.10 s	3.92×10^{-8}	2.85×10^{-7}	5.84×10^{-5}	4.30×10^{-6}	1.35×10^{-8}	3.19×10^{-8}
⁶⁹ Fe	0.17 s	1.22×10^{-8}	9.57×10^{-8}	2.35×10^{-5}	1.44×10^{-6}	5.87×10^{-9}	2.13×10^{-8}
⁷⁰ Fe	>150 ns	3.24×10^{-9}	2.82×10^{-8}	8.21×10^{-6}	3.49×10^{-7}	1.84×10^{-9}	8.87×10^{-9}
⁷¹ Fe	>150 ns	4.92×10^{-10}	5.15×10^{-9}	1.92×10^{-6}	4.97×10^{-8}	1.83×10^{-10}	2.81×10^{-9}
⁷² Fe	>150 ns	7.15×10^{-11}	1.07×10^{-9}	2.92×10^{-7}	5.16×10^{-9}	2.28×10^{-11}	5.29×10^{-10}
⁷³ Fe		5.54×10^{-12}	8.33×10^{-11}	3.91×10^{-8}	9.58×10^{-10}		6.95×10^{-11}
⁷⁴ Fe			3.49×10^{-12}	2.95×10^{-9}	4.43×10^{-11}		5.92×10^{-12}
⁷⁶ Fe				5.54×10^{-12}			
⁶⁶ Co	0.233 s	2.81×10^{-8}	2.69×10^{-7}	1.49×10^{-4}	1.25×10^{-6}	1.15×10^{-7}	2.44×10^{-8}
⁶⁷ Co	0.425 s	2.00×10^{-7}	1.30×10^{-6}	3.42×10^{-4}	1.18×10^{-5}	1.86×10^{-7}	8.23×10^{-8}

⁶⁸ Co	0.18 s		2.47×10^{-7}	1.52×10^{-6}	4.12×10^{-4}	1.61×10^{-5}	3.08×10^{-7}	1.92×10^{-7}
⁶⁹ Co	0.27 s		3.25×10^{-7}	2.08×10^{-6}	3.74×10^{-4}	1.59×10^{-5}	4.66×10^{-7}	3.12×10^{-7}
⁷⁰ Co	0.15 s		2.09×10^{-7}	1.39×10^{-6}	3.02×10^{-4}	9.81×10^{-6}	3.61×10^{-7}	3.36×10^{-7}
⁷¹ Co	0.21 s		1.48×10^{-7}	1.14×10^{-6}	1.67×10^{-4}	4.36×10^{-6}	1.29×10^{-7}	2.77×10^{-7}
⁷² Co	0.09 s		5.80×10^{-8}	6.02×10^{-7}	6.09×10^{-5}	1.28×10^{-6}	4.13×10^{-8}	1.42×10^{-7}
⁷³ Co	>150 ns		2.21×10^{-8}	2.21×10^{-7}	1.99×10^{-5}	7.85×10^{-7}	6.80×10^{-9}	5.05×10^{-8}
⁷⁴ Co	>150 ns		3.00×10^{-9}	2.44×10^{-8}	3.69×10^{-6}	1.07×10^{-7}	7.26×10^{-10}	1.18×10^{-8}
⁷⁵ Co	>150 ns		3.81×10^{-10}	3.42×10^{-9}	5.15×10^{-7}	1.36×10^{-8}	5.50×10^{-11}	1.72×10^{-9}
⁷⁶ Co			2.53×10^{-11}	3.53×10^{-10}	4.42×10^{-8}	1.08×10^{-9}	2.15×10^{-12}	1.79×10^{-10}
⁶⁶ Ni	54.6 h		5.78×10^{-9}	4.95×10^{-8}	2.84×10^{-5}	8.07×10^{-8}	6.78×10^{-8}	3.35×10^{-9}
⁶⁷ Ni	21 s		9.04×10^{-8}	5.03×10^{-7}	1.43×10^{-4}	1.95×10^{-6}	2.29×10^{-7}	2.76×10^{-8}
⁶⁸ Ni	29 s		4.19×10^{-7}	2.18×10^{-6}	3.72×10^{-4}	7.42×10^{-6}	1.13×10^{-6}	1.50×10^{-7}
⁶⁹ Ni	11.4 s		1.12×10^{-6}	5.97×10^{-6}	7.31×10^{-4}	1.74×10^{-5}	3.67×10^{-6}	5.65×10^{-7}
⁷⁰ Ni	6.0 s		2.78×10^{-6}	1.46×10^{-5}	1.29×10^{-3}	2.92×10^{-5}	9.27×10^{-6}	1.46×10^{-6}
⁷¹ Ni	2.56 s		4.35×10^{-6}	2.57×10^{-5}	1.58×10^{-3}	3.07×10^{-5}	7.49×10^{-6}	2.88×10^{-6}
⁷² Ni	1.57 s		7.60×10^{-6}	5.63×10^{-5}	1.32×10^{-3}	2.69×10^{-5}	8.50×10^{-6}	3.75×10^{-6}
⁷³ Ni	0.84 s		7.13×10^{-6}	4.95×10^{-5}	1.00×10^{-3}	4.26×10^{-5}	3.49×10^{-6}	3.40×10^{-6}
⁷⁴ Ni	0.9 s		4.58×10^{-6}	2.48×10^{-5}	4.41×10^{-4}	1.90×10^{-5}	1.35×10^{-6}	2.08×10^{-6}
⁷⁵ Ni	0.6 s		1.53×10^{-6}	8.87×10^{-6}	1.49×10^{-4}	6.65×10^{-6}	2.64×10^{-7}	8.33×10^{-7}
⁷⁶ Ni	0.24 s		5.02×10^{-7}	4.36×10^{-6}	3.20×10^{-5}	1.76×10^{-6}	3.94×10^{-8}	2.36×10^{-7}
⁷⁷ Ni	>150 ns		5.64×10^{-8}	4.08×10^{-7}	5.41×10^{-6}	6.70×10^{-7}	3.45×10^{-9}	4.08×10^{-8}
⁷⁸ Ni	>150 ns		5.03×10^{-9}	2.57×10^{-8}	5.34×10^{-7}	1.57×10^{-7}	2.38×10^{-10}	8.40×10^{-9}
⁸⁰ Ni			1.56×10^{-12}	1.28×10^{-11}	1.86×10^{-9}	5.36×10^{-10}		2.10×10^{-11}
⁸² Ni					1.02×10^{-12}			
⁶⁶ Cu	5.120 min		1.43×10^{-11}	1.13×10^{-10}	6.41×10^{-7}	1.96×10^{-10}	1.38×10^{-9}	3.30×10^{-11}
⁶⁷ Cu	61.83 h		9.68×10^{-10}	5.08×10^{-9}	7.23×10^{-6}	1.58×10^{-8}	1.56×10^{-8}	7.18×10^{-10}

Table 56.7 (Continued)

Fission product	Half-life	²³⁵ U Thermal	²³⁵ U Fast	²³⁵ U High	²³⁸ U Fast	²³⁹ Pu Thermal	²⁵² Cf Spontaneous
⁶⁸ Cu	31.1 s	3.15 × 10 ⁻⁹	1.37 × 10 ⁻⁸	7.70 × 10 ⁻⁶	4.33 × 10 ⁻⁸	4.97 × 10 ⁻⁸	2.94 × 10 ⁻⁹
^{68m} Cu	3.75 min	7.36 × 10 ⁻⁹	3.71 × 10 ⁻⁸	3.51 × 10 ⁻⁵	1.17 × 10 ⁻⁷	1.16 × 10 ⁻⁷	6.86 × 10 ⁻⁹
⁶⁹ Cu	2.85 min	1.14 × 10 ⁻⁷	5.57 × 10 ⁻⁷	1.86 × 10 ⁻⁴	1.16 × 10 ⁻⁶	1.66 × 10 ⁻⁶	8.98 × 10 ⁻⁸
⁷⁰ Cu	4.5 s	1.49 × 10 ⁻⁷	6.05 × 10 ⁻⁷	1.07 × 10 ⁻⁴	1.05 × 10 ⁻⁶	2.19 × 10 ⁻⁶	1.40 × 10 ⁻⁷
^{70m} Cu	47 s	4.46 × 10 ⁻⁷	2.15 × 10 ⁻⁶	6.08 × 10 ⁻⁴	3.71 × 10 ⁻⁶	6.58 × 10 ⁻⁶	4.20 × 10 ⁻⁷
⁷¹ Cu	19.5 s	3.48 × 10 ⁻⁶	1.78 × 10 ⁻⁵	1.90 × 10 ⁻³	1.38 × 10 ⁻⁵	2.12 × 10 ⁻⁵	2.57 × 10 ⁻⁶
⁷² Cu	6.6 s	1.27 × 10 ⁻⁵	7.83 × 10 ⁻⁵	3.42 × 10 ⁻³	2.87 × 10 ⁻⁵	5.23 × 10 ⁻⁵	7.92 × 10 ⁻⁶
⁷³ Cu	4.2 s	4.71 × 10 ⁻⁵	2.61 × 10 ⁻⁴	5.71 × 10 ⁻³	1.24 × 10 ⁻⁴	7.11 × 10 ⁻⁵	1.70 × 10 ⁻⁵
⁷⁴ Cu	1.594 s	6.82 × 10 ⁻⁵	2.87 × 10 ⁻⁴	5.65 × 10 ⁻³	1.36 × 10 ⁻⁴	6.30 × 10 ⁻⁵	2.52 × 10 ⁻⁵
⁷⁵ Cu	1.224 s	1.01 × 10 ⁻⁴	4.36 × 10 ⁻⁴	4.38 × 10 ⁻³	1.41 × 10 ⁻⁴	4.42 × 10 ⁻⁵	2.59 × 10 ⁻⁵
⁷⁶ Cu	0.641 s	8.28 × 10 ⁻⁵	5.21 × 10 ⁻⁴	2.26 × 10 ⁻³	9.79 × 10 ⁻⁵	1.66 × 10 ⁻⁵	1.90 × 10 ⁻⁵
⁷⁷ Cu	0.469 s	4.45 × 10 ⁻⁵	2.24 × 10 ⁻⁴	9.36 × 10 ⁻⁴	1.22 × 10 ⁻⁴	5.43 × 10 ⁻⁶	8.90 × 10 ⁻⁶
⁷⁸ Cu	342 ms	1.09 × 10 ⁻⁵	3.75 × 10 ⁻⁵	2.35 × 10 ⁻⁴	7.98 × 10 ⁻⁵	9.79 × 10 ⁻⁷	4.94 × 10 ⁻⁶
⁷⁹ Cu	188 ms		4.66 × 10 ⁻⁶	4.60 × 10 ⁻⁵	2.98 × 10 ⁻⁵	1.13 × 10 ⁻⁷	9.46 × 10 ⁻⁷
⁸⁰ Cu	>150 ns	5.25 × 10 ⁻⁸	2.54 × 10 ⁻⁷	5.52 × 10 ⁻⁶	2.82 × 10 ⁻⁶	7.23 × 10 ⁻⁹	9.56 × 10 ⁻⁸
⁸¹ Cu			9.36 × 10 ⁻⁹	3.47 × 10 ⁻⁷	3.14 × 10 ⁻⁷	2.80 × 10 ⁻¹⁰	9.15 × 10 ⁻⁹
⁸² Cu		1.48 × 10 ⁻¹⁰	1.62 × 10 ⁻¹⁰	2.21 × 10 ⁻⁸	2.49 × 10 ⁻⁸	3.36 × 10 ⁻¹²	5.64 × 10 ⁻¹⁰
⁶⁶ Zn	Stable			1.39 × 10 ⁻⁹		3.50 × 10 ⁻¹²	
⁶⁷ Zn	Stable		4.54 × 10 ⁻¹²	3.62 × 10 ⁻⁸	8.05 × 10 ⁻¹²	9.94 × 10 ⁻¹¹	1.79 × 10 ⁻¹²
⁶⁸ Zn	Stable	4.74 × 10 ⁻¹¹	2.12 × 10 ⁻¹⁰	5.41 × 10 ⁻⁷	2.74 × 10 ⁻¹⁰	3.65 × 10 ⁻⁹	6.55 × 10 ⁻¹¹
⁶⁹ Zn	56.4 min	2.48 × 10 ⁻¹⁰	9.79 × 10 ⁻¹⁰	6.10 × 10 ⁻⁷	9.72 × 10 ⁻¹⁰	1.64 × 10 ⁻⁸	2.99 × 10 ⁻¹⁰
^{69m} Zn	13.76 h	1.06 × 10 ⁻⁹	4.78 × 10 ⁻⁹	4.94 × 10 ⁻⁶	4.75 × 10 ⁻⁹	7.01 × 10 ⁻⁸	1.28 × 10 ⁻⁹
⁷⁰ Zn	>5 × 10 ¹⁴ years	3.03 × 10 ⁻⁸	1.20 × 10 ⁻⁷	4.91 × 10 ⁻⁵	7.53 × 10 ⁻⁸	1.50 × 10 ⁻⁶	2.57 × 10 ⁻⁸

^{71}Zn	2.45 min	7.71×10^{-8}	3.01×10^{-7}	3.22×10^{-5}	9.80×10^{-8}	1.46×10^{-6}	5.55×10^{-8}
$^{71\text{m}}\text{Zn}$	3.96 h	3.29×10^{-7}	1.47×10^{-6}	2.61×10^{-4}	4.79×10^{-7}	6.24×10^{-6}	2.37×10^{-7}
^{72}Zn	46.5 h	6.10×10^{-6}	3.05×10^{-5}	1.17×10^{-3}	3.64×10^{-6}	5.82×10^{-5}	2.22×10^{-6}
^{73}Zn	23.5 s	4.63×10^{-5}	2.08×10^{-4}	4.22×10^{-3}	3.80×10^{-5}	1.65×10^{-4}	1.11×10^{-5}
^{74}Zn	95.6 s	2.51×10^{-4}	8.36×10^{-4}	9.01×10^{-3}	1.17×10^{-4}	4.42×10^{-4}	3.82×10^{-5}
^{75}Zn	10.2 s	7.67×10^{-4}	2.57×10^{-3}	1.52×10^{-2}	2.79×10^{-4}	6.84×10^{-4}	9.38×10^{-5}
^{76}Zn	5.7 s	1.84×10^{-3}	1.19×10^{-2}	1.77×10^{-2}	5.35×10^{-4}	8.62×10^{-4}	1.64×10^{-4}
^{77}Zn	2.08 s	3.14×10^{-3}	1.15×10^{-2}	1.70×10^{-2}	1.67×10^{-3}	6.76×10^{-4}	1.93×10^{-4}
^{78}Zn	1.47 s	3.56×10^{-3}	8.56×10^{-3}	1.04×10^{-2}	3.26×10^{-3}	4.40×10^{-4}	2.72×10^{-4}
^{79}Zn	0.995 s	1.64×10^{-3}	2.62×10^{-3}	5.02×10^{-3}	3.32×10^{-3}	1.29×10^{-4}	1.36×10^{-4}
^{80}Zn	0.545 s	2.42×10^{-4}	7.08×10^{-4}	1.52×10^{-3}	1.04×10^{-3}	3.30×10^{-5}	3.76×10^{-5}
^{81}Zn	0.29 s		7.24×10^{-5}	2.51×10^{-4}	3.37×10^{-4}	3.55×10^{-6}	9.76×10^{-6}
^{82}Zn	>150 ns	1.08×10^{-5}	6.44×10^{-6}	4.24×10^{-5}	9.30×10^{-5}	1.75×10^{-7}	1.70×10^{-6}
^{83}Zn	>150 ns	6.32×10^{-8}	2.46×10^{-7}	4.41×10^{-6}	9.35×10^{-6}	4.91×10^{-9}	2.68×10^{-7}
^{84}Zn		1.22×10^{-6}	7.17×10^{-9}	2.24×10^{-7}	6.56×10^{-7}	1.03×10^{-10}	1.28×10^{-8}
^{86}Zn		2.28×10^{-10}		1.09×10^{-10}	3.67×10^{-10}		1.05×10^{-11}
^{67}Ga	3.2612 days			1.79×10^{-11}			
^{68}Ga	67.61 min			6.64×10^{-10}		2.03×10^{-12}	
^{69}Ga	Stable		1.08×10^{-12}	1.67×10^{-8}	1.06×10^{-12}	1.79×10^{-10}	1.71×10^{-12}
^{70}Ga	21.14 min	1.47×10^{-11}	5.65×10^{-11}	3.58×10^{-7}	4.02×10^{-11}	7.77×10^{-9}	7.77×10^{-11}
^{71}Ga	Stable	9.39×10^{-10}	3.84×10^{-9}	5.09×10^{-6}	1.03×10^{-9}	1.36×10^{-7}	2.35×10^{-9}
^{72}Ga	14.10 h	3.86×10^{-8}	1.62×10^{-7}	4.72×10^{-5}	1.86×10^{-8}	2.39×10^{-6}	4.74×10^{-8}
^{73}Ga	4.86 h	1.21×10^{-6}	4.75×10^{-6}	3.91×10^{-4}	6.16×10^{-7}	2.21×10^{-5}	6.00×10^{-7}
^{74}Ga	8.12 min	1.46×10^{-5}	4.24×10^{-5}	1.86×10^{-3}	5.06×10^{-6}	1.24×10^{-4}	5.05×10^{-6}
^{75}Ga	126 s	1.93×10^{-4}	5.02×10^{-4}	6.89×10^{-3}	3.52×10^{-5}	5.83×10^{-4}	3.01×10^{-5}
^{76}Ga	32.6 s	1.05×10^{-3}	4.69×10^{-3}	1.77×10^{-2}	1.61×10^{-4}	1.54×10^{-3}	1.22×10^{-4}

Table 56.7 (Continued)

Fission product	Half-life	²³⁵ U Thermal	²³⁵ U Fast	²³⁵ U High	²³⁸ U Fast	²³⁹ Pu Thermal	²⁵² Cf Spontaneous
⁷⁷ Ga	13.2 s	4.08 × 10 ⁻³	1.65 × 10 ⁻²	3.75 × 10 ⁻²	1.40 × 10 ⁻³	3.78 × 10 ⁻³	3.42 × 10 ⁻⁴
⁷⁸ Ga	5.09 s	1.03 × 10 ⁻²	2.61 × 10 ⁻²	5.22 × 10 ⁻²	6.31 × 10 ⁻³	5.51 × 10 ⁻³	1.13 × 10 ⁻³
⁷⁹ Ga	2.847 s	1.71 × 10 ⁻²	3.16 × 10 ⁻²	5.90 × 10 ⁻²	1.84 × 10 ⁻²	5.49 × 10 ⁻³	1.37 × 10 ⁻³
⁸⁰ Ga	1.697 s	1.17 × 10 ⁻²	2.08 × 10 ⁻²	4.29 × 10 ⁻²	1.47 × 10 ⁻²	3.63 × 10 ⁻³	9.63 × 10 ⁻⁴
⁸¹ Ga	1.217 s	8.18 × 10 ⁻³	9.96 × 10 ⁻³	1.77 × 10 ⁻²	1.48 × 10 ⁻²	1.51 × 10 ⁻³	6.41 × 10 ⁻⁴
⁸² Ga	0.599 s	6.26 × 10 ⁻³	2.37 × 10 ⁻³	7.69 × 10 ⁻³	1.13 × 10 ⁻²	2.02 × 10 ⁻⁴	3.01 × 10 ⁻⁴
⁸³ Ga	0.308 s	1.92 × 10 ⁻⁴	4.69 × 10 ⁻⁴	2.14 × 10 ⁻³	3.94 × 10 ⁻³	2.29 × 10 ⁻⁵	1.35 × 10 ⁻⁴
⁸⁴ Ga	0.085 s	1.11 × 10 ⁻²	3.83 × 10 ⁻⁵	2.87 × 10 ⁻⁴	8.60 × 10 ⁻⁴	1.35 × 10 ⁻⁶	1.85 × 10 ⁻⁵
⁸⁵ Ga	>150 ns	5.88 × 10 ⁻⁷	2.23 × 10 ⁻⁶	2.43 × 10 ⁻⁵	9.65 × 10 ⁻⁵	2.86 × 10 ⁻⁸	2.85 × 10 ⁻⁶
⁸⁶ Ga	>150 ns	3.28 × 10 ⁻⁵	4.85 × 10 ⁻⁸	1.05 × 10 ⁻⁶	5.74 × 10 ⁻⁶	1.18 × 10 ⁻⁹	1.33 × 10 ⁻⁷
⁶⁹ Ge	39.05 h			4.65 × 10 ⁻¹²			
^{71m} Ge				4.36 × 10 ⁻⁹		1.00 × 10 ⁻¹⁰	
⁷² Ge	Stable	3.64 × 10 ⁻¹¹	1.36 × 10 ⁻¹⁰	1.97 × 10 ⁻⁷	6.88 × 10 ⁻¹²	1.29 × 10 ⁻⁸	9.59 × 10 ⁻¹¹
⁷³ Ge	Stable	2.38 × 10 ⁻⁹	8.51 × 10 ⁻⁹	3.53 × 10 ⁻⁶	5.38 × 10 ⁻¹⁰	2.40 × 10 ⁻⁷	2.65 × 10 ⁻⁹
^{73m} Ge	0.499 s	5.59 × 10 ⁻¹⁰	1.74 × 10 ⁻⁹	4.36 × 10 ⁻⁷	1.10 × 10 ⁻¹⁰	5.62 × 10 ⁻⁸	6.21 × 10 ⁻¹⁰
⁷⁴ Ge	Stable	1.67 × 10 ⁻⁷	4.19 × 10 ⁻⁷	4.44 × 10 ⁻⁵	1.84 × 10 ⁻⁸	5.60 × 10 ⁻⁶	7.24 × 10 ⁻⁸
⁷⁵ Ge	82.78 min	6.81 × 10 ⁻⁷	1.44 × 10 ⁻⁶	3.04 × 10 ⁻⁵	4.23 × 10 ⁻⁸	7.88 × 10 ⁻⁶	1.48 × 10 ⁻⁷
^{75m} Ge	47.7 s	4.56 × 10 ⁻⁶	1.05 × 10 ⁻⁵	3.50 × 10 ⁻⁴	3.10 × 10 ⁻⁷	5.27 × 10 ⁻⁵	9.90 × 10 ⁻⁷
⁷⁶ Ge	0.8 × 10 ²⁵ years	1.30 × 10 ⁻⁴	4.71 × 10 ⁻⁴	2.26 × 10 ⁻³	5.04 × 10 ⁻⁶	5.12 × 10 ⁻⁴	1.15 × 10 ⁻⁵
⁷⁷ Ge	11.30 h	5.96 × 10 ⁻⁴	3.18 × 10 ⁻³	1.01 × 10 ⁻²	1.02 × 10 ⁻⁴	2.32 × 10 ⁻³	6.94 × 10 ⁻⁵
^{77m} Ge	52.9 s	8.91 × 10 ⁻⁵	4.33 × 10 ⁻⁴	7.57 × 10 ⁻⁴	1.38 × 10 ⁻⁵	3.47 × 10 ⁻⁴	1.04 × 10 ⁻⁵
⁷⁸ Ge	88.0 min	6.94 × 10 ⁻³	2.21 × 10 ⁻²	3.41 × 10 ⁻²	1.50 × 10 ⁻³	1.18 × 10 ⁻²	6.21 × 10 ⁻⁴
⁷⁹ Ge	18.98 s	2.33 × 10 ⁻²	5.37 × 10 ⁻²	8.67 × 10 ⁻²	1.05 × 10 ⁻²	2.98 × 10 ⁻²	1.74 × 10 ⁻³

⁸⁰ Ge	29.5 s		1.02×10^{-1}	1.37×10^{-1}	1.42×10^{-1}	2.34×10^{-2}	5.49×10^{-2}	2.91×10^{-3}
⁸¹ Ge	7.6 s		1.26×10^{-1}	1.46×10^{-1}	1.38×10^{-1}	5.63×10^{-2}	5.51×10^{-2}	4.60×10^{-3}
⁸² Ge	4.60 s		1.26×10^{-1}	1.50×10^{-1}	1.45×10^{-1}	1.24×10^{-1}	2.71×10^{-2}	5.39×10^{-3}
⁸³ Ge	1.85 s		4.79×10^{-2}	7.68×10^{-2}	1.03×10^{-1}	1.15×10^{-1}	8.04×10^{-3}	6.39×10^{-3}
⁸⁴ Ge	0.947 s		1.90×10^{-2}	3.01×10^{-2}	3.52×10^{-2}	8.48×10^{-2}	1.86×10^{-3}	2.40×10^{-3}
⁸⁵ Ge	535 ms		2.13×10^{-3}	4.91×10^{-3}	7.89×10^{-3}	2.84×10^{-2}	1.08×10^{-4}	1.06×10^{-3}
⁸⁶ Ge	>150 ns		6.29×10^{-1}	5.42×10^{-4}	9.21×10^{-4}	6.10×10^{-3}	1.75×10^{-5}	1.42×10^{-4}
⁸⁷ Ge	~0.14 s		2.20×10^{-3}	3.16×10^{-5}	9.11×10^{-5}	3.77×10^{-4}	9.34×10^{-7}	2.02×10^{-5}
⁸⁸ Ge	>150 ns		5.20×10^{-5}	1.38×10^{-6}	7.20×10^{-6}	4.15×10^{-5}	2.72×10^{-8}	1.59×10^{-6}
⁷² As	26.0 h				7.70×10^{-11}		1.65×10^{-12}	
⁷³ As	80.30 days				3.84×10^{-9}		1.43×10^{-10}	1.05×10^{-12}
⁷⁴ As	17.77 days		4.99×10^{-12}	1.09×10^{-11}	1.90×10^{-8}		2.03×10^{-9}	1.91×10^{-11}
^{74m} As			1.16×10^{-11}	2.95×10^{-11}	8.67×10^{-8}	1.53×10^{-12}	4.73×10^{-9}	4.46×10^{-11}
⁷⁵ As	Stable		2.56×10^{-9}	5.48×10^{-9}	2.20×10^{-6}	1.37×10^{-10}	2.68×10^{-7}	2.79×10^{-9}
⁷⁶ As	1.0778 days		1.65×10^{-7}	5.48×10^{-7}	3.21×10^{-5}	5.60×10^{-9}	5.53×10^{-6}	7.56×10^{-8}
⁷⁷ As	38.83 h		4.31×10^{-6}	1.90×10^{-5}	3.68×10^{-4}	4.35×10^{-7}	9.89×10^{-5}	1.40×10^{-6}
⁷⁸ As	90.7 min		1.30×10^{-4}	2.85×10^{-4}	2.78×10^{-3}	1.54×10^{-5}	9.88×10^{-4}	2.77×10^{-5}
⁷⁹ As	9.01 min		2.66×10^{-3}	2.85×10^{-3}	1.65×10^{-2}	3.45×10^{-4}	8.02×10^{-3}	1.90×10^{-4}
⁸⁰ As	15.2 s		1.37×10^{-2}	1.64×10^{-2}	6.21×10^{-2}	1.98×10^{-3}	3.19×10^{-2}	7.80×10^{-4}
⁸¹ As	33.3 s		6.09×10^{-2}	6.83×10^{-2}	1.68×10^{-1}	1.39×10^{-2}	1.03×10^{-1}	2.88×10^{-3}
⁸² As	19.1 s		1.29×10^{-1}	7.39×10^{-2}	1.68×10^{-1}	3.68×10^{-2}	5.68×10^{-2}	4.00×10^{-3}
^{82m} As			2.71×10^{-2}	7.39×10^{-2}	1.68×10^{-1}	3.68×10^{-2}	5.68×10^{-2}	4.00×10^{-3}
⁸³ As	13.4 s		2.91×10^{-1}	3.07×10^{-1}	5.63×10^{-1}	2.41×10^{-1}	1.15×10^{-1}	2.32×10^{-2}
⁸⁴ As	3.24 s		1.97×10^{-1}	2.76×10^{-1}	4.60×10^{-1}	3.61×10^{-1}	6.57×10^{-2}	2.19×10^{-2}
⁸⁵ As	2.021 s		1.21×10^{-1}	2.07×10^{-1}	2.59×10^{-1}	3.77×10^{-1}	1.43×10^{-2}	2.60×10^{-2}
⁸⁶ As	0.945 s		1.99×10^{-2}	5.89×10^{-2}	7.81×10^{-2}	2.27×10^{-1}	6.00×10^{-3}	9.35×10^{-3}

Table 56.7 (Continued)

Fission product	Half-life	²³⁵ U Thermal	²³⁵ U Fast	²³⁵ U High	²³⁸ U Fast	²³⁹ Pu Thermal	²⁵² Cf Spontaneous
⁸⁷ As	0.56 s	5.05 × 10 ⁻²	1.68 × 10 ⁻²	2.04 × 10 ⁻²	4.97 × 10 ⁻²	1.27 × 10 ⁻³	3.78 × 10 ⁻³
⁸⁸ As	>150 ns	1.24 × 10 ⁻¹	2.01 × 10 ⁻³	4.32 × 10 ⁻³	1.66 × 10 ⁻²	1.02 × 10 ⁻⁴	8.64 × 10 ⁻⁴
⁸⁹ As		1.54 × 10 ⁻⁴	2.10 × 10 ⁻⁴	5.00 × 10 ⁻⁴	3.47 × 10 ⁻³	4.55 × 10 ⁻⁶	1.09 × 10 ⁻⁴
⁷⁵ Se	119.779 days			1.20 × 10 ⁻⁹		9.06 × 10 ⁻¹¹	
⁷⁶ Se	Stable	3.04 × 10 ⁻¹¹	9.35 × 10 ⁻¹¹	4.43 × 10 ⁻⁸		7.06 × 10 ⁻⁹	4.42 × 10 ⁻¹¹
⁷⁷ Se	Stable	2.75 × 10 ⁻¹⁰	1.02 × 10 ⁻⁹	1.02 × 10 ⁻⁷	1.11 × 10 ⁻¹¹	3.88 × 10 ⁻⁸	2.98 × 10 ⁻¹⁰
^{77m} Se	17.36 s	1.84 × 10 ⁻⁹	7.48 × 10 ⁻⁹	1.18 × 10 ⁻⁶	8.16 × 10 ⁻¹¹	2.60 × 10 ⁻⁷	2.00 × 10 ⁻⁹
⁷⁸ Se	Stable	2.47 × 10 ⁻⁷	6.21 × 10 ⁻⁷	2.44 × 10 ⁻⁵	1.20 × 10 ⁻⁸	1.17 × 10 ⁻⁵	1.20 × 10 ⁻⁷
⁷⁹ Se	295000 years	1.10 × 10 ⁻⁵	1.38 × 10 ⁻⁵	3.35 × 10 ⁻⁴	6.89 × 10 ⁻⁷	1.99 × 10 ⁻⁴	1.94 × 10 ⁻⁶
^{79m} Se	3.92 min	1.65 × 10 ⁻⁶	1.88 × 10 ⁻⁶	2.52 × 10 ⁻⁵	9.40 × 10 ⁻⁸	2.97 × 10 ⁻⁵	2.90 × 10 ⁻⁷
⁸⁰ Se	Stable	4.89 × 10 ⁻⁴	4.27 × 10 ⁻⁴	3.28 × 10 ⁻³	1.51 × 10 ⁻⁵	3.25 × 10 ⁻³	2.42 × 10 ⁻⁵
⁸¹ Se	18.45 min	1.04 × 10 ⁻³	5.26 × 10 ⁻⁴	1.42 × 10 ⁻³	3.53 × 10 ⁻⁵	3.16 × 10 ⁻³	2.92 × 10 ⁻⁵
^{81m} Se	57.28 min	6.93 × 10 ⁻³	3.86 × 10 ⁻³	1.63 × 10 ⁻²	2.59 × 10 ⁻⁴	2.11 × 10 ⁻²	1.95 × 10 ⁻⁴
⁸² Se	0.83 × 10 ²⁰ years	3.71 × 10 ⁻²	4.02 × 10 ⁻²	1.01 × 10 ⁻¹	4.88 × 10 ⁻³	8.76 × 10 ⁻²	1.55 × 10 ⁻³
⁸³ Se	22.3 min	1.43 × 10 ⁻¹	1.56 × 10 ⁻¹	3.52 × 10 ⁻¹	2.79 × 10 ⁻²	1.19 × 10 ⁻¹	9.01 × 10 ⁻³
^{83m} Se	70.1 s	3.35 × 10 ⁻²	3.19 × 10 ⁻²	4.39 × 10 ⁻²	5.71 × 10 ⁻³	3.71 × 10 ⁻²	2.11 × 10 ⁻³
⁸⁴ Se	3.10 min	6.31 × 10 ⁻¹	5.94 × 10 ⁻¹	7.19 × 10 ⁻¹	1.74 × 10 ⁻¹	3.27 × 10 ⁻¹	2.55 × 10 ⁻²
⁸⁵ Se	31.7 s	4.47 × 10 ⁻¹	5.34 × 10 ⁻¹	4.99 × 10 ⁻¹	2.46 × 10 ⁻¹	2.05 × 10 ⁻¹	3.75 × 10 ⁻²
^{85m} Se		4.47 × 10 ⁻¹	5.31 × 10 ⁻¹	4.95 × 10 ⁻¹	2.36 × 10 ⁻¹	2.01 × 10 ⁻¹	3.75 × 10 ⁻²
⁸⁶ Se	15.3 s	8.36 × 10 ⁻¹	1.23 × 10 ⁰	7.23 × 10 ⁻¹	8.35 × 10 ⁻¹	2.93 × 10 ⁻¹	6.70 × 10 ⁻²
⁸⁷ Se	5.50 s	7.31 × 10 ⁻¹	6.75 × 10 ⁻¹	4.70 × 10 ⁻¹	8.48 × 10 ⁻¹	1.37 × 10 ⁻¹	7.11 × 10 ⁻²
⁸⁸ Se	1.53 s	2.68 × 10 ⁻¹	4.47 × 10 ⁻¹	2.54 × 10 ⁻¹	5.42 × 10 ⁻¹	4.20 × 10 ⁻²	4.42 × 10 ⁻²
⁸⁹ Se	0.41 s	4.86 × 10 ⁻²	1.22 × 10 ⁻¹	7.53 × 10 ⁻²	3.34 × 10 ⁻¹	5.03 × 10 ⁻³	1.53 × 10 ⁻²

⁹⁰ Se	>150 ns	1.27×10^{-2}	2.39×10^{-2}	1.44×10^{-2}	1.06×10^{-1}	1.22×10^{-3}	4.15×10^{-3}
⁹¹ Se	0.27 s	6.66×10^{-4}	9.59×10^{-4}	1.45×10^{-3}	1.88×10^{-2}		5.84×10^{-4}
⁹² Se		4.17×10^{-5}	5.51×10^{-5}	1.15×10^{-4}	1.98×10^{-3}	2.26×10^{-6}	6.09×10^{-5}
⁹⁴ Se	>150 ns	1.71×10^{-8}	1.58×10^{-8}	2.31×10^{-7}	6.41×10^{-6}	2.28×10^{-7}	2.35×10^{-7}
⁹⁶ Se		1.28×10^{-11}	3.08×10^{-12}	8.98×10^{-11}	2.47×10^{-9}	4.76×10^{-12}	1.55×10^{-10}
^{79m} Br	4.86 s	1.04×10^{-9}	1.19×10^{-9}	6.70×10^{-7}	5.11×10^{-11}	1.91×10^{-7}	1.22×10^{-9}
^{80m} Br	4.4205 h	1.11×10^{-7}	8.95×10^{-8}	1.54×10^{-5}	2.93×10^{-9}	1.10×10^{-6}	3.62×10^{-8}
⁸¹ Br	Stable	8.86×10^{-6}	5.87×10^{-6}	2.88×10^{-4}	2.54×10^{-7}	2.67×10^{-4}	1.20×10^{-6}
⁸³ Br	2.40 h	1.95×10^{-2}	3.18×10^{-3}	3.55×10^{-2}	2.89×10^{-4}	1.71×10^{-2}	4.29×10^{-4}
⁸⁴ Br	31.80 min	1.86×10^{-2}	8.42×10^{-3}	3.49×10^{-2}	1.50×10^{-3}	2.73×10^{-2}	9.17×10^{-4}
^{84m} Br	6.0 min	1.67×10^{-2}	1.79×10^{-2}	1.24×10^{-1}	3.19×10^{-3}	4.85×10^{-2}	1.63×10^{-3}
⁸⁵ Br	2.90 min	2.35×10^{-1}	1.84×10^{-1}	5.01×10^{-1}	3.95×10^{-2}	1.48×10^{-1}	1.92×10^{-2}
⁸⁶ Br	55.1 s	2.30×10^{-1}	2.25×10^{-1}	4.26×10^{-1}	9.14×10^{-2}	1.89×10^{-1}	2.10×10^{-2}
^{86m} Br		2.30×10^{-1}	2.24×10^{-1}	4.26×10^{-1}	9.14×10^{-2}	1.89×10^{-1}	2.10×10^{-2}
⁸⁷ Br	55.65 s	1.27×10^0	1.43×10^0	1.14×10^0	6.57×10^{-1}	5.53×10^{-1}	1.10×10^{-1}
⁸⁸ Br	16.29 s	1.39×10^0	1.67×10^0	1.63×10^0	9.00×10^{-1}	4.66×10^{-1}	1.69×10^{-1}
⁸⁹ Br	4.40 s	1.04×10^0	1.33×10^0	1.20×10^0	1.62×10^0	3.44×10^{-1}	1.50×10^{-1}
⁹⁰ Br	1.91 s	5.53×10^{-1}	7.26×10^{-1}	5.66×10^{-1}	1.34×10^0	2.13×10^{-1}	1.09×10^{-1}
⁹¹ Br	0.541 s	2.24×10^{-1}	1.36×10^{-1}	1.48×10^{-1}	7.59×10^{-1}	1.98×10^{-2}	4.14×10^{-2}
⁹² Br	0.343 s	2.68×10^{-2}	2.09×10^{-2}	3.03×10^{-2}	2.34×10^{-1}	2.46×10^{-3}	1.20×10^{-2}
⁹³ Br	102 ms	3.09×10^{-3}	6.42×10^{-2}	1.16×10^{-3}	5.01×10^{-2}	6.59×10^{-3}	2.53×10^{-3}
⁹⁴ Br	70 ms	1.66×10^{-4}	8.14×10^{-5}	4.23×10^{-4}	7.90×10^{-3}	2.71×10^{-3}	3.58×10^{-4}
⁹⁶ Br	>150 ns	1.91×10^{-6}	2.28×10^{-7}	1.16×10^{-6}	3.52×10^{-5}	6.20×10^{-7}	1.91×10^{-6}
^{83m} Kr	1.83 h	1.55×10^{-6}	8.47×10^{-7}	3.66×10^{-5}	3.15×10^{-8}	2.90×10^{-5}	3.01×10^{-7}
⁸⁵ Kr	3.934.4 days	2.55×10^{-2}	3.09×10^{-3}	2.74×10^{-2}	1.99×10^{-4}	1.00×10^{-2}	4.60×10^{-4}
^{85m} Kr	4.480 h	5.89×10^{-3}	6.34×10^{-4}	3.39×10^{-3}	4.08×10^{-5}	2.36×10^{-3}	1.08×10^{-4}

Table 56.7 (Continued)

Fission product	Half-life	²³⁵ U Thermal	²³⁵ U Fast	²³⁵ U High	²³⁸ U Fast	²³⁹ Pu Thermal	²⁵² Cf Spontaneous
⁸⁷ Kr	76.3 min	4.63 × 10 ⁻¹	3.50 × 10 ⁻¹	7.34 × 10 ⁻¹	3.47 × 10 ⁻²	2.84 × 10 ⁻¹	2.24 × 10 ⁻²
⁸⁸ Kr	2.84 h	1.73 × 10 ⁰	1.25 × 10 ⁰	1.32 × 10 ⁰	3.68 × 10 ⁻¹	7.47 × 10 ⁻¹	8.81 × 10 ⁻²
⁸⁹ Kr	3.15 min	3.44 × 10 ⁰	2.56 × 10 ⁰	2.28 × 10 ⁰	6.46 × 10 ⁻¹	1.10 × 10 ⁰	1.74 × 10 ⁻¹
⁹⁰ Kr	32.32 s	4.40 × 10 ⁰	4.02 × 10 ⁰	2.50 × 10 ⁰	1.85 × 10 ⁰	1.10 × 10 ⁰	3.35 × 10 ⁻¹
⁹¹ Kr	8.57 s	3.16 × 10 ⁰	2.92 × 10 ⁰	1.65 × 10 ⁰	2.62 × 10 ⁰	6.97 × 10 ⁻¹	3.16 × 10 ⁻¹
⁹² Kr	1.840 s	1.66 × 10 ⁰	1.35 × 10 ⁰	8.25 × 10 ⁻¹	2.50 × 10 ⁰	3.09 × 10 ⁻¹	2.36 × 10 ⁻¹
⁹³ Kr	1.286 s	4.86 × 10 ⁻¹	3.05 × 10 ⁻¹	2.06 × 10 ⁻¹	1.43 × 10 ⁰	6.37 × 10 ⁻²	1.30 × 10 ⁻¹
⁹⁴ Kr	0.33 s	8.68 × 10 ⁻²	6.19 × 10 ⁻²	7.32 × 10 ⁻²	7.34 × 10 ⁻¹	2.15 × 10 ⁻²	4.89 × 10 ⁻²
⁹⁵ Kr	0.78 s	7.19 × 10 ⁻³	2.26 × 10 ⁻²	1.17 × 10 ⁻²	1.27 × 10 ⁻¹	1.11 × 10 ⁻³	1.10 × 10 ⁻²
⁹⁶ Kr	>50 ms	3.78 × 10 ⁻²	2.31 × 10 ⁻³	1.35 × 10 ⁻³	3.42 × 10 ⁻²	8.16 × 10 ⁻³	1.98 × 10 ⁻³
⁹⁷ Kr	>150 ns	2.97 × 10 ⁻⁵	1.15 × 10 ⁻⁴	1.07 × 10 ⁻⁴	8.02 × 10 ⁻⁴	1.61 × 10 ⁻³	1.99 × 10 ⁻⁴
⁹⁸ Kr		1.63 × 10 ⁻³	4.32 × 10 ⁻⁶	6.46 × 10 ⁻⁶	2.60 × 10 ⁻⁴	2.24 × 10 ⁻⁷	1.72 × 10 ⁻⁵
¹⁰⁰ Kr	>150 ns	1.15 × 10 ⁻⁶	9.60 × 10 ⁻¹⁰	5.36 × 10 ⁻⁹	3.66 × 10 ⁻⁷	6.52 × 10 ⁻¹¹	2.69 × 10 ⁻⁸
⁸⁷ Rb	4.81 × 10 ¹⁰ years	2.50 × 10 ⁻³	1.33 × 10 ⁻³	2.04 × 10 ⁻²	1.44 × 10 ⁻⁴	1.47 × 10 ⁻²	3.38 × 10 ⁻⁴
⁸⁸ Rb	17.78 min	2.23 × 10 ⁻²	5.48 × 10 ⁻²	1.55 × 10 ⁻¹	2.02 × 10 ⁻³	5.73 × 10 ⁻²	3.66 × 10 ⁻³
⁸⁹ Rb	15.15 min	2.05 × 10 ⁻¹	3.90 × 10 ⁻¹	5.92 × 10 ⁻¹	8.86 × 10 ⁻²	2.55 × 10 ⁻¹	2.00 × 10 ⁻²
⁹⁰ Rb	158 s	1.39 × 10 ⁻¹	1.29 × 10 ⁻¹	1.68 × 10 ⁻¹	2.81 × 10 ⁻²	1.41 × 10 ⁻¹	1.75 × 10 ⁻²
^{90m} Rb	258 s	7.07 × 10 ⁻¹	6.89 × 10 ⁻¹	1.35 × 10 ⁰	1.41 × 10 ⁻¹	6.04 × 10 ⁻¹	7.48 × 10 ⁻²
⁹¹ Rb	58.4 s	2.23 × 10 ⁰	2.01 × 10 ⁰	2.52 × 10 ⁰	6.75 × 10 ⁻¹	1.38 × 10 ⁰	2.24 × 10 ⁻¹
⁹² Rb	4.492 s	3.13 × 10 ⁰	2.79 × 10 ⁰	2.93 × 10 ⁰	1.47 × 10 ⁰	1.61 × 10 ⁰	3.47 × 10 ⁻¹
⁹³ Rb	5.84 s	3.07 × 10 ⁰	3.41 × 10 ⁰	2.20 × 10 ⁰	2.62 × 10 ⁰	1.36 × 10 ⁰	5.03 × 10 ⁻¹
⁹⁴ Rb	2.702 s	1.57 × 10 ⁰	1.89 × 10 ⁰	1.33 × 10 ⁰	2.54 × 10 ⁰	7.04 × 10 ⁻¹	4.54 × 10 ⁻¹
⁹⁵ Rb	377.5 ms	7.64 × 10 ⁻¹	8.98 × 10 ⁻¹	5.27 × 10 ⁻¹	1.60 × 10 ⁰	4.32 × 10 ⁻¹	2.68 × 10 ⁻¹

⁹⁶ Rb	202.8 ms	1.68×10^{-1}	2.28×10^{-1}	1.51×10^{-1}	1.17×10^0	3.91×10^{-2}	1.27×10^{-1}
⁹⁷ Rb	169.9 ms	3.79×10^{-2}	5.37×10^{-2}	3.01×10^{-2}	8.86×10^{-2}	5.36×10^{-3}	3.44×10^{-2}
⁹⁸ Rb	114 ms	2.36×10^{-3}	5.35×10^{-3}	4.57×10^{-3}	8.44×10^{-2}	6.78×10^{-4}	8.20×10^{-3}
¹⁰⁰ Rb	51 ms	3.48×10^{-2}	1.55×10^{-5}	2.45×10^{-5}	1.25×10^{-3}	2.06×10^{-6}	1.05×10^{-4}
^{87m} Sr	2.815 h	2.51×10^{-7}	9.79×10^{-8}	1.01×10^{-5}	2.73×10^{-9}	5.77×10^{-6}	8.99×10^{-8}
⁸⁸ Sr	Stable	7.68×10^{-5}	3.64×10^{-5}	1.83×10^{-3}	1.16×10^{-6}	6.79×10^{-4}	1.50×10^{-5}
⁸⁹ Sr	50.53 days	1.75×10^{-2}	8.32×10^{-4}	1.76×10^{-2}	4.63×10^{-5}	1.51×10^{-2}	2.29×10^{-4}
⁹⁰ Sr	28.79 years	7.37×10^{-2}	3.43×10^{-2}	1.12×10^{-1}	1.12×10^{-3}	9.69×10^{-2}	2.94×10^{-3}
⁹¹ Sr	9.63 h	2.51×10^{-1}	6.85×10^{-1}	5.07×10^{-1}	1.17×10^{-2}	3.86×10^{-1}	1.78×10^{-2}
⁹² Sr	2.71 h	1.08×10^0	1.61×10^0	1.25×10^0	1.03×10^{-1}	1.02×10^0	8.14×10^{-2}
⁹³ Sr	7.423 min	2.57×10^0	2.14×10^0	2.38×10^0	5.45×10^{-1}	2.14×10^0	2.36×10^{-1}
⁹⁴ Sr	75.3 s	4.51×10^0	3.79×10^0	2.92×10^0	1.51×10^0	2.92×10^0	5.47×10^{-1}
⁹⁵ Sr	23.90 s	4.54×10^0	4.37×10^0	2.71×10^0	3.18×10^0	2.61×10^0	7.67×10^{-1}
⁹⁶ Sr	1.07 s	3.57×10^0	4.38×10^0	1.81×10^0	4.13×10^0	1.82×10^0	8.88×10^{-1}
⁹⁷ Sr	429 ms	1.72×10^0	2.37×10^0	8.67×10^{-1}	2.86×10^0	7.87×10^{-1}	6.02×10^{-1}
⁹⁸ Sr	0.653 s	8.08×10^{-1}	1.04×10^0	3.16×10^{-1}	2.27×10^0	3.27×10^{-1}	3.71×10^{-1}
⁹⁹ Sr	0.269 s	1.33×10^{-1}	2.16×10^{-1}	7.55×10^{-2}	9.94×10^{-1}	3.75×10^{-2}	1.35×10^{-1}
¹⁰⁰ Sr	202 ms	8.15×10^{-3}	3.56×10^{-2}	1.03×10^{-2}	3.04×10^{-1}	6.76×10^{-3}	3.52×10^{-2}
¹⁰¹ Sr	118 ms	4.49×10^{-3}	2.56×10^{-3}	1.20×10^{-3}	4.80×10^{-2}	2.89×10^{-4}	5.66×10^{-3}
¹⁰² Sr	69 ms	1.73×10^{-4}	1.67×10^{-4}	1.07×10^{-4}	6.28×10^{-3}	8.03×10^{-6}	4.78×10^{-4}
¹⁰⁴ Sr		1.31×10^{-7}	6.93×10^{-8}	6.47×10^{-7}	2.02×10^{-5}	9.44×10^{-9}	1.08×10^{-6}
^{89m} Y	15.28 s	1.88×10^{-7}	6.74×10^{-8}	4.63×10^{-5}	2.68×10^{-9}	6.95×10^{-6}	1.34×10^{-7}
⁹⁰ Y	64.00 h	8.97×10^{-6}	4.59×10^{-6}	1.01×10^{-3}	2.43×10^{-7}	1.93×10^{-4}	6.01×10^{-6}
⁹¹ Y	58.51 days	3.30×10^{-4}	1.72×10^{-4}	9.07×10^{-3}	8.88×10^{-6}	2.48×10^{-3}	1.08×10^{-4}
⁹² Y	3.54 h	7.15×10^{-2}	2.90×10^{-3}	3.95×10^{-2}	2.33×10^{-4}	4.51×10^{-2}	1.24×10^{-3}
⁹³ Y	10.18 h	1.09×10^{-1}	2.07×10^{-1}	2.96×10^{-1}	3.96×10^{-3}	1.74×10^{-1}	1.07×10^{-2}

Table 56.7 (Continued)

Fission product	Half-life	²³⁵ U Thermal	²³⁵ U Fast	²³⁵ U High	²³⁸ U Fast	²³⁹ Pu Thermal	²⁵² Cf Spontaneous
⁹⁴ Y	18.7 min	3.90×10^{-1}	6.77×10^{-1}	8.44×10^{-1}	3.39×10^{-2}	6.75×10^{-1}	5.96×10^{-2}
⁹⁵ Y	10.3 min	1.11×10^0	1.18×10^0	1.80×10^0	2.23×10^{-1}	1.68×10^0	1.98×10^{-1}
⁹⁶ Y	5.34 s	2.24×10^{-1}	1.33×10^{-1}	1.63×10^{-1}	7.28×10^{-2}	2.49×10^{-1}	5.45×10^{-2}
^{96m} Y		2.02×10^0	1.35×10^0	2.56×10^0	7.36×10^{-1}	2.24×10^0	4.91×10^{-1}
⁹⁷ Y	3.75 s	3.14×10^0	3.03×10^0	2.94×10^0	2.52×10^0	2.96×10^0	8.70×10^{-1}
⁹⁸ Y	0.548 s	1.11×10^0	1.39×10^0	1.21×10^0	1.51×10^0	1.19×10^0	6.43×10^{-1}
^{98m} Y	2.0 s	1.11×10^0	1.39×10^0	1.21×10^0	1.51×10^0	1.19×10^0	6.43×10^{-1}
⁹⁹ Y	1.470 s	1.95×10^0	2.25×10^0	1.34×10^0	3.74×10^0	1.44×10^0	1.15×10^0
¹⁰⁰ Y	735 ms	5.67×10^{-1}	8.70×10^{-1}	4.33×10^{-1}	2.93×10^0	3.45×10^{-1}	7.78×10^{-1}
¹⁰¹ Y	0.45 s	2.78×10^{-1}	2.83×10^{-1}	1.19×10^{-1}	1.46×10^0	8.40×10^{-2}	3.36×10^{-1}
¹⁰² Y	0.30 s	2.68×10^{-1}	4.58×10^{-2}	2.55×10^{-2}	5.22×10^{-1}	6.12×10^{-3}	8.26×10^{-2}
¹⁰³ Y	0.23 s	2.58×10^{-3}	5.55×10^{-3}	4.35×10^{-3}	1.33×10^{-1}	1.01×10^{-3}	1.78×10^{-2}
¹⁰⁴ Y	180 ms	5.68×10^{-4}	2.32×10^{-4}	7.19×10^{-4}	1.63×10^{-2}	7.34×10^{-5}	1.64×10^{-3}
⁹³ Zr	1.53×10^6 years	1.37×10^{-4}	4.93×10^{-5}	3.84×10^{-3}	2.17×10^{-6}	1.69×10^{-3}	4.25×10^{-5}
⁹⁴ Zr	Stable	1.95×10^{-2}	1.29×10^{-3}	2.88×10^{-2}	6.46×10^{-5}	3.01×10^{-2}	6.61×10^{-4}
⁹⁵ Zr	64.032 days	1.27×10^{-1}	1.48×10^{-2}	1.51×10^{-1}	1.25×10^{-3}	1.25×10^{-1}	5.87×10^{-3}
⁹⁷ Zr	16.744 h	1.09×10^0	5.61×10^{-1}	1.31×10^0	1.02×10^{-1}	1.58×10^0	1.66×10^{-1}
⁹⁸ Zr	30.7 s	2.57×10^0	2.04×10^0	2.37×10^0	4.86×10^{-1}	2.92×10^0	5.87×10^{-1}
⁹⁹ Zr	2.1 s	3.58×10^0	3.36×10^0	2.90×10^0	1.47×10^0	3.76×10^0	1.25×10^0
¹⁰⁰ Zr	7.1 s	4.98×10^0	4.89×10^0	2.09×10^0	3.30×10^0	4.78×10^0	2.06×10^0
¹⁰¹ Zr	2.3 s	2.79×10^0	3.41×10^0	1.28×10^0	4.00×10^0	2.33×10^0	2.20×10^0
¹⁰² Zr	2.9 s	1.78×10^0	2.22×10^0	6.30×10^{-1}	4.09×10^0	1.22×10^0	1.45×10^0
¹⁰³ Zr	1.3 s	4.99×10^{-1}	6.26×10^{-1}	2.45×10^{-1}	2.64×10^0	2.23×10^{-1}	8.43×10^{-1}

^{104}Zr	1.2 s	8.28×10^{-2}	1.16×10^{-1}	7.66×10^{-2}	1.01×10^0	6.10×10^{-2}	2.24×10^{-1}
^{105}Zr	0.6 s	1.16×10^{-1}	5.49×10^{-4}	2.32×10^{-2}	2.13×10^{-1}	6.41×10^{-3}	3.91×10^{-2}
^{106}Zr	>150 ns	1.68×10^{-6}	2.74×10^{-5}	4.87×10^{-3}	7.29×10^{-4}	1.83×10^{-4}	6.07×10^{-3}
^{108}Zr	80 ms	3.10×10^{-10}	1.85×10^{-8}	6.11×10^{-5}	8.82×10^{-7}	4.55×10^{-7}	1.44×10^{-5}
^{110}Zr	>150 ns	9.29×10^{-9}	4.34×10^{-8}	2.62×10^{-7}	1.59×10^{-10}		5.81×10^{-9}
$^{93\text{m}}\text{Nb}$	16.13 years	8.49×10^{-10}	2.12×10^{-10}	5.57×10^{-7}	6.95×10^{-12}	9.89×10^{-8}	1.93×10^{-9}
^{95}Nb	34.991 days	1.06×10^{-4}	4.42×10^{-6}	1.18×10^{-3}	2.30×10^{-7}	5.65×10^{-4}	9.12×10^{-6}
$^{95\text{m}}\text{Nb}$	3.61 days	2.48×10^{-5}	9.05×10^{-7}	1.46×10^{-4}	4.70×10^{-8}	1.32×10^{-4}	2.14×10^{-6}
^{97}Nb	72.1 min	1.08×10^{-2}	2.17×10^{-3}	3.36×10^{-1}	1.94×10^{-4}	6.51×10^{-2}	1.76×10^{-3}
$^{97\text{m}}\text{Nb}$	58.7 s	2.45×10^{-3}	4.44×10^{-4}	4.16×10^{-2}	3.98×10^{-5}	1.53×10^{-2}	4.12×10^{-4}
^{98}Nb	2.86 s	1.16×10^{-1}	1.78×10^{-2}	2.52×10^{-1}	2.53×10^{-3}	1.33×10^{-1}	1.62×10^{-2}
$^{98\text{m}}\text{Nb}$	51.3 min	3.86×10^{-2}	5.02×10^{-3}	4.45×10^{-2}	7.12×10^{-4}	4.45×10^{-2}	5.41×10^{-3}
^{99}Nb	15.0 s	3.00×10^{-2}	1.24×10^{-2}	6.56×10^{-2}	2.54×10^{-3}	7.50×10^{-2}	9.33×10^{-3}
$^{99\text{m}}\text{Nb}$	2.6 min	4.07×10^{-1}	1.42×10^{-1}	7.54×10^{-1}	2.92×10^{-2}	8.81×10^{-1}	1.07×10^{-1}
^{100}Nb	1.5 s	3.19×10^{-1}	2.48×10^{-1}	6.57×10^{-1}	9.62×10^{-2}	7.50×10^{-1}	2.85×10^{-1}
$^{100\text{m}}\text{Nb}$	2.99 s	3.19×10^{-1}	2.48×10^{-1}	6.57×10^{-1}	9.62×10^{-2}	7.50×10^{-1}	2.85×10^{-1}
^{101}Nb	7.1 s	1.92×10^0	1.36×10^0	1.74×10^0	6.89×10^{-1}	3.46×10^0	1.30×10^0
^{102}Nb	1.3 s	1.58×10^0	1.73×10^0	1.85×10^0	1.75×10^0	3.08×10^0	2.04×10^0
^{103}Nb	1.5 s	1.41×10^0	1.81×10^0	1.55×10^0	3.12×10^0	2.70×10^0	3.06×10^0
^{104}Nb	4.9 s	5.70×10^{-1}	7.14×10^{-1}	8.82×10^{-1}	2.87×10^0	1.16×10^0	2.15×10^0
^{105}Nb	2.95 s	1.39×10^{-1}	2.77×10^{-1}	4.29×10^{-1}	1.80×10^0	4.94×10^{-1}	9.99×10^{-1}
^{106}Nb	1.02 s	1.57×10^{-2}	4.35×10^{-2}	1.91×10^{-1}	5.94×10^{-1}	3.49×10^{-2}	4.41×10^{-1}
^{107}Nb	330 ms	2.31×10^{-3}	1.02×10^{-2}	5.25×10^{-2}	1.45×10^{-1}	9.78×10^{-3}	9.02×10^{-2}
^{108}Nb	0.193 s	9.00×10^{-5}	8.19×10^{-4}	1.24×10^{-2}	1.74×10^{-2}	9.32×10^{-4}	1.02×10^{-2}
^{109}Nb	0.19 s	4.84×10^{-4}	1.57×10^{-3}	2.27×10^{-3}	1.53×10^{-3}	1.78×10^{-9}	7.99×10^{-4}
^{110}Nb	0.17 s	1.53×10^{-5}	5.54×10^{-5}	2.98×10^{-4}	1.11×10^{-4}		3.97×10^{-5}

Table 56.7 (Continued)

Fission product	Half-life	²³⁵ U Thermal	²³⁵ U Fast	²³⁵ U High	²³⁸ U Fast	²³⁹ Pu Thermal	²⁵² Cf Spontaneous
⁹⁵ Mo	Stable	4.94 × 10 ⁻¹⁰	1.50 × 10 ⁻¹⁰	1.14 × 10 ⁻⁶	3.22 × 10 ⁻¹²	9.34 × 10 ⁻⁸	1.78 × 10 ⁻⁹
⁹⁹ Mo	65.94 h	4.28 × 10 ⁻²	7.24 × 10 ⁻⁴	2.73 × 10 ⁻²	4.57 × 10 ⁻⁵	3.75 × 10 ⁻²	1.14 × 10 ⁻³
¹⁰⁰ Mo	0.95 × 10 ¹⁹ years	7.30 × 10 ⁻²	1.07 × 10 ⁻²	1.03 × 10 ⁻¹	9.71 × 10 ⁻⁴	1.42 × 10 ⁻¹	1.48 × 10 ⁻²
¹⁰¹ Mo	14.61 min	1.86 × 10 ⁻¹	6.93 × 10 ⁻²	3.05 × 10 ⁻¹	1.03 × 10 ⁻²	1.38 × 10 ⁻¹	8.93 × 10 ⁻²
¹⁰² Mo	11.3 min	6.51 × 10 ⁻¹	3.65 × 10 ⁻¹	7.13 × 10 ⁻¹	8.10 × 10 ⁻²	1.76 × 10 ⁰	4.64 × 10 ⁻¹
¹⁰³ Mo	67.5 s	1.04 × 10 ⁰	7.97 × 10 ⁻¹	1.27 × 10 ⁰	3.73 × 10 ⁻¹	3.81 × 10 ⁰	1.47 × 10 ⁰
¹⁰⁴ Mo	60 s	1.13 × 10 ⁰	1.20 × 10 ⁰	1.27 × 10 ⁰	1.08 × 10 ⁰	4.29 × 10 ⁰	2.83 × 10 ⁰
¹⁰⁵ Mo	35.6 s	6.68 × 10 ⁻¹	9.17 × 10 ⁻¹	1.01 × 10 ⁰	2.00 × 10 ⁰	3.51 × 10 ⁰	3.02 × 10 ⁰
¹⁰⁶ Mo	8.4 s	3.59 × 10 ⁻¹	4.79 × 10 ⁻¹	8.68 × 10 ⁻¹	1.88 × 10 ⁰	2.17 × 10 ⁰	3.47 × 10 ⁰
¹⁰⁷ Mo	3.5 s	1.21 × 10 ⁻¹	2.66 × 10 ⁻¹	5.09 × 10 ⁻¹	1.23 × 10 ⁰	5.86 × 10 ⁻¹	2.01 × 10 ⁰
¹⁰⁸ Mo	1.09 s	3.02 × 10 ⁻²	1.07 × 10 ⁻¹	2.63 × 10 ⁻¹	5.07 × 10 ⁻¹	2.15 × 10 ⁻¹	6.67 × 10 ⁻¹
¹⁰⁹ Mo	0.53 s	1.55 × 10 ⁻²	4.19 × 10 ⁻²	1.09 × 10 ⁻¹	1.68 × 10 ⁻¹	5.92 × 10 ⁻³	1.48 × 10 ⁻¹
¹¹⁰ Mo	0.30 s	3.89 × 10 ⁻³	1.12 × 10 ⁻²	3.25 × 10 ⁻²	6.20 × 10 ⁻²	8.32 × 10 ⁻⁶	2.31 × 10 ⁻²
¹¹¹ Mo	>150 ns	2.28 × 10 ⁻⁴	6.98 × 10 ⁻⁴	7.44 × 10 ⁻³	1.75 × 10 ⁻²	2.53 × 10 ⁻⁷	1.42 × 10 ⁻³
¹¹² Mo	>150 ns	9.65 × 10 ⁻⁶	4.41 × 10 ⁻⁵	1.12 × 10 ⁻³	2.24 × 10 ⁻³	5.95 × 10 ⁻⁹	5.34 × 10 ⁻⁵
¹¹⁴ Mo	>150 ns	4.40 × 10 ⁻⁹	4.58 × 10 ⁻⁸	1.24 × 10 ⁻⁵	8.26 × 10 ⁻⁶	5.44 × 10 ⁻⁷	6.24 × 10 ⁻⁹
¹¹⁶ Mo			5.85 × 10 ⁻¹²	3.93 × 10 ⁻⁸	1.22 × 10 ⁻⁸	1.16 × 10 ⁻¹¹	
⁹⁹ Tc	211,100 years	1.23 × 10 ⁻⁷	4.85 × 10 ⁻⁸	8.15 × 10 ⁻⁵	1.99 × 10 ⁻⁹	1.20 × 10 ⁻⁵	5.48 × 10 ⁻⁷
^{99m} Tc	6.015 h	2.89 × 10 ⁻⁸	9.94 × 10 ⁻⁹	1.01 × 10 ⁻⁵	4.07 × 10 ⁻¹⁰	2.81 × 10 ⁻⁶	1.29 × 10 ⁻⁷
¹⁰⁰ Tc	15.8 s	5.59 × 10 ⁻⁶	2.37 × 10 ⁻⁶	8.59 × 10 ⁻⁴	1.56 × 10 ⁻⁷	3.07 × 10 ⁻⁴	2.53 × 10 ⁻⁵
¹⁰¹ Tc	14.22 min	1.61 × 10 ⁻⁴	7.61 × 10 ⁻⁵	6.06 × 10 ⁻³	5.99 × 10 ⁻⁶	1.24 × 10 ⁻²	4.46 × 10 ⁻⁴
¹⁰² Tc	5.28 s	9.55 × 10 ⁻³	4.88 × 10 ⁻⁴	1.65 × 10 ⁻²	6.88 × 10 ⁻⁵	3.37 × 10 ⁻²	2.94 × 10 ⁻³
^{102m} Tc		9.55 × 10 ⁻³	4.88 × 10 ⁻⁴	1.65 × 10 ⁻²	6.88 × 10 ⁻⁵	3.37 × 10 ⁻²	2.94 × 10 ⁻³

^{103}Tc	54.2 s	8.22×10^{-2}	9.43×10^{-3}	1.31×10^{-1}	2.15×10^{-3}	2.53×10^{-1}	5.66×10^{-2}
^{104}Tc	18.3 min	9.26×10^{-2}	3.16×10^{-2}	2.37×10^{-1}	1.58×10^{-2}	5.42×10^{-1}	4.31×10^{-1}
^{105}Tc	7.6 min	4.85×10^{-2}	7.47×10^{-3}	4.06×10^{-1}	7.81×10^{-2}	1.59×10^0	2.10×10^0
^{106}Tc	35.6 s	2.68×10^{-2}	1.03×10^{-2}	5.10×10^{-1}	2.52×10^{-2}	1.83×10^0	2.19×10^0
^{107}Tc	21.2 s	2.24×10^{-2}	2.57×10^{-2}	6.24×10^{-1}	6.65×10^{-2}	1.82×10^0	3.63×10^0
^{108}Tc	5.17 s	2.38×10^{-2}	2.24×10^{-2}	6.70×10^{-1}	7.63×10^{-2}	6.26×10^{-1}	3.33×10^0
^{109}Tc	0.86 s	1.34×10^{-2}	3.39×10^{-2}	5.98×10^{-1}	8.18×10^{-2}	4.04×10^{-1}	1.89×10^0
^{110}Tc	0.92 s	1.16×10^{-2}	3.05×10^{-2}	3.82×10^{-1}	7.88×10^{-2}	4.02×10^{-2}	8.55×10^{-1}
^{111}Tc	0.30 s	4.49×10^{-3}	1.20×10^{-2}	1.96×10^{-1}	4.27×10^{-2}	6.70×10^{-3}	1.76×10^{-1}
^{112}Tc	0.29 s	6.86×10^{-4}	2.47×10^{-3}	6.91×10^{-2}	2.34×10^{-2}	6.09×10^{-4}	2.29×10^{-2}
^{113}Tc	0.17 s	1.40×10^{-4}	4.85×10^{-4}	2.09×10^{-2}	7.80×10^{-3}	7.87×10^{-5}	1.64×10^{-3}
^{114}Tc	0.15 s	7.01×10^{-6}	4.50×10^{-5}	4.23×10^{-3}	1.39×10^{-3}	2.65×10^{-4}	3.87×10^{-5}
^{116}Tc	90 ms	6.31×10^{-9}	9.15×10^{-8}	7.56×10^{-5}	2.39×10^{-5}	1.46×10^{-7}	4.55×10^{-10}
^{101}Ru	Stable	1.62×10^{-8}	6.41×10^{-9}	1.19×10^{-5}	1.87×10^{-10}	2.43×10^{-6}	1.90×10^{-7}
^{102}Ru	Stable	9.76×10^{-7}	3.96×10^{-7}	1.59×10^{-4}	1.62×10^{-8}	7.65×10^{-5}	7.61×10^{-6}
^{103}Ru	39.26 days	2.36×10^{-5}	9.94×10^{-6}	1.48×10^{-3}	7.57×10^{-7}	1.26×10^{-3}	1.31×10^{-4}
^{104}Ru	Stable	3.27×10^{-4}	1.59×10^{-4}	5.04×10^{-3}	2.01×10^{-5}	2.44×10^{-2}	3.14×10^{-3}
^{105}Ru	4.44 h	1.11×10^{-7}	1.01×10^{-7}	9.91×10^{-3}	3.60×10^{-4}	4.54×10^{-2}	6.83×10^{-2}
^{106}Ru	373.59 days	9.07×10^{-7}	8.70×10^{-7}	3.75×10^{-2}	3.89×10^{-7}	3.24×10^{-1}	2.08×10^{-1}
^{107}Ru	3.75 min	4.94×10^{-6}	8.41×10^{-6}	9.84×10^{-2}	5.09×10^{-6}	8.37×10^{-1}	8.72×10^{-1}
^{108}Ru	4.55 min	1.67×10^{-5}	4.91×10^{-5}	2.23×10^{-1}	3.04×10^{-5}	1.28×10^0	1.98×10^0
^{109}Ru	34.5 s	1.71×10^{-3}	4.00×10^{-3}	4.24×10^{-1}	1.58×10^{-4}	9.96×10^{-1}	2.99×10^0
^{110}Ru	11.6 s	9.89×10^{-3}	2.32×10^{-2}	5.62×10^{-1}	7.84×10^{-4}	5.74×10^{-1}	3.62×10^0
^{111}Ru	2.12 s	1.18×10^{-2}	2.78×10^{-2}	6.13×10^{-1}	1.09×10^{-2}	2.45×10^{-1}	2.26×10^0
^{112}Ru	1.75 s	9.92×10^{-3}	2.88×10^{-2}	4.77×10^{-1}	2.84×10^{-2}	9.21×10^{-2}	9.39×10^{-1}
^{113}Ru	0.80 s	6.05×10^{-3}	1.55×10^{-2}	3.19×10^{-1}	3.04×10^{-2}	3.77×10^{-2}	2.13×10^{-1}

Table 56.7 (Continued)

Fission product	Half-life	²³⁵ U Thermal	²³⁵ U Fast	²³⁵ U High	²³⁸ U Fast	²³⁹ Pu Thermal	²⁵² Cf Spontaneous
¹¹⁴ Ru	0.53 s	1.73 × 10 ⁻³	7.07 × 10 ⁻³	1.45 × 10 ⁻¹	2.05 × 10 ⁻²	1.58 × 10 ⁻²	1.90 × 10 ⁻²
¹¹⁵ Ru	740 ms	2.57 × 10 ⁻⁴	1.45 × 10 ⁻³	3.34 × 10 ⁻²	9.85 × 10 ⁻³	1.80 × 10 ⁻³	1.18 × 10 ⁻³
¹¹⁶ Ru	400 ms	2.46 × 10 ⁻⁵	2.03 × 10 ⁻⁴	1.37 × 10 ⁻²	3.43 × 10 ⁻³	1.95 × 10 ⁻⁴	2.29 × 10 ⁻⁵
¹¹⁷ Ru	300 ms	2.52 × 10 ⁻⁶	1.52 × 10 ⁻⁵	2.78 × 10 ⁻³	5.43 × 10 ⁻⁴	8.56 × 10 ⁻⁶	3.71 × 10 ⁻⁷
¹¹⁸ Ru	>150 ns	6.92 × 10 ⁻⁸	6.89 × 10 ⁻⁷	3.97 × 10 ⁻⁴	9.00 × 10 ⁻⁵	2.23 × 10 ⁻⁷	2.26 × 10 ⁻⁸
¹¹⁹ Ru	>150 ns	6.55 × 10 ⁻¹⁰	1.36 × 10 ⁻⁸	4.06 × 10 ⁻⁵	4.98 × 10 ⁻⁶	3.11 × 10 ⁻⁹	4.47 × 10 ⁻¹¹
¹²⁰ Ru	>150 ns	3.03 × 10 ⁻¹⁰	1.83 × 10 ⁻¹⁰	3.24 × 10 ⁻⁶	1.89 × 10 ⁻⁷	3.33 × 10 ⁻¹¹	
¹²² Ru				6.41 × 10 ⁻⁹	6.30 × 10 ⁻¹¹		
¹²⁴ Ru				3.11 × 10 ⁻¹²			3.51 × 10 ⁻⁹
¹⁰¹ Rh	3.3 years	3.26 × 10 ⁻¹¹		2.37 × 10 ⁻¹⁰		8.95 × 10 ⁻¹²	
^{101m} Rh	4.34 days			1.92 × 10 ⁻⁹		3.82 × 10 ⁻¹¹	3.61 × 10 ⁻¹²
^{103m} Rh	56.114 min	4.27 × 10 ⁻¹⁰	1.50 × 10 ⁻¹⁰	1.58 × 10 ⁻⁷	7.86 × 10 ⁻¹²	2.23 × 10 ⁻⁷	9.48 × 10 ⁻⁹
¹⁰⁵ Rh	35.36 h		6.16 × 10 ⁻⁸	4.08 × 10 ⁻⁶	4.46 × 10 ⁻⁸	1.38 × 10 ⁻⁴	5.53 × 10 ⁻⁵
^{105m} Rh	43.0 s		8.40 × 10 ⁻⁹	3.55 × 10 ⁻⁷	6.08 × 10 ⁻⁹	2.07 × 10 ⁻⁵	8.27 × 10 ⁻⁶
¹⁰⁶ Rh	29.80 s			1.45 × 10 ⁻⁴		2.22 × 10 ⁻⁴	5.92 × 10 ⁻⁴
^{106m} Rh	131 min			1.45 × 10 ⁻⁴		2.22 × 10 ⁻⁴	5.92 × 10 ⁻⁴
¹⁰⁷ Rh	21.7 min			1.75 × 10 ⁻³		7.62 × 10 ⁻²	1.58 × 10 ⁻²
¹⁰⁸ Rh	16.8 s		6.81 × 10 ⁻¹²	4.44 × 10 ⁻³	1.81 × 10 ⁻¹²	1.98 × 10 ⁻²	5.73 × 10 ⁻²
^{108m} Rh			6.81 × 10 ⁻¹²	4.44 × 10 ⁻³	1.81 × 10 ⁻¹²	1.98 × 10 ⁻²	5.73 × 10 ⁻²
¹⁰⁹ Rh	80 s	2.06 × 10 ⁻⁶	5.25 × 10 ⁻⁶	1.88 × 10 ⁻²	6.24 × 10 ⁻¹¹	3.62 × 10 ⁻²	6.52 × 10 ⁻¹
^{109m} Rh		2.06 × 10 ⁻⁶	5.25 × 10 ⁻⁶	1.88 × 10 ⁻²	6.24 × 10 ⁻¹¹	3.62 × 10 ⁻²	2.54 × 10 ⁻¹
¹¹⁰ Rh	3.2 s	5.65 × 10 ⁻⁵	1.33 × 10 ⁻⁴	5.35 × 10 ⁻²	1.73 × 10 ⁻⁹	1.54 × 10 ⁻²	6.72 × 10 ⁻¹
^{110m} Rh		5.65 × 10 ⁻⁵	1.33 × 10 ⁻⁴	5.35 × 10 ⁻²	1.73 × 10 ⁻⁹	1.54 × 10 ⁻²	6.75 × 10 ⁻¹

¹¹¹ Rh	11 s	8.80×10^{-4}	2.08×10^{-3}	2.51×10^{-1}	1.45×10^{-4}	4.43×10^{-2}	2.46×10^0
¹¹² Rh	3.45 s	2.30×10^{-3}	6.05×10^{-3}	4.80×10^{-1}	1.80×10^{-3}	3.57×10^{-2}	2.39×10^0
¹¹³ Rh	2.80 s	6.84×10^{-3}	1.46×10^{-2}	6.00×10^{-1}	7.70×10^{-3}	4.35×10^{-2}	1.95×10^0
¹¹⁴ Rh	1.85 s	5.03×10^{-3}	1.55×10^{-2}	5.83×10^{-1}	1.59×10^{-2}	3.20×10^{-2}	5.60×10^{-1}
¹¹⁵ Rh	0.99 s	3.63×10^{-3}	1.35×10^{-2}	2.91×10^{-1}	2.23×10^{-2}	1.79×10^{-2}	1.71×10^{-1}
¹¹⁶ Rh	0.68 s	8.69×10^{-4}	4.81×10^{-3}	2.60×10^{-1}	2.05×10^{-2}	6.73×10^{-3}	2.26×10^{-2}
¹¹⁷ Rh	0.44 s	4.65×10^{-4}	1.85×10^{-3}	1.17×10^{-1}	1.15×10^{-2}	1.43×10^{-3}	2.15×10^{-3}
¹¹⁸ Rh	>150 ns	3.63×10^{-5}	2.46×10^{-4}	3.86×10^{-2}	5.14×10^{-3}	1.26×10^{-4}	3.54×10^{-4}
¹¹⁹ Rh	>150 ns	1.86×10^{-6}	2.68×10^{-5}	9.28×10^{-3}	1.12×10^{-3}	8.17×10^{-6}	5.11×10^{-6}
¹²⁰ Rh	>150 ns	2.39×10^{-6}	1.08×10^{-6}	1.73×10^{-3}	1.43×10^{-4}	2.75×10^{-7}	3.94×10^{-9}
¹²¹ Rh	>150 ns	1.44×10^{-8}	4.28×10^{-8}	2.19×10^{-4}	1.07×10^{-5}	9.09×10^{-9}	
¹²² Rh	~50 ms	2.85×10^{-10}	8.12×10^{-10}	2.04×10^{-5}	6.17×10^{-7}	1.31×10^{-10}	
¹²³ Rh		8.52×10^{-12}	1.37×10^{-11}	1.32×10^{-6}	2.62×10^{-8}		1.44×10^{-12}
¹²⁴ Rh		1.04×10^{-12}		6.23×10^{-8}	5.60×10^{-10}		1.43×10^{-6}
¹⁰⁵ Pd	Stable			1.52×10^{-8}	3.75×10^{-7}	2.42×10^{-8}	1.07×10^{-8}
¹⁰⁶ Pd	Stable			2.15×10^{-7}		9.15×10^{-7}	6.22×10^{-7}
¹⁰⁷ Pd	6.5×10^6 years			6.43×10^{-7}		6.81×10^{-6}	9.21×10^{-6}
^{107m} Pd	21.3 s			2.42×10^{-6}		1.27×10^{-5}	1.71×10^{-5}
¹⁰⁹ Pd	13.7012 h	2.94×10^{-10}	7.01×10^{-10}	7.60×10^{-5}		1.41×10^{-7}	2.83×10^{-3}
^{109m} Pd	4.696 min	5.46×10^{-10}	1.56×10^{-9}	2.86×10^{-4}		2.61×10^{-7}	5.26×10^{-3}
¹¹⁰ Pd	Stable	2.15×10^{-7}	5.08×10^{-7}	2.33×10^{-3}		4.43×10^{-6}	6.05×10^{-2}
¹¹¹ Pd	23.4 min	2.54×10^{-6}	5.17×10^{-6}	2.61×10^{-3}	3.85×10^{-8}	8.14×10^{-6}	1.21×10^{-1}
^{111m} Pd	5.5 h	4.72×10^{-6}	1.15×10^{-5}	9.81×10^{-3}	8.58×10^{-8}	1.51×10^{-5}	1.71×10^{-1}
¹¹² Pd	21.03 h	1.28×10^{-4}	2.98×10^{-4}	4.75×10^{-2}	9.92×10^{-6}	9.47×10^{-5}	7.45×10^{-1}
¹¹³ Pd	93 s	1.16×10^{-3}	2.04×10^{-3}	1.48×10^{-1}	1.68×10^{-4}	3.74×10^{-4}	2.39×10^0
¹¹⁴ Pd	2.42 min	4.16×10^{-3}	9.57×10^{-3}	3.05×10^{-1}	1.42×10^{-3}	1.21×10^{-2}	1.82×10^0

Table 56.7 (Continued)

Fission product	Half-life	²³⁵ U Thermal	²³⁵ U Fast	²³⁵ U High	²³⁸ U Fast	²³⁹ Pu Thermal	²⁵² Cf Spontaneous
¹¹⁵ Pd	25 s	7.13 × 10 ⁻³	1.82 × 10 ⁻²	3.22 × 10 ⁻¹	5.29 × 10 ⁻³	2.15 × 10 ⁻²	1.70 × 10 ⁰
¹¹⁶ Pd	11.8 s	6.82 × 10 ⁻³	2.63 × 10 ⁻²	5.97 × 10 ⁻¹	1.48 × 10 ⁻²	3.59 × 10 ⁻²	8.19 × 10 ⁻¹
¹¹⁷ Pd	4.3 s	8.77 × 10 ⁻³	2.42 × 10 ⁻²	5.64 × 10 ⁻¹	2.28 × 10 ⁻²	2.22 × 10 ⁻²	2.92 × 10 ⁻¹
¹¹⁸ Pd	1.9 s	3.18 × 10 ⁻³	1.51 × 10 ⁻²	4.07 × 10 ⁻¹	2.88 × 10 ⁻²	8.63 × 10 ⁻³	1.27 × 10 ⁻¹
¹¹⁹ Pd	0.92 s	4.35 × 10 ⁻⁴	4.52 × 10 ⁻³	2.19 × 10 ⁻¹	1.84 × 10 ⁻²	1.65 × 10 ⁻³	8.49 × 10 ⁻³
¹²⁰ Pd	0.5 s	2.71 × 10 ⁻³	9.36 × 10 ⁻⁴	9.08 × 10 ⁻²	8.39 × 10 ⁻³	2.43 × 10 ⁻⁴	4.05 × 10 ⁻⁴
¹²¹ Pd	>150 ns	4.73 × 10 ⁻⁵	1.04 × 10 ⁻⁴	2.68 × 10 ⁻²	2.01 × 10 ⁻³	2.47 × 10 ⁻⁵	8.11 × 10 ⁻⁷
¹²² Pd	>150 ns	4.77 × 10 ⁻⁶	1.00 × 10 ⁻⁵	6.04 × 10 ⁻³	4.16 × 10 ⁻⁴	1.62 × 10 ⁻⁶	3.32 × 10 ⁻¹⁰
¹²³ Pd	>150 ns	3.99 × 10 ⁻⁷	4.79 × 10 ⁻⁷	9.54 × 10 ⁻⁴	5.36 × 10 ⁻⁵	3.62 × 10 ⁻⁸	1.78 × 10 ⁻⁶
¹²⁴ Pd	~0.2 s	2.73 × 10 ⁻⁷	2.34 × 10 ⁻⁸	1.12 × 10 ⁻⁴	4.26 × 10 ⁻⁶		1.42 × 10 ⁻⁴
¹²⁵ Pd				8.79 × 10 ⁻⁶	2.07 × 10 ⁻⁷		4.53 × 10 ⁻⁶
¹²⁶ Pd				6.79 × 10 ⁻⁷			6.06 × 10 ⁻¹²
¹²⁸ Pd		1.34 × 10 ⁻¹²		5.75 × 10 ⁻⁹			
¹³⁰ Pd		6.79 × 10 ⁻¹¹	2.56 × 10 ⁻¹²	3.96 × 10 ⁻¹²			
^{106m} Ag	8.28 days			1.18 × 10 ⁻¹¹		8.06 × 10 ⁻¹²	1.27 × 10 ⁻¹¹
¹⁰⁷ Ag	Stable			3.92 × 10 ⁻¹¹		1.26 × 10 ⁻¹⁰	3.37 × 10 ⁻¹⁰
^{107m} Ag	44.3 s			4.51 × 10 ⁻¹⁰		8.44 × 10 ⁻¹⁰	2.26 × 10 ⁻⁹
^{110m} Ag	249.76 days	2.28 × 10 ⁻¹²	6.48 × 10 ⁻¹²	4.14 × 10 ⁻⁶			1.25 × 10 ⁻⁴
¹¹¹ Ag	7.45 days	1.24 × 10 ⁻¹⁰	2.88 × 10 ⁻¹⁰	5.11 × 10 ⁻⁶			4.53 × 10 ⁻⁴
^{111m} Ag	64.8 s	8.28 × 10 ⁻¹⁰	2.11 × 10 ⁻⁹	5.88 × 10 ⁻⁵	3.32 × 10 ⁻¹²	3.27 × 10 ⁻¹²	3.03 × 10 ⁻³
¹¹² Ag	3.130 h	8.29 × 10 ⁻⁷	1.51 × 10 ⁻⁷	6.14 × 10 ⁻⁴	1.83 × 10 ⁻⁹	5.86 × 10 ⁻¹¹	3.60 × 10 ⁻²
¹¹³ Ag	5.37 h	5.42 × 10 ⁻⁷	7.80 × 10 ⁻⁷	3.33 × 10 ⁻⁴	1.79 × 10 ⁻⁸	1.81 × 10 ⁻¹⁰	2.94 × 10 ⁻²
^{113m} Ag	68.7 s	3.62 × 10 ⁻⁶	5.72 × 10 ⁻⁶	3.83 × 10 ⁻³	1.31 × 10 ⁻⁷	1.21 × 10 ⁻⁹	1.96 × 10 ⁻¹

^{114}Ag	4.6 s		9.17×10^{-4}	8.58×10^{-5}	1.96×10^{-2}	4.95×10^{-6}	1.50×10^{-4}	9.13×10^{-1}
^{115}Ag	20.0 min		1.93×10^{-4}	3.72×10^{-4}	2.29×10^{-2}	3.22×10^{-5}	7.15×10^{-4}	4.39×10^{-1}
$^{115\text{m}}\text{Ag}$	18.0 s		1.37×10^{-3}	3.72×10^{-4}	2.29×10^{-2}	3.22×10^{-5}	7.15×10^{-4}	5.38×10^{-1}
^{116}Ag	2.68 min		4.74×10^{-3}	1.30×10^{-3}	8.98×10^{-2}	2.64×10^{-4}	3.82×10^{-3}	6.50×10^{-1}
$^{116\text{m}}\text{Ag}$	8.6 s		7.65×10^{-4}	1.30×10^{-3}	8.98×10^{-2}	2.64×10^{-4}	3.82×10^{-3}	5.37×10^{-1}
^{117}Ag	72.8 s		1.52×10^{-3}	5.09×10^{-3}	1.77×10^{-1}	1.44×10^{-3}	9.45×10^{-3}	5.00×10^{-1}
$^{117\text{m}}\text{Ag}$	5.34 s		1.52×10^{-3}	5.09×10^{-3}	1.77×10^{-1}	1.44×10^{-3}	9.45×10^{-3}	5.15×10^{-1}
^{118}Ag	3.76 s		3.42×10^{-3}	7.23×10^{-3}	2.71×10^{-1}	4.44×10^{-3}	9.88×10^{-3}	2.97×10^{-1}
$^{118\text{m}}\text{Ag}$	2.0 s		2.99×10^{-3}	7.23×10^{-3}	2.71×10^{-1}	4.44×10^{-3}	9.88×10^{-3}	2.94×10^{-1}
^{119}Ag	2.1 s		7.25×10^{-3}	1.86×10^{-2}	6.18×10^{-1}	1.84×10^{-2}	1.44×10^{-2}	1.93×10^{-1}
^{120}Ag	1.23 s		8.75×10^{-4}	9.38×10^{-3}	5.41×10^{-1}	2.26×10^{-2}	5.68×10^{-3}	7.95×10^{-2}
^{121}Ag	0.79 s		2.58×10^{-3}	4.80×10^{-3}	3.51×10^{-1}	1.79×10^{-2}	2.39×10^{-3}	1.90×10^{-2}
^{122}Ag	0.520 s		6.68×10^{-4}	1.20×10^{-3}	1.82×10^{-1}	1.02×10^{-2}	4.65×10^{-4}	4.68×10^{-3}
^{123}Ag	0.293 s		2.75×10^{-4}	2.80×10^{-4}	6.74×10^{-2}	4.30×10^{-3}	4.76×10^{-5}	3.34×10^{-3}
^{124}Ag	0.172 s		5.52×10^{-4}	3.65×10^{-5}	1.89×10^{-2}	1.02×10^{-3}	6.16×10^{-10}	2.42×10^{-3}
^{125}Ag	166 ms		1.66×10^{-9}	2.35×10^{-9}	3.61×10^{-3}	1.75×10^{-4}	4.98×10^{-11}	2.03×10^{-4}
^{126}Ag	107 ms		4.75×10^{-10}	1.85×10^{-10}	6.86×10^{-4}	9.44×10^{-9}	3.87×10^{-12}	1.98×10^{-7}
^{127}Ag	79 ms		1.58×10^{-10}	3.90×10^{-11}	9.31×10^{-5}	1.19×10^{-9}		
^{128}Ag	58 ms		1.12×10^{-11}	1.52×10^{-12}	2.28×10^{-5}	7.10×10^{-11}		
^{130}Ag	~50 ms		6.66×10^{-6}	1.45×10^{-7}	9.41×10^{-8}		1.70×10^{-8}	1.23×10^{-10}
$^{111\text{m}}\text{Cd}$	48.50 min				2.66×10^{-8}			2.46×10^{-6}
^{112}Cd	Stable		1.06×10^{-9}	1.15×10^{-11}	1.12×10^{-7}			1.00×10^{-4}
^{113}Cd	7.7×10^{15} years		2.59×10^{-10}	3.59×10^{-10}	1.67×10^{-6}	1.61×10^{-12}		5.51×10^{-4}
$^{113\text{m}}\text{Cd}$	14.1 years		8.68×10^{-10}	1.35×10^{-9}	1.03×10^{-5}	6.04×10^{-12}		1.85×10^{-3}
^{114}Cd	Stable		7.65×10^{-8}	1.26×10^{-7}	1.33×10^{-4}	1.23×10^{-9}	2.22×10^{-7}	1.98×10^{-2}
^{115}Cd	53.46 h		9.00×10^{-7}	6.44×10^{-7}	1.02×10^{-4}	1.06×10^{-8}	2.03×10^{-6}	1.23×10^{-2}

Table 56.7 (Continued)

Fission product	Half-life	²³⁵ U Thermal	²³⁵ U Fast	²³⁵ U High	²³⁸ U Fast	²³⁹ Pu Thermal	²⁵² Cf Spontaneous
^{115m} Cd	44.56 days	5.53 × 10 ⁻⁶	2.42 × 10 ⁻⁶	3.99 × 10 ⁻¹	3.98 × 10 ⁻⁸	6.80 × 10 ⁻⁶	4.10 × 10 ⁻²
¹¹⁶ Cd	>1.2 × 10 ²¹ years	3.00 × 10 ⁻⁵	5.45 × 10 ⁻⁵	6.39 × 10 ⁻³	1.56 × 10 ⁻⁶	2.56 × 10 ⁻⁴	9.83 × 10 ⁻²
¹¹⁷ Cd	2.49 h	1.12 × 10 ⁻⁴	1.22 × 10 ⁻⁴	3.87 × 10 ⁻³	6.04 × 10 ⁻⁶	4.52 × 10 ⁻⁴	4.38 × 10 ⁻²
^{117m} Cd	3.36 h	3.73 × 10 ⁻⁴	4.59 × 10 ⁻⁴	2.38 × 10 ⁻²	2.27 × 10 ⁻⁵	1.51 × 10 ⁻³	1.47 × 10 ⁻¹
¹¹⁸ Cd	50.3 min	1.72 × 10 ⁻³	3.83 × 10 ⁻³	9.28 × 10 ⁻²	2.86 × 10 ⁻⁴	3.90 × 10 ⁻³	2.72 × 10 ⁻¹
¹¹⁹ Cd	2.69 min	2.45 × 10 ⁻³	5.84 × 10 ⁻³	1.14 × 10 ⁻¹	9.15 × 10 ⁻⁴	7.66 × 10 ⁻³	8.91 × 10 ⁻²
^{119m} Cd	2.20 min	2.25 × 10 ⁻³	5.84 × 10 ⁻³	1.14 × 10 ⁻¹	9.15 × 10 ⁻⁴	7.66 × 10 ⁻³	8.91 × 10 ⁻²
¹²⁰ Cd	50.80 s	8.39 × 10 ⁻³	2.39 × 10 ⁻²	4.16 × 10 ⁻¹	7.48 × 10 ⁻³	2.14 × 10 ⁻²	1.56 × 10 ⁻¹
¹²¹ Cd	13.5 s	7.24 × 10 ⁻³	2.68 × 10 ⁻²	5.52 × 10 ⁻¹	1.61 × 10 ⁻²	2.25 × 10 ⁻²	9.79 × 10 ⁻²
¹²² Cd	5.24 s	1.19 × 10 ⁻²	2.73 × 10 ⁻²	6.44 × 10 ⁻¹	2.66 × 10 ⁻²	1.69 × 10 ⁻²	8.34 × 10 ⁻²
¹²³ Cd	2.10 s	1.01 × 10 ⁻²	1.52 × 10 ⁻²	5.28 × 10 ⁻¹	2.80 × 10 ⁻²	5.00 × 10 ⁻³	3.34 × 10 ⁻²
¹²⁴ Cd	1.25 s	1.21 × 10 ⁻²	8.87 × 10 ⁻³	3.35 × 10 ⁻¹	2.09 × 10 ⁻²	2.74 × 10 ⁻⁴	1.10 × 10 ⁻²
¹²⁵ Cd	0.65 s	5.55 × 10 ⁻³	5.22 × 10 ⁻⁴	1.48 × 10 ⁻¹	9.77 × 10 ⁻³	6.95 × 10 ⁻⁵	2.69 × 10 ⁻³
¹²⁶ Cd	0.506 s	8.08 × 10 ⁻³	1.92 × 10 ⁻⁴	6.67 × 10 ⁻²	8.13 × 10 ⁻⁴	2.30 × 10 ⁻⁵	2.33 × 10 ⁻⁴
¹²⁷ Cd	0.37 s	8.16 × 10 ⁻³	1.06 × 10 ⁻⁴	2.03 × 10 ⁻²	4.12 × 10 ⁻⁴	8.87 × 10 ⁻⁶	9.83 × 10 ⁻⁹
¹²⁸ Cd	0.28 s	3.55 × 10 ⁻³	2.30 × 10 ⁻⁵	8.31 × 10 ⁻³	1.28 × 10 ⁻⁴	3.96 × 10 ⁻⁶	3.35 × 10 ⁻⁹
¹²⁹ Cd	0.27 s	7.24 × 10 ⁻⁷	3.76 × 10 ⁻⁶	2.05 × 10 ⁻³	4.78 × 10 ⁻⁵	1.14 × 10 ⁻⁷	8.37 × 10 ⁻⁷
¹³⁰ Cd	0.20 s	8.78 × 10 ⁻²	1.12 × 10 ⁻³	1.99 × 10 ⁻⁴	5.57 × 10 ⁻⁶	1.55 × 10 ⁻⁴	8.83 × 10 ⁻⁶
¹³¹ Cd	~0.18 s	1.38 × 10 ⁻²	9.78 × 10 ⁻⁵	1.38 × 10 ⁻⁵	2.92 × 10 ⁻⁷	9.35 × 10 ⁻⁶	6.68 × 10 ⁻⁷
¹³² Cd			1.61 × 10 ⁻⁶	5.34 × 10 ⁻⁷	1.82 × 10 ⁻⁴	5.68 × 10 ⁻⁷	7.06 × 10 ⁻⁸
¹³⁴ Cd		9.33 × 10 ⁻¹¹	3.02 × 10 ⁻¹⁰	2.06 × 10 ⁻¹⁰	9.37 × 10 ⁻⁸	2.14 × 10 ⁻¹¹	3.80 × 10 ⁻⁹
¹³⁶ Cd					3.37 × 10 ⁻¹²		
¹¹² In	14.97 min			8.79 × 10 ⁻¹²			3.57 × 10 ⁻⁹

^{112m}In	20.56 min			7.11×10^{-11}					1.52×10^{-8}
^{113m}In	99.476 min			3.53×10^{-10}					2.92×10^{-7}
^{114}In	71.9 s			1.29×10^{-8}				1.86×10^{-12}	8.70×10^{-6}
^{114m}In	49.51 days			7.31×10^{-8}				5.57×10^{-12}	2.61×10^{-5}
^{115}In	4.41×10^{14} years	1.63×10^{-10}		1.01×10^{-6}		1.31×10^{-12}		1.41×10^{-9}	9.51×10^{-5}
^{115m}In	4.486 h	3.82×10^{-11}		1.24×10^{-7}		3.73×10^{-11}		3.30×10^{-10}	2.23×10^{-5}
^{116m}In	54.29 min	3.85×10^{-9}		1.16×10^{-5}		5.82×10^{-9}		1.11×10^{-7}	1.24×10^{-4}
^{117}In	43.2 min	3.66×10^{-7}		2.06×10^{-4}		5.68×10^{-7}		7.02×10^{-6}	6.84×10^{-4}
^{117m}In	116.2 min	8.59×10^{-8}		2.55×10^{-5}		1.16×10^{-7}		1.90×10^{-9}	1.60×10^{-4}
^{118}In	5.0 s	5.06×10^{-6}		1.54×10^{-3}		1.03×10^{-5}		5.77×10^{-5}	2.64×10^{-3}
^{118m}In	4.45 min	1.69×10^{-6}		2.71×10^{-4}		2.89×10^{-6}		1.92×10^{-5}	8.81×10^{-4}
^{119}In	2.4 min	4.72×10^{-4}		9.00×10^{-3}		1.69×10^{-4}		7.24×10^{-4}	3.37×10^{-3}
^{119m}In	18.0 min	1.59×10^{-5}		1.11×10^{-3}		3.46×10^{-5}		1.70×10^{-4}	7.89×10^{-4}
^{120}In	3.08 s	3.15×10^{-4}		2.01×10^{-2}		5.27×10^{-4}		1.61×10^{-3}	1.54×10^{-3}
^{120m}In	46.2 s	3.15×10^{-4}		2.01×10^{-2}		5.27×10^{-4}		1.61×10^{-3}	1.54×10^{-3}
^{121}In	23.1 s	2.47×10^{-3}		1.07×10^{-1}		4.12×10^{-3}		9.81×10^{-3}	5.70×10^{-4}
^{121m}In	3.88 min	3.24×10^{-4}		1.33×10^{-2}		8.43×10^{-4}		2.30×10^{-3}	1.34×10^{-4}
^{122}In	1.5 s	1.26×10^{-3}		1.49×10^{-1}		5.39×10^{-3}		1.10×10^{-2}	1.68×10^{-4}
^{122m}In	10.8 s	1.26×10^{-3}		1.49×10^{-1}		5.39×10^{-3}		1.10×10^{-2}	1.68×10^{-4}
^{123}In	5.98 s	3.91×10^{-3}		4.70×10^{-1}		1.92×10^{-2}		1.94×10^{-2}	3.34×10^{-3}
^{123m}In	47.8 s	2.51×10^{-4}		5.81×10^{-2}		3.94×10^{-3}		4.56×10^{-3}	7.83×10^{-4}
^{124}In	3.11 s	3.39×10^{-3}		7.25×10^{-1}		2.85×10^{-2}		3.47×10^{-2}	9.46×10^{-3}
^{125}In	2.36 s	4.72×10^{-3}		3.51×10^{-1}		1.84×10^{-2}		1.71×10^{-2}	3.66×10^{-3}
^{125m}In	12.2 s	4.72×10^{-3}		3.51×10^{-1}		1.84×10^{-2}		1.71×10^{-2}	3.66×10^{-3}
^{126}In	1.60 s	3.30×10^{-3}		7.04×10^{-1}		2.91×10^{-2}		2.94×10^{-2}	7.98×10^{-3}
^{127}In	1.09 s	4.12×10^{-2}		2.29×10^{-1}		3.30×10^{-2}		2.40×10^{-2}	2.38×10^{-3}

Table 56.7 (Continued)

Fission product	Half-life	²³⁵ U Thermal	²³⁵ U Fast	²³⁵ U High	²³⁸ U Fast	²³⁹ Pu Thermal	²⁵² Cf Spontaneous
^{127m} In	3.67 s	6.25 × 10 ⁻³	3.30 × 10 ⁻²	2.29 × 10 ⁻¹	3.44 × 10 ⁻²	2.40 × 10 ⁻²	2.38 × 10 ⁻³
¹²⁸ In	0.84 s	2.63 × 10 ⁻²	3.93 × 10 ⁻²	3.05 × 10 ⁻¹	7.83 × 10 ⁻²	6.91 × 10 ⁻²	3.32 × 10 ⁻³
¹²⁹ In	0.61 s	2.75 × 10 ⁻²	1.66 × 10 ⁻²	8.13 × 10 ⁻²	6.74 × 10 ⁻²	5.14 × 10 ⁻³	4.88 × 10 ⁻³
^{129m} In	1.23 s	2.53 × 10 ⁻²	1.66 × 10 ⁻²	8.13 × 10 ⁻²	6.74 × 10 ⁻²	5.14 × 10 ⁻³	4.88 × 10 ⁻³
¹³⁰ In	0.29 s	9.42 × 10 ⁻³	8.59 × 10 ⁻²	3.97 × 10 ⁻²	7.51 × 10 ⁻²	3.32 × 10 ⁻²	1.02 × 10 ⁻²
¹³¹ In	0.28 s	1.11 × 10 ⁻²	3.75 × 10 ⁻²	7.16 × 10 ⁻³	2.68 × 10 ⁻²	8.35 × 10 ⁻³	2.62 × 10 ⁻³
¹³² In	0.205 s	6.23 × 10 ⁻³	1.81 × 10 ⁻³	7.53 × 10 ⁻⁴	6.45 × 10 ⁻²	1.57 × 10 ⁻³	5.14 × 10 ⁻⁴
¹³³ In	165 ms	1.71 × 10 ⁻⁴	2.70 × 10 ⁻⁴	5.21 × 10 ⁻⁵	7.40 × 10 ⁻³	3.81 × 10 ⁻⁵	1.95 × 10 ⁻⁴
¹³⁴ In	140 ms	3.47 × 10 ⁻⁶	5.97 × 10 ⁻⁶	2.25 × 10 ⁻⁶	4.92 × 10 ⁻⁴	8.95 × 10 ⁻⁷	2.59 × 10 ⁻⁵
¹³⁶ In		1.68 × 10 ⁻¹⁰	6.87 × 10 ⁻¹⁰	1.33 × 10 ⁻⁹	2.70 × 10 ⁻⁷	2.82 × 10 ⁻¹¹	1.43 × 10 ⁻⁸
¹¹⁸ Sn	Stable	4.10 × 10 ⁻⁹	6.96 × 10 ⁻⁹	3.48 × 10 ⁻⁶	2.13 × 10 ⁻¹¹	1.32 × 10 ⁻⁷	1.16 × 10 ⁻⁶
^{119m} Sn	293.1 days	1.14 × 10 ⁻⁷	2.59 × 10 ⁻⁷	3.99 × 10 ⁻⁵	1.90 × 10 ⁻⁹	3.68 × 10 ⁻⁶	1.44 × 10 ⁻⁶
¹²⁰ Sn	Stable	3.00 × 10 ⁻⁶	8.88 × 10 ⁻⁶	4.24 × 10 ⁻⁴	1.29 × 10 ⁻⁷	7.28 × 10 ⁻⁵	2.21 × 10 ⁻⁷
¹²¹ Sn	27.03 h	3.58 × 10 ⁻⁴	2.90 × 10 ⁻⁵	5.29 × 10 ⁻⁴	8.75 × 10 ⁻⁷	2.20 × 10 ⁻⁴	6.28 × 10 ⁻¹¹
^{121m} Sn	55 years	2.79 × 10 ⁻⁵	8.24 × 10 ⁻⁵	2.41 × 10 ⁻³	2.49 × 10 ⁻⁶	5.40 × 10 ⁻⁴	1.54 × 10 ⁻¹⁰
¹²² Sn	Stable	3.65 × 10 ⁻⁴	1.08 × 10 ⁻³	1.68 × 10 ⁻²	5.23 × 10 ⁻⁵	5.26 × 10 ⁻³	
¹²³ Sn	129.2 days	8.04 × 10 ⁻⁴	3.96 × 10 ⁻³	5.53 × 10 ⁻²	3.33 × 10 ⁻⁴	1.04 × 10 ⁻²	2.07 × 10 ⁻⁶
^{123m} Sn	40.06 min	3.10 × 10 ⁻⁴	1.39 × 10 ⁻³	1.21 × 10 ⁻²	1.17 × 10 ⁻⁴	4.24 × 10 ⁻³	8.44 × 10 ⁻⁷
¹²⁴ Sn	Stable	1.07 × 10 ⁻²	2.55 × 10 ⁻²	2.05 × 10 ⁻¹	2.69 × 10 ⁻³	4.36 × 10 ⁻²	2.27 × 10 ⁻³
¹²⁵ Sn	9.64 days	8.54 × 10 ⁻³	2.28 × 10 ⁻²	4.95 × 10 ⁻¹	6.79 × 10 ⁻³	5.45 × 10 ⁻²	4.46 × 10 ⁻³
^{125m} Sn	9.52 min	1.05 × 10 ⁻²	8.00 × 10 ⁻³	7.78 × 10 ⁻²	2.38 × 10 ⁻³	2.23 × 10 ⁻²	1.82 × 10 ⁻³
¹²⁶ Sn	~100000 years	4.45 × 10 ⁻²	6.79 × 10 ⁻²	9.29 × 10 ⁻¹	1.63 × 10 ⁻²	1.69 × 10 ⁻¹	1.77 × 10 ⁻²
¹²⁷ Sn	2.10 h	8.67 × 10 ⁻²	1.76 × 10 ⁻¹	1.02 × 10 ⁰	4.96 × 10 ⁻²	3.04 × 10 ⁻¹	6.97 × 10 ⁻²

^{127}mSn	4.13 min	7.92×10^{-3}	6.17×10^{-2}	2.24×10^{-1}	1.74×10^{-2}	1.27×10^{-1}	2.85×10^{-2}
^{128}Sn	59.07 min	3.01×10^{-1}	4.54×10^{-1}	1.37×10^0	2.04×10^{-1}	5.45×10^{-1}	1.75×10^{-1}
^{129}Sn	2.23 min	2.30×10^{-1}	5.50×10^{-1}	1.16×10^0	6.25×10^{-1}	6.91×10^{-1}	2.88×10^{-1}
$^{129\text{m}}\text{Sn}$	6.9 min	1.96×10^{-1}	1.91×10^{-1}	2.55×10^{-1}	2.20×10^{-1}	2.89×10^{-1}	1.18×10^{-1}
^{130}Sn	3.72 min	1.08×10^0	1.32×10^0	8.20×10^{-1}	1.65×10^0	9.40×10^{-1}	3.62×10^{-1}
^{131}Sn	56.0 s	8.81×10^{-1}	1.39×10^0	3.69×10^{-1}	2.29×10^0	6.08×10^{-1}	2.96×10^{-1}
^{132}Sn	39.7 s	5.92×10^{-1}	3.21×10^{-1}	1.01×10^{-1}	1.88×10^0	4.84×10^{-1}	1.38×10^{-1}
^{133}Sn	1.45 s	1.38×10^{-1}	1.38×10^{-1}	1.90×10^{-2}	6.73×10^{-1}	3.43×10^{-2}	6.26×10^{-2}
^{134}Sn	1.12 s	1.77×10^{-2}	1.66×10^{-2}	2.22×10^{-3}	1.82×10^{-1}	3.84×10^{-3}	1.51×10^{-2}
^{135}Sn	530 ms	6.27×10^{-4}	1.62×10^{-3}	1.69×10^{-4}	1.90×10^{-2}	1.43×10^{-4}	1.24×10^{-3}
^{136}Sn	0.25 s	1.57×10^{-5}	3.24×10^{-5}	9.17×10^{-6}	1.42×10^{-3}	1.93×10^{-6}	8.67×10^{-5}
^{137}Sn	190 ms	1.86×10^{-5}	3.74×10^{-7}	3.16×10^{-7}	6.33×10^{-5}	4.35×10^{-8}	2.44×10^{-6}
^{138}Sn		3.29×10^{-9}	1.75×10^{-8}	1.08×10^{-8}	2.21×10^{-6}	3.79×10^{-10}	6.66×10^{-8}
$^{120\text{m}}\text{Sb}$		1.30×10^{-10}	4.56×10^{-10}	3.19×10^{-7}	2.83×10^{-12}	2.47×10^{-8}	
^{123}Sb	Stable	5.17×10^{-6}	3.00×10^{-5}	9.56×10^{-4}	7.33×10^{-7}	4.60×10^{-4}	3.17×10^{-12}
^{124}Sb	60.20 days	7.61×10^{-6}	1.75×10^{-4}	3.41×10^{-3}	6.68×10^{-6}	5.00×10^{-5}	4.87×10^{-5}
$^{124\text{m}}\text{Sb}$	93 s	2.42×10^{-6}	1.75×10^{-4}	3.41×10^{-3}	6.68×10^{-6}	5.00×10^{-5}	4.87×10^{-5}
^{125}Sb	2.75856 years	2.74×10^{-5}	3.80×10^{-5}	3.30×10^{-2}	1.53×10^{-4}	6.58×10^{-4}	1.13×10^{-3}
^{126}Sb	12.46 days	6.51×10^{-4}	7.92×10^{-5}	9.02×10^{-2}	6.82×10^{-6}	1.37×10^{-3}	6.72×10^{-4}
$^{126\text{m}}\text{Sb}$	19.15 min	1.72×10^{-3}	1.09×10^{-4}	6.80×10^{-2}	9.42×10^{-6}	2.34×10^{-3}	1.14×10^{-3}
^{127}Sb	3.85 days	7.09×10^{-3}	2.47×10^{-3}	4.41×10^{-1}	2.03×10^{-4}	2.76×10^{-2}	2.68×10^{-3}
^{128}Sb	9.01 h	1.07×10^{-2}	4.35×10^{-3}	4.13×10^{-1}	9.00×10^{-4}	6.21×10^{-2}	5.57×10^{-3}
$^{128\text{m}}\text{Sb}$		6.37×10^{-3}	6.01×10^{-3}	3.09×10^{-1}	1.24×10^{-3}	5.74×10^{-2}	9.48×10^{-3}
^{129}Sb	4.40 h	6.41×10^{-2}	6.08×10^{-2}	1.57×10^0	3.24×10^{-2}	3.81×10^{-1}	1.72×10^{-1}
^{130}Sb	39.5 min	2.15×10^{-1}	1.52×10^{-1}	1.17×10^0	8.07×10^{-2}	5.87×10^{-1}	1.64×10^{-1}
$^{130\text{m}}\text{Sb}$	6.3 min	3.57×10^{-1}	2.09×10^{-1}	8.80×10^{-1}	1.11×10^{-1}	5.92×10^{-1}	2.80×10^{-1}

Table 56.7 (Continued)

Fission product	Half-life	²³⁵ U Thermal	²³⁵ U Fast	²³⁵ U High	²³⁸ U Fast	²³⁹ Pu Thermal	²⁵² Cf Spontaneous
¹³¹ Sb	23.03 min	1.65 × 10 ⁰	1.50 × 10 ⁰	2.15 × 10 ⁰	9.37 × 10 ⁻¹	1.90 × 10 ⁰	9.95 × 10 ⁻¹
¹³² Sb	2.79 min	1.30 × 10 ⁰	1.72 × 10 ⁰	5.63 × 10 ⁻¹	1.44 × 10 ⁰	1.86 × 10 ⁰	7.06 × 10 ⁻¹
^{132m} Sb		8.63 × 10 ⁻¹	1.54 × 10 ⁰	8.80 × 10 ⁻¹	1.27 × 10 ⁰	5.45 × 10 ⁻¹	5.11 × 10 ⁻¹
¹³³ Sb	2.5 min	2.26 × 10 ⁰	1.52 × 10 ⁰	6.99 × 10 ⁻¹	3.10 × 10 ⁰	1.17 × 10 ⁰	1.06 × 10 ⁰
¹³⁴ Sb	0.78 s	7.17 × 10 ⁻¹	4.88 × 10 ⁻¹	2.11 × 10 ⁻¹	2.56 × 10 ⁰	3.99 × 10 ⁻¹	5.58 × 10 ⁻¹
¹³⁵ Sb	1.68 s	1.45 × 10 ⁻¹	2.46 × 10 ⁻¹	4.15 × 10 ⁻²	1.02 × 10 ⁰	6.66 × 10 ⁻²	1.46 × 10 ⁻¹
¹³⁶ Sb	0.923 s	1.15 × 10 ⁻²	1.40 × 10 ⁻²	5.76 × 10 ⁻³	2.39 × 10 ⁻¹	2.92 × 10 ⁻³	3.02 × 10 ⁻²
¹³⁷ Sb	>150 ns	7.43 × 10 ⁻²	8.41 × 10 ⁻⁴	5.15 × 10 ⁻⁴	3.83 × 10 ⁻²	2.75 × 10 ⁻⁴	2.50 × 10 ⁻³
¹³⁸ Sb	>150 ns	3.92 × 10 ⁻⁵	1.14 × 10 ⁻⁴	4.37 × 10 ⁻⁵	4.06 × 10 ⁻³	6.51 × 10 ⁻⁶	2.03 × 10 ⁻⁴
¹³⁹ Sb	>150 ns	1.40 × 10 ⁻⁶	3.90 × 10 ⁻⁶	2.41 × 10 ⁻⁶	3.14 × 10 ⁻⁴	1.74 × 10 ⁻⁷	1.03 × 10 ⁻⁵
^{125m} Te	57.40 days	2.30 × 10 ⁻¹¹	4.05 × 10 ⁻¹¹	2.32 × 10 ⁻⁴	2.02 × 10 ⁻⁷	4.78 × 10 ⁻⁹	4.73 × 10 ⁻⁵
¹²⁶ Te	Stable	8.25 × 10 ⁻¹⁰	1.25 × 10 ⁻⁹	3.08 × 10 ⁻³	8.73 × 10 ⁻¹²	1.36 × 10 ⁻⁷	1.06 × 10 ⁻⁵
¹²⁷ Te	9.35 h	9.92 × 10 ⁻⁹	1.10 × 10 ⁻⁸	3.32 × 10 ⁻³	1.02 × 10 ⁻¹⁰	7.36 × 10 ⁻⁷	6.14 × 10 ⁻¹⁰
^{127m} Te	109 days	2.43 × 10 ⁻⁸	3.13 × 10 ⁻⁸	1.51 × 10 ⁻²	2.90 × 10 ⁻¹⁰	1.80 × 10 ⁻⁶	1.50 × 10 ⁻⁹
¹²⁸ Te	7.7 × 10 ²⁴ years	1.72 × 10 ⁻⁴	9.46 × 10 ⁻⁷	4.97 × 10 ⁻²	2.43 × 10 ⁻⁸	4.26 × 10 ⁻⁵	1.51 × 10 ⁻⁷
¹²⁹ Te	69.6 min	5.73 × 10 ⁻⁶	4.14 × 10 ⁻⁶	4.01 × 10 ⁻²	4.06 × 10 ⁻⁷	1.96 × 10 ⁻⁴	1.80 × 10 ⁻⁴
^{129m} Te	33.6 days	1.40 × 10 ⁻⁵	1.18 × 10 ⁻⁵	1.83 × 10 ⁻¹	1.16 × 10 ⁻⁶	4.79 × 10 ⁻⁴	4.41 × 10 ⁻⁴
¹³⁰ Te	>0.79 × 10 ²¹ years	5.79 × 10 ⁻²	2.40 × 10 ⁻²	6.68 × 10 ⁻¹	5.29 × 10 ⁻⁵	2.05 × 10 ⁻¹	3.07 × 10 ⁻²
¹³¹ Te	25.0 min	9.70 × 10 ⁻²	7.54 × 10 ⁻²	2.92 × 10 ⁻¹	3.55 × 10 ⁻⁴	4.51 × 10 ⁻¹	6.95 × 10 ⁻²
^{131m} Te	30 h	2.33 × 10 ⁻¹	2.24 × 10 ⁻¹	1.16 × 10 ⁰	3.65 × 10 ⁻²	8.70 × 10 ⁻¹	2.36 × 10 ⁻¹
¹³² Te	3.204 days	1.53 × 10 ⁰	1.07 × 10 ⁰	2.55 × 10 ⁰	4.71 × 10 ⁻¹	2.25 × 10 ⁰	7.77 × 10 ⁻¹
¹³³ Te	12.5 min	1.15 × 10 ⁰	2.62 × 10 ⁰	5.37 × 10 ⁻¹	8.01 × 10 ⁻¹	1.77 × 10 ⁰	5.24 × 10 ⁻¹
^{133m} Te	55.4 min	2.99 × 10 ⁰	2.05 × 10 ⁰	2.44 × 10 ⁰	1.96 × 10 ⁰	2.89 × 10 ⁰	1.28 × 10 ⁰

^{134}Te	41.8 min	6.22×10^0	6.02×10^0	2.18×10^0	3.95×10^0	4.40×10^0	2.35×10^0
^{135}Te	19.0 s	3.22×10^0	2.47×10^0	1.04×10^0	4.62×10^0	2.19×10^0	1.78×10^0
^{136}Te	17.63 s	1.32×10^0	1.02×10^0	3.55×10^{-1}	3.53×10^0	5.06×10^{-1}	9.12×10^{-1}
^{137}Te	2.49 s	3.92×10^{-1}	1.61×10^{-1}	7.93×10^{-2}	1.57×10^0	1.29×10^{-1}	2.33×10^{-1}
^{138}Te	1.4 s	6.62×10^{-2}	1.09×10^{-1}	1.64×10^{-2}	5.50×10^{-1}	1.17×10^{-2}	5.41×10^{-2}
^{139}Te	>150 ns	6.66×10^{-3}	9.79×10^{-3}	2.21×10^{-3}	1.21×10^{-1}	8.13×10^{-4}	8.22×10^{-3}
^{140}Te	>150 ns	1.69×10^{-2}	9.04×10^{-4}	1.10×10^{-4}	1.86×10^{-2}	1.41×10^{-4}	8.48×10^{-4}
^{142}Te		2.07×10^{-6}	1.40×10^{-6}	5.53×10^{-7}	9.27×10^{-5}	5.67×10^{-7}	3.47×10^{-6}
^{129}I	1.57×10^7 years			3.53×10^{-3}		3.85×10^{-10}	4.08×10^{-9}
^{131}I	8.02070 days	3.92×10^{-3}	1.08×10^{-3}	1.20×10^{-1}	7.89×10^{-10}	2.29×10^{-2}	1.41×10^{-3}
^{132}I	2.295 h	1.83×10^{-2}	1.02×10^{-2}	7.80×10^{-1}	1.99×10^{-2}	2.66×10^{-1}	2.11×10^{-2}
^{133}I	20.8 h	1.65×10^{-1}	3.84×10^{-1}	1.66×10^0	1.89×10^{-1}	1.11×10^0	2.19×10^{-1}
^{134}I	52.5 min	5.00×10^{-1}	7.45×10^{-1}	1.09×10^0	4.39×10^{-1}	1.44×10^0	3.31×10^{-1}
^{134m}I	3.60 min	3.64×10^{-1}	3.38×10^{-1}	1.73×10^0	3.18×10^{-1}	1.18×10^0	5.83×10^{-1}
^{135}I	6.57 h	2.93×10^0	3.60×10^0	3.13×10^0	1.35×10^0	4.29×10^0	1.85×10^0
^{136}I	83.4 s	1.32×10^0	1.85×10^0	1.23×10^0	1.33×10^0	1.25×10^0	1.36×10^0
^{136m}I	46.9 s	1.25×10^0	1.45×10^0	1.22×10^0	1.34×10^0	1.64×10^0	9.32×10^{-1}
^{137}I	24.5 s	2.62×10^0	2.40×10^0	1.29×10^0	3.53×10^0	2.30×10^0	1.57×10^0
^{138}I	6.49 s	1.42×10^0	1.25×10^0	5.11×10^{-1}	3.12×10^0	1.27×10^0	1.00×10^0
^{139}I	2.280 s	7.71×10^{-1}	4.60×10^{-1}	1.96×10^{-1}	2.06×10^0	3.19×10^{-1}	4.10×10^{-1}
^{140}I	0.86 s	1.37×10^{-1}	1.11×10^{-1}	2.34×10^{-2}	8.69×10^{-1}	5.94×10^{-2}	1.16×10^{-1}
^{141}I	0.43 s	4.07×10^{-2}	1.69×10^{-2}	2.65×10^{-3}	2.57×10^{-1}	7.04×10^{-3}	2.77×10^{-2}
^{142}I	~0.2 s	5.86×10^{-3}	2.26×10^{-3}	7.26×10^{-4}	4.19×10^{-2}	2.47×10^{-3}	3.75×10^{-3}
^{131m}Xe	11.934 days	3.48×10^{-7}	2.41×10^{-7}	9.09×10^{-4}	3.16×10^{-9}	3.00×10^{-5}	1.66×10^{-7}
^{132}Xe	Stable	4.22×10^{-5}	1.71×10^{-5}	1.63×10^{-2}	1.79×10^{-6}	1.53×10^{-3}	2.44×10^{-5}
^{133}Xe	5.243 days	6.66×10^{-4}	1.46×10^{-3}	3.01×10^{-2}	4.18×10^{-4}	9.45×10^{-3}	6.68×10^{-4}

Table 56.7 (Continued)

Fission product	Half-life	²³⁵ U Thermal	²³⁵ U Fast	²³⁵ U High	²³⁸ U Fast	²³⁹ Pu Thermal	²⁵² Cf Spontaneous
^{133m} Xe	2.19 days	1.89 × 10 ⁻³	4.23 × 10 ⁻³	1.42 × 10 ⁻¹	1.22 × 10 ⁻³	3.38 × 10 ⁻²	1.64 × 10 ⁻³
^{134m} Xe	290 ms	2.46 × 10 ⁻²	1.37 × 10 ⁻²	3.92 × 10 ⁻¹	1.90 × 10 ⁻³	1.71 × 10 ⁻¹	2.60 × 10 ⁻²
¹³⁵ Xe	9.14 h	7.85 × 10 ⁻²	1.20 × 10 ⁻¹	4.54 × 10 ⁻¹	1.12 × 10 ⁻²	3.14 × 10 ⁻¹	1.86 × 10 ⁻¹
^{135m} Xe	15.29 min	1.78 × 10 ⁻¹	1.86 × 10 ⁻¹	9.96 × 10 ⁻¹	1.57 × 10 ⁻²	7.52 × 10 ⁻¹	2.25 × 10 ⁻¹
¹³⁷ Xe	3.818 min	3.19 × 10 ⁰	3.53 × 10 ⁰	2.68 × 10 ⁰	1.08 × 10 ⁰	3.68 × 10 ⁰	2.59 × 10 ⁰
¹³⁸ Xe	14.08 min	4.81 × 10 ⁰	4.68 × 10 ⁰	2.65 × 10 ⁰	2.04 × 10 ⁰	3.93 × 10 ⁰	3.63 × 10 ⁰
¹³⁹ Xe	39.68 s	4.32 × 10 ⁰	3.79 × 10 ⁰	1.88 × 10 ⁰	3.28 × 10 ⁰	2.79 × 10 ⁰	3.50 × 10 ⁰
¹⁴⁰ Xe	13.60 s	3.51 × 10 ⁰	2.59 × 10 ⁰	9.13 × 10 ⁻¹	4.04 × 10 ⁰	1.54 × 10 ⁰	2.55 × 10 ⁰
¹⁴¹ Xe	1.73 s	1.22 × 10 ⁰	8.80 × 10 ⁻¹	2.61 × 10 ⁻¹	2.98 × 10 ⁰	4.73 × 10 ⁻¹	1.00 × 10 ⁰
¹⁴² Xe	1.22 s	4.34 × 10 ⁻¹	5.67 × 10 ⁻¹	9.09 × 10 ⁻²	1.53 × 10 ⁰	1.41 × 10 ⁻¹	3.68 × 10 ⁻¹
¹⁴³ Xe	0.30 s	5.30 × 10 ⁻²	6.36 × 10 ⁻²	1.76 × 10 ⁻²	4.39 × 10 ⁻¹	1.18 × 10 ⁻²	4.18 × 10 ⁻²
¹⁴⁴ Xe	1.15 s	6.05 × 10 ⁻³		1.83 × 10 ⁻³	1.23 × 10 ⁻¹	7.43 × 10 ⁻⁴	1.16 × 10 ⁻²
¹⁴⁵ Xe	900 ms	7.16 × 10 ⁻⁵	8.51 × 10 ⁻⁴	1.41 × 10 ⁻⁴	1.30 × 10 ⁻²	5.67 × 10 ⁻⁵	1.12 × 10 ⁻³
¹⁴⁶ Xe		1.06 × 10 ⁻⁵	3.40 × 10 ⁻⁵	6.07 × 10 ⁻⁶	9.35 × 10 ⁻⁴	1.53 × 10 ⁻⁶	6.50 × 10 ⁻⁵
¹⁴⁸ Xe		1.10 × 10 ⁻⁹	6.21 × 10 ⁻⁹	2.62 × 10 ⁻⁹	1.82 × 10 ⁻⁶	9.09 × 10 ⁻¹¹	4.30 × 10 ⁻⁸
¹⁵⁰ Xe					2.89 × 10 ⁻¹⁰		3.31 × 10 ⁻¹²
¹³² Cs	6.479 days	7.38 × 10 ⁻⁸	2.62 × 10 ⁻¹⁰	4.37 × 10 ⁻⁵	2.85 × 10 ⁻¹¹	2.98 × 10 ⁻⁷	6.65 × 10 ⁻¹⁰
¹³⁵ Cs	2.3 × 10 ⁶ years	4.91 × 10 ⁻⁴	2.06 × 10 ⁻⁴	6.05 × 10 ⁻²	3.71 × 10 ⁻⁵	1.26 × 10 ⁻²	2.07 × 10 ⁻³
¹³⁷ Cs	30.07 years	6.00 × 10 ⁻²	2.28 × 10 ⁻¹	9.48 × 10 ⁻¹	1.12 × 10 ⁻²	5.97 × 10 ⁻¹	6.93 × 10 ⁻¹
¹³⁸ Cs	33.41 min	2.43 × 10 ⁻¹	5.54 × 10 ⁻¹	6.65 × 10 ⁻¹	3.02 × 10 ⁻²	3.08 × 10 ⁻¹	5.73 × 10 ⁻¹
^{138m} Cs	2.91 min	2.23 × 10 ⁻¹	1.15 × 10 ⁻¹	6.65 × 10 ⁻¹	3.02 × 10 ⁻²	5.93 × 10 ⁻¹	3.01 × 10 ⁻¹
¹³⁹ Cs	9.27 min	1.31 × 10 ⁰	2.10 × 10 ⁰	2.36 × 10 ⁰	3.47 × 10 ⁻¹	2.32 × 10 ⁰	1.83 × 10 ⁰
¹⁴⁰ Cs	63.7 s	2.07 × 10 ⁰	3.05 × 10 ⁰	2.60 × 10 ⁰	8.87 × 10 ⁻¹	2.28 × 10 ⁰	2.77 × 10 ⁰

¹⁴¹ Cs	24.84 s	2.92×10^0	3.49×10^0	2.20×10^0	1.91×10^0	2.87×10^0	3.79×10^0
¹⁴² Cs	1.684 s	2.28×10^0	2.27×10^0	1.32×10^0	2.28×10^0	1.40×10^0	2.53×10^0
¹⁴³ Cs	1.791 s	1.40×10^0	1.20×10^0	5.65×10^{-1}	2.39×10^0	6.80×10^{-1}	7.43×10^{-1}
¹⁴⁴ Cs	0.994 s	4.18×10^{-1}	3.80×10^{-1}	1.48×10^{-1}	1.74×10^0	1.58×10^{-1}	5.49×10^{-1}
¹⁴⁵ Cs	0.594 s	7.56×10^{-2}	1.37×10^{-1}	2.87×10^{-2}	5.56×10^{-1}	2.80×10^{-2}	1.49×10^{-1}
¹⁴⁶ Cs	0.321 s	7.64×10^{-3}	1.52×10^{-2}	3.31×10^{-3}	1.17×10^{-1}	2.13×10^{-3}	2.58×10^{-2}
¹⁴⁸ Cs	146 ms	1.31×10^{-5}	4.06×10^{-5}	1.06×10^{-5}	2.46×10^{-3}	1.51×10^{-6}	1.54×10^{-4}
¹⁵⁰ Cs	>50 ms	1.99×10^{-9}	1.13×10^{-8}	5.02×10^{-9}	4.81×10^{-6}	6.34×10^{-10}	1.15×10^{-7}
^{137m} Ba	2.552 min	1.33×10^{-4}	6.30×10^{-5}	1.76×10^{-2}	6.56×10^{-6}	4.52×10^{-3}	9.08×10^{-4}
¹³⁹ Ba	83.06 min	6.88×10^{-2}	2.01×10^{-2}	3.81×10^{-1}	2.77×10^{-3}	2.26×10^{-1}	1.45×10^{-1}
¹⁴⁰ Ba	12.752 days	4.88×10^{-1}	2.36×10^{-1}	9.56×10^{-1}	2.66×10^{-2}	1.48×10^0	5.16×10^{-1}
¹⁴¹ Ba	18.27 min	1.66×10^0	1.56×10^0	1.84×10^0	2.26×10^{-1}	1.83×10^0	1.11×10^0
¹⁴² Ba	10.6 min	3.01×10^0	2.66×10^0	2.27×10^0	6.89×10^{-1}	3.08×10^0	2.70×10^0
¹⁴³ Ba	14.5 s	4.10×10^0	3.61×10^0	2.13×10^0	1.74×10^0	2.89×10^0	4.40×10^0
¹⁴⁴ Ba	11.5 s	3.98×10^0	3.01×10^0	1.32×10^0	2.46×10^0	2.16×10^0	3.37×10^0
¹⁴⁵ Ba	4.31 s	1.87×10^0	2.32×10^0	6.06×10^{-1}	2.58×10^0	8.03×10^{-1}	2.06×10^0
¹⁴⁶ Ba	2.22 s	9.14×10^{-1}	1.15×10^0	1.78×10^{-1}	1.98×10^0	2.38×10^{-1}	9.81×10^{-1}
¹⁴⁷ Ba	0.893 s	2.46×10^{-1}	2.43×10^{-1}	3.24×10^{-2}	8.45×10^{-1}	3.53×10^{-2}	2.50×10^{-1}
¹⁴⁸ Ba	0.612 s	2.22×10^{-2}	3.86×10^{-2}	3.97×10^{-3}	2.49×10^{-1}	2.64×10^{-3}	4.80×10^{-2}
¹⁴⁹ Ba	0.344 s	1.03×10^{-3}	2.56×10^{-3}	2.97×10^{-4}	4.73×10^{-2}	2.17×10^{-4}	4.04×10^{-3}
¹⁵⁰ Ba	0.3 s	5.02×10^{-5}	1.49×10^{-4}	1.38×10^{-5}	5.43×10^{-3}	1.20×10^{-5}	3.27×10^{-4}
¹⁵² Ba	~0.1 s	1.49×10^{-8}	8.22×10^{-8}	1.14×10^{-8}	1.50×10^{-5}	5.36×10^{-9}	3.77×10^{-7}
¹⁵⁴ Ba			3.65×10^{-12}	1.96×10^{-12}	7.11×10^{-9}		4.37×10^{-11}
¹³⁹ La	Stable	2.27×10^{-5}	8.92×10^{-6}	6.66×10^{-3}	8.10×10^{-7}	1.03×10^{-3}	4.07×10^{-4}
¹⁴⁰ La	1.6781 days	5.22×10^{-3}	2.04×10^{-4}	3.34×10^{-2}	2.48×10^{-5}	1.02×10^{-2}	5.03×10^{-3}
¹⁴¹ La	3.92 h	1.85×10^{-2}	4.66×10^{-3}	1.86×10^{-1}	4.45×10^{-4}	7.21×10^{-2}	3.72×10^{-2}

Table 56.7 (Continued)

Fission product	Half-life	²³⁵ U Thermal	²³⁵ U Fast	²³⁵ U High	²³⁸ U Fast	²³⁹ Pu Thermal	²⁵² Cf Spontaneous
¹⁴² La	91.1 min	9.65 × 10 ⁻²	2.99 × 10 ⁻²	5.01 × 10 ⁻¹	5.26 × 10 ⁻³	2.99 × 10 ⁻¹	4.14 × 10 ⁻¹
¹⁴³ La	14.2 min	3.80 × 10 ⁻¹	8.65 × 10 ⁻¹	1.05 × 10 ⁰	4.48 × 10 ⁻²	8.15 × 10 ⁻¹	1.05 × 10 ⁰
¹⁴⁴ La	40.8 s	1.07 × 10 ⁰	1.85 × 10 ⁰	1.49 × 10 ⁰	2.11 × 10 ⁻¹	1.31 × 10 ⁰	1.86 × 10 ⁰
¹⁴⁵ La	24.8 s	1.92 × 10 ⁰	1.24 × 10 ⁰	1.54 × 10 ⁰	7.09 × 10 ⁻¹	1.70 × 10 ⁰	2.51 × 10 ⁰
¹⁴⁶ La	6.27 s	1.49 × 10 ⁰	1.33 × 10 ⁰	1.08 × 10 ⁰	1.27 × 10 ⁰	1.16 × 10 ⁰	2.39 × 10 ⁰
¹⁴⁷ La	4.015 s	6.43 × 10 ⁻¹	1.12 × 10 ⁰	4.83 × 10 ⁻¹	1.48 × 10 ⁰	6.11 × 10 ⁻¹	1.94 × 10 ⁰
¹⁴⁸ La	1.26 s	3.36 × 10 ⁻¹	4.22 × 10 ⁻¹	1.49 × 10 ⁻¹	1.09 × 10 ⁰	1.17 × 10 ⁻¹	9.86 × 10 ⁻¹
¹⁴⁹ La	1.05 s	7.99 × 10 ⁻²	1.26 × 10 ⁻¹	2.89 × 10 ⁻²	6.64 × 10 ⁻¹	3.63 × 10 ⁻²	2.34 × 10 ⁻¹
¹⁵⁰ La	0.51 s	1.04 × 10 ⁻²	1.89 × 10 ⁻²	3.56 × 10 ⁻³	2.14 × 10 ⁻¹	5.21 × 10 ⁻³	5.51 × 10 ⁻²
¹⁵¹ La	>150 ns	1.03 × 10 ⁻³	2.37 × 10 ⁻³	3.19 × 10 ⁻⁴	4.48 × 10 ⁻²	4.79 × 10 ⁻⁴	6.14 × 10 ⁻³
¹⁵² La	>150 ns	4.53 × 10 ⁻⁵	1.37 × 10 ⁻⁴	2.09 × 10 ⁻⁵	5.81 × 10 ⁻³	2.41 × 10 ⁻⁵	5.59 × 10 ⁻⁴
¹⁵³ La	>150 ns	1.42 × 10 ⁻⁶	5.95 × 10 ⁻⁶	1.01 × 10 ⁻⁶	6.50 × 10 ⁻⁴	8.51 × 10 ⁻⁷	2.59 × 10 ⁻⁵
¹⁵⁴ La	~0.1 s	1.46 × 10 ⁻⁸	8.00 × 10 ⁻⁸	2.60 × 10 ⁻⁸	2.83 × 10 ⁻⁵	1.82 × 10 ⁻⁸	6.18 × 10 ⁻⁷
^{139m} Ce	54.8 s	7.03 × 10 ⁻¹⁰	2.25 × 10 ⁻¹⁰	9.57 × 10 ⁻⁶	1.02 × 10 ⁻¹¹	2.40 × 10 ⁻⁷	1.02 × 10 ⁻⁷
¹⁴¹ Ce	32.508 days	4.99 × 10 ⁻⁶	3.22 × 10 ⁻⁵	1.74 × 10 ⁻³	9.05 × 10 ⁻⁸	2.29 × 10 ⁻⁴	1.08 × 10 ⁻⁴
¹⁴² Ce	>5 × 10 ¹⁶ years	1.76 × 10 ⁻⁴	7.12 × 10 ⁻⁵	1.22 × 10 ⁻²	3.64 × 10 ⁻⁶	3.57 × 10 ⁻³	1.57 × 10 ⁻³
¹⁴³ Ce	33.039 h	3.13 × 10 ⁻²	1.39 × 10 ⁻³	6.31 × 10 ⁻²	9.01 × 10 ⁻⁵	2.67 × 10 ⁻²	1.64 × 10 ⁻²
¹⁴⁴ Ce	284.91 days	3.45 × 10 ⁻²	1.68 × 10 ⁻²	2.16 × 10 ⁻¹	1.43 × 10 ⁻³	1.16 × 10 ⁻¹	1.01 × 10 ⁻¹
¹⁴⁵ Ce	3.01 min	8.54 × 10 ⁻²	9.18 × 10 ⁻²	5.14 × 10 ⁻¹	1.27 × 10 ⁻²	4.56 × 10 ⁻¹	3.47 × 10 ⁻¹
¹⁴⁶ Ce	13.52 min	5.83 × 10 ⁻¹	4.27 × 10 ⁻¹	8.50 × 10 ⁻¹	8.71 × 10 ⁻²	1.04 × 10 ⁰	1.01 × 10 ⁰
¹⁴⁷ Ce	56.4 s	9.98 × 10 ⁻¹	7.65 × 10 ⁻¹	8.89 × 10 ⁻¹	2.64 × 10 ⁻¹	1.22 × 10 ⁰	1.91 × 10 ⁰
¹⁴⁸ Ce	56 s	1.24 × 10 ⁰	1.16 × 10 ⁰	6.50 × 10 ⁻¹	7.46 × 10 ⁻¹	8.90 × 10 ⁻¹	2.35 × 10 ⁰
¹⁴⁹ Ce	5.3 s	6.98 × 10 ⁻¹	7.58 × 10 ⁻¹	3.05 × 10 ⁻¹	8.43 × 10 ⁻¹	5.62 × 10 ⁻¹	1.50 × 10 ⁰

¹⁵⁰ Ce	4.0 s	3.92×10^{-1}	4.57×10^{-1}	9.37×10^{-2}	8.60×10^{-1}	2.78×10^{-1}	9.41×10^{-1}
¹⁵¹ Ce	1.02 s	9.90×10^{-2}	1.37×10^{-1}	2.15×10^{-2}	4.56×10^{-1}	6.31×10^{-2}	2.92×10^{-1}
¹⁵² Ce	1.4 s	2.05×10^{-2}	3.54×10^{-2}	3.62×10^{-3}	1.84×10^{-1}	1.18×10^{-2}	7.45×10^{-2}
¹⁵³ Ce	>150 ns	1.70×10^{-3}	3.93×10^{-3}	4.58×10^{-4}	5.58×10^{-2}	1.06×10^{-3}	1.02×10^{-2}
¹⁵⁴ Ce	>150 ns	9.12×10^{-5}	2.46×10^{-4}	3.10×10^{-5}	8.00×10^{-3}	8.57×10^{-5}	7.33×10^{-4}
¹⁵⁵ Ce	>300 ns	2.55×10^{-6}	1.17×10^{-5}	1.61×10^{-6}	8.47×10^{-4}	3.46×10^{-6}	5.40×10^{-5}
¹⁵⁶ Ce	~0.15 s	5.73×10^{-8}	4.15×10^{-7}	6.39×10^{-8}	5.45×10^{-5}	1.23×10^{-7}	2.93×10^{-6}
¹⁵⁷ Ce	~0.05 s	4.59×10^{-10}	6.64×10^{-9}	1.67×10^{-9}	2.19×10^{-6}	1.79×10^{-9}	5.90×10^{-8}
¹⁵⁸ Ce		3.87×10^{-12}	9.25×10^{-11}	3.18×10^{-11}	4.98×10^{-8}	1.86×10^{-11}	8.75×10^{-10}
¹⁶⁰ Ce					6.06×10^{-12}		
¹⁴³ Pr	13.57 days	4.50×10^{-7}	1.61×10^{-7}	3.99×10^{-4}	6.36×10^{-9}	3.36×10^{-5}	2.27×10^{-5}
¹⁴⁴ Pr	17.28 min	1.43×10^{-6}	4.81×10^{-7}	2.08×10^{-4}	3.00×10^{-8}	3.66×10^{-5}	3.80×10^{-5}
^{144m} Pr	7.2 min	1.28×10^{-5}	4.86×10^{-6}	3.26×10^{-3}	3.03×10^{-7}	3.29×10^{-4}	3.42×10^{-4}
¹⁴⁵ Pr	5.984 h	3.33×10^{-4}	1.45×10^{-4}	2.04×10^{-2}	1.14×10^{-5}	5.78×10^{-3}	4.25×10^{-3}
¹⁴⁶ Pr	24.15 min	3.62×10^{-3}	1.83×10^{-3}	8.41×10^{-2}	2.15×10^{-4}	1.95×10^{-2}	3.07×10^{-2}
¹⁴⁷ Pr	13.4 min	3.60×10^{-1}	1.53×10^{-2}	2.13×10^{-1}	2.48×10^{-3}	1.39×10^{-1}	1.81×10^{-1}
¹⁴⁸ Pr	2.29 min	7.77×10^{-2}	5.59×10^{-2}	3.69×10^{-1}	1.75×10^{-2}	6.18×10^{-1}	5.41×10^{-1}
¹⁴⁹ Pr	2.26 min	2.97×10^{-1}	1.49×10^{-1}	4.09×10^{-1}	7.70×10^{-2}	5.68×10^{-1}	9.29×10^{-1}
¹⁵⁰ Pr	6.19 s	2.18×10^{-1}	1.90×10^{-1}	2.94×10^{-1}	1.91×10^{-1}	5.09×10^{-1}	1.30×10^0
¹⁵¹ Pr	18.90 s	2.39×10^{-1}	2.19×10^{-1}	1.62×10^{-1}	2.81×10^{-1}	3.72×10^{-1}	1.07×10^0
¹⁵² Pr	3.63 s	1.03×10^{-1}	1.20×10^{-1}	6.57×10^{-2}	2.86×10^{-1}	1.60×10^{-1}	6.96×10^{-1}
¹⁵³ Pr	4.28 s	3.67×10^{-2}	5.48×10^{-2}	2.06×10^{-2}	2.44×10^{-1}	4.93×10^{-2}	2.61×10^{-1}
¹⁵⁴ Pr	2.3 s	5.02×10^{-3}	7.91×10^{-3}	3.54×10^{-3}	8.82×10^{-2}	9.70×10^{-3}	5.33×10^{-2}
¹⁵⁵ Pr	>300 ns	6.73×10^{-4}	1.66×10^{-3}	4.54×10^{-4}	2.96×10^{-2}	1.43×10^{-3}	1.15×10^{-2}
¹⁵⁶ Pr	>300 ns	4.07×10^{-5}	1.48×10^{-4}	4.63×10^{-5}	5.25×10^{-3}	1.30×10^{-4}	1.82×10^{-3}
¹⁵⁷ Pr	~0.3 s	1.65×10^{-6}	1.11×10^{-5}	3.06×10^{-6}	7.04×10^{-4}	7.19×10^{-6}	1.08×10^{-4}

Table 56.7 (Continued)

Fission product	Half-life	²³⁵ U Thermal	²³⁵ U Fast	²³⁵ U High	²³⁸ U Fast	²³⁹ Pu Thermal	²⁵² Cf Spontaneous
¹⁵⁸ Pr	~0.2 s	3.75×10^{-8}	4.04×10^{-7}	1.45×10^{-7}	4.66×10^{-5}	1.96×10^{-7}	4.82×10^{-6}
¹⁵⁹ Pr	~0.1 s	4.88×10^{-10}	1.02×10^{-8}	3.74×10^{-9}	2.18×10^{-6}	4.13×10^{-9}	1.93×10^{-7}
¹⁶⁰ Pr		2.82×10^{-12}	9.11×10^{-11}	8.47×10^{-11}	5.76×10^{-8}	4.76×10^{-11}	4.55×10^{-9}
¹⁴³ Nd	Stable	4.80×10^{-12}	1.37×10^{-12}	2.39×10^{-7}		2.91×10^{-9}	2.54×10^{-9}
¹⁴⁴ Nd	2.29×10^{15} years	9.57×10^{-9}	1.29×10^{-8}	5.52×10^{-6}	5.10×10^{-12}	1.37×10^{-7}	1.27×10^{-7}
¹⁴⁵ Nd	Stable	5.55×10^{-8}	1.83×10^{-8}	8.34×10^{-5}	5.34×10^{-10}	5.93×10^{-6}	4.34×10^{-6}
¹⁴⁶ Nd	Stable	3.19×10^{-6}	1.22×10^{-6}	9.06×10^{-4}	3.90×10^{-8}	8.11×10^{-5}	9.21×10^{-5}
¹⁴⁷ Nd	10.98 days	6.72×10^{-5}	2.81×10^{-5}	5.93×10^{-3}	1.43×10^{-6}	1.59×10^{-3}	1.43×10^{-3}
¹⁴⁸ Nd	Stable	9.93×10^{-4}	5.18×10^{-4}	2.58×10^{-2}	3.59×10^{-5}	1.37×10^{-2}	1.33×10^{-2}
¹⁴⁹ Nd	1.728 h	6.81×10^{-3}	3.46×10^{-3}	6.95×10^{-2}	4.97×10^{-4}	4.98×10^{-2}	5.80×10^{-2}
¹⁵⁰ Nd	$>6.8 \times 10^{18}$ years	3.27×10^{-2}	2.02×10^{-2}	1.20×10^{-1}	4.26×10^{-3}	1.74×10^{-1}	1.45×10^{-1}
¹⁵¹ Nd	12.44 min	7.95×10^{-2}	5.35×10^{-2}	1.55×10^{-1}	1.78×10^{-2}	2.92×10^{-1}	5.60×10^{-1}
¹⁵² Nd	11.4 min	1.41×10^{-1}	1.13×10^{-1}	1.45×10^{-1}	5.37×10^{-2}	3.70×10^{-1}	8.28×10^{-1}
¹⁵³ Nd	31.6 s	1.11×10^{-1}	1.02×10^{-1}	1.06×10^{-1}	1.11×10^{-1}	2.40×10^{-1}	7.99×10^{-1}
¹⁵⁴ Nd	25.9 s	5.80×10^{-2}	5.66×10^{-2}	4.34×10^{-2}	1.13×10^{-1}	1.51×10^{-1}	4.19×10^{-1}
¹⁵⁵ Nd	8.9 s	1.75×10^{-2}	2.50×10^{-2}	1.31×10^{-2}	9.22×10^{-2}	5.07×10^{-2}	2.43×10^{-1}
¹⁵⁶ Nd	5.49 s	4.70×10^{-3}	9.08×10^{-3}	3.27×10^{-3}	4.69×10^{-2}	1.60×10^{-2}	1.05×10^{-1}
¹⁵⁷ Nd	>300 ns	4.85×10^{-4}	1.60×10^{-3}	5.30×10^{-4}	1.61×10^{-2}	2.18×10^{-3}	1.77×10^{-2}
¹⁵⁸ Nd	>300 ns	5.19×10^{-5}	2.62×10^{-4}	6.12×10^{-5}	3.35×10^{-3}	2.19×10^{-4}	2.28×10^{-3}
¹⁵⁹ Nd	~0.7 s	1.77×10^{-6}	1.67×10^{-5}	3.96×10^{-6}	4.37×10^{-4}	1.19×10^{-5}	2.54×10^{-4}
¹⁶⁰ Nd	~0.3 s	5.04×10^{-8}	7.06×10^{-7}	2.23×10^{-7}	3.77×10^{-5}	5.06×10^{-7}	1.74×10^{-5}
¹⁶¹ Nd	~0.2 s	6.16×10^{-10}	1.30×10^{-8}	1.07×10^{-8}	1.74×10^{-6}	1.13×10^{-8}	7.31×10^{-7}
¹⁶² Nd		3.48×10^{-12}	1.08×10^{-10}	2.67×10^{-10}	4.43×10^{-8}	1.75×10^{-10}	1.88×10^{-8}

^{163}Nd				5.56×10^{-12}	1.56×10^{-9}	1.31×10^{-12}	3.05×10^{-10}
^{164}Nd					3.88×10^{-11}		3.65×10^{-12}
^{145}Pm	17.7 years			3.18×10^{-8}		2.00×10^{-10}	2.42×10^{-10}
^{146}Pm	5.53 years	4.50×10^{-10}	7.23×10^{-12}	9.42×10^{-7}		7.89×10^{-9}	1.59×10^{-8}
^{147}Pm	2.6234 years	2.49×10^{-9}	8.62×10^{-10}	1.66×10^{-5}	2.85×10^{-11}	6.49×10^{-7}	7.42×10^{-7}
^{148}Pm	53.08 h	3.87×10^{-6}	1.64×10^{-6}	1.35×10^{-3}	1.18×10^{-7}	2.43×10^{-4}	2.86×10^{-4}
^{150}Pm	2.68 h	3.00×10^{-5}	2.51×10^{-5}	9.03×10^{-4}	3.29×10^{-6}	1.15×10^{-3}	1.92×10^{-3}
^{151}Pm	28.40 h	6.42×10^{-4}	3.19×10^{-4}	1.90×10^{-2}	4.85×10^{-5}	1.08×10^{-2}	2.15×10^{-2}
^{152}Pm	4.12 min	1.39×10^{-3}	8.25×10^{-4}	2.09×10^{-2}	2.13×10^{-4}	1.67×10^{-2}	6.06×10^{-2}
$^{152\text{m}}\text{Pm}$	7.52 min	1.39×10^{-3}	8.25×10^{-4}	2.09×10^{-2}	2.13×10^{-4}	1.67×10^{-2}	6.06×10^{-2}
^{153}Pm	5.25 min	8.80×10^{-3}	6.50×10^{-3}	7.07×10^{-2}	2.86×10^{-3}	6.83×10^{-2}	2.17×10^{-1}
^{154}Pm	2.68 min	5.41×10^{-3}	3.67×10^{-3}	3.32×10^{-2}	3.75×10^{-3}	4.49×10^{-2}	2.98×10^{-1}
$^{154\text{m}}\text{Pm}$		5.41×10^{-3}	3.67×10^{-3}	3.32×10^{-2}	3.75×10^{-3}	4.49×10^{-2}	2.55×10^{-1}
^{155}Pm	41.5 s	1.26×10^{-2}	1.20×10^{-2}	4.44×10^{-2}	1.85×10^{-2}	9.21×10^{-2}	4.40×10^{-1}
^{156}Pm	26.70 s	7.06×10^{-3}	8.71×10^{-3}	2.56×10^{-2}	2.26×10^{-2}	6.21×10^{-2}	4.58×10^{-1}
^{157}Pm	10.56 s	2.93×10^{-3}	5.75×10^{-3}	9.61×10^{-3}	2.16×10^{-2}	2.74×10^{-2}	2.00×10^{-1}
^{158}Pm	4.8 s	7.06×10^{-4}	2.02×10^{-3}	2.57×10^{-3}	1.08×10^{-2}	6.39×10^{-3}	6.91×10^{-2}
^{159}Pm	2 s	1.06×10^{-4}	5.34×10^{-4}	4.03×10^{-4}	4.10×10^{-3}	1.22×10^{-3}	2.04×10^{-2}
^{160}Pm	~ 2 s	7.55×10^{-6}	5.42×10^{-5}	5.46×10^{-5}	8.95×10^{-4}	1.26×10^{-4}	3.90×10^{-3}
^{161}Pm	~ 0.7 s	4.40×10^{-7}	4.53×10^{-6}	6.43×10^{-6}	1.28×10^{-4}	1.04×10^{-5}	4.41×10^{-4}
^{162}Pm	~ 0.5 s	6.80×10^{-9}	9.61×10^{-8}	3.96×10^{-7}	9.18×10^{-6}	4.16×10^{-7}	3.10×10^{-5}
^{163}Pm	~ 0.2 s	1.82×10^{-10}	1.64×10^{-9}	2.00×10^{-8}	1.06×10^{-6}	1.19×10^{-8}	1.43×10^{-6}
^{164}Pm		1.66×10^{-12}	4.01×10^{-11}	7.28×10^{-10}	7.57×10^{-8}	1.72×10^{-10}	4.77×10^{-8}
^{165}Pm				1.68×10^{-11}	3.54×10^{-9}	2.22×10^{-12}	9.64×10^{-10}
^{146}Sm	10.3×10^7 years			8.85×10^{-11}			
^{147}Sm	1.06×10^{11} years			4.31×10^{-9}		1.83×10^{-11}	3.28×10^{-11}

Table 56.7 (Continued)

Fission product	Half-life	²³⁵ U Thermal	²³⁵ U Fast	²³⁵ U High	²³⁸ U Fast	²³⁹ Pu Thermal	²⁵² Cf Spontaneous
¹⁴⁹ Sm	> 2 × 10 ¹⁵ years	1.71 × 10 ⁻¹⁰	5.72 × 10 ⁻¹¹	2.66 × 10 ⁻⁶	1.57 × 10 ⁻¹²	8.19 × 10 ⁻⁸	1.20 × 10 ⁻⁷
¹⁵⁰ Sm	Stable	1.22 × 10 ⁻⁸	4.57 × 10 ⁻⁹	3.06 × 10 ⁻⁵	1.71 × 10 ⁻¹⁰	2.54 × 10 ⁻⁶	4.19 × 10 ⁻⁶
¹⁵¹ Sm	90 years	4.75 × 10 ⁻⁷	1.63 × 10 ⁻⁷	2.57 × 10 ⁻⁴	7.76 × 10 ⁻⁹	3.85 × 10 ⁻⁵	8.56 × 10 ⁻⁵
¹⁵² Sm	Stable	9.65 × 10 ⁻⁶	4.09 × 10 ⁻⁶	1.42 × 10 ⁻³	2.50 × 10 ⁻⁷	4.30 × 10 ⁻⁴	1.32 × 10 ⁻³
¹⁵³ Sm	46.284 h	8.01 × 10 ⁻⁵	4.19 × 10 ⁻⁵	5.89 × 10 ⁻³	4.94 × 10 ⁻⁶	2.12 × 10 ⁻³	6.56 × 10 ⁻³
¹⁵⁴ Sm	Stable	4.73 × 10 ⁻⁴	2.09 × 10 ⁻⁴	1.32 × 10 ⁻²	4.39 × 10 ⁻⁵	9.38 × 10 ⁻³	4.19 × 10 ⁻²
¹⁵⁵ Sm	22.3 min	1.31 × 10 ⁻³	7.93 × 10 ⁻⁴	1.97 × 10 ⁻²	3.12 × 10 ⁻⁴	2.13 × 10 ⁻²	9.59 × 10 ⁻²
¹⁵⁶ Sm	9.4 h	3.03 × 10 ⁻³	2.31 × 10 ⁻³	2.56 × 10 ⁻²	1.21 × 10 ⁻³	4.46 × 10 ⁻²	1.01 × 10 ⁻¹
¹⁵⁷ Sm	482 s	2.67 × 10 ⁻³	3.16 × 10 ⁻³	2.12 × 10 ⁻²	2.96 × 10 ⁻³	4.11 × 10 ⁻²	2.85 × 10 ⁻¹
¹⁵⁸ Sm	5.30 min	2.40 × 10 ⁻³	4.07 × 10 ⁻³	1.24 × 10 ⁻²	4.26 × 10 ⁻³	2.93 × 10 ⁻²	2.45 × 10 ⁻¹
¹⁵⁹ Sm	11.37 s	7.42 × 10 ⁻⁴	2.16 × 10 ⁻³	4.45 × 10 ⁻³	3.86 × 10 ⁻³	1.21 × 10 ⁻²	1.76 × 10 ⁻¹
¹⁶⁰ Sm	9.6 s	2.11 × 10 ⁻⁴	8.34 × 10 ⁻⁴	1.38 × 10 ⁻³	2.29 × 10 ⁻³	3.99 × 10 ⁻³	8.67 × 10 ⁻²
¹⁶¹ Sm	4.8 s	2.83 × 10 ⁻⁵	1.53 × 10 ⁻⁴	3.79 × 10 ⁻⁴	7.74 × 10 ⁻⁴	7.80 × 10 ⁻⁴	2.49 × 10 ⁻²
¹⁶² Sm	~2 s	2.03 × 10 ⁻⁶	1.38 × 10 ⁻⁵	5.56 × 10 ⁻⁵	1.64 × 10 ⁻⁴	1.11 × 10 ⁻⁴	4.57 × 10 ⁻³
¹⁶³ Sm	~1 s	1.37 × 10 ⁻⁷	5.52 × 10 ⁻⁷	6.64 × 10 ⁻⁶	4.87 × 10 ⁻⁵	7.95 × 10 ⁻⁶	5.78 × 10 ⁻⁴
¹⁶⁴ Sm	~0.5 s	6.04 × 10 ⁻⁹	6.21 × 10 ⁻⁸	5.94 × 10 ⁻⁷	1.09 × 10 ⁻⁵	4.17 × 10 ⁻⁷	5.22 × 10 ⁻⁵
¹⁶⁵ Sm	~0.2 s	2.55 × 10 ⁻¹⁰	2.66 × 10 ⁻⁹	3.39 × 10 ⁻⁸	1.45 × 10 ⁻⁶	1.40 × 10 ⁻⁸	2.98 × 10 ⁻⁶
¹⁶⁶ Sm		6.43 × 10 ⁻¹²	9.64 × 10 ⁻¹¹	1.29 × 10 ⁻⁹	1.75 × 10 ⁻⁷	4.35 × 10 ⁻¹⁰	1.29 × 10 ⁻⁷
¹⁶⁷ Sm			1.64 × 10 ⁻¹²	4.47 × 10 ⁻¹¹	1.32 × 10 ⁻⁸	3.46 × 10 ⁻¹²	3.03 × 10 ⁻⁹
¹⁶⁸ Sm					6.36 × 10 ⁻¹⁰		4.63 × 10 ⁻¹¹
¹⁵¹ Eu	Stable	2.49 × 10 ⁻¹⁰	9.55 × 10 ⁻¹⁰	3.39 × 10 ⁻⁷		4.55 × 10 ⁻⁹	1.89 × 10 ⁻⁸
^{152m} Eu	9.3116 h	1.36 × 10 ⁻¹⁰	4.68 × 10 ⁻¹¹	2.47 × 10 ⁻⁶	2.19 × 10 ⁻¹²	6.79 × 10 ⁻⁸	4.35 × 10 ⁻⁷
¹⁵³ Eu	Stable	2.33 × 10 ⁻⁷	4.60 × 10 ⁻⁹	5.03 × 10 ⁻⁵	3.03 × 10 ⁻¹⁰	2.51 × 10 ⁻⁶	1.38 × 10 ⁻⁵

¹⁵⁴ Eu	8,593 years	1.94×10^{-7}	6.21×10^{-8}	3.01×10^{-4}	8.25×10^{-9}	2.80×10^{-5}	2.58×10^{-4}
¹⁵⁵ Eu	4,7611 years	2.63×10^{-6}	1.10×10^{-6}	1.06×10^{-3}	2.11×10^{-7}	1.93×10^{-4}	1.72×10^{-3}
¹⁵⁶ Eu	15,19 days	1.62×10^{-5}	8.28×10^{-6}	3.27×10^{-3}	2.38×10^{-6}	1.18×10^{-3}	9.92×10^{-3}
¹⁵⁷ Eu	15,18 h	6.35×10^{-5}	4.74×10^{-5}	6.13×10^{-3}	1.96×10^{-5}	3.46×10^{-3}	3.50×10^{-2}
¹⁵⁸ Eu	45.9 min	1.28×10^{-4}	1.39×10^{-4}	7.80×10^{-3}	7.76×10^{-5}	5.38×10^{-3}	1.48×10^{-1}
¹⁵⁹ Eu	18.1 min	1.56×10^{-4}	2.89×10^{-4}	6.15×10^{-3}	2.19×10^{-4}	6.84×10^{-3}	1.31×10^{-1}
¹⁶⁰ Eu	38 s	9.03×10^{-5}	2.28×10^{-4}	4.13×10^{-3}	3.20×10^{-4}	4.59×10^{-3}	1.57×10^{-1}
¹⁶¹ Eu	26 s	4.54×10^{-5}	1.53×10^{-4}	2.51×10^{-3}	3.01×10^{-4}	2.77×10^{-3}	1.06×10^{-1}
¹⁶² Eu	10.6 s	6.99×10^{-6}	2.79×10^{-5}	8.29×10^{-4}	1.51×10^{-4}	8.63×10^{-4}	4.70×10^{-2}
¹⁶³ Eu		1.94×10^{-6}	4.20×10^{-6}	2.23×10^{-4}	1.22×10^{-4}	2.07×10^{-4}	1.52×10^{-2}
¹⁶⁴ Eu	~2 s	2.01×10^{-7}	1.06×10^{-6}	4.70×10^{-5}	6.51×10^{-5}	2.52×10^{-5}	3.52×10^{-3}
¹⁶⁵ Eu	~1 s	3.87×10^{-8}	1.95×10^{-7}	6.43×10^{-6}	2.60×10^{-5}	3.04×10^{-6}	5.43×10^{-4}
¹⁶⁶ Eu	~0.4 s	2.50×10^{-9}	1.74×10^{-8}	5.98×10^{-7}	8.16×10^{-6}	2.39×10^{-7}	6.30×10^{-5}
¹⁶⁷ Eu	~0.2 s	2.24×10^{-10}	1.38×10^{-9}	5.08×10^{-8}	2.01×10^{-6}	6.93×10^{-9}	4.05×10^{-6}
¹⁶⁸ Eu		2.85×10^{-12}	2.81×10^{-11}	2.67×10^{-9}	2.70×10^{-7}	1.23×10^{-10}	1.75×10^{-7}
¹⁶⁹ Eu			1.14×10^{-12}	1.27×10^{-10}	2.36×10^{-8}	2.27×10^{-12}	3.22×10^{-9}
¹⁷⁰ Eu				2.42×10^{-12}	1.16×10^{-9}		9.78×10^{-11}
¹⁵¹ Gd	124 days			4.06×10^{-11}			
¹⁵³ Gd	240.4 days			4.32×10^{-8}		2.17×10^{-10}	2.35×10^{-9}
¹⁵⁵ Gd	Stable	4.08×10^{-10}	1.33×10^{-10}	5.84×10^{-6}	8.04×10^{-12}	1.66×10^{-7}	2.68×10^{-6}
¹⁵⁶ Gd	Stable	1.43×10^{-8}	3.92×10^{-9}	4.41×10^{-5}	3.57×10^{-10}	3.94×10^{-6}	4.76×10^{-5}
¹⁵⁷ Gd	Stable	1.48×10^{-7}	6.50×10^{-8}	2.08×10^{-4}	8.04×10^{-9}	2.90×10^{-5}	4.69×10^{-4}
¹⁵⁸ Gd	Stable	1.48×10^{-6}	8.78×10^{-7}	6.09×10^{-4}	1.11×10^{-7}	1.52×10^{-4}	5.58×10^{-3}
¹⁵⁹ Gd	18,479 h	3.71×10^{-6}	4.48×10^{-6}	1.10×10^{-3}	9.06×10^{-7}	4.53×10^{-4}	1.24×10^{-2}
¹⁶⁰ Gd	$>1.3 \times 10^{21}$ years	1.01×10^{-5}	1.51×10^{-5}	1.62×10^{-3}	4.25×10^{-6}	9.67×10^{-4}	3.74×10^{-2}
¹⁶¹ Gd	3,66 min	1.11×10^{-5}	2.26×10^{-5}	2.13×10^{-3}	1.06×10^{-5}	1.26×10^{-3}	5.95×10^{-2}

Table 56.7 (Continued)

Fission product	Half-life	²³⁵ U Thermal	²³⁵ U Fast	²³⁵ U High	²³⁸ U Fast	²³⁹ Pu Thermal	²⁵² Cf Spontaneous
¹⁶² Gd	8.4 min	6.79 × 10 ⁻⁶	1.59 × 10 ⁻⁵	1.52 × 10 ⁻³	1.63 × 10 ⁻⁵	1.19 × 10 ⁻³	6.10 × 10 ⁻²
¹⁶³ Gd	68 s	3.81 × 10 ⁻⁶	4.71 × 10 ⁻⁶	8.77 × 10 ⁻⁴	3.20 × 10 ⁻⁵	5.99 × 10 ⁻⁴	4.68 × 10 ⁻²
¹⁶⁴ Gd	45 s	1.49 × 10 ⁻⁶	4.33 × 10 ⁻⁶	4.10 × 10 ⁻⁴	4.70 × 10 ⁻⁵	2.22 × 10 ⁻⁴	2.58 × 10 ⁻²
¹⁶⁵ Gd	10.3 s	6.14 × 10 ⁻⁷	1.64 × 10 ⁻⁶	1.27 × 10 ⁻⁴	4.44 × 10 ⁻⁵	5.96 × 10 ⁻⁵	9.96 × 10 ⁻³
¹⁶⁶ Gd	~7 s	1.66 × 10 ⁻⁷	5.78 × 10 ⁻⁷	2.75 × 10 ⁻⁵	3.82 × 10 ⁻⁵	1.59 × 10 ⁻⁵	2.92 × 10 ⁻³
¹⁶⁷ Gd	~3 s	3.68 × 10 ⁻⁸	1.04 × 10 ⁻⁷	5.55 × 10 ⁻⁶	2.34 × 10 ⁻⁵	1.08 × 10 ⁻⁶	4.87 × 10 ⁻⁴
¹⁶⁸ Gd	~0.3 s	2.18 × 10 ⁻⁹	9.35 × 10 ⁻⁹	7.02 × 10 ⁻⁷	9.32 × 10 ⁻⁶	6.99 × 10 ⁻⁸	5.74 × 10 ⁻⁵
¹⁶⁹ Gd	~1 s	1.19 × 10 ⁻¹⁰	9.47 × 10 ⁻¹⁰	8.15 × 10 ⁻⁸	2.15 × 10 ⁻⁶	3.29 × 10 ⁻⁹	2.86 × 10 ⁻⁶
¹⁷⁰ Gd		2.68 × 10 ⁻¹²	4.36 × 10 ⁻¹¹	3.85 × 10 ⁻⁹	3.48 × 10 ⁻⁷	8.09 × 10 ⁻¹¹	2.44 × 10 ⁻⁷
¹⁷¹ Gd			1.23 × 10 ⁻¹²	1.80 × 10 ⁻¹⁰	3.42 × 10 ⁻⁸	2.40 × 10 ⁻¹²	9.05 × 10 ⁻⁹
¹⁷² Gd				9.81 × 10 ⁻¹²	8.13 × 10 ⁻⁹		2.17 × 10 ⁻¹⁰
¹⁵³ Tb	2.34 days			3.34 × 10 ⁻¹²			
¹⁵⁵ Tb	5.32 days			3.11 × 10 ⁻⁹		4.65 × 10 ⁻¹²	2.43 × 10 ⁻¹⁰
¹⁵⁶ Tb	5.35 days			5.73 × 10 ⁻⁸		2.63 × 10 ⁻¹⁰	1.17 × 10 ⁻⁸
^{156m} Tb	24.4 h			3.65 × 10 ⁻⁹		2.92 × 10 ⁻¹¹	1.30 × 10 ⁻⁹
¹⁵⁷ Tb	71 years	4.93 × 10 ⁻¹²	1.48 × 10 ⁻¹²	7.22 × 10 ⁻⁷		8.17 × 10 ⁻⁹	3.82 × 10 ⁻⁷
¹⁵⁸ Tb	180 years	1.20 × 10 ⁻¹⁰	4.83 × 10 ⁻¹¹	4.79 × 10 ⁻⁶	4.38 × 10 ⁻¹²	9.99 × 10 ⁻⁸	1.20 × 10 ⁻⁵
^{158m} Tb	10.70 s	1.33 × 10 ⁻¹¹	4.77 × 10 ⁻¹²	3.06 × 10 ⁻⁷		1.11 × 10 ⁻⁸	1.33 × 10 ⁻⁶
¹⁵⁹ Tb	Stable	1.70 × 10 ⁻⁹	1.27 × 10 ⁻⁹	2.16 × 10 ⁻⁵	1.45 × 10 ⁻¹⁰	1.28 × 10 ⁻⁶	8.08 × 10 ⁻⁵
¹⁶⁰ Tb	72.3 days	2.84 × 10 ⁻⁸	1.12 × 10 ⁻⁸	2.11 × 10 ⁻⁵	1.89 × 10 ⁻⁹	6.28 × 10 ⁻⁶	6.73 × 10 ⁻⁴
¹⁶¹ Tb	6.906 days	5.96 × 10 ⁻⁸	7.66 × 10 ⁻⁸	2.30 × 10 ⁻⁴	1.58 × 10 ⁻⁸	2.85 × 10 ⁻⁵	2.71 × 10 ⁻³
¹⁶² Tb	7.60 min	4.52 × 10 ⁻⁸	6.49 × 10 ⁻⁸	1.82 × 10 ⁻⁴	3.49 × 10 ⁻⁸	3.12 × 10 ⁻⁵	3.43 × 10 ⁻³
^{162m} Tb		4.52 × 10 ⁻⁸	6.49 × 10 ⁻⁸	1.82 × 10 ⁻⁴	3.49 × 10 ⁻⁸	3.12 × 10 ⁻⁵	3.43 × 10 ⁻³

^{163}Tb	19.5 min	2.14×10^{-7}	1.57×10^{-7}	4.49×10^{-4}	4.37×10^{-7}	1.01×10^{-4}	1.28×10^{-2}
^{164}Tb	3.0 min	1.80×10^{-7}	3.16×10^{-7}	4.53×10^{-4}	1.68×10^{-6}	7.75×10^{-5}	1.65×10^{-2}
^{165}Tb	2.11 min	2.81×10^{-7}	4.53×10^{-7}	3.05×10^{-4}	4.78×10^{-6}	6.33×10^{-5}	1.51×10^{-2}
^{166}Tb	21 s	1.54×10^{-7}	3.20×10^{-7}	1.45×10^{-4}	9.87×10^{-6}	3.55×10^{-5}	1.04×10^{-2}
^{167}Tb	19.4 s	1.34×10^{-7}	2.12×10^{-7}	6.52×10^{-5}	1.69×10^{-5}	7.45×10^{-6}	4.14×10^{-3}
^{168}Tb	8.2 s	1.73×10^{-8}	3.97×10^{-8}	1.89×10^{-5}	1.56×10^{-5}	1.09×10^{-6}	1.24×10^{-3}
^{169}Tb	~2 s	4.07×10^{-9}	1.62×10^{-8}	5.14×10^{-6}	9.93×10^{-6}	1.76×10^{-7}	1.57×10^{-4}
^{170}Tb	~3 s	2.24×10^{-10}	1.74×10^{-9}	5.79×10^{-7}	4.05×10^{-6}	1.03×10^{-8}	3.62×10^{-5}
^{171}Tb	~0.5 s	2.92×10^{-11}	2.18×10^{-10}	6.43×10^{-8}	1.20×10^{-6}	1.12×10^{-9}	3.59×10^{-6}
^{172}Tb		1.05×10^{-12}	1.05×10^{-11}	8.59×10^{-9}	7.60×10^{-7}	4.07×10^{-11}	2.35×10^{-7}
^{157}Dy	8.14 h			2.32×10^{-10}			2.60×10^{-11}
^{159}Dy	144.4 days			4.36×10^{-8}		2.59×10^{-10}	4.72×10^{-8}
^{160}Dy	Stable	1.93×10^{-12}	1.20×10^{-12}	3.78×10^{-7}		4.68×10^{-9}	1.13×10^{-6}
^{161}Dy	Stable	2.51×10^{-11}	2.15×10^{-11}	2.67×10^{-6}	1.37×10^{-12}	5.53×10^{-8}	1.23×10^{-5}
^{162}Dy	Stable	2.03×10^{-10}	1.73×10^{-10}	1.02×10^{-5}	2.15×10^{-11}	4.39×10^{-7}	8.24×10^{-5}
^{163}Dy	Stable	1.24×10^{-9}	5.18×10^{-10}	2.83×10^{-5}	3.87×10^{-10}	1.74×10^{-6}	4.09×10^{-4}
^{164}Dy	Stable	4.78×10^{-9}	4.70×10^{-9}	6.44×10^{-5}	4.94×10^{-9}	4.48×10^{-6}	1.32×10^{-3}
^{165}Dy	2.334 h	1.53×10^{-8}	1.41×10^{-8}	8.89×10^{-5}	3.54×10^{-8}	7.24×10^{-6}	2.61×10^{-3}
$^{165\text{m}}\text{Dy}$	1.257 min	2.29×10^{-9}	1.93×10^{-9}	6.69×10^{-6}	4.82×10^{-9}	1.08×10^{-6}	3.90×10^{-4}
^{166}Dy	81.6 h	3.98×10^{-8}	4.68×10^{-8}	9.84×10^{-5}	2.61×10^{-7}	1.48×10^{-5}	4.86×10^{-3}
^{167}Dy	6.20 min	7.51×10^{-8}	6.64×10^{-8}	9.58×10^{-5}	1.19×10^{-6}	6.38×10^{-6}	4.51×10^{-3}
^{168}Dy	8.7 min	3.64×10^{-8}	4.62×10^{-8}	6.04×10^{-5}	3.16×10^{-6}	2.83×10^{-6}	3.20×10^{-3}
^{169}Dy	39 s	1.74×10^{-8}	3.77×10^{-8}	3.62×10^{-5}	4.78×10^{-6}	9.71×10^{-7}	9.60×10^{-4}
^{170}Dy	~30 s	3.73×10^{-9}	1.50×10^{-8}	9.22×10^{-6}	5.43×10^{-6}	1.77×10^{-7}	5.49×10^{-4}
^{171}Dy	~6 s	1.09×10^{-9}	4.01×10^{-9}	2.31×10^{-6}	3.72×10^{-6}	4.43×10^{-8}	1.37×10^{-4}
^{172}Dy	~3 s	1.77×10^{-10}	7.73×10^{-10}	7.28×10^{-7}	6.61×10^{-6}	5.62×10^{-9}	2.30×10^{-5}

Table 56.7 (Continued)

Fission product	Half-life	²³⁵ U Thermal	²³⁵ U Fast	²³⁵ U High	²³⁸ U Fast	²³⁹ Pu Thermal	²⁵² Cf Spontaneous
¹⁶¹ Ho	2.48 h			2.84×10^{-9}		3.07×10^{-12}	2.85×10^{-9}
^{161m} Ho	6.76 s			2.14×10^{-10}			4.25×10^{-10}
^{162m} Ho	67.0 min			2.34×10^{-8}		5.16×10^{-11}	4.22×10^{-8}
¹⁶³ Ho	4,570 years			1.75×10^{-7}		9.58×10^{-10}	7.27×10^{-7}
^{163m} Ho	1.09 s			1.31×10^{-8}		1.43×10^{-10}	1.09×10^{-7}
¹⁶⁴ Ho	29 min			1.84×10^{-7}		2.11×10^{-9}	2.16×10^{-6}
^{164m} Ho	37.5 min			8.38×10^{-7}		4.93×10^{-9}	5.05×10^{-6}
¹⁶⁵ Ho	Stable	2.05×10^{-11}	1.12×10^{-11}	3.55×10^{-6}	1.30×10^{-11}	4.76×10^{-8}	4.41×10^{-5}
¹⁶⁶ Ho	26.83 h	4.03×10^{-11}	2.23×10^{-11}	1.46×10^{-6}	6.54×10^{-11}	5.64×10^{-8}	6.00×10^{-5}
^{166m} Ho	1,200 years	9.41×10^{-11}	6.03×10^{-11}	6.66×10^{-6}	1.77×10^{-10}	1.32×10^{-7}	1.40×10^{-4}
¹⁶⁷ Ho	3.1 h	1.03×10^{-9}	5.23×10^{-10}	1.83×10^{-5}	3.75×10^{-9}	2.93×10^{-7}	4.20×10^{-4}
¹⁶⁸ Ho	2.99 min	1.16×10^{-9}	8.53×10^{-10}	2.52×10^{-5}	2.74×10^{-8}	2.91×10^{-7}	7.33×10^{-4}
¹⁶⁹ Ho	4.7 min	2.23×10^{-9}	2.82×10^{-9}	3.28×10^{-5}	1.29×10^{-7}	3.12×10^{-7}	5.14×10^{-4}
¹⁷⁰ Ho	2.76 min	4.93×10^{-10}	1.18×10^{-9}	9.00×10^{-6}	1.91×10^{-7}	5.83×10^{-8}	3.48×10^{-4}
^{170m} Ho	43 s	4.93×10^{-10}	1.18×10^{-9}	9.00×10^{-6}	1.91×10^{-7}	5.83×10^{-8}	3.48×10^{-4}
¹⁷¹ Ho	53 s	1.07×10^{-9}	2.31×10^{-9}	9.65×10^{-6}	7.48×10^{-7}	8.87×10^{-8}	4.04×10^{-4}
¹⁷² Ho	25 s	3.69×10^{-10}	8.68×10^{-10}	6.76×10^{-6}	3.12×10^{-6}	2.41×10^{-8}	1.63×10^{-4}
¹⁶⁵ Er	10.36 h			1.35×10^{-8}		2.11×10^{-11}	6.02×10^{-8}
¹⁶⁶ Er	Stable			7.45×10^{-8}		3.14×10^{-10}	7.39×10^{-7}
¹⁶⁷ Er	Stable	1.10×10^{-12}		3.70×10^{-7}		1.05×10^{-9}	3.59×10^{-6}
^{167m} Er	2.269 s			2.78×10^{-8}		1.57×10^{-10}	5.36×10^{-7}

¹⁶⁸ Er	Stable	6.79×10^{-12}	2.74×10^{-12}	1.28×10^{-6}	1.76×10^{-11}	4.32×10^{-9}	1.92×10^{-5}
¹⁶⁹ Er	9.40 days	3.27×10^{-11}	2.26×10^{-11}	3.76×10^{-6}	2.37×10^{-10}	1.11×10^{-8}	3.39×10^{-5}
¹⁷⁰ Er	Stable	6.42×10^{-11}	8.31×10^{-11}	4.59×10^{-6}	2.37×10^{-9}	1.35×10^{-8}	1.15×10^{-4}
¹⁷¹ Er	7.516 h	1.58×10^{-10}	1.88×10^{-10}	5.25×10^{-6}	1.26×10^{-8}	2.27×10^{-8}	1.59×10^{-4}
¹⁷² Er	49.3 h	2.20×10^{-10}	2.71×10^{-10}	7.96×10^{-6}	1.62×10^{-7}	1.91×10^{-8}	1.48×10^{-4}
¹⁶⁶ Tm	7.70 h			6.56×10^{-11}			1.59×10^{-10}
¹⁶⁷ Tm	9.25 days			8.61×10^{-10}			2.44×10^{-9}
¹⁶⁸ Tm	93.1 days			6.73×10^{-9}		1.58×10^{-12}	3.17×10^{-8}
¹⁶⁹ Tm	Stable			4.67×10^{-8}		1.52×10^{-11}	1.59×10^{-7}
¹⁷⁰ Tm	128.6 days			1.37×10^{-7}		4.53×10^{-11}	1.39×10^{-6}
¹⁷¹ Tm	1.92 years			3.53×10^{-7}	8.52×10^{-12}	2.71×10^{-10}	4.91×10^{-6}
¹⁷² Tm	63.6 h	1.68×10^{-12}	1.13×10^{-12}	1.08×10^{-6}	3.09×10^{-10}	5.40×10^{-10}	1.15×10^{-5}
¹⁶⁸ Yb	Stable			3.33×10^{-12}			4.48×10^{-12}
¹⁶⁹ Yb	32.026 days			5.33×10^{-11}			5.42×10^{-11}
^{169m} Yb	46 s			4.01×10^{-12}			8.11×10^{-12}
¹⁷¹ Yb	Stable			2.51×10^{-9}			1.47×10^{-8}
¹⁷² Yb	Stable			1.84×10^{-8}		1.94×10^{-12}	9.16×10^{-8}
¹⁷¹ Lu	8.24 days						1.27×10^{-12}
^{171m} Lu	79 s						1.27×10^{-12}
¹⁷² Lu	6.70 days			1.54×10^{-11}			2.19×10^{-11}
^{172m} Lu	3.7 min			1.54×10^{-11}			2.19×10^{-11}

Empty cell: no data are available

References

- Bé M-M, Coursol N, Duchemin B, Lamé J, Morillon C, Piton F, Browne E, Chechev V, Helmer R, Schönfeld E (1999a) Table De Radionucléides. CEA Saclay, DIMRI/LNHB, Gif-sur-Yvette
- Bé M-M, Duchemin B, Browne E, Wu S-C, Chechev V, Helmer R, Schönfeld E (1999b) Table De Radionucléides, Comments on Evaluations. CEA Saclay, DIMRI/LNHB, Gif-sur-Yvette
- Bearden JA (1967) *Rev Mod Phys* 39:78–124
- Browne E, Bé M-M, Mac Mahon TD, Helmer RG (2001) Report on the activities of the decay data evaluation project, Report CEA-R-5990, CEA, Saclay. <http://www.nucleide.org/DDEP.htm>
- CODATA (2003) CODATA internationally recommended values of the fundamental physical constants 1998, National Institute of Standards and Technology, Gaithersburg. <http://physics.nist.gov/cuu/constants>
- DDEP (2003) Homepage of the decay data evaluation project, Laboratoire National Henri Becquerel, BNM-CEA Saclay. <http://www.nucleide.org/DDEP.htm>
- Deslattes RD, Kessler EG Jr, Indelicato P, Billy LD, Lindroth E, Anton J (2003a) *Rev Mod Phys* 75:35–99
- Deslattes RD, Kessler EG Jr, Indelicato P, de Billy L, Lindroth E, Anton J, Coursey JS, Schwab DJ, Olsen K, Dragoset RA (2003b) X-Ray transition energies, National Institute of Standards and Technology, Gaithersburg. <http://physics.nist.gov/PhysRefData/XrayTrans>
- England TR, Rider BF (1994) Report LA-UR-94-3106, ENDF-349, Los Alamos National Laboratory, Los Alamos
- Firestone RB, Shirley VS, Baglin CM, Chu SYF, Zipkin J (1996) Table of isotopes, vol 1–2, 8th edn. Wiley, New York
- Helmer RG, van der Leun C (2000) *Nucl Instrum Meth A* 450:35
- IAEA (1991) X-ray and gamma-ray standards for detector calibration, Report IAEA-TECDOC-619, IAEA, Vienna
- IAEA (2002) Third research co-ordination meeting of the IAEA coordinated research project on update of X- and gamma-ray decay data standards for detector calibration and other applications, Report INDC (NDS)-437, IAEA, Vienna. <http://www.nds.iaea.org>
- IAEA (2003) X- and gamma-ray decay data standards for detector calibration and other applications, Report IAEA-TECDOC, IAEA, Vienna. http://www.nds.iaea.org/xgamma_standards/
- Mohr PJ, Taylor BN (1999) *J Phys Chem Ref Data* 28(6):1713
- Mohr PJ, Taylor BN (2000) *Rev Mod Phys* 72(2):351
- Schönfeld E, Janssen H (2000) *Appl Radiat Isot* 52:595
- Schönfeld E, Rodloff G (1999) Energies and relative emission probabilities of K X-rays for elements with atomic numbers in the range from $Z = 5$ to $Z = 100$, Report PTB-6.11-1999-1, PTB, Braunschweig
- Tuli JK (2000) Nuclear wallet cards, 6th edn. Brookhaven National Laboratory, Upton, New York. <http://www.nndc.bnl.gov/wallet/>

Volume 6

Nuclear Energy Production and Safety Issues



57 Technical Application of Nuclear Fission

J. O. Denschlag

Universität Mainz, Mainz, Germany

57.1	<i>Introduction</i>	2617
57.2	<i>Historical Aspects</i>	2617
57.2.1	Oklo	2617
57.2.2	First Attempts to Build Artificial Reactors	2620
57.3	<i>General Principles of Reactor Design</i>	2622
57.3.1	Thermal and Fast Reactor Types – Neutron Physics in a Reactor	2622
57.3.1.1	Thermal Neutrons	2623
57.3.1.2	Epithermal Neutrons (Resonance Region)	2623
57.3.1.3	Fast (Unmoderated) Fission Neutrons	2624
57.3.2	Neutron Moderation	2625
57.3.3	Buildup Reactions	2628
57.3.4	The Fission Factor (η)	2631
57.3.5	The Criticality Factor – Neutron Multiplication Factor k	2632
57.3.6	Reactor Kinetics	2633
57.3.6.1	The Subcritical State	2634
57.3.6.2	The Supercritical State	2635
57.3.6.3	The Critical State	2635
57.3.7	Critical Size	2637
57.4	<i>Specific Nuclear Reactors and Other Nuclear Devices</i>	2638
57.4.1	Research Reactors	2638
57.4.2	Reactors for Power Stations	2640
57.4.2.1	The Pressurized Water Reactor (PWR)	2640
57.4.2.2	The Boiling Water Reactor (BWR)	2646
57.4.2.3	The RBMK Reactor	2646
57.4.2.4	The Fast Breeder Reactor (FBR)	2648
57.4.2.5	The Concept of the Accelerator-Driven System (ADS)	2651
57.4.3	Nuclear Weapons	2654
57.5	<i>The Nuclear Fuel Cycle</i>	2655
57.5.1	Manufacture of the Fuel and Fuel Elements	2656
57.5.2	Reprocessing of Spent Nuclear Fuel	2658
57.5.3	Storage of Nuclear Waste	2659

57.6 *Summary* 2660

57.7 *Editors' Notes* 2660

Abstract: The chapter is devoted to the practical application of the fission process, mainly in nuclear reactors. After a historical discussion covering the natural reactors at Oklo and the first attempts to build artificial reactors, the fundamental principles of chain reactions are discussed. In this context chain reactions with fast and thermal neutrons are covered as well as the process of neutron moderation. Criticality concepts (fission factor η , criticality factor k) are discussed as well as reactor kinetics and the role of delayed neutrons. Examples of specific nuclear reactor types are presented briefly: research reactors (TRIGA and ILL High Flux Reactor), and some reactor types used to drive nuclear power stations (pressurized water reactor [PWR], boiling water reactor [BWR], Reaktor Bolshoi Moshchnosti Kanalny [RBMK], fast breeder reactor [FBR]). The new concept of the accelerator-driven systems (ADS) is presented. The principle of fission weapons is outlined. Finally, the nuclear fuel cycle is briefly covered from mining, chemical isolation of the fuel and preparation of the fuel elements to reprocessing the spent fuel and conditioning for deposit in a final repository.

57.1 Introduction

The impact of nuclear fission on the human way of life is due to the fact that the fission process can be organized in such a way that a self-propagating chain reaction proceeds. This is because the one neutron normally required to induce a fission reaction in a nucleus, like ^{235}U or ^{239}Pu , sets free two to three neutrons that can induce new fission reactions (see [Chap. 4 in Vol. 1](#)). Therefore, in contrast to all other nuclear reactions observed before, macroscopic amounts of matter (up to tons) can undergo nuclear reactions with dramatic consequences. In nuclear reactors (power stations), large amounts of fissile material are burned producing a substantial part of the world's supply of electric energy. Nuclear reactors are used for the mass production of radioisotopes required in medical diagnosis and therapy and in modern technology. Research reactors are used as intense sources of neutrons allowing for neutron diffraction studies that have contributed immensely to the knowledge of the structure of molecules important to chemistry and biology or to the development of new materials. On the other hand, nuclear weapons have changed the military and political equilibrium between nations.

57.2 Historical Aspects

57.2.1 Oklo

A surprising answer to the question as to when the first nuclear reactor was operating was found in the year 1972 by a group of scientists working for the French nuclear weapons program: the first nuclear reactor was operating 2 billion years ago in Africa in a place now called Oklo in the state of Gabon (IAEA 1975; Cowan 1976; Roth 1977).

Different sites have since been found west of Franceville, Gabon, in which the fission reaction occurred. These sites possess rich ore deposits of nearly pure $\text{UO}_2/\text{U}_3\text{O}_8$ that have been formed hydrolytically. Nuclear fission took place in an area containing 500 t of uranium that – at the time – was about 4% in ^{235}U . (Due to the shorter half-life of ^{235}U [7.0×10^8 years] relative to ^{238}U [4.5×10^9 years], the content of ^{235}U in natural uranium has sunk meanwhile to the present value of 0.7%.) The most important of the natural reactors was in operation for at

least 150,000 years and resulted in a production of energy of about 15,000 megawatt-years (MW-years). This would correspond to the output of a modern nuclear power station over a 5-year period.

The discovery of the reactors reminds one of a detective novel. The initial observation was an irregularity in UF_4 , an intermediate product: some samples of UF_4 analyzed on 25 April 1972 showed a weak deficit in ^{235}U (0.7171% differing from the natural value of 0.7207%). (UF_4 is oxidized by F_2 to form UF_6 , a stable compound with a sublimation point of 56°C , which is then used for isotopic enrichment in the diffusion process.) After this first alarm had sounded, evoking the possibility that natural uranium had been thinned by depleted material and, hence, the possibility of fraud or divergence, other samples, a few days later, showed values even less than 0.71%. (Later, in specific samples even values of 0.296% were observed.) The puzzle could however be fairly quickly solved as a large stock of samples of all the batches, from the mined ores to the end products, had been saved. It was soon clear that the low values of ^{235}U were present already in the original ore and the ore could not possibly have been manipulated.

The idea for a possible reason came from the observation that the deficits in ^{235}U (and even deficiencies larger than previously observed) were correlated to the content of the ore in uranium. Such a correlation is to be expected since the criticality depends directly on the amount and concentration of uranium and an ongoing fission process would consume the isotope ^{235}U . In later studies the isotopes produced in fission or their decay products could be detected (IAEA 1975; De Laeter 1988). The composition and amount of fission products allowed for a calculation of the total amount of uranium that underwent fission and, hence, the total amount of energy set free.

As an illustration of the way to disentangle the events that had taken place 2 billion years ago, the measurement of the neodymium isotopes (142–146, 148, and 150) will be presented. It is important to know that neodymium remained in the rocks without migrating. In addition, it is advantageous that the content of natural neodymium in the minerals is small. This content could be determined since ^{142}Nd is practically not formed in nuclear fission. As it results from the systematics of fractional fission yields (see [Chap. 4 in Vol. 1](#)), the (independent, direct) yield of ^{142}Nd is very small. An alternative formation by the β decay of more neutron-rich nuclides of the same mass (i.e., isobars) is not possible because the direct precursor ^{142}Ce is stable. Consequently, the content of the mineral in ^{142}Nd reflects the amount of natural neodymium not produced by fission. Using the known isotopic composition of natural neodymium, the contributions of natural origin of all neodymium isotopes could be subtracted. This is illustrated in [Table 57.1](#) (Columns 1–3).

In addition to correcting the concentrations for Nd of natural origin, corrections have to be made due to neutron capture by Nd isotopes in such a natural reactor. The process is particularly pronounced for ^{143}Nd , which, due to its high neutron capture cross section of $\sigma = 3.25 \times 10^{-22} \text{ cm}^2$, is transformed to ^{144}Nd to a noticeable extent. Correction of column (3) for this effect results in the values given in column (4). A comparison of the values in column (4) with corresponding values obtained from the neutron-induced fission of ^{235}U shown in column (5) shows nearly perfect agreement.

The correction required for the amount of ^{144}Nd (Column 3 and 4) is based on a total neutron dose (fluence) of $1.5 \times 10^{21} \text{ n/cm}^2$ and, hence, gives an estimate for this value.

The total amount of fission reactions that have occurred and the corresponding total amount of energy set free could be calculated from the amount of neodymium from fission (or other fission products) using the known fission yields. It was determined that the energy produced was the value of 15,000 MW-years given above.

■ Table 57.1

Isotopic composition of neodymium of different provenience (at%) (1) Natural Nd; (2) Sample from Oklo; (3) Sample from Oklo after correction for natural Nd; (4) Column (3) corrected for neutron capture; (5) Nd from the fission of ^{235}U

A	(1)	(2)	(3)	(4)	(5)
142	27.11	1.4	0.0	0.0	0.0
143	12.17	22.1	22.6	28.6	28.84
144	23.85	32.0	32.4	26.4	26.50
145	8.30	17.5	18.0	19.0	18.87
146	17.22	15.6	15.6	14.6	14.42
148	5.73	8.0	8.1	8.1	8.26
150	5.62	3.4	3.3	3.3	3.12

The energy set free allows the calculation of the amount of uranium that underwent fission. The deficit in ^{235}U found today (present natural content 0.7207% minus the experimentally determined content) is too small by about a factor of 5. Using the variation of the isotopic ratio of ^{235}U to ^{238}U (that can be calculated from the respective half-lives), one can determine the time when the natural reactors were operating. The result is 2×10^9 years before present. At that time the ^{235}U content in natural uranium amounted to 3.6% – a concentration used in present-day light-water reactors. A few corrections have to be taken into account in these calculations. First, in a natural reactor, like in present-day artificial reactors, some fast neutrons can induce fission also in ^{238}U . In addition, part of the ^{238}U is converted to ^{239}Pu through neutron capture and subsequent β decays. The plutonium can undergo fission itself or – in case of low neutron flux – decay to ^{235}U . Finally, as will be discussed later, in about 17% of the cases the excited nucleus of $^{236}\text{U}^*$ formed by the neutron capture of ^{235}U will not undergo fission but will emit a γ ray and form long-lived ^{236}U ($T_{1/2} = 2.3 \times 10^7$ years). In the time span of the 2×10^9 years since these reactors stopped working this uranium isotope has decayed to ^{232}Th . This thorium isotope was also found at the reactor site.

A question arises with regard to maintaining long-term stable operation of the natural reactors. As it will be pointed out below, a reactor of the given composition can operate only with thermal neutrons, i.e., the neutrons emerging from the fission reaction with an energy around 2 MeV have to be slowed down to thermal energies. In the Oklo reactors water served as a moderator. The amount of water present within the reactor zone determined the reactivity of the reactors. If sufficient water was present, the neutrons were well moderated and the fission rate was high. This led to an increase of the temperature in the zone and to an evaporation of water, hence decreasing the neutron moderation and fission rate. Consequently, the reactor zone cooled down allowing water to enter again. A new cycle then started.

The arguments raised above were also used to estimate the duration of the operation of natural reactors. Using the known heat conductivity of the minerals in the zones one can estimate that the maximum power of the reactors was about 0.1 MW in order to allow sufficient water to be present. For a total energy of 15,000 MW-years this corresponds to a duration of 150,000 years. This value is a lower limit because it cannot be excluded that due to some external influences, like the lack of sufficient water, the reactors were stopped for some periods.

Besides being of academic interest, Oklo is a model for very old deposits of fission products and of ^{239}Pu , and allows for a study of the long-term behavior of radioactive elements in nature. The study reveals that plutonium, in spite of the presence of water, did not show a migration in the loamy sediments. Even a relatively mobile element, like strontium, that is ecologically important due to its long-lived isotope ^{90}Sr (28.5 years) remained essentially within the reactor zone until it had decayed (IAEA 1975; Cowan 1976).

57.2.2 First Attempts to Build Artificial Reactors

Not even a year after the discovery of nuclear fission it became established that in the process neutrons were set free (Anderson et al. 1939; von Halban jun et al. 1939) opening the way to chain reactions and to speculations concerning the production of almost unlimited amounts of energy (Flügge 1939).

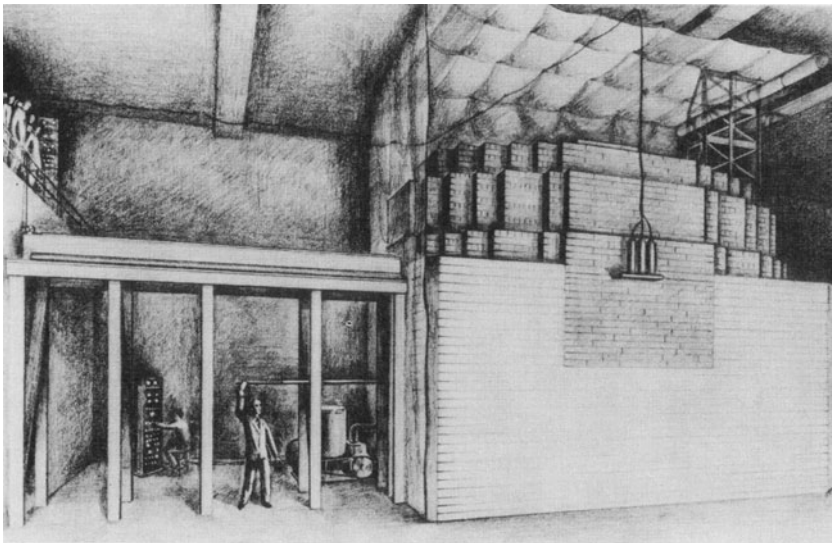
Only 3 years later, in 1942, Fermi set up a test version of a nuclear reactor (under the west stands of Stagg Field, University of Chicago). Unfortunately no photograph exists of this reactor. [▶ Figure 57.1](#) shows a sketch of the set up.

Initially, it was planned to build an array of blocks of natural uranium metal surrounded by blocks of graphite. Since the amount of metallic uranium available was not sufficient, at last mainly uranium dioxide was used (total amount: 40 t of uranium and 385 t of graphite). When the critical state was nearly reached, the control rod was pulled out slowly and in portions while the neutron flux was measured continuously. The record of the neutron flux just before reaching criticality is shown in [▶ Fig. 57.2](#).

One observes that as the control rod is removed little by little, an increase in neutron flux takes place that leads to a new equilibrium value. As it will be pointed out quantitatively later,

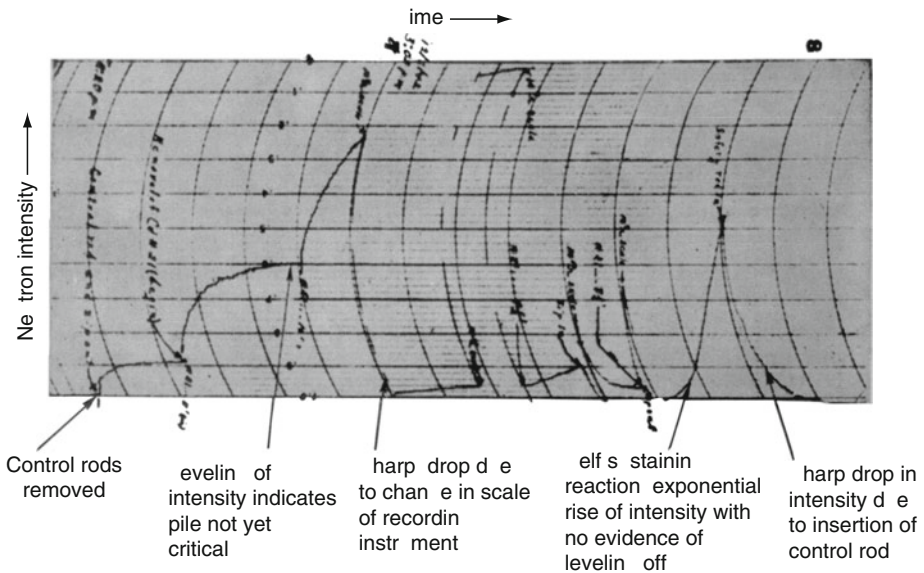
■ **Fig. 57.1**

An artist's conception of the first chain-reacting assembly built under the west stands of Stagg Field, University of Chicago (Glasstone 1967)



■ Fig. 57.2

Record of neutron intensity obtained with the first chain-reacting system on 2 December 1942 (Glasstone 1967)



the reactor operates in this region as an amplifier (amplifying the neutron flux from a small neutron source kept inside). At the position marked “self-sustaining reaction” an exponential rise of the neutron flux with no indication of leveling off is observed. The reactor is said to have reached criticality (or better to have passed criticality by a minute amount). Without outside interference its power will increase indefinitely.

At this point the chain reaction was interrupted by introducing the control rod in order not to expose the participants to dangerous levels of radiation from this unshielded reactor.

Some attempts to build a nuclear reactor were also made in Germany during World War II in the city of Haigerloch near Tübingen. The concept was based on a combination of heavy water (D_2O) and natural uranium. The location was later transformed into the museum “Atom Museum, Haigerloch” with a display of the initial setup. It also commemorates the “Alsos” project in which US troops in a holdup action had collected scientists and material circumventing the German–French front line.

Today the type of heavy-water-moderated reactor with natural uranium still exists in the form of the CANDU-reactor (CANadian Deuterium Uranium reactor). The graphite-moderated reactor of Fermi has found application mostly in the former Soviet Union (RBMK Series). Of these reactors reactor block No. 4 in Chernobyl has become ill famed for the most severe accident in reactor history (see ▶ Sect. 55.5.3.2 in Chap. 55, Vol. 5). The reactor type that has been generally adopted due to technical and economical reasons is the light-water-moderated reactor based on uranium with an enrichment of 3–4% in ^{235}U . It has been realized in two modifications: the boiling water reactor (BWR) and the pressurized water reactor (PWR). An alternative that is theoretically very tempting but has encountered many difficulties in realization is the fast breeder reactor (FBR).

The principle of reactor operation and the different reactor types will be discussed in the following. Neutrons are the most important agent in driving a reactor. Also neutrons for the scientist are the most important product of a research reactor, because they can be used for various analytical purposes (neutron activation analysis, structural analysis through neutron diffraction, etc.). Therefore, at first, some neutron physics will be presented as of relevance for the existing two main types of reactors (“thermal” and “fast”).

57.3 General Principles of Reactor Design

57.3.1 Thermal and Fast Reactor Types – Neutron Physics in a Reactor

The difference between thermal (e.g., light-water reactors) and fast reactors (fast breeder, nuclear weapons) is in the energy of the neutrons inducing the fission reaction. The reason for the distinction is the reaction cross sections for fission in ^{235}U (^{239}Pu) and for competing (n,γ)-reactions mainly in ^{238}U , the main component of the fuel elements.

For neutron energies from thermal (0.025 eV) up to about 1 eV, the fission cross section of ^{235}U and ^{239}Pu is about 100 times higher than the parasitic (n,γ)-cross section of ^{238}U that consumes neutrons without contributing to the chain reaction. In the energy range from 10 to 10^4 eV on the other hand, the (n,γ)-cross section of ^{238}U is by about a factor of 10 higher than the fission cross section of ^{235}U and ^{239}Pu . At neutron energies above 10^4 eV, and particularly above 10^6 eV, the fission cross section dominates again (Choppin and Rydberg 1980; Mughabghab et al. 1981). The consequence is that a chain reaction – in a mixture of about 3% ^{235}U (or ^{239}Pu) and 97% ^{238}U – is possible at low neutron energies (<1 eV) and at high energies (> 10^5 eV), but at intermediate energies the neutrons required to maintain a chain reaction are absorbed by the reaction of $^{238}\text{U}(\text{n},\gamma)^{239}\text{U}$. Consequently, a reactor must be built in such a way that neutrons, originating from the fission reaction, with an energy of about 2 MeV are moderated down to energies below 1 eV as fast as possible, or alternatively any moderation of the neutrons must be avoided. These two (ideally) disjunct energy ranges are distinctive features of the two main types of reactors, i.e., “thermal” and “fast.” Energy spectra of neutrons in different chain reacting systems are shown in [Fig. 57.3](#).

A typical neutron spectrum in a light-water reactor can be compared to the spectra of neutrons (a) as they originate from the fission reaction, (b) as they are found in a fast reactor, and (c) in a fission weapon. As it is customary, in [Fig. 57.3](#) the relative number of neutrons is multiplied by their energy and the product “flux energy” is plotted as a function of the neutron energy. Hence the line parallel to the “neutron energy” axis and labeled “thermal reactor” represents an exponential decrease of the absolute flux over 8 decades.

In principle, in a reactor, three components of the neutron energy spectrum ([Fig. 57.3](#)) can be distinguished (Erdtmann 1976; Erdtmann and Petri 1986):

1. Completely moderated, “thermal” neutrons (Maxwell distribution in [Fig. 57.3](#))
2. Epithermal neutrons (roughly “thermal reactor” from 0.5 eV to ~0.1 MeV)
3. Fast (unmoderated) neutrons

These three components are found in practically every reactor. Each one of these components has a well-defined energy distribution that will be described next. The contributions of the components vary from reactor to reactor. The distribution designated “Thermal Reactor” in

Fig. 57.3

Neutron spectra of some chain-reacting systems (Choppin and Rydberg 1980). The vertical axis shows the “flux energy,” i.e., the product of neutron flux and neutron energy¹.

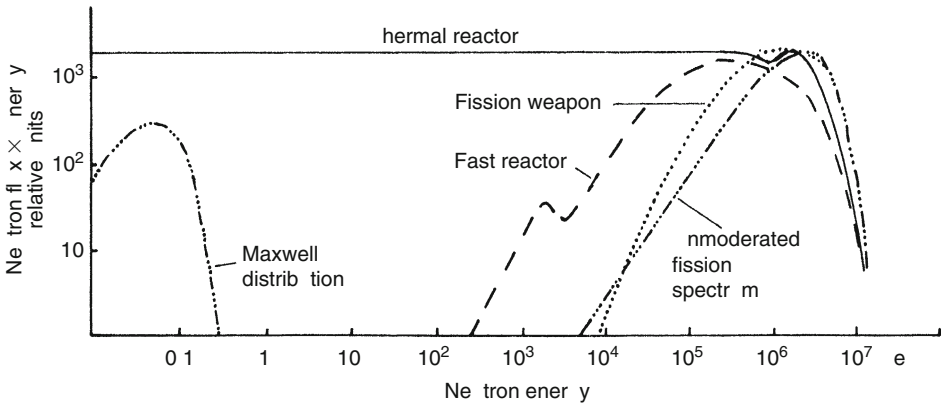


Fig. 57.3 represents a fairly “hard” neutron spectrum. Normally, the Maxwell distribution of the fully moderated neutrons dominates the spectrum at low neutron energies.

57.3.1.1 Thermal Neutrons

The spectrum of thermal neutrons is characterized by an equilibrium of the neutrons’ kinetic energy with that of the surrounding moderator. Like for any gas the speed distribution can be described by the “Maxwell equation”:

$$\frac{dn}{du} = \frac{4n}{u_0^3 \sqrt{\pi}} u^2 \exp\left(-\frac{u^2}{u_0^2}\right) \quad (57.1)$$

where n is the number density of neutrons, u is the speed, and u_0 is the most probable speed of neutrons (at $T = 20^\circ\text{C}$ $u_0 = 2,200$ m/s). The most probable velocity of 2,200 m/s corresponds to a neutron kinetic energy of

$$E_n = \frac{m_n u_0^2}{2} = 0.0253 \text{ eV} \quad (57.2)$$

where m_n is the mass of neutron.

57.3.1.2 Epithermal Neutrons (Resonance Region)

The neutron flux above 0.5 eV is characterized by an $1/E$ law. This also appears in Fig. 57.3 showing that the product of neutron flux and energy is constant from 10^{-2} eV up to 10^5 eV (“thermal reactor”). This dependence allows for a convenient definition of a nominal flux of epithermal neutrons ϕ_{epi} and the corresponding reaction cross sections (resonance integrals).

Generally, the “gross” rate constant R of a reaction induced by neutrons of different energies can be calculated by the following integral:

$$R = \int_0^{\infty} \varphi(E) \sigma(E) dE \quad (57.3)$$

where $\sigma(E)$ denotes the cross section of the reaction in question as a function of neutron energy, and $\varphi(E)$ describes the distribution of the neutron flux along the energy axis². For epithermal neutrons in particular one can write

$$R = \phi_{\text{epi}} \int_{0.5 \text{ eV}}^{\infty} \frac{\sigma(E)}{E} dE \equiv \phi_{\text{epi}} I \quad (57.4)$$

where

$$\phi_{\text{epi}} = \varphi(E)E = \text{const.} \quad (57.5)$$


due to the $1/E$ law. The value of the integral I is called the resonance integral. Resonance integrals are properties of nuclides and may be found in tables (Erdtmann 1976; Mughabghab et al. 1981) like the reaction cross sections for thermal neutrons. They may be used for the determination of the flux of epithermal neutrons (ϕ_{epi}) in any reactor or in different locations of the reactor core. Experimentally, R is measured by activating a monitor with known thermal neutron cross section and known resonance integral in the interesting reactor location. The activation is done twice: (1) after wrapping the sample in a sheet of Cd (0.7 mm thick) and (2) without Cd. The cadmium sheet absorbs thermal neutrons but has (nearly) no interaction with epithermal (epi-cadmium) neutrons. Consequently, irradiation (1) gives information on the epithermal flux and irradiation (2) reflects the effect of the sum of epithermal and thermal flux. The thermal neutron flux can be obtained from the difference.

The information on thermal and epithermal neutron flux is important for diagnostic purposes in any reactor. It is particularly important in research reactors that are used for neutron activation analysis.

57.3.1.3 Fast (Unmoderated) Fission Neutrons

The flux of unmoderated neutrons as a function of their energy, $\varphi_f(E)$, where the subscript f stands for fast neutrons, may be described by Watt's equation (Watt 1952) as given in (Erdtmann 1976):

$$\varphi_f(E/\text{MeV}) = \frac{0.484}{\text{cm}^2 \text{ s MeV}} \exp(-E/\text{MeV}) \sinh \sqrt{2E/\text{MeV}}. \quad (57.6)$$

The function is shown in  Fig. 57.3 (“unmoderated fission spectrum”). These fast neutrons, generally, play no role for the usual (n, γ) -reactions because the (n, γ) -cross sections become very small at neutron energies above 100 keV. Instead, in this energy range (n, p) -, (n, α) -, $(n, 2n)$ -, and (n, n') -reactions become important. The latter are threshold reactions, i.e., their cross sections are zero up to a certain neutron energy (threshold energy) and are then a function of the neutron energy.

Again, the reaction rate constant (R_f) may be described as the integral of the product of neutron flux distribution and the cross section as a function of neutron energy:

$$R_f = \int_{E_{th}}^{\infty} \varphi_f(E) \sigma(E) dE \quad (57.7)$$

where E_{th} is the threshold energy. The integration can also be carried out from zero to infinity as the integral amounts to zero below E_{th} .

The cross-section curves $\sigma(E)$ are usually called excitation functions and the curves of the differential products $\varphi(E)\sigma(E)$ are the response functions. In measuring R_f and assuming relation (4.6), one can measure effective cross sections (σ_f) for unmoderated fission neutrons:

$$\sigma_f = \frac{R_f}{\int_0^{\infty} \varphi_f(E) dE} = \frac{\int_0^{\infty} \varphi_f(E) \sigma(E) dE}{\int_0^{\infty} \varphi_f(E) dE}. \quad (57.8)$$

The integral in the denominator is sometimes abbreviated as ϕ_n resulting in the simple relation:

$$\sigma_f = \frac{R_f}{\phi_n}. \quad (57.9)$$

From a measured value of R_f , Eq. (57.9) allows one to calculate the mean reaction cross section for the respective nuclide. Correspondingly, one may determine the integral of the unmoderated neutron flux ϕ_n if the mean reaction cross section is known. Values of σ_f are available in tabulated form (Erdtmann 1976; Mughabghab et al. 1981). The value of ϕ_n varies as a function of the location in the reactor core (irradiation position) but is constant for a well-defined location at a given reactor power.

As pointed out above, the energy distribution of the neutrons in a reactor may be described by the sum of three components belonging to thermal, epithermal, and unmoderated neutrons. The reactor is characterized by the different contributions of these three components.

In a thermal reactor, it is important to slow down the neutrons quickly and effectively avoiding losses due to parasitic (n,γ)-reactions. In the following section, this moderation of neutrons will be discussed.

57.3.2 Neutron Moderation

The neutrons originate from the fission process with an energy of about 2 MeV, and they are moderated predominantly by elastic collisions with the atomic nuclei present in the reactor core. At first the central collision will be discussed. The laws of conservation of momentum and energy are valid:

$$m_n u_n + m_A u_A = m_n u'_n + m_A u'_A, \quad (57.10)$$

$$\frac{m_n u_n^2}{2} + \frac{m_A u_A^2}{2} = \frac{m_n u'^2_n}{2} + \frac{m_A u'^2_A}{2} \quad (57.11)$$

where m_n and m_A denote the mass of the neutron and that of the collision partner with mass number A , respectively, u_n and u_A are the respective velocities, and unprimed and primed velocities refer to velocities before and after collision, respectively.

■ **Table 57.2**

Velocity u'_n of a neutron – after a central collision with an atom of mass number A – relative to its initial velocity u_n , calculated using ► Eq. (57.12)

A	1	2	12	238
$(u'_n/u_n)_c$	0	−0.33	−0.85	−0.992

In the “laboratory system,” the velocity of the target atom (i.e., the collision partner of neutron) before collision can be considered being $u_A = 0$. Since the masses of the neutron and the moderator atom are approximately proportional to their mass numbers 1 and A , respectively, ► Eqs. (57.10) and (► 57.11) can be rearranged to give the relation:

$$\left(\frac{u'_n}{u_n}\right)_c = \frac{1 - A}{1 + A}, \quad (57.12)$$

where the subscript c is to remind that the ratio in parentheses is calculated for central collision.

In the following ► Table 57.2, a few examples are calculated for the velocity of the neutron after a collision relative to the velocity before the collision as a function of the mass of the collision partner (central collision).

A neutron after a (central) collision with a proton (of identical mass) is at rest, i.e., has lost all of its kinetic energy. In collisions with heavier atoms the neutron bounces back (therefore the negative sign) and conserves part of its speed. In a collision with ^{238}U the neutron bounces back with 99.2% of its initial speed, corresponding to 98.4% of its initial kinetic energy.

It is obvious from this simple discussion that water (H_2O) with its two hydrogen atoms (protons) must be (and is, indeed) a very good moderator. For the general case of a noncentral collision, the following equation applies:

$$\frac{u'_n}{u_n} = \frac{\sqrt{1 + A^2 + 2A \cos \theta}}{1 + A} \quad (57.13)$$

where θ is the angle between the incoming neutron and the outgoing collision partner. For the special case of $\theta = 180^\circ$ (central collision) ► Eq. (57.13) is identical to ► Eq. (57.12).

One observes that for both central and noncentral collisions the relative decrease in speed $u'_n/u_n = k$ is independent of the speed (or the energy) of the neutron and only depends on the mass ratio. Correspondingly, for the energy $E'_n/E_n = k^2$ is valid. Frequently the energy loss is characterized by the quantity $\xi_\theta = \ln(E_n/E'_n)$. Again, ξ is independent of E . For the central collision one can write:

$$\xi_c = \ln \left(\frac{1 - A}{1 + A} \right)^2. \quad (57.14)$$

An integration (i.e., averaging) of all collision angles results in the relation (Smith 1965)

$$\xi = 1 + \frac{\alpha}{1 - \alpha} \ln \alpha \quad (57.15)$$

where

$$\alpha = \left(\frac{1 - A}{1 + A} \right)^2. \quad (57.16)$$

Note that for ${}^1\text{H}$ $\alpha = 0$ and therefore [Eq. \(57.15\)](#) yields $\xi = 1$ as one can easily verify using l'Hospitals rule for the limit $\alpha \rightarrow 0$. The average number of collisions required for a fission neutron of about 2 MeV energy to be moderated to thermal energy is given by the equation

$$n = \frac{1}{\xi} \ln \frac{E_n^0}{E_n} \quad (57.17)$$

where E_n^0 and E_n are the mean energies of fission neutrons (~ 2 MeV) and of thermal neutrons (0.025 eV; see [Eq. \[57.2\]](#)), respectively. Typical values of ξ and of n are given in [Table 57.3](#).

The table illustrates the advantage of light elements as moderators. The moderating qualities of a substance depend, however, on other factors too. The “slowing down power” (SDP) of a moderator includes the scattering cross section for neutrons (σ_s) and the number density (N_s) of scattering atoms (in number of atoms per cubic centimeter [cm^3], for instance):

$$\text{SDP} = \xi \sigma_s N_s. \quad (57.18)$$

Generally, the quantities σ_s and SDP depend on the neutron energy and the values given are averages for the region of epithermal energies. Moderators, in addition to the scattering cross section, possess an absorption cross section, σ_a , for (n, γ)-reactions, etc. Obviously, the absorption cross section of a good moderator should be small.

A quantitative description of the moderating properties including neutron absorption is given by the “moderating ratio” (MR):

$$\text{MR} = \xi \frac{\sigma_s}{\sigma_a}. \quad (57.19)$$

If a moderator is composed of different nuclides/elements, then the properties of the nuclides must be averaged. The properties of some compounds used as moderators are given in [Table 57.4](#).

The quality of the moderators as characterized by MR ([Table 57.4](#)) decreases in the order of $\text{D}_2\text{O} > \text{C} > \text{Be} > \text{H}_2\text{O}$. In a commercial reactor many other factors like the price and the phase (liquid/solid) have to be taken into account. In practice H_2O is used in most reactors together with a fuel enriched in ${}^{235}\text{U}$ (3–4%). Reactors operating with natural uranium rely on D_2O as a moderator.

Table 57.3

Values of the average logarithmic energy decrement ξ , as defined by [Eq. \(57.15\)](#), and of n , the average number of collisions required to moderate a neutron from an initial energy of 2 MeV to thermal energy as defined by [Eq. \(57.17\)](#), for various elements of interest in reactor technology

Nuclide	A	ξ_{tot}	n
${}^1\text{H}$	1	1.00	18
${}^2\text{H}$ (D)	2	0.725	25
${}^4\text{He}$	4	0.425	43
${}^{12}\text{C}$	12	0.158	115
${}^{16}\text{O}$	16	0.120	151
${}^{238}\text{U}$	238	0.0084	2,166

■ **Table 57.4**

Moderating properties of different compounds: scattering cross section for epithermal neutrons (σ_s , in barn); absorption cross section for thermal neutrons (σ_a in barn); average logarithmic energy decrement ξ ; slowing down power (SDP) (cm^{-1}) and moderating ratio (MR)

Compound	σ_s	σ_a	ξ	SDP	MR
H ₂ O	49	0.66	0.927	1.52	69
D ₂ O	10.6	0.00092	0.510	0.181	5,880
Be	5.9	0.009	0.209	0.15	137
C	4.7	0.0045	0.158	0.06	165

The time required for moderation differs according to the number of collisions involved. Average values for the thermalization from an initial energy of about 2 MeV are 40 μs for light water, 150 μs for graphite, and 2.1 ms for lead.

For the thermal reactor it is important that the moderation of the neutrons takes place in as short a time as possible in order to avoid the capture of these neutrons in the (n,γ) -resonances along the way.

57.3.3 Buildup Reactions

In the following, neutron capture reactions that lead to a buildup of heavier nuclides (actinides) will be discussed. As has been mentioned before, inside a reactor, in addition to neutron-induced (n,f) -fission reactions, neutron-capture (n,γ) -reactions take place. The products arising primarily from neutron capture in ^{235}U , ^{238}U , and ^{239}Pu (^{236}U , ^{239}U , and ^{240}Pu , respectively) can undergo further reactions like other neutron capture reactions, as well as β decay, α decay, neutron-induced fission, etc. The possible reactions and their cross sections or half-lives are given in [Fig. 57.4](#).

It appears that starting with uranium a number of neutron capture reactions take place. Subsequent reactions of β decay lead to elements with higher atomic number – in [Fig. 57.4](#) up to Cm ($Z = 96$). The buildup of new heavier isotopes is stopped by the fact that some show α decay and others undergo fission. The kinetics of transformation in α decay, β decay, and isomeric transitions characterized by their half-lives follow the well-known exponential law (see [Chap. 7 in Vol. 1](#)):

$$N = N_0 e^{-\lambda t} \quad (57.20)$$

where N_0 and N denote the initial number of atoms and the number of atoms after time t , respectively, λ is the decay constant that is inversely proportional to the half-life $T_{1/2}$ as

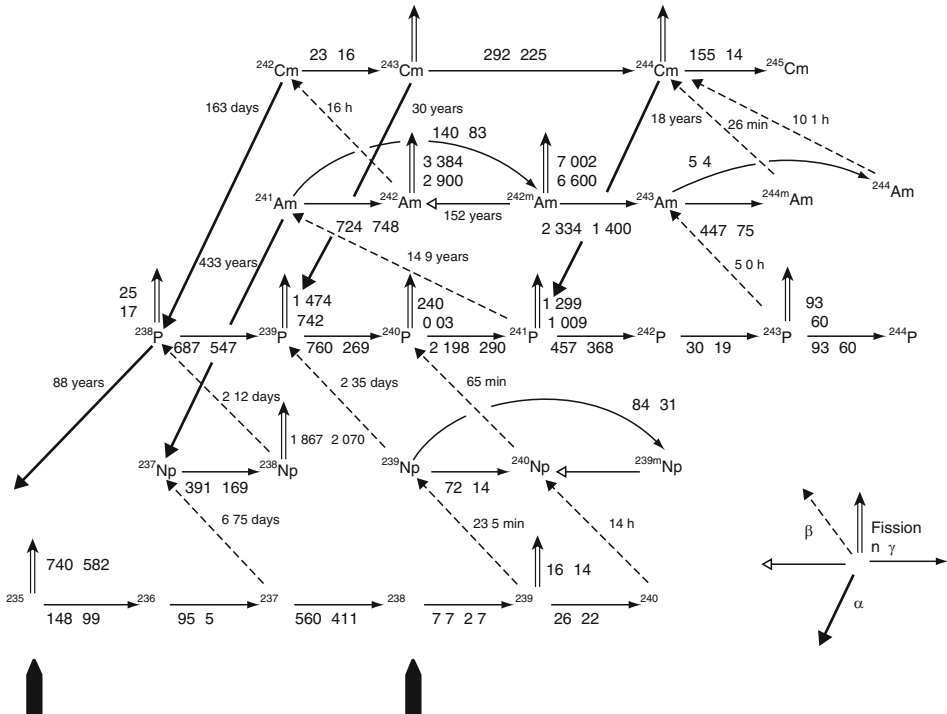
$$\lambda = \frac{\ln 2}{T_{1/2}}. \quad (57.21)$$

For longer decay chains or for a situation of a continuous production of a mother isotope the reader may be referred to the classical system of radioactive growth and decay curves as given in textbooks of radiochemistry. (See also [Eqs. \[38.29\] and \[38.30\] in Chap. 38, Vol. 4.](#))

The situation is similar for neutron-induced fission- and (n,γ) -reactions characterized by cross sections (σ). In a constant neutron flux also an exponential law is realized. The “decay

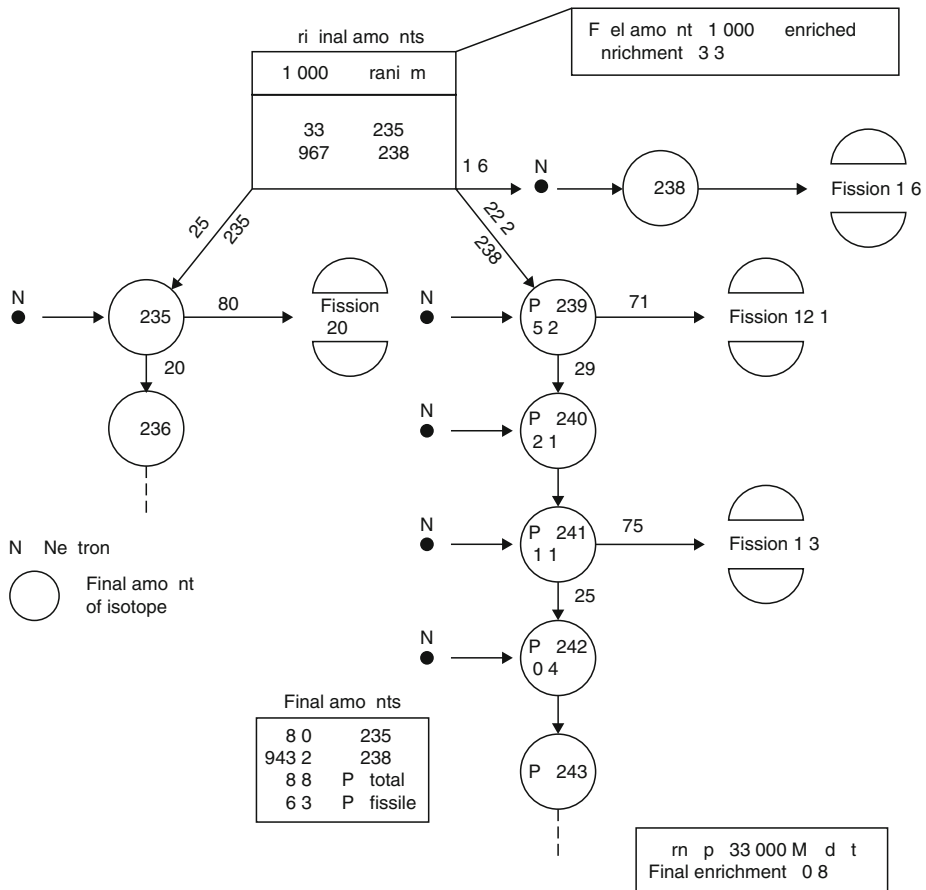
Fig. 57.4

Nuclear reactions and decays occurring by neutron irradiation of uranium. Numbers along the decay paths (α , β , IT) are half-lives (where m is for minute). Numbers along reaction paths ((n, γ) , fission) are cross sections (in barns) for a neutron spectrum of a standard-power light-water reactor, cross sections in parentheses are for thermal neutrons (0.025 eV). (The different arrows are explained by the insert in the lower right corner.) (Choppin and Rydberg 1980)



As it appears from [▶ Fig. 57.4](#), there are numerous other buildup reactions. Among those are the very important formation of ^{239}Pu from ^{238}U by neutron capture and two successive β decays. [▶ Figure 57.4](#) also indicates that a number of the products built up are undergoing fission after neutron capture.

Fig. 57.5
Reaction products in a light-water power reactor after a burn-up of 33,000 MWd/t of fuel (Choppin and Rydberg 1980)



After the burn-up indicated, the amount of ^{235}U that underwent fission is 20 kg. In addition, 1.6 kg of ^{238}U was fissioned by fast neutrons. The amount of 22.2 kg of ^{238}U captured neutrons and decayed to ^{239}Pu . Of this 12.1 kg underwent fission again. Of the remaining 10.1 kg of ^{239}Pu , 5.2 kg remained as such until the end of exposure, the rest of 4.9 kg captured more neutrons forming $^{240,241,242,243}\text{Pu}$. Some ^{241}Pu (1.3 kg) underwent fission. Finally 5 kg of ^{235}U captured a neutron and transformed to ^{236}U without undergoing fission. Therefore, of the 33 kg of ^{235}U present initially, 8 kg remain in the spent fuel and of the 967 kg of ^{238}U , 943.2 kg remain. Instead 8.8 kg of Pu have been formed of which 6.3 kg are fissile ^{239}Pu and ^{241}Pu . In addition, there are 5 kg of ^{236}U and about 35 kg of fission products (formed by the fission of 21.6 kg of uranium and 13.4 kg of plutonium). The total amount of fissionable material remaining in the spent fuel is 14.3 kg (8.0 kg of ^{235}U and 6.3 kg of $^{239,241}\text{Pu}$). This may be recovered by reprocessing.

Therefore, in a typical light-water reactor a considerable amount of new fissionable material is produced. In a breeder reactor more fissionable material is produced from ^{238}U than is consumed in the reactor.

Hence, some of the (n,γ) -reactions that are parasitic in establishing a chain reaction are advantageous from the standpoint of an economic use of uranium.

However, in constructing a reactor, the primary question is at first whether a chain reaction (or a critical assembly) can be established. This question will be discussed in the following section. It can be described by the fission factor (η).

57.3.4 The Fission Factor (η)

A chain reaction is in principle possible if in a substance the number of neutrons set free by fission divided by the number of neutrons required to maintain the fission process is at least equal to 1. This number is designated by η . It is defined by the following equation:

$$\eta = v \frac{\sigma_f}{\sigma_f + \sigma_c} \quad (57.24)$$

where σ_f and σ_c denote the fission cross section, and the capture cross section for (n,γ) -reaction, respectively, and v is the average number of neutrons emitted after fission. Values of σ_f , σ_c , v , and η for the most important fissile nuclides are given in [Table 57.5](#) for thermal and fast neutrons (1 MeV). The highest value of η is obtained for the fission of ^{239}Pu by fast neutrons. A chain reaction with pure ^{238}U is possible neither with thermal neutrons nor with fast ones. For mixtures weighted averages of the cross sections and v values have to be used. Consequently, one obtains

$$\eta = \frac{v_1 f_1 \sigma_{f1} + v_2 f_2 \sigma_{f2}}{(f_1 \sigma_{f1} + f_2 \sigma_{f2}) + (f_1 \sigma_{c1} + f_2 \sigma_{c2})} \quad (57.25)$$

where f_1 and f_2 are the fractions of components 1 and 2, respectively.

Considering, e.g., natural uranium (a mixture of 0.71% of ^{235}U and 99.29% of ^{238}U) and thermal neutrons, the fission factor obtained from [Eq. \(57.25\)](#) is $\eta = 1.33$. Here, a chain reaction is still possible but neutron losses in the moderator and in the construction materials must be kept very small. This requires the use of a very good moderator like D_2O (see above). For a typical light-water reactor fuel (3% in ^{235}U) a value of $\eta = 1.83$ is obtained.

■ Table 57.5

Cross sections for (n,γ)-reactions (σ_c in barn) and neutron-induced fission reactions (σ_f in barn); average total number of neutrons emitted after fission (ν) (Choppin and Rydberg 1980) and fission factor (η) for various fission reactions induced by thermal and fast neutrons (1 MeV)

Neutron	Nuclide	σ_c	σ_f	ν	η
Thermal neutrons	^{233}U	48	531	2.49	2.28
	^{235}U	99	582	2.42	2.07
	^{238}U	2.7	0	0	0
	^{239}Pu	269	742	2.87	2.11
	^{241}Pu	368	1,009	3.00	2.20
Fast neutrons (1 MeV)	^{233}U	0.08	1.95	2.59	2.49
	^{235}U	0.11	1.25	2.58	2.37
	^{238}U	0.17	0.017	2.85	0.26
	^{239}Pu	0.09	1.65	3.02	2.86

Besides neutron capture in the fuel, other parasitic reactions play a role. They will be discussed in the following with respect to the practical case of reactor construction and operation. In this context a criticality factor is defined.

57.3.5 The Criticality Factor – Neutron Multiplication Factor k

As it was shown before, the condition for the establishment of a chain reaction is that at least one of the neutrons originating from fission is inducing a new fission reaction. This condition is expressed by the neutron multiplication factor k (also called criticality factor). k is defined as

$$k = \frac{\text{number of neutrons in generation 2}}{\text{number of neutrons in generation 1}} \quad (57.26)$$

In order to maintain a chain reaction, k has to be at least one. A state of the reactor with $k > 1$ is called supercritical. For every generation of neutrons the reactor power increases by the factor k . The duration of a generation is the average time span between the birth of a neutron and its capture. This time span in a thermal reactor is mainly determined by the time it takes the neutron to be moderated down to thermal energy (usually about 40 μs , see ▶ Sect. 57.3.2) and to diffuse to an absorption site. In a state of exactly $k = 1$ the reactor is called “critical.” The reactor power is constant. A state with $k < 1$ is called subcritical. This topic will be discussed further below (reactor dynamics). The neutron cycle includes a number of steps that have been partly studied already but that will be discussed here in the context of a full neutron cycle.

Assuming that 100 neutrons are captured in the fuel of a reactor with uranium enriched to 3% ^{235}U , $\eta = 1.83$ (see above) and $\nu = 2.42$ (▶ Table 57.5) results in 183 neutrons (second generation) from $(183/2.42) = 76$ fission events (and 24 (n,γ)-capture reactions of ^{235}U and ^{238}U). The 183 neutrons are fast neutrons, which are able to induce fission in ^{238}U producing additional neutrons. This is described by the “fast fission factor” (ϵ). Assuming that $\epsilon = 1.03$, the neutron number increases to $183 \times 1.03 \approx 188$. The neutrons are moderated through

collision with the water molecules. During moderation some neutrons ($\sim 5\%$) diffuse out of the reactor volume and are lost. Thus, the surviving fraction (also called the “leakage factor” of fast neutrons) is $A_f = 0.95$. A number of 179 neutrons are left.

Mainly in the energy range of 1 to 10^4 eV these neutrons undergo (n, γ)-absorption reactions in the moderator, in the construction elements of the reactor and in the fuel (absorption resonances, especially in ^{238}U). This loss can be estimated to amount to 20%. The “resonance escape probability” p therefore amounts to $p = 0.8$, leaving ($179 \times 0.8 \approx$) 143 neutrons. After reaching thermal energy the neutrons diffuse through the reactor core. During this time different effects can take place:

(1) Some neutrons diffuse outside the reactor core and get caught in the construction elements of the reactor. Assuming again a loss of 5%, the surviving fraction (i.e., the “leakage factor”) of thermal neutrons is $A_{th} = 0.95$, i.e., $143 \times 0.95 \approx 136$ neutrons are left. (2) Some thermal neutrons are caught within the reactor core by interaction with the moderator, the construction elements of the reactor, some samples to be activated in irradiation positions, and finally with the control rods and some content of boron in the coolant. The fraction of neutrons that escapes these absorption reactions is called the thermal utilization factor ($f = 0.74$). By moving the control rods this factor can be varied as to maintain a criticality of $k = 1$ and, hence, to leave 100 neutrons for the next cycle. In summary of this discussion the following equation results:

$$k = \eta \varepsilon p f A_f A_{th} \quad (57.27)$$

where η is the fission factor (see [Eq. \[57.24\]](#) or [\[57.25\]](#)), ε is the fast fission factor, p is the resonance escape probability, f is the thermal utilization factor, A_f is the survival of epithermal diffusion loss, and A_{th} is the survival of thermal diffusion loss.

An important point for the safety of reactors is the influence of the core temperature on k , i.e., on the reactivity. Water-moderated reactors can be built to have a negative temperature coefficient: an increase in temperature/power will lead to steam bubbles near the fuel elements and to a decrease in moderation. If the reactor has been designed a little undermoderated, a drop in moderation will bring about a drop in reactivity (k). Such a reactor will be naturally stable against undesired changes in power. One may recall the discussion of the Oklo reactor at the beginning of the chapter.

Other reactors do not have this feature. The Russian developed reactor type RBMK-1000, for instance, is based on neutron moderation in graphite and heat transport by water. Under certain conditions of low power it has a positive temperature reactivity coefficient and this was – among many other reasons – also responsible for the largest accident in reactor history (Chernobyl, 1986).

57.3.6 Reactor Kinetics

The evolution of the generated power after a change in the reactivity is an important point for the control of nuclear reactors. For this purpose, the duration of a neutron generation, i.e., the average lifetime τ of a neutron (from its formation in fission until its capture) is important. Values for these “neutron cycles” in different types of fission assemblies are given in [Table 57.6](#).

■ **Table 57.6**

Average time of neutron cycle in different fission assemblies

Type of assembly	Time of neutron cycle (τ/s)
Thermal reactor	10^{-3} to 10^{-4}
Fast reactor	10^{-6} to 10^{-7}
Nuclear weapons	10^{-8} to 10^{-9}

The time of the neutron cycle in the thermal reactor is mainly determined by the time required to bring the neutrons to thermal energy. This requirement does not exist in the fast reactor and in nuclear weapons. Therefore the cycle times are shorter in these two latter cases.

At every pass of the neutron cycle the number of neutrons (and so the power of the reactor) changes by the factor k . Hence, the change in the absolute number of neutrons per unit of time (dN/dt) is

$$\frac{dN}{dt} = \frac{N(k-1)}{\tau} + K \quad (57.28)$$

where N is the number of neutrons, K is the contribution of a (starter) neutron source that is usually present in any fission assembly ($K = \text{const.}$). For integration ▶ Eq. (57.28) can be rewritten as

$$\int \left(\frac{N(k-1)}{\tau} + K \right)^{-1} dN = \int dt \quad (57.29)$$

Integration of ▶ Eq. (57.29) results in

$$N = \left(N_0 + \frac{K\tau}{k-1} \right) \exp \left[\frac{(k-1)t}{\tau} \right] - \frac{K\tau}{k-1}. \quad (57.30)$$

For the discussion of ▶ Eq. (57.30) three special cases can be distinguished. (1) $k < 1$; the reactor is subcritical, the reactor works as an “amplifier.” (2) $k = 1$; the reactor is critical; the reactor power is constant (the contribution of K is small and can be neglected). (3) $k > 1$; the reactor is supercritical, the reactor power increases exponentially.

57.3.6.1 The Subcritical State

With $k < 1$; $N_0 = 0$, ▶ Eq. (57.30) becomes:

$$N = \frac{K\tau}{1-k} \exp \left[-\frac{(1-k)t}{\tau} \right] + \frac{K\tau}{1-k} \quad (57.31)$$

or

$$N = \frac{K\tau}{1-k} \left\{ 1 - \exp \left[-\frac{(1-k)t}{\tau} \right] \right\}. \quad (57.32)$$

Table 57.7
Amplification of neutron flux by a reactor in a subcritical status at various values of k

K	$N_{\infty}/(K\tau)$
0.1	1.1
0.5	2
0.9	10
0.99	100

The neutron number (reactor power) shows an increase approaching exponentially an equilibrium value of

$$N_{\infty} = \frac{K\tau}{1-k}. \quad (57.33)$$

This “leveling” is exactly what was observed by Fermi when the first artificial reactor was approaching criticality (see [Fig. 57.2](#)). For k between 0 and 1, N_{∞} is larger than $K\tau$. The reactor works as an amplifier. The amplification factor depends on the value of k . This is shown in [Table 57.7](#).

57.3.6.2 The Supercritical State

With $k > 1$ (K can be neglected) [Eq. \(57.30\)](#) becomes:

$$N = N_0 \exp \left[\frac{(k-1)t}{\tau} \right] \quad (57.34)$$

This corresponds to an unlimited exponential increase of N (number of neutrons and reactor power). The behavior is shown in [Fig. 57.6](#) for $k = 1.1$ and may be compared there with the behavior in the subcritical state ($k = 0.5$ and 0.9).

57.3.6.3 The Critical State

The critical state is characterized by a neutron multiplication factor $k = 1$. With this condition [Eq. \(57.30\)](#) becomes $N = N_0$. (The contribution of the constant neutron source K used for starting purposes can be neglected since K is six to seven orders of magnitude smaller than N in an operating reactor.)

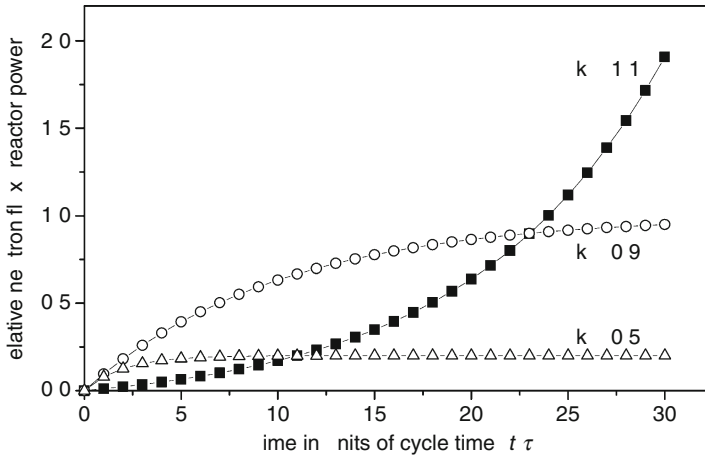
The quantity $\tau/(k-1)$ is usually called the reactor period. It is given by the time of the neutron cycle (τ), which is a constant for a given reactor and is determined mainly by the properties of the moderator. It is also determined by the criticality value k that varies, e.g., as a function of the position of the control rods.

A nuclear weapon is a fission assembly with a very short neutron cycle time: $\tau = 10^{-9}$ s. The criticality factor in a fission weapon is near $k = 2$. From these parameters and [Eq. \(57.34\)](#) it can be easily estimated that the fission reaction in a bomb is over in less than 10^{-7} s.

For a thermal reactor ($\tau = 10^{-4}$ s) and for a value of $k = 1.005$ one calculates also a dramatic increase in reactor power in only 1 s of $e^{50} = 5 \times 10^{21}$! The question therefore arises how a reactor can be controlled if its power changes so drastically for a small change in k ?

■ Fig. 57.6

Evolution of the reactor power with time (in units of the time span τ of the neutron cycle) (a) in a subcritical state ($k = 0.5$ and 0.9) and (b) in a supercritical state ($k = 1.1$). The curves are meant to show the time behavior of the reactor power (neutron flux). Quantitatively the curves for $k = 0.5$ and 0.9 are not directly comparable with the curve for $k = 1.1$



The answer is the existence of “delayed neutrons.” A small fraction of the neutrons emitted from the fission process is not set free promptly from the fission products, but is emitted only as a consequence of the β decay of some fission products that feed excited levels in the daughter nucleus with an excitation energy higher than the binding energy of the last neutron. In these cases the excited (daughter) nucleus may give off its excitation energy not in the form of γ rays but by emission of a neutron. These neutrons appear “delayed” with respect to the birth of the fragment in the fission process. They appear actually with the half-life of their β -active precursors. These half-lives range from about 0.1 s up to 55 s (e.g., ^{87}Br decays with a half-life of 55 s [partly] to ^{86}Kr and a neutron). The fraction of these “delayed neutrons” is small. For the thermal neutron-induced fission of ^{235}U it amounts to a fraction of $\beta = 0.0065$ of the total amount of neutrons. (Unfortunately, it has become customary to designate the fraction of delayed neutrons by the letter β . This β should not be confused with β decay!) This small fraction does, however, have consequences for the control of reactors.

As long as the value of k remains smaller than $1 + \beta$ (i.e., < 1.0065 for ^{235}U) the time of the neutron cycle is determined by the time regime of the delayed neutrons. The neutron cycle time therefore lies between 0.1 and 55 s (depending on the value of k within the limits mentioned) rather than being 10^{-4} s. Assuming a value of $\tau = 1$ s, a calculation like the one performed above for $k = 1.005$ leads to a much smaller increase in reactor power per second ($e^{0.005} \approx 1.005$). Under these conditions, an increase of 10% in reactor power takes 19 s. Reactors must always be built in such a way that the construction makes it impossible to reach a criticality of $k > 1 + \beta$ (“prompt criticality”). This is a basic law of reactor construction since Fermi’s first test reactor. In fact, this is how western reactors are designed. In the reactor at Chernobyl, which was destroyed in an explosion, “prompt criticality” was not made physically impossible. It was only forbidden by regulations that were not followed on the day of the accident. As a result, the reactor exploded.

In this context, it is worth remembering the natural reactor at Oklo discussed at the beginning of this article. Apparently the increase in reactivity due to the influx of water was limited to $k < 1.0065$. Otherwise an explosion would have been the consequence.

57.3.7 Critical Size

The formation of neutrons in a reactor is a function of the volume filled by the fuel. The loss of neutrons by diffusion depends on the surface area of this volume. The ratio of volume to surface area depends on the shape. The largest ratio is found for a sphere. Therefore, Fermi chose a spherical configuration for the first test reactor. However, the ratio of volume to surface area is also a function of the size. The larger the sphere, the better (i.e., larger) is the ratio of volume to surface area.

Consequently, there exists a minimum size of a configuration with fissile material to obtain $k = 1$. This size is called the “critical size.” It depends on many factors: the nature of the fissile material, the geometrical arrangement, the presence of a reflector, the presence of a moderator, and the density of the fissile material. A few typical values are given in ▶ Table 57.8 for metallic samples of a spherical shape without moderator and surrounded by a reflector (20 cm of ^{238}U).

A few values of critical masses of aqueous solutions of the sulfates of the nuclides in a spherical configuration, but without reflector, are given in ▶ Table 57.9.

The critical masses serve only as a rough guide. They can be considerably lower if, e.g., the density is increased by extremely high pressures. This is particularly so for metallic actinides in fission bombs.

After this section covering the principles of chain reactions and of reactor operation, the following sections will be dedicated to the concepts of existing reactors. Since nuclear fission weapons are in principle fast reactors, they will also be briefly covered.

■ Table 57.8
Critical masses of different fissile nuclides (pure) in a spherical configuration, metallic state without moderator, surrounded by a reflector (20 cm of ^{238}U)

Nuclide	Critical mass/kg
^{235}U	22.8
^{233}U	7.5
^{239}Pu	5.6

■ Table 57.9
Critical masses of different fissile nuclides in the form of sulfates in aqueous solution, in a spherical configuration, without reflector

Nuclide	Critical mass
^{235}U	820 g in 6.3 l of water
^{233}U	590 g in 3.3 l of water
^{239}Pu	510 g in 4.5 l of water

57.4 Specific Nuclear Reactors and Other Nuclear Devices

In the following, the most important types of reactors will be discussed briefly. In principle, a distinction has to be made between research reactors and reactors of nuclear power stations. The latter ones are built to produce heat for conversion into electric energy. Research reactors are used as intense neutron sources; the energy set free, necessarily, is not used. Actually energy production in a research reactor is normally disturbing rather than helpful. Therefore, research reactors are generally small and compact. More detailed information, comprehensible also for the nonspecialist, may be found in IAEA (2000) for research reactors and in Zech (1988) concerning reactors for nuclear power stations.

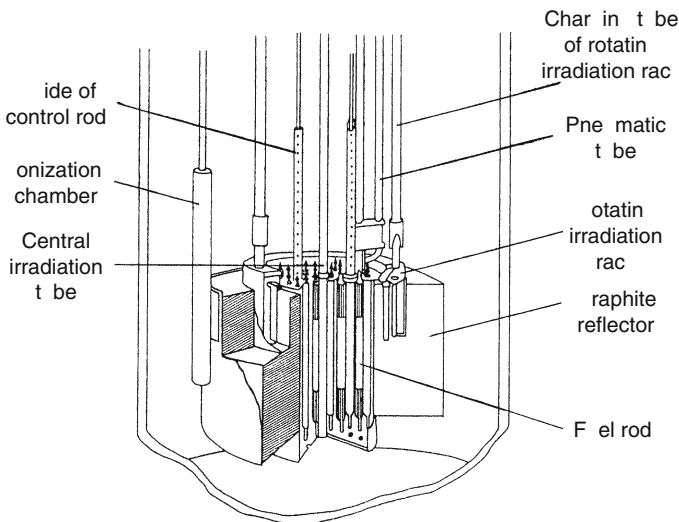
In 2000 the number of research reactors operating worldwide was 288. A detailed survey is given in IAEA (2000). (A database for research reactors is maintained by the International Atomic Energy Agency – IAEA – in Vienna and is accessible through the Internet; see IAEA [2003].) It is not possible to discuss all the different types of research reactors here. The following presentation will be limited to two interesting examples.

57.4.1 Research Reactors

Most of the research reactors are “swimming-pool” reactors. The reactor core is immersed in a water basin, which is open on top. The water has the task of moderating the neutrons, cooling the fuel elements, absorbing the radiation from the core and, nevertheless, giving easy access to the reactor core. Because even thick layers of water are transparent, a visual inspection of the reactor core during operation is possible. As an example of a widely used small research reactor a sketch of the TRIGA reactor is given in [Fig. 57.7](#). (TRIGA stands for Training, Research,

Fig. 57.7

TRIGA reactor, sketch of the reactor core with surrounding water tank and cylindrical graphite reflector with rotating irradiation rack. These and other important parts of the core are designated in the sketch (Berwanger 1965)



Industry, General Atomic, indicating three important fields of application and the – former – manufacturer located in San Diego, California, USA.)

In addition to the reactor core, several irradiation facilities are shown: a rotating rack for 40 samples with a tube of access to these irradiation positions, a pneumatic tube, and a central irradiation tube. The neutron flux at a typical nominal power of 100 kW amounts to $4 \times 10^{12} \text{ s}^{-1} \text{ cm}^{-2}$ in the central irradiation tube. The ionization chamber shown allows for a measurement of the neutron flux (the reactor power).

The TRIGA reactor has an interesting feature, namely that it can produce short and very intense bursts of neutrons. This is due to a particular composition of its fuel elements that are made of an alloy of zirconium (91% by mass) with uranium (8% by mass enriched to 20% ^{235}U) and hydrogen (1% by mass corresponding to 50 atom%). Due to the hydrogen content, the fuel elements contribute directly to the moderation of neutrons. A heating of the fuel elements shifts the energy spectrum of the neutrons to higher values. In order to induce a neutron burst, one control rod is removed rapidly from the reactor core. This way, the reactor is made prompt critical. The reactor power rises to 250 MW within milliseconds. Simultaneously, the fuel elements heat up to a temperature of about 300°C and the energy spectrum of the neutrons is shifted into the region of absorption resonances of ^{238}U . Therefore, the reactivity of the reactor drops drastically followed by the reactor power and the neutron flux. Hence, the quick removal of the control rod, mentioned above, results in a short spike of the neutron flux of 100 ms duration with an integrated neutron fluence of $10^{14} \text{ n cm}^{-2}$. This special feature of the TRIGA reactor allows production and study particularly of short-lived nuclides.

Generally the main areas of application of the small research reactors are the following:

- (1) Neutron activation analysis. (See [▶ Chap. 30 in Vol. 3.](#)) Samples are activated inside the reactor. Characteristic radiations given off after (or during) activation are measured. From these measurements one can deduce the elements that are present in the samples and calculate their respective quantities. This analysis is very selective and in many cases shows an extreme sensitivity. Frequently it does not require a chemical sample preparation, thus excluding errors introduced by such procedures. Therefore, neutron activation is frequently used to calibrate or validate other analytical procedures and to detect small traces of elements of specific interest.
- (2) Production of radionuclides as tracers for research, industry, and medicine (see Vol. 4).
- (3) Study of neutron-induced reactions, like (n, γ) -reactions or the fission process itself.

In addition to the many small research reactors, the high-flux reactor of the Institut Laue-Langevin (ILL) in Grenoble and another high-flux reactor (FRM-II) that is under construction in Munich shall be mentioned here. The ILL-Reactor will be discussed briefly. It is devised to produce a maximum neutron flux. For this purpose one has to concentrate a maximum of fission events in a minimum of space. The main problem is to remove the heat due to the fission reactions from such a small volume. The technical solution is to use a single fuel element (for high mechanical stability). This cylindrical fuel element (diameter: 41 cm, length: 1.48 m) resembles a turbine. Inside the outer mantle it contains an inner tube with a diameter of about 27 cm. The fuel consists of 9 kg of highly enriched uranium (93% ^{235}U). A thin layer of the fuel is welded between two slightly curved plates of aluminum (7 cm \times 90 cm, 1.3 mm thick). A total of 280 such plates are inserted into slits between the outer and inner tube of the fuel element and are maintained there in radial geometry.

The reactor has a power of 54 MW. The small size of the reactor core provides an unusually high neutron flux of $10^{15} \text{ s}^{-1} \text{ cm}^{-2}$. The high power density requires very effective cooling. A total amount of $2,010 \text{ m}^3$ of heavy water (D_2O) is pumped through the turbine-like fuel

element described above. The linear speed of the water is 15 m/s. The main control rod can be inserted into the opening of the inner cylinder. The high neutron flux (1,000 times the flux of the TRIGA reactor described above) allows for additional uses of this reactor:

1. Structural analysis of pure organic or biological samples by neutron scattering
2. Detailed analysis of nuclear fission using the mass separator Lohengrin (see [▶ Chap. 4 in Vol. 1](#))
3. Analysis of the properties of cold and hot neutrons, and the decay properties of the neutron
4. Production of radioactive beams for the synthesis of heavy nuclei and for the questions of the nucleosynthesis in stars

Numerous other research reactors with a neutron flux higher than the TRIGA reactor but not as high as the ILL reactor are used on a routine basis for the production of radionuclides such as $^{99}\text{Mo}/^{99\text{m}}\text{Tc}$, ^{131}I , and other radionuclides for medical diagnosis and treatment. Intense γ -ray sources based on ^{60}Co used for external medical radiation treatment and industrial applications are produced in these reactors.

57.4.2 Reactors for Power Stations

In order to illustrate the economic importance of nuclear energy, some statistics shall be cited. The total number of nuclear power stations operating worldwide at the end of 2001 was 439. In addition, 33 power stations were under construction. The (net) output of electricity of nuclear origin at the end of 2001 amounted to 354,639 MWe (Atomwirtschaft 2002; Deutsches Atomforum 2002). (The abbreviation MWe stands for megawatt electrical power. At an efficiency of about 33% in the conversion of thermal into electrical power, 1 MWe corresponds to about 3 MWth of thermal energy.) Assuming an average price of €0.05/kWh, this corresponds to a yearly turnover of €150 billion (or USD).

The vast majority (80%) of the reactors mentioned are light-water-moderated reactors (LWR). The LWR subdivide in 60% PWR and 20% BWR. The remaining 20% of the reactors are divided among CANadian Deuterium Uranium reactor (CANDU), Reaktor Bolshoi Moshchnosti Kanalny (RBMK), large power channel reactor, gas-cooled reactor (GCR), advanced gas-cooled reactor (AGR), and fast breeder reactor (FBR).

In the following, the PWR will be discussed in some detail, followed by a brief discussion of the similar BWR. The RBMK and FBR will be presented as quite different possibilities. Finally, the accelerator-driven system (ADS) will be outlined as an attractive possibility for the future.

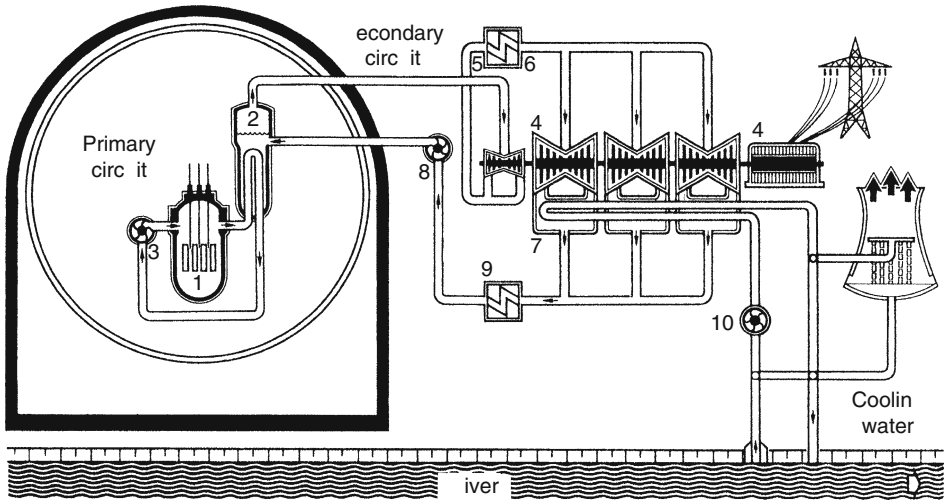
57.4.2.1 The Pressurized Water Reactor (PWR)

As it appears from the numbers given above, the pressurized water reactor has become the most frequently used reactor type for electric power stations. A schematic sketch is shown in [▶ Fig. 57.8](#).

The PWR possesses a double cooling circuit. The primary circuit with the main pumps (3) in [▶ Fig. 57.8](#) passes (light) water along the fuel rods. The water takes over the heat evolved.

Fig. 57.8

Schematic sketch of nuclear power station with a pressurized water reactor; (1) reactor, (2) steam generator, (3) main pump for primary cooling circuit, (4) turbines/generator, (5) steam drum, (6) superheater, (7) condenser, (8) feed water pump, (9) preheater, (10) cooling water pump (Zech 1988)



The thermal energy is transferred to a secondary circuit in a heat exchanger (2). The secondary circuit drives the turbines (4) coupled to the generator (4, right).

Generally, two kinds of turbines are used in sequence. A first smaller turbine is driven by high-temperature/high-pressure steam and secondary larger turbines are exposed to steam of lower temperature/pressure. Before entering the secondary turbines, the vapor must be “dried,” i.e., droplets of condensed water must be removed, because their mechanical impact would rapidly destroy the secondary turbines. The drying of the vapor is made by mechanically removing water droplets (5) and subsequent heating (6).

Behind the turbines, the vapor has to be condensed. This is done by a third cooling circuit, which ultimately dumps the thermal energy into a river or to the air by evaporation of water in a cooling tower. An efficient cooling is important for a good efficiency of the power plant.

Thermodynamically the maximum efficiency of a thermal engine is given by

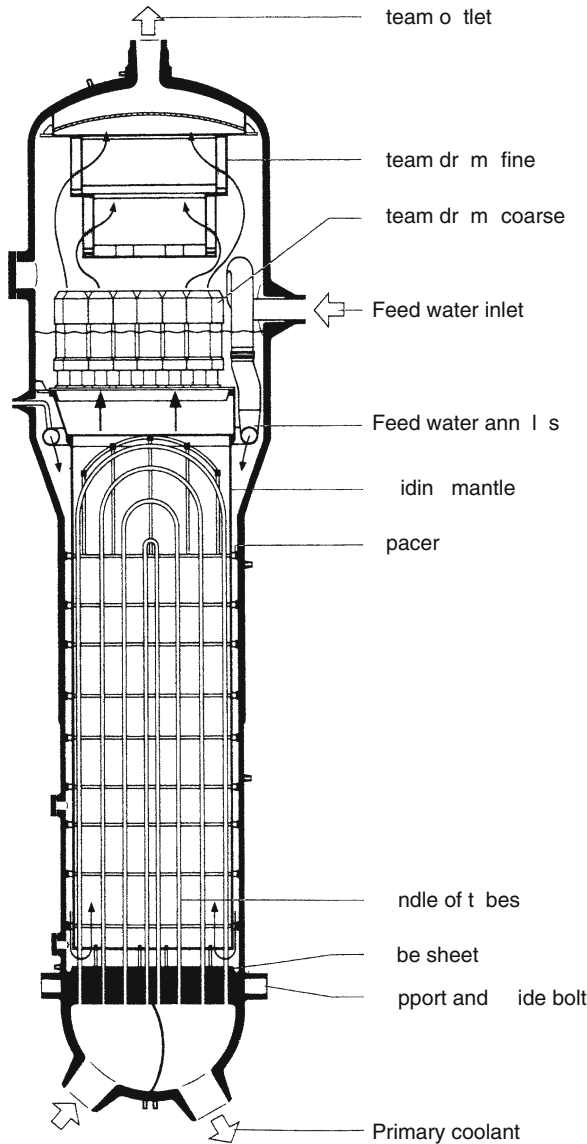
$$\eta = \frac{T_1 - T_2}{T_1} \quad (57.35)$$

where T_1 and T_2 are the temperature of the steam entering the turbine and leaving it, respectively. The condensed water is pumped back to the heat exchanger (2) using pump (8). A heat exchanger is shown in Fig. 57.9 separately. It also contains equipment to remove water droplets from the vapor.

The reactor core contains the fuel elements (Fig. 57.10). A fuel element consists of between 200 and 400 thin tubes of a zirconium alloy (about 1 cm diameter and up to 5 m long) filled with pellets of UO_2 .

■ Fig. 57.9

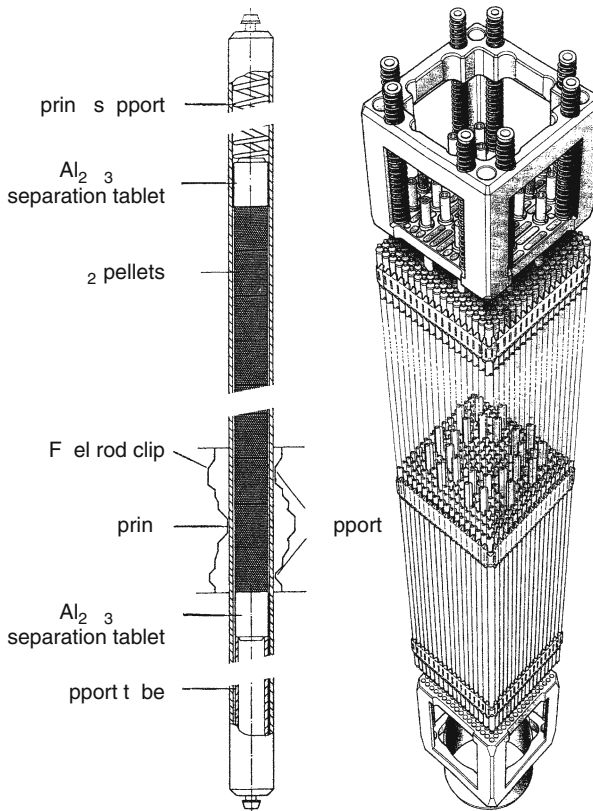
Heat exchanger of a PWR (height about 20 m) (Zech 1988)



At the top and bottom of every fuel rod, a volume is available to accept (rare) gases produced in fission. The uranium in this type of reactor is enriched to 3–4% ^{235}U . When fission occurs the highly energetic fission fragments are stopped in the fuel, heating up the fuel rods. These give off the thermal energy to the surrounding stream of water. Twenty-four rods in every fuel element remain empty for the introduction of the control rods (made from material with high neutron absorption cross sections like Ag, In, Cd, and B) for regulation of the reactor.

■ Fig. 57.10

Left: Fuel rod (diameter 10 mm) containing UO_2 pellets in a cladding of zircaloy or stainless steel.
Right: Fuel element containing an array of 18×18 fuel rods (Zech 1988)



An additional coarse regulation takes place through the addition of boric acid to the water of the primary cooling circuit. The neutron source(s) introduced for a reliable start of the reactor are also housed in these rods of the fuel elements.

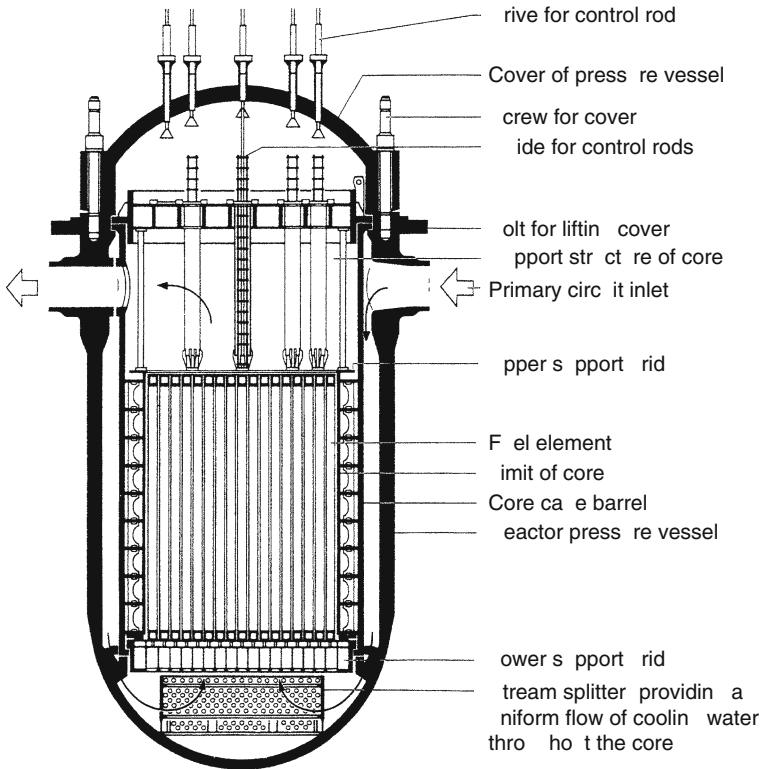
A typical pressure vessel of a pressurized water reactor is shown in ► Fig. 57.11. The height of the pressure vessel for a typical power station of 1,300 MWe generally is 12 m. The thickness of the cylindrical wall amounts to 25 cm. The tank is designed to withstand pressures of 175 bar and a temperature of 350°C. Typical parameters of a PWR are listed in ► Table 57.10.

A nuclear reactor of this size contains an “inventory” of radioactive nuclides that can contaminate large areas – as demonstrated by the reactor accident of Chernobyl in April 1986. Therefore, at least in reactors in Western countries, a number of measures are taken to securely enclose the radioactive inventory. The fission products are surrounded by several barriers:

1. They are enclosed in the matrix of uranium dioxide, a ceramic material resistant to high temperatures and mechanical shock. The uranium dioxide is canned in fuel rods made of stainless steel or “zircaloy,” an alloy consisting mainly of zirconium.
2. The fuel elements are enclosed in a pressure tank (25 cm of steel).

■ Fig. 57.11

Schematic sketch of a pressure vessel of a pressurized water reactor (Zech 1988)



3. The pressure tank is surrounded by walls of concrete (1.5–2 m thick) aimed mainly – under normal operating conditions – at absorbing the radiations from the reactor core.
4. This biological shield normally sits inside a “containment,” a large spherical steel tank (wall thickness 4 cm).
5. This steel tank is surrounded by a dome of concrete (wall thickness 2 m).

In the reactor that exploded in Chernobyl, the barriers (2), (4), and (5) were missing. One problem in the discussion of reactor safety is the fact that a nuclear reactor produces a large amount of heat (3,700 MWth) and about 1% of this thermal energy (=37 MWth) is given off even after a shutdown of the reactor, due to the β decay of the radioactive nuclides.

Consequently, the reactor must be cooled even after shutdown and even in case of an accident. Therefore several independent cooling systems are incorporated. The worst accident that is considered (maximum credible accident “MCA”) is the complete shearing off of the primary circuit line. If this should occur, then a mixture of steam and air would be blown into the containment for a time span of 12 s (blowdown phase). When the pressure falls below 26 bar, water tanks maintained at this pressure automatically would empty into the reactor vessel from both sides (high and low temperature) of the circuit. If this water should evaporate or leak out again, at a pressure of 10 bar, a pump would provide water from other reservoirs. Water leaking out from the primary circuit will have to accumulate on the bottom of the

■ Table 57.10

Typical parameters of a pressurized water reactor (PWR) (GKN-II, Neckarwestheim, Germany)

Quantity	Value	Unit
Thermal power at heat exchanger	3,782	MWth
Electric power	1,300	MWe
Number of fuel elements	193	
Number of fuel rods per fuel element	236 or 300	
Geometrical arrangement of fuel rods in a fuel element	16 × 16 or 18 × 18	
Diameter of fuel rods	0.75 or 9.5	mm
Height of active core	3.9	m
Total mass of uranium	103,000	kg
Mean enrichment in first core	1.9, 2.5, 3.2	mass% ²³⁵ U
Mean enrichment in exchanged rods	3 to 4	mass% ²³⁵ U
Pressure in primary circuit	158	bar
Circulation rate of water	18,800	kg/s
Water temperature at reactor entrance	291	°C
Water temperature at reactor exit	326	°C
Pressure in secondary circuit	65	bar
Steam temperature	280	°C
Circulation rate of steam	2,050	kg/s

containment vessel. Circulating pumps are available there that would pump the water back into the reactor vessel through heat exchangers.

Since this is a handbook of nuclear *chemistry*, a short comment will be made here on chemical tasks in a nuclear power plant. A detailed treatment of the chemical and radiochemical problems encountered in nuclear power stations (PWR and BWR) can be found in the literature (Lin 1996). One important task is the surveillance and control of the cooling circuits, in particular the primary cooling circuit.

As has been mentioned before, the control of the reactor power is partly solved by the addition of boric acid to the primary coolant. A regulation of the reactor by control rods necessarily creates an inhomogeneous neutron field and consequently an inhomogeneous heat evolution in the reactor core. The addition of boric acid to the cooling water results in a very homogeneous load of the reactor core. The dosing of boric acid and its addition to, and removal from, the water is an important chemical task. Boric acid changes the pH of the water that would lead to corrosion if it were not balanced by the addition of basic substances (e.g., LiOH) in the right amount. Radiolysis of water creates elemental oxygen (and hydrogen) in the water of the primary circuit³. To prevent corrosion, extra hydrogen is added to the water. Some longer-lived radioactive corrosion products (like ⁶⁰Co, $T_{1/2} = 5.3$ years) are transported with the primary circuit and may be deposited at undesired locations. This has to be controlled and avoided. Small amounts of tritium diffuse through the cladding of the fuel rods and tritium and fission noble gases penetrate through pinholes. The same is true for some fission iodine,

particularly during power changes (transients) and at shutdown of the reactor. The iodine is found as different species and in various compounds. Decontamination of externally contaminated parts removed from the reactor or decontamination of spills is another task of a radiochemist.

The water of the primary circuit always contains trace amounts of fission products. These may stem from a small outer contamination of the fuel rods by traces of uranium. (The total surface area of the fuel rods exposed to the primary coolant amounts to about 7,000 m², equal to the size of a soccer field.) The fission products may also stem from pinholes in a fuel rod. The measurement of the fission product spectrum and the nuclidic composition allows the radiochemist to decide between the two possibilities. Consequently, the defective fuel rod can be isolated and removed.

Finally, the nonradioactive water used in the secondary circuit and in the third circuit has to be conditioned (removal of calcium bicarbonate and other mineral salts). Waters discharged have to be checked for radioactive and nonradioactive components. Frequently, all the water that has been in contact with radioactive material is released only after distillation!

After this more detailed discussion of the pressurized water reactor, some other types of reactors will also be treated briefly.

57.4.2.2 The Boiling Water Reactor (BWR)

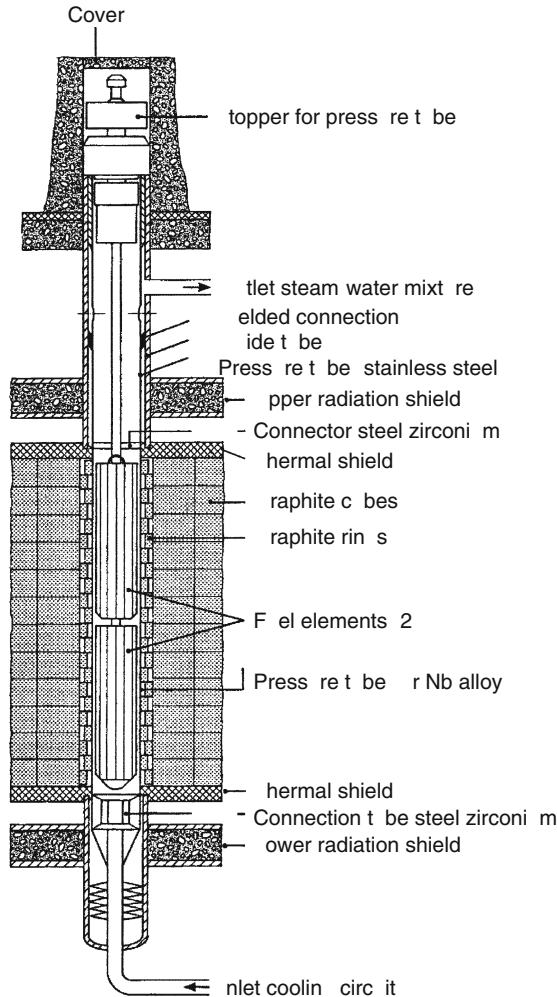
The main difference between the BWR and the PWR is that the former possesses only one cooling circuit. Therefore, the water of the primary cooling circuit is directly driving the turbines. This has the disadvantage that the turbines have to be shielded in order to protect the personnel from the radioactive water. The radioactivity of the steam from the primary circuit is not due to the presence of fission products, because these remain inside the fuel elements, or to (n,γ)-activated corrosion products, because they do not enter into the vapor phase, but to the nuclide ¹⁶N, an emitter of hard γ rays of 6.1 MeV with a half-life of 7.13 s. It is produced inside the reactor core from the oxygen of the cooling water by the following reaction: ¹⁶O (n,p) ¹⁶N. Despite of its short half-life, ¹⁶N reaches the turbines because of the high circulation speed of the water/steam system. Two advantages of the BWR compared with the PWR are that no loss of thermal energy takes place at a heat exchanger and that the absence of a heat exchanger makes a more compact configuration possible and, hence, a smaller containment vessel is needed.

57.4.2.3 The RBMK Reactor

The RBMK reactor has been developed in the former Soviet Union, and has become known in the West mostly because of the Chernobyl accident (GRS 1996). Quite a number of reactors of this type, slightly modified, are still operating in the area of the former Soviet Union. The reactor uses the principle of the BWR. It has, however, neither reactor vessel nor containment. The reactor vessel is replaced by 1,661 pressure tubes. As shown in [Fig. 57.12](#) each pressure tube houses two fuel elements in series. Each fuel element consists of an array of 18 fuel rods. The cooling water enters the pressure tubes from below and exits above as a mixture of water with, on the average, 14.5% steam. The outlet of the 1,661 pressure tubes are united in two

■ Fig. 57.12

Schematic representation of a pressure tube of the RBMK-1000 reactor. The pressure tube contains two fuel elements (above and below). A fuel element consists of a bundle of 18 fuel rods. The pressure tube houses the stream of cooling water. The sketch is not to scale: the diameter of the pressure tube is 88 mm, its length is a total of 22 m, of which 9 m are above the core and 5 m are below and contain no fuel. The pressure tube is surrounded by graphite, which serves as a moderator for the neutrons. The number of such pressure tubes forming the reactor core is 1,661 (GRS 1987; GRS 1996)



pressure tanks where the separation of steam and water takes place. The steam drives the turbines as described for the PWR above. The water is pumped back to the pressure tubes. As opposed to the PWR or BWR in the RBMK reactor, the moderation of the neutrons takes (mostly) place in the graphite elements housing the pressure tubes (► Fig. 57.12). Further details of the reactor are given in ► Table 57.11.

■ Table 57.11

Typical parameters of the RBMK-1000 (Chernobyl version)

Type:	Boiling water/pressure tube reactor
Moderator	Graphite
Cooling agent	H ₂ O
Power, thermal	3,200 MWth
Power, electric	1,000 MWe
Fuel	UO ₂
Total amount of uranium	190 t
Enrichment	2% ²³⁵ U
Height of reactor core	7 m
Diameter of reactor core	11.8 m
Pressure tubes: number	1,661
Pressure tubes: outer diameter	88 mm
Pressure tubes: wall thickness	4 mm
Temperature of moderator	550–700°C
Flow rate of cooling water circulated	37,600 t/h
Water temperature at core entrance	270°C
Water temperature at core exit	284°C
Steam pressure	70 bar
Flow rate of steam circulated	5,780 t/h

This reactor type has some advantages (e.g., no requirement for a pressure tank, which is technologically difficult to manufacture, and the possibility to exchange fuel rods during reactor operation). It has several drawbacks (e.g., a difficulty to control power; under some conditions, a positive temperature coefficient of the reactivity; a decrease in safety due to missing reactor tank and containment). The main problem that led to the accident was however that it was possible for a benevolent but ignorant operating crew to override security measures. Hence, the reactor entered into a state that necessarily led to an explosion. The crew of operators reached this state simply by violating written regulations and by bridging electrical safety switches. In the reactors in Western countries even for a malevolent crew it would not be possible from the layout of the structure to bring a reactor to a similar condition.

57.4.2.4 The Fast Breeder Reactor (FBR)

The idea of a breeder reactor is to dramatically extend the resources available to fission reactors. While the reactors described above “burn” essentially the isotope ²³⁵U, which contributes only 0.7% to the natural uranium, a breeder reactor can convert more ²³⁸U to fissile ²³⁹Pu than it consumes ²³⁵U (or ²³⁹Pu). Therefore, in principle, nearly 100% of the uranium can be used for

energy production rather than 0.7% (^{235}U). This would be more than a factor 100 gained in resources. If it is assumed that the amount of ^{235}U available on earth could provide mankind with energy for about 30 years, the use of such breeder reactors could extend this span to about 3,000 years. In practice, however, the factor gained is smaller than 100.

1. As shown before (see [Fig. 57.5](#)), in a light-water reactor some breeding also occurs and ^{239}Pu contributes to fission so that in practice about 1% of the uranium is used rather than 0.7%.
2. In addition, due to side reactions like the formation of heavier plutonium isotopes 100% of the natural uranium cannot be converted to fissile plutonium isotopes in the breeder technology. However, even the (pessimistic) assumption of a factor of 30 would extend the availability of uranium from 30 to 900 years.

Therefore, the fast breeder technology has been developed in different countries on an experimental or pilot-project scale. It has been shown that the fast breeder reactor (FBR) can be operated safely. However, presently it is not attractive economically because sufficient ^{235}U is available to produce nuclear energy at a lower cost. The FBR is certainly an option for the future when other resources become more scarce.

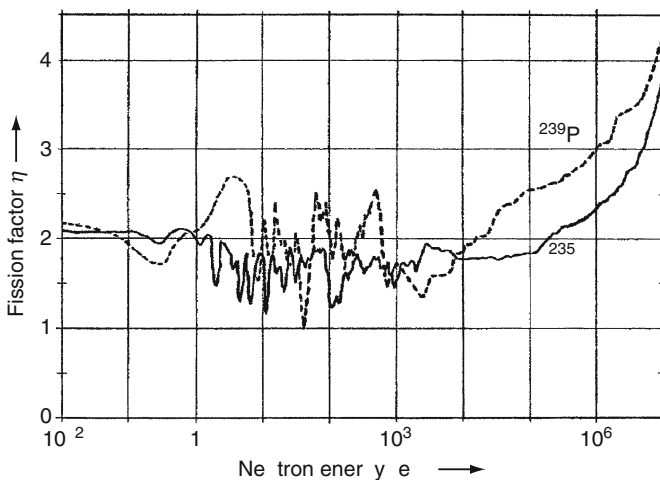
Breeding more fissile material than is used up in the chain reaction requires a fission factor $\eta \geq 2$ (see [Sect. 57.3.4](#)). One neutron is needed for the chain reaction and the second neutron is required for the reaction $^{238}\text{U} (n, \gamma) ^{239}\text{U}$ (decaying to ^{239}Pu).

The dependence of η for the fission of ^{235}U and ^{239}Pu on the neutron energy is given in [Fig. 57.13](#). It appears that η values clearly higher than 2 are found only for neutron energies of $>3 \times 10^4$ eV for ^{239}Pu and $>10^6$ eV for ^{235}U . Consequently, a breeder reactor based on these nuclides must operate with fast neutrons (FBR).

Hence, a moderator is not only not required but should be carefully avoided. Therefore, in a fast reactor one should not use water (or any compound containing hydrogen) even for

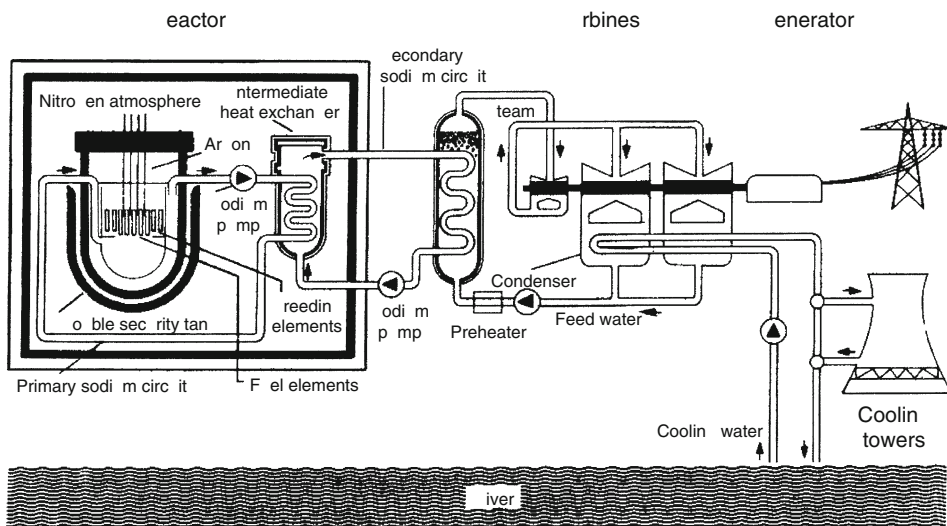
Fig. 57.13

Fission factor η as a function of the neutron energy for the fission of ^{235}U and ^{239}Pu (Zech 1988)



■ Fig. 57.14

Schematic sketch of a nuclear power station based on a liquid-sodium-cooled fast breeder reactor (Zech 1988)



cooling purposes. In the FBRs that have been built so far, metallic sodium has been used as a coolant. A schematic sketch of a nuclear power station based on a FBR is shown in [Fig. 57.14](#).

The sketch in [Fig. 57.14](#) reflects basically the setup of the German SN-300. The French Superphénix is similar with the difference that the main pump is located within the reactor tank. Because of the strong (n, γ) -activation of sodium, the reactor possesses three cooling circuits. The primary circuit containing radioactive ^{24}Na from the reaction $^{23}\text{Na}(n, \gamma)^{24}\text{Na}$ inside the core transfers the thermal energy to a second circuit with nonradioactive sodium. This one transfers the energy to a water/steam circuit that drives the turbines and the generator.

A chemist understands that tons of metallic and highly radioactive sodium at high temperature are a challenge. Therefore special attention has to be paid to the reactor tank. It has a double wall with an alarm system that will go off when sodium leaks out of the inner tank. The tank has no connections to tubes. All tubes enter from above the level of the sodium. Nevertheless most of the technical problems that arose with existing pilot plants were related to sodium.

Some characteristics of the German FBR SNR-300 (Kalkar) which has been built to demonstrate the feasibility of the technique are described in the following section.

The fuel rods (length 2.5 m, diameter 6 mm, stainless steel cladding) in the upper 400 mm contain tablets of UO_2 . In the middle part (950 mm long), which represents the fission zone, they contain tablets of a mixture of UO_2/PuO_2 . The lower part (400 mm) again is filled with UO_2 tablets. The upper and lower parts practically serve as breeding zone only. Some additional characteristics are given in [Table 57.12](#). Further information can be found in Zech (1988).

■ Table 57.12

Some characteristics of the German fast breeder reactor SNR-300 (Kalkar)

Power, thermal	762 MWth
Power, electric	295 MWe
Number of fuel elements	205
Number of fuel rods in fuel element	166
Diameter of fuel rod	6 mm
Active height of core	950 mm
Fuel	PuO ₂ /UO ₂ tablets
Content of fissile Pu in fuel	24% (inner zone fuel elements) 33% (outer zone fuel elements)
Amount of fissile Pu in core	1,150 kg
Number of breeding elements	96
Number of rods in breeding element	61
Composition of breeding material	UO ₂
Circulation rate of Na (1st circuit)	3,552 kg/s
Pressure at entrance/exit of core	9.3/1.3 bar
Temperature at entrance/exit of core	377/546°C
Circulation rate of Na (2nd circuit)	3,264 kg/s
Pressure at entrance/exit	13.6/10.2 bar
Temperature at entrance/exit	335/520°C
Pressure of steam	160 bar
Temperature of steam	495°C

57.4.2.5 The Concept of the Accelerator-Driven System (ADS)

The idea of a reactor driven by an accelerator seems strange at first sight. Why combine a complicated instrument (reactor) with an even more complicated one (accelerator)? Looking more closely a number of advantages appears.

The basic idea is to use a beam of protons (energy: 1–1.6 GeV, beam current: 5–20 mA) impinging on a large target of molten heavy metal (e.g., Pb) as an intense source of neutrons. It costs on the average about 30 MeV of proton energy to produce a free neutron (as a result of a sequence of spallation reactions). Hence, one can calculate that a proton beam of 1 GeV and 10 mA will produce a total number of about 2×10^{20} n/s (corresponding to a neutron flux of about $6 \times 10^{15} \text{ cm}^{-2} \text{ s}^{-1}$ at a distance of 50 cm). These extra neutrons fed into a fissioning system open up a number of possibilities that are otherwise not available due to the scarce neutron balance especially in thermal neutron fission (see ▶ Sect. 57.3.4, values of η). The extra neutrons may be used (1) for (n,γ)-reactions with the purpose to breed new fissioning nuclei or to transform long-lived radioactive isotopes into shorter-lived ones; (2) to operate the reactor in a subcritical state, e.g., with $k = 0.95$ rather than $k = 1$; (3) to selectively destroy by fission

undesired nuclides like some isotopes of plutonium or other transuranium elements that have a potential for weapons and are ecologically problematic.

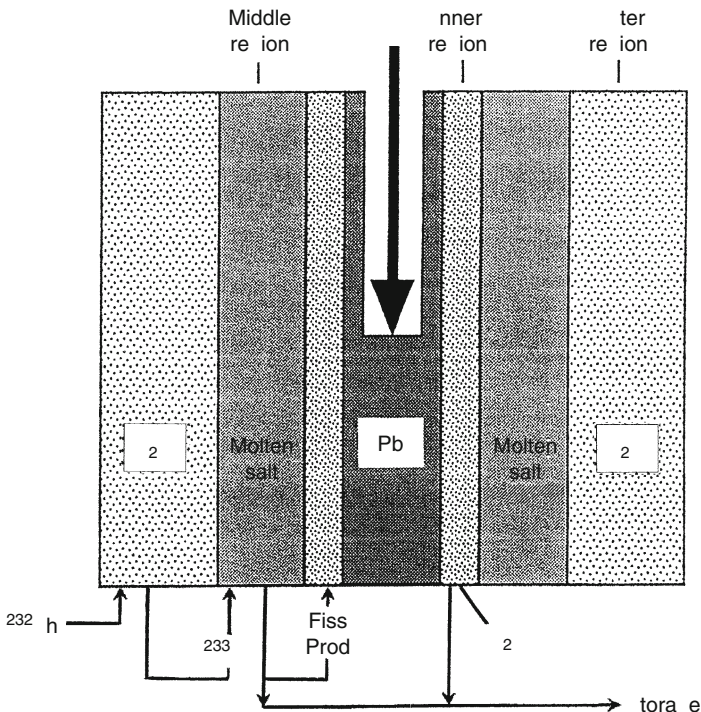
There are different variants of the basic idea. A survey is given in IAEA (1997). In the following, the concept proposed by Bowmann et al. (1992) will be outlined, which would open up the way to using ^{232}Th as a fertile material that could be transformed into the fissile uranium isotope ^{233}U . The approach is illustrated in ► Fig. 57.15. A beam of highly energetic protons (1.6 GeV) from an accelerator is directed onto a target of Pb.

In the target a very high flux of neutrons of about $10^{16} \text{ cm}^{-2} \text{ s}^{-1}$ is produced. The target is surrounded by a moderator (D_2O at a temperature of $40^\circ\text{C}/70^\circ\text{C}$ inlet/outlet), which contains actinides to be burned in the high neutron flux and fission products to be converted into less long-lived products by neutron capture.

Outside the inner region (D_2O) a subcritical assembly of fissile material in the form of a melt of fluorides (LiF/BeF_2 containing $^{233}\text{UF}_4$ or fluorides of other fissile nuclides at a temperature of $500/700^\circ\text{C}$ inlet/outlet) is circulated producing the thermal energy required to drive the turbines. The operation of the core in a subcritical state ($k = 0.97$) increases the safety of the reactor. As it has been shown before (see ► Sect. 57.3.6), the reactivity window for safe operation of a critical reactor is given by $1 + \beta$ (where β is the fraction of delayed neutrons).

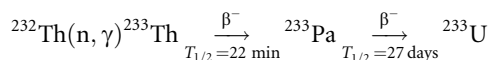
► Fig. 57.15

Schematic sketch of the target assembly and core of an accelerator-driven system (ADS) (Bowmann et al. 1992)



The value of β amounts to 0.0065 for ^{235}U but only to 0.0028 for ^{233}U . In a state with $k = 0.97$ this window is increased to 0.0328, i.e., to more than ten times the value of a corresponding critical state. One may also compare the time behavior of the pilot reactor in Chicago (► Fig. 57.2). After insertion of some reactivity, at $k < 1$ the reactor is self-stabilizing (leveling); at $k > 1$ an indefinite exponential increase in power is observed.

The outermost region (► Fig. 57.15) is again filled with heavy water and contains a solution of salts of ^{232}Th that would undergo the following breeding reaction:



The ^{233}U bred is subsequently put into the fluoride melt in order to undergo fission. The proposed system has a number of additional advantages. (1) It is estimated that about 10% of the electricity produced from the reactor is sufficient to operate the accelerator. (2) The available thorium resources are larger than those of uranium and since thorium would be 100% burned it would provide mankind with energy for centuries. (3) Mining of thorium is easier and ecologically less problematic than mining of uranium. (4) The fission of thorium produces considerably less of the problematic transuranium elements (Np, Pu, Am, etc.).

There are, however, serious problems to be overcome for the realization of the proposal. The main problem of the proposed project is chemical. ^{233}Pa has to be “milked” daily from the breeding area because otherwise it would react to produce ^{234}Pa , which would decay to nonfissile ^{234}U . In addition, fission products would have to be separated in short intervals from the highly radioactive fluoride melt.

Another problem is corrosion due to the hot fluoride melt. Previous experience with the Molten Salt Reactor Experiment (MSRE) at the Oak Ridge National Laboratory (Weinberg 1970) seem to indicate, however, that these problems can be overcome.

The problems mentioned above are certainly the reason why, recently, more modest proposals have been put forth (Bowman 1998).

They concentrate on the removal of neptunium, plutonium, americium, and curium by fission from spent LWR fuel elements. For this purpose, the spent fuel elements would be first converted to fluorides (including their cladding of Zr). This way, uranium could be removed as volatile UF_6 and could be recycled. The remaining ZrF_4 , fluorides of the transuranium elements and nonvolatile fission products could be mixed with NaF. The molten mixture of salts would be passed through an ADR core in such a way (one slow pass) that at the back-end fissile nuclides would have been burned. The output mixture could be deposited without any further chemical treatment. Such a deposit could not be misused for fabrication of weapons and would have no risk of becoming critical again under any external conditions. Such an ADS is proposed for a size of 750 MWth and would produce enough electricity to operate the accelerator and to cover its own cost by selling the remaining power. Recently, some groups have reported studies concerning the chemistry of fluoride melts useful for the project (Ignatiev et al. 2000; Laidler and Bresee 2000; Uhlir 2000; Marecek et al. 2001; Mel'nik et al. 2001; Tanaka et al. 2001; Uhlir et al. 2001). The concept discussed above is based on thermal neutrons moderated by graphite.

Other concepts are based on fast neutrons (Rubbia 1997) and claim to have the advantage that long-lived fission products are also destroyed. Therefore, a geological storage is no longer

needed and could be replaced by a storage of the treated waste in steel canisters for a time span of 300 years. This latter technique resembles the operation of FBRs and, due to the better neutron economy, it could perhaps be realized also without accelerator.

In any case, there are quite a number of options to produce nuclear energy for mankind while existing resources become scarce. Nevertheless it is also certain that these options still require large investments into scientific explorations.

Since weapons based on nuclear fission (“atomic bombs”) are in principle fast homogeneous reactors, the following section is dedicated to the principle of nuclear weapons.

57.4.3 Nuclear Weapons

There are two different kinds of nuclear weapons. Weapons based on the fission process (“atomic bombs”) and weapons based on the nuclear fusion reaction (“hydrogen bombs”). The fusion weapons get most of their energy from a fusion process of light nuclides (like deuterium) to helium. Fusion weapons contain a small fission bomb that serves to heat the fusion matter to a temperature of about 10^8 K required for the start of the fusion process.

A fission bomb is a homogeneous reactor of metallic ^{235}U or ^{239}Pu that can reach a very high reactivity (criticality factor $k = 1.5$ to 2 ; see [Sect. 57.3.5](#)) and possesses a very short neutron cycle time ($\tau = 10^{-8}$ to 10^{-9} s, see [Sect. 57.3.6](#)).

For the values given of k and τ it can be easily estimated using [Eq. \(57.34\)](#) that any amount of fissile material present would be consumed within a time span of 10^{-7} s. In this process the following energy would be set free (using an average value of 170 MeV of [prompt] energy per fission fragment):

$$E_X/J = 1.602 \times 10^{-19} \frac{m_U}{M_U} N_A E_p / \text{eV} \quad (57.36)$$

where E_X/J is the total (prompt) energy set free in joules, m_U is the mass of ^{235}U fissioned, M_U is the molar mass of ^{235}U (~ 235 g/mol), N_A is the Avogadro constant ($6.022 \times 10^{23} \text{ mol}^{-1}$), E_p/eV is the amount of prompt energy set free per fission in eV ($\sim 1.7 \times 10^8$), and the numerical factor is the value of the coefficient converting eV to J.

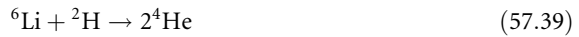
For 1 kg of ^{235}U ($m_U = 1,000$ g) the result is $E_X = 7 \times 10^{13}$ J. The energy of explosive devices is usually measured in tons of trinitrotoluene (TNT), a conventional explosive. An amount of 1,000 t of TNT corresponds to 4×10^{12} J. Hence, the fission of 1 kg ^{235}U corresponds to slightly less than 20 kt of TNT.

Schematically, the construction of a fission weapon is as follows. Fissile material (pure ^{235}U or ^{239}Pu) in a subcritical arrangement, distributed over a larger volume, is compacted rapidly using conventional explosives. The compacting can take place by approaching two parts in a tube-like arrangement (“canon type”) or several parts in a spherical arrangement (“concentric type”). At the moment of highest density (highest value of k), a neutron source is switched on that starts the fission reaction. The total power set free increases exponentially over a time span of about 10^{-6} s. Due to this exponential time law nearly the whole energy is set free at the very end of the time span. The explosion of the bomb causes a sharp descent of k beyond the maximum, interrupting the chain reaction. Most of the power of about 10^{20} W is set free, while the bomb disintegrates within a time span of 10^{-7} s. An early start of the chain reaction has to be avoided because this would lead to a disintegration of the bomb before its full power has been reached. In any case, two extremely fast processes are competing: the chain reaction

and an explosive disintegration of the supercritical system which then becomes subcritical again. Both processes occur on a timescale of about 10^{-8} s. Hence, the development of a very efficient and well-controllable conventional explosive system is as important as the availability of highly enriched ^{235}U or pure ^{239}Pu . Fortunately, this makes it difficult to build atomic bombs that possess an effective explosive power.

A thermonuclear bomb contains a small fission bomb in the middle serving to ignite the fusion reactions. A thermonuclear bomb produces two peaks of power: a first peak is due to the fission bomb and a second peak is due to the fusion reactions.

The light elements undergoing fusion are deuterium, tritium, and lithium. At temperatures of $T = 10^7$ to 10^8 K, the following reactions take place:



Very large thermonuclear bombs possess an additional outer layer of ^{238}U . It undergoes fission by the fast neutrons originating from the fusion process and this way sets free additional energy.

The so-called neutron bomb that does not have large destructive power but kills by radiation is based on reaction (38). It is obvious from momentum conservation and the relative mass of the neutron and the α particle that the neutron will carry away 80% of the total energy released. The fraction of the energy taken by the α particle – due to the strong interaction of the charged particle with the surroundings (see [Sect. 8.2 in Chap. 8, Vol. 1](#)) – will be converted to heat and hence to mechanical and thermal destruction, whereas 80% of the energy transferred to the neutron, due to the less frequent interaction of neutrons with matter, will contribute to harmful and long-ranged radiation of fast neutrons – except for the case of the presence of water (liquid, or in the form of dense clouds) where neutron bombs are of limited effect ([Sect. 57.3.2](#)). It would certainly be preferable that nuclear weapons are never be used again.

57.5 The Nuclear Fuel Cycle

The discussion of the fuel cycle will be limited here to uranium or plutonium. Other fuel cycles, which may become important due to new alternate reactor concepts like thorium-based accelerator-driven reactors, will not be the subject of the following section.

The fuel cycle starts with the mining of the uranium. It continues with its chemical isolation, possibly an isotopic enrichment of ^{235}U (see [Chap. 51 in Vol. 5](#) on “Isotope Separation”), the manufacture of the fuel elements, and their use in the reactor. If a final storage of spent fuel elements as such, as practiced in some countries, is not preferred, the cycle continues with a dissolution of the fuel elements. The remaining uranium and the newly formed plutonium are separated from the fission products. Plutonium can be reintroduced into the reactor in the form of Mixed OXide (MOX) fuel elements. Uranium has to pass through an enrichment plant in order to increase the content of ^{235}U from about 0.8% in the spent fuel to about 3%. The enriched fraction will be returned to new fuel elements.

■ **Table 57.13**

Survey on resources of uranium (1997). The resources (in units of 1,000 t) are given separately for well-known and less well-known sites (assured resources/additional estimates) and for different estimated prices of mining (\$/per kg of uranium) (NEA 1997)

	Assured resources		Additional estimates	
	<80 \$/kg	<130 \$/kg	<80 \$/kg	<130 \$/kg
Australia	622	93	136	44
Kazakhstan	439	162	196	63
USA	110	251		
Canada	331	0	99	
South Africa	218	52	66	22
Namibia	156	31	91	17
Brazil	162	0	100	
Russia	145		36	
Ukraine	46	38	17	30
Uzbekistan	66	17	39	7
Niger	70	0	1	
Mongolia	62	0	21	
Others	107	112	31	81
Total	2,534	756	833	264

The depleted fraction may be used in a breeder reactor. The separated fission products will have to go to some final deposit.

57.5.1 Manufacture of the Fuel and Fuel Elements

Uranium is found in the Earth's crust in a concentration of $2.7 \times 10^{-4}\%$ and is therefore more copious than, e.g., silver with $0.07 \times 10^{-4}\%$. However, most of the uranium is very uniformly distributed in small concentrations among granites. Rich deposits are seldom. These originate from secondary processes: pegmatites of hydrothermal origin in upper regions of granites and, especially, sediments of $\text{UO}_2/\text{U}_3\text{O}_8$ from the erosion and weathering of granites.

The prospecting of uranium mines is facilitated by the radioactivity of uranium and its daughter products. Uranium deposits are usually judged by their size and by the price it costs to extract a kilogram of uranium. A survey of the worldwide resources of uranium is given in

► [Table 57.13](#).

The yearly consumption of uranium in 1996 was 60,500 t (NEA 1997). It has remained nearly constant since. From this number and the values in ► [Table 57.13](#) (figuring an efficiency of mining of about 90% and a future constant use) one may estimate that the “assured resources” will last for about 50 years (from 1997 on). An expected increase in consumption

would decrease the number accordingly. A transition to the breeding technology would however guarantee a supply for more than 1,000 years.

Mining of uranium takes place in open pits or underground, depending on the location (and origin) of the deposits. For underground mines it is important to have a good ventilation (at least ten times higher than in conventional mining) because the radon isotopes, formed in the decay of uranium, emanate into the mines and create a risk of lung cancer for the workers. Dust of uranium minerals contains radium isotopes that are dangerous bone seekers.

In order to isolate uranium, the mined ore is broken, milled, and extracted by one of two procedures. One of the extraction procedures uses a basic solution of sodium carbonate and sodium bicarbonate. The other one is an acidic procedure using sulfuric acid and sodium chlorate. The latter procedure dominates today and will be briefly discussed here. It has the ecological advantage that radium which ends up in the tailings is left there in the very insoluble form of radium sulfate.

The milled ore is leached for 6–12 h in sulfuric acid. The supernatant is decanted or filtered from the remaining ore. The solution is passed through an anion-exchange column where uranium is fixed and most of the other metals (except iron) pass through. Uranium and iron are eluted subsequently from the column. A solution of calcium hydroxide is added to the solution. This way, iron(III)hydroxide is precipitated and filtered off. Uranium is then precipitated as ammonium diuranate $((\text{NH}_4)_2\text{U}_2\text{O}_7)$ by adding NH_4OH . The yellow precipitate is filtered off (“yellowcake”).

For use in reactors operating with natural uranium, the yellowcake can be converted to UO_2 by heating it under reducing conditions. It may then be incorporated directly into the corresponding fuel elements. For use in reactors working with enriched uranium, the UO_2 has to be converted to UF_6 . For this purpose, UF_4 is first prepared by reacting UO_2 with HF . The UF_4 is then oxidized by elemental fluorine to UF_6 . Other variants of these procedures cannot be discussed here in detail and the interested reader is referred to the literature (e.g., Pickert and Zech 1981).

The compound UF_6 is fairly reactive and hydrolyzes with water. The most important property of UF_6 is its low sublimation point of 56.5°C , which makes it suitable for a separation of the isotopes ^{235}U and ^{238}U in the gas phase.

There are three procedures that are used for the enrichment of ^{235}U (Choppin and Rydberg 1980; Pickert and Zech 1981): (1) gas diffusion process, (2) gas centrifugation process, and (3) nozzle process. All three processes use the fact that UF_6 with the isotope ^{235}U is lighter by three mass units than the compound with ^{238}U .

In the gas diffusion process, UF_6 in gaseous form is pumped along some microporous diaphragms, and the fact that $^{235}\text{UF}_6$ diffuses more rapidly through the diaphragm than $^{238}\text{UF}_6$ is used.

In the gas centrifuge process, light molecules are enriched at the center and heavy ones at the outside of a rotating vessel. The size of a single centrifuge is about 1 m in length and about 40–80 cm in diameter. Rotational speeds are around 1,000 rpm. Details are not published but it is estimated that about ten stages are required to enrich ^{235}U from 0.7% to 3%. For comparison, a diffusion plant would require about 1,200 stages.

In the nozzle-type enrichment method, a fast stream of gas is blown through a nozzle along the wall of a curved surface. The heavier molecules concentrate on the outside of the curved surface and the lighter ones toward the center, where they can be skimmed off. The nozzle-type setup may be looked at as a stationary centrifuge. About 500 stages are required to enrich ^{235}U from 0.7% to 3%. Further details of these processes are found in Choppin and Rydberg (1980)

and Pickert and Zech (1981). Due to the military importance of such enrichment plants, many details are kept secret.

After enrichment, the UF_6 is collected in a reaction tank. There it is converted to ammonium uranyl carbonate ($(\text{NH}_4)_4[\text{UO}_2(\text{CO}_3)_3]$) by adding water, carbon dioxide, and ammonium hydroxide. The ammonium uranyl carbonate precipitates from the aqueous solution, is filtered, and thermally decomposed into UO_3 . The uranium trioxide is reduced to UO_2 using hydrogen gas at 550°C . The UO_2 is pressed into tablets that are sintered at $1,700^\circ\text{C}$ for 3 h forming very hard tablets of ceramic character. They are ground to a tolerance of ± 10 or $\pm 25\ \mu\text{m}$. These tablets are filled into tubes of zircaloy (an alloy with $>90\%$ Zr) up to 5 m long and about 1 cm in diameter. The tubes are flooded with helium and closed by welding. Some head space is left in the fuel rods to allow the expansion of fission product gases (► Fig. 57.10). Finally, the fuel rods are assembled in racks forming the fuel elements to be mounted inside the reactor core. Details differ from reactor to reactor.

57.5.2 Reprocessing of Spent Nuclear Fuel

After the use of the fuel elements in the reactor, there are two options for the treatment: (a) final storage as intact fuel rods and (b) reprocessing. The option (a) is simple and needs no further discussion here. Reprocessing seems, however, preferable from two standpoints: ecologically, it is better to remove the long-lived and dangerous plutonium before the final storage of the waste. In addition, reprocessing is also preferable from the standpoint of making full use of the valuable energy resources of mankind.

In any case, a cooling-down phase of at least 100 days (preferably a few years) is normally observed in a tank adjacent to the reactor core. The fuel rods are then packed into special containers, e.g., “CASTOR.” These containers may undergo an additional waiting time of “intermediate storage” on the premises of the power station. Finally, for case (b) above, they will be transported to the reprocessing plant.

The principle of reprocessing is as follows (“PUREX process”). The process starts with cutting the fuel rods in pieces of about 5 cm length. The fuel (UO_2/PuO_2) is dissolved in half-concentrated nitric acid. Radioactive aerosols and radio-iodine set free in the process are retained in filters (aerosols in mechanical filters, iodine in filters impregnated with silver nitrate). Fission rare gases (mainly ^{85}Kr , $T_{1/2} = 10.5$ years) may be condensed in cold charcoal filters and filled later into steel cylinders.

After filtration of insoluble rest products, the solution containing the remaining fission products, uranyl nitrate, and plutonium nitrate is submitted to an extraction cycle with a solution of 30% of tri-*n*-butyl-phosphate in kerosene. Uranium and plutonium pass to the organic phase and the fission products remain in the aqueous solution. Since a high decontamination factor of 10^{-7} has to be realized for fission products in the U/Pu fraction, the extraction steps are repeated many times using some mixer-settler units or some countercurrent extraction columns (Choppin and Rydberg 1980; Pickert and Zech 1981).

For the separation of uranium and plutonium in the organic phase, the plutonium is reduced (by Fe(II) sulfamate or other reducing agents) to the oxidation state III and is eluted to a new aqueous phase. Finally, uranium is stripped from the organic phase into a solution of dilute nitric acid. Further purification procedures that cannot be detailed here, follow for all the fractions discussed. Ample information is found in the literature (see, e.g., Choppin and Rydberg 1980; Pickert and Zech 1981).

Finally, plutonium in the form of PuO_2 together with UO_2 will be used for the manufacture of new MOX-fuel elements. Uranium with a remaining content of about 0.8% in ^{235}U will return to the enrichment plant. The fission products will go to final storage as described in the next section.

57.5.3 Storage of Nuclear Waste

There are several possibilities for storing the highly radioactive waste from nuclear power stations. Decisions (or no decisions) are made on a national basis and depend on the geological and climatic conditions as well as on the political situation in the different nations. Here only two options will be presented that reflect the broad range of possibilities.

One of the big questions is about the untreated fuel elements mentioned at the beginning of [Sect. 57.5.2](#). The US government has decided for a “once through fuel cycle,” i.e., it has chosen to deposit untreated fuel elements. In addition to political reasons, the decision was made because of the availability of an appropriate repository site: Yucca mountain in the desert of New Mexico. It is isolated from population centers (distance to the nearest large community, Las Vegas: 150 km) and surrounded by a military area and by land owned by the federal government. The repository is planned in a tunnel at a depth of 300 m below ground level. It is located in an arid area 300 m above the ground water level. The mountain consists of welded and non-welded tuff with good isolating properties. A number of (21) fuel elements are planned to be sealed in canisters of stainless steel (Type 316NG) covered with an especially corrosion-resistant alloy (Alloy 22). Tuff has strong adsorbing properties that limit transport of radionuclides even in the unlikely event that (1) the fuel elements would be defective, (2) the steel canister mentioned would be broken, or (3) water would flood the tunnel.

Further information on this project can be found on the Internet (DOE 2003). In early 2003, the site was ready to accept spent fuel elements, but a decision to use it as a final repository had not yet been made. Hence, spent fuel elements and some high-level radioactive waste in the United States are presently stored in 131 different locations in 39 states.

The other option to be discussed, in the following section, is the final storage of high-level waste (HLW) after chemical treatment, i.e., after removal of uranium and plutonium. For this purpose, the solutions of nitrates of the fission products have to be brought to dryness, converted to oxides, mixed with some glass-forming agents (SiO_2 , B_2O_3 , TiO_2 , CaO , and others), and melted at temperatures of 900–1,200°C. At these temperatures, highly resistant borosilicate glasses are formed. The content in fission products amounts to about 20%. The glass may be put into steel containers and solidified there. Alternatively small glass beads can be prepared. Again the glass beads are poured into a steel canister. Liquid lead is added to fill the space between the glass beads. This procedure guarantees a good flux of heat to the outside and adds to the stability of the assembly. The total volume of such highly active waste amounts to 2.5–3 m³ per year per nuclear power station of 1,000 MWe.

In Germany it is planned to take the canisters to the rock-salt deposits of Gorleben (near Lüchow-Dannenberg). These rock-salt formations are unchanged over a period of 100 million years. It can be assumed that such deposits will remain unchanged for at least the next few million years. It is planned to use horizontal corridors (length about 1,000 m) drilled in a depth of about 800 m below ground level. From these corridors, vertical holes (50 m deep and 30 cm in diameter) will be drilled into the salt. These holes will be filled with the waste canisters up to about 10 m below the corridors. The rest will be filled with salt and concrete. One such bore

hole can take the waste that one nuclear power station (1,200 MWe) produces in 1 year. The distance of the bore holes along the corridors will be about 10–20 m. When all the boreholes of a corridor are occupied, the corridor itself will be refilled with salt and other parallel corridors, beside, above, or below will be drilled. The salt has the property to flow under pressure. Any space will fill up again with time.

The actual situation is that the exploration of the repository has been finished. Similar to the situation in the United States, no decision has been made to start depositing waste canisters. Wastes returning from the French reprocessing factory in Cap de La Hague or from the British plant in Sellafield are stored above ground in an interim storage unit.

57.6 Summary

Nuclear fission is a process of high scientific, technical, and military relevance. This is due to the fact that a self-propagating chain reaction can be achieved. Research reactors are an invaluable tool for the scientist. Nuclear power stations provide mankind with energy presently worth 150 billion dollars/euros per year (about 16% of the world's consumption of electric energy). This energy does not contribute to the ecologically relevant production of CO₂. Nuclear energy has, however, the problem that an absolutely safe storage of radioactive waste for extremely long times must be guaranteed. Strategies have been developed that come close to this goal. Recently, additional approaches have been proposed to definitely solve this problem (at least to a large extent) by burning the most dangerous waste products (actinides and, possibly, some long-lived fission products) in ADS. Fission has, however, a negative side. Atomic bombs have taken a terrible toll of human lives in Hiroshima and Nagasaki. Fortunately these weapons have never been used again and it is hoped that a state using such weapons would have to expect consequences from the community of nations that would make their use unattractive and render their possession useless.

57.7 Editors' Notes

1. Owing to the logarithmic energy scale, the equidistant points of the horizontal axis represent units of “lethargy,” i.e., $\ln(E_0/E)$, where E_0 is the initial energy of neutrons. Note, however, that the direction of the lethargy axis is the opposite of the energy axis: the higher the energy, the lower is the lethargy and vice versa (p. 2623).
2. The quantity $\varphi(E)$, representing an un-normalized “density function” of the energy of neutrons – see [Sect. 9.2.1 in Chap. 9, Vol. 1](#), has the dimension of flux density per energy, i.e., $\text{cm}^{-2} \text{s}^{-1} \text{eV}^{-1}$. This is in accord with the unit of R , which turns out to be s^{-1} (p. 2624).
3. See for some details of radiolysis of water as a reactor coolant in [Sect. 23.6.3 of Chap. 23, Vol. 3](#) on “Radiation Chemistry” (p. 2645).

Acknowledgments

The author would like to thank Dr. H. Braun and Dr. K. Eberhardt for several valuable hints. Special thanks are due to Dr. Nancy Hecker-Denschlag and Dr. Peter Black for their help in the English formulation of the text.

References

- Anderson HL, Fermi E, Szilard L (1939) *Phys Rev* 56:284
- Atomforum D (2002) *Kernenergie Aktuell* 2002, Report: Leaflet: ISSN 1435–4063. Deutsches Atomforum, Bonn
- Atomwirtschaft (2002) *Atomwirtschaft (Atw)*, 47:263
- Berwanger G (1965) *Atomkernenergie* 10:451
- Bowman CD (1998) *Ann Rev Nucl Part Sci* 48:505
- Bowmann CD, Arthur ED et al (1992) *Nucl Instrum Meth Phys Res A* 320:336
- Choppin GR, Rydberg J (1980) *Nuclear chemistry, theory and applications*. Pergamon, Oxford
- Cowan GA (1976) *Sci Am* 235:36
- De Laeter JR (1988) *Mass Spectrom Rev* 7:71
- DOE (2003) <http://www.ocrwm.doe.gov/ymfp/sr/faq.pdf>
- Erdtmann G (1976) *Neutron activation tables*. Verlag Chemie, Weinheim
- Erdtmann G, Petri H (1986) *Nuclear activation analysis: fundamentals and techniques*. In: Elving PJ (ed) *Treatise on analytical chemistry*. Wiley, New York
- Flügge S (1939) *Die Naturwissenschaften* 23/24:403
- Glasstone S (1967) *Sourcebook on atomic energy*. von Nostrand, Princeton
- GRS (1987) *Neuere Erkenntnisse zum Unfall im Kernkraftwerk Tschernobyl*. Report: GRS-S-40, Gesellschaft für Anlagen- und Reaktorsicherheit (GRS), Garching, Germany
- GRS (1996) *Tschernobyl-Zehn Jahre danach; Der Unfall und die Sicherheit der RBMK-Anlagen*. Report: GRS-121 (ISBN 3-923875-74-6), Gesellschaft für Anlagen- und Reaktorsicherheit, Garching, Germany
- IAEA (1975) *Le Phenomène d'Oklo*. Libreville, Gabun (International Atomic Energy Agency, Vienna)
- IAEA (1997) *Feasibility and motivation of hybrid concepts for nuclear energy generation and transmutation*. In: *Proceedings of the international atomic energy agency technical committee meeting*, Madrid, 17–19 September 1997 (International Atomic Energy Agency, Vienna)
- IAEA (2000) *Nuclear research reactors in the world*. International Atomic Energy Agency, Vienna
- IAEA (2003) <http://www.iaea.org/worldatom/rddb/>
- Ignatiev V, Zakirov R, Grebenkine K (2000) *Molten salts as possible fuel fluids for TRU fuelled systems, actinide and fission product partitioning and transmutation*. In: 6th information exchange meeting, Nuclear Energy Agency, Madrid
- Laidler JJ, Bresee JC (2000) *Pyrochemical processing of irradiated transmuter fuel, actinide and fission product partitioning and transmutation*. In: 6th information exchange meeting, Nuclear Energy Agency, Madrid
- Lin CC (1996) *Radiochemistry in nuclear power reactors*. National Academy Press, Washington, DC
- Marecek M, Novy P, Uhler J (2001) *Technological verification of fluoride volatility method for front-end of molten salt transmutation reactor fuel cycle*, Global 2001. In: *International conference on: back end nuclear fuel cycle: from research to solutions*, Paris
- Mel'nik ML, Bychkov AV, Kormilitsyn MV, Babikov LG, Ponomarev LL (2001) *Nuclear fuel reprocessing for cascade subcritical molten salt reactor*, Global 2001. In: *International conference on: back end nuclear fuel cycle: from research to solutions*, Paris
- Mughabghab SE, Divadeenam M, Holden NE (1981) *Neutron cross sections*. Academic, New York
- NEA (1997) *Uranium, resources, production and demand*. Nuclear Energy Agency, Organisation for Economic Co-Operation and Development (OECD), Paris
- Pickert F-K, Zech H-J (1981) *Brennstoffkreislauf*. Deutsches Atomforum, Bonn
- Roth E (1977) *J Radioanal Chem* 37:65
- Rubbia C (1997) *CERN concept of ADS, feasibility and motivation of hybrid concepts for nuclear energy generation and transmutation*. In: *Proceedings of the international atomic energy agency technical committee meeting*, Madrid, 17–19 September 1997, edited by IAEA
- Smith CMH (1965) *Textbook of nuclear physics*. Pergamon, Oxford
- Tanaka H, Kawamura F, Nishimura T, Kamiya M (2001) *Design study on advanced reprocessing systems for fuel cycle*, Global 2001. In: *International conference on: back end nuclear fuel cycle: from research to solutions*, Paris
- Uhler J (2000) *R&D of pyrochemical partitioning in the Czech Republic, actinide and fission product partitioning and transmutation*. In: 6th information exchange meeting, Nuclear Energy Agency, Madrid
- Uhler J, Priman V, Vanicek J (2001) *Fluoride partitioning R&D programme for molten salt transmutation reactor systems in the Czech Republic*, Global 2001. In: *International conference on: back end nuclear fuel cycle: from research to solutions*, Paris
- Von Halban jun H, Joliot F, Kowarski L (1939) *Nature* 143:470
- Watt BE (1952) *Phys Rev* 87:1037
- Weinberg AME (1970) *Nucl Appl Technol* 8:102
- Zech H-J (1988) *Kernreaktoren*. Verlag Inforum, Bonn



58 Developments and Tendencies in Fission Reactor Concepts

E. O. Adamov¹ · Y. Fujiie²

¹Research and Development Institute of Power Engineering (NIKIET),
Moscow, Russia

²Tokyo Institute of Technology, Tokyo, Japan

58.1	<i>Editors' Introduction</i>	2666
58.2	<i>Future: The Extrapolation of Past and Present</i>	2667
58.2.1	Introduction	2667
58.2.2	Requirements on the Advanced Nuclear Energy System	2668
58.2.2.1	Peaceful Use of Nuclear Energy	2668
58.2.2.2	Harmonization with Nature	2669
58.2.2.3	Effective Utilization of Resources and Environmental Preservation	2670
58.2.2.4	Safety Assurance	2671
58.2.3	Foresight of Expected Form in Future	2672
58.2.3.1	Self-Consistent Nuclear Energy System (SCNES)	2672
58.2.3.2	Fast Reactor and Related Fuel Cycle	2673
58.2.3.3	An Expected Nuclear Energy System	2674
58.2.3.4	Advanced Nuclear Reactors	2676
58.2.4	Light Water Reactor (LWR)	2677
58.2.4.1	Development Results for LWRs	2677
58.2.4.2	Large LWRs as Base-Load Power Supply	2678
58.2.4.3	Use of MOX in LWRs	2678
58.2.4.4	Multipurpose Use of Medium-and-Small-Sized Reactors	2679
58.2.4.5	Supercritical-Water-Cooled Reactor (SCWR)	2682
58.2.5	High Temperature Gas-Cooled Reactor (HTGR)	2683
58.2.5.1	Features of HTGR	2684
58.2.5.2	Hydrogen Production by HTGR	2684
58.2.5.3	HTGR as a Power Reactor	2686
58.2.5.4	Safety of HTGR	2686
58.2.5.5	Development Status of HTGR	2687
58.2.5.6	High Temperature Gas-Cooled Fast Reactors	2689
58.2.6	Sodium-Cooled Fast Reactor (SFR)	2690
58.2.6.1	Features of FR	2690
58.2.6.2	Reactor Core of SFR	2691
58.2.6.3	System Configuration of SFR	2691

58.2.6.4	Safety of SFR	2692
58.2.6.5	Safety Studies and the Results	2694
58.2.6.6	Comparison of SFR types	2695
58.2.6.7	Development Status of SFR	2697
58.2.7	Molten-Salt Reactor (MSR)	2702
58.3	<i>Future: A More Radical Picture</i>	2702
58.3.1	From Advanced Traditional Reactors to New Reactor Concepts	2702
58.3.2	Fast Reactors with a Closed Fuel Cycle as a Basis of Large-Scale Nuclear Power	2704
58.3.2.1	Fast Reactor of Natural Safety	2707
58.3.2.2	Choice of Coolant and Fuel for Fast Reactors in Large-Scale Nuclear Power	2709
58.3.2.3	Lead-Cooled Fast Reactor with an On-Site Fuel Cycle	2713
58.3.2.4	Fuel Cycle of Fast Reactors	2717
58.3.2.5	Technological Consolidation of the Nonproliferation Regime	2721
58.3.3	Generation IV Nuclear Energy Systems	2722
58.3.3.1	Gas-Cooled Fast Reactor System	2723
58.3.3.2	Molten-Salt Reactor System	2724
58.3.3.3	Supercritical-Water-Cooled Reactor System	2727

Abstract: This chapter describes, in two parts, new-generation nuclear energy systems that are required to be in harmony with nature and to make full use of nuclear resources. The issues of transmutation and containment of radioactive waste will also be addressed. After a short introduction to the first part, ▶ Sect. 58.1.2 will detail the requirements these systems must satisfy on the basic premise of peaceful use of nuclear energy. The expected designs themselves are described in ▶ Sect. 58.1.3. The subsequent sections discuss various types of advanced reactor systems. ▶ Section 58.1.4 deals with the light water reactor (LWR) whose performance is still expected to improve, which would extend its application in the future. The supercritical-water-cooled reactor (SCWR) will also be shortly discussed. ▶ Section 58.1.5 is mainly on the high temperature gas-cooled reactor (HTGR), which offers efficient and multipurpose use of nuclear energy. The gas-cooled fast reactor (GFR) is also included. ▶ Section 58.1.6 focuses on the sodium-cooled fast reactor (SFR) as a promising concept for advanced nuclear reactors, which may help both to achieve expansion of energy sources and environmental protection thus contributing to the sustainable development of mankind. The molten-salt reactor (MSR) is shortly described in ▶ Sect. 58.1.7. The second part of the chapter deals with reactor systems of a new generation, which are now found at the research and development (R&D) stage and in the medium term of 20–30 years can shape up as reliable, economically efficient, and environmentally friendly energy sources. They are viewed as technologies of cardinal importance, capable of resolving the problems of fuel resources, minimizing the quantities of generated radioactive waste and the environmental impacts, and strengthening the regime of nonproliferation of the materials suitable for nuclear weapons production. Particular attention has been given to naturally safe fast reactors with a closed fuel cycle (CFC) – as an advanced and promising reactor system that offers solutions to the above problems. The difference (not confrontation) between the approaches to nuclear power development based on the principles of “inherent safety” and “natural safety” is demonstrated.

Abbreviations ABWR, Advanced BWR; ALWR, Advanced LWR; ANL, Argonne National Laboratory; ANTARES, AREVA New Technology based on Advanced gas-cooled Reactor for Energy Supply; APWR, Advanced PWR; ATWS, Anticipated transient without scram; AVR, Arbeitsgemeinschaft Versuchsreaktor; BR, Breeding ratio; BREST, Lead-cooled Fast Reactor of Natural Safety; BWR, Boiling water reactor; CBR, Core breeding ratio; CDA, Core disruptive accident; CEFR, Chinese Experimental Fast Reactor; CFC, Closed fuel cycle; CPS, Control and protection system; CRBR, Clinch River Breeder Reactor; DFR, Dounreay Fast Reactor; EBR, Experimental Breeder Reactor; ECCS, Emergency core cooling system; EPR, European Pressurized Reactor; ESBWR, Economic simplified boiling water reactor; FA, Fuel assemblies; FBTR, Fast Breeder Test Reactor; FCA, Fast critical assembly; FFTE, Fast Flux Test Facility; FP, Fission product; FR, Fast reactor; GFR, Gas-cooled fast reactor; GIF, Generation IV International Forum; GT-MHR, Gas turbine-modular helium reactor; HCDA, Hypothetical core disruptive accident; HENDEL, Helium ENGINEERING DEMONSTRATION Loop; HTGR, High temperature gas-cooled reactor; HTR-10, 10 MW high temperature gas-cooled test reactor; HTR-10GT, HTR-10 with gas turbine; HTR-PM, High temperature reactor-pebble-bed module; HTTR, High temperature engineering test reactor; IAEA, International Atomic Energy Agency; IGR, Impulse graphite reactor; INES, International nuclear event scale; INF, Irradiated nuclear fuel; IRWST, In-containment refueling water storage tank; IS, Iodine–Sulfur; KNK, Kompakte Natriumgekühlte Kernreaktoranlage; LFR, Lead-cooled fast reactor; LOCA, Loss-of-coolant accident; LWR, Light water reactor; MA, Minor actinide; MHTGR, Modular high temperature gas-cooled reactor;

MOX, Mixed oxide; *MSBR*, Molten-salt breeder reactor; *MSR*, Molten-salt reactor; *MSRE*, Molten-Salt Reactor Experiment; *NE*, Neutron excess; *NNC*, National Nuclear Center; *NPP*, Nuclear power plant; *NRC*, Nuclear Regulatory Commission; *PBH*, Potential biological hazard; *PBMR*, Pebble bed modular reactor; *PFBR*, Prototype fast breeder reactor; *PFR*, Prototype fast reactor; *PUREX*, Plutonium Uranium Recovery by EXtraction; *PWR*, Pressurized water reactor; *SASS*, Self-actuated shutdown system; *SBWR*, Simplified boiling water reactor; *SCNES*, Self-Consistent Nuclear Energy System; *SCWR*, Supercritical-water-cooled reactor; *SEFOR*, Southwest Experiment Fast Oxide Reactor; *SFR*, Sodium-cooled fast reactor; *SNR*, Schneller Natriumgekühlter Reaktor; *THTR*, Thorium high-temperature reactor; *TRU*, TRAnsUranic; *ULOF*, Unprotected LOss of Flow; *UTOP*, Unprotected transient over power; *VHTR*, Very high temperature gas reactor; *VHTRC*, Very high temperature reactor critical assembly

58.1 Editors' Introduction

When the project of the second edition was about to be launched by Springer, the Editors of the Handbook had several questions to answer and one of these being how to complete Prof. Denschlag's excellent introduction to the "Technical Application of Nuclear Fission" with the new tendencies and designs of energy production by fission. It has also been realized that some countries were underrepresented among the authors of the first edition compared to their contribution to nuclear science. Fortunately, two experts of nuclear energy production, the Authors of this chapter, have accepted the Editors' invitation to cooperate.

The Editors are well aware that it is rather unusual to write an editorial introduction to one particular chapter; however, in this case it seems to be appropriate and desirable. The reason is that this chapter is at least as much about the future of (nuclear) energy production as about its present (and to some extent its past).

Although there are cases in the history of science when fiction writers like H. G. Wells (in "The World Set Free," written in 1914) predicted scientific and technical breakthroughs (to an accuracy of a few years) such as the discovery of artificial radioactivity or even the first operation of a full-scale nuclear power plant (NPP) (see Wagar 2004). However artistic prophesies that have come true are retrospectively selected and interpreted in a way that is meant to astonish the reader of the present. And if such a prophecy never comes true, it will be forgotten, and no harm is done.

Real scientific writing like this chapter is different. Writing about the past is writing about facts that can be either correct or not. And the scientific community – or even the Editors of this Handbook – can easily judge this. In this respect, there is a resemblance with nonfiction writing like history.

Predictions are a different matter. First of all, they are difficult to make – *especially about future* as Niels Bohr put it in 1957 (who was probably not the first person to use this crack in history). Poor predictions about science will not be easily forgotten either. And this makes it risky for the scientist. If science is connected with an important and controversial industry like in this case, where future depends on politics and public opinion, things become even more difficult. This may cause two equally excellent experts of the same area to have different views (or visions?) about the future, which is also influenced by their characters and personal backgrounds.

For the above reasons, the Editors of the Handbook have decided to split this chapter to two complementary parts with the first one written by Prof. Fuji-ie and the second by Prof. Adamov, and let them express their views as they will. Future will decide whose extrapolation turns out to be more accurate.

58.2 Future: The Extrapolation of Past and Present

The following part has been written by Prof. Y. Fuji-ie.

58.2.1 Introduction

It can be said that civilization is at the turning points to change from that based on chemical reactions to that based on nuclear reactions. The civilization based on chemical reactions started when mankind succeeded in controlling fire in nature and getting heat and light from it, thus making use of the energy produced by chemical reactions. The heat and light enabled mankind to settle down and live from farming as well as cattle breeding in the neighborhood of rivers in the ancient civilization of Orient.

The nature on the Earth has made joint work with sunshine to form the biosphere where a closed system for material flow was possible among plants and animals. However, the industrial revolution about 200 years ago introduced mechanical energy and electricity with steam engines and electric generators. Underground fossil fuel was used without reverse processes of oxidation. It is said global warming due to carbon dioxide urges mankind to find new energy resources other than fossil fuel.

The civilization based on nuclear reactions on the other hand started at the end of the nineteenth century when Röntgen discovered X-rays and analyzed their characteristics. X-rays have been used in various fields of science and technology with success. However, the first application of nuclear energy was made as atomic bombs dropped in Hiroshima and Nagasaki to result in massive deaths of the public and destruction of the cities.

Total abolition of nuclear weapons has not yet been achieved in these decades and there are some countries that have raised suspicions by conducting nuclear testing and obtaining nuclear weapons. Nevertheless, it is good news that nuclear weapons have never been used in wars in these decades exceeding more than half a century.

The aims of nuclear energy development are the following: (1) energy supply to support the civilization, (2) conversion of fertile material to fuel, and (3) creation of knowledge opening the fields and areas for new cutting-edge applications.

Humankind has already succeeded in the first stage of nuclear power development, i.e., electric power generation with fission reactors, especially with light water reactors (LWRs) obtaining excellent safety records. It has taken the latter half of the twentieth century since Dwight D. Eisenhower's speech "Atoms for Peace." However, the issues concerning material conversion and treatment of nuclear waste have been left to this century.

The main efforts in this century therefore must be concentrated to material conversion and management, which mean the realization of nuclear fuel cycle. Practically the following two steps are considered: (1) an LWR fuel cycle that leads to advanced reactors such as the sodium fast reactor (SFR) and (2) an advanced nuclear energy system with related fuel cycle. The second step is more concerned with nuclear material and sensitive to nuclear arms. Therefore, the nuclear menace shall be fully concerned, and individuals as well as organizations in the nuclear community shall make up their minds to develop advanced nuclear energy system exclusively for peaceful use. Advanced nuclear energy system shall be developed for future prosperity of mankind and limited only to peaceful purposes.

The nuclear energy system shall be developed as a "harmonious" system to satisfy the requirements to be discussed in [Sect. 58.1.2](#), fully utilizing the assets of nuclear fission

reactions, i.e., about three neutrons in number and 200 MeV of energy released per reaction. This means not only that nuclear energy should serve just as an energy source but also that issues related to radioactive waste and waste heat should be mitigated to harmonize with the society and the natural environment.

Considering that civilization is supported by science and technology, nuclear science and technology including nuclear energy systems will have to mature into a comprehensive science and technology that supports civilization at the basis. In this century, it is essential to establish the nuclear energy system as harmonious as to be accepted by the society (Fuji-ie 1992, 2005).

In this part, some concepts that are considered promising as advanced nuclear energy systems are described. Reactor type classification in [Sects. 58.1.4](#), [Sect. 58.1.5](#), and [Sect. 58.1.6](#) is basically done by coolant materials. The LWR is selected as an existing reactor system that has succeeded in commercialization and still has a potential to improve its performance and extend the applicable fields ([Sect. 58.1.4](#)). The high temperature gas-cooled reactor (HTGR) is discussed with emphasis on the potential of an efficient and multipurpose use of nuclear energy, including hydrogen production ([Sect. 58.1.5](#)). Focus is placed on the SFR as the promising concept for advanced nuclear energy systems to achieve both expansion of energy sources and environmental protection to contribute to the sustainable development of mankind ([Sect. 58.1.6](#)).

Although the lead-cooled fast reactor (LFR) is not dealt with in this part, it is also a promising advanced FR and will be introduced in the second part by Prof. Adamov. In addition, several topics of international importance, such as nonproliferation, are treated in his part. Other advanced reactors, such as the gas-cooled fast reactor (GFR), the super critical water-cooled reactor (SCWR), and the molten-salt reactor (MSR), are briefly introduced in [Sects. 58.1.4](#), [Sect. 58.1.5](#), and [Sect. 58.1.7](#), respectively.

58.2.2 Requirements on the Advanced Nuclear Energy System

This section considers the requirements for an advanced nuclear energy system as well as for the R&D that will meet these requirements (Fuji-ie 1995).

58.2.2.1 Peaceful Use of Nuclear Energy

The reminiscence of Hiroshima and Nagasaki warns mankind to use nuclear energy exclusively for peaceful purposes. It is worthwhile to note the report of Prof. Dr. Takashi Nagai who contributed the emergency rescue of the atomic bomb victims at Nagasaki in October 1945 (Nagai 2000).

“Everything was finished. Our mother land was defeated. Our university had collapsed and classrooms were reduced to ashes. We, one by one, were wounded and fell. The houses we lived in were burned down, the clothes we wore were blown up, and our families were either dead or injured. What are we going to say? We only wish to never repeat this tragedy with the human race.

We should utilize the principle of the atomic bomb. Go forward in the research of atomic energy contributing to the progress of civilization. A misfortune will then be transformed to good fortune. The world civilization will change with the utilization of atomic energy. If a new and fortunate world can be made, the souls of so many victims will rest in peace.”

The peaceful use of nuclear energy has been accelerated by the statement of the US president, Dwight D. Eisenhower, “Atoms for Peace” in December 8, 1953 (Eisenhower 1953).

“The United States knows that if the fearful trend of atomic military build-up can be reversed, this greatest of destructive forces can be developed into a great boon, for the benefit of all

mankind. The United States knows that peaceful power from atomic energy is no dream of the future. The capability, already proved, is here today. Who can doubt that, if the entire body of the world's scientists and engineers had adequate amounts of fissionable material with which to test and develop their ideas, this capability would rapidly be transformed into universal, efficient and economic usage?... The more important responsibility of this atomic energy agency would be to devise methods whereby this fissionable material would be allocated to serve the peaceful pursuits of mankind. Experts would be mobilized to apply atomic energy to the needs of agriculture, medicine and other peaceful activities. A special purpose would be to provide abundant electrical energy in the power-starved areas of the world."

Recent world interests on nuclear energy are directed also to the peaceful use of nuclear energy through nonproliferation and still forward to abolition of atomic bombs. An example of this movement is the speech of the US President, Barack Obama delivered in Prague on April 5, 2009 (The Huffington Post 2009), who won the Nobel Peace Prize later "for his extraordinary efforts to strengthen international diplomacy and cooperation between peoples" (Nobelprize.org 2009), and another example is the statement by the United Nations (UN Security Council 2009).

Scientifically, research and discussion concerning nonproliferation is directed to change the properties of nuclear fuel with mixing in addition to plutonium transuranium and others to result in small explosion potential for a nuclear weapon (Saito 2005; Kessler 2007). The other direction of nonproliferation is to ask the nations that want to develop nuclear energy to keep safeguards actions guided by the International Atomic Energy Agency (IAEA).

58.2.2.2 Harmonization with Nature

The principle of science and technology in the twenty-first century must shift from a focus on utilization to a priority on harmony with the society and the environment.

For the energy system to harmonize with nature, it should function in a manner similar to the ecological energy system like the biosphere that maintained a balance in the preindustrial era. An important aspect of the biosphere is that it has the potential to maintain a closed circulation of materials through the coexistence of animals and plants. Therefore, it would be meaningful to establish a similar system within the assets of nuclear fission reaction. The biosphere is not closed in energy; it absorbs energy from sunshine and releases the excess back to space. However, it has the potential to be a closed system for the circulation of materials. On the other hand, the fossil energy system cannot maintain the closed circulation of materials because it does not have the capability of dissolving carbon dioxide that the plant has.

While a nuclear energy system inherently generates no carbon dioxide, it does generate radioactive materials. From the scientific point of view, it is necessary to evaluate the feasibility of a nuclear energy system to contain radioactive material in a room, transmute it to nonradioactive or short-lived radioactive material with state-of-the-art science and technology, and release no radioactive waste to the natural environment, i.e., the achievement of full recycle and zero emission should be the expected final goal. With continuous efforts to reach this goal, one can design a nuclear energy system that harmonizes with nature and is accepted by the society.

Then, as quite naturally assumed, questions will arise such as these. Is it possible to have a nuclear energy system that utilizes resources efficiently without producing radioactive waste? Can nuclear energy provide a solution?

To begin with, one should study the possibility of satisfying such a requirement from a scientific standpoint. If it is scientifically possible, then one should consider how and with

what technology it can be done; what is scientifically possible is not necessarily achievable technologically with 100% efficiency. Since technology must always consider efficiency, the energy can never be converted with 100% efficiency and it always involves some energy losses.

Although nuclear fission reaction does not occur between long-lived actinide nuclei and thermal neutrons in LWRs, it does with fast neutrons. Since nuclear fission reduces radioactive waste, it is beneficial in terms of a lowered environmental burden rather than effective utilization of resources. Cross section ratios of fission to capture of actinide nuclides have been compared between the dominant neutron energy range of a fast reactor (FR) and that of an LWR. The results show that the ratios of cross section for minor actinide (MA) nuclides of the FR in particular are one or more orders of magnitude larger than those of the LWR. Therefore, neutrons of the FR can burn more actinide nuclides in the core.

Since the transuraniums are convertible into fissile materials and burnable, the next issue concerning radioactive waste is efficiency in material separation and nuclear reaction, briefly, technological efficiency. This is precisely an issue of technology and method. Even though the current efficiency level is far from satisfactory, further R&D may improve it.

As the other source of radioactivity of FR, R&D should be focused on the long-half-life fission products (FPs). Studies have been just started to transmute long-half-life radioactive fission products or to shorten half-lives. Although further studies are necessary, it seems to be possible to solve this problem. For example, nuclide separation technology may be improved in efficiency with facilities such as lasers as well as particle accelerators.

58.2.2.3 Effective Utilization of Resources and Environmental Preservation

One of the neutrons released by fission reaction is used for the next fission reaction. The other neutrons, i.e., surplus neutrons, are available for producing new nuclear fuel through absorption by fertile materials such as ^{238}U and ^{232}Th , except for those absorbed by other elements or leaking out of the reactor core. In other words, the surplus neutrons can transmute fertile materials to fissile ones.

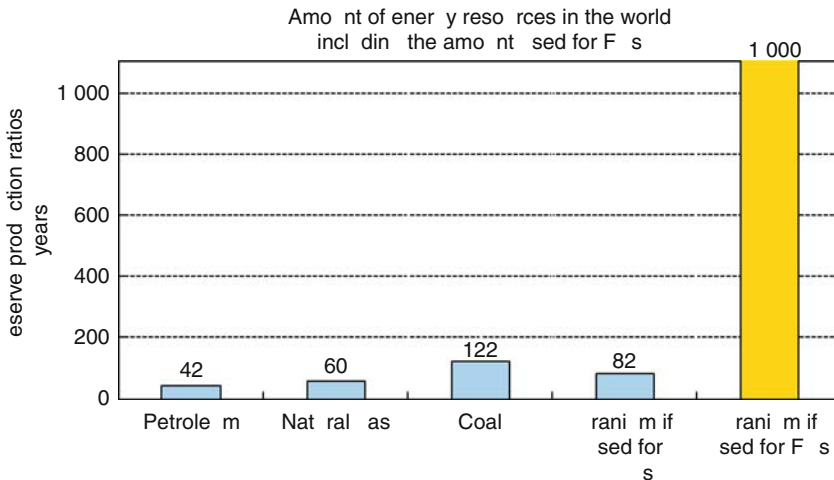
Higher fuel production, i.e., fuel breeding, is expected if the ratio of produced fuel to consumed one is greater than unity, while fossil fuel relying on chemical reactions does not have this feature. If such a system is built, it is very likely that low-quality uranium and uranium in seawater will become resources, while they have been less useful for the LWR cycle. Thus, the system is expected to ensure stable energy supply for mankind over a long period of time, imposing no practical restriction in resources (🔗 Fig. 58.1).

If the consumption of uranium continues at the current level and is used only for LWRs, the uranium resources for energy sources will be available for less than 100 years. However, if the nuclear fuel cycles are established and fuel breeding is achieved in FRs, then the duration of the use of uranium resources will be extended to several thousand years. In addition, if uranium in seawater becomes usable, the duration of use will exceed more than a million years. To that end, it is important to build nuclear reactors that can breed fuel and to develop nuclear fuel cycles, which can efficiently extract reusable nuclear fuel materials after burning.

Nuclear burning of higher-order plutonium isotopes and minor actinide nuclides, which are difficult to burn in LWRs and therefore turn into waste, in nuclear reactors or particle accelerators, will greatly contribute to reducing the effects of radioactive waste, even if it may bring little benefit as an energy source. It is also beneficial to eliminate the radioactivity of fission products with long half-lives by converting them into stable nuclides.

■ Fig. 58.1

Significance of developing fast reactors (FRs) (OECD/NEA, IAEA 2007; OECD/NEA 2009). The reserve-to-production ratios of petroleum, natural gas, and coal were evaluated by dividing the ascertained recoverable reserves by the amount of production in 2008. The ratios of uranium were evaluated by dividing the reserves by the annual demand in 2006 because uranium is easy to reserve and therefore the amounts of production and demand are not correlative. If the price level rises suddenly because of huge demand, recoverable reserves may increase (This is said to be more likely for natural gas)



Reducing the effects of radioactivity takes considerable time. For instance, if the aim is to reduce the radioactivity of nuclear waste to the same level as that of the natural uranium ores within a millennium, a typical time length for civilization, it is necessary to consider this issue in conjunction with geological storage of waste.

In order to achieve such a goal, it will be necessary not only to focus on the nuclear reactor but also on its nuclear fuel cycle of material management; i.e., to consider the nuclear energy system as a whole.

Developing a nuclear energy system that would keep radioactive materials within the system itself and minimizing the generation of radioactive waste would make it possible to suppress the environmental effects to a socially acceptable level. Since nuclear fuel has high energy density, the amount of necessary material and generated radioactive material corresponding to unit energy production are overwhelmingly smaller than those of fossil fuel. Nuclear energy systems have greater potential benefit for the environment.

58.2.2.4 Safety Assurance

Safety assurance is one of the most important factors in the establishment of both the advanced and current nuclear energy systems in society. The release of radioactive materials into the environment has to be prevented in accidents, as well as in normal operational conditions. For a nuclear energy system aiming at both fuel production and the transmutation of radioactivity, the safety assurance with a focus on high performance of the reactor core is essential. It is therefore important to develop the nuclear energy system that minimizes the risk of severe core damage.


The appropriate combination of inherent safety features and engineered ones should be necessary to prevent the extension of anticipated transients and also postulated accidents within the system. As an example of inherent safety features, one should mention Doppler reactivity that is effective against criticality events, which is a basis to ensure the reactor shut down function. Natural circulation is also an inherent safety feature to enhance the cooling capability of the reactor core. The nuclear energy system should be designed in such a way that severe core damage leading to the release of massive amounts of radioactive materials could be avoided.

It is also essential that these high-level measures for ensuring safety should be easy to understand not only to a limited number of professionals, but also to the general public. While explaining technical matters in non-technical language is a challenge, no matter how high the safety level ensured by the system is, society is unlikely to understand or accept complex descriptions. Therefore, it is important to demonstrate that the system really possesses the inherent and engineered safety features and encourage the public to listen to the professionals. Modern nuclear technology cannot be established with disregard for professional expertise.

58.2.3 Foresight of Expected Form in Future

58.2.3.1 Self-Consistent Nuclear Energy System (SCNES)

A system concept, which (1) seeks to produce an amount of fuel more than or equal to that consumed, (2) contains all the radioactive material produced in the system (spatial containment), and (3) brings it safe for human life within finite lengths of time (temporary containment), would be regarded as a “Self-Consistent Nuclear Energy System (SCNES).” Such a system can be defined as a nuclear energy system that provides mankind with safe and stable energy for long periods of time and exhibits consistency for the management and treatment of radioactive materials produced through energy supply.

The SCNES proposed in 1992 as the scientific concept for the expected nuclear energy system in the future civilization shall simultaneously satisfy at least the following four requirements, as shown in  Fig. 58.2:

- Effective utilization of energy : highly efficient and multipurpose utilization of energy.
- Fuel production: long-term security of resources.
- Transmutation and isolation of radioactivity: containment of radioactive materials in time and space.
- Safety assurance: practical elimination of release of radioactive materials at normal operation and accidental conditions.

The developers of nuclear energy systems have made a steady effort aiming to satisfy the requirements of the SCNES, but they failed to satisfy all the requirements simultaneously. Since it may take a long time to reach the expected goal of the development of the SCNES itself, a step-by-step approach is recommended with the following stages of development:

1. Plutonium burning/producing FR that will be incorporated into the LWR-leading power generation system with its potential for reducing the burden to the environment and sustainable usage of nuclear energy.
2. Actinides cycle FR that can recycle the whole of plutonium as well as other minor actinides.
3. Expected nuclear energy system, i.e., the SCNES, where the elimination of radioactive fission products is pursued.

Fig. 58.2

Concept of Self-Consistent Nuclear Energy System (SCNES); from (Fujiie 2005)

Requirements for the expected
nuclear energy system

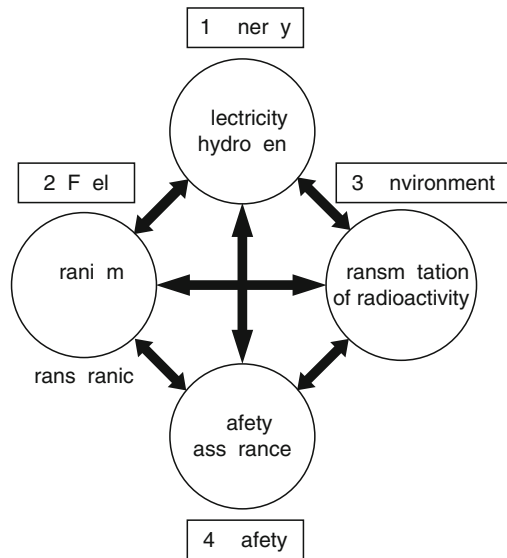
Learn from nature

An expected nuclear energy
system in harmony with nature
should be a materially closed
ecological system with functions
similar or equivalent to the
biosphere ecological system



Full utilization of nuclear
resources recycling

Transmutation and containment
of radioactive waste
zero emission



In this step-by-step approach, it is essential to promote the R&D of the nuclear fuel cycle including reprocessing. Several methods such as advanced aqueous reprocessing and dry reprocessing have potential for the nuclear fuel recycle technologies as a whole. These methods also reduce the environmental burden. The PUREX (Plutonium Uranium Recovery by EXtraction) process focuses on extracting plutonium and has been proven in LWR reprocessing. Dry reprocessing, developed in the USA and Russia has been proven effective for transuranium other than plutonium. Nuclear fuel cycle technologies should also be considered in terms of nuclear nonproliferation, utilization of resources, and reduction of the environmental burden. It is desirable to advance R&D not only for the extraction of specified elements including plutonium with high-purity as is the case with the PUREX process, but also for the elemental separation of transuranium elements with appropriate purity and for the collective separation of them together with minor actinides. In other words, shifting from high-decontamination to low-decontamination is one of the future directions.

58.2.3.2 Fast Reactor and Related Fuel Cycle

It can be said that objective-oriented nuclear reactions such as nuclear fission, absorption, and transmutation occur in a nuclear fission reactor whereas material balance can be kept through separation and mixing of nuclides in a nuclear fuel cycle to satisfy the requirements as discussed in Sect. 58.1.3.3. Here, the important point is that about three neutrons generated from a nuclear fission in the FR core have potential to satisfy the requirements for each stage of the above step-by-step development (Table 58.1). One neutron is indispensable for the nuclear chain reaction for any development stage. More than one neutron among the excess neutrons are needed for fuel production at the stage (1), and further neutrons are required to burn actinides at the stage (2), and transmute radioactive fission products into stable or

■ **Table 58.1**

Neutron balance in fast reactor and thermal neutron reactor (Fuji-ie 1998)

Items	Fast reactor	Thermal neutron reactor ^a	Remarks
Neutrons produced per fission	2.9	2.9	
Neutrons consumed per fission			
Energy production	1.0	1.0	For chain reaction
Capture by fissile material	0.13	0.40	
Fuel production	0.85	1.3	Breeding ratio = 1
Fission product (FP) transmutation	0.30	0.30	Half life of FP \geq 1 year
Others	0.20	0.20	Parasitic absorption by structure material and coolant
Total	2.48	3.25	
Scientific feasibility of SCNES	○	×	Produced > Consumed

^a Estimated for an light water reactor (LWR) with mixed oxide (MOX) fuel.

short-lived nuclides at the stage (3). In particular, the feasibility for the stage will depend on how to separate fission products.

Meanwhile, future technological progress may make the recovery of radioactive fission products possible. In order to efficiently transmute radioactive fission products into stable or short-lived nuclides, it is important to use excess fission neutrons effectively. However, neutrons may be in short supply when elements are separated through chemical processes alone, because not only the intended radioactive nuclides but also their stable isotopes absorb neutrons. If radioactive nuclides alone are isolated (isotope separation), many more types of nuclides can be transmuted without excessive neutron absorption (► [Table 58.2](#)). It clearly shows the importance of nuclear fuel cycle in a new nuclear energy system. In such a system, radioactive fission products would be isolated not at the elemental level but at the isotopic level with, e.g., a laser, and also nuclear spallation neutrons would be utilized with particle accelerators to increase the number of neutrons. Some studies to develop technologies of isotope separation and accelerators have been in progress. However, considering the current technical levels, more advanced R&D is necessary to commercialize these technologies.

58.2.3.3 An Expected Nuclear Energy System

Imagine a nuclear energy system in future, a system derived from the successful pursuit of scientific potential on the basis of the discussions thus far. The flow of fuel materials and energy in the expected nuclear energy system would be something like the example shown in ► [Fig. 58.3](#).

Natural uranium employed in the system causes its own nuclear fission in the reactor. On the other hand, the fertile material, ^{238}U , is converted to nuclear fuel material by nuclear transmutation, which is utilized as an energy source as well. In addition, radioactive materials

reprocessing. Thus, most energy is required for uranium enrichment and reprocessing including isotope separation and multi-recycling of long-lived fission products, though the fraction of energy spent for such purposes could be limited to 1% at most (Arie et al. 2007). The fundamentals of adjusting fuel material in a nuclear fuel cycle are separating/mixing materials, elements, and nuclides.

Transuraniums generated by fuel burning include fissile material (e.g., ^{239}Pu and ^{241}Pu) and fertile material (e.g., ^{240}Pu , ^{242}Pu , and minor actinides), separated and recovered in a fuel cycle facility, and then recycled as fuel materials. Basically, transuraniums are assumed to be transmuted into fissile materials in a reactor at some stage and eventually to undergo fission reactions.

Then, fission products could be separated into radioactive and nonradioactive products with the state-of-the-art nuclear technology like lasers and particle accelerators to be called for in the fuel cycle facility. After that, radioactive fission products with short half-lives could be kept within the system until they decay to nonradioactive nuclides, and those fission products with long half-lives could be transmuted into nonradioactive products.

Nuclear R&D should seek ways to technologically achieve this scientific potential with concrete methods.

58.2.3.4 Advanced Nuclear Reactors

It is worthwhile to make a brief review of advanced nuclear reactors including advanced LWRs (ALWRs) and Generation-IV reactors.

During the coming half century, advanced LWRs will not only play an important role as the producers of base-load electricity but their field of application will also be expanded. Thus far, LWRs have been a reliable energy source with exhibiting superior safety performance and high economic efficiency of larger reactors. Their significance as power reactors will not change in the future. In addition to the practical accomplishment of large reactors to date, marine reactors were developed in the past as a power source and they have been used successfully in submarines and icebreakers for some time now. Because of this development, it is expected that these reactors will be developed as a medium-and-small-sized LWR allowing for marine reactors with good controllability. Furthermore, it is expected that nuclear reactors capable of unmanned operation, long plant life, and low output will be developed for various locations including remote areas.

Development of FRs is important in particular because they are expected to deliver high performance in fission reactions.

The Generation IV International Forum (GIF) was chartered in July 2001 to lead the collaborative efforts of the world's leading nuclear technology nations to develop next-generation nuclear energy systems to meet the world's future energy needs. Six types of the reactors are investigated as the GEN-IV system, which has features aiming at performance improvement, new applications of nuclear energy, and/or more sustainable approaches to the management of nuclear materials. Enhanced sustainability is achieved primarily through adoption of a closed fuel cycle (CFC) with reprocessing and recycling of plutonium, uranium, and minor actinides in FRs including the SFR and LFR.

Above all, the SFR has been developed as the most promising FR system in the world so far. The concept of SFR will be presented in [Sect. 58.1.6](#). The LFR will be introduced in the part written by Prof. Adamov.

High temperature systems offer the possibility of efficient process heat applications and eventually hydrogen production. This approach provides significant reduction in waste

disposal and uranium resource requirements (GIF Overview 2009). Especially, the very high temperature gas reactor (VHTR) pursues another direction of R&D, i.e., further utilization of nuclear energy by converting it into not only electrical energy but also, in the future, environmentally friendly forms. Hydrogen energy is a typical example of this form. Converting nuclear energy into hydrogen energy has very high potential for non-carbon dioxide emission systems, but the conversion requires a high-temperature thermal source. As a solution for this conversion, the VHTR, which has been called as a high temperature gas-cooled reactor (HTGR) is under development. This is a good example showing that civilization based on nuclear reactions can integrate technologies based on chemical reactions developed so far.

58.2.4 Light Water Reactor (LWR)

58.2.4.1 Development Results for LWRs

There are two types of LWRs: the pressurized water reactor (PWR) and the boiling water reactor (BWR). The PWR pressurizes the primary coolant, light water, flowing in the reactor vessel at approximately 16 MPa to avoid its boiling, heats it to about 320°C by the heat generated in the core, sends it to the steam generator where the secondary coolant (light water) is boiled, and finally generates electricity by driving the turbine generator with the steam at high temperature and pressure. Although the system of the PWR tends to be slightly complex since it is equipped with a secondary cooling system, it has an advantage in preventing radiation leaks to the outside because the secondary coolant water is basically free of radioactivity. Shippingport 1, a research reactor with 60 MW output in electricity (hereinafter referred to MWe), was very different from the later standardized PWRs with regard to the positions of the inlet and outlet nozzles for the reactor vessel and with regard to the setting of the steam generator. However, after 1965, the PWR power plants started operation one after another, and the technology has been developed to establish today's basic style of the PWR. As the capacity of plants became larger, the standard has shifted from two loops at the 600 MWe class and three loops at the 900 MWe class to four loops at the 1,100–1,300 MWe classes.

On the other hand, the BWR heats the primary cooling water with heat generated in the core and generates steam in the reactor at approximately 7 MPa and 280°C. Then, this steam drives the turbine generator directly to generate electricity. Although the BWR requires careful handling of radioactive steam, because it uses the generated steam directly to generate electricity, it has the advantage of simplifying plant configuration. The first commercial BWR was Dresden 1 in the USA, which started full-power operation in 1967. This reactor was somewhat different from today's BWRs, including a cooling system that adopted a dual cycle method, i.e., a combination of direct and indirect cycles. Later, BWRs had some improvements that included a change to a single cycle method by placing the steam drum in the reactor vessel, the reduction of fuel cost through increased burnup, the downsizing of the containment vessel, and the multiplexing of the emergency core cooling system (ECCS). These improvements have brought today's basic style.

As of January 1, 2009, the number of nuclear power plants around the world is 432, and their total output is 390 GW in electricity. PWRs account for about 60% and BWRs for about 20% of the total. This means LWRs account for around 80% of reactors and serve as the major nuclear power plant worldwide (Japan Atomic Industrial Forum Inc 2009).

If one looks over the world, there are many construction plans for LWRs, and thus the era of LWRs will be continued for the coming 5 decades at least.

58.2.4.2 Large LWRs as Base-Load Power Supply

After LWRs have been established in society as the commercial reactors, more improvements are planned to produce advanced PWRs (APWRs) and advanced BWRs (ABWRs) for higher safety and better economy.

As for APWRs, the USA designed the AP600 with 600 MWe output that adopts a passive containment cooling system. Later, an improved version with better economy, the AP1000, was designed to produce 1,000 MWe output. French and German industries have developed the European Pressurized Reactor (EPR) with 1,600 MWe output. It has adopted passive safety features against severe accidents, easy operation, and economic competitiveness through a plant life of 60 years. An EPR is being built in Finland, with operation scheduled in 2010. The major features in EPR design include preventing the extension of core melting during the severe core damage by enhancing the cooling capability for the molten materials. If the molten material should diffuse to the outside of the reactor vessel, then it would be channeled to an area specially designed to stabilize it and set adjacent to the reactor pit. Beside this area, an in-containment refueling water storage tank (IRWST) is provided to supply cooling water to cool the hot molten material. These features will strengthen the integrity of the reactor vessel in case of severe core damage and thus the safety enhancement can be achieved. In Japan, the advanced PWRs are now under preparation as Tsuruga Power Station Units 3 and 4, with operation scheduled in 2016 and 2017, respectively. They have some improvements including high reliability steam generators, powerful function of engineering safety facilities, and a lower probability of core damage.

On the other hand, the world's first two ABWRs have been constructed and are in operation in Japan. These are Kashiwazaki-Kariwa Units 6 and 7, which started operation in 1996 and 1997, respectively. Later, Hamaoka Unit 5 started operation, in 2005, and Shika Unit 2 started in 2006. The major feature of the ABWR is an internal pump for recirculation placed directly in the bottom of the reactor pressure vessel instead of the conventional method of external recirculation. As a result, large-diameter piping for recirculation is no longer necessary. In addition, the ECCS is composed of three independent systems. These features can always maintain the sufficient coolant level for the reactor core even in case of pipe rupture accidents with the ECCS functions, so that the risk of loss-of-coolant accident (LOCA) can be practically eliminated and thus the safety and reliability are improved. The USA, taking advantage of experience in development and operations of LWRs, has developed the simplified boiling water reactor (SBWR). It is a reactor with 670 MWe output and strengthened passive safety design that includes a core cooling system by natural circulation that does not employ recirculation pumps. Furthermore, a large-scale reactor, the economic simplified boiling water reactor (ESBWR) with 1,590 MWe output has been developed. Currently, the ESBWR is being evaluated for regulatory approval and is scheduled to start operation in 2015.

58.2.4.3 Use of MOX in LWRs

In the LWR, in addition to ^{235}U , ^{238}U undergoes fission reaction naturally with fast neutrons and is transmuted into ^{239}Pu and ^{241}Pu in the core and utilized as fuel. Thus, an idea is considered to reprocess the spent fuel from the LWR, extract plutonium and uranium from it, mix them to fabricate MOX fuel and reuse it as fuel for the LWR.

Plutonium is produced in the reactor core during operation, and the original fuel naturally transmutes into MOX fuel as the operation continues. The form of the MOX fuel is not

particularly different in composition and configuration from past LWR fuels produced in the improvement process. Europe has 20 years of experience of utilizing MOX fuel.

Reprocessing LWR fuel to fabricate MOX fuel for reuse in LWRs is the first step in the nuclear fuel cycle. Ideally, this process can increase the utilization factor of natural uranium by 50% compared with the case of a once-through LWR fuel cycle. Methods of loading MOX fuel in LWRs are being studied. The representative methods include the loading of 1/3 MOX fuel in the core to avoid a significant change in the existing LWR core characteristics, and full loading of MOX fuel over the core following modification based on the ABWR core design. The construction of an ABWR that allows for full loading of MOX fuel over the core started in May 2008, at Ohma, Japan, and is scheduled to start operation in 2014.

The contributions of uranium and plutonium to power generation according to the MOX fuel loading rates are compared in [Fig. 58.4](#). In the case of uranium fuel with an initial enrichment of 3.7% uranium shows a greater contribution than plutonium, 65:35, in terms of the average value during the fuel service period. The ratios are 55:45 and 50:50 in the case of 1/4 and 1/3 MOX fuel in the core, respectively. The plutonium contribution reaches up to 80% when loading MOX fuel over the core. Plutonium use in thermal neutron reactors like LWRs is expected to lead not only to an effective utilization of resources but also to significant achievements toward the establishment of a nuclear fuel cycle based on FRs.

58.2.4.4 Multipurpose Use of Medium-and-Small-Sized Reactors

Conditions on Locating Plants Nearby

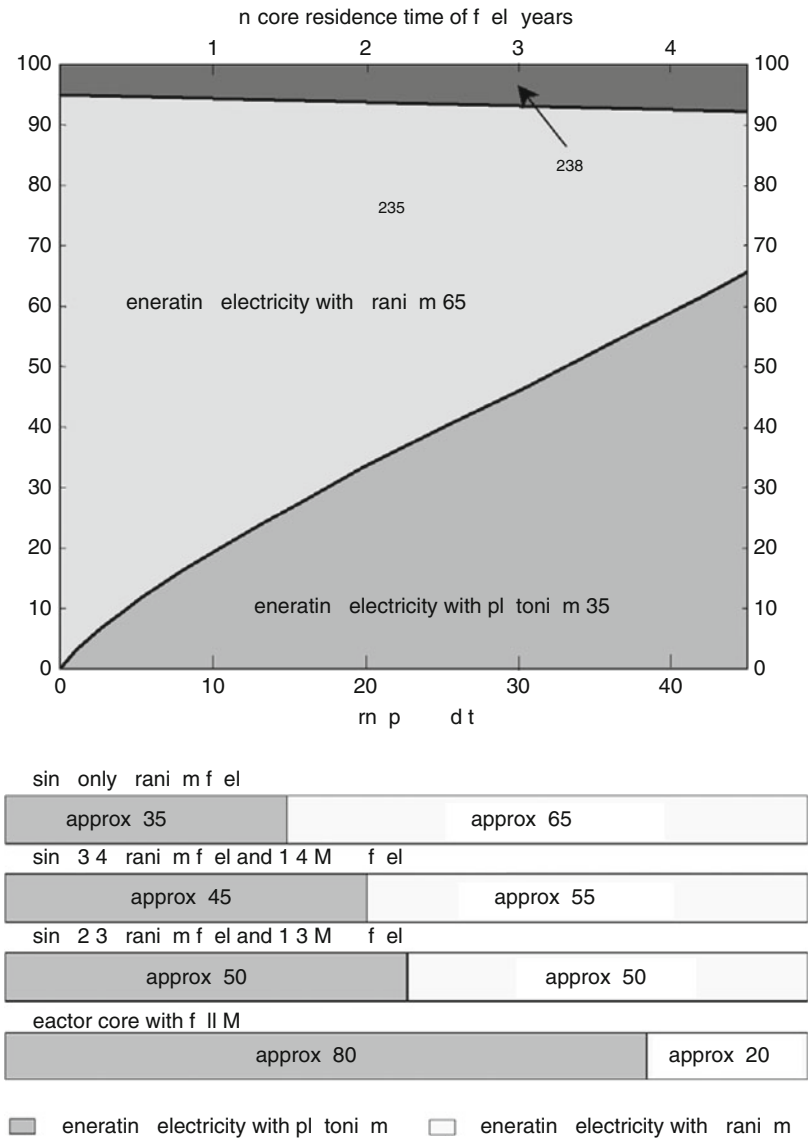
When one looks back on the R&D up to the twentieth century, improvements in product quality and reduction of cost were often achieved through economy of scale. The same is true for nuclear power plants. The power output of early reactors, particularly LWRs, was some 300 MWe. The current ABWRs and APWRs can generate around five times as much as the early reactors and have improved reliability and economy. In this way, nuclear power plants as a whole have contributed to higher self-sufficiency in energy supply. However, such development has brought with it huge systems and complex technology, which has made it difficult to gain people's understanding and trust. In addition, it is a natural trend to locate such large systems in remote areas, where the cost of land is less, and people living in urban areas receive greater benefit. This has been recognized socially as "macro benefit and micro non-benefit" and has created obstacles to plant construction. Accordingly, a compromise is sought through plans that call for medium-and-small- sized reactors nearer to cities.

When developing countries first employ nuclear energy as an energy source, large reactors are not necessarily appropriate in most cases from the perspective of power-line installation and consumption balance. Under these conditions, medium-or-smaller-sized plants with even higher reliability and better economy are expected. This completely differs from past planning, which focused on the achievement of reliability and economy through larger plant design. Obviously, totally different thinking is necessary for R&D in this direction.

Simple and Easy-to-Understand Safety Principles

There are two ways of thought in relation to medium-and-small-sized reactors. One is to make full use of high technology to produce a high-performance nuclear energy system. The other is to omit many parts from the system by using various natural laws and operating with a larger time constant at a slow pace. In other words, there are two choices, a high-technology system or

Fig. 58.4
Efficient use of resources by using plutonium for thermal neutron reactors (ratios of uranium and plutonium generating electricity); from (Sugisaki 2002)



a donkey system, i.e., a low-tech system with slow response. The high-tech system is intended to improve reliability and integrity by progressively adopting high-performance equipment in conjunction with the development of technology. However, with this approach only, a medium-and-small-sized reactor may not achieve performance as high as a large one. Therefore, additional measures may be required. For example, efficiency and quality could be achieved at the same time by installing a ready-made or prefabricated system. That is,

systems could be standardized and plants could be fabricated in sections or as an integrated system off-site. When the site is prepared, the sections or the integrated system can then be transported and installed. Such a system could work as well as the order-made system for the current large reactors, which are assembled piece by piece on site by a forest of cranes. Also, new methods for nonproliferation may be worth consideration, such as a cassette system for fuel exchange handling, because nonproliferation should be a key factor regarding the installation of nuclear power plants near cities. One possible direction should be the construction of standardized small-or-medium-sized reactors that have good flexibility near cities.

The low-tech system, i.e., a donkey system, is the opposite. It requires less manpower, although it still needs more than natural reactors. Because of needing little maintenance and having potential for a continuous operation for a decade without fuel replacement, it can be sited in an isolated island or in a remote area. Of course, it would be necessary to design the reactor to be robust to disturbance and less dependent on control system operations. It may be easier to understand it as a typical passive safety system. For example, reactor control against disturbance does not require a rapid response as in the case of control rods but expects reactivity feedbacks, such as the Doppler effect to work. Additionally, natural circulation, which is driven by buoyancy force generated by difference in coolant temperature, should be employed in such reactors rather than pumps.

What is mentioned above is obviously expected for the nuclear energy in the twenty-first century. Some concepts about FRs as well as LWRs have already been suggested, and their design studies have also been carried out. It is expected that these concepts will be developed and used to create the above mentioned nuclear energy systems: the safety systems to be described more simply, the economical nuclear energy systems to be placed near metropolises, and the power supply systems in remote areas far from transmission networks. These ideas are also applicable to other systems such as reprocessing plants; instead of one large plant that can reprocess spent fuel for tens of reactors, the installation of smaller plants is under discussion along with the discussion on advanced fuel cycle concepts.

Marine Reactors

The use of nuclear reactors to drive ships has been promoted particularly among nautical nations. Commercial marine reactors include the Savannah in the USA, the Otto Hahn in Germany, and the Mutsu in Japan. They experienced marine operation but unfortunately the development had been cancelled after several years. Nuclear-powered ships require free access to ports in the world, but unfortunately there were no sufficient number of ports to make the marine reactor's operation feasible. Some countries had accepted to prepare the ports, but doing this would still take time.

As for the features of nuclear-powered vessels, the Mutsu had a displacement of about 10,000 tons. Its reactor produced 35 MW of thermal power to deliver speeds of 18 knots. Meanwhile, the marine reactors were required to withstand incomparably severer load changes than land-based reactors. For example, they were required to be capable of increasing power from base load to full power in 30 s to avoid collision. The Mutsu was able to meet most performance requirements during operation, including experimental voyage.

Although nuclear submarines are not the main theme of this handbook, they can keep running underwater for a long time without emitting carbon dioxide or the need for oxygen for propulsion. Several hundred nuclear submarines have been built for military use in Russia and the USA, and their performance has resulted in proof of the high safety performance of LWRs. Marine reactors had been also applied to icebreakers operated in USSR/Russia over 50 years. Nuclear-powered aircraft carriers are equipped with several nuclear reactors.

58.2.4.5 Supercritical-Water-Cooled Reactor (SCWR)

The SCWR is composed of a high-temperature, high-pressure, water-cooled reactor, which operates above the thermodynamic critical point of water (22.1 MPa, 374°C) to achieve a high thermal efficiency. Since the coolant does not change phase in the SCWR, the balance-of-plant is considerably simplified and directly coupled to the energy conversion equipment.

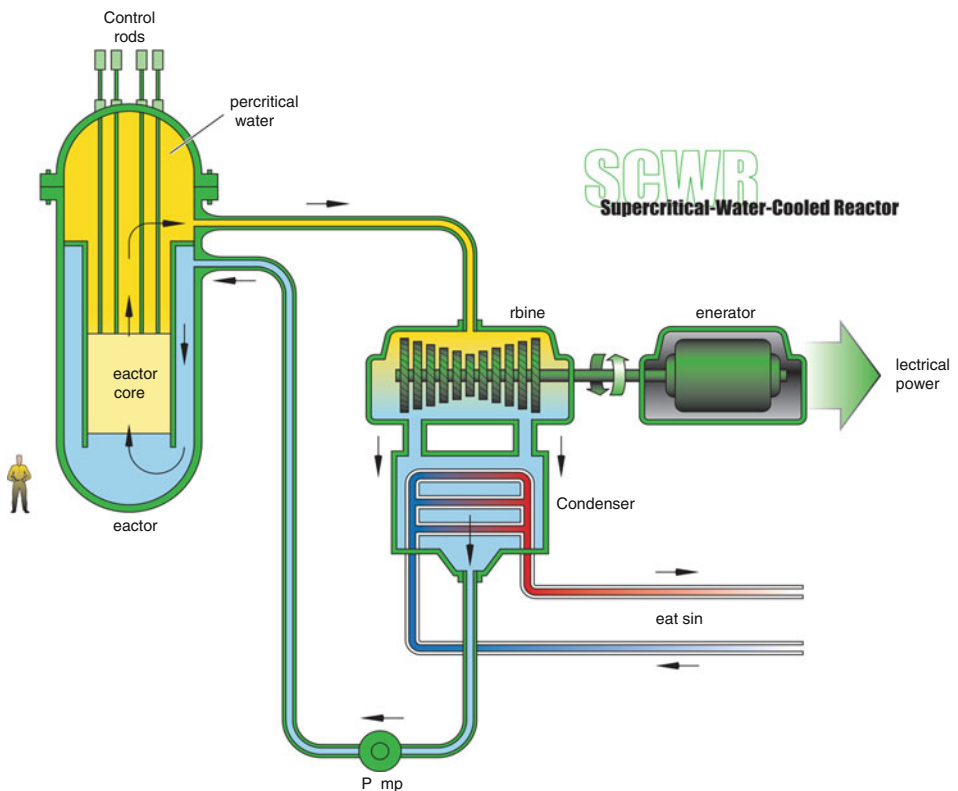
A design example is a system of 1,700 MWe with an operating pressure of 25 MPa and a reactor outlet temperature of 510°C, which is expected to range up to 550°C (► Fig. 58.5). This feature enables ca. 44% of thermal efficiency, which is about one third higher than current LWRs. Passive safety features are incorporated similar to those of simplified BWRs.

In terms of neutron spectrum and fuel cycle, there are two options of the SCWR: the first is a thermal neutron reactor, and the second is an FR-based closed fuel cycle coupled with full actinide recycle based on advanced aqueous processing. Using fast neutrons will be advantageous for achieving sustainability to be aimed for the Generation IV reactor because of their potential to produce at least as much fissile material as it consumes.

Challenges for the SCWR are a feasible core design, accurate estimation of the heat transfer coefficient, and material development for the fuel and core structure for sufficient

► Fig. 58.5

Supercritical-water-cooled reactor (SWCR) (U.S. DOE Nuclear Energy Research Advisory Committee and the Generation IV International Forum 2002)



corrosion-resistance under the SCWR conditions. The low density of supercritical water will need an additional neutron moderator in the thermal neutron reactor option. For the FR option, potential of a positive void reactivity coefficient and design basis loss-of-coolant accidents should be taken into account in the system design.

58.2.5 High Temperature Gas-Cooled Reactor (HTGR)

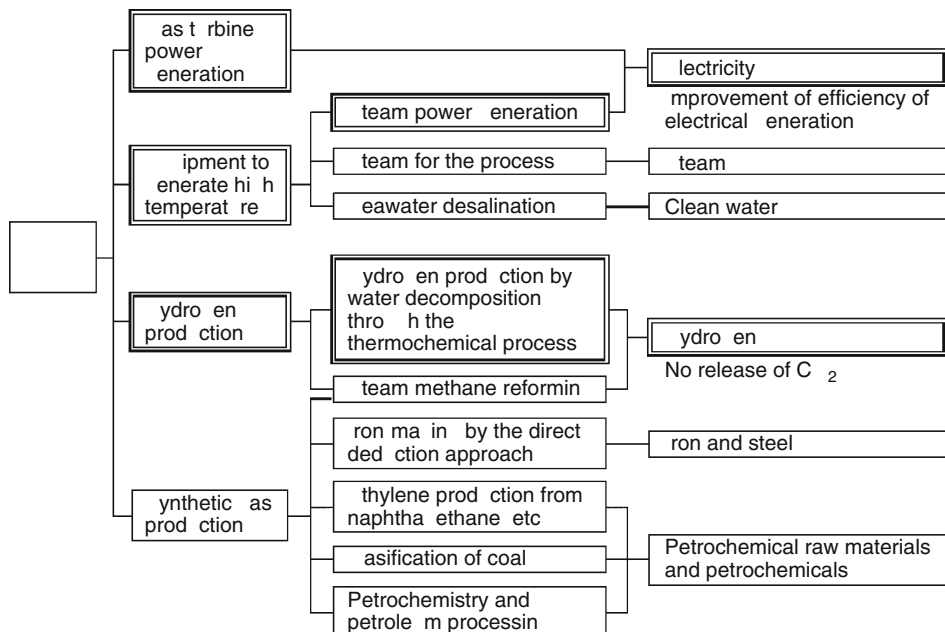
If one could say that the purpose of FRs is to achieve both expansion of energy sources and environmental preservation to contribute to the sustainable development of mankind, the aim of HTGRs is to contribute by offering efficient and multipurpose source of energy, especially chemical energy in form of hydrogen.

If the coolant temperature of a reactor can be raised to more than 700°C, it would not only improve power generation efficiency but also increase the applicability of the reactor as a heat source for purposes such as the generation of hydrogen by thermochemical decomposition of water. If the temperature could be raised to nearly 1,000°C, it would improve thermal efficiency and allow the reactor to be used in chemical and metallurgical industries. [Figure 58.6](#) shows heat utilization assumed in HTGRs. The double-line-boxes in the figure show the particular features of HTGRs.


HTGRs in Japan were originally developed as a substitute for active carbon in blast furnaces used for iron manufacture. This substitution of resources with heat was recognized as a point of compatibility between energy and substance.

Fig. 58.6

Heat utilization of the high temperature gas-cooled reactor (HTGR); from (Fuji-ie 2005)



58.2.5.1 Features of HTGR


A distinctive feature of the HTGRs is its fuel, which differs from the fuel used in LWRs and FRs.  *Figure 58.7* shows a coated particle fuel (approximately 1 mm in diameter), which consists of an oxidative microparticle of uranium or thorium dioxide coated with pyrolytic carbon or silicon carbide. The fuel coating works as a containment vessel. This coated particle exhibits excellent safety characteristics such as the capability to keep radioactive material within itself in up to around 600 MWth module type HTGRs, being a basic element to determine the features of HTGRs. The coated particle is further covered with graphite to moderate neutrons. Therefore, the reactor core becomes larger than that of LWRs; however, the larger size provides the advantage of larger heat capacity.

The typical HTGR fuels are the pebble-bed type, which is a graphite sphere, and the block type fuel; i.e., a graphite block into which coated particles are inserted (Saito et al. 1994). The former is generally suitable for high temperature operation because the fuel spheres circulate slowly in the reactor and each fuel sphere is exposed to high temperature in the reactor for a similar length of time.

As for the coolant, helium, a chemically inactive gas, is used. It is compatible with the structural material and graphite, and it contributes to the reactor's high-temperature features.

58.2.5.2 Hydrogen Production by HTGR

Considering the future utilization of energy, hydrogen production by HTGRs is of particular interest (Ogawa et al. 2009). Distributed energy is typically used in, e.g., batteries and electric cars, and such items do not always require large-sized power reactors, to achieve good economy. This type of advanced nuclear power aims to produce hydrogen by converting the thermal energy generated in nuclear reactors.

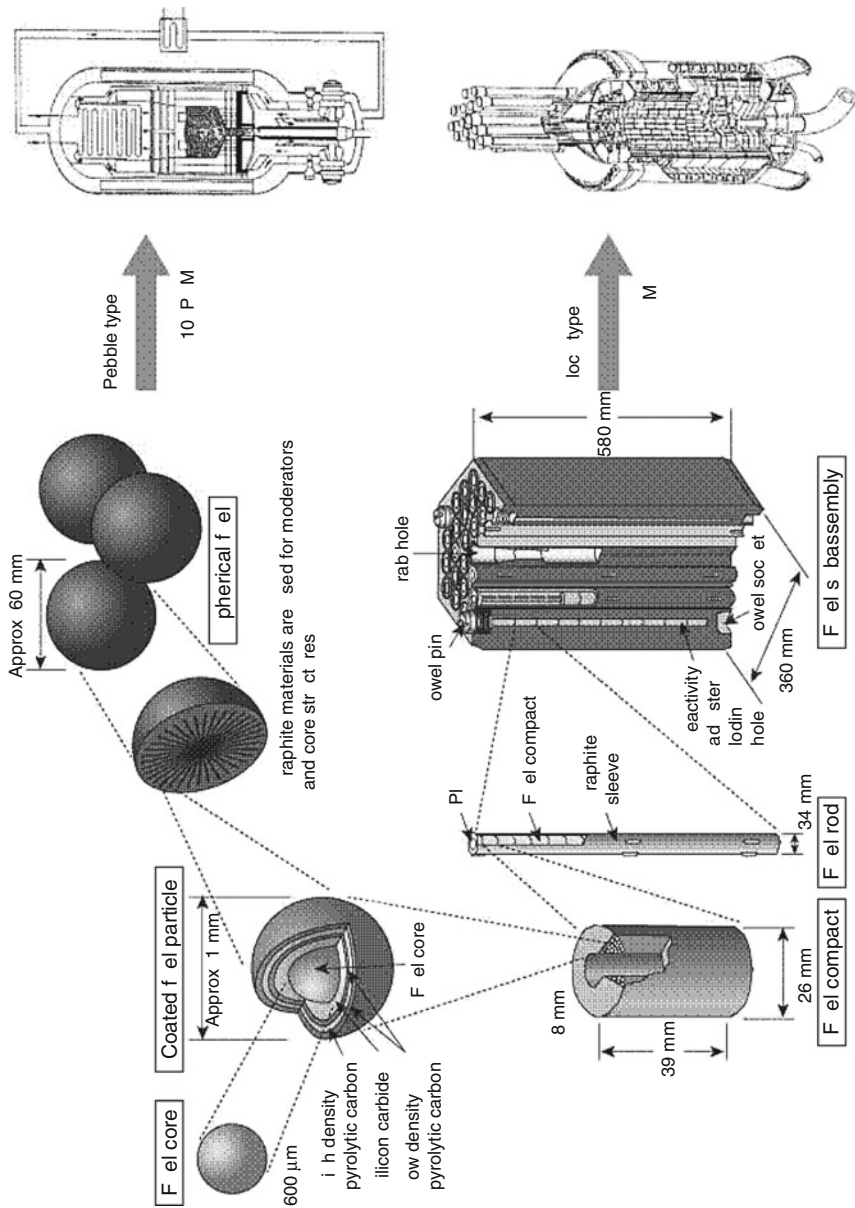
High temperature nuclear reactors are advantageous for hydrogen production because they do not use fossil material as energy source, and thus the direct decomposition of water is not accompanied by the release of carbon dioxide. Hydrogen production by HTGRs may be performed by thermochemical cycles like the Iodine–Sulfur (IS) process shown in  *Fig. 58.8*. In the IS process, water reacts with iodine and sulfur dioxide exothermically to produce hydrogen iodide and sulfuric acid, which are then thermally decomposed to produce hydrogen and oxygen, respectively, using high temperature maintained by nuclear energy. The thermal decomposition reactions also produce iodine and sulfur dioxide, which can be used again in the initial reaction, thereby the chemical cycle of water-splitting is completed. The thermochemical cycles offer a means for direct conversion of nuclear heat to chemical energy of hydrogen (Onuki et al. 2009).

There are a couple of questions concerning hydrogen production arising at this point. How much hydrogen production will be necessary, and how much thermal output is expected from HTGRs to produce all the hydrogen needed? Is it economical at all to produce hydrogen with nuclear reactors?

For example, suppose that cars are powered with hydrogen or fuel cells instead of gasoline and that carbon dioxide reduction laws are enacted requiring all vehicles operated in the city to be carbon dioxide free. The current annual consumption of gasoline in Tokyo is equivalent to about 600,000 tons of hydrogen. In order to provide this quantity of hydrogen, about 60 small reactors with a thermal output of 100 MW will be required. Owing to the safety features of

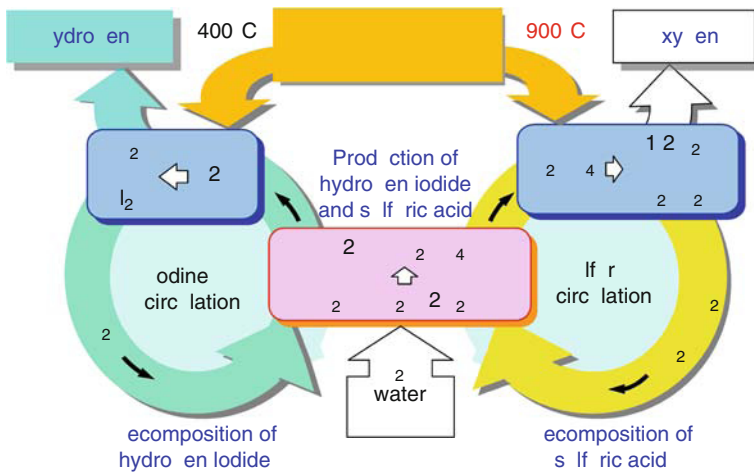
Fig. 58.7

HTGRs and Fuel Forms; from (Japan Atomic Energy Research Institute 1998)



■ Fig. 58.8

Thermochemical water-splitting cycle using iodine and sulfur (Onuki et al. 2009)



HTGRs, it is quite possible to locate them near metropolises in accordance with urban demand. Since the transportation of hydrogen is costly, it would be important to produce hydrogen near points of demand.

58.2.5.3 HTGR as a Power Reactor

As a high-temperature thermal source capable of 950°C, the HTGR offers a more effective way of generating electricity. Because the HTGR can generate steam at higher temperature than the LWR, e.g., the steam turbines will work with significantly higher efficiency.

Another possibility is to develop a direct gas turbine system at high temperature and pressure to increase the efficiency. Since helium has small cross section for neutron capture and is also chemically inactive, no induced radioactivity and no corrosion products can be expected in the coolant. Furthermore, the oxidative microparticle fuel coated with layers such as pyrolytic carbon or silicon carbide is expected to prevent the release of the fission gas into the coolant. Eventually the HTGR is suited to adopt the direct cycle, i.e., the gas turbine cycle, which allows building a more compact electric-power facility than the indirect cycle with a steam turbine system. While the thermal efficiency of electricity generation by steam turbine is about 40%, the gas turbine cycle can increase the efficiency up to ca. 50%.

A set of these compact multiple HTGRs can be referred to as modular type, and an example is the pebble bed modular reactor (PBMR) with the electricity generation of 165 MWe by gas turbine, which can be extended to a medium or large power station by adopting several modules (Koster et al. 2003).

58.2.5.4 Safety of HTGR

The HTGR's "shutdown," "cooling," and "containment" capabilities are as follows. HTGR shutdown using thermal neutrons raises no particular issues except in the case of air or water

ingress. The HTGR also has favorable features for core cooling. The HTGR is robust against high temperature because the fuel particles used are covered with layers of graphite. The sublimation temperature of graphite is as high as 3,500°C, and graphite can keep radioactive materials up to temperatures of about 1,600°C. This temperature is higher than the allowable maximum temperature of the fuel cladding of the LWR and FR, which ranges from approximately 900°C to 1,200°C. Moreover, the graphite in the HTGR has a large thermal capacity, and the power density of the HTGR is several dozen times smaller than that of the LWR. Therefore, a feature of the HTGR is that the temperature rises slowly in response to changes in the reactor output power. Consequently, even if a piping failure causes a helium leak and loss of coolant, the temperature would rise slowly because fuel heat is released through graphite blocks with large heat capacity. This means that engineered safety features such as the ECCS for LWRs, is, therefore, unnecessary. Temperatures in an HTGR during the accident will not exceed the temperature limit against the accidents but be brought under control naturally, representing its high level of safety.

As described, a notable feature of the HTGR using thermal neutrons is that the core is unlikely to melt. On the other hand, graphite oxidation due to the piping failure can be an important safety issue in the HTGR. That is, when a piping failure may occur in the main coolant pipe or in the heat exchanger, the air or steam would flow into the core. Because of its high temperature, the graphite would be damaged by oxidization and generates carbon monoxide. Against the air ingress, the confinement system is provided to restrict the amount into the core, which will mitigate oxidization and suppress the generation density of carbon monoxide to be sufficiently less than the detonation limit. Against the steam ingress, the primary helium system will be kept at higher pressure than the secondary water-steam system or a rapid blowdown system for the water-steam system is provided to mitigate the amount into the core. The gas turbine system is a favorable energy conversion system for the HTGR to eliminate the potential risk of the steam ingress. As a result of air ingress, however, the release of gaseous fission products from the oxidized fuel will be restricted to satisfy the allowable limit, which is equivalent to that for the LWR.

58.2.5.5 Development Status of HTGR

The UK developed coated particle fuel resisting high temperature for HTGRs in 1956. This marked a turning point in the construction of a demonstration reactor in the UK named Dragon. In Germany, an experimental reactor for electricity generation named AVR (Arbeitsgemeinschaft Versuchs Reaktor) has been developed. Its thermal output was 15 MW and it used pebble bed fuel with a diameter of approximately 6 cm. It has successfully operated at a 950°C gas temperature at the core outlet and achieved high availability for around 20 years. Germany has also aggressively performed R&D for a commercial HTGR for electricity generation and cogeneration. In addition, they have studied use of the heat generated by HTGRs to turn coal and lignite, plentiful resources in Germany, into forms such as gas or liquid, which are easy to use and environmentally friendly. Based on experience with the AVR, the thorium high-temperature reactor (THTR) began its operation in 1986. It was a prototype reactor for electricity generation using (Th,U)O₂ fuel with highly enriched ²³⁵U, and its electrical output was 300 MWe. However, it was in operation for only about 3 years because the government had opposed nuclear power, which was a situation similar to that faced by the fast reactor SNR-300.

On the other hand, the USA adopts a block type fuel element in HTGRs. In this fuel element, coated particle fuel and graphite powder are mixed and sintered, then shaped into thin rods, and loaded and sealed into holes in a hexagonal column-shaped graphite block. The experimental

reactor Peach Bottom, designed for electricity generation, started operation in 1967, with power output of 42 MWe. Later, the coated particle fuel was improved, however, operation ceased finally in 1974. In 1981, a demonstration reactor Fort St. Vrain, designed for electricity generation, started operation with a power output of 342 MWe and achieved nearly 40% thermal efficiency. However, repeated small troubles prevented it from maintaining high availability, and the operation ceased in 1989. The USA has also studied the feasibility of large HTGRs with scale merit of economy in mind. Later, however, they shifted to the development of small modular HTGRs such as the gas turbine-modular helium reactor (GT-MHR) (Note: The GT-MHR is an HTGR with improved economy, aiming for high efficiency power generation. In this reactor, high-temperature helium coolant is led to a gas turbine combined with a small power generation unit.). The designs take advantage of the HTGR's coated particle fuel, which resists high temperature. Therefore, even if a piping break causes the loss of core coolant, the heat from the reactor vessel can be dissipated through radiation and will not lead to fuel melting.

The Republic of South Africa aims at the commercialization of a PBMR (thermal power of a little over 200 MW, outlet temperature of approximately 750°C) that employs the technologies of the German pebble-bed type reactor. The national utility ESKOM started development in 1993, and PBMR Ltd. was founded in 1999. The construction schedule of the demonstration plant envisions commissioning in or near 2018.

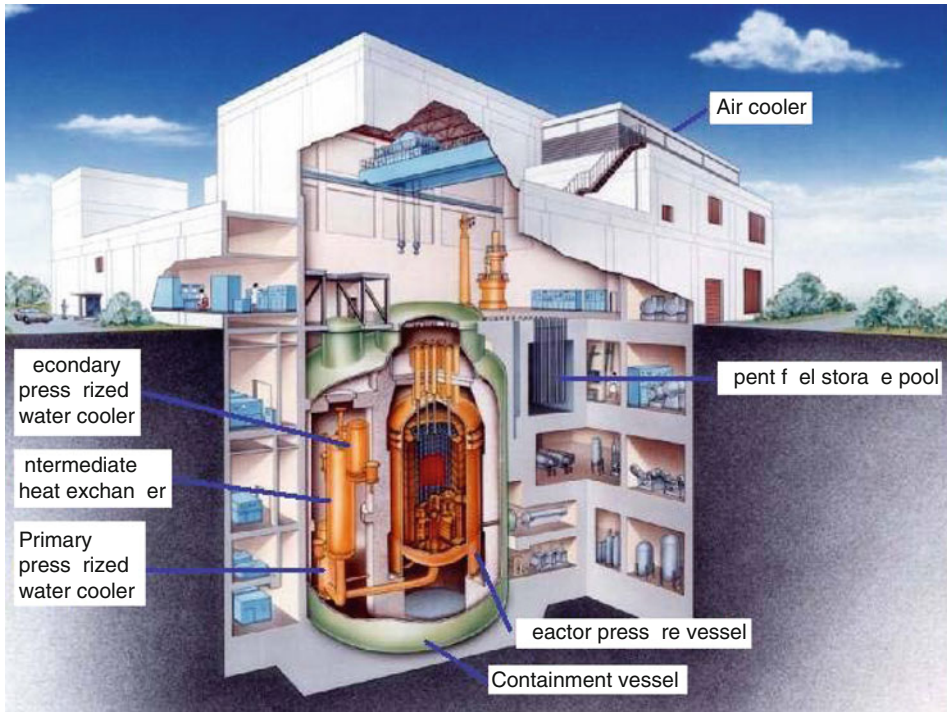
In China, the 10 MW high temperature gas-cooled test reactor (HTR-10) (thermal power of 10 MW, outlet temperature of 700°C, pebble-bed type) was built with help from Germany. The reactor reached first criticality in 2000 and achieved full power operation in 2003. Presently, the 10 MW high temperature reactor with gas turbine (HTR-10GT) project, aiming at construction of a helium gas turbine power generation system, is underway to study key issues of helium gas turbine technology. In addition, construction of a demonstration plant, high temperature reactor-pebble bed-module (HTR-PM) (electric power of 210 MWe, outlet temperature of 700°C), is underway with completion scheduled for or near 2013.

In Japan, a new reactor project was launched in 1969. Its purpose is to employ HTGRs not only in power generation but also to apply it to steel manufacture and chemical engineering. R&D has been carried out to establish a technological base for HTGRs and to further advance their development. First, the Helium ENGINEERING DEMonstration Loop (HENDEL), a facility for research and testing, had been built for advanced basic study on high temperature technology, and a critical facility VHTRC (very high temperature reactor critical assembly) had been constructed and put into operation. Further, the high temperature engineering test reactor (HTTR) has been constructed, targeting thermal output of 30 MW and an outlet temperature of 950°C (► Fig. 58.9). The reactor achieved full power operation with a helium temperature of 850°C in 2000, and achieved operation at 950°C in 2004. Currently it is operating smoothly, and research and testing are being carried out for other possible applications such as hydrogen production. As for hydrogen production, bench-scale water-splitting was performed by IS process and the chemical reactors such as sulfuric acid decomposer equipped with ceramic heat exchanger have been developed aiming at demonstration of nuclear hydrogen production using HTTRs.

In France, R&D for the ANTARES (AREVA New Technology based on Advanced gas-cooled Reactor for Energy Supply: thermal power of 600 MW, outlet temperature of 850°C, annular core with hexagonal block-type fuel assemblies) is in progress in collaboration with design vendors, utilities, and research institutes. This project is based on the modular high temperature gas-cooled reactor (MHTGR) designed through collaboration with vendors in France, Germany, and the USA, as well as the GT-MHR designed by Russian and US vendors, with the participation of Japanese vendors. The ANTARES aims at an indirect cycle to provide

■ Fig. 58.9

High temperature engineering test reactor (HTTR); from (Japan Atomic Energy Research Institute 1998)



a flexible heat source; either heat supply or cogeneration, with no change in the loop configuration, and is expected to achieve deployment earlier than other technologies that have more development problems to be solved. This R&D started in 2001 and envisions the main results on the problems related to the feasibility being obtained by 2010.

While coated particle fuel has excellent high-temperature durability and is suitable for HTGRs, it is difficult to recycle this type of fuel. That is, mainly due to the fact that this fuel is covered by multilayers of coating material, the fuel cannot be dissolved by nitric acid, which is used to reprocess fuel in LWRs, and it is hard to extract useful nuclear fuel materials from the spent fuel. Therefore, a measure to address this problem has been considered in the development of fuel for HTGRs. The proposal is to enable the complete use of the fuel constituents by remarkably improving burnup. Even in this case, it is difficult to burn higher-order plutonium isotopes and MAs in a thermal reactor, and long-lived radioactive material is contained in the spent fuel. Thus, a concept and methodology have been required, which may lead to commercialize the fuel cycle.

58.2.5.6 High Temperature Gas-Cooled Fast Reactors

For fuel utilization by recycling, a high temperature GFR featuring a helium gas coolant and fast neutrons is being studied. Although R&D is at the basic stage, some types of fuel and cladding

combinations, which do not moderate neutrons as effectively as graphite, are under discussion. For example, the use of particle fuel coated with titanium-group material, which has superior resistance to high temperature, is being considered. Another example is a fuel pin whose cladding tube is made of metallic materials that have a high melting point such as niobium.

A direct gas turbine system working with helium is being considered for GFRs. (Helium, being an inert gas, is advantageous to safety; and the recent technological advances in the gas turbine are expected to progress.)

There is, however, some concern about safety. Since the fuel enrichment is more than 20%, the output density of core fuel tends to be larger than that of thermal neutron reactors like LWRs. In addition, fuel particles without graphite have much less heat capacity, and the high fuel enrichment causes lower Doppler reactivity at the rise of fuel temperature. Because of these factors, it is difficult to ensure a slow temperature rise at an accident, which is possible for HTGR operated with thermal neutrons. Moreover, the countermeasures for core disruptive accidents (CDAs) should be investigated to prevent significant energetics due to concentrating motions of molten fuel and to ensure a long-term stable cooling capability for molten fuels.

The GFR with related fuel cycle is aiming at the sustainable utilization of fuel resources by recycling, as well as multiple utilization and high thermal efficiency, and it may develop new-generation nuclear energy systems that serve as an efficient use of nuclear energy resource and that can harmonize with the environment.

58.2.6 Sodium-Cooled Fast Reactor (SFR)

58.2.6.1 Features of FR

The FR has been emphasized as a leading advanced nuclear reactor following the LWR since the beginning of nuclear energy development. As fast neutrons have high neutronic potential, the FRs are greatly expected to make desired nuclear reactions, which will be capable of expanding the efficient utilization of uranium, transmuting radioactive nuclides into nonradioactive or short-lived ones and managing the quantity and the toxicity of radioactive material within the duration of civilization.

To enable the functions above, the FR system should consist of two parts. One is the reactor where requested reactions should occur and the other is the nuclear fuel cycle where material selections and treatments of materials, elements, and nuclides suitable to feed the reactor core can be made. The necessary functions and the material selection are summarized in the following three Subsections.

Plutonium, instead of ^{235}U , is a main contributor to the nuclear reactions in FRs where mixture of plutonium and uranium is used as fuel. Simple metallic fuel is a candidate to achieve better FR core performance than oxide fuel due to its higher fuel density, which has been employed in the LWR. Carbide and nitride fuels are also considered.

The core configuration without a moderator becomes compact and gives a high power density. The coolant should be less interactive with neutrons, and high thermal conductivity as well as heat transport capability is recommended for an efficient transformation of thermal energy through narrow flow channels. Candidates for the coolant include liquid metals such as sodium and lead, gases such as helium and water including supercritical water.

➤ *Table 58.3* shows comparison of the properties of water, sodium, and helium.

■ Table 58.3

Comparison of the properties of water, sodium, and helium (Iwanami Shoten 1998)

Items		Water	Sodium	Helium
Nuclear	Neutron moderation power	High	Low	Low
Thermal	Melting point °C/Boiling point °C (atmospheric pressure)	0°C/100°C	98°C/880°C	−272°C/ −269°C
	Specific heat (kJ/kg°C)	5.43 ^a	1.30 ^b	5.19 ^c
	Thermal conductivity (W/m°C)	0.57 ^a	66.1 ^b	0.340 ^c
Hydraulics	Density (kg/m ³)	738 ^a	826 ^b	2.38 ^c
	Dynamic viscosity (10 ^{−6} m ² /s)	0.123 ^a	0.281 ^b	19.6 ^c
Others	Chemical activity	Low	High	None
	Clarity	Clear	Opaque	Clear
	Compatibility with materials	Generates corroded products	Easy to prevent corrosion	Favorable

^aat 287°C, 7 MPa.^bat 527°C, 1 kPa.^cat 727°C, 5 MPa.

58.2.6.2 Reactor Core of SFR

The reactor core serves to materialize the potential of nuclear reactions and has configuration so as to meet the above-mentioned requirements. The core configuration highly depends on the nuclear fuel cycle such as reprocessing methods and depends on the types of fuel loading; single-region core or multi-region one according to the purposes of the reactor. The main purposes for the core to achieve are to release energy by nuclear fissions, produce new fuel, and transmute radioactive material into short-lived or nonradioactive material. In the development to date, blanket fuel has been provided for fuel production. The core of “Monju,” which is a Japanese prototype FR, is shown in [Fig. 58.10](#) as an example of a sodium-cooled fast reactor core. In Monju, the blanket region is arranged to surround the core fuel region axially and radially so that it can produce fuel material of plutonium. Furthermore, a plan is also investigated to place test fuel to burn minor actinides. Neutron shielding subassemblies are located outside the blanket region. MOX fuel is utilized, which consists of ²³⁹Pu and depleted uranium and has a plutonium enrichment of around 20%. The blanket fuel composed of depleted uranium is arranged on the top, bottom, and circumferential regions of the core, and ²³⁸U in the blanket fuel absorbs neutrons leaking from the core to produce new core fuel.

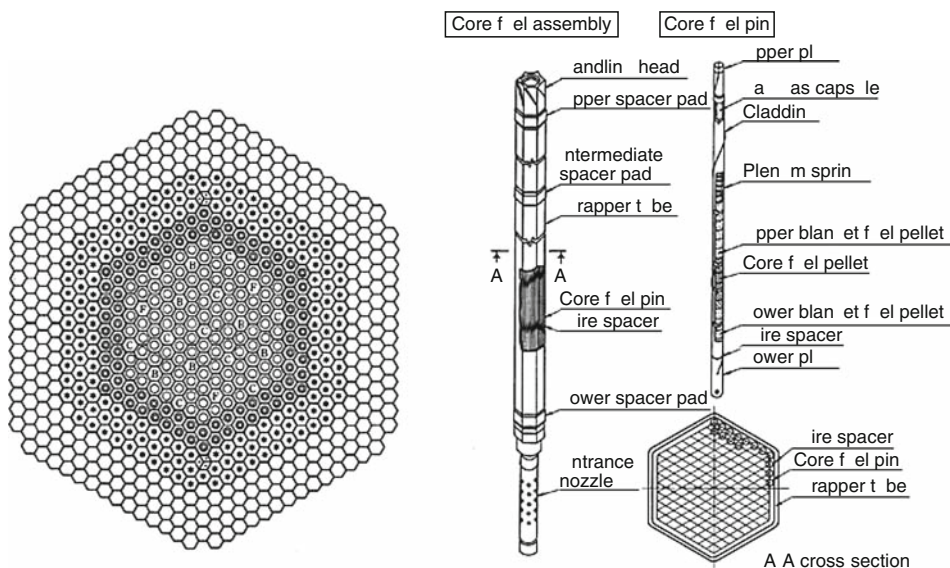
58.2.6.3 System Configuration of SFR

The system of SFRs is configured to have a process of generating electricity with a high-temperature coolant flowing from the reactor core, i.e., a mechanism by which heat is generated, extracted, and turned into electric power (see [Fig. 57.14 in Chap. 57 of this Volume](#)).

The system configuration varies depending on the method of generating electricity: a steam turbine, a gas turbine, or others. As for sodium cooling, the sodium–water reaction has to be

■ Fig. 58.10

The core of the Japanese prototype fast breeder reactor (PBFR) "Monju"; from (Power Reactor and Nuclear Fuel Development Corporation 1980)



avoided so as not to influence the reactor safety. So far, SFRs have adopted an intermediate sodium system between the primary sodium system and the steam-generating system.

Since the boiling point of sodium at atmospheric pressure is as high as 880°C, the SFR does not require pressurization of the core in principle. The reactor outlet temperature ranges from 510°C to 550°C, which is higher than that of the PWR (~325°C) by 200°C or more. This means that the SFR has great potential for high temperature and conversion efficiency. The thermal efficiency of the SFR can be improved to more than 40% compared to around 35% achieved by the LWR.

58.2.6.4 Safety of SFR

The FR and the LWR have a system that concentrates energy and radioactive material in the core. Therefore, the concepts on safety assurance based on the “defense in depth” principle are also basically the same. However, FR core configuration is not designed to have reactivity maximum configuration and any relocation of core material could increase reactivity (positive reactivity insertion), whereas LWR cores are arranged in the reactivity maximum configuration. Therefore hypothetical core disruptive accidents (HCDAs) are reviewed in the licensing process even though their occurrence probability is negligibly small. As the safety of FRs, the SFR’s safety will be mainly treated here.

Shutdown

Like in LWRs, two independent reactor shutdown systems are installed to protect the reactor core, where safety characteristics of SFRs or LWRs have been taken into account. Concerning the safety characteristics for “shutdown,” the Doppler coefficient of the FR is slightly smaller than that of the LWR. The Doppler coefficient is an important factor from the overpower transient point of view.

When sodium is used as a coolant, the operating pressure is low, and it is unnecessary to assume accidents such as control rod ejection, which may occur in a high pressure operation system like the LWR. In the SFR, an inadvertent control rod withdrawal is anticipated due to the failure of the power control system, which gives no rapid reactivity insertion but a continuous one. Thus, the effect of the control rod withdrawal is not significant, although the Doppler reactivity of the SFR is smaller than that of the LWR. On the other hand, the sodium coolant has the advantages of a large temperature margin for the boiling point and high thermal conductivity.

Based on the above design efforts for the essential safety functions, the occurrence probability of severe accidents can be equivalent to or less than 10^{-6} per reactor years as is similar to the modern LWR. Nevertheless, further efforts to strengthen the passive prevention capability have been devoted in the SFR in addition to the inherent safety features around the 1980s. During this period, passive safety arguments against the anticipated transient without scram (ATWS) have been made in the USA, Europe, and Japan. No detection signals or no driving force is required in the passive mechanism and there are fewer uncertainties to analyze their effectiveness.

In Europe, the thermal expansion (elongation) of the drivelines for the absorber rods was selected as the most promising passive mechanism within the frame of the European Fast Reactor project. This mechanism is reliable with containing less uncertainty due to the axial elongation behaviors of the drivelines of absorber rods. This mechanism would need a rather longer period, and thereby the temperature increase rate should be mitigated by other design measures, e.g., longer halving time for the flow coast down. Nevertheless, the absorber rods will be pushed in by the force created by the thermal expansion and thus suitable to the freestanding core design (Edelmann et al. 1994).

In Japan, the self-actuated shutdown system (SASS) has been developed as a passive safety feature (Takamatsu et al. 2007; Nakanishi et al. 2008) using the phenomena that electromagnetic force of the control rod latch will be lost when alloy temperature exceeds the Curie point. Several kinds of in-sodium transient testing have been carried out together with in-pile experiments in the experimental fast reactor “Joyo.” This mechanism is effective to the robust restraint core, which is designed for seismic requirements.

Cooling

Concerning the cooling of the reactor core, loss-of-coolant accident due to piping breach, which is treated as the major accident in high-pressure systems of LWRs, is no more a significant issue in SFRs, since SFR is a low-pressure system. The ECCS, which is significant also for the safety of LWRs, is not required. Instead, a guard vessel is set outside of the reactor vessel to prevent loss of sodium coolant from the core in SFR.

In the SFR, high potential for natural circulation of sodium coolant due to large buoyancy force can be expected because of large temperature difference of coolant between the inlet and the outlet of the core. In this manner, the SFR has more favorable features for “cooling” than those of the LWR.

Containment

The third essential safety function for safety assurance is “containment” of radioactive materials. Similar to the LWR, the SFR has multiple containment systems, such as pellet, cladding, primary coolant boundary, guard vessel, and containment against the release of fission products. Especially when the guard piping may be adopted both for primary and secondary cooling systems together with guard vessels, these outer boundaries and vessels will play an important role as the first containment. Instead of guard pipes, an inert gas can be filled inside the containment.

58.2.6.5 Safety Studies and the Results

Studies on Reactor Core Safety

The safety issues of nuclear energy systems are discussed sometimes from the viewpoint of the inherent and passive safety characteristics of the system. The essential safety question concerning FRs is how to avoid radioactive material release to the environment during meltdown of the core.

The problem of dealing with the consequences of CDAs – that can be possibly caused by unprotected transient over power (UTOP) and unprotected loss of flow (ULOF) – is an issue in the safety licensing process even though the occurrence probability is negligible. Conservative assumptions predict significant energy release by reactivity insertion due to the compaction of molten fuel. In SFR licensing process, primary coolant boundaries and confinement are required to accommodate the CDA consequences.

One of the advanced measures against CDAs is to avoid energy release. Considering the low occurrence probability, it is not possible to equip a system with active elements whose failure probability is about 10^{-2} per demand. Activation of the safety system should be based on using physical properties like melting point and material relocations by the driving forces such as fission gases and steel vapors. Therefore, a concept of fuel subassembly in which molten fuel discharge from the core is enhanced has been developed to prevent the formation of molten fuel pool and its resultant compaction, and thus energy release due to reactivity insertion can be excluded from the CDA scenario. This safety concept meets the safety requirements for the SCNES.

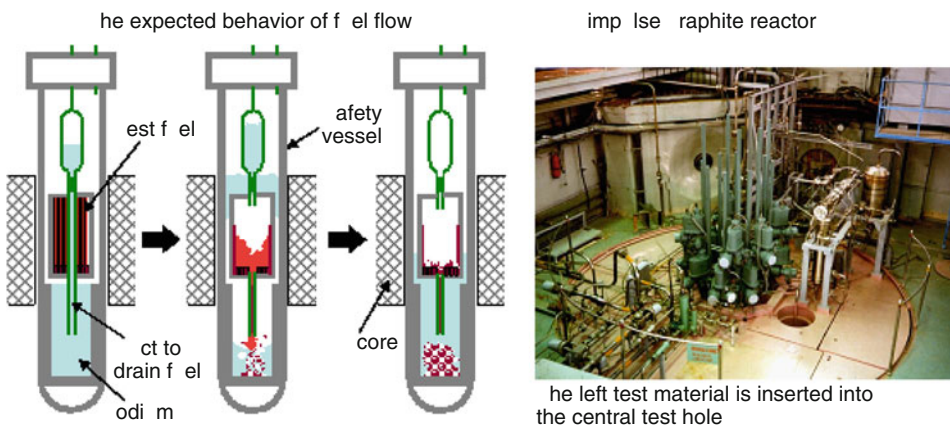
A research program for re-criticality-free core with existent reactor was fixed and tested in an impulse graphite reactor (IGR), in the collaboration between Kazakhstan NNC (National Nuclear Center) and Japan Atomic Energy Agency. It succeeded to obtain positive experimental results (Inagaki et al. 1998; Niwa et al. 2005, 2007; Fuji-ie 1992, 2006) (see Fig. 58.11).

Safety Concern About Chemical Reactivity of Sodium

The disadvantage of using sodium as a coolant is a recurring question of plant design because of its chemical reactivity.

Fig. 58.11

The test to validate a measure to avoid re-criticality during core disruption; from (Fuji-ie 2005). The test has been conducted in international cooperation between National Nuclear Center of the Republic of Kazakhstan and Japan Atomic Energy Agency



There is concern that sodium fire may be caused by sodium leaking out from the piping and vessels. As for a sodium leak, all pipes and vessels in the containment vessel are generally covered with guard pipes and vessels or filled with inert gas. However, sodium leaks from outside the containment vessel could cause sodium combustion and damage the reactor building. Fortunately, sodium outside the containment vessel is only secondary sodium without radioactive contamination.

In fact, the sodium leak that occurred at “Monju” involved the secondary heat transport system, which means that the leaked sodium was not radioactive. Therefore, no radioactive material was released to the environment by the sodium leak and the safety facilities were not affected. Knowledge about sodium fire has been accumulated through operation experiences. So far, there have been about 150 sodium leak events in the UK, France, Germany, and the former Soviet Union. However, no reports have been released of safety facility damage due to the sodium leak or combustion, and the reactors that experienced the sodium leakage were repaired and successfully resumed their operations.

Chemical problems arise when sodium and water react with each other in case of heat transfer tube failure in the steam generator. The secondary sodium exchanges heat with pressurized water in the steam generator, and the high-temperature steam drives the turbines. Therefore, if a failure should occur in the heat transfer tube of the steam generator where the pressurized water flows, then the pressurized water will vigorously react with the sodium in the steam generator and the failure would propagate. The chemical reaction of sodium and water generates hydrogen. As a result, pressure loading is imposed and may damage the intermediate heat exchanger in the reactor cooling system. Further measures have been taken to provide for early detection of water leak caused by the heat transfer tube failure, as well as rapid drain of the pressurized water out of the steam generator to stop the water leak. Experimental research on the propagation of the break caused by the chemical reaction of sodium and water has provided knowledge with which system integrity can be ensured against pressure loading.

In February 1987, in the prototype fast reactor (PFR) in the UK, the heat transfer tube of the steam generator (superheater) was damaged by its fretting caused by flow-induced vibration at the rated operation, and the water leaked out of the tube. Even though the hydrogen detector had been out of order during the operation and no quick depressurization systems were provided for the water/steam system to prevent the propagation of the damage to the surrounding, the burst disks on the sodium water reaction pressure relief system ruptured passively and the reactor was safely shutdown without any impact on the primary cooling system. After that, modifications were made such as automatic connection of the hydrogen detection system triggered by the trip signal, and providing a quick blowdown system for the superheater, and the reactor successfully resumed operation about half a year later.

58.2.6.6 Comparison of SFR types

SFRs are generally categorized into loop and pool types. The features and achievements of loop/pool type FRs are summarized in [Table 58.4](#). Generally, it is found that construction of loop type FRs tends to be more expensive than pool type FRs due to larger mass of components and larger building size for piping system. From the viewpoint of primary sodium accommodation, the pool type FRs seem to have a simpler primary sodium boundary since primary sodium is contained in the reactor vessel. The loop type FRs have advantages concerning reliability and inspection capability. Separated compact components such as the reactor vessel, primary pump, and intermediate heat exchanger, will allow reliable off-site manufacturing and preservice

■ Table 58.4

Comparison between loop type and pool type fast reactors (FRs)

Item	Loop type	Pool type
Safety	No vibration source, such as pumps, in the reactor vessel	Primary sodium is unlikely to leak out because it is contained in the reactor vessel
	Need to take measures on the assumption of sodium leak from the primary piping	Need to take measures against the failure of flow path inside the reactor vessel
Reliability (structural reliability)	Compact-sized reactor vessel is favorable from the seismic viewpoint	Moderate thermal transient due to large heat capacity
	The reactor vessel can be assembled in factory to provide higher reliability	Significant volume of the reactor vessel
	Good accessibility to components	The reactor vessel must be assembled at the reactor site due to its large diameter
		Need for adequate quality assurance concerning the welding of the reactor vessel
		Difficulty in accessing the components installed inside the reactor vessel
		Difficulty in inspection of structures that form the flow path inside the reactor vessel
Potential for improved economy through simplification of the secondary system	Elimination or simplification of the secondary system can be easily achieved by adopting a highly reliable steam generator	
Reactors	EBR-I, Fermi, SEFOR, CRBR, FFTF (USA)	EBR-II (USA)
	DFR (UK)	PFR (UK)
	Rapsodie (France)	Phenix, Superphenix (France)
	KNK-II, SNR-300 (Germany)	BN-600 (Russia)
	BOR-60, BN-350 (Russia)	PFBR (India)
	FBTR (India)	
	CEFR (China)	
	JOYO, Monju (Japan)	

inspection. From the viewpoint of in-service inspection, loop type FRs could inspect and monitor primary sodium boundaries outside the reactor vessel, while pool type FRs have difficulties to inspect and monitor complicate in-vessel structures under sodium.

Such a comparison of reactor types has been performed over a long period, and both types have been really adopted for FRs in various countries. Loop configuration has been well

adapted in all experimental reactors such as Experimental Breeder Reactor-I (EBR-I), South-west Experimental Fast Oxide Reactor (SEFOR), Fast Flux Test Facility (FFTF), Dounreay Fast Reactor (DFR), Rapsodie, Kompakte Natriumgekühlte Kernreaktoranlage-II (KNK-II), BOR-60, BN-350, Fast Breeder Test Reactor (FBTR), Chinese Experimental Fast Reactor (CEFR), and Joyo. And prototype reactors such as Clinch River Breeder Reactor (CRBR), SNR-300 and Monju have adopted the configuration as well. Among these loop type FRs, Monju and Joyo are only available plants that will restart. Regarding prototype and demonstration FRs, a larger number of pool type FRs, including PFR (UK), Phenix and Superphenix (France), BN-600 (Russia), and prototype fast breeder reactor (PFBR) (India), were adopted. In India, a prototype pool type FR of 500 MWe power output is under construction expecting their first criticality in 2010.

58.2.6.7 Development Status of SFR

FR as a Base-Load Power Supply

FR development started in the USA and the former Soviet Union, followed by European countries: France, Germany, and the UK, and Asian countries: India and Japan.

► [Table 58.5](#) shows the current status of FR development in the world. Although not all of them are at the same stage, generally speaking, the technology level has already reached the stage at which commercial reactors can be built. At the beginning of FR development, the USA was the front-runner and led the world. The USA has constructed an experimental fast reactor, EBR-I with 200 kW power output. It is well known as the first reactor in the world to generate electricity, a feat that was accomplished in 1951 (see ► [Fig. 58.12](#)).

The reactor that first succeeded in generating electricity was not the LWR, which has been commercialized, but the FR. Thereafter in the USA, many FRs such as the Enrico *Fermi* Atomic Power Plant, EBR-II and FFTF were constructed and operated. Test data have been accumulated from these reactors through R&D for core fuel, structural materials, neutronic characteristics of core, safety, and so on. CRBR with 380 MWe power output passed the safety review in 1975, and the construction began. However, the nuclear policy changed during President Carter's administration, and the construction was called off.

Then, Europe came to the forefront. The UK constructed and operated PFR, the first prototype FR in Europe, following DFR. Now, the PFR has finished its roles and is in the process of decommissioning. Meanwhile, France constructed and operated a demonstration reactor Superphenix based on the experience of construction and operation of Rapsodie and Phenix, but it is closed.

France in particular has operational experience with a commercial scale fast reactor, Superphenix, with 1,300 MWe power output. In Germany, although a steam-cooled fast reactor had been considered, they have actually developed SFRs, beginning with the experimental reactors, KNK-I and II. Then, a prototype reactor, SNR-300, with 327 MWe power output was constructed. It had the same plant concept as the prototype reactor Monju in Japan. However, the provincial government where SNR was constructed opposed its operation in 1986, and it was dismantled.

In the former Soviet Union, many experimental reactors have been constructed and operated. In Aqtau, Kazakhstan, BN-350 started operation both to generate power and to produce fresh water in 1973 and operated until 2000. In Beloyarsk, Russia, BN-600 with 600 MWe power output started operation in 1981 and continues operation up to now.

Table 58.5
Fast reactors (FRs) that have been developed worldwide (Japan Atomic Industrial Forum Inc 2009; IAEA 2006)

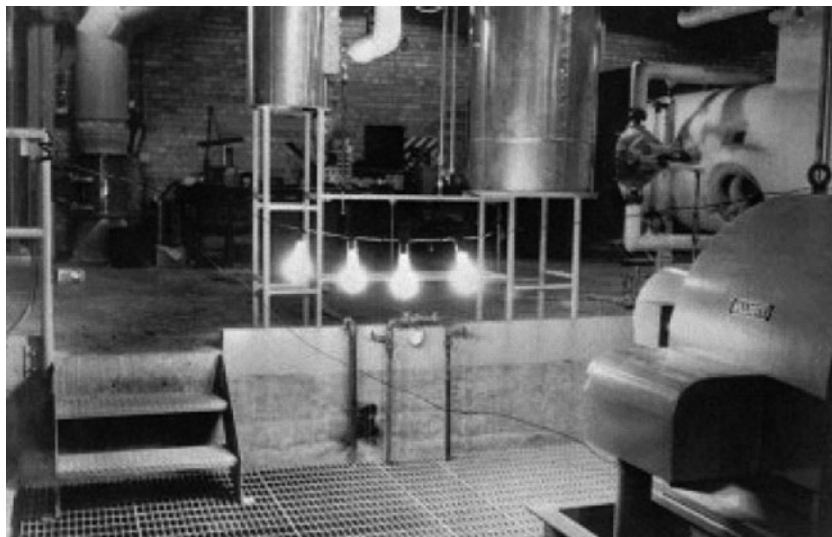
Country	Reactor name	Thermal/ electric output (MW)	Objective	Year of starting construction	Year of the first criticality	Present state	Reactor structure	Fuel	Avg. burnup (MWd/kg)	Reactor inlet/outlet temperature (°C)	Breeding ratio
USA	EBR-I	1.2/0.2	Experiment	1946	1951	Closed	Loop	U	–	230/322	–
	EBR-II	62.5/20	Experiment	1958	1961	Closed	Pool	U	20	371/473	–
	E. Fermi	200/61	Experiment	1956	1963	Closed	Loop	U+10%Mo	6	288/427	1.16
	SEFOR	20/–	Experiment	1965	1969	Closed	Loop	PuO ₂ –UO ₂	2	371/438	–
	FFTF	400/–	Experiment	1970	1980	Closed	Loop	PuO ₂ –UO ₂	45	360/503	–
UK	DFR	60/15	Experiment	1954	1959	Closed	Loop	U+7%Mo	25	230/350	–
	PFR	600/270	Prototype	1966	1974	Closed	Tank	PuO ₂ –UO ₂	67	399/560	0.95
France	Rapsodie	40/–	Experiment	1962	1967	Closed	Loop	PuO ₂ –UO ₂	65	400/515	–
	Phenix	563/250	Prototype	1968	1973	Operating	Pool	PuO ₂ –UO ₂	40	395/560	1.16
	Superphenix	3,000/1,240	Demonstration	1976	1985	Closed	Pool	PuO ₂ –UO ₂	70	395/542	1.18
	BN-350 ^a	1,000/350	Prototype	1964	1972	Closed	Loop	UO ₂	38	300/500	1.0

Russia ^a	BR-1	0.03/–	Experiment		1955	Closed	Loop	Pu			
	BR-2	0.2/–	Experiment		1956	Dismantled	Loop	Pu			
	BR-5	5/–	Experiment	1957	1958	Dismantled	Loop	PuO ₂ -UC,UN			
	BR-10	10/–	Experiment	1971	1973	Closed	Loop	PuO ₂ -UC,UN			
	BOR-60	55/12	Experiment	1964	1968	Operating	Loop	UO ₂	330/545	–	
	BN-600	1,470/600	Demonstration	1967	1980	Operating	Pool	UO ₂	62	380/550	0.85
	BN-800	2,100/800	Demonstration	2002	2012	Under construction	Pool	PuO ₂ –UO ₂		354/547	0.98
	KNK-II	60/–	Experiment	1966	1977	Closed	Loop	PuO ₂ –UO ₂	75	360/525	–
Germany	SNR-300	762/327	Prototype	1973	–	Abandoned	Loop	PuO ₂ –UO ₂	57	377/546	–
India	FBTR	42.5/15	Experiment	1972	1985	Operating	Loop	(U, Pu)C	30	380/515	–
	PFBR	1,250/500	Prototype	2004	Planned as 2010	Under construction	Pool	PuO ₂ –UO ₂	77	397/547	
China	CEFR	65/25	Experiment	2000	Planned as 2005	Under construction	Pool	PuO ₂ –UO ₂	100	360/530	–
Japan	Joyo	140/–	Experiment	1970	1977	Operating	Loop	PuO ₂ –UO ₂	50	370/500	1.06
	Monju	714/280	Prototype	1985	1994	Suspended	Loop	PuO ₂ –UO ₂	80	397/529	1.20

^aFormer Soviet Union

■ Fig. 58.12

Experimental Breeder Reactor- I (EBR-I), the FR that succeeded in generating electricity for the first time in the world. Then, four light bulbs were lit (Argonne National Laboratory 2002)



This achieves a reliable operation with average plant availability more than 70% since 1980. The construction of an SFR called BN-800 with 800 MWe output had been suspended for an extended period, but construction has restarted. A study on a lead-cooled FR is being carried out.

In Japan, the experimental fast reactor “Joyo” started operation in 1975 following the criticality test equipment called fast critical assembly (FCA). Joyo has run irradiation tests for domestic fuel material and increased the core thermal output as well. At the beginning of operation, the thermal output of the core was 100 MW. Currently, it employs a third-generation core, called the MK-III, with 140 MW thermal output.

The prototype fast breeder reactor “Monju” was constructed in 1990. The output operation had been carried out and preparations for the full-power operation were being made (► Fig. 58.13). However, it caused sodium leaks from the secondary system on December 8, 1995 and the operation has been suspended. As of 2009, the overall plant and its functions, including long-stopped as well as improved facilities, have been checked, and preparations to restart operation are under way.

Multipurpose Use of Medium-and Small-Sized FRs

A small SFR, commonly referred to as the 4S (Super Safe, Small, and Simple), is under development with the aim of commercialization in the early 2010s (► Fig. 58.14). The reactor is intended to serve as a dispersed supply source of power and heat for local areas with an electric output of 10–50 MWe. This reactor is designed for continuous operation up to 30 years without refueling by steadily driving upward a removable radial reflector surrounding the core. This also has the advantage of nuclear nonproliferation because it is capable of sealed operation with no need to unseal the reactor for maintenance. This can be achieved by a reactor internal structure composed only of passive components, such as an electromagnetic pump with no active parts for in-vessel coolant circulation. There have also been studies on the application of

Fig. 58.13

Prototype fast breeder reactor Monju; from (Fuji-ie 2005)

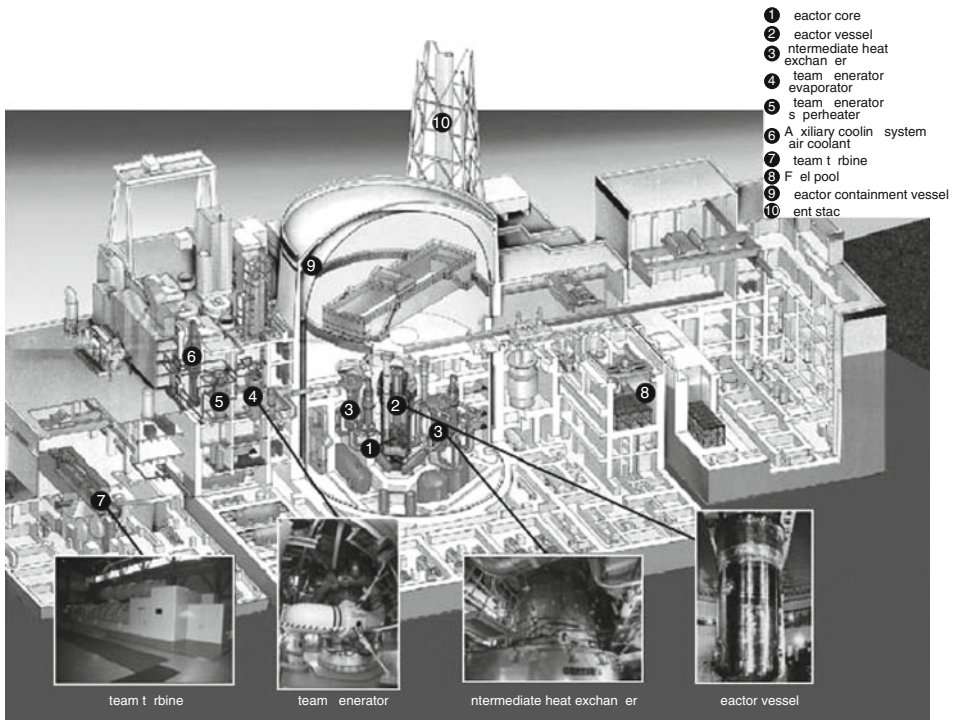
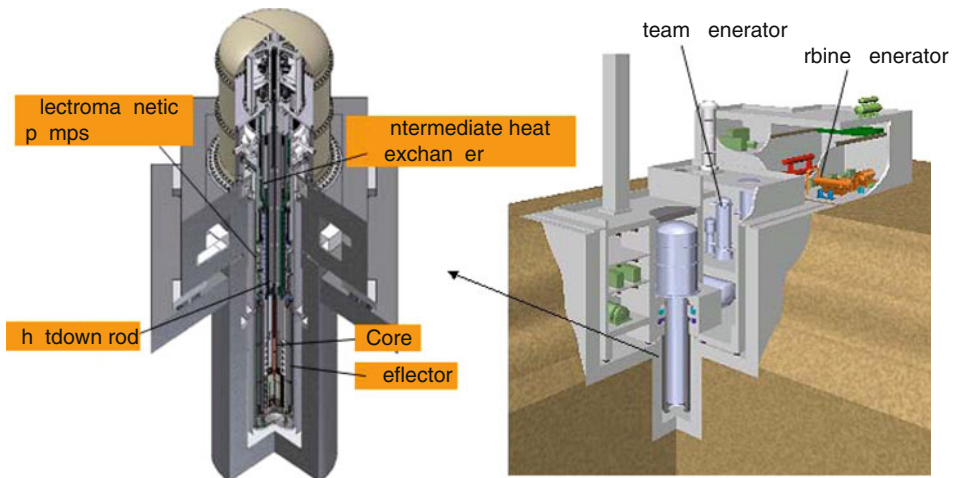


Fig. 58.14

Bird's-eye view of the 4S plant (Matsuyama et al. 2009; Tsuboi et al. 2009)



nuclear energy to steam supply to extract crude oil from oil sand in Canada. The 4S has been attracting attention as a candidate for this application.

58.2.7 Molten-Salt Reactor (MSR)

This type of reactor uses molten salt as a fuel and a coolant that circulates in the reactor. The neutrons produced by fission reaction in the circulation process are moderated by graphite so that the system features an epithermal to thermal neutron spectrum. The heat generated in the molten salt is transferred to a secondary coolant system through an intermediate heat exchanger, and then through a tertiary heat exchanger to the power conversion system. The excellent heat transport properties of molten salt can contribute to a smaller reactor building and a higher thermal power output.

A representative application of the MSR concept is thorium reactor, and MSRE (Molten-Salt Reactor Experiment) with thermal output of 8 MW was developed by Oak Ridge National Laboratory in the USA and had been operated from 1966 to 1969. In the thorium reactor, the breeding of fissile nuclide, ^{233}U , can be achieved through prevention of parasitic absorption by fission products and ^{233}Pa , a nuclide generated in the process of producing ^{233}U from ^{232}Th . After that, molten-salt breeder reactor (MSBR) with electric output of 1,000 MWe was designed in the 1970s. At that time, there were technological issues to be solved for commercialization, such as necessity of developing material that is durable under the system environment of high temperature molten salt. Other issues were shielding and remote handling against high intensity of gamma rays from the thorium molten salt coolant.

The following example is an MSR plant with a power level of 1,000 MWe, which has been proposed as a reference GEN-IV MSR in GIF aiming at actinide burning with continuous recycling (US DOE and GIF 2002) (see [Fig. 58.15](#)). The reactor can use ^{238}U or ^{232}Th as a fertile fuel dissolved as fluorides in the molten salt. Due to the thermal or epithermal spectrum of the fluoride MSR, ^{232}Th is favorable for achieving the highest conversion performance. It operates above 700°C of coolant outlet temperature, which affords improved thermal efficiency, i.e., 40–50%. The coolant outlet temperature can be improved up to 850°C for the purpose of hydrogen production.

58.3 Future: A More Radical Picture

The following part has been written by Prof. E.O. Adamov.

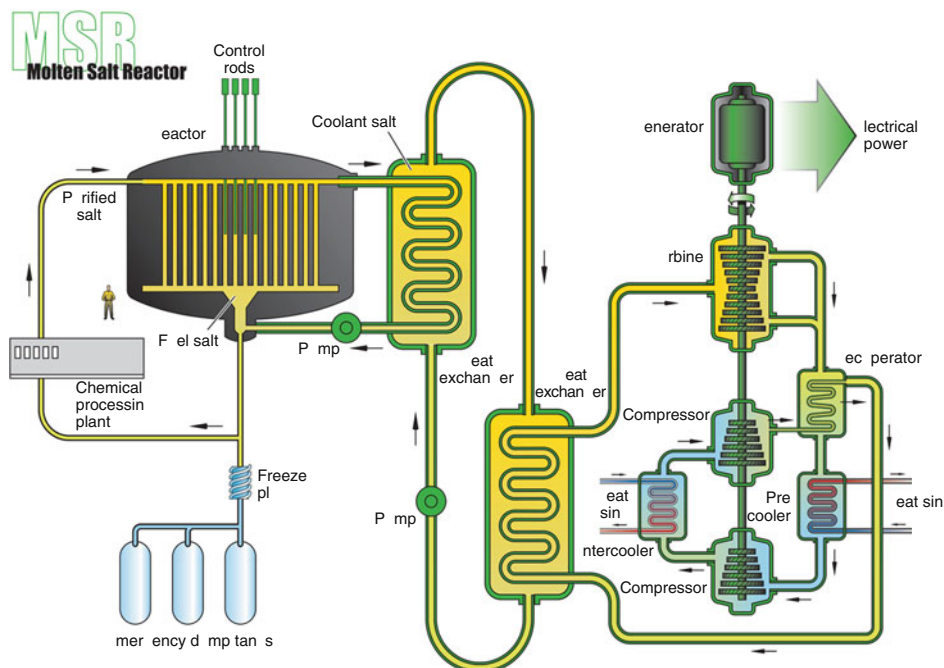
58.3.1 From Advanced Traditional Reactors to New Reactor Concepts

Nuclear power met the close of the twentieth century with accomplishments far more modest than those predicted. According to the projections of 1975, the industry was to build up its total installed capacity to a level of about 1,500 GWe by the end of the century, whereas the actual capacity came merely to 370 GWe (net). The output of the almost 50-year effort in thermo-nuclear fusion never reached the stage of practical use.

The trust in nuclear power safety was shaken by three major accidents at nuclear power plants: Windscale (UK, 1957), Three-Mile Island (USA, 1979), and Chernobyl (USSR, 1986). Public consciousness, which associated nuclear energy with the tragic experience of its military

Fig. 58.15

Molten-salt reactor (MSR) (U.S. DOE Nuclear Energy Research Advisory Committee and the Generation IV International Forum 2002)



application in 1945 against Japan, was more willing to accept myths about the consequences of these rare accidents than scientifically proved information about their actual impacts on life and environment. Nuclear energy uses remained practically confined to electricity production, with the district heating, high-grade heat generation, and transport left entirely to fossil fuels.

The concern about proliferation of nuclear weapons grew dramatically by the end of the century, while the monitoring functions of the IAEA are greatly complicated by the fact that the nuclear fuel enrichment technology is integral to its radiochemical reprocessing both for peaceful and military applications. The environmental requirements gained priority and cast doubt on the adequacy of technologies for treatment of nuclear materials (bituminization, cementation, and vitrification), which retain various levels of radioactivity after irradiation, considering the need for proving their efficiency over periods commensurable with geological epochs.

Wide practical application was found only by vessel-type (PWR, BWR) and pressure-tube (RBMK, CANDU) reactors. The gas-cooled graphite-moderated reactors, which gave rise to nuclear power in Europe (UK, France), are being phased out of operation. Among the wide range of alternative reactor concepts considered, few reactors passed the test of operation at pilot, demonstration, and semicommercial plants, including several fast neutron reactors (BN-350 and BN-600 in the former USSR, Phenix and Superphenix in France, Monju in Japan), as well as high-temperature reactors in Germany (AVR, THTR-300), Japan (HTTR), and the USA (Fort St. Vrain, Peach Bottom-1).

Nuclear power development was slowed down by discovery of new fossil fuel fields (mainly offshore deposits), appearance of new exploitation technologies, and introduction

of energy-saving measures, which decreased the energy demand growth rates, and was hampered by a significant rise in the capital costs of nuclear power plant construction. Further growth of nuclear power with traditional reactor systems will be unavoidably limited by the reserves of natural uranium, of which only 1% is actually used in energy generation by thermal neutron reactors.

Analysis of the realities observed at the turn of the century suggested the inevitability of predominant use of nuclear energy (from both fission and fusion) in resolving the problems of energy supply for sustainable development. Such countries as China and India are already demonstrating the priority of nuclear over other sources of electricity in their current national energy programs. A similar approach was taken in the Strategy of Nuclear Power Development in the Russian Federation, approved by the Russian Government in 2000. The attitude toward nuclear power is changing in the UK, Eastern Europe, and in the European Union as a whole. The US initiative on advanced reactor systems (Generation IV) and the resumed work on the closed fuel cycle, previously banned by law for nonproliferation reasons, are strong evidence of the USA returning to the nuclear option.

After a long period of decline, renewed interest in nuclear power development is observed, which manifests itself so far in resumed efforts to step up construction of nuclear plants, mostly with the well-proven PWRs and BWRs.

However, there is no avoiding the fact that the conditions for a new start of nuclear power are very much different from those of the industry's early days, considering primarily the requirements for safety, environmental quality, and proliferation resistance. Besides, assuming that nuclear energy will be used on a large scale, the industry can no longer afford using uranium reserves as inefficiently as thermal-neutron reactors do. In the USA, analysis of the situation formed after the three mile island nuclear power plant (USA) (TMI) accident led to the concept of "inherent safety" (Weinberg et al. 1985). In Russia, the concept of "natural safety" was developed, which applied both to the reactor design and to the nuclear fuel cycle (Orlov et al. 1992). Japan came up with the concept of "Self-Consistent Nuclear Energy System (SCNES)" (Fuji-ie 1992). It is for this reason that the nuclear community is considering both the earlier and the new reactor designs and fuel cycle concepts, provided they can meet the current requirements better than the existing plants will ever do.

Description of specific concepts will precede an overview of the position that nuclear power came to by the end of the twentieth century.

58.3.2 Fast Reactors with a Closed Fuel Cycle as a Basis of Large-Scale Nuclear Power

Thermal reactors developed for military purposes do not have enough neutrons to resolve the problems of fuel availability and safety on the industrial scale of power production.

Thermal reactors use less than 1% of uranium (^{235}U and a little of ^{238}U converted to Pu), wherefore suitable for this purpose are only the richest ores (currently estimated at ~ 17 Mt) with the metal content of $\sim 10^{-3}$ and up, whose reserves are much smaller than those of coal, oil, and gas. The safety problems of these reactors include reactivity variations with fuel burning, which are vastly larger than the delayed neutron fraction and thus pose the risk of a runaway (Chernobyl), accumulation of radioactive waste, as well as separation of U isotopes and separation of U from Pu during fuel reprocessing, which are potential proliferation hazards.

Fermi must have doubted the potential of thermal reactors for future energy production as he proposed a fast reactor (FR) for this purpose (Fermi 1944) – a reactor with a large excess of neutrons over the amount required for maintaining a chain reaction. Neutron excess (NE) is the key physical resource for dealing with the problems of fuel and, as is apparent now, of safety, given an adequate choice of technological tools:

$$NE = \frac{v_{\text{fis}} - 1 - \alpha + f(v_{\text{fer}} - 1)}{1 + \alpha} \quad (58.1)$$

where v_{fis} , v_{fer} – number of neutrons per fission of a fissile and a fertile nucleus, respectively; α – losses due to radiative absorption by a fissile nucleus; f – contribution from threshold fission of a fertile nucleus.

The breeding ratio (BR) of fissile nuclei (Pu , ^{233}U) from fertile nuclei (^{238}U , ^{232}Th) appears as $BR = NE - A$, with A standing for losses through absorption in structural components and fission products, and through leakage.

With NE in fast reactors reaching 2.3 as against ~ 1 in thermal reactors (1.2 in the ^{232}Th – ^{233}U cycle), it is easy to attain full reproduction ($BR \approx 1$) and even breeding ($BR > 1$) of fissile ^{239}Pu or ^{233}U , with U (Th) used up completely. If such is the case, lean ores are also usable, even if it is hundreds of times more expensive to mine them. Reactivity varies little in an equilibrium operation mode ($BR \approx 1$) where actinides (except for ^{238}U) come to equilibrium rather than accumulate, while separation of Pu from U is ruled out, and so will be U isotope separation in due time.

Use of cheap and inexhaustible U and Th fuel, whose calorific value is 3 million times greater than that of coal, may open a new era in human history. With the average U and Th content in the Earth crust estimated at 4×10^{-6} t and 10^{-5} t, respectively, their reserves of $\sim 10^{14}$ t in the strata down to 2 km are so great that even a thousandth part of them will last for millions of years.

As early as 1951, first nuclear electricity was produced at the experimental fast reactor EBR-I, but both this reactor and the E. Fermi Plant suffered accidents in the 1960s, and in the 1980s the USA stopped the construction of fast reactors and the work on a closed fuel cycle for nonproliferation reasons.

In the USSR, A.I. Leipunsky came to the idea of fast reactors in 1949, and took the lead in development of such machines. In the 1970s, the BN-350 was built, which operated for 25 years, followed by the BN-600, which is still in service.

Power plants with fast reactors were also constructed in France and the UK but saw no further development in either country mostly for the reason that those reactors proved to cost much more than their thermal counterparts. The closed fuel cycle (CFC) of nuclear power plants with fast reactors was never brought into practice. So, nuclear power based on fast reactors failed to evolve into a common business in the market of energy and investments. As regards fuel, including the problems of radioactive waste and nonproliferation, even with thermal reactors nuclear power is still unable to take over any significant part of global energy production. Its share of $\sim 7\%$ in terms of fuel (16% of electricity) has little effect on the growing consumption of fossil fuel and CO_2 emissions on the planet.

The idea of developing nuclear power based on fast reactors met with no success in the twentieth century. The industry, which started with thermal reactors of military origin in the 1950s, declined into stagnation, despite a steep rise in fossil fuel prices, as early as the 1970s in the USA and in the 1980s, after the Chernobyl accident, in Russia and Europe.

The third oil crisis in the past 30 years reawakened interest in building power plants with thermal reactors in a number of countries. Nuclear power has long grown from a sphere of science into that of engineering and industry, pragmatically focusing today on building nuclear plants with thermal reactors, their improvement, and marketing. For this reason, it appears necessary to recur to the original concept of nuclear power based on fast reactors, to analyze the reasons for the failure of the earlier efforts, and to correct the mistakes made.

Pragmatism prevailed over all other considerations in nuclear power engineering during the decades of the industry's efforts to survive. The first attempt to revise in a radical way the traditional nuclear engineering approaches after the Three-Mile-Island accident was made by a well-known American physicist A. Weinberg in his book "The Second Nuclear Era. A new start for nuclear power" (Weinberg et al. 1985). His principles of "inherent safety" were rather oddly taken by the engineering community: all the operating nuclear power plants (NPPs) were claimed to comply with such principles. Having found its way into the Nuclear Regulatory Commission (NRC) regulations, the requirement of "inherent safety" led to further increase of capital costs associated with provision of additional safety barriers in new US reactor designs. After the Chernobyl accident, Russian physicists led by V. Orlov developed the "natural safety" approach, which has much in common with Weinberg's principles. Both concepts require that high safety should not be sought by designing more and more complicated engineered features or by increasing their number but should rely on the fullest possible use of the laws of nature (hence the new concept is referred to as "natural safety"). On the other hand, there is a significant difference between the two approaches, which makes it impossible to reconcile the old engineering solutions with the new concept. As applied to nuclear reactors, *this concept does away with classification of accidents into design-basis and beyond-design-basis events and may not be extended to a design (or an operating plant) where an accident requiring local public evacuation is possible*. As regards the fuel cycle, the *concept of natural safety calls for radiation-equivalent management of nuclear materials, for elimination of the technologies posing the greatest proliferation hazards (isotope separation and enrichment, reprocessing of irradiated fuel with extraction of weapons-grade plutonium), and provides for substantial reduction of nuclear material transportation*, especially long-distance hauls. It is worth noting that there is much in common between the concept of "natural safety" (Russian approach, Orlov et al. 1992) and the idea of "harmonization with nature," which is central to the Japanese concept of "Self-Consistent Nuclear Energy System, SCNES" (Fuji-je 1992, 2005).

Fermi created the first thermal reactor, but it was not this reactor type that he proposed for power production (this was done later by "pragmatists"). His idea was a fast reactor with high NE and $BR > 1$, which would open the way for a new power industry consisting of inexpensive nuclear plants using cheap and inexhaustible fuel. The first nuclear power plants were but little more expensive than conventional ones, but their cost grew fourfold in the 1970s due to the safety requirements introduced by the NRC, and the US companies stopped building new nuclear plants. Later, the TMI and Chernobyl accidents happened and the general public, who had been apprehensive of nuclear energy since the first use of nuclear weapons, was turned strongly against nuclear power.

Having certain doubts about nuclear power (with its huge radioactivity and production of "nuclear explosives") and seeing no good way to ensure safety, Fermi suggested that Argonne National Laboratory (ANL) should develop the fast reactor concept so that the first reactors of this type would be started on Pu from natural uranium-fueled thermal reactors, with the ones to follow them relying on the surplus Pu (given $BR > 1$) for their first cores. He did think about

enriched uranium, too, but his conclusion – with the Oak Ridge facility yet to be built – was that nuclear power would be better off without energy-intensive U isotope separation (i.e., diffusion method used at that time in the USA).

It was not until the 1980s that the main reason for the failure of the earlier effort to create fast reactor plants became clear. It lies in the very concept of a fast breeder reactor with $BR > 1$ and using plutonium from irradiated fuel of thermal reactors for the first cores. In fact, the uranium consumption and the separation work required for starting up fast reactors on enriched uranium are much smaller than in the case of using plutonium from thermal reactors for the same purpose. Hence, it is possible to give up high rates of Pu breeding, while the “excessive” neutrons may be used for and the design effort aimed at bringing out and employing the natural safety qualities of fast reactors, including waste management and proliferation resistance, with the cost of nuclear plants reduced.

To correct the mistakes made in the past and to move toward large-scale nuclear power with fast reactors as its basic component it is essential to give up the fast breeder reactor in favor of a “naturally safe” fast reactor of pool-type configuration, with high-density fuel of equilibrium composition ($BR \approx 1$), moderate power density, and heat removal by noncombustible high-boiling coolant, providing transmutation of minor actinides, and having an on-site closed fuel cycle.

Within the next 2 decades, when mostly thermal reactors will be built in the world, it is necessary to develop and bring in new fast reactors of natural safety with a closed fuel cycle, which can pave the way for large-scale nuclear power in the twenty-first century.

58.3.2.1 Fast Reactor of Natural Safety

Having created the first thermal reactor, Fermi came up with the idea of a fast reactor with a large neutron excess and $BR > 1$, which held the promise of large-scale energy production at inexpensive nuclear plants using inexhaustible fuel.

In elaborating this idea of Fermi's, specialists of the ANL (USA) chose metallic fuel and lightweight sodium as coolant (Na–K in the EBR-I reactor). In the USSR, Leipunsky considered Pb–Bi and gas but decided on Na (Pb–Bi found its first application in reactors of nuclear submarines in the 1950s.) As regards fuel, he gave preference to heat-resistant ceramics.

Starting with the BR-5 reactor (PuO₂ fuel, Na-coolant, 1959, USSR), fast reactors have run on oxide fuel, proven already in thermal-neutron machines (Shippingport NPP, USA, 1957). But high-density, heat-conducting ceramics were much better for such reactors from the viewpoint of attaining, among other things, the in-core Pu breeding ratio of ~ 1 (with fuel operation in equilibrium), which is why, beginning in 1965, the BR-5(10) used U monocarbide and, later (in 1983), mononitride fuel. The subsequent BN-350 and BN-600 reactors relied on enriched UO₂, as construction of a plant for fabrication of mixed U–Pu fuel, including its nitride and metallic varieties, had been stopped.

Plutonium extraction by organic agents from aqueous solutions of irradiated U was first practiced for weapons production and was later applied for reprocessing of NPP fuel. It was clear, though, that the aqueous process, requiring long fuel cooling, would add vastly to the duration of the closed fuel cycle and to the consumption of Pu in starting up a fast reactor; it reduces drastically the breeding rates and leads to safety problems in transportation of fissile and radioactive materials to the remote reprocessing facility. Therefore, in the 1960s, efforts were undertaken in the USA (Idaho) and in Russia (NIAR, Dimitrovgrad) to study “dry”

reprocessing of fast reactor fuel on the nuclear plant sites. Such processes never came into industrial practice as the fast reactor development program was terminated.

By the 1980s, Russia had nuclear submarines with reactors cooled by Pb–Bi eutectic and work was in progress to develop a concept of naturally safe fast reactors that could have the features studied since the 1950s–1960s but not applied in the early fast reactors, such as,

- Nitride fuel with $BR \approx 1$, no uranium blanket, small reactivity variations with fuel burning (optimal $BR \approx 1.05$), fuel composition designed to require no U, and Pu separation in reprocessing (merely addition of ^{238}U)
- “Dry” electrochemical reprocessing of irradiated fuel on the NPP site after relatively short cooling, a factor of ~ 3 smaller consumption of Pu (or enriched U) for reactor startup, and radical reduction of fresh and irradiated fuel transportation
- Moderate power density, Pb coolant instead of combustible Na with its small boiling margin, a widely spaced fuel lattice instead of the close-packed one chosen for the moderating Na, Pb temperature gain reduction, and increase in its temperature at the core inlet upward of 400°C with a margin to Pb melting, no fuel assembly shrouds (as in PWR with a widely spaced lattice)
- Austenitic steels replaced by the ferritic–martensitic steels practically proven in nuclear submarines, low-swelling, and resistant to lead action

This made it possible for Russia to initiate development (Adamov and Orlov 1992) of a fast reactor named lead-cooled fast reactor of natural safety (BREST), i.e., a pilot 300 MWe reactor (for trying out, e.g., equilibrium operation) and the first-of-the-kind 1,200 MWe power unit, with the R&D effort to support it, aimed at demonstration of the new fast reactor and its closed fuel cycle within the normal period of ~ 20 years.

Deterministic exclusion (assured negligible probability) of the most dangerous accidents involving prompt criticality excursion, loss of cooling, fires and explosions with catastrophic radioactive releases, upsetting of the natural radioactivity level in radioactive waste disposal, together with exclusion of U and Pu separation in reprocessing and – later, gradually – of U isotope separation – all add up to make the safety of nuclear power convincing and to simplify the “defense in depth” (against residual risks).

Changeover from chemical to physical treatment to remove fission products from fuel (based on mass difference and using plasma) will render illicit Pu extraction impossible, which will make this technology eligible for transfer to the countries that seek to develop their own nuclear power for self-sufficiency in energy supply. This will allow attaining the long-declared objective of the “universal and total ban and elimination of nuclear weapons.” It is at this point that the world community will be entitled and able to stop any secret Pu extraction from irradiated fuel in places other than those legally established. If they see prospects for independent development of their national nuclear power based on fast reactors, certain countries may accept for the time being the services of nuclear states or of international centers for uranium enrichment, reprocessing of thermal-reactor fuel, and fabrication of the first cores of fast reactors.

Technical and political palliatives do restrain but have failed to prevent the propagation of nuclear weapons. If consistently implemented for nuclear reactors and, especially, for the fuel cycle, the concept of natural safety can technologically strengthen the non-proliferation regime under the conditions of a large-scale nuclear power industry in the twenty-first century (Adamov et al. 1995).

58.3.2.2 Choice of Coolant and Fuel for Fast Reactors in Large-Scale Nuclear Power

Selection of Coolant

Analysis of the characteristics of liquid-metal coolants, such as sodium (Na), lead (Pb) and lead-bismuth eutectic (Pb-Bi), makes it possible to decide on the coolant for the new fast reactor considered as a basic component of large-scale nuclear power, which will be capable of taking over the greater part of the electricity generation increase and, possibly, of providing for other energy-intensive processes.

In safety terms, the noncombustible, high-boiling ($T_{\text{boil}} \approx 1,750^{\circ}\text{C}$) and only slightly activated Pb has obvious advantages over the flammable, low-boiling ($T_{\text{boil}} \approx 890^{\circ}\text{C}$), and easily activated Na. The lower melting temperature of Na, and of Pb-Bi as a matter of fact, offers no preference over Pb as both these coolants necessitate external heating prior to the initial startup of the reactor. It will take relatively short operation at full power to have the decay heat high enough to keep both sodium and lead liquid when the reactor is shut down. Neither expensive engineered features are required for sealing the Pb coolant circuit, as distinct from sodium-cooled reactors (SFRs), nor are safeguard vessels, nor additional (intermediate) circuits, nor fast-acting cutoff devices, which are used for mitigating the consequences of Na leaks and of its contacts with air and water leading to fires and radioactive releases. Moreover, the above advantages promise a higher economic efficiency of the lead-cooled fast reactor (LFR).

Neutron moderation in Pb, with its high atomic weight, is much less than in lightweight Na, while absorption is equally low. Therefore, in contrast to Na, a larger Pb fraction in the core owing to greater fuel lattice pitch will cause practically neither softening of the neutron spectrum nor decrease of the core breeding ratio (CBR), i.e., the ratio between Pu generation in capture of fertile ^{238}U neutrons, and its fission rate. Given $\text{CBR} \approx 1$, Pu breeding fully makes up for its burnup in the core, which is important in regard to both safety (small reactivity margin) and self-supply of fuel. Small reactivity variations with fuel burning in the LFR as compared to other reactors, with $\text{CBR} < 1$, allow a considerable increase in the time of reactor operation without refueling or rearrangement of fuel assemblies (FA). In this case, the fuel lifetime is limited not so much by the reactivity margin as by the service life of fuel rods and assemblies and other structural components of the LFR, which depends on the irradiation, corrosion, and other processes affecting their integrity and performance.

With a wider-spaced fuel lattice in the LFR it is possible to increase the coolant flow area and to reduce its velocity. As a result, the hydraulic resistance and the pumping power requirements in the LFR are a factor of 3–5 smaller than in the SFR. The lead coolant temperature gain reduced down to $100\text{--}120^{\circ}\text{C}$ allows raising its temperature at the core inlet to $400\text{--}420^{\circ}\text{C}$ and providing a sufficient margin to its crystallization point ($T_{\text{cryst}} = 327^{\circ}\text{C}$). Even so, the fuel cladding temperature in the “hot spot” will not exceed 650°C , whereas in the sodium-cooled reactors it is higher than 700°C .

A decrease in the Na density and a drop of its level in the core cause reactivity and power growth, and Na boiling may lead to a quick criticality excursion with possible fuel failure and release of radioactivity. In the case of lead, such an accident is impossible due to the high temperature of Pb boiling, which exceeds the temperature of core failure. Besides, when the core is surrounded by a lead reflector, whose level depends on that in the core, its leaks and the core uncovering result in increase of neutron leakage, input of negative reactivity, and shutdown of the reactor (Adamov et al. 1997).

As compared with Pb, Na has better mass heat capacity and heat conduction, permitting removal of heat fluxes at high unit power of the reactor, which is essential for high rates of fuel burning and Pu production. These advantages dictated the priority of the sodium-cooled fast reactor in the 1950s, when ambitious plans were made for nuclear power development – in the absence of Pu and with insufficiently explored uranium reserves – and a short Pu doubling time was regarded as the most important characteristic of fast reactors providing for the growth of nuclear generating capacities. Today, however, considering the great Pu quantities (2,300–2,500 t) accumulated in the “spent” (or, more correctly, irradiated) fuel of thermal reactors, this purpose is no longer on the agenda. Besides, in order to reduce positive density and void effects of reactivity in a high-power sodium-cooled fast reactor, the designers had to resort to considerable flattening of the core, where it is difficult to provide $\text{CBR} \approx 1$. As a result, for self-supply of Pu alone, a perceptible part of it was to be produced in a uranium blanket, with its resulting quality making it fit for nuclear weapons – in contradiction to the nonproliferation requirement.

Failure of the sodium coolant circuit and its long exposure to the atmosphere lead to a fire and, consequently, to a 24-h release of $\sim 10^5$ Ci accounted for by ^{24}Na alone. Further Na burning will cause cooling interruption and fuel melting with release of $\sim 10^7$ – 10^8 Ci, depending on the reactor power level and the time of fuel irradiation. Such an accident is classed as Level 7 of the International nuclear event scale (INES) and involves inevitable evacuation of the local residents with prolonged isolation of the territory (ISTC 2001; Orlov et al. 2003).

Although the SFR operation record and the design experience show such reactors to meet the current safety requirements, there is still a risk of an accident with Na burning or boiling and with large radioactive releases. Moreover, the probability of such an accident and the safety costs will grow with the increase in the scale of the nuclear power industry based on these reactors.

The main problems with Pb today are the needs for improving the coolant technology and testing the chosen structural steels for corrosion resistance in lead at its operating temperatures, which has been largely done already on test facilities with a positive outcome both for the core and for the coolant circuit materials. As in the case of Pb–Bi eutectic used in reactors of nuclear submarines, corrosion resistance is sustained by control of oxygen concentration, kept within a fairly narrow range. At the same time, it is important to note that though considerable upward or downward departures from the nominal oxygen regime are possible during operation for hundreds of hours, they will not result in dangerous corrosion intensification. Nevertheless, the problem of maintaining the required oxygen concentration throughout the lead circuit and the problem of damage to oxide films under thermal and radiation impacts, call for further tests under conditions brought as close as possible to the operating ones.

An advantage of the Pb–Bi eutectic over Pb is its lower crystallization temperature of 125°C , which allows operation in a lower temperature range, where the corrosion problems of structural materials may be fairly easily solved (and, in fact, have been solved already). The Pb–Bi eutectic was considered as a coolant option for fast reactors back in the 1950s, but preference was given to Na, mainly for the reason of its better thermal properties. Pb–Bi was used for cooling ships’ reactors, and Russia – as the only country to have operated such facilities – has unique technologies for working with this coolant.

The problems of structural material corrosion and slagging in Pb–Bi were resolved by choosing an appropriate oxygen regime, as well as by monitoring and maintaining the coolant quality. The main objective today is to demonstrate the possibility of increasing the operating coolant temperatures for the selected structural materials, which is necessary for the future reactors.

The current high price of Bi and its very limited prospected resources are prohibitive for building large-scale nuclear power on reactors with Pb–Bi coolant. The total capacity of a nuclear power industry using mostly such reactors and relying on the explored, estimated, and economically acceptable global reserves of Bi would not be more than 50–70 GWe. For operation of Pb–Bi-cooled reactors, it is necessary to solve the problem of α -active ^{210}Po in their maintenance and repairs. Moreover, ^{210}Po brings about the risk of large radioactive releases in the event of the circuit failure due to, e.g., an act of sabotage. If the reactor vessel head were opened while Pb–Bi is still in the liquid form, the 24-h release of ^{210}Po would come to $\sim 6 \times 10^4$ Ci, which, considering the radiation (biological) hazard of ^{210}Po , is commensurable with the radiological consequences of an accident involving Na burning (Tupper et al. 1991; Orlov et al. 2003).

Considering that the lead-cooled fast reactor will show its chief merits at the power level of at least 300 MWe, Pb–Bi is being considered for cooling self-contained transportable small modular reactor facilities designed to serve as power sources in remote and hard-to-reach regions. The reactor core protection preventing access to fuel, the CBR of ~ 1 , which allows refueling-free operation with a small reactivity margin for as long as ~ 20 – 30 years, the thermal parameters making Pb–Bi fit for natural circulation, all are significant advantages from the viewpoint of proliferation resistance and safety. Besides, cooling by natural circulation of Pb–Bi offers a good possibility of simplifying the coolant circuit design, which may facilitate building such reactors in developing countries.

The natural occurrence of Pb is ~ 200 times as great as that of Bi, its explored recoverable reserves and global production ($\sim 2 \times 10^8$ t and $\sim 3 \times 10^6$ t per year, respectively) are $\sim 1,000$ times larger, while the price is a factor of 3–7 lower. Besides, the specific radioactivity of Pb–Bi coolant caused by its activation, though largely providing the radiation safety of the reactor, is $\sim 1,000$ times as high as that of Pb coolant, and the corrosivity of Pb–Bi is also higher in the operating temperature range of (~ 400 – 600°C) of lead.

Thus, comparison between Na, Pb, and Pb–Bi as candidate liquid–metal coolants shows Pb to be the best option for the fast reactors that are considered as a possible basic component of the future large-scale nuclear power industry.

Selection of Fuel

After successful use of PuO_2 in the first core of the BR-5 reactor in Russia, oxide fuel found application in the fast power reactors (BN-350, BN-600). However, it was clear in the late 1950s already that fuel of higher density and heat conduction has a number of advantages in a fast reactor. These advantages include smaller critical inventory and higher CBR; lower operating temperatures of the fuel and its larger melting margin; smaller release of fission gas from fuel, its smaller pressure on the fuel cladding; higher reliability of fuel rods; and, finally, smaller amounts of thermal energy accumulated in fuel, which may be released in an accident with loss-of-coolant circulation and result in its boiling with possible vapor explosion. For this reason, beginning in the 1960s, carbide and nitride fuels were studied, using them as the main fuel in several charges of the BR-5 reactor and later of the BR-10 reactor.

In the USA, even the first fast reactors, EBR-1 and EBR-2, ran on metallic fuel, i.e., U–Pu–Zr alloy and, with the experience gained, it was intended to use this fuel in the IFR – a fast power reactor with a closed fuel cycle (Wade and Chang 1988).

Admittedly, the experience of using the advanced fuels in fast reactors is by far less substantial than that obtained in operation of oxide fuel. Nevertheless, for all the importance of the previous experience and the maturity of the technology, choice of fuel for the innovative fast reactor of the future large nuclear power will be dictated by the requirements of high safety and economic efficiency.

If oxide fuel is used, its low density will make it possible to attain $\text{CBR} \approx 1$ only with relatively high power and large dimensions of the reactor core, or with very low power densities. Low heat conduction of oxides leads to high operating temperatures, small fuel melting margins, poor confinement of gaseous and volatile fission products in the fuel matrix, and high power effect of reactivity ($\Delta\rho_N \gg \beta_{\text{eff}}$); it also requires fuel rods of a small diameter, which adds to their fabrication costs.

The disadvantages of metallic fuel are its considerable swelling in burning, which calls for high alloying and porosity, and the existence of phase transitions at temperatures as low as those approaching the operating temperatures of lead. Phase transitions of metallic fuel and, especially, its interaction with steel claddings with formation of easily melted eutectic (510°C for Pu, 710°C for U, and 750°C for U + 15%Pu + 10%Zr), are responsible for small margins to fuel failure in accidents with temperature growth. Lead reacts with metallic fuel to form U and Pu plumbates.

With the priority given to reliable fuel operation in the reactor, to confinement of radioactive products, and to prevention of fuel failure in accidents, two types of fuel, i.e., carbides and nitrides, were considered for the concept of lead-cooled fast reactors. Both types have high density and heat conduction, they are both resistant to thermal decomposition, show little swelling at moderate operating temperatures and good confinement of fission gas. This – given a gas plenum in fuel rods for collection of fission products and a small heat-conducting gap between fuel and cladding – makes it possible to reduce significantly stresses in the claddings and the risk of their failure. The properties of high-density and heat-conducting fuel combined with those of lead coolant ensure full Pu reproduction in the core and a small magnitude of the power effect of reactivity, which allows operation with the total reactivity margin as small as $\sim 1 \beta_{\text{eff}}$, excluding accidents with prompt criticality excursion in case of inadvertent input of positive reactivity caused, e.g., by spontaneous withdrawal of Control and protection system (CPS) rods (ISTC 2001).

The choice of mononitride fuel for fast reactors was dictated by its certain, if small, advantages over carbides from the viewpoint of density, swelling, and confinement of fission gas. An important factor in the final decision made in favor of mononitrides was the higher pyrophorosity of monocarbide, which causes problems in fuel fabrication and handling of irradiated fuel with failed claddings (Rogozkin et al. 2003).

It should be noted, though, that mononitride fuel shows considerable parasitic absorption of neutrons in the $^{14}\text{N}(\text{n,p})^{14}\text{C}$ reaction, which results in an impaired neutron balance and in formation of environmentally hazardous ^{14}C . However, it is possible to overcome this drawback by using nitrogen enriched with ^{15}N in the future, as well as by catching carbon and fixing it in stable chemical compounds during fuel reprocessing. A later changeover to mononitride with enriched nitrogen having low neutron absorption and moderation, allows counting on a perceptible economic gain owing to a reduced mass of fuel inventory despite the high cost of ^{15}N (ISTC 2001).

58.3.2.3 Lead-Cooled Fast Reactor with an On-Site Fuel Cycle

The concept of an innovative fast reactor with lead coolant and nitride fuel, under development at present, implies that beyond-design-basis accidents should be excluded through consistent implementation of the principles of natural safety, i.e., by using the natural properties of a fast reactor, of its high-boiling coolant chemically passive in contact with air and water, and of the high-density, heat-conducting fuel, which allow operation of the reactor with a small reactivity margin commensurable with $1 \beta_{\text{eff}}$. Losses of coolant are prevented by the pool-type reactor design and its boiling, by passive removal of decay heat.

This concept is essentially different from the concepts of the reactors currently in operation and under development in its radically new approach to safety. Instead of addition of expensive engineered features and systems, safety relies mostly on fundamental natural behavior patterns and processes, feedbacks, physical and chemical properties inherent in a fast reactor, its fuel, coolant, and other components. Also important in this respect are the design solutions that allow using to the utmost the natural safety properties.

However, there is no identifying natural safety with absolute safety, which means that all possible accidents are ruled out. Natural safety implies exclusion of accidents with large radioactive releases requiring evacuation of the local people. Technical accidents involving failure or breakdown of systems and components may still happen but their radiological consequences, if any, will never be dangerous. They can lead, though, to a prolonged shutdown but are, in any case, limited to losses no greater than the cost of the plant. Such accidents are events of economic significance, and protection against them should be provided – as for other dangerous facilities – by defense in depth, while the ensuing economic losses may be taken care of by appropriate allocations for insurance.

It will not be a great exaggeration to say that the high cost of present-day NPPs is largely a price paid for their safety, and the safety requirements will inevitably get bigger because the probability of accidents will rise with growth of the nuclear power scale. With the principle of natural safety put into effect, it will be possible to reconcile the usually conflicting requirements for NPP safety and economic efficiency. The level of insurance costs for facilities of natural safety will be by far lower than that for, e.g., contemporary NPPs, where allowance is made for the losses associated with possible public evacuation, damage to human health, and isolation of contaminated land areas (ISTC 2001; Adamov and Orlov 1997).

For the properties of natural safety to be fully and consistently implemented, it is not only nitride fuel and lead coolant but also certain other options that should be translated into the reactor design, such as:

- Fuel inventory that should be made up so as to provide a small (comparable to $1 \beta_{\text{eff}}$) total reactivity margin due to compensation of burnup of fissile nuclides by their full reproduction (the optimal CBR being roughly equal to 1.05) and owing to the small power effect of reactivity.
- Widely spaced fuel lattice with a large coolant flow area – for reducing its velocity to 2 m/s and the hydraulic losses, to 0.10–0.15 MPa, as well as for increasing the amount of heat removed by natural circulation.
- Highly heat-conducting fuel rods – for reducing the maximum operating fuel temperature to $T < 1,000^\circ\text{C}$, which provides a small (less than 7%) fission gas release from fuel and its low pressure on claddings, as well as a relatively small amount of thermal energy in fuel.

- Fuel claddings made of ferritic–martensitic chromium steel which will show radiation and corrosion resistance in liquid lead.
- Absence of uranium blankets, replaced by lead reflector with a better albedo, which improves the power distribution, provides for negative void and density effects of reactivity, and rules out production of weapons-grade plutonium.
- Coolant flow rate feedback to power, provided passively by lead columns in special channels adjacent to the core, where the lead level varies with the flow rate, hence changing neutron leakage.
- Reactor shutdown in the event of loss of forced circulation or abnormally high coolant temperature at the core outlet, produced by insertion of absorber rods of passive threshold action.
- Passive and unlimited in time removal of residual heat directly from the lead circuit by natural circulation of air through air-cooled heat exchangers, with the heated air vented to the atmosphere.
- Lead coolant circuit of high heat capacity, capable of accumulating heat during accidents and transients without a perceptible increase in the temperature of the core and safety-related circuit components.
- Coolant circulation pattern, which prevents steam (in case of steam generator leakage) and gas bubbles from getting into the core and ensures inertial coolant flow in the event of pumps' trip.

The characteristics of a lead-cooled fast reactor and of its closed fuel cycle (CFC) allow operation with fuel of equilibrium composition. This mode of operation features full reproduction of fissile nuclides in the core ($\text{CBR} \approx 1$), irradiated fuel reprocessing in the closed fuel cycle, refabrication of fuel and its return to the reactor, with the reprocessing limited to removal of fission products without separating Pu and minor actinides (MA) from the mix (U–Pu–MA). Plutonium and minor actinides have practically the same mass and isotopic composition in the loaded (fresh) and unloaded (irradiated) fuel. In the long run, it is only ^{238}U that burns out, whose loss is made up for by depleted U during fuel fabrication. Ideally, operation in the equilibrium fuel mode implies roughly equal reactivity margins at the beginning and at the end of the refueling interval, referred to as the cycle, with allowance made for all the processes – fuel burning and swelling, cladding corrosion, deformation of fuel rods and fuel assemblies, etc. – that accompany the reactor operation.

The fuel type considered for the first core of the fast reactor is nitride of depleted U mixed with Pu and MA, whose composition corresponds to that of PWR's irradiated fuel after its reprocessing and subsequent cooling for ~ 20 years.

The reactor is planned to operate in cycles, which are equal to the time between periodical fuel replacements. At the end of the first and second cycles, additional fuel with the composition similar to that of the first core will be loaded into the reactor. The fuel assemblies retrieved from the core at the end of each irradiation cycle are placed in the in-pile storage, where they will be cooled for the duration of the next cycle, to be then sent to the CFC facilities for reprocessing. The time of irradiated fuel reprocessing and of new fuel fabrication is also equal to the cycle duration. Thus, as early as the beginning of the fourth cycle, the core will receive fuel assemblies containing its own reprocessed fuel, which was unloaded after its irradiation during the first cycle. If the cycle duration is assumed to be 1 year and the fuel lifetime, 5 years, by the beginning of the eighth cycle (after ~ 7 years) the reactor will be loaded only with its own irradiated and reprocessed fuel and will start operating in an equilibrium fuel mode.

An example of an innovative lead-cooled fast reactor of natural safety is the pilot 300 MWe reactor BREST-OD-300, which is being developed in Russia (ISTC 2001; Adamov et al. 1997).

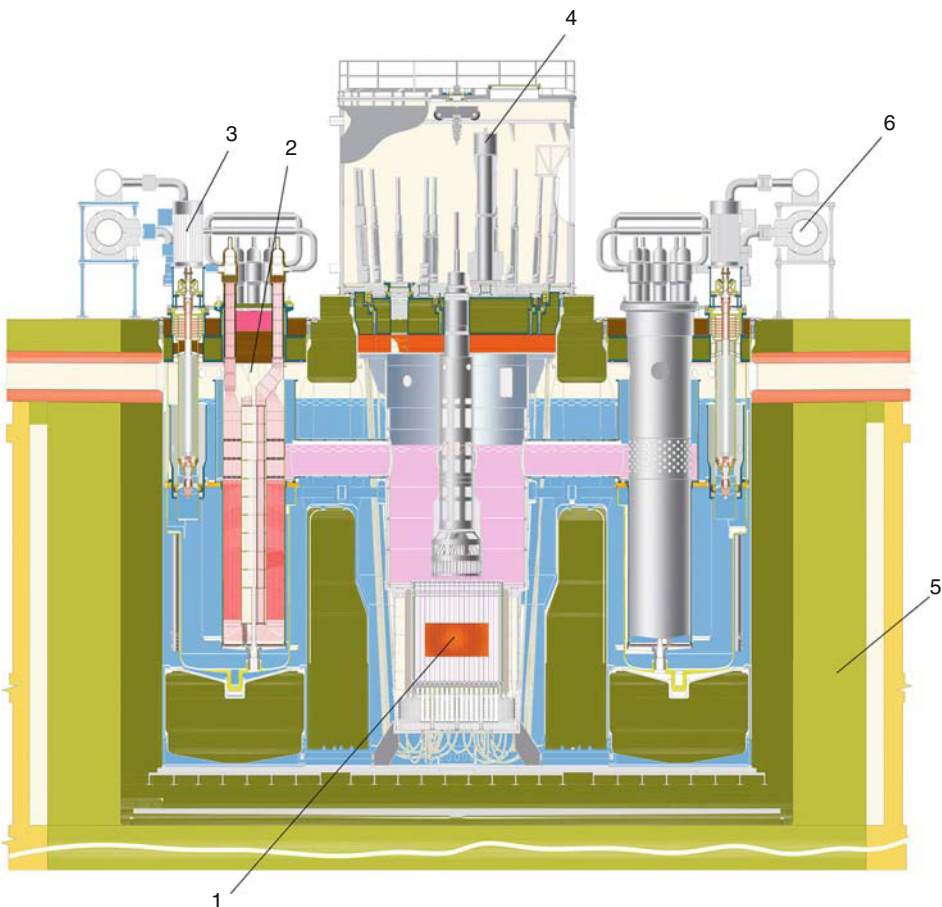
Use of the chemically inert and high-boiling lead coolant allows giving up the three-circuit arrangement of heat removal in favor of a two-circuit system.

The reactor facility of pool design, which incorporates the core with reflectors and control rods, the lead coolant circulation circuit with steam generators, pumps, equipment of the fuel reloading system, as well as safety and auxiliary systems, is arranged in a steel-lined thermally insulated concrete vault (► Fig. 58.16). The concrete temperature is maintained within the permissible limits by natural circulation of air.

Lead circulation in the core and steam generators is provided by a difference in the “cold” and “hot” coolant levels produced by the pumps rather than by the pressure set up by them. There will be no variation of the lead flow in the steam generators if one or several pumps should stop, and

■ Fig. 58.16

BREST-OD-300 reactor: 1 – reactor core; 2 – steam generator; 3 – pump; 4 – reloading machine; 5 – reactor vault; 6 – cooling system



inertial flow will be provided in the event of a quick pump trip owing to leveling of the coolant surfaces. To mitigate the consequences of possible breaks in the steam generator tubes, the primary circuit is designed to have an integral loop configuration, with the steam generators and the main circulation pumps placed outside the reactor vessel. Such a configuration together with the arrangement of lead circulation and steam venting from the reactor vault via hydraulic locks into the confinement system and then on through filters to the atmosphere, prevents any dangerous ingress of steam into the core and overpressure of the reactor vault.

The low pressure in the concrete vault of the reactor and the relatively high temperature of lead freezing, which contributes to self-healing of possible cracks in the concrete, rule out the possibility of large lead leakage, loss of cooling, and fuel melting.

Fuel assemblies (FA) and reflector blocks are reloaded with the aid of rotary plugs, using the in-pile reloading machine and a set of mechanisms for out-of-pile handling.

The reactor core is built of fuel assemblies with the same fuel composition and fuel rod pitch. Radial equalization of the FA power and the coolant temperature gains relies on profiling of the fuel inventory and lead flow, with the former provided by using fuel rods of a smaller diameter in the central assemblies and those of a larger diameter in the peripheral ones. The equalized distributions are kept stable owing to the same fuel composition in all assemblies, subject to the condition of $\text{CBR} \approx 1$.

Considering the small reactivity margin, some control elements are arranged around the core, which operate by changing neutron leakage. In the same space lead-filled channels are located, which passively provide feedbacks from the coolant flow in the core to the reactivity and reactor power.

The central tubes of fuel assemblies located in the middle of the core accommodate hydraulically driven absorber rods made of WB_2 sinking in lead. These rods serve the purpose of reactivity compensation and also perform the function of the reactor safety system, which operates passively in the event of coolant flow interruption or increase of its temperature at the core outlet.

The natural properties of lead coolant and mononitride fuel and the neutronic characteristics of the fast reactor combined with the design of the core and cooling circuits raise the BREST reactor to a radically different level of safety and provide for its stable behavior without involving active safety features in the severe accidents unmanageable in any one of the existing reactors, such as:

- Spontaneous withdrawal of control rods.
- Trip of all pumps in the primary (lead) circuit.
- Trip of all pumps in the secondary circuit.
- Reactor vessel failure.
- Breaks of the secondary circuit pipelines.
- Total loss of power, with cooling required for unlimited time, etc.

Even in the most severe accident with coolant circuit failure and direct contact of lead with the atmosphere, the ensuing toxic and radioactive releases would correspond merely to Level 5 on the international scale of events at NPPs (INES), which is an accident dangerous for the environment but not requiring evacuation of the local population (ISTC 2001; Orlov et al. 2003).

With the fast reactor operating in a closed fuel cycle, the fuel quantity running through the cycle is largely determined by the duration of the external (to the reactor) part of the CFC. Therefore, in order to reduce the time and costs required for cooling of irradiated fuel and for

transportation of irradiated and reprocessed fuel, as well as for providing trouble-free operation, radiation safety and proliferation resistance, the external part of the BREST-OD-300 fuel cycle should be arranged on the power plant site (► Fig. 58.17). Besides the reactor facility, the turbine hall and all the NPP structures, the site is expected to accommodate the facilities for fuel reprocessing and for fabrication of replacement fuel assemblies. On the site, there may also be a facility for long-term (150–200 years) monitored cooling of radioactive waste so that it can be subsequently buried without upsetting the radiation balance of the Earth.

In the future, electricity production at large NPPs is likely to remain the main application of nuclear energy. This factor and the reduction of unit costs with increase in the power and number of nuclear units were the reasons for conceptual study of a 1,200 MWe lead-cooled fast reactor as a candidate basic component of a large-scale nuclear power mix. The BREST-OD-300 being developed as a prototype of the BREST-1200 reactor, their design and engineering features are largely similar, as may be seen from the data of ► Table 58.6 (ISTC 2001; Adamov et al. 1997).

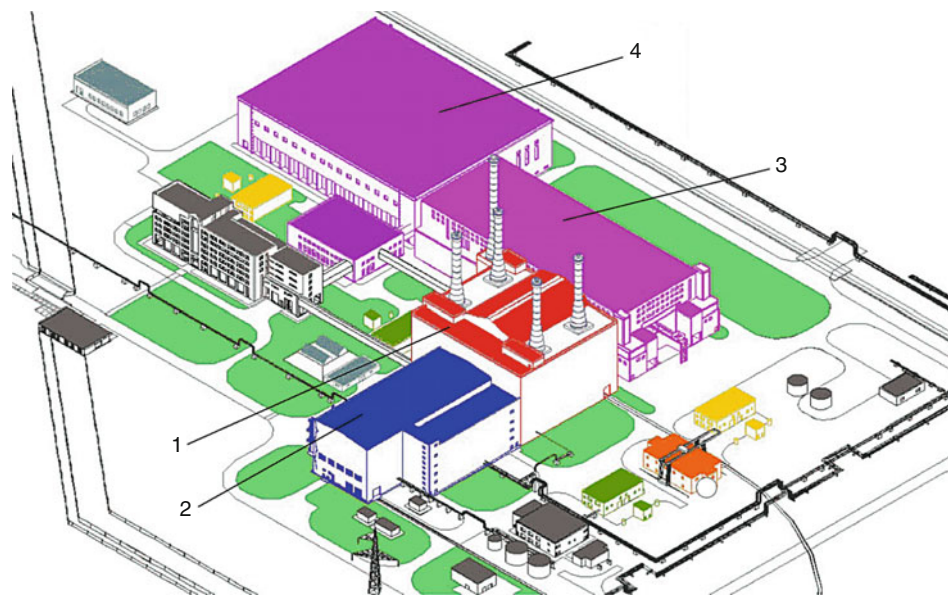
58.3.2.4 Fuel Cycle of Fast Reactors

Introduction of fast reactors with a closed nuclear fuel cycle into the nuclear power industry can radically change the current approaches to fuel supply and management of long-lived radwaste.

A fast reactor produces more nuclear fuel than it burns during operation, due to irradiation of the fertile ^{238}U isotope. All the depleted uranium that now has no use in the nuclear power

► Fig. 58.17

Nuclear power complex with BREST-OD-300 reactor: 1 – reactor; 2 – turbine unit; 3 – radioactive waste storage and treatment complex; 4 – on-site nuclear fuel cycle complex



■ Table 58.6

Technical characteristics of BREST-OD-300 and BREST-1200

Characteristics	BREST-OD-300	BREST-1200
Thermal power, MW	700	2,800
Electric power, MW	300	1,200
Core diameter, mm	2,300	4,755
Core height, mm	1,100	1,100
Fuel rod diameters, mm	9.4; 9.8; 10.5	9.4; 9.8; 10.5
Fuel rod pitch, mm	13.0	13.0
Core fuel	(U+Pu+MA)N	(U+Pu+MA)N
Core charge, (U+Pu+MA)N, t	16	63.9
Charge of (Pu+MA) / ($^{239}\text{Pu} + ^{241}\text{Pu}$), t	2.1/1.5	8.56/6.06
Fuel lifetime, years	5	5 ÷ 6
Refueling interval, years	1	1
CBR	~1.05	~1.05
Maximum fuel burnup, % h. a. (heavy atoms)	10.2	10.2
Total effect of reactivity, % $\Delta K/K$	0.35	0.31
Lead inlet/outlet temperature, °C	420/540	420/540
Maximum fuel cladding temperature, °C	650	650
Maximum lead velocity, m/s	1.8	1.7
Steam temperature at steam generator inlet/outlet, °C	340/520	340/520
Pressure at steam generator outlet, MPa	24.5	24.5
Net efficiency of power unit, %	43	43
Design service life, years	30	60

industry may be processed to serve as reactor fuel; if so, the fuel resources available to nuclear power will increase 100 times (whereas less than 1% of the mined natural uranium is actually used today).

In production of fuel for a fast reactor, uranium – natural or depleted – is only needed to make up for the fission products separated during reprocessing of irradiated nuclear fuel (INF), which accounts for about 10% of the “fresh” fuel mass. For a thermal reactor, natural uranium is enriched to a required level, with roughly 10% of the mined uranium going into fuel, while its remaining 90% ends up in the tails of enrichment processes and is not involved in energy generation.

Thus, the consumption of natural or depleted uranium in producing fuel for a fast reactor is roughly a factor of 100 less than for a thermal reactor, and therefore much less expensive natural uranium may be used for making up fast reactors. It should be also taken into account that the existing quantities of depleted uranium are large enough already to serve as makeup fuel for a mix of fast reactors for several hundreds of years, so that natural uranium mining for the makeup purposes may be at least suspended.

The long-term radiation hazard of irradiated nuclear fuel is accounted for mostly by actinides. Given INF cooling for 60–60,000 years, the governing part is played by plutonium and americium, while longer cooling would bring neptunium to the fore, with a relatively small contribution from curium. To reduce the long-term radiation hazard of actinides, it is proposed to subject them to transmutation (to “burn” them in fuel).

A fast reactor can burn Np, Am, and Cm without any additional fuel consumption, including not only those produced in its own fuel but also in the fuel of thermal reactors. The final objective of transmutation is to convert long-lived actinides into fission products, as fission-free irradiation turns some actinides into others, and long-lived actinides will not disappear. Unless fission occurs, irradiation, e.g., of ^{237}Np ($T_{1/2} = 2.14 \times 10^6$ years) results finally in formation of the $^{234}\text{U} - ^{238}\text{U}$ isotopes, among which ^{234}U is the shortest-lived one ($T_{1/2} = 2.46 \times 10^5$ years), which means that long-lived activity will not be significantly decreased. Conversion of actinides into fission products can effectively reduce long-lived radioactivity.

Transmutation of long-lived nuclides (actinides and fission products) in the fuel cycle of fast reactors should proceed, at least, until the biologically equivalent activity of the waste to be buried declines to that of the natural uranium consumed (this condition is referred to as equivalence in terms of radiation and biological hazards). Notably, such equivalence may be attained both by the time of burial and within a historically short and reliably predicted period of, e.g., 200–1,000 years. This approach allows reasonably minimizing the mass and hazard of long-lived waste, while the specific conditions of waste disposal should meet the national regulatory requirements.

In the currently used open fuel cycle, with irradiated fuel recognized as mere waste, radiation equivalence is achievable only after 100,000–500,000 years of its cooling.

Based on the earlier studies (Adamov and Orlov 1992; Adamov et al. 1992, 1996, 1997), it was shown that radiation equivalence is feasible if radioactive waste is stored for 100–1,000 years, provided the nuclear power industry introduces a fuel cycle with transmutation, which will have the following key features:

- Reprocessing of the whole INF quantity from thermal reactors with specified partitioning for transfer of Pu, Np, Am, Cm, and other long-lived fission products into the fuel cycle of fast reactors.
- Operation of fast reactors in a closed fuel cycle to burn the bulk of actinides and to transmute long-lived fission products in the course of their operation.
- Thorough treatment of the radioactive waste subject to disposal to remove Pu, Am, and some other long-lived nuclides.
- Interim storage of highly active waste before its final disposal.

In setting up a fuel cycle with transmutation and seeking proper environmental protection, it is appropriate to modify the uranium mining process so that the associate highly radioactive radium and thorium could be co-extracted together with natural uranium for subsequent transmutation in fast reactors.

Possibilities for implementation of this fuel cycle concept may be illustrated by two scenarios:

Scenario 1 – Only thermal reactors are developed and built.

Scenario 2 – Using the reprocessed fuel of thermal reactors, a system of fast reactors develops, with all Pu, Np, Am, and Cm from INF of the former transferred into the fuel cycle of the latter. By the end of the twenty-first century, the energy output of the system of fast reactors is two times that of the thermal reactor mix.

Scenarios 1 and 2 assume availability of all the above components of the fuel cycle with transmutation, including cooling of radioactive waste before burial.

As new fast reactors are built and started on Pu, Np, Am, Cm from INF of thermal reactors, the previously accumulated irradiated fuel peters out. Transmutation of Pu, Np, Am, and Cm from INF of fast reactors and replacement of INF (disposed of in the open cycle of thermal

reactors) by the radioactive waste from regeneration of thermal and fast reactor fuel have a significant positive effect on the potential biological hazard (PBH) of long-lived waste produced by the nuclear power industry (Fig. 58.18).

It was assumed in the calculations that reprocessing of thermal and fast reactor fuel would give rise to waste with the following percentage of certain elements relative to the reprocessed fuel mass: Sr, Tc, I, and Cs each accounting for 0.1%; U and Cm, for 0.1%; Pu and Am, for 0.01%, and the rest coming to almost 100%.

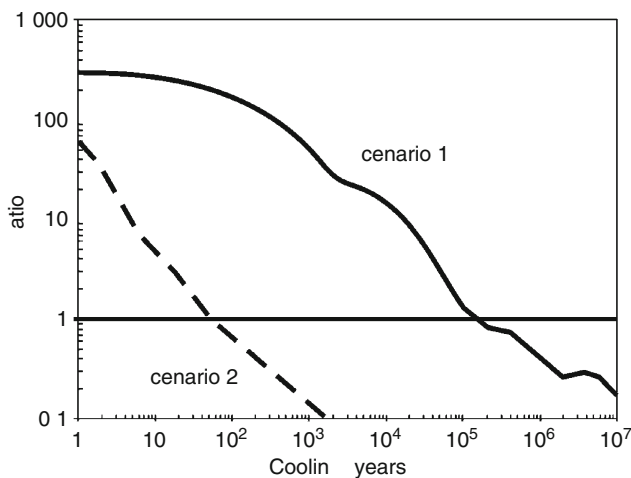
Whereas the potential biological hazard (PBH) of thermal reactors' irradiated fuel declines to that of the natural uranium consumed by them (radiation equivalence) after about 10^5 years of cooling, it takes only 50 years for the PBH of the waste generated in INF reprocessing to reach a radiation-equivalent level. The proportion of elements going to waste during reprocessing is an effective control parameter for attaining radiation equivalence; it will decrease with the time of fast reactor operation.

Analysis of the radiation balance in a closed cycle of nuclear power plants suggests strategic decisions for management of the long-lived waste components. However, this is but the first step in developing a scientific groundwork for environmentally acceptable nuclear power. The next step is to prove the long-term environmental safety of the sites chosen for final disposal of radioactive waste, attainable by preserving the local radiation balance and by providing a likeness to natural conditions (Lopatkin et al. 2003). This requirement could be best met on the uranium mining sites. However, provision of a local balance need not be treated as an imperative requirement. Waste may be also disposed of in repositories specially built in deep rocks, which would offer better confinement of radioactive elements as compared with natural uranium fields.

The main current approach to proving the environmental safety of waste burial sites relies on numerous barriers to keep in high specific radioactivity. Safety is not easily, if at all, demonstrable where the time required for cooling of INF from thermal reactors reaches 10^4 – 10^6 years.

■ Fig. 58.18

Ratio between the potential biological hazard (PBH) (through ingestion) of the natural uranium accumulated in the irradiated fuel of thermal reactors by the year 2100 (*Scenario 1*) and that of radioactive waste (*Scenario 2*)



Allowance for the migration conditions, i.e., for temporary retention of a radionuclide on the way from its burial place to the biosphere, permits easing the requirements for the radiation balance attainment, which in this case may be more appropriately referred to as the radiation balance between waste components and natural uranium with allowance for migration. Consideration of all these circumstances shows that a perceptible radiation imbalance between waste and feed materials is tolerable at the time of waste disposition in a deep repository. It will change to a balance within the time required for the waste components to cover the distance from the deep repository to the biosphere. Clearly, the repository depth and the rock structure at the burial site are the parameters that, if appropriately chosen, can facilitate attainment of the required balance and reduce the time required for it. In terms of radiation equivalence with allowance for migration in waste disposal, the traditional approach to the burial safety involves a highly conservative judgment, which assumes that all the barriers in the path of radioactive nuclides have failed and these elements will migrate to the biosphere with groundwater.

58.3.2.5 Technological Consolidation of the Nonproliferation Regime

The Nonproliferation Treaty and the international safeguards to support it failed, unfortunately, to stop new countries from getting possession of nuclear weapons. The effectiveness of political measures would be largely enhanced, if the processes of potential danger from the viewpoint of nuclear proliferation were phased out with development of the new nuclear technology. Such processes include the following:

- Separation of U isotopes (enrichment).
- Production of weapons-grade Pu in uranium blankets.
- Extraction of Pu and/or ^{233}U from irradiated fuel.
- Long-term storage of INF.
- Storage of extracted Pu.
- Transportation of weapons-grade and irradiated nuclear materials over large distances.

A nuclear power industry built with the currently available technologies in a nonnuclear country to the level of 5–10 GWe and following a long-term development program, may sooner or later encourage such nations to create facilities for isotope separation and extraction of Pu (or ^{233}U) as well as other, associated facilities of the fuel cycle. The international nuclear fuel cycle centers, proposed by the presidents of Russia and the USA some time ago, could prevent the worldwide sprawl of such technologies. But it is a far from easy business to harmonize the day-to-day relations between a large national nuclear energy complex and a foreign supplier of fuel cycle services, especially if the national energy security is at stake. Establishment of such centers within international jurisdiction would provide, perhaps, an optimal answer to this problem.

The most important objective of the new nuclear technology under development is to make the peaceful nuclear power free from the need for the elements that are dangerous from the viewpoint of proliferation of nuclear weapons. If this is achieved, annual circulation of large nuclear fuel masses will no longer be a proliferation hazard, and the attention of international monitoring agencies may be then focused on preventing creation of illegal facilities for uranium enrichment and for extraction of Pu and ^{233}U .

This objective may be accomplished by developing nuclear power with fast reactors as its basic component, which will feature full fuel reproduction in the core without breeding

blankets. Fast reactors operating in a closed uranium–plutonium fuel cycle, will have no need of uranium enrichment, and this process may be phased out in due course. The first cores of fast reactors will be fabricated by clearing the plutonium storage places and the irradiated fuel pools of the present-day NPPs. The initial Pu separation and the fabrication of first cores for fast reactors, using plutonium or enriched uranium, should take place at the facilities of the Nuclear Club countries or at international nuclear technology centers.

The nonproliferation regime may be technologically supported in the fuel cycle of a fast reactor with full fuel reproduction in the core owing to the following:

- Presence of transmutable actinides and fission products in fuel (about 1% after treatment) facilitates its protection against theft in all the links of the fuel cycle.
- Full Pu reproduction in the core ($\text{CBR} \approx 1$) requires no U blankets, which excludes in-pile weapons-grade Pu production and the need for its separation.
- Similar composition of the fuel unloaded from and loaded into the reactor core, requires no separation or addition of plutonium, with possible correction the fuel composition by adding ^{238}U to make up for its burnout.
- The fuel cycle complex is arranged on the NPP site, which excludes diversion of nuclear materials outside, eliminates the need for long-distance transportation and handover, and reduces the risk of accidents and thefts.
- The reactor design should rule out any possibility of loading target materials for production of weapons-grade fissile elements.

In fast reactors, the uranium–plutonium fuel of equilibrium composition is unfit for production of nuclear weapons. Its breeding properties are worse than those of uranium 20% enriched in ^{235}U (the IAEA limit). Absence of plutonium and uranium separation in all stages of the fuel cycle guarantees proliferation resistance.

The ^{238}U isotope burns out in the closed fuel cycle of a fast reactor, while plutonium is an integral and inseparable part of fuel (a “catalyst” for burning) and stays at all times incorporated in highly active materials. The international fuel cycle centers are expected to provide services to nuclear power complexes with fast reactors of the proposed type by producing only the first-core fuel and the makeup fuel, required for bringing NPPs into service, till the fuel cycle is closed. For the rest of the time, the plants will rely for their operation on the fuel they will breed, and will be independent from the foreign fuel suppliers.

58.3.3 Generation IV Nuclear Energy Systems

The ten countries (Argentina, Brazil, Canada, France, Japan, the Republic of Korea, the Republic of South Africa, Switzerland, the UK, and the USA) have joined together to form the Generation IV International Forum (GIF) to develop future-generation nuclear energy systems that can be licensed, constructed, and operated in a manner that will provide competitively priced and reliable energy products while satisfactorily addressing nuclear safety, waste, proliferation, and public perception concerns. Subsequently, the GIF Charter was signed by Euratom in 2003, and the People’s Republic of China and the Russian Federation, both in 2006.

The objective for Generation IV nuclear energy systems is to have them available for international deployment about the year 2030, when many of the world’s currently operating nuclear power plants will be at or near the end of their operating licenses.

Basic goals for Generation IV are defined in the four broad areas of sustainability, economics, safety and reliability, and proliferation resistance and physical protection:

- *Sustainability* (effective fuel utilization, development of new energy products that can expand nuclear energy's benefits beyond electrical generation, improved waste management, and demonstration of its safe long-term storage, minimal environmental impacts).
- *Economics* (competitive life cycle and energy production costs, low financial risks comparable to other energy projects, practical applications other than power production – hydrogen, process heat, district heating, potable water).
- *Safety and reliability* (safe and reliable operation, improved accident management and minimization of consequences, investment protection, and reduced need for off-site emergency response).
- *Proliferation resistance and physical protection* (effective proliferation resistance of nuclear energy systems through improved design features and other measures, increasing physical protection against terrorism by increasing the robustness of new facilities).

From more than 100 various proposals, six promising reactor systems were selected by GIF experts for further R&D within the framework of Generation IV (DOE 2002):

- Gas-cooled fast reactor (GFR) system
- Lead-cooled fast reactor (LFR) system
- Molten-salt reactor (MSR) system
- Sodium-cooled fast reactor (SFR) system
- Supercritical-water-cooled reactor (SCWR) system
- Very-high-temperature reactor (VHTR) system

The solutions in physics and design of SFR and VHTR (HTGR) were discussed in the first part of the chapter. The second part of the chapter deals with the innovative approaches to development of naturally safe fast reactors with a closed fuel cycle, including LFR, which is treated as the main line in establishment of large-scale nuclear power. The other three reactor systems selected for the Generation IV Project are briefly discussed below.

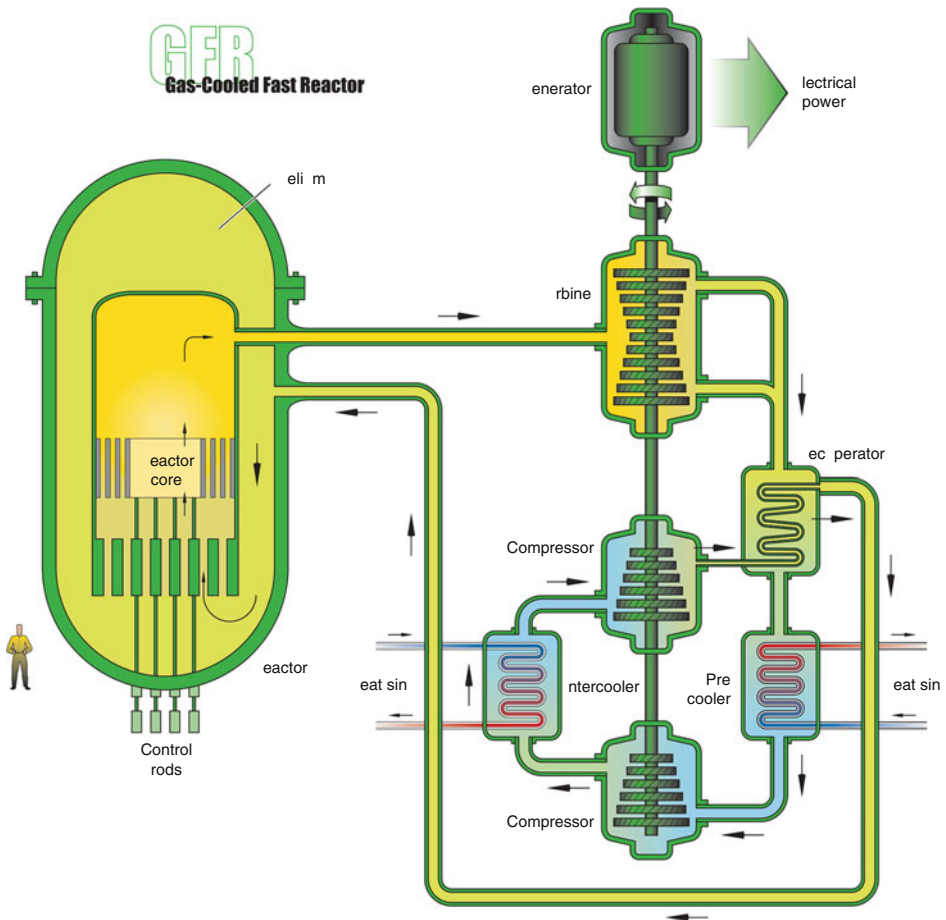
58.3.3.1 Gas-Cooled Fast Reactor System

The gas-cooled fast reactor (GFR) system features a fast-spectrum helium-cooled reactor (➤ Fig. 58.19) and closed fuel cycle. Like thermal-spectrum helium-cooled reactors such as the GT-MHR and the PBMR, the high outlet temperature of the helium coolant makes it possible to deliver electricity, hydrogen, or process heat with high conversion efficiency. The GFR uses a direct-cycle helium turbine for electricity and can use process heat for thermochemical production of hydrogen. Through the combination of a fast-neutron spectrum and full recycle of actinides, GFRs minimize the production of long-lived radioactive waste isotopes. The GFR's fast spectrum also makes it possible to utilize available fissile and fertile materials (including depleted uranium from enrichment plants) two orders of magnitude more efficiently than thermal spectrum gas reactors with once-through fuel cycles. The GFR reference assumes an integrated, on-site spent fuel treatment, and refabrication plant.

A summary of design parameters for the GFR system is given in the ➤ Table 58.7.

The GFR system is top ranked in sustainability because of its closed fuel cycle and excellent performance in actinide management. It is rated good in safety, economics, and in proliferation resistance and physical protection. It is primarily envisioned for missions in electricity

■ Fig. 58.19

Gas-cooled fast reactor (GFR)

production and actinide management, although it may be able to also support hydrogen production. Given its R&D needs for fuel and recycling technology development, the GFR is estimated to be deployable by 2025.

58.3.3.2 Molten-Salt Reactor System

The molten-salt reactor (MSR) system features an epithermal to thermal neutron spectrum and a closed fuel cycle tailored to the efficient utilization of plutonium and minor actinides. A full actinide recycle fuel cycle is envisioned. In the MSR system, the fuel is a circulating liquid mixture of sodium, zirconium, and uranium fluorides. The molten salt fuel flows through graphite core channels, producing a thermal spectrum. The heat generated in the molten salt is transferred to a secondary coolant system through an intermediate heat exchanger, and then through another heat exchanger to the power conversion system (● Fig. 58.20). Actinides and

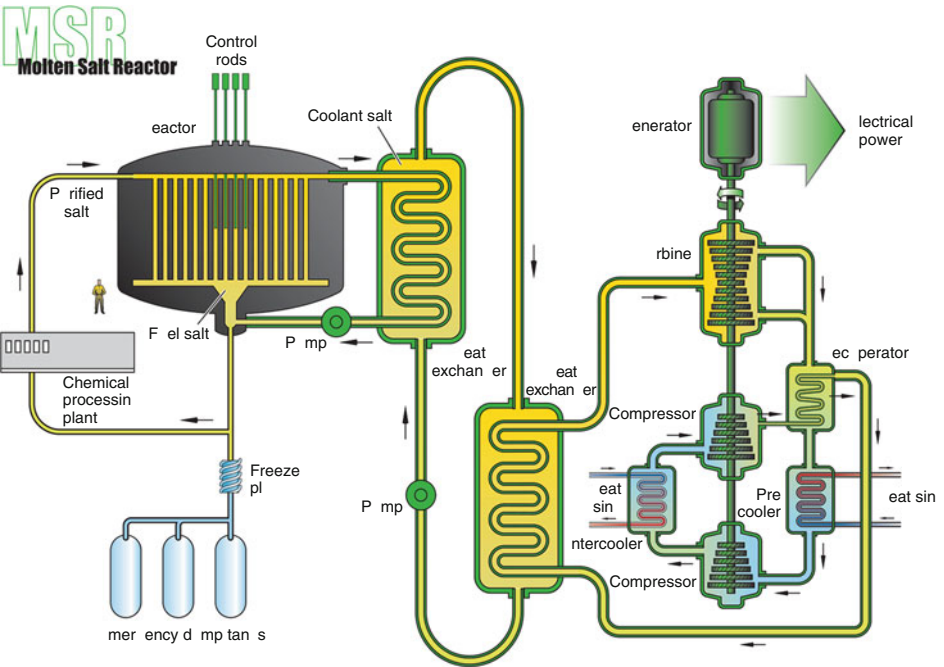
Table 58.7

Design parameters for the gas-cooled fast reactor (GFR) system

Reactor parameters	Reference value
Reactor power	600 MWth
Net plant efficiency (direct cycle helium)	48%
Coolant inlet/outlet temperature and pressure	490°C/850°C at 90 bar
Average power density	100 MWth/m ³
Reference fuel compound	UPuC/SiC (70/30%) with about 20% Pu content
Volume fraction, Fuel/Gas/SiC	50/40/10%
Conversion ratio	Self-sufficient
Burnup	5% FIMA (fissions per initial metal atoms)
Damage	60 dpa

Fig. 58.20

Molten-salt reactor



most fission products form fluorides in the liquid coolant. The homogenous liquid fuel allows addition of actinide feeds with variable composition by varying the rate of feed addition. There is no need for fuel fabrication. The reference plant has a power level of 1,000 MWe. The system operates at low pressure (<0.5 MPa) and has a coolant outlet temperature above 700°C, affording improved thermal efficiency.

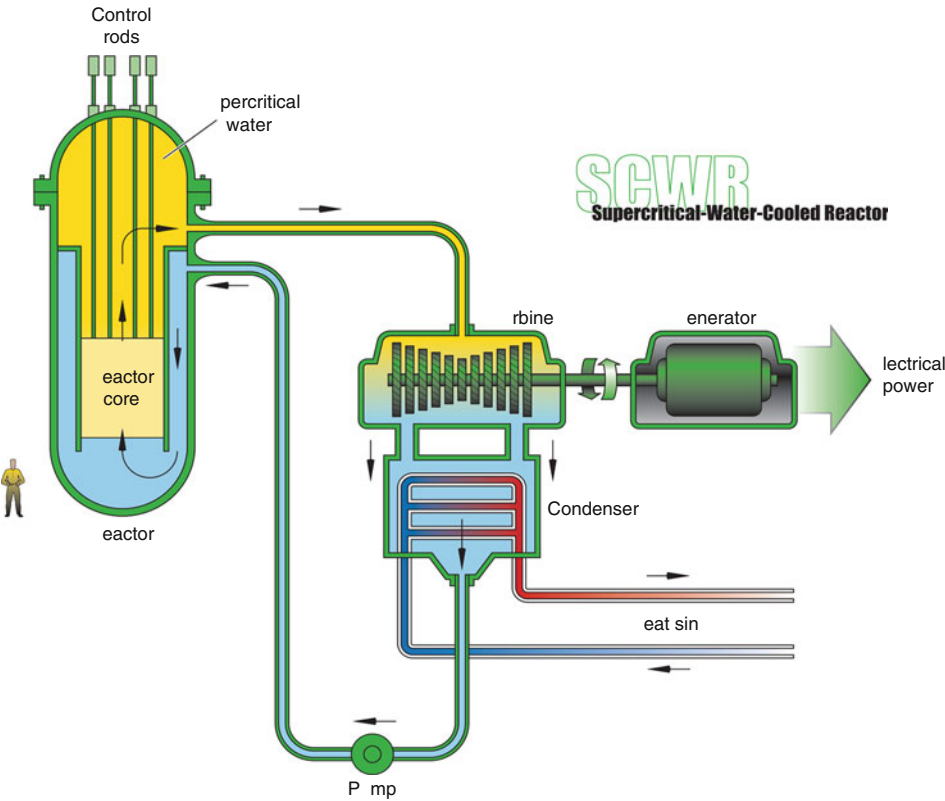
Table 58.8

Design parameters for the molten-salt reactor (MSR)

Reactor parameters	Reference value
Net power	1,000 MWe
Power density	22 MWth/m ³
Net thermal efficiency	44–50%
Fuel-salt	
Inlet temperature	565°C
Outlet temperature	700°C (850°C for hydrogen production)
Vapor pressure	<0.1 psi (pound-force per square inch)
Moderator	Graphite
Power cycle	Multi-reheat recuperative helium Brayton cycle
Neutron spectrum burner	Thermal actinide

Fig. 58.21

Supercritical-water-cooled reactor (SWCR)



The MSR system is top ranked in sustainability because of its closed fuel cycle and excellent performance in waste burn-down. It is rated good in safety, and in proliferation resistance and physical protection, and it is rated neutral in economics because of its large number of subsystems. It is primarily envisioned for missions in electricity production and waste burn-down. Given its R&D needs for system development, the MSR is estimated to be deployable by 2025.

A summary of the reference design parameters for the MSR is given in the ► [Table 58.8](#).

58.3.3.3 Supercritical-Water-Cooled Reactor System

The supercritical-water-cooled reactor (SCWR) (► [Fig. 58.21](#)) system features two fuel cycle options: the first is an open cycle with a thermal neutron spectrum reactor; the second is a closed cycle with a fast-neutron spectrum reactor and full actinide recycle. Both options use a high-temperature, high-pressure, water-cooled reactor that operates above the thermodynamic critical point of water (22.1 MPa, 374°C) to achieve a thermal efficiency approaching 44%. The fuel cycle for the thermal option is a once-through uranium cycle. The fast-spectrum option uses central fuel cycle facilities based on advanced aqueous processing for actinide recycle. The fast-spectrum option depends upon the materials' R&D success to support a fast-spectrum reactor.

In either option, the reference plant has a 1,700-MWe power level, an operating pressure of 25 MPa, and a reactor outlet temperature of 550°C. Passive safety features similar to those of the simplified boiling water reactor are incorporated. Owing to the low density of supercritical water, additional moderator is added to thermalize the core in the thermal option. Note that the balance-of-plant is considerably simplified because the coolant does not change phase in the reactor.

■ **Table 58.9**

Designs parameters for the supercritical-water-cooled reactor (SCWR) system

Reactor parameters	Reference value
Plant capital cost	\$900/KW
Unit power and neutron spectrum	1,700 MWe
Net efficiency	44 %
Coolant inlet and outlet temperatures and pressure	280°C/510°C/25 MPa
Average power density	100 MWth/m ³
Reference fuel	UO ₂ with austenitic or ferritic–martensitic stainless steel, or Ni-alloy cladding
Fuel structural materials, cladding structural materials	Advanced high-strength metal alloys are needed
Burnup	~45 GWD/MTHM (gigawatt-day/metric tons of heavy metal)
Damage	10–30 dpa (displacements per atom)
Safety approach	Similar to advanced light water reactors (ALWRs)

A summary of design parameters for the SCWR system is given in the ► [Table 58.9](#).

The SCWR system is highly ranked in economics because of the high thermal efficiency and plant simplification. If the fast-spectrum option can be developed, the SCWR system will also be highly ranked in sustainability. The SCWR is rated good in safety, proliferation resistance, and physical protection. The SCWR system is primarily envisioned for missions in electricity production, with an option for actinide management. Given its R&D needs in materials compatibility, the SCWR system is estimated to be deployable by 2025.

Acknowledgments

Prof. Y. Fuji-ie is grateful to Mr. Shoji Kotake and Mr. Nariaki Uto for their support through his contributing part of the chapter especially for the section on sodium-cooled fast reactor. The author is grateful also to Dr. Kazuo Arie, Dr. Masurou Ogawa, Dr. Kazuhiko Kunitomi and Dr. Kaoru Onuki for their contribution on HTGRs including valuable discussion on advanced nuclear energy system.

Prof. E. Adamov would like to thank Prof. V. Orlov and Drs. V. Smirnov, A. Lopatkin, and A. Dzhalavayan for their significant contribution to this chapter.

The chapter could not be completed without their contributions.

References

- Adamov EO, Orlov VV (1992) Nucl Engng Int 37(454):42–44
- Adamov EO, Orlov VV (1997) Nucl Eng Des 173:33–41
- Adamov EO, Ganey IKh, Orlov VV (1992) Atomnaya Energiya 73(1):44–50 (in Russian)
- Adamov EO, Mihailov VN, Dyakov AF, Velikhov EP (1995) New concept of nuclear involvement in overcoming world energy problems. In: 16th WEC Congress, Tokyo, Japan, 8–13 October 1995
- Adamov EO, Ganey IKh, Lopatkin AV et al (1996) Atomnaya Energiya 81(6):409–415 (in Russian)
- Adamov EO, Orlov VV, Filin AI, Leonov VN, Smirnov VS, Tsikunov VS (1997) Nucl Eng Des 173:143–150
- Argonne National Laboratory (Winter 2002) Early Argonne reactor lit the future of the nuclear power industry. Logos 20, November 1, http://www.anl.gov/Media_Center/logos20-1/ebri.htm
- Arie K et al (2007) In: Proceedings of the international conference on advanced nuclear fuel cycles and systems (GLOBAL 2007), Boise, Idaho, USA, September 2007, pp 310–317
- DOE (2002) A technology roadmap for generation IV nuclear energy systems. GIF-002-00, December 2002. U.S. DOE Nuclear Energy Research Advisory Committee and the generation IV international forum, http://www.ne.doe.gov/genIV/documents/gen_iv_roadmap.pdf
- Edelmann M et al (1994) Nucl Technol 107:3–14
- Eisenhower D (1953) Atoms for peace. <http://www.americanrhetoric.com/speeches/dwightdeisenhoweratomsforpeace.html>
- Fuji-ie Y (1992a) Society in the 21st century and nuclear energy civilization – creation of universal energy. Denki Shimbun, Tokyo (in Japanese)
- Fuji-ie Y (1992b) In: Proceedings of the international conference on design and safety of advanced nuclear power plants (ANP'92), Tokyo, Japan, October 1992, pp 11.3-1–11.3-9
- Fuji-ie Y (1995) Nuclear energy – the way to comprehensive nuclear science and technology. Denki Shimbun, Tokyo (in Japanese)
- Fuji-ie Y (1998) Nuclear energy for recycling-oriented civilization – perspective and long-term prospect. Denki Shimbun, Tokyo (in Japanese)
- Fuji-ie Y (2005) Nuclear energy – learning and assimilating the nature. ERC, Tokyo, pp 279–304 (in Japanese)
- Fuji-ie Y (2006) Can nuclear energy system support civilized society in the 21st century: atom Wirtschaft, Germany, February 2006, pp 106–114
- Gif Overview (2009) <http://www.gen-4.org>
- IAEA (2006) Fast reactor database: IAEA-TECDOC-1531
- Idaho National Laboratory (2005) <http://nuclear.inl.gov/deliverables/docs/gen-iv-10-yr-program-plan.pdf>
- Igashira M, Ohsaki T (2002) Prog Nucl Energy 40: 555–560

- Inagaki T, Fuji-ie Y et al (1998) Role and approach to the recriticality elimination with utilizing the in-pile test reactor of IGR. In: Second international conference on non-proliferation problems
- ISTC (2001) ISTC Project # 1418, final report, 2001, Natural safety fast neutron lead-cooled reactor for large scale nuclear power, Adamov EO, Orlov VV (eds) NIKIET, Moscow
- Iwanami Shoten (Tokyo) (1998) Physics and chemistry dictionary, 5th edn (in Japanese)
- Japan Atomic Energy Research Institute (1998) The present status of research and testing in high temperature engineering
- Japan Atomic Industrial Forum Inc. (2009) World nuclear power plants 2009
- Kessler G (2007) Nucl Sci Eng 155:53–73
- Koster K et al (2003) Nucl Eng Des 222:231–245
- Lopatkin AV, Velichkin VI, Nikipelov BV, Poluektov PP (2003) Atomnaya Energiya 92(4):308–317 (in Russian)
- Matsuyama S et al (2009) In: Proceedings of 2009 international congress on advances in nuclear power plants (ICAPP'09), paper ID 9198, Tokyo, Japan, May 2009
- Nagai T (2000) Atomic bomb rescue and relief report (trans: Kuo AF). Nagasaki Association for Hibakushas' Medical Care, Nagasaki (original report written 1945)
- Nakanishi S et al (2008) In: Proceedings of 2008 international congress on advances in nuclear power plants (ICAPP'08), paper ID 8224, Anaheim, CA, USA, June 2008
- Niwa H et al (2005) In: Proceedings of the international conference on advanced nuclear fuel cycles and systems (GLOBAL 2005), paper No. 498, Tsukuba, Japan, October 2005
- Niwa H et al (2007) Safety implications of the eagle experimental results for the fact project. In: International conference on nuclear power of Republic Kazakhstan. Kurchatov, Republic of Kazakhstan
- Nobelprize.org (2009) http://nobelprize.org/nobel_prizes/peace/laureates/2009/
- OECD/NEA (2009) BP statistical review of world energy, June 2009
- OECD/NEA, IAEA (2007) Uranium 2007: resources, production and demand
- Ogawa M et al (2009) Present status of HTGR and hydrogen production development in JAEA. In: 4th NEA information exchange meeting on nuclear production of hydrogen, Oakbrook, IL, USA, April 2009
- Onuki K et al (2009) Energy Environ Sci 2:491–497
- Orlov VV, Avrorin EN, Adamov EO et al (1992) Atomnaya Energiya 72(4):317–329 (in Russian)
- Orlov VV, Smirnov VS, Leonov VN, Sila-Novitsky AG et al (2003) Deterministic safety of BREST reactors. In: Proceedings of the ICONE-11, Shinjuku, Tokyo, Japan, 20–23 April 2003, p 180
- Power Reactor and Nuclear Fuel Development Corporation (1980) Application for reactor establishment license for the fast breeder reactor monju power plant
- Rogozkin BD, Stepenova NM, Proshkin AA (2003) Atomnaya Energiya 95(3):208–221 (in Russian)
- Saito M (2005) Multicomponent self-consistent nuclear energy system: protected plutonium production by transmutation of minor actinides. In: Workshop on future nuclear systems and fuel cycles. Karlsruhe, Germany
- Saito S et al (1994) Design of high temperature engineering test reactor (HTTR), JAERI 1332
- Sinha RK, Kakodkar A (2006) Nucl Eng Des 236:683–700
- Sugisaki T (2002) Private communication
- Takamatsu I et al (2007) J Nucl Sci Technol 44(3):511–517
- The Huffington Post (2009) http://www.huffingtonpost.com/2009/04/05/obama-prague-speech-on-nu_n_183219.html
- Tsuboi Y et al (2009) In: Proceedings of 2009 international congress on advances in nuclear power plants (ICAPP'09), paper ID 9214, Tokyo, Japan, May 2009
- Tupper RB et al (1991) Polonium hazards associated with lead bismuth used as a reactor coolant. In: Proceedings of the international conference on fast reactors and related fuel cycles, vol IV, Kyoto, Japan, October 28–November 1 1991, pp 5–6
- U. S. DOE Nuclear Energy Research Advisory Committee and the Generation IV International Forum (2002) A technology roadmap for generation IV nuclear energy systems. (http://www.ne.doe.gov/genIV/documents/gen_iv_roadmap.pdf)
- UN Security Council (2009) S/RES/1887
- Wade DC, Chang I (1988) Nucl Sci Eng 100:507
- Wagar WW (2004) H. G. Wells: traversing time. Wesleyan University Press, Middletown, p 144
- Weinberg AM, Spiewak I, Barkenbus JN (1985) The second nuclear era. A new start for nuclear power. Praeger Publishers, New York



59 Nuclear Power Sources for Space Systems

N. E. Kukharkin · N. N. Ponomarev-Stepnoi · V. A. Usov

Russian Research Center “Kurchatov Institute”, Moscow, Russia

59.1	<i>Introduction</i>	2732
59.2	<i>Reactor Power Sources</i>	2733
59.2.1	Onboard Reactor Power Sources	2733
59.2.1.1	Thermoelectric Nuclear Power Systems	2733
59.2.1.2	Thermionic Nuclear Power Systems	2740
59.2.2	Nuclear Power Propulsions	2745
59.2.2.1	Programs of the NPP Development in the USSR and the USA and the Achieved Results	2745
59.2.2.2	The Russian Concept of the Model NPP Designs	2747
59.2.3	Nuclear Power Propulsion Systems (NPPS)	2749
59.3	<i>Radioisotope (Radionuclide) Power Sources</i>	2751
59.3.1	Radioisotope Thermoelectric Generators (RTGs)	2751
59.3.1.1	The Choice of Radionuclides and the Methods of RTG Manufacturing	2752
59.3.1.2	Purpose. Classification. Basic Requirements and RTG Performances	2753
59.3.1.3	Examples of RTG Designs for Terrestrial and Space Applications	2755

Abstract: This chapter contains the information about nuclear power sources for space systems. Reactor nuclear sources are considered that use the energy of heavy nuclei fission generated by controlled chain fission reaction, as well as the isotope ones producing heat due to the energy of nuclei radioactive decay. Power of reactor nuclear sources is determined by the rate of heavy nuclei fission that may be controlled within a wide range from the zero up to the nominal one. Thermal power of isotope sources cannot be controlled. It is determined by the type and quantity of isotopes and decreases in time due to their radioactive decay. Both, in the reactor sources and in the isotope ones, nuclear power is converted into the thermal one that may be consumed for the coolant heating to produce thrust (Nuclear Power Propulsion System, NPPS) or may be converted into electricity (Nuclear Power Source, NPS) dynamically (a turbine generator) or statically (thermoelectric or thermionic converters). Electric power is supplied to the airborne equipment or is used to produce thrust in electric (ionic, plasma) low-thrust engines. A brief description is presented of the different nuclear systems with reactor and isotopic power sources implemented in Russia and the USA. The information is also given about isotopic sources for the ground-based application, mainly for navigation systems.

59.1 Introduction

The opportunity to employ nuclear power (power released by fissioning heavy nuclei and power released in radioactive decay) in space systems became evident as early as in the middle of the twentieth century. After the creation of atomic weapon both in the USA and in the USSR, practical studies of possible lines and patterns of atomic power sources for different space missions were initiated (Snyder 1961).

It is known that the advantages of nuclear power manifest themselves where continuous operation and comparatively high power are needed. In space applications, it is a great advantage that a small amount of nuclear fuel produces a large amount of energy. Solar power systems provide for a continuous lifetime, but large surfaces of solar cell panels are needed to increase power output, which is a limiting factor.

Nuclear power sources (NPSs) are classified first of all according to the type of the nuclear conversion taking place in them:

- In reactor power sources, energy is released by heavy nuclei fissioning in controlled chain reactions.
- In isotope power sources (actually: radionuclide sources), energy of radioactive decay of nuclei is used. The radionuclides themselves are products of fission or activation due to irradiation by neutrons.

Energy released in reactor sources is higher by orders of magnitude. The energy output depends on the reactor power and can be controlled.

Energy release in isotope sources depends on the type and quantity of the radionuclide used. The rate of decay cannot be controlled. Only the quantity of energy directed to the conversion system can be changed.

59.2 Reactor Power Sources

Reactor power sources are subdivided into two types:

- Onboard power sources. Electric power generated by them powers the instrumentation in space vehicles; it serves system survival and the operation of electric jet engines of low propulsion.
- Nuclear reactor engines. Fission energy is used for the heating of propellant to produce a jet thrust.

Hybrid patterns such as power propulsion systems are also feasible.

59.2.1 Onboard Reactor Power Sources

The advantages of these systems are as follows:

- Compact size.
- Independence of the distance to the Sun and of the vehicle orientation to the Sun.
- Maneuverability, the opportunity to operate at different power levels including increased power.
- Tolerance to cosmic radiation exposure.

At the current status of solar power sources, the advantages in mass-dimensions characteristics of those manifest themselves at the level of their electric power of several tens of kilowatts (for unmanned space vehicles).

The nuclear power unit (NPU) and the automatic control system (which is protected by radiation shielding and located in the instrumentation module at some distance from NPU) are the basic components of nuclear power systems.

The basic components of the nuclear power unit are as follows: the reactor, the system of power conversion, the system of power transfer (the coolant loop), the system of heat removal into the environment, and the unit of radiation protection.

Both dynamic (machinery) and static (non-machinery) conversion systems, that is, thermoelectric and thermionic ones, are considered as systems for the power conversion (production).

As static systems are more common in practice, the information about those will be given in the following sections.

59.2.1.1 Thermoelectric Nuclear Power Systems

The distinguishing feature of space power systems is that they operate at high temperatures because excess heat can only be removed into the environment by radiation. As the radiator surface (and weight) is limited, the temperature level of the whole system gets high. Therefore, high-temperature semi-conductors, silicon and germanium, are the elements of the thermoelectric converter.

Heat generated in the reactor is supplied to the hot ends of the elements; excess heat is removed to the radiator and rejected into the environment.

According to the methods of heat supply and removal, there are different configurations that have been implemented by developers in different countries (USSR and the USA):

- The configuration with the reactor, converter, and radiator arranged within one unit with heat transfer by heat conduction and radiation (without a coolant) is characteristic of the reactor-converter “Romashka,” USSR (Millionshchikov et al. 1964).
- In NPS SNAP-10A (USA), the converter has been combined with the radiator. Heat has been transferred from the reactor by a liquid-metal coolant (Johnson et al. 1966).
- In NPS “Buck” (USSR), the converter was an individual unit. Heat was removed from the reactor to the radiator also by a liquid-metal coolant – Na-K eutectics (Gryaznov 1999).

Each configuration has definite advantages and disadvantages. For instance, the system “Buck,” which was successfully employed in space, had a high-power output.

Thermoelectric Reactor-Converter “Romashka”

“Romashka,” as a terrestrial model, was the first NPS with a thermoelectric converter turning nuclear reactor heat into electric power. It was brought to electric power in August 1964 at the terrestrial facility of Kurchatov Institute and operated successfully about 15,000 h producing 6,100 kWh of electric power. Its basic characteristics are summarized in [Table 59.1](#) (Gverdtseteli et al. 1969; Kukharkin et al. 2008).

The basic NPS unit is a high-temperature fast-nuclear reactor (NR) ([Fig. 59.1](#)) in which heat generated in the core is transferred by conduction and radiation to the converter adjacent

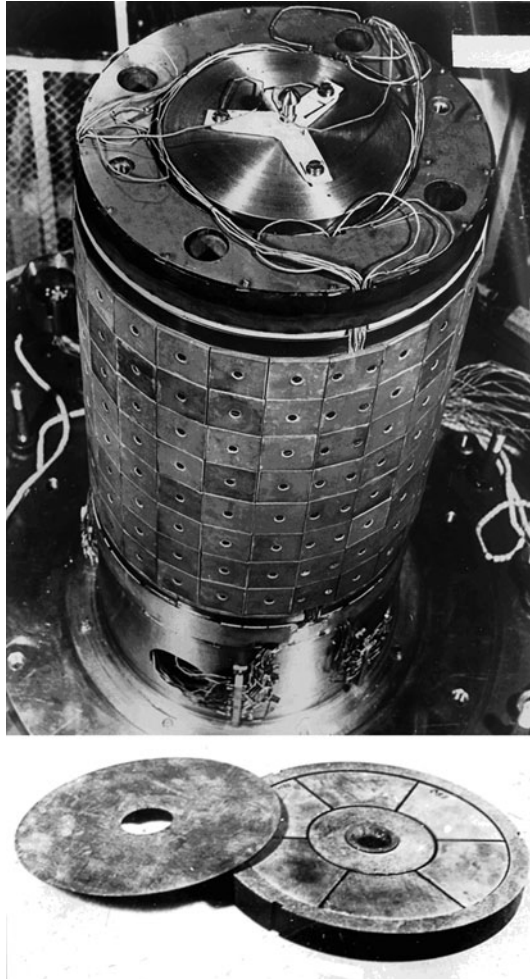
Table 59.1

The “Romashka” NPS basic characteristics

Core diameter/height	241/351 mm
Radial reflector outer diameter/height	483/553 mm
Reactor load mass by ^{235}U	49 kg
Total mass (without drives and control rods)	635 kg
Effective thermal power (without taking into account the end wall spread of heat)	28.2 kW
Electrical output (at start-of-life)	460–475 W
A coefficient of electrical power reduction over a lifetime of 15,000 h	0.8
Operating voltage	21 V
Maximum temperature of the	
Core center	2,173 K
Radial reflector outer surface	1,233 K
Hot ends of thermopiles	1,088 K
Cold ends of thermopiles	858 K
Mounting of radiating fins	823 K
Neutron flux in the core center	$9.2 \times 10^{12} \text{ n/cm}^2 \text{ s}$
Neutron leakage from the reactor	$3 \times 10^{12} \text{ n/cm}^2 \text{ s}$

■ Fig. 59.1

Reactor “Romashka” and fuel element



to the outer surface of a radial reflector. The reactor core comprises a stack of 11 fuel elements (FEs); the segmented FEs consists of discs of uranium bicarbide with 90% enriched uranium. This is located within a graphite package, so built that a significant part of heat from the core goes through the package body, thus reducing the temperature drop in uranium bicarbide.

A cylindrical radial beryllium reflector encloses the reactor. A graphite bushing is located between the core and reflector coated with silicon carbide and beryllium oxide providing the compatibility of materials at high ($\sim 1,473$ K) operating temperatures. Graphite plates also coated with beryllium oxide preventing the interaction of beryllium with the converter keyboard and reducing beryllium evaporation are located at the reflector 24-hedral outer surface.

The reactor end reflectors are also made of beryllium. The high-temperature heat insulation made of foam graphite and graphitized fabric is mounted on the reactor end walls to

reduce heat transfer. The reactor design and employed materials provide its long-term operation at high temperatures (up to 2,173 K in the center of the core and between 1,273 and 1,373 K on the reflector outer surfaces) that ensures the optimum operational conditions for the high temperature silicon–germanium converter.

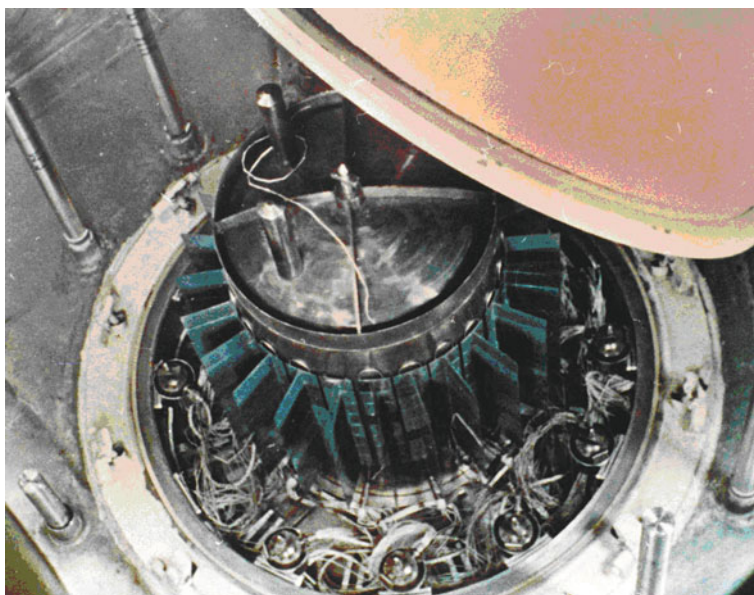
The converter consists of 1,536 pairs of thermopiles made of silicon–germanium alloy (Si: 85% by mass, Ge: 15% by mass) with n- and p-conductivity. Each module of 16 thermopiles is mounted on the inner surface of the hermetically sealed steel vessel. To provide for a good contact on the reactor heating, each module is pressed on the reflector by gas bellows elements. On the hot side, the keyboard consists of molybdenum plates, on the cold one – of copper bridges. To prevent an electric contact (shorting), insulating plates of beryllium oxide are used on the hot and cold sides. The excess heat is removed from the reactor-converter by shaped enamel-coated copper fins with an emissivity of at least 0.9 (► Fig. 59.2).

The reactor control system consists of four rods located in the radial reflector and in the lower movable end reflector. Two rods are used for automatic and manual control, whereas the other two, together with the movable reflector, are used for the protection in case of emergency. The negative temperature coefficient of the reactor reactivity allows operating for a long time without the interference of the control system. Only some deterioration of electric power necessitated increasing of thermal power up to a new level.

The “Romashka” system testing confirmed the opportunity of a durable lifetime for thermoelectric elements under the conditions of neutron and gamma radiation exposure. Electrical power reduction over the lifetime of 15,000 h was determined by 1.5 times increase of the converter internal resistance (mainly, of the contact one) with 1.17 times increase of the thermoelectromotive force. Studies showed that the temperature annealing without irradiation resulted in significant restoration of properties.

■ Fig. 59.2

Pilot thermoelectric plant “Romashka”



Nuclear Power System SNAP-10A (USA)

SNAP-10A was the first power system in the World with a nuclear reactor launched in space. It was put into a near-earth 1,300 km orbit on April 3, 1965. The flight lasted 43 days and then the NPS was shut down by a radio command from Earth because of malfunctions in the electric circuits of the spacecraft (Johnson et al. 1966; Wetch 1990).

➤ Figure 59.3 shows the SNAP-10A NPS schematics. ➤ Figure 59.4 presents the system's general view.

A thermoelectric generator (TEG, for its performances see ➤ Table 59.2) and radiator are arranged in one unit.

Heat is supplied from the reactor with TEG by the eutectic sodium and potassium alloy, which is circulated by a conduction electromagnetic pump having a self-contained Pb-Te thermogenerator. The main TEG consists of 120 modules. The coolant heated in the reactor comes through the module pipeline heating hot ends of thermoelements. Thermoelements are connected in sequence by copper bridges along the hot side and by aluminum plate-type radiators along the cold one. The converter-radiator mounting assemblies are welded to the space frame surface that represents the system's basic load-bearing element.

The nuclear reactor and shield are mounted on the upper bearing ring of the load-bearing unit.

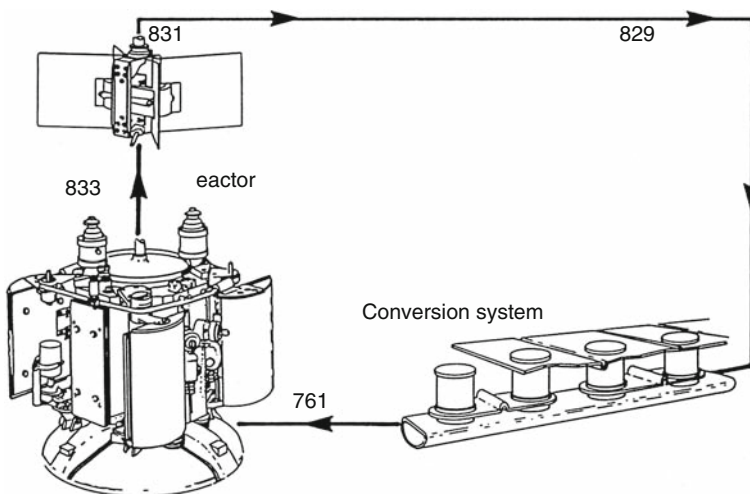
The shield represents a steel container filled with cold-pressed lithium hydride. The thermoelectric generator and other units of the system are located behind the shield. The SNAP-10A NPS maximum diameter is 1.5 m, height is 3.65 m, and mass is 450 kg.

The core consists of 37 fuel rods of 3.18 cm diameter combining the functions of neutron-induced fission and moderation. Fuel rods are made of a homogeneous mixture of enriched uranium and zirconium hydride. They are tightly packed into a cylinder vessel of 22.7 cm diameter and 40 cm height. A beryllium reflector and tiltable semi-cylindrical controls being the part of the reflector are located at the vessel outer side.

Loading of ^{235}U is 4.3 kg, the reactor mass is 125 kg.

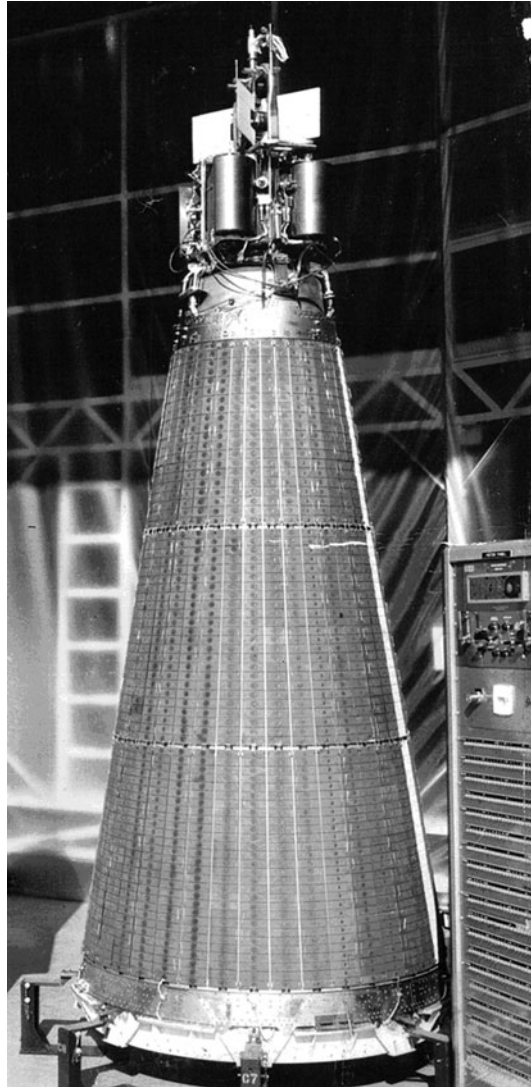
■ Fig. 59.3

Reactor SNAP-10A conversion scheme



■ Fig. 59.4

Space nuclear thermoelectric plant SNAP-10A



For safety purposes, the reflector can be ejected on radio command from the Earth in case of an abnormal operation or automatically on the entry into dense layers of the atmosphere.

Space Thermoelectric System “Buk”

The “Buk” space thermoelectric system was created in the USSR at the end of the 1960s. Between 1970 and 1988, there were more than 30 launches of these systems on “Kosmos” launch vehicles (Gryaznov 1999, Mashinostroyenie Entsiklopediya). The system was operated at low orbits about 300 km high.

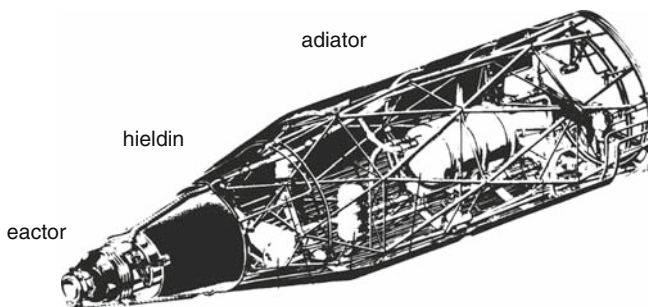
■ **Table 59.2**

TEG performances

Inlet coolant temperature	803 K
Reactor thermal power	34 kW(t)
Radiator average temperature	588 K
Average temperature drop in thermoelectric material	170 K
Q-factor of thermoelements	$0.58 \times 10^3/\text{K}$
Number of thermoelements	1,440
Operating voltage	28.5 V
Electric power (at the lifetime beginning)	540 W
Conversion total efficiency	0.016
Mass of the TEG 120 modules	68 kg
Radiator total area	5.8 m^2

■ **Fig. 59.5**

Space nuclear thermoelectric plant “Buk”



➤ **Figure 59.5** presents the “Buk” system’s general view. The “Buk” NPS consists of the nuclear reactor, the shield, the radiator with the TEG inside located in series along the nuclear reactor axis.

A small fast reactor is used as a power source, the core of which contains more than 30 fuel rods. The fuel is a highly enriched uranium-molybdenum alloy. Longitudinally movable control rods are placed in the beryllium side reflector.

A two-loop heat removal system uses a eutectic alloy of sodium and potassium as coolant. The first loop coolant, heated up to about 1,000 K, is supplied into the TEG located in a cylindrical casing. The second loop coolant removes the excess heat to the radiator.

The TEG has two independent sections: the main one for the spacecraft users and the auxiliary one for the power-to-conduction type electromagnetic pumps used for both coolant loops. There are two cascade thermoelectric converters in the TEG.

The reactor thermal power is about 100 kW(th), the maximum electric power is about 3 kW. The “Buk” NPS lifetime was extended in operation to several thousands of hours by which time the efficiency was reduced down to 0.9 of its start-of-life value.

The operation in low orbits required two safety systems.

The basic safety system is intended for moving the nuclear spacecraft into a long-term disposal orbit at a height of more than 850 km. The lifetime of the system moved to this orbit is quite enough for the nuclear reactor fission products to decay to the level of natural radioactivity.

The second back-up system provides for the aerodynamic dispersion of a fuel composition with fission products into the upper layers of the Earth atmosphere into particles the sizes of which are sufficiently small to pose no excess radiological hazard to the population and environment.

Problems of Power Increase

A low-efficiency coefficient is a disadvantage of nuclear power systems with TEGs. In case of need to increase power up to several tens of kilowatts, it is necessary to increase the temperature drop in the generator. The temperature increase is limited by the liquid-metal loop capabilities. In this case, lithium technologies are to be employed. The temperature decrease on cold junctions results in a sharp enlargement of the radiator surface. This explains the fact that the development of the SP-100 NPS in the USA has been unfinished.

With the current state-of-the-art of solar generators, thermogenerators with electric power of less than 30 kW become noncompetitive.

The foresight of these trends led to the necessity to develop nuclear power systems with a thermionic converter.

59.2.1.2 Thermionic Nuclear Power Systems

The merits of thermionic converters lie in the fact that they operate at higher temperatures, have smaller dimensions and higher efficiency. They may be located inside the reactor core as their cathodes may serve as claddings of fuel elements making a thermionic fuel element (TFE). In this case, the high-temperature coolant loop is eliminated. These designs were developed in the USSR.

There are other possible layouts too, such as the NPS with the outrigger generator, heat to which is supplied by a high-temperature lithium coolant, and other advanced patterns with heat supply by heat pipes (HP) providing a minor temperature drop. These patterns, along with built-in TFEs developed in the USSR, were investigated in the USA.

Built-in TFEs may be divided into two types: single-cell and multi-cell ones. In a single-cell TFE, the thermionic cell is of the same length as the core or TFE. In a multi-cell TFE, several thermionic cells are located along the TFE length. In the USSR, both layouts of 5–10 kW electric power were developed (and created) on a competitive basis. They used thermal neutron reactors with a zirconium hydride moderator.

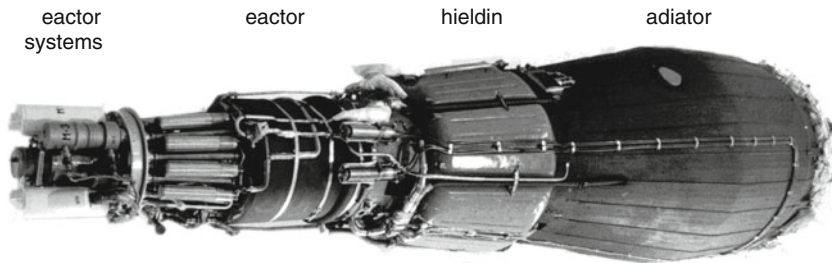
Simultaneously, studies were performed to justify the opportunity to create a more powerful (~500 kW) system in which a fast reactor was considered as a power source.

Space Nuclear Power System “Topaz” with Multi-Cell TFEs

The system development started in the 1960s. In 1970–1973, first time in the world, three prototypes of thermionic reactor-converters with multi-cell TFEs underwent terrestrial electrical testing. Then, after the testing of the fourth prototype employing TFEs with single-crystal molybdenum emitters coated with single-crystal tungsten, the creation of the “Topaz” NPS for

■ Fig. 59.6

Space nuclear thermionic plant “Topaz”



the experimental space vehicle (SV) started (Mashinostroyeniye Entsiklopediya, Kuznetsov et al. 1974; Gryaznov et al. 1989). ➤ Figure 59.6 presents the “Topaz” NPS layout.

The unit for cesium vapor supply, of the control system drivers, the reactor-converter, the reactor shielding, and the radiator are located in series along the system axis.

The automatic control system (ACS) is located in the instrumentation module and connected to the NPS systems by electrical service lines.

The core consists of several tens of TFEs and four zirconium hydride moderator discs. Fission gas is vented from multi-cell TFEs to the interelectrode gap (IEG). TFEs are electrically connected so that they form the operating section and the pump section. TFEs are electrically connected at both ends in cesium vapor. The operation section terminal electrical output is about 6 kW.

Rotating beryllium drums with boron carbide cover plates located in the side reflector provide the control. Each group of controls has its own drive.

The system of cesium vapor generation and supply providing its venting through the TFE interelectrode gap is employed.

The lithium hydride single-component radiation shielding is placed in the hermetically sealed steel cask.

The radiator has a load-carrying capacity and serves as a structural component. It is designed as a system of D-shaped tubes welded into the ring-type collectors and supported by the load-bearing elements. The tubes' plate surface is soldered to the radiator steel ferrule having a high emissivity coating. The sodium–potassium coolant cooling TFEs anodes transfers heat to the steel ferrule. The radiator emissivity ensures rejection in space of at least 170 kW (th) at the coolant temperature at the radiator inlet up to 880 K.

The NPS “Topaz” is 4.7 m long of 1.3 m maximum diameter and ~1,200 kg mass.

Starting from 1979, three nuclear-power tests of the NPS with the ACS were performed during terrestrial running tests. The last test lasted for about 7,000 h. During the tests, a conversion efficiency degradation by ~ 20% was found, which was attributed mainly to hydrogen outflowing from the moderator units and penetrating into the IEG. Hydrogen presence resulted in the plasma losses and extraneous heat removal into the IEG.

Two “Topaz” NPSs were tested in flight in 1987–1988 with the spacecrafts “Cosmos-1818” and “Cosmos-1867.” Spacecrafts were placed in a circular operational orbit at a height in excess of 800 km. NPSs were operated for 5 months and about 1 year, respectively. The initial values of the systems' parameters after bringing to a nominal power were close to those obtained in the terrestrial tests. However, by the end of tests, the efficiency degraded by 25%.

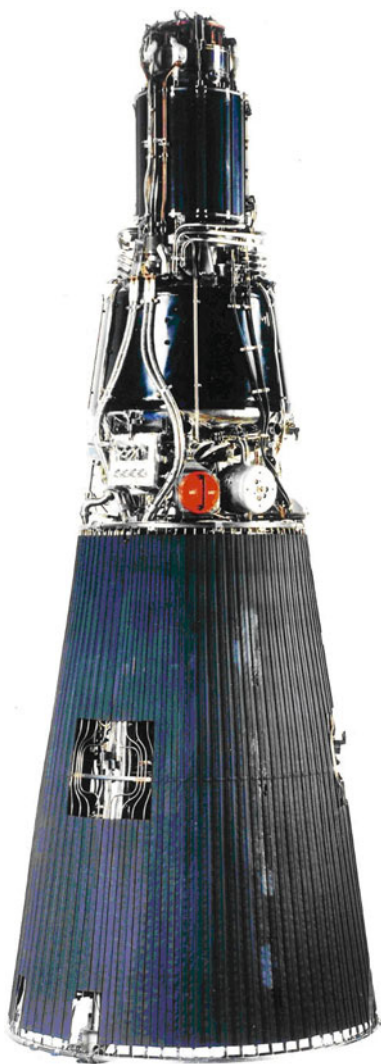
Space Nuclear Power System “Yenisey” with Single-Cell TFEs

Development of the “Yenisey” NPS (“Topaz-2”) was initiated at the end of the 1960s. As it can be seen from ▶ Fig. 59.7, its layout is close to that of the “Topaz” NPS. The system is 3.9 m long of 1.4 m diameter and 1,000 kg mass. Its distinctive feature is the employment of single-cell TFEs that allowed to simplify the perfection of units and the NPS as a whole and to establish better hygienic conditions for the thermionic converter operation (Ponomarev-Syepnoi et al. 1993; Kukharkin et al. 1999; Nikitin et al. 2000; Kukharkin et al. 2008).

A single-crystal molybdenum alloy coated with single-crystal tungsten (enriched in tungsten-184 isotope as it has the lowest cross section for neutron capture of all the W isotopes) was

■ Fig. 59.7

Space nuclear thermionic plant “Yenisey”



used as the emitter material. The collector was made of the polycrystalline molybdenum alloy. The emitter units have central orifices. Pellets of uranium dioxide of 96% enrichment in U-235 may be loaded through the orifice at any stage of the system preparation. Tungsten electrical heaters may be inserted instead of nuclear fuel to perform the system-running tests without nuclear heating and to check the system output parameters at the stage of system manufacturing. These orifices allow removing fission gas into space that facilitates the cathode integrity.

There are 37 TFEs in the reactor core (► Fig. 59.8). Three of those supply electric current to the pump section. The remaining 34 TFEs supply electric current to the operating section. The electrical connection is at the reactor, both ends in a helium chamber. The electrical power on the operating section terminals ranges from 4.5 kW up to 5.5 kW at the voltage of about 30 V.

The ACS controls the system. Nine of 12 control drums located in the reflector are controlling members and are actuated by one automatic control (AC) drive located behind the radiation shielding.

Three controls of the emergency protection system are actuated by their own drives operating only on bringing the reactor to power.

The original system for generation and wick feed of cesium vapors is employed. Cesium vapor is rejected into space through the controlled throttle. Depending on cesium flow rate, the necessary pressure is settled in the volume of interelectrode gaps. Cesium is heated by the liquid metal loop.

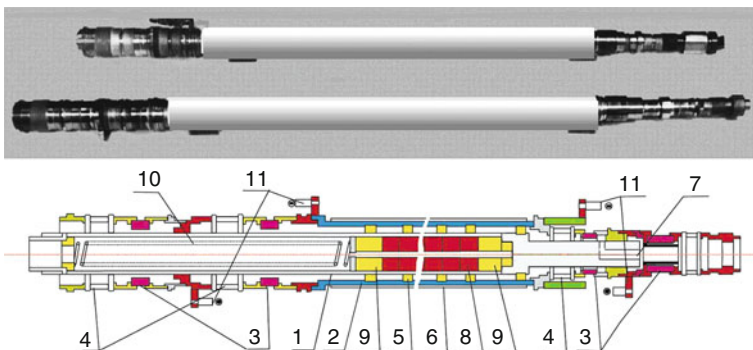
The radiator consists of round finned tubes forming a conical surface joined to the frame. The outer surface of fins has a special coating increasing the emissivity.

The hydrogen retention system, based on the protection of the moderator units and the reactor inner cavities by special coatings with special gas supplied into these cavities to replenish and recover the coatings became an important distinction of the “Yenisey” NPS. This system allowed extending the system lifetime significantly.

The “Yenisey” NPS underwent a whole cycle of the terrestrial running tests including off-line tests of units and systems and mechanical, vibration, thermal physic, electrical, and power tests of models and prototypes. In the course of running tests, the opportunity was taken to

■ Fig. 59.8

Thermionic channel “Yenisey”: 1, Emitter; 2, Collector; 3, Metal-ceramic units; 4, Bellows units; 5, Spacers; 6, External insulation; 7, Cesium input; 8, Fuel; 9, End reflector; 10, Retaining device; 11, Current leadouts



replace nuclear fuel in single-cell TFEs by electric heaters that allowed simulating all basic operational modes of the NPS without nuclear fuel.

Between 1975 and 1986, six terrestrial nuclear power tests that lasted from 3,000 up to 14,000 h confirmed the rated performances. On the basis of these tests and on a series of off-line tests of TFEs, the system predicted lifetime was not less than 3 years.

The main difficulties occurring in the course of durable terrestrial running tests were associated with the maintaining of operational ability of facilities' systems providing the conditions close to the flight ones.

The “Yenisey” NPS did not undergo flight tests.

Russian-American Cooperation

Tests and further development of the NPS with single-cell TFEs were continued in 1991–1996 under the agreement between the SPI/ISP (USA) and Russian developers approved by the Governments of both countries. Two models of the “Yenisey” NPS (named in the USA as “Topaz-2”) were tested in the new-built facilities with electric heating at University of New-Mexico and in Albuquerque. Specialists from Russia, USA, Great Britain, and France took part in these tests. The results of tests confirmed the required parameters (Nickitin et al. 1992; Topaz 1995; Andreev et al. 1995; Wetch et al. 1997).

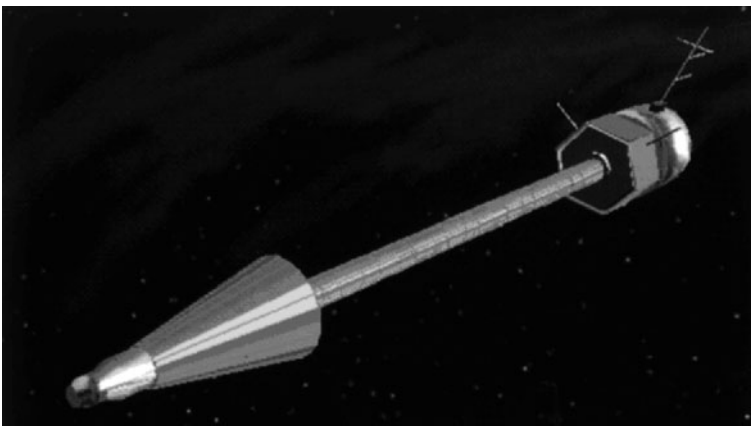
Successful tests gave grounds to the American specialists to start development of the experimental space system NEPSTP with the “Topaz-2” NPS and electrical jet-propulsion engines of different types to transfer a space vehicle from a radiation-safe orbit to the geostationary one ($H = 36,000$ km) (► Fig. 59.9), and to start development of the SPACE-R thermionic NPS of 40 kW electrical power using the “Topaz-2” technology.

Though the “Topaz” program was not fulfilled in a full scope, it was an example of cooperation between Russia and the USA and promoted the achievements in new technology knowledge.

Works on the TFEs perfection and increase of their power are being continued in Russia.

■ Fig. 59.9

American space nuclear power system NEPSTR with “Topaz-2”



59.2.2 Nuclear Power Propulsions

This section considers nuclear power propulsions (NPPs) in which the propellant heated up to a high temperature expels through the nozzle creating a jet thrust. They are intended for a delivery of space vehicles to the near-earth high orbits, to the Moon and to the solar system planets. As compared to chemical jet engines, the NPP specific impulse is more than two times higher. Among other propellants, hydrogen is preferred that is stored in liquid state on the SV board. Though the ratio of thrust to the engine mass of the NPP is less than that of the oxyhydrogen liquid engine, the mass of delivered payload is two times higher due to the exceeding specific impulse and relatively low propellant consumption.

Different reactor layouts were studied for the employment in the NPP. According to the set of developed technologies and obtained study results, NPPs with a solid-core reactor are best prepared for the practical application. Though, along with those, the NPPs with a gas-core reactor were studied theoretically and experimentally in the USSR and in the USA.

59.2.2.1 Programs of the NPP Development in the USSR and the USA and the Achieved Results

The NPP development started in the USA and USSR almost simultaneously in the mid-1950s, but the American researchers managed to demonstrate the feasibility of their ideas somewhat earlier (Dyakov et al. 1985; Demyanko et al. 1993; Deniskin et al. 1993; Bennet et al. 1994; Ponomarev-Stepnoy et al. 1999).

During 1955–1973, under the national program ROVER/NERVA 20 NPP reactors (of the KIVI, NRX, Phoebus, Pewee, XE series) of 100–5,000 MW rated power to produce thrust of 2×10^6 – 1.1×10^7 N were developed in the USA and tested at the nuclear site Nevada. The program of running tests was focused on the integrated testing of the whole system.

The concept of the American NPP reactor was based on the homogeneous graphite core stacked up of hexagonal fuel elements with a turnkey size 19 mm having 19 orifices for hydrogen flowing through. Microparticles of uranium bicarbide dispersed in a graphite matrix served as the fuel. The average temperature for hydrogen heating up to 2,280–2,550 K and the thrust specific impulse of 8100–8500 m/s were achieved in tests.

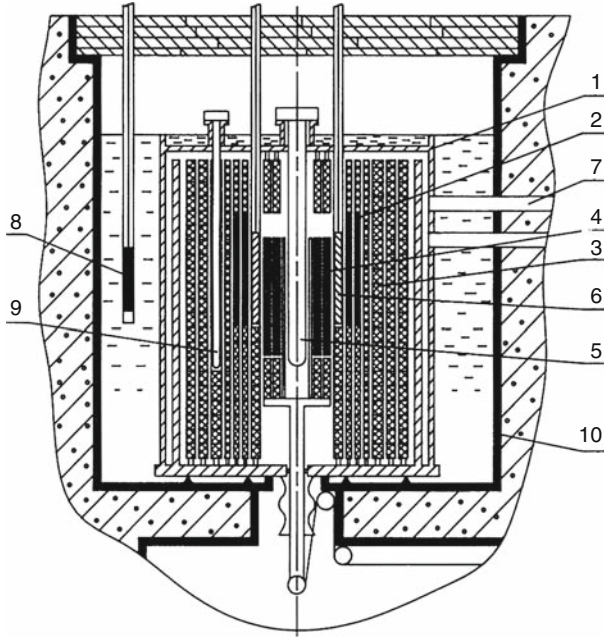
Another line of the NPP development was chosen in the USSR. The program was based on the creation of the technology, production, and testing basis for the element-by-element individual running tests of the engine basic units and systems and for their finishing in tests of the reactor models and engine as a whole. All this allowed reducing expenses significantly.

An impulse graphite reactor IGR (➤ Fig. 59.10) with a central channel to test fuel assemblies at the NPP transient operation modes and a research reactor IVG-1 (➤ Fig. 59.11) to test full-scale fuel assemblies (FA) of nuclear rocket engines of 3×10^5 – 4×10^6 N and higher thrust were built at the Semipalatinsk nuclear test site. Further, an experimental NPP model of a low thrust was mounted at the same site.

The concept of Russian NPP reactors was based on a heterogeneous structure consisting of fuel assemblies located in the moderator units. High-temperature compositions of uranium carbide and refractory metals (UC-ZrC-NbC, UC-ZrC) were employed as FAs materials allowing to achieve the level of hydrogen heating up to 2,900–3,100 K and to increase the thrust specific impulse up to 9,000–9,500 m/s. The heterogeneous structure allowed to perform

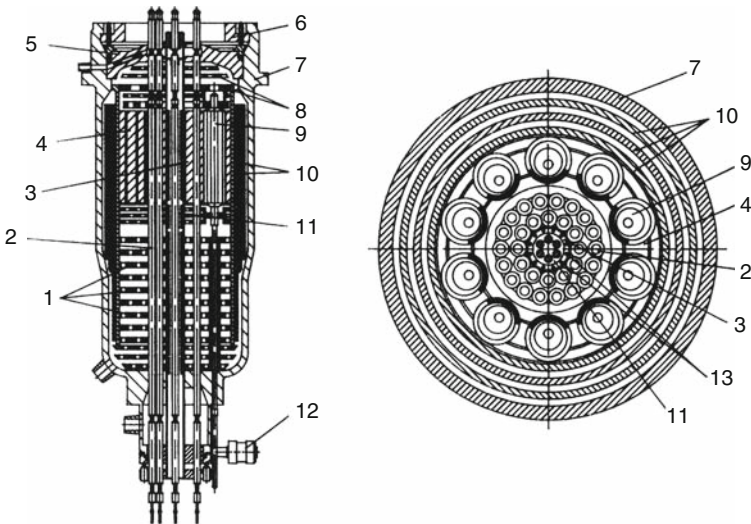
■ Fig. 59.10

Reactor IGR: 1, Reactor vessel; 2, Core; 3, Reflector; 4, Mobile core; 5, Experimental channel; 6, Control rod; 7, Helium pipeline; 8, Ionization chamber; 9, Experimental channel; 10, Water tank



■ Fig. 59.11

Reactor "IVG-1": 1, Fe-H₂O shielding; 2, Fuel channels; 3, Centre insertion; 4, Reflector; 5, Cover; 6, Lock; 7, Vessel; 8, Upper shields; 9, Control drums (CD); 10, Side shields; 11, Experimental channel; 12, CD driver; 13, Reactivity compensation rods



running tests of the reactor's most crucial component (FA) individually. The components were tested in the IGR and IVG-1 reactors.

The IVG-1 test facility was commissioned in 1975. By 1990, about 150 FAs of more than ten modifications including a set of FAs for the IRGIT prototype reactor for the low-thrust NPP were tested at that facility. In the course of these tests, the following parameters were achieved:

Temperature of hydrogen heating in a FA	2,600–3,100 K
• A single FA lifetime	4,000 s
• Number of times of a single FA bringing to power	12
• Rate of a FA heating-cooling	150 K/s
Density of power rate in fuel elements	35 kW/cm ³

No losses of FAs operational abilities were established in the tests.

► [Table 59.3](#) presents the NPP comparative performances achieved in the USSR and USA.

59.2.2.2 The Russian Concept of the Model NPP Designs

Characteristic features are a heterogeneous core and a modular structure that allow simplifying the reactor and NPS running tests.

The reactor is a channel-tank type unit in which a core, a side reflector with rotating control drums and internal protection are located. A nozzle chamber is located below the reactor.

The core comprises fuel assemblies, the moderator, and complementary nuclear safety rods (on delivery to the supporting orbit). FA consists of a bundle (► [Fig. 59.12](#)) of densely packed carbide-graphite elements and of twisted carbide FEs of different compositions based on uranium enriched up to 90%. This design allows reducing the nonuniformity of power deposition and the coolant temperature at the FA outlet.

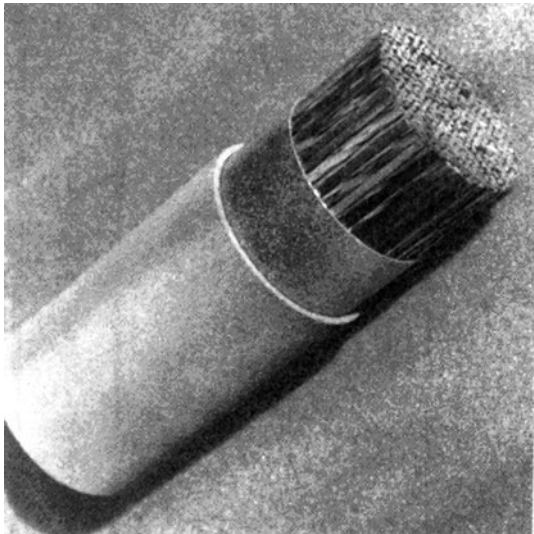
Yttrium hydride or zirconium hydride may be used as a moderator. Boron carbide or alloys of rare earth elements (Eu, Gd, Hf) serve as absorbing elements in control drums. The beryllium reflector is sectional (at high temperatures, beryllium oxide may be also employed).

■ [Table 59.3](#)

NPP performances achieved in the USSR and the USA

Performances	USSR	USA
Power, MW	230 (IVG1)	4,100 (Phoebus 2A)
Propulsion, MN	~0.15 (IVG1)	≈0.93 (Phoebus 2A)
Hydrogen flow rate, kg/s	16 (IVG1)	120 (Phoebus 2A)
Specific propulsion pulse, m/s	~9,500 (IVG1)	≈8,480 (Pewee)
Coolant outlet average temperature, K	3,100 (IVG1)	2,550 (Pewee)
Average power density in the core, kW/cm ³	15 (IVG1)	2.3 (Pewee)
Maximum density of power rate in fuel, kW/cm ³	35 (IVG1)	5.2 (Pewee)
Lifetime at the nominal power, s	4,000 (IVG1)	6,540 (NF1)
Maximum number of start-ups	21 (IVG1)	28 (XE)

■ Fig. 59.12
Bundle of fuel elements



Materials for the reactor load-bearing elements are chosen with regard to the specified operation conditions (pressure, consistency with hydrogen, irradiation conditions). Both nitrogen-doped chromium-nickel steels and alloys of the Fe-Cr-Ni system containing Mo, Nb, Al, and Ti may be employed. The compositions $\text{ZrH}_{1.85} + \text{LiH}$, $\text{ZrH}_{1.85} + \text{B} + \text{LiH}$, $^{238}\text{U} + \text{LiH}$ are the candidates for the radiation shielding. The shielding forms a shadow cone with $10^\circ\text{--}30^\circ$ angle.

As applied to space missions (a CV delivery to the geostationary orbit, cargo delivery to the Moon, Mars), different NPPs with the thrust between 5 kN and 10^4 kN, total time of the engine operation 1–6 h at 10–20 start-ups were put under consideration. Due to the difficulty to perform running tests of powerful engines, the opportunity to employ a bunch of engines for spacecrafts was considered.

The NPP design performances for the Moon and Mars exploration are as follows:

Reactor type	Intermediate
• Propellant	Hydrogen
• Thrust-specific impulse	9,400–9,550 m/s
• Thrust of the NPP single module	6.8×10^4 N
• The NPP module reactor thermal power	340 MW(t)
• Propellant flow rate	7.1 kg/s
• Propellant temperature in the nozzle chamber	2,900–3,100 K
• Propellant pressure in the nozzle chamber	6 MPa
• Fuel	Solid solutions of UC-ZrC-C, UC-ZrC, UC-ZrC-NbC

• Uranium enrichment	90%
• ^{235}U loading	20.1 kg
• Moderator	$\text{ZrH}_{1.85}$
• Neutron flux in the core	$1.2 \times 10^{19} \text{ cm}^2/\text{s}$
• Efficiency of controls:	
Control drums	5.6%
Nuclear safety rods	9.8%
Thrust to the NPP mass ratio (without hydrogen tanks)	24–31 N/kg

59.2.3 Nuclear Power Propulsion Systems (NPPS)

Nuclear power propulsion systems (NPPS) in contrast to onboard sources and NPPs discussed in [Sects. 59.2.1](#) and [59.2.2](#), respectively, may perform both functions: generate electric energy for the spacecraft's onboard needs and/or heat the propellant producing thrust (Pupko et al. 1991; Kolganov et al. 1993; Ponomarev-Stepnoi and Usov 1995; Ponomarev-Stepnoi et al. 1995, 1996, 2003, 2005).

They may be developed on the basis of both the NPP and the onboard nuclear power system technologies. The NPPS reactor is operated in two modes: either continuous power or short propulsion. Power levels at those modes differ by 3–4 orders of magnitude.

In the NPPS based on the NPP technology, the reactor is successfully combined with a dynamic power conversion system operating in a closed gas turbine Brayton cycle (helium and xenon) or in a potassium steam turbine Rankine cycle.

[Figure 59.13](#) illustrates the layout of the NPPS with a dynamic converter operating in the Brayton cycle. This layout is considered to be the prospective one for the manned Martian mission. Its performances for the power mode are as follows:

Reactor thermal power	90 kW
• Coolant	98.3% Xe + 1.7% He
• Coolant flow rate	1.13 kg/s
• Coolant temperature at the reactor inlet/outlet	1,190/1,500 K
• Maximum pressure in the power conversion loop	1.0 MPa
• Electric power	25 kW
Brayton cycle efficiency	28.6%

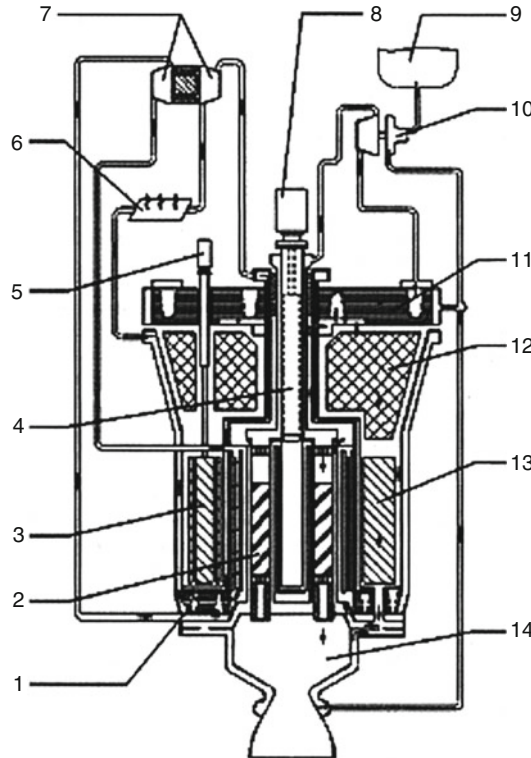
The system performances for the propulsion mode correspond to those of the NPP operating with hydrogen.

The planned lifetime in the mode of electric power production employing intermediate reactors is 3 years. On extending the lifetime up to 10 years, fast reactors are the best choice.

The NPPS based on the NPP technology are effective at high-altitude near-earth orbits as electric power sources. With the NPPS thrust of about 500 kN, time of delivery to the geostationary orbit will be 6–10 h.

■ Fig. 59.13

Nuclear power propulsion system (NPPS): 1, Recuperator; 2, Fuel assembly; 3, Control drum (CD); 4, Nuclear safety rod (NSR); 5, CD Drive; 6, Radiator; 7, Turbogenerator; 8, NSR Drive; 9, Hydrogen Tank; 10, Turbo-pump; 11, Hydrogen recuperator; 12, Shielding; 13, Reflector; 14, Nozzle



The NPPs based on thermionic reactor converters may also become the basis for nuclear power propulsion systems. There are two possible development lines:

- Power increase and employment of electrical jet engines to produce thrust.
- Development of bimodal reactors.

The NEPSTP project carried out in the USA by the APL incorporating Russian space NPS “Yenisey” and different electrical jet engines either American or Russian ones may serve as an illustration of the first development line. The long duration (about half a year) of a payload delivery to the geostationary orbit is a disadvantage of this system, though its readiness is of the highest degree.

The system based on the bimodal reactor in which electric power is generated in a thermionic converter and thrust is produced by hydrogen expelled through the core (TFE) will allow significantly shorter time of delivery to high-altitude orbits.

Thus, the employment of the NPPS based on the NPS with dynamic power conversion system is preferable for missions of fast delivery (especially, in case of manned interplanetary flights), but for the cargo carrying, the NPPS based on the NPS with the electric jet propulsion system is preferred.

59.3 Radioisotope (Radionuclide) Power Sources

Power released in these sources is associated with radioactive decay of different radionuclides generated either on fission in nuclear reactors or on neutron irradiation of stable isotopes (Corliss and Harvey 1964).

In this case, it is impossible to control power-deposition processes. Power starts to be generated as soon as the radionuclide is produced. It decreases exponentially and is determined by the amount and the decay constant of the radionuclide. Thus, safety issues concerning these sources are crucial not only in the course of their operation but also at the stages of their production, of power-source assembling, storage, pre-starting procedures, and after decommissioning.

This section considers the radioisotope sources of electricity though they may be employed in space systems for the thrust production similar to the reactor sources. It is obvious that power of these sources is significantly lower than that of the reactor NPS.

Radioisotope sources of electric power are divided into two types according to the principle of electricity production: sources not employing a thermal cycle and sources employing that. The first ones are ordinarily termed as nuclear batteries.

Nuclear batteries are well suited to terrestrial applications; however, they are less applicable in space. They are divided into three categories:

- Single-stage batteries with a direct charge accumulation, that is, batteries with a direct conversion of radioactive decay energy into electricity.
- Two-stage batteries in which decay energy goes into the generation of a charge-free carrier (batteries with the p-n junction, Volta effect, secondary electron emission).
- Three-stage batteries in which decay energy goes into the production of photoradiation converted into electricity (photovoltaic arrays).

Let us consider sources employing a thermal cycle in more detail.

59.3.1 Radioisotope Thermoelectric Generators (RTGs)

These generators (which should be properly called radionuclide thermoelectric generators – a term rarely used) convert almost all energy of charged particles (α , β) and gamma-quanta into heat on their deceleration in the radioactive material and in the cladding of the capsule containing this material (Radioizotopnye istochniki elektricheskoy energii 1978; Turi et al. 1991).

This capsule with the radioactive material is called a radiation heat source (RHS). Heat may be produced in dynamic or static cycles using the temperature difference between RHS and environment. Similar to the reactor sources, static conversion systems, particularly thermoelectric ones, were widely used both in the USSR and in the USA. Systems on their basis have been named as radioisotope thermoelectric generators (RTG).

The RTG basic units include the radiation heat source (RHS), thermoelectric unit (TEU), radiation shielding (RS), and radiator. (Space systems need radiators also to cool them.) RTGs' merits are determined by the following unique properties: spontaneous release of thermal power, its direct conversion into electricity, a simple design, high-energy output, a long lifetime, the opportunity of employment practically in all scopes of activities: under water, at the surface of the Earth and planets, and in space.

In the USA, RTGs were mostly used in space systems. In the USSR, they were widely employed in navigation.

59.3.1.1 The Choice of Radionuclides and the Methods of RTG Manufacturing

A wide range of radioactive nuclides (► [Table 59.4](#)) may be employed for RTGs as power sources. According to the fabrication method, they may be divided into four groups (Radioizotopnye istochniki elektricheskoy energii 1978, Mashinostroyenie Entsiklopediya):

- ^{90}Sr , ^{147}Pm , ^{144}Ce , and ^{137}Gs are produced from nuclear wastes (fission products).
- ^{60}Co , ^{170}Tm , ^{192}Ir , and ^{210}Po are generated in nuclear reactors on the neutron irradiation of targets made of stable ^{59}Co , ^{169}Tm , ^{191}Ir , and ^{209}Bi .
- ^{227}Ac and ^{232}U are produced by the neutron irradiation of uranium-cycle by-products such as ^{226}Ra , ^{230}Th , and ^{231}Pa .
- ^{238}Pu , ^{242}Cm , and ^{244}Cm are generated in the course of the irradiation of plutonium-cycle by-products ^{237}Np , ^{241}Am , and ^{243}Am .

Nuclear wastes are the most readily available and cheapest raw materials for the production of radioactive nuclides in large amounts. The nuclides ^{210}Po and ^{60}Co of the second group are the most advanced ones both in their production method and in their properties. The production

■ **Table 59.4**

Radionuclides with a half-life between 100 days and 100 years

Nuclide	$T_{1/2}$	Specific activity ^a Ci/g	Nuclide	$T_{1/2}$	Specific activity ^a Ci/g
^3H	12.26 years	9,700	^{171}Tm	1.9 years	1,100
^{22}Na	2.58 years	6,320	^{192}Ir	74.4 days	9,170
^{45}Ca	164 days	17,750	^{194}Os	1.9 years	980
^{60}Co	5.27 years	1,140	^{204}Tl	3.56 years	490
^{85}Kr	10.3 years	410	^{210}Po	138.4 days	4,500
^{90}Sr	28.4 years	139	^{227}Ac	21.7 years	75
^{106}Ru	1 year	3,400	^{228}Th	1.9 years	829
^{110}Ag	253 days	4,700	^{232}U	73.6 years	21
^{113}Cd	5.1 years	620	^{235}Np	410 days	1,360
^{125}Sb	2 years	1,440	^{238}Pu	87.5 years	17
^{134}Cs	2.07 years	1,300	^{242}Cm	162.5 days	3,340
^{137}Cs	30 years	87	^{244}Cm	18.4 years	80
^{144}Ce	284.4 days	3,200	^{248}Cf	350 days	1,510
^{147}Pm	2.62 years	930	^{249}Ci	360 days	1,460
^{155}Eu	1.7 years	1,360	^{250}Cf	10.9 years	130
^{170}Tm	128.5 days	6,000	^{252}Cf	2.9 years	650

^aSpecific activity of the real radioisotope fuel is determined by the content (%) of the respective nuclide

of radionuclides of the third and fourth groups is associated with a series of technological difficulties both in the production of initial materials and in their processing after the irradiation. ^{238}Pu and ^{244}Cm are the best candidates for the creation of the durable lifetime sources of electricity.

59.3.1.2 Purpose. Classification. Basic Requirements and RTG Performances

According to the application environment, RTGs are grouped into terrestrial, marine, and space ones (Mashinostroyeniye Entsiklopediya, Corliss and Harvey 1964; Radioizotopnye istochniki elektricheskoy energii 1978).

Terrestrial RTGs are usually placed at the distant and hard-to-reach areas to supply electric power to scientific equipment or beacons of different purposes. They are distinguished by simplicity of fabrication and maintenance. These generators employ, as a rule, cheap fuel with a long half-life (^{90}Sr or mixed fission products). ▶ Table 59.5 presents the basic performances of these RTGs fueled by ^{90}Sr .

Marine RTGs are used as the sources of electricity for subsea buoys and lighthouses. ▶ Table 59.6 comprises the performances of these systems.

Space RTGs are employed as the power supply for the equipment and instrumentation of space vehicles operating in near-Earth orbits, on the Moon, Mars and other planets, and their satellites.

In the USSR, RTGs operated in artificial satellites (AS) of the “Kosmos-84” series. In the USA, 38 RTGs of different design and power were launched in space between 1961 and 1977. Later, a unified GPHS RTG with ^{238}Pu fuel pellets and thermal power of 300 W was developed

■ Table 59.5

Basic performances^a of some terrestrial RTGs

RTG type, country	W W	U V	t year	Efficiency %	W_{sp} , W/kg	Mass kg	Dimensions mm
Beta-M, Russia	10	14	10	4.2	0.017	550	660 × 655
Efir-MA, Russia	30	35	10	4.2	0.023	1,250	815 × 1,430
Angara, Russia	12		10	4.8	0.1	120	-
Gong, Russia	18	14	10	6	0.03	600	730 × 945
Gorn-M, Russia	66	7,14,28	10	6.3	0.066	1,000	820 × 1,270
Gloria-10, Russia	10	7,14	10	6.9	0.069	260	650 × 650
Gloria-20, Russia	20	7,14	10 (20)	7.2	0.076	280	650 × 850
Gloria-40, Russia	40	7,14	10 (20)	7.9	0.132	400	550 × 1,000
Gloria-60, Russia	60	7,14,28	10 (20)	8.1	0.152	460	650 × 1,200
Gloria-80, Russia	80	7,14,28	10 (20)	8.2	0.147	800	850 × 1,000
Gloria-120, Russia	120	7,14,28	10 (20)	8.4	0.19	850	850 × 1,230
BUP-500, USA	610	28	5.5	8.5	0.18	3,300	1,392 × 1,392

^aRadionuclide – ^{90}Sr . Designations: W = electric power; U = voltage; t = lifetime; W_{sp} = specific electric power

■ **Table 59.6**

Basic performances of some RTGs designed for marine applications

RTG type, country	Radio-nuclide	W W	U V	t year	Efficiency %	W_{sp} W/kg	Mass kg	Depth of submergence m	Application
SNAP-7A, SNAP-7C, USA	^{90}Sr	11.6	5	10	4.5	0.014	850	0	Navigation beacons
SNAP-7B, SNAP-7D, USA	SrTiO_3	68	12	10	4.7	0.033	2,090	0	Lighthouse
SNAP-7E, USA	^{90}Sr	6.5	4.5	5	3.3	0.0064	1,020	6,850	Subsea buoys
SNAP-21, USA	^{90}Sr	14	3.5	5	6.9	0.064	227	7,000	Subsea buoys
SNAP-23, USA	^{90}Sr	88	28	10	7.1	0.19	450	7,000	Subsea buoys

■ **Table 59.7**

Basic performances of some space RTGs

RTG type, country	Radionuclide	W W	U V	t year	Efficiency %	W_{sp} W/kg	Mass kg	Application
SNAP-3A, USA	^{238}Pu	2.7	-	5	5.0	1.5	2.1	AS
SNAP-9A, USA	^{238}Pu	25	-	5	5.1	2.2	12.3	AS
SNAP-19B, USA	$^{238}\text{PuO}_2$	28	4.75	3–5	6.0	2.1	13.6	AS
SNAP-27, USA	$^{238}\text{PuO}_2$	73	16	5	5.0	2.3	31.7	Moon station
Transit-RTG, USA	$^{238}\text{PuO}_2$	35	-	-	4.2	2.6	13.5	AS
SNAP-19, USA	$^{238}\text{PuO}_2$	42	-	5	6.3	3.0	14	AS
MHW-RTG, USA	$^{238}\text{PuO}_2$	160	-	12	6.7	4.2	38.1	AS
Orion-1, Russia	^{210}Po	22	-	0.6		2.7	8.2	AS
"Angel," Russia	^{238}Pu	0.1	15	10	1.2	0.2	0.5	SV
GPHS-RTG, USA	$^{238}\text{PuO}_2$	300	-	8–10	9.0	7.0	42.9	SV
Margarita-20, France	^{90}Sr	12.5	-	5	4.7	1.6	8	SV

that supplied electric power for space vehicles (SV) in flights to Jupiter, Saturn, and other planets. ➤ [Table 59.7](#) contains the basic performances of space RTGs.

The basic common requirements imposed on RTGs of different purposes are as follows: a high efficiency and electric power density, long lifetime, reliability, and sufficiently high operating temperatures of the conversion system. Strong gamma-radiation requiring heavy

shielding must be eliminated. The following special requirements are imposed on space-based RTGs: the mass and dimensions must be minimized; the radiator temperature must be optimized to provide the removal of excess heat into the environment.

59.3.1.3 Examples of RTG Designs for Terrestrial and Space Applications

In the course of the RTGs' development, the general concept took into account their purpose. The following units and materials were developed and fabricated for the terrestrial RTGs (Mashinostroyeniye Entsiklopediya, Radioizotopnye istochniki elektricheskoy energii 1978; Turi et al. 1991; Schock et al. 1999):

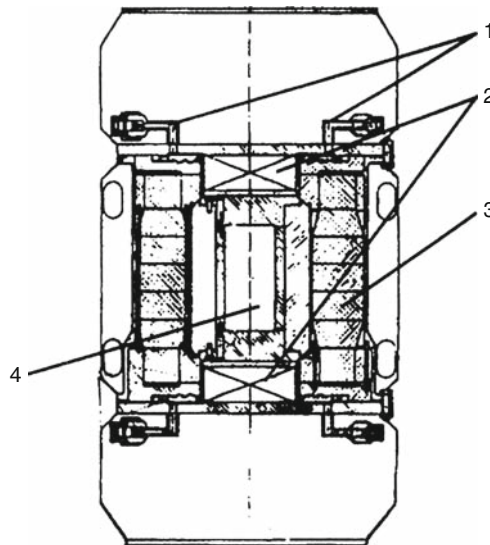
- A parametric series of unified RHS designs based on strontium titanate of 20–100 W thermal power, 0.8 W/cm^3 volumetric heat generation, $800\text{--}900^\circ\text{C}$ operating temperature, and 11.5 year lifetime.
- Medium-temperature two-stage thermal-electric batteries (TEBs) of 8–9% efficiency, $400\text{--}500^\circ\text{C}$ operating temperature, electric power of 2–159 W, and 10 year lifetime.
- High-temperature refractory alloy based on depleted uranium (U+Mo) for gamma-shielding. The operating temperature is $700\text{--}800^\circ\text{C}$, lifetime is 10 years, density $\geq 17 \text{ g/cm}^3$.
- Fibrous thermal-insulating material with the operating temperature 800°C , coefficient of heat conduction 0.04 W/m/K , lifetime 15 years, density $0.30\text{--}0.35 \text{ g/cm}^3$.

The RTGs of the “Gong,” “Gorn,” “Heli,” and “Gloria” types (Fig. 59.14) were developed on the basis of these units.

These RTGs employ multibank plate TEBs enclosed in hermetically sealed casings located at the RHS upper and/or lower end with the combined radiation shielding and prestressed

■ Fig. 59.14

RIG “Gloria 40”: 1, Cooling system; 2, Thermogenerator; 3, Insulation; 4, RHS



thermal insulation. The available heat factor is 85–92%, efficiency is 7–8%, lifetime amounts to 10–15 years, electric power ranges between 10 and 15 W, voltage is 7, 14, 28 V, specific power is 0.08–0.2 W/kg.

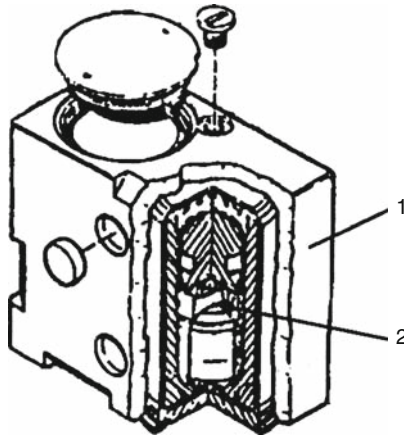
The low-power RTGs fueled with ^{238}Pu were mainly developed in the USSR for medical purposes.

The RTGs for space applications were developed largely in the USA. Unified generators and their units (modules) were also created there.

Their design can be illustrated by the American GPHS-RTG thermoelectric generator (► Fig. 59.15) employing ~ 20 heat-source modules (► Fig. 59.16). The RTG of this design may supply electricity to space vehicles exploring the solar space under almost all programs.

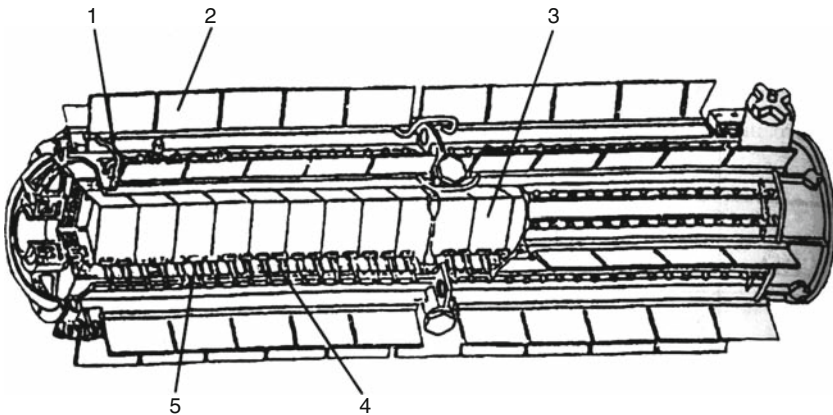
■ Fig. 59.15

Radioisotopic heat source (RHS): 1, Graphite cover; 2, $^{238}\text{PuO}_2$ pellet



■ Fig. 59.16

Radioisotopic thermoelectric generator GPHS-RTG: 1, Coolant tubes; 2, Radiator edge; 3, RHS modules; 4, Thermoelectric element; 5, Insulation



According to their simple and reliable design, mass-dimension characteristics, and lifetime, space RTGs with electric power ranging from fractions up to hundreds of watts are the best power sources for space vehicles. The GPHS-RTG, the USA basic space RTG, based on ^{238}Pu with electric power $W = 300\text{ W}$ has a specific electric power $W_{\text{sp}} = 7\text{ W/kg}$. The RTG lifetime for the flights into deep space comprises 8–10 years.

References

- Andreev PV, Galkin AY, Zhabotinsky EE et al (1995) Electrical propulsion units based on Topaz-type thermionic nuclear power systems for information satellite systems. In: Proceedings of the 12th Symposium on space nuclear power systems, Pt. 1, Albuquerque NM, pp 335–339
- Bennet G et al (1994) Prelude to the future: A brief of nuclear thermal propulsion in the United States. In: A critical review of space nuclear power and propulsion 1984–1993. AIP Press, New York, pp 221–267
- Corliss WR, Harvey DG (1964) Radioisotopic Power Generation, Prentice Hall, Englewood Cliffs, NJ
- Demyanko YuG, Kostylev AM, Fedotov RA (1993) Nazemnaya obrabotka yadernykh raketnykh dvigateley s tverdogaznym reaktorom v SSSR. Raketnaya kosmicheskaya tekhnika. Nauchno-tekhnicheskyy sbornik, 1(134). Raketnye dvigateli i energeticheskiye ustanovki. Sistemy i sredstva bortovoy energetiki. M.: NIITP, 45–54
- Deniskin VP, Dyakov YeK, Nezhevenko LB et al (1993) Rezultaty razrabotki i ispytany TVS aktivnykh zon reaktorov yard. Tezisy doklada 3-y otraslevoyy konferentsii “Yadernaya energetika v kosmose. Yadernye raketnye dvigateli.” Podolsk, 27–32
- Dyakov YeK, Podladchikov YuN, Popov YeB, et al (1985) Problemy razrabotki TVS yard i dvigatelno-energeticheskikh ustanovok na baze yard. Raketno-kosmicheskaya tekhnika. Nauchno-tekhnicheskyy sbornik, ser. IV, 1(86):29–40
- Gryaznov GM (1999) Kosmicheskyye yadernye energeticheskiye ustanovki. Yadernoy nauke i tekhnike Rossyi 50 let. Tr. Ubileynoy Konferentsii. Ministerstvo Rossiyskoy Federatsii po atomnoy Energii. Moskva. Izdat
- Gryaznov GM, Zhabotinsky YeE, Zrodnikov AV et al (1989) Termoemissionnyye reaktory-preobrazovateli kosmicheskikh yaeu. Atomnaya Energiya 66(6): 374–377
- Gverdstiteli IG, Kukharkin NE, Ponomarev-Stepnoy NN, Usov VA (1969) Osnovnye rezultaty 15000-chasovykh ispytany vysokotemperaturnogo reaktora-preobrazovatela “Romashka” – V sb.: Doklady 4-y Amerikanskoy konferentsii po preobrazovaniyu energii. Washington
- Johnson RA, Morgan WT, Rocklin SR (1966) SNAP-10A - First reactor in space. SAE J 74(3):92–96
- Kolganov VD, Smetannikov VP, Ulasevich VK et al (1993) Mesto reaktora IVG1 v perspektivnoy programme sozdaniya yard dlya Marsianskoy ekspeditsii. Tezisy doklada 3-y otraslevoyy konferentsii “Yadernaya energetika v kosmose. Yadernye raketnye dvigateli. Podolsk, pp 427–436
- Kukharkin NE, Nechayev YuA et al (1999) Energoresursnyye kharakteristiki odnoelementnykh EGK, proshedsikh yaderno-energeticheskyye ispytaniya v sostave reaktornykh blokov ustanovki “Topaz-2.” Tezisy doklada 5-y Mezhdunarodnoy konferentsii “Yadernaya energetika v kosmose.” Podolsk. p 44
- Kukharkin NE, Ponomarev-Stepnoy NN, Usov VA (2008) Kosmicheskaya yadernaya energetika (yadernye reaktory s termoelektricheskimi i termoemissionnyymi preobrazovaniyem – “Romashka” i “Enisey”). Moskva, Izdat
- Kuznetsov VA, Gryaznov GM, Artyukhov GYa et al (1974) Razrabotka i sozdaniye termoemissionnykh yaeu “Topaz”. Atomnaya Energiya 36(6):450–457
- Mashinostroyeniye Entsiklopediya. Tom IV-25. Mashinostroyeniye yadernoy tekhniki. Kniga 2. Kosmicheskyye reaktornyye ustanivki
- Millionshchikov MD, Kukharkin NE, Ponomarev-Stepnoy NN, Usov VA, et al (1964) Vysokotemperaturnyy reaktor - preobrazovatel “Romashka” – Atomnaya energiya, 17(5):329–336
- Nikitin VP, Ogloblin BG, Sinkevich VG (1992) Special features and results of the TOPAZ-2 nuclear power system tests and with electric heating. 9th Symposium on space nuclear power systems, Pt. 1, Albuquerque NM, pp 41–46
- Nikitin VP, Ogloblin BG, Sokolov YeN, Ponomarev-Stepnoy NN, Kukharkin NE, Usov VA, Nikolayev YuV (2000) Kosmicheskaya yadernaya energeticheskaya ustanovka “Enisey.” Atomnaya energiya, 88(2):95–108
- Ponomarev-Stepnoy NN, Usov VA (1995) Conceptual design of the bimodal nuclear power system based on the “Romashka” type reactor the thermionic energy conversion system. In: 12th Symposium on

- space nuclear power systems. USA, Albuquerque, 1995
- Ponomarev-Stepnoi NN, Usov VA et al (1995) Conceptual design of the bimodal nuclear power and propulsion system based on the "Topaz-2" reactor with the modernized single-Cell TFE. In: 12th Symposium on space nuclear power systems, USA, Albuquerque, 1995
- Ponomarev-Stepnoi NN, Usov VA et al (1996) Bimodal space nuclear power system with fast reactor and Topaz-2 type single cell TFE. In: 13th symposium on nuclear power and propulsion, Pt. 3, 1077–1081
- Ponomarev-Stepnoy NN, Talyzin VM et al (1999) Raboty po sozdaniyu otechestvennogo yard. Atomnaya energiya, 86(4):296
- Ponomarev-Stepnoy NN, Talyzin VM, Usov VA (2000) Rossyskiye kosmicheskiye yadernye energeticheskiye ustanovki i yadernye raketnye dvigateli. – Zhurnal Nuclear News, dekabr
- Ponomarev-Stepnoy NN, Kukharkin NE, Usov VA, Talyzin VM, Pavshuk VA (2003) Rossyskiye kosmicheskiye yadernye energeticheskiye ustanovki i yadernye raketnye dvigateli. Perspektivy ispolzovaniya energodvigatelnykh ustanovok i tekhnologii ikh sozdaniya dlya mirnykh primeneny. – V sb.: Doklady 10-go mezhdunarodnogo seminaru po kosmicheskim dvigatelyam 10-JWC. Italiya, g.Lerika
- Ponomarev-Stepnoy NN, Pavshuk VA, Usov VA (2005) Rossyskiy opyt razrabotki yadernykh energoustanovok i yadernykh raketnykh dvigateley pervogo pokoleniya – kak osnova sozdaniya perspektivnykh energodvigatelnykh kompleksov dlya mirnykh issledovaniy blizhnego i dalnego kosmosa. – V sb.: Doklady mezhdunarodnogo astronavticheskogo kongressa. Japan, Fukuoka, October 2005, 47/S35, 13
- Ponomarev-Syepnoi NN, Usov VA et al (1993) Space nuclear power system based on thermionic reactor with single-cell TFEs. In: 10th Symposium on space nuclear power and propulsion, Pt. 3
- Pupko VYa, Vizgalov AV et al (1991) Fast neutron thermionic-converters for high-power space nuclear systems. In: 8th symposium on space nuclear power and propulsion, Pt. 3, pp 657–661
- Radioizotopnye istochniki elektricheskoy energii (1978) Pod redaktsiyey G.M. Fradkina. M.: Atomizdat, 304
- Schock A et al (1999) Design and analysis of RTGs for CRAF and cassini missions. In: Proceedings of the 8th Symposium on space nuclear power systems, Pt. 2, Albuquerque NM, 938–953
- Snyder NW (ed) (1961) Space power systems. Academic Press, New York, London
- Topaz (1995) Topaz International Program. Booz.Allen & Hamilton, Arlington, VA
- Turi DA, Dzhonson RA et al (1991) Kosmicheskaya radioizotopnaya programma ssha. Perevod s anglyskogo. Otrasleyaya yubileyay konferentsiya "Yadernaya energetika v kosmose": Tezisy dokladov. Obninsk, Ch.P., 31–52
- Wetch JR (1990) History of space nuclear power short course notes. In: 7th Symposium on space nuclear power. Albuquerque, New Mexico
- Wetch JR, Britt EJ et al (1997) Low-cost space fission power systems utilizing US and former Soviet Union experience and technology. In: 14th symposium on space nuclear power and propulsion, Pt. 3, 1309–1315

60 Technical Developments for Harnessing Controlled Fusion

G. Veres¹ · S. Zoletnik¹ · W. Jacob²

¹KFKI Research Institute for Particle and Nuclear Physics, Budapest, Hungary

²Max-Planck-Institut für Plasmaphysik, Bereich Materialforschung, AG Reaktive Plasmaprozesse, Garching, Germany

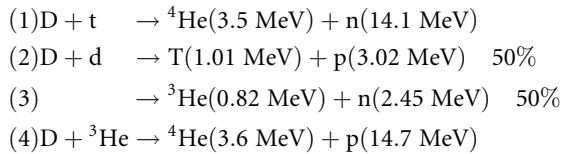
60.1	<i>The Necessary Conditions for Fusion Energy Production</i>	2760
60.1.1	Sources and Sinks of Power	2760
60.2	<i>Inertial Confinement Fusion</i>	2763
60.3	<i>Basic Schemes of Magnetic Confinement</i>	2766
60.4	<i>Technology of Magnetic Confinement Fusion Devices</i>	2769
60.5	<i>Plasma–Wall Interaction in Nuclear Fusion Devices</i>	2775
60.5.1	Basic PSI Processes	2778
60.5.2	Physical Sputtering	2779
60.5.3	Chemical Erosion	2782
60.5.4	Chemical Sputtering	2783
60.5.5	Redeposition and Co-Deposition	2785
60.5.6	Edge Plasmas in Magnetically Confined Fusion Devices	2786
60.5.7	Other PWI Processes	2788
60.6	<i>Prospects of Practical Application</i>	2790

Abstract: This chapter gives the conditions for achieving power production using nuclear fusion reactions. The two basic schemes for plasma confinement, inertial and magnetic, are briefly considered and the present technical solutions are outlined. The physical and chemical processes taking place between the hot plasma and the containing vessel wall are discussed in more detail. At the end of the chapter, the present status of research and the planned future development plans are summarized.

60.1 The Necessary Conditions for Fusion Energy Production

Inevitably, the final goal of nuclear fusion research is to create such conditions that $P_{\text{out}} > P_{\text{in}}$, that is, the power P_{in} necessary to run a fusion-based power station, must be smaller than the power output P_{out} of the station. From a global perspective, this inequality is *the* necessary condition for efficient fusion energy production. However, it is clear that in the everyday work, this inequality is too general and so practically meaningless. More practical necessary conditions are needed (see later on), which can serve as reachable targets during the developments.

In [Chap. 6 of Vol. 1](#), it was shown that sustained fusion reactions can only take place in a high-temperature thermal medium called plasma. It was also shown – and here it shall be repeated for convenience – that the most important nuclear reactions are at the present stage of research. Note that below (as throughout this chapter), element symbols refer to bare nuclei without the electron shell – a special notation common in the field of fusion.



As also shown in [Fig. 6.3](#) in Chap. 6 of Vol. 1, of the above mentioned chapter, the $\text{D}(\text{t}, \text{n}){}^4\text{He}$ reaction (DT reaction in short) is distinguished by the lowest plasma temperature needed and by the highest fusion probability. Consequently, this reaction is the most promising one, and therefore it will be dealt with almost exclusively throughout the rest of this chapter.

To derive the necessary conditions for fusion energy production, one needs to list and calculate all the sinks and sources of power both in the DT reaction and in the power station as a whole.

60.1.1 Sources and Sinks of Power

The energy generated in the course of a DT reaction is released in the form of the kinetic energies of the created particles. In the DT reaction, two particles are generated: an alpha particle and a neutron. Bearing no electrostatic charge, the neutrons rarely collide with plasma particles and, therefore, transfer only a negligible fraction of their kinetic energy to the plasma medium before leaving it. The alpha particle on the other hand, depending on the plasma parameters (density, size, etc.), can deposit a considerable fraction – in an optimum situation up to 100% – of its energy to the plasma.

Therefore, from a fusion reactor point of view, the utilization of the energy of alpha particles is different from that of the neutrons. The alpha particles' energy can and must be used for plasma heating (alpha heating), whereas the neutrons' energy must be absorbed

outside the plasma and converted to some useful form of energy (e.g., by heating steam generators and driving turbines with the steam in order to generate electricity). In the DD reactions, the situation is similar, but in the case of the D-He reaction all resulting particles are charged, therefore more energy is kept in the plasma.

At present, the problems, both technical and physical, connected with the maintenance of a proper energy balance of the plasma, are far more difficult to solve than the absorption of neutrons in a mantle that surrounds the plasma. Before continuing the topic of utilization of neutrons, the power balance for the plasma will be treated below.

A simple expression for the requirements for positive energy balance shall be derived below by assuming homogenous plasma with volume V . The volumetric rate (number per volume per time) of fusion reactions is

$$f = n_D n_T \langle \sigma v \rangle = \frac{1}{4} n_e^2 \langle \sigma v \rangle. \quad (60.1)$$

Here it was assumed that there are no ions other than the fuel ions present (i.e., no impurities and no helium ash), and that D and T are present in the optimal 50–50% mixture. n_D , n_T , and n_e are the deuterium, tritium, and electron densities, respectively, and $\langle \sigma v \rangle$ is the Maxwellian-averaged fusion reaction rate at the temperature T as given in [▶ Chap. 6 of Vol. 1](#).

The volumetric rate of alpha heating is f times E_α , the energy of the alpha particle (neutrons escape). Assuming alpha particle energy deposition with 100% efficiency:

$$P_\alpha = \frac{1}{4} n_e^2 \langle \sigma v \rangle \cdot E_\alpha. \quad (60.2)$$

The losses of power from the plasma can be very diverse: radiation losses (line radiation and bremsstrahlung) and losses associated with plasma particles lost to walls of the plasma container due to the imperfect confinement. To characterize the integral effect of all possible power losses, a quantity τ_E , called *energy confinement time* is introduced as

$$\tau_E = \frac{W}{P_{\text{loss}}}. \quad (60.3)$$

Here W is the total energy content of the plasma and the energy confinement time measures the rate at which a system loses energy to the environment. Supposing equal electron and ion temperatures T and a 50–50% D-T mixture, the total energy content of a hypothetical homogeneous plasma with volume V can be given as $W = 3n_e k_B T V$.

A self-sustaining fusion plasma requires $P_{\text{loss}} < P_\alpha$, that is,

$$\frac{3n_e k_B T}{\tau_E} V < \frac{1}{4} n_e^2 \langle \sigma v \rangle \cdot E_\alpha V. \quad (60.4)$$

Or, after rearrangement

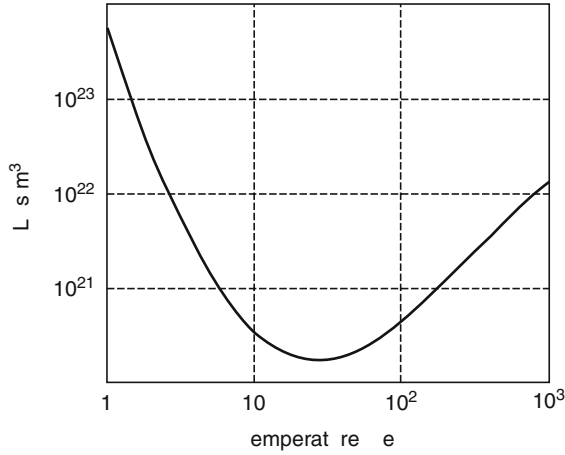
$$L \equiv \frac{12 k_B T}{E_\alpha \langle \sigma v \rangle} < n_e \tau_E. \quad (60.5)$$

The L -function, named after J.D. Lawson, has an absolute minimum as a function of temperature ([▶ Fig. 60.1](#)).

The minimum of the L -function occurs at temperature about 25 keV (approximately 250 million K) and has a value of approximately $1.5 \times 10^{20} \text{ s/m}^3$. Substituting this value into [▶ Eq. \(60.5\)](#), one gets the so-called Lawson criterion (Lawson 1957)

■ Fig. 60.1

The D-T L-function has a minimum around 25 keV plasma temperature



$$n_e \tau_E > 1.5 \times 10^{20} \text{ s m}^{-3}. \quad (60.6)$$

In the above treatment, it was assumed that alpha heating compensates all the losses from the plasma. This condition is called *ignition*. One can set similar Lawson condition for various $Q = P_f/P_{\text{loss}}$ values. Abundantly used is the case when the total (alpha + neutron) fusion power reaches the losses, that is $Q = 1$. This condition is called *breakeven*. In a given experiment, the value of the product $n_e \tau_E$ and its deviation from the minimum requirement is a measure of fusion performance. From the above derivation, it is clear that the actual value of the number before the factor 10^{20} s m^{-3} in the Lawson criterion depends on the plasma temperature. In the early decades of controlled fusion research, the fusion performance of the plasmas was so far from the Lawson criterion that its use was satisfactory. In the recent years, however, the use of another quantity called *fusion triple product* $T_i n_e \tau_E$ became more popular, because it also contains the ion temperature T_i and describes the Lawson criterion off the optimal temperature as well:

$$T_i n_e \tau_E > 2.5 \times 10^{21} \text{ keV s m}^{-3}. \quad (60.7)$$

This expression is valid sufficiently close to the minimum of the L -function where $\langle \sigma v \rangle$ can be approximated with a quadratic function.

Looking at the Lawson criterion, one can immediately see that there are two basic ways to satisfy it:

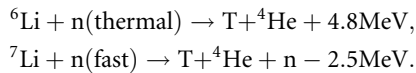
1. Creating a sufficiently high plasma density and confining the plasma for a rather short time, or
2. Maintaining a rather low plasma density and achieving a suitably long confinement.

Although not necessarily only these two options exist, nowadays the main stream of research concentrates on these two solutions. In case (1), the confining “force” is simply the inertia of the plasma against expansion. This method is called *inertial confinement fusion* (ICF), which speaks of confinement times of the order of nanoseconds and plasma densities on the order of 10^{31} m^{-3} . In the case of method (2), the confinement is reached with magnetic fields

(*magnetic confinement fusion*, MCF) as charged particles (D and T) gyrate around the magnetic field lines, and no perpendicular motion is present in zero order. Here, typical number densities are around 10^{20} – 10^{21} m⁻³ and energy confinement times of the order of 1 s.

Before going any further and discussing the two main confinement schemes, the problem of utilization of fusion-born neutrons needs to be considered briefly.

The DT reaction involves one deuterium and one tritium ion. Deuterium is abundantly present in water: every 6,500th hydrogen atom is deuterium. On the other hand, Tritium – because of its radioactive half-life of 12.32 years – is negligibly present in nature, and so must be produced artificially. And here the neutrons come into play. Lithium occurs in notable percentages everywhere in the mantle of Earth, and the following two nuclear reactions can very conveniently be used to breed tritium:



Both reactions produce tritium although the first reaction generates energy while the second one consumes it. In addition, natural lithium comprises 7.4% ⁶Li and 92.6% ⁷Li. Even though there is a much larger fraction of ⁷Li, nuclear data show that the ⁶Li reaction is much easier to initiate and as a result, it is this reaction that dominates in the breeding process.

With respect to the ⁶Li reaction, if there were no loss of neutrons, then each neutron produced during DT fusion and consumed in this reaction would produce one new tritium. In a practical reactor, however, there are always some unavoidable neutron losses. Thus, some form of neutron multiplication is required. Also needed is a method of slowing down the high-energy fusion neutrons since the ⁶Li reaction is most easily initiated with thermal, low-energy neutrons.

The breeding of tritium is envisaged in a mantle (called breeding blanket) that surrounds the chamber where the fusion plasma is confined.

In the following sections, the inertial and magnetic confinements shall be examined separately.

60.2 Inertial Confinement Fusion

As shown in the previous section, the inertial confinement scheme involves creation of very high densities for very short times. A small piece of solid or liquid material (a *fuel pellet*) is compressed by intense beams of energy (called *driver*) to the desired densities, and the confinement is simply achieved by the finite free expansion time of the compressed pellet.

Interest in the peaceful uses of inertial confinement fusion emerged later than that in magnetic confinement fusion, because until powerful laser or ion beams were developed and became available to civil researchers in the late 1960s, only an A-bomb's explosion could serve as a driver.

The sequence of events in inertial confinement can briefly be described as follows. A small pellet of radius less than ~5 mm and containing the fuel mixture (DT, in this case) is symmetrically struck from several directions by intense pulses of energy from either a laser or an ion beam. Absorption of this energy below the pellet's surface leads to local ionization and plasma formation. The consequence of these processes is an outward-directed mass transfer by ablation and – by a rocket type reaction – an inward-directed pressure wave leading to the compression and heating of the target. With the temperature and fuel density sufficiently

high, the fusion reactions will start and the pellet disassembles in a micro-explosion. The pellet can be further heated by the alpha particles originating from the DT reaction provided the density is high enough so as they can be slowed down inside the pellet. (Slowing down of fusion neutrons would need unreasonably high densities.) The disassembly typically takes place in a time interval of less than 10^{-8} s, corresponding to the propagation of a pressure wave across the pellet with sonic speed.

For inertial confinement fusion, a criterion equivalent in meaning to the Lawson criterion but different in form is applicable, which considers time integrated quantities during the whole fusion burn process rather than the steady-state conditions in the original Lawson criterion. For the simple calculations below, uniform compression of a pellet is considered. Suppose that ignition and fusion burn conditions are attained when the pellet containing N_0 atoms has a radius of R_0 .

From this time on, the pellet freely expands with the sound speed, which is $c_s = \sqrt{k_B T_e / m_i}$. To get the corresponding Lawson criterion, it shall be assumed that the pellet consists of a 50–50% deuterium-tritium mixture and the $\langle \sigma v \rangle$ fusion rate is constant during the expansion; as a first approximation, the consumption of fuel during the explosion shall not be taken into account. The number of reactions in the whole pellet during time dt is $N_f = N_D n_T \langle \sigma v \rangle dt$. The *burn fraction* f (i.e., the ratio of the burnt fuel to its initial quantity) during the expansion time is

$$f = \frac{1}{N_D} \int_0^\infty N_f dt = \langle \sigma v \rangle \int_0^\infty \frac{N_0/2}{(4\pi/3)(R_0 + c_s t)^3} dt = \frac{\langle \sigma v \rangle}{4c_s} n_0 R_0, \quad (60.8)$$

where n_0 is the initial number density of hydrogen atoms (deuterium and tritium) at $t = 0$. At around 20–25 keV temperature the ratio $\langle \sigma v \rangle / c_s$ is approximately constant, so the burn fraction is proportional to $n_0 R_0$ or, in other words, to $\rho_0 R_0$. The larger the pellet and the higher its initial density, the larger is the attainable burn fraction. Taking into account the consumption of fuel during expansion, the burn fraction is limited to around 30%, which gives the Lawson criterion for ICF in the form (Gil 1981):

$$\rho R > 0.3 \text{ g/cm}^2. \quad (60.9)$$

In principle, this criterion can be satisfied with $R = 1$ cm and $\rho = 0.3 \text{ g/cm}^3$. However, in this case, the generated fusion energy is uncontrollably high: equivalent to some few tens of megatons of TNT. Therefore, if the energy released from the implosion of one fuel pellet is limited to about 100 MJ from practical considerations, the necessary density is 300 g/cm^3 , which is very difficult to achieve, given the DT liquid density is only 0.2 g/cm^3 . This calls for a 10-times linear compression of the initial fuel.


Beside the burn fraction, another important parameter of inertial fusion experiments is the *target gain*. Assuming that the fusion reactions are initiated in a homogeneous target compressed to the necessary density and fusion temperature in the 10 keV range, the energy gain from the process is the ratio of the 17.6 MeV energy released in the reaction to the $2 \times 10 \text{ keV}$ energy of the DT fuel, giving about 1,000. Given the present efficiency of lasers - which is of the order of a few percent-, the losses in target drive, and the conversion efficiency to electricity, this number is not very high. A more efficient operation mode is when only the center of the target is heated and ignited, for example, by shock waves. In this case, a burning front can be driven by the fusion-generated alpha particles and the target gain can be higher.

The years of experience with inertial confinement have shown the importance of several processes and phenomena:

- It is essential that during compression, the illumination of the target by the driver be extremely homogeneous and symmetrical. If the illumination by *direct drive* is not satisfactory, conversion of the direct radiation into a secondary radiation might be a solution (*indirect drive*, see below).
- The inner core should reach a high density very quickly before thermal conductivity or shock wave preheats the central region to cause an internal pressure build-up that opposes the compression.
- The absorption characteristics of short-wavelength laser radiation are better than those of long-wavelength radiation. This calls for the development of effective, short-wavelength laser radiation sources.
- Laser-based drivers transfer their energy predominantly to electrons, and these energetic electrons can preheat the fuel pellet, which is again an undesirable process.
- Accelerators transfer the energy with better efficiency to the ions and can therefore be significantly more efficient than lasers. This provides some appeal for the use of light or heavy ion accelerators for driver purposes, although focusing of charged particle beams is an issue.

To reduce the minimally required temperature after the compression of fuel pellets, a new scheme, the *fast ignition* (Meyer-ter-Vehn 2001), is currently under investigation. In this scheme, in contrast to conventional *central ignition*, the driver compresses the fuel to a temperature just lower than required for fusion, and the pre-compressed fuel is ignited by a very powerful short-wavelength laser of femtosecond pulse duration. The main advantage of this scheme is that the compression of the fuel pellet to lower temperatures than that in the case of central ignition requires substantially less energy, and so the ratio of the generated to the used energy (the “efficiency” of the scheme) is much better.

As mentioned earlier, a very homogeneous and symmetrical target illumination is one of the keys to success in inertial confinement research. This follows from the fact that the interface between the accelerated solid state and the ablating plasma is subject to Rayleigh-Taylor instability, as a heavy material is leaning on the more tenuous plasma. The instability grows exponentially from an initial perturbation caused by nonuniformities. Better than 1% uniform compression reduces the initial perturbation to such a level that, in the final stage, the pellet is still sufficiently compressed. The quest to reach uniform ablation has led to what is known as indirect drive (Lindl 1995). The distinction between this approach and the direct drive is as follows.

The indirect drive target consists of both a fuel pellet and a small cylindrical cavity, inside which the pellet is located (see  Fig. 60.2).

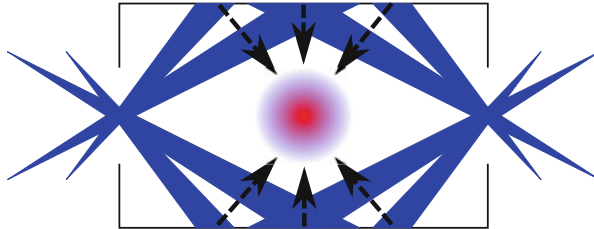
The cylindrical vessel, known as a *hohlraum* (from the German word for cavity), is a few centimeters long, is made of a high-*Z* material such as gold, and has windows that are transparent to the driver on each end. Then, instead of requiring all the driver’s beams to strike symmetrically on the pellet – as in direct drive – the beams enter both ends of the *hohlraum* obliquely and ablate the inner surface of the cavity. The high-*Z* material of the *hohlraum* emits X-rays, and by focusing the driver beams to appropriate points in the cavity, the resulted irradiation of the pellet is highly symmetric.

Crucial aspects of the indirect drive are (inter alia)

- Finding the optimum pointing position of the driver beam.
- Overcoming the difficulties and costs of target manufacturing.
- Increasing the overall efficiency of the energy coupling from the driver to the fuel pellet.

■ Fig. 60.2

The indirect drive target system, showing the fuel pellet, the hohlraum and the driver beams with the resulting X-rays



Another studied variant of the indirect drive scheme is wire array Z-pinch drive (Olson 2005). In this scheme, the pellet is enclosed inside a cylinder formed by an array of metal (typically tungsten) wires. A short and powerful current pulse of several MA is driven in the wires, which transforms them into thin plasma filaments confined by the magnetic field formed around the current channels (pinch effect). The plasma filaments are further heated by the current into the 100 eV temperature range. This way, an X-ray radiation hohlraum is formed, as in indirect-drive laser fusion experiments. The potential advantage of the wire-array drive is the better overall coupling efficiency of energy from electricity to X-ray radiation. For wire array experiments, this is expected to be at least 10%, while for present laser technology, even the conversion efficiency to the driver laser light is much less.

One last word on inertial confinement: the protection of a future reactor chamber from radiation and debris released in the micro-explosion is a unique and challenging aspect of ICF reactor design. Other challenges of this field include pellet handling and positioning in the chamber, protection of mirrors and other optical elements, etc.

60.3 Basic Schemes of Magnetic Confinement

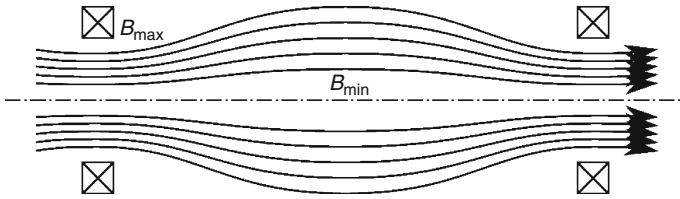
In ICF, the main technical and physical difficulties are associated with the requirement to reach a certain threshold density, whereas the confinement time is given by the process itself. In MCF, the situation is inverted: required densities are rather easy to achieve, while required confinement times are very difficult. It has to be stressed that the MCF scheme basically aims at steady-state operation; the energy confinement time is not the lifetime of the plasma but is related to the magnitude of power losses.

The basic idea of magnetic confinement is that charged particles – like the deuterium and tritium nuclei in a fusion plasma – can move freely along the lines of a magnetic field, but the same ions move very slowly (with *drift velocities* only) across the field.

In the early years of magnetic confinement research, *open configurations* were constructed, which essentially means that the magnetic field lines did not close onto themselves inside the experimental device, but only outside. In *mirror configurations* (see ► Fig. 60.3), a magnetic field gradient is applied at the ends of the vessel. It can be shown that an adiabatic invariant of the motion of charged particles in magnetic field is their magnetic moment: $\mu = mv_{\perp}^2 / (2B)$, where m is the mass of the particle, v_{\perp} is the magnitude of its velocity component normal to the

■ Fig. 60.3

The concept of a magnetic mirror configuration



local magnetic field, and B is the magnitude of the magnetic flux density. To conserve the magnetic moment and the total energy $E_{\text{tot}} = [mv_{\parallel}^2/(2B) + \mu]B$ at the same time, the particles must decelerate along the field lines while approaching the high- B regions. These high- B areas are called magnetic mirrors. The ratio of the maximum magnetic induction B_{\max} to the magnetic induction B_0 in the plasma confinement region limits the class of confined particles to those where $v/v_{\perp} < B_{\max}/B_0$. This defines a so-called loss cone in particle velocity space from which particles can escape from the mirror device. The loss cone is gradually populated by collisions between particles and the overall result is a continuous particle and energy loss reducing the confinement time. Some versions of the mirror configuration (tandem mirror) aim at adding electrical barriers to the ends of the devices so as the mirror loss is reduced. However, the end losses from mirror devices remain relatively high.

To reduce the parallel losses, *closed configurations* were developed. In these, the magnetic field lines close onto themselves at least in some finite plasma volume (the *confined region*). Concerning this closed magnetic field geometry, one point needs to be specially emphasized:

According to Shafranov's virial theorem (Shafranov 1966), there are no self-confining magnetic equilibria; the plasma in equilibrium must necessarily "lean against" some mechanical structure – that is, there is no plasma equilibrium with currents only, and no mechanical constraints. It is clear that the plasma must be manipulated ultimately and confined with external magnetic fields, and the mechanical structure that supports the external coils generating the magnetic field is finally the cause of the confinement.

In the followings, the plasma will be considered to be in equilibrium.

Following the Magnetohydrodynamics (MHD) theory, the equation of equilibrium (the equation of force balance) is

$$\mathbf{J} \times \mathbf{B} = \nabla P. \quad (60.10)$$

Here P is the plasma pressure, \mathbf{J} is the current density flowing both inside the plasma and in some coils of some mechanical structure, and \mathbf{B} is the resulted magnetic induction.

► Equation (60.10) states that both \mathbf{J} and \mathbf{B} must be perpendicular to ∇P . This means that \mathbf{J} and \mathbf{B} must lie on a surface with no components perpendicular to it. Then, the question arises: What can the shape of the surface to which the \mathbf{J} and \mathbf{B} are bound be. The answer is a consequence of the Poincaré–Hopf theorem, namely, that the surface must have the form of a topological torus, where the field lines lie on nested surfaces, and there are no field lines connecting one surface with the other.

► Equation (60.10) does not determine the total current density, only its component normal to \mathbf{B} (take the cross product of the first equation with the magnetic induction!). To

have the total current, one also needs the charge conservation equation, $\nabla \cdot \mathbf{J} = 0$, which, in turn, implies the existence of a parallel current (i.e., parallel to the magnetic induction). The existence of a parallel and a perpendicular current at the same time means that the lines of both \mathbf{J} and \mathbf{B} must be helical, that is, wind around the torus.

The measure of this helical nature is the so-called *rotational transform*. For field lines closing upon themselves, the rotational transform is the number of toroidal turns (the long way around the torus) necessary for the magnetic field line at the given magnetic surface to reach its original poloidal position (i.e., make one turn the short way around).

At this point, it has to be stressed that equilibrium configurations are not necessarily stable at the same time: some equilibria are not stable at all, and a fast growing instability destroys the plasma within fractions of a microsecond.

During the past 50 years of magnetic fusion research, there have been many different toroidal configurations with rotational transform constructed and exploited (see, e.g., Braams and Stott 2000), but currently two special configurations seem to be most promising and form the mainstream of the research: the *stellarators* and the *tokamaks*. In this chapter, only these two types will be introduced.

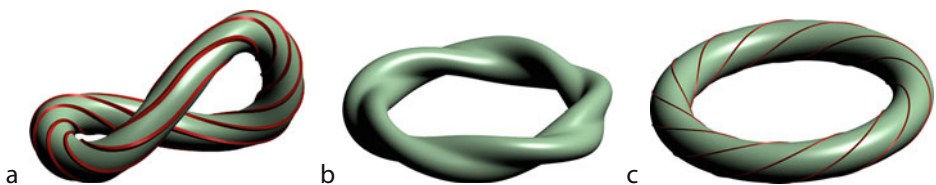
In a stellarator, the rotational transform of the magnetic field is produced by external coils only. External coils alone cannot produce rotational transform in an axisymmetric configuration. Here, the axis of symmetry is the major axis of an ideal (geometrical) torus. Due to this reason, stellarator devices must be non-axisymmetric either by a 3D distortion of the torus (e.g., ▶ Fig. 60.4a) or by non-axisymmetric external coils (▶ Fig. 60.4b). However, there are always some in-plasma currents driven by the plasma itself that distort the externally applied (vacuum) field, which can be taken into account in the design of the machine. The stellarator concept dates back to 1958 (Spitzer 1958), when L. Spitzer, Jr. had shown how to create rotational transform in current-free closed field-line systems. Modern stellarator designs make use of advances in computer technology to optimize the magnetic field geometry following some criteria. These optimization techniques can be very much different leading to vastly different configurations.

The tokamak concept was created in the early 1950s by I.Y. Tamm and A.D. Sakharov (Sakharov 1951; Tamm 1951), but, due to political reasons, their work had not been known in the west until 1958. In a tokamak, the rotational transform is created by the (poloidal magnetic field of the) plasma current itself that is driven in the toroidal direction. This toroidal current drive is a basic requirement of the tokamak configuration.

At the beginning of this section, it was mentioned that the achievement of the required density in MCF is rather easy. This is true, but one also wants to achieve a density as high as possible to maximize the fusion power. However, the density, unfortunately, cannot be

■ Fig. 60.4

Figure-eight stellarator (a), classical stellarator (b), tokamak (c)



arbitrarily high, because instabilities set in that destroy or decrease the efficiency of the confinement. To be more precise, the key parameter governing the instability threshold is not the density itself, but the ratio of the plasma kinetic pressure to the pressure of the magnetic field. This quantity is called *plasma beta*

$$\beta = \frac{P}{B^2/2\mu_0}, \quad (60.11)$$

and the instability limit associated with this quantity is called the beta limit.

In tokamaks, due to the externally driven plasma current, beside the beta-limit, there is another factor limiting the operational space. Namely, the magnitude of the plasma current should not exceed a given value. A practical quantification of the rotational transform is the *safety factor* denoted by q and expressing the ratio by how many times the field lines twist the long way around the torus while winding in the short one, $q \propto B_{\text{tor}}/B_{\text{pol}}$. In tokamaks, the poloidal field is produced by the driven plasma current alone, and so the safety factor is proportional to the inverse of the current. If the safety factor drops below a given value (i.e., the current is too high), a fatal instability called kink instability develops that terminates the discharge.

When the tokamaks appeared in the 1960s, most of the countries and laboratories switched to tokamak research, and abandoned or rebuilt their stellarators into tokamaks. The overwhelming success of tokamaks lies in their robust equilibrium within the operational space and relative simplicity of design. Achieved values of the fusion triple product had doubled every 1.8 years and now (in 2010) it is believed, that the first fusion reactors will be tokamak based.

The stellarator research, although cut back 50 years ago, had not been stopped. Stellarators have two advantages compared to tokamaks: as there is no driven current, (1) stellarators are better candidates for steady-state operation; and (2) they lack the current driven instability. The drawback of stellarators is that they require a very sophisticated design and state-of-the art industrial technology. At the time of writing of this chapter, stellarators seem to have their share on fusion reactor market as second-generation devices.

Later in this chapter, the role of the aspect ratio (the ratio of the major radius of a torus to its minor one) in the technology of fusion devices will be emphasized. It is to mention, that those configurations that have an aspect ratio close to unity (compact devices) have a larger beta limit and so a more favorable possible fusion performance.

60.4 Technology of Magnetic Confinement Fusion Devices

After 50 years of research and development, modern magnetic fusion devices are complex industrial-like objects where physics research meets technological development. This section gives an overview of the key technologies used in fusion research.

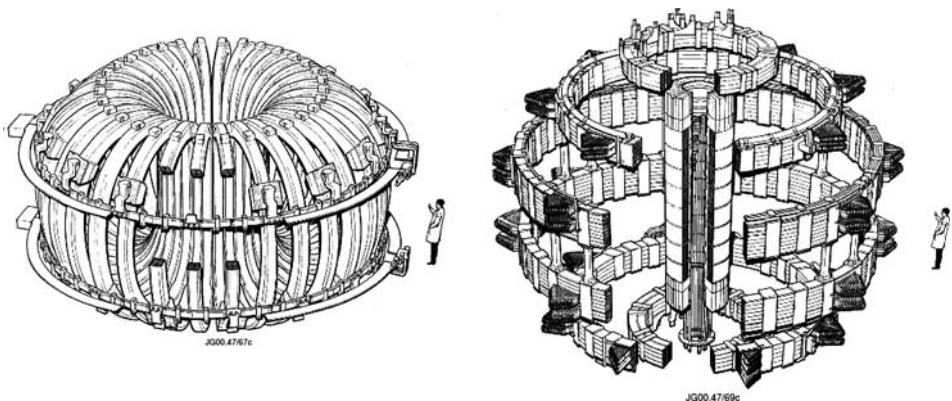
Most of the power flux from DT fusion plasmas will be carried by neutrons that slow down in the blanket of the device in a typically 1 m thick layer. As the final aim of fusion research is the construction of GW class power plants, practical power flux handling limits set the volume of the blanket into the $1,000 \text{ m}^3$ order of magnitude. This means the device linear size must be in the 10 m range. Present day fusion experiments do not produce substantial fusion powers; therefore, their sizes can be much smaller: the torus major radius (R) is 2–3 m, while the minor radius is typically 0.5–1 m.

As shown in the previous sections, the $3nk_B T$ kinetic pressure of fusion plasmas acts on the magnetic coil system, which finally operates as some kind of container. Engineering practice limits the pressure in several meter size systems maximum to the 100-atmosphere range, and as the plasma temperature is set by the fusion processes to 10^8 kelvins, the plasma density cannot be higher than 10^{-4} atmospheric density, that is, about 10^{21} particles per cubic meter. Additionally, this tenuous hydrogen gas should also be clean as the plasma bremsstrahlung radiation increases with the square of the ion charge (Chen 1984). One percent contamination in the $Z = 10$ –20 range would increase the radiation loss by 1–10 times, therefore, the base pressure of the plasma container should be in the 10^{-6} mbar range at most. This is high vacuum condition although requirements are not as strict as in many laboratory solid-state experiments. Standard high-vacuum practices (Kohl 1995) are a must in fusion experiments, including two-stage pumping with rotary, turbomolecular and/or cryogenic pumps, baking, and other wall-conditioning techniques. Cleanliness of the vacuum vessel inner wall is extremely critical; therefore, plasma–wall interaction will be discussed separately in the following section.

The magnetic field is generated by coil systems located outside the vacuum vessel. As described before, the plasma beta is limited by instabilities; therefore, magnetic fields in the Tesla range are required. The toroidal component of the magnetic field is the dominant one, which is generated by a set (15–20) of coils surrounding the vacuum vessel (► Fig. 60.5). Coil currents must be in the 1–10 MA range. Taking into account the available space and the conductivity of copper, the power needed for maintaining the magnetic field is in the several 100 MW range even for larger present-day fusion devices. This amount of power cannot be continuously extracted from the coils; therefore, copper coil devices operate in pulses lasting less than a minute. Copper coil technology would also prohibit positive energy balance for a fusion power plant; therefore, superconductive coils must be used on the long term. Several experimental devices have been built using superconductive coils (Tore Supra Team 1999) and experience shows that standard liquid-helium cooled superconductive technology can meet the requirements for fusion power plants. However, for plasma confinement studies superconductive technology is not absolutely required. As shown above, the energy confinement time is

► Fig. 60.5

The toroidal (left) and poloidal(right) coil set of JET (Wesson 2000a) (Copyright EFDA-JET)



in the second range, therefore a few-second pulse (achievable with copper coils) can be considered as steady state from the confinement point of view.

Additionally to the toroidal field coils, plasma stability and shape control requires poloidal field (PF) coils as well. Part of the PF coil set is a central solenoid, which can produce a magnetic flux increase along the axis of symmetry of the torus. The current in the toroidal field coils is essentially DC during operation, but the PF coils must be operated dynamically to counteract expansion of the plasma ring by plasma pressure and plasma current and to set the required plasma shape. Some lower current correction coils are also installed in order to compensate for small field distortions caused by tolerances in the mechanical construction. Additional coils can be placed inside the toroidal field coils for creating divertors, as described in the following section.

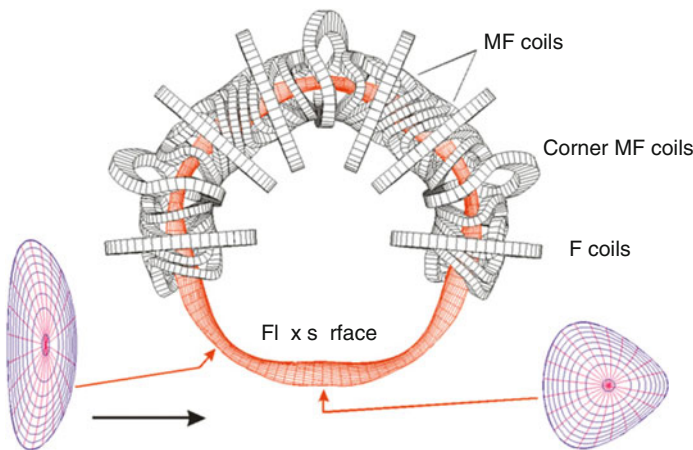
The strong magnetic fields and high coil currents induce huge forces on the coils, in the 10 T/m range; therefore, mechanical stability of the coil system is a key issue.

In stellarators, coil geometries are more complex. ▶ [Figure 60.6](#) shows Wendelstein 7-AS, a partly optimized modular stellarator (Hirsch et al. 2008) with copper coils. In stellarators, all coil currents can be operated as DC, but due to the shape, the forces might be more difficult to handle.

As soon as good vacuum conditions are achieved and the magnetic field is established, the working gas (typically deuterium in present-day devices) is introduced into the vacuum chamber with a pressure in the 10^{-2} Pa range. Ionization (breakdown) is achieved either by inductively inducing a toroidal electric field (via the central solenoid in the case of tokamaks) or by intense micro- or radiofrequency electromagnetic waves. In the case of tokamaks, the breakdown is followed by a current ramp-up phase in which the toroidal plasma current reaches the value required for establishing the rotational transform. To drive the current, the magnetic flux is increased inside the opening of the torus in time by increasing the current in the central solenoid coil. The induction lines emerging from the central solenoid can be closed around the torus either with or without an iron core. During the ramp-up phase, the

■ **Fig. 60.6**

Coil set and plasma cross sections in the Wendelstein 7-AS stellarator (Hirsch et al. 2008)
(Copyright IOP)



poloidal-field coils need to be carefully controlled to keep the plasma column in place and achieve the required plasma shape. In the case of stellarators, the startup procedure is simpler as no plasma current is required for the target magnetic configuration and both breakdown and heating are achieved by electromagnetic waves.

In tokamaks during the ramp-up phase, the plasma current ohmic heating power heats the plasma to 0.1–1 keV temperature. The value of the toroidal plasma current is set by the magnetic configuration, therefore the ohmic heating power is determined by the plasma resistance R . Unfortunately $R \propto T_e^{-3/2}$ and thus with increasing electron temperature T_e the heating power is decreasing. This effect limits the plasma temperature to a few keV with ohmic heating alone, and therefore fusion conditions cannot be reached.

As soon as plasma with at least a few hundred eV temperature is achieved, additional heating should be applied to reach fusion (10–20 keV temperatures). Several electromagnetic wave heating schemes that are capable of delivering up to several 10 MW power have been developed. The key in these schemes is to launch a wave into the plasma, which propagates into a region where a resonance occurs with the cyclotron motion of particles and at least part of the wave energy is converted to thermal particle motion. In a plasma, a large number of waves can propagate, but, depending on frequency, polarization, magnetic field, and plasma density, there are several regions where these waves are non-propagating. Due to the curved geometry, the toroidal magnetic field decreases as $B_t \propto 1/R$, and therefore, the cyclotron frequency $f_c = eB/(2\pi m)$ also depends on R . The results of the above are lines of resonances and areas of non-propagating zones for a given wave frequency in the cross-section of the plasma. Additionally, at the boundary of non-propagating zones, wave conversion can take place, whereas energy is transferred from one type of wave propagating on one side of the region to a different but identical frequency wave propagating on the other side. Different heating schemes can be designed making use of detailed knowledge of these wave propagation features (Wesson 2000b).

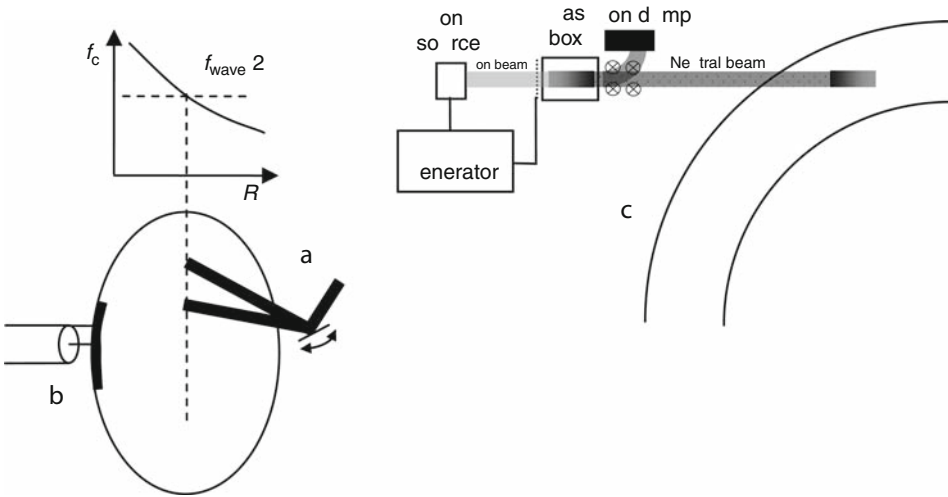
Two wave heating schemes are used most often in fusion experiments; *Electron Cyclotron Resonance Heating* (ECRH) relies on the cyclotron motion of the electrons. In most implementations, an electromagnetic wave with twice the electron cyclotron frequency is launched from the outer side of the torus. The wave can freely propagate to the plasma layer where $2f_c = f_{\text{wave}}$ and a considerable part of it is absorbed there (► Fig. 60.7). Typical frequencies are 50–170 GHz, where the wavelength is in the millimeter range. The waves can be transmitted in several centimeters or 10-cm wide beams using mirrors and launched into the plasma through highly transparent, cooled windows. With suitably aligned steering mirrors, the absorption volume can be moved to different locations along the minor radius. As the temperature quickly equilibrates along magnetic surfaces, ECRH can change the plasma temperature well localized to a certain minor radius range.

The microwaves for ECRH are generated by powerful gyrotron devices (Nusinovich 2004), which convert the energy of an electron beam to the electromagnetic wave. Gyrotrons developed for fusion application can currently reach up to 1–2 MW power at 140–170 GHz for a few seconds or somewhat lower power in CW (continuous wave) mode. It is expected that 1–2 MW CW gyrotrons can soon be developed with about 50% overall wave generation efficiency (Kasugai et al. 2006). Several of such gyrotrons are used on a single fusion device to reach ECRH heating power in the 10 MW range (Erckmann et al. 2007).

As the thermal coupling between the electron and ion fluids is relatively loose and losses through the electron fluid can be high (Doyle et al. 2007) ECRH is not the most efficient way of heating the ions. This task can be more efficiently done by waves resonating in the ion cyclotron

■ Fig. 60.7

Fusion heating schemes: (a) ECRH (b) ICRH (c) NBI



range of frequencies (10s of MHz). Unfortunately, at this frequency the wavelength is larger than the device size, therefore quasi-optical propagation is not possible and heating cannot be so localized as in the case of ECRH. Due to the above reason, *Ion Cyclotron Resonance Heating* (ICRH) uses a different approach. A simple loop antenna is placed inside the vacuum vessel, close to the plasma. Electromagnetic waves are generated by high-power amplifiers and transmitted to the antenna via coaxial lines. The difficulty in ICRH is to match the coupling impedance of the wave to the plasma with the impedance of the transmission line, otherwise the wave is reflected back into the waveguide. The coupling impedance depends on the plasma to antenna distance and the plasma conditions as well; therefore, it can easily change during a plasma discharge. Another problem of ICRH antennas is the strong electric field arising close to the antenna at the plasma edge. This can accelerate ions to high speeds, which bombard either the antenna or other structures in the vacuum vessel. The resulting impurities enter the plasma and increase its radiation. Nevertheless, by careful choice of the materials utilized in the antenna and surrounding structures and by optimizing the wave coupling several MW of ICRH power can be injected into the plasma.

Another, even more powerful ion heating mechanism is *Neutral Beam Injection* (NBI). In this, a low-temperature plasma ion source (Brown 2004) is placed to a high, typically 50–100 kV electric potential. An ion beam is extracted from it and accelerated by the high voltage. The beam passes through a gas box, where ions pick up electrons from gas atoms by charge exchange process (Dolan 2000) and therefore they become neutralized. The neutralization efficiency is energy dependent, typically 50–80%. The residual ion beam is bent by a magnet and its energy damped in an ion dump. The neutralized high-energy atomic beam penetrates the magnetic field of the fusion device and in the plasma it gets ionized by collisions with plasma particles. The fast ions are confined by the magnetic field and they form a high-energy ion population, which gradually slows down and heats the plasma thermal ions and electrons. The overall efficiency of an NBI system depends on several parameters, but 30–50% can be typically reached. NBI is the most effective ion heating method on present day devices capable

of delivering several 10 MW of power. For reactor-scale devices, the NBI technique needs further development. In a large and dense plasma, the penetration of a 100 keV neutral beam is insufficient; therefore, the energy needs to be increased to 0.5–1 MeV. At this energy, the efficiency of the charge exchange process is negligible; therefore, positive ions cannot be used as ion source. As an alternative, negative-ion sources are being developed (Brown 2004) where an additional electron is loosely bound to the atom. This can easily be removed in the neutralization cell, therefore negative-ion NBI is expected to be a powerful tool for reactor-scale plasma heating.

In tokamaks, the helical magnetic field structure is generated by the current flowing in the plasma loop. As described above, this current can be driven inductively for a few tens of seconds, or – with careful design – up to a few hundred seconds. However, for DC current drive inductive technique is unsuitable. For current drive purpose, most of the above described heating techniques can be applied with some modification. For instance, an ECRH wave directed in one direction in the torus is capable of driving an asymmetric electron velocity distribution, thus driving toroidal current. The current drive efficiency of various heating schemes have been assessed for present day devices and a technique called *Lower Hybrid Current Drive* (LHCD) (Gormezano 1986) was found to be the most suitable. This relies on generating waves in the plasma with frequencies in the 1 GHz range. A special waveguide array is placed close to the plasma whereby appropriate phasing of the individual waveguides can launch a wave with high B -parallel wave vector component. These waves can capture plasma electrons and produce a high-energy B -parallel tail in their velocity distribution, thus drive a toroidal current. However, LHCD is best applicable at low plasma densities; therefore, it is not clear whether reactor-scale devices can make use of it. For fusion reactors, a more promising candidate is the Neutral Beam Current Drive (NBCD), where heating neutral beams injected in one toroidal direction drive the current. With this technique, up to 1 MA current drive has been demonstrated (Oikawa et al. 2001) albeit with a power comparable to the total NBI heating power.

In addition to external current drive, the high-pressure fusion plasma itself can drive a so-called *bootstrap current* (Peeters 2000). This is generated by the radial pressure gradient, and therefore it is negligible in the center of the plasma and cannot be used for full current drive, but can substitute 50–70% of the total current in future high-pressure tokamak plasmas.

After the development of the above-mentioned heating techniques, a general tendency called *power degradation* was observed. This means that regardless of the heating technique used, the energy confinement time of the plasma becomes inversely proportional to the heating power (Doyle et al. 2007), that is, confinement deteriorates with heating power. With detailed experimental studies, it was also found that the local heat transport coefficient is an instantaneous function of the heating power and not the local plasma parameters (Stroth et al. 1996). A spontaneous transition to an improved confinement state, called *H-mode*, was found (Wagner 2007) and reproduced on both tokamaks and stellarators. The H-mode is considered as the candidate operating scenario of a fusion reactor.

The above findings are in contrast to neoclassical transport theory (Helander and Sigmar 2002), which predicts diffusive transport across the magnetic field lines, with heat and particle diffusivity coefficients dependent on local plasma parameters. As even the magnitude of the experimentally found transport coefficients is much higher than the neoclassical result, it is believed that heat and particle transport in fusion plasmas is dominated by small-scale plasma turbulence driven by spatial inhomogeneities of various plasma parameters. This is called anomalous transport. According to the present understanding, the turbulent state is a dynamic equilibrium of interacting small-scale waves and flows (Diamond et al. 2005): waves excite ExB

flows across the magnetic field and these flows tear turbulent eddies apart before they can cause transport. Several elements of this process have been found experimentally (Fusjisawa 2008). Such a system often settles to a state close to some critical gradient where avalanches can cause fast nonlocal response to external perturbations. Recent simulations of turbulence in fusion plasmas give reasonable predictions (Doyle et al. 2007) but it is thought that still a long time is needed until reliable predictions can be given to transport in magnetically confined fusion plasmas.

In the above-described turbulent plasma state, the H-mode is a state where a strong DC flow develops at the plasma edge and inhibits turbulent transport. As shearing of flow means a continuous radial change of the flow velocity, the affected layer must have a limited extent. This is called the pedestal, a few centimeters radial range at the plasma edge. In the pedestal region, transport is close to the neoclassical prediction and the temperature and density exhibit steep gradients, called transport barrier. The gradient can be so steep that pressure- and current-driven MHD instabilities can develop and periodically open up the pedestal for a short time. These are called *Edge Localized Modes* (ELM), and they are a key element of an H-mode plasma. Without ELMs, the He ash could not be extracted through the pedestal. Under certain circumstances, internal transport barriers (ITB) can also be induced in deeper layers of the plasma, further improving H-mode confinement quality. As turbulent transport is not fully understood quantitatively, the physics of H-mode and ELMs are also at the infancy of their understanding.

For the study and control of fusion plasmas, the confinement parameters need to be measured. For this purpose, a large collection of plasma diagnostic tools have been developed (Hutchinson 2002) utilizing a broad choice of physical effects and technical tools. Simple magnetic loops and coils can measure external components of the magnetic and electric fields. At the plasma edge, measurements with immersed probes can provide valuable information, but in the plasma core, no material probes can be used. This region is only accessible with laser, microwave, or atomic beam probes, or the radiation of the plasma at microwave, visible, infrared, and X-ray wavelength can be used. Based on the above techniques, at present key plasma parameters (density, electron and ion temperature, electric potential, flow velocity, current density, radiation intensity, etc.) can be measured with temporal and spatial resolution. Depending on the technique, there are inherent constraints on spatial and temporal resolution; therefore, multiple techniques are often used for even the same plasma parameters. A special class of diagnostics have been recently developed for the study of plasma turbulence, where microsecond temporal, sub-percent amplitude, and at least centimeter spatial resolution is needed at the same time.

Control of plasma parameters is becoming more and more critical as plasmas approach reactor conditions. In present-day experiments, only a few parameters are actively controlled, such as mean density, plasma current (in tokamaks), and plasma shape, but with the improved theoretical understanding of the turbulent transport in plasmas, it is becoming increasingly important to control profiles as well. For this purpose, some real-time data evaluation and intelligent control schemes have already been demonstrated (Felton et al. 2005).

60.5 Plasma–Wall Interaction in Nuclear Fusion Devices

Introductory remarks

This section deals with plasma–wall-interaction (PWI) processes in magnetically confined fusion (MCF) devices only. In inertial confinement fusion (ICF), the interaction is

unidirectional in the sense that during the nanosecond-timescale fusion process, no interaction can take place between the plasma and the chamber wall. However, debris from the micro-explosion and fusion reaction products will reach the wall and cause the same, if not greater, damage as in MCF. At present, little is known about these effects.

An area of particular interest for MCF is the understanding of physical and chemical processes in the boundary plasma and the interaction of this boundary plasma with the surrounding walls. It has been shown earlier that fusion plasmas cannot be maintained at sufficiently high temperatures if they are allowed to come into contact with the surrounding walls. On the other hand, a fusion device cannot be run without a certain degree of plasma–wall interaction. Two indispensable functions have to be assured by plasma–wall-interaction processes: The power generated in the core plasma has to be transferred through the wall to the cooling medium, and the ash of the fusion reaction, that is, helium, has to be removed from the core plasma.

Plasma–wall interaction comprises a large variety of physical, chemical, nuclear, and thermo-mechanical processes. In this respect, the term “plasma–wall interaction” (PWI) is the more general phrase including all these various processes, while the term “plasma–surface interaction” (PSI) more specifically concentrates on the physical and chemical interaction processes at the surface of plasma-facing components. While the PSI processes depend only on the plasma-facing material (PFM), that is, the material used at the surface of wall components, and the impinging power and particle fluxes, PWI is also strongly influenced by the choice of other materials used for the fabrication of wall components and the corresponding physical and material aspects. The latter is particularly important for the thermo-mechanical behavior of wall components and the nuclear processes caused by the immense neutron flux.

The field of PWI is challenging, multifaceted, and highly interdisciplinary. It comprises research fields such as plasma physics, surface physics, solid-state physics, atomic and molecular physics, nuclear physics, chemistry, materials science, and mechanical engineering. In the following, focus will be put on the PSI processes at the plasma-facing surfaces, because they are of special importance for the operation of fusion plasmas. The selection of a specific plasma-facing material is closely linked to the operational scenario of the plasma and vice versa. Some other aspects of PWI will shortly be presented at the end of this section. Basic questions related to plasma–material interaction in magnetically confined fusion are discussed in the textbook of Naujoks (2006).

Three aspects of PSI processes have to be considered. The first and most important is impurity generation. Particle fluxes impinging on the surface of surrounding walls can cause material release. If these released species are transported into the core plasma, they contribute to plasma dilution and increase of radiation. If the impurity fraction in the core exceeds certain limits, the thermonuclear plasma will be extinguished. Therefore, reducing the plasma impurity fraction is an important aim of the control of PSI processes. Second, net erosion has to be taken into account as a lifetime-limiting process for plasma-facing components. Third, fuel species that are permanently retained in plasma-facing materials contribute to the total fuel inventory in the device. In particular, tritium is an issue in that respect, because the total tritium handling allowance in a nuclear fusion plant will be limited by regulatory authorities. Consequently, the tritium inventory in the device has to be minimized.

In MCF, a toroidal magnetic field is applied to isolate the hot fusion plasma (= *plasma core*) from the surrounding walls. It has already been discussed in [Sect. 60.3](#) that a field line in the core does not close with itself after one cycle around the torus but makes an infinite number of cycles and forms a so-called magnetic surface. The confining field in the core comprises nested

toroidal magnetic surfaces that have no intersection with the wall. The toroidal field is in the range of 2–5 tesla, while the poloidal component is about a factor of 10 lower. The D–T fuel mixture has to be heated to temperatures on the order of 10 keV or more. Fusion reactions can occur only in this fully ionized core plasma. The products of a D–T reaction are a ^4He nucleus with about 3.5 MeV and a neutron with about 14 MeV (see ▶ Sect. 60.1). As described above, the chargeless neutron can pass the surface layers of the wall with virtually no interaction. Charged particles of the thermal plasma-particle population are bound to the magnetic surfaces within a Larmor radius; therefore, they can leave the core plasma only by cross-field transport. Fast particles such as ^4He nuclei have Larmor radii in the 5–10 cm range and some plasma waves or nonideal magnetic fields might cause them to reach the wall. In addition to the charged-particle load, there are always some neutralized plasma species that can leave the plasma and interact with the surface of the wall.

In contrast to the core plasma, magnetic field lines in the boundary plasma do have intersections with the wall. The core and boundary plasma are separated by the so-called last closed flux surface (LCFS = surface defined by those magnetic field lines that do not yet have an intersection with the wall). Charged-particle transport parallel to the magnetic field is much more efficient than either the above-described neoclassical or anomalous transport acting perpendicular to the field. Therefore, charged species that leave the core plasma across the LCFS and enter the boundary plasma are quickly transported along the field lines to the wall. This transport parallel to the magnetic field occurs in a rather thin plasma sheath of the order of about 1 cm. This layer, denominated *scrape of layer* (SOL), carries most of the particles and power leaving the core plasma to the walls. Consequently, the power and particle fluxes at those wall areas where the SOL strikes a surface are extremely high. Strong electric fields also build up in the sheath layer due to the different mobility of electrons and ions, which cause charge separation. The resulting ExB flows and instabilities make the SOL a complex plasma layer. Basic SOL physics is thoroughly discussed in the textbook by P. Stangeby (2002). Most work to date has focused on the investigation of the tokamak concept, this being particularly true for the study of SOL physics. However, the basic physical processes and the related PSI problems are very similar in a stellarator (Hirsch et al. 2008).

In present-day MCF devices, investigations are almost exclusively carried out using hydrogen and deuterium. It remains a challenge to extrapolate present-day results on transport, operational scenarios, or plasma–wall-interaction processes to future devices working with D–T mixtures. A detail that cannot be studied in H–D mixtures is the physics of fast alpha particles in the core plasma. On the one hand, the fast alpha particles produced by the fusion reaction have to be confined sufficiently long to allow them to transfer their kinetic energy to the other plasma species (alpha heating). This thermalization contributes substantially to plasma heating. On the other hand, after thermalization they quickly have to be removed from the core plasma because they are a plasma impurity and would eventually quench the fusion plasma. Removal of He from the core plasma is strongly determined by SOL and PSI processes. Particle and energy confinement in the core plasma has to be sufficiently high, but as just discussed, particle confinement must not be too good to allow for removal of the ^4He particles and other possible impurities.

In the boundary plasma or edge plasma, the plasma density and temperature are much lower than in the core. The areas where the SOL hits the wall are relatively small so that the particle and power flux densities to these areas are very high. Plasma–wall-interaction processes are mainly determined by these areas. Two concepts have been developed to control plasma–surface interaction to some extent. The first one is the *limiter concept*. The limiter is

a compact solid component that intersects the magnetic field lines in the main chamber. It limits the plasma and protects other wall areas. Consequently, in such a setup the LCFS position is determined by the position of the limiter. The second concept is the *divertor concept*. The boundary plasma is guided by the magnetic field to somewhat remote target plates (divertor plates) so that the dominant PSI region is, compared with a limiter machine, further away from the core plasma. In contrast to the limiter setup, the LCFS position in a divertor setup is determined by the magnetic field. It, therefore, allows a higher flexibility in shaping the plasma. In a divertor device, the magnetic surface that defines the LCFS is called *separatrix*. **► Figure 60.8** shows a sketch of a limiter and divertor setup. In most cases, limiters are also used in divertor machines to protect special components in the main chamber, but not to define the LCFS position. Particle energies and particle fluxes onto limiter and divertor surfaces differ significantly. Divertor and limiter machines also differ in some other aspects of SOL physics.

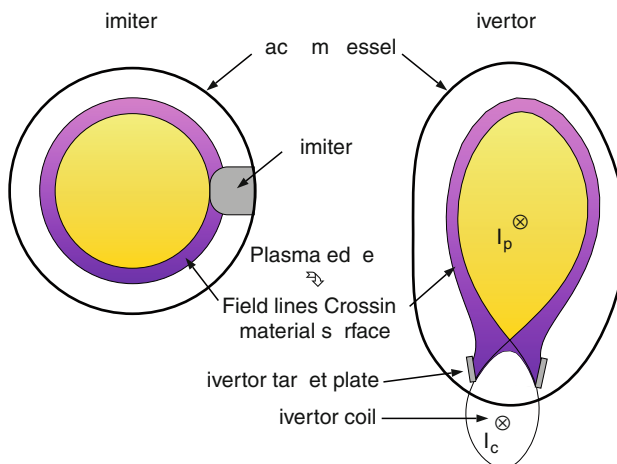
60.5.1 Basic PSI Processes

Before discussing the plasma–surface–interaction processes (PSI processes) in a MCF device, it is favorable to briefly discuss the most important microscopic processes. Note that these processes are basic in the sense that they occur whenever energetic or reactive species interact with solid surfaces. These processes are in no way restricted to PSI processes in a fusion device. For example, such processes are exploited in many technical plasma applications or occur in different kinds of ion–solid interaction.

The basic PSI processes can be divided in two major classes: processes due to energetic species and processes due to low-energy (thermal) species. The term energetic species is often

■ Fig. 60.8

Schematic representation of the cross section of a thermonuclear plasma device in a limiter and divertor configuration. In the divertor configuration, the edge plasma is guided to the divertor with the magnetic field created by additional divertor coils (Figure by courtesy of Karl Krieger, IPP)



used synonymously for ions and vice versa, but in the parameter space relevant here, energetic neutrals undergo identical interactions with surfaces as ions. In MCF, energetic neutrals contribute substantially to the energetic particle flux to the surface, because charge exchange collisions between ions and neutrals in the boundary plasma produce energetic neutrals.

The interaction of energetic species with surfaces is dominated by physical processes due to momentum transfer by collisions. The most important microscopic processes are *physical sputtering*, *implantation*, and *reflection*. Other processes that can also occur are *material mixing* and *preferential sputtering*, (Behrisch 1981, 1983; Behrisch and Wittmaack 1991; Behrisch and Eckstein 2007). Thermal species with low energies do not have sufficient kinetic energy to trigger physical processes, but they can react with surface species through chemical reactions. This process will be called *chemical erosion*. There is no unambiguous definition of thermal species and what is meant by low energy, but in the present context it is useful to consider species with energies well below typical surface binding energies or chemical bond energies as thermal species. This means that one should consider species with kinetic energies below about 1 eV as low-energy or thermal species. This use of the phrase thermal should not be confused with a thermal energy distribution of species in hot fusion plasma. With respect to surface interactions, species with thermal energy distributions corresponding to temperatures of about 10 keV are very energetic. A third class of process can occur if energetic and chemically reactive species interact simultaneously with the surface. This process is named *chemical sputtering*. These three different classes of PSI process and their relevance for MCF are discussed to some more detail in the following subsections.

60.5.2 Physical Sputtering

Physical sputtering is a well-understood process that is made use of in many technical applications. In MCF, however, it is an unwanted but unavoidable process. Physical sputtering is a process that occurs if energetic species impinge on a surface. It is caused by momentum transfer from the impinging projectiles to target atoms. It takes place for all target materials and incident particles with energy above certain threshold energy. This threshold energy depends strongly on the mass ratio of the projectile-target combination and lies in the range of about 30 to a few 100 eV.

Physical sputtering was thoroughly reviewed by Eckstein (2007). Various aspects of physical sputtering can be excellently modeled by computer simulations (Eckstein and Urbassek 2007). In systems where the interaction is dominated by kinetic processes, excellent agreement between experimental data and simulation results is generally achieved (Eckstein 2007). Simulation codes for physical sputtering, which are based on the binary collision approximation, are TRIM.SP (Eckstein 2007) and SRIM (Ziegler et al. 1985). Physical sputtering depends on the angle of incidence and, to some extent, on the surface roughness (Eckstein 2007). As long as the temperature is well below the melting point of the material, physical sputtering shows negligible temperature dependence (Schmid et al. 2006). However, for carbon a strong increase of the sputtering yield close to the sublimation temperature was reported. This process was named radiation-enhanced sublimation (RES) (Roth et al. 1982).

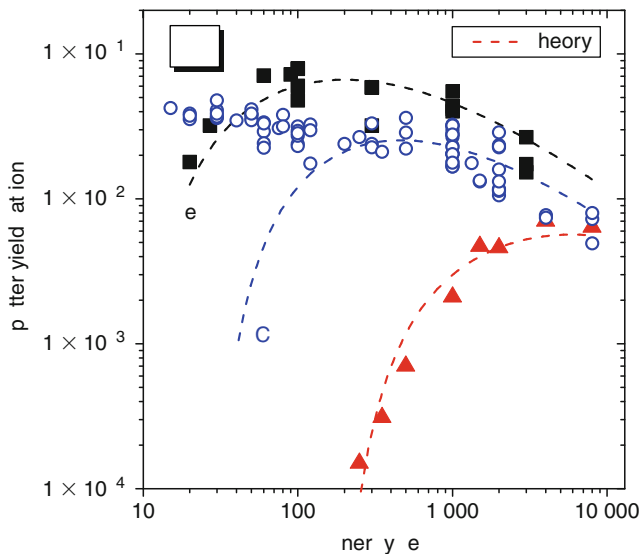
Sputtered particles originate predominantly from the topmost surface layer. In general, they are monatomic and have mean energies in the eV range. If chemical reactions between projectile and target atoms start to play a role or if activated surface atoms can react with neutral species from the ambient atmosphere, the situation becomes more complicated. These

chemical reactions can cause an increase as well as a decrease of the sputtering yield. The reaction products can have a lower surface binding energy compared with the pure material and, consequently, are more easily sputtered so that the sputtering yield increases. Alternatively, they can have a higher surface binding energy and, as a consequence, the sputtering yield decreases. The latter is, for example, the case for oxygen, carbon, or nitrogen bombardment of various metals where metal oxides (Al_2O_3 , SiO_2 , TiO_2 , etc.), carbides (TiC , WC , SiC , etc.), and nitrides (TiN) are formed. Such chemical processes create a significant problem for the reliable control of reactive sputtering processes as recently discussed by Sproul et al. (2005).

The sputtering yield combined with the maximum tolerable concentration of the sputtered species in the core plasma (Stangeby 2002) is one of the most important selection criteria for plasma-facing materials. The actual choice for ITER (International Thermonuclear Experimental Reactor) is to use beryllium as PFM for the main chamber wall and tungsten and/or carbon in the divertor. Furthermore, it is anticipated that the only possible option for a future power reactor will be tungsten. The sputter yields of Be, C, and W due to bombardment with deuterium are presented in ▶ Fig. 60.9. From these three materials, tungsten has the lowest sputter yield and the highest threshold energy. Due to the large difference in atomic mass between deuterium and tungsten (~ 2 u versus ~ 184 u), deuterium can, in a binary collision, transfer only a small amount of its kinetic energy to tungsten. The maximum transferable energy in a central collision is given by the kinematic factor, $\gamma = 4 M_1 M_2 / (M_1 + M_2)^2$; for the combination deuterium (D) on tungsten (W), $\gamma = 0.043$; for H (i.e., ^1H) on W, $\gamma = 0.022$; and for T on W, $\gamma = 0.063$. This is the main reason for the high threshold energy. As a consequence of

■ Fig. 60.9

Sputtering yields of the plasma-facing materials Be, C, and W due to bombardment with the hydrogen isotope deuterium (normal incidence, 300 K). The lines are model results describing physical sputtering only. While data for Be (squares) and W (triangles) show good agreement with the physical sputtering model, data for C (circles) deviate strongly at low particle energies (lower than 100 eV). This is due to chemical sputtering



the higher γ factor of T compared with D, the sputter yield for T will be slightly higher than for D. The corresponding γ values for D impinging on the other plasma-facing materials C and Be are 0.49 and 0.60, respectively.

The threshold energy for sputtering of tungsten by deuterium impact is about 230 eV (Eckstein 2007). With increasing energy, the sputter yield increases monotonically reaching values in the range of a few times 10^{-3} at energies of several keV. The data are well described by TRIM.SP simulations and other analytical descriptions of physical sputtering. The sputter yield for beryllium is high already for low energies. The threshold energy for D on Be is about 9 eV (Eckstein 2007). It reaches a maximum at about 100 eV (maximum yield is about 0.7). For higher energies, the yield decreases again. Similar to the sputtering of W, the sputter yield of Be is well described by the corresponding model curve. The sputtering of Be and W by D is dominated by physical sputtering.

In contrast to Be and W, the sputtering of C by D shows a disagreement between model and experiment. While for energies higher than about 200 eV, good agreement can be found between data and model, model and data deviate strongly for lower energies. The measured yields remain high also for low energies, while the model predicts a strong decrease with decreasing energy. Even below the threshold energy for physical sputtering of about 28 eV, the sputter yield is still increasing with decreasing ion energy. The existing data show no threshold for this process. The reason for this disagreement at low energies is due to the fact that the sputtering of carbon by hydrogen isotopes at low projectile energies is dominated by chemical sputtering effects. These will be discussed further below. Physical sputtering effects seem to dominate only for energies higher than about 200 eV.

Impurity sputtering and selfsputtering: The data in [Fig. 60.9](#) describe the physical sputtering for deuterium impact. The other species that contributes dominantly to the impinging particle flux in a fusion device, tritium, shows, according to model predictions, very similar behavior. However, the yield is slightly higher due to the higher mass of T. In addition to fuel species, impurity ions also contribute to the energetic particle flux from the boundary plasma. With respect to physical sputtering, two effects have to be considered. First, in contrast to hydrogen isotopes, impurity ions can be multiply charged. Therefore, they can gain higher energies due to acceleration in the plasma sheath. For example, in present fusion devices with carbon walls, the dominant impurity species is carbon and the dominant charge state of carbon ions is 4 so that impinging C^{4+} ions will gain four times the energy in the plasma sheath compared with the impinging fuel ions. In addition, due to the higher mass the kinematic factor (γ) of these species is significantly higher than that of D. For tungsten as surface material, the γ value of D is 0.043 while that of C is 0.23. That means that even a small impurity fraction in the impinging flux may contribute with a similar (or even larger) amount to the total sputtered flux as the fuel ions. The situation becomes particularly critical if the corresponding impurity species is identical to the wall species. In this case – this process is called selfsputtering – the kinematic factor equals to 1, the sputtering yield can be very high and so, a runaway situation may occur.

Other processes related to the impact of energetic species on PFMs are reflection and implantation. Impinging energetic species may be reflected due to collision with surface atoms. Depending on the kinematic factor and the scattering angle, they will transfer a certain fraction of their kinetic energy to the surface. In general, reflected species are neutral and are thus not guided by the magnetic field. Reflected species will penetrate the boundary plasma and will finally be ionized by an inelastic collision with a plasma electron. The penetration depth depends strongly on the energy of the species after reflection. The higher the mass of the target atom, the higher its mean energy after reflection. In particular, hydrogen isotopes

reflected from a tungsten surface have much higher mean energies than those reflected from carbon or beryllium surfaces. This is one reason why plasma edge physics is closely linked to the chosen surface material.

Impinging species that are not reflected penetrate into the solid. They are decelerated due to interaction with the electrons and nuclei of the target and finally come to rest. The penetration depth depends on the projectiles energy and on the specific projectile-target combination. With increasing fluence, the local concentration of implanted species in the target material increases. The maximum tolerable local concentrations depend critically on the specific chemical and physical interactions between target atoms and projectiles. If this maximum concentration is reached, other physical processes will set in. The implanted species may diffuse to the surface and be reemitted, may diffuse into the bulk of the material, or, in extreme cases, lead to local bubble formation. Apart from that, in particular hydrogen in tungsten or other metals may significantly deteriorate the mechanical and other physical properties of the material. Such material-related issues of PSI in MCF have recently been reviewed by Federici et al. (2001).

60.5.3 Chemical Erosion

Chemical erosion is the process initiated by chemical reactions between thermal neutral species and surface atoms. Out of the three nuclear fusion materials, only carbon is subject to chemical erosion with a variety of impinging species. The most important interaction in that respect is that of atomic hydrogen with carbon. Some other species play an additional role. In particular, the interaction of oxygen with carbon has to be considered. The underlying microscopic processes are in general thermally activated so that chemical erosion exhibits strong temperature dependence. Further, it does not require impact of high-energy projectiles. This lack of threshold energy is the major difference to physical sputtering. Erosion processes involving chemical reactions have recently been reviewed by Jacob and Roth (2007).

The atomistic steps of the interaction of hydrogen atoms with carbon surfaces were investigated in detail by Küppers and coworkers (Küppers 1995). Using a thin amorphous hydrogenated carbon layer as model system, they revealed and quantified the individual steps in the erosion process. According to their model, hydrogen atoms attack even at low temperatures sp^2 -hybridized carbon atoms at the edges of graphitic planes or with broken bonds. Via different intermediate steps, the surface is increasingly hydrogenated and most of the surface carbon atoms are rehybridized to sp^3 . This hydrogenation reaction is not thermally activated, but proportional to a cross section for the addition of hydrogen. Further impinging atomic hydrogen will abstract bonded hydrogen via formation of H_2 molecules producing an intermediate radical stage with a broken bond at the surface or add to an existing broken bond. In steady state, hydrogen abstraction and hydrogen addition lead to an equilibrium concentration of broken bonds of about 2–4% of the available surface sites. With increasing temperature, different thermally activated processes become possible and at temperatures around 400 K chemical erosion can occur. The sp^3 hydrocarbon complexes in the neighborhood of broken bonds can be desorbed by simultaneously reforming a C–C double bond with the neighboring free bond, thus returning to the graphitic sp^2 hybridization. This process has a lower activation energy than the release of a similar hydrocarbon complex on a site with no neighboring free bond. On a fully hydrogenated surface, the hydrogen abstraction reaction leading to a broken (dangling) bond is the rate-limiting step for chemical erosion. With further increasing

temperature, bonded hydrogen can be thermally released thus interrupting the hydrogenation process. This hydrogen release process becomes significant at temperatures above about 600 K and leads to a reduction of chemical erosion. Thus, the erosion rate will exhibit a maximum at intermediate temperatures. For typical experimental parameters, this maximum occurs around 600 K. The dominant release product of this process is CH_4 , but it contributes only about 1/3 of the total carbon erosion yield. Hydrocarbon species containing more than one C atom contribute the remaining 2/3. The product spectrum is very rich and species with up to 6 C atoms were detected.

60.5.4 Chemical Sputtering

Chemical sputtering is defined as “a process whereby ion bombardment causes or allows a chemical reaction to occur which produces a particle that is weakly bound to the surface and hence easily desorbed into the gas phase” (Jacob and Roth 2007). The erosion process depends on both the kinetic energy and the chemical reactivity of the impinging species. In general, chemical sputtering is used to describe an increase of the sputtering yield compared to physical sputtering. As mentioned before, chemical effects can also lead to a decrease of the sputtering yield. Such chemical effects are usually not subsumed under the phrase chemical sputtering. Ion bombardment can trigger two mechanisms. Either it can lead to creation of reactive sites at the surface, which in turn interact with chemically reactive species to produce volatile species, or it can break the terminal bond of a surface group thus leading to ejection of this group. While in the first case the desorbing species have a kinetic energy distribution mostly determined by the surface temperature, in the latter case the species is ejected with substantial kinetic energy in the range of a few eV.

Chemical sputtering is characterized by a number of different experimental observations:

- The process depends strongly on the projectile–target combination.
- Molecules containing projectile and target atoms are formed.
- The threshold energy is substantially lower than for physical sputtering.
- The sputtering yield shows pronounced temperature dependence.
- Chemical sputtering yields are substantially higher compared with physical sputtering data or predictions from computer simulations. In contrast, data for physical sputtering with noble gases or self-sputtering (target and projectile atoms are identical) are, in general, in excellent agreement with such model predictions.

Chemical sputtering with the emphasis on the sputtering of carbon by hydrogen isotopes was recently thoroughly reviewed by Jacob and Roth (2007). If a carbon-containing surface is bombarded with hydrogen ions, the dominant erosion products are hydrocarbon species. The process is thermally activated and exhibits similar temperature dependence as chemical erosion (see preceding section). The position of the maximum, T_{max} , depends on the ion energy and on the ion flux. As can be seen in ► Fig. 60.9, the yield for sputtering of C by D (circles) remains high even at the lowest energies.

The elementary processes for the chemical sputtering mechanism are as follows. Impinging ions break carbon–carbon bonds at the surface and within the ion penetration range. Locally available hydrogen reacts with these broken bonds, forming C–H bonds and thus stabilizing them. Consecutive C–C bond breaking and C–H bond formation processes lead to the production of stable, volatile hydrocarbon entities, and/or loosely bound terminal groups at

and below the surface (within the ion penetration range). Finally, the formed volatile hydrocarbon molecules or erosion precursors are either desorbed directly due to ion impact or first diffuse to the surface and desorb there. At room temperature, subsurface hydrocarbon species can desorb only from a limited near-surface layer of the order of 2 nm.

On the basis of this model, a mathematical description was devised that is able to consistently describe all experimental observations, which can be extrapolated to other projectiles. In particular, the model correctly reproduces experimentally observed isotope dependence for bombardment with H and D and allows extrapolation to tritium (Hopf and Jacob 2005). The chemical sputtering yield of carbon due to bombardment with D is about a factor of 2 higher than that of H. Due to the higher mass of tritium, the predicted chemical sputtering yield of tritium will be about 50% higher than that for deuterium (Hopf and Jacob 2005).

It has to be mentioned here that similar effects as for bombardment of carbon surfaces with hydrogen isotopes are observed if a carbon surface is bombarded by any kind of energetic species in the presence of atomic hydrogen. In such a situation, the energetic species provides the kinetic energy required to break bonds and the chemical reactivity is provided by the atomic hydrogen species (Jacob and Roth 2007).

Another species that causes chemical sputtering of carbon and is of relevance for MCF is oxygen. On the one hand, oxygen is an almost unavoidable impurity in any vacuum system mostly introduced in the form of water; on the other hand, this process is relevant for the removal of redeposited carbon layers in fusion devices (see below). It is interesting to note that the interaction of oxygen with carbonaceous layers is also of significant relevance in different technological applications, for example, in microelectronics (ashing, resist stripping), for modification or patterning of polymers using oxygen plasmas, and for sterilization. If carbon materials are bombarded with energetic oxygen ions (Jacob 2007), the impinging oxygen is trapped or reemitted in the form of CO and CO₂. At 300 K, the saturation concentration of oxygen in graphite is 0.25 O/C. At 300 K and ion energies higher than 50 eV, the chemical sputtering yield is around 0.7 removed C atoms per impinging O atom. In the range from 50 eV to 10 keV, the yield increases slightly with increasing energy. For energies higher than 500 eV, it is even higher than 1 due to the increasing contribution of physical sputtering. The maximum of the yield occurs at about 3 keV. For energies lower than 50 eV, the yield decreases significantly. Erosion of carbon surfaces due to impinging oxygen impurities is an issue of significant relevance for fusion, because dissociation of the released CO and CO₂ species in the edge plasma produces new oxygen ions and neutrals, which again can erode carbon so that oxygen atoms can participate multiple times in an erosion process. This contributes to lifetime problems of carbon PFCs in areas where significant oxygen fluxes may reach the surface. Therefore, the oxygen impurity content in a fusion device with carbon PFCs has to be minimized.

Oxygen plasmas can be used to remove redeposited hydrocarbon films. In oxygen plasmas, not only energetic oxygen ions, but also reactive excited neutral oxygen species such as O atoms and ozone may interact with the surface. At present, the determining microscopic processes are not well known, but experimental results indicate that a synergism between ion bombardment and O₂ molecules exists and may play a significant role in this process. Very high erosion yields can be achieved with oxygen-containing plasmas on areas that receive a sufficiently high ion flux. In fact, for the time being this is the most effective method for removing carbon and hydrocarbon layers. For removal of hydrocarbon layers in fusion devices, neutral species are of particular importance. On surfaces having no direct plasma contact, so-called remote areas, ion-induced processes cannot prevail because such areas receive no ion bombardment. In such

situations, erosion has to be driven by neutral species from the plasma. Possible candidates are oxygen atoms, ozone, or excited oxygen molecules. The erosion efficiency of neutral activated oxygen species was investigated by Schwarz-Selinger et al. (2009a, b). They found that the erosion caused by activated species from the plasma increases with increasing temperature by about two orders of magnitude and follows an Arrhenius-type dependence on substrate temperature with effective activation energy of 0.25 eV (temperature range 290–580 K). The precise nature of the activated species is, however, still unknown. Nevertheless, removal of redeposited hydrocarbon films in fusion devices seems to be possible at elevated surface temperatures. However, before this method can be really applied in future devices, many accompanying problems – such as collateral damage during cleaning and removal of oxygen from the vacuum system after oxygen treatment – have to be solved.

60.5.5 Redeposition and Co-Deposition

Eroded species can redeposit; this process is generally called redeposition. Redeposition can occur very close to the place of erosion or in areas very far away. The details of this process depend on a great number of different parameters. Only surface atoms transformed by PSI processes into chemically stable volatile species can be transported to the vacuum pumps and be pumped away. All other species will remain inside the vacuum vessel. They only will be transported from one location to another. On plasma-facing surfaces, the probability is high that a redeposited species will be eroded again. The long-range transport of first-wall materials in a fusion device is usually due to a series of many erosion-deposition cycles. Redeposition reduces the net erosion rate and contributes, therefore, to the extension of the component lifetime in net erosion areas. The fuel inventory in PFMs in net erosion areas is only due to implantation and diffusion into the bulk. On the other hand, in net deposition areas, a constantly growing layer of eroded material will redeposit and a certain amount of fuel species will be incorporated in the growing film. The amount of retained fuel species depends on the chemical affinity to incorporate hydrogen during film growth. In addition, due to PSI processes thermodynamically metastable phases may be formed. For instance, implantation of energetic hydrogen species into the growing film may lead to higher hydrogen concentrations than incorporation due to adsorption and surface reactions. The incorporation of fuel species into a growing redeposited film is usually named co-deposition because hydrogen isotopes are not film-forming species and are only deposited together with film-forming species.

On all surfaces, there is an ongoing competition between erosion and deposition processes. The answer to the question where net erosion and net deposition areas occur depends on the impinging particle fluxes and on the transport of eroded species through the edge plasma. In general, the higher the ion energy and the higher the ion flux density the higher is the probability that erosion exceeds deposition. These are net erosion areas. In contrast, high fluxes of depositing species and low ion energies are indicative of net deposition areas.

Sputtered metal or carbon atoms have sticking probability close to 1 and stick on the next surface they come in contact with. If they are ionized during their transport through the boundary plasma and impinge as ions on the surface, the sticking probability is also very close to 1. Consequently, they will redeposit only on areas that have direct line of sight to the erosion area or on so-called plasma-wetted areas, that is, surfaces that have direct contact with the boundary plasma. On the other hand, surfaces that are neither in direct line of sight nor plasma-wetted will receive a negligible flux of sputtered atoms.

Hydrocarbon species, the erosion products of chemical erosion and chemical sputtering of carbon surfaces, lead to much more complex redeposition phenomena. Stable species such as methane do not stick at surfaces and may be transported to the vacuum pumps and thus removed from the vacuum system. However, they may be dissociated or ionized during their transport through the boundary plasma and thus they may become redeposited. Furthermore, some of the released products may already be radical species. The sticking of such hydrocarbon radicals can vary over orders of magnitude from 10^{-4} for CH_3 radicals to about 0.8 for C_2H radicals (Jacob 2005). Low-sticking neutral species can survive many wall collisions and can, therefore, be transported to remote areas in the fusion device before they become redeposited. As re-erosion on such areas is typically negligible, this process leads to deposition of stable hydrocarbon films with typical hydrogen fractions of 50%. These redeposited hydrocarbon films constitute a constantly growing D and T reservoir and are a major safety concern. Based on present knowledge, long-term tritium retention in ITER will be dominated by tritium bound in such redeposited hydrocarbon films.

60.5.6 Edge Plasmas in Magnetically Confined Fusion Devices

As said before, the core and edge plasmas are separated by the LCFS (= separatrix in divertor devices). The core plasma is fully ionized. The plasma number density, n_e , in the core is of the order of 10^{20} – 10^{21} m^{-3} and the plasma temperature, T_e , is of the order of 10 keV. The plasma number density in the boundary plasma or edge plasma, n_e , is of the order of 10^{19} – 10^{20} m^{-3} , decaying exponentially toward the walls. T_e is in the range of 1–100 eV.

The main chamber wall of a fusion device will be exposed to large fluxes of charge exchange (CX) neutrals. These CX neutrals are produced if a neutral hydrogen atom collides with an energetic ion from the plasma. While charged species are confined by the magnetic field, energetic neutrals are no longer confined and will impinge on the surrounding walls. In fusion devices, this CX flux is a significant contribution to the total flux of energetic species reaching the main chamber wall. The particle energies of the CX species can be very high (beyond 1 keV) (Stangeby 2002) and the corresponding physical sputtering of wall material is an unavoidable process in a fusion device. The sputtered species can penetrate and contaminate the core plasma. Impurity radiation cools the core plasma. Because the radiated energy increases strongly with the atomic number Z , much lower concentrations of high- Z atoms than low- Z atoms are acceptable in the core plasma. While, for example, beryllium concentrations of the order of 10^{-2} are tolerable, only about 10^{-5} are tolerable for tungsten (Stangeby 2002). On the other hand, the sputtering yield of Be is much higher than that of W (► Fig. 60.9). On the main chamber walls, the tradeoff between high sputtering yield and high tolerable concentration has led to the decision to use Be as PFM. However, it is also clear that Be is no option for a future power reactor. For this purpose, tungsten will have to be used and plasma scenarios will have to be developed to allow operation of fusion plasmas with a tungsten first wall. The local CX flux depends on the neutral density. Consequently, it is high where the neutral density is high and that is around the main recycling areas. For a fusion device employing the limiter concept (see ► Fig. 60.8), this means that the limiter and the surrounding areas are exposed to a high CX flux. In addition, the limiter is in this case the main interaction area for PSI and suffers a high ion flux. Since the limiters in a limiter machine are inevitably close to the core plasma, the energies of the impinging ions and CX neutral are rather high so that the sputtering yields are also rather high. Consequently, limiters produce a lot of impurities. Due to the proximity to the

LCFS, these impurities have a very high probability to penetrate the core plasma and contribute strongly, therefore, to plasma contamination. As a result, the limiter concept is no option for future fusion devices.

Almost all modern fusion devices rely on the divertor concept and all planned devices comprise a divertor. The divertor was initially a separate chamber to which the boundary plasma was diverted by additional divertor coils. In the divertor, the plasma is guided onto target plates. The dominant and most important process at the target plate is neutralization. The impinging plasma ions are neutralized and reemitted into the gas phase. Therefore, the neutral gas pressure in the divertor is substantially higher than in the main chamber. The pump ducts to the vacuum pumps are located underneath the divertor to pump the neutral gas. Naturally, the pumped gas is dominantly composed of fuel species, but in addition, the helium ash and other volatile impurities will be removed in this way. The pumped fuel will be recycled in the gas handling facility and pumped impurities will be permanently removed. The other important function of the divertor is to handle the arriving power flux. This will be discussed further below.

Depending on the type of plasma-facing material, surface temperature, and mean energy of the impinging particle flux, different basic PSI processes can occur. In ITER, it is presently foreseen to use either carbon and tungsten in combination in different areas of the divertor, or only tungsten alone. Due to the co-deposition issue, carbon does not seem to be a realistic choice for future power reactors. Energetic species impinging on the divertor target plates will lead to physical sputtering. This process occurs for carbon as well as for tungsten surfaces. For carbon, in addition to physical sputtering, chemical erosion and chemical sputtering contribute to target plate erosion. Due to the higher density in the divertor (compared with the main chamber), mean particle energies are much lower than at a limiter surface. The lower particle energies, however, are compensated by larger fluxes, since the total power flux to the wall has to be maintained. However, the sputter yield decreases over proportional with decreasing energy, so that the total sputtered flux is lower in the divertor concept. In addition, to reach the core plasma, released species from the target plate have to migrate through the incoming plasma flux. The probability is high that species are ionized due to interaction with the boundary plasma and are transported back to the target plate where they might be redeposited. The probability for a species eroded from the divertor surface to enter the core plasma is much lower than for a species created at a limiter surface. In summary, the contribution of PSI processes to plasma contamination is much lower in a divertor device than in a limiter device. Consequently, all next-step fusion devices will operate with a divertor.

Different divertor operational scenarios exist. At low divertor density, particle transport processes are dominated by charged species, which are guided by the magnetic field. The power flux is dominated by the kinetic energy of the impinging ions. Due to the high ion flux density in the region where the separatrix strikes the target plates ("strike point"), the power flux is strongly localized. This strong localization can create extreme conditions for plasma-facing materials at the divertor target plates. Predictions for ITER yield power flux densities of the order of 10 MW/m^2 for normal steady-state phases. During off-normal events such as ELMs (see below), these power flux densities can increase by factors of 5–10 and to even higher values for disruptions (see below). No component can tolerate such power fluxes so that this low-density scenario is not compatible with requirements for a future power reactor.

This challenge can be overcome if the divertor is operated at higher density. Inelastic collisions between electrons and heavy particles decrease the electron temperature, so that mean particle energies decrease. With increasing density, the number of collisions of ions with

neutrals further increases. This causes cross field transport and tends to broaden the strike area of the plasma ions on the target plate. In addition, CX collisions produce fast neutrals that also contribute to a distribution of the energetic particle flux onto a larger area. At sufficiently low electron temperature and sufficiently high neutral density, volume recombination (i.e., electrons and protons recombine to form neutral hydrogen atoms and molecules) sets in. The neutral flux is again distributed to a larger area, but, even more important, hydrogen atoms and molecules can radiate line radiation, which then contributes to cooling of the divertor plasma. Emission of radiation goes into the full solid angle, so that enhanced radiation is a very efficient concept to distribute the power flux to a much larger area. Consequently, the local power flux density around the strike point position is significantly reduced if a substantial fraction of the power flux can be converted into radiation. At high divertor density, n_e can reach values of 10^{21} m^{-3} . Under such conditions, electron temperature is 1 eV and below.

The cooling of the divertor plasma due to enhanced radiation, the so-called radiative cooling, can be systematically exploited by the intentional injection of impurities into the divertor plasma. For example, argon, neon, or nitrogen are considered for injection into the divertor plasma to reduce the power flux in ITER to tolerable limits.

60.5.7 Other PWI Processes

Another requirement that plays an important role in plasma–wall interaction in MCF devices is the handling of the extreme power-flux densities. This is a substantial challenge for the plasma-facing materials and the design of the components to be used in the divertor. As an example, ITER is designed for a fusion power of 500 MW. Twenty percent of this power is generated in the form of energetic alpha particles that are used to heat the core plasma. With an additional foreseen external heating power of about 73 MW, the total heating power that has to be removed via PWI processes and to be conducted to the heat sinks of the cooling system of the wall components is of the order of 170 MW. Since the radial extend of the SOL is only of the order of a centimeter and most of this heating power is transported along the SOL to the target plates in the divertor, the local power densities at the target plate are extremely high. Inclining the target plates can increase the strike area by about a factor of 6. Nevertheless, the total strike area is still only about 6–8 m². In the ITER reference scenario, it is estimated that about half of the total heating power is convected to the target plates leading to a mean power density of 10 MW/m². The other half of the heating power is distributed onto the whole inner-wall area of about 680 m² dominantly by radiation. The corresponding power density of about 0.1 MW/m² can easily be removed by active cooling. Neutrons deploy their energy much deeper in the wall, therefore they are not considered as a plasma–wall interaction problem here.

Prototype components for divertor elements, which can reliably remove the predicted power flux densities of about 10 MW/m², have been produced and successfully tested (Samm 2008). However, the impact of transient effects such as disruptions and ELMs impose a further very serious challenge for the integrity of divertor components (Federici et al. 2001). These events may cause surface damage and high erosion losses due to surface melting and melt layer losses, surface vaporization, cracking, and spallation. A disruption is the usually unplanned sudden termination of the plasma current that may occur if operational limits of plasma confinement are exceeded. One but not the only example of such an operational limit is the density limit. A disruption always leads to the sudden loss of plasma confinement and the

complete stored energy in the plasma is dumped onto the first wall. Typical thermal quench times anticipated for ITER are several milliseconds. The spatial distribution of the power is hard to predict, but based on present experience a substantial fraction goes to the divertor. This means that maximum power loads during disruptions are more than a factor of 10 up to 100 higher than the above-mentioned mean power density of 10 MW/m². Since ITER will be an experimental device, it must be able to withstand a few disruptions. On the other hand, disruptions have to be completely avoided in future power reactors. Avoidance and mitigation strategies for disruption are explored to extent the lifetime of in-vessel components (Federici et al. 2001).

As described in the previous section, ELMs are edge-localized instabilities occurring during H mode plasma operation. ELMs are repetitive transient phenomena with a typical duration of some 10⁻⁴ s and lead to a periodic expulsion of particles and power from the core plasma into the SOL and finally onto the surfaces of the divertor target and the first wall. ELMs seem to be required to avoid impurity accumulation in the core plasma.

Three different types of ELMs exist. Type I ELMs lead to large power loads. They have a large amplitude and relatively low frequency. Up to 10% of the stored energy in the main plasma can be ejected during one type I ELM. The spatial distribution is inhomogeneous, but most energy is dumped to the inner divertor target plates. This extreme power flux can cause melting of the surface, even for tungsten, and lead to melt layer loss (evaporation and splashing). It is obvious that this has severe consequences for the involved plasma-facing materials and components. Plasma operation with type I ELMs is not compatible with lifetime requirements of a power reactor and has to be avoided. Type II ELMs are relatively uncommon. They have a rather low energy content and pose no problems for wall materials. For practical purposes, they play no role. Type III ELMs have a much higher frequency than type I ELMs (0.1–1 kHz) and lower amplitude (about 1% of energy content). They are compatible with material requirements and are the favored operational mode for ITER. Mitigation methods for type I ELMs and triggering of type III ELMs are actively investigated. However, different types of ELMs occur in different plasma-operation scenarios. The best confinement is coupled to large type I ELMs, while small-ELM regimes have their price in confinement quality. The choice of plasma operation scenario is therefore a compromise between tolerable divertor load and good confinement.

A further aspect of PWI is the fact that plasma-facing materials and structural materials have in general different requirements. The plasma-facing materials are optimized for lifetime, low impurity generation, and low tritium inventory, which require low atomic number or low sputtering yield. On the other hand, structural materials have to guarantee the structural stability of divertor and first-wall components and must be able to conduct the impinging energy fluxes to the cooling system. In general, this leads to a different choice for PFM and structural material. This allows a higher flexibility in designing plasma-facing components, but creates also new problems. Since, in general, thermal expansion coefficients of different materials differ, significant stresses are created at the interfaces of different materials. This represents a major challenge for the development of joining methods and remains a very active and important field of material science and for the further development for MCF.

Certain consequences of PSI processes – apart from sputtering and deposition – have strong implications for the properties of the materials of the first wall as well. Important issues in this context are the change of material properties due to implantation of hydrogen as well as radiation damage and transmutation due to neutron irradiation. Such material-related topics have recently been reviewed in depth by Federici et al. (2001).

60.6 Prospects of Practical Application

Present day fusion devices are practically plasma confinement experiments, albeit at sizes and power close to fusion reactor needs. As discussed in [Sect. 60.1.1](#), positive energy balance requires good enough thermal insulation of the plasma, which is characterized by the energy confinement time τ_E . As this single parameter includes all kinds of losses (radiation, conduction, particles), it cannot be described in an easy analytical form. Even at the present state of research, it cannot be derived from first principle simulations. Due to the complexity, empirical scalings have been established on the basis of experiments (ITER 2007). For the energy confinement time, the most often used IPB98(y,2) scaling is a regression fit to a compilation of selected well characterized H-mode confinement results from 19 present and past tokamak experiments (ITER 2007) in the form:

$$\tau_E = 0.0562 I_p^{0.93} B_t^{0.15} n^{0.41} P^{-0.69} R^{1.97} \varepsilon^{0.58} \kappa_a^{0.78} M^{0.19}, \quad (60.12)$$

where I_p is the plasma current in MA, B_t is the toroidal field in tesla, n is the plasma-electron density in units of 10^{19} particles/m³, P is the heating power in MW under stationary conditions (which equals the power loss from the plasma), R is the torus major radius, $\varepsilon = a/R$ is the inverse aspect ratio, a is the mean plasma minor radius, κ_a is the plasma elongation defined as the ratio of the plasma cross section to $a^2\pi$, and M is the mean ion mass relative to hydrogen H (¹H). This scaling has been established mostly in deuterium discharges but the weak atomic-mass dependency makes one hope it is applicable to DT plasmas as well.

Although IPB98(y,2) is dimensionally incorrect and hides complex physical processes, it is very useful for a first estimation for the performance of a future device. Similar scalings have been established for stellarators as well, for example, ISS95/04 (Yamada 2005). Other scalings provide the H-mode access and other necessary conditions. Limits on certain parameters or parameter combinations arising from understood physics or empirical scalings bound the operating space of the devices. This prevents changing the parameters in, for example, IPB98(y,2) independently. For example, the increase of density (n) would be beneficial for the confinement time and volume fusion power ($P_f \propto n^2$) as well. However, for tokamaks, but not for stellarators, the so-called Greenwald empirical disruption limit represents an upper bound for the density in the form $n_{\max} \propto I_p/\pi a^2$. Therefore, operation close to the density limit means an effective $\tau_E \propto I_p^{1.34}$ scaling, which would call for increasing the plasma current. On the other hand, the rotational transform in tokamaks is $q = (B_t 2\pi a^2)/(R\mu_0 I_p)$ and it must be above 2 because of the well-understood magnetohydrodynamic kink-instability limit. Therefore, at high density, high current, fixed plasma geometry, and heating, the scaling effectively becomes $\tau_E \propto B_t^{1.49}$, that is, finally, a high magnetic field is required. Ultimately, the technical limit on the magnetic field strength renders the IPB98(y,2) scaling a function of geometrical parameters and the power only. Of course, the device size and the needed power are again interdependent, but in any case the increase of the major radius R and the inverse aspect ratio $\varepsilon = a/R$ is beneficial, calling for large and compact devices.

Following IPB98(y,2), present day fusion devices are not capable of reaching positive energy balance simply due to their size. The largest tokamak devices are just about to reach the breakeven limit in DT plasma, but in reality, this is not demonstrated as the neutron flux during high-power DT operation, which would activate the device and would inhibit manned access for a considerable period of time. Only two devices were capable of operating in DT mixture: TFTR (Strachan 1997) in USA and JET (Keilhacker 1999) in Europe. The larger and

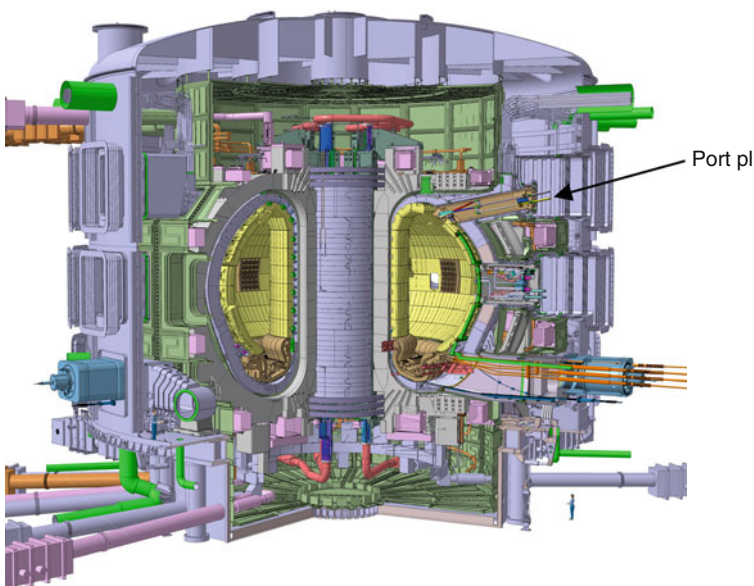
even presently operational JET devices demonstrated $Q = 0.2$ – 0.3 in quasi steady-state operation and up to 0.55 transiently. Comparison between pure deuterium and DT discharges confirmed that Q can be reliably calculated for DT discharges on the basis of deuterium ones.

According to the scaling, a device at twice the size of the presently largest tokamak (JET) could reach about $Q = 10$, and at nearly three times the size, it would ignite (Jacquot 1999), that is, alpha heating would replace the external heating. To reach that condition, an international tokamak device has been proposed already in 1985 (Braams and Stott 2000). By 1998, the engineering design of an $R = 8$ m tokamak was completed (ITER 1999) with full superconducting coil set and all technical equipment capable of demonstrating fusion ignition for few 100 s long pulses. Due to financial problems, this device could not be built, but a downscaled version of the plans at $R = 6.2$ m was created by 2001 (Aymar et al. 2002). This is the basis of ongoing efforts, which are generally hoped to conclude latest by 2020, in the startup of the ITER experiment.

It is important to understand that ITER (● Fig. 60.10) will not be a fusion reactor, but a combined plasma confinement and fusion technology experiment. From the plasma physics point of view, it should demonstrate plasma operation under reactor conditions with $Q = 10$ in 500 s pulses. The plasma current would be driven inductively. Long pulse operations are planned with noninductive current drive at about $Q = 3$ fusion performance. ITER should demonstrate plasma operation with dominant alpha particle heating and should be capable of exploring diagnostics and plasma control schemes toward a reactor.

However, it will utilize techniques, which will not be possible on a reactor due to the continuous operation and/or higher neutron dose. From the technology point of view, one important aim is to demonstrate tritium-breeding technologies. ITER will not be self-sustaining of tritium as only a few test blanket modules (TBM) will be installed for the testing

■ Fig. 60.10
Cutaway view of ITER



of various technologies (Giancarli et al. 2006). Several competing concepts will be explored: water or helium gas cooled mixture of lithium-silicate and beryllium pebbles or lithium-lead liquid.

ITER will have 73 MW external heating capability and 500 MW fusion-power production is expected. This is quite a large technological step compared to JET, which is similar in construction. The most important difference is that ITER will be a nuclear device with several hundred kW/m^2 neutron power deposited in the blanket. This is a major hurdle for heating and diagnostics devices, which will have to place all sensitive components behind shielding and must cool all structures seen by the neutron flux. Nearly all of such equipment will be installed in port plugs, which can be removed by remote handling equipment as maintenance operations can be carried out only in hot cells.

ITER will be able to test plasma confinement and key technologies needed for a fusion reactor but will not be able to test how structural materials behave under the extreme neutron dose expected in a fusion reactor. Most of the difference in the dose comes from the fact that ITER will operate in short pulses only, while a fusion reactor will have to have a high availability. The expected irradiation damage to structural materials in a fusion reactor will also be much higher than in present-day fission reactors for two reasons. Firstly, in a fission reaction only a few percent of the energy is taken away by the neutrons, while in a fusion one 80%. Secondly, the fusion plasma is tenuous and therefore all neutrons reach the wall of the reaction chamber. This neutron load will certainly cause serious damage to the materials, but the nature of this is largely unknown as fission reactors can simulate the fusion neutron load only to a certain extent.

Another question for materials' scientists is the activation of structural materials by neutrons. As no radioactive material is generated in a fusion reactor, the careful choice of the structural materials would allow minimization of the nuclear waste production to rather low levels. For this purpose, a special fusion steel called EUROFER97 has been developed and characterized inside fission reactors up to 30 displacement per atom (dpa) dose (Lindau et al. 2005). The results indeed show that after about 100 years, the fusion reactor components could be recycled as nonradioactive materials. Concerning the neutron damage, an irradiation with fusion-relevant neutron spectrum must be carried out up to the ~ 150 dpa level expected in a reactor. For this, an accelerator-based device called IFMIF (Moeslang et al. 2006) is being designed. It would generate 14 MeV neutrons by firing two deuterium beams onto a liquid lithium target. Small material samples would be investigated and, based on the results, the materials for fusion power plants could be designed. Some experts also consider the construction of steady-state $Q < 1$ tokamak devices as neutron sources for testing full fusion reactor components.

Even if using special fusion materials, it cannot be expected that the blanket of the fusion power plant would survive the full lifetime of the reactor. At present, it is estimated that the blanket and the divertor will have to be replaced every 2–5 years. This is a major intervention, which has to be done completely with remote handling operations, as the materials will be strongly activated. It has been found that the engineering design of the blanket system is extremely important and will largely determine the time needed for blanket replacement (Ihli et al. 2007), and through this the availability of the power plant.

In addition to the status of magnetic confinement fusion, it is worth briefly considering the status of inertial confinement fusion developments as well. This field has been combined with military research for the study of materials under extreme conditions experienced during nuclear bomb explosions; therefore, its progress was only partly visible to the public. However, recently two major laser ICF facilities are being built or operated: Laser Megajoule (LMJ)

(Cavailler 2005) in France and the National Ignition Facility (NIF) (Hammel 2006) in USA. Both of them are expected to demonstrate positive energy balance processes (breakeven) in a few years time. This is going to be a major achievement of many decades of laser fusion research, but similarly to ITER, it is not going to demonstrate practical energy production. Several technical challenges need to be solved for the construction of an ICF-based power plant. At present, lasers can fire only a few times a day; for a fusion reactor, 10 Hz CW operation would be needed. Similar development is necessary in the efficiency of the lasers, which need to reach about 10%, an increase of an order of magnitude from present systems. Automated 10 Hz production of precise, multilayer pellets at low price (a few 10 Eurocents) seems to be a comparable challenge. Wall damage, especially in the case of highly sensitive high-power optical elements is also a major issue, in this context IFE shares the problems of MCF. These technological issues have been considered in the past in less depth by the IFE community, but the demonstration of breakeven will certainly give a boost to these developments. One important proposed experiment is the HIPER project (HIPER 2007), which aims at testing the fast ignitor concept described above. NIF, LMJ, and HIPER would test the physics and technology for the IFE-based energy production power plant.

In the MCF field, the results from ITER and IFMIF would provide the basis of the construction of a demonstration magnetic fusion power plant dubbed DEMO. There is no agreement yet on how such a device would look in detail. Several conceptual studies have been concluded on fusion power plants during the past decades. They are based on different tokamak variants (Najbadi et al. 2003, 2006; EFDA 2005), stellarators (Raffray 2007), and assume different blanket technology (EFDA 2005). These studies indicate that fusion energy production would be possible at a cost comparable to present energy prices. However, all of these studies make assumptions on the solution of several problems, which will be available only after ITER or even later. The key elements have been described in the sections above, here they are listed just for reference. The problem of structural material damage will be addressed in IFMIF. The selection of plasma-facing materials is a major issue, which will partly be tested in ITER albeit DEMO might impose higher heat loads and the long-term issues might also pose problems. The control of plasma operation at a desired operational point might require advanced current drive, heating, and diagnostic techniques. Although some of these are readily available, their operation in the harsh nuclear environment of DEMO might be problematic or at least require further development. This leads to the final difficulty, the complexity of the fusion device. A fusion power plant assumes simultaneous operation of a large number of components, which are all extremely complex themselves. No matter which of the two basic concepts wins (i.e., IFE or MFE) one thing for sure is: reliability, robust engineering design, and good management are going to be key issues in the construction and operation of fusion power plants, as these devices will be most probably the most complex instruments humankind has ever devised.

References

-
- | | |
|--|--|
| Aymar R, Barabasci P, Shimomura Y (2002) Plasma Phys Controlled Fusion 44:519 | Behrisch R, Eckstein W (2007) Sputtering by particle bombardment IV, topics in applied physics, vol 110. Springer, Berlin |
| Behrisch R (1981) Sputtering by particle bombardment I, topics in applied physics, vol 4. Springer, Berlin | Behrisch R, Wittmaack K (1991) Sputtering by particle bombardment III, topics in applied physics, vol 64. Springer, Berlin |
| Behrisch R (1983) Sputtering by particle bombardment II, topics in applied physics, vol 42. Springer, Berlin | |

- Braams CM, Stott PE (2000) Nuclear fusion: half a century of magnetic confinement fusion research. Institute of Physics Publishing, Bristol
- Brown IG (2004) The physics and technology of ion sources. Wiley, New York
- Cavailler C (2005) Plasma Phys Controlled Fusion 47: B389
- Chen FF (1984) Introduction to plasma physics and controlled fusion. Plenum Press, New York
- Diamond P et al (2005) Plasma Phys Controlled Fusion 47:R35
- Dolan TJ (2000) Fusion research: principles, experiments and technology. Pergamon, Oxford
- Doyle EJ et al (2007) Nucl Fusion 47:S18
- Eckstein W (2007) Sputtering yields in "Sputtering by Particle Bombardment IV". In: Behrisch R, Eckstein W (eds) Topics in applied physics, vol 110. Springer, Berlin, pp 33–187
- Eckstein W, Urbassek HM (2007) Computer simulation of the sputtering process in "Sputtering by Particle Bombardment IV". In: Behrisch R, Eckstein W (eds) Topics in applied physics, vol 110. Springer, Berlin, pp 21–31
- EFDA (2005) Final report on conceptual power plant study, EFDA report EFDA-RP-RE-5.0
- Erckmann W et al (2007) Fusion Sci Technol 53:279
- Federici G, Skinner CH, Brooks JN, Coad JP, Grisolia C, Haasz AA, Hassanein A, Philipps V, Pitcher CS, Roth J, Wampler WR, Whyte DG (2001) Plasma–material interactions in current tokamaks and their implications for next step fusion reactors. Nucl Fusion 41:1967–2137
- Felton R et al (2005) Fusion Eng Des 74:561
- Fusjisawa A (2008) Nucl Fusion 49:013001
- Giancarli L et al (2006) Fusion Eng Des 81:393
- Gil RD (1981) Plasma physics and nuclear fusion research. Academic, London/New York
- Gormezano G (1986) Plasma Phys Controlled Fusion 28:1365
- Hammel BA (2006) Plasma Phys Controlled Fusion 48: B497
- Helander P, Sigmar DJ (2002) Collisional transport in magnetized plasmas. Cambridge University Press, Cambridge
- HIPER (2007) Technical background and conceptual design report 2007, www.hiper-laser.org/docs/tdr/hipertr2.pdf
- Hirsch M et al (2008) Major results from the Stellarator Wendelstein 7-AS. Plasma Phys Controlled Fusion 50(053001):204
- Hopf C, Jacob W (2005) Bombardment of graphite with hydrogen isotopes: a model for the energy dependence of the chemical sputtering yield. J Nucl Mater 342:141–147
- Hutchinson I (2002) Principles of plasma diagnostics. Cambridge University Press, Cambridge
- Ihli T et al (2007) Fusion Eng Des 82:2705
- ITER (2007) Nucl Fusion 47:S1–S413
- ITER (1999) ITER final design report, ITER EDA Documentation Series No.14, IAEA, Vienna
- Jacob W (2005) Redeposition of hydrocarbon layers in fusion devices. J Nucl Mater 337–339:839–846
- Jacob W, Roth J (2007) Chemical sputtering in "Sputtering by Particle Bombardment IV". In: Behrisch R, Eckstein W (eds) Topics in applied physics, vol 110. Springer, Berlin, pp 329–400
- Jacquot J (1999) Nucl Fusion 39:235
- Kasugai A et al (2006) Fusion Eng Des 81:2791
- Keilhacker M (1999) Nucl Fusion 39:209
- Kohl W (1995) Handbook of materials and techniques for vacuum devices. AIP Press, Woodbury
- Küppers J (1995) Surf Sci Rep 22:249–321
- Lawson JD (1957) Proc Phys Soc B 70:6
- Lindau R et al (2005) Fusion Eng Des 75:989
- Lindl J (1995) Phys Plasmas 2:3933
- Meyer-ter-Vehn J (2001) Plasma Phys Controlled Fusion 43:A113
- Moeslang A et al (2006) Fusion Eng Des 81:863
- Najbadi F et al (2003) Fusion Eng Des 65:143
- Najmabadi F et al (2006) Fusion Eng Des 80:3
- Naujoks D (2006) Plasma–material interaction in controlled fusion. Springer, Berlin
- Nusinovich G (2004) Introduction to the physics of gyrotrons. Johns Hopkins University Press, Baltimore/London
- Oikawa T et al (2001) Plasma Phys Controlled Fusion 41:1575
- Olson C (2005) Fusion Sci Technol 47:633
- Peeters AG (2000) Plasma Phys Controlled Fusion 42: B231
- Raffray AR (2007) Fusion Sci Technol 54:725
- Roth J, Bohdansky J, Wilson KL (1982) Erosion of carbon due to bombardment with energetic ions at temperatures up to 2000 K. J Nucl Mater 111–112:775–780
- Sakharov AD (1951) In: Leontovich MA (ed, 1958) Plasma physics and the problem of controlled thermonuclear reactions. English translation: Pergamon, 1961, Oxford
- Samm U (2008) Plasma-wall interaction in magnetically confined fusion plasmas. Fusion Sci Technol 53:223–228
- Schmid K, Baldwin M, Doerner R (2006) Modelling of thermally enhanced erosion of beryllium. J Nucl Mater 348:294–301
- Schwarz-Selinger T, Genoese F, Hopf Ch, Jacob W (2009a) Carbon removal from tile-gap structures with oxygen glow discharges. J Nucl Mater 390–391:602–605
- Schwarz-Selinger T, von Toussaint U, Hopf Ch, Jacob W (2009b) Fuel removal from tile gaps with oxygen discharges: reactivity of neutrals. Phys Scr T138(014009):8
- Shafranov VD (1966) Rev Plasma Phys 2:103

- Spitzer L Jr (1958) *Phys Fluids* 1:253
- Sproul WD, Christie DJ, Carter DC (2005) Control of reactive sputtering processes. *Thin Solid Films* 491:1–17
- Stangeby PC (2002) *The plasma boundary of magnetic fusion devices*. Institute of Physics Publishing, Bristol
- Strachan JD (1997) *Plasma Phys Controlled Fusion* 39: B103
- Stroth U et al (1996) *Plasma Phys Controlled Fusion* 38:611
- Tamm IY (1951) In: Leontovich MA (ed, 1958) *Plasma physics and the problem of controlled thermonuclear reactions*. English translation: Pergamon, 1961, Oxford
- Tore Supra Team (1999) *Fusion Eng Des* 46:313–322
- Wagner F (2007) *Plasma Phys Controlled Fusion* 49:B1
- Wesson J (2000a) *The science of JET, JET open publication*. See www.jet.efda.org
- Wesson J (2000b) *Tokamaks*. Clarendon Press, Oxford
- Yamada H (2005) *Nucl Fusion* 45:1684
- Ziegler JF, Biersack JP, Littmark U (1985) *Stopping and range of ions in solids*. Pergamon, New York (See also: <http://www.srim.org/>)



61 Radioactive Waste Management

P. A. Baisden · C. E. Atkins-Duffin

Lawrence Livermore National Laboratory, Livermore, California, USA

61.1	<i>Radioactive Wastes</i>	2799
61.1.1	Classification of Radioactive Waste	2800
61.1.1.1	Exempt Waste	2800
61.1.1.2	Low-Level Waste (LLW)	2800
61.1.1.3	Intermediate-Level Waste (ILW)	2800
61.1.1.4	High-Level Waste (HLW)	2800
61.2	<i>The Nuclear Fuel Cycle</i>	2801
61.2.1	Options in the Fuel Cycle That Impact Waste Management	2801
61.2.1.1	Material Balance in the Nuclear Fuel Cycle	2802
61.3	<i>The Front-End of the Nuclear Fuel Cycle</i>	2802
61.3.1	Uranium Mining and Milling	2803
61.3.2	Conversion to UF ₆	2804
61.3.3	Enrichment	2804
61.3.4	Fuel Fabrication	2805
61.3.5	Commercial Nuclear Power Generation	2805
61.3.6	Fast Reactors	2807
61.4	<i>The “Back-End” of the Nuclear Fuel Cycle</i>	2808
61.4.1	Spent Fuel	2808
61.4.2	Fuel Reprocessing	2811
61.4.2.1	PUREX, the Industry Standard	2812
61.4.2.2	Vitrification	2814
61.4.2.3	Recycling plutonium as mixed-oxide fuel (MOX)	2814
61.4.2.4	Recycling U	2816
61.4.3	Direct Disposal of High-Level Waste	2816
61.4.3.1	Geologic Disposal	2817
61.5	<i>Partitioning and Transmutation (P&T)</i>	2818
61.5.1	Transmutation of Minor Actinides	2819
61.5.2	Transmutation of the Long-Lived Fission Products	2822
61.5.3	Strategies for the Transmutation of Minor Actinides and Long-Lived Fission Products	2823
61.5.4	Partitioning Schemes for the Minor Actinides and Long-Lived Fission Products	2825
61.5.4.1	Improved PUREX Process	2825

- 61.5.4.2 Aqueous Schemes for the Separation of Minor Actinides from HLW from PUREX 2826
- 61.5.4.3 Advantages of Nonaqueous Processes for Partitioning and Transmutation 2828
- 61.5.5 Transmutation Devices for the Advanced Fuel Cycle 2830
- 61.5.5.1 Future of P&T 2831
- 61.6 *Editors' Notes* 2832

Abstract: Issues related to the management of radioactive wastes are presented with specific emphasis on high-level wastes generated as a result of energy and materials production using nuclear reactors. The final disposition of these high-level wastes depends on which nuclear fuel cycle is pursued, and range from once-through burning of fuel in a light water reactor followed by direct disposal in a geologic repository to more advanced fuel cycles (AFCs) where the spent fuel is reprocessed or partitioned to recover the fissile material (primarily ^{235}U and ^{239}Pu) as well as the minor actinides (MAs) (neptunium, americium, and curium) and some long-lived fission products (e.g., ^{99}Tc and ^{129}I). In the latter fuel cycle, the fissile materials are recycled through a reactor to produce more energy, the short-lived fission products are vitrified and disposed of in a geologic repository, and the minor actinides and long-lived fission products are converted to less radiotoxic or otherwise stable nuclides by a process called transmutation. The advantages and disadvantages of the various fuel cycle options and the challenges to the management of nuclear wastes they represent are discussed.

61.1 Radioactive Wastes

Radioactive wastes, like most other waste forms, contain a variety of materials differing widely in chemical composition, physical state, and origin, either naturally occurring or man-made. This range of materials necessitates equally variant strategies for managing the waste while protecting humans and the environment and being attentive to social and economic considerations.

There are two major sources of radioactive waste both derived from the industrial production of radionuclides: (1) wastes derived from the production of material to support the manufacture of nuclear weapons, often referred to as *defense waste*; (2) wastes resulting from the generation of nuclear power, often referred to as *civilian waste*. There is also nuclear waste associated with other industrial practices (e.g., medical radionuclide production, X-ray sources, or neutron sources) and general scientific research, but the volume and resultant hazard level from these sources is considerably less than from either of the two primary sources.

A number of schemes exist for the classification of nuclear wastes. Most simply, they can be separated by level of radioactivity (high, intermediate, or low) and by type of radiation (alpha, beta, gamma, or X-ray). Further classification often contains information about the physical nature of the waste, either solid or liquid, or the half-life of the contained material (short or long-lived). Another characteristic of radioactive waste that must be considered when developing waste management strategies is the thermal heat content of the waste. The half-life of the radioactive materials determines how long the waste requires management and the total amount of radioactivity as well as the heat content dictate how to handle the waste.

There are two general principles or options that are used to manage both radioactive and nonradioactive wastes. These are (1) to concentrate and isolate wastes (i.e., *concentrate-and-contain*) and, (2) to dilute to regulatory-accepted levels and then discharge the wastes to the environment (i.e., *dilute-and-disperse*).

A third option, which is unique to the management of radioactive wastes, is *delay-and-decay*. In this case, the waste is stored and allowed to decay until the level of radioactivity has decreased to a more manageable, or even background, level.

A number of good, general references about radioactive waste generation and management are available, e.g., see ref. Web (2003a).

61.1.1 Classification of Radioactive Waste

61.1.1.1 Exempt Waste

Exempt waste, sometimes identified as “below regulatory concern”, contains very low concentrations of radioactivity. The associated radiological hazards are generally considered to be negligible as they are less than naturally occurring radioactivity.

61.1.1.2 Low-Level Waste (LLW)

LLW is generated from hospitals, laboratories and industry, as well as from the nuclear fuel and defense program cycle. It comprises paper, rags, tools, clothing, filters, and other lightly contaminated materials that contain small amounts of mostly short-lived radionuclides. It is not dangerous to handle, but must be disposed of more carefully than normal garbage. Often it is buried in shallow monitored landfill sites. To reduce its volume, it can be compacted or incinerated (in a closed container) before disposal. Worldwide it constitutes 90% of the volume but only 1% of the radioactivity associated with all radioactive waste.

61.1.1.3 Intermediate-Level Waste (ILW)

ILW contains higher amounts of radioactivity and may require the use of special shielding to assure worker safety. It typically contains materials like resins, filters, chemical sludge, reactor components, and contaminated materials from reactor decommissioning. It may be solidified in concrete or bitumen for disposal. Generally, short-lived waste (mainly from reactors) is buried, but long-lived waste (from reprocessing nuclear fuel) is usually subject to deep geologic disposal. Worldwide it makes up 7% of the volume and has 4% of the radioactivity of all radioactive wastes.

61.1.1.4 High-Level Waste (HLW)

HLW generally refers to materials requiring permanent isolation from the environment. It frequently arises as a by-product of nuclear power generation (reprocessing streams or spent fuel) or from the isolation of fissile radionuclides from irradiated materials to be used in nuclear weapons production. When nuclear fuel from reactor operations (civilian or defense) is chemically processed, the radioactive wastes include highly concentrated liquid solutions of nuclear fission products. Typically, these waste streams are solidified either in a glass (vitrification) or in another matrix. Both the liquid solutions and the vitrified solids are considered HLW. If the nuclear fuel is not processed, it too, is considered as HLW and must be dispositioned. The path most often proposed is direct, deep geologic isolation.

Although the relative amount of HLW is small with respect to the total volume of radioactive waste produced, it contains 95% of the radioactivity.

HLW in the form of spent nuclear fuel or vitrified reprocessing waste generates intense levels of both radioactivity and heat, requiring heavy shielding and thermal cooling during its

handling and storage. Frequently wastes are stored in cooling ponds or vaults prior to their disposal. While stored, both the temperature and radioactivity of the wastes gradually decrease, simplifying their handling and disposal considerably.

Wastes that contain large quantities of alpha-bearing materials require similar isolation in their ultimate disposal. These wastes are sometimes referred to as transuranic (TRU) or higher actinide wastes and do not generate the thermal heat described above. These wastes are produced in volumes greater by a factor of 5–10 than the HLW previously discussed.

The disposal of HLW is an urgent public policy issue. These political aspects have led to the need for the nuclear community to demonstrate the feasibility and safety of HLW disposal and, in some countries, to implement laws that require operational HLW disposal capability in the next 10–50 years. Many European countries, the USA, and Japan have programs dedicated to the disposal of HLW. Currently, all HLW produced to date is being stored; no permanent disposal has yet occurred.

61.2 The Nuclear Fuel Cycle

Since the dominant sources of all radioactive wastes are associated with energy production via nuclear reactors, it seems prudent to discuss nuclear waste in the context of the nuclear fuel cycle. The nuclear fuel cycle consists of all the relevant activities that must be undertaken to produce electricity from nuclear reactions. The schematic of the nuclear fuel cycle is shown in

• Fig. 61.1.

When discussing how to manage wastes from the nuclear power industry, it is often convenient to break the fuel cycle up into two parts: The *front-end* consists of all the activities beginning with mining and milling up through and including burning the uranium fuel in a nuclear reactor. The remaining activities or *back-end* of the nuclear fuel cycle is where the vast majority of the waste is generated and managed.

As the term nuclear fuel cycle suggests, the standard scenario envisioned by the nuclear power industry was to reprocess the spent fuel because uranium and plutonium would be recovered and recycled to generate additional energy. In addition, by recovering uranium and returning it to the fuel cycle, the demand for new uranium as well as the need for enrichment services could be reduced by about 30% compared to “once-through” fuel management (Choppin et al. 1995). The advantage of reprocessing with respect to waste management is of course, the large reduction in volume (factor of ~100) of the materials to be disposed of as HLW. Some countries, most notably the USA and Canada, have elected not to reprocess fuel, and thus not to close the fuel cycle.

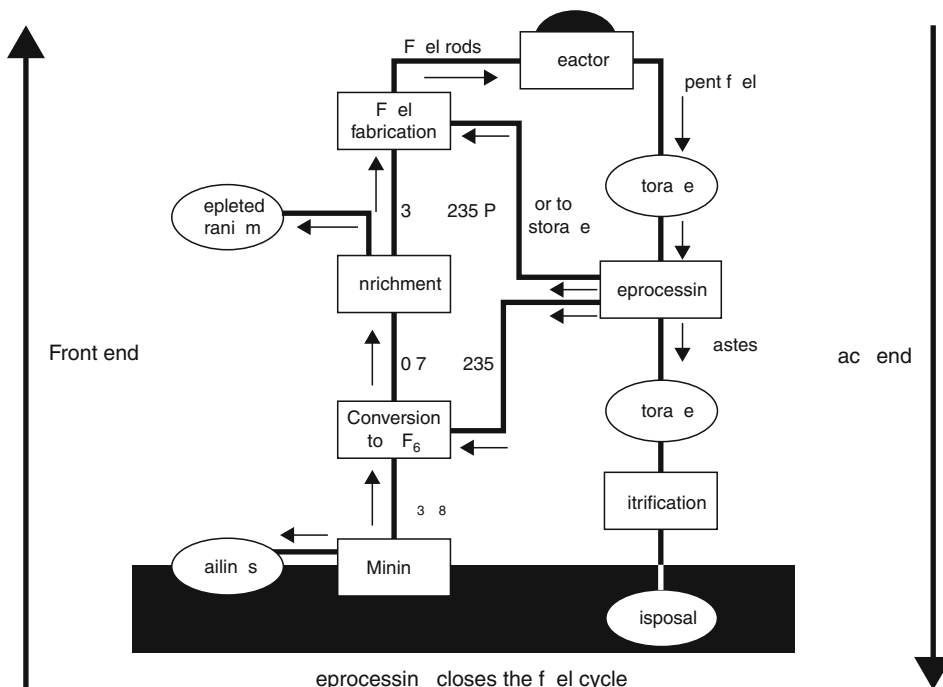
61.2.1 Options in the Fuel Cycle That Impact Waste Management

The three major *back-end* fuel cycle options currently under consideration by various countries are the following:

- Once through cycle with direct disposal of spent fuel as HLW.
- Reprocessing fuel cycle (RFC) with mixed oxide (MOX) recycle of U and Pu in light water or fast breeder reactors (FBRs) and disposal of HLW.

■ Fig. 61.1

Schematic of the nuclear fuel cycle (Courtesy of the World Nuclear Association (Web 2003b))



- Advanced fuel cycle (AFC), an extension of RFC in which the wastes are partitioned and some are transmuted (P&T) to reduce the long-term radiotoxicity.¹

These variations in the fuel cycles each have different advantages and disadvantages and pose different challenges to the management of nuclear wastes that vary in nature and complexity. The sections on “Spent Fuel,” “Fuel Reprocessing,” and “Partitioning and Transmutation” discuss these variations in more detail.

61.2.1.1 Material Balance in the Nuclear Fuel Cycle

A material balance of the nuclear fuel cycle gives one a sense of the quantities of nuclear materials and wastes that are generated and must be managed. Table 61.1 shows the balance of materials in the nuclear fuel cycle needed for the operation of a typical 1,000 MWe power plant.²

61.3 The Front-End of the Nuclear Fuel Cycle

This section describes the wastes generated at each point in the fuel cycle and strategies for handling them. A general discussion is also available in ref. Web (2003c).

Table 61.1

Balance of materials in the nuclear fuel cycle needed for the operation of a typical 1,000 MWe power plant. Uranium concentrations are sometimes expressed in terms of U_3O_8 content (U_3O_8 is a mixture of two uranium oxides, approximately as they occur in nature). Pure U_3O_8 product contains about 85% uranium by mass. Concentrate is 80% U, enrichment to 4% U-235 with 0.3% tails assay, 80% load factor for reactor, core load 72 t U, refueling annually with one third replaced

Fuel cycle step	Nuclear materials handled
Mining	22,400 t of 1% uranium ore
Milling	280 t of uranium oxide concentrate (with 224 t U)
Conversion	331 t UF_6 (with 224 t U)
Enrichment	35 t UF_6 (with 24 t enriched U) – balance is “tails”
Fuel fabrication	27 t UO_2 (with 24 t enriched U)
Reactor operation	7,000 million kW h (7 TW h) of electricity
Spent fuel	27 t containing 240 kg Pu, 23 t U (0.8% U-235), 720 kg fission products, also some transuranium elements

Courtesy of the World Nuclear Association (Web [2003b](#)).

61.3.1 Uranium Mining and Milling

Uranium is a naturally occurring ore that can be excavated or recovered using in situ techniques. The decision as to which mining method to use for a particular deposit is governed by the nature of the ore body, safety, and economic considerations. When excavation is chosen either underground mining or open pit technologies is utilized. In general, open pit mining is used where deposits are close to the surface while deeper deposits require underground mining. Owing to access considerations, open pit mining results in large quantities of materials having to be removed. In contrast, underground mining operations exhibit small surface disturbances, with much less material having to be removed. Examples of open pit uranium mining include the Ranger mine in the Northern Territory of Australia and many of Canada's older mines (e.g., at Cluff Lake, Key Lake, and Rabbit Lake). Examples of underground mines include the Olympic Dam mine in Southern Australia, which also produces copper and some gold and silver, as well as the newer mines in Canada, McArthur River and Cigar Lake. McArthur River and Cigar Lake are somewhat atypical underground mines because they contain a very high-grade ore. Thus, these mines require special remote handling equipment.

An increasing proportion of the world's uranium now comes from in situ leaching, where oxygenated groundwater is circulated through a very porous ore body to dissolve the uranium and bring it to the surface. In situ leaching may be with slightly acidic or with alkaline solutions to keep the uranium in solution. With in situ leach mining, dissolved materials other than uranium are simply returned to their underground location. The uranium is then recovered from the solution as in a conventional mill.

At the mill, usually located close to the mine, the ore is crushed and ground to a fine slurry. Sulfuric acid, in which uranium is soluble, is used to leach the product from the bulk material. The residue, consisting of undissolved solids (waste rock) is referred to as the tailings. This material contains most of the radioactivity including radium and toxic materials such as heavy

metals. Frequently the tailings are pumped into engineered ponds designed to retain the solids and prevent any seepage of the liquid. Eventually the tailings may be returned to the mine or covered with rock and clay, then replanted with vegetation. The tailings are about ten times more radioactive than typical granites.

The uranium is recovered from the sulfuric acid solution by precipitation with a base. The resulting product, uranium oxide (U_3O_8) is often referred to as “yellowcake” and is only mildly radioactive. Yellowcake generally contains more than 80% uranium by weight in contrast to the original ore that may have contained as little as 0.1% uranium.

61.3.2 Conversion to UF_6

Although the uranium concentration has been raised substantially in the milling operation, the relative abundance of the fissile isotope, ^{235}U , is too low. Natural uranium contains about 0.7% by weight ^{235}U . To sustain a nuclear reaction in most commercial power reactors, the fuel must be enriched to about 3.5%. Enrichment is often with gaseous feedstock achieved by converting U_3O_8 to the gaseous UF_6 . Uranium conversion plants that produce UF_6 as a feedstock for enrichment processes are currently in operation in both Europe and North America.

61.3.3 Enrichment

Using uranium hexafluoride as the feedstock, the enrichment process exploits the 1% mass difference between the ^{235}U and the ^{238}U isotopes. The USA constructed the first enrichment facilities in Oak Ridge, Tennessee using gaseous diffusion technology. Over time, the technology has transitioned to gas centrifugation.³ In this process, the feedstock is supplied to a rotating cylinder where the heavier isotope is moved to the outer part of the cylinder because of the gravitational field. The lighter isotope is then fed to the next stage in the process and enrichment is realized in a multistep process. The centrifugation process also consumes less power per unit of product.

A newer, potentially more economic technology that has been explored in the USA, France, and Australia is laser isotope separation (LIS).⁴ This technology depends on the use of laser photons to selectively excite and ionize only the ^{235}U isotope in a mixture and the use of a magnetic field to preferentially extract ^{235}U away from the more dominant ^{238}U isotope.

During enrichment, every ton of uranium hexafluoride processed yields about 130 kg of enriched UF_6 (about 3.5% ^{235}U) and 870 kg of “depleted” UF_6 (mostly ^{238}U). The enriched UF_6 is subsequently converted at specialized fuel fabrication facilities into uranium dioxide (UO_2) powder and pressed into fuel pellets. The “depleted uranium” has found use in its metal form as counterweights in yacht keels, as antitank ammunition or radiation shielding, since it is only slightly radioactive (less radioactive than natural uranium) and 1.7 times more dense than lead.

Not all commercial power reactors require the uranium fuel to be enriched. A small number of reactors, notably the Canadian CANDU reactors, can operate using natural uranium because they use heavy water (D_2O) rather than light water (H_2O) as the neutron moderator. Additionally, some early British gas-cooled reactors do not require enriched uranium.

61.3.4 Fuel Fabrication

At the fuel fabrication facility, enriched UF_6 is converted to uranium dioxide (UO_2) powder that is pressed into small ceramic pellets and sintered at a high temperature (over $1,400^\circ\text{C}$). These pellets are inserted into thin tubes, usually of a zirconium alloy (zircaloy) or stainless steel, to form fuel rods. The rods are then sealed and assembled in clusters to form fuel elements or assemblies for use in the core of the nuclear reactor. Some 25 t of fresh fuel is required each year by a 1,000 MWe reactor.

61.3.5 Commercial Nuclear Power Generation

Nuclear power produces energy by splitting the atom, most notably ^{235}U or ^{239}Pu . Energetically, when these nuclides split or fission, the resulting pieces called fission fragments have a combined rest mass less than the parent nuclide. The difference in mass is converted to energy during the fission process and this process of transforming matter directly into energy results in the release of about 200 MeV of energy (or 3.2×10^{-11} J) for every atom that fissions. (By capturing the fission products this energy is converted to heat and used to drive turbines to produce electricity.) In contrast, the burning of fossil fuels involves only the breaking of chemical bonds, and as a result, only 4 eV or 6.5×10^{-19} J/molecule of CO_2 is released for the combustion of carbon. Thus, the great advantage of nuclear power is its ability to extract a tremendous amount of energy from a small volume of fuel (Beller and Rhodes 2000). A second major advantage of nuclear power is related to the inherent characteristics of the fuel itself. Aside from its potential use in nuclear weapons, uranium ore has little use for humankind other than for the production of electricity. In contrast, fossil fuels can potentially be used for a wide variety of applications from the production of pharmaceuticals to various important synthetic materials production and to transportation. A third inherent advantage of nuclear power is that under normal operations, energy is produced with minimal environmental impact in terms of air and water pollution compared with burning of fossil fuel, particularly coal. Fossil fuels release large quantities of CO_2 and sulfur and nitrogen oxides (acid rain) to the atmosphere and substantial amounts of fly ash as solid waste. Energy created by splitting the atom does not produce these greenhouse gases.

Presently, nuclear energy provides over 16% of the world's total electricity as base load power. Approximately 435 commercial nuclear reactors operating in 31 countries produce this electricity with a total generating capacity of over 350 GWe. Of the existing commercial power reactors shown in [Table 61.2](#), the overwhelming majority (>99%) are thermal reactors, which means that fission is induced by low energy, thermal neutrons (~ 0.025 eV). Of the thermal reactors, greater than 80% are light water reactors (LWRs). In a LWR, normal hydrogen in water is used as the moderating material that, by successive scattering events, reduces the energy of the neutrons born in the fission event from approximately 2–3 MeV to the thermal regime (~ 0.025 eV). If the neutrons are not moderated, as in a fast reactor, a much harder or more energetic neutron spectrum (10s to 100s of keV) is used to induce fission.

Several hundred uranium dioxide fuel assemblies make up the core of a reactor. For a reactor with an output of 1,000 MWe, a typical core contains about 75 t of low-enrichment uranium ($\sim 3.5\%$ ^{235}U). During the operating cycle of a nuclear reactor, several competing processes determine the final radionuclide inventory in the spent fuel. These processes are

■ **Table 61.2**

Types of commercial nuclear reactors

Reactor type	Main countries	Number	GWe	Fuel	Coolant	Moderator
Pressurized water reactor (PWR)	USA, France, Japan, Russia	252	235	Enriched UO_2	Water	Water
Boiling water reactor (BWR)	USA, Japan, Sweden	93	83	Enriched UO_2	Water	Water
Gas-cooled reactor (Magnox & AGR)	UK	34	13	Natural U (metal), Enriched UO_2	CO_2	Graphite
Pressurized heavy water reactor "CANDU" (PHWR)	Canada	33	18	Natural UO_2	Heavy water	Heavy water
Light water graphite reactor (RBMK)	Russia	14	14	Enriched UO_2	Water	Graphite
Fast neutron reactor (FBR)	Japan, France, Russia	4	1.3	PuO_2	Liquid sodium	None
Other	Russia, Japan	5	0.2			
Total		435	364			

Courtesy of the World Nuclear Association (Web [2003d](#)).

- Neutron-induced fission, a process that produces energy and two fission products for each atom that fissions.
- Neutron capture, a process that produces an isotope of the same element but of one mass unit higher.
- Radioactive decay. (In a nuclear reactor, there are two primary modes of decay, beta minus decay and alpha decay. For the process of beta minus decay, a nucleus of mass number A and atomic number Z is transformed into another nucleus of mass number A but with atomic number $Z + 1$. Alpha decay, on the other hand, results in the loss of a helium nucleus leaving the original nucleus four A units and two Z units lighter.)

Consequently, in a nuclear reactor, fission products as well as isotopes of heavier elements are produced. These heavy elements are formed by the neutron capture followed by beta decay and are often referred to as the transuranic elements. Because the fission process is asymmetric,⁵ the products of the fission reaction tend to distribute themselves around mass 83–105 (light fragment) and mass 129–149 (heavy fragment). Some of the more common light fragments are ^{85}Kr , ^{90}Sr , ^{95}Zr , ^{99}Tc , and the corresponding heavy fragments are ^{129}I , ^{137}Cs , ^{144}Ce , and ^{147}Nd .

To maintain efficient performance over the reactor volume for nominally 1,000 MWe LWR, about one third or about 25 t of spent fuel is removed from the reactor core every year or so, the spent fuel being replaced with fresh fuel. However, over time, the concentration of fission fragments and heavy elements in a fuel bundle will increase to the point where it is no longer practical to continue to use the fuel. Therefore, after 24–36 months the core is removed from the reactor.

61.3.6 Fast Reactors

Fast reactor technology was developed during the same time frame that thermal reactor technology was being pursued for commercial power production. Since less than 1% of the energy content of mined uranium is realized in burning uranium in conventional LWRs, the initial motivation for fast reactors was to breed plutonium from uranium to maximize uranium fuel utilization. In order to exploit a higher fraction of the energy content of uranium, Pu could be produced in fast “breeder” reactors (FBRs) by placing a “blanket of uranium” around the core. In the blanket, ^{238}U would capture fast neutrons and produce more Pu than consumed in the reactor. In fact, of the order of 70% of all ^{238}U placed in a fast reactor can be converted to ^{239}Pu . Since the natural abundance of ^{238}U is 99.3%, this conversion results in the production of an almost infinite supply of fissile fuel for future generations.

There are several major differences in the design and operation of fast reactors compared with thermal reactors. First, in a fast reactor, no moderator is used and neutrons induce fission at or near the energies created (~ 2 MeV or neutron speed $u = 2 \times 10^7$ m/s). Although fast reactors do not require a moderator, they do require a coolant. Since water is such an efficient neutron moderator, it cannot be used as a coolant; therefore, liquid metals such as sodium, lead, or lead-bismuth or gases, such as helium and carbon dioxide have been used. Second, because neutrons travel at such high speeds in fast reactors, the probability of neutrons escaping to the surroundings is much higher. As a result of this “neutron leakage,” fewer neutrons are available to react with other fissile nuclei to sustain the chain reaction in fast reactors. To overcome this problem, fast reactor fuel contains a higher ratio of fissile-to-fertile nuclides/isotopes.⁶ Common fast reactor fuel is either highly enriched ^{235}U or a mixture of Pu and ^{238}U . Because Pu has a rather low, fast neutron absorption cross section, a loading of Pu of at least 20–30% is required. The remaining 70–80% of the fuel is ^{238}U .

In the mid-1980s, because the expected shortage of uranium never materialized and uranium remained abundant and cheap, the need for fast reactors to breed plutonium was no longer compelling or economical. This, along with concerns related to the potential proliferation of plutonium, caused interest in fast reactors to wane. This happened just as large prototype demonstration fast reactors such as the BN-600 (600 MWe) in Russia (1980) and the Superphenix (1,240 MWe) in France (1985) started coming online. About the same time, 1984, the USA initiated the Integral Fast Reactor Program, a fast reactor concept developed by Argonne National Laboratory (ANL) in conjunction with an industrial partner, General Electric Corp. This program was built on the successful operation of ANL's experimental breeder reactor, EBR-II, a liquid metal (Na) cooled fast reactor and its associated pyrochemical process that enabled the practical recycling of a metallic alloy fuel. However, for political reasons (in 1977, under President Carter reprocessing was halted in the USA because of proliferation concerns about Pu) and economic reasons (readily available supply of low-cost uranium) the USA terminated its fast reactor program in 1994. Likewise, the Superphenix reactor in France was shut down about 5 years later in 1999. The Japanese currently have the most active FBR program in the world with both the Joyo (100 MWth, where MWth stands for megawatts of thermal power) and the Monju (280 MWe) reactors still in operation.

61.4 The “Back-End” of the Nuclear Fuel Cycle

61.4.1 Spent Fuel

To first order, the specific amounts of fission products and transuranic nuclides produced during the operating cycle of a nuclear reactor will depend on the original composition of the fuel and how the reactor is operated. This includes the energy (thermal or low energy, or fast or high energy) and the flux density of the neutrons (number of neutrons/unit area/unit time) inducing the reactions and, the exposure time or time the reactor is in operation. The result is a wide range of radioactive species found in the spent fuel:

- Fission products that range in half-life from very short, days or less, to those that are very long-lived, hundreds of thousands to millions of years. ➤ [Table 61.3](#) lists some of the longer-lived fission products of concern for waste management.
- Unreacted uranium, primarily ²³⁵U and ²³⁸U along with ²³⁶U ($T_{1/2} = 2.4 \times 10^7$ years) formed by neutron capture on ²³⁵U.
- Isotopes of the heavier actinides including Np, Pu, primarily as ²³⁹Pu, and isotopes of Am and Cm.

In general, by volume the uranium isotopes represent about 95% of LWR spent fuel, the fission products ~3.4%, all the plutonium isotopes about 1%, and the minor actinides (MAs) (minor actinides = Np, Am, and Cm) about 0.6%. Of the plutonium isotopes, the fissile isotopes ²³⁹Pu + ²⁴¹Pu account for about two third of the total mass. From ➤ [Table 61.4](#), the nominal isotopic composition of plutonium resulting from the operation of LWRs at discharge is roughly A: 238 (2.5%), 239 (57.7%), 240 (24.3%), 241 (11.5%), and 242 (4.0%).

The relative amounts of the various actinide nuclides in spent fuel as a function of time after discharge from a pressurized water reactor (PWR) are shown in ➤ [Fig. 61.2](#).⁷

The nuclidic and elemental composition of spent fuel will vary depending on the history of operation of the reactor and the extent of fuel burnup where *burnup* is usually expressed in terms of *megawatt-days per metric ton* (MW d/t). As a result, the radionuclide content of spent fuel from thermal reactors can vary in composition not only from reactor type to reactor type (pressurized water reactor, boiling water reactor, high-temperature gas reactor, etc.) but also

■ **Table 61.3**

Some long-lived fission products from a thermal reactor (a typical PWR) after 10 years of cooling of spent UO₂ fuel containing 1 t of U (3.2% enriched) with 33 MW d/kg U burnup at an average flux of $3.24 \times 10^{18} \text{ n m}^{-2} \text{ s}^{-1}$

Fission product	Half-life/year	Activity (TBq/t U)
⁹⁹ Tc	2.13×10^5	0.484
¹²⁹ I	1.57×10^7	0.0012
¹³⁵ Cs	3.0×10^6	0.0098
⁹³ Zr	1.5×10^6	0.068
¹²⁶ Sn	1.0×10^5	0.029
⁷⁹ Se	6.5×10^4	0.0151

Data taken from ref. Choppin et al. (1995).

■ **Table 61.4**

Major and minor actinide content of spent LWR fuel (NAS 1996). Uranium-fueled 1,000 MWe PWR, 150 days after discharge (Benedict et al. 1981)

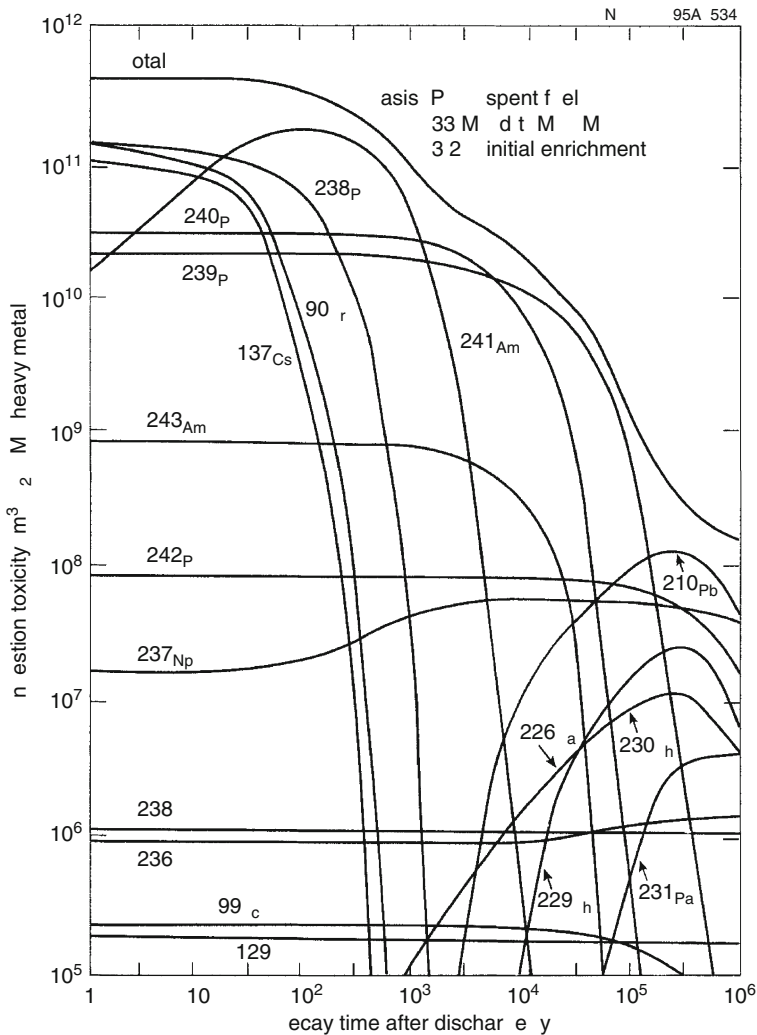
Actinide isotope	Half-life/year	Kg/year in spent fuel
²³⁴ U	2.5×10^5	3.1×10^0
²³⁵ U	7.1×10^8	2.1×10^2
²³⁶ U	2.4×10^7	1.1×10^2
²³⁷ U	1.8×10^{-2}	9.1×10^{-7}
²³⁸ U	4.5×10^9	2.6×10^4
²³⁷ Np	2.1×10^6	2.0×10^1
²³⁹ Np	6.4×10^{-3}	2.0×10^{-6}
²³⁶ Pu	2.6×10^0	2.5×10^{-4}
²³⁸ Pu	8.6×10^1	6.0×10^0
²³⁹ Pu	2.4×10^4	1.4×10^2
²⁴⁰ Pu	6.6×10^3	5.9×10^1
²⁴¹ Pu	1.3×10^1	2.8×10^1
²⁴² Pu	3.8×10^5	9.7×10^0
²⁴¹ Am	4.6×10^2	1.3×10^0
^{242m} Am	1.5×10^2	1.2×10^{-2}
²⁴³ Am	7.9×10^3	2.5×10^0
²⁴² Cm	4.0×10^{-1}	1.3×10^{-1}
²⁴³ Cm	3.2×10^1	2.0×10^{-3}
²⁴⁴ Cm	1.8×10^2	9.1×10^{-1}
²⁴⁵ Cm	9.3×10^3	5.5×10^{-2}
²⁴⁶ Cm	5.5×10^3	6.2×10^{-3}

from reactor to reactor of the same type. In general, reactors operated to a higher fuel burnup will result in an increase in the content of both the fission products and transuranic elements in the spent fuel. Of course, longer irradiation times will result in the production of more long-lived fission products.

The relative levels of dominant fission products and some actinides elements in spent fuel in terms of ingestion radiotoxicity as a function of decay time after discharge from a PWR is also shown in ► *Fig. 61.2*. In the short-term, fission products with half-lives of 30–50 years dominate spent nuclear fuel and represent the most limiting radiological factor impacting the design of a repository for spent fuel. This is due to the intense gamma radiation and the resulting decay heat associated with the fission products. The heat load initially comes from the decay of ¹³⁷Cs ($T_{1/2} = 30$ years) and ⁹⁰Sr ($T_{1/2} = 28$ years). Since the spent fuel is both highly radioactive and thermally hot, it is usually stored in special cooling ponds on the reactor site. The cooling ponds are water-filled basins with geometrically arranged racks to hold the fuel element to prevent criticality. These cooling ponds serve two purposes. First, the water absorbs the heat from the spent fuel and second, it serves as a radiation barrier to shield workers from the intense radiation.

■ Fig. 61.2

Relative ingestion radiotoxicity of representative fission products and some actinides in spent fuel as a function of time after discharge from a pressurized water reactor (PWR) (NAS 1996) (Courtesy of the Oak Ridge National Laboratory, managed by UT-Battelle, LLC, for the U.S. Department of Energy (1995))



Cooling times can vary depending on the ultimate fate of the spent fuel. Because of the lack of or nonexistence of reprocessing capacity, spent fuel is being held at reactor sites for of the order of 7–10 years. At some sites, spent fuel has been stored in such ponds for over 20 years. For reactor sites in the USA where reprocessing is not an option, the strain on spent fuel storage capacity is problematic for the commercial power industry. Requirements now include the construction of additional wet storage capacity or building containment for above ground dry cask storage for fuel that has been allowed to cool in cooling ponds for at least 1 year. For dry

cask storage, spent fuel is loaded into steel casks that are either welded or bolted shut after an inert gas blanket has been placed over the spent fuel. The casks are then placed in a metal or concrete vault that serves as the radiation shielding. Centralized storage facilities either exist, or are being built, in some countries to manage the spent fuel until it is ultimately taken for reprocessing or prepared for permanent disposal.

After about 100 years, 99% of heat load comes from the decay of the actinides. In fact, strategies for long-term management of spent fuel may require a cooling period of 40–50 years to reduce the heat load on a repository. By storing spent fuel for this period of time in above ground wet or dry storage facilities, the radioactivity decreases to about 0.1% of its original value. After this cooling period, the spent fuel will be easier to handle but nonetheless require encapsulation in appropriate corrosion resistant containers for its long-term management in the repository.

61.4.2 Fuel Reprocessing

In the Reprocessing Fuel Cycle (RFC) option, the unused uranium and the plutonium produced in the reactor are recovered leaving the minor actinides with the fission products as HLW. (The radiotoxicity of these wastes will be significantly less than that of the spent fuel although the toxic lifetime is determined by the minor actinides – neptunium, americium, curium – and, to a lesser extent, by some of the long-lived fission products content of the waste.) As mentioned previously, this was the scenario initially envisioned by the nuclear power industry to reprocess fuel for two reasons:

- Uranium and plutonium would be recovered and recycled to make more energy.
- The volume of material to be disposed of as HLW would be significantly reduced since uranium and plutonium combined comprise about 97% of mass of spent fuel.

Compared with the strategy of once-through burning of fuel in an LWR followed by direct disposal in a repository, the most effective way to reduce the total mass of HLW is to remove the uranium and plutonium, store the uranium, burn the plutonium to make energy, vitrify the remaining waste, and dispose of it as HLW in a repository. In addition, if the uranium is recovered, re-enriched, and returned to the LWR fuel cycle, there is the side benefit of reducing the demand for mining and milling new uranium and the need for enrichment services by about 30%.

In the late 1960s and early 1970s, the combination of the value of the recovered uranium and plutonium, the reduced volume of HLW, and the reduced demand for new uranium and enrichment services appeared to offset the cost of reprocessing, which was considered economically viable. Nevertheless, from the point of view of the USA, uranium is cheap and highly enriched uranium from the weapons stockpiles of both the USA and Russia is available in sufficient supply to be downblended, i.e., mixed with either natural or depleted uranium to make fuel for LWRs for the near future. (Albright 1992; Albright et al. 1997) For this reason and because of concerns about proliferation of nuclear materials, especially plutonium, the USA continues its policy not to reprocess. On the other hand, reprocessing facilities are in operation in the UK at Sellafield (THORP), in France at La Hague and Marcoule, and in Russia at Chelyabinsk (Mayak). Smaller plants are also in operation in India and Japan. Through the years, over 75,000 t of commercial spent fuel has been processed to recover uranium and plutonium worldwide and the annual capacity now stands at about 5,000 t per year (Web 2003e). The nonreusable part of the spent fuel, the fission products, and the minor

actinides, are currently being incorporated into glass and allowed to solidify inside corrosion-resistant canisters through a process called vitrification. The operation of a 1,000 MWe reactor would generate about 12 canisters of vitrified waste annually, each containing about 400 kg of highly radioactive glass (Web [2003f](#)).

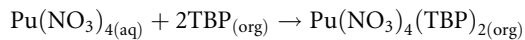
61.4.2.1 PUREX, the Industry Standard

Currently aqueous techniques are the main industrial-scale separation methods used in the nuclear power industry. Continuous processes, such as solvent extraction, are preferred over semicontinuous processes such as ion exchange in the nuclear industry because of the volume of materials to be processed and because continuous processes are typically more efficient, more reliable, and show less degradation in high radiation fields. The main steps that are involved in reprocessing spent fuel from commercial (primarily, zircaloy clad, uranium-oxide) fuels include the following: removal of the cladding and dissolution of the oxide fuel using the head-end treatment; chemical separation of U and Pu from the majority of the fission products in what is called the first extraction cycle in the partitioning stage, where Pu is separated from U; purification of the individual fractions of U and Pu using a multiple cycle process; and finally, conversion of the nitrates of U and Pu to metal-oxides.

The gaseous and volatile fission products (primarily Kr, Xe, I₂, and tritium as T₂ and HTO, and RuO₄) are released in the head-end step and treated in an off-gas scrubber system using sodium-hydroxide. Further removal of I₂ may be accomplished by passing the off-gas through filters impregnated with either silver nitrate or potassium-iodide. The recovered iodine is commonly disposed of as a liquid effluent and discharged to the sea. (Raisbeck et al. [1995](#)). Of the rare gases, only ⁸⁵Kr poses a problem because it is produced in significant quantities and it has a relatively long 10.7 year half-life. In contrast, the other Kr and Xe isotopes have considerably shorter half-lives and decay within about a year. The most common method for removal of ⁸⁵Kr is to cryogenically trap it with liquid N₂, separate it, and store it after fractional distillation. In most cases, the gaseous effluents from reprocessing are released directly into the atmosphere in a controlled fashion, although this practice is becoming less favorable.

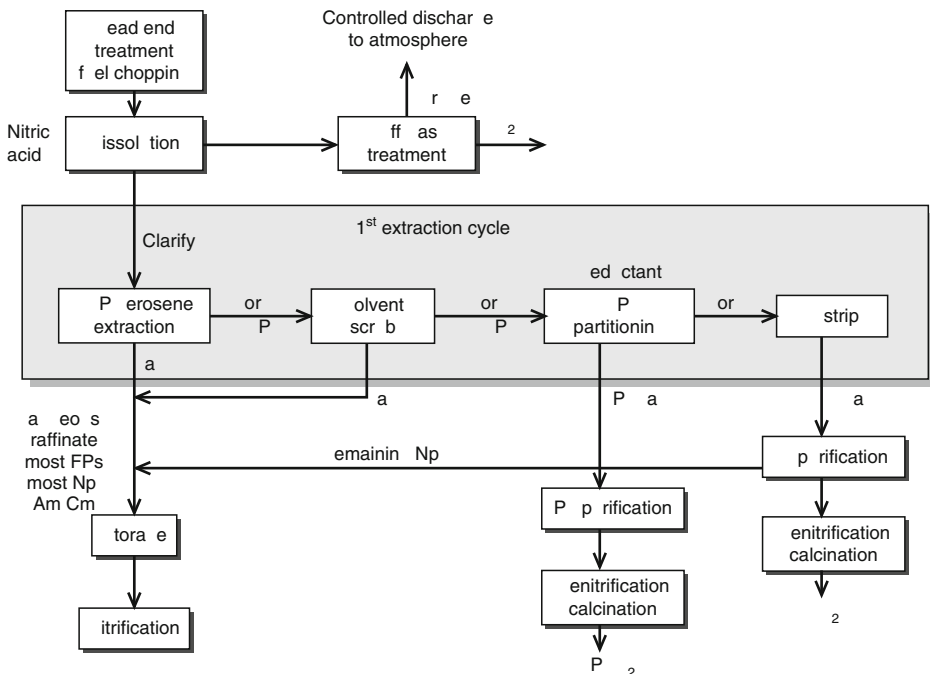
Presently, the PUREX process (Plutonium Uranium Redox EXtraction) is universally employed as the preferred aqueous chemical processing technology for reprocessing irradiated/spent fuels. PUREX has also been the primary separation technology used to separate U and Pu from production reactor fuels in the weapons programs for defense applications. PUREX is a wet chemical process that uses tributyl phosphate (TBP) in kerosene (or dodecane) to co-extract U(VI) and Pu(IV) from a strongly acidic nitrate solution (3–4 M HNO₃) leaving the bulk of the nonvolatile fission products, including the trivalent lanthanides, in the aqueous phase (Culler [1956](#)). The cladding hulls are not dissolved but rather recovered from the dissolver, checked for residual U and Pu, and then disposed of as high-level solid waste. Because Am and Cm exist in aqueous solution as 3+ cations, they are not extracted by TBP and thus behave like the 3+ lanthanides. For comparison, the combined mass of Am and Cm is about one tenth that of the lanthanides, and the lanthanides represent about one third of the total mass of the fission product inventory in spent fuel. Neptunium, whose stable oxidation state is +5 under these high acidity conditions, is extracted only slightly by TBP.

In the partitioning stage of the PUREX process, Pu is reduced to the +3 state by the addition of a reductant (U(IV) or Fe(II) sulfamate), to allow back extraction into a fresh aqueous phase. The U, as U(VI), the residual U(IV), and the small amount of Np extracted during the first



where the subscripts (aq) and (org) indicate the aqueous and the organic liquid phase, respectively. The PUREX process yields two product streams, one containing chemically purified uranium and the other, chemically purified plutonium. The major waste stream is generated in the first PUREX extraction cycle and contains the vast majority of the fission products, the minor actinides, and small amounts of uranium and plutonium lost during processing. This waste stream is often referred to as the aqueous raffinate from the first extraction cycle. By definition, this is a high-level liquid waste stream. The schematic diagram of the PUREX process is shown in [Fig. 61.3](#).

Schematic diagram of the PUREX process



Residual quantities of minor actinides and fission products that are removed from the purification parts of the cycle are usually reduced in volume and then combined in the aqueous raffinate HLW stream. The cladding hulls are managed as high-level solid waste by packaging them in drums and storing the drums in a dry disposal site.

During the PUREX process, solvents undergo radiolysis and degrade as a result of the intense radiation arising primarily from fission product decay. In modern PUREX plants, most solvents are treated to remove these degradation products and then recycled back in to the process. For example, dibutyl- or monobutylphosphate are degradation compounds formed by the radiolysis of TBP. Since these compounds form strong complexes with many of the fission products as well as plutonium, they must be removed from the TBP/kerosene phase as time goes on; otherwise, the desired levels of decontamination will not be achieved in the first extraction cycle. Normally, the compounds are removed by washing the TBP organic phase with successive aqueous phases containing sodium carbonate, sodium hydroxide, and then dilute nitric acid.

Similarly, nitric acid is treated and recycled reducing the aqueous waste generated in the overall process. These wastes can be further reduced by the proper choice of equipment. For example, centrifugal contactors, which can achieve high extraction efficiencies while minimizing the contact time between the aqueous and organic phases, are commonly used to reduce solvent degradation in the first extraction cycle where radiolysis is most problematic. Because of the costs associated with waste disposal, as a matter of economics and sound business practice, considerable attention is paid to eliminating or reducing the number and volume of waste streams in modern PUREX plants. The pursuit of any option involving reprocessing requires building and operating geologic repositories because fission products or alpha-bearing waste from reprocessing are forms of HLW that will require isolation. For an in-depth discussion of the treatment of spent nuclear fuel, see ref. Choppin and Rydberg (1980).

61.4.2.2 Vitrification

High-level liquid waste must be solidified before disposal. Typically, this is achieved by calcining the aqueous HLW waste stream resulting from reprocessing the spent fuel. Calcining converts the aqueous waste into a dry powder containing the radioactivity. The powder is incorporated into borosilicate glass to immobilize the waste. The resulting glass mixture is poured into stainless steel canisters, typically holding hundreds of kilograms of glass. A year's supply of waste from a 1,000 MWe reactor is contained in 5 t of such glass, or about 12 canisters, 1.3 m high and 0.4 m in diameter (Web 2003f). With appropriate shielding, these canisters can be readily transported and stored. This material is also slated for geologic disposal.

61.4.2.3 Recycling plutonium as mixed-oxide fuel (MOX)

Reprocessed plutonium can be used as fuel in specially modified LWRs. With minor modifications, typically adding more control rods to manage the reactivity over the reactor volume, LWRs can be configured to operate using fuel consisting of both uranium and plutonium-oxide or what is termed mixed-oxide or MOX fuel. Over the past 10 years, specially licensed reactors in France, Germany, Switzerland, and Belgium have used MOX fuel to generate electricity. Japan plans to have one third of its 53 reactors using MOX by 2010 (Web 2003g).

MOX fuel is made by mixing plutonium with depleted uranium, a by-product of the uranium enrichment process, or with natural uranium. Two sources of plutonium are available. The first is reprocessed plutonium from commercial spent fuel and the second is weapons-grade plutonium surplus from the nuclear stockpiles of both the USA and Russia (Albright 1992; Albright et al. 1997). These sources, reactor-grade plutonium and weapons-grade plutonium, differ in the content of ^{239}Pu and the minor plutonium isotopes, especially ^{240}Pu . Commercial reactor-grade plutonium is nominally about 55–60% ^{239}Pu and has a relatively high amount ~20–25% of ^{240}Pu whereas weapons-grade plutonium contains greater than 95% ^{239}Pu and a minor amount of ^{240}Pu .

MOX fuel fabrication facilities are currently operating in France, Belgium, the UK, India, and Japan and collectively produce about 460 t per year (Web 2003b). For the fabrication of MOX fuel, the “age” of the plutonium, or rather the time since the plutonium was last separated from americium, is very important. ^{241}Am , which results from the decay of short-lived ^{241}Pu ($T_{1/2} = 14.4$ years), builds up at a rate of about 2 parts per million per month or about 0.5% per year. Because ^{241}Am emits a 60 keV γ ray, additional shielding and remote handling is required during MOX fabrication if the ^{241}Am content becomes greater than 5–6%. As a result, MOX is usually made with recently reprocessed plutonium.

As part of a long-term strategy for reducing the inventory of weapons-grade plutonium, both the USA and Russia expect to construct MOX fabrication facilities in their respective countries and eventually burn plutonium in LWRs. Fabrication plants using weapons-grade plutonium will have to incorporate additional controls to prevent possible diversion of plutonium that is not required at other MOX plants.

In practice, MOX fuel can be made with fairly high (>50%) loadings of plutonium, but to burn such a fuel would require specially designed reactors. Loadings of the order of 5% (for weapons-grade Pu) to 7% (for LWR reprocessed Pu) are more common for use in modified LWRs. The characteristics of MOX fuel containing 5–7% plutonium are very similar to those of the more conventional (4–5% enriched) uranium-oxide fuel. As a result, MOX fuel can be substituted for part of a reactor’s fuel loading without any significant changes in the reactor’s operating conditions and performance. However, reactors burning MOX will typically limit the MOX loading to about one third of the fuel assemblies in the core.

Since most plutonium isotopes have small thermal neutron fission cross sections, the minor actinides build up in the fuel over time and the recycling of plutonium in LWRs has serious limitations. Nonetheless, burning plutonium in MOX fuel using conventional LWRs has two advantages (1) economically, burning plutonium in the reactor produces usable energy and, (2) burning plutonium reduces the inventory and thus prevents the accumulation of separated plutonium resulting from reprocessing commercial power reactor spent fuel. If weapons-grade plutonium is burned as MOX fuel, there are additional advantages over and above reducing the inventory of weapons-grade plutonium. The first is that while in the reactor, the weapons-grade plutonium in the fuel would be protected against diversion by the intense radioactive field of the fission products. This is similar to the argument used by those who are against any reprocessing of fuel and claim that by not reprocessing, plutonium left in spent fuel is protected against proliferation by the fission products in the fuel or what is called the “spent fuel standard” (NAS 1994). Second, while in the reactor, the isotopic composition of the weapons-grade Pu would be degraded and eventually closely resemble reactor-grade plutonium (ca. 65% ^{239}Pu + ^{241}Pu and high ^{240}Pu content). Burning plutonium in MOX fuel reduces the overall radiotoxicity compared with untreated LWR spent fuel but the resulting minor actinides and fission products will nonetheless require disposition in a geologic

repository. Within the commercial nuclear power community, recycling of plutonium in MOX fuel in LWRs is viewed as a mature industry.

61.4.2.4 Recycling U

The uranium recovered from the reprocessing of commercial spent fuel usually contains about 1% ^{235}U , and because the PUREX process does not remove 100% of the fission products and other actinides, reprocessed uranium is slightly more radioactive than natural uranium. The increased radioactivity is primarily due to the presence of other α -emitting contaminants. (According to the International Atomic Energy Agency, IAEA 1977, the level of fission products in reprocessed uranium cannot exceed 19 MBq/kg of U. Similarly, reprocessed U can contain no more than 250 kBq/kg U of other non-uranium alpha activity.) During irradiation, the level of ^{234}U increases over that found in natural uranium. In addition, ^{232}U , not present in natural uranium, is produced by the decay of 2.85 year ^{236}Pu . Although the total accumulation of ^{232}U is small, it decays with a 72-year half-life by α emission down through a chain of other α - and γ -ray emitters including the 1.9 year ^{228}Th . The decay chain finally culminates with ^{208}Tl , a hard γ -ray emitter. The long-lived ^{236}U ($T_{1/2} = 2.4 \times 10^7$ years) is also produced by the (n, γ) reaction on ^{235}U but adds little to the α -activity. The (n, γ) reaction on ^{236}U produces the 6.75 d ^{237}U isotope that decays by beta-emission to ^{237}Np . This decay occurs during storage prior to reprocessing and does not impact the radioactivity associated with reprocessed uranium. In addition to these uranium isotopes, small amounts of plutonium and neptunium left in the uranium fraction after reprocessing add to the α -activity of reprocessed uranium.

For reprocessed uranium to be used again in a reactor, it must again be enriched to about 3.5%. Because new uranium is in plentiful supply, it has not been necessary to re-enrich uranium recovered from reprocessing to meet the requirements for new fuel. If and when it becomes necessary to enrich reprocessed uranium, the potential occupational hazard associated with UF_6 conversion, enrichment, and fuel fabrication processes due to the small amounts of residual fission products in the uranium will have to be addressed.

61.4.3 Direct Disposal of High-Level Waste

At the current time, all the spent fuel identified as waste, all reprocessing waste, and all waste resulting from the isolation of fission products remains in storage as no disposal sites have been established. In the interim, extended storage, either at reactor sites or in a more centralized location, is considered an acceptable waste management strategy. A number of disposal options have been or are being considered including the following:

- Geologic disposal:
 - Subsurface burial (hard rock such as granite, clay, salt, unsaturated tuff)
 - Disposal on the ocean floor in some kind of highly engineered containment.
 - Disposal in glaciated areas, in Antarctica for example.
- Ocean dilution.
- Disposal into space.
- Nuclear transmutation, the conversion of long-lived radionuclides into shorter-lived or even stable nuclides.

Each of these options has serious political, environmental, and/or technical issues that must be addressed. Among the options discussed for disposing of these materials, an international consensus has emerged that deep geologic disposal is the most appropriate means for isolating such wastes permanently from man's environment (NAS 1957).

61.4.3.1 Geologic Disposal

The basic concept of geologic disposal is to contain and isolate the HLW from the environment for an extended (up to tens of thousands of years) period of time. A strategy known as "*defense-in-depth*" is employed in most proposed repository designs. In simple terms, this concept relies on a series of redundant barriers to increase reliability in the safety argument. These barriers generally include (1) the leach-resistant waste form, (2) corrosion-resistant containers into which the wastes are encapsulated, (3) special radionuclides and groundwater-retarding materials placed around the waste containers, commonly referred to as backfill, and (4) the host geological formation. These barriers both retard the transport of radionuclides in groundwater flow, and serve to isolate the waste from man's environment.

It is anticipated that geologic disposal of HLW will be preceded by some period of interim storage, either at the reactor site, at a centralized location or at the disposal site, during which time the temperature and radioactivity of the HLW will decrease systematically. This is in fact the situation by default as no current disposal site exists. Transport of the waste materials from the storage location to the disposal site will be necessary. Under consideration are specially constructed collision-and fire-resistant shipping casks, transported via designated ship, train, or truck. Each national program must address its specific issues. Some type of waste packaging is planned. Liquid wastes resulting from isolation of the fission products or reprocess will need to be solidified before transport, packaging, or disposal.

Conceptually, waste packages will be lowered down vertical shafts or transported into the repository through sloping, horizontal tunnels. Once at the repository, the waste packages will be emplaced into holes predilled into the sides or floor of the repository using equipment developed for this purpose. In some concepts, these holes will then be backfilled with suitable material. Filling the repository may require anywhere from 10 to 50 years or more, depending on the national program. Finally, the repository itself may be backfilled and sealed, including all shafts, boreholes, and tunnels that may have been drilled during repository construction. With a suitable choice of waste packaging, backfill, and geological environment, the radioactive materials should remain isolated from man's environment for many tens of thousands of years.

The long-term safety of HLW disposal can be systematically assessed through predictive modeling of the gradual failure of the engineered barriers (i.e., the waste form, waste package, and backfill) and the subsequent transport to man's environment of radionuclides by groundwater flow. Such safety assessments must be based on a good physical understanding of the fundamental processes involved in the release and transport of radionuclides, as well as those acting on, or likely to act on, the repository and the geological formation. In addition, the potential interplay (coupling) between these processes must be understood. Finally, substantial site monitoring efforts will be needed, involving the collection of data at the surface as well as in situ, at the proposed repository location.

Each country with an interest in HLW disposal is conducting or collaborating on long-term, extensive scientific research programs to understand how better to dispose of this waste

and to understand the possible long-term consequences of the disposition. These enduring missions cover the areas of geology, geochemistry, geophysics, hydrology, materials science, radiochemistry, design engineering, safety analysis, and risk analysis. Several countries have constructed underground research facilities in support of their national programs, including Belgium (Mol), Sweden (Stripa), Germany (Gorleben), Switzerland (Grimsel), and the USA (Yucca Mountain).

There is extensive technical literature in many international, peer-reviewed journals covering the range of technical, political, and risk issues that are being studied by the national programs. The reader is also directed to the Internet web pages of the various national programs to understand the specific conditions and constraints each is striving to understand.

61.5 Partitioning and Transmutation (P&T)

The third and most futuristic back-end option to the nuclear fuel cycle is termed the advanced fuel cycle (AFC). The AFC not only closes the fuel cycle but also offers a potential way around the long-term hazards of radioactive wastes by significantly reducing the radiotoxic inventory. In the AFC option, in addition to the removal of uranium and plutonium, a complex series of aqueous chemical and/or nonaqueous metallurgical operations are performed to selectively remove the minor actinides (minor actinides are neptunium, americium, and curium, and small amounts of the heavier actinides) and some of the long-lived fission products (long-lived fission products are principally, technetium, and iodine) from the HLW before vitrification and disposal. This process is called *partitioning*. Once the minor actinides and long-lived fission products are removed from the waste stream, the idea is to convert them into less radiotoxic or otherwise stable isotopes by a process called “*transmutation*” or “*incineration*.” Transmutation involves using nuclear reactions and processes such as neutron capture followed by fast radioactive decay, (n,2n) reactions with energetic neutrons, or neutron-induced fission to achieve the desired transformation. Transmutation can be accomplished through a combination of LWRs, fast reactors (configured either as breeders or as minor actinide or transuranic [TRU] “burners”), and subcritical, accelerated-based transmutation devices.

In a recent report by the Nuclear Energy Agency (OECD/NEA 2002), a group of experts determined that a 100-fold reduction in the actinide content of HLW would be the minimum requirement for any partitioning and transmutation strategy to be technically viable. Similar arguments have been put forward by experts in the USA, France, and the UK. In the NEA report, this level was set in on the basis of reducing the radiotoxicity of the HLW (assuming uranium-oxide fuel with an average burnup of 50 GW d/t HM and reprocessed 4 years after discharge from the reactor, where HM stands for heavy metal) remaining after removal of 99.9% of the U and Pu, to the natural toxicity level for LWRs that is the equilibrium radiotoxicity of the natural uranium required to fabricate the fuel. Without partitioning and transmutation, this level would be reached by spent fuel after a few hundred thousand years (➤ Fig. 61.2). However, by decreasing the actinide content as defined above, this level would be reached in about 1,000 years – within a time span as pointed out in the report, “during which the HLW container can be expected to fulfill its safety function.” A transmutation scheme that includes only the recycle of plutonium and not the minor actinides, will reduce the long-term radiotoxicity of the waste only by about a factor of five. Therefore, plutonium and the minor actinides have to be considered together for any transmutation scheme to be beneficial. It should be further recognized that any fuel cycle strategy involving partition and transmutation

but not including breeding of plutonium only addresses the long-term waste issues but does nothing to improve the resource utilization of uranium.

61.5.1 Transmutation of Minor Actinides

For the purpose of transmutation, the minor actinides of concern in spent fuel are neptunium, americium, and curium although small amounts of the higher actinides, berkelium, californium, einsteinium, and fermium can be made under the right conditions. The reaction pathways leading to the production of the transuranium elements are given in [Fig. 61.4](#).

For the minor actinides, the transmutation process consists of the capture of one or more neutrons until a more fissionable isotope is formed. For the actinides, the most important transmutation reaction is fission because it results in the removal of the isotope from the minor actinide inventory and replaces it with two typically shorter-lived, less toxic fission fragments. With more energetic neutrons, the $(n,2n)$ reaction is also useful because this reaction transforms fertile actinides with low fission probabilities to more fissile actinides with higher fission probabilities. Neutron capture reactions that produce less fissionable isotopes merely add to the inventory of minor actinides.

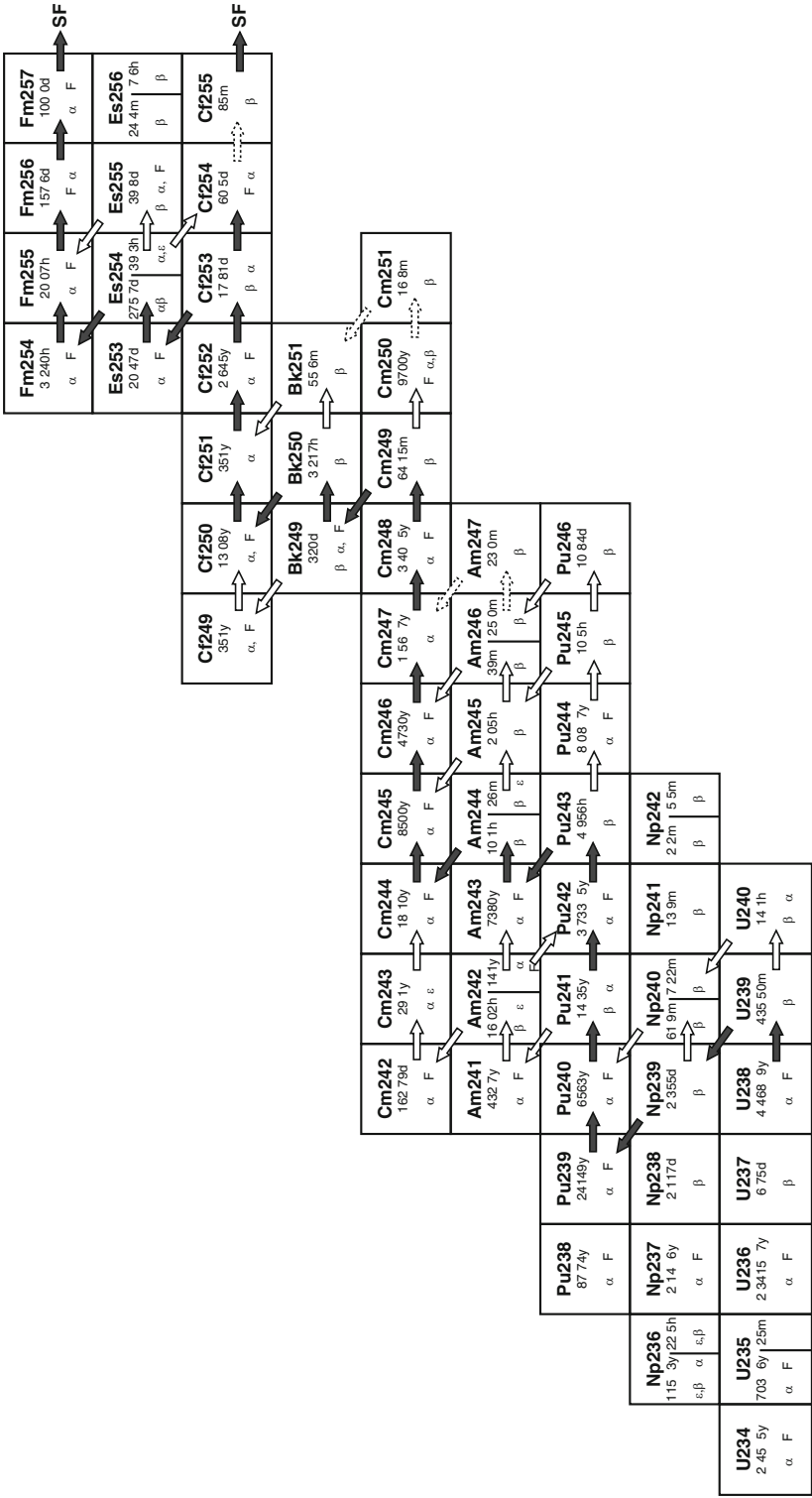
Conventional LWRs alone cannot be used to transmute minor actinides because thermal neutrons are not as effective for inducing the fission reaction. As a result, minor actinides (especially, non-fissile even isotopes of plutonium) build up as a function of time. Therefore, thermal reactors tend to preferentially produce minor actinides. Fast reactors or fast neutron spectrum devices on the other hand tend to more effectively destroy the minor actinides because the probability of fission for both the even and odd isotopes of plutonium fission with fast neutrons is considerably higher than with thermal neutrons. Thus, fast reactors are heavily preferred for the recycle of plutonium and the ultimate complete destruction of all of the minor actinides.

Transmutation of neptunium, which exists as a single isotope ^{237}Np with a half-life of about 2 million years, is possible in both thermal and fast reactors through either homogeneous or heterogeneous means though there seems to be no clear advantage to the heterogeneous route. Putting neptunium in either LWR- UO_2 or MOX fuel, then burning it homogeneously with UO_2 or as a mixture of UO_2 and PuO_2 does not present any significant problems with respect to reactor operation at small loadings (a few percent). Fuel fabrication though is a bit more difficult because ^{237}Np decays to protactinium-233 and ^{233}Pa emits a number of penetrating γ rays that require additional shielding. For conventional UO_2 fuel fabrication, the addition of neptunium adds significantly to both the alpha activity and gamma radiation levels. For MOX fuel fabrication the impact is much less as the presence of neptunium does not add as much to the alpha activity as to the gamma radiation level. However, upon multiple recycling of MOX fuel, neutron capture on ^{237}Np leads to the build up of the short-lived ^{238}Pu ($T_{1/2} = 88$ years).

Plutonium-238 decays by alpha emission with a high decay energy and thus adds considerably to the heat load during processing. Also, because of the high decay energy, neutron emission from (α,n) reactions on light elements from the decay of ^{238}Pu leads to other complications not only for fuel fabrication but also for transportation and storage of fuel. The transmutation of ^{237}Np is important because it is considered to be the dominant long-term dose contributor in performance assessments for geologic repositories in oxidizing environments such as Yucca Mountain in the USA.

Fig. 61.4

Neutron capture pathways of importance for the production of actinides (NAS 1996) (Reprinted with permission from Nuclear Wastes, Technologies for Separations and Transmutation, p. 22, courtesy of the National Academy Press, Washington, DC)



For the transmutation of americium, there are primarily two isotopes with which to be concerned in developing any transmutation scheme. They are ^{241}Am ($T_{1/2} = 460$ years) and the longer-lived ^{243}Am ($T_{1/2} = 7,900$ years) produced by the beta decay of ^{241}Pu and ^{243}Pu , respectively. The 152 year $^{242\text{m}}\text{Am}$ isotope, formed by the (n,γ) reaction on ^{241}Am is also of importance because its decay leads to ^{242}Cm . Curium-242 with its very short 163 d half-life is the most intense α -emitting nuclide in spent fuel. Successive neutron captures on ^{243}Am followed by beta decay lead to the production of curium with masses of 244, 245, and 246. The transmutation pathways for the production and destruction of Am isotopes are shown in

► Fig. 61.4.

As mentioned previously, because of the emission of 60 keV γ rays from the decay of ^{241}Am , fuel fabrication involving substantial quantities of Am is not compatible with using conventional facilities involving contact handling conventional glove-box methods. Instead, a shielded facility with equipment modified to operate remotely will be required. For these reasons, the transmutation of americium via specially prepared heterogeneous targets appears to be the preferred method while transmutation of neptunium in MOX fuels may be more than adequate. The transmutation of ^{241}Am in particular is important because it is the parent of long-lived ^{237}Np .

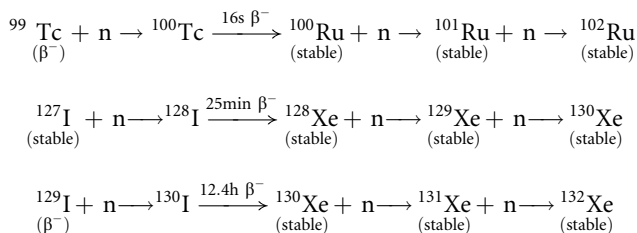
The transmutation of curium in reactors poses yet another set of problems compared with neptunium and americium because the curium isotopes have both shorter half-lives and higher spontaneous fission branches. In spent fuel, ^{242}Cm ($T_{1/2} = 163$ d) is by mass about 100 times less abundant than the 18 year ^{244}Cm isotope, but its specific activity is about six times higher. Both the high specific activity and the neutron intensity associated with curium makes handling operations and fuel fabrication much more difficult than even americium. The situation is made more interesting because the curium isotopes decay primarily by α emission to produce isotopes of plutonium. Curium-242 α -decays to ^{238}Pu , ^{243}Cm to ^{239}Pu , ^{244}Cm to ^{240}Pu , and ^{245}Cm to ^{241}Pu , etc. For the case of transmuting the most abundant curium isotope by mass in spent fuel, ^{244}Cm , the in-growth of ^{240}Pu causes problems because of its low thermal fission cross section. As a result, transmutation of ^{244}Cm in a LWR is not practical. If, however, curium were to be stored for about 100 years, it would decay to $\sim 2\%$ of its original amount and then the remaining decay product, ^{240}Pu , could be transmuted in a fast reactor along with normal plutonium recycling operations.

When developing transmutation scenarios for the minor actinides (MAs), consideration of their transmutation yield in reactors using either thermal or fast neutrons is important, but not the only factor that must be taken into account. Of equal or even more importance is the impact of loading of MAs on the operation of the reactor. For example, the neutron economy over the reactor volume must be considered as well as issues related to reactivity such as spikes or transients and the associated safety parameters covering situations such as loss-of-coolant incidents. For a discussion of the impacts on reactor performance caused by the loading of minor actinides, see Chap. 2 in ref. OECD/NEA (1999).

With respect to the partitioning stage, in addition to the total amount or inventory of a given nuclide to be transmuted, other factors have to be considered. Several factors become important when determining the optimum partitioning flow sheet. Some of these factors include process chemical yield and/or loss of material, product purity or effectiveness of the separation with respect to fission products and other actinides, impact of decay properties in terms of decay heat and neutron emission and, of course, the generation of secondary wastes. For a more detailed discussion of challenges associated with partitioning actinides for transmutation see Subchapter 3.4 in ref. OECD/NEA (2002).

61.5.2 Transmutation of the Long-Lived Fission Products

The fission products that are the most important long-term risks associated with spent fuel are technetium, (exists only as ^{99}Tc), iodine, and possibly cesium. See [Table 61.3](#) for a list of other long-lived fission products. The transmutation process for fission products is basically the capture of a neutron (or several neutrons) followed by beta decay until a less toxic (shorter-lived) or stable isotope is formed. For technetium (i.e., for β^- decaying ^{99}Tc with $T_{1/2} = 2.13 \times 10^5$ years) and iodine (i.e., stable ^{127}I and β^- decaying ^{129}I with $T_{1/2} = 1.6 \times 10^7$ years), the transmutation can be accomplished in thermal reactors through the following pathways:



For both technetium and iodine, capture of a single neutron followed by β^- decay results in the production of stable isotopes of ruthenium and xenon, respectively. Further, as the irradiation proceeds, additional neutrons can be captured but these products are also stable. In practice, the transmutation of technetium and iodine in conventional thermal reactors will be difficult for several reasons. First, because these are major fission products, they are produced in high yield and thus result in large inventories that must be separated from the HLW and transmuted. Second, the thermal neutron capture cross sections are not particularly large and therefore much higher neutron fluxes are required to significantly reduce the inventory in a reasonable amount of time. Third, the available neutron flux from conventional LWRs is too small (10^{13} neutrons $\text{cm}^{-2} \text{s}^{-1}$) to achieve the required level of transmutation in a reasonable length of time.

For cesium, the problematic isotope is ^{135}Cs but transmutation is possible by capture of a neutron followed by beta decay to produce the stable ^{136}Ba isotope. However, ^{135}Cs is not the only cesium isotope present in spent fuel. The short-lived ^{137}Cs ($T_{1/2} = 30$ years) isotope and stable ^{133}Cs are both present in about the same amount as ^{135}Cs . In theory, you can transmute ^{137}Cs to produce ^{138}Ba , which is stable, but the intense gamma radiation from ^{137}Cs makes fabrication of transmutation targets or mixing cesium back into fresh fuel impractical. On the other hand, transmuting stable ^{133}Cs creates more ^{135}Cs by neutron capture on ^{133}Cs to form ^{134}Cs . Because ^{134}Cs does not decay immediately but rather has a half-life of about 2 years, it would be present long enough in the reactor to capture another neutron and produce more ^{135}Cs . The only way around the problem of producing additional ^{135}Cs from ^{133}Cs would be to first isotope separate ^{133}Cs from ^{135}Cs before beginning the transmutation. This process is not practical for two reasons: (1) the highly radioactive ^{137}Cs isotope would make handling the material extremely difficult and (2) isotope separation is a very costly process. Similar arguments can be made for transmuting the long-lived isotopes of zirconium (^{93}Zr), selenium (^{79}Se), and tin (^{126}Sn).

Although some of the long-lived fission products have thermal neutron capture cross sections suitable for transmutation in reasonable irradiation times, others do not and would require reactors with very high neutron fluxes to reduce inventories significantly. As a result, dedicated reactors with large thermal fluxes and/or dedicated accelerator-driven systems

(ADSs) with thermal neutron fluxes of the order of 10^{16} neutrons $\text{cm}^{-2} \text{s}^{-1}$ are being proposed.⁸ Fast neutron capture cross sections for most long-lived fission products are several orders of magnitude smaller than those for thermal neutrons making transmutation by fast reactors less appealing. Again, because of the relatively low transmutation rates for long-lived fission products, transmutation of these radionuclides is expected to be very expensive.

In general, transmutation of long-lived fission products, although theoretically possible, is very difficult. It will require significant development to be successful, and economically, is not very compelling. Fission products under transmutation conditions are only consumers of neutrons, and unlike the actinides, they do not produce additional neutrons useful for transmutation. Consequently, the product of the capture cross section and the neutron flux must ensure faster neutron capture than the decay rate of the radionuclide for it to be a realistic candidate for transmutation. For this reason, without prior isotopic separation the transmutation of only a few long-lived fission products, namely iodine and technetium and, possibly ^{107}Pd , are feasible. Thus, the most prudent way to minimize the long-term radiological impact of most long-lived fission products is to separate and immobilize them in specially designed, stable waste forms.

61.5.3 Strategies for the Transmutation of Minor Actinides and Long-Lived Fission Products

A number of different strategies for transmuting the minor actinides have been suggested. In general, the different approaches depend on trade-offs between the effectiveness of the partitioning steps (chemical yields and acceptable losses of the desired elements) and the degree of transmutation that can be achieved by various types of devices.

Currently, there are two schools of thought on the transmutation of actinides present in LWR spent fuel. The first addresses in a systematic way the *utilization of plutonium* as an energy source and the management of the minor actinides as a waste product. It also allows for advances in technology to be incorporated in the process as they become available. In this scenario, the fuel cycle is closed in an evolutionary way. In successive steps, beginning with recycling plutonium in LWRs and then later, in fast reactors using MOX fuel and conventional reprocessing technology, plutonium is recovered and burned to produce energy. The final steps involve different methodologies aimed at significantly reducing or eliminating the inventory of minor actinides. One of the ways is to gradually reduce the inventory of minor actinides by irradiating them as special targets (heterogeneous recycling) in conventional reactors. In the end, however, dedicated fast spectrum devices with multiple recycling enabled by nonaqueous or “pyroprocessing” must be implemented to completely eliminate the minor actinides.

The second approach is quite different – to never separate plutonium and the minor actinides during the processing of LWR fuel. Here, the principal driver is to reduce the risk for proliferation of plutonium rather than reduce the long-term radiological impact of commercial spent fuel. The waste stream in this case contains all of the transuranic (TRU) elements and is managed as a single unit. To accomplish the transmutation of this waste stream, a “TRU burner” is required that operates in a closed cycle where the wastes are recycled multiple times. Further, to be effective, nonaqueous chemical processing will be necessary to minimize the time between irradiations and shorten the overall recycle time. The main difference between the nonaqueous scheme in the evolutionary approach and this one is that in the former, plutonium would first be removed by conventional wet chemical processing and only the minor actinides sent forward and later reprocessed using nonaqueous methods.

The waste stream from the IFR concept was designed to contain only fission products and little or no transuranium elements. In the IFR concept, the reactor and the reprocessing/fuel fabrication facilities are colocated and all fuel handling operations from fueling and defueling through reprocessing and fuel fabrication are all carried out remotely behind extensive shielding. This process allows fuels that are much more radioactive to be handled safely and reduces any vulnerability associated with proliferation of plutonium in a truly closed fuel cycle.

Because of wide use of thermal reactors and its associated infrastructure for power production, it is unlikely that in the future the nuclear industry will ever move toward a strategy based solely on fast reactors. It is more likely that the industry will evolve to “reactor parks” where thermal and fast reactors are used to generate power as well as manage the resultant wastes that are produced.

61.5.4 Partitioning Schemes for the Minor Actinides and Long-Lived Fission Products

In order to realize the AFC and significantly reduce the inventories of minor actinides and possibly, certain long-lived fission products, advances are required in the chemical processes used to separate or partition these elements from spent fuel. Two approaches are being considered. One is based on aqueous processes that are either variations or extensions of the conventional PUREX process. The other is based on nonaqueous processes. (Coops et al. 1983) In some of the AFC scenarios, combinations of both aqueous and nonaqueous processes are envisioned. For example, in addition to separating uranium and plutonium for recycle as fuel, aqueous processes could be used for the initial separation of selected long-lived fission products and the minor actinides from spent fuel. Nonaqueous processes have a clear advantage in transmutation schemes requiring multiple recycle in dedicated transmutation devices where minimizing the time between fuel discharge and fuel reprocessing is critical. This is because aqueous processes cannot accommodate the decay heat and the intense radiation fields from “fresh” spent fuel. In addition to developing new chemical processes, a significant amount of development is needed to make targets of minor actinides and long-lived fission products compatible with the appropriate transmutation devices.

61.5.4.1 Improved PUREX Process

Over the past 10 years, modifications to the PUREX process have made it possible to more effectively separate neptunium. To effect the efficient separation of Np within the conventional PUREX process, Np is oxidized to VI state by nitrous acid and is extracted in the first cycle along with U and Pu into the organic phase. The extracted Np(VI) follows the uranium stream and is later separated during the second purification cycle of uranium. In the RFC, the neptunium is sent to vitrification and disposed of as HLW; but in an AFC option, the neptunium can be blended with MOX fuel or fabricated into special targets for later transmutation. The other minor actinides, americium and curium cannot be separated by reasonable modifications to the PUREX process. These elements will require the addition of special processing steps to separate them from the PUREX high-level waste stream.

Modifications to the traditional PUREX process can also lead to the separation of two of the long-lived fission products, technetium and iodine. During dissolution, 10–20% of the

technetium remains as an insoluble residue with the noble metals Ru, Rh, and Pd with the cladding hulls. The technetium that *does* dissolve in the nitric acid is Tc(VII) in the TcO_4^- form and is extracted by TBP. Subsequently, technetium can then be scrubbed from the organic phase. Iodine is released as a gas in the dissolution step and is separated by simply trapping it from the off-gas. Like Am and Cm, other fission products of potential concern with respect to waste disposal, Cs and Sr, and probably Pd, Se, and Sn cannot be removed by reasonable modifications to the PUREX process. However, separation schemes to remove Sr and Cs from HLW using crown ethers, calixarenes, zeolites, and dicarbollides are currently under investigation (Horwitz et al. 1990, 1991; Esimantovskii et al. 1992; Kumar et al. 1997; Dozol et al. 2000; Jain et al. 1995; Selucky et al. 1979).

The reprocessing of conventional LWR-MOX fuel with a view of recycling the transuranium elements (TRU) and burning them either in fast reactors or in dedicated transmutation devices is conceptually possible in present PUREX reprocessing plants. The same PUREX process used for the removal of transuranium elements from HLW from the reprocessing of once-through LWR- UO_2 fuel from conventional nuclear power plants can be used for MOX. However, reprocessing of MOX fuel is more difficult because the radiotoxicity is about eight times higher for MOX compared with once-through spent LWR- UO_2 fuel. Subsequent reprocessing of recycled MOX fuel will undoubtedly require dedicated facilities with more shielding and remote handling capabilities and new, nonaqueous processes.

61.5.4.2 Aqueous Schemes for the Separation of Minor Actinides from HLW from PUREX

A number of aqueous processes to separate minor actinides from HLW are under investigation in various laboratories around the world (Mathur et al. 2001; Horwitz and Schulz 1999; Musikas 1999; Madic 2000). Some of these processes are relatively mature and have been tested on a pilot plant-scale with either simulated or actual wastes while others are in their infancy. By far, the largest number of separation schemes have been developed to separate the trivalent lanthanide elements, Ln(III), from the trivalent actinide elements, An(III) in HLW. This separation is difficult not only because the Ln(III) behave similarly to the An(III) (are similar in size and exist as 3+ cations in aqueous solution) but also because they are present in HLW in quantities that are a factor of 10 higher than the amount of Am and Cm combined. In addition, the Ln(III) constitute about one third of the total mass of all the fission products in the HLW stream from PUREX. If the An(III) are to be efficiently transmuted, it is important that Ln(III) be removed because some Ln(III) have high thermal neutron absorption cross sections and thus would interfere with the process. Once the Ln(III)–An(III) are separated from the remaining fission products, the An(III) are normally selectively stripped in a second step. In some waste management strategies, Am and Cm would be handled and either transmuted or stored separately. Under this scenario, the separation of Am from Cm would be required. However, separating Am from Cm is even more difficult because both are trivalent cations in solution and their ionic radii differ by only 0.1–0.2 nm. (Shannon 1976; Shannon and Prewitt 1969, 1970)

The *TRUEX process*, developed at ANL in the early 1980s (Schulz and Horwitz 1988; Mathur et al. 1995), was found to be a very efficient process for co-extracting the An(III) with the Ln(III) from HLW. The process uses a phosphine oxide derivative, CMPO(*n*-octyl-phenyl-di-isobutyl-carbamoylmethyl-phosphine-oxide) to co-extract the An(III)–Ln(III)

elements from a strong nitric acid solution. As a result, the TRUEX process is directly applicable to the HLW stream coming from PUREX. Although selective stripping steps can be used to remove Am and Cm, coupling TRUEX to a process such as TALSPEAK results in the best An(III)–Ln(III) separation. The *TALSPEAK process*, developed at Oak Ridge National Laboratory (ORNL) in the 1960s (Weaver and Kappelmann 1964; Kolarik et al. 1972; Liljenzin et al. 1984; Persson et al. 1984) uses HDEHP (di-ethyl-hexyl-phosphoric acid), an acidic organophosphorus extractant, to co-extract the An(III)–Ln(III) and then the An(III) are selectively stripped by contacting the organic phase with an aqueous phase containing a strong complexing agent such as glycolic acid or DTPA (di-ethylenetriamine-pentaacetic acid). Since the complexing agent forms a stronger complex with the An(III), the An(III) are back extracted into the aqueous phase leaving the Ln(III) behind. The Japanese developed a similar process to co-extract an An(III)–Ln(III) and then to selectively strip the An(III) using DPTA. The Japanese process (Tachimori et al. 1979, Tachimori and Nakamura 1982; Morita et al. 1991) used *DIDPA* (di-isodecylphosphoric acid) for the co-extraction step.

Other processes that are being investigated for the co-extraction of An(III) and Ln(III) include TRPO and DIAMEX. *TRPO* under development in China (Zhu et al. 1989) uses a trialkyl phosphine oxide to co-extract the An(III)–Ln(III) from a solution containing low to moderate concentrations of nitric acid (~ 1 M) and then back extracts both into a high nitric-acid solution. The high nitric-acid medium makes it difficult to subsequently separate the An(III) from the Ln(III). The *DIAMEX* (DIAMide EXtraction), developed in a collaborative effort by France and UK, (Musikas and Hubert 1987; Cuillerdier et al. 1991; Musikas and Schultz 1992; Weigl et al. 2001) uses non-phosphorous-based compounds, the malonamides as extractants. These extractants appear to be similar in efficiency to CMPO but offer the advantage of producing no solid secondary waste because the diamide extractants upon combustion yield only carbon dioxide and water.

In addition to TALSPEAK and DIDPA, other separation schemes of note that are being developed for separating the An(III) from the Ln(III) include those based on ligands with nitrogen-donor atoms such as tripyridyltriazine and ligands with sulfur-donor atoms such as Cyanex 301, a commercial product consisting primarily of bis (2,4,4-trimethylpentyl) dithiophosphinic acid. (Vitorge 1984; Musikas 1984, 1985; Ensor et al. 1988; Chen et al. 1996; Zhu 1995)

For the separation of Am from Cm, the only processes that offer promise are SESAME and one based on the precipitation of Am(V). *SESAME*, being developed in both France and Japan, is a process by which, under strong oxidizing conditions, Am(III) is oxidized to Am(VI) and then separated from Cm(III) by extraction. The French work (Donnet et al. 1997; Chartier et al. 1998) uses a heteropolyanion catalyst coupled with electrolysis to affect the oxidation. Ammonium persulfate is used for the same purpose in the SESAME process by the Japanese (Madic 2000). Am(V) produced either chemically or electrochemically and then precipitated as a double carbonate is the basis for the other process (Yakovlev and Gorbenko-Germanov 1956).

There are advantages and disadvantages to all of the processes just described. Some are easier to implement than others. Some require adjustment of parameters such as pH or nitrate concentration. Some have problems with third phase formation and solvent degradation or become impractical for industrial applications because of the limited loading capacities of the extractants. In all cases, however, adding separation steps to the PUREX process to remove the minor actinides will generate additional secondary waste streams that will have to be managed.

61.5.4.3 Advantages of Nonaqueous Processes for Partitioning and Transmutation

Alternatives to aqueous processing or “dry” or nonaqueous processing techniques have been tried but none, until recently, have been used on a “true” industrial scale for fuel reprocessing. Examples of these include separations based on (1) differences in volatility of the halides, especially fluorine compounds; (2) molten salt (liquid–liquid) extraction where fuel dissolved in a molten salt is then contacted with a heat resistant low volatility second phase such as 100% TBP or a liquid metal; and, (3) electrorefining, where controlling the cell potential results in removal of a metal from a molten salt by the selective deposition (reduction) on a cathode.

Probably the most inviting and challenging R&D area impacting waste management for the advanced fuel cycle is the development of nonaqueous processes. Because of the higher burnup needed for transmutation as well as the need for multiple recycling with minimum cooling time between fuel discharge and reprocessing, nonaqueous processes offer several important advantages. Nonaqueous processes are much more radiation resistant compared with aqueous processes and thus they can be used to reprocess spent fuel after considerably shorter cooling periods. Other advantages include the potential to produce much smaller quantities of secondary waste and waste forms suitable for long-term disposal, the ease of recycling of reagents used in separations, and finally, the compactness of equipment reduces the physical size of the plant needed, thus capital costs are reduced. Currently, the major drawback is that separation factors are usually smaller requiring multiple stages to achieve the relatively high levels of decontamination. Also, processes must be conducted under highly controlled atmospheres, e.g., dry argon, to avoid hydrolysis and precipitation reactions. Nonaqueous processes typically have a rather limited throughput because these are usually operated as batches rather than as continuous processes. However, this is not a severe limitation in a transmutation scenario because after the initial processing of the spent fuel, the volume of material to be processed once the transmutation cycle begins is only a fraction of the initial fuel volume.

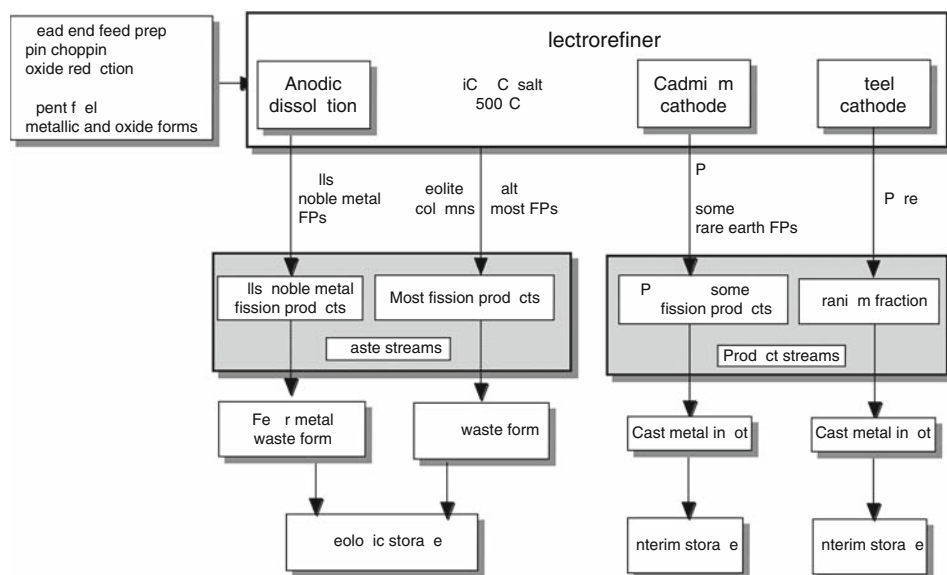
Nonaqueous Processing: Electrometallurgical Treatment: ANL

Currently, nonaqueous separation schemes are under investigation in several countries including the USA, Russia, and Japan. Probably the most advanced nonaqueous processing scheme to date has been developed at ANL (NAS 2000). This process termed “electrometallurgical processing” has been demonstrated on the engineering scale and used recently by ANL to successfully process driver fuel and blanket spent fuel from the Experimental Breeder Reactor (EBR-II). EBR-II *driver fuel* consists of highly enriched uranium metal alloyed with about 10% Zr and clad in stainless steel. The *blanket fuel* is depleted uranium metal that also uses stainless steel cladding.

Briefly, the electrometallurgical treatment, shown schematically in ► Fig. 61.6, involves chopping the spent fuel into small pieces and placing it in an anode basket inside an electrorefiner vessel containing a LiCl/KCl salt mixture heated to about 500°C. Prior to electrolysis, an oxidant such as CdCl₂ or UCl₃ is added to the salt. Upon passage of a constant electrolysis current between the anode basket and a steel cathode, elements that form very stable chloride compounds (e.g., actinides, alkali, alkaline earth, and rare earth elements) dissolve into the salt leaving the less stable chloride compounds (e.g., Cd, Fe, Nb, Mo, and noble metals) with the cladding hulls in the anode basket.

■ Fig. 61.6

Schematic diagram of ANL's nonaqueous electrometallurgical process used to reprocess spent fuel from an experimental fast breeder reactor (EBR-II) (NAS 2000) (Reprinted with permission from Electrometallurgical Techniques for DOE Spent Fuel – Final Report, p. 21, courtesy of the National Academy Press, Washington, DC)



The electrolysis is carried out under controlled current conditions such that principally U^{3+} is reduced to the metal at the cathode. After a period of time, the cathode is removed from the electrorefiner and the U metal is harvested after the adhering salt is removed by volatilization in a vacuum furnace. The U is then cast into an ingot in a high-temperature furnace and stored. ANL also demonstrated a variation to this flow sheet that uses a liquid Cd cathode in addition to the steel cathode. The Cd cathode permitted the separation of Pu, the transuranium elements, and some rare earth fission products from the salt. Without the Cd cathode, these elements remained along with most of the fission products in the salt. The salt was subsequently processed by adding zeolite, heating to adsorb the salt into the zeolite, adding glass, and then hot isostatically pressing the mixture to form a glass-bonded sodalite ceramic waste form. The cladding hulls, noble metal fission products, and any unoxidized material that remained in the anode basket were subjected to removal of adherent salt by volatilization and converted to a metallic waste form by adding more Zr and cast into an ingot in a furnace.

By changing the head end treatment steps, other types of fuel can be accommodated in this nonaqueous process. For example, an initial Li/Li₂O step can be added to convert oxide fuel to the metallic form. To be compatible with the electrometallurgical treatment just described, the electrorefiner requires the spent fuel to be in a metallic form.

This electrometallurgical process with some modifications and additional development could be used in transmutation schemes involving other fuel types such as metal-oxides and nitrides and in situations where cooling periods as short as 3–5 months are required. ANL has already developed an electrochemical head end process to convert oxide fuel to the metallic form by reducing the oxide in a LiCl/Li₂O molten salt bath. The resulting metal fuel could then

be electrorefined using the process just described for EBR-II fuel. For an in-depth description and assessment of ANL's electrometallurgical process for the processing of EBR-II core and blanket fuel, see (NAS 2000).

A variation of the PUREX process is being proposed by the US Department of Energy as a possible alternative partitioning scheme for the transmutation of wastes. This aqueous process called *UREX*, only removes uranium from spent commercial LWR fuel and leaves plutonium in the HLW stream with the other minor actinides and fission products. Nonaqueous pyroprocessing, a variation of the ANL electrorefining process, is then proposed to be used to separate both the plutonium and minor actinides so that they can be transmuted in an ADS. For further information related to potential modifications of this process for other accelerator transmutation of waste applications, see ANL-99/15 (1999).

61.5.5 Transmutation Devices for the Advanced Fuel Cycle

For the AFC to be most effective and reduce the inventory of minor actinides at a reasonable rate, dedicated devices that produce a “hard” or “fast” neutron spectrum will be required. Such devices include the advanced liquid metal reactors (ALMRs), a fast reactor configured to operate as an actinide “incinerator” rather than “breeder” and accelerator-driven systems (ADSs). Fast reactor technology discussed earlier in this chapter is relatively mature whereas the development of ADS is in its infancy. Accelerator-based waste transmutation programs are ongoing in France, Japan, USA, and CERN.

An ADS facility consists of (1) a high power proton accelerator; (2) a subcritical target that produces a high neutron flux upon bombardment with high-energy protons; (3) a blanket system that utilizes this intense source-driven neutron flux to fission actinides and transmute fission products; and, a support chemical processing plant. The heart of the system is the subcritical target where an intense (>100 mA), high-energy (1–2 GeV) proton beam impinges on a high Z target to produce neutrons in a process called spallation. The effectiveness of an ADS target is usually given by the number of neutrons produced per incident proton and is linearly proportional to both the atomic number and density of the target. For this reason, targets such as molten lead or lead/bismuth eutectic are being proposed as the spallation source. Accelerator-driven systems producing 40 or more neutrons per incident proton are also being proposed. The waste material is loaded into the blanket where it is “incinerated” by capturing one of the neutrons causing it either to fission or to be converted to a short-lived or stable isotope. This process therefore reduces the radiotoxic inventory of the waste material. The heat produced from the transmuter, (the combination of the target and blanket) can then be used to generate power, $\sim 10\%$ of which can be used to run the accelerator, and the remaining 90% can be put on the power grid.

Unlike fast reactors that operate on the criticality principle where the nuclear reaction is sustained, ADS systems are subcritical. When the proton beam is off in an ADS, no neutrons are created and no nuclear reaction occurs. An often overlooked key component of an ADS is the supporting chemical processing plant. Within the plant, separation processes are used to first partition the spent fuel to obtain the waste material that is introduced into the ADS and then later to support multiple recycle, fuel fabrication, and finally the production of the final waste forms acceptable to a geologic repository. All of these activities are crucial to the success of transmutation using ADS and considerable R&D is needed to make this a reality.

For an in-depth comparison of fast reactors and accelerator-driven systems for transmutation of actinides and long-lived fission products, see (OECD/NEA 2002). For more information on accelerator transmutation of waste (ATW) program in the USA, see refs. Jarvinen et al. (1992), LANL (1999), and DOE (2001).

61.5.5.1 Future of P&T

Japan, France, and the USA are the most active pursuers of partitioning and transmutation technologies. In addition, several international groups (NEA, IAEA, and the EC) are pursuing studies. Each organization regularly publishes its progress, status, and future activities, with many of these reports being available on the respective Web sites.

Japan has recently completed Phase I of their program, having demonstrated a P&T process with expected performance. R&D work is being conducted by JNC, JAERI, and CRIEPI. This work will need to be coordinated with the restructuring of the FBR program. The Japanese are proposing cooperation among domestic and international organizations to efficiently use experimental facilities that will be needed in the R&D program. It is anticipated that the P&T R&D plan will be reviewed again in 2005, especially with respect to FBR's being used jointly for power generation and transmutation.

France's goal is to demonstrate the scientific feasibility of transmutation in various reactor types by 2006. This includes the feasibility of downstream separation from reprocessing and conditioning of separated long-lived radionuclides. These are joint collaborative efforts with government, industry, and academia. Progress is reviewed annually by the National Evaluation Commission.

In the past several years, the US program has changed significantly. The program's budget doubled from fiscal year 2000 to 2001 and allowed for an expanded experimental program. The new program *Advanced Accelerator Application* (AAA) combines two former programs: the defense Accelerator Production of Tritium (APT) and the civilian Accelerator Transmutation of Waste (ATW). AAA has four principal objectives:

- Demonstrate the practical performance of an accelerator-driven subcritical multiplier;
- Demonstrate the viability of transmutation for waste and spent fuel management;
- Enhance the Nation's nuclear science and advanced technology education infrastructure;
- Provide a more robust backup tritium production capability for national security.

The accelerator-driven test facility (ADTF) envisioned to be operational by 2010 will be the program's focal facility.

Within the EC, a technical working group has been established to develop a 10-year R&D plan for ADS. The goals of their activities are to

- Reduce the risks associated with radioactive waste using transmutation;
- Develop a technical plan that could lead to a demonstration of experimental ADS in 10 years;
- Identify advantages this program could have in the nuclear community, and how competence can be maintained.

Several reports discuss, in greater detail, the various national programs (NEA 2000, 2002; DOE 2001). In response to continued growth in population and economic prosperity, and growing understanding of both resource limits and environmental impacts of fossil fuel use, it is likely that nuclear power use will grow substantially, both nationally and globally over the

next half century. If so, advanced nuclear power systems must be designed and deployed to meet modern safety and security standards, meet nonproliferation imperatives, and resolve the lingering nuclear waste issue. Current US energy policy points toward continued and increasing use of nuclear energy, and acknowledges the potential benefits of moving to advanced fuel cycles. DOE⁹ has begun a cooperative effort with industry for near term deployment of new nuclear reactors in the USA. These plants would be current technology (Generation-III) and require little R&D. However, it only makes sense to attack the barriers to building new nuclear power plants if society intends to use large amounts of nuclear energy for a long time. Sustained, large-scale use of nuclear energy creates the need to transition to a sustainable fuel cycle, where uranium is recycled and used entirely, and both plutonium and minor actinides are cycled to minimize the long-term environmental hazard of the waste. Several DOE programs are moving toward R&D on advanced nuclear fuel cycles and advanced (Generation-IV) reactor systems. At some scale of nuclear energy deployment, fuel cost, availability, waste management cost, and capacity will create a compelling need for a fully closed fuel cycle, which maximizes the energy derived from fissionable resources and minimizes wastes. While it is not yet known at what point this will become compelling, it is known that it will take many decades to complete the transition to such a sustainable nuclear fuel cycle.

61.6 Editors' Notes

1. Radiotoxicity of a radionuclide is inversely proportional to its maximum permissible concentration, MPC. Ingestion radiotoxicity – see the vertical axis of [Fig. 61.2](#) – can be expressed as a minimum of water that is still drinkable if the unit mass of the substance containing the given radionuclide is dissolved in it (p. 2802).
2. MWe means megawatts of electric power (p. 2802).
3. For more details on gaseous diffusion and gas centrifugation see [Sects. 51.4.4 and 51.4.5, respectively, in Chap. 51, Vol. 5](#), on “Isotope Separation” (p. 2804).
4. For details of LIS see [Sect. 51.7.3 in Chap. 51, Vol. 5](#) (p. 2804).
5. See [Fig. 4.10 in Chap. 4, Vol. 1](#), on “Nuclear Fission” (p. 2806).
6. A fertile nuclide by definition means a non-fissile nuclide, which, however, can be converted into a fissile nuclide via neutron-induced nuclear reactions (p. 2807).
7. What [Fig. 61.2](#) actually shows is the ingestion radiotoxicity of the various nuclides. However, larger radiotoxicity means larger activity/number of atoms/mass of the given radionuclide per mass unit, i.e., the shapes of the curves are also characteristic of the relative amounts of radionuclides (p. 2808).
8. For more details about ADS see [Sect. 61.5.5 in this Chapter](#), and [Sect. 57.4.2.5 in Chap. 57 of this volume](#) on “Technical Application of Nuclear Fission” (p. 2823).
9. DOE means US Department of Energy (p. 2832).

Acknowledgments

The authors would like to thank Prof. W. F. Kinard and Dr. W.G. Halsey for their insightful comments made during the preparation of the manuscript. The authors also gratefully acknowledge the technical editing efforts of Ms. D. Schliech and Ms. K. Ramirez for their

careful attention to detail in preparing this document in the proper camera-ready format. This work was performed under the auspices of the US Department of Energy by the Lawrence Livermore National Laboratory under Contract No. W-7405-Eng-48.

References

- Albright D (1993) World inventory of plutonium and highly enriched uranium, 1992. Oxford University Press, New York
- Albright D, Berkhout F, Walker W (1997) Plutonium and highly enriched uranium 1996: world inventories, capabilities, and policies. Oxford University Press, New York
- ANL-99/15 (1999) A technology roadmap for developing ATW technology, Separations and waste form technology, September 1999
- Beller D, Rhodes R (2000) The need for nuclear power. *Foreign Affairs* 79:30
- Benedict M, Pigford T, Levi HW (1981) Nuclear chemical engineering, 2nd edn. McGraw Hill, New York
- Chartier D, Donnet L, Adnet JM (1998) *Radiochimica Acta* 83(3):129
- Chen J, Zhu Y, Jiao R (1996) *Sep Sci Technol* 31:2723
- Choppin GR, Rydberg J (1980) Nuclear chemistry, theory and applications. Pergamon, Oxford
- Choppin GR, Rydberg J, Liljenzin JO (1995) *Radiochemistry and nuclear chemistry, theory and applications*. Butterworth-Heinemann, Great Britain
- Coops MM, Knighton JB, Mullins LJ (1983) Pyrochemical processing of plutonium. In: Carnall WT, Choppin GR (eds) *Plutonium chemistry*, ACS symposium series, vol 216. American Chemical Society, Washington DC, pp 381–400
- Cuillerdier C, Musikas C, Hoel P, Nigond L, Vitart X (1991) *Sep Sci Technol* 26(9):1229
- Culler FL (1956) Reprocessing of reactor fuel in blanket materials by solvent extraction. In: Bruce FR, Flether IM, Hyman HH, Katz KJ (eds) *Process chemistry, Progress in nuclear energy, Series III, Vol 1*. McGraw Hill, New York, pp 172–194
- DOE (2001) United States Department of Energy, Office of Nuclear Energy, Science and Technology and Coordinated with the National Nuclear Security Administration. Report to Congress — The Advanced Accelerator Applications Program Plan, US Government Printing Office, Washington DC
- DOE/RW-0519 (1999) A roadmap for developing accelerator transmutation of waste (ATW) technology, A report to congress, October 1999
- Donnet L, Adnet JM, Faure N, Bros P, Brossard Ph, Josso F, (1999) The development of the SESAME process. In: *Proceedings of the fifth OECD/NEA information exchange meeting on actinide and fission product partitioning and transmutation*, Mol, Belgium, 25–27 November 1998
- Dozol JF, Dozol M, Macias RM (2000) *J Incl Phenom Macro Chem* 38(1–4):1
- Ensor DD, Jarvinen GD, Smith BF (1988) *Solv Extr Ion Exch* 6:439
- Esimantovskii VM, Galkin BY, Lazarev LN, Lyubtsev RI, Romanovskii VN, Shishkin DN (1992) Technological tests of HAW partitioning with the use of chlorinated cobalt dicarbolyde (CHCODIC), Management of secondary wastes. In: Post RG (es) *Proceedings of the symposium on waste management*, Arizona Board of Regents, Tuscon, pp 801–804
- Horwitz EP, Schulz WW (1999) Solvent extraction in the treatment of acidic high-level liquid waste: where do we stand? In: Bond AH, Dietz ML, Rogers RD (eds) *Metal ion separation and preconcentration: progress and opportunities*, ACS symposium series, vol 716, American Chemical Society, Washington DC, pp 20–50
- Horwitz EP, Dietz ML, Fisher DE (1990) *Solv Extr Ion Exch* 8:557
- Horwitz EP, Dietz ML, Fisher DE (1991) *Solv Extr Ion Exch* 9:1
- International Atomic Energy Agency (IAEA) (1977) *Regional nuclear fuel cycle centres*, Vienna, Austria
- Jain S, Ramaswamy M, Theyyunni TK (1995) Removal of strontium from low level waste using zeolite 4A. In: *NUCAR 95: proceedings of the nuclear and radiochemistry symposium*, Kalpakkam, India, 21–24 February 1995
- Jarvinen GD, Marsh SF, Smith BF, Yarbrow SL, Yates M, Walker RB (1992) Baseline actinide blanket processing flowsheet for the ATW program, LA-UR-92-63, Los Alamos National Laboratory, Los Alamos
- Kolarik E, Koch G, Kuesel HH, Fritsch J (1972) Separation of Americium and Curium from highly radioactive waste solution, KFK-1553, Karlsruhe Nuclear Research Center, Karlsruhe, Germany
- Kumar A, Mohapatra PK, Pathak PN, Manchanda VK (1997) Dicyclohexano 18 Crown 6 in butanol-octanol mixture: a promising extractant of Sr(II) from nitric acid medium. *Talanta* 4:387
- LANL (1999) Roadmap for the development of accelerator transmutation of waste: target and blanket system

- Liljenzin JO, Persson G, Svantesson I, Wingefors S (1984) *Radiochimica Acta* 35:155
- Madic C (2000) Overview of the hydrometallurgical and pyro-metallurgical processes studied worldwide for the partitioning of high active nuclear wastes in actinide and fission partitioning and transmutation, Madrid, OECD/NEA
- Madic C, Hudson MJ, Liljenzin JO, Glatz JP, Nannicini R, Facchini A, Kolarik Z, Odoj R (2000) New partitioning techniques for minor actinides, Final Report, EUR 19149
- Mathur JN, Murali MS, Iyer RH, Ramunujam A, Dhami PS, Gopalakrishnan V, Rao MK, Badheka LP, Banerji A (1995) *Nucl Technol* 109:219
- Mathur JN, Murali MS, Nash KL (2001) *Solv Extr Ion Exch* 19(3):357
- Morita Y, Tani S, Kubota M (1991) Separation of transuranic elements from high-level waste by extraction with diisodecyl phosphoric acid. In: The third international conference on nuclear fuel reprocessing and waste management, Recod'91, Vol 1, Sendai, Japan
- Musikas C (1984) Actinide-lanthanide group separation using sulfur and nitrogen donor extractants. In: International chemistry congress of Pacific Basin societies, CEA-Conf-7706, Honolulu
- Musikas C (1985) Actinide/lanthanide group separation using sulphur, and nitrogen donor extractants. In: Choppin GR, Navratil JD, Shulz WW (eds) *Actinide/lanthanide separations*, World Scientific, Philadelphia, pp 19–30
- Musikas C (1999) Review of possible technologies for actinide separations using other extractants than TBP, NATO SCI. Ser., Ser. 2 53, Chemical Separation Technologies and Related Methods of Nuclear Waste Management, pp 99–122
- Musikas C, Hubert H (1987) *Solv Extr Ion Exch* 5:877
- NAS (1957) The disposal of radioactive waste on land. National Academy Press
- NAS (1994) Management and disposal of excess weapons plutonium. National Academy of Sciences. Committee on International Security and Arms Control, National Academy Press, Washington DC, p 34
- NAS (1996) Nuclear wastes, technologies for separations and transmutation. National Academy Press
- NAS (2000) Electrometallurgical techniques for DOE spent fuel – final report. National Academy Press
- OECD/NEA (1999) Actinide and fission product partitioning and transmutation proceedings of the fifth international information exchange meeting, Mol, Belgium, 25–27 November 1998
- OECD/NEA (2001) Actinide and fission product partitioning and transmutation sixth international information exchange meeting, Madrid, Spain, 11–13 December 2000
- OECD/NEA (1998) Status and assessment report of actinide and fission product partitioning and transmutation, OECD Report NEA/PTS/DOC
- OECD/NEA (2000) Nuclear energy agency, Organisation for economic co-operation and development. Actinide and fission product partitioning and transmutation, NEA Press, Paris
- OECD/NEA (2002) Accelerator-driven systems (ADS) and fast reactors (FR). In: Advanced nuclear fuel cycles: a comparative study, NEA Press, Paris
- Persson G, Wingefors S, Liljenzin JO, Svantesson I (1984) *Radiochimica Acta* 35:163
- Persson G, Svantesson S, Wingefors S, Liljenzin JO (1986) *Solv Extr Ion Exch* 2:89
- Raisbeck GM, Yiou F, Zhou ZQ, Kilius LR (1995) *J Marine Syst* 6(N5-6):561
- Schulz WW, Horwitz EP (1988) *Sep Sci Technol* 23:1191
- Selucky P, Rais J, Kyr M (1979) Study of the possibility of using dicarbollides to extract cesium and strontium from waste radioactive solutions, *Ustav Jad. Vyzk., [Rep.]* (1979), (UJV 5069) pp 58
- Shannon RD (1976) *Acta Cryst* A32:751
- Shannon RD, Prewitt CT (1969) *Acta Cryst* B25:925
- Shannon RD, Prewitt CT (1970) *Acta Cryst* B26:1046
- Tachimori S, Nakamura H (1982) *J Nucl Sci Technol* 19(4):326
- Tachimori S, Sato A, Nakamura H (1979) *J Nucl Sci Technol* 16(6):434
- Vitorge P (1984) Lanthanides and trivalent actinides complexation by tripyridyl, triazine, Applications to liquid-liquid extraction, CEA-R-5270
- Weaver B, Kappelmann FA (1964) Talspeak: a new method of separating Americium and Curium from lanthanides by extraction from an aqueous solution of aminopolycarboxylic acid complex with a monoacidic phosphate or phosphonate, ORNL-3559, Oak Ridge National Laboratory, Oak Ridge
- Web (2003a) <http://www.nea.fr/rwm/>; <http://www.world-nuclear.org/info/inf04.html>; <http://www.iaea.org/NewsCenter/Focus/RadWaste/index.html>; <http://www.nrc.gov/waste/hlw-disposal.html>
- Web (2003b) <http://www.world-nuclear.org/info/inf03.html>
- Web (2003c) <http://www.wise-uranium.org/index.html>
- Web (2003d) <http://www.world-nuclear.org/info/inf32.html>
- Web (2003e) <http://www.world-nuclear.org/info/inf69.html>
- Web (2003f) <http://www.world-nuclear.org/education/wast.html>
- Web (2003g) <http://www.world-nuclear.org/info/inf29.html>
- Web (2003h) <http://www.wise-uranium.org/efac.html>
- Weigl M, Geist AM, Gompfer K, Kim JI (2001) *Solv Extr Ion Exch* 19(2):215

Yakovlev GN, Gorbenko-Germanov DS (1956) Coprecipitation of Americium (V) with double carbonates Uranium (VI) or Platinum (vi) with Potassium. In: Proceedings of the 1st United Nations international conference on peaceful uses of atomic

energy, Vol 7, International Atomic Energy Agency, Vienna

Zhu Y (1995) *Radiochimica Acta* 68:95

Zhu Y, Song C, Xu J, Yang D, Lui B, Chen J (1989) *Chinese J Nucl Sci Eng* 9:141



62 Nuclear Forensic Materials and Methods

I. D. Hutcheon · P. M. Grant · K. J. Moody

Livermore National Laboratory, Livermore, CA, USA

62.1	<i>Introduction</i>	2839
62.1.1	Nuclear Smuggling	2839
62.1.2	Historic Considerations	2840
62.1.3	Facets of Nuclear Forensic Analysis	2841
62.1.3.1	Improvised Nuclear Device (IND) and Radiologic Dispersal Device (RDD)	2841
62.1.3.2	Pre-det and Post-det	2842
62.1.3.3	Source and Route	2843
62.2	<i>Chemical Aspects of Nuclear Forensic Science</i>	2843
62.2.1	Commonly Used Chemical Methods in the Radiochemical Forensic Laboratory	2844
62.2.2	Tracers in Inorganic Analysis	2847
62.2.3	Radiochemical Milking	2850
62.2.4	Reagent Blanks	2851
62.3	<i>Radionuclide Chronometry</i>	2852
62.3.1	Chronometry Versus Age-Dating	2852
62.3.2	Granddaughters and the Detection of Spoofing	2855
62.3.3	Detection of Incomplete Fuel Reprocessing	2856
62.4	<i>Analytical Methods</i>	2856
62.4.1	Application of Radiochemical Procedures	2856
62.4.2	Preparation of Counting Sources	2857
62.4.3	Radiation Counting Systems	2858
62.4.3.1	Nuclear Counting	2859
62.4.3.2	Particle Detection	2860
62.4.3.3	Tritium Analysis	2861
62.4.4	Imaging and Microscopy	2863
62.4.4.1	Optical Microscopy	2863
62.4.4.2	Scanning Electron Microscopy	2864
62.4.4.3	Transmission Electron Microscopy	2865
62.4.4.4	Electron Microprobe Analysis	2865
62.4.4.5	X-Ray Microanalysis	2865
62.4.5	Isotope Mass Spectrometry	2866
62.4.5.1	Isotope-Ratio MS	2866
62.4.5.2	Element MS	2867

62.4.5.3 MS and In Situ Microanalysis 2868

62.4.6 Organic GC-MS 2870

62.4.6.1 General and Applications 2870

62.4.6.2 Sample Prep 2871

62.4.6.3 Spectral Reduction and Compound Identification 2872

62.5 Special Nuclear Materials 2872

62.5.1 Natural Versus Synthetic Materials 2873

62.5.2 Separation of Uranium Isotopes and ²³⁵U Enrichment 2873

62.5.3 Nuclear Reactors and the Production of Plutonium and ²³³U 2877

62.5.4 Recovery and Purification of Special Nuclear Materials from
Reactor Products 2879

62.5.5 Heavy Element Metals and Alloys 2881

62.6 Case Studies 2884

62.6.1 Overview 2884

62.6.2 Hoax: Nonradioactive – Source Analyses Only 2885

62.6.3 Hoax: Radioactive – Source Analyses Only 2885

62.6.4 Incident: Natural Radioactivity – Source Analyses Only 2886

62.6.5 Real: Radioactive – Source and Route Analyses 2887

Abstract: A short history and treatment of the various aspects of nuclear forensic analysis is followed by a discussion of the most common chemical procedures, including applications of tracers, radioisotopic generators, and sample chronometry. Analytic methodology discussed includes sample preparation, radiation detection, various forms of microscopy, and mass-spectrometric techniques. The chapter concludes with methods for the production and treatment of special nuclear materials and with a description of several actual case studies conducted at Livermore.

Abbreviations *amu*, Atomic mass unit; *AMDIS*, Automated Mass Spectral Deconvolution and Identification System; *CBRN*, Chemical, Biologic, Radiologic, Nuclear; *CBRNE*, CBRN + Explosives; *CCD*, Charge-coupled detector; *CSI*, Crime-scene investigation; *DOE*, Department of Energy (US); *D-38*, Depleted uranium ($^{235}\text{U} < 0.72\%$); *EDS*, Energy-dispersive spectrometry (X-ray); *EMIS*, Electromagnetic isotope separation; *EMPA*, Electron microprobe analysis; *FTIR*, Fourier-transform infrared spectroscopy; *GC-MS*, Gas chromatography-mass spectrometry; *GDMS*, Glow-discharge mass spectrometry; *HDEHP*, di-2-ethylhexyl orthophosphoric acid; *HE*, High explosives; *HEU*, High-enriched uranium; *HPGe*, High-purity germanium; *ICP-MS*, Inductively coupled-plasma mass spectrometry; *IND*, improvised nuclear device; *IRMS*, Isotope-ratio mass spectrometry; *LA-ICPMS*, Laser ablation ICP-MS; *LEPS*, Low-energy photon spectroscopy; *LEU*, Low-enriched uranium; *LLNL*, Lawrence Livermore National Laboratory (US); *LSC*, Liquid scintillation counting; *MOX*, Mixed-oxide; *MC-ICPMS*, Multicollector ICP-MS; *NBC*, Nuclear, Chemical, Biologic; *NFA*, Nuclear forensic analysis; *NIST*, National Institute of Standards and Technology (US); *Oralloy*, Oak Ridge alloy (nominal 93.5% ^{235}U); *PUREX*, Pu-U extraction; *PWR*, Pressurized-water reactor; *RAP*, Radiologic Assistance Program (US); *RDD*, Radiologic dispersal device; *SEM*, Scanning electron microscopy; *SIMS*, Secondary-ion mass spectrometry; *SNM*, Special nuclear material; *SPME*, Solid-phase microextraction; *TBP*, Tributyl phosphate; *TEM*, Transmission electron microscopy; *TIMS*, Thermal-ionization mass spectrometry; *TNT*, Trinitrotoluene; *WDS*, Wavelength-dispersive spectrometry (X-ray); *WMD*, Weapons of mass destruction; *XRD*, X-ray diffraction (spectrometry); *XRF*, X-ray fluorescence (spectrometry)

62.1 Introduction

62.1.1 Nuclear Smuggling

The end of the Cold War in 1991 was accompanied by the disassembly of the USSR into a dozen independent countries. The ensuing social instabilities and decline in safeguarding special nuclear material (SNM) resulted in elevated occurrences of nuclear smuggling and sales of radioactive contraband on the international black market (Williams and Woessner 1996; Stone 2001). The large majority of these trafficking incidents to date have been scams or hoaxes, but seizures of significant quantities of weapons-grade or weapons-usable SNM have occurred.

During the mid-1990s, interdictions of weapons-usable SNM were characterized by relatively large quantities and frequencies. For example, in 1994, three reported seizures were indicative. In St. Petersburg, Russia, 3.05 kg of 90% high-enriched uranium (HEU), likely from Elektrostal in the Russian Federation, was confiscated from three perpetrators by the Federal Security Service. Later in the year, the German BND conducted a successful undercover

operation that resulted in the arrest of a Colombian national (with ties to a drug cartel) and two Spaniards. They had smuggled 560 g of mixed U/Pu-oxide and 210 g of ^6Li -enriched Li metal into the Munich airport in a lead-reinforced suitcase. The Pu component was approximately two-thirds of the mixed-oxide (MOX) powder and was enriched to 87.6% in ^{239}Pu . Finally, 2.7 kg of 88% HEU, probably stolen from Obninsk, were intercepted in a parked car in Prague.

By the beginning of the new millennium, however, seizures of worthy material became less frequent and the associated SNM specimens less substantial. Similar to the world of illicit drug trafficking, the tactic of nuclear smuggling seemed to evolve toward the presentation of smaller samples for technical analysis by possible customers, with the claim of much larger available quantities secured elsewhere. Thus, 4 g of 73% HEU in the trunk of a car was interdicted at the Bulgaria–Romania border in 1999. From the forensic analyses of the nuclear material, as well as those of the accompanying collateral evidence, the SNM was most likely derived from the former Soviet Union (Moody et al. 2005). The smuggler claimed that he had obtained the U specimen in Moldova, and a very similar seizure occurred in Paris 2 years later.

The most recent episodes of nuclear smuggling cited in the open literature have occurred in Georgia (Sokova and Potter 2008). In 2003, guards at the Georgia–Armenia border arrested a man with 170 g of $\sim 90\%$ HEU. Three years later, in a sting operation in Tbilisi, Georgian security forces arrested a Russian national and accomplices and confiscated ~ 80 g of $\sim 90\%$ HEU. The origin of these materials is still unknown or unconfirmed, but is suspected to be Russia from the ensuing investigations.

62.1.2 Historic Considerations

Although some investigators have asserted that nuclear forensic analysis (NFA) is a new science, invented at the Institute for Transuranium Elements, Karlsruhe, in March 1992 (e.g., Mayer et al. 2007), such claims are based merely on the start of analysis of smuggled nuclear materials by a non-weapons laboratory. The authors believe this view to be an unduly narrow definition of NFA and prefer a broader perspective. In fact, the contemporary methods and analytes of interest in NFA derive largely from Cold War nuclear weapons programs and intelligence operations. Although advances in instrumentation (such as ICP-MS and SIMS) have improved analytic capabilities in the current era, measured species have remained largely unchanged, with some exceptions for novel application areas such as specimen chronometry and geolocation.

Indeed, the first presently unclassified NFA activities with tangible results were likely those conducted by Enrico Fermi at the first nuclear weapon test, the US Trinity event on July 16, 1945. He made the first prompt explosive yield estimate by measuring the displacement of small pieces of paper dropped as the blast wave passed (Rhodes 1986, p. 674). A few hours later, Fermi and Herb Anderson sampled Trinity ground zero in lead-lined tanks equipped with trap doors in the floor to sample post-shot debris from the crater. Later NFA (radiochemical) gave a yield of 18.6 kt for Trinity (Rhodes 1986, p. 677). (1 kt of TNT = 4.184 TJ.)

Three weeks later, Kazuo (Paul) Kuroda made fallout measurements after the detonation of a “new kind of bomb” over the Aioi Bridge in Hiroshima, and correctly deduced that ^{235}U was the fissile fuel in *Little Boy*. Such activities are most definitely considered within the scope of NFA today.

Indeed, a broader view of the discipline would also incorporate one of the more impressive NFA investigations ever conducted. In 1972, French scientists measured a 0.003% discrepancy

in uranium isotopic composition in ore from the Oklo mine in Gabon, Central Africa. The ensuing investigation into prehistoric geologic conditions, existing Nd and Ru isotopic residues, and other considerations led to the stunning forensic inference of a natural nuclear reactor that had operated at an average power output of ~ 100 kW for a few hundred thousand years approximately 2 billion years ago (Cowan 1976).

The present authors both applied and developed NFA techniques within the US nuclear test program from the early 1980s to the cessation of testing in 1992, but the authors were but third-generation radiochemistry staff at the Livermore and Los Alamos National Laboratories. The true pioneers of NFA came much earlier. The results of their investigations were classified and therefore not published in the open literature, but such restriction did not negate the enterprise.

The narrow view of NFA would also exclude the authors' investigation into the January 1992 fatal explosion of a purported "cold fusion" apparatus. Although cold fusion was (and is) not mainstream nuclear science, the authors consider it their first NFA in the public domain, and it comprised both nuclear source forensic exhibits and associated collateral evidence (Grant et al. 1995a, b).

62.1.3 Facets of Nuclear Forensic Analysis

What is true of late, however, is that NFA has attracted international attention beyond the confines of weapons laboratories and intelligence agencies. A driving force behind this elevated political and public interest has been the confluence of increased transnational terrorism, indiscriminant use of chemical and biologic weapons of mass destruction (WMD) against civilian populations, suicide bombers in general (September 11, 2001 in particular), and widespread popularity of the CSI television series. One consequence of this focused attention by persons of diverse backgrounds has been the delineation of various NFA activities into categories based on effort areas.

62.1.3.1 Improvised Nuclear Device (IND) and Radiologic Dispersal Device (RDD)

While nuclear smuggling, nonproliferation, weapons diagnostics, and other topics are all of interest in NFA, two formidable weapon types are of special concern. The improvised nuclear device (IND) is a hypothetical, ad-hoc apparatus, fabricated by a subnational group or rogue nation, containing fissionable and perhaps fusionable materials, and designed to produce a nuclear explosion. A nuclear weapon stolen from a weapons state would generally also be considered an IND and within the purview of this area of concern. A radiologic dispersal device (RDD) is also a terrorist contrivance that contains radioactive material(s). However, the radionuclide(s) need not have nuclear yield potential, and the design is intended to disperse the material within its near environment via conventional high explosives (HE).

Because of the enormous difficulty and expense to produce either HEU or weapons-grade plutonium, an IND is considered a low-probability threat. However, it is one with potentially catastrophic consequences. Just the opposite is true of an RDD. The widespread commercial availability of large industrial radiation sources, such as ^{60}Co , ^{90}Sr , ^{137}Cs , ^{192}Ir , and others,

makes the prospect of an RDD attack much higher probability, but with greatly diminished effects in comparison to an IND.

Some nations addressing nuclear terrorism are heavily focused on the IND threat, choosing to weight the possible consequences of such an attack over the probability of its occurrence. This choice is reflected in their level of funding, training, and exercises for nuclear counterterrorism, which include NFA. Other nations are completely focused on the RDD danger, playing the probability odds for their preparedness posture.

The adopted nomenclature for these effort areas is somewhat contrived. Despite the fact that both the IND and RDD depend on radioactive substances at their core, the non-fissionable isotopes have been labeled “rad” materials, while SNM is differentiated as “true” nuclear stuff. Thus the clumsy term “rad-nuke” has entered the lexicon to arbitrarily divide radionuclides into categories based on terrorist end use or terror-induced results. (Does ^{239}Pu in an IND metamorphose into rad material if the device fizzles, but the HE disperses the device across the neighborhood? The answer, apparently, is yes.) Consequently, an original all-WMD acronym, “NBC” (for nuclear, biologic, and chemical), has today become “CBRN” or “CBRNE” (explosives) as descriptors for various national technical units, expert panels, government offices, and trade magazines.

62.1.3.2 Pre-det and Post-det

Another line of demarcation separates whether an IND or RDD was successfully exploded (a post-detonation scenario), or whether the device was interdicted or failed to fire (pre-detonation situation). This differentiation reflects very different incident consequences, as well as the ensuing NFA.

For an IND, the post-det world is predominantly an extrapolation of methods and measurements from radiochemical and other diagnostics developed during nuclear weapons testing. Assays are typically made of residual actinide species, major and high-value-minor fission products, and induced activation products. These data allow inferences or conclusions about device composition, design, performance, near environment, and other characteristics. Analyses of a post-det RDD would also have roots in historic radiochemistry, and would be supplemented by conventional forensic analyses. The latter would include high-explosive residues, perpetrator-specific specimens (DNA, hair, latent prints), and other possible evidence (tool marks, fibers, paints, tapes, paper, etc.). The problem of contaminated evidence (conventional criminalistics examinations of radioactively tainted exhibits) is likely most acute for a post-det RDD, as a successful IND should vaporize any such specimens proximate to the device.

The pre-det investigation of either an IND or RDD would seek to detect many of the same radionuclear analytes as for a post-det inquiry. Therefore, materials analysis of IND components would focus on actinide species and their isotopic ratios to estimate threat credibility. Fission products, perhaps at trace levels, could provide clues about radiochemical separation tactics used for reprocessed material. Even activation products, if the nuclear pit contained Pu, might supply information on the time elapsed since a device was assembled.

Much more NFA is possible in a pre-det investigation. Interrogation of nuclear source materials in an IND would additionally investigate, for example, device design, metal

components and their trace-element compositions, densities, alloying species, initiator, possible boost apparatus, and general metallurgy. With inputs of measured forensic data and physical design, performance potential of the weapon may be assessed via detailed computer calculations. Analyses of collateral criminalistics evidence would also be paramount in this situation.

For an RDD in either scenario, collection and analyses of conventional forensic specimens would be most important because attribution of the radioactive source would be less imperative than for an IND. Criminalistics examinations would be the most likely to identify and locate the perpetrators.

62.1.3.3 Source and Route

Pre-det investigations of smuggled nuclear samples at Livermore have been conveniently divided into source and route (or pathway) efforts for optimum information return. Source analyses allow assessments of the identity and quality of the nuclear material, as well as perhaps its origin, production modality, and supply potential. Route analyses are the province of criminalistics examinations and geolocation measurements. They provide insights into the identities of the traffickers, their methods and habits, pathway(s) of the material after legitimate control was lost, frequency of shipment, and potential end-user applications. More detailed discussion of source and route forensic analyses can be found in (Moody et al. 2005).

Some NFA investigators believe that too much focus is placed on the IND post-det scenario at present. Their opinion is that, should such a catastrophe become reality, the counterterrorism enterprise of any organization had failed in a most fundamental way, and perhaps more assets should have been devoted to enhanced surveillance, improved radiation instrumentation, device detection, etc. A similar view is sometimes expressed for source NFA in the pre-det arena. Although very important to know the identity and isotopic composition of a radioactive threat, additional source analyses would perhaps provide nuclear production details, facility identification, and the time since last chemical processing. However, were the material or an assembled weapon stolen, such source information would likely be but nominally productive in attribution efforts. Indeed, only pre- or post-det (RDD) route analyses have the potential to identify terrorist personnel and places of interest, a point sometimes unappreciated by NFA programmatic efforts.

62.2 Chemical Aspects of Nuclear Forensic Science

Radiochemical separations are the backbone of much of nuclear forensic science, since they provide a means by which small forensic signatures may be isolated from an overwhelming radiochemical background due to the sample matrix. This is particularly important for chronometry, where one compares analyte concentrations that can differ by 15 orders of magnitude or more. For the measurement of the relative concentrations of analytes that are isotopes of different chemical elements, the key issue is accurate chemical yielding. When two or more analytes of the same element have vastly different concentrations, standard chemical separations cannot address the issue of dynamic range; in this case, a collection of techniques known as radiochemical milking can be used to determine the minor isotope.

62.2.1 Commonly Used Chemical Methods in the Radiochemical Forensic Laboratory

Chemical methods apply to the separation and purification of radioactive substances in the same way they apply to stable substances. A radiochemical separation is judged in terms of both the yield and the purity of the separated material; this is particularly important when analyte concentrations are low or contaminant levels are high. Purity and fractional recovery are often evaluated with the tracer technique. Radiochemical and mass spectrometric detection methods are quite sensitive, and it is possible to work with trace amounts of analyte. However, radiochemical procedures involving the presence of an isotopic carrier (which can also function as a tracer) are often simpler to design than are carrier-free procedures; losses from adsorption on vessel walls or suspended particles may negatively affect the recovery of the analyte in a tracer-level sample.

In any chemical separation scheme, the original sample becomes divided into at least two fractions through the application of a driving force across a functional boundary in such a way that the resulting fractions have a chemical fingerprint that is distinctly different from that of the initial sample. Typical driving forces are concentration gradients, solvent flow, or electrochemical potential. Typical separation boundaries include immiscible liquid–liquid or liquid–solid interfaces. The effectiveness of the separation of contaminant A from desired material B can be expressed in terms of a decontamination factor D :

$$D = \{[A]_i \times [B]_i\} / \{[A]_f \times [B]_f\}, \quad (62.1)$$

where $[A]_i$ and $[B]_i$ are the concentrations of A and B in the initial sample, and $[A]_f$ and $[B]_f$ are their concentrations in an isolated chemical fraction of A or B. The decontamination factor can be calculated for one or more steps in a chemical process or for the process as a whole.

Separation by precipitation is a procedure that is familiar to most chemists, and is a common method used in the analytical chemistry laboratory. At the tracer level, where the concentration of an analyte nuclide is small, the concentration in solution before precipitation is too low to permit precipitation by exceeding the solubility of even the most insoluble of compounds. It is necessary that a carrier be present that can be removed from solution by precipitation.

There are two types of carrier (Hahn 1936). The first is referred to as an isotopic carrier, and is a compound of the element of which the trace analyte is an isotope. For instance, 12.8-day ^{140}Ba can be carried from solution by adding a soluble barium salt, mixing to give a uniform solution, and precipitating BaSO_4 with the addition of a soluble sulfate. The second is termed a non-isotopic carrier, or co-precipitant. In the elements beyond bismuth, where there are no stable nuclides, co-precipitation is particularly important. Non-isotopic carriers are often used to separate “weightless” radioactive material when it is necessary to retain a high specific activity. An example of co-precipitation: ^{140}La is a 40 h activity that builds up to transient equilibrium in samples containing ^{140}Ba . It is carried on BaSO_4 , which is a non-isotopic carrier for tracer lanthanum. The amount of ^{140}La carried on BaSO_4 can be decreased through the addition of a lanthanum isotopic carrier, which holds the ^{140}La in solution.

With radiochemical forensic samples, isotopic carrying is used mainly for yielding; the presence of excess isotopic carrier can interfere with subsequent mass-spectrometric and radiation-counting measurements. Non-isotopic carrying, however, has many applications to the radiochemical analysis of the actinides. Iron hydroxide is very effective in carrying the

actinides. Lanthanum fluoride is often used to concentrate plutonium, americium, and curium from large solution volumes; it is a poor carrier of uranium. Typically, these precipitates are separated from their associated mother liquids through centrifugation and decantation rather than by filtration, unless a counting source is being prepared.

Solvent extractions are also commonly performed in the radiochemical forensic laboratory. Unlike precipitation, solvent extraction does not require visible amounts of material for success; in fact, if a carrier is present, the analyst must pay attention to the solubility of the analyte in the various phases. Generally, liquid–liquid extraction systems involve intimate contact between immiscible liquid phases, which leads to a partitioning of the analytes between the two phases.

The extent to which a given solute B distributes itself between organic and aqueous phases is usually represented by a partition coefficient, P :

$$P = [B]_{\text{org}}/[B]_{\text{aq}}, \quad (62.2)$$

where $[B]_{\text{org}}$ and $[B]_{\text{aq}}$ are the concentrations of analyte B in the organic and aqueous phases, respectively. For an ideal system, in which the solutes do not alter the properties of the solvents, and where solvent immiscibility is not affected as a result of the extraction, the partition coefficient is independent of the amount of analyte present. With carrier present, there are very few extracting systems that approach the ideal (Grahame and Seaborg 1938; Myers et al. 1950). P tends to decrease with an increase in temperature. The use of volumes of different size also affects P ; this is particularly important in partition chromatography. P is also affected by the addition of an inert diluent to the organic phase.

The solvent extraction method with which the analytical chemist is most familiar involves placing both liquid phases in a separatory funnel and agitating by hand to effect the partition; due to issues of contamination control and limited solution volumes, this implementation is little used in nuclear forensic analysis. Often, phases are mixed in a capped centrifuge cone using a vortex mixer; this is particularly convenient in a gloved box, where the loss of manual dexterity impedes the manipulation of a separatory funnel and stopcock. Phase separation is facilitated through the use of a centrifuge.

Reversed-phase partition chromatography is a special case of solvent extraction: An extractant is attached to an immobile support, and an immiscible mobile phase flows past. Molecular species containing the analyte partition between the two phases. It is usually the organic phase that is attached to the support and the aqueous phase that flows (Hulet 1964; Bark et al. 1967). The standard solvent extraction processes are carried out on the column. The organic phase is distributed on the surface of small, equally sized particles that are placed in a glass tube, called a chromatographic column.

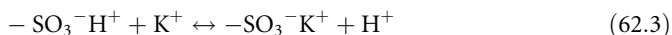
The radioanalytical chemist finds several applications of the use of solvent extractions as mass-reduction steps prior to performing chromatographic procedures, particularly following non-isotopic carrying steps, or for samples whose dissolution included a substrate or container. For example, if iron hydroxide has been used as a co-precipitant, the subsequent removal of the iron can be accomplished by extraction from a hydrochloric acid solution into hexone (methyl isobutyl ketone). Nickel can be removed from a nitric acid solution by extraction into a chloroform solution of dimethylglyoxime.

Extractions involving the chelating agent thenoyltrifluoroacetone (TTA) in an organic solvent are particularly useful in the isolation of uranium, neptunium, and plutonium from nitric acid solutions; some of the radiochemical milking experiments used to determine the

concentrations of small amounts of ^{236}Pu , ^{232}U , ^{233}U , or ^{243}Am in the presence of much larger amounts of other isotopes of the same elements begin with a TTA extraction. Extractions involving organophosphorus compounds leave residual phosphates in the aqueous phase that can interfere with subsequent purification steps; consequently, this class of reagents, used in procedures that are common in the chemical industry, is rarely employed in the nuclear forensic laboratory.

Ion exchange is a powerful technique for the radiochemical isolation of most of the species of interest to the nuclear forensic analyst (Hyde 1956; Katz and Seaborg 1957). Ion-exchange resins usually consist of a cross-linked styrene-divinylbenzene polymer to which ionizable functional groups are attached. These materials are fabricated into small spherical beads over which an aqueous solvent is passed. Optimal separations are obtained when the beads are all approximately the same size, which helps prevent channeling of the solvent through a column packed with the beads. Resin beads are available in most mesh sizes from about 18 mesh down to colloidal size, but most resins of use in the radioanalytical laboratory are between 100 and 200 mesh ($\sim 0.152\text{--}0.075\text{ mm}$).

Resins are classified as either cation-exchangers or anion-exchangers, depending on the nature of the incorporated functional groups, which are derived from strong or weak acids or bases. A typical strong cation-exchange resin contains sulfonic acid groups, which exchange a coordinated hydrogen ion for another cation under the proper conditions. For example:



Similarly, a typical strong anion-exchange resin contains quaternary amine bases, which exchange hydroxyl ions with anions from the solvent, for example,



The capacity of the resin for binding analyte ions is usually expressed in terms of milliequivalents per milliliter of wet resin, and depends on the structure of the polymer and the nature of the functional group. For a standard strong anion-exchange resin, a typical capacity is 1.2 meq/ml; for a strong cation-exchanger, a typical capacity is 2.0 meq/ml.

Because of the limited chemical capacity of most resins, an increase in the size of the sample being processed often requires an increase in the size of the chromatographic column. This limits the size of samples input to chromatographic steps to less than a gram. However, the intrinsically high separation factors and high chemical yields attainable with column chromatography make this technique among the most powerful available to the radioanalyst (Girardi and Pietra 1976).

There are two techniques for separating ions by means of an ion-exchange column, referred to as “elution” and “chromatographic.” In the elution technique, ions are adsorbed from a solution that is passed through the column. Some ions have no affinity for the resin and pass through the column unhindered, while others interact strongly with the resin and are adsorbed in a narrow band at the top of the column. This is often used as a concentration step from large solution volumes. In chromatographic ion exchange, the solution of ionic species is passed through the column and the ions migrate down the column at rates dependent on their affinities for the functional groups on the resin. The most weakly adsorbed ions are the ones that appear first in the effluent. The successful separation of the analytes from one another depends on loading the sample in a small volume. Many cation-exchange procedures operate on the chromatographic principle.

The isolation of a chemical fraction is only the first part of a radiochemical analysis. The relative concentrations of the analytes must be measured, a chemical yield applied, and the absolute concentrations of the analytes in the original sample must then be derived. Chronometric determinations can be based directly on relative concentrations, often with smaller propagated errors. Concentration data arise from mass spectrometry or by radiation counting. Samples submitted for mass spectrometry typically require no special handling beyond the requirements of cleanliness; these samples are submitted in small volumes of dilute nitric acid or as a dry deposit, preferably in a Teflon container. For radiation counting, the geometric extent of the radionuclide sample, and whether liquid or solid, affects the efficiency of the detector and the accuracy with which the concentrations of the radionuclides can be determined.

62.2.2 Tracers in Inorganic Analysis

The basis of the application of radiochemical separations to the measurement of concentrations involves the use of tracers to follow the yield of an element through a chemical process. A tracer may consist of a short-lived radionuclide, measured through radiation counting, or a long-lived or stable separated nuclide that can be measured through mass spectrometry. The tracer nuclide is usually selected so as not to be present among the analytes, or is added in excess to significantly change the relative concentration of that isotope. A tracer is usually added to a nuclear forensic sample by the analyst, but there are cases in which it arises in situ through decay processes. The nuclear forensic analyst's main use of the tracer technique involves the determination of the efficiency of a series of general chemical operations, such as precipitation, filtration, solvent extraction, ion-exchange chromatography, volatilization, etc.

The identity and amount of a radioactive tracer that should be added to a particular sample depend on several factors. The analyst must be careful to add enough tracer activity that it can be accurately measured in the final sample; this includes considerations of decay during chemical separation and purification prior to counting, the efficiency of the radiation counter for detecting the characteristic emissions of the tracer nuclide, and the level of activity of any radioactive sample analytes that might interfere with the observation of the tracer. Similarly, the analyst must not add so much tracer that it overwhelms the signature of the other nuclides of the same element or causes extra purification issues if it spreads into another chemical fraction. In traditional radiochemistry, quantities of radionuclides that are quite undetectable by ordinary means emit easily detectable levels of radiation; in the nuclear forensic laboratory, it is often assumed that a "weightless" amount of a radionuclide is added as a tracer activity.

Use of a radioactive tracer to determine a chemical yield is part of a broad suite of techniques known as "isotope dilution": The analyst wishes to measure the amount of a stable element X in a sample from which a pure chemical fraction of X can be only incompletely separated. A tracer aliquot containing a known mass of X (M_X), labeled with a radioactive isotope of X characterized by radioactivity of a known intensity (C), is added to the sample. A separation is performed to obtain a pure sample of X of mass M_S and a measured radioactive intensity of C' which is less than C due to losses in the separation procedure; M_S is determined by any suitable standard quantitative-analysis method (e.g., gravimetry of a stoichiometric compound of X). The specific activity of the chemical fraction, C'/M_S , is equal to the specific activity of the element X in the mixture after tracing but prior to

separation, $C/(M_X + M_0)$, where M_0 is the mass of element X in the original sample. This yields the isotope dilution formula

$$M_0 = (C/C')M_S - M_X. \quad (62.5)$$

When the tracer aliquot contains only a “weightless” quantity of X, one arrives at the classical tracer equation

$$M_S/M_0 = C'/C; \quad (62.6)$$

The fraction of the initial activity C present in the final sample is equal to the fraction of the initial mass M_0 in that sample.

With the introduction of sensitive mass spectrometric techniques, the tracer concept has been expanded to include the use of long-lived radionuclides and separated stable isotopes. Often, an element may not have an available isotope with properties suitable for radiation counting (e.g., Ne or Al). In experiments in which a mass spectrometric measurement is to be performed on the analytes, incorporation of a more appropriate tracer, rather than a radiometric tracer, may be expedient, since it relieves the analyst of an unnecessary measurement. For example, in forensic radiochemistry, one is frequently required to measure the isotopic content of a mixture of naturally occurring isotopes in a uranium fraction through mass spectrometry; this is a consequence of the long half-lives of the uranium isotopes, which makes the radiation counting of small samples difficult. Since the mass-spectrometric measurement must be made anyway, one often avoids adding tracer aliquots of 69-year ^{232}U or 6.7-day ^{237}U , both of which are easily measured through their radioactivity, and add instead 1.6×10^5 -year ^{233}U or 2.34×10^7 -year ^{236}U tracer. If a known amount of ^{233}U (M_{233}) is added to the original sample, which contained no ^{233}U to begin with, then the amount of ^{238}U (M_{238}) in the original sample can be determined from the isotopic ratio of $^{238}\text{U}/^{233}\text{U}$ in the chemical fraction:

$$M_{238} = M_{233} \times \left(^{238}\text{U}/^{233}\text{U} \right)_{\text{atom}} (238/233), \quad (62.7)$$

where the factor $(238/233) = 1.0215$ converts the $^{238}\text{U}/^{233}\text{U}$ atom ratio determined by mass-spectrometric atom counting to a mass ratio.

Even when the sample contains ^{233}U as an analyte, the use of ^{233}U as a tracer is not precluded. In this case the techniques of isotope dilution are called a “spiked/unspiked” analysis. The sample is subdivided quantitatively into two or more aliquots. One of these aliquots is traced with a known amount of ^{233}U (the spiked fraction), while a second aliquot is untraced (the unspiked fraction); since the results of the analysis of the unspiked fraction enter the determination only through an isotope ratio, the aliquot need not be quantitative. A purified uranium fraction is recovered from each sample, and they are then analyzed by mass spectrometry. The unspiked isotope ratio, $(^{238}\text{U}/^{233}\text{U})_{\text{atom,U}}$, and the spiked isotope ratio $(^{238}\text{U}/^{233}\text{U})_{\text{atom,S}}$, combined with the mass of ^{233}U in the tracer aliquot, M_T , can be used to determine the mass of ^{238}U in the spiked aliquot, M_{238} :

$$M_{238} = M_T(238/233) \left[\left(^{238}\text{U}/^{233}\text{U} \right)_{\text{atom,U}} \times \left(^{238}\text{U}/^{233}\text{U} \right)_{\text{atom,S}} \right] / \left[\left(^{238}\text{U}/^{233}\text{U} \right)_{\text{atom,U}} - \left(^{238}\text{U}/^{233}\text{U} \right)_{\text{atom,S}} \right] \quad (62.8)$$

Isotope ratios measured in the unspiked sample can be used with M_{238} to determine the masses of each of the other uranium isotopes in the sample.

Another example involving the use of a mass tracer: Gallium is commonly alloyed with plutonium in weapons applications; the admixture of a small amount of gallium stabilizes the δ -plutonium metallic phase, which is more workable than is α -phase plutonium. Though there are appropriate radioactive isotopes for classical tracer applications (e.g., 78 h ^{67}Ga or 14 h ^{72}Ga), these nuclides are often not available on a convenient schedule. Natural gallium consists of two stable isotopes, ^{69}Ga (60.1%) and ^{71}Ga (39.9%), so tracing with stable isotopes is possible. Separated stable isotopes have also been used to determine the concentration of iron in plutonium. Since nominally separated isotopes are usually not completely monoisotopic, the mathematics of calculating a chemical yield becomes more complicated; a recursion relationship is often set up, which converges in two-to-three iterations.

When a given nuclide is used to trace the yield of its element in a chemical reaction, the fundamental assumption is that the chemical state of all isotopes of the same element is identical; this is ensured through mixing and performing isotopic-exchange reactions. In tracer chemistry, it is important that there be no isotopic fractionation. If a significant period of time has elapsed between the characterization of the concentration of the tracer nuclide and the measurement of its concentration in the final sample, then an appropriate radioactive decay correction must be applied.

In a simple chemical apparatus, isotopic fractionation occurs by two mechanisms. The first is isotopic disequilibrium, in which the mass difference between the isotopes causes a significant difference between the equilibrium constants or rates of reactions in which the two isotopic species are involved. The magnitude of the isotopic fractionation is greater for traced elements in which there is a large fractional difference between the mass number of the tracer and that of the traced element; this effect is considered negligible for isotopes of all elements with atomic numbers >10 (Duncan and Cook 1968).

The second mechanism by which isotopic fractionation can occur is through hot-atom chemistry. In a radioactive decay process, the daughter nuclide is often formed with an energy in excess of its surroundings, attaining an oxidation state differing from both its precursor atom and from other isotopes of the same element already in solution or in the sample matrix. This can be demonstrated by an example: The main isotope of neptunium present in a heavy element sample is 2.14×10^6 -year ^{237}Np . It is usually present at a concentration that requires chemical purification prior to detection and quantification. Consequently, a yield tracer is required to relate the concentration in the final fraction to that of the original sample. For this purpose, 2.35-day ^{239}Np is used. A common way of tracing with ^{239}Np is to add an aliquot of α -decaying 7,400-year ^{243}Am , in which the ^{239}Np decay daughter is in secular radioactive equilibrium. In this way the analyst can “cheat” the decay process; the concentration of ^{239}Np does not begin decaying with its characteristic half-life until a chemical separation from americium disrupts the equilibrium. During this time, the analyst can ensure that exchange has taken place between the sample atoms and the tracer atoms; however, the separation must be effected immediately after the isotopic exchange because of hot-atom chemistry. The ^{239}Np concentration in equilibrium is constant, but is not stagnant. The ^{239}Np atoms that decay are constantly replaced by ^{239}Np atoms supplied by the ^{243}Am decay process, which may not be in the same oxidation state or chemical form as the other neptunium atoms. This can result in the chemical yields of ^{239}Np and ^{237}Np in a purified neptunium fraction being unequal. For truly precise tracing of neptunium, the ^{239}Np tracer should be chemically purified from ^{243}Am prior to addition to the experimental sample and isotopic exchange.

The chemical behavior of trace elements can be unpredictable (Lavrukhina et al. 1967); to avoid these effects, “carriers” are added to the sample. Under the proper conditions, an added carrier can serve the function of a tracer. If several milligrams of an element are placed in solution with a radionuclide that is one of its isotopes, and a stoichiometric compound exists such that the element concentration can be determined by weight, the gravimetric yield of the carrier can be applied to the radionuclide (Ruzicki 1968). This was a popular technique in the determination of the yields of the rare-earth fission products; aliquots containing known amounts of the rare earths were added to dissolved reactor targets, after which the individual rare earths were isolated, precipitated as oxalates, and fired to stoichiometric oxides. The chemical yields determined from the weights of the samples were applied to the radionuclide concentrations determined from radiation counting to give the final fission-product yields.

62.2.3 Radiochemical Milking

The dynamic range in the measurement of nuclide concentrations required by chronometry makes it impossible to perform accurate age assessments without radiochemical separations. However, when the nuclide to be determined is present as a minor component in an overwhelming concentration of isotopes of the same element, chemical separations are of limited use. In these instances, the method of radiochemical milking has proven to be valuable.

In a milking experiment, a purified sample is prepared of the element that includes the trace nuclide to be measured. The time at which the sample was purified must be well characterized. The sample is set aside for a predetermined length of time to allow radioactive decay to partially replenish the daughter activities. At an accurately determined time, the daughter activities are isolated from the parent activities and are purified; the decay interval and the half-lives of the nuclides relate the isotope ratios among the daughter activities to the isotope ratios among the parent activities. If one or more concentrations of the parent isotopes are known, and the daughter of the nuclide to be quantified can be observed and measured, the concentration of the “invisible” isotope of the parent element can be determined.

This is best illustrated by an example: The ^{236}Pu content of a plutonium sample cannot be directly measured by any means at the analyst’s disposal. Even though ^{236}Pu has a relatively short half-life (2.858 years), its characteristic decay γ -rays are weak; its emitted α particles are of higher energy than are the α particles emitted by the other plutonium isotopes, but its decay rate is so low compared to the decay rates of the other isotopes that it is not possible to fabricate a source from which one can observe the ^{236}Pu peak in the α spectrum over random pileup events.

Several tenths of a gram of weapons-grade plutonium is required for the measurement. The sample is dissolved in nitric acid containing a drop of hydrofluoric acid and is evaporated to a moist deposit, after which it is dissolved in warm 0.5 M HNO_3 (containing nitrite ion); plutonium is extracted into 0.02 M TTA in benzene, leaving the uranium and americium decay daughters behind in the aqueous phase. The organic phase is scrubbed several times with 0.5 M HNO_3 , discarding the aqueous phase each time; the time of the last solvent-extraction phase separation is recorded as the uranium-plutonium separation time. The plutonium sample, still in the organic solvent, is capped and set aside. After a month, the sample is agitated with 0.5 M HNO_3 , and the aqueous phase is retained as the uranium fraction; this sample contains the uranium atoms that grew into the plutonium sample as a consequence of radioactive decay during the storage period. The uranium fraction is further purified from residual plutonium and is then volatilized onto a platinum counting plate.

Two uranium activities are observed in the α -particle pulse-height spectrum taken of the uranium sample, ^{234}U (from the decay of ^{238}Pu) and ^{232}U (from the decay of ^{236}Pu). The ratio of the α -decay rates of $^{236}\text{Pu}/^{238}\text{Pu}$ in the original sample are related to the ratio of the daughter concentrations through their half-lives and the in-growth time; the milking technique takes advantage of the shorter half-lives of ^{236}Pu and ^{232}U relative to ^{238}Pu and ^{234}U , respectively, to produce an activity ratio that is more amenable to measurement.

Other examples of measurements made possible by radiochemical milking include the following:

1. Plutonium recovered via the PUREX process often contains a trace quantity of 7,400-year ^{243}Am , a reactor flux indicator that is an artifact of incomplete fuel reprocessing. The decay signature of ^{243}Am is quickly overwhelmed and obscured by the in-growth of 430-year ^{241}Am from the decay of 14-year ^{241}Pu . In a purified americium sample, the 2.4-day ^{239}Np daughter of the α decay of ^{243}Am quickly approaches radioactive equilibrium with the mother activity while the 2.1×10^6 -year ^{237}Np daughter of ^{241}Am α decay grows into the sample slowly, and linearly, with time. A neptunium sample, separated from purified americium at a well-defined time, can be used to determine the $^{243}\text{Am}/^{241}\text{Am}$ concentration at the time that the americium was isolated from plutonium.
2. The amount of 1.6×10^5 -year ^{233}U in a sample of enriched uranium can be a key signature of the enrichment process that produced the material. Unfortunately, ^{233}U has virtually the same α -decay energy as does 2.4×10^5 -year ^{234}U , and is usually present at such a low concentration as to preclude a sufficiently accurate mass spectrometric determination. The value of $^{233}\text{U}/^{234}\text{U}$ in enriched uranium can be determined using a double-milking technique, in which a large purified uranium sample is allowed to decay for several months, after which thorium is isolated and purified. The relative amounts of the thorium isotopes in this sample are not favorable for measurement; however, after a month, radium is isolated from the thorium sample and the relative activities of ^{224}Ra , ^{225}Ra , and ^{226}Ra can be related to the relative concentrations of ^{232}U , ^{233}U , and ^{234}U , respectively, in the original sample. The limiting accuracy of the technique depends on the ability of the analyst to establish the separation time of radium from the thorium sample; from milked fractions, the present authors have made ^{233}U concentration measurements with uncertainties of less than 10%.

Radiochemical milking procedures are very labor-intensive and require large amounts of sample and in-growth periods of long duration. This causes a considerable delay in the return of analytical data. The fundamental accuracy of the technique depends on how well separation times and in-growth periods can be established. When sequential milkings are performed, the activities in the second milk step are no more than, and usually significantly less than, those in the first milk step; this can result in counting fractions that emit radiation with so little intensity that an accurate measurement is problematic.

62.2.4 Reagent Blanks

Chemicals of normal reagent-grade purity suffice for the separation of analytes that do not occur in nature; there should be no important impact on the analyses of samples of neptunium, plutonium, americium, or curium, provided reagent volumes are kept small so that mass is not introduced into the final samples. For all other analytes, reagents that

have been double-distilled in Teflon should be used, even in the early stages of the chemistry, and contact with glass should be minimized; reagent-grade chemicals and glass both contain significant levels of uranium and thorium. Small quantities of commercial-grade chemicals of sufficient volatility can usually be vacuum-distilled in the radioanalytical laboratory.

The reagent blank can negatively impact a chronometric analysis. For example, ^{242}Pu has a small concentration in most plutonium samples, and is also usually the plutonium analyte with the longest half-life (3.8×10^5 years). The daughter of its radioactive decay is 4.5×10^9 -year ^{238}U , which is the major isotope of uranium in the reagent blank. As a result of the combination of these factors, a reasonable age cannot be reliably determined from the $^{242}\text{Pu}/^{238}\text{U}$ chronometric pair; the derived age is always significantly longer than that calculated from the other plutonium chronometers. If reagents of sufficient purity are used, one can interpret the excess ^{238}U as an indicator of the industrial process that resulted in the plutonium sample. The uranium content of reagent-grade chemicals can obliterate this signature.

In the analysis of actinide metal samples, the interpretation of the trace constituents are also affected by the reagents. Reduction to metal is usually performed by reaction of the actinide salt with alkaline-earth metals; the solvated ions of these materials are significant components of the reagent blank, as are the impurities that are common in the alkaline earths.

62.3 Radionuclide Chronometry

Using a variety of techniques, the radiochemical analyst measures the concentrations of various radioactive and stable nuclides in a nuclear forensic sample. The resultant table of concentrations is the radioanalytical “fingerprint” of the sample. However, unlike an actual fingerprint, which is interpreted by comparison with a database, the fingerprint of a sample of special nuclear material is forged by the methods used in its creation, and information about the origin of the material can be obtained from scientific principles by the informed analyst.

From experience, the present authors have found that examination of a table of concentrations that are the primary result of a nuclear forensic measurement campaign is seldom illuminating. The uranium and plutonium data are best examined as isotope ratios. Nuclides that grow into any radioactive sample are best presented as a “time since purification,” the chronometric age of the material. Generally, any mixture of heavy-element isotopes will incorporate several chronometers, and deviations among the resulting ages can be attributed to incomplete chemical processing, or to an intentional attempt to fool the analyst (spoofing). Examination of a table of ages calculated from the concentration data is the most convenient way of interpreting information on the relative concentrations of nuclides related by radioactive decay.

62.3.1 Chronometry Versus Age-Dating

The rate of decay of a pure sample of a large quantity of radionuclide is proportional to the number of atoms in the sample, with the constant of proportionality being the characteristic decay constant, λ :

$$-dN/dt = \lambda N \quad (62.9)$$

This leads to the law of simple radioactive decay,

$$N = N_0 \exp(-\lambda t) \quad (62.10)$$

and consequently to the Bateman equations that describe in-growth, sequential decays, and more complicated decay schemes (see [Chap. 7 in Vol. 1](#)). Here, N_0 is the original number of atoms in the sample at a reference time defined as $t = 0$, and N is the number of atoms that remain after a time t . If this equation is solved for the time-interval required for one half of the atoms to decay ($N = N_0/2$), one obtains the half-life ($t_{1/2}$) associated with the radionuclide, which depends only on the decay constant:

$$t_{1/2} = \ln 2 / \lambda \quad (62.11)$$

This leads to the concept of a radionuclide sample acting as a clock, and radiometric chronometry.

Chronometry is related to radioactive dating (see [Chap. 17 in Vol. 2](#)), but is not exactly the same thing. In age-dating, the analyst measures the concentration of a radioactive nuclide relative to the concentration of a reference isotope of the same element, usually very long-lived or stable. If the isotope ratio at a given time is known, the measurement of the change of that isotope ratio at a later time, taking into account the half-lives of the nuclides involved, determines the age. The limitation of the technique is that it cannot be used to measure ages that are much smaller than the half-life of the shorter-lived nuclide; for small values of the age, uncertainties in the measurement of the isotope ratio are larger than the change in the ratio due to decay. An example: The half-life of ^{14}C is 5,730 years, making it convenient for the determination of the age of samples that span the range of human civilization. The ratio of the concentrations of ^{14}C and stable ^{13}C changes by a factor of 2 every 5,730 years; if the analyst knows the zero-time isotope ratio, $^{14}\text{C}/^{13}\text{C}$ at measurement time determines the age of the sample on the time scale of millennia. If, however, the analyst is working with a sample that is only a year old, the change in the $^{14}\text{C}/^{13}\text{C}$ value is only 0.013%; consequently, the accuracy of the measurement must be better than that or the data cannot be interpreted as an age other than as a limit. (This particular example is somewhat complicated in actual practice due to the bomb pulse of ^{14}C injected into the biosphere by atmospheric nuclear testing.)

In chronometry, the age of the sample is defined not in terms of the decay of a parent nuclide, but rather as the in-growth of a daughter activity. Radionuclides that are linked to one another by the processes of radioactive decay have relative concentrations that can be calculated with the Bateman equations, which express the simple laws of radioactive decay and in-growth. If there exists a time at which all the descendant radionuclides have been removed from the mother material, that time can be determined through the measurement of the relative concentrations of the mother and daughter nuclides at a later time. The time interval between the purification of the sample and the subsequent analysis of the sample is defined as the “age” of the material at the analysis time. The technique does not apply when the half-life of the daughter nuclide involved in the determination is significantly shorter than the elapsed time.

This technique offers two distinct advantages when working with long-lived nuclides: (1) the initial concentration ratio of the parent nuclide relative to a reference isotope need not be known; and (2) the in-growth of the daughter activity is roughly linear with age.

The major drawback is that an accurate age determination requires that at some reference time the daughter of the radioactive decay of the parent was completely removed from the material by a chemical procedure. The α decay of 24,100-year ^{239}Pu results in the in-growth of 7.04×10^8 -year ^{235}U . In a chemically purified sample of ^{239}Pu , the change in the ^{239}Pu

concentration in a year is 0.003%; in an age-dating experiment, this would be hard to observe. If the ^{235}U is quantitatively isolated from a 1 g ^{239}Pu sample after a year, the fraction will contain 28 μg of ^{235}U , easily quantifiable by either radiation counting or mass spectrometry. If the in-growth period is twice as long, twice as much ^{235}U can be isolated.

A sample consisting of mixed uranium or plutonium isotopes provides the means of measuring the age of the sample through as many as a dozen different chronometers. If the sample was completely purified at the reference time, all of the chronometers should yield the same age. The present authors usually find that in a plutonium sample all the $^{232}\text{U}/^{236}\text{Pu}$, $^{234}\text{U}/^{238}\text{Pu}$, $^{235}\text{U}/^{239}\text{Pu}$, and $^{236}\text{U}/^{240}\text{Pu}$ chronometers yield the same age (as they should, since the removal of each uranium isotope from a plutonium sample should be equally effective). When these ages agree with those determined from $^{241}\text{Am}/^{241}\text{Pu}$ and $^{230}\text{Th}/^{238}\text{Pu}$, which are chronometric pairs that can be measured with great precision and are based on the chemical properties of elements different than those of uranium, it is inferred that the sample was completely purified at the time of separation. However, for the US weapons-grade plutonium, the authors often find that $^{241}\text{Am}/^{241}\text{Pu}$ gives a significantly larger value for the age than do the uranium isotopes. The only reasonable explanation for this is that the procedure for removing the uranium isotopes from the plutonium sample was less effective in removing americium from the material. This means that at any later time, there will be more ^{241}Am in the plutonium sample than can be explained by in-growth, making it appear as if the decay process had been proceeding for a longer time, resulting in a value for the age that is too large.

In general, the decay properties of the radionuclides are known with greater accuracy than are the concentrations that the analyst is likely to measure. The uncertainties associated with the chronometric atom concentration ratios represent almost the entire uncertainty budget associated with the age determination. However, these error bars do not translate directly to identical error bars on the derived sample ages; that is, a 5% error bar on the value of a concentration ratio does not necessarily translate into a 5% error bar on the age, instead being dependent on the functional form relating the age and the ratio.

The chronometry of plutonium samples is not limited to nuclides related by α and β decay. The mass-240 plutonium isotope decays almost completely by α emission; however, one in every 1.7×10^7 decays is by spontaneous fission. In spontaneous fission, the parent atom subdivides into two similar, but not identical, daughter atoms, with the yield being distributed over products covering a wide range of atomic numbers and masses (Laidler and Brown 1962). The intrinsic radioactivity of plutonium is high enough that 1 g of weapons-grade plutonium containing 6% ^{240}Pu by mass undergoes approximately 1,500 spontaneous-fission decays every minute. Krypton and xenon are gaseous elements that are chemically inert. The chemical properties of the fission-product Kr and Xe nuclides provide an opportunity to determine a sample age more associated with metallurgy than with chemical reprocessing: Plutonium is converted to the metal from a salt at some time after the last chemical purification step. Most of the fission products and the daughters of α and β decays are chemically reactive species; even fairly volatile elements will be retained to some extent in the melt; however, the inert gases will be completely flushed out of the melt by the by-product process gases. The subsequent in-growth of Kr and Xe by spontaneous fission defines the casting time of a metal sample. Since the isotopic distributions of fission-product Kr and Xe are different than those of the naturally occurring gases, a small admixture of the natural isotopes can be deconvoluted. However, the measurement becomes impossible in the presence of a significant amount of air, which must be rigorously excluded in the early stages of the analytical procedure; 1 cm^3 of air at standard temperature and pressure contains 3×10^{13} atoms of Kr and 2×10^{12} atoms of Xe. This can

introduce a background that would interfere with the observation of the radiogenic species through mass spectrometry.

The ratio of the concentrations of nuclides that are related by radioactive decay is interpreted as an age through the application of the rate laws, which are formulated in terms of characteristic decay constants, which are related to half-lives as discussed above. Radioactive decay is a statistical process, and in the limit of a small number of decays of atoms, the rate laws break down and the statistics of small numbers dominates (Schmidt et al. 1984). (See [▶ Fig. 9.10 in Chap. 9, Vol. 1.](#)) Measurement of the product of a small number of decays and interpretation of that measurement as an age is the fundamental limitation of the technique at short times.

62.3.2 Granddaughters and the Detection of Spoofing

The radiochemical analyst should always measure multiple chronometric concentration ratios to guard against intentional misdirection (“spoofing”). An individual signature can be introduced into the sample during its fabrication; this can mislead the analyst if that is the only measurement performed. For instance, someone might implement the idea of adding americium to their plutonium stream with the intent of making the material look older than it really is. Material whose apparent age could be demonstrated to predate a known reprocessing era would have to be attributed to another source. Adding ^{241}Am to a plutonium sample would deceive nondestructive γ -spectrometry measurements in common use by the safeguards community, but it would not deceive a full forensic analysis of multiple chronometers.

To fool the forensic analyst, the fabricator would have to successfully predict the suite of chronometric signatures that would be quantified. In the absence of this information, it would be necessary to modify them all. To adjust the age of the uranium chronometers in a sample of plutonium of US weapons-grade composition, a peculiar mixture of uranium isotopes containing $\sim 2\%$ ^{234}U , 79% ^{235}U , and 19% ^{238}U (all in atomic percent) would have to be added, in an amount necessary to match the ^{241}Am chronometer. If a significant amount of this material is added, the fabricator must concern himself or herself with the distribution of the contaminant throughout the matrix of the plutonium. Uranium isotopes arising through decay processes should be distributed uniformly with the parent plutonium isotopes. Uranium added to the process solutions before precipitation and calcination might end up inhomogeneously mixed in the final product. Furthermore, if added through insertion into the metallurgical process, the uranium contaminant is more likely to concentrate in the slag than in the billet. Adding uranium to the host metal in the form of a melt is of limited use since uranium is not very soluble in molten plutonium.

Imagine that the fabricator has solved the technical problem of distributing americium and the uranium isotopes through the plutonium matrix, uniformly and in the proper proportions, so as to make it look older. He must still consider the second- and third-order chronometers (involving granddaughter and great-granddaughter decay products, respectively). If he wants to make the ^{238}Pu in a freshly separated plutonium sample appear to be 8 years old, the $^{234}\text{U}/^{238}\text{Pu}$ value must be adjusted to 0.0653. The $^{230}\text{Th}/^{238}\text{Pu}$ value must be adjusted simultaneously to 7.54×10^{-7} . To make a sample of ^{238}Pu appear to be 8 years older, it is necessary to add ^{234}U that is 4.07 years old in order to match the concentrations comprising the ^{230}Th chronometer; however, even if this is done, the resultant $^{226}\text{Ra}/^{238}\text{Pu}$ signature will still be off by 24%.

The difficulty of uniformly dispersing the required amounts of properly aged contaminants to achieve a consistent false age makes it essentially impossible to fool a full forensic analysis. When samples are large (or old) enough, the determination of second- and third-order chronometers makes spoofing prohibitively difficult.

62.3.3 Detection of Incomplete Fuel Reprocessing

The incomplete removal of a daughter nuclide from a sample containing its parent activity will result in the value of the age determined from that chronometric pair being too large. This can be thought of as being analogous to traveling to a different time zone without resetting one's watch. The unremoved daughter will be in excess of what has grown into the sample, making it appear as if in-growth had occurred for a longer time, until the sample becomes so old that the daughter activity approaches secular equilibrium with the parent. This means that, in addition to the detection of spoofing, a chronometric analysis based on several pairs of genetically related nuclides can be a sensitive way of obtaining details about the chemical processes used to produce the analytical sample.

The authors' experience has been that US weapons-grade plutonium, which is produced via the PUREX process, always contains a small excess of americium and a larger excess of neptunium relative to the uranium chronometers that result in a consistent, smaller age. One might speculate that the americium was in fact completely removed, but at an earlier time than was the uranium, giving it extra time to grow into the sample; however, trace amounts of ^{243}Am have been observed in plutonium samples, which does not arise in the radioactive decay of mixed long-lived plutonium isotopes. The ^{243}Am can only be present if it is residual from the original spent reactor fuel, where it was produced in neutron reactions on ^{242}Pu ; therefore, americium was never completely removed from plutonium in the PUREX process. However, PUREX is much more effective at removing fission products; the authors have performed several consistent chronometric determinations from the measurements of $^{125}\text{Sb}/^{240}\text{Pu}$ and $^{137}\text{Cs}/^{240}\text{Pu}$.

62.4 Analytical Methods

62.4.1 Application of Radiochemical Procedures

Radioanalytical chemistry is a destructive technique. It is always advisable to save some portion of the sample if there is enough material to do so. Before radiochemical analysis, classical forensic measurements (e.g., fingerprinting and isolation of hair and pollen) should be performed, and particles for morphological measurements should be segregated from the bulk. It must be remembered that the sample is not necessarily uniform, and significant fractionation of the bulk material should be avoided. The radiochemical sample itself can be subjected to nondestructive assay by γ -ray spectrometry and neutron counting, and in the past the authors have heated this sample prior to dissolution to obtain a specimen for organic gas chromatography. The results of measurements made on the sample prior to dissolution can be related to the subsequent radiochemical analysis by quantitative dissolution of an accurately weighed solid sample, followed by dilution to a precisely measured solution volume or weight.

A radiochemical analysis begins with the creation of an analytical mother solution from the sample. The quantitative dissolution of a solid sample to create a stable solution can be the most difficult part of the radiochemical analysis. Since the results of individual radiochemical procedures are related back to this “pot” solution based on a “per-volume” or “per-gram-solution” basis, it is critical that the product of the dissolution procedure is as close to a true solution as possible; if there is a possibility of colloidal material, the solution should be agitated during aliquoting, if possible. Samples of plutonium and uranium metal dissolve readily in hydrochloric acid, but even with heating, often leave a residue. If chronometry beyond that involving the heavy elements is to be performed, collection of the noble gases and volatile fission products should be accomplished during the dissolution of plutonium metal samples. The addition of nitric acid to uranium residuals, followed by digestion, can result in a solution since most uranium salts dissolve readily in nitric acid. Plutonium oxide will not necessarily dissolve completely in nitric acid, particularly if it has been high-fired. Any sample containing a significant amount of plutonium must be treated with hydrofluoric acid, no matter what the initial chemical form; invisibly small colloidal plutonium oxide particles are stable against reactions with most mineral acids, and their presence interferes with the chemistry. For most actinide samples, the preferred pot solution matrix is hydrochloric acid with a concentration between 2 and 6 M. If the matrix of the analytical sample is other than a metal or a mixture of the salts of the heavy elements, the ingenuity of the analyst may be taxed in preparing the analytical pot. The primary rule in the preparation of the pot is to avoid more than trace quantities of fluoride or phosphate in the stock solution, as these can interfere with the subsequent chemical purification steps.

Chemical yields are determined from tracer activities added to the analytical aliquots; however, the yields can also be determined from short-lived activities that are present in the sample due to secular radioactive equilibrium. For example, the chemical yield of uranium can be determined from the recovery of an added ^{232}U tracer activity, but in plutonium samples it can also be determined from ^{237}U : There is a 0.00245% branch for the decay of ^{241}Pu by α -particle emission. If it is known that the plutonium sample was last purified more than a month ago, one can assume that 6.75-day ^{237}U in the analytical samples is in equilibrium with ^{241}Pu , with a concentration defined by the branching ratio of activity(^{237}U)/activity(^{241}Pu) = 2.45×10^{-5} . Similarly, radium is traced with 3.66-day ^{224}Ra , in secular equilibrium with the decay of 1.9-year ^{228}Th . Use of intrinsic short-lived radionuclides as tracers requires that the time at which they were isolated from their parent activities is known precisely.

62.4.2 Preparation of Counting Sources

Samples for α counting must be sufficiently thin so that range straggling does not impact the widths of the peaks in the α spectrum. This is accomplished by the purification of α -emitting chemical fractions to minimize mass. In the case of long-lived α emitters like the isotopes of uranium and thorium, care must be taken to balance the decay rate of the analyte against its mass. Distribution of an α -emitting sample over a larger area helps alleviate this problem, until the dimensions of the source became comparable to the area subtended by the counter, at which point the counting geometry reduces counting efficiency. Samples for absolute α -particle intensity measurements must be mounted on the same substrate as is the calibration standard (usually platinum), so that the “back-bounce” of α particles emitted into the sample substrate and scattered backward into the detector volume is the same.

Samples for α counting are prepared by stippling, by vacuum volatilization, or by electrodeposition. In stippling, the substrate is warmed and small drops of a solution containing the analyte are delivered from a transfer pipet, making sure that the activity is distributed over the substrate in a quasi-uniform fashion. Stippling can be quantitative, with 100% of the analyte transferred from the solution to the substrate, but the preparations are of inferior quality for spectrometric measurements. In vacuum volatilization, the analyte solution is dried on a tungsten filament and mounted in vacuum between two electrodes. The filament is then heated white-hot through the sudden application of an electric current, resulting in the analyte being volatilized from the filament and onto a substrate mounted above it. The technique is not quantitative, with losses (often more than 50%) caused by some of the volatilized analyte not encountering the substrate foil; however, it results in uniform, thin deposits that are very appropriate for α spectrometry. In electrodeposition (Aumann and Muellen 1975; Muellen and Aumann 1976), the analyte is dissolved in a plating solution that is placed in a cell whose bottom surface incorporates the conductive sample substrate; an electrode is suspended in the solution, a current is passed through the cell, and the analyte is electrodeposited onto the substrate. Electrodeposition (also called “electroplating” or “molecular plating”) can be nearly quantitative and results in a thin, uniform counting source appropriate for spectrometry, but the technique is labor-intensive and time-consuming. In all three cases, activity can be fixed to the substrate and extraneous mass removed by passing the final sample through a Bunsen burner flame (except in cases of elements, e.g., polonium, that are volatile at low temperatures).

There have been advances in α -source preparation using functionalized surfaces (Gonzalez and Peterson 2009) and co-precipitation on special filters (Sill and Williams 1981). These methods show promise, but information is still needed on the longevity of archived samples and the availability of appropriate efficiency standards.

Gamma- and X-ray-emitting samples can be prepared in a variety of ways, including those listed above for α counting. The penetrating nature of the radiation allows the analyst to prepare γ sources in a variety of different media and geometrical configurations. One of the standard geometries is 10 ml of solution in a cylindrical plastic vial with a lateral cross section of 10 cm². If a γ -ray source must be counted close to a detector, its physical dimensions relative to those of the detector should be small or benchmarked against a radionuclide standard of the same physical extent. Low-energy photons are attenuated by matter more severely than are high-energy photons, with high-atomic-number materials being more effective attenuators than low-atomic-number materials; the attenuation coefficients for photons below 100 keV are not perfectly known for the heavy elements. Thus, the analyst should not try to quantify low-energy photon emission through a lead sample container, but a plastic container or a volume of dilute aqueous solution is effective for this application. Solutions of radionuclides that are counted for γ rays must be stable; any precipitation taking place during the count changes the source geometry and adversely impacts the accuracy with which the concentration of radionuclides can be determined.

62.4.3 Radiation Counting Systems

A modern nuclear forensic analysis relies heavily on instrumentation. A well-equipped laboratory will have the means for making a variety of inorganic, isotopic, and organic analyses, in addition to having the support of a counting facility for radiation measurements.

62.4.3.1 Nuclear Counting

In addition to survey instrumentation, the radiochemical forensic lab requires basic radiation-counting support in order to monitor the progress of certain chemical separations. For example, the performance of a methanolic nitric acid separation of Am and Cm on an anion-exchange column is not always reproducible. In operation, the column eluent is collected as a sequence of small samples in a number of glass centrifuge cones. Americium, which emits γ radiation in its decay, follows curium off the column, and is located in the eluent stream with the aid of a laboratory radiation counter.

The authors have found that most general radiochemical separations can be successfully monitored with only three counters: (1) a flow-through argon-gas (or P10-gas: Ar with 10% CH₄) proportional counter for detecting α particles; (2) a flow-through methane-gas proportional counter for detecting β particles; and (3) a NaI(Tl) well counter for detecting γ rays. The first two counters output to scalars; the third counter yields γ -ray spectra that may utilize a multichannel analyzer with a display that permits peak identification and integration.

Quantitative nuclear counting measurements take place in a dedicated nuclear counting facility, close enough to the forensic laboratory for convenience, yet sufficiently isolated so that the radiation field and loose contamination associated with radiochemical operations do not affect the background levels. For the optimum detection of marginal signatures, a counting lab is often located underground to attenuate the cosmic-ray background. Air-conditioning is required; cryogenic- and counting-gas effluents must be removed; and the reliable operation of gas-filled counters requires a stable temperature. The counting facility must have separate electrical circuits, isolating the counting equipment from non-counting apparatus (e.g., vacuum pumps and the transient use of power tools). Since electrical noise impacts detector performance, the circuit for the counters should be filtered, should have sufficient battery backup power to survive power transients, and an auxiliary electric generator for longer outages. If the power to the detectors is interrupted, it should only be restored in an approved fashion; this is usually implemented with a cutoff circuit.

The counting laboratory requires plumbing for the supply of counting gases (principally Ar, P10, and methane); they are supplied at the pressures required by the counters (slightly above atmospheric pressure for flow-through proportional counters and ~ 1.5 bar for gridded ion chambers), with flows that are controlled by needle valves on the counters themselves. Counting gases should be delivered through metal tubes with in-line ceramic electrical insulators; plastic tubes eventually fail and should be avoided. Gases supplied in pressurized cylinders often contain a measurable quantity of 3.8-day ^{222}Rn , which can interfere with the low-level detection of ^{238}Pu and ^{241}Am α particles, as they are emitted with a similar energy. A supply of counting gases should be maintained, and no cylinder should be used until it has been stored for at least 2 weeks to allow ^{222}Rn decay.

Vacuum is also required in the counting laboratory, and these lines should be supplied with cold traps to prevent pump oil from back-streaming and depositing on sensitive counting apparatus (e.g., surface-barrier detectors).

Generally, α -particle counters do not require shielding for nuclear forensic applications; residual contamination in a low-level chemical fraction and nuclides that recoiled into the detector from previous counting sources are always more important contributions to the detector background than the natural radiation environment. Shielding from cosmic rays and environmental radiation (i.e., photons from ^{40}K and the natural U and Th decay chains) is required in the operation of γ - and X-ray counters. A thickness of 20 cm of Pb is sufficient for

this purpose, particularly if the counting lab is underground. However, cosmic-ray interactions with intervening structural materials and the shielding itself produce *bremsstrahlung* and neutrons that can adversely impact the detector background. The fluorescence of lead produces X-rays, and it is normal practice to line the interior of a Pb shield with layers of Cd, Cu, and Al, in that order. An air gap around the detector (~ 30 cm in any direction) can provide a decrease in the intensity of photons and electrons that have been down-scattered into the 150–200 keV range (Watt and Ramsden 1964).

Shielding should be constructed from low-background materials. Modern steels are often recycled and can contain 5.3-year ^{60}Co , introduced either by fallout from atmospheric nuclear weapons testing in the 1950s and 1960s, or by the improper disposal of γ irradiators (Lubenau and Yusko 1995; 1998). Natural sources of Pb contain 22-year ^{210}Pb , a member of the ^{238}U decay series; even though chemical recovery of Pb removes the U that is always present in the ore, it does not eliminate ^{210}Pb . The decay of ^{210}Pb results in the in-growth of 5-day ^{210}Bi (which emits 1.1 MeV β particles and, consequently, *bremsstrahlung*) and 138-day ^{210}Po (which emits α particles) until transient equilibrium is established. Batches of Pb from different sources are contaminated with ^{210}Pb to varying degrees (Alessandretto et al. 1993). Older materials are preferred in fabricating shielding for low-background counting applications, as the radionuclide content of these materials has been reduced by decay. Steel from World War I battleships and Pb ballast from eighteenth-century Spanish vessels are in high demand for low-background counting enclosures.

Quite often, the number of samples generated in a nuclear forensic analysis outnumbers the available radiation counters, requiring temporary storage. Counting samples should be stored in a shielded container near the laboratory door, both to prevent transfer of loose contamination and to avoid increasing the backgrounds of operating counters. Automated sample changers improve the throughput of a radiation counter. When a given analysis is completed, the sample is removed from the counter and replaced with another sample without requiring off-shift staff. Sample changers for α and β counters consist of a rotary turret; the detector itself is mounted behind a collimating shield so that the radiations emitted by nearby samples do not admix with those emitted by the current sample. Sample changers for γ counters usually consist of a turret or a belt coupled to an elevator; following the completion of an analysis, the sample is lowered into its position on the turret, the next sample is rotated into position, and is subsequently raised to proximity with the detector. In this way, intervening shielding material and distance effectively eliminate the radioactive emissions of other samples from the detector background. The efficiency of any radiation counter is dependent upon the position of the source relative to the detector volume during an analysis. For counters where efficiency is an issue, the turret or turret/elevator must deliver a sample to a well-defined location. Close-in counting can result in pileup and summing effects, which should be avoided whenever possible.

62.4.3.2 Particle Detection

Beta-Particle Counters

While useful for characterizing the performance of chemical separations in the laboratory, β counting is rarely employed as a quantitative technique. Most β -emitting analytes also emit γ rays, which are characteristic of the decaying nuclides; however, there are activities (including long-lived fission products such as ^{99}Tc and ^{147}Pm , and other potential analytes such as ^{14}C and ^3H) that β decay without accompanying photon emission. A set of attenuating Al foils of

various thicknesses can facilitate the identification of β -emitting nuclides in samples assayed with a gas-filled proportional counter. Access to a single β counter with an eight-position sample turret is recommended.

Alpha-Particle Counters

Alpha counting is used extensively in the nuclear forensic analysis of U, Pu, and other actinides. Windowless gas-proportional detectors are insensitive to decay energy and generate a scalar value defined by the absolute α -decay rate of a sample and the length of the count. Since the counter efficiency is often $\sim 50\%$, these are called 2π counters. Spectral data taken with Si surface-barrier detectors or gridded ionization (Frisch-grid) chambers can be used to divide the total decay rate obtained from 2π counting into contributions from the individual nuclides. Frisch-grid detectors, where the sample is inserted directly into the counting gas, have high efficiencies and are therefore useful for counting low-activity sources. However, conversion-electron summing can adversely affect the spectral peak shape when counting Am or Np isotopes. Solid-state detectors suffer less from electron-summing effects, and high-activity sources can be counted if the turret is designed so that samples can be backed away from the detector. Counting labs should maintain at least two 2π counters with four- or six-position turrets, four Si surface-barrier detectors with six-position turrets, and four Frisch-grid counters with six-position turrets.

Gamma-Ray Counters

Though a wide variety of high-purity Ge (HPGe) counters are commercially available, nuclear forensic measurements can be performed with two different detector types: a coaxial detector with an Al window and a nominal efficiency relative to standard NaI(Tl) of 30–40%, and a LEPS planar detector with a Be window. Downward-looking detector-dewar geometry is compatible with the implementation of an elevator/turret sample changer. Well-type detectors can be valuable to check the performance of chemistry procedures, but the attendant summing effects makes them of little use for quantitative γ -ray spectrometry. Many HPGe detectors are available with an incorporated annular, low-resolution photon detector to suppress Compton events. Events that take place in the Compton annulus coincident in time with an event in the HPGe detector are used as a criterion for excluding it from the spectrum. In this way, the continuum under low-energy photopeaks is reduced, which increases the precision with which low-energy photons can be measured in the presence of more intense high-energy photons. A nuclear-forensic counting laboratory should maintain at least three coaxial detectors, one with Compton suppression and at least one with a LEPS-type detector, each equipped with a multi-position sample changer.

Neutron Counters

Most of the utility of neutron counting is in the interrogation of a sample upon receipt, before the shipping container is opened. Neutron emission from a questioned sample could signal the presence of Pu. Spontaneously fissioning nuclides should be introduced into the counting facility only in limited quantity, as neutrons are penetrating and damage the function of HPGe detectors. Neutrons also potentially increase the background in the counting facility via nuclear activation reactions with surrounding materials.

62.4.3.3 Tritium Analysis

The $A = 3$ hydrogen isotope, tritium (^3H or T), is utilized in nuclear weapons as a component of thermonuclear fuel. Tritium is also widely used in industry and medicine, both as a source of

luminescence in wristwatches and building exit signs, and as an isotopic label in a wide variety of radiopharmaceuticals (Moskalev 1968; Cronkite 1979). Along with ^{241}Am in smoke detectors, T is a weapon-relevant material that is commercially distributed and could be diverted into proliferant channels.

Approximately 2,400 Ci of T are produced per electric MW in a heavy-water-moderated, CANDU-type reactor, a result of the continuous high-flux neutron irradiation of large quantities of deuterium (^2H or D) (Wong et al. 1984):



The small capture cross-section ensures that the product T will always be dilute relative to the other isotopes of hydrogen. Though this material can constitute a contamination hazard, it is of little use in the weapons world without prohibitively expensive isotope enrichment. The neutron irradiation of the minor ^3He component ($1.4 \times 10^{-4}\%$) of natural He (Firestone and Shirley 1996)

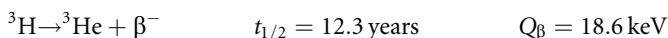


or enriched ^6Li targets



are both means of producing T in high concentration relative to the other isotopes of hydrogen. T-bearing material from any of these sources could appear on the black market.

In most of its chemical forms, T is highly dispersible, which is a serious problem when it is handled by persons with little or no training. Fortunately, the low energy of the β particles emitted in T decay [with a range of $\sim 0.5 \mu\text{m}$ in tissue (Moskalev 1968)], results in very low specific radiotoxicity.



However, this same property makes the detection and quantitation of T problematic. Since most radionuclides decay with the generation of more ionization than does T, and since no γ rays are emitted in its decay, other radionuclides present in a sample can mask the detection of low concentrations of tritium. As a result, the determination of T almost always involves a chemical step: either the preparation of a purified “hydrogen” sample (usually water) for direct radiation counting (Reinig et al. 1976) or the isolation of a helium fraction (containing the decay product ^3He) from the sample headspace after a defined in-growth interval for a mass-spectrometric measurement (Surano et al. 1992). These techniques and others (Chiarappa-Zucca et al. 2002) are also used for environmental monitoring, which can be quite relevant for the detection of T smuggling.

A nuclear forensic laboratory may encounter T in its molecular form (gaseous), but is most likely to encounter it in a liquid form. These samples can be aqueous (in which T is incorporated in either the water molecule or, in the case of radiopharmaceuticals, the solute) or organic. Organic T can be released in the form of water through a variety of wet or dry oxidation methods: Examples of wet oxidation include the destruction of the organic material with H_2O_2 in the presence of a ferrous-ion catalyst and the digestion of mixtures following the addition of HClO_4 . The evolved water fraction will contain hydrogen atoms from the reagents, which may impact the analytic data, depending on the method. Dry oxidation (combustion) is accomplished by heating the sample in the presence of oxygen; the gas-phase combustion products are passed over hot copper oxide, resulting in water that condenses in a cold-trap collector.

Liquid scintillation counting (LSC) is the usual method applied for the direct measurement of T radioactivity. Samples in which T is the major source of radioactivity are introduced into a scintillation cocktail. Prior conversion to water, followed by distillation to purify the sample from other radionuclides, is the preferred forensic method unless the analyst is certain that no other radionuclides are present. LSC on T-bearing aqueous specimens involves the use of an appropriate emulsifier to distribute the sample throughout the organic scintillator without degradation in performance. LSC calibration standards are available from NIST, and compensation for the efficiency change caused by the introduction of varying amounts of sample solution into the scintillator is discussed in Sansoni and Kracke (1971).

An indirect method for determination of T involves the quantitation of the T decay daughter, ^3He (Surano et al. 1992), a standard chronometric technique. An aqueous sample is cycled between 90°C and liquid-nitrogen temperature, evacuating and discarding the headspace gas each time, with the end of the last degassing cycle defining the beginning of the interval of in-growth of the daughter. After the in-growth period, the headspace gas is collected during the heating and cooling of the sample, and is introduced into a mass spectrometer. The number of daughter atoms produced during a well-defined in-growth interval and the length of that interval define the number of T atoms in the analytical specimen. The technique is sufficiently specific that very little sample preparation is necessary for aqueous samples. As few as 10^5 atoms of ^3He can be determined to an accuracy of a few percent. When the number of questioned samples to be analyzed is limited and the number of atoms of T in each sample is fairly large, this technique is superior to LSC; however, LSC is the preferred method when high sample throughput is required. There are advantages and disadvantages to both LSC and ^3He MS for the analysis of very dilute samples, however (Surano et al. 1992; Chiarappa-Zucca et al. 2002).

62.4.4 Imaging and Microscopy

The nuclear forensic analyst is conversant with instrumental techniques, but visualization of the features of a sample is particularly satisfying and can usually be performed nondestructively. The rapid identification and characterization of specimens without the compromise of integrity is the fundamental starting point of many forensic investigations. The unaided human eye can resolve features on the order of 50–100 μm in size; the role of microscopy is to provide a magnified image of a sample, allowing the observation of features requiring increased resolution. Microscopy techniques in nuclear forensic science use photons and electrons to probe the chemical, physical, and structural compositions of samples at spatial resolutions ranging from <1 Å to tens of micrometers. The nuclear forensic analyst most commonly uses forms of optical and electron microscopy for imaging.

62.4.4.1 Optical Microscopy

Light microscopy is one of the discipline's primary characterization techniques. It allows the forensic scientist to quickly address that most fundamental question, "what does the sample look like?" before proceeding with more extensive, often destructive, analyses. At all levels of sophistication (from hand lenses to compound microscopes), optical microscopy reveals

details of shape and size, color, surface morphology and texture, corrosion, tool marks, wear patterns, surficial coatings, and mineralogy (Davidson and Feigelson 1957; Horrocks 1974). The stereomicroscope and the polarizing microscope are both extensively used in the radio-chemical forensic laboratory. Both produce a magnified sample image through the use of a dual array of lenses (objective and eyepiece). The stereomicroscope produces three-dimensional images at relatively low magnification ($\sim 2\text{--}100\times$), and the subdivision of specimens into aliquots for subsequent analyses is facilitated by this instrument. The polarizing microscope, which can readily magnify an image to $1,000\times$, passes light through a set of polarizing filters to gain additional information about the nature of the sample from optical properties such as anisotropy, crystallinity, pleochroism, and birefringence. The wavelength of the incident light limits the resolution of an image: theoretically, the resolution of conventional microscopes is as good as 200 nm, but values better than 1 μm are rarely achieved. Both stereo and polarizing microscopes can be modified for digital photography, and an excellent description of the uses of optical microscopy in forensic science is given in Pluta (1988) and Peteraco and Kubic (2004).

62.4.4.2 Scanning Electron Microscopy

Optical microscopy is simple to use as little or no sample preparation is required, and samples can be analyzed rapidly. Despite these advantages, the most commonly used imaging tool in the nuclear forensic laboratory is not the optical microscope. Scanning electron microscopy (SEM) offers superior resolution and provides direct measurement of elemental compositions when combined with X-ray analysis. In SEM, a finely focused beam of electrons of energy $\sim 0.5\text{--}30$ keV is rastered over a sample. Sample preparation affects the quality of SEM images. Specimens must be compatible with the high vacuum of the SEM, and insulating materials must be coated with a thin conductive layer (usually 2–10 nm of Au, Pd, or C). With standard thermionic filament sources, image resolution is limited to ~ 10 nm, which translates to a maximum magnification of $\sim 100,000\times$. With field-emission electron sources, a resolution of 1 nm can be achieved (a maximum magnification of $1,000,000\times$). The interrogation of a questioned sample is limited by the physical dimensions of the SEM specimen chamber, typically <10 cm.

Backscattered electrons, secondary electrons, Auger electrons, and X-rays and other photons arise in the interaction of the incident electron beam with the sample. The intensity of one or more of these types of emission is measured as a function of raster position, resulting in the construction and display of an image of the sample. Each type of emission conveys different information about a sample, and morphologic or compositional information can be revealed in an image through choice of the appropriate detection mode (Reimer 1985; Newbury et al. 1986; Reed 1996). Secondary electrons arise from inelastic collisions between incident electrons and atomic electrons, and they sample only the outer few nanometers of the surface, providing information about sample topology. Backscattered electrons have energies comparable to that of the incident electron beam, and provide information about the mean atomic number of the sample; they are used to map the spatial distribution of phases of disparate chemical composition (Krinsley et al. 1998). Qualitative and quantitative information about chemical composition is carried by the characteristic X-rays of the elements (Reimer 1985; Newbury et al. 1986; Reed 1996).

62.4.4.3 Transmission Electron Microscopy

Transmission electron microscopy (TEM) is difficult to use and requires elaborate and time-consuming sample preparation; nevertheless, it provides a unique capability for ultrahigh spatial resolution (~ 0.1 nm, or $\sim 2,000\times$ that obtained by optical microscopy). It can reveal information about the microstructure of the sample via electron diffraction. TEM is capable of an extremely wide range of magnification (from $\sim 100\times$ to several million times) and provides information on extremely fine structural details, but at the expense of tight restrictions on sample thickness. A variety of techniques, from simple crushing to elaborate ion-beam milling, are used to produce electron-transparent specimens of the required thickness (Braverman et al. 1988; Anderson 1990). Just as in SEM, characteristic X-rays are generated by the interaction of the incident electron beam with the sample. X-ray analysis can be combined with TEM imaging and diffraction to provide comprehensive information about the internal microstructure of a questioned specimen, with nanometer spatial resolution (Joy et al. 1986).

TEM involves the use of a focused beam of high-energy (100–400 keV) electrons. The beam passes through a very thin sample (<250 nm thick) (Hirsch et al. 1971; Wenk et al. 1976; Reimer 1984; Joy et al. 1986) and scattered electrons are delivered to the detector (normally a high-resolution CCD) by a series of magnetic lenses. Imaging and diffraction modes are available in TEM: In imaging mode the incident electrons illuminate a region of the sample and produce a magnified image. The contrast in TEM images arises from several different mechanisms, and images may provide information on sample thickness, sample crystallinity, crystal orientation, and the density of defects and deformations. In diffraction mode the incident electrons produce an electron diffraction pattern, similar to an X-ray diffraction pattern, which can be indexed by modified X-ray diffraction procedures to identify solid phases at an extremely fine spatial scale.

62.4.4.4 Electron Microprobe Analysis

Electron microprobe analysis (EMPA) provides quantitative chemical characterization of spatially resolved areas of specimens. Element-specific X-rays are generated when a focused beam of energetic electrons (5–25 keV) strikes the sample. EMPA has many similarities to SEM (Newbury et al. 1986; Reed 1996); however, EMPA uses much higher beam currents (several hundreds of nanoamperes (nA)), which result in correspondingly poorer spatial resolution. EMPA uses both energy- and wavelength-dispersive spectrometers to measure the intensity of the characteristic elemental X-rays; elements from Be to Pu can be assayed, with accuracies approaching 1% and detection limits from 50 to 200 $\mu\text{g/g}$. Accurate quantitation requires flat, well-polished samples with stringent limitations on the magnitude of topographic features (Lister 1978). As with SEM, insulating materials must be coated with a conductive material prior to EMPA analysis; carbon is normally used to minimize absorption of low-energy X-rays.

62.4.4.5 X-Ray Microanalysis

The spectrum of characteristic X-rays generated by the interaction of energetic electrons with a sample in SEM, TEM, or EMPA is determined by the elemental composition of

that sample. These X-rays provide the means to measure elemental concentrations for most solid samples, including small particles. Characteristic X-rays are emitted with precisely defined energies, and are distinct from the continuum of X-ray energies found in *bremsstrahlung* (Newbury et al. 1986; Goldstein et al. 1992). These X-rays may be analyzed by either of two methods: energy-dispersive X-ray spectrometry (EDS) uses a semiconductor detector (usually Si(Li)) to simultaneously measure the energy and intensity of X-rays over a broad energy range (0.1–15 keV), and can detect elements from B to Pu. Detection limits of 0.1% can be achieved for silicate and oxide materials. Wavelength-dispersive spectrometry (WDS) uses an analyzing crystal. Incident X-rays are diffracted according to the Bragg principle, and they are dispersed according to wavelength rather than energy. Only X-rays satisfying the relation ($n\lambda = 2d \sin\theta$) are constructively reflected into a detector. WDS provides much higher energy resolution (eV compared to >100 eV) and much higher signal-to-noise ($\sim 10\times$) than EDS, but analyses tend to take longer and the instrument is much more expensive. WDS detects elements from Be to Pu and can achieve detection limits of 0.01% (Newbury et al. 1986; Goldstein et al. 1992).

62.4.5 Isotope Mass Spectrometry

Mass spectrometry (MS) is a workhorse of nuclear forensic analysis. Different instruments provide the means of measuring the isotopic, elemental, and molecular abundances of a wide variety of materials with high sensitivity, precision, and accuracy. In a mass spectrometer, a portion of a sample is converted into positively or negatively charged ions that are separated and analyzed according to their respective mass-to-charge ratios. Mass spectrometers are specialized instruments, and are usually classified according to the method of ion generation (e.g., thermal ionization, electron-impact ionization, or plasma ionization) and the type of mass analyzer (e.g., magnetic sector or radio-frequency quadrupole) (Duckworth et al. 1986; White and Wood 1986; Johnstone and Herbert 2002). A nuclear forensic investigation may employ as many as nine different types of mass spectrometers, depending on the analytic requirements for a given sample. Described below are the characteristics of the instruments most commonly used in nuclear forensic analyses.

62.4.5.1 Isotope-Ratio MS

Isotope-ratio mass spectrometry is used to determine the relative isotopic abundances of major and trace elements. Mass spectrometric methods are able to measure the relative concentrations of both radioactive and stable isotopes with a precision and accuracy of better than 0.001%. To achieve measurements of this quality, isotope-ratio MS relies almost exclusively on magnetic-sector instruments operated in temperature-controlled laboratories (Becker and Dietze 2000).

In thermal-ionization mass spectrometry (TIMS), samples consist of fg–ng quantities of chemically separated and purified analyte dissolved in a small volume (typically 1–10 μl). The solution is deposited on a refractory metal filament (e.g., high-purity W or Re), where it is evaporated to dryness. The filament is then heated to temperatures of 1,000–2,500°C in the ion source by resistive heating. If the ionization potential of the analyte is low compared to the work function of the filament, some of the analyte atoms will be ionized and emitted from the filament surface. TIMS ion sources commonly incorporate a second filament arranged

opposite that bearing the sample; evaporated neutral atoms and molecules are ionized on the hot surface of the second filament. Nearly all TIMS instruments employ single-focusing, magnetic-sector mass analyzers in which the electrostatically accelerated ions are separated according to their respective mass-to-charge ratios. TIMS instruments incorporate as many as 12 detectors (Faraday-cup and/or electron-multiplier modules) for the simultaneous collection of all isotopes of interest. TIMS achieves a precision for isotope-abundance ratios exceeding 1 part in 100,000 (Platzner 1997; Becker 2003; Richter and Goldberg 2003) through the accurate measurement of ion currents between 10^{-9} and 10^{-18} A. TIMS is the preferred technique for U and Pb isotope measurements.

Sample preparation for TIMS is time-consuming and labor-intensive; development of the techniques for purification, concentration, and filament-loading, specific to each element, can take months to develop and perfect. As a result, TIMS has been replaced by multi-collector, inductively coupled, plasma-source mass spectrometers (MC-ICPMS) in many laboratories. In MC-ICPMS, a sample is dissolved in an acid solution, which is nebulized in a spray chamber and aspirated into an Ar plasma. The analyte dissociates into its atomic constituents and ionizes in the high temperature of the plasma (5,000–8,000 K). Ionization proceeds with very high efficiency (>90% for elements with a first ionization potential of <8 eV). Positive ions are extracted from the plasma with a wide range of energies (up to several hundred electron volts), and MC-ICPMS instruments use either a gas-filled collision cell or double-focusing mass spectrometry to achieve adequate mass resolution and abundance sensitivity. Unlike a thermal ionization source, the plasma source is not adequately stable, requiring MC-ICPMS instruments to simultaneously collect and quantitate the different analyte masses to achieve high precisions and accuracies. The ion detection systems are similar to those used in TIMS. The detection limits for MC-ICPMS are generally <1 pg/g (10^{-12} g/g) and can reach the 10^{-15} g/g range for favorable elements. Precision and accuracy compare favorably to TIMS (Linge and Jarvis 2009). By virtue of its high-efficiency ion source, MC-ICPMS has enabled a wide spectrum of isotope-ratio measurements in nuclear forensic analysis (Wallenius et al. 2002).

Neither TIMS nor MC-ICPMS is applicable to the analysis of electronegative elements (C, N, O, and S) or noble gases (He, Ne, Ar, Kr, and Xe), whose isotope ratios are best measured with instruments known collectively as (gas-source) isotope-ratio mass spectrometers (IRMS). The analyte is prepared in a gaseous state (Duckworth et al. 1986; White and Wood 1986; Beyerle et al. 2000) and introduced into the ion source. An intense beam of 50–70 eV electrons induces ionization via electron impact (collisions between electrons and gas molecules). Positive ions are extracted from the source and mass-analyzed. A dual inlet system provides a parallel, intermittent source of gas of known isotopic composition, and the isotopic analysis of the unknown analyte is related to that of the standard. Stable-isotope MS requires milligram or larger samples, resulting in the determination of isotope ratios with precisions and accuracies of 0.01–0.1%. Noble-gas mass spectrometers use specially modified ion sources that have very small internal volumes to minimize analytical blanks, yet provide high efficiency for the ionization of chemically resistant analytes. Noble-gas spectrometers can achieve zeptomole (10^{-21} mole) detection limits.

62.4.5.2 Element MS

In contrast to isotope-ratio MS, elemental-composition MS provides analyses of relative elemental concentrations, and greater emphasis is placed on measurement of a wide variety

of disparate materials, rather than achieving very high accuracy. Accuracies of 1–10% are considered acceptable, compared to 0.001–0.01% for isotope ratios.

The low detection limits and multielement capability of inductively coupled, plasma-source mass spectrometry (ICP-MS) make it a technique of choice for nuclear forensic analysis. Acid solutions of analytes are nebulized in a spray chamber and aspirated into an Ar plasma. For rapid, multielement analysis of elements at trace and ultra-trace concentrations, ICP-MS is an optimum method, provided that solid samples are easily dissolved to produce aqueous solutions (Duckworth et al. 1986; Brundle et al. 1992; Linge and Jarvis 2009). Most commercial ICP-MS instruments use an rf quadrupole mass analyzer that can scan through a wide mass range very quickly (a measurement across 1–300 atomic mass units (amu) takes less than 1 s). Higher precision can be obtained through time-averaging multiple scans. A quadrupole has lower precision and stability than a magnetic-sector analyzer, but provides adequate mass resolution for most nuclear forensic applications. Detection limits are element dependent, on the order of 0.1–10 pg/l, with analyte requirements in the fg–ng range. The extraordinary sensitivity of ICP-MS is particularly important in nuclear forensic analysis for detecting ultra-trace quantities of long-lived actinides, and provides an advantage over α -spectroscopy of at least 1,000 \times for plutonium isotopes. Isotope dilution methods (Linge and Jarvis 2009) can improve the accuracy of trace-element analyses by ICP-MS to 2–5%. Simple sample-introduction methods for hyphenated techniques operating at near-atmospheric pressure (e.g., laser ablation, high-performance liquid chromatography, gas and ion chromatography, and capillary electrophoresis) have enabled ICP-MS to become a particularly versatile tool for many types of nuclear forensic investigation.

62.4.5.3 MS and In Situ Microanalysis

Most nuclear forensic samples are physically and chemically heterogeneous, while the MS techniques discussed in preceding paragraphs pertain to analyses of homogeneous bulk samples. Complementary techniques involving in situ microscale isotope and trace-element analyses also play a pivotal role in nuclear forensic investigations.

The most widely used technique for spatially resolved analysis of isotope and trace-element abundances is secondary-ion mass spectrometry (SIMS). The technique can be applied to any solid sample, and counterfeit currency, golf-ball-size pieces of metal, and sub-micrometer-sized grains of U-oxide have all been analyzed with SIMS (Wilson et al. 1989; Zinner 1989; Brundle et al. 1992; Ireland 1995; Vickerman 1998; Tamborini and Betti 2000; Gillen and Bright 2003). In SIMS, a focused, primary ion beam, typically O_2^+ , Cs^+ , or O^- , is used to sputter a sample surface. These primary ions have sufficient energy (keV) to penetrate a few nanometers into the surface of a sample and generate positive and negative secondary ions characteristic of the material. These secondary ions are produced with a broad energy distribution (maximum at a few electron volts and extending out to hundreds of electron volts), which requires the use of double-focusing mass analyzers. SIMS can be used to measure the concentration of any element, from H to Pu, over a dynamic range of more than nine orders of magnitude. The sputtering process is very matrix-dependent, making the limitation to accurate SIMS quantitation the acquisition of matrix-matched standards with sputtering behavior similar to that of the unknown analytes. If an appropriate standard is available, the accuracy of trace-element analyses by SIMS is \sim 2–10% (Wilson et al. 1989). The precision and accuracy

of isotope-ratio measurements are typically 0.02–0.4%, depending on ion yield and relative isotope abundances (Zinner 1989; Ireland 1995). Since the sputtering of chemically complex samples generates large numbers of molecular ions, a SIMS analysis that meets the needs of the nuclear forensic analyst requires a mass resolving power ($m/\Delta m > 5,000$) sufficient to separate elemental ions from molecular species of the same nominal mass (e.g., $^{24}\text{Mg}^{16}\text{O}^+$ and $^{40}\text{Ca}^+$ at mass 40).

Two SIMS operational modes are depth-profiling (used to observe changes in chemical or isotopic composition as a function of depth beneath a surface) and microprobe-mapping (used to observe changes in elemental and isotopic distributions across a sample surface). Both involve rastering the primary ion beam across the sample in a manner similar to that of the electron beam in SEM. The secondary-ion signal is correlated with the position of the primary ion beam where the secondary ions were generated. Sputtering of the sample by the primary beam produces a record of isotope and chemical variations in three dimensions (Ireland 1995). Resolution is determined by the lateral extent of the primary beam and can be as good as 50 nm with the NanoSIMS. Depth resolution is typically 1–2 nm. Another SIMS mode is bulk analysis (in which a static primary beam produces maximum sensitivity while sacrificing depth and lateral resolution); detection limits are generally in the range of 1–100 ng/g. Isotope-ratio measurements are carried out in analogous fashion, but with special attention to sample charging and alignment of the secondary ion beam in the mass spectrometer.

Isotope-ratio and impurity-concentration measurements of particle samples are most effectively conducted by SIMS. By virtue of its accurately focused primary beam, the operational characteristics of SIMS for micrometer-scale particles, most often weighing >1 pg, are precisions and accuracies of better than 0.5% (Ranebo et al. 2009). Real-world investigations often require consideration of complex environmental matrices (of little or no forensic value) for but a few Pu- or U-bearing particles. SIMS particle-search mode can find and analyze such important specimens. These searches may be performed in ion-microscope mode via a defocused ion beam (>100 μm diameter), or with the microprobe method previously discussed. Fully automatic particle searches, requiring only operator sample loading, may be executed to delineate interesting grains within a complex population of thousands of particles of ordinary constitution (Ranebo et al. 2009). Use is made of a conducting substrate, such as a polished, high-purity graphite disk or a double-sided, gummed support, for SIMS particle analyses.

Laser-ablation, inductively coupled-plasma mass spectrometry (LA-ICPMS) is an instrumental technique in which a laser-ablation cell and optical microscope supplant the spray chamber/nebulizer apparatus of a standard ICP-MS instrument. Subsamples of questioned material are ablated from a solid sample via laser (often a pulsed Nd-YAG tuned to 266 or 213 nm). Ablated specimens are transported in a stream of Ar to a plasma torch for ionization and mass discrimination as per solution ICP-MS. Only minimal sample prep is required, and few restrictions are placed on the nature of questioned solid samples (Brundle et al. 1992; Vickerman 1998). While laser spot sizes can be reduced to several micrometers, sensitivity is degraded as a result, and usual spatial resolutions are on the order of 10–100 μm . Matrix-matched standards are also necessary for accurate trace-element and isotopic quantitative analyses in LA-ICPMS. Depending on the quality of such primary standards, LA-ICPMS accuracies are typically 1–10%, with limits-of-detection in the parts-per-billion (ppb) range (► Table 62.1).

■ **Table 62.1**

Analytic methods for nuclear forensic analysis (adapted from Kristo et al. 2006)

Technique		Information return		Typical detection limit	
Bulk samples					
Radiochemistry		Isotopic		10 ⁴ atoms	
TIMS		Isotopic		pg-ng/g	
ICP-MS		Isotopic elemental		pg-ng/g	
GDMS		Isotopic elemental		pg-μg/g	
XRF		Elemental		0.01 wt%	
XRD		Molecular		~2 at.%	
Technique		Information return		Spatial resolution	
Microscopy					
Optical		Images		0.5 μm	
SEM		Images		1 nm	
TEM		Images		0.1 nm	
Technique	Information return		Typical detection limit		Spatial resolution
Microanalysis					
LA-ICPMS	Elemental isotopic		pg-ng/g		10–100 μm
SIMS	Elemental isotopic		1–100 ng/g		0.05–10 μm
SEM/EDS	Elemental		0.2–2 at.%		0.1 μm
EMPA	Elemental		0.01 at.%		1 μm

62.4.6 Organic GC-MS

62.4.6.1 General and Applications

Organic chemistry applications are often overlooked within the realm of NFA, a discipline highly skewed toward inorganic and isotopic measurements. However, an RDD or pre-det IND would dictate HE analyses, as would questioned specimens acquired from suspected hydrodynamic experiments for nuclear proliferation activities. Organic species can also be significant in pre-det route analyses, comprising target analytes in trace-evidence samples, inks, papers, adhesives, lubricants, and diverse materials for chemical “fingerprinting.” Although assorted organic instrumental techniques have been applied in specific NFA investigations, because of the sensitivity and specificity, as well as application to extremely complex sample matrices, the most versatile and valuable organic protocols in the authors’ laboratory have been based on GC-MS.

Complete textbooks are available on the general practice of GC-MS, and references with a specific forensic focus may be found as well (e.g., Yinon 1987; Saferstein 2002; Stafford 2005). The sensitivity of the technique is in the range of nanograms/liter (ng/l) for general analyses, improving to picograms/liter (pg/l) for selected-ion monitoring. Chemical separations of complex mixtures are accomplished by temperature-programmed capillary chromatography,

while exact identifications of eluted analytes are performed via compound ionization and mass spectrometry, in conjunction with reference standards and/or comparison libraries. Material profiling via GC-MS also has good potential for intelligence applications because it retains chemical information, in contrast to, for example, trace-element characterization of inorganic solids. Thus, minor components of a GC-MS spectrum positive for HE, in addition to contributing to the material fingerprint, may also be indicative of synthesis precursors, reaction by-products, side-reaction pathways, or other reactant/product impurities. Such data may often prove insightful for attribution of the synthetic method, process conditions, and (if very fortunate) perhaps the production lab.

62.4.6.2 Sample Prep

Sample-preparation practices for GC-MS can be grouped into several distinct categories based on complexity and separation tactic. The simplest technique is merely sampling a questioned vapor phase with a gas-tight syringe and introducing the specimen directly into the injection port of the GC.

Somewhat more involved, but similar in practice, is solid-phase micro-extraction (SPME; Pawliszyn 1997). SPME is a vehicle for the non-exhaustive extraction of volatile and semi-volatile species that is based on the partitioning of analytes between sample, sample headspace, and SPME fiber. The fiber consists of a glass substrate coated with specific chemical sorbent(s), and is available in several commercial variants depending on the nature of the sample and the diagnostic analytes. Protected within the barrel of a syringe needle, after exposure the SPME fiber is introduced directly into the GC injection port for thermal desorption and ensuing chromatography. Thermal equilibration of fiber with sample is typically performed over 20–30 min; collection and species concentration are performed simultaneously; no solvents are required; there is no hazardous waste stream; and potentially dangerous quantities of toxic materials are reduced to the nanogram (ng)–microgram (μg) levels appropriate to GC-MS analysis.

In contrast, solvent extraction is the most labor-intensive and chemically involved procedure for routine GC-MS sample prep, but it is also the most thorough. A questioned liquid or solid specimen is exhaustively extracted with suitable solvent, this process often aided by sonication. Methylene chloride (CH_2Cl_2) is an excellent reagent for removing nonpolar organic species from solid or aqueous samples. To increase the suite of analytes to a more expansive mix of general polar and nonpolar organic compounds, a solvent mixture of CH_2Cl_2 with acetone or an alcohol has proven effective. However, acetone alone is the reagent of choice for more selective extraction of nitro-based HE species. After volume reduction of the solution, with concomitant analyte concentration, the extract is injected into the GC.

Some polar species can be difficult to chromatograph, but such compounds may often be chemically derivatized to enhance the separation and detection of eluted analytes. Derivatization is a chemical reaction with an added reagent to produce specific products clearly derived from the reactants, but with improved GC-MS analytic properties. Thus, TMS (trimethylsilane) derivatives of alcohols are synthesized with *bis*(trimethylsilyl) trifluoroacetamide, primary and secondary amines are reacted with acylation reagents, and many other analogous reactions are likewise possible. Derivatives may also be implemented in conjunction with SPME, and derivatization reactions can be performed on-fiber.

62.4.6.3 Spectral Reduction and Compound Identification

The result of a GC-MS analysis is a large data file containing MS fragment-ion measurements (m/z^+ values and associated intensities) as a function of retention time of analytes on the GC column. If the investigator is interested only in compounds for which he/she has reliable primary standards, identifications based on matching retention times and corresponding ion-fragmentation patterns can be exact. Accurate quantitation may also be performed in this case by measuring a calibration curve (typically GC peak area versus known analyte concentration) and interpolating questioned-specimen empirical data between points on the fitted calibration function. However, as the CAS Registry currently comprises more than 50 million chemical substances, and the NIST/EPA/NIH (NIST08) MS database, for example, contains but 192,000 compounds, known comparison standards are generally not readily available for all analytes of potential interest to a forensic analysis. Consequently, an investigator often relies primarily on the evaluated match of experimental mass spectra with those in one or more comparison libraries.

Although GC-MS spectral analyses and compound identification can be performed manually, the effort can be tedious, inefficient, and problematic for highly complex chromatograms. The authors' laboratory makes productive use of a software package developed by the US Department of Defense and NIST for international treaty verification. The Automated Mass Spectral Deconvolution and Identification System (AMDIS) incorporates several algorithms to distill pure component spectra and associated data from intricate chromatograms, and then uses that information to assess whether the component can be attributed to a known compound in the reference database.

The authors use two primary AMDIS outputs to assess the degree of confidence of a potential identification. The first is the net match factor; it is the final match quality value for the correspondence between the deconvoluted empirical component and library spectra (perfect match $\equiv 100$). The other is the purity parameter, which is the fraction of the total ion signal at component maximum scan attributed to the deconvoluted component. For reporting purposes, the customarily used acceptance criteria in the authors' laboratory are: match factor $\geq \sim 80$ and purity $\geq \sim 60\text{--}70\%$. However, an identification with lower purity will sometimes be included if, in the estimation of an experienced analyst, the corresponding match factor is sufficiently high and individual interpretation of the experimental spectrum justifies it. (Analogous to computer-automated dermatoglyphic fingerprint matching, final assessment of a GC-MS spectrum by a skilled mass spectroscopist is essential for high-quality results.) However, an absence of a suitable standard reference material for confirmatory empirical measurements (both MS ion-fragmentation profile and GC retention time) requires that the analyst establish an identification largely reliant on a database match. Consequently, even though determination of a chemical species only via AMDIS may be believed to be a virtual certainty, a conservative forensic analyst will nevertheless label such identification as "tentative" only.

62.5 Special Nuclear Materials

The Atomic Energy Act of 1954 defines "special nuclear materials" (or SNM) as ^{233}U , plutonium, or uranium enriched in ^{235}U . These are the fissile isotopes (nuclides that undergo fission with high probability when irradiated with neutrons of any energy) that can be

produced in quantity, and the fundamental principle of nuclear nonproliferation efforts is limiting access to these materials. Of the three, only ^{235}U occurs in nature, where it constitutes $\sim 0.72\%$ of naturally occurring uranium; most of the balance of natural uranium consists of ^{238}U , which fissions efficiently only through interactions with high-energy (>1.2 MeV) neutrons. The boundary between low-enriched uranium (LEU) and highly enriched uranium (HEU) is arbitrarily set at 20% ^{235}U , where the well-reflected critical mass drops below 100 kg. The production of macroscale ^{239}Pu and ^{233}U is accomplished through reactor-irradiation of ^{238}U and ^{232}Th , respectively, and chemically recovering and purifying the desired product. While not part of the definition, SNM is usually assumed to refer to “weapons-grade” materials, in which the majority of the elemental content is the fissile isotope.

Nuclear forensic principles apply to all three of the special nuclear materials, including uranium of any enrichment (or depletion) in ^{235}U . They can also be applied to other materials arising in the nuclear fuel cycle (e.g., ^{237}Np , ^{241}Am) and to the natural-composition feed materials (uranium and thorium).

62.5.1 Natural Versus Synthetic Materials

Uranium and thorium are widely distributed in the earth’s crust, with average concentrations of ~ 2 and 8 ppm, respectively (Grainger 1958; Boyle 1982; Frondel et al. 1967; Wills 1997). Over 100 different uranium-based minerals are known, but deposits of high-grade ore (like uraninite and pitchblende, with as much as 70% uranium by weight) are rare. Most of the world’s supply of recovered uranium has been extracted from ores with a uranium content of only about 0.2% . Conversely, the mineralogy of thorium is less varied, and deposits of its principal mineral, monazite, are fairly common. The thorium content of pure monazite is typically between 5% and 10% .

Enrichment of ^{235}U (increasing its fractional concentration relative to ^{238}U) is one of three methods for producing fissile fuel for a nuclear explosive device. The other two involve the operation of nuclear reactors and the capture of neutrons by either ^{232}Th (to make ^{233}U) or ^{238}U (to make ^{239}Pu). The enrichment of ^{235}U is a difficult process, conducted on a very large scale. The production of uranium that is enriched in ^{235}U must necessarily be accompanied by the production of uranium that is depleted in ^{235}U . Enriched uranium and depleted uranium are synthetic materials, derived from natural uranium through the action of Man. While ^{233}U and ^{239}Pu are long-lived ($t_{1/2} = 1.59 \times 10^5$ years and $24,100$ years, respectively), neither exists in nature in significant concentration. Plutonium and ^{233}U are also synthetic materials; the mixtures of nuclides that make up a sample of either are defined by the engineering processes that give rise to the material. The presence of ^{233}U and/or ^{239}Pu in a sample can only come about through anthropogenic nuclear processes.

62.5.2 Separation of Uranium Isotopes and ^{235}U Enrichment

Natural uranium can be used as fuel in a nuclear reactor; however, as the proportion of ^{235}U increases, the ease with which a fission reactor can be used as an energy source increases. Modern light-water-moderated reactors are fueled by uranium enriched in ^{235}U from 0.71% (natural) to $3\text{--}5\%$. For greater ^{235}U enrichments, the size of a reactor for a given power level can decrease; reactors for ship propulsion use starting enrichments of at least 10% to minimize

the size and weight of the power plant, while submarines use fuels enriched to 90% or more (materials considered weapons-usable).

The mass number of the uranium nucleus influences the chemistry of the atom to which it is central by a miniscule amount; as a result, separation of uranium isotopes cannot be accomplished through the application of the standard chemical techniques used to purify or separate chemical substances. (See [▶ Chap. 15, Vol. 2](#) on isotope effects and [▶ Chap. 51, Vol. 5](#) on isotope separation in general.) Isotope separation must take advantage of those properties that are modified by changes in the number of neutrons in the nucleus. Most enrichment technologies currently used or under study rely on differences in mass, manifested either through differences in inertia (electromagnetic isotope separation) or the distribution of velocities at thermal equilibrium (gaseous diffusion, centrifugation, and aerodynamic techniques). All of these techniques take volatile compounds of uranium (such as UF_6) as feed material. Other techniques involve the interaction of laser light with an atomic or molecular vapor (laser isotope separation). The narrow frequency width of the delivered photons allows the selection of certain hyperfine electronic transitions that vary among the different isotopes of the element.

While other materials have been used as feed to uranium-enrichment processes, the most widely used volatile compound of uranium is the hexafluoride. At room temperature, UF_6 is a colorless solid with a density of 5.1 g/cm^3 . It sublimates at atmospheric pressure, and at room temperature has a vapor pressure of ~ 100 torr. The main disadvantage of working with UF_6 is its high chemical reactivity. It reacts vigorously with water, but is not very reactive with dry air. UF_6 reacts with most metals; however, nickel, copper, and aluminum are resistant. This holds only for pure UF_6 ; the presence of even small amounts of HF increases the rate of attack on even the resistant metals.

Electromagnetic isotope separation (EMIS) machines are often called Calutrons (Nier et al. 1940). The expense of running Calutrons is prohibitive, as they are inefficient in their consumption of both energy and resources, so the technique was abandoned in the United States in favor of gaseous diffusion. Though the method has drawbacks, it does offer the advantage of producing small quantities of weapons-usable materials almost immediately.

In EMIS techniques, a uranium-bearing volatile compound is introduced as a gas into an ion source, in which the molecules are destroyed and $+1$ uranium ions are produced. These ions are extracted and accelerated by means of an electrical potential of a few kilovolts. The initial thermal energy differences are relatively unimportant, so that ions of the same mass are deflected to virtually the same extent. The path radius of a particular ion is proportional to the square root of its mass. The separation of the masses can be related to the separation of the ion orbits at the point of collection. A homogeneous magnetic field provides for first-order focusing, so that if products with the same mass are emitted from the ion source over a small range of angles and velocities, they arrive at the same location after traveling through 180° of the path imposed by the magnetic field; the separated isotopes are usually harvested at the 180° position.

Another method that has been used to enrich uranium on the industrial scale is thermal diffusion (Vasaru 1975). Under the influence of a temperature gradient, the heavier molecular component of a mixture of two isotopes will tend to concentrate at the lower temperature. A thermal diffusion apparatus consists of two concentric, chemically resistant vertical tubes, where the inner tube carries high-temperature steam and the outer tube is jacketed and cooled by circulated water. The annular space between the two tubes is very narrow, less than 1 mm in thickness. UF_6 is introduced into the annulus between the two tubes at a pressure of

200 atmospheres, required to keep the UF_6 in the liquid phase near the hot inner wall. Lighter molecules tend to move toward the inner wall and rise to the top of the apparatus, while heavier molecules move outward and downward. The stringent requirements on the tolerances of the apparatus and the limited throughput make this method inferior to other diffusion-based enrichment technologies, and it has been abandoned.

Gaseous diffusion is the most widely used method for enriching uranium (Massignon 1958; Gowing 1964; Villani 1979), though it is being supplanted by gas-centrifuge technology. Gaseous diffusion has a proven efficacy and reliability, and is used in large-scale production facilities in several countries. Gaseous diffusion can be used as an enrichment method because the thermal equilibrium principle requires that all molecules of a gas mixture in equilibrium with its surroundings have the same average kinetic energy. Therefore, lighter molecules travel faster and strike the container walls more frequently than do heavier ones. As a consequence, a minute hole in the wall of the container, provided it is small enough to prevent the bulk outflow of the gas as a whole, will allow the passage of a larger proportion of light molecules than heavy ones, weighted by their relative concentrations. For uranium hexafluoride gas, made up of $^{235}\text{UF}_6$ and $^{238}\text{UF}_6$, the molecular masses are 349 and 352, respectively, and the ratio of average velocities is $(352/349)^{1/2} = 1.0043$, with $^{235}\text{UF}_6$ moving faster than $^{238}\text{UF}_6$.

The porous diffusion barrier is the central apparatus of the enrichment process. The holes in the barrier must have a characteristic diameter that is smaller than the mean free path of the molecule to be separated; if collisions between molecules can occur with significant frequency within the barrier, equipartition of energy will render the barrier ineffective. Also, the barrier must be thin enough so that it has adequate permeability at low pressure and be chemically resistant to hot UF_6 vapor. Diffusion barrier is usually fabricated in the form of tubes into which the UF_6 gas is introduced. These tubes are bundled, and the bundles are housed in cylindrical diffusers, each of which is associated with a compressor for manipulating and repressurizing the enriched gas that flows through the walls of the barrier tubes into interstitial space. There is also a heat exchanger for ensuring that adiabatically compressed or expanded UF_6 gas is at thermal equilibrium and never heats to the point that it becomes dangerously reactive or cools to a temperature at which it freezes; the gas is heated significantly by compression.

Gaseous diffusion operates at temperatures above and pressures below the UF_6 triple point, near 70°C and 0.5 atmospheres. Since the difference in average velocities between $^{235}\text{UF}_6$ and $^{238}\text{UF}_6$ is small, the enrichment that can be obtained in any single separation cell is minimal. The actual performance of a gaseous diffusion cell depends not only on the relative masses of the UF_6 molecules, but also on the pressure and temperature of the gas and the permeability, size, and geometrical configuration of the barrier. For instance, if the operating pressure of the cell increases, the mean free path of the UF_6 atoms gets shorter and the probability of molecular collisions inside the barrier pores increases; this reduces the efficiency of the barrier, though the flow of gas through the barrier is increased.

Typically, the input flow of UF_6 is adjusted so that roughly half of the feed diffuses through the walls of the barrier tubes into interstitial space, becoming enriched (product), while the rest remains in the tubes, becoming depleted (tails). To obtain significant enrichments, this process must be repeated multiple times (Krass et al. 1983). In a “cascade” of diffusion cells, the product of one enrichment cell is used as feedstock for another. The cascade is “simple” if the tails are discarded; the cascade is “countercurrent” if the tails are reintroduced as feed in a lower enrichment stage. Simple cascades are not used because of the potentially profligate waste of uranium. After the initial start up of a countercurrent cascade, feed material is introduced only in the amount necessary to balance the withdrawal of product and tails.

Early in the history of the US gaseous-diffusion plants, a shortage of uranium made it necessary to use material as cascade feedstock that had been recovered from reactor applications. This resulted in the cascades being contaminated with the nonnatural uranium isotopes ^{236}U , ^{233}U , and ^{232}U , a contamination that persists to this day due to the long cascade residence times for a given uranium atom. Incomplete fuel reprocessing resulted in significant amounts of Np, Pu, and Tc (all of which have volatile fluorides) being introduced into the cascade as contaminants in the feedstock.

Another way in which uranium can be enriched is by means of the gas centrifuge (London 1961; Olander 1978; Villani 1979). If a polyisotopic gas is subjected to an intense centrifugal force, the heavier molecules will move preferentially to the periphery of the rotor, producing a partial enrichment of the lighter molecules near the center of the apparatus. The separation factor increases with the centrifugal force supplied by the motion of the centrifuge and decreases with an increase in temperature. The separation factor also increases with the mass difference between the molecules, unlike gaseous diffusion where it increases with mass ratio; therefore, centrifugation is as effective a technique for heavy elements as for light ones.

The enrichment gain from a single centrifuge unit can be more than an order of magnitude greater than that for a gaseous diffusion cell, but the technical challenges associated with operating high-speed centrifuges are substantial. For instance, the required centrifugal acceleration to the wall of the rotor is more than 10^5 times the acceleration of gravity; issues of material strength are clearly important. It is still necessary to operate a centrifuge-based plant in cascade, requiring both the removal of product and tails and the introduction of feedstock with the centrifuge running at speed. The technical difficulty of the problem has taken many years to address, only recently bringing centrifuges into competition with gaseous diffusion as an enrichment technology. The mass load of a given centrifuge is limited by the necessity that the UF_6 remain in the gas phase under the operating conditions of the apparatus; otherwise there will be no diffusion and, consequently, no enrichment. If it is assumed that the pressure at the wall of the rotor during operation of the centrifuge must remain below 100 torr (the UF_6 vapor pressure at room temperature), then the resulting pressure at the center of the rotor comprises a good vacuum. The initial gas load of a stationary centrifuge with a radius of 10 cm must remain below 3.6×10^{-4} atmosphere so that the pressure at the rotor wall during operation does not induce a phase change; this is the limitation of the maximum load of UF_6 in a given centrifuge unit. A cascade of gas centrifuges draws considerably less power per unit of enrichment work than does a gaseous diffusion cascade, but operates in pretty much the same way. Uranium enrichment by gas centrifuge is economical on a smaller scale than is gaseous diffusion.

Similarly, structured cascades should result in the same $^{234}\text{U}/^{235}\text{U}$ isotopic signature from centrifuges as from gaseous diffusion; however, centrifuge plants have been competing with diffusion plants only recently, so they are not expected to be contaminated with the nonnatural uranium isotopes that persist in the products of gaseous diffusion. A sample of enriched uranium in which the relative enrichments of ^{234}U and ^{235}U are about the same, but in which ^{236}U is absent, is quite likely the product of a gas centrifuge plant.

Aerodynamic enrichment techniques have been demonstrated on the industrial scale (Becker et al. 1981; Grant et al. 1977). The separation of isotopes is produced by the centrifugal force applied to a stream of gas through deflection by a solid barrier. The feed gas is composed of UF_6 diluted in a much larger amount of a light auxiliary gas, usually hydrogen. The method provides a high stage throughput with a reasonably high single-stage separation factor, and offers the advantage that the technology is less complicated than that in high-speed centrifuges.

This is an emerging technology, and at this time the forensic radiochemist is unlikely to encounter a large sample of uranium enriched in ^{235}U by this technique.

Uranium can be enriched in ^{235}U through laser isotope separation (LIS). Lasers produce large numbers of photons, all having nearly the same frequency. Atomic or molecular ionization or excitation can be stimulated by these photons, but the process occurs with high probability only when the energies of transition and the photon are closely matched, relative to the energy widths associated with each. The energy associated with a given transition is broadened by collisions in a high pressure gas, and by the motions of the individual molecules toward or away from the photon source (Doppler effect). Still, with careful preparation, it is possible to selectively excite atoms or molecules of one of the isotopes of uranium in the presence of the others (Boehm et al. 1978; Villani 1979; Letokov 1979; Krass et al. 1983). Selective excitation of one isotopic species in the presence of one or more others requires a laser that is tunable with a precision of one part in 10^5 . This can be accomplished by modern dye lasers. In LIS, single-stage separation factors have been so good that reactor fuel compositions have been obtained in a single pass.

The isotopic signature of enriched uranium arising from LIS is more like that occurring in EMIS than from any of the cascade techniques. Both ^{234}U and ^{238}U should be depleted relative to ^{235}U in the product. The value of $^{234}\text{U}/^{238}\text{U}$ will depend on the frequency width of the laser beams as well as line broadening in the target atoms or molecules determined by the experimental setup.

An issue that all enrichment methods have in common is criticality safety during the later stages of procedures resulting in highly enriched ^{235}U . The danger of an accidental criticality can be eliminated if the concentration of enriched uranium in a single location is kept below the critical amount. Critical mass is also dependent on chemical form, density, geometrical configuration, and the presence of neutron reflectors or moderators; in general, successful forensic measurements can be made on samples that have masses that are far below the concerns of criticality. For the forensic radiochemist, the limitation on batch size may mean a greater variability in isotopic signatures between samples of highly enriched uranium than between samples of low-enriched uranium.

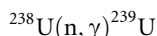
62.5.3 Nuclear Reactors and the Production of Plutonium and ^{233}U

A nuclear reactor is a device in which the fission process is controlled, either to produce power, radionuclides, or both. All nuclear reactors depend upon an initial load of fuel that contains fissile materials. Absorption of a neutron by a fissile nucleus produces another fission event with high probability, accompanied by the emission of more neutrons. If one of the neutrons emitted in each fission induces another fission, the number of neutrons in each succeeding “generation” will remain constant and the neutron economy is balanced. This is referred to as a self-sustaining chain reaction, and is the normal operating condition of a nuclear reactor. (See [Chaps. 57](#) and [58](#) in this Volume.)

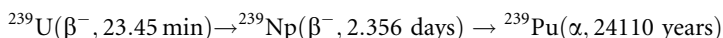
Fission-produced neutrons can be absorbed by any of the materials present in the reactor, with relative probabilities proportional to the neutron-absorption cross sections of the nuclei in the materials. Even for the fissile nuclides, neutron-capture reactions compete favorably with neutron-induced-fission reactions. For example, low-energy neutron irradiation of a sample of ^{235}U results in the production of ^{236}U about half as often as it results in fission. Fuel containing the fissile actinides always contains some of the even-mass actinide nuclides as well, which are

called “fissionable” since the neutrons present in the reactor can cause fission in these nuclides with only low probability.

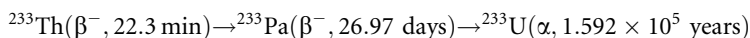
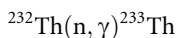
Power reactor fuel usually consists of uranium enriched in fissile ^{235}U to the level of a few percent; the balance is fissionable ^{238}U , which does not initially contribute much to the production of fissions in the reactor fuel. The ^{238}U in the fuel preferentially captures a neutron, resulting in the production of ^{239}U :



The nuclide ^{239}U is short-lived and decays to ^{239}Np , which in turn decays to ^{239}Pu , a fissile material:



If the reactor runs long enough that a significant fraction of the initial ^{238}U is transmuted into ^{239}Pu , the neutron economy must be corrected for fissions arising in neutron reactions with ^{239}Pu . ^{238}U is a “fertile” material under these conditions, since it produces fissile fuel under neutron irradiation. The other common fertile material is ^{232}Th , which produces ^{233}U in much the same way:



This is the origin of a separate fuel cycle, involving thorium and ^{233}U .

The reactor components of greatest interest to the forensic radiochemist are the “clean” fissionable material that constitutes fresh nuclear fuel, and the neutron-irradiated fuel that is the result of nuclear reactor operation. The design of the reactor determines both the ingoing fuel composition and the outgoing fuel isotopic content (Glasstone and Sesonske 1967).

The spent fuel from a nuclear reactor is a mixture of nuclides in which the percentage of each is a function of the isotopic content of the starting material, the temperature of the core and moderator, the period of irradiation, the energy distribution of the incident neutrons, and the radioactive half-lives of the nuclides produced. Fuel efficiency in production reactors is less important than is the isotopic composition of the plutonium product. Particularly important is the minimization of the amount of ^{240}Pu produced relative to ^{239}Pu ; ^{240}Pu has undesirable nuclear properties for use in nuclear explosives. The operation of a plutonium production reactor is often incompatible with the economical production of power, unless the reactor design permits refueling during power production.

With short reactor irradiation times, relatively pure ^{239}Pu is formed from natural or low-enriched uranium. The cross section for thermal neutron capture by ^{239}Pu is about 1,020 barns, and a sizable fraction produces ^{240}Pu rather than fission:



Consequently, when a fuel element containing uranium is subjected to a prolonged exposure to thermal neutrons, the amount of ^{240}Pu formed begins to increase relative to ^{239}Pu . The product ^{240}Pu is fissionable rather than fissile, and neutrons are captured to form ^{241}Pu ,



Higher-mass plutonium isotopes are produced by subsequent neutron captures. A fuel element in a plutonium production reactor is usually removed when $^{240}\text{Pu}/^{239}\text{Pu}$ is between

0.05 and 0.07, at which point there is generally considerable reactivity left in the fuel. In a natural-uranium-fueled reactor, this limits the burn-up of the initial uranium content of the fuel (sum of all isotopes) to 0.1–0.2%; in other words, at fuel discharge, ~99.8% of the original uranium remains in the form of uranium isotopes.

The plutonium recovered from irradiated uranium is always composed of a mixture of plutonium isotopes, providing the basis for “fingerprinting” the material. At very low burn-ups (low integrated neutron flux), ^{239}Pu dominates the mixture. At higher burn-ups, the concentrations of the other plutonium isotopes become more significant. For weapons applications, a compromise is struck between the production of unwanted plutonium isotopes and the inefficient use of the uranium starting material. Different countries strike somewhat different balances in defining the ^{240}Pu content of weapons-grade plutonium.

The ^{233}U – ^{232}Th fuel cycle offers many potential advantages in the generation of power when compared to reactors fueled with ^{235}U or ^{239}Pu ; even so, it is only a small factor in the nuclear power industry (Wymer 1968; Dukert 1970). This is mainly because thorium does not exhibit a fissile isotopic form in nature. A reactor cannot be fueled with thorium alone; thorium must be used in conjunction with one of the fissile materials as fuel. Another problem with the ^{233}U – ^{232}Th fuel cycle is the side production of ^{232}U . It has a half-life of ~70 years, so its intrinsic radioactivity is quite high, and one of the decay daughters (^{208}Tl) emits a 2.6-MeV γ ray, which is very hard to attenuate with shielding because of its very high energy. Even though the dose associated with freshly purified ^{233}U (containing ^{232}U) is low, a large sample quickly grows in dangerous amounts of daughter activities. Otherwise, the production of ^{233}U for weapons applications has many parallels with the production of plutonium. Irradiations tend to be of short duration at high flux, in order to minimize the buildup of undesirable uranium isotopes (including ^{232}U).

Analogous to plutonium produced in reactors, ^{233}U contains variable amounts of all the other uranium isotopes; this is particularly important when ^{235}U has been used to jump-start the breeding process. The heavier uranium isotopes eventually provide an avenue to the production of the plutonium isotopes, which may be dominated by ^{238}Pu rather than ^{239}Pu .

The application of nuclear forensic techniques to samples of purified heavy elements is well developed; however, when applied to unseparated spent reactor fuel, the methods become more complicated. The radionuclide content of a spent fuel sample is not controlled solely by radioactive decay, but is strongly influenced by neutron-induced transmutation. Chronometry based on the decay of the light plutonium isotopes cannot be performed due to the initial presence of an overwhelming quantity of uranium. The isotopic distribution of the plutonium isotopes and the concentration of fission products can provide a means by which the degree of transmutation can be estimated, unless the material started out as MOX fuel (where reprocessed plutonium is incorporated into fuel fabricated from uranium with insufficient fissile content to support the reactor application). More study is needed to extend the methodology to unprocessed fuel.

62.5.4 Recovery and Purification of Special Nuclear Materials from Reactor Products

Reprocessing is a general term that refers to the chemical recovery of a product heavy element following irradiation of fertile target material within an isotope production apparatus. A nuclear reactor is most often used for isotope production, with neutrons inducing the

desired nuclear transformations. For example, ^{237}Np targets are reprocessed for ^{238}Pu , and ^{232}Th blankets around breeder reactors are reprocessed for ^{233}U . The most important reprocessing efforts, contemporary and historic, have focused on the isolation of plutonium from irradiated uranium.

Most of the radioactivity in freshly discharged reactor fuel is due to the decays of the fission products (except for thorium-based fuels, where a significant fraction of the external dose is due to the decay of the daughters of ^{232}U). During the reactor irradiation, short-lived radioactive species quickly reach equilibrium concentrations, where the rate of loss due to decay (or neutron reactions) balances the rate of production. Products with half-lives comparable to, or longer than, the reactor irradiation interval continue to build up in the fuel. When reactor operations stop, radioactive decay provides a substantial reduction in total radioactivity over the next few months, leaving only longer-lived and stable species to be removed by fuel reprocessing.

Chemistry used in the recovery of plutonium from irradiated fuel must provide a separation from all these elements, other fission and activation products, and the actinides (including a large amount of unburned uranium), and still provide a complete recovery of plutonium. The same issues apply to the recovery of uranium from spent thorium fuel. Most of the processes must be performed remotely due to the intense radiation field associated with the spent fuel. As in the enrichment of uranium, the batch size in the later steps of the reprocessing procedure, where the fissile product has become more concentrated, is limited by the constraints of criticality safety. There is a balance between maximizing the yield of the precious fissile product and minimizing the concentrations of contaminant species left in the final product. These residual contaminants, which can be detected at very small concentrations using standard radiochemical techniques, provide a fingerprint of the industrial process used to recover the material.

A number of reprocessing methods have been used for the recovery of plutonium, and some are still undergoing active research. These techniques have included co-precipitation (e.g., with LaF_3 , BiPO_4), molten-salt extraction (in KCl , NaCl , MgCl_2), ion exchange, and fluoride volatility. However, the most-developed separation methods have been based on solvent extraction and are known by names such as PUREX, Redox, Halex, and Butex (Campbell and Burch 1990; Sood and Patil 1996). The Butex process, at one time employed at the Windscale works in Great Britain, involves a solvent extraction with dibutyl carbitol; the plutonium product was prone to contamination with fission-product ruthenium, for which the decontamination factor was only $\sim 10^3$. The Hexone process, used at the Hanford works in the early 1950s, involves a solvent extraction with methylisobutylketone; the plutonium product was characterized by contamination with fission product Zr , Nb , and Ce , for which the decontamination factors were $\sim 10^5$. Given an analytical sample of only tens of milligrams, the contaminant species from both processes are nevertheless readily observable in a clean chemical fraction by their emitted radiations.

Variants of the Purex (Pu-U Reduction EXtraction) process are the most widely used plutonium-reprocessing schemes worldwide. Purex on the industrial scale began at the US Savannah River Plant in 1954 and replaced the Redox process at the Hanford works in 1956; every country that has produced significant quantities of plutonium has exploited the method. In Purex, the organic extractant is tributyl phosphate (TBP). In addition to optimum complexation properties for nuclear analytes of interest, TBP has a low aqueous solubility and is chemically and radiolytically stable. The density of TBP (0.98 g/cm^3) is so close to that of water that it is common to dilute it in a lower density solvent. It is completely miscible with common organic solvents (e.g., kerosene, *n*-dodecane) at ordinary temperatures.

In preparation for a Purex separation, spent fuel undergoes decladding, after which the fuel matrix is dissolved in nitric acid. The oxidation state of the plutonium in solution is adjusted to Pu(IV) by the addition of a reagent such as NaNO_2 , N_2O_4 , or hydroxylamine. Pu(IV) and U(VI) are then extracted as $\text{Pu}(\text{NO}_3)_4 \cdot 2(\text{TBP})$ and $\text{UO}_2(\text{NO}_3)_2 \cdot 2(\text{TBP})$, respectively, into the TBP-bearing organic phase. This first step provides an effective decontamination from the fission products and the trivalent actinides. Ferrous sulfamate is then added to reduce Pu(IV) to Pu(III), after which it is back-extracted into another aqueous solution, separating uranium from plutonium. Another TBP extraction of the aqueous plutonium product stream provides additional decontamination from unwanted byproducts. The Pu(III) is then oxidized to Pu(IV) to prepare it for concentration from nitric acid solution by anion exchange, after which it is reduced and precipitated as PuF_3 . Subsequent roasting in an oxygen atmosphere converts the plutonium to the storage form, a mixture of PuF_4 and PuO_2 . PuO_2 is also produced through precipitation with hydrogen peroxide or oxalic acid, followed by calcination. Uranium is stripped from the initial TBP phase into a low-acid medium and subjected to a second extraction cycle for further purification. The purified uranium solutions are concentrated by evaporation, after which thermal denitration results in UO_3 as a final product for storage.

The recovery of uranium from irradiated thorium is also accomplished using a TBP extraction procedure, called Thorex (Long 1978). The main difference compared with Purex is that in Thorex the valuable fissile material is uranium, and care must be taken in both efficiency of recovery and limitation of batch size (criticality safety), while in Purex the uranium fraction is usually less valuable and it exhibits a ^{235}U enrichment that does not present a severe criticality concern. Another difference is that neither the uranium product nor the thorium matrix are oxidized or reduced from their initial valences. As with Purex, there is a built-in decay time before Thorex can be performed, required by the 27-day half-life of ^{233}Pa decay to fissile ^{233}U .

In a two-cycle Purex procedure, the recoveries of both Pu and U are on the order of 99.9%; the Pu/U separation factor is 10^6 . The literature reports that plutonium decontamination factors from the fission products are $\sim 10^8$, and that the only long-lived impurities detected in the final product are ^{93}Zr , ^{99}Tc , and ^{106}Ru . However, the authors' experience has been that the light rare earths (mainly La and Ce), thorium, neptunium, and the trivalent actinides (Am and Cm), which exhibit some degree of complexation in nitrate media (Guseva and Tikhomirova 1979), are present in a gram-sized plutonium sample at concentrations that are detectable by radiochemical means.

62.5.5 Heavy Element Metals and Alloys

The fuel in most nuclear reactors is in the form of a heat-resistant ceramic. The main use of the metallic forms of the special nuclear materials is as fuel in nuclear explosive devices. Consequently, interdiction of a metal sample is the “smoking gun” that points to a weapons application.

Even though there are substantial differences between the metallic properties of plutonium and uranium, there are a number of similarities, both in chemical properties and in methods of production. Both metals build up oxide coatings on exposure to air, resulting in their passivation. Consequently, strong nitric acid will not attack either of the metals without the presence of a complexing agent. Uranium and plutonium are pyrophoric in bulk, burning

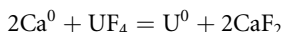
with an intense white light. Fine powders of both metals (which can be produced by hydriding/dehydriding) can spontaneously ignite unless protected from air. Both metals exist in more than one solid allotropic form, and make a very limited number of intermetallic solutions; powder metallurgy techniques have been developed to produce useful alloys from materials that are insoluble in the molten elements (Warner 1953, Vol'skii and Sterlin 1970).

Uranium is a dense silvery metal. It is malleable, ductile, and slightly paramagnetic. Though it does not form many solid solutions, it forms a wide range of intermetallic compounds. Uranium metal is a poor electrical conductor, with conductivity only about one half that of iron. It is also semi-plastic, and tends to yield under load.

Uranium metal displays three allotropic forms between room temperature and its melting point at 1,135°C. The orthorhombic α phase exists at temperatures up to 668°C. Uranium metal is rolled only in this easily worked α phase, otherwise cracking occurs. At temperatures over 500°C the metal starts to soften, but heat generated in working the metal can cause transformation into the complex tetragonal β phase, which is hard and brittle; β -phase uranium exists at temperatures between ~668°C and 776°C. Above 776°C, uranium metal displays the body-centered-cubic γ phase; the metal is quite soft at these temperatures, deforming under its own weight. Consequently, the γ phase is easiest to extrude. Hot uranium metal reacts with steel dies and rollers; therefore other materials are used in its manipulation.

Impurities in a uranium sample can strongly affect the phase-transition temperatures. Both α and β phases of uranium are complex, and do not form many solid solutions; conversely, the γ phase forms extensive solid solutions. For instance, addition of molybdenum to uranium metal at 2% concentration causes the β phase to completely disappear and stabilizes the γ phase sufficiently that it can be preserved at room temperature by rapid quenching. Important alloys of uranium include U-Mo, which is fairly chemically inert and has applications in the aircraft industry; U-Nb and U-Nb-Zr, with applications in the nuclear industry; and U-Ti, a very strong alloy.

The formation of the halides of Ca and Mg are favored over the formation of the halides of uranium at all temperatures up to 1,500°C; therefore, the reaction of a uranium tetrahalide with Ca^0 or Mg^0 will proceed exothermically to produce uranium metal. However, UCl_4 , UBr_4 , and UI_4 are deliquescent and air-reactive; practicality dictates that the production of uranium metal involves the reaction of UF_4 with either Mg^0 or Ca^0 :



The reaction of Ca^0 with UF_4 is sufficiently exothermic that both CaF_2 and U^0 reaction products are molten; the equivalent Mg^0 reaction is less exothermic, so the reaction must be initiated at an elevated temperature to result in molten products. CaF_2 and MgF_2 are not soluble in molten uranium, so the reaction produces a dense metallic uranium phase and a lower-density salt phase; unreacted starting materials are more soluble in the salt phase and concentrate there. After cooling, the salt cake can be physically separated from the metal product and discarded.

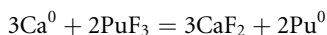
The reaction of Ca^0 or Mg^0 with UO_2 produces uranium metal powder, a consequence of the refractory character of the CaO or MgO reaction products that interfere with the formation of a molten metal billet. Ca^0 is preferred over Mg^0 , which results in the formation of a U^0 powder of finer particles at a lower chemical yield; the smaller powder size increases the pyrophoricity hazard. Metal powder is also formed in the electrolysis of UCl_3 or UF_4 dissolved

in a molten KCl/NaCl, or KUF₅ or UF₄ dissolved in molten CaCl₂/NaCl, both under an argon atmosphere; particle size is governed by the temperature and the electrolytic current density. Very fine uranium powder results from a hydriding/dehydriding process, but the pyrophoricity of the final product makes it difficult to use.

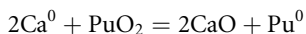
Plutonium metal is a poor conductor of both heat and electricity. The electrical resistivity of α -phase plutonium is the highest of all metals, almost that of a semiconductor. The metal has six solid allotropic forms below its melting point at 640°C. This prevents solid unalloyed plutonium metal from being used in sustained applications where heat is generated (e.g., nuclear fuel elements); the expansion that occurs in going from α phase to δ phase is greater than that occurring in any other metal except tin. Monoclinic α -phase plutonium is stable at temperatures up to 115°C, and has a density of 19.8 g/cm³. It is hard and brittle and difficult to machine. From 115°C to 185°C, the body-centered monoclinic β phase is stable. From 185°C to 310°C, the orthorhombic γ phase is stable. Phase changes between α - and β -Pu and between β - and γ -Pu are sluggish, taking place over several degrees. From 310°C to 452°C, the face-centered-cubic δ phase is stable, which is easy to machine, roll, and extrude. It is one of the few materials that contracts on heating (negative linear expansion coefficient). From 452°C to 480°C, the cubic-close-packed δ' phase is stable, and between 480°C and the melting point (640°C) the body-centered-cubic ϵ phase is stable.

Plutonium forms refractory compounds with A-subgroup metals and metalloids, but only the δ and ϵ phases exhibit an affinity for solid solutions. Most δ -phase solid solutions can be retained at room temperature by rapid quenching. Significant solid solutions in the other Pu phases are rare; Np and Pu are mutually soluble in the α phase, and Th and U mix with Pu in both the β and γ phases. Alpha-phase plutonium is highly reactive with oxygen, while δ -phase plutonium alloys are not as reactive.

The methods of producing plutonium metal are similar to those used in the production of uranium metal. The best reactants are PuF₄ and either Ca⁰ or Mg⁰. PuF₃ can also be reduced by the alkaline earth metals under an argon atmosphere:



I₂ is often added as an accelerant (“booster”). The reaction products are molten, and the mutually insoluble phases are separated mechanically after cooling. Plutonium metal is also produced by the reaction of PuCl₃ with Ca⁰; however, even though the melting points of the products are lower, the reaction is considerably less exothermic and requires the addition of a booster. Plutonium metal can also be produced in the reaction of Ca⁰ or Mg⁰ with PuO₂:



This chemical system is fluorine-free, which reduces the neutron background in the laboratory caused by ¹⁹F(α ,n) reactions. The final product consists of small beads of the metal, coated with the CaO reaction product that prevents the formation of a billet. The beads are recovered by treatment with dilute acetic acid, followed by a nitric acid wash.

Plutonium metal is often purified by electrolytic refining; the plutonium sample is immersed in a molten chloride salt under an inert atmosphere, comprising the anode in an electrolytic cell. Liquid Pu metal is collected on the surface of a tungsten cathode and drips off into a collector. Transition-metal contaminants remain in the residue of the anode, and rare earths and other actinides concentrate in the molten salt. The yield of purified Pu metal can be as high as 97%. Zone melting is also used to purify metallic plutonium; the plutonium is fabricated into a bar along which a high-temperature zone is passed. As the melt zone is moved

along the bar, impurities tend to concentrate in the melt. After repeated passes, the ends of the bar contain most of the impurities and are discarded.

Plutonium alloys can be prepared by melting and mixing the constituent metals; however, it is possible to introduce oxides or halides of plutonium to a melt of the alloying element if it is sufficiently reducing, and may remove the need for an inert atmosphere while producing the alloy. Important δ -phase weapon alloys are made by adding PuF_3 to molten Ga or Al.

62.6 Case Studies

62.6.1 Overview

Although relevant exercises have been conducted, and Cold War nuclear weapons programs provide validated analytic platforms, there have been no actual post-det terrorist incidents involving an IND or RDD to date. Consequently, no technical investigations in the contemporary embodiment of nuclear forensic analysis exist for an actual post-det situation, and all discussed case studies necessarily focus on interdicted, pre-det materials. (However, a nuclear accident that is perhaps exemplary of maximum-credible consequences of successful terrorist activities was the uncontrolled criticality and resultant explosion of the Soviet RBMK power reactor at Chernobyl in 1986.)

Over 1993–2008, the IAEA recorded >1,500 incidents of worldwide nuclear trafficking in their database. Of course, not all of these cases involved perilous radioactive materials; less than half were actual seizures, and most were scams, but on the order of 15–20 of them entailed weapons-usable SNM. However, some scams on the nuclear black market have been so incredible that one seriously questions the technical competence of such individuals, even if they manage to actually obtain dangerous materials.

One such hoax is the “red-mercury” phenomenon. This mythical substance is alleged to induce the detonation of a thermonuclear bomb without requiring the inconvenience of developing a primary fission trigger (in its nuclear embodiment). The record of red-Hg sales indicates that it has also been offered as a substance for guided-missile control, gravity bombs, antiradar coatings, enriched-U production, heat conduction, and medicines. A specification sheet accompanying one such suite of samples analyzed at Livermore claimed a density of $>20 \text{ g/cm}^3$ and the presence of Lr as a transuranic impurity. But the longest-lived isotope of Lr has a half-life of only $\sim 3 \text{ h}$, and it can be produced only a few atoms at a time through heavy-ion irradiation of an actinide target. Despite such nonsense, however, red-Hg scams have a history dating to 1979, involve significant sums of money, and persist to the present day (indicating that underestimating the knowledge base of some nuclear profiteers and end-users may be difficult to do).

The rest of this section will give an overview of selected nuclear casework conducted at Lawrence Livermore National Laboratory (LLNL) during the 1990s. These investigations provide examples of various types of material specimens and scams that, despite their age, remain representative of the nature of questioned samples analyzed today. The time that has lapsed since primary investigation is indicative that they have been adjudicated; ongoing investigations and more recent cases remain restricted as a matter of laboratory policy and agreements with submitting agencies.

62.6.2 Hoax: Nonradioactive – Source Analyses Only

In 1996, US federal law enforcement requested accelerated forensic analyses of a small (0.37 g) fragment of gray metal, to be conducted in real time during an ongoing operation. The material was being advertised as a sample of a larger available quantity – a substance that could substitute for HEU in an atomic weapon. The specimen was determined to be high-purity Sc, and it was characterized at macro, minor, trace, and ultra-trace concentrations of diverse species by a comprehensive suite of analytic techniques. A full description of these various analyses, with photographs, tables, and figures, has been previously published in the refereed literature (Grant et al. 1998a).

Forensic radiochemical assays of a suite of heavy elements (Ra, Ac, Th, Pa, U, Np, Pu, Am, and Cm) were negative, with the exception of ^{230}Th at trace level. Th-230 is a daughter product of the decay of natural U and was present at a specific activity of (2.21 ± 0.74) dpm/g. As its half-life is not sufficiently long for independent existence derived from primal nucleosynthesis, the presence of ^{230}Th in the Sc specimen was indicative of a prior association with U (although only 0.15 ppm of residual U remained in the sample). Indeed, the commercial recovery of Sc from U-mining operations is an historic endeavor (Lash and Ross 1961; McGinley and Facer 1976).

Metallurgical examination of the Sc suggested that it originated in a casting pour. Quantitative assay of 55 elements revealed C, P, Cr, and Fe as the major impurities, and the presence of relatively high P concentration (0.3%) also supported a former connection to U mining or processing. Phosphoric acid, TBP, and HDEHP are often used in these enterprises. No fissionable species or weaponization indicators were detected in the specimen. Although Sc is chemically similar to U, their nuclear properties are quite different, and to assert its use as substitute HEU was clearly a hoax.

As passing interest, anomalous characteristics for which no clear explanation emerged were also observed for this particular sample. These included the enrichments of several parts-per-million-level lanthanides over their natural values by appreciable factors and the presence of synthetic, odd-chain fatty acids.

62.6.3 Hoax: Radioactive – Source Analyses Only

Attempts by subnational (and perhaps some national) groups to acquire nuclear materials for use in weapons projects created a cottage industry in illicit-material hoaxes, driven principally by the lure of large prospective profits. One such persistent scam, centered in Southeast Asia, trades in specimens of irregularly shaped metal alleged to be ^{235}U . These pieces often have markings of “uranium,” “made in USA,” a serial number, the skull-and-crossbones symbol, and others.

Such a metal object was discovered while cleaning an office in a consulate in 1996, and it had markings identical to those in illicit sales casework that had been assessed by LLNL in 1988. The sample was proffered by a local military official as nuclear-weapons-grade HEU. Although “lost” in the embassy for 8 years, the part submitted for analysis in 1996 was derived from the 1988 investigation and may actually be the specimen that began the Southeast Asian uranium scam.

This questioned sample was at least radioactive, and it weighed 8.96 kg. It had a complex shape, and a number of arc-shaped scratches on the surface led to the suggestion that it may

have been part of a hinge, possibly from a shipping container. The density was measured to be 17 g/cm^3 . Material composition was “U-10Moly,” an alloy of U with 9.9 wt% Mo, and it had been electroplated with a thin ($90 \text{ }\mu\text{m}$) surface layer of pure ($>99\%$) Ni. The U was significantly depleted (D-38) to $\sim 0.3 \text{ wt}\%$, but not to the modern D-38 standard: concentrations of the minor U isotopes were too elevated. Chronometry gave the last chemical purification of the U as $1961 \pm 3 \text{ years}$. An open-source, primary reference for this investigation is Grant et al. (1998b).

No evidence could be found for an association of use or fabrication of the item by the nuclear industry. The part had been made by the National Lead Company of New York, but the company was out of business. The D-38 specimen was most likely a component of an aircraft counterweight unit, and was probably military in origin.

62.6.4 Incident: Natural Radioactivity – Source Analyses Only

In 1998, a high-school student in the San Francisco Bay Area purchased a vial of yellow powder at a local flea market. It was labeled “97% pure uranium.” The student brought the material to school, where a teacher recognized it as a potential sample of yellowcake. The teacher confiscated the material and gave the entire specimen to knowledgeable staff at UC Berkeley, which then requested assistance from the Department of Energy (DOE) Oakland Office for sample identification. DOE deployed a regional RAP team (Internet 2009) to transport the sample to the Livermore Forensic Science Center.

Primary containment of the specimen was a snap-top plastic vial $\sim 3 \text{ cm}$ in diameter and 8.5 cm long. It was nearly full of the questioned powder, which weighed $\sim 100 \text{ g}$. Secondary containment during RAP transport was a coffee can, while an outer container consisted of a cardboard box. Exposure rate readings ($\beta + \gamma$) were $\leq 0.1 \text{ mR/h}$ at the surfaces of both the box and the coffee can, and was $\sim 0.5 \text{ mR/h}$ at the wall of the primary vial. No external α radioactivity was detected.

The material was a light-yellow, very fine powder, without the “wet” appearance associated with U nitrates or chlorides. It was insoluble in water and did not appreciably affect the pH of the supernatant liquid, but it readily dissolved in only slightly acidified solution. Approximately 0.2 g was quantitatively dissolved in 25 ml of dilute HNO_3 , and suitable aliquots were analyzed by γ -ray and α spectrometry.

No radionuclides, other than the naturally occurring isotopes of U and their daughters, were measured in excess of background activities in any of the α or γ spectra. The weighted averages and 1s uncertainties of empirical data from these counting results were $^{235/238}\text{U} = (7.02 \pm 0.04) \times 10^{-3}$ and $^{234/238}\text{U} = (5.11 \pm 0.03) \times 10^{-5}$ (mass ratios). Additionally, upper limits were placed on the following isotopic ratios with ^{238}U : $^{232}\text{U} (\leq 7 \times 10^{-13})$, $^{232}\text{Th} (\leq 1.5 \times 10^{-3})$, $^{239}\text{Pu} (\leq 4 \times 10^{-10})$, and $^{238}\text{Pu} (\leq 8 \times 10^{-13})$. Further, quantitative dilution gave the concentration of U in the oxide powder as $(0.744 \pm 0.022) \text{ g U/g specimen}$.

Thus, the questioned material was a U salt with an isotopic composition very close to that of natural abundance. Based on the chemical behavior, its color, and the grams-per-gram assay, it is likely that the specimen was, in fact, anhydrous uranyl hydroxide or yellowcake ($0.78 \text{ g U/g sample}$). Although a relatively routine investigation, the officials involved requested and received expedited, overnight analyses. Apparently, the innocuous student was at some risk for potential legal repercussions had the material been other than natural U.

62.6.5 Real: Radioactive – Source and Route Analyses

A Turkish national was stopped by Bulgarian border guards in 1999, who then discovered a Pb container secreted in the trunk of the car. The Pb shield contained a yellow cushioning material, paper molding, and, at the center, a sealed-glass ampoule with gray-black powder inside. A full rendering of the timeline, case details, photographs, tables, and figures for this investigation may be found in Moody et al. (2005). This was perhaps the most complete and expansive interrogation of illicit nuclear material ever conducted to that point, including both source and route forensic analyses, and it served as an exemplar for subsequent nuclear forensic investigations undertaken at LLNL.

The black powder weighed ~ 4 g, had a density of 2.1 g/cm^3 , and appeared effectively homogeneous under stereomicroscope examination. X-ray diffraction analysis identified the material as predominantly U_3O_8 , with a much lesser component consisting of a hydrated uranyl fluoride compound. Quantitative analysis of 72 elements (from Li to Th) by ICP-MS and other techniques measured the total impurity level between 500 and 800 ppmw, indicative of a batch reprocessing operation. SEM and TEM measurements revealed that the oxide powder comprised extremely friable, loosely compacted clumps of $<100 \text{ }\mu\text{m}$ in size. Much smaller particles made up the clumps, and were characterized by a very fine grain-size distribution of <0.1 to $\sim 1 \text{ }\mu\text{m}$, with the mean size of an empirical measurement of 816 grains being $\sim 160 \text{ nm}$. Such particle size was unusual within the authors' experience, in that it is unnecessary for operations in US facilities and constitutes a considerable respiratory hazard.

Radiochemical analyses of the sample disclosed that it had been recovered from reactor-irradiated material. Quantitative measurements were made of ^{232}U – ^{236}U and ^{238}U , and ^{234}U was enriched to 1.1 wt% and ^{236}U to 12 wt%. The enrichment of ^{235}U was 73 wt%, making the specimen weapons-usable material. This was clearly no hoax.

The sample also contained ppb levels of Pu and ^{237}Np , and high ^{238}Pu content was consistent with reactor burn-up of light-mass U isotopes. The residual fission products ^{134}Cs , ^{137}Cs , and ^{125}Sb were also detected, providing supplemental evidence of reactor irradiation and reprocessing. The absence of other fission products gave some clues to the reprocessing chemistry.

With the forensic actinide measurements as input, and the assumption of a simple cross-section model, the isotopic composition of the starting material could be computationally reconstructed. The results were $^{235}\text{U} = 90\%$, $^{238}\text{U} = 9\%$, and $^{234}\text{U} = 1\%$. The material had been used as fuel in a nuclear reactor, and the reactor type was light-water research or propulsion (in fact, a pressurized-water reactor (PWR)). The high ^{236}U concentration signified a long irradiation history that had consumed $\sim 50\%$ of the initial ^{235}U .

Two Pu and seven U radiochronometers were measured to determine the time elapsed since the sample was last chemically processed. All but one chronometer were reasonably consistent, and the weighted average of the data was (6.46 ± 0.14) years before the LLNL assay date of April 17, 2000. The processing date was therefore approximately October 30, 1993, with an uncertainty of <2 months (2s). Only ^{237}Np from ^{241}Pu – ^{237}Np was present in large excess over the in-growth concentration, and it gave an anomalous age of ~ 130 years. Reprocessing was thus less successful in removing trivalent species (e.g., PUREX). The ^{241}Pu – ^{241}Am contaminant age was the same as the U age, indicating that Pu was also likely present during purification and not introduced later. There was no evidence of spoofing.

Forensic analyses of the collateral route evidence were also important for attribution in this case. The yellow material inside the Pb shield was determined via FTIR and GC-MS to be paraffin wax (C_nH_{2n+2}). Gel-permeation chromatography measured a MW ~ 390 Da and an average C number ~ 26 . The distinctive yellow color was due to an appreciable loading (64–77 wt%) of $BaCrO_4$ of 1–4 μm size dispersion. The organic component was characterized by SPME/GC-MS, and the result was a chemical fingerprint consisting of 47 individual species, with five naphthalene varieties being relatively unusual compounds.

Assessment of the wax was facilitated by the fact that the inorganic $BaCrO_4$ is seldom used by Western countries today because of the environmental toxicity of Cr. However, it is used as yellow pigment in paint, ceramics, and other applications, as well as an oxidizer in energetic materials in South America, Asia, and Eastern Europe.

Optical microscopy of the paper in the mold liner, as well as a gummed label on the Pb, was used to identify and quantitate the hardwood and softwood fibers composing the papers. The species of trees represented included Scotch pine, spruce, aspen, alder, and birch. The fibers were determined to be definitely not North American, inconsistent with those found in Western Europe or Scandinavia, but consistent with an Eastern European origin.

Metallurgy of the Pb shield concluded that it had been cast in a crude mold, probably sand, and fashioned by hand. Exterior markings gave clear evidence of coarse hand-filing for contouring and smoothing, but no indication of the use of machine tools. The Pb was an alloy containing ~ 5 wt% Sb to increase metal malleability. The isotopic composition of the Pb was inconsistent with mining operations in the United States, but similar to ores obtained from Asia or Europe.

In contrast to the Pb container, the glass ampoule represented skilled craftsmanship. The material composition was consistent with commercial soft borosilicate glass.

Overall attribution of this sample attempted to integrate the various forensic results into a self-consistent picture. The HEU was definitely not of US origin, as an initial enrichment of 90% ^{235}U is distinctly different from the $\sim 93.5\%$ composition of US Oralloy. This conclusion was further supported by the extremely fine grain-size distribution. Moreover, while the collateral pathway indicators (paraffin wax, paper composition, and Pb-shield isotope ratios) both excluded and implicated multiple regions of the world, Eastern Europe was linked as a potential source of materials by all of these diverse analyses.

Comprehensive attribution of the Bulgarian HEU is still incomplete. However, a ^{235}U enrichment of 89–90% was the material standard employed by the USSR for its nuclear weapons and nuclear power programs and, in conjunction with the other forensic analyses, connects the former Soviet Union to the likely origin of this sample.

References

- | | |
|---|---|
| <p>Alessandretto A, Allegretti F, Brofferio C, Camin DV, Remonesi O, Fiorini E, Giuliani A, Pavan M, Pessina G, Pizzini S, Previtali E, Sverzellati P, Zanotti L (1993) Nucl Inst Meth Phys Res B83:539</p> <p>Anderson RM (ed) (1990) Specimen preparation for transmission electron microscopy II, MRS Symposium Proceedings, Vol. 199, Materials Research Society, Pittsburgh PA</p> | <p>Aumann DC, Muellen G (1975) Nucl Inst Methods 115:75</p> <p>Bark LS, Duncan G, Graham RJT (1967) Analyst 92:347</p> <p>Becker JS (2003) Spectrochim Acta B 58:1757</p> <p>Becker JS, Dietze H-J (2000) Int J Mass Spectrom 197:1</p> <p>Becker EW, Noguiera-Batista P, Voelcker H (1981) Nucl Technol 52:105</p> <p>Beyerle U, Aeschbach-Hertig W, Imboden DM, Baur H, Graf T, Kipfer R (2000) Environ Sci Technol 34:2042</p> |
|---|---|

- Boehm HDV, Michaels W, Weitkamp C (1978) *Optics* Comm 26(2):178
- Boyle RW (1982) *Geochemical prospecting for thorium and uranium deposits*. Elsevier, Amsterdam
- Braverman JC, Anderson RM, McDonald ML (eds) (1988) *Specimen preparation for transmission electron microscopy I. MRS Symposium Proceedings, Vol. 115*, Materials Research Society, Pittsburgh PA
- Brundle CR, Evans CA Jr, Wilson S (1992) *Encyclopedia of materials characterization*. Butterworth-Heinemann, Boston
- Campbell DO, Burch WD (1990) *J Radioanal Nucl Chem Articles* 142(1):303
- Chiarappa-Zucca ML, Dingley KH, Roberts ML, Velsko CA, Love AH (2002) *Anal Chem* 74:6285
- Cowan GA (1976) *Sci Am* 235(1):36
- Cronkite EP (1979) Tritium and other labeled organic compounds incorporated in genetic material. National Council on Radiation Protection and Measurements, Washington DC
- Davidson JD, Feigelson P (1957) *Int J Appl Rad Isotop* 2:1
- Duckworth HE, Barber RC, Venkatasubramanian VS (1986) *Mass spectrometry*. Cambridge University Press, Cambridge
- Dukert JM (1970) *Thorium and the third fuel*. Oak Ridge, TN, US Atomic Energy Commission/Division of Technical Information
- Duncan JF, Cook GB (1968) *Isotopes in chemistry*. Clarendon, Oxford
- Firestone RB, SHIRLEY VS (eds) (1996) *Table of isotopes*, 8th edn. Wiley, New York
- Fronzel JW, Fleischer M, James RS (1967) *Glossary of uranium and thorium bearing minerals*, 4th edn. Geological Survey Bulletin #1250, U.S. Government Printing Office, Washington, D.C
- Gillen G, Bright D (2003) *Scanning* 25:165
- Girardi F, Pietra R (1976) *At Energy Rev* 14:521
- Glasstone S, Sesonske A (1967) *Nuclear reactor engineering*. Van Nostrand, Princeton
- Goldstein JI, Newbury DE, Echlin P, Joy DC, Romig ADJR, Lyman CE, Fiori C, Lifshin E (1992) *Scanning electron microscopy and X-ray microanalysis: a text for biologists, materials scientists, and geologists*. Plenum, New York
- Gonzalez ER, Peterson DS (2009) *J Radionucl Nucl Chem* 282:543
- Gowing M (1964) *Britain and atomic energy (1939–1945)*. McMillan, London
- Grahame DC, Seaborg GT (1938) *J Am Chem Soc* 60:2524
- Grainger L (1958) *Uranium and thorium*. George Newnes, London
- Grant WL, Wannenburg JJ, Haarhoff PC (1977) The cascade technique for the South African enrichment process. *AIChE Symposium Series* 73.
- Grant PM, Whipple RE, Andresen BD (1995a) *J Foren Sci* 40:18
- Grant PM, Whipple RE, Bazan F, Brunk JL, Wong KM, Russo RE, Andresen BD (1995b) *J Radioanal Nucl Chem Articles* 193:165
- Grant PM, Moody KJ, Hutcheon ID, Phinney DL, Haas JS, Volpe AM, Oldani JJ, Whipple RE, Stoyer N, Alcaraz A, Andrews JE, Russo RE, Klunder GL, Andresen BD, Cantlin S (1998a) *J Foren Sci* 43:680
- Grant PM, Moody KJ, Hutcheon ID, Phinney DL, Whipple RE, Haas JS, Alcaraz A, Andrews JE, Klunder GL, Russo RE, Fickies TE, Pelkey GE, Andresen BD, Kruchten DA, Cantlin S (1998b) *J Radioanal Nucl Chem* 235:129
- Guseva LI, Tikhomirova GS (1979) *J Radioanal Chem* 52:369
- Hahn O (1936) *Applied radiochemistry*. Cornell University Press, Ithaca, NY
- Hirsch PB, Howie A, Nicholson RB, Pashley DW, Whelan MJ (1971) *Electron microscopy of thin crystals*. Butterworths, London
- Horrocks DL (1974) *Applications of liquid scintillation counting*, Chap. 6. Academic, New York
- Hulet EK (1964) *J Inorg Nucl Chem* 26:1721
- Hyde EK (1956) Radiochemical separation methods for the actinide elements. In: *Proceedings of the International Conference on the peaceful use of atomic energy*, Geneva, 1955. A/CONF. 8/7, New York: United Nations, p 281
- Internet, 2009, <http://www.nv.doe.gov/library/factsheets/RAP.pdf>; http://nnsa.energy.gov/emergency_ops/1709.htm
- Ireland TR (1995) *Adv Anal Geochem* 2:1
- Johnstone RAW, Herbert CG (2002) *Mass spectrometry basics*. CRC, Boca Raton, FL
- Joy DC, Romig AD, Goldstein JL (eds) (1986) *Principles of analytical electron microscopy*. Plenum, New York
- Katz JJ, Seaborg GT (1957) *The chemistry of the actinide elements*. Wiley, New York
- Krass AS, Boskma P, Elzen B, Smit WA (1983) *Uranium enrichment and nuclear weapon proliferation*. Taylor and Francis, New York
- Krinsley DH, Pye K, Boggs S Jr, Tovey NK (1998) *Backscattered scanning electron microscopy and image analysis of sediments and sedimentary rocks*. Cambridge University Press, Cambridge
- Kristo MJ, Smith DK, Niemeyer S (2006) *Model action plan for nuclear forensics and nuclear attribution*. IAEA Nuclear Security Series No. 2, International Atomic Energy Agency, Vienna
- Laidler JB, Brown F (1962) *J Inorg Nucl Chem* 24:1485
- Lash LD, Ross JR (1961) *J Metals* August 1961:555
- Lavrukhina AK et al (1967) *Chemical analysis of radioactive materials*. CRC, Cleveland, Ohio
- Letokov VS (1979) *Nature* 277:605
- Linge KL, Jarvis KE (2009) *Geostand Geoanal Res* 33:445
- Lister B (1978) *The preparation of polished sections*. Rep. No. 78/27, Institute of Geological Science, London

- London H (1961) Separation of isotopes. George Newnes, London
- Long JT (1978) Engineering for nuclear fuel reprocessing, Chap. 3. American Nuclear Society, La Grange Park, IL
- Lubenau JO, Yusko JG (1995) *Health Phys* 68:440
- Lubenau JO, Yusko JG (1998) *Health Phys* 74:293
- Massignón D (1958) Proceedings of Second UNO Geneva Conference on Peaceful Uses of Atomic Energy, Vol 4. UNO, New York
- Mayer K, Wallenius M, Fanghanel T (2007) *J Alloys Compounds* 444–445:50
- McGinley FE, Facer JF (1976) Uranium ore processing, STI/PUB/453. International Atomic Energy Agency, Vienna, pp 181–190
- Moody KJ, Hutcheon ID, Grant PM (2005) Nuclear forensic analysis. CRC/Taylor & Francis, Boca Raton, FL
- Moskalev YuI (ed) (1968) Tritium oxide. Atomizdat, Moscow
- Mueller G, Aumann DC (1976) *Nucl Inst Methods* 128:425
- Myers RJ, Metzler DE, Swift EH (1950) *J Am Chem Soc* 72:3767
- Newbury D, Joy DC, Echlin P, Fiori CE, Goldstein JI (1986) Advanced scanning electron microscopy and X-ray microanalysis. Plenum, New York
- Nier AO, Booth ET, Dunning JR, Grosse AV (1940) *Phys Rev* 57:546
- Olander DR (1978) *Sci Am* 239(2):37
- Pawliszyn J (1997) Solid-phase microextraction: theory and practice. Wiley-VCH, New York
- Peteraco N, Kubic T (2004) Color atlas and manual of microscopy for criminalists, chemists, and conservators. CRC, Boca Raton, FL
- Platzner IT (1997) Modern isotope ratio mass spectrometry. In: Chemical Analysis, Vol 145. Wiley, Chichester
- Pluta M (1988) Advanced light microscopy. Elsevier, Amsterdam
- Ranebo Y, Hedberg PML, Whitehouse MJ, Ingenerid K, Littmann S (2009) *J Anal Atom Spectrom* 24:277
- Reed SJB (1996) Electron microprobe analysis and scanning electron microscopy in mineralogy. Cambridge University Press, Cambridge
- Reimer L (1984) Transmission electron microscopy: physics of image formation. Springer, Berlin
- Reimer L (1985) Scanning electron microscopy. Springer, Berlin
- Reinig WC, Hutchinson JMR, Koranda JJ, Moghissi AA, Osbourne RV, Ostlund HG (1976) Tritium measurement techniques, NCRP report 47. National Council on Radiation Protection and Measurements, Washington DC
- Rhodes R (1986) The making of the atomic bomb. Simon & Schuster, New York
- Richter S, Goldberg SA (2003) *Int J Mass Spectrom* 229:181
- Ruzicki J (1968) Stoichiometry in radiochemical analysis. Pergamon, New York
- Saferstein R (2002) In: Saferstein R (ed) Forensic science handbook, Vol I, 2nd edn. Prentice-Hall, Upper Saddle River, NJ, pp 117–159
- Sansoni B, Kracke W (1971) Rapid determination of low-level alpha and beta activities in biological material using wet ashing by OH radicals. In: Rapid methods for measuring radioactivity in the environment. International Atomic Energy Agency, Vienna
- Schmidt K-H, Sahm C-C, Pielenz K, Clerc H-G (1984) *Z Phys A* 316:19
- Sill CW, Williams RL (1981) *Anal Chem* 53:412
- Sokova EK, Potter WC (2008) Illicit nuclear trafficking: collective experience and the way forward, STI/PUB/1316. International Atomic Energy Agency, Vienna, pp 405–423
- Sood DD, Patil SK (1996) *J Radioanal Nucl Chem Articles* 203(2):547
- Stafford DT (2005) In: Saferstein R (ed) Forensic Science handbook, Vol II, 2nd edn. Prentice-Hall, Upper Saddle River, NJ, pp 81–109
- Stone R (2001) *Science* 292:1632
- Surano KA, Hudson GB, Failor RA, Sims JM, Holland RC, Maclean SC, Garrison JC (1992) *J Radioanal Nucl Chem* 161:443
- Tamborini G, Betti M (2000) *Mikrochim Acta* 132:411
- Vasaru G (1975) Separation of isotopes by thermal diffusion. Rumanian Academy, 1972, Bucharest, distributed by USERDA, report ERDA-tr-32
- Vickerman JC (1998) Surface analysis – the principal techniques. Wiley, Chichester
- Villani S (ed) (1979) Uranium enrichment, Topics in Applied Physics, Vol 35. Springer, Berlin
- Vol'skii AN, Sterlin YAM (1970) Metallurgy of plutonium. Israel Program for Scientific Translation, Jerusalem
- Wallenius M, Morgenstern A, Apostolidis C, Mayer K (2002) *Anal Bioanal Chem* 374:379
- Warner JC (ed) (1953) Metallurgy of uranium and its alloys. US Atomic Energy Commission Technical Information Service, Oak Ridge, TN
- Watt DE, Ramsden D (1964) High sensitivity counting techniques. Macmillan, New York
- Wenk H-R, Champness PE, Christie JM, Crowley JM, Heuer AH, Thomas G, Tighe NJ (eds) (1976) Electron microscopy in mineralogy. Springer, Berlin
- White FA, Wood GM (1986) Mass spectrometry. Wiley, New York
- Williams P, Woessner PN (1996) *Sci Am* 274(1):40
- Wills BA (1997) Mineral processing technology, 6th edn. Butterworth/Heinemann, Oxford
- Wilson RG, Stevie FA, Magee CA (1989) Secondary ion mass spectrometry: a practical handbook for depth profiling and bulk impurity analysis. Wiley-Interscience, New York

- Wong KY, Khan TA, Guglielmi F (1984) Canadian tritium experience. Ontario Hydro, Toronto
- Wymer RG (ed) (1968) Thorium fuel cycle. In: Proceedings of the Second International Thorium Fuel Cycle Symposium, Gatlinburg, TN, 1966. US Atomic Energy Commission/Division of Technical Information, Oak Ridge, TN
- Yinon J (ed) (1987) Forensic mass spectrometry. CRC, Boca Raton, FL
- Zinner E (1989) Isotopic measurements with the ion microprobe. In: Shanks WC, Criss R (eds) U.S. Geological Survey Bulletin 1890. Government Printing Office, Washington DC: U.S, pp 145–162



63 Nuclear Safeguards Verification Measurement Techniques

M. Zendel¹ · D. L. Donohue¹ · E. Kuhn² · S. Deron² · T. Bíró³

¹International Atomic Energy Agency, Vienna, Austria

²Retired from the International Atomic Energy Agency, Vienna, Austria

³Institute of Isotopes, HAS, Budapest, Hungary

63.1	<i>Introduction</i>	2896
63.2	<i>Safeguards Verification Measurement Procedures</i>	2898
63.2.1	Diversion Strategy	2899
63.2.2	Type of Material	2899
63.2.3	Significant Quantity	2899
63.2.4	Type of Facility	2900
63.2.5	Material Balance Area and Measurement Points	2900
63.2.6	Material Stratification for Sampling	2900
63.2.7	Type of Defect	2901
63.2.8	Sampling Plan	2901
63.2.9	Inspection Activities for Safeguards Verification Measurements	2901
63.2.10	Inspection Frequency	2902
63.2.11	Detection Probability	2902
63.2.12	Safeguards Approach	2903
63.2.13	Classification of Methods	2903
63.2.13.1	Nondestructive Assay	2903
63.2.13.2	Destructive Analysis	2904
63.2.14	Evaluations of Accountability Verification Measurements	2904
63.3	<i>Non-Destructive Assay (NDA)</i>	2905
63.3.1	Introduction	2905
63.3.2	Safeguards Environment and Measurement Conditions	2907
63.3.3	Gamma Ray Spectrometry	2909
63.3.3.1	Gamma Ray Detectors	2909
63.3.3.2	Low-Resolution Gamma Spectroscopy (LRGS)	2911
63.3.3.3	High-Resolution Gamma Spectroscopy (HRGS)	2913
63.3.4	Neutron Counting Techniques	2915
63.3.4.1	Neutron Detectors	2915
63.3.4.2	Gross Neutron Counting	2917
63.3.4.3	Neutron Coincidence Counting	2918
63.3.4.4	Multiplicity Coincidence Counting	2921
63.3.4.5	Active Neutron Coincidence Counting	2922

63.3.5	Spent Fuel Measurement	2923
63.3.5.1	Gamma Methods	2924
63.3.5.2	Neutron Methods	2925
63.3.5.3	Combined Gamma/Neutron Methods	2926
63.3.5.4	Optical Methods	2927
63.3.6	Unattended NDA Systems	2928
63.3.6.1	Unattended Gamma-Based NDA Systems	2930
63.3.6.2	Unattended Neutron-Based NDA Systems	2931
63.3.6.3	Other Unattended NDA Systems	2934
63.3.7	Other NDA Techniques	2935
63.3.7.1	Physical Property Measurement	2935
63.3.7.2	Calorimetric Techniques	2937
63.3.7.3	X-Ray Measurements	2938
63.3.7.4	Analytical NDA Techniques at Laboratories	2940
63.3.8	New and Novel Technologies	2941
63.3.8.1	New Technologies	2941
63.3.8.2	Novel Technologies	2944
63.4	<i>Laboratory Analysis for Nuclear Material Accountability Verifications ...</i>	2950
63.4.1	Introduction	2950
63.4.2	Bulk Measurement, Sampling, Conditioning, and Shipment of Safeguards Inspection Samples	2950
63.4.2.1	Spent Fuel Solutions	2951
63.4.2.2	Uranium Hexafluoride in Pressurized Cylinders	2952
63.4.2.3	Plutonium Oxide Powders	2954
63.4.2.4	Uranium Dirty Scrap Materials	2956
63.4.3	Safeguards Analytical Laboratories	2957
63.4.3.1	Off-Site Laboratories	2957
63.4.3.2	On-Site Laboratories	2958
63.4.4	Isotopic Analysis	2960
63.4.4.1	Isotopic Analysis by Mass Spectrometry	2960
63.4.4.2	²³⁸ Pu Abundance by Alpha Spectrometry	2967
63.4.4.3	Gamma Spectrometry of Nuclear Material Samples	2970
63.4.5	Elemental Assay	2971
63.4.5.1	Ignition Gravimetry of U, Pu, Th	2971
63.4.5.2	Uranium Titration	2972
63.4.5.3	Plutonium Titration	2973
63.4.5.4	Controlled Potential Coulometry of Plutonium	2975
63.4.5.5	Isotope Dilution Assays	2978
63.4.5.6	Spectrophotometric Determination of Hexavalent Plutonium	2982
63.4.5.7	X-ray Absorption and Fluorescence Spectrometry	2983
63.4.5.8	Assay of Alternative Nuclear Materials	2984

63.5	<i>Environmental Sampling and Analysis to Verify the Completeness of State Declarations</i>	2985
63.5.1	Introduction	2985
63.5.2	Sampling, Conditioning, and Shipment of IAEA Safeguards Environmental Inspection Samples	2988
63.5.2.1	Cotton Swipe and Other Swipe Materials	2988
63.5.2.2	Air Filters	2989
63.5.2.3	Water, Soil, Vegetation, and Biota Samples	2990
63.5.2.4	Process and Structural Materials	2991
63.5.3	Safeguards Analytical Laboratories	2991
63.5.3.1	Clean Laboratory for Safeguards	2991
63.5.3.2	The Network of Analytical Laboratories (NWAL) of the IAEA	2994
63.5.4	Sample Screening Methods	2994
63.5.4.1	Gamma Spectrometry	2995
63.5.4.2	X-Ray Fluorescence Spectrometry	2995
63.5.5	Bulk Sample Analysis	2995
63.5.5.1	Tracers	2996
63.5.5.2	Sample Preparations and Separations	2997
63.5.5.3	Thermal Ionization Mass Spectrometry	2998
63.5.5.4	Inductively Coupled Plasma Mass Spectrometry	2998
63.5.6	Particle Analysis	2999
63.5.6.1	Sample Preparation	3000
63.5.6.2	Thermal Ionization Mass Spectrometry	3000
63.5.6.3	Secondary Ion Mass Spectrometry	3001
63.5.6.4	Scanning Electron Microscopy with X-Ray Spectrometry	3002

Abstract: This chapter deals with the “nuclear safeguards” verification system and describes procedures and measurement methods that allow the safeguards inspectorates/authorities to verify that nuclear materials or facilities are not used to further undeclared military activities. These procedures and methods provide the strong technical basis upon which the safeguards inspectorates/authorities issue their conclusions and receive the broadest international acceptance regarding the compliance of participating states with their obligations.

63.1 Introduction

Nuclear safeguards stands for the “methods developed to safeguard the peaceful activities against diversion of nuclear material by the risk of early detection – controlling nuclear material as a measure of arms reduction” (IAEA 1985). More specifically, IAEA safeguards has been described as a comprehensive set of internationally approved technical and legal measures, applied by the IAEA, to verify the political undertakings of states not to use nuclear material to manufacture nuclear weapons and to deter any such use (IAEA 1998b). *Nuclear material* is defined as any source material (natural uranium, depleted uranium and thorium, excluding uranium ore) or special fissionable material (plutonium-239, uranium-233, uranium enriched in the isotopes 235 or 233) (IAEA 2002, No. 4.1) encountered in the applications of nuclear energy. Nuclear safeguards systems have been introduced because of the fears raised by the devastating effects of the nuclear bombs detonated over Hiroshima and Nagasaki at the end of the Second World War in August 1945 (Fisher 1997).

This chapter focuses on safeguards verification techniques and does not address other important safeguards measures such as containment and surveillance, near real time accountancy (NRTA), collection and analysis of satellite imagery, and “external information” on national programs and international trade and exchanges. These measures merit separate chapters outside the scope of this handbook. The chapter emphasizes the procedures and methods used to verify the accuracy of declared inventories and flows of nuclear materials but also those involving trace elements in “environmental samples” and novel technologies searching for undeclared nuclear material and activities. All procedures and methods (except new and novel technologies) discussed here are implemented by the IAEA and to a great extent by national or regional inspectorates.

In the wake of the arms race, which started between the Atlantic Alliance and the Soviet Union, the United Nations set up the International Atomic Energy Agency (IAEA) in 1957. The UN delegated to IAEA the task of promoting the peaceful uses of atomic energy and establishing an international safeguards system, with the aim to stop the proliferation of nuclear weapons and foster disarmament. Yet up to 1971, IAEA was limited to exercise its safeguards on nuclear materials or facilities that were acquired through its technical assistance or were placed voluntarily in its custody (IAEA 1961; IAEA 1968). The nuclear Non-Proliferation Treaty (NPT) (IAEA 1970), which was open for signature in 1968, earmarked a major step toward a global international safeguards system. As of 2010, more than 190 states have become signatories of the treaty, covering indeed the dominant part of nuclear activities in the world. NPT entered into force in 1970. It requires the signatories to enter a safeguards agreement with the IAEA, whereby they renounce to nuclear weapons and place all their nuclear materials under IAEA control. Based on its Statute, the IAEA obtained approval of its NPT safeguards system (IAEA 1971) in 1971. NPT assures the international community that all nuclear materials and activities under safeguards outside the so-called Nuclear Weapon States (the five states that possessed nuclear weapons when the NPT entered into force: China, France,

Soviet Union (now Russia), United Kingdom, and United States of America) are used exclusively for peaceful purposes, contributing to dispel mistrust among states (IAEA 2002). With the expulsion of Iraqi armed forces from the territory of Kuwait in early 1991, the UNSCOM Special Commission and the IAEA (UNSC687 resolution) uncovered a comprehensive nuclear weapon program that Iraq had failed to declare in breach of its commitments as party to NPT. This led the IAEA member states to endorse a strengthening of IAEA safeguards measures providing the framework to detect undeclared nuclear material and activities. In 1997, the IAEA Board approved the model of “Additional Protocols (AP)” (IAEA 1997), and by 2009, the IAEA had concluded APs with 136 states and the European Atomic Energy Community (EURATOM). The AP spells out measures beyond the scope of INFCIRC-26, -66 or -153 type agreements providing broader access for the inspectorate to virtually all locations where nuclear material is handled or suspected and to detailed information on the state’s nuclear activities. The combination of activities under the comprehensive safeguards agreement and AP could determine that a state’s nuclear program is for peaceful purpose only and has been completely and correctly declared. This has drastically changed the safeguards system toward an information driven, state-level approach whereby the IAEA concludes for a state with increased confidence that no nuclear material has been diverted from declared sites and that there is no evidence of clandestine nuclear activities elsewhere. This state-level approach takes into account all available information to the IAEA such as inspection results, design information verification, open source evaluation including tracking of black-market nuclear networks, satellite imagery and environmental sampling.

EURATOM, instituted as early as 1958 by its six founding states (Belgium, France, Germany, Italy, Luxembourg and the Netherlands), established a comprehensive international nuclear safeguards system soon after the signature of a US-EURATOM Cooperation Agreement (1959). Argentina and Brazil set up a joint safeguards inspectorate (ABACC) in 1991. IAEA safeguards agreements foresee operating safeguards state systems of accounting and control over nuclear materials (SSAC). Partnerships between the SSACs, ABACC, EURATOM, and the IAEA are a strong factor in optimizing the resources of all parties, while the IAEA retains the capability to reach independent conclusions. With the indefinite extension of the NPT in 2005, the IAEA has been confirmed into its responsibilities in the operation and strengthening of a worldwide nuclear safeguards system in cooperation with the relevant national and regional institutions and the United Nations Organization.

International safeguards systems have certainly succeeded in limiting proliferation of nuclear weapons, but the world is still a long way from being free from their menace. Most non-nuclear weapons states are weary of unfair burden upon those subject to NPT, while nuclear weapon states appear reluctant to progress toward nuclear disarmament. A few states continue to use this as an argument for not signing NPT at the cost of mistrust by neighboring countries and international community. Others like Israel consider that existing safeguards systems or other treaties are not sufficient to ensure their national security and refuse to renounce to nuclear weapons. Serious conflicts in the Middle East, in the Korean peninsula, and Asia make much current headlines about further risks of proliferation. International safeguards, evidently, can at best contribute to build and maintain international confidence. However, their effectiveness (but also their limitations) had a positive impact on the negotiations of the successive arms limitation treaties and on the declaration of seven Nuclear Weapon Free Zones: the Antarctic (1961), Space (1967), South America (Tlatelolco Treaty 1968), Seabeds and Ocean Floors (1972), the Pacific (Rarotonga Treaty 1986), South East Asia (Bangkok Treaty 1995), and Afrika (Pelindaba 1996). The signatories of the four regional

treaties have the obligation to enter comprehensive safeguards agreements with the IAEA. Synergies between nuclear safeguards measures and future progresses toward a global nuclear disarmament, could be considered for the IAEA and CTBTO – the UN organization created for the control of the compliance with the Comprehensive Nuclear Weapon Test Ban Treaty, yet under ratification – as both are based in Vienna. The IAEA has acquired vast experience in safeguards verification techniques. It may be called to take on new roles in the future, such as verifying fissile material from dismantled weapons or verifying compliance with a potential global ban on the production of fissile material for weapons. It could thus contribute to both nonproliferation and disarmament.

The IAEA and a commission of eminent persons (IAEA 2008) have recently reviewed IAEA activities to meet future challenges up to 2020 and beyond. The increasing spread of nuclear material, technology, and know-how may pose increased proliferation risks in a globalized world. Safeguards, which will remain a core mission for the IAEA, must be further strengthened to cope with expanded growth and spread of nuclear power generation – and particularly, the establishment of new facilities for uranium enrichment, spent-fuel reprocessing, or processing of direct-use nuclear material. This will require new technologies to make safeguards more effective and efficient. Multilateral fuel-cycle centers and proliferation-resistant nuclear facilities could facilitate future safeguards implementation.

Meeting future challenges will require a robust IAEA “toolbox” containing: the necessary legal authority to gather information and carry out inspections, state-of-the-art technology, particularly for the detection of clandestine nuclear activities, a high-caliber workforce, and sufficient resources.

63.2 Safeguards Verification Measurement Procedures

The safeguards systems, based on regional and international treaties, consist of activities at the headquarters and on-site inspections to verify that states comply with their obligations derived from the related specific agreements. At Headquarters, state reports and declarations are being received and evaluated in context with all other available information such as inspection data, open source information and satellite imagery to assess the peaceful nature of a state’s nuclear program. Databases on nuclear material inventories and transfers are being maintained. In addition, inspection data acquired from implementing technical devices in the field are being archived and used for preparing and coordinating on-site inspections. On-site inspections are performed to independently verify nuclear material and activities and are considered the most powerful tool for safeguards purposes.

The *technical objective* of NPT is “the timely detection of diversion of significant quantities of nuclear material from peaceful nuclear activities to the manufacture of nuclear weapons and other nuclear explosive devices or for purposes unknown and deterrence of such diversion by risk of early detection” (IAEA 2002). To this aim, safeguards inspectorates regularly physically verify the inventories and transfers of declared nuclear materials subject to safeguards agreements. The type and amount of nuclear material are thereby inspected by direct physical and/or analytical measurements, using in the first place the nuclear characteristics of the material (emitted gamma or neutron radiation, isotopic composition, etc.) but also other “non-nuclear”-type measurements, such as weighing, calorimetry, Cherenkov radiation detection, etc. The goal is to verify the correctness and completeness of the nuclear material accountancy reports of the state and to confirm that no “safeguards significant quantities” of nuclear

materials are missing. In addition, IAEA inspectors are authorized to take “environmental samples” in specified locations within or near nuclear facilities in states having signed an “additional protocol,” which defines means for the IAEA to confirm the absence of signatures of undeclared activities in the facility process or its environment. All these measures are implemented in close cooperation with the facility operator and the state or regional safeguards authorities, but in a way that guarantees that the IAEA can draw its own independent conclusions.

International safeguards systems have thus two basic pillars, the first one being the state’s declaration regarding the nuclear activities and nuclear material inventory and accountancy in the nuclear facilities in the state, the second being a complex verification system to confirm that the state’s accountancy system and its declarations are both correct and complete. The state accountancy reports are expected to be based on operator’s own accountability data.

The following definitions and descriptions are used in order to quantify and qualify the inspection goals (IAEA 2002).

63.2.1 Diversion Strategy

Diversion of nuclear material, a particular case of noncompliance, could include:

The undeclared removal of declared nuclear material from a safeguarded facility.

The use of a safeguarded facility for the production of undeclared nuclear material (e.g., production of high enriched uranium in an enrichment plant or plutonium in a reactor through irradiation).

The use of nuclear material specified and placed under safeguards in such a way as to further any military purpose (applicable to specific safeguards systems).

The diversion strategy is a hypothetical scheme, which the diverter could consider to divert nuclear material or to misuse items subject to safeguards. It could include one or more concealment methods, i.e., actions to reduce the probability of detection, such as tampering safeguards equipment or accountancy, falsifying documents and declarations, etc. Verification principles, methods, and procedures are designed to uncover possible diversion strategies according to the type of nuclear material and the characteristics of the facility.

63.2.2 Type of Material

Nuclear material is classified according to the element contained and, for uranium the degree of enrichment. Six classes are defined at this time: plutonium (Pu), high enriched uranium (HEU), uranium-233 (^{233}U), depleted uranium (DU), natural uranium (NU), low enriched uranium (LEU), and thorium (Th).

63.2.3 Significant Quantity

To set a target for the quantification of the inspection goal, the IAEA currently adopts the following quantities (► [Table 63.1](#)) called “significant quantities” (SQs) as estimates of the amount of material that would be sufficient to manufacture a nuclear explosive device.

■ **Table 63.1**

IAEA Significant Quantities (SQs)

Material type	Isotopic composition	SQ
HEU	$^{235}\text{U} > 20\%$	25 kg ^{235}U
LEU	$^{235}\text{U} < 20\%$	75 kg ^{235}U
Natural U (NU)	$^{235}\text{U} = 0.7\%$	10 t NU
Depleted U	$^{235}\text{U} < 0.7\%$	20 t DU
^{233}U		8 kg ^{233}U
Plutonium	$< 80\% \text{ } ^{238}\text{Pu}$	8 kg Pu
Thorium		20 t Th

63.2.4 Type of Facility

Safeguards procedures vary also according to the type of facility and the physical form under which nuclear materials appear. Two types of facilities are considered.

Item facility: Power reactors (Light Water Reactor (LWR), On-load Reactor (OLR)), Research Reactor (Material Testing Reactor (MTR), Fast Breeder Reactor (FBR), (TRIGA) and Critical Assemblies, Nuclear Material Storage (dry and wet).

Bulk handling facility: fuel fabrication, reprocessing, conversion, and enrichment.

63.2.5 Material Balance Area and Measurement Points

A material balance area (MBA) defines an area in or outside of a facility such that:

- The quantity of nuclear material in each transfer into or out of each MBA can be determined.
- The physical inventory of nuclear material in each MBA can be determined when necessary, in accordance to specified procedures.

A key measurement point (KMP) is a location where nuclear material appears in a form that may be measured to determine material flow or inventory.

In addition to the above, whenever the state has accepted the additional measures foreseen in the model protocol INFCIRC/540, IAEA inspectors are granted access to “location-specific” environmental sampling points where they may take samples of air, water, vegetation, soil, smears, etc., to confirm the absence of undeclared nuclear material or activities at the specified location (IAEA 1997).

63.2.6 Material Stratification for Sampling

In order to make a meaningful statistical evaluation of the results of accountancy verifications, the inspector’s measurements must be planned in a way, which will provide independent estimates of the overall measurement uncertainties. All factors influencing these uncertainties must be considered, such as the material type and form, the sampling procedure, and the measurement method. According to theory and experience, the inspectorate detection

capability is optimal if the materials (items, batches, and lots) being verified are grouped into “material strata” having similar features, and physical and chemical properties. In practice, the inspector and the operator agree on a common stratification.

63.2.7 Type of Defect

A difference between the declared amount of nuclear material or nonnuclear material and the material actually present for verification purposes is called a *defect*. *Gross defect* refers to an item or batch that has been falsified to the maximum extent possible so that all or most of the nuclear material is missing (e.g., a spent fuel (SF) assembly is substituted with a dummy assembly containing no nuclear material).

Partial defect refers to an item or batch that has been falsified in such a way that some fraction of the declared amount is yet actually present.

Bias defect refers to an item or batch that has been slightly falsified so that only a small fraction of the declared amount is missing.

63.2.8 Sampling Plan

The term sample has two meanings:

- In statistical sampling, a sample is a subset of items selected from a defined group (population) of items.
- In material sampling for analysis, a sample is a small quantity of material taken from one item or container for measurement.

Statistical sampling plan procedures are applied to determine, in a given stratum, the number of items to be verified by each of the relevant measurement methods (nondestructive assay (NDA), weighing, sampling, and destructive analysis (DA)). The sampling plan is based on inspection by attributes and ensures that – based on the assumption that the operator’s declaration has been falsified by the goal amount – at least one defect will be correctly identified as a defect with probability $(1-\beta)$, where β is the nondetection probability. The preselected value of $1-\beta$ is typically 90% for high and 20% for low probability levels. The goal amount is usually 1 SQ (see [Sect. 63.2.3](#)).

63.2.9 Inspection Activities for Safeguards Verification Measurements

The physical verification activities consist of the following steps (IAEA 1997, 2004):

1. Advance planning of an inspection is done at the inspectorate headquarter or inspectors’ regional office and includes:
 - (a) A review of the facility design information and the accountancy reports.
 - (b) A stratification of the declared nuclear material available for verification in groups or “strata” of items of similar characteristics at each KMP.
 - (c) A statistical sampling plan for each material stratum to ensure a predetermined detection probability for the specific types of verification measurements and defect testing.

- 2. During inspection at the facility:
 - (a) For each KMP:
 - (i) Selected items or batches are measured using NDA.
 - (ii) Their weight or volume are determined, the operator’s scales or tanks calibration and declared tare weights are confirmed.
 - (iii) Statistically significant defects in the above tests are investigated.
 - (iv) Material samples are taken, as required by the sampling plan, and conditioned, to ensure that the integrity of the analytical information is maintained during transport.
 - (b) Environmental samples are taken at each “environmental sampling point,” as specified in the sampling plan.
- 3. The samples are analyzed in the laboratory selected by the inspectorate.
- 4. The inspection data and the results of the analyses are collected and evaluated statistically, usually at the inspectorate headquarter.

63.2.10 Inspection Frequency

A minimum time necessary for manufacturing a nuclear explosive device has been defined according to the material *category*, its irradiation status and suitability for conversion into components of nuclear explosive devices. *Direct use material* (such as Pu containing less than 80% ²³⁸Pu, HEU and ²³³U) can be used without transmutation or further enrichment. *Unirradiated material* does not contain substantial amounts of fission products thus it requires less time and effort to be converted to components of nuclear explosive devices than irradiated direct use material like spent reactor fuel. *Indirect use material* (DU, NU, LEU and Th) must be further processed to produce direct use material.

These categories set the period of time used as the objective for timely detection of a diversion (timeliness component of the inspection goal) and govern the *inspection frequencies* (number of inspections per year). Material categories and typical inspection frequencies are shown in [▶ Table 63.2](#).

63.2.11 Detection Probability

Because safeguards systems cannot in practice cover all material during an inspection, the inspectors take only random samples of the total population for verification. The goal is to assure that the detection probability for detecting a defect (a falsified or missing item, a certain

■ **Table 63.2**
Material categories and typical inspection frequencies

Material category	Material type	Inspection frequency
Direct use material unirradiated*	Purified Pu, HEU	1 month
Direct use material irradiated	Spent fuels	3 months
Indirect use material	(²³⁵ U < 20%, NU, DU, Th)	1 year

quantity missing from items or bulk material) applied to each material stratum is not below a predetermined level.

63.2.12 Safeguards Approach

The type of the safeguards agreement and facility, as well as all the above factors are taken into consideration when the safeguards approach for the particular facility is prepared. This approach will determine also the verification methods and the instruments that will be installed permanently at facilities and applied during inspections or used in the analytical laboratories on samples taken by the inspectors.

63.2.13 Classification of Methods

► [Table 63.3](#) lists the four classes of methods and instruments implemented for safeguards verification measurements.

63.2.13.1 Nondestructive Assay

A nondestructive assay is a measurement of the nuclear material content or of the element or isotopic concentration of an item without producing significant physical or chemical changes in the item. It is generally carried out by observing the radiometric emission or response from the item and by comparing that emission or response with a calibration based on essentially similar items whose contents have been determined through destructive analysis. There are two broad categories of NDA:

- (a) *Passive assay*, in which the measurement refers to spontaneous emissions of neutrons or gamma rays or to the total decay energy.
- (b) *Active assay*, in which the measurement refers to a stimulated emission (e.g., neutron- or photon-induced fission).

■ [Table 63.3](#)

Classification of methods and instruments

Class	Implementation mode
NDA unattended mode	Instruments permanently installed, possibly combined with remote monitoring via satellites or other communication means
NDA attended mode	Instruments kept at the facility or hand-carried/shipped by the inspector
Nuclear material sample DA	samples taken at the facility and shipped to an analytical laboratory for elemental and isotopic assay of fissile element
Environmental sampling	Environmental samples, mainly swipes taken from inside or outside surfaces at facilities or any other location, analyzed in specialized laboratories for signatures of potential undeclared activities

63.2.13.2 Destructive Analysis

Determination of nuclear material content and, if required, of the isotopic composition of chemical elements present in the sample. Destructive analysis normally involves destruction of the physical form of the sample. In the context of IAEA safeguards, determination of the nuclear material content of an item sampled usually involves:

- (a) Measurement of the mass of the sample.
- (b) The taking of a representative sample.
- (c) Sample conditioning (if necessary) prior to shipment to the Safeguards Analytical Laboratory for analysis.
- (d) Processing of the sample to the chemical state required for the analysis (e.g., dissolution in nitric acid).
- (e) Determination of the concentration of the nuclear material (U, Pu, Th) present in the sample (i.e., elemental analysis) using techniques such as chemical titration, controlled potential coulometry, gravimetric analysis, isotope dilution mass spectrometry, and K-edge densitometry.
- (f) Determination of the isotopic abundance ratios of U or Pu isotopes (i.e., isotopic analysis) using, inter alia, techniques such as mass spectrometry, gas mass spectrometry, and thermal ionization mass spectrometry.

63.2.14 Evaluations of Accountability Verification Measurements

The majority of the nuclear material samples, collected during safeguards inspections and sent to an analytical laboratory for measurements, serve several purposes. (i) They are taken to verify the correctness of declarations for the amounts of nuclear material (element (U, Pu, Th) and isotope amounts (^{235}U , ^{233}U)) in inventories and in transfers into or out of a facility; (ii) The analytical results obtained for the verification samples are also evaluated for the purpose of verifying the quality and functioning of the operators' measurement systems; these should "...conform to the latest international standards or be equivalent in quality to such standards" (IAEA 1972).

The operator-declared data and the measurement results, obtained for the inspection samples, are stored in the inspectorate in a central operator-inspector database where they can be accessed for subsequent evaluations (IAEA 2004). This database also contains the results of verification measurements by nondestructive assay (NDA) methods.

In the IAEA data analysis, various statistical techniques (IAEA 1998a) are used to derive separate estimates of the operator's and inspector's uncertainty parameters based on the collection of historical operator-inspector differences. The results of these evaluations are "performance values," typical for a specific facility and for each stratum (material type) and measurement method combination. The actually observed "verification measurement performance" is then used for the planning (sample size calculations), the conduct (establishing reject limits), and the evaluation (material balance) of inspections in a given facility.

The nuclear material contained and processed in a facility is stratified into items or batches that have similar physical and chemical characteristics. Grouping the material into strata simplifies verification and makes it possible to formulate the sampling plans needed to verify a material balance and to calculate its uncertainty. In calculating sampling plans, generally

three levels of “defects” (differences between the declared amount of nuclear material and the material actually present) are considered. In most situations NDA measurements serve for the purpose of detecting “partial and gross defects,” while sampling for DA copes with the detection of “bias defects.”

The sample size for a stratum defines the number of items to be verified in order to be able to draw conclusions about the total population. The total sample size can then be allocated among the accountancy verification methods for gross, partial and bias defects (IAEA 1998a; Jaech and Russell 1991). The uncertainty values generally used are the verification performance estimates for the given facility and strata. The International Target Values could serve as a substitute (IAEA 2001).

For every inspection, the analytical results are evaluated by an operator–inspector paired comparison. Differences exceeding the 3-sigma limits, calculated from the respective verification performance estimates, are classified as discrepant and subject to further investigations.

The “material unaccounted for” (MUF) over a “material balance period,” declared by the operator for each “material balance area” and its statistical significance are examined, where:

$$MUF = PB + X - Y - PE$$

with PB being the beginning inventory, X the sum of all inventory increases, Y the sum of all inventory decreases, PE the ending inventory.

For the declared MUF , its uncertainty σ_{MUF} is calculated from the verification performance estimates, as derived from the historical operator–inspector differences for this facility. The declared MUF is expected not to exceed $3 \times \sigma_{MUF}$; otherwise it is concluded that MUF is statistically significant. The calculated σ_{MUF} value is also compared to the International Standard of Accountancy (IAEA 2002, No 6.35) which is based on the operating experience at the various types of bulk handling facilities and defines the uncertainty with which a facility operator is expected to be able to close a material balance. If σ_{MUF} is larger, it is concluded that the facility measurement system does not meet this standard. In both cases, a significant finding will trigger follow-up evaluations, and activities with respect to the facility accountancy and measurement system will be initiated.

For all samples collected during inspections, the analytical results and their evaluation will be reported to the corresponding state as part of an inspection statement. Any significant finding in the material balance evaluations will also be reflected in the annual Safeguards Implementation Report.

63.3 Non-Destructive Assay (NDA)

63.3.1 Introduction

Nondestructive assay (NDA) for safeguards describes analytical techniques to measure, check, and verify the amount of nuclear material or of the elemental or isotopic concentration of an item without producing significant physical or chemical changes in the item. It allows inspectors to determine both the quantity and composition of nuclear material without ever sampling it directly. Ultimately, NDA techniques provide for the independent verification of the total amount of nuclear material held at a nuclear facility. The main nuclear materials of interest are uranium (U) and plutonium (Pu). Usually, no single measurement method can

directly determine the total amount of either Pu or U and only a combination of appropriate NDA techniques provide the total mass of the respective element.

The most widely used NDA instruments rely on the detection of nuclear radiation such as gamma rays and/or neutrons. Physical measurement techniques are also used with available instruments that measure heat, weight, liquid volume, thickness, and light emission/absorption. These physical techniques may be applied by themselves, or they may be used in combination with other nuclear measurements to provide quantitative measurements of the nuclear material. The general reference on the theory and application of passive NDA (PANDA) is given by reference (Reilly et al. 1991) and its addendum (Reilly et al. 2007).

The development of NDA instruments for the measurement of nuclear materials has evolved over many years. Various national and international institutions have developed NDA techniques with the goal of increasing the technical competence of safeguards systems. NDA instruments range in size and complexity from small portable units for use by safeguards inspectors during on-site verification of nuclear materials, to large in situ NDA systems designed for routine in-plant use (e.g., plant operator equipment, subject to independent authentication). Most of the NDA equipment has to withstand demanding environments such as high radiation fields, variable humidity, and high and low temperatures. In addition, such equipment must be reliable with consistently reproduced performance when operated by different users.

In general, NDA techniques are less expensive, nonintrusive on the operation of the nuclear facility, less time consuming than destructive analysis (DA) techniques, and are amenable to automation. NDA measurements can be performed on large quantities of nuclear material without breaching the container or containment of the material. Principally, NDA significantly reduces the need for DA sampling. However, the accuracy associated with NDA verification measurements is generally less than it would be if the items were verified at the final process stage at which sampling for DA and direct measurement of the nuclear material content become possible.

In many instances, NDA is the only technically feasible solution to perform verification, e.g., for valuable finished products (such as fresh fuel assemblies/pins) and also when direct access to nuclear material is impossible or undesirable (e.g., spent fuel). NDA measurements can be made outside of glove boxes, transport containers, on solutions inside processing systems, and on materials packaged for storage and disposition. NDA methods are also well suited to the verification of inhomogeneous bulk materials such as waste, where representative DA sampling cannot be performed. NDA offers another important advantage over traditional DA methods: measurements can be performed in a timely manner, both in situ and during inspection activities.

In the context of neutron and gamma-ray measurements, NDA techniques used by the inspectorate can be categorized as *passive* NDA or *active* NDA. Passive NDA refers to techniques that measure radiation emitted spontaneously from nuclear material. This method is often applied to Pu samples, because of the large spontaneous fission rate of the even-even Pu isotopes. Active NDA, on the other hand, refers to techniques that measure induced radiation responses from a sample, often using an external neutron source. These active methods are usually applied to perform uranium measurements where the spontaneous fission rate is low.

In addition to the quantitative measurements performed by an inspector, in some cases a qualitative measurement (attribute testing) is sufficient, e.g., simply confirming the presence of a representative isotope based on a typical gamma ray.

63.3.2 Safeguards Environment and Measurement Conditions

Safeguards inspectors routinely use NDA to perform the verification of nuclear materials present in the complete range of nuclear fuel cycle facilities. Today, a broad range of modern NDA instruments and techniques are available for the detection, identification, assay and verification of nuclear material in a wide variety of physical and chemical forms. The IAEA alone has authorized over 100 different types of NDA instruments for inspection use, while several NDA instruments are under evaluation and others under development (IAEA 2003; Zendel 2008). If safeguards verification is to be effective, inspectors have to perform independent measurements in order to verify declared material quantities. Selection of the correct equipment for a particular measurement task is a very important part of inspection activities and a thorough knowledge of an NDA technique's capability to meet the goal of the inspection activity is required. A high level of standardization of NDA equipment can reduce implementation costs significantly because less maintenance and training is required.

The diversity of nuclear materials present in the large variety of nuclear facilities to be safeguarded necessitates an equally diverse “toolbox” of NDA instrumentation. Nuclear material can be grouped into two main types: bulk material and item material. The first group comprises powders, pellets, solutions, scrap, and metals contained in various process and storage containers, whereas the second group consists mainly of fuel elements and pins in various storage configurations. Further distinctions are made in respect of the strategic value of the nuclear material as unirradiated direct use (e.g., Pu-oxide and mixed oxide (MOX) powders), irradiated direct use (e.g., spent fuel), and indirect use material (depleted, natural and low enriched uranium).

The hardware and software of an NDA system depend on the specific conditions (e.g., environment, sample matrix, etc.) of the measurement task. In most cases, different NDA instruments are required to obtain the total quantity for a given nuclear material sample. Only a combination of the results of several calibrated NDA techniques provides for a credible assessment of the type and quantity of nuclear material.

The nature of a particular inspection activity may require the customization of equipment and methods applied. The equipment and method should be simple and user friendly, and should provide results in a short time period, because the available inspection time is usually very limited. Furthermore, emphasis is placed on compact, lightweight, rugged, and reasonably priced equipment, which can be carried by the inspectors and thus remain completely under their control.

For large and complex facilities, the inspectorates require facility resident and specific safeguards equipment systems with features for attended, unattended, and remotely controlled operations. Some of the safeguards systems are integrated in the process equipment of the facility. The dimensions of the measurement head (the sensor) for these systems are often strongly conditioned by factors like sample geometry, plant requirements and detection efficiency, all of which factors impose boundary conditions that demand an individual design.

Calibration is necessary in all quantitative NDA measurements to relate measured responses (e.g., neutron coincidence rate or specific gamma intensity) to nuclear material characteristics. An accurate measurement depends crucially on the effective calibration of measurement instrumentation. This calibration is based on similar items whose nuclear material content is very accurately known. The resulting calibration functions including all necessary correction factors (such as those relating to neutron multiplication or gamma-ray

absorption effects) are incorporated into the software or firmware associated with a given measurement technique. In certain specific cases, the procurement and use of standards that are nominally identical to the measured items is possible. The use of calibration standards on a one-to-one basis is, in general, not feasible. Other alternatives, such as predictive modeling methods based on Monte Carlo calculations (mainly with the code MCNP (Monte Carlo Nuclear Particle)) are being increasingly employed for the prediction of responses for given samples under well-defined conditions (Bourva et al. 2007; Lebrun et al. 2007). A recent version of the Monte Carlo code, MCNPX (Monte Carlo Nuclear Particle Extended), can directly simulate the singles, doubles, and triples count rates from a known neutron source (see ► Sect. 63.3.4.3). In addition to meeting the urgent practical need for the reduction of the number of calibration standards, a good computational method, once developed, could play an important role in helping to identify false physical standards.

Measurement accuracy and quality control (QC) are important issues and require a regular measurement control program to provide standards against which to check the measurement performance of equipment. Normalization standards are applied independently of calibration standards to verify that an instrument is working properly and providing authentic data. Such a standard may be: (a) a well-characterized radiation source (e.g., ^{252}Cf source for neutron coincidence counters or sources of known energy and intensity for gamma spectrometers); or, (b) a properly authenticated sample of plant-specific material that has been kept under safeguards seal.

In some instances, safeguards inspectorates do not own the NDA equipment and need to share the instruments with third parties, e.g., operators. In this case, documented joint-use procedures should define arrangements for data sharing, authentication, recalibration and use of standards and software, maintenance, repair, storage, and transportation.

Sensors, together with their electronics and data generators, are security critical components, as they are the prime sources of independent safeguards data. Therefore, any unauthorized access to potentially vulnerable components must be prevented by containing these components in tamper-indicating housings and by restricting their servicing, repair, and replacement to inspectorate staff. A sensor mounted with its data generator in a single tamper-indicating enclosure constitutes a “smart sensor.”

NDA measurements are usually performed on a well-stratified inventory grouping items with similar weights, locations, and properties together. The inspector applies a random sampling plan based on the number of items per stratum, the measurement performance of the selected NDA instrument, the significant quantity and the non-detection probability. For verification purposes, random sampling plans are calculated to detect three types of defects: gross, partial, and bias. In some cases, where it is not possible to take samples or to obtain representative samples (e.g., inhomogeneous material such as dirty scrap), partial defect NDA measurements are performed in lieu of bias defect tests. The rejection limit for a given NDA measurement is set at three-sigma level of the performance-based measurement errors. Performance-based measurement errors are derived from the collection of historical operator–inspector differences obtained for each MBA/stratum/measurement method combination. The performance-based measurement error provides the overall uncertainty combining all sources of uncertainties associated with the measurement (Aigner et al. 2002; IAEA 2001). Real performance values for NDA techniques applied to safeguards have been reviewed extensively (Guardini et al. 2004).

The hypothesis of the random sampling plan is based on the assumption that no defect and hence no “outlier” is present in the stratum; otherwise the verification of the stratum has failed.

In most cases, partial and bias defect testing by NDA are accomplished through the application of destructive analysis (DA) methods to random samples derived from the selected items.

63.3.3 Gamma Ray Spectrometry

Most nuclear materials of concern to safeguards emit gamma rays that can be used for identification and quantitative measurement purposes. Gamma-ray devices measure the energy and intensity of gamma rays emitted from nuclear material. The transmitted gamma ray intensity is mainly a function of gamma ray energy, absorber composition, absorber thickness, and measurement geometry – each of these parameters must be carefully considered in the final analysis. Spectral analysis of emitted radiation identifies the type of a nuclear material by its characteristic gamma rays. Further analysis of selected gamma ray intensities provides quantitative characteristics such as enrichment and isotopic composition. In some cases, additional parameters must be measured (e.g., active length, weight, etc.) to calculate the total mass of the element.

The gamma spectrometry technique, used in nuclear safeguards for measuring enrichment, requires less expensive equipment than the mass spectrometry technique and the equipment required is very easy to operate and maintain. Gamma spectrometry techniques, if properly implemented, can offer very precise results within relatively short measurement times. Both low- and high-resolution gamma-spectrometric measurements are essential verification tools for safeguards purposes. Main attributes of various gamma ray-detector systems are listed in

➤ [Table 63.4](#).

63.3.3.1 Gamma Ray Detectors

Three main types of instruments are presently used for gamma spectrometry: inorganic scintillation counters (usually activated sodium iodide – NaI – crystals), semiconductor detectors (usually high-purity germanium – HPGe – crystals), and gas-filled detectors (e.g., high-pressure xenon ionization chambers). In all cases, the interaction of a gamma ray with the detector results in an electrical signal, whose intensity is proportional to the energy of the incoming gamma ray. The signal is amplified, processed in a pulse processing electronic chain, counted, and analyzed by a multichannel analyzer (MCA). The resulting gamma spectrum (which shows the number of events as a function of gamma energy) exhibits isotope-characteristic gamma peaks. Finally, the spectrum is analyzed using specialized software, performing peak fitting, background subtraction, peak intensity calculation, external or intrinsic calibration and calculation of the relative isotopic abundances.

Semiconductor detectors change their conductivity upon the impact of radiation by producing a flow of free electrons (n-type) or positive holes (p-type) in the semiconductor material. This results in a collection of charge at the electrodes, when a voltage is applied to the semiconductor. Germanium detectors presently offer the best resolution but must be cooled by liquid nitrogen – they are capable of resolving complex gamma spectra and determining the isotopic composition of essentially all nuclear materials present in the nuclear fuel cycle. Recently, electrically cooled HPGe became available with sufficient resolution to measure the isotopic composition of Pu-samples. These systems are especially important for future unattended and remote systems as well as for field applications where liquid nitrogen is not available.

■ **Table 63.4**

Gamma-ray systems

System	Detector	Verification task	Typical performance values (%) ^a
HRGS	HPGe	²⁴⁰ Pu-effective (%) in fresh PuO ₂ , MOX, scrap	0.3–1
		²⁴⁰ Pu-effective (%) in fresh fuel	1
		Uranium enrichment in UF ₆ cylinder	2 (LEU)-10 (DU)
HM-5	NaI	Search and Identify nuclear material	Attribute
		Active length	0.5 cm
		²³⁵ U enrichment in fresh fuel (NAIGEM)	3
MMCN		²³⁵ U enrichment powder/pellets	3
UBVS		²³⁵ U enrichment in UO ₃	3
MMCC	CdZnTe	²³⁵ U enrichment in fresh fuel assemblies	5
FMAT		Fresh MOX assemblies underwater	Attribute
IRAT		Irradiated nonfuel items	Attribute
SFAT		Spent fuel (no movement required)	Attribute
CBVB		Spent fuel bundles (CANDU)	Attribute
CBVS		Spent fuel bundles in stacks (CANDU)	Attribute
SMOPY	CdZnTe + FC	LWR spent fuel	5(attribute/consistency)
CRPS	CdZnTe (+FC)	Radiation profiling of dry storage casks	Attribute
HSGM	IC	Dose rate of irradiated items	Attribute
FDET	IC + FC	Burnup and SF confirmation	10(attribute/consistency)

^aAverage measurement time ~300 s.

Room temperature semiconductor detectors – cadmium/zinc/telluride (CdZnTe) and CdTe detectors in particular – have a proven record in safeguards verification measurements and related applications and have been in use for more than 15 years (Arlt et al. 1992, 1993; Arlt and Rundquist 1996). Peltier-cooled CdTe detectors operated at just below 0°C can achieve a resolution at relatively low gamma-ray energies (<200 keV), which are sufficient to perform selected isotopic measurements for uranium and plutonium. Silicon-pin photo diodes can serve as detectors for X-ray and gamma ray photons. They are used as gamma monitors in high-radiation fields. CdZnTe and CdTe detectors are ideal for field measurements and for the design of small detection probes that can be operated in close proximity to the items to be verified, even if there are space restrictions. They have become the most versatile room temperature gamma detectors, complementing the classical NaI and liquid nitrogen-cooled germanium detectors, by providing a medium resolution and a reasonable efficiency. In many cases, the use of these detectors has helped to increase both the efficiency and effectiveness of NDA methods applied in the nuclear safeguards field.

Scintillation detectors consist of a scintillator (usually inorganic crystals such as NaI) and a photomultiplier tube. The scintillator emits light upon the absorption of radiation. This light

is collected and converted into an electronic signal by a photomultiplier tube. Scintillation detectors operate at room temperature and are cheaper and more robust than germanium detectors. Scintillation counters have a low energy resolution, but high detection efficiency. However, they experience a distinct shift with temperature changes and need to be stabilized frequently. Improving detection capability, specifically resolution and sensitivity, is a continuous challenge. Recently, LaCl_3 and LaBr_3 scintillation detectors have been introduced (Synthfeld et al. 2006). This type of detector combines an improved detector sensitivity relative to CdZnTe detectors with a reasonable resolution (2% at 122 keV), in comparison with $\text{NaI}(\text{Tl})$ detectors of the same size. LaBr_3 detectors are already commercially available and implemented for isotope identification and are employed in uranium enrichment applications that profit from their superior resolution and sensitivity.

Gas-filled detectors record ionization of the gas in the chamber caused by the gamma interaction. The ion current is proportional to the amount of energy deposited by the gamma ray. Gas detectors feature long-term stability that cannot be matched by scintillator or solid-state detectors because the charge transport properties of the gas are not significantly affected by changes in temperature and the effects of radiation. This high stability is very important for detectors in unattended monitoring applications, where background temperature and radiation varies significantly. High-pressure xenon ionization chambers have emerged recently as gamma-ray spectrometers.

63.3.3.2 Low-Resolution Gamma Spectroscopy (LRGS)

Low-resolution gamma spectroscopy (LRGS) is simple to use and easy to implement under field conditions. LRGS applications in safeguards range from performing the quantitative verification of enrichment levels to the purely qualitative detection of spent fuel attributes and the presence of nuclear material.

Mini multichannel analyzers connected to NaI detectors (MMCN) are routinely used to verify the enrichment of uranium in powders and pellets (Arlt et al. 1997). The basic measurement procedure involves viewing a uranium sample through a collimator with a NaI detector. The enrichment is deduced from the intensity of gamma rays attributed to ^{235}U (e.g., gamma ray at 186 keV). Under a well-defined geometry, the measured count rate of the 186 keV photons is proportional to the ^{235}U abundance. Because of the strong attenuating properties of uranium compounds, infinite thickness for the 186 keV gamma rays is required and achieved with rather thin samples (3 mm for uranium metal, 15 mm for UF_6). The standardized procedure controls the geometry and utilizes specially designed support stands with collimators to provide a quantitative assessment of enrichment within minutes. The technique works very well for pure and homogeneous uranium materials.

Mini multichannel analyzers connected to CdZnTe detectors (MMCC) are the preferred instruments for fresh fuel verification giving more credible results than NaI -based systems (Arlt et al. 1993, 1997). The probe of the CdZnTe based system is less than 1 cm in diameter and can be inserted into the water tube or control rod guide tube of fuel assemblies and can therefore be implemented entirely in situ without any problems arising from interference resulting from radiation emitted by adjacent fuel assemblies.

In many instances, qualitative results are sufficient to characterize the nuclear material (e.g., Spent Fuel Attribute Tester (SFAT) to confirm the presence of the ^{137}Cs peak at 662 keV as

an attribute for spent fuel). In some cases, the absence of specific gamma rays confirms the absence of a particular nuclear material or distinguishes between nuclear and nonnuclear material (e.g., irradiation attribute tester (IRAT) used to confirm absence of nuclear material in closed containers stored in spent fuel ponds).

The handheld monitor (HM-5, Fieldspec) is a battery-powered, digital, low-resolution, gamma spectrometer (Jung et al. 2007). The HM-5 is a lightweight, easy to operate and very frequently used instrument for safeguards purposes. This device combines various functions such as dose rate measurement, source search, isotope identification, enrichment measurement. It uses a small scintillation NaI detector and energy selective electronics with a digital display. The HM-5 is a typical instrument for attribute measurements (if background permits) and capable of detecting different energy ranges of gamma rays, allowing qualitative verification of the presence of either plutonium or uranium in unirradiated nuclear material. The HM-5 is used to measure the active length of light water reactor (LWR) fuel assemblies. The measured length combined with data on uranium mass per unit of length, obtained from a neutron coincidence collar, enables the inspector to determine the total uranium mass in the fuel assembly. Recently, enhancement of the HM-5 has enabled it to measure the enrichment of unirradiated uranium materials. The instrument is also widely used as a key tool during complementary access (CA) activities to confirm the absence of undeclared nuclear materials (► Fig. 63.1).

The Fresh MOX Attribute Tester (FMAT) consists of a stainless steel cylinder housing shielding and collimation, a CdZnTe detector and a preamplifier (Aparo et al. 1999). A multiwire cable connects the waterproof measurement cylinder with a data acquisition/control unit (operated above water). The FMAT is used to verify fresh mixed oxide (MOX) fuel stored in spent fuel ponds awaiting loading to the reactor core. It clearly distinguishes between

► Fig. 63.1

Hand-held low-resolution gamma spectrometer (HM-5, Fieldspec)



the gamma rays of ^{235}U (186 keV) and ^{241}Pu (208 keV) and measures key plutonium gamma rays to evidence that an interrogated item exhibits the unique characteristics of fresh MOX.

The Uranium Bottle Verification System (UBVS) is an integrated system combining a weighing scale and NaI detector for ^{235}U enrichment measurement of reprocessed UO_3 in large storage bottles. An inspector determines the weight of the bottle ($\sim 1,300$ kg for full bottles) utilizing a dedicated scale. The weighing scale platform is sealed in a tamper-proof enclosure and is connected via a tamper-proof conduit to the measurement cabinet where the weighing terminal is stored. An ultrasonic gauge (ULTG) is used to measure the thickness of the bottle wall to allow for the attenuation correction of the subsequent enrichment measurement. The enrichment level is measured using either a calibrated HM-5 or a calibrated NaI detector connected to a multichannel analyzer. The acquired spectra are evaluated using a special computer code (NaIGEM). The code calculates the ^{235}U enrichment by a peak-fitting technique and allows for wall thickness and matrix corrections. A simple evaluation of the 186 keV peak by regions of interest alone would fail due to the strong interference of ^{228}Th stemming from the ^{232}U decay. Therefore, the masses for ^{235}U and U total composition are derived from a combined evaluation of the weighing results, the enrichment and the uranium concentration in UO_3 .

63.3.3.3 High-Resolution Gamma Spectroscopy (HRGS)

High resolution gamma spectroscopy (HRGS) is widely used in safeguards to verify the isotopic composition of plutonium or uranium in unirradiated nuclear material. The isotopic information for plutonium (^{238}Pu , ^{239}Pu , ^{240}Pu , ^{241}Pu , ^{242}Pu and ^{241}Am) is needed for neutron assays to convert measured neutron responses stemming from a limited number of Pu-isotopes (including Am) to total plutonium mass. Similarly, the heat output measured by calorimetry is correlated with the Pu-isotopics to obtain the total mass of Pu. Plutonium emits a complex spectrum of X- and γ -rays that are interpreted using dedicated software (Multi-Group Analysis (MGA)) (Gunnink 1990) either embedded in the multichannel analyzer software or as a stand-alone application. MGA mainly exploits the complex 94–104 keV region. MGA calculates the abundances of ^{238}Pu , ^{239}Pu , ^{240}Pu , and ^{241}Pu (^{242}Pu has indistinct gamma rays and is estimated from isotopic correlation). The abundances of ^{241}Am and, if present in the Pu sample, ^{235}U and ^{237}Np , and their respective element ratios are determined simultaneously.

The TARGA software contains an upgraded version of MGA as an engine, and provides a comparison tool for operator-declared and inspector-measured values. An alternative method – fixed energy response function analysis with multiple efficiencies (FRAM) – considers the higher energies, requiring specific hardware settings (Sampson et al. 2003). This allows for measurements in containers with steel wall thickness of greater than 10 mm.

The measurement of uranium samples usually involves only two main isotopes – ^{235}U and ^{238}U – providing the uranium enrichment of the sample. The spectral analysis of the γ -spectra is performed using a modified MGA code – MGAU (Gunnink et al. 1994). HRGS is used to determine the ^{235}U enrichment of uranium hexafluoride (UF_6) in shipping cylinders. In this case, low-resolution gamma ray systems would fail to provide accurate assays due to the complexity of the gamma spectra caused by the presence of additional radionuclides (e.g., ^{228}Th) stemming from natural decay chains plated on the container walls. In addition, for feed (Natural Uranium) and tails (Depleted Uranium) cylinders, the signal-to-noise ratio for the 186 keV peak with LRGS exceeds measurement tolerances and, therefore, HRGS is needed.

High Purity Germanium (HPGe) detectors cooled by liquid nitrogen are the backbone of HRGS applied by Safeguards. The Pu-sample is placed, in its original packaging, on a planar HPGe detector, acquiring a spectrum in the energy range 0–614 keV within 300–1,000 s. The spectrum is then analyzed using MGA code. Typical precisions and accuracies range between 0.5% and 2% reliability for all isotope abundances except ^{242}Pu .

The content of nuclear material in waste drums is usually very low and not homogeneously distributed. However, bulk-handling facilities such as reprocessing and fuel fabrication plants often accumulate a huge number of waste containers that together contain significant amounts of nuclear material. Representative sampling for DA is not feasible and NDA is the only means of determining the content of nuclear material in the waste. This is also true for the determination of holdup in bulk facilities. Although several NDA methods exist to tackle the problem of holdup accounting in bulk facilities, the related measurement uncertainties often exceed the specified goal.

The Segmented Gamma Scanner (SGS-IQ3) is a commercially available gamma assay system and uses transmission-corrected passive assay techniques to determine isotopics and to quantify individual isotopes (usually ^{239}Pu or ^{235}U) within items of scrap and waste (Booth et al. 1997; Mayer et al. 2004). The SIQ3 system utilizes a 15 cm, 4π low background, steel shield with three collimated HPGe detectors (coaxial) to perform quantitative gamma assay measurements in combination with three additional HPGe detectors (planar, optimized for low energy and high resolution) to measure the plutonium isotopics. Three transmission sources are mounted opposite the coaxial detectors to perform the transmission measurements. The quantities are determined both by summing the transmission-corrected result for each detector, and by summing the spectra and performing a quantitative assay based on the average density of the drum.

The in situ object counting system (ISOCS) is an intrinsically, numerically calibrated gamma spectrometry system incorporating a well-characterized HPGe detector (Bronson and Young 1997). The system is commercially available and is used to verify nuclear materials, in particular uranium, contained in holdup and waste. The calculation of the efficiency versus energy function is based on user-defined models that take into account all physical parameters describing geometry and sample matrix. The acquired gamma spectrum is analyzed using calibration information. The ISOCS calibration method is a powerful tool enabling calibration of the detector for a wide variety of source geometries and activity distributions.

The cascade header enrichment meter (CHEM) is another application that uses HPGe detection to qualitatively confirm the absence of HEU in centrifuge cascade header pipes of enrichment plants (Close et al. 1998). The technique uses an external radiation source (^{57}Co) and a special collimated HRGS with specific software to control, perform, and evaluate X-ray fluorescence (XRF) and passive measurements. The XRF measurement provides the amount of total uranium in the UF_6 gas. The deposit on the inside surface of a header pipe requires two measurements of the ^{235}U gamma ray at 186 keV with different geometries to determine the amount of ^{235}U in the gas alone. The level of enrichment of uranium in the gas of the header pipe can then be determined independently of the gas pressure.

Gamma/X-Ray/Weighing (GXW) method can simultaneously determine plutonium element concentration and isotopic composition both in solid and liquid samples from a single HRGS measurement (Dragnev et al. 1997; Parise et al. 2003). It exploits the full spectroscopic information contained in a gamma spectrum from a plutonium sample using several gamma-spectrometric analysis techniques such as enrichment-meter-type measurements and passive X-ray fluorescence analysis (XRF). In combination with weighing, this method determines the total Pu content in a sample.

63.3.4 Neutron Counting Techniques

NDA based on neutron measurements plays an important role in the qualitative and quantitative analysis of nuclear material, in particular plutonium in bulk and item form. Plutonium samples have a high rate of spontaneous fission neutrons, while uranium samples are typically interrogated using an induced fission neutron signature.

Neutrons are primarily emitted from nuclear material in three ways:

1. Spontaneous fission of uranium, plutonium (in particular involving even isotopes of plutonium), and curium (in spent fuel).
2. Induced fission from fissile isotopes of uranium and plutonium, typically by means of a low-energy neutron source.
3. α -particle induced reactions, involving light elements such as oxygen and fluorine.

Contamination of the plutonium-bearing materials with other spontaneous fission nuclides (e.g., ^{244}Cm) will strongly interfere with the neutron assay. ^{244}Cm is the strongest neutron emitter and accounts for more than 95% of the neutrons in spent fuel although the share of curium is only about 0.5% of the plutonium content.

A few ppm of ^{244}Cm will lead to a significant overestimation of the result. However, ^{244}Cm is an important “tagging” nuclide that could be used for neutron measurements in combination with known concentration ratios of curium, plutonium and uranium (Rinard and Menlove 1997). This technique can be applied only if chemical processes do not change the element ratio, i.e., there is no separation. This is the case for determining plutonium and uranium composition in selected process wastes, e.g., the leaching process of spent fuel or vitrification process.

Falsification of the neutron count by adding a neutron source (such as ^{252}Cf) could fool the neutron assay equipment. However, the subsequent presence of ^{252}Cf in the product would be a serious problem and a very strong indicator of attempted spoofing.

Main attributes of various neutron detector systems are listed in [Table 63.5](#).

63.3.4.1 Neutron Detectors

Neutrons can only be detected by indirect methods, e.g., via nuclear reactions producing charged particles. The electrical signal produced by the resulting charged particles can then be processed by the detection system.

^3He gas detectors are the most commonly used neutron detectors in safeguards. The detection principle is based on the $^3\text{He} (n, p) ^3\text{H}$ reaction. This reaction produces a proton with recoil energy of 732 keV that ionizes the surrounding gas and generates an electronic signal. Thermal neutrons have a high absorption cross section for the $^3\text{He}(n, p)^3\text{H}$ reaction. The neutron absorption cross section decreases with orders of magnitude as the neutron energy increases, hence moderation of neutrons is essential to achieving a reasonable detection efficiency of the counting system. ^3He gas detectors have been proven robust and effective. They are commercially available with various diameters, lengths, and gas pressures.

BF_3 detectors are occasionally used based on the $^{10}\text{B}(n, \alpha)^7\text{Li}$ reaction. BF_3 detectors are less sensitive to gamma radiation fields but are less efficient. Recently, solid-state neutron radiation devices with boron carbide diodes have been developed, which demonstrate very promising potential for future applications such as miniaturized handheld neutron detection devices.

■ Table 63.5

Neutron systems

System	Detector	Measurement task	Typical performance values (%) ^a
HLNC	³ He	Pu in PuO ₂	0.5(pure)-3(scrap)
		Pu in MOX	3–5
		Pu in pins/assemblies	1
INVS		Pu in small samples (powder, pellets, liquids)	1.5
		Pu in MOX scrap	2.5
FPAS		Pu in fresh MOX pins	2
GBAS		Pu in in-process materials	5–10
BNCN		Pu in fast critical assembly fuel plates	5
DRNC		Pu in fast critical assembly fuel drawers	3
UFBC		Pu in Powders, MOX pins and fresh FBR fuel	1–2
UWCC		Pu in fresh MOX fuel assemblies (underwater)	2–3
SFCC		Pu in spent fast breeder reactor fuel (underwater)	8
WCAS		Pu in large waste container	11
WDAS		Pu in waste drums	8
PNCC		Pu under various field conditions	
PSMC		Pu in impure samples (MOX)	2
ENMC		Pu in pure samples (MOX)	0.5
		Pu in impure samples (MOX scrap)	2–3
UNCL		²³⁵ U in LWR fresh fuel	2–4
AWCC		²³⁵ U in HEU, bulk UO ₂ and pellets	3–5
		²³⁵ U in LWR fuel	1–5(burnable poison)
AEFC		²³⁵ U in spent fuel from research reactors	10
SFNC	Fission chamber	Presence of spent fuel	Attribute

^aAverage measurement time ~300 s.

Fission chambers have a thin layer of ²³⁵U plated on the inner wall of a gas-filled chamber. Neutrons will cause fission of ²³⁵U producing high-energy fission fragments (~90 MeV). The fission fragments cause ionization in the stopping gas, which could then be transformed to an electronic signal. The fission chambers have the highest tolerance versus gamma dose rates (up to roughly 10⁴ Gy/h) of any of the available neutron detectors because the short ranging fission fragments deposit a much larger quantity of energy in the stopping gas in comparison to the gamma rays. They are the only neutron detectors capable of measuring highly active spent fuel. The inherently low efficiency of fission chambers is compensated for by the large number of neutrons available for counting.

^3He and BF_3 detectors are sensitive to high gamma radiation fields, which produce a high pile-up and mask the neutron signal. Under such conditions, fission chambers are used.

Plastic and liquid (organic) scintillators are often used for fast-neutron detection because of their fast response and modest cost. Their function is based on the elastic scattering of the neutron on light elements (mostly carbon and hydrogen). The proton absorbs the kinetic energy from the neutron, producing heat and visible light. The visible light is collected in a photomultiplier tube coupled to the scintillator and converted to an electronic pulse. However, gamma radiation also produces visible light while interacting with the scintillator. This sensitivity to gamma radiation severely limits the application of scintillators in the selective neutron detection process.

Europium-activated lithium iodide (enriched in ^6Li) as a scintillator can detect neutrons and gammas simultaneously (Mukhopadhyaya and Mchugh 2004; Syntfeld et al. 2005). Neutrons are detected via the reaction $^6\text{Li}(n, t)\alpha + 4.78 \text{ MeV}$. The high-energy pulses from the neutron events can be well discriminated from the pulses stemming from the interactions with the gamma radiation.

63.3.4.2 Gross Neutron Counting

Gross neutron counting for safeguards purposes is applied in searching for undeclared nuclear material and activities, process monitoring, measuring holdup in glove boxes, and in the assay of spent fuel.

The handheld neutron monitor (HHNM) is a portable ($\sim 4 \text{ kg}$) neutron detection device with three ^3He proportional neutron counters, a GM counter and integrated electronics, which provide a means of searching for and localizing neutron radiation sources. A measurement sequence consists of background and verification measurements. When a predetermined threshold is exceeded, the detector triggers an alarm and records the relevant information.

The DG-5 is a portable device for gamma and neutron detection using a liquid scintillator. The presence of neutrons is a strong indicator of nuclear material and activities. Neutrons are difficult to shield by heavy metals in contrast to gamma radiation. They need lightweight elements to lose their energy and be absorbed while gamma radiation would penetrate this neutron shield to a large extent. Therefore, safeguards inspectors use the DG-5 to scan for undeclared nuclear material and activities.

The spent fuel plutonium canister counter (SPCC) is designed to operate underwater and to count neutrons emitted from natural uranium spent fuel rods stored in dry stainless steel canisters (Menlove et al. 2002). The counter uses three ^3He detectors located inside watertight and Pb-shielded pipes spaced 120° apart and surrounding a cylindrical cavity. SPCC determines ^{240}Pu mass from total neutron counts corrected for background, ^{238}U spontaneous fission and multiplication.

The portable neutron uranium holdup (PNUH) monitor system is a neutron counting system to determine the quantity of uranium holdup within the cascade halls of an enrichment plant (Beddingfield and Menlove 2002). PNUH is custom built and the detector head is a polyethylene-moderated assembly with 25 ^3He neutron proportional tubes. PNUH measures the total neutron signals at various prescribed locations. Measurement data are acquired with standard INCC software and evaluated with specialized PNUH software using distributed source term analysis (DSTA).

63.3.4.3 Neutron Coincidence Counting

During fission, multiple neutrons (multiplicity $\sim 2\text{--}3$ for plutonium) are emitted contemporaneously from the splitting nucleus. Because they arrive in the detector simultaneously, these neutrons can be distinguished from all other neutrons (e.g., those produced by (α, n) reactions or by neutron generators), which are not correlated in time. The fission neutrons are referred to as coincident neutrons. The neutrons emitted by a plutonium-bearing sample consist of spontaneous fission neutrons from even-even plutonium isotopes ($^{238,240,242}\text{Pu}$), from the interaction of α -particles with low- Z elements (e.g., O, C, F, Al, etc.) and induced fissions from $^{239,241}\text{Pu}$ ("multiplication effect") caused by thermalized spontaneous fission neutrons and (α, n) neutrons. The spontaneous fission rates are sufficiently high to permit direct measurement of the fission neutrons (passive neutron counting). Emitted neutrons are moderated and then detected with ^3He tubes. Amptek circuits amplify the output pulses from the ^3He tubes and convert the pulses above a discriminator threshold to digital pulses.

The ^3He neutron counters detect all neutrons arising from both (α, n) and fission reactions. Sophisticated pulse processing electronics, called neutron coincidence counting circuits (shift register), measure the number of neutrons that are detected within a predefined time interval (gate width), and differentiate between time correlated (coincidence) neutrons emitted from the fission events and single neutrons created as a result of α -particle interactions. The measured coincident neutrons (doubles) are proportional to the mass of the even-even Pu isotopes ($^{240}\text{Pu}_{\text{effective}} = 2.43\ ^{238}\text{Pu} + ^{240}\text{Pu} + 1.69\ ^{242}\text{Pu}$).

The absolute plutonium mass is determined from the mass of ^{240}Pu effective and the isotopic abundances. Induced fissions exhibit higher neutron multiplicity than the spontaneous fission events; hence, they contribute to the enhancement of coincidence response and introduce nonlinearity in the response for higher amounts. The plutonium content of samples in this type of measurement can typically range from the gram level up to several kilograms. Standard methods have been developed for multiplication corrections.

The main parameters characterizing neutron coincidence are the average neutron lifetime (die-away time τ , typically $\sim 50\ \mu\text{s}$) and the neutron detection efficiency (ε) in terms of their magnitude and uniformity. High detection efficiency is important for coincidence counting because the probabilities of detecting dual and triple coincidences are proportional to ε^2 and ε^3 , respectively. A flat spatial efficiency profile is needed to obtain comparable results for different sample positions, dimensions, and filling heights. A short die-away time is important as it minimizes the accidental coincidence count rate from any high background of random neutrons. Both parameters are influenced by the moderator. Reducing the moderator may decrease detection efficiency and die-away time. Less-moderated counter assemblies detect neutrons before thermalization (epithermal counters) and therefore have a significantly reduced die-away time ($\tau \approx 22\ \mu\text{s}$).

The detector system is calibrated using known standards that are subject to DA sampling. Two calibrations are normally used:

- (a) "Passive" calibration curve (using measured doubles versus ^{240}Pu -effective mass). This calibration curve provides the most accurate results for measurement situations where the singles neutron background has a significant uncertainty. This is especially true for small samples where the neutron multiplication is small. For this mode of calibration, a well-matched set of standards is required and the multiplication is built into the calibration curve.

- (b) “Known-Alpha” multiplication calibration curve can be used when the material is pure. Then the α -factor (ratio of the uncorrelated to spontaneous fission neutron events) is accurately predicted by the isotopic ratios. Impurities, e.g., fluorine, moisture, significantly change the calculated neutron response. This mode of measurement always has the best statistical precision and the calibration curve is a straight line.

Interactive software (e.g., IAEA neutron coincidence counting (INCC)) functions as a hardware interface, controlling setup for the coincidence counting electronics. The software supports the inspector in setting calibration and measurement parameters and inputting sample data (e.g., Pu isotopics, declared mass of plutonium, etc.) based on the operator’s declaration or inspector’s own analysis. The code updates the input to the date of measurement providing decay-corrected values for the operator–inspector data comparison. The actual assay cycle is preceded by a sequence of normalization and background measurement cycles. Each sequence must pass all built-in quality control criteria for acceptable results. When the measurements are completed, the Pu mass is calculated based on the selected calibration parameters and the measured neutron count rates (singles, doubles, and triples) and an operator–inspector difference for the plutonium mass along with propagated errors is recorded. The computer routine facilitates the re-evaluation of results using different measurement parameters, e.g., change of calibration curve or using different data sets of isotopics.

The neutron measurements are influenced by a number of physical and environmental factors such as filling heights, changes in density, presence of nearby reflectors and additional neutron sources. These factors could change the number of neutrons available to induce fission and hence lead to false coincident events.

The same coincidence measurement technique is used for “active neutron counting techniques” whereby the fissile isotopes are irradiated by neutrons from an external source to induce fission. The resulting multiple induced fission neutrons are then measured using standard coincidence counting methods to separate the signals from induced fission neutrons from the signals caused by single neutrons. The active neutron counting technique measures the fissile isotopes of uranium (^{235}U) and plutonium (^{239}Pu , ^{241}Pu).

The high-level neutron coincidence counter (HLNC) has a detector head composed of a polyethylene cylinder with an embedded array of 18 ^3He tubes (Krick and Menlove 1979). The moderator slows down the energetic neutrons to thermal velocities. The words “high-level” are included in the name because the counting and sorting electronics can perform at a high rate, such as 100,000 cps of single neutrons. The HLNC is specifically designed to measure high spontaneous fission neutron rates from samples containing up to several kilograms of plutonium.

The HLNC is the basic model – a whole “family” of instruments exists with various measurement configurations to fit shape and size of the item being measured (Menlove 1983; Menlove et al. 1994). In most instances, these systems are facility resident or integrated into the facility process and can be operated either in attended or unattended mode. The counter is used to measure plutonium in bulk material (e.g., PuO_2 , mixed $\text{PuO}_2 - \text{UO}_2$ (MOX)) or plutonium in unirradiated MOX fuel assemblies and pins (► Fig. 63.2).

The inventory sample counter (INVS) is a small counter within the HLNC family (Miller et al. 1991; Sprinkle et al. 1993) with a high neutron counting efficiency (35%), designed to minimize perturbation from moisture, bagging, or other matrix materials in the sample. It is used to perform high-precision measurements of small plutonium samples, such as process samples, e.g., Pu pellets, powders, and solutions in vials. The samples are weighed with high accuracy ($\sim \pm 0.1$ mg) and the plutonium result is then extrapolated to the total item quantity.

■ Fig. 63.2

High-level neutron coincidence counter (HLNC)



The Universal Fast Breeder Counter (UFBC) is a thermal neutron coincidence counter designed to assay FBR fuel assemblies and other types of plutonium fuel (Menlove et al. 1984). UFBC has 7.0% efficiency using 12 ^3He tubes surrounded by polyethylene and a thin cadmium sleeve. The uniform counting (flat response) region in the detector head (141 cm high and 30.5 cm in diameter) is 105 cm. UFBC can measure assemblies with plutonium loadings of up to 16 kg (24% Pu).

The fuel pin assay system (FPAS) is used to determine the Pu-content of fresh MOX fuel pins stored on trays with results that correspond to greater than 2% with the declared data (Cowder and Menlove 1982; Miller et al. 1989). FPAS has a relatively flat response for 1.2 m. The system primarily operates in attended mode by the inspector identifying and checking the positioning of the pin tray in the counter. The system could be transformed to an unattended system using a robotic conveyor for the tray delivery/removal in combination with a radiation-triggered ID camera to record the tray identification.

The glove box assay system (GBAS) measures the in-process material of plutonium in a specific process glove box (Miller et al. 1989). This system is a very large coincident neutron counting system (160 cm high, 100 cm long, and 7.6 cm wide) that can be positioned and raised to cover the front and back sides of very tall MOX process glove boxes. Six slabs were originally installed in pairs on either side of a glove box. Each slab contains twenty 152 cm ^3He tubes. Monte Carlo calculations were used to design the detector and study its response before installation. GBAS can be moved into place around randomly selected glove boxes containing large amounts of MOX materials in process. Experience has shown a measurement uncertainty of $\sim 5\%$ for neutron assay.

The birdcage neutron coincidence counter (BCNC) verifies plutonium content in fast critical assembly fuel plates stored in containers called birdcages (Krick et al. 1985a).

A birdcage can store up to 2 kg of plutonium. Neutron coincidence measurements are performed without removing the fuel plates from the birdcages. The custom-designed detector body consists of 20 ^3He proportional counter tubes embedded in polyethylene, providing an efficiency of about 5%.

The drawer neutron counter (DRNC) has been designed to perform the assay of plutonium in fast critical assembly fuel drawers (Krick and Menlove 1980). Eight tubes (2.5 cm diameter by 91 cm active length) were used in the system. The principal feature of the neutron coincidence detector is a 7 cm by 7 cm by 97 cm detector channel, which provides a uniform neutron detection efficiency of 16% along the central 40 cm of the channel.

The underwater coincidence counter (UWCC) is a transportable system for measuring fresh MOX fuel stored under water (Eccleston et al. 1998). It is a modified version of a standard Fork detector (FDET) whereby the ionization and fission chambers have been replaced with sensitive ^3He tubes embedded in a high-density polyethylene measurement head. The UWCC measures neutrons coming from a segment of the MOX fuel in “multiplication corrected” coincidence mode and provides total Pu, once the isotopics and the active fuel length are known.

The waste crate assay system (WCAS) measures plutonium content of large waste containers for high- and low-activity waste (Menlove et al. 2001). WCAS is a passive neutron coincidence counter operating in 4π geometry and can work in high radiation fields up to 110 R/h. The system employs a combination of shielded and unshielded ^3He detectors (98 ^3He tubes in total) embedded in a polyethylene matrix and has a detection efficiency of $\sim 10\%$. For the low active waste, all tubes are used to determine ^{240}Pu effective by the coincidence rates. The high active waste measurement utilizes only the shielded tubes (78 mm steel) to obtain ^{244}Cm contents by the singles rates. The amount of plutonium and ^{235}U in the wastes are calculated with Cm/Pu ratio and Cm/ ^{235}U ratios, known from the stream average ratios at the waste generating sites. WCAS has a small ^{252}Cf source of known source strength that can be positioned in an automated sequence at a fixed number of locations adjacent to the waste container wall. The measurement with and without source provides a matrix correction factor for a given configuration. WCAS can measure a wide range of plutonium masses from a few milligrams to tens of kilograms within a matrix of 4,000 kg of mixed metal waste.

The waste drum assay system (WDAS) measures the residual small plutonium amounts of in-process wastes in 200 liter drums. The system uses a modified neutron coincidence counter with a counter comprising 60 ^3He tubes ($\sim 20\%$ efficiency) with low background. WDAS applies the add-a-source correction technique that corrects for the effects of the waste matrix on neutrons (Menlove et al. 1993, Menlove 1995). A small ^{252}Cf source is placed in various positions near the external surface of the sample drum. The changes in the ^{252}Cf coincidence counting rate provide a matrix correction for the plutonium inside the drum.

The portable neutron coincidence counter (PNCC) consists of four individual slab detectors with four ^3He tubes each that can operate in multiple modes and configurations (Thornton et al. 2006). The detector is lightweight and portable (~ 15 kg) to address flexibility of measurement requirements for various field environments. PNCC has about 12% detection efficiency.

63.3.4.4 Multiplicity Coincidence Counting

Normal coincidence counting techniques rely on the detection of two coincident neutrons (doubles) and making an assumption based either on the multiplication or on the (α , n) neutron rate. These two analysis methods – passive calibration and known-alpha – require

traceable calibration standards and the results can be subject to bias due to changes in sample multiplication or composition; however, they are useful for identifying these changes in the material.

Multiplicity counting uses the additional information from events when three coincident neutrons are emitted per fission (triples) (Ensslin et al. 1998). This additional information is obtained from the measurable multiplicity distribution and allows solving all three unknowns, namely, ^{240}Pu -effective mass, multiplication, and the (α, n) neutron rate. Therefore, the mass of plutonium in the sample can be calculated directly without making any assumptions about its chemical and physical composition. Multiplicity counting can be applied to all plutonium samples, but is beneficial primarily in measuring impure samples. For some material categories (e.g., small Pu samples, process residues with high (α, n) neutron rate) multiplicity counting may not be helpful because of the limited precision of the triple coincidences. Multiplicity counting requires high efficiency as the detected triples rate is proportional to the efficiency cubed. The counters are designed to minimize die-away time and deadtime. Conventional coincidence counters can be used for multiplicity analysis, but their lower efficiencies and longer die-away times lead to very long counting times.

The plutonium scrap multiplicity counter (PSMC) is a high-efficiency neutron multiplicity counter with cadmium lining designed for measuring impure samples such as MOX scrap materials (Nakajima et al. 1997). The PSMC contains 80 ^3He -filled tubes (at 4-atmosphere fill pressure) arranged in four rings embedded in polyethylene and has an efficiency of $\sim 55\%$.

Epithermal-neutron multiplicity counters (ENMCs) use ~ 120 high-pressure ^3He tubes (10 atm) in closely packed rings with less moderator material (Langner et al. 2006; Asano et al. 2006). The higher pressure and the large number of tubes capture more of the thermalized and epithermal neutrons resulting in an efficiency of about 65%. The reduced thickness of high-density polyethylene shortens the neutron die-away time to only 22 μs . This combination improves the statistical precision by a factor of 5–20 compared with traditional thermal-neutron counters depending on the characteristics of the samples (Stewart et al. 2000). Sufficient counting statistics are important for unfolding the multiplicity distribution to determine the triples. In addition, the singles background rate must be accurately measured and shielding used on the outside of the neutron detector to reduce the singles neutron background. The background for doubles and triples is very small and relatively constant. Although designed for multiplicity counting, ENMC is a very powerful “normal” neutron coincidence counter due to its high efficiency and optimized design parameters. In some cases, statistical errors for small samples have been reduced to less than 0.15% using an ENMC; in impure samples, the statistical error dominates the systematic error and can be as high as 3% (over 100 min measurement time).

63.3.4.5 Active Neutron Coincidence Counting

The fissile isotopes of uranium (^{235}U) and plutonium (^{239}Pu , ^{241}Pu) can be measured using “active neutron counting techniques.” This technique uses an external neutron source to induce fission in the fissile plutonium and uranium content of the sample. The multiple induced fission neutrons are then measured using standard coincidence counting methods. The technique is mainly applied to determine the mass of ^{235}U in uranium-bearing samples (from LEU to HEU) in powder, metal, pellets, fresh fuel elements, and waste drums. It can be operated either with or without a cadmium liner (fast or thermal mode).

The uranium neutron coincidence coLLar (UNCL) can be operated in either an active or a passive mode to measure the ^{235}U and the ^{238}U mass per unit length of LWR fuel assemblies (Menlove 1981). UNCL has four polyethylene slabs that surround a central cavity where a fuel assembly is placed for measurement. ^3He tubes are embedded in three of the four slabs. The fourth polyethylene slab contains a cylindrical well for the AmLi neutron source. The active mode uses neutrons from a low-intensity (5×10^4 n/s) AmLi neutron source to cause fission of ^{235}U in the fuel and the neutrons from induced fission in ^{235}U are counted using coincidence electronics. When no interrogation source is present, the passive neutron-coincidence count rate from spontaneous fission gives a measure of ^{238}U linear mass density (g/cm). The UNCL measures only one section of the fuel, approximately 40 cm long. The measured coincidence neutron rate is proportional to the ^{235}U mass per unit length. Together with a measurement of the active length of fuel (e.g., using an HM-5), the UNCL can verify the operator-declared total ^{235}U content of a fuel assembly. Measurements on pressurized water reactor (PWR) and boiling water reactor (BWR) assemblies have demonstrated that, for measurements of similar fuel assemblies used for calibration, the overall accuracy for assay of ^{235}U linear density is 1–2%. For absolute measurements, using calibration parameters from other facilities and fuel assemblies, the accuracy is in the range of 2–4%, depending on how closely the standards match the assemblies assayed and how precisely calibration has been performed. When operated in passive mode, the UNCL can be used to confirm ^{238}U linear density to within 10%. The ^{235}U sensitivity enables detection of a removal or substitution of three to four rods in a PWR assembly and a single rod in a BWR assembly. Assemblies containing Gd as a neutron poison need to be analyzed using a poison correction factor calculated by Monte Carlo simulations (Menlove and Pieper 1987).

The active well coincidence counter (AWCC) is designed to measure ^{235}U in HEU metals, bulk UO_2 materials and light water reactor (LWR) fuel pellets (Krick et al. 1985b; Menlove et al. 1996). The AWCC has 42 ^3He tubes in two rings, achieving an efficiency of about 36%. The system uses two AmLi neutron sources, each mounted in one of the end plugs of the assay chamber of the coincidence counter body. The neutron sources induce fissions in isotopes not having significant spontaneous fission activity, e.g., ^{235}U . The induced-fission neutrons of the sample are quantified with standard coincidence counting techniques. The use of the AWCC to verify total ^{235}U content provides an important advantage over gamma-ray techniques for some applications (e.g., for large and/or heterogeneous samples). The high neutron penetrability permits the AWCC to measure the entire ^{235}U content of a sample rather than just the surface layer that would be measured using gamma-ray techniques. The AWCC can be operated either with or without a cadmium liner (thermal or fast mode). Although designed for active neutron assay, it is also a good passive neutron counter if the AmLi sources are removed.

63.3.5 Spent Fuel Measurement

NDA methods are presently the only feasible means of verifying spent fuel. Several instruments are available for measuring spent fuel assemblies stored underwater. Direct measurement of plutonium and uranium in spent fuel is normally impossible because the primary neutron and gamma signals come from higher actinides (e.g., spontaneous fission neutrons from the ^{242}Cm and ^{244}Cm isotopes) and fission products. The measurement of gamma and neutron radiation from spent fuel assemblies can be used to confirm various attributes and to estimate burnup, which can be correlated to the quantity of plutonium in the assembly. The variability of the fuel

designs is a challenge for the adaptation of these techniques, particular in the area of the quantitative verification of irradiated fuel from research reactors that might contain HEU.

The most powerful verification tools for spent fuel in wet storage are the improved Cherenkov viewing device (ICVD), safeguards MOX python (SMOPY) device and the FORK detector (FDET). The ICVD is a nonintrusive instrument based on the detection of Cherenkov light specific to high irradiation effects in water caused by spent fuel. SMOPY and FDET measure total neutron and gamma radiation simultaneously. A passive gamma emission tomograph is currently being tested to be able to detect defects at a pin level.

63.3.5.1 Gamma Methods

The spectrometric performances of CdZnTe detectors, their robustness, and simplicity are key to their wide application for the verification of irradiated materials in spent fuel (Lebrun et al. 2000; Lebrun and Carchon 2003).

High-resolution gamma spectrometric measurements from fission products have also been used to estimate burnup. The fission product nuclide must be long-lived in comparison to the fuel irradiation time. The measured gamma-ray intensity must be corrected for cooling time decay; if the cooling time is not known, it can be estimated from the relative activities of various fission products. Errors can be greatly reduced by measuring the ratio of the activities of two nuclides having a known dependence on burnup. Although capable of giving good estimates of burnup, this method is time consuming, because of the need to place detector systems underwater and to move each fuel assembly to the detector position for verification to be performed.

The spent fuel attribute tester (SFAT) is a routine inspection instrument for gross defect detection. It provides a qualitative verification of the presence of spent fuel through the detection of particular fission product gamma rays – either from ^{137}Cs (662 keV) for fuel which has cooled for longer than 4 years or from ^{144}Pr (2,182 keV) for fuel with shorter cooling time (Carrasco et al. 1997). The equipment comprises a stainless steel watertight housing containing a collimated NaI, CdTe, or CdZnTe detector that can be submerged in a storage pond. SFAT takes measurements from the top of a fuel assembly as it sits on top of the underwater storage rack and does not require movement of the fuel. The SFAT is applied where Cherenkov viewing cannot provide conclusive verification (e.g., for low burnup or long cooling time, where the Cherenkov radiation is too weak or where the water in the storage pond is not clear enough).

The irradiated item attribute tester (IRAT) differentiates irradiated nonfuel items from irradiated fuel items that are stored in spent fuel storage ponds (Aparo et al. 1999). It consists of a stainless steel cylinder housing shielding and collimation, a miniature CdZnTe detector, and a preamplifier. A multiwire cable connects the measurement cylinder (watertight) and data acquisition/control unit (operated above water). The IRAT detects gamma radiation characteristic of either fission products contained in spent fuel or activation products contained in irradiated structural materials. The IRAT uses the detection of key fission product gamma rays as evidence that an item being measured has the characteristics of spent fuel. A statistical test compares the measured gamma ray spectrum to a background measurement in order to determine if a certain gamma emitter is present. The presence of such fission/activation products serves as evidence that an item once underwent fission (^{137}Cs for cooling time > 4 years; ^{144}Pr , ^{137}Cs , ^{134}Cs , or $^{95}\text{Zr/Nb}$ cooling time < 4 years) or, in the case of a structural item, was once exposed to a significant neutron flux (^{60}Co). The measurement with

Fig. 63.3**The irradiated item attribute tester (IRAT)**

IRAT requires movement of the spent fuel as the detector approaches the item from the side. IRAT is very similar to FMAT with differences in the collimator part and the type of CdZnTe detector (► Fig. 63.3).

The high-sensitivity gamma monitor (HSGM) is an enhanced underwater survey meter, consisting of a Geiger–Mueller probe and a microprocessor unit. It measures gamma and X-rays in the 60 keV to 3 MeV range over a total dose rate range of 1 mSv/h (0.1 mR/h) to 300 Sv/h (30,000 R/h). The HSGM is powered by an internal chargeable battery (or by facility power if the battery is discharged beyond a certain level). The technique provides a qualitative confirmation of irradiated items. The method cannot readily distinguish between irradiated nonfuel items and genuine spent fuel items, as it only detects the radioactivity of each item. It does not provide any information on burnup, cooling time, plutonium content, or any other quantitative property. In contrast to ICVD or SFAT, each item to be verified must be isolated from neighboring items. Thus, movement of items is a requisite unless a sufficient separation already exists.

The CANDU (CANada Deuterium Uranium) spent fuel bundle verifier for baskets (CBVB) employs a highly collimated and shielded CdTe, suspended on an automatic winch whose speed can be set for scanning either storage baskets or stacks. It verifies the presence of irradiated CANDU fuel bundles stacked in baskets under water.

The CANDU bundle verifier for stacks (CBVS) moves vertically along the space between columns of trays (10 cm gap) of spent fuel and uses a CdZnTe detector for bundle identification (Ahmed et al. 2001). It employs thick lead shielding to protect the electronics and detector. The CBVS is unable to verify the spent fuel at the bottom layer of a stack due to limited accessibility of a large-size detector part through the funnel structure. During inspection, the tray must be moved. In addition, the large size of the scanning part is both heavy and difficult to handle.

63.3.5.2 Neutron Methods

The advanced experimental fuel counter (AEFC) is used for the characterization of spent fuel from research reactors stored underwater (Menlove et al. 2007). The AEFC can be operated in

either passive neutron mode or active neutron mode, using an AmLi neutron source to generate fissions in the fuel item. The counter is transportable (~ 70 kg) and consists of a polyethylene moderator containing six boron-lined ^3He tubes with a lead shield surrounding the measurement cavity (117 mm in diameter) to reduce the gamma dose to acceptable levels. The radiation tolerant ^3He tubes are embedded in the moderator forming two different measurement sets. One set (inner row) measures neutron coincidences to distinguish fission neutrons from background. The second set (outer row) is placed further back within the polyethylene moderator and is therefore much less sensitive to AmLi neutrons than to fission neutrons, so that the signal is approximately proportional to the fission rate in the fuel item. The detector also contains a collimated ionization chamber to record the gamma emission profile correlated with the relative burnup of the measured item.

The spent fuel coincident counter (SFCC) is an underwater neutron coincident counter for the verification of operator-declared plutonium content in canned fast breeder reactor spent fuel (Bytchkov et al. 2001; Lestone et al. 2002). The SFCC is hermetically sealed; it operates ~ 5 m below water level in a fixed position in a spent fuel storage pond. SFCC has a ring of 20 ^3He tubes embedded in polyethylene ($\sim 15\%$ detection efficiency) and shielded from fission product gamma rays by a 7 cm thick lead ring. A single ionization chamber measures the gamma-ray dose from the spent fuel to determine the appropriate operational parameters to avoid gamma-ray pile effects in the ^3He tubes. The plutonium isotopics are calculated based upon validated burnup chains code and specially developed iterative software in combination with MCNP modeling converts the measured single and double neutron count rates to plutonium mass. An inspector is guided by the software through all measurement, evaluation and decision making (accepted/rejected) processes. The SFCC easily distinguishes irradiated fuel from nonfuel items, which are loaded to the reactor to replace discharged assemblies.

The spent fuel neutron counter (SFNC) is a prototype neutron-detector system that verifies closely packed spent fuel assemblies stored in a spent fuel pond (Ham et al. 2002). The system contains a fission chamber moderated by a polyethylene cylinder housed in a watertight stainless steel enclosure. The SFNC measures total neutron signals from long-cooled spent fuel assemblies while in their storage position, without requiring them to be moved. The technique can detect a missing fuel assembly. These measurements are performed underwater in a gap between four assemblies.

63.3.5.3 Combined Gamma/Neutron Methods

The ratio of neutron to gamma ray data, when combined with other complementary information, is used to characterize a particular type of fuel. To simplify the verification of spent fuel, a technique involving gross gamma ray and neutron measurements can be used.

The Fork DETector (FDET) measures gross gamma and neutrons from a spent fuel assembly, which can be correlated with the operator's declared data on burnup and cooling time (Halbig et al. 1985). Separate detector heads are used to measure BWR- fuel and PWR-type fuel. The system is operated in the spent fuel pond and consists of a microprocessor-controlled, battery-operated electronics unit, a preamplifier, 5–6 meter long pipes to support the detector underwater, and a special watertight measuring head. This head has two pairs of fission chambers for neutron counting and a single pair of ionization chambers for the total gamma flux, which form a fork-type measurement cavity. The pairing of detectors on two sides of an assembly minimizes the sensitivity to assembly-detector geometry and burnup

asymmetries. The operator has to move the fuel assembly to the measurement cavity. Interactive software prompts the user through the measurement procedure and simultaneously collects neutron and gamma data. The software can also support unattended measurements.

The safeguards MOX Python (SMOPY) device combines gross neutron counting with low-resolution gamma spectroscopy to characterize any kind of spent fuel (Lebrun et al. 2001). The SMOPY uses online interpretation tools for the evaluation of measurement data. The system contains a well-shielded and collimated CdZnTe gamma detector and a fission chamber. It is placed over the storage hole of the spent fuel assembly. The assembly is lifted through the open measurement cavity and it can either be scanned or selective parts measured. The SMOPY can verify and distinguish irradiated MOX fuel from LEU fuel and can confirm the burnup of a spent fuel assembly.

The SMOPY device can also be operated in active mode using an AmLi source. This has been successfully demonstrated for the underwater verification of canisters containing residues of irradiated HEU. This application is based on total neutron counting and detects the difference between active background and active background plus induced fissions.

The cask radiation profiling system (CRPS) records radiation profiles (“fingerprints”) from spent fuel storage containers at the time of positioning casks in the dry silo and compares them with a fingerprint taken at the time of subsequent verification (Thevenon et al. 2008). A collimated and calibrated CdZnTe detects gamma spectra in scanning mode while ascending down the verification tube at constant speed. The verification tube is adjacent to the silo and ranges from the top to the bottom. The position information of the detector is provided by a pulser, which emits a signal for every constant interval rotation of the motor’s winch wheel that drives the detector within the verification tube. All raw data are acquired and processed with dedicated software on the inspector’s laptop.

The CRPS provides a tool to reverify a dry storage cask in its storage position to demonstrate that the cask content has not changed (in the event of loss of continuity of knowledge) or as a part of periodic routine requirements for reverification. The maintenance and/or restoration of continuity of knowledge of a spent fuel dry storage container by a reproducible fingerprint require a systematic management of fingerprints over a long period. A database has been developed for the storage and evaluation of fingerprints to secure and effectively compare fingerprints while taking into account decay and changes in the measurement hardware configuration. Automatic unfolding of the radiation profiles to count the number of baskets loaded in the storages is also possible. The CRPS could be run with a pair of detectors to perform neutron (fission chamber) and gamma profiling.

63.3.5.4 Optical Methods

The improved Cherenkov viewing device (ICVD) is the instrument most commonly used by safeguards inspectors to verify spent fuel (Trepte et al. 1996). Observation of the Cherenkov radiation from irradiated reactor fuel assemblies is used to obtain qualitative confirmation of the presence of spent fuel in storage pools. Cherenkov radiation, which results from the interaction of the intense beta radiation from spent fuel with the water in the storage pool, varies in intensity and – for highly active fuel – can be seen in darkness with the naked eye. For fuel with low burnup and/or long cooling times, the Cherenkov intensity is very low, but can be seen using a light-amplifying capability in the night vision device. The ICVD employs light filtering techniques (e.g., ultraviolet filters). Special photo cathodes have been developed with

appropriate spectral sensitivity for Cherenkov light to minimize background light interference and even permit use of the ICVD under normal facility lighting.

Observation of the Cherenkov radiation from irradiated reactor fuel assemblies is used to obtain qualitative confirmation (attribute testing) of the presence of spent fuel in storage by scanning rows of assemblies from the pool bridge. Characteristic patterns formed by the arrangements of rods and holes in fuel assemblies have to be observed to ensure a valid verification. A well-trained inspector can easily detect the presence of an inactive “dummy assembly” surrounded by highly active neighbors.

ICVD cannot be used when fuel is stored in canisters. Furthermore, absorption and reflection of the Cherenkov light caused by additives or particles in the water and its turbulence in spent fuel ponds may result in failure to verify the spent fuel. It is also difficult to see fuel assemblies that are double-stacked in the storage pool.

The digital Cherenkov viewing device (DCVD) is used to verify assemblies with long cooling times and/or low burnups, which have weak Cherenkov signals that cannot be seen with a standard ICVD (Chen et al. 2006a). Apart from its higher sensitivity, the DCVD can record and document individual scans for subsequent reanalysis. It has the potential to quantify the Cherenkov glow from spent fuel assemblies as a function of irradiation history and cooling time. Further development efforts to enable partial defect detection are promising (Chen et al. 2006b).

The optical fiber radiation probe system (OFPS) is used to verify irradiated bundles in the spent fuel bay of CANDU stations (Kim et al. 2006). The OFPS consists of a scanning actuator, an optical fiber scintillator coupled to a flexible optical fiber, data acquisition electronics, and a PC.

The use of an optical fiber scintillator for CANDU spent fuel verification has the benefit of detecting gross gamma rays in storage ponds without being hindered by the funnel structure. Gamma rays from the spent fuel interact with the optical fiber scintillation media to produce ionization, which subsequently leads to the emission of fluorescent light (~ 400 nm) of the doped Ce^{3+} in the optical fiber. Since the optical fiber scintillator is both highly resistant to radiation and able to withstand high temperature and humidity, more precise and safe measurement is possible in between bundles of a tray. In high radiation fields, the optical fiber cable itself emits light from radiation interactions. Therefore, the signal from the cable has to be compensated by a second optical fiber cable (without scintillation media). The detector can be placed between bundles (1.5 cm gap). The verification system performs gross gamma measurements supporting the re-verification of CANDU spent fuel bundles stored in ponds without requiring movement of the horizontal storage trays.

63.3.6 Unattended NDA Systems

Modern nuclear facilities are increasingly automated with the aim of decreasing both personnel exposure and production costs. Owing to automation, direct access to nuclear material may be limited for both the operator and the inspectorate. Unattended NDA systems generate measurement data without requiring the presence of an inspector. The data acquired are routinely collected from measurement cabinets after a certain period or are transmitted remotely to an external location (such as an inspector's office). Main attributes of various unattended NDA systems are listed in [Table 63.6](#).

A combination of containment and surveillance (C/S) data with synchronized NDA data is a very powerful tool to monitor nuclear processes while C/S or NDA data in isolation have less

■ Table 63.6

Unattended NDA systems

System	Detector	Main measurement task	Typical performance values (%) ^a
VIFM	VIFB: solid state Si	Counts SF bundles (fuelling machine → SF pond)	Attribute
	VIFC: solid-state Si & FC	Counts SF bundles from core to fuelling machine	Attribute
SEGM	Si-Pin	Monitors cask loading into dry storage silo	Attribute
ISVS	Xe-IC + ³ He	CoK spent fuel receipts to spent fuel pond	Attribute
IHVS	IC + ³ He	CoK of spent fuel from pond to dissolver	Attribute
PCAS	³ He	Pu in PuO ₂ , MOX in canister	1–2
IPCA	³ He	Pu in MOX in canister	0.85
	3 HPGe	²⁴⁰ Pu-effective (%), U/Pu ratio	
(A)MAGB	³ He	Pu powder/pellets/scrap in process container	4.5
	HPGe	²⁴⁰ Pu-effective (%), U/Pu ratio	
FAAS	³ He	Pu in final fresh MOX assemblies	1.8
VWCC	³ He	U, Pu in vitrified highly active waste via ²⁴⁴ Cm	5–25
VCAS	FC + IC	U, Pu in vitrified highly active waste via ²⁴⁴ Cm	5–25
ENGM	24 ³ He	Pu in fresh MOX (receipt)	Attribute
CCRM	³ He + NaI	CoK of fresh MOX fuel between ENGM and EVRM	Attribute
EVRM	³ He + NaI	CoK of MOX fuel between EVRM and core	Attribute
EXGM	¹⁰ B + 2 IC	CoK of spent MOX fuel to and from spent fuel pond	Attribute
PIMS	142 ³ He	Pu in powder process area	6
RHMS	3 ³ He	Pu, U in leached hulls via ²⁴⁴ Cm	5–25
TCVS	³ He	Pu in MOX canisters temporary stored in process	<6
HMMS	³ He	Pu, U in hulls via ²⁴⁴ Cm	5–25
DCPD	³ He	CoK of Pu canister movements	Attribute
DSNC	³ He	Pu, U in high active, dry reprocessing material via ²⁴⁴ Cm	5
DSNM	³ He	CoK of rear access ports of glove boxes	Attribute
ATPM	Temperature/flow	Power monitoring of research reactors	Attribute
MUND	³ He	Monitoring of fuel transfer casks	Attribute
SMMS	Pressure/temperature	Volume determination/balancing of solutions	0.05

^aAverage measurement time ~300 s.

value. These systems help to decrease overall inspection effort and are capable of monitoring routine activities involving nuclear material, such as the complete process of loading, transferring, and storing spent fuel in dry storage silos.

The main drawback of these automated systems is their predictability. In most safeguards approaches, this drawback is compensated for by unannounced or short-notice inspections on a random basis. Most unattended NDA systems are part of the HLNC family. Other systems use low-resolution gamma detectors either in combination or as a stand-alone application.

Recently, a large reprocessing facility has been commissioned and the safeguards instrumentation in place has set a new technological standard in terms of the networking and integration of different unattended verification systems and C/S systems covering the complete process and storage areas (Johnson et al. 2001, 2004).

63.3.6.1 Unattended Gamma-Based NDA Systems

The VXI integrated fuel monitor (VIFM) is used at CANDU stations to monitor and count fuel bundles discharged from the reactor (Bot et al. 1997; Truong et al. 2001). The system employs radiation hardened solid-state gamma detectors with self-authenticating/tamper-indicating circuitry. The VIFM uses an autonomous data acquisition module (ADAM) to acquire data from the radiation sensors. High operational reliability, great dynamic detection sensitivity (to include all operational possibilities), and insensitivity to power outages are some of the important features of the system. The VIFM has three subsystems:

- A VIFM core discharge monitor (VIFC) detects discharges of spent fuel from a reactor core into the fuelling machine. Both neutron (normal on-power discharge signal) and gamma ray intensities are continuously monitored by solid-state silicon gamma detectors and an array of fission chambers for neutron counting. High dose (~ 2 Mrad) tolerant electronics are employed to withstand the strong radiation fields. An inspector, evaluating the monitoring data, is able to identify in a straightforward, unambiguous manner the abrupt but characteristic changes in count rate associated with fuel bundle discharges, regardless of the operational status of the reactor. Because of the linear increase in background signal, the system can also track the operating power level of the reactor.
- A VIFM bundle counter (VIFB) counts irradiated fuel bundles as they are transferred between the fuelling machine and the spent fuel bay(s). Collimated gross gamma counters detect each fuel bundle as it passes. The proper placement of detectors and the use of the appropriate evaluation algorithm for the facility enable the device to count the bundles as they pass and, to record the direction in which the bundles are moving.
- A VIFM Yes/No monitor (VIFD) determines if any irradiated fuel has been discharged through access ports that are not part of the normal discharge path.

The silo entry gamma monitor (SEGM) monitors the final loading of dry storage containers into a final silo storage location (Zendel et al. 2006). The SEGM consists of a pair of pin-diode gamma silicon detectors, which are inserted at different levels into the verification tubes available for each silo, thereby providing direction-sensitive verification of the silo loading. The detectors are installed before the start of the transfer campaign in all of the silos that will be used for that campaign. The cables from several silos (up to 8) are routed to a common electronics cabinet, where the resulting data is logged. The maximum length of the signal cables connecting the electronic cabinet to the detectors is 200 m. The data can be extracted either

locally or remotely via a standard Ethernet link. The detectors are removed by inspectors and replaced by seals after each silo has been completely filled and the top cover welded.

The integrated spent fuel verification system (ISVS) consists of time synchronized CCTV cameras and radiation detectors, which verify the receipt of spent fuel assemblies received into a facility, unloaded from the transport cask and transferred into storage ponds (Yokota et al. 1998). The radiation detectors, a high-pressure Xe ionization chamber for gammas and a ^3He tube for neutrons, are assembled with preamplifiers and shielding inside a watertight tube. Each channel is equipped with two tubes at each side to provide redundancy for improved system reliability and to enable verification of the direction of spent fuel moving into the temporary storage pit or returning to the unloading pit.

The integrated head-end verification system (IHVS) is intended to maintain continuity of knowledge on spent fuel assemblies moving from the spent fuel storage area to the shearing machine, as well as the removal of hulls drums to waste storage (Yoshida et al. 2005). The system employs radiation-tolerant camera(s) and radiation detectors (CRD) contained in a cylindrical body, which is installed into the shielding wall itself and also contains internal shielding to reduce the dose rate to meet requirements at the exterior of the cell. Each CRD has one ^3He neutron detector and two ion chambers to detect the radiation of a spent fuel assembly in a respective cell. The cameras provide identification and monitoring of transfer routes. The IHVS comprises 14 CRD devices covering the feeding, sharing, and hulls drumming cells.

The continuous enrichment monitor (CEMO) monitors the absence of HEU production in selected gaseous centrifuge facilities and delivers qualitative Go-No-Go information to the inspectorate (Packer 1991; Packer et al. 1997). The CEMO determines the content of U-235 from the intensity of the 186 keV peak using NaI detectors fixed on the product header pipes and correlating the pressure of the gaseous UF_6 with a transmission measurement (radioactive X-ray transmission source: ^{109}Cd (~20–50 keV)). The enrichment is then calculated based on these two parameters. The system operates continuously and transmits remotely (twice a day) state of health and alarm messages in the event that LEU is not confirmed or when a system fault occurs.

63.3.6.2 Unattended Neutron-Based NDA Systems

Continuously operating, unattended and custom-designed NDA systems are being implemented at plutonium handling facilities (e.g., reprocessing, conversion, and fabrication plants) to monitor and determine the plutonium content in various process stages. The main components of these systems are modified HLNC counters tailored to the specification of the material container and process environment. In general, the detectors operate in continuous mode with data dumps every minute. Radiation triggered ID cameras generate time stamped video records, which the inspector can correlate with the raw measurement data.

The plutonium canister assay system (PCAS) determines the content of plutonium in MOX and pure oxide powders in cans contained in a specific transport container (four cans per canister) (Menlove et al. 1986). The system can be integrated into an operator's material handling system and continuous measurement cycles are performed, which are evaluated at the end of a given collection period. Thereby, continuous verification of the flow of canisters can be performed without inspectorate intervention. For inventory verification, an inspector provides an electronic list of canisters to be verified and the operator transfers the selected

canister to the PCAS during shift work without an inspector being present. At the end of a verification campaign, the inspector collects the verification data for evaluation.

The improved plutonium canister assay system (IPCA) is a neutron coincidence detector with provision for the simultaneous measurement of Pu isotopics by HRGS (Abhold et al. 2001). The neutron detector uses a double ring of ^3He tubes for the determination of ^{240}Pu effective mass contained in MOX canisters. The HRGS includes three Ge detectors that determine isotopic composition including the U/Pu ratio. A digital camera, automatically triggered by neutrons, records the canister ID during these measurements. The IPCA is designed to determine the mass of plutonium and uranium in MOX canisters with an uncertainty better than 0.85% for a range of 5–16 kg of plutonium. This performance significantly reduces the random sample size for destructive analysis.

The material accountancy glove box counter (MAGB) provides the plutonium content in specific process containers, handled in the glove boxes of the automated process (Menlove et al. 1993). The system consists of two slab detectors viewing the load cell of a process glove box, where the container filled with either feed powder, pellets, or scrap is placed. A radiation-triggered camera identifies the process container and creates a time stamped video ID record. An upgraded version (AMAGB) employs an HPGe system for the determination of isotopics and U/Pu ratio.

The MOX fuel assembly capsule assay system (FAAS) determines plutonium content in the final assembly contained in a storage capsule. Coupled to the automated capsule transfer system, it provides information about the movements of fuel into and out of the product storage (Menlove et al. 1993). It is designed to assay the complete active zone of the assembly with plutonium loadings up to 10 kg and can accommodate 5 m long capsules that contain the fuel assemblies. The unshielded detector body has 12 ^3He tubes and an efficiency of $\sim 16\%$. In addition, the continuous mode gives a time history of movements of neutron source material in the vicinity. The FAAS is augmented with a surveillance system to meet verification requirements.

The vitrified waste coincidence counter (VWCC) is used at a vitrification facility to quantify plutonium and uranium present in canisters of vitrified highly active nuclear waste that is not suitable for further nuclear use (Beddingfield et al. 1998). The system contains five ^3He tubes shielded by 100 mm of lead. The efficiency is 0.5–1.0% depending on the distance between the detector and the canister. The VWCC calibration is based upon Monte Carlo computer modeling. The upper limit for Pu as a measured discard in vitrified waste is in the order of 5 g in a 10 kg matrix, which can be easily measured by the VWCC. The individual components are all radiation hardened to allow for proper operation in this strong radiation environment. The coincidence counting rates are used to determine the amount of ^{244}Cm , which is the dominating neutron contributor. The inspector will then apply the Pu/Cm and U/Cm mass ratios that have been analytically determined for each batch from an aliquot taken from the input tank of the melter. These ratios do not change during the vitrification process and hence Cm can be used as a tag for the mass of plutonium and uranium. The total rates will be used to verify sample-to-sample uniformity.

The vitrified waste canister assay system (VCAS) is intended to determine the residual uranium and plutonium content in canisters of vitrified high-level spent-fuel reprocessing waste prior to the termination of safeguards on this material. It consists of five neutron detectors (two ^{235}U fission chambers, two ^{238}U chambers and a bare ^{235}U chamber sensitive to thermal neutrons) and one gamma detector (ionization chamber, meant to authenticate the presence of gamma radiation). In contrast to the VWCC, the VCAS uses ^{235}U fission chambers

to determine the ^{244}Cm content by singles (totals) neutron counting. The plutonium and uranium contents are calculated from Pu/Cm and U/Cm ratios (determined in the feed solution to the melter). In addition, vitrification of the waste solution is verified by measurement of the neutron spectrum (using the ratio of counting rates in ^{235}U and ^{238}U fission chambers). The fill level of the canister is determined by a comparison of count rates from top and bottom ^{235}U fission chambers. The neutron radiation data will be integrated with cameras that monitor the measurement station and verify the canister ID.

The entrance gate monitor (ENGM) is a passive neutron coincidence collar detector permanently installed at the entrance to the fresh fuel transfer route of a fast breeder reactor (Hashimoto et al. 1994; Iwamoto et al. 1997). The detector head has four groups of ^3He with six tubes each. Fresh fuel assemblies entering the reactor facility must pass through the ENGM so that their Pu content can be verified. Therefore, the ENGM is the system that verifies the amount of fresh fissile fuel in an assembly and serves as the first detector in a sequence of detector systems that follow the movement of fuel assemblies within the reactor facility.

The cask car radiation monitor (CCRM) consists of a ^3He detector and NaI detector installed close to the surface of the cask car. By measuring neutron and gamma doses, the monitor is able to distinguish between fresh fuel and spent fuel as well as between other items (e.g., irradiated reflectors and control rods). The monitor controls the flow of fresh fuel between ENGM and the ex-vessel transfer machine radiation monitor (EVRM) and the flow of spent fuel from the EVRM to the spent fuel storage via the exit gate monitor (EXGM). It further monitors any movements of spent fuel retrieved from the spent fuel pond via the EXGM.

The EVRM has the same detection features as the CCRM. It controls the flow of assemblies to and from the core.

The EXGM is a watertight detector assembly including a lead shielded ^{10}B detector and two ionization chambers located underwater, close to the spent fuel transfer equipment, where spent fuel is taken to the storage racks. The direction of the transfer is monitored by two gamma detectors, placed above and below the neutron detector.

The plutonium inventory monitoring system (PIMS) is a network of 142 ^3He neutron detectors in moderating enclosures, which are installed in a plutonium-powder process area at fixed positions outside of process glove boxes and the ventilation system (Simpson et al. 1998; Parvin 2007; Whitehouse et al. 2004). The collected neutron counts are processed in a matrix approach to image the neutron field of the process area. Any change to the in-process inventory will be detected and can be accounted for on a near real-time basis. The PIMS will also be used to verify the clean out and to measure any residual material. The PIMS is operator-owned equipment used jointly with the inspectorate. Appropriate authentication measures are therefore in place to validate the measurement results.

The Rokkasho hull monitor system (RHMS) consists of three ^3He detectors embedded in the operator's hull monitor system and determines uranium and plutonium content in canisters of leached hulls at the Rokkasho Reprocessing Plant. The operator uses a sophisticated system with both passive and active interrogation. The safeguards detectors are operated independently of the operator's system, using the passive phase of the measurement cycle to register total neutrons (singles) from ^{244}Cm . The plutonium and uranium content can then be calculated from the Pu/Cm and U/Cm ratios derived from the associated dissolver solution.

The temporary canister verification system (TCVS) verifies the inventory of plutonium in MOX canisters in temporary storage positions located in glove boxes. It consists of NDA measurement stations on both sides of the storage glove boxes using an array of ^3He tubes. The TCVS is capable of quantifying 0.1–30 kg Pu in MOX powder and continuously records

data to monitor the movement of canisters (e.g., actual storage position and whether a full canister is coming from a different process step). Quantitative results are needed at specific inventory times achieving measurement uncertainties for partial defect testing (i.e., better than 6% at 1 sigma).

The hulls monitoring and measurement system (HMMS) measures the neutron emitted from spontaneous fission of ^{244}Cm in the hull drum, and calculates the amount of Pu and U contained in the hull drum using the ratios of $^{244}\text{Cm}/\text{Pu}$ and $^{244}\text{Cm}/\text{U}$ arrived at by applying a calculation code.

The directional canister passage detector (DCPD) is intended to verify the movement of MOX canisters. Each monitor comprises a double neutron ^3He tube in a polyethylene moderator supported by surveillance. The system determines whether a canister follows the normal process route (e.g., when and where the MOX canister came from and when the canister left the process area). All other possible movement combinations should be flagged by the system.

The Direct Use of PWR spent fuel in CANDU (DUPIC) safeguards neutron counter (DSNC) is a well-type neutron coincidence counter with 18 ^3He detectors configured with appropriate shielding, which measures all types of highly active materials from the dry reprocessing process for CANDU bundles (Menlove et al. 1997). It derives plutonium and uranium contents from the measured ^{244}Cm contents. Plutonium- and uranium-curiu ratios are determined from burnup calculations (Origen code) validated by HRGS scanning. The DSNC is operated remotely in a hot cell.

The DUPIC safeguards neutron monitor (DSNM) monitors the rear access ports of the process glove boxes through total neutron monitoring using ^3He detectors (Kim 2007).

The mobile unit for neutron detection (MUND) is an all-in-one neutron detection system for data collection and storage capable of running on battery power (Zendel et al. 2006). The unit is based on a ^3He detector mounted inside a polyethylene moderator slab. The preamplifier, HV supply, discriminator, recording electronics, and battery are all integrated inside a single, sealable enclosure. Two redundant data loggers record the data produced by the detector. The MUND collects data for more than 8 weeks without service. For servicing purposes, the device is removed from its measurement location, data are downloaded from the internal electronics, and batteries are recharged. The system has been specifically designed to perform the unattended monitoring of fuel transfer flasks. It is not intended for use in high-radiation environments. Once installed, an MUND is usually serviced by replacing the unit with a fully recharged one.

The mobile monitoring system for container transport (MMCT) consists of radiation monitoring, video surveillance, GPS location equipment, and smart power management to monitor the transfer of spent fuel via railcar (Lucero et al. 2004). The radiation sensors detect the spent fuel assembly during the loading, transfer and unloading process. The detector enclosure contains the detector assembly, which comprises six ^3He neutron tubes and two ionization chambers. The system is capable of acquiring safeguards data continuously for more than 1 week under harsh environmental, outdoor conditions (e.g., -20°C) without requiring recharging of the batteries.

63.3.6.3 Other Unattended NDA Systems

The advanced thermo-hydraulic power monitor (ATPM) is a monitoring system that can measure the actual thermal power produced by a reactor to confirm the declared operation in

nuclear research reactors (Araujo et al. 2001). The ATPM is a complete system comprising ultrasonic flow and temperature sensors mounted on primary cooling loop elements, together with a data collection and evaluation system housed in a tamper-indicating 19" industrial cabinet, which can be located up to 300 meters from the sensor location. The ATPM measures the reactor-coolant inlet and outlet temperatures and the coolant flow through the reactor core. These parameters are used to calculate the energy flow rate and the total energy produced in the reactor. The result of this calculation is then used to determine if substantial amounts of fissile material might have been generated in the reactor or, to confirm its declared operation.

The solution measurement and monitoring system (SMMS) uses high-accuracy and authenticated pressure and temperature measurement devices installed on selected process tanks to determine the volume, density, and temperature of the respective solution (Ehinger et al. 2004). The instruments are connected directly to the pneumatic dip-tube measurement lines of the tanks. The monitoring data exhibits temporal changes caused, for example, by filling, holding, sparging, sampling, and transferring activities. The system evaluation software discriminates between these characteristic changes and other disturbances and alerts the inspector to any unexpected operations. SMMS provides continuity of knowledge for plutonium-bearing materials in the solution process and supports the verification of nuclear material inventory, inventory changes, and other transfers. The SMMS software automatically decides whether a process follows its declared operation based upon the observed volume, density, and temperature data.

The IPCA Load Cell (IPLC) is an unattended load cell system intended to measure independently, the weight of MOX powder canisters with a relative accuracy of greater than 0.05%. The IPLC includes three load cells located on top of the IPCA system – raw data is collected and processed through an amplifier and dedicated software. The typical weights to be measured are between 200–300 kg.

63.3.7 Other NDA Techniques

This category of instrument comprises systems that measure physical properties such as weight, volume, absorption of light, sound velocity and heat. Weighing is performed to determine the net weight of an item or batch that is selected as a sample for verification. It is normally applied in conjunction with other accountancy verification methods in order to determine the quantity of nuclear material within the sample. Volume and concentration measurements, in conjunction with other verification methods, are carried out extensively in reprocessing plants to derive amounts of materials contained in solutions. An ultrasonic thickness gauge determines the thickness of container walls and is needed to correct for gamma ray attenuation. Measurement of decay heat can indicate the presence of spent fuel or, when measured in a calorimeter, can quantify pure plutonium samples. Laser-based technologies are becoming increasingly important, providing new and novel verification and detection tools for current and future safeguards activities (Zendel et al. 2007).

Main attributes of various further measurement systems are listed in [Table 63.7](#).

63.3.7.1 Physical Property Measurement

The load cell-based weighing system (LCBS) is used for weighing large uranium hexafluoride (UF₆) product cylinders (Dermendjiev et al. 1983). Cylinders are weighed with the LCBS

■ Table 63.7

Other measurement systems

System	Detector	Verification task	Typical performance values (%)
ICVD	Light amplifier for Cherenkov light	Spent fuel (cooling time <10 years)	Attribute
DCVD	Digital light amplifier for Cherenkov light	Spent fuel (low burnup, long cooling time >10 years)	Attribute
OFPS	⁶ Li-doped fibers	CANDU spent fuel bundles	Attribute
LCBS	Strain gauge	Weighing of UF ₆ cylinders	0.1
ULTG	Ultrasonic sensor	Measurement of wall thicknesses	0.3
PPMD	Pressure sensor	Volume in tanks	0.01
CALO	Temperature sensitive resistance sensor	Pu in nuclear material	0.4
XRFA	Si detector	Characterization of metals, alloys, minor and trace elements	Attribute
KEDG	HPGE transmission measurement	Pu, U concentration in solutions (>50 g/l)	0.2
HKED	XRF + KEDG	Pu, U in input solutions (IAT)	0.6 (U), 1.0 (Pu)
		Pu, U in product solutions (OAT)	0.3 (U), 0.9 (Pu)
COMPUCEA	LaBr ₃ + Si	U in unirradiated solutions	0.2
HFLS	Tunable laser + spectrophotometer	Detection of nuclear activities involving UF ₆	Sensitivity > 0.1 ppm
UFLS	Tunable laser + spectrophotometer	²³⁵ U-Enrichment in UF ₆	[0.15 (LEU)-0.7 (DU)] ^a
LIBS	Laser + spectrophotometer	Confirming past nuclear activities and absence of undeclared activities by trace analysis	Attribute
LIDAR	Laser + spectrophotometer	Detecting signatures of nuclear activities	Attribute
XRFS	X-ray detector	U, Pu, Np, Th, Am concentrations	1
OSAS	Alpha spectrometer	Pu in diluted solutions (<10 mg/l)	
OSCA	³ He + HKED	Cm/Pu/U ratio in input/HALW solutions	
OSDM	Frequency oscillator	Density of solutions	0.04

^aTarget accuracy.

attached to a crane. The load cell senses the weight of the suspended product cylinder and results are indicated on a display unit. After assembly and setup (requiring 20–30 minutes), weighing time is typically 3–5 minutes per cylinder with an accuracy of greater than 0.1%.

The ultrasonic thickness gauge (ULTG) is a small and simple instrument designed for measuring metal thickness. The measurement principle is based on measuring the time interval

from sound emission to reception of the echo and then multiplying this interval by the material-specific sound velocity. Silicone grease is used as couplant to eliminate any air between the sensor and measurement surfaces. The ULTG is required to measure the wall thickness of containers to allow correction for variations in the attenuation of the 186 keV gamma peak. The ULTG cannot determine multiple layers and measures only the outer layer.

Portable pressure measurement device (PPMD) is a lightweight carry-on type instrument comprising digital pressure modules (DPM) packed together with a power supply in a tamper-indicating enclosure (Landat et al. 1997). The PPMD can be connected to the level, density, and reference probes of a tank in parallel to an operator's own equipment. The sensor data are used to independently verify the volume of solutions in various storage and process tanks.

The 3D laser range finder (3D-LRF) is in routine use for design information verification (DIV) activities involving the largest reprocessing plant under safeguards (Agboraw et al. 2006). The system is capable of confirming within an accuracy of millimeters that no structural changes have occurred since the previous scanning and, of highlighting changes that may have occurred, in particular, to maintain continuity of knowledge (CoK) of the interiors of hot cells especially on various piping arrangements. For this purpose, baseline scans – called reference scans – are performed during the plant construction; subsequent verification scans taken during periodic inspection activities are compared to the original references.

The ground penetrating radar technology (GPRT) is based on the transmission and reflection of electromagnetic pulses. It represents a nonintrusive means of surveying sites for the identification and/or verification of structural elements. GPRT uses pulses of electromagnetic radiation in the microwave band (UHF/VHF frequencies) of the radio spectrum, and reads the reflected signal to detect subsurface structures and objects without drilling, probing, or otherwise breaking the ground surface. Applications include the detection of hidden objects and structures (Carchon et al. 2006).

63.3.7.2 Calorimetric Techniques

Calorimeters measure the heat produced by a sample of nuclear material, whereby the heat originates primarily from the α -decay of the isotopes making up the nuclear material. Calorimeters have traditionally been fabricated using a sensor of nickel wire wound around a measurement chamber (Bracken et al. 2002). The nickel wire provides a temperature-sensitive resistance leading to highly accurate and precise electrical measurements of the power produced by a sample. Calorimeters are calibrated with ^{238}Pu heat sources or plutonium samples with known mass and isotopic composition. Calorimetric assay is the most precise and accurate NDA measurement method for plutonium products (>100 grams).

Plutonium samples always contain a mixture of isotopes: ^{238}Pu , ^{239}Pu , ^{240}Pu , ^{241}Pu , and ^{242}Pu . The nuclide ^{241}Am is also present in most plutonium-bearing items. The amount of heat produced per gram of each nuclide is a known physical quantity ("specific power") based on the decay rate and decay energy of the isotope. The major contributors to the heat produced are ^{238}Pu and ^{241}Am . The measurement of the total heat in a calorimeter coupled with the measurement of the relative abundance of the individual nuclides in the sample (nuclidic/isotopic composition) provides the elemental mass in the sample. Calorimetry and neutron coincidence counting are complementary assay techniques that provide high assurance of correct and valid measurements. The calorimeter has the advantage being insensitive to geometry, matrix and humidity. However, measurements using calorimeters are very time

consuming in contrast to neutron measurements. Therefore, calorimetry is barely used by international safeguards but widely used in domestic safeguards to quantify plutonium and americium in plutonium bearing items.

63.3.7.3 X-Ray Measurements

X-ray emission is characteristic of the element while gamma-ray emission is characteristic of the isotope. Plutonium and uranium, as atoms with high atomic numbers, absorb energy at distinctive energies (e.g., the K-edge for Pu is at 121.8 keV as discussed below), associated with the energies needed to dislodge electrons from their innermost electron shells.

The X-ray fluorescence analyzer (XRFA) is a light, portable, and commercially available instrument (1.4 kg) for the characterization of metals, alloys, and possible dual-use materials by means of X-ray fluorescence (XRF). It is used by safeguards inspectors to verify the correctness and completeness of the presence of declared materials and the absence of undeclared ones. The measurement principle is based on irradiating the sample material by an X-ray photon field generated by an X-ray tube (no radioactive source!) and then measuring the characteristic X-ray fluorescence spectrum emitted by the sample using a high-performance Peltier-cooled Si-PiN detector. XRF can determine semi-quantitatively the relative concentrations of major, minor, and trace elements with atomic masses from 9 (fluorine) through 89–103 (the actinide elements) in various types of samples without requiring any sample preparation (► Fig. 63.4).

K-EDGE X-ray densitometry (KEDG) measures the photon transmission through a liquid sample at two energies that bracket as closely as possible the K-absorption edge energy of the element of interest. The K-absorption edge energy represents an element-specific signature. The logarithmic ratio of the photon transmission measured below and above the absorption edge is directly proportional to the volume concentration of the measured element for a well-defined sample cell. For plutonium, radioactive sources from ^{75}Se ($E_\gamma = 121.1$ keV) and ^{57}Co ($E_\gamma = 122.2$ keV) are used as transmission sources. These γ -ray energies very closely bracket the 121.8 keV electron-binding energy of the K shell of plutonium. The majority of the K-edge

■ Fig. 63.4

X-ray fluorescence analyzer (XRFA)



densitometers used for safeguards are now equipped with an X-ray generator that acts as a photon source for the transmission measurement. The high photon strength provided by an X-ray tube allows measurements to be performed on highly radioactive samples. The method is very selective and is one of the most accurate NDA techniques, but the determination of Pu may be biased by the presence of a minor actinide element of lower atomic number, such as U. It is therefore best used for relatively concentrated solutions (>50 g/l) of plutonium in product solutions, input solutions, and process solutions (in-line measurements).

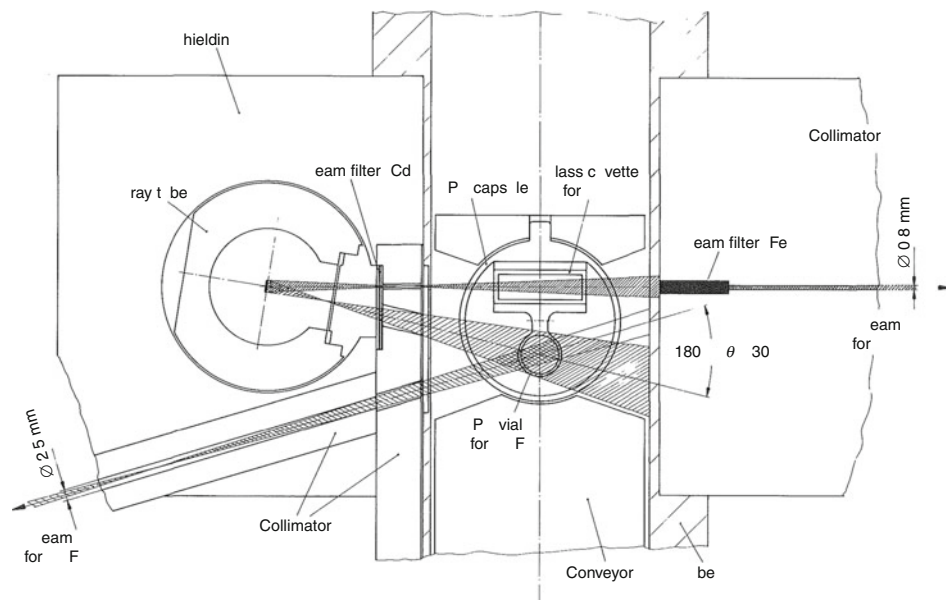
Hybrid K-edge (HKED) is a technique used for measuring the concentration of U and Pu in mixed solutions by combining X-ray fluorescence and K-edge densitometry. Depending on the concentration of plutonium and uranium, the higher element concentration is identified by K-edge measurement and the lower concentration from the ratio of Pu/U of the XRF. HKED has become a standard technique to analyze solutions samples containing U and/or Pu over a concentration range from 0.5 to 400 g/l in reprocessing plants. In addition, HKED is also used to determine Np in the presence of fission products.

The X-Ray beam in KEDG-mode passes through a sample cell with a known path length and an HPGe detector measures the absorption at the K-edge to determine the concentration, based on the calibration of the system with solution standards. Located at a backward angle of 150° relative to the beam, a second HPGe detector can measure the X-Ray spectrum generated by the elements in the sample. K-edge densitometers equipped with an X-ray generator are usually resident and attached to shielded or unshielded glove boxes for sample handling (► Fig. 63.5).

Combined procedure for uranium concentration and enrichment assay (COMPUCEA) is a transportable system used to perform accurate on-site analytical measurements of elemental

► Fig. 63.5

The hybrid K-edge densitometer



assay and enrichment of liquid, unirradiated uranium samples (Ottmar et al. 2007). Solid uranium samples require preparation by quantitative dissolution of the sample. The system is portable and can be used at room temperature. The technique combines absorption edge spectrometry to establish the uranium concentration (L-edge for uranium: 17.17 keV) and a ^{235}U -enrichment spectrometer based on LaBr_3 . The L-edge technique uses a small X-ray generator of low energy and an ultrahigh-resolution Si gamma detector operated under modest Peltier cooling.

63.3.7.4 Analytical NDA Techniques at Laboratories

Some of the NDA verification techniques on samples of nuclear material taken during a safeguards inspection are carried out at specialized analytical laboratories, for example, the Safeguards Analytical Laboratory (SAL) at Seibersdorf in Austria or the On-Site Laboratory (OSL) at the Rokkasho Reprocessing Plant in Japan. Commercially available and customer-specific equipment is used to determine amounts and isotopic compositions of plutonium and uranium in inspection samples, having various chemical and physical forms, to supplement or replace destructive analysis. A parallel analysis of one and the same sample by NDA and DA serves the quality assurance of the analytical methods and control of the results.

High-resolution gamma spectrometry (HRGS) determines enrichment in uranium bulk samples by relating the gamma results to the total U content of the sample that has been assayed by titration or other methods such as IDMS or KEDG. In the absence of radioisotope interferences, the results have a precision and accuracy ranging between 0.5% rel. for natural and 0.2% rel. for enriched U. At OSL, HRGS is applied to Pu sampled from the output accountancy tank (OAT) to determine the isotopic composition, if the sample is not subjected to mass spectrometry. Additionally, Np in U and in Pu product samples can be determined. HRGS is used at SAL to screen all Pu samples as they are received.

X-Ray fluorescence spectrometry (XRF) is a non-portable XRF diagnostics tool, measuring well-characterized emissions from various elements (ranging from sodium to the highest elements on the periodic chart) when they are stimulated by x-rays. It provides the amounts of each element present (but not individual isotopes) within microgram detection limits. XRF is used to simultaneously determine concentrations of Th, U, Np, Pu, and Am. The XRF technique is applied if the element concentration to be determined falls below the useful range for K-edge measurements ($<40\text{g/l}$). It provides quantitative concentration measurements down to concentration levels of about 0.5 g/l. The quantitative evaluation of XRF measurements for concentrations is not as straightforward as for KEDG, e.g., matrix effects, but the technique is very accurate in performing element ratio measurements to determine the concentration of a minor element relative to the concentration of a major element known from a K-edge measurement.

The hybrid K-edge densitometry (HKED) at OSL is the main instrument to analyze solutions samples from the input accountability tank (IAT) and output accountability tank (OAT) containing U and/or Pu over a concentration range from 0.5 to 400 g/l. The KEDG-mode is applied down to 40 g/l and the XRF-mode down to 0.5 g/l U or Pu. Thus, the evaluation of KEDG and XRF spectra of a sample from the IAT yields the concentration of U (KEDG alone), the U/Pu ratio (XRF alone), and the Pu concentration (KEDG and XRF combined).

The OSL Alpha Spectrometer (OSAS) estimates plutonium in diluted solutions containing less than 10 mg/l of plutonium. An α -source can be made from the sample through a simplified

drop deposition method, followed by combustion. Spectra with higher resolution are obtained by electro-deposition, a method that is also preferred due to safety reasons (namely, using a furnace in a glove box is avoided). The sum activity of $^{239}\text{Pu} + ^{240}\text{Pu}$ is measured with an α -detector and the Pu concentration of the sample is estimated by comparing the α -count rate of the unknown sample with the count rate of a known standard reference source.

The OSL-curium neutron analyzer (OSCA) is a neutron coincidence counter that measures ^{244}Cm in solutions. At OSL, the system is integrated within a Hybrid-K-Edge (HKED) enclosure. The OSCA associated with HKED or isotope dilution mass spectrometry (IDMS) will provide analytical data to establish the $^{244}\text{Cm}/\text{Pu}$ and $^{244}\text{Cm}/\text{U}$ ratios in IAT solutions or in high active liquid waste solutions.

The OSL-density meter (OSDM) measures the density of solutions to estimate accurately the mass of a solution contained in a sampled vessel/container. OSDM measures the frequency of an oscillating tube filled with the solution sample. The instrument is calibrated by measuring the frequency of oscillation using air, water, or liquid density standards. A sample solution is injected, or drawn, into the temperature-stabilized tube and a built-in computer automatically converts the frequency measurement into a density reading.

63.3.8 New and Novel Technologies

Emerging and future needs for safeguards verification require state-of-the-art equipment and innovative technological solutions to meet current and future verification challenges (Khlebnikov et al. 2006a; Annese et al. 2009; Tolk et al. 2007). The early detection of undeclared facilities, activities and materials has become a major safeguards task. It plays a primary role in providing independent safeguards conclusions on the completeness and correctness of a state's nuclear program. The increasing complexity and automation of nuclear facilities as well as new facility types require new approaches and advanced instrumentation. The verification system has to be further developed taking full account of advances in present safeguards verification techniques ("new technologies") and through the exploration of innovative technologies that are either already available or investigated in other branches of science and technology fields not traditionally related to safeguards ("novel technologies"). In particular, capabilities to detect nuclear activities (e.g., reprocessing or enrichment) from a distance are of prime interest and require a new toolbox for the inspectorate. In many cases, safeguards implementation involves unannounced inspections and complementary access (CA) requiring detection devices to search for nontraditional elements/nuclides (such as americium, neptunium, beryllium, and tritium) that could indicate the presence of a clandestine nuclear weapons program. Instruments for these specific types of verification activities often need to be made available to inspectors at very short notice. Such equipment must be multipurpose, robust, portable, and easy to operate to allow the inspector to readily perform numerous tasks within the short time span of each particular verification activity, including the search for indicators of undeclared nuclear materials and activities.

63.3.8.1 New Technologies

New technologies for safeguards purposes could address missing capabilities in routine verification tools and could enhance the effectiveness and efficiency of present verification systems. Instrumentation based on new technologies might be in its final development stage

but not yet available for routine safeguards implementation. Such equipment will be authorized for routine use subject only to a careful assessment of aspects (including its expected performance, usability, and affordability) and the completion of a successful field test. New sensors for nuclear material detection and characterization, process monitoring equipment/techniques and analytical equipment are the main new technology drivers. Various efforts are underway to develop techniques for the direct verification of plutonium in spent fuel (Tobin et al. 2008, 2009).

The *superconducting gamma spectrometer* is a cryogenic, ultrahigh energy resolution γ -ray spectrometer, operated at temperatures of $T \approx 0.1$ K (Ali et al. 2006, 2008). It can be characterized as a cryogenic gamma-ray micro-calorimeter, which measures the energy of radiation from increase in temperature upon absorption of a γ -ray. The detector consists of a highly sensitive, cryogenic transition-edge sensor (TES) coupled to a tin γ -ray absorber. The TES is a Mo/Cu multilayer sensor capable of determining the energy of a single γ -photon with extremely high precision – it operates in the narrow temperature range of the transition from superconducting to normal state. An individual sensor element is 1.5×1.5 mm by 0.25 mm thick. To achieve reasonable counting statistics, detector arrays with many sensors are used (Hoover et al. 2009). The system offers an order of magnitude improvement in energy resolution over conventional high-purity Ge (HPGe) detectors. It could be used for accurate enrichment measurements and Pu-isotopics.

The *differential die-away self-interrogation (DDSI) technique* is a recently conceived NDA technique for quantifying the total fissile and fertile content in spent fuel (Menlove et al. 2009) using a modified ^3He coincidence counter. In DDSI, the spontaneous fission neutrons from ^{244}Cm that are present in the assembly act as the interrogating source. After each spontaneous fission event, the neutron time distribution is analyzed to determine the fast and slow neutron distributions from the spontaneous and induced fissions in the sample, respectively. Fissile mass is determined from the fissions induced by reflected thermal neutrons originating from the spontaneous fission reaction. The sensitivity of the fissile mass measurement is enhanced by measuring the sample with and without a cadmium liner between the sample and the surrounding moderator (“passive-neutron albedo reactivity (PNAR)”). The fertile mass is determined from the multiplicity analysis of the neutrons detected soon after the initial triggering neutron is detected.

Self-interrogation neutron resonance densitometry (SINRD) uses the unique neutron-resonance cross-sectional structure for fissionable nuclides such as ^{235}U , ^{233}U , ^{239}Pu , and ^{241}Pu . Its sensitivity is based on using the same fissile materials in the sample and in the fission chamber because the effect of resonance absorption lines in the transmitted flux is amplified by the corresponding (n,f) reaction peaks in the fission chamber (LaFleur et al. 2008, 2009). The amount of resonance absorption of these neutrons in the spent fuel can be measured using ^{235}U and ^{239}Pu fission chambers placed adjacent to the assembly.

^{252}Cf interrogation with prompt neutron detection (CIPN) is a lightweight, active interrogation instrument/detector, similar in size and shape to the FORK detector (Scheer et al. 2009). The main difference between CIPN and a FORK detector is the introduction of an interrogating ^{252}Cf source adjacent to the fuel and opposite to the fission-chamber detector region. Two gross-neutron measurements are performed: a background measurement (without ^{252}Cf) and an active assay with the ^{252}Cf source next to the fuel. Fissile content is quantified using the measured neutron multiplication in the assembly.

The *delayed neutron technique* quantifies the fissile content in a spent fuel assembly by measuring the delayed neutrons emitted by fission fragments after active interrogation by

a neutron burst (~ 1 s) from a neutron generator (Scheer et al. 2009). The generator stops after 1 s and starts again after another second. In between, the delayed neutrons are being measured and multiple interrogation/measurement cycles are performed to gain sufficient counting statistics.

Self-induced X-ray fluorescence (XRF) can be used to quantify the Pu content in spent fuel (Charlton et al. 2009). The radioactive decay in the spent fuel leads to self-induced XRF of uranium and plutonium atoms in the fuel and resulting X-rays are then emitted by the fuel. It has been demonstrated by measurements and simulations that the Pu/U atom ratio at the surface of a fuel pin can be measured in an appropriately designed and implemented instrument using the 103.7 keV K X-ray from Pu.

Lead slowing-down spectroscopy (LSDS) is an active interrogation technique that has been used for several decades in cross-sectional measurements. It can provide independent Pu isotopic mass without operator-declared information about the spent fuel (Gavron et al. 2009). In typical operation, a neutron source provides a pulse of neutrons close to the center of a large block of lead. The neutrons are moderated slowing down gradually. The incoming neutrons from the slowing down process will induce fission in the fuel placed in the center of the lead block and high-energy fission- neutrons are emitted. An annular ring of fission chambers selectively measures the higher-energy fission neutrons as a function of the time after the neutron pulse. Potential threshold fission chamber types include those lined with ultra pure ^{238}U (to minimize the contributions from ^{235}U) and those based on ^{232}Th . New time-spectra analysis methods are applied to determine the fissile mass of $^{239,241}\text{Pu}$ and ^{235}U .

A new on-line monitoring system featuring Raman and ultraviolet-visible-near infrared (UV-vis-NIR) spectroscopy methods combined with a Coriolis and conductivity probes provides immediate chemical data and flow parameters of high-level radioactive waste streams (Bryan et al. 2009). This allows real time monitoring of the solvent extraction flow sheets for quick detection of undeclared activities with fissile isotopes present in the radiochemical streams during reprocessing activities. The proof-of-principle has been successfully demonstrated for on-line monitoring of U (VI), nitrate, and HNO_3 by using Raman spectroscopy and on-line monitoring of Np, Pu, Nd, for both aqueous and organic phases, using Vis/NIR.

The multi-isotope process (MIP) monitors spent nuclear fuel reprocessing facilities on-line, nondestructively, and in near real time (Orton et al. 2009). The method is based upon the measurement of distribution patterns of a suite of indicator (radioactive) isotopes present within particular process streams. Distribution patterns, monitored on-line by gamma spectrometry, are compared in near real time to patterns representing “normal” process conditions using multivariate pattern recognition software. The MIP monitor is sensitive to minor alterations in major process variables including acid and organic ligand concentration. Therefore, it might be used to confirm the declared operation of a reprocessing plant, providing additional information on reactor type, burnup, and cooling time.

The laser-based optical and chemical imager (LOCI) is a unique instrument that combines accurate isotope ratio analyses obtained both by laser desorption Fourier transform ion cyclotron resonance mass spectrometry (FTICR-MS) and by LIBS without any sample preparation (Scott and McJunkin 2009). A single photon ionization (SPI) process is implemented allowing near 100% ionization efficiency for elements and compounds with ionization energies less than 10.5 eV. The FTICR-MS and LIBS isotope capability coupled with LOCI's wide mass range, mapping capability, high resolution, and automated data collection as well as data interpretation offers an alternative to the labor-intensive bulk analysis of traditional methods,

such as TIMS. This capability will be very useful for environmental samples and for determining the burnup rates within fuel elements.

Electrochemically modulated separations (EMS) is a technique that relies on electrochemical redox adjustment and surface chemistry to effect isolation and accumulation of Pu at a target electrode (Clark et al. 2006; Duckworth et al. 2009). EMS may be a rapid and cost-effective means of performing Pu separations that has implications for DA and NDA, simplifying laboratory separations and allowing NDA for input accountancy tanks.

Automated radioanalytical chemistry can provide near real time monitoring of reprocessing plant operations (O'Hara et al. 2009). A sequential injection chromatography system for the separation and analysis of Am, Pu, and Np isotopes is integrated in a modular system that automates the complete sample analysis process, from initial sample preparation to final data reporting.

The laser item identification system (L2IS) is capable of monitoring all transfers of UF₆ cylinders between process areas (Poirier et al. 2009). L2IS uniquely identifies each cylinder through exploring the unique microstructure of each cylinder's surface with different lasers. It has been demonstrated that every cylinder has a unique "fingerprint" that remains intact even under extreme environmental conditions. The L2IS system is composed of a portable unit, operated in attended mode, and a fixed installed unit, operated without inspector presence. The portable unit acquires the fingerprints of a given set of feed cylinders intended to be used over the coming months and the fixed system monitors the flow of previously identified cylinders in a transfer corridor.

63.3.8.2 Novel Technologies

Novel Technologies aim to provide access to a wider range of methods and instruments in support of safeguards implementation by adapting technologies already available or being developed in other branches of science and technology fields but not used for safeguards. Such technologies could significantly contribute to the early detection of undeclared nuclear activities and material. Typical examples include the determination of an undeclared location previously used for storing radioactive material, forensics of materials found on-site and evidence of nuclear fuel-cycle process activities at suspected locations. In contrast to new technologies, safeguards equipment based on novel technologies is in its early stage of development and may not be readily available within a short time frame. Several promising technologies based on laser spectrometry and optically stimulated luminescence (OSL), anti neutrino detection, nuclear magnetic resonance (NMR), atmospheric gas sampling, and analysis and various electromagnetic systems have been identified (Khlebnikov et al. 2006b; Whichello et al. 2009). Nanotechnology in its various forms such as nano-electronics, nano-electromechanical systems, ultra-small, highly sensitive, and selective sensors (Morrison et al. 2007) could significantly contribute to novel technologies. A novel suite of smart safeguards verification systems can be expected with unique detection features allowing at the same time further miniaturization of the equipment. The most impressive advance allowed for by nanotechnology development is the possibility of autonomous smart sensor networks. These networks could support safeguards monitoring functions by capturing data, processing and transmitting information, and communicating with other sensors in potentially hostile environments.

Optically stimulated luminescence (OSL) is capable of de-trapping radiation-induced excitation energy accumulated during the irradiation of a surface (Kosierb 2007). The release

of this energy could be stimulated by various types of lasers in the visible and infrared frequency ranges. The intensity of the resulting photon emission is proportional to the radiation dose absorbed by the material, unveiling information on the former presence of a radioactive source. The detection system uses a charge-coupled device (CCD) camera attached to a photomultiplier. The optical part of the detector has to be optimized to decouple the larger signal, emanating from the optical pump, from the smaller signal emitted by the sample. Samples collected by the inspectors are analyzed by OSL, indicating the previous presence of stored nuclear materials and thereby presenting the potential to disclose undeclared activities.

OSL could also be used for container verification. Luminescent phosphor additives, ionized by radiation, are mixed with paints or clear coats and are applied to the surface of a container (Miller et al. 2009). The OSL phosphors luminesce in proportion to the ionization radiation dose and the intensity of excitation light. The OSL coatings/additives will be invisible to the naked eye, but could be seen using an InGaAs infrared detector. The OSL additives would tag the container and reveal an attempt to tamper with the container and therefore increase the confidence that its integrity had not been compromised.

Tunable diode laser spectroscopy (TDLS) systems are tuned to access specific regions of the mid-infrared spectrum where most gases of interest such as UF_6 have strong absorption while common gases, such as oxygen and nitrogen, do not. TDLS systems have the potential to determine ^{235}U enrichment in UF_6 gas and to indicate the presence of HF gas, a by-product of enrichment activities.

The HF detector laser system (HFLS) is a portable instrument for HF gas detection, designed for easy operation in airborne and ground-based mobile searches for enrichment activities. The HFLS is built as a backpack unit allowing continuous air monitoring while leaving the inspector's hands free. A tunable diode laser shines through a multipass cell, which is continuously collecting air gas. The detector then analyzes the unique absorption lines caused by the HF gas in the cell. The instrument is very sensitive and can measure HF concentrations of >0.1 ppb. The system provides a very quick measurement and identification with high spectral resolution in the infrared range.

The UF_6 detector based on laser spectrometry (UFLS) is an on-site analytical instrument based on TDLS. It measures the enrichment of UF_6 samples (Lebrun et al. 2008). The system has passed feasibility study and is now under development for field use. It determines the concentration of ^{235}U and ^{238}U in UF_6 on-site with an accuracy of greater than 1% for ^{235}U enrichment. The precise measurement of the isotopically broadened absorption peaks of ^{235}U and ^{238}U requires a mid-IR laser with wide single-mode tuning ranges, better than 4 cm^{-1} of continuous tuning at $1,290\text{ cm}^{-1}$ and less tuning at 852 cm^{-1} . In comparison with mass spectrometry, UFLS does not require a highly trained specialist to perform measurements. It is hoped that the instrument will partly replace the need for DA and thereby will improve verification timeliness and reduce inspection resources.

Laser-induced breakdown spectroscopy (LIBS) is being applied for a novel complementary access instrument based on the detection of gaseous and solid signatures and indicators of nuclear fuel cycle processes (Kosierb 2007; IAEA 2009b). LIBS is an atomic emission spectroscopy technique that utilizes a pulsed, well-focused laser to create a micro-plasma on the sample surface (Salmon et al. 2008). The resulting light emission spectrum of the decaying vapor plume has well-known specific emission lines that are analyzed by an integrated spectrometer. The spectroscopic profile is compared to those in its library to determine the composition of the material. LIBS can perform the analysis of elemental composition and trace analysis of solid

■ Fig. 63.6

Laser-induced breakdown spectroscopy (LIBS)

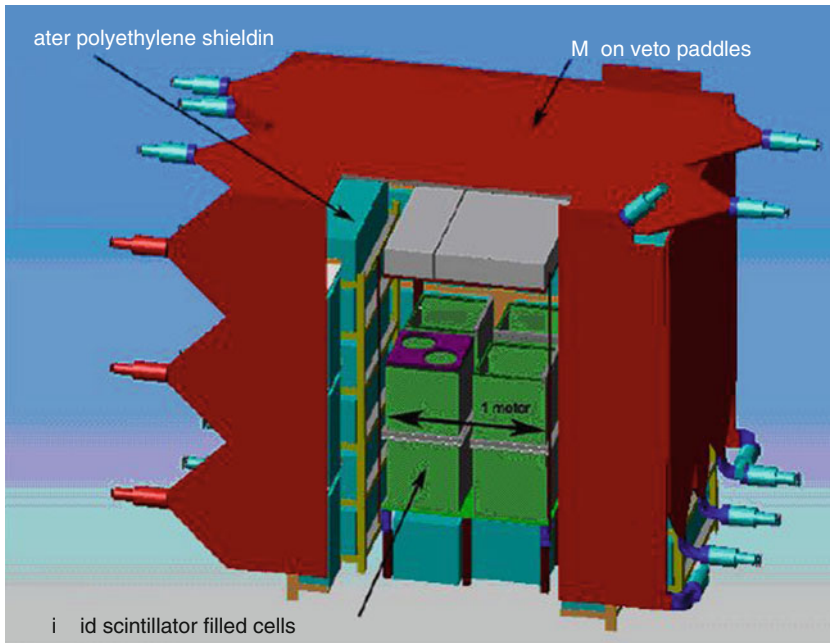


materials to confirm past nuclear activities and the absence of undeclared activities, and is therefore considered as a possible screening device to reduce the number of environmental samples (► Fig. 63.6).

The light detection and ranging (LIDAR) system may remotely sense the presence of characteristic gaseous compounds emanating from nuclear fuel cycle (NFC) processes into the atmosphere (IAEA 2006b). LIDAR might be capable of analyzing emissions and detecting fingerprints of undeclared nuclear activities from a distance of some kilometers of a suspected site by using a mobile LIDAR laboratory in its vicinity. A laser, tunable to precise wavelengths, selectively stimulates such airborne molecules. A light-sensitive telescope scans the atmosphere, detecting the presence of the stimulated molecules. For safeguards purposes, differential absorption LIDAR (DIAL) is particularly interesting. This technology sends laser pulses tuned on two different wavelengths to the atmosphere – one specific to the strongly absorbing molecule, the other less absorptive as a reference – and then analyzes the intensity of light scattered back over time. The signals are processed providing the transmission both on and off a molecular absorption feature to give a measure of the concentration.

The *antineutrino detector* can measure the plutonium content of an online nuclear reactor core, may provide effective power and burn-up to confirm that reactors are operating as declared (Bernstein et al. 2003; Bowden et al. 2007; IAEA 2009c). Antineutrinos are produced in nuclear reactors when uranium and plutonium atoms fission into neutron-rich fragments that undergo successive beta decays. A common detection scheme uses the inverse beta decay reaction producing a closely timed coincident neutron and positron – these are detectable in a scintillator that is shielded from background radiation. Despite the small cross section, the abundant antineutrino production of the core allows for high statistical detection with modestly sized detectors (1 m^3) at practical standoff distances (tens of meters). When an antineutrino collides with a proton, it produces a positron and a neutron. The interaction of these two particles creates the antineutrino signature – two relatively intense flashes of light that occur so close in time to one another that they appear to be almost simultaneous (► Fig. 63.7).

■ Fig. 63.7

The antineutrino detector

The Fourier-transform infrared system (FTIR) is a well-known spectroscopic technique based on the absorption of infrared photons that excite vibrations of molecular bonds. Molecules such as U_3O_8 , UO_2 , UO_3 , ThO_2 , have characteristic absorption bands in the infrared region that can be used like a fingerprint to detect their respective presence. FTIR radiometry has become a relatively mature and reliable method for the identification and measurement of chemicals emitted from stacks and its potential for passive standoff detection of nuclear material is under investigation (Puckrin and Thériault 2006).

Electromagnetic wave gradiometer technology can be used to detect underground electrically conductive structures or paths such as clandestine tunnels (Matter 2003). Primary low-frequency electromagnetic (EM) waves induce electrical current flow in conductive paths located underground. Conductive paths are abundant in underground operating structures, such as electrical power cables or air ventilation pipes, or conductive paths such as the moist conductive soil layer that commonly surrounds tunnels with high humidity and condensation. The transmitter can be located above ground (either in a fixed location or carried by an inspector) or underground in a borehole. The induced current flow generates a secondary magnetic wave that is retransmitted through the ground and measurable on the surface above the underground structure using a gradiometer antenna array with a narrow band synchronous receiver. The signal is scanned on the surface and a plot of its magnitude yields a profile showing the structure's centerline and depth information.

Nuclear magnetic resonance (NMR) could measure the $^{235}\text{U}/^{238}\text{U}$ ratio accurately and therefore it could be used to detect clandestine enrichment at a declared facility, applying mature NMR technology (Pepper et al. 2007; Magnelind et al. 2009). NMR provides

a quantitative measure of the number of nuclei of a given isotope in a given sample. The NMR signature of materials is measured in ultralow magnetic fields and at ultralow frequencies. The method has the potential of quickly and accurately (possibly at the fraction of a percent level) measuring the amounts of ^{238}U and ^{235}U in each and every cylinder containing feed, tails, and product, as well as monitoring the flow of UF_6 in the cascade area. The benefits of NMR include that it is nonintrusive and no source is required.

Acoustic wave analysis technology may provide a viable containment verification tool (Goldfarb 2007). Acoustic waves are disturbances in mechanical vibrations in solids, liquids, or gases. The interpretation of acoustic waves can unveil subtle structural changes in materials, including cracks, pits, voids, gaps, bends, and changes in density and elasticity. A monitoring system with a network of acoustic sensors may be useful to detect abnormal process operations.

The *speckle laser interferometric application* could detect hidden underground structures or other non-visible items (Mersch 2007; Nothdurft and Yao 2005). The system uses subtle differences in surface response to coherent light and requires significant interpretive analysis. It subtracts a picture taken from a surface illuminated by laser light (background picture) from subsequent pictures taken after “disturbing the surface,” e.g., by a small underground detonation. The effect of the observed subsurface disturbance on the surface is a function of the hidden subsurface features.

Remote sensing in satellite imagery and “stereo mapping” could be further developed to enhance interpretation of site activities using the broad potential of satellite imagery data ranging from panchromatic, multispectral, hyperspectral to radar for site description and change detection (Niemayer 2009). A satellite could view the earth in different spectral bands covering the visible and infrared band. It could measure local ground and water temperatures to an absolute accuracy of 1 K. By further investigating other portions of the electromagnetic spectrum, it may be possible to detect and identify the location of an undeclared nuclear activity, e.g., to detect the waste heat from a clandestine plutonium production reactor. Hyperspectral data allow for a quantitative estimation of geophysical and geochemical characteristics of the earth’s surface and is therefore useful for assessing, e.g., surface cover changes due to drilling, mining, and milling activities.

Atmospheric gases sampling and analysis can provide useful information about the existence and nature of ongoing nuclear activities. ^{85}Kr could be indicative of reprocessing activities (Kalinowski et al. 2006; IAEA 2006a). For each kilogram of plutonium reprocessed, some 10–35 TBq of ^{85}Kr are typically released into the atmosphere. This evidence can be detected from a distance, varying from hundreds of meters to some kilometers, depending on meteorological conditions. The technique uses air sampling with a cryo-absorption device to concentrate the fraction of noble gases. The amount of ^{85}Kr is determined either by low-level counting of the β -radiation, by accelerator driven mass spectrometry or by atom-trap trace analysis (ATTA).

Micro seismic monitoring can detect any abnormal underground activities that could indicate unauthorized design changes and containment breaches in final nuclear depositories (Saari and Lakio 2008). It consists of several seismic sensors grouped in a network to monitor remotely excavation-induced micro-earthquakes and explosions occurring inside the local geology of nuclear repositories. The system can also detect early the drilling activity of a tunnel-boring machine trying to excavate an access tunnel to the depository from outside (Saari and Lakio 2009).

Microelectromechanical systems (MEMS) have the potential for creating miniature bench-top laboratories on a chip (Janssens-Maenhout and Nucifora 2007). Such miniaturized

chemical laboratories could provide real-time chemical detection of trace elements in vapor and they could be tailored to detect many classes of chemicals, providing a quick indication of the presence of a class of selected chemicals in the field. MEMS would work with sensors that would use polymer or gel-coated silicon devices to trap targeted chemicals, and then send the agents through fluidic channels to on-chip arrays of surface-acoustic-wave detectors (SAWs). The sensors can be “pre-tuned” to targets of interest, during fabrication, by careful selection of absorption layer and can perform spectroscopic measurements. A follow-on device would integrate the fluidics, sensors, and support electronics on a single device.

Detectors, sensitive to hydrogen fluoride and other fluorine-containing gases (Moritz et al. 1999; Filippov et al. 2007) are of safeguards interest for indicating possible enrichment activities. These types of sensors are based on the Pd-LaF₃-SiO₂-Si structure that generates a signal resulting from the electrochemical reaction with the fluoride on the surface of the sensor. The lower detection limit offered by this technology has been estimated at around 0.05 ppm of HF. It can be assumed that a device based on this semiconductor sensor is able to register directly both UF₆ and further products resulting from its degradation.

Other sensors are composed of nanostructured materials such as carbon nanotubes and metal oxide nanowires. These materials have a controlled pore size and an increased adsorptive capacity due to the large surface area enabling the selective uptake of gaseous species. The absorption can lead to a measurable change in some specific properties, e.g., conductance, capacitance, etc. (Li et al. 2003).

Nanocomposite scintillators utilizing nanocrystals of known scintillator and detector materials will allow for the production of large composites of the nanocrystals with an expanded variety of attainable shapes and sizes (Del Sesto et al. 2007; McKigney et al. 2007). These nanocomposite materials are expected to have improved properties with respect to the properties of the bulk single crystal scintillators from which they are derived. Preliminary measurements show that nanophosphor materials have a significantly higher light output (by a factor of 3) than single-crystal materials of the same weight. This translates to greater scintillation efficiency. In addition, a shift toward longer wavelengths is observed in both the photoluminescence excitation and emission of the nanomaterial with a smaller overlap of the excitation and emission spectra, enhancing the energy resolution of the nanocrystal material.

Nanocomposite semiconductors such as nanowires arrays of CdZnTe can be used for detecting low-energy gamma rays (Gandhi et al. 2008). The CdZnTe compound semiconductor is electrodeposited in the form of nanowires onto a TiO₂ nanotubular template. The preliminary results indicate that the CZT nanowire arrays can be used as radiation detector materials at room temperature with a much lower bias potential (0.7–2.3 V) as compared to the 300–500 V applied to bulk detector materials.

Solid-state neutron detectors using silicon nanopillars (Cheung et al. 2006) are being developed. The space between the silicon nanopillars is completely filled with ¹⁰B-enriched material using chemical vapor deposition (CVD). The incident neutrons are converted by the nuclear reaction ¹⁰B(n, α)⁷Li to α-particles, which are collected and detected by the silicon (Nikolic et al. 2007). The coin-sized detector has achieved a thermal neutron detection efficiency of 20% and neutron/gamma discrimination of 10⁵, which are comparable to the parameters of a ³He-based detector. Such detectors could be arranged in flexible arrays and could be directly attached to a moderator. They could also replace ³He tubes. Another attractive application combines recent advancements in ultrawide band radio frequency identification (RFID) technology with such neutron detectors (Nekoogar et al. 2009). The RFID neutron tags can be used for neutron monitoring. They are totally passive and will operate indefinitely

without battery power. The tag is compact; it can be directly mounted on metal, and has high performance in dense and cluttered environments.

Miniaturized wireless semiconductor devices can form sensor networks – also known as smart dust (Sailor and Link 2005). These devices are millimeter- to micrometer-sized multifunctional packages, combining a sensor (e.g., optical, chemical, vibration, or radiation) with computing and communication capabilities. A large number of these packages can be integrated to form an “Internet-like” network. The devices could be inexpensively mass-produced using conventional silicon fabrication techniques coupled with nanotechnology. Potential applications for safeguards may include the monitoring of facilities and inventories, measuring temperature profiles and detecting undeclared process activities via chemical signatures.

63.4 Laboratory Analysis for Nuclear Material Accountability Verifications

63.4.1 Introduction

One diversion scenario is the removal of small amounts of material over a longer period, masking under the measurement uncertainties the slow accumulation of “significant quantities” of material in a “protracted diversion.” This can involve small underestimates in the declaration of inputs, small overestimates of the outputs, or inflated estimates of measurement uncertainties by the operator. *Destructive analysis* (DA) remains the basic tool to detect such potential actions by analyzing independent samples obtained by the inspectors during physical inventory or material flow verifications, based on a random sampling plan. The inspection samples are most often shipped for analysis to specialized laboratories operated by or on behalf of the inspectorate. In the case of some large bulk-handling facilities, inspectorate specialists will analyze the inspection samples locally or on the plant site at a dedicated laboratory. Inspectors may perform additional inspections and request other samples for the purpose of verifying the quality of the measurement systems and providing independent estimates of the measurement uncertainties. The inspectorate laboratories supply also certified materials, which are submitted to the operator laboratory as part of external analytical quality control measures. They also prepare and/or certify spikes for isotope dilution assays and physical or chemical standards for the calibration of portable or installed instruments used for on-site verification measurements.

The accountability measurements of the facility operators and the verification measurements by the inspectorate are expected to meet internationally accepted standards of precision and accuracy (IAEA 2001), which were defined by an international panel of analytical chemists and data evaluation specialists and are reviewed at regular intervals.

63.4.2 Bulk Measurement, Sampling, Conditioning, and Shipment of Safeguards Inspection Samples

A prerequisite for accurate destructive analysis is a strict representativity of the sample, when it is taken, and its proper conservation during its handling at the plant and its shipment to the analytical laboratory. If the purpose of the sampling is to verify material accountability, the

weight or volume of the material to be sampled must be measured just before sampling and recorded. Operator's installations and procedures are normally used for bulk measurements of weights or volumes and sampling for verifications.

A validation of operator sampling installations and procedures is therefore done during the initial design information verifications and associate inspectors, sampling specialists, and analysts of the inspectorate laboratory. The sampling installations and procedures should comply with internationally accepted standards and technical norms. Inspector's samples of plutonium and spent fuel samples must frequently be pretreated, diluted, conditioned, and packaged so that the amount of radioactive material per package complies with international air transport regulations (IATA 2003). Because of their small size, the composition of inspection samples is prone to be affected by humidity, air oxidation or evaporation. The inspectorates select and qualify, therefore, carefully the vessels in which inspection samples are taken, conditioned, and shipped in a way to ensure their integrity until they reach the laboratory. The vessels should be chemically inert and should not break during transport. Their tare should be stable over time and varying atmospheric conditions, and it must be possible to close or cap them hermetically, so that a weight control may detect potential changes in the composition of the sample between its taking and its analysis and permit their correction, when necessary. Plastic vessels are used for samples of solutions or sintered pellets and dense metal. Glass vessels are chosen for powder and most other samples. The sampling vessels, the sample vials and their handling must always remain under inspectors' supervision and control. Document STR69 (IAEA 2004) describes the precautions and procedures adopted for obtaining reliable DA inspection samples from most types of materials subject to nuclear safeguards.

Sampling is not recommended in the case of finished or intermediate products from which analytical samples cannot be taken without destroying a valuable manufactured item (e.g., rods, bundles, assemblies). It is also undesirable on very heterogeneous materials in small quantities from which representative samples cannot be taken without unreasonably great effort and expense, and therefore sampling may not lead to meaningful results. Verifications of the accountability of the above materials will rely on NDA methods, combined with C/S measures. However, when the weight or volume of the material cannot be measured, the taking and analysis of a sample may still be justified for verifying the operator's measurement system.

The procedures are designed to yield at least duplicate results, which allow estimating the uncertainties resulting from subsampling and conditioning steps. Four examples are outlined below.

63.4.2.1 Spent Fuel Solutions

In spent fuel reprocessing plants, inspection samples of spent fuel (SF) solutions are taken from tanks equipped with means to homogenize the solution, by air sparging or mechanical stirring, and to measure the weight of the solution, using strain gauges, or its level and volume, usually with dip tube systems and differential manometers (ISO 1996a). During normal plant operation, this is done solely at the input accountability tank for material flow verification. Inventory verifications are scheduled when the plant is idle and most fuel material is removed from the process areas. Only storage tanks may need then to be measured and sampled.

The norm ISO18213 gives detailed recommendations concerning accountability tank installations and procedures for volume calibration and measurement (ISO 2007b). It reflects the results of extensive experience collected at a number of spent fuel reprocessing plants

(CETAMA 1997; Hunt et al. 1994; Janin 2006). For accurate bulk measurements and representative sampling, the “dead volumes” of ancillary pipes should be negligible compared to the volume of the bulk solution, and the heel remaining at the bottom of the tank after it is emptied should be minimized. Such tanks are subject to initial calibration before the start of plant operation and typically verified once a year (Janin 2006).

Primary samples of 3–5 ml are withdrawn from a sampling pot through which an airlift circulates the bulk solution, while the tank is stirred (ISO 1995a). The operator collects a sequence of primary samples in evacuated 5–10 ml vials, capped with a synthetic rubber septum. The inspector selects one of the primary sampling vials and witnesses its subsequent subsampling and conditioning. Occasionally, the inspector may request replicate primary samples to check their representativity. This can be done on the spot by witnessing a measurement of their density and comparing the results with the density of the bulk solution measured with the dip tubes in the tank, after referring all values to the same temperature (ISO 1995b).

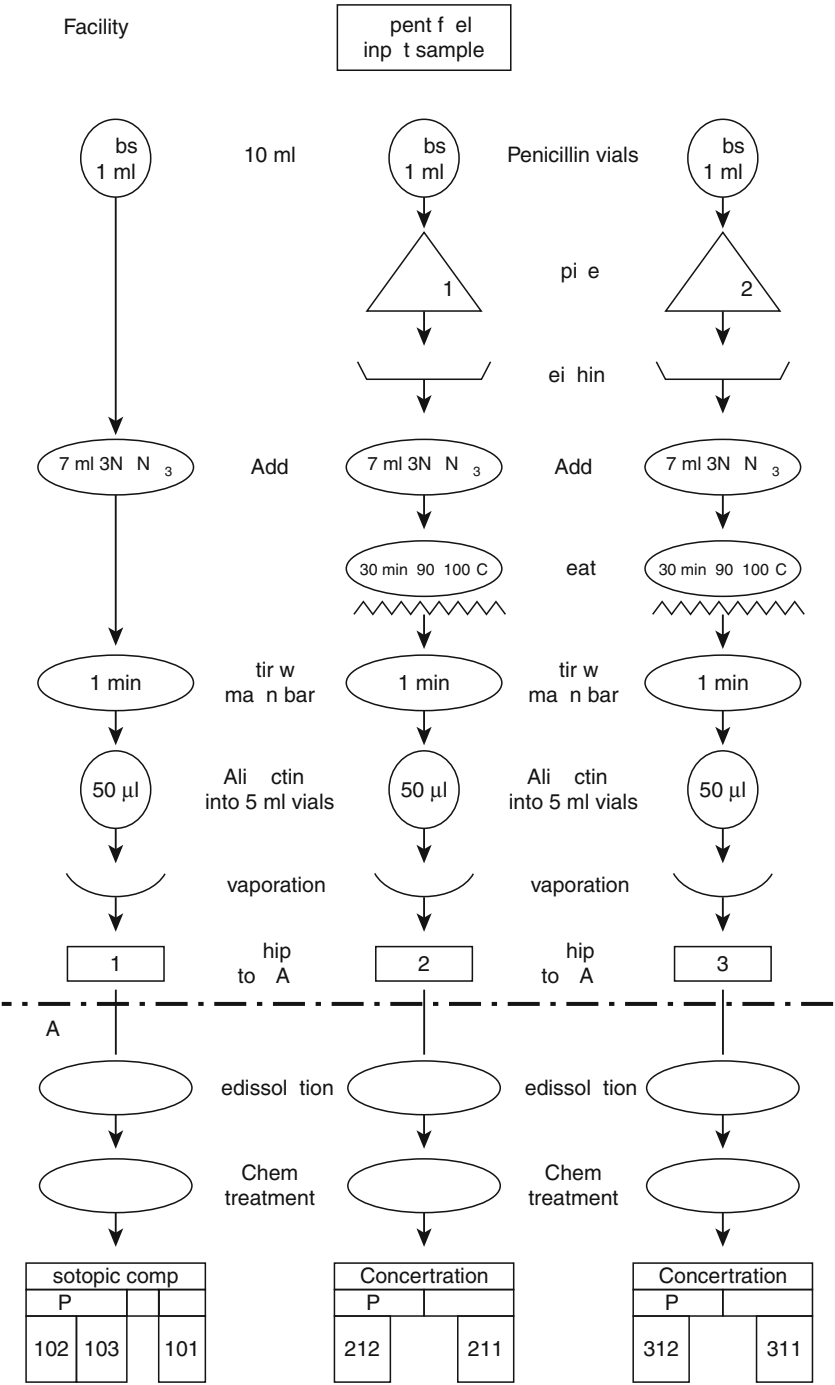
The large-size-dried (LSD) spike procedure is the standard IAEA procedure for the preparation and analysis (see section “Isotope Dilution Mass Spectrometry”) of high burnup spent fuel samples with a ^{239}Pu abundance lower than 80% by isotope dilution mass spectrometry (IDMS). The procedure for sample conditioning at the facility and the measurement scheme followed in the laboratory are outlined in [Fig. 63.8](#). The first of the three subsamples is intended for isotopic analysis and is transferred into an empty 10 ml penicillin vial. The second and third subsamples, intended for elemental assay, are transferred into separate 10 ml penicillin vials, which contain certified amounts of a mixed U/Pu tracer. The latter two subsamples are weighed to an accuracy of ± 0.0005 g or better. The tracers are re-dissolved with nitric acid; the subsamples are diluted to about 7 ml and homogenized. An aliquot of about 50 μl of each diluted subsample is transferred into a clean and empty penicillin vial of 5 ml and dried carefully. The penicillin vials are capped and inserted in a small lead pot. The lead pots are bagged out and packed in a tin can. Several tin cans may be packaged in a single Type A container, which is air flown to the inspectorate laboratory.

63.4.2.2 Uranium Hexafluoride in Pressurized Cylinders

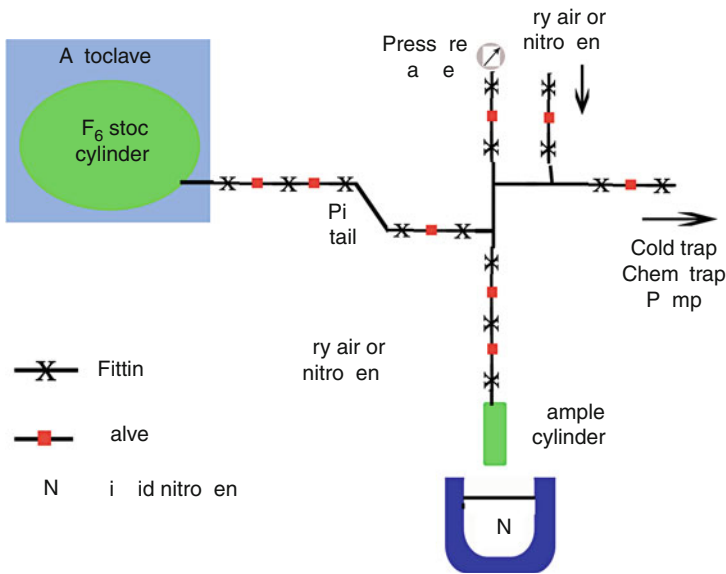
Bulk measurement of UF_6 in isolated UF_6 cylinders consists of determining the gross weight of the cylinder on a suitable scale just before sampling and then subtracting the known tare. To obtain a representative sample suitable for elemental uranium assay, the cylinder is placed in an autoclave, connected to a stainless steel vacuum rig ([Fig. 63.9](#)), heated and kept at 93–113°C throughout a prescribed period and during sampling. After complete homogenization, a measured portion of UF_6 is withdrawn from the liquid phase via a “pigtail” and transferred into a large primary sample bottle. The convection currents in the liquid UF_6 readily achieve isotopic homogeneity. However, chemical homogeneity is more difficult to reach in the presence of insoluble particles or volatile impurities. Excessive volatile impurities are vented to the process before weighing and sampling the cylinder.

The primary sample bottle is transferred to the operator’s laboratory and mounted on a subsampling station ([Fig. 63.10](#)). The UF_6 is liquefied and a subsample of 1 to 5 g is collected again from the liquid phase (ANSI 1972; ISO 1996b) into a finger tube ([Fig. 63.11](#)), which is weighed and shipped to the inspectorate laboratory. If the subsample is not issued from homogeneous liquid phases, only the uranium isotopic analysis will provide a meaningful result. In such a case, it is recommended to skip the elemental uranium assay.

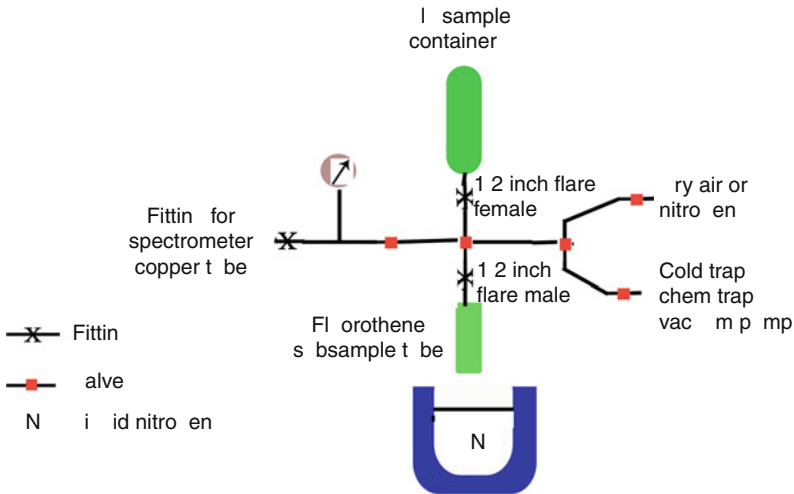
Fig. 63.8
Standard sample preparation and measurement scheme for spent fuel samples of high burnup (IAEA 2004)



■ Fig. 63.9
Outline of a system for the sampling of UF₆ cylinders (IAEA 2004)



■ Fig. 63.10
System for subsampling Liquid UF₆ from a primary sample cylinder (ANSI 1972)



63.4.2.3 Plutonium Oxide Powders

PuO₂ powders readily exchange atmospheric moisture and carbon dioxide, particularly on their surface. With the precautions described below, the shipper's and the receiver's data were in

■ Fig. 63.11

UF₆ subsampling tubes (IAEA 2004)

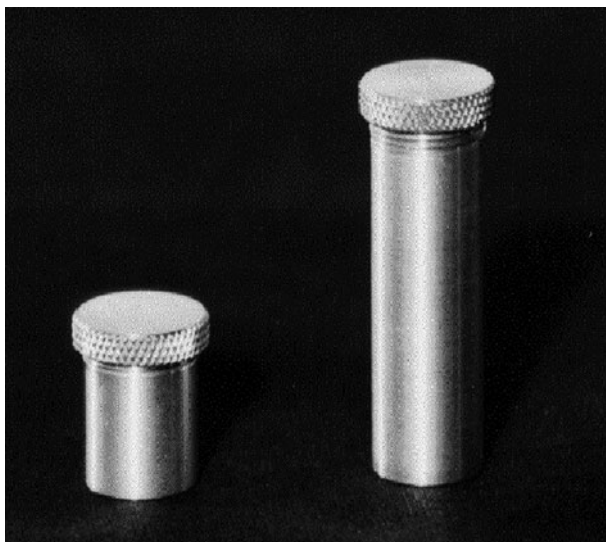
excellent agreement, with uncertainties of the order of 0.07% over a large number of shipments of plutonium oxide between the plants of La Hague in France and Sellafield in the United Kingdom (Swinburn and McGowan 1976). The operator's sampling and subsampling procedures must conform to internationally accepted standards (ISO 1993). Special care is further required in the conditioning of inspector's subsamples to minimize the atmospheric effects and to allow a correction for changes in the chemical composition before the sample reaches the inspectorate laboratory.

The selected can of powder is weighed just before sampling. A large primary sample is collected in a tared and gas-tight flask, under a dry controlled atmosphere in the glove box where the material is processed or stored. The primary sample flask should be transferred immediately to a subsampling glove box where its gross weight is measured on an analytical balance and recorded. Just prior to subsampling, the sample flask is shaken vigorously; the gross weight is checked and recorded. Duplicate subsamples of about 1 g are weighed to ± 0.5 mg or less into tared vessels.

These vessels can be small glass tubes, like the inserts of the BC4 and BC5 brass containers (► Fig. 63.12), whenever one can use a Type B package carrying several grams of plutonium to ship a load of samples. These containers were actually designed and qualified for use with the PAT2 container, which had received approval for the shipment of Type B quantities of Pu samples to or from the USA (Kuhn et al. 1982). Their compact size make them very attractive for shipments of gram size Pu samples in any Type B container.

■ Fig. 63.12

BC5 and BC4 brass vials with glass tube insert (IAEA 2004)



In other cases, the subsamples are dissolved in nitric acid in the operator's analytical laboratory. An aliquant of each subsample, carrying about 4 mg of plutonium, is taken into a 5 ml penicillin vial and dried carefully to form an adherent film of nitrate salt on the bottom of the vial. The two aliquants are intended for elemental assays. Another fraction of at least one subsample is usually prepared for isotopic analysis and dried as above. With current products issued from high burnup spent fuel, some 20 penicillin vials could be packed together into a single Type A container and flown to SAL.

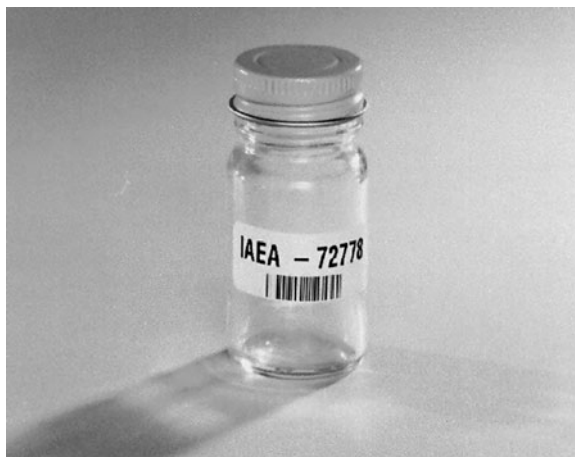
63.4.2.4 Uranium Dirty Scrap Materials

Uranium scrap materials in cans or hoppers are expected to be heterogeneous in element concentration and isotopic composition, and tend to change in composition upon exposure to atmosphere. As far as possible, the content of the container to be verified should be carefully mixed just before sampling. The item is weighed on a suitable scale immediately before duplicate samples of relatively large size are taken by collecting material from various spots in the bulk of the material.

Each sample of about 30 g is introduced into a tared glass bottle, which is immediately capped tightly and weighed. Metal-capped bottles used in the pharmaceutical industry (► Fig. 63.13) are ideal for this purpose as their tare is very stable and the cap inner PE lining insures a very tight closure. The same bottles are used to take and ship gram size samples of uranium compounds in powder form, like UO_2 products or yellow cake. The samples are packed without further handling in an "Excepted" or "Type A" package and flown to the inspectorate laboratory.

■ Fig. 63.13

Glass bottle for samples of uranium oxide powders and scrap (IAEA 2004)



63.4.3 Safeguards Analytical Laboratories

63.4.3.1 Off-Site Laboratories

The concept of IAEA's safeguards analytical services (Lopez-Menchero et al. 1976) foresaw that the agency would establish and operate a fully equipped safeguards analytical laboratory (SAL). The analytical capability of SAL was to be such that samples taken from any key measurement point of the fuel cycle could be analyzed and that the results of these analyses would meet the requirements of safeguards accounting verification.

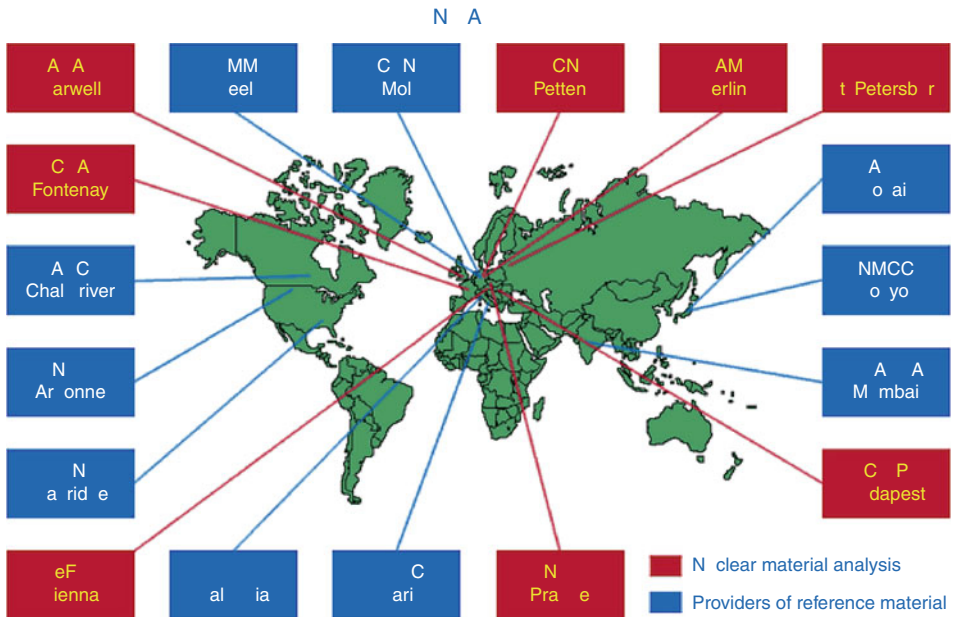
To accommodate the 5,000 samples that were anticipated annually, SAL was to become part of a network of analytical laboratories (NWAL), along with existing laboratories nominated by member states for this purpose at the request of the IAEA. This approach was selected for reasons of economy and flexibility of services, but also because it provided the possibility of checking the accuracy of the analyses of actual inspection samples by comparing results obtained by different verification laboratories. Such an intercomparison was to become an important feature of the quality control program that the IAEA maintains to ensure the quality of measurements made by SAL and the network. Other safeguards systems operate in a similar way, which indeed strengthen the credibility of the verification measurements. After the successful completion of the PAFEX-1 and PAFEX-2 tests, IAEA NWAL became operational in 1975 (● Fig. 63.14).

In order to preserve the confidentiality of their origin, all IAEA inspection samples are sent first to the IAEA Laboratories in Seibersdorf (Austria), from where a number of them are redispached to NWAL, in accordance with instructions of the inspectorate. In 1975, about 480 samples, mostly uranium products but also a few of plutonium dioxide, were analyzed. A maximum was reached in 1990 with 1,600 samples, including uranium, plutonium, and spent fuel samples received and analyzed (Deron et al. 1994).

Safeguards analytical laboratories use essentially the same sorts of techniques and equipment as research and plant laboratories for nuclear material isotopic and elemental assay and

■ Fig. 63.14

The IAEA Network of Analytical Laboratories in the 1980s



material accountability. DA has the advantage that the sample is treated in a way to optimize the conditions of its final measurement. However, advances made in NDA measurements have found many applications in laboratories too, as can be seen in ▶ Sects. 63.4.3, ▶ 63.4.4, and ▶ 63.5.

63.4.3.2 On-Site Laboratories

With the planning and construction of large spent fuel reprocessing or mixed U/Pu oxide fuel fabrication plants with annual throughputs close to 1,000 “Significant Quantities,” the safeguards inspectorates planned minimal laboratory facilities directly on site. Their justification is to reduce strongly the number of samples of sensitive materials, which need to be shipped to distant laboratories, and to obtain analytical results faster, by eliminating long shipment times. Much research went into developing and testing robotized equipment to perform DA treatment and measurements automatically (Brandalise et al. 1994; Takahashi et al. 1994; Zahradnik and Swietly 1996) for their eventual installation at on-site laboratories.

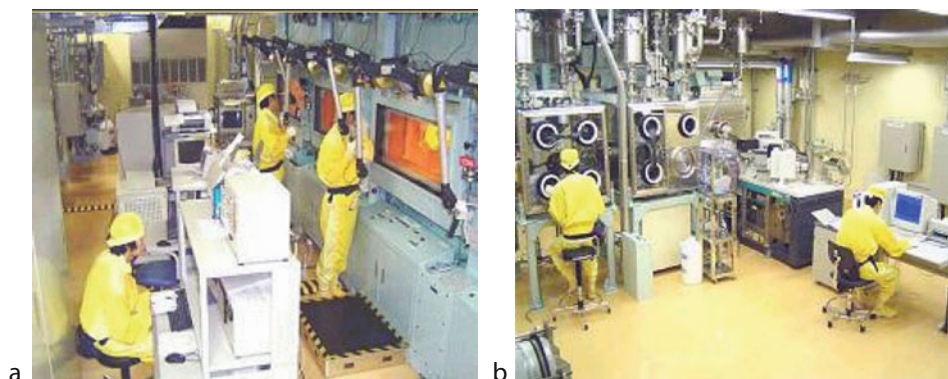
EURATOM set up on-site laboratories in La Hague in France (Regnier et al. 1994) and in Sellafield in the UK (Schneider et al. 1999). The Japanese state system and the IAEA operate jointly an On-Site Safeguards Analytical Laboratory (OSL) at the Rokkasho-Mura Reprocessing Plant (RRP) in Japan (Zahradnik-Gueizelar et al. 2007; Iwamoto et al. 2006). The latter includes (Matsuo 2008) a high activity laboratory handling spent fuel and high active waste samples in hot cells, a medium activity laboratory equipped with shielded glove boxes where plutonium and uranium products are measured and subsampled (▶ Fig. 63.15), a low

activity laboratory for chemical separations and alpha spectrometry, and a mass spectrometry laboratory (🔗 [Table 63.8](#)).

The pneumatic *sample transfer system* within OSL/RRP is connected to the operator's automatic sampling and sample transfer systems. Inspection sampling jugs are fed into the

■ **Fig. 63.15**

OSL facilities at RRP. (a) Hot cells; (b) Glove Boxes (Matsuo 2008)



■ **Table 63.8**

OSL/RRP analytical equipment (Midorikawa et al. 2006)

Laboratory area	Sample handling equipment	Analytical instruments	Treatment/measurement	See section
High activity	Hot cells	HKED	U, Pu, Np concentration	14.3.1
		OSCA	^{244}Cm	14.3.1
		Density meter	Solution density	
		Balance	Subsampling/spiking	
		Pu(VI) Spectrophotometer	Pu concentration < 10 g/l	14.4.5.5
		FP separation unit	Free U, Pu from FP	
Medium activity	Shielded glove boxes	HKED	U, Pu concentration	14.3.1
		Density meter	Solution density	
		Balance	Subsampling/spiking	
		HRGS	Pu isotopics	14.3.1
Low activity	Glove boxes	Separation robot	U, Pu separation	
		Alpha spectrometer	$^{238}\text{Pu}/(^{239}\text{Pu} + ^{240}\text{Pu})$ and Pu concentration < 10 mg/l	14.4.4.2
Mass spectrometry	Glove boxes	TIMS	U, Pu isotopics and content by IDMS	14.4.4.1, 14.E4.5.5.2

system from a jug-feeding machine installed in OSL/RRP. Authentication of inspectors' jugs is further ensured by *inspector passage detectors* tracking the inspectors' jugs between their departure from OSL, their arrival at the automatic sampling bench, and their return to OSL. Correlation with information from the operator-declared data and the *automatic sampling authentication system* confirm the authenticity of the inspector samples (Duhamel et al. 2004).

63.4.4 Isotopic Analysis

63.4.4.1 Isotopic Analysis by Mass Spectrometry

A *mass spectrometer* consists of three main components, which are kept under high vacuum: an ionization source, a mass analyzer, and a detector assembly (➤ Fig. 63.16). Ionization of the analyte may be produced by thermal ionization, inductively coupled plasma, or other means. The mass analyzer separates the ions according to their electrical charge and kinetic energy. It can be a time-of-flight system, a quadrupole, an electromagnetic sector, an accelerator, or another kind of mass filter. Electromagnetic sectors offer better mass resolutions and isotope abundance sensitivities than cheaper quadrupole analyzers and are therefore preferred to obtain the accuracies required for safeguards isotopic DA measurements.

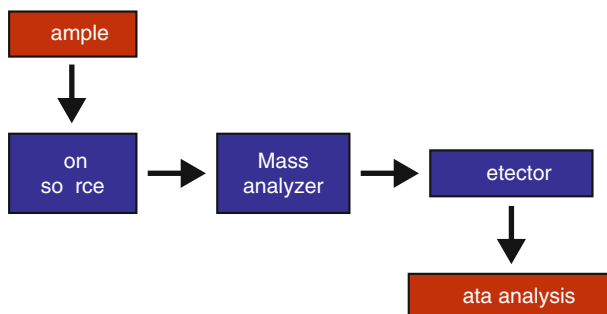
Isotopic Analysis by Thermal Ionization Mass Spectrometry

Thermal ionization mass spectrometers (TIMS) with magnetic sector are thus the basic instruments for Pu and U isotopic analysis in safeguards inspection samples. The performance of commercial instruments has improved tremendously, particularly in the last 30 years, in terms of vacuum capability, design of the ionization source and detector assembly, stability of electrical supplies, sensitivity and linearity of ion current amplifiers, and includes full automatization of the measurement and data reduction.

In modern instruments, the *ionization source* is equipped with a turret, which may hold 13 to MS filament assemblies (Tuttas et al. 1998). Each assembly carries one or two side filaments, usually in platinum or tungsten, and a center rhenium ionization filament. A 1 µl or less of sample solution containing 0.05 to 1 µg of uranium or 5–100 ng of plutonium is loaded onto a side filament, and dried electrically under controlled conditions to obtain a reproducible

■ Fig. 63.16

Main components of a mass spectrometer



oxide deposit. The loaded turret is mounted inside the ionization source and the ionization source cavity is evacuated to 10^{-4} Pa or less. The samples are degassed in sequence before starting a cycle of measurements as follows.

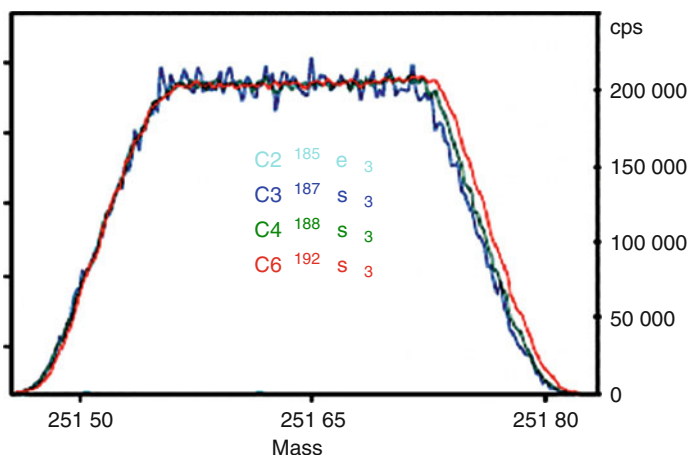
The temperature of the center ionization filament is raised to about $2,500^{\circ}\text{C}$ and maintained at a constant value within 10°C , preferably under optical pyrometer control. The temperature of the sample is raised stepwise; molecular species volatilize and break down partially to produce U or Pu atoms. Impacts with electrons emitted by the center filament produce positive ions, which are extracted by a set of electrostatic focusing lenses under high voltage, and injected into the mass analyzer. The magnetic field of the analyzer is adjusted to collect the major analyte isotope ions in the center of the selected ion current detector. Focusing of the ion beam is adjusted to obtain a maximum intensity of the major isotope ion current. The instrument and its tuning are optimized to obtain a very flat top with sharp edges when scanning across an isotope ion peak (🔗 Fig. 63.17).

Various approaches have been devised to increase the *thermoionization efficiency*, such as electro-codeposition of actinides and platinum on the sample filament (Rokop et al. 1982), the resin bead loading technique (Walker and Smith 1979), or carburization (Jakopic et al. 2008). All these methods are said to facilitate the reduction of the sample species into atoms and enhance their ionization. An electrically heated cavity as sample holder installed in the source turret of a commercial mass spectrometer (Riciputi et al. 2002) yields also amazing increases of the ionization efficiency up to 5 and 7%.

Ions captured in a *faraday cup* detector produce very low electrical currents, typically below 1 pA, which flow across a very large resistor to yield voltage signals in the range of 0.1–100 mV. The linearity of the response of faraday cups, the stability of the signal and the signal-to-noise ratio were greatly increased with the introduction and improvements of digital voltage amplifiers, the use of 10^6 M Ω voltage drop resistors, instead of the 10^5 M Ω resistors used earlier (Tuttas et al. 1998). In standard designs, the image of the exit slit of the ionization source, focused on the ion detector entry slit, has the same size than the source slit. Operating

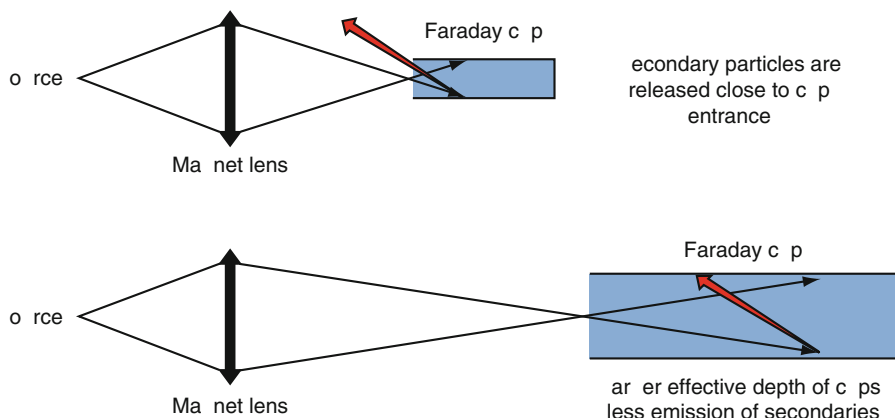
🔗 Fig. 63.17

Typical scan over isotope ion peaks measured with compact discrete-dynode detectors



■ Fig. 63.18

Increased magnification reduces losses of secondary ions within faraday cups



with a magnification of $\times 2$ instead of $\times 1$, and installing deeper faraday cups (Thermo Fisher Scientific: Triton 2005) provide greater space to install multidetectors and decrease the loss of secondary ions, minimizing thereby between-cup differences (► Fig. 63.18).

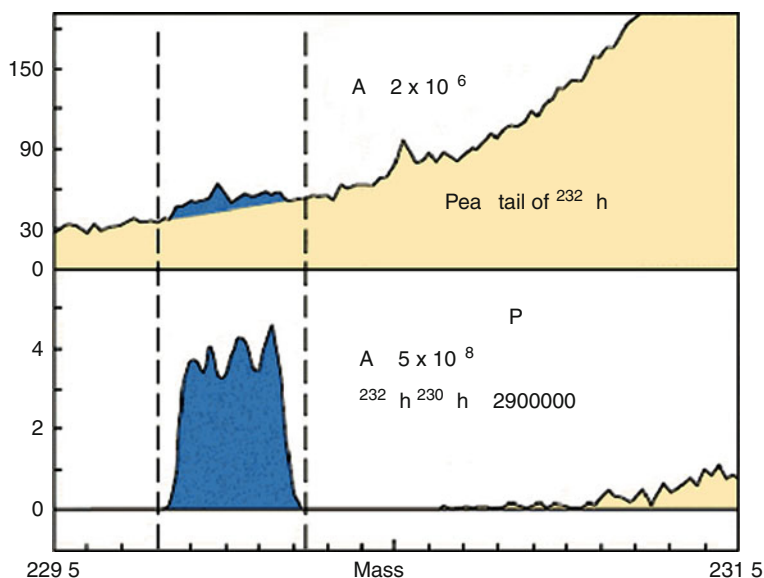
Minor isotopes or samples of very small size, typically in ng range or below, are measured with *ion multipliers* rather than with faraday cups. Three types of ion multipliers may be used: Daly scintillation detectors (Daly 1960), discrete-dynode multipliers (DNM), or continuous electron multipliers (“channeltrons”), with amplifications of 10^4 – 10^8 . Channeltrons are very compact but have a narrower dynamic range than DNMs. The output signal of the ion multiplier can be used to measure the instantaneous intensity of the ion beam as it is done with the faraday cup signal. Alternatively it serves to count the number of ions hitting the detector, using pulse counting technology. Channeltrons with a diameter of 2 mm, faraday cups, 3.5 mm in diameter, or 7 mm wide discrete-dynode detectors exist now. *Multidetector assemblies* with 8–12 detectors can be built with such devices (Tuttas et al. 2005). The individual detectors are spaced in a way to allow a simultaneous collection of the ion currents of isotopes of interest, namely ^{233}U , ^{234}U , ^{235}U , ^{236}U , ^{238}U and/or ^{238}Pu , ^{239}Pu , ^{240}Pu , ^{241}Pu , ^{242}Pu and ^{244}Pu . The ion synchronous collection eliminates the effects of changes in thermionic emission and time drift of the ion currents. This improves the reproducibility of the results and shortens the duration of a measurement, but raises the question of checking the relative ion sensitivity of the various detectors when using a multi-ion-detector thermal ionization mass spectrometer (MIC/TIMS).

Highest *isotope abundance sensitivity* is needed to measure well very minor isotopes, e.g., to determine the age of a uranium sample (Wallenius et al. 2001). Use of tandem magnetic sectors or addition of an energy filter (Thermo Fisher Scientific, Patent 1993) like a retarding potential quadrupole lens (RPQ) (► Fig. 63.19) would do the job.

All processes in the course of the loading of the sample and its TIMS measurement may entail small *isotopic fractionation* effects, which bias isotope ratio measurements. This is particularly the case during sample evaporation and ionization within the ionization source, which favor the lighter isotopes. These effects are globally corrected via a *mass discrimination factor* determined by measuring U and Pu isotopic standards, such as the ones listed in ► Table 63.9, under exactly the same conditions than actual samples are.

■ Fig. 63.19

Isotope abundance sensitivity with and without a retarding potential quadrupole



■ Table 63.9

Recommended uranium and plutonium isotopic reference materials for the determination of mass discrimination in isotopic analyses

Supplier	Reference	Certified ratio	Certified value (a)
IRMM Geel (Belgium) (IRMM 2008)	EC-NRM-199	$^{233}\text{U}/^{238}\text{U}$	1.00001 (30)
		$^{235}\text{U}/^{238}\text{U}$	1.00015 (20)
	IRMM-074/1	$^{233}\text{U}/^{238}\text{U}$	1.02711 (26)
		$^{235}\text{U}/^{238}\text{U}$	1.000254 (15)
	IRMM-3636	$^{233}\text{U}/^{236}\text{U}$	1.01906 (16)
	IRMM-290a/A2	$^{239}\text{Pu}/^{242}\text{Pu}$	1.013450 (82)
NBL Argonne (USA) (NBL 2008)	NBL-U500	$^{235}\text{U}/\text{TotU}$	0.49696 (50)
		$^{238}\text{U}/\text{TotU}$	0.49711 (50)
	NBL-128	$^{239}\text{Pu}/^{242}\text{Pu}$	0.99937 (26)
	NBL-137	$^{239}\text{Pu}/^{240}\text{Pu}$	0.24131 (39)
CETAMA Bagnols (France) (CETAMA 2009)	MIRF-01	$^{239}\text{Pu}/^{242}\text{Pu}$	0.9783 (5)
	MIRF-02	$^{233}\text{U}/^{236}\text{U}$	0.9681 (10)

Note (a): The figures in parentheses represent the expanded standard uncertainties on the last decimal figures of the certified values, with $k = 2$.

In the standard *data collection scheme*, the isotopic ion beams are collected sequentially on a *single detector* by changing the magnetic field of the mass analyzer or the accelerating voltage of the ionization source. The mass spectrum of interest is scanned repeatedly in a way that allows to account for the changes in the rate of ion emission with time. *Peak jumping* is the preferred scanning scheme when the measurement is done in automatic mode. With *multidetector* the magnetic field and accelerating voltage are kept constant and the various isotope ions are collected simultaneously but in separate detectors. Ion current changes with time no longer perturb the measurement. However, as said above, it is necessary to verify that all detectors have the same response, or ion sensitivity, or otherwise to correct for differences (Ramakumar and Fiedler 1999).

Total evaporation is very effective in minimizing the isotope discrimination effect. In this scheme, the sample is heated progressively and the isotope ion currents are collected as early as possible after the beginning of the ion emission. Data are collected until the sample has been totally exhausted. Total evaporation is readily applied in multi-detection mode (Callis and Cappis 1996; Aggarwal et al. 1999), but can also be used in single detection mode (Fiedler 1995). The method permits the analysis of samples much smaller than required for conventional techniques using Faraday collectors. Reproducibilities of 0.02% RSD and less have been obtained for U and Pu isotope ratios (Callis and Abernathy 1991).

The value of the isotope ratio is derived from the ratio of the measured ion currents, or their integral, corrected for the isotope discrimination effects as shown in the example below:

$$n(^{236}\text{U})/n(^{238}\text{U}) = (1 - 2k)I(^{236}\text{U})/I(^{238}\text{U}) \quad (63.1)$$

where $n(^{236}\text{U})/n(^{238}\text{U})$ is the ratio of ^{236}U and ^{238}U isotopes to be determined, $I(^{236}\text{U})/I(^{238}\text{U})$ is the ratio of the measured ion currents, or their integral, k is the mass discrimination factor per mass unit.

As said above, the factor k is obtained by measuring for example an isotopic reference material with certified $^{235}\text{U}/^{238}\text{U}$ ratio

$$k = (R/R(I) - 1)/3 \quad (63.2)$$

where R is the certified value of the isotope ratio $n(^{235}\text{U})/n(^{238}\text{U})$ of the reference material $R(I)$ is the ratio $I(^{235}\text{U})/I(^{238}\text{U})$ of the measured ion currents.

Ion fractionation can be very effectively corrected by an *internal calibration* after spiking a uranium sample with a mixture of isotopes of certified ratio, like IRMM-3636 (Richter et al. 2008) or CETAMA-MIRF-02, or spiking a plutonium sample with a certified mixture of ^{242}Pu and ^{244}Pu isotopes. Several batches of mixtures of ^{236}U , ^{233}U , ^{242}Pu , and ^{244}Pu isotopes were prepared for isotopic and IDMS assays of spent fuel solution samples using the method of internal calibration (Stepanov et al. 1990b). Calibration of such spikes could now be done to an accuracy of $\pm 0.05\%$ (1s) against isotopic standards certified to $\pm 0.03\%$ or less, like the $^{233}\text{U}/^{235}\text{U}/^{238}\text{U}$ reference materials IRMM-74/7-10 with low ^{233}U abundance. Unfortunately, there exists yet no mixture of ^{239}Pu and ^{240}Pu isotopes certified on a purely gravimetric basis.

The results reported in Stepanov et al. (1990b) led to suspect that some small differences between laboratories may be due to uncorrected differences in detector sensitivities or errors therein, at the laboratories using MIC/TIMS instruments. On commercial MIC/TIMS, a program measures the relative gains of the various amplifier chains. A program connecting a given amplifier chain sequentially with the various ion detectors, called *virtual amplifier*, corrects for differences between amplifier chains. Yet it is also necessary to measure the ratios of the *ion capture efficiencies* of the various cups or ion multipliers. This may be done by

producing a very steady ion beam, often the rhenium ion beam emitted by the ionization filament, and programming the instrument to peak jump from one collector to the next. More convincing but more tricky is to load a very accurately characterized mixture of three or more isotopes of the element of concern (Fiedler and Donohue 1988). The isotope ratios are measured in multidetection mode while the isotope ion spectrum is shifted by one detector in successive steps. ➤ **Table 63.10** describes a sequence of steps which may be used with a mixture of ^{239}Pu , ^{240}Pu , ^{242}Pu and ^{244}Pu isotopes, available with reference material UK Pu5/92138 issued by AERE, Harwell (Hamilton et al. 1989). The isotope fractionation at each step is corrected by reference to the certified isotope ratios. The idea was further developed by Dubois et al. into a *dynamic multidetection* measurement mode (Dubois et al. 1989), which practically eliminates mass fractionation effects and possible mismatches of cup efficiencies with a 2-isotope internal standard and MIC/TIMS. According to the results presented, precisions and accuracies of 0.01% are achievable with this procedure. An ultimate refinement has been introduced by performing total evaporation measurements with peak tailing correction in dynamic multicollection mode, using a MIC/TIMS with magnetic sector equipped with a dispersion quadrupole (Goldberg et al. 2002; Richter and Goldberg 2003).

High-accuracy measurements require very sophisticated instruments and measurement procedures, but *isobaric interference* of ^{238}U on ^{238}Pu measurement, and that of ^{241}Am on ^{241}Pu also deserve great attention. These can be minimized by taking advantage of different atomization kinetics. Actually in resin bead measurements the ^{238}U interference is corrected by collecting ^{235}U isotopes during the Pu measurement (Walker and Smith 1979). It is now becoming practical to do so with commercial MIC/TIMS (Aggarwal and Alamelu 2005). Yet in order to achieve best results it is customary to perform a careful chemical separation and to eliminate uranium contaminations. Chemical treatment is unavoidable in IDA to ensure a *complete isotope exchange* (see section “Isotope Dilution Mass Spectrometry”). A *chemical separation* follows to provide U and Pu fractions in a clean and controlled matrix. When analyzing spent fuel samples the separation serves also to yield samples free from fission products, which do not need to be handled in a high activity laboratory (see ➤ Sect. 63.4.2.2).

■ **Table 63.10**

Example of a sequence of measurements of a 4-Pu isotope mixture for the determination of relative ion efficiencies of the 7 faraday cups of a MAT 261 mass spectrometer

Step	Faraday cup number						
	8	7	6	5	4	3	2
1			239	240		242	244
2		239	240		242		
3	239	240		242		244	
4				239	240		
5					239	240	242
6					239	240	242
7				239	240		
8	239	240		242		244	
9		239	240		242		
10			239	240		242	244

Proven valency adjustment and separation procedures are outlined below.

- (a) *ISO 8299 procedure* (ISO 2005b): Reduce plutonium to Pu(III) and Pu(IV) in 7 M nitric acid with Fe(II), reoxidize to Pu(IV) with nitrite, then adsorb U and Pu in 7 M nitric acid on a quaternary ammonium anion exchange column, elute fission products, Am and other potential interferences with 7 M nitric acid before collecting the uranium fraction; finally reduce Pu on the column to Pu(III) with hydroxylamine and elute it with the same reagent.
- (b) *ISO 15366 procedure* (ISO 1999): Reduce and reoxidize Pu in 3 M nitric acid as in the previous procedure, adsorb Pu and U on a TOPO impregnated silicagel column, wash out fission products, Am and other potential interfering species with 3 M nitric acid, then condition the column with 1.7 M nitric acid before reducing Pu on the column with a freshly prepared solution of 0.1 M HI/1.7 M HNO₃; elute Pu with the HI/HNO₃ reagent, and finally wash out U with water.
- (c) *LANL procedure* (Marsh et al. 1974): Oxidize Pu to Pu(VI) by fuming the sample with HClO₄, re-dissolve the sample in 12 M HCl and adsorb U and Pu on a quaternary ammonium anion exchange column, elute fission products, Am and other interfering species with 12 M HCl; then reduce Pu on the column and elute it with a reducing solution of 0.1 M HI/12 M HCl; finally wash out U with dilute 0.1 M HCl.
- (d) *UTEVA procedure* (Morgenstern et al. 2002): In 6 M HNO₃/0.3% H₂O₂ a sample of spent nuclear fuel is expected to contain Am(III), Pu(IV) with 13% Pu(III), Np(IV), and U(VI) along with the fission products. In this medium Pu, Np and U are adsorbed on a liquid ion exchanger column (UTEVA), while the fission product and Am are not retained. Pu is fully reduced to Pu(III) and eluted with 2 M HNO₃/0.002 M ascorbic acid. Then Np is recovered with a 2 M HNO₃/0.1 M oxalic acid eluent. Finally, U is eluted with 0.007 M ammonium oxalate.
- (e) *The resin bead procedure* (Marsh et al. 1981): An aliquot of sample containing about 1 mg of U and/or 10 µg of Pu is adjusted to 8 M HNO₃ and subjected to a redox valency adjustment with Fe(II) and nitrite as in procedures (a) and (b). The sample is equilibrated with about 10 anion exchange resin beads of around 300 µm diameter. Each bead collects about 10 ng of U and/or Pu and is mounted on a mass spectrometer filament for a sequential measurement of the Pu and U isotopic compositions.

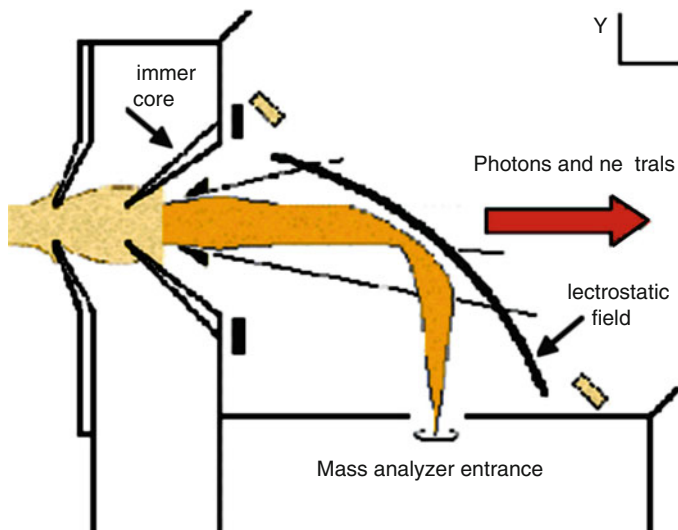
Isotopic Analysis by Inductively Coupled Plasma Mass Spectrometry

While the ionization filament in a TIMS may be heated to a maximum temperature of 2,500°C, inductively coupled plasma reach temperatures of 15,000–20,000°C and have much higher ionization efficiency. A pneumatic nebulizer serves to inject sample solutions directly into the plasma. Inductively coupled plasma mass spectrometers (ICP-MS) have thus become powerful tools in trace and ultra-trace analyses with detection limits down to 1 ppq or less. ➤ [Section 63.4.5.8](#) refers to ICP-MS applications in measuring alternative nuclear materials, Am, Np, and Cm, and ➤ [Sects. 63.5.2](#) and [63.5.5.4](#) dwell upon their use in environmental analyses for safeguards.

Commercial ICP-MS equipped with magnetic sectors and multidetection could meet the requirements of safeguards accountancy verifications (Pereira de Olivera et al. 2008). Prior chemical separations of the nuclear elements are, however, of benefit to reduce isobaric interferences by the numerous polyatomic ions generated by the plasma source. An elegant solution is to attach a liquid chromatography unit in line with the ICP source (Guenther-Leopold et al. 2005). Double focusing mass filters or diverse energy filter components

■ Fig. 63.20

The Varian 90° deflector (Elliott et al. 2005)



overcome some of the interferences. Collision reaction cells (Varian 2009) are also common accessories to segregate polyatomic ions and might improve the isotopic analysis of actinides too. Ion multiplier detectors should be protected against impacts from high-energy photons and neutral particles, as done with the 90° deflector of Varian (Elliott et al. 2005) (► Fig. 63.20).

Active research in safeguards applications of ICP-MIC-SFMS is thus to be expected in DA of nuclear fuels as well as in environmental analyses.

63.4.4.2 ^{238}Pu Abundance by Alpha Spectrometry

Isobar ^{238}U can be a source of positive bias in the determination of ^{238}Pu isotopic abundance by mass spectrometry despite prior chemical separation of the two elements. In this respect, eluting Pu before U is advantageous (see section “Isotopic Analysis by Thermal Ionization Mass Spectrometry,” procedures (b)–(d)). Great attention must be placed anyway to minimize sources of blanks due to low levels of natural uranium in most chemical reagents and mass spectrometry filaments. It is therefore still customary to perform ^{238}Pu measurement by alpha spectrometry in parallel with mass spectrometry.

^{238}Pu abundance in safeguards samples varies between 0.001% in so called weapon grade plutonium to over 1.5% in plutonium from high burnup spent fuel. A typical alpha spectrum (Bagliano et al. 1991) obtained with an ion-impact detector with a resolution of 12 keV is shown in ► Fig. 63.21. The presence of Am-241 with alpha rays in the range of 5.39–5.49 keV will yield high results. ► Table 63.11 lists the relevant nuclear data. The accuracy of the alpha spectrometry of plutonium depends strongly upon the chemical preparation of the sample, the production of carrier-free alpha sources, the counting geometry, the detector resolution, and the method used to correct for the tailing of the ^{239}Pu and ^{240}Pu alpha peaks.

Fig. 63.21

Typical plutonium alpha spectrum (Bagliano et al. 1991)

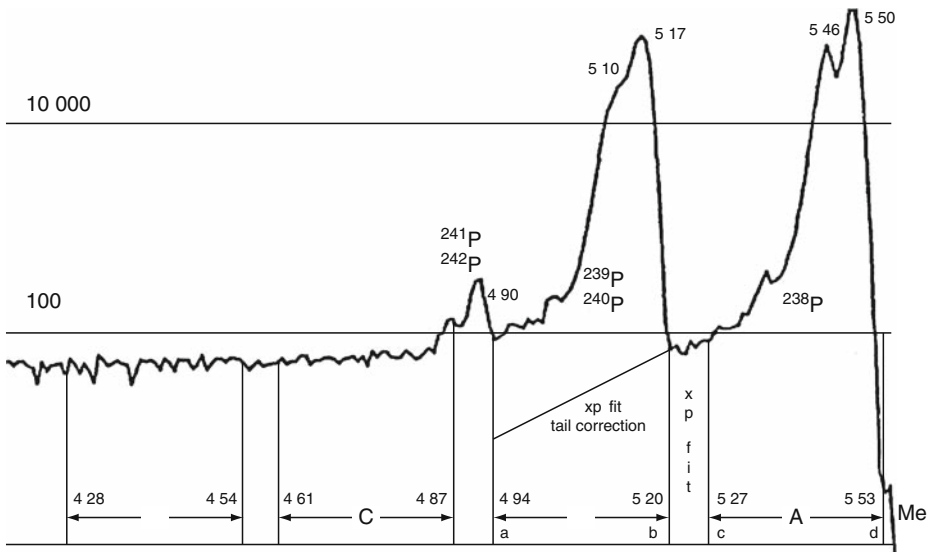


Table 63.11

Relevant nuclear data (Nichols et al. 2008)

Nuclide	Half-life [year]	Radiation	Energy [keV]	Emission probability [%]
^{238}Pu	87.74	α	5,456.3	28.29
	± 0.03		5,499.03	69.3
^{239}Pu	24,110	α	5,105.5	11.94
	± 30		5,144.3	17.11
			5,156.6	70.77
^{240}Pu	6,561	α	5,123.68	27.16
	± 7		5,168.17	72.74
		β^-	20.78	100.00
^{241}Pu	14.290	α	4,853.0	0.0003
	± 0.006		4,896.3	0.002
^{242}Pu	373,000	α	4,858.1	23.49
	$\pm 3,000$		4,902.2	76.48
^{244}Pu	8.00×10^7	α	4,546	19.4
			4,589	80.5
^{241}Am	432.6 ± 0.6	α	5,388.2	1.660
			5,442.8	13.1
			5,485.56	84.45
		γ	59.54	35.9
			26.34	2.27

The separation of ^{241}Am deserves particular attention, when the ^{241}Pu abundance is high and when a long time has elapsed since the plutonium fuel material was produced. This is the case with samples of high burn-up spent fuel. The standard anion exchange method described in section “Isotopic Analysis by Thermal Ionization Mass Spectrometry,” para. (a) is well suited for the purpose, as Pu is eluted long after Am, fission products and U are. It is a good practice, nevertheless, to measure the ^{241}Am gamma emission at 60 keV in the separated Pu fraction to verify that it will not bias the results.

The aim of the source preparation is to obtain very thin, smooth, and uniform deposit to minimize the effects of self-absorption and retrodiffusion, which alter the resolution of the alpha spectrum. Some of the methods are listed below:

Electrodeposition on polished platinum or stainless steel disks, with a variety of supporting electrolytes (ISO 2007d; Ingelbrecht et al. 1997; Amoudry and Silly 1984; Hallstadius 1984; Lally and Glover 1984).

Vacuum sublimation on glass (Amoudry and Eloy 1984).

Drop deposition, usually with addition of spreading agents such as tetraethyleneglycol (ISO 2005c; Miguel et al. 1984).

Deposition on a mass spectrometry filament to perform alpha and mass spectrometry measurement on the same filament (Strebin and Robertson 1977).

The deposit should not carry more than 10–20 $\mu\text{g}/\text{cm}^2$ of matter to minimize self-absorption (Amoudry and Silly 1981). The support material must have a finely polished surface and be inert to corrosion. Support material of high atomic weight reduces retrodiffusion of alpha rays. Gold-plated copper or steel support produces sources of resolution down to 12 keV. Several publications report comparisons of different methods of source preparation (Aggarwal et al. 1985; Lally and Glover 1984).

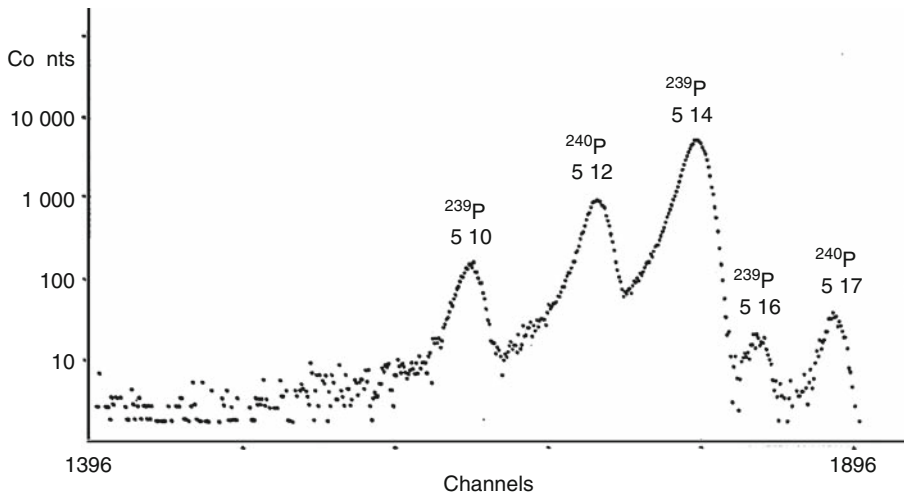
The spectrum of alpha radiation may be measured in a gas proportional counter or a gridded ionization chamber (Bortels et al. 1985), but semiconductor detectors are more commonly utilized in nuclear fuel analyses. The properties of Si detectors for alpha spectrometry have been studied extensively (Bortels et al. 1994, 1993; Bortels 1991; Bortels and Bauer 1990a, 1990b; Aggarwal et al. 1988). Particle implanted passivated silicon (PIPS) detectors nowadays present resolutions down to 9 keV (► Fig. 63.22), which permit, with a favorable geometry (Amoudry and Silly 1981), a deconvolution of the ^{239}Pu and ^{240}Pu alpha peaks in the range of 5.0–5.2 keV (Amoudry and Burger 1984). The counting chamber is kept under reduced pressure of 0.5 Pa or less during measurement.

A number of elaborate peak fitting algorithms have been proposed to correct for the tailings and deconvolute overlapping peaks (Raab and Parus 1994; Babeliowsky and Bortels 1993; Garcia-Torano 1990; Amoudry 1983). *Deconvolution* of the ^{239}Pu and ^{240}Pu peaks is not normally done to measure the ^{238}Pu abundance in safeguards samples, as more precise results are obtained by combining the alpha activity ratio $^{238}\text{Pu}/(^{239}\text{Pu} + ^{240}\text{Pu})$ with the $^{240}\text{Pu}/^{239}\text{Pu}$ isotope ratio measured by mass spectrometry. The $^{238}\text{Pu}/^{239}\text{Pu}$ isotope ratio is calculated according to ► Eq. (63.3):

$$R_8 = R_\alpha T_8 (T_9^{-1} + R_0 / T_0) \quad (63.3)$$

where R_8 is the $^{238}\text{Pu}/^{239}\text{Pu}$ isotope ratio, R_α the $^{238}\text{Pu}/(^{239}\text{Pu} + ^{240}\text{Pu})$ alpha activity ratio, R_0 the $^{240}\text{Pu}/^{239}\text{Pu}$ isotope ratio measured by mass spectrometry, T_8 , T_9 , T_0 are the half-lives of isotopes ^{238}Pu , ^{239}Pu , ^{240}Pu , respectively.

■ Fig. 63.22

Alpha spectrum of a $^{239}\text{Pu}/^{240}\text{Pu}$ mixture obtained with a PIPS detector of 9 keV resolution

A simple algorithm is sufficient to correct the ($^{239}\text{Pu} + ^{240}\text{Pu}$) alpha activity for the tailing of the ^{238}Pu peaks, such as a “linear decrease,” an “exponential decrease” (ED), or a GP (geometric progression) tail correction. Results obtained using the GPRANL code (Gunnink et al. 1984), the ED or GP correction methods agree within 0.3% of the mass spectrometry results, as long as the $^{238}\text{Pu}/(^{239}\text{Pu} + ^{240}\text{Pu})$ alpha activity ratio stays below 5 (Bagliano et al. 1991; Aggarwal et al. 1980; Ramaniah et al. 1980). In these cases, and with sources of suitable quality, the counts around 5.17 MeV, at the ^{239}Pu and ^{240}Pu peaks, should be at least 300 to 500 times larger than the counts in the valley around 5.25 MeV. Then tailing corrections will not exceed 0.2 to 0.5%.

At present, IAEA SAL estimates at 0.4% the total uncertainty (1s) of its determinations of ^{238}Pu abundance in safeguards samples by a combination of alpha and mass spectrometry taking into account the contributions of short and long term measurement reproducibility, calibration, and nuclear data uncertainties.

63.4.4.3 Gamma Spectrometry of Nuclear Material Samples

Gamma ray spectrometry is widely used in safeguards laboratories to measure the isotopic abundance of various U and Pu isotopes but also their concentration, as well as the concentration of “alternative nuclear elements” (see Sect. 14.4.4.8) fission and decay isotopes (Parus and Raab 1996; Parus et al. 1987). Laboratory applications make use of the developments of NDA technology mentioned in ► Sect. 63.3.1, but are usually part of DA procedures.

The ^{235}U abundance of LEU products is determined with a total uncertainty of 0.13% (1s) by measuring the 186 keV gamma rays with a NaI or GeLi well detector on 5 ml solutions containing a well-known amount of uranium, close to 0.5 g. The volume of the sample and synthetic calibration test solutions, their acid and U concentrations are kept in a very narrow range so that the self-absorption and counting geometry be constant factors or minor variations be accurately

corrected. The technique is a good back up to mass spectrometry in case of a pile up of samples. Alternatively, the procedure can be used to measure U concentration of samples with known ^{235}U abundance, when the accuracy of a titration is not required.

High-resolution gamma spectrometry (HRGS) is routinely used as screening and quality control tool in processing nuclear material as well as environmental samples (see ▶ Sect. 63.5.3.1). In IAEA/SAL vials of Pu product samples are all subject to gamma spectrometry before any wet chemical treatment is undertaken. Estimates of elemental and isotopic composition of U, Pu, Am, or other relevant radioisotopes serve to orient further processing and are recorded for later use. The gamma spectrometry data help to select the optimal spike for IDMS or IDAS, when spiking is to be done in the laboratory. On the whole, U and Pu isotopic gamma results will be matched with the mass spectrometric assays to exclude any gross error in the analytical process. Gamma rays at 60 keV will detect ^{241}Am , which may remain in the separated Pu fractions, before alpha and mass spectrometry (see ▶ Sects. 63.4.4.1 and ▶ 63.4.4.2). Fission products are also measured in spent fuel samples when inspectors want to verify burn-up data.

The MGA (Wang et al. 1999; Buckley et al. 2000) and MGAU (Gunnink et al. 1994) gamma spectroscopy softwares, designed for the low-energy region, are used commonly for measurements of Pu and U in product or scrap samples, while general surveys of fission products require measurement over the entire energy range and call usually upon commercial softwares (Canberra 2009a, 2009b).

63.4.5 Elemental Assay

63.4.5.1 Ignition Gravimetry of U, Pu, Th

Ignition gravimetry remains the most reliable and accurate analytical method for elemental assay, especially if gram size samples are available. It is most easily applied for the analysis of nuclear grade oxides of uranium, plutonium or thorium, or to samples that can be readily transformed into an oxide, such as powders and solutions of nitrate salts (Rodden 1953; ISO 1987a, 1987b, 2003, 2004b, 2007). The sample in oxide form is ignited, usually in a platinum crucible, to a temperature between 870 and 1,250°C, depending on the element, for 1 hr periods to reach a constant weight and the formation of a stoichiometric oxide. The average relative atomic mass of uranium or plutonium, W , must be derived from their measured or known isotopic composition. The total mass fraction of nonvolatile impurities, ε , remaining in the ignited oxide must also be measured or known with a suitable precision and accuracy. The mass fraction, C , of the analyte, M , ($M = \text{U, Pu or Th}$), is derived from ▶ Eq. (63.4):

$$C = m_o(1 - \varepsilon)G/m_s \quad (63.4)$$

where m_o is the mass of ignited oxide, m_s the mass of the sample, G the gravimetric factor calculated with ▶ Eq. (63.5):

$$G = xW/(xW + yW_o) \quad (63.5)$$

where $W_o = 15.9994$ is the relative atomic mass of oxygen, and M_xO_y is the stoichiometric molecular formula of the ignited oxide, with $M = \text{U, Pu or Th}$.

A precision of 0.05% or less is expected if the sample contains less than 0.05% nonvolatile impurities. Random uncertainties may increase to 0.15% if the impurity content reaches 0.5%.

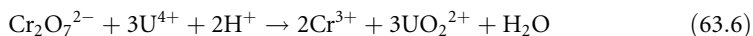
Deviations of the ignited oxide from stoichiometry lead to systematic errors, which should not exceed 0.1%. Systematic errors may also come from calibration errors in the impurity analyses and from systematic errors due, e.g., to uncertainties in their chemical form. The result carries a positive bias, if an impurity, although present, is not measured or detected.

Less pure materials may be analyzed by ignition gravimetry after a suitable chemical purification. For example, thorium in ores, alloys or other materials may be separated by precipitation as oxalate (Scott 1939; Ewing and Banks 1948; Willard and Gordon 1948; Kall and Gordon 1953), which is then ignited to ThO_2 at 95°C. However, the extra steps bring additional random as well as systematic errors.

63.4.5.2 Uranium Titration

Most uranium titration procedures rely on the redox properties of the U(VI)/U(IV) couple. In early redox titration methods, U(VI) was reduced with Ti(III), Cr(II), Pb, Cd amalgam or a Jones reductor. Most of these procedures are not very selective, require a prior removal of nitrate, or operate at elevated temperatures and under inert atmosphere. Samples of nitric solutions, adjusted to 1N HNO_3 and 2N H_2SO_4 , can be titrated directly by Ce(IV) with o-phenanthroline as colorimetric end point indicator, after Ti(III) reduction (Corpel and Regnaud 1962). The method was adapted to a gravimetric titration by Cr(VI) with amperometric end point (Nair et al. 1996) and applied to diluted dissolver solutions, containing 100–300 µg of uranium, with burnup of up to 10,000 MWd/t. Uranium can be titrated potentiometrically with Fe(II) from strong phosphoric acid medium (Rao and Sagi 1962). Fe(II) and W(VI) do not interfere, but V(V), Mo(VI), and Cr(II) do. A fast and very selective procedure was derived from the latter, based on the reduction of U(VI) by an excess Fe(II) in a phosphoric acid medium, the catalytic destruction of the excess Fe(II) by nitric acid in the presence of molybdate, followed by a dilution and a titration with a standardized solution of dichromate with a colorimetric end point detection (Davies and Gray 1964). Out of 23 species, only Ag(I), V(IV), or V(V) appear to interfere appreciably. In the Davies & Gray/NBL-modified procedure a potentiometric titration with vanadyl ion as electrochemical indicator replaced the colorimetric titration (Eberle et al. 1970). This procedure is widely used for accountability and safeguards verification measurements. ISO 7097-1 describes its application to a gravimetric titration of aliquants of samples of uranium nitrate solutions, metal, oxides and hexafluoride of nuclear grade, containing about 50 mg of uranium (ISO 2004a). The overall process is equivalent to a titration of U(IV) with dichromate according to

Eq. (63.6) below:



The mass fraction of uranium in the sample, C_U , in g/g, is equal to:

$$C_U = WT(m_c/2m_a) \quad (63.7)$$

where W is the relative atomic mass of the uranium in the sample, T the titer of the dichromate solution in equivalent/gram, m_c the mass of dichromate solution used to reach the end point, in gram, m_a the mass of sample aliquant used in the titration, in gram.

The final titration is usually performed with a commercial automatic volumetric titrator. Gravimetrically calibrated burettes yield coefficients of variation of 0.05% or less for the overall uncertainties of random or systematic nature in the assays of samples of uranium and mixed

■ Fig. 63.23

IAEA-SAL robotized system for the treatment and titration of uranium samples by the NBL modified Davies & Gray method (Aigner and Aigner 1994)



uranium/plutonium products. Robot systems (● Fig. 63.23) automatize the entire process, including the redox steps preceding the titration, and run reliably unattended overnight with the same precision and accuracy than with the semi automatic procedure (Aigner and Aigner 1994). A scaled down procedure processes 5–25 mg aliquants of uranium with no loss of precision (Slanina et al. 1976). The Davies & Gray procedure is sufficiently selective to be applicable to the determination of uranium in dissolver solutions from spent fuel reprocessing plants.

The dichromate titrant is particularly attractive as its solutions are very stable as long as they are stored in hermetic vessels, and can be calibrated directly versus primary standards, namely, NIST 136f dichromate (Montgomery and Sanerwein 2008) and NBL 112A (NBL 2008) or CETAMA MU2 (CETAMA 2009) uranium metal. Nonetheless, NBL felt compelled to replace dichromate by Ce(IV), which is not listed as a toxic chemical (Zebrowski et al. 1995; ISO 2007a).

63.4.5.3 Plutonium Titration

Plutonium titrations take general advantage of the properties of the Pu(III)/Pu(IV) or Pu(IV)/Pu(VI) electrochemical couples. Microvolumetric titrations of mg amounts of plutonium with potentiometric end point detection were widely used in the past (Metz 1957; Fudge et al. 1960).

Plutonium was often reduced to Pu(III) with an excess Ti(III), which was titrated colorimetrically (Corpel and Regnaud 1962) to Pu(IV) with Ce(IV), after destroying the excess Ti(III). The method was adapted to a sequential amperometric titration of U and Pu in samples of breeder reactor fuel materials (Chadwick and McGowan 1972). 500 mg samples of Pu metal

can be dissolved in 6N HCl to obtain Pu(III), which is titrated spectrophotometrically with Ce(IV) in presence of ferroin with uncertainties of $\pm 0.07\%$ (Caldwell et al. 1962). 50–140 mg samples of Pu metal, dissolved in 4N sulfuric acid and reduced to Pu(III) on a Jones reductor, may be titrated gravimetrically with Cr(VI) using two polarized gold electrodes to detect the end point, with a coefficient of variation of 0.05% and 100.01% recovery (Pietri and Baglio 1960). In a more selective method, Pu is reduced to Pu(III) with an excess Cu(I) in a solution of HCl/sulfamic acid and aluminum chloride. Fe(II) and the excess Cu(I) are reoxidized by Cr(VI) up to a potentiometric end point. Sulfuric and phosphoric acid are then added to lower the Pu(III)/Pu(IV) redox potential, so that Pu(III) can be titrated with Cr(VI) without oxidizing chloride (Davies and Townsend 1974).

Another group of methods relies on a prior oxidation of plutonium to Pu(VI) by fuming perchloric acid (Waterbury and Metz 1959), argentic oxide (Drummond and Grant 1966), sodium bismuthate (Charyulu et al. 1984), or Ce(IV) (MacDonald and Savage 1979). In the so-called AgO-method, a longtime accountability method at many bulk handling plants, the excess AgO is destroyed by sulfamic acid, an excess standardized ferrous sulfate is added to reduce Pu(VI) to Pu(IV) and the excess Fe(II) backtitrated with Ce(IV) by potentiometry with polarized electrodes (Corpel and Regnaud 1966) or by amperometry with Cr(VI) (Cherry et al. 1968). However, Ag^+ , coming from the destruction of AgO, oxidizes a fraction of the excess Fe(II) and introduce a very reproducible bias of 0.2%. The titrant therefore must be standardized against a Pu standard solution treated in the same way than the samples (Cauchetier et al. 1975). ^{241}Am gives also a positive bias for Am/Pu ratios above 0.02 because of a partial oxidation of Am or the presence of radiolytic H_2O_2 (Spevackova et al. 1978). Unfortunately, Cr interferes, yielding high results in case of corrosion of process tanks.

A method, free from Fe or Cr interference, (MacDonald and Savage 1979) involves a prior oxidation of plutonium to Pu(VI) with an excess of Ce(IV). Sulfamic acid is added to avoid side reactions with nitrites. Fluoride residues from the dissolution of solid samples are complexed by addition of Al(III). The excess Ce(IV) is then reduced by a slight excess of arsenite in the presence of Os(VIII) as catalyst. Excess As(III) is oxidized by permanganate, also in a very quantity. Finally, oxalic acid is added to reduce the excess Mn(VII). Pu(VI) is then reduced quantitatively to Pu(IV) with Fe(II) and the excess Fe(II) backtitrated with Cr(VI). All steps are followed potentiometrically and carefully timed. The Pu mass fraction, C_{Pu} , in g/g, in the sample aliquant submitted to titration is calculated according to the following equation:

$$C_{\text{Pu}} = W(T_{\text{f}}m_{\text{f}} - T_{\text{c}}m_{\text{c}})/2m_{\text{a}} \quad (63.8)$$

where W is the relative atomic mass of the plutonium in the sample, T_{f} the titer of the Fe(II) solution, in equivalent/g, m_{f} the mass of Fe(II) solution, in g, T_{c} the titer of the dichromate solution in equivalent/g, m_{c} the mass of dichromate solution used to reach the end point, in g, m_{a} the mass of sample aliquant used in the titration, in g.

A scaled down procedure, applicable to the titration of 4 mg of plutonium, was set up at IAEA/SAL with the assistance of Dounreay (MacDonald and Savage 1987) and of the Nuclear Research Institute in Řež (CSSR) (Kuvik 1991). This made possible to receive and titrate samples of Pu products taken in Japanese facilities, as only mg amounts of plutonium can be air flown from Japan in Type A packages. The process including the preliminary redox steps, was automatized to achieve coefficients of variation of 0.05% (Kuvik et al. 1992; Ronesch et al. 1992). 23 species do not interfere, but vanadium does quantitatively, and Np partially. The test sample should carry less than mg-amounts of nitrite, fluorosilicate, and iodate. The effect of americium remains to be studied (ISO 2000).

63.4.5.4 Controlled Potential Coulometry of Plutonium

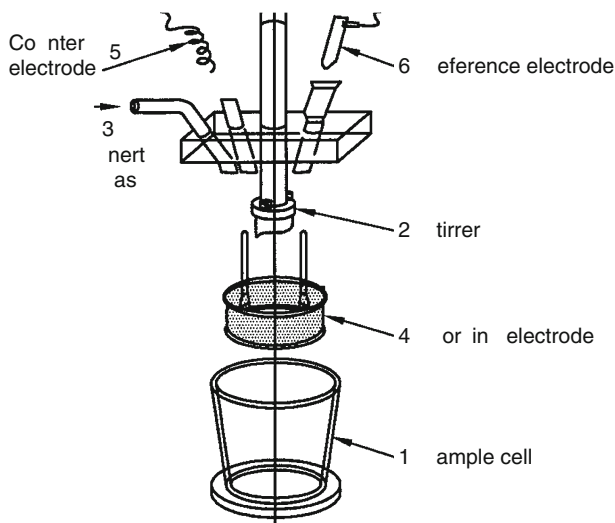
Before operational amplifiers became available, constant current coulometry (CCC) was used more often than controlled potential coulometry (CPC) because the instrumentation was so much simpler. CCC continued to be used for highly precise U determinations in very pure materials (Goode et al. 1967; Malinowski 1967; Merciny et al. 1981).

In CPC, the *measurement cell* (► Fig. 63.24) consists of a sample cell [1], a working electrode [4], a counter electrode compartment [5], and a reference electrode compartment [6]. A *potentiostat* supplies an electrolysis current between the working and the counter electrode in a way to maintain a chosen difference of potential between the working and the reference electrodes. Normally, a Pu assay involves two steps: first, the potential of the working electrode is set to a value leading to the reduction of Pu to Pu(III); the electrode potential is then changed to a value required to reoxidize Pu(III) to Pu(IV). The reduction and reoxidation potentials are selected to reach near quantitative electrolysis of plutonium while minimizing the electrolysis of possible interfering species. A *current integrator* measures the quantity of electricity needed to achieve the reoxidation of Pu(III) to Pu(IV) and relates it to the amount of plutonium.

Dilute sulfuric (Shults et al. 1959; Jackson et al. 1980), nitric (Holland et al. 1998), perchloric (Metz and Waterbury 1962), hydrochloric (Shults 1963), or phosphoric acid (Bärring and Jönsson 1970) have been used as *supporting electrolyte*. The choice of the supporting electrolyte determines the magnitude of interferences from potential impurities (Milner and Phillips 1974): iron interferes stronger in nitric acid than in sulfuric acid, but little or not in hydrochloric acid, as indicated by the Pu(III)/Pu(IV) and Fe(II)/Fe(III) formal potentials (► Table 63.12). Oxygen removal is also a greater challenge with sulfuric acid than with nitric acid.

■ Fig. 63.24

CPC cell



■ **Table 63.12**

Formal potentials of Fe(II)/Fe(III) and Pu(III)/Pu(IV) redox couples, volt versus standard calomel electrode (SCE)

Electrolyte	Concentration	Potential Fe(II)/Fe(III)	Potential Pu(III)/Pu(IV)	Difference
H ₂ SO ₄	0.5M		0.492	
HNO ₃	0.9M	0.66	0.668	0.01
HClO ₄	1M	0.53	0.73	0.20
HCl	2.5M	0.446	0.705	0.259
	5.5M	0.372	0.686	0.315
	7.4M	0.323	0.640	0.317

Chemistry may be combined with CPC to improve selectivity. For example (Jackson et al. 1980) applying the chemistry of the Davies and Townsend titration (see ▶ Sect. 63.4.4.3), Pu is first reduced electrolytically to Pu(III) in an hydrochloric/sulfamic acid mixture along with iron and other potential interfering species. Iron and a number of the other impurities are reoxidized next without reoxidizing Pu(III). Finally, phosphate is added to lower the redox potential of the Pu(III)/Pu(IV) couple to permit a quantitative electrooxidation of Pu(III) to Pu(IV), without oxidizing chloride ions. The procedure is very selective and is applicable to Pu determinations in the presence of uranium in 10:1 U/Pu molar ratio.

CPC at a solid electrode has also been applied to determine uranium (Davies et al. 1970; Phillips and Crossley 1978), which is reduced from U(VI) to U(IV) with electrogenerated Fe(II). The approach has been used for sequential coulometry of U and Pu (Angeletti et al. 1969; Davies et al. 1970; Fardon and McGowan 1972; Phillips and Crossley 1978).

Controlled potential reduction of Pu(VI) to Pu(IV) has also been used to avoid iron interference, but plutonium must be oxidized chemically by AgO, Ce(IV) or fuming HClO₄ prior to its coulometric determination (Shults 1963).

The characteristics of a coulometric method depend also upon the *choice of the working electrode*. Electrode double-layer charging, surface oxide formation, hydrogen evolution at low potential, and electrode or electrolyte oxidation at higher potentials contribute to the background current and depend upon the electrode material and the electrolyte. Mercury pool electrodes have been used for uranium coulometry, but efficient stirring of the solution/electrode interface is difficult to achieve. Long electrolysis times lead to uncertainties in the background current correction. Faster electrolysis is achieved with solid working electrodes such as a Pt gauze electrode (Shults et al. 1959; Shults 1960; Jackson et al. 1980), or a gold mesh electrode (Holland et al. 1998). Glassy carbon was used as indicating electrode in Pu titrations and CPC of iron, chromium, uranium, and neptunium was done with a glassy carbon crucible as working electrode (Plock and Vasquez 1969). Electrochemical reactions at solid electrodes may be slowed down considerably by adsorption or deposition of trace species in solution. Pretreatment and storage of the electrode must be subject to well-validated procedures in order to maintain or restore the electroactive properties of the working electrode. Samples having undergone an ion exchange purification carry resin degradation species, which accelerate electrode “poisoning.” This effect is overcome by fuming the purified sample in concentrated sulfuric acid before performing the CPC measurement.

The *design of the electrolysis cell* is a critical parameter. The objective is to achieve a fast and rigorous removal of dissolved oxygen, to maintain accurate control of the potential of the

working electrode, to achieve near-quantitative electrolysis in the shortest possible time, and to minimize diffusion and leakages between the working electrode compartment and the counter electrode and reference electrode compartments. The working electrode compartment being usually a small cylindrical glass vessel, ideal control of the electrode potential would require a perfect cylindrical symmetry of the working electrode, the counterelectrode, and the mechanical stirrer. Full symmetry never exists in practice, as either the counterelectrode (Holland et al. 1998) or the stirrer is off center (Jackson et al. 1980). It is essential to locate the tip of the reference electrode compartment in a region of highest current density and as close as possible to the surface of the working electrode, in order to best control the electrochemical reactions occurring there (Harrar 1968; Harrar 1987; Harrar and Shain 1996). The larger the ratio of the area of the working electrode to the volume of the test solution, the faster is the electrolysis. Wrapping several layers of platinum or gold gauze as the working electrode is probably not so much increasing the effective area of the electrode but decreases the volume of the test solution. Yet the benefit is partially offset by the increase of the capacitive component of the background current. Analysts deploy much ingenuity in devising special designs of the mechanical stirrer to reach the fastest stirring rate without solution splashing.

Modern electronics will meet the following essential *instrumental requirements* (Holland et al. 1998). For assays of up to 15 mg of plutonium, the potentiostat should be able to supply a current output of 250 mA or more, in order to observe an exponential decay of the coulometric current at the outset of the electrolysis. The potential control circuitry should be fast enough to raise the control potential by 1 V within a millisecond with less than 1 mV overshoot. The selected potential should remain stable to ± 1 mV during measurements. The meter measuring the difference of potential between the working and reference electrodes should have an input impedance of $10^{11} \Omega$ or more. The current integrator should cover a range of 50 μA to 100 mA with a linearity of 0.005% or less. It is recommended to include in the equipment an adjustable constant current supply with a stability of 0.002% to perform an electrical calibration of the current integrator with an accuracy of 0.01%. If room temperature varies excessively, the instrument should be located in a temperature-controlled cabinet to limit electronic drift to the above values.

The norm ISO 12183 incorporates the latest technological experience (ISO 2005d). It describes the coulometric assay of 4 to 15 mg aliquants of plutonium in 0.9M nitric acid, using a gold working electrode. The current integrator is calibrated electrically. A blank is measured first under conditions similar to those used for a plutonium sample. The plutonium test aliquant is weighed into a coulometric cell, fumed to dryness with sulfuric acid and re-dissolved with the blank solution. The test solution is degassed and about 99.9% of the plutonium reduced to Pu(III). The rest potential of the working electrode is measured. The potential of the working electrode is raised to oxidize Pu(III) to Pu(IV). The electrooxidation current is integrated until about 99.9% of the electrolysis is completed. The quantity of electricity used in the oxidation and the rest potential of the working electrode at the end of the oxidation are recorded. The fraction, f , of plutonium electrolyzed is calculated according to the Nernst equation. Stopping the electrolyses before their completion shortens the process and reduces the background current correction and its uncertainty. With automatic coulometers, like the ones described by Jackson et al. (1980) and Phillips et al. (1977), uncomplete electrolysis is not usually corrected mathematically but via a chemical calibration against plutonium reference materials. The Harwell instrument (Phillips et al. 1977) was equipped with an automatic sample changer.

Pd, Ir, Pt, Au interfere but are normally not of concern in nuclear fuel materials. Interference of Fe or Np can be corrected if their content is measured or known and their atom ratio to

plutonium does not exceed 0.005. A confidence interval of 0.1 to 0.2% is achievable for a single determination of plutonium at a confidence level of 0.95. This includes the contribution of uncertainties of systematic character, which should not exceed 0.03%. The uncertainties will increase if the sample must be purified by a suitable chemical separation before applying the coulometric measurement (Pietri et al. 1981; Mitchell et al. 1990). The accuracy of the procedure is verified by measuring aliquants of standard plutonium solutions.

With increasing concerns about the treatment of radioactive wastes, CPC of plutonium or uranium in sulfuric or nitric acid is becoming more attractive, as titration procedures like the Davies&Gray or the McDonald&Savage methods yield complex liquid wastes, which are difficult to condition.

63.4.5.5 Isotope Dilution Assays

Isotope dilution analysis (IDA) involves mixing an aliquant of the sample with an aliquant of an artificially enriched isotope of the element to be analyzed. The content of the latter in the original sample is derived from the results of the isotopic analysis of the mixture compared to the isotopic compositions of the sample and of the enriched isotope. The term “spiking” is often used to refer to the mixing step. The aliquant of enriched isotope added to the sample is also commonly called a “spike.” IDA is used in particular for the determination of uranium, plutonium, or thorium in solutions of irradiated nuclear fuels. It has also been used for an independent measurement of the total volume or mass of solution in accountability tanks of chemical processing plants.

Radiometric Isotope Dilution Assay Techniques

Gamma spectrometry could readily be used to determine uranium with good accuracy by spiking the sample with a uranium spike of sufficiently different ^{235}U abundance, and measuring the 185 keV gamma ray emission of the ^{235}U isotope before and after spiking with enriched ^{235}U . Alpha and gamma spectrometry were shown to be applicable to the IDA of plutonium (Mayer et al. 1995; Parus and Raab 1996) measuring the ratio of the ^{238}Pu activity to the sum of the ^{239}Pu and ^{240}Pu activities. The $^{238}\text{Pu}/(^{239}\text{Pu} + ^{240}\text{Pu})$ alpha activity ratios should not exceed 5 in the spiked and unspiked samples (Ramaniah et al. 1980; Parus et al. 1992), when determining Pu concentrations by isotope dilution alpha spectrometry (IDAS). A plutonium containing 95% of ^{239}Pu or more and less than 0.01% of ^{238}Pu is a convenient spike for IDAS of high burnup plutonium samples holding, e.g., 1% of ^{238}Pu and 50% of ^{239}Pu , just as it is too for isotope dilution mass spectrometry (IDMS). Use of a ^{238}Pu spike is recommended only when the ^{238}Pu isotope abundance does not exceed 0.1% in the unspiked sample. Precautions required to reach accuracies of a few percent by IDAS were described in ► Sect. 63.4.4.2.

Isotope Dilution Mass Spectrometry

Although the technique is more expensive than radiometry, mass spectrometry is, however, the preferred method for IDA of samples of nuclear materials taken for accountability verifications. Traditionally, separated or highly enriched isotopes, absent from the samples or only present as minor isotopes, such as ^{233}U , ^{242}Pu , ^{244}Pu or ^{230}Th were used as spike material in isotope dilution mass spectrometry. IDMS is the standard operator method for the accountability of nuclear materials in input solutions of irradiated nuclear fuels. The method involves taking a representative sample from the input accountability tank and diluting it accurately 100–1,000-fold in a heavily shielded cell. A portion of the diluted solution is transferred to

a medium activity laboratory where it is subsampled and mixed with an accurately measured aliquot of a calibrated dilute spike solution.

IDMS is also the basic technique for safeguards verification measurements on spent fuel solutions and active liquid wastes from reprocessing plants, although it may be used too for the verification of the composition of any sample taken in the nuclear fuel cycle. At first, the IAEA used ^{233}U and ^{242}Pu spikes in the form of a dried nitrate carrying about 1 mg of uranium and 10 μg of plutonium in a sealed penicillin vial. The inspector witnessed the taking of the primary sample, its dilution and requested the weighing of a milliliter of the diluted input solution into duplicate dried spike vials. The inspector witnessed further the heating of the subsamples with nitric acid to re-dissolve the mixed spike, their drying, the capping of the penicillin vials, their bagging out and packaging in Type A containers, which were air flown to Seibersdorf.

- (a) *The resin bead method.* In the resin bead method (Carter et al. 1976) a few beads of anion exchange resin are used to retrieve minute amounts of the unspiked and spiked samples, and transferred to the safeguards laboratory. At the analytical laboratory, a single bead of each sample is mounted on the filament of a thermal ionization mass spectrometer to measure plutonium and uranium sequentially. It was hoped that such resin bead samples may be air mailed to SAL in Seibersdorf in accordance with the regulations of the international air transport association (IATA) and the universal postal union (UPU) valid in 1985. It is essential to achieve full chemical equilibrium between the sample and the spike before adsorbing plutonium on resin beads. According to (Marsh et al. 1981) ferrous sulfamate and nitrite are the most effective reagents to do this. The optimized procedure was tested successfully at La Hague (Cesario et al. 1987) and at the reprocessing plant in Tokai Mura in the frame of the TASTEX program (Walker et al. 1981); the test samples having been sent by registered air-mail or shipped as “excepted” air cargo. Current international air mailing of radioisotopes (UPU 2009) have become more restrictive but shipping resin bead samples of irradiated fuel samples as “excepted” air cargo remains possible (IATA 2010). Yet, this attractive approach has not been implemented further, mainly because the preparation of the samples, although simple, requires more handling by the plant operator and therefore more efforts from the inspector for witnessing or authenticating these operations.
- (b) *Spiking undiluted spent solution samples.* Actually, enriched ^{235}U and low burnup plutonium with a ^{239}Pu abundance of 95% or higher are very suitable spikes for the assay of samples of industrial nuclear materials. Alloy chips containing about 50 mg of 20–90% enriched ^{235}U and 2 to 4 mg of plutonium with a high ^{239}Pu abundance, known as *UPu metal spikes*, were used by EURATOM inspectors to spike samples of concentrated input solutions directly (Debievre and Van Audenhove 1976). The homogeneity of the alloys is considered a limiting factor in the accuracy of their certification. A similar method based on the use of *Al capsules* holding a dried mixture of uranyl and plutonium nitrate suitable for spiking a sample of the concentrated input solution (Koch et al. 1976). Both techniques avoid the need for an accurately measured dilution and its independent verification. It is also claimed that an effective valency cycling and isotopic equilibration of the plutonium is achieved during the re-dissolution of the metal alloy or the aluminum capsule. A small fraction of the spiked solutions containing 1–10 μg of plutonium are taken, dried, and shipped to the safeguards laboratory.
- (c) *The large size dried spike method.* In the large-size dried spike (LSD) procedure, selected by the Nuclear Material Control Centre Laboratory (NMCC) in Tokai Mura and the

IAEA (Kuno et al. 1989), the spike is a mixture of uranylene and plutonium nitrate carefully dried in a 10 ml penicillin vial. For the assay of spent fuel solutions and MOX products with U/Pu ratios around 100:1, each vial contains about 50 mg of uranium-enriched just below 20% in ^{235}U and 2 mg of plutonium with a ^{239}Pu abundance of 95% or more. Calculations (Laszlo et al. 1991) and experience show that these amounts are appropriate to reach relative uncertainties around 0.1% in a single measurement of samples carrying about 100 mg of depleted uranium and 1 mg of high burn plutonium with a ^{239}Pu abundance of 50%.

The mass of uranium or plutonium, m , in the sample aliquant, in g, is derived from \bullet Eq. (63.9) below:

$$m = S(I_s/I)(R_s - R_m)/(R_m - R) \quad (63.9)$$

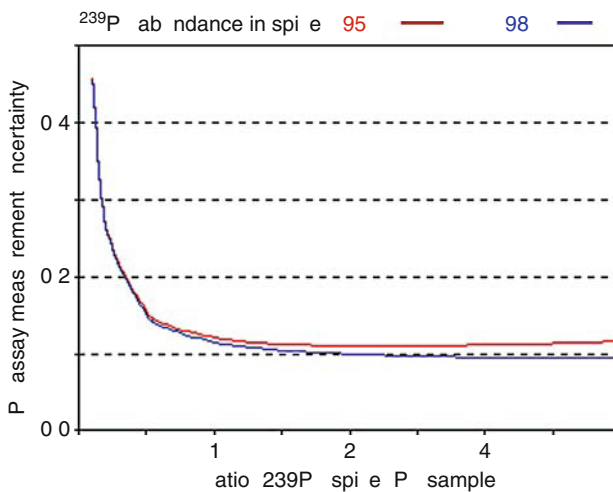
where S is the mass of spike plutonium added to the sample aliquant, in g, I_s is the ^{235}U or ^{239}Pu isotopic abundance in the spike, in weight %, I is the ^{235}U or ^{239}Pu isotopic abundance in the sample, in weight %, R , R_s , R_m are the $^{235}\text{U}/^{238}\text{U}$ or $^{240}\text{Pu}/^{239}\text{Pu}$ isotope ratios, respectively in the sample, spike, and their mixture.

The diagrams in \bullet Fig. 63.25 assume that the $^{240}\text{Pu}/^{239}\text{Pu}$ atom ratios in the unspiked and spiked samples can be measured with a relative uncertainty of 0.05%. The uranium enrichment should not exceed 20% so that the spike does not come in the category of high enriched uranium (HEU), subject to stricter safeguards controls, and will not be allowed in facilities, which are not licensed for the processing of HEU materials.

- (d) *Preparation and certification of LSD spikes.* NMCC and IAEA SAL jointly prepare a stock solution by dissolving metal standards of natural or depleted uranium (NBL112A, EC101, CEA-MU2 or JAERI-U4), HEU (NBL-NRM116) and plutonium with high ^{239}Pu abundance (NBL 126, EC 201, CEA-MP2 or NBS 949) and mixing them to obtain a concentration of about 2 mg/g of plutonium and 50 mg/g of uranium with a ^{235}U abundance just below 20%. The titers are calculated from the “make-up” data and the certificates of the source

\bullet Fig. 63.25

Random measurement uncertainty of the plutonium assay using the LSD spike, as a function of the ratio of mass of ^{239}Pu spike and mass of Pu in sample



metals. The titers are verified (Doubek et al. 1991) by mass spectrometric analyses of the isotopic compositions, potentiometric titration of uranium and potentiometric titration, or controlled potential coulometry of plutonium in accordance to ISO 10980 (ISO 2005b).

The advantage of the LSD spikes is that they can be prepared from primary reference materials more easily than UPu alloy spikes. On the other hand, the dissolution of the LSD spike with the spiked sample does not bring the benefit of a redox equilibration of the sample and spike plutonium, as the dissolution of metallic spikes does. It is therefore essential to avoid losses of LSD spiked samples after their drying in the plant laboratory and until their chemical treatment at the safeguards laboratory. As a quality assurance measure, a number of LSD spikes shipped to a plant under safeguards are returned unused to the verification laboratory in order to check that the spikes are not damaged during shipments or storage.

LSD spikes of certified isotopic and element compositions are available from IRMM since the 1970s (IRMM 2008; Verbruggen et al. 2008a). Automatic equipment (Verbruggen et al. 2008b) was installed to boost the production, also starting from certified metal reference materials.

- (e) *Analytical measurement procedures.* At the safeguards laboratory, the unspiked and spiked samples are re-dissolved in nitric acid and undergo a chemical valency adjustment to achieve isotopic equilibration between the sample and the spike. Uranium and plutonium are separated from each other and from interfering isobares or species altering the ionization and/or fractionation pattern of uranium or plutonium during their measurement by thermal ionization mass spectrometry. Alternative chemical treatments were described in Sect. 63.4.3.1 about isotopic analysis by mass spectrometry. The procedure follows essentially the international standard ISO 8299 (ISO 2005a) with an expected precision and accuracy of 0.1% or better. The calculations are also in line with the mathematical model described by (Kipphardt et al. 2004).
- (f) *Verifications of tank volumes.* For an independent verification of the total mass or volume of solution of nuclear material in accountability tanks of chemical processing plants a known amount, Σ , of a tracer element is added to the nuclear fuel solution in the tank. Only elements which do not disturb the plant process can be used as tracers. They should also be absent or present only in low concentrations in the nuclear material solution. Natural lithium (Bokelund 1970), magnesium (Mathew et al. 1976), and lutetium (Bokelund et al. 1996) have been used as tracers in demonstration exercises. The tank is carefully mixed after the addition of the tracer, the solution is sampled, the sample is diluted by a factor K , and aliquants of the diluted sample are then spiked with ^6Li , ^{26}Mg or ^{176}Lu enriched isotope. Li, Mg, or Lu is separated after a chemical equilibration step. A blank sample, taken prior to the addition of the tracer in the tank, is treated in the same way to determine the isotopic composition and the concentration of Li, Mg, or Lu, which may be present initially in the tank solution. The concentration of added tracer, T , observed in the tank solution, is derived from the dilution factor, K , TIMS measurements of the isotope ratios $^6\text{Li}/^7\text{Li}$, $^{26}\text{Mg}/^{24}\text{Mg}$ or $^{175}\text{Lu}/^{176}\text{Lu}$ in the blank sample, in the tracer and in the sample collected after the addition of the tracer in the tank, and the isotopic compositions of the blank and the tracer. The mass of the solution, M , in the tank is equal to:

$$M = \Sigma / T \quad (63.10)$$

The diluted sample can also be spiked with an enriched isotope of uranium, plutonium, or thorium to determine by IDMS its concentration in nuclear fuel element, C_d ,

along with its concentration in added tracer, T_d . The total mass of nuclear fuel element present in the tank, NF , is readily calculated according to ▶ Eq. (63.11):

$$NF = \Sigma \times C_d / T_d \quad (63.11)$$

This estimate is independent of the dilution factor, K , which does not need to be measured.

Risks of sample contamination are high with Li or Mg tracers and isotopic fractionation is large during lithium TIMS measurements.

Neodymium has been considered as an alternative tracer (Debievre 1997), as it is a fission product present in measurable concentrations in spent fuel solutions and can serve as in situ spike. The accuracy of TIMS measurements is now so good that it could be practical to use enriched ^{235}U or ^{233}U as a tracer for the direct measurement of the total content of fissile material in a tank, skipping altogether the verification of the volume or mass of solution in the tank (Debievre and Perrin 1991).

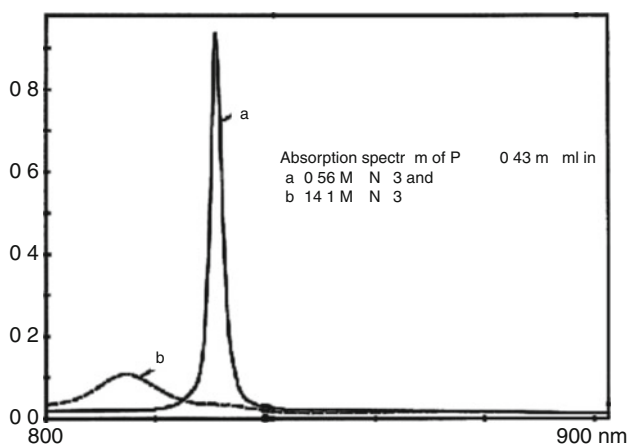
Nonetheless, the efficiency of the mixing of the tracer and the fuel solution, the impact of solution trapped in ancillary tubes and a number of other points remain to be investigated, so that the procedure has rarely been implemented in safeguards verifications up to now.

63.4.5.6 Spectrophotometric Determination of Hexavalent Plutonium

The absorption peak by PuO_2^{2+} ions at 831 nm is the basis of selective Pu determinations (ISO 2009; Cauchetier 1981). Pu in nitric acid solutions is quantitatively oxidized to Pu(VI) with ceric nitrate or argentic oxide AgO . A recording double-beam spectrophotometer is used to scan the absorption spectrum between 800 and 860 nm (Schmieder et al. 1970). The absorption peak at 831 nm is very sharp with a half height width of 26 Å (▶ Fig. 63.26). The peak height is proportional to the concentration of plutonium in the sample up to 0.55 g/l, provided that the spectrophotometer has a resolution of 4 Å or less and the scanning speed is slow enough to allow the recorder to complete a full scale excursion while scanning across the absorption peak.

■ Fig. 63.26

Pu(VI) absorption peak at 831 nm (Schmieder et al. 1970)



The method is calibrated against Pu standard solutions treated in the same way than the unknown samples.

Acidity, anions and temperature affect the oxidation of plutonium and the Pu(VI) extinction coefficient (Savage et al. 1986). Oxidation by Ce(IV) is less prone to anion interferences than AgO oxidation. The acidity should preferably not exceed 2 N when using Ce(IV) as the oxidant, except in the presence of phosphates. Yet for a long time AgO was the preferred oxidizing agent at La Hague, particularly in the assay of dissolver solutions containing always a significant fraction of fine solids (Patigny 1982). The extinction coefficient of Pu(VI) decreases by 0.7% with an increase of 0.1 M in nitrate concentration. It decreases too with temperature by 0.5% per °C. All these parameters must be carefully controlled and be the same for the treatment and measurement of the samples and calibration standards.

Pu(VI) spectrophotometry is actually used in many instances at spent reprocessing plants, including in their accountability programs (Grison 1980; Holland and Dorsett 1986). Fiber optics has eased its applications to analyses in glove boxes and hot cells (Schott 1984). Diode-array spectrophotometers should find applications in process control and safeguards (Cauchetier et al. 1985), as the optical spectra give abundant information on the species present in process solutions. Pu and U spectrophotometry is amenable to automation (Jackson et al. 1976). Use of Nd(III) as internal standard and authentication tag was validated for on-site safeguards measurements of plutonium in highly active waste solutions in spent fuel reprocessing plants by Pu(VI) spectrophotometry (Surugaya et al. 2008). A reproducibility of 10% should be achievable for plutonium concentrations around 10 mg/l. The limit of detection varies between 0.1 mg/l and 2mg/l depending upon the authors.

Higher reproducibilities and accuracies of 0.06–0.1% were obtained (Nikitina et al. 2007) with a two-channel photometer for the characterization of ^{240}Pu , ^{242}Pu or ^{244}Pu spikes or their mixtures. The two channels are centered on the Pu(VI) absorption peak at 831nm and in a region of low absorbance at 720 nm. The ratio of the light intensities in the two channels is taken as a measure of the plutonium light absorption. The technique was proposed for the determination of U, Pu, and fission products such as Nd and Rh in dissolver solutions (Stepanov et al. 2002) with expected reproducibilities of 0.1 to 0.25%. LSD spikes containing around 50 mg of 20% enriched uranium and 2 mg of plutonium have been verified with the same technique and precision. With such a capability, the technique would qualify as a bias defect detection method.

63.4.5.7 X-ray Absorption and Fluorescence Spectrometry

In the 1970s (Pella and von Baeckman 1969; von Baeckman 1971), an instrument was developed for the automatic dilution and L-X-ray fluorescence analysis (XRFA) of U and Pu in spent fuel solutions with a precision and accuracy of about 1%.

The *hybrid K-edge densitometer* (HKED) turned out to find quicker applications for safeguards verifications (Ottmar et al. 1986; Ottmar and Eberle 1991) at the input of spent fuel reprocessing plants, as the sample needs neither a dilution nor any treatment before measurement. The technique, considered as an NDA method and described in ▶ Sect. 63.3.1, is installed in particular in on-site analytical laboratories and operated by analytical chemists on duty there. Operators have found the instrument so practical and reliable that they use it in their nuclear material accountability program (Brousse et al. 1993). The HKED fluorescence channel is also used for DA of Th or mg-size Pu samples,

measuring the Th/U or Pu/U ratios against a uranium “internal standard” (Ottmar et al. 1991; Doubek et al. 1994).

L X-ray fluorimetry with commercial XRF analyzers has been applied to determine U, Th and Pu in oxides and mixed oxides dissolved in borax or polyphosphate glass beads with 0.3% reproducibility. Average relative differences of $\pm 0.2\%$ were observed with results of titrations or gravimetric assays with standard deviations of 0.5% on the differences (Bagliano et al. 1991). The technique has the advantage of yielding only solid wastes and no liquid waste. These instruments are also powerful tools to determine the overall chemical composition of mixed fuels, alloys, nuclear scrap, sludges, fuel cladding, and structural components, etc. Analyses of impurities in ignited oxides are an important component of U, Th, and Pu gravimetric determinations (Sect. 63.4.4.1). Checks of the chemical purity of reagents and samples at key analytical steps are another application of X-ray fluorimetry to the control of the quality of DA procedures.

63.4.5.8 Assay of Alternative Nuclear Materials

The irradiation of nuclear fuels in the reactors produce important amounts of fissile isotopes such as ^{237}Np , ^{241}Am , and ^{243}Cm , besides Pu. Since 1993, the IAEA is called to take these isotopes into consideration in its safeguards duties, as a category of “alternate nuclear materials” (ANM), which might be used to fabricate nuclear explosives (Charlton and Stanbro 2001; Bathke et al. 2009). To guard against such misuses, it was agreed at present to verify that undeclared production of these isotopes does not remain concealed. This is done through an evaluation of the flow sheet of the chemical processing plants (Koch et al. 1997; Rance et al. 2007) and the verification that the process is not modified to allow a separation of ANMs. To perform such “flow sheet verifications” the inspectors must be able to use at least some qualitative or semiquantitative tools to confirm that ANMs are not present in unexpected steps or amounts in the processes. Safeguards focuses particularly on ^{237}Np , which is a long-lived nuclide, as it is expected to be easier to use to produce alternate nuclear fuels or nuclear explosives.

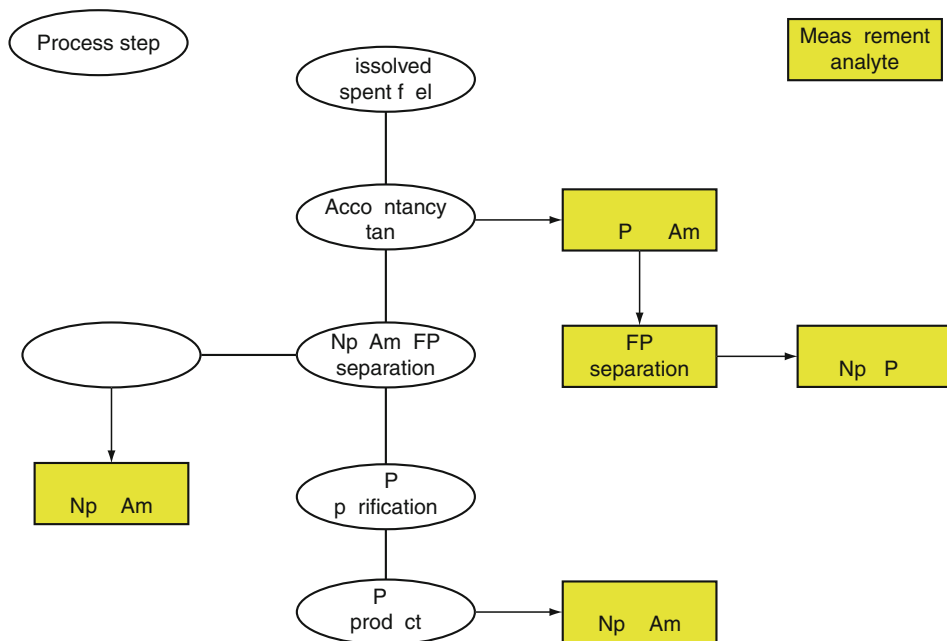
An attractive proposal is to combine U, Pu, Am verifications by HKED with a simple DA measurement of Np/Pu ratios (Ottmar et al. 2001) at spent fuel reprocessing and Pu fuel fabrication plants (Fig. 63.27).

A large arsenal of “conventional” methods exists for measurements that are more elaborate whenever this would be needed. Separated ANMs can be assayed by gravimetry, titration, or coulometry (Crossley 1988). Smaller or more dilute materials may be analyzed by spectrophotometry (ISO 1997; Kageyma et al. 2001), L X-ray fluorimetry (Benony et al. 1994), IDMS (Efurd et al. 1986), IDAS (Aggarwal et al. 2005) or isotope dilution gamma spectrometry (IDGS) (Sus et al. 1996). Gamma (Ludwig et al. 2008) or alpha spectrometry (ISO 2007c; Sus et al. 1998), differential pulse polarography (Cauchetier 1978), laser-induced fluorimetry (Stepanov et al. 1990a; Aleksandruk et al. 1991) are applicable to very dilute materials. The sensitivity of laser-induced photoacoustic spectrophotometry (LIPAS), developed to investigate actinide chemistry in dilute solutions, would allow to determine Am down to 10^{-8} M and Np down to 10^{-7} M (Ewart et al. 1987), with careful control of the oxidation state and chemical forms.

A review of “nonconventional” methods (Rosenberg 1992) concludes that ICPMS can be the most attractive and versatile instrument as it already is in environmental analyses (Varga et al. 2006), when combined with modern chromatographic separations (Vajda et al. 2009).

■ Fig. 63.27

Proposed scheme for the control of alternative nuclear materials at a spent fuel reprocessing plant with the HKED (Ottmar et al. 2001)



63.5 Environmental Sampling and Analysis to Verify the Completeness of State Declarations

63.5.1 Introduction

Starting from the inception of international safeguards under INFCIRC-66 and -153 type agreements, the main emphasis of IAEA safeguards inspections was to verify that declared nuclear material placed under safeguards was accounted for and had not been diverted for non-peaceful purposes. Concerns about the existence of undeclared nuclear materials or activities in states subject to comprehensive safeguards agreements were not directly addressed by the IAEA, with the assumption being that any such activities would be detected by other means. The IAEA's involvement in such investigations began with the implementation of United Nations Security Council Resolution 687 (United Nations Security Council 1991) following the expulsion of Iraqi armed forces from the territory of Kuwait in early 1991. UNSCR 687 entered into force on April 3, 1991, and specified that the IAEA, in conjunction with a UN Special Commission (UNSCOM), would carry out inspections inside Iraq for the destruction, removal, or rendering harmless of all "nuclear weapons or nuclear-weapons-usable material or any subsystems or components or any research, development, support or manufacturing facilities related to the above." The IAEA, in turn, set up an Action Team consisting of safeguards inspectors and experts, supplemented by experts supplied by its member states, to carry out these inspections aimed at understanding all aspects of the Iraqi nuclear activities carried out prior to 1991 in breach of their safeguards undertakings under the NPT.

The IAEA Action Team inspections in Iraq began in May, 1991, and continued until December 1998 during which time a number of previously unknown nuclear facilities and processes came to light, including the uranium recovery from phosphate ores at Al Jesira and Al Qaim, the electromagnetic isotope separation facilities at Al Tarmiya and Ash Sharqat, the centrifuge facility at Al Furat and the nuclear weapon design and explosive test facility at Al Atheer (Dillon 2002). The details of this undeclared nuclear development program were painstakingly pieced together from physical evidence (buildings and equipment), interviews with Iraqi scientists, documents seized by the inspectors and, last but not least, by measuring small traces of nuclear material in so-called “environmental samples” taken at known and suspected nuclear facilities in Iraq (Donohue and Zeissler 1993; Zeissler and Donohue 1995). The collection and analysis of such environmental samples were a completely new activity for the IAEA. It exposed the agency to a number of developments that had been carried out in the member states prior to that time. Among these were methods for sampling radioactive effluents in waterways, for taking swipe samples of dust in buildings and from equipment as well as the analysis of such samples by highly selective and sensitive methods such as the fission-track method combined with thermal ionization mass spectrometry (FT-TIMS).

The uncovering of the Iraqi undeclared nuclear program starting in 1991 demonstrated that the traditional nuclear accountancy-based safeguard system applied up to that time needed to be strengthened. Addressing the *correctness* of the states’ declarations was not a protection against a state that was determined to carry out undeclared nuclear activities for the production of special nuclear materials and with the intention of hiding this from IAEA safeguards inspectors. This revelation convinced the IAEA and its member states of the need to develop new approaches and tools to provide additional assurances about the *completeness* of the states’ declarations and the absence of undeclared materials and activities. The efforts to strengthen agency safeguards in light of these events was embodied in the Program 93+2, which was initiated in 1993 and was planned to finish in time to provide input to the NPT Review and Extension Conference planned for 1995 (IAEA 1994, 1995, 1996). Program 93+2 studied a number of strengthening measures such as the use of third-party or open-source information, use of satellite imagery and import-export information, as well as the logistics and optimized use of environmental sampling and analysis.

The environmental sampling activities under Program 93+2 focused on 12 field trials in which a wide variety of environmental samples were taken around known nuclear facilities in 11 member states (see ► Table 63.13).

The main conclusions from these field trials were that nuclear activities, especially those involving large amounts of nuclear or radioactive materials were detectable in the environment at distances of 10–20 kilometers by use of water, sediment, biota, and vegetation samples. However, the dilution effects were found to be large and the signatures were often mixed with global fallout or releases from other facilities. These effects tend to reduce the usefulness of such sampling for safeguards purposes and to raise the question of the cost-effectiveness of such sampling on a regular basis to detect undeclared activities in a wide-area approach (i.e., where the exact source of effluents is not known a priori). However, the field trials did demonstrate the utility and cost-effectiveness of swipe sampling inside facilities; the complete details of declared activities could be revealed by sensitive and selective analysis of such samples (see ► Sects. 63.5.5 and ► 63.5.6).

In parallel with the 93+2 field trials, the IAEA designed and constructed a special Clean Laboratory for Safeguards in Seibersdorf, Austria (see ► Sect. 63.5.3.1), which went into full operation in 1996. In the years since 1996, the environmental sampling for safeguards program

■ Table 63.13

Field trials of environmental sampling for safeguards under Program 93+2

Country	Facility	Date	Conclusions
Sweden	Power reactors, Research center	Sept 1993	Fission and activation products were seen in effluent water released in a coastal area
Hungary	Power reactor	Oct 1993	Elevated fission and activation products in a river were possibly due to Chernobyl accident
USA	Enrichment plant	Mar 1994	Enriched uranium could be seen in vegetation, water and sediment at a distance of several km
Japan	Reprocessing plant	Apr 1994	No clear indication of reprocessing could be seen in water released in a coastal area
South Africa	Enrichment plant	Apr 1994	Enriched uranium particles were seen in vegetation and swipes from vegetation as well as in swipes from inside buildings
Australia	Research center	Apr 1994	Enriched uranium used as targets for medical isotope production could be seen in swipe samples as well as depleted uranium used in research activities
Argentina	Enrichment plant	May 1994	Swipe sampling in buildings showed depleted and enriched uranium particles typical of enrichment operations
Indonesia	Research center	May 1994	Low levels of fission and activation products were seen in water and vegetation. Swipe samples taken in buildings showed low and high-enriched uranium particles from research and medical isotope production activities
Republic of Korea	Research center	June 1994	Water samples showed both depleted and enriched uranium associated with research and fuel fabrication activities. Swipe samples from buildings showed depleted and low-enriched uranium particles
UK	Reprocessing	Sept 1994	Fission products associated with fuel reprocessing were seen in water and vegetation; uranium particles found in swipe samples from process buildings were diagnostic of the processes carried out
Netherlands	Enrichment Plant	Dec 1994	No signatures of enrichment could be found in water, sediment, biota, or vegetation, but swipe samples from inside buildings showed depleted and enriched uranium particles representative of enrichment operations.
Japan	Enrichment	Mar 1995	No signatures of enrichment were found outside the facility, but swipe samples from inside buildings showed clear signatures of enrichment operations

has grown in terms of the number of samples taken and the number of facilities that have been sampled. Protocols have been implemented for all aspects of the program, including sample kit production, sample taking and shipment, screening, analysis at SAL/CL or in the network of analytical laboratories (NWAL) in the agency's member states, as well as the evaluation of the data and drawing of safeguards conclusions (IAEA 2005). Between 300 and 700 swipe samples

are taken each year by agency inspectors and each sample is subjected to screening and detailed analysis at two separate laboratories in order to obtain cross confirmation about the presence of any unexpected or undeclared nuclear materials present. The following sections give a detailed picture of the environmental sampling process.

63.5.2 Sampling, Conditioning, and Shipment of IAEA Safeguards Environmental Inspection Samples

63.5.2.1 Cotton Swipe and Other Swipe Materials

The basic IAEA swipe sampling kit (see [Fig. 63.28](#)) consists of six cotton wipers, which are 10 × 10 cm in size. Mini-grip bags of two different sizes are included to individually bag and double-bag the swipes after sampling; this double-bagging is the principle means to stop cross-contamination of the sample from that point onward. Each sampling kit also contains two pairs of clean-room latex gloves, a sample data sheet, pen, and extra labels. The kits are prepared in a Class 100/ISO Class 5 work area that is monitored before and after each batch

Fig. 63.28
Standard cotton swipe sampling kit



of kits is prepared to ensure that the cleanliness class is not exceeded. In addition, swipes are taken of the workbench before and after sample kit preparation and these swipes are analyzed by bulk and particle methods to detect unusually high levels of U or Pu or the presence of particles containing these elements. A certain number of unused kits from each production batch are also archived in case of future questions about their cleanliness. Finally, the cotton wipers used in making the kits are subjected to destructive (bulk) analysis whenever a new batch is received; typical levels of U in the wipers are from 1–3 ng whereas Pu is below the detection limits of the most sensitive techniques available (less than approximately 1 fg).

A second type of swipe material (designated Type-J) consists of cellulose material similar to filter paper with a circular center part of 2.5 cm diameter. These cellulose wipers are used to take swipe samples inside hot cells. Four wipers, attached to a plastic holder, are introduced into the hot cell of interest and used by the remote manipulators to take a swipe sample. Upon exiting the bank of hot cells, usually through a glove box, one of the wipers is detached and given to the facility operator for making radioactivity measurements that will determine the shipment conditions for the remaining three wipers that are sent back to the IAEA in Austria. Each of the three hot cell swipes is packaged in a plastic bottle that is bagged in a polyethylene mini-grip bag or heat-sealed in plastic (so-called bag-out) before being placed in a Pb or stainless steel container to provide a minimum of shielding for energetic beta or gamma radiation. The three shielded samples are then placed in a special sealable aluminum can and eventually in a steel drum or other container that is licensed for transport of excepted or type-A quantities of radioactive materials.

The Type-J wipers are also used to take samples in a certain enrichment facility under safeguards in a nuclear weapons state. The wiper is inserted in a special metal fitting (a so-called Koshelev fitting) that is part of the pipe-work connected to the enrichment cascade. Therefore, this sample comes into contact with the UF_6 gas in the pipe-work and can be used to detect the presence of material with higher ^{235}U enrichment than declared.

63.5.2.2 Air Filters

During the IAEA Action Team inspections in Iraq (see [Sect. 63.5.1](#)), a variety of sampling media were tested, in the context of non-site-specific or wide-area environmental sampling. In addition, various field trials of wide-area environmental sampling were carried out in which high-volume air samplers were employed. One such sampler is shown in [Fig. 63.29](#). It consists of a high-volume air blower system pulling ambient air through a 20×30 cm paper filter. Typical air volumes sampled by such devices are in the range 40–900 m³ per hour. Deployment of air filter samplers in a safeguards role presents the following challenges:

Each sampler must be supplied with electrical power and is subject to interruptions if used in an unattended mode.

Cameras or other systems would be needed to ensure that the sampler is not tampered with. Clogging of the filter medium with sand or high dust loading would limit the duty cycle between filter changes.

Analysis of the resulting filter samples would be possible by nondestructive methods such as gamma spectrometry or X-ray fluorescence but these do not represent the most sensitive methods. Bulk analysis would be affected by the high dust loading of the filter and perhaps by the filter material itself, e.g., glass-fiber filters would be difficult to destroy chemically

■ Fig. 63.29

High-volume air sampler



and would add unwanted elements. Particle analysis would present similar difficulties as with soil sampling.

Use of high-volume air samplers in a wide-area sampling scheme would be prohibitively expensive because a “grid” of samplers would be needed with samples collected every week, representing many hundreds or thousands of samples per year for a medium-sized area (for example, Iraq has an area of 438,000 km²).

For the reasons listed above, as well as owing to the large dilution effects that can be expected as a plume of effluent leaves a nuclear facility and travels down-wind, high-volume air sampling was not chosen as a routine sampling method for IAEA safeguards. The IAEA reserves the right to implement such wide-area sampling under the additional protocol (IAEA 1997) in those cases where it is both feasible and cost-effective.

63.5.2.3 Water, Soil, Vegetation, and Biota Samples

Samples of the true “environment” such as water from rivers and lakes, sediment, biota, vegetation, and soil, were taken in Iraq by the IAEA Action Team in the period 1991–1998 and during the field trials carried out under Program 93+2. Protocols and sampling equipment were developed and tested for these different sample types. One such device was a high-volume water sampling system based on a sample collection cartridge connected to a water pump powered by a 12 V battery, as shown in ▶ Fig. 63.30. The cartridge contains a paper filter to trap particulates and radionuclides adsorbed on particles and a mixed ion exchange bed to remove dissolved species such as ¹³⁷Cs. The flow rate through such a sampler is in the range of 200–300 liters per hour.

Fig. 63.30**High-volume water sampler and cartridge**

Sampling of soil, vegetation, and water-borne biota for safeguards purposes was performed during the 93+2 field trials using ad hoc methods developed at the time. Plastic mini-grip bags were used for soil and vegetation and 1 liter wide-mouth plastic bottles were used for biota sampling. A more systematic study of such sampling methods was carried out and special protocols were developed (Rose et al. 1997). Since that time, these types of samples have rarely been taken by IAEA inspectors and, therefore, will not be covered here in detail.

63.5.2.4 Process and Structural Materials

There is no limit to the types of materials that might be taken as safeguards samples in the search for undeclared activities. Elemental impurities can be used to trace the origin of nuclear materials through various stages of a technological process such as mining of uranium ore, concentration of the uranium in the form of yellowcake, conversion of yellowcake to UO_2 , further conversion to UF_6 for enrichment, etc. Elemental impurities are removed at each stage, until nuclear grade purity is achieved, but certain elements may be reintroduced coming from the reagents or vessels used. Although such information may be used to match two or more known materials, the sampling uncertainties and batch-to-batch nonreproducibility will make absolute source attribution much more difficult.

63.5.3 Safeguards Analytical Laboratories

63.5.3.1 Clean Laboratory for Safeguards

The role of the clean laboratory (CL) for safeguards as well as the structure of IAEA's environmental sampling for safeguards (ESS) program are described elsewhere

(Deron et al. 1996; Donohue 1998, 2002; IAEA 2003). The clean laboratory (CL) consists of two zones; the first zone of approximately 100 m² is maintained at a cleanliness level of “Class-100,000” according to the US Federal Standard 209E or ISO Class 8 according to the ISO Standard 14644-1. The CL is equipped for the measurement of samples using instrumental methods such as thermal ionization mass spectrometry (TIMS), inductively coupled plasma mass spectrometry (ICP-MS), scanning electron microscopy (SEM) in combination with X-ray spectrometry (XRS) and high-resolution gamma spectrometry (HRGS). A higher class of cleanliness is maintained in the second zone of the CL, also of approximately 100 m² area, where work surfaces are kept at US Class 100/ISO Class 5 for the chemical treatment of swipe samples and the production of certified clean sampling kits.

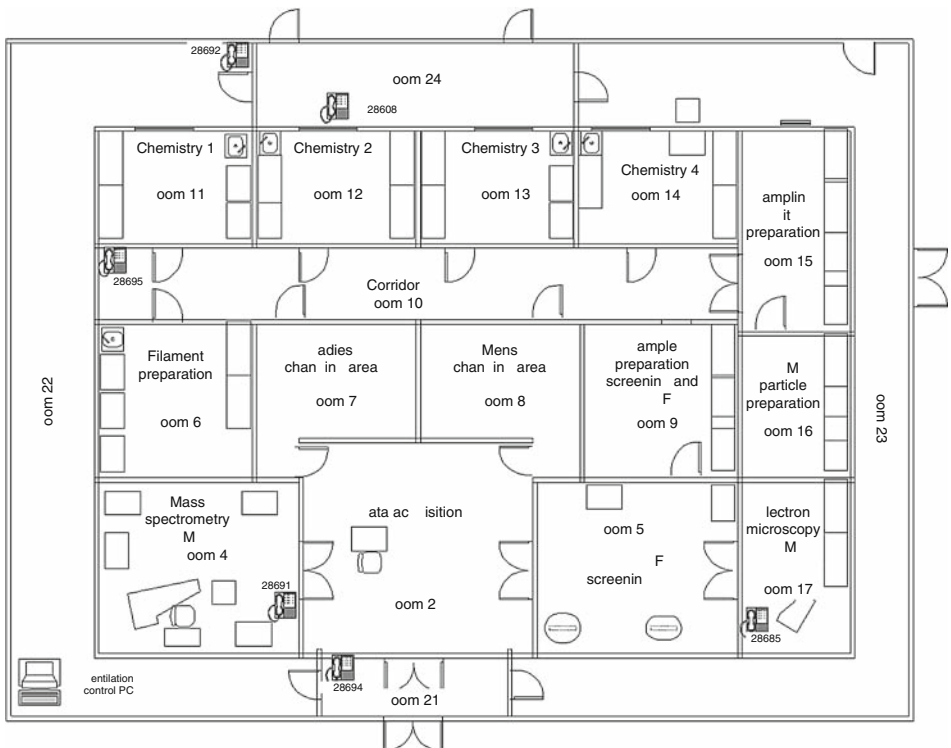
The CL was constructed in 1995 and entered into full operation in 1996 at the same time that the agency began to implement environmental sampling for safeguards (ESS) as a routine tool under existing legal authority. A floor plan of the CL is shown in [Fig. 63.31](#).

The CL was designed to support the following activities:

1. Preparation and certification of clean sampling kits and supplies for taking environmental samples. The number of sampling kits produced per year is approximately 1,000.
2. The receipt, book-in and recoding of up to 1,000 environmental samples per year. After initial cleaning of the outer sample bags and screening by high-resolution gamma

Fig. 63.31

Floor plan of the IAEA Clean Laboratory for Safeguards



spectrometry (HRGS) and X-ray fluorescence spectrometry, the samples are kept in archival storage until a detailed analytical request is received. It is IAEA policy to retain in the archive at least one subsample of every environmental sample received for an indefinite period. For this reason as well as others, it is sometimes necessary to split subsamples; this is done in a glove bag inside a Class-100 clean-air bench in order to avoid cross contamination.

3. Detailed bulk analysis of environmental samples according to an analytical request. Bulk analysis (see [Sect. 63.5.5](#)) refers to the complete dissolution of the subsample (usually a cotton or cellulose swipe), chemical treatment and measurement of U and Pu by thermal ionization mass spectrometry (TIMS, see [Sect. 63.5.5.3](#)) or inductively coupled plasma mass spectrometry (ICP-MS, see [Sect. 63.5.5.4](#)). Element concentrations are measured using the isotope dilution mass spectrometry (IDMS) method. In addition to U and Pu, the element Am is sometimes measured using either ICP-MS or alpha spectrometry.
4. Particle analysis of environmental samples by secondary ion mass spectrometry (SIMS, see [Sect. 63.5.6.3](#)) or scanning electron microscopy in combination with X-ray spectrometry (SEM-XRS, see [Sect. 63.5.6.4](#)). The SEM-XRS instrument and its sample-preparation area are located in the clean laboratory, but the SIMS instrument is not. Sample preparation for SIMS can be carried out in the CL, but a small dedicated clean-room at US Class-100/ISO-Class 5 cleanliness level is colocated with the instrument to avoid potential cross contamination when transporting the prepared sample planchets to the instrument. The SEM-XRS method is also supported in the CL by an array of optical microscopes equipped with micromanipulation systems for picking up particles of interest prior to further treatment such as chemical analysis and isotopic measurement by TIMS or ICP-MS.

In general, the CL is operated as a mixed-flow clean-room facility, meaning that the Class-100/ISO Class 5 areas are the workbenches and fume cupboards in the various rooms, rather than the entire room. A laminar flow of clean air falls from high-performance particulate (HEPA) filters in the suspended ceiling of the room and is directed to the work area by plastic curtains. Certain clean laboratories in the network employ full laminar flow in the rooms at US Class 10/ISO Class 4 cleanliness conditions. The most sensitive measure of effectiveness is the blank levels of U and Pu that can be achieved, rather than the chosen cleanliness class. Blanks consist of the following types:

1. Reagents used in the chemical treatment of the samples for bulk analysis (“process blank”). These are typically ultra-pure mineral acids such as HNO_3 or HCl as well as reducing agents such as HBr or HI and highly pure water (18 M Ω).
2. Blanks of the swipe sample matrix (“swipe blank”) after each processing step. The swipe blank contains the process blank as well as any U, Pu or interfering elements contained in the swipe material. The cotton wipers chosen for swipe sampling are generally quite low in U content – 1–5 ng per wiper – and the Pu content is not measurable by bulk analysis: it is believed to be below 1 fg (the most likely source would be Pu from nuclear weapons fallout).
3. Blanks of the air in a clean-room laboratory or other working area (“room blank”). These are collected in a petri dish of approximately 100 cm² area that is left exposed on a surface for 1–2 weeks. Then, U and Pu are recovered with concentrated HNO_3 , spiked with tracers of ²³³U and ²⁴²Pu, and subjected to bulk analysis by ICP-MS. Typical values in a Class 100/ISO Class 5 working area are in the range 0.1–0.2 fg/cm² – hour for U and below the detection limit of the ICP-MS method for Pu (estimated to be 10⁴ times lower).

The IAEA Clean Laboratory for Safeguards is certified annually to meet the specified cleanliness standards by an outside organization.

63.5.3.2 The Network of Analytical Laboratories (NWAL) of the IAEA

The IAEA collaborates with a number of laboratories in the member states that form a network dedicated to the analysis of environmental samples for safeguards. ▶ [Table 63.14](#) lists the members of this network and the analytical services they offer.

63.5.4 Sample Screening Methods

Screening of incoming environmental samples is performed to obtain information that will guide the further detailed analysis and to assist in the shipment of samples to the NWAL. Samples that are known to be radioactive for the purposes of shipment from the field to the IAEA are delivered directly to the nuclear laboratory of SAL for screening and archival storage because the CL is not licensed to handle such materials. All samples known to be below the limits for radioactive shipment purposes are delivered to the CL where they are screened,

■ **Table 63.14**

Member laboratories of the IAEA NWAL for environmental sample analyses. Techniques in use by the NWAL include FT-TIMS = fission-track thermal ionization mass spectrometry, AMS = accelerator mass spectrometry, SIMS = secondary ion mass spectrometry, HRGS = high-resolution gamma spectrometry, TIMS = thermal ionization mass spectrometry, ICP-MS = inductively coupled plasma mass spectrometry, SEM = scanning electron microscopy

Laboratory	Particle analysis	Bulk analysis
U.K. Atomic Energy Authority – Aldermaston, U.K.	FT-TIMS	
QinetiQ – Malvern, U.K.	SIMS	
Australian Nuclear Science and Technology Organization, Lucas Heights, Australia		AMS
Air Force Technical Applications Center – Patrick Air Force Base, Florida, U.S.A	FT-TIMS	
U.S. Department of Energy – Oak Ridge National Laboratory, Los Alamos National Laboratory, Pacific Northwest National Laboratory, Lawrence Livermore National Laboratory		HRGS, TIMS and ICP-MS
Commissariat à l’Énergie Atomique, Bruyères-le Chatel, France	FT-TIMS	
European Commission Joint Research Centre Institute for Transuranium Elements, Karlsruhe, Germany	SIMS	HRGS, TIMS and ICP-MS
Khlopin Radium Institute, St. Petersburg, Russian Federation		HRGS, TIMS
Laboratory for Microparticle Analysis, Moscow, Russian Federation	SIMS	
Japan Atomic Energy Research Institute, Tokai-mura, Japan	SIMS, SEM, FT-TIMS	HRGS, TIMS

archived, analyzed, or transferred to the NWAL. The limits for declaring a sample as radioactive for the purposes of shipment are described in the International Air Transport Authority (IATA 2010) regulations, which are based on the IAEA Regulations for the Safe Transport of Radioactive Materials (IAEA 2009a). So-called “cold” or non-radioactive environmental samples can actually contain a measurable amount of alpha, beta, or gamma radioactivity as long as they fall below the limits given in the above regulations. This is why HRGS screening is performed on all environmental samples received, regardless of their status under the shipping regulations.

63.5.4.1 Gamma Spectrometry

Screening of all environmental samples is performed by HRGS either in the CL for “cold” samples or in the nuclear laboratory of SAL for “radioactive” samples (Parus et al. 2003; Carchon et al. 2007). Cotton swipes and cellulose (Type-J) swipes are placed in a Marinelli beaker to maximize collection efficiency. The samples are measured with a coaxial Ge detector system in the CL for a typical measurement time of 6 hours. Samples that are known to be more active are measured in SAL at greater distance from the detector or for shorter periods using gamma spectrometers with high-purity planar Ge detectors.

The range of gamma-ray energies measured with these systems is from 20 keV to 2,620 keV, which allows the measurement of most fission and activation products expected to be found in environmental samples. The nuclides of interest, their half-lives and main gamma-ray energies are shown in ▶ [Table 63.15](#). The data from HRGS screening are evaluated with commercial software using energy and efficiency calibration data from the measurement of reference material samples. The result is a report for each sample of those nuclides that were detected above the detection limit or the minimum detectable amount for all other nuclides of interest.

63.5.4.2 X-Ray Fluorescence Spectrometry

In addition to the HRGS screening that is performed on all environmental samples received by the IAEA, X-ray fluorescence (XRF) screening is performed on all “cold” samples in the CL to detect significant amounts of U. This screening is useful for the CL and network laboratories in their further processing of the samples in case the amount of U present represents an increased risk of cross contamination. The equipment for this screening consists of a 100 W X-ray generator with Rh anode and end-window configuration, a robotic arm for manipulation of the samples (usually a single cotton swipe in a plastic bag held in a metal frame), and two X-ray detectors (a high-purity Ge detector and a Si(Li) detector). The Si(Li) detector is equipped with an energy filter (Bragg filter using single-crystal graphite strips) tuned to the L-alpha energy of U (13.6 KeV). This system, referred to as “Tripod I,” has a detection capability of approximately 35 ng/cm² for U with a 4 hour measurement time and the data can be displayed as an elemental map.

63.5.5 Bulk Sample Analysis

The purpose of bulk analysis is to detect U and Pu at the lowest possible levels and to measure both their concentration and isotopic composition. This process involves destruction of the

■ **Table 63.15**

List of radionuclides expected in environmental samples

Nuclide	Half-life	γ -line (keV)	Nuclide	Half-life	γ -line (keV)
⁵¹ Cr	27.7 days	320.1	¹²⁴ Sb	60.2 days	602.7(1,691)
⁵⁴ Mn	312.1 days	834.8	¹²⁵ I	59.41 days	35.5
⁵⁷ Co	271.8 days	122.1	¹²⁵ Sb	2.758 a	427.9
⁵⁸ Co	70.8 days	810.8	^{125m} Te	57.4 days	35.5(109.3)
⁵⁹ Fe	44.5 days	1,099.3	^{127m} Te	109 days	88.3
⁶⁰ Co	5.27 a	1,332.5	^{129m} Te	33.6 days	459.6
⁶⁵ Zn	244.3 days	1,115.5	¹³¹ I	8.02 days	364.5
⁷⁵ Se	119.8 days	264.7	¹³⁴ Cs	2.062 a	604.7
^{91m} Nb	60.9 days	1,204.7	¹³⁷ Cs	30.017 a	661.6
^{92m} Nb	10.15 days	934.4	¹⁴⁰ Ba	12.75 days	537.3
^{95m} Nb	86.6 h	235.7	¹⁴⁰ La	1.678 days	1,596.2
⁹⁵ Nb	34.97 days	765.8	¹⁴¹ Ce	32.5 days	145.4
⁹⁵ Zr	64.02 days	756.7	¹⁴⁴ Ce, ¹⁴⁴ Pr	284.89 days	696.5
⁹⁹ Mo	65.94 h	739.5	¹⁵² Eu	13.54 a	121.78
^{99m} Tc	6.01 h	140.5	¹⁵⁴ Eu	8.59 a	1,274.4
^{102m} Rh	2.9 a	475.1	¹⁵⁵ Eu	4.76 a	86.5(105.3)
¹⁰³ Ru	39.26 days	497.1	¹⁹² Ir	73.83 days	205.8(484.6)
¹⁰⁶ Ru, ¹⁰⁶ Rh	373.6 days	621.9(511.9)	²⁰³ Hg	46.6 days	279.2
^{108m} Ag	418 a	722.9(433.9)	²³¹ Th	25.52 h	25.64
¹⁰⁹ Cd	462.6 days	88.03	^{234m} Pa	1.17 min	1,001.03
^{110m} Ag	249.8 days	657.8	²³⁴ Th	24.1 days	63.29
^{121m} Te	154 days	212.2	²³⁴ U	2.455E+5 a	53.2
¹²¹ Te	16.78 days	573.1	²³⁵ U	7.038E+8 a	185.71
¹²² Sb	2.70 days	564.2	²³⁷ Np	2.14E+6 a	86.48
^{123m} Te	119.7 days	159.0	²³⁹ Pu	24,110 a	129.30
¹²⁴ I	4.18 days	602.7	²⁴¹ Am	432.2 a	59.54

sample matrix (usually cotton or cellulose swipes) by high-temperature ashing followed by dissolution in strong mineral acid. The resulting solution is split in two equal parts and one part is kept as an archive in case problems should occur with the other fraction. The fraction of the original solution to be measured is split again into portions that will result in U and Pu concentration determination by use of the IDMS method and fractions that will be processed for U and Pu isotopic composition measurements.

63.5.5.1 Tracers

The primary tracers used for bulk analysis are shown in ► [Table 63.16](#). They are produced by the Institute for Reference Materials and Measurements in Geel, Belgium.

■ Table 63.16

Tracers used for isotope dilution mass spectrometry

Tracer	Isotope ratio	Isotope amount ratio
IRMM-057 (^{233}U Spike)	$^{234}\text{U}/^{233}\text{U}$	0.000352 (14)
	$^{235}\text{U}/^{233}\text{U}$	0.000004124 (29)
	$^{236}\text{U}/^{233}\text{U}$	0.0000000434 (14)
	$^{238}\text{U}/^{233}\text{U}$	0.00001043 (21)
IRMM-044 (^{242}Pu Spike)	$^{238}\text{Pu}/^{242}\text{Pu}$	0.000009 (6)
	$^{239}\text{Pu}/^{242}\text{Pu}$	0.000827 (4)
	$^{240}\text{Pu}/^{242}\text{Pu}$	0.000108 (4)
	$^{241}\text{Pu}/^{242}\text{Pu}$	0.000009 (4)
	$^{244}\text{Pu}/^{242}\text{Pu}$	0.000015 (4)

Note: IRMM-057 certificate date February 2003; IRMM-044 validity date 30.06.1989.

63.5.5.2 Sample Preparations and Separations

The procedure for chemical separation of these various aliquots is based on anion exchange and solvent extraction chromatography using AG MP-2 anion exchange resin in HNO_3 medium and UTEVA (Eichrom Corp.) in HNO_3 and HCl media. The basic steps in a bulk-analysis preparation scheme are listed below (Shinonaga 2008):

1. The swipe is placed in a covered quartz tube and ashed in an oven at 600°C for 8–10 h. A blank swipe and an empty quartz tube are treated at the same time to provide the swipe and process blank values.
2. The ash is dissolved in 16 M HNO_3 and dried and re-dissolved several times. It is then treated with H_2O_2 and aqua regia to complete the oxidation and sample destruction process and a “mother” solution is re-dissolved in 8 M HNO_3 .
3. The mother solution is split into 3 parts; 20% will be used for U IDMS and ^{238}Pu analysis by TIMS, and alpha spectrometry, respectively. Forty percent will be used for U isotopic analysis, and Pu elemental and isotopic analysis by IDMS (there is no un-spiked Pu fraction and Pu isotopic composition will be estimated by isotopic stripping of the ^{242}Pu spike). The rest (40%) of the solution is kept as an archive.
4. High-purity isotopic spikes of ^{233}U (IRMM-057) and ^{242}Pu (IRMM-044) are added to the 20% and 40% fractions, respectively, and the isotopes are equilibrated by repeated drying and re-dissolution in 16 M HNO_3 and treatment with H_2O_2 .
5. Resin columns containing AG MP-2 and UTEVA are prepared in nitrate form in 8 M HNO_3 . The sample fraction is loaded on the MP-2 column in 8 M HNO_3 and rinsed further with 8 M HNO_3 with the eluate going into the UTEVA column. The MP-2 column is further processed for Pu analysis and the UTEVA column is further processed for U analysis.
6. The Pu is eluted from the MP-2 column with a mixture of 9 M HCl and 1 M HI , then the Iodine is removed by repeated fuming with 10 M HCl . This Pu fraction is further cleaned using an MP-2 column in the chloride form and elution with $\text{HCl-H}_2\text{O}_2$ and HBr . This fraction is finally taken up in 16 M HNO_3 .

7. The U on the UTEVA column is eluted with 0.05 M HCl, dried and re-dissolved in 10 M HCl. This fraction is then further purified with an MP-2 column in the chloride form at a molarity of 10 M HCl. The U is finally eluted with 0.05 M HCl, dried, and converted to the nitrate form with 16 M HNO₃.

63.5.5.3 Thermal Ionization Mass Spectrometry

The measurement of U IDMS and U isotopic fractions from the chemical separation shown above are performed on a Thermo-Fisher Triton mass spectrometer equipped with a single-ion counting detection system (Thermo Fischer Scientific: Triton 2005). Therefore, a peak-jumping measurement scheme is used along with manual sample filament heating procedure to optimize the signal intensity prior to data acquisition. Depending on signal intensity, one or two blocks of data are taken – consisting of 20 scans each. A single block takes approximately 20 minutes. The isotopes of U from 233 to 238 are symmetrically scanned to cancel out drift in signal intensity during the scan. Typical count rates for a 1–2 ng filament loading are 20,000–50,000 ion counts per second for the major isotope present.

63.5.5.4 Inductively Coupled Plasma Mass Spectrometry

In the past decade, ICP-MS instruments have become sufficiently sensitive and stable to offer an attractive alternative to the traditional TIMS measurements for bulk analysis of U and, especially, Pu. The ICP-MS method offers the advantage that samples are presented to the instrument in solution form which eliminated the filament-loading step and filament-blank considerations that are seen with TIMS. An additional advantage is the more constant sensitivity of the ICP plasma ion source and the absence of interference effects that suppress ionization of the element of interest. On the other hand, the ICP source produces a much larger number of molecular ion interferences that affect the accuracy of a Pu measurement, especially at near the detection limit (low parts per quadrillion, ppq). The best approach for these interferences is to remove all possible interfering elements during the chemical preparation of the samples. In any case, the potential interferences must be measured at some point during the analysis of a sample to ensure that they are below the threshold for significant contribution to the masses of interest (²³⁸Pu through ²⁴⁴Pu). In those cases where the interfering elements are above this threshold, a correction can be made for them, based on the “formation co-efficient” that relates the ion signal of the interfering element to the production of molecular species at the mass of a plutonium isotope. This correction procedure will naturally increase the uncertainty of the final Pu isotopic data, in some cases significantly.

The ICP-MS instrument used in the IAEA Clean Laboratory is the Thermo-Finnigan Element 2. It uses a magnetic sector double-focusing mass spectrometer with single-ion counting detector system and peak-jumping data collection. The quoted sensitivity with a concentric nebulizer is 10⁹ cps per ppm, which gives a theoretical sensitivity of 1 ppq for elements that do not suffer molecular interference effects. Special de-solvating nebulizers such as the Apex Q (Elemental Scientific Corp.) can improve the sensitivity further.

63.5.6 Particle Analysis

Early in the environmental sampling program of the IAEA it was recognized that the analysis of individual micrometer-sized particles was a source of unique information about nuclear materials and activities. ▶ [Table 63.17](#) shows the calculated composition of 1 μm diameter particles coming from various nuclear processes. Thus, it can be seen that a pure particle of natural U oxide (“NU”) contains about 10^{10} U atoms in total and that when this particle is irradiated in a reactor, approximately 5 million atoms of ^{239}Pu would be created. Furthermore, a particle of high-enriched uranium (“HEU”) would produce only small numbers of ^{231}Pa and ^{232}Th daughter atoms in 10 years of decay. To be able to “age-date” such a particle would involve measurement of these small components, something which is currently not possible with the most sensitive techniques.

The above considerations show that particles contain small amounts of material, but that the major isotopes would be easily measurable by sophisticated methods such as TIMS or ICP-MS. One of the most challenging aspects of particle analysis for safeguards is the methods used to locate the particles of interest in a “sea” of uninteresting environmental materials such as minerals and organic particles like pollen and fibers. The detection and location of particles containing fissile nuclides such as ^{235}U and ^{239}Pu can be accomplished by the fission-track technique (Fleischer et al. 1975). This method is based on creating a close contact between the particles and a polycarbonate plastic surface (Lexan) which is then irradiated in a nuclear reactor at high thermal neutron fluence (approximately $1 \times 10^{15} \text{ n/cm}^2$) for several minutes. During this irradiation, atoms of the fissile isotopes will undergo fission and the energetic fission fragments will leave damage tracks in the plastic material. After separation of the particle layer from the Lexan, it is etched in NaOH solution to make the damage tracks visible under an optical microscope. The selectivity of this method is very high because no other particles will leave such tracks and the number of tracks compared to the size of the particle gives a clue to the presence of enriched U or Pu because natural U with a ^{235}U content of 0.7% only leaves a small number of tracks in comparison. The fission-track method has been

■ **Table 63.17**

Composition of typical 1 μm diameter particles found in nuclear facilities

Nuclide	NU	Irradiated NU (700 MWD/T)	LEU (4%)	Irradiated LEU (30 GWD/T)	HEU (93%)	Decay of HEU (10 years)
U-238	9,900 M	9,900 M	9,600 M	9,310 M	600 M	
U-236	<1	1.2 M	<1	45 M	<1	
U-235	72 M	64 M	400 M	155 M	9,300 M	
U-234	550 K	530 K	3,600 K	2,500 K	100 M	
Pu-239		5.5 M		57 M		
Pa-231						92
Th-230						2,820

Note: GWD/T = gigawatt-days per ton; MWD/T = megawatt days per ton; LEU 4% = low-enriched uranium with 4% abundance of ^{235}U .

combined with thermal ionization mass spectrometry (FT-TIMS) to provide a powerful method to locate particles containing U or Pu and then to measure their isotopic composition with high sensitivity and accuracy. A calculation of the number of U atoms needed to produce one fission track in Lexan under nominal irradiation conditions is about 10^7 or 4 fg, keeping in mind that a 1 μm diameter particle would contain about 5 pg of U. Furthermore, if such a particle can be manipulated and mounted on a filament for measurement by TIMS, the efficiency of ion collection would be in the range of 0.1–1%, i.e., one ion detected for every 100–1,000 atoms loaded. A particle containing 10^{10} atoms would therefore provide a minimum of 10^7 ions at the mass spectrometer output. Thus, minor isotopes such as ^{234}U or ^{236}U could be measured with counting-statistics limited accuracy of several percent relative and the ^{235}U could be measured with less than 1% relative uncertainty. These calculations are borne out by actual measurement data from the network laboratories that perform FT-TIMS measurements (Stetzer et al. 2004; Park et al. 2006; Usuda et al. 2006).

63.5.6.1 Sample Preparation

Most particle-analysis methods (SEM, SIMS and FT-TIMS) require the removal of particles from the swipe substrate and deposition on a flat surface. In the case of FT-TIMS, the particles are removed by ultrasonic treatment in a suitable suspension medium such as ethanol or siloxane. The suspension is then mixed with collodion and dried as a thin layer on the Lexan plastic for irradiation. After irradiation, this collodion layer can be peeled off to allow chemical etching of the fission tracks in the plastic. The collodion layer can also be replaced on the Lexan after etching with a slight offset so that the particles and tracks are visible under a light microscope at magnification 250–500. Replacement of the collodion layer is not necessary if a comparator microscope is available that allows viewing two objects (i.e., the collodion layer and the Lexan with tracks) simultaneously.

For both SEM and SIMS, the only requirement is that particles should be deposited on a polished flat and conducting surface; pyrolytic graphite planchets with a diameter of 2.5 cm are frequently used. The particles are deposited from suspension or can be deposited using a vacuum extractor system in which the planchet acts as an impactor in a flow of gas with the particles entrained. The one disadvantage of the vacuum extractor is that many particles bounce off the planchet and often a type of sticking agent (polyisobutylene in nonane) is applied and later removed by heating at 250°C. In all procedures where ultrasonic removal and suspension in an organic liquid are used, care must be taken to avoid cutting the swipe material because it results in many organic fibers on the planchet that can accumulate charge and deflect the electron or ion beam of the final measurement instrument. Care is also needed in all methods of particle deposition to avoid too thick a deposit where particles are on top of each other or too close together to allow unambiguous measurements. An optimal spacing between particles is 10–20 μm .

63.5.6.2 Thermal Ionization Mass Spectrometry

The basic processes in TIMS, which apply equally to the measurement of particles, have been published elsewhere (Duckworth et al. 1986). In TIMS, the particle is deposited on a pure metal filament; typical filament materials are W, Ta, and Re which have been purified by

zone-refining to greater than 99.99% purity in order to remove possible U background. In the vacuum system of the mass spectrometer, the filament is heated by passing a current of several amperes through it until it reaches a temperature of 1,400–1,800°C. At these temperatures, the elements Pu and U tend to evaporate from the particle in contact with the filament surface and a certain fraction of these atoms will leave as positive ions. The ratio between neutral and ionic species is given by the Saha-Langmuir equation (Duckworth et al. 1986):

$$N_+ = N_0 \exp[e(\omega - \varphi)]/kT, \quad (63.12)$$

where N_+ is the number of positive ions produced, N_0 is the number of neutral atoms produced, $e\varphi$ is the ionization potential of the element, $e\omega$ is the work function of the surface, k is the Boltzmann constant, and T is the absolute temperature of the filament surface.

The main challenge of single-filament TIMS is that there is a competition between evaporation of the analyte atoms and their ionization; a higher temperature favors ionization but accelerates the loss of material from the filament. In situations where the amount of sample element is severely limited, this competition is a serious challenge. Use of separate evaporation and ionization filaments allows the analyst to better control both processes but the geometrical coupling between the two filaments separated by about 1 cm means that the overall ionization efficiency is reduced. Under the best of circumstances, the ion production efficiency of a thermal ion source is in the range 0.1 to 1% (ions collected per atom loaded). The sensitivity of TIMS for low levels of actinide elements has been demonstrated in many laboratories (Elliott et al. 2006; Buerger et al. 2009; Kraiem et al. 2010).

Modern TIMS instruments combine a single magnetic sector with multi-ion detection systems, although the use of multiple ion counters is not yet mature and many laboratories continue to use a single-ion counting detector and peak jumping. Use of multiple Faraday collectors is a mature technology with excellent methods to inter-calibrate the collectors, but the ion signals and consequent sample amounts must be high for this method and it is not commonly used with ultra-low amounts (pg-ng) as found in environmental samples. Use of a reverse polarity quadrupole filter before the ion-counting detector is also used to reduce the tailing of ions from major isotopes, thus improving the abundance sensitivity from a value of 10^6 to around 10^8 .

63.5.6.3 Secondary Ion Mass Spectrometry

A description of the basic operation of a SIMS instrument is also found elsewhere (Duckworth et al. 1986). The basic principle is the bombardment of the sample surface with energetic ions (typically O_2^+ at 10–15 keV of energy). The interaction of these ions with the sample atoms results in sputtering of material from the surface. A small fraction of the sputtered material is in the form of positive secondary ions, which can be accelerated into an ion lens and analyzed in a double-focusing mass spectrometer. Raster scanning of the primary ion beam and synchronous display of the detected ions will provide an ion image showing local concentrations of that isotope. The ion microscope produces a similar image through stigmatic imaging of the secondary ions and their detection by a position-sensitive ion detector system. In the case of particle analysis, the particles removed from a swipe sample are deposited on a flat conductive surface and illuminated by the primary ion beam. The ion image of this field (typically $150 \times 150 \mu m^2$) will show the presence of particles in the 0.5–10 μm diameter range that contain, e.g., either ^{235}U or ^{238}U . Mathematically comparing these two images will yield the

“enrichment” of the particles. Measurement of an area on the planchet of 1 cm^2 using fields of $150 \times 150 \text{ }\mu\text{m}$ in size takes approximately 6–8 hours.

The sensitivity of SIMS for U particles is limited by the secondary-ion production and extraction efficiency, which is approximately 0.1% under typical measurement conditions (Tamborini et al. 2004). Therefore, a U particle of $1 \text{ }\mu\text{m}$ diameter containing 10^{10} total U atoms would be expected to yield approximately 10^7 ions of the major isotope (^{238}U) and approximately 10^5 ions of the minor isotope (^{235}U) under ideal conditions. Practical considerations such as pre-sputtering and duty cycle would reduce these values by as much as a factor of 10. The result is that the enrichment or ratio of $^{235}\text{U}/^{238}\text{U}$ can only be measured with 1–5% uncertainty for a pure U particle that is $1 \text{ }\mu\text{m}$ in size. Realistic particles encountered in environmental samples are frequently smaller or less pure, and certain interference effects can also reduce the quality of such data. An obvious improvement is offered by a large-geometry SIMS instrument like the Cameca IMS-1280 that has significantly higher sensitivity and resolution to reduce the effects of molecular ion interferences (Ranebo et al. 2009).

63.5.6.4 Scanning Electron Microscopy with X-Ray Spectrometry

Another method to locate particles containing elements of interest is the scanning electron microscope combined with energy-dispersive X-ray spectrometry (SEM-XRS). The SEM instrument used in the clean laboratory consists of a JEOL 6490 SEM with Oxford INCA X-ray spectrometer. The software supplied with this instrument allows an automated search capability in which a specified area of the sample planchet is sequentially scanned in fields of approximately $100 \times 100 \text{ }\mu\text{m}$. The backscattered electron detector is used to detect particles containing high-Z (atomic number) elements. When such a particle is detected, the energy-dispersive X-ray spectrum of the particle is accumulated for a specified time such as 10 s, the resulting spectrum is stored and the search continues. At the end of an analysis, which may take many hours, the data can be sorted according to the element of interest and particles revisited for further analysis, either by energy-dispersive XRS or wavelength-dispersive XRS, which is capable of measuring elemental composition with reasonable accuracy down to element ratios of 1 part per thousand (0.1%). Particles identified in this way can be manipulated inside the vacuum system of the SEM or offline with an optical microscope and further analysis can be carried out by bulk, SIMS, or other mass spectrometric methods to obtain a complete elemental and isotopic analysis of a single interesting particle.

References

- Abhold ME, Baker MC, Bourret S, Polk P, Vo DT, Ishikawa M, Sao Y, Uchikoshi S, Yokota Y (2001) In: 42nd INMM annual meeting, Indian Wells
- Agboraw E, Johnson S, Creusot C, Poirier S, Saukkonen H, Chesnay B, Sequeira V (2006) In: IAEA symposium on international safeguards, IAEA-CN-148/200, Vienna, Austria
- Aggarwal SK, Alamelu D (2005) Novel approach for determining ^{238}Pu by TIMS using IEC method. *Int J Mass Spectrom* 241:83
- Aggarwal SK, Chitambar SA, Kavimandan VD, Almaula AI, Shah PM, Parab AR, Sant VL, Jain HC, Ramaniah MV (1980) Precision and accuracy in the determination of $^{238}\text{Pu}/(^{239}\text{Pu} + ^{240}\text{Pu})$ alpha activity ratio by alpha spectrometry. *Radiochim Acta* 27(1):1–5
- Aggarwal SK, Choursiya G, Duggal RK, Singh CP, Rawat AS, Jain HC (1985) A comparative study of different methods of preparation of sources for alpha spectrometry of plutonium. *Nucl Instrum Methods Phys Res A* 238(2/3):463–468

- Aggarwal SK, Duggal RK, Shah PM, Rao R, Jain HC (1988) Experimental evaluation of the characteristic features of passivated ion implanted and surface barrier detectors for alpha spectrometry of plutonium. *J Radioanal Nucl Chem Ar* 120(1):29–39
- Aggarwal SK, Fiedler R, Deron S (1999) Isotope ratio measurements for plutonium in isotopic reference materials by thermal ionisation mass spectrometry (TIMS) using total evaporation technique. In: *Proceedings of eighth ISMAS symposium on mass spectrometry, Mumbai, vol 2*, pp 863–868
- Aggarwal SK, Alamelu D, Mirashi NN, Shah PM (2005) A comparison of alpha spectrum evaluation methods for the determination of $^{241}\text{Am}/^{243}\text{Am}$ alpha-activity ratio using alpha spectrometry, NUCAR-2005. In: *Proceedings of DAE-BRNS symposium on nuclear and radiochemistry Mumbai (India)*, Bhabha Atomic Research Centre 2005, pp 491–492(729 pp)
- Ahmed I, Arlt R, Hiermann A, Ivanov V, Qasim KG (2001) In: *IAEA symposium on international safeguards, IAEA-SM-367/7/03/P*
- Aigner H, Aigner M (1994) Design and operation of a robot for NBL modified Davies/Gray potentiometric titration method applied to U product samples, IAEA-SM-333/143P, IAEA, Vienna
- Aigner H, Binner R, Kuhn E, Blohm-Hieber U, Mayer K, Guardini S, Pietri C, Rappinger B, Mitterrand B, Reed J, Mafra-Guidicini O, Deron S (2002) *ESARDA Bulletin* 31:39–68
- Aleksandruk VM, Babaev AS, Dem'yanova TA, Stepanov AV (1991) Fluorescent determination of neptunium in plutonium, EUR-13686, 13. In: *Annual symposium on safeguards and nuclear material management, Avignon, France, 14–16 May*, pp 215–218(745 pp)
- Ali S, Terracol SF, Drury OB, Friedrich S (2006) *Nucl Instrum Methods Phys Res A* 559:542–544
- Ali S, Hau ID, Niedermayr TR, Friedrich S (2008) *J Radioanal Nucl Chem* 276(3):749–753
- Amoudry F (1983) SMMA alpha spectrum deconvolution code, CEA-N-2366
- Amoudry F, Burger P (1984) Determination of $^{239}\text{Pu}/^{240}\text{Pu}$ isotopic ratio by high resolution alpha-particle spectrometry, alpha-particle spectrometry and low-level measurement, Harwell, 10–13 May 1983, CEA-CONF-6775; *Nucl Instrum Methods Phys Res* 223:360
- Amoudry F, Eloy JF (1984) Alpha sources deposit by sublimation, CEA-N-2362, (Sep 1983). *Int J Appl Radiat Isot* 35:259
- Amoudry F, Silly M (1981) Method for processing alpha spectra adapted for measuring plutonium, americium and curium by isotopic dilution. In: *ICRM meeting on alpha-spectrometry, Geel, 14–16 Oct 1981, Proceedings, CEA-CONF-6116*, p 28
- Amoudry F, Silly M (1984) Method of alpha-particle spectrometric analysis applied to the measurement of plutonium, americium and curium. *Int J Appl Radiat Isot* 35:259
- Angeletti LM, Bartscher WJ, Maurice MJ (1969) *Z Anal Chem* 246:297
- Annese C, Monteith A, Whichello J, Swinhoe M, Tobin S, Koskelo M, Tolk K (2009) *J Nucl Mater Manag* 37(4):49–60
- ANSI (1972) American National Standard N15.7, ANSI
- Aparo M, Arenas Carrasco J, Arlt R, Bytchkov V, Esmailpour K, Heinchen O, Hiermann A (1999) In: *21st ESARDA annual meeting: symposium on safeguards and nuclear material management, Sevilla, Spain*, pp 351–360
- Araujo J, Madueme G, El-Osery I, Aparo M (2001) In: *42nd INMM annual meeting, Indian Wells*
- Arlt R, Rundquist DE (1996) *Nucl Instrum Methods Phys Res A* 380:455
- Arlt R, Czock K-H, Rundquist DE (1992) *Nucl Instrum Methods Phys Res A* 322:575
- Arlt R, Rundquist DE, Bot D, Siffert P, Richter M, Khusainov A, Ivanov V, Chrunov A, Petuchov Y, Levai F, Desi S, Tarvainen M, Ahmed I (1993) In: *Proceedings Material Research Society symposium, April 1993, San Francisco, USA, vol 302*, pp 19–29
- Arlt R, Beguier J, Czock K-H, Frankl M, Murakami K, Starovich S, Tolba A (1997) In: *IAEA symposium on international safeguards, IAEA-SM-351/160*
- Asano T, Ninagawa J, Fujiwara S, Takahashi S, Nakajima S, Sato T, Menlove HO, Rael DD (2006) In: *IAEA symposium on international safeguards, IAEA-CN-148/51*
- Babeliowsky T, Bortels G (1993) ALFA: a program for accurate analysis of complex alpha-particle spectra on a PC. *Appl Radiat Isot* 44(10–11):1349–1358
- Bagliano G, Capps J, Deron S, Parus JL (1991) The SAL-IAEA in agency's safeguards measurement system activity in 1990, IAEA/AL/041, IAEA, Vienna
- Bärring NE, Jönsson G (1970) Controlled potential coulometric determination of the oxygen-metal ratio in mixed uranium-plutonium oxides. *Anal Chim Acta* 50:229
- Bathke G, Wallace RK, Hase KR, Jarvinen GD, Ireland JR, Ebbinghaus BB, Johnson MW, Sleaford BW, Bradley KS, Collins BA, Prichard AW, Smith BW (2009) The attractiveness of materials in advanced nuclear fuel cycles for various proliferation and theft scenarios. In: *GLOBAL 2009 congress: the nuclear fuel cycle: sustainable options and industrial perspectives, Paris, 6–11 Sep, Proceedings*, p 422
- Beddingfield DH, Menlove HO (2002) *Nucl Instrum Methods Phys Res A* 485(3):797–804
- Beddingfield DH, Menlove HO, Iwamoto T, Tomikawa H (1998) In: *39th INMM annual meeting, Naples*

- Benony G, Pouyat D, Roche C, Cerdan F, Florestan J (1994) X-rays fluorescence spectroscopy with energy dispersion and Bragg reflector: application to actinide solution analysis. In: CEA-N-2756, meetings of gamma and X 93 spectrometry, Saint-Rémy-les-Chevreuse, France, 12–14 Oct 1993, Proceedings, pp 103–107(422 pp)
- Bernstein A, Estrada J, Greaves M, Hagmann C, Lund J (2003) In: 44th INMM annual meeting, Phoenix
- Bokelund H (1970) Investigation of reprocessing input measurement using tracer techniques-Final report for the period, ETR-266, Eurochemic, Belgium, IAEA-R876-F, IAEA, 15 Dec 1960–14 July 1970
- Bokelund H, Deron S, Dratschmidt HH, Foggi C, Hamilton WI, Jones TL, Kinney J, Neuilly M, Reed WJ, Taylor GE, Smith DH, Weh R (1996) An international collaboration exercise on the calibration of a model reprocessing plant accountancy (CALDEX) tank using a lutetium tracer. ESARDA Bulletin 26:1
- Booth L, Gillespie B, Seaman G (1997) In: 5th nondestructive assay/nondestructive examination waste characterization conference, Salt Lake City
- Bortels G (1991) Status of high-resolution alpha-particle spectrometry using Si detectors, EUR-1368613. In: Annual symposium on safeguards and nuclear material management, Avignon, France, 14–16 May, pp 159–163(745 pp)
- Bortels G, Bauer P (1990a) Non-linearity of silicon detectors for particle radiation, 40. annual convention 1990 of the Austrian physical society. Salzburg Univ, Austria, p 106(142 pp)
- Bortels G, Bauer P (1990b) Response of Si detectors to electrons, deuterons and alpha particles. Nucl Instrum Methods Phys Res A 299(1–3):205–209
- Bortels G, Budtz-Joergensen C, Knitter HH (1985) Assaying of targets for nuclear measurements with a gridded ionization chamber. Nucl Instrum Methods Phys Res A 236(3):630–640
- Bortels G, Steinbauer E, Bauer P, Biersack JP, Burger P (1993) Calculation of the resolution function of silicon detectors for alpha particles. In: 43rd annual convention of the Austrian Physical Society at the Technical University, Graz (Austria), 20–24 Sep 1993, p 76(206 pp)
- Bortels G, Steinbauer E, Bauer P, Biersack JP, Burger P, Ahmad I (1994) A survey of the physical processes which determine the response function of silicon detectors to alpha particles. Nucl Instrum Methods Phys Res A 339(1–2):102–108
- Bot D, Keeffe R, Messner R (1997) In: 19th ESARDA annual symposium on safeguards and nuclear material management, Montpellier
- Bourva LCA, Carchon R, Vukadin Z, Lebrun A, Zendel M, Koestlbauer M (2007) In: 48th INMM annual meeting, Tucson
- Bowden NS, Bernstein A, Allen M, Brennan JS, Cunningham M, Estrada JK, Greaves CMR, Hagmann C, Lund J, Mengesha W, Weinbeck TD, Winant CD (2007) Nucl Instrum Methods Phys Res A 572: 985–998
- Bracken D, Biddle R, Carrillo L, Hypes P, Rudy C, Schneider C, Smith M (2002) Los Alamos national laboratory report, LA-13867-M
- Brandalise B, Ougier M, Wellum R, Wojnowski D, Koch L, Wagner HG (1994) In: Robotized equipment for the on site analysis of fissile material, IAEA-SM-333/37, International Nuclear Safeguards, Vienna, Proceedings, vol 1, p 755
- Bronson FL, Young B (1997) In: Proceedings of 5th non-destructive assay and nondestructive examination waste characterization conference, Salt Lake City, Utah, pp 342–352
- Brousse T, Delaunay J, Grandin P, Vian A, Doutreligne P (1993) Use of an hybrid “K-edge” spectrometer for determination of U and Pu, CEA-N-2756. In: Meeting of gamma and X 93 spectrometry, Saint-Rémy-les-chevreuses
- Bryan SA, Levitskaia TG, Lines AM, Billing JM, Casella AJ, Johnsen AM, Peterson JM, Thomas EM (2009) In: 2nd Japan-IAEA workshop on advanced safeguards technology for the future nuclear fuel cycle, Tokaimura
- Buckley WM, Friensehner A, Twomey T, Kreek SA, Lanier RG, Parker WE, Martinez D, Wang TF, Ruhter W, Keyser R, Sangsingkeow P (2000) Full range MGA plutonium isotopic analysis using single Ge detector, UCRL-JC-137275
- Buerger S, Riciputi L, Bostick D, Turgeon S, Mchay E, Lavelle M (2009) Int J Mass Spectrom 286:70
- Bytchkov V, Lavender C, Aparo M, Koulikov I, Vallejo Luna J, Koudriachov A, Murakami K (2001) In: Symposium on international safeguards, IAEA-SM-367/14/04
- Caldwell CE, Grill LF, Kurtz RG, Miner FJ, Moody NE (1962) Anal Chem 34(3):346–348
- Callis EL, Abernathey RM (1991) High precision isotopic analysis of uranium and plutonium by total sample volatilization and signal integration. Int J Mass Spectrom 103:93
- Callis EL, Capps JH (1996) Total evaporation in thermal ionization mass spectrometry, AECL-11342. In: Proceedings of the 2nd Alfred O. Nier symposium on inorganic mass spectrometry, Durango, pp 24–26(160 pp)
- Canberra (2009) Genie 2000 basic spectroscopy software, application note C37150. Canberra Industries
- Canberra (2009) Genie 2000 gamma analysis software, model S501, application note. Canberra Industries
- Carchon R, Jung S, Ayalew T, Lebrun A, Zendel M, Antoine C (2006) In: 11th international conference on ground penetrating radar, Columbus Ohio

- Carchon R, Moeslinger M, Bourva L, Bass C, Zendel M (2007) Nucl Instrum Methods Phys Res A 579(1):380–383
- Carrasco JA, Bytchkov V, Dubreuil A, Yim S, Arlt R, Esmailpour K (1997) In: Symposium on international safeguards, IAEA-SM-351/149
- Carter JA, Walker RL, Eby RE, Pritchard CA (1976) In: Simplified method for preparing micro samples for simultaneous isotopic analysis of uranium and plutonium, IAEA-SM-201/9, Safeguard Nuclear Materials 1975, Proceedings, vol 2, p 461
- Cauchetier P (1978) In: Determination of microamounts of neptunium by differential pulse polarography, CEA-CONF-4410, Radiochemical conference: 9, Piestany, Czechoslovakia, 12–15 Sep
- Cauchetier P (1981) Dosage spectrophotométrique du neptunium. Anal Chim Acta 24:443
- Cauchetier P, Guichard C, Regnaud F (1975) Note sur l'utilisation de l'oxyde d'argent (II) dans le titrage du plutonium. Anal Chim Acta 80:188
- Cauchetier P, Guichard C, Wagner JF (1985) Spectrophotométrie des éléments transuraniens dans le retraitement, CEA-CONF-7999. In: Karlsruhe international conference on analytical chemistry in nuclear technology, Karlsruhe
- Cesario J, Chevalier C, Dubois JC (1987) Combined use of the resin bead technique and a multi-isotopic tracer for assay by isotopic dilution of uranium and plutonium in spent fuel solutions. In: Proceedings of an international symposium on nuclear material safeguards held in Vienna, IAEA-SM-293/5, IAEA, Vienna, 10–14 Nov 1986, vol 1, pp 705–717 (769 pp)
- Cetama (1997) Input tank calibration exercise at La Hague, Dossier des mesures in situ, DOMIS, CETAMA, France
- Cetama (2009) Catalogue of reference materials, CETAMA, CEA/MARCOULE, BP 17171, 30207 Bagnols-sur-Cèze Cedex (France), <http://www-cetama.cea.fr>, <http://www-cetama.cea.fr/scripts/home/publigen/content/templates/show.asp?P=331&L=FR&ITEMID=8>
- Chadwick PH, McGowan IR (1972) Determination of plutonium and uranium in mixed oxide fuels by sequential redox titration. Talanta 19:1335
- Charlton SW, Stanbro WD (2001) Monitors for the prediction of alternate nuclear material concentrations for pressurized water reactor spent fuel. Nucl Technol 136(1):24–36
- Charlton WS, Strohmeier D, Stafford A, Saavedra S, Hoover AS, Rudy C (2009) In: Proceedings of 31st annual meeting of ESARDA, Vilnius, Lithuania
- Charyulu MM, Rao VK, Natarajan PR (1984) Potentiometric determination of plutonium by sodium bismuthate oxidation. Talanta 31:1109
- Chen JD, Axell K, Gerwing AF, Parcey DA, Kosierb R, Larsson M, Lindberg B, Vinnå F (2006b) In: IAEA symposium on international safeguards, IAEA-CN-148/69
- Chen JD, Gerwing AF, Parcey DA, Kosierb R, Larsson M, Axell K, Hildingsson L, Lindberg B, Vinnå F (2006a) In: 47th INMM annual meeting, Nashville
- Cherry J, Holmes J, Williams JJB (1968) Analytical method for the determination of plutonium by amperometric titration (argentic oxidation, ferrous reduction), PG-Report-832, UKAEA, Sellafield
- Cheung CL, Nikolic RJ, Reinhardt CE, Wang TF (2006) Nanotechnol 17:1339–1343
- Clark WJ Jr, Park SH, Bostick DA, Duckworth DC, Van Berkel GJ (2006) Anal Chem 78:8535
- Close DA, Johnson WS, Kandarian RM, Kerr PL, Moss CE, Romero CD (1998) Los Alamos National Laboratory report, LA-UR-98-1211
- Corpel J, Regnaud F (1962) Cérimétrie en milieu nitrique, application au dosage du fer, de l'uranium et du plutonium. Anal Chim Acta 27:36
- Corpel J, Regnaud F (1966) Dosage du plutonium par potentiométrie à intensité constante: application au combustible de rapsodie. Anal Chim Acta 35:508
- Cowder L, Menlove HO (1982) Los Alamos National Laboratory report, LA-9493-M (ISPO-178)
- Crossley D (1988) Analysis of NpO₂ samples for Np content by controlled potential coulometry, AEA Technology PLC, Didcot
- Daly NR (1960) Scintillation type mass spectrometer ion detector. Rev Sci Instrum 3(31):264–267
- Davies W, Gray WA (1964) A rapid and specific titrimetric method for the precise determination of uranium using iron(II) sulphate as reductant. Talanta 11:1203
- Davies W, Townsend M (1974) UKAEA-TRG report 2463
- Davies W, Gray W, Mcleod KC (1970) Coulometric determination of uranium with a platinum electrode. Talanta 17:937
- Debievre P (1997) Personal communication, Geel
- Debievre P, Perrin R (1991) Why should we do some more isotope-specific thinking in measurements for safeguards. In: 13th annual symposium on safeguards and nuclear material management, Avignon, 14–16 May 1991, Proc. EUR-13686, pp 187–193 (745 pp)
- Debievre P, Van Audenhove J (1976) Accurate procedure to safeguard the fissile material content of input and output solutions of reprocessing plants, (IAEA-SM-201/108), Safeguard Nuclear Materials 1975, IAEA, Vienna, Proceedings, vol 2, p 493
- Del Sesto RE, McKigney EA, Cooke DW, Muenchausen RE, Ott KC, Gilbertson RD, McCleskey TM, Bacrania ML, Jacobsohn G, Burrell AK, Bennett BL, Sitarz SC, Smith JF (2007) Nucl Instrum Methods Phys Res A 579(1):15–18
- Dermendjiev E, Lauppe W, Schinzer F (1983) In: Proceedings of an international symposium on

- recent advances in nuclear material safeguards, IAEA-SM-260/41
- Deron S, Donohue D, Bagliano G, Kuhn E, Sirisena K (1994) The IAEA's analytical capabilities for safeguards, IAEA-SM-333/221. In: international nuclear safeguards 1994, Vienna, Proceedings, vol 1, p 717
- Deron S, Donohue DL, Perrin R (1996) A clean laboratory for safeguards, IAEA Yearbook, 1996. International Atomic Energy Agency, p E5
- Dillon GB (2002) The IAEA in Iraq, past activities and findings, IAEA Bulletin 44(2): 13–16
- Donohue DL (1998) *J Alloy Comp* 271–273:11
- Donohue DL (2002) *Anal Chem* 74:28A; IAEA (1992) IAEA inspections and Iraq's nuclear capabilities, IAEA/PI/A35E
- Donohue DL, Zeissler R (1993) *Anal Chem* 65:359A
- Doubek N, Jammet G, Zoigner A, Deron S, Bagliano G, Tsutaki Y, Hatakenaka T, Ohuchi T, Tohmine K, Falta G (1991) Preparation and validation of a large size dried spike: batch SAL-9951, IAEA/AL/040, Vienna
- Doubek N, Ottmar H, Eberle H (1994) Analysis of mg size Pu samples with X-ray fluorescence analyzer, IAEA-SM-333/142P. In: Symposium international nuclear safeguards 1994, Proceedings, IAEA, Vienna, vol 1, p 816
- Dragnev T, Barnes B, Deron S, Parus J, Raab W, Mojaev V, Majorov V, Close DA, Parker JL (1997) In: Symposium on international safeguards, IAEA-SM-351/116
- Drummond JL, Grant RA (1966) Potentiometric determination of plutonium by argentic oxidation, ferrous reduction and dichromate titration. *Talanta* 13:477
- Dubois JC, Eliot E, Retali G (1989) Development of dynamic multicollection for uranium and plutonium analysis in thermal ionisation mass spectrometry. In: 11th Symposium on safeguards, ESARDA, Luxembourg, 30 May 1989–1 June 1989, CEA-CONF-9901
- Duckworth H, Barber R, Venkatarasubramanian V (1986) *Mass spectrometry*, 2nd edn. Cambridge University Press, Cambridge
- Duckworth DC, Arrigo L, Liezers M, Douglas M (2009) In: 2nd Japan-IAEA workshop on advanced safeguards Technology for the future nuclear fuel cycle, Tokai-mura, Japan
- Duhamel G, Kuhn E, Zahradnik-Gueizelar P (2004) Establishing the joint IAEA/JSGO/NMCC safeguards on-site laboratory for the Rokkasho Reprocessing Plant. In: 7th conference on facility operations-safeguards interface, Charleston
- Eberle et al (1970) Modified potentiometric procedure, New Brunswick Laboratory report 252
- Eccleston GW, Menlove HO, Abhold AE, Baker MC, Pecos JM (1998) Los Alamos National Laboratory report LA-UR-98-3302
- Efurd DW, Drake J, Roensch FR, Cappis JH, Perrin RE (1986) Quantification of neptunium by isotope dilution mass spectrometry, LA-10701-MS
- Ehinger M, Chesnay B, Creusot C, Damico J, Johnson S, Wuester J, Masuda S, Kajii M (2004) International conference on facility operations-safeguards interface, Charleston
- Elliott S, Kalinitchenko I, Hoss T (2005) Innovative high sensitivity 90-degree reflecting ICP-MS ion optics for routine sample analysis, advance note, Varian
- Elliott N, Bickel G, Linauskas S, Paterson L (2006) *J Radioanal Nucl Chem* 267:637
- Ensslin N, Harker W, Krick M, Langner D, Pickrell M, Stewart J (1998) Los Alamos National Laboratory report, LA-13422-M
- Ewart FT, Mcmillan JW, Pollard PM, Thomason HP, Liezers M (1987) The development of a laser-induced photoacoustic facility for actinide speciation, AERE-R-12875
- Ewing RE, Banks CV (1948) Analysis of thorium-chromium mixtures. *Anal Chem* 20:233
- Fardon JB, McGowan IR (1972) Controlled potential coulometry: application of a secondary reaction to the determination of plutonium and uranium at a solid electrode. *Talanta* 19:1321
- Fiedler R (1995) Total evaporation measurements: experience with multi-collector instruments and a thermal ionization quadrupole mass spectrometer. *Int J Mass Spectrom Ion Processes* 146–147:91–97
- Fiedler R, Donohue D (1988) Pocket sensitivity calibration of multicollector mass spectrometers. In: Symposium on trace element analysis by mass spectrometry, Regensburg, 30 Sep 1987–2 Oct 1987; Fresenius Z *Anal Chem* 331(2):209–213
- Filippov VI, Moritz W, Terentjev AA, Vasiliev AA, Yakimov SS (2007) *IEEE Sens J* 7(2):192–196
- Fisher D (1997) History of the International Atomic Energy Agency, the first forty years, STI/PUB/1032, IAEA, Vienna
- Fleischer R, Price P, Walker R (1975) *Nuclear tracks in solids*. University of California Press, Berkeley
- Fudge AJ, Wood AJ, Banham MF (1960) Report AERE-R 3264
- Gandhi T, Raja KS, Misra M (2008) *Proc SPIE* 6959:695904-1
- Garcia-Torano E (1990) Numerical methods to analyze alpha spectra and application to the study of neptunium 237 and neptunium 236. PhD thesis, INIS-mf-12666, Universidad Complutense de Madrid, Dept. de Fisica Atomica, Molecular nuclear, p 217
- Gavron A, Smith LE, Ressler JJ (2009) *Nucl Instrum Methods Phys Res A* 602(2):581–587
- Goldberg SA, Richter S, Schwieters H (2002) Improved environmental and forensics measurements using multiple ion counters in isotope ratio mass spectrometry, IAEA-CN-98/3/07. In: International conference on advances in destructive and non-destructive analysis for environmental monitoring

- and nuclear forensics, Karlsruhe, 21–23 Oct 2002, synopses, p 128
- Goldfarb M (2007) In: International safeguards workshop advanced sensors for safeguards. Santa Fe, New Mexico
- Goode GC, Herrington J, Johns WT (1967) High precision analysis of nuclear materials by controlled current coulometry: determination of uranium. *Anal Chim Acta* 37:44
- Grisson J (1980) *Analisis* 8(8):354
- Guardini S, Arlt R, Bickel M, Carchon R, Chard P, Iievlev S, Lebrun A, Levai F, Li TK, Lu MS, Mafra O, Mclelland P, Morel J, Ottmar H, Peerani P, Rackam J, Ruhter W, Thauel B, Tiitta A, Schwalbach P, Swinhoe M (2004) *ESARDA Bulletin* 32:12–54
- Guenther-Leopold I, Wernli B, Waldis JK, Kopajtic Z (2005) Measurement of Pu isotope ratios in nuclear fuel samples by HPLC/MC/ICPMS. *Int J Mass Spectrom* 242:195
- Gunnink R (1990) Lawrence Livermore National Laboratory report, UCRL-LR-103220, vol 1
- Gunnink R, Ruhter WD, Niday JB (1984) GRPANL: a program for deconvoluting and interpreting complex peak clusters, UCRL-898765. In: International conference on nuclear methods in environmental and energy research, Mayaguez, Puerto Rico
- Gunnink R, Ruhter WD, Miller P, Goerten J, Swinhoe M, Wagner H, Verplancke J, Bickel M, Abousahl S (1994) MGAU: a new analysis code for measuring ^{235}U enrichments in arbitrary samples, UCRL-JC-114713. In: IAEA symposium on international safeguards, IAEA-SM-333/88
- Halbig JK, Bosler GE, Klosterbuer SF, Rinard PM (1985) Los Alamos National Laboratory report, LA-UR-85-3735
- Hallstadius L (1984) Methods for the electrodeposition of actinides. *Nucl Instrum Methods Phys Res A* 223:266
- Ham Y, Bosler G, Vones J, Gryntakis E, Abedin-Zadeh R, Peixoto O (2002) In: 43rd INMM annual meeting, Orlando, Florida
- Hamilton FE, Knight AP, Maidment I, Thomas AM, Wood AJ (1989) The preparation and characterisation of a 3:3:3:1 mixture of ^{239}Pu : ^{240}Pu : ^{242}Pu : ^{244}Pu for use as an isotopic reference material for mass spectrometric analysis, UK safeguards R&D Project, SRDPR155, Harwell Laboratory, UK
- Harrar JE (1968) Platinum working electrode for controlled potential coulometry, UCRL-50417
- Harrar JE (1987) Analytical controlled potential coulometry. *Trends Anal Chem* 6:152
- Harrar JE, Shain L (1996) *Anal Chem* 38:1148
- Hashimoto Y, Arlt R, Saringer G, Janov J, Halbig JK, Klosterbuer SF (1994) In: IAEA symposium on international safeguards, IAEA-SM-333/51
- Holland MK, Dorsett RS (1986) Improved laboratory assays of plutonium and uranium for SRP purification and finishing processes, DP-MS-86-4327. In: Annual meeting of the Institute of Nuclear Materials Management, New Orleans, p 9
- Holland MK, Cordaro JV, Fields TC, Reeds GE (1998) Automated controlled potential coulometer for the IAEA. In: Proceedings of the 6th international conference on nuclear engineering, San Diego
- Hoover AS, Bacrania MK, Hoteling NJ, Karpius PJ, Rabin MW, Rudy CR, Vo DT, Beall JA, Bennett DA, Doriese WB, Hilton GC, Horansky RD, Irwin KD, Ullom JN, Vale LR (2009) *J Radioanal Nucl Chem* 282:227–232
- Hunt BA, Dworschak H, Cuypers M, Foggi C (1994) Volume and mass measurement techniques in large and small tanks for research and development and training at the Joint Research Centre Ispra Establishment, IAEA-SM-333/70P, International nuclear safeguards 1994, Proceedings, vol 1, p 801
- IAEA (1961) The agency's safeguards system, IAEA, INFCIRC/26
- IAEA (1968) The revised IAEA safeguards system, IAEA, INFCIRC/66 (1965), Rev. 2 (1968)
- IAEA (1970) The treaty on the non-proliferation of nuclear weapons (NPT) 1968, IAEA INFCIRC/140
- IAEA (1971) The structure and content of agreements between the agency and states in connection with NPT, IAEA, INFCIRC/153
- IAEA (1972) The structure and content of agreements between the agency and states required in connection with the treaty on the non-proliferation of nuclear weapons, INFCIRC/153 (Corrected). IAEA, Vienna
- IAEA (1985) International safeguards and the non-proliferation of nuclear weapons, IAEA, IAEA/GI/AH.E85-10942
- IAEA (1994) GOV/INF/759. Available at <http://www.govatom.iaea.org>
- IAEA (1995) GOV/2784. Available at <http://www.govatom.iaea.org>
- IAEA (1996) GOV/2863. Available at <http://www.govatom.iaea.org>
- IAEA (1997) Model protocol additional to the agreement between the state and the IAEA for the application of safeguards, INFCIRC/540 (Corrected), IAEA
- IAEA (1998a) Statistical concepts and techniques for IAEA Safeguards, fifth edition, IAEA/SG/SCT/5. IAEA, Vienna
- IAEA (1998b) The evolution of IAEA safeguards, international nuclear verification series no. 2, IAEA, Vienna
- IAEA (2001) International target values 2000 for measurement uncertainties in safeguarding nuclear materials, STR-327, International Atomic Energy Agency, Vienna

- IAEA (2002) IAEA safeguards glossary (2001 edn), International nuclear verification, series no. 3, IAEA, Vienna
- IAEA (2003) International nuclear verification series no. 1 (revised), ISBN 92-0-109403-5
- IAEA (2004) Destructive analysis and evaluation services for nuclear material accountability verifications, STR-69, rev. 5, IAEA, Vienna
- IAEA (2005) STR-348
- IAEA (2006a) In: Technical meeting on noble gas monitoring sampling and analysis for safeguards, STR-351, International Atomic Energy Agency, Vienna
- IAEA (2006b) In: Technical meeting on application of laser spectrometry techniques in IAEA safeguards, STR-352, International Atomic Energy Agency, Vienna
- IAEA (2008) Reinforcing the global nuclear order for peace and prosperity: the role of the IAEA to 2020 and beyond, International Atomic Energy Agency
- IAEA (2009a) Regulations for the Safe Transport of Radioactive Material, 2009 Edition of Safety Requirements, IAEA Safety Standards Series No. TS-R-1
- IAEA (2009b) Experts and users advisory meeting on laser induced breakdown spectroscopy for safeguards applications, STR-362, Vienna
- IAEA (2009c) In: Focused workshop on antineutrino detection for safeguards applications, STR-361, Vienna, 28–30 Oct 2008
- IATA (2003) Dangerous goods regulations, 44th edn. IATA, Montreal
- IATA (2010) Dangerous goods regulations, 51st edn. IATA, Montreal
- Ingelbrecht C, Moens A, Eykens R, Dean A (1997) Improved electrodeposited actinide layers. *Nucl Instrum Methods Phys Res A* 397(1):34–38
- IRMM (2008) Catalogue of isotopic reference materials. IRMM, European Commission, Joint Research Centre, Retieseweg 111, B-2440, Geel. http://irmm.jrc.ec.europa.eu/html/reference_materials_catalogue/catalogue/IsotopicRM_Catalogue_Jun2008.pdf
- ISO (1987a) Determination of plutonium content in plutonium dioxide (PuO_2) of nuclear grade, gravimetric method ISO 8300, 1st edn. ISO, Geneva
- ISO (1987b) Determination of plutonium in solutions of pure plutonium nitrate, gravimetric method, ISO 8425, 1st edn. ISO, Geneva
- ISO (1993) Guidelines for plutonium dioxide sampling in a nuclear reprocessing plant, ISO11482. ISO, Geneva
- ISO (1995a) Recommendations for representative sampling of spent fuel dissolver solution for uranium and plutonium concentration determination, N-334E14, ISO/TC85/SC5/WG3. ISO, Geneva
- ISO (1995b) Verification of samples of uranyl or plutonium nitrate solutions by density measurements, ISO-11597. ISO, Geneva
- ISO (1996a) Slow bubble technique for accurate measurement of liquid height in accountancy vessels equipped with dip tubes, ISO 13463. ISO, Geneva
- ISO (1996b) Subsampling of uranium hexafluoride in the liquid phase, ISO 9894, 1st edn. ISO, Geneva
- ISO (1997) Determination of neptunium in nitric acid solutions by molecular absorption spectrophotometry, ISO-13465-1997(E). ISO, Geneva
- ISO (1999) Chemical separation and purification of uranium and plutonium in nitric acid solutions for isotopic and isotope dilution analysis by solvent chromatography, ISO 15366:1999. ISO, Geneva
- ISO (2000) Determination of milligram amounts of plutonium in nitric acid solutions. Potentiometric titration with potassium dichromate after oxidation by Ce(IV) and reduction by Fe(II) , ISO 8298, 2nd edn. ISO, Geneva
- ISO (2003) Determination of uranium in uranyl nitrate solutions of nuclear grade quality, gravimetric method, ISO7476. 2nd edn. ISO, Geneva
- ISO (2004a) Determination of uranium in solutions, hexafluoride and solids: iron(II) reduction/potassium dichromate oxidation titrimetric procedure, ISO 7097-1, 1st edn. ISO, Geneva
- ISO (2004b) Uranium dioxide powder or pellets, determination of uranium and oxygen to uranium ratio using the gravimetric method with impurity correction, ISO12795. 1st edn. ISO, Geneva
- ISO (2005a) Determination of isotopic and elemental uranium and plutonium concentrations of nuclear materials in nitric acid solutions by thermal ionization mass spectrometry, ISO 8299, 2nd edn. ISO, Geneva
- ISO (2005b) Verification of the titer of reference solutions used in the determination of element concentration, ISO 10980. ISO, Geneva
- ISO (2005c) Préparation des sources de plutonium et détermination du rapport isotopique $^{238}\text{Pu}/^{239}\text{Pu}$ par spectrométrie alpha, ISO 11483:2005. ISO, Geneva
- ISO (2005d) Determination of plutonium by controlled potential coulometry, ISO-12183. ISO, Geneva
- ISO (2007a) Determination of uranium in solutions, uranium hexafluoride and solids, iron(II) reduction/ cerium(IV) oxidation titrimetric method, ISO 7097-2, 1st edn. ISO, Geneva
- ISO (2007b) Tank calibration and volume determination for nuclear material accountancy, ISO18213-1 to 6. ISO, Geneva
- ISO (2007c) Nuclear fuel technology – alpha spectrometry – part 1: determination of neptunium in uranium and its compounds, ISO-21847-1-2007(E). ISO, Geneva
- ISO (2007d) Spectrométrie alpha: détermination du plutonium dans l'uranium et ses composés, ISO 21847-2. ISO, Geneva

- ISO (2009) Determination of plutonium in nitric acid solutions by spectrophotometry, ISO 9463:2009. ISO, Geneva
- Iwamoto T, Hashimoto Y, Nagamatsu K, Tomura N, Menlove HO, Halbig JK, Klosterbuer SK, Wenz TR, Abedin-Zadeh R, Ammann P, Elomaa P (1997) In: Symposium on international safeguards, IAEA-SM-351/96
- Iwamoto T, Ebata T, Fujimaki K, Ai H (2006) Extensive cooperation in establishment and installation of safeguards system at RRP, IAEA-CN-148/109
- Jackson DD, Hodgkins DJ, Hollen RM, Rein JE (1976) Automatic spectrophotometer for plutonium and uranium determination, LA-6091. In: Safeguarding nuclear materials, symposium, IAEA-SM-201/18, IAEA, Vienna, Oct 1975, Proceedings, vol 2, pp 91–105
- Jackson DD, Hollen RM, Roensch FR, Rein JE (1980) Controlled potential coulometric determination of plutonium with hydrochloric and sulfamic acid electrolyte and phosphate complexation. *Anal Chim Acta* 117:205
- Jaech JL, Russell M (1991) Algorithms to calculate sample sizes for inspection sampling plans, STR-261, rev.1. IAEA, Vienna
- Jakopic R, Richter S, Kuehn H, Aregbe Y (2008) Isotope ratio measurements of pg-size plutonium samples using TIMS in combination with the “Multiple Ion Counting” and filament carburization, INIS-FR-09-0127. In: Atalante 2008: nuclear fuel cycle for a sustainable future, Montpellier, France, 19–23 May
- Janin V (2006) Calibration check in accountancy tanks at Rokkasho-mura reprocessing plant, IAEA-CN-148/198. In: Symposium on international safeguards, Vienna, 16–20 Oct
- Janssens-Maenhout G, Nucifora S (2007) *Nucl Eng Des* 237(2007):1209–1219
- Johnson SJ, Abedin-Zadeh R, Pearsall C, Chesnay B, Creusot C, Ehinger M, Kuhn E, Robson N, Higuchi H, Takeda S, Fujimaki K, Ai H, Uehara S, Amano H, Hoshi K (2001) In: IAEA symposium on international safeguards, IAEA-SM-367/8/01
- Johnson SJ, Chesnay B, Pearsall C, Fujimaki K, Iwamoto T (2004) In: 7th international conference on facility operations-safeguards interface, Charleston
- Jung S, Carchon R, Hammerschmied R, Zendel M, Hanks D, Schwalbach P, Puttaert (2007) In: 48th INMM annual meeting, Tucson
- Kageyama T, Sugaya SI, Kono S, Higuchi H, Endo H, Kowata M, Noda Y (2001) Determination of neptunium in neptunium-uranium-plutonium mixed oxide fuel by spectrophotometry, JNC-TN-8400-2001-026
- Kalinowski MB, Daerr H, Kohler M (2006) Measurements of krypton-85 to detect clandestine plutonium production. *INESAP information bulletin no.* 27, pp 9–12
- Kall HL, Gordon L (1953) Quantitative insolubility of thorium oxalate. *Anal Chem* 25:1256
- Khlebnikov N, Whichello J, Parise D (2006a) In: 47th INMM annual meeting, Nashville
- Khlebnikov N, Parise D, Whichello J (2006b) In: IAEA symposium on international safeguards, IAEA-CN-148/32, Vienna
- Kim HD (2007) In: JAEA-IAEA workshop on advanced SG techniques for NFC, Tokyo
- Kim JS, Park IJ, Ahn GH, Min GS, Lebrun A (2006) In: IAEA symposium on international safeguards, IAEA-CN-148/72
- Kipphardt H, Debievre P, Taylor PDP (2004) New mathematical models with associated equations for IDMS. *Anal Bioanal Chem* 378:330–341
- Koch L, Arenz HJ, Von Baeckman A, Cricchio A, De Meester R, Romkowski M, Van Der Stijl E, Wilhelmi M (1976) Improvements and experience in the analysis of reprocessing samples, safeguard nuclear materials 1975, vol 2. IAEA, Vienna, p 449
- Koch L, Betti M, Cromboom O, Mayer K (1997) Nuclear material safeguards for P and T. In: Global '97: international conference on future nuclear systems, Yokohama, Tokyo, 5–10 Oct, Proceedings, pp 876–878 (1588 pp)
- Kosierb R (2007) JAEA-IAEA workshop on advanced safeguards technology for the future nuclear fuel cycle, Tokai-mura, Japan
- Kraiem M, Mayer K, Gouder T, Seibert A, Wiss T, Thiele H, Hiernaut J-P (2010) *Int J Mass Spectrom* 289:108
- Krick MS, Menlove HO (1979) Los Alamos National Laboratory report, LA-7779-M (ISPO-53)
- Krick MS, Menlove HO (1980) Los Alamos National Laboratory report, LA-8404-MS (ISPO-97)
- Krick MS, Menlove HO, Zick J, Ikonomou P (1985b) Los Alamos National Laboratory report, LA-10382-MS (ISPO-219)
- Krick MS, Menlove HO, Ramalho A (1985a) Los Alamos National Laboratory report, LA-10430-M (ISPO-234)
- Kuhn E, Deron S, Aigner H, Andersen JA (1982) Reduced-size plutonium sample processing and packaging for the PAT-2 package, SAND-82-1371C. In: CONF-820713-12, Institute of Nuclear Materials Meeting, Washington, 19–21 Jul
- Kuno Y, Takeda S, Sato S, Akiyama T, Tsutaki Y, Suzuki T, Kuhn E, Deron S, Sirisena K (1989) Reprocessing plant input accountability measurements – a new and simplified spiking technique, the large size dried spike. *Trans Am Nucl Soc* 60:229–230
- Kuvik V (1991) The MacDonald and Savage titrimetric procedure scaled down to 4 mg sized plutonium samples. *Anal Chim Acta* 256:163
- Kuvik V et al (1992) Optimization of the automatized MacDonald and Savage method, IAEA/AL/068. IAEA, Vienna

- Lafleur AM, Charlton WS, Menlove HO, Swinhoe M (2008) LA-UR-08-03798
- Lafleur AM, Charlton WS, Menlove HO, Swinhoe M (2009) In: 31st ESARDA annual meeting, Vilnius
- Lally AE, Glover KM (1984) Source preparation in alpha spectrometry. *Nucl Instrum Methods Phys Res A* 223(2/3):259–265
- Landat D, Hunt BA, Koehne W, Franssen F, Hope D (1997) In: 38th INMM annual meeting, Phoenix
- Langner DG, Kroncke KE, Marlow JB, Menlove HO, Swinhoe MT (2006) In: INMM 47th annual meeting, Nashville
- Laszlo G, De Ridder P, Goldman A, Cappi J, Debievre P (1991) Optimal sample to tracer ratio for isotope dilution mass spectrometry: the poly-isotopic case, EUR-1368613. In: Annual symposium on safeguards and nuclear material management, Avignon, Proceedings, pp 219–223
- Lebrun A, Carchon R (2003) IAEA-STR-333
- Lebrun A, Bignan G, Szabo JL, Arenas-Carrasco J, Arlt R, Dubreuil A, Esmailpur-Kazerouni K (2000) *Nucl Instrum Methods Phys Res A* 448(3):598–603
- Lebrun A, Merelli M, Szabo J-L, Huver M, Arlt R, Arenas-Carrasco J (2001) In: IAEA symposium on international safeguards, IAEA-SM-367/14/03
- Lebrun A, Bourva L, Belian A, Langner D, Zendel M (2007) In: Proceedings of the 29th ESARDA annual symposium on safeguards and nuclear material management, Aix-en-Provence
- Lebrun A, Ryzhikov V, Zendel M, Nadezhinskii A, Grigorev G, Mechold L (2008) In: 49th INMM annual meeting, Nashville
- Lestone JP, Pecos JM, Rennie JA, Sprinkle JK, Staples P, Grimm KN, Hill RN, Cherradi I, Islam N, Koulikov J, Starovich Z (2002) *Nucl Instrum Methods Phys Res A* 490(1–2):409–425
- Li J, Lu Y, Ye Q, Cinke M, Han J, Meryyappan M (2003) *Nano Lett* 3(7):929–933
- Lopez-Mencherero E, Ryzhov MN, Clark B, Szabo E, Beetle TM, Deron S (1976) Analytical services for agency safeguards (IAEA-SM-201/98), Safeguarding nuclear materials, Vienna, Proceedings, vol 2, pp 73–90
- Lucero RL, Glidewell DD, Bartberger JC, Perlinski AW (2004) In: INMM 45th annual meeting, Orlando
- Ludwig R, Raab W, Dashdondog J, Balsley S (2008) Np analysis in IAT-samples containing <10 microgram Pu. In: Atalante 2008: nuclear fuel cycle for a sustainable future, INIS -FR-09-0139, Montpellier, 19–23 May
- Macdonald A, Savage DJ (1979) Plutonium accountancy in reprocessing plants by ceric oxidation, ferrous reduction and dichromate titration. In: IAEA conference on nuclear safeguards technology, Vienna, Oct 1978, Proceedings, vol 1, p 651
- Macdonald A, Savage DJ (1987) A method for the determination of plutonium in plutonium concentrates solutions by ceric oxidation, ferrous reduction and amperometric titration with dichromate, UKAEA report ND-R-1516(D), Dounreay
- Magnelind PE, Matlashov AN, Volegov PL, Espy MA (2009) *IEEE Trans Appl Supercond* 19(3):816–818, Part 1
- Malinowski J (1967) Precise determination of uranium in pure metal and uranium compounds by constant current coulometry. *Talanta* 14:283
- Marsh SF, Ortiz MR, Abernathy RM, Rein JE (1974) Improved 2-column ion exchange separation of plutonium, uranium and neodymium in mixed U/Pu fuels for burn up measurements, LA5568
- Marsh SF, Abernathy RM, Rein JE (1981) Evaluation of treatments to attain isotopic equilibration of plutonium preceding the resin bead technique for mass spectrometric assay analysis of spent reactor fuel. In: Minutes 4th SALE participants meeting, Argonne, p 218; *Anal Lett* 13:1487
- Mathew CK, Jain HC, Kavimandan VD, Aggarwal SK (1976) An independent method for input accountability in reprocessing plants (MAGTRAP). In: Safeguarding nuclear materials, Proceedings of the symposium, IAEA-SM-201/87, IAEA, Vienna, Oct 1975, vol II, p 485
- Matsuo Y (2008) Nuclear fuel cycle projects in Rokkasho-Mura. In: International conference Atalante 2008, Montpellier
- Matter JC (2003) In: ESARDA-INMM workshop on safeguards perspectives for a future nuclear environment, Como
- Mayer RL II, Rollen HY, Gillespie B, Hordijk L (2004) In: INMM 45th annual meeting, Orlando
- Mayer K, Ingelbrecht C, Peetermans F (1995) Development of an isotopic seal for tagging reprocessing input solutions. *Trans Am Nucl Soc* 72(suppl1):32a
- Mckigney EA, Sesto RED, Jacobsohn LG, Santi PA, Muenchausen RE, Ott KC, McCleskey TM, Bennett BL, Smith JF, Cooke DW (2007) *Nucl Instrum Methods Phys Res A* 579:15–18
- Menlove HO (1981) Los Alamos National Laboratory report, LA-8939-MS (ISPO-142)
- Menlove HO (1983) In: ESARDA fifth annual symposium on safeguards and nuclear material management, Versailles, pp 231–240
- Menlove HO, Pieper JE (1987) LA-10827-MS (ISPO-258)
- Menlove HO, Eccleston GW, Swansen JE, Goris P, Abedin-Zadeh R, Ramalho A (1984) Los Alamos National Laboratory report, LA-10226-11 (ISPO-215)
- Menlove HO, Adams EL, Dahn E, Ramalho A (1986) Los Alamos National Laboratory report, LA-10615-M (ISPO-216)
- Menlove HO, Miller MC, Ohtani T, Seya M, Takahashi S (1993) Los Alamos National Laboratory report, LA-UR-93-1860

- Menlove HO, Krick MS, Langner DG, Miller MC, Stewart JE (1994) In: Symposium on international safeguards, IAEA-SM-333/94
- Menlove HO (1995) Los Alamos National Laboratory report, LA-UR-95-1989
- Menlove HO, Siebelist R, Wenz TR (1996) Los Alamos National Laboratory report, LA-13073-MS (ISPO-384)
- Menlove HO, Rinard PM, Kroncke KE, Lee YG (1997) Los Alamos National Laboratory report, LA-13239-MS
- Menlove HO, Rinard PM, Li TK, Romero M, Franco JB, Hiruta K, Nasuno S (2001) In: Proceedings of the 8th NDA waste characterization conference, Denver
- Menlove HO, Ecclestone GW, Veal KD, Abushady Y, Azmi S, Dinov K, Zendel M (2002) Los Alamos National Laboratory report LA-UR-02-3677
- Menlove HO, Swinhoe MT, Lebrun A, Lafolie R, Godfrey R, Roach D, Everton C (2007) In: 29th ESARDA annual meeting: symposium on safeguards and nuclear material management, Aix en Provence
- Menlove HO, Menlove SH, Tobin SJ (2009) Nucl Instrum Methods Phys Res A 602:588–593
- Merciny S, Fattyn-Fauville G, Swennen L, Duyckaerts G (1981) Constant current coulometric determination of uranium in pure metal. *Anal Chim Acta* 129:113
- Mersch S (2007) In: International safeguards workshop advanced sensors for safeguards, Santa Fe, New Mexico
- Metz CF (1957) *Anal Chem* 29:1748
- Metz CF, Waterbury GR (1962) In: Kolthoff IM, Elving PJ (eds) *Treatise on analytical chemistry*, part II, vol 8. Interscience, New York, pp 302–303
- Midorikawa M, Sato Y, Hara S, Konno K, Iwanaga M (2006) The on-site laboratory for the Rokkasho reprocessing plant in Japan, IAEA-CN-148/103
- Miguel M, Delle Site A, Deron S, Raab W, Swietly H (1984) Preparation of drop deposited plutonium sources on porcelain support, results and limit of alpha spectrometric analyses. *Nucl Instrum Methods Phys Res* 223:270
- Miller MC, Menlove HO, Augustson RH, Ohtani T, Seya M, Takahashi S, Abedin-Zadeh R (1989) In: INMM 30th annual meeting, Orlando
- Miller MC, Menlove HO, Seya M, Takahashi S, Abedin-Zadeh R (1990) In: INMM 31st annual meeting, Los Angeles
- Miller MC, Menlove HO, Abdel-Hallm A, Hassan B, Kestleman A (1991) Alamos National Laboratory report, LA-12112-M (ISPO-329)
- Miller SD, Tanner J, Simmons K, Conrady M, Benz J (2009) In: 2nd Japan-IAEA workshop on advanced safeguards technology for the future nuclear fuel cycle, Tokai-mura
- Milner GWC, Phillips G (1974) In: Nürnberg HW (ed) *Electroanalytical chemistry*. Wiley, London
- Mitchell WG, Spaletto MI, Lewis K, Soriano MD, Smith MM (1990) Effect of ion exchange purification on the determination of plutonium at NBL, NBL-323
- Montgomery RR, Sauerwein JC (2008) Standard Reference Material Catalog, NIST SP-260-168, 133 pp
- Morgenstern A, Apostolidis C, Carlos-Marquez R, Mayer K, Molinet R (2002) Single-column extraction chromatographic separation of U, Pu, Np and Am. *Radiochim Acta* 90:81
- Moritz W, Bartholomäus L, Roth U, Filippov V, Vasiliev A, Terentjev A (1999) *Anal Chim Acta* 393:49–57
- Morrison M, Charpentier A, Teichert O, Singh K, Joseph T, Malsch I (2007) “Nanotechnology and Civil Security”, nanoforum consortium, tenth nanoforum report
- Mukhopadhyaya S, Mchugh HR (2004) *Proc SPIE* 5198:73
- Nair PR, Xavier M, Mathew KA, Shah PM, Aggarwal SK, Jain HC (1996) A simple, rapid and accurate electrochemical method for uranium determination in dissolver solution of irradiated fuel. *ESARDA Bulletin* 26:22
- Nakajima K, Ishikawa S, Mcelroy RD, Davidson DR, Menlove HO (1997) In: 19th ESARDA annual symposium on safeguards and nuclear material management, Montpellier
- NBL (2008) Catalogue of reference materials, New Brunswick Laboratory, Argonne. http://www.nbl.doe.gov/html/certified_reference_materials.htm
- Nekoogar F, Dowla F, Wang TF (2009) In: 2nd Japan-IAEA workshop on advanced safeguards technology for the future nuclear fuel cycle, Tokai-mura
- Nichols AL, Aldama DL, Verpelli M (2008) IAEA handbook nuclear data for safeguards, INDC (NDS)-0534. IAEA, Vienna. <http://www-nds.iaea.org/sgnucdat/a2.htm>
- Niemayer I (2009) *J Nucl Mater Manag* 37(4):41–48
- Nikitina SA, Stepanov AV, Grigor'eva MG, Gogoleva TD, Pantelev Y (2007) Application of a method of precision spectrophotometry with internal standardization for certification of plutonium and plutonium containing reference materials. In: Romanovskij VN (ed) *Proceedings of Khlopin Radium Institute Sankt-Peterburg*, vol 2007, pp 103–110 (218 pp)
- Nikolic RJ, Conway AM, Reinhardt CE, Graff RT, Wang TF, Deo N, Cheung CL (2007) In: IEEE nuclear science symposium conference record, N24-342, Honolulu, pp 1577–1580
- Nothdurft R, Yao G (2005) *Opt Express* 13(25): 10034–10039
- O'hara MJ, Farawila AF, Grate JW (2009) In: 2nd Japan-IAEA workshop on advanced safeguards technology for the future nuclear fuel cycle, Tokai-mura
- Orton CR, Fraga CG, Douglas M, Christensen RN, Schwantes JM (2009) In: 2nd Japan-IAEA workshop

- on advanced safeguards technology for the future nuclear fuel cycle, Tokai-mura
- Ottmar H, Eberle H (1991) The hybrid k-edge densitometer/k-xray fluorimeter: principle, design, performance, report kfk 4590, Karlsruhe
- Ottmar H, Eberle H, Matussek P, Michel-Piper I (1986) Report KfK 4012, Karlsruhe
- Ottmar H, Eberle H, Doubek N, Raab W, Parus JL (1991) Analysis of Th-U, U-Pu and Pu solutions with the hybrid K-edge/XRF analyzer. In: 13th ESARDA annual meeting: symposium on safeguards and nuclear material management, Ispra, Avignon, May 1991, Proceedings, pp 149–157
- Ottmar H, Mayer K, Morgenstern A, Abousahl S (2001) Demonstration of measurement technologies for neptunium and americium verification in reprocessing, IAEA-SM-367/14/07/P. In: Symposium on international safeguards: verification and nuclear material security, IAEA, Vienna
- Ottmar H, Eberle H, Abousahl S, Albert N, Schorlé H (2007) In: 29th ESARDA annual symposium on safeguards and nuclear material management, Aix-en-Provence
- Packer TW (1991) In: 13th ESARDA annual symposium on safeguards and nuclear material management, Avignon, France.
- Packer TW, Wormald M, Charlier C, Bush W, Cherradi I (1997) In: IAEA symposium on international safeguards, IAEA-SM-351/169
- Parise D, Frazzoli FV, Brunetti G, Dragnev T, Lebrun A, Guardini S, Ravazzani A (2003) In: 25th ESARDA annual meeting: symposium on safeguards and nuclear material management. Stockholm
- Park Y, Song K, Pyo H, Lee M, Jee K, Kim W (2006) Nucl Instrum Methods Phys Res A 557:657
- Parus JL, Raab W (1996) Determination of plutonium in nuclear materials with a combination of alpha and gamma spectrometry. Nucl Instrum Methods Phys Res A 369:588
- Parus JL, Raab W, Donohue D, Deron S (1987) Analysis of Pu containing materials by gamma spectrometry. Inorg Chim Acta 140:283–284
- Parus JL, Raab W, Swietly H, Cappis J, Deron S (1992) On the capability of isotope dilution alpha spectrometry in the determination of plutonium concentration. Nucl Instrum Methods Phys Res A 312:278
- Parus J, Kierzek J, Raab W, Donohue DL (2003) J Radioanal Nucl Chem 258:123
- Parvin D (2007) In: JAEA-IAEA workshop on advanced safeguards technology for the future nuclear fuel cycle, Tokai-mura
- Patigny P (1982) In: Proceedings of the 4th annual ESARDA symposium – petten, Pays-Bas
- Pella PA, Von Baekman AV (1969) X-ray spectrometric determination of uranium and plutonium in solutions of spent nuclear fuels. Anal Chim Acta 47:431
- Pepper S, Queirolo A, Zendel M, Whichello J, Annese C, Griebel J, Griebel R (2007) In: USSP-IAEA workshop on advanced sensors for safeguards, report no. BNL-79695-2007-CP, Upton
- Pereira de Oliveira O, Sarkis JES, Ponzevera E, Alonso A, De Bolle W, Quétel C (2008) Evaluating the accuracy of uranium isotope amount ratio measurements performed by a quadrupole and a multi-collector magnetic sector inductively coupled plasma mass spectrometers for nuclear safeguards. In: Atalante 2008: nuclear fuel cycle for a sustainable future, Montpellier, 19–23 May
- Phillips G, Crossley D (1978) Recent development in the application of controlled potential coulometry to the determination of plutonium and uranium. In: Proceedings of the symposium in Vienna, IAEA-SM-231/56, IAEA, Vienna, vol 2, p 665
- Phillips G, Newton DA, Wilson JD (1977) An automatic controlled potential coulometer. J Electroanal Chem 75:77
- Pietri CE, Baglio JA (1960) Talanta 6:159
- Pietri CE, Freeman BP, Weiss JR (1981) Quantitative ion exchange separation of plutonium from impurities, NBL-298
- Plock CE, Vasquez J (1969) Use of glassy carbon as a working electrode in controlled potential coulometry. Talanta 16:1492
- Poirier S, Langlands D, Zendel M, Moeslinger M, Sequeira V (2009) In: 31st ESARDA annual meeting, Vilnius
- Puckrin E, Thériault J-M (2006) Defence R&D Canada – Valcartier, TN 2006-120
- Raab W, Parus JL (1994) The measurement of $^{240}\text{Pu}/^{239}\text{Pu}$ and $^{238}\text{Pu}/^{239}\text{Pu}$ isotopic ratios by alpha-particle spectrometry. Nucl Instrum Methods Phys Res A 339:116
- Ramakumar KL, Fiedler R (1999) Calibration procedures for a multicollector mass spectrometer for cup efficiency, detector amplifier linearity, and isotope fractionation to evaluate the accuracy in the total evaporation method. Int J Mass Spectrom 184(2–3):109–118
- Ramaniah MV, Jain HC, Aggarwal SK, Chitambar SA, Shah PM, Almaula AI, Kavimandan VD, Parab AR, Sant VL (1980) Isotope dilution alpha spectrometry for the determination of plutonium concentration in irradiated fuel dissolver solution: IDAS and R-IDAS, BARC-1046
- Rance P, Chesnay B, Killeen T, Murray M, Nikkinen M, Petoe A, Plumb J, Saukkonen H (2007) Neptunium flow-sheet verification at reprocessing plants. In: Proceedings of GLOBAL 2007 conference on advanced nuclear fuel cycles and systems, La Grange Park (United States), ANS, 13 Sep 2007, pp 346–352(1873 pp)
- Ranebo Y, Hedberg PM, Whitehouse M, Ingeneri K, Littmann S (2009) J Anal Atom Spectrosc 24:277

- Rao GG, Sagi SR (1962) A new titrimetric reagent: iron(II) in a strong phosphoric acid medium, titration of uranium(VI) at room temperature. *Talanta* 6:715
- Regnier J, Saverot P, Chare PJ, Schenkel R, Saglini JC, Wagner HG (1994) Mise en oeuvre des garanties dans une usine de retraitement moderne (IAEA-SM-333/62), International Nuclear Safeguards 1994, Proceedings, vol 2, pp 35–48
- Reilly D, Ensslin N, Smith H (1991) US Nuclear Regulatory Commission, NUREG/CR-5550, LA-UR-90-732
- Reilly D et al. (2007) Addendum to passive nondestructive assay of nuclear materials. Electronic resource: <http://www.lanl.gov/orgs/n/n1/panda/index.shtml>
- Richter S, Goldberg SA (2003) Improved techniques for high accuracy isotope ratio measurements of nuclear materials using thermal ionization mass spectrometry. *Int J Mass Spectrom* 229:181–197
- Richter S, Alonso-Munoz A, Eykens R, Jacobsson U, Kuehn H, Verbruggen A, Aregbe Y, Wellum R, Keegan E (2008) Isotopic composition of natural Uranium samples, measurement using new $n(^{233}\text{U})/n(^{236}\text{U})$ double spike IRMM-3636. *Int J Mass Spectrom* 269:145
- Riciputi LR, Ingeneri KB, Hedberg PMI (2002): Enhanced ionization efficiency using the high efficiency cavity source implemented on a magnetic sector TIMS, IAEA-CN-98/5/25P. In: International conference on advances in destructive and non-destructive analysis for environmental monitoring and nuclear forensics, Karlsruhe, extended synop, 128, 106, Proc IAEA, Vienna, Oct 2002, 347–353(392 pp)
- Rinard PM, Menlove HO (1997) In: 19th ESARDA annual symposium on safeguards and nuclear material management, Montpellier
- Rodden CJ (1953) Analytical chemistry of uranium. *Anal Chem* 25(11):1598
- Rokop DJ, Perrin RE, Knobloch GW, Armijo VM, Shields WR (1982) Thermal ionization mass spectrometry of uranium with electrodeposition as a loading technique. *Anal Chem* 54(6):957–960
- Ronesch K et al (1992) The Macdonald and savage titrimetric procedure for plutonium scaled down to the milligram level – automated procedure for routine analysis of safeguards samples containing 2 to 5 mg plutonium, IAEA/AL/59. IAEA, Vienna
- Rose CL, McKay WA, Halliwell CM, Watterson JD, Toole J (1997) SDRP-R246, AEA Technology PLC, Oxfordshire
- Rosenberg RJ (1992) Non-conventional measurement techniques for the determination of some long-lived radionuclides produced in nuclear fuel, VTT-TIED-1357
- Saari J, Lakio A (2008) Posiva working report 2008-39
- Saari J, Lakio A (2009) Posiva working report 2009-03
- Sailor MJ, Link JR (2005) *Chem Commun* (11):1375–1383
- Salmon L, Menut D, Lacour J-L, Vors E, L'hermite D, Gallou C, Sirven J-B, Mauchien P (2008) Atalante 2008: nuclear fuel cycle for a sustainable future, Montpellier
- Sampson T, Kelley T, Vo D (2003) Los Alamos National Laboratory report, LA-14018
- Savage DJ, Gunn JB, Drummond JL (1986) The effect of anions on Pu(VI) spectrophotometry. In: International conference on analytical chemistry in nuclear technology, Karlsruhe, ND-R-1258(D), Proceedings, 3–6 Jun 1985, p 21
- Scheer MA, Tobin SJ, Sandoval NP, Hu J, Menlove HO, Swinhoe MT (2009) In: 2nd Japan-IAEA workshop on advanced safeguards technology for the future nuclear fuel cycle, Tokai-mura
- Schmieder H, Kuhn E, Ochsenfeld W (1970) The absorption spectra of Pu(III), Pu(IV), Pu(VI), U(IV), and U(VI) in nitric acid and in tri-n-butyl phosphate-n-alkane solutions and their application in the automatic process control. KFK-1306
- Schneider HG, Merten M, Ottmar H, Cromboom O, Brandalise B, Mayer K, Hilton LC, Janssens W, Daures P, Koch L (1999) Pre-OSL: the means to test and optimize the technical operation of the On-Site Laboratory Sellafield (OSL), IAEA-SM-351/104. In: IAEA symposium on international safeguards, Vienna IAEA 1999, p 17(1990 pp)
- Schott R (1984) In: Proceedings of the 6th annual ESARDA symposium, Venice, paper 7–12, p 461
- Scott WW (1939) Standard methods of chemical analysis, vol 1, 5th edn. Van Nostrand, New York, p 298
- Scott JR, Mcjunkin TR (2009) In: 2nd Japan-IAEA workshop on advanced safeguards technology for the future nuclear fuel cycle, Tokai-mura
- Shinonaga T (2008) Analytical instructions for uranium and plutonium in environmental swipe samples (internal IAEA procedure SALCLI.5100, IAEA)
- Shults WD (1960) Controlled potential coulometric titration of plutonium. Application to PFR samples, ORNL-2921
- Shults WD (1963) Application of controlled potential coulometry to the determination of plutonium, (Pu(VI) to Pu(IV)). *Talanta* 10:833
- Shults WD, Hobbs BB, Blevin EL, Thomason PF (1959) Progress report on the analysis of dissolver solutions by controlled potential coulometric titration, ORNL-2776
- Simpson JCB, Clark PA, Nicols OP, Whitehouse KR (1998) Proceedings of the tripartite seminar on nuclear material accounting and control at radiochemical plants, Obninsk
- Slanina J, Bakker F, Lingerak WA (1976) Accurate potentiometric titration of 5–25 mg uranium, IAEA-SM-

- 201/65. In: Proceedings of the symposium, Vienna 1975, vol 2, p 157
- Spevackova V, Guichard C, Cauchetier P (1978) Influence de l'americium-241 sur la détermination du plutonium par la méthode à l'oxyde d'argent(II). *Anal Chim Acta* 96:189
- Sprinkle JK Jr, Menlove HO, Miller MC, Russo PA, Jorgensen C (1993) In: 15th ESARDA annual meeting: symposium on safeguards and nuclear material management, Rome
- Stepanov AV, Aleksandrjuk VM, Babaev AS, Demyanova TA, Preobrazhenskaya EB, Nikitina SA (1990a) Determination of uranium and neptunium by laser-induced time resolved spectrofluorimetry. In: 12th radiochemical conference, Marianske Lazne, 7–11 May; *Radioisotopy* 31(5–6):267
- Stepanov A, Byelaev B, Buljanitsa L, Lovtaus A, Ryzhinskii M, Eliot E, Dubois JC, Retali G, Tamberg T, Deron S, Capps J, Fiedler R, Swietly H, Aigner H, Jaech J (1990b) A $^{233}\text{U}/^{236}\text{U}/^{242}\text{Pu}/^{244}\text{Pu}$ spike for isotopic and isotope dilution analysis by mass spectrometry with internal calibration, IAEA-AL-23 (Rev.1990-01-02)
- Stepanov AV, Nikitina SA, Karasev VT, Belyaev BN, Stepanov DA, Pevtsova EV, Bogoroditskij AB (2002) Precise spectrophotometric method for the determination of U, Pu, Nd, and Rh using the principle of internal standardization. *Radiokhimiya* 44(2):165–169
- Stetzer O, Betti M, Van Geel J, Erdmann N, Kratz J-V, Schenkel R, Trautmann N (2004) *Nucl Instrum Methods Phys Res A* 525:582
- Stewart JE, Menlove HO, Mayo DR, Geist WH, Carrillo LA, Herrera GD (2000) Los Alamos National Laboratory report, LA-13743-M
- Strebin RS Jr, Robertson DM (1977) Alpha-energy and mass analyses of plutonium from a single sample mount. *J Radioanal Nucl Chem* 40(1–2):213
- Surugaya N, Taguchi S, Sato S, Watahiki M, Hiyama T (2008) Spectrophotometric determination of plutonium in highly radioactive liquid waste using an internal standardization technique with Neodymium(III). *Anal Sci* 24(3):377
- Sus F, Parus JL, Raab W (1996) Determination of neptunium in plutonium and mixed uranium-plutonium samples by isotope dilution gamma-spectrometry with ^{243}Am as a spike. *J Radioanal Nucl Chem* 211(2):363–374
- Sus F, Krtil J, Malek Z, Beran M (1998) Determination of trace radioactivity of thorium, uranium, neptunium, plutonium, americium, and curium in swipes and environmental samples, *Nucleon*, vol 1, pp 13–22
- Swinburn KA, McGowan IR (1976) IAEA-SM-201/63. In: Proceedings of the IAEA symposium, Oct 1975, vol 2, p 133
- Synthfeld A, Moszynski M, Arlt R, Balcerzyk M, Kapusta M, Majorov M, Marcinkowski R, Schotanus P, Swoboda M, Wolski D (2005) *IEEE Trans Nucl Sci* 52(6):3151–3156
- Synthfeld A, Arlt R, Gostilo V, Loupilov A, Moszynski M, Nassalski A, Swoboda M, Wolski D (2006) *IEEE Trans Nucl Sci* 53(6):3938–3943
- Takahashi M, Uchikoshi S, Midorikawa M, Adachi T (1994) Development of a digital-analogue robotic system for input solution and mixed oxide samples, IAEA-SM-333/53, International Nuclear Safeguards 1994, Proceedings, vol 1, p 761
- Tamborini G, Donohue DL, Ruedenauer F, Betti M (2004) *J Anal At Spectrom* 19:1
- Thermo Fisher Scientific, Patent (1993) Retarding Potential Quadrupole Lens (RPQ), Patent no. US 5180913, Thermo Fisher Scientific, Bremen
- Thermo Fisher Scientific Triton (2005): Thermal ionization mass spectrometer, neptune, multicollector ICP-MS, Thermo Fisher Scientific, Bremen. http://www.thermo.com/eThermo/CMA/PDFs/Various/File_26979.pdf
- Thevenon JB, Lebrun A, Ferey T, Fauvel D, Aujames P (2008) *ESARDA Bulletin* 40:13–25
- Thornton A, Menlove HO, Charlton W, Miller M, Rael C (2006) In: INMM 47th annual meeting, Nashville
- Tobin SJ, Demuth SE, Fensin ML, Hendricks JS, Menlove HO, Swinhoe MT (2008) In: INMM 49th annual meeting, LA-UR-08-03763, Nashville
- Tobin SJ, Charlton WS, Ehinger MH, Fensin ML, Hoover AS, Menlove HO, Quiter BJ, Rajasingam A, Sandoval NP, Saavedra SE, Strohmeier D, Swinhoe MT, Thompson SJ (2009) In: 31st ESARDA annual meeting, Vilnius
- Tolk K, Mangan D, Glidewell D, Matter J, Whichello J (2007) *J Nucl Mater Manag* 35(4):101–110
- Trepte O, Hildingsson L, Chen JD, Burton GR, Young GJ, Attas EM (1996) Swedish and Canadian safeguards support programs to IAEA under IAEA task JNT A00704, SKI-R-96-45
- Truong QS, Keeffe R, Ellacott T, Desson K, Herber N (2001) In: IAEA symposium on international safeguards, IAEA-SM-367/8/08/P
- Tuttas D, Schwieters JB, Quaas N, Bouman C (1998) Improvements in TIMS high precision isotope ratio measurements for small sample sizes. Application note: 30136, Thermo Fisher Scientific, Bremen
- Tuttas D, Schwieters JB, Bouman C, Deerberg M (2005) New compact discrete dynode multipliers integrated into the thermo scientific TRITON variable multicollector array. Application note: 30192, Thermo Fisher Scientific, Bremen
- United Nations Security Council (1991) Text of UNSC Resolution 687. Available at <http://www.fas.org/news/un/iraq/sres/sres0687.htm>

- UPU (1985) Universal postal convention, UPU international bureau, Berne
- Usuda S, Yasuda K, Saito-Kokubu Y, Esaka F, Lee C-G, Magara M, Sakurai S, Watanabe K, Hirayama F, Fukuyama H, Esaka K, Iguchi K, Miyamoto Y, Chai J-Y (2006) *Int J Environ Anal Chem* 86:663
- Vajda N, Toervenyi A, Kis-Benedek G, Kim CK (2009) Development of extraction chromatographic separation procedures for the simultaneous determination of actinides. *Radiochim Acta* 97(1):9–16
- Varga Z, Stefanka Z, Suranyi G, Vajda N (2006) Rapid methods for the determination of long-lived radionuclides in environmental samples by ICP-SFMS and radioanalytical techniques. *Czech J Phys* 56(supplD):D177–D182
- Varian (2009) Principles and performance of the CRI for the Varian 820-MS (pdf, 365 KB)
- Verbruggen A, Bauwens J, Eykens R, Kehoe F, Kühn H, Jacobsson U, Richter S, Aregbe Y (2008a) Preparation and certification of IRMM-1027k, Large-Sized Dried (LSD) spike, EUR 23539 EN-2008, JRC 483248, IRMM/JRC, Geel
- Verbruggen A, Bauwens J, Jakobsson U, Eykens R, Wellum R, Aregbe Y (2008b) An automated system for the preparation of Large Size Dried (LSD) spikes. In: *Atalante 2008: Nuclear fuel cycle for a sustainable future*, Montpellier
- Von Baekman AV (1971) Determination of uranium and plutonium in solutions of spent nuclear fuels by X-ray fluorescence analysis, IAEA-SM-133/81. In: *Symposium on progress in safeguards technology*, Karlsruhe 1970, Proceedings IAEA, Vienna, vol 2, pp 45–49
- Walker RL, Smith DH (1979) In: *Analysis of plutonium and uranium by the resin bead-mass spectrometric method* ANS topical conference, Kiawah Island, Nov 1979, CONF-791117-24
- Walker RL, Smith DH, Musick WR, Carter JA, Donohue DL, Deron S, Asakura Y, Kagami K, Irinouchi S, Masui J (1981) Resin bead mass spectrometry, results of a resin bead field experiment-TASTEX-J, SALE participants meeting, Argonne, Minutes, p 208
- Wallenius M, Morgenstern A, Nicholl A, Fiedler R, Apostolidis C, Mayer K (2001) Age determination of highly enriched uranium, IAEA-SM-367/5/07. In: *Symposium on international safeguards: verification and nuclear material security*, Vienna, Proceedings, p 1396
- Wang TF, Raschke KE, Ruhter WD, Kreek SA (1999) MGAHI: a plutonium gamma-ray isotopic analysis code for nondestructive evaluation, ANS 1999 winter meet, Long Beach, 14–18 Nov 1999; *Trans Am Nucl Soc* 81:234–236
- Waterbury GR, Metz CF (1959) *Anal Chem* 31:1144
- Whichello J, Annese C, Monteith A (2009) In: *2nd Japan-IAEA workshop on advanced safeguards technology for the future nuclear fuel cycle*, Tokai-mura
- Whitehouse K, Carr E, Sim D, Morris G, Tolk K (2004) In: *7th international conference on facility operations-safeguards interface*, Charleston
- Willard HB, Gordon L (1948) Thorium in monazite sand. *Anal Chem* 20:165
- Yokota Y, Ishikawa M, Matsuda Y, Tsujino K, Abhold ME, Buck SE, Ianakiev K, Klosterbuer SF, Marks T (1998) In: *39th INMM annual meeting*, Naples
- Yoshida H, Koizumi K, Ishikawa M, Kudo K, Hiyama T, Swinhoe M, Abhold M (2005) In: *INMM 46th annual meeting*, Phoenix
- Zahradnik P, Swietly H (1996) The robotized chemical treatment of diluted spent fuel samples prior to isotope dilution analysis. *Nucl Meth Chem Isot Anal* 204:145
- Zahradnik-Gueizelar P, Kuhn E, Johnson S, Duhamel G, Radecki Z, Kuno Y (2007) Authentication and sample chemistry: a new approach at the rokkasho reprocessing plant on-site laboratory. In: *Proceedings of an international safeguards symposium*, IAEA, Aug 2007, pp 681–688(888 pp)
- Zebrowski et al. (1995) Evaluation of procedure with ceric titrant, New Brunswick Laboratory report 332
- Zeissler R, Donohue DL (1995) *J Radioanal Nucl Chem* 194:229
- Zendel M (2008) *Int J Nucl Sci Technol* 4:72–80
- Zendel M, Khlebnikov N, Aparo M (2006) In: *IAEA symposium on international safeguards*, IAEA-CN-148/31
- Zendel M, Haas E, Khlebnikov N, Monteith A, Parise D, Poirier S, Ryzhikov R, Whichello J (2007) In: *29th ESARDA annual symposium on safeguards and nuclear material management*, Aix-en-Provence



Index

A

- A-bomb, 1861
- Absolute activity, 246, 334, 335
- Absorbed dose, 2152, 2154, 2218–2227, 2230–2231, 2242, 2243, 2288, 2295–2299, 2301–2313
- Absorbed fractions, 2182
- Absorber thickness, 1413, 1420
- Absorption coefficient, 526
- Absorption (attenuation) of gamma photons, 420
- ACAR spectra, 1476–1478
- $^{225}\text{Ac}/^{213}\text{Bi}$ generator, 1944, 1960, 1964–1967
- Acceleration tube, 2345–2346
- Accelerator driven system (ADS), 2651–2654
- Accelerator mass spectrometry, 2462–2485, 2491, 2495, 2500
- Accelerator production of tritium (APT), 2831
- Accelerators, 1268–1270, 1281, 1292, 1309, 1317–1320, 1323, 1326
- Accelerator transmutation of waste (ATW), 2831
- Accelerator, types of, 1905
- Accepted units, 477, 479
- Accidents, nuclear, 2507
- Acetone, 1952–1953, 1982, 1987, 2005, 2125, 2153
- Acetyl carnitine, 2000
- Acetyl coenzyme A, 2000
- Acetylene, 1298, 1360
- Acoustic oscillations, 628
- Actinide concept, 818, 820, 823, 846–850
- Actinide contraction, 850
- Actinides, 23, 24, 30, 94, 226, 290, 291, 316
- Actinide series, 926
- Actinides, metallic properties of, 859
- Actinium, 5, 6, 226, 227, 488
- Actinium ($4n+3$) series, 339, 345
- Action levels, in nuclear emergency, 2558
- Activable tracers, 1764
- Activated complex, 717, 718
- Activation analysis, 1553–1612, 1674–1678
- Activation cross section, 1867, 1870, 1871
- Activation kinetics, 353
- Activation methods, 1555, 1562–1563, 1591, 1595
- Activation reactions, 1555–1560, 1564, 1565, 1580, 1604
- Activity concentration, 334
- AcuTect, 2102
- Acute myeloid leukemia (AML), 1965
- Acyclic bifunctional chelators, 2147–2152
- Addition theorems, 453
- Additive property of activity, 416
- Adiabatic calorimetry, 2310
- Administration, distribution, metabolism, excretion (ADME), 2080–2081
- ADOR, 796
- Adsorption enthalpy, 934, 936, 946, 963, 965, 977, 978, 984–988, 990–994
- Adsorption temperature, 2433, 2440–2443, 2446–2448
- Advanced accelerator application (AAA), 2831
- Advanced fuel cycle (AFC), 2802, 2830–2832
- Advanced photon source (APS), 1742
- Aerodynamic isotope separation, 2383–2384
- AES. *See* Auger emission spectrometry
- After effect, 1434–1436, 1439
- $^{109\text{m}}\text{Ag}$, 1943, 1955
- Age determinations, 16, 27
- Age-momentum correlation (AMOC), 1480–1481
- AIDA, 937, 939, 941, 954
- Akagenite, 1424, 1425
- ^{26}Al , 2464, 2476–2479, 2496, 2499
- Alaga rules, 95
- ALCHEMY II, 866
- Aldehydes, 1987, 1997, 1998, 2002–2003, 2035, 2039, 2046, 2058
- Aliovalent charge states, 1434
- Aliquat, 947, 967–969
- Alkali elements, 2440
- Alkali halide crystals, 1292
- Alkaline earth metals, 227–230
- Alkenes, ^{11}C -labeled, 1986, 1993, 1996
- Alkylating agents, 1986, 2049
- Alkyl chlorides, bromides and iodides, 1299
- Alkyl halides, 1986, 1987, 1992–1994, 2003
- Allowed transitions, 119, 129, 131–135, 357–361
- Alpha-alpha mother-daughter decays, 982
- Alpha-alpha parent-daughter correlation, 882, 936
- Alpha decay, 64, 112–123
- Alpha-decay energies, 64
- Alpha-HIB. *See* Alpha-hydroxy-isobutyric acid
- Alpha-hydroxy-isobutyric acid (Alpha-HIB), 85, 836, 928, 947, 966, 1962
- Alpha-L-alanine, 2306, 2307
- Alpha-nucleus interaction, 117
- Alpha partial half-lives, 116
- Alpha particle clustering, 187, 213
- Alpha particle counters, 2861
- Alpha particle energies, 778, 942, 976, 987, 1019–1023
- Alpha particle method (APM), 1681
- Alpha particles, 485, 521, 522
- Alpha particle sources, 2574
- Alpha-ray measurement, 1770–1771

- Alpha spectroscopy, 937, 939
 Alsos project, 2621
 Alumina generator, 1884–1897, 1951, 1957, 1963, 1964, 2075, 2076
 Alvarez structure, 2355
 Alzheimer's disease, 2045, 2046
 Americium, 18, 22, 819, 823, 850, 853–857, 861, 865, 867
 Amides, 1994, 1997, 1998, 2041, 2051, 2092, 2096, 2099, 2110–2111, 2136, 2154, 2158, 2172
 Amino acids, 1989, 2000–2004
 AML. *See* Acute myeloid leukemia
 Amsterdam density functional (ADF), 867
 Analogue approach, 2098, 2103
 Analysis of hydrogen, 1661–1663
 Angiocardiology, 1955, 1958
 Angioplasty, 1950, 1954–1958, 1962, 1964
 Angular correlation of annihilation radiation (ACAR), 1475–1480
 Angular distribution, 159–161, 177, 180, 189, 202
 Anion-exchange column, 950, 952, 954
 Anion-exchange resin, 950–958, 968, 970, 983
 Annealing, 25
 Annihilation, 1269, 1273, 1448, 1454, 1455, 1462–1483, 1487, 1509–1511, 1638, 1641–1642, 1653, 1768, 1847
 Annihilation peak, 2271, 2272, 2569
 Annihilation radiation, 1463, 1475–1478
 Annual effective dose, 2237, 2531–2533, 2537, 2541, 2542
 Anomalous lead dating, 811–812
 Anomalous scattering, 1519
 Anthropogenic radioactivity, 2511
 Antibaryonic, 625
 Antibody, 1883, 1889, 1890, 1893, 1948, 1959, 1964, 2055, 2074, 2080, 2091, 2096–2104, 2132, 2146–2155, 2159, 2161, 2165–2167, 2171, 2180, 2183–2192
 Antigen, 1883, 2184–2191, 2197, 2202, 2203
 Antigen-mAb system, 2188
 Antihydrogen, 1509–1511
 Antileptons, 42
 Antimatter, 618, 625–627
 Antimatter galaxies, 461
 Antiparticles, 461–462, 469
 Antiprotonic atoms, 1487, 1503, 1507–1509
 Antiprotonic helium, 1496, 1497, 1507–1509
 Antiquarks, 42, 43, 463
 APD detector. *See* Avalanche photodiode detector
 APM. *See* Alpha particle method
 Apollo-12 basalts, 796
 Apparatus for continuous determination of distribution ratios in solvent extraction (AKUFVE), 2412–2415
 Appearance energy, 1335, 1362–1363
 APS. *See* Advanced photon source
 Aqueous chemistry, 937–943, 981
 Aqueous raffinate, 2813
 Aqueous solutions, 1283–1291, 1301, 1305–1306, 1310–1311, 1315, 1320, 1326, 1435, 1769, 1780, 1785, 1788
 Arachidonic acid, 1999, 2005
 ARCA II system, 2412
 Argon-39, 764–767, 770–773
 Argon/argon dating, 765
 Argon-40, radiogenic, 766, 767, 781, 782
 Arithmetic mean, 404
 Aromatic compounds, 1988, 2125, 2128, 2131
 Aromatic hydrocarbons, 1276, 1287, 1289, 1292–1299, 1318
⁷²As, 1905, 1943–1948
 Associated particle method (APM), 1683
 Astatine, 13
 Astrophysical S-factor, 642
 Asymmetric complexes, 2099
 Asymmetric fission, 258
 Asymmetric mass distribution, 254, 260
 Asymmetric mass split, 20
 Asymmetric syntheses, 2002, 2003, 2035, 2101
 Asymmetry energy, 212, 213, 232, 233
 Asymmetry parameter, 1400, 1407, 1419–1420, 1440, 1490, 1492, 1517
 Asymptotic behavior, 347, 349, 352
²¹¹At, 1929, 1931, 1944, 1960, 2181–2182, 2185, 2186, 2199–2201
 Atlantis II hot brine, 1012
 Atmospheric nuclear tests, 2540, 2541
 Atomflot, 2522
 Atomic bomb, 2245, 2507, 2654, 2655, 2660
 Atomic-electron binding energies, 504–510
 Atomic mass, 487, 492, 540, 609
 Atomic mass units, 482, 492, 540
 Atomic number, 487, 514–520
 Atomic units, 477, 480
 Atomic vapor laser isotope separation (AVLIS), 2400
 Atomic weapons, transport of, accidents, 2551
 Atomic weight, 487, 491–504
 'Atoms for Peace' Conference, 18
 ATP pump, 2081
 Attenuation corrections, 1535
^{195m}Au, 1944, 1955, 1958–1959
¹⁹⁸Au colloid, 2180, 2187
 Auger cascades, 275
 Auger effect, 388, 390–392
 Auger electrons, 390–392, 1888, 1928–1930, 1959, 1960, 1966, 2181, 2203
 Auger emission spectrometry (AES), 1609, 1745
 Auger process, 1341
 Auger spectra, 391, 392
 Auger transitions, 1496, 1507
 Automated Rapid Chemistry Apparatus (ARCA), 2412
 Autoradiograph, of lung tumor, 2183–2184
 Autoradiography, 1634, 1767, 1770, 1790
 Avalanche detectors, 2265
 Avalanche photodiode detector (APD) detector, 1449, 1453–1456
 Average energy isotope effect, 1352

Averted dose, 2558, 2560
 AVF cyclotron, 2351, 2359
 Avogadro's constant, 367, 483

B

¹²⁸Ba, 1944, 1945, 1949
 BABI, 794
 Back-bending effect, 92
 Back-end, of nuclear fuel cycle, 2808–2818
 Backfill, 2817
 Background counts, 418
 Backing-off, 1280
 Backscattering spectrometry, 1680, 1745
 Backscatter peak, 2272
 β -amyloid plaques, 2045, 2046
 Barium, 4, 5, 10, 20, 227–230, 488
 Barium carbonate, 1783
 Barkas effect, 369, 371
 Barn, 157, 181
 Barrier curvature parameter, 904
 Baryon density, 630–635
 Baryon number violation, 626
 Baryons, 459, 463, 472
 Baryon to photon ratio, 630, 634
 BAT, 1953, 2161, 2163
 Batch yield, 1909, 1918, 1919, 1923, 1924
 Bateman equations, 345, 346, 675, 676, 1878, 1879
 BATO, 2083, 2087
 BCS theory, 70
¹⁰Be, 2476–2478, 2482
 Beam extraction, 2336–2337
 Beam time, 1538, 1568, 1611
 Becquerel, unit of activity, 334, 478
 Beer–Lambert law, 1280
 Benzaldehydes, 1989, 2040, 2049, 2050, 2059
 Benzene, 1276, 1286, 1298, 1307, 1361, 1779
 Benzodiazepine receptors, 2007, 2008, 2032, 2048, 2125
 Benzyl-TETA-HSA, 1950
 Berkeley gas-filled separator (BGS), 1015
 Berkelium, 22, 820, 823, 826, 850, 856, 857, 865
 Bernoulli distribution, 411–415, 430, 438
 Bernoulli trials, 405, 411, 414, 415, 443
 Beryllium–7, Beryllium–10, 742, 771–772
 Bessel function, 1395, 1413
 Beta-CIT, 2006, 2007, 2105, 2127, 2139, 2140
 Beta-decay, 64, 73, 123–136
 Beta-decay energies, 64
 Beta-decay probability, 117, 129, 135, 358
 Beta-particle counters, 2860–2861
 Beta-particle emitters, 1889, 2196–2198
 Beta-ray measurement, 1769–1770
 Beta stability, 685, 686
 Beta transition, 72
 Betatron, 2357
 Betatron oscillations, 2357–2359
 Bethe–Bloch curve, 369

Bethe–Bloch equation, 365–371, 374, 376, 382
 Bethe formula, 296
 Bhabha scattering, 376
²¹²Bi, 1944, 1965, 1966, 2145, 2149, 2199, 2201, 2202
²¹³Bi, 1929, 1941, 1944, 1960, 1964–1967, 2145, 2149, 2151, 2161, 2185, 2199, 2202, 2203
 Bifunctional chelates, 2198
 Bifunctional chelating, 1890, 1961
 Bifunctional chelator (BFC), 1967, 2074, 2092–2100, 2110, 2144, 2146–2175
 Bifunctional labeling chemistry, 2143–2175
 Bifunctional prochelator, 2153, 2158–2161
 Big Bang, 28, 150, 207, 615–618, 630–633, 636, 658, 764
 Bimodal fission, 841, 844
 Binding energy, 44, 45, 48, 50–52, 58, 61, 64, 67, 73, 85, 107, 108, 111–113, 504, 514, 540
 Binding-site barrier, 2184
 Binomial distribution, 405, 411, 414–417, 423, 424, 430, 434, 435, 443, 446
 Biological microbial enrichment, 2401
 Biological molecules, 1310–1313, 1325
 Biosynthetic methods, 1980
 BIPM, 476
 Bismuth germanate (BGO), 2278, 2285
 Black-disk model, 158
 Black hole, 621, 629, 641, 652, 658
 Blackness effect, 1413
 Blobs, 1274
 Bloch-state, 1465–1466, 1471
 Blood-brain barrier (BBB), 1981, 1995, 2010, 2027, 2085, 2086, 2105
 Blood flow agents, 2084–2087
 Blood flow measurements, 1348
 Blood pool imaging, 1950
 Bohrium, 24, 25, 883, 885, 892, 926–929, 983–986, 1012, 1014
 Bohr magneton, 55, 127, 484, 485
 Bohr–Mottelson formula, 93
 Boiling water reactor (BWR), 2621, 2640, 2645–2647
 Bolton and Hunter reagent, 2136
 Boltzmann–Uehling–Uhlenbeck (BUU) formalism, 203
 Bolus injection, 1954, 1959
 Bombesin, 2057, 2060, 2103, 2197
 Bond-breaking model, 1505, 1506
 Bond rupture, 1308, 1334, 1335, 1340, 1356, 1435
 Bone marrow toxicity, 2198
 Bonn potential, 50
 Boric acid, 2643, 2645
 Born approximation, 183, 299, 370
 Born–Oppenheimer approximation, 703, 706, 707
 Boron neutron captures therapy, 2004
 Bose–Einstein distribution, 1387
 Bosons, 458, 459, 462–468, 470–472
⁷⁶Br, 1919–1922
⁷⁷Br, 1905, 1943, 1955, 2204
 Brachytherapy, 1888, 1889, 2538

- Bragg additivity, 372, 379
 Bragg curve, 371, 373
 Bragg's law, 1526–1528, 1531
 Brain imaging, 2084, 2086, 2087, 2105
 Brain receptor-targeting, 2106
 Branched alkanes, 1296
 Branching decay, 338–341, 355, 676
 Branching ratio, 1034
 Breakeven, 2762, 2790, 2793
 Breakthrough, 1942, 1946, 1949–1959, 1963, 2076, 2082
 Breakthrough of parent nuclide, 1942
 Breeder reactors, 2631, 2648–2651, 2700
 Breed plutonium, 2807
 Breit–Wigner, 173, 174
 Bremsstrahlung, 376, 378, 380, 388, 390
 Brilliance, 1448, 1454, 1456, 1741, 1742, 1758
 Broecker scale, 737
 BTP system, 854
 Bubble model, 1469
 Bulk sample, 1622, 1625, 1654
 Bursts of X-rays, 655–656
 Butyrophenone neuroleptics, 2034
- C**
 Cadmium ratio (CR), 1877, 1878
 Cage effect, 1360
 Calibration standards, 2566, 2863, 2908, 2922, 2986
 Californium, 22, 24, 820, 822, 823, 826, 850, 856, 857
 Calixarene agents, 1967
 Calorimeters, 2937–2938
 Calorimetry, 2308–2310
 Calutrons, 2378
 CANadian Deuterium Uranium reactor (CANDU-reactor), 2621–2640
 Cancer, 2045, 2047–2049, 2056
 Cancer radiotherapy, 1267
 Capacitive liner, 2344, 2346
 Capillary Mössbauer spectroscopy, 1435–1436
 Capture cross sections, 225
 Carbanion, 1984–1985, 1993, 2003, 2026, 2029
 Carbohydrates, 1992, 2004–2005
 Carbon burning, 639, 643–647
 Carbon cycle, 729, 734, 741–743
 Carbon-14 dating, 784, 786, 789
 Carbon fixation, 722
 Carbon, hydrogen, oxygen, and nitrogen (CHON) principle, 2424–2425
 Carbon monoxide, 1979, 1981, 1983, 1992–1998
 Carbon-nitrogen-oxygen (CNO) cycle, 331, 332
 Carbonylations, 1992, 1993, 1996–1998
 Carbonyl compounds, 1996, 1997, 2025
 Carbonyl functionality, 1981, 1989–1990, 2005
 Cardiac function, 1955
 Cardiac PET, 1954
 Cardiolite, 2081–2083
 Cardiotec, 2083, 2084
 Carrier-free, 334
 Carrier, of tracers, 1765–1766
 Cascade decay, 1496, 1565
 Cascade generators, 2343
 Cassiopeium, 1014
 CASTOR, 2658
 Catcher foil, 1686
 Catecholborane, 2128
 Cation-exchange column, 820, 950–954
 Cation-exchange resin, 950–952, 960, 982, 983
 Cauchy distribution, 434, 438–442
 CCD detector, 1489, 1684, 1752
 CD. *See* Cyclodextrin
¹⁰⁹Cd, 1943, 1955
 χ^2 distribution, 397, 430, 433, 436–438, 451, 452, 454
¹³⁴Ce, 1944, 1945, 1949, 1966, 1967
 Cellulose, 1311–1314, 1636, 1711
 CEMS. *See* Conversion electron Mössbauer spectroscopy
 CEMS detectors, 1431–1432
 Central attractive well, 152
 Central ignition, 2765
 Central limit theorem, 402, 405–410, 416, 432, 434, 438, 443–445
 Central nuclear interaction potentials, 47
 Central potential, 46, 65, 96, 147, 164, 284
 Centrifugal barrier, 154–156
 Centrifugal contactors, 2409, 2423
 Centrifugal extractors, 2408, 2409
 Centrifugation, 2382–2383
 Cerebral blood flow, 2084–2090
 Ceretec, 2085–2086
 Ceric sulfate dosimeter, 2291–2292
 Certified reference materials (CRMs), 1576, 1583, 1607, 1637, 1663, 1667
 Cesium, 2336, 2420, 2464
 (²³²Th) chain, 669
 (²³⁵U) chain, 671, 687
 (²³⁷Np) chain, 672
 (²³⁸U) chain, 670
 Chain elements, chemistry of, 687
 Chain reaction, 17–20, 231, 263, 447
 Chain scission, 1307
 Chain yields, 245–264
 Chance coincidences, 427
 Chance for a positive result, 429
 Chandrasekhar limit, 655
 Channeling effect, 1719–1721
 Channeltron, 1432
 Characteristic function, 400–404, 410, 420, 430, 432, 436–438
 Charge coupled device (CCD), 1489, 1683–1684, 1691, 1752
 Charge distribution, after nuclear decay, 1334–1343, 1396, 1398–1400
 Charged particle activation analysis (CPAA), 1567–1568, 1583

- Charged-particle-induced reactions, 156, 157
Charge plunger experiment, 275–276
Charge radii, 57–59, 67, 111
Charge-transfer reaction, 184
Charm, 42, 464
Chart of the nuclides, 61–63, 70, 133
Chelate extraction, 2407
Chelators, 1967–1968, 2057, 2077, 2078, 2084,
2092–2104, 2106, 2108, 2110, 2113–2114, 2144–2175,
2197, 2203
Chemical dosimeters, 2290–2297
Chemical equilibria, 700, 704–708, 716, 1778–1780, 1783
Chemical evolution of a galaxy, 615, 661–662
Chemical isomer shift, 1397–1399, 1404–1406, 1440
Chemical processing, of irradiated material, 1904,
1911–1914
Chemical reactivity, 1908, 1914, 2024, 2025
Chemical separation, 1908, 1909, 1912, 1914, 1923,
1928,–1931
Chemical stability, 1880, 2077, 2078
Chemoselective conjugation, 2054–2058
Cherenkov counter, 1504, 1770
Cherenkov radiation, 368, 376, 377, 382–383
Chernobyl, 2506–2511, 2515, 2517, 2522, 2524, 2527,
2547–2528, 2549, 2550
Chiral centers, 2002, 2003, 2085, 2088
Chirality, 2002
Chloramine-T, 2124, 2127–2129, 2132–2134, 2136
Chlorine–36, 770, 772–773
Cholecystokinin B, 2193
Chondrites, 660, 735, 767, 777, 796
Chopper, 1531, 1545, 1650, 1657, 1659, 1701
Chromatogram, 2394
Chromatography, 692, 713, 859, 928, 933–937, 940, 944,
945, 947, 950, 959–968, 978–980, 984, 994, 1021,
2393–2397
CHUR, 796
CHX-substituted DTPA, 1961
CINDA. *See* Computer Index of Neutron Data
CKM mixing matrix, 470
¹¹C-labeled compounds, 1979, 2002–2009, 2061
¹¹C-labeled tracers, 1980
Classical cyclotron, 2350
Classical electron radius, 467, 484
Clebsch–Gordan coefficients, 1411
Climate indicators, 754–755
Climate Long-Range Investigation and Mapping
(CLIMAP), 733, 739, 746
Climatic changes, 728, 731, 733, 735, 739, 740, 743, 744,
747–748
Climatic optimum of the Pliocene, 750
Climatic response, 729, 744–746
Cloud muo, 1490
Clover detector, 1649, 1726–1727
Clover-Ge-BGO detector system, 1726
Clusius–Dickel column, 2379
Cluster-configuration shell model, 121
Cluster decay, 839
Clustering, 107–111, 120–122, 137
Cluster model, 41, 107, 108, 110, 120
[¹¹C]Methyl iodide, 1980–1986, 1989–1996, 1999,
2003–2005, 2047
CMP, CMPO system, 853
CNO cycle, 641–645, 654, 656
CNS receptor binding molecules, 2091, 2096
Cobalt, complexes of, 1361, 1365
COBE satellite, 616, 628
Cockcroft–Walton source, 2343, 2344
Co–57 decay scheme, 1393
Coenzyme A, 2000
Coherent and incoherent scattering, 1522–1523, 1533,
1538
Coherent elastic scattering, 1526–1527, 1535
Coherent scattering, 387
Coincidence circuit, 336, 427
Coincidence loss, 2277
COLD, 986, 987, 991, 993
Cold fusion, 881, 885–889, 908, 911–915, 1012,
1013, 1024
Cold neutrons, 1624, 1631, 1664, 1666
Cold tower, 2387, 2388
Collective rotation, 85, 92, 176
Collimator, 1631, 1633, 1641, 1645–1647
Collision dynamics, 202–204
Color, 41, 42, 330, 356, 442, 463–466, 472
Color center, 2298
Committed doses, 2219, 2223, 2229–2230, 2242
Common lead, 809, 811
Comparative half-life, 132, 357
Comparator method, 1568, 1569, 1576–1577, 1602
Compartmental model, 2021
Competing acceptors model, 1434, 1435
Competing reaction channels, 1906
Complete fusion, 188, 190, 199
Complete fusion of heavy ions, 889
Complex chemistry, 2414–2415
Composite detectors, 2285–2286
Composite nucleus, 148–151, 156–159, 190–192, 204
Compound nucleus (CN), 147, 149, 151, 157, 172, 190,
192, 199, 201
Compound semiconductors, 2278
Compton continuum, 2271, 2285
Compton edge, 385
Compton effect, 384–387
Compton scattering, 1627, 1637, 1638, 1641, 1642, 1651
Compton suppression, 1621, 1638, 1641, 1647–1650,
1659
Computational chemistry, 818, 865–867
Computed tomography (CT), 1936, 1946, 1947, 1953,
2010, 2085, 2089, 2144, 2535, 2537
Computer Index of Neutron Data (CINDA), 1834
Concentration factor, 2508, 2522, 2526, 2561

- Concordia and discordia, 807–809
Concordia diagram in dating, 808
Conductivity, 2295–2296
Confidence level, 468
Confinement time, 2761–2763, 2766, 2767
Confocal imaging, 1751–1756
Conservation laws, 79, 119, 135, 147, 148, 459, 462, 466, 470
Constituents, 41–44, 51, 107
CONTIN, 1475
Continental glaciation, 736–737
Continuous distribution, 124, 398, 400, 403, 404, 407, 409, 437
Conversion electron Mössbauer spectroscopy (CEMS), 1430–1433
Conversion electrons, 75–84
Conversion electron sources, 2573, 2575
Conversion factors for energy equivalent quantities, 485–487
Convolution, 407, 409–411, 430, 441, 444
Copernicium (Cn), 24, 879, 884, 888, 891–893, 911, 926, 929, 990–994, 1014, 2454
Copper–67, 1884, 1898–1899, 2196–2197
Core temperature, influence on reactivity, 2633
Coriolis antipairing effect, 94
Cork injection, 2438, 2439
Coronary restenosis, 1950
Corona triode, 2346
Correlated α - α mother-daughter decays, 982
Correlated decay chains, 985
Correlation coefficient, 301
Correlation functions, for nuclear scattering, 1523–1525
Corrosion resistance, 1791
Cosi fan tutte, 248, 265
Cosine effect, 1421
Cosmic microwave background radiation (CMBR), 616–619, 621, 624, 625, 629, 630, 636
Cosmic neutrino background, 630
Cosmic radiation, 2505, 2528–2529, 2534, 2557
Cosmic radionuclides, 2529
Cosmic ray dose rate, latitude distribution of, 2529
Cosmic-ray induced reaction, 151
Cosmic rays, 2242, 2478, 2479, 2516, 2528–2529
Cosmochronology, 15–16, 27–29
Cosmogenic radionuclides, 770–773
Cosmological and SN radionuclides, 2475
Cosmological constant, 623, 624, 636
Cosmological parameters, 616, 619, 624
Coster–Kronig electrons, 2203
Coulomb barrier, 152–158, 161, 177, 187, 192, 198, 202, 641, 642, 649, 685, 889, 892, 909, 911, 1023
Coulomb capture ratios, 1495
Coulomb correction, 130, 378, 388
Coulomb energy, 185, 230–237, 283, 328
Coulomb excitation, 153, 154, 177, 180–182, 185
Coulomb interaction, 1271, 1274, 1395, 1396
Coulomb potential, 153, 165, 234, 325, 326, 466
Coulomb scattering, 324–326
Counterstream cascades, 2373–2375
Counting efficiency, 1623, 1627, 1636, 1642, 1645, 1653, 1654
Counting gas, 1431, 1770, 1780
Coupled accelerator, 2356
Coupled resonances, 2359–2360
Covariance, 407, 408, 412
CPTA, 2161, 2163, 2171
CPT invariance, 461–462, 469
CP-violation, 469, 470, 626
CR. *See* Cadmium ratio
Cranked shell model, 99, 101
Critical density, 619, 630, 633, 634
Critical distance, 1274, 1275
Critical energy, 367, 378–380
Criticality factor, 2632–2633, 2635, 2654
Critical mass, of fissile nuclides, 2637
Critical size, 2637
Critical state, 2620, 2635–2637, 2653
Cross-couplings, 1994–1996
Cross-linking, 1302, 1306–1314
Crossover decays, 685
Cross section, 156–162, 166–169, 173–185, 188–193, 199, 201, 204, 214–218
Cryofurnace, 1438
Crystal defects, 1466, 1481–1482
¹²⁸Cs, 1944, 1945, 1949
CSDA range, 521, 522, 528, 530–533, 538, 540
¹¹C-syntheses methods, 1983–2002
[¹¹C]tamoxifen, 1984
⁶²Cu, 1919, 1943, 1945, 1950, 2144, 2145, 2149
⁶⁴Cu, 1864, 1865, 1881, 1905, 1914, 1919–1922, 1928, 1931, 2144, 2145, 2149, 2164, 2165
⁶⁷Cu, 1862–1865, 1880–1882, 1898, 1899, 1905, 1928–1931, 2144, 2145, 2149, 2171, 2195–2197
Cu(I) assisted radioiododebromination, 2126
[⁶²Cu]ATSM, 1950
Cumulative activity, 1939, 1940
Cumulative yield, 245, 252
Cuprate mediated coupling reactions, 1993
Cuprates, 1985, 1993, 1994, 1999
[⁶²Cu]PTSM, 1950, 2145
Curie, unit of activity, 334, 480
Curing of polymer coating, 1309
Curium, 18, 22, 24, 819, 823, 826, 830, 846, 850, 856, 857, 867
Cushioning collision model, 1336
Cyanations, 1993, 1994
Cyanex–301 system, 855–856
Cyanide, 1983, 1990–1993, 2002–2004, 2014, 2078, 2106, 2111
Cyanogen bromide, 1991, 1992
Cyclic accelerators, 2321, 2341, 2348, 2357
Cyclodextrin (CD), 1335, 1373, 1374

Cyclohexane, 1276, 1277, 1294–1298, 1356
 Cyclopentadienyl, 2098, 2099, 2106
 8-Cyclopentyl-3-(3- ^{18}F fluoropropyl)-1-propylxanthine (^{18}F CPFPX), 2045, 2046
 Cyclopropane, 1277, 1360, 1372
 Cyclotron, 1904–1931, 2322–2327, 2331–2332, 2335, 2348–2352, 2358–2362
 Cyclotron production of radionuclides, 1906, 1907, 1911
 Cyclotron, types of, 1905
 Cytotoxicity, 1960, 2199, 2204

D

DADS, 2086
 Damped/dissipative collision (deep-inelastic), 187–190
 Dark energy, 621–625
 Dark matrix, 1748
 Dark matter, 472
 Darmstadtium, 24, 884, 887, 891, 892, 1013, 1014
 DAT. *See* Dopamine transporter agents
 Daughter nuclide, 1939, 1941–1946, 1949, 1955, 1958, 1967
 Davydov–Filippov model, 96
 DC. *See* Damped/dissipative collision (deep-inelastic)
 D-D and D-T reactions, 1682, 1683, 1834–1835, 1846
 Dead time, 443–445, 453, 2261, 2263
 De Broglie wave length, 157, 173, 187, 202
 Debye length, 325–329
 Debye model, 1386–1389, 1415
 Debye–Scherrer cone, 1528
 Debye temperature, 1387, 1413, 1415, 1441
 Debye–Waller factor, 1527
 Decarboxylation of alanine, 1780
 Decay after activation, 352–353
 Decay chains, 342–346, 356, 1013–1023
 Decay constant, 6, 11, 78, 109, 115, 118, 129, 136, 218, 246, 322, 335–341, 346, 351–358, 361, 420, 424–427, 451, 1870–1871, 1878, 1906, 1937, 1941
 Decay energies, 609, 1034
 Decay gamma rays, from thermal neutron capture, 1810–1834
 Decay law, 6, 362, 424
 Decay modes, 1034
 Decay products, 1915, 1929, 1936, 1964–1965, 1967
 Decay schemes, 12, 112, 113
 Decay series, 5–8, 13, 339, 342, 344, 345, 351, 355
 Deceleration parameter, 622, 623
 Deciles, 404
 Deconvolution, 403, 409–411
 Deep inelastic collisions, 187, 188
 Deep Sea Drilling Project (DSDP), 733
 Defense waste, 2799
 Deformation alignment, 96–98
 Deformed nuclei, 21, 63, 70–73, 81, 85, 89–96, 98–101, 119, 122–123, 156, 180, 182, 289
 Deformed-shell nuclei, 905

Degrees of freedom, 93, 146–149, 162, 190, 194, 198, 207, 214, 239, 299, 436–438, 452–454, 461
 Delayed coincidence, 336
 Delayed fission, 841–843
 Delayed neutrons, 245, 247, 258, 2636, 2704, 2942–2943
 DeMoivre–Laplace theorem, 434–436
 Dendrochronology, 785, 788–789
 De novo inhibitor, 2092
 Density effect correction, 367–369
 Density function, 337, 375, 398–404, 407–411, 420–422, 427–439, 442–445, 450
 Density functional method, 862, 866, 943
 Dental practice, 2556
 Dental radiography, 2536
 Deoxyribonucleic acid (DNA), 1310–1311, 1325, 1894, 2042, 2043, 2199, 2204, 2205
 Depleted uranium, 2421, 2423
 Depletion depth, of Si detectors, 2266
 Deprenyl, 2008, 2040
 Depth profiling, 1608, 1611, 1683, 1685, 1687, 1712, 1716, 1717, 1722, 1723, 1730–1732
 Depth selective CEMS (DCEMS), 1432
 Desferrioxamine-B (DFO), 2151–2152
 Detailed balance, 174
 Detection efficiency, 1431, 1449, 1476, 1490, 1560, 1573, 1578, 1582, 1648, 1650, 1698–1699, 1706, 1725–1727, 1731
 Detection limit, 1627–1629, 1637, 1647, 1650, 1663
 Detection limit, PIXE, 1698–1700, 1708–1710
 Detector calibration, 2566–2575
 Detector damage, 1634
 Detector efficiency calibrations, 2573
 Detectors, 1449, 1452–1456
 Detector signal, 427, 440, 446
 Determination of boron, 1661, 1663, 1667
 Deuterium, 630, 633–636, 700, 702–706, 711–714, 718, 720–723, 728, 732, 735, 744, 751
 Deuteron, 9, 13, 17, 19, 44, 45, 48, 50, 162, 184, 292, 298, 300, 306, 311, 321, 485, 631, 642, 690, 691
 Deuteron-induced γ -ray emission (DIGE), 1710, 1724, 1728
 De Vries effect, 787
 DFO. *See* Desferrioxamine-B
 Diagnostic administrations of radiopharmaceuticals, 2538
 Diagnostic radiology, 2535–2537, 2553–2556
 Diagnostic radionuclides, nuclear properties, 2145
 DIAMide EXtraction (DIAMEX), 2827
 DIANE, 1685
 Diaryliodonium salts, 2038–2039
Diatide, 2102
 Dichromate dosimeter, 2292–2293
 Differential cross section, 1556, 1557
 Differential distribution function, 398
 Differential oscillation strength, 1273
 Diffuse scattering, 1526–1529

- Diffusion, 1765, 1771, 1777, 1783–1785, 1789, 1790
Diffusion coefficient, 2435, 2436
Diffusion in liquids and solids, 1493, 1784–1785
Difunctional precursors, 1987
DIGE. *See* Deuteron-induced γ -ray emission
Digital pulse processing, 1743
Digital signal processing (DSP), 1639–1640
3,4-Dihydroxy-L-phenylalanine (DOPA), 2000, 2002, 2027, 2028, 2031, 2036, 2061
Diisobutyl carbinol (DIBC), 966
Dilatancy model, 807
Dimensional analysis, 399, 428
Dimercaptosuccinic acid (DMSA), 1963, 2087–2089
Diogenes, 270
Dioximes, 2083, 2085
Dirac equation, 461
Dirac–Fock (DF) calculations, 519
Dirac–Fock calculations, multiconfiguration, 943
Dirac–Slater Discrete Variational Method (DS DVM), 943
Direct drive, 2765, 2766
Direct labeling approach, 2074, 2100–2101
Direct radioiodination, 2128–2131, 2136, 2138, 2140
Direct reactions, 149, 156–158, 160, 161, 182–185, 199
Discovery of new elements, criteria for, 916
Discrete distribution, 398, 400, 434
Disintegration rate, 334, 335
Disorder model, 1366
Dispersion parameters, 401, 403, 441
Displacement laws, 6
Disposal into space, of high-level waste, 2816
Dissociative character, 2449
Distance measurements, 621–625, 636
Distillation, 2371–2374, 2377, 2378, 2380–2382, 2384–2392, 2395
Distillation apparatus, 1912
Distribution coefficients, 931, 939–942, 947, 949, 955, 958, 960, 969–971
Distribution function, 203, 398–401, 404, 407, 409, 420–422, 426, 432–434, 438, 444
Disulfide, 2079, 2080, 2088, 2092, 2100, 2101, 2132, 2189
DMSA. *See* Dimercaptosuccinic acid
DNA. *See* Deoxyribonucleic acid
DNR. *See* Dynamic neutron radiography
Dole effect, 735–736
DOPA. *See* 3,4-Dihydroxy-L-phenylalanine
Dopamine-D₁ and D₂ receptors, 2005, 2006
Dopamine transporter agents (DAT), 2105–2106
Doppler-broadening spectroscopy, 1477–1478
Doppler effect, 1391, 1406, 1472
Doppler shift, 1383, 1393–1394, 1404, 1406, 1414, 1472
Doppler speed, 1394, 1799
Dose assessment, 2010
Dose coefficients, 2226–2230
Dose constant, 1886–1899
Dose deposition, within tumor, 2183, 2187
Dose evaluation, 2289
Dose limits, 2223, 2238, 2241, 2242, 2247
Dose linearity, 2011
Dose rate, 1889–1890, 1894–1967, 2144, 2185, 2186, 2199
Dose response, 2010
Dosimetry, 1282–1283, 1292, 1856, 1923, 1924, 1948–2051, 2081, 2180, 2196, 2288–2313
Dosimetry reactions, 1845–1846
DOTA, 1889, 1890, 1947, 1949, 1952, 1953, 1961, 1967, 1968, 2103, 2144, 2148, 2154, 2155, 2158–2164, 2167–2174, 2186, 2194, 2197, 2198, 2202, 2203
DOTA-peptides, 1949, 1952, 2163, 2168, 2197
DOTETE, 2173–2175
Double beta decay, 357
Double crystal monochromator, 1742, 1744
Double neutron capture, 1884, 1896–1897
Doubly exotic atoms, 1500
Doubly magic deformed region, 1014
Doubly magic nucleus, 888, 902, 911, 1006
Dowex 50*8, 1021
Dpm, 334
Dps, 334
Drug development, 1979, 2010–2012
Drugs, detection and identification, 1679–1682, 1851
Dry cask storage, 2927
Dry distillation, 1882, 1887, 1899, 1912, 1923, 2122, 2200
DTPA, 1890, 1891, 1898, 1949, 1961, 1962, 1964, 1967, 2076, 2087, 2088, 2103, 2110, 2147, 2149–2152, 2159–2161, 2166–2173, 2194, 2197–2200, 2202, 2205
Dubna gas-filled recoil separator (DGFRS), 1016
Dubnium, 23–25, 926, 928, 929, 942, 960–969, 1012, 1014, 1021
Dumbbell, 224, 244, 245, 250, 251, 261, 272
Duoplasmatron, 2326–2327, 2336, 2341
Duty factor, 2362
DV-DFS method, 867
¹⁶⁵Dy, 1864, 1881, 1962, 2186, 2187, 2196, 2198
¹⁶⁶Dy, 1864, 1944, 1959, 1962, 1966–1968, 2145, 2149
[Dy–166]DTPA, 1967
¹⁶⁶Dy/¹⁶⁶Ho generator, 1944, 1959, 1962, 1966–1968
Dynamical hindrance, 827, 911
Dynamic neutron radiography (DNR), 1684
Dynamics of condensed phases, 1518
Dynamics of ions in solutions, 1457
Dynamic structure factor, 1518, 1523–1525, 1533, 1538
Dynamitron, 2344–2345
Dynodes, 441, 447, 448
- ## E
- EBIS, 2324, 2325, 2333–2335
EBIT, 2324, 2325, 2333–2335
EC. *See* Electron capture
ECD. *See* Ethylene-cysteine dimere
EDTA. *See* Ethylenediaminetetraacetic acid
EDTMP, 2186, 2202

- Effective dose, 1911, 1916
Effective dose commitments, 2541–2542, 2546
Effective dose, to the population, sources of, 2567–2557
Effective means, 402
Effective thickness, 1393–1395, 1413, 1420, 1425, 1427
Efficiency, of a thermal engine, 2641
Einsteinium, 22, 24, 820–821, 823, 826, 850, 856, 857
Einstein model, 1386, 1387
Einstein temperature, 1386
Elastic recoil detection (ERD), 1712–1722
Elastic recoil detection analysis (ERDA), 1712
Elastic scattering, 150, 168–170, 177–180, 185, 188
Electric charge distribution, 1334, 1340–1342, 1400
Electric field gradient (EFG) tensor, 1400, 1402
Electricity, of nuclear origin, 2640
Electric moments, 53–56
Electric monopole interaction, 1396–1399, 1404
Electric quadrupole interaction, 1395, 1396, 1400–1402, 1407, 1412
Electrochemical cells, 2063
Electrochemical deposition, 994
Electromagnetic interaction, 43, 49, 60, 75, 77, 79, 111, 128, 465, 466, 470
Electromagnetic separation, 2371, 2378
Electromagnetic transition, 56, 73, 75, 76, 79–82, 96, 103
Electro migration, 2401
Electron beam ion source (EBIS), 2324, 2325, 2333–2334
Electron capture (EC), 11, 12, 16, 22, 62, 123, 124, 131, 133, 150, 272, 338, 341, 354, 357, 359, 390, 1287, 1302, 1338–1340, 1343, 1376, 1393, 1433, 1434, 1436, 1596, 1676, 1770
Electron configuration, 487–491
Electron cyclotron resonance (ECR), 2324, 2330–2333
Electron cyclotron resonance ion sources (ECRIS), 2324, 2325, 2329–2336
Electronic absorption, 1391, 1434
Electron irradiation, 1270, 1281, 1282, 1317, 1323
Electron microprobe analyzer, 1704
Electron multiplier, 1432
Electron paramagnetic resonance (EPR), 2305–2308
Electron-photon showers, 390
Electrons, 481, 483, 487, 521, 522, 527–531, 540
Electron scavenging, 1276, 1277
Electron sources, 2573
Electron spin resonance (ESR), 764, 773–774
Electron transfer reaction, 1782
Electronvolt energy unit, 477, 479, 540
Electrophilic ^{18}F , 1916–1917, 2026–2032
Electrophoresis, 1275, 1346, 1363–1365, 1710, 1711
Electrostatic accelerators, 2325, 2338–2348, 2356
Electrostatic analyzer, 2467, 2468, 2473, 2489
Electroweak interaction, 470
Element 110, 1008, 1009, 1012–1014
Element 111, 1013
Element 112, 1010, 1013–1015
Element 113, 881, 884, 888, 911, 915, 1022
Element 114, 878, 884, 888, 891
Element 115, 884, 888, 891, 1020, 1021, 1025
Element 116, 884, 888, 891, 911, 1017, 1018, 1020, 1023, 1025
Element 118, 878, 881, 885, 891, 892, 911, 915, 916, 1023, 1025–1027
Element 120, 1025
Elemental analysis, 1674–1677, 1680–1683, 1686, 1688
Elemental assay, 2952, 2956, 2957, 2971–2985
Elementary particles, 457–473, 615, 621, 625–627
Elementary pattern, 1422–1424
Element-specific dynamics, 1448, 1454, 1457
Elements 107 through 112, 1012–1015
Elimination reaction, 1994
El Niño/Southern Oscillation (ENSO), 741, 746, 788
Elution curve, 693, 694, 820–822, 953–957, 968, 981, 1785, 1786
Emanation, 1784
Emission Mössbauer spectroscopy, 1433–1435
Emittance, 2325, 2337, 2363–2364
Empirical variance, 406
Emulsions, 16
ENAA. *See* Epithermal neutron activation analysis
End of bombardment (EOB), 1885, 1886, 1890, 1891, 1898, 1899, 1906, 1947
Endoradiotherapeutic agents, 2180, 2182, 2184–2188, 2196, 2197
Endoradiotherapy (ERT), 1929, 1943, 1944, 1959, 1960, 1966, 2180–2182, 2199
Endothermic, 150
Energy deposition, 1270–1275, 1308
Energy domain, 1448, 1449, 1453
Energy loss, mean logarithmic, 1354
Energy monitors, 1846
Energy resolution, 1384, 1391, 1432, 1455, 1478, 1539, 1545, 1549, 1573, 1574, 1621, 1638, 1640–1643, 1726, 1728, 1742, 1743, 1768
Energy standards, 2566–2575
Enhanced stability, 839, 905, 906, 916
Enriched uranium, from weapons stockpiles, 2811
Enrichment, biological, 2401
Enrichment factor, 1345
Enrichment of radioisotopes, 1342–1348
Enrichment of ^{235}U , 2400, 2422, 2554
Environmental monitoring, 2228, 2302, 2303, 2506
Environmental radioactivity, 2506
Enzymatic synthesis, 2000, 2001, 2061
Enzymes, 2000, 2002, 2005–2009
Enzymes as catalysts, 2000–2002
EOB. *See* End of bombardment
EON, EOZ, 267–269
Epibatidine, 2008, 2041
Epithelial flux, 1872, 1874, 1877, 1879, 1890
Epithelial neutron activation, 1557
Epithelial neutron activation analysis (ENAA), 1565, 1566, 1676

- Epithermal neutrons, 1864, 1874–1875, 1877, 2622–2624, 2628
- Equilibrium dose constant, 1886, 1889, 1899
- Equilibrium time, 2377
- Equivalent dose, 2219–2229, 2239, 2242, 2246, 2249
- ^{169}Er , 2187, 2195
- Error calculation of the count rate, 428
- Error function (erf), 432
- Error propagation, 407–413
- ERT. *See* Endoradiotherapy
- 1/e rule, 338, 346
- Escape probability, of neutrons, 2633
- ESRF. *See* European synchrotron radiation facility
- Esters, 1993–1999, 2003, 2005, 2032, 2039, 2046, 2052–2054, 2060, 2083, 2086, 2089, 2135, 2154, 2155, 2158, 2166, 2167
- Estimate, of half-life, 899, 908, 1017
- Estimation of the mean life, 422
- Estradiol, 2005, 2045, 2092, 2093, 2098, 2186
- Ethanol-monochlorobenzene dosimeter, 2294–2295
- Ethylbromide, 1345, 1361
- Ethylene, 1276, 1277, 1293, 1294, 1306, 1307, 1315, 1323, 1325, 1351, 1360, 1363
- Ethylene-cysteine dimere (ECD), 2085, 2086, 2089
- Ethylenediaminetetraacetic acid (EDTA), 1951, 2147, 2149, 2151
- ^{151}Eu , 1409, 1437, 1450, 1580, 1795, 1807, 1849
- European synchrotron radiation facility (ESRF), 1739, 1741–1744, 1746, 1751–1753, 1758
- Evaporation, 214
- Even-odd effect, staggering of the isotopes, 719, 720
- EXAFS. *See* Extended X-ray absorption fine structure
- Exchange distillation, 2371, 2377, 2384–2392
- Exchange reactions, 1765, 1766, 1780–1784, 1789
- Excitation energy, 63, 311
- Excitation energy, of recoil reaction products, 1352
- Excitation function, 158–161, 192, 196, 201, 1904–1907, 1910, 1914–1916, 1925, 1930
- Exciton model, 201, 202
- Exempt waste, 2800
- Exothermic, 150, 151
- Exotic atoms, 1485–1511
- Exotic hydrogen atoms, 1493, 1498–1500
- Exotic nuclear decay, 838–841
- Exotic radionuclides, isolation of, 2411–2413
- Expectation value, 397, 404–406, 408, 413, 414, 417, 420, 430, 432, 436, 438
- Expected value of linear combinations, 407
- Explosive burning, 648, 650–653, 655, 656
- Explosive nucleosynthesis, 648, 651, 658
- Explosives, detection and identification, 1660, 1682
- Exponential distribution, 401, 408, 420–431, 438–440, 443, 444, 446
- Exponential law of decay, 334–338, 421, 423, 424–426
- Exponential probability density, 898
- Exposure pathways, 2227
- Extended X-ray absorption fine structure (EXAFS), 861–863, 865, 1750, 1756–1758
- External beam radiation, 2180
- Extracted beam, 1908–1910, 1925
- Extraction chromatography, 713, 947, 960, 966
- Extraction systems, 2332, 2336, 2337, 2407–2408
- Extra push, 686, 827, 911
- ## F
- $^{18}\text{F}]\text{AlF}^{2+}$, 2057
- $^{18}\text{F}]\text{altanserin}$, 2034, 2035
- Faraday cups, 2463, 2469–2470, 2489
- Fast breeder reactor (FBR), 2621, 2640, 2648–2651, 2654
- Fast fission factor, 2631–2632, 2649
- Fast fission neutrons, 2632–2633
- Fast ignition, 2765
- Fast neutron, 1834–1851, 1863–1867, 1875, 1880, 1884, 1898–1899
- Fast neutron activation analysis (FNAA), 1565, 1604, 1676
- Fast neutron reaction data, 1834–1851
- Fast reactors, 2673–2674, 2687, 2693, 2696, 2704–2723, 2807, 2818, 2819, 2823–2826, 2830, 2831
- Fatty acids, 1987, 1993, 1999, 2004–2005, 2123–2126
- Favorskii reaction, 1780
- ^{18}F -click cycloadditions, 2050
- $^{18}\text{F}]\text{CPFPX}$. *See* 8-Cyclopentyl-3-(3- ^{18}F)fluoropropyl)-1-propylxanthine
- FDA. *See* Food and drug administration
- ^{52}Fe , 1919, 1921, 1922, 1943–1947
- ^{57}Fe , 1457, 1794
- ^{60}Fe , 2476, 2481–2485, 2495, 2499
- Febetron accelerator, 1269
- Fenske equation, 2375
- Fermi energy, 146, 151, 153, 162, 170–173, 198, 201–204
- Fermi-gas model, 146, 198, 202
- Fermi integral function, 357–359
- Fermions, 458–465, 468–472
- Fermi transition, 132, 133
- Fermium, 20, 22, 23, 820–823, 826, 850
- Ferrihydrite, 1426
- Ferroelectricity, 715
- Ferromagnetic interaction, 1416
- Fertile actinides, 2819
- Fertile nuclide, 2807, 2832
- Few nucleon systems, 50, 110–111
- $^{18}\text{F}]\text{F}_2$, 2024, 2026–2034, 2043
- f -factor, 1388, 1412–1413, 1429
- $^{18}\text{F}]\text{FDDNP}$, 2045, 2046
- $^{18}\text{F}]\text{FDG}$, 2027, 2041–2043, 2053, 2054, 2063
- 6- $^{18}\text{F}]\text{FDOPA}$, 2027–2032, 2035, 2036, 2061
- $^{18}\text{F}]\text{FDOPA}$, 2028
- $^{18}\text{F}]\text{FET}$. *See* O-(2- ^{18}F)fluoroethyl)-L-tyrosine

- [^{18}F]FLT, 2043, 2044
 ^{18}F Fluoracylation, 2054
[^{18}F] Fluoride, 2024, 2026, 2030–2034, 2038, 2041–2047, 2053, 2055, 2057–2063
[^{18}F] Fluorobenzaldehyde, 2039, 2057, 2058
[^{18}F] Fluorocarazolol, 2050
 ^{18}F -Fluorodemetalation, 2029–2030
2-[^{18}F] Fluoro-deoxy-D-glucose, 2024, 2027, 2041–2043
 ^{18}F -Fluoroethylation, 2047–2049
O-(2-[^{18}F]fluoroethyl)-L-tyrosine ([^{18}F]FET), 2043, 2045
2-[^{18}F] Fluoro-L-tyrosine, 2030, 2031, 2035, 2036
4-[^{18}F] Fluoro-meta-L-tyrosine, 2035, 2036
[^{18}F] Fluoromethylation, 2046, 2047
[^{18}F] FMISO, 2045, 2046
Fictitious isochrons, 793–794
Field flutter, 2359
Field index, 2358, 2360
Field quanta, 42, 43
Film dosimeters, 2229, 2289, 2300–2302
Fine structure constant, 367, 483, 1398, 1462, 1495
Fingerprint method, 1421, 1442
Finite-range droplet model (FRDM), 52, 228, 230
First-order quantum correction, VPIE, 710
First pass radionuclide angiography (FPRNA), 1943–1944, 1955–1958
Fissile actinides, 2819, 2877–2878
Fissility parameter, 234–238, 250, 251, 269, 272, 274
Fission barrier, 233–235, 237, 238, 242, 244, 251, 276
Fission cross section, 1867
Fission factor, 2631–2633, 2649
Fission fragments, 252, 298, 300, 2285
Fission isomers, 239, 242, 272–277
Fission neutron spectrum, 1558
Fission path, 17, 152, 243, 244, 255, 282, 305
Fission product yields, 2575–2611
Fission spectrum, 2249, 2575, 2624
Fission track dating, 764, 774, 775
Fitting function, 435, 436, 449
Fitting nuclear spectra, 424, 448–453
Fitting parameters, 449, 451
 ^{18}F -labeled aromatic systems, non-activated, 2036
 ^{18}F -labeled compounds, 2043, 2062, 2063
 ^{18}F -labeled peptides and proteins, 2051–2058
Flavones, 1998
Flavor, 625, 645
Florentium, 690
Flow rate, 1791
Fluence monitor, 1834, 1846
Flumazenil, 2007, 2008, 2048, 2049
Fluorescence yields, 511, 515
Fluorimetry, 2304, 2305
Fluorination, 2024–2051, 2053, 2063
Fluorine, 488
Fluorine substituent effects, 2024–2025
Fluorometaraminol, 2030, 2031
Flux monitoring, 1860, 1877–1878
Flux of solar neutrinos, 185
Flux perturbation factor, 1677
FNAA. *See* Fast neutron activation analysis
[^{18}F]N-methylspiperone, 2034, 2035
Foil activation, 1634
Fokker–Planck equation, 190
Food and drug administration (FDA), 1959, 2084–2085, 2102, 2151, 2201
Food chain, 2524–2527, 2559
Food irradiation, 1323–1324
Formaldehyde, 1989, 1992, 2002
Formazan, 2293, 2294, 2307
Form factor, 166
Forward recoil elastic spectroscopy (FRES), 1712–1713
Fourier transform, 170, 403
Fractile, 404
Fractionated crystallization, 228, 230
Fractionation, 637, 659, 660, 705–709, 711–713, 720, 722, 723, 728–731, 736–738, 749, 757, 778, 779, 782, 784, 790, 794, 800, 802, 806, 814, 815
Fractionation factor, deuterium, 2389
Fragmentation path, 1350
Francium, 13
Fraunhofer scattering, 180
Free radical, 1275, 1277, 1299, 1302–1305, 1308, 1310, 1315, 1324, 1465, 1466, 1470
Frenkel equation, 2433
Frenkel pair, 1337, 1362, 1363
FRES. *See* Forward recoil elastic spectroscopy
Fresnel scattering, 180
Fricke dosimeter, 2290–2291
Front-end, of nuclear fuel cycle, 2802–2807
Fructose, 2002
 ^{18}F -Si compounds, 2059
Fuel cycle, 2667, 2671, 2673–2676, 2679, 2681–2682, 2689–2691, 2704–2724, 2727
Fuel fabrication, 2544, 2553, 2555
Fuel pellet, 2762–2766
Fuel reprocessing, 2509, 2511, 2514, 2522, 2545, 2546, 2555
Fuel rod, 2643, 2646, 2650, 2658, 2712, 2713, 2716, 2737, 2917
Fullerenes, 1335, 1375–1376, 1530, 1661, 1785, 1786
Full width at half maximum (FWHM), 404, 432, 438, 442, 1382, 1385, 1394, 1413, 1573, 1643, 1754
FUN, 794
Fundamental constants, 477, 481–487
Fundamental constituents of matter, 41, 42
Furifosmin, 2082, 2112
Fusion energy production, 2760–2763, 2793
Fusion of hydrogen to helium, 638, 644
Fusion reactions, 929, 930
Fusion triple product, 2762, 2769
FWHM. *See* Full width at half maximum

G

- ^{67}Ga , 1905, 1911, 1924, 1925, 1928, 1930–1931, 2145, 2146, 2149, 2158, 2204
- ^{68}Ga , 1910, 1915, 1919, 1931, 1940–1946, 1950–1954, 2023, 2145, 2146, 2149, 2152, 2158
- [^{68}Ga]BAT-TECH, 1953
- GACEMS. *See* Glancing angle CEMS
- [^{68}Ga]DOTA-DPhe¹-Tyr³-octreotide, 1952, 1953
- [^{68}Ga]DOTATOC. *See* [^{68}Ga]DOTA-DPhe¹-Tyr³-octreotide
- GafChromic, 2301
- Galactic cosmic rays (GCRs), 652
- Galaxies, chemical evolution of, 615, 661–662
- Gamma decay, 75–84, 117, 127, 359–361
- Gamma distribution, 430–432, 437, 444
- Gamma-ray counters, 2861
- Gamma-ray detectors, 2909–2911
- Gamma-ray energies, 682
- Gamma-ray measurement, 1768–1769
- Gamma ray sources, 2566–2575
- Gamma-ray spectrometry, 2909–2914
- Gamma-soft nuclei, 95, 103
- Gamow–Condon–Gurney formula, 356
- Gamow–Teller transition, 132, 133
- Gamow wave function, 362
- Gancyclovir, 2028
- Gas centrifugation, 2371, 2381, 2383
- Gas chemistry, 2430, 2449, 2453
- Gas chromatography, 2393–2397
- Gas-cooled fast reactor system, 2669, 2689–2690, 2723–2725
- Gas diffusion process, 2657
- Gaseous diffusion, 2875, 2876
- Gas filled magnet, 2468–2471
- Gas filled separators, 885, 893, 895
- Gas ionization detectors, 2471–2472
- Gas jet, 832–836, 839, 882, 897, 916, 933, 936, 938, 941–944, 952, 976
- Gas-liquid chromatography, 2393–2396
- Gas-phase separations, 932, 944
- Gas-solid chromatography, 2393
- Gas-solid interaction, 2454
- Gas target, 1910–1912, 1916–1917, 1920, 1956, 1983
- Gauge bosons, 42, 470, 472
- Gauge symmetry, 461, 466
- Gauge transformations, 461
- Gaussian98, 866
- Gaussian distribution, 260, 400, 434
- Ge detector, 1595, 1634, 1674, 1726, 1743, 1766, 1768–1769, 1776, 1790
- $^{68}\text{Ge}/^{68}\text{Ga}$ generator systems, 1936, 1940–1946, 1950–1952
- Geiger–Müller, 2260–2264
- Geiger–Nuttall plot, 355, 356
- Geiger–Nuttall rule, 355, 357
- Gel-effect, 1304
- Gel-type generators, 1897, 1957, 1963
- Geminate recombination, 1274, 1277
- Generating function, 400–403, 412–414, 417, 447
- Generator-derived therapeutic radionuclides, 1936, 1959–1966
- Generators, 1859, 1885, 1919, 1935–1968, 2074–2077, 2144, 2201–2203
- Gene therapy, 2028, 2029
- Genetically related radioactive materials, 674
- Genotoxicity, 2011
- Geochemical Ocean Sections Study (GEOSECS), 787, 788, 803
- Geochronometer, 770, 774, 775, 779, 784, 803–804, 807
- Geologic disposal, of high-level waste, 2816–2818
- Geologic thermometer, 728–732
- Geometric cross section, 157, 169
- Geometric mean, rule of, 710
- g-factor, 1439, 1799–1810
- Giant haloes, 778
- Giant resonances, 89, 181
- Gibbs' phase rule, 2405
- GICEMS. *See* Grazing incident ^{57}Fe CEMS
- GIM mechanism, 464
- Glancing angle CEMS (GACEMS), 1432
- Global fallout, 2509, 2513, 2518, 2520, 2522, 2539–2553
- Globally dispersed radionuclides, 2527, 2540, 2545–2546
- Global Network for Isotopes in Precipitation (GNIP), 747
- Glucitol, 2002
- Glucose, 1856, 1947, 1956, 1959, 2004, 2005, 2041, 2042, 2051, 2135
- Gluon, 465–467, 472, 626–629
- Glutamine, 2304
- Glycolytic metabolism, 2042
- Glycoprotein IIb/IIa, 2102
- GM counter, 1766–1770, 1780
- GMP standard. *See* Good manufacturing practice (GMP) standard
- Gold, 1562, 1579, 1589, 1591, 1594, 1604, 1634, 1747, 1775, 1809
- Goldanskii–Karyagin effect, 1420
- Good manufacturing practice (GMP) standard, 2122
- Goodness of fit, 397, 450, 451
- Grafted polymers, 1309–1311
- Graphite calorimeter, 2312
- Gravitational clustering of matter, 628–629
- Gravitational interaction, 41, 45
- Gravitational settling, 2524
- Gravity, 43, 330, 458, 465, 482
- Gray, 2219, 2224, 2227
- γ -ray linear attenuation coefficient, 520
- Grazing angle, 180, 188–190
- Grazing incident ^{57}Fe CEMS (GICEMS), 1432
- Grignard reagents, 1982, 1983, 1986–1989, 1992, 1994, 1999, 2004, 2029

Ground-state deformation, 902
Groundwater, age of, 798
Group theory, 459
GS plant, 2385, 2387, 2388
GS process, 2387–2389
Guanidine, 1983, 1991, 2030, 2031, 2055, 2125, 2140, 2186, 2201
Guidance levels, 2238, 2242
G-value, 1274, 1281–1284, 1291, 1303, 1307, 1313
Gyromagnetic ratio, 55, 76

H

Hadronic atoms, 1487, 1495, 1496, 1499–1509
Hadrons, 458, 462, 463, 466, 467, 471, 472
Hahnium, 928, 1012
Half-life, of fission products, 2576–2611
Half-thickness, 520, 524, 525
Halfwidth, 404, 422, 439, 441, 445
Haloacetophenones, 2034
Halobenzonitriles, 2034
Halo, giant, 778
Halogens, hot atom chemistry of, 1356–1359, 1365
Halogens, physicochemical data of, 2025
Halo nuclei, 205
Hamada–Johnston potential, 47, 48
Hamburger synchrotronstrahlungslabor (HASLAB), 1745
Hard collision, 1271, 1273
Hard-core potentials, 48
Harmine, 2012, 2013
Harmonic mean, 402, 452
Hartree–Fock method, 67
Hartree–Fock–Slater values, 519
Hassium, 24, 25, 879, 884–887, 892, 893, 900–905, 915, 917, 919, 926, 929, 936, 986–990, 1012, 1014
HASLAB. *See* Hamburger synchrotronstrahlungslabor
HDEHP, 1588, 1893, 1961
Health hazards, of radiation exposure, 1882
Heat exchanger, of a PWR, 2642
Heavy element topology, 1026
Heavy-ion accelerators, 878, 892
Heavy-ion collisions, 180, 204–207
Heavy ion emission, 679, 685–686
Heavy-ion induced reactions, 826
Heavy ion reaction products (SHIP), 1012–1016, 1024
Heavy water, 704, 705, 710–716, 721–722
Heavy water production, 2385–2386
Heck reaction, 1996, 1998
HEHA, 2148, 2159–2162, 2203
Height equivalent per theoretical plate (HETP), 2381, 2390, 2435
Heisenberg's uncertainty relation, 128
Helioseismology, 645, 659
Helium burning, 639, 645–648
Helium gas jet, 882, 897

Henry's Law, 2394
Hepatoma, in the liver, 2181
Hertzprung–Russel diagram, 638–639
Hesse–Rübartsch method, 1427
Heterobifunctional reagents, 2135–2136
Heterodyne detection method, 1448–1452
Heterogeneous recycling, 2823
Hevesy's tracer concept, 1855, 1942, 2022
¹⁸²Hf, 2476, 2483–2484
^{195m}Hg, 1944, 1955, 1958, 1959
Higgs boson, 468–470, 472
Higgs effect, 626
Higgs field, 468, 627
Higgs mechanism, 466–470, 472
High-current accelerators, 918
High-dose dosimetry, 2290, 2294, 2297, 2303–2305
High-flux reactor, 2639
High-level waste (HLW), 2800–2801, 2811, 2814–2818, 2822, 2825–2827, 2830
Highly radioactive waste, 2659
High mobility cations, 1296
High-performance liquid chromatography (HPLC), 859, 937–940, 1275, 1592, 1785
High-purity germanium detectors, 1628, 1638, 1639
High-resolution monochromator, 1455
High temperature gas-cooled reactor (HTGR), 2668, 2677, 2683–2690, 2723
His-tagged recombinant scFv, 2098
HMPAO, 2085–2086, 2091
¹⁶⁶Ho, 1864, 1881, 1944, 1959, 1962, 1966–1968, 2145, 2149, 2187, 2196, 2198
[¹⁶⁶Ho]DOTMP, 1962
[¹⁶⁶Ho]DTPA, 1962
¹⁶⁶Ho-ferric hydroxide, 1962
Holmes/Houtermans model, 809–812
Horizontal distillation, 2430
Hot atom chemistry, 1334–1376
Hot atom reaction, 1335, 1337, 1348, 1354, 1359–1370, 1376
Hot Big Bang, 616
Hot fusion, 881, 882, 887, 888, 908, 913, 915, 1012, 1013, 1016, 1024
Hot spot, of particle beam, 2363
Hot tritium reaction, 1335, 1336, 1350, 1351, 1356
Hot zone concept, 1363
Hot-zone model, 1335, 1366
HPLC. *See* High-performance liquid chromatography
HSA. *See* Human serum albumin
Hubble law, 621, 623, 629
Human serum albumin (HSA), 1950, 2055
Hydrated electron, 1275, 1276, 1283–1291, 1312, 1316, 1319
Hydrazine, 1927, 2057, 2097
2-Hydrazino-nicotinic acid (HYNIC), 2057, 2076, 2096–2097, 2103, 2114
Hydroboration, 2127, 2128

- Hydrocarbons, 1274–1277, 1287, 1289, 1292–1300, 1307, 1315–1318
- Hydrodynamical model, 85
- Hydrogen abstraction reaction, 1285, 1306, 1312, 1350, 1352, 1370
- Hydrogen atom, 1277, 1287, 1291, 1295, 1300, 1306, 1311, 1312, 1316, 1319, 1326, 1336, 1467, 1493, 1498–1500, 1503–1506, 1532
- Hydrogen bomb, 2551
- Hydrogen bond, 1504–1506
- Hydrogen bond effect, 1505
- Hydrogen burning, 638–648, 654, 656
- Hydrolysis, 850, 854, 937, 947–949, 961, 966, 971, 972, 983
- Hydroxyl radical, 1284, 1287–1291, 1319
- HYNIC. *See* 2-Hydrazino-nicotinic acid
- Hyperfine interactions, 1395–1404, 1407, 1421, 1422
- Hyperons, 42
- Hypothetical decay, 429
- Hypoxia, 1950, 2022, 2027, 2045, 2046, 2061, 2089, 2090, 2146
- I**
- ^{120g}I, 1907, 1921–1924, 2122
- ¹²²I, 1886, 1919, 1943, 1945, 1948, 1949
- ¹²³I, 1886, 1907, 1911, 1912, 1919, 1922–1926, 1930, 1948, 1959, 2122–2131, 2135–2140, 2166, 2204
- ¹²⁴I, 1886, 1905–1909, 1919–1928, 1931, 2023, 2122, 2123
- ¹²⁵I, 1864, 1865, 1886, 1893–1896, 1922, 1923, 1926, 2122, 2123, 2128–2130, 2133–2136, 2170, 2183, 2186, 2204, 2205
- ¹²⁹I, 2464, 2476, 2480–2481, 2491
- ¹³¹I, 1855, 1859–1861, 1864, 1865, 1882, 1886–1887, 1900, 1919, 1924, 2122–2125, 2130, 2180–2183, 2186, 2194–2197
- ¹³²I, 1936, 1943
- IAEA significant quantities, 2900
- ICEMS. *See* Integral CEMS
- Ice, radiation chemistry of, 1291–1292
- Ice volume effect, 731, 737
- ICRP. *See* International Commission on Radiological Protection
- Icru sphere, effective dose, 2220, 2224
- Ideal cascade, for uranium isotope separation, 2376
- ID18F configuration, 1744
- IFR concept, 2824, 2825
- IgG molecule, schematic structure of, 2188–2191
- Illium, 690
- Imaging plate, 1685, 1770, 1790
- Impact induced multiple ligand abstraction (IMULA), 1366
- Impact parameter, 154–158, 182, 187–189, 202–206
- Implantation reactions, 1337–1370
- Impulse graphite reactor, 2745–2747
- Impurity Mössbauer spectroscopy, 1434
- IMULA. *See* Impact induced multiple ligand abstraction
- ^{110m}In, 1913, 1915, 1924, 1943, 1945, 1948, 2055
- ¹¹¹In, 1905, 1911, 1924, 1925, 1928, 1930, 1948, 1953, 1955, 2110, 2145, 2149–2151, 2154, 2158, 2166, 2194, 2197, 2204, 2205
- ^{113m}In, 1943, 1955
- ^{114m}In, 1864, 1888–1890, 2196
- Incineration, 2818
- Incoherent scattering, 1522–1524, 1532–1538, 1666
- Incomplete fuel reprocessing, 2851, 2856, 2876
- Incomplete fusion, 191, 192, 199
- Incompressibility, 147, 182, 184, 203, 207–212
- In-core irradiation, 1571
- Incremental heating, 766–768
- Indefatigability and exponential distribution, 420
- Independence of random variables, 406
- Independent decays, 338
- Independent yields, 263–267
- Indirect drive, 2762, 2765, 2766
- Individual dose, 1947, 2183
- INDO method, 866
- Indoor exposure, 2530
- Induced pattern, 1422–1425
- Inductively coupled plasma-mass spectrometer (ICP-MS), 2462, 2480, 2485–2492, 2500
- Industrial radiography, 2556
- Industrial use of radiation, 2556–2557
- Inelasticity, 1535–1536
- Inelastic scattering, 169, 180, 185, 188–189, 211
- Inertial confinement fusion, 2763–2766
- Inflationary epoch, 618, 619, 625
- In-flight separation, 878, 893
- Infusion, 1954, 1956, 1958
- Inhalation, 1956, 2011, 2012
- Inhibitor, 1468, 1991, 2008, 2012, 2040, 2043, 2091–2092
- Inorganic solids, radiation chemistry of, 1291–1292
- Instability, towards fission, 233, 234
- Instrumental neutron activation analysis (INAA), 1562, 1565, 1569–1583
- Insulated core transformers, 2344
- Insulator stack, 2345
- Integral CEMS (ICEMS), 1432
- Integral distribution function, 399
- Integral fast reactor (IFR), 2807, 2824
- Integrated approach, 2079, 2101–2102
- Interacting boson models, 42, 101, 106
- Interaction barrier, 158
- Interaction boson, 41, 42, 106, 462
- Interaction matrix element, 128, 133
- Interference effects, in coherent scattering, 1522–1523
- Intermediate-level waste (ILW), 2800
- Intermolecular isotope effect, 716
- Internal beam, 1908, 1910
- Internal conversion, 12, 76, 78, 79, 82, 360
- Internal conversion coefficient (ICC), 514–520, 1799

- Internal electron-positron pair emission, 76
Internal standard method, 1635, 1707, 1711
International Commission on Radiological Protection (ICRP), 2144, 2145
International reactor dosimetry file (IRDF), 1845
International System of Units (SI), 476–482, 485, 491
Interquantile range, 404
Interquartile range, 404, 432, 438, 439
Interstage flow, 2375, 2376, 2387
Interstitial fluid pressure, in tumor, 2184
Interventional radiology, 2535–2536
Intervention, in nuclear emergency, 2558–2560
Intervention levels, 2560
Intrachelating agents, 2205
Intramolecular isotope effect, 716
Intranuclear cascade, 19, 203
Intranuclear cascade model, 202, 203
Intravenous bolus injection, 1954
Intrinsic quadrupole moments, 56, 57, 64
Intruder states, 87, 88
Inventory of radioactive nuclides, 2643
Inverse isotope effect, 710, 716
In vivo generator, 1962, 1965–1968
Iodine, 8, 14, 26, 489
Iodine–129 (^{129}I), 1407–1409, 1450, 1597–1598, 1771, 1794
Iodine administration, 2559
Iodine prophylaxis, 2232
Iodine, radioisotopes of, 1906–1908, 1923, 2122–2123
Iodine/xenon dating, 775
Iodogen Iodo-beads, 2132
Ion accelerators, 1697–1733
Ion beam analytical (IBA) methods, 1705, 1712, 1716, 1719–1724, 1729, 1731
Ion exchange, 2404–2426
Ion-gamma reactions, 1726–1727
Ionic polymerization, 1304, 1305
Ion implantation, 1368, 1375, 1482, 1611
Ion-ion reactions, 1288, 1724–1729, 1731
Ionium (thorium–230) dating, 800
Ionium/protactinium dating, 801
Ionization, 2321–2325, 2329, 2333, 2334
Ionization chambers, 2262–2263, 2266
Ionization cross section, 2322, 2323
Ionization energy, 368, 377, 378
Ionization energy loss, 377, 378
Ionization of atoms, mechanisms for, 1340
Ionization potential, 856, 1275, 1276, 1340, 1468, 1469
Ionizing radiation, 2262, 2278, 2288, 2290, 2295, 2296, 2302, 2303, 2308
Ion-molecule reaction, 1294–1297, 1308, 1336, 1357
Ion pair extraction, 2407–2408
Ion sources, 2321–2337, 2339–2341, 2345, 2346, 2349–2350, 2356, 2358
Ion trap (EBIT), 2333–2334
 $^{191\text{m}}\text{Ir}$, 1864, 1944, 1955, 1958
IRDF. *See* International reactor dosimetry file
Irradiation capsule, 1570, 1571, 1601
Irradiation of food, 1323–1324
Island of SHE stability, 1014
Island of stability, 668, 673–674
Island of Superheavy Elements, 1007
Isobar, definition, 1034
Isobaric analogue state, 184
Isobars, 1034
Isochron, 27, 297
Isochronous cyclotron, 2350–2352, 2358, 2361, 2362
Isochrons, fictitious, 793
Isolation of exotic radionuclides, 2411–2413
Isomer, definition, 1034
Isomeric ground state, 275, 291
Isomeric impurities, 1907, 1923
Isomeric Mössbauer excitation, 1448–1449
Isomeric states, 77, 81–84, 136
Isomerism, 6, 291
Isomers, 1034
Isomer shift, 1397–1399, 1404–1407, 1414, 1415, 1417, 1421, 1422, 1426, 1437, 1440
Isomer shift conversion, 1437
Isonitrile ligands, 2082
Isonitriles, 2003, 2082
Isopropyl chloride, 1360, 1361
Isospin, 44, 48, 49, 61, 111, 205, 461–464, 466, 468, 469, 472
Isothermal gas chromatography, 935, 944, 962, 979, 985
Isotone, definition, 1034
Isotones, 1034
Isotope, definition, 5, 7, 1034
Isotope dilution analysis, 26, 1786–1788, 1791
Isotope effects, 699–723
Isotope enrichment, 2422–2433
Isotope exchange, 705–708
Isotope exchange equilibria, 705
Isotope exchange, monothermal, 2386–2387
Isotope exchange reaction, 706
Isotope fractionation, 706, 707, 711–713, 720–723
Isotope incoherence, 1522
Isotope mass spectrometry, 2866–2870
Isotope online separations, 2451
Isotopes, 487–504, 1034
Isotope separation, 17, 2371–2401
Isotopic abundances, 487, 491
Isotopic analysis, 2904, 2952, 2956, 2960–2971, 2978, 2981, 2997, 3002
Isotopic chronostratigraphy, 729, 748–750
Isotopic compositions, 487–504, 1034
Isotopic dilution, 1982–1983, 1987
Isotopic mixtures, 711
Isotopic molecules, 2371, 2389
Isotopic paleoclimatology, 727–759

Isotopic substitution, 1536, 1537, 1540, 1542
 Isotopologue, 700
 Isotopomers, 700
 Isotopy, 5

J

JNS, 769
 JOIDES, 751
 Joint distribution function, 406–407
 Joint Institute of Nuclear Research (JINR), 1016

K

³⁸K, 1905, 1912, 1919
 Kaonic atoms, 1487
 Kapton, 1471, 1702, 1739
 Kerma, 2219, 2224
 Kidney, function, imaging, 2087, 2089
 KIE. *See* Kinetic isotope effect
 Kinematic separation, 893
 Kinetic isotope effect (KIE), 715, 2008, 2014
 Kinetic spectrophotometry, 1278, 1280
 Kinetic stability, 1953, 1967–1968, 2077, 2098, 2150, 2171–2174
 Kinetic theory analysis, 1335, 1353
 KIO₃, 2130
*k*₀ method, 1562, 1577–1583, 1598
 Knock-on electrons, 373, 374
 Knockout reactions, 162, 169–172, 178, 179, 185–187, 205
^{81m}Kr, 1920, 1927, 1930–1931, 1943, 1955, 1956
 Kronecker delta, 1400
 Kryptofix 2.2.2, 2033, 2061
 Krypton–81 and krypton–85, 773
 Kryptonate, 1791
*k*₀ standardization, 1636, 1654
 Kurie plot, 129, 130
 K X-rays, 511–514
 Kyshtym, 2549

L

¹³⁴La, 1944, 1945, 1949, 1966
 Labeled precursors, 1980, 1983–1993, 2002, 2043, 2046, 2136
 Labeling chemistry, 1979–2014, 2074–2114, 2143–2175
 Labeling mAbs and their fragments, 1948, 2188, 2190–2192, 2197, 2200–2203
 Labeling position, 1979, 1981, 1989, 1993, 2000–2009, 2023, 2026
 Labeling, position-specific, 1980–1981
 Labeling synthesis, 1981–1983, 1991, 1993, 2000, 2013
 Labeling techniques, 26
 Lactoperoxidase, 2132–2135
 Laddertron, 2343
 Landau tail, 373
 Lanthanides, nuclear properties of, 2145
 Lanthanum/cerium dating, 775

Laplace equation, 1400
 Large-scale homogeneity, 618
 Large scale separations, 2380–2382
 Laser isotope separation (LIS), 2397–2401
 Lattice vibration, 1381, 1386–1388, 1413, 1420, 1441, 1448, 1454, 1456, 1531
 Laue method, 1528, 1531
 1/*ν* Law, 1622, 1624
 Law of diminishing returns, 218
 Law of large numbers, 405
 Law of the Unconscious Statistician, 400
 Lawrence Livermore National Laboratory (LLNL), 1016, 1017, 1020, 1021, 1025, 1026
 Lawrencium (103), 23, 24, 822–823, 850, 851, 866, 926, 1252
 Lawson criterion, 2762–2764
 Leach mining, 2803
 Lead–204, 809
 Lead-cooled fast reactor, 2668, 2676, 2708–2717, 2723
 Lead–210 dating, 801
 Leading-edge discriminator, 1474
 Leakage factor, 2633
 Leakage spectra, 1688–1691
 Leak problem, 1791
 LEP experiments, 468
 Lepidocrocite, 1423
 Leptons, 459, 462–465, 470, 472, 625–627
 Lethargy, 1879
 Level densities, 120, 175, 193, 276–277, 306
 Level density parameter, 175, 176, 194–197, 209, 214
 Level width, 173
 LFC. *See* Loss-free counting
 Li, 151, 185–187, 205, 214
 Libby's model, 1336
 LiF dosimeter, 2298
 Lifetime distribution, 336, 337, 420, 421, 424, 446
 Light water reactor (LWR), 2667–2674, 2676–2693, 2697
 Likelihood function, 450
 Limiting distributions, 453
 Lindberg–Lévy version of the central limit theorem, 434
 Linear accelerators, 2354–2355
 Linear attenuation coefficient, 420, 520
 Linear dose-response, 2011
 Linear energy transfer (LET), 2185, 2199, 2204
 Linear mixing rule, 1274, 1305
 Linear momentum transfer (LMT), 199
 Lioluminescence, 2302
 Lipids, 1312–1313, 1323
 Liquid chemical dosimeters, 2290, 2297
 Liquid drop energy, 74, 242, 285
 Liquid drop model (LDM), 232–235, 238, 239, 242–243, 250
 Liquid scintillators, 2278, 2281–2284
 Liquid structure, 1519, 1533–1535
 Liquid targets, 1910–1912, 1914
 Lithium amides, 1998

Little disorder model, 1366
Live time clocks (LTC), 1603
Location parameters, 397, 400, 422
Location sensitive analysis, 1608–1612
Lohengrin, 248, 249, 260, 265, 269, 272
Long-lived fission products, 2808, 2822–2830
Lorentzian curve, 1382
Lorentzian distribution, 434
Loss-free counting (LFC), 1572, 1574, 1578, 1603
Low-energy excited isomers, 361
Low energy photon (LEP) detector, 1271, 1676
Low-level waste (LLW), 2800
Low radiation doses, biological effects of, 2023–2024, 2088, 2199, 2204
Low-seniority scheme, 70
LSC, 942
LTC. *See* Live time clocks
¹⁷⁷Lu, 1864, 1889–1894, 1947, 2144–2149, 2158, 2195–2197
Luminescence, 2302–2305
Luminosity of stars, 622–624, 638, 639
Lunar rocks, 769
LUNI, 794
Lutetium/hafnium dating, 776
Lyoluminescence (LL), 2303–2304
Lyoluminescent dosimeters (LLDs), 2303–2304

M

MACHO, 620
Macrocyclic bifunctional chelators, 1953, 1967–1968, 2144, 2148, 2151–2165, 2171, 2172
Macromolecules, labeling of, 1991, 1992, 2184
Macroscopic microscopic model, 902, 907
Magic angle, 1419, 1733
Magic nuclei, 52, 70, 85, 89, 244
Magic numbers, 13, 22, 57, 62–68, 75, 81, 82, 95, 113, 115, 182, 240, 286, 783, 1006, 1008
Magnetic analyzer, 2467–2469, 2473, 2498
Magnetic beam analyzer, 2346
Magnetic confinement fusion, 2769–2775
Magnetic dipole interaction, 1395, 1402–1403, 1410–1412
Magnetic field reversal, 734
Magnetic isotope effect, 719
Magnetic moments, 42, 55–56, 127
Magnetic quantum number, 1400, 1403, 1467
Magnetic resonance imaging (MRI), 2010, 2080, 2085, 2089, 2114
Magnetic sextet, 1409, 1418
Magnetic spectrometer, 1510, 1722, 1732–1733
Magnetic splitting, 1403, 1408–1418, 1426, 1433, 1439–1442
Magnetic trap, 2331
Magnitude, 616, 620, 622–624, 630, 634, 646, 651, 654
Magnon, 1531, 1538
Main-sequence stars, 638, 642, 644, 654, 655
Malonic esters, 1993, 2003–2005, 2154
Manganese dating, 777
Manhattan Project, 13, 17
Man-made chemical elements, 336, 929
Mannheim's impurity theory, 1457
Mannitol, 2002, 2043
Mannose, 2004–2027
Mantle (of Earth), 791
MAO, 2008, 2012, 2013, 2040
Marine reactors, 2676, 2681
Markov chains, 447–448
Mass asymmetry, 20, 193, 195, 250
Mass attenuation coefficient, 520–523
Mass attenuation length, 389
Mass defect. *See* Mass excess
Mass diffusion, 2401
Mass-energy absorption coefficient, 520, 526, 540
Mass-energy conservation, 150–152
Mass excess, 150, 540–609, 1862
Mass extinctions, 729, 734, 735, 753–756
Massey conditions, 1494
Mass function, 398–400, 403, 415, 426, 434
Mass-independent isotope effects, 719
Massive transfer, 192
Mass, non-baryonic, 637
Mass number, 487, 504, 540
Mass parabola, 338, 340
Mass radii, 59–60
Mass separation, 248, 264–265
Mass separator, 246, 248, 260, 265, 272
Mass spectrometer, time-of-flight, 916
Mass spectrometry, spectroscopy, 16, 492
Mass unit, 229, 334
Mass-yield curves, 252–256
Mass-yield distribution, 844
Mass yields, 224, 245, 247, 248, 258, 262, 263, 265
Masurium, 690
Mathematical expectation, 397
Matrix activity, removal of, 1587
Matter-antimatter asymmetry, 618, 625–627
Maximum activity, 218, 349
Maximum credible accident (MCA), 2644
Maximum likelihood estimate of the expected value, 406
Maximum likelihood principle, 449–450
Maximum permissible concentration (MPC), 2832
Maxwell equation, 2623
MBB, 769
MCDF, 943
Mckay equation, 1781
MDR1. *See* Multidrug resistance
Mean absolute deviation, 404
Mean dead time, 444
Mean-field, 147, 152, 172, 173, 177, 187–192, 198, 200, 202–205, 207, 211
Mean free path, 127, 173, 203, 207, 389, 420, 520
Mean frequency, 426–428, 430, 431, 444
Mean implantation energy (MIE), 1369, 1370

- Mean life, 78, 336, 337, 339, 346, 348, 351, 421–423
Mean logarithmic energy loss, 1354
Mean signal frequency, 444
Mean square displacement, 1386–1388, 1413
Mean square velocity, 1388
Mean time, 108, 338, 346
Median, 400
Medical exposure, 2533–2539
Medical internal radiation dose (MIRD), 2230–2232
Medical radionuclides, 1859–1931, 2451
Medical uses of radiation, 2539, 2555–2556
Megawatt electrical power (MWe), 2547
Megawatts of thermal power (MWth), 2640, 2644, 2645, 2648, 2651, 2653, 2684, 2725, 2727, 2776, 2807
Meitnerium (109), 24, 882, 884, 885, 887, 892, 897, 898, 994, 1012, 1014, 1259
MeLi. *See* Methyllithium
MELT, 1475
Membrane pervaporation, 2377, 2401
Memory effect, 1308, 1309
Memorylessness of exponential distribution, 427, 428, 444
Mendelevium (101), 23, 821–823, 850, 1248
Mercaptoacetyl-glycine (MAG₃), 2088, 2092, 2094, 2096, 2104, 2110
Mercury, 1319, 1320, 1591, 1605, 1775, 1787, 1809
Merit function, 452, 453
Mesic molecules, 1500, 1504
Meson factories, 1488
Meson field theories, 49–50
Mesonic atoms, 1487
Mesons, 459, 462–464
Mesoscopic length scales, 1539–1541
Mesterolone, 1999
Metabolism, 1855–1856, 1959, 1999, 2004, 2010, 2011, 2022–2025, 2031, 2041–2042, 2080–2081, 2086, 2185–2186
Metabolism, of radionuclides, 2230, 2525
Metallicity (in astronomy), 624, 635, 636, 661, 662
Metalloenes, 1373, 1374
Metallofullerene, 1375, 1785, 1786
Metals, radiation chemistry of, 1269, 1286, 1288, 1292, 1300, 1309, 1310, 1314–1316, 1319, 1320
Metal wear, 1791
Metamorphic veil, 783
Metastatic cancer, 2047, 2049, 2181
Meteoric water line, 735–736
Meteorites, 791, 794
Meteoritic inclusions, 659–661
Methane, 1276, 1277, 1293, 1356–1358, 1431, 1543
Methionine, 2002–2004, 2010, 2062, 2110, 2132, 2133
Methyl iodide, 1980–1996, 1999, 2003–2005, 2047
Methyl isobutyl ketone (MIBK), 965
Methylisocyanate, 1990
Methyllithium (MeLi), 1985–1986, 2005, 2029
Methyl triflate, 1985
Microanalysis, 1739, 1740, 1745–1746
Micro-autoclave, 1992, 1997
Microautoradiography, 1770, 1784
Microbeam channels, 2347–2348
Microdosing, 2010–2011
Microenvironment, 1404, 1413, 1421–1424, 1427, 1434, 1435
Microfluidic flow chemistry, 2063
Micro PIXE, 1703–1705, 1707
Microscopic dynamics, 1454, 1517, 1519, 1537–1539
Microscopic X-ray fluorescence analysis, 1738–1758
Microtron, 2356–2357
Microwave dielectric heating, 1980, 2022, 2059
Microwave ion source, 2328–2330
Microwaves, to speed-up a reaction, 1980
Micro XRD, 1750
MIE. *See* Mean implantation energy
Mike, the first U.S. thermonuclear device, 1006
Miniaturization of synthesis equipment, 1980
Minor actinides, 2424
Mirror configurations, 2766, 2767
Mirror nuclei, 184
Misonidazole, 2061, 2089
Missing mass, 619, 636
Mixed-oxide fuel (MOX), 2425
Mixer-settlers, 2408, 2409, 2416, 2417
Mixing process, 1791
Mixing ratio, 78, 81
^{52m}Mn, 1943, 1945, 1947
⁵³Mn, 276, 2479–2480, 2497, 2499
⁹⁹Mo, 1859–1861, 1864, 1865, 1881, 1884–1887, 1900, 1924–1925, 1936–1937, 1939, 1943, 1956–1959, 1963, 2074–2076, 2122
Mode converter, 2261
Model function, 448–449
Moderating ratio (MR), 2627, 2628
Moderation, of neutrons, 2617, 2619, 2625–2628, 2633, 2639, 2691, 2709, 2737, 2915, 3647
Moderator isotope effect, 1352, 1353
Moderators, 1336, 1350–1359
Molar activity, 334
Molar cross section, 1557
Molar volume isotope effect, 714
Molecular dynamics, 187, 198, 203
Molecular rocket, 1335, 1373–1375
Molecular solid, 1482–1483
Molecular target, identification of, 2186
MOLFDIR, 866, 867
Molière distribution, 375
Molten salt reactor (MSR), 2668, 2702, 2703, 2723–2727
Molten Salt Reactor Experiment (MSRE), 2653, 2666, 2702
Molybdenum–99, 1859, 1861, 1883–1886, 1919, 1957, 1989, 1992, 2075
Momenta of a distribution, 401
Moments of inertia, 92, 94, 287, 301, 308

Momentum conservation, 11, 112, 156, 246–249, 252
⁹⁹Mo/^{99m}Tc generator system, 1937, 1939, 1943, 1956–1957, 1959, 1963
 Monoamino-monoamido (MAMA) chelators, 2106
 Monochromator, 1278, 1279, 1455, 1458, 1544–1545, 1547, 1548, 1739, 1742, 1744
 Monoclonal antibody (mAb), 2183, 2187–2192
 Monothermal isotope exchange, 2386–2387
 Monte Carlo transport simulations, 2182
 MORB, 780
 Mössbauer absorption type spectra using synchrotron radiation, 1453
 Mössbauer effect, 1381, 1382, 1385–1389, 1438, 1439
 Mössbauer–Lamb factor, 1388, 1393, 1412–1416, 1419, 1420, 1427, 1430
 Mössbauer line, 1385, 1390
 Mössbauer nuclides, 1794–1799
 Mössbauer parameters, 1404–1422, 1424, 1426, 1435, 1436
 Mössbauer peak intensity, angular dependence of, 1411
 Mössbauer periodic table, 1389
 Mössbauer polarometry, 1435
 Mössbauer source, 1436, 1448, 1449, 1453
 Mössbauer species, 1395, 1414, 1421, 1422, 1427, 1436
 Mössbauer spectrometers, 1428–1429
 Mössbauer spectroscopy, 439, 441, 1379–1442, 1448, 1449, 1453, 1454, 1733
 Mössbauer spectrum, 1389–1395, 1397, 1401, 1403, 1406–1411, 1419, 1421, 1422, 1424, 1428, 1429, 1433, 1434, 1439, 1440
 Most probable value, 400, 415, 418, 437
 MOX fuel, 2814–2816, 2819, 2821, 2823, 2825, 2826
 MRI. *See* Magnetic resonance imaging
 Multi-column technique (MCT), 950, 954
 Multiconfiguration Dirac–Fock calculations, 943
 Multicusp ion source, 2325, 2328, 2329, 2336
 Multidrug resistance (MDR1), 2112–2113
 Multielemental analysis, simultaneous, PIXE, 1708
 Multifragmentation, 196–198
 Multi-gamma calibration sources, 2570
 Multi-gamma sources, 2274, 2573
 Multiple foil activation method, 1688, 1845, 1846
 Multiple scattering, 1535, 1721
 Multiple separations, 676
 Multiple step series, 676
 Multiplication by a ‘photomultiplier’, 441
 Multiplication factor, 2262
 Multipolarity, 75, 76, 78, 80, 357, 361, 1411, 1412
 Multipole mixing ratio, 1440
 Multipole radiation, 1411, 1418
 Multistage leads, 812
 Multitracer technique, 1769, 1773–1777, 1785, 1790
 Multivariate statistical techniques, 1743
 Muon, 1487, 1489–1494, 1496, 1499–1500, 1531, 1532
 Muon capture, 1495, 1499, 1500

Muon catalyzed fusion (μ CF), 1500–1501
 Muonic atoms, 1496, 1497, 1500–1502
 Muonic hydrogen, 1499, 1500
 Muonium, 1485–1511
 Muon polarization, 1489–1494
 Muon spin rotation (μ SR), 1490–1493
 Mylar, 1368, 1438, 1471, 1725
 Myocardial imaging agents, 2080–2085, 2091, 2108–2109, 2112
 Myocardial perfusion, 1947, 1953, 1954, 1957, 2081
 Myoview, 2083

N
²²Na, 1463, 1464, 1471, 1474, 1479–1481
 Na–22 decay scheme, 1463, 1464
 Na(Ti), 2280
n-alkanes, 1296–1299, 1307
 Nano generator, 1967
 NanoSIMS 50, 2498–2499
 Natural decay chain, 2185, 2201
 Natural isotopic abundance, 487
 Natural lifetime, 173
 Natural line width, 1382, 1386, 1391, 1394, 1413, 1420, 1799
 Natural radioactive decay series, 667–687
 Natural radioactive sources, 2276
 Natural reactor, Oklo, 2617, 2637
 Natural units, 477, 480
 Natural uranium, 2617–2621, 2627, 2631, 2649, 2657, 3648
N-chlorosuccinimide, 2128
¹⁴⁰Nd, 1905, 1930, 1944, 1945, 1949, 1966–1968
 NDP. *See* Neutron depth profiling
¹⁴⁰Nd/¹⁴⁰Pr generator, 1944, 1945, 1949, 1955, 1966–1968
 Negatron, 11, 357
 Neodymium, 2482, 2483
 Neon burning, 639, 647, 648
 Neptunium (93), 14, 17, 18, 24, 489, 818–819, 823, 836, 846, 850, 852, 856–862, 879, 1235
 Neptunium (*4n+1*) series, 343, 805
 Neptunium, transmutation of, 2819, 2821
 Nernst’s distribution law, 2405
 Neuroblastoma, 2103
 Neuroendocrine tumors, 1947, 1953, 2002, 2056, 2193, 2201
 Neuroreceptor, 2104–2108
 Neurotensin, 2054, 2098, 2103, 2193
 Neutrino, 11, 16, 29, 41, 42, 124–128, 133, 134, 185, 357, 459, 464, 469, 470, 472, 2285
 Neutrino detector, 645
 Neutrino families, 632
 Neutrino oscillations, 645
 Neutrino wave function, 128
 Neutron abundance, 631

- Neutron activation analysis (NAA), 1555, 1562–1570, 1573, 1574, 1579, 1582–1594, 1597–1607, 1674, 1676, 1678, 1846–1849
- Neutron attenuation, 1688–1691
- Neutron bomb, 2655
- Neutron capture, 818–826, 841
- Neutron-capture (n, γ) reactions, 151, 157, 173–176, 184, 192
- Neutron counters, 2861
- Neutron counting techniques, 2915–2923
- Neutron cross sections, 1535, 1556, 1558, 1564, 1568, 1572, 1576, 1580, 1600, 1606, 1626, 1631, 1660, 1688, 1799–1810, 1834–1846
- Neutron cycle, 2632–2636, 2654
- Neutron depth profiling (NDP), 1608–1611, 1683, 1685
- Neutron detectors, 2915–2917
- Neutron diffraction, time-of-flight (TOF), 1531, 1657, 1665, 1680, 1713, 1719, 1722
- Neutron-drip line, 184
- Neutron flux, 175, 218
- Neutron generators, 1674–1691
- Neutron guides, 1621, 1631
- Neutron halo, 60, 185, 1503
- Neutron imaging, 1682–1685
- Neutron-induced fission, 1865
- Neutron-induced reactions, 1834, 1851
- Neutron inelastic scattering, 1865, 1884, 1897–1898
- Neutron moderation, 2617, 2619, 2625–2628, 2633, 2691, 2709
- Neutron multiplication factor, 2632–2635
- Neutron optics, 1525
- Neutron physics, in a reactor, 2622–2625
- Neutron powder diffraction, 1528–1531, 1535, 1539, 1547, 1548
- Neutron radiography (NR), 1634, 1682–1685
- Neutron reaction data, 1799–1851
- Neutron reflection, 1679
- Neutron reflectometry, 1525, 1541–1542
- Neutron resonance radiography (NRR), 1683
- Neutron-rich nuclei, 22, 31, 62, 137, 261, 268, 355
- Neutron scattering, 1515–1549, 1635, 1654
- Neutron separation energy, 540, 609
- Neutron skin, 1503
- Neutron sources, 1518, 1528, 1531, 1542–1544
- Neutron spectrum, in a light water reactor, 2622
- Neutron spectrum, of nuclear reactors, 1872–1875
- Neutron spin-echo spectroscopy, 1539
- Neutron star, 641, 648, 651–658
- Neutron star matter, 657
- Neutron-to-proton ratio, 629–631
- Neutron transmission, 1860, 1869–1871
- Neutron yields, 252
- New region of enhanced stability, 905
- Newton's equations, 628
- NGDW, 740
- ^{66}Ni , 1943, 1966, 1967
- Nickel dating, 777
- Nicotine, 2008, 2011–2012
- Nilsson model, 71, 72
- NIST, 476
- Nitrido, 2084, 2099, 2108, 2109
- Nitroalkanes, 1987, 1988, 1993
- Nitro blue tetrazolium (NBT), 2294
- Nitrogen–14, 784
- Nitroimidazole, 2089, 2090
- Nitromethane, 1988, 1989, 2004
- NMR spectroscopy. *See* Nuclear magnetic resonance
- Nobelium (102), 23, 822–823, 838, 850, 866, 879, 1250
- No-carrier-added (n.c.a.), 334, 2437
- NODASA, 2171, 2172
- Non-baryonic, 616, 619–623, 636, 637
- Nondestructive analysis (NDA), 2905–2923
- Nondestructive assay (NDA), 2903
- Non-equilibrium, in radioactive decay, 346–352
- Nonequilibrium processes, 198–202, 205
- Non-isotopic carrier, of tracer, 1766
- Non-isotopic tracer, 1763–1764, 1771
- Non-linear stage, 628
- Non-proliferation treaty, 2896
- Non-relativistic, 622, 625, 626, 629, 658
- Normal distribution, 398, 402–405, 408–410, 416–420, 430–438, 441–451, 454
- Normalized distributions, 398
- Normalizing factor, 399
- Normal random numbers, 435, 438, 439
- NOTA (1,4,7-triazacyclononane-N,N',N''-triacetic acid), 2057, 2148, 2158, 2164
- Nova, 640, 654–656
- Nozzle process, 2657
- Nozzle separator, 2385
- ^{237}Np decay chain, 1964
- NR. *See* Neutron radiography
- NRR. *See* Neutron resonance radiography
- Nuclear absorption cross section, 1799
- Nuclear accidents, 2507, 2539
- Nuclear army facilities, 2549
- Nuclear astrophysics, 16, 146, 159, 205, 328
- Nuclear batteries, 2751
- Nuclear bomb tests, atmospheric, 1215
- Nuclear Bragg scattering, 1448
- Nuclear bremsstrahlung, 378
- Nuclear chain reaction, 17
- Nuclear charge distribution, 262–270, 272
- Nuclear charge radius, 1399
- Nuclear chemistry, 20, 30
- Nuclear chemistry, small scale, 2410–2421
- Nuclear cluster decay, 342
- Nuclear data furnace code, 1716
- Nuclear decay, 112–123
- Nuclear density, 44, 64, 201, 204, 210, 215
- Nuclear devices, 2638–2655
- Nuclear elastic scattering, 1860

- Nuclear emergency, 2558–2560
Nuclear emulsions, 16
Nuclear equation of state, 203, 207–216
Nuclear excitation by electronic transfer, 1449
Nuclear facilities, 2507, 2515, 2517, 2539–2553
Nuclear fission, 223–277, 2617–2660
Nuclear forces, 41–50, 59, 61, 64, 65, 68
Nuclear forensic analysis, 2840–2843, 2845, 2858–2861, 2866–2868, 2870, 2884
Nuclear forensic methods, 2870
Nuclear fuel cycle, 2655–2660, 2801–2818, 2832
Nuclear fusion, 319–332
Nuclear industry, 2812, 2824, 2825, 2882, 2886
Nuclear isomerism, 6
Nuclear landscape, 21, 148, 205
Nuclear levels, 152, 241, 515
Nuclear lighthouse effect, 1448
Nuclear magnetic moment, 1799
Nuclear magnetic resonance (NMR) spectroscopy, 2012, 2013, 2084, 2089, 2129, 2175
Nuclear magneton, 55, 56
Nuclear mass, 51–52, 59, 73, 85, 124, 540–609
Nuclear medicine, 2539, 2547, 2553, 2556
Nuclear molecules, 189
Nuclear moments, 44, 56–57
Nuclear potential energy, 152–154
Nuclear power, advantage of, 2805
Nuclear power plant, chemical tasks, 2645
Nuclear power production, 2527, 2543–2547
Nuclear power propulsions, 2745–2749
Nuclear power propulsion system (NPPS), 2749–2750
Nuclear power source (NPS), 2731–2757
Nuclear properties of transactinide elements, 1023–1025
Nuclear quadrupole moment, 1799
Nuclear reaction, 9–10, 19–20
Nuclear reaction analysis (NRA), 1722–1732
Nuclear reaction cross section, 1906–1907, 1925
Nuclear reactor, 18, 161, 224
Nuclear resonance, 1381–1386, 1435–1438, 1448, 1453, 1455, 1729
Nuclear resonant elastic scattering, 1449–1454
Nuclear resonant excitation spectroscopy, 1448
Nuclear resonant forward scattering, 1448
Nuclear resonant inelastic and quasi-elastic scattering, 1448, 1454–1458
Nuclear rotation, 55, 89, 93–101
Nuclear safeguards, 2893–3002
Nuclear scattering, 1519, 1521, 1523, 1530
Nuclear shells, 902
Nuclear size, 57–60
Nuclear smuggling, 2839–2841
Nuclear spectra, 448–453
Nuclear spectroscopy, 451–453
Nuclear spin, 1386, 1400–1402, 1409, 1412, 1418, 1439, 1452, 1522, 1799
Nuclear spin isotope effect, 719
Nuclear temperature, 148, 176, 224, 244, 269
Nuclear testing, 2510–2511, 2540, 2541
Nuclear transitions, 75–84
Nuclear transmutation, of high-level waste, 2800–2801
Nuclear vibration, 85–89
Nuclear waste, 2659–2660
Nuclear weapon materials, 2542–2543
Nuclear weapon tests, 2506–2507, 2511, 2517–2519, 2522
Nuclear Zeeman effect, 1403, 1408
Nucleon knockout reactions, 162, 178, 179, 185–187
Nucleon–nucleon, 148, 149, 152, 162, 163, 170, 172, 198–207
Nucleophilic aliphatic substitutions, 2041–2046
Nucleophilic aromatic substitutions, 2030, 2034–2040, 2061
Nucleosynthesis, 28–29, 31, 615, 630–634, 642, 645, 648–659, 661
Nucleosynthesis by spallation, 652
Nucleosynthesis in binary star systems, 652–657
Nucleosynthesis of carbon and oxygen, 645–647
Nuclide, definition, 1034
Nuclide production, 2410–2411
Nuclidic purity, 1766, 1772
 N_xS_{4-x} ligands, 2092, 2096
- O**
- Observed activity, 335, 338, 427
Occupational radiation exposure, 2552–2557, 2560
Ocean dilution, of high-level waste, 2816
Octreoscan, 1953, 2166
Octreotide, 2186, 2194, 2201, 2205
OER. *See* Oxygen enhancement ratio
Oeschger counter, 764, 770, 773, 775, 784, 785, 797
O-(2-[^{18}F]fluoroethyl)-L-tyrosine, 2043
Off-specular scattering, 1541
Oklo, natural reactor, 20, 2617–2620, 2633, 2637
OLGA, 935
Once-through burning, 2799, 2811
Once-through cycle, 2679, 2723, 2727
Oncologic applications, 1936, 1959
On-column preparations and closed loops, 1980
One-atom-at-a-time chemistry, 928
One-pion exchange nucleon–nucleon potential, 49
One-pot and on-line procedures, 1980
Onsager's theory, 1274
Opioid receptors, 2008, 2048
Optical active center, 2094. *See also* Chirality
Optical activity, 703
Optical approximation, 1273
Optical model, 158, 164–170, 177–179, 193
Ore gap, 1468
Organ dose, 2083, 2089, 2190, 2193
Organic chemical dosimeter, 2294–2297
Organic compounds, radiation chemistry of, 1292–1293
Organic liquid scintillator, 2282
Organic molecules, radiation chemistry of, 1292
Organic synthesis, 1980, 2098

- Organocuprates, 1994, 1999
 Organometallic compounds, 995
 Organometallic reagent, 1993
 Ornithine, 2003
 Ortho-para conversion, 1470, 1472
ortho-Ps, 1467–1470
¹⁹¹Os, 1864, 1882, 1944, 1955, 1958
 Oscillation strength, 1273
 Oscillometric measurement, 2295, 2296
 Osmium, 1365–1368, 1595, 1808
 Osmium/osmium dating, 777
 Over-expressed receptors, 2102, 2110, 2193
 Oxalate, 1946, 1951, 1958, 2033, 2034, 2063
 Oxyanions, 1364–1365, 1661
 Oxygen burning, 639, 643, 645–647
 Oxygen enhancement ratio (OER), 1687
 Ozone isotope effect, 720
- P**
- ³²P, 1855, 1859, 1882, 1889, 2180, 2187, 2196, 2198
 Pair distribution function (PDF), 1524, 1529
 Pair emission, 76, 360
 Pairing energy, 51, 52, 233, 283, 340
 Pairing interaction, 45, 70, 122
 Pair production, 366, 374, 384–390, 1638
 Pair production length, 390
 Paleoceanographic changes, 751
 Paleoclimatology, 728
 Paleotemperature, 728–731, 737–741, 755
 Palladium, 1993–1998, 2038, 2126
 Palomares, 2551
 Pancreatic polypeptide, 2103
 Parabolic rule, 68, 89
 Paramagnetic materials, 1416
para-Ps, 1467–1470
 Parasitic beam, 1910
 Parent-daughter alpha-alpha correlation, 882
 Parent-daughter correlations, 28
 Parent/daughter pairs, 1966
 Parent-daughter relationship, 1767–1768
 Parent radionuclide, 1861, 1919, 1936–1938, 1941, 1942, 1955, 1959, 1966, 2075
 Paris potential, 49–50
 Parity, 44, 45, 56, 60, 66, 67, 79, 84, 86, 100–103, 119, 132–136, 469
 Partial cross sections, 1866, 1867
 Partial decay constant, 115, 339, 341, 355
 Partial decay rates, 339
 Partial fission half-lives, 900
 Partial half-lives, 82, 108, 113–116, 124, 355, 361
 Partial pair distribution functions (PPDF), 1534
 Partial PDOS as distinguished by electronic states, 1458
 Partial phonon density of states, 1455–1457
 Partial production cross sections, 1654, 1659, 1810
 Participant, 156, 204, 205, 208
 Participant-spectator, 201, 204–205
 Participant-spectator reactions, 204–205
 Particle accelerators, 2321, 2348, 2449
 Particle beam, focusing, 2337
 Particle currents, 462
 Particle evaporation, 201
 Particle implanted passivated silicon (PIPS), 2969, 2970
 Particle-induced X-ray emission (PIXE), 1568, 1697–1712, 1723, 1725, 1728–1731, 1733, 1745
 Particle-rotor model, 96–97
 Particle-vibration coupling, 89
 Particulates, radiolabeled, 2181, 2186, 2187
 Partitioned fission yield, 2540
 Partition function ratio, 707
 Partitioning, 2802, 2812, 2818–2832
 Partitioning and transmutation, 2407, 2409, 2424–2425
 PAS. *See* Principal axis system
 Patient doses, 2535–2536
 Pattern analysis, 1422–1424
 Pauli blocking, 202
 Pauli principle, 46, 63, 66, 68, 146, 162, 173, 458, 463
²¹²Pb, 1944, 1965, 1966
 PCAA. *See* Pre-concentration activation analysis
¹⁰³Pd, 1864, 1911, 1928–1931, 1960, 1961, 1967
¹¹²Pd, 1943, 1966, 1967
 PDB, 732
 PDF. *See* Pair distribution function
 PDF analysis, 1529
 Peak shape, 1643, 1651, 1652
 PELAN. *See* Pulsed elemental analysis with neutrons
 Pelletron, 2343, 2466
 Penetration factor, 118–120
 Penning ion gauge (PIG), 2324–2331, 2336, 2350
 Penning (PIG) ion source, 2327–2328, 2350
 Penning trap, 1507–1508, 1510
 PEPA, 2148, 2159–2161
 Peptide labeling, 2039, 2040, 2056
 Peptide nucleic acid (PNA), 2055
 Peptides, 1312, 1883, 1889, 1893, 1949, 1964, 2003, 2050–2059, 2102–2104, 2131–2136, 2163, 2192–2194
 Peptides and antibodies, 2100
 Percentiles, 401, 404
 Perfusion agents, 2078–2081, 2084–2086, 2090–2091
 Perfusion ⁶²Cu complexes, 1945, 1950, 2145
 Perfusion imaging, 1945, 1949, 1954, 2084
 Periodic system of elements, 226
 Periodic table of elements, 492
 Permanent implants, 1894
 Perrhenate, 1963, 1964
 Personnel monitoring, 2228, 2233–2234
 Perspex dosimeter, 2299–2301
 Pertechnetate, 1957
 Perturbation theory, 1401, 1404
 PET-microdosing, 2011
 PET-radiopharmaceuticals, 2022, 2041
 PFTNA. *See* Pulsed fast-thermal neutron analysis
 PGAA. *See* Prompt gamma activation analysis

- PGE. *See* Platinum group elements
- Pharmacodynamics, 2010, 2012
- Pharmacokinetics, 2010, 2011, 2185
- Pharmacology, 1948, 2011
- Phase equilibria, 708–713
- Phase problem, 1527, 1541
- Phonon density of states, element specific, 1448, 1455–1458
- Phonon energy spectrum, 1448, 1455, 1456
- Phosgene, 1981, 1983, 1990, 2005, 2006
- Phosphates, 1311, 1315, 1316, 1337, 1345, 1363, 1364, 1589–1593
- Phosphorus–32, 15, 1363–1364, 1588, 1589, 1604, 1664, 1771, 1800
- Photocathode, 2278–2281
- Photochemical isotope separation, 2397–2401
- Photodisintegration, 631, 642, 648, 651, 656
- Photoelectric absorption, 1637, 1638
- Photoelectric effect, 384–388, 390
- Photoelectric peak, 445–447
- Photographic dosimeters, 2298
- Photoionization, 2399
- Photomultiplier tube (PMT), 2279–2281
- Photon activation analysis (PAA), 1562, 1568–1569, 1583, 1588
- Photon attenuation, 389, 390
- Photon emitters, 1904, 1924–1927
- Photon-photon interaction, 388–389
- Photon spectrometer, 2268
- Photostimulated luminescence (OSL), 2298
- Photosynthesis, 15, 25, 723, 1789, 1790
- Photosynthetic carbon fixation, 738
- PHRS. *See* Pulse height response spectrometer
- Phtalocyanines, 1345
- Pick-off annihilation, 1469–1472
- Pickup, 182, 184
- Pile-up, 2261, 2276, 2280
- Pile-up losses, 1603
- Pion, 162, 465
- Pion capture, 1504–1506
- Pionic atoms, 1487, 1498–1500, 1503–1506
- Pionic hydrogen atoms, 1500, 1503–1506
- Pipeline, 1680, 1791
- Pitchblendes, 814
- PIXE. *See* Particle-induced X-ray emission
- PIXE chambers, 1700–1702, 1712
- Planetary orbital changes, 733
- Plasma, 320–323, 2321–2337
- Plasma beta, 2769, 2770
- Plasma energy, 367
- Plasma frequency, 328, 329
- Plasma parameter, 322, 325–329
- Plasma physics, 320, 324–330
- Plasma protein binding, 2011, 2023
- Plasmatron, 2326–2327
- Plastic scintillators, 2281
- Platinum group elements (PGE), 1594–1595
- Platzman's optical approximation, 1272–1273
- Pleochroic haloes, 764, 778–779
- Plural scattering, 1713, 1716–1717, 1721
- Plutonium–238, 2417, 2509–2514, 2518, 2551, 2552, 2574
- Plutonium (94), 17, 18, 22, 24, 30, 818, 819, 823, 826, 844, 846, 850–853, 856–864, 867, 1236, 1315
- Plutonium and uranium refining by extraction (PUREX) process, 853
- PMMA dosimeter, 2299–2300
- PNA. *See* Peptide nucleic acid
- PnAO, 2085, 2089–2090
- Pneumatic tube systems for transport, 1570
- p-nuclides, 648, 651
- Point kernel approach, 2183
- Poisson approximation, 416, 445, 449, 453
- Poisson distribution, 408, 411, 416–422, 426, 427, 434, 443, 449–452
- Poisson process, 427, 430, 431, 443, 444
- Poisson statistics, 1603, 1653, 1767
- Polarizer, 1546, 1549
- Polarometry, 1435
- Polonium, 4, 5, 13
- Polonium/lead dating, 779
- Polyethylene, 1307–1310, 1314, 1325, 1581–1582, 1678, 1685, 1768
- Polyethylene films, in dosimetry, 2299
- Polymer irradiation, 1307
- Polymerization, 1293, 1302–1316
- Polymers, 1471, 1474, 1479, 1482
- Polymethylmethacrylate dosimeters, 2299–2300
- Polysaccharides, 1311–1312
- Position-specific labeling, 1980–1981
- Positive-ion scavengers, 1277
- Positron, 1462–1483
- Positron annihilation, 1462–1483
- Positron beams, 1479–1480
- Positron branching, 1921, 1924, 1945, 1947
- Positron emission tomography (PET), 27, 30, 1979–1982, 2002, 2005, 2007, 2010–2013, 2022–2027, 2041–2042, 2047, 2049, 2057
- Positron emitters, 1463, 1886, 1904, 1906, 1910, 1912, 1915–1924, 1930, 1945–1955, 2023, 2146
- POSITRONFIT, 1475
- Positronium (Ps), 1273, 1466–1475, 1482, 1483, 1487, 1489, 1492, 1493
- Positron lifetime, 1464, 1473–1475, 1480–1484
- Positron lifetime spectroscopy, 1473–1475
- Positron sources, 1463, 1464, 1471–1472
- Potassium/argon dating, 781
- Potassium/calcium dating, 783
- Potassium–40 dating, 781
- Potential energy surface, 243
- Potentiometric measuring system, 2292
- pp-chain, 642–645
- PPDF. *See* Partial pair distribution functions
- ¹⁴⁰Pr, 1944, 1945, 1949, 1966–1968

- Pre-concentration activation analysis (PCAA), 1584, 1592–1593
- Preequilibrium, 199, 201
- Preorganization, 2151, 2174
- Preparative radiochemistry, 2440, 2443, 2449–2451
- Pressure chamber, 1438
- Pressure tube, schematic representation, 2647
- Pressure vessel, of a PWR, 2644
- Pressurized water reactor (PWR), 2621, 2640–2647
- Pre-tinning, 2100, 2101
- Primary interfering reaction, 1604
- Primary isotope effect, 715
- Primary parent, 342–345
- Primary precursors, 1980–1983
- Primordial abundances, 633–636
- Primordial nucleosynthesis, 629–637
- Principal axis system (PAS), 1400, 1411–1412, 1419
- Probabilistic interpretation for the decay constant, 425
- Probability density, 375, 398
- Probability integral isotope effect, 1352, 1353
- Process calorimeters, 2289, 2311
- Prochelator, 2148, 2153, 2154, 2158–2161, 2168
- Production cross section, 879, 882, 885–888, 891, 909, 911, 915
- Production of nuclear weapons, 2540, 2543
- Product yields, 201, 245, 248, 252
- Progesterone, 1999, 2005, 2093, 2101, 2205
- Projected dose, 2558
- Projected range, 521, 533–540
- Projectile fragmentation, 205
- Proliferation, of tumors, 2010, 2182
- Promethium (61), 13, 490, 690–698
- Promethium (61), discovery of, 692, 1148
- Prompt criticality, 2636, 2708, 2712
- Prompt gamma activation analysis (PGAA), 1561–1566, 1571, 1572, 1600, 1619–1667
- Prompt gamma neutron activation analysis (PGNAA), 1680, 1681
- Prompt gamma radiation, 1621–1625, 1638
- Prompt gamma rays, 1556, 1560, 1568, 1660, 1680
- Prompt neutron, 245, 257
- Prompt neutron yields, 252
- Prompt radiation analysis, 1678–1682, 1834
- Proportional counters, 2262–2266
- Propyl chloride, 1360, 1361
- Prosthetic groups, 2040, 2046–2057
- Protactinium-233, 2819
- Protecting effect, in radiation chemistry, 1299
- Protection of workers for intervention in nuclear emergency, 2560
- Proton drip line, 22, 136, 137
- Proton induced γ -ray emission (PIGE), 1710, 1728–1731
- Proton-proton (p-p) chain, 331, 641–645
- Proton-rich nuclei, 21, 22, 62, 136, 205
- Protons, 487, 521–536, 540
- Proton separation energy, 540, 609
- Proton spectrum, 1727
- Ps. *See* Positronium
- ^{244}Pu , 2476, 2482–2485, 2494, 2495
- Pulmonary ventilation, 1861, 1955, 1956
- Pulsed elemental analysis with neutrons (PELAN), 1681
- Pulsed fast-thermal neutron analysis (PFTNA), 1681
- Pulse dosimetry, 1282–1284
- Pulse height response spectrometer (PHRS), 1688, 1690
- Pulse radiolysis, 1269, 1275–1283, 1286, 1288, 1291, 1300, 1301
- PUREX process, 2658, 2812–2816, 2825–2827, 2830
- Pyridines, 1998, 2039–2042, 2055, 2098, 2104, 2107
- Pyrogallol-formaldehyde resin, 1951
- Pyroprocessing, 2823, 2830
- Pyruvate, 2000, 2061
- ## Q
- Q_β systematics, 889, 901
- Quadrupole doublet, 1419
- Quadrupole moment, 54
- Quadrupole splitting, 1401, 1407–1410, 1414–1416, 1422, 1426, 1427, 1433, 1439–1442
- Quadrupole vibrations, 86, 87
- Quality assurance (QA), 1575, 1583, 1600, 1607, 1656, 1666–1667
- Quality control, 1595, 1601
- Quantile, 401, 404, 437
- Quantum beats, 1449, 1458
- Quantum chemical calculations, 943, 949
- Quantum chromodynamics (QCD), 50, 109
- Quantum correction, VPIE
- Quantum mechanical tunneling effect, 1335, 1371–1373
- Quantum molecular dynamics, 187
- Quantum numbers, 66, 104, 177
- Quark, 625–629
- Quark confinement, 464, 466
- Quark model, 462–464
- Quark structure, 44
- Quartiles, 404
- Quartz distillation apparatus, 1912
- Quasar spectra, 636
- Quasi-elastic Mössbauer spectroscopy, 1454
- Quasi-elastic neutron scattering, 1538
- Quasielastic scattering, 185
- Quasifission, 710
- Quinoxaline, 1991
- Q-values, 150–153, 156, 192, 540, 609, 1861, 1862
- ## R
- ^{224}Ra , 1965, 2201, 2202
- ^{226}Ra , 1864, 1929, 1936, 1944, 1964, 1965
- Raclopride, 2006, 2007
- Rad. *See* Roentgen absorbed-dose
- Radial distribution function, 1534–1537
- Radial wave equation, 65, 166
- Radiation-and matter-dominated eras, 618

- Radiation chemistry, 1267–1326
Radiation counting systems, 2858–2863
Radiation damage, 1482, 1625, 1685, 1686, 1725, 1756, 1834
Radiation detectors, 2259–2286
Radiation dose, 1773
Radiation effects, in polymers, 1291, 1306–1310
Radiation exposure, occupational, 2557
Radiation length, 367, 375, 379–381
Radiation loss, 368, 369, 378, 380
Radiation processing, 1267, 1283, 1292, 1309, 1313, 1314, 1317–1326
Radiation protection, 2505–2560
Radiation resistance, 1961
Radiation synovectomy, 2187
Radiation synthesis, 1313–1315
Radiation technologies, 1313, 1317
Radiation types, 5
Radiation yield, 522, 528
Radiative neutron capture, 1622, 1860
Radical polymerization, 1267, 1313, 1317, 1324, 1325
Radical scavengers, 1276, 1277, 1309, 1323, 1336, 1361
Radioactive beams, 846, 847
Radioactive carbon, 1359
Radioactive contamination, 2520, 2522
Radioactive dating, 668, 764–815
Radioactive debris, 2540
Radioactive decay, 333–362, 1860, 1878, 1937–1941, 1960, 1964, 1981
Radioactive decay chains, 667–687
Radioactive decay, of superheavy elements, 778
Radioactive effluents, environmental transport of, 2521–2527
Radioactive equilibrium, 346–352
Radioactive inventory, 2643
Radioactive-ion sources, 2334–2335
Radioactive multitracers, 1773–1777
Radioactive projectile beams, 187
Radioactive series, 805
Radioactive source, natural, 2886
Radioactive tracer, 1763–1791
Radioactive waste, 2238, 2421, 2425–2426, 2507, 2509, 2543, 2549, 2551
Radioactive waste management, 2799–2832
Radioactivity, 2646, 2656, 2666, 2670–2673, 2686, 2703, 2706–2711, 2719, 2720, 2740, 2799–2803, 2811, 2814, 2816, 2886, 2925, 2989, 2995
Radioactivity accumulation, 1344
Radioanalytical chemistry, 2417–2420
Radiobiology, 1687–1688
Radiobromine, 1357
Radiocarbon, 764, 770, 784–790, 796
Radiocarbon dating, 784, 785, 788
Radiochemical activation analysis (RAA), 1583–1599
Radiochemical methods, 245
Radiochemical milking, 2845, 2850–2851
Radiochemical purity, 1766
Radiochemical separations, 2843, 2847, 2850, 2859
Radiochemical yield, 1345
Radiochemical yields, in aromatic nucleophilic substitutions, 2034, 2039
Radiochemistry, 3–31
Radiochemistry, preparative, 2440, 2443, 2449–2451
Radiochromatography, 1770, 1771
Radiochromic dye, 2296–2297
Radiochromic film dosimeters, 2300–2302
Radioelements, 689–698
Radio-frequency ion sources, 2325, 2328
Radio frequency quadrupole (RFQ), 2355–2356
Radiogenic argon–40, 781, 782
Radiography, 2527, 2535, 2536, 2552–2557
Radioimmunoassay, 26
Radioimmunotherapy, 1888, 1889
Radioiodinated compounds, 2122–2140
Radioiodination, 1886, 2056, 2121–2140, 2188, 2200
Radioiododeboronation, 2127–2128
Radioiododebromination, 2125, 2126
Radioiododehalogenation, 2125–2126, 2136, 2139, 2140
Radioiododeiodination, 2125
Radioiododestannylation, 2126–2128, 2135, 2136, 2140
Radioiododethallation, 2123–2124, 2136, 2140
Radioiododetriazeneation, 2131
Radioisotopes, 1855, 1893, 1906–1908, 1923, 1925, 1928, 1930, 1942, 1948, 1958, 2063, 2102, 2122–2123, 2136, 2144, 2161
Radioisotope thermoelectric generators, 2751–2757
Radioisotopic analysis, 1577
Radiolabeled particulates, 2186, 2187
Radiolabeling, 1883
Radiolanthanides, 1882, 1949, 1955, 1956, 2144, 2199
Radiological emergencies, 2558–2559
Radioluminography, 1770
Radiolysis, 1914, 1942, 1965, 2169
Radiometals, 2143–2175
Radiometric analysis, 1786–1789
Radiometric titration, 1788
Radionuclide chronometry, 2852–2856
Radionuclide, cosmogenic, 770
Radionuclide generator, 1936, 1939–1943, 1952, 1959, 1960
Radionuclide generator systems, 1859
Radionuclide mixtures, 338
Radionuclide production, 1936, 2547, 2557
Radionuclides, 2144–2151, 2161, 2165, 2166, 2170, 2173, 2505–2534, 2538–2552, 2556–2559
Radionuclide sources, 1267, 1268
Radionuclides, positron emitting, 1463
Radionuclide therapy, 2180–2205
Radionuclidic contamination, 1894
Radionuclidic impurity, 1924, 1947
Radiopharmaceutical chemistry (RPC), 1943, 1944
Radiopharmaceuticals, 1335, 1371, 2074–2092, 2099–2114, 2517, 2538

- Radiosensitivity, of tumors, 2182
Radiotherapeutics, 2180–2194, 2198, 2200
Radiotherapy, 2180–2182, 2185–2188, 2190–2205, 2539
Radiotoxicity, 1894
Radiotracer synthesis, 1979–1983
Radium, 4–6, 10
Radon, 2233–2243, 2527, 2528, 2531–2534, 2543, 2553, 2554, 2557
Radon and its decay products, 2531–2532, 2554
Radon isotopes, 675
Rain washout, 2524
Rapid chemical separation, 835
Rapidity, 206
Rapid synthetic method, 1979
Rare earth elements (REE), 1555, 1594–1596, 1665–1667, 1775
Rate coefficients, of chain propagation, 1303
Rayleigh scattering, 384–387
Rayleigh separation, 2373
⁸¹Rb, 1905, 1912, 1919, 1920, 1927, 1930, 1943, 1955, 1956
⁸²Rb, 1910, 1915, 1919, 1920, 1931, 1936, 1943, 1945, 1954
^{82m}Rb, 1919, 1920
RBE. *See* Relative biological effectiveness
RBMK, nuclear reactor, 2646–2648
⁸¹Rb/^{81m}Kr generator, 1943, 1955, 1956
¹⁸⁶Re, 1864, 1889, 1913, 1928–1930, 2089, 2114, 2144, 2181, 2195, 2197
¹⁸⁸Re, 1864, 1889, 1896, 1897, 1944, 1954, 1957, 1959, 1962–1964, 2114, 2144, 2187, 2196, 2198
Reaction at equilibrium, 1783
Reaction channel, 1906
Reaction cross sections, 1845, 1850
Reaction gas chromatography, 934, 945, 979, 980
Reaction kinetics, 1780–1781
Reaction rate, 147, 161, 194
Reaction zone, 1363–1366
Reactivity, 2619, 2633, 2637, 2639, 2648, 2652–2654, 2672, 2681, 2683, 2690–2694, 2704, 2705, 2708–2718, 2736, 2746, 2783, 2784, 2814, 2821, 2874, 2879
Reactivity integral, 1355, 1356
Reactor core safety, 2694
Reactor design, general principles, 2622–2637
Reactor inventory, 2643
Reactor kinetics, 2633–2637
Reactor operation, 2544, 2546, 2553, 2555
Reactor-produced radionuclides, 1859, 1862, 1864, 1883
Reactor products, 2879–2881
Reactors, breeder, 2631, 2648, 2649, 2656, 2973
Reactors, fast, 2622–2625, 2634, 2637, 2649, 2667, 2668, 2670, 2673–2674, 2687–2725, 2807, 2818–2825, 2830, 2831
Reactor shutdown, 2692, 2714
Reactor sources, 1536, 1541–1548
Reactors, thermal, 2424
Reactor water, 2416–2417
Receptor binding, 1908, 2074, 2091, 2094, 2096, 2101, 2104, 2107, 2108, 2190, 2194
Receptors, 1995, 2005–2009
Receptor specific agents, 2084
Reciprocal lattice, 1526–1531
Recoil after alpha decay, 685
Recoil atom reaction yield, 1334, 1361
Recoil-decay tagging, 910, 918
Recoil energy, 1334, 1337–1342, 1361–1369, 1373, 1374
Recoil implantation, 1335, 1368–1370
Recoil labeling, 26, 1980
Recoilless emission of γ rays, 25
Recombinant scFv, 2101
Recovery, of generator parent radionuclides, 1959
Recycling plutonium, 2676, 2814–2816, 2823
Recycling uranium, 2676, 2816
Red giants, 639, 647, 654
Redshift, 616, 618, 622–624, 629, 636
[¹⁸⁸Re]DTPA, 1964
Reduced mass, 118, 120
Reduced matrix element, 1411
Reduced partition function ratio, 707, 709
Reduced transition probability, 78, 118
Reducing agent, 1992, 2080–2084, 2088, 2100, 2132, 2133
REE. *See* Rare earth elements
Re-entry reaction, 1335, 1336
Reference materials, 1576, 1583, 1587, 1591, 1593, 1607
Reflection cross section, of thermal neutrons, 1678
Reflection geometry, in Mössbauer spectroscopy, 1429–1432
Refractive index, 382, 383, 1525, 1541–1544, 1740
Refractory lining wear, 1791
Region of interest (ROI), 1651, 1729
Regulatory peptides, 2192–2193
¹⁸⁸Re labeled antibody, 1964
¹⁸⁸Re labeled anti-CD66, 1964
¹⁸⁸Re labeled HEDP, 1963
¹⁸⁸Re labeled lipiodol, 1964
Relative atomic mass, 487, 491–504, 540
Relative biological effectiveness (RBE), 1687, 2199, 2204
Relative χ^2 , 438
Relative deviation, 412
Relative width, 404, 405
Relativistic effects, 926, 927, 945, 948, 983, 994
Relativistic factor, 367
Relativistic quantum-chemical calculations, 866
¹⁸⁸ReMAG3, 1964
Renal function, 2087–2089
Renewal processes, 442–447
Reprocessed uranium, 2816
Reprocessing fuel cycle (RFC), 2801, 2802, 2811, 2825
Reprocessing of nuclear fuel, 2423, 2658–2659
Repulsive Coulomb interaction, 152
Research reactors, 1621, 1628, 1635, 1665, 2539, 2547

- Residual dose, 2558
Residual interaction, 45, 69
Residual solvent analysis, 2013
RESOLUTION, 1475
Resolution of scintillation detectors, 436
Resolving time, 427
Resonance absorption, 1383–1388, 1391–1394, 1407, 1435, 1453
Resonance capture, 1868
Resonance counters, 1433
Resonance escape probability, 2633
Resonance integrals, 1799–1810
Resonance reactions, 75
Resonance scattering, 1519
Resonances, coupled, 2359–2360
Resonant ionization mass spectrometry (RIMS), 2462, 2485, 2491–2495, 2499, 2500
Rest energy, 43, 44, 49, 265, 365, 388
Rest mass, 29, 124–127, 150, 367
Retention, 14, 25
Retention time, 973
Reverse kinematics, 184, 200, 205, 214
Reverse Monte Carlo for powder patterns (RMCPOW), 1530
Reverse Monte Carlo (RMC) modeling, 1529, 1536–1537
RGD, 2054, 2056, 2060, 2102, 2103
Rhenium–188, 1365–1368, 1595, 1808, 1883, 1896, 1962, 1963
Rhenium/osmium dating, 790
Rietveld refinement, 1529, 1531, 1535
Rift valley, 793
Rigid triaxial rotor, 96
RIKEN, 1014, 1022
Ring-closure reactions, 1986, 1998, 2005
RMCPOW. *See* Reverse Monte Carlo for powder patterns
²²²Rn, 1936, 1944
Roche lobe, 653
Roentgen absorbed-dose (Rad), 1282, 1886, 1888–1890, 1896, 1899
Roentgenium, 24, 884, 887, 892, 1013, 1014
Root mean square (rms), 58, 211, 402, 452
Rotating crystal method, 1528
Rotating wheel technique, 832
Rotational energy, 155
Rotational excitations, 76, 92, 275, 8791
Rotation alignment, 97–99
Rotational states, 90–94, 109
Rotation group, 460, 461
Rotation-vibration coupling, 96
Round robin exercises, 1745
RPC. *See* Radiopharmaceutical chemistry
rp-process, 655–658
r-process, 642, 648–651, 656–661
Ru–99, 1794
Rubidium/strontium dating, 791
Rule of the geometric mean, 710
Rutherford backscattering spectroscopy (RBS), 1710–1731
Rutherfordium (104), 23–26, 882, 883, 892, 926–929, 937, 942–960, 976, 1012, 1014, 1253
Rutherford, unit of activity, 458
- S**
Saddle point, 244, 245
Safeguards inspection samples, 2950–2960
Safeguards verification measurements, 2901–2902
Safety factor, 2769
Samarium/neodymium dating, 795
Sample screening methods, 2994–2995
Sandostatin, 2166
Sargent rule, 357
Satellites, nuclear accidents, 2551–2552
Saturation factor, 218
SAVE, 787
¹¹⁸Sb, 1943, 1945, 1948
⁴⁴Sc, 1943–1947
Scaled events, 431
Scale energy, 30, 367
Scaler signals, 431
Scanning particle microprobe (SPM), 1703, 1704, 1725
Scattering cross section, 1867, 1869, 1874
Scattering length, 1500, 1503, 1519–1522, 1525, 1532, 1536, 1540, 1541, 1544, 1545
Scattering vector, 1522, 1525, 1526, 1536, 1539–1541
Scavenger, 1275–1277, 1285, 1293, 1309, 1323, 1336, 1350, 1361, 1362, 1468, 1599, 1955, 1958
Scavenging techniques, 1303
Schematic structure, 640
Schottky–Frenkel defects, 774
Schrödinger equation, 46, 65, 118, 119, 166, 284
Schwinger–Lüders–Pauli theorem, 134
Scintillation cocktail, 1769
Scintillation detector, 21, 436, 446
Scintillators, 2278–2286
⁷²Se, 1905, 1943, 1945, 1947
⁷³Se, 1905, 1919–1922, 1947
^{77m}Se, 1943, 1955
Seaborgium (106), 23, 25, 882, 883, 892, 926, 929, 936, 969–983, 1012, 1014, 1256
Sealed tube accelerator, 1681
Secondary interfering reaction, 1604–1605
Secondary ion mass spectrometry (SIMS), 2462, 2497–2499
Secondary isotope effects, 715, 716
Secondary precursors, 1981–1993, 2023, 2049–2050
Secondary yields, 245
Second order Doppler shift, 1404, 1406, 1414
Secular equilibrium, 342, 346–349, 352, 1938–1941
Selection rules, 79, 80, 119, 133, 135
Selectivity coefficient, 2410
Selenium, 1590, 1591, 1605, 1711, 1752, 1753, 1802, 1947, 1997, 1998, 2822
Self-absorption, 1623, 1625, 1635, 1654

- Self-consistent nuclear energy system (SCNES), 2672–2674, 2694, 2704, 2706
- Self-shielding, 1623, 1625, 1635, 1654
- Self-shielding factor, 1559, 1580
- Semi-adiabatic calorimeter, 2309, 2311
- Semiconductor dosimeters, 2312–2313
- Semiconductors, radiation chemistry of, 1269, 1291, 1292, 1314, 1429, 1434, 1456, 1469, 1480, 1481, 1489, 1555, 1573, 1586, 1589, 1590, 1595, 1611, 1621, 1637, 1638, 1653, 1678, 1686, 1687, 1725, 1739, 1743
- Separation energies, 540–609
- Separation factors, 705, 709, 2371–2383, 2386, 2387, 2389, 2392–2397, 2407, 2423, 2425, 2479, 2482, 2483
- Separation in-flight, 881, 882, 893–897
- Separation of element groups, 1586–1588
- Separation unit, 2372, 2382, 2384, 2401
- Separative stages, 2371, 2374
- Separator for Heavy Ion reaction Products (SHIP), 885, 888, 891, 894–897, 916
- Serotonergic system, 2007
- Serum proteins, 2087, 2174
- SESAME, 2827
- Sestamibi, 2081–2084, 2108, 2112
- SF decay, 990
- Shadowing parameter, 1355, 1356
- Shape of the photoelectric peak, 445–447
- SHE, 916, 1009
- Shell closures, 240, 242, 251, 256, 266, 267
- Shell correction energies, 902, 903
- Shell effects, 674, 902
- Shell model, 52, 56, 57, 60, 63–75, 84, 85, 92, 99, 101–104, 109–111, 120, 121, 132, 239–243, 250
- Shell structure, 21, 25, 76, 92, 93, 238, 284, 305, 360
- Shielding, radiation, 2232, 2240
- SHIP, 837, 881, 894, 897, 937, 1012
- SHIPTRAP, 917
- Shirley factor, 1399
- Short-lived Isotopes Studied by the AKufve technique (SISAK), 2412–2413, 2426
- Short-lived radionuclides, 2430–2432, 2449
- Shot noise, 1279, 1280
- Si avalanche photodiode, 1449
- SI base units, 476–479
- SI derived units, 476–479
- Si(Li) detector, 2267, 2269
- Siegbahn notation, 511
- Sievert, 2219, 2254
- Silicon-32, 773
- Silicon burning, 639–642, 648
- Silicon detector, 2266, 2285, 2471
- Silicon detector, position sensitive, 897
- Silicon diodes, 2312, 2313
- Silicon surface barrier detector, 1609
- Silver, 1319, 1593–1594, 1664, 1666, 1747, 1770, 1775, 1779, 1790, 1804
- Simulation of nuclear spectra, 435
- Single-atom chain, statistical analysis, 898
- Single-atom chemistry, 30, 929
- Single-atom decay chains, 882, 897
- Single atom scattering, 1518–1520
- Single photon emission computed tomography (SPECT), 1856, 1904–1907, 1919, 1922–1926, 1930, 1942–1944, 1948, 1953, 2084, 2114, 2139
- SI prefixes, 478, 481
- Site-specific phonon densities of states, 1458
- Skyrme–Hartree–Fock, 905, 906
- Slanting beams, 1910, 1911, 1928, 1929
- SLAP, 729, 731
- Sleptons, 472
- Slowing down power (SDP), 2627, 2628
- ¹⁴⁶Sm, 2476, 2482–2483
- ¹⁵³Sm, 1864, 1881, 2145, 2149, 2186, 2187, 2195–2198
- Small angle neutron scattering (SANS), 1539–1541, 1545
- Small Angle Separator System (SASSY), 1012
- SMOW, 731
- ¹¹⁰Sn, 1943, 1945, 1948
- ¹¹³Sn, 1898, 1943, 1955
- ^{117m}Sn, 1863–1865, 1897, 1898, 1905
- Sn–119, 1794
- SNOW, 731
- Snow and ice chronology, 802
- Sodium-cooled fast reactor (SFR), 2668, 2676, 2690–2702, 2709, 2710, 2723
- Soft collision, 1273
- Solar abundances, 650, 653, 659, 661
- Solar neutrino, 29, 185, 645
- Solar neutrino problem, 645
- Solid dosimeters, 2297–2298, 2307–2308
- Solid reaction, 1783–1784
- Solid-state detectors, 2471, 2473
- Solid targets, 1910–1914, 1925
- Solid-waste disposal and transport, 2546–2547
- Solubility, 1285, 1308, 1312, 1319, 1763, 1765, 1779–1780
- Solubility isotope effect, 711
- Solubility of heavy water, 712
- Solvating reagent, 2407
- Solvation parameters, 1980
- Solvent extraction, 2404–2426
- Solvent isotope effect, 716
- Somatostatin receptor, 2194, 2205
- Sonication, to speed-up a reaction, 1980
- Sophisticated radiochemical separations, 1936, 1942
- Source-screen distance (SSD), 1688
- Sources of radiation, 1268–1270, 1317, 1323, 1324
- Spallation, 19, 28, 652, 2353, 2356, 2476, 2478, 2481, 2509
- Spallation sources, 1543, 1657
- Spallogenic products, 2430, 2439
- S-parameter, 1478
- Special decay modes, 136–137
- Speciation, 2415–2416
- Specific activity, 334
- SPECT. *See* Single photon emission computed tomography

- Spectators, 185, 204–206
Spectral power distribution, 617
Spectrophotometry, 1275, 1278, 1280, 1593
Spectrum evaluation, 1424–1427
Spectrum point, 398, 400, 409, 424, 435, 448–453
Specular reflection, 1541
Spent fuel measurement, 2923–2928
Spent nuclear fuel, 2423–2425, 2898, 2901, 2906, 2907, 2911, 2912, 2915–2917, 2923–2935, 2942, 2943, 2951–2953, 2956–2958, 2964, 2967–2973, 2979, 2982–2985
Spin-echo spectroscopy, 1539
Spin incoherence, 1522
Spin, nuclear, 719
Spin-orbit coupling, 162
Spin-spin relaxation, 1441, 1442, 1491
Spontaneous electrodeposition, 1899
Spontaneous fission, 235–238, 244, 247, 251, 253, 259, 261, 266–268, 274, 361, 821–826, 832, 839, 841–845
Spontaneous fission tracks, 2453
Spoofing, 2855–2856
SPring–8, 1449, 1450, 1742
s-process, 649
Spur model, 1273, 1466–1469
Spur, of ionized or excited molecules, 1273–1274
Squarks, 472
⁸²Sr, 1905, 1910, 1919, 1931, 1943, 1945, 1954
⁹⁰Sr, 1864, 1936, 1943, 1956, 1959–1962, 2144
 μ SR. *See* Muon spin rotation, 1490–1493
⁹⁰Sr/⁹⁰Y generator, 1943, 1959, 1961
SSD. *See* Source-screen distance
Stability valley of nuclei, 354
Stable isotope as tracer, 1764
Standard adsorption enthalpy, 985–988, 990–992
Standard atomic weights, 492, 504
Standard candles, 622, 624, 636, 655
Standard conditions, 1414, 1636
Standard deviation, 403
Standardization, 408
Standard model, 457–473, 625–627
Standard normal distribution, 430, 433, 435
Standard normal random variable, 408, 435
Standard radionuclides, 2573
Standard reduction potentials, 1285, 1290
Standard sources, for alpha particles, 2574–2575
Standard sublimation enthalpy, 986, 994
Stark effect, 241
Statistical nature of radioactive decay, 362
Statistical samples, 400
Steel, 1268, 1422, 1424, 1433, 1442, 1588, 1589, 1605, 1606, 1656, 1682, 1684, 1791
Stellarator, 2768–2774, 2777, 2790, 2793
Stellar evolution, 615, 637–641, 654–658
Stellar nucleosynthesis, 637–652
Stereoselective reaction, 2086
Sterilization, 1267, 1311, 1314, 1323–1326
Sternheimer factor, 1415, 1441
Steroid, 1993, 2004–2005, 2012
Stille and Suzuki couplings, 1983, 1993–1996
Stochastic effects, 2220, 2242–2246, 2254–2256
Stochastic processes, 397, 427, 442–448
Stockpiling, 1028
Stony meteorites, 767, 784, 810
Stopping power, 367–372, 376, 378, 380, 520–540
Storage, of nuclear waste, 2659–2660
Storage rings, 2353–2355
Stragglings, 1611, 1721, 1722, 1731, 1732
Strangeness, 463
Stripping, 182, 184, 216
Strong charge, 463
Strong decay gamma rays, 2568, 2570
Strong interaction, 46, 50, 465
Strontium, 1592, 1778, 1803
Strutinsky's method, 285
SU(2), 461, 462, 466, 468, 472
SU(3), 102–107, 395, 461, 466, 472
Sub-barrier fission, 311–315
Sub-barrier fusion, 185
Subcellular range, 2203, 2204
Subclinical disease, therapy, 1964
Sublimatogram, 1369
Sub-surface muon, 1489–1490, 1493
Successive decays, 1941
Succinimidyl 3-(tributylstannyl)benzoate, 2135
Suess effect, 787, 788
Sulphonamides, 1989
Summing of events, 1603
Sun, 637, 639
Sunna film, 2308
Superactinide, 1008, 1009
Superallowed transitions, 133
Superconductivity, 626
Supercritical media, 1980
Supercritical state, 2635, 2636
Supercritical water-cooled reactor (SCWR), 2668, 2682–2683, 2723, 2726–2728
Superexcited molecules, 1273
Superheavy elements (SHEs), 23, 487, 492, 878, 879, 882, 899, 904–907, 915–919, 1006–1028
Superheavy nuclei, 879, 882, 893, 898, 905–909
SuperHILAC, 1011, 1012
Supermicroautoradiography, 1770
Supermirror, 1632
Supernova, 639, 641, 655
Superphénix, 2650, 2696, 2697, 2703, 2807
Supersymmetric models, 472
Surface area determination, 1789
Surface energy, 230–233, 236, 237
Surface muons, 1489–1490, 1493
Surface reaction, 1442, 1783
Survival curve, 2204
Swimming-pool reactors, 2638

- 3j symbol, 1411, 1412, 1418
 Symmetric fission, 258
 Symmetry breaking, 61, 468
 Synchrocyclotron, 2350, 2352, 2361
 Synchrotron, 2325, 2334, 2352–2354, 2357, 2361, 2364, 2365
 Synchrotron Mössbauer sources, 1448, 1453
 Synchrotron oscillations, 2361
 Synchrotron radiation, 1448–1458, 1738–1758
 Synchrotron radiation source (SR), 1737–1758
 Synergy, 2408
 Synthetic multilayers, 1742
 Szilard–Chalmers process, 14, 1342–1360, 1863
- T**
^{178m}Ta, 1944, 1955–1958
 Taagepera–Nurmia formula, 356
 Table of nuclides, 1034–1261
 Tandem accelerator, 2462–2467
 Tandem mode, 1910
 Tandetron, 2344, 2345
 Tapered cascade, 2372, 2375
 Target-and recoil chamber, 932, 933
 Target construction, 1908, 1914, 1931
 Targeted radionuclide therapy, 2180, 2181, 2187, 2191
 Targeted radiotherapeutics, 2180–2202
 Targeted radiotherapy, 1960, 2145, 2165, 2185–2188, 2190–2205
 Targeting vehicle, in radionuclide therapy, 2186
 Target-projectile interactions, 177
 Targetry, 1904, 1908–1911, 1916, 1923, 1925, 1928
 Tat-peptides, 2103
 Tau, 42
¹⁴⁹Tb, 2199, 2200
^{94m}Tc, 1907, 1913, 1919, 1924
^{99g}Tc, 2077
^{99m}Tc, 1855, 1856, 1859–1861, 1865, 1884–1886, 1919, 1924, 1925, 1937, 1939, 1943, 1956–1959, 1963, 2073–2114
¹¹⁸Te, 1943, 1945, 1948
¹³²Te, 1936, 1943
 Technecard, 2082
 TechnesScan, 2088
 Technetium (43), 13, 26, 690–692, 696–698, 1099
 Technetium chemistry, 2074, 2076, 2085, 2113
 Technetium-99m generator, 26
 Teflon, 1307, 1588, 1633, 1647, 1774
 Teletherapy, 2538
 Temperature anisotropy, 616
 Temperature profiles, 2432, 2433, 2453
 Tensor interaction, 187
 Terminal stack, 2345
 Ternary fission, 245, 270–272
 Terrestrial radiation, 2530–2534
 Terrigenic helium, 798
 Testosterone, 2005, 2093
 Tetrazolium dosimeter, 2293–2294
 Tetrazolium salts, 2293, 2301
 Tetrofosmin, 2083, 2112
 Texture, 1412, 1419, 1420, 1437, 1528, 1733
²²⁸Th, 1965, 2201
²²⁹Th, 1936, 1960, 1964, 1965, 2203
 Thallium(III) trifluoroacetate (Tl(TFA)₃), 2123
 Therapeutic application, of radionuclides, 1854, 2196
 Therapeutic radiometals, nuclear properties, 2144, 2145
 Therapeutic radionuclides, 1919, 1924, 1928–1931
 Therapeutic tracers, 1959
 Thermal broadening, 1383–1385
 Thermal diffusion, 2371, 2377–2380, 2401
 Thermal diffusion columns, 2378–2380
 Thermal equivalent neutron flux, 1624, 1653
 Thermal history, 627
 Thermal ionization mass spectrometry (TIMS), 2462, 2485, 2495–2500
 Thermalization of positrons, 1464–1466, 1469
 Thermal neutron activation analysis (TNAA), 1564–1565, 1676, 1677
 Thermal neutron cross section, 1557, 1578–1580
 Thermal neutrons, 145, 174, 225, 248, 266, 1799–1834, 1861–1864, 1868, 1869, 1872–1878, 1880, 1889–1891, 1898, 2619, 2622–2624, 2627–2633, 2636, 2651
 Thermal reactor, 1860, 1876–1877, 2424, 2622–2625, 2634, 2704–2708, 2719, 2720, 2805–2808, 2822, 2825
 Thermal scan, 1428, 1435
 Thermal utilization factor, 2633
 Thermionic nuclear power systems, 2740–2745
 Thermionic reactor converters, 2741, 2750
 Thermochromatogram, 2430, 2432, 2436
 Thermochromatographic apparatus, 2432
 Thermochromatographic column (TCC), 2430–2433, 2438, 2440, 2451, 2452
 Thermochromatographic technique, for batch separation of ¹⁸⁸Re, 1963
 Thermochromatography, 928, 933–936, 944, 962, 972–976, 986, 991–995, 2430–2454
 Thermoelectric generator (TEG), 2737, 2751–2757
 Thermoelectric nuclear power systems, 2733–2740
 Thermoluminescence, 764, 796–797
 Thermoluminescent dosimeters (TLDs), 2228, 2278, 2286, 2302–2303
 Thermonuclear bomb, 2655, 2884
 Thermonuclear test, 1007
 Thick target yield, 1906, 1909, 1915, 1916, 1922–1925, 1928, 1942, 1947–1950, 1959, 2024
 Thin-absorber approximation, 1394, 1426, 1427
 Thin-layer activation, 1791
 Thiocyanate dosimeter, 1283
 Thomas–Fermi radius, 378
 Thomson scattering, 384, 387
 Thorium, 1568, 1592–1593, 1597
 Thorium-232, as a fertile material, 2652, 2670, 2878

- Thorium-230 dating, 803
 Thorium ($4n+0$) series, 342
 Thoron, 2531–2534
 Three Mile Island, 2547
 Threshold energy, 151, 156
 Threshold reaction, 2624
 Thule, 2551
 Thymidine, 1893, 2002, 2005, 2006, 2042, 2043, 2051, 2074, 2105, 2204
 ^{44}Ti , 1905, 1943–1946
 Time differential Mössbauer emission, 1435, 1436
 Time domain, 1448, 1449, 1452
 Time-of-flight (TOF), 897, 1531–1532, 1538, 1542–1546, 1657, 1665, 1680, 1713, 1845
 Time-of-flight detector, 2473, 2484, 2494
 Time-of-flight mass spectrometer, 916
 Time spectrum, 1449, 1452, 1474, 1475, 1507, 1681, 1744
 Timing uncertainties, 1602
 $^{117\text{m}}\text{Tin}$, 1884, 1897–1898
 TiOA, 939
 Tissue-equivalent dosimetry, 2294
 Tiuxetan, 1959, 2151
 ^{201}TL , 1905, 1911, 1925–1927, 1930, 1959, 2081, 2082
 TL dating, 796
 TL dosimeters, 2234, 2302
 TL materials, UV treatment of, 2303
 TNAA. *See* Thermal neutron activation analysis
 TODGA system, 853–854
 Tokamak, 2768–2777, 2790–2793
 Tommsdorf-effect, 1304
 TOSCA, 1532, 1538
 Total cross section, 1866–1869
 Total ICC, 514–520
 Total reaction cross-section, 157–159, 189, 217
 Total reflection, 1738, 1740, 1744, 1754
 Toxic effects of radiation, 2180
 Toxic elements, in foodstuffs, 1591
 Toxicity, 721, 2147, 2170, 2201, 2203
 Traceability, 1607
 Trace element analysis, 1562, 1584
 Tracer concept, of Hevesy, 1942
 Tracer principle, 1855, 2022
 Tracers, 2410, 2847–2850, 2857
 Tracer technique, 1763–1791
 Track detectors, 2234, 2432, 2452
 Track-etched detector, 1678
 Transactinide chemistry, 423
 Transactinide elements, 926–931, 934, 976, 2431, 2432, 2442, 2451–2454
 Transactinides, 1014, 1023–1025
 Transfer factor, 2521, 2524, 2525
 Transfermium Working Group, 882, 892, 898
 Transfer reactions, 170, 179, 184, 185
 Transformed pattern, 1422–1427
 Transient equilibrium, 347, 348, 1938–1940
 Transition metal mediated reactions, 1993–1999
 Transition radiation, 368, 376, 382–384
 Transition rate, 80–81
 Transition states, 289, 313
 Transition state (TS) structure, 2014
 Transmission coefficients, 158, 168, 190, 191, 195
 Transmission integral, 1394, 1424, 1427, 1439
 Transmission spectrum, 441
 Transmutation, 2816–2832
 Transport, of nuclear waste, 2522
 Transport simulations, 2182
 Transuranic (TRU), 2666, 2673, 2675, 2801, 2818, 2823–2826
 Transuranic (TRU) burners, 2818, 2823
 Transuranium elements, 10, 14, 24, 818–867
 Transuranium metals, 855
 Transverse flow, 206, 207
 Triaxial rotor, 96
 Triboluminescence, 2302
 Tributylphosphate (TBP), 853
 Tributylstannylation, 2126–2127
 Triflates, 1985, 1987, 1994, 1997, 1998, 2036, 2038, 2041, 2057
 TRIGA reactor, 2412, 2638–2640
 Trinitrotoluene (TNT), 2540, 2542, 2654, 2839
 Triphenylmethane dye, 2296, 2300
 Triphenyl tetrazolium chloride (TTC), 2293, 2294, 2301, 2307
 TRITA, 2148, 2154, 2157
 Tritiogenic ^3He , 798
 Tritium activity, 2540
 Tritium analysis, 2861–2863
 Tritium dating, 797
 TRODAT, 2105–2107
 Tropical year, 2567
 Trouton's rule, 2390
 TRPO, 2827
 Tryptophan, 2132, 2192
 TTO, 787
 Tumor radiosensitivity, 2182
 Tunneling effect, quantum mechanical, 717, 1371–1373
 Type Ia, 622, 624, 636, 640, 655
 Type II, 639–641
 Tyrosine, 2131–2136, 2191, 2192
- U**
 U(1), 461, 466, 472
 ^{233}U , 1936, 1960, 1964
 Ultrashort-lived nuclides, 1571
 Unattended NDA Systems, 2928–2935
 Unbiased estimate, 406, 452
 Uncertainty principle, 78, 225, 389, 462, 466
 Uncorrelated random variables, 407
 Underground nuclear tests, 2541, 2542
 Undermoderated reactor, 2633

Undulator, 1742, 1744
 Unified atomic mass unit, 150, 477, 479, 487
 Unimodal distribution, 400
 Units of activity, 334
 Universal constants, 482
 Universal Linear Accelerator (UNILAC), 1011, 1012
 Unmoderated neutron, 2622–2625
 Unresolved resonance region, 1868
 UNSCEAR, 2215, 2218, 2236, 2242, 2243, 2513, 2517, 2527–2546, 2549–2555
 Uranium, 1315, 1334, 1499, 1592–1593, 1597, 1598, 1604, 1658, 1660, 1698
 Uranium-234 dating, 803
 Uranium-238 dating, 803
 Uranium enrichment and conversion, 2544, 2554
 Uranium, fission products, 1855, 1936
 Uranium hexa-fluoride (UF_6), 2377, 2381–2383, 2400–2401, 2544, 2554
 Uranium mining and milling, 2554
 Uranium production, 2405, 2408, 2422
 Uranium series, 800
 Uranium ($4n+2$) series, 344
 Uranium tetra-fluoride (UF_4), 2449, 2544
 Uranium, thorium based dating, 352
 Uranium/thorium/lead dating, 804
 Uranium/xenon, uranium/krypton dating, 813
 Urea, 1990, 1998, 2005

V

Vacancy cascade, 1341
 Van de Graaff accelerator, 2342
 van der Waals force, 232
 Van Hove correlation function, 1523, 1524
 Vapor pressure curve, 933
 Vapor pressure isotope effects, 708
 Vascular recirculation, 1955
 VASSILLISSA, 1016
 Velocity calibration, 1428, 1429
 Velocity filter SHIP, 894
 Velocity selector, 1545, 1549
 Ventricular function, 1955, 1958
 Vibrational density of states, of Fe-57 in Al, 1457
 Vitamins, 2110–2112
 Vittrification, 2802, 2813, 2814, 2824
 Voigt function, 1425
 Volatile compounds, 2430, 2439–2446, 2448–2449, 2451, 2452
 Volatility, 2378, 2440, 2446–2449, 2452, 2453
 Volcanoes, 802
 Volume energy, 232, 233
 VPIE, 708

W

¹⁷⁸W, 1944, 1955–1958
¹⁸⁸W, 1864, 1889, 1896, 1897, 1936, 1944, 1957, 1959, 1962–1964

Walden inversion, 1782
 Warman–Asmus–Schuler equation, 1277
 Water calorimeter, 2309–2312
 Water clean-up, 2425
 Water-moderated reactors, 2621, 2630, 2633, 2640, 2873
 Water radiolysis, 1306, 1310, 1321, 1326
 Water targets, 1910, 1911, 1914, 1917, 1918
 Watertightness, 1791
 Watt's equation, 2624
 Wavelength-dispersive crystal spectrometer, 1710
 WAY 100635, 1981, 1998, 2007, 2106
 Weak bosons, 465–468, 470
 Weak decoupling, 629–632
 Weak freeze-out, 630–632
 Weak interaction, 134–135, 464–470, 625–627, 633, 642
 Weak isospin, 463–466, 469, 472
 Weak plasma coupling, 323
 Weighted least squares method in nuclear spectroscopy, 451–453
 Weinberg angle, 470
 Weizsäcker formula, 51
 Westcott g-factors, 1622, 1799
 White dwarf, 639, 641, 646, 654–656
 Whole-rock dating, 768, 813
 Wideröe structure, 2354
 Wien velocity filter, 2467–2468
 Wiggler, 1742
 Wigner–Eckart theory, 1411
 Wilets–Jean model, 95
 WIMP, 621, 637
 Window method, 1427
 Windscale, 2550
 Wittig reaction, 1986, 1996, 2004
 Wittig reagents, 1986
 WKB approximation, 118, 288
 Woods–Saxon potential, 74, 239, 240, 286, 287
¹⁸⁸W/¹⁸⁸Re generator, 1944, 1957, 1959, 1962–1964
 W-values, 1275

X

X-ray absorption, 1746–1747, 1750, 1755
 X-ray absorption fine structure (XAFS), 818, 858, 861–865
 X-ray absorption near edge structure (XANES), 1742, 1744, 1750, 1756–1758
 X-ray absorption spectroscopy (XAS), 1739, 1742, 1750, 1751, 1756–1758
 X-ray burst, 655–656
 X-ray diffraction (XRD), 1739–1741, 1750, 1756, 1758
 X-ray energies, 510–515
 X-ray fluorescence analysis (XRF), 1657, 1707, 1737–1758
 X-ray fluorescence microtomography (XFCT), 1739, 1750–1758

X-ray imaging, 1755
X-ray intensities, 510–515
X-ray photoelectron spectroscopy (XPS), 1376,
1738, 1745
X-ray scattering, 1518, 1519, 1525, 1526, 1537, 1662
X-ray standards, 2566

Y

⁸⁶Y, 1905, 1919, 1924, 1928, 1931, 2145, 2149
⁹⁰Y, 1859, 1864, 1871, 1889, 1919, 1924, 1928, 1943, 1947,
1959–1962, 2144–2151, 2158, 2169, 2181, 2182, 2186,
2187, 2196–2199
Yellow cake, 2422, 2554

Yield curves, 244, 248, 250
Yield purity, 1911, 1914, 1924

Z

Zeeman effect, 241
Zeolite, 1483, 1530
Zero-point energy approximation, 710
Zevalin, 1959, 2151
Zirconium, 2419, 2423, 2442, 2548, 2639–2643, 2724,
2737, 2824
⁶²Zn, 1919, 1936, 1943, 1945, 1950, 2145
Zp-model, 266–268
z-scores, 1607

